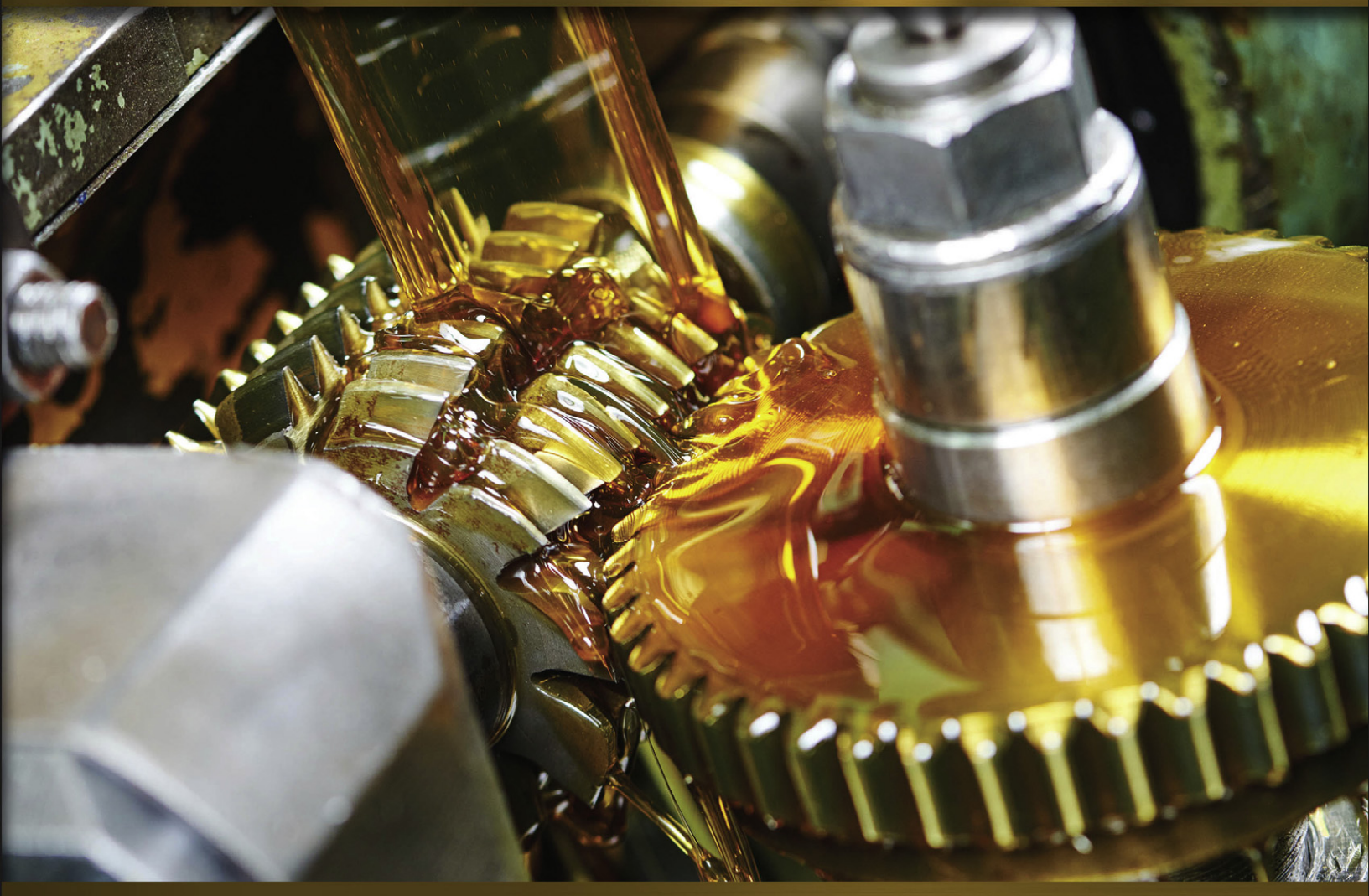
COMPREHENSIVE MATERIALS FINISHING

Volume 1: Finish Machining and Net-Shape Forming



Volume Editor **Imtiaz A. Choudhury**

Editor-in-Chief **M.S.J. Hashmi**

About the pagination of this eBook

This eBook contains a multi-volume set.

To navigate this eBook by page number, you will need to use the volume number and the page number, separated by punctuation or a space.

Refer to the Cumulative Index and match the page reference style exactly in the Go box at the bottom of the screen.

COMPREHENSIVE MATERIALS FINISHING

COMPREHENSIVE MATERIALS FINISHING

EDITOR-IN-CHIEF

MSJ HASHMI

Dublin City University, Dublin, Ireland

VOLUME 1

FINISH MACHINING AND NET-SHAPE FORMING

VOLUME EDITOR

IMTIAZ A CHOUDHURY

University of Malaya, Kuala Lumpur, Malaysia



ELSEVIER

Amsterdam • Boston • Heildelberg • London • New York • Oxford
Paris • San Diego • San Francisco • Singapore • Sydney • Tokyo

Elsevier
The Boulevard, Langford Lane, Kidlington, Oxford OX5 1GB
225 Wyman Street, Waltham MA 02451

Copyright © 2017 Elsevier Inc. All rights reserved

No part of this publication may be reproduced or transmitted in any form or by any means, electronic or mechanical, including photocopying, recording, or any information storage and retrieval system, without permission in writing from the publisher. Details on how to seek permission, further information about the Publisher's permissions policies and our arrangements with organizations such as the Copyright Clearance Center and the Copyright Licensing Agency, can be found at our website: www.elsevier.com/permissions.

This book and the individual contributions contained in it are protected under copyright by the Publisher (other than as may be noted herein).

Notices
Knowledge and best practice in this field are constantly changing. As new research and experience broaden our understanding, changes in research methods, professional practices, or medical treatment may become necessary.

Practitioners and researchers may always rely on their own experience and knowledge in evaluating and using any information, methods, compounds, or experiments described herein. In using such information or methods they should be mindful of their own safety and the safety of others, including parties for whom they have a professional responsibility.

To the fullest extent of the law, neither the Publisher nor the authors, contributors, or editors, assume any liability for any injury and/or damage to persons or property as a matter of products liability, negligence or otherwise, or from any use or operation of any methods, products, instructions, or ideas contained in the material herein.

Library of Congress Cataloging-in-Publication Data
A catalog record for this book is available from the Library of Congress

British Library Cataloguing-in-Publication Data
A catalogue record for this book is available from the British Library

ISBN 978-0-12-803249-7

For information on all publications visit our website at http://store.elsevier.com



Publisher: Oliver Walter
Acquisition Editor: Ruth Ireland
Content Project Manager: Gemma Tomalin
Associate Content Project Manager: Joanne Williams
Designer: Matthew Limbert

Printed and bound in Canada

EDITOR-IN-CHIEF



Saleem Hashmi is emeritus professor in the School of Mechanical & Manufacturing Engineering at Dublin City University, Ireland. He founded the School in January 1987, in addition to setting up the Materials Processing Research Centre (MPRC), a research centre of excellence in the field of materials processing.

In 1990, Professor Hashmi established Advances in Materials and Processing Technologies (AMPT), a much-needed international conference in materials processing. He continues to be the chairperson of the steering committee for this series of conferences. In 1998 he was appointed as editor-in-chief of Elsevier's *Journal of Materials Processing Technology* and continued in this role until 2008.

In 1995, Professor Hashmi was awarded the higher doctorate degree of DSc, by the University of Manchester, the highest academic degree any university in the UK can award.

Professor Hashmi has supervised or co-supervised 112 PhD and 55 MEng research students to successful completion. Over the years he has also acted as an external examiner and expert assessor for PhD candidates and engineering departments with universities in Ireland, the UK, India, Pakistan, Bangladesh, Hong Kong, Canada, Australia, and Malaysia. He has published in excess of 460 papers and 25 books so far.

Professor Hashmi was the editor-in-chief for Elsevier's 13-volume major reference work *Comprehensive Materials Processing* which was published in 2014.

He has been appointed as the editor-in-chief for Elsevier's *Materials Science and Materials Engineering Reference Module*, a 14-section online resource comprising around 3500 reviewed articles. This launched in December, 2015 and is constantly being updated.

VOLUME EDITORS



Imtiaz Ahmed Choudhury is currently a professor at the Department of Mechanical Engineering, University of Malaya (UM), and has been with UM since 1996. He received his Bachelor degree in Mechanical Engineering from Bangladesh University of Engineering and Technology (BUET), MEng from Asian Institute of Technology (AIT), Thailand, and MSc in Mechanical Engineering from Arizona State University, USA. He obtained his PhD from Dublin City University. He started his career as an assistant engineer in a gas transmission and distribution company, Dhaka, Bangladesh. He worked as a maintenance engineer in a power station for 3 years in Libya. He started his academic career in 1982 as an assistant professor in an engineering college, Bangladesh. Since then, he has been working in academia. Imtiaz's research interests include traditional/nontraditional machining with vegetable oil-based lubricant, tool condition monitoring, machining difficult-to-cut and high strength materials, injection molding and application and use of solar energy. He has been a member of a panel of judges for the SME innovation award 2011–2013, Malaysia, under the category of "Manufacturing Sector." He was a Senate member of the University of Malaya. He has authored and coauthored about 100 papers in referred journals, more than 60 conference papers and some book chapters published in Elsevier works. He has also been a reviewer of various international journals. Imtiaz is a Fellow of Institution of Mechanical Engineers, UK (IMechE), and a life Fellow of Institution of Engineers, Bangladesh (IEB). He is a chartered engineer, UK (CEng).



Professor Shahjahan Mridha was born in Bangladesh and obtained his BSc and MSc in Metallurgical Engineering at the Bangladesh University of Engineering & Technology (BUET), Dhaka, and PhD at the University of Leeds in UK (1980) on Gas Nitriding of Low Alloy Steels. Since 1972 he has worked at the Department of Metallurgical Engineering, BUET for 20 years as a faculty member except for 1986–1987 where he was a Commonwealth Academic Staff member at the University of Birmingham, UK, working on Plasma Nitriding.

Professor Mridha was a senior research fellow at the University of Strathclyde, UK from 1989–1994 and worked on laser processing of aerospace materials in collaboration with UK Ministry of Defence. In late 1994 he moved to Nanyang Technological University (NTU) in Singapore where he was employed as an associate professor until 2001, working on semiconductor materials, composite and intermetallic coatings.

In January 2002 he joined the International Islamic University Malaysia (IIUM) as professor, later assuming the position of Head of the Department of Manufacturing and Materials Engineering. He left IIUM in July 2012 to join the Department of Mechanical and Aerospace Engineering at the University of Strathclyde (UK) as a Leverhulme Trust Professor, and remains there presently as visiting professor.

Professor Mridha has published more than 150 journal and conference papers. His research contributions are primarily on microstructure–properties relationships, semiconductor materials and surface modification of light alloys and steel using high power laser and TIG torch melting technology. He is the pioneer of TIG torch techniques for surface coating applications. Professor Mridha is subject editor of the *Metallic Materials* section in Elsevier's *Reference Module in Materials Science and Materials Engineering* launched in December 2015.

In addition to his academic career, Professor Mridha worked as an international consultant for the United Nations Industrial Development Organization (UNIDO) from 2001 until 2007, delivering expert advice and training to engineers working in manufacturing industries in the Indian and African continents.



Bekir Sami Yilbas is a distinguished professor in the Mechanical Engineering Department, King Fahd University of Petroleum and Minerals, Saudi Arabia. He received his PhD in Mechanical Engineering from Birmingham University, and was awarded a doctorate of Engineering at Birmingham in 2005 due to his significant contribution to his field of study. He has received numerous awards as recognition of his research work. Some of these include President of India's Prize for 1988 by Indian Royal Engineering Society, Technology Prize for 1990 by Science and Technology Foundation in Turkey, Best Research Award for 1997, 2002, 2007 by King Fahd University of Petroleum and Minerals, Silver Jubilee Medal by Silesian University of Technology, Donald Julius Groen Prize for 2007 by Institution of Mechanical Engineers (IMechE), Distinguished University Professor award at King Fahd University of Petroleum and Minerals, 2008 – present by King Fahd University of Petroleum and Minerals, Professor W. Johnson International Gold Medal for 2008 by Advances in Materials and Processing Technologies (AMPT) Steering Committee, Professor Fryderyk Staub Golden Owl Award by World Academy of Metals and Manufacturing, Almarai's Distinguished Scholar Prize by King Abdulaziz City of Science and Technology.

Bekir Sami Yilbas has published 720 journal papers in reputable international journals and presented over 100 papers at international conferences. He has 12 patents issued and is the subject editor of *Arabian Journal of Science and Engineering* and editor of *Journal of Fluids*. He has served as an editorial board member of international journals, including the *International Journal of Machine Tool and Manufacture Design, Research and Application, International Journal of Subsurface Sensing Technologies and Applications, Journal of Materials Processing Technology, Journal of Achievements in Materials and Manufacturing Engineering, International Journal of Nanomanufacturing*, and *Archives of Materials Science and Engineering*, and has received numerous awards as recognition of his research work.

CONTRIBUTORS TO VOLUME 1

AA Abdullahi
University of Malaya, Kuala Lumpur, Malaysia and Federal University of Technology, Minna, Nigeria

MY Ali
International Islamic University Malaysia, Kuala Lumpur, Malaysia

SNA Aziz
University of Malaya, Kuala Lumpur, Malaysia

M Azuddin
University of Malaya, Kuala Lumpur, Malaysia

R Bahar
International Islamic University Malaysia, Kuala Lumpur, Malaysia

KC Bala
Federal University of Technology, Minna, Nigeria

SK Chaubey
Indian Institute of Technology Indore, Indore, India

S Chinchanikar
Vishwakarma Institute of Information Technology, Pune, India

IA Choudhury
University of Malaya, Kuala Lumpur, Malaysia

SK Choudhury
Indian Institute of Technology Kanpur, Kanpur, India

YA El-Shekeil
Universiti Putra Malaysia, Serdang, Malaysia

Fengfeng Jeff Xi
Ryerson University, Toronto, ON, Canada and Shanghai University, Shanghai, P.R. China

S Gencalp Irizalp
Celal Bayar University, Manisa, Turkey

M Hourmand
University of Malaya, Kuala Lumpur, Malaysia

Hui Ye
Xiamen University, Xiamen, China

WNP Hung
Texas A&M University, College Station, TX, USA

MSA Hussin
University of Malaya, Kuala Lumpur, Malaysia

NK Jain
Indian Institute of Technology Indore, Indore, India

Jian Wang
Fine Optical Engineering Research Center, Chengdu, China

SA Lawal
Federal University of Technology, Minna, Nigeria

SS Lawal
Federal University of Technology, Minna, Nigeria

I Maher
University of Malaya, Kuala Lumpur, Malaysia and Kafrelsheikh University, Kafrelsheikh, Egypt

H Marashi
University of Malaya, Kuala Lumpur, Malaysia

N Nahar
University of Malaya, Kuala Lumpur, Malaysia

MB Ndaliman
Federal University of Technology, Minna, Nigeria

MY Noordin
Universiti Teknologi Malaysia, Johor Bahru, Malaysia

Y Nukman
University of Malaya, Kuala Lumpur, Malaysia

AC Petare
Indian Institute of Technology Indore, Indore, India

Qiao Xu
Fine Optical Engineering Research Center, Chengdu, China

Qinghua Zhang
Fine Optical Engineering Research Center, Chengdu, China

MM Ratnam
Universiti Sains Malaysia, Nibong Tebal, Penang, Malaysia

N Saklakoglu
Celal Bayar University, Manisa, Turkey

T Saleh
International Islamic University Malaysia, Kuala Lumpur, Malaysia

SM Sapuan
Universiti Putra Malaysia, Serdang, Malaysia

AAD Sarhan
University of Malaya, Kuala Lumpur, Malaysia and Assiut University, Assiut, Egypt

M Sayuti
University of Malaya, Kuala Lumpur, Malaysia

Shuai Guo
Shanghai University, Shanghai, P.R. China

Z Taha
University Malaysia Pahang, Pekan, Malaysia

KF Tamrin
University of Malaya, Kuala Lumpur, Malaysia

Tianyan Chen
Fujian Chuanzheng Communications College, Fuzhou City, China

Yaguo Li
Fine Optical Engineering Research Center, Chengdu, China

BS Yilbas
King Fahd University for Petroleum and Minerals, Dhahran, Saudi Arabia

CONTENTS OF ALL VOLUMES

VOLUME 1 – Finish Machining and Net-Shape Forming

Conventional Finish Machining

1.1 Factors Affecting Surface Roughness in Finish Turning *MM Ratnam* 1

1.2 Effect of Cutting Variables on Boring Process: A Review *SA Lawal, MB Ndaliman, KC Bala, and SS Lawal* 26

1.3 Finish Machining of Hardened Steel *SK Choudhury and S Chinchanikar* 47

1.4 Review of Gear Finishing Processes *NK Jain and AC Petare* 93

1.5 Robotic Polishing and Deburring *Fengfeng Jeff Xi, Tianyan Chen, and Shuai Guo* 121

1.6 Precision Grinding, Lapping, Polishing, and Post-Processing of Optical Glass *Yaguo Li, Qinghua Zhang, Jian Wang, Qiao Xu, and Hui Ye* 154

Advances in Finish Machining

1.7 Techniques to Improve EDM Capabilities: A Review *H Marashi, AAD Sarhan, I Maher, and M Sayuti* 171

1.8 Natural Fiber-Reinforced Composites: Types, Development, Manufacturing Process, and Measurement *SM Sapuan, KF Tamrin, Y Nukman, YA El-Shekeil, MSA Hussin, and SNA Aziz* 203

1.9 Effect of Electrical Discharge Energy on White Layer Thickness of WEDM Process *I Maher, AAD Sarhan, and H Marashi* 231

1.10 Micro-EDM Drilling of Tungsten Carbide Using Microelectrode with High Aspect Ratio to Improve MRR, EWR, and Hole Quality *M Hourmand, AAD Sarhan, MY Noordin, and M Sayuti* 267

1.11 Micromachining *MY Ali and WNP Hung* 322

1.12 Laser Machining Processes *BS Yilbas* 344

1.13 ELID Grinding and EDM for Finish Machining *T Saleh and R Bahar* 364

Finishing Process Using Net Forming

1.14 Laser Peening of Metallic Materials *S Gencalp Irizalp and N Saklakoglu* 408

1.15 Micro Plastic Part Filling Capabilities through Simulation and Experiment: A Case Study on Micro Gear Shape *M Azuddin, Z Taha, and IA Choudhury* 441

1.16 Net-Shape Microfabrication Technique by Micrometal Powder Injection Molding *AA Abdullahi, N Nahar, M Azuddin, and IA Choudhury* 466

1.17 Review of Miniature Gear Manufacturing *NK Jain and SK Chaubey* 504

VOLUME 2 – Surface and Heat Treatment Processes

2.1 Fundamentals of Heat Treating Metals and Alloys *MK Banerjee* 1

2.2 Hardenability of Steel *AK Bhargava and MK Banerjee* 50

2.3 Carburizing: A Method of Case Hardening of Steel *MMA Bepari* 71
2.4 Surface Hardening by Gas Nitriding *K Farokhzadeh and A Edrisy* 107
2.5 Laser Beam Processing for Surface Modifications *BS Yilbas* 137
2.6 Surface Induction Hardening *J Barglik and A Smalcerz* 154
2.7 Recent Advances in Mechanical Surface Treatment *S Ismail, Q Ahsan, and ASMA Haseeb* 171
2.8 Heat Treatment of Commercial Steels for Engineering Applications *MK Banerjee* 180
2.9 Heat Treatment of Tool Steels *RA Mesquita, CA Barbosa, and AR Machado* 214
2.10 Heat Treatment of Cast Irons *I Chakrabarty* 246
2.11 Thermal Treatment for Strengthening Titanium Alloys *A Sinha, S Sanyal, and NR Bandyopadhyay* 288
2.12 Heat Treatment of Aluminum Alloys *HMMA Rashed and AKM Bazlur Rashid* 337
2.13 Solutionizing and Age Hardening of Aluminum Alloys *G Quan, L Ren, and M Zhou* 372
2.14 Heat-Treating Copper and Nickel Alloys *AK Bhargava and MK Banerjee* 398
2.15 Cryogenic Treatment of Engineering Materials *T Slatter and R Thornton* 421

VOLUME 3 – Surface Coating Processes

3.1 Electroless Plating of Pd Binary and Ternary Alloys and Surface Characteristics for Application in Hydrogen Separation *AM Tarditi, ML Bosko, and LM Cornaglia* 1
3.2 Tuning of the Microstructure and Surface Topography of Hot-Dip Galvanized Coatings *SMA Shibli and R Manu* 25
3.3 Surface Finish Coatings *P Sahoo, SK Das, and J Paulo Davim* 38
3.4 Residual Stresses in Thermal Spray Coating *AFM Arif, KS Al-Athel, and J Mostaghimi* 56
3.5 Laser Texturing of Materials and Surface Hydrophobicity *BS Yilbas* 71
3.6 Surface Texture Properties of Co–Ni Alloys Formed with Unipolar and Bipolar Plating *J Vazquez-Arenas, I Romero-Ibarra, RH Lara, and FS Sosa-Rodríguez* 86
3.7 HVOF Coating of Nickel Based Alloys: Surface and Mechanical Characteristics *BS Yilbas* 96
3.8 Laser-Based 3D Printing and Surface Texturing *A Selimis and M Farsari* 111
3.9 Hydrophobicity and Surface Finish *A Owais, M Khaled, and BS Yilbas* 137
3.10 Atomizers and Finish Properties of Surface Coatings *R Ray and P Henshaw* 149
3.11 Gas Nitriding of H13 Tool Steel Used for Extrusion Dies: Numerical and Experimental Investigation *SS Akhtar, AFM Arif, and BS Yilbas* 158
3.12 Hot-Dip Galvanizing Process *F Ozturk, Z Evis, and S Kilic* 178
3.13 Finishing and Post-Treatment of Thermal Spray Coatings *MM Verdian* 191
3.14 High Velocity Oxy-Fuel Spraying and Surface Finish *H Singh, M Kaur, and N Bala* 207
3.15 Electroless Plating as Surface Finishing in Electronic Packaging *MA Azmah Hanim* 220
3.16 Hard Coatings on Cutting Tools and Surface Finish *H Caliskan, P Panjan, and C Kurbanoglu* 230
3.17 Topological Evaluation of Surfaces in Relation to Surface Finish *P Demircioglu* 243

3.18 Evaluation of Surface Finish Quality Using Computer Vision Techniques *I Bogrekci and P Demircioglu* 261

3.19 Effect of Surface Roughness on Wetting Properties *H Mojiri and M Aliofkhazraei* 276

3.20 Surface Preparation and Adhesion Tests of Coatings *M Jokar and M Aliofkhazraei* 306

3.21 Powder Metallurgical Processing of NiTi Using Spark Plasma Sintering *K McNamara, J Butler, AA Gandhi, and SAM Tofail* 336

3.22 Spark Plasma Sintering of Lead-Free Ferroelectric Ceramic Layers *M Karimi-Jafari, K Kowal, E Ul-Haq, and SAM Tofail* 347

3.23 Electrochemical Processing and Surface Finish *NK Jain and S Pathak* 358

Index 381

CONTENTS OF VOLUME 1

Preface xvii

Introduction to Finish Machining and Net-Shape Forming xix

VOLUME 1 – Finish Machining and Net-Shape Forming

Conventional Finish Machining

1.1 Factors Affecting Surface Roughness in Finish Turning *MM Ratnam* 1

1.2 Effect of Cutting Variables on Boring Process: A Review *SA Lawal, MB Ndaliman, KC Bala, and SS Lawal* 26

1.3 Finish Machining of Hardened Steel *SK Choudhury and S Chinchanikar* 47

1.4 Review of Gear Finishing Processes *NK Jain and AC Petare* 93

1.5 Robotic Polishing and Deburring *Fengfeng Jeff Xi, Tianyan Chen, and Shuai Guo* 121

1.6 Precision Grinding, Lapping, Polishing, and Post-Processing of Optical Glass *Yaguo Li, Qinghua Zhang, Jian Wang, Qiao Xu, and Hui Ye* 154

Advances in Finish Machining

1.7 Techniques to Improve EDM Capabilities: A Review *H Marashi, AAD Sarhan, I Maher, and M Sayuti* 171

1.8 Natural Fiber-Reinforced Composites: Types, Development, Manufacturing Process, and Measurement *SM Sapuan, KF Tamrin, Y Nukman, YA El-Shekeil, MSA Hussin, and SNA Aziz* 203

1.9 Effect of Electrical Discharge Energy on White Layer Thickness of WEDM Process *I Maher, AAD Sarhan, and H Marashi* 231

1.10 Micro-EDM Drilling of Tungsten Carbide Using Microelectrode with High Aspect Ratio to Improve MRR, EWR, and Hole Quality *M Hourmand, AAD Sarhan, MY Noordin, and M Sayuti* 267

1.11 Micromachining *MY Ali and WNP Hung* 322

1.12 Laser Machining Processes *BS Yilbas* 344

1.13 ELID Grinding and EDM for Finish Machining *T Saleh and R Bahar* 364

Finishing Process Using Net Forming

1.14 Laser Peening of Metallic Materials *S Gencalp Irizalp and N Saklakoglu* 408

1.15 Micro Plastic Part Filling Capabilities through Simulation and Experiment: A Case Study on Micro Gear Shape *M Azuddin, Z Taha, and IA Choudhury* 441

1.16 Net-Shape Microfabrication Technique by Micrometal Powder Injection Molding *AA Abdullahi, N Nahar, M Azuddin, and IA Choudhury* 466

1.17 Review of Miniature Gear Manufacturing *NK Jain and SK Chaubey* 504

PREFACE

Finish manufacturing processes are final stage processing techniques which are deployed to bring products to a stage where they are ready for marketing and putting in service. Over recent decades, a number of finish manufacturing processes have been developed by researchers and technologists. Some of these new processes have been documented and illustrated both individually and collectively in relation to application in specific areas. The advancement of tools of physics has resulted in considerable changes to these processes, and the precision with which they can be applied. The reporting of these developments are sometimes fragmentary, and this reference work provides a more connected and thorough review of these processes.

Comprehensive Materials Finishing is the primary reference source for researchers at different levels and stages in their career both in academia and industry. This reference work encompasses the knowledge and understanding of many experts into a single, comprehensive work. Containing a combination of review articles, case studies, and research findings resulting from research and development activities in both industrial and academic domains, this reference work focuses on how some of these finish manufacturing processes are advantageous for a broad range of technologies. These include applicability, energy and technological costs, and practicability of implementation. A wide range of materials such as ferrous, nonferrous, and polymeric materials are covered.

This work details the three foremost and distinct types of finishing processes: surface treatment, finish machining processes, and surface coating processes. Surface treatment refers to properties of a material being modified without otherwise changing the physical dimensions of the surface. Finish machining processes involve a small layer of material being removed from the surface by various machining type processes to render improved surface characteristics. Surface coating processes are where the surface properties are improved by adding fine layer(s) of materials with superior surface characteristics to improve the service life of the surface being coated. Each primary surface finishing process is presented in a separate volume, comprising chapters on many of the following relevant specific processes as follows:

Volume 1: Finish Machining and Net-Shape Forming: developments in conventional finish machining processes (honing, lapping, polishing, burnishing, and deburring), fine grinding, free EDM, laser finishing, electrical discharge grinding (EDG), electro-chemical honing (ECH), electrochemical discharge grinding (ECDG), electrochemical grinding (ECG), electrochemical turning (ECT), micro-machining process, and high-speed machining.
Volume 2: Surface and Heat Treatment Processes: This contains aspects of heat treatments, stress relieving, annealing, normalizing, hardening, tempering, austempering, martempering, carburizing (pack, liquid, gas, and post carburizing treatments), nitriding (gas and plasma), salt bath (boriding, chromizing, cyaniding, and carbonitriding), phase transformation of the outer surface (induction, flame, laser, electron beam, and anodizing).
Volume 3: Surface Coating Processes: Plating (electroplating, alloys (bronze/brass and others), chromium, dense chromium, copper and tin, gold, silver and other precious metals, zinc and nickel, electroforming, electroless nickel, hot dip galvanizing, selective/brush plating, surface finish coatings, air spray painting, and chemical vapor deposition (CVD)).

Finishing processes are at the core of successful production of marketable products and address recent progress in materials finishing technologies and science as well as covering recent developments in specific manufacturing processes involved with finishing of products for applications in all areas of engineering, biomedical, environmental, health and safety, and monitoring and control. The in-depth study of these finishing processes as presented in these volumes will assist scientists and engineers in the selection, design, and usage of materials, whether required in small- or large-scale uses across industries.

The initiations for this project began in 2014 and by January, 2015, I had selected the volume editors – Bekir Yilbas, Imtiaz Choudhury, and Shahjahan Mridha and we met with Gemma Tomalin, Joanne Williams, and Graham Nisbet at the Elsevier office in Oxford to finalize the table of contents and plan the project. Throughout 2015, the volume editors and I worked resolutely to select topics to be covered, invite authors, and review their manuscripts, eventually getting all content ready for production by the end of 2015. In 2016, authors returned their proof corrections and final files were produced. To create a work of this scale, the most in-depth reference ever published on materials finishing processes and surface engineering, relies on a collaboration of authors, editors, and the team at Elsevier. I would like to thank the many dedicated authors, whose contributions will be an essential reference for materials scientists and engineers. Each chapter has been reviewed by one of the volume editors, leading experts in their fields, whose knowledge and expertise have proved invaluable. I am indebted to each volume editor and their dedication to making their volume an exhaustive and relevant resource for the scientific community for many years to come. Finally, on behalf of myself and the volume editors, I would like to thank Gemma Tomalin and Joanne Williams at Elsevier for their support, cooperation, and good humor throughout this project – from the first meeting in early 2015, to the publication mid-2016.

MSJ Hashmi
Editor-in-Chief
Dublin City University, Dublin, Ireland

INTRODUCTION TO FINISH MACHINING AND NET-SHAPE FORMING

The finish machining process is used to produce precise dimensions and surfaces to improve the aesthetics and sales value of manufactured products. Some common, popular methods of machining are honing, lapping, polishing, burnishing, and deburring.

The honing process is used mainly to obtain precise surface finishing of holes (internal surface) and external cylindrical surfaces or flat surfaces. Compared with grinding, the honing process is a low-speed operation producing cooler chips, with little or no damage/distortion of the material surface. Honing, an abrasive finishing operation, removes material from the internal or external surface of a part. This process is capable of high material removal rates and offers advantages of low-cost equipment. An accuracy of 0.001 mm can be obtained in a wide range of materials.

Lapping is an abrasive finishing operation used on flat or cylindrical surfaces. It utilizes a rough chemical-mechanical-polishing technique for an improved surface finish and accuracy and provides better wear life of a part. It is intended to only remove approximately 0.01 mm of material. The lap, which is usually made of softer material, is attached to an abrasive material or may be used with a slurry to cut harder material.

Burnishing is a cold working process primarily used to polish internal surfaces by utilizing plastic deformation and without actual removal of metal. As the tool passes through a work part, pressure is generated and exceeds the yield point of the work part, this results in the material exhibiting plastic flow. This allows the high spots to be flattened out and the valleys to be filled in. Cold working causes the work part to harden and produces a wear- and corrosion-resistant surface with a mirror-like finish.

Polishing is a process by which a smooth, glossy, and finished surface is produced either by fine-scale abrasive removal or by softening and smearing of surface layers by frictional heating during polishing. Chemical mechanical polishing uses a ceramic slurry in a sodium hydroxide solution when a chemically reactive surface (silicon wafer) is polished.

Thin ridges or small parts sticking to the newly machined surface, known as burrs, generally develop during machining along the edges of the work part. Deburring is the removal of these burrs, and there are various deburring processes available. Deburring is important for functionality, quality, aesthetics, and the smooth operation of work pieces.

Finish machining and net-shape forming of micro-parts are being investigated more because the demand for high-precision components (such as for the aerospace and automotive industry and for medical implants and instruments) has necessitated using micro-machining and net-forming techniques as opposed to conventional methods, which may lead to material wastage. Materials, processing conditions, tools, and machinery are some of the key factors that influence the manufacturing of quality products. These factors have received increased attention because of their roles in creating quality products. Over the years, advancements in micro-machining have been made through the application of light amplification by stimulated emissions of radiation (LASER), which is referred to as laser beam machining (LBM). Similarly, net-shape techniques such as die forming, investment casting, powder injection molding (PIM), and, more recently, additive layer manufacturing (ALM) comprising 3D printing using metal and plastic have been found to be cost-effective for micro-fabrication of intricate and complex micro-parts.

It is now clear that the use of conventional machining has been constrained because of the intricate shape and micro/nano size of the feature's design, as has the emergence of advanced engineering materials. Therefore, stringent micro-fabrication techniques are required. Some commonly used techniques involve boring, such as ultrasonic-assisted lapping, gear honing, polishing, electrical discharge machining (EDM), laser beam machining (LBM), etching, coning, and micro-injection molding (μIM). These techniques are presented in this volume in two chapters covering μIM.

Chapters in This Volume

1.1 Factors Affecting Surface Roughness in Finish Turning
1.2 Effect of Cutting Variables on Boring Process: A Review
1.3 Finish Machining of Hardened Steel
1.4 Review of Gear Finishing Processes
1.5 Robotic Polishing and Deburring
1.6 Precision Grinding, Lapping, Polishing, and Post-Processing of Optical Glass
1.7 Techniques to Improve EDM Capabilities: A Review
1.8 Natural Fiber-Reinforced Composites: Types, Development, Manufacturing Process, and Measurement
1.9 Effect of Electrical Discharge Energy on White Layer Thickness of WEDM Process
1.10 Micro-EDM Drilling of Tungsten Carbide Using Microelectrode with High Aspect Ratio to Improve MRR, EWR, and Hole Quality
1.11 Micromachining

1.12 Laser Machining Processes
1.13 ELID Grinding and EDM for Finish Machining
1.14 Laser Peening of Metallic Materials
1.15 Micro Plastic Part Filling Capabilities through Simulation and Experiment: A Case Study on Micro Gear Shape
1.16 Net-Shape Microfabrication Technique by Micrometal Powder Injection Molding
1.17 Review of Miniature Gear Manufacturing

The volume contains chapters on finish machining, EDM/WEDM, gear manufacturing, micro-machining, laser machining, and net-shape micro-fabrication techniques. The content of each chapter is sufficient to give the reader background information about comprehensive finishing and net-shape forming techniques. Furthermore, the chapters are arranged to provide a progressive understanding of the various techniques as applied in practice. Therefore, it is expected that the reader will find this volume to be a great source for pertinent information on comprehensive finishing and net-shape forming.

Concluding Remarks

The contributions by the authors of this volume are excellent pieces of information relevant to researchers, technologists, students, and industrialists. Current research trends as well as research outlooks in the fields of comprehensive finishing and net-shape forming are presented in this volume.

Acknowledgments

The editor expresses his deep appreciation and gratitude to all the authors and co-authors of the chapters featured in this volume for their commitment, hard work, and comprehensive contributions in various areas related to materials finishing and net-shape forming. In addition, the invitation by Elsevier through Prof. M.S.J. Hashmi to create this project is greatly appreciated. Thank you to the production team, authors, and various institutions, as well as to your employers for this wonderful support.

The editor greatly acknowledges the support provided by the University of Malaya through Research Projects UMRG RP020/2012A and FRGS FP066–2015A.

IA Choudhury
University of Malaya, Kuala Lumpur, Malaysia

1.1 Factors Affecting Surface Roughness in Finish Turning

MM Ratnam, Universiti Sains Malaysia, Nibong Tebal, Penang, Malaysia

© 2017 Elsevier Inc. All rights reserved.

1.1.1	**Introduction**	1
1.1.2	**Factors due to Machining Conditions**	1
1.1.2.1	Factors due to Cutting Fluids and Method of Fluid Application	1
1.1.2.2	Factors due to Tool Vibration	4
1.1.3	**Factors due to Cutting Tool**	6
1.1.3.1	Tool Geometry	6
1.1.3.2	Tool Wear	9
1.1.3.3	BUE	11
1.1.3.4	Tool Coating	12
1.1.4	**Effect of Machining Parameters**	13
1.1.5	**Effect of Workpiece Material**	17
1.1.6	**Optimization Studies and Development of Surface Roughness Prediction Models**	19
1.1.7	**Summary**	22
References		23
Relevant Websites		25

1.1.1 Introduction

Turning is a common metal removal process in which a single-point cutting tool is moved relative to a rotating cylindrical workpiece on a machine tool. The major application of turning is in the removal of bulk material from the workpiece to achieve the required dimensions. This is known as rough turning, or simply as roughing. However, turning is increasingly used to produce good surface finish in processes known as finish turning. This is done typically to avoid or reduce secondary processes such as grinding or lapping, thus saving production costs. Finish turning usually involves turning using the tip or the curved nose area of the cutting tool insert. The depth of cut is usually less than the nose radius of the cutting tool. The objective of finish turning is to produce products of high-dimensional precision with good surface finish quality.

The surface finish quality of a product is usually assessed in terms of its surface roughness. The roughness of a machined surface is considered as one of the main characteristics of the product as it greatly influences the fatigue life, coefficient of friction, wear resistance, and subsequently the reliable function of the product during service. There are many factors that affect the surface finish quality of a workpiece in turning. These factors can be broadly divided into the following four main categories:

1. Factors due to machining conditions, such as dry turning, wet turning, type of cutting fluid, method of cutting fluid application, chatter vibration, and machine tool rigidity.
2. Factors due to cutting tool parameters, such as tool nose radius, nose angle, tool edge preparation (honed or chamfered), rake angle, side edge cutting angle, cutting tool material, and tool coating.
3. Factors due to machining parameters, such as feed rate, cutting speed, and depth of cut.
4. Factors due to workpiece material properties, such as hardness, microstructure, grain size, composition, and internal defects.

The research work carried out in the past to understand how the various factors affect the surface finish quality of the workpiece in turning is reviewed in this chapter. A greater emphasis is given to the more recent work in this rapidly advancing field which in influenced by the development of modern instrumentation and data analysis techniques. Previous works to optimize the process parameters to obtain the best surface finish and to predict the surface roughness are reviewed. Potential areas for further research that can provide new insights into the effect of the various factors in more detail are suggested at the end of the chapter.

1.1.2 Factors due to Machining Conditions

1.1.2.1 Factors due to Cutting Fluids and Method of Fluid Application

Cutting fluids serve as lubricants as well as heat removal agents during turning. They are used to reduce friction and tool wear, improve surface finish, reduce energy consumption, reduce thermal distortions, facilitate chip removal, reduce tendency of built-up edge (BUE) formation, and protect the newly machined surface from environmental corrosion effects. Cutting fluids are also known as metalworking fluids, coolants, or simply as lubricants. A detailed treatment of the subject on metal cutting fluids is given by Byres.[1]

Extensive research has been carried out in the past three decades to study the effect of the type of cutting fluid and the method of fluid application on the surface finish of various types of workpiece materials during turning. The cutting fluids used in these studies can be classified into four main categories according to their chemical formulation. They are mineral oils, soluble oils (emulsified oils), synthetic (chemical) fluid, and semisynthetic fluids. Cutting oils without further dilution or additives are known as neat oil or straight oil. Besides mineral and chemical-based fluids, vegetable oils, being biodegradable,

have the potential to reduce waste treatment costs and health hazards associated with the petroleum-based oils. Therefore, several researchers have investigated the effect of various bio-based cutting fluids on the surface finish quality in turning. The four common methods of applying the cutting fluid to the cutting zone are by flood filling, jet impingement, mist, and minimum quantity lubricant (MQL). The effects of the fluid application methods on the surface roughness of the finished workpiece have been studied by a number of researchers.

The effect of different cutting fluids on surface finish and tool wear during turning of AISI 304 steel using a carbide tool was investigated by Xavior and Adithan.[2] The authors studied three types of cutting fluids, namely soluble oil (emulsion), neat (mineral) cutting oil, and coconut oil. Coconut oil was chosen as one of the cutting fluids due to its lower onset temperature of thermal degradation compared to sunflower and sesame oils.[3] In their machining experiments the feed rate was varied from 0.1 to 0.35 mm rev^{-1}. Their results showed that at a low feed rate (0.2 mm rev^{-1}) coconut oil and soluble oil produced similar surface finish but neat oil resulted in slightly higher roughness values. At higher feed rates (0.35 mm rev^{-1}) coconut oil produced the best surface finish when compared to the other two fluids. A difference in the average roughness (R_a) of 1.0 μm was obtained at a feed rate of 0.35 mm rev^{-1} when comparing turning carried out using straight oil and coconut oil. This observation was attributed to the much lower tool flank wear when the machining was carried out using coconut oil as the cutting fluid. The authors reported that the lower viscosity of coconut oil allowed easier flow of the cutting fluid thus enabling better removal of the heat at the tool–workpiece interface.

Lawal *et al.*[4] prepared new oil-in-water emulsion cutting fluids by mixing three different types of oils (palm kernel oil, cottonseed oil, and mineral oil) separately with water and additives such as anticorrosion agent, antioxidant, and biocide. The water-to-oil ratio used for each case was 9:1. The turning tests were performed on AISI 4340 alloy steel. Their results showed a general trend of improvement of surface roughness when using palm kernel oil and cottonseed oil-based cutting fluids compared to mineral oil-based cutting fluid. The authors attributed this finding to the reduction in cutting force when using bio-based fluids. This in turn was explained in terms of the formation of a high-strength boundary film that resulted from the high proportion of fatty acids in the bio-based fluids.

MQL refers to the use of a very small quantity of cutting fluid, typically at flow rates of 50–500 ml h^{-1}, which is directed to the cutting zone via nozzles or channels built inside the tool holder. The concept of using MQL (also known as near-dry lubrication or micro-lubrication) in machining was suggested more than a decade ago as a means of overcoming the problems related to the airborne cutting fluid particles that pose health hazards. MQL also leads to significant saving in cutting fluids and reduces workpiece/tool/machine cleaning cycle time. Khan *et al.*[5] studied the effects of MQL using vegetable oil-based cutting fluid on the turning performance of AISI 9310 alloy steel compared to completely dry and wet turning. The MQL was supplied by passing air at high pressure into a mixing chamber that drew a controlled amount of fluid. The mixture was directed at high velocity to the chip–tool interface

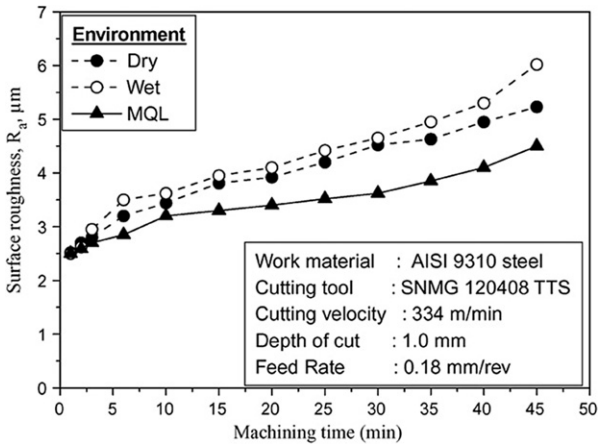


Figure 1 Effect of various cooling conditions on surface roughness.[5]

through a nozzle. Their results (**Figure 1**) show that turning using MQL produced better surface finish compared to dry or wet turning. After 45 min of machining time an improvement of 29% in the average roughness was observed compared to the wet turning. The improvement observed, however, depended on the work-tool materials and was achieved mainly by controlling the deterioration of the auxiliary cutting edge by abrasion, chipping, and formation of BUE. The surface roughness improved effectively due to the reduction of wear and damage to the tool tip due to the application of MQL.

de Angelo Sanchez *et al.*[6] investigated the effect of different methods of cutting fluid application on the turning of difficult-to-cut machine steel (SAE EV-8). The author compared three different methods of fluid application, namely overhead flood filling, MQL, and pulverization. The cutting fluid used for the flood fill was a semisynthetic fluid while that used for MQL was vegetable oil. Pulverization was achieved by using a high-pressure nozzle. Among the methods compared the authors found that the application of cutting fluid jet directed to the chip–tool interface resulted in increased tool life and decreased cutting force, thus improving the surface finish. However, when the reduction in tool wear is the main objective the authors reported that the conventional method of flood filling was more efficient. Shokoohi *et al.*[7] studied the combined effect of MQL and precooling of the workpiece on surface roughness and other effects such as power consumption and chip formation. The machining was carried out on hardened and tempered AISI 1045 steel. The workpiece was precooled using CO_2 as the cryogenic agent. The cutting fluid was made by mixing sunflower oil with water and a small amount of antibacterial agent. The authors reported that the application of the precooling process along with using MQL with the new coolant resulted in the improvement of the surface finish. This was attributed to the colder cutting zone due to the efficient penetration of the oil into the tool–workpiece interface.

Since the conventional cooling methods, such as flood filling and high-pressure jets, are unable to ensure the penetration of the fluid to the chip–tool interface, Sohrabpoor *et al.*[8] used MQL strategy during the turning of AISI 4340 stainless steel. The authors compared four strategies of lubrication namely dry

cutting, air cool, wet with pure liquid lubricant, and MQL. They observed a maximum improvement in surface finish (a decrease in R_a from approximately 27 μm for dry cutting to 6 μm using MQL) at a feed rate of 0.28 mm rev^{-1} and spindle speed of 1000 rev min^{-1}. The improvement observed was explained in terms of the reduced wear at the auxiliary (minor) cutting edge of the tool. Hadad and Sadeghi[9] found that the MQL nozzle position has an important influence on the performance of MQL turning. Oil mist supplied to both the rake and flank faces prevented the adhesion of chip in low temperature and the lubrication effect helped to improve the surface finish.

Amini *et al.*[10] used the term near-dry machining (NDM) to describe MQL and observed a slight decrease in the average roughness compared to dry turning. The authors carried out their experiment by turning AISI 4142 steel. They investigated the effect of several parameters involved in the NDM method, namely flow rate, air pressure, frequency of sending the lubricant, and the nozzle position. Directing the fluid to the machining zone enabled friction to be reduced thus decreasing the machining temperature and preventing formation of BUE and therefore reducing tool wear. However, there were no obvious correlations between the flow rate and the surface roughness or between the frequencies of sending lubricant with the surface roughness.

Extremely high temperatures generated during high-speed turning have detrimental effects on machining. High temperatures not only limit tool life but also deteriorate surface finish by inducing tensile residual stresses, distortions due to thermal gradients and micro-cracks. This problem can to some extent be alleviated using cutting fluids that effectively reduce the cutting temperature. However, since cutting fluid may not remove the extent of the heat efficiently Dilip Jerold and Pradeep Kumar[11] attempted using a cryogenic coolant to reduce the cutting temperatures to lower than those achievable using the conventional coolants. The efficiency of using CO_2 cryogenic coolant was compared to that of dry and wet machining with respect to the surface roughness and other parameters. The workpiece material used was AISI 1045 steel. The authors reported that the use of cryogenic cooling reduced the cutting temperatures by 5–22%. The surface finish improved by 5–25% in the cryogenic cutting condition compared to wet cutting.

Dhar and Kamaruzzaman[12] carried out a similar study by using liquid nitrogen jet as the coolant during the turning of AISI 4037 steel. The results were compared with dry machining and with machining using soluble oil as the coolant. After a machining time of 60 min the average surface roughness (R_a) produced under cryogenic cooling decreased by about 40% and 25% compared to wet and dry cooling, respectively. The authors attributed the reduction in the surface roughness to the reduction in the auxiliary (minor) flank wear due to the retention of tool hardness through the reduction in temperature by the liquid nitrogen jet impinging along the auxiliary edge. Liquid nitrogen, however, is expensive and increases the overall machining cost. Moreover, due to its extremely low temperature (− 196 °C) liquid nitrogen can precool the workpiece significantly thus resulting in thermal micro-cracks.

Dilip Jerold and Pradeep Kumar[13] investigated the effect of carbon dioxide as the cutting fluid in turning AISI 316 stainless steel. Compared to dry machining the CO_2 machining resulted in improvement of surface finish by 57%, while compared to wet machining the improvement was 52%. These observations were made at a cutting speed of 94 m min^{-1} and feed rate of 0.143 mm rev^{-1}. Significant improvement in surface roughness was observed at other feed rates and cutting speeds as well though the difference was more pronounced at higher feeds. The better surface finish obtained when machining using CO_2 as the coolant was explained in terms of the better chip breakability and less accumulation of the chips near the cutting zone. This reduced the frictional contact of the chips with the finished workpiece.

The addition of twisted nematic liquid crystals to mineral oil-based cutting fluids has been found to reduce the coefficient of friction of the friction pairs up to five times.[14] The liquid crystal was selected from a homologous series of fatty acid esters of cholesterol. The liquid crystals were completely melted in the cutting fluid before machining. A reduction in the surface roughness was observed as shown in **Figure 2**. This behavior was explained in terms of the double action of liquid crystalline additive which leads to the reduction of the friction coefficient in the tool–chip–workpiece interface zones.

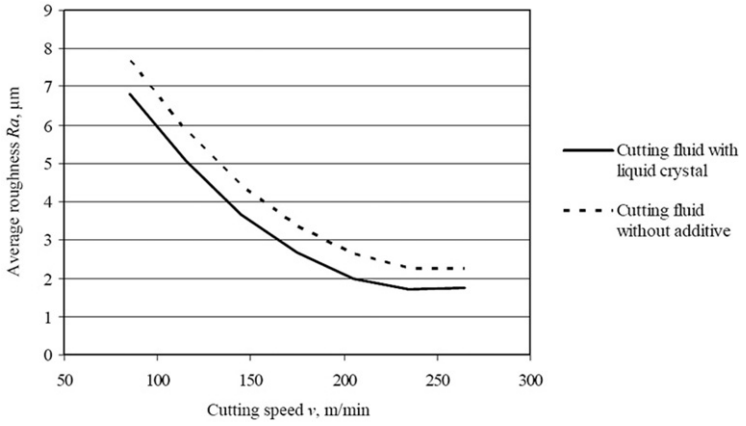


Figure 2 Effect of liquid crystal addition to cutting fluid on average roughness R_a.[14]

The larger molecules of the liquid crystal provided better protection from the direct metal contact.

Ozcelik *et al.*[15] found that the inclusion of 8% of extreme pressure (EP) additive to canola-based cutting fluids resulted in approximately 35% reduction in the average roughness of the workpiece compared to the mineral-based cutting fluid. The EP additive is absorbed into the surface of the workpiece and decreased the shear stress. The authors also reported that a reduction of 24% in average roughness was obtained when compared to semisynthetic cutting fluid. However, a 12% addition of EP increased the average roughness. Although the 8% of EP additive decreased the shear stress on the machine surface, the BUE increased with the increase in the EP additive.

Although many researchers have investigated various types of fluids as lubricants in turning only a few of them have explored the possibility of using solid powders as the lubricants. Srikiran *et al.*[16] used nano-crystalline graphite powder as a lubricant during the turning of AISI 1040 steel using tungsten carbide inserts. The feed rate was varied from 0.05 to 0.125 mm rev^{-1}, the cutting speed was varied from 51 to 192.6 m min^{-1}, while the depth of cut was varied from 0.25 to 1 mm. Four levels of each parameter were considered in their experiments. The authors reported that the decrease in the size of nano-particles caused the cutting forces and tool–chip interface temperature to increase. This effect caused the surface roughness to deteriorate. Vamsi Krishna *et al.*[17] investigated the performance of boric acid and graphite as solid lubricants during the turning of AISI 1040 steel. A considerable reduction in the cutting forces, coefficient of friction between chip and tool interface and average flank wear was observed. These lead to the reduction in the surface roughness of the finished workpiece. Boric acid was found to perform well compared to graphite. The main drawback of using solid powders as lubricants is, however, due to the ease with which the particles get airborne, thus posing health hazards to personnel and possible damage to sensors in the machine tool.

Vamsi Krishna *et al.*[18,19] also used boric acid solid lubricant of 50 nm particle size as suspension in SAE-40 and coconut oil and studied the lubricating properties during the turning of AISI 1040 steel with a carbide tool. The results were compared with pure SAE-40 oil and coconut oil as lubricants. The reduction in surface roughness observed was attributed to the better lubricating action caused by the nano-boric acid suspensions. The suspension caused a reduction in the frictional forces between the tool and the workpiece thereby reducing the temperatures developed, hence decreasing tool wear, and resulting in improved surface finish quality.

The addition of nanoparticles, such as graphite, molybdenum sulfide (MoS_2), copper (Cu), copper oxide (CuO), alumina (Al_2O_3), etc., to cutting fluids has been shown to improve the lubrication properties of the fluid. The nanoparticles not only act like miniature balls in reducing the coefficient of friction but help to conduct away heat more efficiently. Several researchers have explored the addition of nanoparticles to cutting fluids, thereafter known as nanofluids. Amrita *et al.*[20] evaluated the performance of a new nanofluid prepared by adding nanographite powder to soluble oil as the base fluid. The lubricating properties of the conventional cutting fluid (soluble oil) and nanofluid were evaluated by using the four-ball tests. The turning experiments were carried out on AISI 1040 steel. The nanofluid was applied using MQL application at a flow rate of 10 ml min^{-1}. The nozzle was placed 1 cm from the tool–workpiece interface to ensure that the fluid mist enters the interfaces properly. The results of the wear tests showed that inclusion of the graphite nanopowder reduced the coefficient of friction by about 3.5%. The reduction was attributed to the lubricating properties of the lamellar structure which causes the particles to align along the direction of movement and slide over one another. MQL application with nanofluid caused the surface roughness to decrease by 28% compared to MQL without the graphite nanoparticles.

Sayuti *et al.*[21] applied a mist of SiO_2 nano-lubricant by compressed air in the turning of AISI 4140 hardened steel. The optimum SiO_2 nano-lubrication parameter to achieve the lowest tool wear and the best surface finish were investigated. The authors prepared the nano-lubricant by adding SiO_2 nanoparticles with an average size of 5–15 nm to mineral oil. An MQL system equipped with thin-pulsed jet nozzle controlled by using a variable speed control valve was used in their experiments. The best surface finish was obtained using 0.5%wt nanoparticle concentration due to the reduction in the coefficient of friction at the tool–chip interface. The surface roughness was found to increase at higher SiO_2 additions. The authors attributed this behavior to the large number of nanoparticles that transfer additional kinetic energy to the workpiece surface and dissipate more heat.

From the investigations carried out in the past on the effectiveness of various cutting fluids used in turning it is obvious that some types of cutting fluids are better than others as far as surface finish quality is concerned. Vegetables oils have good potential to replace mineral and chemical-based cutting fluids due to their biodegradability and good lubricating and heat removal properties. The effect of the extended use of vegetable oils due to oxidation and bacterial contamination need further study before bio-based oils becomes widely acceptable as cutting fluids. The addition of nanoparticles has also produced an improvement in the surface finish in many turning applications.[22] The improvement, however, depended on several factors such as concentration of nanoparticles, method of fluid application, direction of jet, etc. It is not possible to compare the experimental work published in the literature to determine the best type of nanofluid (nanoparticle and base fluid combination) to obtain the best surface finish quality. This because the surface finish depends on numerous other parameters, such as cutting parameters (particularly, feed rate, and cutting speed), workpiece material, tool geometry, and machine tool rigidity. These parameters were different among different researchers.

1.1.2.2 Factors due to Tool Vibration

Vibrations are unavoidable during turning. Many factors can lead to vibrations, such as the variation of cutting forces, unbalanced masses in the machine tool, and sources outside the machine tool. In modern turning machines the level of vibration caused by the machine tool is kept to a minimum by careful design and by the use of vibration dampers. Thus, the main source of vibration during cutting is tool chatter. Tool chatter results from the violent relative motion between

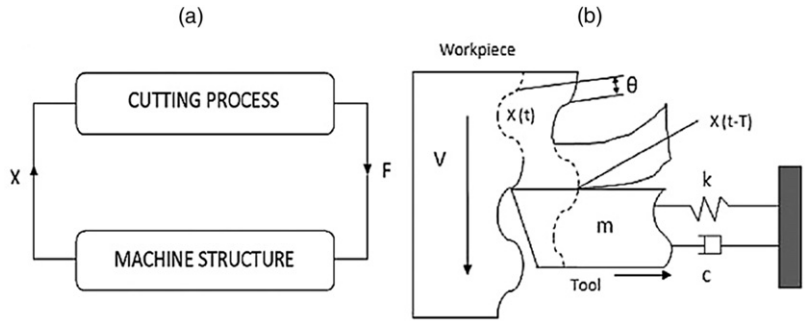


Figure 3 (a) Machine tool and cutting process interaction and (b) mechanism of regeneration.[23]

the cutting tool and the workpiece which is aggravated by tool wear, tool chipping, abnormal chip formation, and surface defects. Chatter vibration is well known to lead to poor surface finish.

Chatter vibration results from the forces generated during the dynamic cutting process and can be divided into primary chatter and secondary chatter. Primary chatter is caused by friction between the tool–workpiece interface and thermo-mechanical effects. Secondary chatter is caused by the regeneration of a wavy surface on the workpiece (see **Figure 3**). Regenerative chatter vibration which occurs at the frequency of the most dominant mode of the machine tool structure has been found to be the most destructive of all other vibrations that occur during turning. The presence of chatter vibration during turning can be recognized by the chatter marks on the machined surface, the appearance of chips produced as well as from the noise generated. Chatter vibration generally leads to reduced productivity of the machine tool.

A review of chatter vibration research in turning is provided by Siddhpura and Paurobally.[23] The authors reviewed 144 papers that deal with chatter stability prediction, chatter detection, and chatter control techniques. Although no papers that correlate chatter vibration with the surface roughness was reviewed, the authors discussed a limited number of papers in which the effects of chatter vibration on tool wear were investigated. In the presence of vibration the cutting speed and chip cross-section has been found to vary, thus affecting tool life.[24] The magnitude of this effect was reported to be large even when the impact of tool loading was excluded. Increased tool wear has also been found to aggravate chatter vibration thus leading to further increase in wear.[25] Kayhan and Budak[26] found experimentally that chatter causes 50–80% reduction in the tool life based on the flank wear limit of 0.2 mm. Siddhpura and Paurobally[23] identified establishing a theoretical relationship between chatter vibration and tool wear as a potential scope for further research. Since tool wear, primarily tool nose wear, has significant effect on the surface roughness the theoretical relationship, once established, can be extended to include the surface roughness parameters.

Very little work has been reported in the literature to correlate the level of chatter vibration directly with surface roughness. Since chatter vibration is a complex phenomenon influenced by a multitude of factors, such as material properties, especially the material microstructure, cutting parameters, cooling methods, tool wear, etc., it is difficult to investigate the effect of vibration on surface roughness in isolation. Lin and Chang[27] studied the effects of vibrations on the surface finish by simulation and experiment. The authors developed a topography simulation model to simulate the surface profile after turning. The effects of the relative motion between the cutting tool and the workpiece together with the effects of tool geometry were incorporated into their model to predict the resultant surface geometry. The authors reported that both the vibration frequency and the vibration amplitude have strong effects on the surface roughness values. They showed that the ratio of the vibration frequency to the spindle rotation speed has a greater effect on the surface roughness than the vibration frequency alone. They noticed that the effects of the radial vibration component on the surface roughness were more significant compared to either the tangential or the axial vibration components. The surface roughness for the surface finish profile generated with the tangential direction vibration was found to increase as the vibration amplitude increased. Although the axial-direction vibration generally degraded the surface finish their results showed that the surface roughness did not always increase as the vibration amplitude increased.

Wang *et al.*[28] investigated the influence of tool-tip vibration on the surface roughness in ultraprecision single-point diamond turning (SPDT). SPDT is used to produce products having very fine surface finish such as optical and medical components. The authors carried out face turning on a polycrystalline copper specimen using a depth of cut of 10 μm under mist coolant. Their results showed that the relative tool-work displacement during turning process is mainly due to the high-frequency tool-tip vibration. This was found to be the dominant factor affecting roughness of the machined surface.

Although vibration has not been correlated directly with surface finish, the effect of vibration on tool wear and tool life has been investigated by several researchers.[29–31] Dimla[29] used vibration features to monitor tool wear in turning. The machining was carried out on EN24 steel using coated inserts and the vibration signals were measured on-line. The authors correlated the measured tool wear forms, namely flank, nose and notch wear, to the features in the vibration signal in the time and frequency domains. They found that the time domain features were more sensitive to the cutting conditions while the frequency domain features correlated well with the tool wear. Their results showed that all three (x, y, and z) components of vibrations were sensitive to the nose and

flank wear forms although the direct correlation between the vibration amplitude and the tool wear was not investigated.

The effect of tool edge wear on the cutting forces and vibrations in 3D high-speed finish turning of nickel-based super alloy Inconel 718 was investigated by Fang *et al.*[30] Since in high-speed finish machining the feed rate is in the same order of magnitude as the tool dimensions, the tool edge wear dominates the wear pattern. The authors analyzed the cutting vibrations that accompany the dynamic tool edge wear using the fast Fourier transform (FFT) and the wavelet transform. They concluded that the FFT method is not best suited to analyze the cutting vibrations caused by the tool edge wear. However, the discrete wavelet transform showed that the vibration amplitude increased as the tool edge wear increased. As mentioned by the authors the scope of their work did not include the study of surface roughness caused by vibrations. Bhuiyan *et al.*[31] used acoustic emission (AE) and vibration signature in turning to investigate the tool wear, chip formation, and surface roughness of the workpiece under different cutting conditions. The effect of vibration on tool wear was found to depend on the chip formation. The tool wear was maximal for the up curled and side curled chip formation. Others have also reported that the severity of chatter decreases the tool life significantly.[32]

In most of these studies the researchers have reported that the tool wear is accompanied by a gradual increase in the chatter vibration whereas sudden tool failure is indicated by an abrupt increase in the vibration amplitude. Since tool wear and tool failure have detrimental effects on the workpiece surface finish an increase in chatter vibration will also have a detrimental effect on the surface finish. Bonifacio and Diniz[33] investigated the correlation between the wear of coated carbide tools and the growth of surface roughness during the turning of AISI 4340 steel by monitoring the vibration of the cutting tool. The authors attached two accelerometers onto the tool holder. The first accelerometer measured the vibration in the cutting direction while the second measured the vibration in the feed direction. Coated cemented carbide tools with three layers of coatings ($TiC + Al_2O_3 + TiN$) were used in their experiments. The parameters used to measure the surface roughness were R_a and R_{max}. The authors concluded that it is not the absolute value of the vibration signal that is important but its change. They recommended that the strategy of automatically establishing the end of tool life is to compare the instantaneous vibration signal with an initial or an intermediate value of the signal. Under all machining condition when the difference between the signals is higher than a predefined value this indicates the time for the tool change.

1.1.3 Factors due to Cutting Tool

1.1.3.1 Tool Geometry

Due to the direct contact of a cutting tool with the machined part the tool itself has the major influence on the roughness of the finished workpiece. There are several factors related to tool that affect the surface roughness of the workpiece. These are: (1) tool geometry (nose radius, rake angle, edge preparation, etc.), (2) tool material (tungsten carbide, ceramic, etc.), (3) tool condition (new or worn), and (4) tool finishing (coating). Dogra *et al.*[34] reviewed 72 published papers that discuss the effect of the tool geometry variation on finish turning in general. The authors pointed out that the cutting edge geometry, which comprises the chamfer angle, chamfer width, and edge hone, has a significant effect on the surface finish and the surface integrity. However, most of the literature reviewed by the authors focused on the effect of the tool geometry on the cutting dynamics, the chip formation, and the machining stability rather than its effect on the surface finish.

Simplified analytical expressions are available for the theoretical average roughness R_a and peak-to-valley roughness R_t as a function of the feed rate and the nose radius assuming that only the rounded nose is involved in the machining. These expressions are given by[35]

$$R_a = \frac{f^2}{32r} \quad [1]$$

and

$$R_t = \frac{f^2}{8r} \quad [2]$$

where f is the feed rate (rev mm^{-1}) and r is the tool nose radius (mm).

Equations [1] and [2] show that for a constant feed the surface roughness is indirectly proportional to the tool nose radius. Therefore, it can be deduced from these equations that in order to reduce the surface roughness the nose radius should be increased. However, there is an upper limit to the nose radius beyond which the cutting forces will increase substantially thus increasing tool wear, particularly groove wear, and introducing vibrations. This in turn will cause the surface finish to deteriorate.

Gokkaya and Nalbant[36] investigated the effects of different insert radii of cutting tools besides other parameters, such depth of cut and different feed rates, on the surface quality of the workpieces. AISI 1030 steel was machined using a CNC turning lathe under dry conditions. Three different insert radii (0.4, 0.8, and 1.2 mm) of cemented carbide cutting tools coated with three layers of coating materials were used in their study. The authors reported that the minimum average roughness was obtained when using a cutting tool of maximum radius (1.2 mm). The surface roughness improved by 293% when the insert radius was increased by 200% (from 0.4 to 1.2 mm). For each depth of cut ranging from 0.5 to 2.5 mm in steps of 0.5 mm and for every feed rate tested the average roughness value was found to decrease when the tool nose radius was increased from 0.4 to 1.2 mm. The greatest decrease in surface roughness was observed at the highest feed rate of 0.35 mm min^{-1}. The difference, however, was not significant at a feed rate of 0.15 mm min^{-1}. The decrease in roughness with increase in nose radius follows an inverse trend as predicted by the theoretical relationship given by eqn [1]. The authors' results show that the effect of vibration at large nose radius does not have a dominant effect on the surface finish for the range of nose radii and cutting parameters tested. Thus, as a rule-of-thumb a larger nose radius should be selected to obtain a better surface finish.

The effect of the tool nose radius on surface finish as well as the tool wear and the cutting forces during tuning of hardened AISI 52100 steel (61 HRC) was investigated by Chou and Song.[37] Ceramic inserts with tool nose radii ranging from 0.8 to 2.4 mm were used in their experiments. The surface finish and tool flank wear were recorded periodically using the stylus profilometer and an optical microscope. The cutting forces during machining were measured using a triaxial force transducer. The author also examined the formation of white layer (phase transformation structures) at the hard turned surface. Their findings show that the tangential force increased only slightly when the nose radius was increased. The increase, however, was more obvious at higher feed rates, whereby an increase in the tangential force of about 20% was noticed. The specific cutting energy, given by the tangential force divided by the uncut chip area, was found to generally increase with the nose radius, particularly at lower feed rates. However, a tool with a larger nose radius was found to produce finer surface finish.

According to the ISO 3685 (1993) standard[38] the manufacturing tolerance allowed on the nose of a cutting tool insert is $0.10r_e$ where r_e is the nominal radius. The 10% deviation allowed in the radius by the standard causes a significant deviation in the shape of the nose profile from that of a perfectly circular profile as reported by Chian and Ratnam.[39] The authors extracted the nose profile of six inserts (total of 18 tool edges) and found that the radius deviated up to 20.3% of the nominal radius. Sung *et al.*[40] showed that the deviation of the true nose profile from that of a geometrically circular profile has a significant effect on the surface roughness of the machined workpiece. Using simulation study alone the authors showed that during ideal 'machining', i.e., in the absence of vibration and tool wear, the deviation in the nose radius causes the maximum peak-to-valley roughness R_t to deviate as much at 32.7% while causing the average roughness R_a to deviate by a maximum of 19.8%. The authors have also shown experimentally that when the turning was carried out under identical conditions using the same batch of inserts, the slight radius variation from one tool to another causes R_t to vary as much as 41.8% while causing R_a to vary by 29.3%. This variation in roughness values was attributed to the random variation in the nose profile due to the radius tolerance allowed in the ISO 3685 standard. Thus, it is important to ensure that the profile tolerance is kept to a minimum especially in tools used for precision turning and finishing operations.

Besides tool nose radius another important factor that has been shown to influence the surface roughness is cutting edge preparation. Cutting edge preparation is particularly important in finish turning because the feed rate used is usually in the same order of magnitude as the cutting edge geometry. Moreover, most of the tool–workpiece interaction takes place along the cutting edge. The effect of cutting edge preparation on surface roughness is best studied in hard turning. Hard turning involves workpiece hardness values typically in the range from 45 to 70 HRC. The tool edge geometry is critical in hard turning because tools with superior edge strength are necessary to withstand the large tool stresses produced during machining. Cutting tools typically have chamfered, honed, or chamfered and honed edges as illustrated in **Figure 4**.

Thiele and Melkote[41] investigated the effect of tool geometry on the surface finish during the hard finish turning of AISI 52100 steel. The authors characterized the edge geometry of each insert to measure the edge features and conducted the turning operations on a rigid machine tool with high spindle accuracy to minimize errors of vibration and run-out. The cutting tools used were made of cubic boron nitride (CBN). These types of tools are commonly used in hard-turning operations. The tool edges used were 'up-sharp' edges, i.e., without strengthening of edges but having finite edge hone, honed, chamfered and chamfers with hones. One up-sharp edge, two-honed edges (intermediate and large), and one chamfer with up-sharp edge were used in their experiments. The radii of the hones were measured using a coordinate measuring machine. The results obtained by the authors when machining a workpiece of 41 HRC hardness showed that tools with smaller hone (22.86 μm) produced better surface finish compared to tools with larger hone (121.92 μm). At a feed rate of 0.15 mm rev^{-1} the R_a value decreased from 1.1 to 0.7 μm, i.e., a drop of 36%. The drop in R_a, however, decreased when the hardness of the workpiece increased to 57 HRC. This observation was explained in terms of the interaction between the chip and the tool along the cutting edge at various feed rates. At low feed rates the ratio of the undeformed chip thickness to the edge geometry is the lowest and the plowing action dominates the cutting process for each type of edge preparation. This effect causes the surface roughness to increase. At higher feed rates the ratio of undeformed chip thickness to edge hone radius increases. The contribution of shearing increases as the contribution of the plowing action decreases thus resulting in better surface finish. For any given feed rate the authors reported that the plowing effect increases with the edge hone radius.

Ozel *et al.*[42] investigated the effects of cutting edge geometry and several other factors on the surface roughness in finish hard turning of AISI H13 steel. Cubic boron nitrite inserts with two distinct edge preparation were used in their study. Since CBN inserts have lower toughness than common

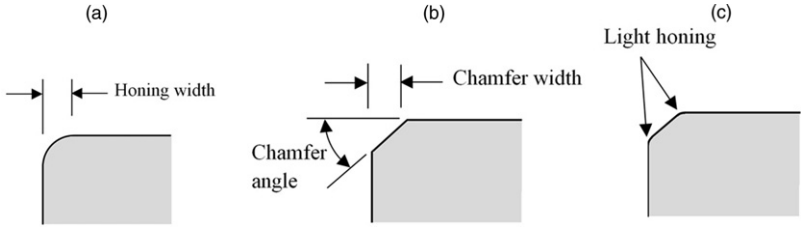


Figure 4 Different type of tool edge preparation: (a) Honed, (b) chamfered, and (c) honed and chamfered.

tool materials and is prone to chipping, proper edge preparation was essential to increase the cutting edge. The authors investigated the CBN inserts with two distinct representative types of edge preparation, i.e., chamfered and honed. The chamfered inserts had 20° chamfer angle and 0.1 ± 0.03 mm chamfer width while the honed inserts had an average radius of 10.5 ± 4.0 μm. At the cutting speed of 100 m min^{-1} the authors found that there was no significant difference in the average roughness (R_a) for feed rates of 0.05 and 0.1 mm rev^{-1}. But, at a higher feed rate (0.2 mm rev^{-1}) machining with honed insert produced significantly lower roughness. The roughness decreased from 1.4 to 0.4 μm. The results were somewhat different at the higher cutting speed of 200 m min^{-1}. The honed insert produced better surface finish at feed rates of 0.05 and 0.1 mm rev^{-1} compared to chamfered edge. But, the roughness at 0.2 mm rev^{-1} from the two insert types was almost similar. These observations were, however, made when cutting a workpiece having hardness value of 54.7 HRC. For a fixed feed rate of 0.2 mm rev^{-1} the authors observed that the surface finish showed improvement for the materials having hardness of 51.3 and 54.7 HRC when machining using the honed inserts. However, this observation was reversed at the lowest feed rated tested (0.05 mm rev^{-1}), i.e., chamfered edge geometry resulted in better surface finish at higher hardness and cutting speed.

Davoudinejad and Noordin[43] investigated the effect of chamfer and honed edge geometry on surface roughness and other factors during turning of hardened DF-3 tool steel (58 HRC) using PVD-TiN-coated mixed ceramic inserts. Good surface finish was obtained using chamfered tool at feeds and speeds ranging from 0.125 to 0.05 mm rev^{-1} and 155 to 210 m min^{-1}, respectively. A larger difference in the average roughness was observed at lower feeds (0.05 to 0.125 mm rev^{-1}). The average improvement obtained was 36%. Thus, the effect of the cutting edge geometry was more significant at smaller feed rates. At higher feed rates tool fracture at the tip of the insert in the chamfered tool caused unstable surface roughness.

The nose edge in the conventional cutting inserts is made up of only one radius. In an attempt to improve the surface finish tool manufactures have introduced inserts having a series of radii that make up the cutting edge. This type of inserts are known as wiper inserts or multiple radii inserts. The wiper edge is made up of a large main radius which is complemented by a number of smaller radii (**Figure 5**). The extended cutting edge at the tool corner is carefully designed to 'wipe' off the miniscule peaks and valleys usually left behind by the conventional insert after the machining. The wiper inserts allow machining at much higher feed rates than the conventional inserts to attain the same level of surface finish. However, due to the larger contact area between the tool and the workpiece, wiper inserts exert a larger force on the workpiece compared to the conventional inserts.

Surfaces produced by wiper inserts and conventional inserts were compared by Elbah *et al.*[44] during hard turning of AISI 4140 steel. Unlike in most previous studies whereby only one roughness parameter is considered, the authors compared the surface in terms of R_a, R_z (average peak-to-valley height), and R_t. All three parameters showed a significant drop (up to 2.5 times) when the machining was carried out using the wiper

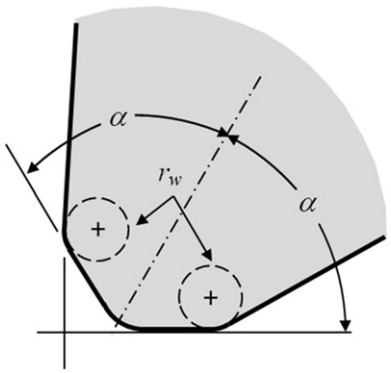


Figure 5 Wiper tool edge design (tool angle = 2α, wiper circle radius = r_w).

inserts. This is due to the smearing effect of the extended cutting edge in the wiper design. The 2-D profile along the feed direction for the conventional insert showed a very repeatable form of peaks and valleys whereas the profile for the wiper insert was random in nature.

Correia and Davim[45] also compared the performance of wiper inserts with conventional inserts during the turning of AISI 1045 steel. The authors evaluated several surface roughness parameters, namely R_a, R_{zD}, R_{3z}, R_a/R_q, R_q/R_t, and R_a/R_t. No significant difference in R_a, R_{zD}, R_{3z}, and R_q was observed at a low feed rate (0.075 mm rev^{-1}). This implied that at very low feed rates finish machining with the wiper inserts produced similar roughness when compared to machining using the conventional inserts. However, at higher feed rates (0.15 and 0.25 mm rev^{-1}) the wiper inserts produced better surface finish. Reduction of about 40 and 60% in the R_a value was reported at the feed rates of 0.15 and 25 mm rev^{-1}, respectively. The other roughness parameter also showed similar drop when the machining was carried out using the wiper inserts.

Ceramic and ceramic composite tools have been found to produce good surface finish due to the high-hot hardness and wear resistance of the ceramic material. Grzesik and Wanat[46] investigated the characteristics of surface roughness produced in turning of hardened low-chromium alloy steel using mixed alumina–titanium ceramic tools equipped with both conventional and wiper edge. The cutting speed was kept constant at 100 m min^{-1} and after each pass the surface finish was measured using a stylus profilograph. A set of 2D roughness parameter were also obtained using a shop-floor roughness tester. The authors analyzed 12 amplitude, spacing, hybrid, and functional parameters. In comparing the average roughness R_a and peak-to-valley roughness R_t the authors reported that at very low feed rates (<0.1 mm rev^{-1}) both the wiper and the conventional inserts produced very similar roughness values. At higher feed rates (>0.2 mm rev^{-1}) the wiper insert produced significantly lower roughness. For instance, at the feed rate of 0.4 mm rev^{-1}, conventional insert produced a R_a value of 5.47 μm while the wiper insert produce R_a of 0.69 μm. A significant drop in the R_t was also observed when using the wiper insert at a feed rate of 0.4 mm rev^{-1}. The authors' results are similar to those reported by Correia and Davim.[45]

The best quality surface finishing in the order of nanometers can be produced by using SPDT. This process is also known as ultraprecision turning. Ultraprecision turning is normally used to produce optical components like lenses and high-precision molds. The cutting edge radius in typically in the range of 50 nm and the positional accuracy and dynamic stability of the machine tool are in the order of 1 to 10 nm. Tauhiduzzaman and Veldhuis[47] studied the effect of tool geometry on surface roughness in SPDT. Single crystal diamond tools were used to perform face turning. Tools with two different nose radii (0.50 and 1.50 mm) were compared. In addition, a specially designed tool with a combined radius of 0.50 and a 0.50 mm flat secondary region was also tested. The authors reported that oblique cutting with a larger nose radius tool produces more chip thinning near the trailing edge of the tool. This in turn reduces the uncut chip thickness and results in better surface finish. This was, however, true only at a feed rate 50 μm rev^{-1}. At lower feed rates the severe chip thinning resulted in more side flow. The more edge serrated chip resulted in poorer surface finish. These observations were, however, depended largely upon the microstructure of the material.

The rake angle in a tool is known to affect chip flow and thus influence surface finish. Positive rake angle causes chips to flow upwards along the rake face while negative rake angles subject chips to compressive stresses. Negative rake angles can lead to micro-cracking and poor surface finish. Ranganath and Vipin[48] studied the effect of rake angle on surface roughness in CNC turning. The tools selected were cemented carbide insert having three combinations of nose radius (0.4, 0.8, and 1.2 mm) and positive rake angles of 16°, 18°, and 20°. At a depth of cut of 0.2 mm and feed rate of 0.05 mm rev^{-1} the authors found that the average roughness decreased from 1.8 to 1.6 μm. The decrease, however, was less at higher feed rates.

Gupta and Kumar[49] investigated the surface roughness during turning of glass fiber-reinforced composite by varying several process parameter independently. Cutting tools having rake angle of $-6°$, 0°, and $+6°$ were used in the machining. Their results showed that the best surface finish ($R_a = 1.793$ μm) was produced when using tool with rake angle of 0°. The rake angle of $-6°$ produced slightly higher roughness compared to the tool rake angle of 6°. Since the maximum variation in R_a was only 0.048 μm the results obtained from machining the glass fiber composite does not lead to a firm conclusion.

1.1.3.2 Tool Wear

Tool wear is the gradual loss of tool material that leads to a change in the shape of the cutting tool from its original shape. Extremely high temperatures and stresses are generated during cutting due to the metal-to-metal rubbing action which aggravates wear. Wear of the cutting tool changes the part of the tool edge geometry that is directly in contact with the machined workpiece. Since the cutting tool leaves an imprint on the workpiece any changes in the tool nose profile due to wear will directly influence the surface finish. However, most researchers' measured flank wear along the major cutting edge and related the flank wear to surface roughness. This is because the major flank wear is the tool life criterion defined in the ISO3685 (1993) standard.[38] According to the standard the maximum width of the flank wear land $VB_{B(\max)} = 0.6$ mm if the flank is not regularly worn. If the flank is regularly worn the criterion for tool life is based on the average width of flank wear $VB_B = 0.3$ mm. Although the major flank of a cutting tool is not directly in contact with the finished surface, increased flank wear increases the cutting force and introduces tool chatter which leads to deterioration in surface finish. Extensive research has been carried out in the past to study wear and surface roughness in turning. However, there are not many papers in which the direct correlation between wear and surface roughness has been investigated. In such situations the relationship between the two variables can only be inferred by comparing the surface roughness and the tool wear plotted separately against other variables such as feed rate or machining time.

The tool wear–surface roughness relationship is not a simple relationship but depends on several compounding factors which include the dynamics of machining and the stability of the machine tool. Pavel *et al.*[50] investigated the effect of tool wear on surface roughness for the case of continuous and intermittent hard turning. For continuous cutting the authors reported that as the tool wear increased the peaks of the roughness profile became higher while the valleys between the peaks flattened. This observation was due to the rapid increase in the notch wear to a steep groove much deeper than other abrasion marks. A different behavior, however, was observed during the intermittent cutting. The average roughness R_a showed only a small increase at the beginning of the cutting and then started to decrease even below the initial value recorded with a new tool. This behavior was explained in terms of the widening of the notch wear and the flattening of the nose radius due the combined action of cutting and interruptions. The shocks caused by the intermittent cutting lead to a very irregular surface profile. Although the surface finish improved with tool wear the authors observed a negative effect at very high levels of wear ($VB_{\max} > 0.15$ mm).

Grzesik[51] compared the effect of wear on three differently shaped ceramic cutting on the surface roughness during turning of hardened steel (HRC 50–60). Conventional and wiper ceramic inserts were used in the study. A set of 2-D roughness parameters as well as amplitude distribution function, bearing curve parameters were analyzed. The notch wear along the minor flank edge (trailing edge) produced substantial modification of the surface irregularities. The average roughness R_a and the peak-to-valley roughness R_z were found to increase gradually with the tool flank wear. The wiper insert, however, produce better surface finish particularly at a lower feed rate (0.1 mm rev^{-1}) compared to the standard insert or wiper insert at twice the feed rate. The smoothing action of the wiper insert also caused the RMS average slope $R_{\Delta q}$ to increase only from 2.4° to 10° during 21 min of machining compared to an increase from 6.6° to 15.2° when using the conventional insert.

Other researchers have also observed that surface roughness generally increased with the tool flank wear. Bhuiyan and Choudhury[52] monitored the vibration frequency signal and found that as the flank wear increased the frequency of vibration along the feed direction decreased until a flank

wear of 0.129 mm. Beyond this the frequency increased continuously until tool failure. The frequency of vibration in the radial direction, however, was found to increase steadily with the increase in nose wear except at the critical point of tool wear when chip breakage occurred. The trend of surface roughness was found to be similar to that of tool wear. When the tool wear rate was steady the trend of surface roughness was also steady. When the tool wear became rapid there was a rapid increase in the surface roughness.

Kilickap *et al.*[53] investigated the effect of tool wear on surface finish during turning of homogenized SiC-p reinforced aluminum metal-matrix composite (MMC). Three different cutting speeds (50, 100, and 150 m min^{-1}), feed rates (0.1, 0.2, and 0.3 mm rev^{-1}), and depths of cuts (0.5, 1.0, and 1.5 mm) were used in their study. Both TiN-coated and uncoated inserts were used in the dry turning. When the machining was carried out using uncoated inserts the authors found that the surface roughness decreased at higher cutting speeds. Coated inserts produced a similar trend only at higher depths of cut. At a low depth of cut and a high feed rate the reverse trend was observed when the machining was done using the coated inserts. But, generally, coated tools produced lower surface roughness. The authors' experimental results also showed that depth of cut had the least influence on the surface roughness.

Tool wear and surface roughness effects during turning are often investigated when studying the machinability of materials. Good machinability is often characterized by good surface finish and high surface integrity of the machined part, minimum tool wear or increase tool life, low cutting forces, and power requirements as well as easy chip control. Sahin *et al.*[54] investigated the machinability of 2024 aluminum alloy reinforced with Al_2O_3 particles using varying size and with the fraction of particles up to 30 wt.% under different cutting conditions. A constant depth of cut of 2 mm and feed rate of 0.1 mm rev^{-1} were used while the cutting speed was varied between 100, 160, and 210 mm rev^{-1}. Two types of cutting tools were used in their experiments, namely TiN-coated tool and TP30 tool. The tool wear was measured using an optical tool microscope to determine the degree of the flank and crater wear. The damage and wear features were also observed using a scanning electron microscope. The average roughness R_a and the maximum peak-to-valley roughness R_{max} were measured using a stylus instrument. The average roughness versus cutting speed data obtained by the authors showed different trends for different particle sizes and different percentage reinforcements. Without the particle addition the average roughness and tool life decreased with increasing cutting speeds. With 30% addition of 16 μm Al_2O_3 particle the reverse trend was observed. The increase in surface roughness of the workpiece at higher speed was attributed to the increased chipping of the tool and the loss of the coated layer.

Sahoo and Sahoo[55] studied the machinability of AISI 4340 steel in terms of the flank wear, surface roughness, chip morphology, and the cutting forces in finish hard turning using uncoated and multilayer coated TiN and ZrCN carbide inserts at a cutting speed of 150 m min^{-1} and feed of 0.15 mm rev^{-1}. The depth of cut was 0.4 mm. The flank wear and the average roughness R_a increased gradually with the machining time while machining using TiN-coated inserts. The uncoated insert, however, showed significant increase in flank wear and a tool life of only 1 min whereas the surface roughness showed significant fluctuation. This behavior was explained in terms of the failure of the uncoated insert by chipping which eventually lead to deterioration of the surface finish quality.

In spite of the advances in tool materials, such as whisker-reinforced ceramics and CBN, for cutting high-strength materials like nickel-based alloys, the coated cemented carbides are still widely used in the industry due to their lower costs. Cantero *et al.*[56] analyzed tool wear mechanism in the finish turning of Inconel 718 in both dry and wet turning using coated-cemented carbide inserts. Inconel 718 is one of the most commonly used Ni alloy in manufacturing aerospace components due to their excellent mechanical properties and corrosion resistance. The authors carried out turning tests on a lathe equipped with a dynamometer for cutting force measurements. Coated carbide inserts having 80° tip angle and 0.4 mm nose radius were used in the machining. The surface quality was assessed using a roughness tester. Five measurements of the average roughness R_a at four different points on the machined surface were recorded. The authors reported that different wear mechanisms occurred during the turning – notching and chipping being the most common. They also observed material adhesion in all their wear tests resulting in BUE formation. The notch formation and chipping were explained in terms of the combination of aggressive conditions involved during the machining of Ni alloys, leading to strain hardening at elevated temperatures. Machining at high speeds was found to accelerate diffusion wear mechanism thus resulting in flank and crater wear. The authors found that the average roughness was maintained in a reasonable range in both dry and wet turning conditions. The roughness values for dry turning was, however, more dispersed compared to wet turning. The dispersion is likely due to chipping of the tool caused by the high temperatures during the dry turning.

Ozel *et al.*[57] investigated surface finish and tool flank wear in the finish turning of AISI D2 steel (60 HRC) using ceramic wiper multi-radii insert. The author found that at very low feed rates, for example, 0.05 mm rev^{-1}, the surface roughness remained almost constant at different machining time although the flank wear increased. At higher feed rates (0.1 and 0.15 mm rev^{-1}) the average roughness increased with the tool flank wear. The authors also developed multiple linear regression models and neural network models for surface roughness and tool flank wear prediction.

Since tool wear is known to influence surface finish the value of surface roughness can be used to establish the moment to change the tool in finish turning. But, studies carried out by several authors show that flank wear or nose wear formation alone is not sufficient to explain the surface roughness variation with cutting time. Shahabi and Ratnam[58] showed that although the tool nose wear increased gradually with machining time the average roughness R_a decreased and then increased. This observation was true at all the feed rates tested by the authors (0.2, 0.25, 0.3, and 0.4 mm rev^{-1}). The authors attributed the decrease in roughness during the initial stage of machining to the gradual growth of nose wear which causes flattening of the roughness profile. As the cutting progresses the growth of the notch wear causes the roughness to increase. Nevertheless, other researchers have shown that the average surface roughness generally increased with increasing flank wear.[49–51,59,60]

In most of the published literature, researchers investigated the effect of tool wear indirectly on a single roughness parameter. The most common parameter considered is the average roughness R_a. The usual justification given by the researchers is that R_a is the most common parameter used in the industry for roughness assessment. But, since R_a is an amplitude parameter that merely provides the average deviation of the surface profile above a mean line the subtle changes in the surface texture due to machining may not be captured by this parameter. R_a is not capable of differentiating between 'spiky' and 'scratched' surfaces. Thus, in some studies the increase in tool wear produced an increase in surface roughness while in the others the trend is reversed. In the continuous hard turning of 1117 hardened steel (62 ± 1 HRC) using PCBN inserts the results reported by Pavel *et al.*[50] showed that R_a increased by a maximum of only about 1.2 μm whereas R_z and R_{pk} (reduced peak height) showed maximum increase of approximately 6.1 and 5.4 μm. Compared to average roughness, R_z and R_{pk} had the most significant deviation from the initial values at the start of machining.

Kumar and Ratnam[61] introduced three new roughness parameters that are unique to turning, namely (1) average slope of profile peaks (Φ_p), (2) average slope of profile valleys (Φ_v), and (3) the relative length of profile (R_{rl}). These parameters are defined as follows:

(a) Average slope of the profile peaks (Φ_p): The mean angle between the tangents drawn on each half of the peak and is measured along the assessment length (**Figure 6(a)**). The parameter is given by:

$$\Phi_{\mathrm{p}} = \frac{1}{N}\sum_{i=1}^{n}\Phi_i \qquad [3]$$

(b) Average slope of profile valleys (Φ_v): The average slope of profile valleys (Φ_v) is defined as the mean angle between the tangents drawn on each half of valley and is measured along the assessment length (**Figure 6(a)**). This parameter is given by:

$$\Phi_{\mathrm{v}} = \frac{1}{N}\sum_{i=1}^{n}\Phi_i \qquad [4]$$

(c) Relative length ratio of the peaks (R_{rl}): The ratio of the length measured below the each peaks at the level selected above the mean line (**Figure 6(b)**). It measures the horizontal characteristics of the peak deviation from its apex. This parameter is determined from the following equation:

$$R_{\mathrm{rl}} = \frac{\frac{1}{N}\sum_{i=1}^{n} L_i}{\frac{1}{N}\sum_{j=1}^{n} L_j} \qquad [5]$$

The authors showed that these three parameters have good correlation with the tool nose wear compared to the other roughness parameters. The average slope of the profile peaks (Φ_p) was found to have a linear and high negative correlation ($R^2 = 0.9762$) with the nose wear. This trend was attributed to the flattening of the roughness profile as the tool gets increasing worn out during turning.

In correlating the tool wear to the surface roughness almost all researchers measured flank wear defined as $VB_{\max}$ (**Figure 7**). But, flank wear does not provide comprehensive information about tool wear during finish turning because most of the cutting takes place at the tool nose corner. Kwon *et al.*[62] proposed tool wear models that gages the tool wear pattern more accurately. Their model considers the wear in the nose area instead of the flank wear. The authors demonstrated using their models as well as experimentally that surface roughness increases with the tool nose wear. A more rapid increase in surface roughness was observed at a higher feed rate.

1.1.3.3 BUE

Another major factor that affects surface roughness and is closely related to tool wear is the BUE formation. BUE is formed under low cutting speeds due to the shearing action of

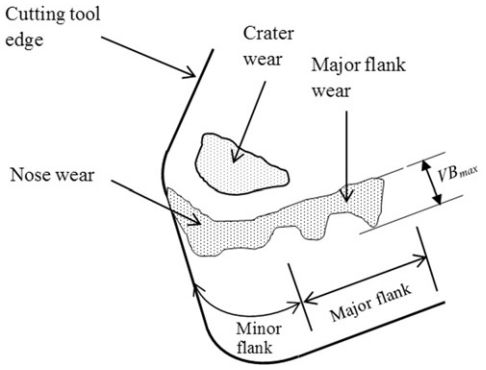


Figure 7 Dominant wear types in cutting tool insert.



Figure 6 Variables used in calculating (a) the profile slope (b) relative length.[61]

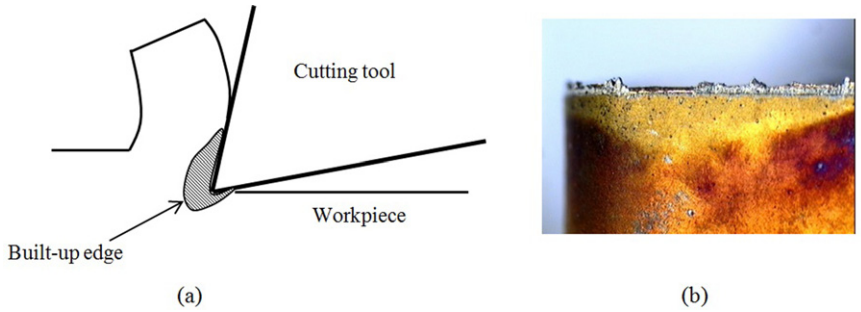


Figure 8 Built-up edge on cutting tool: (a) schematic diagram, (b) photograph to tool. https://www.secotools.com/en/Global/presscentre/Left/Archive-2014/Identifying-and-addressing-eight-common-insert-failure-modes/

the cutting tool. The workpiece material undergoes plastic deformation, melts and adheres close to the tip of the cutting tool at the rake face (see **Figure 8**). Ductile and low hardness materials like aluminum, some high-temperature alloys, and some MMCs have tendency to form BUE on the cutting tool. Low cutting speeds and absence of coolant are among the main factors that contribute to BUE formation. A three-stage cyclic dynamic process is usually involved in the formation of the BUE. These are: (1) the initiation of the BUE at the tool–chip interface, (2) the growth of the BUE to a certain size with various shapes and geometry, and (3) the breakage and disappearance of the BUE. This cyclic process repeats itself throughout the machining operation and has a significant effect on the cutting force, the cutting temperatures, tool wear, tool life, and the surface roughness and dimensional accuracy of the finished product.[63]

Since the BUE can easily tear off during turning some of the torn materials can get attached to the workpiece surface thus affecting the surface finish quality of the workpiece. BUE formation can also lead to changes in the dimensions of the machined product due to the changes in the depth of cut, increased vibration, and the rapid fluctuation in cutting forces. These lead to further deterioration of the surface finish. Fang *et al.*[64] investigated the quantitative relationship between the BUE formation and the cutting vibrations. The authors carried out a set of cutting experiments over a wide range of cutting conditions on 2024-T351 aluminum alloy commonly used in the industry. They analyzed the vibration signals generated from the machining in both the time and the frequency domains. Their results showed that three distinct BUE regions that are characterized by different pattern of cutting vibrations exist. The authors showed that a statistical parameter known as kurtosis can be used to distinguish between the steady and unsteady BUE formation. The authors found that in the steady BUE region the process of formation of the BUE is accompanied by increased vibration magnitude. Although no study on the effect of the BUE formation on surface finish was carried out it is obvious that the increased vibration during turning will lead to increased waviness of the finished surface.

Since BUE formation is a dynamic phenomenon its direct effect on the surface roughness of the workpiece has not been investigated widely. Most researchers select the machining parameters, machining conditions, such as use of proper cutting fluids, to avoid the formation of BUE. Although a new coated tool can avoid BUE formation, wear of the coating during machining can lead to formation of the BUE.[65] Gomez-Parra *et al.*[66] studied the mechanism of built-up layer and BUE formation, their evolution and influence on the dry turned surface quality of aeronautical aluminum alloys. Machining tests were carried out on UNS A92024 (Al–Cu) and UNS A97050 (Al–Zn) alloy cylindrical bars. Uncoated and TiN-coated inserts were used as cutting tools. The cutting speed was varied from 45 to 170 mm min^{-1} while the feed rate was varied from 0.05 to 0.3 mm rev^{-1}. The depth of cut was fixed at 1.0 mm. The results produced by the authors showed that the average roughness (R_a) decreased along the cutting length. The authors explained this observation in terms of the increase in the thickness of the BUE which causes reduction of the tool position angle. An increase in the feed was found to increase the intensity of the adhesion effects. These results, however, seem to disagree with the general understanding of the effect of BUE on surface roughness. The surface finish is known to deteriorate due to the presence of BUE thus increasing the surface roughness. But, the authors' results showed the opposite trend. This could be because the material that had adhered to the tool was still intact and had not torn off during the single pass of the cutting tool.

The BUE effect on tool wear during the turning of medium and high-strength steels at low cutting speeds was investigated by Cassier *et al.*[67] The authors used AISI 1020, AISI 1045, and AISI 4140 steel bars as the workpiece material in their experiments. To ensure BUE formation the authors used dry cutting with low depth of cut (0.4 mm) and low cutting speeds (4–10 m min^{-1}). The authors noted that a total of 13 out of 72 experiments showed BUE formation for the uncoated tools. However, since BUE formation is a dynamic process they caution that this finding does not imply that the other tools did not undergo BUE formation. They also observed that BUE formation was more common on tools used to cut AISI 1045 steel though greater BUE formation occurred on tools used to machine AISI 1020 steel. The greater tendency of BUE formation on the AISI 1020 steel was attributed to the ductility of the material. The formations of BUE lead to increased abrasive wear and poorer surface finish. The coated tools, however, did not show any sign of BUE formation.

1.1.3.4 Tool Coating

The development of coated cutting tools was initiated by the development of new alloys and engineered materials and the

difficulty associated with machining these materials effectively and economically. Coated tools have high wear resistance, are less susceptible to BUE formation and can be used to cut hard materials at high cutting speeds. The commonly used coating materials are titanium nitride (TiN), titanium carbide (TiC), titanium carbonitride (TiCN), and aluminum oxide (Al_2O_3). The coatings are usually applied using the chemical vapor deposition (CVD) and the physical vapor deposition (PVD) techniques. The coating thickness typically varies from 2 to 10 μm.

Gokkaya and Nalbant[68] investigated the effect of cutting tool coatings on the surface roughness of AISI 1015 steel. Four different cemented carbide tools were compared, namely uncoated, coated with AlTiN, coated with TiAlN using PVD, and 3-layer coating with the outermost layer coated with TiN. Five different cutting speeds (50, 73, 102, 145, and 205 m min^{-1}) and two feed rates (0.24 and 0.32 mm rev^{-1}) were used in their study. The authors reported that lower average roughness was obtained by using the three-layer coated insert. Lowering the cutting speed by 33% improved the surface finish by about 69%.

Thakur *et al.*[69] investigated the effect of cutting speed and tool coating deposited by CVD on the machined surface roughness, tool wear characteristics, chip morphology, and chip reduction coefficient during turning of Inconel 825. The turning experiments were carried out using uncoated cemented carbide and CVD multilayer coated (TiN/TiCN/Al2O3/ZrCN) inserts at a constant feed rate of 0.198 mm rev^{-1} and depth of cut of 1 mm. Their results showed that the CVD multilayer coated tool resulted in the deterioration in surface finish as the cutting speed was increased from 50 to 125 m min^{-1}. The average roughness R_a increased from approximately 0.6 to 2.7 μm. The surface roughness obtained using the uncoated insert, however, was almost constant at different cutting speeds. The increase in the surface roughness with the cutting speed was explained by the formation of BUE. This was due to (1) higher surface roughness of the coated inserts and (2) increased edge radius of the CVD coated inserts. The authors concluded that surface roughness could not be improved using the CVD multilayer coated tool under the machining conditions tested.

Yigit *et al.*[70] compared the performance of multilayer coated carbide tool when turning spheroidal graphic cast iron with uncoated tools. TiCN/TiC/Al2O3/TiN multilayered coatings with different thicknesses were fabricated on WC substrate using high-temperature CVD. In all the cutting speed tested (125, 150, 175, and 200 m min^{-1}) the authors found that the best surface finish was produced by the multilayer coated tool having a total coating thickness of 10.5 μm. This was explained in terms of the decreased flank wear and cutting forces for the coated tools compared to the uncoated tool.

Nalbant *et al.*[71] investigated the surface roughness effects of coating method, coating material, cutting speed, and feed rate on the machining of AISI 1030 steel. Uncoated, PVD- and CVD-coated cemented carbide inserts were used in their study. The authors used five different feed rates (0.25, 0.30, 0.35, 0.40, and 0.45 mm rev^{-1}) and three different cutting speeds (100, 200, and 300 m min^{-1}). The depth of cut was kept at 2 mm. At 200 mm min^{-1} cutting speed and 0.25 mm rev^{-1} feed rate the TiN coated with PVD method produced surface roughness of 2.16 μm, TiAlN-coated PVD method produced 2.3 μm while AlTiN coated with PVD provided 2.46 μm. The authors reported that increasing the number of coating layers decreased the friction coefficient and therefore decreased the average roughness of the workpiece. TiN-coated cutting tool produced the lowest roughness whereas the uncoated tool produced the highest roughness. The difference between the average roughness for TiN-coated and uncoated inserts was, however, only 13.5% while that between TiAlN-coated and uncoated insert was only 1.8%. Thus, for the range of cutting parameters tested no significant difference in the average roughness can be observed between the coated and the uncoated tools.

From the published literature it can be noted that machining with coated tools generally improved the surface finish. Uncoated tools have greater tendency to wear by abrasion and adhesion especially at lower cutting speeds. This leads to the formation of BUE thus affecting the surface finish. Coated tools, however, fail mainly by abrasion. The coated tools, in general, experience lesser wear compared to the uncoated tool and this decreases the effects of vibration and tool chatter. However, when the coating is worn the possibility of formation of BUE increases.[66]

1.1.4 Effect of Machining Parameters

The three most common machining parameters that have significant influence on the surface finish and the dimensional accuracy of the machined product and have been studied extensively in the past are the feed rate, cutting speed, and the depth of cut. These three parameters are the most easily controlled parameters compared to other parameters in a turning operation. The manner in which these parameters influence surface finish depends greatly on other factors such as the material property of the workpiece, the type of cutting tool used during machining, the presence or absence of cutting fluid, the method to fluid application, and the stability of the machine tool. Researchers have generally study the effect of the three main machining parameters on the surface roughness in relation to a specific type of workpiece material and often by using a particular type of cutting tool. Many researchers have investigated the effects of the cutting parameters on other factors besides surface roughness, such as tool wear, cutting force, temperatures, BUE formation, and vibration in addition to surface finish. Many of these studies have been carried out with the aim of finding the optimum parameters that produces the best surface finish quality. Previous works on optimization studies are reviewed in greater detail in Section 1.1.6. The focus of this section is to understand the manner in which the various machining parameters, particularly the feed rate, the cutting speed, and the depth of cut, affect the surface roughness of the machined workpiece.

Aouici *et al.*[72] investigated the influence of cutting parameters on the surface roughness and cutting forces in hard turning of X38CrMOV5–1 (50 HRC) using CBN tool. Using analysis of variance (ANOVA) the authors investigated the combined effects of three cutting parameters, namely cutting speed, feed rate, and depth of cut on the surface roughness parameters (R_a, R_t, and R_z) and cutting force components. Each

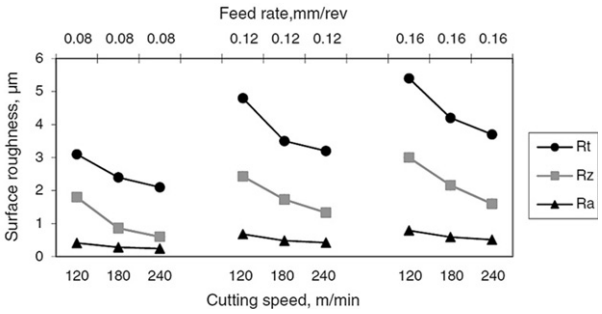


Figure 9 Effect of cutting speed on surface roughness at various feed rates.[72]

cutting parameter was varied in three different levels. The cutting speeds used were 120, 180, and 240 m min^{-1}, feed rates were 0.08, 0.12, and 0.16 mm rev^{-1} while the depths of cut were 0.15, 0.30, and 0.45 mm. Their results (**Figure 9**) showed that the surface roughness increased with increasing feed rate. All three roughness parameters generally decreased with the increasing cutting speed, the percentage decrease being higher at a higher feed rate. The peak-to-valley roughness along the assessment length R_t showed the most significant change compared to R_a and R_z.

Rafai and Islam[73] investigated the effects of the cutting speed, feed rate, and the depth of cut on the dimensional accuracy and the surface finish in dry turning of AISI 4340 (30 HRC) steel. The cutting tool used was cobalt-coated carbide insert with a corner radius of 0.8 mm. The cutting speeds selected were 54, 150, and 211 m min^{-1}, the feed rates were 0.11, 0.22, and 0.33 mm rev^{-1} and the depths of cut were 0.5, 1.0, and 1.5 mm. The surface finish was assessed using the average roughness parameter R_a to enable comparison with the published results. The authors reported that the extent of the influence of feed rate on surface roughness was much higher compared to the influence of the cutting speed and depth of cut. For practical machining operations the authors recommend that the cutting speed and depth of cut can be overlooked provided that the cutting speed is high enough to prevent the formation of BUE.

Many studies to determine the optimal cutting conditions to produce the best surface finish have been carried out by varying the three main machining parameters, namely cutting speed, feed rate, and depth of cut. Gunay and Yucel[74] applied the Taguchi method to determine the optimum surface roughness in the turning of high-alloy white cast iron. Their objective was to minimize the average roughness R_a. The ANOVA was used to determine the statistical significance of the cutting parameters. The workpiece material used was Ni-Hard materials of two different hardness values (50 and 62 HRC). The smaller-the-better performance characteristic for R_a was applied to obtain the optimal cutting parameters based on the signal-to-noise (S/N) ratio. Two type of inserts, namely ceramic and CBN were used in their study. The cutting speeds were 50, 100, and 150 m min^{-1}, feed rates were 0.05, 0.075, and 0.1 mm rev^{-1} while the depths of cut were 0.25, 0.50, and 0.75 mm. The authors reported that the R_a value increased with the increasing depth of cut at 50 m min^{-1} cutting speed for ceramic tool. At a cutting speed of 100 m min^{-1} no significant variation in R_a with the depth of cut was observed. The variation of R_a with the depth of cut, however, was not regular when the cutting was carried out using the CBN tool. At the higher cutting speed of 150 m min^{-1} neither of the cutting tools showed a regular tendency with the depth of cut. The authors attributed the irregular tendency to the randomized distribution of the feed rate due to the design of the experiment. The R_a value was found to increase linearly as the feed increased from 0.05 to 0.1 mm rev^{-1} for machining of the Ni-Hard material with 62 HRC. The authors reported that the smallest R_a obtained was 0.280 µm at 100 m min^{-1} cutting speed and 0.5 mm depth of cut.

Asilturk and Akkus[75] also carried out a study similar to that of Gunay and Yucel[74] using the Taguchi method. Their objective was to optimize turning parameters to minimize surface roughness. Unlike Gunay and Yucel's work the authors measured R_a as well as R_z. The machining was carried out on a hardened AISI 4140 (51 HRC) steel using coated carbide inserts. The cutting speeds tested were 90, 120, and 150 m min^{-1}, the feed rates were 0.18, 0.27, and 0.36 mm rev^{-1} while the depths of cut were 0.2, 0.4, and 0.6 mm. The authors used the Taguchi method and L_9 orthogonal array to reduce the number of experiments. Although the authors did not discuss in detail how each parameter affected the surface finish they reported that the best R_a and R_z values were obtained at the following optimum conditions: 120 m min^{-1} cutting speed, 0.18 mm rev^{-1} feed rate, and 0.4 mm depth of cut.

Kumar *et al.*[76] investigated the effect of cutting speed, feed rate, and depth of cut on the cutting force and surface roughness during dry turning of Al-4.5%Cu/Ti MMC. The Ti content was varied from 5 to 10%. The cutting inserts used were uncoated cemented carbide tools. Turning tests were carried out under three different cutting speeds (40, 80, and 120 m min^{-1}), three feed rates (0.12, 0.24, and 0.36 mm rev^{-1}), and three depths of cut (0.5, 0.75, and 1.0 mm). After each machining run the authors measured the average surface roughness R_a of the workpiece using an optical profiling system with a scan length of 50 µm. The authors reported that the surface roughness of all machined samples with different Ti content were higher at the minimum cutting speed of 40 m min^{-1} and lowest at the higher cutting speed of 120 m min^{-1}. They explained the better surface finish at higher cutting speed in terms of the lesser amount of BUE formed at higher machining speeds thus leading to better surface finish of the samples during the dry turning.

Due to the lack of a comprehensive study on the surface integrity of nimonic C-263 alloy in turning Ezilarasan *et al.*[77] investigated the surface integrity parameters in the turning of this alloy. This material has high content of Nickel (54%) and is used in the manufacture of hot combustion parts such as gas turbines for aerospace applications. The authors used whisker-reinforced ceramic cutting tools. The machining experiments were carried out under dry cutting conditions by varying the cutting parameters. The cutting speeds used were 125, 190, and 250 m min^{-1}, feed rates were 0.102 and 0.143 mm rev^{-1}, and the depth of cut was 0.75 mm. The cutting forces were measured using a three-axis dynamometer while the surface roughness was measured using a surface profilometer. As expected the average surface roughness R_a generally increased

with the feed rate. The authors' results showed that higher cutting speeds produced lower roughness values. The surface roughness also generally increased with the machining time, but the best surface finish (lowest surface roughness) was obtained at 190 m min^{-1}. The higher surface roughness at low speeds was attributed to the tendency to form BUE. The authors concluded that the best cutting condition for the alloy is 0.012 mm rev^{-1} feed rate and 190 m min^{-1} cutting speed.

Kini and Chincholkar[78] studied the effect of varying the machining parameters in turning on the surface roughness and the material removal rate for 30 filament wound glass fiber reinforced polymer in turning using coated tungsten carbide inserts under dry cutting conditions. The authors developed empirical models for the surface roughness and material removal rate using factorial design experiments. In developing the models the authors used two values of cutting speed (59.94 and 133.2 m min^{-1}), two feed rates (0.1 and 0.4 mm rev^{-1}), two depths of cut (0.1 and 0.2 mm), and cutting tools having two different nose radii (0.4 and 1.2 mm). Only one value of surface roughness, namely average roughness R_a was measured. For a constant cutting speed the authors' results showed that the average roughness decreased when the feed rate was increased from 0.1 to 0.4 mm rev^{-1}. This result contradicts those of many other researchers. The surface roughness did not show any trend with the cutting speed. The authors did not explain this behavior as their work was focused on developing the models. Nevertheless, the authors concluded that the feed rate is the main influencing factor on surface roughness followed by depth of cut.

Equations [1] and [2] show that the theoretical surface roughness of the finished workpiece varies as a square of the feed rate. Thus, good surface finish can be obtained by using a small feed rate. But, the machining time will increase leading to increased production cost. The effects of cutting speed and depth of cut on the surface roughness are not so straight forward but depend on many other factors. In machining 7075 Al alloy with 10 wt.% SiC composite Bushan *et al.*[79] found that the surface roughness decreased more or less linearly with cutting speed when using carbide or PCD inserts. The cutting speeds used in their experiment were 180, 200, 220, and 240 m min^{-1}, the feed rates were 0.1, 0.2, 0.3, and 0.4 mm rev^{-1}, while the depths of cut were 0.5, 1.0, 1.5, and 2.0 mm. The decrease in surface roughness (R_a) with the increase in cutting speed was higher when using the PCD insert. Similar observations were made when the machining was carried out on SiC composites. A sharp increase in the surface roughness of both materials was observed when the feed rate was increased. Their results depicted an approximately parabolic relation as predicted by the theoretical relation given by eqns [1] and [2]. The surface roughness also increased with increasing depths of cut due to the increased flank wear.

Unlike the findings of many others, some researchers observed a decrease in surface roughness with increase in cutting speeds. Suresh and Basavarajappa[80] developed a surface response model as a function of cutting parameters in the turning of hardened AISI H13 steel (55 HRC) using PVD coated ceramic tools under different cutting conditions. The cutting speeds used were 42, 80, 140, and 238 m min^{-1}, the feed rates were 0.04, 0.08, 0.14, and 0.20 mm rev^{-1} and the depths of cut were 0.05, 0.15, 0.30, and 0.45 mm. The surface roughness parameter measured was R_a. The authors concluded that cutting speed has the most dominating effect over tool wear followed by feed rate and depth of cut, whereas feed rate is the most significant factor influencing surface roughness followed by depth of cut and cutting speed. Better surface finish at higher cutting speeds was attributed to the lower vibration and lower cutting and thrust forces generated at higher speeds. According to the authors, another factor that contributed to the lower surface roughness at higher speeds is caused by the less heat that was dissipated to the workpiece surface as the heat was swept away by the flowing chips. The minimal surface roughness was obtained with the combination of low feed rate, low depth of cut, and high cutting speed.

Dwivedi *et al.*[81] investigated the effect of turning parameters on surface roughness of A356 alloy with 5% SiC composite produced by electromagnetic stir casting. The cutting speeds used in the study were 100, 145, and 190 m min^{-1}, the feed rates were 0.14, 0.19, and 0.24 mm rev^{-1} while the depths of cut were 0.2, 0.4, and 0.6 mm. The cutting tools used in the machining experiments were tungsten carbide inserts. Their results agreed with those of many other researchers, whereby higher cutting speed results in better surface finish (lower average roughness). They explained this observation in terms of the increased surface temperature of workpiece, which caused softening of the material thus lowering the resistance offered by the material against the tool. The authors noted that as the feed rate increased from the lower to the upper limit the surface roughness increased. The higher material removal rate increased the friction between the tool and the workpiece material. This in turn increased the surface roughness of the workpiece. The authors also noted that the surface roughness increased as the depth of cut increased. This was due to the higher chip thickness. The authors concluded that the best combination of parameters for the lowest surface roughness was cutting speed of 190 m min^{-1}, feed of 0.14 mm rev^{-1}, and depth of cut of 0.20 mm.

Unlike the surface roughness versus cutting speed trend report by many researchers, Qu *et al.*[82] reported the opposite trend. In dry cutting of aluminum bronze alloy using uncoated and coated cemented carbide inserts the authors noticed that the lowest surface roughness was recorded at the lowest cutting speed. As cutting speed increased the surface roughness increased to a maximum value between 16 and 33 m min^{-1}. This increase was attributed to the formation of BUE, which induced sever vibration and scratch effect. From 33 to 126 m min^{-1}, however, the surface roughness decreased due to the weakening forming condition of the BUE. Beyond 126 m min^{-1} the roughness increased again due to sever tool wear resulting in high cutting temperature and forces. With the increase of feed rate, however, the authors noticed that the surface roughness increased monotonically as predicted by theory. However, at higher feed rates the difference between the experimental and theoretical roughness increased. This deviation was explained in terms of the larger cutting force and the increased vibration at higher feed rates thus resulting in more violent vibration of the machine tool structure. The surface roughness versus depth of cut plot had a minimum point at a depth of cut of about 1 mm. The authors explained

the appearance of the minimum point in terms of the 0.4 mm nose radius of the cutting tool. For cutting depths less that 0.4 mm the authors explained that the nose tends not to fully take part in the cutting. The small angle between the workpiece and the cutting tool decreased the amount of heat generated. Furthermore, the heat transfer from the workpiece to the tool decreased thus decreasing the temperature of the workpiece and increasing the temperature of the tool.

Lalwani *et al.*[83] investigated the effect of cutting parameters, namely cutting speed, feed rate, and depth of cut, on the cutting forces and surface roughness in finish hard turning of MDN250 steel using coated carbide insert tool. The MDN250 is a special class of high-strength steel that differs from the conventional steels. MDN250 steel is hardened by metallurgical reaction that does not involve the use of carbon. Three different cutting speeds (55, 74, and 93 m min^{-1}), three different feed rates (0.04, 0.08, and 0.12 mm rev^{-1}), and three depths of cut (0.1, 0.15, and 0.2 mm) were used in their experiments. A single value of roughness parameter (R_a) was measured using an optical surface profilometer. The authors concluded that the feed rate and depth of cut are the most significant factors that influence surface roughness, whereas cutting speed does not have a significant effect on surface roughness.

The influence of the three main turning parameters on the machinability of homogenized Al–Cu/TiB_2 MMC was investigated by Senthil *et al.*[84] The authors used six different cutting speeds (50, 100, 200, 300, 400, and 500 m min^{-1}), six different feed rates (0.05, 0.15, 0.25, 0.45, 0.65, and 0.85 m min^{-1}), and five different depths of cut (0.3, 0.3, 0.9, 1.2, and 1.5 mm). TiB_2-coated inserts were used in the turning experiments. The authors noted a significant drop in the surface roughness from 50 to 100 m min^{-1} cutting speed. Thereafter, the roughness remained more or less constant. The surface roughness value appeared to increase rapidly with increasing feed. The surface roughness was affected only slight by the increase in the depth of cut. The R_a values were within 3–4 μm at different depths of cut.

In most of the studies carried out to investigate the effect of cutting parameters on surface finish the researchers carried out the experiments under dry cutting or a single type of cooling method. Fratila and Caizar[85] investigated the combined effect of the cutting parameters and the cooling method on the surface quality of AISI 1045 steel during finish turning. The authors used dry cutting, minimal quantity lubrication as well as flood cooling. The insert type used was carbide. The cutting speeds used were 62, 90, and 204 m min^{-1}, the feed rates were 0.196, 0.226, and 0.306 mm rev^{-1} and the depths of cut were 0.25, 0.5, and 1.0 mm. Unlike most researcher, the authors measured three roughness parameters, namely R_a, R_z, and R_q (root mean square of the roughness profile). The experimental data were analyzed using ANOVA and F-test to determine the main effects of the process parameters and to establish the optimum process conditions. The analysis showed that the surface quality of the workpiece is strongly influenced by the cutting depth and less influenced by the feed rate. The authors found no significant differences between the roughness parameters and cooling methods.

The friction and lubrication behavior of femoral heads used in bone implants are affected by the surface roughness and the sphericity. Thus, precision finishing of these implants are important. Uddin[86] presented the effect and optimization of the key machining parameters in finish turning of metallic femoral heads. The objective of the investigation was to achieve the best surface roughness and sphericity. The study was carried out using ANOVA. Three different cutting speeds (200, 250, and 300 mm min^{-1}), three different feed rates (0.1, 0.2, and 0.3 mm rev^{-1}), and three different depths of cut (0.2, 0.3, and 0.5 mm) were selected in their L_n orthogonal experimental study. The average surface roughness (R_a) and sphericity (S_p) were measured in each case. The workpiece material was AISI 316L steel. The tools used were diamond-shaped tungsten carbide insert. As in many other machining studies the authors reported that the feed rate is the most significant factor affecting the surface roughness. As the feed rate was increased the surface roughness also increased. Unlike the work of Fratila and Caizar[85] the authors did not notice a marked change in the surface roughness due to changes in the cutting speed and depth of cut.

Chauhan and Dass[87] carried out a study to optimize the machining parameters when machining Grade-5 titanium using PCD (polycrystalline diamond) tools using response surface methodology (RSM). RSM is a set of mathematical and statistical techniques useful for modeling and analysis of problems in which the response of interest is affected by several parameters and the objective is to optimize this response. The machinability performance was evaluated in terms of the average surface roughness (R_a) and the tangential force. The cutting speeds used were 30, 50, and 70 m min^{-1}, feed rates were 0.05, 0.10, and 0.15 mm rev^{-1} while the depths of cut were 0.15, 0.20, and 0.25 mm. The approach angle of the tool was varied from 60° to 90°. Although the authors did not discuss the trends of roughness versus cutting parameters their results showed that the R_a value increased with cutting speed and feed rate and decreased with decrease in the approach angle and depth of cut. The decrease in surface roughness was attributed to the increased friction effect of the chip which lead to increased temperature and stress on the nose of the cutting tool.

Patel and Patel[88] investigated the effect of different cutting parameters (cutting speed, feed rate, and depth of cut) on the surface roughness and the power consumption in the turning of 6036 Al alloy TiC MMC using PCD tools. The cutting speeds used were 63, 103, and 170 m min^{-1}, the feed rates were 0.107, 0.215, and 0.313 mm rev^{-1} and the depths of cut were 0.3, 0.6, and 0.9 mm. The results showed that surface roughness increased almost linearly with feed rate while the depth of cut had minimum effect on surface roughness. The surface roughness, however, decreased with increasing cutting speeds. The decrease was higher at a higher depth of cut.

Khidhir and Mohamed[89] analyzed the effect of cutting parameters on surface roughness and tool wear during the machining of nickel-based hastelloy-276. The RSM method was used to find the combination of factors that gave the optimal response. The cutting speeds used were 150, 200, and 250 m min^{-1}, the feed rates were 0.15, 0.2, and 0.25 mm rev^{-1} while the depths of cut were 0.5, 1.0, and 1.5 mm. The average surface roughness (R_a) was the responding variable. The authors noted that the surface roughness was higher at

lower cutting speed. The surface roughness was lower at higher cutting speeds.

Table 1 provides a summary of the cutting parameters, workpiece material, cutting tools, and the roughness parameters used in many of the literatures related to studies on the effect of machining parameters on surface roughness. It is not surprising to notice that in the order of listing the three common machining parameters the depth of cut is always listed the last. The depth of cut has been found by most researchers to have the least significant effect on the surface roughness while the feed rate has the most significant effect. In most of these studies the authors measured only one roughness parameter, namely R_a. Since R_a represents the average height of the surface profile and the gradual tool wear by abrasion alters the profile height only slightly other parameters that are more sensitive to changes in profile height, particularly the bearing area curve parameters, are expected to exhibit a more accurate trend.

1.1.5 Effect of Workpiece Material

Among the material characteristics that have direct influence on the surface finish are the hardness, grain size, residual surface stresses, subsurface defects, and impurities. The effects of material on the surface finish are usually investigated in terms of the machinability of materials. Machinability is assessed in terms of the surface finish quality, power consumption, chip formation, tool life, and dimensional accuracy of the machined part. Soft and ductile materials like aluminum though very easy to machine tend of form BUE on the cutting tool thus leading to poor surface finish. But, since ductile materials have limited structural applications most metal cutting are done on their alloys.

Among the various material characteristics that affect surface finish the most easily studied characteristic is hardness of the workpiece material. Compared to other characteristics hardness can be easily measured using a hardness tester, such as the Rockwell or Brinell hardness tester. Horváth and Drégelyi-Kiss[90] analyzed the surface roughness of two types of aluminum alloys, namely AS12 eutectic alloy (64 HB) and AS17 hyper-eutectic alloy (114 HB) in fine turning. Two types of inserts, normal (ISO) and wiper, were used in their experiment. The machining parameters were varied as shown in Table 2. The average surface roughness R_a of AS12 alloy was found to vary in the range 0.363–220 μm for wiper insert and 0.284–1.763 μm for the ISO insert. In the case of AS17 the roughness ranges was 0.351–1.040 μm for the wiper and 0.428–1.677 μm for the ISO insert. Their results showed that the average roughness decreased slightly when the hardness of the material increased. The results obtained by Thiele and Melkote[41] during the turning of through-hardened AISI 52100 steel bars also showed slight improvement in the surface finish when machining the harder material (57 HRC) compared to the softer material (41 HRC) under the same machining conditions. The authors used CBN inserts with different cutting edge preparations. The steel bars were heat treated to three desired hardness values (41 HRC, 47 HRC, and 57 HRC). At a feed of 0.05 mm rev^{-1} the thrust force when cutting the harder material (57 HRC) using 93 and 121 μm honed inserts was much higher than when turning the 41 HRC material.

Chinchanikar and Choudhury[91] investigated the effect of workpiece hardness and other factors, namely cutting parameters and type of tool coating, on the different machinability aspects like tool life, surface roughness, cutting force, and chip morphology during the turning of hardened AISI 4340 steel at three different hardness (35, 45, and 55 HRC). Using a hardening and tempering process the authors maintained the maximum variation in hardness of the material to within 1 HRC. The cutting inserts used were cemented carbide inserts coated with a single layer of TiAlN- and CVD-coated multilayer $TiCN/Al_2O_3$. The authors noted a significant improvement in the surface roughness when machining hardened AISI 4340 steel at 45 HRC compared to 35 HRC under all the machining conditions tested. The better surface finish was explained in terms of the chip morphology whereby polished and bright chip back surface showed minimum friction due to the lower cutting forces, thus resulting in better surface finish quality.

Unlike the results observed by Horváth and Drégelyi-Kiss[90] and Chinchanika and Choudhury[91] the results obtained by Ozel *et al.*,[42] however, showed the opposite trend. The authors studied the effect of workpiece hardness among other factors on the surface roughness of AISI H13 steel. They compared the average roughness R_a obtained when turning 51.3 and 54.7 HRC steels. Their results showed that for the same cutting speed and tool edge geometry the harder material produced slightly higher average roughness. Although no explanation was offered it appears that the difference in hardness values between the two materials is too small to produce a significant difference in the surface roughness.

Unlike hardness, material microstructure has a greater influence on the surface finish particularly in very high-precision turning where the depth of cut is in the order of a few micrometers. Tauhiduzzaman and Veldhuis[47] studied the effect of material microstructure including grain boundary density and presence of inclusions, on surface geometry in ultraprecision SPDT. SPDT has the potential of reducing the amount of post process polishing required to fulfill the final product specifications. Controlled studies were performed on samples whose microstructure was refined through mechanical strain hardening processes. The depth of cut used in the face turning operation was 2 μm. The authors reported that 54% strain hardening improved surface roughness by reducing plastic side flow and spring back effect. The strain hardening also introduced dislocations and the high density of dislocations allows the material to fracture easily during machining. However, 82% strain hardening produced voids, fractures, and pitting in the finished surface thus leading to poorer surface finish.

In the work reported by Kumar *et al.*[76] it was found that at a high cutting speed (120 m min^{-1}) the MMC having the lowest Ti content (5%) produced the best surface finish ($R_a = 1.7$ μm) and the MMC having 10% Ti content produce the worst surface finish ($R_a = 2.3$ μm). Although the authors did not explain the exact reason for the higher surface roughness when using 10% Ti content it is believed that the higher percentage of the hard TiC reinforcement caused a larger number of broken particulates and voids to be formed at during the turning operations.

Table 1 Parameters used in previous investigations on effect of machining parameters on surface roughness

References	*Cutting parameters*	*Workpiece material (hardness)*	*Cutting tool*	*Roughness parameters*
Aouici *et al.*[72]	v=120, 180, 240 m min^{-1} f=0.08, 0.12, 0.16 mm rev^{-1} d=0.15, 0.30, 0.45 mm	X38CrMOV5–1 (50 HRC)	CBN	R_a R_t R_z
Rafai and Islam[73]	v=54, 154, 211 m min^{-1} f=0.11, 0.22, 0.33 mm rev^{-1} d=0.5, 1.0, 1.5 mm	AISI 4340 steel (30 HRC)	Cobalt-coated carbide	R_a
Gunay and Yucel[74]	v=50, 100, 150 m min^{-1} f=0.05, 0.075, 0.1 mm rev^{-1} d=0.25, 0.50, and 0.75 mm	Ni-Hard material (50 HRC, 62 HRC)	Ceramic and CBN	R_a
Asilturk and Akkus[75]	v=90, 120, 150 m min^{-1} f=0.18, 0.27, 0.36 mm rev^{-1} d=0.2, 0.4, 0.6 mm	AISI 4140 steel (51 HRC)	Al_2O_3; TiC-coated carbide	R_a R_z
Kumar *et al.*[76]	v=40, 80, 120 m min^{-1} f=0.12, 0.24, 0.36 mm rev^{-1} d=0.5, 0.75, 1.0 mm	Al-4.5%Cu/Ti MMC	Uncoated cemented carbide	R_a
Ezilarasan *et al.*[77]	v=125, 190, 250 m min^{-1} f=0.102, 0.143 mm rev^{-1} d=0.75 mm	Nimonic C-263 alloy (32, 28, 320 HV)	Whisker-reinforced ceramic	R_a
Kini and Chincholkar[78]	v=59.94 and 133.23 m min^{-1} f=0.1 and 0.4 mm rev^{-1} d=0.1 and 0.2 mm	Glass fiber-reinforced polymer	Coated tungsten carbide	R_a
Bushan *et al.*[79]	v=180, 200, 220, 240 m min^{-1} f=0.1, 0.2, 0.3, 0.4 mm rev^{-1} d=0.5, 1.0, 1.5, and 2.0 mm	7075 Al alloy	Cemented carbide, PCD	R_a
Suresh and Basavarajappa[80]	v=42, 80, 140, 238 m min^{-1} f=0.04, 0.08, 0.14, 0.20 mm rev^{-1} d=0.05, 0.15, 0.30, 0.45 mm	Hardened AISI H13 steel (55 HRC)	PVD coated ceramic	R_a
Dwivedi *et al.*[81]	v=100, 145, 190 m min^{-1} f=0.14, 0.19, 0.24 mm rev^{-1} d=0.2, 0.4, 0.6 mm	A356 alloy with 5% SiC composite	Tungsten carbide	R_a
Qu *et al.*[82]	v=33–88 m min^{-1} f=0.05–0.21 mm rev^{-1} d=0.4–1.2 mm	Aluminum bronze alloy (169 HB)	Cemented carbide	R_a
Lalwani *et al.*[83]	v=55, 74, 93 m min^{-1} f=0.04, 0.08, 0.12 mm rev^{-1} d=0.1, 0.15, 0.2 mm	MDN250 steel	Coated carbide	R_a
Senthil *et al.*[84]	v=50, 100, 200, 300, 400, 500 m min^{-1} f=0.05, 0.15, 0.25, 0.45, 0.65, 0.85 m min^{-1} d=0.3, 0.3, 0.9, 1.2, 1.5 mm)	Al–Cu/TiB_2 MMC	TiB_2 coated	R_a
Fratila and Caizar[85]	v=62, 90, 204 m min^{-1} f=0.196, 0.226, 0.306 mm rev^{-1} d=0.25, 0.5, 1.0 mm	AISI 1045 steel (187 HB)	Carbide	R_a R_z R_q
Uddin[86]	v=200, 250, and 300 mm min^{-1} f=0.1, 0.2, and 0.3 mm rev^{-1} d=0.2, 0.3, and 0.5 mm	AISI 316L steel	Tungsten carbide	R_a
Chauhan and Dass[87]	v=30, 50, and 70 m min^{-1} f=0.05, 0.10, and 0.15 mm rev^{-1} d=0.15, 0.20, and 0.25 mm	Grade-5 titanium (36 HRC)	PCD	R_a
Patel and Patel[88]	v=63, 103, and 170 m min^{-1} f=0.107, 0.215, and 0.313 mm rev^{-1} d=0.3, 0.6, and 0.9 mm	6036 Al alloy TiC metal matrix	PCD	R_a

Akasawa *et al.*[92] investigated the effect of microstructure and hardness on the machinability of medium-carbon chrome–molybdenum steel. The authors measured the surface roughness of the workpiece, cutting force, and chip hardness as the measures of machinability. The samples used in the tests were made from the original hot-rolled steel. The processing parameter during the heat treatment and the cold drawing were controlled to produce samples having different microstructures. The 'as hot-rolled' sample had ferrite and pearlite structure with some martensite. The annealed and cold-drawn sample had ferrite matrix with partially spheroidized cementite particles. The normalized (annealed and air

Table 2 Machining parameters[90]

Cutting speed (m min^{-1})	500	667	1250	1833	2000
Feed rate (ISO insert) (mm rev^{-1})	0.05	0.058	0.085	0.112	0.12
Feed rate (wiper insert) (mm rev^{-1})	0.1	0.116	0.17	0.224	0.24
Depth of cut (mm)	0.2	0.267	0.5	0.733	0.8

cooled) sample has ferrite and pearlite structure. The quenched and tempered sample had tempered martensite structure. All the samples, except for the as hot-rolled sample, had almost the same hardness. Unlike most other researchers the authors measured the R_y roughness parameter instead of the usual R_a parameter. R_y is defined as the maximum roughness height within a sampling length. The authors noted that the formation of BUE when machining the low-alloy medium-carbon steel specimens depended on the microstructure of the workpiece material although the hardness was about the same. The annealed and cold-drawn workpiece having ferrite matrix with spheriodized cementite formed BUE only in narrow cutting conditions and produced the best surface finish. The authors also noted that surface finish of the normalized workpiece was the worst among the samples tested in dry machining due to the BUE formation.

1.1.6 Optimization Studies and Development of Surface Roughness Prediction Models

The papers reviewed thus far show that it is possible to achieve the optimum surface finish quality required on a product by carefully controlling the input process parameters and the machining conditions. Since the three main machining parameters, namely the feed rate, cutting speed, and the depth of cut, can be easily controlled by the user during the finish turning many researchers have carried out optimization studies in order to determine the machining parameters that can produce the best surface finish quality in addition to minimizing tool wear. Most of the optimization studies have been combined with the development of surface roughness prediction models. Besides changing the cutting parameters several researchers have attempted to optimize other variables such as tool geometry, workpiece material, and cutting conditions in order to obtain the minimum surface roughness.

Davim[93] studied the influence of cutting conditions on the surface finish based on the techniques of Taguchi. The objective of the study was to establish a correlation between the cutting velocity, feed rate, and the depth of cut with the surface roughness parameters R_a and R_t. The correlation between the process parameters and each roughness variable was obtained by using multiple linear regressions. The workpiece material used in the study was free machining steel (9SMnPb28k) while the tool material was cemented carbide. The cutting speeds used in the study were 71, 141, and 283 mm min^{-1}, the feed rates were 0.1, 0.16, and 0.25 mm rev^{-1} while the depths of cut were 0.5, 0.75, and 1.00 mm. Thus, the three-level Taguchi experimental design consisting of 27 experiments was used in the study. The ANOVA analysis showed that the cutting velocity had greater influence on the roughness followed by the feed rate, while the depth of cut had no significant influence on the surface roughness. The interaction between cutting velocity and feed rate was reported to be the most important compared to the other analyzed parameters. Although the author did not identify the optimum parameters to produce the best surface finish their regression models were able to predict R_a and R_t accurately with errors lesser than those obtained from the geometric theoretical model.

Singh and Venkateswara Rao[94] carried out an experimental investigation to study the effect of the tool geometry, namely the effective rake angle and nose radius, and the cutting conditions (cutting speed and feed rate) on the surface finish during hard turning of AISI 52100 steel. This material is commonly used in the manufacture of ball and roller bearings. The workpiece was heat treated to obtain a hardness of 58 HRC. Mixed ceramic inserts having nose radii of 0.4, 0.8, and 1.2 mm were selected in their study. The effective rake angles were 6°, 16°, and 26°. The cutting speeds used were 100, 150, and 200 m min^{-1} while the feed rates were 0.10, 0.20, and 0.32 mm rev^{-1}. The depth of cut was kept constant at 0.2 mm. Based on the experimental results the authors developed second and third order mathematical models for the average surface roughness using RSM. They optimized the surface roughness models by using genetic algorithm (GA). The GA provided the minimum values of surface roughness and their respective optimal input machining parameters. The lowest surface roughness of 0.4866 μm was achieved using the following parameters: 200 m min^{-1} cutting speed, 0.1 mm feed rate, 6° effective rake angle, and 1.2 mm nose radius.

Unlike many other researchers who optimized the cutting parameters to obtain the best surface finish, Neseli *et al.*[95] optimized the cutting tool geometry parameters for the same effect. The specimen used in their study was AISI 1040 steel. The cutting inserts used were Al_2O_3 coated tools. In all their experiments the depth of cut, cutting speed, feed rate were fixed at 1.5 mm, 150 m min^{-1}, and 0.15 mm rev^{-1}, respectively. The tool geometry parameters varied were the nose radius (0.4, 0.8, and 1.2 mm), the approach angle (60°, 75°, and 90°), and the rake angle (−9°, −6°, and −3°). The authors used RSM to develop a quadratic prediction model for R_a using their experimental data. The L_{27} Taguchi standard orthogonal array was adopted as the experimental design. Using ANOVA the authors showed that the most dominant factor affecting R_a is the tool nose radius, which accounted for 51.45% contribution of the total variation. This was followed by the approach angle (18.24%) and rake angle (17.74%). The optimum combination of the tool geometry parameters to obtain the minimum surface roughness was: 0.4 mm tool nose radius, 60° approach angle, and −3° rake angle. An interesting observation made by the authors is the way in which the nose radius affects the surface roughness of the machined surface. Unlike the predictions of theory and the findings of many other researchers, whereby the increase in tool radius caused the surface roughness to decrease, the authors reported the opposite trend, i.e., as the tool nose radius increased the

surface roughness also increased. The authors explained this behavior in terms of the increased contact length of tool-workpiece during the cutting. The increased contact length caused chatter vibration and therefore increased the surface roughness. However, this explanation was not supported by any experimental data.

Since the surface roughness of the workpiece is strongly correlated with cutting parameters such as insert nose radius, feed rate, and depth of cut, Nalbant *et al.*[96] varied these three parameters to obtain the best surface finish quality. Since surface roughness is not strongly correlated with the cutting speed, therefore the authors did not include this parameter in their study. The workpiece material was AISI 1030 steel while the cutting tools were TiN-coated tools. The authors applied the Taguchi method for the parameter design. The cutting speed was kept fixed at 300 m min^{-1} while the feed rates were varied in three stages, namely 0.15, 0.25, and 0.35 mm rev^{-1}. The radii of the inserts used were 0.4, 0.8, and 1.2 mm, whereas the depths of cut were 0.5, 1.5, and 2.5 mm. The machining performance measure used by the authors was the average roughness R_a. The authors used the L_9 orthogonal array with 26 degrees of freedom. The results reported by the authors are similar to those of many other researchers, i.e., the insert radius and feed rate are the most significant cutting parameters affecting surface roughness. Based on the lower-the-better signal-to-noise ratio and ANOVA the authors concluded that the optimal cutting parameters for surface roughness are: 1.2 mm insert radius, 0.15 mm rev^{-1} feed rate, and 0.5 mm depth of cut.

Many studies on the machining of MMCs have shown that minimizing the surface roughness of such composites is difficult.[97,98] This is due to factors such as the morphology, distribution, and volume fraction of the reinforcement phase as well as the matrix properties. Palanikumar and Karthikeyan[99] studied the various factors affecting surface roughness in the machining of Al/SiC particulate composite using the experimental design concept. The factors considered in their investigation were the % volume fraction of SiC, cutting speed, depth of cut, and the feed rate. All four parameters were varied in two stages. The volume fractions of SiC used were 10% and 25%, the cutting speeds were 50 and 150 m min^{-1}, the depths of cut were 0.5 and 0.15 mm and the feed rates were 0.1 and 0.5 mm rev^{-1}. Assessing the factors and their effect on the surface roughness was carried out using response graphs, normal probability plots, and the ANOVA technique. For the analysis the authors concluded that the optimal conditions to obtain the minimum surface roughness (1.66 μm) were: high cutting speed (150 m min^{-1}), high % volume fraction of SiC (25%), low depth of cut (0.50 mm), and flow feed rate (0.10 mm rev^{-1}).

Hasçalık and Çaydaş[100] carried out an optimization study during the turning of commercial Ti–6Al–4 V alloy using the Taguchi method. In addition to the optimization study, the authors also studied the effect of the machining parameters on the surface roughness and tool life. The cutting speed, feed rate, and depth of cut were varied in three levels. The cutting speeds used were 30, 60, and 90 m min^{-1}, the feed rate were 0.15, 0.25, and 0.35 mm rev^{-1} while the depths of cut were 0.5, 1.0, and 2.0 mm. The smaller-the-better (SB) criterion for the surface ratios was used in their signal-to-noise ratio analysis using ANOVA. An L_9 orthogonal array with four columns and nine rows was used in the experimental design. The optimal machining parameters for the lowest surface roughness was obtained at 90 m min^{-1} cutting speed, 0.15 mm rev^{-1} feed rate, and 0.5 mm depth of cut. The authors also identified the feed rate as the main factor that has the highest significance on the surface roughness. Feed rate was reported as 1.72 more significant compared to depth of cut. They reported that the cutting speed did not have any significant effect on the surface roughness.

Most researchers have used the tool wear in addition to the surface roughness as the performance measures while optimizing the machining parameters. Hagiwara *et al.*,[101] however, considered the chip breakability and surface roughness as the optimization criteria during the contour finish turning of AISI 1045 steel. According to the authors the chip breakability comprises four major factors, namely the chip shape and size, side flow, side curl, and up curl. However, the authors considered only the chip shape and chip size as the chip breakability factor takes care of the side flow, side curl, and up curl factors. The authors conducted full factorial experiments using a range of feed rates (0.04, 0.70, 0.10, 0.13, and 0.16 m rev^{-1}) and a range of depths of cut (0.2, 0.6, 1.2, and 2.0 mm). Unlike in straight turning the effective depth of cut varies along the surface of the workpiece due to the deep slopes in the machined part. The authors reported that although a small constant feed tend to produce good surface finish but the chip breakability was so poor that the surface quality deteriorated. On the contrary, a large feed rate produced good chip breakability but gave poor surface finish. The constant feed of 0.10 mm rev^{-1}, however, produced better surface roughness in most the machined segments of the workpiece.

Muthkrishnan and Davim[102] used two modeling techniques to predict the surface roughness, namely the ANOVA method and artificial neural network (ANN), in the machining of Al–SiC MMC. Both methods provide a systematic and effective approach for the optimization of the cutting parameters. The cutting speed used by the authors ranged from 100 to 600 m min^{-1}, while two feeds rates (0.108 and 0.200 mm rev^{-1}) were selected. The depths of cut used were 0.25, 0.5, and 0.75 mm. The average surface roughness R_a was measured at three different locations of the machined workpiece using a roughness tester. Using ANOVA the authors reported that the feed rate had the highest physical as well as statistical influence on the surface roughness (51%) followed by the depth of cut (30%) and the cutting speed (12%). Based on the signal-to-noise ratio the authors determined the optimum factors to obtain the best surface finish. The data collected from the machining experiments were used to train a three-layer ANN network with a 3–10–1 configuration (3 nodes in the input layer, 10 nodes in the hidden layer, and 1 node in the output layer). The authors reported that the output of the ANN model matched closely with the results of direct measurement of the surface roughness of the workpiece. Since the ANN method consumes less time and produces higher accuracy the authors concluded that optimization using ANN is the most effective approach to obtain the best surface finish compared to ANOVA.

The optimization of cutting parameters and the prediction of surface roughness involve highly constrained nonlinear dynamic optimization problem that can only be solved by

complete enumeration. Raj and Naboothirir[103] developed an improved genetic algorithm (IGA) to optimize the cutting parameters for predicting the surface roughness. The IGA method includes a stochastic crossover technique and an artificial initial population scheme to provide a faster search mechanism. The IGA was equipped with an improved evolutionary direction operator that can efficiently search and actively explore solutions. The authors applied the IGA method to predict the effect of tool geometry, namely nose radius, and cutting parameters (cutting speed, feed rate, and depth of cut) on the surface roughness in the dry turning of SS 420 metal. They compared the proposed IGA method with the conventional GA used in the previous studies. Each of the four parameters used in the study had three levels. To reduce the number of experiments the authors used the Taguchi's robust design and L_{27} orthogonal array method. The feed rates used were 0.059, 0.159, and 0.26 mm rev^{-1}. The cutting speeds were 39.269, 60.475, and 94.247 m min^{-1} while the depths of cut were 0.4, 0.8, and 1.2 mm. The nose radii were 0.4, 0.8, and 1.2 mm. The mathematical models for the average roughness R_a was developed using regression analysis in RSM. The results showed that the IGA optimization method was able to predict the machining parameters that results in much lower surface roughness compared to the conventional GA method.

In the optimization study carried out by Chauhan and Dass[87] (Section 1.1.4) the authors developed a quadratic regression model for the surface roughness using RSM based on their experimental data. The ANOVA analysis was used to test the significance of the regression model, to test the significance of individual model coefficients, and to test for the lack-of-fit. The regression model was then used to predict the surface roughness within the limits of the factors investigated by the authors. They carried out three confirmation experiments for the surface roughness and tangential force. The results of the ANOVA and confirmation tests showed that the quadratic model was able to predict the average roughness accurately within the prediction interval of 95%. However, the authors did not identify the combination of machining parameters and approach angle that produced the best surface finish.

Process optimization is necessary especially in processes where the desired output depends on the complex interaction of numerous parameters. Since surface finish is affected in varying degrees by several factors reviewed in this chapter, it is necessary to determine the combination of factors that produces the best surface finish quality. Homami *et al.*[104] used a full factorial design for the design of experiment to optimize cutting parameters, namely feed rate, cutting speed, nose radius, and approach angle, in order to obtain the desired optimum value of the surface roughness. Full factorial design is a design of experiment in which every level of each factor appears with every level of every other factor. The authors used ANN for modeling the system and GA for the optimization of the cutting parameters. The workpiece material was Inconel 718 (331 HRB) and the cutting tools used were TiAlN-coated tungsten carbide inserts. The nose radii used were 0.8, 1.2, and 1.6 mm while the approach angles were 45° and 75°. The cutting speeds and feed rates used in their investigation were, respectively, 45, 55, and 65 m min^{-1} and 0.2, 0.25, and 0.3 mm rev^{-1}. Using the GA the authors identified that the optimum parameters for the Inconel 718 as 45 m min^{-1} cutting speed, 0.22 mm rev^{-1} feed rate, 1.6 mm tool nose radius, and 60°approach angle. This combination of parameters produced the minimum surface roughness of 0.5498 μm.

Khamel *et al.*[105] investigated the effects of the three common process parameters, namely cutting speed, feed rate, and depth of cut, on the performance characteristics such as tool life, surface roughness, and cutting forces. The workpiece material was AISI 52100 (60 HRC) while the cutting tool was CBN inserts. For the three-level experimental design using L_{27} Taguchi method the cutting speeds used were 100, 140, and 200 m min^{-1}, the feed rates were 0.08, 0.12, and 0.16 mm rev^{-1} while the depths of cut were 0.2, 0.4, and 0.6 mm. The authors investigated the combined effects of the process parameters on the performance characteristics using ANOVA. The optimization technique associated with the RSM quadratic models was used as the multi-objective optimization approach. The authors reported that the feed rate and cutting speed have strong influence on the surface roughness and tool life. About 64% of the total variation of the surface roughness was due to the feed rate. The depth of cut, however, had maximum influence on the cutting forces. Simultaneous optimization of the tool life, surface roughness, and cutting forces was achieved with a cutting speed of 168 m min^{-1}, feed rate of 0.08 mm rev^{-1}, and depth of cut of 0.22 mm.

Batish *et al.*[106] investigated the influence of five independent process parameters during the hard turning of EN31, SAE8260, and EN9 tool steels. The parameters considered were the material hardness, feed rate, cutting speed, and the combination of cutting tool nose radius and depth on the machining forces and surface roughness. Each factor was varied in three levels resulting in 10 degrees of freedom. The L27 orthogonal array was used to determine the combination of the parameters to be investigated. The hardness of the material were 50, 55, and 60 HRC, the cutting speeds were 75, 110, and 150 m min^{-1}, the feed rates were 0.03, 0.06, and 0.1 mm rev^{1}, nose radii-depth of cut combinations were 0.4–0.075, 0.4–0.15, and 0.8–0.15 (mm-mm). The GA method was used to optimize all the responses. The authors reported that only the feed rate significantly affected the surface roughness while the material hardness had no significant effect.

The surface roughness of the workpiece and the cutting forces are usually considered as the main quality attributes of a turned workpiece. Since in most of the optimization methods the researchers do not evaluate each parameter, Gok[107] applied variance analysis to grey relational grades (GRA) of the factor levels to discover interactions between the machining parameters relating to the surface roughness and cutting forces. Unlike the Taguchi method which is designed to optimize single response characteristics the GRA method is able to optimize multiple outcomes. The attributes evaluated by the author are R_a, R_t, F_f, and F_c where F_f and F_c are the feed force and cutting force, respectively. Prediction models for surface roughness and cutting force were developed using the response surface analysis. The author noted that the optimal combination of machining parameters using response optimization are the values of the largest cutting velocity (200 m min^{-1}), values of the smallest depth of cut (0.5 mm), and feed rate

(0.125 mm rev^{-1}). This finding agrees with those of many other researchers as well as that predicted by the theory, namely the lowest surface roughness is achieved by using a small feed rate.

The review of the optimization studies show that many researchers have attempted to optimize the three main cutting parameters, namely the cutting speed, feed rate, and the depth of cut, in order to achieve the best surface finish quality, i.e., minimum surface roughness. The only difference between their works is the choice of the workpiece material, the cutting tools, and the range of the parameters investigated. The approaches used are also similar, namely the Taguchi experimental design and ANOVA analysis, to carry out the experimental plan and to determine the most influential factor that affects the surface roughness. The prediction models have been developed mostly using the RSM, GA, or ANN or a combination of these methods. In most cases the researchers reported that high cutting speeds and low feed rates produced better surface finish. The effect of the depth of cut on the surface finish depends on other factors such as workpiece material and chip formation. In the machining of glass fiber reinforce plastic composite material, Palanikumar[108] reported that a high depth of cut produced lower surface roughness while in the machining of Al/SiC MMC Manna and Bhattacharyya[109] reported that an increase in the depth of cut increases the surface roughness. Radhika *et al.*[110] also reported that the surface roughness increases as the depth of cut increased during the machining of aluminum hybrid MMC. Nevertheless, in all the reported studies the optimization models developed by the researchers were able to predict the optimum combination of input variables in order to obtain the best surface finish quality.

1.1.7 Summary

The objective of the finish turning process is to avoid or reduce the secondary finishing processes such as grinding, lapping, and polishing. However, this chapter has shown that numerous and complex interrelated factors govern the final surface finish quality produced by the finish turning process. Although it is not possible to list these factors in the order in which they produce the best surfaces based on the published literature, it is possible to identify certain factors that can generally be considered as those contributing to a good surface finish. The combination of low feed rate, low depth of cut, large nose radius, an efficient lubricant, and turning using a very rigid machine tool will likely lead to good surface finish in most steels. The use of wiper inserts instead of the conventional inserts could also results in good surface finish. Harder materials can produce better surface finish but this depends on the microstructure of the material as well as the machining parameters. Some composites and metal-matrix materials appear to produce better surface finish when machined at greater depths of cut.

In spite of the extensive research carried out in the past, there are several areas that need further investigation in order to arrive at a more in-depth understanding of the effect of the various factors reviewed. The following areas are identified as examples of potential areas for further research:

a. Effect of the chip breaker design on surface finish
   Chip breakers can reduce cutting pressure and enable chips to be removed more easily during the turning process. In materials that produce long curly chip an effective chip breaker can break up the chips, facilitate easily chip removal thus avoiding interference with the machining process. An understanding of the effect of chip breaker design on surface finish in the cutting of different types of material under different machining conditions will provide significant insight into the effectiveness of chip breaker design. This type of study can be done using simulation software such as DEFORM 3D and can be verified experimentally.
b. Effect of BUE formation on surface roughness
   BUE is known to be detrimental to the surface finish. However, the direct influence of material, cutting parameters, and formation of BUE on surface roughness has not been studied in any depth. Since the formation and destruction of BUE are dynamic processes it will be interesting to see how the surface roughness changes during the machining. An in-process method of monitoring the various roughness parameters as proposed by Kumar and Ratnam[61] will be useful for such type of studies.
c. Investigation on factors affecting surface roughness using other roughness parameters
   A review of the available literature shows that the centerline average roughness (R_a) is the most common roughness parameter studied in the past. There are, however, over 70 amplitude, spacing, hybrid, and functional roughness parameters that can be used to characterize a surface more accurately that the most common R_a parameter.[111] The effect of the various factors on some or most of these roughness parameters have not been studied in the past. The conflicting observations made by researchers when studying the effect of the various factors on surface roughness could be overcome by selecting the parameter that is most suited to the turning process.
d. Effect of nanoparticle addition in vegetable oil-based cutting fluids
   The addition of nanoparticles in cutting fluids has shown to be effective in improving the surface finish in turning. Most researchers have used chemical or mineral oil-based cutting fluids in their studies. The effect of adding nanoparticle in vegetable oils as cutting fluids, however, has been relatively unexplored. The effect of the particle size and amount of nanoparticles added to the fluid on the machining performance is a potential area for further investigation.
e. Optimization of machining parameters to minimize tool nose wear
   It is well known that the tool nose edge plays a significant role in the surface finish quality of the workpiece. However, no previous work has been found where researchers attempt to optimize the machining or other parameters in order to minimize the tool nose wear.

See also: 1.3 Finish Machining of Hardened Steel

References

1. Byers, J. P. *Metalworking Fluids*, 2nd ed.; CRC Press: New York, 2006.
2. Xavior, M. A.; Adithan, M. Determining the Influence of Cutting Fluids on Tool Wear and Surface Roughness During Turning of AISI 304 Austenitic Stainless Steel. *J Mater. Proc. Tech.* **2009**, *209* (2), 900–909.
3. Jayadas, N. H.; Prabhakaran Nair, K. Coconut Oil as Base Oil for Industrial Lubricants – Evaluation and Modification of Thermal, Oxidative and Low Temperature Properties. *Tribol. Int.* **2006**, *39*, 873–878.
4. Lawal, S. A.; Choudhury, I. A.; Nukman, Y. Evaluation of Vegetable and Mineral Oil-In-Water Emulsion Cutting Fluids in Turning AISI 4340 Steel with Coated Carbide Tools. *J. Cleaner Prod.* **2014**, *66*, 610–618.
5. Khan, M. M. A.; Mithu, M. A. H.; Dhar, N. R. Effects of Minimum Quantity Lubrication on Turning AISI 9310 Alloy Steel Using Vegetable Oil-Based Cutting Fluid. *J. Mater. Proc. Tech.* **2009**, *209* (15–16), 5573–5583.
6. de Angelo Sanchez, L. E.; Palma, G. L.; Ioan, M.; Modolo, D. L.; Nalon, L. J.; Santos, A. E. Effect of Different Methods of Cutting Fluid Application on Turning of a Difficult-to-Machine Steel (SAE EV-8). *Proc. Inst. Mech. Eng., Part B: J. Eng. Manuf.* **2013**, *227* (2), 220–234.
7. Shokoohi, Y.; Khosrojerdi, E.; Rassolian, S. B. H. Machining and Ecological Effects of a New Developed Cutting Fluid in Combination with Different Cooling Techniques on Turning Operation. *J. Cleaner Prod.* **2015**, *94*, 330–339.
8. Sohrabpoor, H.; Khanghah, S. P.; Teimouri, R. Investigation of Lubricant Condition and Machining Parameters while Turning of AISI 4340. *Int. J. Adv. Manuf. Tech* **2014**, *76* (9–12), 2099–2116.
9. Hadad, M.; Sadeghi, B. Minimum Quantity Lubrication-MQL Turning of AISI 4140 Steel Alloy. *J. Cleaner Prod.* **2013**, *54*, 332–343.
10. Amini, S.; Khakbaz, H.; Barani, A. Improvement of Near-Dry Machining and Its Effect on Tool Wear in Turning of AISI 4142. *Mater. & Manuf. Proc.* **2015**, *30* (2), 241–247.
11. Dilip Jerold, B.; Pradeep Kumar, M. Experimental Investigation of Turning AISI 1045 Steel Using Cryogenic Carbon Dioxide as the Cutting Fluid. *J. Manuf. Proc.* **2011**, *13* (2), 113–119.
12. Dhar, N. R.; Kamruzzaman, M. Cutting Temperature, Tool Wear, Surface Roughness and Dimensional Deviation in Turning AISI-4037 Steel Under Cryogenic Condition. *Int. J. Mach. Tools & Manuf.* **2007**, *47* (5), 754–759.
13. Dilip Jerold, B.; Pradeep Kumar, M. Machining of AISI 316 Stainless Steel Under Carbon-Dioxide Cooling. *Mater. & Manf. Proc.* **2012**, *27* (10), 1059–1065.
14. Mokšin, V.; Vekteris, V. Effectiveness of Twisted Nematic Liquid Crystals as Water Based Cutting Fluid Additive and Tap Lubricant. *Mechanika* **2011**, *17* (5), 570–575.
15. Ozcelik, B.; Kuram, E.; Huseyin Cetin, M.; Demirbas, E. Experimental Investigations of Vegetable Based Cutting Fluids with Extreme Pressure during Turning of AISI 304L. *Tribol. Int.* **2011**, *44* (12), 1864–1871.
16. Srikiran, S.; Ramji, K.; Satyanarayana, B.; Ramana, S. V. Investigation on Turning of AISI 1040 Steel with the Application of Nano-Crystalline Graphite Powder as Lubricant. *Proc. Inst. Mech. Eng., Pt. C: J Mech. Eng. Sci.* **2013**, *228* (9), 1570–1580.
17. Vamsi Krishna, P.; Srikant, R. R.; Nageswara Rao, D. Experimental Investigation to Study the Performance of Solid Lubricants in Turning of AISI 1040 Steel. *Proc. Inst. Mech. Eng., Pt. J: J. Eng. Tribol.* **2010**, *224* (12), 1273–1281.
18. Vamsi Krishna, P.; Srikant, R. R.; Nageswara Rao, D. Experimental Investigation on the Performance of Nanoboric Acid Suspensions in Sae-40 and Coconut Oil during Turning of AISI 1040 Steel. *Int. J. Mach. Tools & Manf.* **2010**, *50* (10), 911–916.
19. Vamsi Krishna, P.; Nageswara Rao, D. Performance Evaluation of Solid Lubricants in Terms of Machining Parameters in Turning. *Int. J. Mach. Tools & Manuf.* **2008**, *48* (10), 1131–1137.
20. Amrita, M.; Srikant, R. R.; Sitaramaraju, A. V. Performance Evaluation of Nanographite-Based Cutting Fluid in Machining Process. *Mater. & Manuf. Proc.* **2014**, *29* (5), 600–605.
21. Sayuti, M.; Sarhan, A. A. D.; Salem, F. Novel Uses of SiO_2 Nano-Lubrication System in Hard Turning Process of Hardened Steel AISI 4140 for Less Tool Wear, Surface Roughness and Oil Consumption. *J. Cleaner Prod.* **2014**, *67*, 265–276.
22. Sharma, A. K.; Tiwari, A. K.; Dixit, A. R. Progress of Nanofluid Application in Machining: A Review. *Mater. & Manf. Proc.* **2015**, *30* (7), 813–828.
23. Siddhpura, M.; Paurobally, R. A Review of Chatter Vibration Research in Turning. *Int. J. Mach. Tools & Manuf.* **2012**, *61*, 27–47.
24. Tobias, S. A. Machine Tool Vibration Research. *Int. J. Mach. Tool Des. & Res.* **1961**, *1*, 1–14.
25. Chiou, Y. S.; Chung, E. S.; Liang, S. Y. Analysis of Tool Wear Effect on Chatter Stability in Turning. *Int. J. Mech. Sci.* **1995**, *37*, 391–404.
26. Kayhan, M.; Budak, E. An Experimental Investigation of Chatter Effects on Tool Life. *Proc. Inst. Mech. Eng., Pt. B: J. Eng. Manuf.* **2009**, *223*, 1455–1463.
27. Lin, S. C.; Chang, M. F. A Study on the Effects of Vibrations on the Surface Finish Using a Surface Topography Simulation Model for Turning. *Int. J. Mach. Tools & Manuf.* **1998**, *38*, 763–782.
28. Wang, H.; To, S.; Chan, C. Y. Investigation on the Influence of Tool-Tip Vibration on Surface Roughness and Its Representative Measurement in Ultra-Precision Diamond Turning. *Int. J. Mach. Tool. Manu.* **2013**, *69*, 20–29.
29. Dimla Snr., D. E. The Correlation of Vibration Signal Features to Cutting Tool Wear in a Metal Turning Operation. *Int. J. Adv. Manuf. Tech.* **2002**, *19* (10), 705–713.
30. Fang, N.; Pai, P. S.; Mosquea, S. Effect of Tool Edge Wear on the Cutting Forces and Vibrations in High-Speed Finish Machining of Inconel 718: An Experimental Study and Wavelet Transform Analysis. *Int. J. Adv. Manuf. Tech.* **2011**, *52* (1–4), 65–77.
31. Bhuiyan, M. S. H.; Choudhury, I. A.; Dahari, M. Monitoring the Tool Wear, Surface Roughness and Chip Formation Occurrences Using Multiple Sensors in Turning. *J. Manuf. Sys.* **2014**, *33* (4), 476–487.
32. Clancy, B. E.; Shin, Y. C. A Comprehensive Chatter Prediction Model for Face Turning Operation Including Tool Wear Effect. *Int. J. Mach. Tools & Manuf.* **2002**, *42* (9), 1035–1044.
33. Bonifcio, M. E. R.; Diniz, A. E. Correlating Tool Wear, Tool Life, Surface Roughness and Tool Vibration in Finish Turning with Coated Carbide Tools. *Wear* **1994**, *173*, 137–144.
34. Dogra, M.; Sharma, V. S.; Dureja, J. Effect of Tool Geometry Variation on Finish Turning – A Review. *J. Eng. Sci. Technol. Rev.* **2011**, *4* (1), 1–13.
35. Whitehouse, D. *Surfaces and Their Measurement*, 1st ed.; Hermes Penton Ltd.: London, 2002.
36. Gökkaya, H.; Nalbant, M. The Effects of Cutting Tool Geometry and Processing Parameters on the Surface Roughness of AISI 1030 Steel. *Mater. & Des.* **2007**, *28* (2), 717–721.
37. Chou, Y.; Song, H. Tool Nose Radius Effects on Finish Hard Turning. *J. Mater. Process. Tech.* **2004**, *148*, 259–268.
38. ISO3685, International Standard. *Tool Life Testing with Single Point Turning Tools*. ISO: Geneva, 1993.
39. Chian, G. J.; Ratnam, M. M. Determination of Tool Nose Radii of Cutting Inserts using Machine Vision. *J. Sens. Rev.* **2011**, *31* (2), 0260–2288.
40. Sung, A. N.; Ratnam, M. M.; Loh, W. P. Effect of Tool Nose Profile Tolerance on Surface Roughness in Finish Turning. *Int. J. Adv. Manuf. Technol.* **2015**, *76*, 2083–2098.
41. Thiele, J. D.; Melkote, S. N. Effect of Cutting Edge Geometry and Workpiece Hardness on Surface Generation in the Finish Hard Turning of AISI 52100 Steel. *J. Mater. Proc. Tech.* **1999**, *94*, 216–226.
42. Ozel, T.; Hsu, T.-K.; Zeren, E. Effects of Cutting Edge Geometry, Workpiece Hardness, Feed Rate and Cutting Speed on Surface Roughness and Forces in Finish Turning of Hardened AISI H13 Steel. *Int. J. Adv. Manuf. Technol.* **2005**, *25*, 262–269.
43. Davoudinejad, A.; Noordin, Y. Effect of Cutting Edge Preparation on Tool Performance in Hard-Turning of DF-3 Tool Steel with Ceramic Tools. *J. Mech. Sci. & Tech.* **2014**, *28* (11), 4727–4736.
44. Elbah, M.; Yallese, M. A.; Aouici, H.; Mabrouki, T.; Rigal, J.-F. Comparative Assessment of Wiper and Conventional Ceramic Tools on Surface Roughness in Hard Turning AISI 4140 Steel. *Measurement: J. Int. Meas. Conf.* **2013**, *46* (9), 3041–3056.
45. Esteves Correia, A.; Paulo Davim, J. Surface Roughness Measurement in Turning Carbon Steel AISI 1045 using Wiper Inserts. *Measurement: J. Int. Meas. Conf.* **2011**, *44*, 1000–1005.
46. Grzesik, W.; Wanat, T. Surface Finish Generated in Hard Turning of Quenched Alloy Steel Parts using Conventional and Wiper Ceramic Inserts. *Int. J. Mach. Tool. Manu.* **2006**, *46*, 1988–1995.
47. Tauhiduzzaman, M.; Veldhuis, S. C. Effect of Material Microstructure and Tool Geometry on Surfacegeneration in Single Point Diamond Turning. *Prec. Eng.* **2014**, *38* (3), 481–491.
48. Ranganath, M. S.; Vipin, V. P. Effect of Rake Angle on Surface Roughness in CNC Turning. *Int. J. Adv. Res. & Innov.* **2014**, *2* (2), 522–530.
49. Gupta, M.; Kumar, S. Investigation of Surface Roughness and MRR for Turning of UD-GFRP using PCA and Taguchi Method. *Int. J. Eng. Sci. Technol.* **2015**, *18*, 70–81.

50. Pavel, R.; Marinescu, I.; Deis, M.; Pillar, J. Effect of Tool Wear on Surface Finish for a Case of Continuous and Interrupted Hard Turning. *J. Mater. Proc. Tech.* **2005**, *170*, 341–349.
51. Grzesik, W. Influence of Tool Wear on Surface Roughness in Hard Turning using Differently Shaped Ceramic Tools. *Wear* **2008**, *265*, 327–335.
52. Bhuiyan, M. S. H.; Choudhury, I. A. Investigation of Tool Wear and Surface Finish by Analyzing Vibration Signals in Turning ASSAB-705 Steel. *Mach. Sci.& Technol.* **2015**, *19*, 236–261.
53. Kılıckap, E.; Cakır, O.; Aksoy, M.; Inan, A. Study of Tool Wear and Surface Roughness in Machining of Homogenized SiC-p Reinforced Aluminium Metal Matrix Composite. *J. Mater. Proc. Tech.* **2005**, *164–165*, 862–867.
54. Sahin, Y.; Kok, M.; Celik, H. Tool Wear and Surface Roughness of Al_2O_3 Particle-Reinforced Aluminium Alloy Composites. *J. Mater. Proc. Technol.* **2002**, *128*, 280–291.
55. Sahoo, A. K.; Sahoo, B. Experimental Investigations on Machinability Aspects in Finish Hard Turning of AISI 4340 Steel using Uncoated and Multilayer Coated Carbide Inserts. *Measurement* **2012**, *45*, 2153–2165.
56. Cantero, J. L.; Dıaz-Alvarez, J.; Miguelez, M. H.; Marın, N. C. Analysis of Tool Wear Patterns in Finishing Turning of Inconel 718. *Wear* **2013**, *297*, 885–894.
57. Ozel, T.; Karpat, Y.; Figueira, L.; Davim, J. P. Modelling of Surface Finish and Tool Flank Wear in Turning of AISI D2 Steel with Ceramic Wiper Inserts. *J. Mater. Process. Tech.* **2007**, *189*, 192–198.
58. Shahabi, H. H.; Ratnam, M. M. In-Cycle Monitoring of Tool Nose Wear and Surface Roughness of Turned Parts using Machine Vision. *Int. J. Adv. Manuf. Technol.* **2009**, *40*, 1148–1157.
59. Diniz, A. E.; Liu, J. J.; Dornfeld, D. A. Correlating Tool Life, Tool Wear and Surface Roughness by Monitoring Acoustic Emission in Finish Turning. *Wear* **1992**, *152* (2), 395–407.
60. Jia, P.; Zhou, M. Tool Wear and Its Effect on Surface Roughness in Diamond Cutting of Glass Soda-Lime. *Chinese J. Mech. Eng. (English Ed.)* **2012**, *25* (6), 1224–1230.
61. Kumar, B. M.; Ratnam, M. M. In-Process Measurement of Surface Roughness using Machine Vision with Sub-Pixel Edge Detection in Finish Turning. *Int. J. Prec. Eng. & Manuf.* **2014**, *15* (11), 2239–2249.
62. Kwon, Y.; Ertekin, Y.; Tseng, T.-L. Characterization of Tool Wear Measurement with Relation to the Surface Roughness in Turning. *Mach. Sci. &Tech.* **2004**, *8* (1), 39–51.
63. Nakayama, K.; Shaw, M. C.; Brewer, R. C. Relationship between Cutting Forces, Temperatures, Built-Up Edge and Surface Finish. *CIRP Annals* **1966**, *14*, 211–223.
64. Fang, N.; Srinivasa Pai, P.; Mosquea, S. The Effect of Built-Up Edge on the Cutting Vibrations in Machining 2024-T351 Aluminum Alloy. *Int. J. Adv. Manuf. Technol.* **2010**, *49*, 63–71.
65. Pálmai, Z.; Csernák, G. Effects of Built-Up Edge-Induced Oscillations on Chip Formation during Turning. *J. Snd. & Vib.* **2013**, *332* (8), 2057–2069.
66. Gomez-Parra, A.; Alvarez-Alcon, M.; Salguero, J.; Batista, M.; Marcos, M. Analysis of the Evolution of the Built-Up Edge and Built-Up Layer Formation Mechanisms in the Dry Turning of Aeronautical Aluminium Alloys. *Wear* **2013**, *302*, 1209–1218.
67. Cassier, Z.; Prato, Y.; Muñoz-Escalona, P. Built-Up Edge Effect on Tool Wear When Turning Steels at Low Cutting Speed. *J. Mater. Eng. & Perform.* **2004**, *13* (5), 542–547.
68. Gökkaya, H.; Nalbant, M. The Effects of Cutting Tool Coatings on the Surface Roughness of AISI 1015 Steel Depending on Cutting Parameters. *Turk. J. Eng. & Env. Sci.* **2006**, *30* (5), 307–316.
69. Thakur, A.; Gangopadhyay, S.; Maity, K. P. Effect of Cutting Speed and CVD Multilayer Coating on Machinability of Inconel 825. *Surf. Eng.* **2014**, *30* (7), 516–523.
70. Yigit, R.; Findik, F.; Çelik, E. Performance of Multilayer Coated Carbide Tools When Turning Cast Iron. *Turk. J. Eng. & Env. Sci.* **2009**, *33* (3), 147–157.
71. Nalbant, M.; Gokkaya, H.; Toktas, I.; Sur, G. The Experimental Investigation of the Effects of Uncoated, PVD-and CVD-Coated Cemented Carbide Inserts and Cutting Parameters on Surface Roughness in CNC Turning and Its Prediction using Artificial Neural Networks. *Rob. & Comp.-Int. Manf.* **2009**, *25*, 211–223.
72. Aouici, H.; Yallese, M. A.; Belbah, A.; Elbah, M. M. Experimental Investigation of Cutting Parameters Influence on Surface Roughness and Cutting Forces in Hard Turning of X38CrMoV5–1 with CBN Tool. *Sadhana* **2013**, *38* (3), 429–445.
73. Rafai, N. H.; Islam, M. N. An Investigation into Dimensional Accuracy and Surface Finish Achievable in Dry Turning. *Mach. Sci. & Technol.* **2009**, *13*, 571–589.
74. Gunay, M.; Yucel, E. Application of Taguchi Method for Determining Optimum Surface Roughness in Turning of High-Alloy White Cast Iron. *Measurement* **2013**, *46*, 913–919.
75. Asiltürk, I.; Akkus, H. Determining the Effect of Cutting Parameters on Surface Roughness In Hard Turning using the Taguchi Method. *Measurement* **2011**, *44* (9), 1697–1704.
76. Kumar, A.; Mahapatra, M. M.; Jha, P. K. Effect of Machining Parameters on Cutting Force and Surface Roughness of In Situ Al–4.5%Cu/TiC Metal Matrix Composites. *Measurement* **2014**, *48*, 325–332.
77. Ezilarasan, C.; Senthil Kumar, V. S.; Velayudham, A. Effect of Machining Parameters on Surface Integrity in Machining Nimonic C-263 Super Alloy using Whisker-Reinforced Ceramic Insert. *J. Mater. Eng. & Perform.* **2013**, *22* (6), 1619–1628.
78. Kini, M. V.; Chincholkar, A. M. Effect of Machining Parameters on Surface Roughness and Material Removal Rate in Finish Turning of 30_ Glass Fibre Reinforced Polymer Pipes. *Mater. & Des.* **2010**, *31*, 3590–3598.
79. Bhushan, R. K.; Kumar, S.; Das, S. Effect of Machining Parameters on Surface Roughness and Tool Wear for 7075 Al Alloy SIC Composite. *Int. J. Adv. Manuf. Technol.* **2010**, *50*, 459–469.
80. Suresh, R.; Basavarajappa, S. Effect of Process Parameters on Tool Wear and Surface Roughness during Turning of Hardened Steel with Coated Ceramic Tool. *Proc. Mat. Sci.* **2014**, *5*, 1450–1459.
81. Dwivedi, S. P.; Kumar, S.; Kumar, A. Effect of Turning Parameters on Surface Roughness of A356/5% SIC Composite Produced by Electromagnetic Stir Casting. *J. Mech. Sci. & Technol.* **2012**, *26* (12), 3973–3979.
82. Qu, S.; Sun, F.; Zhang, L.; Li, X. Effects of Cutting Parameters on Dry Cutting of Aluminum Bronze Alloy. *Int. J. Adv. Manuf. Technol.* **2014**, *70*, 669–678.
83. Lalwani, D. I.; Mehta, N. K.; Jain, P. K. Experimental Investigations of Cutting Parameters Influence on Cutting Forces and Surface Roughness in Finish Hard Turning of MDN250 Steel. *J. Mater. Proc. Technol.* **2008**, *206*, 167–179.
84. Senthil, P.; Selvaraj, T.; Sivaprasad, K. Influence of Turning Parameters on the Machinability of Homogenized Al–Cu/TiB_2 In Situ Metal Matrix Composites. *Int. J. Adv. Manuf. Technol.* **2013**, *67*, 1589–1596.
85. Fratila, D.; Caizar, C. Investigation of the Influence of Process Parameters and Cooling Method on the Surface Quality of AISI-1045 during Turning. *Mater. & Manuf. Proc.* **2012**, *27*, 1123–1128.
86. Uddin, M. S. On the Influence and Optimisation of Cutting Parameters in Finishing of Metallic Femoral Heads of Hip Implants. *Int. J. Adv. Manuf. Technol.* **2014**, *73*, 1523–1532.
87. Chauhan, S. R.; Dass, K. Optimization of Machining Parameters in Turning of Titanium (Grade-5) Alloy using Response Surface Methodology. *Mater. Manuf. Process.* **2012**, *27*, 531–537.
88. Patel, P. R.; Patel, V. A. Effect of Machining Parameters on Surface Roughness and Power Consumption for 6063 Al Alloy TiC Composites (MMCs). *Int. J. Eng. Res. & Applicat.* **2012**, *2* (4), 295–300.
89. Khidhir, B. A.; Mohamed, B. Analyzing the Effect of Cutting Parameters on Surface Roughness and Tool Wear When Machining Nickel Based Hastelloy – 276. *IOP Conf. Series: Mater. Sci. Eng.* **2011**, *17*, 012043.
90. Horváth, R.; Drégelyi-Kiss, Á. Analysis of Surface Roughness of Aluminum Alloys Fine Turned: United Phenomenological Models and Multi-Performance Optimization. *Meas.: J. Int. Meas. Conf.* **2015**, *65*, 181–192.
91. Chinchanikar, S.; Choudhury, S. K. Investigations on Machinability Aspects of Hardened AISI 4340 Steel at Different Levels of Hardness using Coated Carbide Tools. *Int. J. Refrac. Met. & Hard Mater.* **2013**, *38*, 124–133.
92. Akasawa, T.; Fukuda, I.; Nakamura, K.; Tanaka, T. Effect of Microstructure and Hardness on the Machinability of Medium-Carbon Chrome–Molybdenum Steel. *J. Mater. Proc. Technol.* **2004**, *153–154*, 48–53.
93. Paulo Davim, J. A Note on the Determination of Optimal Cutting Conditions for Surface Finish Obtained in Turning using Design of Experiments. *J. Mater. Process. Technol.* **2001**, *116*, 305–308.
94. Singh, D.; Venkateswara Rao, P. Optimization of Tool Geometry and Cutting Parameters for Hard Turning. *Mater. Manuf. Process.* **2007**, *22* (1), 15–21.
95. Neseli, S.; Yaldız, S.; Turkes, E. Optimization of Tool Geometry Parameters for Turning Operations Based on the Response Surface Methodology. *Measurement* **2011**, *44*, 580–587.
96. Nalbant, M.; Gokkaya, H.; Sur, G. Application of Taguchi Method in the Optimization of Cutting Parameters for Surface Roughness in Turning. *Mater. Design* **2007**, *28*, 1379–1385.

97. Monaghan, J. M. The Use of Quick Stop Test to Study the Chip Formation of An Sic/Al Metal Matrix Composite and Its Matrix Alloy. *Process. Adv. Mater.* **1994**, *4*, 170–179.
98. Hoecheng, H.; Yen, S. B.; Ishihara, T.; Yen, B. K. Fundamental Turning Characteristics of Tribology Favored Graphite/Aluminium Alloy Composites. *J. Comp. A* **1997**, *28A*, 813–818.
99. Palanikumar, K.; Karthikeyan, R. Assessment of Factors Influencing Surface Roughness on the Machining of Al/SiC Particulate Composites. *Mater. & Des.* **2007**, *28*, 1584–1591.
100. Hasçalık, A.; Çaydaş, U. Optimization of Turning Parameters for Surface Roughness and Tool Life Based on the Taguchi Method. *Int. J. Adv. Manuf. Technol.* **2008**, *38*, 896–903.
101. Hagiwara, M.; Chen, S.; Jawahir, I. S. Contour Finish Turning Operations with Coated Grooved Tools: Optimization of Machining Performance. *J. Mater. Process. Technol.* **2009**, *209*, 332–342.
102. Muthukrishnan, N.; Paulo Davim, J. Optimization of Machining Parameters of Al/SiC-MMC with ANOVA and ANN Analysis. *J. Mater. Process. Technol.* **2009**, *209*, 225–232.
103. Ansalam Raj, T. G.; Narayanan Namboothiri, V. N. An Improved Genetic Algorithm for the Prediction of Surface Finish in Dry Turning of SS 420 Materials. *Int. J. Adv. Manuf. Technol.* **2010**, *47*, 313–324.
104. Homami, R. M.; Tehrani, H. M.; Movahedi, B.; Azimifar, F. Optimization of Turning Process using Artificial Intelligence Technology. *Int. J. Adv. Manuf. Technol.* **2014**, *70*, 1205–1217.
105. Khamel, S.; Ouelaa, N.; Bouacha, K. Analysis and Prediction of Tool Wear, Surface Roughness and Cutting Forces in Hard Turning with CBN Tool. *J. Mech. Sci. & Tech.* **2012**, *26* (11), 3605–3616.
106. Batish, A.; Bhattacharya, A.; Kaur, M.; Singh, M. C. Hard Turning: Parametric Optimization using Genetic Algorithm for Rough/Finish Machining and Study of Surface Morphology. *J. Mech. Sci. & Tech.* **2014**, *28* (5), 1629–1640.
107. Gok, A. A New Approach to Minimization of the Surface Roughness and Cutting Force Via Fuzzy TOPSIS, Multi-Objective Grey Design and RSA. *Measurement* **2015**, *70*, 100–109.
108. Palanikumar, K. Cutting Parameters Optimization for Surface Roughness in Machining of GFRP Composites using Taguchi's Method. *J. Reinforced Plastics & Comp.* **2006**, *25* (16), 1739–1751.
109. Manna, A.; Bhattacharyya, B. Investigation for Optimal Parametric Combination for Achieving Better Surface Finish During Turning of Al/SiC-MMC. *Int. J. Adv. Manuf. Technol.* **2004**, *23*, 658–665.
110. Radhika, N.; Subramaniam, R.; Senapathi, S. B. Machining Parameter Optimisation of an Aluminium Hybrid Metal Matrix Composite by Statistical Modelling. *Ind. Lub. & Tribol.* **2013**, *65* (6), 425–435.
111. Gadelmawla, E. S.; Koura, M. M.; Maksoud, T. M. A.; Elewa, I. M.; Soliman, H. H. Roughness Parameters. *J. Mater. Proc. Technol.* **2002**, *123* (1), 133–145.

Relevant Websites

http://americanmachinist.com/turning-surface-finishes-calculator
American Machinist.
http://www.cimindustry.com/article/tooling/10-tips-to-improve-surface-finish
Canadian Industrial Machinery Magazine.
http://www.digitalsurf.com/en/guideprofileparameters.html
Digital Surf.
http://www.machinerylubrication.com/Read/29574/choose-cutting-oil
Machinery Lubrication.
http://www.mmsonline.com/articles/inserts-for-difficult-materials
Modern Machine Shop.
http://www.productionmachining.com/articles/implementing-wiper-inserts-to-maximize-productivity
Production Machining Magazine.
http://compositemachining.org/2014/10/how-choice-of-rake-angle-will-affect-surface-finish/
Sandvik Coromant.
https://www.secotools.com/en/Global/presscentre/Left/Archive-2014/Identifying-and-addressing-eight-common-insert-failure-modes/
Seco Tools.
http://todaysmachiningworld.com/magazine/how-it-works-cutting-fluids/
Today's Machining World.

1.2 Effect of Cutting Variables on Boring Process: A Review

SA Lawal, MB Ndaliman, KC Bala, and SS Lawal, Federal University of Technology, Minna, Nigeria

© 2017 Elsevier Inc. All rights reserved.

1.2.1	**Introduction**	26
1.2.2	**Factors Affecting Boring Operation**	27
1.2.3	**Application of Boring Process in the Building of Tunnel**	39
1.2.3.1	Ground–Equipment–Support Interactions	41
1.2.3.2	Boring and Thrusting	41
1.2.3.2.1	Restart after standstill	42
1.2.3.2.2	Immobilization during ongoing excavation	42
1.2.3.2.3	Tunnel support	42
1.2.3.2.4	Single and double shielded TBMs	42
1.2.3.3	Counter Measures	42
1.2.4	**Future Research Direction in Boring Operation**	43
1.2.5	**Conclusions**	44
References		44

1.2.1 Introduction

Boring is a process of enlarging a hole size that was already made by drilling, or casting to the designed dimension. The enlargement of hole can be made by means of a single point cutting tool or a boring head containing multiple tools. The boring of an engine cylinder or of a gun barrel is an example of such process. In boring, either the boring head/bar can be rotated or the workpart can be rotated. Boring machines or boring mills usually rotate the boring bar against a stationary workpiece. Also in turning machines, boring can be performed where the boring bar attached to the tool post remains stationary against a rotating workpiece held in the lathe chuck. The boring bar with insert attached to it is fed into an existing hole. Depending on material, type of tool insert, and cutting conditions, the chip formed may either be continuous or discontinuous. The surface produced is known as bore. Surface roughness in boring may vary between 0.0002 and 0.006 mm. With the advancement of machining technology, the limitations of boring with respect to geometric accuracy and material hardness have been diminishing. With new grades of carbide and ceramic tool inserts, the accuracy of boring and surface quality has increased. The hole produced may either be straight or tapered. The work holding devices used lathe could be either three-jaw chuck, the four-jaw chuck, the collet, or the faceplate. For round or hexagonal workpieces, three-jaw chuck is used while four-jaw chuck and collet are used for irregular-shaped workpieces.

In boring of steels, vibration of tool and workpiece are the important limiting factor for volume of metal removed and machining efficiency. In boring operations, the length of boring bar is kept long, resulting in vibrations leading to tool failure, poor surface finish, and chatter. The ratio of length to diameter of boring bar is one of the important factors that is responsible for tool vibration. It has been established that boring bars with a high length–diameter ratio tend to chatter.[1] In the industry where metal cutting operations such as turning, milling, boring, and grinding take place, degrading vibrations are a common problem. In internal turning operation, vibration is a pronounced problem, as long and slender boring bars are usually required to perform the internal machining of workpieces. Tool vibration in internal turning frequently has a degrading influence on surface quality, tool life, and production efficiency, and will also result in severe environmental issues such as high noise levels. Boring bar vibrations are usually directly related to the lower order bending modes of the clamped boring bar.[2,3]

The concern today in the manufacturing industry is the vibration induced by metal cutting, for example, turning, milling, and boring operations. Turning operation and especially boring operations are associated with serious vibration-related problems. To reduce the problem of vibration and ensure that the desired shape and tolerance are achieved, extra care must be taken with production planning and in the preparations for the machining of a workpiece. The vibration problem associated with metal cutting thus has considerable influence on important factors such as productivity, production costs, etc. Hence, the need for thorough investigation of the factors that cause vibrations in machining operation is therefore an important step toward solving the problem. In internal turning, the metal-cutting process is carried out in predrilled holes or holes in cast, etc. The dimensions of the workpiece hole generally determine the length and limit the diameter or cross-sectional size of the boring bar.

Usually, a boring bar is long and slender and is thus sensitive to excitation forces introduced by the material deformation process in the turning operation. The boring bar is generally the weakest link in the boring bar–clamping system of the lathe. The boring bar motion may vary with time. This dynamic motion originates from the deformation process of the work material. The motion or vibration of the boring bar influences the result of the machining in general, and the surface finish in particular. Tool life is also likely to be influenced by the resulting vibrations. The tool vibrations during turning are usually denoted 'self-excited chatter' or 'tool

 doi:10.1016/B978-0-12-803581-8.09148-7

vibration.' Depending on the driving force of the tool vibration, the vibration is generally divided into one of two categories: regenerative chatter and non-regenerative chatter (primary chatter).[4–7] Primary chatter may arise from different physical causes, for example, random excitation of the tool holder's eigen frequencies due to plastic deformation of workpiece material and/or friction between the tool and the cut material, the tendency of the cutting force excitation to change with the cutting speed, and the dynamic effects of the geometry of the cutting tool on the cutting process, etc.[4,7,8] Regenerative chatter is induced by the undulation on the surface of the workpiece which is produced during previous successive cuts.[4,9]

During an internal turning operation, the cutting tool and the boring bar are subjected to a prescribed deformation as a result of the relative motion between the tool and workpiece both in the cutting-speed direction and feed direction. As a response to the prescribed deformation, the tool is subjected to traction and thermal loads on those faces that have interfacial contact with the workpiece or chip. In the metal-cutting process, during which chips are formed, the workpiece material is compressed and subjected to plastic deformation. This results in considerable strain and strain rates in the primary deformation zone. **Figure 1** shows a typical boring operation process.

Also, the dynamic properties of a boring bar installed in a lathe are influenced by the boundary conditions imposed by the clamping of the bar.[2,10] A number of theories concerning the machine tool chatter and the behavior of the dynamic system have been developed explaining tool vibration during turning operations.[4,11–13] In 1946, the principles of the traditional theory of chatter in simple machine-tool systems was worked out by Arnold[11] based on experiments carried out in a rigid lathe, using a stiff workpiece but a flexible tool holder. In this way he was able to investigate chatter under controlled conditions. Later in 1965, Tobias[4] presented an extensive summary of results from various researchers concerning the dynamic behavior of the lathe, the chatter theory, and further developed the chatter phenomena considering the chip-thickness variation and the phase lag of the undulation of the surface. Also, in the same year, Merritt[12] discussed the stability of structures with *n*-degrees of freedom, assuming no dynamics in the cutting process; they also proposed a simple stability criterion.

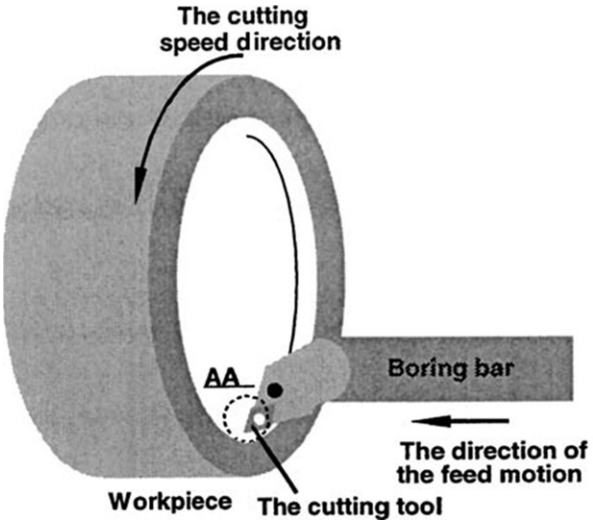


Figure 1 Boring operation.[2]

1.2.2 Factors Affecting Boring Operation

Like any other machining operations, output results are determined by the cutting conditions such as cutting speed, feed rate, depth of cut (DOC), type of tool, tool geometry, cutting fluid type, and method of application, machining type and materials. Hence, researchers have employed some of these cutting conditions to investigate how they affect the boring operation in terms of surface finish, cutting force, too wear, tool vibration, dimensional accuracy, etc. Akesson *et al.*[14] investigated the dynamic properties of boring bars concerning different clamping conditions. The experimental setup and subsequent measurements were carried out on a Mazak SUPERQUICKTURN – 250 M computer numerical control (CNC) turning center. The CNC lathe has 18.5 kW spindle power and a maximal machining diameter of 300 mm with 1005 mm between the centers, a maximal spindle speed of 400 revolutions per minute (rpm) and a flexible turret with a tool capacity of 12 as shown in **Figure 2**.

Two different boring bars were used in the experiment. The first boring bar used in the modal analysis was a standard 'non-modified' boring bar, WIDAXS40TPDUNR15F3D6G. The second boring bar used was a modified boring bar, based on the standard WIDAXS40TPDUNR15 boring bar with an accelerometer and an embedded piezo-stack actuator. The accelerometer was mounted 25 mm from the tool tip to measure the vibrations in the cutting-speed direction (y-). This position was as close as possible to the tool tip, but at a sufficient distance to prevent metal-chips from the material removal process from damaging the accelerometer. The standard WIDAXS40TPDUNR15 boring bar was manufactured using material 30CrNiMo8 (AISI4330), which is a heat treatable steel alloy (for high strength). Shaker excitation was used for the experimental modal analysis of the boring bars. The utilized spectrum estimation parameters and excitation signals' properties were determined. A frequency range covering the significant part near the resonance frequencies was selected, i.e., -100 to -200 Hz around the resonance peaks. The coherence values for the involved transfer paths at each eigen frequency were greater or equal to 0.996.

A number of different phenomena were observed during the experimental modal analysis of the boring bars for various configurations and setups. For instance, large variations were observed in the first resonance frequencies of the boring bar for different tightening torques of the clamp screws. Also, the order in which the clamp screws were tightened (first from the upper side of the boring bar or first from the underside of the boring bar) had a significant impact on, for example, the fundamental bending resonance frequencies. The results from the experimental modal analysis of the two boring bars demonstrate that the different controlled clamping conditions in the experiments yield different dynamic properties of the

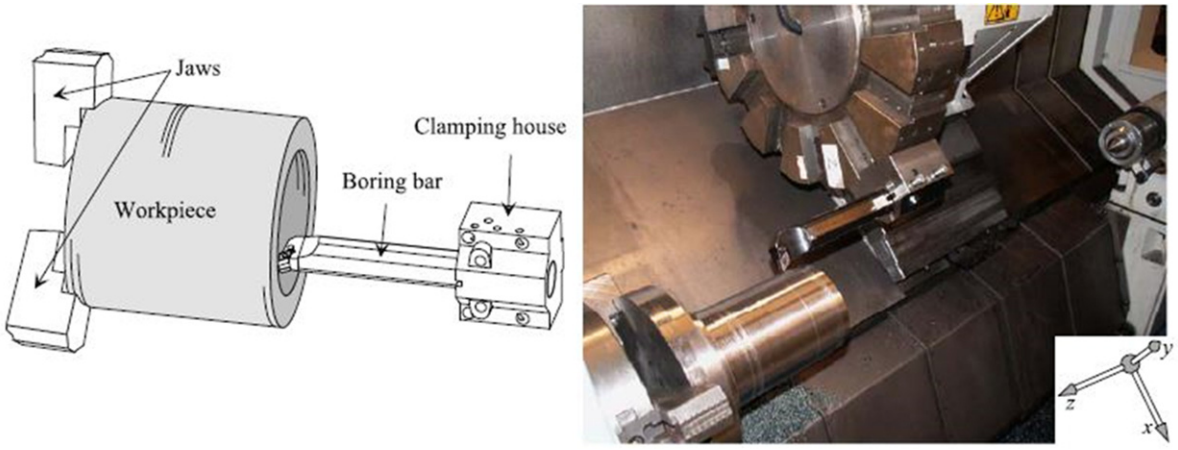


Figure 2 (a) An internal turning setup with a workpiece clamped in a shuck to the left and a boring bar clamped in a clamping housing to the right. (b) The room in the Mazak SUPERQUICKTURN – 250 M computer numerical control lathe where machining is carried out.[14]

clamped boring bars. Hence, the different clamping conditions result in different boundary conditions along the clamped part of the boring bar. It was also established that a boring bar clamped in a standard clamping housing with clamping screws is likely to have a nonlinear dynamic behavior. The standard clamping housing with clamp screws is the likely source of the nonlinear behavior. Multi-span Euler–Bernoulli models of a clamped boring bar incorporating pinned or elastic support boundary conditions approximating the flexibility of the actual screw clamping of the boring bar end inside the clamping housing provide significantly higher correlation with experimental modal analysis results compared to a traditional fixed-free Euler–Bernoulli model.

The fundamental boring bar resonance frequencies decrease with increasing excitation level. However, with regard to the behavior of relative damping as a function of excitation force level; the results from the standard boring bar indicate that the relative damping for the first mode increases with increasing excitation force level, while the relative damping for the second mode decreases with increasing excitation force level. Also, the results from the modified boring bar give an ambiguous indication of the effects on damping properties and the clamp screw tightening torque appears to affect the nonlinear behavior of the boring bar. The investigation shows that the number of clamping screws, the clamping screw diameter sizes, the screw tightening torques, and the order the screws are tightened has a significant influence on a clamped boring bars eigen frequencies and its mode shapes orientation in the cutting speed – cutting depth plane. The results indicated that multi-span Euler–Bernoulli beam models with pinned boundary condition or elastic boundary condition modeling the clamping are preferable as compared to a fixed-free Euler–Bernoulli beam for modeling dynamic properties of a clamped boring bar. It also demonstrated that a standard clamping housing clamping a boring bar with clamping screws imposes nonlinear dynamic boring bar behavior.

Rao *et al.*[1] evaluated the cutting tool condition monitoring by analyzing surface roughness, workpiece vibration, and



Figure 3 Workpiece.[1]

volume of metal removed for AISI 1040 steel in boring. The experiment was conducted on CNC lathe DX200 model, with tool inserts of DNMG150608 and DNMG150604 having nose radii of 0.8 and 0.4 mm respectively. The metal used in this experiment was AISI1040 with length of 90 mm, outer diameter of 100 mm, and inner diameter of 56 mm as shown in Figure 3.

The following sequential procedure was used to carry out the experiment under dry conditions.

1. Each test was started with a fresh cutting edge with one test condition (trials) and machining stopped at the end of each pass. After each pass the DOC was increased by 0.2 mm (fixed DOC was given in each pass) until the tool failed.
2. Vibration signals from the rotating workpiece were measured in the machining process using LDV.
3. After each pass the tool insert was removed and flank wear and crater wear were measured with machine vision system.
4. After each cut the workpiece was also removed and its surface roughness measured on Talysurf.

5. The steps one to four to be continued until the tool failed and beyond that two or three passes performed on the workpiece to observe the behavior of tool wear.
6. A new workpiece and new tool insert were loaded to the machine and the above steps were followed with a new working condition.
7. In each trial, surface roughness, volume of metal removed, and time and amplitude of workpiece vibrations were identified when the tool failed based on flank wear. The above procedure was followed for all the trials and in each trial the cutting parameters were changed as given in the **Table 1**.

Taguchi, analysis of variance (ANOVA) and regression analysis methods were used to analyze the experimental data to find out the effect and contribution of cutting parameters. According to selected orthogonal array eight experiments (trials) were conducted with two levels of cutting parameters such as workpiece rotational speed, tool insert nose radius, and feed rate. The results show that in each trial of experiment, a strong correlation among the dependent and independent variables was found. A noncontact monitoring system was used with Laser Doppler Vibrometer to observe vibration of workpiece during machining. Tool life was evaluated by analyzing surface roughness, amplitude of workpiece vibration, and volume of metal removed with the help of Taguchi, ANOVA, and regression analysis. The following results were observed during the experiment.

1. Vibration amplitudes of workpiece are found to be increased along with the progression of the tool wear.
2. Nose radius (45.81%) is the significant parameter for affecting the amplitude of workpiece of vibration.
3. Feed rate (55.57%) is the significant parameter for affecting the surface roughness.
4. Feed rate (51.26%) is the significant parameter for affecting the volume of metal removed.

Andren *et al.*[3] studied the identification of motion of cutting tool vibration in a continuous boring operation – correlation to structural properties. The experimental modal analysis and the operating deflection shape (ODS) analysis were carried out on a Mazak SUPER QUICK TURN – 250 M CNC turning center. It has 18:5 kW spindle power and a maximum machining diameter of 300 mm; with 1007 mm between the center. The cutting operations were performed as an external turning operation using the WIDAX S40TPDUNR15 boring bar. The measurements were divided into two different categories: modal analysis and ODS analysis of the boring bar. In the modal analysis measurement the following equipment were used: (1) 14 PCB 333A32 accelerometers, (2) OSC audio power amplifier, USA 850, (3) Ling Dynamic Systems shaker V201, (4) Bruel and Kjær 8001 impedance head, (5) Bruel and Kjær NEXUS conditioning amplifier 2692, (6) HP VXI E1432 front–end data acquisition unit, and (7) PC with IDEAS Master Series version 6. The ODS data were collected using less sensitive accelerometers than those used in the modal analysis measurement. For the ODS analysis, the boring bar vibration was measured during a continuous cutting operation and data were collected using the following measuring equipment: (1) 14 PCBU353B11 accelerometers, (2) HP VXI E1432 front–end data acquisition unit, and (3) PC with IDEAS Master Series version 6.

Table 1 Test trails for boring[1]

S/N	*Speed (m min^{-1})*	*Feed (mm rev^{-1})*	*Nose radius (mm)*
1	210	0.10	0.8
2	210	0.16	0.8
3	170	0.10	0.8
4	170	0.16	0.8
5	210	0.10	0.4
6	210	0.16	0.4
7	170	0.10	0.4
8	170	0.16	0.4

The experimental modal analysis of the boring bar with modified clamping resulted in two identified modes. The first mode in the cutting depth direction had a resonance frequency of 570 Hz; and a relative (viscous) damping of 1.85%. The second mode in the cutting-speed direction had a resonance frequency of 595 Hz and a damping of 0.84%. The damping of the first mode was noted to be slightly larger than prior to the modification of the clamping. The two modes were well separated as defined by the cross MAC value and the synthesized frequency response functions corresponded well with the measured functions. From the ODS results, it was apparent that vibrations of the boring bar were dominating in the cutting-speed direction during a continuous cutting operation. The deformation pattern of the boring bar was according to the ODS measurement dominating in the cutting-speed direction at both resonance peaks. The ODS resulted in eigen frequencies at a somewhat lower frequencies compared with the modal analysis.

Saindane *et al.*[15] investigated the effect of vibration damping in boring operation using passive damper. Boring bar of 16 mm × 16 mm cross section and 200 mm long of WIDAX make was used. The boring operations were carried out on a lathe machine as shown in **Figure 4** using EN9 as workpiece material. The workpiece was mounted on the lathe using a four-jaw chuck. The machining parameters were selected based on the manufacturers recommendations and were changed according to the proposed conditions. Also the cutting speed, length of passive damper on boring bar, and overhang length were varied as shown in **Table 2** and experiments were conducted to analyze the effect of vibration on deflection of boring bar.

The boring operation was carried out for 51 mm internal diameter using passive dampers of nylon and polyurethane. Fast Fourier transform (FFT) analyzer and accelerometer were used to obtain various results for the experiments and the deflections were measured in terms of acceleration by accelerometer as shown in **Table 3**.

It was observed that the proposed method was an innovative to reduce the deflection of the boring bar in boring operation. The results proved the passive damping technique has vast potential in the reduction of deflection and depend on the DOC. Passive dampers are also relatively cheaper than other damped boring bars.

Khatake and Nitnaware[16] studied the mitigation of vibration using passive damper in machining. The study involved the use of particle damper, which is a passive damping concept

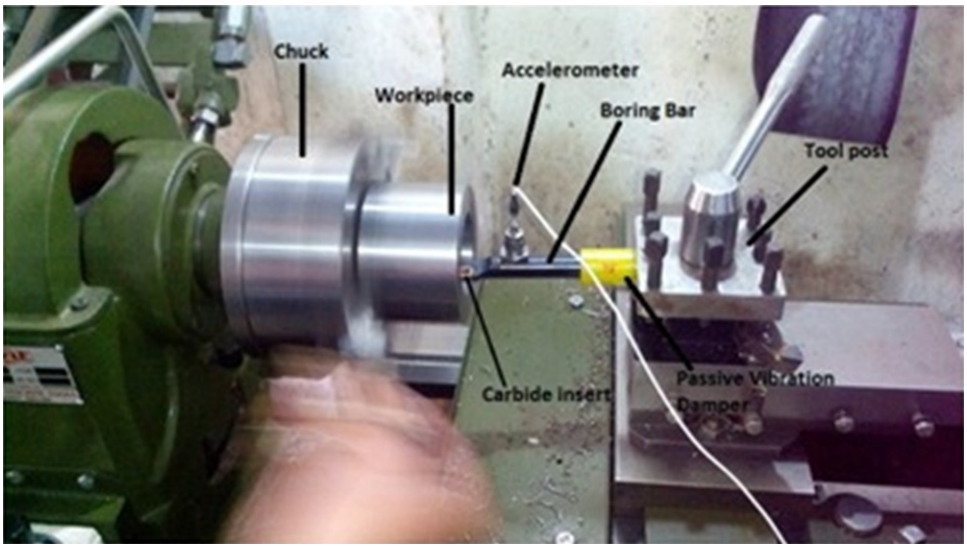


Figure 4 Experimental set up of boring bar with passive damper and accelerometer.[15]

Table 2 Experimental conditions[15]

S/No	*Cutting speed (rpm)*	*Feed rate (mm rev^{-1})*	*Depth of cut (mm)*	*Overhanging of the boring bar (mm)*	*Material used for damping*	*Percentage of overhang damped*	*Length of passive damper*
1	100	0.02	1	100	Nylon	3	30
2	100	0.02	1	120	PU	6	72
3	100	0.04	2	100	Nylon	6	60
4	100	0.02	2	120	PU	3	36
5	120	0.02	2	100	PU	3	30
6	120	0.04	2	120	Nylon	6	72
7	120	0.04	1	100	PU	6	60
8	120	0.04	1	120	Nylon	3	36

Table 3 Experimental results[15]

S/No	*Without damper (mm)*	*With damper of polyurethane (μm s^{-2})*	*With damper of nylon (μm s^{-2})*
1	28	22	25
2	50	40	30
3	40	50	30
4	25	28	40
5	24	25	23
6	40	30	20
7	25	22	18
8	48	35	20

that uses metal or ceramic particles or powders of small size that are placed inside cavities within or attached to the vibrating structures. Metal particles of high density such as lead or tungsten steel are the most common materials for better damping performance. In contrast to viscoelastic materials which dissipate the stored elastic energy particle damping treatment focuses on energy dissipation in a combination of collision, friction, and shear damping. It involves the potential of energy absorption and dissipation through momentum exchange between moving particles and vibrating walls, friction, impact restitution, and shear deformations. It is an attractive alternative in passive damping due to its conceptual simplicity, potential effectiveness over broad frequency range, temperature, and degradation insensitivity and very low cost. The principle adopted in the study was to enhance the damping capability, minimizing the loss in static stiffness through implementation of passive damper.

Boring bar of 20 mm × 20 mm cross section and 200 mm long of WIDAX make was used on EN9 workpiece material. The boring operations were carried out on CNC center lathe. The workpiece was mounted using a pneumatic chuck. The machining parameters such as feed rate (0.09 mm min^{-1}), DOC (0.6 mm^{-1}), clamping pressure (10 bar), etc., were selected based on the manufacturers recommendations and were kept constant for all the samples used. Only the cutting speed, passive damper position on boring bar, and overhang length were changed as shown in **Table 4**. Boring was carried out for 110 mm internal diameter using newly designed tool and conventional tool. The evaluation criteria were the dynamic characteristics, frequency, and damping ratio, of the machining system, as well as the surface roughness of the machined workpieces.

Table 5 shows the results obtained for cutting speed of 210 rpm, DOC of 0.6 mm and feed rate of 0.09 mm min^{-1}.

Table 4 Experimental conditions[16]

Boring tool	*BT1*	*BT2*	
Overhang length L (mm)	30	60	90
Position of passive damper	Vertical	Horizontal	
Cutting speed (rpm)	70	140	210

Table 5 Experimental results[16]

S/N	*Overhang length of boring bar (mm)*	*Surface finish (μm) without passive damper*	*Surface finish (μm) with passive damper*	
			Vertical	*Horizontal*
1	30	2.63	2.41	2.63
2	60	2.59	2.51	1.46
3	90	2.80	3.19	3.25

The result shows that the results prove the passive damping technique has vast potential in the reduction of tool chatter. It is therefore concluded that passive damping has a good effect in improving surface finish in boring operation and significant improvement was observed between the results of surface finish obtained using boring bar without passive damper and boring bar with passive damper.

Kadu *et al.*[17] formulated a mathematical model for the investigation of tool wears in boring machining operation on cast iron using carbide and cubic boron nitride tools. The process of formulation of mathematical model for optimizing the tool life in casting machining operation and its analysis in this study involved two levels for each independent parameter taken. In tool life optimization process, the objective of the experiment was used to gather information through experimentation for formulation of mathematical model for cast iron machining operation. During cast iron machining operations, the measurement of tool life, surface finish, bore size variation, operation time, and spindle load was measured using meter scale, surface finish tester, digital dia. test plug gauges, digital stopwatch, and current in percentage amp. Energy and time were measured using energy meter and stopwatch respectively. Pilot experiments were performed to select test envelope and test points of process parameters for experimental design. These process parameters as shown in **Table 6** were used in experimental design for the investigation of process parameters like cutting speed, nose radius, length, diameter, and material of the cutting tool, cutting fluid pressure, and concentration and DOC for casting machining operation. The observed values for tool life, surface finish, bore size variation, operation time, and spindle load were recorded for formulation of mathematical model. In casting machining operation observations were taken out at two levels for each independent parameter.

One hundred and twenty-eight experiments were designed on the basis of sequential classical experimental design technique that has been generally proposed for engineering applications.[18] The basic classical plan consists of holding all but one of the independent variables constant and changing this one variable over its range. The main objective of the experiments consists of studying the relationship between 09 independent process parameters with the 05 dependent responses for tool life optimization. Simultaneous changing of all 09 independent parameters was cumbersome and confusing. Hence all 09 independent process parameters were reduced by dimensional analysis. Buckingham's π theorem was adapted to develop dimensionless π terms for reduction of process parameters. This approach helps to better understand how the change in the levels of any one process parameter of a π terms affects 05 dependant responses for cast iron boring machining operation. Out of five response/dependant variables two dependant variables cutting time and surface roughness were evaluated. A combination of the levels of parameters, which lead to maximum, minimum, and optimum response, can also be located through this approach. Regression equation models of tool life were optimized by mini–max principle.[19]

The authors observed that (1) the dimensionless π term have provided the idea about combined effect of process parameters in that π terms. A simple change in one process parameter in the group helped the manufacturer to maintain the required torque (*To*) and surface roughness (*Ra*) values so that to get increased tool life. (2) The mathematical models developed with dimensional analysis for different combinations of parameters for cutting speed, nose radius, length, diameter, and material of the cutting tool, cutting fluid pressure and concentration, and DOC can be effectively utilized for cast iron boring machining operations. (3) The computed selection of cast iron boring machining operation parameters by dimensional analysis provides effective guidelines to the manufacturing engineers so that they can minimize *To* and *Ra* for higher performances. (4) The models have been formulated mathematically for the Indian conditions. The comparison of values of dependent term obtained from experimental data, mathematical model, and ANN. From the values of percentage errors, it seems that the mathematical models can be successfully used for the computation of dependent terms for a given set of independent terms. Indian industries can use the data for calculation cutting time, tool life, surface roughness, bore size variation, and spindle load estimation for cast iron boring machining operations.

Badadhe *et al.*[20] conducted an experiment to optimize the cutting parameters in boring operation. Four parameters, i.e., spindle speed, feed, DOC, and length–diameter (L/D) ratio of boring bar were considered as input variables. **Tables 7** and **8** show the input factors and levels used in the experimental design and experimental matrix of 3^4 orthogonal array respectively. Total nine runs (L_9) were conducted during one trial. Trials were repeated to check the consistency in the output. Cutting trials were conducted on Kirloskar make (Enterprise-500) center lathe machine. AISI 1041 carbon steel cylinders with 100 mm outside diameter, 85 mm inside diameter, and 75 mm length were used as workpieces.

Standard boring bars with Widax tool holder S25TPCLNR12F3, S20SSCLCR09T3, and S16QSCLCR09T3 along with cemented carbide inserts having radius 1.2 mm were used for metal cutting. Surface finish was measured offline by using HOMMELWERKE TURBO RAUHEIT V 6.14, Swiss make surface recorder having 0.8 mm cut-off and 4.8 mm sample length. The ANOVA was carried out to find the significant factors and their individual contribution in the response function, i.e., surface roughness.

Table 6 Test envelope and test points for cast iron boring machining operation[17]

Pi term	*Equation*	*Test envelope*	*Test points*	*Independent variable with its own range*
$\prod_1$	Tool geometry parameters: $\left(\frac{LD_{pc}NR}{D^3}\right)$	(0.000162–0.0012096)	0.000162 0.000227 0.00025 0.00028 0.000324 0.00035 0.000392 0.000432 0.000454 0.0005 0.00056 0.000605 0.0007 0.000784 0.000864 0.00121	L, mm – 175,270 Dpc, mm – 0.5,0.7 NR, mm – 0.4,0.8 D, mm– 50,60
$\prod_2$	Cutting speed: $\left(\frac{Vc}{(Dg)^{0.5}}\right)$	(0.46923–0.706782)	0.469237 0.514024 0.645201 0.706782	*g*, mm sec^{-2} – 9810 *D*, mm – 50,60 Vc-mm sec^{-2} – 360,495
$\prod_3$	Coolant concentration and pressure: $\left(\frac{g.Cc}{PcD^5}\right)$	(4.21E-06–1.88E-05)	4.21E-06 5.05E-06 6.31E-06 7.57E-06 1.05E-05 1.26E-05 1.57E-05 1.88E-05	*g*, mm sec^{-2} – 9810 Pc-N mm^{-2} – 10,15 D,mm-50,60, Cc N mm^{-3} – 5, 6
$\prod_4$	Material Hardness: $\left(\frac{Hm}{Pc}\right)$	(1831.2–4414.5)	1831.2 2746.8 2943 4414.5	Hm, N mm^{-2} Tn Carbide – 27468 cubic boron nitride-44145 Pc, N mm^{-2}–10,15

Table 7 Experimental levels[20]

S/No	*Control variables*	*Level 1*	*Level 2*	*Level 3*
A	Spindle speed (rpm)	54	140	224
B	Feed rate (mm rev^{-1})	0.045	0.36	0.676
C	Depth of cut (mm)	0.5	0.75	1
D	L/D ratio for boring bar (mm)	4	5	6.25

Table 8 Basic Taguchi L_9 (3^4) orthogonal array[20]

Run	*A*	*B*	*C*	*D*
1	1	1	1	1
2	1	2	2	2
3	1	3	3	3
4	2	1	2	3
5	2	2	3	1
6	2	3	1	2
7	3	1	3	2
8	3	2	1	3
9	3	3	2	1

The averages of surface roughness values obtained during each trial (Ra_1 and Ra_2) and the Signal-to-Noise (S/N) ratio calculated for the criteria of lower-the-better are shown in **Table 9**.

The optimal values of the input factors *A*, *B*, *C*, and *D* were obtained from S/N ratio as shown in **Table 10** using the lower the better characteristic. The S/N ratio for spindle speed is higher at level 3, similarly for others the values are feed 1, DOC 2, and L/D ratio 1. Hence the optimal combination of control factors were given as 3-1-2-1 and this is represented on the plot of **Figure 5**.

ANOVA was carried out to check the significant contribution of each input factor in response function. **Table 11** shows the results of the ANOVA for surface roughness. It can be observed from the ANOVA result, that the parameters A, B, and D are having significant contribution of 28%, 30%, and 36% respectively in the response function (*Ra*) whereas the parameter C has relatively less contribution and thus is of less importance.

The study shows that the control factors had varying effects on the response variable and the use of the Taguchi parameter design technique was considered successful as an efficient method to optimize machining parameters in a boring operation.

Table 9 Experimental results for surface roughness and calculated value for S/N ratio[20]

Run	*A*	*B*	*C*	*D*	*Ra*	*S/N ratio*
1	54	0.045	0.5	4	3.63	−11.1981
2	54	0.36	0.75	5	11.30	−21.0616
3	54	0.676	1	6.25	13.70	−22.7344
4	140	0.045	0.5	6.25	5.97	−15.5195
5	140	0.36	0.75	4	6.82	−16.6757
6	140	0.676	1	5	10.20	−20.1720
7	224	0.045	0.5	5	4.59	−13.2363
8	224	0.36	0.75	6.25	7.66	−17.6846
9	224	0.676	1	4	2.99	−9.5134

Table 10 Calculated mean S/N ratios[20]

Level	*A*	*B*	*C*	*D*
1	−18.33	−13.32	−16.35	−12.46
2	−17.46	−18.47	−15.36	−18.16
3	−13.48	−17.47	−17.55	−18.65
Delta	4.85	5.16	2.18	6.18
Higher S/N ratio	3	1	2	1

Moetakef-Imani and Yussefian[21] studied the dynamic simulation of boring process. The study involved the use of a boring bar with 20 mm diameter and 140 mm length ($L/D=7$) to implement the machining tests. Carbide inserts with 0.4 mm nose radius and flat rake face were used to machine the aluminum 6061 tubes. The dynamic properties of boring bar and geometrical properties of the cutting tool are presented in **Tables 12** and **13** respectively.

The cutting speed, feed rate, and radial DOC were in the range of 70–110 m min^{-1}, 0.08–0.24 mm rev^{-1}, and 0.2–4 mm respectively. Cutting force components were measured in three orthogonal directions by a KISTLER9255b dynamometer. The dynamic simulation program was also implemented for every corresponding machining experiment. For the sake of comparison between the experimental measurements and numerical simulations, two different cutting tests were presented. The cutting conditions for these two cutting experiments are shown in **Table 14**.

The DOC was set to 0.5 and 4 mm for tests *A* and *B* respectively. All other conditions for these tests are equal. In order to validate the proposed method, 30 boring experiments were conducted. **Figure 6** shows the algorithm for dynamic simulation of boring process.

Measured and predicted cutting force components for boring with machining conditions of test A are depicted in **Figure 7**. When the tool first engaged the cut, it undergoes transient vibrations. But after several revolutions, the cutting process becomes stable and the tool continues to vibrate periodically with relatively constant amplitude.

So the condition of test A was stable and chatter-free cutting machining operation. The simulated peak frequency occurred at 672 Hz with a deviation of 12.94% above the measured value of 594 Hz. It was observed that the deviation resulted from the over estimation of the eigen frequencies by the Euler–Bernoulli beam equation. When the results of cutting force components measured by a dynamometer was compared with the simulated results by the proposed algorithm. The measured values of the cutting force components in x, y, and z direction were predicted by 9%, 2%, and 12% errors in magnitude. This amount of error was consistent with the validity interval of $\pm 10\%$ for the cutting force computation[22] which could be due to the cutting force coefficient computations.

Experimental and simulated cutting force components in time domain for the condition of test B are shown in **Figure 8**. It was observed from the measured data that the machining process was unstable with chattering frequency around 573 Hz. In case of chatter, measured force components oscillate randomly and grow rapidly to large amplitudes. It could be seen from **Figure 8** that the simulated results had also predicted the incidence of chatter vibrations. Although the model was capable of truly predicting the chatter occurrence for the conditions of test B, the variation of simulated and measured cutting force amplitudes is increased.

This is due to the fact that the measured cutting force components have been amplified by chatter frequency.[23] As a consequence of high-vibration amplitudes, the actual geometrical angles of the cutting tool will change from their nominal values. It is well known that the variation of cutting tool angles will affect the cutting force components significantly.[22,24] The high-reciprocating velocity of the tool tip makes the cutting process be accompanied with the plunging of the tool in to the workpiece. The high acceleration of the tool increases the effect of the tool inertia forces on dynamometer measurements. All of these will make the prediction of dynamic characteristic of the process under chatter vibration almost impossible. However, for any dynamic model the correct prediction of chatter onset is enough since no practical machining operation will be carried out under chatter conditions.

The researchers were able to develop a model to simulate the dynamics of boring process. The developed model relies on the novel algorithms of geometrical modeling. In contrast to the previous models that were only able to predict the stability region, this model computes the dynamic cutting force components and frequencies in stable boring operation. The performed cutting experiments have shown that the cutting force components and the vibration frequencies in chatter-free dynamic boring operation could be predicted within $\pm 15\%$ error margin. The model is valid for both finishing (DOC$<r$) and roughing (DOC$>r$) boring processes. The model is also able to predict the chatter onset in boring

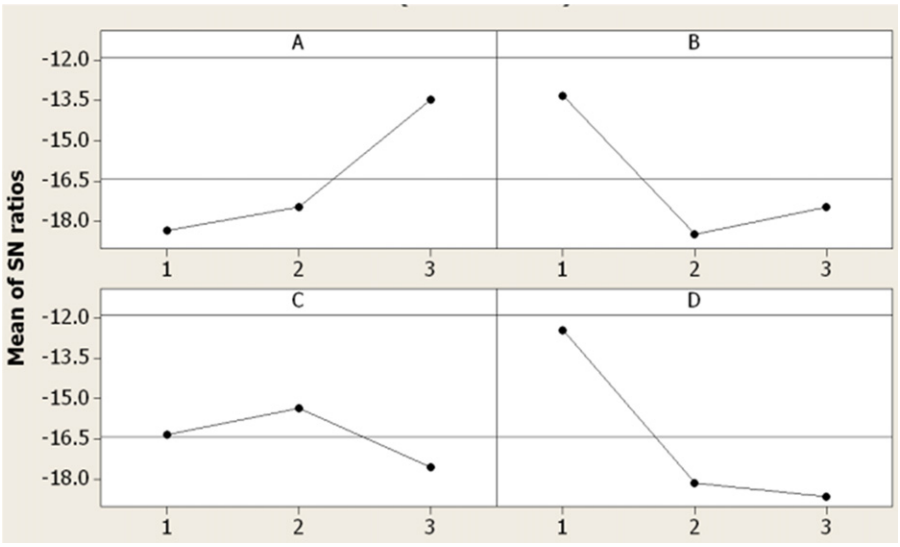


Figure 5 Plots for mean S/N ratios for *A*, *B*, *C*, and *D*.[20]

Table 11 Results of the ANOVA for surface roughness[20]

Source of variation	df	*Sum of squares*	*Mean square*	*F-ratio*	*Contribution (%)*
Spindle speed (A)	2	60.30	30.15	59.66	27.65
Feed rate (B)	2	66.02	33.01	65.33	30.28
Depth of cut (C)	2	8.48	4.24	8.39	3.89
L/D ratio (D)	2	78.65	39.32	77.82	36.07
Error	9				
Total	17				

Table 12 Dynamic properties of boring bar[21]

Parameter	L_e *(m)*	L *(m)*	ξ_y	w_{1y} *(Hz)*
Value	0.1535	0.14	0.025	620

Table 13 Geometrical specifications of the cutting tool[21]

Parameter	L *(m)*	r *(mm)*	α_s *(deg)*	α_b *(deg)*	c_s *(deg)*	c_e *(deg)*
Value	0.14	0.4	−5	0	−3	32

Table 14 Geometrical specifications of the cutting tools for tests A and B[21]

Parameter	*Depth of cut (mm)*	c *(mm rev^{-1})*	V *(m min^{-1})*	*DO (mm)*	*Result*
Test A	0.5	0.14	95	30.5	Stable
Test B	4	0.14	95	30.5	Chatter

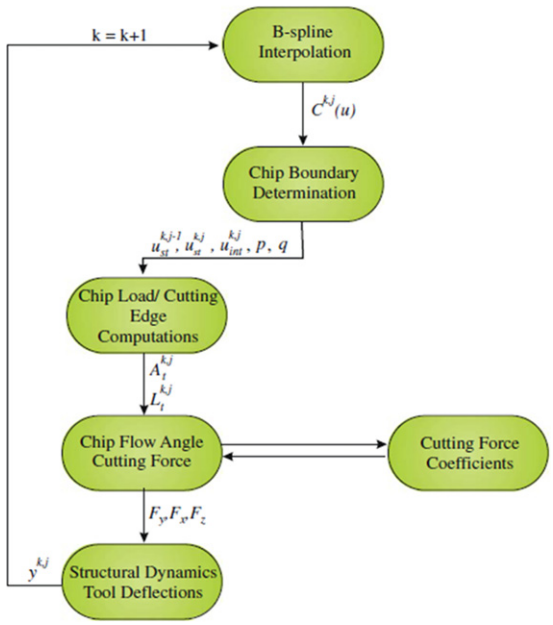


Figure 6 Algorithm for dynamic simulation of boring process.[21]

operation. Due to the nonlinear geometry of the edge, the influence of DOC and feed rate is interrelated and should not be separately investigated. The instantaneous chip load is computed to incorporate the effect of DOC and feed rate. The influence of geometrical properties (like tool angles and nose radius) as well as structural and process parameters could be investigated using this model. The stability and efficiency of the process depends on the combined effect of all these

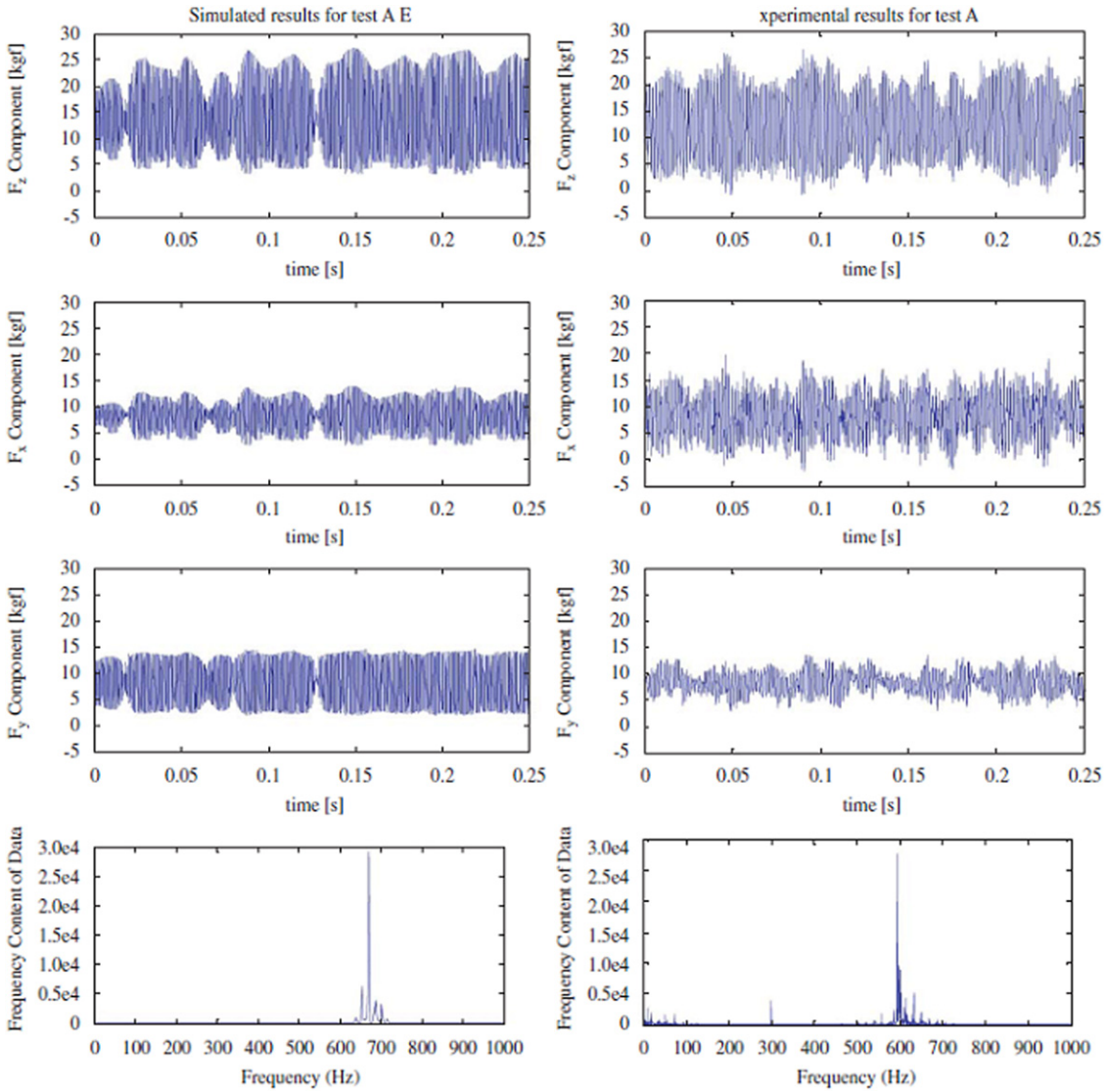


Figure 7 Experimental and simulated cutting force values for test A.[21]

parameters. Hence, the proposed model provides a better understanding of a certain boring process.

Byung-Kwon Min *et al.*[25] studied the use of smart boring tool for process control. The experiment involved the evaluation of the performance of the tool tip servo under real machine tool operating conditions, cutting tests were performed using a stationary Smart Tool boring bar and rotating workpiece. For the cutting test, an aluminum workpiece made from thick wall tube with a 180 mm diameter hole was used. The Smart Tool boring bar was attached to a turning machine tool post and the workpiece was attached to spindle. The tool tip position measurement was recorded to the memory of the controller computer. The spindle speed was 510 rpm corresponding to a cutting speed of 4.8 m s^{-1}. The feed rate was 0.21 mm rev^{-1}. Step response and sine wave tracking were conducted. The purpose of the step response experiment was to determine what tolerances could be maintained in the position of the tool tip relative to the fixture, as well as the effects of cutting on the transient response of the tool tip servo. The purpose of the sine wave tracking experiment was to verify the ability of the system to follow sinusoidal references during cutting. This is similar to the objective of isolating the tool tip motion from boring bar vibration. The model parameters and monitoring variables for the experiments are shown in **Tables 15** and **16**.

Figure 9 illustrates the geometry of finish boring process. As can be seen, if the center of the pre-boring hole and the finish boring tool position are offset due to fixture misalignments, the DOC of the boring process becomes a periodic function that is repeated with every revolution of the spindle.

Tool breakage also results in the deviation of the cutting force from the normal cutting force generated by the boring process. Cutting force is a monotonic function of the DOC and feed rate.[26] Consequently, if the feed is maintained constantly and if the cutting force is accurately measured, the geometric profile of the cutting surface can be estimated from the force data. Cutting tool insert breakage can be monitored in a cutting force changes. For a boring process, the radial direction

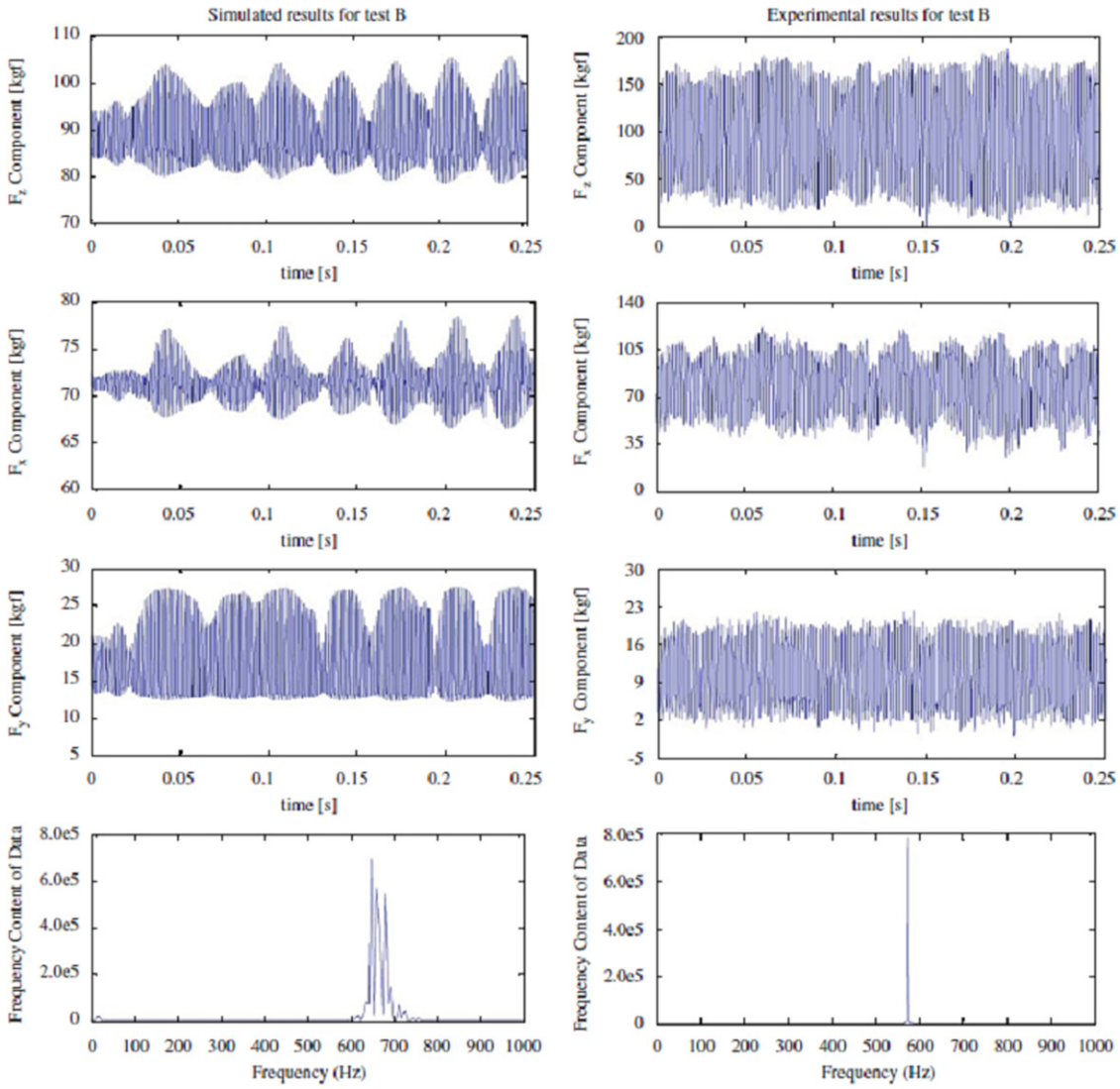


Figure 8 Experimental and simulated cutting force values for test B.[21]

component of the cutting force dramatically increases immediately after tool fracture or chipping.[27] Considering the small cutting force generated by finishing process, an excessive rise in the radial cutting force generally indicates finish tool breakage, if the force is bigger than that observed in workpiece misalignment error which will be detailed in the rest of this section.

Based on above observation, the monitoring of fixture misalignment and tool breakage of the Smart Tool boring process can be carried out with force pattern recognition. The radial cutting force estimation described in the previous section has been considered as a method for the monitoring of the Smart Tool boring process. The cutting force estimated by Smart Tool during a single rotation is compared with the radial cutting force measured by a tool dynamometer. The cutting force estimated by Smart Tool during a single rotation is compared with the radial cutting force measured by a tool dynamometer in a polar plot in **Figure 10(a)**. Cutting speed was 2.0 m s^{-1} and feed rate was 0.083 mm per revolution. A random cutting profile was used to evaluate dynamic performance of the estimator. The difference between the Smart Tool estimation and the tool dynamometer measurement was less than 10% of the cutting force and, thus, the cutting force based on disturbance estimation could be used to detect both the dynamic and the static cutting forces.

Figure 10(b) shows the polar plot of cutting force during a normal boring process operation. **Figures 10(c)** and **10(d)** show the case of workpiece misalignment error and the event of tool breakage respectively. Cutting condition of 2 m s^{-1} cutting speed and 0.083 mm per revolution federate was used for all experimental data. 0.25 mm DOC is used for normal cutting and 0.25 mm desired DOC with 1.27 mm offset was used for misalignment experiment. For the tool breakage experiments, inserts with a 2.0 mm notch was used to expedite breakage. For the normal operation, as can been in **Figure 10(b)**, the cutting force has not deviated more than 10 N from its mean value of 25.96 N and the center of the force plot is close to the center of the graph. The response from misaligned cutting

Table 15 Model parameters[25]

Variable	*Value*
Piezoelectric actuator	
Young's modulus Y_{33}^E (Pa)	4.8×10^{10}
Strain constant d_{33} (m V^{-1})	5.5×10^{-8}
Maximum voltage V_{max} (V)	100
Density m_p (kg m^{-3})	7500
Maximum current I_{max} (A)	2.0
Area A_p (m^2)	1.0×10^{-4}
Length l_p (m)	0.4
Tool tip translation mechanism	
Width T(m)	0.025
Mass M_m (kg)	0.15
Length l (m)	0.016
Damping b_m (N s/m)	0.025
Length Dl (m)	0.01
Young's modulus E_t (Pa)	2×10^{11}
Boring bar	
Moment of inertia I (m^2 kg)	7.1×10^{-7}
Young's modulus E_b (Pa)	2×10^{11}
Ultimate strength S_{ut} (N)	1.4×10^{11}
Damping b_b (N s m^{-1})	0.013
Yield strength S_e (N)	3.4×10^{10}

Table 16 Monitoring variables[25]

Process status	*a*	*b*	*R (129.80)*	*r (5.19)*	*θ*
Normal	1.08	0.50	25.96	1.19	24.95
Workpiece misalignment	30.79	− 29.17	24.79	42.58	− 43.44
Tool breakage	5.09	3.34	150.93	6.78	29.48

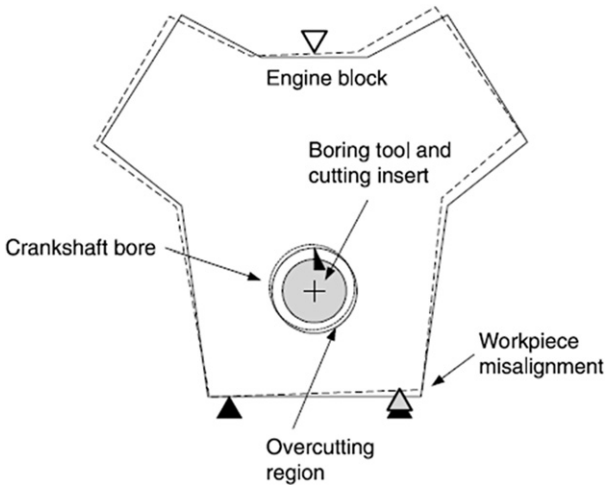


Figure 9 Nonuniform depth of cut due to workpiece misalignment error.[25]

plotted in Figure 10(c) also shows regular cutting force, but the center of the force plot is shifted from the graph center. The small partial circle in the plot is due to the negative reaction force of the tool when the cutting insert lost the contact with workpiece. The tool breakage recorded in Figure 10(d) shows the chaotic behavior of the cutting force with huge force value. As can be seen the plots in Figure 8, it is obvious that the different process failures have different force patterns. Therefore, if the difference between the force patterns can be specified quantitatively, monitoring of these failures is possible.

In this experiment, the R and r values calculated from 10 most recent revolutions are used. The R is equal to mean value cutting force. Therefore, regardless of existence of workpiece misalignment error, the excessive R value bigger than critical value is due to tool breakage. The critical cutting force of the tool breakage must be determined by experiment. In this experiment, it is set to 129.80 N which is 500% of measured cutting force, 25.96 N, from normal operation plotted in Figure 10(b). As far as the mean cutting force R is smaller than critical value, the bigger r value indicates workpiece misalignment error. The threshold of r value is also determined by experiment. In the experiment, it is set to 5.19 N which is 20% of normal operation cutting force. This also means threshold of the offset is approximately 20% DOC, even though that is not exact number due to nonlinear relation between cutting force and DOC. From a and b values, which are x and y-directional components of the radial cutting force, the misalignment direction of the hole can be found. The a, b, R, r, and direction of least square center.

The authors were able to develop a mechatronic metal cutting tool to improve the accuracy and flexibility of line boring machining in the automotive industry. Laser position sensors and piezoelectric actuator were integrated into the rotating body of the boring tool, and to compensate the boring bar droop and effects of cutting forces, a fast tool servo utilizing feedback control of the boring tool insert position was designed and embedded in the rotating tool assembly. In addition to position control, a self-monitoring algorithm that utilizes disturbance estimator was put together in the controller. Self-monitoring capability is an important feature in automated machine tool systems and it is more critical when sophisticated mechatronics is used to control the process. This chapter has proposed a tool monitoring method that utilizes the process information and estimated cutting force during tool tip servo control. A new measurement technique of the cutting force based on disturbance estimation was developed and integrated into a sensorized boring tool. The proposed cutting process monitoring method was effective to detect tool failure as well as process failure due to workpiece misalignment errors which occurred in the boring process. The force measurement by the proposed method matches well with the conventional force measurement using a tool dynamometer. The developed accurate cutting force estimation method is not only useful for process failure monitoring, but it is also useful as a substitute for tool dynamometers, especially in cases where the tool dynamometer is difficult to be placed, such as in a rotating tool tip.

Kanase Sandip *et al.*[28] conducted an experiment on the improvement of surface roughness (*Ra*) value of boring operation using passive damper. The workpiece was mounted using a pneumatic chuck in CNC turning center and the clamping pressure was set at 10 bars. The machining parameters like feed, DOC, clamping pressure, etc., were selected based on the manufacturers recommendations and were kept

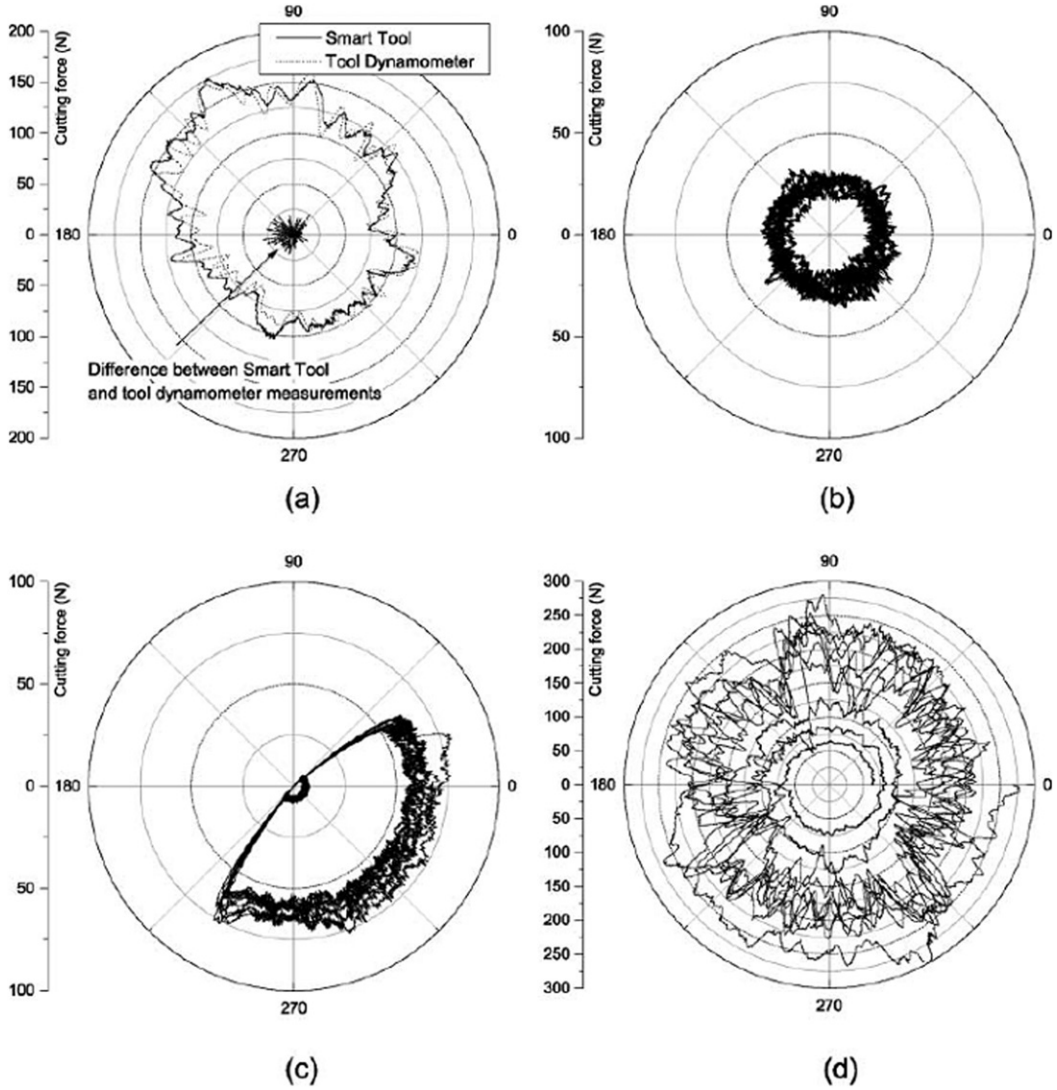


Figure 10 Cutting force measured at Smart Tool. Depth of cut 0.25 mm; feed rate 0.083 mm rev^{-1}; cutting speed 2 m s^{-1}. (a) Comparison with tool dynamometer measurement, (b) normal cutting, (c) workpiece misaligned (tool offset 1.27 mm), and (d) tool breakage.[25]

Table 17 Experimental parameters[28]

Boring tool	BT_A	BT_B	
Overhang length L (mm)	40	80	120
Impact damper position	Vertical	Horizontal	
Clearance CL (mm)	0.4		
Spindle rotation N (rpm)	80	160	240
Feed rate S (mm min^{-1})	0.9		
Depth of cut t (mm)	0.6		



Figure 11 Sample workpiece.[28]

constant for all the samples used. Only the cutting speed, passive damper position on boring bar, and overhang length was changed. The recommended cutting speed, feed, DOC, etc., are shown in **Table 17**. Boring was carried out for 105 mm internal diameter as shown in **Figure 11**.

Twenty five numbers of experiments were conducted to analyze the effect of vibration on surface finish. Boring bar of 20 mm × 20 mm cross section and 200 mm long of WIDAX make was used. The boring operations were conducted on CNC turning center of ACE make using EN9 workpiece material. A Mitutoyo SJ-201P apparatus was used to determine the surface roughness of the bored surface. **Tables 18–21** show the results obtained for all the experiments conducted under different conditions.

Table 18 Surface roughness without passive damper (cutting speed 240 rpm, doc 0.6 mm and feed rate 0.09 mm min^{-1})[28]

S/No	Test A	Overhang length (mm)	Response (surface roughness, R_a)		
			1	2	3
1	3	40	2.72	2.72	2.73
2	2	80	2.37	2.47	2.69
3	5	120	2.82	2.90	2.60

The results proved the passive damping technique has vast potential in the reduction of tool chatter. Also the suppression in tool chatter by using impact damper boring bars was very significant. Boring bars with impact damping are also relatively cheaper than other damped boring bars. It is therefore concluded that impact damping has a good effect in improving surface finish in boring operation.

Pardeep Kumar *et al.*[29] conducted an experiment to analysis and optimized the parameters that affect bore deviation (BD) in boring process. A systematic method as outline in the form of flow chat as shown in **Figure 12** was used to optimize the cutting parameters to achieve minimum BD of the Crankcase made up of grade FG 260 of IS: 210–1978.

Randomization of the run order and analysis sequences was carried out according to the run order by Design Expert software 9.0. Full factorial design of three factors with two having three levels and one factor having two levels which consist of 18 runs were adopted. The overall experimental results corresponding to each run generated by the software are shown in **Table 22**. The machining response that was analyzed was BD. All data obtained was then used as input to the Design Expert software 9.0 for further analysis, according to steps outline for full factorial with optimal design.

Design Expert software was used to analyze the results obtained in order to identify the significant factors and interactions between the factors under studied. ANOVA provides information of analysis of variance and case statistics for further interpretation as shown in **Table 23**. Normal probability plot, main effect plot, and interaction plot for the dependent parameters that significantly affect the response were obtained to show the reliability of the results obtained from the experiment.

From the experiment, it has been observed that the existing parameters for finish tappet bore was cutting speed (137 m min^{-1}), feed rate (0.1 mm rev^{-1}), and cutting allowance (0.5 mm^{-1}), whereas for the same dimensions the optimum cutting parameters was cutting speed (160 m min^{-1}), feed rate (0.3 mm rev^{-1}), and cutting allowance (0.3 mm^{-1}). Further, on comparing the values of BD of existing and optimum parameters, the BD was 0.021 mm when the experiments were performed with existing cutting parameters whereas BD obtained with optimum parameters was about 0.015 mm. Therefore there was an approximately 40% of reduction in BD by employing the optimum parameters.

1.2.3 Application of Boring Process in the Building of Tunnel

Boring process is not only restricted to workshop, in fact, it has been applied in the building of tunnels for transportation purpose. Since the need for infrastructure to handle the intercity transportation of people and goods has steadily increased. The construction of such facilities often requires the excavation of long, deep tunnel such as the base tunnels of the Alptransit Project in Switzerland,[30] the Brenner Base tunnel between Austria and Italy,[31] the Lyon-Turin tunnel between France and Italy,[32] or the Gibraltar Strait tunnel between Spain and Morocco.[33] The application of boring process in this complex operation involved a large special engineering machine for tunnel boring known as tunnel boring machine (TBM). In using TBM, it has been observed that several factors affect its operation. Robbins[34] stated that, it was always impossible to find a route that will avoid the problem of excavating in difficult geological zones with a sufficient degree of certainty. The extent and frequency of the difficulties encountered can be decisive in terms of economical viability or even in terms of the technical feasibility of a TBM drive. And in some cases, a very great potential damage, a single event can cast the entire project into doubt. The length and the number of critical stretches are very important in this respect. Short tunnel stretches with unfavorable but well-known geological conditions are not particularly risky for the economic success of a TBM drive provided that adequate countermeasures are planned in advance.[35]

TBM performance can be affected by geological conditions in a great variety of ways.[36] For instance, boreability problems in hard rock, steering difficulties or severe vibration of the cutter head due to mixed face or blocky rock conditions, major water inflows, cave-ins ahead of the tunnel face, or unstable excavation walls in highly fractured or weathered rock as well as crossing fault zones may represent difficult tunneling conditions. ITA[37] observed that squeezing ground conditions may also slow down or obstruct TBM operation and sometimes even call into question the feasibility of a TBM drive. Because of the nature of this complexity in mechanized tunneling, the need for well funded, thorough investigation of the risks, the technical feasibility, and the cost of TBM application cannot be overemphasized. Hence, it is not surprising that the question of TBM applicability in squeezing conditions has kept engineers busy for more than 30 years.[38–40] Due to the increased economic importance of mechanized tunneling associated with the demand for long-deep tunnels, the application of boring operation is particularly relevant today.

Ramoni and Anagnostou[41] carried out a comprehensive literature search on case histories involving TBMs under squeezing conditions in order to identify the specific problems associated with the use of TBMs. They observed that squeezing behavior may become problematic at different distances behind the tunnel face. Hence, the specific potential hazards concern both the machine area (sticking of the cutter head, jamming of the shield) and the back-up area (e.g., jamming of the back-up equipment, inadmissible convergences of the bored profile, damage to the tunnel support). In addition to the difficulties that are directly caused by squeezing behavior, adverse events such as clogging of the cutter head, insufficient bracing of the grippers, or instabilities of the face or the tunnel wall may also occur when boring through weak ground. It was equally difficult or even impossible to distinguish the different phenomena from each other. For example, when driving through poor-quality ground it may remain uncertain if the

Table 19 Surface roughness with passive damper (boring bar overhang length: 40 mm, depth of cut: 0.6 mm, and feed rate: 0.09 mm min^{-1})[28]

S/No	Speed (rpm)	Test No.	Vertical position			Test No.	Horizontal position		
			Response (surface finish R_a in μm)				Response (surface finish R_a in μm)		
			1	2	3		1	2	3
1	80	7	3.16	3.30	3.28	14	3.29	3.46	3.31
2	160	4	2.70	2.61	2.65	15	2.96	2.78	2.94
3	240	6	2.37	2.39	2.51	23	2.76	2.79	2.73

Table 20 Surface roughness with passive damper (boring bar overhang length: 80 mm, depth of cut: 0.6 mm, and feed rate: 0.09 mm min^{-1})[28]

S/No	Speed (rpm)	Test No.	Vertical position			Test No.	Horizontal position		
			Response (surface finish Ra in μm)				Response (surface finish Ra in μm)		
			1	2	3		1	2	3
1	80	1	2.61	2.40	2.50	16	3.14	3.27	3.35
2	160	8	2.56	2.37	2.31	21	2.38	2.47	2.71
3	240	9	2.61	2.40	2.50	22	1.26	1.38	1.56

Table 21 Surface roughness with passive damper (boring bar overhang length: 120 mm, depth of cut: 0.6 mm, and feed rate: 0.09 mm min^{-1})[28]

S/No	Speed (rpm)	Test No.	Vertical position			Test No.	Horizontal position		
			Response (surface finish Ra in μm)				Response (surface finish Ra in μm)		
			1	2	3		1	2	3
1	80	13	3.23	3.29	3.11	19	3.30	3.13	3.20
2	160	11	2.41	2.51	2.30	24	2.80	2.61	3.07
3	240	10	3.23	3.29	3.11	25	2.99	3.35	3.09

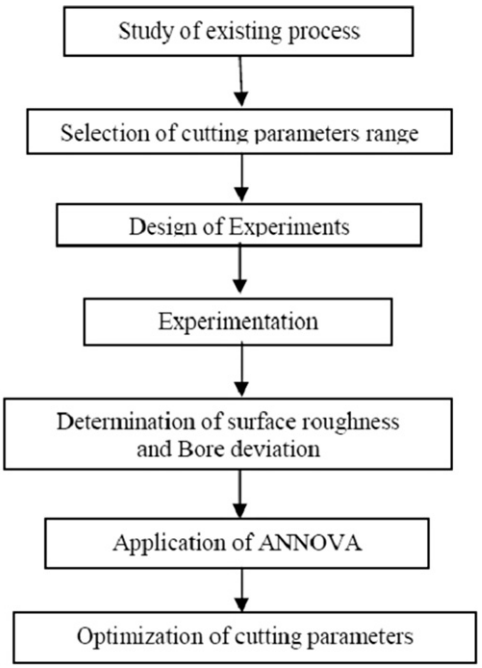


Figure 12 Flow Chart of Experimental Method.[29]

Table 22 Design of Experimental set up[29]

Run	Factor 1 (A)	Factor 2 (B)	Factor 3 (C)	Response
	Cutting allowance (mm)	Cutting speed (m min^{-1})	Feed rate (mm rev^{-1})	Bore deviation (μ)
1	0.3	120	0.1	0.017
2	0.5	120	0.1	0.022
3	0.3	140	0.1	0.02
4	0.5	140	0.1	0.019
5	0.3	160	0.1	0.018
6	0.5	160	0.1	0.02
7	0.3	120	0.2	0.021
8	0.5	120	0.2	0.021
9	0.3	140	0.2	0.02
10	0.5	140	0.2	0.021
11	0.3	160	0.2	0.016
12	0.5	160	0.2	0.019
13	0.3	120	0.3	0.023
14	0.5	120	0.3	0.022
15	0.3	140	0.3	0.021
16	0.5	140	0.3	0.021
17	0.3	160	0.3	0.014
18	0.5	160	0.3	0.015

Table 23 ANOVA for bore deviation[29]

Sources	*Sum of square*	df	*Mean square*	*F-value*	*Desirability*
Means vs. Total	6.806E-003	1	6.806E-003		
Linear vs. means	5.356E-005	3	1.785E-005	4.55	
2FI vs. Linear	3.146E-005	3	1.049E-005	4.92	Suggested
Quadratic vs. 2FI	7.556E-006	2	3.778E-006	2.14	Aliased
Residual	1.587E-005	9	1.764E-006		
Total	6.914E-005	18	17.59		

ground pressure acting upon the TBM is due to squeezing or raveling behavior.[35]

A marked difference exists between conventional and mechanized tunneling as a result of the magnitude of the potentially problematic deformations. Due to the geometrical constraints imposed by the equipment, even convergences as small as one or two decimeters may lead to difficulties in the machine or in the back-up area of a TBM drive Kovári.[42] Again, experience in some stretches of the Gotthard Base Tunnel has shown that hard but highly fractured rocks may also exhibit relevant deformations and challenge TBM tunneling, particularly if encountered at great depths. Tunneling experience shows that the ground deformations may develop very rapidly and very close to the working face. In such a situation, the achieved gross advance rate would play a secondary role (the TBM would become jammed even if operated at the highest feasible speed). Furthermore, standstills of TBM operation cannot be completely avoided.[39,43] Besides adverse ground conditions, unpredictable stops due to technical problems (e.g., electric power stoppages, mechanical breakdowns of the TBM, problems in the back-up system) have to be considered. For example, during the excavation of the Evinos–Mornos Tunnel (Greece) the cutter head of one of the gripper TBMs ($D=4.20$ m) became jammed during an excavation standstill which was caused by an interruption of the electric power supply.

When tunneling by a single shielded TBM (or a double shielded TBM in the so-called (auxiliary mode), the tunnel support (lining by precast segments) forms part of the thrusting system. There have been negative experiences in cases where a proper backfilling of the segmental lining was not achieved. For example, the double shielded TBM ($D=2.91$ m) that excavated a part of the Stillwater Tunnel (USA) probably became trapped in squeezing ground because of the impossibility of fully utilizing its installed thrust force. Firstly, it was not possible to drive the double shielded TBM in the 'gripper mode' and secondly, the improperly backfilled segmental lining was not able to withstand the combined loading of ground pressure and thrust force generated in the 'auxiliary mode.' In this case there was a further difficulty in relation to the telescopic part of the shield, which had a smaller diameter than the front and the rear shield, favoring the accumulation of loose material in this area, and thus leading to an increase in the friction that had to be overcome when moving the double shield. Similar problems also arose with gripper bracing, the backfilling of the segmental lining, and the telescopic part of the shield during the excavation of the Los Rosales tunnel (Colombia, double shielded TBM, $D=3.54$ m). Possible problems in the back-up area include inadmissible convergences of the bored profile or damage to the tunnel support. Such problems are basically the same as in conventional tunneling, the main differences being that in conventional tunneling (1) there is the option of excavating a considerably larger profile in the critical stretches (in order to accommodate the deformations) and (2) there is also more flexibility concerning the location of support installation (stabilization measures can be taken practically wherever and whenever required).

In TBM tunneling, the space available for ground deformations and tunnel support is largely predetermined by the fixed geometry of the excavated cross section. The possibility of enlarging the boring diameter locally is very limited (up to 30 cm, if at all possible). Besides the typical problems mentioned above, jamming of the back-up equipment is an additional hazard scenario to be considered, particularly for gripper TBMs. This has been experienced, for example, during the excavation of the Strada Section of the Tavanasa–Ilanz Tunnel (Switzerland, gripper TBM, $D=5.20$ m), in the Northern Section of the Vereina Tunnel (Switzerland, gripper-TBM, $D=7.64$ m), and, recently, in the Faido Section of the Gotthard Base Tunnel (Switzerland, gripper-TBM, $D=9.43$ m).

In furtherance of their research, Ramoni and Anagnostou[44] extensively studied the TBMs under squeezing conditions under the following subheadings:

1.2.3.1 Ground–Equipment–Support Interactions

They identified the relevant interfaces between the main system components and understanding their interactions was very important to an assessment of the critical situations. This might affect the performance, or even the feasibility of a TBM drive taking into consideration the peculiarities of existing TBM types with respect to thrusting systems, tunnel support, the presence or absence of a shield, and the achievable gross advance rate. They observed that the large number of interfaces between ground, tunneling equipment, and support in combination with the possibility of conflicting requirements and feedback effects introduces a high level of complexity, which necessitates an efficient mapping of the system and of its interfaces in order to identify and analyze the relevant interactions.

1.2.3.2 Boring and Thrusting

They have observed that the jamming of the TBM represents a major hazard as it may lead to serious damage, necessitating lengthy standstills for freeing or repairing the machine. Besides being important from a practical point of view, this potential problem is also theoretically very interesting and has attracted several research efforts over recent years. The researchers that have work in this area includes Graziani *et al.*,[45] Ramoni and Anagnostou,[46,47] and Sterpi and Gioda.[48] Ramoni and Anagnostou[44] further investigated the following conditions as it affects boring and thrusting.

1.2.3.2.1 Restart after standstill

If the ground behavior is time dependent, which is very common for squeezing conditions, a radial ground pressure may develop upon the machine during a standstill. In order to resume TBM operation, i.e., to move the TBM forwards and to rotate the cutter head, the thrusting system must be able to cope with the frictional forces acting upon the cutter head and the shield (Figure 13). In order to move the TBM forwards, both the installed thrust force and the bearing capacity of the thrusting system must be higher than the frictional resistance (static friction).

The frictional resistance was observed to increase with the radial pressure acting upon the machine (which may be high in the case of squeezing ground) and with the size of the loaded area (i.e., with the diameter and length of the cutter head and of the shield). However, it depends on the type of the ground and on the surface roughness of the cutter head and of the shield as they are relevant with respect to the skin friction coefficient.

1.2.3.2.2 Immobilization during ongoing excavation

TBM immobilization during the boring process can be seen as equivalent to the borderline case of a zero net advance rate. In the case of intensively squeezing ground, however, one should bear in mind that before the machine moves forwards the extrusion of the core has first to be compensated. Under normal conditions (characterized by the usual values for penetration and rotational speed), the effect of the core extrusion is small, but it may become relevant in the case of a low-penetration rate or a low-rotational speed. In extreme cases, the cutter head penetrates and rotates without moving forward (the penetration is used-up just for removing the axially deforming ground at the working face).

1.2.3.2.3 Tunnel support

Maidl *et al.*[49] stated that the application of tunnel support usually took place at two locations: in the machine area and later in the back-up area at a distance of 30–60 m behind the tunnel face. The locations of the support installation are determined by the design of the tunneling equipment. In the back-up area it is generally possible to install the tunnel support without slowing down the rate of TBM progress. Support application in the machine area, however, interferes considerably with TBM operation because, as a rule, it necessitates a halt of the machine. Furthermore, the support in the machine area may influence the ground pressure acting upon the shield. According to Schneider *et al.*,[50] particularly critical in this respect is the zone between the first and the second tunnel support installation points. In order to reduce the risk of problems in this area (e.g., jamming of the back-up equipment, inadmissible convergences of the bored profile, damage to the tunnel support) the installation of a higher quantity of tunnel support may be needed in the machine area, and this, as said before, will affect general TBM performance.

1.2.3.2.4 Single and double shielded TBMs

The differences between single and double shielded TBMs include the TBM length, the thrusting system, the tunnel support, and the advance rate. Single shielded TBMs are longer than gripper machines. As the area exposed to the squeezing pressure is larger, a higher frictional resistance has to be overcome and, consequently, all other parameters being equal, the risk of shield jamming is higher. The disadvantage of a longer shield is, nevertheless, not of absolute significance because single shielded TBMs usually have a higher installed thrust force than gripper TBMs.

1.2.3.3 Counter Measures

In order to influence system behavior, counter measures are as follows (1) cutter head, (2) geometry, (3) overboring, (4) shield, (5) thrust force and torque, (6) back-up equipment, and (7) tunnel support. While the tunnel support was studied under (1) practically rigid supports, (2) yielding supports, (3) deformable longitudinal joint elements, and (4) on the appropriate support concept.

In conclusion, the authors observed that, the result of a complex interaction between the ground, the tunneling equipment (TBM and back-up) and the support affect the TBM performance. Hence, the factors resulting from the three main

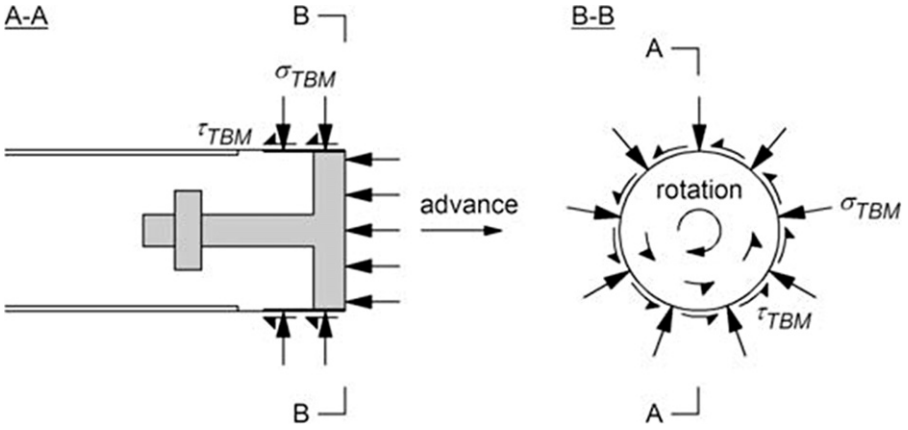


Figure 13 Loads acting on the TBM at restart (the shear and normal stresses at the face apply only in the case of a significant core extrusion). Ramoni, M.; Anagnostou, G. Tunnel Boring Machines under Squeezing Conditions. *Tunn. Undergr. SP. Technol.* **2010**, *25*, 139–157.

components of the system affect the TBM drive simultaneously and are usually coupled with each other.

Huo *et al.*[51] investigated the effect of disk cutters plane layout design of the full-face rock TBM based on different layout patterns. The study involved formulation of a nonlinear multi-objective mathematical model with multiple constraints for the disk cutters plane layout design, and analyses the characteristics of a multi-spiral layout pattern, a dynamic star layout pattern, and a stochastic layout pattern. The emphasis was put on the study of superiority of three different layout patterns as shown in **Figure 14**.

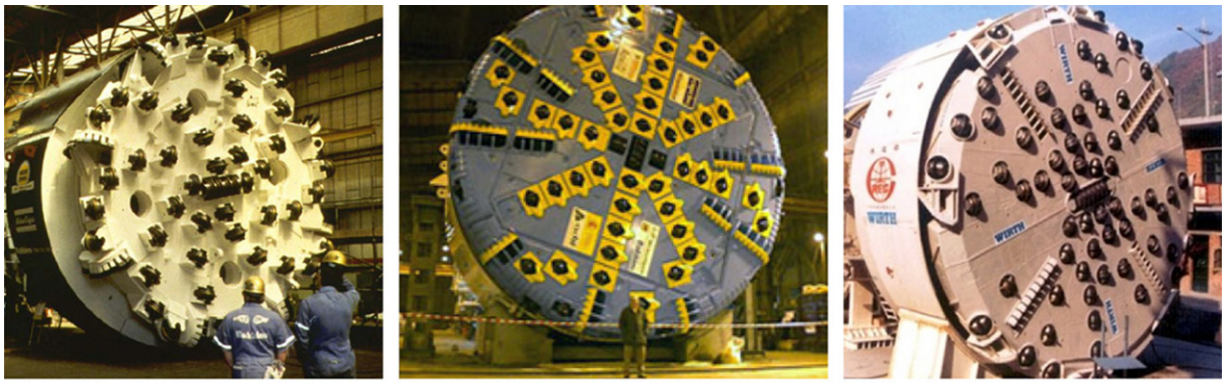
Different layout patterns were adopted in practice during the layout design of the disk cutters, while taken into consideration the engineering technical requirements and the corresponding structure design requirements of the cutter head. Genetic algorithm was employed to solve a disk cutter's multi-spiral layout problem and a cooperative coevolutionary genetic algorithm (CCGA) utilized to solve a disk cutter's star or stochastic layout problems. An instance of the disk cutter's plane layout design was solved by the proposed methods using three different kinds of layout patterns. Experimental results showed the effectiveness of the method of combining the mathematical model with the algorithms, and the pros and cons of the three layout patterns. Some of the observations made were as follows (1) the quality of plane layout design of the disk cutters for the full-face rock TBM directly affects the balance of force distribution on the cutter head during excavation, (2) the layout design of the disk cutters belongs to a complex optimization problem, so there was a need to make use of the advanced optimization methods to solve the problem, (3) the multi-spiral layout pattern can make the disk cutters distribute more evenly on the cutter head and can improve the stress distribution of the cutter head, and (4) the stochastic layout pattern can provide infinite possible solution space for the layout of the disk cutters and can produce the best solutions with the best performance indices.

1.2.4 Future Research Direction in Boring Operation

Available literatures in boring operation have shown a gap that needs to be investigated in order to fully appreciate how the various input factors affect the output factors or variables. Studies have shown that cutting fluid types and method of its application could affect the outcome of an investigation during machining processes.[52,53] Efforts have been concentrated on how vibrations, ratio of length to diameter affects the results of boring operation and not much have been reported on how cutting fluids type or it methods of applications affect boring operation. Even when cutting fluids are used, it is never discussed as a factor that could affect the outcome of the result. For instance, Chang[54] used two nose radii in his work to evaluate the effect of vibrations on tool life and surface roughness. He found that surface roughness and tool wear were strongly affected by the vibration amplitude and frequency and that improper tool geometry and nose radius will produce more vibrations than the DOC. Huang and Chen[55] discovered that two types of vibrations may occur in machining, such as forced vibration and self excited vibration. Forced vibration was noted to be associated with bad gear drives, unbalanced machine-tool components, misalignment, or motors and pumps, etc., while self-excited vibration occurred due to chatter which was caused by the interaction of the chip removal process and the structure of the machine tool and resulted in disturbances in the cutting zone.

Similarly, Lin and Chang[56] studies show that vibrations have strong correlation with surface roughness, when effects of vibration signals on tool wear, surface quality, and machining time were studied. Bernardos and Vosniakos[57] investigated the relative motion between cutting tool and workpiece on the surface finish profile, using the ratio between vibration frequency and spindle rotational speed. While, Salgado *et al.*[58] studied the cutting parameters such as feed rate, spindle speed, DOC, tool nose radius, nose angle, and vibration data which are the input information for evaluation of tool life by adopting two levels of spindle speed, feed rate, and nose radius. Korkut and Kucuk[59] had proved that the best length to diameter ratio that results in less vibration in boring process is three. They obtained minimum vibration of tool and workpiece when the value of L/D ratio was taken as three. Tool failure in boring was identified by observing higher power consumption, poor surface finish, dimensional inaccuracy, appearance of a burnishing band on machined surface, tool vibrations, workpiece vibration, etc.

A lot of experimental and analytical studies have been employed to study boring bar dynamics and most researches



(a) Multi-spiral layout pattern (b) Star layout pattern (c) Stochastic layout pattern

Figure 14 Different layout patterns of the disk cutters.[51]

were usually carried out on dynamic modeling of cutting dynamics and concentrated on the prediction of stability limits. Parker[60] investigated the stability limit of a slender boring bar in external longitudinal turning, experimenting with alternative regenerative cutting conditions at different cutting speeds and inclination angles. The vibration was measured in the cutting-speed and cutting-depth direction. He developed a two-degrees-of freedom analytical model of the boring bar with two input forces, one proportional to the variation of chip thickness and the other proportional to the penetration velocity. Based on boring bar point receptance estimates, the modal constants of the model were determined. Stability limits were predicted with the aid of the model; these were then compared with the experimental results. However, there was a wide range of cutting speeds resulting in extensive vibration in the cutting-speed direction, which was not predicted by the model. The experimental results indicated that the direction of vibration was either in the cutting-speed direction or in between the cutting speed and cutting depth direction.

Rao *et al.*[61] introduced an analytical dynamic boring force model which included the instantaneous variation of chip cross-sectional area under dynamic conditions. They produced a continuous system model of boring dynamics based on their dynamic boring force model and an uniform Euler–Bernoulli cantilever beam with a circular cross section. They studied boring with a zero side cutting edge angle and calculated chatter frequencies (fundamental eigen frequency of the boring bar) and amplitudes; these were then compared with the experimental results. They claim that their model correlates well with the experimental results.

Jayaram *et al.*[62] attempted to model the chatter stability limit in boring using a simplified analytical model of boring bar dynamics based on the direct point receptance functions and a linear regenerative cutting force model for three orthogonal directions. Jayaram *et al.*[40] claimed that estimates of the direct point receptances were produced based on hammer-excitation. Moreover, they experimentally determined stability limits for turning to validate their model. Kuster *et al.*[63] developed a computer simulation model of boring bar dynamics based on a three-dimensional model of regenerative cutting. Using the knowledge of the radius of curvature of the cutting tool tip as a base, their model differentiates between roughing and finishing in boring.

Marui *et al.*[64] investigated primary chatter of boring bars (with a rectangular cross section) and a tool holder shank using experiments in which they cut the top of a square thread in external longitudinal turning operations. The displacement of the boring bars was measured in both the cutting-speed and cutting-depth direction. With respect to the tool holder shank, both the cutting force and the displacement were measured in the cutting-speed direction. They used displacement and force as a function of time and chatter mark on the workpiece as well as displacement versus displacement to study primary chatter. They found that the vibration of the tool was dominating in the cutting-speed direction. The frequency of this self-excited vibration was slightly lower than the first natural frequency in the cutting-speed direction of both the boring bars and the tool holder shank. While, Taskesen[65] used a closed-loop feedback circuit in on-line vibration control system to measure the relative vibration between workpiece and cutting tool. He used root mean square of workpiece vibration velocity to evaluate the tool life.

1.2.5 Conclusions

It has been established that one of the important factors that affect manufacturing cost is the cost of tooling; therefore any reduction in tooling cost will result in the reduction of manufacturing cost. This reduction in tooling cost can be achieved through proper selection of tool material, tool geometry, cutting speed, feed rate, DOC, and cutting fluids. Following the literature review on effect of cutting parameters during boring operation, it is observed that experimental investigation of the effect of cutting fluid types and its method of application in boring operation still remain an area of research that has not been studied.

Thus, it is of importance to investigate the effect of cutting fluids on the dynamic properties of the clamped boring bar, surface roughness, and tool wear during boring operation in order to gain further understanding of the dynamic behavior of clamped boring bars in the boring process. It is equally observed from literature that the TBM performance depends on a very complex interaction between the ground, the tunneling equipment (TBM and back-up), and the support. Hence, these factors resulting from the three main components of the system affect the TBM drive simultaneously and are usually coupled with each other.

See also: 1.1 Factors Affecting Surface Roughness in Finish Turning. 1.3 Finish Machining of Hardened Steel

References

1. Rao, K. V.; Murthy, B. S. N.; Rao, N. M. Cutting Tool Condition Monitoring By Analyzing Surface Roughness, Workpiece Vibration and Volume of Metal Removed for Aisi 1040 Steel in Boring. *Measurement* **2013**, *46*, 4075–4084.
2. Andren, L.; Håkansson, L.; Brandt, A.; Claesson, I. Identification of Dynamic Properties of Boring Bar Vibrations in a Continuous Boring Operation. *Mech. Syst. Signal Process.* **2004**, *18* (4), 869–901.
3. Andren, L.; Håkansson, L.; Brandt, A.; Claesson, I. Identification of Motion of Cutting Tool Vibration in a Continuous Boring Operation – Correlation to Structural Properties. *Mech. Syst. Signal Process.* **2004**, *18* (4), 903–927.
4. Tobias, S. A. *Machine Tool Vibration*; Blackie: London, 1965.
5. Kato, S.; Marui, E. On the Cause of Regenerative Chatter Due to Workpiece Deflection. *J. Eng. Ind.* **1974**, *96* (1), 179–186.
6. Khraisheh, M. K.; Pezeshki, C.; Bayoumi, A. E. Time Series Based Analysis for Primary Chatter in Metal Cutting. *J. Sound. Vib.* **1995**, *180* (1), 67–87.
7. Hamdan, M. N.; Bayoumi, A. E. An Approach to Study the Effects of Tool Geometry on the Primary Chatter Vibration in Orthogonal Cutting. *J. Sound. Vib.* **1989**, *128* (3), 451–469.
8. Sturesson, P.-O. H.; Hakansson, L.; Claesson, I. Identification of the Statistical Properties of the Cutting Tool Vibration in a Continuous Turning Operation–Correlation to Structural Properties. *J. Mech. Syst. Signal. Process.* **1997**, *11* (3), 459–489.
9. Tlusty, J. Analysis of the State of Research in Cutting Dynamics. *Ann. CIRP* **1978**, *27*, 583–589.
10. Scheuer, J.; Kansson, L.H.; Claesson, I. Modal Analysis of a Boring Bar using Different Clamping Conditions. In *Proceedings of the Eleventh International Congress on Sound and Vibration*; ICSV11: St. Petersburg, Russia, 2004.

11. Arnold, R. N. Mechanism of Tool Vibration in Cutting of Steel. *Proc. Inst. Mech. Eng.* **1946**, *154* (1), 261–284.
12. Merritt, H. E. Theory of Self-Excited Machine-Tool Chatter, Contribution to Machine-Tool Chatter, Research–1. *J. Eng. Ind., Trans. ASME* **1965**, *87* (4), 447–454.
13. Thompson, R. A. The Modulation of Chatter Vibrations. *J. Eng. Ind.* **1969**, *91* (3), 673–677.
14. Akesson, H.; Smirnova, T.; Hakansson, L. Analysis of Dynamic Properties of Boring Bars Concerning Different Clamping Conditions. *Mech. Syst. Signal. Pr.* **2009**, *23*, 2629–2647.
15. Saindane, G.; Jakikore, A.; Umbarkar, A. Experimental Investigation of Vibration Damping in Boring Operation Using Passive Damper. *Int. J. Res Eng. Adv. Technol.* **2014**, *2* (3), 1–3.
16. Khatake, P.; Nitnaware, P. T. Vibration Mitigation Using Passive Damper in Machining. *Int. J. Mod. Eng. Res. Technol.* **2013**, *3* (6), 3649–3652.
17. Kadu, R. S.; Awari, G. K.; Sakhale, C. N.; Modak, J. P. Formulation of Mathematical Model for the Investigation of Tool Wears in Boring Machining Operation on Cast Iron Using Carbide and CBN Tools, 3rd International Conference on Materials Processing and Characterisation (ICMPC 2014). *Procedia Mater. Sci.* **2014**, *6*, 1710–1724.
18. Schenck, H., Jr. *Theory of Engineering Experimentation*; Mc Graw Hill: New York, NY, 1961.
19. Modak, J. P.; Bapat, A. R. Formulation of Generalised Experimental Model for a Manually Driven Flywheel Motor and Its Optimization. *Appl. Ergon.* **1994**, *25* (2), 119–122.
20. Badadhe, A. M.; Bhave, S. Y.; Navale, L. G. Optimization of Cutting Parameters in Boring Operation. *IOSR J. Mech. Civ. Eng.* **2005**, *2320–334X*, 10–15.
21. Moetakef-Imani, B.; Yussefian, N. Z. Dynamic Simulation of Boring Process. *Int. J. Mach. Tool. Manu.* **2009**, *49*, 1096–1103.
22. Yussefian, N. Z.; Moetakef-Imani, B.; El-Mounayri, H. The Prediction of Cutting Force for Boring Process. *Int. J. Mach. Tool. Manu.* **2008**, *48*, 1387–1394.
23. Lazoglu, I.; Atabey, F.; Altintas, Y. Dynamics of Boring Processes: Part III – Time Domain Modeling. *Int. J. Mach. Tool. Manu. 42* **2002**, 1567–1576.
24. Komanduri, R.; Lee, M.; Raff, L. M. The Significance of Normal Rake in Oblique Machining. *Int. J. Mach. Tool. Manu.* **2004**, *44*, 1115–1124.
25. Min, B. K.; O'Neal, G.; Koren, Y.; Pasek, Z. A Smart Boring Tool for Process Control. *Mechatronics* **2002**, *12*, 1097–1114.
26. Koren, Y.; Ko, T. R.; Ulsoy, A. G. Tool Wear Estimation Under Varying Cutting Conditions. *Trans ASME, J. Dyn. Syst. Control* **1991**, *113* (2), 300–307.
27. Shiraishi, M. Scope of In-Process Measurement, Monitoring and Control Techniques in Machining Processes – Part 1: In-Process Techniques for Tools. *Precis. Eng.* **1988**, *10* (4), 179–189.
28. Kanase Sandip, S.; Patil Jaydeep, S.; Jadhav Sainand, M. Improvement of Ra Value of Boring Operation Using Passive Damper. *Int. J. Eng. Sci.* **2013**, *2* (7), 103–108.
29. Kumar, P.; Oberoi, J. S.; Singh, C.; Dhiman, H. Analysis and Optimization of Parameters Affecting Bore Deviation in Boring Process. *Int. J. Innov. Tech. Res.* **2014**, *2* (3), 967–972.
30. Kovári, K. The Two Base Tunnels of the Alptransit Project: Lötschberg and Gotthard. In *Worldwide Innovations in Tunnelling, STUVA-Tagung '95, Stuttgart, Forschung + Praxis 36*. Alba Fachverlag GmbH + Co.KG: Düsseldorf, 1995; pp. 23–29.
31. Bergmeister, K. Brenner Base Tunnel: Link Between Munich and Verona. *Tunnel* **2007**, *1/2007*, 9–20.
32. Nasri, V.; Fauvel, P. Lyon-Turin Long and Deep Railway Tunnel Project. In *Rapid Excavation and Tunnelling Conference*, SME IncSeattle: Littleton, CO, 2005; pp. 531–543.
33. Pliego, J. M. Open Session – The Gibraltar Strait Tunnel. An Overview of the Study Process. *Tunn. Undergr. SP. Technol.* **2005**, *20* (6), 558–569.
34. Robbins, R. J. Large Diameter Hard Rock Boring Machines: State of the Art and Development in View of Alpine Base Tunnels. *Felsbau* **1992**, *10* (2), 56–62.
35. Kovári, K. Rock Deformation Problems When using Full-Facing Cutting Equipment in Rock, Part 1. *Tunnel* **1986**, *3/86*, 236–244.
36. Barla, G.; Pelizza, S. TBM Tunnelling in Difficult Ground Conditions. In *GeoEng2000 – International Conference on Geotechnical & Geological Engineering, Melbourne*; Vol. 1; Technomic Publishing Company Inc.: Lancaster, 2000; 1471–1489.
37. ITA. Long Traffic Tunnels at Great Depth. In *ITA Working Group N-17 – Long Tunnels at Great Depth*; ITA: Lausanne, 2003.
38. Prader, D. Beispiele von Druckerscheinungen im Tunnelbau. In *Internationales Symposium für Untertagbau, Luzern, Schweizerische Gesellschaft für Boden– und Felsmechanik Zürich*; 1972; pp. 82–98.
39. Lombardi, G. Bau von Tunneln bei grossen Verformungen des Gebirges. In *Tunnel 81, Internationaler Kongress, Düsseldorf, Band 2, Messegesellschaft mbH NOEWA Düsseldorf und Deutsche Gesellschaft für Erd – und Grundbau e.V. Essen*, 1981; pp. 351–384.
40. Robbins, R.J. The Application of Tunnel Boring Machines to Bad Rock Conditions. In *Rock Mechanics: Caverns and Pressure Shafts, ISRM Symposium, Aachen*, Vol. 2; A.A. Balkema: Rotterdam, 1982; pp. 827–836.
41. Ramoni, M.; Anagnostou, G. Experiences and Basic Considerations on TBM Tunnelling in Squeezing Ground. In *Research Project FGU 2007/005, Report 090201 (Revision B) of the Institute of Geotechnical Engineering (IGT) of the ETH Zurich to the Swiss Federal Roads Office (FEDRO)*, 2009.
42. Kovári, K. Rock Deformation Problems When using Full-Facing Cutting Equipment in Rock, Part 2. *Tunnel* **1986**, *4/86*, 289–298.
43. Gehring, K. H. Design Criteria for TBM's with Respect to Real Rock Pressure. In *Tunnel Boring Machines – Trends in Design & Construction of Mechanized Tunnelling, International Lecture Series TBM Tunnelling Trends*, Hagenberg, A.A. Balkema, Rotterdam, Brookfield, 1996; pp. 43–53.
44. Ramoni, M.; Anagnostou, G. Tunnel Boring Machines under Squeezing Conditions. *Tunn. Undergr. SP. Technol.* **2010**, *25*, 139–157.
45. Graziani, A.; Capata, A.; Romualdi, P. Analysis of Rock-TBM-Lining Interaction in Squeezing Rock. *Felsbau Magazin* **2007**, *25* (6), 23–31.
46. Ramoni, M.; Anagnostou, G. The Effect of Advance Rate on Shield Loading in Squeezing Ground. In *Underground Space – The 4th Dimension of Metropolises, ITA World Tunnel Congress 2007, Prague*, Vol. 1, 2007a; Taylor & Francis Group: London; pp. 673–677.
47. Ramoni, M.; Anagnostou, G. Numerical Analysis of the Development of Squeezing Pressure During TBM Standstills. In *The Second Half Century of Rock Mechanics, 11th Congress of the International Society for Rock Mechanics (ISRM), Lisbon*, Vol. 2, 2007b; Taylor & Francis Group: London; pp. 963–966.
48. Sterpi, D.; Gioda, G. Ground Pressure and Convergence for TBM Driven Tunnels in Visco-Plastic Rocks. In *ECCOMAS Thematic Conference on Computational Methods in Tunnelling, EURO:TUN 2007*; Vienna University of Technology, 2007; p. 89.
49. Maidl, B.; Schmid, L. R.; Ritz, W.; Herrenknecht, M. *Tunnelbohrmaschinen im Hartgestein*; Ernst & Sohn Verlag für Architektur und technische Wissenschaften GmbH: Berlin, 2001.
50. Schneider, E.; Home, L.; Sänger, B.; Kolb, S. Innovative Concept for Constructing the Brenner Base Tunnel with Previously Produced Exploratory Tunnel. *Tunnel* **2007**, *1/2007*, 21–33.
51. Junzhou Huo; Wei Sun; Jing Chen; Xu Zhang. Disc Cutters Plane Layout Design of the Full-Face Rock Tunnel Boring Machine (TBM) Based on Different Layout Patterns. *Comput Ind Eng* **2011**, *61*, 1209–1225.
52. Lawal, S. A.; Choudhury, I. A.; Nukman, Y. Application of Vegetable Oil-Based Metalworking Fluids in Machining Ferrous Metals – A Review. *Int. J. Mach. Tool. Manu.* **2012**, *52*, 1–12.
53. Lawal, S. A.; Choudhury, I. A.; Nukman, Y. A Critical Assessment of Lubrication Techniques in Machining Processes: A Case for Minimum Quantity Lubrication Using Vegetable Oil-Based Lubricant. *J. Clean. Prod.* **2013**, *41*, 210–221.
54. Chang, F. X. An Experimental Study of the Impact of Turning Parameters on Surface Roughness. In *Proceedings of the Industrial Engineering Research Conference, Paper No. 2036, GA*, 2001.
55. Huang, L. H.; Chen, J. C. A Multiple Regression Model to Predict In-Process Surface Roughness in Turning Operation via Accelerometer. *J. Ind. Technol.* **2001**, *17* (2), 2–7.
56. Lin, C. S.; Chang, F. M. A Study on the Effects of Vibrations on the Surface Finish using a Surface Topography Simulation Model for Turning. *Int. J. Mach. Tool. Manu.* **1998**, *38* (7), 763–778.
57. Bernardos, P. G.; Vosniakos, G. C. Predicting Surface Roughness in Machining: A Review. *Int. J. Mach. Tool. Manu.* **2003**, *43*, 833–844.
58. Salgado, D. R.; Alonso, F. J.; Cambero, I.; Marcelo, A. In-Process Surface Roughness Prediction System using Cutting Vibrations in Turning. *Int. J. Adv. Manuf. Tech.* **2009**, *43*, 40–51.
59. Ihsan Korkut; Yilmaz Kucuk. Experimental Analysis of the Deviation from Circularity of Bored Hole Based on the Taguchi Method. *J. Mech Eng.* **2010**, *56* (5), 340–346.
60. Parker, E. W. Dynamic Stability of a Cantilever Boring Bar with Machined Flats Under Regenerative Cutting Conditions. *J. Mech. Eng. Sci.* **1970**, *12* (2), 104–115.

61. Rao, P. N.; Rao, U. R. K.; Rao, J. S. Towards Improved Design of Boring Bars Part 1: Dynamic Cutting Force Model with Continuous System Analysis for the Boring Bar. *Int. J. Mach. Tool. Manu.* **1988**, *28* (1), 33–44.
62. Jayaram, S.; Iyer, M. An Analytical Model for Prediction of Chatter Stability in Boring. *Trans. NAMRI/SME* **2000**, *28*, 203–208.
63. Kuster, F. Cutting Dynamics and Stability of Boring Bars. *Ann. CIRP* **1990**, *39* (1), 361–366.
64. Marui, E.; Ema, S.; Kato, S. Chatter Vibration of Lathe Tools. Part 1: General Characteristics of Chatter Vibration. *J. Eng. Ind., Trans. ASME* **1983**, *105*, 100–106.
65. Taskesen, A. Computer Aided Nonlinear Analysis of Machine Tool Vibrations and Developed Computer Software. *Math. Comput. Appl* **2005**, *3*, 377–385.

1.3 Finish Machining of Hardened Steel

SK Choudhury, Indian Institute of Technology Kanpur, Kanpur, India
S Chinchanikar, Vishwakarma Institute of Information Technology, Pune, India

© 2017 Elsevier Inc. All rights reserved.

1.3.1	**Introduction**	47
1.3.1.1	Soft-Part and Hard-Part Machining	47
1.3.1.2	Qualitative Comparison of Hard-Part Turning with Grinding	48
1.3.1.3	Applications and Machining Characteristics of Hardened Steels	50
1.3.1.3.1	Hardened steels: Hardness $\leq$ 45 HRC	50
1.3.1.3.2	Hardened steels: Hardness in the range of 45–70 HRC	50
1.3.2	**Equipment and Tooling**	51
1.3.2.1	Machine Tools: Applications of Hard Machining Processes	51
1.3.2.1.1	Industrial applications	53
1.3.2.1.1.1	Complete machining of flanges	53
1.3.2.1.1.2	Machining of gears: compact manufacturing system	53
1.3.2.1.1.3	Vertical pick-up turning machines	54
1.3.2.1.1.4	Combination (hybrid) technology	54
1.3.2.1.1.5	Scroll-free turning	55
1.3.2.2	Cutting Tool Materials	55
1.3.2.3	Cutting Edge Geometry: Macro- and Micro-Geometry of the Insert	56
1.3.3	**Finish Machining of Hardened Steel: Physical Aspects**	58
1.3.3.1	Cutting Forces	58
1.3.3.2	Chip Formation	60
1.3.3.3	Tool–Chip Interface Temperature	61
1.3.3.4	Tool Wear Patterns and Mechanisms	63
1.3.3.5	Surface Integrity	66
1.3.3.5.1	Surface roughness	66
1.3.3.5.2	RSs	70
1.3.3.5.3	White layer effect	72
1.3.3.5.4	Cutting errors and dimensional accuracy	74
1.3.4	**Modeling of Hard Machining Processes**	75
1.3.4.1	Modeling of Cutting Force	75
1.3.4.2	Modeling of Tool Wear Progression	76
1.3.4.3	Modeling of RSs	78
1.3.5	**Hard Machining: Application of Different Cooling Techniques**	80
1.3.5.1	Dry, Semidry, and Cryogenic Machining	80
1.3.5.2	Application of Vegetable Oils and Solid Lubricants	83
1.3.6	**Optimization Studies in Machining of Hardened Steel**	86
References		88
Relevant Websites		92

1.3.1 Introduction

Higher production rates in shorter lead-times with continuous quality improvement, dry machining techniques, and constant demand for increased metal cutting performance from difficult-to-machine workpiece materials are continuously increasing. Among users in recent years, demands for extremely tough and hard steels also known as ultrahigh strength steels (UHSS) are continuously increasing. These grades of steel finds application in landing gear components, rocket cases, air frame fittings, heavy vehicle crank shafts, connecting rods, spindles, and power transmission gears. A significant research being undertaken to consider replacing Inconel engine shafts with UHSS in the aerospace industry. However, in the hardened state, these steels are amongst the difficult-to-machine workpiece materials which create ever new challenges for machining operations and place very high demands for high performance cutting tools. The hardness and alloying content makes these grades of steel difficult to machine, the generated temperature being high.

1.3.1.1 Soft-Part and Hard-Part Machining

The term hardened steel is often used for medium or high carbon steel. Hardened steel is designed to be resilient and tough to penetrate by suitable heat-treatment process, namely hardening and tempering processes. Both these processes are used hand in hand when hardening steel. The process begins

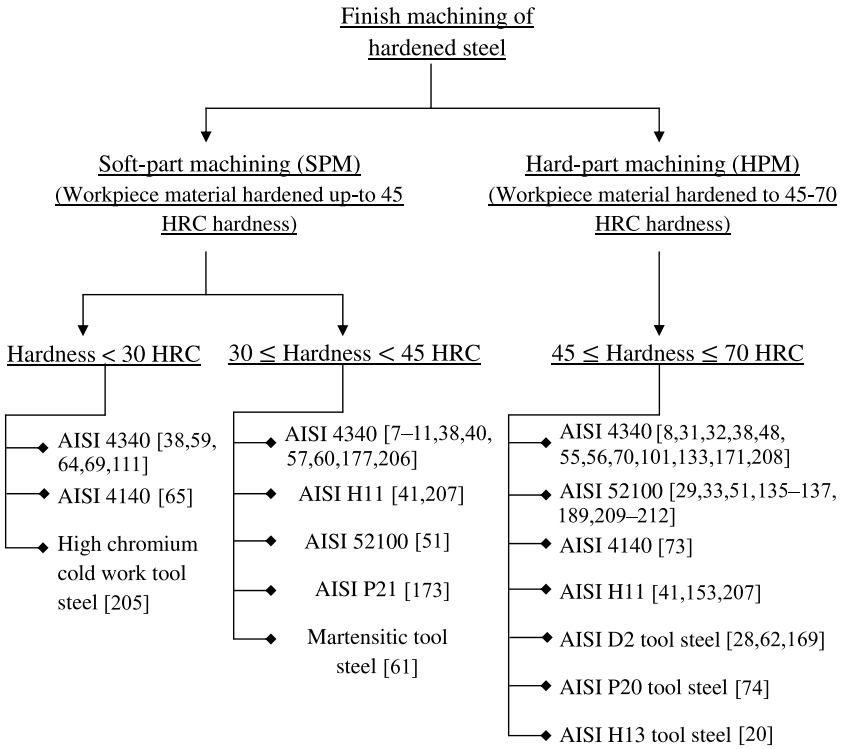


Figure 1 Attempts made by various researchers while soft and hard machining of hardened steel. Modified from Ref. [3].

with hardening wherein a piece of metal is heated gradually until it reaches a high temperature (a temperature that causes it to turn red). Next, the piece of metal is removed and placed directly into cool water. The steel is now very hard, but many times this process leaves the steel very brittle and susceptible to breaking during use. Tempering reduces the hardness of the forged steel very slightly but improves the toughness. In tempering process, steel is heated until it turns the indicative blue color and then allowing the new hardened and tempered steel to cool on its own. The final result of exactly how hard the steel will become depends on the amount of carbon present in the metal.[1]

Today, finish machining of hardened steel which is being stimulated interactively by new cutting tool materials and improved machining processes is categorized as soft-part machining (SPM) and hard-part machining (HPM). SPM is a process wherein a workpiece material hardened up to 45 HRC hardness is easily machined with the advancement in the cutting tool materials and machine tools. On the other side, machining of hardened steels having hardness in the range of 45–70 HRC is considered under HPM.

Sandvik Coromant, the world-leading manufacturer of cutting tools, commented that HPM has become a viable manufacturing process for mass production and is able to meet industry productivity goals of higher quality and shorter cycle times with advent of super-hard cutting tool materials such as cubic boron nitride (CBN) and aluminum oxide ceramics and new optimized machines.[2] Although, HPM has been mostly attempted by various researchers with CBN and ceramic tools, attempts also have been made using coated carbide tools with the development in the cemented carbide grades, coating materials and coating deposition technologies as an economical alternative to costly CBN and ceramic tool materials.[3] A summary of various researchers work which were performed at different levels of work material hardness categorized as SPM and HPM is shown in **Figure 1**.

Researchers have tried to investigate the specific cutting characteristics in terms of cutting forces, surface roughness, tool life, chip morphology, residual stresses (RSs), the changes of subsurface microstructure (so-called white layer), and the tool–chip interface temperature considering the effects of cutting parameters, tool materials, different coatings, and tool geometry under dry and/or semidry and/or flood cooling environment during finish machining of hardened steels while many of them have ventured to characterize the wear phenomenon. Important conclusions of their work for a given tool–workpiece combination are given in Section 1.3.3.

1.3.1.2 Qualitative Comparison of Hard-Part Turning with Grinding

Hard-part turning (HPT) in comparison to grinding offers many advantages. Traditionally, grinding processes are employed for finishing operations on the machine parts with hardness value in excess of 60 HRC. However, HPT using tools with geometrically cutting edges can produce comparable surface finish with the desired accuracy. HPT with a single point cutting tool can produce complex contours as against the costly form wheels are required in case of grinding. Moreover, it is possible to perform multiple operations with single

setup when using HPT resulting in excellent positional accuracy, reduced part handling, and less risk of part damage in comparison to grinding. Further, HPT is mostly carried out under dry cutting condition which reduces costs for coolant, its maintenance or disposal as against grinding waste while grinding.[2,4]

In particular, better production control in terms of reduced manufacturing costs, production time, and higher product quality can be achieved while HPT by employing proper tool geometry, using rigid and stable machine tools and by providing proper clamping to workpiece, tool holder and insert for maximum rigidity. Depending on part geometry, a reduction of machining time and cost of well over 70% can be achieved while maintaining accuracy and surface finish when employing HPT in comparison to grinding.[2] Qualitative comparison of HPT with grinding in terms of overall product quality, process flexibility, material removal rate, subsurface damage, RSs, process reliability, setup time, environmental compatibility, and shape and dimension accuracy is shown in Figure 2.

HPM is widely used in automotive, roller bearing, hydraulic, and die and mold industries. HPT finds application in finish turning of gearwheels, gear shafts, bearing rings, and other transmission parts. Hard milling, hard broaching, and hard reaming processes are widely used in the die and mold industry. In general, HPT is widely accepted as a best replacement to costly grinding operations as it provides a relatively high accuracy for many hard parts and cost benefits. However, issues related to surface integrity, especially undesirable patterns of RSs and the changes of subsurface microstructure, so called white layer, which reduces fatigue life of turned surfaces are need to be considered for hard-part turned surfaces.[6] A group of researchers experimentally investigated and mathematically modeled the performance measures such as surface roughness, RSs, and the changes of subsurface microstructure (so-called white layer) considering the effects of cutting parameters, tool materials, different coatings, and tool geometry during finish machining of hardened steels. Important conclusions of their work are given in Sections 1.3.3 and 1.3.4.

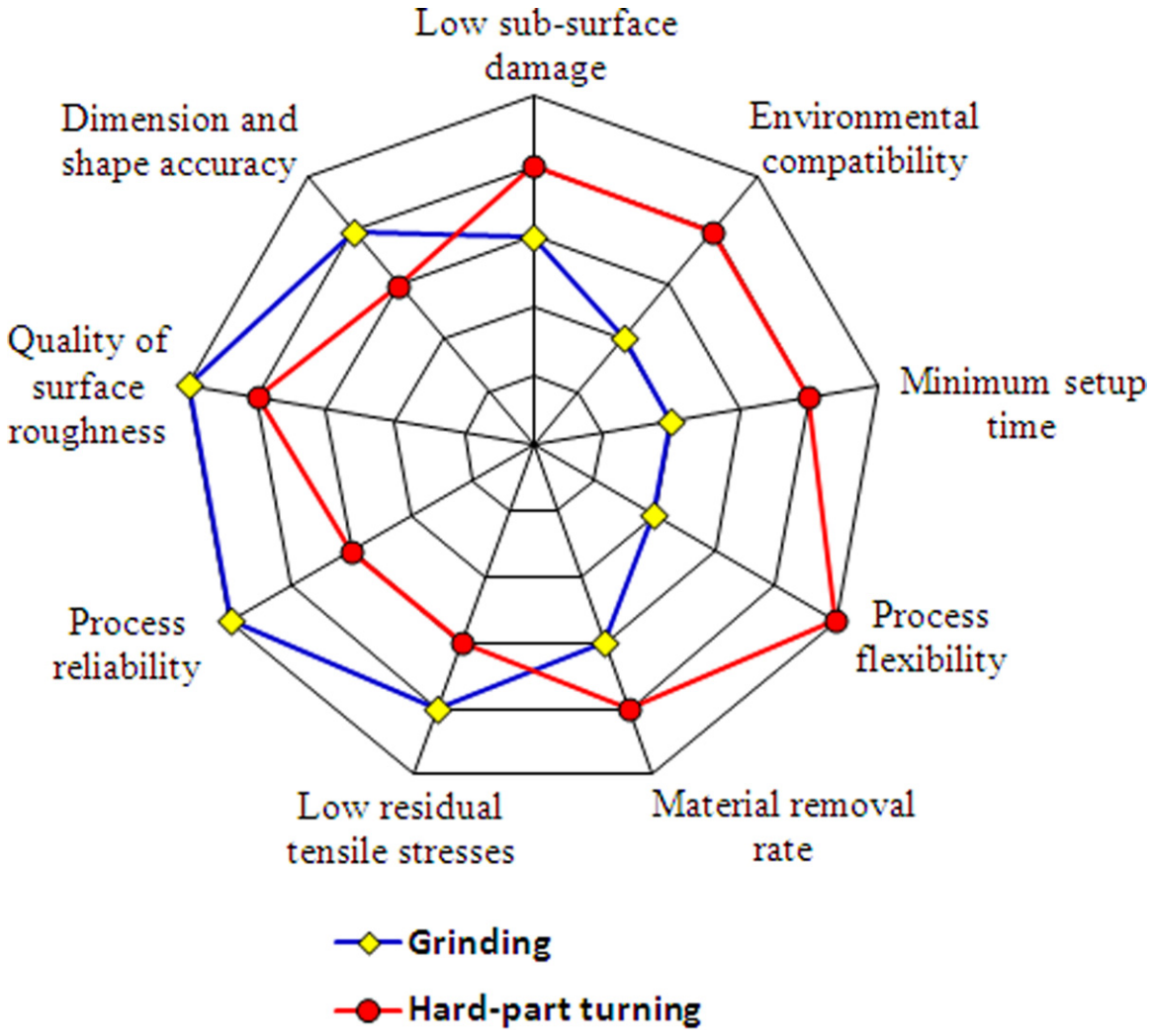


Figure 2 Qualitative comparison of hard-part turning (HPT) with grinding. Modified from Ref. [5].

1.3.1.3 Applications and Machining Characteristics of Hardened Steels

Finish machining of hardened steels is greatly affected with the type of cutting tool material and macro- and micro-geometry employed for the cutting inserts. It has been reported that higher workpiece hardness imposes certain restrictions on cutting conditions to be employed during machining to have better tool life, dimensional accuracy, and surface finish. Further, machining performance largely depends upon the physical properties and chemical compositions of the workpiece and the cutting tool materials, especially the coating materials and their characteristics in case of coated tools. The machining aspects such as chip formation, heat generation and tool wear differ substantially while machining of hardened steel at different levels of hardness.[7–11] Applications of hardened steels at different levels of hardness are given in **Table 1**.

1.3.1.3.1 Hardened steels: Hardness ≤ 45 HRC

With the advent of the new cutting tool materials and improved machining processes, today, machining of hardened steel having hardness up to 45 HRC is being considered as SPM. Sufficient research has been carried out to investigate the effect of work material hardness and cutting parameters on the machining performance using uncoated/coated carbide, ceramic, and CBN tool inserts. Attempts also have been made by various researchers to predict worn tool cutting forces and tool wear progression given the cutting conditions, tool geometry, workpiece, and cutting tool material properties. In view of increasing laws and directives governing industrial safety and environmental protection, a group of researchers evaluated machining performance of hardened steel under dry and/or near-dry and/or flood-cooling environment. Based on the literature review on machining of hardened steel and leading tool manufacturer catalogs, machining characteristics of various types of hardened steels having hardness in the range of 20–45 HRC is given in **Table 2**.

1.3.1.3.2 Hardened steels: Hardness in the range of 45–70 HRC

The concept of HPT (45–70 HRC) has gained considerable attention in the recent past in metal cutting as it can apparently replace the traditional process cycle, which comprises rough turning, heat treatment, and finish grinding. HPT was introduced to increase the flexibility and ability to manufacture complex geometries. Gearwheels, bearing rings, and other transmission parts are typical applications for HPT. Machining characteristics of hardened steels which include high speed steels (HSS), die steels, bearing steels, alloy steels, and case hardened steels having hardness in the range of 45–70 HRC is given in **Table 3**.

Hardened steels have good dimensional stability combined with high resistance to tempering. However, machining of these materials is considered as difficult-to-cut materials and care must be taken to select the correct cutting conditions. In order to withstand higher cutting forces and higher cutting temperatures in the HPM, rigid machine tools with adequate power, very hard and tough tool materials with appropriate tool geometry, tool holders with high stiffness and appropriate

Table 1 Applications of various types of hardened steels[3,12]

Type of hardened steel	*Applications*
Case hardened steels (55–62 HRC)	Gears, shafts, bearings, nozzles, bushes, clutch sleeves, and constant velocity (CV) joints
Bearing steels (58–62 HRC)	Bearing housings, roller bearings, fuel injector nozzles, ball bearings, and hub units
Cold work tool steels (45–65 HRC)	Cold extrusion tools, stamping tools, dies, punches and tools for the manufacture of screws, nuts, and bolts
Hot work tool steels (45–58 HRC)	Extrusion dies, tool and dies, punches, and drop forging die
High manganese steels (200–400 BHN)	Crushing cones, railway components, deflector plates, and mineral processing equipment
High tensile steels (45–56 HRC)	Jet engine mounting, helicopter camshaft gears, landing gear components, and air frame fittings
High speed steels (HSS) (58–66 HRC)	Tool and dies, thread rolling dies, pressure rolls, high temperature bearings, metal cutting tools such as milling cutters, drills, taps, and threading dies

Table 2 Machining characteristics of hardened steels: Hardness ≤45 HRC[3]

Type of steel	*Machining characteristics*
Low-carbon (<0.3% C)	Soft and gummy, difficult chip control, and high-speed machining is possible
Free-machining steels (<220 HB)	Easy to machine using higher cutting speed and high depth of cuts, difficult chip control
Medium and high carbon steels, alloy steels, and tool steels (≤35 HRC)	Higher content of chromium, nickel, and molybdenum: greater tendency to work harden Higher nickel content: more difficult to control chip Higher carbon and alloy content: generally difficult to machine Higher carbon content: more abrasive, achieves good surface finish, and lower speeds
Alloy steels and tool steels (36–45 HRC)	Greater tendency to work harden, more difficult to control chips, hard to break chips, and increased abrasive wear

Table 3 Machining characteristics of hardened steels: hardness in the range of 45–70 HRC[3,12]

Type of hardened steel	*Machining characteristics*
Case hardened steels (55–62 HRC)	While machining of these steels it is important to make sure that machining is taking place in the hard case zone as machining into the soft core may reduce the cutting tool performance. Mostly, polycrystalline cubic boron nitride (PCBN) and ceramic tools are preferred for machining
Bearing steels (58–62 HRC)	Bearing steels are slightly hyper eutectic with a carbon content of about 1%. The microstructure is martensitic with embedded carbides. Due to the abrasiveness of the material, wear resistant grades, mostly, PCBN and ceramic tools are preferred for machining
Cold work tool steels (45–65 HRC)	Cold work tool steels are highly abrasive and the embedded carbides lead to increase crater wear on cutting tools. These steels are difficult to machine as they are wear resistant and a lot of heat is generated during machining
Hot work tool steels (45–58 HRC)	These steels are known for high hot tensile strength, toughness, and wear resistance. Most of the alloying elements in these steels are carbide formers. Tool wear is mostly dominated by crater wear and edge chipping
High manganese steels (200–400 BHN)	These steels have a tendency to work harden. Always machine beneath the skin of the component as tool wear accelerates during machining of the actual skin. Tool life reduces by using too low feed rates and notching occurs when using higher feed rates
High tensile steels (45–56 HRC)	These steels are known for their toughness and capability of obtaining high tensile strength in the heat-treated condition. It is suggested to use low cutting speeds and sharp positive tool geometries to prevent surface abuse and carbon depletion
High speed steels (HSS) (58–66 HRC)	These steels known for high strength, hardness, good wear resistance, and high edge sharpness. A high abrasion resistance and toughness characteristic of these steels generates high temperatures at the cutting edge. Most dominant wear modes are crater wear and notching which can be reduced by lowering the cutting speed and the feed rate, respectively

cutting conditions are some of the prerequisites.[2] Sufficient research has been carried out by the researchers using uncoated/coated CBN, polycrystalline cubic boron nitride (PCBN), and ceramic and carbide tool inserts while HPM. However, CBN inserts win the race in all respects as they exhibit better tool life at toughest cutting conditions due to their high and stable hardness,[13] and its lower solubility for steel material of the machined workpiece.[14] The next section describes the equipment and tooling requirement, especially, the macro- and micro-geometry of the cutting insert for various operations (turning, milling, drilling, broaching, reaming, and threading) while finish machining of hardened steel.

1.3.2 Equipment and Tooling

1.3.2.1 Machine Tools: Applications of Hard Machining Processes

Machining of the steels in the hardened/soft condition primarily depends upon the workpiece configuration, production volume, and amount of the material to be removed. In general, roughing operation wherein up to 30% of the work material is removed from the blank is carried out under soft-state condition. After a workpiece is roughed in the soft state, it is heat-treated to get the required hardness. However, heat treatment usually creates problems with workpieces being twisted, bent, or otherwise out of shape. Machining to the finished size in hardened state allows making a part with higher accuracy and better dimensional characteristics compared to parts heat-treated after machining.[15]

With the advent of the modern machine tools and advanced cutting tool materials, nowadays, it is feasible to machine the workpiece entirely from a hardened state. However, the degree of machine rigidity, rigid spindle tooling and tool holders, hydrostatic guideways, polymer composite reinforcement bases, and high dynamic stiffness, which determines low levels of vibration over a wide frequency range dictate the degree of hard machining accuracy and the quality of surface finish.[16] A solid machine tool, one with bridge construction and a rigid spindle and hand-scraped machine surfaces as they are more accurate and better at dampening vibration than conventionally ground surfaces plays a large part in the level of success of hard machining. High machine rigidity and stability will minimize the impact of variable cutting force on the surface profile produced. This results in a better process capability. All vertical pick-up turning machines from EMAG have a machine base made of MINERALIT® polymer concrete which has eight times better damping properties than gray cast iron. In particular, in case of hard machining small depths of cut (0.05–0.3 mm) and feed rates (0.05–0.2 mm rev^{-1}) are used resulting in small undeformed chip thickness and the ratio of the undeformed chip thickness to the radius of the cutting edge. The geometrical relationship leads to larger effective negative rake angle and as a result extremely high pressure is generated to remove material in the vicinity of the cutting edge. Moreover, a large corner radius causes the components of the resultant cutting force to be high in conjunction with extreme high thermal stresses which demands for an absolute stable and rigid process.[17]

Machining operations performed on hardened steel (turning, milling, drilling, boring, reaming, and threading) found applications in automotive, aerospace, bearing, and die/mold industries as shown in **Figure 3**. Today, HPM is often combined with high-speed machining (HSM) using computerized numerical control (CNC) machine tools.[6] A stable machine structure and dynamic axes based on a completely new modular machine concept are the outstanding features of the modern CNC vertical turning machines which make it possible to utilize various production technologies for soft and hard machining with integrated automation and a pick-up spindle.

Not only machine stability, but also rigidity and thermal stability are vital components in producing an accurate and

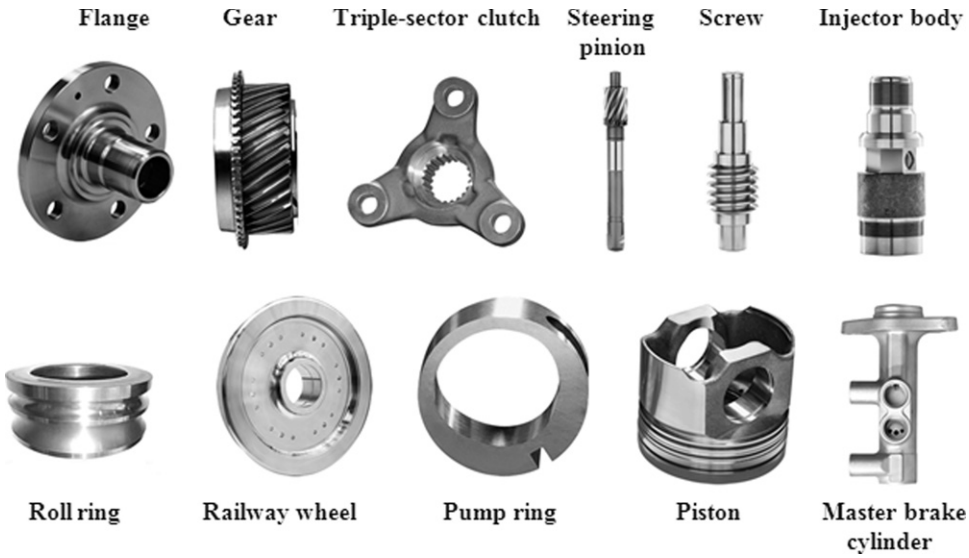


Figure 3 Industrial applications of hard-part machining. Modified from Ref. [17].

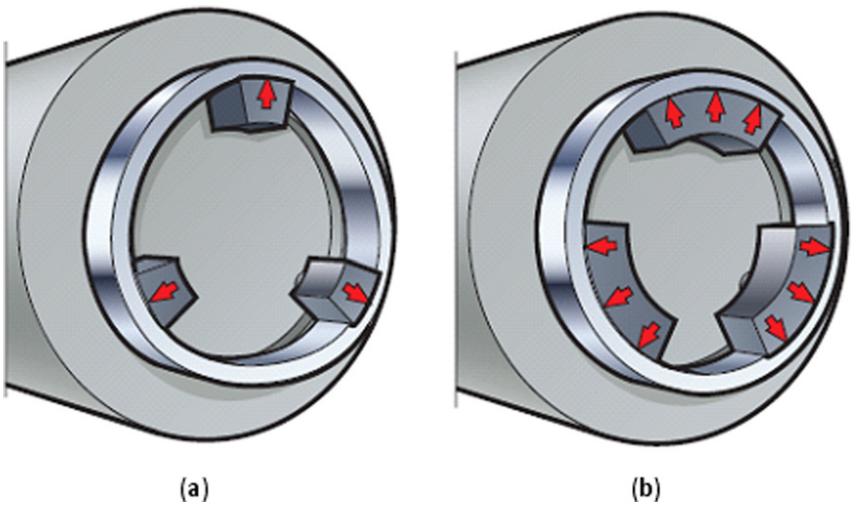


Figure 4 Clamping of thin-walled parts using (a) ordinary three-point jaws and (b) wide jaws. Modified from Ref. [2].

high-quality finished part. Heat generated at any place in the machine affects the tolerance of the workpiece, so it must be controlled accurately. Removing heat by cooling the spindle or transporting it away in heat-containing chips will pay dividends in better tolerances. In this respect, vertical lathes (pick-up machines) with no resting place for chips to accumulate are good examples of 'thermostable machining systems'.[2] In order to control thermal distortion of the machine tool structure, nowadays, machine tools are equipped with a thermal distortion stabilizing system which circulates a temperature-controlled fluid through the main components of the machine. This system is usually employed for high-precision machining applications such as die and mold parts that require long duration cutting. To isolate heat and vibrations from spindle drive, spindle and drive motor are connected coaxially by the diaphragm coupling that provide the spindle carriage with a smooth, vibration free, and rotationally accurate ride.[16] Guiding accuracy and positioning accuracy of the carriage are also become vital and an important criteria to consider in case of hard machining processes.

The ability to accurately rotate the workpiece is vital for achieving close dimensional tolerances. Workpiece clamping especially, thin-walled components place very stringent requirements on clamping. Hard machining of thin-walled parts is often subjected to part distortion which can be eliminated by gripping the part using multiple contacts on the chuck.[16] Ordinary three-point jaws can distort the roundness of thin-walled work-piece due to local excessive clamping forces (**Figure 4(a)**). As against, gripping thin-walled work-piece using wide jaws distribute clamping forces over a larger area for better machining with narrower dimensional tolerances (**Figure 4(b)**).[2] Magnetic work-holding devices are also

more commonly used due to sufficient clamping force and consistent part location for complete 3D machining in a single setup with improved accuracy and better surface finish.[16]

Usually, a length-to-diameter ratio of up to 2:1 is used for workpieces supported on one end only. However, with additional tailstock support, this ratio can be extended. Properly aligned headstock and tailstock promotes maximum rigidity and add extra dimensional stability as shown in Figure 5.[2]

Further, added strength for tool holder and insert clamping brings additional rigidity to process while machining of hardened steels. It is always desired to keep the overhang as short as possible or, if feasible, use a rigid tool with a large cross-section as deflection of the tool holder increases by the cube of the added overhang. In addition to a requirement of strong tool holder, hard machining also requires a rigid means of clamping inserts to tool holder. CoroTurn® RC clamping for negative inserts and CoroTurn® 107 for positive inserts provide this rigidity by clamping the insert in two directions, combining downward forces with insert positioning accuracy as shown in Figure 6.

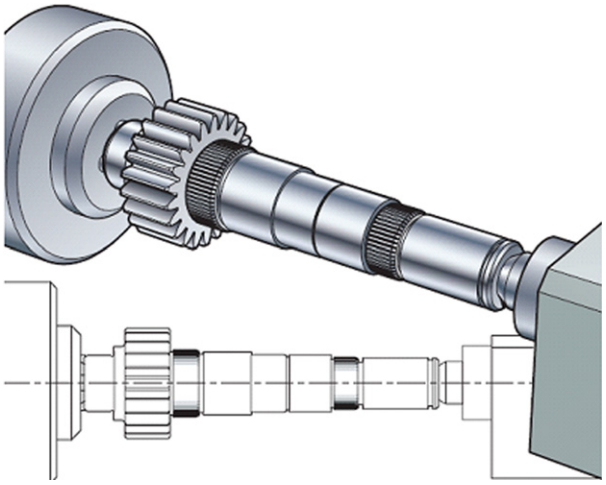


Figure 5 Properly aligned headstock and tailstock promote rigidity. Modified from Ref. [2].

1.3.2.1.1 Industrial applications

1.3.2.1.1.1 Complete machining of flanges

'Downsizing' remains the focus of industrial production, in regards to car engines, in the energy industry or also general mechanical engineering. Machining of ever smaller and more precise components in the hardened/soft state, such as flanges has become possible with modern CNC machine tools such as EMAG's vertical turning lathes as shown in Figure 7(a).[17] The design of these machines provides a high degree of flexibility to apply different production technologies for soft and hard machining which has become the basis for success when machining a wide range of flanges.

1.3.2.1.1.2 Machining of gears: compact manufacturing system

A demand on the manufacture of transmission components such as shafts, gears, planetary gears, and plate carriers at the highest precision continues to increase. Modern gearboxes are becoming smaller while the number of speed-gears increases, leading to a general increase in the quantity of all gears and toothed components. With innovative machine designs by the gearing specialists from EMAG have expedited developments in the production of transmission systems such as, vertical pick-up turning machine (VL 2) for the fast and precise machining of gears, pick-up gear hobbing machine for the fast hobbing and deburring of gears (VLC 200 H) (Figure 7(b)), vertical chamfering machine (VLC 100 C), and laser-welding machine (ELC 160) for the joining of synchronizing ring and transmission gear.

The integrated automation system, using a pick-up spindle in VLC 200 H, ensures short idle times and reduced cost-per-piece. It is perfectly prepared for integration into manufacturing systems. These machines have a body made of high-grade MINERALIT® polymer concrete, which is thermally stable and provides excellent damping properties, resulting in extended tool life and super surface finishes. The KOEPFER gantry loader, equipped with V-grippers, forms the basis of the automation system of these machines. Long-time magazines, like the recirculating storage conveyor, make sure that machines are running for a number of hours and are not only suitable for both wheel- and shaft-type components, but can also be reset without much effort. The capacity of a gravity-based magazine and thus the

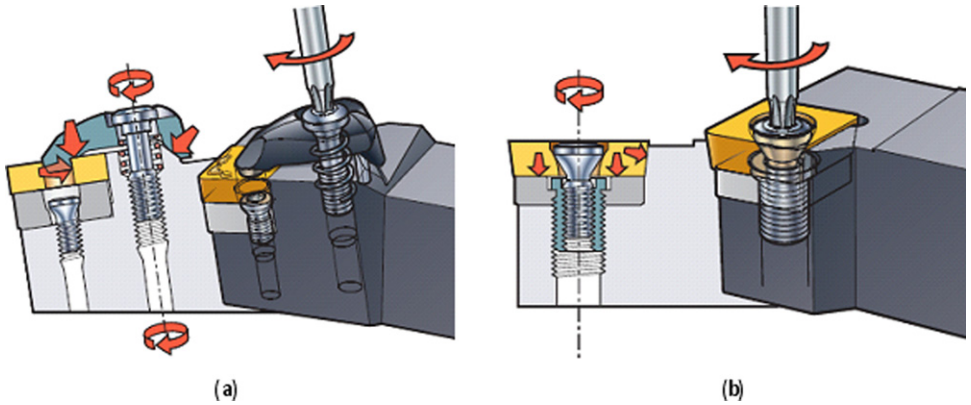
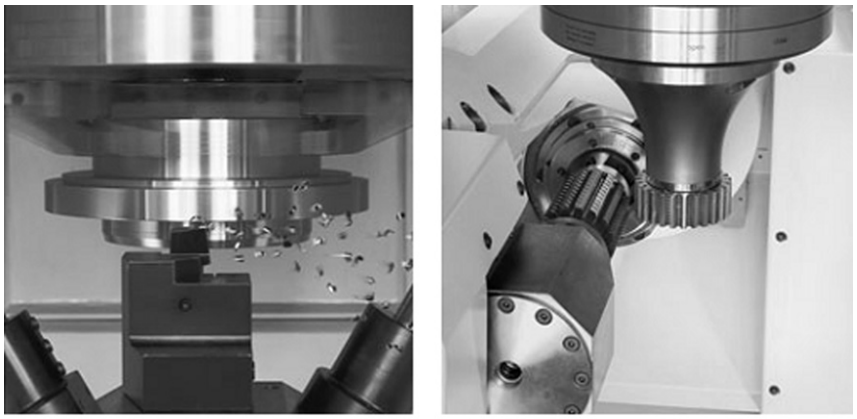
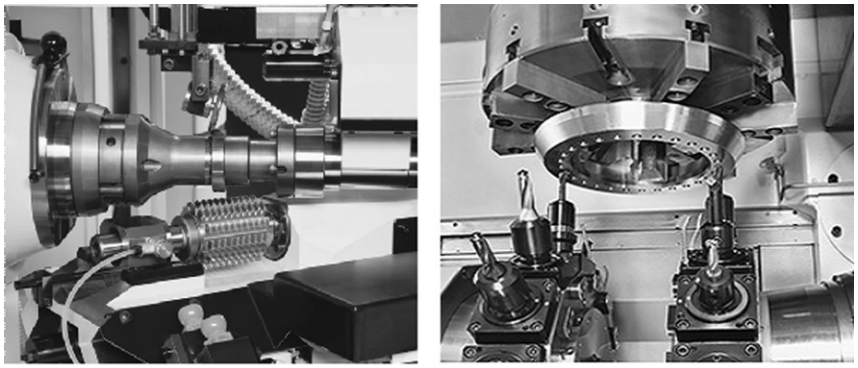


Figure 6 (a) CoroTurn RC clamping for negative inserts and (b) CoroTurn 107 for positive inserts which are held in place with a screw clamp system. Modified from Ref. [2].



(a) (b)

Figure 7 (a) Vertical pick-up turning machine and (b) pick-up gear hobbing machine. Modified from Ref. [17].



(a) (b)

Figure 8 (a) Compact shifting milling head for processing of screws (b) vertical machining center: drilling. Modified from Ref. [17].

autonomy of these machines can be greatly enhanced with the use of multiple feeding rails.[17]

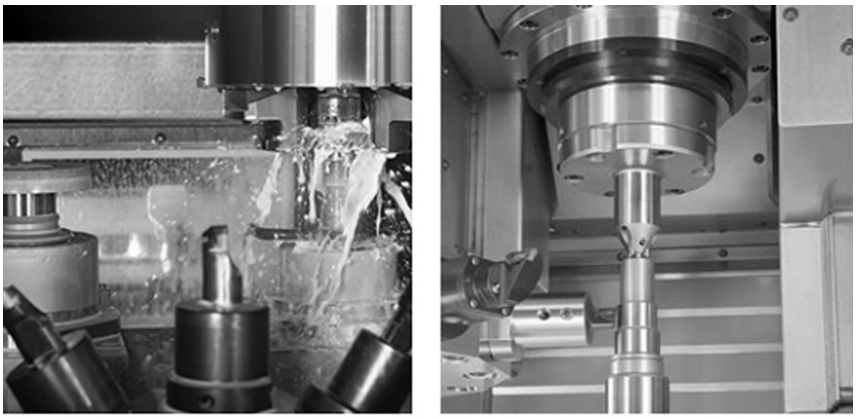
1.3.2.1.1.3 Vertical pick-up turning machines

Vertical turning with suspended spindle also called vertical pick-up turning machines are primarily used in the manufacture of large batches of high-quality metal components. In these machines the work-spindle takes over both the work-holding function for the machining process and the automation process. The highly stable vertical turning machines are being used in the production of gearwheels, sprockets, sliding sleeves, components for CVTs, link pins, connecting rods, rockers, bearing rings, and piston rings as shown in **Figure 8**. This vertical design of the machine offers ideal chip-flow conditions and makes dry machining, an uncomplicated process. Another advantage of these machines is its stability and their vibration resistant design which is obtained through their polymer concrete base and the firmly integrated tooling system to the machine base.[17]

1.3.2.1.1.4 Combination (hybrid) technology

Every year up to two billion gears are produced worldwide, the larger part by gear cutting for transmission systems for the automotive industry. Earlier, requirements of complex gear geometries and exceptional geared components quality was attained with a relatively long process chain, namely turning, gear cutting, and deburring, with each process allocated to a different machine. However, today, gear cutting, turning and deburring operations are integrated in a single setup which offers customers a much quicker alternative for gear production. The vertical machines EMAG VSC 400 WF and VLC 250 WF have all processes integrated in a single setup, resulting in increase in productivity dramatically.[17]

These days, the combination of hard turning and grinding is performed on a single machine, to great effect, to reduce cycle times. Moreover, the process combination (hard turning and grinding) allows greater flexibility and improved component quality. A typical example of combination machining is the machining of gearwheels as shown in **Figure 9(a)**. The shoulders are finish hard turned and the bore and cone are pre-turned and finish-ground because of the high demands made on their quality. To achieve this, the machine has been equipped with two grinding spindles, one of which is designed to machine the bore, with the second one machining the external sections of the component. Another example of the



(a) (b)

Figure 9 (a) A combination of hard turning and grinding and (b) scroll-free turning. Modified from Ref. [17].

combination technology is the machining of scroll-free seats of a pressure ring. To have its outside diameter scroll-free surface it is pre-turned and then finish-ground and its face is hard finish-turned. Another interesting example of this technology is the machining of nuts with internal ball tracks, as used in ball screws. The EMAG VSC, equipped with *Y*- and *B*-axis allows the hard turning of the face, the O/D and the shoulder of the nut and grinding of the internal thread on the ball track. The high-precision *B*-axis allows the setting of the lead angle of the thread, whilst the *Y*-axis serves as in-feed axis for the machining of the ball track. The advantage of this concept over conventional, sequential processes is that all quality-defining surfaces can be machined in a single setup. Re-clamping errors that affect in particular the alignment of face and O/D to the center line of the ball groove are thus avoided.[17]

1.3.2.1.1.5 Scroll-free turning

The Scroll-free Turning process is a process wherein turning tool carries out a rolling motion which offers new opportunities in the machining of precision components. The cutting edge of an inclined CBN wheel moves over the rotating workpiece and the cutting speed is generated by the workpiece rotation as shown in **Figure 9(b)**. With the movements of tool and workpiece overlaid, the contact point of the cutting edge continuously moves along the component surface. The process is very fast, about five to six times faster than that of hard turning processes and about two to three times that of grinding, and impresses with outstanding surface finishes without any trace of scoring marks.[17]

1.3.2.2 Cutting Tool Materials

Machining is a major manufacturing process that is being stimulated interactively by new cutting tool materials, improved machining processes, and government regulations. Diminishing component size and weight, enhanced surface quality, tighter tolerances, and high manufacturing accuracies and reduced costs are the key drivers to the progress of cutting technology.[6] These key drivers have a direct influence on the primary inputs to the cutting process, namely, the cutting tool material, cutting tool geometry and its design, cutting parameters, the workpiece material, and the cutting fluid.[18] A wide range of cutting tool materials is available with the variety of properties, performance capabilities, and cost. These include HSS, cemented carbides (WC), cermets, ceramics (alumina and silicon nitrides), PCBN, and polycrystalline diamond (PCD).

Cemented carbides are the most common cutting tool materials currently in use and are now the material of choice for more than half of all cutting tools produced worldwide, particularly for machining harder materials at higher speeds. HSS are used in a wide variety of cutting operations requiring complex tool shapes such as drills, reamers, taps, broaches, and milling cutters. Cemented carbides are made by powder metallurgy methods using a number of different carbides, namely, tungsten carbide, titanium carbide, tantalum carbide and niobium carbide, and tough metals of the iron group as binders, mostly, cobalt. The percentage of hard particles in carbide tool materials can vary from about 60 to 90%. Some of the developments in the field of carbides are cobalt enrichment, i.e., increasing the concentration of cobalt binder phase near the surface to improve the toughness within the layer keeping the core material hard. Cermet is the collective name for cemented carbides (CERamic plus METal) that have hard particles based on titanium carbide, titanium carbonitride, and/or titanium nitride rather than tungsten carbide. In comparison to cemented carbides, cermets have higher abrasive wear resistance, high hot hardness and better chemical stability, and low tendency for oxidation wear. However, strength and toughness are lower than cemented carbides.[6]

Ceramic tool materials have found applications principally in turning and milling of cast irons, super-alloys, and in finishing of hardened materials. For cutting tools, two kinds of ceramic composite materials based on aluminum oxide and silicon nitride are used. In general, ceramics exhibit high hardness and chemical inertness and hence, wear by adhesion and chemical erosion is almost eliminated except for few selected materials. PCBN which is also termed simply as CBN is significantly harder than cemented carbide or ceramics and is the only material having exceptional hot hardness. CBN has found its main application in the machining of hard ferrous

materials where temperature in the cutting zone is relatively high due to its high hot hardness. PCD is the hardest material we know of and possess superior abrasive resistance compared to any other cutting materials. However, the biggest limitation of PCD inserts is its chemical affinity to ferrous materials. PCD inserts provide premium performance mainly in the machining of highly abrasive aluminum alloys with higher silicon content, low tensile strength nonferrous or nonmetallic material and magnesium, copper, zinc, and the alloys of these metals.[6]

However, in practice no single material exhibits all of the desirable properties for a tool material as the surface and bulk requirements of a cutting tool during machining are entirely different and conflicting. The surface of the cutting tool should be hard, should have low thermal conductivity and low coefficient of friction and should be chemically inert. On the other hand, the bulk should have high thermal conductivity to quickly carry away the heat penetrated into the cutting tool. The bulk material of cutting tool should be sufficiently stronger and tougher to prevent chipping or fracture of the tool under impact forces. Moreover, temperature generated during dry machining is very high, which the uncoated cutting tools cannot sustain. In order to satisfy the conflicting and different requirements of the tool surface and core, coated cutting tools were developed. Coated cutting tools highly contributed in conservation of coating materials as coating generally requires a very thin film to be deposited on cutting tool substrate, which are generally a few microns thick.

Different types of cutting tool materials employed by the researchers while machining of hardened steels at different levels of work material hardness is shown in Figure 10. It can be seen that mostly coated carbide tools were employed by the researchers while machining of hardened steel having hardness up to 45 HRC. However, it can be seen that machining of hardened steel having hardness beyond 45 HRC were mostly attempted by the researchers under dry cutting conditions using ceramic and PCBN tools. A significant contribution of coated carbide tools can also be seen to machine tough and hard steels having hardness in the range of 45–65 HRC.[3]

1.3.2.3 Cutting Edge Geometry: Macro- and Micro-Geometry of the Insert

From last decade, demands for the precision cutting tools which can enhance productivity and quality of workpieces while finish machining of hardened steels are increasing. For an integral and systematic development of a precision cutting tool, four aspects are considered, namely cutting tool material (substrate), coating technology which can enhance the properties of the substrate, macro-geometry which can ease chip transportation, chip breaking and handling, and cutting edge preparation for specific application.[19] The geometry of the cutting edge, in terms of nominal radius and the microstructuring of the tool face and tool flank has relevant influence on the performance of the precision cutting tool.

In order to define the adequate cutting edge geometry and preparation for a specific application, it is required to consider the following aspects, namely, initial condition of the cutting edge, type of machining process, process parameters, size effect and/or micro-machining aspects, workpiece material, tool material (substrate), cutting tool macro-geometry, and required coating as shown in Figure 11.

For finish machining of hardened steel, the cutting geometry is generally characterized by a large negative rake angle, a reinforced edge chamfer to avoid the chipping off of the cutting edge due to large compressive stresses, and the cutting edge radius which is generally obtained by honing. The tool geometry is generally divided in macro- and micro-geometry of the insert. The macro-geometry of the cutting tool is related to the design and optimization of cutting angles, tool flank and tool face angles, corner radius of the tool, radius of the chamfered corner, and chip-breakers to facilitate the chips flow and evacuation, to support the mechanical and thermal loads generated in the cutting process with adequate lubrication during machining. Cutting edge preparation (micro-geometry of the tool) consists of modifying the micro-topography of the cutting edge in terms of roughness and texture of the flank and face surfaces of the tool so as to enhance the performance and reliability of the cutting tool and the quality of the workpiece.[19]

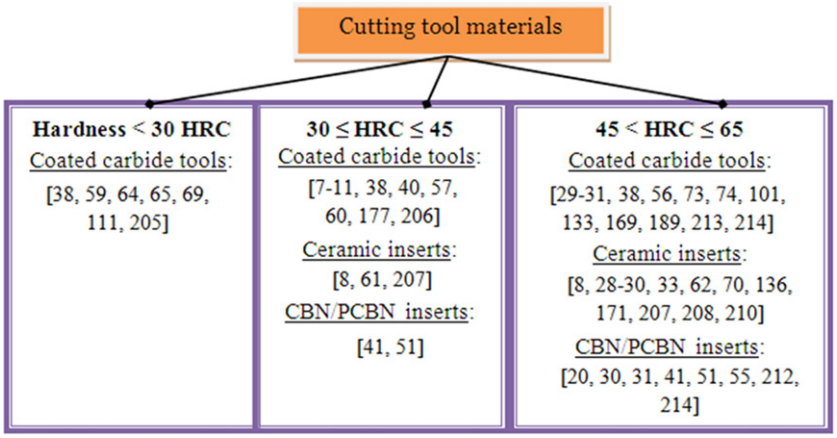


Figure 10 Attempts made by researchers while machining of hardened steel at different levels of hardness using different cutting tool materials. Modified from Ref. [3].

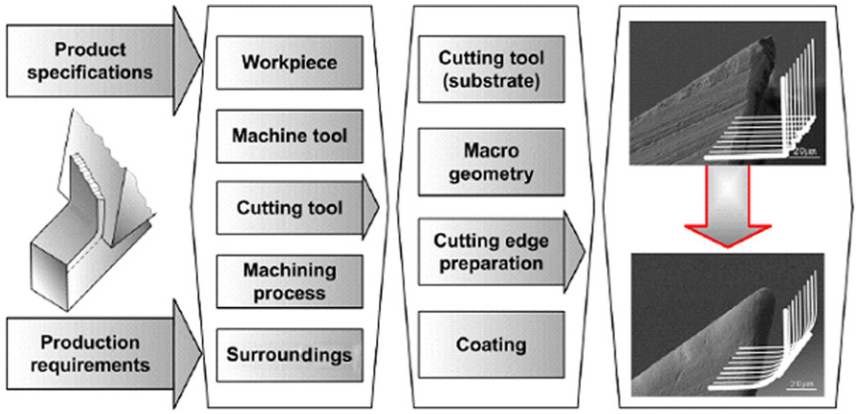


Figure 11 General aspects of cutting edge preparation.[19]

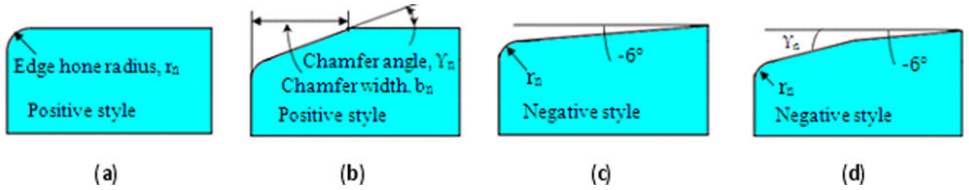


Figure 12 (a) Honed edge, positive insert (b) chamfered and honed edge, positive insert, (c) honed edge, negative insert, and (d) chamfered and honed edge, negative insert.[3]

Macro-geometry comprises of insert size, shape/point angle, and corner radius which is usually determined based on requirement of cutting edge strength (higher corner radius provides more toughness to cutting edge), entering angle versus requirements regarding versatility and cutting power. The micro-geometry usually refers to cutting edge geometry. Two edge geometries are more commonly used while machining of hardened steel, especially when using PCBN inserts. They are honed edges and chamfered and honed edges. In honed edges a small radius is applied to cutting edge and in chamfered and honed edges a chamfer is ground along the edge and the edge is honed afterwards. For PCBN inserts, usually, chamfer angle varies between 10° and 30°, chamfer width varies between 0.05 and 0.25 mm and corner radius varies between 0.015 and 0.050 mm. To have a strong edge, generally, PCBN inserts having negative top rake angle are used. However, to have a stronger cutting edge while machining a hardened steel additional chamfer and edge hone is provided as shown in **Figures 12(a)–12(d)**.[3]

Proper selection and application of cutting edge preparation is one of the basic ingredients as edge geometry and micro-topography of tool surfaces play an important role for a successful development of precision cutting tools.[19] With this view, in recent years, substantial efforts have been made by the researchers in understanding the effects of the edge preparation during finish machining of hardened steels and micro-machining. It has been observed that insert micro-geometry has significant impact on the workpiece surface properties and performance of the cutting tool.[20–24] Ozel *et al.*[22] during their investigations on hard turning with uniform and variable edge design PCBN inserts while turning of hardened AISI 4340 steel observed that variable micro-geometry tool design reduces the heat generation along the tool cutting edge. Further, they observed that lower values of tool wear and plastic strain on the machined workpiece with the use of a variable micro-geometry insert in comparison to uniform micro-geometry insert as shown in **Figure 13**. In another study, Karpat and Ozel[25] experimental and simulation study of analysis concluded that a honed micro-geometry insert results in lower cutting forces, hence lower flank wear values as against chamfered micro-geometry inserts.

Selection of different micro-geometries, namely wiper, chamfer, and hone is depending upon specific application while deciding HPM strategy. In general, a standard radius produces a certain surface finish at a certain feed rate. As against, a wiper radius can produce the same finish profile at twice the feed rate, or twice as good a finish profile at the same feed rate. Leading tool manufacturers have optimized wiper geometry of CBN inserts in terms of lower cutting forces and better surface integrity for specific applications. Virtually, for finish inserts with a chamfer micro-geometry is preferred to enhance the machining performance during machining of hardened steel. In addition, chamfered with a honed edge is less sensitive to chipping and generally performs more consistently.[2] It is reported that high surface quality can be achieved by using wiper insert geometry.[26,27] Galoppi *et al.*[14] observed that PCBN inserts provided with wiper geometry result in lower tool life as against conventional ones. Similar observation was reported when using ceramic inserts.[27] However, Gaitonde *et al.*[28] observed that ceramic inserts provided with wiper geometry result in better tool life and surface finish as against conventional ones.

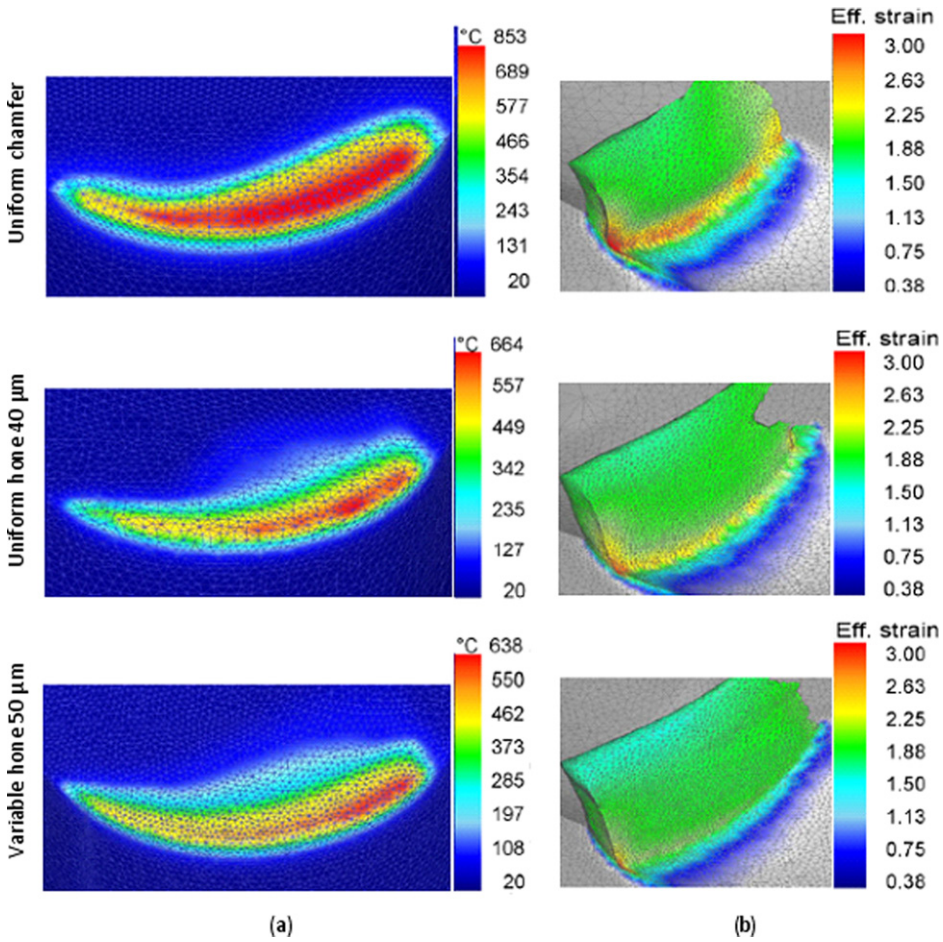


Figure 13 Simulated results of (a) temperature distributions and (b) chip formation and strain fields using PCBN inserts with different micro-geometry.[22]

From **Figure 10**, it can be seen that the researchers performed hard machining (45–65 HRC) using mostly PCBN and ceramic tool materials. However, in view of inflexibility of fabricating PCBN inserts with complex tool geometries and the prohibitive cost of PCBN inserts, a group of researchers performed hard machining using coated carbide tools.[3] Attempts also have been made by the researchers to compare the machining performance of coated ceramic and carbide inserts with uncoated CBN and ceramic inserts when machining hardened steels.[29,30] The work reported shows that the sintered carbide tool is more suitable for turning a workpiece of lower hardness ($\leq$45 HRC). However, coated carbide inserts designed with proper macro- and micro-geometries could become a viable alternative to costly ceramic and CBN inserts while finish machining of hardened steel which is discussed in detail in next section.

1.3.3 Finish Machining of Hardened Steel: Physical Aspects

The researchers have worked on many facets of machining of hardened steel to investigate the effects of cutting parameters, tool materials, and tool geometry on different machinability aspects like, the tool life, surface integrity, cutting forces, chip morphology, and the tool–chip interface temperature. Many of the researchers have ventured to characterize the wear phenomenon under dry and/or semidry and/or flood cooling environment. Compared to SPM, in HPM, the uncut chip thickness is often on the same order of magnitude as tool edge dimension which directly influences the physical aspects of the machining process in terms of cutting forces, the quality of the workpiece (surface finish, surface and subsurface material structure, and RSs), and tool wear and wear mechanisms. With a view to have clear understanding of the changing behavior of physical aspects of finish machining of hardened steel considering the effect of work material hardness, cutting parameters, and tool materials is discussed in following subsections.

1.3.3.1 Cutting Forces

In general, the cutting forces in HPM of a steel component are about doubled than the forces employed while SPM at the same cutting data. High cutting forces also means higher specific cutting force, but, in the context of conventional

machining, in finish HPM, the depth of cut is only of 0.1–0.2 mm which is lower than the tool nose radius, cutting forces are rather low, typically in the range of 50–200 N. However, in roughing of hardened steel the forces are considerably higher, and can reach up to several thousands Newton. There is almost a linear relationship exists between cutting forces and both feed rate and depth of cut.[2,31,32]

Normally, the force conditions in hard turning were different from those in conventional turning, i.e., the radial force was dominant in comparison to the tangential force.[25,33–36] But with variable hone edge radius, the tangential force becomes more than radial force thus increasing the efficiency of cut.[22] However, while finish hard turning of AISI 52100 (100Cr6) steel with CBN 7020 insert, when cutting was limited within the tool nose, radial force component was found to be predominant.[34] Such finding is in contradiction with what is known from conventional turning that the radial force component is 0.3–0.5 times the cutting force component. Consequently, the radial force cannot be neglected in characterizing static and dynamic behaviors of such machining system.[37]

Aneiro *et al.*[31] observed that the depth of cut had the greatest influence on force and temperature. Tool life observed was particularly long for the TiCN/Al_2O_3/TiN-coated carbide tool. However, it was about half of the tool life of PCBN tool at similar cutting conditions, but, claimed that hard machining with coated carbides is justified as PCBN tool prices are, probably, more than twice that of coated carbide price. Suresh *et al.*[32] claimed that hard turning of AISI 4340 (48 HRC) with multilayer CVD-coated TiN/TiCN/Al_2O_3 cemented carbide tool has several benefits over grinding process such as, reduction of processing costs, increased productivity, and improved material properties. The analysis of results concluded that the optimal combination of low feed rate and low depth of cut with high cutting speed is beneficial for reducing machining force. Higher values of feed rates are necessary to minimize the specific cutting force.

Lima *et al.*[38] evaluated the performance of multilayer TiCN/Al_2O_3/TiN-coated carbide inserts in order to investigate the applicability of these inserts to machining of hardened AISI 4340 steel at different levels of hardness 23, 35, 42 and 50 HRC, respectively. Their study concluded that coated carbide tools were unable to machine 50 HRC workpiece, even at light metal removal rates. Experimental results indicated that the relationship between the hardness of the work material and the machining force was not straightforward. The cutting force presented higher values followed by the thrust and feed force. Luo *et al.*[39] observed higher cutting forces for the ceramic tool than those of the CBN tool during their investigation of the variation of the cutting forces with the hardness of the work material. They found that the principal cutting force and thrust force decreased with the increase of hardness, and at about HRC50, the cutting force starts to increase.

Chinchanikar and Choudhury[9,11,40] also observed higher cutting forces for harder workpiece and for CVD-applied multilayer MT-TiCN/Al_2O_3/TiN-coated carbide tool in comparison to PVD-applied single-layer TiAlN-coated carbide tool during machining of hardened AISI 4340 steel at different levels of hardness (**Figure 14**). However, cutting forces were observed by them to be reduced and become nearly equal to that of the softer material at higher cutting speed when coupled with higher feed and higher depth of cut. Their study of analysis concluded that lower cutting forces employed for PVD-coated tools could be attributed to a positive cutting edge style employed for PVD-coated tool in comparison to negative, stable cutting edge style for CVD-coated tool (**Figure 15**) and the characteristics of the PVD-applied coating process which produces very smooth and bright coating surface with a low coefficient of friction between the tool face and the chips.

Aouici *et al.*[41] experimental study on hard turning of AISI H11 steel, hardened to 40, 45, and 50 HRC, respectively, using CBN tools also showed that the cutting force components were influenced principally by depth of cut and workpiece hardness. In HPT, higher cutting forces employed at low cutting speeds were observed to be reduced when cutting speed was increased.[42–45] This may be due to the fact that at high speeds the cutting temperature is very high that results in thermal softening of the workpiece material thereby reducing the cutting forces required for machining. Gaitonde *et al.*[28] explored the consequences of machining parameters on various machining responses in view of hard turning as a potential alternative to costly grinding operations. Results of their experimental analysis during turning of high chromium AISI D2 cold work tool steel using wiper ceramic inserts concluded that the machining force was highly sensitive to feed rate and machining time. The specific cutting force was highly sensitive to machining time while higher values of feed rates were necessary to minimize the specific cutting force.

In finish machining of hardened steel, the undeformed chip thickness is comparable to the cutting edge radius of the

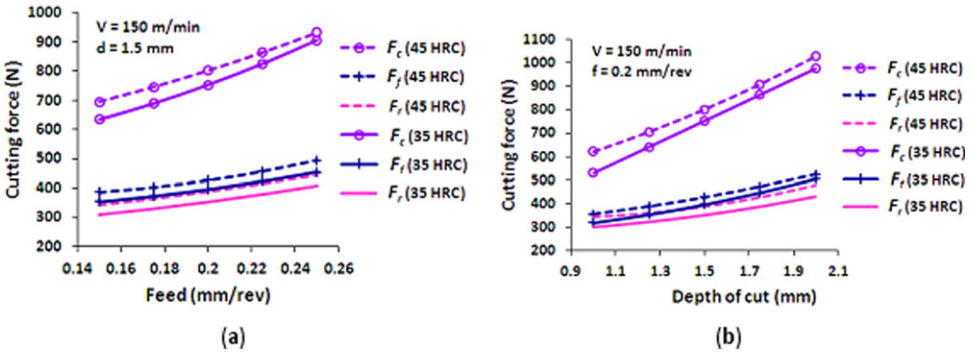


Figure 14 Effect on cutting forces (F_c: tangential force, F_f: feed force and F_r: radial force) by (a) feed and (b) depth of cut.[11]

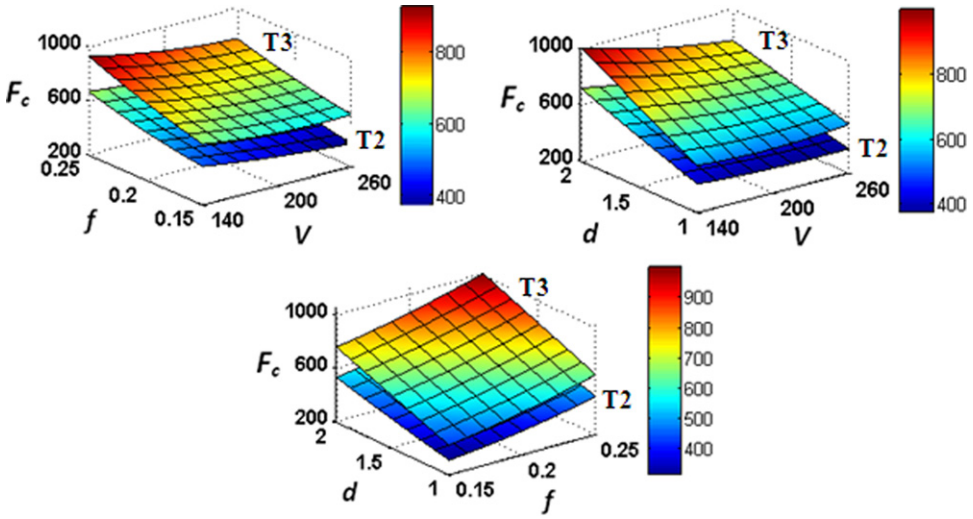


Figure 15 3D response surfaces showing effect of cutting conditions on tangential force (letter T2 and T3 shows response surfaces for PVD-coated and CVD-coated tools, respectively).[40]

tool and grain size of the material which consumes more energy as a round cutting edge of the tool tends to remove a solid grain of the workpiece material. As against, in macroscale machining, the cutting edge of the tool is assumed to be perfectly sharp. Furthermore, it is assumed that there is no contact between the cutting tool and workpiece at the tool flank due to sharp cutting edge and hence, frictional force at the interface is therefore neglected. However, there exists a friction zone at the tool flank in case of finish machining of hardened steel due to elastic recovery of the newly machined surface of the workpiece at the tail end of the of the cutting edge. Hence there exist three deformation zones named primary, secondary, and tertiary deformation zones as against primary and secondary deformation zones in case of macroscale machining.[46]

The force required to overcome tertiary deformation zone does not contribute to the chip removal and hence is commonly named as plowing force. The plowing force is proportionally very small compared to the forces generated in the primary and secondary deformation zones due to the large values of the undeformed chip thickness employed in the macroscale machining. However, in case of finish machining of hardened steel, the magnitude of the plowing force becomes proportionally considerable due to the lower value of overall cutting force and hence can no longer be neglected.[46] With this view, Bhokse *et al.*[47] investigated varying contribution of chip formation and plowing cutting forces at different cutting conditions during hard turning of AISI 52100 alloy steel. They found contribution of chip formation cutting force in the range of 60–70% in total cutting force in comparison to plowing force. However, at lower values of depth of cut, they observed plowing forces has become predominant as compared to chip formation forces. Further, they found that variation in the chip formation force was more prominent in comparison to plowing cutting force with the increase in cutting speed, feed, and depth of cut.

From the available literature it has been observed that sufficient studies were made on the machining of hardened steel alloys. Several studies are available wherein cutting parameters were optimized for surface roughness or cutting force(s) or both. However, in most of the studies, tool life being an important factor was not considered while optimizing the cutting conditions. Experimental observations from several studies indicate that all the three components of cutting forces are higher for harder work material. However, forces were observed to be reduced and become nearly equal to that of the softer material at higher cutting speed when coupled with higher feed and higher depth of cut. In almost all the studies cutting forces get affected mostly by depth of cut (nearly 60–70% contribution) followed by feed (nearly 25–30% contribution) and cutting speed has little influence. In finish machining of hardened steel (depth of cut: 0.1–0.3 mm, less than tool nose radius), the radial component of cutting force has been observed to be largest in magnitude followed by the tangental and feed forces. Moreover, the magnitude of the plowing force becomes proportionally considerable in case of finish machining of hardened steel. The contribution of chip formation cutting force observed in the range of 60–70% in total cutting force. However, at lower values of depth of cut, plowing force has become predominant as compared to chip formation force. More investigations on force and friction conditions through modeling attempts are required to be taken up to characterize the static and dynamic behaviors of HPM process.

1.3.3.2 Chip Formation

Chips produced during machining significantly influence the surface finish of the workpiece, tool life, and overall cutting operation. A group of researchers reported that the formation of chips (form of chip) was strongly influenced by the work material hardness, type of tool, and cutting conditions, especially the feed rate.[9,39,48,49] More closely curled chips are produced in case of harder workpiece, which are hard to break and might be one of the reasons for employing higher cutting

forces for harder workpiece as discussed in Section 1.3.3.1.[9] Jerold and Pradeep Kumar[50] also observed higher cutting forces for closely curled chips in comparison to loose arc chips while turning AISI 1045 steel. In general, snarled long ribbon-chips or snarled tubular-chips are produced at low feed rate when turning steel hardened to 35 HRC and at higher feed rate, short spiral or loose arc chips are obtained when turning softer workpiece (35 HRC) and short helical chips when turning harder workpiece (45 HRC).[9]

Chips form and shape (morphology) produced during machining also significantly changes with the machining time or with the progress of tool wear and has a prominent effect on the quality of the workpiece produced.[48] Attainment of surface finish during machining of hardened steel can be explained in terms of chip morphology. The typical free and back surfaces of the chip produced using two different coated tools (T2 and T3) are shown in **Figures 16(1)–16(8)**. More or less polished back and smooth free surfaces can be seen on the chip produced when using PVD-coated tool T2. However, rough back surface showing some parallel stripes and damaged free surface of the chip can be seen when using CVD-coated tool T3. Polished and bright back surface of the chip obtained when using coated tool shows that minimum friction was offered by tool T2 during machining, which resulted in lower cutting forces and hence, better surface finish as against the higher values of cutting forces and surface roughness when using CVD-coated tool (T3).[9]

It has been observed that when steel in the hardness range of 10–50 HRC were cut, continuous chip was produced with a decrease in cutting forces with increase in hardness in this range of hardness.[51] Increase in steel hardness (10–50 HRC) raises the chip–tool interface temperature which softens the steel resulting in an increase in the shear angle in turning. This leads to a decrease in the chip thickness reducing the tool/chip contact area and hence, contributes to the reduction in cutting force. However, when the hardness exceeds 50 HRC, chip segmentation appears and the cutting forces increase. When harder material is machined, the fracture strain becomes lower, and when it becomes lower than a certain limit, fracture becomes predominant and concentrated shear occurs intermittently at the shear area.[51] Segmented chips are also produced when machining softer material at higher cutting speeds as shown in **Figure 17**. SEM micrographs of the chips of the EN 24 steel of hardness 40 and 45 HRC are shown in **Figures 18(a)** and **18(b)**. It can be seen that the chip of EN 24 steel with 40 HRC is smooth and without serrations whereas the chip of EN 24 steel with 45 HRC has serrations.[49]

1.3.3.3 Tool–Chip Interface Temperature

Heat generated in machining operation is an important factor in addressing metal cutting issues like dimensional accuracy, surface integrity, and tool life. In machining of hardened steels, higher workpiece hardness generates higher temperatures in the cutting zone which have a very strong influence on the workpiece surface quality and the tool wear rate. Therefore, measurement of the chip–tool interface temperature during machining and develop a mathematical model to establish the effect of various key factors of machining on temperature will be extremely valuable and represents a key issue.[10]

Over the past century, several conduction techniques like tool–chip thermocouple, embedded thermocouple, thermocolors, and radiation techniques like infrared thermometry, pyrometry have been developed to evaluate the chip–tool interface temperature arising in the cutting zone during machining. However, tool–work thermocouple technique is widely used during metal cutting due to its ease of implementation and low cost as compared to other techniques as shown in **Figure 19(a)**.[10,31,52,53] In order to establish the relationship between the electromotive force (emf) generated and the corresponding temperature, a schematic of calibration setup is shown in **Figure 19(b)**. A tool–work thermocouple

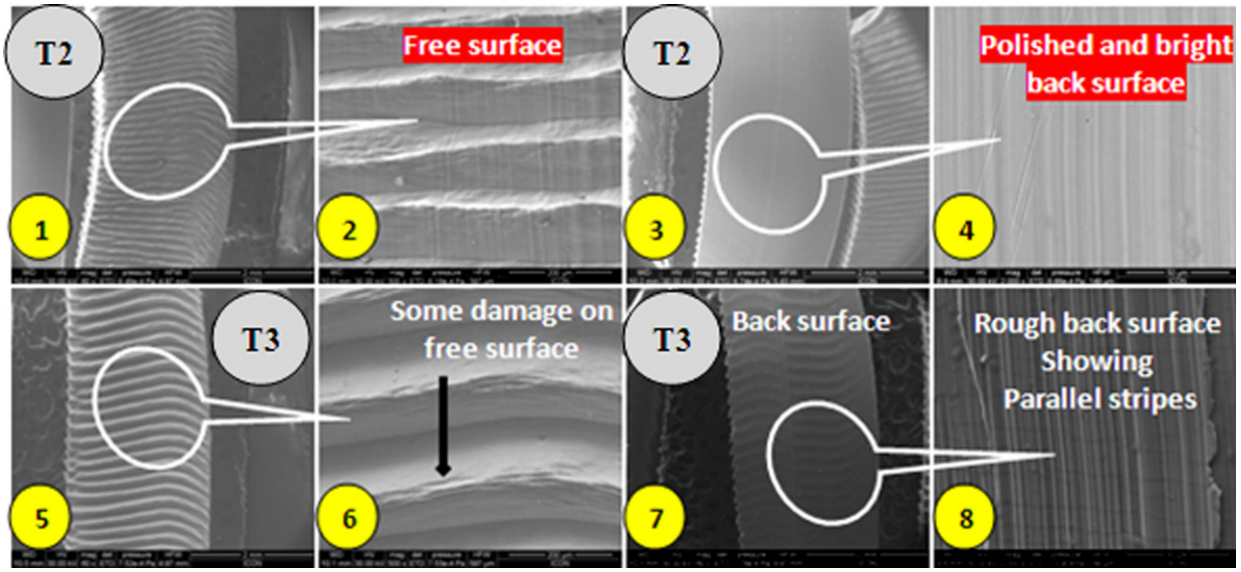


Figure 16 SEM images of the chip surfaces (1) (2) free surface (using T2), (3) (4) back surface (using T2), (5) (6) free surface (using T3), and (7) (8) Back surface (using T3).[9]

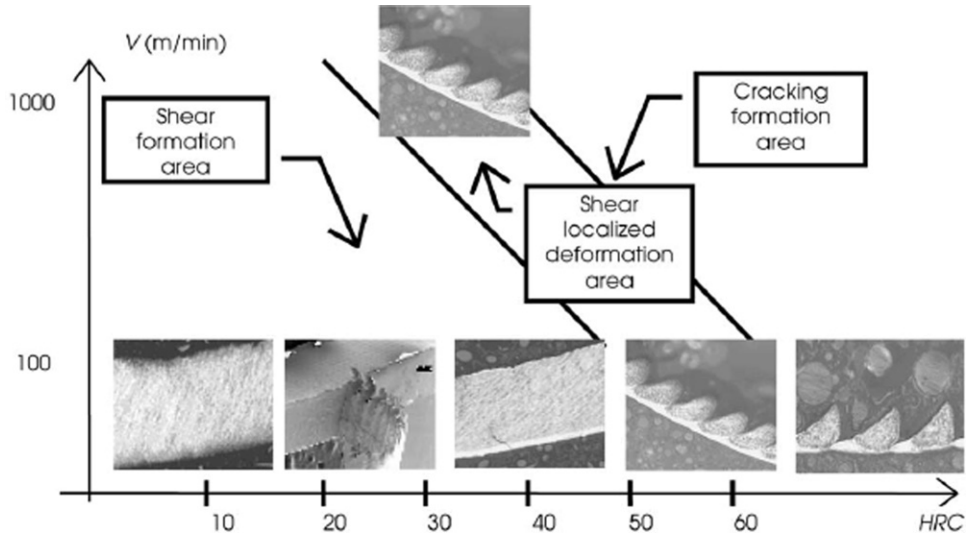


Figure 17 Chip morphology according to the hardness and the cutting speed.[51]

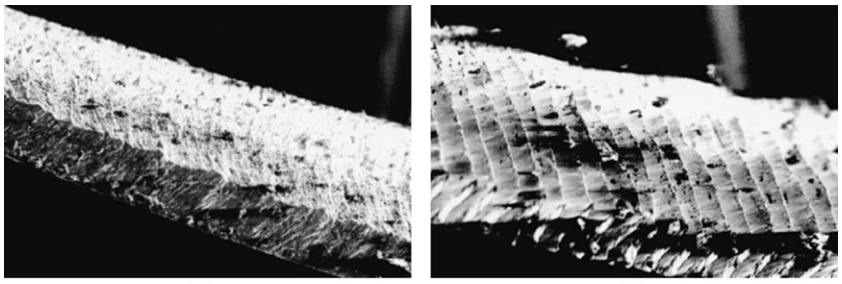


Figure 18 SEM micrograph of the chip of EN 24 steel with (a) 40 HRC and (b) 45 HRC.[49]

junction is formed using a tool and a long continuous chip. The tool and chip junction is heated at different temperature which can be measured by using standard K-type thermocouple wire connected to temperature indicator. Emf generated between the hot and cold junction can be monitored by a digital multimeter. The linear relationship obtained for AISI 1045 and AISI 304 workpieces when using different cutting tools is shown in **Figure 20(a)**.

The chip–tool interface temperature was observed to be more influenced by thermal properties of the workpiece and tool coating.[10,53,54] Most of the studies concluded that the tool–chip interface temperature increases with the increase in cutting speed, feed, and depth of cut. However, interface temperature decreases with the increase in tool nose radius.[31,36,52] Chinchanikar *et al.*[10] observed that the tool–chip interface temperature is higher for harder work material which gets affected mostly by cutting speed followed by feed and depth of cut having the negligible influence on chip–tool interface temperature. In cutting process analysis, values of the cutting speed are often replaced by corresponding values of the thermal number. This is because the cutting speed influences the contact temperature and cutting energy more intensively than other process variables.[54]

It can be seen (**Figure 20(b)**) that the temperatures calculated for the same values of thermal number differ substantially for uncoated and coated tools, especially in the case of stainless steel. At higher values of the thermal number, the reduction of the average tool–chip interface temperature occurs more intensively when a fourfold coating is applied. The main reason why the maximum temperatures occur at different thermal numbers is that the diffusivities of steels used are different.[54]

Noncontact radiation techniques like infrared thermometry, pyrometry have been used to evaluate the chip–tool interface temperature. However, accuracy of the results depends upon the exact values of the emissivity of the cutting tool material and temperature of the radiating surface. Further, when the chip flows at a high speed along the rake face, these methods give erratic results during the measurement of exact temperature on the rake/flank face with the help of infrared rays due to accessible issue. Metallographic techniques like observing the microstructural changes of the cutting tool/workpiece after cutting can be used to find the temperature near the rake face. However, this technique is laborious and time consuming. Further, this technique is applicable to only those tool materials that exhibit a change in the microstructure with temperature.[10]

The finite element method (FEM) simulations of Cohelo *et al.*[55] study showed that temperature at the tool–chip interface was stable and as high as 800 °C when using TiAlN-based

coated and uncoated PCBN tools (Figure 21) while finish turning of hardened AISI 4340 steel (52 HRC).[55] The simulation results of their study indicate that the temperature at the PCBN substrate is always lower than at the surface. The coating layer not only prevents heat from going to the substrate, but it works as an additional barrier to keep the substrate at lower temperature. As the presence of coating layer creates an additional thermal resistance between workpiece and the tool, resulting in lowering temperature at the substrate, demands for coated cutting tools while finish machining of hardened steels are continuously increasing. However, tool wear patterns and wear mechanisms of different coated tools have significant effect on quality of workpiece machined while machining of hardened steels is discussed in the following section.

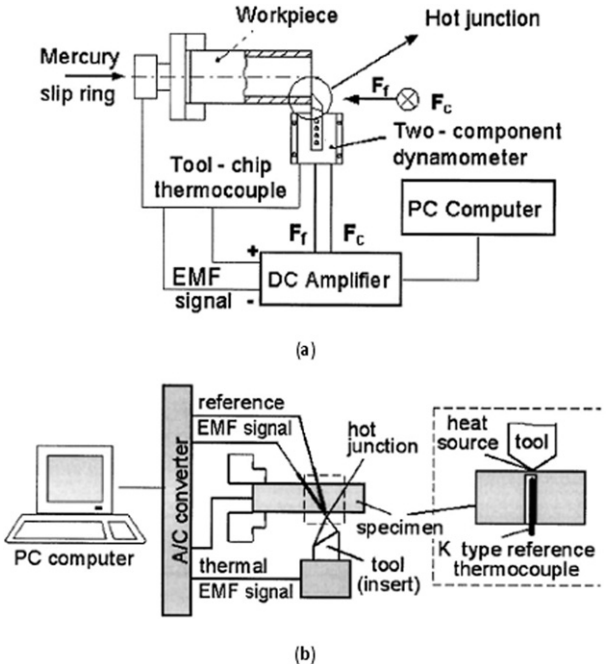


Figure 19 (a) Tool–work thermocouple setup and (b) thermoelectric calibration setup.[54]

1.3.3.4 Tool Wear Patterns and Mechanisms

Finish machining of hardened steels having hardness in the range of 50–65 HRC is mostly carried out using uncoated/coated PCBN tools as they exhibit better tool life at toughest cutting conditions due to their high and stable hardness,[13] and its lower solubility for steel material of the machined workpiece.[14] However, in view of inflexibility of fabricating PCBN inserts with complex tool geometries and the prohibitive cost of PCBN inserts, More *et al.*[56] investigated and compared the machining performance in terms of tool wear, surface roughness, and cutting forces of the cBN–TiN-coated carbide inserts with commercially available PCBN-tipped inserts during turning of hardened AISI 4340 steel (53 HRC). They observed less crater wear when using cBN–TiN-coated inserts than that of the PCBN inserts because of the lubricity of TiN coating layer on the cBN–TiN inserts. They also observed a good surface finish and a tool life of about 18 min per cutting edge as against 32 min with PCBN inserts. The cutting forces for the cBN–TiN-coated carbide inserts were observed slightly higher than those of the PCBN inserts due to a slightly larger nose radius and a rough surface associated with the cBN–TiN-coated inserts. A cost analysis performed by them, based on a single cutting edge, shows that the cBN–TiN-coated carbide tools are capable of reducing machining costs, and, therefore, will be an important complement to PCBN compact tools for finish machining of hardened steels.

Chinchanikar and Choudhury[9,57] also observed better tool life by CVD-applied multilayer MT-TiCN/Al_2O_3/TiN-coated carbide tool due to thick coating and claimed that the protective Al_2O_3 oxide layer formed during cutting has protected the CVD-coated tool from severe abrasion at elevated temperatures. In HPT with PCBN tools, the wear mechanisms

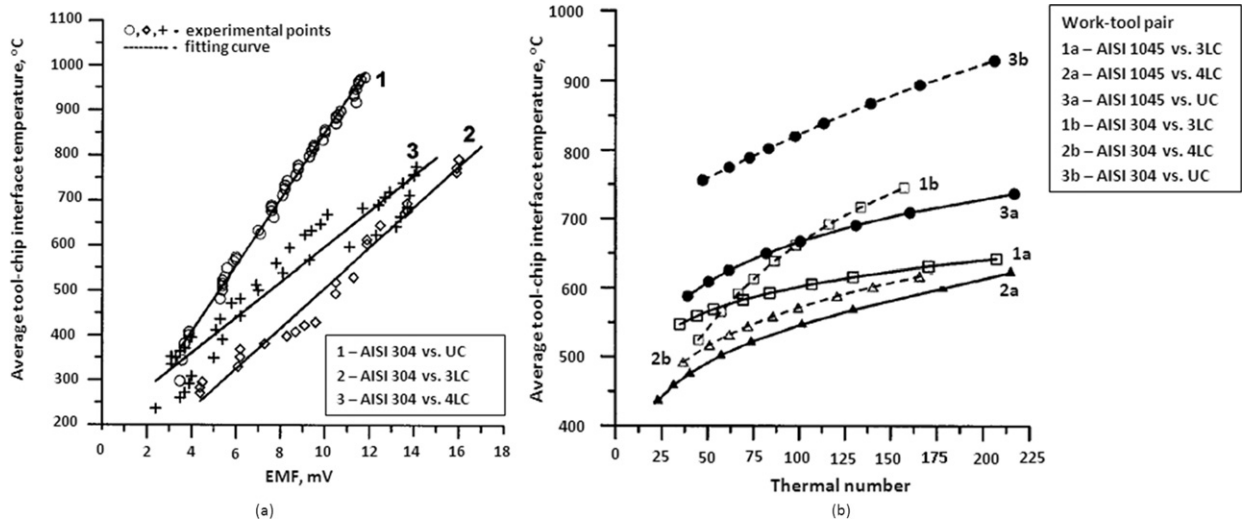


Figure 20 (a) Thermoelectric calibration plots for AISI 304 and (b) dependence of tool–chip interface temperature on thermal number (tool codes: P20 uncoated carbide-UC; TiC/Al_2O_3/TiN-3LC: TiC/TiCN/Al_2O_3/TiN-4LC.[54]

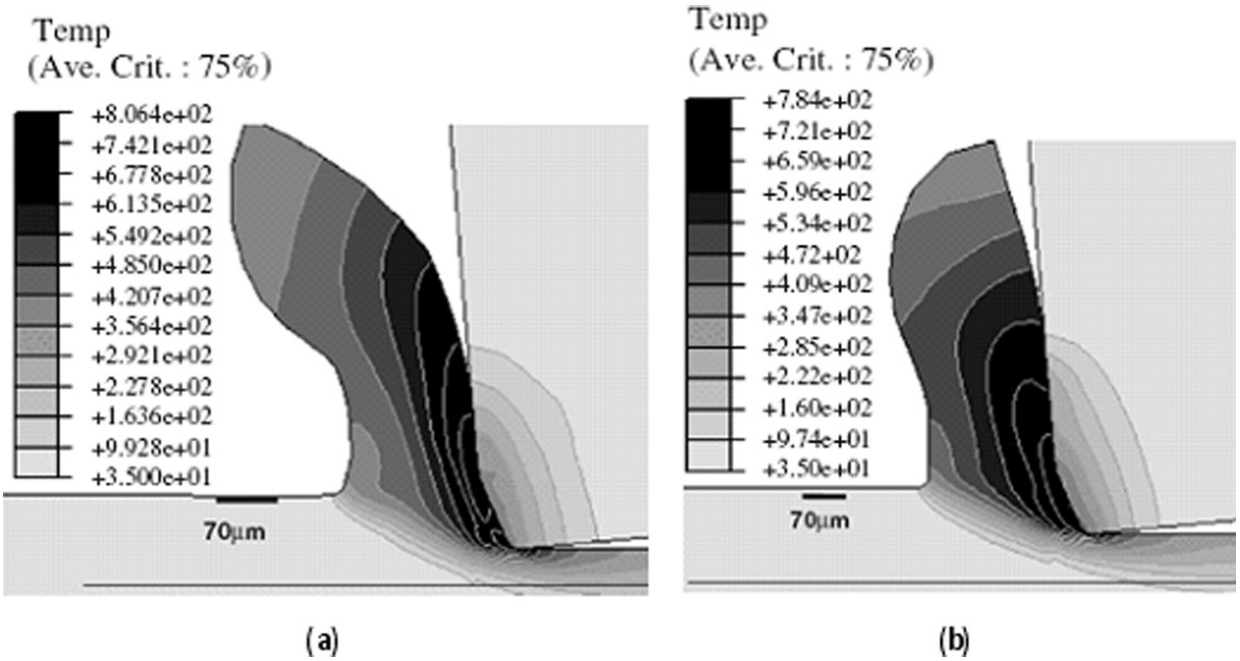


Figure 21 Temperatures obtained from finite element method simulation for (a) uncoated PCBN tool and (b) TiAlN-coated PCBN tool.[55]

depend not only on the chemical composition of the PCBN, and the nature of the binder phase, but also on the hardness value and above all on the microstructure (percentage of martensite, type, size, composition of the hard phases, etc.) of the machined work material.[51] Park and Kwon[58] experimental study also concluded that the hardness of the coating is the most important requirement to resist flank wear against abrasion. A group of researchers proposed the tool life model in a generalized form of the extended Taylor's law as a function of the cutting parameters and of the workpiece hardness. They found that cutting speed followed by the work material hardness as having the most significant effect on flank wear progression during machining of hardened steel.[7,40,48,51,57,59,60]

Coelho *et al.*[55] claimed that TiAlN-nanocoated PCBN tool is a better choice while finish turning of hardened AISI 4340 due to a combination of high hardness and the presence of an oxidizing layer produced by TiAlN coating at the lower cutting temperature range as against cutting temperature range of higher than 1000 °C required for AlCrN coated PCBN tool. They observed that the use of coatings on PCBN substrate bring benefits to tool life, extending it up to 38%, from 17.8 to 24.5 km, using TiAlN-nano coating, within the tested cutting conditions. With the other coatings employed by them, TiAlN and AlCrN, the tool life was extended up to 21 and 11.8%, meaning to 21.6 and 19.9 km, respectively, within the tested cutting conditions. The higher hot hardness of the TiAlN-nano at the temperature on the interface, have delayed tool wear, lasting longer than TiAlN. They found that the performance of AlCrN was not as good as the other coatings, since within the cutting conditions; temperature was below its oxidizing range. The typical wear pattern observed by them for different tools is shown in **Figure 22**.

Several attempts have been made by machining of hardened steels using cermet and ceramic tools. Noordin *et al.*[61] obtained longest tool life when cutting with cermet insert at low cutting speed and feed rate during dry turning of martensitic stainless tool steel (43–45 HRC). However, in all other instances, multilayer carbide inserts outperformed cermet inserts. Lima *et al.*[62] observed higher flank wear rate with mixed alumina inserts when using a cutting speed of 220 m min^{-1} and feed rate of 0.15 mm rev^{-1}. Further, they observed in contrast to the coated carbide and PCBN tools tested against AISI 4340 steel, that the mixed alumina tool failed by spalling when machining under higher cutting conditions. Ghani *et al.*[63] observed that the cutting edge of TiN-coated carbide tools take longer time from the crack initiation to fracturing than that of uncoated cermets tools, especially at higher values of cutting speed, feed, and depth of cut. However, at lower values of cutting speed, feed, and depth of cut, uniform and gradual wear on the flank face of uncoated cermets was observed by them in comparison to the TiN-coated carbide tools during end milling of hardened AISI H13 tool steel (50 ± 3 HRC).

Sufficient efforts have been made by the researchers to understand the wear mechanisms of cutting tools while machining of hardened steel. Avila *et al.*[64] experimental results during turning of quenched and tempered AISI 4340 steel with coated tools showed the presence of three wear mechanisms, namely, one possessing a lower wear rate, related to the wear of the coating; the second one, more severe, associated with the wear in the absence of the coating in the crater wear region, and the third one associated with the wear of the uncoated tool. They found the highest wear rate with the TiAlN followed by TiN- and TiCN-coated carbide tools and claimed that the high amount of aluminum in the coating, which resulted in a high hardness and low toughness film, is mainly responsible for the high wear rate. Moreover, they claimed that comparatively lower adhesion of the TiAlN film to the substrate also contributed to its poor performance.

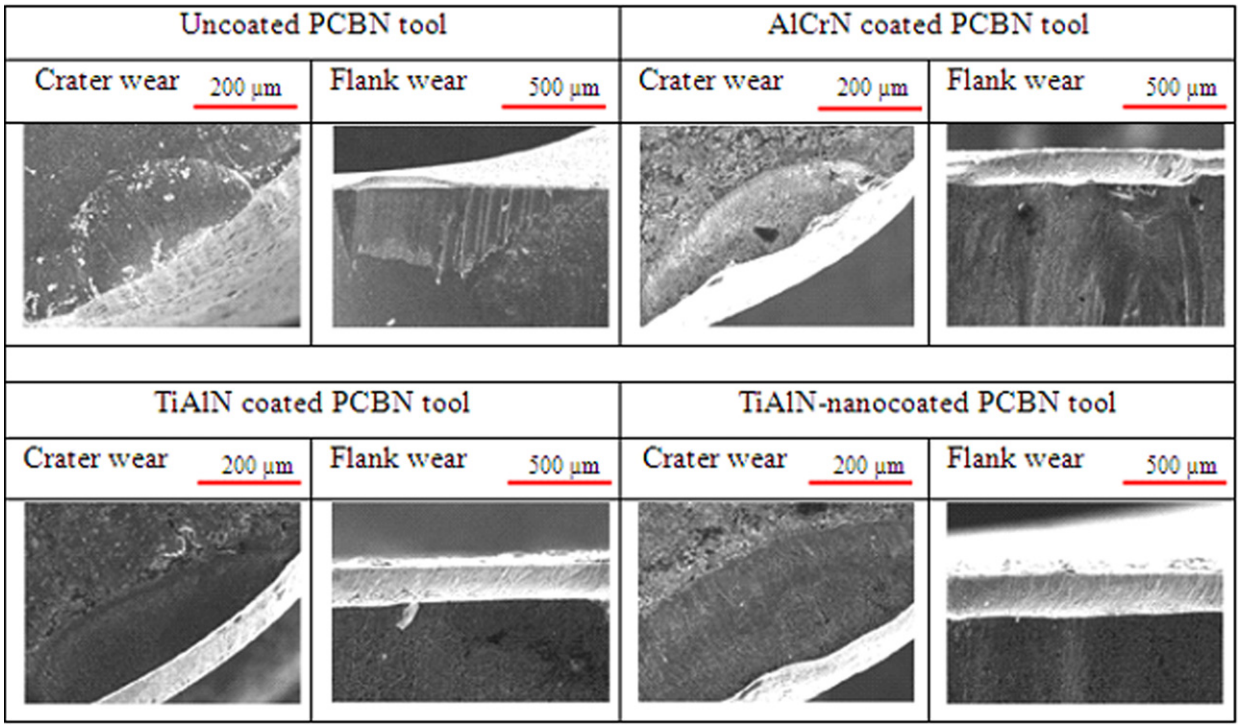


Figure 22 Aspect of cutting edges after wear (finish turning at cutting speed of 150 m min^{-1}, feed and depth of cut of 0.07 mm rev^{-1} and 0.2 mm, respectively).[55]

Khrais and Lin[65] also observed that flank wear proceeded through three levels: initial break-in wear, gradual wear, and catastrophic wear and claimed that the TiAlN-coated carbide inserts demonstrate best performance under dry condition with any cutting speeds less than 260 m min^{-1} while turning of hardened AISI 4140 steel. Chubb and Billingham[66] systematic examination of worn inserts using optical and scanning microscopy revealed that the cutting performance was initially controlled by wear on the flank face which was predominantly of an abrasive type, but was superseded on coating breakthrough by a combined diffusion/abrasion mechanism. On the rake face they observed coating breakdown due to thermal cracking that resulted in removal of small regions of the coating, which in turn allowed direct substrate–metal interaction and hence, enhanced diffusion wear.

Poulachon *et al.*[51] during their study on wear mechanisms of PCBN tool, obtained the progression of the tool wear for different cutting conditions as shown in **Figure 23**. They observed crater wear appears first when the cutting speed is higher. They claimed that the binder of the tool is abraded by hard carbide particles of 100Cr6 steels (i.e., chromium carbides) which leads to CBN grains detachment from the bond. Moreover, an increase in cutting speed leads to an increase in cutting temperature which thus, accelerates the tool wear rate.

Luo *et al.*[39] experimental results of analysis during dry turning of AISI 4340 also concluded that the main wear mechanism for the CBN tools was the abrasion of the binder material by the hard carbide particles of the workpiece. However, adhesive and abrasive wear were observed by them as dominant wear mechanisms when using the ceramic tools. They observed that the carbide tool was unable to cut for more than 5 min due to fracture of the cutting edge while turning a workpiece having hardness above 45 HRC. Moreover, they observed usable cutting time of less than 1 min as carbide tool failed almost immediately at a higher work hardness of 55 and 60 HRC. The work reported shows that the sintered carbide tool is more suitable for turning a workpiece of lower hardness.

Chinchanikar and Choudhury[9,57] investigated the tool wear patterns and wear mechanism(s) considering the effect of workpiece hardness, cutting parameters, and type of coating. They observed a severe damage at the nose of the tool, pitting on the rake and flank faces resulting in exposing the tool substrate, coating delamination, crater wear and metal adhesion at the end of cutting when turning AISI 4340 steel (45 HRC) using CVD-coated MT-TiCN/Al_2O_3/TiN-coated carbide tool (**Figure 24(a)**). The fine abrasive marks and metal adhesion can be seen from the magnified view of **Figure 24(a)** as shown in **Figure 24(b)**. After a brief cutting, this adhered metal gets dislodged and comes out as a loose fragment along with the coating material, resulting in pitting on the flank and rake faces, subsequently exposing the tool substrate.

However, adhesion was observed as a prominent wear mechanism when turning comparatively softer AISI 4340 steel (35 HRC).[9,57] Removal of the adhered workpiece material from the tool surface due to fast flowing chips is responsible for fragmentation of tool material. On the other hand, abrasion was observed as a prominent wear mechanism when turning softer material at higher cutting speeds.[9] **Figure 24(c)** reveals deep abrasion marks covered with metal adhesion on flank face of MT-TiCN/Al_2O_3/TiN-coated carbide tool. This adhered metal eventually being plucked from the tool surfaces

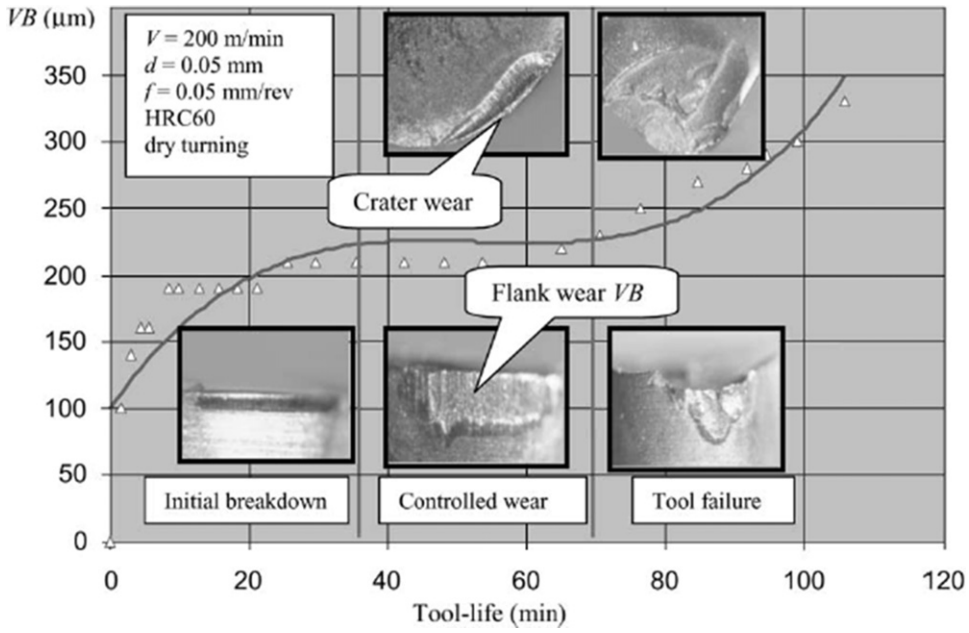


Figure 23 Tool wear rate progression.[51]

under high sliding speed resulted in forming shallow pockets as seen in Figure 24(d). Removals of the hard particles from the tool flank surface which are responsible for cutting are shown by marked circles in Figure 24(e). These hard particles get entrapped between the machined surface and the tool while machining, subsequently rub the flank surface of the cutting tool indicating the signs of three-body abrasion wear.[9]

Rapid deterioration of the cutting edge, eventually leading to catastrophic failure, is normally observed just after the removal of the coating layer(s), especially, when using PVD-applied single-layer TiAlN-coated carbide tool.[9,57] Comparatively smooth flank surface of PVD-coated single-layer TiAlN carbide tool (Figure 24(f)) as against the rough flank surface of CVD-coated multilayer MT-TiCN/Al_2O_3/TiN carbide tool after delamination of the coating (Figure 24(e)), shows better adhesion strength of the MT-CVD TiCN (bottom most) coating layer to the tool substrate. Complete spalling of the coating from the flank and rake faces and plastic deformation of the cutting edge can be seen from Figure 24(f). High compressive stresses clubbed with high cutting speed results in plastic deformation of the cutting edge which affects the dimensional accuracy and quality of the machined surface. A rough surface in the crater wear region (Figure 24(f)) indicates a severe wear mode which might have occurred by diffusion and adhesion wear mechanisms that are active on the rake face. Moreover, interdiffusion of tool and workpiece elements (Fe and Co) resulting in weakening of the binder. This causes fracturing of small elements of the tool which are being carried away along with the chips resulting in the formation of rough surface in the crater.

In the machining of hardened steel alloys, tool wear adversely affects the surface integrity of the machined surface and dimensional accuracy and is need to be considered while optimizing the cutting conditions for cutting forces and surface finish. Surface integrity of the machined surface in terms of the surface finish achieved, RSs, white layer effect, dimensional accuracy, and optimization studies are discussed in following sections.

1.3.3.5 Surface Integrity

It is well acknowledged that the functional performance of a manufactured component is heavily influenced by the quality and reliability of the surface produced in terms of topography and surface layer characteristics. With a view to address the growing demand on component performance, reliability and durability, sufficient efforts have been made by the researchers to investigate the effect of the process parameters and type of tool on the nature of the surface alterations produced and hence, on product's functional performance during machining of hardened steel.[67] Surface integrity is the surface condition of a workpiece after being manufactured and is generally expressed in terms of topography characteristics and surface layer characteristics. The topography includes surface roughness, waviness, form errors, and surface flaws. The surface layer characteristics include local plastic deformation, RSs, cracks, hardness, and phase changes. Surface integrity of the machined component is drastically deteriorated with the use of improper selection of process variables during machining, dull tools, improper amount, and type of coolant or lubrication.[68]

1.3.3.5.1 Surface roughness

Surface roughness is the measure of the finely spaced micro-irregularities on the surface texture which is composed of three components, namely roughness, waviness, and form. Every machining operation leaves characteristic evidence on the machined surface. Ideal surface roughness is a function of only feed and geometry of the cutting tool which can be achieved in the absence of the built-up edge, chatter, and inaccuracies in the machine tool movements. The theoretical surface

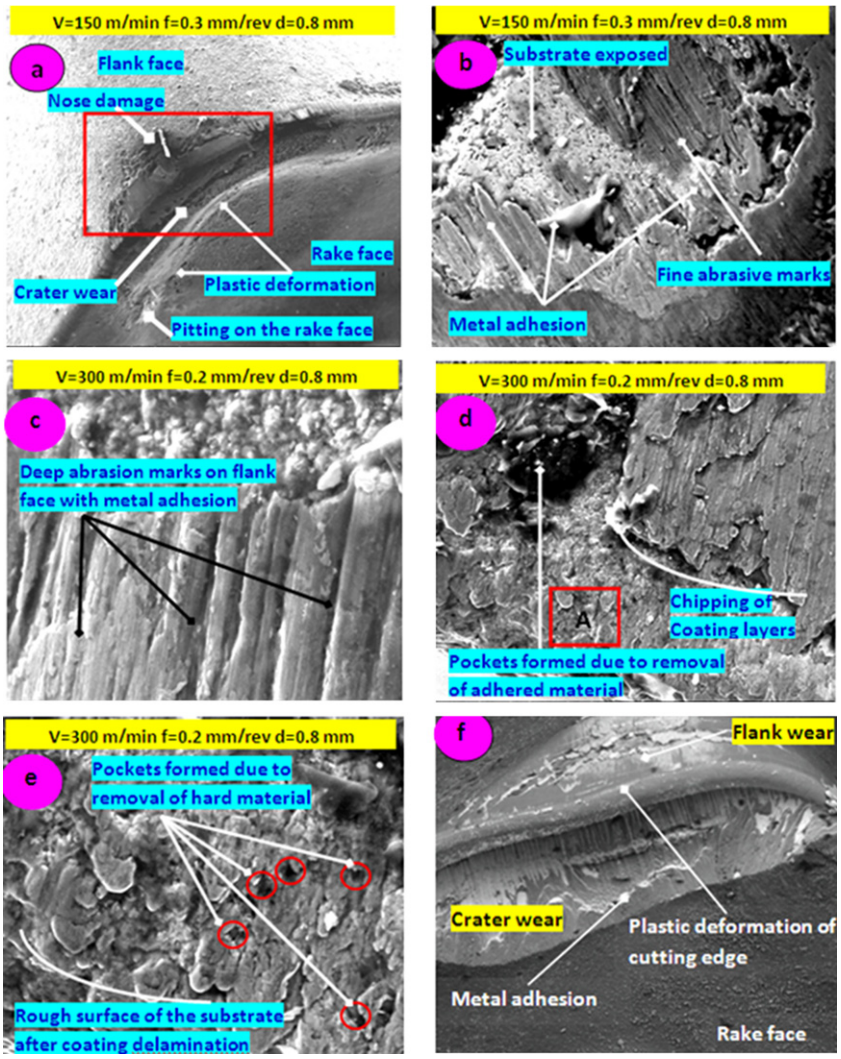


Figure 24 SEM images of (a) (b) CVD-coated tool and its magnified (workpiece with 45 HRC), (c), (d), and (e) flank face, clearance face and its magnified view (workpiece with 35 HRC hardness), and (f) PVD-coated single-layer tool (workpiece with 35 HRC hardness).[9]

roughness parameter, R_a, can be given as $R_a = (0.0321\ f^2)/r_\varepsilon$, where, '$f$ 'is the feed rate in mm rev^{-1} and 'r_ε' is the insert radius.[56]

The ability of a manufacturing operation to produce a surface roughness depends on many factors such as the machining variables (cutting speed, feed, and depth of cut), the tool macro- and micro-geometries (nose radius, rake angle, side cutting edge angle (SCEA) and type of cutting edge such as chamfered, honed, and a combination of chamfered and honed), workpiece and tool material combination and their mechanical properties, quality and type of the machine tool used, auxiliary tooling and the amount and type of lubrication at the point of cutting and vibrations present between the workpiece, machine tool and cutting tool. A small change in any of the above factors can have a significant effect on the surface produced.

Surface roughness is an important characteristic of the surface integrity of machined parts, and correlated to the tool wear as well as feed rate.[69,70] Dogra *et al.*[71] during their investigation on continuous and interrupted finish hard turning observed that the R_a values with the CBN tool were in the range of 0.3–0.7 μm and with carbide inserts they were in the range of 0.35–1.3 μm with the selected tool wear criterion ($VB_{max} = 200$ μm), indicating that the roughness values are comparable with grinding (less than 1.6 μm). **Figures 25(a)** and **25(b)** show the values of surface roughness obtained by them with progression of machining time in continuous and interrupted turning, respectively, at different cutting speeds. It can be seen that the roughness obtained with CBN inserts in continuous turning increased marginally with the progression of machining time, while with carbide inserts it increased rapidly just after the tool wear criterion reached. However, at higher cutting speed ($V = 190$ m min^{-1}), significant increase in the surface roughness can be seen when using CBN tool. At higher cutting speed, formation of shallow pockets on the cutting edge was observed by them, which altered the shape of the tool nose, causing increase in roughness value. As against, at higher cutting speed, a drastic increase in the roughness

value can be seen with carbide tool due to rapid wear and chipping off of the tool. Under all the cutting conditions tested, they observed higher values of the surface roughness with carbide tools than those produced with CBN tools. However, this effect can be seen as more prominent for interrupted surface in comparison to continuous surface. Their study of analysis concluded that the difference in roughness obtained was mainly dependent on tool wear.

Asilturk and Akkus[73] observed that the feed rate together with the interaction effects of the feed rate and cutting speed as well as the depth of cut and cutting speed had the most significant effect on surface roughness during turning of hardened AISI 4140 steel (51 HRC) with Al_2O_3 and TiC-coated carbide tools. Cakir *et al.*[74] also found that feed rate had the greatest influence on surface roughness, followed by cutting speed and depth of cut had no significant effect during turning of AISI P20 tool steel (52–55 HRC). They observed higher values of surface roughness, which further increased at higher cutting speed when using CVD-applied multilayer TiCN/Al_2O_3/TiN carbide insert in comparison to PVD-applied single-layer TiAlN-coated carbide insert which showed almost no variation in surface roughness at higher cutting speeds.

When machining hardened steel at comparatively lower hardness (35 HRC), it is reported that the surface roughness gets affected significantly at higher values of feed and depth of cut. However, this effect was less prominent in case of harder workpiece. This may be because of reduction in cutting forces occurred due to softening of the harder material at higher feed and depth of cut. As against, this effect was more prominent when using PVD-coated tool as growing crater wear observed for these tools reduces the metal available to support the tool, which promotes more chatter. Surface roughness presented lower values when using PVD-coated tools (**Figure 26**), which can be attributed to minimum friction offered by these tools to flowing chips. Chips produced when using PVD-coated tool showed more or less polished back and smooth free surfaces as against chips produced showed a rough back surface showing some parallel stripes and damaged free surface when using CVD-coated tool as shown in **Figure 16**. Polished and bright chip back surface obtained with PVD-coated tool shows that minimum friction was offered by these tools during cutting which resulted in lower cutting forces and hence, produced better surface finish.[9,11,40] The typical surface roughness contours for PVD (T2) and CVD-coated (T3) tools as shown in **Figure 27**.

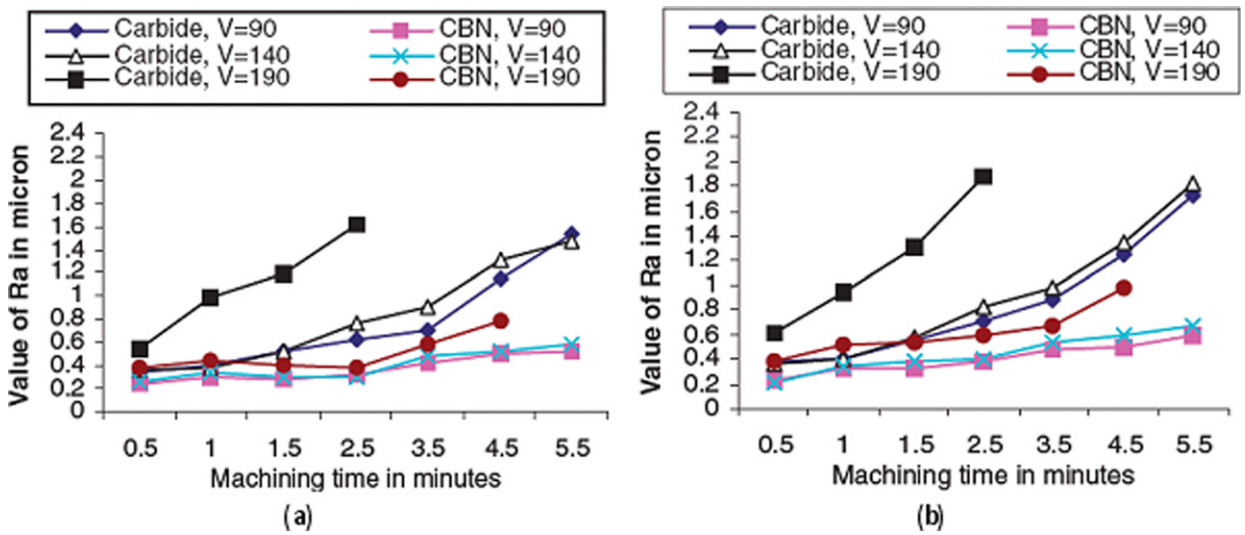


Figure 25 Progression of roughness for (a) continuous surface and (b) interrupted surface.[72]

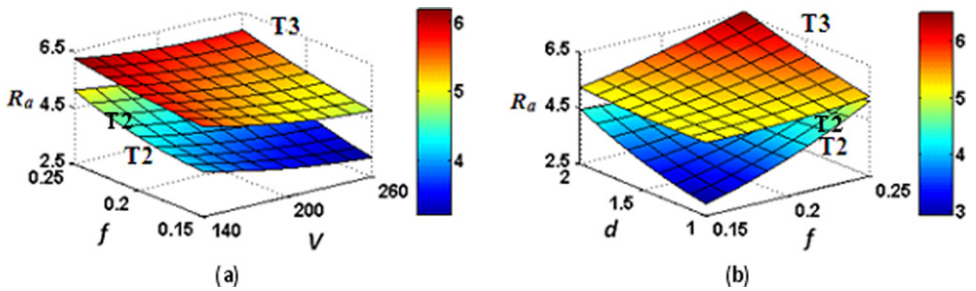


Figure 26 3D response surfaces showing effect of cutting conditions on surface roughness (letter T2 and T3 shows response surfaces for PVD-coated and CVD-coated tools, respectively).[40]

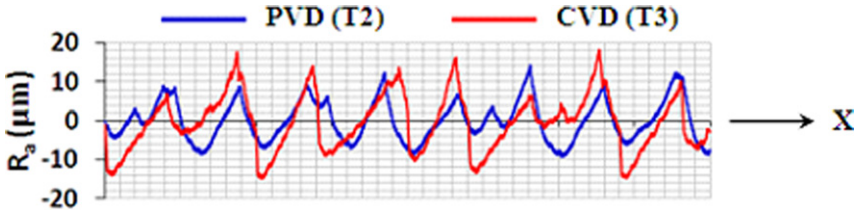


Figure 27 Surface contour plots obtained by T2 and T3 at $V=200$ m min^{-1}, $f=0.2$ mm rev^{-1}, and $d=1.5$ mm (X-axis shows evaluation length of 4 mm).[40]

From Figure 26, it can be seen that surface roughness decreases with increase in cutting speed. However, this effect can be seen as more prominent for PVD-coated tools (T2). However, surface roughness increases with increase in the values of feed and depth of cut, which is in line with the classical theory of metal machining. Interaction effect of $f \times d$ can be seen as more prominent for T2, indicating that surface roughness obtained with this tool is more sensitive to cutting conditions, especially feed and depth cut. At higher feed and depth of cut, the force components increase sharply resulting into more vibrations and hence chatter marks remaining on the machined surface. However, this effect can be seen as more prominent when using T2 as growing crater wear observed for these tools reduces the metal available to support the tool, which promotes more chatter. In summary, when surface finish is a criterion for tool selection, PVD-applied single-layer TiAlN-coated carbide tool is the better option during finish machining of hardened AISI 4340 steel. However, values of higher feed and depth of cut is to be avoided in this case.[40]

Yusuf and Motorcu[72] developed the first- and second-order surface roughness models for turning with TiN-coated carbide tools using response surface methodology (RSM). They observed feed rate followed by cutting speed are the main influencing factors on the surface roughness while depth of cut was insignificant. Noordin *et al.*[75] investigated the effects of cutting speed, feed, and SCEA of the cutting edge, on cutting force and surface roughness, while machining with coated carbide tools. They observed that feed is the most significant factor on the surface roughness. However, secondary contributions by the second order of SCEA^2 and the interaction effect of feed and SCEA, was also observed by them during turning of AISI 1045 steel. Lalwani *et al.*[76] investigated the effect of cutting parameters on surface roughness in finish hard turning of MDN250 steel using coated ceramic tool. They observed that surface roughness do not vary much with cutting speed. However, feed rate, interaction effect between feed rate and depth of cut and interaction effect between speed and depth of cut were observed as having prominent effect on surface roughness.

Senthil kumar *et al.*[49] observed better performance of the Ti [C,N]-mixed alumina inserts in terms of surface finish than that of zirconia toughened alumina (zirconia particles dispersed in alumina matrix) ceramic cutting tool during machining of hardened steel EN24 steel. They found that the flank wear generally does not affect the performance of the surface finish while using ceramic cutting tools, until it does not affect the nose region of the tools. Further, they observed that the surface roughness exhibited a rising trend, up to certain time of machining beyond which there was an improvement in surface finish which could be attributed to the nose-associated transformation toughening of zirconia toughened alumina ceramic cutting tool.

If hard turning is to be a viable replacement for finish grinding operations, it must be capable of producing surface finishes comparable to grinding with the R_a and R_z parameters in the range of 0.1–1 μm and 2–4 μm, respectively.[77–79] From Figure 28, it can be seen that the Rz values provided that CBN-based tools produce more stable surface finish in comparison to Al_2O_3–TiC composite based ones while continuous turning of different steels at depths of cut of 0.1–0.3 mm and for feed rates ranging from 0.04 to 0.15 mm rev^{-1}.[79] Depending on the steel grade machined the peak-to-valley height varies approximately between 2 and 7 μm for ceramic tools (Figure 28(a)) and from 1.5 to 3.5 μm for CBN tools (Figure 28(b)). Figure 29 shows the scanning electron microscopy (SEM) images of the quality of the surface observed during turning of AISI 4340 alloy steel using coated carbide tool for two different depth of cuts (0.8–1 mm) at cutting speed of 260 m min^{-1} and feed of 0.1 mm rev^{-1}. The improved surface finish for lower depth of cut of 0.8 mm can be clearly evidenced from Figure 29(a) as compared to surface finish obtained at higher depth of cut of 1 mm (Figure 29(b)). The study of analysis while hard turning using coated carbide tool concluded that the surface roughness is sensitive to variations in feed rate and depth cut at lower values of cutting speed it is found to be insensitive to variations in machining time.[80]

In hard turning, it is reported that the built up edge is never observed due to the poor ductility of the workpiece material and the high cutting temperature generated by the cutting process. Thus, the profile of the generated on the workpiece surface is the conjugate profile of the cutting edge.[51] High abrasiveness of the hardened workpiece combined with the higher cutting temperatures employed during machining of hardened steel induce a rapid tool wear. It has been reported that the worn flank surfaces of the tool increases the cutting forces and particularly the thrust force as the tool penetration in the work material becomes difficult due to the flank wear.[51,57] Usually, cutting forces and surface roughness get affected with the progression in tool wear. Many of the cases, especially in finish machining of hardened steel, tool life is considered to be over when surface roughness exceeds beyond the specified limit. However, Poulachon[51] reported that the increase in surface roughness due to tool wear appears later than the increase in thrust force as shown in Figure 30, i.e., the thrust force is more prominently get affected with the tool wear and could be a better choice for tool wear monitoring in comparison to surface roughness.

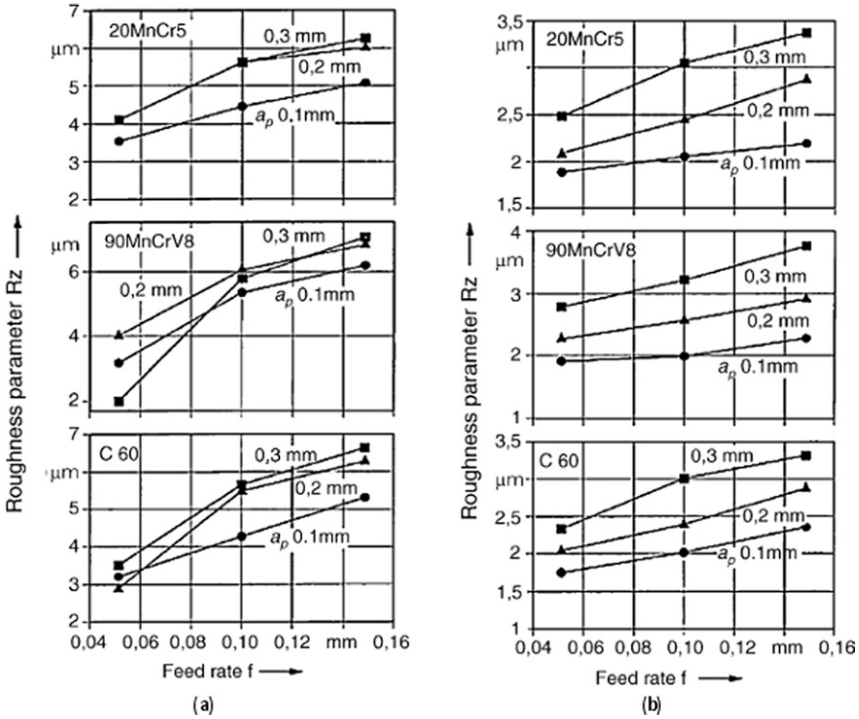


Figure 28 Influence of feed rate on roughness parameter R_z using (a) mixed ceramics and (b) CBN tool. Hardness of workpiece: 20MnCr5 (55–60) HRC, 90MnCrV8 (59–62) HRC, C60 (52–55) HRC (cutting speed: 140 m min^{-1} for ceramic ISO-CNGA 120408 inserted tools; 170 m min^{-1} for CBN ISO-DMCW 11T308 inserted tools).[79]

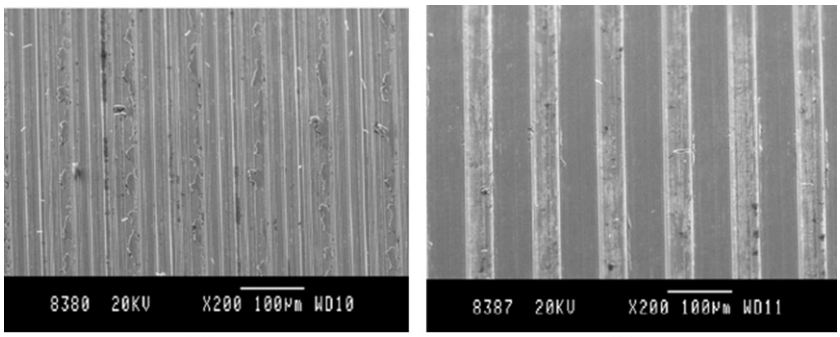


Figure 29 SEM images of the surface quality observed during turning of AISI 4340 high strength low alloy steel at varying depth of cut (a) d=0.8 mm and (b) d=1 mm.[80]

1.3.3.5.2 RSs

In general, machining (turning, milling, grinding, drilling, broaching, etc.) is a term used to describe the removal of material from a workpiece. Machining processes are known for being complex due to the diversity of physical phenomena involved, such as large elastic–plastic deformation, complicated contact/friction conditions, thermo-mechanical coupling and chip separation mechanisms.[81,82] The stress produced in the workpiece surface as a result of machining is called RSs, which especially tensile in nature significantly affect the fatigue life, fracture resistance, and stress corrosion of the component. The level of generated RSs depends on the machined material, tool flank wear, shape of the cutting edge, and the process parameters used. In hard turning, RS can be generated by mechanical, thermal, and phase transformation changes.[71]

HPM is mostly used as a finishing process and hence, it is imperative to study about the machining parameters which affect the magnitude and nature of the RSs as they can enhance or impair the functional behavior of a machined part. It is possible to generate tailor-made stresses on hard turned surfaces by effectively controlling cutting parameters so as to get prolonged service life of component.[83] Hard turning with a sharp cutting tool generates a unique 'hook' shaped RS profile characterized by compressive RS at the surface and maximum compressive RS in the subsurface,[84,85] but as tool wears out, the nature of the surface RSs changes to tensile that reduces

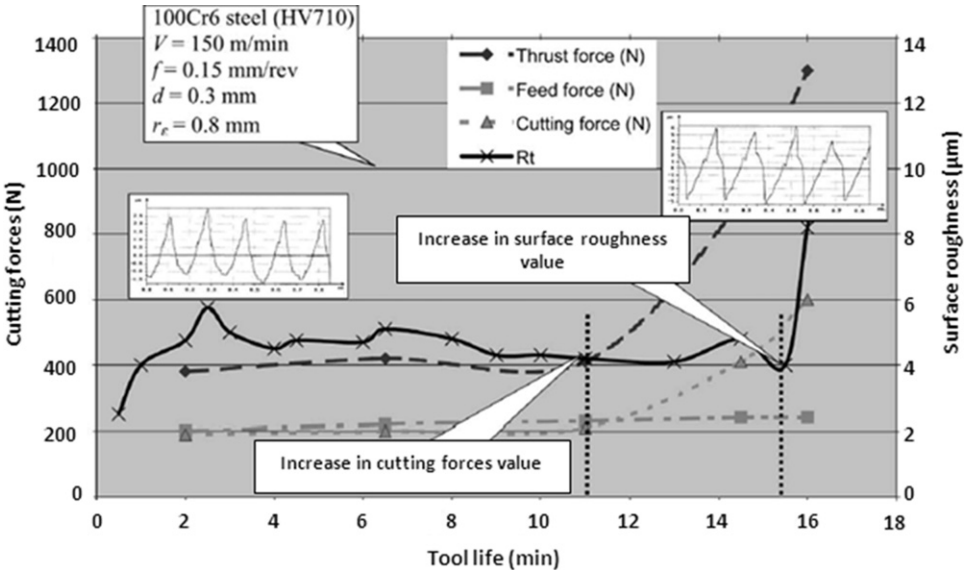


Figure 30 Cutting force and surface roughness progression as a function of the tool wear.[51]

fatigue life of component. This is one of the major areas of concern in hard turning.

Matsumoto *et al.*[86] also observed compressive RSs in a deep subsurface, contributing a long fatigue life of hard-part component. They found that the tool edge geometry was having the most dominant factor in deciding the RS profile while hard turning of case carburized steel (58–62 HRC) using PCBN tool. Further, they observed that increase in cutting speed increases the tensile RSs on the surface. As against, higher feed generated compressive stresses while a high negative rake angle produced more compressive stresses. Javidi and Rieger[87] found that the nose radius and feed rate as most critical parameters to control RSs. They observed that RSs became more compressive with the increase in feed rate. However, decrease in compressive RSs was observed by them with increase in the tool nose radius. However, ploughed depth also found as a major influencing factor in producing the machining-induced RS profile and a unique hook shaped RS profile is produced when the ploughing depth reached a threshold (critical) value.[85]

It has been observed that the microstructural phenomena associated with white and dark layers formation influenced the RS distribution. Further, it is claimed that better prediction of RS could be achieved by incorporating such microstructural changes in the RS model.[88] Thiele *et al.*[89] investigated the effects of tool edge preparation and material hardness on surface RS during finish hard turning of AISI 52100 steel with PCBN tool. Their study of analysis concluded that a large edge hone radius (~120 μm) and a chamfer tool (24.5 μm) produces more compressive RSs than small edge hone tools (~20 μm). They found low residual tensile stresses with small edge hone tools for workpiece hardness of 41 HRC and compressive RS for higher workpiece hardness of 57 HRC. Hua *et al.*[90] during their investigation on RSs considering the effect of tool geometry, cutting process parameters, and material hardness show that an optimal combination of a large-hone edge with a chamfer at an aggressive feed rate favors an increase in compressive RSs in both axial and circumferential directions.

Figure 31 shows the RS generated during turning of continuous (c), interrupted (I), and fully interrupted (FI) surfaces at cutting speed of 190 m min^{-1} with the carbide and CBN tools. It can be seen that with both the tools (190-C condition), the maximum compressive RS observed beneath the machined surface was larger in magnitude and also deeper in the subsurface. A tensile RSs can be seen only for a few microns beneath the machined surface which can be removed by any super-finishing process to avail the advantage of fatigue life of the component.[71,87] However, for compressive RS on the surface, the magnitude of the compressive RS beneath the machined surface and its penetration in the subsurface can be seen low.

The circumferential RSs observed on the exposed surface with varying flank during turning of continuous and fully interrupted surfaces with both tools as shown in **Figure 31(c)**. For all the cases with fresh tools or when maximum flank wear reached 100 μm, compressive RS was observed on the surface of the machined workpiece. With increase in the flank wear, shifting of compressive RSs to tensile stresses can be seen which could be attributed to an increased thermal effect due to rubbing between the worn tool flank and the workpiece surface.[91] It can be seen that almost zero RS on the surface could be obtained by limiting the maximum flank wear up to 100 μm.

It is reported that turning with CBN tool results in tensile RS of lower magnitude in comparison to carbide tools which could be attributed to high thermal conductivity of CBN tools and thus low thermal damage on the machined surface in comparison to carbide tools. Moreover, the chamfer and honed edge geometry of CBN tools resulting in reduction of tensile RS produced on the surface.[91,92] At higher cutting speed higher cutting temperatures generated in the cutting zone either shifts the nature of the RSs from compressive to less compressive or toward tensile. However, this effect was observed more prominently with carbide tools in comparison to CBN tools.[71] Previous investigations on the effects of flank

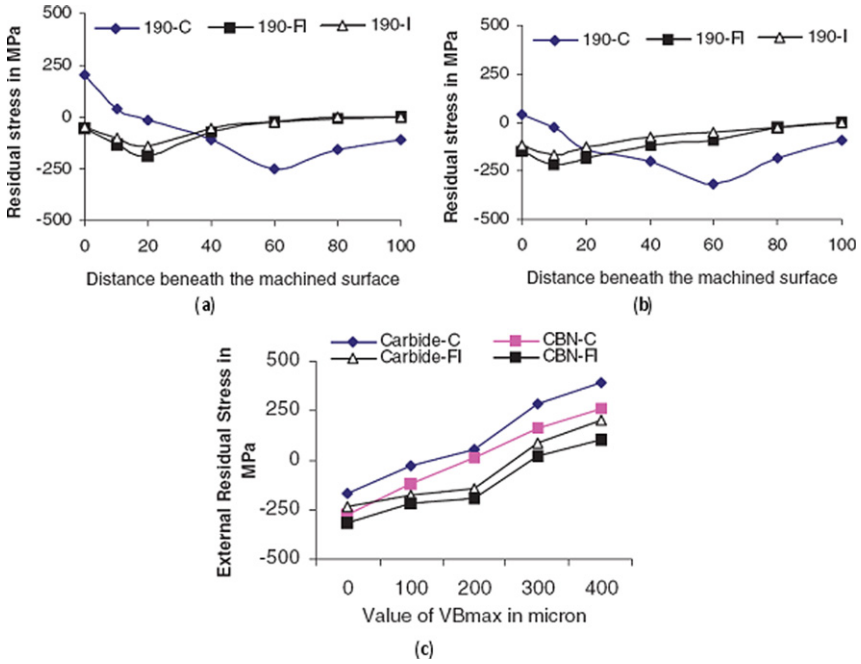


Figure 31 Residual stress generated at $V=190$ m min^{-1} as VB_{max} reaches 200 μm with (a) carbide tool, (b) CBN tool, and (c) effect of flank wear on external residual stress generated.[71]

wear indicate that an increase in flank wear results in a shifting of the surface RS toward tensile stress values. Also, increasing flank wear shifts the maximum compressive stress deeper in the subsurface layer.[93,94]

From above it can be deduced that a favorable surface integrity in terms RSs is very important in finish machining of hardened steel as it can be decisive for tool change. Components requiring good fatigue strength can be severely affected if the HPM process is not controlled effectively. A worn tool and a high cutting speed generate tensile RSs which can be detrimental while deciding the fatigue life of the component. Hard turned surfaces are more repeatable while the ground surface are more random in nature due to random distribution and shape of cutting edges of the abrasive grains that gives a upper hand to the hard turning.[37] In general, the performance of carbide tools was comparable with that of CBN at low and medium cutting speeds in terms of the type of RS observed on the surface.

1.3.3.5.3 White layer effect

Workpiece surfaces, especially hard-part machined surfaces, usually exhibit surface alterations under the circumstance of excessive flank wear or aggressive cutting conditions that are referred as white layers.[93,94] White layers can be resulted from severe plastic deformation and grain refinement or by phase transformations as a result of rapid heating and quenching.[95] White layer is denominated due to their white appearance, has a high hardness, ultrafine grains, and resists metallurgical etching. It is basically a rehardened structure, which can reach up to 10 μm deep increasing with the size of the flank wear land.[96]

White layers are produced due to the occurrence of martensitic phase transformation, particularly at higher cutting speeds. However, occurrence of mechanically induced grain refinement at low cutting speeds owing to severe deformation.[97] Tool flank wear and cutting speed which led to an increase in temperature at the cutting zone are dominant factors for formation of white layer in hard turning.[98] Therefore, chances of white layer generation can be minimized by controlling the temperature in the cutting zone. It has been observed that the thickness of the white layer generated with CBN tools was somewhat less than that produced with carbide tools. This effect could be attributed to greater thermal conductivity of CBN tools in comparison to that of carbide tools.[71] It has been found that the thickness of the white layer generated for continuous surfaces increases with cutting speed.[98,99] However, white layer was not observed while machining of interrupted and fully interrupted surfaces which could be attributed to discontinuity in heat propagation through the workpiece surface due to interruptions and generation of an air flux through the slots on the surface, which helps in limiting the temperature of the workpiece and the tool.[71]

A typical white layer obtained during hard-part of machining is shown in **Figure 32**. A white layer followed by dark-etching layer having thickness of about 13–17 μm, respectively can be seen. It can be seen that the white layer has an unresolvable feature, the dark-etching layer has very fine precipitates and the bulk exhibits a pearlite microstructure. Rough surface profile observed could be attributed to machining-induced vibration due to an imperfect workpiece holding device used.[96,100]

A thin white layer formed during hard turning of AISI 4340 steel (50–52 HRC) using cBN–TiN-coated carbide tool can be seen from SEM micrograph (**Figure 32**). The white layer formed approximately of 1 μm thick shows that the intensive

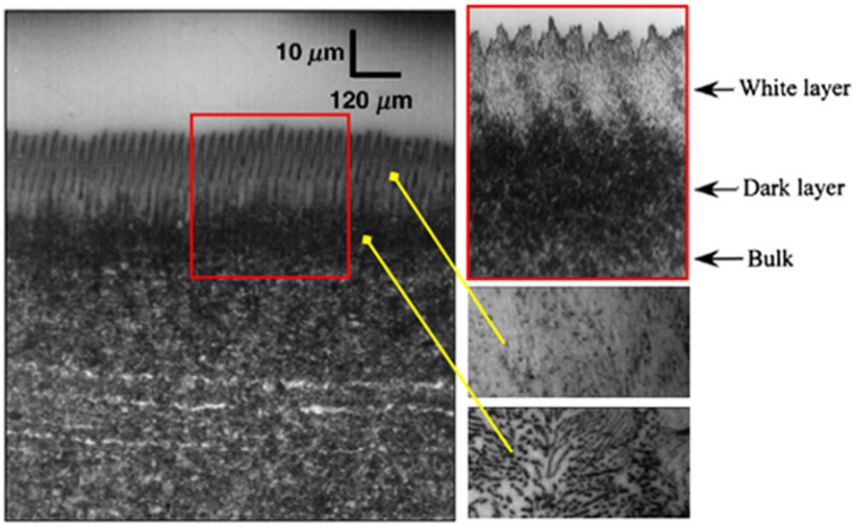


Figure 32 Phase transformed structures of a machined hard surface.[96,100]

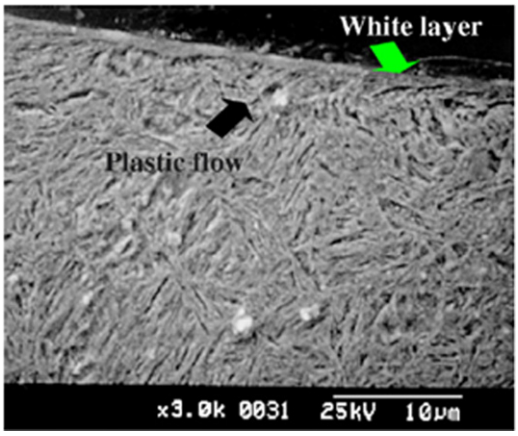


Figure 33 SEM micrograph showing the white layer and plastic flow in the subsurface (5% nital etchant).[101]

heating which was sufficient to produce a phase change at the surface followed by subsequent rapid cooling occurred at the workpiece–tool interface. Heating occurred due to the high energies involved in the hard turning and rapid cooling occurred mainly from conduction and partially from convection. A subsurface plastic flow in the circumferential direction of the workpiece can be also seen from **Figure 33**. This effect could be attributed to excessive shear associated with the negative rake angle (-5°) and nose radius (0.8 mm) of the tool.[101]

White layers are formed as a consequence of high friction energy and heat generated during machining which significantly influenced by the tool wear and magnitude of cutting speed employed during the process. At higher cutting temperature, martensite present in steel structure gets transformed into the austenite forming the white layer. Tool wear increases with increase in cutting speed and hence, thickness of the white layer. However, a group of researchers observed at higher cutting speeds, decrease in the white layer depth and its hardness. This may be due to the fact that at high cutting speeds the temperature of the workpiece material reduces as maximum heat is carried away with fast flowing chips.[34,102] Ramesh *et al.*[97] found that white layers produced were largely due to grain refinement induced by severe plastic deformation when using low-to-moderate cutting speeds. As against, at higher cutting speeds, the white layer formation was mainly due to thermally driven phase transformation. They observed that white layers found to be comprised of very fine (nano-scale) grains compared to the bulk material which increases the hardness of the layer.

Properties of white layers produced from HPT and grinding processes are fundamentally different in terms of surface structure characteristics, micro-hardness, microstructure, and chemical composition. A turned white layer is etching resistant, has much more strained and retained austenite than the ground white layer. The micro-hardness profile obtained from HPT and grinding processes is almost same. However, ground white layer observed to be 40% harder and the thickness ratio of dark to white layer is much larger than the white layer in turning.[98] Smith *et al.*[103] observed that the presence of white layer did not adversely affect fatigue life and that, on average, the hard turned surface performed as well or even better than the ground surface. The results of analysis of their study concluded that the effect of RS on fatigue life was more significant than the effect of white layer during hard turning of AISI 52100 steel.

However, Schwach and Guo[104] observed that a white layer induced by hard turning was very detrimental to rolling contact fatigue (RCF) as it increased tensile RSs. They found almost six times more life for a component which was free of white layer than life obtained with a white layer component. Steel with fine microstructure showed thicker white layer in comparison to steels with coarse microstructure. Moreover, the carbon content in the white layer was observed to increase with time and with increasing layer thickness.[105] A negligible white layer was observed at higher cutting speeds while hard turning of H13 steel with CrTiAlN and CrTiAlN/MoST-coated carbide tools. This could be attributed to lower workpiece and tool temperatures due to low friction coefficient of coated tools. Moreover, coated tools resulted in reduced and more

homogeneous hardening effects compared to uncoated tool.[106] It is reported that white layer increased with increase in both cutting speed and feed rate. As against, dark layer decreased with increase in cutting speed, while it remained almost constant or slightly decreased when feed rate was increased.[99]

The white layer formation occurring only with a worn tool in service is undoubtedly a phase transformation process at near austenizing temperature or even below when accompanied with high strain rates. Negative tool geometry and high feed rates tend to increase white layer formation. A group of researchers observed that the surface integrity (white layer formation, micro-hardness and surface roughness) achieved with carbide tools was comparable with that of CBN tools and they found no discernible difference in hardness between the white layer and bulk material using coated carbide tool in comparison to CBN tool[107] which shows that the coated carbide tools could be complementary to PCBN tools in finish hard turning. According to some researchers white layer does not have any significant effect on fatigue strength but it is RSs on the machined surface which were detrimental while some have directly observed white layer as the culprit for reducing fatigue strength of component.[37]

1.3.3.5.4 Cutting errors and dimensional accuracy

Finishing operations are carried out to achieve the desired surface finish and dimensional accuracy of a machined component. Deflections caused by cutting forces are generally the main source of dimensional error in machining. This is especially the situation when long and flexible tools are used. As the machining operations are the last operations in the process chain, the cost of scrapping the workpiece in the finishing stage due to dimensional inaccuracies is high. Tool wear, cutting forces, and cutting temperature are the key factors that affect the part accuracy and process stability and reliability. To achieve high surface finish and high dimensional accuracy a rigid setup of the machine tool system is recommended. The stiffness of the machine tool and the tool holders should be high enough to avoid static and dynamic deflections.[108]

In an attempt to analyze the geometrical accuracy, investigations on the parts produced in series in terms of measurement of size deviations, out-of-roundness, cylindricity error, and parallelism error. It was observed that as compared to grinding, cylindricity error obtained was on the higher side for hard turning, but, still workable. However, the parallelism was better in hard turning. Flatness error obtained was observed to be adequate in hard turning. As against, it was very high in grinding. Also, the axial run-out was much higher in grinding in comparison to hard turning. Thus hard turning seemed to be a better option while the ground gear did not fulfill the requirements prescribed in the drawing because of its large flatness error.[109] Cutting parameters such as cutting speed, feed rate, and depth of cut have significant influences on the three quality characteristics, namely dimensional error, surface roughness, and circularity. A hybrid predictive model recently proposed by Jawahir and Wang[110] for optimum cutting parameter selection could be a viable option to optimize all three quality characteristics during finish machining of hardened steel.

For any process to be accepted by the industry it should be robust and accurate as far as the performance is concerned. Attempts have been made by the researchers to investigate process accuracies and the sources of errors to establish the reliability of the hard turning process as a substitute to finish grinding. Zhuo *et al.*[71] observed that the tool wear, cutting forces and temperature induced by the cutting process on the cutting tool and workpiece are the major error drive factors in a precision hard turning as shown in Figure 34.

In plain turning, the diameter of the machined component generally deviates from its desired value along the length of job. This could be attributed to change in the effective depth of cut due to several reasons which include wear taking place at the tool nose, overall compliance of the machine–fixture–tool–work (M–F–T–W) system and thermal expansion of the job during machining followed by cooling. Therefore, variation in diameter produced would be governed by limiting the cutting temperature with effective design of M–F–T–W system. With the increase in cutting temperature, the rate of flank wear and thermal expansion of the workpiece increases resulting in more dimensional inaccuracy. By properly selecting the type of cooling technique dimensional deviations of the machined component can be controlled.[111] Cryogenic cooling provided remarkable benefit in respect of controlling the increase in diameter of the finished job with machining time, as can be seen in Figure 35.

It has been reported that the use of machine tool with polymer concrete bed improved the machining performance in terms of reduced tool wear and better surface finish due to its outstanding damping and high rigidity in comparison to cast iron bed.[112] Tool wear, especially flank wear has a significant effect on the quality of the surface produced. In general, while machining of hardened steel, the dimensional errors measured in axial/radial directions can increase up to 25 μm for the flank wear of 0.2 mm. Moreover, higher cutting temperature employed during process (800–1000 °C) resulting in substantial thermal expansions of cutting edge of the tool and the workpiece. In particular, at cutting speed of 160 m min^{-1} and feed and depth of cut of 0.05 mm rev^{-1} and

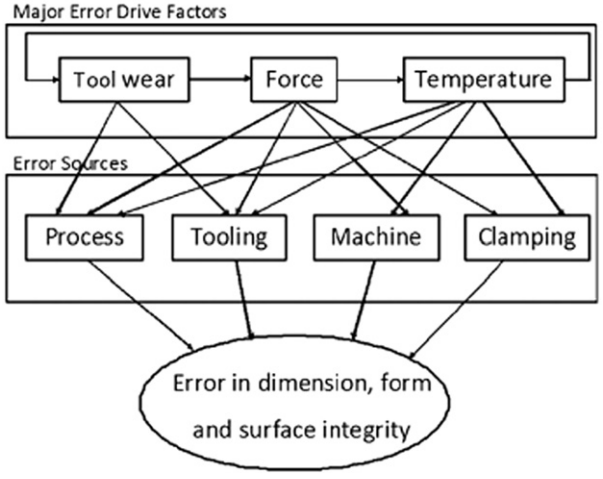


Figure 34 Major error driver factors and error sources in precision hard turning.[107]

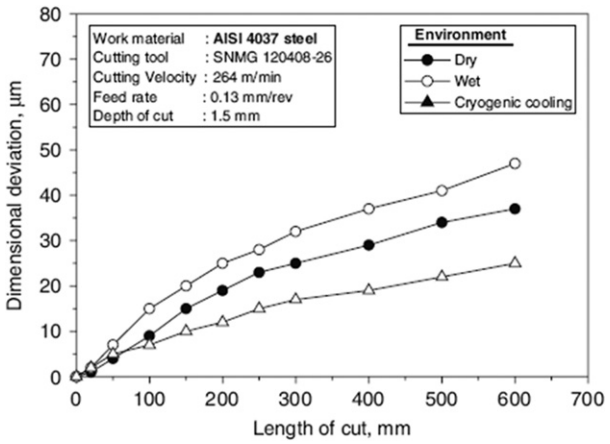


Figure 35 Variation in change in dimension with cutting-length under different conditions.[111]

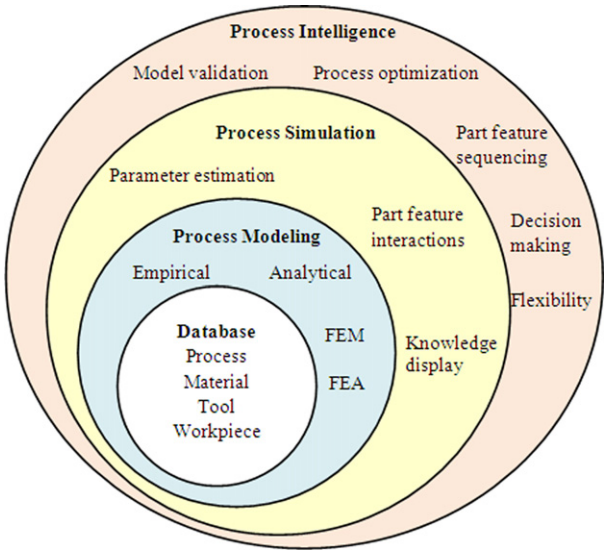


Figure 36 Process data and models drive design and manufacturing decisions with increasing levels of complexity.[115]

0.05 mm, thermal expansion of the CBN tool tip and workpiece can reach up to 10–15 µm, respectively.[107]

It is important to choose a nose radius that is smaller than the cutting depth as this has the same effect as choosing the correct entering angle. If the nose radius is too large it will push the tool in the radial direction and affect the dimensions of the component. Wiper inserts act as a large nose radius and will generally need a bit more care when applying it to internal turning.[113] In manufacturing of the bores, heat removal is more difficult than when machining external surfaces. So there may be chances of thermal distortions. A finite element based model which was developed for the simulation of thermal deformation in the hard turning of small bores indicated that thermal distortion did not have a significant effect on the machining accuracy, as the deviation in diameter caused by the heat remained below 0.001 mm.[114]

However, in internal turning operations and specially in finishing, the machining conditions are difficult. The workpiece is sometimes thin-walled and flexible, and the internal turning is often performed by using long boring bars with relatively low stiffness. Machining of deep cavities or with long overhangs is prone to vibration problems. One way to overcome this is to reduce the depth of cut, the speed or the feed. However, losing productivity in favor of keeping the process running is not beneficial. The use of a Silent Tool when going deeper into a bore, will retain, or in many cases improve productivity with a high-quality surface finish, closer tolerances and improved tool life even when working with boring bars with large overhangs. Silent Tools is a family of products for internal turning, milling, boring, and drilling. These products are tuned to work on overhangs beyond the limitation of solid steel and solid carbide shanks. They are easy to operate and are very flexible due to the wide variety of back-end and front-end couplings.[113]

From above it is evident that with effective control on error sources, HPM could achieve the level of desired geometrical accuracies. It can even surpass the grinding capabilities if executed carefully. Since machining with a severely worn tool affects the dimensional accuracy and surface finish and replacing the tool well before the end of its life affects the machining economy. Several attempts made by the researchers to model the cutting forces, flank wear progression and RSs during machining of hardened steel which will be discussed in next section.

1.3.4 Modeling of Hard Machining Processes

Nowadays, with the increasing trend toward maximizing productivity and higher material removal rates, the ability to predict the cutting performance is embedded in the road map for cutting technology. Manufacturing evolution, i.e., the design-to-manufacturing cycle is strongly driven by the database of information on process, tooling, materials and workpiece requirements as shown in Figure 36. Evidently, process data and appropriate models can drive design and manufacturing decisions to achieve goals with increasing levels of complexity.[115]

Predictive models which are capable of predicting quantitatively the influence of the magnitude of one or more input parameters on the magnitude of one or more output parameters are of special importance in the finish machining of hardened steel in view of to predict process results, such as, tool life, surface finish/integrity of the component being machined and forces on the tool and/or workpiece. Moreover, predictive models could be used to find ways of optimizing the processes, to obtain new knowledge of process steps and process design and to derive capabilities of process monitoring and control from this.[6] Considerable amount of modeling efforts have been undertaken to predict machining performance namely, tool wear, tool life, surface roughness, cutting forces/power, and part accuracy. Also, significant attempts have been made by the researchers in developing safer and secure operating conditions for machining, selection of appropriate tooling, and accessories such as jigs and fixtures to avoid machining chatter and vibrations.[67]

1.3.4.1 Modeling of Cutting Force

The understanding of the cutting forces considering the tool wear is important in addressing metal cutting issues such as

dimensional accuracy, surface finish, white layer effect, and RSs in finish machining of hardened steel. Several studies have concluded that in the machining of hardened steels higher workpiece hardness demands for higher cutting forces and hence generates higher temperature in the cutting zone that has a very strong influence on the tool wear, surface integrity, and workpiece quality.[8–11,38] Furthermore, determination of cutting forces, prior to machining is important because through these forces the power requirements of the machine tool and the cutting tool properties can be estimated.

However, it is imperative to estimate shear plane angle and friction parameters in order to calculate cutting forces. The single shear plane model has been criticized over the years. However, the infinite strain rate, assumption of the rigid, perfectly plastic workpiece material and the perfectly sharp cutting edge of the tool are the major inherent drawbacks of the single shear plane model.[116] Moreover, most of the analyses presented pertained only to orthogonal cutting.[117,118] A 3D analysis has been presented by Usui *et al.*[119–121] and Oxley[122] considering the secondary cutting edge and tool nose radius effects, which is of course the most usual in practice. However, both Oxley's and Usui's models require stress and strain data at the strain rate and temperature encountered in metal machining.

Mechanistic modeling, a combination of analytical and experimental modeling techniques, for cutting force is also presented by a group of researchers, a review of which can be found in Ehmann *et al.*[123] As this kind of modeling is not purely analytical and based on metal cutting mechanics, such an approach avoids the complications of incorporating parameters such as shear angle and friction angle, by using experimental force data and it is suitable for practical machining processes which are mostly oblique cutting in nature.[124] Attempts have been made to introduce the effect of the secondary cutting edge to predict the chip-flow direction for turning operations. A group of researchers.[125–127] predicted the cutting forces while using a sharp tool considering the effect of tool geometry complexity. They observed better prediction of cutting forces by replacing actual cutting edge of tools with nose radius with an equivalent cutting edge.

Although, several cutting force models have been developed, very few have considered the effect of tool wear on cutting forces.[33,118,128,129] Moreover, most of the models have used CBN/ceramic inserts as a tool material during machining of hardened steel. Chinchanikar and Choudhury[57] studied the interrelationship between the tool wear and cutting forces within the different phases of the tool life through mathematical modeling during turning of hardened AISI 4340 steel. They observed that the feed and radial components of cutting force are more influenced by tool wear and increase sharply when rapid deterioration of the cutting edge takes place. Huang and Liang[33] developed an analytical model for predicting the cutting forces due to flank wear under hard turning conditions by extending Waldorf's orthogonal force modeling approach. Model predictions showed better agreement with the experimental results. Worn tool cutting forces were obtained by summing up the predicted forces without any tool wear and the forces due to the flank wear alone. They observed that the predicted forces match better in the tangential cutting direction and the axial direction than in the radial direction with the progress of tool flank wear. In another study, Li and Liang[128] found that the cutting forces under near dry machining could reduce 10–20% cutting forces compared with the forces under dry machining conditions when cutting the AISI 1045 with uncoated carbides, suggesting that lubricating has a stronger effect on cutting forces than cooling under these conditions as shown in **Figure 37**.

Smithey *et al.*[129] developed a model for worn tool cutting forces in 3D cutting operations to show the growth of the plastic flow region at the tool flank during dry turning of AISI 4140 steel with TiN-coated carbide inserts. Sharp tool cutting forces were obtained by the authors using a mechanistic force model that showed an excellent agreement with the experimental results. However, the said model may not be applicable to other tool and work combinations. In another study, Huang and Liang[130] presented the ploughing effect in a mechanistic model to calculate the total 2D cutting forces in shallow cuts during hard turning. Chip formation forces were predicted by transforming the 3D cutting geometry into an equivalent 2D cutting geometry. Finally 3D cutting forces were estimated by geometric transformation. The proposed model was calibrated and validated using experimental machining data for finish turning of hardened 52100 steel. The Johnson–Cook equation was used by them to represent the workpiece material properties of hardened 52100 steel. The developed model showed prediction accuracy with experimental results within 15%.

From the available open literature, it has been observed that cutting forces could be better predicted by replacing actual cutting edge of tools with nose radius with an equivalent cutting edge.[125,127,131,132] Further, it has been observed that model prediction accuracy, especially when employed shallow cuts during finish machining of hardened steel, could be increased by summing up the ploughing forces and the chip formation forces. Several studies concluded that machining of hardened steels using coated carbide tools could become an economical alternative to costly CBN and ceramic tool materials.[31,32,56,71,133] Therefore, development of a reliable model which can predict the cutting forces considering tool wear effect in the finish machining of hardened steel using coated tools will be extremely valuable and needs to be taken.

1.3.4.2 Modeling of Tool Wear Progression

In finish machining of hardened steel, prediction of the tool wear progression will be extremely valuable since the machining with a severely worn tool, especially at the flank faces (flank wear), affects the dimensional accuracy, surface finish, and replacing the tool well before of its tool life affects the machining economy. Significant efforts have been made by several researchers in understanding and modeling the tool wear progression and wear mechanisms like abrasion, adhesion and diffusion in metal cutting as shown in **Table 4**.

Studies available in the literature,[38,41,152] confirming a strong influence of cutting force and temperature on the tool wear rate through different tool wear mechanisms like abrasion, adhesion, and diffusion. It is reported that during machining of hardened steels higher cutting temperatures in the range of 800–950 °C are generated in the cutting zone.

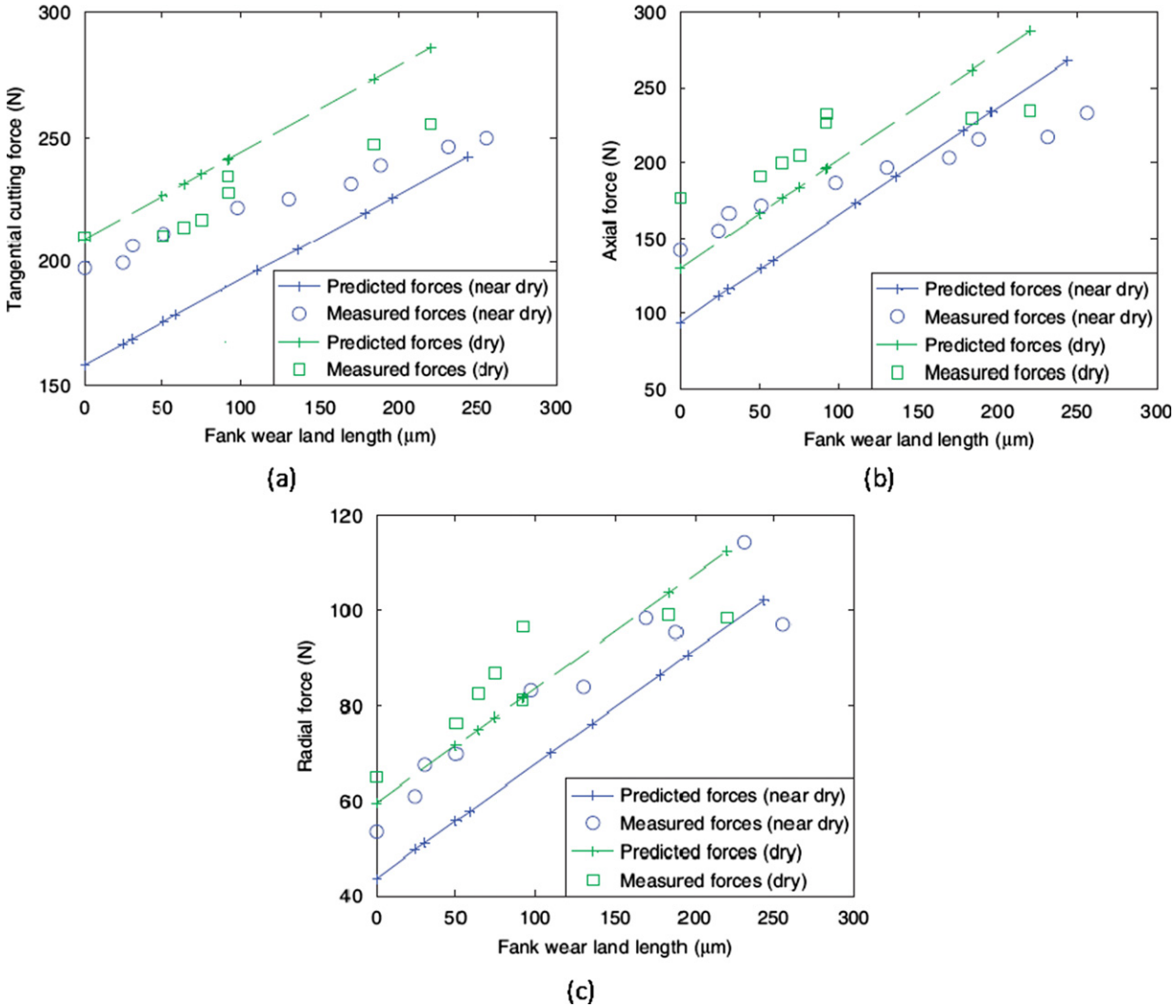


Figure 37 Model and experimental results of cutting forces under dry and near dry cutting (cutting speed of 91.5 m min^{-1} and feed and depth of cut values of 0.076 2 and 0.762, respectively.[128]

Tool wear, especially when using coated carbide tools during finish machining of hardened steel having hardness in the range of 50–65 HRC, is the main hurdle in the wide implementation of these tools in the industry.[3]

Abrasion and adhesion are usually predominant wear mechanisms when machining hardened steel. Abrasion wear is more prominent in case of turning harder workpiece. As against, adhesion wear is more prominent when turning softer workpiece. It has been observed that the contribution of abrasion wear increases and that of adhesion wear decreases with the machining time. However, the contribution of diffusion wear has been observed to increase at higher cutting speeds.[7] It is generally agreed that tool wear criteria in the range of 0.15–0.2 mm (flank wear length) is more realistic during finish machining of hardened steel as beyond this tool wear criteria tool failure occurred by chipping off of the cutting edges instead of progressive growth of tool wear.[7,60] Huang and Dawson[135] developed a model to predict crater wear depth of CBN tool incorporating abrasion, adhesion, and diffusion wear mechanisms. The proposed model was experimentally validated by them in finish turning of hardened 52100 bearing steel.

Singh and Rao[136] developed prediction model for flank wear of ceramic inserts in finish turning of hardened AISI 52100 steel. They found that abrasive and adhesive wear mechanisms as predominant mechanisms. However, abrasive wear was observed by them decreasing at higher cutting speeds and adhesive wear increasing as cutting speed increases. They also found that the contribution of diffusive wear mechanism increases at higher cutting speeds. However, when using CBN tool in finish hard turning of hardened AISI 52100 steel, Huang and Liang[147] observed adhesion as the main wear mechanism. On the other hand, they observed chemical diffusion as a dominant wear mechanism over extended periods of machining under aggressive cutting conditions as shown in **Figure 38**. Mechanical wear model which was modeled considering abrasion and adhesion as dominant wear mechanisms could be used to predict the flank wear progression and failure points of uncoated and ceramic-coated PCBN during finish turning of hardened steel.[134]

Table 4 Attempts made by various researchers in modeling of tool wear[3]

Researchers	*Tool wear model*
Chinchanikar and Choudhury[7]	Developed flank wear progression model considering abrasion, adhesion, and diffusion wear mechanisms in turning hardened AISI 4340 steel using multilayer-coated carbide tool
Chinchanikar and Choudhury[60]	Developed empirical models to predict flank wear of multilayer-coated carbide tool in turning AISI 4340 steel hardened at two different levels of hardness
Dawson and Kurfess[134]	Developed flank wear progression model considering abrasion and adhesion as dominant wear mechanisms
Huang and Dawson[135]	Developed model to predict crater wear depth of CBN tool incorporating abrasion, adhesion, and diffusion wear mechanisms
Singh and Rao[136]	Developed flank wear prediction model of ceramic inserts in hard turning considering abrasion, adhesion, and diffusion as dominant wear mechanisms
Kramer[137]	Developed wear rate model for coated tools considering abrasive wear and the chemical dissolution as dominant wear mechanisms
Singh and Vajpayee[138]	Developed flank wear model considering abrasion as dominant wear mechanism
Choudhury *et al.*[139]	Developed flank wear model in the machining of EN 24 steel using high speed steel (HSS) tools
Bhattacharya and Ham[140]	Developed flank wear model considering adhesion as a dominant wear mechanism
Molinari and Nouari[141]	Developed crater wear model considering diffusion wear as a dominant mechanism in high speed cutting processes
Wong *et al.*[142]	Suggested comprehensive equations for flank and crater wear
Haddag and Nouari[143]	Carried out tool wear and heat transfer analyses in dry machining based on multisteps numerical modeling
Halila *et al.*[144]	Developed wear model considering abrasive particles embedded at the interface between tool and chip
Luo *et al.*[145]	Developed flank wear rate model combining cutting mechanics simulation and an empirical model
Kannatey-Asibu[146]	Developed flank wear rate model considering adhesion and diffusion as dominant wear mechanisms while machining of AISI 1045 steel using tungsten carbide cutting tool
Huang and Liang[147]	Developed CBN tool flank wear rate model as a function of tool/workpiece material properties and cutting parameters in finish hard turning of hardened steel
Kwon[148]	Developed predictive models for flank wear that explicitly incorporate cutting temperature and physical properties of coatings and work materials
Kramer and Judd[149]	Presented quantitative models for the relative abrasive and chemical dissolution wear rates of potential tool coating materials
Palanisamy and Shanmugasundaram[150]	Developed regression and artificial neural network (ANN) models to predict tool wear in hard turning
Dureja[153]	Developed flank and crater wear models using response surface methodology (RSM)

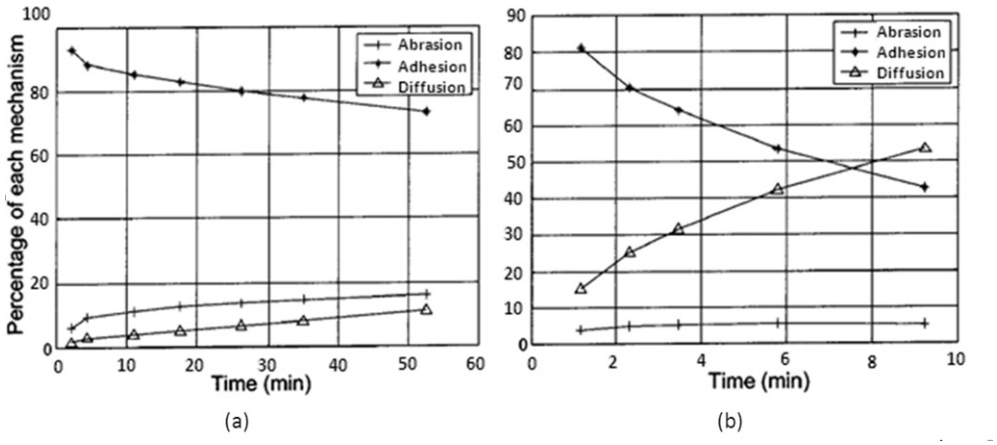


Figure 38 Contribution percentage of different wear mechanisms when using feed and depth of cut of 0.114 mm rev^{-1} and 0.203 mm and at cutting speed of (a) 1.21 m s^{-1} and (b) 2.29 m s^{-1}.[147]

Very few attempts have been made by the researchers to model the flank wear progression of coated carbide tool in machining of hardened steel as models developed are mostly applicable when using CBN or ceramic tools. The analysis of most of the studies concluded that tool wear increases with the increase in cutting speed, feed, and effective rake angle. However, cutting speed followed by feed was reported to be having most prominent effect on tool wear in comparison to depth of cut.[7,60,136,151,153] On the other hand, tool wear was reported to slightly decreasing with the increase in nose radius.[136]

1.3.4.3 Modeling of RSs

Considerable amount of modeling efforts have been undertaken to predict machining performance namely, tool wear,

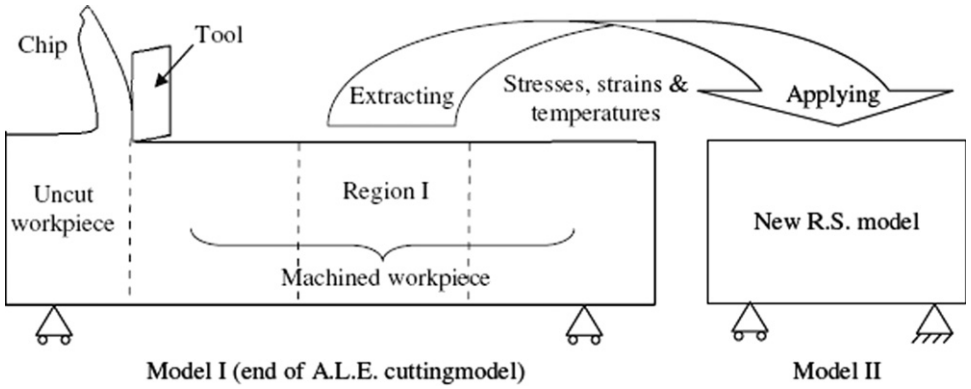


Figure 39 Schematic implementation of the modified RS approach.[162]

tool life, surface roughness, cutting forces/power, and part accuracy. Also, significant attempts have been made by the researchers in developing safer and secure operating conditions for machining, selection of appropriate tooling and accessories such as jigs and fixtures to avoid machining chatter and vibrations.[67] RS profile in a component is often considered as the critical characteristic as it directly affects the fatigue life of a machined component. Predictive models for RSs are among the fastest growing research topics in several research groups owing to its correlation with the fatigue life of the machined components.[154]

The desired RSs in the machined surfaces can be obtained by selecting correct cutting conditions, tool geometry and other process parameters. The service life of a machined product will heavily depend on the machining-induced RSs and would be of paramount importance in the overall enhancement of product sustainability. The computational methods such as numerical modeling using finite element methods have been widely used to predict machining-induced RSs, despite the questions surrounding the validity of the various assumptions made and the material constitutive relationships being incorporated in these models.[67] Moreover, its high computational cost has been always an issue. Hua *et al.*[155] investigated through numerical modeling the effects of cutting conditions, tool edge configuration, and the work material hardness on the axial and circumferential RSs in hard turning of bearing steels using commercial FEM software. The effect of cutting conditions, tool geometry parameters such as rake angle, tool nose radius and tool edge configurations with chamfer on RSs was investigated using a thermo-elastic–plastic finite element model.[156–159] Outeiro *et al.*[160] investigated using FEM the role of size effect on RSs and the microstructural transformation of the machined layer.

El-Axir[161] developed experimental-based model to predict turning-induced RSs in five different materials. The proposed model developed by them fitted the experimental data with a high degree of accuracy and determines both the location and depth of the maximum RS. In this study, tensile strength of material, cutting speed, and feed rate were considered as input parameters affecting RS distribution. Further, it was postulated that the RS profile along the depth beneath surface is a polynomial function of the depth beneath surface and the coefficients of this polynomial are, in turn, functions of the input parameters.

Nasr *et al.*[162] presented a modified FE approach to predict machining-induced RSs using commercial FE software (ABAQUS™). In order to cut down the computational time from days as in case of the traditional approach to just few minutes, a modified approach was developed. The flow chart for both the traditional and modified approaches can be referred from.[162] In the traditional approach, the same model is left to relax and cool down to predict RSs. However, in the modified approach, only the machined workpiece is modeled, while the chip, tool, and uncut workpiece are not considered. **Figure 39** shows a schematic for the implementation of the modified approach, where the workpiece parameters (stresses, strains, and temperature) are exported from the cutting model and imported to the new RS model. Four different workpiece materials (AISI H13, AISI 316L, AISI 52100, and AISI 4340) were used by them to validate the predicted results of their model with the experimental results which were obtained under similar cutting conditions. They observed predicted results in reasonable agreement with experimental results.

Agrawal and Joshi[163] developed an analytical model to predict the RSs in orthogonal machining of AISI 4340 steel. Predicted results of the RSs obtained by them are in good (86–88%) agreement with the experimental values in the *X*- and *Y*-directions. They found that the RS is greatly affected by the process parameters such as feed, cutting speed, machining temperature, and tool design parameters, such as edge radius as shown in **Figures 40–42**.

The analysis of their study concluded as follows:

- The tensile RSs on the machined surface decrease with an increase in the edge radius. However, the compressive RSs below the machined surface increase with an increase the edge radius.
- The tensile RSs on machined surface increase with an increase in the cutting speed and observed to decrease with increase in the depth of cut. However, below the surface, the compressive RSs increase with increase in the depth of cut.

The predictions of RSs are most critical on the machined aerospace components for the safety of the aircraft. With this view, Lazoglu *et al.*[164] presented an analytical model to predict the RSs which was validated with the measured experimental results obtained in machining of the high strength engineering

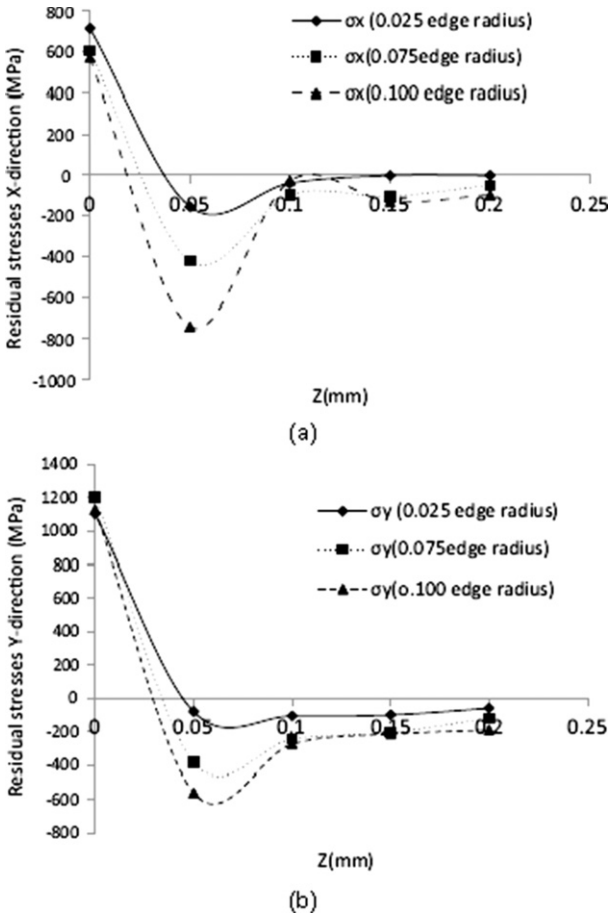


Figure 40 Effect of tool edge radius on residual stresses in (a) *X*-direction (σ_x) and (b) *Y*-direction (σ_y).[163]

material Waspaloy. They employed an enhanced analytical elasto-plastic model using the superposition of thermal and mechanical stresses on the workpiece, followed by a relaxation procedure. By changing the material properties and cutting conditions, the algorithm suggested by them could be easily applied to different materials.

The analytical model of RS in orthogonal cutting proposed by Jiann is an important tool for RS prediction in orthogonal cutting.[165] However, a significant error in the prediction accuracy has been observed for the surface RSs. With this view, Qi *et al.*[166] developed an improved analytical model to predict RSs in orthogonal cutting. The simulation results obtained for RSs by their model were compared with the Jiann's model and the simulation results of the two models are compared with the experimental results in cutting AISI 1045 steel. The authors observed better prediction accuracy in comparison to Jiann's model and claimed that the developed model could provide favorable conditions for the optimization of cutting parameters.

Ulutan *et al.*[167] developed an analytical model for prediction of RSs which is verified with experimental measurements of RSs on bearing steel 100Cr6 (JIS SUJ2) in the literature. Thermal field of workpiece which was determined using a finite-difference-based technique was used by them in the thermo-mechanical model of the RSs. Stresses resulting from thermal and mechanical loading were obtained by them using an analytical elasto-plastic model and a relaxation procedure. With the analytical model presented by them, the RSs could be predicted with acceptable accuracy and quite fast.

Predictive models for surface and subsurface, covering RSs, microstructural and metallurgical alteration, variations in mechanical properties, micro-crack development and growth, etc., are urged as significant owing to their correlation with the fatigue life of a product.[168] Nevertheless, the gaps in the experimental and predicted values point to the opportunity for the future work. The gap may be reduced by better definition of the physical phenomena at tool–chip, tool–work, and tool edge radius interfaces in a machining process.[166]

1.3.5 Hard Machining: Application of Different Cooling Techniques

Green cutting will become an important tendency of machining with environment consciousness enhanced laws and regulations consummated. At present, green cutting technology includes dry machining, semidry machining using minimum quantity lubrication (MQL), compressed air cooling, cryogenic machining, and solid lubrication. Dry cutting involves heat dissipation without coolants and for machining of harder materials, it demands high performance cutting tools. MQL technology is close to dry cutting technique, which is between dry and wet machining wherein a small quantity of cutting fluid mixed with compressed air access the contact zone between tool and chip as shown in **Figure 43**.[3]

1.3.5.1 Dry, Semidry, and Cryogenic Machining

Finish machining of hardened steel is almost cited in literature using dry cutting, because the increase of the temperature makes chip deformation and shearing of the hardened material, easier. Moreover, since the process is performed usually at high speed, most of the heat is carried away by the chip flowing at a high speed making the use of cutting fluid redundant. It is reported that HSM of hardened steels under flood coolant condition lowers the tool life due to formation of severe thermal cracks.[169] However, the complete absence of lubrication creates problems in chip transportation and causes an increase of tool–chip and tool–workpiece friction. On the other hand, the use of abundant cutting fluid has the advantages of providing chip transportation, reducing friction, and cooling the workpiece. In machining of hardened steel, the application of abundant cutting fluid does not allow the workpiece to soften, which is good for the process. Moreover, the use of cutting fluids increases the cost of cutting process and poses a serious problem to the preservation of the environment and human health. Therefore, MQL may represent a compromise between the dry cutting and wet cutting.[3]

Chinchanikar and Choudhury[48] during their investigation on finish turning of hardened AISI 4340 steel (54–57 HRC) using differently coated carbide tools observed that improvement in tool life of almost 20–25% under MQL in comparison to dry turning as shown in **Figure 44**. However, this effect was

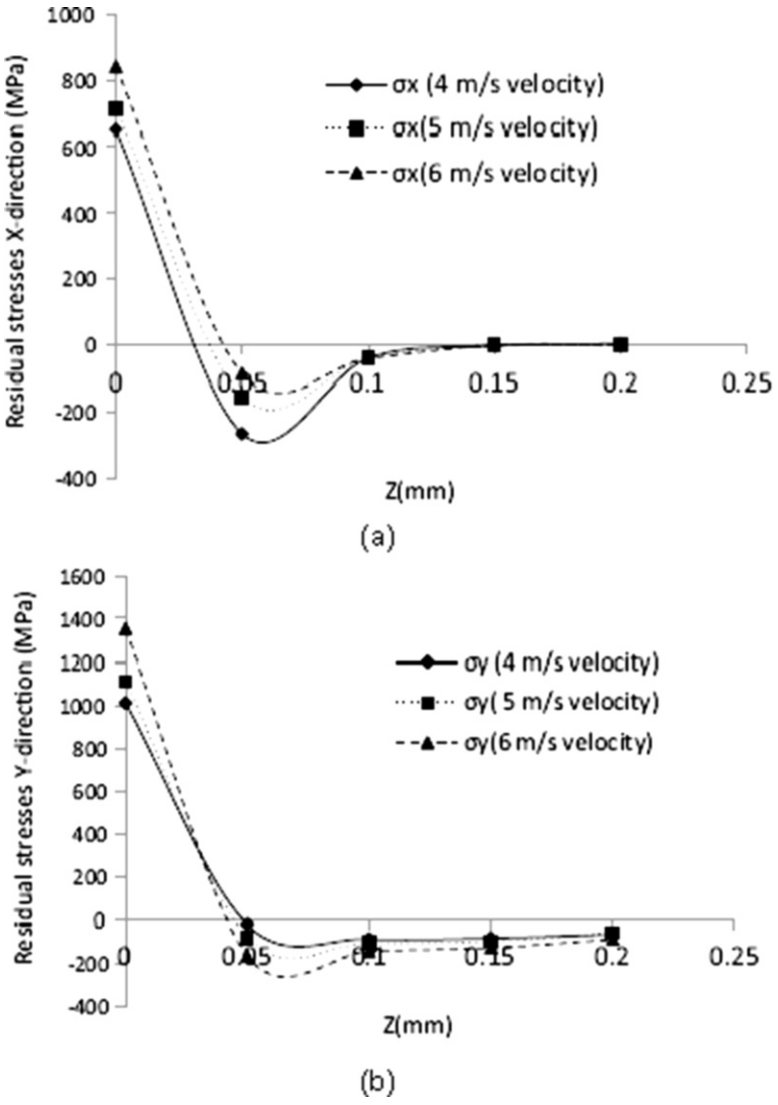


Figure 41 Effect of cutting speed on residual stresses in (a) *X*-direction (σ_x) and (b) *Y*-direction (σ_y).[163]

observed by them more prominent at higher cutting speed of 150 m min^{-1}. The tool nose wear width progression with machining time and the tool images indicating tool condition at the end of cutting under dry and MQL cutting conditions are shown in **Figure 45**. Nose wear, chipping off at the nose and clearance face was observed as a dominant wear forms under both dry and MQL cutting conditions.

The cooling and lubricating technique employed during machining significantly improves the surface properties. Avila and Abrao[171] observed that during turning of hardened AISI 4340 steel using mixed alumina inserts emulsion-based fluid without mineral oil and dry cutting provide better results in comparison to synthetic fluid and emulsion containing mineral oil. In general, machining under MQL improves tool life due to better cooling and lubricating effects in comparison to machining under dry and wet conditions. However, effectiveness of the cooling and lubricating technique to a large extent depends on the cutting parameters, namely the cutting speed and feed rate.[172]

Machining under MQL provides extra oxygen resulting in the formation of a protective oxide layer in between the chip–tool interface which acts as a diffusion barrier. However, there exists an optimal cutting speed at which a stable protective oxide layer can be formed. When cutting speed is lower than this speed, there is less oxide layer and the improvement of tool life is less apparent. As the cutting speed is far beyond the optimal value, the protective layer is absent and the thermal cracks are apt to occur at the cutting edge due to large fluctuation of temperature. Therefore, by properly selecting cutting parameters under MQL the tool life could be effectively improved.[173] It is reported that the tool flank wear and the cutting temperature were effectively reduced due to the lubricant percolating in mist and wet cutting. In dry cutting, the tool wear width was at its maximum near the boundary of the depth of cut, whereas for the mist and wet cutting methods the tool wear was almost flat.[174]

Khan *et al.*[175] observed a significant improvement in tool life under MQL as MQL-assisted in lowering the tool wear rate

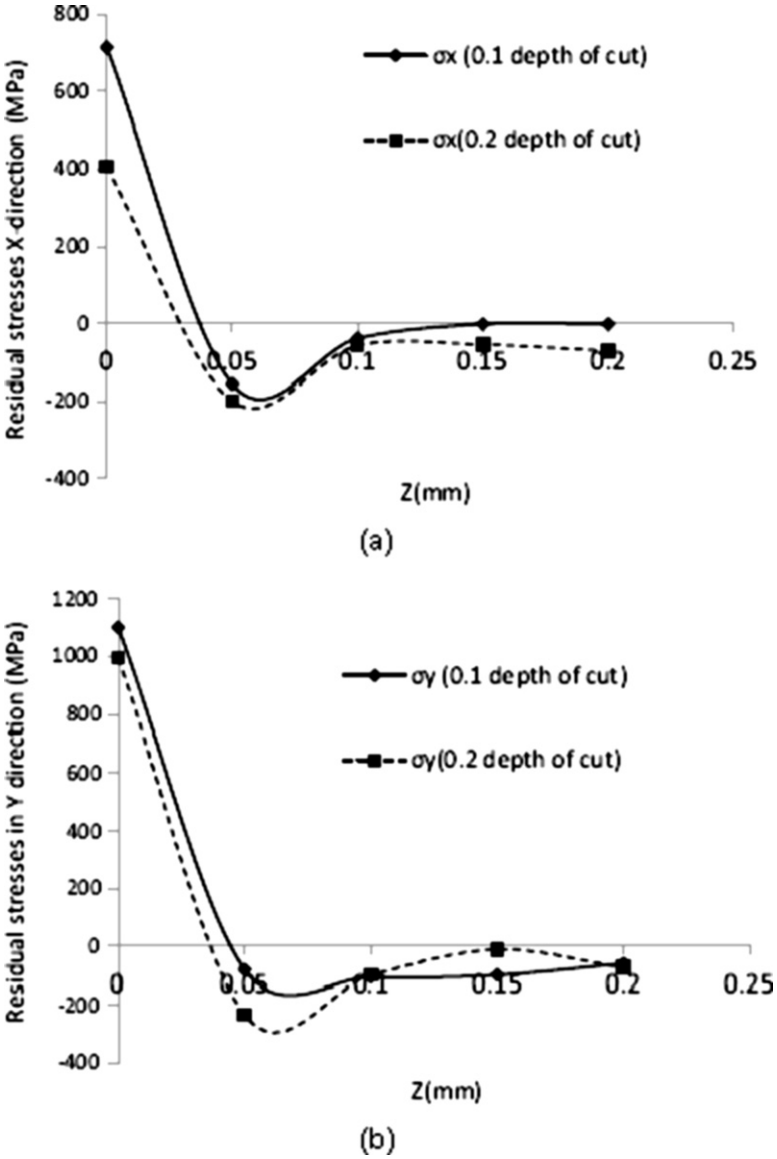


Figure 42 Effect of depth of cut on residual stresses in (a) *X*-direction (σ_x) and (b) *Y*-direction (σ_y).[163]

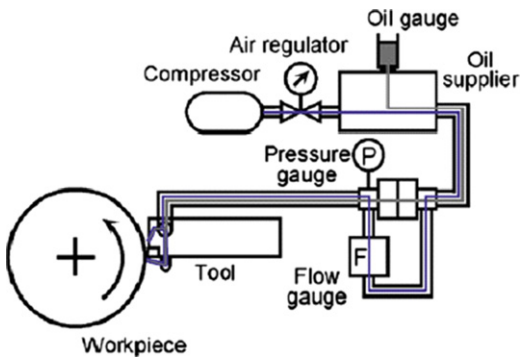


Figure 43 Schematic view of the components of a MQL system.[170]

due to abrasion, adhesion and diffusion type thermal sensitivity wear. Moreover, they found that MQL eliminates built-up edge formation and reduces deep grooving and hence, catastrophic failure of the cutting tools. Varadarajan *et al.*[176] during their investigation on hard turning developed a fluid application system by which a thin pulsed jet of cutting fluid at high velocity was applied at the immediate cutting zones. They observed superior performance in terms of cutting force, tool life, surface finish, cutting ratio, cutting temperature, and tool–chip contact length during MQL in comparison to that of dry and conventional wet turning.

Vikram Kumar and Ramamoorthy[177] also found better machining performance in terms of cutting force, temperature, and surface finish under MQL than that of dry and conventional wet turning. Dhar *et al.*[69] observed significant reduction in tool wear rate and surface roughness under MQL mainly through reduction in the cutting zone temperature and favorable change in the chip–tool and work–tool interaction as shown in **Figure 46**. In another study,[111] they found that MQL-assisted machining results in lower cutting temperature,

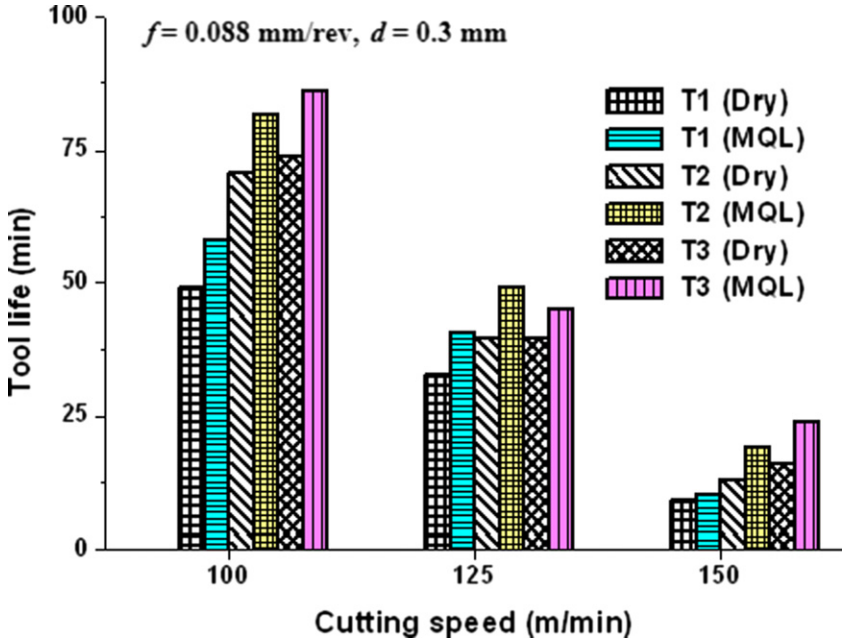


Figure 44 Histogram showing tool life for differently PVD-coated carbide tools, T1: AlTiN coated, T2: Multilayer TiAlN/TiSiN coated, and T3: AlTiCrN coated.[48]

lower cutting force and hence, resulting in lower dimensional deviation.

On the other hand, a group of researchers observed that dry machining leads to the lowest values of tool wear and surface roughness, while the minimal quantity of lubricant technique does not provide any advantage over dry hard turning.[20,62,74] Bruni *et al.*[20] investigation also showed that MQL technique did not significantly reduce the tool wear, whilst wet cutting produced the worst surface finish. Attanasio *et al.*[178] observed similar tool life under dry cutting conditions and under MQL applied on the rake. However, MQL applied on the flank surface resulted in reducing tool wear and hence, in increasing tool life. Finally, they concluded that although, MQL gives some advantage during turning operation, but it presents some difficulty in exactly reaching the lubricant at the cutting zone.

Although, dry and semidry machining are the most commonly used machining techniques which complement to reduce or eliminate the use of conventional cutting fluids, chilled air, and cryogenic machining techniques also have been found to be a complete alternative for cutting fluids due to the difficulties in machining difficult-to-machine materials. Cryogenic machining is a term referred to machining operations conducted at very low temperatures (lower than 120 K) using a super cold medium, usually liquefied gases.[179] Schwach *et al.*[180] investigated the effect of cryogenic cooling during hard turning of AISI 52100 steel and AISI D2 steel using CBN and ceramic tools. The effect of cryogenic liquid nitrogen cooling, tool and workpiece materials, and cutting speeds on white layer formation were investigated. It was found that with cryogenic cooling ceramic tools performed well and resulted in thinner white layer than conventional CBN dry hard turning. It was also observed that hard turning without coolant include surface softening and more fluctuation of RSs. Liquid nitrogen cooling resulted in retention of material hardness, flatter stress gradients, and elimination of tensile stresses in case of hard turning with alumina inserts.

1.3.5.2 Application of Vegetable Oils and Solid Lubricants

In the twenty-first century, with environment consciousness enhanced laws and regulations consummated, green cutting will become an important tendency of machining. Although, cutting fluids are beneficial in the industries, today their uses have become more and more prevalent around the world as they are contaminated with metal particles and degradation products which create health and environmental issues.

From last decade, vegetable oil-based cutting fluids are getting more and more attention in industry as they are renewable, biodegradable, nontoxic and have high viscosity and high flash point.[181] Among users, rapeseed,[182] canola,[183] and coconut oils[184–186] are mostly preferred as vegetable oil-based cutting fluids to alleviate problems faced by workers such as skin cancer and inhalation of toxic mists in the working environment when using mineral oil-based lubricants.[187] Ozcelik *et al.*[188] experimental study during turning using sunflower oil, canola oil, semisynthetic, and mineral-based oils also concluded that mineral and semisynthetic cutting fluids could be replaced by vegetable-based oils.

A group of researchers made great effort to compare machining performance under dry cutting, wet cutting, and cutting with vegetable-based oils. Chinchanikar *et al.*[189] performed hard turning of AISI 52100 steel (60–62 HRC) PVD-coated nanolaminated TiSiN–TiAlN carbide tool under dry, with water-based and coconut oil-based cutting fluids. Experimental observations of their study indicate that hard turning under dry condition produced lower values of surface roughness. However, at higher cutting speeds hard turning using coconut oil showed lower values of surface roughness.

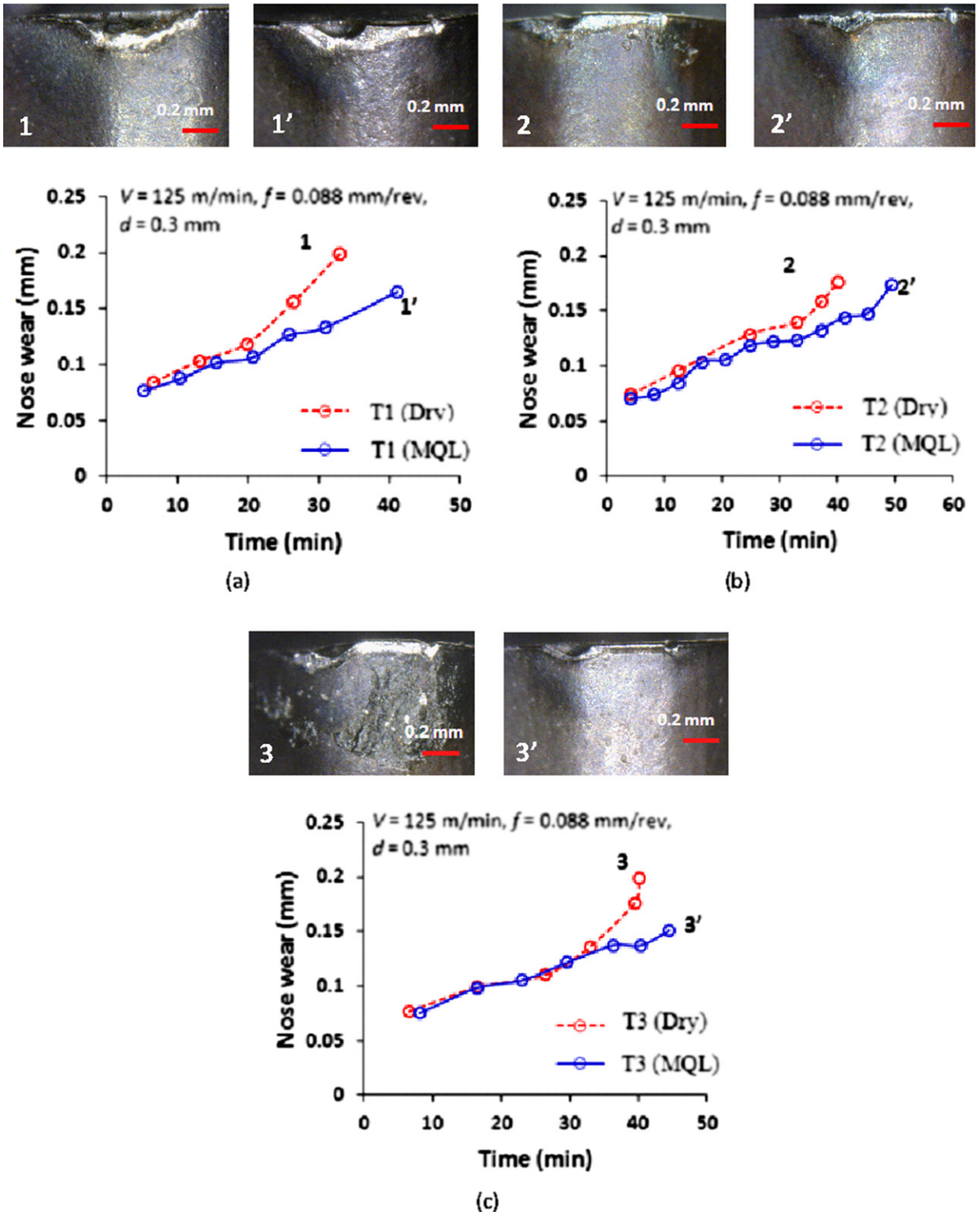


Figure 45 Nose wear with time of cutting under dry and MQL cutting condition at V=125 m min^{-1}, f=0.088 mm rev^{-1} and d=0.3 mm (a) AlTiN (T1), (b) multilayer TiAlN/TiSiN (T2), and (c) AlTiCrN (T3). Tool images indicate tool condition at the end of cutting shown by numbers.[48]

The coconut oil also found to be more effective in lowering surface roughness at higher values of feed and depth of cut. They observed that surface roughness gets affected mostly by feed and increased when cutting speed exceeds 150–160 m min^{-1} irrespective of the cooling mediums used. However, this effect can be seen as more prominent when turning under dry cutting conditions as shown in Figure 47.

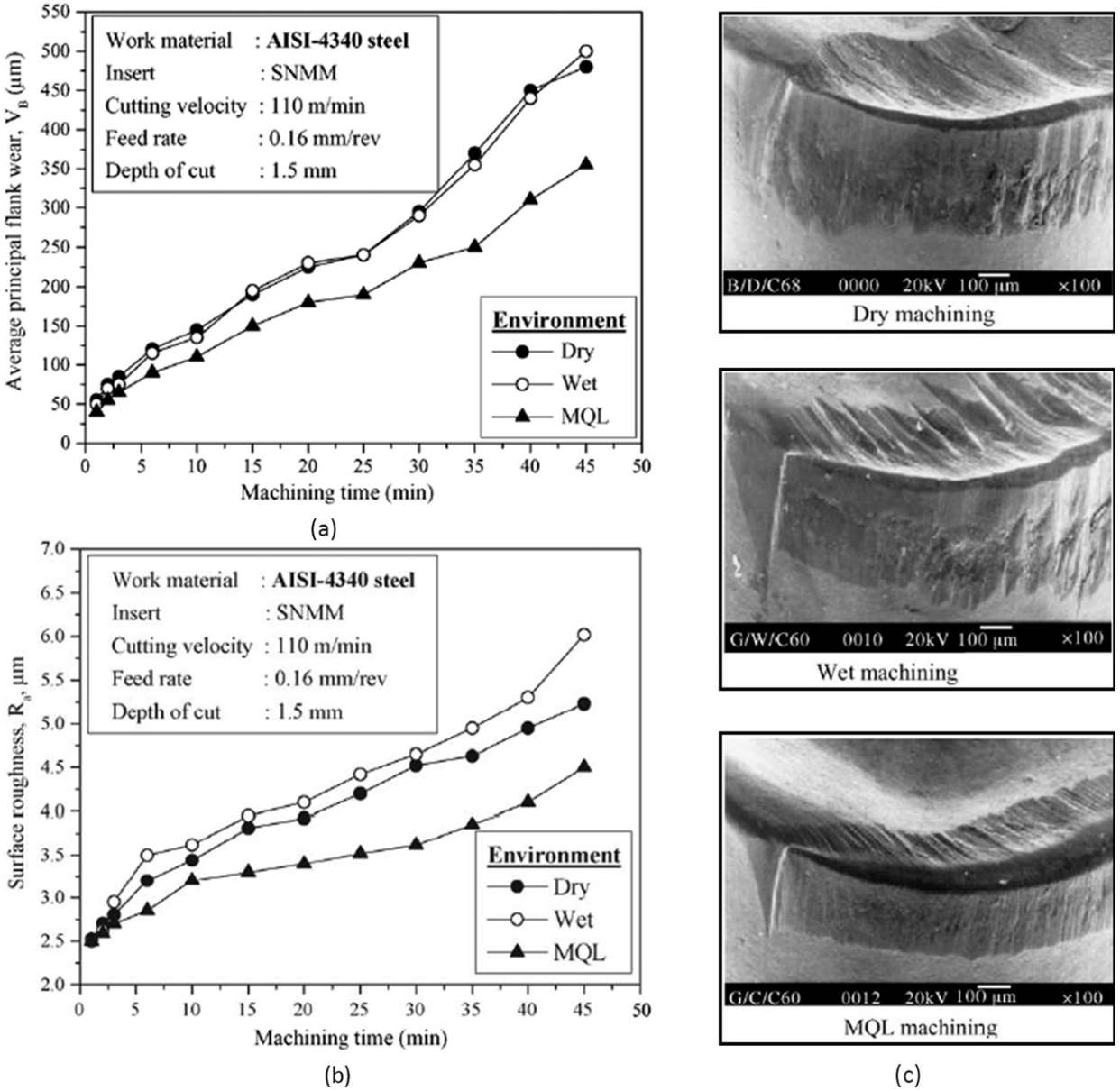


Figure 46 (a) Growth of average principal flank wear, V_B, (b) surface roughness with progress of machining, (c) SEM views of the worn out insert after machining 45 min.[69]

Xavior and Adithan[184] observed better performance in terms of lower tool wear and improved surface finish when using coconut oil in comparison to emulsion and neat cutting oils during turning of AISI 304 stainless steel. Ojolo *et al.*[190] observed better performance during turning with groundnut oil in comparison to coconut oil, palm kernel oil, and shear butter oil. Further, they found that the performance of vegetable-based cutting fluids depend on the workpiece material and cutting parameters employed during machining.

With a view to have eco-friendly and user-friendly alternatives to conventional cutting fluids, a group of researchers performed machining using solid lubricants as a cooling medium. It is reported that, solid lubricants, if employed properly, limits the cutting temperature by effectively removing the heat from the machining zone. Rao and Krishna[191] investigated and compared the machining performance in terms of cutting forces, tool wear, tool temperature, and surface roughness under the lubricating action of boric acid and compared with dry and wet machining. They reported that the use of boric acid as solid lubricant is advantageous over dry and wet machining.

Singh and Rao[192] investigated the effect of molybdenum disulfide solid lubricant on surface roughness while hard turning of bearing steel. Experimental results of their study indicate that a considerable improvement in the machining performance when using solid lubricant as compared to dry hard turning. In another study, Singh and Rao[193] explored the use of solid lubricants during hard turning while machining

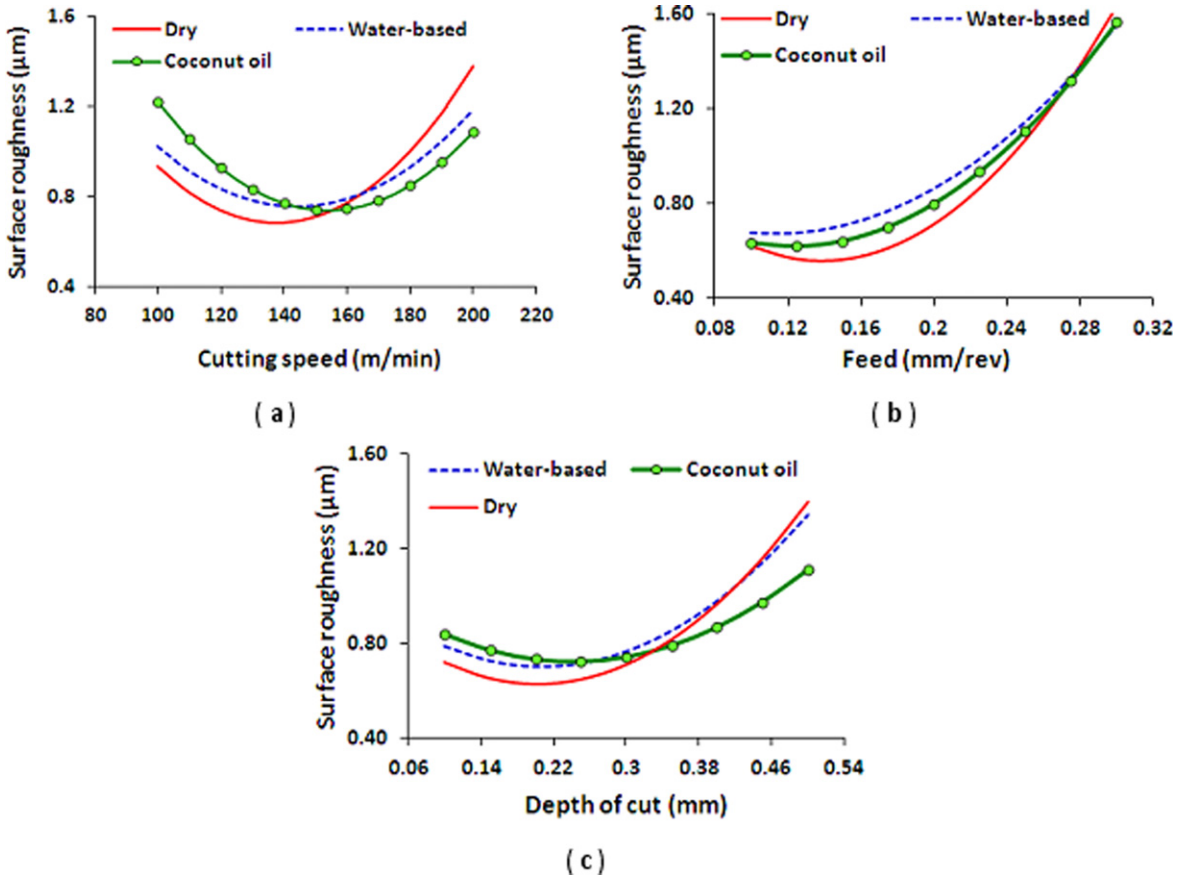


Figure 47 Effect on surface roughness under dry cutting, wet cutting, and cutting with vegetable-based oils by (a) cutting sped, (b) feed, and (c) depth of cut.[189]

bearing steel with mixed ceramic inserts at different cutting conditions and tool geometry. Results show considerable improvement from 8 to 15% in the surface finish with the use of solid lubricants as compared to dry hard turning. Experimental results of their study showed the superiority of the molybdenum disulfide hard turning over the graphite-assisted hard turning. Surface roughness value went down initially with increase in speed and then started increasing with the further increase in cutting speed. This might be due to increase in tool wear rate at higher speeds. Surface roughness was found to be increasing with increase in feed. Surface finish first improved with increase in effective rake angle, but, on further increasing rake angle, it deteriorated due to increase in forces. Increase in nose radius also improved surface finish. Their work emphasizes that the proper selection of the solid lubricants along with cutting conditions and tool geometry is essential for achieving the overall improvement in hard turning process. The solid lubricant-assisted hard turning may become a viable alternative to the dry and wet hard turning process.

Hard turning is mostly performed without coolant, but if lubrication and some cooling methods are used, it may prove beneficial for the process. It reduces abrasion and adhesion, thereby reducing rate of flank wear propagation which is the major cause of increase in workpiece temperature and formation of white layer at machined surface.[37] From the literature review, it has been observed that researchers have made a great effort to obtain eco-friendly and user-friendly alternatives to conventional cutting fluids using vegetable-based oils, solid lubricants, compressed air, and MQL technique. However, very few studies are reported on using coolants in hard turning while most works do without it. Moreover, there is disagreement between researchers about the use of coolants in hard turning so the area is still open for further investigations. New developments in the cutting tool materials and coating technology has brought some advantageous conditions for application of MQL in the machining of hardened steels. However, the major factor in this technology is to ensure cutting fluid accessing cutting zone and confirm minimal quantity of lubricant.

1.3.6 Optimization Studies in Machining of Hardened Steel

Finish machining of hardened steels by turning is receiving increasing attention especially in automotive and bearing industries. HPT offers a number of potential benefits over traditional grinding and has, nonetheless, several unique characteristics, as segmented chip formation and microstructural alterations at the machined surfaces, fundamentally different from conventional turning.[194] Moreover, HPT reduces processing time, the production cost, and setup time,

besides an adequate surface roughness. Furthermore, many of its process responses are predictable such as tool wear, tool life, quality of machined surface, and amount of material removed.[195]

One of the major problems in industries is to cut down the manufacturing cost without sacrificing the quality of the components as economy of machining operation plays a key role in competitiveness in the market. As a consequence of this, in any process planning of metal parts, modern sophisticated machine tools need optimization procedure for the selection of process parameters. Optimization in turning means determination of the optimal set of machining parameters such as cutting speed, feed rate, and depth of cut to satisfy the objectives within the operational constraints. These objectives may be desired roughness of the machined surface and RSs, minimum white layer thickness and dimensional deviation, minimum tool wear and maximum metal removal rate or any weighted combination of both.[196] However, in practice, parameter settings that are optimal for one defined objective function may not be particularly suited for another objective function. This results in an important optimization problem to define parameter settings given multiple. Therefore, the simultaneous consideration of multiple objectives, especially conflicting objectives with their different relative priorities need to be considered for efficient hard turning operation.[197]

Optimal selection of process parameters by formulating and solving as a multi-objective optimization problem has been analyzed with varying degree of generality by many researchers. A group of researchers analyzed multi-objective optimization problem in hard turning by combining neural network modeling with optimization methods. Effect of process parameters on the machining responses such as tool wear, surface integrity in terms of surface roughness, RSs, and microstructure alterations can be better understood by neural network modeling. Usually, evolutionary algorithms (EAs) such genetic algorithms (GAs) and particle swarm optimization (PSO) are preferred for optimization of neural network based models.[197,198] These days, with the availability and affordability of high-speed computers, optimization techniques based on EAs are becoming more popular in engineering design and manufacturing activities.[196]

Karpat and Ozel[197] presented multi-objective optimization of hard turning process using CBN tool. Objective of their study was to obtain optimum process parameters to limit tool wear and surface roughness and maximize the productivity while hard turning. A neural network model was developed by them to predict the surface roughness and tool wear. PSO algorithm was used to obtain optimum cutting speed, feed rate, and tool edge geometry. Results of their analysis concluded that the combined neural network and PSO system was capable of generating optimal process parameters and could be used successfully in the multi-objective optimization of hard turning. Tandon *et al.*[198] optimized machining parameters in end milling to minimize machining time by combining a feed forward neural network force model with PSO.

Pytlak[199] attempted multi-objective optimization of hard finish turning of 18HGT steel using CBN tool with wiper geometry. The cutting parameters such as cutting speed, feed and depth of cut were optimized to obtain minimum unit production cost, production time per unit and resultant cutting force. The multi-objective optimization was carried out by them with the application of traditional method of weights, as well as the modified distance method (MDM) based on evolutionary computations (EC). The authors claimed that the multi-objective optimization based on EC (the MDM method) quickly and effectively finds Pareto set of solutions. However, they pointed out that the large numbers of solutions obtained in the Pareto set seem to be one of the greatest disadvantages and the selection of a single solution from the set requires additional information about the decision maker's preferences. Finally, from the optimal sets obtained of Pareto solutions, the best solution was selected with the aid of the hierarchical optimization method. The results of their multi-objective optimization study show that in order to assure low unit production cost, low values of cutting force and to comply with constraints related to the surface roughness, the cutting speed of 119 m min^{-1} and the values of feed and depth of the cut of 0.3 mm rev^{-1} and 0.1 mm, respectively, to be adopted during hard finish turning of 18HGT steel using CBN tool with wiper geometry.

Ganesan *et al.*[200] during their investigation on continuous profile multi-pass machining obtained optimal machining parameters for minimum production time subject to a set of practical constraints such as cutting force, power and dimensional accuracy, and surface finish. They formulated process model using nontraditional algorithms such as GA and PSO. Their study shows that PSO produced better results in comparison to GA. Attempts also have been made to solve multi-objective optimization problem in turning by using multi-objective differential evolution (MODE) algorithm and nondominated sorting genetic algorithm (NSGA-II).[196] MODE and NSGA-II are the improved population-based search and optimization techniques which are widely used by the researchers in engineering design application.[201]

Yang and Natarajan[196] presented the optimum set of input parameters namely cutting speed, feed rate, and depth of cut during a single-pass turning of EN24 steel with tungsten carbide tool. Objective of their study was to minimize the tool wear and maximize the metal removal rate subjected to the temperature and surface roughness constraints. The regression models, developed for tool wear, temperature, and surface roughness were used for the problem formulation. In their study, the nondominated solution set which was obtained from MODE was compared with NSGA-II using the performance metrics and reported. They found 100 wider solutions with the NSGA-II algorithm. As against, the MODE algorithm was observed to be having lack of solution diversion. However, they observed that the MODE algorithm performed better than NSGA-II with fewer values of algorithm effort (AE) and optimizer overhead (OO).

Paiva *et al.*[202] presented a novel multi-objective optimization method based on the concept of multivariate mean square error (MMSE) approach in turning of hardened AISI 52100 steel. This novel approach combines principal component analysis (PCA) with RSM focusing a multidimensional nominal-the-best (NBT) problem. The results and confirmation runs of their study show that the MMSE approach outperforms the desirability method applied in the optimization of the 52100 hard turning. However, the solutions obtained

from MMSE and RSM-desirability function approach were not very different in practical terms.

Over the years, many researchers have developed algorithms based on classical techniques such as least-squares (LS) and many others for the domain engineering applications.[11] A desirability function approach presented by Derringer and Suich[203] is one of them, which is employed for simultaneous optimization of response variables. When using this approach, each response variable is transformed into desirability function (D_i), which is a dimensionless number ($0 \leq D_i \geq 1$). '0' indicates the completely undesirable level of response. '1' indicates the completely acceptable level of response. With this approach, optimization of several response variables (R_i) are converted into optimization of single desirability function, 'D_m' which is the geometric mean of the desirability of several responses and has to be optimized with respect to process variables.[11,40]

Chinchanikar and Choudhury[11] obtained the optimum values of process variables (cutting speed, feed, and depth of cut) in order to get the better tool life, minimum cutting forces and minimum surface roughness during turning of hardened AISI 4340 steel at two different levels of hardness, namely, 35 and 45 HRC, when using multilayer CVD-coated TiCN/Al_2O_3/TiN carbide tool. Optimization study was carried out by them in two different modules; the first module generates a set of solutions which ensures minimum surface roughness and cutting forces. The second module selects a most optimum cutting condition among the solutions generated in module 1, which gives better tool life. They found that lower feed and depth of cut values of 0.15 mm rev^{-1} and 1 mm and cutting speed of 235 and 144 m min^{-1}, while turning, namely, 35 and 45 HRC workpiece using CVD-applied multilayer-coated carbide tool, are the optimum cutting parameters which ensures minimum cutting forces, minimum surface roughness and better tool life. In another study, Chinchanikar and Choudhury[40] obtained a cutting speed of 176 m min^{-1} and lower values of feed and depth of cut of 0.15 mm rev^{-1} and 1 mm is the optimum cutting condition which ensures minimum cutting forces, minimum surface roughness and better tool life when using PVD-coated single-layer TiAlN carbide tool during turning of AISI 4340 steel (35 HRC).

Aouici *et al.*[41] presented the optimal manufacturing conditions subjected to minimum values of the cutting forces and surface roughness during the hard turning of hot work steel (AISI H11) using CBN 7020 tool. They obtained optimized surface roughness in the range of 0.327–0.34 μm and cutting force components in the axial direction of 33.91–38.78 N, radial direction in the range of 90.12–102.38 N and tangential direction of 63.85–77.57 N for the cutting speed in the range of 189–197 m min^{-1} and at lower values of feed and depth of cut of 0.08 mm rev^{-1} and 0.15 mm, respectively. In another study, tool geometry combination in terms of nose radius, rake and approach angles was optimized to obtain minimum surface roughness.[204] In this study, optimum cutting insert geometries obtained are found to be tool nose radius of 0.4 mm, approach angle of 60° and rake angle of −3° and the optimized surface roughness parameter obtained of 1.829 4 μm.

Sufficient efforts have been made by the researchers to obtain optimal cutting parameters for optimizing the various responses during machining of hardened steels. However, in most of the studies cutting parameters were optimized considering surface roughness or cutting forces or both. The tool life, being an important aspect was not considered while optimizing the cutting conditions. Moreover, most of the studies available are applicable for CBN/ceramic tools. Very few attempts have been made by the researchers by using coated carbide tools in the machining of hardened steel. On the other hand, process responses which are very important in finish machining of hardened steel such as RSs, white layer effect, and dimensional variation are rarely considered while optimizing the cutting conditions and further studies are required in this domain using coated carbide tools.

See also: 1.1 Factors Affecting Surface Roughness in Finish Turning

References

1. Available from: http://en.wikipedia.org/wiki/Hardened_steel (accessed 15 February 2016).
2. Coromant Sandvik. Available from: http://www2.coromant.sandvik.com/coromant/pdf/Hard_part_turning/C-1040-069.pdf (accessed 15 February 2016).
3. Chinchanikar, S.; Choudhury, S. K. Machining of Hardened Steel: Experimental Investigations, Performance Modeling and Cooling Techniques: A Review. *Int. J. Mach. Tools Manuf.* **2015**, *89*, 95–109.
4. Erdel, B. P. *High-Speed Machining*; S.M.E.: Dearborn, MI, 2003.
5. Klocke, F.; Brinksmeier, E.; Weinert, K. Capability Profile of Hard Cutting and Grinding Processes. *CIRP Ann.* **2005**, *54* (2), 557–580.
6. Grzesik, W. *Advanced Machining Processes of Metallic Materials*; Elsevier: Oxford, 2008.
7. Chinchanikar, S.; Choudhury, S. K. Predictive Modeling for Flank Wear Progression of Coated Carbide Tool in Turning Hardened Steel Under Practical Machining Conditions. *Int. J. Adv. Manuf. Technol.* **2014**, doi:10.1007/s00170-014-6285-6.
8. Pal, A.; Choudhury, S. K.; Chinchanikar, S. Machinability Assessment through Experimental Investigation During Hard and Soft Turning of Hardened Steel. *Procedia Mater. Sci.* **2014**, *6*, 80–91.
9. Chinchanikar, S.; Choudhury, S. K. Investigations on Machinability Aspects of Hardened AISI 4340 Steel at Different Levels of Hardness Using Coated Carbide Tools. *Int. J. Refract. Met. Hard Mater.* **2013**, *38*, 124–133.
10. Chinchanikar, S.; Choudhury, S. K.; Kulkarni, A. P. Investigation of Chip–Tool Interface Temperature During Turning of Hardened AISI 4340 Alloy Steel Using Multi-Layer Coated Carbide Inserts. *Adv. Mat. Res.* **2013**, *701*, 354–358.
11. Chinchanikar, S.; Choudhury, S. K. Effect of Work Material Hardness and Cutting Parameters on Performance of Coated Carbide Tool When Turning Hardened Steel: An Optimization Approach. *Measurement* **2013**, *46*, 1572–1584.
12. Seco. Available from: http://www.secotools.com/CorpWeb/switzerland/Downloads/Drehen/GB_PCBN_TechGuide_IV_Inlay_LR.pdf (accessed 15 February 2016).
13. Ezugwu, E. O.; Da Silva, R. B.; Bonney, J.; Machado, A. R. Evaluation of the Performance of CBN Tools When Turning Ti–6Al–4V Alloy with High Pressure Coolant Supplies. *Int. J. Mach. Tools Manuf.* **2005**, *45*, 1009–1014.
14. Galoppi, G. S.; Filho, M. S.; Batalha, G. F. Hard Turning of Tempered DIN100Cr6 Steel with Coated and No Coated CBN Inserts. *J. Mater. Process. Technol.* **2006**, *179*, 146–153.
15. Practicalmachinist. Available from: http://www.practicalmachinist.com/vb/cutting-tools/requirements-milling-hardened-steels-236637/ (accessed 15 February 2016).
16. Paulo Davim, J. *Machining: Fundamentals and Recent Advances*; Springer, Verlag London Limited: London, 2008.
17. Available from: http://www.emag.com/workpieces.html (accessed 2 April 2016).
18. Byrne, G.; Dornfeld, D.; Denkena, B. Advancing Cutting Technology. *CIRP Ann.* **2003**, *52* (2), 483–507.

19. Rodriguez, C. J. C. *Cutting Edge Preparation of Precision Cutting Tools by Applying Micro-Abrasive Jet Machining and Brushing*; Kassel University Press GmbH: Kassel, 2009.
20. Ozel, T.; Hsu, T. K.; Zeren, E. Effects of Cutting Edge Geometry, Workpiece Hardness, Feed Rate and Cutting Speed on Surface Roughness and Forces in Finish Turning of Hardened AISI H13 Steel. *Int. J. Adv. Manuf. Technol.* **2005**, *25*, 262–269.
21. Toenshoff, H.; Wobeker, H. G.; Brandt, D. Hard Turning – Influences on the Workpiece Properties. *Trans. NAMRI* **1995**, *23*, 215–220.
22. Ozel, T.; Karpat, Y.; Srivastava, A. Hard Turning with Variable Micro-Geometry PcBN Tools. *CIRP Ann. – Manuf. Technol.* **2008**, *57*, 73–76.
23. Thiele, J. D.; Melkote, S. N. The Effect of Tool Edge Geometry on Workpiece Subsurface Deformation and Through Thickness Residual Stresses for Hard Turning of AISI 52100 Steel. *Trans. NAMRI* **1999**, *27*, 135–140.
24. Chou, Y. K.; Evans, C. J.; Barash, M. M. Experimental Investigation on CBN Turning of Hardened AISI 52100 Steel. *J. Mater. Process. Technol.* **2002**, *124*, 274–283.
25. Karpat, Y.; Ozel, T. 3D FEA of Hard Turning: Investigation of PCBN Cutting Tool Micro-Geometry Effects. *Trans. NAMRI/SME* **2007**, *35*, 1–8.
26. Ozel, T.; Karpat, Y.; Figueira, L.; Davim, J. P. Modelling of Surface Finish and Tool Flank Wear in Turning of AISID2 Steel with Ceramic Wiper Inserts. *J. Mater. Process. Technol.* **2007**, *189*, 192–198.
27. Noordin, M. Y.; Zainal, A. M.; Kurniawan, D. Hard Turning of Cold Work Tool Steel Using Wiper Ceramic Tool. *J. Mek.* **2008**, *25*, 92–105.
28. Gaitonde, V. N.; Karnik, S. R.; Figueira, L.; Davim, J. P. Analysis of Machinability during Hard Turning of Cold Work Tool Steel (Type: AISI D2). *Mater. Manuf. Process.* **2009**, *24* (12), 1373–1382.
29. Sahin, Y. Comparison of Tool Life between Ceramic and Cubic Boron Nitride (CBN) Cutting Tools When Machining Hardened Steels. *J. Mater. Process. Technol.* **2009**, *209* (7), 3478–3489.
30. Sales, W. F.; Costa, L. A.; Santos, S. C.; Diniz, A. E.; Bonney, J.; Ezugwu, E. O. Performance of Coated, Cemented Carbide, Mixed-Ceramic and PCBN-H Tools When Turning W320 Steel. *Int. J. Adv. Manuf. Technol.* **2009**, *41*, 660–669.
31. Aneiro, F. M.; Coelho, R. T.; Brandao, L. C. Turning Hardened Steel Using Coated Carbide at High Cutting Speeds. *J. Braz. Soc. Mech. Sci. Eng.* **2008**, *30* (2), 104–109.
32. Suresh, R.; Basavarajappa, S.; Samuel, G. L. Some Studies on Hard Turning of AISI 4340 Steel Using Multilayer Coated Carbide Tool. *Measurement* **2012**, *45*, 1872–1884.
33. Huang, Y.; Liang, S. Y. Modeling of Cutting Forces Under Hard Turning Condition Considering Tool Wear Effect. *J. Manuf. Sci. Eng.* **2005**, *127* (2), 262–270.
34. Yallese, M. A.; Chaoui, K.; Zeghib, N.; Boulanouar, L.; Rigal, J. Hard Machining of Hardened Bearing Steel Using Cubic Boron Nitride Tool. *J. Mater. Process. Technol.* **2009**, *209*, 1092–1104.
35. Zhou, J. M.; Andersson, M.; Stahl, J. E. The Monitoring of Flank Wear on the CBN Tool in the Hard Turning Process. *Int. J. Adv. Manuf. Technol.* **2003**, *22*, 697–702.
36. Fnides, B.; Aouici, H.; Yallese, M. A. Cutting Forces and Surface Roughness in Hard Turning of Hot Work Steel X38CrMoV5-1 Using Mixed Ceramic. *Mechanika* **2008**, *2* (70), 73–78.
37. Bartarya, G.; Choudhury, S. K. State of the Art in Hard Turning. *Int. J. Mach. Tools Manuf.* **2012**, *53*, 1–14.
38. Lima, J. G.; Avila, R. F.; Abrao, A. M. Turning of Hardened AISI 4340 Steel Using Coated Carbide Inserts. *Proc. Inst. Mech. Eng. B-J. Eng. Manuf.* **2007**, *221*, 1359–1366.
39. Luo, S. Y.; Liao, Y. S.; Tsai, Y. Y. Wear Characteristics in Turning High Hardness Alloy Steel by Ceramic and CBN Tools. *J. Mater. Process. Technol.* **1999**, *88*, 114–121.
40. Chinchanikar, S.; Choudhury, S. K. Experimental Investigations to Optimise and Compare the Machining Performance of Different Coated Carbide Inserts. *Proc. Inst. Mech. Eng. B-J. Eng. Manuf.* **2014**, *228* (9), 1104–1117.
41. Aouici, H.; Yallese, M. A.; Chaoui, K.; *et al.* Analysis of Surface Roughness and Cutting Force Components in Hard Turning with CBN Tool: Prediction Model and Cutting Conditions Optimization. *Measurement* **2012**, *45*, 344–353.
42. Ebrahimi, A.; Moshksar, M. M. Evaluation of Machinability in Turning of Micro-Alloyed and Quenched-Tempered Steels: Tool Wear, Statistical Analysis, Chip Morphology. *J. Mater. Process. Technol.* **2009**, *209*, 910–921.
43. Lin, H. M.; Liao, Y. S.; Wei, C. C. Wear Behavior in Turning High Hardness Alloy Steel by CBN Tool. *Wear* **2008**, *264*, 679–684.
44. Bouacha, K.; Yallese, M. A.; Mabrouki, T.; Rigal, J. Statistical Analysis of Surface Roughness and Cutting Forces Using Response Surface Methodology in Hard Turning of AISI52100 Bearing Steel with CBN Tool. *Int. J. Refract. Met. Hard Mater.* **2010**, *28*, 349–361.
45. Yan, H.; Hua, J.; Shivpuri, R. Numerical Simulation of Finish Hard Turning for AISI H13 Die Steel. *Sci. Technol. Adv. Mater.* **2005**, *6*, 540–547.
46. Hashmi, M. S. J. *Comprehensive Materials Processing*; ISBN: 978-0-08-096533-8 Elsevier Ltd.: Amsterdam, 2014.
47. Bhokse, V.; Chinchanikar, S.; Anerao, P.; Kulkarni, A. Experimental investigations on Chip Formation and Plowing Cutting Forces during Hard Turning. In *4th International Conference on Materials Processing and Characterization at GRIET Hyderabad*, ICMPC; India; 13th–14th March; 2015.
48. Chinchanikar, S.; Choudhury, S. K. Hard turning Using HiPIMS-Coated Carbide Tools: Wear Behavior Under Dry and Minimum Quantity Lubrication (MQL). *Measurement* **2014**, *55*, 536–548.
49. Senthil Kumar, A.; Raja Durai, A.; Sornakumar, T. Machinability of Hardened Steel Using Alumina Based Ceramic Cutting Tools. *Int. J. Refract. Met. Hard Mater.* **2003**, *21*, 19–117.
50. Jerold, B. D.; Pradeep Kumar, M. Experimental Investigation of Turning AISI 1045 Steel Using Cryogenic Carbon Dioxide as the Cutting Fluid. *J. Manuf. Process.* **2011**, *13*, 113–119.
51. Poulachon, G.; Moisan, A.; Jawahir, I. S. Tool-Wear Mechanisms in Hard Turning with Polycrystalline Cubic Boron Nitride Tools. *Wear* **2001**, *250*, 576–586.
52. Korkut, I.; Boy, M.; Karacan, I.; Seker, U. Investigation of Chip-Back Temperature During Machining Depending on Cutting Parameters. *Mater. Des.* **2007**, *28*, 2329–2335.
53. Grzesik, W. Experimental Investigation of the Cutting Temperature When Turning with Coated Index Able Inserts. *Int. J. Mach. Tools Manuf.* **1999**, *39*, 355–369.
54. Grzesik, W.; Nieslony, P. Thermophysical-Property-Based Selection of Tool Protective Coatings for Dry Machining of Steels. *J. Manuf. Sci. Eng.* **2003**, *125*, 689–695.
55. Coelho, R. T.; Ng, E. G.; Elbestawi, M. A. Tool Wear When Turning Hardened AISI 4340 with Coated PCBN Tools Using Finishing Cutting Conditions. *Int. J. Mach. Tools Manuf.* **2007**, *47*, 263–272.
56. More, A. S.; Jiang, W.; Brown, W. D.; Malshe, A. P. Tool Wear and Machining Performance of cBN–TiN Coated Carbide Inserts and PCBN Compact Inserts in Turning AISI 4340 Hardened Steel. *J. Mater. Process. Technol.* **2006**, *180*, 253–262.
57. Chinchanikar, S.; Choudhury, S. K. Wear Behaviors of Single-Layer and Multi-Layer Coated Carbide Inserts in High Speed Machining of Hardened AISI 4340 Steel. *J. Mech. Sci. Technol.* **2013**, *27* (5), 1451–1459.
58. Park, K. H.; Kwon, P. Y. Flank Wear of Multi-Layer Coated Tool. *Wear* **2011**, *270*, 771–780.
59. Chakraborty, P.; Asfour, S.; Cho, S. Modeling Tool Wear Progression by Using Mixed Effects Modeling Technique When End-Milling AISI 4340 Steel. *J. Mater. Process. Technol.* **2008**, *205*, 190–202.
60. Chinchanikar, S.; Choudhury, S. K. Modeling and Evaluation of Flank Wear Progression of Coated Carbide Tools in Turning Hardened Steels. *Int. J. Manuf. Technol. Manag.* **2013**, *27* (1/2/3), 4–17.
61. Noordin, M. Y.; Venkatesh, V. C.; Sharif, S. Dry Turning of Tempered Martensitic Stainless Tool Steel Using Coated Cermet and Coated Carbide Tools. *J. Mater. Process. Technol.* **2007**, *185*, 83–90.
62. Lima, J. G.; Avila, R. F.; Abrao, A. M.; Faustino, M.; Paulo Davim, J. Hard Turning: AISI 4340 High Strength Alloy Steel and AISI D2 Cold Work Tool Steel. *J. Mater. Process. Technol.* **2005**, *169* (3), 388–395.
63. Ghani, J. A.; Choudhury, I. A.; Masjuki, H. H. Wear Mechanism of TiN Coated Carbide and Uncoated Cermets Tools at High Cutting Speed Applications. *J. Mater. Process. Technol.* **2004**, *153–154*, 1067–1073.
64. Avila, R. F.; Godoy, C.; Abrao, A. M.; Lima, M. M. Topographic Analysis of the Crater Wear on TiN, Ti(C,N) and (Ti,Al)N Coated Carbide Tools. *Wear* **2008**, *265*, 49–56.
65. Khrais, S. K.; Lin, Y. J. Wear Mechanisms and Tool Performance of TiAlN PVD Coated Inserts During Machining of AISI 4140 Steel. *Wear* **2007**, *262*, 64–69.
66. Chubb, J. P.; Billingham, J. Coated Cutting Tools – A Study of Wear Mechanisms in High Speed Machining. *Wear* **1980**, *61*, 283–293.
67. Saoubi, R. M.; Outeiro, J. C.; Chandrasekaran, H.; Dillon, O. W., Jr.; Jawahir, I. S. A Review of Surface Integrity in Machining and Its Impact on Functional Performance and Life of Machined Products. *Int. J. Sustain. Manuf.* **2008**, *1* (1/2), 203–236.
68. Available from: http://en.wikipedia.org/wiki/Surface_integrity (accessed 15 February 2016).

69. Dhar, N. R.; Kamruzzaman, M.; Ahmed, M. Effect of Minimum Quantity Lubrication (MQL) on Tool Wear and Surface Roughness in Turning AISI-4340 Steel. *J. Mater. Process. Technol.* **2006**, *172*, 299–304.
70. Oliveira, A. J.; Diniz, A. E.; Ursolino, D. J. Hard Turning in Continuous and Interrupted Cut With Pcbn and Whisker-Reinforced Cutting Tools. *J. Mater. Process. Technol.* **2009**, *209*, 5262–5270.
71. Dogra, M.; Sharma, V.; Sachdeva, A.; Suri, N. M. Tool Life and Surface Integrity Issues in Continuous and Interrupted Finish Hard Turning with Coated Carbide and CBN Tools. *Proc. IMechE, Part B: J. Eng. Manuf.* **2012**, *226* (3), 431–444.
72. Yusuf, S.; Motorcu, A. R. Surface Roughness Model for Machining Mild Steel with Coated Carbide Tool. *Mater. Des.* **2005**, *26*, 321–326.
73. Asilturk, I.; Akkus, H. Determining the Effect of Cutting Parameters on Surface Roughness in Hard Turning Using the Taguchi Method. *Measurement* **2011**, *44*, 1697–1704.
74. Cakir, M. C.; Cihat, E.; Ilker, D. Mathematical Modeling of Surface Roughness for Evaluating the Effects of Cutting Parameters and Coating Material. *J. Mater. Process. Technol.* **2009**, *209*, 102–109.
75. Noordin, M. Y.; Venkatesh, V. C.; Sharif, S.; *et al.* Application of Response Surface Methodology in Describing the Performance of Coated Carbide Tools When Turning AISI 1045 Steel. *J. Mater. Process. Technol.* **2004**, *145*, 46–58.
76. Lalwani, D. I.; Mehta, N. K.; Jain, P. K. Experimental Investigations of Cutting Parameters Influence on Cutting Forces and Surface Roughness in Finish Hard Turning of MDN250 Steel. *J. Mater. Process. Technol.* **2008**, *206*, 167–179.
77. Grzesik, W.; Wanat, T. Comparative Assessment of Surface Roughness Produced by Hard Machining with Mixed Ceramic Tools Including 2D and 3D Analysis. *J. Mater. Process. Technol.* **2005**, *169*, 364–371.
78. Dawson, Ty. G.; Kurfess, T. R. Tool Life, Wear Rates, and Surface Quality in Hard Turning. *Trans. NAMRI/SME* **2001**, *29*, 175–182.
79. Patz, M. Drehen statt Schleifen. *Werkstatt und Betrieb* **1995**, *128*, 1052–1056.
80. Suresh, R.; Basavarajappa, S.; Gaitonde, V. N.; Samuel, G. L. Machinability Investigations on Hardened AISI 4340 Steel Using Coated Carbide Insert. *Int. J. Refract. Met. Hard Mater.* **2012**, *33*, 75–86.
81. Stenberga, N.; Proudian, J. Numerical Modelling of Turning to Find Residual Stresses. *Procedia CIRP* **2013**, *8*, 258–264.
82. Vaz, M.; Owen, D. R. J.; Kalhori, V.; Lundblad, M.; Lindgren, L. E. Modelling and Simulation of Machining Processes. *Arch. Comput. Methods Eng.* **2007**, *14*, 173–204.
83. Gunnberg, F.; Escursell, M.; Jacobson, M. The Influence of Cutting Parameters on Residual Stresses and Surface Topography during Hard Turning of 18MnCr5 Case Carburised Steel. *J. Mater. Process. Technol.* **2006**, *174*, 82–90.
84. Warren, A. W.; Guo, Y. B. Characteristics of Residual Stress Profiles in Hard Turned versus Ground Surfaces with and without a White Layer. *J. Manuf. Sci. Eng.* **2009**, *131*, 1–10.
85. Guo, Y. B.; Anurag, S.; Jawahir, I. S. A Novel Hybrid Predictive Model and Validation of Unique Hook-Shaped Residual Stress Profiles in Hard Turning. *CIRP Ann. – Manuf. Technol.* **2009**, *58*, 81–84.
86. Matsumoto, Y.; Hashimoto, F.; Lahoti, G. Surface Integrity Generated by Precision Hard Turning. *CIRP Ann. – Manuf. Technol.* **1999**, *48* (7), 59–62.
87. Javidi, A.; Rieger, U.; Eichlseder, W. The Effect of Machining on the Surface Integrity and Fatigue Life. *Int. J. Fatigue* **2008**, *30*, 2050–2055.
88. Umbrello, D.; Outeiro, J. C.; M'Saoubi, R.; Jayal, A. D.; Jawahir, I. S. A Numerical Model Incorporating the Microstructure Alteration for Predicting Residual Stresses in Hard Machining of AISI 52100 Steel. *CIRP Ann. – Manuf. Technol.* **2010**, *59*, 113–116.
89. Thiele, J. D.; Melkote, S. N.; Peascoe, R. A.; Watkins, T. R. Effect of Cutting-Edge Geometry and Workpiece Hardness on Surface Residual Stresses in Finish Hard Turning of AISI 52100 Steel. *ASME J. Manuf. Sci. Eng.* **2000**, *122*, 642–648.
90. Hua, J.; Shivpuri, R.; Chenga, X.; Bedekara, V.; Matsumoto, Y.; Hashimoto, F.; Watkin, T. R. Effect of Feed Rate, Workpiece Hardness and Cutting Edge on Subsurface Residual Stress in the Hard Turning of Bearing Steel Using Chamfer + Hone Cutting Edge Geometry. *Mater. Sci. Eng. A* **2005**, *394* (1–2), 238–248.
91. El-Wardany, T. I.; Kishway, H. A.; Elbestawi, M. A. Surface Integrity of Die Material in High Speed Hard Machining, Part 2: Microhardness Variations and Residual Stresses. *Trans. NAMRI/SME* **2000**, *122*, 632–641.
92. Hua, J.; Umbrello, D.; Shivpuri, R. Investigation of Cutting Conditions and Cutting Edge Preparations for Enhanced Compressive Subsurface Residual Stress in the Hard Turning of Bearing Steel. *J. Mater. Process. Technol.* **2006**, *171* (2), 180–187.
93. Konig, W.; Klinger, M.; Link, R. Machining Hard Materials with Geometrically Defined Cutting Edges-Field of Application And Limitations. *Ann. CIRP* **1990**, *39* (1), 61–64.
94. Tonshoff, H. K.; Arendt, C.; Ben Amor, R. Cutting of Hardened Steel. *Ann. CIRP* **2000**, *49* (2), 547–566.
95. Griffiths, B. J. Mechanism of White Layer Generation with Reference to Machining Processes and Deformation Processes. *ASME J. Tribol.* **1987**, *42*, 145–152.
96. Chou, Y. K. Surface Hardening of AISI 4340 Steel by Machining: A Preliminary Investigation. *J. Mater. Process. Technol.* **2002**, *124*, 171–177.
97. Ramesh, A.; Melkote, S. N.; Allard, L. F.; Riester, L.; Watkins, T. R. Analysis of White Layers Formed in Hard Turning of AISI 52100 Steel. *Mater. Sci. Eng. A* **2005**, *390* (1–2), 88–97.
98. Guo, Y. B.; Sahni, J. A. Comparative Study of Hard Turned and Cylindrically Ground White Layers. *Int. J. Mach. Tools Manuf.* **2004**, *44*, 135–145.
99. Umbrello, D.; Filice, L. Improving Surface Integrity in Orthogonal Machining of Hardened AISI 52100 Steel by Modeling White and Dark Layers Formation. *Ann. CIRP* **2009**, *58*, 73–76.
100. Chou, Y. K.; Evans, C. J. White Layers and Thermal Modeling of Hard Turned Surfaces. *Int. J. Mach. Tools Manuf.* **1999**, *39*, 1863–1881.
101. Jiang, W.; More, A. S.; Brown, W. D.; Malshe, A. P. cBN–TiN Composite Coating for Carbide Inserts: Coating Characterization and Its Applications for Finish Hard Turning. *Surf. Coat. Technol.* **2006**, *201*, 2443–2449.
102. Bosheh, S. S.; Mativenga, P. T. White Layer Formation in Hard Turning of H13 tool steel at High Cutting Speeds Using CBN Tooling. *Int. J. Mach. Tools Manuf.* **2006**, *46*, 225–233.
103. Smith, S.; Melkote, S. N.; Lara-Curzio, E.; Watkins, T. R.; Allard, L.; Riester, L. Effect of Surface Integrity of Hard Turned AISI 52100 Steel on Fatigue Performance. *Mater. Sci. Eng. A* **2007**, *459*, 337–346.
104. Schwach, D. W.; Guo, Y. B. A Fundamental Study on the Impact of Surface Integrity by Hard Turning on Rolling Contact Fatigue. *Int. J. Fatigue* **2006**, *28*, 1838–1844.
105. Poulachon, G.; Albert, A.; Schluraff, M.; Jawahir, I. S. An Experimental Investigation of Work Material Microstructure Effects on White Layer Formation in PCBN Hard Turning. *Int. J. Mach. Tools Manuf.* **2005**, *45*, 211–218.
106. Aramcharoen, A.; Mativenga, P. T. White Layer Formation and Hardening Effects in Hard Turning of H13 Tool Steel with CrTiAlN and CrTiAlN/MoST-Coated Carbide Tools. *Int. J. Adv. Manuf. Technol.* **2008**, *36*, 650–657.
107. Zhou, J. M.; Andersson, M.; Stahl, J. E. Identification of Cutting Errors in Precision Hard Turning Process. *J. Mater. Process. Technol.* **2004**, *153–154*, 746–750.
108. Sorby, K. High Accuracy Turning with Long Boring Bars. In *International Conference on Sustainable Manufacturing and Operations Management*, 2013; pp. 41–44.
109. Kundrak, J.; Karpuschewski, B.; Gyani, K.; Bana, V. Accuracy of Hard Turning. *J. Mater. Process. Technol.* **2008**, *202*, 328–338.
110. Jawahir, I. S.; Wang, X. Development of Hybrid Predictive Models and Optimization Techniques for Machining Operations. *J. Mater. Process. Technol.* **2007**, *185*, 46–59.
111. Dhar, N. R.; Kamruzzaman, M. Cutting Temperature, Tool Wear, Surface Roughness and Dimensional Deviation in Turning AISI-4037 Steel Under Cryogenic Condition. *Int. J. Mach. Tools Manuf.* **2007**, *47*, 754–759.
112. Bruni, C.; Forcellese, A.; Gabrielli, F.; Simoncini, M. Hard Turning of an Alloy Steel on a Machine Tool with a Polymer Concrete Bed. *J. Mater. Process. Technol.* **2008**, *202*, 493–499.
113. Coromant Sandvik. Available from: http://www2.coromant.sandvik.com/coromant/pdf/Silent_tools/Silent_tools.pdf (accessed 15 February 2016).
114. Bana, V.; Karpuschewski, B.; Kundrak, J.; Hoogstrate, A. M. Thermal Distortions in the Machining of Small Bores. *J. Mater. Process. Technol.* **2007**, *191*, 335–338.
115. Stein, J., Dornfeld, D.A. Integrated Design and Manufacturing for Precision Mechanical Components. In *Proceedings of 1st International Conference on Integrated Design and Manufacturing, PRIMECA, Nantes, France*, 1996; pp. 195–204.
116. Astakhov, V. P. On the Inadequacy of the Single-Shear Plane Model of Chip Formation. *Int. J. Mech. Sci.* **2005**, *47*, 1649–1672.
117. Li, B.; Wang, X.; Hu, Y.; Li, C. Analytical Prediction of Cutting Forces in Orthogonal Cutting Using Unequal Division Shear-Zone Model. *Int. J. Adv. Manuf. Technol.* **2011**, *54*, 431–443.
118. Waldorf, D. J.; DeVor, R. E.; Kapoor, S. G. A Slip-Line Field for Ploughing During Orthogonal Cutting. *J. Manuf. Sci. Eng.* **1998**, *120*, 693–699.

119. Usui, E.; Hirota, A.; Masuko, M. Analytical Prediction of Three Dimensional Cutting Process, Part 1, Basic Cutting Model and Energy Approach. *J. Eng. Ind.: ASME* **1978**, *100*, 222–228.
120. Usui, E.; Hirota, A. Analytical Prediction of Three Dimensional Cutting Process, Part 2, Chip Formation and Cutting Force with Conventional Single-Point Tool. *J. Eng. Ind.: ASME* **1978**, *100*, 229–235.
121. Usui, E.; Shirakashi, T.; Kitagawa, T. Analytical Prediction of Three Dimensional Cutting Process, Part 3, Cutting Temperature and Crater Wear of Carbide Tool. *J. Eng. Ind.: ASME* **1978**, *100*, 236–243.
122. Oxley, P. L. B. *The Mechanics of Machining: An Analytical Approach to Assessing Machinability*; Ellis Horwood: Chichester, 1989.
123. Ehmann, K. F.; Kapoor, S. G.; DeVor, R. E.; Lazoglu, I. Machining Process Modeling: A Review. *J. Manuf. Sci. Eng.: ASME* **1997**, *119*, 655–663.
124. Markopoulos, A. P. *Finite Element Method in Machining Processes*; pp. VIII, 92 Springer: London, 2013.
125. Hu, R. S.; Mathew, P.; Oxley, P. L. B.; Young, H. T. Allowing for End Cutting Edge Effects in Predicting Forces in Bar Turning with Oblique Machining Conditions. *Proc. Inst. Mech. Eng. Part C* **1986**, *200* (C2), 89–99.
126. Young, H. T.; Mathew, P.; Oxley, P. L. B. Allowing for Nose Radius Effects in Predicting the Chip Flow Direction, and Cutting Forces in Bar Turning. *Proc. Inst. Mech. Eng. Part C* **1987**, *201* (C3), 213–226.
127. Wang, J.; Mathew, P. *Prediction of Chip Flow Direction and Cutting Forces in Oblique Machining with Nose Radius Tools Report 1988/IE/5*; University of New South Wales, 1988.
128. Li, K.-M.; Liang, S. Y. Modeling of Cutting Forces in Near Dry Machining Under Tool Wear Effect. *Int. J. Mach. Tools Manuf.* **2007**, *47*, 1292–1301.
129. Smithey, D. W.; Kapoor, S. G.; DeVor, R. E. A Worn Tool Cutting Force Model for Three-Dimensional Cutting Operations. *Int. J. Mach. Tools Manuf.* **2000**, *40*, 1929–1950.
130. Huang, Y.; Liang, S. Y. Force Modelling in Shallow Cuts with Large Negative Rake Angle and Large Nose Radius Tools – Application to Hard Turning. *Int. J. Adv. Manuf. Technol.* **2003**, *22*, 626–632.
131. Young, H. T.; Mathew, P.; Oxley, P. L. B. Allowing for Nose Radius Effects in Predicting the Chip Flow Direction, and Cutting Forces in Bar Turning. *Proc. Inst. Mech. Eng. C: J. Mech. Eng. Sci.* **1987**, *201* (C3), 213–226.
132. Arsecularatne, J. A.; Mathew, P.; Oxley, P. L. B. Prediction of Chip Flow Direction and Cutting Forces in Oblique Machining with Nose Radius Tools. *Proc. Inst. Mech. Eng. B: J. Eng. Manuf.* **1995**, *209*, 305–315.
133. Sahoo, A. K.; Sahoo, B. Experimental Investigations on Machinability Aspects in Finish Hard Turning of AISI 4340 Steel Using Uncoated and Multilayer Coated Carbide Inserts. *Measurement* **2012**, *45* (8), 2153–2165.
134. Dawson, T. G.; Kurfess, T. R. Modeling the Progression of Flank Wear on Uncoated and Ceramic-Coated Polycrystalline Cubic Boron Nitride Tools in Hard Turning. *J. Manuf. Sci. Eng.* **2006**, *128* (1), 104–109.
135. Huang, Y.; Dawson, T. G. Tool Crater Wear Depth Modeling in CBN Hard Turning. *Wear* **2005**, *258*, 1455–1461.
136. Singh, D.; Rao, P. V. Flank Wear Prediction of Ceramic Tools in Hard Turning. *Int. J. Adv. Manuf. Technol.* **2010**, *50*, 479–493.
137. Kramer, B. M. A Comprehensive Tool Wear Model. *CIRP Ann.* **1986**, *35*, 67–70.
138. Singh, C. K.; Vajpayee, S. Evaluation of Flank Wear on Cutting Tools. *Wear* **1980**, *62*, 247–254.
139. Choudhury, S. K.; Eswar Kumar, A.; Ghosh, A. Scheme of Adaptive Turning Operations. *J. Mater. Process. Technol.* **1999**, *87*, 119–127.
140. Bhattacharya, A.; Ham, I. Analysis of Tool Wear- Part 1: Theoretical Models of flank Wear. *J. Eng. Ind.* **1969**, *91*, 790–798.
141. Molinari, A.; Nouari, M. Modeling of Tool Wear by Diffusion in Metal Cutting. *Wear* **2002**, *252*, 135–149.
142. Wong, T.; Kim, W.; Kwon, P. Experimental Support for a Model-Based Prediction of Tool Wear. *Wear* **2004**, *257* (7–8), 790–798.
143. Haddag, B.; Nouari, M. Tool Wear and Heat Transfer Analyses in Dry Machining Based on Multi-Steps Numerical Modeling and Experimental Validation. *Wear* **2013**, *302* (1–2), 1158–1170.
144. Halila, F.; Czarnota, C.; Nouari, M. Analytical Stochastic Modeling and Experimental Investigation on Abrasive Wear When Turning Difficult to Cut Materials. *Wear* **2013**, *302* (1–2), 1145–1157.
145. Luo, X.; Cheng, K.; Holt, R.; Liu, X. Modeling Flank Wear of Carbide Tool Insert in Metal Cutting. *Wear* **2005**, *259*, 1235–1240.
146. Kannatey-Asibu, E. A Transport-Diffusion Equation in Metal Cutting and its Application to Analysis of the Rate of Flank Wear. *J. Eng. Ind.* **1985**, *107*, 81–89.
147. Huang, Y.; Liang, S. Y. Modeling of CBN Tool Flank Wear Progression in Finish Hard Turning. *J. Manuf. Sci. Eng.: ASME* **2004**, *126* (1), 98–106.
148. Kwon, P. Predictive Models for Flank Wear on Coated Inserts. *J. Tribol.* **2000**, *122* (1), 340–347.
149. Kramer, B. M.; Judd, P. K. Computational Design of Wear Coatings. *J. Vac. Sci. Technol. A* **1985**, *3* (6), 2439–2444.
150. Palanisamy, P.; Shanmugasundaram, S. Modelling of Tool Wear and Surface Roughness in Hard Turning Using Regression and Artificial Neural Network. *Int. J. Mach. Mach. Mater.* **2008**, *4* (1), 76–94.
151. Chinchanikar, S.; Choudhury, S. K. Comparative Evaluations of Tool Nose Wear Progression Under Dry and Near-Dry Cutting Conditions during Hard Turning Through Experimentation and Mathematical Modeling. In *5th International and 26th All India Manufacturing Technology Design and Research (AIMTDR-2014) Conference, India*; 2014.
152. Huang, Y.; Liang, S. Y. Cutting Forces Modeling Considering the Effect of Tool Thermal Property-Application to CBN Hard Turning. *Int. J. Mach. Tools Manuf.* **2003**, *43*, 307–315.
153. Dureja, J. S. Optimisation of Tool Wear during Hard Turning of AISI-H11 Steel Using TiN Coated CBN-L Tool. *Int. J. Mach. Mach. Mater.* **2012**, *12* (1/2), 37–53.
154. Sasahara, H. The Effect on Fatigue Life of Residual Stress and Surface Hardness Resulting from Different Cutting Conditions of 0.45%C Steel. *Int. J. Mach. Tools Manuf.* **2005**, *45*, 131–136.
155. Hua, J.; Umbrello, D.; Shivpuri, R. Investigation of Cutting Conditions and Cutting Edge Preparations for Enhanced Compressive Subsurface Residual Stress in the Hard Turning of Bearing Steel. *J. Mater. Process. Technol.* **2006**, *171* (2), 180–187.
156. Dogra, M.; Sharma, V. S.; Dureja, J. Effect of Tool Geometry Variation on Finish Turning – A Review. *J. Eng. Sci. Technol. Rev.* **2011**, *4* (1), 1–13.
157. Sasahara, H.; Obikawa, T.; Shirakashi, T. The Prediction of Effects of Cutting Condition on Mechanical Characteristics in Machined Layer. In *Advancement of Intelligent Production*; Usui, E., Ed.; Elsevier: Amsterdam, 1994; pp. 473–478.
158. Sasahara, H.; Obikawa, T.; Shirakashi, T. FEM Analysis of Cutting Sequence Effect on Mechanical Characteristics in Machined Layer. *J. Mater. Process. Technol.* **1996**, *62*, 448–453.
159. Sasahara, H.; Obikawa, T.; Shirakashi, T. Prediction Model of Surface Residual Stress within a Machined Surface by Combining Two Orthogonal Plane Models. *Int. J. Mach. Tools Manuf.* **2004**, *44*, 815–822.
160. Outeiro, J. C.; Kandibanda, R.; Pina, J. C.; Dillon Jr., O. W.; Jawahir, I. S. Size Effect in Machining and Its Influence on Product Sustainability. In *Proceeding of the 15th Life Cycle Engineering Conference, LCE 2008*; Sydney; 2008.
161. El-Axir, M. H. A Method of Modeling Residual Stress Distribution in Turning for Different Materials. *Int. J. Mach. Tools Manuf.* **2002**, *42*, 1055–1063.
162. Nasr, M. N. A.; Ng, E.-G.; Elbestawi, M. A. A Modified Time-Efficient FE Approach for Predicting Machining-Induced Residual Stresses. *Finite Elem. Anal. Des.* **2008**, *44*, 149–161.
163. Agrawal, S.; Joshi, S. S. Analytical Modelling of Residual Stresses in Orthogonal Machining of AISI4340 Steel. *J. Manuf. Process.* **2013**, *15*, 167–179.
164. Lazoglu, I.; Ulutan, D.; Alaca, B. E.; Engin, S.; Kaftanoglu, B. An Enhanced Analytical Model for Residual Stress Prediction in Machining. *CIRP Ann. – Manuf. Technol.* **2008**, *57*, 81–84.
165. Su, J.-C.; Young, K. A.; Srivatsa, S.; Morehouse, J. B.; Liang, S. Y. Predictive Modeling of Machining Residual Stresses Considering Tool Edge Effects. *Prod. Eng.* **2013**, *7* (4), 391–400.
166. Qi, Z.; Li, B.; Xiong, L. Improved Analytical Model for Residual Stress Prediction in Orthogonal Cutting. *Front. Mech. Eng.* **2014**, *9* (3), 249–256.
167. Ulutan, D.; Alaca, E.; Lazoglu, I. Analytical Modelling of Residual Stresses in Machining. *J. Mater. Process. Technol.* **2007**, *183*, 77–87.
168. Joshi, K.; Venkatachalam, A.; Jawahir, I. S. A New Methodology for Transforming 3R Concept into 6R Concept for Improved Product Sustainability. In *Proceedings of IV Global Conference on Sustainable Product Development and Life Cycle Engineering, Sao Carlos, Brazil*; 2006.
169. Kang, M. C.; Kim, K. H.; Shin, S. H.; Jang, S. H.; Park, J. H.; Kim, C. Effect of the Minimum Quantity Lubrication in High-Speed End-Milling of AISI D2 Cold-Worked Die Steel (62 HRC) by Coated Carbide Tools. *Surf. Coat. Technol.* **2008**, *202* (22–23), 5621–5624.
170. Kamata, Y.; Obikawa, T. High Speed MQL Finish-Turning of Inconel 718 with Different Coated Tools. *J. Mater. Process. Technol.* **2007**, *192–193*, 281–286.
171. Avila, R. F.; Abrao, A. M. The Effect of Cutting Fluids on the Machining of Hardened AISI 4340 Steel. *J. Mater. Process. Technol.* **2001**, *119*, 21–26.
172. Leppert, T. Effect of Cooling and Lubrication Conditions on Surface Topography and Turning Process of C45 Steel. *Int. J. Mach. Tools Manuf.* **2011**, *51*, 120–126.

173. Liao, Y. S.; Lin, H. M. Mechanism of Minimum Quantity Lubrication in High-Speed Milling of Hardened Steel. *Int. J. Mach. Tools Manuf.* **2007**, *47*, 1660–1666.
174. Sung Jung, H. E. O. Environmentally Conscious Hard Turning of Cemented Carbide Materials on the Basis of Micro-Cutting in SEM (2nd Report): Stress Turning with Three Kinds of Cutting Tools. *J. Mech. Sci. Technol.* **2009**, *23*, 1959–1966.
175. Khan, M. M. A.; Mithu, M. A. H.; Dhar, N. R. Effects of Minimum Quantity Lubrication on Turning AISI 9310 Alloy Steel Using Vegetable Oil Based Cutting Fluid. *J. Mater. Process. Technol.* **2009**, *209*, 5573–5583.
176. Varadarajan, A. S.; Philip, P. K.; Ramamoorthy, B. Investigations on Hard Turning with Minimal Cutting Fluid Application (HTMF) and Its Comparison with Dry and Wet Turning. *Int. J. Mach. Tools Manuf.* **2002**, *42*, 193–200.
177. Vikram Kumar, C. H. R.; Ramamoorthy, B. Performance of Coated Tools during Hard Turning Under Minimum Fluid Application. *J. Mater. Process. Technol.* **2007**, *185*, 210–216.
178. Attanasio, A.; Gelfi, M.; Giardini, C.; Remino, C. Minimal Quantity Lubrication in Turning: Effect on Tool Wear. *Wear* **2006**, *260*, 333–338.
179. Shokrani, A.; Dhokia, V.; Newman, S. T. Environmentally Conscious Machining of Difficult-to-Machine Materials with Regard to Cutting Fluids. *Int. J. Mach. Tools Manuf.* **2012**, *57*, 83–101.
180. Schwach, D. W.; Guo, Y. B. Feasibility of Producing Optimal Surface Integrity by Process Design in Hard Turning. *Mater. Sci. Eng. A* **2005**, *395*, 116–123.
181. Maleque, M. A.; Masjuki, H. H.; Sapuan, S. M. Vegetable-Based Biodegradable Lubricating Oil Additives. *Ind. Lubr. Tribol.* **2003**, *55* (3), 137–143.
182. Belluco, W.; De Chiffre, L. Performance Evaluation of Vegetable-Based Oils in Drilling Austenitic Stainless Steel. *J. Mater. Process. Technol.* **2004**, *148*, 171–176.
183. Lawal, S. A.; Choudary, I. A.; Nukman, Y. Application of Vegetable Oil-Based Metal Working Fluids in Machining Ferrous Metals – A Review. *Int. J. Mach. Tools Manuf.* **2012**, *52*, 1–12.
184. Xavior, M. A.; Adithan, M. Determining the Influence of Cutting Fluids on Tool Wear and Surface Roughness During Turning of AISI 304 Austenitic Stainless Steel. *J. Mater. Process. Technol.* **2009**, *209*, 900–909.
185. Jayadas, N. H.; Nair, P. K.; Ajithkumar, G. Tribological Evaluations of Coconut Oil as an Environment-Friendly Lubricant. *Tri. Int.* **2007**, *40*, 350–354.
186. Krishna, V. P.; Srikant, R. R.; Rao, D. N. Experimental Investigations on the Performance of Nanoboric Acid Suspensions in SAE-40 and Coconut Oil During Turning of AISI 1040 Steel. *Int. J. Mach. Tools Manuf.* **2010**, *50*, 911–916.
187. John, J.; Bhattacharya, M.; Raynor, P. C. Emulsions Containing Vegetable Oils for Cutting Fluid Application. *Colloids Surf. A: Physicochem. Eng. Asp.* **2004**, *237*, 141–150.
188. Ozcelik, B.; Kuram, E.; Cetin, M. H.; Demirbas, E. Experimental Investigations of Vegetable Based Cutting Fluids with Extreme Pressure During of AISI 304L. *Tribol. Int.* **2011**, *44*, 1864–1871.
189. Chinchanikar, S.; Salve, A. V.; Netke, P.; More, A.; Kendre, S.; Ramesh Kumar Comparative Evaluations of Surface Roughness During Hard Turning under Dry and with Water-Based and Vegetable Oil-Based Cutting Fluids. *Procedia Mater. Sci.* **2014**, *5*, 1966–1975.
190. Ojolo, S. J.; Amuda, M. O. H.; Ogunmola, O. Y.; Ononiwu, C. U. Experimental Determination of the Effect of Some Straight Biological Oils on Cutting Force During Cylindrical Turning. *Rev. Mater.* **2008**, *13* (4), 650–663.
191. Rao, N.; Krishna, V. Performance Profiling of Boric Acid as Lubricant in Machining. *J. Braz. Soc. Mech. Sci. Eng.* **2008**, *30* (3), 239–244.
192. Singh, D.; Rao, P.V. Improvement in Surface Quality with Solid Lubrication in Hard Turning. In *Proceedings of the World Congress on Engineering 3*; London, UK; 2008.
193. Singh, D.; Rao, P. V. Performance Improvement of Hard Turning with Solid Lubricants. *Int. J. Adv. Manuf. Technol.* **2008**, *38*, 529–535.
194. Huang, Y.; Chou, Y. K.; Liang, S. Y. CBN Tool Wear in Hard Turning: Survey on Research Progresses. *Int. J. Adv. Manuf. Technol.* **2007**, *35*, 443–453.
195. Tamizharasan, T.; Sevaraj, T.; Haq, A. N. Analysis of Tool Wear and Surface Finish in Hard Turning. *Int. J. Adv. Manuf. Technol.* **2006**, *28*, 671–679.
196. Yang, S. H.; Natarajan, U. Multi-Objective Optimization of Cutting Parameters in Turning Process Using Differential Evolution and Non-Dominated Sorting Genetic Algorithm-II Approaches. *Int. J. Adv. Manuf. Technol.* **2010**, *49*, 773–784.
197. Karpat, Y.; Ozel, T. Swarm-Intelligent Neural Network System (SINNS) Based Multi-Objective Optimization of Hard Turning. *Trans. NAMRI/SME* **2006**, *34*, 611–618.
198. Tandon, V.; El-Mounayri, H.; Kishawy, H.; End Milling, N. C. Optimization Using Evolutionary Computation. *Int. J. Mach. Tools Manuf.* **2002**, *42*, 595–605.
199. Pytlak, B. Multicriteria Optimization of Hard Turning Operation of the Hardened 18HGT Steel. *Int. J. Adv. Manuf. Technol.* **2010**, *49*, 305–312.
200. Ganesan, H.; Mohankumar, G.; Ganesan, K.; Ramesh Kumar, K. Optimization of Machining Parameters in Turning Process Using Genetic Algorithm and Particle Swarm Optimization with Experimental Verification. *Int. J. Eng. Sci. Technol.* **2011**, *3* (2), 1091–1102.
201. Saravanan, R.; Ramabalan, S.; Ebenezer, N. G. R.; Natarajan, R. Evolutionary Bi-Criteria Optimum Design of Robots Based on Task Specifications. *Int. J. Adv. Manuf. Technol.* **2009**, *41*, 386–406.
202. Paiva, A. P.; Paiva, E. J.; Ferreira, J. R.; Balestrassi, P. P.; Costa, S. C. A Multivariate Mean Square Error Optimization of AISI 52100 Hardened Steel Turning. *Int. J. Adv. Manuf. Technol.* **2009**, *43*, 631–643.
203. Derringer, G.; Suich, R. Simultaneous Optimization of Several Response Variables. *J. Qual. Technol.* **1980**, *12*, 214–219.
204. Neseli, S.; Yaldiz, S.; Turkes, E. Optimization of Tool Geometry Parameters for Turning Operations Based on the Response Surface Methodology. *Measurement* **2011**, *44*, 580–587.
205. Sahoo, A. K.; Sahoo, B. Surface Roughness Model and Parametric Optimization in Finish Turning Using Coated Carbide Insert: Response Surface Methodology and Taguchi Approach. *Int. J. Ind. Eng. Comput.* **2011**, *2*, 819–830.
206. Chinchanikar, S.; Choudhury, S. K. Characteristics of Wear, Force and Their Inter-Relationship: In-Process Monitoring of Tool within Different Phases of the Tool Life. *Procedia Mater. Sci.* **2014**, *5*, 1424–1433.
207. Dureja, J. S.; Gupta, V. K.; Sharma, V. S.; Dogra, M. Wear Mechanisms of Coated Mixed-Ceramic Tools during Finish Hard Turning of Hot Tool Die Steel. *Proc. Inst. Mech. Eng. C: J Mech. Eng. Sci.* **2010**, *224*, 183–193.
208. Mandal, N.; Doloi, B.; Mondal, B.; Das, R. Optimization of Flank Wear Using Zirconia Toughened Alumina (ZTA) Cutting tool: Taguchi Method and Regression Analysis. *Measurement* **2011**, *44*, 2149–2155.
209. Umbrello, D.; Micari, F.; Jawahir, I. S. The Effects of Cryogenic Cooling on Surface Integrity in Hard Machining: A Comparison with Dry Machining. *CIRP Ann. – Manuf. Technol.* **2012**, *61*, 103–106.
210. Aslantas, K.; Ucun, I.; Cicek, A. Tool Life and Wear Mechanism of Coated and Uncoated Al_2O_3/TiCN Mixed Ceramic Tools in Turning Hardened Alloy Steel. *Wear* **2012**, *274–275*, 442–451.
211. Huang, Y.; Liang, S. Y. Modeling of CBN Tool Flank Wear Progression in Finish Hard Turning. *J. Manuf. Sci. Eng.* **2004**, *126* (1), 98–106.
212. Diniz, A. E.; Ferreira, J. R.; Filho, F. T. Influence of Refrigeration/Lubrication Condition on SAE 52100 Hardened Steel Turning at Several Cutting Speeds. *Int. J. Mach. Tools Manuf.* **2003**, *43*, 317–326.
213. Kurniawan, D.; Noordin, M. Y.; Sharif, S. Hard Machining of Stainless Steel Using Wiper Coated Carbide: Tool Life and Surface Integrity. *Mater. Manuf. Process.* **2010**, *25*, 370–377.
214. Dogra, M.; Sharma, V. S.; Sachdeva, A.; Suri, N. M. Finish Hard Turning of Continuous and Interrupted Surfaces with Cubic Boron Nitride (CBN) and Coated Carbide Tools. *Mater. Manuf. Process.* **2012**, *27*, 523–530.

Relevant Websites

http://www.emag.com/workpieces.html
EMAG.
http://www.practicalmachinist.com/vb/cutting-tools/requirements-milling-hardened-steels-236637/
Practical Machinist.
http://www2.coromant.sandvik.com/coromant/pdf/Hard_part_turning/C-1040-069.pdf
Sandvik Coromant.
http://www2.coromant.sandvik.com/coromant/pdf/Silent_tools/Silent_tools.pdf
Sandvik Coromant.
http://www.secotools.com/CorpWeb/switzerland/Downloads/Drehen/GB_PCBN_TechGuide_IV_Inlay_LR.pdf
SECO.
http://en.wikipedia.org/wiki/Hardened_steel
http://en.wikipedia.org/wiki/Surface_integrity

1.4 Review of Gear Finishing Processes

NK Jain and AC Petare, Indian Institute of Technology Indore, Indore, India

© 2017 Elsevier Inc. All rights reserved.

1.4.1	**Introduction**	94
1.4.2	**Microgeometry of Gears**	95
1.4.3	**Materials, Manufacturing and Quality of Gears**	97
1.4.4	**Gear Finishing Processes**	98
1.4.4.1	Gear Grinding	98
1.4.4.1.1	Types of gear grinding	98
1.4.4.1.2	Form or non-generative grinding	98
1.4.4.1.3	Generative grinding	99
1.4.4.1.3.1	Generative grinding using threaded wheel	100
1.4.4.1.3.2	Generative grinding using cup-shaped wheel	100
1.4.4.1.3.3	Generative grinding using dish-shaped wheel	100
1.4.4.1.3.4	Generative grinding using rack-tooth worm wheel	100
1.4.4.1.4	Selection of parameters	101
1.4.4.1.5	Advantages	101
1.4.4.1.6	Limitations	101
1.4.4.1.7	Applications	101
1.4.4.2	Gear Lapping	101
1.4.4.2.1	Advantages	102
1.4.4.2.2	Limitations	102
1.4.4.2.3	Applications	103
1.4.4.3	Gear Honing	103
1.4.4.3.1	External Honing	104
1.4.4.3.2	Internal honing	104
1.4.4.3.3	Advantages of internal honing over external honing	104
1.4.4.3.4	Advantages	105
1.4.4.3.5	Limitations	105
1.4.4.3.6	Applications	105
1.4.4.4	Gear Shaving	105
1.4.4.4.1	Mechanism of gear shaving	106
1.4.4.4.2	Types of gear shaving	107
1.4.4.4.2.1	Axial or conventional gear shaving	107
1.4.4.4.2.2	Diagonal gear shaving	108
1.4.4.4.2.3	Tangential or underpass gear shaving	108
1.4.4.4.2.4	Plunge gear shaving	108
1.4.4.4.3	Advantages	109
1.4.4.4.4	Limitations	109
1.4.4.4.5	Applications	109
1.4.4.5	Gear Burnishing	109
1.4.4.5.1	Advantages	111
1.4.4.5.2	Limitations	111
1.4.4.5.3	Applications	111
1.4.4.6	Conventional Finishing Processes for Conical Gears	111
1.4.4.6.1	Finishing of conical gears by grinding	111
1.4.4.6.1.1	Generative gear grinding	111
1.4.4.6.1.2	Form or non-generative gear grinding	111
1.4.4.6.2	Finishing of conical gears by lapping	112
1.4.4.7	Gear Finishing by AFM	112
1.4.4.7.1	Working principle of AFM process	112
1.4.4.7.2	Types of AFM process	112
1.4.4.7.2.1	One-way AFM	112
1.4.4.7.2.2	Two-way AFM	112
1.4.4.7.2.3	Orbital AFM process	113
1.4.4.7.3	AFM machines	113
1.4.4.7.4	Components of an AFM machine	113

1.4.4.7.5	AFM parameters	115
1.4.4.7.6	Gear finishing by AFM	115
1.4.4.7.7	Advantages	115
1.4.4.7.8	Limitations	116
1.4.4.7.9	Applications	116
1.4.5	**Comparative Evaluation**	117
Acknowledgments		117
Appendix A		118
References		119
Relevant Websites		120

1.4.1 Introduction

Gear is a modified form of a wheel. It is the second most important machinery element after the wheel. Gears can be classified according to following three criteria: (1) according to configuration: external and internal gears; (2) according to axes of transmission; (a) for transmission of power and/or motion between two parallel shafts: straight toothed spur gear, single helical, and double helical or herringbone gears, (b) for transmission of power and/or motion between two intersecting shafts: bevel gears (straight-tooth, spiral-tooth, zero-bevel, crown, and miter type), (c) for transmission of power and/or motion between nonparallel and nonintersecting shafts: spiral gears, hypoid gears, worm and worm wheel; and (3) according to pattern of rotation; (a) rotation to rotation, (b) rotation to translation and vice-versa. Gear drives are preferred for various power and motion transmission purposes due to their compactness and higher reliability. Annually more than 10 billion gears are manufactured and consumed in various applications in almost all the industries.[1] Some worth mentioning are:

- automobile (i.e., cars, trucks, tractor, motor-cycles, scooter, etc.),
- transportation (i.e., buses, train, subways, mine cars, etc.),
- aerospace (i.e., high speed aircraft engine),
- marine (i.e., high power high speed marine engine, navy fighting ships),
- control systems (i.e., gun, helicopter, tanks, radars application),
- earth moving vehicles,
- different types of machine tools,
- oil and gas industry (i.e., oil platforms, pumping station, drilling sites, refineries and power stations),
- industrial application (i.e., power transmission; construction equipment, agriculture machinery, equipment and machines used in mining, cement manufacturing, steel manufacturing, food processing, sugar manufacturing and other industries),
- home appliances (i.e., washing machine, food mixtures, fans, etc.), and
- mechanisms, toys and gadgets.

Despite of excellent market position there are some increasing requirements for further improvement in gear drives, namely: (1) improvement of power density and transmitted power; (2) reduction in running noise, toxic emission, and price; (3) increase in reliability and service life time; (4) easy disposal and material recycling of the used gears; and (5) integration of electronic systems such as data acquisition, logical control, integrated safety system.[2] Gear failure is an unpredictable and catastrophic phenomenon and there are various reasons responsible for different types of gear failures. Gear failure can be categorized into two types, i.e., failure related to lubrication and failure related to non-lubrication. **Table 1** presents different modes of the gear failures.

Table 1 Different modes of gear failures[3]

Failures related to lubrication		*Failures related to non-lubrication*		
Overload	*Bending fatigue*	*Hertzian fatigue*	*Wear*	*Scuffing*
1. Brittle fracture 2. Ductile fracture 3. Plastics deformation ● Cold flow ● Hot flow ● Indentation ● Rippling ● Ridging ● Bending	1. Low cycle fatigue (<1000 cycles to failure) 2. High cycle fatigue (>1000 cycles to failure)	1. Pitting ● Initial ● Superficial ● Destructive ● Spalling 2. Micro-pitting ● Frosting ● Gray stanning ● Peeling 3. Sub-case fatigue	1. Adhesion 2. Abrasion 3. Corrosion 4. Fretting	1. Scoring 2. Galling 3. Seizing 4. Welding

Table 2 Surface quality related parameters of a gear which affect its various performance aspects

To improve service life and operating performance	*To reduce noise and transmission error*
Reduce parameters of surface roughness (i.e., R_a, R_{max} and R_z) on the tooth flank	
Improve wear characteristics by reducing sliding coefficient of friction and friction forces	Eliminate microgeometry errors
Improve the microstructure	Remove sharp corners from gear tooth
Increase the fatigue life	Increase the wear resistance

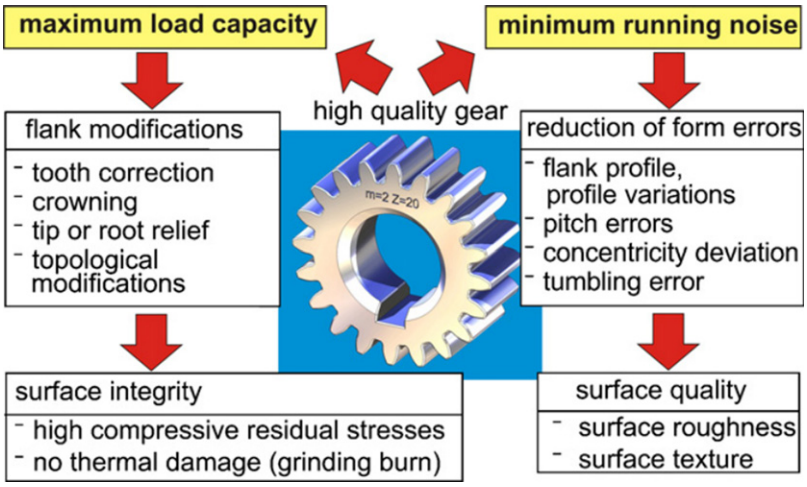


Figure 1 Different goals of a gear finishing process. Reprinted with permission from Ref. [2]. Elsevier © 2008.

Prevention of premature failures of the gears requires careful consideration of interrelationship between following factors: (1) gear tooth geometry; (2) gear tooth motion; (3) gear tooth forces (static and dynamic); (4) gear material; (5) lubricant characteristics (physical and chemical); (6) operating environment; and (7) tooth surface quality. Among these, first six factors are related to the design and use environment of the gears, whereas the last factor depends on the surface quality of the gears. Surface quality of gears is evaluated in terms of surface finish, microgeometry, i.e., form errors, and wear characteristics. Poor surface quality, i.e., errors in microgeometry and poor surface finish of gear tooth are the major source of noise generation particularly at higher running speed, errors in motion transfer, excessive wear, backlash between the meshing gear pairs and large dynamic forces during power transmission.[3] All these factors reduce the power to be transmitted and incorrect velocity ratios. Microgeometry of gear teeth is the most dominant factor among the causes of gear noise generation, contributing approximately 20% to it. Other contributing factors include: gear teeth surface finish (10%), accuracy of assembly (15%), gear material, gear design, lubrication of gears, bearing, motor and variation of load, driving condition, shaft alignment, wear, surface damage and gearbox configuration.[4] **Table 2** presents the surface quality related parameters of a gear that affect its service life, operating performance, transmission errors, and noise reduction.[5] It can be concluded from this table that gear tooth surface should have very good surface quality for smooth, noiseless power and/or motion transmission and to improve the load carrying capacity.

Increasing demands for different types of gears have motivated researcher to investigate and improve their surface quality using different conventional and advanced gear finishing processes. Surface quality of the gear tooth can be significantly enhanced by using a proper gear finishing process. **Figure 1** presents the different goals of a gear finishing process. These goals can be classified in two major categories namely: (1) improvement in surface quality and reduction in errors in microgeometry (i.e., form errors) to minimize the running noise; and (2) flank medications and improving surface integrity to maximize load capacity.[4,6]

1.4.2 Microgeometry of Gears

Microgeometry of gears is very important due to its effect on service life, low noise emission, high load carrying capability and transmission efficiency of the gears. Errors in microgeometry has two components form errors and location errors. **Figure 2** illustrates different components of errors in microgeometry of a gear and their effects on various performance aspects of a gear.

Form errors has two components, which are namely error in profile and lead of a gear. Total profile error or deviation (F_a) defines the form and location of the involute profile and it is evaluated perpendicular to the involute profile from root

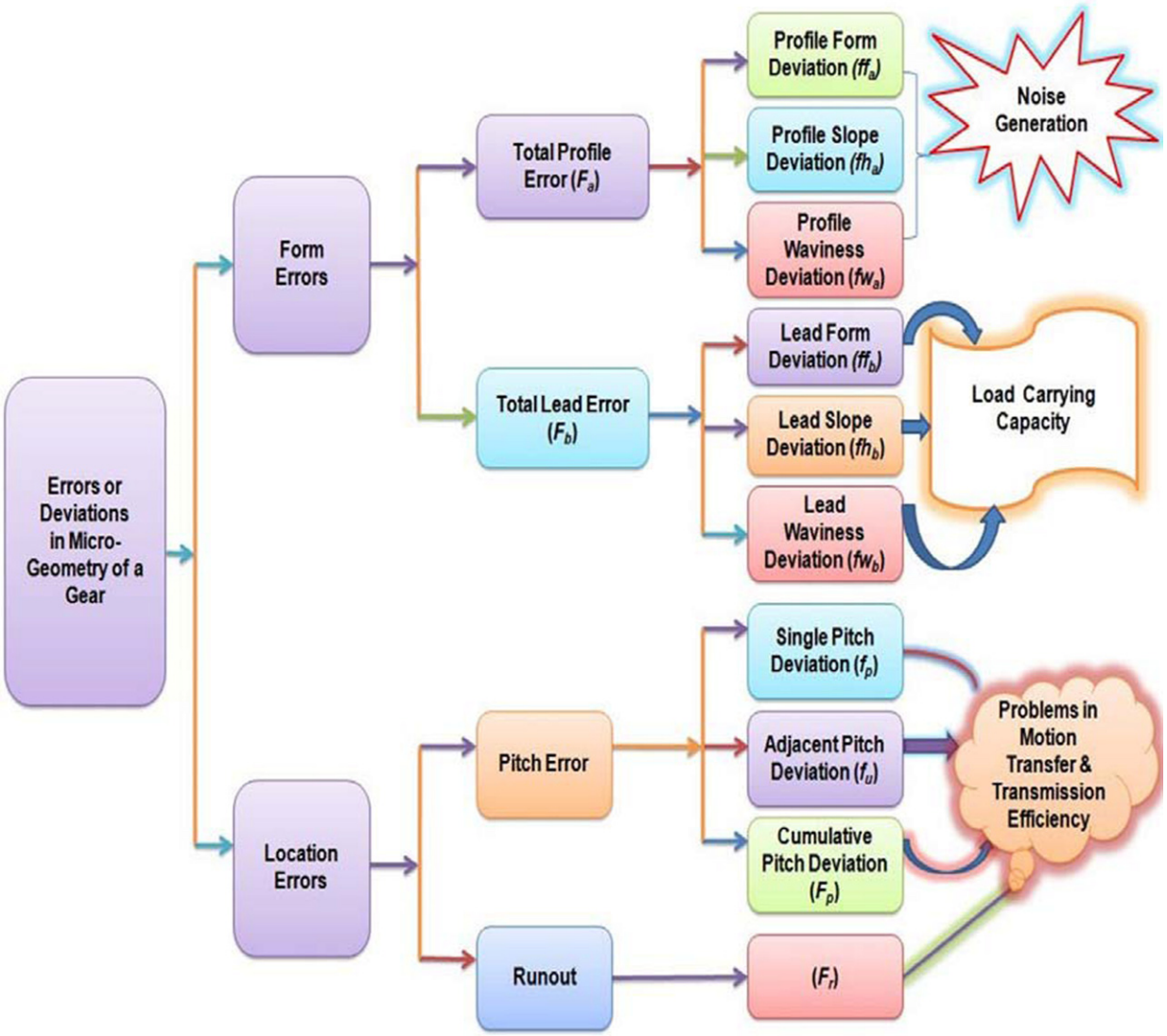


Figure 2 Different components of errors or deviations in microgeometry of a gear and their effects.

to tip. It determines noise generation characteristics of a gear. Total profile error is sum of two components: (1) profile form deviation (ff_a): it is a difference between nominal involute form to actual involute form; and (2) profile angle deviation (fh_a): it is a difference between nominal involute angle to actual involute angle. Total lead error or deviation (F_b) defines the form and location of the tooth flank and it is evaluated at the middle of the tooth height along the tooth width. It determines load carrying capacity of gear. Total lead error is sum of two components: (1) lead form deviation (ff_b): it is a difference between nominal lead form line to actual lead form line; and (2) lead angle deviation (fh_b): it is a difference between nominal helix angle to actual helix angle. Location errors are associated with pitch and runout of gear. These errors affect motion transfer characteristics and transmission efficiency of a gear. The characteristics of pitch error or deviation are evaluated at the middle of the tooth height along the pitch circle and describe the middle location of all right and left flanks with respect to each other. It has three components: (1) single pitch deviation (f_p) is the difference between the actual and nominal angular positions of two respective flanks on the two consecutive gear teeth; (2) adjacent pitch deviation or pitch-to-pitch deviation (f_u) is the maximum difference between the angular deviations of any two adjacent right flanks or left flanks; and (3) cumulative pitch deviation or index error (F_p) is the difference between the summation of the theoretical values of pitches and summation of the actual values of the pitches over all the teeth of a gear. Runout error (F_r) is the maximum difference between the actual radial positions of all teeth measured with respect to their nominal radial position. It describes the radial location of all teeth with respect to the pitch circle and is evaluated at the middle of the tooth height along the pitch circle.

1.4.3 Materials, Manufacturing and Quality of Gears

Materials used for manufacturing the gears depend on various types of selection criteria such as application, shape, size, service, peripheral speed, required accuracy, type of manufacturing process, load carrying capacity, wear resistance, allowable stress, etc. Following are some guidelines which can be used for selecting a gear material[6]:

- Cast iron is a popular gear material due to its good wear resistance, good lubrication, relatively good machinability, and ease of producing complicated shapes by casting it. It is used for manufacturing large gears of complicated shapes.
- Steel is sufficiently strong and possess good resistance to abrasive wear of the gears.
- Cast steel is used where stress on gear is higher and gear geometry is difficult to fabricate.
- Plain carbon steels are used for manufacturing the gears for industrial applications due to combination of their high toughness and high strength.
- Alloy steels are used where higher gear tooth strength and lower wear of gear flank surface are desired.
- Aluminum is used for manufacturing light-weight gears.
- Nonmetallic materials are used for manufacturing gears for noiseless operation at higher peripheral speeds.

Conventional gear manufacturing processes are classified in two major categories, i.e., generative type and non-generative type gear manufacturing. Table 3 presents different gear manufacturing processes of each category. Conventional manufacturing processes of gears do not yield acceptable surface quality thus failing to meet the requirements of the end users. For example, gears manufactured by hobbing and shaping have tool marks and scallops on the gear tooth surface. Post-manufacturing heat treatment to improve gear hardness also adversely affects the surface quality of the gears. Therefore, a proper gear finishing process becomes necessary to ensure better surface quality of the gear teeth to eliminate the imperfections/discontinuities occurred during gear manufacturing and heat treatment processes such as small pits, burrs, scratches, cut marks, etc. and to attain the required surface quality.

There are different international standards for expressing gear quality. Some worth mentioning standards are Deutsches Institut fur Normung (DIN) of Germany, American Gear Manufacturing Association (AGMA) of USA, Japanese International Standard (JIS) of Japan, Korean Standard (KS) of South Korea, Italian Organization of Standardization (UNI) of Italy and British Standards Society (BSS) of UK. Two most commonly used standards in the industries to define the gear quality are AGMA 3900 and DIN 3963.[1,6] Table 4 presents typical applications of the gears of different quality expressed on both AGMA 3900 and DIN 3963 standards.

Table 3 Different types of gear manufacturing processes

Gear manufacturing processes		
Conventional gear manufacturing processes		*Special and advanced gear manufacturing processes*
Generative type	*Non-generative type*	
1. Hobbing 2. Shaping 3. Milling 4. Broaching 5. Bevel gear generating	1. Casting 2. Powder metallurgy 3. Forming ● Stamping ● Extrusion ● Forging ● Hot Embossing	1. Gleason method 2. Template gear cutting 3. EDM and micro-EDM (μ-EDM) 4. WEDM and micro-WEDM (μ-WEDM)

Table 4 Typical applications of gears according to their quality[1]

Designation	*Gear quality*		*Typical applications*
	AGMA 3900	*DIN 3963*	
AA: Ultra-high accuracy	14 or 15	2 or 3	Military navigation, precision, instruments, computer, and equipment
A: High accuracy	12 or 13	4 or 5	Instruments, aircraft engines, turbines, professional cameras,
B: Medium-high accuracy	10–11	6–7	Precision machine-tool speed drives, automotive transmissions, and high-speed machinery
C: Medium accuracy	8–9	8–9	
D: Low accuracy	6 or 7	10 or 11	Appliances, hand tools, pumps, Commercial clocks, farm machines,
E: Very low accuracy	4 or 5	12	fishing reels, hoists, and slow–speed machinery

1.4.4 Gear Finishing Processes

Different gear finishing processes can be grouped into following two categories (1) conventional gear finishing processes such as gear grinding, gear lapping, gear honing, gear shaving, and gear burnishing; and (2) unconventional or advanced gear finishing processes such as abrasive flow machining (AFM), electrochemical finishing (ECF), electrochemical honing (ECH), electrochemical grinding (ECG), hybrid finishing processes, etc. The selection of an appropriate gear finishing process depends on various factors such as gear material hardness, productivity, need, and type of finishing. **Table 5** summarizes applicability of four conventional finishing processes for gears.

1.4.4.1 Gear Grinding

Gear grinding process uses a properly formed and dressed grinding wheel, which finishes the gear teeth flanks by abrading action of the fine abrasives. It is performed during the manufacturing cycle of gears to achieve certain desired characteristics in the finished gears. Heat treatment processes have tendency to thermally distort the gears thus deteriorating their tooth accuracy. This necessitates hard finishing of the gear teeth. Grinding is an effective means of finishing the heat-treated high-hardness steels (having hardness 40 HRC and above). Therefore, grinding is used to correct the thermal distortions and to improve the surface finish and microgeometry of the gears. Generally, it removes very small of material from precut gears to make gear teeth more accurate for various engineering applications.[8]

Wear of the grinding wheel is an important aspect. As the sharp cutting edges of the abrasives wear out, the cutting forces on these abrasive grains increase until either the abrasive grains fracture thus revealing new sharp cutting edges or the abrasive grains are pulled out from the grinding wheel thus exposing new abrasive grains. Essentially, if the process were perfect then the grinding wheel would be self-sharpening. Even though grinding wheel wear is an accepted phenomenon, but very high grinding wheel wear rate will not only result in wheel replacement but also in other nonproductive preparatory operations for a grinding wheel such as trueing, dressing, and profiling. Grinding or G-ratio (ratio of volume of the work material removed to volume of the grinding wheel wear) is a measure of grinding efficiency. Values of G-ratio can range from less than one to several hundred, depending on these variables.[8]

Another distinguishing feature of the grinding process is the fractional amount of time the abrasive grain is actually generating the chips in comparison with the total time this grain is in contact with the workpiece material. Three distinct phenomena have been recognized to occur as the abrasive grain comes in contact with and leaves contact with the work surface. They are rubbing, plowing, and cutting. The actual cutting or chip formation may be occurring for only about 30% of the time the abrasive grains and the workpiece are in contact. The force at which the transition from rubbing and plowing to cutting occurs is called the *threshold force*. When the machine holding the grinding wheel and the workpiece, exert a force in excess of this threshold force, grinding process will happen. There are essentially two techniques for grinding the gears: form grinding and generating type grinding.[8,9] The parameters affecting the grinding process and their types with advantages and limitations are presented in the following sections.

1.4.4.1.1 Types of gear grinding

Gear grinding can be classified as form or non-generative grinding or generative grinding according to shape of the grinding wheel used. **Table 6** presents different versions of the gear grinding process. **Figure 3** depicts working principle of form and generative grinding of a gear.

1.4.4.1.2 Form or non-generative grinding

Form grinding of gears uses a specially manufactured abrasive grinding wheel whose circumference is profiled to have involute form by a diamond dressing tool as shown in **Figure 3**. This special form of the wheel fits in the space between two consecutive teeth of a gear. When this wheel is given rotary motion then flank surfaces and root of two adjacent gear teeth are ground. Indexing motion given the workpiece gear ensures grinding of the all the teeth of the workpiece gear. According to abrasive material of the grinding wheel, it can be further classified in two categories, i.e.,

Table 5 Applicability of different conventional finishing processes for gears[7]

Gear grinding can be used when	*Gear shaving can be used when*	*Gear lapping can be used when*	*Gear honing can be used when*
• More material is to be removed • For gears having more pressure angle • For gears having large face width and module • For gears requiring higher accuracy in profile and lead • Presence of thermal distortions • For mixed volume and frequent changeovers	• For finishing high volume of small gears • For heat treated gears having poor accuracy in profile and lead • Minor thermal distortions are present • For mixed volume and frequent changeovers	• For finishing the mating gears in a pair using suitable lapping medium • Minute corrections in involute profile, helix angle, runout or index error are desired • Dimensionally accurate gear with high tolerance is required • Excellent surface quality is required	• Less material is to be removed • For gears having high contact ratio, low pressure angle, and long addendum • Removing nicks and burrs • Minor corrections in gear microgeometry are required • Resistance to wear and pitting is to be improved • High surface finish

ceramic form grinding which uses ceramic as abrasive. Most commonly used ceramics are aluminum oxide (Al_2O_3) and silicon carbide (SiC). It is used to grind the harder material normally (60 HRC or above), and borazon form grinding which uses cubic boron nitride (CBN) as abrasives. Figure 4 depicts different versions of form grinding of a spur gear using single form grinding wheel (Figure 4(a)), multiple form grinding wheels (Figure 4(b)), and straddle grinding wheel (Figure 4(c)).One of the primary advantages of form grinding of gears is that various simple and compound forms of the gear teeth can be ground using manufacturing the specially designed grinding wheel whose form has to be changed with change in module, pressure angle, and even number of gear teeth. Form grinding can be used for finishing spur gears, single helical gears, straight bevel gears, worm and worm wheel, and internal gears.[4,8–9]

Table 6 Different versions of the gear grinding process[1]

Gear grinding	
Form grinding	*Generative grinding*
1. Ceramic form grinding 2. Borazon form grinding	1. Threaded wheel 2. Cup-shaped wheel 3. Dish-shaped wheel (Saucer process) 4. Rack-tooth worm wheel 5. Generative grinding of bevel gears

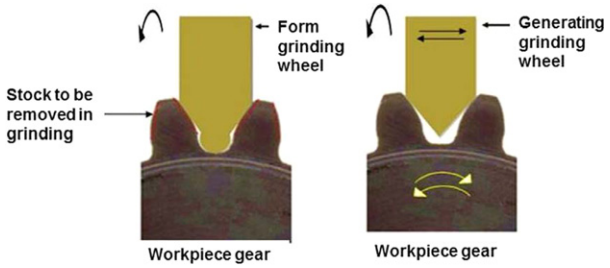


Figure 3 Comparison of form grinding and generative grinding of a gear.[1]

Estimation of grinding time in form grinding: the time required to grind a gear depends on three major factors: (1) time for rough grinding, (2) time for finish grinding, and (3) time to dress the grinding wheel. In addition, there are some handling times. The time required for rough or finish grinding may be calculated by following equation.

$$\text{Grinding time (minutes)} = \frac{\text{No. of gear teeth} \times \text{Number of cuts}}{\text{cycles per minute}}$$

Number of cuts is the ratio of amount of the gear material available for grinding and amount of material ground per cut.

1.4.4.1.3 Generative grinding

Generating grinding of gear is performed using a grinding wheel (or wheels) whose flanks imitate a toothed rack which rolls over the reference circle of the gear forming the involute flank. The grinding wheel performs three motion rotation about its own axis, tangential to gear pitch circle which shifts and turns and axial along the tooth width. It is commonly used for gear with module 0.5–10 mm. Generative grinding

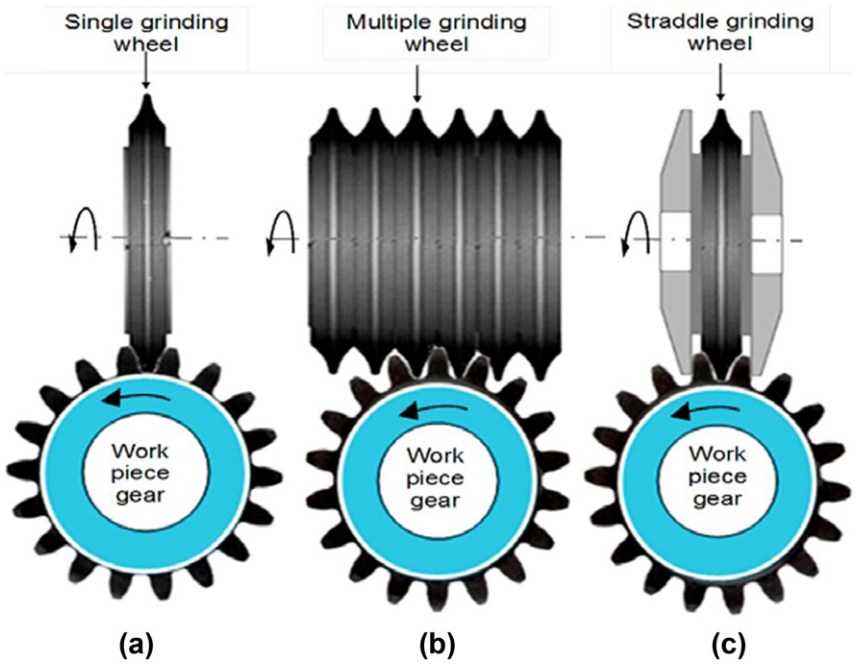


Figure 4 Different versions of form grinding of a spur gear using (a) single form grinding wheel; (b) multiple form grinding wheels; and (c) straddle grinding wheel.[3]

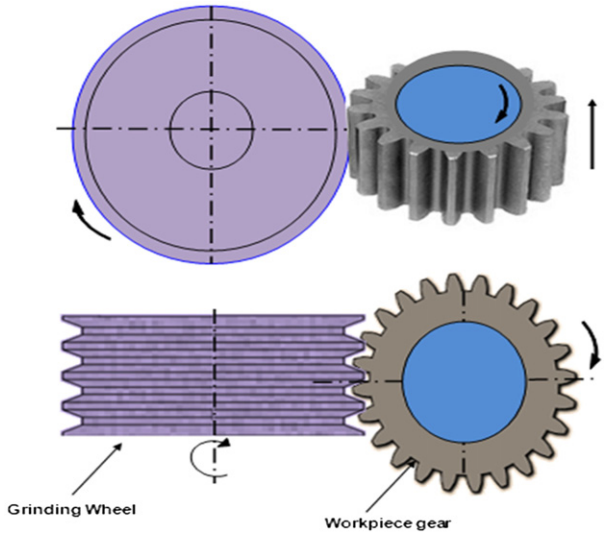


Figure 5 Schematic of generative grinding of a gear using threaded grinding wheel.[4]

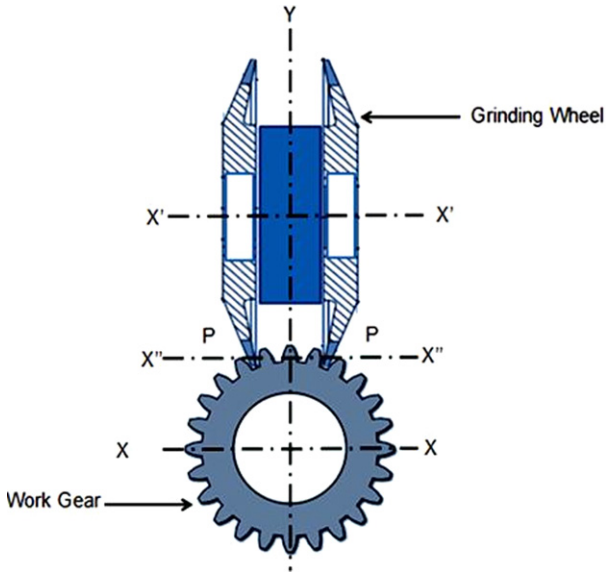


Figure 6 Schematic of generative grinding of a gear using cup-shaped grinding wheel.

has following four versions according to type of the grinding wheel used: threaded wheel, cup-shaped wheel, dish-shaped (saucer) wheel, and rack-tooth worm wheel.[8–10] These are described in following sections.

1.4.4.1.3.1 Generative grinding using threaded wheel

Figure 5 depicts schematic of generative grinding using a threaded grinding wheel. The finishing mechanism of this process is similar to gear hobbing with only difference that a threaded grinding wheel is used in place of the hob cutter. The workpiece gear mounted is on an arbor. Ratio of speed of workpiece gear and grinding wheel is equal to ratio of number of teeth on the workpiece gear and number of thread start on the wheel. Generally, operating speed of the threaded grinding wheel is chosen as 25 m s^{-1}. Gear quality produced by this process depends on the indexing mechanism. This process can be used for generative grinding of external spur or helical gears.

1.4.4.1.3.2 Generative grinding using cup-shaped wheel

In this process the gear is rolled against a cup-shaped grinding wheel, the sides of which are beveled at an angle equal to the pressure angle of the gear teeth. The grinding wheel moves in a straight line along the gear tooth width grinding the flank surfaces of two teeth as depicted in **Figure 6**. Soft grinding wheel without coolant is used to minimize grinding wheel wear. Spur and helical gears up to 457 mm (or 18″) pitch diameter can be ground by this process.

1.4.4.1.3.3 Generative grinding using dish-shaped wheel

This process uses two dish-shaped grinding wheels which are either inclined at 15°–20° with each other or parallel to each other and are mounted on a simulated rack as shown in **Figure 7**. This process is used when higher productivity, exact profile and longitudinal modification are required. Lack of uniform transition between gear tooth flank and root is the main limitation of this process.

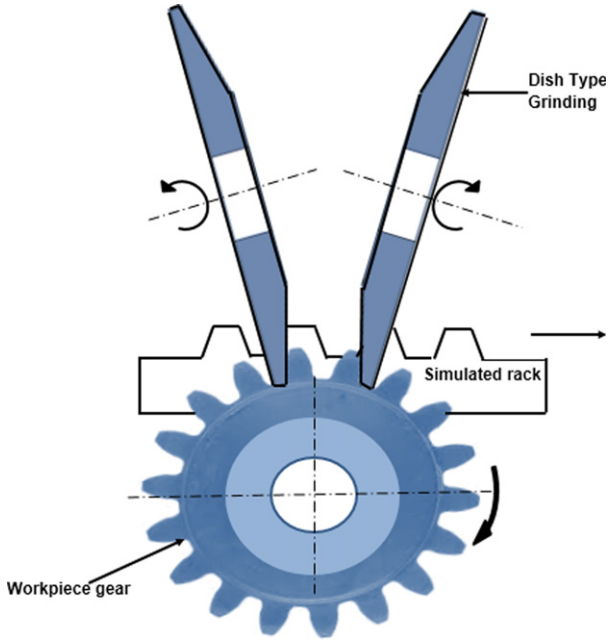


Figure 7 Schematic of generative grinding of a gear using dish-shaped grinding wheel.[3]

1.4.4.1.3.4 Generative grinding using rack-tooth worm wheel

Figure 8 shows schematic of working of this process in which workpiece is mounted on a vertical arbor or in a fixture that fits between the centers of the machine. The grinding wheel is dressed to have shape of a conventional or CBN-plated rack-tooth worm. For grinding the helical gears, the workpiece holding slide of the machine is set at an angle equal to the helix angle of the gear. The workpiece gear is rotated by a motor that is synchronized with motor of the grinding wheel. Al_2O_3 or SiC as abrasive can be used to prevent burning of

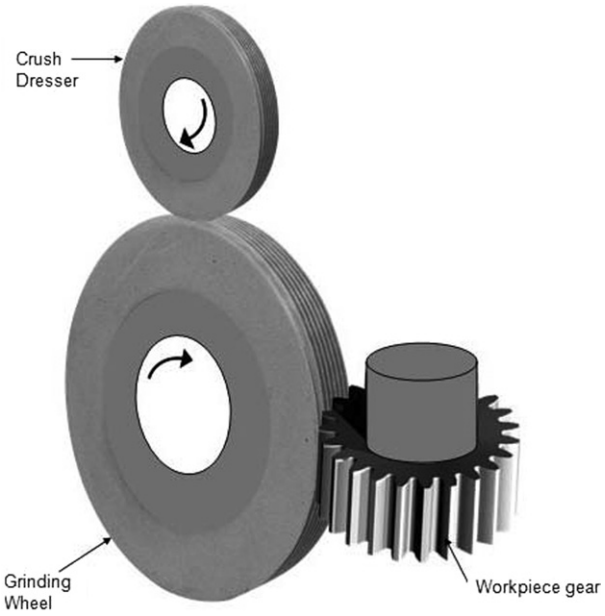


Figure 8 Schematic of generative grinding of a gear using a rack-tooth worm wheel.[3]

the hardened gear teeth. But, this result in more breakdowns of the grinding wheel and loss of correct tooth profile. Grinding accuracy mainly depends on careful dressing of the wheel. Generally, special diamond wheel are used for dressing the grinding wheel. Gear quality mainly depends on profile of the rack-tooth on the grinding wheel, accuracy of dressing operation, and accuracy of diamond wheel used for dressing.

1.4.4.1.4 Selection of parameters

A grinding wheel is basically a precision tool composed of abrasive grains held together by a bonding material. The abrasive grains provide the wheel with its cutting ability which helps in finishing the material to the required dimensional accuracy and surface finish. Material of grinding wheels becomes more important in case of gear grinding due to need of high precision in terms of surface finish and material removal rate (MRR). Al_2O_3, SiC, and CBN are the most commonly used abrasives. Synthesis of these abrasives allows accurate control of their form and physical characteristics.[10] Grinding wheel speed is an important parameter during gear grinding. Increase in grinding wheel speed keeping other parameters constant, reduces grinding forces and roughness, and increases life of redressed grinding wheel and specific energy consumption. **Table 7** presents the details of abrasives, grinding wheel speed, and depth of cut for different gear materials.

Grinding fluid is also considered as one of the important parameter of the process. It removes heat and chips and helps in improving grinding wheel life and enhancing the gear tooth finish. It minimizes possibilities of burning of gear surfaces. Generally, mineral base sulfochlorinated or sulfurized oils are used. Plain soluble-oil emulsions and chemical solutions have also been reported to give satisfactory performance for many gear grinding applications.[4,8,9]

1.4.4.1.5 Advantages

- Gear grinding is fast and is able to provide micro-finish.
- Microgeometry errors can be correct by using a properly shaped grinding wheel.
- It is the only finishing process other than gear honing which can finish hardened gears having hardness value more than 40 HRC.[4]
- It is only productive process for finishing the conical gears.

1.4.4.1.6 Limitations

- Grinding results in two major undesirable effects namely: grinding burns caused by high temperature damage surface integrity of the ground gears and can even sometime lead to gear failure through tooth breakage and transverse grind lines on the finished surface which cause noise and vibration of the gears.
- Additionally, ground gear teeth have detects such as fine cracks, thermal distortion, and uneven stress distribution over the gear tooth surface. To detect these defects magnetic particle inspection and macro-etching with dilute nitric acid inspection is required which is costly.[4,8–11]
- Gear grinding is unable to finish some special gears such as inner gears, multi-joint gears and large-size gears.[8–10]
- Abrasive grains lose their cutting ability due to wear necessitating redressing of grinding wheel.
- Control of rate of heat generation is required to eliminate cracking and burning of gear surface. This requires use of cutting fluid and frequent dressing of grinding wheel which increases cost of finishing.[8]
- Gear grinding is an expensive, complex process, and comparatively low productivity process due to smaller MRR.[4,8–11]

1.4.4.1.7 Applications

- Frequently used to finish tooth profile of different type of gears of hard material which have been heat treated to a high hardness level after gear cutting.
- Gear grinding can finish spur, helical and conical gears.

1.4.4.2 Gear Lapping

Lapping is a fine finishing process which uses a lapping medium between the workpiece and a lapping tool rotating at a very low speed (<80 rpm). Lapping medium is chalky paste consists of abrasive particles having mesh size from 300 to 900 (i.e., abrasive particle size ranging from 17 to 51 μm) and a carrier fluid. Al_2O_3, SiC, boron carbide, and diamond powder are the most commonly used abrasives. Oil, grease, water, and kerosene are the mostly commonly used carrier fluid. Lapping tool should be made of a material softer than the workpiece material. Fine grain cast iron is the most commonly used material for making the lapping tool. However, cloth (for lapping of hardened materials for metallographic examination), copper (for lapping of diamond), leather, wood, brass, steel, and glass can also be used.[12] Shape of the lapping tool should be complementary of the desired shape of workpiece. There are two versions of lapping process: free-abrasive

Table 7 Details of abrasives, grinding wheel speed, and depth of cut for different gear materials[3]

Gear material	*Abrasive*	*Grinding wheel speed (m min^{-1})*	*Depth of cut (mm/pass)*
Hardened and case hardened steel	Aluminum oxide (Al_2O_3)	1700–2000	0.038
Nitrided gears	Silicon carbide (SiC)	1700–2000	0.13–0.25
High speed steel	Cubic boron nitride (CBN)	3000	0.13–0.25

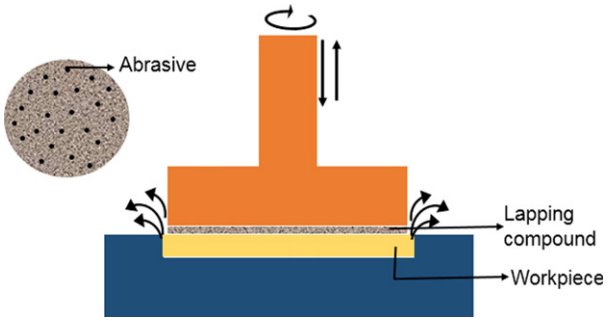


Figure 9 Schematic of a typical lapping process.

lapping and fixed-abrasive lapping.[1,4] In the **free-abrasive** lapping process, lapping medium is supplied between the lapping tool and workpiece. This is one of the most accurate finishing processes causing the least amount of damage to the workpiece due to use of a rigid lapping tool which can be tailored to suit a particular material. In the **fixed-abrasive** lapping process, abrasive particles are bonded to either to a film or to a paper. An abrasive lapping film has various abrasive particles bonded to a thin, uniform polyester film and is capable of producing a highly finished surface. SiC papers are much thicker than the films and can create rounded edges on the workpiece.[4]

Figure 9 depicts working of a typical lapping process in which a lapping tool is pressed against the workpiece and moved back and forth in a figure of eight or in other motion pattern over the workpiece surface. Abrasive particles remove the workpiece material and soft lapping tool is not worn away because abrasives get embedded in its surface instead of moving across it. Sometimes lapping can be performed by hand also but, for greater accuracy and consistency machines are preferred. Lapping of soft materials is difficult as abrasives may get embedded. Centerless lapping machine is used for lapping small cylindrical parts such as piston pins, ball-bearing races, etc. Two alternative cutting mechanisms have been suggested for material removal by lapping: (1) for a hard lapping tool, abrasive particles roll, knead, and slide between the lapping tool and workpiece removing material from both the surfaces; and (2) for a soft lapping tool, abrasive particles are embedded to the lapping tool surface and material removal action is similar to the grinding process.

Gear lapping finishes the mating gears simultaneously by running them together in the presence of the lapping medium which is supplied continuously under pressure. Smaller gear is used as the driver and the larger gear is as the driven member. The necessary tooth contact load is applied by driven gear for a very short duration. Since, gear lapping finishes the mating gears simultaneously therefore no stock allowance is provided on the mating gears for their finishing by lapping. Before starting lapping process both gears are ground by hand grinder to remove nicks and burrs. Lapping removes very small amount of material when the matting gears are rotated and their direction of rotation is changed thus imparting them a very fine finish, very high accuracy and achieving the desired contact pattern.[4,13] There are four important parameters namely lapping pressure, size of abrasive particles, concentration of abrasive in the lapping medium, and lapping speed that affect performance of the lapping process. Coarser abrasives are used for gears having a coarse pitch and finer grits are used for gears having a fine pitch. Generally, abrasives having 280 mesh size are used for lapping of the spiral bevel gears and 400 mesh size for lapping the hypoid gears. Reduction in noise level between the mating gears is criteria for successfully lapping.

1.4.4.2.1 Advantages

- Gear lapping improves wear properties of gear teeth.
- It is less damaging than grinding. It can even remove subsurface damage caused by sawing or grinding.
- Lapping improves flatness, parallelism and gives very surface finish.
- Lapping finishes products to a very high value of dimensional accuracy imparting tolerance values generally less than 2.5 μm over all the lapped surfaces.
- Lapping machines can be adjusted to lap gears with shaft angles of 0°–180°.
- Minor corrections in tooth bearing shape and position can be obtained through lapping.

1.4.4.2.2 Limitations

- Gear lapping corrects only minute errors in the involute profile, helix angle, tooth spacing, and concentricity produced during either manufacturing or heat treatment of the gears.
- It finishes the mating gears is a pair which cannot be interchanged with the members of any other similar pair.
- It is a very slow process and is costly as compared to other finishing methods. Material removal in lapping usually ranges from 0.003 to 0.03 mm but many reach up to 0.08–0.1 mm in certain cases.
- Low MRR and nonuniform lapping over tooth surface result poor correction in profile error.[14]

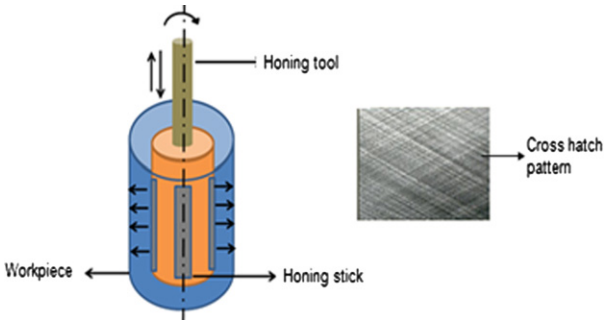


Figure 10 Working principle of finishing of internal cylinders by honing process.

1.4.4.2.3 Applications

- Gear lapping can finish spur, helical and conical gears but it is mainly used for finishing spiral bevel gears and hypoid gears.[15]
- Lapping is used to produce optical lenses, metallic bearing surfaces, gauges, and other parts requiring very good finishes and extreme accuracy.
- Lapping process is used to produce dimensionally accurate specimens to high tolerances (generally less than 2.5 μm uniformity).
- Lapping can also be used to finish bearings, guideways of lathe and planer, poppet and plug valves, silphon type seals, piston and cylinder walls, and relieving of the hot bearings.

1.4.4.3 Gear Honing

Finishing of internal cylinders by conventional honing process uses a honing tool having equally spaced bonded abrasive sticks protruding on its periphery as shown in **Figure 10**. They are held against the workpiece with a controlled light pressure usually exercised by small springs. The honing tool is provided a combination of rotatory and reciprocating motion and is regulated in such a way that a given point on the honing stick does not trace the same path repeatedly. This produces a fine surface finish having cross-hatched lay pattern.[16] Angle of this cross-hatch lay pattern depends on the ratio of rotary to reciprocating motion. This lay pattern helps in retaining the lubricating oil in the lengthwise and circumferential direction of the workpiece, in improving frictional resistance and uniformly distributing the load. Surface finish depends on (1) type and size of abrasives used; (2) honing pressure applied; (3) rotational speed; (4) speed of reciprocation; and (5) length and position of stroke. A cutting fluid is used to remove chips and keep temperature low. There are different versions of honing process for finishing different type of product as mentioned in **Table 8**.

Gear honing is hardened gear finishing process which also improves their noise characteristics. It was used for the first time in 1970s to remove transportation damages on hardened tooth flanks. It uses an abrasive-impregnated helical gear-shaped tool which is run in tight mesh with the hardened gear in a cross-axes relationship. The workpiece gear is driven by the honing tool at high speeds (up to 1000 sfpm) while being traversed back and forth across the honing tool in a path parallel to the axis of the workpiece gear to ensure finishing of its entire face width. The workpiece gear is driven in both directions during the honing cycle. Conventional honing oil used as a coolant, lubricant, and a medium to flush away the wear debris. Amount of material removed from the workpiece gear ranges from 0.013 to 0.05 mm. Honing gives higher dimensional accuracy, fine finish of gear flank surfaces with cross-hatch lay pattern, minor corrections in tooth irregularities, and improved noise and wear characteristics of the hardened gears.[18–21]

The honing gear material must have the capability to yield the gear profile as well as hold its shape under pressure. Generally, it is a mixture of plastic resins (polyurethane and epoxy matrix) and abrasive grains and is formed in a precision mold. **Table 9** presents commonly used abrasives for different gear materials. The abrasives are bonded together by vitrified, resinoid, or metallic type bonds. The bond must be strong enough to hold the abrasive grains but should not be so hard that it rubs workpiece gear deteriorates its quality rather than improving it. Abrasive grain size generally depends on the

Table 8 Different versions of the honing process and their applications[17]

Version of honing process	*Applications*
Longitudinal honing	Connecting rod holes, brake drum, cylinder liners, correct out-of-roundness or circularity, taper, boring tool marks, bell mouth, and barrel and axial distortion in workpiece
Short-stroke honing (fine honing)	Crank shaft, rotor shaft
Surface honing	Rollers, guideways, and guide rails
Profile honing	Tracks of inner and outer ball-bearing rings

Table 9 Commonly used abrasives for different gear materials[1,2,4]

Gear material	*Abrasive*
Steels	Al_2O_3
CI and nonferrous materials	SiC
steels (soft and hard), Ni- and Co-base super alloys, stainless steels, Br–Cu-alloy and Zr	CBN
chromium plating, carbides, ceramics, glass, CI, brass, bronze, and surfaces nitrided to depths greater than 30 μm	Diamond

Table 10 Size of abrasive for different combinations of circular pitch and surface roughness[3]

Circular pitch of gear (mm)	*Surface roughness (μm)*	*Mesh of abrasives*
≤16	0.75–0.89	60
16–20	0.63–0.75	100
>20	0.38–0.50	180
>20	0.25–030	280
>20	0.075–0.10	500

Table 11 Details of different honing tools used in gear honing[21]

Type	*Composition of honing tool and use*	*Surface roughness*
Standard type honing tool	Mixture of variety of resin and abrasives used for shaved and heat treated gears. Improves tooth spacing and runout	0.2–0.35 μm
AA ground honing tool	Mixture of variety of resin and abrasives with precise tooth form. Improves tooth spacing and runout	0.2–0.25 μm
Polishing type honing tool	Consist of a flexible, porous polyurethane material. Polishing achieved by use of abrasive liquid compound	0.1–0.15 μm

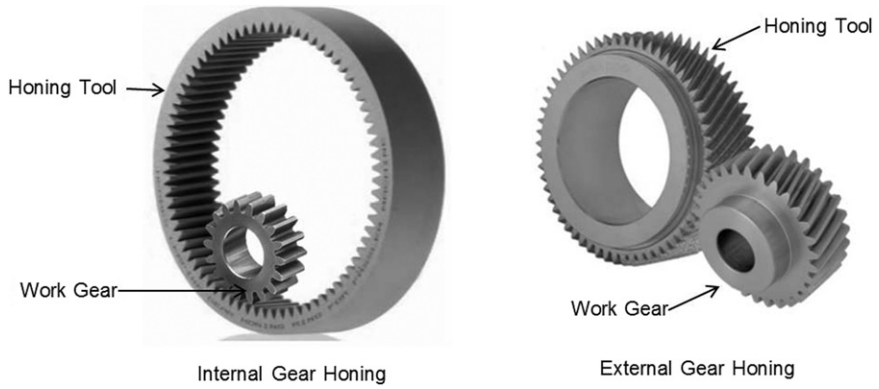


Figure 11 Concept of internal and external honing for finishing a gear.

desired value of MRR and surface finish.[1,2,4] Generally, it varies from 60 to 500 mesh number. **Table 10** presents size of abrasives for different combinations of circular pitch of gears and surface roughness. Type of honing gear depends on the workpiece gear material, finishing method, application requirement, and available machine capacities. Size of honing gear ranges from 3.5″ (for internal gears) to 14″ while face width ranging from 0.5 to 2 in. **Table 11** presents the various tools used in honing of gear teeth.[4,21]

Two basic methods are used to hone the gear teeth. One is the zero-backlash method and the other is called the constant-pressure method. The zero-backlash method is used for hardened gears made within commercial tolerance specifications. The constant-pressure method is used to hone the gear teeth on hardened gears produced to dimensions outside commercial tolerance ranges. Depending on relative position of the honing and workpiece gears, gear honing can be performed either as (1) external honing; or (2) internal honing. **Figure 11** illustrates their concept.

1.4.4.3.1 External Honing

In this process, honing and workpiece gears mesh with each other in a cross-axis arrangement with constant center distance. Gear tooth are finished from root to the tip and direction of rotation of the honing gear is reversed for finishing the second flank as shown in **Figure 12**.

1.4.4.3.2 Internal honing

Figure 13 shows schematic of internal honing process for finishing an external spur gear. In this process, a large-size

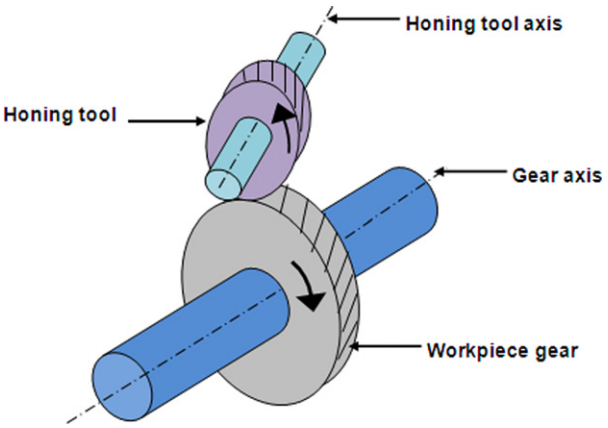


Figure 12 External honing of a single helical gear.

internal helical gear made of a ceramic material is used as honing tool which has cross-axis meshing with the workpiece gear held between the centers of the honing machine. Axis of the honing gear can be varied to match the required crossed-axis angle meshing arrangement with workpiece gear. The gear honing machine has provision of back and forth traverse along the workpiece gear axis finishing a gear having large face width.

1.4.4.3.3 Advantages of internal honing over external honing

- Internal honing has higher traverse contact ratio as compared to external honing. It results in balanced contact pressure,

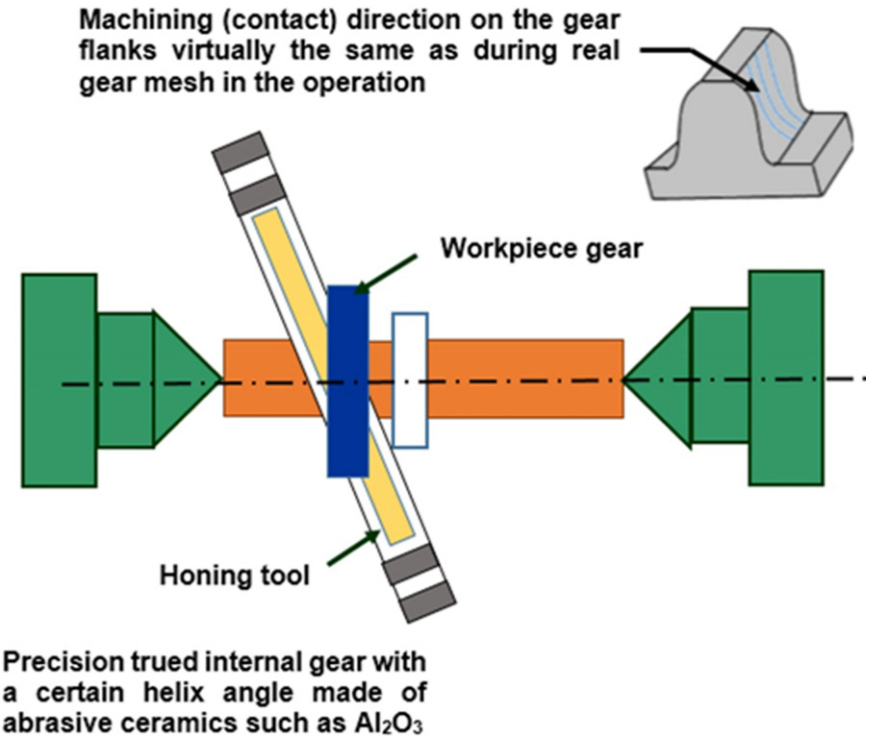


Figure 13 Internal honing of an external spur gear.[19]

good tooth form, large honing stroke, reduced adjacent and accumulated pitch error, and reduced radial runout.
- Internal honing gives higher accuracy.
- Internal honing tool has higher stability as compared to external honing tool. It offers more resistance against breaking.

1.4.4.3.4 Advantages

- Honing generates a tribologically superior surface which retains lubricating oil on contact surface thus reducing friction and minimizing wear of the contact surfaces under load.[22]
- Functional characteristics of the gears such as geometric accuracy, dimensional accuracy, roughness, lay pattern and integrity can be improved by gear honing.
- It reduces or corrects geometric errors induced by previous manufacturing or finishing processes.
- It does not increase tooth surface temperature, nor does it produce heat cracks and burned spots nor it reduce skin hardness.
- It does not generate internal stresses.
- It does not cold work or alters the microstructure of the gear materials.
- Low cost and economical process of gear finishing.

1.4.4.3.5 Limitations

- Limited life of honing gear tool.
- Honing time increases as error in tool shape increases.

1.4.4.3.6 Applications

- Can be used for finishing hardened external and internal gears.
- For improving geometric accuracy and surface conditions and to remove nicks and burrs.[22]
- For minor corrections in tooth shape which increases wear resistance and reduces noise generation.
- Honing can do crowning of gears also.

1.4.4.4 Gear Shaving

Gear shaving removes a small amount of material from the workpiece gear to correct errors in its profile, pitch, helix angle, eccentricity, and improves surface finish of the gear.[4,23] by using a specially shaped shaving cutter which is similar to a helical gear having serrated cutting edges as shown in Figure 14.

The shaving cutter and workpiece gear are pressed to make proper meshing contact and center distance between cutter and workpiece gear is reduced incrementally. The shaving cutter rotates in a tight mesh with the workpiece gear either in parallel or crossed-axes arrangement. The meshing between cutter and workpiece gear is flexible to obtain any desired value of cross-axes angle.[23] The rotary motion between the workpiece gear and shaving cutter is performed in both directions (i.e., clockwise and anticlockwise) during the finishing cycle and material removal takes place in the form of hair-like chip.[24–25] The workpiece gear is reciprocated parallel to its axes across the face of the cutter and fed up into the cutter with each stroke of the table. Cutting action in gear shaving includes fine cutting and finishing caused by a land of

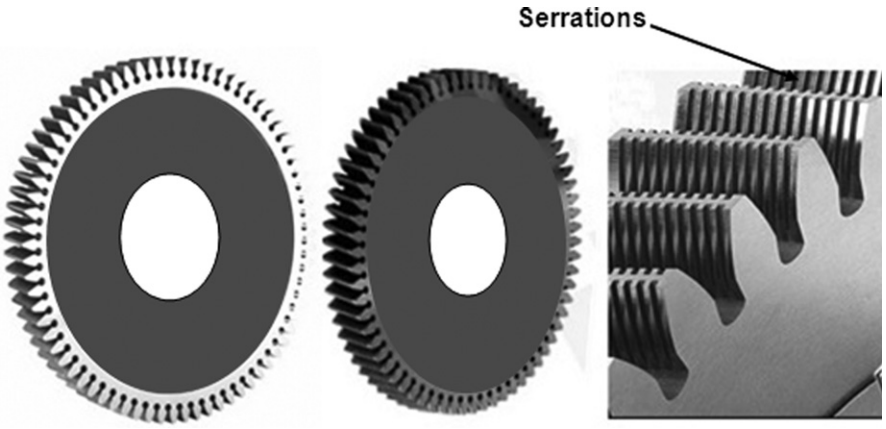


Figure 14 Photographs showing (a) gear shaving cutters (b) serration of shaving cutter.

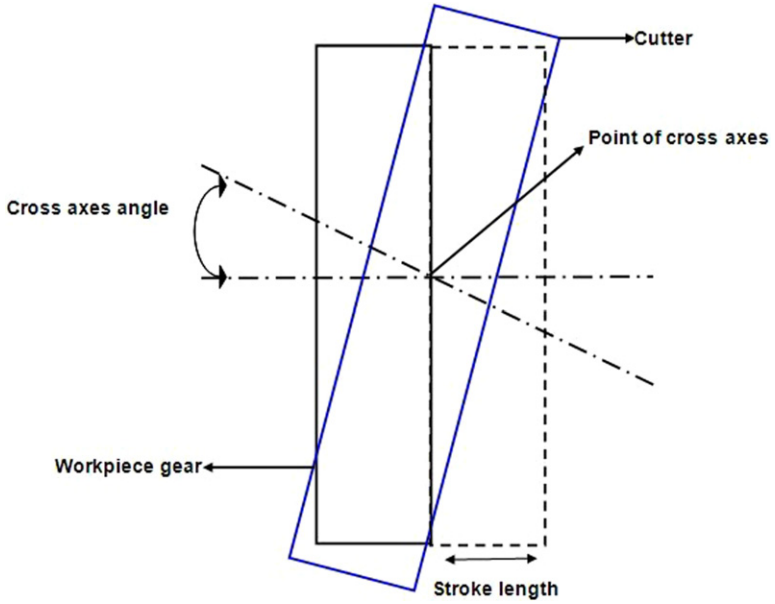


Figure 15 Schematic of cross-axes arrangement in the gear shaving process.[4]

the shaving cutter. Gear shaving process differs from other finishing processes in many aspects. Main difference is the use of geometrically defined cutting edges in gear shaving. Other differences include negative clearance angles, very small chips (height: 50–150 μm, length: 100–400 μm), low thermal load on the cutting edge due to low cutting speeds and chip thicknesses, and strongly varying load on cutting edge and clearance face.[26]

1.4.4.4.1 Mechanism of gear shaving

There is a difference between the helix angle of the gear shaving cutter and that of the workpiece gear which causes them to rotate in different planes. This difference between their axes is called cross-axes angle and is approximately equal to the difference in their helix angles. Figure 15 depicts cross-axes arrangement in the gear shaving process. Value of cross-axes angle in the range from 10° to 15° usually yields better accuracy and surface finish of the gear tooth.[27] Higher value of cross-axes angle may result in large amount of material removal by cutting action but it lowers down the width of contact zone which reduces the cutting action itself. An axial motion is provided to the workpiece gear to enable penetration of the cutting edges of the shaving cutter. Extra care should be taken care to avoid the direct contact between shaving cutter and the gear root fillet because it may adversely affect the accuracy of the involute.

Selection of material for the gear shaving cutter is one of the most important parameters in gear shaving. It depends on the hardness of the workpiece gear. Generally, hardened high speed steel (HSS) of M2 or M7 grades is used in many gear finishing applications while, T15 or M30 grades of HSS is used for conditions where higher red hardness is required. Carbide shaving cutters are used to achieve the high quality finishing of workpiece gear made of difficult to machine

materials. A fresh shaving cutter can finish around 80 000 gears. It can be redressed around four to ten times and the cutter life has been estimated to finish approximately 1500 gears per sharpening cycle.[4] Shaving stock or allowance is another important aspect of the gear shaving process. Sufficient shaving allowance should be provided on the gear to achieve good finish and accuracy by gear shaving. **Table 12** presents the standard shaving allowances for different size of gears.

1.4.4.4.2 Types of gear shaving

Gear shaving is classified according to type of the shaving cutter and type of relative motion between shaving cutter and workpiece gear. According to type of the shaving cutter, gear shaving can be classified as rotary shaving or rack shaving as depicted in **Figure 16**. Rotary shaving method uses a pinion shaped shaving cutter with serrated teeth, while rack shaving uses rack type shaving cutter having serrated teeth.

In the rack shaving process, the rack type shaving cutter is reciprocated under the workpiece gear and infeed takes place at the end of each stroke. Since, is impractical to have rack longer than 20 in (508 mm) therefore 6 in (or 152 mm) is the maximum diameter of gear that can be shaved by this process.

In the rotary shaving process, the cutter has serrated gear teeth ground in such a way that teeth profile will conjugate with that of the gear to be shaved. The shaving cutter rotates while meshing with the workpiece gear thus scraping off or shavings little amount of material from the workpiece gear.[28] There is no indexing mechanism involved in this process. Shaving cutter is the driver and the workpiece gear is the driven member. Rotary gear shaving is done in the green or soft state of the gear, i.e., prior to heat treatment. This process has the ability to modify the pinion geometry to compensate for the distortions that occur during heat treatment. The rotary gear shaving is further classified in four categories namely axial or conventional, diagonal, tangential or under pass and plunge. The basic difference between these versions of rotary shaving is type of relative motion between workpiece gear and shaving cutter.[26] Following paragraphs briefly describe these different versions of rotary shaving.

Table 12 Recommended shaving allowance for pre-shaved gears[1]

Gear size		*Shaving allowance on tooth thickness (mm)*	
Module	*Pitch*	*Minimum*	*Maximum*
1.6	16	0.025	0.050
2.5	10	0.038	0.075
4	6	0.050	0.100
12	2	0.075	0.150

1.4.4.4.2.1 Axial or conventional gear shaving

There are two independent motions in the axial or conventional type of rotary gear shaving: first is tight rotational meshing between the workpiece gear and shaving cutter and second one is the traverse motion of the shaving cutter along the axis of the workpiece gear as shown in **Figures 17**.[28,29] Length of traverse is generally 1.6 mm greater than the face width of the workpiece gear and it is adjusted to ensure finishing of entire face width of the gear.[27] Crowning of the gear teeth can be done using the built-in crowning mechanism in the gear shaving machine.

This process is suitable for gears having wider face width. It can improve the roughness of tooth flanks and can decrease the individual pitch error by 30% but, it cannot correct cumulative pitch error or index error in fact in some cases a shaved gear may have cumulative pitch error increased because it creates flank grooves in the middle of tooth profiles.[31]

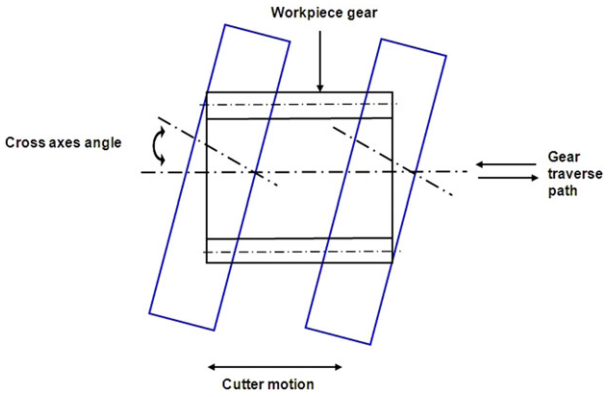


Figure 17 Schematic of axial or conventional type of rotary gear shaving.[30]

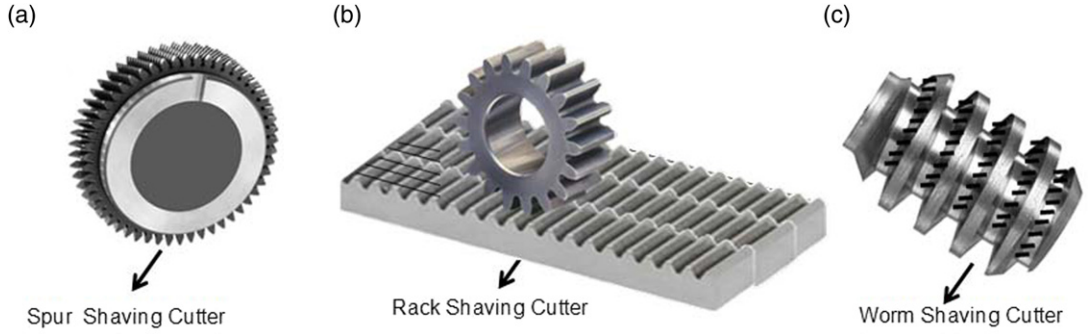


Figure 16 Types of gear shaving cutters (a) spur gear type; (b) rack type; and (c) worm type.

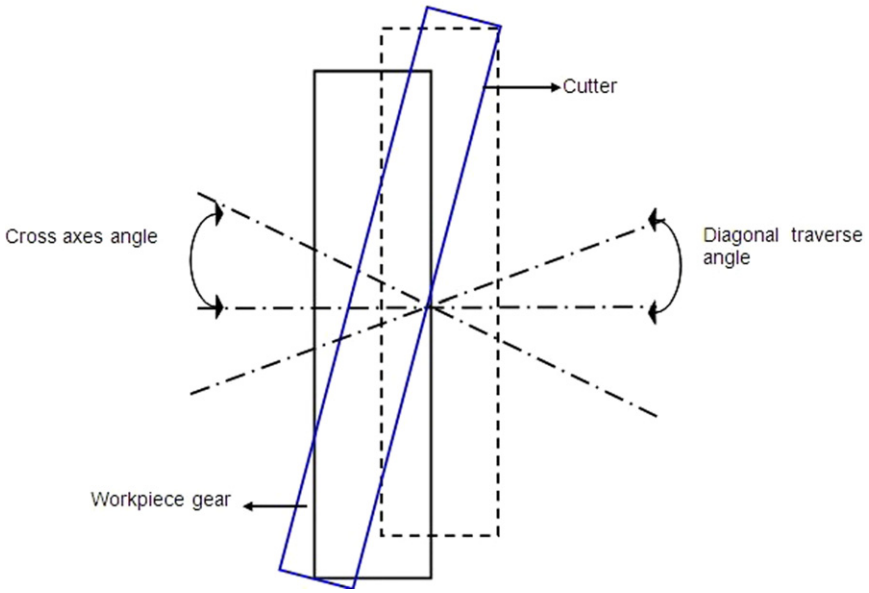


Figure 18 Schematic of diagonal type of rotary gear shaving.[4]

1.4.4.4.2.2 Diagonal gear shaving

In diagonal type rotary gear shaving, face width of gear and shaving cutter has a special relationship with diagonal traverse angle and there is a relative motion between the shaving cutter and workpiece gear as shown in **Figure 18**. Width of shaving cutter depends upon face width of the workpiece gear and diagonal traverse angle. Diagonal traverse angle varies from 30° to 60° to obtain optimum conditions of cutting speed and quality of workpiece gear.[32] Wide face width of workpiece gear and narrow shaving cutter restrict the diagonal traverse to a small angle. Increasing the cutter face width permits increase in the diagonal angle. Crowning of the gear teeth is accomplished by rocking the machine table by providing the sum of traverse angle and crossed-axes angle. As the traverse angle approaches to 90°, machine controlled crowning is no longer possible then it is obtained by modifying shaving cutter only. A special cutter with differentially staggered gashes becomes essential when the traverse angle is above 60° to have effective shaving of the entire tooth surface.

In this process, wear of shaving cutter is uniform hence increasing its life.[27] This process can reduce shaving time up to 50%. It is mainly used for medium and high-production rate. It can be used for finishing shoulder gears also.[27]

1.4.4.4.2.3 Tangential or underpass gear shaving

In this process, workpiece gear is rolled into the shaving cutter teeth and moved in radial direction at right angle to its axis in forward and return stroke from an initial center distance to the desired final center distance as shown in **Figure 19**. For this, width of the shaving cutter should be more than face width of the workpiece gear. Pitch surface of the cutter is given a hyperboloid form (concave curvature) to ensure proper contact across the full face width of workpiece gear. Concave pitch surface on the shaving cutter is obtained by negative longitudinal crowning of its teeth. A special shaving cutter with mutually staggered gashes is required to clean the shaved gear teeth.

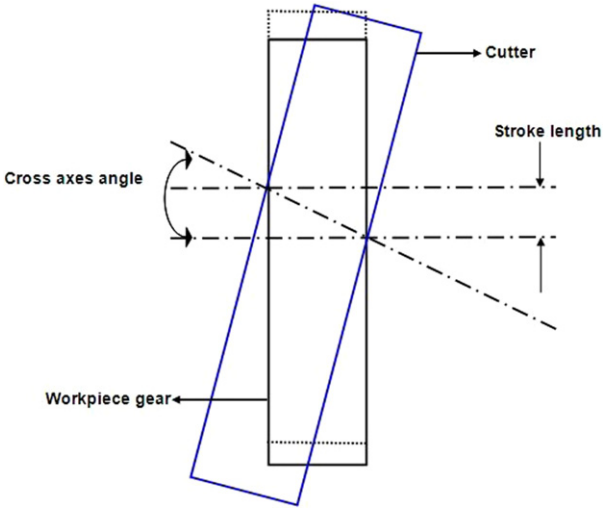


Figure 19 Schematic of tangential or underpass type of rotary gear shaving.[4]

Stroke length in this process is smaller than that for axial and diagonal type gear shaving processes consequently shaving time is less as compared to these versions of rotary gear shaving process. Since, the pivot point of the shaving cutter moves along the entire face width of the workpiece gear resulting in its uniform wear which increases shaving cutter life. This process is most suitable for shoulder gears with critical clearance between the gear and the shoulder.[27]

1.4.4.4.2.4 Plunge gear shaving

This process does not require any translational motion of shaving cutter or workpiece gear because workpiece gear is plunged into the shaving cutter. Chip thickness value in this process is in the range of 2–10 μm depending on the feed rate and the gear data.[32] Theoretical pitch surface of the shaving cutter used in this process

is a hyperboloid with a hollow tooth form.[33] There is line contact between shaving cutter tooth surface and workpiece gear tooth surface whereas other versions of rotary gear shaving have point contact between them. Consequently, this process requires wider shaving cutters with special tooth flank geometry. This restricts value of crossed-axes angle in the range from 10° to 20°. Advantages of this process are simple machine structure, increased productivity, good accuracy, and longer cutting life. Since, stroke length of shaving cutter is very short therefore shaving time in process is the least.[34] The time required to shave a gear of a car gearbox with diagonal shaving is approximately 1 min, while with plunge shaving typically it only takes 10 s.[22] Therefore, this process is generally used for finishing gear in mass production due to low finishing cost and short machining time.[34–36]

1.4.4.4.3 Advantages

- Gear shaving improves gear tooth surface finish and concentricity of the tooth profile, modifies tooth form and eliminates danger of tooth end load concentration in service.
- It can give same surface finish as given by gear grinding (R_a from 0.4 to 0.6 μm).[36]
- It can reduce errors in microgeometry of the hobbed and shaped gear by 65–80%. Gear quality of DIN class 6 or 7 can be achieved routinely with low finishing cost and high process reliability. While, gear quality up to DIN standard 4 can be achieved with extra care during pre-shaving and shaving processes and maintaining workpiece characteristics favorable to shaving process.[37]
- It provides profile modifications that improve noise and load carrying capacity of gear. Profile modifications can be incorporated in either axial or transverse plane and small errors of lead can be corrected readily.[32]
- It can minimize thermal distortions caused by heat treatment.
- It is faster and economical gear finishing process.[38]

1.4.4.4.4 Limitations

- Gear shaving can finish either unhardened gears or gears having hardness value up to 40 HRC only.
- Shaved gears have a step mark left on gear teeth the end of the involute profile which causes excessive noise, wear, and vibration.[39]
- Shaving causes more material removal from the gear tooth surface around pitch points of a gear. This adversely affects gear tooth surface finish and their transmission quality specially when they have true involute profile.[40–41]

1.4.4.4.5 Applications

- Gear shaving is generally used for finishing of soft gears while shaving followed by some surface hardening and then lapping for soft but precision gears.[26]
- It is widely used for finishing spur, helical and worm wheels of moderate size.
- It can be used to remove hobbing scallops and other irregularities produced by gear hobbing process.[36]
- It can be used to provide crowned tooth or a tapered tooth which are required to avoid end bearing condition.

Outcome of gear shaving process depends upon various factors such as workpiece gear material, its geometry, shaving allowance, shaving cutter and its material, shaving process parameters, and shaving machine related parameters. **Table 13** presents summary of Influence of different workpiece gear related parameters on different aspects of gear shaving process.

1.4.4.5 Gear Burnishing

Gear burnishing finishes a gear by plastic deformation rather than material removal. In this process, workpiece gear is rolled under pressure while meshing accurately with ground, polished and hardened master gears (known as burnishing die) of high accuracy and surface finish. As the burnishing die (driver) start engaging with the workpiece gear (driven), the sliding action occur along the line of action from top of burnishing die tooth toward its pitch point on approach side as shown in **Figure 20(a)** and from pitch point toward root of

Table 13 Influence of workpiece gear related parameters on different aspects of gear shaving process[36]

Workpiece gear related parameter	*How it affects*		
	Shaving cutter	*Shaving parameters*	*Shaving machine*
Gear material	Type of steel used	Type of shaving process	Type of machine
Gear geometry parameters (i.e., module, pressure angle, number of teeth, helix angle, faces width)	Hardness and structure of the steel (heat treatment quality)	Feed and cutting speed	Machine in good conditions and of medium life
Shaving allowance	Serrations characteristics (dimension and finish, especially of side walls)	Cross-axes angle	Type of the clamping fixtures for gear and cutter
Pre-shaving condition (type of manufacturing process, microgeometry, etc.)	Manufacturing accuracy and precision in re-sharpening	Number of passes	Old machine in bad condition
Post-shaving gear accuracy, profile and helix corrections	Geometry characteristics (i.e., bore, faces, etc.)	Type of lubrication	–
Single open gear or cluster gear with shank (and danger of flexion)	Accurate design (even contacts, number of teeth, outside diameter)	–	–

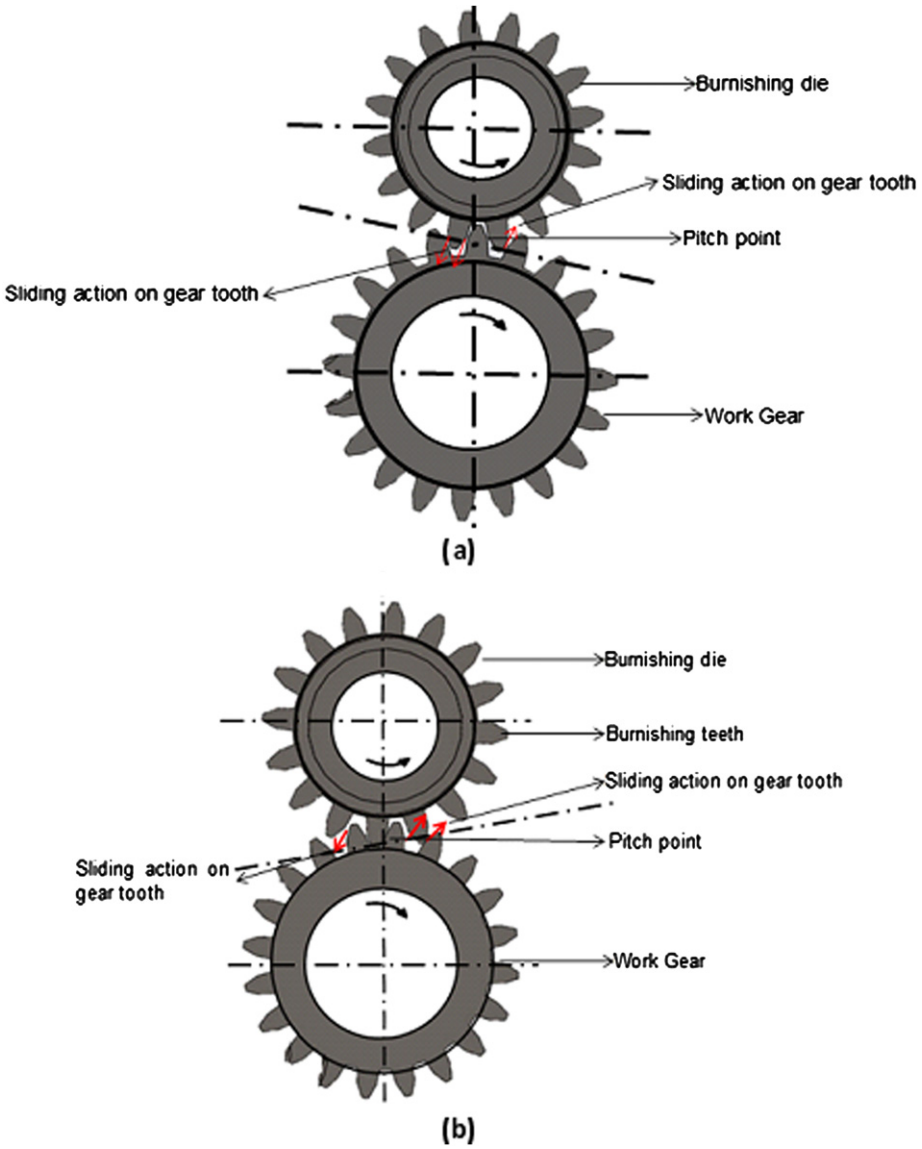


Figure 20 Sliding action in gear burnishing process: (a) approach side; and (b) recession side, of the burnishing die teeth.[4]

tooth on recession side as shown in **Figure 20(b)**. These changes in sliding action compresses the workpiece gear from root toward pitch point on approach side and from pitch point toward top on recession side. Changes in direction of sliding causes more material to be displaced on the recession side as compared to approach side approximately in the ratio of 3:1.[4,42] The workpiece gear is finished by smearing off the minute irregularities from its teeth surfaces by cold plastic deformation along line of contact which also helps in improving the surface integrity of the workpiece gear by inducing compressive residual stresses in it.[42] Accuracy and quality of gear burnishing is affected by amount of material flow and hardness of the workpiece gear material. Stock allowances given on workpiece gear also affect its accuracy and quality. Gear burnishing dies are generally made of special fatigue and impact resistant high speed steel. **Figure 21** depicts photographs some gear burnishing dies.

Gear burnishing machines are generally either single-die or double-die type. Selection criteria include rigidity, strength, high speed loading, die-phasing, independent adjustment for die axis and die positioning. Arrangement of workpiece gear and burnishing dies for single-die and double-die gear burnishing machine are shown in **Figures 22(a)** and **22(b)**, respectively.

In a single-die gear burnishing machine the workpiece gear is mounted on the roller steady rest in between head stock and tail stock while burnishing die is mounted on a heavy duty gearhead above the workpiece gear. The die is driven by an electric motor which in turn rotates workpiece gear due to tight meshing with it. Direction of rotation of the burnishing die is reversed during the burnishing process to provide balanced

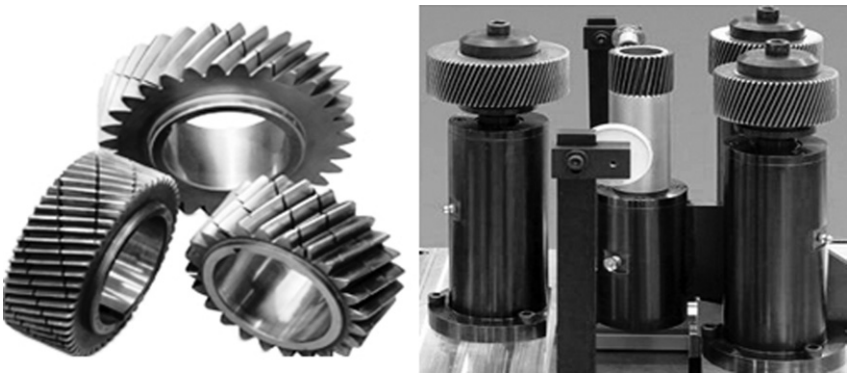


Figure 21 Photographs of some gear burnishing dies.[43]

material flow on the leading and trailing side of a gear tooth. Lubrication is provided to get the desired surface quality and to prevent abrasion of the workpiece gear.[4,32] In a double-die gear burnishing machine, the workpiece gear is sandwiched between fixed upper burnishing die and hydraulically fed lower burnishing die. Arbor of the workpiece gear is rotated by a hydraulic motor slightly slower or faster than the speed of die to ensure clash-free engagement. Amount of upward movement of the lower die controls gear finishing.

1.4.4.5.1 Advantages

- Burnishing is very fast finishing process for producing smooth surface compared to shaving and honing for finishing same dimension gear due to very short finishing times (i.e., 5–10 s) for the gear.[44]
- It can finish both external and internal gears.
- It removes or reduces nicks and burrs from the gear teeth.
- It improves surface integrity and fatigue life of the gears.
- Longer life of burnishing dies (typically 500 000–750 000 cycles) and their lower maintenance cost makes it very suitable for mass production.[44]

1.4.4.5.2 Limitations

- Burnishing can finish only unhardened gears.
- It cannot improve tooth position, tooth profile, lead, spacing, or concentricity.
- Since, it is a localized cold-working operation therefore it may result in some undesirable effects such as localized surface stresses and nonuniform surface characteristics.
- Cost of burnishing dies is higher as compared to the cutter used shaving and grinding.
- Causes damage when a large portion of workpiece gear tooth is rolled over.

1.4.4.5.3 Applications

- For finishing the helical gears.
- For improving fatigue strength of gears teeth.
- For improving gear tooth profile and gear noise.
- For improving gear quality and surface finish.

1.4.4.6 Conventional Finishing Processes for Conical Gears

Due to complex geometry of conical gears, only two conventional gear finishing processes namely gear grinding and gear lapping can be used for finishing them. There is minor difference in working principle of these two gear finishing processes when they used for conical gears as mentioned below. Other details of these two processes are same as described earlier.

1.4.4.6.1 Finishing of conical gears by grinding

Grinding is very accurate and precise process for finishing the conical gears and can finish gear having hardness value up to 92 HRC. It can attain surface roughness values in the range of 0.25–0.76 μm; gear quality of DIN standard 6–7 normally and DIN standard 2–3 with extra care. But, it is very complex and costly process. Moreover, it causes two major undesirable effects namely: grinding burns caused by high temperature damage surface integrity of the ground gears and can even sometime lead to gear failure through tooth breakage and transverse grind lines on the finished surface which cause noise and vibrations of the gears. There are two versions of gear grinding which can be used for finishing conical gears. They are generative grinding and form grinding.[4]

1.4.4.6.1.1 Generative gear grinding

In this process, the workpiece gear is run in mesh with a cup-shaped grinding wheel and relative motion between the workpiece gear and the grinding wheel finishes flank surfaces and root of the gear teeth. Al_2O_3 or CBN as abrasives and vitrified or resinoid as bond are most commonly used for manufacturing cup-shaped grinding wheel. It is used for finishing hypoid and spiral gears. It provides accurate tooth spacing, concentricity, and profile.

1.4.4.6.1.2 Form or non-generative gear grinding

Figure 23 shows schematic of 'Waguri method' for finishing the bevel gears which uses a circular grinding wheel with an average point width equal to 0.25–0.50 mm which is less than the slot width of workpiece gear. Grinding wheel rotates about its axis and gears are ground along the line contact between grinding wheel and workpiece gear tooth.

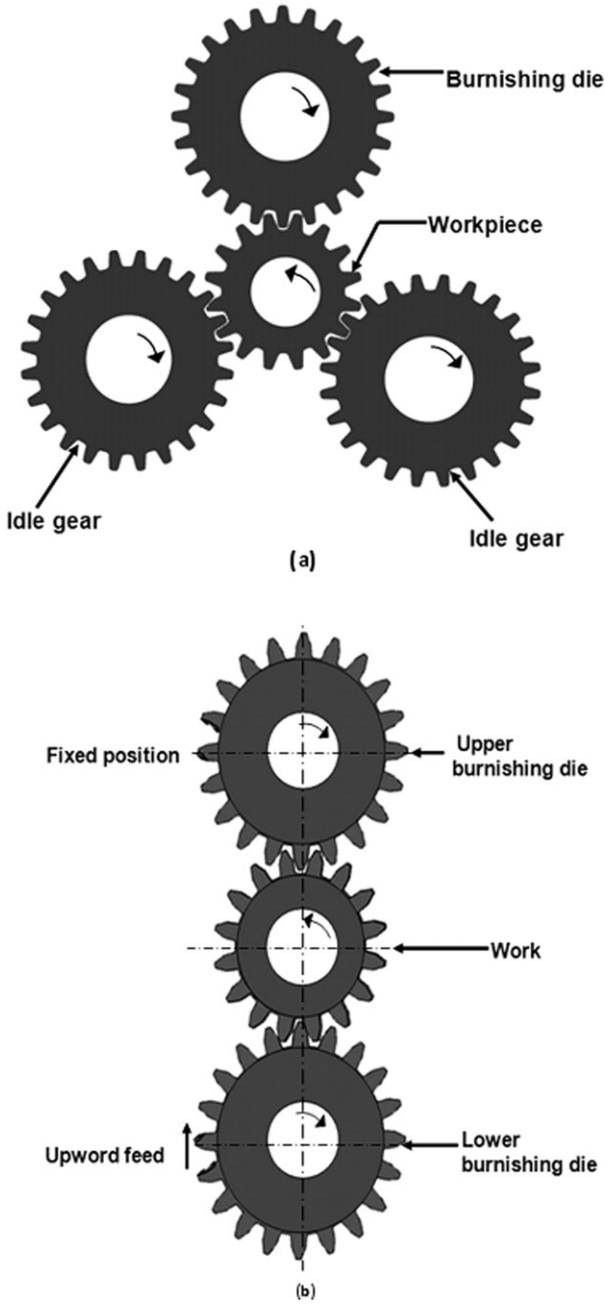


Figure 22 Arrangement of workpiece gear and burnishing dies in (a) single-die gear burnishing machine; and (b) double-die gear burnishing machine.

1.4.4.6.2 Finishing of conical gears by lapping

In this process, small gear (driver) run in mesh with workpiece gear (driven) under tooth contact load and lapping compound is supplied in between them for finishing operation. Lapping is usually used to finish hypoid and spiral bevel gears.[15] **Figure 24** shows the schematic of finishing a spiral bevel gear by the lapping process.

1.4.4.7 Gear Finishing by AFM

In the recent years, developments in materials and manufacturing technology grew up very rapidly so as the demand for better quality product at minimum cost. Major focus of these developments has been on reduction of manufacturing lead time, manufacturing and finishing costs, improving product quality, operating performance, service life, and product reliability. Finishing cost of a product contributes 15–20% toward its total manufacturing cost.[45] As the requirements for surface roughness go below 1 μm value, finishing cost increases very rapidly. AFM process was developed by Extrude Hone Corporation, USA in 1960s with an objective to achieve high surface finish with minimum cost. Initially, it was used for deburring hydraulic control block radar guided acquisition system.[45]

1.4.4.7.1 Working principle of AFM process

AFM is an advanced fine finishing process which is used to polish, deburr, and radius the inaccessible or difficult-to-reach surfaces, complex intricate geometries and edges by flowing abrasive laden viscoelastic self-deformable putty through them. **Figure 25** depicts working principle of AFM process in which abrasive laden viscoelastic self-deformable putty is filled in two vertically opposite cylinders and is extruded back and forth through the passage formed by the workpiece and the tooling or by workpiece alone.[46,47] This causes shearing off surface peaks from the workpiece surface imparting very fine finish to it. More aggressive finishing is done where restriction to flow of the putty is more. Extrusion pressure to medium-containing cylinder is applied by a hydraulic unit or by mechanical means.

1.4.4.7.2 Types of AFM process

Three types of AFM process namely one-way, two-way and orbital have been reported in the literature.[46] The most frequently used version is two-way AFM process.

1.4.4.7.2.1 One-way AFM

This system consists of one hydraulically operated piston-cylinder arrangement, one specially designed medium-containing cylinder and tooling for holding the workpiece as depicted in **Figure 26**. Piston of the hydraulic cylinder pushes the AFM medium causing it to flow through the medium-containing cylinder and through those surfaces of the workpiece which are to be finished, in a closed loop manner. AFM medium is extruded from one side of workpiece in one cycle and then it is collected and reinserted for circulation in the next cycle and this sequence continues till the desired results are obtained. This process causes wastage of AFM medium and finishing time is long.

1.4.4.7.2.2 Two-way AFM

It consists of two oppositely positioned hydraulic cylinders and two cylinders containing AFM medium for extruding the viscoelastic putty through the passage formed by workpiece fixture and tooling (See **Figure 27**). Pistons of the medium-containing cylinders can be moved back and forth either hydraulically or mechanically. Initially, the AFM medium is filled in the lower medium-containing cylinder. Workpiece is clamped in the specially designed fixture positioned between both medium-containing cylinders. The AFM medium is moved back and forth by the pistons of the medium-containing cylinders. Fixture and clamp not only hold the workpiece in position during its finishing by the AFM process but

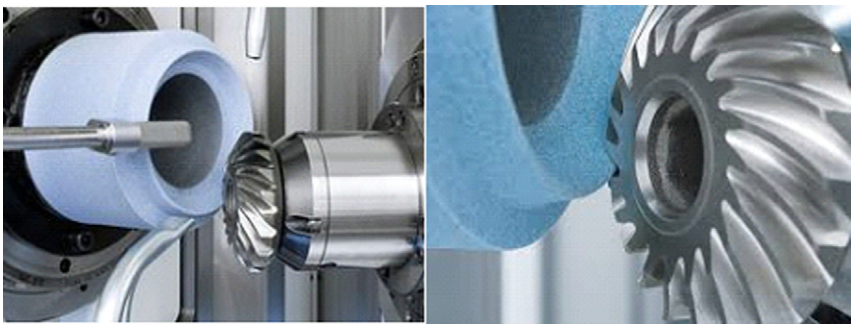


Figure 23 Photographs of Schematic of Waguri method for finishing the bevel and hypoid gear.

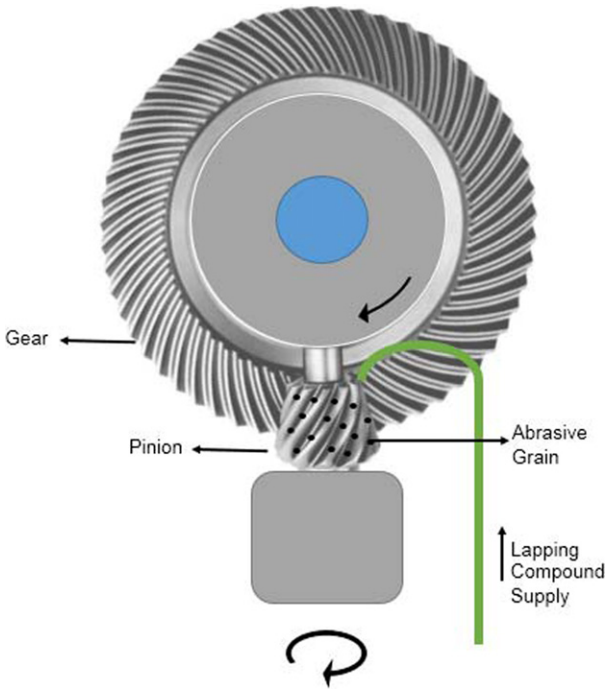


Figure 24 Schematic of finishing a spiral bevel gear by the lapping process.

also direct the AFM medium on those areas of the workpiece which are to be finished. Abrasive particles contained the AFM medium shears off the surface peaks from the workpiece surfaces thus imparting fine finish to them. One complete cycle consist of an upward and downward stroke. The process can either be operated for a fixed number of cycles or till the desired surface finish is achieved.

1.4.4.7.2.3 Orbital AFM process

In this version of AFM, workpiece surface is finished by providing high frequency and low amplitude vibrations to the workpiece as shown in **Figure 28**. The AFM medium is filled in two medium-containing cylinders, workpiece is placed in a fixture positioned between cylinder and orbital vibrations are given to the workpiece in a direction normal to the movement of the AFM medium. Surface finishing takes place due to restrictions created between the workpiece and fixture by orbital vibrations.

1.4.4.7.3 AFM machines

Standard AFM machines have extrusion pressure from 0.69 to 220 bar and flow rate up to 400 l min^{-1}. Modern AFM machines have CNC control and flexibility to hold any complicated internal or external parts with a facility to vary extrusion pressure, number of cycles or strokes, finishing time, flow rate of AFM medium, volume per stroke, etc.[47]

1.4.4.7.4 Components of an AFM machine

Major components of a complete AFM system are machine structure, tooling and abrasive medium.[46–47]

- **Machine structure:** generally, AFM machine has two hydraulic cylinders, two medium-containing cylinders, workpiece fixture, limit switches, supporting structure, pressure control valve, stroke counter, and hydraulic power unit. CNC control system is also provided in modern machines to run machine for mass production as shown in **Figure 29**. AFM medium is moved back and forth from one medium-containing cylinder to other medium-containing cylinder by the pistons of hydraulic cylinders operated by hydraulic power unit. Workpiece is clamped between the medium-containing cylinders through fixture unit.
- **Tooling:** it is very significant part of AFM system because it holds and supports the workpiece during the finishing process. It confines and directs the flow of AFM medium to the appropriate areas of workpiece for deburring, radiusing, and surface improvements and same time it blocks flow of AFM medium into or out of workpiece passages where no finishing is desired. Tooling can be designed to provide more restriction to flow of AFM medium to remove the more material and impart better finishing. Replaceable inserts made of nylon, teflon or hardened steel are used to restrict tooling area. The tooling can be designed to hold single or multiple workpieces for their simultaneous finishing.
- **Medium:** AFM medium is in the form of semi-solid putty having self-deforming ability which is forced through a passageway or restrictions either in one direction or in both directions. It is a mixture of pliable polymer carrier, abrasive grains and lubricating oil. It is resilient enough to act as a self-deforming grinding stone when forced through the workpiece. Commonly used abrasives are alumina, SiC, CBN, and diamond. Size of abrasive

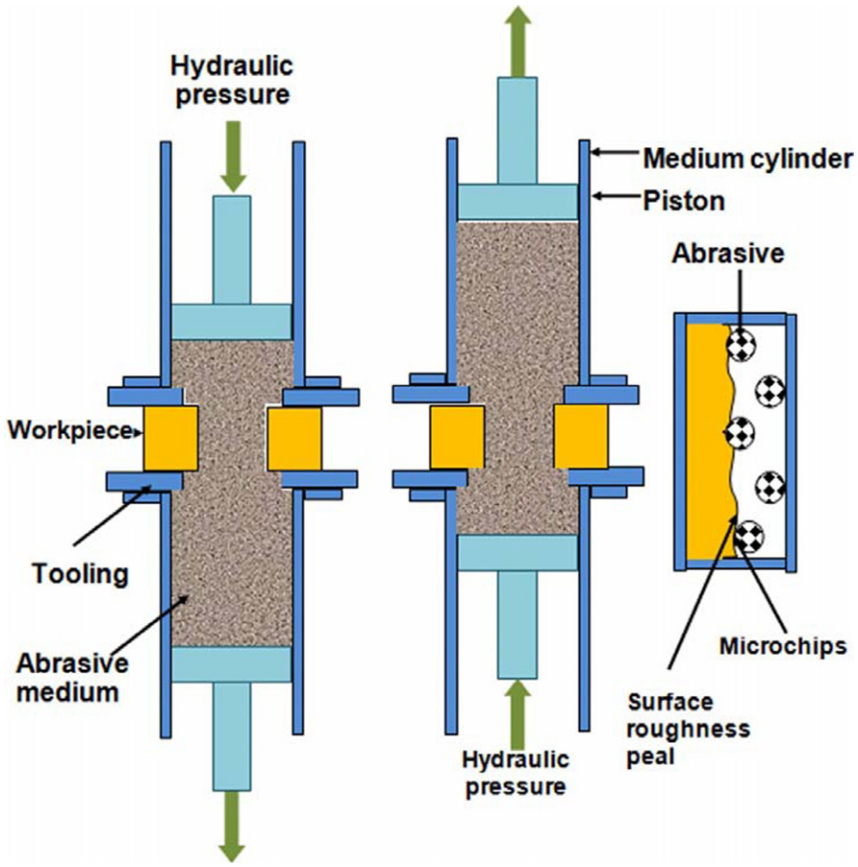


Figure 25 Schematic of working principle of AFM.[47]

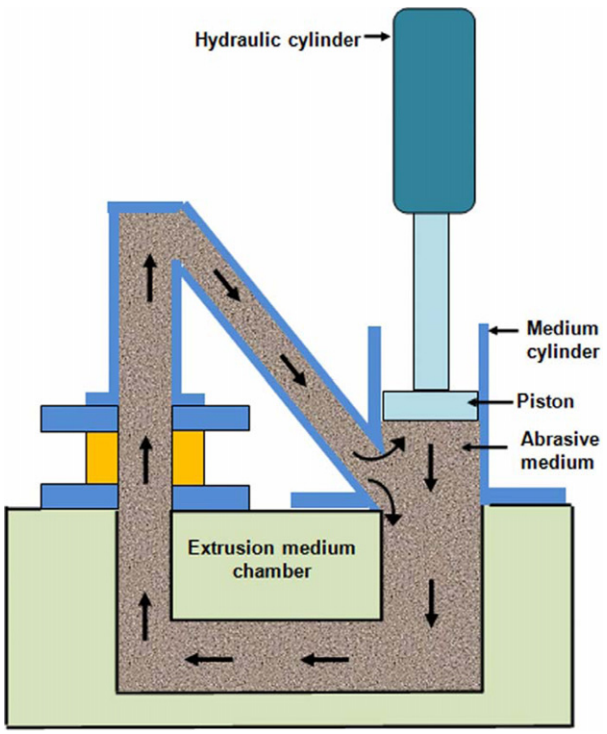


Figure 26 Working principle of one-way AFM process.[46]

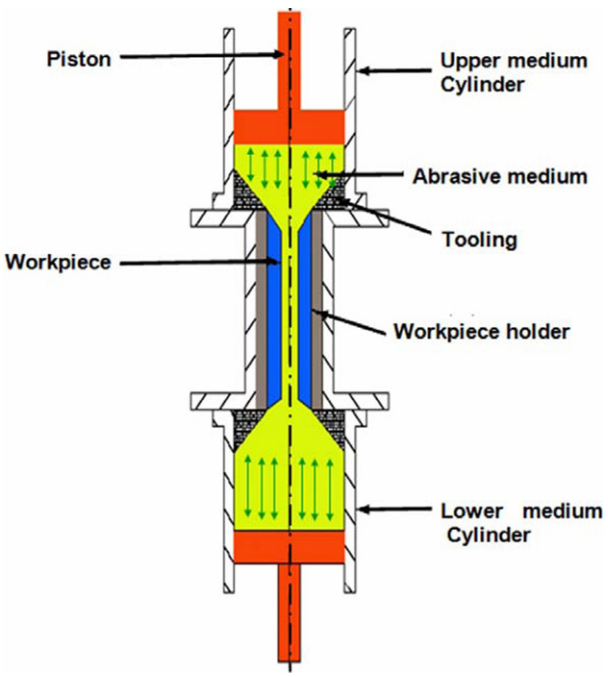


Figure 27 Working principle of two-way AFM process.[48]

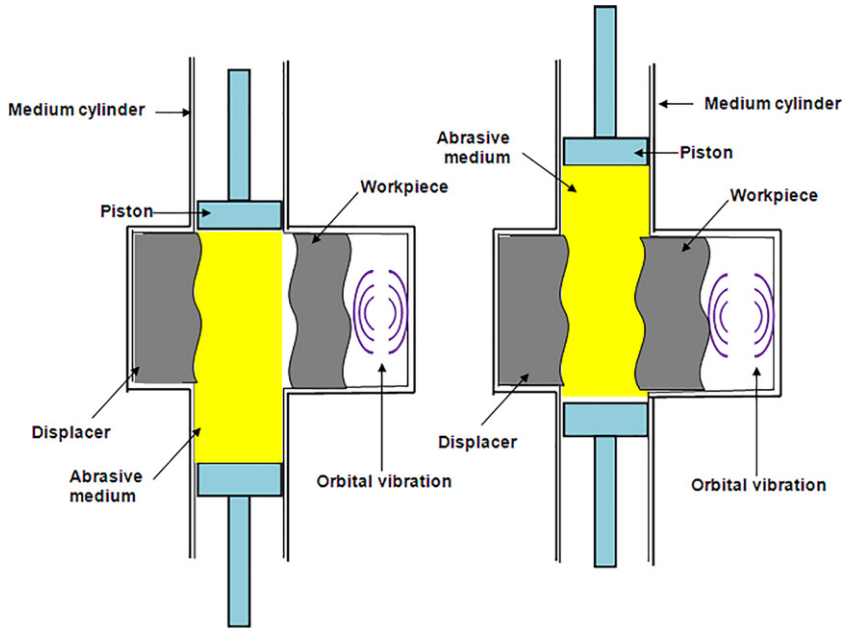


Figure 28 Working principle of orbital AFM process.[47]

particles ranges from 0.005 to 1.5 μm. Different values of viscosity can be obtained by changing ratio of polymer and lubricating oil. Higher viscosity medium is generally used for uniform abrasion and lower viscosity medium is suitable for radiusing the edges. The viscosity and flow rate of medium significantly affect MRR and edge radius size. Low viscosity medium with higher flow rate is applicable for deburring whereas low and steady flow rate is used for uniform material removal in finishing and polishing applications.

1.4.4.7.5 AFM parameters

AFM is a controllable finishing process in which, parameters related to AFM medium, abrasive particles, AFM process, and workpiece can be changed to meet the desired finishing and shaping requirements and MRR. MRR in AFM process depends on the following parameters:[47–49]

- extrusion pressure,
- number of cycles/strokes,
- flow rate of medium,
- viscosity of medium,
- size of abrasive particles,
- concentration of abrasive particles,
- hardness of abrasive particles, and
- geometry and Hardness of workpiece.

1.4.4.7.6 Gear finishing by AFM

AFM has all potential and capabilities to be developed as economical and productive alternative to conventional finishing processes of gears. Recent investigations[50–52] have reported AFM being capable of improving surface finish within a very less time and simultaneously improving microgeometry, service life, and stability of gear. Figure 30 depicts geometry of an unfinished gear manufactured by WEDM and same gear finished by AFM process[50] showing that AFM helped in achieving the required cambered shape of gear tooth. Helical gears finished by Xu *et al.*[51] using AFM have been found to have increased tooth stiffness and load carrying capacity and reduction in contact area, friction and wear of the tooth surface. Venkatesh *et al.*[52] used ultrasonic assisted AFM (UAAFM) for finishing the straight bevel gears and reported improvement in surface finish. Further research is under progress at IIT Indore investigating on finishing of cylindrical and conical gears by AFM.

1.4.4.7.7 Advantages

- AFM is excellent process for finishing inaccessible or difficulty-to-reach areas completing roughing and finishing in one pass.
- It gives average surface roughness values as small as 50 nm with dimensional tolerance as good as ± 5 μm. Thickness of material removed is in the range of 1–10 μm.
- It can produce consistent surface quality with tight tolerances repeatedly.
- Multiple-holes can be finished simultaneously in single setup of AFM process in minimum time. Similar finishing by manual polishing takes very long time and is very costly. A minimum limit on the hole size that can be finished/deburred properly is 0.22 mm and the largest size (or diameter) that has been finished is around 1000 mm.
- Results of finishing multiple parts simultaneously are uniform, repeatable, and predictable. Automated AFM system can finish thousands of parts per day and labor cost reduces to great extent by reducing manual hand work.

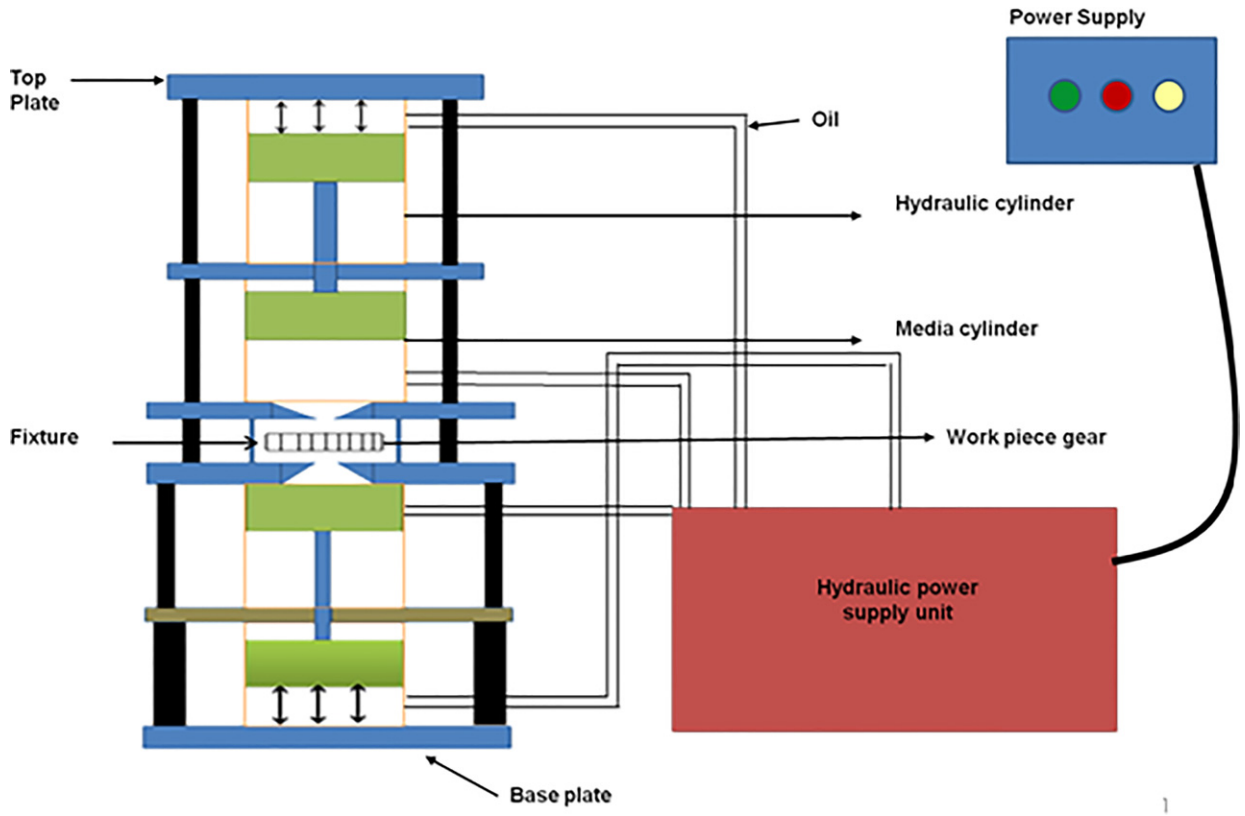


Figure 29 Schematic of a complete AFM system.

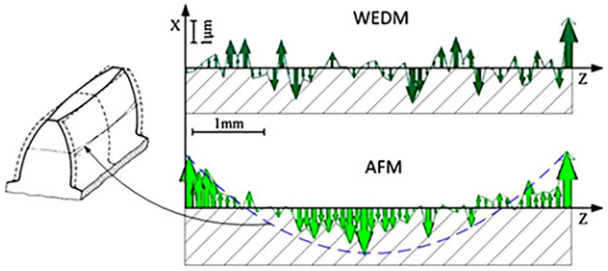


Figure 30 Tooth profile of a gear manufacturing by WEDM and then finished by AFM. Reprinted with permission from Ref. [50]. Springer. © 2014.

- It offers flexibility for change in material, geometry, and dimension of the workpiece, type of AFM medium and abrasives and AFM process parameters thus enabling finishing of variety of parts on same setup by just changing the fixtures for holding workpiece.
- Suitable medium can be used as per finishing requirements.

1.4.4.7.8 Limitations

- Unable to improve surface irregularities like deep scratches, large bumps, out-of-roundness, and taper, etc.
- MRR in AFM is slow hence process is not applicable for mass material removal.

1.4.4.7.9 Applications

AFM finds many finishing applications in different fields. Figure 31 illustrates photographs of some typical components before and after finishing by AFM demonstrating improvement in surface quality the AFM process. Some major applications of AFM process are:

- Finishing of different components used in aerospace, automotive, diesel and turbine engines, i.e., deburring of aircraft valve bodies and spools, fuel spray nozzles, fuel control bodies, airfoil surfaces of impellers, etc.
- Finishing of fluid handling components of the food processing systems.
- Finishing of the components manufactured by additive layer manufacturing processes.
- Finishing common rail pipe fuel system of a diesel engine.[53]
- Finishing of outer rotor surface of the cycloidal pump.[54]
- Modification of surface texture and removal of surface layer which is subjected to mechanical and thermal damage.[46]
- Aerospace applications include removal of the thermal recast layer in the cooling holes of blades and disks, deburring fuel spray nozzles, and polishing cast surfaces of blades, compressor wheels, and impellers.[54]

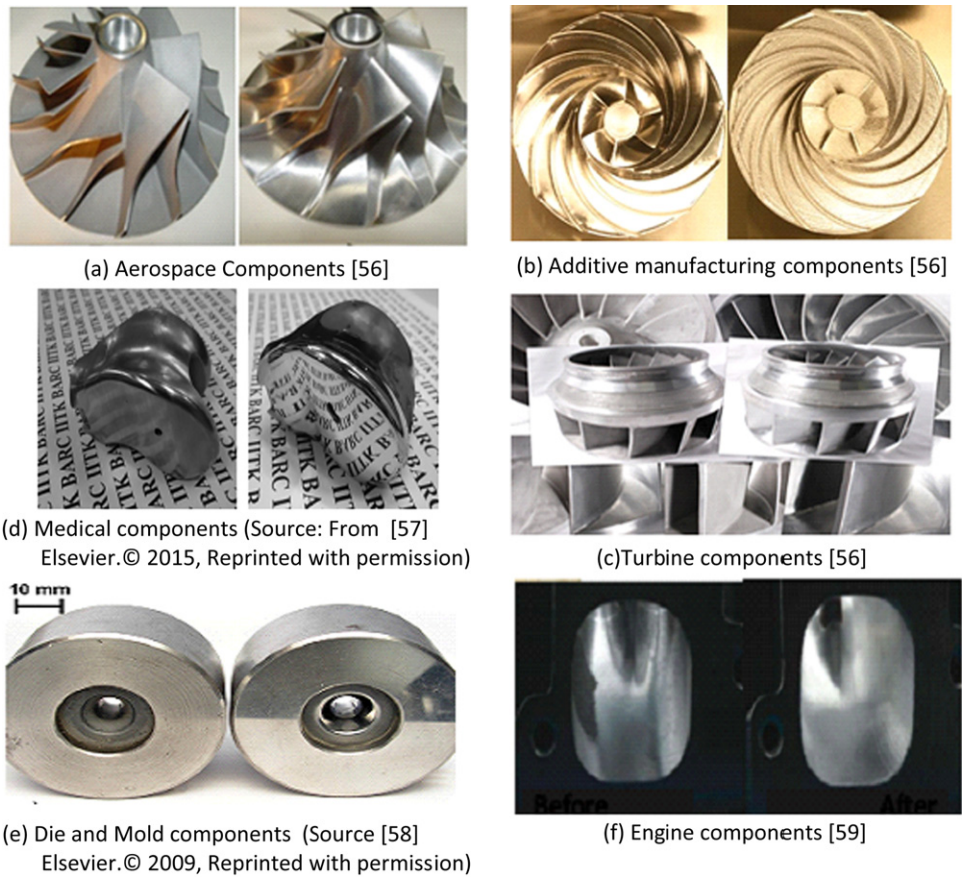


Figure 31 Components before finishing and after finishing by AFM.[56–59]

- Radiusing and deburring of air cooling holes of turbine disk and holes of combustion liner.[55]
- Reworking components to remove coke and carbon deposits, improve surface integrity and enhance eddy current readings.
- Materials ranging from soft aluminum to hard nickel alloys, ceramics, and carbides can be successfully finished with this process. Surface integrity problems such as residual stresses, metallurgical transformations, plastic deformation, tearing and cracking can be reduced or avoided.[46]

1.4.5 Comparative Evaluation

Gears are manufactured according to the given design, drawing, and service requirements. Successful production of gears depends on availability of manufacturing machines, cutting tools, finishing, and heat treatment processes and machines for them. Gear finishing is very critical aspect which affects overall performance of gear after its manufacturing. Various conventional finishing processes such as grinding, lapping, shaving, honing, burnishing, and unconventional or advanced processes such as AFM and ECH can be used to perform finishing of gears. This chapter described these processes in details. Table A1 in Appendix A presents comparative summary of these processes which should help the reader to select a suitable gear finishing process.

Grinding is the oldest process of gear finishing which is used widely in gear industry. This process is capable of giving DIN quality 2–3 with extra care but has certain limitations such as grinding burn, traverse grid line generation which affect surface integrity of the gears adversely. Lapping can produce DIN quality of 6 and the mating gears after lapping cannot be interchanged. Shaving can produce DIN quality 3–4 with extra care but this process is applicable for soft and unhardened gears only. Honing can produce DIN quality 6 with extra care but life of honing tool is limited. AFM is recently developed advanced finishing processes which can finish hard and hardened gears made of both metallic and nonmetallic materials. Some hybrid processes based on AFM for gear finishing are also under development stage.

Acknowledgments

Authors express their sincere gratitude toward all those researchers and authors whose figures have been used in this manuscript and their publishers for permitting to use these figures.

Appendix A

Table A1 Comparison of different processes for finishing the gears

Process	Capabilities	Applications	Limitations
Gear Grinding	• It is very accurate and frequently used gear finishing process • It can finishes gears having hardness value up to 92 HRC • It can do profile modification • It improves accuracy of gears • **Gear quality:** DIN standard 6–7 in normal condition and 2–3 with extra care • **Average surface value:** 0.25–0.80 μm.	• Generally used to finish tooth profile of different types of gears made of hard materials and gears which have been hardened after their manufacturing • For finishing of spur, helical, and bevel gears	• The thermal damage may lead to grinding burn on the gear surface • Generates transverse grind lines on the gear face which increases noise and vibrations of a gear • Redressing of grinding wheels affect form accuracy of a gear • Cost of grinding machine is very high and operation is complicated as it requires skilled machine operator • Take long time in form grinding • Grinding cannot modify some special gears such as an inner gear, multi-joint gears, and very large-size gear
Gear Lapping	• It corrects minute distortion caused due to heat treatment, errors in involute profile, helix angle, spacing, and eccentricity in the hardened gears • Gear tooth contact improves by lapping • **Gear quality:** DIN standard 7 in normal condition, 6 with extra care • **Average surface value:** 0.08–0.25 μm	• For finishing of spur, helical, bevel gear, spiral bevel, and hypoid gears • Usually employed on those gears that has been shaved and hardened	• Longer lapping cycles affects the form accuracy adversely • Only mating gears are lapped in a pair and they cannot be interchanged
Gear Honing	• It improves noise characteristics of the gears • It produces cross-hatch lay pattern on finished gear teeth surface which improves lubricating oil retention • No increase in backlash • High gear quality and improved gear efficiency • Correct the distortion after heat treatment • Improves concentricity • No machining marks in transverse direction • **Gear quality:** DIN standard 7 in normal condition and 6 with extra care • **Average surface roughness:** 0.13–1.25 μm	• For finishing of spur, helical, and bevel gear	• Can be used only for unhardened gears only • Limited life of honing tool • Slow process

Gear Shaving	• It corrects error in index, helical angle, tooth profile, and eccentricity • It increase load carrying capacity of gears • Improve tooth surface smoothness • Reduces gear noise • Eliminates the danger of tooth end load concentration in service • Effectively correct spacing error • Shaving can remove 80% of errors of manufactured gear • **Gear quality:** DIN standard 7 in normal condition and up to 3 with extra care • **Average surface value:** 0.4–0.6 μm	• Widely used for teeth of straight or helical toothed external spur gears and worm wheels of moderate size	• Can be used only for those gears which have hardness up to 40 HRC • High investment cost • Cost of shaving cutter very high • High tool wear
Gear Burnishing	• Improves surface integrity and fatigue life of the gears • Faster than other conventional gear finishing methods • **Gear quality:** DIN standard 7 in normal condition • **Average surface value:** Not available	• For finishing helical gears	• Some undesirable effects such as localized surface stresses and nonuniform surface characteristics are produced due to cold working • Can be used only for soft and unhardened gears only
Gear Finishing by Abrasive Flow Machining (AFM)	• Improves surface roughness and fatigue life • Take less time to finish gear than conventional gear finishing methods • **Gear quality:** not reported • **Average surface value:** not reported	• For finishing of spur, helical, and bevel gears • Both external and internal gears can be finished	• Selection of abrasive and media is major issue • High cost of medium • Specially designed fixture is required to hold gear and direct abrasive putty. This increases cost

See also: 1.6 Precision Grinding, Lapping, Polishing, and Post-Processing of Optical Glass. 1.13 ELID Grinding and EDM for Finish Machining. 1.15 Micro Plastic Part Filling Capabilities through Simulation and Experiment: A Case Study on Micro Gear Shape

References

1. Radzevich, S. P. *Dudley's Handbook of Practical Gear Design and Manufacture*, 2nd ed.; CRC Press: New York, NY, 2012.
2. Karpuschewski, B.; Knoche, H. J.; Hipke, M. Gear Finishing by Abrasive Processes. *CIRP Ann. Manuf. Technol.* **2008**, *57* (2), 621–640.
3. Davis, J. R. *Gear materials, Properties and Manufacture*, 1st ed.; ASM International: Geauga County, OH, 2005.
4. Townsend, D. P. *Dudley's Gear Handbook (The Design, Manufacture and Applications of Gears)*; McGraw Hill Education (India) Private Limited: New Delhi, 2011.
5. Pathak, S.; Jain, N. K.; Palani, I. A. On Use of Pulsed Electrochemical Honing to Improve Micro-Geometry of Bevel Gears. *Mater. Manuf. Process.* **2014**, *29* (11–12), 1461–1469.
6. Goch, G. Gear Metrology. *Ann. CIRP* **2003**, *52* (2), 659–695.
7. Daryani, P. H. *The Art of Gear Fabrication*, 1st ed.; Industrial Press Inc.: Madison Avanue, NY, 2001; pp. 48–71.
8. Ra, S. B. Grinding of Spur and Helical Gears. *Gear Technology Magazine*, 1992; pp. 20–31.
9. Rowe, W. B. *Principles of Modern Grinding Technology*; William Andrew; Elsevier: Oxford, 2009.
10. Marinov, V. *Manufacturing Processes for Metal Products*; Kendall Hunt Publishing Company: Dubuque, USA, 2010; pp. 138–140.
11. Plainte, P. Gear Grinding Comes of Age. *Gear Technology Magazine*, 1995; pp. 32–36.
12. Newman Tools Inc. Available from: www.newmantools.com/lapping/timesaver_booklet.pdf (accessed 3 March 2016).
13. Masseth, J.; Kolivand, M. Lapping and Superfinishing Effects on Surface Finish of Hypoid Gears and Transmission Errors. *Gear Technology Magazine*, 2008; pp. 72–78.
14. Weia, B. Y.; Deng, X. Z.; Fang, Z. D. Study on Ultrasonic-Assisted Lapping of Gears. *Int. J. Mach. Tool. Manuf.* **2007**, *47* (12–13), 2051–2056.
15. Jiang, Q.; Gosselin, C.; Masseth, J. Simulation of Hypoid Gear Lapping. *J. Mech. Design* **2008**, *130* (11), 11260, (1–10).
16. Uhlmann, C.; Spur, G.; Kleinschnitker, M. Honing and Superfinishing. In *Handbook of Ceramics Grinding and Polishing*; Marinescu, I. D., Doi, T. K., Uhlmann, E., Eds.; William Andrew; Applied Science Publisher: Oxford, UK, 2015; pp. 234–262 (Chapter 5).
17. Klocke, F. *Manufacturing Processes 2: Grinding, Honing, Lapping*; Springer–Verlag: Berlin, Heidelberg, 2009; p. 301.

18. Flores, G.; Wiens, A.; Stammen, O. Honing of Gears. *Gear Technology Magazine*, 2014; pp. 60–66.
19. Tonshoff, H. K.; Friemuth, T.; Marzenell, C. Properties of Honed Gears during Lifetime. *Ann. CIRP* **2000**, *49* (7), 431–434.
20. Boyce, M. P., Ed. *Gears and Gas Turbine Engineering Handbook*, 4th ed.; Butterworth-Heinemann: Oxford, 2012 (Chapter 14).
21. Dugas, J. P. Rotary gear honing, *Gear Technology Magazine*, 1987; pp. 36–48.
22. Jones, J. F. *Design for Manufacturability Handbook*; McGraw-Hill Publications: New York, NY, 2004; pp. 4.253–4.286.
23. Radzevich, S. P. Diagonal Shaving of an Involute Pinion: Optimization of the Geometric and Kinematic Parameters for the Pinion Finishing Operation. *Int. J. Adv. Manuf. Technol.* **2007**, *32*, 1170–1187.
24. Radzevich, S. P. On Satisfaction of the Fifth Necessary Condition of Proper Part Surface Generation in Design of Plunge Shaving Cutter for Finishing of Precision Involute Gears. *J. Mech. Design, ASME* **2007**, *129*, 969–980.
25. Watson, H. J. Modern Gear Production, 1st ed.; Pergamon Press: Oxford, UK, 1970; pp. 240–255.
26. Moriwaki, I.; Okamoto, T.; Fujita, M.; Yanagimoto, T. Numerical Analysis of Tooth Forms of Shaved Gear. *JSME Int. J., Series III* **1990**, *33* (4), 608–613.
27. Wordpress. Available from: www.drishtikona.files.wordpress.com/2012/08/ch4.pdf (accessed 3 March 2016).
28. Klocke, F.; Schroder, T. Gear Shaving: Simulation and Technological Studies. In *International Design Engineering Technical Conferences and Computers and Information in Engineering Conference, ASME*, 2003; pp. 257–264.
29. Hsu, R. H.; Fong, Z. H. Analysis of Auxiliary Crowning in Parallel Gear Shaving. *Mech. Mach. Theory* **2010**, *45*, 1298–1313.
30. Mitsubishi Heavy Industries Machine Tool Co., Ltd. Available from: www.mhi-global.com/products/detail/ind_gear_shaving_cutter.html (accessed 3 March 2016).
31. Zhong, J. S.; Qu, L. S. Intelligent Control of the Gear-Shaving Process. *Proc. Inst. Mech. Eng. B: J. Eng. Manuf.* **1993**, *207*, 159–165.
32. Kim, J. D.; Kim, D. S. The Development of Software for Shaving Cutter Design. *J. Mater. Process. Technol.* **1996**, *59*, 359–366.
33. Hsu, R. H.; Fong, Z. H. Theoretical and Practical Investigations Regarding the Influence of the Serration's Geometry and Position on the Tooth Surface Roughness by Shaving with Plunge Gear Cutter. *J. Mech. Eng. Sci., Proc. IMechE, Part C* **2006**, *220*, 1170–1187.
34. Fuentes, A.; Nagamoto, H.; Litvin, F. L.; Perez, I. G.; Hayasaka, K. Computer Methods in Applied Mechanics and Engineering. *Comput. Methods Appl. Mech. Eng.* **2010**, *199*, 1677–1690.
35. Radzevich, S. P. Design of Shaving Cutter for Plunge Shaving a Topologically Modified Involute Pinion. *Trans. ASME* **2003**, *125*, 632–639.
36. Bianco Gianfranco. Available from: www.biancogianfranco.com/Mio%20sito-2-.html (accessed 3 March 2016).
37. Hung, C. H.; Liu, J. H.; Chang, S. L.; Lin, H. J. Simulation of Gear Shaving with Considerations of Cutter Assembly Errors and Machine Setting Parameters. *Int. J. Adv. Manuf. Technol.* **2007**, *35*, 400–407.
38. Natarajan, R.; Rathnasabapthy, C.; Krishnamurthy, R. Surface Durability of Shaved Gears. *Wear* **1987**, *114* (3), 295–308.
39. Kuang, J. H.; Chen, W. L. Determination of Tip Parameters for the Protuberance Pre-Shaving Cutters. *Mech. Mach. Theory* **1996**, *31* (7), 839–849.
40. Jelaska, D. *Gears and Gear Drives*; John Wiley & Sons Ltd: West Susses, 2012.
41. Lv, M.; Yang, X. Design and Manufacture of a Shaving Cutter with Unequal Depth Gashes. *J. Mater. Process. Technol.* **2002**, *129*, 193–195.
42. Groover, M. P. *Fundamentals of Modern Manufacturing: Materials, Processes and Systems*, 4th ed.; John Wiley & Sons Inc.: New York, NY, 2010; p. 544.
43. ITW. Available from: http://itw.njolson.net/GearMachines/BurnishingDies.aspx (accessed 3 March 2016).
44. Boljanovic, V. *Metal Shaping Processes: Casting and Molding, Particulate Processing, Deformation Processes and Metal Removal*; Industrial Press: New York, NY, 2010; pp. 381–384.
45. Petri, K. L.; Billo, R. E.; Bidanda, B. A Neural Network Process Model for Abrasive Flow Machining Operations. *J. Manuf. Syst.* **1998**, *17* (1), 52–64.
46. Fletcher, A. J.; Hull, J. B.; Mackie, J.; Trengove, S. A. Computer Modeling of the Abrasive Flow Machining Process. In *Surface Engineering;* Meguid, S. A., Ed.; Springer: The Netherlands, 1990; pp. 592–601.
47. Sankar, M. R.; Jain, V. K.; Ramkumar, J. *Abrasive Flow Machining (AFM): An Overview*; Indian Institute of Technology: Kanpur, 2008; pp. 1–9.
48. Jain, V. K. *Advanced Machining Processes*; Allied Publisher Private Ltd.: New Delhi, 2002; pp. 57–73.
49. Kennametal. Available from: www.kennametal.com/en/products/precision-surface-solutions/deburring-and-machining-processes/afm-abrasive-flow-machining.html (accessed 3 March 2016).
50. Kenda, J.; Duhovnik, J.; Tavcar, J.; Kopac, J. Abrasive Flow Machining Applied to Plastic Gear Matrix Polishing. *Int. J. Adv. Manuf. Technol.* **2014**, *71*, 141–151.
51. Xu, Y. C.; Zhang, K. H.; Lu, S.; Liu, Z. Experimental Investigations into Abrasive Flow Machining of Helical Gear. *Key Eng. Mater.* **2013**, *546*, 65–69.
52. Venkatesh, G.; Sharma, A. K.; Singh, N.; Kumar, P. Finishing of Bevel Gears Using Abrasive Flow Machining. *Procedia Eng.* **2014**, *97*, 320–328.
53. Zhu, L. F.; Wang, K.; Wu, H.; Xiu, D.; Sun, L. Z. Research on the Methods for Common-Rail Pipe Holes Abrasive Flow Machining. *Appl. Mech. Mater.* **2014**, *721*, 122–126.
54. Xie, W. B.; Zhang, K. H.; Zhang, S. W.; Xu, B. Research on Abrasive Flow Machining for the Outer Rotor of Cycloidal Pump. *Key Eng. Mater.* **2011**, *546*, 50–54.
55. Rhoades, L. J. Abrasive Flow Machining of Turbine Engine Components. In *International Manufacturing Technology (IMT) Conference*, Chicago, IL, 1990.
56. Extrude Hone AFM. Available from: www.extrudehoneafm.com (accessed 3 March 2016).
57. Kumar, S.; Jain, V. K.; Sidpara, A. Nano-Finishing of Freeform Surfaces (Knee Joint Implant) by Rotational Magnetorheological Abrasive Flow Finishing (R-MRAFF) Process. *Precis. Eng.* **2015**, *42*, 1–14.
58. Uhlmann, E.; Mihotovic, V.; Coenen, A. Modelling the Abrasive Flow Machining Process on Advanced Ceramic Materials. *J. Mater. Process. Technol.* **2009**, *209*, 6062–6066.
59. Hacettepe University. Available from: http://yunus.hacettepe.edu.tr/∼selis/teaching/WEBkmu479/Ppt/kmu479Presentations2010/Abrasive_Flow_Machning.pdf (accessed 3 March 2016).

Relevant Websites

www.biancogianfranco.com/Mio%20sito-2-.html
: Bianco Gianfranco.

www.extrudehoneafm.com
: Extrude Hone AFM.

http://yunus.hacettepe.edu.tr/~selis/teaching/WEBkmu479/Ppt/kmu479Presentations2010/Abrasive_Flow_Machning.pdf
: Hacettepe University.

http://itw.njolson.net/GearMachines/BurnishingDies.aspx
: ITW.

www.kennametal.com/en/products/precision-surface-solutions/deburring-and-machining-processes/afm-abrasive-flow-machining.html
: Kennametal.

www.mhi-global.com/products/detail/ind_gear_shaving_cutter.html
: Mitsubishi Heavy Industries Machine Tool Co., Ltd.

www.newmantools.com/lapping/timesaver_booklet.pdf
: Newman Tools Inc.

www.drishtikona.files.wordpress.com/2012/08/ch4.pdf
: Wordpress.

1.5 Robotic Polishing and Deburring

Fengfeng Jeff Xi, Ryerson University, Toronto, ON, Canada and Shanghai University, Shanghai, P.R. China
Tianyan Chen, Fujian Chuanzheng Communications College, Fuzhou City, China
Shuai Guo, Shanghai University, Shanghai, P.R. China

© 2017 Elsevier Inc. All rights reserved.

1.5.1	**Contact Area-Based Path Planning**	121
1.5.1.1	Contact Mechanics	121
1.5.1.2	Contact Area	122
1.5.1.3	Coverage Area Map	124
1.5.1.4	Continuous Polishing Path	124
1.5.1.5	Step-Over Size	126
1.5.1.6	Polishing Path Planning	126
1.5.2	**Surface Roughness Modeling**	130
1.5.2.1	Generation of a Polishing Stone Topography	130
1.5.2.2	Micro Depth of Cut of a Single Grain	131
1.5.2.3	Micro Depth of Cut of a Polishing Tool	132
1.5.2.4	Prediction of Surface Roughness	133
1.5.3	**Contact Stress-Based Control**	134
1.5.3.1	Robotic Polishing/Deburring System	134
1.5.3.2	Contact Stress Modeling	134
1.5.3.3	Friction Torque Modeling	135
1.5.3.4	Polishing Parameter Planning	136
1.5.3.5	Air Cylinder Pressure Control Modeling	137
1.5.3.6	Air Spindle Speed Control Modeling	137
1.5.3.7	Combined Control System	139
1.5.3.8	Pressure Tracking Control	139
1.5.3.9	Robotic Deburring Control	139
1.5.4	**Polishing/Deburring Toolhead Design**	143
1.5.4.1	Hybrid Design	144
1.5.4.2	Toolhead Dynamic Modeling	144
1.5.4.3	Ring Actuator Modeling	147
1.5.4.4	Simulation of Ring Actuator Stiffness	149
1.5.4.5	Experiment on Ring Actuator Stiffness	150
1.5.5	**Conclusions**	152
References		152

1.5.1 Contact Area-Based Path Planning

1.5.1.1 Contact Mechanics

Over the last 30 years or so, a great deal of research has been carried out to develop automated polishing/deburring systems.[1] During polishing, an abrasive tool, such as disk, wheel, stone, belt, and brush, is pressed under a force/pressure against the surface of a part while undergoing a linear or circular reciprocal motion. The pressing interaction between the tool and the part can be modeled using the Hertzian contact theory.[2] The purpose of this modeling is to determine their contact area which represents an effective polishing region.

Contact area is the area generated between two separate nonconforming bodies made of elastic materials under an applied compressive force F, as shown in **Figure 1**. Nonconforming refers to bodies with different profiles and a small contact area relative to the dimensions of the bodies themselves. The upper body is labeled by B_1 and the lower body

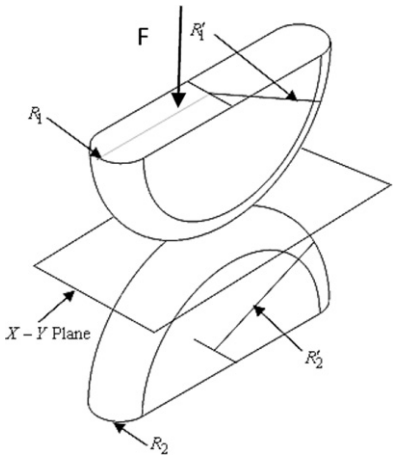


Figure 1 Two contact bodies. Roswell, A. *Modelling for Contact Stress Control in Automated Polishing* (MSc Thesis); Toronto, ON: Ryerson University, 2004.

by B_2. The first point where B_1 and B_2 interact is referred to the initial contact point. If the bodies are assumed to be disks, then each disk has maximum and minimum radii of curvature R_1 and R_1' for the upper disk at the point of contact and R_2 and R_2' for the lower disk. The line of action of the compressive force F is normal to the xy plane, i.e., a tangential plane passing through the point of contact.

Before the compressive force is applied, the separation distance between two points on the surfaces of the bodies and along the line normal to the $x-y$ plane near the point of contact is approximated by.[2]

$$d = Ax^2 + By^2 \quad [1]$$

where x and y are coordinates with the origin at the point of contact, and the constants A and B depend on the principal radii of curvature of both disks at the point of contact as given below

$$A = \frac{1}{4}\left(\frac{1}{R_1}+\frac{1}{R_2}+\frac{1}{R_1'}+\frac{1}{R_2'}\right) - \frac{1}{4}\sqrt{\left[\left(\frac{1}{R_1}-\frac{1}{R_1'}\right)+\left(\frac{1}{R_2}-\frac{1}{R_2'}\right)\right]^2 - 4\left(\frac{1}{R_1}-\frac{1}{R_1'}\right)\left(\frac{1}{R_2}-\frac{1}{R_2'}\right)\sin^2\varnothing} \quad [2]$$

$$B = \frac{1}{4}\left(\frac{1}{R_1}+\frac{1}{R_2}+\frac{1}{R_1'}+\frac{1}{R_2'}\right) + \frac{1}{4}\sqrt{\left[\left(\frac{1}{R_1}-\frac{1}{R_1'}\right)+\left(\frac{1}{R_2}-\frac{1}{R_2'}\right)\right]^2 - 4\left(\frac{1}{R_1}-\frac{1}{R_1'}\right)\left(\frac{1}{R_2}-\frac{1}{R_2'}\right)\sin^2\varnothing} \quad [3]$$

where the angle $\varnothing$ is the intersection angle between planes generated between R_1 and R_2 Note that A and B are related to the geometric shape and configuration of the bodies.

The force F causes elastic deformation of the bodies over the region surrounding the initial point of contact. When the force is applied, the point of contact becomes surface contact and increases with increasing force. The boundary line of the contact surface forms an elliptic area given by

$$\frac{x^2}{a^2}+\frac{y^2}{b^2} = 1 \quad [4]$$

where a and b are the semimajor and semiminor axes of the elliptic contact area. The positive constants a and b determine the shape of the contact area between the disks. a and b are related by $k = b/a$, where b is determined by[2]

$$b = \sqrt[3]{\frac{3kE(k')}{2\pi}(F\Delta)} \quad [5]$$

and

$$\Delta = \frac{1}{A+B}\left(\frac{1-U_1^2}{E_1}+\frac{1-U_2^2}{E_2}\right) \quad [6]$$

where U_1 and U_2 are the Poisson's ratios of the disks, E_1 and E_2 are the modulus of elasticity of body B_1 and B_2, and $k' = \sqrt{1-k^2}$. Note that k is not an exact solution but an approximation given by the following equation:

$$\frac{B}{A} = \frac{\left(\frac{1}{k^2}\right)E(k') - K(k')}{K(k') - E(k')} \quad [7]$$

where $K(k')$ is the complete elliptic integral of first kind

$$K(k') = \int_0^{\frac{\pi}{2}} \frac{d\theta}{\sqrt{1-k'^2\sin^2\theta}} \quad [8]$$

and $E(k')$ is the complete elliptic integral of second kind

$$E(k') = \int_0^{\frac{\pi}{2}} \sqrt{1-k'^2\sin^2\theta}\, d\theta \quad [9]$$

If all model parameters are held fixed (i.e., compressive force, modulus of elasticity, Poisson's ratio), the contact area is a function of one variable, i.e., radius of curvature of the bodies.

1.5.1.2 Contact Area

With the introduction of Hertzian contact theory, the polishing tool is substituted with B_1 and the part surface with B_2. Figure 2 shows a simple yet practical case, where the part has a semi-elliptic cross section area with a semimajor axis $u = 20$ cm and a semiminor axis $v = 10$ cm. The radii of curvatures of the part surface changes in one direction while kept constant in

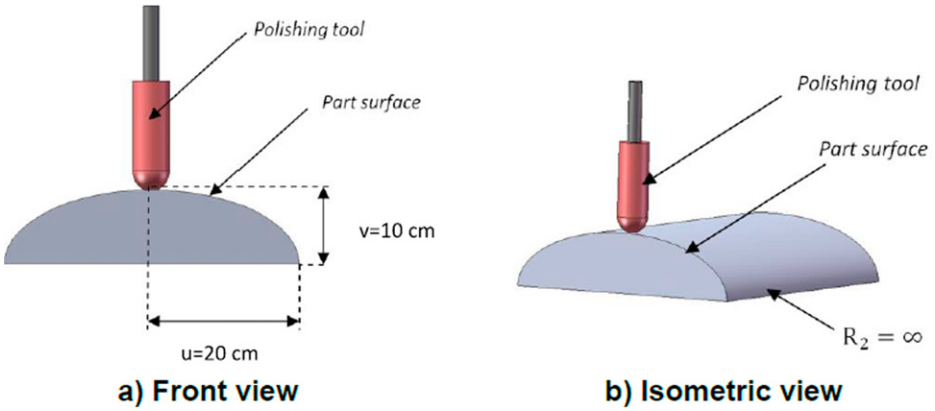


Figure 2 Polishing tool and part. Rososhansky, M. *Coverage Based Tool-Path Planning for Automated Polishing Using Contact Mechanics Theory* (MSc thesis); Toronto, ON: Ryerson University, 2010.

the other, i.e., the maximum radius of curvature of the part surface approaches infinity (i.e., $R_2=\infty$).

The polishing tool under study is assumed to carry a semi-spherical polishing head where the tool tip is tangent to the part surface and its centerline is normal to the part surface. This implies that: (1) equal minimum and maximum radii of the polishing tool (i.e., $R_1=R_1'$); and (2) the angle between planes of principal curvature equals to zero (i.e., $\varnothing=0$).

Substituting the assumption into eqn [2] results in[3]

$$A=\frac{1}{2R_1} \qquad [10]$$

which indicates that A is a function of the principal radius of the polishing tool only and a constant principal radius of the polishing tool implies of a constant A. Following the same procedure for eqn [3] results in[3]

$$B=\left(\frac{1}{2}\right)\left(\frac{1}{R_1}+\frac{1}{R_2'}\right) \qquad [11]$$

which indicates that B is a function of the radii of curvatures of the polishing tool and the part surface. If R_1 is constant then B is a function of R_2' only. Changes in A and B results in changes to the semimajor a and semiminor b of the contact area. Therefore, the contact area changes along the part surface.

The radius of curvature of the part can be calculated as follows

$$R=\frac{|x'y''-y'x''|}{(x'^2+y'^2)^{\frac{3}{2}}} \qquad [12]$$

where x', x'', y', and y'' are the first and second derivatives of x and y, respectively. For an ellipse, it can express $x=u\cos\theta$ and $y=v\sin\theta$. Then, the equation for the radius of curvature of an ellipse is given by

$$R=\frac{uv}{\left(v^2\cos^2\theta+u^2\sin^2\theta\right)^{\frac{3}{2}}} \qquad [13]$$

Figure 3 shows the change in radius versus the location of the polishing tool. This part has a semi-elliptic surface with symmetry along its main axis. The radius of the profile increases from both ends toward the center of the part. The maximum radius occurs at the center where $x=0$ and the minimum radius at both ends where $x=\pm 20$(cm), corresponding to the major axis of elliptic cross section.

In this case, the ratio B/A is a function of R_1 and R_2'. Since R_1 is constant, B/A is a function of R_2' only. As R_2' increases, B/A decreases and vice versa, as R_2' decreases B/A increases. The change in radius affects the semimajor and semiminor axes of the contact area between the polishing tool and the part surface. Therefore, increase in the radius of curvature of the part results in a large contact area. **Figure 4** shows a graph of k vs. tool location along the part surface. The following observations are made:

1. At $x=0$(cm) (Maximum R_2'): k ratio approaches unity implying a circular contact area. Note that $k=1$ implies equal semimajor and semiminor axes which indicate that the equation of an ellipse reduces to the equation of a circle and the contact area is circular.
2. At $x=\pm 20$(cm) (Minimum R_2'): small k ratio implying an elliptic contact area at these points.

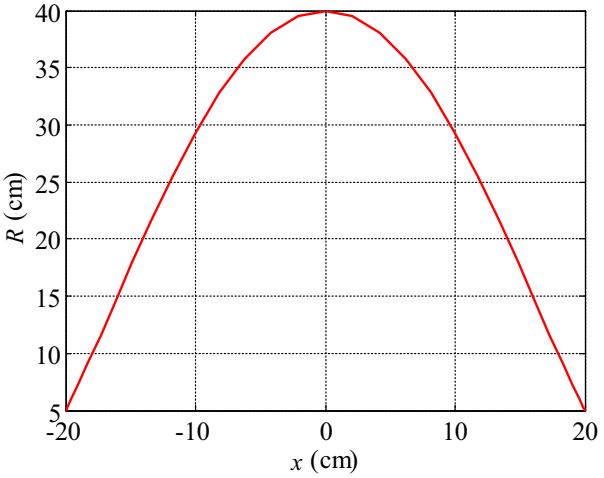


Figure 3 Part surface radius vs. tool location.[3]

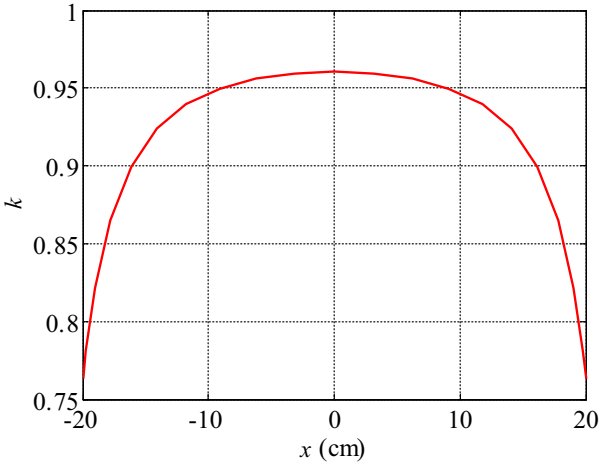


Figure 4 k vs. tool location.[3]

Figure 5 shows a plot of the semimajor axis a and semiminor axis b of the elliptic contact area versus tool locations. The following observations are made:

1. At $x=0$: Small difference between a and b indicating $k\approx 1$. Thus, the contact area resembles a circle.
2. At $x=\pm 20$(cm): Large difference between a and b indicating a small k ratio which implies that the contact area is elliptic.

This figure indicates that for a part with curved profiles the contact area between the polishing tool and the part surface changes with the change in radius of curvature of the part.

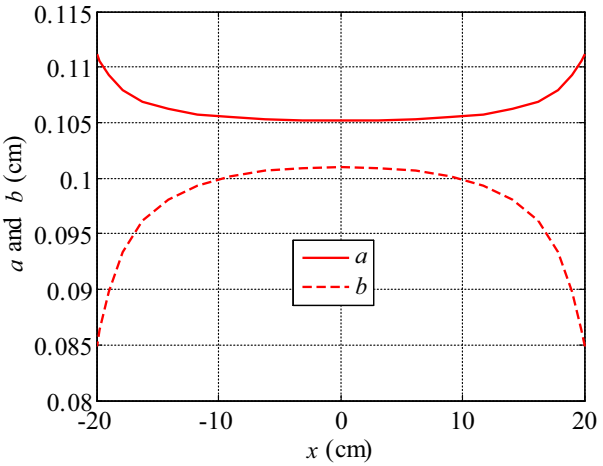


Figure 5 Major axis and minor axis of contact area vs. tool location.[3]

Two conclusions with respect to the contact area between the polishing tool and the part surface are derived from the above discussion:

1. Increase in the radius of curvature of the part results in increase of the contact area between the polishing tool and the part profile.
2. Decrease in the radius of curvature of the part results in decrease of the contact area between the polishing tool and the part profile.

1.5.1.3 Coverage Area Map

Based on the above discussion, a coverage area map (CAM) can be generated along a prescribed polishing path. Here CAM is defined as a two dimensional evidence describing the interaction between the polishing tool and the part surface. For generating the CAM, let N represent a single contact point and CA the corresponding contact area. Any contact point N implies of a contact area CA which is a function of the radius of curvature (i.e., $\forall N \exists \mathrm{CA}(R_1, R'_1, R_2, R'_2)$) as seen in Figure 6.

The polishing path P is a collection of distinct contact points N_i generated by interpolating discretized control points along the part surface. The polishing path for a single raster path is given by

$$P = \{N_1, N_2, \cdots, N_i, \cdots, N_k\} \quad [14]$$

where N_i is the i^{th} contact point along the part surface and N_k is the last contact point. Since, the contact point N_i implies of a corresponding contact area CA_i (i.e., $\forall N_i \Rightarrow \exists \mathrm{CA}_i$), the CAM for a single raster path is given by

$$\mathrm{CAM} = \{\, \mathrm{CA}_1 \quad \mathrm{CA}_2 \quad \cdots \quad \mathrm{CA}_i \quad \cdots \quad \mathrm{CA}_k \,\} \quad [15]$$

where

$$\mathrm{CA}_i = \left\{ (x,y) \middle| \left(\frac{x^2}{a_i^2} + \frac{y^2}{b_i^2} = 1 \right) \right\} \quad [16]$$

Therefore, the Contact Area Map is a set of contact areas where each CA_i is the elliptic contact area generated between the polishing tool and the part surface along the polishing path. The coordinates x and y are defined in the local frame of reference and a_i and b_i are the semimajor and semiminor axes of the contact area.

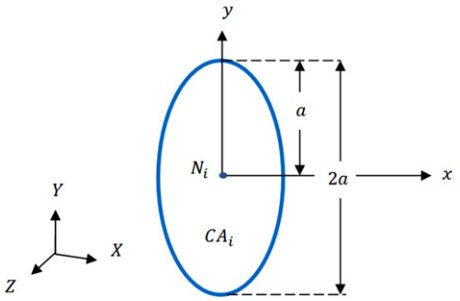


Figure 6 Elliptical contact area at contact point *N*. Rososhansky, M. *Coverage Based Tool-Path Planning for Automated Polishing Using Contact Mechanics Theory* (MSc thesis); Toronto, ON: Ryerson University, 2010.

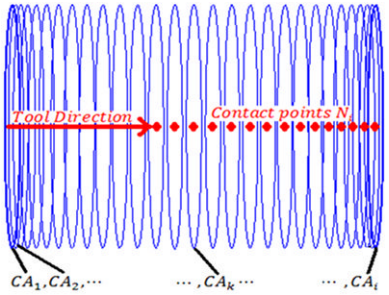


Figure 7 Coverage area for a single raster path. Rososhansky, M. *Coverage Based Tool-Path Planning for Automated Polishing Using Contact Mechanics Theory* (MSc thesis); Toronto, ON: Ryerson University, 2010.

Figure 7 shows the CAM for a single raster path. This is a special case of CAM since all the contact points along the path are in a straight line and the contact area has the same length throughout the path indicating a constant semimajor axis. Generating the CAM only requires the semimajor axis a_i since the semiminor axis b_i has little effect in path definition as long as the polishing tool moves slowly and continuously to provide sufficient overlapping. Therefore, the CAM for a polishing path is given by

$$\mathrm{CAM} = f\begin{pmatrix} a_1 & a_2 & \cdots & a_i & \cdots & a_k \end{pmatrix} \quad [17]$$

The two envelop lines represent the semimajor axis a. The area generated by the boundary lines is the coverage area during polishing. Figure 8 shows the coverage area for a single raster path along the part surface. Note that the boundary lines of the coverage area are straight lines.

1.5.1.4 Continuous Polishing Path

Generating continuous raster path based on CAM is a complicated task but the main idea is that it is a set of all

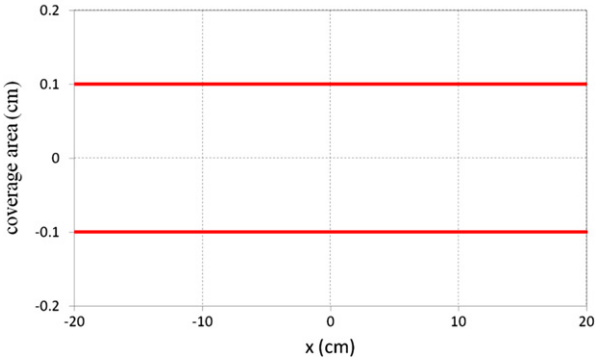


Figure 8 Coverage area for a single raster path. Rososhansky, M. *Coverage Based Tool-Path Planning for Automated Polishing Using Contact Mechanics Theory* (MSc thesis); Toronto, ON: Ryerson University, 2010.

individual raster paths along the part surface as described by

$$\mathrm{CRP} = \{P_1, P_2, \cdots, P_l, \cdots P_j\}^T \quad [18]$$

where CRP stands for continuous raster path. P_1 represents the l^{th} polishing path along the part surface and P_j represents the last polishing path. Using eqn [15] and recalling that every contact point N_{i1} implies of a contact area CA_{i1} results in[3]

$$\mathrm{CAM} = \begin{Bmatrix} \mathrm{CA}_{11} & \mathrm{CA}_{21} & \cdots & \mathrm{CA}_{i1} \\ \mathrm{CA}_{12} & \mathrm{CA}_{22} & \cdots & \mathrm{CA}_{i2} \\ \vdots & \vdots & \cdots & \vdots \\ \mathrm{CA}_{1l} & \mathrm{CA}_{2l} & \cdots & \mathrm{CA}_{il} \\ \vdots & \vdots & \ddots & \vdots \\ \mathrm{CA}_{1j} & \mathrm{CA}_{2j} & \cdots & \mathrm{CA}_{ij} \end{Bmatrix} \quad [19]$$

where l represents the l^{th} polishing path and i represents the i^{th} point along the part surface. Because of $\mathrm{CA}(R_1, R_1', R_2, R_2')$, changes in radii of curvatures result in changes to the contact area.

Figure 9 shows the CAM for a flat surface with constant radii of curvature. This is a special case of CAM since: (1) the contact area is circular indicating that $a_{i1} = b_{i1}$, (2) the contact area remains constant throughout the part surface, i.e., $\mathrm{CA}_{il} = \mathrm{CA}_{il+1}$, and (3) minimum and maximum radii of curvatures approaching infinity $(R_2 = R_2' = \infty)$. Therefore, the vertical distance between consecutive path centers CA_{ik} and CA_{ik+1} remains constant. Note that the contact points were placed farther away from each other so that the contact area will be more visible. In practice, however, the CAM is much denser between contact points.

The step-over size between paths P_1 and P_{i+1} depends on the vertical distance of the boundary between CA_l and CA_{l+1}. The vertical distance of the contact area is twice the semimajor axis (i.e., $2a_{il}$). Thus, the step-over size between P_l and P_{l+1} have a maximum vertical distance of $2a_{il}$ and the Contact Area Map (eqn [19]) can be rewritten

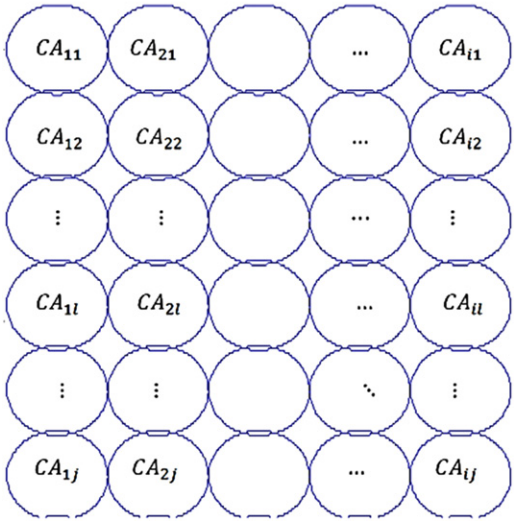


Figure 9 Coverage area map for a flat surface. Rososhansky, M. *Coverage Based Tool-Path Planning for Automated Polishing Using Contact Mechanics Theory* (MSc thesis); Toronto, ON: Ryerson University, 2010.

in terms of the semimajor axis a:

$$\mathrm{CAM} = \begin{Bmatrix} 2\mathrm{a}_{11} & 2\mathrm{a}_{21} & \cdots & 2\mathrm{a}_{i1} \\ 2\mathrm{a}_{12} & 2\mathrm{a}_{22} & \cdots & 2\mathrm{a}_{i2} \\ \vdots & \vdots & \cdots & \vdots \\ 2\mathrm{a}_{1l} & 2\mathrm{a}_{2l} & \cdots & 2\mathrm{a}_{il} \\ \vdots & \vdots & \ddots & \vdots \\ 2\mathrm{a}_{1j} & 2\mathrm{a}_{2j} & \cdots & 2\mathrm{a}_{ij} \end{Bmatrix} \quad [20]$$

Achieving a complete coverage area between two adjacent paths P_l and P_{l+1} the step-over size must have a maximum vertical distance of $2a_{il}$ between centers of contact area to adjacent one. Letting $2a_{ij} = \begin{bmatrix} a_{ij} & a_{ij} \end{bmatrix}^T$ and substituting into [20] results in

$$\mathrm{CAM} = \begin{Bmatrix} \begin{bmatrix} \mathrm{a}_{10} \\ \mathrm{a}_{10} \end{bmatrix} & \begin{bmatrix} \mathrm{a}_{20} \\ \mathrm{a}_{20} \end{bmatrix} & \cdots & \begin{bmatrix} \mathrm{a}_{i0} \\ \mathrm{a}_{i0} \end{bmatrix} \\ \begin{bmatrix} \mathrm{a}_{11} \\ \mathrm{a}_{11} \end{bmatrix} & \begin{bmatrix} \mathrm{a}_{21} \\ \mathrm{a}_{21} \end{bmatrix} & & \begin{bmatrix} \mathrm{a}_{i1} \\ \mathrm{a}_{i1} \end{bmatrix} \\ \begin{bmatrix} \mathrm{a}_{12} \\ \mathrm{a}_{12} \end{bmatrix} & \begin{bmatrix} \mathrm{a}_{22} \\ \mathrm{a}_{22} \end{bmatrix} & \cdots & \begin{bmatrix} \mathrm{a}_{i2} \\ \mathrm{a}_{i2} \end{bmatrix} \\ \vdots & \vdots & & \vdots \\ \begin{bmatrix} \mathrm{a}_{1l} \\ \mathrm{a}_{1l} \end{bmatrix} & \begin{bmatrix} \mathrm{a}_{2l} \\ \mathrm{a}_{2l} \end{bmatrix} & \vdots & \begin{bmatrix} \mathrm{a}_{il} \\ \mathrm{a}_{il} \end{bmatrix} \\ \vdots & \vdots & \ddots & \vdots \\ \begin{bmatrix} \mathrm{a}_{1j} \\ \mathrm{a}_{1j} \end{bmatrix} & \begin{bmatrix} \mathrm{a}_{2j} \\ \mathrm{a}_{2j} \end{bmatrix} & \cdots & \begin{bmatrix} \mathrm{a}_{ij} \\ \mathrm{a}_{ij} \end{bmatrix} \end{Bmatrix} \quad [21]$$

Note that $\begin{bmatrix} \mathrm{a}_{ij} & \mathrm{a}_{ij} \end{bmatrix}^T$ represents the total length of the contact area at the i^{th} discretized point along the j^{th}

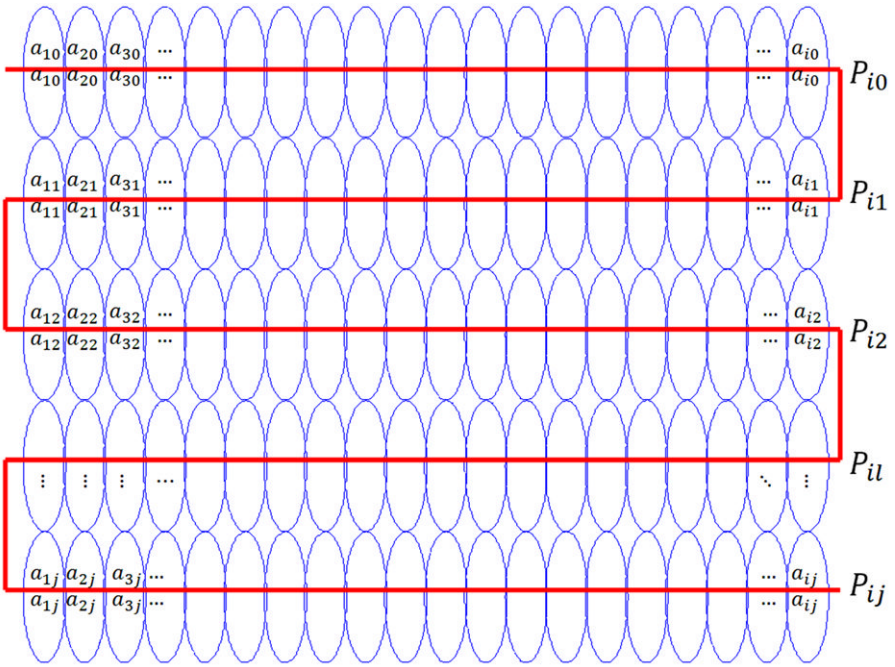


Figure 10 Coverage area map for a continuous polishing path. Rososhansky, M. *Coverage Based Tool-Path Planning for Automated Polishing Using Contact Mechanics Theory* (MSc thesis); Toronto, ON: Ryerson University, 2010.

polishing path. Figure 10 shows a CAM for a continuous polishing path.

1.5.1.5 Step-Over Size

Step-over defines a gap between two adjacent polishing polish paths. A constant step-over size is commonly used in conventional machining including polishing. However, this would result in undesired effects during polishing. If a large step-over size is used, an unpolished region is generated between two paths as shown in Figure 11. This region indicates that the polishing tool did not come in contact with the part surface resulting in a rough surface. Additional pass is required to remove the roughness and guarantee full coverage during polishing. If a small step-over size is used, it results in overlapping between adjacent paths as shown in Figure 12. Overlapping, also called crowding, may degrade the part surface and decrease polishing tool life as the same area is covered more than once. This results in increased production time and manufacturing costs.

To explain more on this effect, an ellipsoid shown Figure 13 is considered for a 3D case, which can be expressed as

$$\frac{x^2}{u^2}+\frac{y^2}{v^2}+\frac{z^2}{w^2}=1 \qquad [22]$$

where, in the simulation, $u=1$(cm), $v=0.6$(cm), and $w=0.8$ (cm) are fixed positive real numbers that determine the shape of the ellipsoid.

The radius of curvature in the xz plane is given by the following eqn [3]

$$K_{xz}=\frac{\overline{A}C_{xz}}{\left(\overline{A}^2\left(\frac{z^2}{c^2}\right)+C_{xz}^2\left(\frac{x^2}{a^2}\right)\right)^{\frac{3}{2}}} \qquad [23]$$

where $\overline{A}=\left[\frac{a^2(b^2-\gamma^2)}{b^2}\right]$ and $C_{xz}=\left[\frac{c^2(b^2-\gamma^2)}{b^2}\right]$ and the radius of curvature in the γz plane is given by the following equation:

$$K_{\gamma z}=\frac{\overline{B}C_{\gamma z}}{\left(\overline{B}^2\left(\frac{z^2}{c^2}\right)+C_{\gamma z}^2\left(\frac{x^2}{b^2}\right)\right)^{\frac{3}{2}}} \qquad [24]$$

where $\overline{B}=\left[\frac{b^2(a^2-x^2)}{a^2}\right]$ and $C_{\gamma z}=\left[\frac{c^2(a^2-x^2)}{a^2}\right]$

Figure 14 shows the CAM for the ellipsoid with both the crowding effect, highlighted in green, and the unpolished area, highlighted in red. For an ellipsoid, the unpolished area and the crowding effect are both present when the step-over size is maintained constant throughout the part surface.

1.5.1.6 Polishing Path Planning

To overcome the problems outlined with constant step-over size, a method based on the CAM is described for the generation of a tool path that guarantees a full coverage area at the contact between the polishing tool and the part surface during robotic polishing. Assume that the γ position of each contact point is given by the recursive equation:

$$P_{ij}=P_{ij-1}+a_{ij-1}+a_{ij} \qquad [25]$$

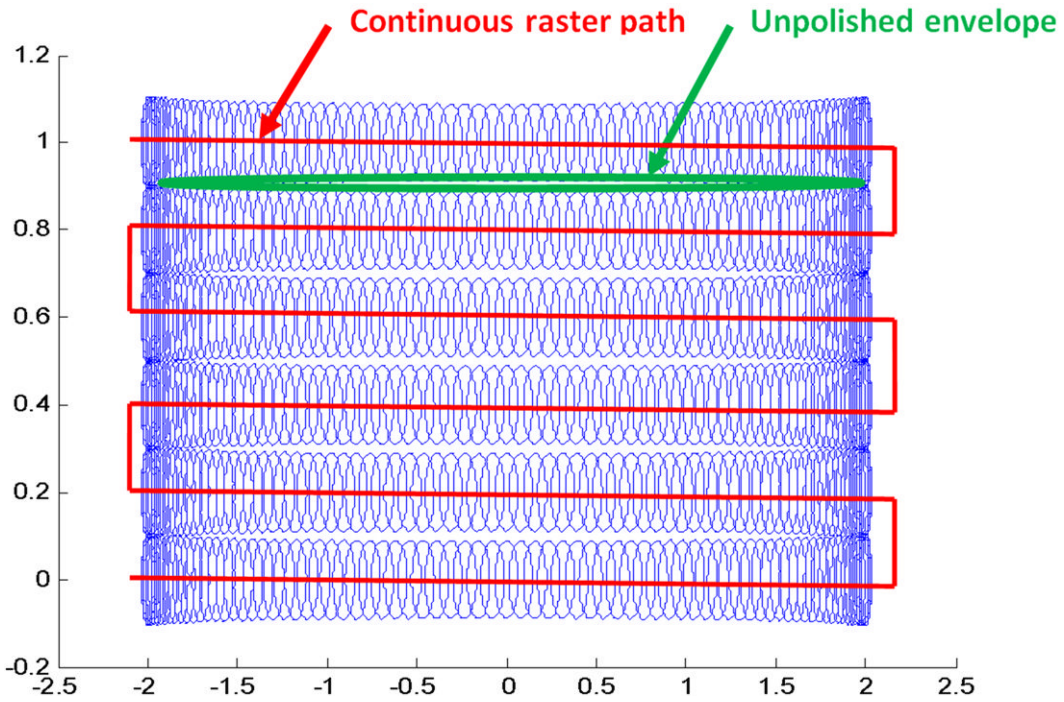


Figure 11 Large step-over size (elliptical cross section, major 2 cm). Rososhansky, M. *Coverage Based Tool-Path Planning for Automated Polishing Using Contact Mechanics Theory* (MSc thesis); Toronto, ON: Ryerson University, 2010.

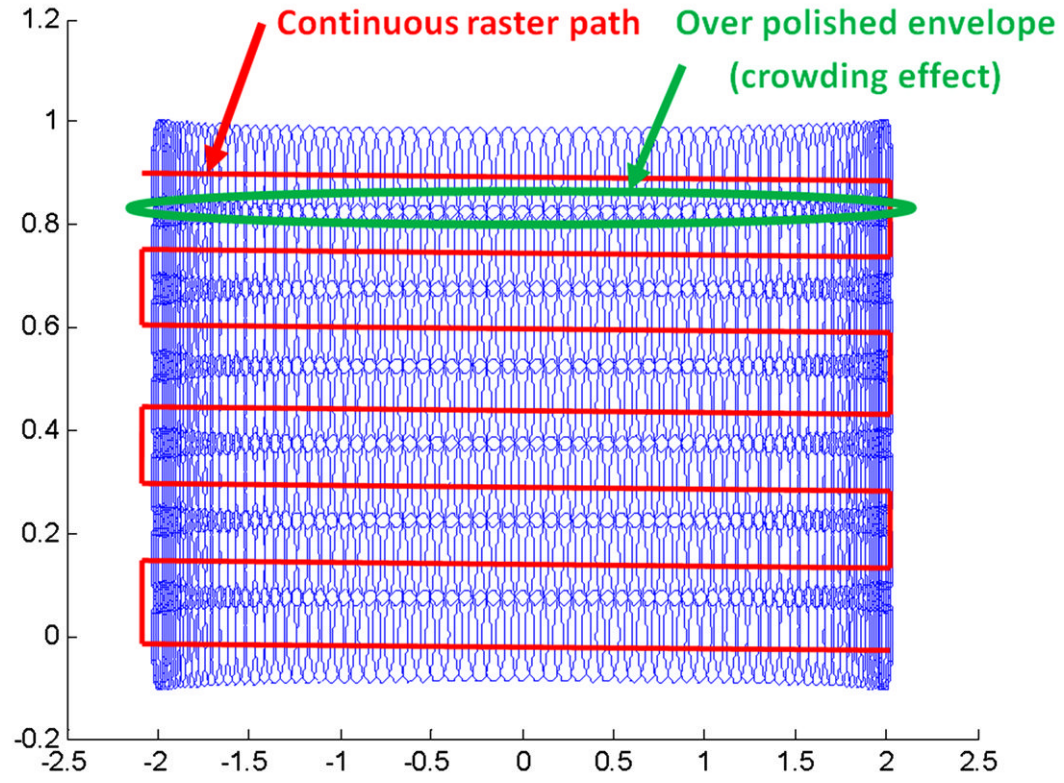


Figure 12 Small step-over size. Rososhansky, M. *Coverage Based Tool-Path Planning for Automated Polishing Using Contact Mechanics Theory* (MSc thesis); Toronto, ON: Ryerson University, 2010.

where P_{ij-1}, P_{ij} are the $j-1^{th}$, j^{th} polishing path respectively, a_{ij-1}, a_{ij} are the semimajor axis of the contact area at the i^{th} element of the $j-1^{th}$, j^{th} polishing path, respectively.

Next, define the base path as the first polishing path generated along the part surface (i.e., $j=0$). The base pass P_{i0} is arbitrarily chosen along the part surface. Adjacent polishing path P_{i1} is generated relative to the base path. The γ position of any polishing path is a function of the boundary of the semimajor axis a. Therefore, the base path is also a function of γ and is defined by:

$$P_{i0}(a_{i0}) = 0 \tag{26}$$

indicating that P_{i0} is a function of a_{i0} defined for the polishing path $j=0$, and is assumed to be a straight line since its γ position is 0; thus, it is ignored. The base path P_{i0} passes through the contact point N_{i0} at the center of the contact area CA_{i0} (i.e., along a_{i0} and not $2a_{i0}$). The γ position of the next polishing path P_{i1} follows eqn [25] as described by $P_{i1}=P_{i0}+a_{i0}+a_{i1}$, where a_{i0} and a_{i1} are the semimajor axes of the first and second contact areas for the i^{th} element. Since, $P_{i0}=0$ the equation reduces to:

$$P_{i1} = a_{i0} + a_{i1} \tag{27}$$

All adjacent polishing tool-paths along the part surface are described by the recursive method as follows:

$$\begin{aligned} P_{i2} &= P_{i1} + a_{i1} + a_{i2} \\ P_{i3} &= P_{i2} + a_{i2} + a_{i3} \\ &\vdots \\ P_{ij} &= P_{ij-1} + a_{ij-1} + a_{ij} \end{aligned} \tag{28}$$

This is a recursive method where determination of a polishing path requires the knowledge of the previous path. Alternatively, eqn [28] is written in the following form:

$$\begin{Bmatrix} P_{i2} \\ P_{i3} \\ \vdots \\ P_{ij} \end{Bmatrix} = \begin{Bmatrix} a_{i0} + 2a_{i1} + a_{i2} \\ a_{i0} + \sum_{j=1}^{j=2} 2a_{ij} + a_{ij} \\ \vdots \\ a_{i0} + \sum_{j=1}^{j=j-1} 2a_{ij} + a_{ij} \end{Bmatrix} \tag{29}$$

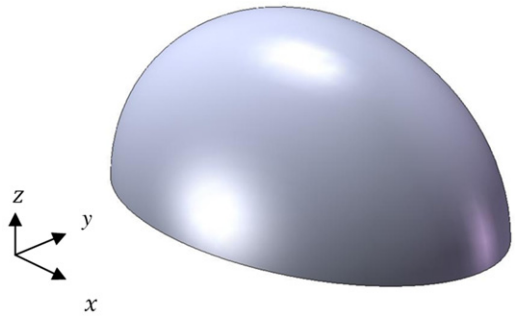


Figure 13 Semi-ellipsoid part surface. Rososhansky, M. *Coverage Based Tool-Path Planning for Automated Polishing Using Contact Mechanics Theory* (MSc thesis); Toronto, ON: Ryerson University, 2010.

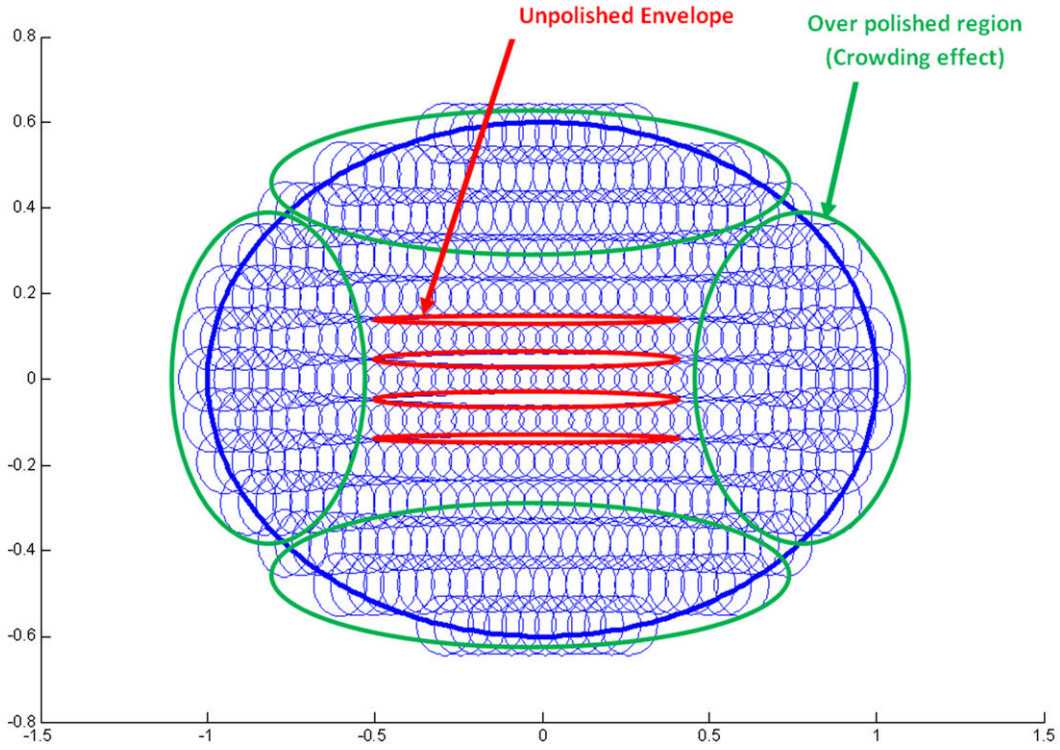


Figure 14 Crowding and unpolished areas for an ellipsoid. Rososhansky, M. *Coverage Based Tool-Path Planning for Automated Polishing Using Contact Mechanics Theory* (MSc thesis); Toronto, ON: Ryerson University, 2010.

In conclusion, the contact points for the polishing path P_{ik} are placed at the γ position as defined by the following equation

$$P_{ij} = \begin{cases} 0 & j = 0 \\ a_{i0} + a_{ij} & j = 1 \\ a_{i0} + \sum_{j=1}^{j=j-1} 2a_{ij} + a_{ij} & j \geq 2 \end{cases} \quad [30]$$

This algorithm guarantees a full coverage area during robotic polishing. The algorithm eliminates the crowding effects and the unpolished envelope identified in the previous section.

Now this algorithm is applied to the parts from the previous section. **Figure 15** shows the modified polishing path of **Figure 11**. In this case the modified CAM shows a full coverage of the part surface. The step-over size between each polishing path is determined by summing up the γ positions of the semimajor axis a. Notice that a small overlap is generated between two adjacent paths. This slight overlap is desired to compensate for imperfections in the polishing tool. Note that the base polishing path is a straight line since the γ position of this path is defined to be at $P_0(a_{ij})=0$. Adjacent paths are summation of the semimajor axis generated at the contact points between the polishing tool and the part surface. Notice that the path becomes more curved for each consecutive polishing path.

Figure 16 shows the modified polishing path for the ellipsoid of **Figure 14**. In this case the modified *CAM* shows a full coverage along the part surface. The step-over size between each polishing path is determined by summing up the γ positions of the semimajor axis a. The base path was defined to be at $\gamma=0$ therefore it is a straight line. Symmetry exists along the x axis since that the part surface was divided into two separate sections. **Figure 16** shows the modified polishing path for the ellipsoid where the radii of curvatures changes in both xz and yz planes for every contact point.

To this end, one may notice that on flat surfaces the radii of curvatures of the part surface approaches infinity and the contact area is circular throughout the polishing path. Therefore, the semimajor axis a_{ik} of any contact point always equals the semimajor axis of adjacent contact point a_{ik+1}. The radii of curvatures of the part surface are constants along the pat surface. Therefore, changing the γ position of any contact point does not affect the contact area.

On part surface where the radius of curvature changes along the x axis but maintained constant along the y axis, the radius of curvature is constant along the γ axis. Therefore, changing the γ position of any contact point does not affect the contact area. However, part surfaces where both radii of curvatures change along the part surface the modified polishing path is complicated to generate. In this case the proposed recursive method still applies, but small modification is required. The complication arises since the radius of curvature constantly changes in both the xz and yz planes. Both planes are functions of x, y, and z axes. Changing the x or y positions of a contact point changes the z position of the contact point. Therefore, the radius of curvature changes which results in different contact areas. **Figure 17** shows a wire frame design of the part surface. Note that changing the position of the contact point from point 1 to point 2 changes the z position of the part surface which results in different radius of curvature. Thus, changing the position of the contact point results in different coverage area.

To generate the modified polishing path that guarantees full coverage area an iterative search method has to be implemented for the recursive method. The search method calculates the semimajor axis a_{ij+1} at a given contact point and adopts itself to the previous semimajor axis a_{ij} until there is no crowding effect or unpolished regions along the part surface.[3]

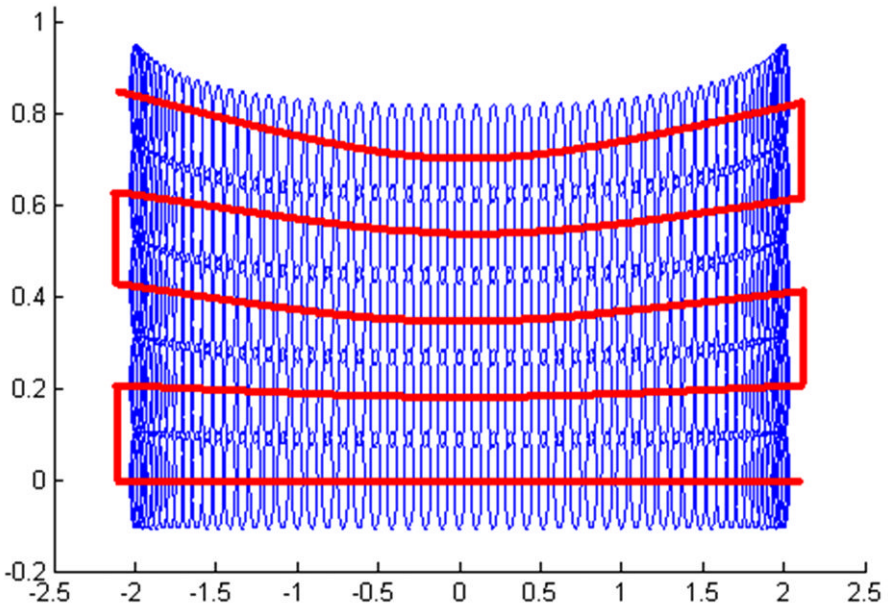


Figure 15 Modified polishing path for **Figure 11**.[4]

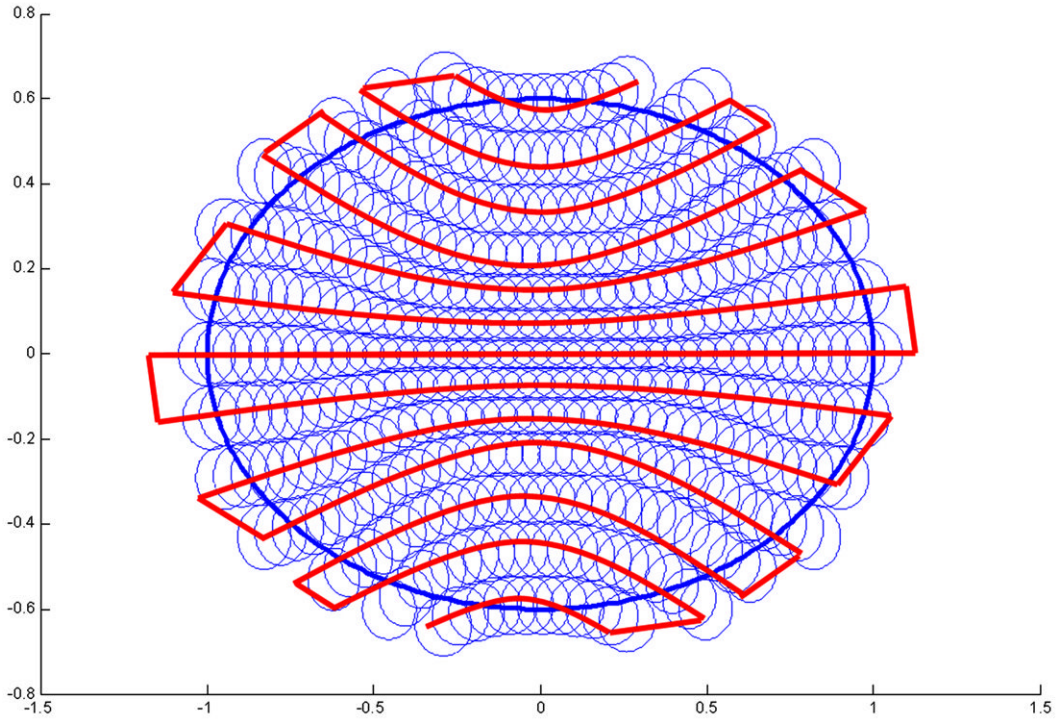


Figure 16 Modified polishing path of Figure 14.[4]

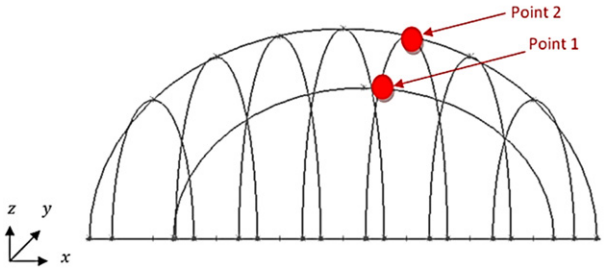


Figure 17 Wire frame design of an ellipsoid. Rososhansky, M. *Coverage Based Tool-Path Planning for Automated Polishing Using Contact Mechanics Theory* (MSc thesis); Toronto, ON: Ryerson University, 2010.

1.5.2 Surface Roughness Modeling

1.5.2.1 Generation of a Polishing Stone Topography

Within the contact area, surface roughness after polishing can be predicated through modeling. The first step is to generate the topography of a polishing tool. The surface roughness of the polished part can be considered as an imprint created by the polishing tool rubbed against the part. Previous experimental research has revealed that the distribution of the grain protrusion heights of an abrasive tool is of a Gaussian distribution.[5] To generate a random distribution for the grain protrusion heights of a polishing stone, the mean value and standard deviation are required. The grid numbers (M) of commonly used polishing stones are $M=320$ for the first stage stoning, $M=400$ for the second stage stoning, and $M=600$ for the final stage stoning. The grain dimension d_g is expressed equal to the aperture opening of the screen according to the following relationship[5]

$$d_{g\max}(mm) = 15.2M^{-1} \quad [31]$$

This grain size is considered as the maximum grain size, denoted by $d_{g\max}$, for a given grit number M. Furthermore, the average grain dimension denoted by $d_{g\text{avg}}$ is related to grit number M (for $M > 40$) as

$$d_{g\text{avg}}(mm) = 68M^{-1.4} \quad [32]$$

From eqns [31] and [32], it can be calculated that for $M=320$, 400, and 600, $d_{g\max}=47.5$, 38, and 25.3 μm, respectively, and $d_{g\ \text{avg}}=21.1$, 15.5, and 8.8 μm, respectively.

Extensive experiments using 3-D stylus instruments and SEM micrographs show that $d_{g\max}$ and $d_{g\text{avg}}$ are very close to the maximum grain protrusion height $h_{\max}$ and the mean grain protrusion height h_{avg}, respectively. Therefore, the mean value and standard deviation for generating the topography of a polishing stone are given as

$$\mu = d_{g\text{avg}} \quad [33a]$$

$$\sigma = \left(d_{g\max} - d_{g\text{avg}}\right)/3 \quad [33b]$$

where μ and σ are the mean value and standard deviation, respectively. From eqns [33a] and [33b], it can be calculated

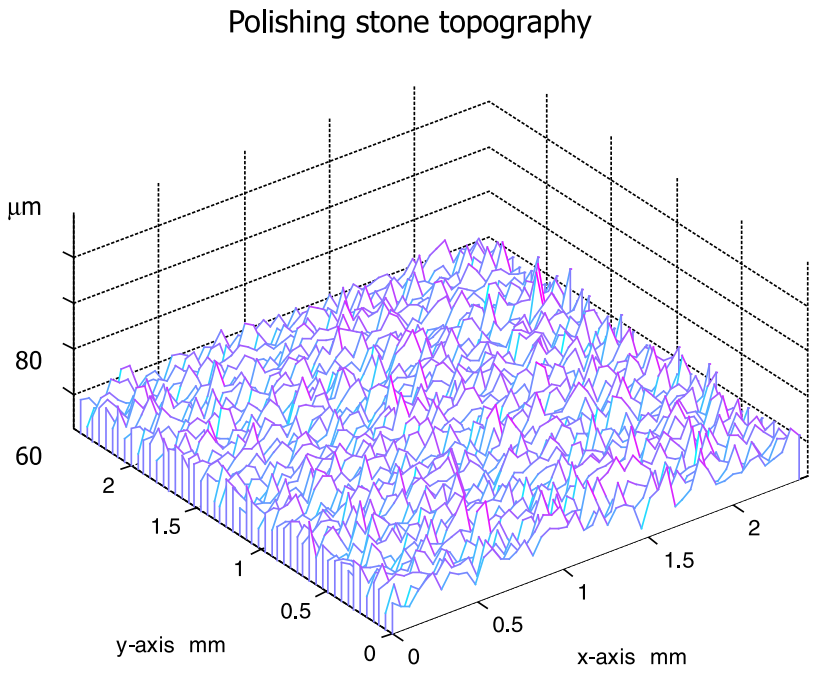


Figure 18 Polishing stone topography. Xi, F.; Zhou, X. Modeling Surface Roughness in the Stone Polishing Process. *Int. J. Mach. Tool. Manu.* **2005**, *45*, 365–372.

that $\mu = 21.1$, 15.5, and 8.8 µm, respectively, and $\sigma = 8.8$, 7.5, and 5.5 µm, respectively, for $M = 320$, 400, and 600.

To generate the topography, the polishing stone is meshed by a grain interval. The grain interval is the distance between two adjacent grains and it is related to the structure number S of the polishing stone. The structure number indicates the volumetric concentration of abrasive grains in the stone. For a given number of S, the density of the stone, V_g (%), may be approximated as[5]

$$V_g = 2(32 - S) \quad [34]$$

In general the distribution of the grain intervals is assumed uniform. The interval Δ can be derived from the following relation

$$\frac{\pi}{6} d_{g\,\mathrm{avg}}^3 = V_g \Delta^3 \quad [35]$$

The left-hand side of eqn [35] indicates the volume of the grains in the polishing stone in terms of the average grain size, and the right-hand side in terms of the density. The two sides should be equal. Therefore, from eqn [35], the grain interval Δ (mm) can be determined as

$$D = 137.9 M^{-1.4} \sqrt[3]{\frac{\pi}{32 - S}} \quad [36]$$

To generate a polishing stone topography, the stone is meshed using the interval determined by eqn [36]. The distribution of the grain protrusion heights is described by a Gaussian distribution with the mean value and standard deviation determined by eqns [33a] and [33b]. **Figure 18** is a simulated polishing stone topography with grit number $M = 400$, showing that the surface of a polishing tool is made of randomly distributed protrusion heights.

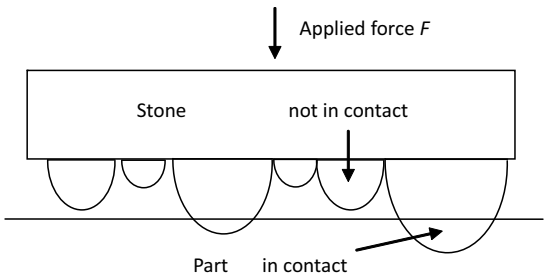


Figure 19 Micro-grain contact model. Xi, F.; Zhou, X. Modeling Surface Roughness in the Stone Polishing Process. *Int. J. Mach. Tool. Manu.* **2005**, *45*, 365–372.

1.5.2.2 Micro Depth of Cut of a Single Grain

Prior to studying the surface roughness of the polished part, the problem of determining the micro depth of cut of a single grain is addressed. Among three types of gain shape: semi-sphere, cone, and prism shape, the semi-sphere shape is adopted because of its commonality for grain modeling.

In the polishing process, the polishing stone is pressed under certain pressure against the part. Though the pressure is applied to the entire polishing stone, it is only concentrated on the grains that are in contact with the part. As shown in **Figure 19**, the contact grains are more protruded than the grains that are not in contact with the part. Due to the highly concentrated pressure on the contact grains, plastic deformation occurs in the contact area, thereby creating micro cuts. Therefore, the polishing cutting mechanism may be modeled based on the plasticity theory, similar to indentation.

Among three methods, Brinell, Vickers, and Rockwell, the Brinell test model is used to determine the micro depth of cut of a single grain. In other words, the grain is modeled as an

indenter inserted in the part. It is assumed that the grain is much harder than the part. For example, the common polishing grain material is aluminum oxide with HB over 1000, while steel is with HB around 300. In the Brinell test model, a hardened ball is pressed into the surface of the material by a standard force. In our polishing model, the hardened ball is replaced by the semi-sphere polishing grain. After the load and the ball have been removed, the diameter of the indentation is measured. The Brinell hardness number (HB) is obtained by dividing the size of the applied force f by the spherical surface area of the indentation A:

$$\mathrm{HB} = \frac{f(kgf)}{A(\mathrm{mm}^2)} \quad [37]$$

where f is the force applied on the grain, and its determination will be discussed later.

The contact area can be obtained by calculation from the values of the radius r_g of the ball and the radius r_c of the indentation, that is

$$A = 2\pi r_g(r_g - \sqrt{r_g{}^2 - r_c^2}) \quad [38]$$

Note that for the grain model, $r_g = d_g/2$, where as mentioned before, d_g is the grain diameter. The following relation holds among r_g, r_c, and h

$$r_g^2 = r_c^2 + (r_g^2 - h)^2 \quad [39]$$

From eqn [39], the micro depth of cut for a single grain can be derived as

$$h = r_g^2 - \sqrt{r_g^2 - r_c^2} \quad [40a]$$

Substituting eqns [37] and [38] into eqn [40a] yields

$$h = \frac{f}{2\pi r_g \mathrm{HB}} \quad [40b]$$

Using eqn [40b], the micro depth of cut of a single grain can be determined given the contact force on the grain and the hardness of the part.

1.5.2.3 Micro Depth of Cut of a Polishing Tool

Knowing how to determine the micro depth of cut of a single grain, two methods can be used to determine the micro depth of cut for a polishing tool. The first one is an average method, simply to estimate the micro depth of cut of multiple grains. This method assumes that all the grains are in contact with the part. In this case, eqn [40b] is used to calculate the average micro depth of cut of the multiple grains. For computing eqn [40b], HB is known if the part material is given, and the average diameter of the grains is equal to μ if the grit number M is given. However, the average force f on each grain is not given and needs to be determined as follows.

$$f = \frac{F}{N} \quad [41]$$

where F is the force exerted on the polishing stone, and N is the total of number of grains.

Table 1 shows the computed average micro depth for $M = 320$, 400, and 600. The grain diameter is determined by eqn [32], the grain interval is determined by eqn [36], the grain force is determined by eqn [41], and the micro depth of cut is determined by eqn [40b]. As shown in Table 2, the results obtained by the average method in fact are the lower bound.[6]

The second method is a search method. Compared to the experimental data, the micro depth of cut determined based on the average method is very small. This discrepancy results from the assumption that all the grains in the contact area are in contact with the workpiece. In reality, however only those protruded grains that are in contact with the workpiece will contribute to the micro depth of cut. Hence, in order to give a more realistic prediction of the surface roughness, it becomes clear that the grain protrusion heights must be considered with different heights obtained from its random distribution.

The basic idea of the search method is to find a solution that the force exerted on the stone is balanced by a number of more protrusion grains in the contact area. Then, these grains are taken as the contact grains to determine the micro depth of cut, while excluding the rest of the grains. Since the grain with the maximum protrusion height cuts off the surface polished by all the other contact grains, it generates the most dominant scallops and its micro depth of cut should be considered first. Then, if the second highest grain does not cut into the scallops generated by the first highest grain, the first scallops will be the final marks. If the second grain does cut, it will change the profile of the first scallops. The process of modifying the surface profile continues with more grains involved in a descending order, and it terminates when no grain cuts into the scallops anymore. Mathematically, the search method is described as follows.

Table 1 Micro depth of cut based on average method

Grit number M	*Grain diameter (μm)*	*Grain interval (μm)*	*Part hardness (HB)*	*Micro depth of cut (μm)*
320	21.1	21.8	300	0.02–0.03
400	15.5	15.9	300	0.01–0.02
600	8.8	9.0	300	0.009–0.01

Source: Rososhansky, M. *Coverage Based Tool-Path Planning for Automated Polishing Using Contact Mechanics Theory* (MSc thesis); Toronto, ON: Ryerson University, 2010.

Table 2 Micro depth of cut – upper bound, lower bound, and search method

Grit number M	*Upper bound (μm)*	*Lower bound (μm)*	*Search method (μm)*
320	47.5	0.02–0.03	0.4–0.8
400	38	0.01–0.02	0.25–0.6
600	25.3	0.009–0.01	0.2–0.5

Source: Rososhansky, M. *Coverage Based Tool-Path Planning for Automated Polishing Using Contact Mechanics Theory* (MSc thesis); Toronto, ON: Ryerson University, 2010.

First, the micro depth of cut of the most protruded gain is determined as

$$h_1 = \frac{F}{\pi d_{g1} \mathrm{HB}} \quad [42]$$

where h_1 is the micro depth of cut of the most protruded grain. Note that in eqn [42], the total stone force is initially applied to the most protruded grain with d_{g1} being its diameter.

After h_1 is obtained, the difference of $(r_{g1}–h_1)$ is compared to r_{g2}. If larger, it means that the first grain will balance the entire stone force. Then search terminates and h_1 is taken as the final micro depth of cut. If smaller, the second most protruded grain will contribute to the force balance. Since the force is distributed proportionally to the area, the stone force will be divided between the two grains as follows:

$$f_i = \frac{F r_{gi}}{\sqrt{\sum_{i=1}^{2} r_{gi}^2}} \quad [43]$$

where $i = 1, 2$. Under the force re-distribution determined from eqn [43], the micro depth of cut of the second most protruded grain will be calculated as

$$h_2 = \frac{f_2}{\pi d_{g2} \mathrm{HB}} \quad [44]$$

Similarly, the difference of $(r_{g2}–h_2)$ is compared to r_{g3}. If larger, it means that the first and second gain will balance the entire stone force. Then search terminates and h_2 is taken as the final micro depth of cut. If smaller, the third most protruded grain will contribute to the force balance.

To this end, the search algorithm can be expressed, first for the force distribution as

$$f_i = \frac{F r_{gi}}{\sqrt{\sum_{i=1}^{k} r_{gi}^2}} \quad [45]$$

where $i = 1, \ldots, k$, and then for the micro depth of cut as

$$h_k = \frac{f_k}{\pi d_{gk} HB} \quad [46]$$

where index k indicates a number of k contact grains. The search terminates when $r_{gk} - h_k > r_{g(k+1)}$.

For the simulation results of the search method provided in **Table 2**, the number of the contact grains is in the range of 100–120 for $M = 320$, 150–180 for $M = 400$, and 220–280 for $M = 600$. The depth of cut determined based on eqn [42] is usually very big because it is based on a single grain contact. If this value is greater than the diameter of the biggest grain, it is considered unrealistic; the reason being that the depth of cut cannot be greater than the size of grains. Therefore, the maximum size of the grain is taken as the upper bound.

The average method, on the other hand, represents the lower bound, which is too small because it is based on all grains contact. The search method provides a realistic prediction that lies in between the two bounds, since it is based on the actual number of contact grains. **Table 2** shows the results of the upper and lower bounds as well as the search method. The force range considered is ~ 10 N.

1.5.2.4 Prediction of Surface Roughness

A realistic way of predicting the surface roughness should be based on the surface roughness of the previous process. In this study, the ball-end milling process is considered as the previous process and the surface roughness of the milled surface can be approximated as[7]

$$R_a = \frac{0.0321 s^2}{r_m} \quad [47]$$

where s is the feed (mm) and r_m (mm) is the radius of the milling tool. The surface roughness of the milling process is in the range of 0.8–5 μm.[7]

In the actual polishing process, the part is first polished by a fine stone ($M = 320$) with a number of strokes till the coarse milling marks are removed and covered by the fine marks left by the stone. This is followed by the second polishing using a finer stone ($M = 400$), and then again followed by the third polishing using an even finer stone ($M = 600$).

Since polishing marks are created by the stone, it would be reasonable to assume that the surface roughness is very close to the micro depth of cut of the contact grains. Based on this assumption, the number of strokes needed to reduce the previous surface roughness to the current one may be calculated as

$$N_s = \left(\frac{G}{2G_k}\right)\left(\frac{R_a^{(j)}}{h^{(j+1)}}\right) \quad [48]$$

where N_s is the number of strokes, G is the number of grains in the contact area, G_k is the number of the contact grains determined from the search method, R_a is the surface roughness value of the previous process, h is the micro depth of cut of the current process, and index j indicates the jth time of polishing.

For example, assume that the surface roughness after milling is around 3 μm. From **Table 2**, the micro depth of cut of the first polishing using the stone of $M = 320$ is around 0.8 μm, which is considered as R_a after the first polishing. The number of strokes is estimated based on eqn [48]. The number of cutting layers is calculated around four, for the reduction from 3 to 0.8 μm. In addition, the grain ratio is needed. As mentioned before, the number of contact grains is around 100 for $M = 320$. The simulation shows that there are around 20 K grains within the contact area. Substituting these values into eqn [48], the number of strokes for the first polishing would be around 400. The similar approach can be used to determine the number of strokes for the second and third polishing. As shown in **Table 3**, the predicted surface roughness is in the same magnitude of the experiment data obtained from the SPI finishing guide.[8]

1.5.3 Contact Stress-Based Control

1.5.3.1 Robotic Polishing/Deburring System

Figure 20 shows a robotic polishing/deburring system developed at Ryerson University that consists of a hybrid robot with an active compliant toolhead. This is a decoupled system because the robot is used solely for motion control and the active compliance toolhead solely for force control. The robot has five axes, composed of a three-axis parallel robot (tripod) and a two-axis gantry. The active compliance toolhead is attached to the moving platform of the robot.

Figure 21 is a control block diagram for the toolhead. There are two control inputs, one for a pressure valve and another for a flow valve. There are two outputs, one being the contact stress and another being the tool spindle speed. The input voltage V_p is supplied to actuate the pressure valve to provide the tool pressure. Simultaneously, the input voltage V_q is supplied to actuate the flow valve to provide a flow rate. The volumetric flow entering the polishing spindle provides a polishing torque. The control method requires the following set of modeling.

Table 3 Comparison with the experiment data

Grit number M	*Predicted* (μm)	*Experiment range*[8] (μm)
320	0.4–0.8	0.7–0.8
400	0.25–0.6	0.5–0.6
600	0.2–0.5	0.25–0.3

Source: Rososhansky, M. *Coverage Based Tool-Path Planning for Automated Polishing Using Contact Mechanics Theory* (MSc thesis); Toronto, ON: Ryerson University, 2010.

1.5.3.2 Contact Stress Modeling

The first one is contact stress modeling, which refers to the pressure (contact stress) arising from two bodies subjected to compressive loading by forcing them together. It is modeled to obtain a relationship between the applied force (the compressive load) and the maximum pressure (maximum compressive stress). The principal stress on the contact surface is given as follows[10]

$$\sigma_{zz} = -\left[\frac{M}{2}\left(\frac{1}{n} - n\right)\right]\frac{b}{\Delta} \qquad [49]$$

where σ_{zz} is the compressive principal stress indicated by the negative sign, and

$$M = \frac{2k}{k'^2 E(k')} \quad , \quad n = \sqrt{\frac{k^2 + k^2(Z/b)^2}{1 + k^2(Z/b)^2}}$$

and the rest of parameters are previously defined in Section 1.5.1. Through simplification for the polishing case, the maximum stress P_0 can be expressed as

$$P_0 = \frac{b}{E(k')\Delta} \qquad [50]$$

The stress distribution within an elliptic contact area is expressed as

$$P_{\text{seg}}(x, y) = P_0[1 - (x/a)^2 - (y/b)^2]^{1/2} \qquad [51]$$

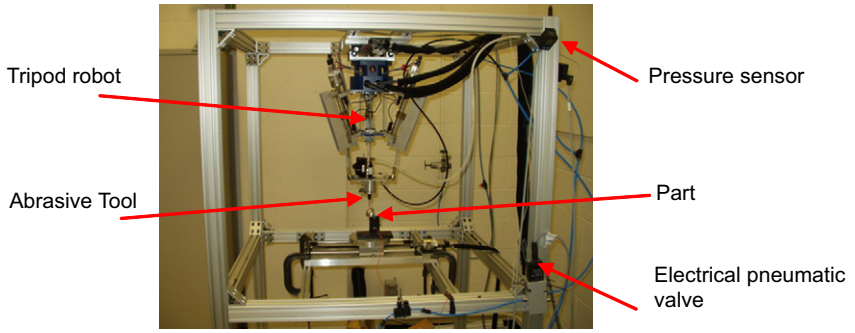


Figure 20 A polishing/deburring robot.[9]

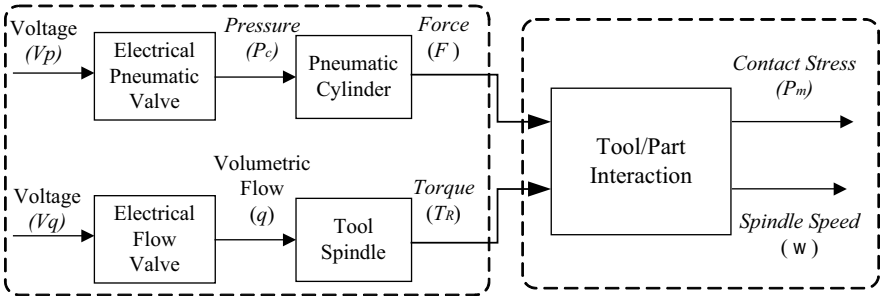


Figure 21 Control block diagram. Liang, L. *Modeling and Control of Automated Polishing/Deburring* (Ph.D. thesis); Toronto, ON: Ryerson University, 2008.

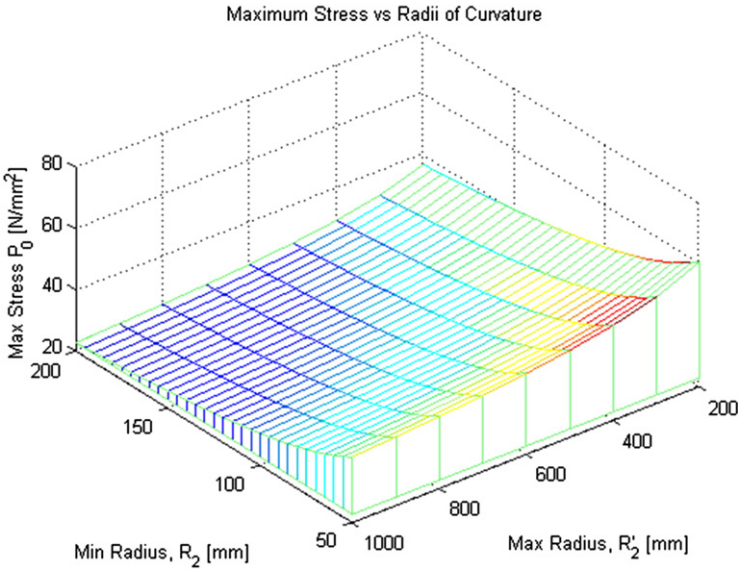


Figure 22 Variation in P_0 versus the radii of curvature. Roswell, A. *Modelling for Contact Stress Control in Automated Polishing* (MSc Thesis); Toronto, ON: Ryerson University, 2004.

The mean stress across the elliptic contact area is derived as

$$P_m = \frac{2}{3}P_0 \qquad [52]$$

In practice, the user specified polishing pressure (stress) is considered as the mean stress. **Figure 22** illustrates the relationship between the maximum stress (P_0) and the radii of curvature (R_2 and R_2') of the part when the applied force remains constant. It can be seen that the stress (pressure) is highest when the radii are smallest.

The mapping of contact stress on the surface radii of curvature proves the applied force cannot remain constant if contact stress is required to be constant. By solving for the force, an equation is obtained for determining the force variation necessary for keeping contact stress P_0 constant.

$$F = \frac{2\pi E^2(k')\Delta^2 {P_0}^3}{3k} \qquad [53]$$

1.5.3.3 Friction Torque Modeling

The second modeling is friction torque which is the minimum torque needed in order to provide reciprocal polishing motion. It is assumed the friction torque is equivalent to the polishing torque necessary to remove material from the part surface. There are two cases: non-Hertzian and Hertzian contact. The first case is to polish a flat surface using a disk, consequently the pressure is assumed constant across the contact region. The second case is for curved tool/part, and the mean pressure is considered. In general, the friction torque is given as

$$T_f = F_{sf}\, r \qquad [54]$$

where $F_{sf}=F_s\mu_k$, $F_s=PA_c$, μ_k is the friction coefficient, P and A_c are the cylinder pressure and area, respectively.

For non-Hertzian contact as shown in **Figure 23**, the contact area is formed when the circular flat polishing tool is in contact with a flat part. Therefore, the radius of the contact area is equivalent to the polishing toolhead's radius. The torque across the circular contact area is double integrated leading to the below:

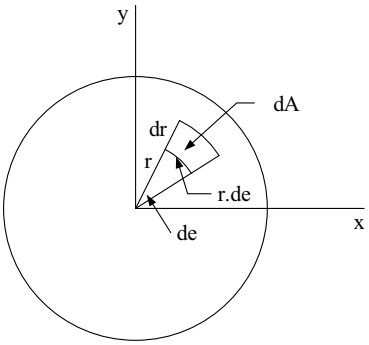


Figure 23 Circular contact area. Roswell, A. *Modelling for Contact Stress Control in Automated Polishing* (MSc Thesis); Toronto, ON: Ryerson University, 2004.

$$T_f = \mu_k P_s \int_0^{2\pi}\int_0^R r^2 \mathrm{d}r\, \mathrm{d}e = \mu_k P_s \frac{R^3}{3} \int_0^{2\pi} \mathrm{d}e = \frac{2}{3}\pi\mu_k P_s R^3 \qquad [55]$$

The first integral (the inner integral) gives the torque per unit radian, while the outer integral provides the total friction torque across 2π radians. This equation can be directly related to the applied polishing force as shown

$$T_f = \frac{2}{3}\mu_k FR \qquad [56]$$

For Hertzian elliptic contact given in **Figure 24**, since the focus is not on the pressure at particular locations within the elliptic contact area, rather on the pressure over the entire elliptic contact area, the pressure at the infinitesimal segment is taken to be the same throughout the contact area. Therefore, the average

or mean pressure is used. Therefore, the torque is given as

$$T_f = \mu_k P_m \int_0^{2\pi} \int_0^R r^2 \mathrm{d}r\, \mathrm{d}e = \mu_k P_m \int_0^{2\pi} \frac{R^3}{3} \mathrm{d}e \qquad [57]$$

where for the elliptic region, R is expressed as $R^2 = a^2\cos^2 e + b^2\sin^2 e$, then the torque is obtained as a function of mean contact stress as

$$T_f = \frac{\mu_k P_m}{3} \int_0^{2\pi} (a^2\cos^2 e + b^2\sin^2 e)^{3/2} \mathrm{d}e$$

$$= \frac{1}{3}\mu_k P_m \pi (a^3 + b^3) \qquad [58]$$

Further manipulation to express the torque as a function of force yields[10]

$$T_f = \frac{2}{9}\mu_k \pi (1 + 1/k) \times \left(\frac{3kF}{2\pi}\right)^{4/3} \times (E(k')\Delta)^{1/3} \qquad [59]$$

Figure 25 shows the friction torque under constant force. This value increases as the ratio of the maximum to minimum principal radius (R_2'/R_2) increases. Figure 26 displays the friction torque under constant contact stress. In this situation, as the contact region becomes less elliptic, i.e., the value of k increases, the friction torque increases.

Investigating the effects of friction torque on the polishing speed is critical to achieving the goal of maintaining a constant speed throughout the polishing process. The two parameters can be related as below

$$\omega = \frac{W}{T_R} \qquad [60]$$

Where W is the supplied power, $T_R = I\dot{\omega} + T_f$ is the resultant tool torque. Then, the rotational speed for the non-Hertzian circular contact is obtained as

$$\omega_C = \frac{W}{\left(I\dot{\omega} + \frac{2}{3}\mu_k F_s R\right)} \qquad [61]$$

and that for the elliptic Hertzian contact as

$$\omega_E = \frac{W}{\left(I\dot{\omega} + \left\{\frac{2}{9}\mu_k \pi (1 + 1/k) \times \left(\frac{3kF}{2\pi}\right)^{4/3} \times (E(k')\Delta)^{1/3}\right\}\right)} \qquad [62]$$

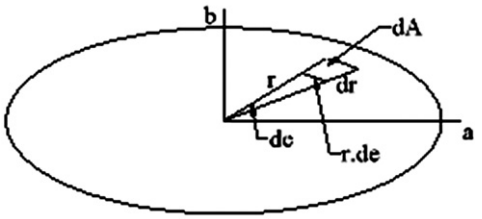


Figure 24 Elliptic contact area. Roswell, A. *Modelling for Contact Stress Control in Automated Polishing* (MSc Thesis); Toronto, ON: Ryerson University, 2004.

1.5.3.4 Polishing Parameter Planning

Equations [52], [61], and [62] show that both contact stress and spindle speed are a function of part geometry. For example, to maintain a constant contact stress throughout polishing, which would provide a uniform polishing quality, the polishing pressure should be computed to vary based on part geometry. Likewise, to maintain a constant spindle speed throughout polishing, which would provide a constant material removal rate, the spindle power should be computed to vary based part geometry as well. The process of planning these parameters is called parameter planning process. Based on the part coordinates obtained through polishing path planning, the polishing pressure (force) and the spindle power are computed.

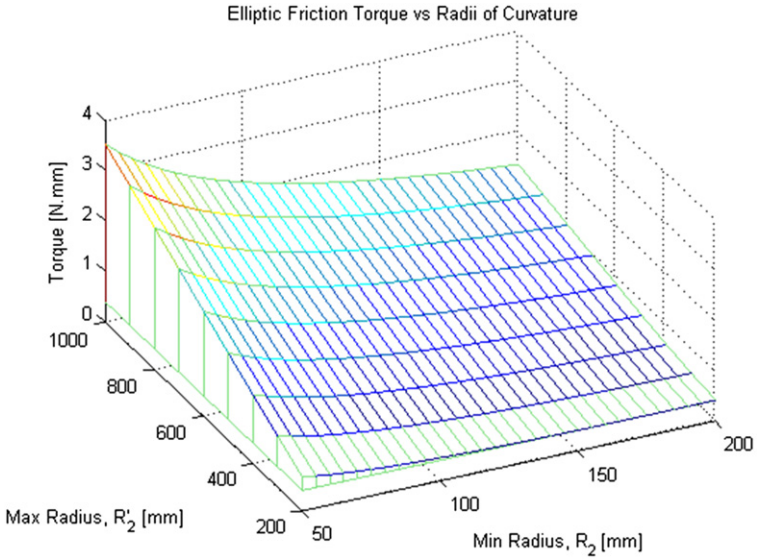


Figure 25 Friction torque under constant force. Roswell, A. *Modelling for Contact Stress Control in Automated Polishing* (MSc Thesis); Toronto, ON: Ryerson University, 2004.

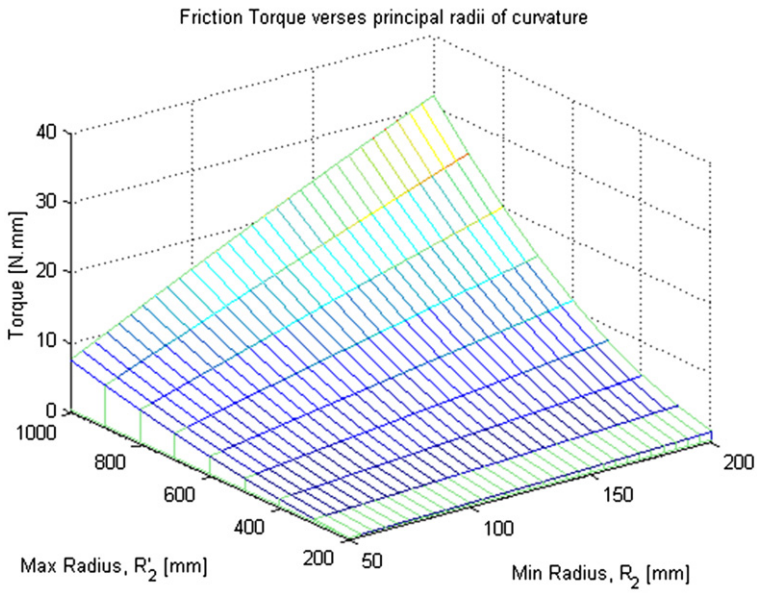


Figure 26 Friction torque under constant contact stress. Roswell, A. *Modelling for Contact Stress Control in Automated Polishing* (MSc Thesis); Toronto, ON: Ryerson University, 2004.

A number of tests were carried out for polishing a curved door stop with and without the application of the pressure planning. Part profiles were measured using a 2-D laser profile scanner (Cobra 2D from Optical Gaging Products Inc.), with accuracy of 10 μm and the dynamic resolution of 1.0 μm. For the constant force case, the pneumatic cylinder pressure was held constant at 2.25 bars. For the constant contact stress case, the parameter planning method was utilized, the pneumatic cylinder pressure varies from 1.71 to 2.30 bars; this range of pressure is according to a 50 N mm^{-2} desired surface contact stress. The 2.30 bars is required when the polishing tool reaches the top of the arc, while the 1.71 bar value is required when polishing the end of the arced edge.

Figure 27 shows the experiment result. Due to slight alignment inaccuracy, there are some measurement errors. Nevertheless, the general tendency is correct. Near the middle of the part (door stop), the radius of curvature is large, i.e., flatter, the constant force (varying contact stress) produced a similar profile to that by the constant stress, and both very close the original profile. However, at both ends where the radii of curvatures become small, the constant force case removed more materials due to high-concentrated force, and the polished profile deviated substantially from the original one. For the constant contact stress case, the polished profile is still very close to the original one. In general, polishing is only meant to improve surface finish not to alter the part geometry (profile).

1.5.3.5 Air Cylinder Pressure Control Modeling

After polishing parameters are planned, polishing control becomes a tracking problem. Similar to robot tracking control after joint motions are planned, polishing tracking control is to track the planned polishing parameters, such as supply pressure. Pressure control modeling is to relate the air cylinder pressure P_c to the control input voltage V_p as below

$$P_c = G_p V_p \quad [63]$$

where G_p is the transfer function relating the input voltage and the cylinder pressure. The relationship between the cylinder pressure P_c and the applied contact force F is given as

$$P_c = \frac{F+f}{A_c} \quad [64]$$

where A_c is the area of the piston inside the cylinder chamber, f is the spring return force of the cylinder which can be obtained through stiffness measurement. The relation between F and the mean contact stress P_m is given as

$$F = \frac{9\pi E^2 (k')\Delta^2 P_m^3}{4k} \quad [65]$$

Under the condition of a constant contact stress P_m, the cylinder pressure P_c can be precomputed from eqns [64] and [65]. Therefore, the control objective is to track the change of the cylinder pressure P_c. **Figure 28** shows a polishing path planning including pressure based on constant contact stress. Standard G-codes are implemented in our polishing/deburring robot, except letter P is used to indicate the cylinder pressure P_c instead of time.

1.5.3.6 Air Spindle Speed Control Modeling

Air spindles are commonly used for polishing and they can be modeled as[11]

$$W = (P_s - P_x)q \quad [66]$$

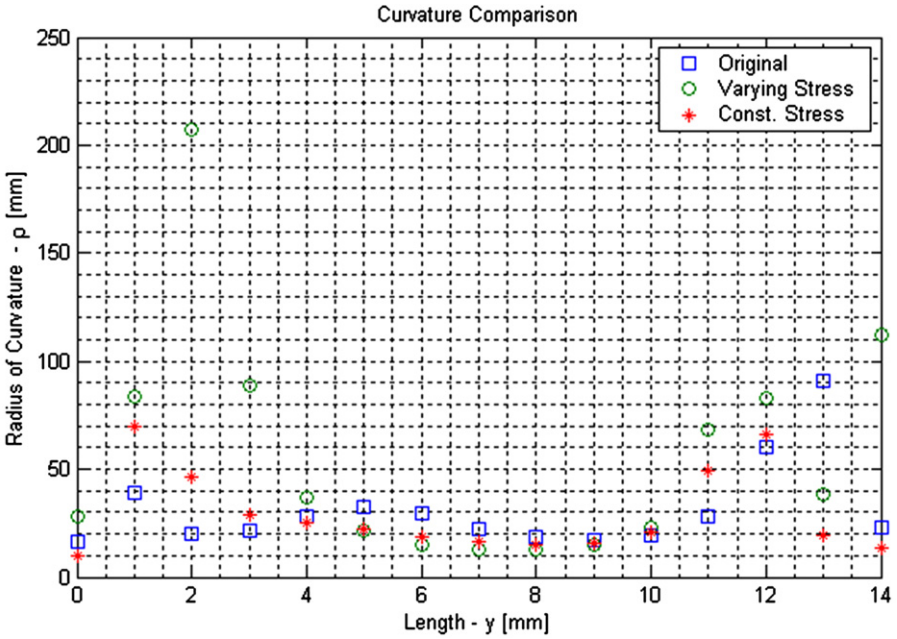


Figure 27 Experiment result between constant force and constant contact stress. Roswell, A. *Modelling for Contact Stress Control in Automated Polishing* (MSc Thesis); Toronto, ON: Ryerson University, 2004.

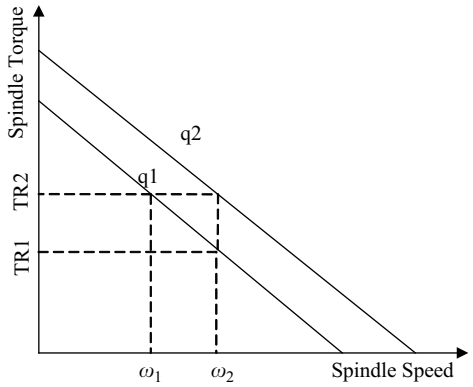


Figure 28 Spindle speed vs. spindle torque. Liang, L. *Modeling and Control of Automated Polishing/Deburring* (Ph.D. thesis); Toronto, ON: Ryerson University, 2008.

where W is the power, P_s represents the supply pressure, P_x is the exhaust pressure, and q is the volumetric flow rate. The resistance of the fluid flow is defined as

$$R_f = (P_s - P_x)/q \qquad [67]$$

Substituting eqn [67] into eqn [66] yields

$$W = Rq^2 \qquad [68]$$

Using eqn [60] and considering power efficiency, the spindle torque can be expressed as

$$T_R = \frac{\eta R_f q^2}{\omega} \qquad [69]$$

By combining with eqn [59] for Hertzian contact, the dynamic equation of the spindle can be derived as

$$I\dot{\omega} = \frac{\eta R_f q^2}{\omega} - \frac{2}{9}\mu_k \pi \left(1 + \frac{1}{k^3}\right)\left(\frac{3kF}{2\pi}\right)^{4/3}(E(k')\Delta)^{1/3} \qquad [70]$$

When the polishing tool rotates at a constant speed, $I\dot{\omega} = 0$, eqn [70] reduces to

$$\omega = \frac{\eta R_f q^2}{\frac{2}{9}\mu_k \pi (1 + \frac{1}{k^3})(\frac{3kF}{2\pi})^{4/3}(E(k')\Delta)^{1/3}} \qquad [71]$$

The spindle does not produce torque at the free running speed, while it exerts a maximum torque when the spindle stalls. The spindle speed can be expressed as a function of output torque T_R by using the following equation

$$\omega = \omega_0\left(1 - \frac{T_R}{T_{\max}}\right) \qquad [72]$$

where $T_{\max}$ is the spindle maximum output torque, ω_0 is the free running speed of the spindle when no load. **Figure 28** shows a speed–torque relation. It can be assumed that the spindle rotates at ω_2 under flow rate q_1, i.e., on the lower line. When geometry changes, under the constant contact stress condition, the friction torque will change from T_{f1} to T_{f2}. Correspondingly, the output torque will change from T_{R1} to T_{R2}. Therefore, the spindle speed is reduced to ω_1. If the spindle speed is required to remain at the original ω_2, the flow rate must be changed from q_1 to q_2, i.e., from the lower line to the upper line. As a result, the spindle speed can be put back from ω_1 to ω_2.

1.5.3.7 Combined Control System

Now by combining eqns [63] and [69], the entire control system corresponding to Figure 21 can be expressed as

$$\begin{bmatrix} F \\ T_R \end{bmatrix} = \begin{bmatrix} G_p A_c & 0 \\ 0 & \dfrac{\eta R_f G_q^2}{\omega} \end{bmatrix} \begin{bmatrix} V_p \\ V_q^2 \end{bmatrix} \quad [73]$$

Noting that $q = G_q V_q$, where G_q is the transfer function of the flow value. This is a decoupled nonlinear control system, corresponding to the left-hand side of Figure 21. The right-hand side of Figure 21 is the tool/part interaction. Under the condition of a constant contact stress P_m, for a given part geometry, the applied contact force F can be determined using eqn [65], which can be directly related to the cylinder pressure P_c through eqn [64]. The goal of the pressure control is to keep actual P_c as close to planned P_c as possible. In other words, this is the problem of pressure tracking control. Under the condition of constant spindle speed ω, for a given part geometry, the flow rate q can be determined through eqn [71]. If only the contact stress is kept constant, then the spindle speed changes with change in part geometry under the constant input V_q. Figure 29 shows this change and the parameters of the geometry for this simulation are taken from the pressure planning given in Table 4. It can be seen that the spindle speed varies under constant flow rate.

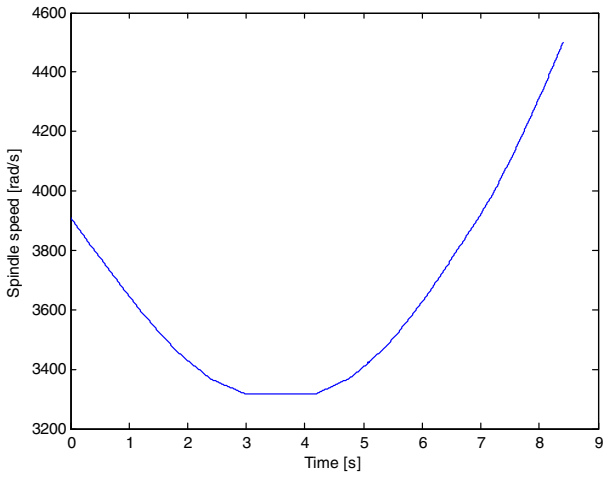


Figure 29 Spindle speed vs. varied geometry. Liang, L. *Modeling and Control of Automated Polishing/Deburring* (Ph.D. thesis); Toronto, ON: Ryerson University, 2008.

1.5.3.8 Pressure Tracking Control

Under the constant contact stress, polishing control is to adjust the cylinder pressure P_c pre-planned based on the part geometry. This control can be treated as the problem of pressure tracking control. In our set up as shown in Figure 30, an active compliance toolhead is made of three spring return pneumatic cylinders (EZH-1.5x6.5–10 from Festo) to provide pressure in the axial direction controlled by a proportional directional control valve (MPYE-5–1/4–010B from Festo) with a response frequency of 100 Hz. A pressure sensor (PENV-A-PS/O-K from Festo) is used to measure the cylinder pressure to form a closed control loop.

A common PID controller can be applied to achieve this control goal. The control block diagram for the pressure tracking is shown Figure 31. The output pressure in the pneumatic cylinders is used as feedback to compare with the desired planned cylinder pressure P_{cd}. The error e is converted to the change of input voltage V_p by using the PID controller. The transfer function for PID control is

$$U(s) = K_{pp} E_p(s) + K_{pi} \frac{E_p(s)}{s} + K_{pd} s E_p(s) \quad [74]$$

where $E_p(s) = P_{cd}(s) - P_c(s)$ and K_{pp}, K_{pi}, and K_{pd} are the proportional gain, integration gain and derivative gain, respectively.

Figure 32 shows the planned cylinder pressure P_c of Table 4. Figure 33 shows the experimental results of the cylinder pressure tracking for the polishing control. From the time at 72 s, the toolhead started being in contact with the part. It ended at the time of 88 s when the tool left contact with the part. It can be seen that the measured cylinder pressure follows the planned cylinder pressure by using a PID controller. The PID controller gains are tuned experimentally to be 0.9, 0.9, and 0.1, respectively.

1.5.3.9 Robotic Deburring Control

Burr is an unwanted material left on the part after cutting. Burr location is generally predictable either at the entrance of cutting or at the exit, with the latter being dominant. However, the burr geometry varies. Burr is commonly measured by burr

Table 4 G-Code with planned pressure parameter

N05	M03							
N110	G01	X2.813	Y18.677	Z-7.544	A-22.2	B0.0	P1.59	F1.0
N120	G01	X2.817	Y17.010	Z-6.940	A-17.3	B0.1	P1.69	F1.0
N130	G01	X2.821	Y15.343	Z-6.500	A-12.7	B0.1	P1.84	F1.0
N140	G01	X2.825	Y13.677	Z-6.209	A-8.5	B0.2	P2.00	F1.0
N150	G01	X2.829	Y12.010	Z-6.050	A-4.5	B0.2	P2.15	F1.0
N160	G01	X2.833	Y10.343	Z-6.010	A-0.8	B0.2	P2.24	F1.0
N170	G01	X2.837	Y8.677	Z-6.075	A 2.9	B0.2	P2.26	F1.0
N180	G01	X2.841	Y7.010	Z-6.230	A 6.7	B0.2	P2.19	F1.0
N190	G01	X2.845	Y5.343	Z-6.469	A10.6	B0.1	P2.06	F1.0
N200	G01	X2.849	Y3.677	Z-6.808	A14.7	B0.1	P1.92	F1.0
N645	M05							

Source: Roswell, A. *Modelling for Contact Stress Control in Automated Polishing* (MSc thesis); Toronto, ON: Ryerson University, 2004.

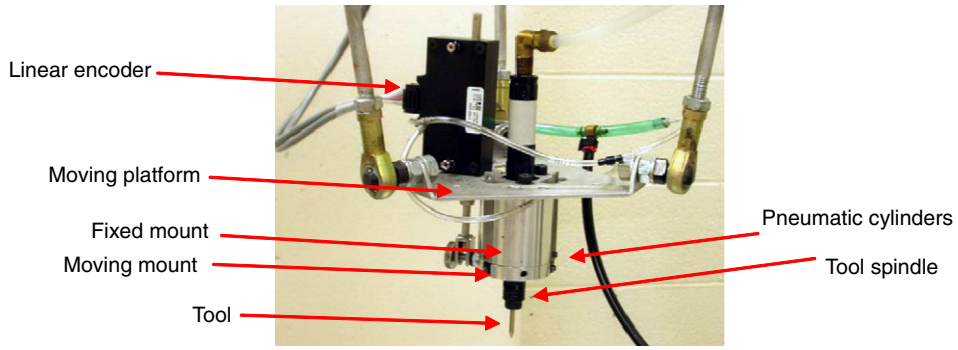


Figure 30 Active compliance toolhead. Liang, L. *Modeling and Control of Automated Polishing/Deburring* (Ph.D. thesis); Toronto, ON: Ryerson University, 2008.

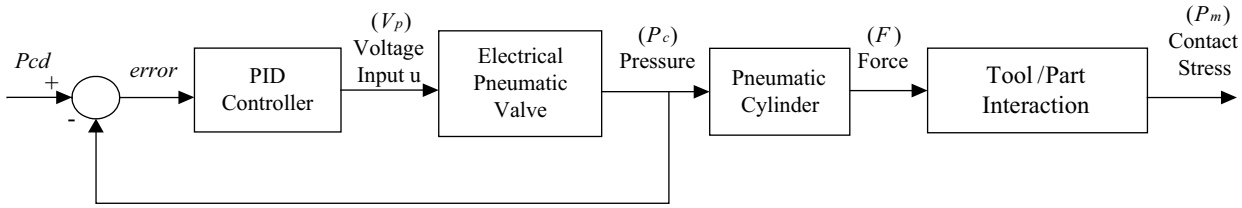


Figure 31 Close loop pressure tracking control block diagram. Liang, L. *Modeling and Control of Automated Polishing/Deburring* (Ph.D. thesis); Toronto, ON: Ryerson University, 2008.

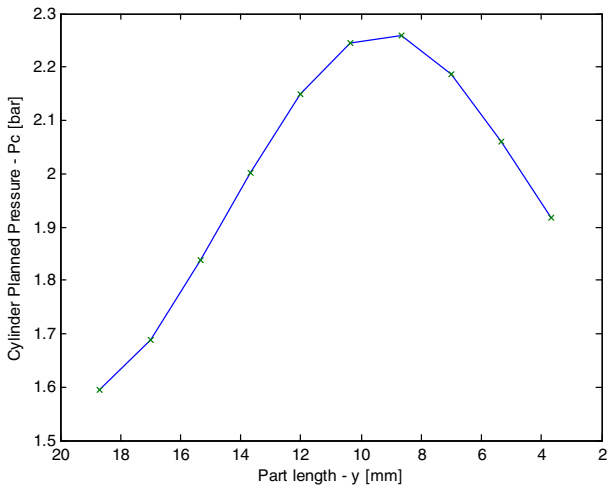


Figure 32 Planned cylinder pressure. Liang, L. *Modeling and Control of Automated Polishing/Deburring* (Ph.D. thesis); Toronto, ON: Ryerson University, 2008.

height and thickness. Some experimental research has been done on milling and drilling. **Table 5** lists the basic types of burr geometry for milling as well as those for drilling. The experiment results[12] show that the depth of cut is the primary factor for the burr height; feed rate and cutting speed are secondary factor for the same tool geometry.

Since burr geometry is generally unknown, a deburring control method is presented with a burr height measurement. A linear encoder shown in **Figure 30** was integrated with our toolhead to form a closed-loop deburring control system.[13] For the development of this control system, a dynamic model of the tool system is described based on the axial compliant tool model, as shown in **Figure 34**.

In deburring, the tool is pressed against the part by three single acting pneumatic cylinders with spring return in the tool axial direction, denoted by z. The tool dynamic model is derived treating the tool system as a spring-damper-mass system subject to the control force and contact force

$$M\ddot{z} + C\dot{z} + Kz = u_p - F \qquad [75]$$

where M is the tool mass, C and K are the damping and stiffness of the spring inside the cylinder, respectively, u_p is the control force, and F is the contact force between the part and the tool. It is noted that the tool axial direction is the tool length direction. In other words, variable z represents the tool length.

The contact force is derived as follows. In light of the micro-cutting model,[6] the average micro depth of cut considering the multiple grains of the abrasive deburring tool can be expressed as

$$h = \frac{F/N}{2\pi r_g \mathrm{HB}} \qquad [76]$$

where HB is the hardness of the part (N mm^{-2}), r_g is the average radius of the grain (mm), and N is the number of grains inside the contact area. Assuming that the part is cut by h for each rotation, then the velocity at which the tool cuts into the part is equal to the spindle rotational speed ω multiplied by h as

$$\dot{z} = \omega h = \frac{\omega F/N}{2\pi r_g \mathrm{HB}} \qquad [77]$$

where the tool rotational speed ω is expressed in rps (revolutions per second). Then the contact force can be derived linearly

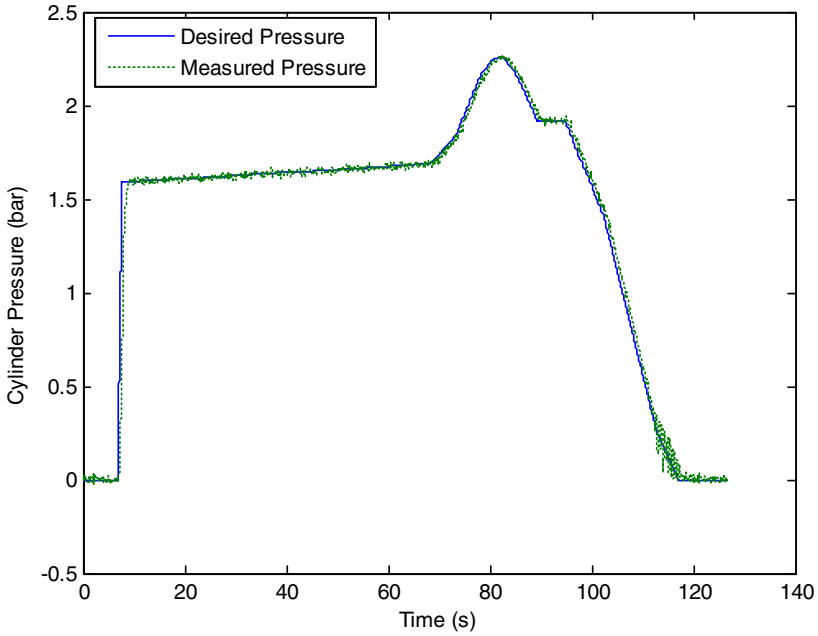
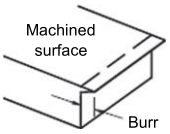
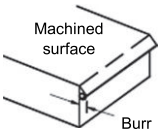
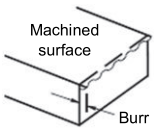
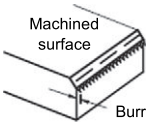
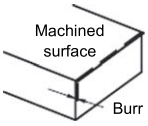
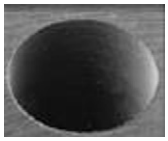
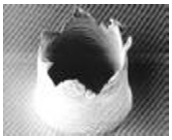
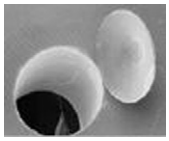


Figure 33 Pressure trajectory tracking. Liang, L. *Modeling and Control of Automated Polishing/Deburring* (Ph.D. thesis); Toronto, ON: Ryerson University, 2008.

Table 5 Burr geometry

Machining method	*Burr geometry*				
Milling	Knife type burr	Wave-type burr	Cur-type burr	Edge breakout	Secondary burr
					
Drilling	Uniform burr	Crown burr	Uniform burr with drill cap	Irregular burr	
					

Source: Liang, L. *Modeling and Control of Automated Polishing/Deburring* (Ph.D. thesis); Toronto, ON: Ryerson University, 2008.

proportional to the tool axial cutting velocity (the same direction as the tool length) as

$$F = C_e\dot{z} \quad [78]$$

where C_e is given as

$$C_e = \frac{2\pi r_g \mathrm{HB}}{\omega} N \quad [79]$$

Substituting eqn [79] into eqn [75] yields the dynamic model of the tool system in terms of tool length variable z as

$$M\ddot{z} + (C + C_e)\dot{z} + Kz = u_p \quad [80]$$

Taking Laplace transform on both sides of eqn [80] yields the tool length response function for the open loop control system as[13]

$$Z(s) = \frac{U_p(s)}{Ms^2 + (C + C_e)s + K} \quad [81]$$

Based on eqn [81], a closed-loop tool length control can be formed for the deburring process and **Figure 35** shows its block diagram. This is the control method based on on-line burr measurement, because the tool length signal is fed back to compare with the desired tool length. The control effort is generated based on the tool length error by applying a tuned PID controller. The transfer function for the proposed tool length control is derived as

$$U_p(s) = K_{zp}E_z(s) + K_{zi}\frac{E_z(s)}{s} + K_{zd}sE_z(s) \quad [82]$$

where $E_z(s) = z_d(s) - z(s)$, K_{zp}, K_{zi}, and K_{zd} are the proportional gain, integration gain, and derivative gain, respectively.

The proposed deburring control based on on-line burr measurement has been implemented on the robotic deburring system described in **Figure 20**. **Figure 36** shows the block diagram for the entire deburring process including control system and tool/part interaction. The complete tool system also includes a pneumatic valve and three pneumatic cylinders that generate the tool force. Due to the high-response rate requirement, a flow valve is used instead of a pressure valve as done traditionally. Since the flow valve exhibits strong nonlinearity, a linearization method is developed to establish a proportional relation between the control voltage and the control force around a set point. The details are presented in Ref.[10]

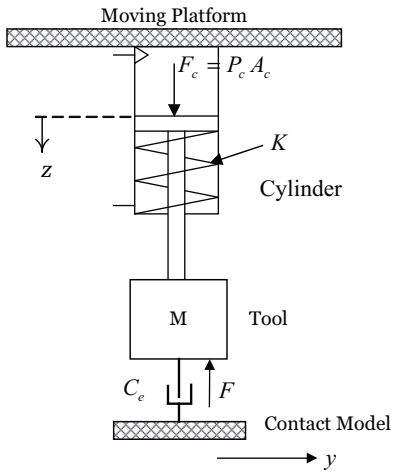


Figure 34 Tool system modeling. Liang, L. *Modeling and Control of Automated Polishing/Deburring* (Ph.D. thesis); Toronto, ON: Ryerson University, 2008.

The first experiment presented here is the deburring of the edge of an aluminum plate. **Figure 37** shows the experiment setup. The control gains K_{zp}, K_{zi}, and K_{zd} for the actual control system are tuned at 0.9, 1, and 0.06, respectively. They are different from the simulation due to uncertainty in the actual control system. Since in this case the nominal tool path is a straight line, the desired tool length is set at a constant value of 4.5 mm. The objective of the proposed control method is to maintain the tool length at 4.5 mm. The experimental result of the deburring control is given in **Figure 38**. It can be seen that the total deburring period is approximately 60 s. The tool encounters the burrs in the first half of period as separated by a vertical dashed line in **Figure 38**. When hitting the burr, the tool is pushed upward to shorten its length, i.e., below 4.5 mm, as shown in the top figure of **Figure 38**. This negative tool length change informs the controller that there is a burr, hence to raise the control voltage to increase the control force, as shown in the bottom figure of **Figure 38**. In the second half, the top edge sags, causing the tool to extend, i.e., above 4.5 mm, as shown in the top figure of **Figure 38**. Correspondingly, the control voltage reduces to decrease the control force to avoid over-cut, as shown in the bottom figure of **Figure 38**. One may notice from **Figure 38** that though the control voltage signal follows the tool length change, the response is not sufficiently sharp. This is due to the long-time delay in the pneumatic system. An electrically actuated tool system would provide a better response rate.

The second experiment is on the same part to investigate the burr reduction rate for our deburring system. **Figure 39** shows the burr height changes after two paths of deburring. The edge profile is measured using a 2-D laser profile scanner. The resolution of the profile scanner is 10 μm in the *z*-direction, i.e., in the same direction as the burr height. It can be clearly seen from **Figure 39** that the burrs are effectively removed by applying the proposed closed-loop tool length control method. At the locations without burrs, the part

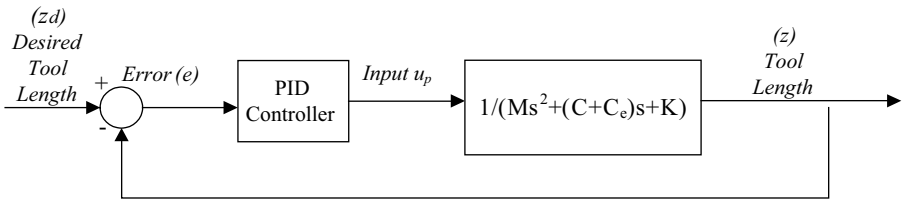


Figure 35 Closed-loop tool length control block diagram. Liang, L. *Modeling and Control of Automated Polishing/Deburring* (Ph.D. thesis); Toronto, ON: Ryerson University, 2008.

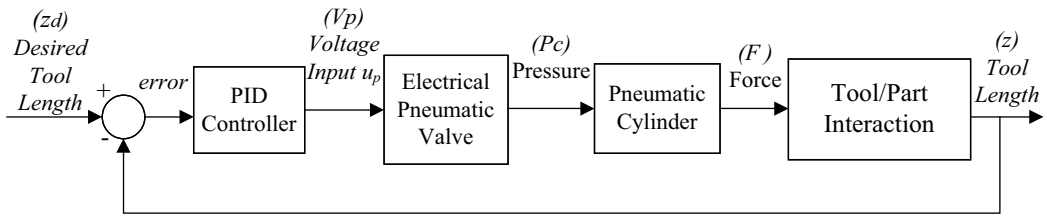


Figure 36 Block diagram for the entire deburring process. Liang, L. *Modeling and Control of Automated Polishing/Deburring* (Ph.D. thesis); Toronto, ON: Ryerson University, 2008.

geometry is maintained as no over-cut, due to the regulation of the tool length. To quantify the burr reduction rate, the mean value and variance of the edge profile are obtained based on the measurement data given in Figure 39. Table 3 lists the calculation results. The mean value represents the average height of the profile, and the variance represents its roughness. It can be seen that the mean value is reduced by 0.08 mm from the first path of deburring and again by 0.03 mm from the second path. Hence the average burr reduction is about 0.05 mm, which is close to 0.06 mm of the simulation. Furthermore, a small variance indicates a smoother part surface. It can be clearly seen from Table 6 that the profile variance value decreases as the number of deburring paths increases, meaning that the edge profile becomes smoother.

The third experiment is on a zigzag path, mimicking the deburring of the fir trees of a turbine disk. The experiment set up is shown in Figure 40. Since this is an in-house prepared test piece, there is no CAD model. Therefore, the reverse engineering-based approach is used to measure and fit the zigzag profile as shown in Figure 41, based on which a tool path is generated as shown in Figure 42.

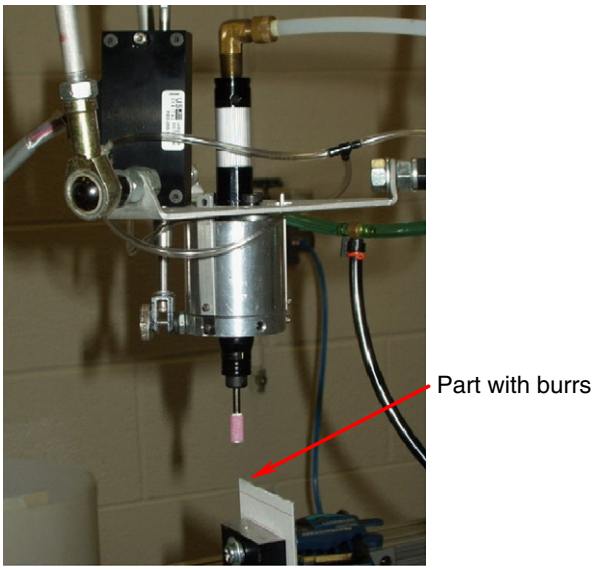


Figure 37 Edge deburring experiment. Liang, L. *Modeling and Control of Automated Polishing/Deburring* (Ph.D. thesis); Toronto, ON: Ryerson University, 2008.

1.5.4 Polishing/Deburring Toolhead Design

Generally, there are two main categories of cutting tools: hard and soft. The former is used for cutting including turning, milling, and drilling, and the latter is used for finishing processes including polishing and deburring. A soft tool has built-in compliance, similar to a human hand, to provide varying stiffness for delicate finishing operation. There are two types of compliance tools: passive usually using springs without control and active using pneumatic actuators with control.

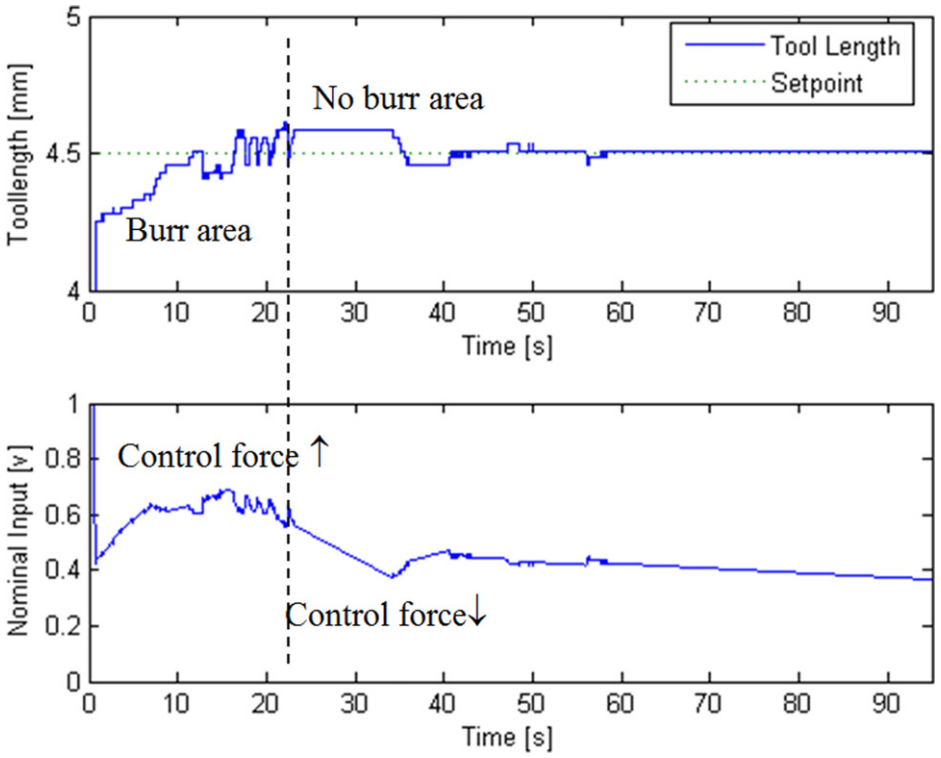


Figure 38 Experimental results of deburring control; top – the time history of the tool length; bottom – the control signal of the pneumatic valve. Liang, L. *Modeling and Control of Automated Polishing/Deburring* (Ph.D. thesis); Toronto, ON: Ryerson University, 2008.

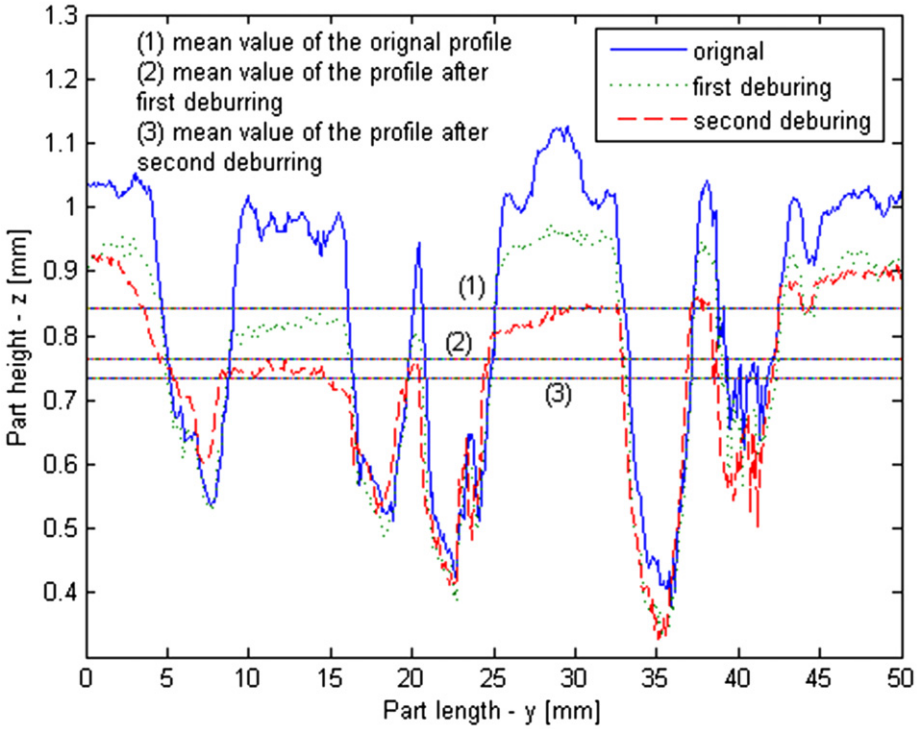


Figure 39 Burr reduction before and after deburring. Liang, L. *Modeling and Control of Automated Polishing/Deburring* (Ph.D. thesis); Toronto, ON: Ryerson University, 2008.

Table 6 Profile variance and mean value before and after deburring

	Profile mean (mm)	*Profile variance*
Original profile	0.8437	0.0414
First deburring	0.7648	0.0302
Second deburring	0.7337	0.0209

Source: Liang, L. *Modeling and Control of Automated Polishing/Deburring* (Ph.D. thesis); Toronto, ON: Ryerson University, 2008.

1.5.4.1 Hybrid Design

The design presented is for active compliance polishing/deburring toolheads. This design must be approached first by the principle of its design, compliance between tool tip and the part. See **Figure 43** below for a diagram of the tool tip contact with the part. This is a 3-D model in which the tool has three stiffness in the *x*, *y*, and *z* axis. An action plane is introduced to combine the *x* and *y* axis to one axis, i.e., the radial direction and the *z* axis is along the axial direction. So the tool model shown in **Figure 43** is for a hybrid model combining both the radial and axial direction.[14,15]

The design of the tool must be actively compliant in both axial and radial directions. As shown in **Figure 44**, the bottom part of the toolhead is for the axial compliance control. This is the same design as shown in **Figure 30**, that is to use three linear pneumatic actuators to control the axial force and is integrated with a linear encoder for the axial height measurement. The top part is for the radial compliance control, through a ring pneumatic actuator integrated with an *x*–*y* angular sensor. The two compliance systems are connected through a gimbal.

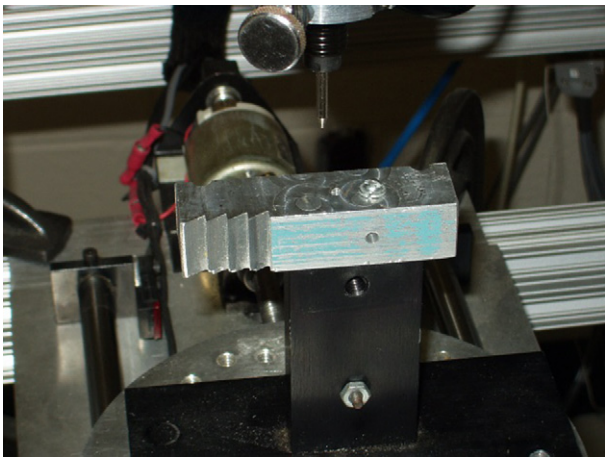


Figure 40 Zigzag path deburring mimicking the fir trees of the turbine disk. Liang, L. *Modeling and Control of Automated Polishing/Deburring* (Ph.D. thesis); Toronto, ON: Ryerson University, 2008.

1.5.4.2 Toolhead Dynamic Modeling

As shown in **Figure 44**, the two gimbal axes are selected to be the *x* and *y* axes. The inner gimbal axis of rotation is the *x* axis

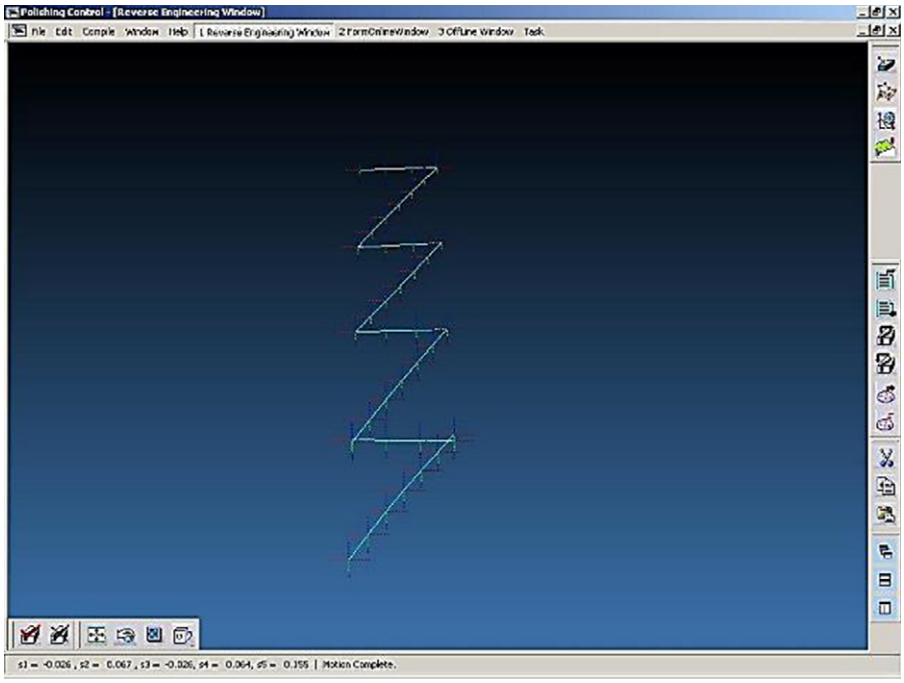


Figure 41 Zigzag path fitting. Liang, L. *Modeling and Control of Automated Polishing/Deburring* (Ph.D. thesis); Toronto, ON: Ryerson University, 2008.

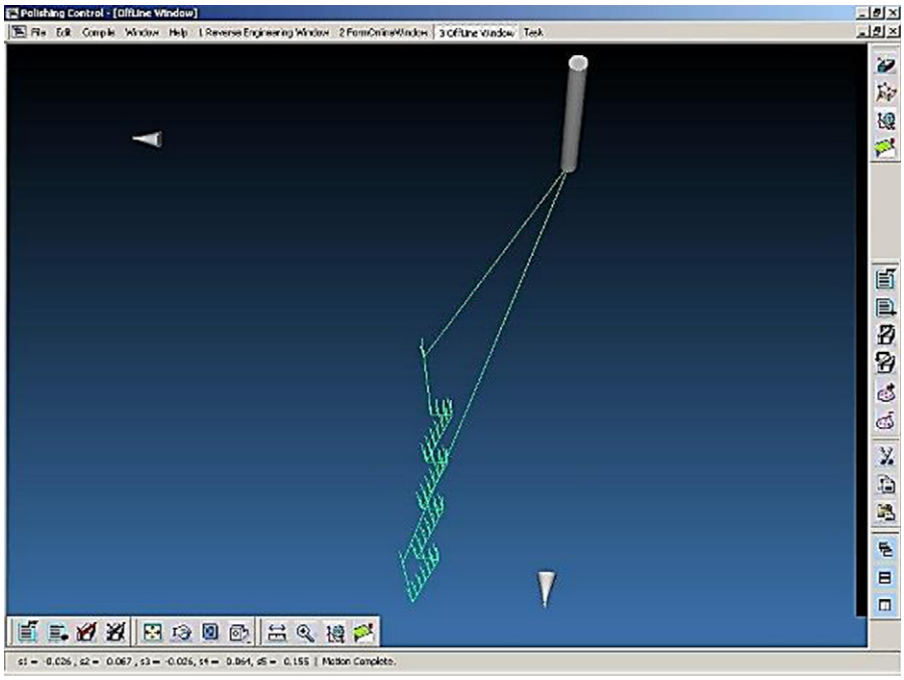


Figure 42 Zigzag tool path planning. Liang, L. *Modeling and Control of Automated Polishing/Deburring* (Ph.D. thesis); Toronto, ON: Ryerson University, 2008.

and the outer gimbal axis is the y axis. Again, the z axis is in line with the axial direction of the tool with the positive direction extending from the gimbal to the tool tip. In the radial direction, the tool's x and y axes are combined into a radial action plane. The action plane rotates parallel to the radial displacement/force direction. During radial actuation of the tool the action plane will describe the tool's full range of motion during manipulation of the radial actuator. **Figure 45** shows a model for the hybrid toolhead.

The tool has two displacements in the radial direction, r_l is the lower radial displacement and r_u is the upper radial displacement. The lower displacement is the displacement of the

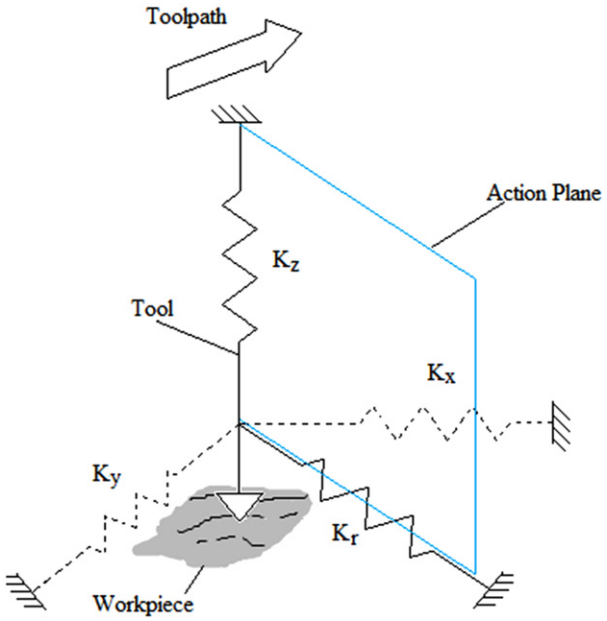


Figure 43 A 3D compliance tool model. Kroeker, J. *Design Analysis & Testing of an Enhanced Radial-Axial Hybrid Compliant Deburring Tool* (MSc thesis); Toronto, ON: Ryerson University, 2014.

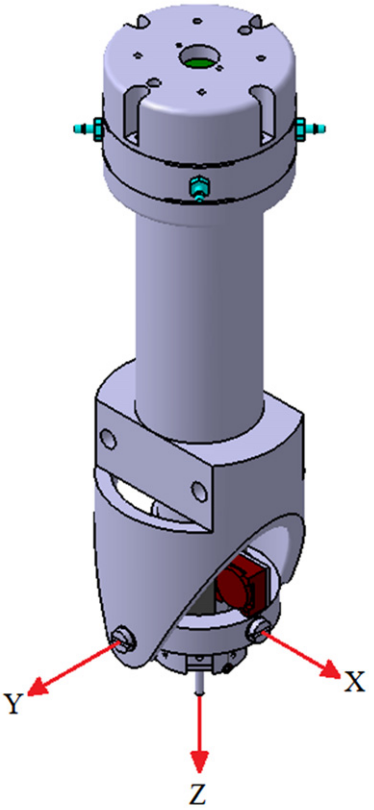


Figure 44 Design of a hybrid axial/radial compliance toolhead. Kroeker, J. *Design Analysis & Testing of an Enhanced Radial-Axial Hybrid Compliant Deburring Tool* (MSc thesis); Toronto, ON: Ryerson University, 2014.

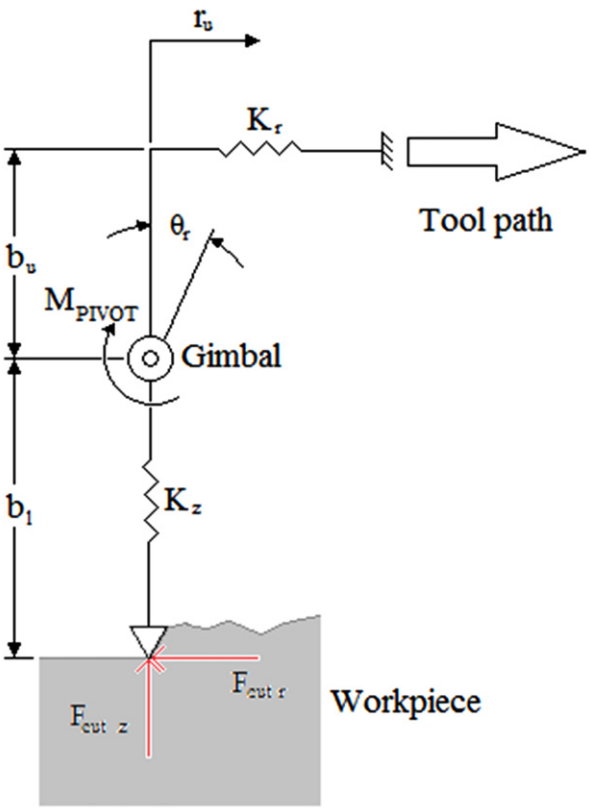


Figure 45 Model of the hybrid tool. Kroeker, J. *Design Analysis & Testing of an Enhanced Radial-Axial Hybrid Compliant Deburring Tool* (MSc thesis); Toronto, ON: Ryerson University, 2014.

tool shaft as a direct result of an encountered burr. The upper displacement is the resultant displacement of the tool shaft at the sensor as the result of the tool tip movement. The tool is split into an upper and lower half, b_l is the distance from the gimbal to the tool tip and b_u is the distance from the gimbal to the center of contact of for the tool shaft and actuator diaphragm. A relationship can be made between the four variables as can be seen in eqn [83].

$$r_l = \frac{b_l}{b_u} r_u \qquad [83]$$

The velocities and accelerations of the upper and lower radial displacements can be expressed by taking the derivative of [83] as

$$\dot{r}_l = \frac{b_l}{b_u} \dot{r}_u \qquad [84]$$

$$\ddot{r}_l = \frac{b_l}{b_u} \ddot{r}_u \qquad [85]$$

The angle of rotation of the tool shaft in the action plane θ_r can be determined by taking the sine of the components for upper and lower sides of the tool as

$$\sin\theta_r = \frac{r_u}{b_u} \qquad [86]$$

Due the scale of the components a small angle approximation can be made as

$$\theta = \frac{r_u}{b_u} \quad [87]$$

Angular velocity and acceleration can be expressed by taking the derivative of [87] as

$$\dot{\theta} = \frac{\dot{r}_u}{b_u} \quad [88]$$

$$\ddot{\theta} = \frac{\ddot{r}_u}{b_u} \quad [89]$$

A summation of the moments about the axis of pivot (M_{PIVOT}) is taken and can be seen in eqn [90].

$$M_{\text{PIVOT}} = M_{\text{RA}} + M_{\text{Cut}} \quad [90]$$

M_{RA} is the moment about the pivot caused by the radial actuator. M_{Cut} is the moment about the pivot caused by the cutting force of the tool tip on the part. Equation [91] further breaks M_{RA} into its respective components the force of the radial actuator (F_{RA}) multiplied by the moment arm (b_u) as

$$M_{\text{RA}} = F_{\text{RA}} b_u \quad [91]$$

The force of the radial actuator can be further broken down into the stiffness of the radial actuator (K_{RA}) multiplied by the radial displacement (r_u) it has traveled. The moment about the pivot due to the cutting force is similar to eqn [91]. They have different moment arms and therefore this yields

$$M_{\text{Cut}} = F_{r-\text{Cut}} b_l \quad [92]$$

Substituting eqns [91] and [92] into eqn [90] and rewriting M_{PIVOT} in terms of inertia will yield

$$\left(\frac{I}{b_l}\right)\ddot{r}_l + \left(K_{\text{RA}}\frac{{b_u}^2}{{b_l}^2}\right) r_l = F_{r-\text{Cut}} \quad [93]$$

Similarly, the axial modeling for the tool is the coupling of the actuator's stiffness with the tool tip and part stiffness relationship. Equation [94] gives the dynamic relationship between the mass of the moving axial component of the tool and stiffness relationship in the axial direction.

$$m_z \ddot{z} + K_z z = F_{z-\text{Cut}} \quad [94]$$

The combination of these two equations yields a complete model for the hybrid toolhead

$$\begin{bmatrix} \frac{I}{b_l} & 0 \\ 0 & m_z \end{bmatrix} \begin{pmatrix} \ddot{r}_l \\ \ddot{z} \end{pmatrix} + \begin{bmatrix} K_{\text{RA}}\frac{{b_u}^2}{{b_l}^2} & 0 \\ 0 & K_z \end{bmatrix} \begin{pmatrix} r_l \\ z \end{pmatrix} = \begin{Bmatrix} F_{r-\text{Cut}} \\ F_{z-\text{Cut}} \end{Bmatrix} \quad [95]$$

Each term is an important part of the dynamic model of the deburring tool. The terms $F_{r-\text{Cut}}$ and $F_{z-\text{Cut}}$ are defined by the tool/part interaction through the Hertzian contact mechanics. The term K_z is defined for the axial stiffness. As mentioned before, the axial actuators are made of three linear pneumatic actuators, and this stiffness is relatively easy to determined by measuring the ratio of the pneumatic cylinder force to its displacement. The term K_{RA} is the stiffness of relationship of the radial actuator. Since this is a ring pnuematic actuator, the stiffness in the radial direction is relatively complex to determine.

1.5.4.3 Ring Actuator Modeling

Figure 46 shows our ring actuator, the base structure being a donut shape ring evenly divided into four chamers. The inner side of each chamber is covered by a diaphragm which is clamped by an arc retainer to follow the circular shape of the hole. The outer side, top and bottom of the ring atuctor are covered with seal. Four air nozzles are used to supply air to four air chambers, which can be controlled under a single valve or separate valves. The stiffness of the ring actuator is determined by these four pressurized diaphragm chambers.

To provide radial compliance, the radial actuator has a 0.125in gap between the unpressurized diaphragm and the centered around the outer diameter of the tool shaft which is fixed to a two-axis gimbal. The gap between the diaphragm and the tool shaft will become filled with the inflated diaphragm upon a demand for pressure. When polishing or deburring, the tool tip will deflect and because of the two-axis gimbal this will cause a radial deflection of the tool shaft within the action plane. The deflection will cause a reactant force on the radial actuator that will be realized by a diaphragm causing a deformation of this diaphragm. The total deformation of the tool shaft will be the resultant of the cutting force and the inflating of the diaphragm due to the air pressure.

For stiffness modeling, hyperelastic material theory is adopted. Hyperelastic materials are defined by a constitutive model which derives the stress–strain relationship from a strain energy density function. Here, an Arruda–Boyce constitutive model is used and given as[16]

$$W_{8\text{ch}} = \frac{N k_B T}{2}\left[\beta\lambda_{\text{chain}} + \sqrt{n}\ln\left(\frac{\beta}{\sinh\beta}\right)\right] \quad [96]$$

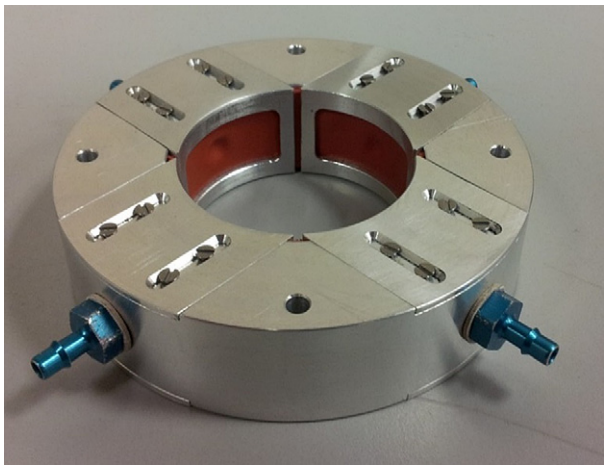


Figure 46 Pneumatic ring actuator. Kroeker, J. *Design Analysis & Testing of an Enhanced Radial-Axial Hybrid Compliant Deburring Tool* (MSc thesis); Toronto, ON: Ryerson University, 2014.

$$\lambda_{\text{chain}} = \sqrt{\frac{I_1}{3}} \quad [97]$$

$$\beta = L^{-1}\left(\frac{\lambda_{\text{chain}}}{\sqrt{n_{\text{chain}}}}\right) \quad [98]$$

where n is the number of chain segments for a hyperelastic material, I_1, is the first invariant of the left Cauchy–Green deformation tensor, k_B is the Boltzmann constant, T is temperature, and N is the number of chains in the network of a cross-linked polymer.

The strain energy density formula can be represented in polynomial form as

$$W_{8\text{ch}} = \mu \sum_{i=1}^{n} \left[\frac{C_i}{\lambda_m^{2i-2}}\left(I_1^i - 3^i\right)\right] \quad [99]$$

The locking stretch of the hyperelastic material is represented by λ_m, and the initial shear modulus is represented by μ. The strain energy density can be expressed in terms of the deformation gradient. The Langevin function is expressed in the series expansion form for the first three terms.

$$\overline{U} = \mu\left\{\frac{1}{2}\left(\bar{I}_1 - 3\right) + \frac{1}{20\beta^2}\left(\bar{I}_1^2 - 9\right) + \frac{11}{1050\beta^4}\left(\bar{I}_1^3 - 27\right) + \ldots\right\} + \frac{K}{2}(J-1)^2 \quad [100]$$

To this end, the stress–strain law for the Arruda–Boyce model is expressed as

$$\sigma_{ij} = \frac{\mu}{J^{5/3}}\left(1 + \frac{I_1}{5J^{2/3}\beta^2} + \frac{33{I_1}^2}{525\beta^4 J^{4/3}} + \ldots\right)\left(B_{ij} - \frac{I_1}{3}\delta_{ij}\right) + K(J-1)\delta_{ij} \quad [101]$$

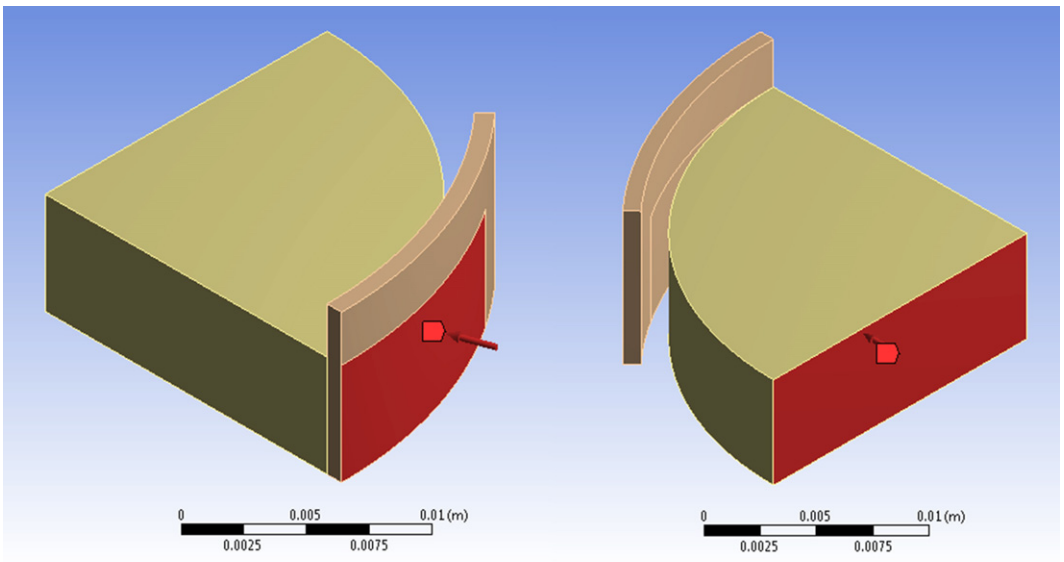


Figure 47 Ring diaphragm model. Kroeker, J. *Design Analysis & Testing of an Enhanced Radial-Axial Hybrid Compliant Deburring Tool* (MSc thesis); Toronto, ON: Ryerson University, 2014.

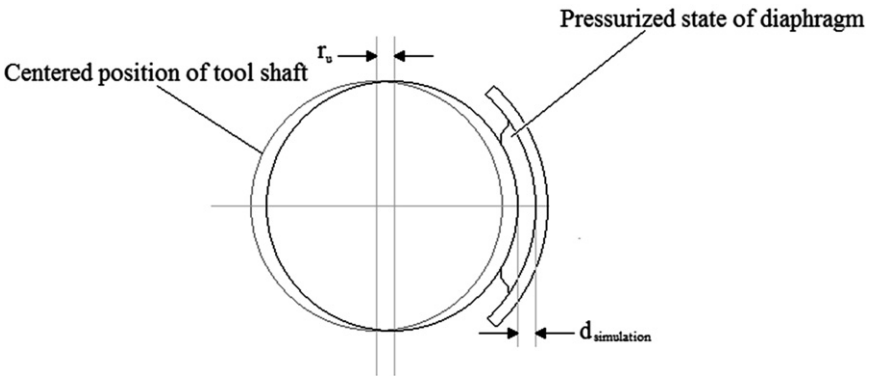


Figure 48 Ring actuator displacement model. Kroeker, J. *Design Analysis & Testing of an Enhanced Radial-Axial Hybrid Compliant Deburring Tool* (MSc thesis); Toronto, ON: Ryerson University, 2014.

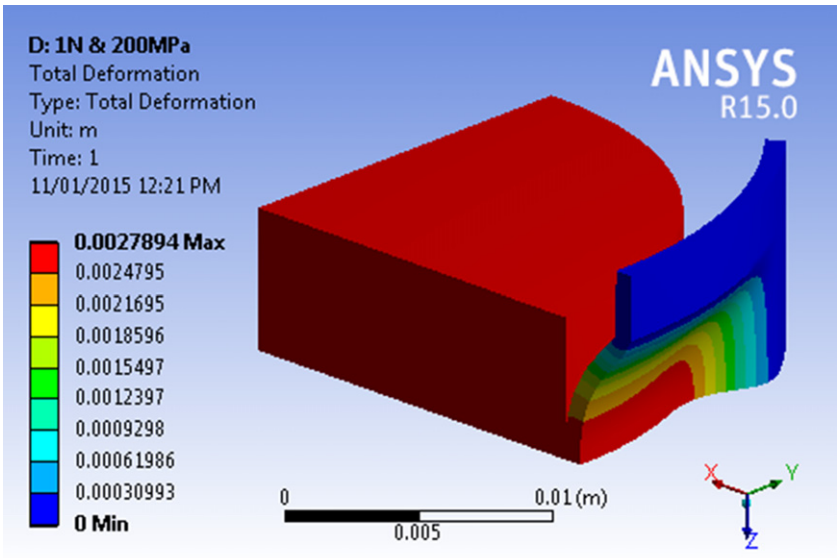


Figure 49 Ring actuator deformation simulation. Kroeker, J. *Design Analysis & Testing of an Enhanced Radial-Axial Hybrid Compliant Deburring Tool* (MSc thesis); Toronto, ON: Ryerson University, 2014.

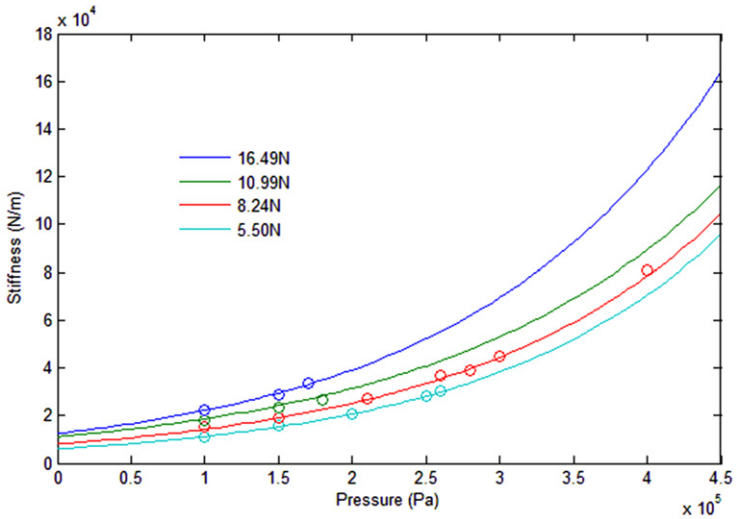


Figure 50 Ring actuator stiffness curves through simulation. Kroeker, J. *Design Analysis & Testing of an Enhanced Radial-Axial Hybrid Compliant Deburring Tool* (MSc thesis); Toronto, ON: Ryerson University, 2014.

The principle stress–strain relationship seen in eqn [101] can be used to define an engineering stress–strain relationship dependent on the type of deformation being modeled, from which the stiffness of the ring actuator might be obtained.

1.5.4.4 Simulation of Ring Actuator Stiffness

Since eqn [101] is difficult to solve, instead a finite element program is used for simulation to determine the stiffness. A tool shaft is assumed rigid and all the deformations are assumed to happen on the diaphragm. The input force is $F_{r-\mathrm{Cut}}$ from the tool tip resulting from cutting. This force is transferred to the actuator through the gimbal to F_{RA}. For our tool design, the gimbal axis to the tool tip b_l is 0.041 m, and the gimbal axis to the radial actuator b_u is 0.225 m.

The diaphragm is modeled as a single curved rectangular body contacting a cylindrical tool. For simplicity, only a chamber is model, which represents a quarter of the whole ring actuator, as shown in **Figure 47**. The force from the tool to the diaphragm is applied to the flat face of the tool shaft cylinder (the area in red on the right image), while the pressure from the back of the diaphragm is applied to the free surface opposite to the contact of the cylinder (the area in red on the left image).

The analysis was completed using large deflection for a nonlinear hyperelastic material analysis. The total deformation of the model was solved for using a static structural analysis

function in ANSYS Workbench. The deformation of the diaphragm, represented by $d_{simulation}$ must be considered with respect to the actual center position of the shaft to determine the displacement of the shaft from the center position represented by r_u. Figure 48 illustrates the relationship between $d_{simulation}$ and r_u.

Figure 49 shows a simulation of the diagram deformation as the result of 1 N of shaft force and 200 MPa of pressure on the diaphragm. Depending on the force and pressure applied, the simulated diaphragm deformation, $d_{simulation}$, may exceed the gap. When this happens, the actual gap value is taken as the maximum shaft displacement.

To determine the stiffness of the ring actuator, the pressure on the diaphragm and force on the shaft were varied within the design requirement. The force on the tool tip was varied between 5.50 and 16.49 N, and the pressure was varied between 100 and 400 MPa. The radial displacement of the tool shaft from the centered position was calculated by subtracting $d_{simulation}$ and the radial thickness of the tool shaft from the total radial distance of the diaphragm. The resulting displacement was used to determine the stiffness of the ring actuator based on the force on the tool shaft. The stiffness values were plotted against pressure based on tool shaft force as shown in Figure 50.

Data from these plots were curve fitted to an exponential function given in eqn [102] with the coefficients for different cutting forces shown in Table 7.

Table 7 Coefficients for stiffness and pressure relationships

Shaft force (N)	a_{exp}	b_{exp} ($\times 10^{-6}$)
5.50	6095	6.12
8.24	8088	5.68
10.99	11030	5.23
16.49	12490	5.72

Source: Kroeker, J. *Design Analysis & Testing of an Enhanced Radial-Axial Hybrid Compliant Deburring Tool* (MSc thesis); Toronto, ON: Ryerson University, 2014.

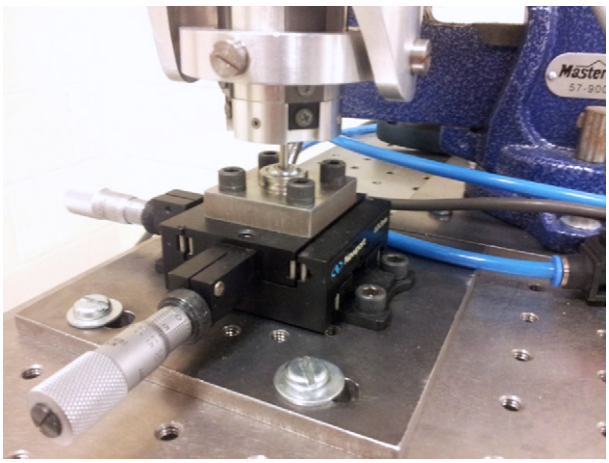


Figure 51 Final calibration rigging. Kroeker, J. *Design Analysis & Testing of an Enhanced Radial-Axial Hybrid Compliant Deburring Tool* (MSc thesis); Toronto, ON: Ryerson University, 2014.

$$\gamma = a_{\exp} e^{b_{\exp} x} \quad [102]$$

1.5.4.5 Experiment on Ring Actuator Stiffness

For experiment, the test tool was mounted to a table vice which was mounted to a rigid testing platform. A calibration setup was designed to achieve this, see Figure 51 for the

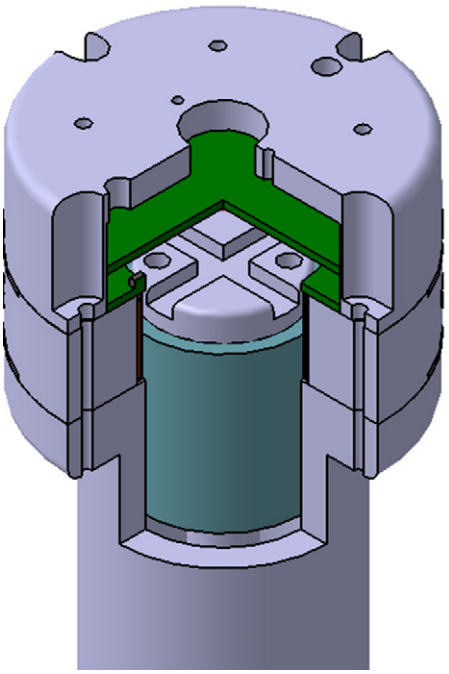


Figure 52 Centering collar (light blue). Kroeker, J. *Design Analysis & Testing of an Enhanced Radial-Axial Hybrid Compliant Deburring Tool* (MSc thesis); Toronto, ON: Ryerson University, 2014.

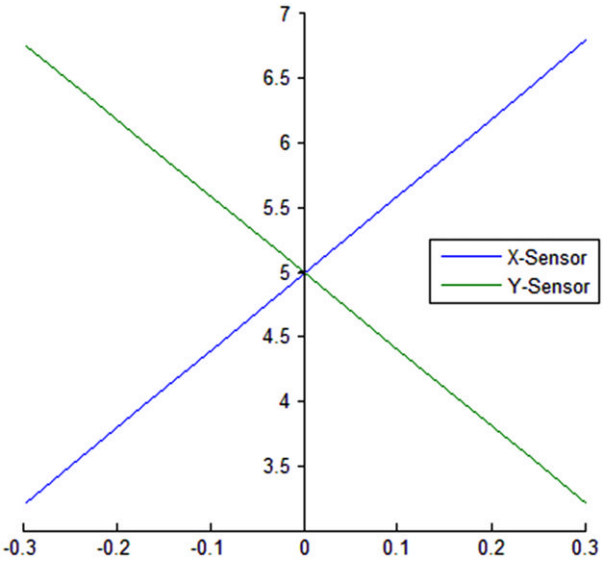


Figure 53 Voltage vs. displacement relationship. Kroeker, J. *Design Analysis & Testing of an Enhanced Radial-Axial Hybrid Compliant Deburring Tool* (MSc thesis); Toronto, ON: Ryerson University, 2014.

calibration stage. A two-axis stage with two micrometers was used to accurately determine the displacement in two degrees of freedom. The tool tip was attached to the stage via a close tolerance ball joint to which the shaft of the tool tip could freely slide within. The final calibration stage was created using adapter plates that linked each component together to the common fixed rigid testing platform.

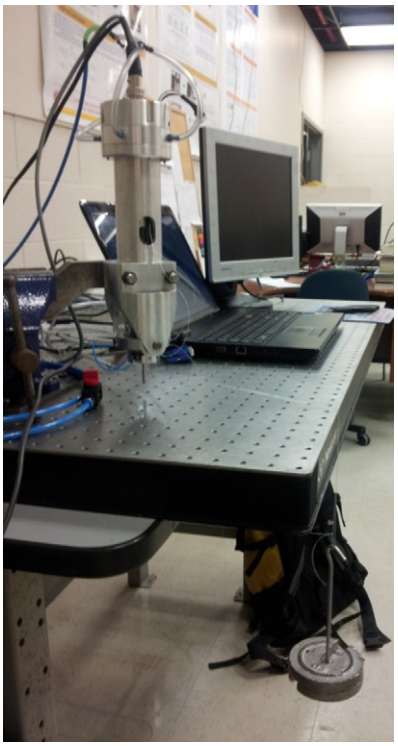


Figure 54 Stiffness testing setup. Kroeker, J. *Design Analysis & Testing of an Enhanced Radial-Axial Hybrid Compliant Deburring Tool* (MSc thesis); Toronto, ON: Ryerson University, 2014.

Calibration was completed on a two-axis stage from Newport with manual micrometers also from Newport. The custom board with two magnetic field sensors were made. Data was collected through a Measurement Computing USB data acquisition unit at 100 samples per second.

A bias was determined for each sensor using a removable plastic collar which fit within the tool between the inner shaft of the tool and the outer casing as can be seen in **Figure 52**. The collar will hold the tool shaft directly in the center to determine a bias. The bias is present due to tolerance stack-ups, magnetic cross-talk, and imperfections in the magnet placement. Once the shaft was centered and the bias determined, the collar could be slid downward and cleared away.

A filter was applied to the signals to reduce the noise within the signals. The calibration data was a combination of measurements from the micrometers and signals recorded from the data acquisition unit. In order to make recording and processing the data as simple as possible a pulse generator was use to record exactly one value of the voltage for both x and y sensors. This allowed time for the micrometers to be set before taking another recording.

The calibration resulted in a linear relationship for each sensor. **Figure 53** shows a plot of voltage vs. displacement, and eqns [103] and [104] are the two linear equations obtained through data fitting. To verify the accuracy of the voltage and displacement relationship the magnetic field sensor was calibrated at 22.5° increments 360° around the tool.

$$x = 5.922V_{x\ \text{sensor}} + 5.0682 \qquad [103]$$

Table 8 Stiffness and pressure exponential curve fitting coefficients

Shaft Force (N)	a_{exp}	b_{exp} $(\times 10^{-6})$
9.35	9298	5.49
13.46	11762	5.47

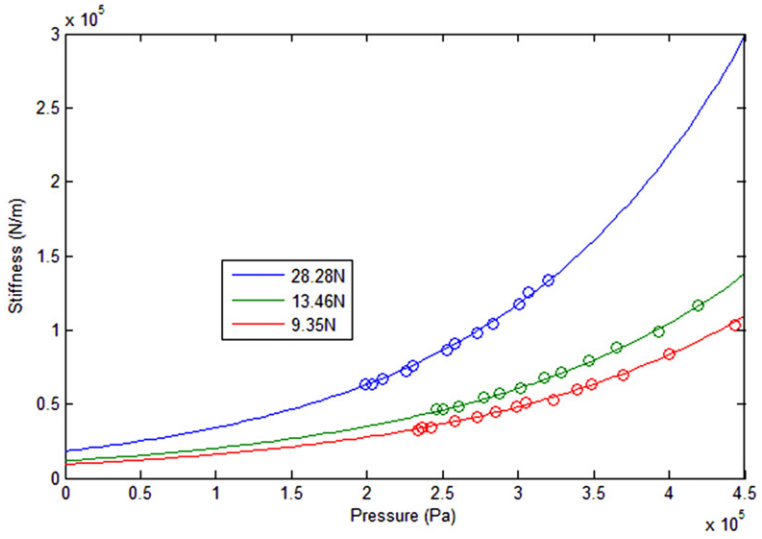


Figure 55 Experimental stiffness and pressure testing results. Kroeker, J. *Design Analysis & Testing of an Enhanced Radial-Axial Hybrid Compliant Deburring Tool* (MSc thesis); Toronto, ON: Ryerson University, 2014.

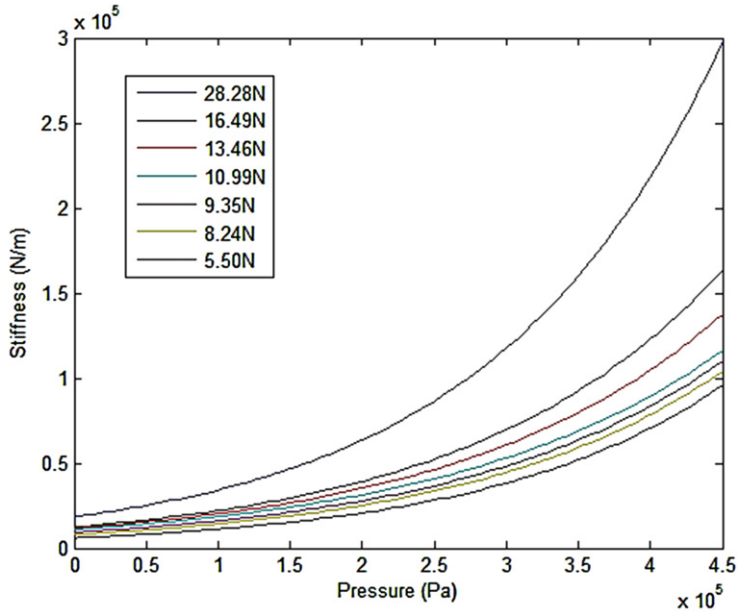


Figure 56 Stiffness vs. pressure relationship for simulation and testing data. Kroeker, J. *Design Analysis & Testing of an Enhanced Radial-Axial Hybrid Compliant Deburring Tool* (MSc thesis); Toronto, ON: Ryerson University, 2014.

$$y = -5.9129V_{y\ \text{sensor}} + 5.0377 \qquad [104]$$

Once calibrated, the tool could be tested for its stiffness behavior. This would be accomplished by loading tool tip and varying the pressure of the ring actuator. Using the calibrated sensor the position in the x and y directions could be recorded. Data was recorded using the same data acquisition unit. The addition of an Omega PX319 pressure transducer was used to accurately measure the pressure on the ring actuator over the duration of data recording. The displacement was measured using the magnetic sensors and converted using the voltage/displacement relationship determined through calibration. Weights were hung from fishing line fixed to the tool tip and left to hang off of the rigid testing table, see **Figure 54** for image of the experimental setup. The mass of each weight was measured and recorded for each test. The tool was pressurized and data recorded. The pressure was varied within the ring actuator and held for small time increments in order to create clear displacement and pressure data sets. Data was recorded continuously and sorted for stable pressure and displacement values.

The stiffness was determined based on the force on the tool tip and the displacement caused as a result of the force and pressure setting. As the pressure was varied for a constant tool tip force a noticeable change of displacement and therefore stiffness was observed. The stiffness and pressure relationships are plotted in **Figure 55**. The plots were curve fitted and like the simulation results and they too appeared to correlate to exponential functions.

The exponential functions were used for fitting the experiment data, with coefficient listed in **Table 8**. **Figure 56** combines between simulation and experiment data for comparison. It can be seen that both follow the same relationship and fall within a logical trend that appears to increase as the shaft force increases.

1.5.5 Conclusions

In this chapter, four fundamental issues for robotic polishing and deburring including contact area-based path planning, surface roughness modeling, contact stress-based control, and polishing/deburring toolhead design have been discussed. The methods developed to deal with these issues are based on contact mechanics. It is shown that the contact area during polishing/deburring between the tool and part varies depending on the geometry of the part, hence leading to a new method presented for polishing/deburring path planning. Then the micro depth of cut within the contact area is modeled leading a method presented for the determination of the surface roughness for the polishing/deburring process. Through further modeling of the relation between the contact stress and the friction force, a control method is developed for controlling the polishing force as well as the spindle speed. This control method is further extended by integrating an on-line sensor forming a closed-loop control for the deburring process. Finally, a design method is presented for the design of a toolhead with two directional compliances, i.e., axial and radial, for active force of the polishing/deburring process. The proposed methods have been tested on a robotic polishing/deburring system developed at Ryerson University.

See also: 1.4 Review of Gear Finishing Processes

References

1. Pessoles, X.; Tournier, C. Automatic Polishing Process of Plastic Injection Molds on a 5-Axis Milling Center. *J. Mater. Process. Technol.* **2009**, *209*, 3665–3673.

2. Roswell, A. *Modelling for Contact Stress Control in Automated Polishing* (MSc thesis); Toronto, ON: Ryerson University, 2004.
3. Rososhansky, M. *Coverage Based Tool-Path Planning for Automated Polishing Using Contact Mechanics Theory* (MSc thesis); Toronto, ON: Ryerson University, 2010.
4. Rososhansky, M.; Xi, F. Coverage-Based Tool Path Planning for Automated Polishing Using Contact Mechanics Theory. Special Issue on Adaptive Manufacturing *SME J. Manuf. Syst.* **2011**, *30*, 144–153.
5. Zhou, X.; Xi, F. Modeling and Predicting Surface Roughness of the Grinding Process. *Int. J. Mach. Tool. Manu.* **2002**, *42*, 969–977.
6. Xi, F.; Zhou, X. Modeling Surface Roughness in the Stone Polishing Process. *Int. J. Mach. Tool. Manu.* **2005**, *45*, 365–372.
7. Schey, J. A. *Introduction to Manufacturing Processes*; McGraw-Hill Book Company: New York, NY, 1987.
8. *SPI Finishing Guide*; Available from: www.moldpolishingc.come/Spi.html (accessed March 1, 2016).
9. Xi, F.; Liao, L.; Mohemad, R.; Liu, K. A Tripod-Based Polishing/Deburring Machine. In *Smart Devices and Machines for Advanced Manufacturing*; Wang, L., Xi, F., Eds.; Springer-Verlag: London, 2008; pp. 189–218, ISBN 978–1–84800–146–6.
10. Roswell, A.; Xi, F.; Liu, G. Modeling and Analysis of Contact Stress for Automated Polishing. *Int. J. Mach. Tool. Manu.* **2006**, *46*, 424–435.
11. Liang, L. *Modeling and Control of Automated Polishing/Deburring* (Ph.D. thesis); Toronto, ON: Ryerson University, 2008.
12. Liao, L.; Xi, F.; Engin, S. Robotic Deburring Based on On-Line Burr Measurement. In *Burrs – Analysis, Control and Removal*; Aurich, J. C., Dornfeld, D., Eds.; Springer-Verlag: Berlin; Heidelberg, 2009; pp. 213–220. ISBN# 9783642005671.
13. Liao, L.; Xi, F.; Liu, K. Modeling and Control of Automated Polishing/Deburring Process Using a Dual-Purpose Compliance Toolhead. *Int. J. Mach. Tool. Manu.* **2008**, *48* (12–13), 1454–1463.
14. Petz, B. *Design Analysis and Testing of a Radial-Axial Hybrid Active Force Compliant Tool Head for Deburring Turbine Engine Components* (MSc thesis); Toronto, ON: Ryerson University, 2011.
15. Kroeker, J. *Design Analysis & Testing of an Enhanced Radial-Axial Hybrid Compliant Deburring Tool* (MSc thesis); Toronto, ON: Ryerson University, 2014.
16. Arruda, E. M.; Boyce, M. C. A Three Dimensional Constitutive Model for the Large Stretch Behavior of Rubber Elastic Materials. *J. Mech. Phys. Solids.* **1993**, *41* (2), 389–412.

1.6 Precision Grinding, Lapping, Polishing, and Post-Processing of Optical Glass

Yaguo Li, Qinghua Zhang, Jian Wang, and Qiao Xu, Fine Optical Engineering Research Center, Chengdu, China
Hui Ye, Xiamen University, Xiamen, China

© 2017 Elsevier Inc. All rights reserved.

1.6.1	**Grinding/Lapping of Optical Glass**	154
1.6.1.1	Loose-Abrasive Grinding	154
1.6.1.1.1	Conventional loose-abrasive grinding	154
1.6.1.1.2	Unconventional loose-abrasive grinding	157
1.6.1.2	Fixed-Abrasive Grinding	158
1.6.2	**Polishing of Optical Glass**	159
1.6.2.1	Loose-Abrasive Polishing	159
1.6.2.2	Fixed-Abrasive Polishing	162
1.6.2.2.1	Fixed-abrasive pad polishing	162
1.6.2.2.2	Fixed-abrasive pellet polishing	162
1.6.2.3	Nonabrasive Polishing	164
1.6.3	**Post-Processing of Optical Glass**	166
1.6.3.1	Wet Chemical Post-Processing	166
1.6.3.2	Dry Post-Processing	167
1.6.4	**Summary**	167
Acknowledgments		168
References		168

1.6.1 Grinding/Lapping of Optical Glass

Grinding is a fundamental process in precision manufacturing where glass is machined to desired surface form and surface roughness is gradually decreased as well. Two sorts of grinding techniques, namely loose-abrasive and fixed-abrasive grinding are available at present to machine glass workpiece. Each type of grinding has a number of embodiments, which are presented in this section.

1.6.1.1 Loose-Abrasive Grinding

1.6.1.1.1 Conventional loose-abrasive grinding

Grinding, which is realized on most occasions in the form of loose-abrasive grinding, is the first step to achieve precision manufacturing of glass. The abrasives, usually harder than glass, for example, SiC, alumina, diamond, etc., are mixed with water and supplied intermittently onto the copper/cast iron laps engraved with regular V-shaped or flat-bottom grooves. The abrasives roll and/or slide against on the surface to fracture and plow glass surface, resulting in material removal and leaving a latent cracked layer.[1]

Material removal rate (MRR), one of the most important aspects in manufacturing, is found to be affected by several factors in loose-abrasive grinding, including supply of abrasives, abrasive size, relative speed, and pressure between glass and grinding tools, etc. The supply of abrasive slurry affects MRR. It is found that increasing the supply of abrasives can result in increased MRR but excessive supply may not necessarily lead to greater MRR, that is to say, there exists an optimum abrasive supply value in excess of which MRR will level off. The optimum supply is a minimum abrasive supply at which the maximum MRR is achieved during grinding of glasses. The optimum supply depends on abrasive size and grinding machines used as well as glass properties to be ground. The phenomenological results apply to various grades of abrasive size and most types of abrasives. Generally speaking, the maximum MRR is greater for coarser abrasives than finer ones and the corresponding optimal supply of abrasives is basically smaller for finer abrasives. The number of the particles of abrasives taking part in material removal will shrink as the supply of abrasive is cut down, so the MRR will also descend accordingly. On the other hand, decreasing the number of particles undertaking the external loading will increase the load upon a single particle of abrasives participating in material removal and therefore the probability of pulverizing the loaded particles, making the size of abrasives smaller, which will also decrease the MRR since smaller abrasives, in general, induce less MRR. **Figure 1** shows variation of MRR as a function of abrasive supply. MRR increases with supply of abrasives, but excessive supply does not increase MRR and there exists an optimum value. The value for coarse abrasives is greater than fine abrasives.

Relative slurry concentration (the ratio of abrasive weight to water weight) also plays an unignorably important role in MRR. MRR is clearly dependent on the relative concentration of abrasives. The MRR appears to increase sharply when the inverse of the ratio is elevated from zero and then slowly falls in loose-abrasive grinding. It is more conspicuous for larger abrasives. Higher concentration will give rise to higher MRR, but further increase in concentration does not get much higher

 doi:10.1016/B978-0-12-803581-8.09152-9

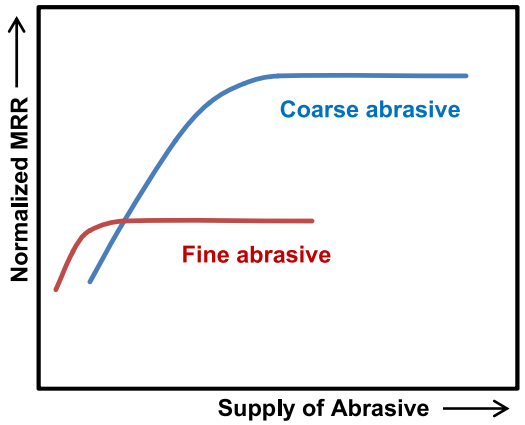


Figure 1 MRR vs. abrasive supply. Too much supply of abrasives does not mean greater MRR. MRR plateaus as abrasive supply exceeds a certain value.[1]

material removal. On the contrary, too high concentration will result in decreased MRR during loose grinding. The results indirectly imply the significant role of water in grinding process and there is a peak value of MRR in the plot of MRR versus concentration. Hence it is suggested to find out the most appropriate concentration and optimal abrasive supply before using a machine for loose-abrasive grinding. The variation of MRR with the concentration of abrasive is presented in Figure 2. The MRR first rises steadily with the concentration of abrasives and decreases for over-concentrated slurry.

The load and relative speed directly dominates MRR. According to well-known Preston's formula,[2] MRR is linearly proportionate to the pressure and relative speed between glass and lapping tools.

$$MRR = kPv$$

where P is the pressure, v is the relative speed, and k is an all-purpose coefficient. k may be decomposed into the following major factors: slurry concentration, abrasive size, abrasive properties, glass properties, properties of grinding tools, etc. MRR is in linear relation to the load exerted onto grinding lap on the condition that the supply of abrasive slurry is sufficient. Increasing the load means the need for increased abrasive supply, in which case the linear relationship also holds. Otherwise, MRR may not increase and even decrease when raising the load on grinding lap. However, MRR may not further rise linearly when load and velocity exceeds a threshold.

Abrasive size has overwhelming effect on MRR in grinding process. Opticians usually use coarse abrasives to elevate MRR and fine abrasives to obtain smooth surface that is ready for polishing process. Loosely speaking, the smaller the abrasives used, the smoother the resultant surface, the less the MRR (for abrasives of the same materials) and the shallower the subsurface damage. The size of abrasives (i.e., grade of abrasives) is chosen consecutively smaller in order to strike a balance between MRR and surface quality. MRR under the optimal supply of abrasive slurry is shown to depend directly on abrasive size for various types of abrasives, especially for fine abrasives. Figure 3 shows MRR-abrasive relationship for

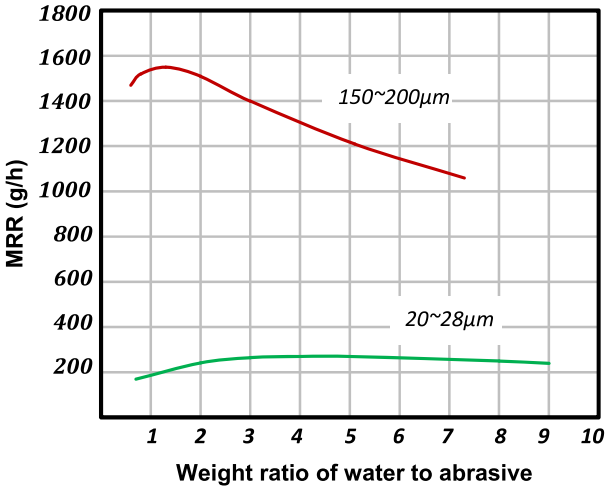


Figure 2 Variation of MRR with concentration of abrasive. An optimal concentration exists at which maximum MRR occurs.[1]

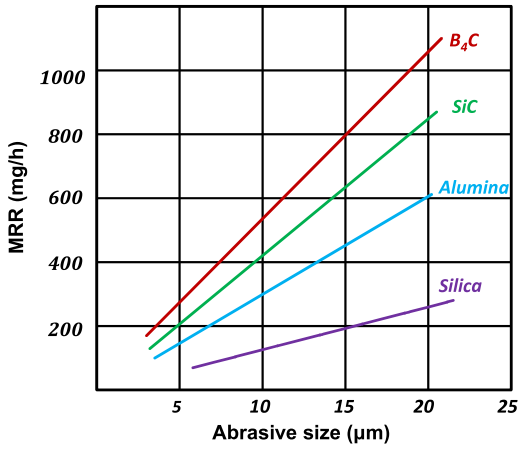


Figure 3 Variation of MRR with abrasive size for various abrasives.[1]

various types of abrasives. MRR is proportional to abrasive size for various abrasives. It is apparent that the properties of abrasives used in grinding process severely exert a big influence on MRR. The hardness of abrasives seems to correlate well with MRR. Figure 4 shows the influence of different micro-hardness of abrasives to MRR. Harder abrasives remove glass much faster than softer ones except garnet which exhibits similar MRR as SiC but with much lower hardness than SiC. An interesting phenomenon is found that MRR is much higher at the beginning of the grinding process where smaller grade abrasives begin to be employed to grind the surface of previous step with larger abrasives. Then MRR gradually lowers with grinding time and approaches a steady level. Figure 5 presents the variation of MRR with grinding time. The following may explain the underlying cause: the much deeper subsurface damage by the previous larger abrasive grinding exists on glass surface and the surface is transferred to finer abrasive grinding which makes the severer cracked layer detached from the surface and results in greater MRR. The characteristic cracked layer of finer abrasive grinding will form and the MRR goes stable as finer grinding process proceeds.

This way, greater MRR lasts for some time within the initial several minutes when glass surface is ready for finer grade grinding.

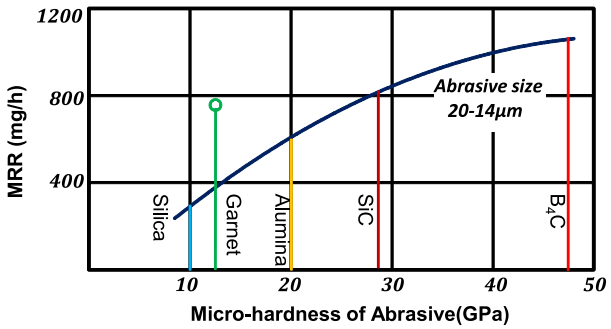


Figure 4 Influence of micro-hardness of abrasive to MRR.[1]

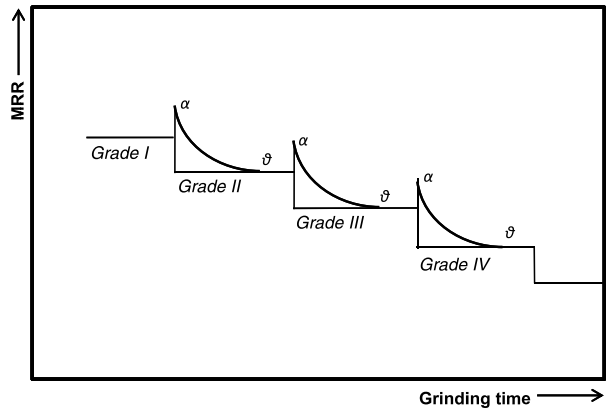


Figure 5 Variation of MRR with grinding time.[1]

Grinding/Lapping tool material also contributes to MRR. A variety of materials have been tested as grinding tool materials for MRR. The tested results plotted in Figure 6 illustrate that MRR is able to be raised by making use of hard grinding plates for soft-to-medium hardness of grinding materials (hardness < 1 GPa). High-hardness grinding materials (hardness > 2 GPa) behave much different from soft-medium ones. The MRR is little influenced by the hardness of grinding materials. The grinding plate will be smoothed when hard grinding plate is utilized, which will cause poor contact with abrasive particles and make the grinding process less effective.

Other two important issues, namely surface roughness and subsurface damage, concern precision manufacturing community, too. The subsurface damage is caused inevitably in the grinding of brittle materials (excluding ductile grinding) because material is removed due to factures in brittle mode. Glass surface is first fractured underneath the contacting point of abrasive with glass when contacting pressure is in excess of the fracture toughness of glass. The factures extend into glass randomly and they are able to grow. Once they intersect one another, glass debris surrounded by the fractures has the potential of detaching from the bulk. In this way, the glass surface is ground away and a surface full of tiny bumps and hollows forms, which can be quantified in terms of surface roughness. Some fractures may not interlace and may be concealed into the glass, which is referred to as subsurface damage. Subsurface damage must be eliminated in many applications because they weaken the strength and worsen the performance of components.

Surface roughness is experimentally verified to be related to the size of abrasives as follows[1]:

$$h \cong \alpha d$$

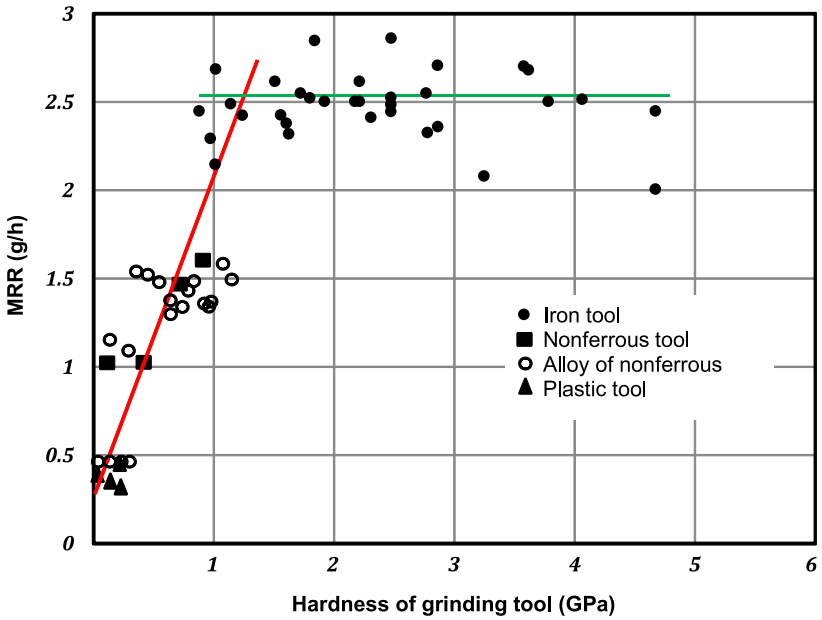


Figure 6 MRR vs. hardness of grinding tool. Greater MRR may be realized by using hard grinding plates. However, extremely hard plates make no difference to MRR.[1]

where h means the peak-to-valley surface roughness, d stands for the maximum size of the abrasive grade utilized to machine the glass, and α is the coefficient, relying on abrasive properties, equal to 0.17 for silica, 0.22 for garnet, and 0.27 for alumina, respectively.[1] This set of plots change much similarly to those of MRR versus abrasive size. It is not difficult to understand that increasing the size of abrasives will make the cracks spread inwards more, which is capable of reaching greater surface roughness and larger MRR as well as deeper subsurface damage. Correspondingly, surface roughness will deteriorate when using hard abrasive to grind glass, similar to MRR with respect to hardness of abrasives. The results for different grinding tools clarify that surface roughness of glass ground by soft grinding tool is slighter than by hard ones, similar to MRR. Plastic tools produce surfaces of lightest surface roughness. But load and velocity make no difference to surface roughness, which is much different from MRR. The mechanism is that surface roughness is governed by the pressure/load exerted on a single particle that is determined by the fracture strength of the particle which relies on the size of the abrasives used. Raising velocity will increase the number of particles per unit time taking part in material removal but does not change the fracture toughness and size. Thus the surface roughness seems not to be affected by velocity between grinding tools and glass workpiece. Likewise, the number of effective particles will rise when increasing load imposed onto grinding tools and furthermore the particles will fracture into smaller ones when the load surpasses the fracture toughness of the particles, leading into more and finer effective particles. Therefore, surface roughness will not be degraded even if the load is elevated. As to subsurface damage, it is found that the depth of subsurface damage is linearly proportional to surface roughness for ground glass, approximately four times peak-to-valley surface roughness in loose-abrasive grinding of glass.[1]

1.6.1.1.2 Unconventional loose-abrasive grinding

Ultrasonics has been used for cleaning for many decades and extended into the field of manufacturing. Abrasives are accelerated via fluid media by an ultrasonic generator. Figure 7 illustrates ultrasonic machining mechanism. The energetic abrasives impinge onto the surface of workpiece and induce material removal. The material removal can be realized in the form of cavitation erosion, sliding against the workpiece surface and hammering of abrasives. The MRR is related to ultrasonic power density, the clearance of ultrasonic horn from workpiece, etc. It is a noncontact grinding technique. The surface roughness of machined workpiece is affected by many factors, like the size and hardness of abrasives used, ultrasonic power, and so forth.

Another grinding process involves fluid jet abrasives. Abrasives are either pre-mixed with fluid (e.g., water) and then accelerated to a very high speed through a nozzle (over tens of m s^{-1}) or entrained and accelerated by a high-pressure jet.[4] The high-speed abrasives impact the glass surface and induce material removal. Because the abrasives are highly energized, the strong force will crack the glass or remove material in ductile or brittle mode depending on the velocity, hardness of abrasives, etc. To get a high-speed jet, the nozzle delivering fluid must be narrow-opened and be wear-resistant to abrasives. Figure 8 shows an abrasive waterjet machining system. MRR and surface roughness is dependent on several parameters, inclusive of hardness and size of abrasives, shape of abrasive grains, flow rate, impinging angles, etc. Generally speaking, harder and larger abrasives will remove material faster, but reach rougher surfaces. Increasing flow rate may also

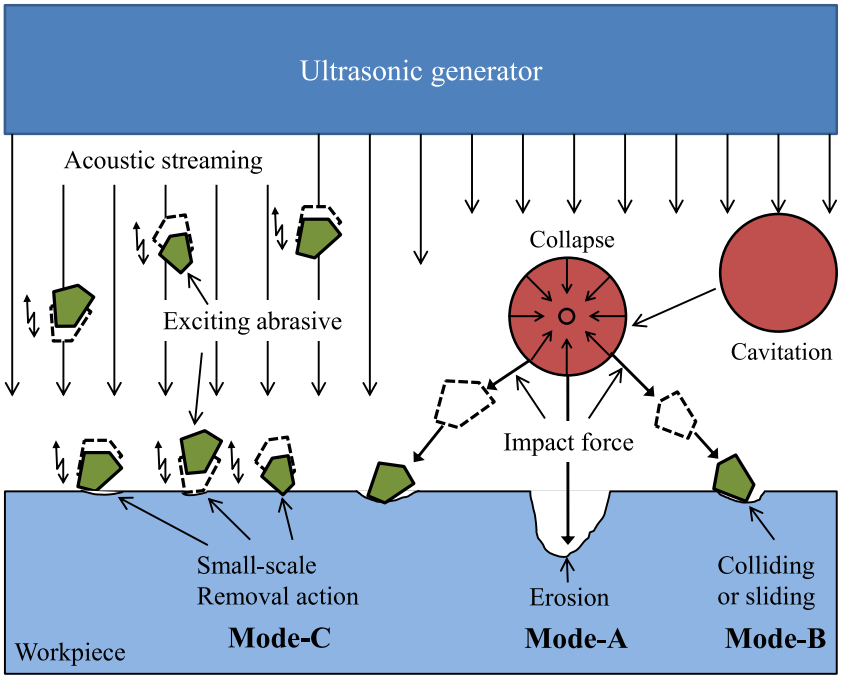


Figure 7 Mechanism of ultrasonic machining: Mode-A, cavitation erosion; Mode-B, collision and sliding due to cavitation collapse force; Mode-C, nanoscale removal by ultrasonics-driven abrasives.[3]

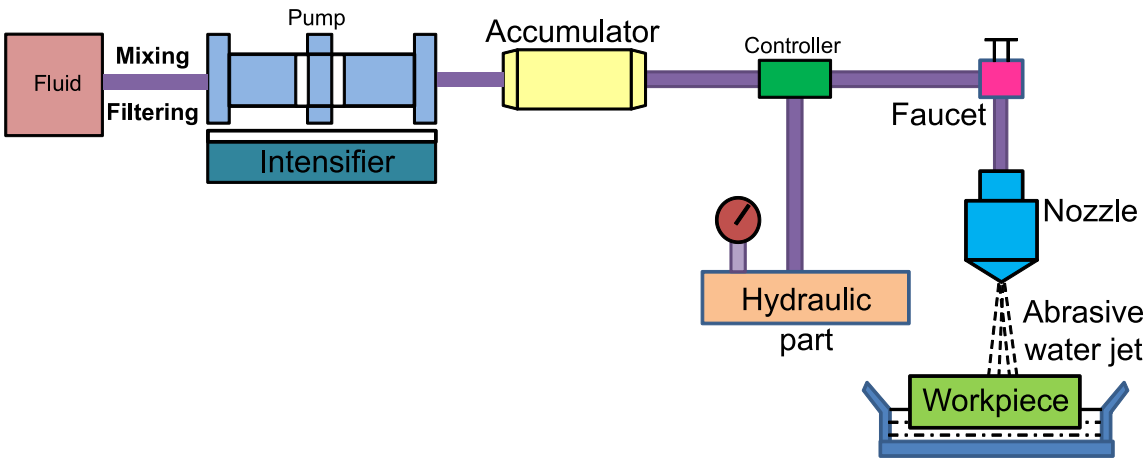


Figure 8 Schematic of an abrasive water jet machining system.[7]

increase MRR and lower surface roughness of workpiece. A potential drawback of the technology is contamination of workpiece surface by abrasives. Fluid jet abrasive polishing can be implemented when soft abrasives like ceria takes the place of hard SiC abrasives. Air abrasive jet grinding is similar to water jet process except that the media through which the abrasives are accelerated is air rather than water, which is sometimes referred to as sandblasting. Sandblasting machines glass surface due to the cracks by particle impacts at high speed. Low speed may not induce material removal and just clean the surface of workpiece. A microscopic photograph of glass surface underwent sandblasting as depicted in **Figure 9** shows that cracks appear around the impact points by abrasives.[5] On many occasions, cracks are undesirable, but a rough surface is preferred by substrates for organic light emitting diodes (OLED) in order to acquire uniform distribution of lighting, which can be realized by sandblasting.[6]

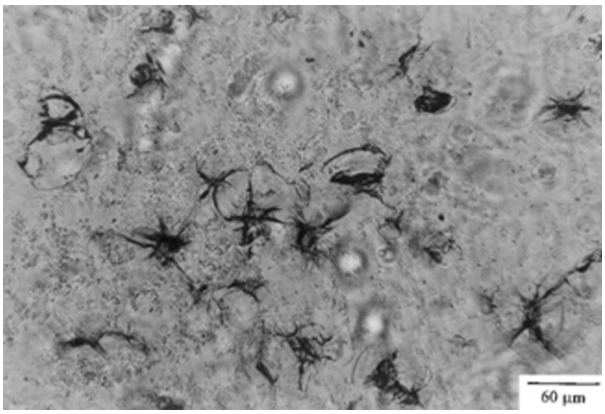


Figure 9 Micrograph of cracks by sandblasting after processing 30 min.[5]

1.6.1.2 Fixed-Abrasive Grinding

Fixed-abrasive grinding involves the use of pellets, pads, or wheels in which hard abrasives are bound. Pellet grinding resembles loose-abrasive grinding, a constant pressure process, except that the abrasives are now fixed into binding materials. The abrasives can be pre-arranged uniformly or even any desired distribution in principle so that material removal distribution can be formatted. The pellets can be formed into plane, spherical surfaces in order to conform to local surface of workpiece. The thing worth pointing out is that surface roughness and subsurface damage is reported to be improved as compared to loose-abrasive grinding and MRR is much better than loose-abrasive grinding. No extra supply of abrasives is needed during grinding process.

Abrasives can be coated onto the side surface of a wheel or top surface of cup wheel (referred to as wheel grinding). **Figure 10** shows a grinding machine with peripheral and cup-wheel grinding heads.[8] There are several types of wheel grinding processes.[9,10] They are categorized as constant feed grinding since feeding rate are prescribed to be constant in these processes. **Figure 11** illustrates various grinding modes.

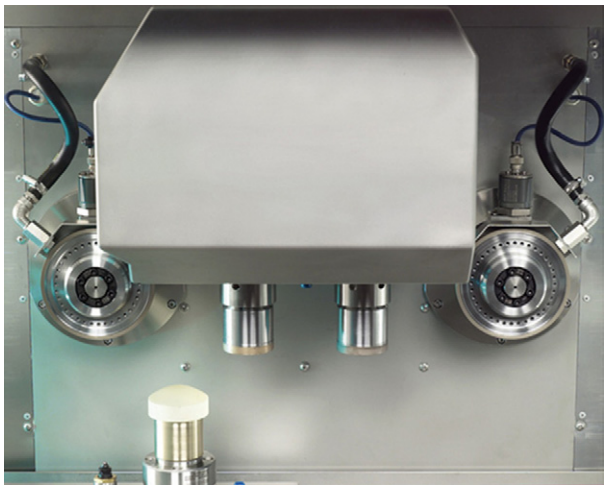


Figure 10 Schneider's SCG100 grinding machine with peripheral and cup-wheel grinding heads.

Many issues are worth research in wheel grinding, for example, bonding materials, abrasive concentration, grinding coolants, wheel wear, etc. Optical community is concerned with surface

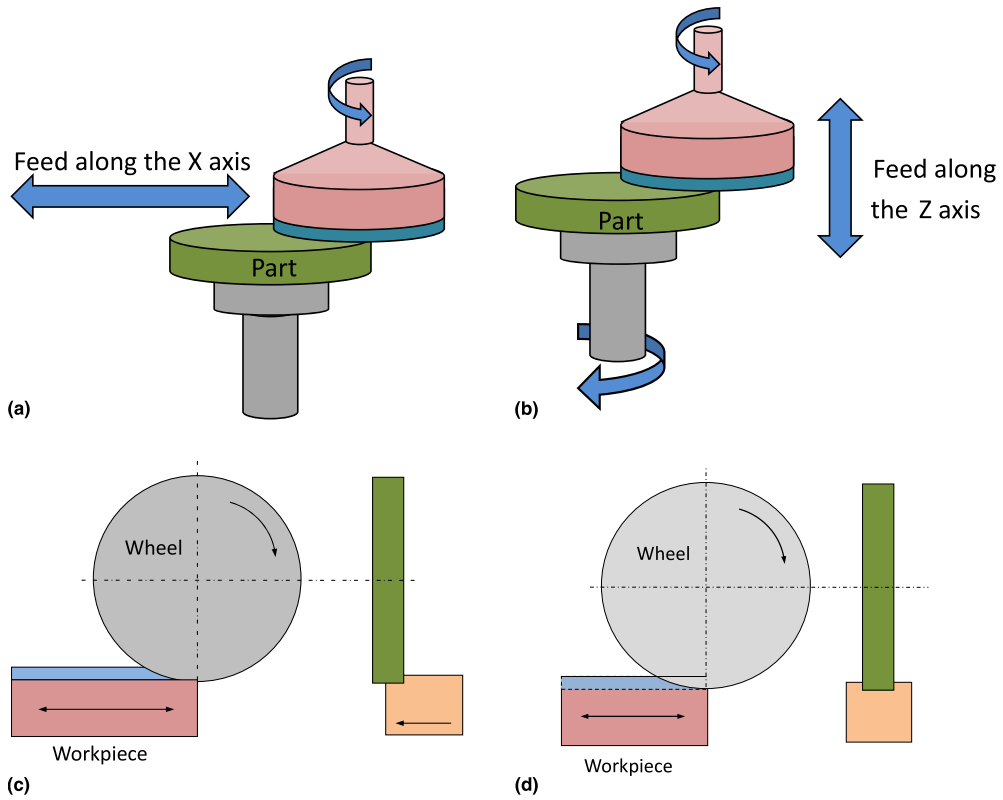


Figure 11 Different grinding modes: (a) vertical feed cup-wheel grinding and (b) horizontal feed cup-wheel grinding[9]; (c) horizontal spindle surface grinder-traverse grinding and (d) horizontal spindle surface grinder-plunge grinding.[10]

quality and subsurface damage of wheel grinding since subsurface damage defines the minimum thickness of material that has to be removed. Schoen[11] compared subsurface damage and surface roughness between fixed-abrasive grinding and loose-abrasive grinding/lapping. They found that surface roughness of fixed-abrasive process is almost one order of magnitude lower than lapping and fixed-abrasive grinding is superior over lapping from the viewpoint of subsurface damage. Figure 12 show that surface roughness and subsurface damage can be remarkably reduced by deterministic microgrinding (DMG). Li *et al.*[12] investigated subsurface damage of fixed-abrasive grinding and found that subsurface damage is predominantly governed by the size of abrasives used while other external factors have marginal effects on subsurface damage; subsurface damage diminishes with decreasing abrasive size in their experiments, unlike the results by Suratwala that smallest abrasives surprisingly increases the subsurface damage depth.[13]

Ultrasonics can be imposed onto grinding wheel or workpiece to get some interesting results. Some results indicate that although machining force is lessened surface roughness may be degraded by incorporating ultrasonics. If the relationship between surface roughness and subsurface damage remains to hold in ultrasonic assisted machining, subsurface damage should be greater upon using ultrasonics, which is undesirable. Electrolytic in-process dressing (ELID) grinding process has successfully applied to the grinding of hard-brittle materials. In ELID grinding, metallic-bonded super-abrasive wheel is capable of being dressed continuously during the course of grinding process so that new abrasives protrude out to grind workpiece smoothly. Because of incessant appearance of new abrasives, MRR can be stabilized and the quality of finished surface is improved compared to conventional grinding process. The grinding force versus stock material removal is much lower than conventional grinding and G-ratio is also much steady and enhanced.[14]

1.6.2 Polishing of Optical Glass

Polishing process follows grinding step to smooth surface to <1 nm and to finalize surface form to specifications. Polishing also relieves subsurface damage left by grinding process. Loose-abrasive polishing is prevailing, but some innovatory technologies have emerged during last several decades. With these novel technologies, polishing process is more deterministic than ever before. These technological innovations as well as conventional polishing processes are introduced in the section.

1.6.2.1 Loose-Abrasive Polishing

Classical loose-abrasive polishing is still widespread on optical shop-floors. It refers to the use of a polishing lap (usually soft metals, pitch, polyurethane, cloth, etc.) on a hardback-plate.[15–17] The polishing lap is pressed against surface of workpiece and relative motion is driven and meanwhile slurry is sprayed. Chemical mechanical polishing (CMP), widely

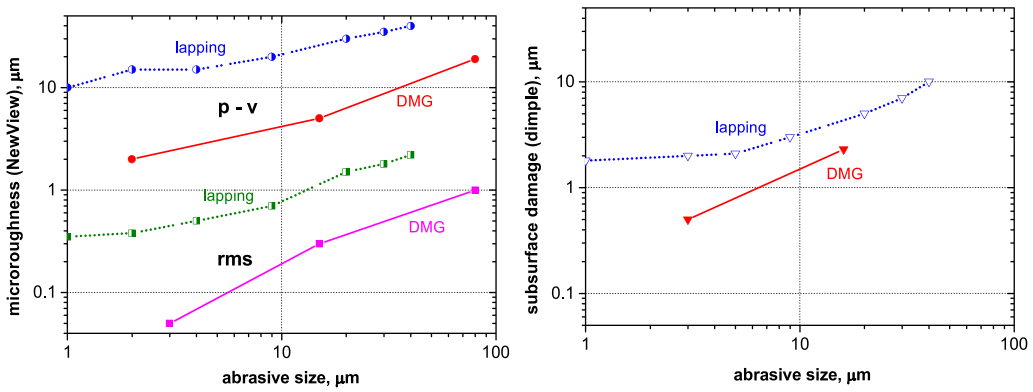


Figure 12 Surface roughness and subsurface damage in deterministic micro-grinding (DMG).[11]

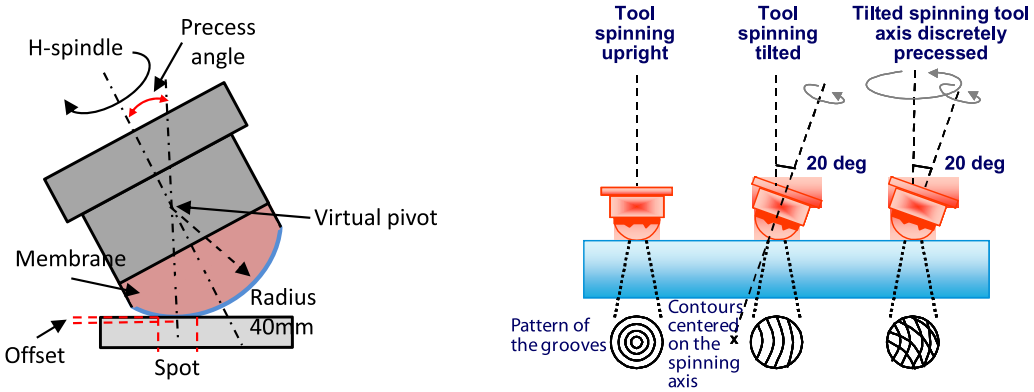


Figure 13 Bonnet polishing head presses with respect to the normal to the workpiece while the head rotates with its axis.[25,26]

used in semiconductor industry, is typical representative of loose-abrasive polishing.[18] In polishing process, chemical action is more prominent than grinding and sometimes is a key factor that makes polishing possible and enables the generation of sub-nanometer smooth surface. Super-smooth surface of glass (surface roughness 0.1 nm) has been obtained by using pitch polishing.[19,20] Modified loose-abrasive polishing, including bowl feed polishing, float polishing and elastic emission machining (EEM) can now produce glass with atomic scale surface.[21–23] Float polishing and EEM are non-contact polishing techniques. As to float polishing, workpiece can be polished due to cavitation in slurry that makes abrasives undulate and thus workpiece can be polished. EEM removes material in elastic mode where abrasives are carried by the motion of fluid induced by the rotation of a polyurethane ball. The abrasives come into contact with glass surface and chemically bond with glass surface. The abrasives are then forced to move owing to the fluid flow and there is a probability that glass bonds will rupture and adhere onto abrasives. In this way, material removal occurs and glass is polished with atomically ultra-smooth surface and damage-free. Polishing tool in EEM has evolved from original sphere type to pipe so that machining efficiency is able to be increased. EEM has been applied successfully to various materials (glass, ceramics, low-expansion glass, silicon, etc.).[24]

Bonnet polishing is a recently developed polishing technique by University College London/Zeeko, UK. **Figure 13** shows working schematic of Bonnet polishing head. The polishing head is an inflated rubber bag onto which membranes (polyurethane pad, etc.) are stuck. The rotation axis of polishing tool is inclined relative to normal line of workpiece so that the material removal function is near Gaussian and the polishing head presses with respect to the normal line of workpiece. The head is compatible with conventional polishing machines. The contacting spot can be varied in size by adjusting the position of the bonnet head. The removal function exhibits excellent linearity with tool speed. This technique can be used to polish flat, spherical, and aspherical surface. The surface roughness of finished workpiece has been down to <0.5 nm (R_a).[27] Afterwards, Zeeko started fluid jet abrasive polishing. Fluid jet polishing is similar to abrasive jet grinding except that soft abrasives are utilized such as ceria.[28] Fluid jet polishing is well suited for polishing complex surface and inner surface otherwise impossible to be reached with conventional methods.[29] The surface roughness of 1 nm is readily achieved.

Field can exert forces onto materials because of the interaction of field-matter. Magnetic materials are subject to forces when they are in a magnetic field. The forces can be taken advantage of to manufacture glass workpiece. This method is named as magnetic abrasive polishing. At first the abrasives and magnetic materials were sintered to produce abrasive of magnetism. Later, conventional abrasives mixed with iron particles were proposed to replace the magnetic abrasives due to complicated procedures of producing magnetic abrasives.[30] During polishing, the magnetos do not come into

direct contact with workpiece and polishing force is conveyed by magnetic particles. The polishing tool is actually flexible and compliant to any surface form. So the merits of magnetic abrasive polishing are the ability to polish internal surface, cylindrical surface, exotic surface, small tube internal surface, microstructures. Figure 14 shows magnetic abrasive polishing where the abrasives are constrained within two magnets. The process is able to polish external and internal surface as well as complex concave and convex surface.

In 1970s, Shlyago *et al.* employed magnetorheological (MR) fluid in the polishing of glass.[31] MR fluid stiffens or solidifies when it is subject to magnetic field and returns to liquid after removing magnetic field. The viscosity of liquid changes significantly with and without magnetic field. The solidified MR fluid can be applied to fabricate glass workpiece. Unlike conventional polishing tool, MR fluid tool will not be worn and is automatically renewed when the magnetic field is alternately turned on or off. This way, the polishing surface of MR tool remains sharp and keeps constant MRR with polishing time. Magnetorheological finishing (MRF) was commercialized by QED Inc., in late 1990s.[32] Figure 15 shows mechanism and process of MRF. When the magnetic field is turned on, magnetic particles lines up and MR fluid stiffens and is sheared to be appropriate to polish workpiece. MRF now can polish a wide range of materials, such as fused silica, BK7, CaF_2, KDP, ZnS, SiC, polymers, etc., and the surface roughness achievable <1 nm. Since it belongs to sub-aperture polishing, precise surface form is possible with few iterations of polishing runs by MRF, indicating MRF is a deterministic polishing process of high-convergence rate. The material removal in MRF is reported to be due to shear stress and the normal load between abrasives and workpiece is little, so subsurface damage that are common in conventional polishing is greatly reduced, which facilitates the enhancement of resistance of optics to laser damage.[33] Figure 16 shows subsurface defects. Few defects are found on the MRF finished surface whilst a great number of pits and tiny scratches are clear on pitch polished surface. The efficacy of improving laser damage resistance has been verified by combining MRF and wet chemical etching or laser conditioning.[34]

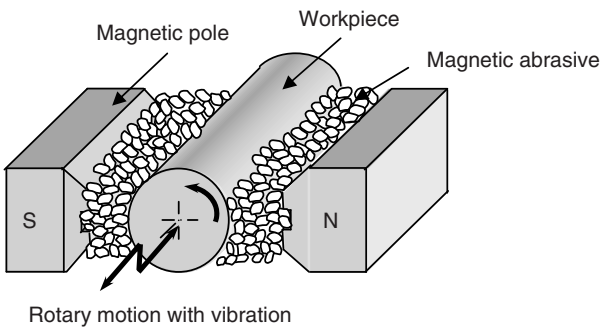


Figure 14 Magnetic abrasive polishing.[30]

Ultrasonics is a common technique in manufacturing society. As it is well known, machining performance, at least MRR, can be improved by introducing ultrasonic vibration into manufacturing processes. The easy-to-implement property adds to the universality of ultrasonics to machining processes. Ultrasonic vibration has been combined with CMP and satisfactory results have been demonstrated.[35] The vibration is superimposed onto a special wafer carrier and the carrier

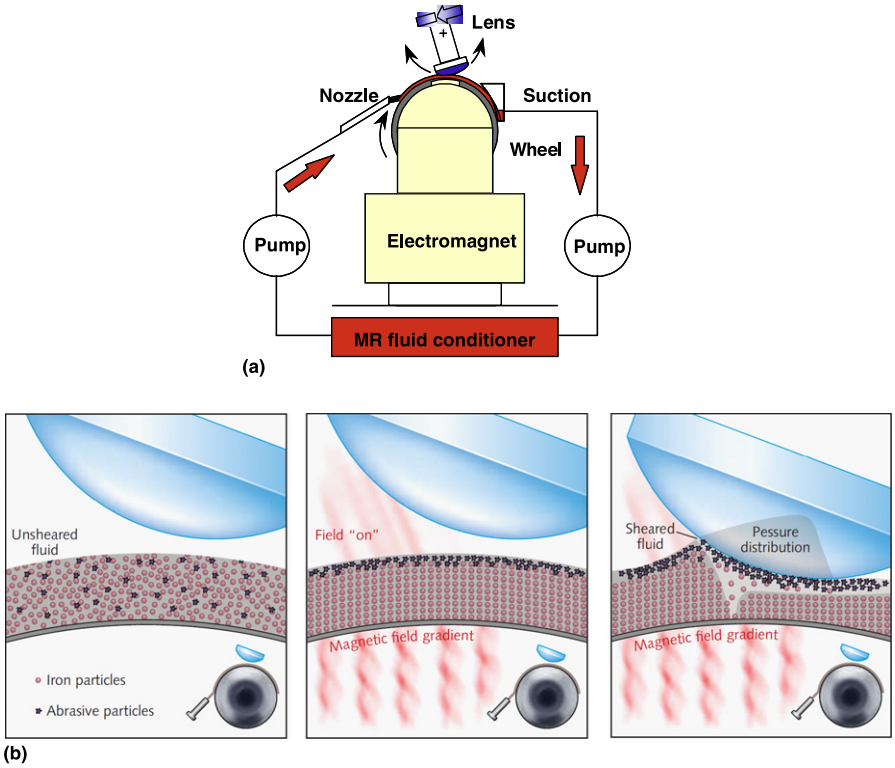


Figure 15 MRF polishing system (a) mechanism of MRF (b) process.[32]

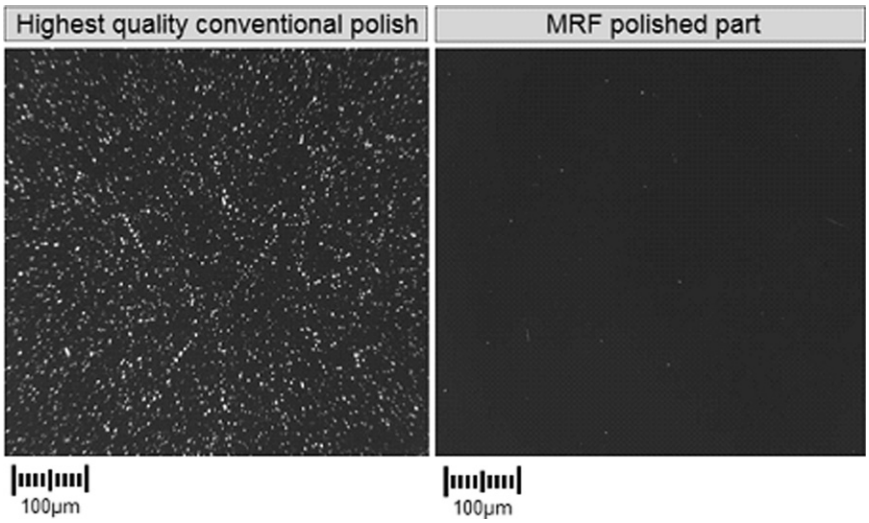


Figure 16 Subsurface defects caused by highest quality conventional pitch polishing and MRF finishing.[34] (with permission of the SPIE).

together with the wafer vibrates in vertical direction. The smoother surface and greater MRR have been confirmed. Although MRR and surface may be improved, expensive ultrasonic apparatus may lag the technique behind.

1.6.2.2 Fixed-Abrasive Polishing

1.6.2.2.1 Fixed-abrasive pad polishing

Loose-abrasive polishing proceeds in the form of pitch lap or pad with continuous or intermittent injection of polishing slurry. The loose-abrasive polishing (well-known as conventional CMP) has been extensively utilized to polish and planarize silicon wafer substrates and patterned wafers.[18] Typical loose-abrasive polishing is comprised of 3 factors: polishing tools, polishing slurry, and workpiece. The process is a three-body system: tool-abrasive-workpiece. The polishing is fulfilled by the interaction among tools, slurry, and glass. The motion of abrasives is stochastic and renders the process unpredictable, resulting in nondeterministic characteristics of the process. Aside from the physical nature of the loose-abrasive process, chemical reaction is considered to be of paramount importance to the polishing processes that employ abrasive softer or equivalent to the workpiece to be polished. This kind of loose abrasive polishing possesses obvious superiorities: generating ultra-smooth surface (surface roughness <1.0 nm), inducing little surface and subsurface damage. However, some innate drawbacks accompany the process, for example, lack of determinism, hard to achieve high uniformity and global flatness, minor 'active' abrasives ($<0.5\%$),[36] etc. Thus bound-abrasive pad polishing (bound-abrasive CMP) was proposed in order to overcome the shortcomings of conventional CMP. In bound-abrasive CMP, polishing abrasives were embedded into polishing pad, made usually of composites like polyurethane, in order to improve polishing performance.

IBM introduced a fixed-abrasive pad to polish magnetic disk substrates more than 30 years ago.[38] The pad is impregnated with diamond abrasives over $>50\%$ by weight. The abrasives are bound within polyurethane and may disintegrate but not detach from the binder during the polishing processes, avoiding the incurrence of deep scratches and the possible erosion of metals. The pad material was further improved to be self-conditioned by using special polymers to keep long-term stability.[39,40] Tani *et al.* developed a kind of high porosity (up to $>$vol. 50%) pad which can relieve pad-loading and accommodate abrasives of wider range of size.[41] Enomoto *et al.* recently proposed a new bound-abrasive polishing tool, consisting of acrylic resin and fiber as well as abrasives.[42] They adopted acrylic resin instead of polyurethane because of high hardness and potential ability to reduce adhesion to abrasives. The results reveal that the surface roughness of finished workpiece is as low as 1 nm for BK7 and the roll-off of the edge is also improved. Noritake Inc., claims a loosely bound-abrasive polishing pad that integrates both the merits of loose abrasive (high MRR, less scratching) and bound-abrasive polishing (smooth polishing).[37] A special type of resin is used as polishing material and the abrasives can be added differently for various substrates as needed. Figure 17 illustrates bound abrasive where the abrasives are loosely held in the pores, which can be silica, ceria, alumina, etc., as needed for various substrate materials.

This type of bound-abrasive polishing is relatively easy to be implemented and do not need much modification to conventional polishing machines. It has demonstrated several superior performances in defect control, flatness as well as controllability. The kind of polishing belongs to more three-body abrasion than two-body system since the abrasives are loosely bound and can be released during the polishing process.

1.6.2.2.2 Fixed-abrasive pellet polishing

If abrasives are firmly bound within a matrix, particularly a hard matrix, the polishing tool is different from the previous type because two-body mode is excited during the polishing process. The matrix can be shaped into a pellet, a grinding wheel or cup wheel, a ring, or bar to form a special distributed polishing tools. Figure 18 shows bound abrasive pad invented by 3M for the application of polishing SOI wafers. The

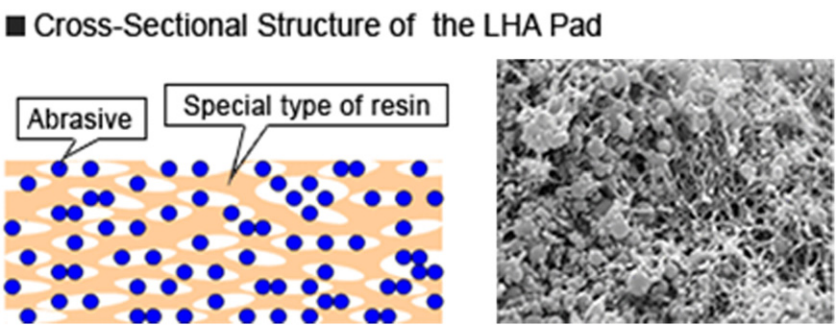


Figure 17 Bound-abrasive pad invented by Noritake.[37]

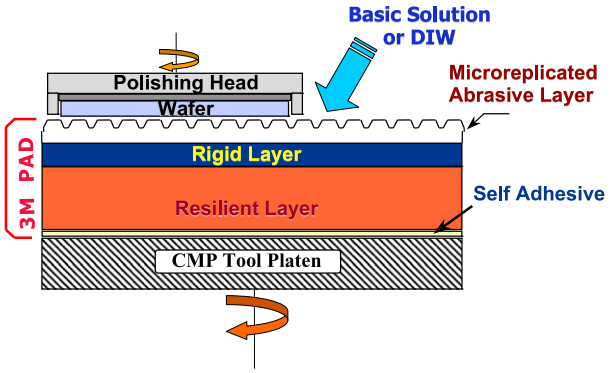


Figure 18 Bound-abrasive polishing pad configuration by 3M.

abrasives are fixed into the top layer that is patterned. The pad is composed of several layers of various materials and the top surface is characterized by molded 'posts' full of abrasives.[43,44] Since the abrasives have been embedded in the 'posts,' there is no need for slurry and only deionized water or basic solution is employed. The possibility of slurry drying and pad glazing is reduced, so the pad dressing is not necessary. It is reported that the planarization rate of bound-abrasive polishing is approximately three times that of conventional loose-abrasive process and the rate is much more stable. Furthermore, better flatness can also be obtained using this type of pads.

Gillman and Jacobs blended ceria and NH_4Cl or alumina in epoxy matrix to fabricate a sort of bound-abrasive polisher in the form of pellets, ring, and a full lap.[45] BK7 glass and fused silica can be polished to RMS surface roughness of ~1 and ~1.5 nm in 30 and 60 min, respectively. The polishers can be applied to polishing flats, spherics as well as aspheric surfaces and is interchangeable in most conventional polishing apparatus. The experiments show that production time may be cut down significantly by means of using the polishers.

Afterwards, Zhou invented a new bound-abrasive polishing tool intended first for the polishing of silicon.[46] The results for silicon substrates validate the effectiveness of polishing technique. Then the technique was extended to polishing quartz glass.[47] The surface can be polished to <0.5 nm (R_a) within 10 min. The process can function in both dry and wet situations with two kinds of polishing tools w/wo micro-pores. Li *et al.* incorporated ultrasonic vibration to bound-abrasive polisher and found MRR can be substantially improved after using vibrations and the surface roughness can be polished down to $R_a \sim 1$ nm.[48,49] Besides external downward load and relative speed, applied voltage and phase difference also impact the MRR and final surface roughness.[50,51] The mechanism of increase in MRR is to some degree explained using a mathematical model.[52] The pulsed impact due to vibrations may play an important role in removing material, especially for originally smooth polished surface. The smooth surface is cracked by the impact of pellet, resulting in degraded surface roughness and much higher MRR as compared to that without vibration.[53] Another reason is reckoned to be the excellent capability of discharging polishing debris that may keep chemical reaction from taking place between abrasives and glass.[52,54] The polishing can proceed with or without water or other liquids, but using water makes the final surface smoother and may lower MRR in some cases.[55] **Figure 19** shows surface roughness of fused silica with bound-abrasive polishing. The vibration-assisted polishing may incur some regular patterns on final surface on the order of nanometers in amplitude and deteriorate surface roughness mildly in most situations.[48–55] Ochiai *et al.*[56–57] have produced bound-abrasive polishing blocks by means of electrophoresis deposition (EPD). The manufactured EPD polishing tools contains ceria or silica and has polished glass to ~1.3 nm. The EPD cannot be used under dry conditions but can progress smoothly in the presence of water and the MRR is fairly high. Bouzid *et al.*[58] fabricated pellets of mixture of ceria and epoxy to polish BK7 glass and found fast reduction in surface roughness to 10 nm RMS within 5 min, very promising in rapid production of precision glass surface.

Another bound-abrasive polishing adopts ice as matrix material to accommodate abrasives.[59] Compared to cast iron and copper, ice possesses low hardness and is able to yield smooth surface of glass. Some materials have been tested for the effects of ice polishing and it shows that silicon wafers can be polished very well of surface roughness, R_a 0.57 nm and R_a 0.37 nm with alumina and ceria abrasives.[60] The copper workpieces were also evaluated to exhibit significant improvement of surface quality.[61] Since the melting point of ice is 0 °C at room pressure, cryogenic apparatus is necessary. With this polishing method, the additional fluid is not needed any more.

Much effect has been made to improve the performance of bound-abrasive polisher and to transfer the technology into industrial applications. Bound-abrasive has succeeded in some respects, for example, the polished surface quality, comparable MRR with loose-abrasive polishing, and the efficient use of abrasive, etc. In addition, slurry is unnecessary any more.

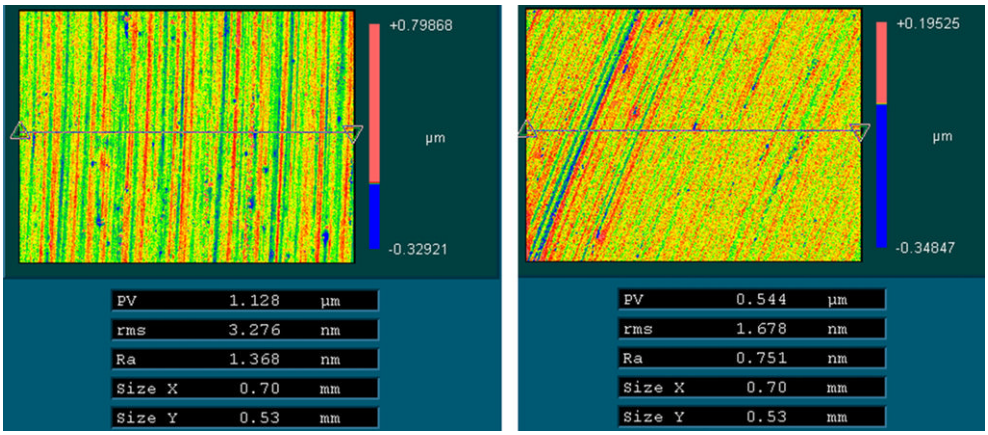


Figure 19 Surface roughness of fused silica with bound-abrasive polishing in dry and wet situations.[55]

The only thing is to supply water in the course of polishing run, which is eco-friendly. The process is much more deterministic and predictable than its loose-abrasive counterpart, but the manufacture of abrasive pellets/polisher is the most pressing issue. The technique will prevail once the cost and the fabrication time is cut down for mass production in that it is easy to implement and is compatible with mainstream machinery.

1.6.2.3 Nonabrasive Polishing

Some methods need not use abrasives to polish glass workpiece and they are listed out in the following. It is known long before that HF solution can etch glass. Therefore, chemical polishing with fluoride solutions is possible.[62] The solution can be HF and HF with additives of strong acids or NH4F. The products of chemical reaction contain gaseous silicofluoride and fluorides of metallic oxides. Polishing rate depends on the concentration of HF and composition of solutions as well as temperature. The subsurface cracks and contamination will be removed, at least ameliorated. Attributed to numerical control, the surface form can be precisely figured if controlled properly and surface roughness of 0.15 nm R_a has been attained for quartz glass with appropriate concentration and compositions.[63]

Plasma etching has been extensively applied in semiconductor for dry etching of thin film and patterning.[64] Most plasma etching processes remove materials due primarily to reactive ion etching (RIE). Researchers of optical fabrication started to employ low-temperature plasma as polishing tool to manufacture glasswares in 1960s and 1970s.[65,66] Glass is polished by chemical reaction in plasma polishing process in plasma-assisted chemical etching (PACE). Material is removed by a restrained reactive gas plasma moving over the surface of workpiece in PACE at low pressure (1–10 Torr). PACE smoothens glass by virtue of chemical reactions and is a type of noncontact polishing technique. Hence no mechanical damage occurs on the finished surface of glass workpiece. For different materials to be polished, different working gases are used. For example, CF_4, SF_6, are potential gases for manufacturing fused silica while for SiC NF_3 may be utilized in PACE.[67] During the course of polishing fused silica, CF_4 will react chemically with SiO_2 to produce gaseous byproduct SiF_4 and CO_2. The PACE will not induce edge distortion because of no solid contact between glass and polishing tool. Moreover, mid-spatial frequency can also be corrected by PACE.[68] Mori *et al.* initiated an atmospheric plasma etching process plasma chemical vaporization machining (PCVM), of which the pressure is nearly 1 atm. **Figure 20** shows PCVM apparatus. Plasma is ignited at the end of a pipe electrode by a RF system in a chamber where workpiece is located. The working gas was chosen to be SF_6 and He for fused silica machining and RF power supply excites plasma.[69] The MRR of PCVM is said $4 \sim 1100$ times faster than conventional smaller pitch polisher when fused silica glass is machined.[69] The attainable surface roughness of final fused silica surface is 0.37 nm RMS.[70] Recently, martial removal rate was further elevated to 0.55 $mm^3\ s^{-1}$ using reactive atom plasma technology.[71] The technology is being used to figure complex surface like continuous phase plate (CPP).[72]

Another nonabrasive polishing involves particle beam. It was found that highly energetic beams can sputter materials as early as 1920s, although it is not until 1960s that ion polishing was proposed.[73,74] The beams are usually composed of ions accelerated to much high energy and bombard the surface of workpiece. The use of energetic ions (e.g., Ar^+ ions) as high as 300 keV to machine materials is referred to as ion beam figuring (IBF). IBF can manufacture a variety of materials, inclusive of optical glass, ceramics, semiconductors, etc. It belongs to noncontact machining techniques and is able to be used for machining very thin workpiece. However, IBF may cause heating and surface roughening and vacuum is necessary, which puts limitations to the application of the technology. Ion beam smoothing will be realized when low-energy ions (<2 keV) is employed. IBS is capable of preparing ultrasmooth surface of <0.2 nm R_q. If ions (Ga^+ ions) are focused by means of electronic and electrical controls and directed toward material surface, focused ion beam (FIB) machining takes place. FIB is able to machine very hard materials and has been applied to dress diamond tools.[75] RAP uses very low-energy beam and processing is mainly by chemical reactions. **Figure 21** shows particle energy for various nonabrasive polishing processes. Different processes use different particle energy. The MRR and surface roughness are found to be relevant to ion energy, incident angle, etc. Ion beam polishing is

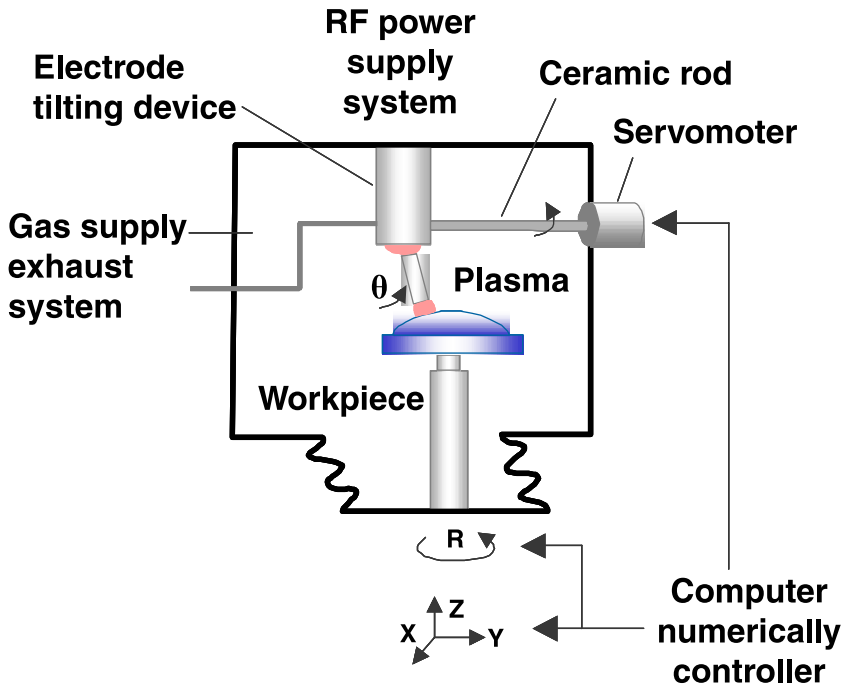


Figure 20 PCVM apparatus.[70]

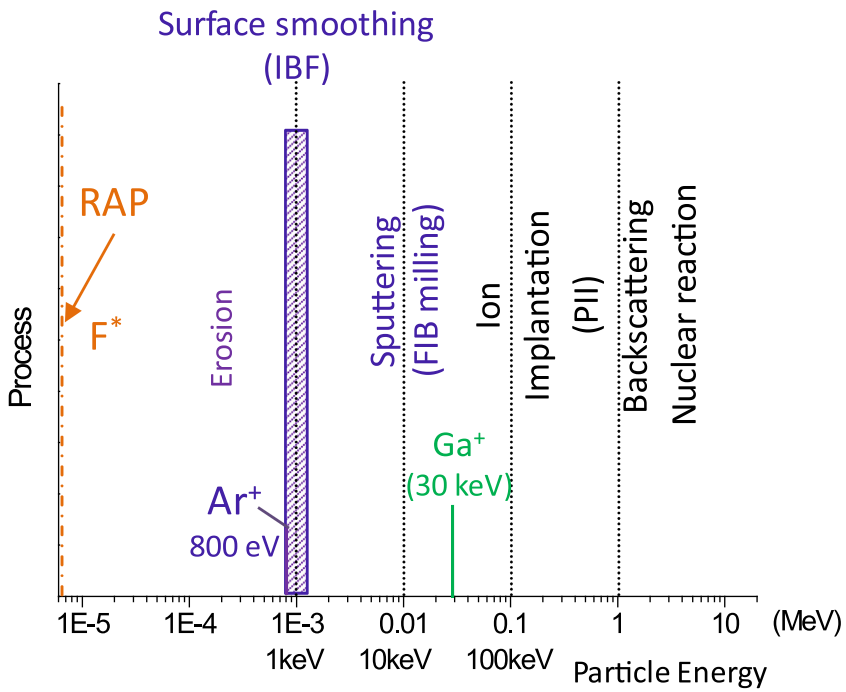


Figure 21 Different processes can be realized with different particle energies.[75]

generally less efficient than plasma polishing in that material is removed physically in ion polishing process while plasma polishing is a chemistry-dependent process.[76] Damage may be incurred in ion polishing process, dependent on ion energy. In general, the lower the energy of the atoms (ions), the less the damage induced by the atoms (ions). But it is difficult to accelerate a single atom (ion) to extremely low energy with conventional technology, so gas cluster ion beam (GCIB) was put forward by Yamada at the beginning of 1990s.[77] Molecular dynamics (MD) simulation demonstrates that material suffers less damage when impinged by larger cluster after undergoing the same acceleration energy.[78] GCIB technology shown in

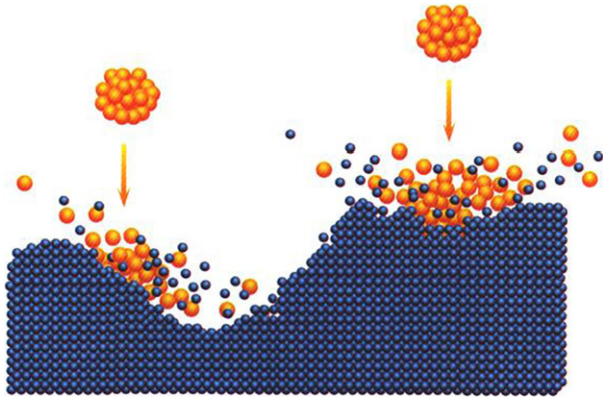


Figure 22 GCIB technology.[81]

Figure 22 accelerates several hundreds or thousands of atoms of singly or doubly charged and thus very low charge-to-mass ratio is practical, which is instrumental in machining material on atom-scale. GCIB ions are composed of a cluster of hundreds or thousands of atoms which are loosely bound. They splinter into smaller cluster or single atom and sputter atoms of workpiece surface. Subsurface of workpiece is impossible to be damaged since the energy of atoms is much low. The clusters can be formed with a wide spectrum of gases and gas mixtures, such as Ar, Xe, O_2, N_2, CH_4, B_2H_6, ethanol, water, C_{60}, etc.[79,80]

Laser polishing is a type of polishing taking advantage of energy field. Mechanism of laser polishing is thermal effect that softens/melts locally glass material and smoothens the surface because of the viscous flow of glass driven by surface tension. CO_2 lasers are a common tool to polish glass. The first laser polishing, to the best of our knowledge, is carried out by Temple who employed continuous wave CO_2 laser (10.6 μm) to polish fused silica for the purpose of increasing damage resistance of glass surface.[82] Vega utilized CO_2 lasers ($\lambda = 10.6$ μm) to reduce surface roughness of glass of 500–~1 nm.[83] Nowak lately pushed surface roughness down to <1 nm from initial ~1 μm using a well-controlled CO_2 laser of 10.6 μm, enabling the technique a precision polishing process.[84] Cracking in laser polishing may be the most important issue in laser polishing, which is due to thermal stress resulting from localized heating and cooling of glass surface. Xiao researched the effect of thermal stress on cracking during laser polishing of various glasses. They preheated samples to ~400 °C with an oven before laser polishing and the results show that thermal expansion coefficient plays a vital role in cracking glass in laser polishing. Glasses with low-expansion coefficient can be laser polished successfully.[85] Laguarta improved spatial and temporal uniformity of CO_2 laser beam to allow the fabrication of high-expansion coefficient glasses by laser polishing.[86] Nowadays, laser manufacturing is increasingly supplanting conventional techniques thanks to its easy-to-use property and versatility.[87]

1.6.3 Post-Processing of Optical Glass

Aside from surface roughness and surface form, resistance to laser damage is an issue of paramount importance for laser optics. The ultraviolet (UV) damage performance of optics has been an obstacle to the development of high-power giant laser systems. The surface damage threshold of fused optics is far lower than its intrinsic damage threshold. It is generally accepted that defects during the processing of optics account for low damage threshold in UV spectrum. Specifically speaking, cracks due to brittle facture of fused silica surface in grinding and/or polishing, metallic contaminants in the course of polishing and organic molecules in the handling and storage of optics play the most significant roles in the UV-nanosecond-laser induced damage. They therefore, must be eliminated so as to improve the damage resistance of optics. To that end, optics must be post-processed to obtain a clean and damage-resistance surface to meet the rigorous requirements of high-power lasers. Some post-processing methods are summarized in the following.

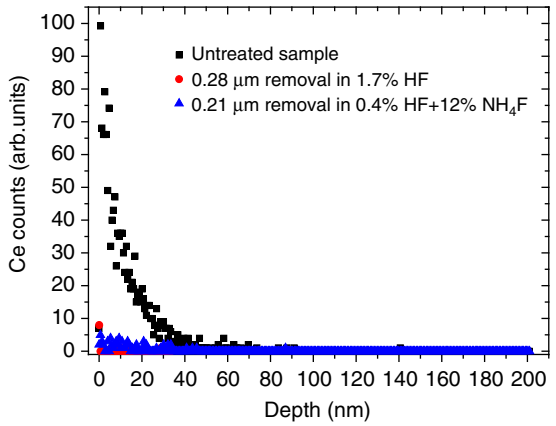


Figure 23 Ce elements on top surface of fused silica as polished and etched slightly with HF solutions.

1.6.3.1 Wet Chemical Post-Processing

It has been known that glass can be eroded by HF solutions at room temperature. Thereby HF solutions are selected to chemically polish glasses as previously stated. In addition, HF can be employed to clean/etch the top surface of polished glass as a thin layer (Beilby layer) covers the finished surface into which contaminants are embedded. Laser damage resistance can rise by means of chemically etching the surface of fused silica because absorptive contaminators in the layer are removed.[88,89] Further etching does not improve damage resistance but decrease damage performance of glass contrarily. There exists an optimum etching thickness where laser damage may be maximized. The thickness ranges from several hundreds of nanometers to several microns.[90–92] More recently, it was shown that nano-crystallites with wide energy gap may be the culprits for laser induced damage even if the bandgap of crystallites is wide enough to be transparent in UV region (355/351 nm). With the etching of glass in HF solutions, contaminants are indeed removed but the possibility for deposition of nano-crystallites also increases, shown in Figure 23.[93] HF etching can slightly clean surface of fused silica. That may account for the up-and-down of laser damage threshold as the etched thickness rises and the nano-crystallites may be the limitations to achieving higher laser damage threshold. As a consequence, dynamic etching was suggested

that ultrasonics and/or megasonics are imposed during the etching of fused silica in order to reduce the deposition of nano-crystallites throughout the course of etching.[94] The method sets a new record in damage threshold of fused silica optical components. **Figure 24** shows damage density as a function of laser irradiance where damage density continues to drop-down after relieving nano-crystalline deposits by ultrasonic/megasonic etching which can trigger laser damage in fused silica.

Glass leaching has been broadly researched by nuclear researchers.[96] Alkaline and alkaline earth ions possess great mobility in glass. Likewise, metallic contamination can be leached out in acid solutions like nitric and chloric acids. The leaching with the mixture of HNO_3 and H_2O_2 can dissolve metallic contamination in top surface of finished fused silica optics. Then the leached optics is subject to laser irradiation at 15 J cm^{-2} Fluence but no damage sites are found and the surface seems intact, indicating leaching is an effective way to reduce metallic contamination and to boost damage resistance of optics. **Figure 25** supports this statement where the surface contains no visible change or modification on leached surface.

1.6.3.2 Dry Post-Processing

Laser processing has been applied to increase damage resistance since 1980s. Temple radiated fused silica surface with a continuous wave CO_2 laser. The irradiated surface was damage-tested by 1064 nm nanosecond lasers. Small spot damage testing results indicate that damage threshold of processed surface is almost the same as the bulk damage threshold. Also, large spot damage tests show ~3–4 times enhancement of damage threshold over original polished surface.[82] Brusasco raster-scanned fused silica with a 10.6 μm CO_2 laser, leading to laser damage threshold from ~10–20 J/cm^2 to 30 J cm^{-2} at 355/351 nm.[98] Brusasco also treated fused silica with 355 nm UV laser of slim lower fluence than damage threshold to reduce damage density of fused silica.[99] Menapace combined MRF, wet etching, and UV laser conditioning to process fused silica optics. The processed optics shows a reduction of four orders in damage density.[33]

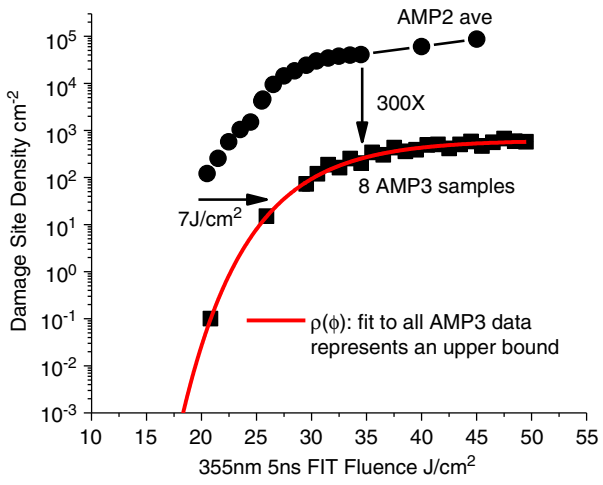


Figure 24 Damage density vs. laser irradiance[95] (with permission of the SPIE).

Ion beams can polish glass as mentioned before and can remove surface contamination as well. Kamimura removed ~90 nm of fused silica with ion beam etching and found that laser damage threshold was doubled from 7 to 15 J cm^{-2} (355 nm, 0.85 ns) when ion-beam voltage was <200 V.[100] Kamimura later chemically etched first and then ion-beam etched fused silica and obtained a threshold 2.8-fold higher than original unprocessed surface.[101,102] Xu and Yan improved damage threshold of fused silica with Ar^+ ion beam etching.[103,104]

Thermal annealing is another way to modify laser damage property of fused silica. Shen annealed fused silica at several temperatures to recover cracks in the surface of optics. The annealing can restore the damage of fractured surface and annealing time and temperature may determine the effect of annealing.[105]

1.6.4 Summary

The entire procedures involved in precision manufacturing of optics for high power laser systems are summarized. Grinding, polishing and post-processing are all indispensable in the fabrication of laser optics, which ensures the usability, operational lifetime, and performance of optics in laser systems. The optical components are first shaped to the desired surface form rapidly in grinding process. However, grinding generally incurs subsurface damage on the topmost surface of ground optics which is detrimental to laser systems and should be removed in subsequent steps. Then polishing process follows in which the surface form and surface quality are further improved and subsurface damage are relieved to designed specifications.

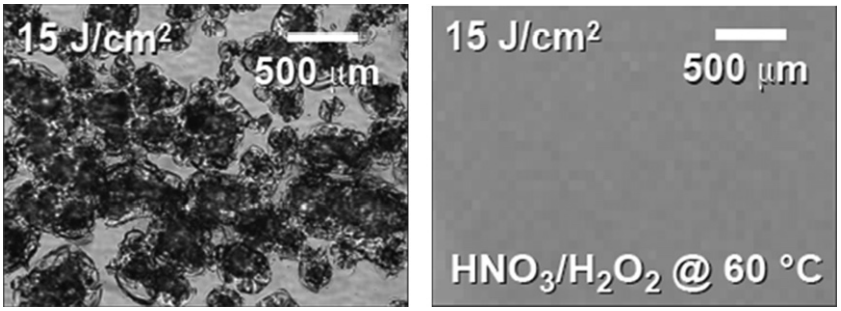


Figure 25 Laser damage morphology with and without HNO_3 leaching[97] (with permission of the SPIE).

Thereafter post-processing mostly enhances the damage performance of optical components to guarantee that the manufactured optical components fulfil the requirements of high power lasers. There are many technologies available in each step. With the development of science and technology, more new techniques will emerge. The intelligent, rapid but atomic controllable and eco-benign manufacturing will be future trends in precision manufacturing.

Acknowledgments

Part of the content by the authors of the references in this chapter is gratefully acknowledged. Some of the work was partially financed by the National Natural Science Foundation of China (No. 51505444), the Foundation of Key Laboratory for Ultra-Precision Manufacturing of China Academy of Engineering Physics (K984–15-JCZ), the Foundation for Development of Science & Technology of China Academy of Engineering Physics (2015B0203032).

See also: 1.5 Robotic Polishing and Deburring

References

1. Kachalov, N. N. *Technology of Grinding and Polishing Sheet Glass* (Mao, W.; Yang, Y., translators); China Industry Press: Peking, 1965 (chapter 3) (in Chinese); Acad. Sci., U.S.S.R: Moscow-Leningrad, 1958 (in Russian).
2. Preston, F. W. The Theory and Design of Plate Glass Polishing Machines. *J. Soc. Glass Technol.* **1927**, *11*, 214–256.
3. Ichida, Y.; Sato, R.; Morimoto, Y.; Kobayashi, K. Material Removal Mechanisms in Non-Contact Ultrasonic Abrasive Machining. *Wear* **2005**, *258*, 107–114.
4. Hashish, M. Comparative Evaluation of Abrasive Liquid Jet Machining Systems. *Trans. ASME, J. Eng. Ind.* **1993**, *115*, 44–50.
5. Bouzid, S.; Bouaouadja, N. Effect of Impact Angle on Glass Surfaces Eroded by Sand Blasting. *J. Eur. Ceram. Soc.* **2000**, *20*, 481–488.
6. Chen, S.; Kwok, H. S. Light Extraction from Organic Light-Emitting Diodes for Lighting Applications by Sand-Blasting Substrates. *Opt. Exp.* **2010**, *18*, 37–42.
7. Khan, A. A.; Ali, M. Y. Application of Silicon Carbide in Abrasive Water Jet Machining. In *Silicon Carbide – Materials, Processing and Applications in Electronic Devices*; Mukherjee, M., Ed.; InTech: Rijeka, 2011; pp. 431–452.
8. Hinn, M.; Pisarski, A. Efficient Grinding and Polishing Processes for Asphere Manufacturing. *Proc. SPIE* **2013**, *8884*.88840I.
9. Blaineau, P.; Laheurte, R.; Darnis, P.; Darbois, N.; Cahuc, O.; Neauport, J. Relations between Subsurface Damage Depth and Surface Roughness of Grinded Fused Silica. *Opt. Exp.* **2013**, *21*, 30433–30443.
10. Malkin, S.; Guo, C. *Grinding Technology: Theory and Applications of Machining with Abrasives*, 2nd ed.; Industrial Press Inc.: South Norwalk, CT, 2008; 372p.
11. Schoen, J. A Tutorial on Deterministic Microgrinding. *Convergence* **1999**, *7*, 1–4.
12. Li, Y.; Zheng, N.; Li, H.; *et al.* Morphology and Distribution of Subsurface Damage in Optical Fused Silica Parts: Bound-Abrasive Grinding. *Appl. Surf. Sci.* **2011**, *257*, 2066–2073.
13. Suratwala, T.; Wong, L.; Miller, P.; *et al.* Sub-Surface Mechanical Damage Distributions During Grinding of Fused Silica. *J. Non-Cryst. Solids* **2006**, *352*, 5601–5617.
14. Ohmori, H.; Katahira, K. Electrolytic In-Process Dressing Grinding of Ceramic Materials. In *Handbook of Advanced Ceramics*; Marinescu, I. D., Ed.; CRC Press: Boca Raton, FL, 2007; pp. 147–178.
15. Li, Y.; Hou, J.; Xu, Q.; Wang, J.; Yang, W.; Guo, Y. The Characteristics of Optics Polished with a Polyurethane Pad. *Opt. Exp.* **2008**, *16*, 10285–10293.
16. Li, Y.; Wang, J. Surface Characteristics of an Optical Component Manufactured with a Polyurethane Lap. *Appl. Opt.* **2009**, *48*, 737–742.
17. Jian, W.; Yinbiao, G.; Yaguo, L.; Qiao, X.; Wei, Y. Research of Optical Flats in Pad Polishing. *Proc. SPIE* **2009**, *7282*. 72820X.
18. Zantye, P. B.; Kumar, A.; Sikder, A. K. Chemical Mechanical Planarization for Microelectronics Applications. *Mater. Sci. Eng. R.* **2004**, *45*, 89–220.
19. Ando, M.; Negishi, M.; Takimoto, M.; Deguchi, A.; Nakamura, N. Super-Smooth Polishing on Aspherical Surfaces. *Nanotechnology* **1995**, *6*, 111–120.
20. Ando, M.; Negishi, M.; Takimoto, M.; *et al.* Super-Smooth Surface Polishing on Aspherical Optics. *Proc. SPIE* **1720**, *1992*, 22–33.
21. Dietz, R. W.; Bennett, J. M. Bowl Feed Technique for Producing Supersmooth Optical Surfaces. *Appl. Opt.* **1966**, *5*, 881–882.
22. Mori, Y.; Yamauchi, K.; Endo, K. Elastic Emission Machining. *Precis. Eng.* **1987**, *9*, 123–128.
23. Namba, Y.; Tsuwa, H.; Wada, R. Ultra-Precision Float Polishing Machine. *Ann. CIRP* **1987**, *36*, 211–214.
24. Kanaoka, M.; Liu, C.; Nomura, K.; *et al.* Processing Efficiency of Elastic Emission Machining for Low-Thermal-Expansion Material. *Surf. Interface Anal.* **2008**, *40*, 1002–1006.
25. Beaucamp, A.; Namba, Y.; Inasaki, I.; Freeman, R. Finishing of Optical Molds to λ/20 by Automated Corrective Polishing. *Ann. CIRP* **2011**, *60*, 375–378.
26. Kim, E. D.; Walker, D. D. Spinning Compliant Tool of Precessions Polishing Technique for Polishing Aspheric Optics. In: *Optical Fabrication and Testing of Optical Society of America*, Tucson, AZ, June 3, 2002. Paper OPDP3.
27. Walker, D. D.; Brooks, D.; King, A.; *et al.* The "Precessions" Tooling for Polishing and Figuring Flat, Spherical and Aspheric Surfaces. *Opt. Express* **2003**, *11*, 958–964.
28. Beaucamp, A.; Freeman, R.; Morton, R.; Ponudurai, K.; Walker, D. D. Removal of Diamond-Turning Signatures on X-Ray Mandrels and Metal Optics by Fluid-Jet Polishing. *Proc. SPIE* **2008**, *7018*, 701835.
29. Kordonski, W. I.; Shorey, A. B.; Tricard, M. Magnetorheological Jet (MR Jet) Finishing Technology. *Trans. ASME, J. Fluids Eng.* **2006**, *128*, 20–26.
30. Shinmura, T.; Takazawa, K.; Hatano, E.; Matsunaga, M. Study on Magnetic Abrasive Finishing. *Ann. CIRP* **1990**, *39*, 325–328.
31. Shlyago, Y. I.; Bibik, E. E.; Evstishenkov, V. S.; Skobochkin, V. E.; Shlyago, O. A. Use of Magnetorheological Liquids with an Abrasive Filler for the Finishing of Glass. *Glass Ceram.* **1978**, *35*, 28–30.
32. Jacobs, S. D. Innovations in Polishing of Precision Optics Part 2. *Convergence* **2003**, *11*, 1–8.
33. Miao, C.; Shafrir, S. N.; Lambropoulos, J. C.; Mici, J.; Jacobs, S. D. Shear Stress in Magnetorheological Finishing for Glasses. *Appl. Opt.* **2009**, *48*, 2585–2594.
34. Menapace, J. A.; Penetrantea, B.; Golinib, D.; *et al.* Combined Advanced Finishing and UV-Laser Conditioning for Producing UV-Damage-Resistant Fused Silica Optics. *Proc. SPIE* **2002**, *4679*, 56–68.
35. Tso, P.-L.; Tung, C. Study on Ultrasonic-Assisted Chemical Mechanical Polishing. *Int. J. Abra. Technol.* **2011**, *4*, 132–139.
36. Bulsara, V. H.; Ahn, Y.; Chandrasekar, S.; Farris, T. N. Mechanics of Polishing. *Trans. ASME, J. Appl. Mech.* **1998**, *65*, 410–416.
37. Noritake. Available from: http://www.noritake.co.jp/eng/company/dev/toryu.html (accessed 19 February 2016).
38. Ottman, J. C.; Shen, J. C. S. Fixed abrasive polishing method and apparatus. US Patent 4393628; 1983.
39. Choi, J. Y.; Do Jeong, H. A study on Polishing of Molds Using Hydrophilic Fixed Abrasive Pad. *Int. J. Mach. Tool. Manuf.* **2004**, *44*, 1163–1169.
40. Kim, H.; Park, B.; Lee, S.; Jeong, H.; Dornfeld, D. Self-Conditioning Fixed Abrasive Pad in CMP. *J. Electrochem. Soc.* **2004**, *151*, G858–G862.
41. Tateishi, T.; Gao, Q.; Tani, Y.; Yanagihara, K.; Sato, H. Development of a High-Porosity Fixed-Abrasive Pad Utilizing Catalytic Effects of TiO_2 on Polyurethane Matrix. *Ann. CIRP* **2006**, *55*, 321–324.
42. Enomoto, T.; Satake, U.; Fujita, T.; Sugihara, T. Spiral-Structured Fixed-Abrasive Pads for Glass Finishing. *CIRP Ann. – Manuf. Technol.* **2013**, *62*, 311–314.
43. Kulawski, M.; Luoto, H.; Henttinen, K.; Suni, I.; Weimar, F.; Makinen, J. Advances in the CMP Process on Fixed Abrasive Pads for the Polishing of SOI-Substrates with High Degree of Flatness. *Mater. Res. Soc. Symp. Proc.* **2004**, *816*, 191–196.
44. Van Der Velden, P. Chemical Mechanical Polishing with Fixed Abrasives Using Different Subpads to Optimize Wafer Uniformity. *Microelectron. Eng.* **2000**, *50*, 41–46.
45. Gillman, B. E.; Jacobs, S. D. Bound-Abrasive Polishers for Optical Glass. *Appl. Opt.* **1998**, *37*, 3498–3505.

46. Zhou, L.; Kawai, S.; Honda, M.; Shimizu, J.; Eda, H.; Yakita, K. Research on Chemo-Mechanical-Grinding (CMG) of Si wafer – 1st Report: Development of CMG wheel. *J. Jpn. Soc. Precis. Eng.* **2002**, *68*, 1559–1563.
47. Zhou, L.; Shiina, T.; Qiu, Z.; Shimizu, J.; Yamamoto, T.; Tashiro, T. Research on Chemo-Mechanical Grinding of Large Size Quartz Glass Substrate. *Precis. Eng.* **2009**, *33*, 499–504.
48. Li, Y.; Wu, Y.; Zhou, L.; *et al.* Chemo-Mechanical Manufacturing of Fused Silica by Combining Ultrasonic Vibration with Fixed-Abrasive Pellets. *Int. J. Precis. Eng. Manuf.* **2012**, *13*, 2163–2172.
49. Li, Y.; Wu, Y.; Wang, J.; Xu, Q.; Yang, W.; Guo, Y. Precision Manufacturing of Fused Silica Glass by Combining Bound-Abrasive Polishing with Ultrasonic Vibration. *Proc. SPIE* **2012**, *8416*, 841606.
50. Li, Y.; Wu, Y.; Zhou, L.; *et al.* Investigation into Chemo-Mechanical Fixed Abrasive Polishing of Fused Silica with the Assistance of Ultrasonic Vibration. *Key Eng. Mater.* **2012**, *523–524*, 155–160.
51. Li, Y.; Wu, Y. Hybrid Polishing of Fused Silica Glass with Bound-Abrasive Polishers in Conjunction with Vibration. *Proc. SPIE* **2012**, *8486*, 84860N.
52. Li, Y.; Wu, Y.; Zhou, L.; Fujimoto, M. Vibration-Assisted Dry Polishing of Fused Silica Using a Fixed-Abrasive Polisher. *Int. J. Mach. Tool. Manuf.* **2014**, *77*, 93–102.
53. Li, Y.; Wu, Y.; Wang, J.; Yang, W.; Guo, Y.; Xu, Q. Tentative Investigation Towards Precision Polishing of Optical Components with Ultrasonically Vibrating Bound-Abrasive Pellets. *Opt. Express* **2012**, *20*, 568–575.
54. Fu, Y.; Li, Y. Glass Polishing with Bound-Abrasive Vibrating Polishing Tools. *J. Optoelectron. Adv. Mater.* **2014**, *16*, 70–75.
55. Zhou, C.; Zhang, Q.; He, C.; Li, Y. Function of Liquid and Tool Wear in Ultrasonic Bound-Abrasive Polishing of Fused Silica with Different Polishing Tools. *Optik* **2014**, *125*, 4064–4068.
56. Ochiai, K.; Nanbu, Y.; Tanaka, F.; Sasaki, T.; Utsunomiya, Y. Study on High-Removal-Rate Mirror Grinding of Optical Glass. *Res. Rep. Saitama Ind. Technol. Cent* **2009**, *7*, 1–5 (in Japanese).
57. Ochiai, K.; Nanbu, Y.; Tanaka, F.; Utsunomiya, Y.; Ikeno, J.; Shibutani, H. Study on Mirror Grinding of High-Performance Glass. *Res. Rep. Saitama Ind. Technol. Cent* **2008**, *6*, 1–4 (in Japanese).
58. Bouzid, D.; Belkhie, N.; Aliouane, T. Optical Glass Surfaces Polishing by Cerium Oxide Particles. *IOP Conf. Ser.: Mater. Sci. Eng.* **2012**, *28*, 012007.
59. Belyshkin, D. V. Using Ice for Polishing Glass and Crystals. *Glass Ceram.* **1966**, *23*, 523–525.
60. Zuo, D.; Sun, Y.; Zhao, Y.; Zhu, Y. Basic Research on Polishing with Ice Bonded Nanoabrasive Pad. *J. Vac. Sci. Technol. B* **2009**, *27*, 1514–1519.
61. Mohan, R.; Babu, N. R. Design, Development and Characterisation of Ice Bonded Abrasive Polishing Process. *Int. J. Abra. Technol.* **2011**, *4*, 57–76.
62. Dyatlova, O. N. Chemical Polishing of Glass. *Glass Ceram.* **1962**, 77–81.
63. Yamamura, K. Development of Numerically Controlled Local Wet Etching. *Sci. Technol. Adv. Mater.* **2007**, *8*, 158–161.
64. Kilby, J. S. Plasma Etch. In *Handbook of Semiconductor Manufacturing Technology*, 2nd ed.; Doering, R., Nishi, Y., Eds.; CRC Press: Boca Raton, FL, 2008; pp. 21.1–21.69.
65. Anderson, G. S.; Mayer, W. N.; Wehner, G. K. Sputtering of Dielectrics by High-Frequency Fields. *J. Appl. Phys.* **1962**, *33*, 2991–2992.
66. Donskoi, A. V.; Dresvin, S. V.; Orlova, M. A.; Osovskii, B. B.; Khait, O. D.; Paushkin, E. V. Plasma Polishing of Surface of Wares Made of Silicate Glass of any Composition. *Glass Ceram.* **1976**, *33*, 162–165.
67. Bollinger, L. D.; Zarowin, C. B. Rapid, Nonmechanical, Damage-Free Figuring of Optical Surfaces Using Plasma-Assisted Chemical Etching (PACE): Part I Experimental Results. *Proc. SPIE* **1988**, *966*, 82–90.
68. Bollinger, D.; Gallatin, G.; Samuels, J.; Steinberg, G.; Zarowin, C. Rapid, Non-Contact Optical Figuring of Aspheric Surfaces with Plasma Assisted Chemical Etching (PACE). *Proc. SPIE* **1990**, *1333*, 44–57.
69. Takino, H.; Yamamura, K.; Sano, Y.; Mori, Y. Removal Characteristics of Plasma Chemical Vaporization Machining with a Pipe Electrode for Optical Fabrication. *Appl. Opt.* **2010**, *49*, 4434–4440.
70. Takino, H.; Shibata, N.; Itoh, H.; *et al.* Fabrication of Optics by Use of Plasma Chemical Vaporization Machining With a Pipe Electrode. *Appl. Opt.* **2002**, *41*, 3971–3977.
71. Fanara, C.; Shore, P.; Nicholls, J. R.; Lyford, N.; Sommer, P.; Fiske, P. A New Reactive Atom Plasma Technology (RAPT) for Precision Machining: The Etching of ULE Optical Surfaces. *Proc. SPIE* **2006**, *6273*, 62730A.
72. Jourdain, R.; Castelli, M.; Shore, P.; Sommer, P.; Proscia, D. Reactive Atom Plasma (RAP) Figuring Machine for Meter Class Optical Surfaces. *Prod. Eng. Res. Dev.* **2013**, *7*, 665–673.
73. Meinel, A. B.; Bashkin, S.; Loomis, D. A. Controlled Figuring of Optical Surfaces By Energetic Ionic Beams. *Appl. Opt.* **1965**, *4*, 1674.
74. Kingdon, K. H.; Langmuir, I. The Removal of Thorium from the Surface of a Thoriated Tungsten Filament by Positive Ion Bombardment. *Phys. Rev.* **1923**, *22*, 148–160.
75. Allen, D. M.; Shore, P.; Evans, R. W.; *et al.* Ion Beam, Focused Ion Beam, and Plasma Discharge Machining. *CIRP Ann. – Manuf. Technol.* **2009**, *58*, 647–662.
76. Somekh, S. Introduction to Ion and Plasma Etching. *J. Vac. Sci. Technol.* **1976**, *13*, 1003–1007.
77. Yamada, I. Cluster Ion Beam Process Technology – 20 Years of R&D History. *Nucl. Instrum. Methods Phys. Res. B* **2007**, *257*, 632–638.
78. Yamada, I. Low-Energy Cluster Ion Beam Modification of Surfaces. *Nucl. Instrum. Methods Phys. Res. B* **1999**, *148*, 1–11.
79. Takaoka, G. H.; Ryuto, H.; Takeuchi, M. Surface Irradiation and Materials Processing Using Polyatomic Cluster Ion Beams. *J. Mater. Res.* **2012**, *27*, 806–821.
80. Seki, T.; Aoki, T.; Tanomura, M.; Matsuo, J.; Yamada, I. Energy Dependence of a Single Trace Created by C_{60} Ion Impact. *Mater. Chem. Phys.* **1998**, *54*, 143–146.
81. Yamada, I.; Matsuo, J.; Toyoda, N.; Kirkpatrick, A. Materials Processing by Gas Ion Beams. *Mater. Sci. Eng. R* **2001**, *34*, 231–295.
82. Temple, P. A.; Lowdermilk, W. H.; Milam, D. Carbon Dioxide Laser Polishing of Fused Silica Surfaces for Increased Laser-Damage Resistance at 1064 nm. *Appl. Opt.* **1982**, *21*, 3249–3255.
83. Vega, F.; Lupon, N.; Cebrian, J. A.; Laguarta, F. Laser Application for Optical Glass Polishing. *Opt. Eng.* **1998**, *37*, 272–279.
84. Nowak, K. M.; Baker, H. J.; Hall, D. R. Efficient Laser Polishing of Silica Micro-Optic Components. *Appl. Opt.* **2006**, *45*, 162–171.
85. Xiao, Y. M.; Bass, M. Thermal Stress Limitations to Laser Fire Polishing of Glasses. *Appl. Opt.* **1983**, *22*, 2933–2936.
86. Laguarta, F.; Lupon, N.; Armengol, J. Optical Glass Polishing by Controlled Laser Surface-Heat Treatment. *Appl. Opt.* **1994**, *33*, 6508–6513.
87. Heidrich, S.; Richmann, A.; Willenborg, E. Development of a Laser Based Process Chain for Manufacturing Free form Optics. *Proc. SPIE* **2012**, *8433*, 84330P.
88. Yoshiyama, J. A Study of the Effects of Polishing, Etching, Cleaving, and Water Leaching on the UV Laser Damage of Fused Silica. *Proc. SPIE* **1998**, *3244*, 331–340.
89. Battersby, C. L.; Sheehan, L. M.; Kozlowski, M. R. Effects of Wet Etch Processing on Laser-Induced Damage of Fused Silica Surfaces. *Proc. SPIE* **1999**, *3578*, 446–455.
90. Ye, H.; Li, Y.; Yuan, Z.; Wang, J.; Yang, W.; Xu, Q. Laser Induced Damage Characteristics of Fused Silica Optics Treated by Wet Chemical Processes. *Appl. Surf. Sci.* **2015**, *357*, 498–505.
91. Ye, H.; Li, Y.; Yuan, Z.; Wang, J.; Xu, Q.; Yang, W. Improving UV Laser Damage Threshold of Fused Silica Optics by Wet Chemical Etching Technique. *Proc. SPIE* **2015**, *9532*, 953221.
92. Wang, J.; Li, Y.; Yuan, Z.; *et al.* Producing Fused Silica Optics with High UV-Damage Resistance to Nanosecond Pulsed Lasers. *Proc. SPIE* **2015**, *9532*, 95320H.
93. Bude, J.; Miller, P.; Baxamusa, S.; *et al.* High Fluence Laser Damage Precursors and Their Mitigation in Fused Silica. *Opt. Exp.* **2014**, 5839–5851.
94. Suratwala, T. I.; Miller, P. E.; Bude, J. D.; *et al.* HF-Based Etching Processes for Improving Laser Damage Resistance of Fused Silica Optical Surfaces. *J. Am. Ceram. Soc.* **2011**, *428*, 416–428.
95. Bude, J.; Miller, P. E.; Shen, N.; *et al.* Silica Laser Damage Mechanisms, Precursors and Their Mitigation. *Proc. SPIE* **2014**, *9237*, 92370S.
96. Bunker, B. C. Waste Glass Leaching Chemistry and Kinetics. *Mater. Res. Soc. Symp. Proc.* **1987**, *84*, 493–507.
97. Miller, P. E. Laser Damage Precursors in Fused Silica. *Proc. SPIE* **2009**, *7504*, 75040X.
98. Brusasco, R. M.; Penetrante, B. M.; Butler, J. A.; Maricle, S. M.; Peterson, J. E. CO_2-Laser Polishing for Reduction of 351-nm Surface Damage Initiation in Fused Silica. *Proc. SPIE* **2002**, *4679*, 34–39.
99. Brusasco, R. M.; Penetrante, B. M.; Peterson, J. F.; Maricle, S. M.; Menapace, J. A. UV Laser Conditioning for Reduction of 351-nm Damage Initiation in Fused Silica. *Proc. SPIE* **2002**, *4679*, 48–55.
100. Kamimura, T.; Nakai, K.; Mon, Y.; *et al.* Improvement of Laser-Induced Surface Damage in UV Optics by Ion Beam Etching ($CsLiB_6O_{10}$ and Fused Silics). *Proc. SPIE* **1999**, *3578*, 695–701.
101. Kamimura, T.; Akamatsu, S.; Yamamoto, M.; *et al.* Enhancement of Surface-Damage Resistance by Removing a Subsurface Damage in Fused Silica. *Proc. SPIE* **2004**, *5273*, 244–249.

102. Kamimura, T.; Akamatsu, S.; Horibe, H.; *et al.* Enhancement of Surface-Damage Resistance by Removing Subsurface Damage in Fused Silica and Its Dependence on Wavelength. *Jpn. J. Appl. Phys.* **2004**, *43*, L1229–L1231.
103. Xu, S.; Zheng, W.; Yuan, X.; Lv, H.; Zu, X. Recovery of Fused Silica Surface Damage Resistance by Ion Beam Etching. *Nucl. Instrum. Methods Phys. Res. B* **2008**, *266*, 3370–3374.
104. Yan, Z.; Liao, W.; Zhang, Y.; *et al.* Optical Characterization and Laser Damage of Fused Silica Optics after Ion Beam Sputtering. *Optik* **2014**, *125*, 756–760.
105. Shen, N.; Miller, P. E.; Bude, J. D.; Laurence, T. A.; Suratwala, T. I.; Wong, L. L. Thermal Annealing of Laser Damage Precursors on Fused Silica Surfaces. *Opt. Eng.* **2012**, *51*, 121817.

1.7 Techniques to Improve EDM Capabilities: A Review

H Marashi, University of Malaya, Kuala Lumpur, Malaysia
AAD Sarhan, University of Malaya, Kuala Lumpur, Malaysia and Assiut University, Assiut, Egypt
I Maher, University of Malaya, Kuala Lumpur, Malaysia and Kafrelsheikh University, Kafrelsheikh, Egypt
M Sayuti, University of Malaya, Kuala Lumpur, Malaysia

© 2017 Elsevier Inc. All rights reserved.

1.7.1	**Introduction**	171
1.7.2	**Brief Overview of the EDM Process**	172
1.7.3	**Ultrasonic Vibration Assisted EDM**	172
1.7.3.1	Tool Vibration	172
1.7.3.2	Workpiece Vibration	173
1.7.3.3	Dielectric Vibration	174
1.7.4	**Dielectric Medium**	175
1.7.4.1	Fluid Dielectric Medium	175
1.7.4.2	Gas Dielectric Medium (Dry EDM)	177
1.7.4.2.1	Near dry EDM	180
1.7.5	**PMEDM**	180
1.7.5.1	Powder Addition to EDM and Micro-EDM	182
1.7.5.1.1	EDM performance improvement	182
1.7.5.1.2	Surface modification	186
1.7.5.2	Powder Mixed Ultrasonic-Assisted EDM	188
1.7.5.3	Powder Mixed Near-Dry EDM	191
1.7.6	**Electrode Modification**	191
1.7.7	**Simulation and Modeling**	193
1.7.7.1	Mathematical Modeling	194
1.7.7.2	Finite Element Method	195
1.7.7.3	Molecular Dynamics Model	197
1.7.7.4	Supporting Vector Machine	197
1.7.7.5	Others	197
1.7.8	**Conclusions**	198
Acknowledgments		198
References		198
Relevant Websites		202

1.7.1 Introduction

Fabrication of machineries with high durability is a necessity for heavy-duty manufacturing components. Electrical discharge machining (EDM) is an advanced manufacturing technique for electrically conductive materials with any hardness property. By converting electrical energy to thermal energy,[1] a series of repeated sparks are generated on the workpiece surface facilitating[2] the material removal through surface material erosion. Great machinability of EDM has introduced this nonconventional technique to several major manufacturing industries included but not limited to aerospace,[3] biomedicine,[4] automotive, die and mold production, etc. Not only prominent cutability of EDM, elimination of any mechanical stress,[5] vibration issues, and chatter[3] are considered as some other advantages.

Despite the complex machining mechanism, EDM abilities have not been fully exploited due to its disadvantages. Primarily, the problem arises from the low material removal rate (MRR) and its inverse relationship with surface quality. Increasing the MRR sacrifices the surface quality of the machined workpiece. Also, repetitive spark between tool and workpiece causes an undesirable erosion of tool material increasing production cost. Furthermore, since the machined surface is exposed to heat and instant cooling by dielectric, surface cracks, heat-affected zone and residual stress[6] are considered as other drawbacks. Hence, presenting new methods to develop EDM capabilities has always been center of attention. Several techniques have been introduced as an enhancement method to boost EDM performance such as implementation of ultrasonic vibration in EDM, alternative tool materials, introducing alternative dielectric mediums, etc.

While there are benefits of EDM, drawbacks hinder widespread implementation of EDM within a majority of groundbreaking fields. To overcome the drawbacks, there are several improvement techniques that have been suggested primarily, the employment of water or gas as dielectric, ultrasonic vibration assisted EDM, and powder mixed electrical discharge machining (PMEDM). Furthermore, modeling and simulation of conventional or enhanced EDM process brings more understanding of the process performance. This chapter thoroughly analyses of accessible investigations through comprehensive

categorization to create a transparent map for further studies on EDM enhancement techniques.

1.7.2 Brief Overview of the EDM Process

The concept of EDM was introduced between World Wars I and II and later, Boris R. and Natalie I. Lazarenko developed the RC-relaxation circuit and servo system unit, which transformed EDM into a dependable machining technique.[7] Currently, EDM performance is considerably enhanced by advanced and sophisticated generators, servo systems, controllers, etc. As shown in Figure 1, a typical electrical discharge machine mainly consists of five core modules: the control unit and generator, servo system, circulation system, dielectric reservoir and pump, machining tank with a workpiece holder, and a X–Y table.

The electrical discharge machine performs the machining action while two important components, the tool and workpiece are immersed in dielectric fluid. Thus, the functionality of EDM is highly dependent on the dielectric fluid characteristics. As shown in Figure 1, the generator initially applies a potential difference between the tool and workpiece while these two components are immersed in dielectric. The servo controller maintains a narrow gap between the tool and workpiece and charging lasts for a predefined period (e.g., 200 μs). Then discharge occurs between the closest points on the tool and workpiece, where the spark strikes the tool and workpiece surfaces and current passes through the gap at a frequency range of 2000–500 000 times per second.[8] The spark's immense heat melts or/and evaporates workpiece material, resulting in the formation of cavities on the surface. Then charge and discharge occur repeatedly to complete machining, printing the electrode's pattern on the workpiece surface. Electrical discharge machines require for the tool electrode to have the exact opposite shape as the one to be printed on the workpiece.

As the EDM material removal mechanism involves surface melting and/or evaporation, no mechanical stress is applied on the workpiece. This feature highlights EDM as a viable tool for manufacturing fragile components, since mechanical stress is avoided on delicate parts with complex structures. Also in microscale manufacturing, EDM produces the finest outcome in terms of precision machining of difficult-to-cut materials with geometrically sophisticated shapes.[9] Machinability of high-hardness conductive materials, mechanical stress elimination, and vibration and chatter problem mitigation[3] are the main advantages of EDM.

1.7.3 Ultrasonic Vibration Assisted EDM

Applying ultra-sonication to different EDM elements appears to substantially boost performance, especially in micro-hole fabrication, as ultrasonic vibration facilitates easier ejection of debris from the gap. The vibration effect on the tool, workpiece, dielectric machining tank, or around the machining area has been shown to produce remarkable outcomes.

1.7.3.1 Tool Vibration

In 1995, the implementation of ultrasonic vibration pulse electro-discharge machining (UVPEDM) positively proved to enable machining of micro-holes in different substrate materials, including engineering ceramics.[10] Pulse discharge in the UVPEDM technique is generated by the ultrasonic vibration of the tool electrode rather than a special pulse generator in traditional EDM. It has been demonstrated that implementing UVPEDM produces higher MRR with low equipment cost and good operational performance. Later, Zhang *et al.*[11] proposed spark erosion by ultrasonic frequency from DC power instead of pulsed power supply where the pulse discharge was produced by the relative motion between the tool and the workpiece and the tool had sinusoidal vibration with ultrasonic frequency, facilitating easier ejection of melted and eroded material from the gap.

Also in drilling small holes ($\leq$1 mm Ø) in low electrical conductivity ceramic-coated nickel alloy, Thoe *et al.*[12] proved that the electrode's ultrasonic vibration achieves higher MRR. However, using a peck drill cycle was necessary to remove debris and maintain the MRR due to the adverse depth/diameter ratio of the hole. By adjusting the operating

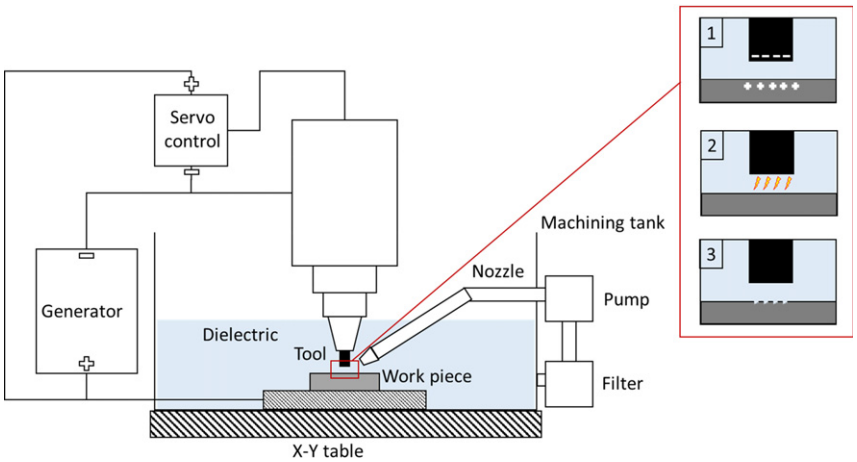


Figure 1 Schematic diagram of electro-discharge machine (1) charging, (2) spark, and (3) cavity formation.

parameters during the transition from ceramic to nickel machining, it was possible to preserve the integrity of any intermediate bonding layer. Although EDM process is suitable for titanium alloys, it is not ideal for small and deep holes because titanium alloys have low heating conductivity and high tenacity.[13] Applying ultrasonic vibration to the tool in micro-hole fabrication by EDM permits drilling holes with a diameter below Ø0.2 mm and depth/diameter ratio of over 15 in titanium alloys.[13] The influence of the tool's ultrasonic vibration on fabricating a micro-hole in nitinol has shown to boost machining efficiency to over 60 times and with no significant increase in electrode wear.[14] Furthermore, numerical simulation revealed that the efficiency improvement is attributed to the strong stirring effect caused by ultrasonic vibration, which results in excellent flushing in the micro-EDM process.

In machining cemented tungsten carbide, tool vibration was observed to significantly increase the MRR compared to conventional EDM at low pulse duration and low discharge current.[15] However, ultrasonic vibration resulted in higher surface roughness and TWR compared with conventional EDM. Additionally, tool vibration in EDM produced higher micro-hardness as well as a thinner heat-affected zone and recast layer on the machined surface.[16] EDM performance was more examined by Wei *et al.*[17] in machining SiC fiber-reinforced SiC matrix composite, which is an advanced ceramic matrix composite (CMC). It was found that implementing tool vibration or deep debris flushing reduced the negative effect of low workpiece conductivity in the EDM process by increasing the MRR and surface quality without increasing the TWR.

A parametric study was carried out on EDM for machining M2-grade high-speed steel using ultrasonic assisted cryogenically cooled copper electrode (UACEDM).[18] As shown in **Figure 2**, the electrode was cooled using liquid nitrogen and ultrasonic vibration was implemented using pulse generator, transducer, and horn. It was revealed that using UACEDM results in lower electrode wear ratio and surface roughness compared to conventional EDM. The electrode shape was also measured and it was found that the shape retention was better in the UACEDM process compared to conventional EDM. Similarly, another investigation[19] addressed the tool wear problem in the EDM process by designing a cryogenically cooled electrode with a tip made of copper (Cu)–titanium carbide (TiC). The performance of the newly formed cermet electrode tip was compared to a conventional copper electrode tip for the UACEDM process. Investigation revealed that the electrode wear ratio and out-of-roundness decreased while MRR and surface roughness increased when a cermet electrode tip was used compared to a conventional tooltip. Furthermore, the crack density and width on the surface machined by cermet tooltip appeared to be less than the specimen machined with a conventional tooltip.[19]

1.7.3.2 Workpiece Vibration

Ultrasonic vibration of workpiece have been taken under consideration by many research studies. Yan *et al.*[20] solved the problem with drilling micro-holes in borosilicate glass by applying ultrasonic vibration to the workpiece to produce precise micro-holes with high aspect ratios (ARs). When drilling a micro-hole with 150 μm diameter and 500 μm depth under appropriate machining parameters, the diameter variations between the entrance and exit could reach about 2 μm. Gao and Liu[21] induced ultrasonic vibration to the workpiece using the setup schematically illustrated in **Figure 3** and revealed that the efficiency increased 8 times compared to conventional micro-EDM for drilling holes in stainless steel with 0.5 mm thickness using a tungsten electrode with 43 mm diameter.

A set of experiments were conducted by Sundaram *et al.*[22] regarding the ultrasonic vibration of the workpiece during EDM. Based on the results, ultrasonic vibration at 60% of the peak power with 3300 pF capacitance appeared to be remarkably effective on achieving the highest MRR. In addition, machining time was found to significantly influence the TWR. Yu *et al.*[23] observed that the planetary movement of the electrode coupled with ultrasonic vibration of the workpiece in EDM micro-hole drilling yielded almost 2.5 times higher MRR than conventional micro-EDM in a high-hardness material. According to the cited research, tool rotation provides an

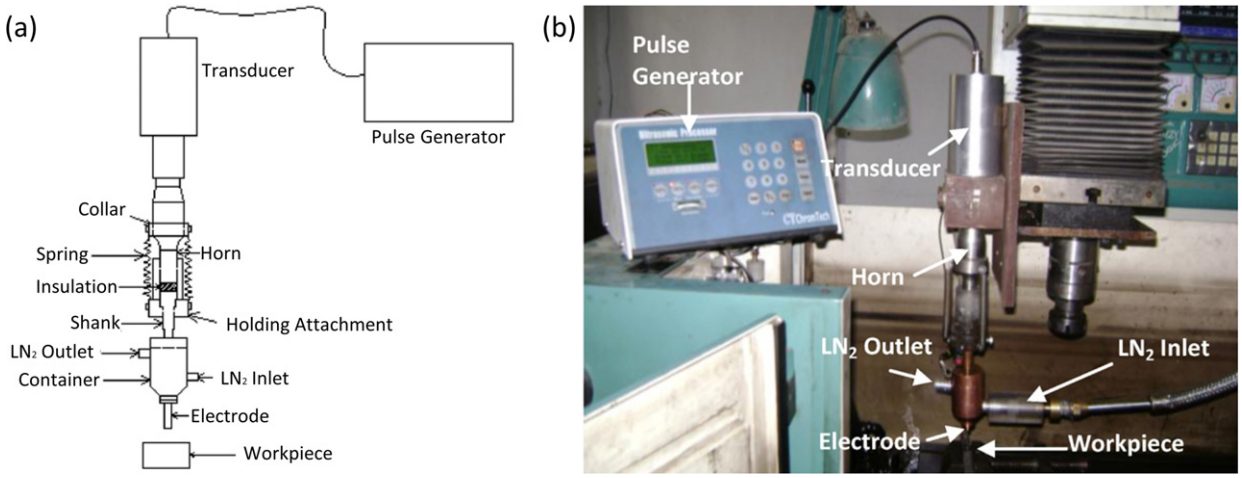


Figure 2 (a) The schematic diagram of vibration assembly and (b) the electrode setup fixed on the electrical discharge machining machine.[18]

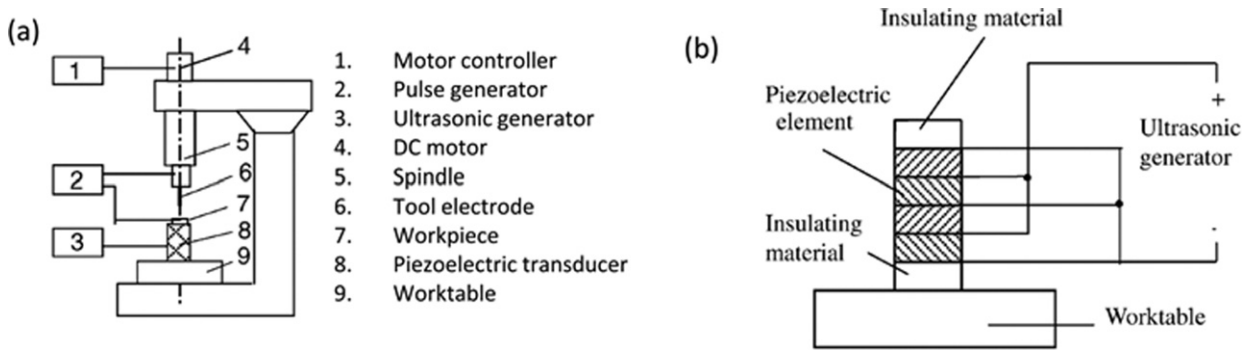


Figure 3 (a) The combined apparatus of ultrasonic and micro-electrical discharge machining and (b) ultrasonic transducer.[21]

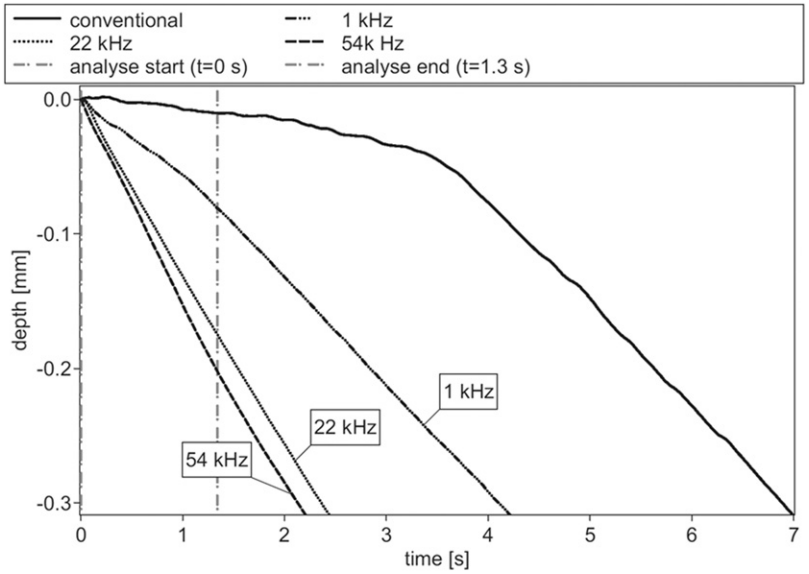


Figure 4 Electrode feed conventional and vibration assisted processes.[24]

uneven gap between the wall of the hole and the electrode, helping the bubbles to scape more easily from the gap. Besides, ultrasonic vibration of the workpiece boosts the penetration of dielectric into the gap, consequently increasing the wetting effect by weakening the boundaries between bubbles and dielectric.

Garn *et al.*[24] studied the effect of vibration on the electrical discharge in the micro-EDM process. Authors explained the micro-EDM boring process as three major subdivisions, the start-up process, the major boring process, and the workpiece breakthrough of the tool electrode. Extensive investigations have shown a delayed start-up process on the workpiece surface for conventional micro-EDM; however, this effect can be reduced by inducing vibration on the workpiece. As shown in Figure 4, the start-up process and machining time is considerably reduced for the vibration assisted EDM process compared with conventional EDM. The cause of this reduction was analyzed by single discharge analysis which also provided a means to investigate the effect of vibration frequency. In a dry EDM process, the implementation of a rotary magnetic field and ultrasonic workpiece vibration were deliberated by Teimouri and Baseri.[25] First, preliminary experiments were carried out to realize the influence of the magnetic field and determine the best tool design from material and geometry perspectives by considering the MRR. Then a parametric study on dry EDM was carried out with a brass tool with two eccentric holes by applying a rotary magnetic field, as selected in preliminary experiments. It was found that the magnetic field has positive effects on MRR and surface roughness and applying ultrasonic vibration results in the achievement of superior MRR.

1.7.3.3 Dielectric Vibration

Besides tool and workpiece vibration, employing vibration around the machining area affects electrical discharge machinability. A system with the ability to apply ultrasonic vibration around the electrode was designed and employed for micro-EDM hole fabrication,[26] which resulted in significant reduction of operational time and tool wear ratio (TWR/MRR). Furthermore, in terms of applying ultrasonic vibration in EDM, Liu *et al.*[27] proposed the production of a hollow nickel microsphere (Figure 5) by placing an ultrasonic transducer around the machining area.

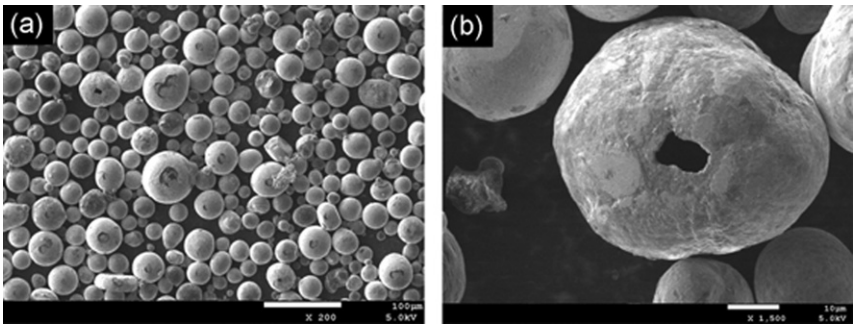


Figure 5 (a) Scanning electron microscope (SEM) micrograph showing a group of spherical microspheres at low magnification under ultrasonic wave; and (b) SEM micrograph of a thin hollowed sphere at high magnification.[27]

1.7.4 Dielectric Medium

The machining gap in EDM is continuously supplied by dielectric medium during the process, which leaves impact of dielectric specifications on the EDM product. It was found that the characteristics of a single discharge are significantly affected by dielectric type,[28] as the energy distribution and plasma diameter are specifically different for different dielectric materials,[29] thus affecting productivity, cost, and quality.[30]

Usually, paraffin-based oil dielectric is used in die-sinking EDM, but it does not provide a healthy machining environment as it releases toxic gases and causes air pollution. Furthermore, hydrocarbon oil decomposes during ignition, discharging harmful vapors such as CO and CH_4.[31] Operating with water or a gas like oxygen[32] have demonstrated to not only have a positive influence on the EDM process but to also provide a healthier working environment for the operators. In addition, the high discharge temperatures decompose kerosene, forming a layer of carbon element that adheres to both machined surface and tool[33] in the machining area. The presence of carbon in the machining gap eventually interrupts the normal discharge, resulting in arcing and short-circuiting.

1.7.4.1 Fluid Dielectric Medium

Dielectric liquid is supposed to form a barrier between the tool and workpiece, cool the machining area and eject debris particles from the machining gap. To find an appropriate liquid for EDM, different types of dielectric fluid have been used and their performance investigated. König and Jörres[34] employed highly concentrated aqueous glycerin solution as dielectric and found that dielectric containing glycerin is more advantageous than hydrocarbon dielectrics when working with long pulse durations and high-pulse duty factors and discharge currents. The glycerin dielectric proved superior to the hydrocarbon medium for roughing under optimized parameters.

Deionized water is one of the best known dielectric liquids for wire EDM due to its advantages over chemical compounds. [35] In order to improve the performance of deionized water as dielectric medium, Leão and Pashby[30] investigated the feasibility of organic compounds with large molecular structure as additives, such as ethylene glycol, glycerin, polyethylene glycol 200, polyethylene glycol 400, polyethylene glycol 600, dextrose, and sucrose. Yan *et al.*[36] modified the titanium workpiece surface by using urea solution in distilled water as dielectric during the process. The nitrogen element decomposed from the dielectric containing urea and migrated to the workpiece forming a hard TiN layer, which resulted in good wear resistance of the machined surface following EDM.

It is found that water-in-oil emulsion as dielectric results in the formation of a recast layer with great surface roughness, thickness, and micro-hardness compared with a recast layer formed in kerosene and deionized water.[37] Both carbide and oxide were identified on the recast layer formed on the samples in water-in-oil emulsion. However, only carbide was detected in the recast layer formed in kerosene. But due to the higher supersaturation of gases in the melted material, the recast layer formed in W/O emulsion possessed more microvoids than that formed in kerosene and deionized water. Zhang *et al.*[28] investigated the material removal characteristics of the EDM process using various dielectrics, including gaseous dielectrics (air and oxygen) and liquid dielectrics (deionized water, kerosene, and water-in-oil (W/O) emulsion). **Figure 6** depicts the craters formed when utilizing various dielectric materials. All geometrical parameters of the craters, including the recast material in the craters, were precisely determined by metallographic method. It appeared that there was a huge difference between the shapes of craters when different dielectrics were implemented. It was found that when using kerosene dielectric, less volume of material was melted compared to other dielectrics.

Jeswani[38] introduced the practice of using water as dielectric[2] and compared the performance of EDM in oil and water. Machining in distilled water exhibited higher MRR and lower wear ratio than in kerosene in a high-pulse energy range. Using distilled water as dielectric resulted in lower machining accuracy, but the obtained surface finish was superior. The machining characteristics of tap water, distilled water, and a mixture of 25% tap and 75% distilled water were inspected by Jilani and Pandey.[39] The results demonstrated that tap water performs more efficiently than deionized water and hydrocarbon oil and there was a possibility of achieving zero electrode wear when using water dielectric and copper tool with negative polarity.

Kruth *et al.*[40] studied the influence of workpiece material, electrode material, and type of dielectric on the surface composition and metallographic phases of the white layer.

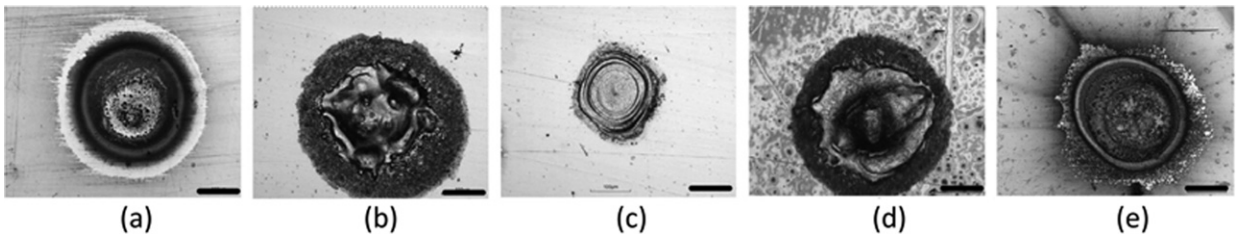


Figure 6 Comparison of the external appearances of craters formed in (a) air; (b) kerosene; (c) deionized water; (d) W/O emulsion; and (e) oxygen. Pulse duration = 105 μs, the length of the scale bar was 100 μm.[28]

Increasing carbon content was observed when using oil dielectric; however, with using water as dielectric, the carbon element formed iron carbides (Fe3C) in columnar, dendritic structures on the surface, which caused decarburization. The white layer contained about 4 times more carbon when using oil dielectric than base material. The white layer of samples machined in water dielectric contained about 50% less carbon than the base material. Also Chen *et al.*[41] verified that utilizing deionized water as dielectric produces higher MRR and lower TWR than kerosene.

Ekmekci *et al.*[42] observed that the amount of austenite phase retained and the intensity of micro-cracks were much less in the white layer of the samples machined in deionized water. In another study, Kang[43] investigated the effects of EDM conditions on the crack susceptibility of a nickel-based super alloy. According to the EDM dielectric fluid and post-EDM processes, such as solution heat treatment, the cracks existing in the recast layer propagated into the substrate when a 20% strain tensile force was applied at room temperature. Unlike the specimens machined in kerosene dielectric, those machined in deionized water after heat treatment underwent oxidation and showed no crack propagation behavior.

Casanueva *et al.*[44] proposed a new power supply for spark erosion based on a series-parallel resonant converter, resulting in great weight and size reduction, which is especially suitable for portable operations. The proposed control attained optimum stable operation when using tap water as dielectric fluid, preventing the generation of undesired impulses and maintaining the distance between the electrode and the workpiece within an optimum, stable range. This technology, initially meant for underwater operations in nuclear plants, may be extended for chip-less metal machining at low cost. Tang and Du[45] used a combination of gray relational analysis and Taguchi method for EDM parameter optimization in machining a Ti–6Al–4V workpiece in tap water dielectric. Under optimum condition, utilizing tap water led to an 87.3% increase in MRR as well as 25.7 and 18.9% reductions in TWR and surface quality, respectively.

Micro-slit EDM using pure water and negative polarity achieved high MRR, low electrode wear, small slit expansion, and low machined burr compared to positive polarity machining.[46] In comparing kerosene with pure water, pure water apparently caused low carbon adhesion to the electrode surface, did not drop the discharge energy and prevents the occurrence of abnormal discharges. Therefore, higher MRR and TWR were detected when using water as dielectric. In continual multi-slit EDM, pure water did not cause carbon element adherence on the electrode surface either, proving the lasting stability of material removal and electrode wear.[46]

Another application with water dielectric achieved complex EDM–electrochemical machining (ECM) machining, where EDM handled the shaping and ECM managed the subsequent finishing using a copper electrode.[47] Two types of EDM and ECM complex machining were taken under consideration: one with a formed electrode, and the other with simple-shape electrode scanning. **Figure 7** demonstrates the formed electrode and its related workpieces after EDM and ECM process, which indicated that after ECM the surface roughness was lowered from 1 μm (**Figure 7(a)**) to 0.6 μm (**Figure 7(b)**). The complex machining with electrode scanning was applied to produce small components of various shapes but without making a formed electrode. The EDM surface of 1 μm average surface roughness (R_a) improved to 0.2 μm R_a by applying ECM. Second, in order to get a smoother surface, a new EDM and ECM-lapping complex machining technology was developed. The surface roughness of a machined hole was improved to 0.07 μm R_a by applying ECM lapping for 2 min. The superior surface finish of the hole was evident with the complex machining technology.

Furthermore, in applying water as dielectric, a hybrid EDM–ECM machine was implemented by Nguyen *et al.*[48] Low resistivity deionized water used as a bi-characteristic fluid enhanced the performance in terms of finishing and machining accuracy. Low feed rate was instigated in the machining technique transition from EDM to EDM. Eventually, the heat-affected zone on the machined workpiece surface was dissolved by the chemical reaction owing to the changing machining characteristics. Thus, a novel hybrid machining process called simultaneous micro-EDM and micro-ECM (SEDCM) was proposed. Additionally, significantly higher surface integrity and dimensional accuracy were achieved when using SEDCM milling.[49] Besides, short voltage pulses localized the dissolution zone for greater precision and remove the micron-thick layer created by discharge craters on the machined surface. The three main factors of SEDCM presented were low-resistivity deionized water, low feed rate and short voltage pulses. SEDCM milling was also investigated.[50] As shown in **Figure 8**, covering the electrode walls with a thin insulating film enabled tool wear compensation during drilling of a blind hole with SEDCM due to the electro-deposition effect during the process.[51]

Using ethanolamine as dielectric medium was signified to facilitate achieving a titanium carbonitride (TiCN) coating by EDM as a result of using a titanium tool electrode and carbon and nitrogen atoms in the dielectric. As shown in **Figure 9**,

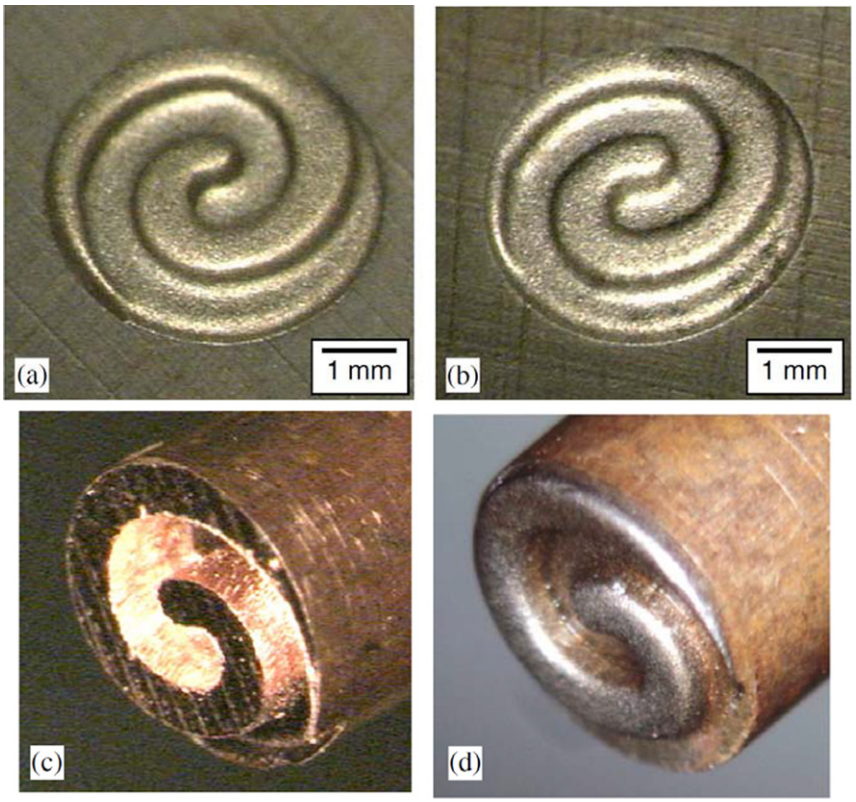


Figure 7 Photo of machined hole: (a) after electrical discharge machining; (b) after electrochemical machining (ECM); and formed electrode: (c) before machining; and (d) after ECM.[47]

a 15 μm thick layer mainly containing a TiC0.3N0.7 phase with fine-grain structure formed, which metallurgically bonded with the steel substrate and enhanced the hardness to 1780 HV for TiCN coating (4 times higher than the TiN coating obtained by magnetron sputtering).[52]

1.7.4.2 Gas Dielectric Medium (Dry EDM)

In 1991, Kunieda *et al.*[32] revealed a new method of improving EDM efficiency by supplying oxygen gas into the gap while using a water-based dielectric. It appeared that the stock removal rate increased due to the enlarged volume of the discharge crater and more frequent occurrence of discharge. Later, dry EDM was introduced as an innovative method, where the fluid dielectric was replaced by a gas medium. This method had positive effects on process performance, such as higher precision and lower electrode wear rate with less residual stress on the machined surface. Govindan and Joshi[53] presented an experimental characterization of material removal in dry electrical discharge drilling technique when using oxygen gas dielectric. According to a six-factor, three-level experiment using L27 orthogonal array, gap voltage, discharge current and electrode rotational speed influenced MRR. In most of the experiments, TWR was found close to zero, however, a predominant deposition of melted and eroded work material on the electrode surface instead of tool wear was evident.

As indicated in dry EDM setup in **Figure 10**, a pipe-shaped tool electrode supplies a pressured gas from the inside to eject debris from the gap. As tool rotation results in higher stabilization and enhanced MRR, a symmetric pipe-shaped tool electrode with inner channel was employed. This method provides a healthier and safer working environment, first by not producing toxic vapor from oil dielectric usage and second, by reducing the risk of fire hazards from flammable oil. Additionally, dry EDM reduces environmental damage as less industrial waste is produced.

Govindan and Joshi[54] presented a comprehensive and quantitative analysis of micro-crack formation, in terms of length, number, and orientation of micro-cracks formed on the machined surfaces in dry EDM. It was stated that average crack length (the best crack factor indicator) was considerably touched by voltage, current, pulse off-time and speed in both, the wall and bottom regions of the dry EDM surface. Furthermore, the causes of surface micro-crack formation were identified as (1) stresses due to contraction of diffused materials on work surface such as tool material (Cu), shield material (Al), carbon (C) and oxygen (O), (2) thermal residual stresses due to temperature gradient between region of sparking and other neighboring region of workpiece, (3) arcing in the interelectrode gap, due to high debris reattachment, and (4) mechanism of sensitization.

Kunieda *et al.*[55] showed that three-dimensional (3D) shapes can be machined very precisely using a special NC tool path that can supply a uniform, high-velocity air flow over the working gap. Furthermore, the MRR was improved as the concentration of oxygen in air was increased due to the heat generated from electrode material oxidation. Kunieda *et al.*[56]

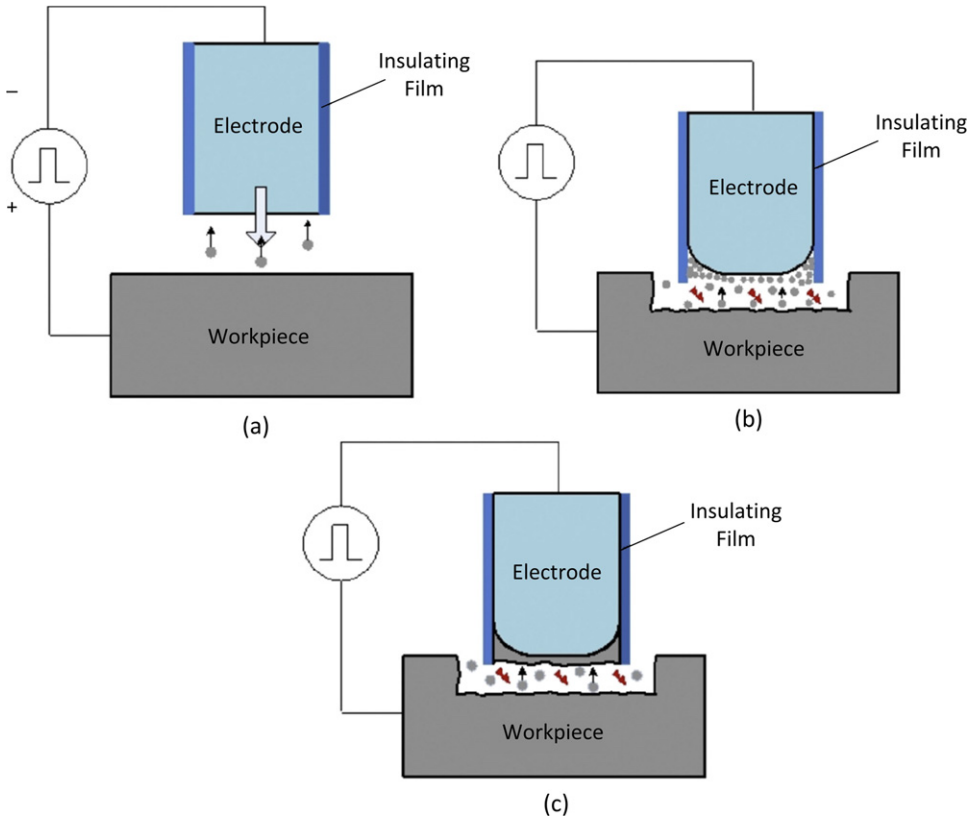


Figure 8 Principle of simultaneous micro-EDM and micro-ECM: (a) electrochemical dissolve, (b) discharge, and (c) discharge and electrodeposition.[51]

described the high-speed EDM milling of 3D cavities using gas as the working fluid. Remarkably small electrode wear and high MRR were obtained, especially when oxygen gas was used in the process. Machining accuracy considerably enhanced when the gas was sucked through the pipe electrode rather than jetted. Yu *et al.*[57] observed that between dry EDM milling, oil EDM milling, and oil die-sinking EDM, and dry EDM milling was the most advantageous for 3D machining of cemented carbide in terms of time and cost. The EDM milling operation with oxygen gas dielectric facilitated higher machining speed and lower TWR than oil EDM milling. In comparing dry EDM with oil die-sinking EDM for machining the same shape using cemented carbide, oil die-sinking EDM exhibited shorter machining time. However, since oil die-sinking requires time for producing electrodes, dry EDM should be more useful in actual production.

Several gaseous dielectric mediums have been proposed for dry EDM application. Roth *et al.*[58] studied process performance concerning MRR using air, CO_2, N_2, and O_2. **Figure 11** demonstrates the measurement of MRR as a function of different flushing gases. The graph shows that O_2 achieved the highest MRR, which is 4 times higher than using air as dielectric, whereas the lowest MRR was produced by N_2. It was evident that the heat energy from oxidation had little effect on the MRR and that the main difference between oxygen and less oxidizing gases was found at different stabilities and time efficiencies of the process.

Although dry EDM has many advantages over conventional EDM, instability and arcing are still serious concerns with the dry EDM process,[59] which have motivated researchers to find solutions for process stability. Kunieda *et al.*[60] presented a piezoelectric actuator with high frequency response to control the gap length in EDM to prevent frequent short-circuit occurrence in dry EDM due to the narrower discharge gap compared with conventional EDM. A hybrid dry EDM process was proposed in a pulsating magnetic field applied tangential to the electric field, to increase the movement of electrons and degree of ionization in the plasma.[61] Implementing the magnetic field in the dry EDM process led to 130% productivity improvement with zero electrode wear compared to dry EDM.

In order to enhance dry EDM process Liqing and Yingjie[62] proposed two methods, first based on oxygen EDM mechanism, a dry EDM approach using oxygen gas mixture followed by performing analysis validation. Second, dry EDM was considered for cryogenically cooled workpieces and the accompanying experiments were prepared. The experimental results showed an increase in the MRR with both oxygen-mixed EDM and cryogenically cooled workpiece techniques along with a decrease in the surface roughness value (R_a) with the latter.

In another study, a thermoplastic composite electrode was used instead of solid graphite to perform fine EDM finishing in air.[63] Employing a thermoplastic composite electrode with air rather than water or oil was efficient, as the peak-valley surface

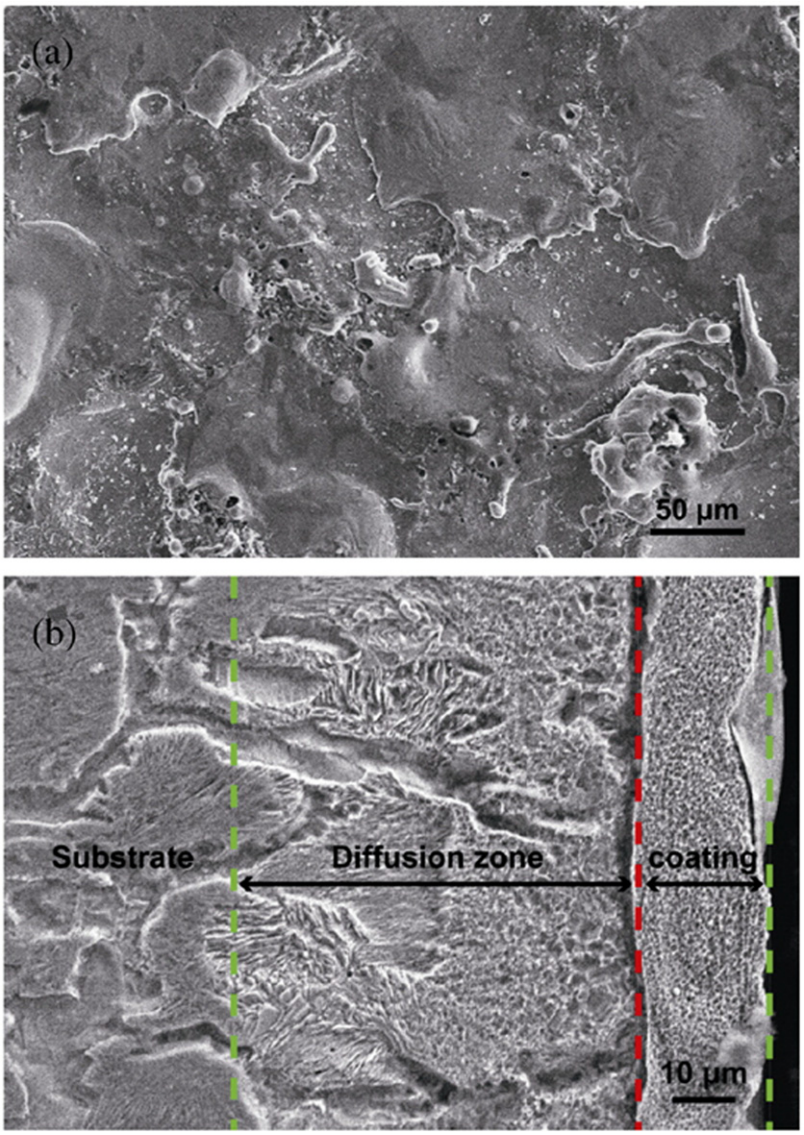


Figure 9 Scanning electron microscope of the top surface (a) and the cross-sectional and (b) morphologies of the deposited coating.[52]

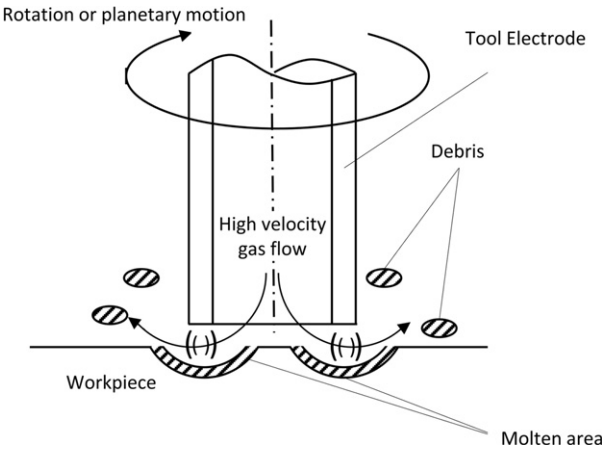


Figure 10 Principle of dry electrical discharge machining.[32]

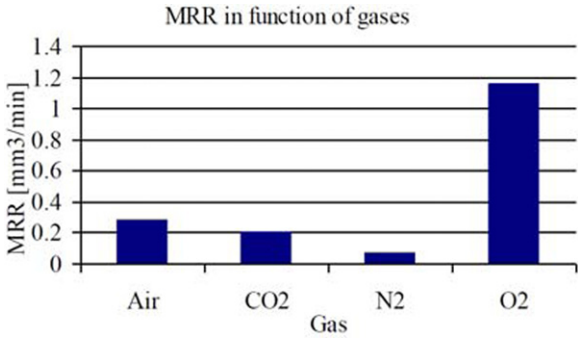


Figure 11 Material removal rate for different flushing gases.[58]

finish of a rough-machined tool steel part is iteratively flattened by 30 μm over three thermoplastic composite electrode forming, and EDM process cycle. Furthermore, abrasive jet

machine (AJM) integrated dry EDM was proposed for dry EDM application, where a pipe-shaped tool electrode supplies the abrasive and dielectric medium.[64] For both 6A and 9A peak current, higher MRR and lower surface roughness were obtained with hybrid AJ-EDM rather than dry EDM. Although increasing the peak current in dry EDM significantly increased the surface roughness, only a moderate increase was detected in the hybrid machining.

1.7.4.2.1 Near dry EDM

Near dry EDM is the EDM process when a mixture of liquid and gas is used as a two phase dielectric fluid where a minimum quantity lubrication (MQL) dispenser is engaged to supply a minimum amount of liquid droplets at a controlled rate to the gap between the workpiece and electrode. Kao *et al.*[65] employed mixture of water and air as the dielectric fluid for near dry EDM. It was indicated that near dry EDM achieves higher MRR, sharper cutting edge, and less debris deposition than dry EDM (Figure 12). In compare of conventional EDM (with liquid dielectric medium), near dry EDM found to obtain higher MRR at low discharge energy with a smaller gap distance. However, due to higher thermal load on electrode, electrode wear increased in near dry EDM. Further, a mathematical model was developed to quantitatively correlate the water–air mixture's dielectric strength and viscosity to the gap distance.

Fujiki *et al.*[66] studied the influence of electrode lead and tilt angles and dielectric fluid flow rate on MRR, tool electrode wear ratio, and surface roughness in near-dry EDM milling process. It was specified that the MRR is linearly proportional to the mass flow rate of air and kerosene mixture, the TWR is inversely related to the mass flow rate of air and kerosene mixture, and the R_a does not have a good correlation with the flow rate of the mixture. Furthermore, a new gap control strategy for five-axis milling using near-dry EDM was presented by Fujiki *et al.*[67] In conventional EDM control strategy only allows the retraction of the electrode in the direction of machining trajectory, which results in inefficient gap control when the electrode is not perpendicular to the workpiece. The new gap controller was capable of retracting the electrode in the direction of its orientation which facilitates more effective expansion of the discharge gap leading to faster recovery of average gap voltage. Experimental results specified a 30% increase in MRR while the TWR and surface roughness were not affected.

1.7.5 PMEDM

Amongst all enhancement techniques, adding powder to dielectric fluid is the most practiced approach in EDM improvement investigations. In PMEDM, adding powder to dielectric in the original circulation EDM system is not a feasible method. One reason is the existence of a filter in the system that may filter out the powder particles, and second, the original EDM circulation system's capacity is too high, which would increase the amount of powder required for the process. Thus, an external circulation system containing a small machining tank with a workpiece holder, pump, stirrer, magnetic filter, pipes, nozzle, etc., enables liquid circulation throughout the process. This circulation system with low dielectric capacity and filtration system enables the constant reuse of powder mixed dielectric (PMD).

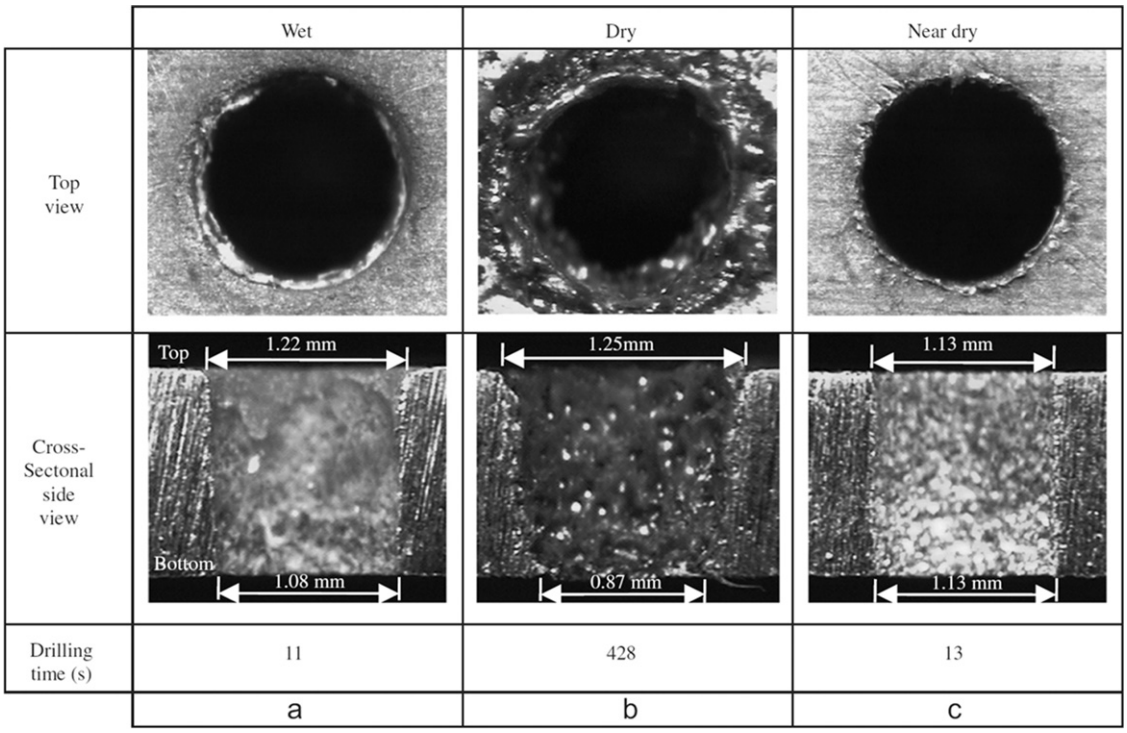


Figure 12 Optical micrographs on holes drilled on 1.27 mm Al6061: (a) wet, (b) dry, and (c) near dry electrical discharge machining conditions.[65]

Figure 13 displays the basic PMEDM dielectric circulation system. The magnetic filter is either placed in the small machining tank or the secondary dielectric reservoir. The powder particles are injected into the process or the process entails filling with the PMD liquid. In order to avoid powder suspension at the bottom of the tank, a stirrer is placed inside the machining tank. In some cases, both the pump and stirrer are located in the same tank in which machining is performed. The distance between the dielectric suction point and nozzle outlet is kept as short as possible (10 in) to ensure the complete suspension of powder in the discharge gap.[68]

To avoid aggregation and sedimentation, and to ensure homogeneous suspension of particles in the dielectric fluid the powder is usually mixed with dielectric by conventional methods like implementing a stirrer in the machining tank[70] or blending the powder with dielectric in advance.[71] With the promising application potential of ultrasonic vibration in EDM, the ultrasonic vibration of the machining tank in PMEDM was proposed to prevent powder suspension during the process.[72]

As shown in Figure 14, in PMEDM, the discharge does not directly strike the workpiece. In fact, the primary discharge

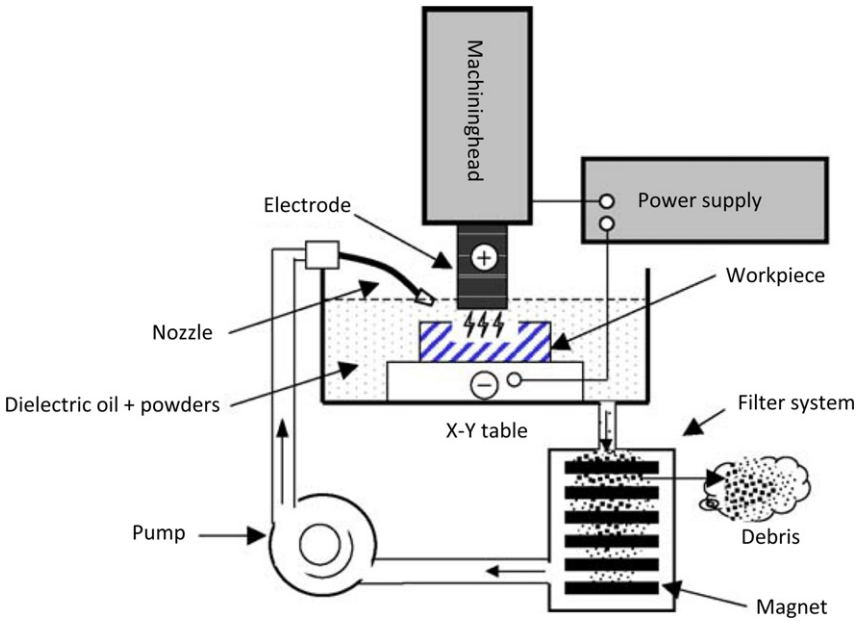


Figure 13 Schematic diagram of a self-designed filter system for the electrical discharge machining process used for the experiments.[69]

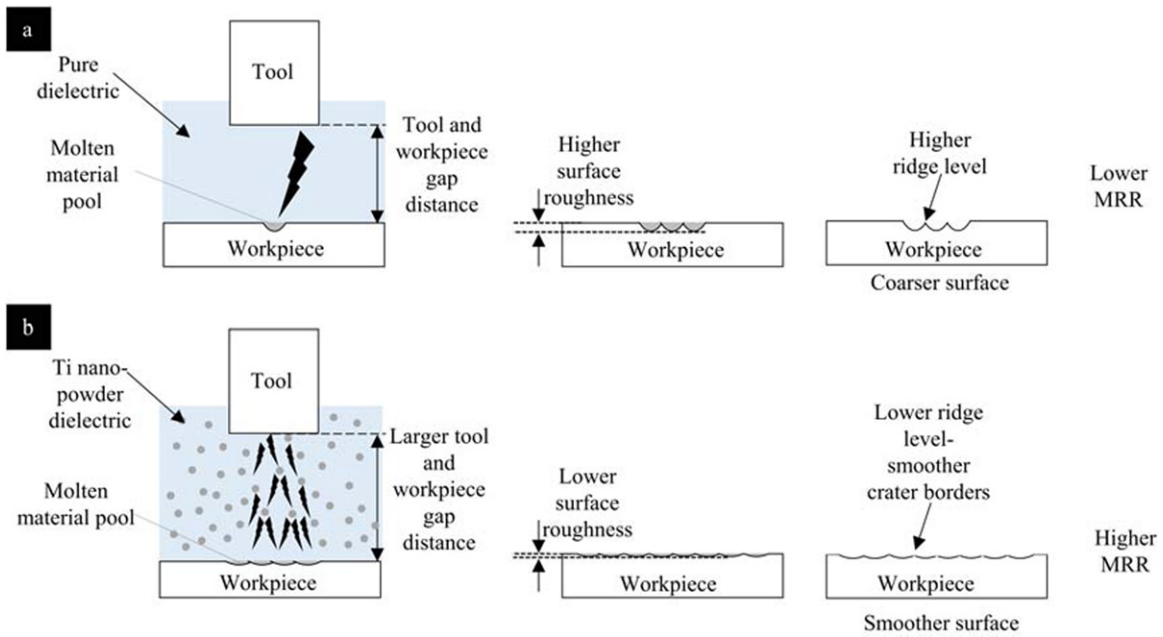


Figure 14 Discharge in (a) electrical discharge machining and (b) powder mixed electrical discharge machining.[76]

occurs between the tool and the conductive powder, after which a wave of diffused discharges hits the workpiece.[73] In the spark gap, powder particles move close to each other to form a chain like structure and build a bridge between the tool and workpiece. This results in declining dielectric insulating strength, leading to higher spark frequency in the gap. It has been proven that adding electrically conductive powder to dielectric increases the gap between the workpiece and tool, leading to energy dispersion and enhanced MRR as well as surface roughness.[2] It has been established that the particles contribute by enlarging the gap between the electrode and workpiece[74] due to the improved dielectric fluid's electrical conductivity.[33] A larger gap results in easier debris ejection from the gap, averting the occurrence of short-circuiting and arcing, subsequently resulting in a more stable machining condition. Greater electrical conductivity triggers more frequent discharges, which results in higher MRR. A larger gap with sparks hitting over the greater distance results in the formation of evenly distributed, 'large and shallow' etched cavities,[75] and ultimately improved surface quality.

1.7.5.1 Powder Addition to EDM and Micro-EDM

Powder particles mixed with dielectric fluid of water or oil in EDM is a common approach to enhance the EDM outcome in terms of machined surface quality as well as machinability. Several powder materials with different particle sizes for machining metallic or ceramic materials have been explored by researchers. Adding powder to dielectric fluid is meant to primarily boost the process by improving the performance factors. The EDM process specification is evaluated using a number of significant parameters like MRR, TWR, and surface quality. Depending on the process and powder specifications, either the machining process is enhanced in terms of process capabilities like increasing MRR or a situation is facilitated whereby EDM is used for new applications like coating. Therefore, research trend in PMEDM and powder mixed micro-EDM is categorized and explained in two parts: EDM performance improvement and surface modification.

1.7.5.1.1 EDM performance improvement

In using powder for EDM improvement techniques, Jeswani[77] observed that adding 4 g l^{-1} of fine graphite powder (10 μm average size) to dielectric increased the MRR and TWR by 60 and 15%, respectively. The TWR fell by about 28%, which is attributed to the decrease in the breakdown voltage of the kerosene dielectric caused by the graphite powder addition. Semi-conductive graphite nano-powder in both milling and sinking EDM of cemented tungsten carbide provided a smooth and defect-free nano-surface,[6] which assists the formation of shallower craters with more homogeneous distribution on the surface, thus producing a high quality glossy surface and reduced surface roughness. Increasing the powder concentration up to a certain level increased the surface quality, which again decreased after an optimum concentration due to the powder settling problem and bridging effect. The bridging effect results in frequent arcing and short-circuiting and may also cause more concentrated discharge energy and carbon accumulation on the workpiece surface, ultimately deteriorating the surface roughness. Nevertheless, the considerable improvement in surface finish, MRR as well as TWR was due to the increased spark gap, uniform discharge and breakdown strength of dielectric, which improved both surface topography and crater distribution.

The ability of EDM in machining high-hardness materials has captured interest to apply EDM in ceramic machining. However, the low conductivity of ceramics is an issue preventing the use of EDM for ceramic component production. According to Liew *et al.*[71] the electrical resistivity concern of reaction bonded (RB)-SiC ceramic is better solved by adding carbon nano-fiber to the dielectric during the μ-EDM process. It has been demonstrated that carbon nano-fibers (**Figure 15**) contribute to improving the machining process of this ceramic, leading to more frequent discharges and consequently higher MRR. As indicated in **Figure 16**, nano-fibers position themselves to form a bridging network between the tool and workpiece. The carbon nano-fibers high electrical conductivity may explain the performance improvement in PMEDM of RB-SiC by the reduced insulating strength of the dielectric, which results in enlarged gap distance.

Adding 10 μm silicon powder to dielectric has been seen to assist with producing high surface quality in a shorter period of time, reducing the surface roughness as well as producing a mirror like surface finish.[74] Although adding silicon powder considerably improved the surface quality, over larger areas the surface quality slightly deteriorated, which is explained by the capacitive effect. The capacitive effect entails higher peak current than the current set on the discharge generator, originating deeper and more irregular craters that increase with increasing electrode area. In order to assess the influence of silicon powder addition to complex shape polishing, a mold cavity with 110 mm width, 45 mm length and 10 mm height was machined. According to the results, the addition of silicon powder significantly enhanced the cavity polishing (**Figure 17**).[74]

Kansal *et al.*[78] studied the effects of process parameters when 20–30 μm silicon powder was added to dielectric. The experiments were performed using a newly designed experimental

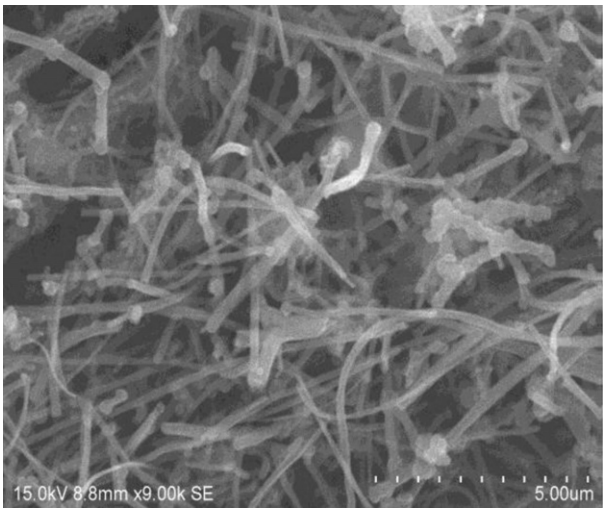


Figure 15 Scanning electron microscope micrograph of carbon nano-fibers.[71]

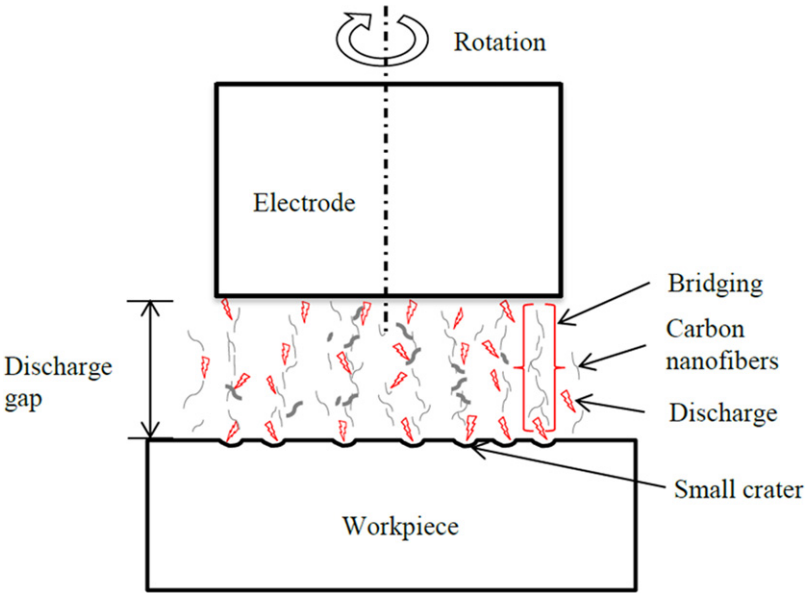


Figure 16 Schematic model of carbon nano-fiber-assisted micro-electrical discharge machining.[71]

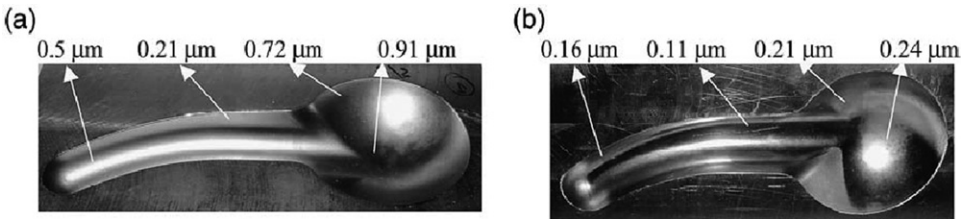


Figure 17 Mold cavity (a) without silicon and (b) with silicon powder for 100 min polishing time.[74]

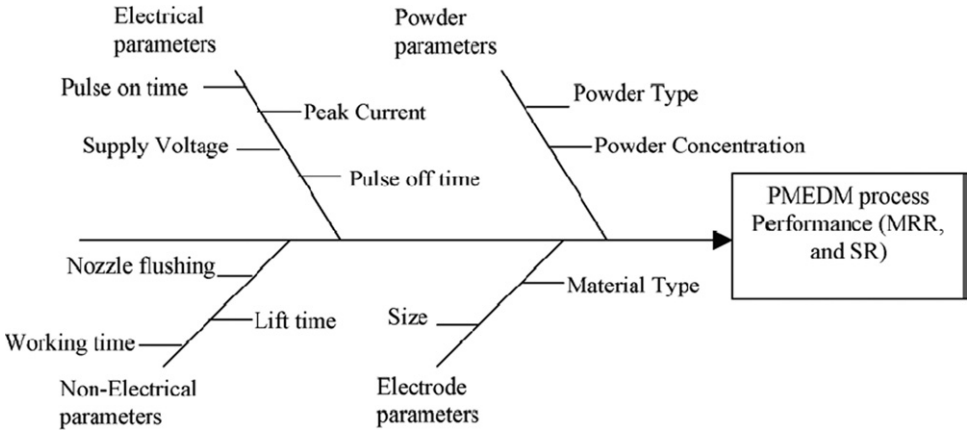


Figure 18 Cause and effect diagram.[78]

setup. Figure 18 shows the Ishikawa cause and effect diagram built for the machining parameters, which signifies that the powder parameters and electrode parameters were the most influential factors on the PMEDM process performance including MRR and surface quality. The analysis of variance (ANOVA) revealed that the peak current and concentration were the most significant parameters affecting MRR and SR.[78]

Kansal *et al.*[79] used ANOVA and obtained the most substantial process parameters along with optimized machining conditions for the EDM process with 30 μm silicon particles added. The most influential parameters introduced were peak current, powder concentration, pulse on-time, pulse off-time, and grain size, with the peak current and silicon concentration being the most critical parameters affecting MRR. Peças and

Henriques[80] observed that utilizing 10 μm silicon particle suspension in dielectric reduced the crater diameter and depth as well as white layer thickness (WLT). Furthermore, the short-circuiting and open circuit abnormal discharge occurring during conventional EDM decreased at 1 g l^{-1} silicon concentration. The optimum powder concentration to achieve the best surface roughness was found to be 2 g l^{-1}, and this effect was evident even at low powder concentrations. The highest efficiency and stability were observed at 2 g l^{-1} and 3 g l^{-1} silicon concentrations, when the abnormal discharge was completely eradicated. For silicon concentrations over 3 g l^{-1}, short-circuiting was detected, which was due to the bridge formation by excessive particles in the gap.

Adding 1 μm aluminum powder to dielectric to obtain fine surface roughness was proposed by Wu *et al.*[81] In order to overcome the electrostatic force that causes Al powder agglomeration, a surfactant was adopted to homogenously mix the powder in dielectric. The desired distribution effect was achieved when 0.1 g l^{-1} of Al powder and 0.25 g l^{-1} of surfactant were added to the dielectric. As shown in **Figure 19**, R_a of 0.172 μm was achieved under the following parameters: positive polarity, 0.3 A discharge current, 1.5 μs pulse duration time, 140 and 90 V gap voltage and 0.25 g l^{-1} surfactant concentration. The surface roughness improved by 60% from 0.434 μm in EDM oil to 0.172 μm in Ti/surfactant-added oil. Additionally, a thinner recast layer of 1–2 μm thickness was achieved compared to 5–8 μm using pure dielectric in EDM.

Zhao *et al.*[75] specified that adding 10 μm of Al powder at 40 g l^{-1} concentration in steel workpiece machining produced large and shallow craters, enhancing the surface roughness more than conventional EDM. However, due to energy loss in the discharge gap and reduced ejecting force on the melted material, the machining efficiency and surface roughness decreased compared to conventional EDM.

It was observed that adding Al powder during EDM of cobalt-bonded tungsten carbide (94WC–6Co) could effectively disperse the discharge energy, thus improving the machining efficiency.[82] Four parameters, namely discharge current, pulse on-time, grain size, and aluminum concentration were investigated. The TWR value tended to decrease with the aluminum powder concentration down to a minimum value, after which it tended to increase. MRR and TWR both increased with an increase in either grain size, current or pulse on-time.

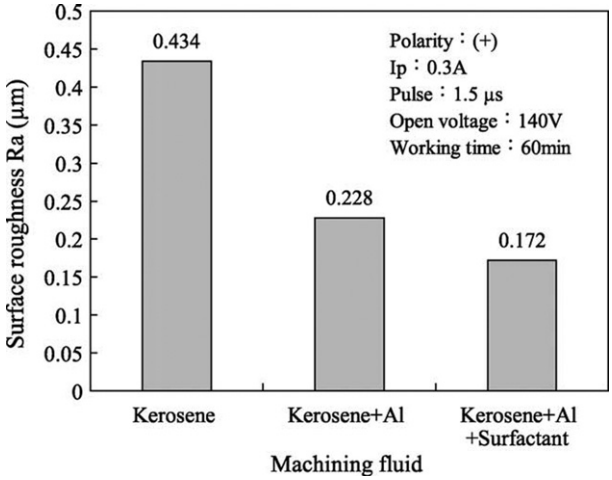


Figure 19 Influence of dielectric on surface roughness.[81]

Utilizing SiC abrasive mixed oil for deep micro-hole fabrication in SUS 304 stainless steel and Ti–6Al–4V titanium alloy plates has been shown to improve the shape precision and surface roughness of micro-holes.[83] An investigation of SiC powder (3 and 5 μm) added to water dielectric verified the MRR augmentation during the micro-slit EDM process.[33] According to this research, SiC powder addition causes bridging effect between the tool and workpiece in the gap besides discharge energy dispersion, thus creating two discrete discharge pulses from a single discharge period that could effectively disperse the discharge energy into several increments. The discharge could then generate minor craters and debris, whereby the minor debris would ease the gap exhaust and accelerate the MRR. The slight craters could lead to the production of refined surface roughness. Hu *et al.*[84] verified that adding SiC (2 μm) particles in the EDM process of Al matrix composites (SiCp/Al) considerably enhanced the machined surface properties compared to conventional EDM, with about 31.5% improvement in surface roughness and almost 100% increase in wear resistance reported.

The effect of alumina powder added to dielectric in machining SKD11 was investigated by Yan and Chen.[85] They determined that the non-conductive alumina powder addition to dielectric does not affect the gap distance, but it significantly affects the EDM characteristics. Under optimum condition, the MRR of SKD11 increased. Surface finish was achieved under the conditions of 1 μm particle diameter, 4 g l^{-1} concentration and 60 rpm electrode rotation speed. In another study, boron carbide was added to both kerosene and water dielectric by Kibria *et al.*[86] MRR, TWR, overcut, diametral variance at the hole's entrance and exit, and surface integrity during machining of titanium alloy (Ti–6Al–4V) were investigated. It was found that using deionized water increased both MRR and TWR, while a thinner white layer was produced than by using kerosene. Moreover, when suspended particles were applied, the MRR increased with deionized water but the TWR decreased with kerosene dielectric. The significant effect of adding boron carbide to deionized water dielectric was evident in enhancing the machining performance in micro-hole fabrication on titanium alloy with micro-EDM.

Through comparative studies on using various powder materials with the same machining conditions, Wong *et al.*[87] investigated the near-mirror phenomenon in EDM when graphite, silicon, aluminum, crushed glass, silicon carbide, and molybdenum sulfite powder particles with the properties shown in **Table 1**. To add powder to the system, the EDM flushing system was modified to add and distribute the powder in the machining gap. Adding powder to dielectric during machining expands the machining gap. The relative machining gaps of the powder materials employed are tabulated in **Table 2**. Particular powder and workpiece combinations were identified for producing mirror like finish or glossy-machined surfaces. Close scrutiny of the mirror-finished surfaces revealed shallow overlapping resolidified disks with smooth rims, unlike typical EDM surfaces that are normally covered with deep craters, pock marks, and globules. It was found that appropriate electrode polarity and pulse parameter settings

and correct combinations of workpiece material and powder characteristics significantly influence the mirror finish condition. It was stated that in order to achieve a mirror-finished surface, it is essential to apply negative polarity. The presence of powder increased machining stability and the surface had well-formed and small overlapping craters. Al powder generated a mirror like finish in machining SKH-51, but not in EDM of SKH-54. Si and C powders seemed to be effective in providing a very fine finish.

In micro-slit EDM, different dielectrics of kerosene, kerosene with aluminum powder, and kerosene with SiC powder were used with a thin copper diskette electrode to machine titanium alloy[88] with the setup exhibited in Figure 20. The effects were investigated on material removal depth, TWR, slit expansion, surface roughness, and the discharging condition waveform. Adding both SiC and Al powder to kerosene resulted in enlarged gap distance between workpiece and tool. The extended gap increased the debris removal rate as well as material removal depth. Moreover, a bridging effect was produced by the added powder drifting throughout the kerosene and, thus facilitating the discharge dispersion in several increments. Therefore, several discharge trajectories were formed within a single input impulse and several discharge spots were created within a discharge impulse as well. The effects caused by the discrete discharge pulses can be elucidated in terms of these effects minimizing the machined debris. The debris could be more easily removed, hence increasing the material removal depth and surface roughness. However, adding powder to kerosene disturbed the carbon nuclides' adhesion to the electrode surface, consequently increasing the electrode wear rate as well as the slit expansion.

Tzeng and Lee[89] studied the effect of aluminum, chromium, silicon carbide, and copper particles addition to dielectric on the EDM performance factors of MRR and TWR. Particle size demonstrated the greatest impact on machining outcome, where the smallest particles (70–80 nm) generated the least increase in spark gap, the highest MRR and the lowest TWR. The results established that increasing the particle size reduces the MRR growth and increases the TWR and spark gap. Chromium was identified to have the highest MRR and lowest TWR, followed by aluminum and then silicon carbide particles. Moreover, the copper particles had no significant influence on EDM performance.

To produce parts for ultrahigh vacuum such as in space environments, Furutani and Shiraki[90] used the lubricant deposition method during finishing EDM. Molybdenum disulfide (MoS_2) powder was added to the working oil to deposit a

Table 1 Powder characteristics[87]

Powder	*Mesh size (degree of purity)*
Graphite	#400 (38 ± 3 μm) (purum powder of 99% purity, ash content: 0.05%)
Silicon	#325 (45 ± 3 μm) (99.5%)
Aluminum	#325 (45 ± 3 μm) (99.5%)
Crushed glass	#10 (2.0 ± 0.07 μm)
Silicon carbide	#8 (2.36 ± 0.08 μm)
Molybdenum sulfide	Typical particle size: 1–3 μm (max 40 μm)

Table 2 Spark gap distances under different powder suspension conditions[87]

Dielectric condition	*Spark gap distance (μm)*
Without powder	10–15
Graphite	45–50
Silicon	33–27
Aluminum	120–160
Crushed glass	10–15
Silicon carbide	80–90
Molybdenum sulfide	44–48

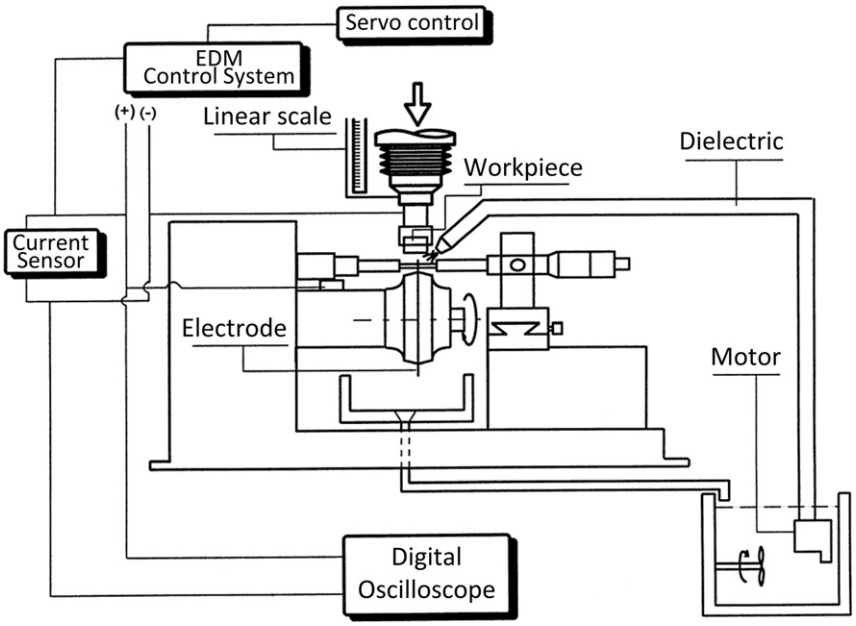


Figure 20 Detailed schematic diagram of the experimental equipment.[88]

lubricant layer on carbon steel and stainless steel. MoS_2 was perfectly deposited under the electrical conditions of high open circuit voltage, small discharge current, short pulse duration, and medium pulse interval. Furthermore, a smoother surface was obtained by adding aluminum powder to the mixture of MoS_2 and working oil. In friction testing, a surface finish achieved with a mixture of MoS_2 and working oil had a smaller friction coefficient than with normal working oil.

The effect of aluminum, chromium, silicon carbide, and copper particle addition on the machined surface quality of an SKD-11 workpiece during the PMEDM process was investigated.[69] The most critical powder characteristic factors governing surface roughness and the recast layer were identified as particle size, particle concentration, particle density, electrical resistivity, and thermal conductivity. It was revealed that the additive particle size influences the surface quality. The smallest particles (70–80 nm) produced the best surface finish, while larger particles reduce the surface roughness. However, particle size has an inverse relationship with the recast layer. The smallest particle size produced the thickest recast layer on the machined surface. Of the additives, Al powder generated the best surface finish and thinnest recast layer on the machined surface, while copper powder additive resulted in the worst surface characteristics.

1.7.5.1.2 Surface modification

In surface modification applications using PMEDM, graphite powder has demonstrated to be more suitable than aluminum powder in increasing the micro-hardness of EN31, H11 as well as high carbon high chromium (HCHCr) die steel workpieces.[91] The copper electrode was the best for EN31 and H11 die steels, whereas the tungsten–copper electrode was better suited for HCHCr steel to achieve higher micro-hardness. There was a nearly 80% increase in micro-hardness after PMEDM. Suspended powder particles deposited on all machined samples, resulting in the formation of a particle-rich phase. According to XRD analysis, a largely amorphous structure formed owing to the high temperature coupled with rapid cooling.

In a similar study,[92] the coated titanium carbide layer enhanced the machined surface hardness by 76.76% from 990 Hv to 1750 Hv with improved surface quality and completeness of tungsten carbide surface using PMEDM. Ti powder was added to the dielectric and the experiment was designed with varying currents and duty cycles, which resulted in modified titanium coating layer thickness. A small number of micro-cracks appeared on the surface, which were filled with and substituted by titanium powder and carbon (a hydrocarbon) that decomposed from the dielectric that acted as a combiner (TiC). As seen in **Figure 21**, at 20 A current and 50% duty factor, a 5 μm coating layer of titanium and carbon with fewer cracks and higher hardness was achieved. Furthermore, in machining AISI D2 steel, adding titanium nano-powder to dielectric diminished the surface micro-cracks, improved the surface morphology and surface roughness, and enhanced the MRR by ~69%. In contrast, elemental analysis signified negligible Ti deposition on the machined surface while the atomic concentration of Ti increased around the crack regions.[76]

The addition of Si, W, and graphite powder to dielectric was tested by Bhattacharya *et al.*[93] Powder concentration, current and pulse on-time were determined as the main factors influencing surface roughness. Of the dielectrics used, kerosene provided superior cooling effect while EDM oil provided better surface finish. Machined surface micro-hardness was influenced by the powder, concentration, current, pulse on-time, and electrode material. Tungsten–copper electrode and tungsten powder resulted in elevated micro-hardness.

The surface of a Ti workpiece was also modified using Ti powder mixed micro-current EDM at various working parameters. At $3\,g\,l^{-1}$ concentration, the surface cracks considerably reduced; however, at $6\,g\,l^{-1}$, no micro-cracks were observed on the modified surface at 0.1 A current and short pulse durations ($\leq$50 s). The recast layer thickness enhanced to approximately 4–11 μm at $6\,g\,l^{-1}$ concentration. Additionally, a TiO phase was detected in the recast layer when Ti powder was used in the dielectric fluid. **Figure 22** indicates that the Ti surface modified at 0.1 A current for 30 and 50 s in $6\,g\,l^{-1}$ concentration of Ti powder dielectric produced a hydrophilicity surface. Hence, an appropriate Ti powder concentration not only prevented the formation of surface cracks but also boosted the Ti surface wettability during micro-current EDM modification.[94]

Sidhu *et al.*[95] investigated the surface modifications of three types of MMC: 65 vol%SiC/A356.2, 10 vol% SiC–5 vol% quartz/Al, and 30 vol%SiC/A359 by PMEDM process. The micro-hardness and surface integrity were evaluated in terms of contributing process parameters. Evidently, the micro-hardness increased primarily with increasing density of reinforced particles in the matrix. There was also a significant amount of metal transfer from the copper electrode during the process as compared to graphite.[95]

Bhattacharya *et al.*[96] investigated the most appropriate parameter settings for rough and finished machined surfaces of EN31, H11, and HCHCr die steel materials in aluminum and graphite PMEDM process. Copper (Cu) electrode with aluminum suspended in dielectric maximized the MRR. Suspending powder in the dielectric resulted in surface modification. Graphite powder exhibited lower MRR but improved surface finish. HCHCr required higher current and pulse on settings to initiate a machining cut and functioned best in combination with a tungsten–Cu electrode and graphite powder for enhanced finish. The MRR for H11 was lower than EN31 but significantly higher than HCHCr under the same process conditions.

Besides surface quality improvement, surface modification by the material transfer during EDM has emerged as a key research area in the last decade. Kumar and Batra[97] investigated the response of three die steel materials, OHNS, D2, and H13 die steels, to surface modification by EDM using tungsten PMD. It was shown that under suitable machining conditions, a considerable amount of powder material transferred to the workpiece surface. Due to the breakdown of hydrocarbon oil during the process, the percentage of carbon element increased. At high plasma temperature, the availability of carbon and tungsten powder resulted in carbide formation. Adequate conditions for material transfer by EDM were found to be low discharge current (less than 5 A), shorter pulse on-time (less than 10 s), longer pulse off-time (more than 50 s) and negative polarity of the tool electrode. Surface alloying

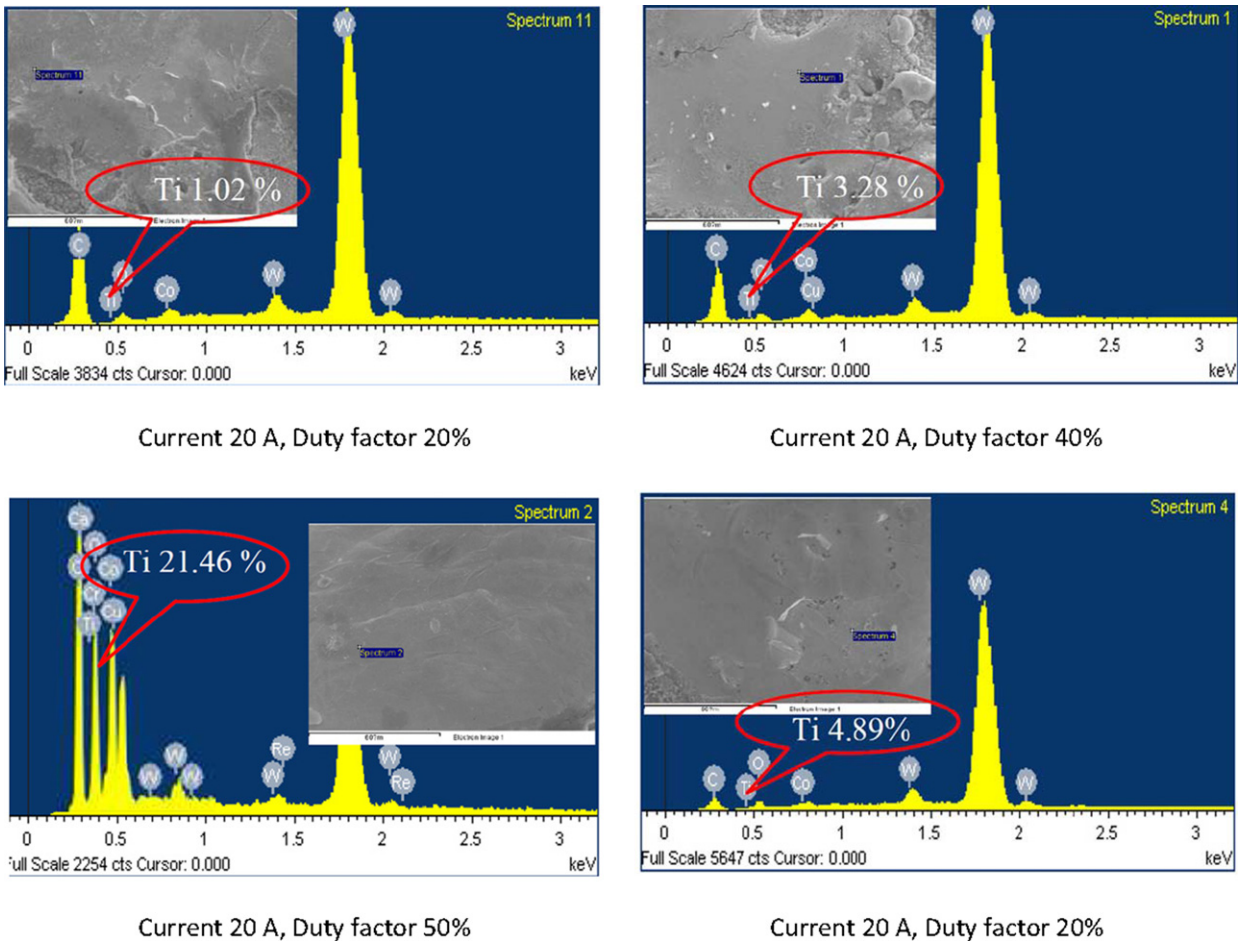


Figure 21 Energy dispersive X-ray spectra of the Ti coating surface.[92]

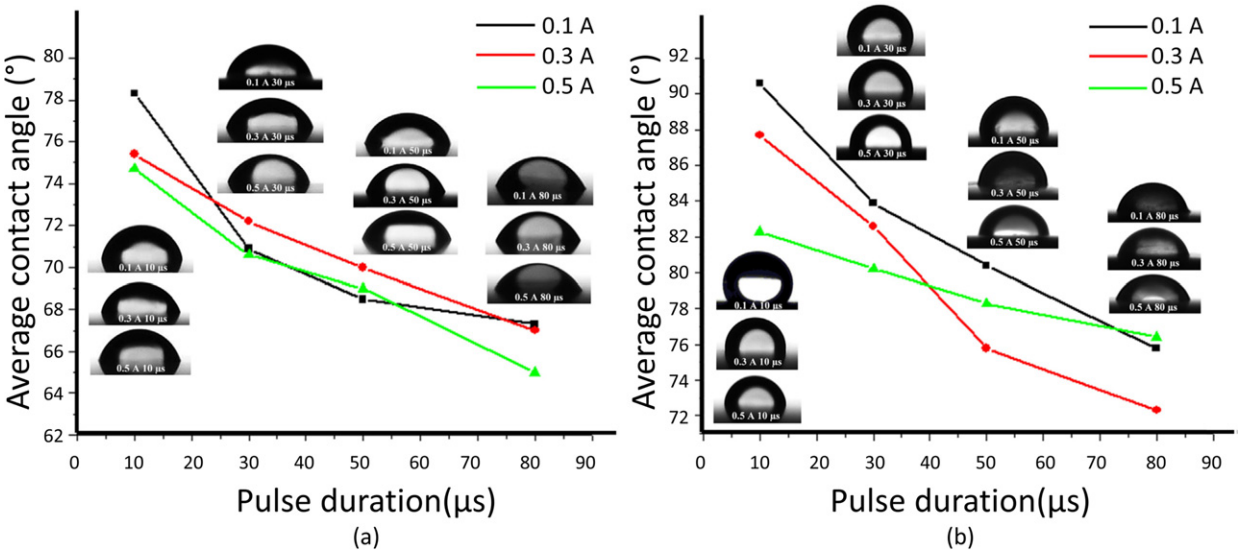


Figure 22 The relationship between the average contact angles and durations of modified Ti at various current levels in deionized water mixed with concentrations of (a) 3 g l^{-1} and (b) 6 g l^{-1} Ti powder dielectric solvent, respectively.[94]

appeared to improve the surface micro-hardness by over 100% for all three workpiece materials. The H13 die steel workpiece surface after machining (Figure 23) had the highest material transfer of 3.25%.

1.7.5.2 Powder Mixed Ultrasonic-Assisted EDM

Ultrasonic-assisted EDM can also be implemented when powder is mixed into dielectric. To enhance the machined surface of Al–Zn–Mg aluminum alloy, USM and PMEDM were combined.[98] SiC particles were added to the dielectric fluid to produce a particle-reinforced mechanism and solid solution strengthened structure to facilitate surface modification in a short working time. According to this research, the combined process of USM and PMEDM can attain an 80 μm deep modified layer on the machined surface of aluminum alloy after 240 s, which can significantly increase the hardness and wear resistance of the machined surface.

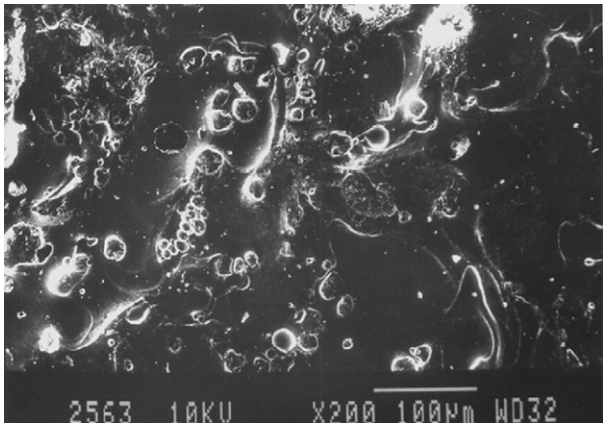


Figure 23 Scanning electron microscope of H13 die steel after machining with tungsten powder mixed dielectric (at $I_p = 4$ A, $P_{on} = 10$ s, and $P_{off} = 85$ s).[97] I_p, peak current; P_{off}, pulse off-time; P_{on}, pulse on-time.

EDM with tool vibration and addition of TiC particles to kerosene dielectric appeared to be considerable factors in the performance of machining Al–Zn–Mg.[70] Figures 24–26 indicate the influence of peak current on MRR, relative electrode wear ratio and surface roughness, respectively. Decomposed Ti particles from TiC added to dielectric migrated to the Al–Zn–Mg surface, resulting in fine grain consolidation during the solidification. Additionally, the penetration of some TiC particles into the machined surface during the process increased the hardness and wear resistance by alloying the external workpiece layer.

Other than applying ultrasonic vibration in PMEDM, workpiece vibration at 1000 KHz frequency overcame the improper ejection of debris from the gap in micro-EDM.[73] Using the setup in Figure 27, workpiece vibration in micro-EDM was investigated with the presence of graphite particles in dielectric. It was revealed that the effect of 55 nm graphite

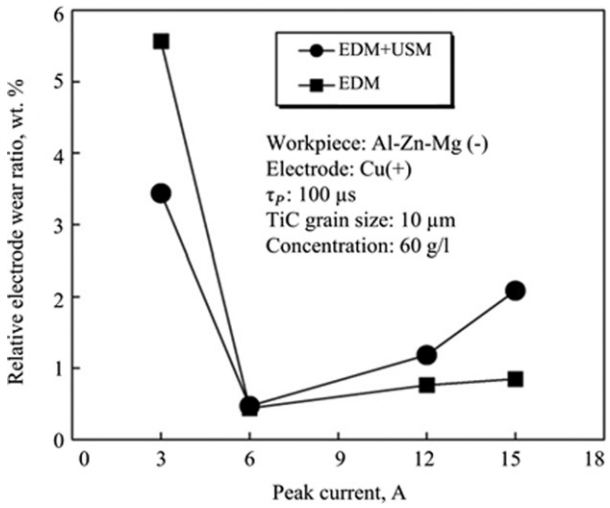


Figure 25 Relation between peak current and relative electrode wear ratio in two processes.[70]

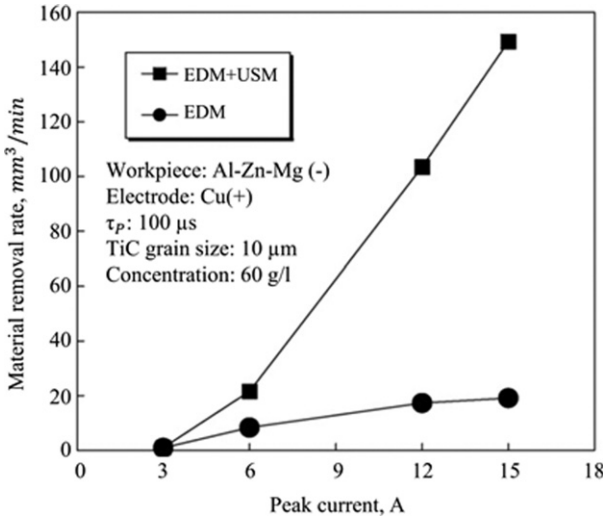


Figure 24 Relation between peak current and material removal rate in two processes.[70]

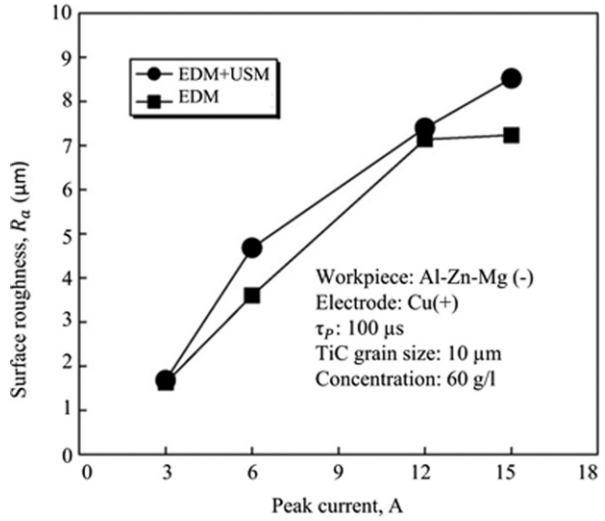


Figure 26 Relation between peak current and surface roughness in two processes.[70]

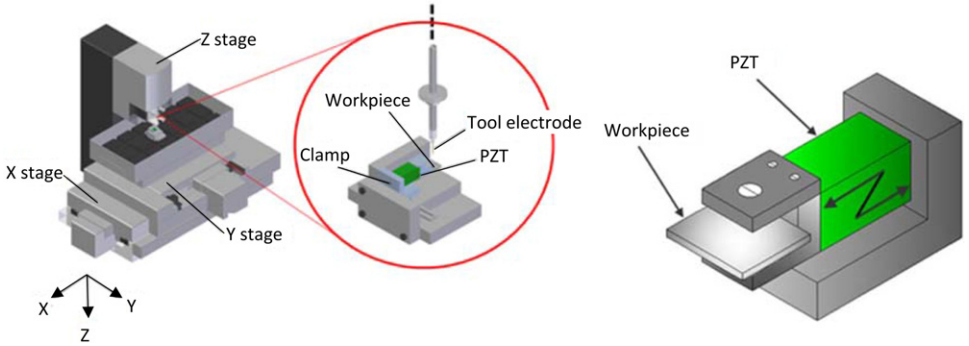


Figure 27 (a) Micro-electrical discharge machining, and (b) vibration additional mechanism using piezoelectric actuator (PZT).[73]

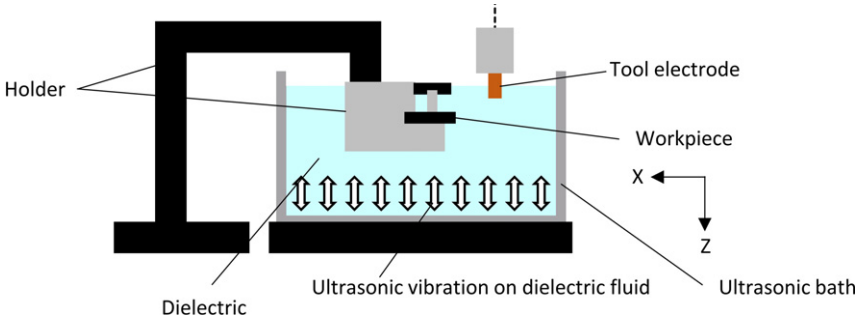


Figure 28 Setup for ultrasonic vibration of dielectric fluid.[99]

addition to dielectric on MRR enhancement was greater than workpiece ultrasonic vibration with 1000 frequency and 1.5 μm amplitude. In three machining conditions, i.e., workpiece vibration, with graphite powder addition, and a combination of both, significantly decreased machining time to a maximum of 6, 20, and 24 times faster than ordinary EDM, respectively. Additionally, the best surface was achieved at 15 g l^{-1} graphite powder concentration.

In PMEDM developments, when a specific powder concentration is added to the dielectric, particles are usually mixed with dielectric using conventional methods like implementing a stirrer in the machining tank[70] or blending the powder with dielectric in advance.[71] Ultrasonic vibration of the dielectric seems to be a means of properly utilizing the powder additive effect during the EDM process. Ultrasonic vibration of the dielectric fluid tank during graphite PMEDM of Silver–tungsten appeared to effectively improve the surface quality, eliminate micro-cracks as well as reducing the machining time by up to 35%.[99] **Figure 28** demonstrates a schematic design of ultrasonic tank vibration-assisted μ-EDM, with a developed independent tool holder and fixture to keep the workpiece in place so it would not be affected by the vibration from the bottom of the tank.

Prihandana *et al.*[72] implemented a PMEDM chamber ultrasonic vibration with 43 KHz frequency. It was reported that the suspension of 2 μm MoS_2 powder in dielectric during vibration-assisted micro-EDM was substantially effective in improving the MRR and surface quality. According to this research, the MRR rose owing to higher powder availability in the gap area as a result of the ultrasonic vibration. The vibration participated more in the discharge action and also diminished the adhesion of debris to the workpiece. **Figures 29** and **30** illustrate the machined surface obtained by micro-EDM processing using a pure dielectric fluid and 2 g l^{-1} MoS_2 powder with ultrasonic vibration of the dielectric fluid, respectively. Comparing these figures signifies the great enhancement in profile depth and machined surface quality by introducing tank ultrasonic vibration associated with MoS_2 powder addition to the dielectric. Moreover, powder addition resulted in a larger spark gap. Thus, easier flushing of debris, increased lubricity in the spark gap, distributed current path on the surface as well as dielectric breakdown are considered other advantages of the MoS_2 contribution to the discharge, which resulted in superior surface quality, free from black carbon spots. Ultrasonic vibration of the dielectric fluid, the addition of micro-MoS_2 powder at a concentration of 5 g l^{-1} and the use of copper as workpiece material are necessity for attaining a high MRR.

In micro-EDM of holes in ceramics, the simultaneous influence of carbon nano-fibers and ultrasonic vibration of the dielectric fluid around the machining area resulted in a hole almost 5 times deeper than using pure oil in a specific period of time.[100] **Figure 31** shows a probe-type oscillator horn designed to place around the machining area. As schematically illustrated in **Figure 32**, ultrasonic vibration of the horn-generated intense ultrasonic waves that traveled through the liquid, generating small cavities that enlarged and then collapsed. Ultrasonic vibration initially assisted to homogeneously mix the carbon nano-fibers with dielectric, and eventually, the cavitation vibration effect resulted in superior

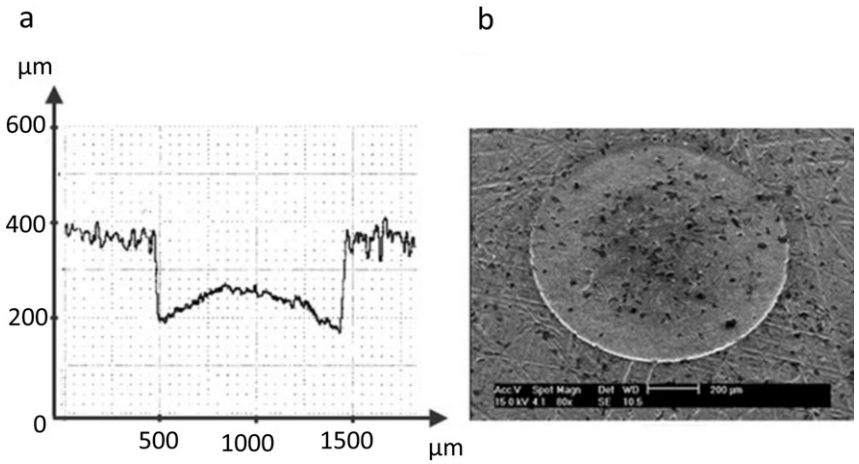


Figure 29 Profile of Cu–W surface with brass as the tool electrode obtained by micro-electrical discharge machining processing using pure dielectric fluid: (a) depth profile and (b) machined surface image.[72]

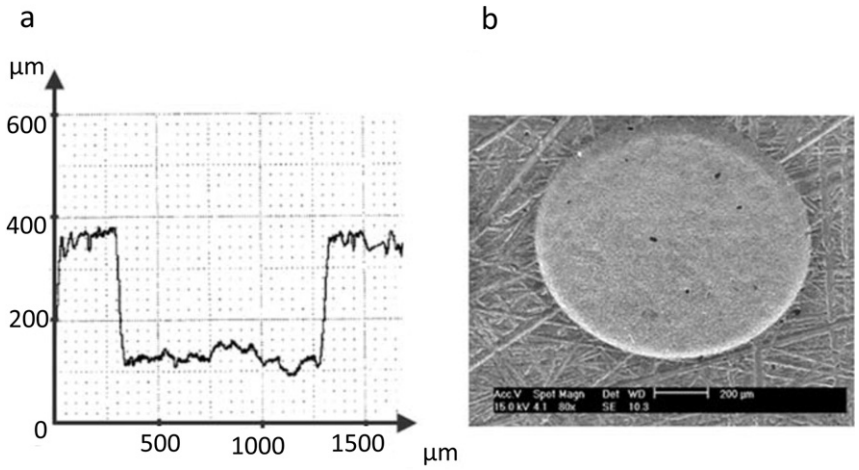


Figure 30 Profile of Cu–W surface with brass as the tool electrode obtained by micro-electrical discharge machining processing using MoS_2 powder with ultrasonic vibration of dielectric fluid and powder concentration of 2 g l^{-1} (a) depth profile and (b) machined surface image.[72]

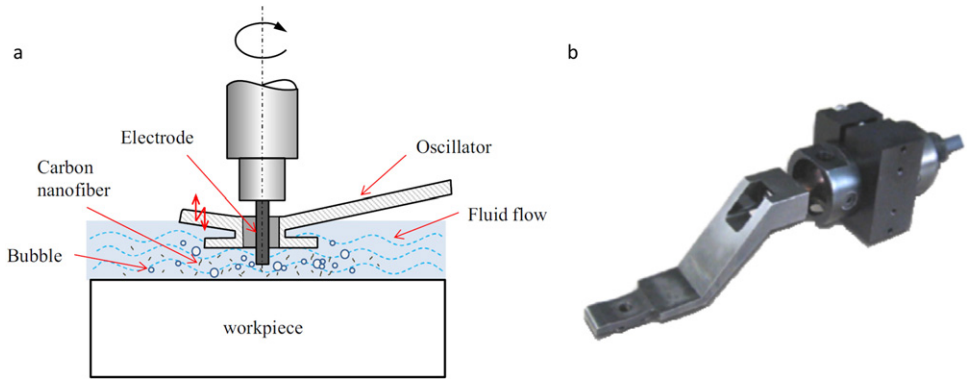


Figure 31 (a) Schematic diagram of the proposed hybrid micro-electrical discharge machining process and (b) photograph of the probe-type oscillator horn used in the experiment.[100]

debris ejection from the gap. The fabricated hole depth was considerably affected by the amplitude of vibration, where 10 µm amplitude achieved the maximum hole depth. On the contrary, the ultrasonic influence was negligible without powder additive. Furthermore, superior surface topography, more accurate geometry, and higher stability were obtained.

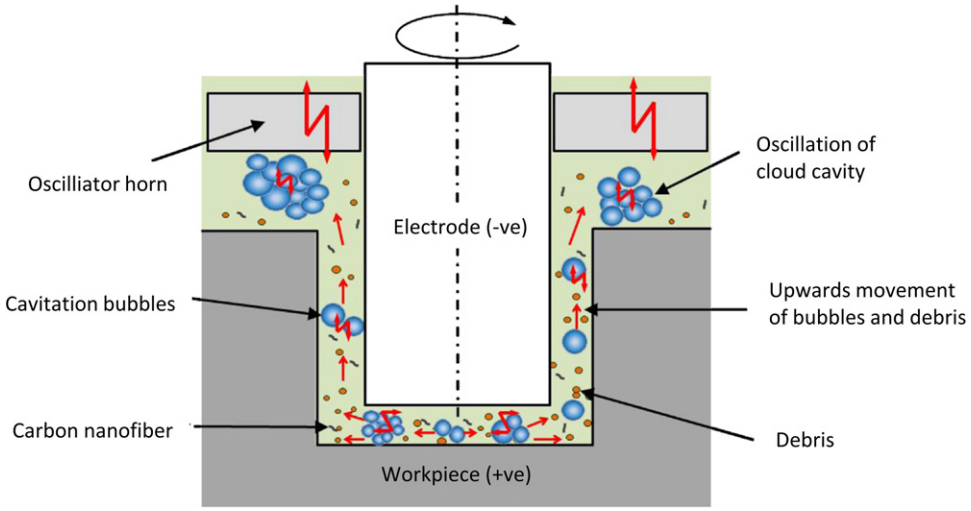


Figure 32 Schematic model of debris removal through cavitation-assisted micro-electrical discharge machining of a deep micro-hole.[100]

1.7.5.3 Powder Mixed Near-Dry EDM

In powder mixed near-dry electrical discharge machining (PMND-EDM), instead of one-phase conventional oil dielectric, a three-phase dielectric medium was proposed including a gas continuous phase (compressed air), liquid dispersed phase (EDM oil), and solid dispersed phase (silicon powder).[101] As a result, the dielectric's deionization effect, spark initiation, and MRR improved owing to the new dielectric breakdown mechanism, which considerably differs from conventional EDM. **Figure 33** shows the effect of peak current, pulse on-time, pulse off-time, flow rate, powder concentration, air pressure, and tool rotational speed on MRR based on the tool material. The optimum silicon powder concentration to achieve the highest MRR was found to be 9 g l^{-1}.

Similarly, in another study on PMND-EDM,[102] focus was on the influence of vital factors affecting MRR, including peak current, pulse on-time, pulse off-time, flow rate, powder concentration, air pressure, and tool rotational speed. As expected, MRR was directly influenced by peak current and pulse on-time due to the discharge energy enhancement. Conversely, increasing the pulse off-time reduced the discharge frequency, resulting in lower MRR. Nevertheless, in PMND-EDM, the deionization and dielectric field strength enhancement of the dielectric medium between tool and workpiece was mainly due to the fluid phase and dispersed silicon powder phase, respectively. It was demonstrated that the enlarged gap improved the deionization effect and facilitated discharge, resulting in higher MRR. Hence, increasing the concentration or flow rate led to higher MRR. Based on the analysis, the order of the various parameters' effects on MRR, from the greatest to the smallest, is as follows: peak current, pulse on-time, pulse off-time, flow rate, powder concentration, air pressure, and tool rotational speed.

Parametric optimization of MRR and TWR in chromium powder (45–55 μm) mixed EDM was investigated in machining EN-8 steel. Average current, duty cycle, electrode angle, and the concentration of chromium powder added to dielectric fluid in EDM were selected as process parameters. As shown in **Figure 34**, experiments were performed on the newly designed experimental setup developed in the laboratory.[103]

A cost-efficient method of fabricating carbon nano-tubes by EDM with 1000 μs pulse duration and 2.5 A peak current in air medium was developed.[104] An EDM was employed to synthesize nano-crystalline powder from scrapped cemented tungsten carbide.[105] Among deionized water, ethanol and kerosene, deionized water was the most suitable liquid for this application.

1.7.6 Electrode Modification

Electrode material and fabrication specifications have a direct impact on machining performance, especially for surface modification and coating purposes, as the tool fabrication method facilitates the coating. Electrical discharge coating refers to using an EDM for coating during the process. Titanium powder was used in EDM with a green compact electrode for surface modification or coating to create a thick TiC layer on the surface.[106] Ti particles in the EDM process of carbon steel (AISI-1049) adhered to the workpiece due to the heat from the discharge, resulting in the growth of a TiC layer. The powder concentration in the gap between the workpiece and a rotational disk electrode had to be kept high to obtain a wider accretion area by using the rotational gear-shaped electrode. A TiC layer with 150 μm thickness and 1600 Hv hardness developed on carbon steel surface when using an electrode with 1 mm diameter. Patowari *et al.*[107] used W–Cu powder metallurgy sintered tools in EDM for surface modification of C-40 grade plain carbon steel. A wide range of layer thicknesses were deposited with an average of 3–785 μm to increase the surface micro-hardness.

Hwang *et al.*[108] proposed multilayer electrodes on EDM for coating applications. A multilayer electrode (MLE) enhanced the composition of Ti and C as well as the surface hardness of the coated layer, reduced the surface roughness and microcracks, and increased electrical discharge stability and coating speed when applied to electrical discharge coatings. Additionally, the abrasion resistance of a coating layer is excellent at room temperature (30 °C) and it can be maintained at high temperature too (400 °C). However, this ability reduces with

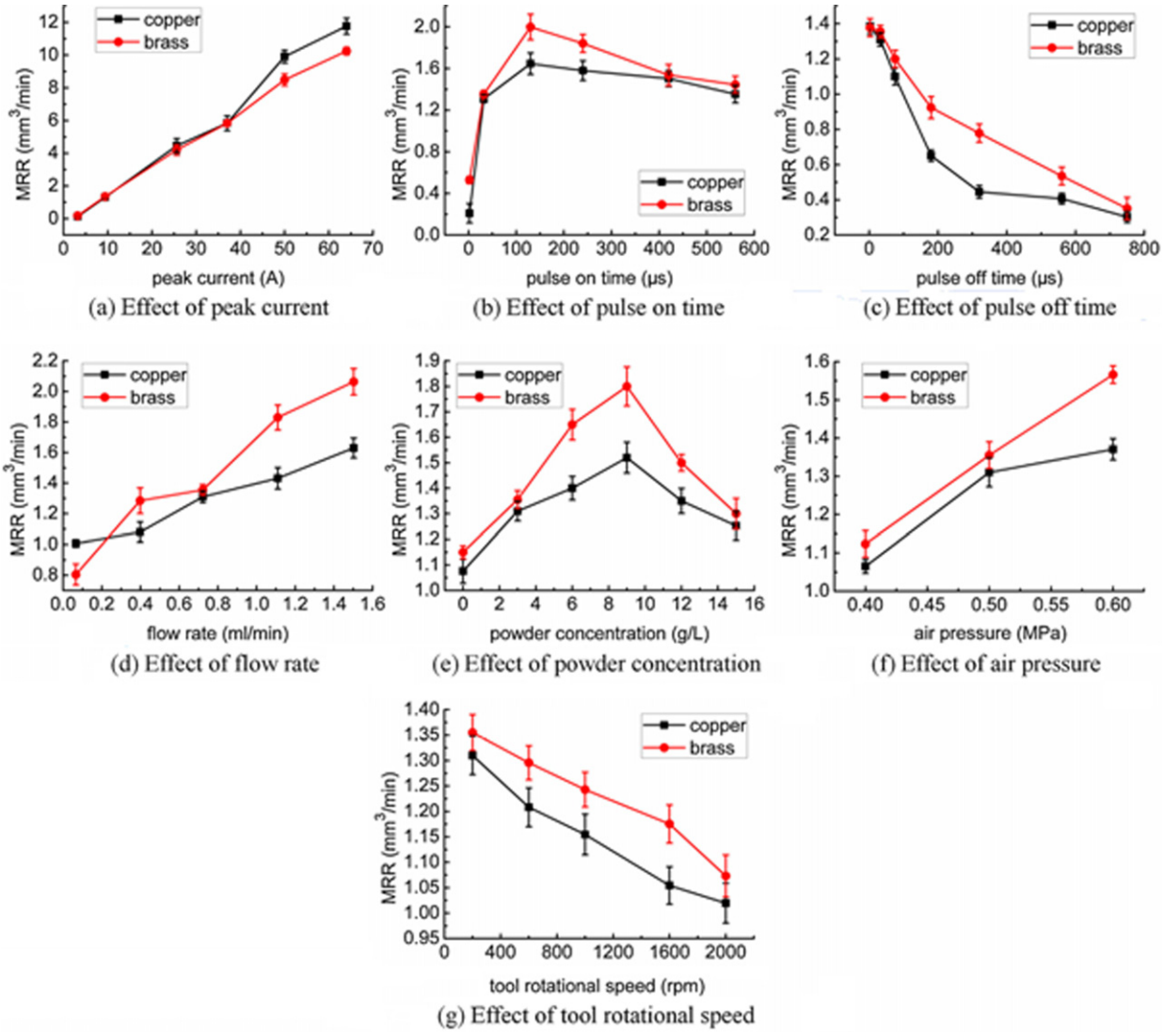


Figure 33 Effect of each process parameter on MRR based on different tool materials.[101]

increasing loading force, which mainly results from the stripping of the substrate (Ni) under the coated layer instead of the coated layer itself.

Suzuki and Kobayashi[109] employed a titanium carbide semi-sintered electrode as the source of coating material in EDM for coating the machined surface where a hard TiC layer formed on the surface owing to material migration from the tool to the surface and adhesion caused by single-pulse discharge. TiC was directly supplied from the electrode to the workpiece surface by single-pulse discharge without the presence of TiC between the electrode and workpiece. It was reported that when a temporary voltage drop occurs during discharge, clustered TiC powder that has maintained its powder form are present in the crater and adhesion is greater compared to when the voltage remains constant. Mohri *et al.*[110] proposed the rapid accretion of a thin electrode material and rapid manufacturing of a thin electrode. Through the explosion process in EDM, the electrode material can be accreted in the workpiece in an instant.

It was found that in low wear setting with EDM, a diamond like amorphous carbonaceous layer builds on the erosion front of the electrode surface in EDM, significantly disturbing the electrode erosion.[111] Parameters including applied current and pulse duration affect the microstructure of this layer, which has lower thermal conductivity and higher hardness compared to the base graphite material. A simple thermal model was proposed to simulate the pulse duration values at which a protective carbonaceous layer forms over the entire frontal surface of the microscale electrodes with a projection area below 1 mm^2. In order to achieve electrical discharge drilling with high AR > 30 micro-holes, implementing a tool with an insulated sidewall was proposed.[112] The concept was to promote the process stability of micro-EDM deep drilling by preventing secondary sparks to facilitate achieving micro-holes with 0.2 mm diameter and up to about 120 AR within 1 h.

Frohn-Villeneuve and Curodeau[113] proposed a new dry die-sinking EDM polishing method using a moldable graphite–polymer composite electrode as tool and evaluated

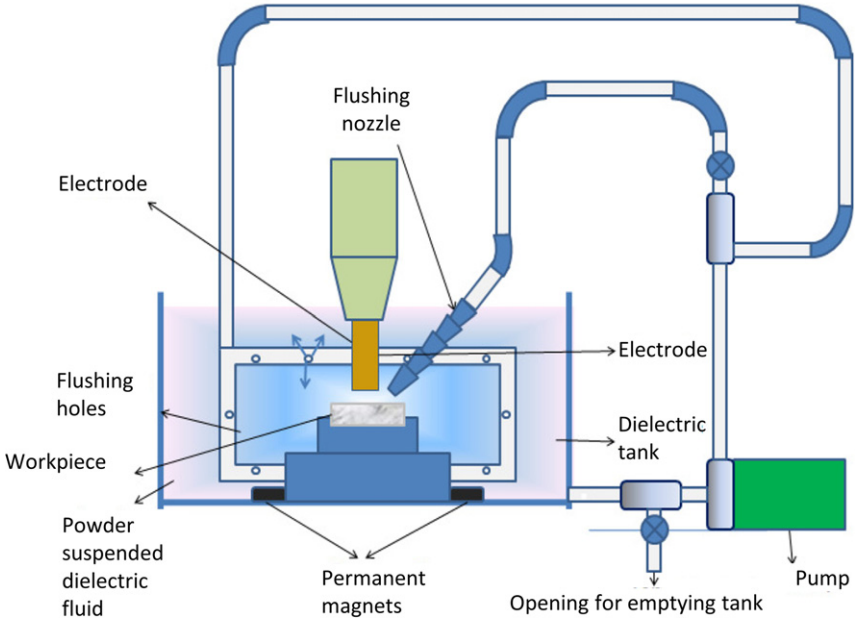


Figure 34 Line diagram of experimental setup.[103]

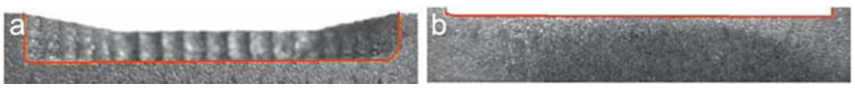


Figure 35 Section view of Ti6Al4V workpieces machined by, (a) a bundled electrode and (b) a die-sinking electrode.[114]

the influence of various process parameters on surface roughness, MRR and electrode relative wear rate. In order to attain higher MRR in EDM, Gu *et al.*[114] presented a bundled die-sinking electrode for machining Ti6Al4V. After studying the performance of this electrode compared to solid die-sinking electrode, the simulation results explained the high performance of the EDM process with a bundled electrode through the use of multi-hole inner flushing to efficiently remove molten material from the interelectrode gap and through the improved ability to apply a higher peak current. Figure 35 shows the cross-section of the surface machined with bundled electrode and die-sinking electrode. Bundled electrodes could tolerate a much higher peak current compared to die-sinking electrode, which resulted in a significantly higher MRR and a comparably lower TWR.

Muralidhara *et al.*[115] proposed a directly coupled piezo-actuated tool feed mechanism which was used to feed the tool and also to sense the tool displacement from a reference position. The hysteresis behavior of the piezoactuator is also integrated through an electromechanical model for estimating the actual tool displacement. Comparing the simulation and experimental results for piezoactuator displacement, a maximum error of 15% was observed. Further, in order to control the tool feed rate during machining, a tool feed controller based on the gap voltage feedback was developed. A contact-based measurement technique was integrated with the tool feed controller to measure the tool wear and the depth of material removed. The experimental results obtained through the contact-based measurement technique were in agreement with the tool-displacement simulations with a maximum error of about 10%.

El-Taweel[116] produced a novel tool electrode material of Al–Cu–Si–TiC composite using powder metallurgy and investigated the relationship of process parameters in EDM of CK45 steel. Titanium carbide percent (TiC%), peak current, dielectric flushing pressure, and pulse on-time as input process parameters and MRR and TWR were selected as output parameters. It was revealed that the new electrode is more sensitive to peak current and pulse on-time than conventional electrodes. The observed optimal process parameter settings based on composite desirability were TiC percent of 18%, peak current of 6 A, flushing pressure of 1.2 MPa, and pulse on-time of 182 μs for achieving maximum MRR and minimum TWR.

1.7.7 Simulation and Modeling

Understanding the discharge incident during the EDM process is a crucial challenge for enhancing process performance fundamentally. Process simulation and modeling and understanding the input parameters' effect on the outcome are beneficial to gaining a clearer vision of the process. Regarding the developed model, the numerically predicted and experimentally obtained values can be compared to evaluate the process behavior and model's estimation efficiency. Thus, the application of numerical modeling and simulation has emerged as a key research area for both prediction and optimization. In this section, numerical

investigations on the EDM process from the past decade are considered.

1.7.7.1 Mathematical Modeling

Fujun *et al.*[117] were the first to establish a universal mathematical model that lays a mathematical foundation for computer simulation, virtual machining and the establishment of real non-sphere machining systems by rotary EDM. The authors presented the shaping principle of machining a non-sphere with a rotary electrode and analyzed in greater detail the functions of a non-sphere machining system with a rotary electrode and the motion laws of machining rotary workpieces. Bleys *et al.*[118] introduced a new wear compensation technique, which incorporated real-time wear sensing based on discharge pulse evaluation, where the tool wear was continuously evaluated during machining, and the actual wear compensation was adapted on the basis of the real-time wear evaluation.

In 2008, Salonitis *et al.*[119] established a thermal-based model for determining the MRR and R_a as a function of the process parameters. The model predicts that an increase in discharge current, arc voltage or spark duration results in higher MRRs and coarser workpiece surfaces. On the other hand, a decrease in idle time increases the MRR with the additional advantage of achieving slightly better surface roughness values. A theoretical thermal model was proposed for the simulation of the die-sinking EDM process. The MRR and R_a were determined with an average deviation of 8.2 and 6.1%, respectively.

A 3D geometric simulation method of micro-EDM milling processes was introduced by Heo *et al.*[120] They presented a *Z*-map algorithm to precisely represent the geometries of a machined workpiece and the evolution of the tool shape caused by tool wear during machining. The micro-EDM milling process was mathematically and geometrically modeled. As illustrated in Figure 36, the performance of the developed simulator was evaluated by comparing the machined actual square cavity results with the simulation results. The developed EDM simulator can be used for tool path generation for tool wear compensation as well as for tool wear prediction.

Mathematical models were developed for modeling and analyzing the effects of process parameters, including discharge current, pulse on-time, duty factor, and capacitance value on the disintegration factor at the entrance edge of a drilled hole in the EDM drilling process of cobalt-bonded tungsten carbide.[121] In order to identify the optimum processing parameter settings, a quadratic model of response surface methodology associated with the sequential approximation optimization method was employed. From the experimental values of up to 95% confidence interval, it was found that the effect of interaction between discharge current and capacitance value had the highest impact on the disintegration factor, followed by capacitance value and the quadratic term of the duty factor. The optimal machining parameters reportedly diminished the disintegration factor by 5.53%.

An empirical model relating to electrical discharge drilling process parameters (working current and pulse on/off-time) was identified to predict the WLT at various hole depths.[122] Via ANOVA and Tukey's honestly significant difference methods, the experimentation outcome was analyzed. It was found that the electrical discharge drilling parameters' influence on the

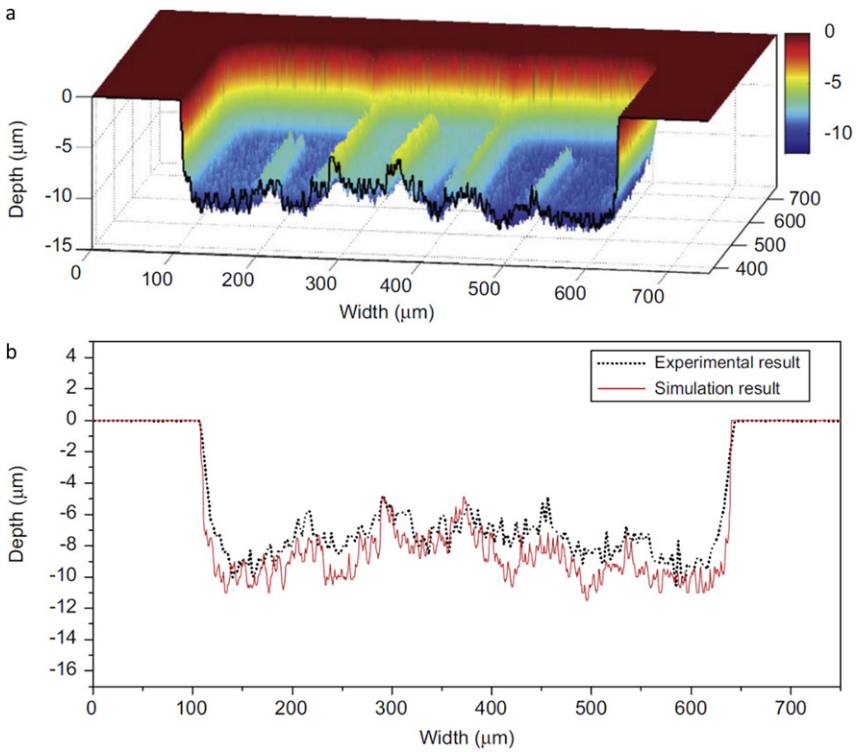


Figure 36 Workpiece surface generation simulation results: (a) graphical cross-sectional view generated by the simulator (solid line shows the contour of the cross-sectional edge) and (b) comparison of real machined and simulated surface profiles.[120]

variation in WLT was around 38–39%, while the impact of hole depth on WLT variation was 17%.

Shabgard *et al.*[123] simulated the temperature distribution over the workpiece and tool surface during a single discharge in the EDM process. The temperature dependency of material properties and the expansion of plasma channel radius were considered in the simulation stage, then the profile of temperature distribution was utilized to calculate the discharge crater dimensions. According to the simulation results, increasing pulse current and pulse on-time have converse effects on the plasma flushing efficiency, as it increases by pulse current and decreases by pulse on-time.

In 2015, Zhang *et al.*[124] proposed a fix-length compensation method. Their initial experiments showed that a cone-shaped tool end formed with this compensation method. Finally, they carried out a set of experiments to validate the simulation accuracy. The results revealed that the relative error of the simulation was below 4% compared to the experimental data under most machining conditions.

1.7.7.2 Finite Element Method

Finite element, a dominant numerical method, is used to find approximate solutions to boundary value problems for partial differential equations. Das *et al.*[125] developed a finite element-based model for EDM, with the ability to consider all process parameters including power input, pulse duration, etc., to predict the transient temperature distribution, liquid- and solid-state material transformation, final crater shape and residual stresses induced in the workpiece as a result of a single-pulse discharge. In 2004, Schulze[126] investigated the crater morphology in different processes and obtained an analytical relation between pulse parameters and roughness. For both single-discharge and a sequence of discharges, simulations of the thermal-affected zones were done. The crater geometry simulation refers exclusively to the thermal influence of the machining surface through the base of the plasma channel.

Process simulation and residual stress analysis for the micro-EDM machining of molybdenum was introduced by Allen and Chen.[127] Material removal was analyzed using a thermo-numerical model, which simulates a single-spark discharge process. Using the numerical model, the influence of important EDM factors including pulse duration on crater dimensions and tool wear percentage was investigated. The results from a coupled thermal-structural finite element analysis also defined how the thermal action of the micro-EDM process affects the machined workpiece surface integrity.

Kansal *et al.*[128] applied the finite element method and developed an axisymmetric two-dimensional (2D) model for powder mixed electric discharge machining. In order to predict the thermal behavior and material removal mechanism in the PMEDM process, the model considered several significant aspects of temperature-sensitive material properties, heat source shape and size (Gaussian heat distribution), heat percentage distribution among the tool, workpiece and dielectric fluid, pulse on/off-time, material ejection efficiency, and phase change (enthalpy). **Figure 37** displays the spark frequency in EDM versus PMEDM. The model initially calculated the temperature distribution in the workpiece material using ANSYS

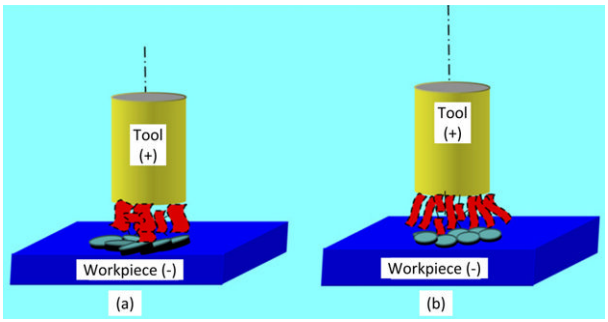


Figure 37 Spark frequency in (a) electrical discharge machining and (b) powder mixed electrical discharge machining.[128]

software and then projected the MRR from the temperature profiles. The effects of various process parameters on the temperature distribution along the workpiece radius and depth were stated. Finally, the model was verified by contrasting the theoretical with experimental MRR values attained.

Hosseini Kalajahi *et al.*[129] performed thermal modeling and finite element simulation of EDM to predict the thermal behavior and material removal mechanism in the EDM process. Several significant characteristics were taken into account, including temperature-dependent material properties, heated zone shape and size (Gaussian heat distribution), energy distribution factor, plasma flushing efficiency, and phase change. Furthermore, the influence of EDM parameters on MRR were inspected by using design of experiments and response surface methodology techniques. Finally, a quadratic polynomial regression model was recommended for MRR, and the model's accuracy was checked by means of analysis of residuals.

By using the finite element scheme, Izquierdo *et al.*[130] numerically calculated the temperature fields within the workpiece generated by the superposition of multiple discharges as they occur during actual EDM operation. According to the results (**Figure 38**), the model can predict surface roughness with less than 6% error. It can also predict MRR well, with less than 3% error. Joshi and Pande[131] proposed a thermo-physical model for die-sinking EDM. The analysis was constructed on realistic assumptions such as Gaussian distribution of heat flux, spark radius equation based on discharge current and discharge duration, latent heat of melting, etc., to predict the crater cavity shape as well as the MRR. Experiments were carried out to study the MRR and crater shapes produced during actual machining.

In another study, Joshi and Pande[132] used both finite element method and artificial neural networks (ANN) and reported the development of an intelligent model for the EDM process. For predicting crater cavity shape, MRR and MRR, a 2D axisymmetric thermal finite element model for single-spark EDM was established based on more realistic assumptions, such as the Gaussian distribution of heat flux, time- and energy-dependent spark radius, and so on. Upon model verification with experimental results, a neural network-based process model was presented for various work tool materials. The ANN model could reportedly precisely predict EDM process responses to selected process conditions.

An axisymmetric 3D thermo-physical model for EDM of titanium alloy was presented by Xie *et al.*[133] The numerical

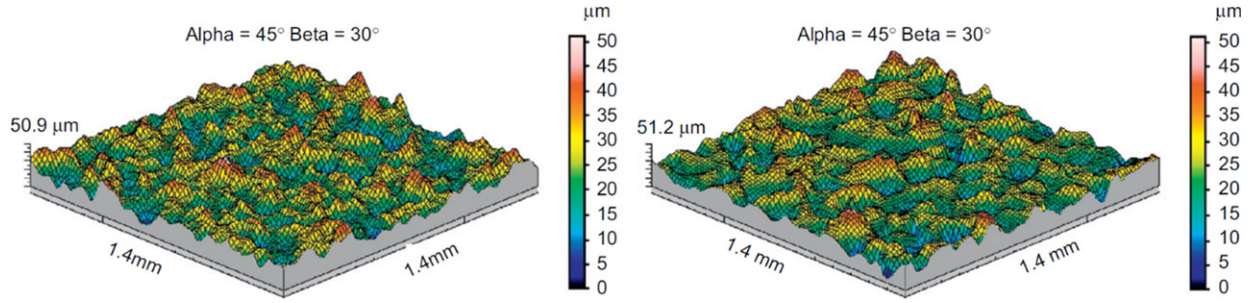


Figure 38 Comparison between simulated (left) and measured (right) surfaces.[130]

simulation of the single-spark discharge of titanium alloy machining in EDM and the influence of various process parameters on the temperature distribution along the workpiece radius were reported. Lastly, the model was verified empirically, demonstrating that it can predict the MRR efficiently. Shabgard *et al.*[134] also proposed an axisymmetric 3D model for temperature distribution in the EDM process. FEM was used to calculate the surface integrity characteristics of AISI H13 tool steel as the workpiece. White layer thickness, heat-affected zone depth, and arithmetical mean roughness consisting of the studied surface integrity features on which the effect of process parameters, including pulse on-time and pulse current were investigated. A comparison between the experimental and numerical results signified good agreement between these two values.

A fundamental study of micro-EDM based on the physics of single spark and electrothermal theory was implemented by Somashekhar *et al.*[135] Regarding a single-discharge crater, the experimental and simulation results were contrasted. The verification process results showed diameter-to-depth ratios of the crater of 2.92 and 2.67, respectively attained from the simulation and the experiment. Based on FEM, the heat flux of the plasma was investigated by comparing the melted material boundary in the crater as achieved by metallographic method and the isothermal surface of the thermal-physical model.[136] Evidently, the Gauss heat source was more consistent with the actual EDM process compared with other heat source types, such as point heat and circular heat sources. Moreover, Somashekhar *et al.*[137] proposed a numerical model based on the finite volume method in order to solve the micro-EDM model equations and predict the influence of spark ratio (spark on/off-time) on the temperature distribution in the material.

The powder-mixed micro-EDM process was analyzed using FEM analysis by taking into account the larger expansion of the plasma channel and reduction in heat flux distributed to the workpiece due to presence of powder particles. Analysis was based on FEMs and the multiple discharge approach. The heat source expansion factor owing to the presence of powder particles was estimated to be 1.07 at 0.02 g l^{-1} powder concentration. The fraction of heat flux to the workpiece found to decrease from 0.24 at 0.02 g l^{-1} to 0.11 at 0.2 g l^{-1} powder concentration. For model validation, simulated R_{max} and recast layer thickness values were compared with their corresponding measured values. The simulated and measured results varied with the same general trend, suggesting that the proposed model for PMD micro-EDM was fundamentally sound.[138]

Balaji and Yadava[139] identified a simulation model to simulate the complex electro-discharge diamond surface grinding (EDDSG) process, which entails simulating each constituent process, namely EDM and surface grinding for temperature and thermal stress distribution. The influence of various dielectric fluids, duty factors and energy partitions during EDM on the temperature distribution and MRR was specified. The prediction results could be used to determine the surface integrity of the machined surface. In another research work, Zhang *et al.*[140] simulated the evolution process of discharge-generated bubbles and investigated the influence of interelectrode distance on the characteristics of the bubbles through material removal mechanism simulation and experiment, respectively. They found that a smaller interelectrode distance can contribute to greater pressure and expansion velocity of the bubbles as well as higher force applied on the tool electrode and workpiece. A smaller interelectrode distance can contribute to a larger volume of both melted and removed material.

Gu *et al.*[114] aimed to identify an effective Ti6Al4V EDM process with a bundled die-sinking electrode. The simulation results explained the high performance of the EDM process with a bundled electrode through the use of multi-hole inner flushing that efficiently removes molten material from the interelectrode gap and through the improved ability to apply a higher peak current. Wang and Han[141] built a 3D model of flow field with liquid, gas, and solid phases for the machining gap in EDM. The mechanisms of debris and bubble movement in the machining gap during consecutive-pulse discharge were analyzed with the model and their movements were observed via experiments. The results showed that the proposed simulation model is feasible. Bubble expansion is the main way that the bubbles escape from the machining gap. Much debris moves outside the machining gap following the excluded bubbles, which is the principal way that the debris is ejected from the machining gap. The bubble expansion becomes stronger with increasing discharge current and pulse on-time.

A comprehensive electro-thermal model of micro-EDM has been used to simulate the crater formation process is presented. This model incorporates realistic machining conditions such as Gaussian distributed heat flux, temperature dependent thermal properties, and expending plasma radius. The heat transfer equation and experimental measurements of a generated crater dimensions are used to determine the energy distribution fraction to the electrodes, a crucial parameter of the micro-EDM modeling. Simulation results show a good agreement with experimental results.[142]

1.7.7.3 Molecular Dynamics Model

Yang *et al.*[143] simulated the formation process of discharge craters in 3D and analyzed the material removal mechanism in EDM using molecular dynamics (MD). They noted that the material removal mechanism in EDM can be explained in two ways: by vaporization and by the bubble explosion of superheated metals. Simulation of the distribution of removed materials from the gap showed that some part of the removed material became debris ejected from the gap, another part settled on the surface of the opposite electrode, and the last part returned to the surface of the electrode from which it was ejected.

Residual stress deteriorates the quality of produced component which might lead to premature failure when mechanical stress is applied. Yang *et al.*[144] simulated the formation mechanism of residual stress and its distribution using molecular dynamics methods. It was found that a larger pressure gradient formed in the melting area during discharge and a larger stress gradient in the melting region and the solid region in contact with the melting area. From the residual stress distribution, it was concluded that the residual stress on the electrode surface is tensile while inside the electrode it is compressive, indicating that cracks can easily generate in the resolidified layer.

Zhang *et al.*[145] used a computational simulation model combining the molecular dynamics simulation model and the two-temperature model for single discharge process in nano-EDM to study the machining mechanism of nano-EDM from a thermal point of view. The melting, cooling and solidifying processes were analyzed. They determined that during melted material cooling, tensile stress of more than 3 GPa arises, which leads to material disintegration. The white layer formation was attributed to the homogeneous solidification. Moreover, the resultant residual stress was analyzed.

Guo *et al.*[146] employed the atomistic–continuum modeling method, in which a two-temperature model and a molecular dynamics simulation model were integrated to construct a simulation model for a cathode in single-discharge micro-EDM process. By analyzing the evolution of temperature, stress, and microstructure of the material as well as the dynamic behavior of the material in the removal process, the mechanisms of the cathode material removal and crater formation were revealed. In addition, the removal process of the cathode material under a combination of pure thermal action and pure electric action was compared with that under the two pure actions, respectively, to analyze the interactive effect between the thermal and electric actions.

1.7.7.4 Supporting Vector Machine

The supporting vector machine was adopted by Zhang *et al.*[147] to establish a micro-EDM process model based on the orthogonal test. A new multi-objective optimization genetic algorithm based on the notion of nondominated sorting was proposed to optimize the processing parameters. Experimental results demonstrated that the proposed multi-objective genetic algorithm method is precise and effective in obtaining Pareto-optimal solutions of parameter settings. The optimized parameter combinations could significantly reduce the processing time while reducing electrode wear. Therefore, the proposed method is suitable for micro-EDM parameter optimization and can also enhance the efficiency and stability of the process.

Aich and Banerjee[148] applied support vector machines to develop a model of the EDM process. The Gaussian radial basis function and e-insensitive loss function were used as kernel function and loss function, respectively. Separate models of MRR and R_a were developed by minimizing the mean absolute percentage error of training data obtained for different sets of support vector machine parameter combinations. Particle swarm optimization was employed for the purpose of optimizing support vector machine parameter combinations. The models thus developed were then tested with disjoint testing data sets. The optimum parameter settings for maximum MRR and minimum R_a were further investigated by applying particle swarm optimization to the developed models.

1.7.7.5 Others

Also in terms of simulation, a geometric simulation model of the EDM drilling process with a cylindrical tool for predicting tool and drilled hole geometries was identified.[149] For accurate geometry simulation, tool motion, sparking gap width, spark frequency, the crater made by a single spark, and the TWR were selected as simulation parameters. The comparison of the prediction results with the actual experimental results revealed that geometry can be predicted within 13% error. The developed model can also be successfully introduced as an offline tool wear compensation method, which enables considering both end and corner wear of a tool with less than 2.9% compensation error.

The spectroscopic measurement of the arc plasma diameter in EDM was explained.[150] Unlike conventional plasma expansion models established based on observations of generated craters and unproven assumptions, it was revealed that arc plasma completes expanding within a few microseconds after dielectric breakdown, while the diameter of the craters grows slowly in comparison with the expansion speed of the arc plasma. Moreover, the increase in arc plasma diameter with rising discharge current or gap width was computed, enabling accurate simulation of discharge crater generation using the newly established heat source model.

In another study, the development of a sinking EDM simulation method by determining discharge locations was described.[151] The simulation repeats the routine modeling of the process of each discharge consisting of determining the discharge location, electrode removal, debris particles generation and displacement, and tool electrode feeding. The experimental results and the electrode shapes and gap width distributions simulated for different working surface areas were coherent.

A thermal model capable of simulating the superposition of successive discharges, which leads to the formation of EDM surfaces, was developed by Izquierdo *et al.*[152] Some process aspects, such as the percentage of discharge energy transferred to the workpiece, plasma channel growth, material removal mechanism, and the influence of convective cooling were discussed. Predictions of the extension of the recast layer and heat-affected layer for both regimes were also determined. Finally, the model was used to predict the extension of the white layer and heat-affected zone. It was observed that the

model performed well, with less than 3 μm prediction error in the analyzed EDM regimes.

In order to facilitate superior debris flushing in EDM, a rotary tool and magnetic field were implemented. Then two adaptive neuro-fuzzy inference system (ANFIS) models were designed to correlate the EDM parameters to MRR and surface roughness using the data generated from experimental observations.[153] To select the best process parameters of magnetic field intensity, rotational speed and product of current and pulse on-time, the continuous ant colony optimization (CACO) technique was used. According to the results, the CACO technique that comprises ANFIS models as objective and constrain functions, can successfully optimize the input conditions of the magnetic field-assisted rotary EDM process.

1.7.8 Conclusions

EDM as one of the most promising technologies for production of difficult-to-cut conductive materials, is the center of attention by researchers in the past decades. This chapter provides a detailed review of the available investigations with comprehensive categorization to build a clear mapping for further research in the area of EDM. The following can be concluded:

- Utilization of water-based dielectric or gas can be a better replacement for oil-based dielectrics since they provide a healthier and safer machining environment. Employing water dielectric produces thinner heat-affected zone and reduces the carbon content in the machining gap. Furthermore, the utilization of gas as dielectric is more cost efficient compared to hydrocarbon oil due to an extremely decreased TWR and reduced cost of dielectric medium compared to employing hydrocarbon oil. Application of water as a dielectric cause lower carbon generation which made it a suitable dielectric fluid, in some cases. Utilization of low resistivity deionized water has shown to facilitate achievement of simultaneous EDM–ECM process.
- Ultrasonic vibration assisted EDM is shown to have substantial impact for enhancing performance factors, where vibration of either tool and workpiece or dielectric results in higher cavitation effect. Majority of studies emphasize on micro-EDM and verified to obtain fabrication of microholes with significantly higher ARs. However, there is room for improvement and exploring the impact of ultrasonic vibration in conventional EDM for fabrication of cavities in complex shapes. Furthermore, the effects of vibration outside the ultrasonic frequency range can be recommended for further research.
- Introduction of ultrasonic vibration in dry EDM is feasible method owing to lack of dielectric fluid in the process. This enhancement seems to be a promising method for commercialization in terms of stability and effectiveness. Ultrasonic vibration have been identified as having higher machining efficiency in PMEDM, initially through homogenously mixing the powder with dielectric and secondly through improving the debris ejection effect throughout the process.
- Mixing powder with dielectric fluid shown to significantly improve the performance of EDM, however, deposition of powder particles at the bottom of the tank is still an issue which was addressed by solutions like ultrasonic vibration of the machining tank or addition of surfactant to dielectric fluid. Future studies should concentrate on introducing new solutions to homogeneously mix the powder with the dielectric liquid to avoid powder suspension at the bottom of the tank.
- The addition of titanium, tungsten, and titanium carbide to dielectric in PMEDM process is appropriate for surface modifications through alloying the external surface, which results in increased surface hardness, wear resistance. These powder materials can have substantial application for coating to address the steel oxidization issues in steel mold and die production manufacturing. In addition, adding conductive powder to dielectric increase the machinability of workpieces with very low conductivity might become possible with PMEDM.
- Although particle size is considered as essential factor in PMEDM investigations, a majority of investigations perform the experiment using micro-level solid particles. Whilst the occasionally available investigations on nano-size additives have obtained prominent outcomes.
- Mathematical modeling, finite element analysis, molecular dynamics model, supporting vector machine are the mostly used methods that could simulation and model the EDM process and its performance efficiently. Simulation and modeling of EDM and understanding the effect of input parameters on the performance factors significantly assist in providing a perfect vision for further enhancements.

Acknowledgments

The authors acknowledge the financial support of University Malaya Research Grant no. PG016-2013B from the University of Malaya, Malaysia.

See also: 1.11 Micromachining

References

1. Tsai, K.-M.; Wang, P.-J. Predictions on Surface Finish in Electrical Discharge Machining Based Upon Neural Network Models. *Int. J. Mach. Tools Manuf.* **2001**, *41* (10), 1385–1403.
2. Mohd Abbas, N.; Solomon, D. G.; Fuad Bahari, M. A Review on Current Research Trends in Electrical Discharge Machining (EDM). *Int. J. Mach. Tools Manuf.* **2007**, *47* (7–8), 1214–1228.
3. Ho, K. H.; Newman, S. T. State of the Art Electrical Discharge Machining (EDM). *Int. J. Mach. Tools Manuf.* **2003**, *43* (13), 1287–1300.
4. Masuzawa, T. State of the Art of Micromachining. *CIRP Ann. – Manuf. Technol.* **2000**, *49* (2), 473–488.
5. Liu, Y.; Wang, J.; Zhao, F.; Wang, Y. Research on Dielectric Breakdown Mechanism of Micro EDM. In *International Conference on Advanced Technology of Design and Manufacture (ATDM 2010)*, November 23–25, 2010; pp. 282–288.
6. Jahan, M. P.; Rahman, M.; Wong, Y. S. Study on the Nano-Powder-Mixed Sinking and Milling Micro-EDM of WC–Co. *Int. J. Adv. Manuf. Technol.* **2010**, *53* (1–4), 167–180.
7. Sommer, C.; Sommer, S. *Complete EDM Handbook*; Advance Publishing, Inc.: Houston, TX, 2005.

8. Jameson, E. C. *Electrical Discharge Machining*; Society of Manufacturing Engineers: Dearborn, MI, 2001.
9. Kibria, G.; Bhattacharyya, B. Analysis on Geometrical Accuracy of Microhole during Micro-EDM of Ti–6Al–4V Using Different Dielectrics. In *International Conference on Advances in Material and Processing Technologies*, 2010; pp. 155–160.
10. Zhixin, J.; Jianhua, Z.; Xing, A. Ultrasonic Vibration Pulse Electro-Discharge Machining of Holes in Engineering Ceramics. *J. Mater. Process. Technol.* **1995**, *53* (3–4), 811–816.
11. Zhang, J. H.; Lee, C. Y.; Lau, W. S.; Ai, X. Spark Erosion with Ultrasonic Frequency. *J. Mater. Process. Technol.* **1997**, *68* (1), 83–88.
12. Thoe, T. B.; Aspinwall, D. K.; Killey, N. Combined Ultrasonic and Electrical Discharge Machining of Ceramic Coated Nickel Alloy. *J. Mater. Process. Technol.* **1999**, *92* (93), 323–328.
13. Wansheng, Z.; Zhenlong, W.; Shichun, D.; Guanxin, C.; Hongyu, W. Ultrasonic and Electric Discharge Machining to Deep and Small Hole on Titanium Alloy. *J. Mater. Process. Technol.* **2002**, *120* (1–3), 101–106.
14. Huang, H.; Zhang, H.; Zhou, L.; Zheng, H. Y. Ultrasonic Vibration Assisted Electro-Discharge Machining of Microholes in Nitinol. *J. Micromech. Microeng.* **2003**, *13* (5), 693.
15. Abdullah, A.; Shabgard, M. R. Effect of Ultrasonic Vibration of Tool on Electrical Discharge Machining of Cemented Tungsten Carbide (WC–Co). *Int. J. Adv. Manuf. Technol.* **2007**, *38* (11–12), 1137–1147.
16. Abdullah, A.; Shabgard, M. R.; Ivanov, A.; Shervanyi-Tabar, M. T. Effect of Ultrasonic-Assisted EDM on the Surface Integrity of Cemented Tungsten Carbide (WC–Co). *Int. J. Adv. Manuf. Technol.* **2008**, *41* (3–4), 268–280.
17. Wei, C.; Zhao, L.; Hu, D.; Ni, J. Electrical Discharge Machining of Ceramic Matrix Composites with Ceramic Fiber Reinforcements. *Int. J. Adv. Manuf. Technol.* **2012**, *64* (1–4), 187–194.
18. Srivastava, V.; Pandey, P. M. Effect of Process Parameters on the Performance of EDM Process with Ultrasonic Assisted Cryogenically Cooled Electrode. *J. Manuf. Process.* **2012**, *14* (3), 393–402.
19. Srivastava, V.; Pandey, P. M. Study of Ultrasonic Assisted Cryogenically Cooled EDM Process Using Sintered (Cu–TiC) Tooltip. *J. Manuf. Process.* **2013**, *15* (1), 158–166.
20. Yan, B. H.; Wang, A. C.; Huang, C. Y.; Huang, F. Y. Study of Precision Micro-Holes in Borosilicate Glass Using Micro EDM Combined with Micro Ultrasonic Vibration Machining. *Int. J. Mach. Tools Manuf.* **2002**, *42* (10), 1105–1112.
21. Gao, C.; Liu, Z. A Study of Ultrasonically Aided Micro-Electrical-Discharge Machining by the Application of Workpiece Vibration. *J. Mater. Process. Technol.* **2003**, *139* (1–3), 226–228.
22. Sundaram, M. M.; Pavalarajan, G. B.; Rajurkar, K. P. A Study on Process Parameters of Ultrasonic Assisted Micro EDM Based on Taguchi Method. *J. Mater. Eng. Perform.* **2007**, *17* (2), 210–215.
23. Yu, Z. Y.; Zhang, Y.; Li, J.; Luan, J.; Zhao, F.; Guo, D. High Aspect Ratio Micro-Hole Drilling Aided with Ultrasonic Vibration and Planetary Movement of Electrode by Micro-EDM. *CIRP Ann. – Manuf. Technol.* **2009**, *58* (1), 213–216.
24. Garn, R.; Schubert, A.; Zeidler, H. Analysis of the Effect of Vibrations on the Micro-EDM Process at the Workpiece Surface. *Precis. Eng.* **2011**, *35* (2), 364–368.
25. Teimouri, R.; Baseri, H. Experimental Study of Rotary Magnetic Field-Assisted Dry EDM with Ultrasonic Vibration of Workpiece. *Int. J. Adv. Manuf. Technol.* **2012**, *67* (5–8), 1371–1384.
26. Ichikawa, T.; Natsu, W. Realization of Micro-EDM Under Ultra-Small Discharge Energy by Applying Ultrasonic Vibration to Machining Fluid. *Procedia CIRP* **2013**, *6*, 326–331.
27. Liu, Y.; Li, X.; Bai, F.; Chen, J.; Wang, Y.; Liu, N. Effect of System Parameters on the Size Distributions of Hollow Nickel Microspheres Produced by an Ultrasound-Aided Electrical Discharge Machining Process. *Particuology* **2014**, *17*, 36–41.
28. Zhang, Y.; Liu, Y.; Shen, Y.; Ji, R.; Li, Z.; Zheng, C. Investigation on the Influence of the Dielectrics on the Material Removal Characteristics of EDM. *J. Mater. Process. Technol.* **2014**, *214* (5), 1052–1061.
29. Zhang, Y.; Liu, Y.; Shen, Y.; Li, Z.; Ji, R.; Cai, B. A Novel Method of Determining Energy Distribution and Plasma Diameter of EDM. *Int. J. Heat Mass Transf.* **2014**, *75*, 425–432.
30. Leão, F. N.; Pashby, I. R. A Review on the Use of Environmentally-Friendly Dielectric Fluids in Electrical Discharge Machining. *J. Mater. Process. Technol.* **2004**, *149* (1–3), 341–346.
31. Zhang, Q. H.; Du, R.; Zhang, J. H.; Zhang, Q. B. An Investigation of Ultrasonic-Assisted Electrical Discharge Machining in Gas. *Int. J. Mach. Tools Manuf.* **2006**, *46* (12–13), 1582–1588.
32. Kunieda, M.; Furuoya, S.; Taniguchi, N. Improvement of EDM Efficiency by Supplying Oxygen Gas into Gap. *CIRP Ann. – Manuf. Technol.* **1991**, *40* (1), 215–218.
33. Chow, H.-M.; Yang, L.-D.; Lin, C.-T.; Chen, Y.-F. The Use of SiC Powder in Water as Dielectric for Micro-Slit EDM Machining. *J. Mater. Process. Technol.* **2008**, *195* (1–3), 160–170.
34. König, W.; Jörres, L. Aqueous Solutions of Organic Compounds as Dielectrics for EDM Sinking. *CIRP Ann. – Manuf. Technol.* **1987**, *36* (1), 105–109.
35. (a) Maher, I.; Eltaib, M. E. H.; Sarhan, A. A. D.; El-Zahry, R. M. Cutting Force-Based Adaptive Neuro-Fuzzy Approach for Accurate Surface Roughness Prediction in End Milling Operation for Intelligent Machining. *Int. J. Adv. Manuf. Technol.* **2015**, *76* (5–8), 1459–1467. (b) Maher, I.; Eltaib, M. E. H.; Sarhan, A. A. D.; El-Zahry, R. M. Investigation of the Effect of Machining Parameters on the Surface Quality of Machined Brass (60/40) in CNC End Milling – ANFIS Modeling. *Int. J. Adv. Manuf. Technol.* **2014**, *74* (1–4), 531–537.
36. Yan, B. H.; Chung Tsai, H.; Yuan Huang, F. The Effect in EDM of a Dielectric of a Urea Solution in Water on Modifying the Surface of Titanium. *Int. J. Mach. Tools Manuf.* **2005**, *45* (2), 194–200.
37. Zhang, Y.; Liu, Y.; Ji, R.; Cai, B. Study of the Recast Layer of a Surface Machined by Sinking Electrical Discharge Machining Using Water-in-Oil Emulsion as Dielectric. *Appl. Surf. Sci.* **2011**, *257* (14), 5989–5997.
38. Jeswani, M. L. Electrical Discharge Machining in Distilled Water. *Wear* **1981**, *72* (1), 81–88.
39. Jilani, S. T.; Pandey, P. C. Experimetnal Investigations into the Performance of Water as Dielectric in EDM. *Int. J. Mach. Tool Des. Res.* **1984**, *24* (1), 31–43.
40. Kruth, J. P.; Stevens, L.; Froyen, L.; Lauwers, B. Study of the White Layer of a Surface Machined by Die-Sinking Electro-Discharge Machining. *CIRP Ann. – Manuf. Technol.* **1995**, *44* (1), 169–172.
41. Chen, S. L.; Yan, B. H.; Huang, F. Y. Influence of Kerosene and Distilled Water as Dielectrics on the Electric Discharge Machining Characteristics of Ti–6A1–4V. *J. Mater. Process. Technol.* **1999**, *87* (1–3), 107–111.
42. Ekmekci, B.; Elkoca, O.; Erden, A. A Comparative Study on the Surface Integrity of Plastic Mold Steel Due to Electric Discharge Machining. *Metall. Mater. Trans. B* **2005**, *36* (1), 117–124.
43. Kang, S. H.; Kim, D. E. Effect of Electrical Discharge Machining Process on Crack Susceptibility of Nickel Based Heat Resistant Alloy. *Mater. Sci. Technol.* **2005**, *21* (7), 817–823.
44. Casanueva, R.; Azcondo, F. J.; Branas, C.; Bracho, S. Analysis, Design and Experimental Results of a High-Frequency Power Supply For Spark Erosion. *IEEE Trans. Power Electron.* **2005**, *20* (2), 361–369.
45. Tang, L.; Du, Y. T. Experimental Study on Green Electrical Discharge Machining in Tap Water of Ti–6Al–4V and Parameters Optimization. *Int. J. Adv. Manuf. Technol.* **2013**, *70* (1–4), 469–475.
46. Lin, C.-T.; Chow, H.-M.; Yang, L.-D.; Chen, Y.-F. Feasibility Study of Micro-Slit EDM Machining Using Pure Water. *Int. J. Adv. Manuf. Technol.* **2006**, *34* (1–2), 104–110.
47. Kurita, T.; Hattori, M. A Study of EDM and ECM/ECM-Lapping Complex Machining Technology. *Int. J. Mach. Tools Manuf.* **2006**, *46* (14), 1804–1810.
48. Nguyen, M. D.; Rahman, M.; Wong, Y. S. Simultaneous Micro-EDM and Micro-ECM in Low-Resistivity Deionized Water. *Int. J. Mach. Tools Manuf.* **2012**, *54–55*, 55–65.
49. Nguyen, M. D.; Rahman, M.; Wong, Y. S. Enhanced Surface Integrity and Dimensional Accuracy by Simultaneous Micro-ED/EC Milling. *CIRP Ann. – Manuf. Technol.* **2012**, *61* (1), 191–194.
50. Nguyen, M. D.; Rahman, M.; Wong, Y. S. Transitions of Micro-EDM/SEDCM/Micro-ECM Milling in Low-Resistivity Deionized Water. *Int. J. Mach. Tools Manuf.* **2013**, *69*, 48–56.
51. Yin, Q.; Wang, B.; Zhang, Y.; Ji, F.; Liu, G. Research of Lower Tool Electrode Wear in Simultaneous EDM and ECM. *J. Mater. Process. Technol.* **2014**, *214* (8), 1759–1768.
52. Xiao, H.; Jie, X.; Zeng, Z.; Li, G. Titanium Carbonitride Coating by Pulsed Electrical Discharge in an Aqueous Solution of Ethanolamine. *Surf. Coat. Technol.* **2014**, *258*, 1006–1010.
53. Govindan, P.; Joshi, S. S. Experimental Characterization of Material Removal in Dry Electrical Discharge Drilling. *Int. J. Mach. Tools Manuf.* **2010**, *50* (5), 431–443.

54. Govindan, P.; Joshi, S. S. Analysis of Micro-Cracks on Machined Surfaces in Dry Electrical Discharge Machining. *J. Manuf. Process.* **2012**, *14* (3), 277–288.
55. Kunieda, M.; Yoshida, M.; Taniguchi, N. Electrical Discharge Machining in Gas. *CIRP Ann. – Manuf. Technol.* **1997**, *46* (1), 143–146.
56. Kunieda, M.; Miyoshi, Y.; Takaya, T.; Nakajima, N.; ZhanBo, Y.; Yoshida, M. High Speed 3D Milling by Dry EDM. *CIRP Ann. – Manuf. Technol.* **2003**, *52* (1), 147–150.
57. Yu, Z.; Jun, T.; Masanori, K. Dry Electrical Discharge Machining of Cemented Carbide. *J. Mater. Process. Technol.* **2004**, *149* (1–3), 353–357.
58. Roth, R.; Kuster, F.; Wegener, K. Influence of Oxidizing Gas on the Stability of Dry Electrical Discharge Machining Process. *Procedia CIRP* **2013**, *6*, 338–343.
59. Xu, M. G.; Zhang, J. H.; Li, Y.; Zhang, Q. H.; Ren, S. F. Material Removal Mechanisms of Cemented Carbides Machined by Ultrasonic Vibration Assisted EDM in Gas Medium. *J. Mater. Process. Technol.* **2009**, *209* (4), 1742–1746.
60. Kunieda, M.; Takaya, T.; Nakano, S. Improvement of Dry EDM Characteristics Using Piezoelectric Actuator. *CIRP Ann. – Manuf. Technol.* **2004**, *53* (1), 183–186.
61. Joshi, S.; Govindan, P.; Malshe, A.; Rajurkar, K. Experimental Characterization of Dry EDM Performed in a Pulsating Magnetic Field. *CIRP Ann. – Manuf. Technol.* **2011**, *60* (1), 239–242.
62. Liqing, L.; Yingjie, S. Study of Dry EDM with Oxygen-Mixed and Cryogenic Cooling Approaches. *Procedia CIRP* **2013**, *6*, 344–350.
63. Curodeau, A.; Richard, M.; Frohn-Villeneuve, L. Molds Surface Finishing with New EDM Process in Air with Thermoplastic Composite Electrodes. *J. Mater. Process. Technol.* **2004**, *149* (1–3), 278–283.
64. Lin, Y.-C.; Chen, Y.-F.; Wang, A. C.; Sei, W.-L. Machining Performance on Hybrid Process of Abrasive Jet Machining and Electrical Discharge Machining. *Trans. Nonferr. Metals Soc. China* **2012**, *22*, s775–s780.
65. Kao, C. C.; Tao, J.; Shih, A. J. Near Dry Electrical Discharge Machining. *Int. J. Mach. Tools Manuf.* **2007**, *47* (15), 2273–2281.
66. Fujiki, M.; Ni, J.; Shih, A. J. Investigation of the Effects of Electrode Orientation and Fluid Flow Rate in Near-Dry EDM Milling. *Int. J. Mach. Tools Manuf.* **2009**, *49* (10), 749–758.
67. Fujiki, M.; Kim, G.-Y.; Ni, J.; Shih, A. J. Gap Control for Near-Dry EDM Milling with Lead Angle. *Int. J. Mach. Tools Manuf.* **2011**, *51* (1), 77–83.
68. Kansal, H. K.; Singh, S.; Kumar, P. Technology and Research Developments in Powder Mixed Electric Discharge Machining (PMEDM). *J. Mater. Process. Technol.* **2007**, *184* (1–3), 32–41.
69. Yih-fong, T.; Fu-chen, C. Investigation into some Surface Characteristics of Electrical Discharge Machined SKD-11 Using Powder-Suspension Dielectric Oil. *J. Mater. Process. Technol.* **2005**, *170* (1–2), 385–391.
70. Chen, Y.-F.; Lin, Y.-C. Surface Modifications of Al–Zn–Mg Alloy Using Combined EDM with Ultrasonic Machining and Addition of TiC Particles into the Dielectric. *J. Mater. Process. Technol.* **2009**, *209* (9), 4343–4350.
71. Liew, P. J.; Yan, J.; Kuriyagawa, T. Carbon Nanofiber Assisted Micro Electro Discharge Machining of Reaction-Bonded Silicon Carbide. *J. Mater. Process. Technol.* **2013**, *213* (7), 1076–1087.
72. Prihandana, G. S.; Mahardika, M.; Hamdi, M.; Wong, Y. S.; Mitsui, K. Effect of Micro-Powder Suspension and Ultrasonic Vibration of Dielectric Fluid in Micro-EDM Processes – Taguchi Approach. *Int. J. Mach. Tools Manuf.* **2009**, *49* (12–13), 1035–1041.
73. Prihandana, G. S.; Mahardika, M.; Hamdi, M.; Wong, Y. S.; Miki, N.; Mitsui, K. Study of Workpiece Vibration in Powder-Suspended Dielectric Fluid in Micro-EDM Processes. *Int. J. Precis. Eng. Manuf.* **2013**, *14* (10), 1817–1822.
74. Peças, P.; Henriques, E. Influence of Silicon Powder-Mixed Dielectric on Conventional Electrical Discharge Machining. *Int. J. Mach. Tools Manuf.* **2003**, *43* (14), 1465–1471.
75. Zhao, W. S.; Meng, Q. G.; Wang, Z. L. The Application of Research on Powder Mixed EDM in Rough Machining. *J. Mater. Process. Technol.* **2002**, *129*, 30–33.
76. Marashi, H.; Sarhan, A. A. D.; Hamdi, M. Employing Ti Nano-Powder Dielectric to Enhance Surface Characteristics in Electrical Discharge Machining of AISI D2 Steel. *Appl. Surf. Sci.* **2015**, *357, Part A*, 892–907.
77. Jeswani, M. L. Effect of the Addition of Graphite Powder to Kerosene Used as the Dielectric Fluid in Electrical Discharge Machining. *Wear* **1981**, *70* (2), 133–139.
78. Kansal, H. K.; Singh, S.; Kumar, P. Parametric Optimization of Powder Mixed Electrical Discharge Machining by Response Surface Methodology. *J. Mater. Process. Technol.* **2005**, *169* (3), 427–436.
79. Kansal, H. K.; Singh, S.; Kumar, P. Effect of Silicon Powder Mixed EDM on Machining Rate of AISI D2 Die Steel. *J. Manuf. Process.* **2007**, *9* (1), 13–22.
80. Peças, P.; Henriques, E. Effect of the Powder Concentration and Dielectric Flow in the Surface Morphology in Electrical Discharge Machining with Powder-Mixed Dielectric (PMD-EDM). *Int. J. Adv. Manuf. Technol.* **2007**, *37* (11–12), 1120–1132.
81. Wu, K. L.; Yan, B. H.; Huang, F. Y.; Chen, S. C. Improvement of Surface Finish on SKD Steel Using Electro-Discharge Machining with Aluminum and Surfactant Added Dielectric. *Int. J. Mach. Tools Manuf.* **2005**, *45* (10), 1195–1201.
82. Kung, K.-Y.; Horng, J.-T.; Chiang, K.-T. Material Removal Rate and Electrode Wear Ratio Study on the Powder Mixed Electrical Discharge Machining of Cobalt-Bonded Tungsten Carbide. *Int. J. Adv. Manuf. Technol.* **2007**, *40* (1–2), 95–104.
83. Lin, Y.-C.; Chow, H.-M.; Yan, B.-H.; Tzeng, H.-J. Effects of Finishing in Abrasive Fluid Machining on Microholes Fabricated by EDM. *Int. J. Adv. Manuf. Technol.* **2006**, *33* (5–6), 489–497.
84. Hu, F. Q.; Cao, F. Y.; Song, B. Y.; *et al.* Surface Properties of SiCp/Al Composite by Powder-Mixed EDM. *Procedia CIRP* **2013**, *6*, 101–106.
85. Yan, B. H.; Chen, S. L. Characteristics of SKD11 by Complex Process of Electrical Discharge Machining Using Liquid Suspended with Alumina Powder. *J. Jpn. Inst.Metals* **1994**, *58*, 1067–1072.
86. Kibria, G.; Sarkar, B. R.; Pradhan, B. B.; Bhattacharyya, B. Comparative Study of Different Dielectrics for Micro-EDM Performance during Microhole Machining of Ti–6Al–4V Alloy. *Int. J. Adv. Manuf. Technol.* **2009**, *48* (5–8), 557–570.
87. Wong, Y. S.; Lim, L. C.; Rahuman, I.; Tee, W. M. Near-Mirror-Finish Phenomenon in EDM Using Powder-Mixed Dielectric. *J. Mater. Process. Technol.* **1998**, *79* (1–3), 30–40.
88. Chow, H.-M.; Yan, B.-H.; Huang, F.-Y.; Hung, J.-C. Study of Added Powder in Kerosene for the Micro-Slit Machining of Titanium Alloy Using Electro-Discharge Machining. *J. Mater. Process. Technol.* **2000**, *101* (1–3), 95–103.
89. Tzeng, Y. F.; Lee, C. Y. Effects of Powder Characteristics on Electrodischarge Machining Efficiency. *Int. J. Adv. Manuf. Technol.* **2001**, *17* (8), 586–592.
90. Furutani, K.; Shiraki, K. Deposition of Lubricant Layer During Finishing Process by Electrical Discharge Machining with Molybdenum Disulfide Powder Suspended in Working Fluid. *JSME Materials and Processing Conference (M&P)* **2002**, *10* (2), 468–473.
91. Batish, A.; Bhattacharya, A.; Singla, V. K.; Singh, G. Study of Material Transfer Mechanism in Die Steels Using Powder Mixed Electric Discharge Machining. *Mater. Manuf. Process.* **2012**, *27* (4), 449–456.
92. Janmanee, P.; Muttamara, A. Surface Modification of Tungsten Carbide by Electrical Discharge Coating (EDC) Using a Titanium Powder Suspension. *Appl. Surf. Sci.* **2012**, *258* (19), 7255–7265.
93. Bhattacharya, A.; Batish, A.; Kumar, N. Surface Characterization and Material Migration during Surface Modification of Die Steels with Silicon, Graphite and Tungsten Powder in EDM Process. *J. Mech. Sci. Technol.* **2013**, *27* (1), 133–140.
94. Chen, S.-L.; Lin, M.-H.; Huang, G.-X.; Wang, C.-C. Research of the Recast Layer on Implant Surface Modified by Micro-Current Electrical Discharge Machining Using Deionized Water Mixed with Titanium Powder as Dielectric Solvent. *Appl. Surf. Sci.* **2014**, *311*, 47–53.
95. Sidhu, S. S.; Batish, A.; Kumar, S. Study of Surface Properties in Particulate-Reinforced Metal Matrix Composites (MMCs) Using Powder-Mixed Electrical Discharge Machining (EDM). *Mater. Manuf. Process.* **2014**, *29* (1), 46–52.
96. Bhattacharya, A.; Batish, A.; Singh, G.; Singla, V. K. Optimal Parameter Settings for Rough and Finish Machining of Die Steels in Powder-Mixed EDM. *Int. J. Adv. Manuf. Technol.* **2011**, *61* (5–8), 537–548.
97. Kumar, S.; Batra, U. Surface Modification of Die Steel Materials by EDM Method Using Tungsten Powder-Mixed Dielectric. *J. Manuf. Process.* **2012**, *14* (1), 35–40.
98. Cherng Lin, Y.; Hwa Yan, B.; Yuan Huang, F. Surface Modification of Al–Zn–Mg Aluminum Alloy Using the Combined Process of EDM with USM. *J. Mater. Process. Technol.* **2001**, *115* (3), 359–366.
99. Prihandana, G. S.; Mahardika, M.; Hamdi, M.; Wong, Y. S.; Mitsui, K. Accuracy Improvement in Nanographite Powder-Suspended Dielectric Fluid for Micro-Electrical Discharge Machining Processes. *Int. J. Adv. Manuf. Technol.* **2011**, *56* (1–4), 143–149.
100. Liew, P. J.; Yan, J.; Kuriyagawa, T. Fabrication of Deep Micro-Holes in Reaction-Bonded SiC by Ultrasonic Cavitation Assisted Micro-EDM. *Int. J. Mach. Tools Manuf.* **2014**, *76*, 13–20.
101. Bai, X.; Zhang, Q.; Zhang, J.; Kong, D.; Yang, T. Machining Efficiency of Powder Mixed Near Dry Electrical Discharge Machining Based on Different

Material Combinations of Tool Electrode and Workpiece Electrode. *J. Manuf. Process.* **2013**, *15* (4), 474–482.
102. Bai, X.; Zhang, Q.-H.; Yang, T.-Y.; Zhang, J.-H. Research on Material Removal Rate of Powder Mixed Near Dry Electrical Discharge Machining. *Int. J. Adv. Manuf. Technol.* **2013**, *68* (5–8), 1757–1766.
103. Ojha, K.; Garg, R. K.; Singh, K. K. Parametric Optimization of PMEDM Process Using Chromium Powder Mixed Dielectric and Triangular Shape Electrodes. *J. Miner. Mater. Charact. Eng.* **2011**, *10* (11), 1087–1102.
104. Tsai, Y. Y.; Su, J. S.; Su, C. Y. A Novel Method to Produce Carbon Nanotubes Using EDM Process. *Int. J. Mach. Tools Manuf.* **2008**, *48* (15), 1653–1657.
105. Shabgard, M. R.; Kabirinia, F. Effect of Dielectric Liquid on Characteristics of WC–Co Powder Synthesized Using EDM Process. *Mater. Manuf. Process.* **2014**, *29* (10), 1269–1276.
106. Furutania, K.; Saneto, A.; Takezawa, H.; Mohri, N.; Miyake, H. Accretion of Titanium Carbide by Electrical Discharge Machining with Powder Suspended in Working Fluid. *Precis. Eng.* **2001**, *25* (2), 138–144.
107. Patowari, P. K.; Saha, P.; Mishra, P. K. Taguchi Analysis of Surface Modification Technique Using W–Cu Powder Metallurgy Sintered Tools in EDM and Characterization of the Deposited Layer. *Int. J. Adv. Manuf. Technol.* **2010**, *54* (5–8), 593–604.
108. Hwang, Y.-L.; Kuo, C.-L.; Hwang, S.-F. The Coating of TiC Layer on the Surface of Nickel by Electric Discharge Coating (EDC) with a Multi-Layer Electrode. *J. Mater. Process. Technol.* **2010**, *210* (4), 642–652.
109. Suzuki, T.; Kobayashi, S. Mechanisms of TiC Layer Formation on High Speed Steel by a Single Pulse in Electrical Discharge Machining. *Electrochim. Acta* **2013**, *114*, 844–850.
110. Mohri, N.; Takezawa, H.; Furutani, K.; Ito, Y.; Sata, T.; New, A. Process of Additive and Removal Machining by EDM with a Thin Electrode. *CIRP Ann. – Manuf. Technol.* **2000**, *49* (1), 123–126.
111. Maradia, U.; Boccadoro, M.; Stirnimann, J.; Kuster, F.; Wegener, K. Electrode Wear Protection Mechanism in Meso–Micro-EDM. *J. Mater. Process. Technol.* **2015**, *223*, 22–33.
112. Ferraris, E.; Castiglioni, V.; Ceyssens, F.; Annoni, M.; Lauwers, B.; Reynaerts, D. EDM Drilling of Ultra-High Aspect Ratio Micro Holes with Insulated Tools. *CIRP Ann. – Manuf. Technol.* **2013**, *62* (1), 191–194.
113. Frohn-Villeneuve, L.; Curodeau, A. Dry Die-sinking EDM with Mouldable Graphite–Polymer Electrode Investigation of Process Parameters and Pulse Identification Methods. *Int. J. Adv. Manuf. Technol.* **2012**, *65* (5–8), 1125–1139.
114. Gu, L.; Li, L.; Zhao, W.; Rajurkar, K. P. Electrical Discharge Machining of Ti6Al4V with a Bundled Electrode. *Int. J. Mach. Tools Manuf.* **2012**, *53* (1), 100–106.
115. Muralidhara; Vasa, N. J.; Makaram, S. Investigations on a Directly Coupled Piezoactuated Tool Feed System for Micro-Electro-Discharge Machine. *Int. J. Mach. Tools Manuf.* **2009**, *49* (15), 1197–1203.
116. El-Taweel, T. A. Multi-Response Optimization of EDM with Al–Cu–Si–TiC P/M Composite Electrode. *Int. J. Adv. Manuf. Technol.* **2008**, *44* (1–2), 100–113.
117. Fujun, R.; Dechen, H.; Dianjun, W. Analysis of Motion Laws of Machining Non-Sphere by EDM with Rotary Electrode. *J. Mater. Process. Technol.* **2004**, *149* (1–3), 323–327.
118. Bleys, P.; Kruth, J. P.; Lauwers, B. Sensing and Compensation of Tool Wear in Milling EDM. *J. Mater. Process. Technol.* **2004**, *149* (1–3), 139–146.
119. Salonitis, K.; Stournaras, A.; Stavropoulos, P.; Chryssolouris, G. Thermal Modeling of the Material Removal Rate and Surface Roughness for Die-Sinking EDM. *Int. J. Adv. Manuf. Technol.* **2008**, *40* (3–4), 316–323.
120. Heo, S.; Jeong, Y. H.; Min, B.-K.; Lee, S. J. Virtual EDM Simulator: Three-Dimensional Geometric Simulation of Micro-EDM Milling Processes. *Int. J. Mach. Tools Manuf.* **2009**, *49* (12–13), 1029–1034.
121. Liu, N.-M.; Chiang, K.-T.; Horng, J.-T.; Chen, C.-C. Modeling and Analysis of the Edge Disintegration in the EDM Drilling Cobalt-Bonded Tungsten Carbide. *Int. J. Adv. Manuf. Technol.* **2010**, *51* (5–8), 587–598.
122. Yildiz, Y.; Sundaram, M. M.; Rajurkar, K. P. Empirical Modeling of the White Layer Thickness Formed in Electrodischarge Drilling of Beryllium–Copper Alloys. *Int. J. Adv. Manuf. Technol.* **2012**, *66* (9–12), 1745–1755.
123. Shabgard, M.; Ahmadi, R.; Seyedzavvar, M.; Oliaei, S. N. B. Mathematical and Numerical Modeling of the Effect of Input-Parameters on the Flushing Efficiency of Plasma Channel in EDM Process. *Int. J. Mach. Tools Manuf.* **2013**, *65*, 79–87.
124. Zhang, L.; Du, J.; Zhuang, X.; Wang, Z.; Pei, J. Geometric Prediction of Conic Tool in Micro-EDM Milling with Fix-Length Compensation Using Simulation. *Int. J. Mach. Tools Manuf.* **2015**, *89*, 86–94.
125. Das, S.; Klotz, M.; Klocke, F. EDM Simulation: Finite Element-Based Calculation of Deformation, Microstructure and Residual Stresses. *J. Mater. Process. Technol.* **2003**, *142* (2), 434–451.
126. Schulze, H. Comparison of Measured and Simulated Crater Morphology for EDM. *J. Mater. Process. Technol.* **2004**, *149* (1–3), 316–322.
127. Allen, P.; Chen, X. Process Simulation of Micro Electro-Discharge Machining on Molybdenum. *J. Mater. Process. Technol.* **2007**, *186* (1–3), 346–355.
128. Kansal, H. K.; Singh, S.; Kumar, P. Numerical Simulation of Powder Mixed Electric Discharge Machining (PMEDM) Using Finite Element Method. *Math. Comput. Model.* **2008**, *47* (11–12), 1217–1237.
129. Hosseini Kalajahi, M.; Rash Ahmadi, S.; Nadimi Bavil Oliaei, S. Experimental and Finite Element Analysis of EDM Process and Investigation of Material Removal Rate by Response Surface Methodology. *Int. J. Adv. Manuf. Technol.* **2013**, *69* (1–4), 687–704.
130. Izquierdo, B.; Sánchez, J. A.; Plaza, S.; Pombo, I.; Ortega, N. A Numerical Model of the EDM Process Considering the Effect of Multiple Discharges. *Int. J. Mach. Tools Manuf.* **2009**, *49* (3–4), 220–229.
131. Joshi, S. N.; Pande, S. S. Thermo-Physical Modeling of Die-Sinking EDM Process. *J. Manuf. Process.* **2010**, *12* (1), 45–56.
132. Joshi, S. N.; Pande, S. S. Development of an Intelligent Process Model for EDM. *Int. J. Adv. Manuf. Technol.* **2009**, *45* (3–4), 300–317.
133. Xie, B.-c.; Wang, Y.-k.; Wang, Z.-l.; Zhao, W.-s. Numerical Simulation of Titanium Alloy Machining in Electric Discharge Machining Process. *Trans. Nonferr. Metals Soc. China* **2011**, *21*, s434–s439.
134. Shabgard, M.; Oliaei, S. N. B.; Seyedzavvar, M.; Najadebrahimi, A. Experimental Investigation and 3D Finite Element Prediction of the White Layer Thickness, Heat Affected Zone, and Surface Roughness in EDM Process. *J. Mech. Sci. Technol.* **2012**, *25* (12), 3173–3183.
135. Somashekhar, K. P.; Mathew, J.; Ramachandran, N. Electrothermal Theory Approach for Numerical Approximation of the μ-EDM Process. *Int. J. Adv. Manuf. Technol.* **2012**, *61* (9–12), 1241–1246.
136. Zhang, Y.; Liu, Y.; Shen, Y.; Li, Z.; Ji, R.; Wang, F. A New Method of Investigation the Characteristic of the Heat Flux of EDM Plasma. *Procedia CIRP* **2013**, *6*, 450–455.
137. Somashekhar, K. P.; Panda, S.; Mathew, J.; Ramachandran, N. Numerical Simulation of Micro-EDM Model with Multi-Spark. *Int. J. Adv. Manuf. Technol.* **2013**, *76* (1), 83–90.
138. Tan, P. C.; Yeo, S. H. Simulation of Surface Integrity for Nanopowder-Mixed Dielectric in Micro Electrical Discharge Machining. *Metall. Mater. Trans. B* **2013**, *44* (3), 711–721.
139. Balaji, P. S.; Yadava, V. Three Dimensional Thermal Finite Element Simulation of Electro-Discharge Diamond Surface Grinding. *Simul. Model. Pract. Theory* **2013**, *35*, 97–117.
140. Zhang, Y.; Liu, Y.; Ji, R.; Zheng, C.; Shen, Y.; Wang, X. Transient Dynamics Simulation of the Electrical Discharge-Generated Bubble in Sinking EDM. *Int. J. Adv. Manuf. Technol.* **2013**, *68* (5–8), 1707–1715.
141. Wang, J.; Han, F. Simulation Model of Debris and Bubble Movement in Consecutive-Pulse Discharge of Electrical Discharge Machining. *Int. J. Mach. Tools Manuf.* **2014**, *77*, 56–65.
142. Shao, B.; Rajurkar, K. P. Modelling of the Crater Formation in Micro-EDM. *Procedia CIRP* **2015**, *33*, 377–382.
143. Yang, X.; Guo, J.; Chen, X.; Kunieda, M. Molecular Dynamics Simulation of the Material Removal Mechanism in Micro-EDM. *Precis. Eng.* **2011**, *35* (1), 51–57.
144. Yang, X.; Han, X.; Zhou, F.; Kunieda, M. Molecular Dynamics Simulation of Residual Stress Generated in EDM. *Procedia CIRP* **2013**, *6*, 432–437.
145. Zhang, G.; Guo, J.; Ming, W.; Huang, Y.; Shao, X.; Zhang, Z. Study of the Machining Process of Nano-Electrical Discharge Machining Based on Combined Atomistic-Continuum Modeling Method. *Appl. Surf. Sci.* **2014**, *290*, 359–367.
146. Guo, J.; Zhang, G.; Huang, Y.; Ming, W.; Liu, M.; Huang, H. Investigation of the Removing Process of Cathode Material in Micro-EDM Using an Atomistic-Continuum Model. *Appl. Surf. Sci.* **2014**, *315*, 323–336.
147. Zhang, L.; Jia, Z.; Wang, F.; Liu, W. A Hybrid Model Using Supporting Vector Machine and Multi-Objective Genetic Algorithm for Processing Parameters Optimization in Micro-EDM. *Int. J. Adv. Manuf. Technol.* **2010**, *51* (5–8), 575–586.
148. Aich, U.; Banerjee, S. Modeling of EDM Responses by Support Vector Machine Regression with Parameters Selected by Particle Swarm Optimization. *Appl. Math. Model.* **2014**, *38* (11–12), 2800–2818.
149. Jeong, Y. H.; Min, B.-K. Geometry Prediction of EDM-Drilled Holes and Tool Electrode Shapes of Micro-EDM Process Using Simulation. *Int. J. Mach. Tools Manuf.* **2007**, *47* (12–13), 1817–1826.

150. Kojima, A.; Natsu, W.; Kunieda, M. Spectroscopic Measurement of Arc Plasma Diameter in EDM. *CIRP Ann. – Manuf. Technol.* **2008**, *57* (1), 203–207.
151. Morimoto, K.; Kunieda, M. Sinking EDM Simulation by Determining Discharge Locations Based on Discharge Delay Time. *CIRP Ann. – Manuf. Technol.* **2009**, *58* (1), 221–224.
152. Izquierdo, B.; Sánchez, J. A.; Ortega, N.; Plaza, S.; Pombo, I. Insight Into Fundamental Aspects of the EDM Process Using Multidischarge Numerical Simulation. *Int. J. Adv. Manuf. Technol.* **2010**, *52* (1–4), 195–206.
153. Teimouri, R.; Baseri, H. Optimization of Magnetic Field Assisted EDM Using the Continuous ACO Algorithm. *Appl. Soft Comput.* **2014**, *14*, 381–389.

Relevant Websites

www.cmmmagazine.com
Commercial Micro Manufacturing International.
www.reliableedm.com/Complete-EDM-Handbook.php
EDM Complete Handbook (Carl Sommer and Steve Sommer).
www.edmtechman.com
EDM Technical Manual.
www.edmtodaymagazine.com
EDM Today Magazine.
www.globalspec.com
HIS Engineering360.

1.8 Natural Fiber-Reinforced Composites: Types, Development, Manufacturing Process, and Measurement

SM Sapuan, Universiti Putra Malaysia, Serdang, Malaysia
KF Tamrin and Y Nukman, University of Malaya, Kuala Lumpur, Malaysia
YA El-Shekeil, Universiti Putra Malaysia, Serdang, Malaysia
MSA Hussin and SNA Aziz, University of Malaya, Kuala Lumpur, Malaysia

© 2017 Elsevier Inc. All rights reserved.

1.8.1 Introduction 204
1.8.2 Overview of Composites 206
1.8.2.1 FRP Composites 206
1.8.2.1.1 Historical development 206
1.8.2.1.2 Definition of composite 207
1.8.2.1.3 Characteristics of composites 207
1.8.2.1.4 Advantages and merits of composites 207
1.8.2.2 Natural FRP Composites 208
1.8.2.2.1 Classification of natural fibers 208
1.8.2.2.1.1 Animal fiber 208
1.8.2.2.1.2 Mineral fiber 208
1.8.2.2.1.3 Plant fiber 209
1.8.2.2.2 Applications of natural fiber composites 210
1.8.2.2.3 Advantages of natural fiber composites 210
1.8.3 Types of Composite Based on Matrix Material 212
1.8.3.1 MMC 212
1.8.3.2 CMC 212
1.8.3.3 PMC 212
1.8.3.3.1 FRP 212
1.8.3.3.1.1 Failure modes 215
1.8.3.3.1.2 Material requirements 215
1.8.3.3.1.3 Applications of FRP 215
1.8.3.3.1.4 Structural applications of FRP 215
1.8.3.3.1.5 Advantages and limitations of FRP 215
1.8.3.3.1.6 Design considerations 216
1.8.3.3.1.7 Disposal and recycling concerns 216
1.8.3.3.2 PRP 216
1.8.4 Manufacturing Process 217
1.8.4.1 Polymers 217
1.8.4.1.1 Polymerization 217
1.8.4.1.2 Polycondensation 217
1.8.4.1.3 Polyaddition 217
1.8.4.2 Natural Fiber-Reinforced Composites 218
1.8.4.2.1 All process description 218
1.8.4.2.1.1 Fiber process 218
1.8.4.2.1.2 Molding process 219
1.8.4.2.1.2.1 Bladder molding 219
1.8.4.2.1.2.2 Compression molding 219
1.8.4.2.1.2.3 Vacuum bagging 220
1.8.4.2.1.2.4 Mandrel wrapping 220
1.8.4.2.1.2.5 Hand lay-up 220
1.8.4.2.1.2.6 Chopper gun 220
1.8.4.2.1.2.7 Filament winding 220
1.8.4.2.1.2.8 Pultrusion 221
1.8.4.2.1.2.9 Resin infusion 221
1.8.5 Machining of Natural Fiber-Reinforced Composite 221
1.8.5.1 Safety Considerations 222
1.8.5.2 Factors Affecting the Cut Quality of Natural Fiber-Reinforced Composites 222
1.8.5.2.1 Kerf width 222
1.8.5.2.1.1 Different in process of kerf 223

1.8.5.2.1.2	Kerf variations	223
1.8.5.2.2	Surface roughness	223
1.8.6	**Application of GRA Technique in Optimization of Cut Characteristics**	224
1.8.6.1	Experimental Methods and Measurements	225
1.8.6.1.1	Cocoa fiber composites	225
1.8.6.1.2	Preparation of cocoa fiber composite	225
1.8.6.1.3	Specification of cutting machine	225
1.8.6.1.4	Selection of cutting parameters	225
1.8.6.1.5	Design of experiments	225
1.8.6.1.6	Evaluation of cut quality characteristics	226
1.8.6.2	Determination of the Optimal Joining Condition	226
1.8.6.2.1	Gray relational analysis	226
1.8.6.2.2	Normalization of original data	226
1.8.6.2.3	Calculation of gray relational coefficient	227
1.8.6.2.4	Calculating the gray relational grade	227
1.8.7	**Conclusions**	228
Acknowledgments		228
References		228
Relevant Websites		230

1.8.1 Introduction

Composite materials are increasingly being used in the automotive manufacturing industry with the aims to reduce fuel consumption and CO_2 emission. A fiber-reinforced polymer (FRP) is a composite material consisting of a polymer matrix imbedded with high-strength fibers, such as glass, aramid, and carbon. Generally, polymer can be classified into two classes, thermoplastics and thermosetting. Thermoplastic materials currently dominate, as matrices for bio-fibers; the most commonly used thermoplastics for this purpose are polypropylene (PP), polyethylene (PE), and poly vinyl chloride (PVC); while phenolic, epoxy, and polyester resins are the most commonly used thermosetting matrices.[1] A lot of research has been done based on fiber-reinforced plastic composites, which is currently going through a transition phase. Material properties and theoretical properties have dominated in every research areas. In achieving fully automated large-scale manufacturing cycles, economical techniques of production are very important with increasing applications. Common problems in the material are due to the anisotropy and non-homogeneity, which is direct to the fiber pulled-out, delamination, burning, and fuzziness. When machined, this composite material is extremely abrasive. Hence the selection of good cutting tool and the cutting condition is very significant in the machining process.[2] For instance, glass-fiber-reinforced plastics (GFRPs) have been widely employed in automobile interior and exterior parts due to excellent mechanical, structural and durability properties at the expense of poor machinability[3] and potential health hazard. Similarly, other synthetic fibers exhibit these shortcomings. The main problem with the glass fiber composite is the non-recyclability and in assembly and production areas of the factory workers have complain about the skin irritation and respiratory diseases due to inhalation of fiber dust. The use of plant fiber will solve this problem. Natural fibers have always found wide applications from the time they gained commercial recognition.

The need of eco-friendly, sustainable, and biodegradable materials for automotive parts has made natural fiber a potential substitute to synthetic fiber.[4] Natural fiber offers numerous benefits which include renewability, less abrasiveness to equipment, low density, unlimited[5] and low weight and cost.[6] The versatility of natural fibers is based on the following desirable material properties:

- Plant fibers are a renewable raw material and their availability is more or less unlimited.
- Very good mechanical properties, especially tensile strength. In relation to its weight, the best bast fibers attain strength similar to that of Kevlar.
- Very good heat, acoustic, and electrical insulating properties.
- Combustibility: products can be disposed of through burning at the end of their useful service lives and energy can simultaneously be generated.
- Biodegradability: as a result of their tendency to absorb water, natural fibers will biodegrade under certain circumstances through the actions of fungi and/or bacteria.
- The abrasive nature of natural fiber is much lower compared to that of glass fiber, which leads to advantages in regard to technical, material recycling, or processing of composite materials in general.
- Reactivity: the hydroxyl groups present in the cell wall constituents not only provide sites for water absorption but also available for chemical modification (e.g., introduce dimensional stability, durability or improved oil/heavy metal absorption properties).

In recent years, Brazil become one of the country that has a large range of natural sources, including natural fibers like banana, coconuts, sisal, cotton, and curaua.[7] *Theobroma cacao L.* (Sterculiaceae) is a scientific name for the cocoa fruit which its natural habitat is the humid tropics. Every year, all the agricultural products like cocoa are harvested and the dried beans must be produced after fermentation to reduce the mass losses

and prevent spoilage. This happens in most tropical countries likes Southeast Asia, South America, West Africa and others.[8] Cocoa beans are used primarily in chocolate manufacturing, but instead of that, cocoa beans also have pharmaceutical and cosmetic importance in industry. The cocoa harvest worldwide production was greater than 3.5 million ton of dry beans which can be seen from October 2008 to September 2009 (ICCO, 2009), and almost 170 530 t of which were produced in Brazil (CEPLAC, 2009). The daily price averaged stated by the International Cocoa Organization (ICCO) was US \$2599 t^{-1} (ICCO, 2010). Meanwhile, the mean annual world billing was more than \$9 trillion, indicating the cocoa agro-industrial sector's great importance around the world. In Malaysia, the plantation of cocoa is over 20 643 ha (Malaysia Koko Board, 2011). Hence, it can be estimated at least 320 000 kg of cocoa pod husk (CPH) is generated after processing.

Nevertheless, along with its great economic importance, cocoa production generates substantial quantities of waste. In this chapter, particular attention is given to CPHs, which are generated after cocoa beans are extracted from the mature cacao fruit and are the main by-product of the cocoa/chocolate industry. Serious disposal problem happened when only 10 t of wet CPHs are generated from each ton of dry beans. In most cases, these husks are underexploited and considered an undesirable waste of the cocoa/chocolate industry. Normally, they are left to rot on the cacao plantation, which can cause environmental problems. Besides producing foul odors, rotting CPHs can propagate diseases, such as black pod rot, when left on the cacao plantations. Conventionally, these organic wastes is shipped away for processing or disposed to landfill. Currently, increases in the production and processing of cocoa beans have generated increasing waste, resulting in million tons of CPHs being disposed of every year. In Brazil and other cocoa-producing countries, processing this cacao waste could provide economic advantages and decrease some of the environmental problems. These large quantities of CPH could yield a large quantity of fibrous materials which might be suitable as alternative resources especially in pulp and paper making industries or automotive application. Because CPHs are readily available, they could be used also to recover value-added compounds such as pectin.[9,10]

In general, natural fibers contain four main components as shown in **Figure 1**, which are cellulose, hemicelluloses, pectin, and lignin. Every percentage of these components varies with the different types of fibers. Growing and harvesting conditions can also affect the variation. For the cellulose, it is a semi-crystalline polysaccharide and is responsible for the hydrophilic nature of natural fibers. Hemicellulose, compared to the cellulose has lower molecular weight and it is fully amorphous polysaccharide. This amorphous have been known as being partially soluble in water and alkaline solutions. Pectin is a polysaccharide like cellulose and hemicellulose. It main function is to hold the fiber together among them. Lignin has lower effect on water absorption and contributes mainly of aromatics unlike hemicellulose. It is an amorphous polymer in the natural fibers components.

In composite material, it consists of materials system composed of a mixture or combination of two or more micro- or macro-constituents that varies in form and chemical composition. Besides, it is essentially insoluble in each other. To improve the material properties such as toughness, stiffness

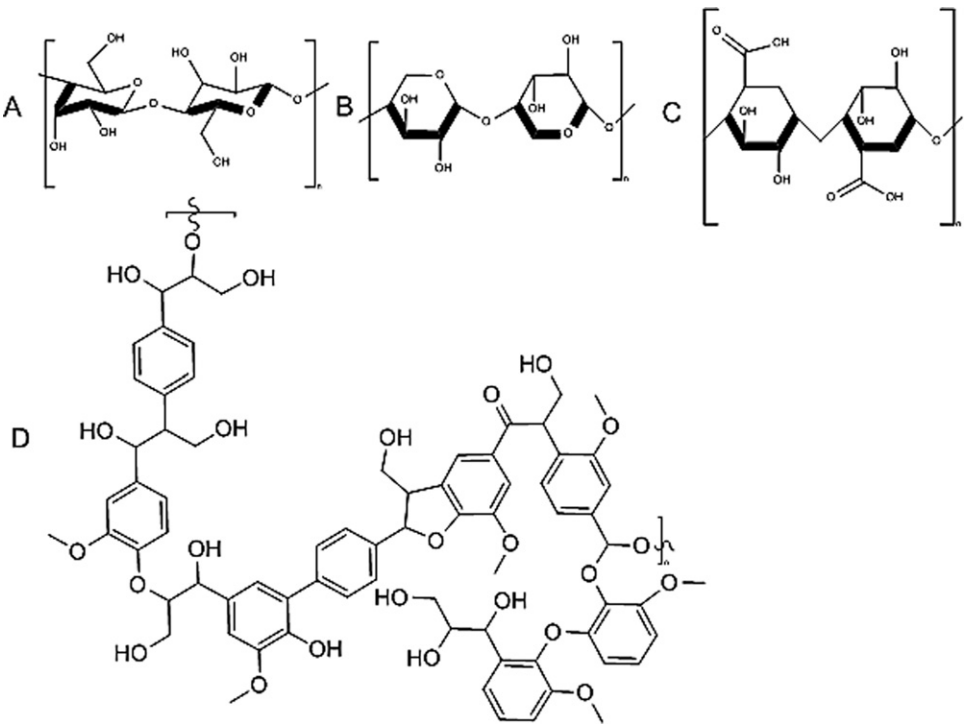


Figure 1 Structural representations of cellulose (a) hemicellulose (b) pectin (c), and lignin (d).[11]

and strength, these composites involve two or more component materials, which are generally combined in an attempt to improve the material properties.

1.8.2 Overview of Composites

In the last three decades, plastics, ceramics, and composite materials have been known as the main emerging materials in our industry. This composite materials have been increased dramatically and the applications have conquering and penetrating the new markets nowadays. Modern composite materials constitute a significant proportion of the engineered materials market ranging from everyday products to sophisticated niche applications. Composites have already proven their worth as weight-saving materials, although the cost is still become the current challenge. Several innovative manufacturing technique currently being used in the composites industry, which is to produce an economically attractive composite components. The cost hurdle is one of the problem and to overcome it, the improvement in manufacturing technology alone is not sufficient, especially for composites.

There must be some vital effort for composites to become competitive with metals, which are effort in design, tooling, quality assurance, manufacturing, material, process and even the program management. The composites industry has begun to recognize that the commercial applications of composites promise to offer much larger business opportunities than the aerospace sector due to the sheer size of transportation industry. Relentlessly, application in composite from aircraft sector to other commercial uses has become outstanding. Penetration of these advanced materials enabled by the introduction of newer polymer resin matrix materials and high-performance reinforcement fibers of glass, carbon, and aramid has witnessed a steady expansion in uses and volume. An expected reduction in costs is due to the increased of the volume.

There are applications that this high-performance FRP can be found such as in composite armoring designed to resist explosive impacts, windmill blades, industrial draft shafts, and fuel cylinders for natural gas vehicles, support beams of highway bridges and even in the paper making rollers. In fact, by using the composites material in the application rather than metals can highly savings in both cost and weight. Examples in applications are cascades for engines, curved fairing and fillets, replacements for welded metallic parts, cylinders, tubes, ducts, blade containment bands, and much more. Their advantages which is lighter construction materials and more seismic resistant structures has placed this composite in high emphasis on the use of new and advanced materials. Besides decreases in dead weight, it also absorbs the shock and vibration through tailored microstructures. Moreover, composites are now extensively being used for rehabilitation or strengthening of preexisting structures that have to be retrofitted to make them seismic resistant, or to repair damage caused by earthquakes or other vibrations of the earth and its crust.

The properties of the composite material can be designed by considering the structural aspects unlike the conventional materials such as steel. Both material and structural design will be involved in the design of the structural component using the composites. Stiffness and thermal expansion which are the properties of the composite can be varied continuously over a broad range of values under the control of the designer. Careful selection of reinforcement type finished product characteristics to be tailored to almost any specific engineering requirement. Material selection is very important whilst the use of composites will be the clear choice. It will depend on many factors such as the lifetime requirements of working, run length which is the number of produced items, complexity of product shape, possible savings in assembly costs and the designer skills and experience in tapping the optimum potential of composites. The use of composites in conjunction with traditional materials may give the best results in some instances.[12]

1.8.2.1 FRP Composites

1.8.2.1.1 Historical development

Since 1950s, the use of non-metallic fibers has been considered as particularly fiber-glass elements which bundled into continuous reinforcing elements. Polymer impregnated bundled fiber-glass fibers has been used as rods for anchorages in tunneling to make advances in polymer development. Nawy *et al.*[13] have conducted an extensive work on the use of bundled and resin-impregnated glass fibers formed into deformed bars as the main reinforcement in element of structure in mid 1960s. Until the late 1970s, the commercial application of bundled and resin-impregnated reinforcement in structural concrete elements was not recognized except for cases where the magnetic fields must be avoided to support the structure. It is important to state at this juncture that the term plastic could be misleading; hence, there is general consensus at this time to define FRP as fiber-reinforced polymer composites.

GFRP reinforcing bars have developed an interest in their using in early 1980s. This was important in supporting the magnetic resonance imaging (MRI) medical equipment or for reinforced concrete surrounding. Such equipment includes sensitive magnets and cannot tolerate the presence of any steel reinforcement. Besides, GFRP reinforcement is more durable and efficient as concrete reinforcement where the environmental and chemical attacks are present. Composite rebar is commonly used in the construction industry like seawalls, roof of decks, base pads for electrical, and equipment of reactor and also the concrete floor slabs in aggressive chemical environment. In Germany history of 1986, the world's first highway bridge had been built using composite reinforcement.

History in United States in 1990s has stated that at least nine major companies have been actively marketing this product since the significant funds have been expended on product evaluation and further development. In addition, glass fiber filaments has become a supplement to concrete matrices to improve the mechanical properties of concrete, but not as a replacement for the main bar reinforcement in supporting structural components. Glass fibers that are alkali resistant are also gaining wide use. These normally contain zirconium (ZrO_2) to minimize or eliminate the alkaline corrosive attack on glass present in the cement paste.

Nylon and PP are examples of synthetic fibers materials which recently begun to be utilized due to availability of information on their mechanical performance in matrix. This

both loose and woven into geotextile form also has better understanding of their structural contribution to crack resistance. The use of carbon fibers as the main reinforcement apart from its use in cement-based composites has grown interest nowadays although the use of other types of non-metallic fibers has been explored. The science of fibrous concrete and composites become an advanced to an extent now and can justify its extended use in years forward.[13]

1.8.2.1.2 Definition of composite

Composite had been broadly defined by world scholars such as Jartiz, Kelly, Beghezan and Van Suchetclan based on its used and applications. Each of it allows us to understand the meaning of composite widely and in depth.

1. The most common meaning of composite has been stated by Jartiz, 'Composites are multifunctional material systems that provide characteristics not obtainable from any discrete material. They are cohesive structures made by physically combining two or more compatible materials, different in composition and characteristics and sometimes in form.' This definition allows anyone to classify among the composites any mixture of materials including the very banal, meaningless mixture. The weakness of this definition does not indicate the specificity of the mixture of materials which is needed to make it distinguishable from any other inappropriate mixture.
2. Kelly had clearly stated that the composites should not be simply regarded as a mixture of two materials. In more appropriate definition, the combination must have its own distinctive significant properties. For example, in terms of strength, resistance to heat or any other desirable quality, it is better that either of the components must be different from either of them.
3. Beghezan defines as 'The composites are compound materials which differ from alloys by the fact that the individual components retain their characteristics but are so incorporated into the composite as to take advantage only of their attributes and not of their short comings,' in order to obtain improved materials.
4. Van Suchetclan explains composite materials as heterogeneous materials consisting of more than one solid phases, which are in intimate contact with each other on a microscopic scale. They can be also regarded as homogeneous materials on a microscopic scale in the sense that any portion of it will have the same physical property.[12]

1.8.2.1.3 Characteristics of composites

In general, composite materials have been divided into two phases. It consists of one or more discontinuous phases embedded in a continuous phase. The continuous phase is known as the 'matrix' whereas the discontinuous phase is usually harder and stronger than the continuous phase and is termed as the 'reinforcement' or 'reinforcing material.' More ductile and less hard can refer to the matrix. It holds the dispersed phase and shares a load with it. Besides, matrix is composed of any of the three basic material types such as polymers, metals, or ceramics. Moreover, the matrix forms the bulk form of the part of product. Meanwhile, for the secondary which embedded in the matrix is a discontinuous phase. Compared to the continuous phase, it usually harder and stronger. It improves the overall mechanical properties of the matrix and gives strengthen to the composites.[14]

Some properties such as their constituent materials, their distribution and the interaction among them are the examples of properties for the composites. It may be the sum of the fraction volume of the properties of the constituents. To improve or to get better properties, the constituent may interact in a synergistic way. The geometry of the reinforcement such as shape, size, and size distribution influences the properties of the composite to a great extent. Besides the nature of the constituent materials stated above, the orientation of the reinforcement and concentration distribution also affect the properties. Spherical, cylindrical, or rectangular cross-sanctioned prisms and platelets are examples of the shape of the discontinuous phase. Meanwhile, the size and size distribution will control the texture of the materials. For the volume fraction, it will determine the interfacial area of the material. All of this three properties; shape of the discontinuous phase, size distribution and the volume fraction plays an important role in determining the extent of the interaction between the reinforcement and the matrix.

Concentration is not only the single most important parameters which influencing the composites properties. Usually, it measured as fraction of weight or volume and determines the contribution of a single constituent to the overall properties of the composites. Apart from that, this concentration also an easily controllable manufacturing variable used to alter its properties.[15]

1.8.2.1.4 Advantages and merits of composites

Advantages of composites compared to their conventional counterparts are the ability to meet various design specifications with significant weight savings and strength-to-weight ratio. The advantages of composite materials compared to conventional ones are as below:

- Composites have a high tensile strength which is 4–6 times higher than that of aluminum or steel (depending on the reinforcements).[16]
- Lower embedded energy compared to other structural metallic materials like aluminum, steel, and etc.
- Composites offer an improved torsional stiffness and impact properties.
- 30–40% lighter compared to other metals, for instance any particular aluminum structures designed to the same functional requirements.
- High fatigue endurance limit (up to 60% of ultimate tensile strength).
- Composites are more versatile than metals and can be tailored to meet complex design requirements and performance needs.[17]
- Composites exhibit long life cycle which offer excellent fatigue, improved impact, and environmental resistance as well as reduce maintenance.
- Composites enjoy reduced life cycle cost compared to metals.
- Composites provide less noise during operation and produce lower vibration transmission than metals.

- Composites exhibit excellent corrosion resistance and fire retardancy.
- Improved appearance with smooth surfaces and readily incorporable integral decorative melamine are other characteristics of composites.
- Composite parts can eliminate joints/fasteners, providing part simplification and integrated design compared to conventional metallic parts.[18]

1.8.2.2 Natural FRP Composites

Natural fiber-polymer composites are made from petroleum or bio-based matrices composed of natural fibers such as kenaf, jute, hemp, pineapple, oil palm empty fruit bunch fibers. Natural fibers are used as reinforcement materials or fillers for the polymer matrices and they readily combine with a thermosetting or thermoplastic matrix.[19] The manufacture of natural-fiber composites includes the use of either a thermoset or thermoplastic polymer binder system combined with the natural-fiber preform or mat. In automotive applications, the most common system used today is thermoplastic PP, particularly for nonstructural components. PP is favored due to its low density, excellent process ability, mechanical properties, excellent electrical properties, and good dimensional stability and impact strength.[20] However, several synthetic thermoplastics are utilized including PE, polystyrene, and polyamides.[21]

Recently, natural FRP composite materials has grow rapidly in terms of their industrial applications and fundamental research. They have such positives properties such as cheap, renewable, completely or partially recyclable, and most important is biodegradable to environment. For plants fiber, they are more and more often applied as the reinforcement of composites and also used as a source of lignocellulosic fibers. Banana, pineapple, kenaf, sisal, ramie, hemp, jute, cotton, flax, bamboo as well as wood are examples for plants fiber, which are normally used nowadays. Wide applications in natural fiber can be seen in their used in transportation, military applications, packaging, consumer products and building or construction industries. Automobiles, railway coaches and aerospace are the examples in transportation application while ceiling paneling and partition boards are two examples that always be used in the building and construction industries. Natural fiber which containing composites are more environmentally friendly. Their advantages like availability, low density, renewability, and price as well as satisfactory mechanical properties have make them an attractive ecological alternative to glass, carbon, and man-made fibers used for the manufacturing of composites.[22]

As stated, natural fibers in Asia such as kenaf have some advantages in terms of cost, density, recyclability, abrasiveness, renewability, and biodegradable over the traditional reinforcement materials. The fiber matrix and the ability to transfer the load from the matrix to the fiber can affect the performance of the fiber-reinforced composites. In addition, one of the key structures in automobiles is the bumpers which protect the passengers from any incoming impact. With proper materials and careful design is very important and should be considered in order to achieve good energy absorbing behavior. Besides that, weight reduction plays an important role in automobiles to achieve the fuel efficiency. Weight reduction can be achieved without compensating the mechanical properties of the traditional materials by considering the safety. Besides, crash worthiness and safety should also be considered as preconditions in light weighting the bumper beam with the introduction of the automotive safety legislation. Furthermore, thermoplastics composites are being used in a variety of application such as mass transit, automotive, and military structures. They have an edge over traditional materials such as steel and aluminum. Variety of good properties like high-specific strength, corrosion resistance, and good damping capacity makes the thermoplastic a highly recommended because of their widely used in the bumper beams long fiber.

Generally, inexpensive polymers, nylon, PE, and PP are matrix elements in the thermoplastic composites. E-glass fiber, also known as lime-alumina-borosilicate glass is commonly being used in the industrial and civil structures and this glass can be obtained from raw materials such as sand.[16] This fiber also categorized in the reinforced material. Lately, long fiber thermoplastic composites show the highest growth rates in the plastic industry, which is approximately 30% per year. The mechanical properties of the long glass fiber thermoplastics can be decided by the fiber length in long glass fiber. By providing hybridization method of natural fiber with glass fiber can improve the mechanical properties of natural-fiber composites.[23]

1.8.2.2.1 Classification of natural fibers

Fibers are materials that similar to pieces of thread- and hair-like class that are continuous filaments or in the pieces of indiscrete elongated shape. They can be spun into filaments, thread, or rope. Besides, they can be used as a components in the composites materials. Furthermore, products can be made such as paper or felt by matting them into sheets. There are two types of fibers. First is from natural fiber and the other one is man-made or synthetic fiber. Natural fibers type include those made from plant, mineral, and animal sources. Also, natural fibers can be classified into three sections which are animal fiber, mineral fiber, and plant fiber.

1.8.2.2.1.1 Animal fiber

Generally, in animal fiber it comprise of protein such as mohair, wool, silk, alpaca, and angora. Examples of the animal fiber are animal hair, silk fiber, and avian fiber which has been divided as below:

- Animal hair (wool or hair): this fiber can be found from hairy mammals animals such as sheeps wool, goat hair, alpaca hair, or horse hair. Cashmere and mohair are the examples for the goat family.
- Silk fiber: this fiber comes from collected dried saliva of bugs or insects during cocoons preparation. Examples of the silk fiber are silk from the silk worms.
- Avian fiber: avian fibers such as feathers which comes from birds.

1.8.2.2.1.2 Mineral fiber

The second natural fiber is mineral fibers. Although it is naturally occurring fiber but it also can be a slightly modified fiber procured from minerals. These can be categorized into

three categories as below:

- Asbestos: asbestos is the only naturally occurring mineral fiber-like serpentine, amphiboles, and anthophyllite.
- Ceramic fibers: examples from the ceramic fiber are glass fibers, aluminum oxide, silicon carbide, and boron carbide. Glass wood and quartz can be categorized into the glass fiber group.
- Metal fibers: aluminum fibers is one of the examples in the metal fiber family.[24]

1.8.2.2.1.3 Plant fiber

Cellulose is the main fiber which contain in the plant fiber. Examples of cellulose fibers are cotton, jute, flax, ramie, sisal, and hemp. In recent times, manufacture of paper and cloth comes from the cellulose fiber. These plant fiber can be divided into several fibers as follows:

- Stalk fiber: stalk fiber comes from the stalk of the plants such as straws of wheat, rice, barley, bamboo, and grass. Tree wood also can be categorized into stalk fiber.
- Leaf fiber: examples of the leaf fiber are sisal and agave and this fiber comes from the leaves of the plant.
- Seed fiber: cotton and kapok are collected from the seed or seed case of the plants.
- Skin fiber: skin fiber can be collected from banana skin, hemp, jute, flax, soybeans, and others. All these fibers have higher tensile strength compared to other fibers. Hence, these fiber can be applied and used for paper, packaging, durable yam, and fabric. Method to collect the fibers are by getting it from the skin or bast surrounding the stem or their respective plant.

Figure 2 shows the classification of plant fibers.

Thermosetting and thermoplastic matrices can be reinforced also by using the natural fibers. This is because the composites require higher performance applications and that is why epoxy, polyester, polyurethane, and phenolic are normally used in natural fiber composites. This examples are belongs to the thermosetting resins matrices. They provide sufficient mechanical properties, in particular stiffness and strength, at acceptably low price levels. Replacing the synthetic fiber by natural fiber is only a first step to consider the ecological aspects of material selection. New materials based on the renewable sources become future development because of the several effects nowadays. The effects such as emission of green house which has free the gases such as CO_2 into the atmosphere and because the finiteness of fossil energy resources has increased the awareness among community to develop new sources.

Two primary physical limits that severely restrict the development of thermoplastic natural-fiber composites are the process temperature and interfacial adhesion between the natural fiber and polymer matrix. This can determine the properties of the physical composite by compatibilizing or couple the blend. There are different between the compatibilization method and the coupling. Coupling is a process in which dissimilar polymers or fillers are made into an alloy by use of external agents called coupling agents. Meanwhile, compatibilization is any operation performed on the fiber and polymer that increases the welling within the blend. This can be achieved by modifying several criteria like polymer matrix, modifying the fiber, adding surface-active agents, and by high shear compounding.[20,25]

The second physical limits are the upper temperature. This include the significant difference between the polymer matrix and the wood surface energy. In natural fiber applications,

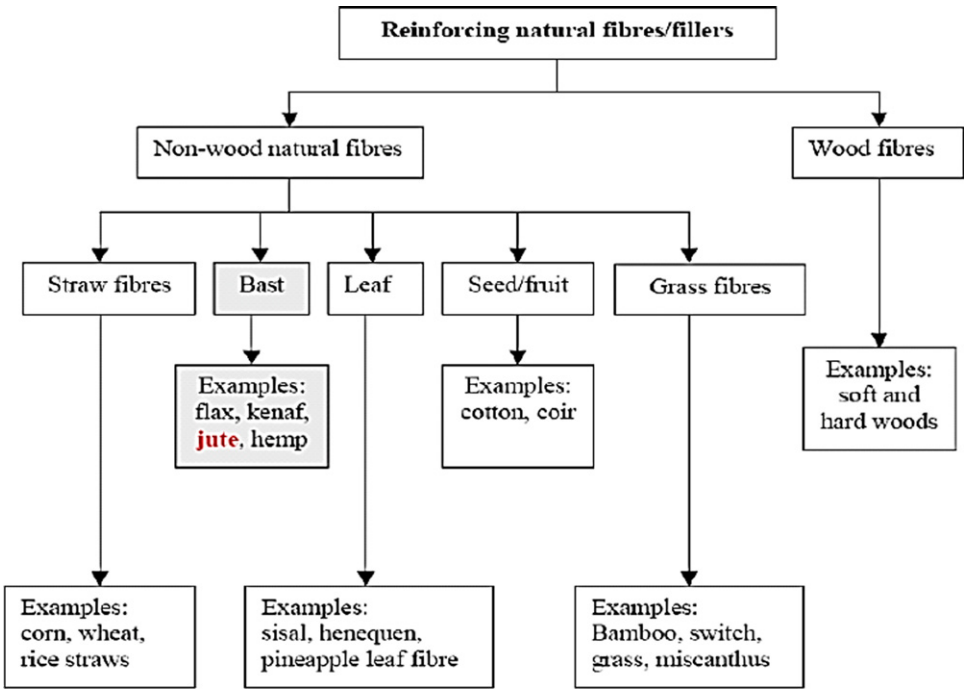


Figure 2 Classification of natural fibers which can be used as reinforcement of polymer.[22]

these process temperature is some kind of limiting factor. The generally perceived upper limit before fiber degradation occurs is on the order of 150 °C for long processing durations, although fibers may withstand short term exposures to 220 °C.[26]

1.8.2.2.2 Applications of natural fiber composites

Many applications involves the natural-fiber composites. It may be very cost-effective material for every applications. Building and construction industry is the popular application for the natural-fiber composites. It parts such as panels for partition and false ceiling, partition boards, wall, floor, window and door frames, roof tiles, mobile or pre-fabricated buildings, and many more. Advantage from the parts is they can be used in times of natural disaster such as earthquakes, cyclones, and floods. Besides that, storage devices also contribute their materials such as post-boxes, gain storage silos, and bio-gas containers. In addition, other applications like furniture, electrical devices, toy, and everyday applications also accounted in everyday life. Besides construction industry, automotive parts under transportation also have higher demand on natural fibers.

There are variety of reasons why natural fibers are the one in the automotive industry. First is because of their low density which can reduce the reduction of weight up to 10–30%. Besides that, they have good acoustic properties that make the mechanical properties of the materials is acceptable. They also have properties that suitable to process for instance low wear on tools. In addition, they are favorable in most aspects like ecobalance for part production and during vehicle operation due to weight savings and also for accident performance which give high stability and less splintering. In the health aspect, they give some benefits compared to glass fibers during production. Besides they can reduced the fogging behavior, the price also give advantages for both the fibers and the applied technologies nowadays.

1.8.2.2.3 Advantages of natural fiber composites

Natural-fibers composite have some main advantages which make them become more popular nowadays. As stated before, these natural fibers constribute to low specific weight than glass fiber and resulting in a higher specific strength and stiffness. Good thermal and acoustic insulating properties also gives them such a good condition. Known as a renewable source, they need less energy in the production process by releasing the oxygen to the environment while using the CO_2. Besides, it is not just can reduce the wear of the tool but also can give a healthier working conditions like no irritation can happen on the skin. Compared to the glass which can causes problem in combustion furnaces, thermal recycling is more possible to be used. Countries which produces low wages will be interested because producible of this fiber are with low investment at low cost.[22]

Automotives become one of the demand sectors in the global market. Their continuing need for the incorporation of natural fiber based materials also creates a simultaneous pressure to address the issue of sustainability. All factors must be taken into action by following the environmentally safe manner. Recent research has focus to the compostable natural-fiber based composites which has been created so that it can be safely disposed of after their intended use without polluting the atmosphere. The history and growth of transportation system shows an enlightening picture of how scientific, technological, social, and economic factors interplay to change the environment in his world. Automotive growth is strongly related to the economic growth that took place in the early part of twentieth century.

Automotive play an important role in the transportation of people both individually and in groups, as well as goods. Large-scale manufacture of these automobiles, operation of the transportation (road) network system, and construction of the required infrastructure has a dominant impact on economic growth of the country.[27] Continuous efforts are on developing newer or alternative materials to achieve cost effectiveness, fuel efficiency, reduced emissions, increased safety, and always with a target on future ability to recycle, or biodegrade. However, today's rising cost of fuel is a major factor in the move to utilize composites for all transport vehicles, and thereby to achieve a light weight construction with an ultimate goal of reduction in fuel consumption and emissions.

According to an estimate, about 25% reduction in the weight of the vehicle is equivalent to a savings of 250 million barrels of crude oil and reduction in CO_2 emissions to the tune of 220 billion pounds per annum. Automobiles today have better fuel economy and safety features than they had 25 years ago. It is estimated that, out of 10 gallons of fuel pumped to the car only 1.7 gallons goes in motion. One way of improvement would be to make the vehicles lighter by using composite based structures. Composites made of two or more materials are superior to their starting materials. FRP composite materials provide a new range of performance materials for an automotive industry. Generally, composites are strong, light, and resistant to corrosion and wear. They have been used in space and military vehicles; performed well, thus could play bigger role in automotives than they do today. As many as 40 automotive components such as trunk and hood liners, floor mats, carpets and padding, speakers, package trays, door panels, and oil and air filters contain fiber products.[28] Natural fibers are about 30–50% lower in density when compared to E-glass fibers and roughly the same as the aramid commercial grade systems.[29]

Furthermore, these fiber based materials can contribute greatly to the automotive manufacturer's final goal constituting weight reduction of 30% and cost reduction of 20%.[30] According to an estimate, there are more than 500 million passenger vehicles in use in this world and about 50 million new cars are produced every year. At an average of 1500 kg of materials for an automobile, the consumption of materials is in the tune of 70 million tons per year. It means, this quantity has to be produced, used and ultimately recycled or disposed at the end of useful life. Nearly as many as 40 automotive components such as trunk and hood liners, floor mats, carpets and padding, speakers, package trays, door panel and oil, and air filters uses fiber products. If these fibers can be replaced by the natural fibers there would be nearly 30% weight reduction and which in turn reduce nearly 20% of cost. However, glass-reinforced plastics exhibit shortcomings such as their relatively high-fiber density (approximately 40% higher than natural fibers), difficulty to machine, and poor recycling properties,

not to mention the potential health hazards posed by glass-fiber in particular.[26,28]

Amounting to a total of only 4000–5000 t in 1996, the use of natural fibers in the European automotive industry has quintuplicate with more than 28 000 t in the year 2000. In this decade, a total use between 50 000 and 100 000 t can be expected in this area. At present time, almost all European automotive producers employ interior parts reinforced by natural plant fibers. Natural fibers are also being used in polyurethane composites. The first commercial example is the inner door panel for the 1999 *S* Class Mercedes-Benz, made in Germany of 35% Baypreg F semi-rigid polyurethane thermoplastic elastomer from Bayer and 65% of a blend of flax, hemp, and sisal. Until now, use of flax, sisal, coconut fiber, cotton, and hemp has been limited to the interiors of DaimlerChrysler vehicles – in upholstery, door paneling, or the rear panel shelf. Elaya and Venkateshwaran[31] conducted experiments on Curacua, jute, coir, ramie, and kenaf with PP mixed at different proportion. The results show that with 50:50% of natural-fiber and polymer ratio provide the better mechanical properties.[31] There are many factors that can influence the performance of natural fiber-reinforced composites. Apart from the hydrophilic nature of fiber, the properties of the natural fiber-reinforced composites can also be influenced by fiber content/amount of filler. In general, high-fiber content is required to achieve high performance of the composites. Therefore, the effect of fiber content on the properties of natural fiber-reinforced composites is particularly significance. It is often observed that the increase in fiber loading leads to an increase in tensile properties. Another important factor that significantly influences the properties and interfacial characteristics of the composites is the processing parameters used. Therefore, suitable processing techniques and parameters must be carefully selected in order to yield the optimum composite products. Generally, the tensile properties of composites are markedly improved by adding fibers to a polymer matrix since fibers have much higher strength and stiffness values than those of the matrices.

In general, higher fiber content is desired for the purpose of achieving high performance of short-FRP composites. It is often observed that the presence of fiber or other reinforcement in the polymeric matrix raises the composite strength and modulus. Therefore, the effect of fiber content on the tensile properties of fiber-reinforced composites is of particular interest and significance for many researchers.[1]

A number of studies demonstrated the effects of fiber loading on mechanical properties (hardness, stiffness, strength, etc.) of natural fiber-reinforced composites. Singha and Rana[32] varied the fiber loading (10–30% by weight) and discovered the optimum tensile strength of Agave fiber-reinforced polystyrene composite at 20% fiber loading. Arrakhiz *et al.*[33] also found a significant increase in the tensile strength of high density polythene after reinforcing with 20% by weight of chemically treated coir fibers. El-Shekeil *et al.*[34] measured that the hardness of kenaf fiber-reinforced thermoplastic polyurethane (TPU) composite increases from 55 to 66 (shore D) as a result of 30% fiber loading. The increase in hardness is attributed to the increase of fiber loading since hardness is a function of the relative fiber volume and modulus of the composites.[35] Similar trend was observed in bamboo fiber filled natural rubber composites.[36] It is noted that machining efficiency of the composite, however, depends on their respective mechanical properties.

The applications of natural fiber-reinforced composites are growing rapidly, due to their inherent properties of light weight, easy availability, and environment friendliness.[37] The mixing of natural fibers with synthetic fibers increases its strength, and it is found to be a good alternative reinforcing material. The banana, sisal, and roselle fiber-reinforced composites are fabricated by the mould method, and the drilling is carried out, using HSS twist drills. From the experiment they found that, the cutting speed, feed rate, and drill diameter are the most significant factors affecting the thrust force. They further observed that the thrust force and torque increases with the increase in the feed rate, and decreases with the increase in cutting speed. Composite materials have become valuable construction materials in the aerospace, defense and automotive industries, due to their higher specific strength, stiffness, and fatigue characteristics. Composite components are joined by mechanical fasteners; and accurate, precise high quality holes need to be drilled to ensure proper and durable assemblies. The drilling of composite materials causes several damages, such as: delamination, fiber-pull out, edge chipping, uncut fibers, and others. It causes poor assembly tolerance, reduces the structural integrity of material, and deterioration of the potential for long-term performance. Drilling is carried out by using the HSS-Co twist drill, the multi construction twist drill, and the brad and spur drill, and reported that the brad and spur drill produced less induced damage around the whole surface, and lesser thrust force than the other two drills. The HSS-Co twist drill is always a bigger delamination factor, which means higher damage in a composite laminate.

Natural fibers have many advantages, such as low density, high-specific strength and modulus, non-abrasiveness, and low cost, when compared to synthetic fibers. Natural fiber-reinforced composite materials are recognized as better materials for structural applications, and the machining of these composites causes a number of problems. In order to overcome these problems an experiment has been carried out by using a cemented carbide end mill cutter and the results are compared with those of the GFRP composites. From the experiment, they found that the delamination factor and surface roughness of the natural fiber-reinforced composites are better than those of glass-fiber-reinforced composites. The effect of cutting speed and feed rate on delamination in drilling glass, hemp, and sandwich fibers-reinforced composites with different fiber volume fractions, is observed by Naveen *et al.*[38] It is found that the damage around the hole is predominant at higher feed rates, and a partial elliptical shape along the direction of fibers. Optimization of the machining parameters in drilling hemp fiber-reinforced composites was carried out by Dilli Babu *et al.*[39] and it was found that the feed rate and cutting speed made the largest contribution to the delamination.

An investigation has been carried out to study the mechanical and machinability characteristics of coir-polyester composites by Jayabal *et al.*[40] They found that the drill diameter of 6 mm and the spindle speed of 600 rpm gave the minimum value of thrust force, torque, and tool wear. An effort has been made for the development of hybrid

composites from natural fibers instead of orthopedic alloys, for internal fixation of fractured bones in the human body by Chandramohan and Marimuthu.[41] From the study it is revealed that composites made from natural fibers are the best materials, when compared with orthopedic composites made from orthopedic materials.[42]

Coir fiber-reinforced composites have been developed; the thrust force, torque, and tool wear during drilling optimized by Jayabal *et al.*[43] An experiment has been conducted to carry out the mechanical and machinability characteristics of glass coir-polyester composites, using factorial design methodology. A regression model is developed for correlating the drilling parameters and their effects by design of experiment techniques, and it is found that the feed rate plays a major role than the other variables. A desirability function based method is applied for optimizing the drilling parameters, based on multiple performance characteristics, by Rajmohan and Palanikumar.[44] The results indicated that the medium spindle speed and lower feed rate are optimum, for the minimum burr height during drilling, and the surface roughness of the hybrid composites.

In the present research, the glass–sisal–jute fibers-reinforced hybrid composites have been developed, and the drilling characteristics of these composites are analyzed, by varying the cutting speed, feed rate, and tool geometry. The results indicated that all the above said parameters affect the drilling characteristics, and subsequently drilling induced damage.[45,46]

1.8.3 Types of Composite Based on Matrix Material

Basically, composite materials can be categorized into three groups on the basis of matrix material. They are:

a. Metal matrix composites (MMC)
b. Ceramic matrix composites (CMC)
c. Polymer matrix composites (PMC)

1.8.3.1 MMC

A lot of advantages such as higher specific modulus, higher specific strength, better properties at elevated temperatures, and lower coefficient of thermal expansion makes the metal matrix a good composite over monolithic metals. Applications for MMC have been widely used such as in combustion chamber nozzle which normally used in rocket and space shuttle. Besides, housings, tubing, cables, heat exchangers, and structural members also part of consideration for wide range of applications.

1.8.3.2 CMC

One of the main objectives in producing CMC is to increase the toughness. Naturally it is hoped and indeed often found that there is a concomitant improvement in strength and stiffness of CMC.[22]

1.8.3.3 PMC

Synthetic polymeric composites are one of the most commonly used matrix materials. Typical examples include glass fiber-reinforced, carbon fiber-reinforced or polymer fiber-reinforced, thermoplastic or thermosetting resins, carbon-reinforced rubber, polymer blends, silica-reinforced resin or mica-reinforced resins, and polymer-bonded or impregnated concrete or wood. Generally, polymer composites are the combinations or compositions that comprise two or more materials as separate phases and at least one of which is a polymer. It is often possible to get unique combinations or levels of properties when combining the polymer with another material such as glass, carbon, or another polymer. Apart from that, it is also often useful to consider as composites such materials as coatings (pigment-binder combinations) and crystalline polymers (crystallites in a polymer matrix).

Generally, wood and bone include in the natural composites which wood can be defined as cellulosic fibers bonded with lignin and bone as mineral bonded with collagen. Otherwise, polymeric compositions cannot be considered as composites if it has very low proportions of pigments or processing aids or compounded with a plasticizer. Meanwhile, typical goal for polymeric compositions are to increase the efficiency of the materials by improving the strength, stiffness or toughness, and also the stability of dimensional. This can be done by embedding particles or fibers in a matrix or binding phase. The next goal is to minimize the price of the filler by using inexpensive and readily available fillers to extend a more expensive or scarce resin. This is very important nowadays as petroleum supplies become costlier and less reliable. Moreover, there are industries which include the use of some filler in their applications such as glass spheres and molybdenum sulfide. Function of fillers is to reduce permeability of materials. On the other hand, glass spheres and molybdenum sulfide is to improve process ability and to make a self-lubricating bearing in incorporation of dry-lubricant particles, respectively.[47]

Particularly, polymers have lower strength and stiffness compared to metals and ceramics. Besides, their mechanical properties are inadequate for a lot of structural purposes. To overcome this, these polymers can be reinforced with other materials so that their disadvantages can be reduced. In the meantime, high pressure is very significant in PMC processed instead of high temperature. High temperature does not require in the processed. Also equipment's required for manufacturing PMC are simpler. Applications for structural in PMC become famous because of the rapid development in this composites industry.

Composites are used because overall properties of the composites are superior to those of the individual components, for example, polymer/ceramic. Composites have a greater modulus than the polymer component but are not as brittle as ceramics. Two types of polymer composites are:

- Fiber-reinforced polymer (FRP)
- Particle-reinforced polymer (PRP)

1.8.3.3.1 FRP

Fibers and matrix are the two main components that made up the fiber-reinforced composites. Commonly, fibers are the main reinforcement and the main source of strength meanwhile for matrix, it glues all the fibers together in shape and besides that, it also transfer stresses between the reinforcing



Figure 3 Schematic illustration of fiber types: unidirectional, chopped, and woven.[48]

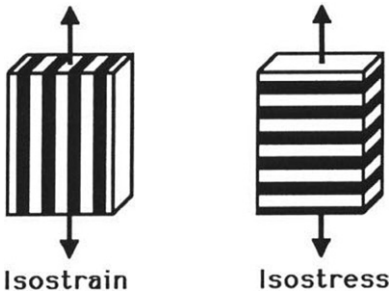


Figure 4 Geometry of idealized unidirectional composite materials.[48]

fibers. Therefore, the functions of fibers are to carry the loads along their longitudinal directions. Occasionally, the fillers also help a lot to smooth the process of manufacturing by adding it to the fibers. Besides, these fillers give special impact properties to the composites and also can reduce the product cost. In fact, fibers are available in three basic forms as shown in Figure 3:

- Continuous fibers are long, straight and generally layed-up parallel to each other.
- Chopped fibers are short and generally randomly distributed (fiber-glass).
- Woven fibers come in cloth form and provide multi-directional strength.

Properties of composite material when combining the fiber and matrix materials may differ from most of engineering materials. This is due to the mechanical properties of composites are highly dependent on the direction in which the loads are applied. Anisotropic, where the material properties are a function of loading direction can include the strength and stiffness of the composites.

From Figure 4, it shows the strength and stiffness are generally much higher along the fiber direction and known as isostrain, while the isostress stated that it is perpendicular to the fiber direction.[49]

- Loading parallel to fiber direction (isostrain).
- Loading perpendicular to fiber direction (isostress).

Composite laminates are formed into a multi-layered structure when combining the individual layers, which is known as lamina. Meanwhile, the continuous fiber composites combine the unidirectional lamina and shows different directions in their fibers oriented as depicted in Figure 5. The combination of fibers aligned turns it into a layered structure with different layers in a laminate. Unidirectional lamina also known as fibers aligned.

Typically, glass fibers, asbestos, carbon/graphite fibers, beryllium, beryllium carbide, beryllium oxide, molybdenum, aluminum oxide, polyamide, natural-fiber, and others is a common based for FRP composites embedded in a matrix of an epoxy or polyester resin. Compared to steel, carbon fiber composites have five times more relative stiffness. It is one of based materials in the reinforced thermosetting resins besides boron and polyaramides. In addition, it also gives high levels of strength and stiffness. Applications such as components in new jet aircraft, boat hulls, and rocket motor cases are normally suited for epoxy and polyester composites because of their excellent properties stated before. Besides that, parts for automobiles and chemical reaction vessels also two examples that can be included in the applications. Polycarbonates, PE, and polyesters are among the resins available as glass-reinforced composition. Although epoxy and polyester resins plays important roles in the properties of reinforced thermosetting resins, there are others significant reinforced thermoplastic resins as well. The properties of reinforced thermoplastics have made these materials a good one to replace with the metals. Less cost, one step fabrication by injection moulding with improved properties has made it possible to apply in applications of appliances, instruments, automobiles, and tools. Polyamide resins are one of the examples for various matrices which show excellent matrices for glass fibers and also give a high-performance composite in the development of other composite systems. Different fibers are of potential interest, including polymers, single-crystal ceramic whiskers, and various metallic fibers. Poly which is also known as vinyl alcohol and sapphire is the example for polymers and single-crystal ceramic whiskers, respectively.

Usually, FRPs are commonly being used in many applications such as in aerospace, construction industries, marine, and automotive parts. As stated before, composite materials are specially or naturally occurring materials which have different physical or chemical properties. Made from two or more constituent materials, these composite materials remain separate and distinct within the finished structure. Most composites have strong, stiff fibers in a matrix which is weaker and less stiff. Example for good properties such as low density is the main objective for strong and stiff component. Commercial material commonly has glass or carbon fibers in matrices based on thermosetting polymers, such as epoxy or polyester resins. After initial production, thermoplastic polymers may be preferred sometimes, since they are moldable. They can be categorized in several classes of composite in which the matrix is a metal or a ceramic. Higher costs in manufacturing become the problems which must have to be overcome and that is why these are still in a developmental stage for the most part. It is often rather complex for adding the fibers or in some cases called particles in these composites. Such examples are improvements may be sought in creep, wear, fracture toughness, and thermal stability. There are varieties of usage for FRP ranging from aircraft, helicopters and spacecraft through to boats, ships and offshore platforms, and to automobiles, sports goods, chemical processing equipment and civil infrastructure such as bridges and buildings. FRP are

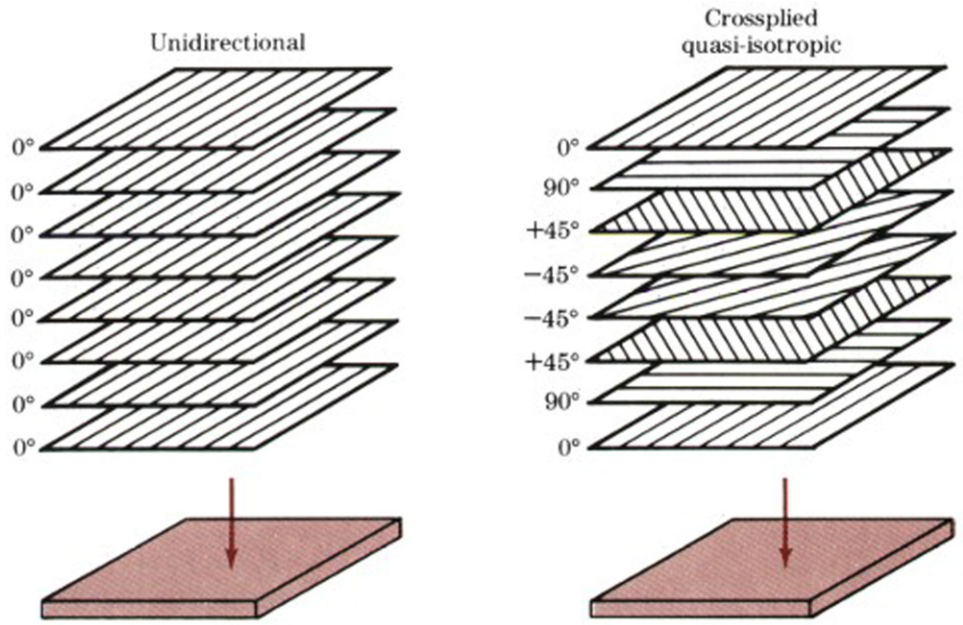


Figure 5 Schematic illustration of lamina being combined to form a laminate.[48]

composites used in almost every type of advanced engineering structure.

The development of new advanced forms of FRP materials has increased the applications of composites over these recent years. FRP materials are famously become established in relatively new market such as in biomedical devices and civil structures. Moreover, this composite continues to grow at an impressive rate as these materials are used more in their existing markets. Carbon nanotubes and nanoparticles can be the examples for new styles of reinforcement and in the developments in high-performance resin systems. FRPs also is a system that are constructed of traditional civil engineering materials, which known as steel and concrete and besides that, it is increasingly being considered as an enhancement to or substitute for infrastructure components. As stated before, the good properties that FRPs have are light weight, no-corrosive, can easily be constructed exhibit high-specific strength and specific stiffness and can be tailored to satisfy performance requirements. Because of their advantageous characteristics, composites have been included in new construction and rehabilitation of structures through its use as reinforcement in concrete, bridge decks, modular structures, formwork, and external reinforcement for strengthening and seismic upgrade. There have been actively studied in numerous research laboratories and professional organizations around the world that the compatibility of FRP to concrete structures as a substitute for steel bars or pre-stressing tendons.

A lot of good properties or high number of advantages for FRP reinforcement such as corrosion resistance, non-magnetic properties, high tensile strength, light weight, and ease of handling. However, besides the good advantages, they generally have cons like relatively poor transverse or shear resistance and have a linear elastic response in tension up to brittle failure. Also, when expose to high temperatures, their resistance to fire is poor. Furthermore, they are more sensitive to stress-rupture effects and will lose significant strength upon bending. Moreover, their cost, whether considered per unit weight or on the basis of force carrying capacity, is high in comparison to conventional steel reinforcing bars or pre-stressing tendons. When view through engineering perspective, the most serious problem that can be detected with the FRP reinforcements are the very low shear strength in the transverse direction and the lack of plastic behavior. This can lead to the rupture of premature tendon, notably when the present of the effects, such as at shear-cracking planes in reinforced concrete beams where dowel action exists. In fact, this dowel action plays a role to reduce shear resistance in the tendon and also to reduce tensile. For the upcoming future, more expectation in continuous improvement is needed and solutions and limitations of use have been offered.

Increasing in the demand and market share will decrease significantly in the unit cost of FRP reinforcements. However, there are applications where FRP reinforcements are cost effective and justifiable, even today. Applications such as the use of FRP meshes or textiles or fabrics in thin cement products and also include the use of bonded FRP sheets or plates in repair and strengthening of concrete structures. Meanwhile, the cost of repair and rehabilitation of a structure is always, in relative terms, substantially higher than the cost of the initial structure. Generally, repair section must be a relatively small volume of repair material yet relatively high commitment in labor. The cost of material becomes secondary because of the labor cost in developed countries significantly so high. Thus, the more the cost-effective in material repair, the highest the performance and durability of the repair material. This indicates that the material cost is not a serious issue in repair. In fact, the FRP repair materials are costly also not a constraining drawback. The argument for FRP composites in a sustainable built environment is questionable when considering the appearing of only energy and material resources on the surface. However,

such a conclusion needs to be evaluated in terms of potential advantages present in use of FRP composites related to considerations such as ocean environments, space systems, defense systems, seismic upgrades, rehabilitating existing structures, and extending their life. Besides that, other examples are longer lasting, higher performance, lighter weight, and higher strength.

FRP composites is one of a sustainable material and because of that, the environmental concerns appear to be a barrier to its feasibility particularly when considering smog, air pollution, acidification associated with its production, and fossil fuel depletion. Additional fact, the structural components of FRP cannot be reused to perform a similar function in another structure unlike steel and timber. That is why the ability to recycle these FRP composites is limited. Nevertheless, direct and indirect benefit may be revealed if the environmental impact of FRP composites in infrastructure applications is evaluated, specifically through the life cycle analysis. Since the first introduced, the composite materials have developed very greatly. However, a number of needs remain before the composite materials can be used as an alternative to conventional materials as part of a sustainable environment.

Ultimately, in order for composites to truly be considered a viable alternative, they must be structurally and economically feasible. Numerous studies regarding the structural feasibility of composite materials are widely available in literature. However, limited studies are available on the economic and environmental feasibility of these materials from the perspective of a life cycle approach, since short term data is available or only economic costs are considered in the comparison. Additionally, the long-term effects of using composite materials needs to be determined. The by-products of the production, the sustainability of the constituent materials, and the potential to recycle composite materials needs to be assessed in order to determine of composite materials can be part of a sustainable environment.

1.8.3.3.1.1 Failure modes

Structural failure can occur in FRP materials when:

- Tensile forces stretch the matrix more than the fibers, causing the material to shear at the interface between matrix and fibers.
- Tensile forces near the end of the fibers exceed the tolerances of the matrix, separating the fibers from the matrix.
- Tensile forces can also exceed the tolerances of the fibers causing the fibers themselves to fracture leading to material failure.[26]

1.8.3.3.1.2 Material requirements

The matrix must also meet certain requirements in order to first be suitable for the FRP process and ensure a successful reinforcement of it. The matrix must be able to properly saturate, and bond with the fibers within a suitable curing period. The matrix should preferably bond chemically with the fiber reinforcement for maximum adhesion. The matrix must also completely envelope the fibers to protect them from cuts and notches that would reduce their strength, and to transfer forces to the fibers. The fibers must also be kept separate from each other so that if failure occurs it is localized as much as possible, and if failure occurs the matrix must also debond from the fiber for similar reasons. Finally, the matrix should be of a plastic that remains chemically and physically stable during and after reinforcement and molding processes. To be suitable for reinforcement material fiber additives must increase the tensile strength and modulus of elasticity of the matrix and meet the following conditions; fibers must exceed critical fiber content; the strength and rigidity of fibers itself must exceed the strength and rigidity of the matrix alone; and there must be optimum bonding between fibers and matrix.

1.8.3.3.1.3 Applications of FRP

FRPs are best suited for any design program that demands weight savings, precision engineering, finite tolerances, and the simplification of parts in both production and operation. A molded polymer artifact is cheaper, faster, and easier to manufacture than cast aluminum or steel artifact, and maintains similar and sometimes better tolerances and material strengths. The Mitsubishi Lancer Evolution IV also used FRP for its spoiler material.[25–27,49,50]

1.8.3.3.1.4 Structural applications of FRP

FRP can be applied to strengthen the beams, columns, and slabs in buildings. It is possible to increase strength of these structural members even after these have been severely damaged due to loading conditions. For strengthening beams, two techniques are adopted. First one is to paste FRP plates to the bottom (generally the tension face) of a beam. This increases the strength of beam, deflection capacity of beam, and stiffness (load required to make unit deflection). Alternatively, FRP strips can be pasted in 'U' shape around the sides and bottom of a beam, resulting in higher shear resistance. Columns in building can be wrapped with FRP for achieving higher strength. This is called wrapping of columns. The technique works by restraining the lateral expansion of the column. Slabs may be strengthened by pasting FRP strips at their bottom (tension face). This will result in better performance, since the tensile resistance of slabs is supplemented by the tensile strength of FRP. In the case of beams and slabs, the effectiveness of FRP strengthening depends on the performance of the resin chosen for bonding.[20,22] Examples of applications and advantages of FRP are shown in the **Table 1** below:

1.8.3.3.1.5 Advantages and limitations of FRP

FRP allows the alignment of the glass fibers of thermoplastics to suit specific design programs. Specifying the orientation of reinforcing fibers can increase the strength and resistance to deformation of the polymer. Glass-reinforced polymers are strongest and most resistive to deforming forces when the polymer fibers are parallel to the force being exerted, and are weakest when the fibers are perpendicular. Thus this ability is at once both an advantage and a limitation depending on the context of use. Weak spots of perpendicular fibers can be used for natural hinges and connections, but can also lead to material failure when production processes fail to properly orient the fibers parallel to expected forces. When forces are exerted perpendicular to the orientation of fibers the strength and elasticity of the polymer is less than the matrix alone. In cast resin components made of glass-reinforced polymers such as unsaturated polyester (UP) and epoxy resin (EP), the

Table 1 Applications and advantages of FRP

Fiber-reinforced polymer	*Application and advantages*
Carbon fiber-reinforced polymers	Rudder of commercial airplane Advantages over a traditional rudder made from sheet aluminum are: ● 25% reduction in weight ● 95% reduction in components by combining parts and forms into simpler molded parts ● Overall reduction in production and operational costs, economy of parts results in lower production costs and the weight savings create fuel savings that lower the operational costs of flying the airplane
Glass fiber-reinforced polymers	Engine intake manifolds are made from glass fiber reinforced PA 66 Advantages over cast aluminum manifolds are: ● Up to a 60% reduction in weight ● Improved surface quality and aerodynamics ● Reduction in components by combining parts and forms into simpler molded shapes Automotive gas and clutch pedals made from glass fiber reinforced PA 66 (DWP 12-13) Advantages over stamped aluminum are: ● Pedals can be molded as single units combining both pedals and mechanical linkages simplifying the production and operation of the design ● Fibers can be oriented to reinforce against specific stresses, increasing the durability and safety[51]

orientation of fibers can be oriented in two-dimensional and three-dimensional weaves. This means that when forces are possibly perpendicular to one orientation, they are parallel to another orientation; this eliminates the potential for weak spots in the polymer.[47]

1.8.3.3.1.6 Design considerations

FRP is used in designs that require a measure of strength or modulus of elasticity those non-reinforced plastics and other material choices are either ill-suited for mechanically or economically. This means that the primary design consideration for using FRP is to ensure that the material is used economically and in a manner that takes advantage of its structural enhancements specifically. This is however not always the case, the orientation of fibers also creates a material weakness perpendicular to the fibers. Thus the use of fiber reinforcement and their orientation affects the strength, rigidity, and elasticity of a final form and hence the operation of the final product itself. Orienting the direction of fibers either, unidirectional, two-dimensionally, or three-dimensionally during production affects the degree of strength, flexibility, and elasticity of the final product. Fibers oriented in the direction of forces display greater resistance to distortion from these forces and vice versa, thus areas of a product that must withstand forces will be reinforced with fibers in the same direction, and areas that require flexibility, such as natural hinges, will use fibers in a perpendicular direction to forces. Using more dimensions avoids this either or scenario and creates objects that seek to avoid any specific weak points due to the unidirectional orientation of fibers. The properties of strength, flexibility and elasticity can also be magnified or diminished through the geometric shape and design of the final product. These include such design consideration such as ensuring proper wall thickness and creating multifunctional geometric shapes that can be molding as single pieces, creating shapes that have more material and structural integrity by reducing joints, connections, and hardware.[25]

1.8.3.3.1.7 Disposal and recycling concerns

As a subset of plastic FR plastics are liable to a number of the issues and concerns in plastic waste disposal and recycling. Plastics pose a particular challenge in recycling processes because they are derived from polymers and monomers that often cannot be separated and returned to their virgin states, for this reason not all plastics can be recycled for re-use, in fact some estimates claim only 20–30% of plastics can be material recycled at all. Fiber-reinforced plastics and their matrices share these disposal and environmental concerns. In addition to these concerns, the fact that the fibers themselves are difficult to remove from the matrix and preserve for re-use means FRP amplify these challenges. FRP are inherently difficult to separate into base a material that is into fiber and matrix, and the fiber-reinforced plastic matrix into separate usable plastic, polymers, and monomers. These are all concerns for environmentally informed design today, but plastics often offer savings in energy and economic savings in comparison to other materials, also with the advent of new more environmentally friendly matrices such as bioplastics and UV-degradable plastics, FRP will similarly gain environmental sensitivity.[26]

1.8.3.3.2 PRP

Particles used for reinforcing include ceramics and glasses such as small mineral particles, metal particles such as aluminum and amorphous materials, including polymers and carbon black. Particles are used to increase the modules of the matrix and to decrease the ductility of the matrix. Particles are also used to reduce the cost of the composites. Reinforcements and matrices can be common, inexpensive materials and are easily processed. Some of the useful properties of ceramics and glasses include high-melting temperature, low density, high strength, stiffness, wear resistance, and corrosion resistance. Many ceramics are good electrical and thermal insulators. Some ceramics have special properties, some ceramics are magnetic materials, some are piezo electric materials, and a few special ceramics are even superconductors at very low temperatures. Ceramics and glasses have one major drawback: they are brittle. An example of particle-reinforced composites is an automobile tire, which has carbon black particles in a matrix of poly-isobutylene elastomeric polymer. Polymer composite materials have generated wide interest in various

engineering fields, particularly in aerospace applications. Research is underway worldwide to develop newer composites with varied combinations of fibers and fillers so as to make them useable under different operational conditions. Against this backdrop, the present work has been taken up to develop a series of polyetheretherketone (PEEK) based composites with glass fiber reinforcement and with ceramic fillers and to study their response to solid particle erosion.[20,22]

Particle-reinforced composites include the most used (by weight) construction material in the world – concrete. Sand (fine particles) and gravel (coarse particles) compose from 60 to 75% of standard concrete.

Note that the particulates (sand and gravel) are combined with the Matrix (cement), which acts as a bonding agent between the particles. The addition of water to a particle-cement mixture results in a complex hydration reaction that produces a network of strong ionic/covalent bonds. The reinforcing particles are generally stiff and hard and restrain deformation of the cement. As with polymers, additives (termed admixtures) are added to concrete to affect its reactions and properties:

- Accelerators speed-up the curing process,
- Retarders slow down the curing process,
- Surface hardeners produce an abrasion resistant surface, etc.[49]

1.8.4 Manufacturing Process

1.8.4.1 Polymers

The linking of small molecules (monomers) to make larger molecules is a polymer. Polymerization requires that each small molecule have at least two reaction points or functional groups. There are two distinct major types of polymerization processes, condensation polymerization, in which the chain growth is accompanied by elimination of small molecules such as H_2O or CH_3OH, and addition polymerization, in which the polymer is formed without the loss of other materials.

1.8.4.1.1 Polymerization

Polymerization, emulsion polymerization any process in which relatively small molecules, called monomers, combines chemically to produce a very large chain-like or network molecule, called a polymer. The monomer molecules may be all alike, or they may represent two, three, or more different compounds. Usually at least 100 monomer molecules must be combined to make a product that has certain unique physical properties – such as elasticity, high tensile strength, or the ability to form fibers – that differentiate polymers from substances composed of smaller and simpler molecules; often, many thousands of monomer units are incorporated in a single molecule of a polymer. The formation of stable covalent chemical bonds between the monomers sets polymerization apart from other processes, such as crystallization, in which large numbers of molecules aggregate under the influence of weak intermolecular forces. Two classes of polymerization usually are distinguished. In condensation polymerization, each step of the process is accompanied by formation of a molecule of some simple compound, often water.

In addition polymerization, monomers react to form a polymer without the formation of by-products. Addition polymerizations usually are carried out in the presence of catalysts, which in certain cases exert control over structural details that have important effects on the properties of the polymer. Linear polymers, which are composed of chain-like molecules, may be viscous liquids or solids with varying degrees of crystallinity; a number of them can be dissolved in certain liquids, and they soften or melt upon heating. Cross-linked polymers, in which the molecular structure is a network, are thermosetting resins (i.e., they form under the influence of heat but, once formed, do not melt or soften upon reheating) that do not dissolve in solvents. Both linear and cross-linked polymers can be made by either addition or condensation polymerization.

1.8.4.1.2 Polycondensation

The polycondensation a process for the production of polymers from bifunctional and polyfunctional compounds (monomers), accompanied by the elimination of low-molecular weight by-products (for example, water, alcohols, and hydrogen halides). A typical example of polycondensation is the synthesis of complex polyester. The process is called homopolycondensation if the minimum possible number of monomer types for a given case participates, and this number is usually two. If at least one monomer more than the number required for the given reaction participates in polycondensation, the process is called copolycondensation. Polycondensation in which only bifunctional compounds participate leads to the formation of linear macromolecules and is called linear polycondensation. If molecules with three or more functional groups participate in polycondensation, three-dimensional structures are formed and the process is called three-dimensional polycondensation. In cases where the degree of completion of polycondensation and the mean length of the macromolecules are limited by the equilibrium concentration of the reagents and reaction products, the process is called equilibrium (reversible) polycondensation.

1.8.4.1.3 Polyaddition

The polyaddition reactions are similar to polycondensation reactions because they are also step reactions, however, without splitting off low-molecular weight by-products. The reaction is exothermic rather than endothermic and therefore cannot be stopped at will. Typical for polyaddition reaction is that individual atoms, usually H-atoms, wander from one monomer to another as the two monomers combine through a covalent bond. The monomers, as in polycondensation reactions, have to be added in stoichiometric amounts. These reactions do not start spontaneously and they are slow. Polyaddition does not play a significant role in the production of thermoplastics. It is commonly encountered with cross-linked polymers. Polyurethane, which can be either a thermoplastic or thermosets, is synthesized by the reaction of multifunctional isocyanates with multifunctional amines or alcohol. Thermosetting EPs are formed by polyaddition of epoxides with curing agents, such as amines and acid anhydrides.

In comparing chain reaction polymerization with the other two types of polymerization the following principal differences should be noted: chain reaction polymerization, or simply called polymerization, is a chain reaction as the name implies. Only individual monomer molecules add to a reactive growing chain end, except for recombination of two radical chain ends or reactions of a reactive chain end with an added modifier molecule. The activation energy for chain initiation is much greater than for the subsequent growth reaction and growth, therefore, occurs very rapidly.[47]

1.8.4.2 Natural Fiber-Reinforced Composites

1.8.4.2.1 All process description

FRP involves two distinct processes, the first is the process whereby the fibrous material is manufactured and formed, and the second is the process whereby fibrous materials are bonded with the matrix during the molding process. Having known the role of design for manufacturing process, this section is now devoted to the manufacturing processes reported to be used in the development of products or components from natural-fiber composites. Ho *et al.*[52] performed extensive literature review composite manufacturing processes that are related natural-fiber composites. They reported that majority of the work related to natural-fiber composites used conventional composite manufacturing processes such injection moulding, compression moulding, resin transfer moulding (RTM), vacuum infusion moulding, and hot press processes. In this chapter only selected manufacturing processes are reviewed.

1.8.4.2.1.1 Fiber process

Fiber preforms are how the fibers are manufactured before being bonded to the matrix. Fiber preforms are often manufactured in sheets, continuous mats, or as continuous filaments for spray applications. The four major ways to manufacture the fiber preform is though the textile processing techniques of weaving, knitting, braiding, and stitching.

- Weaving can be done in a conventional manner to produce two-dimensional fibers as well in a multilayer weaving that can create three-dimensional fibers. However, multilayer weaving is required to have multiple layers of warp yarns to create fibers in the z-direction creating a few disadvantages in manufacturing, namely the time to set up all the warp yarns on the loom. Therefore, most multilayer weaving is currently used to produce relatively narrow width products or high value products where the cost of the preform production is acceptable. Another fiber-reinforced plastic three-dimensional one of the main problems facing the use of multilayer woven fabrics is the difficulty in producing a fabric that contains fibers oriented with angles other than 0° and 90° to each other, respectively.
- The second major way of manufacturing fiber preforms is braiding. Braiding is suited to the manufacture of narrow width flat or tubular fabric and is not as capable as weaving in the production of large volumes of wide fabrics. Braiding is done over top of mandrels that vary in cross-sectional shape or dimension along their length. Braiding is limited to objects about a brick in size. Unlike the standard weaving process, braiding can produce fabric that contains fibers at 45° angles to one another. Braiding three-dimensional fibers can be done using four-steps, two-step, or multilayer interlock braiding. Four step or row and column braiding utilizes a flat-bed containing rows and columns of yarn carriers that form the shape of the desired preform. Additional carriers are added to the outside of the array, the precise location and quantity of which depends upon the exact preform shape and structure required.

  There are four separate sequences of row and column motion, which act to interlock the yarns and produce the braided preform. The yarns are mechanically forced into the structure between each step to consolidate the structure in a similar process to the use of a reed in weaving. Two-step braiding is unlike the four-step process because the two-step includes a large number of yarns fixed in the axial direction and a fewer number of braiding yarns. The process consists of two steps in which the braiding carriers move completely through the structure between the axial carriers. This relatively simple sequence of motions is capable of forming performs of essentially any shape, including circular and hollow shapes. Unlike the four steps process the two steps process does not require mechanical compaction the motions involved in the process allows the braid to be pulled tight by yarn tension alone. The last type of braiding is multi-layer interlocking braiding that consists of a number of standard circular braiders being joined together to form a cylindrical braiding frame. This frame has a number of parallel braiding tracks around the circumference of the cylinder, but the mechanism allows the transfer of yarn carriers between adjacent tracks forming a multilayer braided fabric with yarns interlocking to adjacent layers.

  The multilayer interlock braid differs from both the four-step and two-step braids in that the interlocking yarns are primarily in the plane of the structure and thus do not significantly reduce the in-plane properties of the perform. The four-step and two-step processes produce a greater degree of interlinking as the braiding yarns travel through the thickness of the preform, but therefore contribute less to the in-plane performance of the preform. A disadvantage of the multilayer interlock equipment is that due to the conventional sinusoidal movement of the yarn carriers to form the preform, the equipment is not able to have the density of yarn carriers that is possible with the two-step and four-step machines.
- Knitting fiber preforms can be done with the traditional methods of warp and (weft) knitting, and the fabric produced is often regarded by many as two-dimensional fabric, but machines with two or more needle beds are capable of producing multilayer fabrics with yams that traverse between the layers. Developments in electronic controls for needle selection and knit loop transfer and in the sophisticated mechanisms that allow specific areas of the fabric to be held and their movement controlled. This has allowed the fabric to form itself into the required three-dimensional perform shape with a minimum of material wastage.
- Stitching is arguably the simplest of the four main textile manufacturing techniques and one that can be performed with the smallest investment in specialized machinery.

Basically the stitching process consists of inserting a needle, carrying the stitch thread, through a stack of fabric layers to form a three-dimensional structure. The advantages of stitching are that it is possible to stitch both dry and prepreg fabric, although the tackiness of prepare makes the process difficult and generally creates more damage within the prepreg material than in the dry fabric. Stitching also utilizes the standard two-dimensional fabrics that are commonly in use within the composite industry, therefore, there is a sense of familiarity concerning the material systems. The use of standard fabric also allows a greater degree of flexibility in the fabric lay-up of the component than is possible with the other textile processes, which have restrictions on the fiber orientations that can be produced.

Reinforcing fiber is manufactured in both two-dimensional and three-dimensional orientations:

- Two-dimensional fiber-reinforced polymer is characterized by a laminated structure in which the fibers are only aligned along the plane in x- and y-direction of the material. This means that no fibers are aligned in the through thickness or the z-direction, this lack of alignment in the through thickness can create a disadvantage in cost and processing. Costs and labor increase because conventional processing techniques used to fabricate composites, such as wet hand lay-up, autoclave and RTM, require a high amount of skilled labor to cut, stack and consolidate into a preformed component.
- Three-dimensional fiber-reinforced polymer composites are materials with three-dimensional fiber structures that incorporate fibers in the x-, y-, and z-direction. The development of three-dimensional orientations arose from industry's need to reduce fabrication costs, to increase through-thickness mechanical properties, and to improve impact damage tolerance; all were problems associated with two-dimensional FRP.[47]

1.8.4.2.1.2 Molding process

A rigid structure is usually used to establish the shape of FRP components. Parts can be laid-up on a flat surface referred to as a 'caul plate' or on a cylindrical structure referred to as a 'mandrel.' However, most fiber-reinforced plastic parts are created with a mold or 'tool.' Molds can be concave female molds, male molds, or the mold can completely enclose the part with a top and bottom mold.

The moulding processes of FRP plastics begin by placing the fiber preform on or in the mold. The fiber preform can be dry fiber, or fiber that already contains a measured amount of resin called 'prepreg.' Dry fibers are 'wetted' with resin either by hand or the resin is injected into a closed mold. The part is then cured, leaving the matrix and fibers in the shape created by the mold. Heat and/or pressure are sometimes used to cure the resin and improve the quality of the final part. The different methods of forming are listed below.[51]

1.8.4.2.1.2.1 Bladder molding

Individual sheets of prepreg material are laid-up and placed in a female-style mould along with a balloon-like bladder. The mould is closed and placed in a heated press. Finally, the bladder is pressurized forcing the layers of material against the mould walls. The part is cured and removed from the hot mould. Bladder molding is a closed molding process with a relatively short cure cycle between 15 and 60 min making it ideal for making complex hollow geometric shapes at competitive costs.

1.8.4.2.1.2.2 Compression molding

Compression moulding is a composite manufacturing process normally used to produce composite components in high production volume such as automotive components. There are two types of compression moulding process, i.e., cold compression and hot compression moldings. In this process, for thermosetting matrices, normally an intermediate material called moulding compound is used. It is really a semi-cured composite. Sheet moulding compound and bulk moulding compound (BMC) are two widely used thermosetting-based moulding compounds. For thermoplastic polymer, moulding compound normally used is glass mat thermoplastics (GMT). For preparing composite specimens in the laboratory scale compression moulding, composite pellets are normally prepared using internal mixer and twin screw extruder. In compression moulding process, pressure is applied in cold compression and pressure and temperature in hot compression moulding after the moulding performs are placed in a mould cavity. In cold compression moulding, curing process takes place at room temperature while for hot press it takes place by applying heat to the mould and it in turn being transferred to the composites. Matrices used in this process include UP, vinyl ester and phenolic for thermosetting polymers while among the thermoplastic polymers, PP, polyamide, and PEEK can be used.

Wirawan *et al.*[53] and El-Shekeil *et al.*[54] used laboratory scale compression moulding (**Figure 6**) to prepare composite specimens from sugar cane bagasse and PVC, and kenaf and TPU, respectively. The intermediate materials were made using internal mixer. The intermediate materials were placed into the mould and the heat and pressure were applied to form the composite plates. Hot pressing was then carried out at a temperature around 170 °C for 12.5 min and the mixture

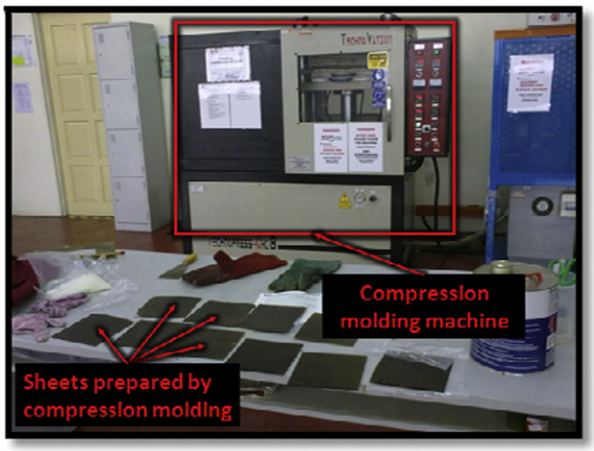


Figure 6 Hot compression moulding machine. Courtesy of Yousuf El-Shekeil.[55]

was cooled under pressure to room temperature. The mechanical and thermal properties of the composites were then determined.

1.8.4.2.1.2.3 Vacuum bagging

Vacuum bagging is one of the processes in the category of prepreg moulding. Another process is called autoclave moulding. The different between these two processes in on the way curing process was done; one in vacuum bag (oven) and the other in an autoclave. Vacuum bagging is a composite manufacturing process that utilizes a vacuum bag to provide compaction pressure and consolidation of plies within the laminate. It is an extended version of hand or wet lay-up process. It also sometimes called vacuum bag moulding.[56] In this process, a mould base is placed horizontally. Then composite prepreg laminates are stacked onto the mould base. Then a series of equipment's and materials are covered onto the composite layers such as release film layer, air-bleeder layer, blocked film layer, and breather layer. Finally, a vacuum bag is placed to cover the composite laminate and all the layers. The vacuum bag is then sealed by means of sealers. Polymer materials that can be used in this process include epoxy, phenolic, and polyimide.

Mariatti and Abdul Khalil[57] used vacuum bagging process to prepare samples of bagasse fiber reinforced UP composites. Two components of bagasse, i.e., rind (outer part) and pith (inner part) were used as reinforcement fibers in composites. The hardener used in this experiment was methyl ethyl ketone peroxide (MEKP). Pressure was applied to the laid-up laminates in order to consolidate the final composites and the bonding between composite plies. Volatiles and trapped air in the laminates were drawn out using vacuum and void contents were minimized. Curing process took place at room temperature. Composite specimens were then tested mechanically to determine tensile, flexural, and impact properties of the composites. Improvements were made on mechanical properties of bagasse fiber UP composites by fiber chemical treatment using sodium hydroxide and acrylic acid.

1.8.4.2.1.2.4 Mandrel wrapping

Sheets of prepreg material are wrapped around a steel or aluminum mandrel. The prepreg material is compacted by nylon or PP cello tape. Parts are typically batch cured by hanging in an oven. After cure the cello and mandrel are removed leaving a hollow carbon tube. This process creates strong and robust hollow carbon tubes.

1.8.4.2.1.2.5 Hand lay-up

Hand lay-up is an open moulding process to produce polymer composite product. This is a labor intensive process where high skill operator is required to perform the fabrication task. A mould release agent is applied onto the mould surface for ease of removing of finished composite products. The laying-up of a component begins with applying gel coat to the mould surface. It is resin rich layer and the purpose is to prevent the fibers appearing on the mould surface. The composites are then prepared by placing a fiber reinforcement and by adding polymer resin onto it. A roller is used to consolidate the composites and composites are made layer by layer. The process is repeated with more layers until the desired thickness is obtained. Then the composites are cured at room temperature or in an oven. Thermosetting resins like UP, vinyl ester, and epoxy are among the most commonly used resins.

Hand lay-up or also known as wet lay-up has been used to produce components from natural-fiber composites for many decades now. Ford had used hand lay-up process to fabricate automotive body from natural fiber-reinforced soya-based polymer composites around a decade ago. Misri *et al.*[58] have used hand lay-up process to develop a small boat from hybrid glass-sugar palm fiber reinforced UP composites. The fabrication work was carried out in association with an established boat builder. This process was labor intensive and required high skill operators to fabricate the boat. The mould was made from glass fiber-reinforced polyester composite and it was developed in such a way that a very high quality surface was obtained. Then mould release agent was placed onto the mould surface to prevent the component sticking to the mould. Then glass fibers were laid-up followed by resin and they were consolidated using a roller. MEKP was used as a hardener. The process is repeated with sugar palm fibers and the process continued, layer by layer until the desired thickness of the composites was achieved. **Figure 7** shows hand lay-up process of hybrid glass-sugar palm fiber composite boat.

1.8.4.2.1.2.6 Chopper gun

Continuous strand of fiber-glass are pushed through a hand-held gun that both chops the strands and combines them with a catalyzed resin such as polyester. The impregnated chopped glass is shot onto the mould surface in whatever thickness the design and human operator think is appropriate. This process is good for large production runs at economical cost, but produces geometric shapes with less strength than other molding processes and has poor dimensional tolerance.

1.8.4.2.1.2.7 Filament winding

Filament winding is a composite manufacturing process to produce components that are normally circular in shape. It can be considered an open mould process and the mould is actually a rotating mandrel. In this process, continuous fiber rovings are being drawn by a puller through a resin bath. The



Figure 7 Hand lay-up process for hybrid glass-sugar palm composite boat. Courtesy of Sairizal Misri.[55]



Figure 8 Pultrusion process of kenaf fiber composites. Courtesy of Mohd Fairuz Abdul Manab.[55]

pre-impregnated composites are in turn being wound around the rotating mandrel. The composites are also being traversed in x-direction so that even distribution of the composites along the length of the mandrel can be achieved. There are three types of winding patterns in the filament winding process, i.e., hoop, helical, and polar windings.

Misri *et al.*[59] developed kenaf fiber reinforced UP composite hollow shafts and studied their mechanical behavior. Continuous kenaf fiber rovings were pulled through a drum type resin bath and the pre-impregnated fiber composites were wound around hollow aluminum rotating mandrel. They studied various properties such as tensile and torsion properties of the composites and such findings were compared with the results of FEA. The major problem with developing filament wound kenaf fiber composites is to obtain consistently smooth surface of shafts. Secondary processing like milling is required.

1.8.4.2.1.2.8 Pultrusion

Pultrusion is a combination of two words; pull and extrusion. The process is similar to extrusion process but in pultrusion, the product is developed by pulling the materials rather than pushing the materials through the die as in the case of extrusion. Continuous fiber rovings or tapes are pulled by means of a puller through a resin bath of thermosetting polymer. Examples of thermosetting polymers that can be used in this process include epoxy, and UP. The resulting impregnated fiber composites leave the resin bath and are being pulled and passed through a series of forming dies. The shape of the final product follows the shape of the cross of the dies and the shape can be circular, rectangular, square, I shaped, and H shaped sections. The composite is also cured in one of the dies. The end products are normally in the form of rods, and bars. At the end of the pultrusion process, the products are cut to the required lengths.

Fairuz *et al.*[60] reported the work on pultruded kenaf fiber reinforced vinyl ester composites using pultrusion process. Kenaf composite rods were produced. In this study, three different parameters were investigated, i.e., speeds, temperatures and filler loadings. Taguchi's design of experiment was used to determine the number of experiments to be conducted. Specimens in the form of rods were produced at three different speeds by fixing temperature and filler loading. Then the same is repeated for different parameters; temperatures and filler loadings. Mechanical properties of the composite rod specimens such as tensile, flexural, and impact properties were tested for each parameter. **Figure 8** shows the pultrusion process of kenaf fiber-reinforced composites.

1.8.4.2.1.2.9 Resin infusion

Fabrics are placed into a mould which wet resin is then injected into. Resin is typically pressurized and forced into a cavity which is under vacuum in the RTM process. Resin is entirely pulled into cavity under vacuum in the VARTM (vacuum assisted resin transfer molding) process. This molding process allows precise tolerances and detailed shaping but can sometimes fail to fully saturate the fabric leading to weak spots in the final shape.

1.8.5 Machining of Natural Fiber-Reinforced Composite

There are various new methods for machining of composites, such as waterjet machining and laser machining. Due to the high cost of such processes, drilling is still used widely as a major secondary machining process, due to the need for structural joining of composites materials. Machining involves the removal of any extra or unwanted material. Some of the most common machining processed are drilling, turning, and milling. Machining of composites brings with it some major problems, including rapid tool wear due to the abrasiveness of composites, fiber fracture, and matrix breaking. Another known nuisance has been delamination, or the breaking of materials fibers, which creates a bad surface finish and caused stress concentrations at such regions. Earlier composites were machined like metals. But poor surface finish and faster tool wear led to the further study of composite machining. Unlike

metals, composites need separate tools and working conditions. Although tools used for machining of metals can still be used for composites, care must be taken to maintain optimum levels of, feed rate, thrust force, and other factors. One of the main advantages of composites has been the fact that an entire part can be manufactured. This minimizes the machining of composites. However with part integration, sometimes composites need to be joined to form a larger part, which means that a certain amount of machining needs to be done for composites too. Since the last decade, a great deal of emphasis has been focused on the development and application of natural fiber-reinforced composite materials in many industries. Needless to say, this called special attention of the automotive industry for the application of many parts such as interior panels. Increased use of natural-fiber composites implies that there is demand for joining of some of the parts together.

Machining of a fiber-reinforced composite depends on the properties of the fibers and the matrix as well as its response to the machining process. In addition, the choice of the specific process depends upon the following factors: type of machining operation, part geometry and size, finish and accuracy requirements, number of parts, diversity of parts including the materials of the parts, availability of appropriate machine and cutting tools, availability of in-house technology, current machining practice, manufacturing schedule, capital requirements and justification for new equipment, and overall costs. Certain machining operations may not be possible at all with some composite materials. For example, it is not possible to machine SiC whisker reinforced alumina with a single-point cutting tool, even with a diamond tool. It may, however, be possible to shape it by diamond grinding or by some of the nonconventional machining processes, such as laser machining or ultrasonic-assisted machining. In other cases more than one process may be candidate processes and the specific process chosen depends on the factors outlined earlier. Of course, the general tendency is to use current machining practices by adopting existing equipment for this application. This is particularly true of composite machining in small manufacturing shops in view of capital limitations for procuring new machinery or new technology. This may not be the case with large companies, such as Boeing, Lockheed, or General Dynamics, where resources are normally available, if justified. Even a particular process chosen now for machining composites may have to be abandoned at a later date because of changes in the factors outlined earlier. For example, the lot size may be increased significantly, necessitating a review of alternate manufacturing processes, or new technology or a technology not currently practiced in the plant may become available or be economically attractive.

1.8.5.1 Safety Considerations

Safety is the main aspect when machining. It can release some finer fractions to atmosphere when machining the fiber-like composites. Besides, it can be very harmful when some of the chemicals from polymer-based composites are released. This is because of the heat and thermal damage when machining take part. In the case of health, it has been established that fibrous materials like asbestos and glass can cause cancer and become suspected agents respectively. Also, there will be other medical problems such as respiratory complications if constant exposure comes from both inorganic fibers and organic compounds, which are released during the machining of polymer-based composites.

It has been reported that fibers used in composites have diameter ranges from 9 to 24 J Lm, with a median length of 10–17 J Lm. Fibers of this size are not respirable and may not reach the lung. If, however, these fibers are longitudinally split during machining they can be potentially harmful. Antonson and Runmark[61] studied the effect of airborne fibrous glass and dust originating from machining-reinforced plastics. They examined the possibility of longitudinal fiber division during machining of reinforced polyester plastic and whether respirable glass fibers can be produced. Their results show that such a division does not occur in the machining of glass-fiber-reinforced polyester composite.

Doyle and Kokasa[62] conducted laser-machining tests on a Kevlar fabric poly (p-phenylene terephthalamide) using a CO_2 laser at a rate of 150 in. min^{-1} and l-kW power. They collected the chemical by-products produced during cutting and analyzed these products using a gas chromotography, mass spectroscopy and found a number of toxic- and cancer-producing compounds. They recommended adequate ventilation and appropriate safety procedures to prevent exposure of personnel to these gases in the laser-cutting facility. In machining GFRPs, they found glass particles. According to Doyle and Kokasa,[62] the *E*-glass fibers vaporize during laser cutting and then condense as small beads ranging from 200 nm to 0.5 μm. Since particles less than 0.5 μm can permeate into the deepest recess of the lungs, they can pose a health danger to the workers in the cutting facility. Konig and Rummenholler[42] investigated, among other things, the safety aspects of the milling of glass and carbon fiber-reinforced plastics. Fine dust particles that can cause respiratory problems were found to be about 1% of the total dust collected during milling. Also, fine dust settles considerably slower than coarser particles, so they could represent a risk to the health of the operator even after the operation is completed.[63]

1.8.5.2 Factors Affecting the Cut Quality of Natural Fiber-Reinforced Composites

Carbon, glass, and aramid are the examples of synthetic fiber-reinforced composites, which become famous in machining sector because of their wide applications in various industries. Besides, the natural fiber-reinforced composite also shows interest and slowly gaining momentum in the machining and cutting nowadays. Generally, the performance and cut quality of the latter composites can be measured in terms of the size of kerf width, surface roughness, burr height, and tool wear. But in this chapter, only two cut quality has been taken into account.

1.8.5.2.1 Kerf width

Kerf width is the width of the material that has been removed during the cutting process. These can be described how much the composite is removed by a saw. This is because every teeth

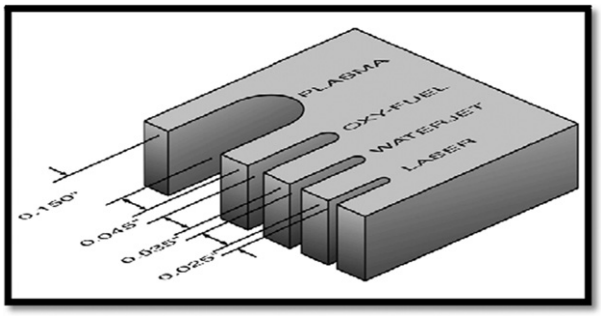


Figure 9 Comparison of kerf width using different types of machine.[64]

on a saw are bent to the side make it remove more material than the width of the saw blade itself. Also, it can prevent the blade from getting stuck in the composites. Recently, when referring to the angle on the edge of the part, some people use that term but it is the incorrect use of the word. Actually, for consistency, the word 'kerf' should only be used when talking about the actual cut width.

1.8.5.2.1.1 Different in process of kerf

Each cutting process removes a different amount of material, or kerf. The more precise processes, like waterjet and laser, remove a smaller amount of kerf, which is one of the reasons they can be more precise. A typical example shown here in **Figure 9**, is for 1/2″ thick mild steel.

Typical kerf width for 1/2″ thick commercial standard:

- Plasma: 0.150‴
- Oxy-fuel: 0.045″
- Waterjet: 0.035″
- Laser: 0.025″

1.8.5.2.1.2 Kerf variations

Not only does kerf width vary from one process to the next but also there are lots of things that affect the kerf width for each process. Of course, as the thickness of material increases, it takes more power to cut through it. In the case of plasma, that means higher current and a larger nozzle. Laser increases power. Oxy-fuel cutting uses a larger nozzle with a wider cutting oxygen stream and hotter preheats. Waterjet uses either a larger nozzle/orifice combination, or a slower cutting speed. Regardless of the process, as the plate gets thicker, the kerf gets wider. There are variations within each process too. For example, when plasma cutting, the actual kerf width depends not only on the cutting current but also on the torch height, speed, and gas settings.

1.8.5.2.2 Surface roughness

There are several types of surface texture which includes roughness, waviness, lay and flaws, see **Figure 10**. Nano roughness and microroughness are the examples for the roughness texture while macroroughness is in waviness part. If we go further into the parts, this roughness are formed by fluctuations in the surface of short wavelengths which characterized by hills and valleys of varying amplitudes and spacings. Hills and valleys also can be defined as local maxima and minima, respectively. Local maxima or known also as asperities are referred to as peaks in a profile and summits in a surface map. Nano- and microroughness include those features intrinsic to the production process. These are considered to include traverse feed marks and other irregularities within the limits of the roughness sampling length. Waviness is the surface irregularity of longer wavelengths and is referred to as macroroughness. Waviness may result from such factors as machine or workpiece deflections, vibration, chatter, heat treatment, or warping strains. Waviness includes all irregularities whose spacing is greater than the roughness sampling length and less than the waviness sampling length. Lay is the principal direction of the predominant surface pattern, ordinarily determined by the production method. Flaws are unintentional, unexpected, and unwanted interruptions in the texture. In addition, the surface may contain gross deviations from nominal shape of very long wavelength, which is known as errors of form. They are not normally considered part of the surface texture.

The evaluation of surface roughness of machined parts using a direct contact method has limited flexibility in handling the different geometrical parts to be measured. Surface roughness also affects several functional attributes of parts, such as friction, wear and tear, light reflection, heat transmission, ability of distributing and holding a lubricant, coating, etc. Therefore, the desired surface finish is usually specified and appropriate processes are required to maintain the quality. Hence, the inspection of surface roughness of the workpiece is very important to assess the quality of a component. Alternately, optical measuring methods are applied to overcome the limitations of stylus method, but they are also sensitive to lighting conditions and noise. The technique proposed in this work, requires no apriority information about the lighting conditions and source of noise. It is important that the specification should include a 'maximum' transverse surface roughness requirement. scanning electron microscopy revealed that the samples with a high surface roughness are heavily damaged by the polishing operation, whilst those with low surface roughness are relatively undamaged, showing only light scoring of the surface.[66,67]

Of these measures, the first two criteria are deemed important from the manufacturing perspective and dependable upon other parameters such as:

- Blade speed,
- Feed rate,
- Fiber loading (fiber content) within the composite, and
- Coolant conditions.

As the number of both measurements and parameters increases, the interactions are becoming increasingly laborious to interpret. The relationships between cut characteristics and processing parameters can be inherently complex and multivariate. This is usually observed in high-volume cutting of numerous fiber composites. Such systems often are called as 'gray.' Gray system theory has been widely used and has shown useful results especially in situations where the data is limited and/or incomplete.[68,69] Besides, it provides an efficient solution to the uncertainty, multi-input and discrete data problem. For example, according to the Taguchi quality design concept, a L18 mixed-orthogonal-array table was chosen for experiments. With both Gray relational analysis (GRA) and statistical method, it is found that the table-feed rate has a significant

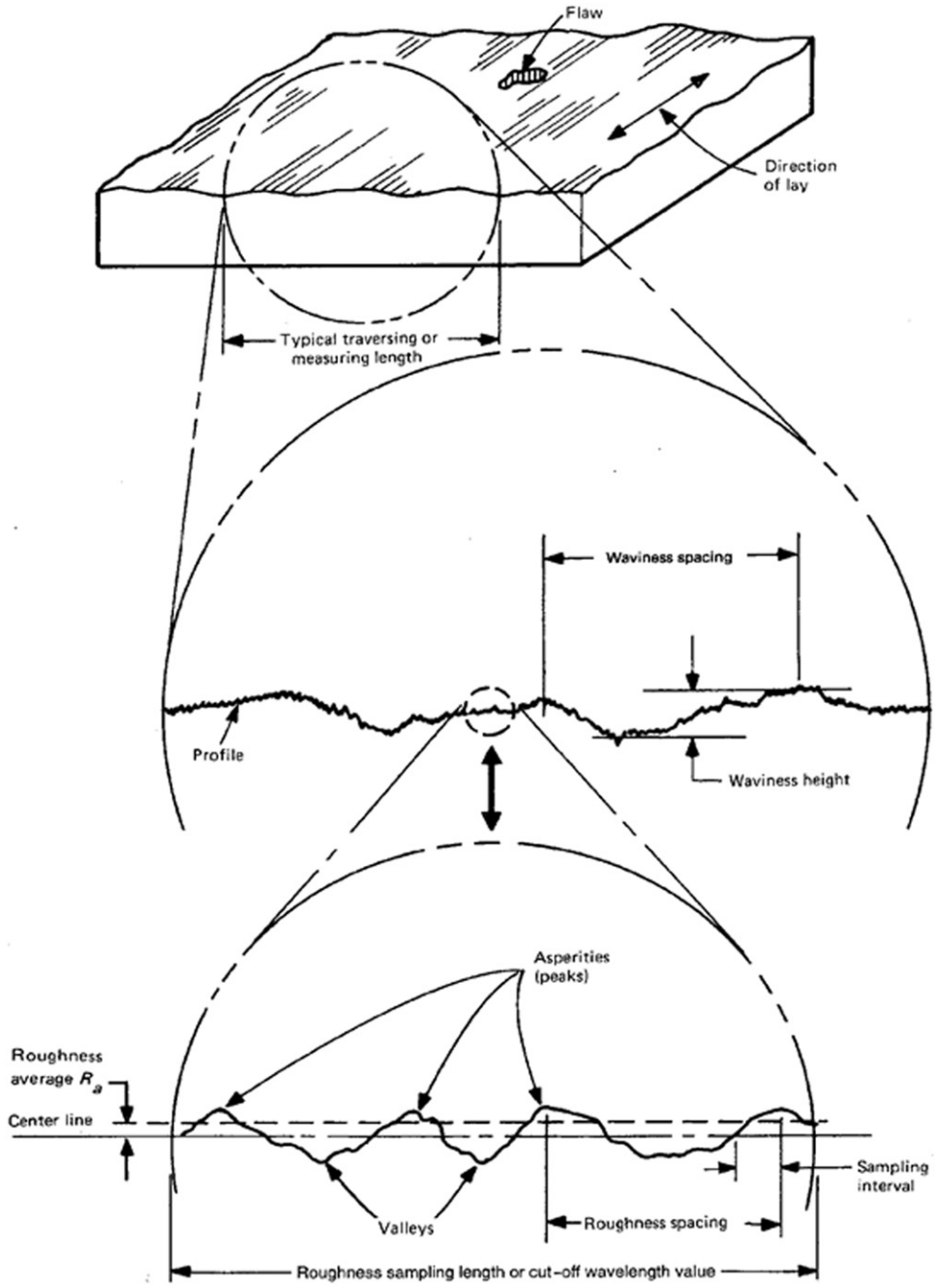


Figure 10 Pictorial display of surface texture.[65]

influence on the machining speed, whilst the gap width and the surface roughness are mainly influenced by pulse-on time. Also, the Gray relational grade will utilize the discrete measurement method to measure the distance.[70]

1.8.6 Application of GRA Technique in Optimization of Cut Characteristics

The purpose of this chapter is to present an efficient method to find the significant parameters affecting machining performance by integrating GRA and statistical method. Also, the optimal machining parameters setting for maximum machining speed and minimum surface roughness can be obtained by applying GRA. Furthermore, it is feasible to obtain optimal machining parameters for a desired surface roughness and maximum metal removal rate by the GRA.

This study concerns the employment of GRA to determine the optimized cut characteristics in precision cutting of CPH fibers-reinforced TPU composites.[71] Polyurethane is widely found in the form of thermoset and thermoplastic properties. Polyurethane thermosets have been reinforced with hard

wood,[72] flax and jute,[73] rice husk,[74] and sisal.[75] However, the study pertaining to natural fiber reinforcement of TPU appears limited to kenaf substrate only.[34,76–79] To the authors' knowledge, there is no published work on CPH fibers-reinforced TPU composites. CPH is a waste product after extracting cocoa bean from cocoa pod and it is abundantly found in Malaysia.[80] Since CPH fiber has properties comparable to synthetic fibers, use of CPH to reinforce TPU has immense economic and environmental benefits.

In this paper, the cut characteristics, namely kerf width (material loss) and surface roughness (surface finish) are optimized as a function of blade speed, feed rate of the blade and cocoa fiber loading in the composite.[81] Minimum size of kerf width signifies minimum material loss whilst low value of surface roughness can be understood as good surface finish. These two important characteristics are desirable to reduce cost associated with post-processing step and minimize waste. Here we report a central composite design (CCD) method in combination with GRA to optimize the cutting process with consideration of the aforementioned multiple cut qualities. The experiment is described in the following section.[82]

1.8.6.1 Experimental Methods and Measurements

1.8.6.1.1 Cocoa fiber composites

Cocoa fiber-reinforced composite was made up of raw CPH and polyester-based TPU. The CPH was obtained from Cocoa Research & Development Centre in Pahang, Malaysia, while TPU was supplied by Bayer Co. (Malaysia) Sdn. Bhd. The main properties of the composite constituents are given in Table 2.

1.8.6.1.2 Preparation of cocoa fiber composite

TPU/CPH composite was initially mixed using Haake Polydrive R600 internal mixer at the optimum processing parameters of 190 °C, 11 min and 40 rpm temperature, time and rotating speed, respectively. Matrix was charged into the mixer until torque was stabilized then fiber was added into the mixer. The sample was preheated for 7 min and then hot pressed for 10 min at 190 °C. The mold was then cold pressed for 5 min. The composite were prepared with different fiber loadings were prepared: 20, 30, and 40% (by weight). It should be noted that as a result of this process, the measured thickness of all composites vary in the region of 3–4 mm.

Table 2 Selected properties of thermoplastic polyurethane

Specific gravity	*Tensile strength*	*Melting temperature*	*Hardness*
1.21	48 MPa*	210 °C	55D

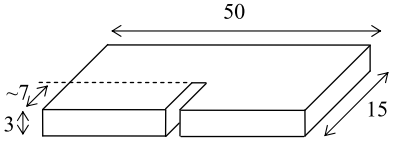


Figure 11 Schematic of a cut profile (dimensions in mm). The cut depth is manually controlled to about 7 mm, i.e., slightly less than the width of the composite.[83]

Finally, the prepared composite was manually cut to the desired dimension as shown in Figure 11.

1.8.6.1.3 Specification of cutting machine

A precision linear saw (Buehler IsoMeT® 5000) was used to precisely cut the composite substrates. It has maximum blade speed of 5000 rpm and maximum feed rate of 19 mm min^{-1}. The saw can be set to virtually cut all sorts of materials including metals, ceramics, composites, laminates, plastic, and biomaterials with minimal deformation. To ensure process repeatability with minimum variation between experiments, the composite was firmly clamped using a custom-made jig. The composite was made stationary throughout the experiment with its surface positioned parallel to the table top. Figure 11 shows the schematic diagram of the cut profile. It was experimentally found that cut depth that is longer than ½ of the width could result in unwanted vibration on both sides of the composites due to their interaction with the blade. Consequently, a large kerf width was formed. For this reason, the depth of the cut was set to be slightly lesser than the sample's width. An abrasive blade of about 450 μm thick was used to perform the cut. In this experiment, no coolant was used since the hydrophilic nature of natural fibers adversely affects the composite properties.[84]

1.8.6.1.4 Selection of cutting parameters

The experiment involved a number of fixed and variable parameters. The fixed parameters are material thickness, blade properties (thickness, diameter, and material) whereas the variables are blade speed, feed rate of the blade, and fiber loading. The selected levels of all parameters are listed in Table 3. Due to conversion from imperial to metric unit, the programmable feed rate values in the machine are no longer integers.

1.8.6.1.5 Design of experiments

A CCD method was used to determine the multi-performance characteristics of cut using precision linear saw. The experimental layout for the cutting process parameters and the corresponding experimental data is presented in Table 4. The first eight experiments composed of 2^3 factorial designs while the center point (experiment number 9) consists of one single set of experimental parameters. Although not explored in this paper, the CCD is often employed in response surface methodology to determine the complex interaction between all parameters while the center point is used to estimate pure error.[85] Mathematical relations will be discussed in the future manuscript. In total, nine experiments were performed.

Table 3 Precision cutting parameters and their levels[82]

Notation	*Parameter*	*Level*		
		−1	*0*	*1*
F	Feed rate (mm min^{-1})	12.1	15.2	18.0
S	Blade speed (rpm)	2500	3500	4500
C	Fiber loading (%)	20	30	40

1.8.6.1.6 Evaluation of cut quality characteristics

In order to evaluate the characteristics of the cut, all specimens are subjected to surface roughness and visual inspections. A digital microscope of $\times 40$ magnification giving a resolution of 0.01 μm on the plane of focus was used for measuring the kerf width. On the other hand, a Perthometer (Mahr) was used for measuring the surface roughness. These two parameters were measured three times for each set of experiment and the averages were calculated and reported in Table 4. In all cases, the width of kerf was measured approximately 500 μm, comparable with the thickness of the blade.

An actual sample featuring the differences in terms of cut characteristics between manual and machine cuts are shown in Figure 12. The characteristics of the machine cut are significantly better with regards to cut straightness and surface roughness.

In addition, variation in the surface roughness with kerf width is also studied (see Figure 13), however, a correlation between the two cannot be established directly. It appears that high-blade speed and high-feed rate at minimum fiber content (experiment number 4) result in large kerf width and high surface roughness. On the other hand, low blade speed and low feed rate at minimum fiber content (experiment number 1) produce small kerf width and low surface roughness. Interestingly, this trend reverses when the composite has maximum fiber content (experiment number 5 and 8).

Table 4 Experimental layout and multi-performance results

Experiment no.	*Run order*	*Cutting parameters*			*Surface roughness,* R_a *(μm)*	*Mean kerf width (μm)*
		F	*S*	*C*		
1	1	−1	−1	−1	1.035	476.19
2	4	1	−1	−1	1.776	494.05
3	6	−1	1	−1	1.534	505.95
4	9	1	1	−1	1.991	553.57
5	2	−1	−1	1	1.382	488.10
6	3	1	−1	1	1.325	500.00
7	7	−1	1	1	1.088	494.05
8	8	1	1	1	0.930	535.71
9	5	0	0	0	1.258	514.88

1.8.6.2 Determination of the Optimal Joining Condition

1.8.6.2.1 Gray relational analysis

Although it is straightforward to determine the optimal parametric configuration (small kerf width with minimum possible surface roughness) by referring to Figure 13, a systematic approach is necessary when one has to machine a number of different composites with varying fiber and parent polymer contents. The complexity to determine the optimum process parameters can be simplified using GRA. GRA is employed to analyze the degree of relation in a discrete progression. The procedure entails the following steps:

1.8.6.2.2 Normalization of original data

The experimental data of kerf width and surface roughness are initially normalized at the scale varying between 0 and 1.0. The desired characteristics of both kerf width and surface roughness are 'lower-the-better' therefore the normalization, x_{ij}, for the 'lower-the-better' quality characteristic can be expressed as:

$$x_{ij} = \frac{\max_j \gamma_{ij} - \gamma_{ij}}{\max_j \gamma_{ij} - \min_j \gamma_{ij}} \quad [1]$$

where γ_{ij} is the ith quality characteristic in the jth experiment. Normalized results with larger values correspond to the better quality. Table 5 shows the normalized results for both types of quality characteristics.

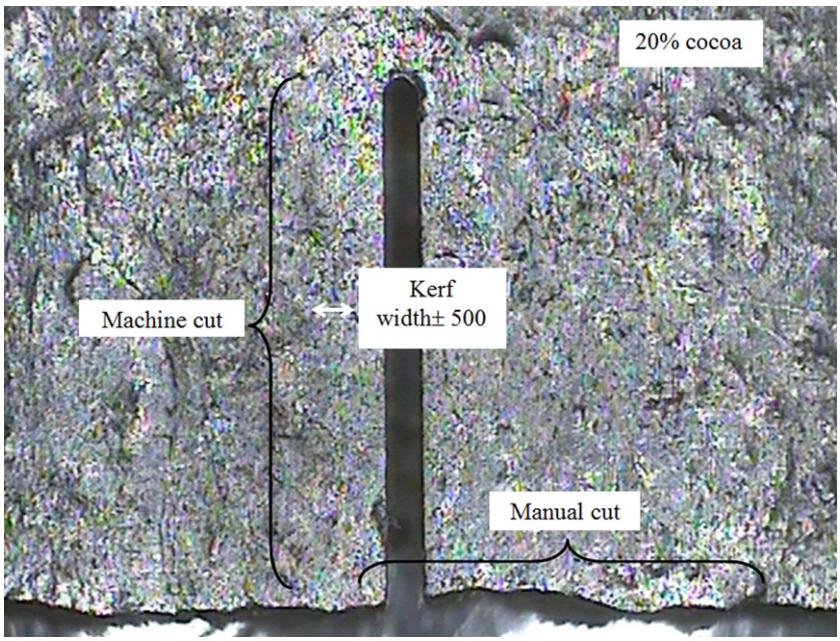


Figure 12 Actual sample showing cut edges between manual and machine cuts.

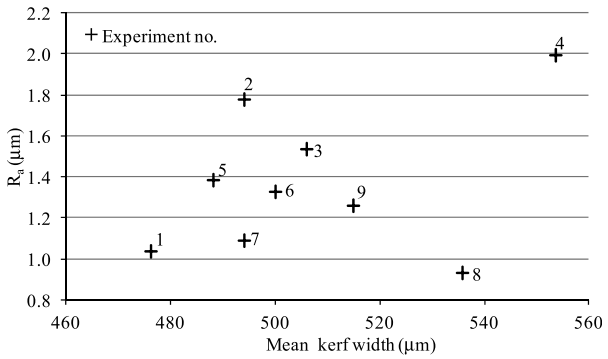


Figure 13 Variation of the surface roughness with kerf width.

Table 5 Data pre-processing of the experimental results.

Experiment no.	*Gray relational generating*	
	Surface roughness (lower-the-better)	*Kerf width (lower-the-better)*
1	0.9010	1.0000
2	0.2026	0.7692
3	0.4307	0.6154
4	0.0000	0.0000
5	0.5740	0.8461
6	0.6277	0.6923
7	0.8511	0.7692
8	1.0000	0.2308
9	0.6909	0.5000

1.8.6.2.3 Calculation of gray relational coefficient

Next, the actual experimental results are compared to an ideal experimental data which can be coined as relational coefficients, ξ_{ij}, and is calculated such that:

$$\xi_{ij} = \frac{\min_i \min_j |x_i^0 - x_{ij}| + \zeta \max_i \max_j |x_i^0 - x_{ij}|}{|x_i^0 - x_{ij}| + \zeta \max_i \max_j |x_i^0 - x_{ij}|} \quad [2]$$

where x_i^0 is the ideal normalized result (i.e., best normalized result = 1.0) for the ith quality characteristics and $\xi[0, 1]$ is distinguishing coefficient. Deng[10] noted that $\xi = 0.5$ is usually applied. **Table 6** lists the gray relational coefficients using equal weights for each set of experiment based on CCD procedure.

1.8.6.2.4 Calculating the gray relational grade

Gray relational grade is an indicator of the multiple quality characteristics. It is calculated by integrating the gray relational coefficients of each experiment using a weighting method and is given by:

$$\gamma_j = \frac{1}{m} \sum_{i=1}^{m} w_i \xi_{ij} \quad [3]$$

where γ_j is the gray relational grade for the jth experiment, w_i is the weighting factor for the ith quality characteristic, and m is the number of quality characteristics. Experiments on the precision cutting were aimed to get small kerf width and low surface roughness. Small kerf width can be understood as minimal material loss while low surface roughness avoids the need of post-processing step to improve edge finish. For the calculation of gray relational grades, the weighting ratio for all qualities is set as:

$$\text{Surface roughness} : \text{kerf width} = 0.5 : 0.5 \quad [4]$$

This implies that both surface roughness and kerf width characteristics have an equal importance in precision cutting process. The allocation of weighting ratio, however, vary and generally depends on some desired machining/manufacturing requirements.[2,3] The resulting grades are tabulated in **Table 7**. Higher values of the gray relational grade signify a close match between the experimental result and the ideal value.

In the present work, experiment number 1 shows best multi-response characteristics out of total 9 experiments having highest gray relational grade (as shown in **Figure 14**). The second highest gray relational grade is represented by experiment number 7. Both experiments number 1 and 7 have equal feed rate of 12.1 mm min^{-1}, however, the blade speed for experiment number 1 is lesser than that of number 7. In addition, the sample in experiment number 1 has minimum fiber content (20% by weight) whereas experiment number 7 has maximum fiber content (40% by weight). By referring to **Figure 14**, it is also clear that experiment number 4 (20% fiber content, high-feed rate, and high-blade speed) has the lowest gray relational grade. On this basis, one may conclude that the effects of fiber content on cut characteristics are insignificant as compared to feed rate and blade speed. This may be attributed to the low abrasiveness of natural fibers as compared to the synthetic fibers, which are very

Table 6 The calculated gray relational coefficients

Experiment no.	*Gray relational coefficients*	
	Surface roughness	*Kerf width*
1	0.8348	1.0000
2	0.3854	0.6842
3	0.4676	0.5652
4	0.3333	0.3333
5	0.5399	0.7646
6	0.5732	0.6190
7	0.7705	0.6842
8	1.0000	0.3940
9	0.6179	0.5000

Table 7 Gray relational grades and its order

Experiment no.	*Gray relational grade*	*Order*
1	0.4587	1
2	0.2674	7
3	0.2582	8
4	0.1667	4
5	0.3261	9
6	0.2981	5
7	0.3637	2
8	0.3485	3
9	0.2795	6

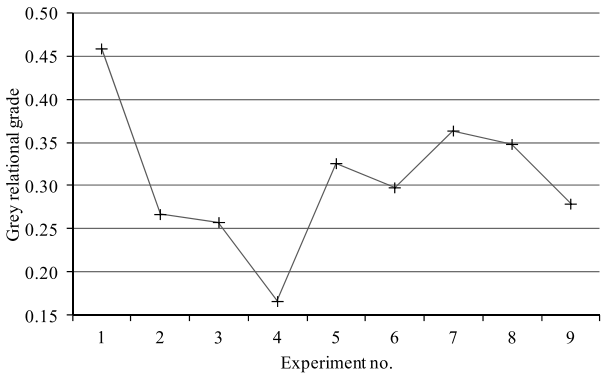


Figure 14 Gray relational grade graph of precision cutting of cocoa fiber composites.

abrasive to the blade. Therefore, variation in fiber loading has insignificant effect on cut characteristics.

1.8.7 Conclusions

Natural fiber-reinforced composites becomes the new options recently to supersede the others synthetic fibers. With higher advantages like biodegradable, renewable, and of course much cheaper makes this natural fibers the main choice in the industrial sector. In this chapter, a CCD method along with GRA was used to determine the optimum precision cutting process parameters having several quality characteristics. The complexity of dealing with a number of variables was simplified using CCD method. The optimum parameters were quantitatively determined based on the highest gray relational grade (experiment number 1). The experiment was performed at minimum feed rate (12.1 mm s^{-1}), minimum blade speed (2500 rpm), and minimum fiber content (20% by weight). The influence of each parameter on cut quality was also discussed. It was found that the feed rate and blade speed have dominant effects compared to the fiber content.

Acknowledgments

The authors wish to thank Universiti Putra Malaysia for granting sabbatical leave to the principal author at Universiti Malaya, Malaysia from October 1, 2013 to June 30, 2014. The project is partially funded by Ministry of Education Malaysia through Exploratory Research Grant Scheme (ERGS) project number ERGS/1-2013/5527190.

See also: 1.12 Laser Machining Processes

References

1. Ku, H.; Wang, H.; Pattarachaiyakoop, N.; Trada, M. A Review on the Tensile Properties of Natural Fiber Reinforced Polymer Composites. *Compos. Part B: Eng.* **2011**, *42*, 856–873.
2. Ferreira, J. R.; Coppini, N. L.; Miranda, G. W. A. Machining Optimisation in Carbon Fibre Reinforced Composite Materials. *J. Mater. Process. Technol.* **1999**, *92–93*, 135–140.
3. Palanikumar, K. Application of Taguchi and Response Surface Methodologies for Surface Roughness in Machining Glass Fiber Reinforced Plastics by PCD Tooling. *Int. J. Adv. Manuf. Technol.* **2008**, *36* (1–2), 19–27.
4. Joshi, S. V.; Drzal, L.; Mohanty, A.; Arora, S. Are Natural Fiber Composites Environmentally Superior to Glass Fiber Reinforced Composites? *Compo. Part A: Appl. Sci. Manuf.* **2004**, *35* (3), 371–376.
5. Mulinari, D. R.; Baptista, C. A. R. P.; Souza, J. V. C.; Voorwald, H. J. C. Mechanical Properties of Coconut Fibers Reinforced Polyester Composites. *Procedia Eng.* **2011**, *10*, 2074–2079.
6. Thakura, V. K.; Thakurb, M. K. Processing and Characterization of Natural Cellulose Fibers/Thermoset Polymer Composites. *Carbohydr. Polym.* **2014**, *109*, 102–117.
7. Arau´jo, J. R.; Waldman, W. R.; De Paoli, M. A. Thermal Properties of High Density Polyethylene Composites with Natural Fibres: Coupling Agent Effect. *Polym. Degrad. Stab.* **2008**, *93*, 1770–1775.
8. Chinenye, N. M.; Ogunlowo, A. S.; Olukunle, O. J. Cocoa Bean (*Theobroma Cacao L.*) Drying Kinetics. *Chil. J. Agricult. Res.* **2010**, *70* (4), 633–639.
9. Vriesmann, L. C.; Amboni, R. D. M. C.; Petkowicz, C. L. O. Cacao Pod Husks (*Theobroma Cacao L.*): Composition and Hot-Water-Soluble Pectins. *Ind. Crop. Prod.* **2011**, *34*, 1173–1181.
10. Daud, Z.; Kassim, A. S. M.; Aripin, A. M.; Awang, H.; Hatta, M. Z. M. Chemical Composition and Morphological of Cocoa Pod Husks and Cassava Peels for Pulp and Paper Production. *Aust. J. Basic Appl. Sci.* **2013**, *7* (9), 406–411.
11. Westman, M. P.; Fifield, L. S.; Simmons, K. L.; Laddha, S. G.; Kafentzis, T. A. *Natural Fiber Composites: A Review*; Pacific Northwest National Laboratory: Richland, Washington, 2010.
12. Chandramohan, D.; Marimuthu, K. A Review on Natural Fibers. *IJRRAS* **2011**, *8* (2), 194–206.
13. Nawy, E. G. *Fundamentals of High-Performance Concrete*, *Technology and Engineering*, 2nd ed.; John Wiley & Sons: United States, 2001.
14. Migliaresi, C. Composites. In *Biomaterials Science: An Introduction to Materials in Medicine*; Ratner, B. D., Hoffman, A. S., Schoen, F. J., Lemons, J. E., Eds.; Elsevier: Boston, 2013; pp. 223–241.
15. Akram, W.; Chaturvedi, S. K.; Ali, S. M. Comparative Study of Mechanical Properties of E-Glass/Epoxy Composite Materials with Al_2O_3, $CaCo_3$, SiO_2 and PBO Fillers. *Int. J. Eng. Res. Technol.* **2013**, *2*, 1029–1034.
16. Bagherpour, S. Fibre Reinforced Polyester Composites. In *Polyester*; El-Din Saleh, H., Ed.; InTech, 2012. ISBN: 978-953-51-0770-5. DOI:10.5772/48697. Available from: http://www.intechopen.com/books/polyester/fibre-reinforced-polyester-composites (accessed 13 April 2016).
17. Trishul, M. A.; Hiremath, V.; Shreyas, P. Production and Testing of Al–Fe_2O_3 Particulate Composite. *Int. Adv. Res. J. Sci. Eng. Technol.* **2015**, *2* (4), 19–24.
18. Biswas, S.; Mittal, A.; Srikanth, G. *TIFAC Composites: A Vision for the Future*; TIFAC: New Delhi, 2009.
19. Abilash, N.; Sivapragash, M. Tensile and Compressive Behaviour of Treated Sisal and Jute Fiber Blended Polypropylene Composite. *J. Polym. Biopolym. Phys. Chem.* **2013**, *1* (1), 1–8.
20. Hardinnawirda, K. *The Effect of Rice Husks as Filler in Polymer Matrix Composites* (Bachelor thesis); Malaysia: Universiti Malaysia Pahang, 2012. Available from: http://umpir.ump.edu.my/4908/1/cd7278_84.pdf (accessed 5 March 2016).
21. Bhardwaj, B. P. The Complete Book on Production of Automobile Components & Allied Products. Available from: https://books.google.com/books?isbn=938103933X (accessed 5 March 2016).
22. Prakash, T. *Processing and Characterization of Natural Fiber Reinforced Polymer Composites* (Bachelor thesis); Rourkela: National Institute of Technology. Available from: http://ethesis.nitrkl.ac.in/1008/1/final_project.PDF (accessed 5 March 2016).
23. Jeyanthi, S.; Rani, J. J. Influence of Natural Long Fiber in Mechanical, Thermal and Recycling Properties of Thermoplastic Composites in Automotive Components. *Int. J. Phys. Sci.* **2012**, *7* (43), 5765–5771.
24. Samivel, P.; Babu, A. R. Mechanical Behaviour of Stacking Sequence in Kenaf and Banana Fiber Reinforced-Polyester Laminate. *Int. J. Mech. Eng. Robot. Res.* **2013**, *2*, 348–360.
25. Vaidya, U. Composites for Automotive, Truck and Mass Transit. Materials, Design and Manufacturing. Available from https://books.google.com/books?isbn=1932078797 (accessed 5 March 2016).
26. Holbery, J.; Houston, D. Natural-Fiber-Reinforced Polymer Composites in Automotive Applications. *JOM* **2006**, *58*, 80–86.
27. Kamath, M. G.; Bhat, G. S.; Parikh, D. V.; Mueller, D. Cotton Fiber Nonwovens for Automotive Composites. *Int. Nonwovens J.* **2005**, *14*, 34–40.

28. Kohan, J. 2011 Boom for Cotton Nonwoven Fibers. Available from: http://english.kohanjournal.com/Articles/363-Boom-for-Cotton-Nonwoven-Fibers.html (accessed 5 March 2016).
29. Gupta, K. M. *Engineering Materials: Research, Applications and Advances*. CRC Press, Taylor and Francis Group: Boca Raton, FL, 2015; 496 pp.
30. Bhat, G., Kamath, M. G., Mueller, D., Parikh, D. V., McLean, M. Cotton-Based Composites for Automotive Applications. GPEC 2004, Paper Abstract No. 15, 2004; pp. 1–8.
31. Elaya, P. A.; Venkateshwaran, N. Natural Fiber-Reinforced Polymer Composites in Automotive Applications – A Review. *IJAEA* **2008**, *1* (6), 68–74.
32. Singha, A.; Rana, R. K. Natural Fiber Reinforced Polystyrene Composites: Effect of Fiber Loading, Fiber Dimensions and Surface Modification on Mechanical Properties. *Mater. Des.* **2012**, *41*, 289–297.
33. Arrakhiz, F.; El Achaby, M.; Kakou, A.; *et al.* Mechanical Properties of High Density Polyethylene Reinforced with Chemically Modified Coir Fibers: Impact of Chemical Treatments. *Mater. Des.* **2012**, *37*, 379–383.
34. El-Shekeil, Y. A.; Sapuan, S. M.; Abdan, K.; Zainudin, E. S. Influence of Fiber Content on the Mechanical and Thermal Properties of Kenaf Fiber Reinforced Thermoplastic Polyurethane Composites. *Mater. Des.* **2012**, *40*, 299–303. doi:10.1016/j.matdes.2012.04.003.
35. Zainudin, E.; Sapuan, S. Impact Strength and Hardness Properties of Banana Pseudo-Stem Filled Unplastisized PVC Composites. *Multidiscip. Model. Mater. Struct.* **2009**, *5* (3), 277–282.
36. Ismail, H.; Shuhelmy, S.; Edyham, M. The Effects of a Silane Coupling Agent on Curing Characteristics and Mechanical Properties of Bamboo Fibre Filled Natural Rubber Composites. *Eur. Polym. J.* **2002**, *38* (1), 39–47.
37. Sathish, S.; Ganapathy, T.; Bhoopathy, T. Experimental Testing on Hybrid Composites Materials. *Appl. Mech. Mater.* **2014**, *592–594*, 339–343.
38. Naveen, P. N. E.; Yasaswi, M.; Prasad, R. V. Experimental Investigation of Drilling Parameters on Composite Materials. *IOSR J. Mech. Civil Eng.* **2012**, *2*, 30–37.
39. Dilli Babu, G.; Sivaji Babu, K.; Gowd, U. M. Optimization of Machining Parameters in Drilling Hemp Fiber Reinforced Composites to Maximize Tensile Strength Using Design Experiments. *Ind. J. Eng. Mater. Sci.* **2013**, *20*, 385–390.
40. Jayabal, S.; Natarajan, U.; Sekar, U. Regression Modeling and Optimization of Machinability Behavior of Glass–Coir–Polyester Hybrid Composite Using Factorial Design Methodology. *Int. J. Adv. Manuf. Technol.* **2011**, *55*, 263–273.
41. Chandramohan, D.; Marimuthu, K. Thrust force and Torque in Drilling the Natural Fiber Reinforced Polymer Composite Materials and Evaluation of Delamination Factor for Bone Graft Substitutes – A Work of Fiction Approach. *Int. J. Eng. Sci. Technol.* **2010**, *2* (10), 6437–6451.
42. Konig, W.; Rummenholler, S. Technological and Industrial Safety Aspects in Milling FRPS. Proc. of the Symposium on Machining of Advanced Composites, Ramulu, M.; Komanduri, R., Eds.; American Society of Mechanical Engineers, (MD-45/PED-66), 1993; pp. 1–14.
43. Jayabal, S.; Natarajan, U. Optimization of Thrust Force, Torque, and Tool Wear in Drilling of Coir Fiber-Reinforced Composites Using Nelder–Mead and Genetic Algorithm Methods. *Int. J. Adv. Manuf. Technol.* **2010**, *51*, 371–381.
44. Rajmohan, T.; Palanikumar, K. Optimization of Machining Parameters for Surface Roughness and Burr Height in Drilling Hybrid Composites. *Mater. Manuf. Process.* **2012**, *27*, 320–328.
45. Singh, I.; Bajpai, P. Machining Behavior of Green Composites: A Comparison with Conventional Composites. In *Green Composites from Natural Resources*; Thakur, V. K., Ed.; CRC/Taylor & Francis: Boca Raton, FL., 2013
46. Jayabal, S.; Natarajan, U.; Sekar, U. Regression Modeling and Optimization of Machinabiliy Behaviour of Glass-Coir-Polyester Hybrid Composite Using Factorial Design Methodology. *Int. J. Adv. Manuf. Technol.* **2011**, *55* (1), 263–273.
47. Martin, A. M. Introduction of Fibre-Reinforced Polymers–Polymers and Composites: Concepts, Properties and Processses. INTECH Institute of Applied Physics, CONICET. Chair of Physical Chemistry II, Physical Chemistry Area. Faculty of Chemistry, Biochemistry and Pharmacy. National University of San Luis. Chaca-buco 917 (CP 5700), San Luis, Argentina, 2013.
48. Gunjavate, P. V.; Chhapakhane, N. K.; Kumbhar, S. B. Experimental Determination of Critical Buckling Load for Glass Composite Laminate. *Int. J. Adv. Eng. Res. Stud.* **2012**, *1*, 106–108.
49. Experiment: Fiber Reinforced Composite Materials. Available from: http://imechanica.org/files/handout8.pdf (accessed 5 March 2016).
50. Kamath, M. G. *Processing and Evaluation of Cotton-Based Composites for Automotive and Other Applications* (Master's thesis); University of Tennessee. Available from: http://trace.tennessee.edu/utk_gradthes/2261 (accessed 5 March 2016).
51. Fibre-Reinforced Plastic. Available from: https://en.wikipedia.org/wiki/Fibre-reinforced_plastic (accessed 5 March 2016).
52. Ho, M.; Wang, H.; Lee, J.; Ho, C.; Lau, K.; *et al.* Critical Factors on Manufacturing Processes of Natural Fibre Composites. *Compos. Part B: Eng.* **2012**, *43*, 3549–3562.
53. Wirawan, R.; Sapuan, S. M.; Yunus, R.; Khalina, A. Properties of Sugarcane Bagasse/Poly (Vinyl Chloride) Composites After Various Treatments. *J. Compos. Mater.* **2011**, *45*, 1667–1674.
54. El-Shekeil, Y. A.; Sapuan, S. M.; Abdan, K.; Zainudin, E. S. Influence of Fiber Content on the Mechanical and Thermal Properties of Kenaf Fiber Reinforced Thermoplastic Polyurethane Composites. *Mater. Des.* **2012**, *40*, 299–303.
55. Sapuan, S. M.; Yusoff, N. B. The Relationship between Manufacturing and Design for Manufacturing in Product Development of Natural Fibre Composites. In *Manufacturing of Natural Fibre Reinforced Polymer Composites*; Salit, M. S., Jawaid, M., Yusoff, N. B., Hoque, M. E., Eds.; Springer International Publishing: Switzerland, 2015; pp. 1–15. doi:10.1007/978-3-319-07944-8.
56. Mayer, R. M. *Design with Reinforced Plastics: A Guide for Engineers and Designers*; The Design Council: London, 1993.
57. Mariatti, J.; Abdul Khalil, S. Properties of Bagasse Fibre-Reinforced Unsaturated Olymer (USP) Composites. In *Research on Natural Fibre Reinforced Polymer Composites*; Salit, Mohd Sapuan, Ed.; UPM Press: Serdang, 2009; pp. 63–83.
58. Misri, S.; Leman, Z.; Sapuan, S. M. A Small Boat From Woven Glass-Sugar Palm Fibre Reinforced Unsaturated Polyester Composite. In *Engineering Composites: Properties and Applications*; Sapuan, S. M., Ed.; UPM Press: Serdang, 2014; pp. 297–312.
59. Misri, S.; Sapuan, S. M.; Leman, Z.; Ishak, M. R. Fabrication and Torsional Behaviour of Filament Wound Kenaf Yarn Fibre Reinforced Unsaturated Polyester Composite Hollow Shafts. *Mater. Des.* **2015**, *65*, 953–960.
60. Fairuz, A. M.; Sapuan, S. M.; Zainudin, E. S.; Aiza, C. N. Study of Pultrusion Process Parameters. *Proceedings of the Postgraduate Symposium on Composites Science and Technology 2014 and the 4th Postgraduate Seminar on Natural Fibre Composites 2014*, 28th January, Putrajaya, Malaysia, 2014; pp. 116–120.
61. Antonsson, A. B.; Runmark, S. Airborne Fibrous Glass and Dust Originating from Worked Reinforced Plastics. *Ame. Ind. Hyg. Assoc. J.* **1987**, *48* (8), 684–687.
62. Doyle, D. J.; Kokasa, J. M. Laser Processing of Kevlar: Hazardous Chemical By-Products. *Proc. of LAMP '87*, Osaka, Japan, 1987; pp. 285–289.
63. Komanduri, R. Machining of Fiber-Reinforced Composites. *Mach. Sci. Technol.* **1997**, *1*, 58–64.
64. What is Cutting Kerf? Available from: http://www.esabna.com/us/en/education/blog/what-is-cutting-kerf.cfm (accessed 5 March 2016).
65. Bhushan, B. *Surface Roughness Analysis and Measurement Techniques*; CRC Press LLC: Boca Raton, FL, 2001. pp. 1–71.
66. Surface Roughness. Available from: http://shodhganga.inflibnet.ac.in/bitstream/10603/6020/12/12_chapter%203.pdf (accessed 5 March 2016).
67. (Technical Data) Surface Roughness. Excerpt from JIS B 0601. Available from: https://th.misumi-ec.com/pdf/tech/mold/09_mo1517.pdf (accessed 7 March 2016).
68. Ju-Long, D. Control Problems of Grey Systems. *Syst. Control Lett.* **1982**, *1* (5), 288–294.
69. Tamrin, K. F.; Nukman, Y.; Sheikh, N. A.; Harizam, M. Z. Determination of Optimum Parameters Using Grey Relational Analysis for Multi-Performance Characteristics in CO_2 Laser Joining of Dissimilar Materials. *Opt. Lasers Eng.* **2014**, *57* (0), 40–47.
70. Rajesh, R.; Anand, M. D. The Optimization of the Electro-Discharge Machining Process Using Response Surface Methodology and Genetic Algorithms. *Procedia Eng.* **2012**, *38*, 3941–3950.
71. El-Shekeil, Y. A.; Sapuan, S. M.; Algrafi, M. W. Effect of Fiber Loading on Mechanical and Morphological Properties of Cocoa Pod Husk Fibers Reinforced Thermoplastic Polyurethane Composites. *Mater. Des.* **2014**, *64*, 330–333.
72. Özgür Seydibeyoğlu, M.; Oksman, K. Novel Nanocomposites Based on Polyurethane and Micro Fibrillated Cellulose. *Compos. Sci. Technol.* **2008**, *68* (3–4), 908–914.
73. Bledzki, A. K.; Zhang, W.; Chate, A. Natural-Fibre-Reinforced Polyurethane Microfoams. *Compos. Sci. Technol.* **2001**, *61* (16), 2405–2411.
74. Rozman, H. D.; Yeo, Y. S.; Tay, G. S.; Abubakar, A. The Mechanical and Physical Properties of Polyurethane Composites Based on Rice Husk and Polyethylene Glycol. *Polym. Test.* **2003**, *22* (6), 617–623.
75. Bakare, I. O.; Okieimen, F. E.; Pavithran, C.; Abdul Khalil, H. P. S.; Brahmakumar, M. Mechanical and thermal Properties of Sisal Fiber-Reinforced Rubber Seed Oil-Based Polyurethane Composites. *Mater. Des.* **2010**, *31* (9), 4274–4280.

76. El-Shekeil, Y.; Sapuan, S.; Khalina, A.; Zainudin, E.; Al-Shuja'a, O. Effect of Alkali Treatment on Mechanical and Thermal Properties of Kenaf Fiber-Reinforced Thermoplastic Polyurethane Composite. *J. Therm. Anal. Calorim.* **2012**, *109* (3), 1435–1443.
77. El-Shekeil, Y. A.; Sapuan, S. M.; Abdan, K.; Zainudin, E. S. Development of a New Kenaf Bast Fiber-Reinforced Thermoplastic Polyurethane Composite. *BioResources* **2011**, *6* (4), 4662–4672.
78. Sapuan, S.; Pua, F-l.; El-Shekeil, Y.; AL-Oqla, F. M. Mechanical Properties of Soil Buried Kenaf Fibre Reinforced Thermoplastic Polyurethane Composites. *Mater. Des.* **2013**, *50*, 467–470.
79. El-Shekeil, Y. A.; Sapuan, S. M.; Khalina, A.; Zainudin, E. S.; Al-Shuja'a, O. M. Influence of Chemical Treatment on the Tensile Properties of Kenaf Fiber Reinforced Thermoplastic Polyurethane Composite. *Exp. Polym. Lett.* **2012**, *6*, 1032–1040.
80. Yusriah, L.; Sapuan, S.; Zainudin, E.; Mariatti, M. Underutilized Malaysian Agro-Wastes Fiber as Reinforcement in Polymer Composites: Potential and Challenges. *J. Polym. Mater.* **2012**, *29*, 2.
81. Onwubolu, G. C. Modelling and Predicting Surface Roughness in Turning Operations Using Hybrid Differential Evolution and the Group Method of Data Handling Networks. *Proceed. Inst. Mech. Eng. Part B: J. Eng. Manuf.* **2008**, *222*, 785–795.
82. Tamrin, K. F.; Nukman, Y.; Choudhury, I. A.; Shirley, S. Multiple-Objective Optimization in Precicion Laser Cutting of Different Thermoplastics. *Opt. Lasers Eng.* **2015**, *67*, 57–65.
83. Alsaeed, T.; Yousif, B. F.; Ku, H. The Potential of Using Date Palm Fibres as Reinforcement for Polymeric Composites. *Mater. Des.* **2013**, *43*, 177–184.
84. Anbukarasi, K.; Kalaiselvam, S. Study of Effect of Fibre Volume and Dimension on Mechanical, Thermal and Water Absorption Behaviour of Luffa Reinforced Epoxy Composites. *Mater. Des.* **2015**, *66*, 321–330, Part A.
85. Tan, Y. Q.; Guo, M.; Zhang, L.; Cao, L. P. Performance Optimization Method of Composite Modified Asphalt Sealant. *J. Highway Transport. Res. Dev. (English ed.)* **2013**, *7* (2), 1–7.

Relevant Websites

http://www.greencorenfc.com/news.htm
GreenCore.
http://www.materialsfinishing.org/index.htm
Institute of Materials Finishing.

1.9 Effect of Electrical Discharge Energy on White Layer Thickness of WEDM Process

I Maher, University of Malaya, Kuala Lumpur, Malaysia and Kafrelsheikh University, Kafrelsheikh, Egypt
AAD Sarhan, University of Malaya, Kuala Lumpur, Malaysia and Assiut University, Assiut, Egypt
H Marashi, University of Malaya, Kuala Lumpur, Malaysia

© 2017 Elsevier Inc. All rights reserved.

1.9.1 Introduction 231
1.9.2 WEDM Process 234
1.9.2.1 Analysis of WEDM Pulse Generator 234
1.9.2.2 Electrical Discharge Machining Wire Electrode 236
1.9.2.2.1 Development of EDM wire electrodes 238
1.9.2.2.2 Plain EDM wires 238
1.9.2.2.2.1 Copper wire 238
1.9.2.2.2.2 Brass wire 239
1.9.2.2.2.3 Aluminum–brass wire 240
1.9.2.2.3 Coated EDM wires 240
1.9.2.2.3.1 Single-layer-coated wires 240
1.9.2.2.3.2 Double-layer-coated wires 241
1.9.2.2.3.3 Multilayer-coated wires 241
1.9.2.2.4 Diffusion-annealed coated wires 243
1.9.2.2.4.1 Alpha phase wires 243
1.9.2.2.4.2 Beta phase wires 243
1.9.2.2.4.3 Gamma phase wires 244
1.9.2.2.4.4 Epsilon phase wires 247
1.9.2.2.5 High tensile strength wires 247
1.9.2.2.5.1 Molybdenum wire 248
1.9.2.2.5.2 Tungsten wire 248
1.9.2.2.5.3 MolyCarb wire 248
1.9.2.2.5.4 Steel core wires 248
1.9.2.2.6 Special wires 249
1.9.2.2.6.1 Abrasive-assisted wire 249
1.9.2.2.6.2 Hot dip galvanized wire 249
1.9.2.2.6.3 Porous electrode wire 249
1.9.3 White Layer and Heat-Affected Zone 250
1.9.4 Experimental Details 251
1.9.4.1 Experimental Design 251
1.9.4.2 Experimental Setup 251
1.9.4.3 Samples Preparation 252
1.9.4.3.1 Titanium alloy grade 5 (Ti6Al4V) preparation 252
1.9.4.3.2 AISI 1050 carbon steel preparation 252
1.9.4.4 Surface Characterization 252
1.9.5 Experimental Results and ANFIS Modeling 253
1.9.5.1 Experimental Results 253
1.9.5.2 ANFIS Model Development 255
1.9.5.3 ANFIS Model Verification 258
1.9.6 ANFIS Modeling Results and Discussion 259
1.9.6.1 Effect of Electrical Parameters on WLT 259
1.9.6.1.1 Brass wire electrode 259
1.9.6.1.2 Coated wire electrode 260
1.9.6.2 Effect of Wire Electrode Parameters on WLT 260
1.9.6.3 Effect of Workpiece Parameters on WLT 262
1.9.7 Conclusions 262
References 263
Relevant Websites 266

1.9.1 Introduction

Wire electrical discharge machining (WEDM) is one of the most commonly known and applied nonconventional machining processes in today's industrial practice. WEDM is an electro-thermal machining process for electrically conductive materials. In this procedure, improvements in WEDM components have rapidly taken place, along with improvements in the control unit.

In WEDM, the cutting tool (wire electrode) never touches the workpiece during the machining process. Because WEDM does not involve cutting forces, it is commonly used in cases requiring low residual stresses. Any electrically conductive material can be cut using WEDM, regardless of the hardness, ranging from public metals, including copper, aluminum, tool steel, and brass, to uncommon new alloys such as tungsten carbide, wafer silicon, cast alloys, Inconel, titanium, carbide, and polycrystalline diamond. Moreover, WEDM can machine high strength, highly corrosive-resistant, highly wear-resistant, and difficult-to-machine materials such as metal matrix composites (MMCs) and cemented carbides.[1] Besides machining electrically conductive materials, some insulating ceramics and nonconductive materials have also been cut with WEDM.[2,3] With WEDM, it is also possible to machine complicated shapes that cannot otherwise be achieved using conventional machining processes, such as turning, milling, and grinding.[4] Applications of WEDM are also found in fuel injector nozzles, extrusion dies, turbine blades, and aircraft engine.[5,6]

The Russian Lazarenko couple was the first to design an electro-discharge machine in 1955.[7] A computer-based numerically controllable component (CNC) wire-cut machine was developed 10 years later. The machine for mass commercial production was constructed in 1969. However, the WEDM machine was able to yield corners with smaller radii in 1972. In the early 1970s, the WEDM machine yield was limited to cutting around 13 $cm^2\ h^{-1}$, which gradually reached 40 $cm^2\ h^{-1}$ by the early 1980s.[1] CNC components played a major role in improving the majority of wire electric discharge controllers for WEDM.

WEDM technology has an increasing demand for machining at higher speeds and with better precision to yield better productivity and superior quality workpieces. Productivity and surface quality are the most important performance parameters of WEDM. Although the productivity affects the cost-efficiency of a process, the quality determines the overall utility of products. The productivity is expressed as cutting speed, whereas the surface quality is defined by surface parameters such as roughness as well as white layer thickness (WLT). These parameters have varying significance depending on the machining process.[8] Productivity increases with increasing spark energy (voltage, current, and pulse duration). However, the increases in discharge voltage, current, and pulse duration play roles in the increasing surface roughness and WLT.[9–11]

In the WEDM process, WLT plays a vital role in the operational characteristics of the part (e.g., fatigue, corrosion, creep life, fracture resistance, surface friction, and coating ability). To achieve a low WLT value, the part must be machined more than once. Therefore, a target WLT is set prior to selecting processing steps that are appropriate for yielding the desired quality.[10] Many investigations were performed by previous researchers, and they observed that the white layer was clear under any cutting condition when water was used as the dielectric fluid.[13,14]

El-Hofy[12] and Levy and Maggi[15] reported the formation of a thin, heat-affected region with thickness of 1 μm and spark energy of 5 μJ, which increased to 25 μm at high spark energy. Moreover, the zone under the machined surface was annealed, producing the white layer. In addition, several molten materials were not discharged into the dielectric fluid, and the heat conduction in most of the workpieces rapidly developed detachments deteriorating the surface integrity. The WLT was developed proportionately with the impact of the discharge energy in the WEDM machining process. The thickness was reported to range from 50 μm for finished machining to approximately 200 μm for high cutting speeds, as shown in **Figure 1**.[12,16]

There are many factors that control the complex WEDM process, as shown in the fishbone diagram (**Figure 2**). These factors can be categorized as electrical (peak current, pulse on-time, pulse off-time, etc.), wire electrode (shape, tension, material, and speed), workpiece (high and material), and nonelectrical (dielectric fluid and flow rate). Any small variations in one of these parameters will affect the cutting quality, including the surface integrity (surface roughness and WLT), and cutting speed.[17] Many research works have reported the best cutting factors to achieve high product quality by decreasing the WLT.[18,19] The WLT has shown an increase following the increase in pulse on-time, and has shown a decrease with the increase of pulse off-time.

In addition, the WLT depends on wire electrode properties such as electrical, mechanical, physical, and geometrical properties. WEDM factors including the mechanical machine theory, machine intelligence, type of pulse generator, and the dielectric flushing system affect the machining performance.

Wires used in WEDM are an important component of the machining process. Copper–zinc alloy (brass) wire electrodes are extensively used as WEDM tools. However, along with current and continuous variations in the manufacturing applications field, there is an expanding demand for higher-performance wire electrodes over traditional wire electrodes made of brass. High-performance wires are known to possess high conductivity and tensile strength with good sparking ability. In practice, coated, porous, composite, and diffusion-annealed wires are categorized as high-performance wires. These wire electrodes are usually made of copper–zinc alloy or steel core with a coating of pure zinc or brass with a small proportion of chromium or high-zinc concentration. Currently, WEDM users are interested in shortening the cutting time without compromising good surface quality of products.[20] A novel and improved version of high-performance WEDM should offer both high cutting rate for productivity and enhanced cutting accuracy to ensure the quality.

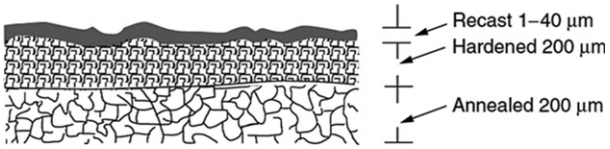


Figure 1 Electrical discharge machining heat-affected zone.[12]

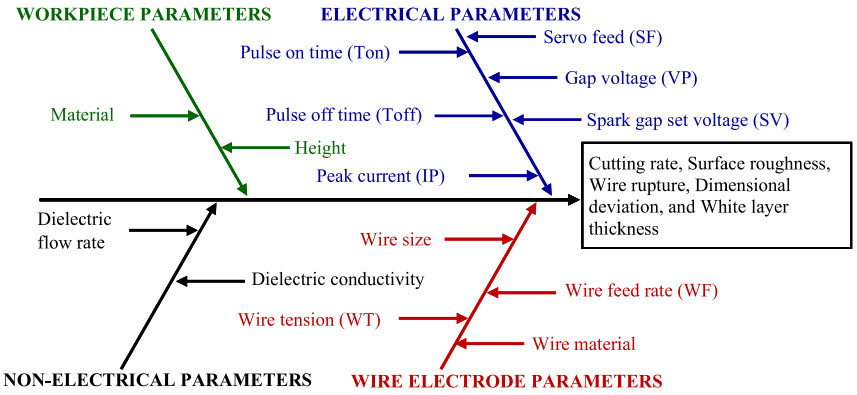


Figure 2 Fishbone diagram of the wire electrical discharge machining factors and performance measures.[17]

The dielectric fluid plays an important role as the working fluid. During cutting, heat from the molten material is rejected into the dielectric fluid. The presence of very small metal particles pollutes the dielectric fluid. This affects the cutting speed and surface integrity because they exist in the spark gap between the workpiece and wire electrode. The dielectric fluid has many functions, such as cooling, cleaning of machined particles, ionization, and electrical insulation. When the voltage reaches the spark gap set voltage, the dielectric fluid ionizes and becomes an electrical conductor. When the spark terminates, the water serves as a coolant and flushes away the machined particles.

Actual WLT monitoring can be accomplished by either an intensive postprocess inspection or a prediction system. Although the postprocess inspection is the easiest to implement, it cannot prevent the parts from being processed before a defective batch is discovered. Ultimately, the WLT prediction system can be used to determine the thickness indirectly.[8] This requires identifying an efficient machining strategy by taking factors affecting the WEDM process into consideration. Furthermore, methods for optimizing the conditions and performance of machining processes should be sought.[21]

There have been prior works that aimed to enhance the process performance based on electro-thermal concepts. These works can be categorized as theoretical,[22,23] numerical,[24,25] or empirical[26,27] and involve performance parameters and guesstimated results associated with the machining process. As mentioned, the generation and distribution of spark energy within the discharge zone determine the WEDM efficiency.[28,29] In practice, spark energy and pulse frequency parameters are varied to obtain efficient control of the WEDM process. However, there remains a challenge in studying the impacts of spark energy and pulse frequency simultaneously on the machining performance. Moreover, discharge parameters need to be low and have a high dielectric flushing rate, which would yield low surface roughness and WLT. This parameter setting eventually decreases the cutting rate in WEDM. Because of this technical trade-off, a set of process parameters fails to obtain a high cutting rate with the least surface defects. Manufacturers should have access to mathematical models for the input parameters and output performance characteristics for effective machining throughputs. The WEDM process is usually modeled after either theoretical or empirical methods.[30] Theoretical models are found to produce high errors when compared to the experimental results. The application and effectiveness of empirical models are limited to certain machining procedures. The relationship between a set of input parameters and output responses is commonly determined using the Taguchi method and response surface methodology (RSM).[31,32] The correlation between input parameters and output measures was studied from a process model developed by a feed-forward neural network.[33] Moreover, machine performance is estimated from an adaptive neuro-fuzzy inference system (ANFIS)-based model of the machining process.[34,35]

In absence of a proper mathematical model, soft computing techniques are efficient. In contrast to traditional computing, these techniques suffer from approximation, partial truth, met heuristics, uncertainty, and inaccuracy. The relationship between input and output parameters can be modeled by soft computing techniques like ANFIS,[36,37] which uses an adaptive neural network to develop a fuzzy inference system. ANFIS can build an input–output mapping model based on both human knowledge as fuzzy if–then rules and known input–output data pairs to train neural networks in a hybrid learning procedure. It provides fuzzy models as a way to learn about the known data set, which estimates parameters of the membership function that allow detection using given input–output data.[38–40]

The following conclusions can be reached after a comprehensive review of the published research works in this field. A few research works have been conducted to discover changes in mechanical properties and surface integrity of the workpiece. Therefore, many options to explore this area for future research remain.[41,42] There are a limited number of studies that involve WLT prediction models.[43] Empirical models have been proposed for a majority of works in surface quality prediction following laboratory experiments. Furthermore, there remains a practical challenge in controlling all factors necessary to yield reproducible results. Hence, the aim of this work was to obtain the best parameters (pulse off-time, pulse on-time, peak current, wire speed, and wire tension) to minimize WLT in the WEDM process. The next goal was to enhance the white layer performance and micro-characteristics in the WEDM process by developing an ANFIS model. In this case, titanium alloy grade 5 (Ti6Al4V)

and AISI 1050 carbon steel-worked materials were cut using brass and coated wire electrodes in the WEDM process.

1.9.2 WEDM Process

WEDM uses electrical discharges to form desired shapes in the manufacturing process, whereas the NC table can make X–Y movements (Figure 3). Due to the involvement of spark and wire burning, it is also termed spark eroding, wire burning, or wire erosion.

WEDM produces a series of electrical discharges between the workpiece and electrode to conduct the machining of the workpiece. Alternating high-frequency current or direct current is discharged through a very small spark gap between the wire electrode to the workpiece with a nonconductive dielectric fluid.[45] The sparks due to discharge can be easily seen instantaneously at the cutting zone (Figure 4) because sparks take place at a rate of more than 100 000 times during 1 s.[12]

1.9.2.1 Analysis of WEDM Pulse Generator

It is possible to attain continuous machining at the time of operating the wire electrode. The spark and burning processes melt and vaporize a small amount of workpiece and wire electrode, resulting in residuals, which are contained in plasma. However, the plasma is a transient state that eventually breaks down at the pulse off-time. The discharged

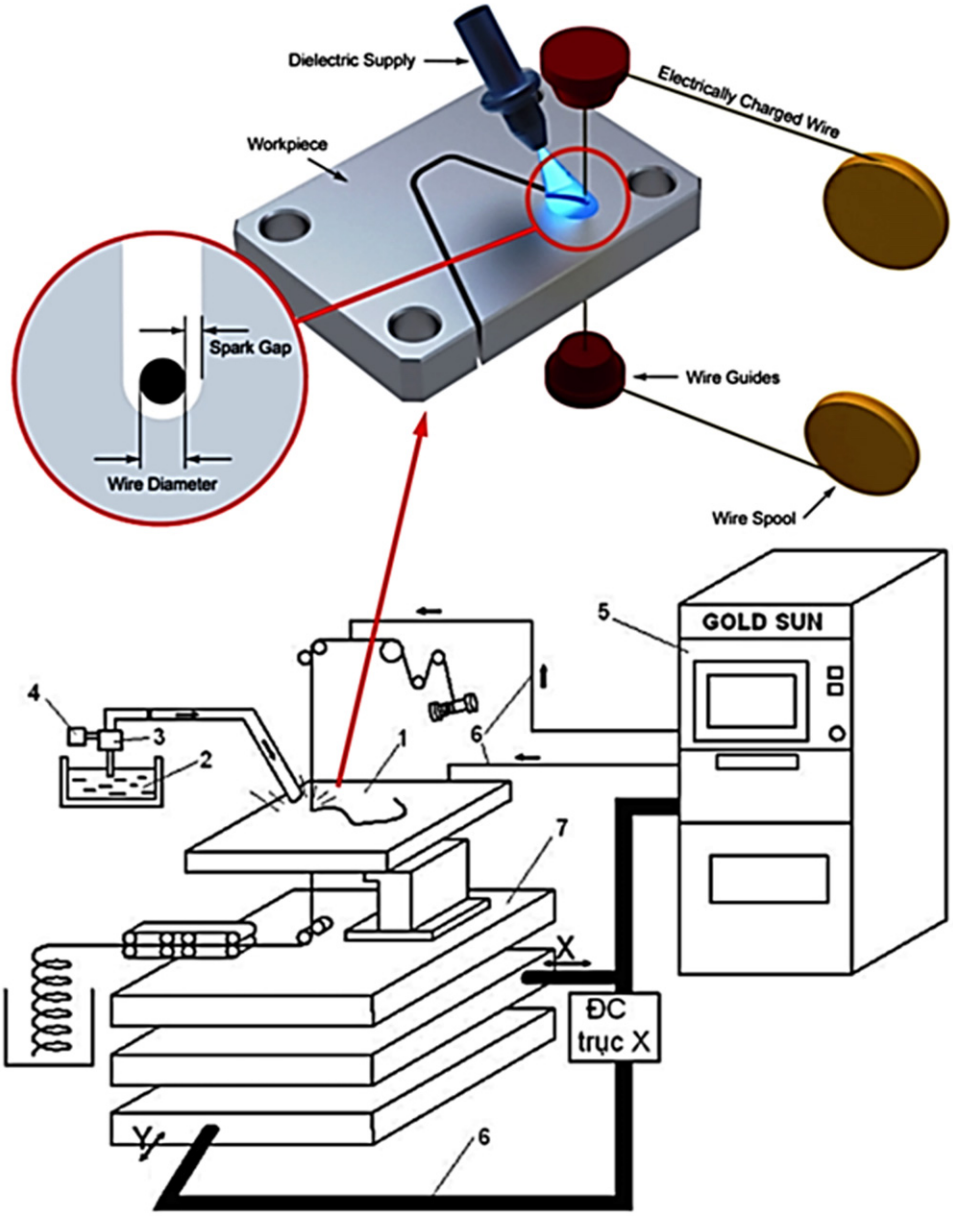


Figure 3 Wire electrical discharge machining–computer controlled machine components (1, workpiece; 2, dielectric fluid; 3, pump; 4, pressure gage; 5, power supply; 6, X–Y control unit; 7, machine table).[44]

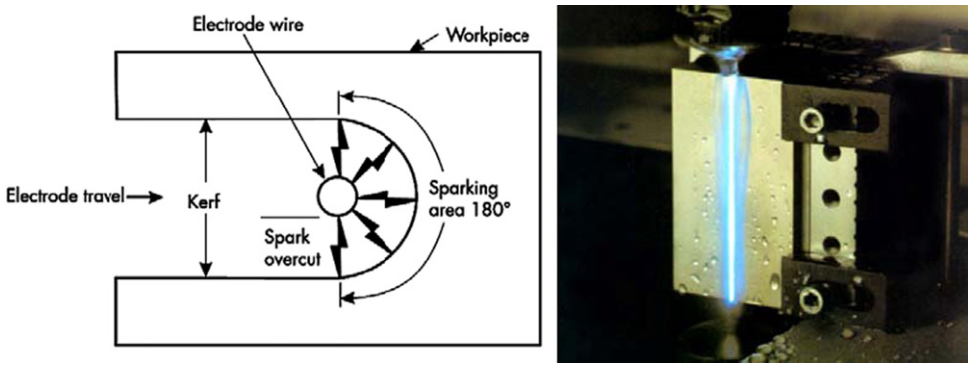


Figure 4 Wire electrical discharge machining discharge sparks.[44]

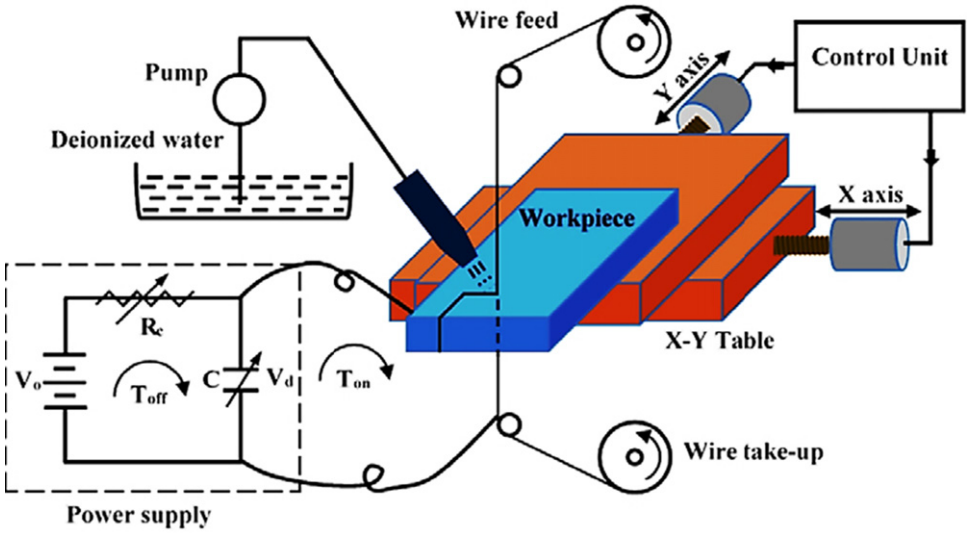


Figure 5 Pulse generator and components of wire electrical discharge machining.

material residues in liquid and vapor states are condensed in solid debris using dielectric fluid. This process repeats in nanoseconds along the length of the wire in the cutting zone.[46] **Figure 5** illustrates the WEDM machine components and a detailed description of the pulse generator used in WEDM.

In a pulse generator, the capacitor is charged from a DC source (V_o). As long as the voltage in the capacitor does not reach the breakdown voltage of the dielectric medium under machining conditions (T_{off}), the capacitor (C) continues to charge. Once breakdown voltage (V_d) is reached, the capacitor starts discharging and a spark is established between the tool and workpiece, leading to machining. Such discharge continues as long as the spark can be sustained. Once the voltage becomes too low (V_d*) to sustain the spark, capacitor charging would continue, as shown in **Figure 6**.[12]

An electrical discharge involves time-varying voltage and current impulses. The following variables are used to determine electric impulses: discharge voltage (V_d), pulse off-time (T_{off}), pulse duration (T_{on}), peak current (IP), pulse cycle time (T_c), pulse frequency (F), and duty factor (DF). The most important WEDM parameters are spark energy and duty factor.

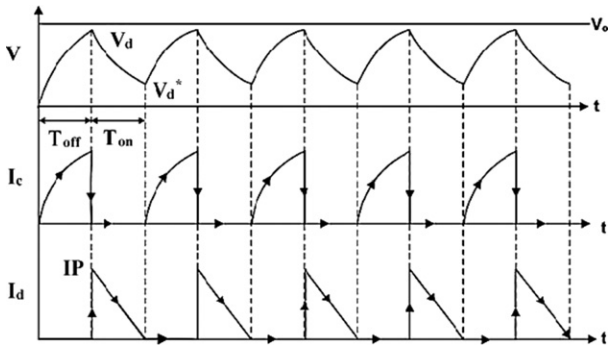


Figure 6 Analysis of RC type electrical discharge machining generator.[12]

The spark energy is defined by electrical energy in each spark, which can be expressed by the following equation:

$$E_s = V_d \times IP \times T_{on} \quad [1]$$

According to eqn [1], spark energy is proportional to three variables: discharge current, the discharge voltage, and pulse

duration. The discharge voltage depends on the properties of the wire electrode and workpiece pair.[47] The spark intensity develops because of discharge current and pulse duration (Figure 7). The spark energy determines the spark size and, hence, the chip size. High spark intensity leads to long sparks, thus increasing the cutting speed and chip size, but deteriorates the surface finishing, as shown in Figure 7(a).[48]

The other most important electrical parameter that significantly influences WEDM performance is the pulse frequency (F), or duty factor (DF). The duty factor determines the weight and number of pulses (eqns [2] and [3]). The duty factor is the percentage of the pulse duration over a total cycle time. In machines with duty factor settings, the pulse interval is set indirectly by setting the pulse duration and duty factor. Pulse frequency is used to set the pulse interval on some machines and to determine the number of chips per second. The pulse frequency and duty factor equations, respectively, are given by:

$$F = \frac{1}{T_{on} + T_{off}} \quad [2]$$

and

$$DF = \frac{T_{on}}{T_{on} + T_{off}} = T_{on} \times F \quad [3]$$

Selecting a spark microsecond cycle time depends on the workpiece thickness, flushing condition, and required surface quality. High pulse frequency leads to short sparks and therefore decreases the chip size (Figure 7(b)). This condition is consequently recommended to improve surface finish. Low pulse frequency leads to long sparks and therefore increases the chip size (Figure 7(a)), so it is recommended for increasing cutting speed.[44]

1.9.2.2 Electrical Discharge Machining Wire Electrode

The wire electrode is the central component of the WEDM system in the process of producing a steady electrical discharge. Therefore, the WEDM performance is largely affected by the wire electrode.[49] Wire rupture is a critical phenomenon that affects the quality and productivity in the WEDM process. It requires some prior knowledge about the characteristics of the wire electrode and workpiece in the cutting process to avoid such rupture for continuous operation of the process.[50] The parameters that define these characteristics are wire tension, thermal load, electrical discharge impact, and flushing rate. The wire rupture is likely to occur when the developed stress exceeds the strength of the wire. The effect of developed stress is determined by factors such as reduction in cross-section reduction and increase in the wire temperature. The wire strength is directly affected by high process temperature and varying thickness of the workpiece, both of which eventually lead to wire rupture.

In early 1970s pure copper wire electrodes were used, compromising the machining accuracy and strength. By the

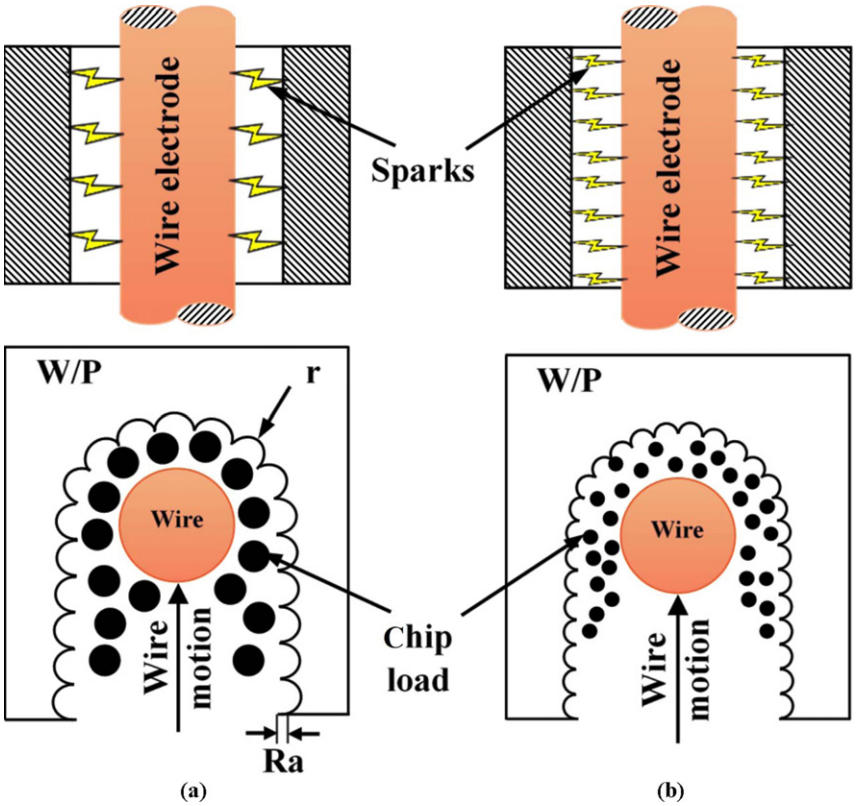


Figure 7 Chip size and load at different spark energy and pulse frequency: (a) high spark energy with low pulse frequency and (b) low spark energy with high pulse frequency.

mid 1970s, brass wire started to replace copper wire electrodes. Following these developments, wire electrodes made of copper and coated with zinc appeared in the machining application in 1980. In the following years, these were replaced by brass wire electrodes coated with zinc, and brass wire electrodes were developed with aluminum or chromium. Since 1990, brass wire electrodes were developed in different compositions to achieve different processing goals. To ensure quality in high-precision cutting, a zinc coating is used over the brass wire electrode and high-speed cutting for productivity is achieved using Cu–50%Zn coating. Subsequently, for higher productivity or cutting speed, wire electrodes made with an increased proportion of zinc have been found to be effective. In cutting thick materials, the heat resistance is improved with the application of brass wire electrodes composed of titanium and aluminum.[51] Moreover, other special wire electrodes were tailored to meet the desired conditions for cutting and characteristics of the workpiece, such as steel, tungsten, molybdenum, abrasive-assisted, and porous wire electrodes.[52]

In practice, the cutting efficiency in the WEDM process relies on complex consideration of mechanical, electrical, geometrical, and physical properties of the wire electrode. However, the overall cutting performance is controlled by several WEDM process factors, such as the mechanical effect, machine intelligence, pulse generator improvements, and the dielectric flushing methods. The following section discusses electrical discharge machining (EDM) wires in terms of their physical properties and their relationships with practical cutting processes.[53,54]

Conductivity determines the transfer of power from the feed source to the target point of cutting. It enables the EDM wire to transfer energy over distances, and thus serves as a key property of the wire. When the cutting process involves an open guide to clear a workpiece obstruction, the distance for power transfer can be considerable. Low conductivity is responsible for a considerable voltage decrease over the distance between the power source and cutting target, which eventually results in power loss at the cutting point. This loss can be significant because the modern power supplies usually produce electric currents more than 100 A. The conductivity values of metals and alloys are determined relative to that of the standard annealed copper based on International Annealed Copper Standard (IACS). Conductivity is expressed as a percentage of IACS, which is 100% for the standard copper wire.[55]

Tensile strength is a mechanical property of the wire that refers to its ability to withstand the applied tension in a cutting procedure aiming at a vertically straight cut.[56] EDM wires with tensile strengths of 900 MPa or more are categorized as 'hard,' whereas 'half-hard' wires possess tensile strengths of approximately 490 MPa and 'soft' wires have tensile strengths less than 440 MPa. In practice, hard wires are used for most cutting processes. However, in taper cutting, hard wire will resist bending at the guide pivot, resulting in faulty taper cutting. In this case, half-hard and soft wires are the primary choices when the taper angle is more than 5°. In general, half-hard and soft wires are not appropriate for automatic threading unless the machine is tailored to work with such wires.[57]

Elongation defines the amount of deformation the wire produces prior to the breakdown. This is a key property of the wire, which is commonly subjected to high-tension load and countless sparks during the cutting process. The percentage of gage length is used to estimate the elongation in a given test. Elongation also determines if a type of wire is more brittle than another. Hard wires possess relatively much less elongation than half-hard wires. Therefore, a brittle wire is more likely to breakdown early due to an overload condition, whereas a more ductile wire may survive in a temporary overload.

Melting point is not listed as a specification parameter for a given wire; however, it plays a significant role during the spark erosion process of the WEDM. In addition, the wire electrode should possess certain resistance to the rapid melting caused by the sparks.

Straightness is rarely specified for EDM wires; however, it plays an important role in successful auto-threading and cutting thicker workpieces.

Flushability indicates the quality of the cut in the WEDM process. Although it is not a specified item for a given wire, better flushability refers to a faster cut by the wire.[58] It depends on the metallurgical property of the alloy components of the wire.

Cleanliness is also not found in the specification of EDM wires. This refers to the quality of the wire being free of contamination. The contamination may appear as dirt from residual metal powder during the drawing process or as drawing lubricant, or may be due to added paraffin prior to spooling. These chemical and metallic contaminants can accumulate over time and eventually clog guides and power feeds or slipping belts or rollers.

Geometrical properties specify the diameter, shape, and coating and layer structure of the given EDM wires. In general, WEDM involves wires with diameters ranging between 0.02 and 0.36 mm. A larger diameter yields an increased supply of pulse energy to the working gap, which improves the overall material removal rate.[59,60] In contrast, micro-WEDM involves ultra-fine wires less than 30 μm in diameter to handle predominantly small pulse energies.[61] Considering the application and process conditions, many patents are available proposing a number of other wire electrode shapes.[62–64] Meanwhile, the high manufacturing cost of modified cylindrical wires limits their usage in practical applications. Improved heat transfer in wire electrodes has been found to yield a 15–20% increase in the cutting rate. Wire electrodes with twisted grooves have been patented to resist sparks occurring at the same point.[65] Regarding their patents, several inventors have disclosed that the change in the direction of the wire's rectangular cross-section played a vital role in moving the generated sparks very near to the workpiece and in preventing hotspots on the wire electrodes during the WEDM process.[66,67] **Figure 8** illustrates several wire shapes that are patented to improve the material removal rate.[65,68]

In 1969, the maximum possible cutting rate was achieved by a 0.15-mm-diameter wire, which was later increased to 0.36 mm. **Figure 9** depicts how the wire diameter is increased every time to facilitate an improved wire electrode for the WEDM process.[69] The effects of several important force factors such as electromagnetic, electrostatic, wire traction, dielectric flushing, and wire feed on the application of the smaller diameter wire electrode (0.03 mm) have been analyzed.[70,71] Prior

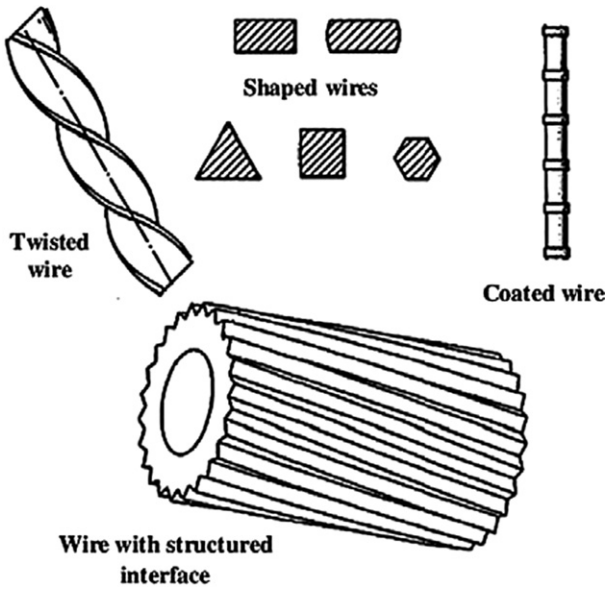


Figure 8 Customized wire shapes.[65,68]

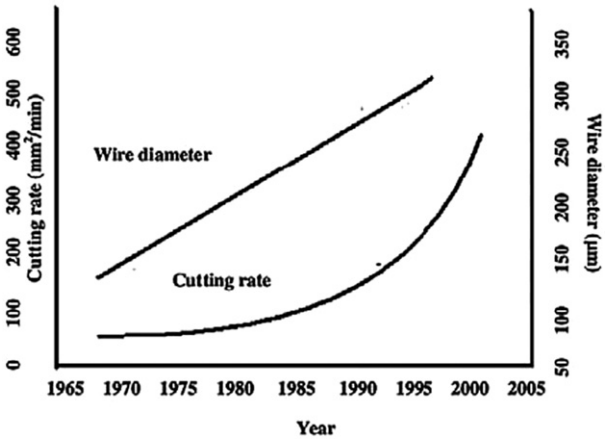


Figure 9 Cutting rate improvement in relation to wire diameters.[74]

works have been conducted to enhance the power supply and transportation system suitable for fine wires with a diameter less than 80 μm.[61,72] To achieve a successful operation, selecting the suitable wire electrode is a very challenging task in WEDM.[73] This requires the study of a variety of wire electrodes to yield the optimal result for this process.

1.9.2.2.1 Development of EDM wire electrodes

The cutting machines in the early 1970s had an extremely low yield, with cutting rates of approximately 21 $mm^2\ min^{-1}$. By the early 1980s, cutting rates increased to 64 $mm^2\ min^{-1}$, whereas the current machines are able to cut at a speed more than 20-times higher than the earliest machines. **Figure 10** shows the advancement rate of WEDM with brass wire and performance of wire electrodes since its development.[69,75–77]

The existing brass-coated wires are in one of the following categories: high falcon (HIF), high hawk (HIH), high eagle (HIE), high sonic (HIS), or high real (HIR).[49] HIS and HIR wire electrodes are suitable for high cutting speed and have been commonly used in applications involving mass production, such as electronic and metal molds for integrated circuit lead frames. However, HIE and HIH wire electrodes were used for high-precision machining and utilized for precise applications such as biomedical and aerospace products. **Figure 11** shows different wire electrodes produced to offer faster cutting speed with improved surface finish and flatness.[79]

The electrical discharge property can be regulated by adding zinc to the wire electrode, which consequently helps to enhance the machining performance. Properties like clarification and heat release can be controlled by alloying conductive elements to the core surface of wire electrodes.[80] Several inventors have considered these properties as the primary control parameters to improve wire electrode performance.[81–83] Prior studies involving plain, alloyed, or coated (zinc-coated, diffusion annealed, etc.) wire electrodes report a significant enhancement in WEDM performance.[84,85] Due to stable discharge, brass wires are the most popular electrodes in machining, but they suffer from low electrical conductivity. The electrical conductivity and heat resistance of the core or coating of the wire have been commonly considered in developing many wire electrodes. Fracture toughness is one of the properties that control the WEDM performance. Fracture toughness is the ability of the wire electrode to resist breakdown and withstand the formation of craters on its surface.[86–88] Wires with high tensile strength are likely to break during the machining process. The issues associated with fracture and electrical conductivity have been addressed using composite materials with the steel core wire electrode. Under the applied preload tension, a discharge may cause a flaw greater than a critical flaw that sets off a catastrophic failure. This event may break an EDM wire, as shown in **Figure 12**.[89] High-strength materials used in EDM wire manufacturing are vulnerable to small flaws because they tend to fail because of their low fracture toughness. Each discharge in the WEDM process results in a flaw in the form of a crater in both the wire and workpiece. These flaws gradually grow larger with the deteriorating flushing conditions and eventually lead to catastrophic wire failure.[90–92]

1.9.2.2.2 Plain EDM wires

The manufacturing of brass wire starts with a continuously cast rod 20 mm in diameter. The rod is made approximately 6 mm round or in a hexagonal cross-section using either a cold-rolled or a cold-drawn procedure. The wire is then shaped approximately 0.9 mm through annealing and drawing by a series of dies. This state is usually termed as a redraw wire. Prior to forming the final size, the wire is redrawn through another series of diamond dies. In the final stage, the wire is resistively annealed or thermally tempered in an inert atmosphere, cleaned, and then spooled.[93–95] According to the convention, the term 'plain' simply refers to the wire that consists of a single homogeneous component without involving coating or alloying of other materials.[57]

1.9.2.2.2.1 Copper wire

Figure 13 shows a copper wire that is the original component in the WEDM process. There was a common notion that the high electric conductivity of copper wire would make it an ideal EDM wire. Unfortunately, copper wire suffers from low

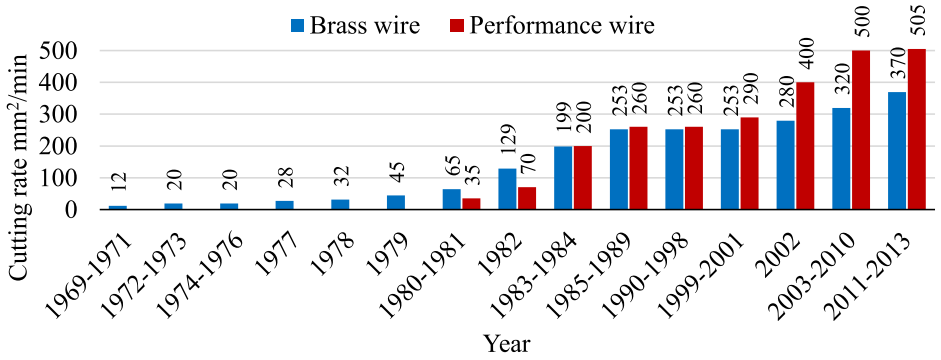


Figure 10 Advancement rate of the wire electrical discharge machining since its development.[78]

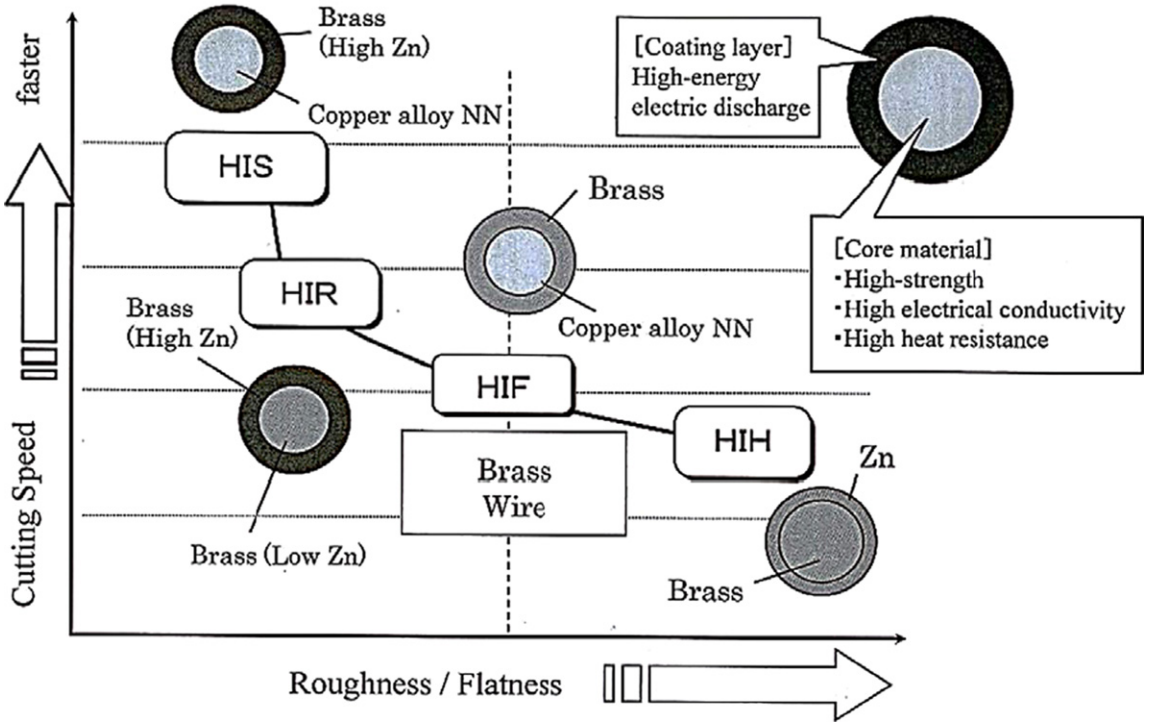


Figure 11 Characterization of electrical discharge wire electrode.[79]

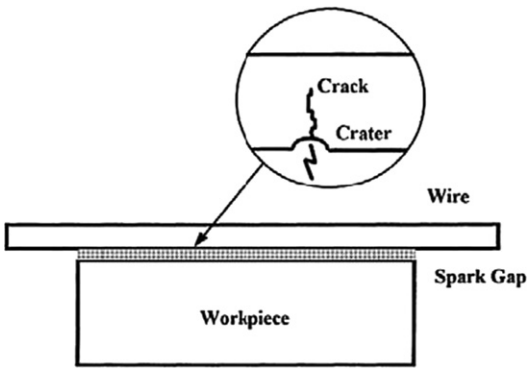


Figure 12 Defect and fracture in the wire electrical discharge machining process.[90–92]

tensile strength, high melting point, and low vapor pressure rating.[96] This became evident at the advent of the second generation of pulse power supplies; hence, brass wire had to take over copper wires in the WEDM process. However, copper wires are occasionally found in applications where the zinc contaminant, contained in either brass or coated wires, is not acceptable.[57,97]

1.9.2.2.2.2 Brass wire

There have been numerous efforts to enhance the performance of wire electrodes. Brass wire is an alloy of copper and zinc, with compositions in the range of 63–65% Cu and 35–37% Zn (**Figure 14**). It has been reported that increasing the proportion of zinc enhances cutting speed and performance.[98]

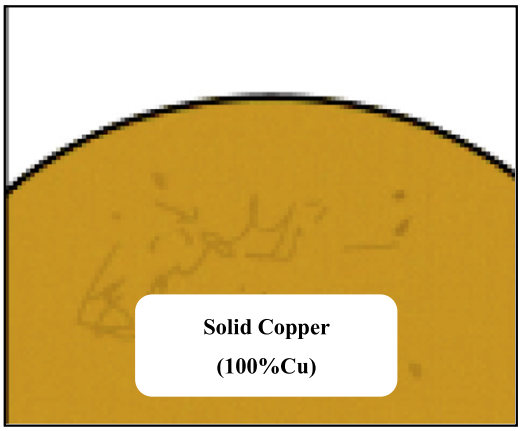


Figure 13 Solid copper wire.[57]

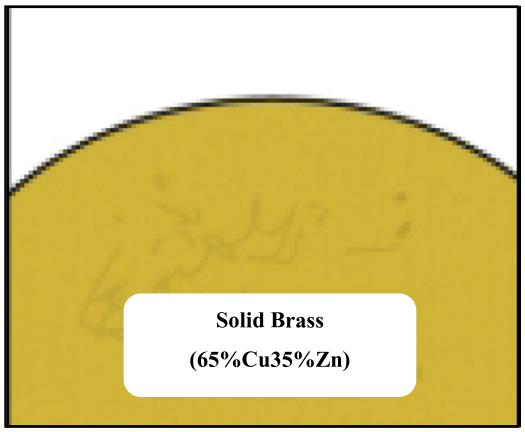


Figure 14 Solid brass wire.[57]

The zinc in the brass wire evaporates during the cutting process and provides more energy yield by cooling the wire. Adding zinc provides significantly higher tensile strength and a greater vapor pressure rating, which compensate for its loss of conductivity. In addition, the dielectric fluid may not be able to clean some zinc particles that will stay between the workpiece and wire electrode gap to facilitate necessary ionization and cutting process.[69] These qualities make brass one of the most popular choices of materials for WEDM electrodes. However, the addition of zinc to any extent significantly reduces the conductivity of the electrode. For example, hard brass wire possesses only 20% of the conductivity of copper wire. Because of the improved flushability with zinc wire, a high-zinc brass composed of Cu60%Zn40% is currently available. This additional zinc content speeds the cutting process up to 5% in some optimized applications.[99] However, zinc proportion more than 40% is not practical for cold-draw wire. The change in the grain structure of wire may make the wire too brittle to process into a fine diameter required for WEDM. In several cases, there can be significant amount of brass deposit on the workpiece after the cutting process, which is more difficult to remove. These findings have encouraged the formation of coated wires.[20,100,101]

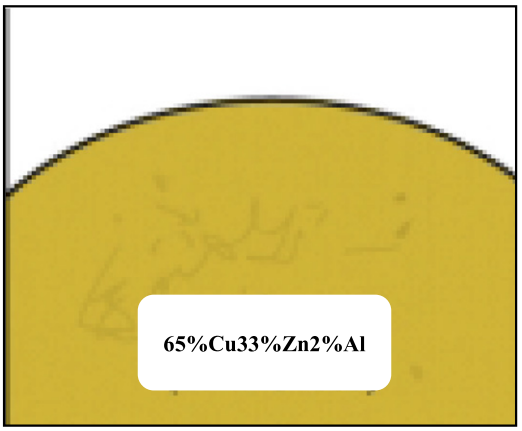


Figure 15 Aluminum–brass alloy wire.[57]

1.9.2.2.2.3 Aluminum–brass wire

A special type of alloy wire is made by alloying a small amount of aluminum with a brass wire, as shown in **Figure 15**. The tensile strength of the wire can be improved by such an alloying process, which can raise the tensile strength as high as 1200 MPa without deteriorating the elongation. These alloyed wires are less prone to damage than the wires made of plain brass.[57]

1.9.2.2.3 Coated EDM wires

US patent US1896613-1933 refers to one of the earliest patents on zinc-coated wires aimed to enhance the cutting performance of EDM wires.[102] Because the limit for raising the zinc content is 40%, zinc is alternatively used to coat the core wire material to enhance the quality of the wire.[103] Coated wires are developed by plating or hot-dipping redrawn wire and then drawing it to the final size. This process is challenging because the zinc surface has to withstand the final drawing process. Currently, the coating is not deposited on the final shape of the EDM wire. The existing wires usually consist of a core made of either brass or copper to facilitate conductivity and tensile strength. In addition, to enhance the spark formation and flush characteristics, pure or diffused zinc is electroplated as the coating on the wire surface.[104–109]

1.9.2.2.3.1 Single-layer-coated wires

One of the earliest strategies used to add zinc to the wire surface is the development of zinc-coated brass wire. One of the standard EDM brass alloy wires consists of zinc coating over the core as thin as 5 μm (**Figure 16**). The zinc-coated brass wire yields a significant increase in the cutting speed over the plain brass wire without compromising with any other important properties.[110] The wire can provide an excellent surface finish when cutting tungsten carbide, and this wire is commonly used to cut polycrystalline diamond and graphite. This wire is also utilized in certain cases where the brass wire creates undesirable plating of brass on the workpiece.

To attain the benefits of the conductivity of copper and flushability of zinc together, zinc-coated copper wire was one of the earliest attempts in the wire development. It does not

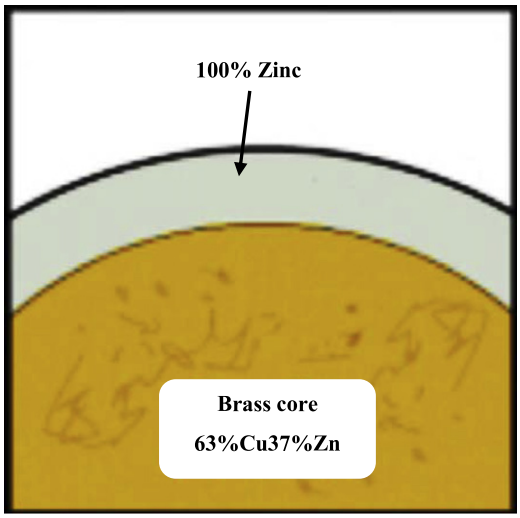


Figure 16 Zinc-coated brass wire.[57]

currently exist in application because the spark penetrates the thin zinc coating and the copper core inside slows the cutting process.[111,112]

US patent US4287404 revealed that electrode wires coated with metals of low vaporization temperature, such as bismuth, tin, zinc, lead, cadmium, antimony, or alloys, protect the core from thermal stress from the electrical discharge. Additionally, it allows an increase in the frequency of electrical discharge without causing damage to the wire.[113] US patent US6300587 refers to a wire electrode with a copper core coated with a peripheral layer. The coating layer is composed of 55.5–75 wt% copper and one or more of the following metals: Zn, Cs, Se, Te, or Mg. The coating layer only forms a natural oxide film.[114] US patent US6348667 is identified as a wire electrode that prevents corrosion, particularly of the noneroded surfaces of the hard metal block. This anticorrosion property is achieved by using a wire electrode in the spark-erosive cutting of hard metals. The coating of the wire consists of either a metal or an alloy. During the cutting process, the outer coating comes loose as small metal particles and remains in the dielectric. However, because these small metal particles are not nobler than the metal contained in the hard metal, the electrochemical corrosion, namely pitting of the hard metal, cannot occur as soon as the small metal particles make contact with the hard metal block. Consequently, the pitting phenomenon in the hard metal block can be avoided. As a rule, the hard metal block consists of cobalt, aluminum, magnesium, zinc, or iron.[115]

1.9.2.2.3.2 Double-layer-coated wires

The wire electrode referred by US patent US4968867 has a core with higher thermal conductivity, an inner coating made of a material with a low boiling point, and an outermost layer of brass offering high mechanical strength. The core of such wires is made of a single metal such as copper, silver, aluminum, or alloys (**Figure 17**). Such wires are found to increase the cutting speed due to several properties, such as the vibration dumping, heat transfer, and resistance to breakage. **Figure 17(a)** shows a cross-sectional view of the first invented sample of the wire electrode. A coating layer (7) covers a core wire (6). In this sample, the coating layer over the core is prepared by brass with 35%Zn, and the core wire is a Cu–Sn alloy with 0.15%Sn. Besides brass, the coating layer is also formed by alloying secondary components such as less than 50%Mg and/or Cd with copper. In another sample of current invention, a wire electrode was designed by considering the area of cross-section of the coating layer that is approximately 50–90% of the entire area of the cross-section of the wire electrode. The larger thickness of the coating layer yields higher tensile strength. The cross-sectional area of the coating layer is approximately 69% of the total cross-sectional area of the wire electrode. In the third embodiment, two layers (7 and 8), one after another, cover the core wire (6), as shown in **Figure 17(b)**. One of the metals, such as Zn, Cd, or Mg, primarily forms the outermost layer because they have a relatively lower boiling point. Accordingly, machining speed can be improved. **Figure 17(c)** shows a cross-sectional view of the fourth embodiment. The outermost layer (9) represents an oxide film in the coating layer (7). This oxide layer can reduce undesired electric discharges at the lateral side of the wire electrode. This realizes a narrow machined groove width. In the fifth embodiment, the wire electrode consists of a core (6) made of Cu alloy, ensuring higher thermal conductivity. A layer on this core (10) is formed by twisting thin wires of brass with high mechanical strength, and the outermost layer (11) is formed by Zn or Zn alloy (**Figure 17(d)**). This design improves the electric discharge characteristics that, in turn, improve the roughness of the workpiece surface. This is because a layer of material with a low boiling point covers an intermediate coating layer with high mechanical strength. **Figure 17(e)** shows a cross-sectional view of the sixth embodiment. The wire electrode has a coating layer (12) of Zn plating on the core surface and an outermost layer (13) formed by brass. A linear material made of a Cu alloy including 0.15%Sn balanced by Cu is subjected to zinc plating to obtain the core wire (6). **Figure 17(f)** presents a cross-sectional view of the seventh embodiment. Here, brass with 35%Zn is used as the coating layer, whereas the core is essentially a Cu alloy including 0.15%Sn balanced by Cu. At least one piano wire may be added in the twisted linear elements to enhance the mechanical strength of the wire electrode.[116]

Patent US4977303 refers to a method of producing an EDM wire electrode that consists of a Cu core with zinc coating. The coated wire is then heated in an oxidizing atmosphere to produce two layers: a copper–zinc alloy layer over the core and a zinc oxide layer over the alloy layer. The resulting electrode wire allows greater current density and traction force, which in turn speeds the cutting yield in the EDM process.[117]

1.9.2.2.3.3 Multilayer-coated wires

US patent US4341939 provides an increase in the cutting speed by eradicating the short circuit phenomenon that reduces the machining performance. In other words, it rapidly affects the transformation of nonerosive short-circuited electrical discharges into electro-erosive effective discharges. The electrode design incorporates a wire core coated with one or more layers of another material and a thin film of nonmetallic material. The thickness of the thin film is sufficient to provide a semi-conductive effect when the film contacts the workpiece

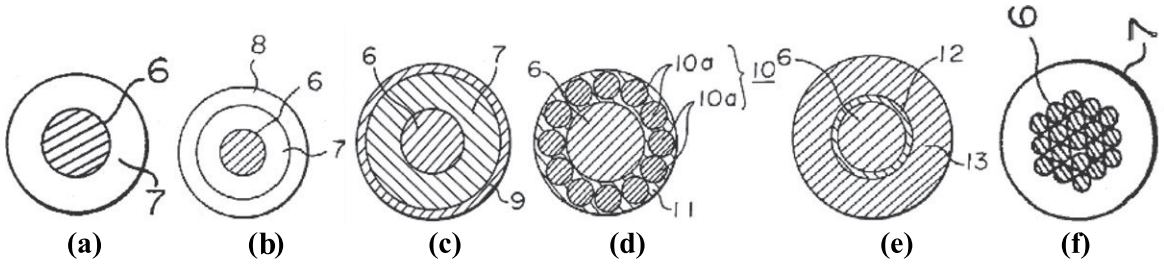


Figure 17 Construction of wire electrodes.[116]

at a small-applied voltage between the electrode wire and the workpiece. However, the film turns into a conductor by electrical and/or thermal breakdown when the applied voltage increases from a few volts to approximately 100 V. The wire has at least a layer of metal with a low vaporization temperature (such as zinc) that is coated with a metal oxide film. The metal layer is treated with electrolytic or thermal oxidization to form a thin film of zinc oxide on the metal surface. **Figure 18(a)** shows a schematic of a cross-section of an electrode wire with a copper core (1) superficially coated with a copper–zinc alloy film (2), which is further layered by a thin film (3) of zinc oxide. The wire core can be made of brass or steel (1), provided that they offer essential qualities such as good electrical conductivity, mechanical strength, and resistance to rupture. Good machining performance has been obtained using bismuth, tin, magnesium, lead, cadmium, antimony, or metal alloys as the coating material. Experiments reveal that satisfactory machining performance can be achieved with other metallic oxides beyond zinc oxide. It has been found useful to create a film of another metal a few microns thick over the zinc coating, where the metal film can be oxidized during the high heating process. The metal oxides known for their semi-conductive properties are CuO, Cu_2O, CdO, In_2O_3, PbO, TiO_2, MnO_2, MgO, and NiO. Nonetheless, dielectric oxides such as $A1_2O_3$ can also be used. There can be nonmetallic films covering the metallic layer surface such as carbides, borides, silicides, sulfides, and nitrides of various metals. **Figure 18(b)** shows the cross-section of a Cu core (1) layered by two copper–zinc superimposed coatings (2 and 4). These coatings are covered with films of zinc oxide in (3) and (5), respectively. As mentioned, heat treatment oxidizes the first coating (2) of 2–4 μm to form a thin film (3) of ZnO. The thin oxide film (3) is then covered with a second zinc coating (4) of approximately 4 μm. A second heat treatment is applied to create a thin film (5) of ZnO covering the surface of the second zinc coating (4). **Figure 18(b)** shows similar phenomena of copper diffusion into zinc and vice versa, as well as coating porosity causing irregularities and coarseness in the outer surface.[118]

The US patent 20080245773 offers a multi-coating EDM electrode wire capable of fast and quality machining in shaping a workpiece without requiring changing the wire.[119] The wire is composed of two or more coating layers with an outer layer of zinc for precision machining and an inner layer of zinc alloy that facilitates fast machining, which in turn offers uninterrupted machining service. Moreover, this type of electrode wire can be produced at a relatively low cost. In addition, discharging occurs at the time of machining a workpiece

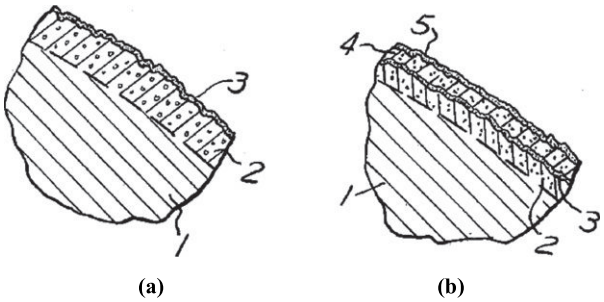


Figure 18 Schematic section of wire electrodes.[118]

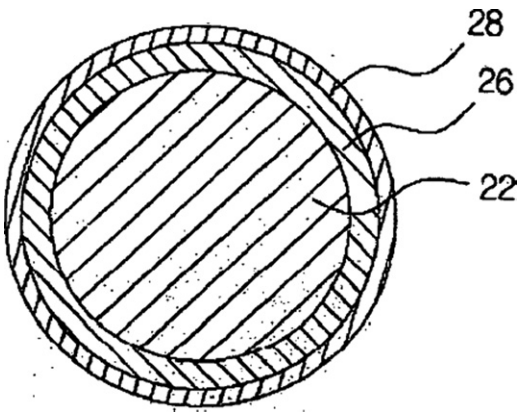


Figure 19 Cross-section of wire electrodes.[119]

without producing debris from the core wire; therefore, the machining work is not interrupted by the electrode wire. **Figure 19** shows the multicoated electrode wire with a core (22) made of copper or brass. The lower layer of coating (26) is made of zinc alloy (CuZn80–CuZn95), which has a higher sublimation point required for fast machining. The upper layer (28) made of zinc alloy (CuZn90–CuZnl00) has a lower sublimation point for precise machining and is formed onto the lower layer (26). Therefore, this wire electrode provides fast and precise machining without interrupting the EDM process.

US patent US5196665-93 was geared toward improving the mechanical strength of electrodes without compromising properties like the heat-shield effect and the elimination of short circuits. The multiple layers on the core surface possess essential properties like high electrical conductivity and low melting and vaporization temperatures in an alternating

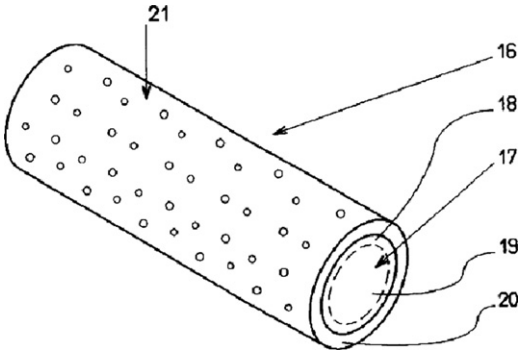


Figure 20 Diagram of wire electrode.[121]

fashion. The alternating layers on the wire electrode surface may form alloys of required structure and composition by diffusing into one another. In this case, the core is made of metal like brass, copper, steel, or copper-clad steel and is coated with layers of zinc, copper, and zinc alloy with 30–60% zinc that are less than 0.5 μm thick.[120] Patent US5721414 developed an electrode wire with a thicker surface layer from diffused copper–zinc alloy following a thermal diffusion method, such that spark erosion machining was accelerated.[121] The wire surface prepared following the patent is just coarse enough for the spark erosion, thus requiring no mechanical surface treatment other than sizing. The wire electrode has a core (17) of copper or copper alloy (19) covered with an upper layer (18) of copper or copper alloy (20) of diffused copper and zinc alloy or copper alloy. The surface layer (20) has a slightly granular surface (21), as shown diagrammatically in **Figure 20**.

1.9.2.2.4 Diffusion-annealed coated wires

In theory, a pure zinc coating would produce the perfect wire with superb flushability. However, in practice, the thin layer of zinc on the core surface is blasted off by electric discharge intensity because of its low melting point. Therefore, zinc hardly gets the chance to provide its full potential.[122] Therefore, the coating should contain a high-zinc content with materials of relatively higher melting points to ensure better adhesion to the core wire. A heat-treating process known as diffusion annealing can obtain this better adhesion. In a diffusion process, atoms transfer from higher to lower concentration regions. The zinc atoms with higher concentration diffuse into the brass, and the copper atoms from the brass diffuse into the zinc. This diffusion process between the core and coating materials eventually produces a zinc–brass alloy that is rich in zinc but possesses a relatively higher melting point and is metallurgically bonded to the core material.[123]

1.9.2.2.4.1 Alpha phase wires

The brass alloy can have several phases suitable for EDM wires, such as alpha, beta, gamma, and epsilon phases, as shown in **Figure 21**.[124] The alpha phase has the highest melting point, which is approximately 910 °C at its highest available zinc content of 35–39 wt%. The beta phase is second to the alpha phase in terms of the melting point, which is approximately 890 °C in a diffusion-annealed coating containing between

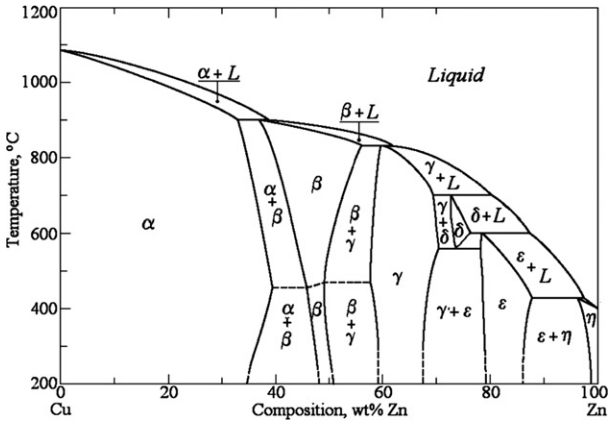


Figure 21 Cu–Zn phase diagram.[124]

40–53 wt% zinc. The gamma phase has the third highest melting point, which is approximately 800 °C in a diffusion-annealed coating containing between 57 and 70 wt% zinc. The epsilon phase has the lowest melting point, which is approximately 550 °C in a diffusion-annealed coating with a typical 85 wt% zinc content.[125]

1.9.2.2.4.2 Beta phase wires

The X-type wire was the earliest type of diffusion-annealed wire, usually termed SWX, Bronco Cut-X, Beta Cut-X, or X-Kut. A beta brass is coated over a pure copper core of this type of wire as shown in **Figure 22(a)**. It combines the advantages of the high conductivity of copper and coherent zinc-rich coating. However, it comes with limitations, such as 50% decrease in tensile strength, poor straightness, and higher cost when compared to solid brass wires. However, it has a significant yield in aerospace applications, offering alloys like inconel and titanium.[126]

Figure 22(b) shows the D-type wire, which is the second diffusion-annealed wire, typically termed Cobra Cut-D or D-Kut. The wire has a copper core alloyed with 20% zinc and a beta brass coating. Its advantages include enhanced conductivity of the 80%Zn to the 20% copper core, a coherent zinc-rich coating, and relatively high tensile strength (800 N mm^{-2}). High production cost is its major shortcoming. This wire yields significantly high productivity in a number of different machines.[57]

Patent US4935594-90 presents a wire electrode that has an erosive wear-resistant outer coating on the common eroding electrode. In **Figure 23**, an eroding electrode has a core (2) 0.1–0.6 mm in diameter. A coating (3) of cadmium, antimony, zinc, bismuth, or an alloy made of these metals can be layered on the core surface (3) (**Figure 23(a)**). Such a wire (1) is best prepared when annealed at 700–850 °C and is cooled to less than 80 °C while passing through a protective gas. In such a way, an altered coating (3′) (**Figure 23(b)**) with the previously mentioned useful properties is achieved. The core (2) of the wire (1′) is made of electrolytic copper with more than 99 wt% copper and a very low oxygen content. A copper–zinc alloy with 79.5–80.5 wt% Cu, with the remainder being Zn, can also be useful in practice. The altered coating (3′) has multiple layers of metallic phases, and its content of metal with a low volatilization temperature gradually decreases from the outer

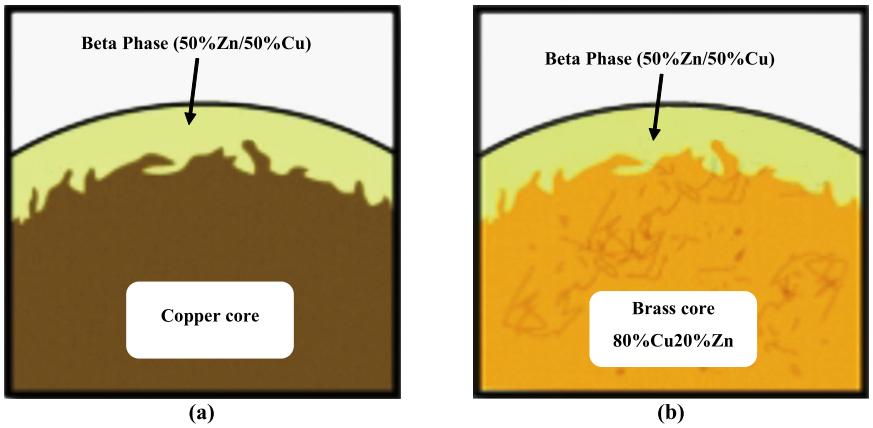


Figure 22 X and D types of wire electrodes.[57]

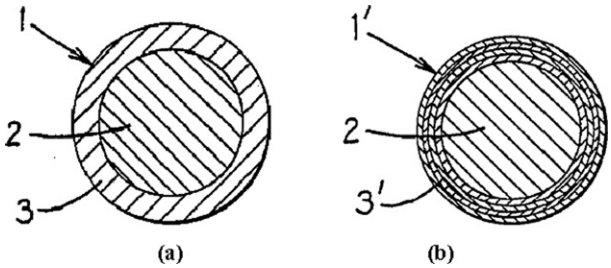


Figure 23 Cross-section of wire before and after the process.[127]

surface to the core of the wire (2). The metallic phase layers include alpha–beta phases and beta–gamma phases.[127]

European patent EP0526361A1 introduced an electrode to obtain high-stability electric discharge during the machining process. The Zn coating is used onto the surface of Cu or Cu alloy wire. The wire is heat-treated to form an outer layer (31) of a homogeneous beta prime phase. In such heat treatment, the temperature is maintained below the beta prime–beta transition temperature of the binary Cu–Zn alloy. Then, the wire is drawn at a drawing ratio more than 100% to obtain an electrode (1), as shown in **Figure 24**. For electro-erosion, the electrode has a Cu–Zn alloy outer layer (3) in the homogeneous beta prime phase free of oxide contents with a junction (32) of low thickness. The wire (20) is primarily made of copper or copper alloyed with at least one of Fe, Co, Ti, P, Mg, Cr, Zr, or Si at a content of between 0.1 and 1 wt%. Alternatively, at least one of the secondary elements such as Al, Sn, or Ni up to 4 wt% overall is also used. The weight concentration of the outer Zn layer (3) is in the range of 46.5%$\pm$1, which is substantially constant throughout its thickness.[128]

Patent US5858136 refers to the copper wire with zinc layer, which is heated at a temperature up to 750 °C to yield a brass beta phase. The heat treatment is continued to ensure complete diffusion of zinc, as shown in **Figure 25(a)**. The temperature is then raised to 950 °C to produce a brass phase, and the Cu core of the wire transforms into a brass alpha phase (**Figure 25(b)**). It offers both benefits of high conductivity and tensile strength.[126]

Patent US7687738 refers to an electrode wire with a single copper core with a diffused zinc alloy coating. The thickness of the coating is more than 10% of the wire diameter. A surface contact film is optionally formed on this coating layer using one of the following elements: Zn, Cu, Ni, Si, or Au. In any of these cases, the spark erosion rate increases by approximately 30% when compared to a brass wire or zinc-plated brass wire of the same diameter. The effect of overall conductivity of the wire on spark erosion performance is another key aspect of this patent. Considering the conductivity property, it is assumed that higher conductivity of the design wire can lead to a higher machining rate because more electrical energy can be supplied from generators that are more powerful. It has been found that such an electrode wire has overall conductivity within the range from 65% IACS to 75% IACS. Conductivity less than 65% IACS is considered inadequate to attain optimum spark erosion cutting performance. At low electrical conductivity, the wire is more prone to breakage due to the impact of heating in the sparking area. This results due to the Joule effect following the reduced cooling related to lower thermal conductivity. Conductivity more than 75% IACS cannot be obtained for this type of electrode wire, because it would restrict the thickness of the diffused layer to less than 10% of the electrode wire diameter. If this procedure fails, then the wire was formed too rigid and brittle and must not be drawn during fabrication. The most recommended overall electrical conductivity of the electrode wire is approximately 69% IACS for a 0.33-mm electrode wire with 35-µm-thick diffused layer (relative thickness approximately 11%). This combination of relative thickness (11%) and overall electrical conductivity (69% IACS) yields good machining performance for wires ranging in diameter from approximately 0.20–0.35 mm.[129]

1.9.2.2.4.3 Gamma phase wires

Gamma phase brass has a higher zinc content than beta phase brass. The brittleness of gamma phase brass typically limits the gamma coating thickness to less than 5 µm. A thicker coating will fracture and strip off during the final drawing process. The brittleness of the gamma phase brass causes discontinuity on the surface as fractures during the final drawing process. This coarse surface improves flushing as the wire passes through the cut, enhancing water flow and scouring debris from the gap, which eventually increases the machining speed. However, the discontinuity in the surface may result in a slightly dirtier surface than other zinc-coated wires.[119] The gamma brass type

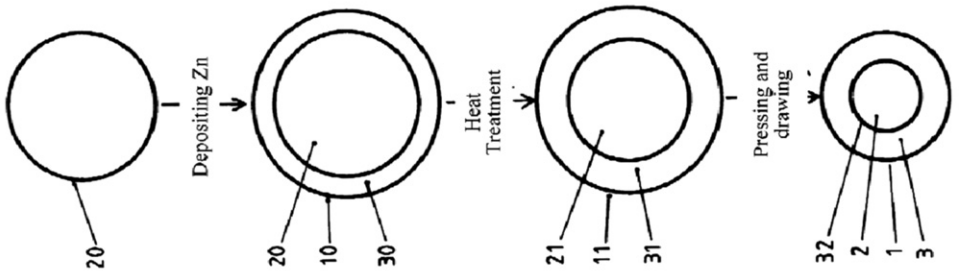


Figure 24 Different processing steps of the wire electrode.[128]

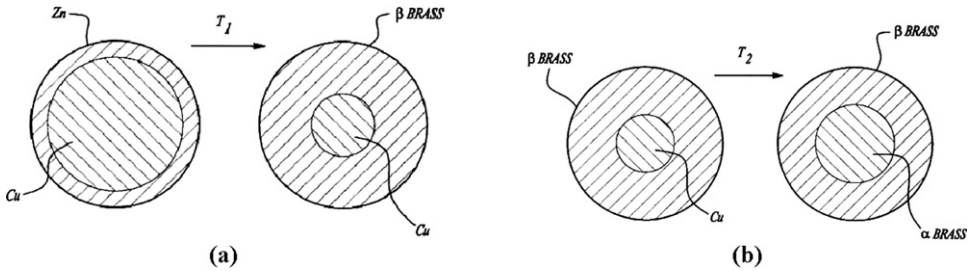


Figure 25 Wires with different coating thickness.[126]

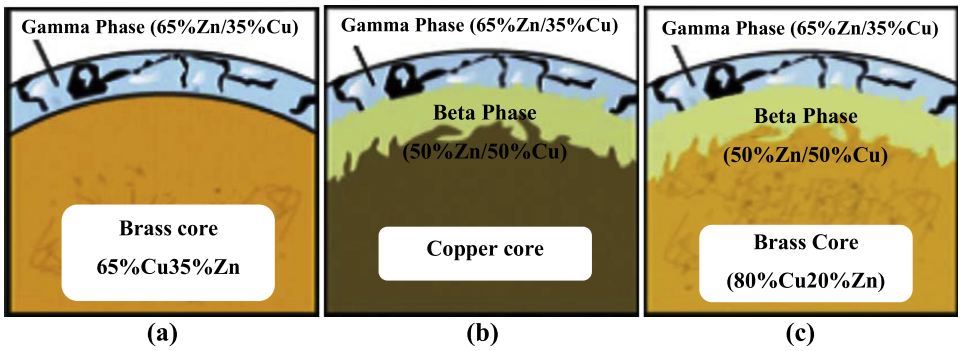


Figure 26 Gamma phase wire electrodes.[57]

of wire consists of a brass core coated with a gamma phase brass outer layer, and it usually has trade names such as Z-Kut, Topaz, Gamma-Z, and Delta Cut. A gamma phase brass coating replaces the pure zinc coating of the zinc-coated brass wire, as shown in **Figure 26(a)**. This construction usually yields 10–25% faster cutting performance than pure zinc-coated wires.[57] Patent US6566622B1 features the wire electrode core made of copper (X-type wire) or copper alloy (D-type wire). Such an electrode is first diffusion heat-treated to yield a beta phase, and then a stabilization treatment is performed to obtain an outer layer of the gamma phase (**Figures 26(b)** and **26(c)**).[130] The application of such electrodes can be similar to those of traditional X and D wire types, but it improves the machining performance by approximately 10%.[131] The diffusion-annealed beta phase brass has a high melting point and is composed of zinc in the range of 45–50%, thus providing excellent tenacity. Gamma wire offers a low-cost method of plating the gamma phase layer over the wire electrode surface. These wires offer an increased removal rate to reduce the cost of rough cuts, which enables them to decrease the cycle time.[132] The upgrades in technology suggested by various inventors have led to numerous efforts to improve gamma-coated wires by using low-temperature diffusion annealing.[114,116] A number of inventors attempted to coat the conductive core with multiple layers of film. The alloys of desired structure and composition are obtained by forming alternating coating layers on the core, where the layers are diffused into one another. These layers offer properties of high conductivity and low melting and vaporization in an alternating fashion.[120,133] The gamma coating phase is subjected to cladding surface passivation to build resistance against corrosion.[134]

Patent US5945010-97 revealed an electrode wire with a coating of a copper–zinc gamma phase alloy or a nickel–zinc alloy. The core of the wire usually contains any one of the following metals: copper, copper-clad steel, or brass. The second coating is formed of a metal such as Zn, Mg, or Al by using

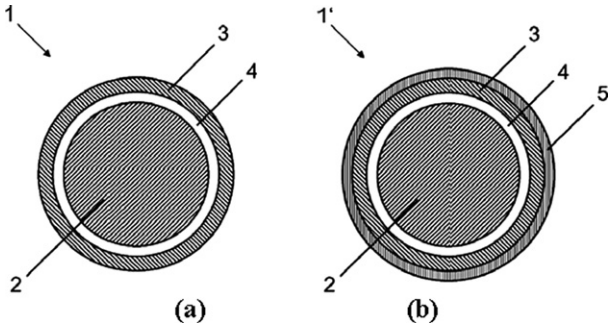


Figure 27 Cross-section of electrode wire.[137]

low-temperature diffusion anneals. The resulting EDM wire offers a faster cutting rate and a surface finish better than traditional wire electrodes. Other pros of the US patent 5945010-99 is achieved by the higher zinc content in the coating compared to the earlier US patent 5945010-97. This results in significantly lower volumetric heat of sublimation for the coating, which leads to more efficient flushing of wire, ensuring sufficient tenacity to survive the EDM erosion process. The tensile strength increases sharply with the formation of the beta phase. With the presence of alpha and beta phases in equal proportion, the tensile strength of brass peaks at a maximum value of 32% zinc content.[135] Considering these factors, patent US5808262 is meant to produce a spark erosion electrode. The core of this wire has relatively lower zinc alpha brass with an outer layer of highly rich zinc beta and gamma brass. This formation offers improved flashability of the electro-erosion process along with relatively higher tensile strength of the electrode core material.[136]

Patent number US2011/0290531A1 refers to a wire electrode (1,1′) for electric discharge cutting processes. The wire electrode (1,1′) has a core (2) made of a metal or metal alloy and a coating (3, 4; 3, 4, 5), at least one (3) of which constitutes a phase mixture of beta brass or beta prime brass and gamma brass, as shown in Figure 27. The beta or beta prime phase and the gamma phase are arranged sequentially in a fine-grained structure. The average size of these grains can be as high as 5 μm. In the preferred embodiment according to Figure 27(b), a core (2) is made of Cu–Zn20% with a coating layer (4) that adjoins the core. The core is primarily made of beta or beta prime brass alloyed with a zinc content of approximately 45 wt%. The coating layer (3) consists of a phase mixture of beta or beta prime brass and gamma brass with a mean zinc content of approximately 53 wt%. The major element of the top layer (5) is zinc oxide. This composition of materials yields a wire electrode (1′) of 750 N mm^{-2} tensile strength and electrical conductivity of approximately 17 m Ωmm^{-2}.[137]

Patent US8338735 has a brass core (1) coated with a gamma phase brass layer (2) with fragmented blocks (2a), between which the core (1) is exposed. The blocks (2a) have E2 thickness with a narrow distribution and they cover more than 50% of the core (1), as shown in Figure 28. This structure forms regular fragments in the coating to facilitate better finishing of the machined parts.[138]

US patent 5762726-98 is known for higher zinc content phases in the copper–zinc constructions. The gamma is a useful phase for EDM wire electrodes because it offers cutting

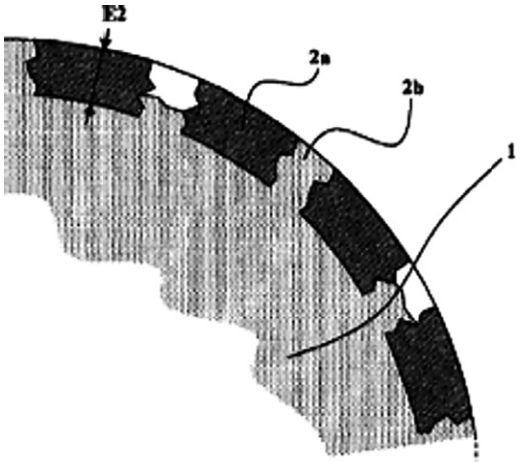


Figure 28 Large-scale diagrammatic view of cross-sectioned wire.[138]

performance superior to that of a wire electrode with a sheath layer over a pure beta phase. The cutting process is made more efficient with the aid of a pure gamma phase when compared to that of the beta phase. The gamma phase, which adds hard inert materials, is rarely produced in a traditional process like long-time diffusion. Therefore, a mixed structure with fractions of alpha, beta, and/or gamma phases is produced. Figure 29(a) shows the initial core of alpha brass and a sheath layer of zinc (eta zinc). Following heat treatment and the shortest possible holding time, another layer is formed between the core and sheath layer, which is termed the epsilon zinc layer (Figure 29(b)). After an increase in the annealing time and diffusion increase, the eta zinc layer transforms into an epsilon zinc layer (Figure 29(c)). It is evident in Figure 29(c) that during the annealing period, a thin gamma brass layer is intermediately formed between the core and epsilon zinc layer. The expansion of the gamma brass layer facilitates the diffusion process of the epsilon zinc layer into the gamma brass layer (Figure 29(d)). A thin layer of beta brass appears at a significantly lower growth rate between the regions of the gamma brass layer and the alpha brass core (Figure 29(e)). Figure 29(f) shows the period when the sheath layer changes to a gamma brass layer. The beta brass sheath layer is developed a little larger in the transitional region between the core and gamma brass sheath layer shown in Figure 29(e). Finally, Figure 29(f) illustrates the final processing state where the eta zinc layer is substantially decomposed and the expansion of the beta crystals results in a thin layer around the core. However, such wire electrodes are not viable in commercial manufacturing due to their failure to resist brittleness in these phases.[139]

There are two requirements in a machining process: speed the machining for a given current and ensure maximum usage of machining current for a given wire diameter. The EDM performance can be improved by using an electrode wire (1) made of copper or brass core (2) a beta brass sub-layer (3) and covered by a coating that combines a fractured gamma brass surface layer (4) (Figure 30). The advantage of beta brass is that it at least partially fills the fractures (5a) in the gamma phase region (5). The beta brass sub-layer may have a relatively smoother surface that facilitates better performance than does

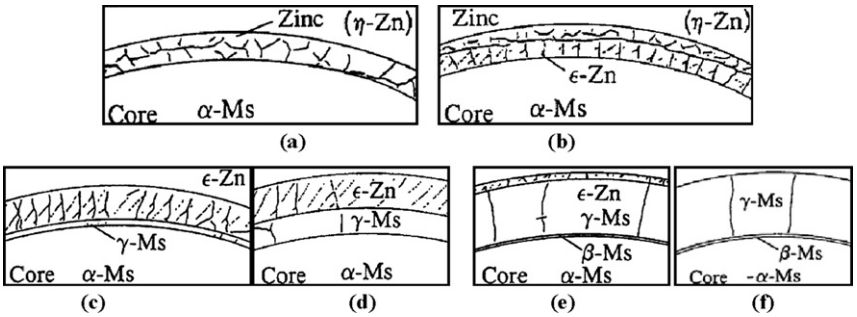


Figure 29 An enlarged representation of the detail of the sheath layer and the core.[139]

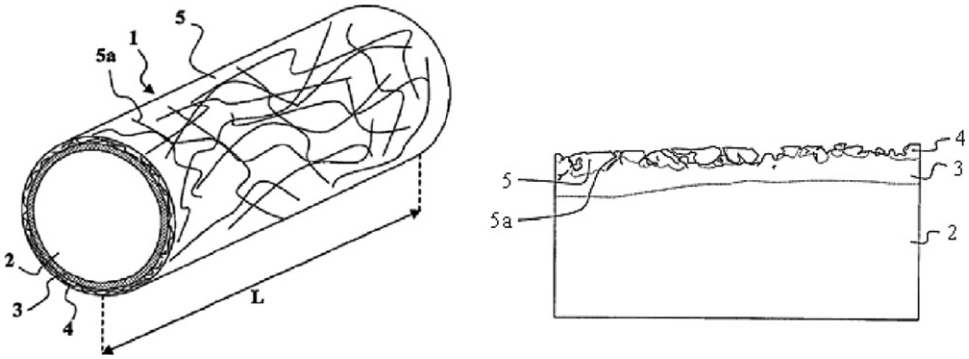


Figure 30 Schematic perspective view and a longitudinal section through an electrical discharge machining wire.[140]

an uneven sub-layer. The thickness of the fractured gamma brass layer is made less than 5% of the wire diameter to facilitate both higher speed and better finish of the machined workpiece.[140]

1.9.2.2.4.4 Epsilon phase wires

The lower melting point is known as one of the limitations of the epsilon phase when compared to beta or gamma phase coatings. However, the limitation is compensated by the higher zinc content in the epsilon phase, which matches the epsilon phase coating performance with that of beta phase coatings while being competitive with gamma phase coating performance. In general, coatings of the epsilon phase yield similar machining performance at a reduced production cost when compared to either beta or gamma phase coatings.[20]

US patent number 20070295695 reveals an EDM wire with a copper core, which is layered with continuous coating of porous epsilon phase brass. Graphite particles are used to fill the porous coating to enhance the performance of epsilon phase coating.[141]

The EDM wire of patent US8067689 consists of an outer layer of gamma phase brass followed by a continuous layer of single zinc or ductile epsilon phase brass. The continuous layer eliminates any discontinuities of the gamma phase and thus exposes a surface of homogeneous electrical properties to the workpiece (**Figure 31**). The epsilon phase brass coating is thinner than that filling the gaps between the gamma particles, which yield high performance with gamma coating. For the purpose of rough cuts, speed is more important than machining accuracy. **Figure 31(a)** shows a brass core (12) coated with a 10-μm-thick layer of zinc (15). The wire is heat-treated for 6 h at a temperature of 1700 °C in a nitrogen atmosphere. The heat-treated wire is shown in **Figure 31(b)**, which shows a coating of gamma phase brass (18) on the high brass core (12). The wire can be plated with a further layer of 10-μm-thick zinc (15), as shown in **Figure 31(c)**, because the nitrogen gas in the heat treatment has a nonoxidizing atmosphere. The brittle gamma phase forms fractured particles (19) in the event of cold drawing of the wire to its final diameter of 0.25 mm, as portrayed in **Figure 31(d)**. However, these particles are encapsulated by the zinc layer (16) on the high brass core (12) because the zinc layer is ductile enough to follow along these particles. The core substrate or its outer surface is also known to add copper content accordingly to the inventor. Therefore, several substrate metals have been considered for this wire design, such as pure copper, brass clad steel, copper-clad steel, brass, brass on copper, brass on copper-clad steel, and brass on brass.[142]

1.9.2.2.5 High tensile strength wires

The electric discharge during the machining process creates electrostatic and electromagnetic forces on the wire electrode. The machined area of the wire electrode is also subjected to a force opposite to the direction of the machining process. During the machining process, all these force factors including the wire vibration can deviate the wire position from its programmed position. This affects the quality and precision of the machining process.[143–146] The deviation of the wire position yields round corners instead of the desired sharp corners.[147] As a result, plain molybdenum or tungsten wires can form because of high tensile strength (>1900 MPa).[61,148] To address the high cost and poor flushability of wires, an improved

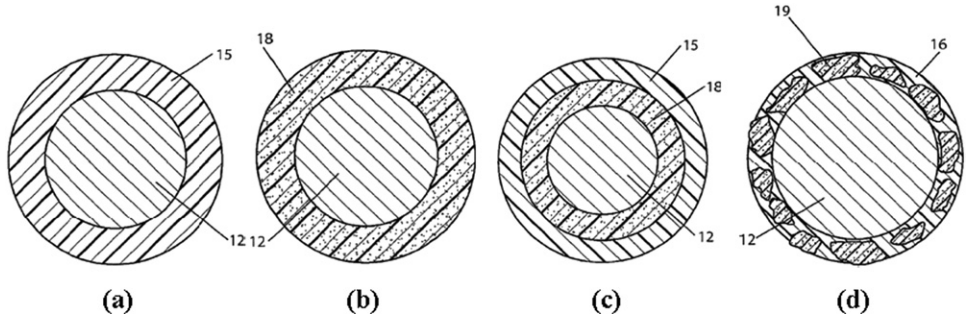


Figure 31 Cross-sectional view of wire.[142]

wire type was developed that is made of a high-strength pearlite steel wire with more than 0.06% carbon content and a layer of copper-free zinc or zinc alloy coating. This yields better precision and accuracy, even under a higher mechanical load.[20,119]

1.9.2.2.5.1 Molybdenum wire

Molybdenum wire is found in very specific applications. To achieve a decent load-carrying capacity in a thin wire, very high tensile strength is required. Moly wire is an excellent candidate in this regard, because it offers both high tensile strength and a high melting point at a diameter of 0.1 mm or less. Unfortunately, this wire suffers from low electrical conductivity and poor flushability. Furthermore, moly wire is very abrasive to power feeds and wire guides, very difficult to auto-thread, and very expensive to produce.[57,72]

1.9.2.2.5.2 Tungsten wire

Tungsten wire is often chosen as a cost-effective option over moly wires for a diameter of 0.05 mm or smaller. In addition, it offers a higher melting point and tensile strength than those of moly wire. Therefore, high-precision machining prefers tungsten wire to moly wire because it requires smaller inner radii within the range of 0.025–0.1 mm. These materials are preferable in high load-carrying capacity requirements, which are not feasible using brass and coated wires at such smaller diameter. However, tungsten and Moly wires are not suitable for thick work because of their numerous shortcomings such as high melting point, limited conductivity, low vapor pressure rating, and slow cutting tendency.[72,149]

1.9.2.2.5.3 MolyCarb wire

For requirements of small wire diameters, a composite wire known as MolyCarb offers competitive advantages. The flushability of moly wire is improved in this type of wire by its graphite and molybdenum oxide mixture coating.[57,150]

1.9.2.2.5.4 Steel core wires

The steel core wire uses a steel core and is typically known by trade names such as Compeed, MicroCut, and MacroCut. The steel core provides excellent tensile strength and ductility, and the intermediate copper layer provides conductivity in addition to a beta phase brass outer layer (**Figure 32**). Steel core wire shows significant resistance to interrupted cuts, breakage for tall workpieces, and poor flushing conditions without compromising exceptional machining performance. However, the steel core has several drawbacks such as straightness issues,

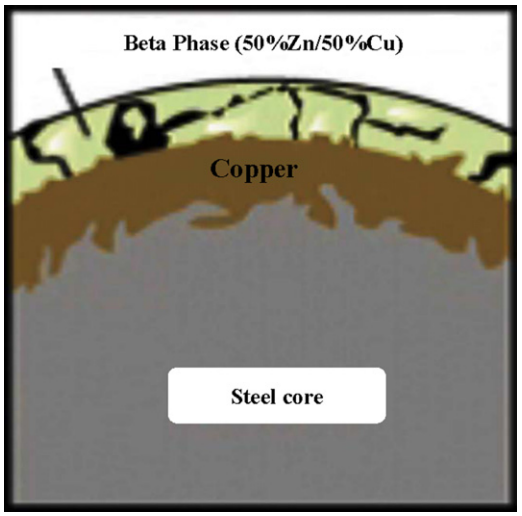


Figure 32 Steel core wire.[57]

high cost, possible damage to scrap choppers, and auto-threadability.[57,140,151]

US patent 4287404-1981 was designed to make the steel core wire effective in the machining process.[111] This invention includes steel core wire with a copper coating and then a coating of a material such as zinc, cadmium, tin, lead, antimony, bismuth, or alloys. This electrode offers good triggering of electrical discharge and reduces the probability of any short circuit. The outcome of this wire electrode is a machining speed higher than that of other conventional electrodes. In addition, Korean patent 10-1-0009194 and US patent US20080245773 offer a wire electrode for electrical discharge machining. These inventions include a steel core coated with copper or a copper–zinc alloy layer of CuZn10–CuZn50.[117] US patent US4686153-87 refers to an electrode wire with a steel core wire coated with conductive metals like copper, along with a surface coating layer of zinc. The average zinc content in the copper–zinc alloy coating is within 10–50 wt%.

The electrode wire (10) in **Figure 33** consists of a copper-clad steel wire (13) with a steel core (11) coated with uniform layers of copper (12) and copper–zinc alloy (14) 0.1–15 μm thick.[121] The wire electrode of US patent 4998552-91 includes a steel core wire with two layers: an inner layer of pure copper and an upper brass layer composed of 50 wt% zinc. The steel core is covered by pure or alloyed copper, which results in higher mechanical strength through a multilayer structure.[20]

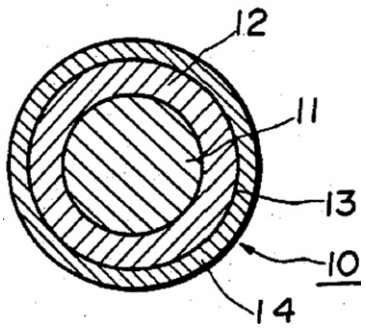


Figure 33 Sectional view of electrode wire.[123]

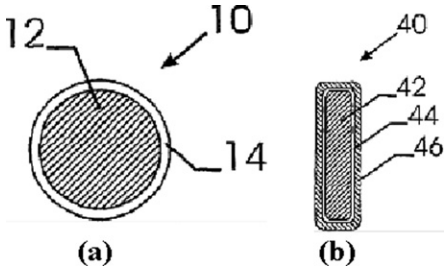


Figure 34 Round and flat electrical discharge machining wires.[152]

US patent 6875943-2005 refers to a high-strength pearlitic steel wire (10) characterized by more than 0.6% carbon and more than 3000 MPa tensile strength. The steel core (12) of the electrode is layered by a copper-free zinc or zinc alloy coating (14). The electrode is effective in applications requiring high-precision machining. Alternatively, a steel strip can be used as shown in **Figure 34(b)**. The wire of the circular cross-section, as shown in **Figure 34(a)**, should preferably have a diameter less than 0.35 mm and can be as low as 0.1, 0.07, or 0.03 mm. Wires with considerably low thickness such as 0.1, 0.05, or 0.02 mm are used as flat wires (40). The pearlitic steel core (42) contributes high strength, whereas the zinc or zinc alloy (Zn–Al alloy) coating (46) offers qualities like heat dissipation and machining functions. The coating with the zinc–aluminum alloy consists of 2 and 10% Al. A rare earth element such as La and/or Ce can be mixed in a proportion between 0.1 and 0.4%. An intermediate layer (44) made of aluminum or silver or alloy, or a nickel or nickel alloy, can be placed between the steel core and zinc or zinc alloy coating. This intermediate layer improves the electrical conductivity of the electrode. In one embodiment of the present invention, an additional layer is formed on the zinc or zinc alloy coating and one of the following materials is used to form this additional layer: graphite or metal oxides like ZnO, TiO_2, $A1_2O_3$, Cr_2O_3, ZrO_2, or Ag.[152]

1.9.2.2.6 Special wires

1.9.2.2.6.1 Abrasive-assisted wire

The EDM wire research currently focuses on achieving higher machining speed and surface integrity. In this regard, US patent 20100012628A1 presents a hybrid wire embedded with electrically nonconducting abrasives, as shown in **Figure 35**. In this process, two-body abrasion is used to improve material removal through electrical erosion. This results in a remarkable

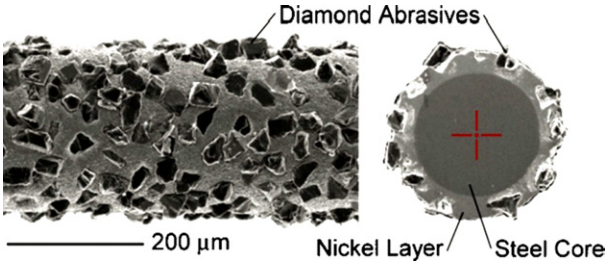


Figure 35 Surface and section of abrasive-assisted wire.[153,154]

improvement in removal rate and ensures better recast surface layer when compared to an equivalent WEDM process. There was negligible recast material present on the machined surfaces. A majority of this process is dedicated to machining steel. However, it may be useful in machining MMCs (such as polycrystalline diamond), which are usually hard to process with WEDM. The abrasion can negatively affect the machining performance, which makes such a process suitable for roughing sequences. Therefore, it is usually developed in a twin-wire machine tool. Although diamond wire can be effective in such work, wire with aluminum oxide abrasives can provide better performance at a lower cost.[153,154]

1.9.2.2.6.2 Hot dip galvanized wire

There are special cases of diffusion-annealed wires with less efficiency because of the nonuniform composition of zinc and alloy.[155] This led to the invention of US patent 20060138091, which involves the hot dip galvanization method. This method is effective for developing a uniform zinc coating on the wire surface.[156] During the first step, the wire goes under a surface-forming process. The coating formation is the next step, and then a second surface-forming process is performed. The final step involves homogeneous heat treatment. This type of wire can prevent harmful contaminants such as disposal of toxic gas and water that are common in traditional methods. In addition, developing a thicker zinc-coated layer eliminates the generation of waste powder and thus improves overall performance of the wire.[157]

1.9.2.2.6.3 Porous electrode wire

Prior studies revealed that the discharge property of diffusion-annealed wire electrodes is improved because of their porous surface infiltrated with graphite.[141] Continuous coating is maintained when the heat-treated wire is cold-drawn. The machining speed increases by at least 15% compared with the traditional zinc-coated wire because of rapid cooling of the wire in a cooling medium. The increased cooling ability is achieved due to the enlarged and porous surface morphology of the wire.[135]

Patent US6482535 refers to a porous EDM wire electrode as shown in **Figure 36**. This invention increases the surface area and inner part of the wire to offer a coated wire for enhanced machining speed. The rapid cooling of the wire is made possible by exposing the inner part to a cooling liquid. The following steps are adopted for this design purpose. First, a core metal with an initial diameter is chosen for a wire. Second, a second metal with a low vaporization point is chosen to perform hot dip galvanization of the core wire by passing it for

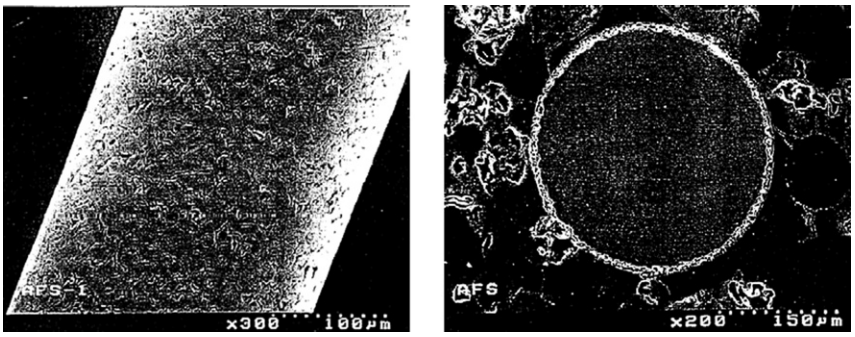


Figure 36 Illustration of the cross-section and surface of porous-coated wire.[103]

a specific time through the molten second metal. Third, an alloy coating by diffusion of both metals is developed, where the second metal is harder and with less elongation than the first metal. Finally, draw the wire with the alloy and coating layers to form a second diameter. This develops cracks in coating layers because of hardness and low elongation of the alloy layer. At this stage, copper or brass with 63–67 wt% copper and 33–37 wt% zinc contents can be alloyed with the first metal. In addition, metals like zinc, aluminum, or tin are viable options to be used as the second metal. The drawing procedure creates cracks in the alloy and coating layers, which characterize the porous nature of the wire.[158]

Similar to many other engineering practices, the selection of an optimal wire for a particular application would most likely be a trade-off for the properties mentioned. As an example, wires with high conductivity are usually low in tensile strength.

1.9.3 White Layer and Heat-Affected Zone

The temperature during electric discharge can go as high as 12 000 °C, which may lead to metallurgical changes in the workpiece surface during the WEDM process.[10] The dielectric fluid fails to remove some of the molten materials, which cool rapidly, and the heat conduction of the workpiece helps it stay hard on the surface. The annealed surface depth is directly determined by the spark energy of the machining process. The depth is reported approximately 50 µm for finish cutting and approximately 200 µm for high cutting rates.[16] In different spark erosion states, a recast layer (white layer) appears with many pockmarks, globules, and cracks of different sizes. Three types of recast layers have been reported. Type 1 represents a single layer less than 10 µm thick, without any distinct feature. Type 2 is an etchable single layer with a thickness of 10–20 µm. Type 3 consists of multiple overlapping hard layers with a thickness of 20 µm or more.[159]

Figure 37 shows the heat-stressed regions of AISI 1050 carbon steel (Figure 37(a)) and titanium alloy grade 5 (Ti6Al4V) materials (Figure 37(b)). Figure 37 illustrates that the heat-stressed regions consist of the white layer and the thermally affected zone.

The white layer forms at the temperature close to the melting point, which is not heated enough to be discharged and flushed away between the wire electrode and workpiece. This layer formation due to unejected and rapidly cooled molten materials during the WEDM process changes the metallurgical structure and properties of the surface layer. The solidified expelled particles may further deposit on the surface before they can be flushed out of the gap. The white layer is heavily contaminated with carbon, which turns it into a structure very different from the base material. The WEDM process expels the hydrocarbons from the electrode and dielectric fluid breakdown and creates extensive carbon particles that penetrate into the molten white layer.

The analysis of microstructure, topography, and composition of AISI 1050 carbon steel was conducted with the aid of scanning electron microscopy (SEM) coupled with energy-dispersive X-ray spectroscopy (EDX), as shown in Figure 38. Table 1 shows a comparative breakdown of the elements present in the AISI 1050 carbon steel base material prior to WEDM and after the white layer formation due to the WEDM. It is evident that there is a significantly high presence of carbon content after the WEDM process when compared to the base material before the WEDM. The heat-affected region lies beneath the white layer. Because this layer is thermally treated at a temperature below the melting point, it is relatively less affected due to the carbon infiltration of the white layer. This heat treatment below the melting point is absorbed by the heat-affected region without causing any alteration in the metallurgical structure of the parent material. Therefore, the WEDM process does not affect the parent material below the heat-affected region.

Figure 39 shows a very high prevalence of micro-cracking in the white layer. These micro-cracks may cause early failure of the material in the case where the white layer becomes too thick and not cleaned through finer finishes or polishing. Furthermore, the micro-cracks are responsible to reduce the corrosion and fatigue resistance of the product. Surface integrity is a major concern for the evaluation of the WEDM performance, and hence the WEDM process should aim to eliminate the formation of such white layers. The micro-cracks form due to the heat stress at the pulse on-time phase of the WEDM cycle. The intensity of micro-cracks is partially determined by the WEDM process, and the thickness of the white layer increases proportionately with the spark energy. The number and size of micro-cracks present in the cavity are also increased due to this process. The affected surface integrity due to the WEDM process can be controlled by the recent power supply technology. The parameters of the power supply that control the surface integrity are voltage, peak current, pulse on-time, pulse off-time, and pulse frequency. Efficient and

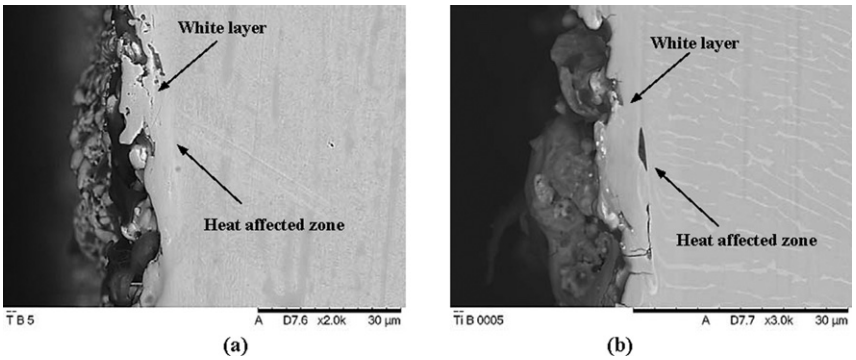


Figure 37 Thermally affected zone of (a) AISI 1050 carbon steel and (b) titanium alloy grade 5.

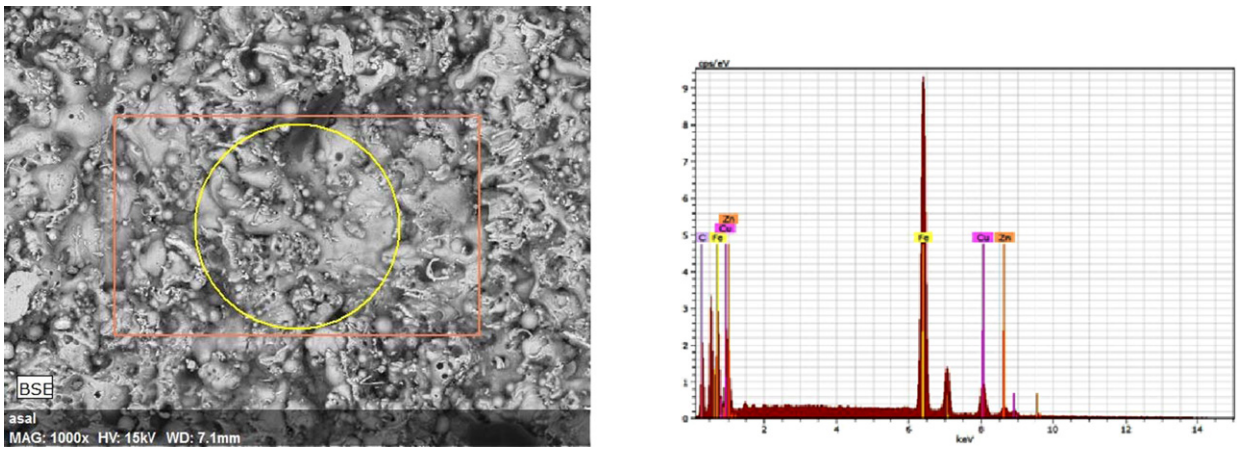


Figure 38 Energy-dispersive X-ray spectroscopy analysis of AISI 1050 carbon steel surface.

Table 1 Elemental analysis of AISI 1050 carbon steel surface before and after wire electrical discharge machining (WEDM)

Element	*C*	*Mn*	*P*	*S*	*Fe*	*Cu*	*Zn*
Before	0.54	0.69	0.03	0.04	98.7	–	–
After WEDM	14.8	–	–	–	63.5	15.8	5.9

balanced control of these power parameters can optimize the WEDM performance and maintain the surface integrity during the stages from roughing to the final finish.

It can be speculated that the intensity of spark energy during the WEDM discharge directly determines the thickness of the white layer and depth of the micro-cracks. The spark energy is gradually lowered from the roughing to the finishing state to reduce the white layer depth and crack formations.

1.9.4 Experimental Details

1.9.4.1 Experimental Design

The design of experiment (DOE) is one of the most powerful tools for experimental planning. It can be used as a great advantage to reduce experimental design changes and cost, as well as to increase design process speed by using statistical methods. The Taguchi method is most important DOE; it provides a simple and effective approach to determine the optimum process parameters. The Taguchi method applies an orthogonal array DOEs and selects a large number of control factors with a reduced number of experiments. In this array, the control factor matrix ensures a balanced contrast between the level and independent distribution among parameters. DOE can play an effective role in identifying impacts of many individual parameters on the system performance. The study of the effect of individual parameter can determine the most influential parameters for the performance measure.[160]

The Taguchi L18 orthogonal array is considered, which involves four machining parameters with three levels and one parameter with two levels, as shown in **Table 2**. Based on an initial investigation, the choice of these parameters is made within the range limit of a running machine without wire breakage.

1.9.4.2 Experimental Setup

A CNC Sodick AQ325L WEDM machine tool is used to conduct the experiment (**Figure 40**). Two different wire electrodes are used for machining titanium alloy grade 5 (Ti6Al4V) and AISI 1050 carbon steel under the machining conditions mentioned in **Table 2**. The characteristics of the two wire electrodes are listed in **Table 3**.

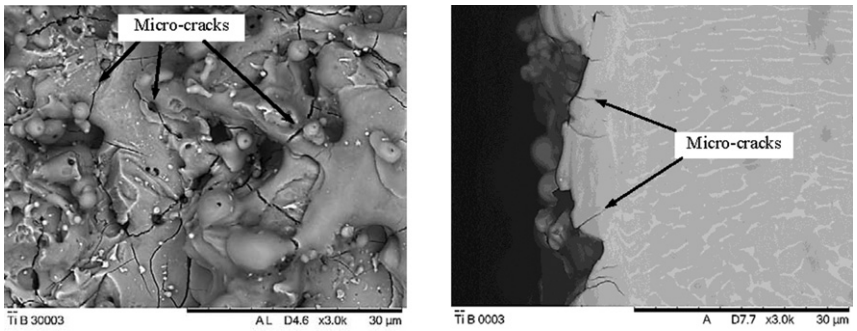


Figure 39 Scanning electron microscopy analysis of (a) Ti6Al4V surface and (b) cross-section illustrating micro-cracks in the white layer.

Table 2 Levels of machining parameters

Machining parameter	*Symbol*	*Units*	*Levels*		
			1	*2*	*3*
Peak current	IP	A	16	17	–
Pulse on-time	T_{on}	µs	0.2	0.3	0.4
Pulse off-time	T_{off}	µs	0.5	0.9	1.3
Wire speed	WS	m min^{-1}	2	4	6
Wire tension	WT	N	3.5	6	10.5

The machining parameters related to the power supply were taken into account to investigate their effect on WLT. These parameters were peak current (IP), pulse width (T_{on}), charging time (T_{off}), wire speed (WS), and wire tension (WT). The machining parameter levels (Table 2) were selected from prior studies, with the working range and levels of the WEDM process parameters following the one-factor-at-a-time method. The other machining parameters were kept constant (main voltage $V_o = 100$ V; spark gap voltage $V_d = 20$ V; flush pressure $= 14$ kgf cm^{-2}; and water resistivity $= 6 \times 10^4$ Ω cm) as recommended by the machine maker.

1.9.4.3 Samples Preparation

The workpiece materials used are titanium alloy grade 5 (Ti6Al4V) and AISI 1050 carbon steel with 100 mm × 100 mm × 20 mm dimensions, which were machined into 5 mm × 5 mm × 20 mm for each specimen. The chemical composition of titanium alloy and was produced by the EDX machine (Table 4) and AISI 1050 carbon steel (Table 1). The electrical resistivity and thermal conductivity of titanium alloy were 17.8×10^{-5} Ω cm and 6.7 W m^{-1} K^{-1}, respectively, and 1.63×10^{-5} Ω cm and 49.8 W m^{-1} K^{-1}, respectively, for AISI 1050 carbon steel.

1.9.4.3.1 Titanium alloy grade 5 (Ti6Al4V) preparation

The samples were ground using P240 (30 s), P320 (40 s), P400 (60 s), P600 (90 s), P800 (120 s), P1200 (180 s), P2500 (210 s), grit silicon carbide paper with a pressure of approximately 9 N, counter rotation of 400 rpm, and plenty of coolant water. Then, the samples were cleaned in ethanol at 30 °C for 15 min using an ultrasonic agitator between the steps. Then, the samples were polished using 9-, 6-, 3-, and 1-µm diamond suspension liquid under 6 N pressure with 7 min of counter rotation at 400 rpm. This was repeated until the surface become smooth (verified with optical microscope (OM) in interference contrast mode).

After polishing, 50 ml of oxide polishing suspension (OPS) with 10 ml H_2O_2 were used for final polishing with 400 rpm counter rotation for 5 min. This was repeated until the microstructure was visible, typically two or three times (checked with OM). Then, the sample surface was washed with dishwashing liquid and water, flushed with ethanol, and dried with a hair dryer. Finally, the samples were etched with Kroll's reagent 5–10 s. The samples were then cleaned in an ultrasonic agitator in acetone at 30 °C for 15 min. Then, samples were carefully rinsed, cleaned in distilled water, and dried to remove contaminants to acquire a uniform surface.

1.9.4.3.2 AISI 1050 carbon steel preparation

The samples were ground using 120 SiC abrasives for stock removal requirements. Once planarity and the area of interest are obtained, one of the standard procedures such as P220 (30 s), P360 (30 s), P800 (30 s), P1200 (60 s), P2400 (90 s), or P4000 (120 s) is applied using grit silicon carbide paper with pressure of approximately 10 N, counter rotation of 400 rpm, and plenty of coolant water. Then, the samples were cleaned in ethanol at 30 °C for 15 min using an ultrasonic agitator between the steps. Then, the samples were roughly polished using 6 and 3 µm diamond suspension liquid with pressure of 6 N, with 5 min of counter rotation at 400 rpm. It is repeated until the surface is smooth (checked with OM in interference contrast mode).

Finally, 0.05 µm alumina suspension liquid with pressure of 5 N was used for the final polishing at 400 rpm counter rotation for 5 min. It was repeated until the microstructure was distinctly visible (checked with OM). Then, the samples surface was washed with distilled water, flushed with ethanol, and dried with a hair dryer. The samples were then cleaned in an ultrasonic agitator in acetone at 30 °C for 15 min. Then, the samples were carefully rinsed, cleaned in ethanol, and dried to remove contaminants to acquire a uniform surface.

1.9.4.4 Surface Characterization

Microscopic surface examinations after each grinding and finishing step were performed using Olumpus BX 61 light OM.



Figure 40 Wire electrical discharge machining machine.

Table 3 Wire electrodes properties

Wire	*Material composition*		*Tensile strength*	*Elongation*	*Electric conductivity*
Brass	CuZn40		1000 N mm^{-2}	1.5%	22% IACS
Coated	Core: CuZn35	Coating: CuZn60	875 N mm^{-2}	2%	20% IACS

Table 4 Chemical compositions of titanium alloy (grade 5)

Element	*Al*	*V*	*Fe*	*O*	*C*	*Ti*
Weight, wt (%)	5.65	3.93	0.13	0.11	0.08	90.1

A SEM combined with EDX (Hitachi tabletop microscope TM3030) was used to examine the surface microstructural and topographical characteristics and WLT of the machined part.

1.9.5 Experimental Results and ANFIS Modeling

1.9.5.1 Experimental Results

The average WLT was calculated for three different measurements at three different places using an image-processing program (ImageJ). 36 Sets of data were used based on DOEs for building and training the ANFIS model, as shown in Table 5. Another four sets were used in a testing step after the training to verify the performance of estimating WLT values.

Table 5 Measured white layer thickness (WLT, in μm) of Ti6Al4V at different machining conditions

Machining parameters					*Performance factors*			*Performance outcomes; WLT (μm)*							
IP (A)	*T_{on} (μs)*	*T_{off} (μs)*	*WS (m min^{-1})*	*WT (N)*	*E_s (μJ)*	*DF (%)*	*F (HZ)*	*Using brass wire*				*Using coated wire*			
								1	*2*	*3*	*Average*	*1*	*2*	*3*	*Average*
16	0.2	0.5	3	3.5	64	28.6	1 428 571	8.96	9.18	8.04	8.73	6.16	4.75	6.07	5.66
		0.9	7	6.0	64	18.2	909 091	7.88	7.38	8.12	7.79	6.28	5.23	3.38	4.96
		1.3	11	10.5	64	13.3	666 667	7.25	6.89	7.14	7.09	5.27	3.52	4.25	4.35
	0.3	0.5	7	3.5	96	37.5	1 250000	9.31	10.14	9.23	9.56	9.93	11.78	8.56	10.09
		0.9	11	6.0	96	25.0	833 333	8.74	7.56	8.47	8.26	7.02	8	7.56	7.53
		1.3	3	10.5	96	18.8	625 000	8.11	7.51	7.58	7.73	6.02	5.58	6.77	6.12
	0.4	0.5	3	6.0	128	44.4	1 111 111	12.36	12.94	11.71	12.34	16.6	16.19	16.25	16.35
		0.9	7	10.5	128	30.8	769 231	11.07	11.41	10.78	11.09	12.25	12.32	13.37	12.65
		1.3	11	3.5	128	23.5	588 235	9.16	10.88	10.17	10.07	11.1	10.65	11.44	11.06
17	0.2	0.5	11	10.5	68	28.6	1 428 571	16.34	16.05	14.53	15.64	7.73	6.08	5.98	6.60
		0.9	3	3.5	68	18.2	909 091	12.27	12.57	13.02	12.62	6.43	5.32	5.37	5.71
		1.3	7	6.0	68	13.3	666 667	9.5	10.72	9.72	9.98	5.56	5.07	4.96	5.20
	0.3	0.5	11	6.0	102	37.5	1 250 000	21.27	20.04	19.39	20.23	11.09	12.68	10.68	11.48
		0.9	3	10.5	102	25.0	833 333	17.79	18.32	16.68	17.60	10.33	11.72	9.78	10.61
		1.3	7	3.5	102	18.8	625 000	16.75	14.93	15.14	15.61	8.73	9.32	7.85	8.63
	0.4	0.5	7	10.5	136	44.4	1 111 111	27.14	26.53	25.28	26.32	20.57	19.38	19.86	19.94
		0.9	11	3.5	136	30.8	769 231	22.93	21.51	20.24	21.56	14	17.58	15.47	15.68
		1.3	3	6.0	136	23.5	588 235	19.84	18.78	17.37	18.66	13.48	13.01	11.65	12.71

1.9.5.2 ANFIS Model Development

The neuro-fuzzy system gathers the benefits of fuzzy systems and offers an explicit and understandable representation of knowledge. However, the neural network involves implicit knowledge that is obtained through learning. The fusion of the concepts of fuzzy logic and neural networks may clarify cognitive uncertainties in manner similar to that of humans. The computational steps involved in the fuzzy-neural system are as follows. First, it builds a fuzzy-neuron based on the concept of biological neuronal morphologies, and then it applies a learning mechanism, as shown in Figure 41. This results in three steps in the fuzzy neural process[161,162]:

- Biological neuron-inspired construction of fuzzy neural models.
- Fuzziness introduced in neural network using synaptic connection models.
- Development of learning algorithms (algorithm to update the synaptic weights).

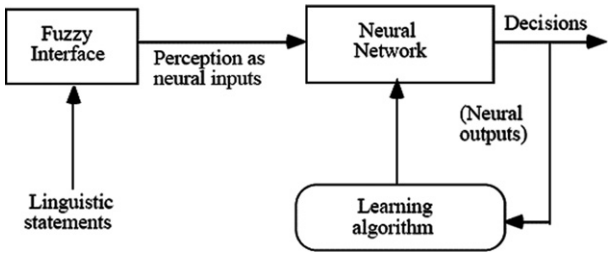


Figure 41 Fuzzy-neural system model.[161]

ANFIS was constructed on the MATLAB platform, and the training data set had 18 readings for each wire electrode, as listed in Table 5. ANFIS was trained using different membership functions. For each wire electrode, the ANFIS model was created using two membership functions for the peak current and three membership functions for other parameters (pulse on-time, pulse off-time, wire speed, and wire tension). The generalized bell-shaped membership functions (gbellmf) yields the minimum training error, which is chosen for training the ANFIS model in this study. The fuzzy rule architecture of the ANFIS involves 18 fuzzy rules produced by the input–output data set following the Sugeno fuzzy model. The training entails 50 cycles of learning using 18 performance measure values. The learning was conducted with an average error of 1.43×10^{-5} and 1.04×10^{-5} for brass and wire electrode with coating, respectively.

ANFIS uses five layers in the network to conduct several steps for fuzzy inference: (1) input parameters; (2) fuzzy set database layer; (3) fuzzy rule base construction; (4) decision-making; and (5) output defuzzification. For simple interpretation of each input variable, we considered two rules and two linguistic values, as shown in Figure 42.

Layer 1: This layer outputs the degree to which the given input conforms with the linguistic label associated with the node. The linguistic terms are represented using gbellmf because of the nonlinear relationship between the cutting parameters and machining performance (Figure 43(a)). A generalized bell MF is specified by three parameters (a, b, c), as shown in

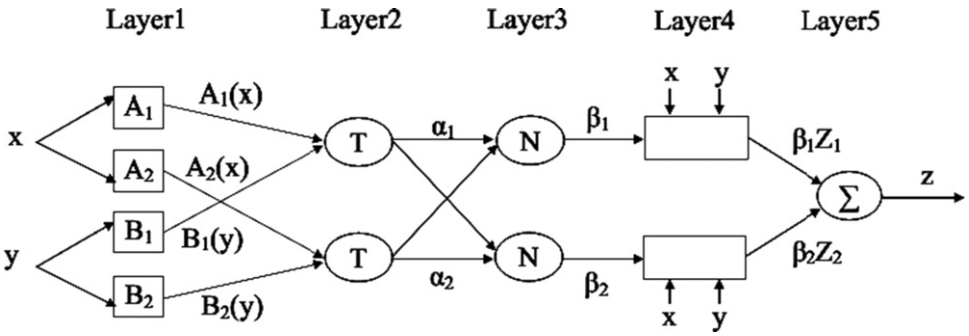


Figure 42 Adaptive neuro-fuzzy inference system architecture for a two-input Sugeno fuzzy model.[161]

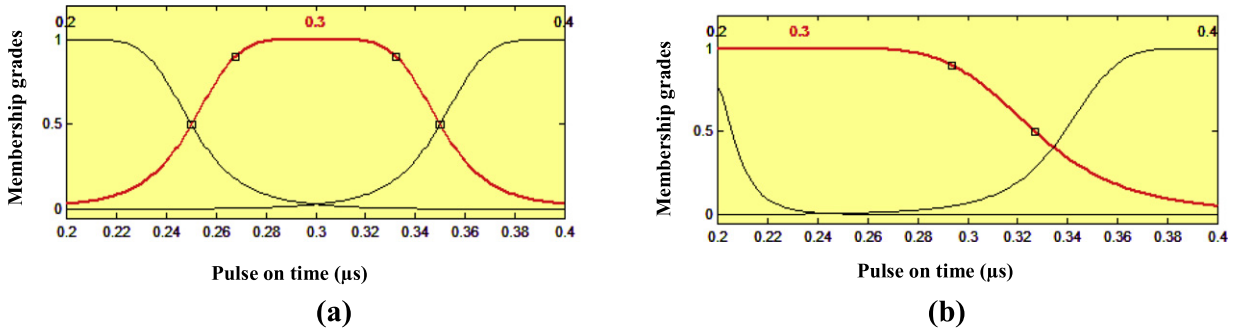


Figure 43 Initial and final membership function of pulse on-time: (a) initial membership function and (b) final membership function.

eqns [4] and [5]. Here, parameter b is usually positive and used to control the slope of the crossover point. Moreover, parameters a and c control the center and width of the MF.

$$A_i(x) = \frac{1}{1 + \left|\frac{x - c_{i1}}{a_{i1}}\right|^{2b_{i1}}} \quad [4]$$

$$B_i(y) = \frac{1}{1 + \left|\frac{y - c_{i2}}{a_{i2}}\right|^{2b_{i2}}} \quad [5]$$

Here (a_{i1}, a_{i2}, b_{i1}, b_{i2}, c_{i1}, c_{i2}) are the model parameters.

With the change in the parameter values, the bell-shaped functions differ consequently (Figure 43(b)). This results in

Table 6 Comparison of measured and predicted white layer thickness (WLT) for Ti6Al4V using brass and coated wire electrodes

Machining parameters					*Using brass wire*			*Using coated wire*		
IP (A)	*T_{on} (μs)*	*T_{off} (μs)*	*WS (m min^{-1})*	*WT (N)*	*Measured WLT*	*Predicted (ANFIS)*	*Error (%)*	*Measured WLD*	*Predicted (ANFIS)*	*Error (%)*
16	0.25	1.1	5	5	13.01	12	7.76	9.11	9.66	6.04
	0.35	0.7	9	8	10.12	10.5	3.75	13.34	12.1	9.30
17	0.25	1.1	5	5	14.23	15.6	9.63	10.03	9.73	2.99
	0.35	0.7	9	8	22.79	23.5	3.12	20.31	18.2	10.39
					Average error		6.07	Average error		7.18

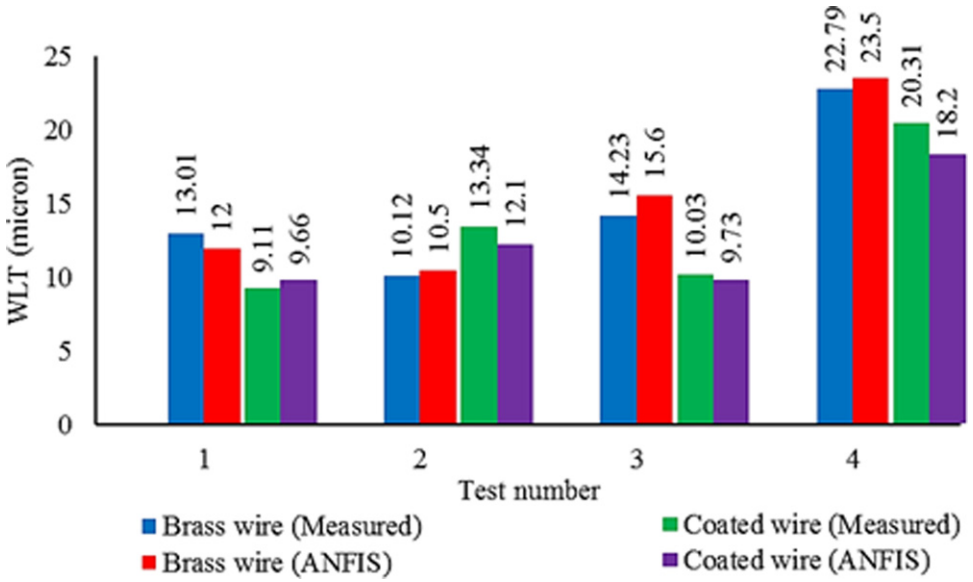


Figure 44 Measurement vs. predicted white layer thickness (WLT) for Ti6Al4V using brass and coated wire electrodes.

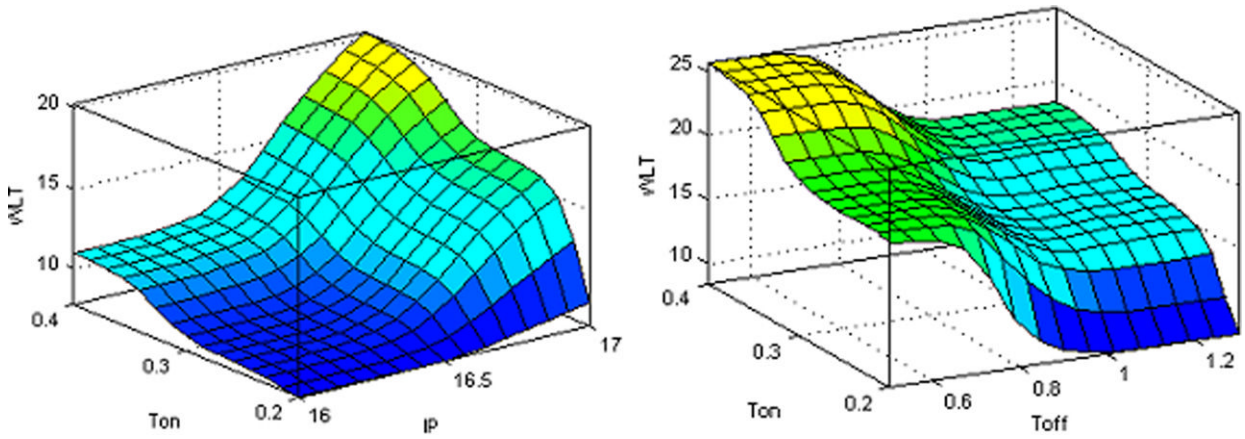
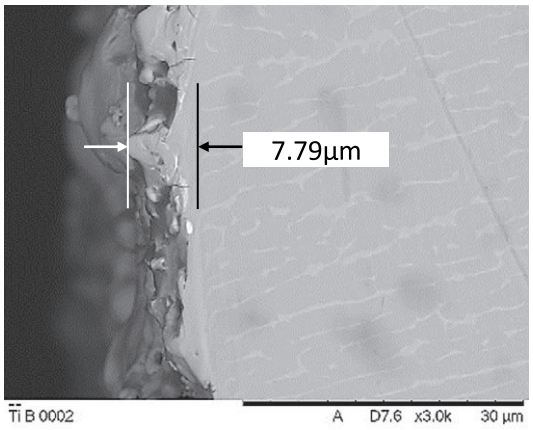
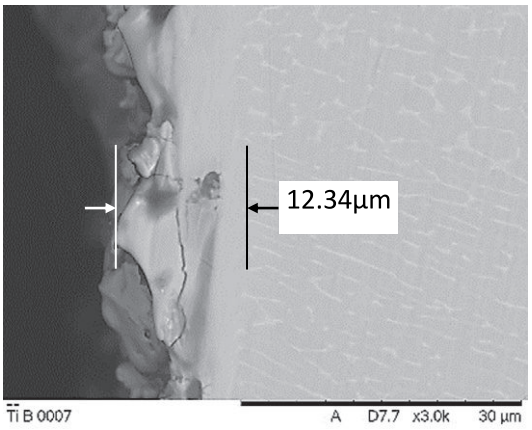
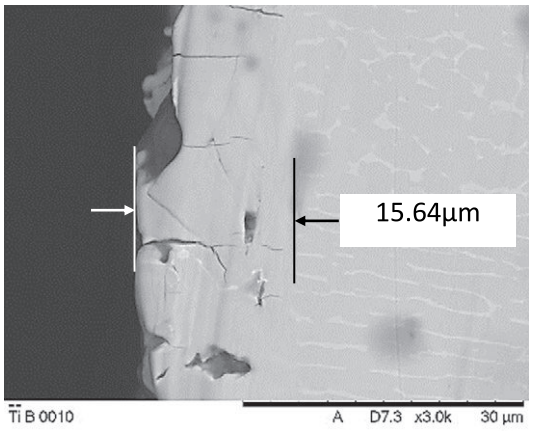
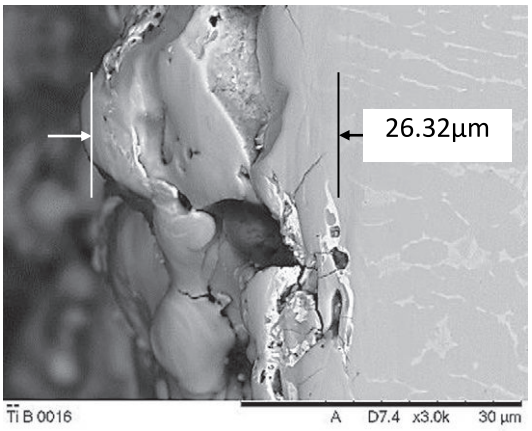


Figure 45 Adaptive neuro-fuzzy inference system model of Ti6Al4V white layer thickness (WLT) in relation to change of electrical parameters of brass wire electrode.

Table 7 The white layer thickness of Ti6Al4V at different peak current and pulse on-time using brass wire

IP	T_{on}	
	0.2	*0.4*
16		
17		

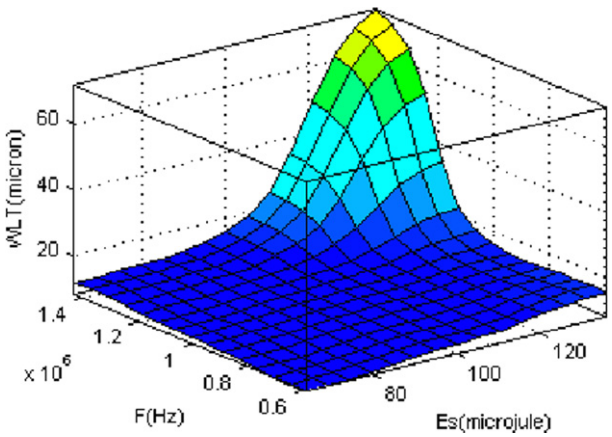


Figure 46 Adaptive neuro-fuzzy inference system model of Ti6Al4V white layer thickness (WLT) in relation to spark energy and pulse frequency of brass wire electrode.

multiple forms of membership functions on linguistic labels A_i and B_i. The parameters of this layer are known as the principal parameters.

Layer 2: Each neuron in layer 2 estimates the strength of firing or activating the associated rule. The outputs from the top and bottom nodes are as follows:

$$\alpha_1 = A_1(x) \times B_1(y) = A_1(x) \wedge B_1(y) \quad [6]$$

$$\alpha_2 = A_2(x) \times B_2(y) = A_2(x) \wedge B_2(y) \quad [7]$$

The two nodes of this layer are labeled by T, because other t-norms are selected to model the logical and the operator. These nodes are termed as rule nodes.

Layer 3: Individual neurons of this layer estimate the normalization of the firing levels with respect to the sum of firing levels. The outputs of the top and bottom neurons are the normalized firing level of the first and second roles, respectively.

$$\beta_1 = \frac{\alpha_1}{\alpha_1 + \alpha_2} \quad [8]$$

$$\beta_2 = \frac{\alpha_2}{\alpha_1 + \alpha_2} \quad [9]$$

Layer 4: Each neuron of this layer estimates the product of the normalized firing levels with the outputs of the individual associated rule.

$$\beta_1 Z_1 = \beta_1(a_1 x + b_1 y) \quad [10]$$

$$\beta_2 Z_2 = \beta_2(a_2 x + b_2 y) \quad [11]$$

Layer 5: Neurons in this layer estimate the total system output by adding all incoming values.

$$Z = \beta_1 Z_1 + \beta_2 Z_2 \quad [12]$$

If a crisp training set $((x^k, y^k), k=1,\ldots, K)$ is known, then descent type methods can be used to train the parameters of the hybrid neural net. The error function for pattern k is given by:

$$E_k = (O^k - Z^k)^2 \quad [13]$$

where O^k is the desired output and Z^k is the estimated output by the neural network.

1.9.5.3 ANFIS Model Verification

Four random readings were considered in the testing data set. The measured WLT values versus predicted values from the ANFIS model are listed in **Table 6**. The plot of four measured WLT values versus predicted values from the ANFIS model is presented in **Figure 44**. This figure presents a comparison of the measured and predicted WLT of Ti6Al4V using brass and coated wire electrodes. There are also proper agreements between the experimental and model predicted values. This close agreement clearly shows that the ANFIS model is useful for predicting and optimizing the WLT under consideration.

To evaluate the fuzzy model, the percentage error E_i and average percentage error E_{av} defined in eqns [14] and [15], respectively, were used.

$$E_i = \frac{|T_m - T_p|}{T_m} \times 100 \quad [14]$$

$$E_{av} = \frac{1}{m}\sum_{i=1}^{m} E_i \quad [15]$$

Here, E_i represents the percentage error for the sample number i, T_m is the measured value, T_p is the predicted value, $i=1,2,3$ denotes the sample number, and E_{av} represents the average percentage error of m sample data.

The obtained average percentage errors are 6.07 and 7.18 for brass and coated wires, respectively. These low error values indicate that the ANFIS-predicted WLT results are almost similar to the actual measurements from the experiment. The error values suggest that the proposed model can predict and optimize the WLT satisfactorily.

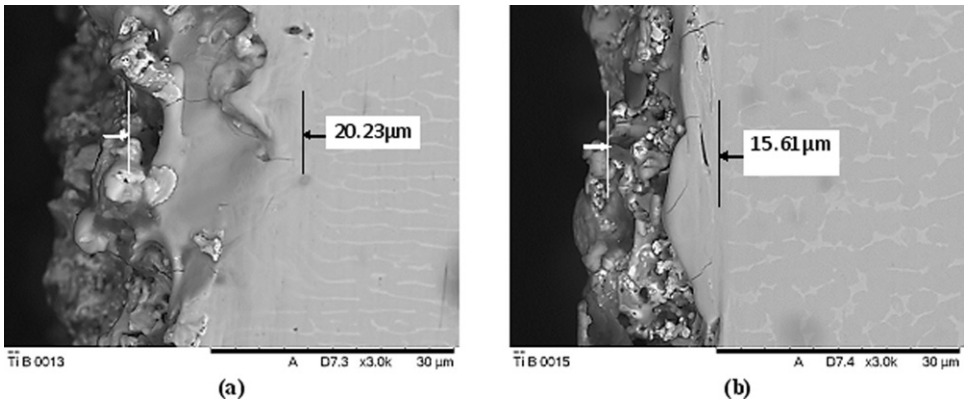


Figure 47 Scanning electron microscopy micrograph of Ti6Al4V white layer thickness using brass wire electrode: (a) low level of pulse off-time and (b) high level of pulse off-time.

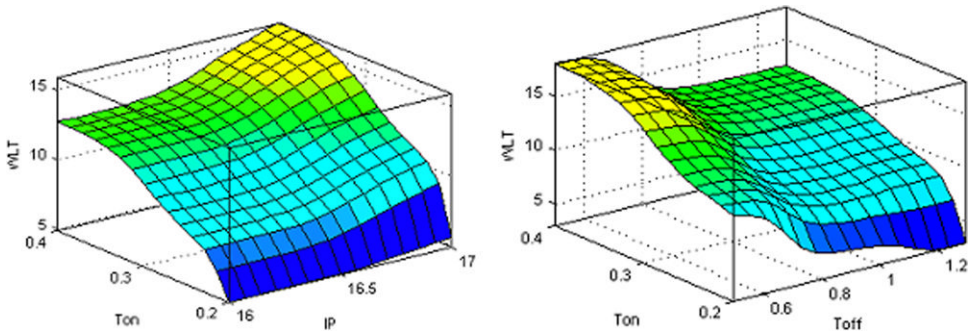
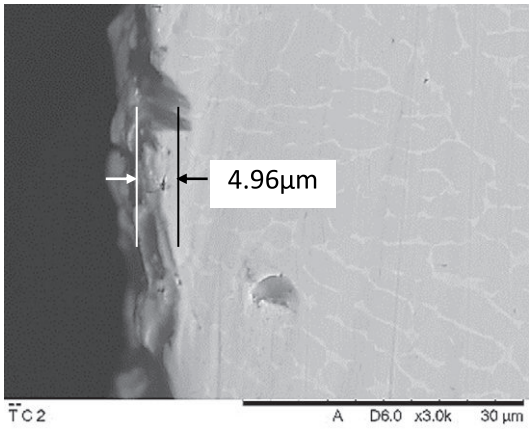
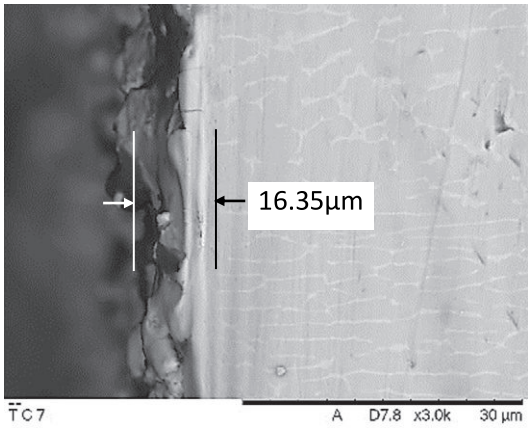
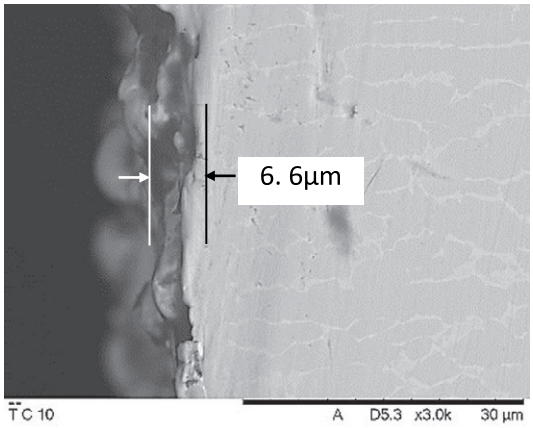
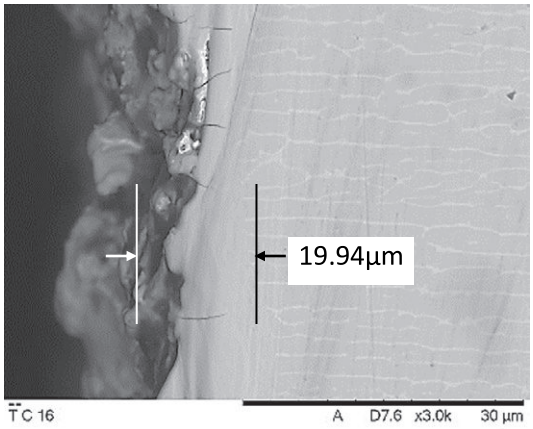


Figure 48 Adaptive neuro-fuzzy inference system model white layer thickness (WLT) in relation to electrical parameter changes of the coated wire electrode.

Table 8 The white layer thickness of Ti6Al4V at different peak current and pulse on-time using brass wire

IP	T_{on}	
	0.2	*0.4*
16		
17		

1.9.6 ANFIS Modeling Results and Discussion

1.9.6.1 Effect of Electrical Parameters on WLT

This section introduces the effect of electrical parameters (pulse on-time, peak current, and pulse off-time) on the WLT of titanium alloy grade 5 (Ti6Al4V) using brass and coated wire electrodes. In addition, the effect of discharge energy and pulse frequency on the WLT was also introduced.

1.9.6.1.1 Brass wire electrode

Figure 45 introduces the effects of the electrical parameters on the WLT of Ti6Al4V based on the ANFIS models of brass wire electrode. **Figure 45** shows that pulse on-time, peak current, and pulse off-time have great effects on WLT, whereby the WLT increases with increasing pulse on-time and peak current but decreases with the increase of pulse off-time.

The same conclusion was obtained from the experimental work, as shown in **Table 7**. It introduces SEM micrographs at $\times 3000$ magnification for the WLT of Ti6Al4V at different pulse on times and peak currents using brass wire electrode. This micrograph verifies that the maximum of WLT is at the highest levels of peak current and pulse on-time. The minimum WLT occurs at the lowest values of pulse on-time and peak current. Increasing peak current and pulse on-time increase the spark energy, as shown in eqn [1]. Hence, the heat produced on the machined surface is increased further, resulting in a larger WLT on the workpiece. Moreover, **Figure 46** and **Table 5** show that during WEDM, the WLT of Ti6Al4V is 3 µm at 40 µJ spark energy and the WLT increases 3 µm linearly for each increase of 20 µJ spark energy at the same duty factor. In addition, the increase of pulse off-time decreases the WLT, as shown in **Figure 46**. This is because the increase of pulse off-time decreases the pulse frequency (eqn [2]). The increase in pulse frequency increases the heat generated on the workpiece surface; therefore, the WLT increases. The same conclusion was obtained from the experimental work, for which the WLT at a low level of pulse off-time ($T_{off}=0.5$ µm or $F=1\,250\,000$ HZ) is 20.23 µm (**Figure 47(a)**) and that at a high level of pulse off-time ($T_{off}=1.3$ µm or $F=625\,000$ HZ) equals 15.61 µm (**Figure 47(b)**). The smallest values of peak current and pulse on-time with the biggest values of pulse off-time appear to be the best choices to obtain a less thick white layer.

1.9.6.1.2 Coated wire electrode

Figure 48 introduces the effects of the electrical parameters on the WLT based on the ANFIS models of coated wire electrode. Figure 48 shows that peak current, pulse on-time, and pulse off-time have a significant impact on WLT. That is, the WLT increases with the increase of the peak current and pulse on-time but decreases with the increase of the pulse off-time.

The same conclusion was obtained from the experimental work, as shown in Table 8. Table 8 introduce SEM micrographs at $\times 3000$ magnification of the WLT at different peak current and pulse on-time using a coated wire electrode. This micrograph verifies that the maximum of WLT is at the highest levels of peak current and pulse on-time, and the least WLT is at the lowest values of pulse on-time and peak current. Moreover, Figure 49 and Table 5 show that during WEDM, a thin WLT of 2 μm at 40 μJ spark energy is produced, and the WLT increases 2 μm linearly for each increase of 20 μJ spark energy at the same duty factor. Moreover, the decrease of pulse frequency decreases the WLT, as shown in Figure 49. The same conclusion was obtained from the experimental work. Here, the WLT at a low level of pulse off-time ($T_{off}=0.5$ μm or $F=1\,250\,000$ HZ) is 11.48 μm (Figure 50(a)), and of high level of pulse off-time ($T_{off}=1.3$ μm or F=625 000 HZ) is equal 8.63 μm (Figure 50(b)). The smallest values of peak current and pulse on-time with the biggest values of pulse off-time appear to be the best choices to obtain a less thick white layer.

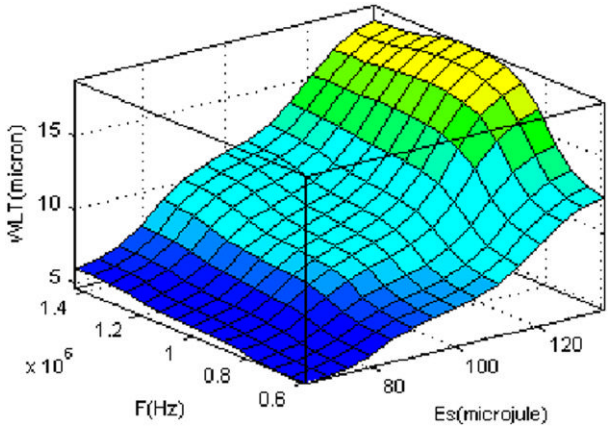


Figure 49 Adaptive neuro-fuzzy inference system model white layer thickness in relation to spark energy and pulse frequency of coated wire electrode.

1.9.6.2 Effect of Wire Electrode Parameters on WLT

This section shows the effects of the wire electrode parameters on the WLT of Ti6Al4V based on the ANFIS models of brass

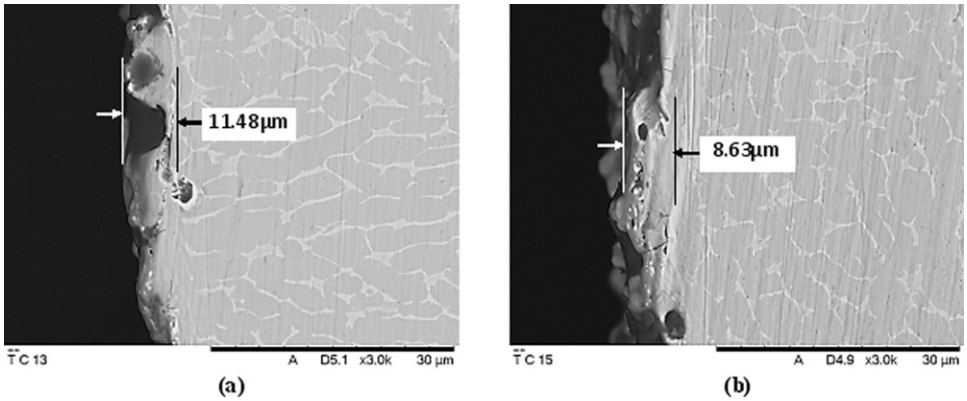


Figure 50 Scanning electron microscopy micrograph of the white layer thickness using coated wire electrode: (a) low level of pulse off-time and (b) high level of pulse off-time.

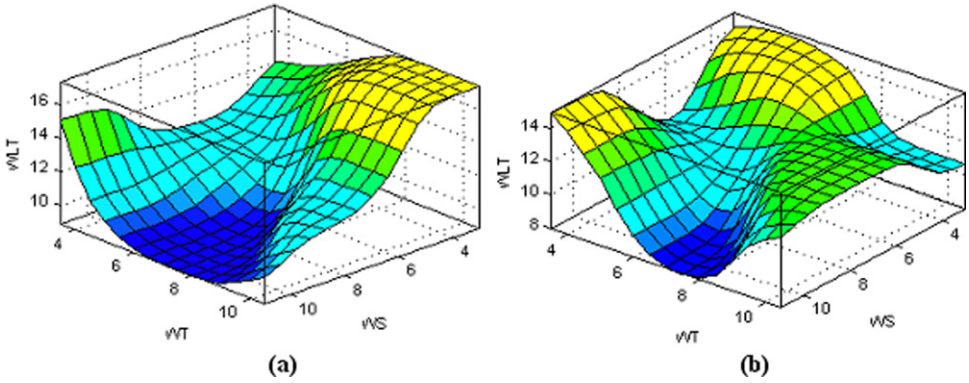


Figure 51 Adaptive neuro-fuzzy inference system model white layer thickness in relation to wire speed and tension parameters change: (a) using brass electrode and (b) using coated wire electrode.

and coated wire electrodes. Figure 51 shows that wire speed has a considerable effect on WLT, but wire tension has a minor effect on WLT. In both cases (brass and coated wires), the WLT decreases with the increase of the wire speed. This is because when the wire speed increases, fresh wire is introduced to the cutting zone, leading to stable cutting by preventing wire rupture. This type of electrode has a considerable effect on maintaining surface integrity. Figures 52(a) and 52(b) show the surface micrograph using brass and coated wire electrodes, respectively, at the same machining parameters. In addition, Figures 53(a) and 53(b) show the WLT using brass and coated wire electrodes, respectively, at the same machining parameters. It can be seen from Figure 52 that the surface finish using coated wire is better than using

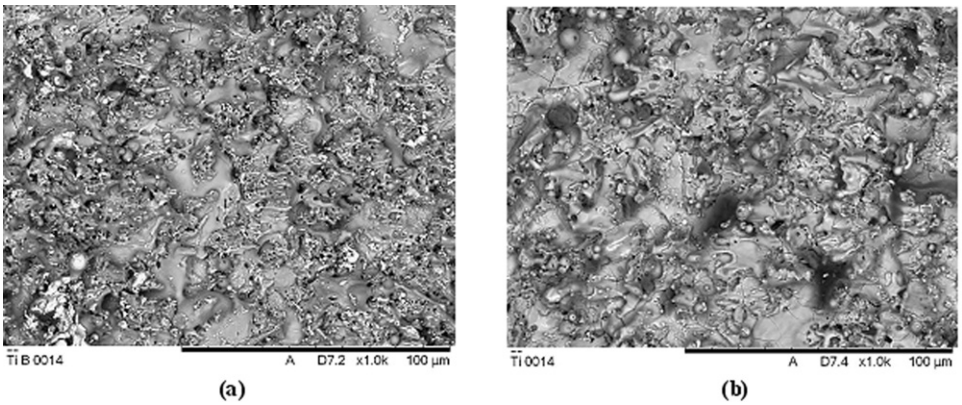


Figure 52 Scanning electron microscopy micrograph of Ti6Al4V surface using (a) brass wire and (b) coated wire electrode.

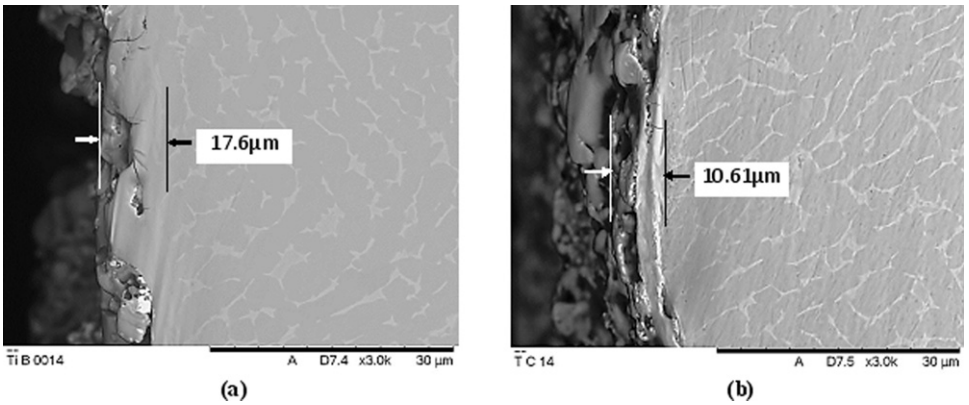


Figure 53 Scanning electron microscopy micrograph of Ti6Al4V white layer thickness using (a) brass wire electrode and (b) coated wire electrode.

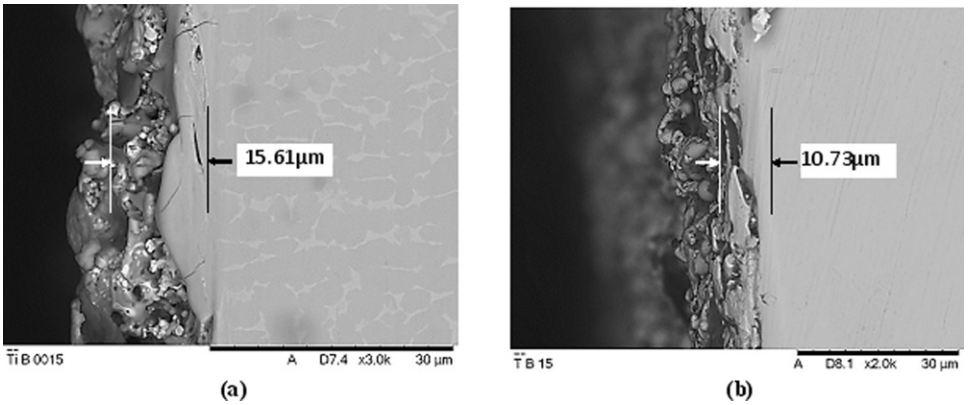


Figure 54 Cross-section of Ti6Al4V and AISI 1050 carbon steel illustrating the thickness and micro-cracks of the white layer in (a) Ti6Al4V titanium alloy and (b) AISI 1050 carbon steel.

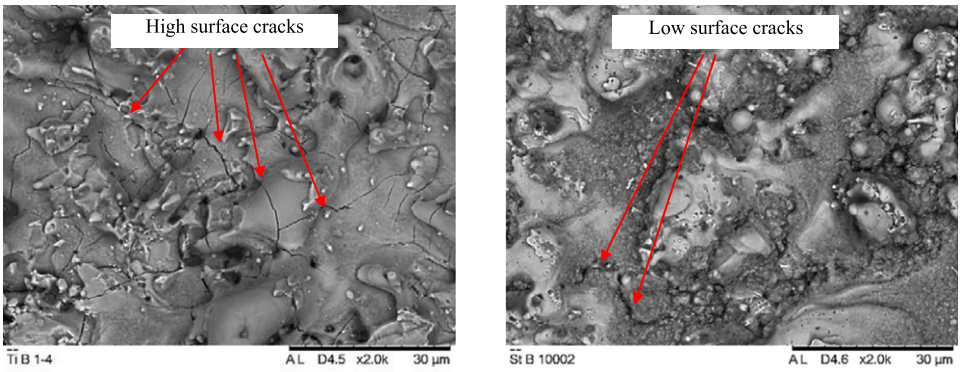


Figure 55 Scanning electron microscopy micrograph of Ti6Al4V and AISI 1050 carbon steel surface illustrating the surface finish and micro-cracks of the white layer of (a) Ti6Al4V titanium alloy and (b) AISI 1050 carbon steel.

a brass wire electrode. Moreover, the WLT obtained using coated wire (**Figure 53(b)**) is smaller than that using brass wire (**Figure 53(a)**).

1.9.6.3 Effect of Workpiece Parameters on WLT

The thermal conductivity of the work metal plays an important role in the surface integrity of WEDM. Metals with high thermal conductivity will usually yield a smaller WLT and less micro-cracking than a lower conductive material. This is because of the higher energy dissipation over the surface of the higher conductive materials. From the experimental work, AISI 1050 carbon steel material has a thinner white layer with less cracks because of its high thermal conductivity and ductile nature when compared to titanium alloy grade 5 (Ti6Al4V), as shown in **Figures 54** and **55**. **Figures 54(a)** and **54(b)** introduce the WLT SEM micrograph of Ti6Al4V and AISI 1050 carbon steel, respectively, at the same machining conditions (IP = 17 A, T_{on} = 0.3 µs, T_{off} = 1.3 µs, WS = 7 m min^{-1}, WT = 3.5 N) using a brass wire electrode. The WLT of Ti6Al4V equals 15.61 µm, and that of AISI 1050 carbon steel equals 10.73 µm. **Figures 55(a)** and **55(b)** introduce the SEM micrograph of Ti6Al4V and AISI 1050 carbon steel surface, respectively, during the same machining conditions (IP = 16 A, T_{on} = 0.2 µs, T_{off} = 0.5 µs, WS = 3 mm min^{-1}, WT = 3.5 N) using a brass wire electrode. There are many more surface cracks in Ti6Al4V than in AISI 1050 carbon steel. In contrast, material with low thermal conductivity cannot act fast enough to dissipate the energy at the neighboring areas, as shown in **Figures 54** and **55**. This allows the spark energy to remain longer, resulting in a thicker white layer with more cracking.

1.9.7 Conclusions

This study investigates the effect of cutting parameters on the WLT of Ti6Al4V and AISI 1050 carbon steel workpieces using brass and coated wire electrodes. Based on these experimental investigations, the peak current, pulse on-time, pulse off-time, and workpiece material are the most influential parameters affecting the WLT formation. The wire speed has a considerable effect, but wire tension has a minor effect on the WLT. A successful empirical model is developed with the aid of ANFIS to predict the relationship between machining parameters (IP, T_{on}, T_{off}, WS, and WT) and the WLT. The training data set for the ANFIS model is built using 36 measured WLT values under different cutting conditions. Four values were used as testing data to verify the models where the average errors were 6.07% using brass wire and 7.18 using coated wire electrode. These results indicate that the ANFIS model with gbellmf is accurate and can be used to predict WLT in WEDM. The ANFIS model is found to be an efficient predictor because of its ability to capture complex nonlinearities and interactions. The ANFIS models settles the peak current, pulse on-time, and pulse off-time as the most influential parameters affecting the WLT. The wire tension and wire speed have minor effect on the WLT. The ANFIS models show that minimum WLT is achieved at the lowest levels of peak current and pulse width, and with the highest level of pulse off-time. In addition, the application of the ANFIS model in the analysis of results in WEDM reveals the following conclusions:

- Low pulse on-time (0.2 µs), low peak current (16 A), high pulse off-time (1.3 µs), high wire speed (11 m min^{-1}), and high wire tension (10.5 N) lead to a smaller WLT for the specific test range.
- By applying the proposed ANFIS, it appears that using a lower spark setting with higher pulse cycle settings will reduce the chip size and produce better flushing. This could lead to less WLT.
- At the same duty factor, the WLT of Ti6Al4V using brass wire equals 3 µm at 40 µJ spark energy and increases 3 µm linearly for each increase of 20 µJ spark energy. WLT using coated wire equals 2 µm at 40 µJ spark energy and increases 2 µm linearly for each increase of 20 µJ spark energy.
- Using a coated wire electrode is better than using brass wire for smaller WLT.
- High thermally conductive metals (AISI 1050 carbon steel) typically have a smaller WLT and less micro-cracking than those of a less conductive material (Ti6Al4V) in WEDM.

See also: 1.11 Micromachining

References

1. Sommer, C.; Sommer, S. *Complete EDM Handbook*; Reliable EDM: Houston, TX, 2013.
2. Mohri, N.; Fukuzawa, Y.; Tani, T.; Sata, T. Some Considerations to Machining Characteristics of Insulating Ceramics-Towards Practical Use in Industry. *CIRP Ann. – Manuf. Technol.* **2002**, *51* (1), 161–164. Available from: http://dx.doi.org/10.1016/S0007-8506(07)61490-5 (accessed March 1, 2016).
3. Kozak, J.; Rajurkar, K. P.; Chandarana, N. Machining of Low Electrical Conductive Materials by Wire Electrical Discharge Machining (WEDM). *J. Mater. Process. Technol.* **2004**, *149*, 266–271.
4. Cheng, X.; Yang, X. H.; Huang, Y. M.; Zheng, G. M.; Li, L. Helical Surface Creation by Wire Electrical Discharge Machining for Micro Tools. *Robot. Comput.-Integr. Manuf.* **2014**, *30* (3), 287–294. Available from: http://dx.doi.org/10.1016/j.rcim.2013.10.010 (accessed March 1, 2016).
5. Kanlayasiri, K.; Boonmung, S. Effects of Wire-EDM Machining Variables on Surface Roughness of Newly Developed DC 53 Die Steel: Design of Experiments and Regression Model. *J. Mater. Process. Technol.* **2007**, *192–193*, 459–464. Available from: http://dx.doi.org/10.1016/j.jmatprotec.2007.04.085 (accessed March 1, 2016).
6. Huang, Y.; Ming, W.; Guo, J.; *et al.* Optimization of Cutting Conditions of YG15 on Rough and Finish Cutting in WEDM Based on Statistical Analyses. *Int. J. Adv. Manuf. Technol.* **2013**, *69* (5–8), 993–1008. doi:10.1007/s00170-013-5037-3.
7. Motoki, M.; Summer, K. Recent EDM. *J. Jpn. Soc. Electr. Mach. Eng.* **1978**, *11*, 2–20.
8. Maher, I.; Ling, L. H.; Sarhan, A. A. D.; Hamdi, M. Improve Wire EDM Performance at Different Machining Parameters – ANFIS Modeling. *IFAC-PapersOnLine* **2015**, *48* (1), 105–110. Available from: http://dx.doi.org/10.1016/j.ifacol.2015.05.109 (accessed March 1, 2016).
9. Yeh, C.-C.; Wu, K.-L.; Lee, J.-W.; Yan, B.-H. Study on Surface Characteristics Using Phosphorous Dielectric on Wire Electrical Discharge Machining of Polycrystalline Silicon. *Int. J. Adv. Manuf. Technol.* **2013**, *69* (1–4), 71–80. doi:10.1007/s00170-013-4995-9.
10. Maher, I.; Sarhan, A. A. D.; Marashi, H.; Barzani, M. M.; Hamdi, M. *White Layer Thickness Prediction in WEDM-ANFIS Modelling, Malaysian International Tribology Conference*, Penang, Malaysia, 2015; pp. 240–241.
11. Marashi, H.; Sarhan, A. A. D.; Maher, I.; Sayuti, M.; Hamdi, M. *Enhanced Surface Roughness of AISI D2 Steel Machined Using Nano-Powder Mixed Electrical Discharge Machining, Malaysian International Tribology Conference*, Penang, Malaysia, 2015; pp. 242–243.
12. El-Hofy, H. *Advanced Machining Processes*; McGraw-Hill: New York, NY, 2005. 10.1036/0071466940.
13. Ramasawmy, H.; Blunt, L.; Rajurkar, K. P. Investigation of the Relationship between the White Layer Thickness and 3D Surface Texture Parameters in the Die Sinking EDM process. *Precis. Eng.* **2005**, *29* (4), 479–490. Available from: http://dx.doi.org/10.1016/j.precisioneng.2005.02.001 (accessed March 1, 2016).
14. Kruth, J. P.; Van Humbeeck, J.; Stevens, L. Micro Structural Investigation and Metallographic Analysis of the White Layer of a Surface Machined by Electro Discharge Machining. In P*roceedings of International Symposium for Electromachining Isem 11*, Les Presses Polytechniques Romandes, Lausanne, Switzerland, 1995; pp. 849–862.
15. Levy, G. N.; Maggi, F. WED Machinability Comparison of Different Steel Grades. *CIRP Ann. – Manuf. Technol.* **1990**, *39* (1), 183–185. Available from: http://dx.doi.org/10.1016/S0007-8506(07)61031-2 (accessed March 1, 2016).
16. McGeough, J. A. *Electro Discharge Machining.* In *Advanced Methods of Machining*; Springer: Dordrecht, 1988.
17. Garg, R. *Effect of Process Parameters on Performance Measures of Wire Electrical Discharge Machining*; National Institute of Technology: Kurukshetra, 2010.
18. Yan, M.-T.; Liu, Y.-T. Design, Analysis and Experimental Study of a High-Frequency Power Supply for Finish Cut of Wire-EDM. *Int. J. Mach. Tools Manuf.* **2009**, *49* (10), 793–796. Available from: http://dx.doi.org/10.1016/j.ijmachtools.2009.04.004 (accessed March 1, 2016).
19. Gökler, M. İ.; Ozanözgü, A. M. Experimental Investigation of Effects of Cutting Parameters on Surface Roughness in the WEDM Process. *Int. J. Mach. Tools Manuf.* **2000**, *40* (13), 1831–1848. Available from: http://dx.doi.org/10.1016/S0890-6955(00)00035-3 (accessed March 1, 2016).
20. Kapoor, J.; Singh, S.; Khamba, J. S. Recent Developments in Wire Electrodes for High Performance WEDM. In *Proceedings of the World Congress on Engineering*, Vol. 2; London, 2010.
21. Huang, J. T.; Liao, Y. S.; Hsue, W. J. Determination of Finish-Cutting Operation Number and Machining-Parameters Setting in Wire Electrical Discharge Machining. *J. Mater. Process. Technol.* **1999**, *87* (1–3), 69–81. Available from: http://dx.doi.org/10.1016/S0924-0136(98)00334-3 (accessed March 1, 2016).
22. Liao, Y. S.; Yu, Y. P. Study of Specific Discharge Energy in WEDM and Its Application. *Int. J. Mach. Tools Manuf.* **2004**, *44* (12–13), 1373–1380. Available from: http://dx.doi.org/10.1016/j.ijmachtools.2004.04.008 (accessed March 1, 2016).
23. Singh, A.; Ghosh, A. A Thermo-Electric Model of Material Removal During Electric Discharge Machining. *Int. J. Mach. Tools Manuf.* **1999**, *39* (4), 669–682. Available from: http://dx.doi.org/10.1016/S0890-6955(98)00047-9 (accessed March 1, 2016).
24. Salah, N. B.; Ghanem, F.; Atig, K. B. Numerical Study of Thermal Aspects of Electric Discharge Machining Process. *Int. J. Mach. Tools Manuf.* **2006**, *46* (7–8), 908–911. Available from: http://dx.doi.org/10.1016/j.ijmachtools.2005.04.022 (accessed March 1, 2016).
25. Izquierdo, B.; Sánchez, J. A.; Plaza, S.; Pombo, I.; Ortega, N. A Numerical Model of the EDM Process Considering the Effect of Multiple Discharges. *Int. J. Mach. Tools Manuf.* **2009**, *49* (3–4), 220–229. Available from: http://dx.doi.org/10.1016/j.ijmachtools.2008.11.003 (accessed March 1, 2016).
26. Dekeyser, W.; Snoeys, R.; Jennes, M. Expert System for Wire Cutting EDM, Based on Pulse Classification and Thermal Modeling. *Robot. Comput.-Integr. Manuf.* **1988**, *4* (1–2), 219–224. Available from: http://dx.doi.org/10.1016/0736-5845(88)90080-4 (accessed March 1, 2016).
27. Lee, C.-S.; Heo, E.-Y.; Kim, J.-M.; Choi, I.-H.; Kim, D.-W. Electrode Wear Estimation Model for EDM Drilling. *Robot. Comput.-Integr. Manuf.* **2015**, *36*, 70–75. Available from: http://dx.doi.org/10.1016/j.rcim.2015.02.001 (accessed March 1, 2016).
28. Gostimirovic, M.; Kovac, P.; Sekulic, M.; Skoric, B. Influence of Discharge Energy on Machining Characteristics in EDM. *J. Mech. Sci. Technol.* **2012**, *26* (1), 173–179. Available from: http://dx.doi.org/10.1007/s12206-011-0922-x (accessed March 1, 2016).
29. Salonitis, K.; Stournaras, A.; Stavropoulos, P.; Chryssolouris, G. Thermal Modeling of the Material Removal Rate and Surface Roughness For Die-Sinking EDM. *Int. J. Adv. Manuf. Technol.* **2009**, *40* (3–4), 316–323. Available from: http://dx.doi.org/10.1007/s00170-007-1327-y (accessed March 1, 2016).
30. Patil, N.; Brahmankar, P. K. Determination of Material Removal Rate in Wire Electro-Discharge Machining of Metal Matrix Composites Using Dimensional Analysis. *Int. J. Adv. Manuf. Technol.* **2010**, *51* (5–8), 599–610. Available from: http://dx.doi.org/10.1007/s00170-010-2633-3 (accessed March 1, 2016).
31. Hewidy, M.; El-Taweel, T.; El-Safty, M. Modelling the Machining Parameters of Wire Electrical Discharge Machining of Inconel 601 Using RSM. *J. Mater. Process. Technol.* **2005**, *169* (2), 328–336.
32. Myers, R. H.; Anderson-Cook, C. M. *Response Surface Methodology: Process and Product Optimization Using Designed Experiments*; John Wiley & Sons: New York, NY, 2009; Vol. 705, p. 680.
33. Tarng, Y. S.; Ma, S. C.; Chung, L. K. Determination of Optimal Cutting Parameters in Wire Electrical Discharge Machining. *Int. J. Mach. Tools Manuf.* **1995**, *35* (12), 1693–1701. Available from: http://dx.doi.org/10.1016/0890-6955(95)00019-T (accessed March 1, 2016).
34. Çaydaş, U.; Hasçalık, A.; Ekici, S. An Adaptive Neuro-Fuzzy Inference System (ANFIS) Model for Wire-EDM. *Expert Syst. Appl.* **2009**, *36* (3, Part 2), 6135–6139. Available from: http://dx.doi.org/10.1016/j.eswa.2008.07.019 (accessed March 1, 2016).
35. Maher, I.; Eltaib, M. E. H.; Sarhan, A. A. D.; El-Zahry, R. M. Cutting Force-Based Adaptive Neuro-Fuzzy Approach for Accurate Surface Roughness Prediction in End Milling Operation for Intelligent Machining. *Int. J. Adv. Manuf. Technol.* **2015**, *76* (5–8), 1459–1467. Available from: http://dx.doi.org/10.1007/s00170-014-6379-1 (accessed March 1, 2016).
36. Maher, I.; Eltaib, M. E. H.; Sarhan, A. A. D.; El-Zahry, R. M. Investigation of the Effect of Machining Parameters on the Surface Quality Of Machined Brass (60/40) in CNC End Milling-ANFIS Modeling. *Int. J. Adv. Manuf. Technol.* **2014**, *74* (1–4), 531–537. Available from: http://dx.doi.org/10.1007/s00170-014-6016-z (accessed March 1, 2016).
37. Maher, I.; Sarhan, A. A. D.; Barzani, M. M.; Hamdi, M. Increasing the Productivity of the Wire-Cut Electrical Discharge Machine Associated with Sustainable Production. *J. Clean. Prod.* **2015**, *108* (Part A), 247–255. Available from: http://dx.doi.org/10.1016/j.jclepro.2015.06.047 (accessed March 1, 2016).
38. Maher, I.; Eltaib, M.E.H.; El-Zahry, R.M. *Surface Roughness Prediction in End Milling Using Multiple Regression and Adaptive Neuro-Fuzzy Inference System*,

International Conference on Mechanical Engineering Advanced Technology For Industrial Production (MEATIP4), Assiut University, Egypt, December 12–14, 2006; pp. 614–620. Available from: http://dx.doi.org/10.13140/RG.2.1.1171.1204 (accessed March 1, 2016).
39. Jang, J.-S. R.; Sun, C.-T.; Mizutani, E. *Neuro-Fuzzy and Soft Computing : A Computational Approach to Learning and Machine Intelligence*; Prentice Hall, Inc.: Upper Saddle River, NJ, 1997; p. xxvi, p. 614.
40. Maher, I. *Surface Roughness Prediction in End-Milling Process*; Assiut University: Assiut, 2008.
41. Newton, T. R.; Melkote, S. N.; Watkins, T. R.; Trejo, R. M.; Reister, L. Investigation of the Effect of Process Parameters on the Formation and Characteristics of Recast Layer in Wire-EDM of Inconel 718. *Mater. Sci. Eng. A* **2009**, *513–514*, 208–215. Available from: http://dx.doi.org/10.1016/j.msea.2009.01.061 (accessed March 1, 2016).
42. Li, L.; Guo, Y. B.; Wei, X. T.; Li, W. Surface Integrity Characteristics in Wire-EDM of Inconel 718 at Different Discharge Energy. *Procedia CIRP* **2013**, *6*, 220–225. Available from: http://dx.doi.org/10.1016/j.procir.2013.03.046 (accessed March 1, 2016).
43. Maher, I.; Sarhan, A. A. D.; Hamdi, M. Review of Improvements in Wire Electrode Properties for Longer Working Time And Utilization in Wire EDM Machining. *Int. J. Adv. Manuf. Technol.* **2015**, *76* (1–4), 329–351. Available from: http://dx.doi.org/10.1007/s00170-014-6243-3 (accessed March 1, 2016).
44. Jameson, E. C. *Electrical Discharge Machining*; Society of Manufacturing Engineers: Dearborn, MI, 2001.
45. Jahan, M. Micro-Electrical Discharge Machining. In *Nontraditional Machining Processes*; Davim, J. P., Ed.; Springer: London, 2013. 10.1007/978-1-4471-5179-1_4.
46. Moulton, D. B. *Wire EDM the Fundamentals*; EDM network: Sugar Grove, IL, 1999. Available from: www.notebookmanuals.com. bestmanual guide (accessed March 1, 2016).
47. Ferreira, J. A Study of Die Helical Thread Cavity Surface Finish Made by Cu–W Electrodes with Planetary EDM. *Int. J. Adv. Manuf. Technol.* **2007**, *34* (11–12), 1120–1132. Available from: http://dx.doi.org/10.1007/s00170-006-0687-z (accessed March 1, 2016).
48. Portt, J. *Introduction to Wire EDM*; John Portt: Ann Arbor, MI, 1992.
49. Aoyama, S. Development of High Performance Wire Electrode for Wire Electric Discharge Machining. *J. Jpn. Soc. Electr. Mach.g Eng.* **2001**, *35*, 46–51.
50. Dauw, D. F.; Beltrami, I. High-Precision Wire-EDM by Online Wire Positioning Control. *CIRP Ann. – Manuf. Technol.* **1994**, *43* (1), 193–197. Available from: http://dx.doi.org/10.1016/S0007-8506(07)62194-5 (accessed March 1, 2016).
51. Paul, C. P.; Kumar, A.; Bhargava, P.; Kukreja, L. M. *Nontraditional Machining Processes – Research Advances*; Springer-Verlag: London, 2013. 10.1007/978-1-4471-5179-1.
52. Ho, K. H.; Newman, S. T.; Rahimifard, S.; Allen, R. D. State of the Art in Wire Electrical Discharge Machining (WEDM). *Int. J. Mach. Tools Manuf.* **2004**, *44* (12–13), 1247–1259. Available from: http://dx.doi.org/10.1016/j.ijmachtools.2004.04.017 (accessed March 1, 2016).
53. Dauw, D. F.; Albert, L. About the Evolution of Wire Tool Performance in Wire EDM. *CIRP Ann. – Manuf. Technol.* **1992**, *41* (1), 221–225. Available from: http://dx.doi.org/10.1016/S0007-8506(07)61190-1 (accessed March 1, 2016).
54. Aoyama, S.; Tamura, K.; Sato, T.; Kimura, T.; Sawahata, K.; Nagai, T. High-Performance Coated Wire Electrodes for High-Speed Cutting and Accurate Machining. *Hitachi Cable Rev.* **1999**, *18*, 75–80.
55. Davis, J. R. *Metals Handbook Desk Edition*, 2nd ed.; ASM International Handbook Committee: Materials Park, OH, 1998.
56. Yan, M.-T.; Huang, P.-H. Accuracy Improvement of Wire-EDM by Real-Time Wire Tension Control. *Int. J. Mach. Tools Manuf.* **2004**, *44* (7–8), 807–814. Available from: http://dx.doi.org/10.1016/j.ijmachtools.2004.01.019 (accessed March 1, 2016).
57. Kern, R. EDM Wire Primer. Available from: http://www.edmtodaymagazine.com/ (accessed March 1, 2016).
58. Cut, X.-X.; Masuzawa, T.; Taniguchi, N. Study on Flushing for EDM (2nd Report) – Analysis and Simulation of the Effect of Jet Flushing for EDM. *J. Jpn. Soc. Electr. Mach. Eng.* **1993**, *27*, 10–22.
59. Gedeon, M. Strip Vs Wire. *Tech. Tidbits* **2011**, *3* (11),
60. Lin, P.; Liao, T.-T. An Effective-Wire-Radius Compensation Scheme for Enhancing the Precision of Wire-Cut Electrical Discharge Machines. *Int. J. Adv. Manuf. Technol.* **2009**, *40* (3–4), 324–331. doi:10.1007/s00170-007-1333-0.
61. Uhlmann, E.; Roehner, M. Investigations on Reduction of Tool Electrode Wear in Micro-EDM Using Novel Electrode Materials. *CIRP J. Manuf. Sci. Technol.* **2008**, *1* (2), 92–96. Available from: http://dx.doi.org/10.1016/j.cirpj.2008.09.011 (accessed March 1, 2016).
62. Groos, H. Wire Electrode for the Spark Erosive Cutting. US 4766280 A, 1988.
63. Walder, G.; Balleys, F. Wire Electrode Arrangement for Electroerosive Cutting. US 5882490 A, 1999.
64. Gonnissen, D.; Van Vooren, W. Electric Discharge Machining Wire. WO Patent 2,001,089,750, 2001.
65. Inoue, K. Traveling-Wire EDM Method. US 4508604 A, 1985.
66. Seong, K. Method of Manufacturing Porous Electrode Wire for Electric Discharge Machining and Structure of the Electrode Wire. WO Patent 1,999,006,183, 1999.
67. Groos, H.; Barthel, B.; Noethe, T.; Dietrich, C. Wire Electrode with a Structured Interface Surface. US 6794597 B2, 2004.
68. Inoue, K. Electroerosive Wire-Cutting Method and Apparatus with a Shaped Wire Electrode. US 4418263 A, 1983.
69. Kaneko, H.; Onoue, M. Electrode Material for Travelling-Wire Type Electrical Discharge Machining. US4424432 A, 3/1, 1984.
70. Makino, Y.; Obara, H.; Ohsumi, T.; Niwa, S. Single Discharging Force and Machining Volume of Wire EDM. *J. Jpn. Soc. Electr. Mach. Eng.* **1995**, *30*, 1–10.
71. Herreroa, A.; Azcaratea, S.; Reesb, A.; Gehringerc, A.; Schothc, A.; Sanchezd, J. A. *Influence of Force Components on Thin Wire EDM*; Whittles Publishing Ltd.: Cardiff, 2008.
72. Ezaki, S.; Hasegawa, H.; Seto, H. Electrode Wire for Electric Spark Cutting. US 5028756 A, 1991.
73. Kern, R. EDM Wire Selection. *EDM Today* **2008**, *1*, 12–16.
74. Kapoor, J.; Singh, S.; Khamba, J. S. High-Performance Wire Electrodes for Wire Electrical-Discharge Machining – A Review. *Proc. Inst. Mech. Eng., Part B: J. Eng. Manuf.* **2012**, *226* (11), 1757–1773. doi:10.1177/0954405412460354.
75. Weng, F. T.; Her, M. G. Study of the Batch Production of Micro Parts Using the EDM Process. *Int. J. Adv. Manuf. Technol.* **2002**, *19* (4), 266–270. doi:10.1007/s001700200033.
76. Sommer, C.; Sommer, S. *Complete EDM Handbook*; Advance Pub: Staten Island, NY, 2005.
77. Sánchez, J. A.; Ortega, N. *Machine Tools for High Performance Machining*; Springer: London, 2009. 10.1007/978-1-84800-380-4_9.
78. Schacht, B. *Composite Wire Electrodes and Alternative Dielectric for Wire Electrical Discharge Machining*; University of Katholieke: Leuen, Belgium, 2004.
79. Aoyama, S.; Kuroda, H.; Seya, O.; Kimura, T.; Sato, T. Development and Applications of High-Strength-High Conductivity Copper Alloy Wire Formed by Continuous Casting and Hot Rolling. *Hitachi Cable Rev.* **2008**, *2*, 102–104.
80. Obara, H.; Ohsumi, T.; Masahashi, Y.; Miyanishi, S.; Hatano, M. Fundamental Study of Accuracy of Wire EDM (6th report) – Study of EDM Conditions and Servo Feed Function of Finish Cut. *J. Jpn. Soc. Electr. Mach. Eng.* **2002**, *36*, 15–23.
81. Otsuka, Y.; Nakai, Y.; Numano, M.; Maruyama, T.; Ohkubo, N.; Kishida, H. Development of High-Speed Electrode Wire for Wire Electro-Discharge Machining. *SEI Tech. Rev.* **2001**, *51*, 133–136.
82. Kuroda, H.; Aoyama, S.; Kimura, T.; Sawahata, K.; Sato, T. Development of High Performance Coated Wire Electrodes for High-Speed Cutting and Accurate Machining. *Hitachi Cable Rev.* **2003**, *22*, 51–56.
83. Hiromitsu, K.; Seigi, A.; Takamitsu, K.; Katsunori, S.; Takahiro, S. Electrode Wires for Wire Discharge Processing with Excellent High Speed and High Precision Processing. *Hitachi Densen* **2003**, *22* (55–60),
84. Morita, M.; Yamauchi, T.; Okada, A.; Uno, Y.; Shimizu, T. Fundamental Study on Coating Wire Electrode for High Performance WEDM (Electrical Machining). In *Proceedings of International Conference on Leading Edge Manufacturing in 21st century: LEM21*; Vol. 2, 2005; pp. 779–782
85. Yamauchi, T.; Okada, A.; Morita, M.; Shimizu, T.; Uno, Y. Development of coating wire electrode for high performance WEDM (1st report) – Fundamental WEDM Characteristics of Coating Wire. *J. Jpn. Soc. Electr. Mach. Eng.* **2005**, *39*, 28–35.
86. Obara, H. The Analysis of Wire Break Down Limitation on Wire Edm (1st Report; Analysis of Water Flow in Cut Groove). *J. Jpn. Soc. Electr. Mach. Eng.* **1989**, *22*, 10–22.
87. Obara, H.; Abe, M.; Ohsumi, T. Prevention of Wire Breakage on Wire EDM – 1st Report: Comparison of Spark Gap Detecting Signals on Wire EDM. *J. Jpn. Soc. Electr. Mach. Eng.* **1997**, *31*, 11–17.
88. Kern, R. Improving Wire EDM productivity. *EDM Today* **2007**, *1*, 10–14.
89. Obara, H.; Yamada, M.; Ohsumi, T.; Hatano, M. Prevention of Wire Breakage During Wire Edm (3rd Report) – Discharge Location and Discharge Voltage in Case of High Current Discharge. *J. Jpn. Soc. Electr. Mach. Eng.* **2002**, *36*, 24–30.

90. Kinoshita, N.; Fukui, M.; Gamo, G. Control of Wire-EDM Preventing Electrode from Breaking. *CIRP Ann. – Manuf. Technol.* **1982**, *31* (1), 111–114. Available from: http://dx.doi.org/10.1016/S0007-8506(07)63279-X (accessed March 1, 2016).
91. Rajurkar, K. P.; Wang, W. M.; Lindsay, R. P. On-Line Monitor and Control for Wire Breakage in WEDM. *CIRP Ann. – Manuf. Technol.* **1991**, *40* (1), 219–222. Available from: http://dx.doi.org/10.1016/S0007-8506(07)61972-6 (accessed March 1, 2016).
92. Luo, Y. F. Rupture Failure and Mechanical Strength of the Electrode Wire Used in Wire EDM. *J. Mater. Process. Technol.* **1999**, *94* (2–3), 208–215. Available from: http://dx.doi.org/10.1016/S0924-0136(99)00107-7 (accessed March 1, 2016).
93. Schuler, G. H. *Metal Forming Handbook*; Springer-Verlag: Berlin; Heidelberg; New York, NY, 1998.
94. Wright, R. N. *Wire Technology: Process Engineering and Metallurgy*, 1st ed.; Butterworth-Heinemann: Oxford, 2010.
95. Kern, R. The Art and Science of Making EDM Wire. Available from: http://www.edmtodaymagazine.com/ (accessed March 1, 2016).
96. Intech, E. EDM Wire: A Reference to Understanding, Selecting and Using Wire on Wire-Cut EDM Machines. *Intech EDM* **1995**, *1*, 1–9.
97. Wang, J.; Ravani, B. Computer Aided Contouring Operation for Traveling Wire Electric Discharge Machining (EDM). *Comput.-Aided Des.* **2003**, *35* (10), 925–934. Available from: http://dx.doi.org/10.1016/S0010-4485(02)00207-5 (accessed March 1, 2016).
98. Prohaszka, J.; Mamalis, A. G.; Vaxevanidis, N. M. The Effect of Electrode Material on Machinability in Wire Electro-Discharge Machining. *J. Mater. Process. Technol.* **1997**, *69* (1–3), 233–237. Available from: http://dx.doi.org/10.1016/S0924-0136(97)00024-1 (accessed March 1, 2016).
99. Antar, M. T.; Soo, S. L.; Aspinwall, D. K.; Jones, D.; Perez, R. Productivity and Workpiece Surface Integrity When WEDM Aerospace Alloys Using Coated Wires. *Procedia Eng.* **2011**, *19*, 3–8. Available from: http://dx.doi.org/10.1016/j.proeng.2011.11.071 (accessed March 1, 2016).
100. Singh, S.; Maheshwari, S.; Pandey, P. C. Some Investigations into the Electric Discharge Machining of Hardened Tool Steel Using Different Electrode Materials. *J. Mater. Process. Technol.* **2004**, *149* (1–3), 272–277. Available from: http://dx.doi.org/10.1016/j.jmatprotec.2003.11.046 (accessed March 1, 2016).
101. Altpeter, F.; Perez, R. Relevant Topics in Wire Electrical Discharge Machining Control. *J. Mater. Process. Technol.* **2004**, *149* (1–3), 147–151. Available from: http://dx.doi.org/10.1016/j.jmatprotec.2003.10.033 (accessed March 1, 2016).
102. Fowle, F. F. Process of Treating Zinc Coated Wire. US 1,896,613, 1933.
103. Groos, H.; Barthel, B.; Noethe, T.; Dietrich, C. Wire Electrode for Spark Erosion Cutting. US 6,781,081 B2, 2004.
104. Kuriakose, S.; Shunmugam, M. S. Characteristics of Wire-Electro Discharge Machined Ti6Al4V Surface. *Mater. Lett.* **2004**, *58* (17–18), 2231–2237. Available from: http://dx.doi.org/10.1016/j.matlet.2004.01.037 (accessed March 1, 2016).
105. Okada, A.; Yamauchi, T.; Arizono, K.; Shimizu, T.; Uno, Y. Development of Coat Wire Electrode for High Performance WEDM (2nd Report) – Fundamental WEDM Characteristices of Φ50 μm Coating Wire. *J. Jpn. Soc. Electr. Mach. Eng.* **2008**, *42*, 12–19.
106. Okada, A.; Yamauchi, T.; Arizono, K.; Uno, Y. Effect of Surface Quality of Brass Coating Wire on Wire EDM Characteristics. *J. Adv. Mech. Des. Syst. Manuf.* **2008**, *2* (4), 735–741.
107. Okada, A.; Yamauchi, T.; Higashi, M.; Shimizu, T.; Uno, Y. Development of Coated Wire Electrode for High-Performance WEDM (3rd Report) – Effects of Wire Surface Unevenness on Wire EDM Characteristics. *J. Jpn. Soc. Electr. Mach. Eng.* **2009**, *43*, 179–186.
108. Okada, A.; Yamauchi, T.; Nakazawa, M.; Shimizu, T.; Uno, Y. Development of Coated Wire Electrode for High-Performance WEDM (4th Report) – Effects of High-Resistance Layer on Wire Electrode on WEDM Characteristics. *J. Jpn. Soc. Electr. Mach. Eng.* **2011**, *45*, 64–70.
109. Kapoor, J.; Singh, S.; Khamba, J. S. Effect of Cryogenic Treated Brass Wire Electrode on Material Removal Rate in Wire Electrical Discharge Machining. *J. Mech. Eng. Sci.* **2012**, *226* (11), 2750–2758. doi:10.1177/0954406212438804.
110. Nourbakhsh, F.; Rajurkar, K. P.; Malshe, A. P.; Cao, J. Wire Electro-Discharge Machining of Titanium Alloy. *Procedia CIRP* **2013**, *5*, 13–18. Available from: http://dx.doi.org/10.1016/j.procir.2013.01.003 (accessed March 1, 2016).
111. Yan, M. T.; Fang, G. R.; Liu, Y. T.; Li, J. R. Fabrication of Polycrystalline Diamond Wheels by Micro Wire-EDM Using a Novel Pulse Generator. *Procedia CIRP* **2013**, *6*, 203–208. Available from: http://dx.doi.org/10.1016/j.procir.2013.03.013 (accessed March 1, 2016).
112. Pérez Delgado, Y.; De Baets, P.; Bonny, K.; *et al.* Influence of Wire-EDM on High Temperature Sliding Wear Behavior of WC10Co(Cr/V) Cemented Carbide. *Int. J. Refract. Metals Hard Mater.* **2013**, *41*, 198–209. Available from: http://dx.doi.org/10.1016/j.ijrmhm.2013.03.013 (accessed March 1, 2016).
113. Convers, D.; Balleys, F.; Pfau, J. Electrode for Electrical Discharg Machining. US 4,287,404, 1981.
114. Nakai, Y.; Yamada, K.; Miyazaki, K.; Inazawa, S.; Ezaki, S.; Kume, T. Wire Electrode for Electro-Discharge Machining and Manufacturing Method Thereof. US 6,300,587 B1, 2001.
115. Baumann, I.; Barthel, B. Wire Electrode for the Spark-Erosive Cutting of Hard Metal. US 6,348,667 B2, 2002.
116. Banzai, M.; Shibata, Y. Wire electrode for Wire Cut Electric Discharge Machinig. US 4,968,867, 1990.
117. Briffod, J. Zinc or Cadmium Coated, Surface Oxidized Electrode Wire for EDM Cutting of a Workpiece; and Method for Forming such a Wire. US 4,977,303, 1990.
118. Briffod, J.-P.; Martin, R.; Pfau, J.; Bommeli, B.; Schnellmann, D. Wire Electrode for Cutting an Electrode Workpiece by Electrical Discharges. US 4,341,939, 1982.
119. Lee, J.-C. Electrode Wire with Multi-Coated Layers for Electrical Discharge Machining and Method of Manufacturing the Same. US 2008/0245773 A1, 2008.
120. Briffod, J.-P. Multi-Layer Electrode Wire and Method for Producing the Same. US 5196665 A, 1993.
121. Lacourcelle, L. Method of Manufacturing a Spark Erosion Electrode Wire. US 5,721,414, 1998.
122. Hermanni, H. Wire Electrode for Use in Spark-Erosive Cutting. US 4924050, 1990.
123. Tominaga, H.; Takayama, T.; Ogura, Y.; Yamaguchi, T. Electrode Wire for use in Electric Discharge Machining and Process for Preparing Same. US 4,686,153, 1987.
124. Baker, H. *ASM Metals Handbook, Volume 3: Alloy Phase Diagrams*; Vol. 3; ASM Intrenational: Materials Park, OH, 1992.
125. Butts, D. A.; Gale, W. F. Equilibrium Diagrams. In *Smithells Metals Reference Book*, 7th ed.; Brandes, E. A., Brook., G. B., Eds.; Butterworth-Heinemann: Oxford; Boston, 1998; pp. 625–644.
126. Briffod, J.P. Process for the Manufacturing of Wires with a Brass Surface, for the Purpose of Wire Electroerosion. US 5,858,136, 1999.
127. Groos, H.; Hermanni, H. Eroding Electrode, in Particular a Wire Electrode for the Sparkerosive Working. US 4,935,594, 1990.
128. Negrerie, M.; Leterrible, P.; Voirin, A. High Performance Electrode Wire for Electric Discharge Machining and Process for Preparing Same. EP 0526361 A1, 1993.
129. Ly, M. Wire for High-Speed Electrical Discharge Machinine. US 7,687,738 B2, 2010.
130. Barthel, B.; Neuser, B. Wire Electrode. US 6566622 B1, 2003.
131. Barthel, B.; Groos, H.; Hermanni, H.; Tauber, K. High-Strength Erosion Electrode. WO Patent 1,998,009,764, 1998.
132. Briffod, J.-p. Wire Electrode for Electroerosion Cutting. EP 0,521,569, 1993.
133. Nakai, Y.; Kishida, H.; Ookubo, N.; *et al.* Wire Electrode for Electro-Discharge Machining. US6291790 B1, 2001.
134. Chiriotti, N.; Pinaya, R.P.; Fluekiger, R. Electrode for Machining a Piece by Electro-Erosion And Its Process for Production. US 6495788 B1, 2002.
135. Tomalin, D. S. Electric Wire for Use in Electric Discharge Machining and Process for Preparing Same. US 5,945,010, 1999.
136. Mukherjee, K.K. Wire Electrode for Electro-Discharge Machining and Method of Manufacturing Same. US 5,808,262, 1998.
137. Baumann, I.; Nöthe, T. Wire Electrodes for Electrical Discharge Cutting. US 2011/0290531 A1, 2011.
138. Ly, M.; Sanchez, G. Electrode Wire for Spark Erosion. US 8,338,735 B2, 2012.
139. Barthel, B.; Groos, H.; Hermanni, H. Wire Electrode and Process for Producing a Wire Electrode, Particular for a Spark Erosion Process. US 5,762,726, 1998.
140. Blanc, P.; Ly, M.; Sanchez, G. Composite Wire for Electrical Discharge Machining. US 8,378,247 B2, 2013.
141. Tomalin, D. S. EDM Wire. US 2007/0295695 A1, 2007.
142. Tomalin, D. EDM Wire. US 8,067,689 B2, 2011.
143. Cut, X.-X; Masuzawa, A.; Fujino, M. Study on Flushing for EDM (1st Report) – Proposal of 2D Small Vibration Method and Scan-Flushing Method. *J. Jpn. Soc. Electr. Mach. Eng.* **1991**, *26*, 1–12.
144. Puri, A. B.; Bhattacharyya, B. Modelling and Analysis of the Wire-Tool Vibration in Wire-Cut EDM. *J. Mater. Process. Technol.* **2003**, *141* (3), 295–301. Available from: http://dx.doi.org/10.1016/S0924-0136(03)00280-2 (accessed March 1, 2016).

145. Tomura, S.; Kunieda, M. Analysis of Electromagnetic Force in Wire-EDM. *Precis. Eng.* **2009**, *33* (3), 255–262. Available from: http://dx.doi.org/10.1016/j.precisioneng.2008.07.004 (accessed March 1, 2016).
146. Okada, A.; Uno, Y.; Nakazawa, M.; Yamauchi, T. Evaluations of Spark Distribution and Wire Vibration in Wire EDM by High-Speed Observation. *CIRP Ann. – Manuf. Technol.* **2010**, *59* (1), 231–234. Available from: http://dx.doi.org/10.1016/j.cirp.2010.03.073 (accessed March 1, 2016).
147. Iwata, Y.; Obara, H.; Ohsumi, T.; Matsuda, Y. Simulation of Wire EDM (1st Report) – Simulating Procedure and Examples-. *J. Jpn. Soc. Electr. Mach. Eng.* **1995**, *29*, 40–48.
148. Okada, A.; Oue, S.; Uno, Y.; Shouji, T.; Fukushima, T.; Terada, O. Development of New CuW Electrode for High-Performance EDM. *J. Jpn. Soc. Electr. Mach. Eng.* **2007**, *41*, 69–76.
149. Kondo, I.; Nishimoto, K. Precisely Process of Wire Electrode EDM. *J. Jpn. Soc. Electr. Mach. Eng.* **1985**, *19*, 12–27.
150. Mujahid, M.; Conrad, R. Molybdenum Base Alloy and Lead-In Wire Made Therefrom. EP 0275580 B1, 1991.
151. Kruth, J. P.; Lauwers, B.; Schacht, B.; van Humbeeck, J. Composite Wires with High Tensile Core for Wire EDM. *CIRP Ann. – Manuf. Technol.* **2004**, *53* (1), 171–174. Available from: http://dx.doi.org/10.1016/S0007-8506(07)60671-4 (accessed March 1, 2016).
152. Gonnissen, D.; Vooren, W.V. Electric Discharge Machining Wire. US 6,875,943 B2, 2005.
153. Menzies, I.; Koshy, P. Assessment of abrasion-assisted material removal in wire EDM. *CIRP Ann. – Manuf. Technol.* **2008**, *57* (1), 195–198. Available from: http://dx.doi.org/10.1016/j.cirp.2008.03.135 (accessed March 1, 2016).
154. Koshy, P.; Menzies, I. Abrasion Assisted Wire Electrical Discharge Machining Process. US 2010/0012628 A1, 2010.
155. Ghodsiyeh, D.; Golshan, A.; Shirvanehdeh, J. A. Review on Current Research Trends in Wire Electrical Discharge Machining (WEDM). *Indian J. Sci. Technol.* **2013**, *6* (2), 154–168.
156. Cheremisinoff, N. P. *Materials Selection Deskbook*; Noyes Publications: Westwood, NJ, 1996.
157. Lee, J.-C. Method of Manufacturing Zinc-Coated Electrode Wire For Electric Discharge Processors Using Hot Dip Galvanizing Process. US 2006/0138091 A1, 2006.
158. Seong, K. C. Porous Electrode Wire for Use in Electrical Discharge Machining and Method of Manufacturing the Same. US 6,482,535 B2, 2002.
159. Tomlinson, W. J.; Adkin, J. R. Microstructure and Properties of Electrodischarge Machined Surfaces. *Surf. Eng.* **1992**, *8* (4), 283–288. Available from: http://dx.doi.org/10.1179/sur.1992.8.4.283 (accessed March 1, 2016).
160. Roy, R. K. *Design of Experments Using Taguchi Approach*; John Wiley & Sons, Inc: New York, NY, 2001.
161. Fuller, R. *Neural Fuzzy Systems*. ESF Series A:443; Åbo Akademis tryckeri: Åbo; 1995.
162. Li, H.; Chen, C. L. P.; Huang, H. P. *Fuzzy Neural Intelligent Systems: Mathematical Foundation and the Applications in Engineering*; CRC Press, LLC: Boca Raton, FL, 2001.

Relevant Websites

http://edmtechman.com/about.cfm
EDM Technical Manual, Poco Graphite, Inc.
http://www.edmtodaymagazine.com/2015/index.php
EDM Today.
http://www.engineersedge.com/edm.shtml
Engineers Edge.
http://www.hitachi-metals.co.jp/e/index.html
Hitachi Metals, Ltd.
http://www.mmsonline.com/
Modern Machine Shop.
http://www.moldmakingtechnology.com/articles/edms-effect-on-surface-integrity
MoldMaking Technology, EDM's Effect on Surface Integrity.
http://www.reliableedm.com/index.php
Reliable EDM.
http://coep.vlab.co.in/index.php?sub=34&brch=105&sim=1028&cnt=2217
Sakshat Virtual Labs.

1.10 Micro-EDM Drilling of Tungsten Carbide Using Microelectrode with High Aspect Ratio to Improve MRR, EWR, and Hole Quality

M Hourmand, University of Malaya, Kuala Lumpur, Malaysia
AAD Sarhan, University of Malaya, Kuala Lumpur, Malaysia and Assiut University, Assiut, Egypt
MY Noordin, Universiti Teknologi Malaysia, Johor Bahru, Malaysia
M Sayuti, University of Malaya, Kuala Lumpur, Malaysia

© 2017 Elsevier Inc. All rights reserved.

1.10.1	**Introduction**	268
1.10.2	**Material Removal Processes**	268
1.10.2.1	Conventional Process	268
1.10.2.2	Nonconventional Process	268
1.10.2.3	Hybridized Process	270
1.10.3	**EDM and Micro-EDM Processes**	270
1.10.3.1	Electrical Discharge Machining	270
1.10.3.2	Sparking and Gap Phenomena in EDM	271
1.10.3.3	Function and Types of Micro-EDM Process	272
1.10.3.4	Pulse Generators/Power Supply	274
1.10.3.4.1	Transistor-type pulse generator	274
1.10.3.4.2	RC-type pulse generator	274
1.10.3.4.3	Pulse waveform and discharge energy	275
1.10.3.5	Electrode Material for EDM	276
1.10.3.5.1	Copper	276
1.10.3.5.2	Copper tungsten	276
1.10.3.5.3	Graphite	276
1.10.3.5.4	Brass	277
1.10.3.5.5	Copper graphite	277
1.10.3.5.6	Zinc alloys	277
1.10.3.5.7	Silver tungsten	277
1.10.3.5.8	Tungsten	277
1.10.3.5.9	Tungsten carbide–cobalt (WC–Co)	277
1.10.3.6	Electrode Material for Micro-EDM	277
1.10.3.7	Dielectric Medium in EDM	278
1.10.3.7.1	Mineral oil	278
1.10.3.7.2	Kerosene	278
1.10.3.7.3	Mineral seal	278
1.10.3.7.4	Transformer oil	278
1.10.3.7.5	Water-based dielectrics	278
1.10.3.7.6	Powder-mixed EDM	278
1.10.3.7.7	Dry EDM	279
1.10.4	**EDM and Micro-EDM Process Parameters**	279
1.10.4.1	EDM Performance Measure (Machining Characteristics)	280
1.10.4.1.1	MRR	280
1.10.4.1.2	EWR	280
1.10.4.1.3	Surface roughness	280
1.10.4.2	Micro-EDM Performance Measure (Machining Characteristics)	280
1.10.4.2.1	MRR	280
1.10.4.2.2	EWR	280
1.10.4.2.3	Overcut	281
1.10.4.2.4	Surface integrity	282
1.10.4.3	Various Fabrication Processes of Microelectrode	282
1.10.4.3.1	WEDG	283
1.10.4.3.1.1	Radial-feed WEDG	283
1.10.4.3.1.2	TF-WEDG	283
1.10.4.3.1.2.1	Principle of TF-WEDG	283
1.10.4.3.1.2.2	Analysis of TF-WEDG	284
1.10.4.3.1.3	Twin-wire EDM system	285
1.10.4.3.1.4	Fabrication of microelectrode for batch production by WEDM	286

1.10.4.3.1.5	Compliant microelectrode arrays were fabricated by WEDM	286
1.10.4.3.1.6	Fabrication of series-pattern micro-disk electrode	288
1.10.4.3.2	Rotating sacrificial disk	290
1.10.4.3.3	Stationary BEDG	290
1.10.4.3.4	MBEDG	291
1.10.4.3.5	Micro-turning process	292
1.10.4.3.6	EDM of micro-rods by self-drilled holes	293
1.10.4.3.7	Reverse EDM	294
1.10.4.3.8	Hybrid process	294
1.10.4.3.8.1	Micro-turning–micro-EDM hybrid machining process	294
1.10.4.3.8.2	Self-drilled holes–TF-WEDG hybrid machining process	296
1.10.4.3.8.3	Continuous machining process of array micro-holes	297
1.10.4.3.8.4	LIGA–micro-EDM hybrid machining process	298
1.10.5	**Prospective on Process Selection**	300
1.10.6	**Methodology**	303
1.10.6.1	Experimental Setup	303
1.10.6.2	Micro-EDM of WC–Co	304
1.10.7	**Results and Discussions**	305
1.10.7.1	Analysis of Results on Micro-EDM of WC–Co	305
1.10.7.1.1	Overcut	305
1.10.7.1.2	MRR and EWR	306
1.10.7.1.3	Surface roughness	311
1.10.7.1.4	Micro-crack	312
1.10.7.1.5	Material migration	314
1.10.8	**Conclusions**	318
Acknowledgment		318
References		318

1.10.1 Introduction

According to the CRIP committee of physical and chemical processes, micro-machining is considered as one of the most fundamental technologies to manufacture and miniaturize products and parts with a dimension between 1 and 999 μm.[1] Miniaturized products and parts are mainly used in biotechnology, information technology, environmental, medical industries, electric devices, miniaturized machines, and so on.[2,3] With the recent advancements in Microelectro Mechanical System, micro-machining is being more and more popular day-by-day.[4] A lot of studies have already been done about the fabrication of functional micro-structure and component.[4,5] Basically, micromachining has been classified into three processes including conventional material removal processes, non-conventional material removal processes, and hybridized processes.

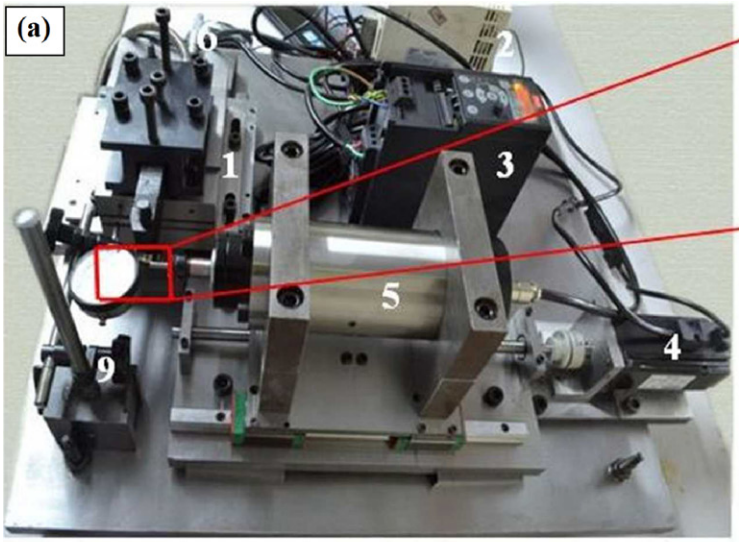
1.10.2 Material Removal Processes

1.10.2.1 Conventional Process

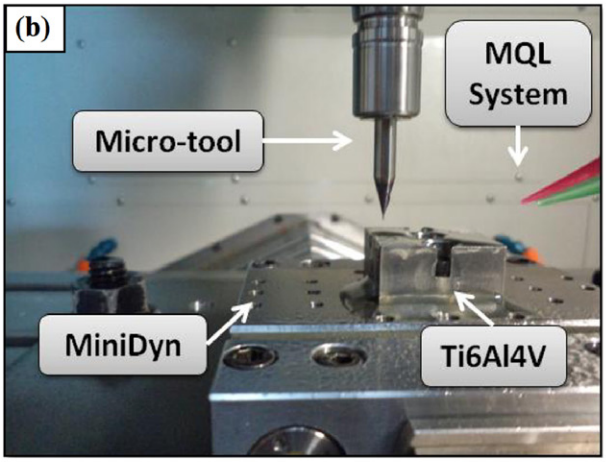
Mechanical force and energy are required for conventional material removal processes where shear force removes the material. Shear refers to simple machining process by physical contact between material and cutting tools.[6,7] Traditional material removal processes such as micro-turning, micro-milling, micro-drilling, and grinding use a single-point diamond cutter or very fine-grit-sized grinding wheels to produce machine parts. They can be used for machining of the most of the materials; for example, ferrous and non-ferrous metals, semiconductors, and plastics. The products with any shape such as flat surfaces, arbitral curvature, long shaft, and so on can be fabricated by conventional material removal processes.[8,9] Figure 1 presents the experimental setup for micro-turning, micro-milling, and micro-grinding.[10–13]

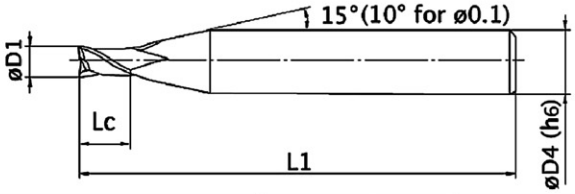
1.10.2.2 Nonconventional Process

In the nonconventional process, other sources of energy such as light energy, spark energy, vibration energy, electrolysis energy, energy beams (laser beam, electron beam, or ion beams), mechanical energy (based on erosion mechanism), etc., are used to remove the material.[7,14–16] Techniques based on energy beams (beam-based micromachining) or solid cutting tools (tool-based micromachining) can be used for micro-machining. There are some constraints due to poor control of 3D structures, low material removal rate (MRR) and low aspect ratio in the beam-based micro-machining by using the laser beam, ion beams, or electron beam. Furthermore, special facilities are required for these processes and the maximum achievable thickness is relatively small.[15,16] Also, due to its quasi-three-dimensional structure, there are some limitations in using photolithography on silicon substrates includes its low aspect ratio and limitation of the work material. High aspect ratio of three-dimensional submicron structures by very high form accuracy can be produced deep X-ray lithography using synchrotron radiation beam (LIGA) process and focused-ion beam machining process. While the special facilities are required for these processes and the

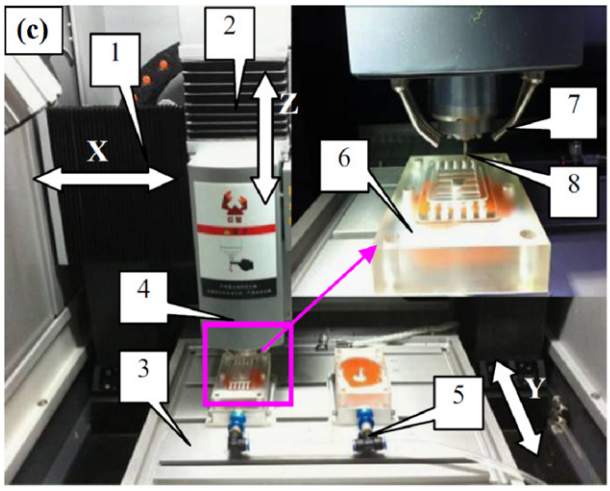


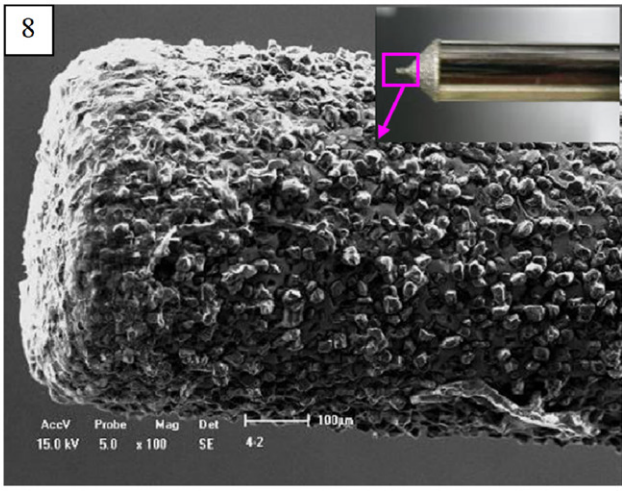
1. Piezoelectric Dynamometer
2. Encoder drive
3. Variable frequency drive
4. Servo motor with encoder
5. Spindle with inbuilt motor
6. Micrometer
7. Coated carbide tool
8. Tool holder
9. Dial gauge





	Symbol	Units	
Corner Geometry		-	S
Coating		-	MS-(AlTi)N
Cutting diameter	*D1*	[mm]	0.2
Shank diameter	*D4*	[mm]	4
Overall length	*L1*	[mm]	40
Length of cut	*Lc*	[mm]	0.3
Number of flutes	*z*	-	2





(1) X feeding device, (2) Z feeding device, (3) Working bench (Y feeding device), (4) Spindle, (5) Vacuum chuck, (6) workingpiece, (7) Coolant water, (8) Micro-grinding tool.

Figure 1 (a) Micro-turning setup,[10] (b) Close view of the micro-milling experimental setup,[11] (c) Micro-grinding system setup.[12,13]

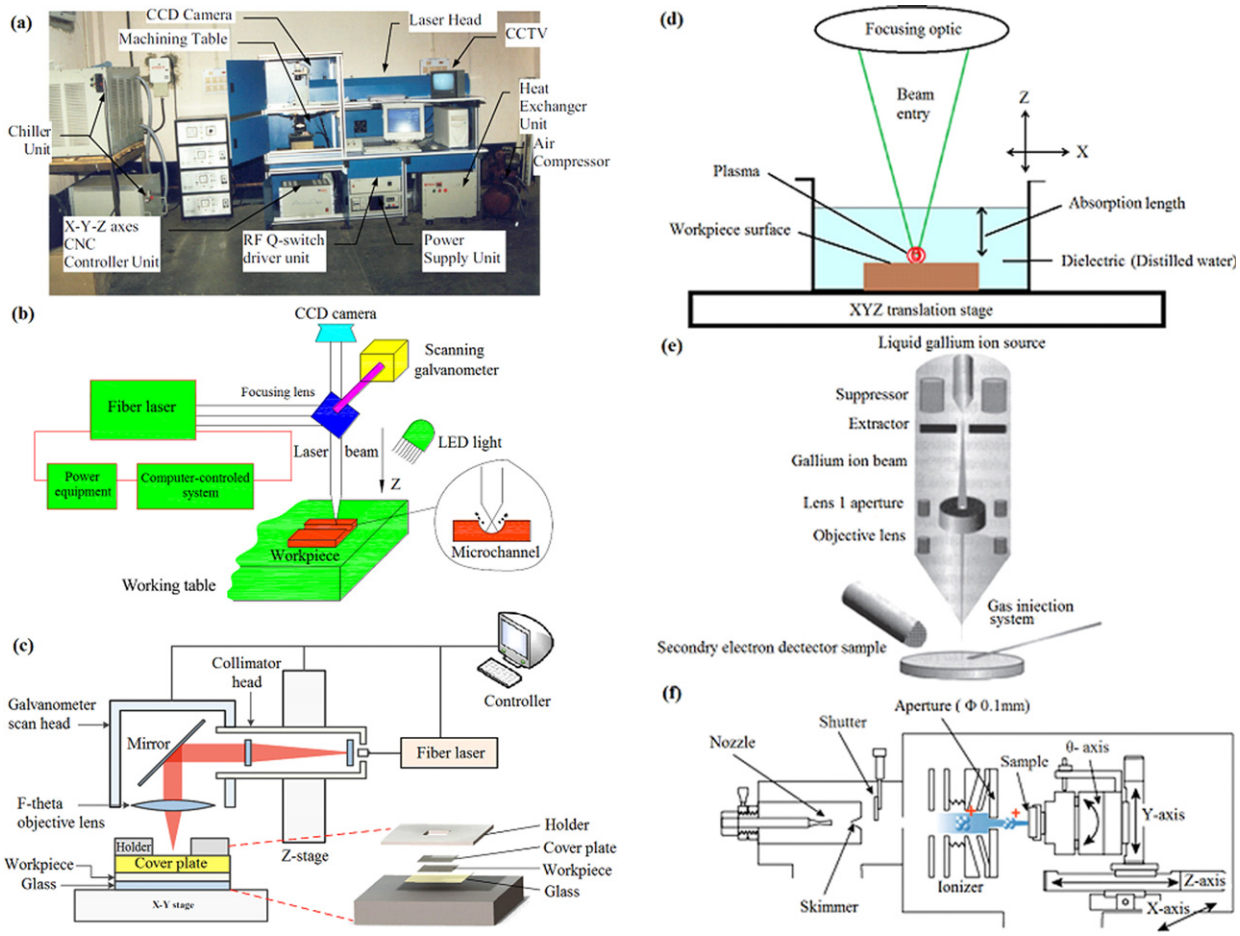


Figure 2 (a) Photographic view of the CNC-pulsed Nd:YAG laser machining system.[17] Schematic of experimental setup for: (b) laser micro-milling process,[18] (c) cover plate laser beam machining,[19] (d) laser induced plasma micro-machining,[20] (e) focused ion beams system,[21] and (f) the gas cluster ion beam irradiation system for precision machining.[22]

maximum thickness is relatively small.[15,16] Figure 2 illustrates the photographic view of the CNC-pulsed Nd:YAG laser machining system[17] and schematic diagram of experimental setup for laser micro-milling process,[18] cover plate laser beam machining (c-LBM),[19] laser induced plasma micro-machining,[20] focused ion beams (FIB) system,[21] and gas cluster ion beam irradiation system for precision machining.[22]

1.10.2.3 Hybridized Process

Hybridized processes are basically a combination of conventional material removal processes (like turning and milling) and non-conventional (such as electrical discharge machining (EDM), wire electrical discharge grinding (WEDG), and electrical discharge grinding (EDG)) to make microstructures with high accuracy. The hybrid material removal process can produce micro-components with almost all kinds of the material, such as metal, plastics, and semiconductors. It can be machined with no limitation of shape; for instance, flat surface, arbitrary curvatures, and long shaft that are needed for the moving parts and guiding structures.[23–26] The hybrid machine which includes microturning, micromilling, micro-EDM, wire electrical discharge machining (micro-WEDM), micro-WEDG, and on machine measurement equipment is shown in Figure 3.

1.10.3 EDM and Micro-EDM Processes

1.10.3.1 Electrical Discharge Machining

EDM is a nonconventional machining process that removes electrical conductive materials according to the thermal energy (melting and partial vaporization of the workpiece) produced by series of sparks occurring between the electrode and workpiece.[27–30] The EDM process is potentially useful for machining materials with various hardness, complex shapes, strength, temperature–resistant, fine surface finish, and accurate dimensions.[27–29,31–33]

Figure 4(a) illustrates that each spark occurs between the workpiece and the closest points of the electrode. The material is removed from both the electrode and workpiece by the spark, which results in an increase of the distance between the electrode and the workpiece at that point. This causes the next spark to occur at the next-closest points between the electrode and workpiece as shown in Figure 4(b). As also can be seen in Figures 4(a) and 4(b), the electrode and workpiece surfaces are quite rough. In fact, all surface finishes have irregular surfaces. Even though the surfaces have only very minute peaks and valleys, these very small changes of dimension allow the EDM spark to occur between the closest peaks.[34]

In EDM, the flow of electricity between the electrode and workpiece introduce the heat in the form of a spark. The main characteristic of the dielectric fluid is that it works as an electrical insulator, until enough voltage is applied to cause it to change into an electrical conductor. The dielectric fluid deionizes when the spark is turned off and the fluid returns to being an electrical insulator. For each spark, this change of the dielectric fluid from an insulator to a conductor, and vice versa occurs as shown in Figure 5.[34]

A small amount of the electrode and workpiece material is vaporized with each spark. The vaporized material is placed in the sparking gap between the workpiece and the electrode in the form of a cloud. The vaporized cloud solidifies when the spark is turned off. Each spark then produces a very tiny hollow sphere of material known as EDM chip (debris) made up of the electrode and workpiece material. Figure 5 illustrates the spark producing the vapor cloud, the cloud in suspension, cloud being cooled and forming into an EDM chip, and removing the chip by flowing dielectric.[34]

The EDM chip must be removed from the sparking area for efficient machining. This removal is performed by flowing dielectric fluid through the sparking gap. Part of the EDM chip is removed by the dielectric fluid and the remaining part solidifies on the electrode surface. As a result, each discharge produces a small crater on both workpiece and tool electrode.[35]

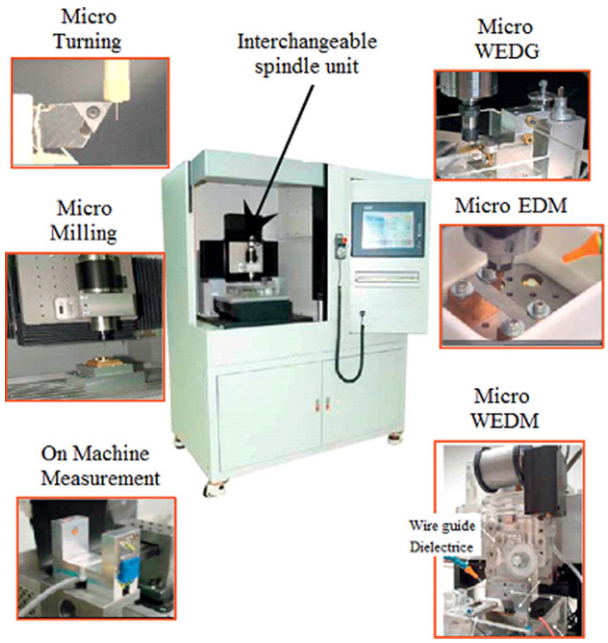


Figure 3 Hybrid machine for multi-processes of micromachining.[3]

1.10.3.2 Sparking and Gap Phenomena in EDM

Rajurkar *et al.* and Kunieda *et al.* reveal that the steps of gap phenomena include the formation of plasma in the dielectric, electrons and ions interaction, heat transfer and material removal by melting and vaporizing, solidified the melting and vaporizing material to debris (chip), flushing the debris, and another spark generation as schematically illustrated in Figures 6(a)–6(c).[36,37]

Figure 6(d) presents a schematic view of the discharge spot. The arc column diameter is considered to increase with the passage of time and equal to the diameter of the generated discharge crater. Electrode materials and dielectric liquid are evaporated, molecules are dissociated, and atoms are ionized, resulting in a rapid expansion of the bubble. As the expansion is confined by the viscosity and inertia of the dielectric fluids, the remaining inside pressure of the bubble gets extremely high level and the boundaries between the bubble and liquid get expanded with the several 10 m s^{-1} of velocity order. It is yet considered that the dielectric liquid has a significant role in the material removal process as the dynamics of the material removal in EDM depends on the high velocity and pressure development in the bubble.[36]

After the end of the discharge duration, ions and electrons are recombined and the dielectric breakdown strength is recovered. The evaporated atoms and molecules are solidified or

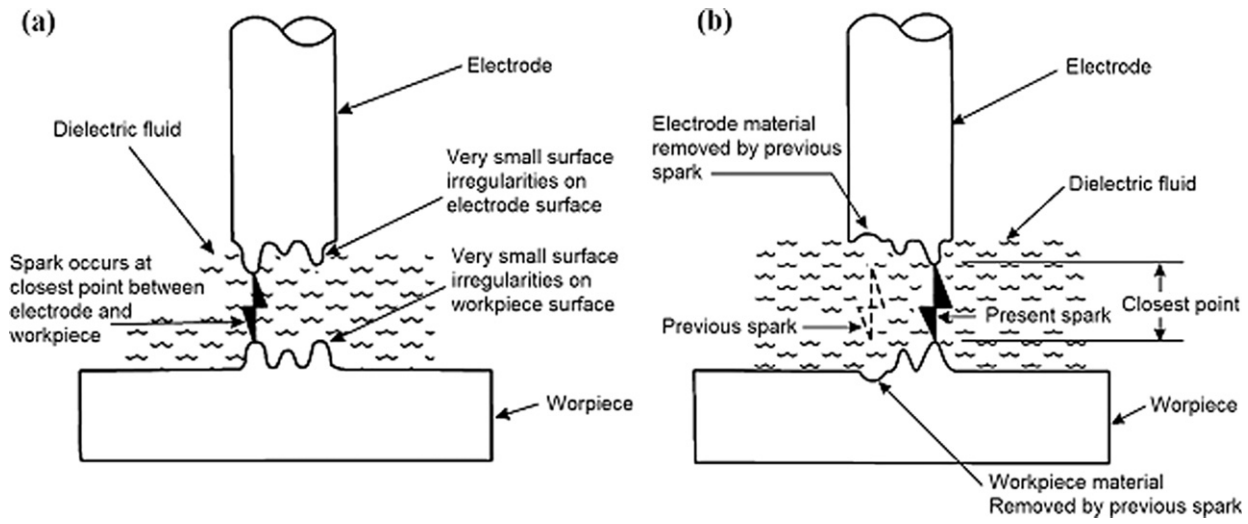


Figure 4 (a) Spark occurs between closest points. (b) Spark movement with a change of closest points.[34]

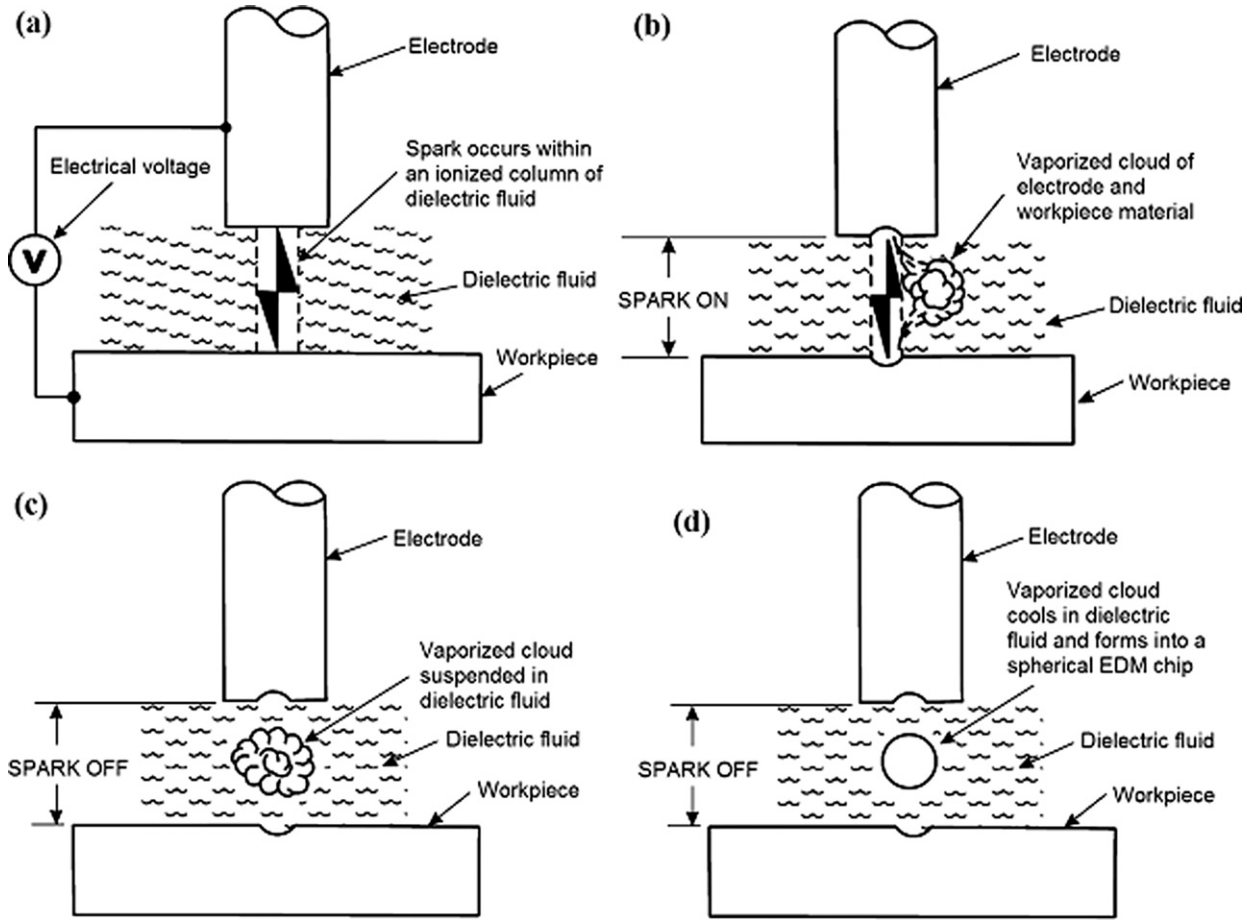


Figure 5 (a) Spark ON: electrode and workpiece material vaporized. (b) Spark OFF: vaporized cloud suspended in dielectric fluid. (c) Spark-OFF: vaporized cloud solidifies to form EDM chip (debris).[34] (d) Spark-OFF: remove the chip by flowing dielectric.

condensed to form debris particles or dielectric liquid, but gases such as hydrogen and methane which are generated by the dissociation of the working oil are left to form a bubble. Since pulse discharge occurs several thousand times or more per second, obviously the gap becomes filled with gas in typical EDM processes. Hundreds of debris particles are generated per single pulse discharge. Melted and evaporated materials are cooled by the dielectric liquid and solidified to form spherical debris particles. Thus, debris particles are removed from the gap with the dielectric liquid and not reattached on the workpiece and electrode surfaces. Furthermore, heat convection in the boundary layers of the dielectric liquid cools the workpiece and electrode surfaces, resulting in machining stability. Thus, the dielectric liquid plays another important role in flushing debris particles and cooling of the gap.[36]

1.10.3.3 Function and Types of Micro-EDM Process

Micro-EDM and EDM have same characteristics but only the size of electrode, discharge energy, and resolution of movement in axis are at the micron level in micro-EDM.[6] The principle functions of the micro-EDM process are micro-mold making, production of die and cavities, and complex three-dimensional shapes in the micron size.[38] In EDM and micro-EDM, no direct contact and negligible force between the workpiece and tool cause to elimination of deformation on the tool, chatter, mechanical stress, and vibration errors during machining.[6,39,40]

A micro-mold cavity has function in mass production of a microcomponent which can be produced by injection molding. Hard-to-machined materials are used for micro-injection that should be machined very accurately and complex shape in three-dimensional forms in the micron range.[3–5] Micro-EDM is one of the effective alternative machining processes that can be used successfully in the production of complicated three-dimensional models using very hard die materials.[3–5] Besides, it is also possible to use for very high-precision machining of the curved surface, slope surface, and thin-sheet materials that are difficult for machining.[1,6,39,41,42] Moreover, a conductive material with any hardness can be machined by micro-EDM without any force. So, micro-mold can be fabricated by using a very thin electrode with controlling of the EDM contour.[3–5]

According to Jahan *et al.*,[43] current micro-EDM technology schematic is shown in **Figure 7**, is used for manufacturing micro-features can be categorized into five different types are as follows:

- Die-sinking micro-EDM, where a microelectrode is used to fabricate its mirror image in the workpiece.

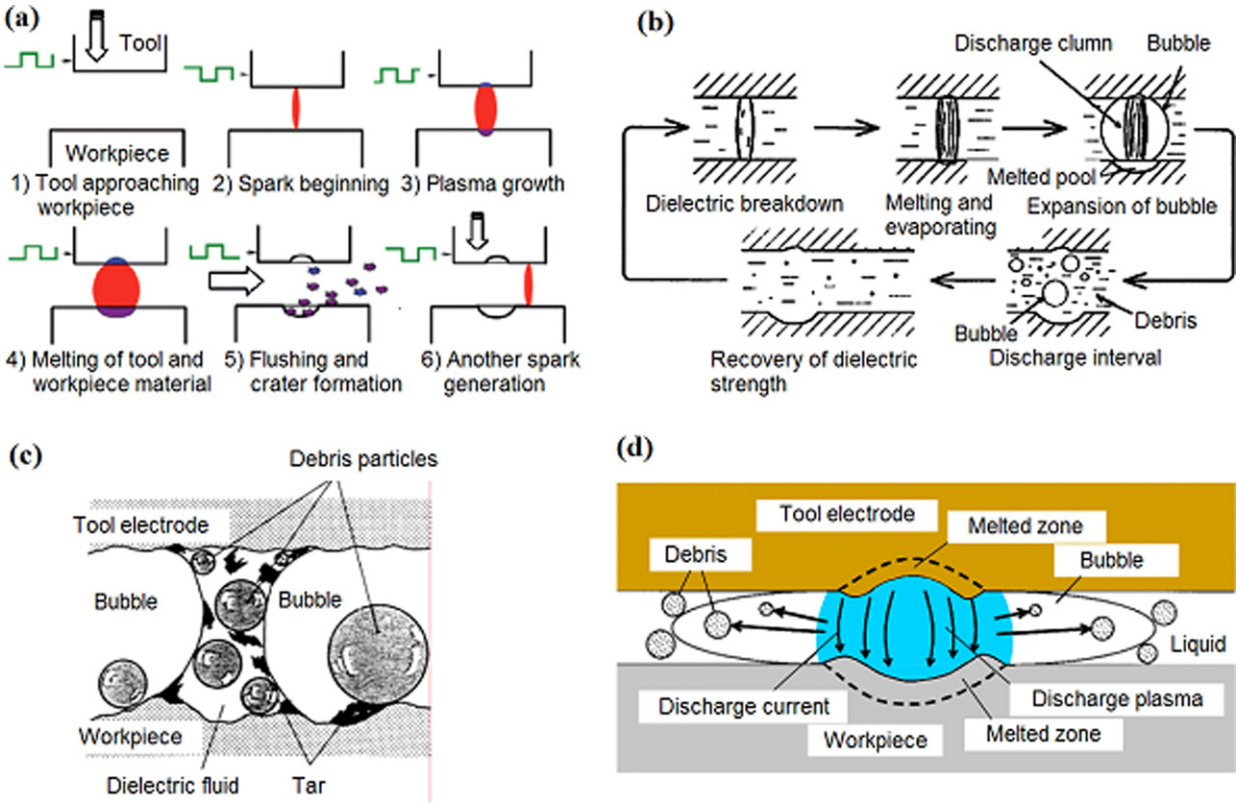


Figure 6 (a) EDM process mechanism (phenomena process).[37] (b) Model of EDM gap phenomena.[36] (c) Schematic view of discharge gap.[36] (d) Discharge phenomena in EDM gap.[36]

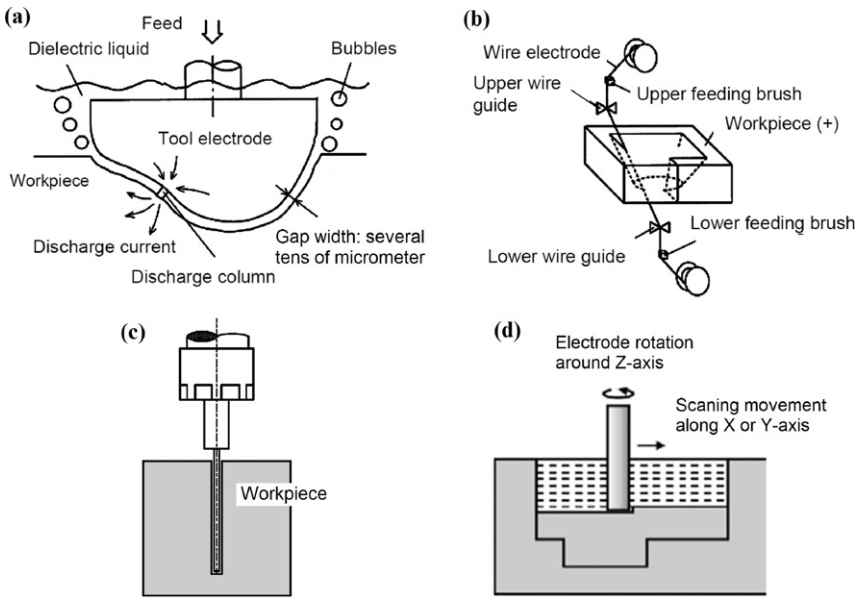


Figure 7 Schematic representation of (a) die-sinking micro-EDM,[36] (b) micro-WEDM,[36] (c) drilling micro-EDM,[5] and (d) milling micro-EDM[44] (all the tools used in different varieties of micro-EDM are in the range of 1–999 mm).[43]

- Micro-wire EDM, in which a wire of diameter less than 0.02 mm is employed to cut through a conductive workpiece.
- Micro-EDM drilling, where microelectrodes are used to 'drill' micro-holes in the workpiece.
- Micro-EDM milling, where microelectrodes are employed to produce 3D cavities by adopting a movement strategy similar to that in conventional milling.
- During micro-EDM, the micro-EDG process is employed to fabricate the microelectrodes on the micro-EDM machine

from a thicker electrode. Different setup and trajectory control of the electrode can be employed in this process included using a 'stationary block,' 'rotating disk,' 'wire EDG (WEDG),' etc.

1.10.3.4 Pulse Generators/Power Supply

Transistor-type pulse generator and resistance capacitance (RC) (relaxation-type) are the two major types of EDM power supply (Figure 8). Among these two types, *RC*-based power supply has gained extensive usage in micro-EDM. Moreover, transistor-type power supply has been employed for the power supply of the conventional EDM.[36,45–47]

1.10.3.4.1 Transistor-type pulse generator

A series of transistors and resistances are connected in parallel between the direct current power supply and the discharge gap in a transistor-type power supply as shown in Figure 8(a). The discharge current flow increases proportionately with the number of transistors switched on at the same time. The Field-effect transistor (FET) operates the gate control circuit by switching it ON or OFF. While generating a single pulse, the gap voltage is monitored to detect the discharge phenomena and the FET is turned OFF after the preset discharge duration.[45]

Transistor-type pulse generators can change the discharge current and the pulse duration based on the required machining characteristics. It provides a very uniform pulse shape resulting in much better control of surface roughness. The resistance across the circuit and the input voltage (*R* and *Vcc* in Figure 8(a)) control the discharge energy in every spark.[45] The smallest UR is obtained by increasing the resistance at around 60 V with voltage settings in transistor-type power supply. If the voltages get lower than 60 V, it will result in unstable discharges.[45–47] It is difficult to minimize the UR frequency because of micro-EDM is fundamentally a discontinuous material removal process but the UR could be minimized significantly by increasing the resistance. The transistor-type pulse generator controls the sparks using microcontroller (decision-making process of the electronics). The micro-controller sets pulse-ON time, pulse-OFF time, signal propagation delay, and the inherent delay of the power transistor. Very fast electronics are used in the setup as all those processes contribute more than few hundred nanoseconds.[36,45,48] This imposes a limit on the shortest pulse duration.[45] Jameson[34] stated that "spark energy is determined by the amount of electrical power contained in each spark, multiplied by the amount of time the electrical power is flowing." The equation for determining spark energy is:

$$E = V \cdot I_p . t_{ON} \quad [1]$$

where, V=voltage e, I_p=current of a single pulse, and t_{ON}=pulse-ON time.

1.10.3.4.2 RC-type pulse generator

Figure 8(b) shows schematic of basic circuit diagram for RC-type pulse generator. Discharge pulse duration in an RC- or relaxation type circuit is dominated by the capacitance of the capacitor and the inductance of the wire connecting the capacitor to the tool and workpiece[37,45,49] and the spark energy (discharge energy) is specified by the used capacitor. The charging and discharging cycle of the capacitor takes place repeatedly.

The capacitor (C) is charged during the charging cycle through the resistor (R) and discharged between the electrode and workpiece during the discharging cycle. The pulse energy (*E*) induced in the gap can be calculated by the following formula;[1,45,46] the gap voltage V_g is assumed to be constant during the discharge cycle.

$$E = 2CV_g(V - V_g) \quad [2]$$

In this equation, the discharge capacitance is denoted by *C* and *V* is the supplied DC voltage. The maximum discharge energy is produced when $V = 2V_g$. The value of maximum discharge energy is $0.5CV^2$, which is equal to the energy stored in the capacitor. In a real application, the RC-type pulse supply will have a stray capacitance between the electric feeders, tool electrode holder, and the work table and the tool electrode and the workpiece. Therefore, the modified form of the above equation is given below[45]:

$$E = 2(C1 + C2)V_g(V - V_g) \quad [3]$$

According to the eqn [3], the minimum achievable discharge energy per pulse is determined by the stray capacitance (*C*2) provided that the value of discharge capacitance (*C*1) is 0. Therefore, it is important to reduce the stray capacitance between the wire and the workpiece in order to decrease the spark energy. A minimum discharge energy is needed in the finishing (final stage of machining) or while machining features at the lower boundary of micro-machining domain.[3,45,49] It can easily produce pulses with high-peak current and short duration which cause to achieve required surface finish with efficient and accurate material removal. On a properly designed equipment, the stray capacitance could be kept as small as around 10–12 pF delivering 0.2-mA peak current and 30-ns wide pulse.[45,50]

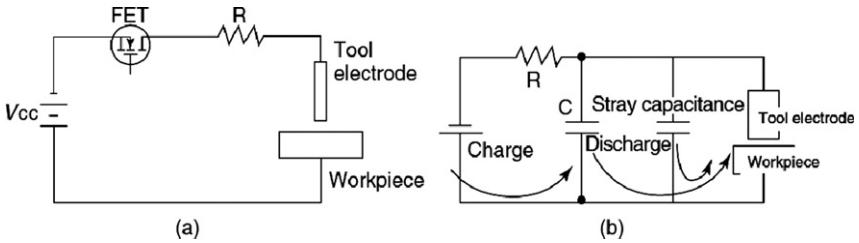


Figure 8 Schematic representation of basic circuit diagram of (a) transistor-type and (b) RC-type pulse generator.[45]

The discharge frequency (discharge repetition rate) depends on the charging time, that is determined by the circuit resistor (R) and this provides for an additional advantage of the RC power supply: when the capacitance is reduced, it also reduces the capacitor charging-up time following a first-order differential equation. The time taken for full charging-up of a capacitor can be calculated by $5 \times RC$ and while $R = 1\,k\Omega$ and $C = 10\,pF$, the full charging time of the capacitor is around 50 ns. Therefore, the value of 'R' should not be very low as arcing can occur instead of sparking and critical resistance that will prevent arcing is desirable.[45,51]

However, the use of RC pulse generator in machining usually results an extremely low MRR. This is due to the fact that the energy per spark is reduced significantly as it depends on the uncontrolled spontaneous discharge frequency bottlenecked by the required capacitor charging time. Moreover, it is difficult to obtain uniform surface finish as the discharge energy varies by depending on the stored electrical charge in the capacitor before dielectric breakdown. In addition, the workpiece can easily be thermally damaged, if the dielectric strength was not properly recovered after the previous discharge and the current continued to flow through the same plasma channel in the gap without charging the capacitor.[45,48]

The basic reason of still using RC-type power supply in micro-EDM is the fact that the charging time for a very small capacitor is much smaller, around few tens of nanoseconds, than the smallest duration of the OFF time that can be reliably achieved using a transistor-type power supply designed using available electronic components. Besides, a transistor power supply would occupy additional time around few tens of nanoseconds for the discharge current to be diminished to zero while an immediate active control of power supply is needed upon short circuit detection. Therefore, the existing high current may pass through the circuit in this additional time and causes damage to fine feature that will be machined in the workpiece.[45]

1.10.3.4.3 Pulse waveform and discharge energy

The pulse generator type determines the discharge energy and pulse shape for the micro-EDM. **Figures 9(a)** and **9(b)**, demonstrate the ideal voltage and current signals for transistor and RC-type pulse generator respectively. The spark energy (discharge energy) of a pulse generator is calculated by its electrical and discharge parameters. MRR, electrode wear ratio (EWR), and surface roughness increase with amplifying of discharge energy.[45] Though used pulse shape in micro-EDM is generally rectangular type, but generators using other pulse shapes have also been developed for various applications.[45,52] For instance, EWR decreased to very low values by initiating trapezoidal pulse shapes in micro-EDM.[45,53]

The open voltage is applied between the tool electrode and the workpiece when the transistors are switched on in the transistor-type pulse generator. But the discharge does not occur instantly. It occurs after the ignition delay time and a discharge current (I_p) is passed through the gap after the dielectric breakdown. The transistors are kept on by the gate control circuit during the discharge time, t_{on}, resulting in a uniform discharge crater size. The transistors are again switched on after the fixed discharge interval t_{off}, while the open voltage is applied between the electrodes.[34,36,45] Equation [1] can be used to calculate the discharge energy per single pulse.

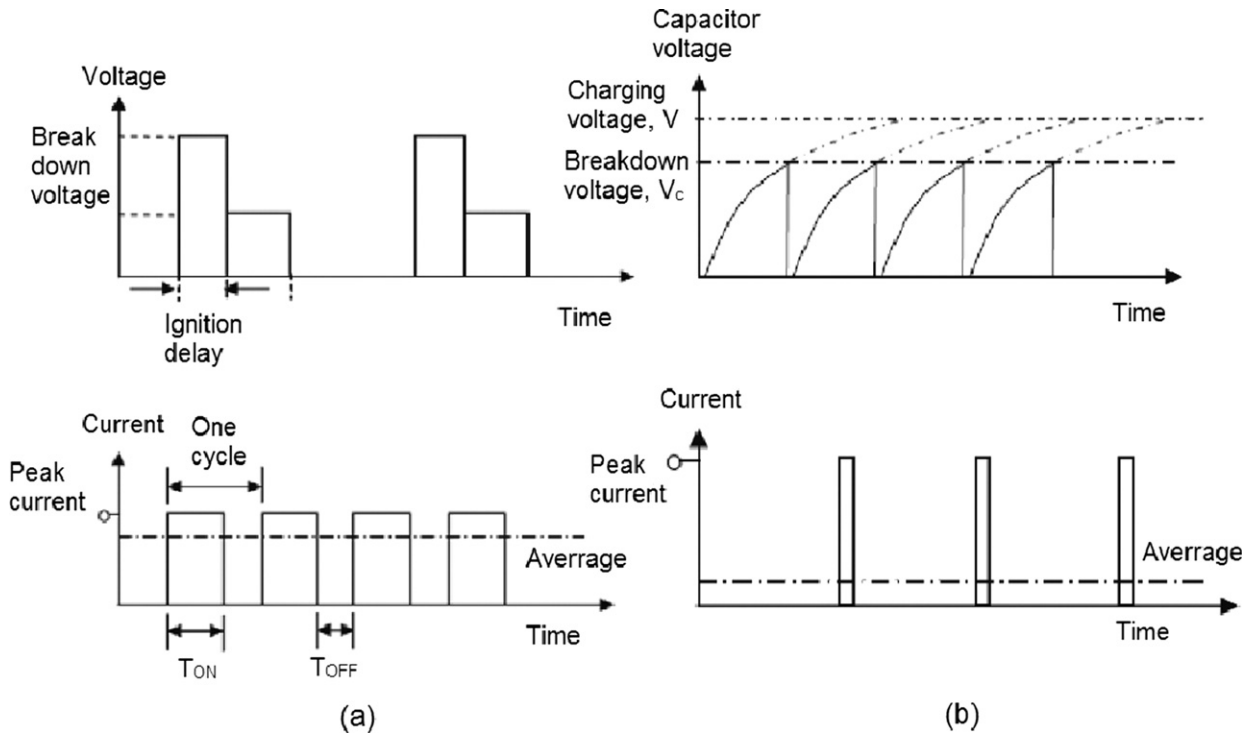


Figure 9 Ideal voltage–time (top) and current–time (bottom) characteristics curve/waveform for (a) transistor-type and (b) RC-type pulse generator.[45,54–58]

The capacitor charging time is considered as the pulse interval or pulse-OFF time, whereas the discharging time is assumed as the pulse-ON time in the RC pulse generator. One of the major characteristics of RC-type pulse generator is that the charging voltage is higher than the breakdown or discharging voltage (V). As a result, sometimes discharging starts before the capacitor is fully charged,[45,48] which generates nonuniform discharge energy. A simplified form of the discharge energy per single pulse, E, can be calculated by eqn [2] where $V=2V_g$

$$E=\frac{1}{2}CV^2 \quad [4]$$

where C is the capacitance used for machining and V is the discharge voltage.[45,59]

1.10.3.5 Electrode Material for EDM

Jameson[34] stated that "electrode materials for EDM must be electrically conductive. However, they should have features such as: high melting point, an ability to be easily machined and low cost." No single electrode material provides all of the desired features for any particular application. The following list of materials is intended as a guide to electrode materials commonly used for die-sinking machines.

1.10.3.5.1 Copper

As Jameson[34] stated "copper is readily available and normally specified as electrolytic-grade or tellurium-copper alloy." Electrolytic grade may be considered as pure copper. Tellurium copper is copper with the element tellurium added and it is equivalent in machinability to free-machining brass. Copper is difficult to grind but has good no-wear-machining characteristics. It is often used for RC power supply operations. Wang and Lin[60] stated that "copper was chosen as electrode for electrical discharge machining of copper tungsten." The physical properties of copper that used by Che Haron[61] are shown in Table 1.

Table 1 Physical properties of copper electrode[61]

Physical properties	*Value*
Electrical resistivity ($\mu\Omega$ cm^{-1})	1.96
Electrical conductivity compared with silver (%)	92
Thermal conductivity (W m K^{-1})	268–389
Melting point (°C)	1083
Specific heat (cal g^{-1} °C)	0.092
Specific gravity at 20 °C (g cm^{-3})	8.9
Coefficient of thermal expansion ($\times 10^{-6}$ °C^{-1})	6.6

1.10.3.5.2 Copper tungsten

Copper–tungsten (CuW) composite is a one kind of self-cooling which is highly resistant to heat corrosion. Phasing can be seen between tungsten and copper in the microstructure of CuW composites because of tungsten and copper have no solid solubility with each other.[62,63] Therefore, CuW composites can be considered as composite material and they are not alloys. CuW composites cannot be created through traditional metal-casting processes and are currently produced through powder metallurgy because of large dissimilation between the melting points of tungsten and copper. Powder metallurgy is gained by compacting pure tungsten powder in a mold (porous), then sintering it under high temperatures and infiltration of liquid copper.[64–66] CuW composites have a high-melting point, corrosion, and abrasion resistance, and act as good conductors for both current and heat.[60] CuW composites possess a very high-melting point with promising corrosion and abrasion resistance, and a good conductor of electricity and heat.[60] The Specification of copper tungsten is shown in Table 2.

Jameson[34] stated that "CuW is often used as an electrode for EDM of tungsten carbide." Lee and Li[68] used copper tungsten as an electrode during the machining of tungsten carbide. Moreover, Soni and Chakraverti[69] found that chemical composition of high-carbon high-chromium die steel (hardened) was changed during EDM machining with rotating copper tungsten (W80, Cu 20) electrode because of the material migration from the electrode. The result of this experiment showed that the migration of tungsten from the tool electrode to the workpiece was higher in blind holes machining rather than in through holes machining. The properties of electrode material are given in Table 3.[68]

1.10.3.5.3 Graphite

Lee and Li[68] used graphite as their electrode material to identify with the comparisons between others electrode in

Table 2 Specification of copper tungsten[67]

Code No.	*Chemical composition %*			*Mechanical properties*				
	Cu	*Impurity*	*W*	*Density (g cm^{-3})*	*Hardness (HB)*	*Resistivity (cm)*	*Conductivity IACS (%)*	*TRS (MPa)*
CuW(50)	50±2.0	0.5	Balance	11.85	115	3.2	54	–
CuW(55)	45±2.0	0.5	Balance	12.30	125	3.5	49	–
CuW(60)	40±2.0	0.5	Balance	12.75	140	3.7	47	–
CuW(65)	35±2.0	0.5	Balance	13.30	155	3.9	44	–
CuW(70)	30±2.0	0.5	Balance	13.80	175	4.1	42	790
CuW(75)	25±2.0	0.5	Balance	14.50	195	4.5	38	885
CuW(80)	20±2.0	0.5	Balance	15.15	220	5.0	34	980
CuW(85)	15±2.0	0.5	Balance	15.90	240	5.7	30	1080
CuW(90)	10±2.0	0.5	Balance	16.75	260	6.5	27	1160

Table 3 Physical properties of copper tungsten electrode[68]

Physical properties	*Value*
Composition	75% tungsten, 25% copper
Density (g cm^{-3})	15.2
Melting point (°C)	3500
Electrical resistivity (μΩ cm^{-1})	5.5
Hardness (HB)	200

Table 4 Physical properties of graphite electrode[68]

Physical properties	*Value*
Density (g cm^{-3})	1.811
Melting point (°C)	3350
Electrical resistivity (μΩ cm^{-1})	1400
Hardness (HB)	10

their researches when machining tungsten carbide. The properties of graphite used in their study are given in **Table 4**. Graphite was found to have high effects on the MRR and on the surface roughness (Ra) when compared to copper and copper tungsten.

1.10.3.5.4 Brass

According to Jameson,[34] brass is readily available. The grade used is normally specified as free machining brass. It has a fairly good wear ratio when machining steel and a very high wear ratio when machining tungsten carbide. Brass is not normally recommended for use with RC-power supplies.

1.10.3.5.5 Copper graphite

Copper graphite is fine-gram graphite that is infiltrated with copper. It has the qualities of graphite, plus the electrical conductivity of copper.[34]

1.10.3.5.6 Zinc alloys

Zinc is rarely used except for coating. It is basically a crystalline metal with moderate ductility and strength. Followed by iron, aluminum, and copper, zinc is the fourth mostly used metal. Many wrought alloys of zinc are available with different alloying elements to improve the strength, ductility, and workability. There are two major group of zinc alloy available for casting. The first one is a standard casting alloy which basically contains zinc with less than 5% aluminum in a hypo-eutectic alloy. The second one is a newer group of hyper-eutectic zinc–aluminum alloys, containing up to 27% of aluminum. Both groups are primarily used in die casting.[70] Jameson reported that[34] zinc alloys may be adopted as an electrode material, but the wear characteristics are very poor.

1.10.3.5.7 Silver tungsten

Silver tungsten (AgW) is a kind of powder metal that combines the high conductivity of silver with the wear resistance of tungsten, to give an unmatched combination of low wear and fine surface finish for EDM applications with fine detail. AgW can be fabricated by the same process as CuW. AgW has some limited range of applications because of its high cost and limited availability.[71]

Table 5 Properties of WC–6%Co[75]

Nominal composition	*94WC–6Co*		
Grain size (in micron size)	*Fine*	*Medium*	*Coarse*
Hardness, HRA	92.5–93.1	91.7–92.2	90.5–91.5
Density, g cm^{-1}	15.0	15.0	15.0
Transverse strength, MPa	1790	2000	2210
Compressive strength, MPa	5930	5450	5170
Modulus of elasticity, GPa	614	648	641
Relative abrasion resistance	100	58	25
CTE, ppm K^{-1}	4.3	4.3	4.3
CTE, ppm K^{-1}, at 1000 °C	5.9	5.4	5.6
Thermal conductivity, W m^{-1} K^{-1}	–	100	121

1.10.3.5.8 Tungsten

Tungsten (W) had been the electrode material of choice for certain limited EDM applications due to the combination of its high density, melting point, and tensile strength. Tungsten has poor electrical conductivity which causes to cut much slower than copper or brass. Also, tungsten is seldom used because of its high cost and very low machinability.[71]

1.10.3.5.9 Tungsten carbide–cobalt (WC–Co)

Tungsten carbide (WC) and its composite (WC–Co) are employed for producing cutting tools, dies, and other special tools and components owing to their high hardness, strength, wear, and corrosion resistance over a wide range of temperatures;[72,73] Also, they can be used as electrode for EDM.[3,74] **Table 5** illustrates the properties of WC–6%Co.

1.10.3.6 Electrode Material for Micro-EDM

The thermal property of the electrode materials has significant influence on the micro-EDM performance as micro-EDM is a thermal process. The electrode with higher heat conductivity has lower temperature on its surface when the heat fluxes from the arc column are equal.[36] Therefore, the materials with higher heat conductivity, melting point, and boiling point are appropriate as microelectrodes. The important properties of the electrode materials, which influence on the micro-EDM process, include melting and boiling temperatures, electrical and thermal conductivity, and specific heat.[54,55,57] **Table 6** demonstrates what kind of materials as microelectrode was used by previous researchers for machining of various materials.

According to Jahan *et al.*,[57] between AgW, CuW, and W electrodes for micro-EDM of WC, AgW electrode produces smoother and defect-free nanosurface with the lowest R_a and R_{max} among the three electrodes. Besides, a minimum amount of material migrates from the AgW electrode to the WC workpiece during the finishing micro-EDM. On the other hand, a CuW electrode achieves the highest MRR followed by AgW and W. In the case of electrode wear, the W electrode has the lowest wear followed by CuW and AgW.

Table 6 Materials of microelectrode for machining various workpieces

Materials of microelectrode	*Materials of workpiece*	*Reference*
Copper tungsten (CuW) Silver tungsten (AgW) Tungsten (W)	WC 10 wt.%Co	57
Tungsten carbide	A block of Uddeholm Stavax ESR tool steel	76
Brass	Nickel–titanium-based shape memory alloy (SMA) with 500 μm thickness	77
Tungsten carbide	Titanium alloy (Ti–6Al–4V)	78
Tungsten carbide	SiC microparticle suspended dielectric on machining Ti–6Al–4 V	79
Tungsten	Inconel 718 alloy	80
Tungsten	RB-SiC material composed of 6H–SiC grains (grain size 1 μm, 88% in volume) and a Si matrix (12% in volume)	81

1.10.3.7 Dielectric Medium in EDM

Basic characteristics required for dielectric used in EDM are high-dielectric strength and quick recovery after breakdown.[82] Sommer[83] stated that "dielectric fluid performs three important functions:

1. The fluid forms a dielectric barrier for the spark between the workpiece and the electrode.
2. The fluid cools the eroded particles between the workpiece and the electrode.
3. The pressurized fluid flushes out the eroded gap particles and removes the particles from the fluid by causing the fluid to pass through a filter system."

The selection of a dielectric fluid is subject to certain conditional as follows[84]:

1. It must be capable of being ionized at a consistence voltage so that its performance is predicted.
2. It must be able to deionizer so that it becomes an efficient insulator during his next build-up of the discharge.
3. There must be no dermatitis.
4. There should be no toxic fumes or excessive smoking.
5. The fluid should inhibit corrosion.
6. The flashpoint of the fluid should be high.
7. The fluid must have low viscosity.

1.10.3.7.1 Mineral oil

Mineral oil or liquid petroleum is a by-product in the distillation of petroleum.[85]

1.10.3.7.2 Kerosene

Kerosene was one of the first popular dielectric oils. Its primary benefit is that it has very low viscosity and flushes very well. Unfortunately, it has many drawbacks like low-flash point, high volatility, odor, and skin reactions. In the 'old days,' there were numerous EDM fires and explosions attributed to the use of kerosene.[85]

1.10.3.7.3 Mineral seal

The name mineral seal oil refers to the fact that it has been derived from sea seal blubber for using in signal lamps and light houses. Mineral seal oil is basically petroleum oil which has many industrial applications. For example, this oil was used as a dielectric fluid in EDM by a number of aerospace companies. In fact, it is listed as potential aerospace dielectric oil in recent times. Unfortunately, it contains some potentially carcinogenic elements, and its use is no longer recommended.[85]

1.10.3.7.4 Transformer oil

Transformer oil is another type of mineral oil-based product which was tailored to be used in EDM as dielectric. Earlier generations of transformer oil were compounded with PCBs. However, transformer oil is not currently being used in EDM.[85]

1.10.3.7.5 Water-based dielectrics

Water is a dielectric fluid which can be used as an alternative to hydrocarbon-based oils. This approach is important to promote a healthy and safe environment while using water in EDM machining. Contemporarily used hydrocarbon oils (i.e., kerosene) release toxic vapor (CO and CH_4) after being decomposed.[86] Research has been carried out over the last 25 years which involves the use of pure water and water with additives.[85,87] Leao and Pashby[88] reported that many works have already been carried out to evaluate the feasibility of adding organic additives such as ethylene glycol, polyethylene glycol 200, polyethylene glycol 400, polyethylene glycol 600, dextrose, and sucrose to improve the properties as well as performance of demonized water as dielectric.

1.10.3.7.6 Powder-mixed EDM

The working principle of powder-mixed EDM (PMEDM) is completely different from the contemporary EDM machining process.[89] An appropriate material in the powder form is mixed into the EDM dielectric. When a suitable voltage is applied, the spark gap filled up with powder particles and the gap distance setup between tool and the work piece increased. The powder particles get energized and act in a zigzag fashion as illustrated in **Figure 10**. These energized particles are accelerated by the supplied electric field and behave as electric conductors. The charged powder particles arrange themselves in clusters beneath the sparking area.[85] This chain formation of charged particles in the dielectric helps to bridge the gap between electrode and workpiece which is responsible for the early explosion. Thus, faster sparking (discharge) takes place and faster erosion from the workpiece surface occurs.[85,90] Adding aluminum powder in the dielectrice results in increased MRR and improved surface roughness during EDM.[27,91]

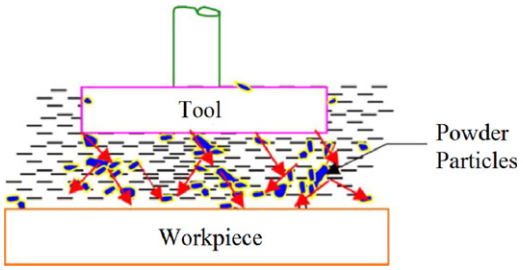


Figure 10 Principle of powder-mixed EDM.[92]

1.10.3.7.7 Dry EDM

In dry EDM, a thin-walled pipe works as tool electrode through which high-pressure gas or air is flown. The high-pressure gas flow to remove the debris from the gap and cools down the inter electrode gap. The technique was invented to decrease the pollution caused by the use of dielectric fluid which leads to production of vapors during machining and the cost to manage the waste.[93]

1.10.4 EDM and Micro-EDM Process Parameters

EDM parameters are categorized into two groups:

1. Electrical parameters:
   - Polarity of the electrode
   - Machining voltage
   - Current
   - Pulse-ON time (duration or pulse time)
   - Pulse-OFF time (non-load voltage or pause time)
   - Duty factor
   - Capacitor.
2. Non-electrical parameters:
   - Flushing pressure of dielectric
   - Rotating speed of the electrode.

The electrode polarity, machining voltage, current, pulse-ON time, pulse-OFF time, duty factor, flushing pressure of dielectric, and rotating speed of the electrode are the parameters are used in transistor-type pulse generator while the electrode polarity, machining voltage, capacitor, flushing pressure of dielectric, and rotating speed of the electrode are the parameters used in RC-type pulse generator. As mentioned before, RC-based power supply has gained extensive usage in micro-EDM.[36,45–47]

The electrode polarity: Electrical polarity of the electrode and workpiece determines the direction of flow for electrons and positive ions. Some EDM manufacturers describe electrode and workpiece polarity as standard and reverse. This description is not acceptable since not all manufacturers use the same polarity for standard and reverse. Because of this, most manufacturers have revised their electrode and workpiece polarity description to specify only electrode polarity as either negative or positive. It is understood, when using this description, that the workpiece is the opposite polarity of that specified for the electrode.[34]

The electrons usually are emitted from the cathode (negative polarity) and move toward the anode (positive polarity) during the micro-EDM process. After that, the metal ions are removed from the anode material due to the electrons which reach the anode surface strike the anode surface. Hence, more materials are removed from the anode's surface rather than the cathode's surface. This is the main reason for earning high MRR when the polarity of electrode is negative during micro-EDM of workpiece with positive polarity.[45]

Discharge voltage: Discharge voltage in the EDM process depends on the spark gap and breakdown dielectric strength. Before flowing electricity, the open gap voltage gets increased till the ionization path is created through the dielectric. As soon as the current starts to flow, the voltage decreases and stabilizes at the working gap level. The predetermined voltage sets the spark gap width between the leading edge of the electrode and workpiece. A higher voltage setting augments the gap, which improves the flushing conditions and helps to stabilize the cut. As the electric field strength improves, tool wear rate (TWR) of MRR and surface roughness amplifies with increasing the open-circuit voltage. However, the after machining effect of varying the open-circuit voltage on surface hardness has been found to be marginal.[52]

Peak current: Peak current is the amount of power used in discharge machining and the ampere (A) is its unit. The current is the most important machining parameter in EDM. During each pulse-ON time, the current amplifies until it reaches a preset level, which is expressed as the peak current, with the augmentation of the current, MRR and electrode wear increase and surface finish deteriorates.[39,52]

Pulse-ON time (duration or pulse time): Pulse-ON time is the time duration that the current is allowed to flow per cycle. Material removal is directly proportional to the amount of energy applied during this pulse-ON time. The spark energy (discharge energy) is controlled by the pulse-ON time and peak current.[94]

Pulse-OFF time (non-load voltage or pause time): Pulse-OFF time is the time duration between the sparks (pulse-ON time). Pulse-OFF time allows the molten material to solidify and to remove debris from the distance between electrode and workpiece (arc gap). This parameter is to affect the speed and the stability of the cut. Thus, using the too short pulse-OFF time causes the sparks to be unstable.[94]

Duty factor: Duty factor is calculated based on following equation.[95]

$$\text{Duty factor} = \frac{\text{Pulse-ON time}}{\text{Pulse-ON time} + \text{Pulse-OFF Time}} \times 100\% \quad [5]$$

Capacitor: The capacitor stores the electrical energy and discharges during the machining. When machining starts as soon as the dielectric breaks down, it discharges the charge stored in the capacitor.[96]

Flushing of dielectric fluid: The dielectric fluid is utilized to flush through the spark gap (the distance between electrode and workpiece) to remove debris (chip) during machining and to keep the dielectric temperature below its flash point.[52] The dielectric flushing during the sparking process has an effect on the EDM performance measures. The flushing during the roughing step influenced the MRR and EWR, while in the finishing step; it influenced the surface roughness. The flushing rate also affects the recast layer and crack density, which can be minimized by obtaining an optimal flushing rate. Moreover, the different properties of the dielectric fluid also play a vital role in flushing away the debris from the machining gap. MRR and

EWR are dependent on the conductivity, breakdown resistance, viscosity, flash point, and safety factors of the dielectric fluids.[52]

Rotating speed of the electrode: The tangential velocities of the electrode amplifies with increasing of the electrode rotating speed, which causes to the dielectric disturbance.[97] The augmentation of the dielectric flow speed helps to remove and flash out debris between the electrode and workpiece (the machined zone). Therefore, it causes to remove higher material from the workpiece.[74]

1.10.4.1 EDM Performance Measure (Machining Characteristics)

1.10.4.1.1 MRR

MRR is calculated based on the volume of material removed from the workpiece divided by machining time.[95]

$$\text{MRR} = \frac{\text{Volume of material removed from workpiece}}{\text{Time of machining}} = \frac{W_b - W_a}{t_m}(\text{g min}^{-1}) \quad [6]$$

where W_b is the weight of workpiece material before machining (g), W_a is the weight of workpiece material after machining (g), and t_m is the machining times (min).

1.10.4.1.2 EWR

EWR is calculated based on the percentage of volume of material removed from the electrode divided by the volume of material removed from the workpiece.[95]

$$EWR = \frac{T_b - T_a}{W_b - W_a} \times 100\% \quad [7]$$

where, T_b is the weight of electrode material before machining (g), T_a is the weight of electrode material after machining (g), W_b is the weight of workpiece material before machining (g), and W_a is the weight of workpiece material after machining (g). Figure 11 illustrates different kinds of electrode wear including: (1) corner wear, (2) end wear, (3) side wear, and (4) volumetric wear[34]:

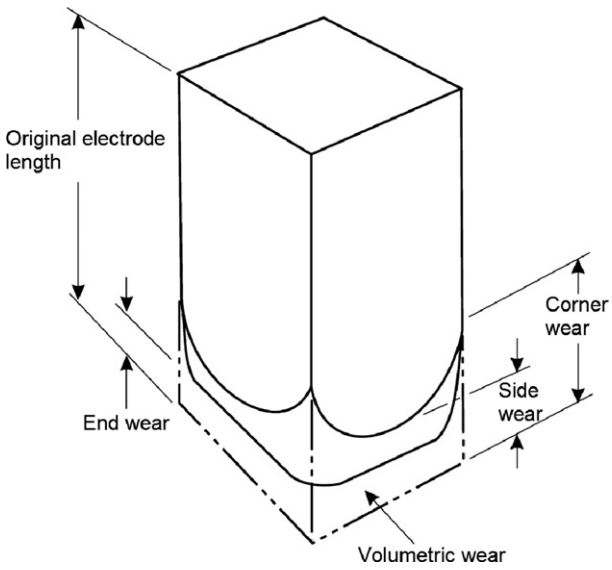


Figure 11 The different kinds of electrode wear.[34]

1.10.4.1.3 Surface roughness

The surface finish is controlled by the number of discharges per second, more often referred to as the frequency sparks. The greater amount of energy applied the greater amount of material removed. However, when greater amounts of current are used larger craters are eroded from the work, causing a rougher surface finish. To maintain increased metal-removal rates and at the same time improve the surface finish, it is necessary to increase the frequency of the discharges. Surface integrity involves the measures of surface roughness, heat affected zone, micro-hardness, micro-crack, residual stress, diffusion of tool material and carbon, and endurance limit.[98]

1.10.4.2 Micro-EDM Performance Measure (Machining Characteristics)

1.10.4.2.1 MRR

Micro-EDM produces the reverse-copied shape of the microelectrode in the workpiece. Figure 12 illustrates the relationship of the micro-hole shape with an microelectrode feed. It is possible the micro-holes shapes were not confirmed because of the microelectrode wear if the microelectrodes did not feed enough. In order to achieve the acceptable micro-holes shape, it is essential to feed the microelectrodes several times as long as the workpiece thickness.[40]

In fact, it is usual to measure the weight differences and convert them into volumes by the materials density. But, this method is inappropriate for micro-EDM as the removed materials is so small (about less than 10 ng) that it is difficult to measure it accurately. So, it is important to measure and calculate removed volume of materials directly.[40] The micro-hole is not an ideal cylindrical one but a tapered one because of the debris moving and the second discharge on the side of micro-hole.[96] MRR is calculated by following equation (the geometry is shown in Figure 13).[96]

$$\text{MRR} = \left\{\frac{\pi}{3}\left[r_{\text{Top}}^2 + r_{\text{Top}}\, r_{\text{Bottom}} + r_{\text{Bottom}}^2\right] \times h\right\} \div t \quad [8]$$

where, r_{Top} is the radius at the entrance side, r_{Bottom} is radius at exit side, h is the workpiece thickness, and t is the machining time to make a micro-hole at a particular setting.

1.10.4.2.2 EWR

Figure 14 demonstrates the different types of wear on the microelectrode. EWR refers to the ratio of amount of

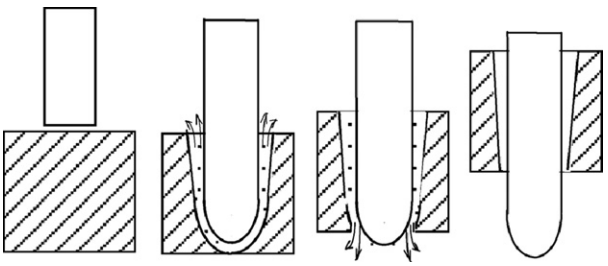


Figure 12 Influence of microelectrode feed on the shape of a micro-hole.[40]

microelectrode removal to the workpiece removal. There are four different methods to determine the EWR which include measuring weight, shape, microelectrode length, and total volume respectively. A popular one is by evaluating volumetric EWR. In fact, it is a usual method to measure the weight differences and then transfer them into the volumes by the density of materials. However, this method is not suitable to evaluate EWR for micro-EDM. As the weight change of the materials in micro-EDM is so small (about less than 10 ng) that it is difficult to determine it accurately. Therefore, it is necessary to directly measure and analyze removed volume.[40]

EWR is computed by following equations respectively.

$$\mathrm{EWR} = \frac{TW}{\mathrm{MRR}} \quad [9]$$

$$TW = \frac{\pi D^2 T}{4t} \quad [10]$$

where TW refers to the volumetric TWR, T refers to the frontal microelectrode wear (bottom wear), D refers to the microelectrode diameter, and t refers to the machining time to make a micro-hole at a particular setting.

The wear morphologies of the fabricated microelectrodes are illustrated in the **Figure 15** after machining micro-holes on the workpiece SUS304 with the same condition. It was reported that strong wear occurs on the corner areas especially for nickel (Ni), titanium (Ti), and iron (Fe) microelectrodes because of the low thermal conductivity. Aluminum microelectrode (Al) had the melting trace after machining of SUS304 and the bending was during machining of iron. Therefore, the very low melting point aluminum has to be taken into consideration. The results show that corner rounding of the microelectrodes is strongly correlated with heat and a great amount of heat stacked at the corner would cause strong wear off.[40]

Tsai and Masuzawa[40] by comparing the microelectrode wears of various materials in micro-EDM found that:

a. The microelectrode volumetric wear ratio gets lower for the microelectrode material with high boiling and melting point with high thermal conductivity. This is independent phenomena for different workpiece materials.
b. Microelectrode corner wear is related to heat diffusion. Therefore, corner rounding is more obvious when the thermal conductivity of the microelectrode remains low.
c. The boiling point of the microelectrode material takes a vital role in wear mechanism of micro-EDM, as high surface temperature and energy density are related to small discharge spot.

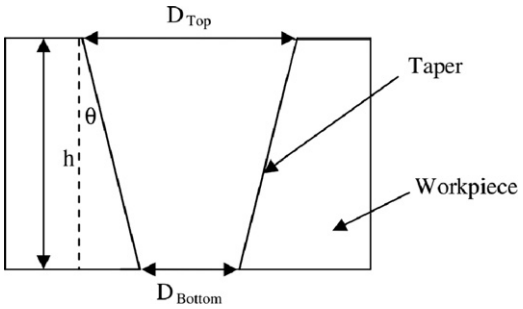


Figure 13 Overview of micro-hole.[96]

1.10.4.2.3 Overcut

The micro-holes overcut were calculated from the distance between the machined micro-holes diameter and the microelectrode diameter. Due to the taper shape of the microelectrode, the overcut was calculated from the average value of the micro-holes entrance and exit side. The overcut is calculated from the following equations (**Figure 13**)[96]:

$$O_c = \frac{D_h - D_t}{2} \quad [11]$$

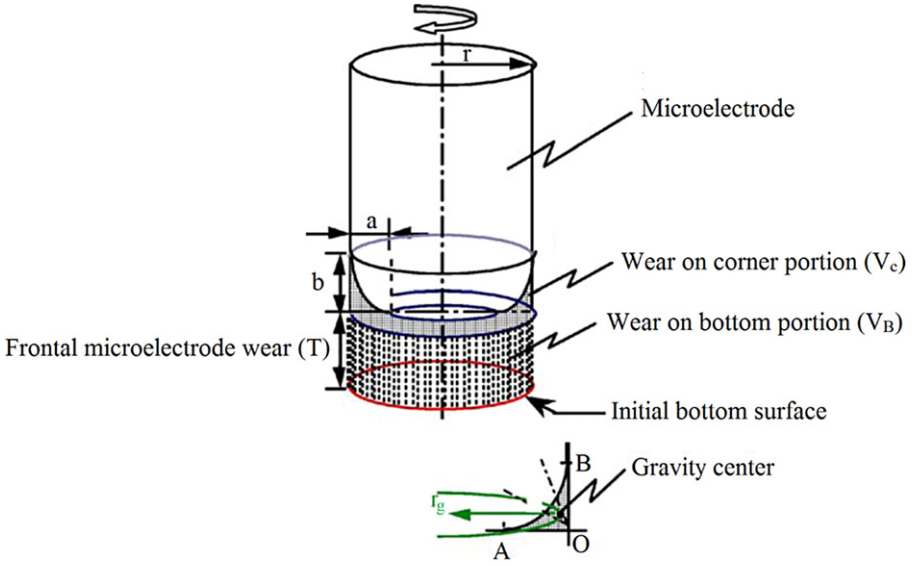


Figure 14 Wear of the microelectrode.[40]

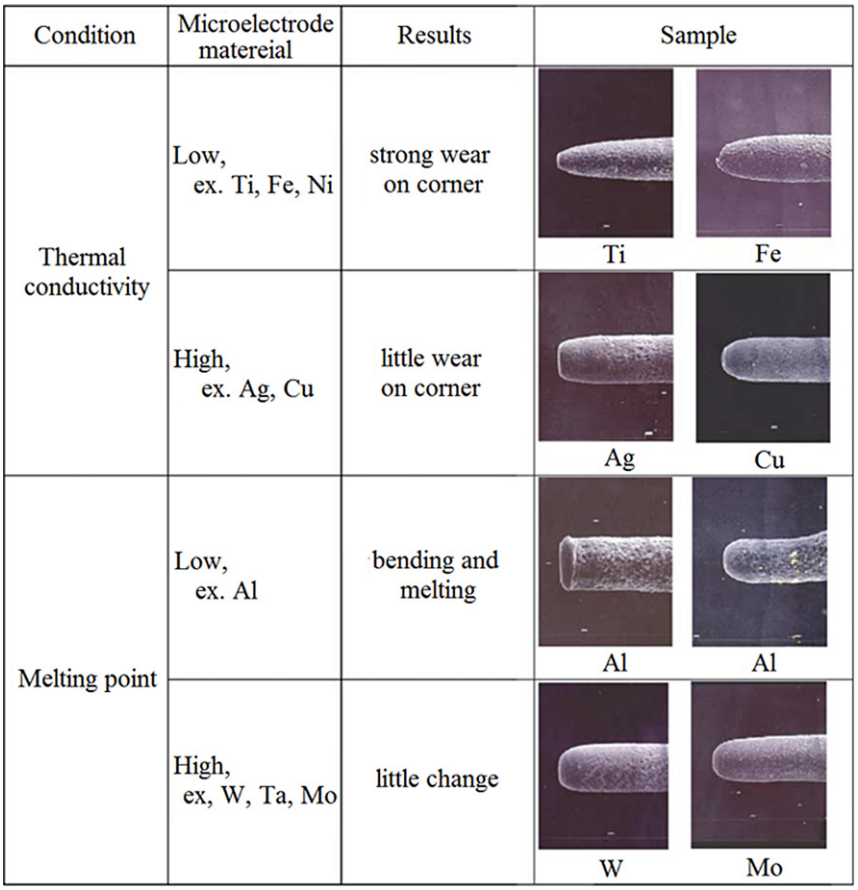


Figure 15 Microelectrode morphology with the thermal properties of materials.[40]

and

$$D_h = \frac{D_{Top} + D_{Bottom}}{2} \quad [12]$$

where O_c is overcut of the micro-holes, D_h is the average diameter of the micro-hole after machining, D_t is the diameter of the microelectrode, D_{Top} is the entrance diameter, and D_{Bottom} is the exit diameter of the micro-hole.

1.10.4.2.4 Surface integrity

Surface integrity involves two aspects: topography characteristics and surface layer characteristics. The topography characteristics are made up of surface roughness, waviness, errors of form, and flaws. The surface layer characteristics that can change through processing are: plastic deformation, residual stresses, heat affected zone, micro-cracks, micro-hardness, phase changes, and recrystallization.

1.10.4.3 Various Fabrication Processes of Microelectrode

Micro-EDM is one the most efficient technologies for fabricating micro-components between nonconventional machining technology. It can be machined ductile, brittle, or super hardened-materials with noncontact process; thus, there is little or almost no force between electrode and workpiece. For micro-EDM process. It is possible to achieve high-precision and high-quality machining with suitable parameters.[4]

It is possible to utilize a very thin and long microelectrode for machining, because of the noncontact nature of EDM. A micro-Milling cutter of down to 50 μm in diameter can be found in the market. However, the length of the tool is usually three to five times of its diameter. Micro-EDM can be used to machine tough die material which micro-Milling is not appropriate to machine them. Although micro-EDM has significant role in the field of micro-machining, EWR and low MRR are some of the disadvantages of micro-EDM. Changing the microelectrode or preparing longer microelectrode from the beginning or fabricating the microelectrode can compensate the wear of microelectrode. Change the microelectrode can reduce the accuracy to the change in setup or re-clamping of the microelectrode; hence, it is not recommended during machining.[4] Consequently, to avoid clamping error in micro-EDM process, microelectrode should be fabricated on the machine. By EDM process using a sacrificial microelectrode can be fabricated a cylindrical microelectrode from an microelectrode thicker than the required diameter.[4]

The fabrication processes of microelectrode are as follows:

1. WEDG
2. Rotating sacrificial disk
3. Stationary block electrical discharge grinding (BEDG)

4. Moving block electrical discharge grinding (MBEDG)
5. Self-drilled micro-hole
6. Revers EDM
7. Micro-turning process
8. Hybrid process.

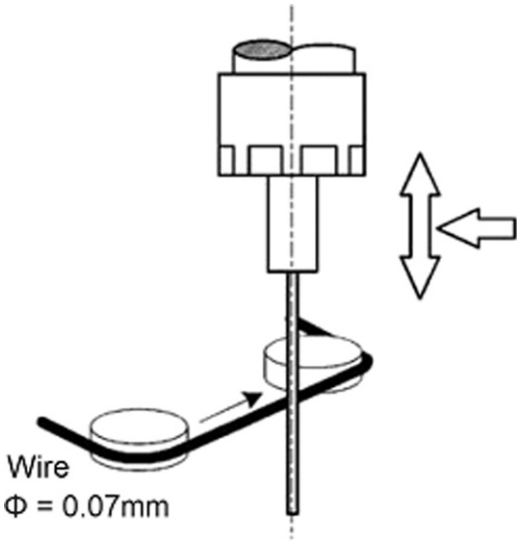


Figure 16 WEDG process.[5]

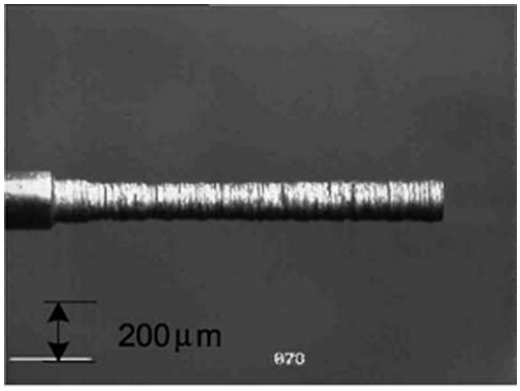


Figure 17 Microelectrode machined using running wire.[5]

1.10.4.3.1 WEDG

WEDG process is known as guided running wire, and it is a typically process for micro-EDM in Figure 16. Figure 17 illustrates typical surface condition of the microelectrode is fabricated by EDM using a running wire. This method is mainly used for micro-EDM machining. The dimensional change of the electrode is theoretically zero, because of using a fresh wire continuously. High-accuracy dimensional can be achieved in micro-EDM by this fact. However, the efficiency of the surface finishing in WEDG method is lower than the rotating electrode process. Because the running wire diameter is only 0.07 mm which is not enough to smoothly finish the machined surface the same as the rotating electrode method with 0.5 mm thickness. Therefore, the speed of the finish machining should be reduced to achieve better surface finishing by using this thin wire.[5] Figure 18 shows the schematic diagram of tangential-feed WEDG (TF-WEDG) compared with conventional radial-feed WEDG. WEDG can fabricate the microelectrode by employing a continuous wire electrode which is fed on a wire guide (Figure 18(a)).[99]

1.10.4.3.1.1 Radial-feed WEDG

Figure 18(b) shows the conventional radial-feed WEDG process. In this process, the microelectrode is positioned to align its central axis in the direction of the symmetry axis ON of wire guide, and during the WEDG method the microelectrode feeds along the radial direction of the guide, namely the direction of axis ON (Y axis). The removal resolution of the microelectrode (the minimum thickness to be removed from microelectrode) is in direct proportion to the motion resolution of Y axis, and the diameter error of machined microelectrode is twice of the positioning error of Y axis (given radial feed S_R, microelectrode diameter decrease Δd, and $\Delta d = 2S_R$). Thus, the alignment error (in X-axis direction) and the positioning error affects directly the machining accuracy of the microelectrode.[99]

1.10.4.3.1.2 TF-WEDG

The TF-WEDG process is proposed to reduce the effect of positioning error during fabricating the microelectrode in order to improve the accuracy.

1.10.4.3.1.2.1 Principle of TF-WEDG

The principle of proposed TF-WEDG method is presented in Figure 18(c). Here, the relative position of the microelectrode

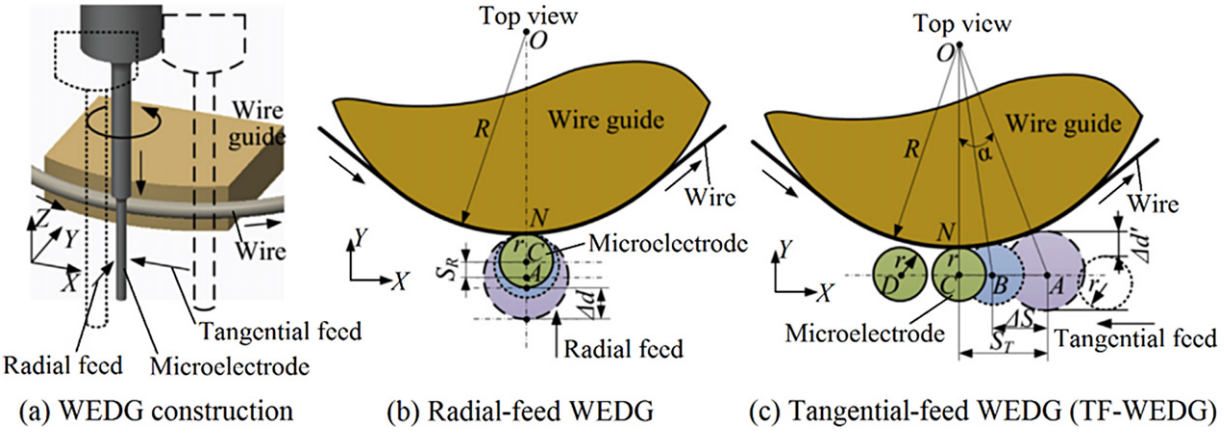


Figure 18 Comparison between radial-feed WEDG and TF-WEDG; (a) WEDG construction, (b) radial-feed WEDG, and (c) TF-WEDG.[99]

and the wire guide with the *Y*-axis is set fixed. During the WEDG process, the microelectrode moves along the tangential *X*-axis direction of the wire-guide arc. In this method for given tangential feed S_T and microelectrode diameter decrease $\Delta d'$, so that $\Delta d' \ll 2 \cdot S_T$ which is detailed in Section 1.10.2.2. Therefore, the removal resolution of the microelectrodes gets improved, and the diameter error of the machined microelectrode can be controlled easily by keeping it lower than the positioning error. Moreover, it is easy to repeatedly achieve a consistent diameter for a numbers of machined microelectrodes by TF-WEDG method by fixing *Y*-axis position and feeding to the position *D*.[99]

1.10.4.3.1.2.2 Analysis of TF-WEDG

Figure 18(c) shows the wire guide which is designed as an arc shape, therefore it properly fit with the wire of TF-WEDG. The microelectrode feeds from the position A to the position B and then to the position C. Therefore, the microelectrode diameter gets reduced during the feeding procedure to obtain a minimum diameter of the microelectrode at the position C. Here the radius of the wire guide and the machined radius of the microelectrode are denoted by *r* and *R* respectively and the distance between the position A and the position C is denoted by S_T. The microelectrodes diameter under different values of S_T can be calculated by using the following equation[99]:

$$d_A = 2(OA - R) = 2\left(\sqrt{(R+r)^2 + S_T^2} - R\right) \qquad [13]$$

The TF-WEDG experimental setup was performed by using wire guide with 1.3 mm radius (*R*). The relations between microelectrode diameter (d_A) and tangential-feed distance (S_T) is shown in **Figure 19** which is calculated by the eqn [13] for machining the microelectrode with diameter of 20, 40, 60, and 80 μm, respectively. As shown in **Figure 19**, when the distance S_T is equal to 120 μm, increments in diameters of four microelectrodes are from 10.72 to 10.96 μm while comparing with $S_T = 0$, and in fact the difference of the increments is only 0.24 μm (10.96 − 10.72 μm). In fact, the slopes of these four curves almost remain the same. Therefore, four conclusions can be drawn as follows: (1) without considering the machined microelectrode diameter, the removed diameter Δd of the microelectrode can be determined only if the distance ΔS is previously given (**Figure 18(c)**). (2) The distance Δd is much smaller than the tangential-feed distance ΔS and the removal resolution is significantly improved. (3) It is evident from **Figure 19** that, the slopes of the curves are gradually decreasing with the reduction in the distance S_T and the removal resolution is higher when the microelectrode is more closer to the symmetric axis of the machine wire guide. (4) It can be seen from the **Figure 18(a)** that the error effect of the horizontal alignment with respect to the wire guide orientation on the removal resolution can be ignored. For instance, if the experimental error is controlled < 5 μm, this could result in the error of microelectrode diameter being smaller than 0.04 μm.[99]

From the analysis mentioned above, it is possible to machine the microelectrode diameter precisely by using the high resolution of TF-WEDG and on-line measurement of the microelectrode diameters. At the position S_T of the micromachining process as shown in **Figure 19**, the required diameter can be machined by feeding the value of ΔS which is calculated by the eqn [13] after the diameter feedback of on-line measurement.[99]

The TF-WEDG method is performed into three steps as presented **Figure 20** in order to earn high-accuracy rate. S_T works as a variable value representing the distance between the microelectrode and the wire-guide axis OO′. $S_T > S1$ in the first step, therefore the axial error of the microelectrode is totally omitted by feeding a large pulse energy. At position A, the microelectrode's diameter is measured by the on-line measurement device and feed based on second step and its diameter is determined by the eqn [13]. $S1 > S_T > S2$ according to the second step (transition step), the microelectrode feeds from the position A to the position B and the calculated diameter is achieved by machining at this position. Then, its diameter is measured again to calculate the feed amount of the final step. $S_T = S3$ is the final step to feed the microelectrode from the position B to the position C, and hence the desired microelectrode is finally fabricated. The final step is a trimming process to obtain a precise diameter and surface. In the second and third steps, the negative polarity machining (the microelectrode with negative polarity) is used for higher material removal and better surface roughness. The microelectrode fabrication will follow this three steps procedure.[99]

In TF-WEDG method, the negative polarity machining increases the material removal from the microelectrode and decreases the surface roughness of the microelectrode. Therefore, it results in an obvious improvement of the surface quality of microelectrode as shown in **Figure 21**. The experimental investigation on the microelectrodes of Φ27 and Φ64 μm are presented in **Figures 22** and **23**, respectively. In the axial direction, the consistency accuracy for one microelectrode is less than 1 μm, and the repeating machining accuracy

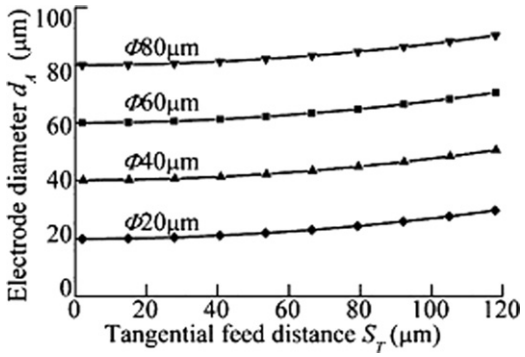


Figure 19 Error analysis of TF-WEDG.[99]

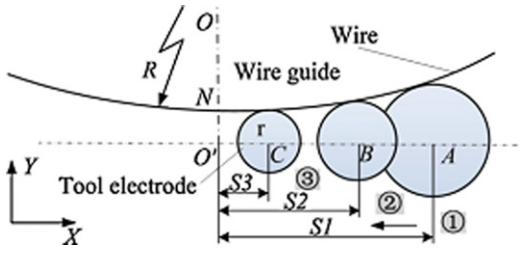


Figure 20 Three steps of TF-WEDG method.[99]

for several microelectrodes is less than 2 μm. The key factors that affect this repeating machining accuracy are the unit stability of WEDG, the geometric errors in the *X*-axis of horizontal straightness with respect to the linear positioning, and the error in the wire diameter.

1.10.4.3.1.3 Twin-wire EDM system

The WEDG technology invented by professor Masuzawa is used to fabricate the microelectrodes. This technology employs an RC pulse generator, which can maintain high accuracy throughout the whole machining process. However, WEDG method needs a lot of time to produce the microelectrodes because of using roughing and finishing steps. On the contrary, a twin-wire EDM system, which includes combined TrC and RC two pulse generators, can be used more efficiently to fabricate microelectrode as shown in **Figure 24**. This system offers only one step to fabricate the microelectrodes.[100]

The twin-wire EDM system works on two isolated wires which move on two v-shaped guides, as shown in **Figure 24**. In this system, two precisely machined copper wire electrodes create two separated pulse generators in one machine. The upper wire is connected a transistor pulse generator which is used for roughing step and another wire is connected an RC pulse generator which is used for finishing step. The transistor type pulse generators equipped with an additional large capacitor provides enough amount of spark energy (discharge energy) to obtain large MRR for roughing step. On the contrary, the RC pulse generator includes a smaller capacitor having reduced stray capacitance to achieve a very low amount

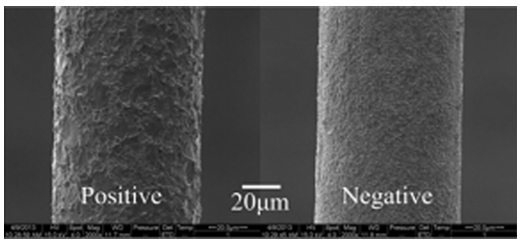


Figure 21 Roughness contrast of positive and negative polarity machining.[99]

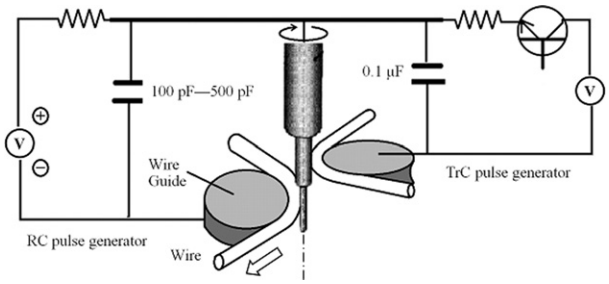


Figure 24 Twin-wire EDM system for the microelectrode fabrication.[100]

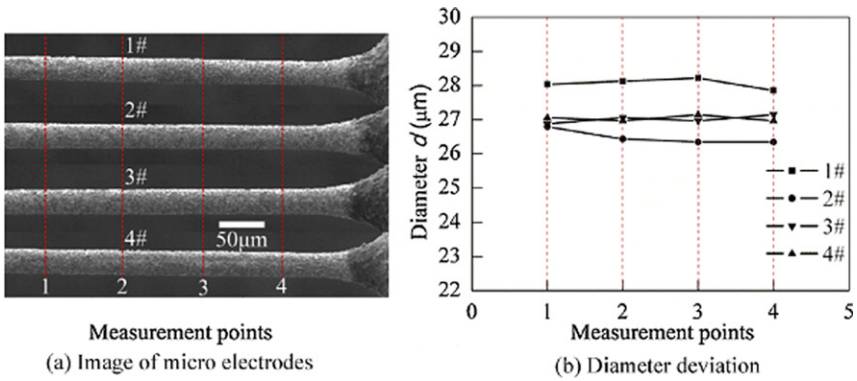


Figure 22 Experimental results of microelectrodes after finishing process (Φ27 μm): (a) image of microelectrodes and (b) diameter deviation.[99]

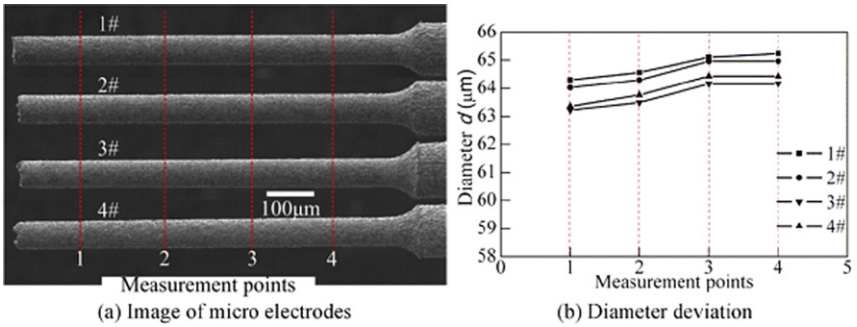


Figure 23 Experimental results of microelectrodes after finishing process (Φ 64 μm): (a) image of microelectrodes and (b) diameter deviation.[99]

of spark energy for finishing step. The lower stray capacitance and small amount of spark energy of an RC pulse generator have made it an essential discharge circuit for machining microelectrodes.[100] By using WEDG technology equipped with an RC pulse generator, it is possible to fabricate microelectrodes with diameters as small as 5 μm.[100,101]

As shown in **Figure 24**, the rod tool spindle at first feeds to the upper wire to shape the microelectrode roughly using a TrC (transistor electro-discharge circuit) electro pulse generator. When the feeding length crosses the gap between those two electrode wires, the twin-wire EDM machining system immediately starts the finish machining through the RC electro pulse generator simultaneously. Conventional EDM machining system that employs transistor type pulse generators required the pulse-ON time, pulse-OFF time, and a duty factor to achieve a high-precision machining. However, the finishing side of the twin-wire EDM machining system determines the accuracy of the microelectrodes without taking the transistor pulse generator into account. This system can produce the straight and thin microelectrodes by using high-precise position control. Fundamentally, twin-wire EDM system can fabricate the precision microelectrodes with various materials.[100]

1.10.4.3.1.4 Fabrication of microelectrode for batch production by WEDM

The micro-WEDM machine was used to manufacture the microelectrode array with high aspect ratio. The microelectrode is clamped on the spindle machine and gradually fed in downward direction against the wire which is moving toward horizontal direction. By this process, raw material of microelectrode (a small metal rod) can be machined to a microstructure array with micro-squared pillars. For producing mass micro-holes, an array of microelectrodes is needed to cut by performing the micro-WEDM process first. **Figure 25** shows the relative wire movement at some stages during the manufacturing. As shown in **Figure 25(a)**, the wire moves at an extremely slow speed from $-X$ to $+X$, while the microelectrode (workpiece) is also moving in downward direction. When all of the layers are machined completely, the workpiece is separated from the wire in the $+Z$ axis direction and then rotated around the Z axis at 90° angle for fabricating the other side as shown in **Figure 25(b)**. After that the fabricated microelectrode array is unclamped from the machine and is mounted directly above the stainless steel plate and then moved slowly toward the downward direction for producing the mass micro-holes array as shown in **Figure 25(c)**. Eventually, the mass micro-holes are machined by using the batch micro-EDM process (**Figure 25(d)**). Finally, the microelectrodes array gets shorter in length than the original one because of the consumption toward the longitudinal microelectrode direction.[102]

Figure 26 illustrates the machined microelectrodes array and also a single microelectrode in microphotograph with the total machining time of 130 and 33 min. These microelectrodes are all uniform and consistent on the tip and the middle. The heights of all the pillars are greater than 700 μm, hence providing a enough amount of compensation in the batch micro-EDM method. **Figure 27(a)** illustrates the results for a single hole as well as a hole array machining. As the fabricated microelectrodes array is not unclamped and reclamped, exceedingly excellent the micro-holes position are attained. **Figure 27(b)** illustrates the regular size of the partial hole.[102]

1.10.4.3.1.5 Compliant microelectrode arrays were fabricated by WEDM

The bending stiffness of the microelectrodes can be reduced by employing wire EDM process. This process has the ability to create real 2D geometries by selectively removing desired material in points that affect the lateral yielding. Flexure, tapered, and spring-like microelectrodes were designed using Pro/MECHANICA (finite element methods) to analyze their various features as shown in **Figure 28**.[103]

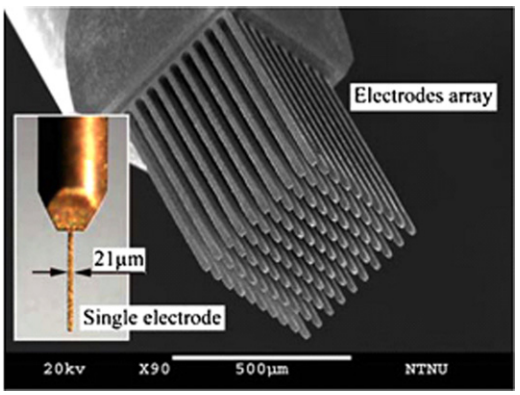


Figure 26 SEM microphotograph of the fabricated single electrode and electrode array.[102]

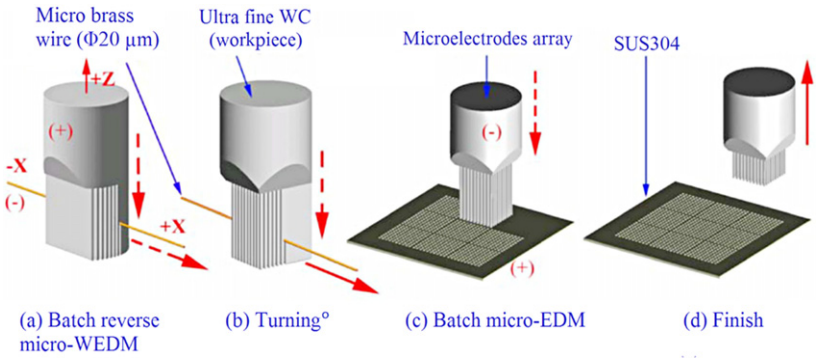


Figure 25 Batch production mode of mass micro-holes.[102]

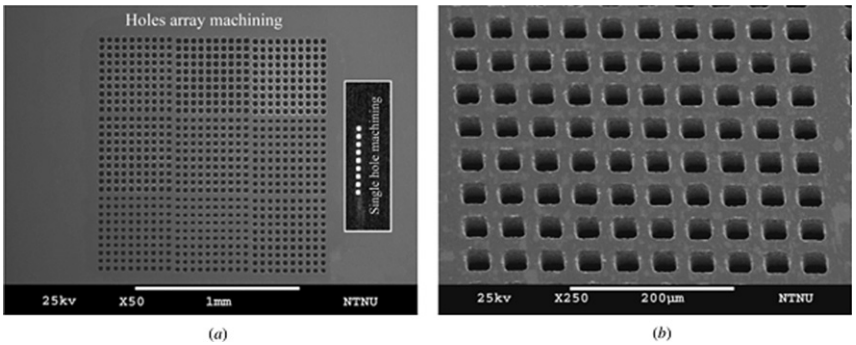


Figure 27 The fabricated micro-hole array (thickness: 30 μm): (a) fabricated single hole and hole array and (b) the partial magnification.[102]

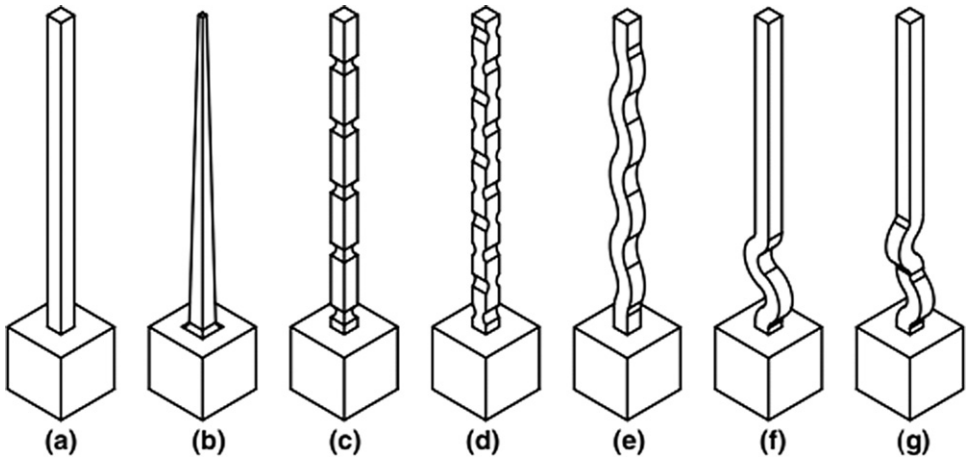


Figure 28 Different microelectrode geometries machined by μ-WEDM process includes: (a) straight, (b) tapered, (c) hour-glass flexures aligned on both sides, (d) hour-glass flexures shifted between both sides, (e) wavy, (f) spring in one horizontal direction, and (g) spring in both horizontal directions.[103]

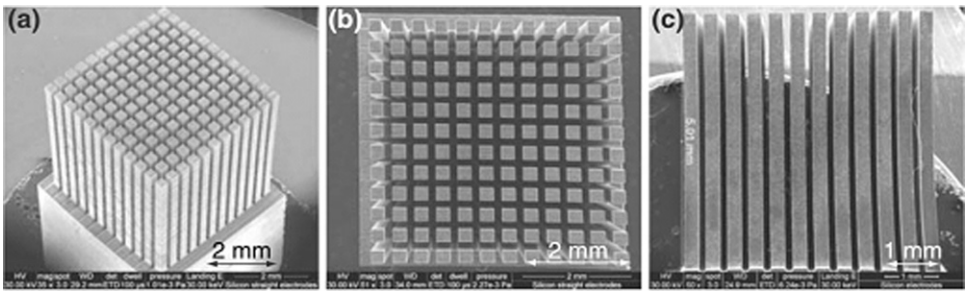


Figure 29 μ-WEDM fabricated straight microelectrode (a) 3D view, (b) top view, and (c) side view.[103]

A tapered microelectrode column with 0.1×0.1 mm tip reduces the bending stiffness by 5 times compared to the straight microelectrode as shown in Figures 28(a) and 28(b). On contrast, flexure feature microelectrodes with circular reliefs having a 0.05 mm depth in each 0.25 mm (Figures 28(c) and 28(d)), are more compliant than the contemporary straight microelectrode by a factor of 4. Besides, lateral rigidity of a straight microelectrode can also be reduced by creating curvatures on it. For instance, the torsional spring-type microelectrode shapes as shown in Figures 28(f) and 28(g) lowers the stiffness by roughly 15%.[103]

Microelectrode arrays of 144 microelectrodes were fabricated into single-crystal silicon blocks with $6 \times 6 \times 10$ mm size. The pitch between two microelectrodes was maintained at 400 μm with a 5 mm microelectrode length. The contemporary straight microelectrodes, shown in Figure 29 possess a 255×255 μm uniform cross section of and a cut achievable in three steps. A roughing step of cutting was accomplished in germanium first with a capacitance and voltage of 9.9 nF and 150 V respectively. This profiling cut made the outlines of the microelectrodes, roughly leaving 10 μm of material on all surfaces. These extended ridges were then retraced with a

capacitance and voltage 3.3 nF of and 150 V respectively. At the next step, the workpiece was rotated at 90° angle. For the other face, the rough cut was eliminated and the finish cut was employed instead. Around 8 h was needed for machining of the entire array.[103]

Similar machining processes were adopted for the microelectrode arrays illustrated in **Figure 30**, that show the μ-WEDM capability to properly trace the complex shapes found in **Figure 28**. The tapered-shaped microelectrode which is depicted in **Figure 30(a)** has a 95×94 μm tip dimension. On contrast, the flexure type microelectrode arrays in **Figures 30(b)** and **30(c)** are machined on square columns with a 250×250 μm cross section. The wavy microelectrode illustrated in **Figure 30(d)** as well as the microelectrodes with the base springs as shown in **Figures 30(e)** and **30(f)** are based on a 220×220 μm cross section for creating larger curvatures.[103]

The μ-WEDM method and subsequent etching were performed to manufacture an microelectrode array which has 144 microelectrodes with 5 mm length. To increase the lateral compliance, the microelectrodes were tapered and machined with a bidirectional spring at the base. After performing the μ-WEDM, the microelectrode array was etched for 1 min in HNO_3:CH_3COOH:HF followed by an another 1 min etching in HNO_3:HF. **Figure 31(a)** shows a SEM image of the microelectrode array and **Figure 31(b)** is a magnified image of the base geometry having a cross section of 100 μm. The two-directional curvatures of the base geometry act as torsional springs. **Figure 31(c)** shows an microelectrode tip that was etched to a very sharp point.[103]

Using μ-WEDM also allows variable the microelectrode lengths to a certain degree. **Figure 32** shows the microelectrode array was manufactured by first machining a v-groove into one side and cutting two chamfers in the other side. This resulted in an array whose tapered microelectrode lengths were from 5 to 9 mm.[103]

1.10.4.3.1.6 Fabrication of series-pattern micro-disk electrode

Schematic diagram of the essential parts of the micro-EDM working system are shown in **Figure 33**. A micro-EDM working system is composed of WEDG method and RC discharge circuit which are mounted on the XYZ stages with a nanometer range positioning accuracy. The stage accuracy this method is

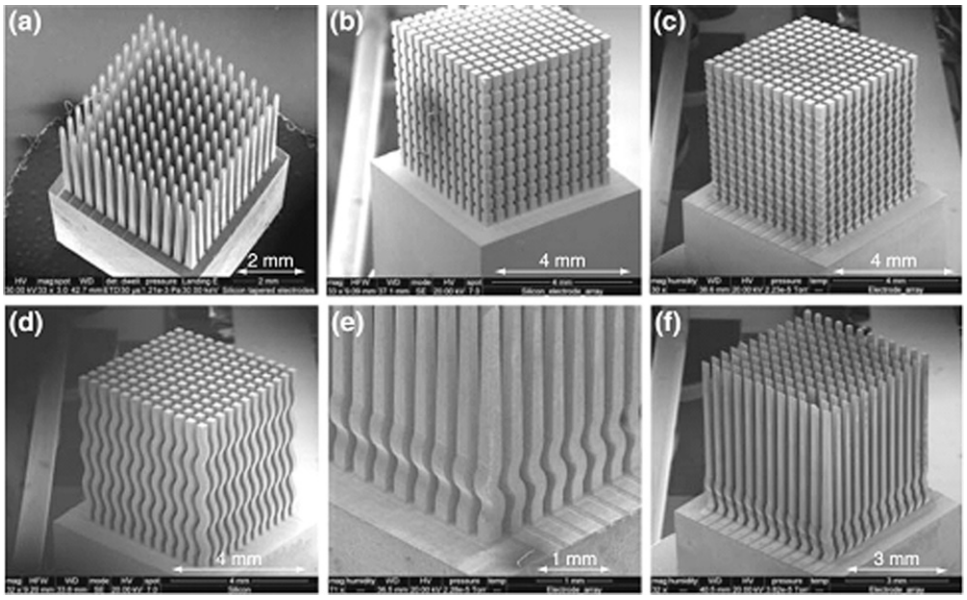


Figure 30 μ-WEDM fabricated microelectrodes with (a) tapers, (b) even flexure, (c) offset flexure, (d) wavy, (e) directional base spring, and (f) unidirectional base spring.[103]

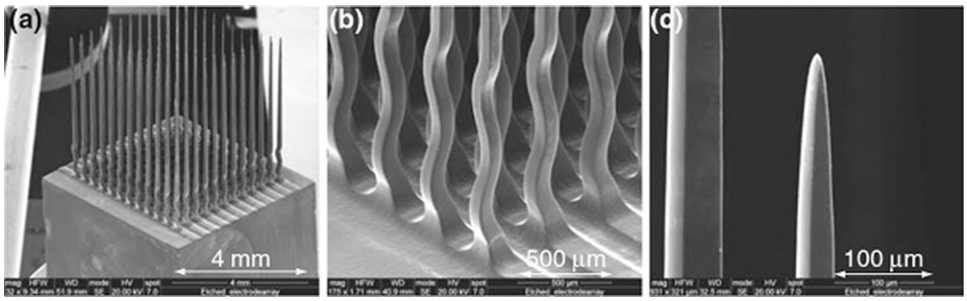


Figure 31 μ-WEDM fabricated (a) tapered microelectrode array, (b) with bidirectional spring at the microelectrode base, and (c) an microelectrode tip etched to a very sharp point.[103]

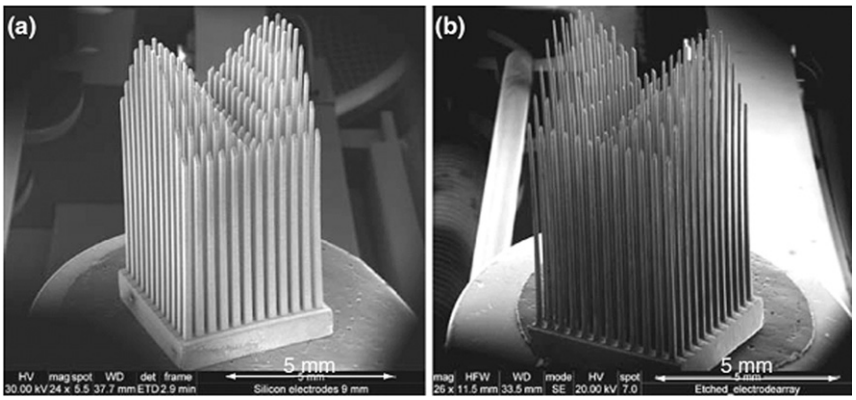


Figure 32 Variable length microelectrode array (a) after μ-WEDM and (b) after etching.[103]

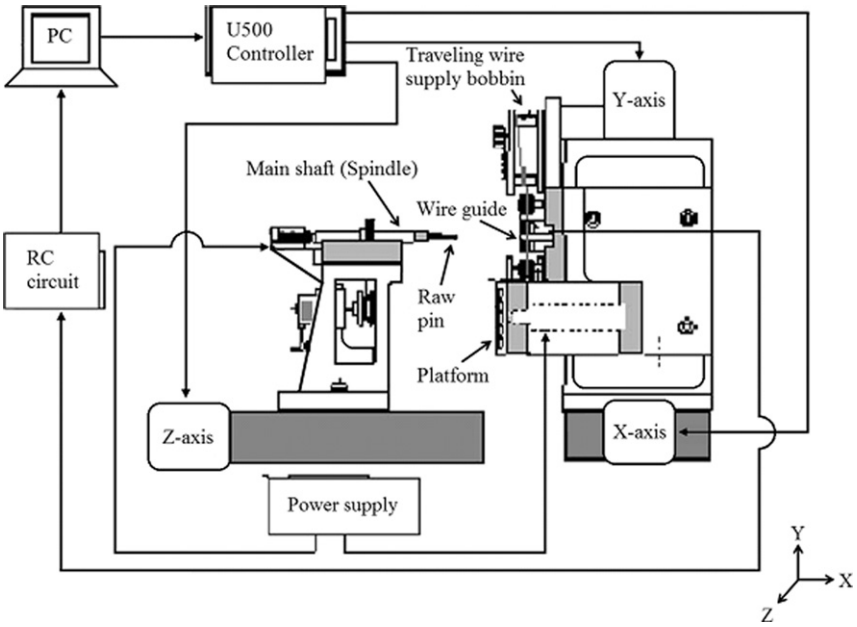


Figure 33 The micro-EDM system configuration.[104]

illustrated in Table 7. In the WEDG process, the tool electrode is basically a wire electrode which travels on a wire guide. By adjusting the discharge voltage and the capacitance at the improving RC discharge circuit, a moderate energy discharge can be obtained to make a micro-component. This method is a free-contact force machining process with a small sparking gap between electrodes.[104]

In the configuration of the micro-EDM working system, a main mandrel shaft is horizontally set on the bearing surface, which is known as horizontal micro-EDM working system. A raw pin can be clamped at the mandrel shaft by a capillary and a ceramic alignment sleeve. The raw pin can be horizontally rotated with the main shaft by means of a transmission motor. As illustrated in Figure 34, the machining can be performed through the sparking discharge between the pin and the wire traveling on the WEDG. The debris is effectively removed from the gap during the machining by gravitational force due to the horizontal position of the pin. U500 controller can control the relative position between the wire electrode and raw pin as shown in Figure 33.[104]

Table 7 Stage accuracy of the horizontal micro-EDM working system[104]

Travel range	*XYZ: 50 × 50 × 50 mm*
Incremental motion	XYZ: 0.1 μm
Velocity range	2–0.0005 mm min^{-1}
Velocity accuracy	±2% RMS
Pitch/yaw/roll	XYZ <20 lrad

The machining procedure of a single micro-disk can be extended into the fabrication of multiple micro-disks as illustrated in Figure 35. However, some factors influence the minimum interval between disks which should be specially noticed and discussed.[104]

Firstly, based on the fabrication procedures outlined, a raw pin can be fabricated into the tool electrode with the

micro-disk by the micro-EDM system illustrated in Figure 33. This tool electrode is rotated with the horizontal rotation on the main shaft by the means of a transmission motor, such tool electrode is called as micro-rotating disk electrode (MRDE).[104]

A polished work-piece plate is placed vertically on the XY table. Before the machining is performed, the positioning detection circuit is employed precisely to detect first position. Moreover, the positioning detection circuit maintains the relative original position between the work-piece surface and outermost MRDE. The MRDE can then be fed into the work-piece from the surface until it reaches the desired depth. A straight line with a micro-slit can thus be formed by means of moving the *Y*-stage which is carrying the workpiece, as schematically presented in Figure 36.[104]

1.10.4.3.2 Rotating sacrificial disk

Figure 37 illustrates the microelectrode fabrication process using a rotating sacrificial electrode. Electrical discharges have caused the erosion on the rotating electrode during the fabrication process. However, the erosion is almost uniformly distributed over the whole electrode perimeter during micro-EDM. The dimensional change of the rotating electrode is almost negligible in microelectrode fabrication by considering the diameter difference between the sacrificial electrode and microelectrode. Moreover, the rotating electrode with 0.5 mm thick provides the same effect as stationary electrode on the surface finish, since its wideness is sufficient to produce a smooth surface, as can be seen in Figure 38.[5]

1.10.4.3.3 Stationary BEDG

Stationary BEDG is the simplest ways to fabricate a micro-electrode. Figure 39 illustrates the fabricated microelectrode using BEDG process. This method can produce the micro-electrode with smooth surface. However, some taper is usually seen in the microelectrode shape and the accuracy is not as good as desired because of the wear occurs on block electrode

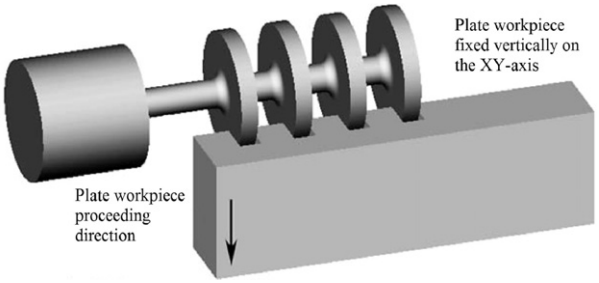


Figure 36 A schematic representation for cutting the micro-slit using the MRDE.[104]

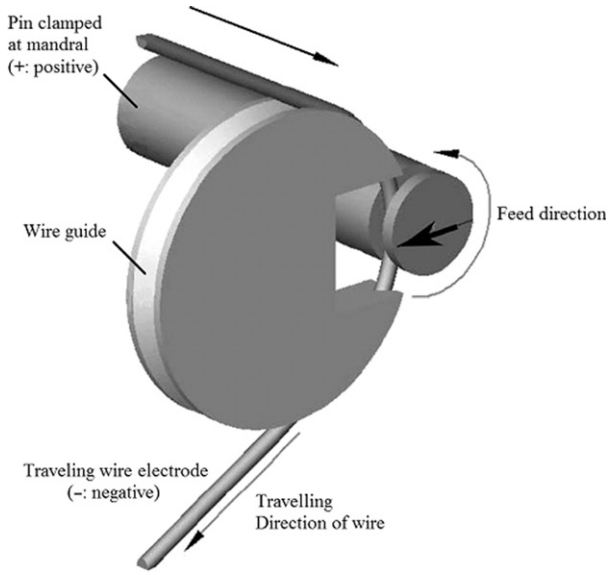


Figure 34 The micro-EDM system configuration.[104]

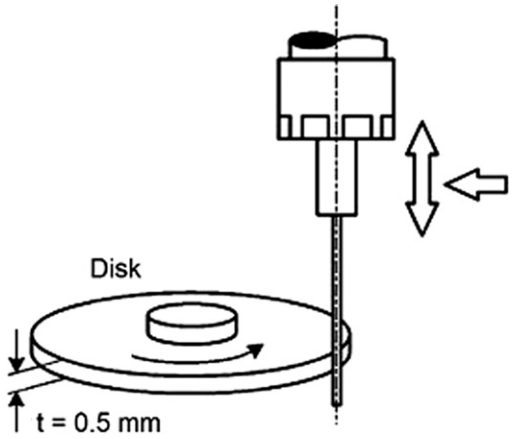


Figure 37 Rotating sacrificial disk.[5]

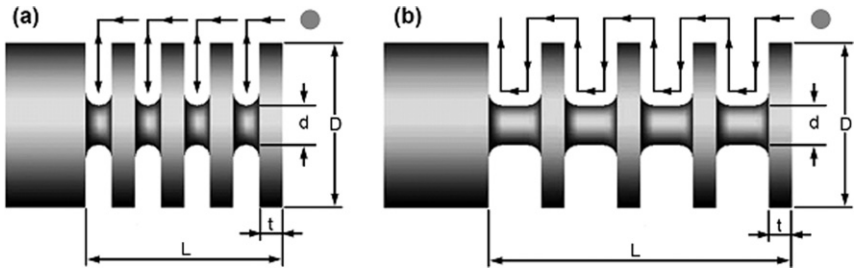


Figure 35 Schematic representation of the tracking path of wire to fabricate the series-pattern micro-disk for (a) a smaller interval or (b) a larger interval between disks.[104]

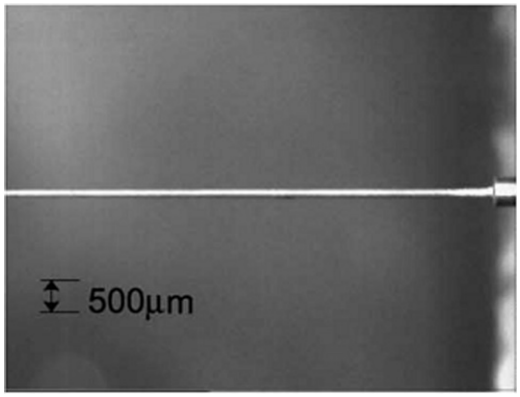


Figure 38 Fabricated microelectrode using rotating disk.[5]

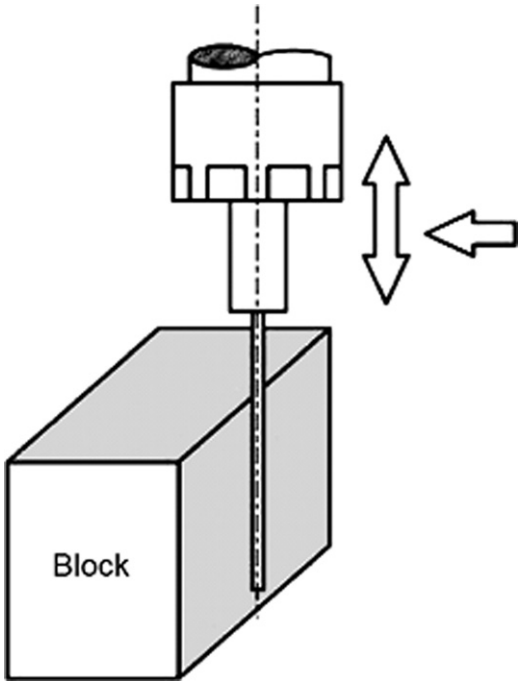


Figure 39 BEDG.[5]

as shown in Figure 40. Since the microelectrode feeds upward and downward during microelectrode fabrication, the lower (tip) portion has a greater chance to face the block electrode, and consequently is subjected to more discharges during the machining. Also, slight tilting of the block electrode toward the microelectrode does not shape to improve the tapered shape. Figures 40 and 41 show tapered and uneven diameter of microelectrode respectively. The block electrode is easy to setup but shape and dimensions of the microelectrode are not easy to control.[5]

1.10.4.3.4 MBEDG

Figure 42 shows the moving BEDG (MBEDG) which is combined the advantage of the rotating sacrificial disk and BEDG methods. Block electrode needs a very simple setup and the surface of the machined microelectrode is generally smooth. However, the precision of shape is not as improved as desired,

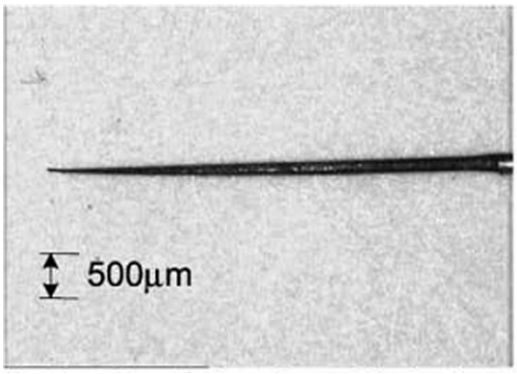


Figure 40 Tapered microelectrode is produced using BEDG.[5]

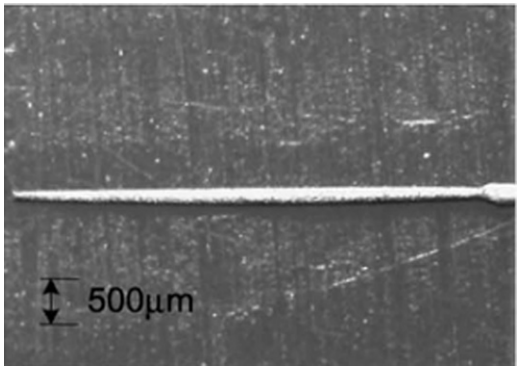


Figure 41 The microelectrode uneven diameter is machined using BEDG.[5]

and the microelectrode generally possesses a tapered shape as a result of the wear in the block electrode. In this fabrication process, the microelectrode in the *Z* axis controlled the EDM gap by the top surface of the block electrode. A relative feed between the microelectrode and the block electrode was employed longitudinally with the block electrode. During the Moving BEDG method, erosion occurred on the moving block electrode by the electrical discharges. However, the erosion occurred almost in a uniform manner over a very larger area of the block electrode. In addition, most of the sparks occurred between the un-machined part of the microelectrode and the top surface of the block electrode. Almost no spark occurs at the side surface of the microelectrode. This produced the not tapered microelectrode with very smooth surface and good accuracy in shape. However, there was difference in the produced microelectrode length which is smaller than the desired length always because of the created groove on the block electrode surface. The difference between the actual length and the desired length of the microelectrodes is almost negligible by considering the machined area between the microelectrode and block electrode.[4]

Figure 43(a) illustrates the CuW microelectrode with about 50 µm diameter and 3 mm length (aspect ratio = 60) was fabricated using BEDG. Figure 43(b) shows the improvement in taperness of the microelectrode which was produced using moving BEDG. Figures 44(a) and 44(b) illustrate the W microelectrodes which were fabricated using BEDG and moving BEDG methods respectively. It is clear that the moving

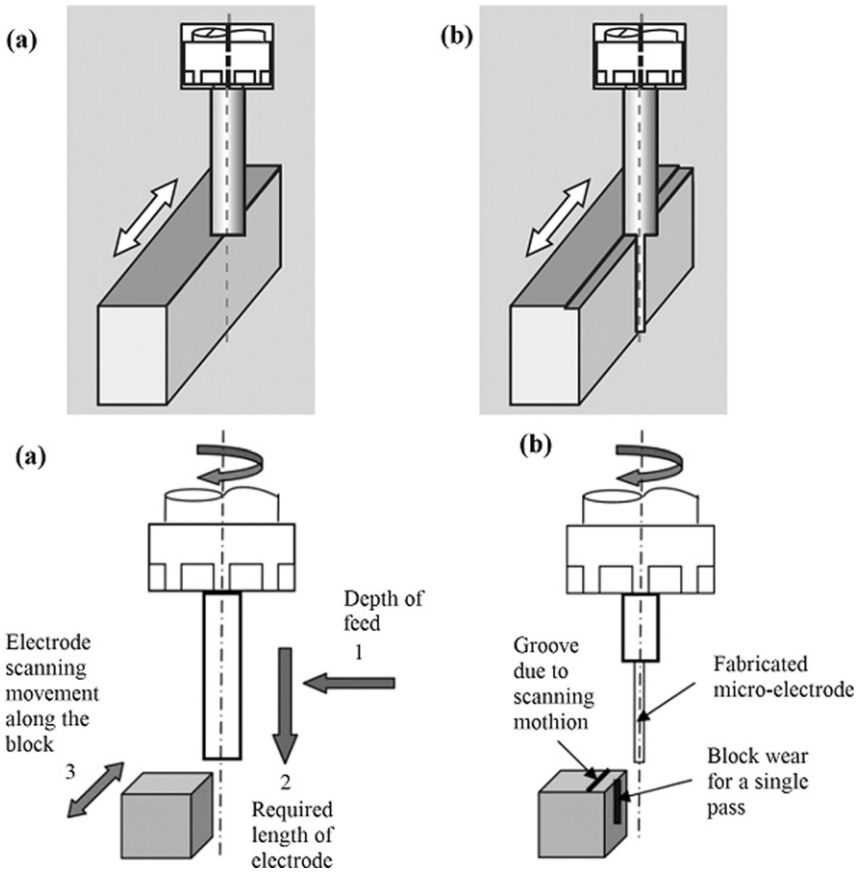


Figure 42 Moving BEDG method for on-machine microelectrode fabrication. (a) At the beginning of moving BEDG. (b) Groove create by erosion.[4,74]

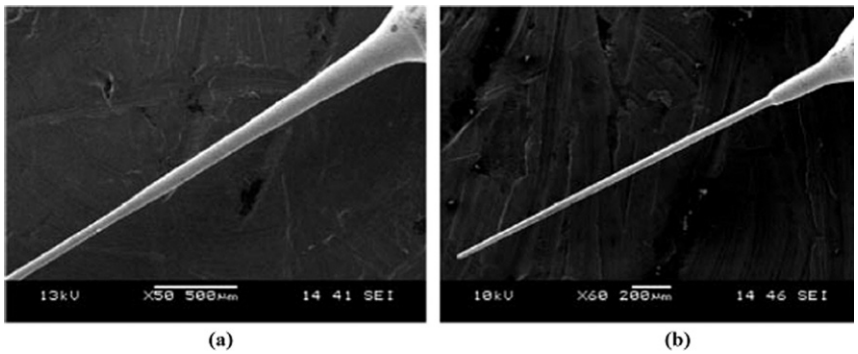


Figure 43 CuW microelectrode; (a) with 50 μm diameter and 3 mm length (aspect ratio = 60) was produced by the BEDG method, (b) with 40 μm diameter and 2 mm length (aspect ratio = 50) was produced by moving BEDG method.[74]

BEDG method can produce less tapered microelectrodes and provides a superior dimensional accuracy.[74]

1.10.4.3.5 Micro-turning process

The main problem that occurs during the micro-turning of the microelectrode is its deflection. Figure 45 illustrates the deflection of end portion of the microelectrode measured using a deflection sensor. Experiments revealed that the microelectrode is bending in normal (X) as well as tangential (Y) direction of the microelectrode contact region. Moreover, the microelectrode deflects toward the rake surface (top surface) of the cutting tool. It is very difficult to get straight microelectrodes below 100 μm diameter band in many cases. The microelectrode either gets broken or starts to wobble due to the excessive cutting force in radial direction on this microelectrode. Figure 46 demonstrates one of this kind of microelectrode which is machined by the conventional micro-turning process.[4]

Figure 47 shows the polycrystalline diamond (PCD) inserts with 100 μm tool nose radius (designed for finishing step or

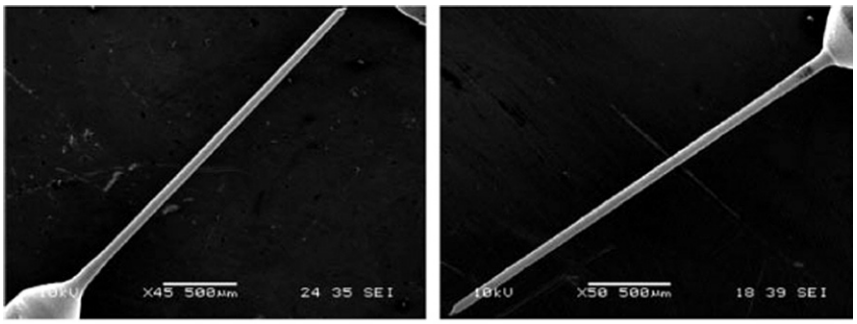


Figure 44 W microelectrode, (a) with 60 μm diameter and 3 mm length (aspect ratio = 50) was produced by the BEDG method, (b) with 40 μm diameter and 3 mm length (aspect ratio = 75) was produced by the moving BEDG method.[74]

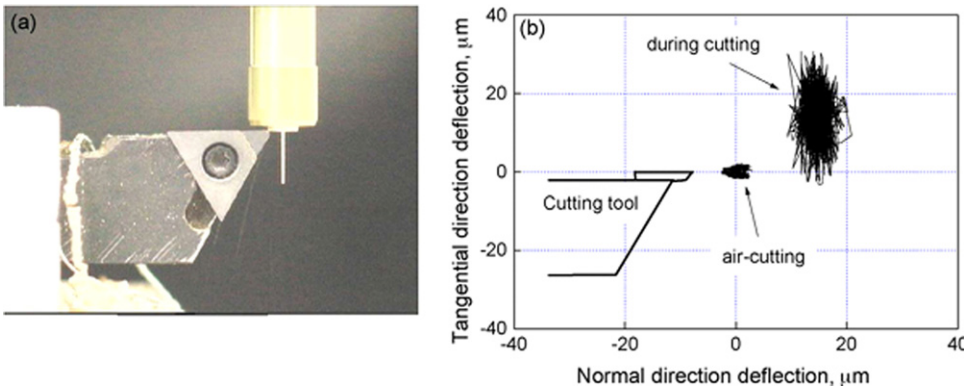


Figure 45 Microelectrode deflection during micro-turning.[4]

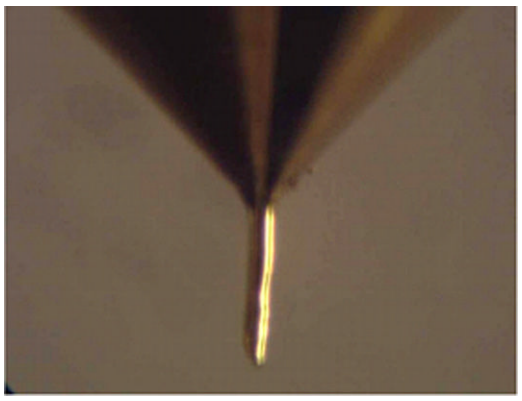


Figure 46 A 100 μm diameter microelectrode was machined by conventional micro-turning.[4]

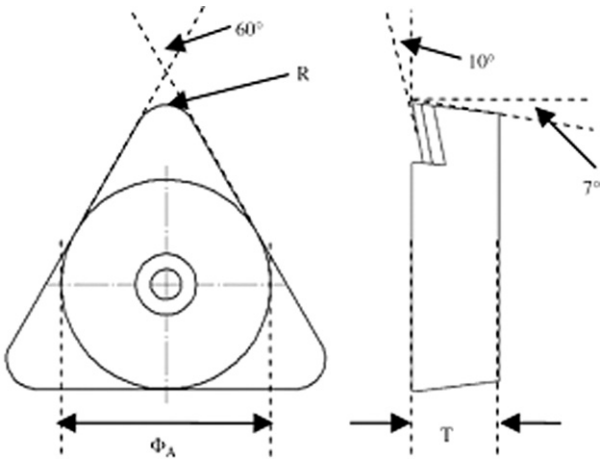


Figure 47 The tool geometry of commercially available PCD inserts for finishing step (light cutting).[4]

light cutting) was used for micro-Turning. This tool nose divides the cutting force on the microelectrode in to two different force components, F_x and F_y as shown in Figure 48(a). Basically the F_y cutting force component performs the actual cutting whereas the F_x component is responsible for the microelectrode deflection. Figure 48(b) illustrates the actual cutting with the commercially available PCD inserts under a tool scope.[4]

1.10.4.3.6 EDM of micro-rods by self-drilled holes

Figure 49 presents the working principle of the developed micro-EDM process. In this process, a rod electrode is rotated with negative polarity and fed into a plate electrode to create a hole. When the rod electrode is returned to its initial place, the axis gets off-centered from the hole center at a certain distance.

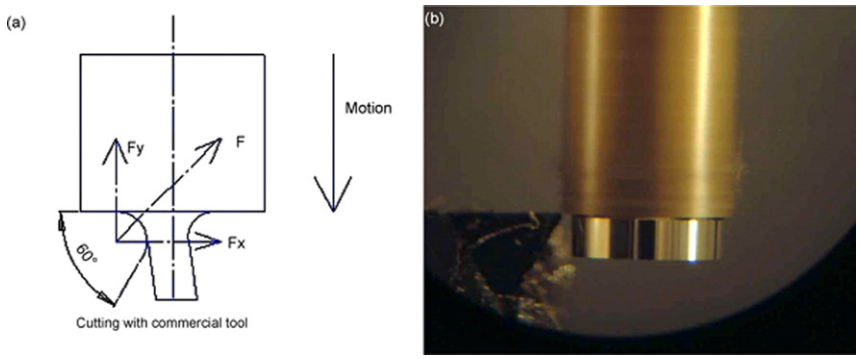


Figure 48 (a) Resolution of cutting forces and (b) actual cutting with the commercially available PCD inserts under a tool scope.[4]

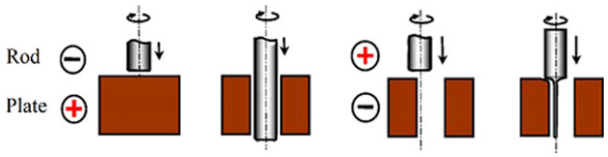


Figure 49 Principle of obtaining micro-rods by self-drilled holes.[105]

Then, the rod electrode polarity is reversed and the rod electrode is fed into the plate electrode either stationary or with rotation. The straight rod electrode (microelectrode) can be achieved if the wear does not occur at the outlet holes even though the inlet holes have already worn out. If the machining gaps between the hole and the electrode are determined before as illustrated in **Figure 50**, the rod electrode with any diameter can be fabricated. With traditional methods, it is essential to measure the machined rod electrode diameter and rectify the starting point of machining from the previous measured results. The benefits of this new process include no adjustment of the starting point is needed and accurate machining efficiency.[105]

Unlike reverse-EDM and WEDG, this process can produce the reference holes with the rod electrode, therefore no reference positioning of the tool electrode to the workpiece is needed. As a result, operation becomes easy and shorter. In addition, stable EDM is achieved because of the wide electrical discharge area compared with WEDG, and complicated shapes can be formed.[105]

Figure 51 shows the fabricated microelectrodes after various machining conditions. **Figure 52** illustrates microelectrodes fabricated by double forming is still taper.[99] **Figure 53** demonstrates the microelectrodes were fabricated by various holes for forming and holes obtained by EDM using these tools.

1.10.4.3.7 Reverse EDM

In micro-EDM, micro-holes, and micro-structures are fabricated by feeding a microelectrode machined by wire EDM or grinding process as illustrated in **Figure 54(a)**. Micro-EDM can be used for fabrication of the micro-holes and microelectrodes. For instance, some holes are fabricated on a metal plate by using EDM. After applying a positive voltage to a workpiece material for machining microelectrodes, the workpiece is fed down to the holes of the metal plate while being machined by EDM. However, the areas around the holes are not machined and remain, getting into a microelectrode at each hole as illustrated in **Figure 54(b)**. This machining process is generally called reverse EDM (REDM). Different microelectrodes shapes can be machined by REDM, which is difficult to fabricate using normal EDM.[106] **Figure 55** depicts examples of multiple microelectrodes and U-shape microelectrode which were fabricated by REDM.

1.10.4.3.8 Hybrid process

1.10.4.3.8.1 Micro-turning–micro-EDM hybrid machining process

As has been described before, all of the microelectrode fabrication processes have their own benefits and disadvantages. The disadvantage of the conventional micro-turning is the transferring the microelectrode to EDM machine. Moreover, rotating sacrificial disk, WEDG, BEDG, moving BEDG, and self-drilled holes are very difficult for automation and are always prone to error. In most cases, the operator is required to check the whole fabrication process and perform manual compensation to find the error. Besides, it takes more than few hours for the electrode fabrication process. For example, it takes about 3–4 h to fabricate a microelectrode with 15 μm diameter and 0.5 mm length using a commercially available 500 μm diameter tungsten electrode with by moving BEDG method. It is a well-known fact that tungsten electrode has negligible wear against stainless steel and 100 holes could be machined on 50 μm thick SUS-304 plate with this microelectrode. A new hybrid machining method for micro-turning can be employed to machine very fine microelectrodes and nearly eliminates all the disadvantages of microelectrode fabrication methods which used micro-EDM machine.[4]

Figure 56 shows the process of turning-EDM hybrid machining. In this type of machining process, EDM is carried by using a microelectrode. Therefore, an electrode of certain length is machined using the micro-turning process. Elimination of clamping error and minimizing the electrode deflection is possible in hybrid machining process, which results in the significant improvement in machining accuracy. When variable diameters of microelectrode are required, turning can significantly save the microelectrode preparation time as compared to the EDM processes. Nonrotational cylindrical micro-components such as key slot or flat bar can also be fabricated using hybrid machining technology with the help of EDM process followed by turning.[4]

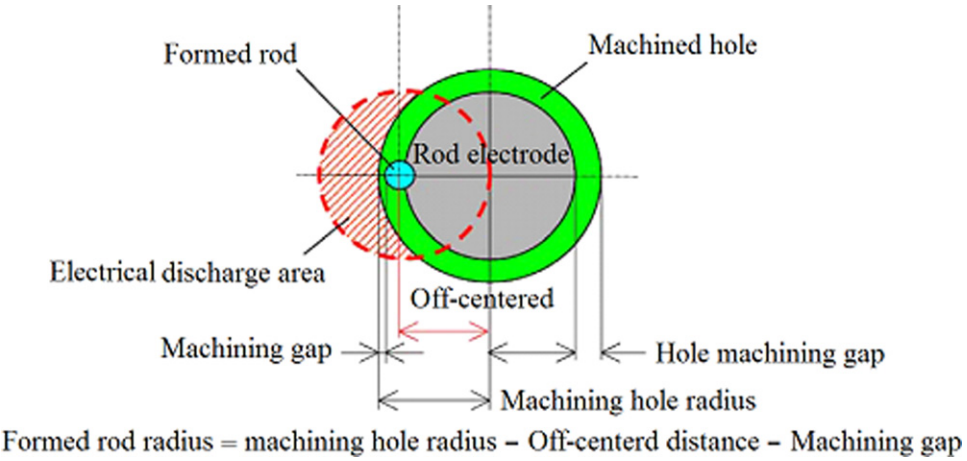


Figure 50 Off-centering concept chart.[105]

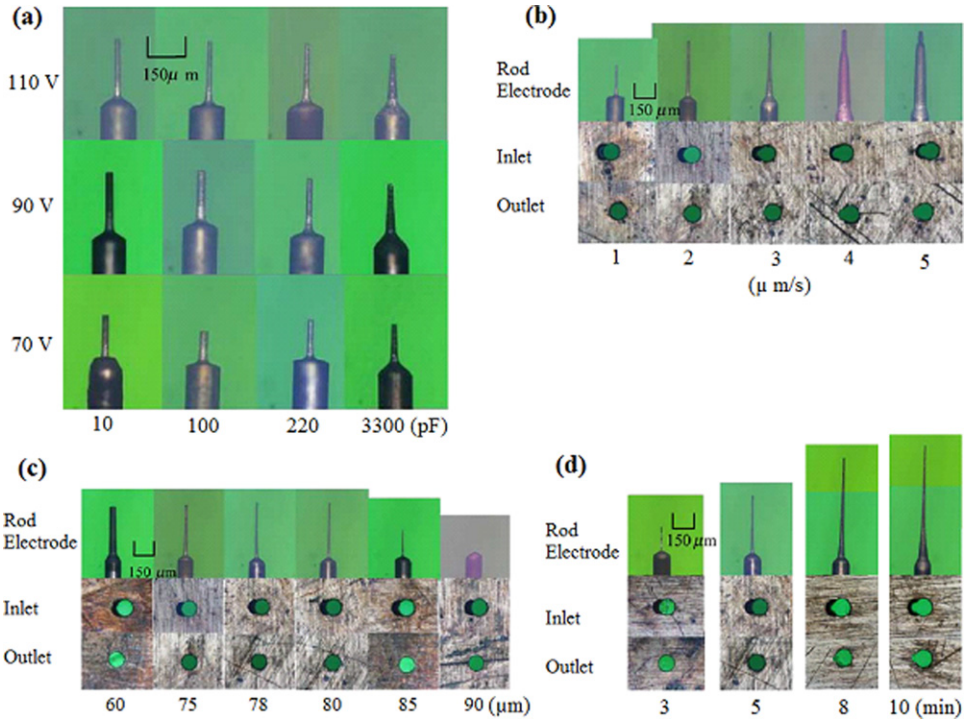


Figure 51 Microelectrodes obtained by (a) varying discharge energy (1 μm s^{-1}, 75 μm, and 5 min), (b) varying feed speed (110 V, 100 pF, 75 μm, and 5 min, (c) off-centering (110 V, 3300 pF, 2 μm s^{-1}, and 5 min, and (d) varying machining time (110 V, 3300 pF, 2 μm s^{-1}, and 78 μm).[105]

As described before, it is always very difficult by microturning to achieve straight microelectrode below 100 μm diameter and in a lot of cases, the microelectrode is either broken or starts to wobble due to excessive radial cutting force on this microelectrode. A commercially available PCD insert can be modified to achieve a very sharp cutting edge which would reduce the F_x component of the cutting force significantly (Figure 57) and thus this makes it possible to achieve straight microelectrode with much smaller diameter.[4] Figure 57 Illustrates the resolution of cutting forces in F_x and F_y components in commercial tool (on the left). Modified tool can reduce the F_x component of cutting force significantly due to sharp cutting edge (on the right).[3]

An approach has been developed to manufacture an ultrasharp-edged tool from the commercially available PCD insert using micro-EDM. A rotating electrode is mounted on the spindle and used to perform micro-EDM (EDG) on the PCD tool edge to produce a very sharp edge.[4] This is illustrated in Figure 58. Table 8 shows the parameters that were used during the tool tip fabrication. Figure 59 shows the

commercially available PCD insert (a) and the modified PCD tool (b). The modified PCD tool has less than 5 mm tool nose radius.

In Figure 60, a microelectrode and the EDG-edged tool used for machining the microelectrode under a tool scope is observed.[4] This has stretched the possibility of micro-turning to an extreme. This method illustrates much improvement on the machining time compared to rotating sacrificial disk, WEDG, BEDG, moving BEDG, and self-drilled holes which takes few hours to fabricate as mentioned earlier. In addition, this method does not require much operator intervention and can mostly be automated due to the less chances of error. Two millimeter long microelectrodes with less than 20 μm diameter have been fabricated very easily. The fabrication process for a 2.0 mm long microelectrode takes less than 10 min.[4] Figure 61(a) shows a microelectrode with 22 μm diameter was produced by micro-turning process and after drilling about 10 holes on 100 μm thick SUS-304 plate.[4] Figure 61(b) demonstrates a graphite microelectrode of 0.5 mm long and 19 μm in diameter that is similarly produced.[3]

1.10.4.3.8.2 Self-drilled holes–TF-WEDG hybrid machining process

Figure 62 shows the hybrid process of self-drilled holes and TF-WEDG holes for the complementary benefits of high efficiency and accuracy. First, the tool electrode with negative polarity drills holes on the plate electrode. Then tool electrode is returned to its initial position and the axis gets off-centered from the hole center at a certain distance. Next, tool electrode polarity changes to the positive and is fed into the plate electrode with rotation in order to machine the microelectrode (rod electrode). The microelectrode is fabricated with dimension close to the desired diameter in the rough machining condition. Finally, TF-WEDG method with the on-line measurement is used to fabricate the accurate microelectrode.[99] A charge coupled device (CCD) is utilized for the on-line measurement.

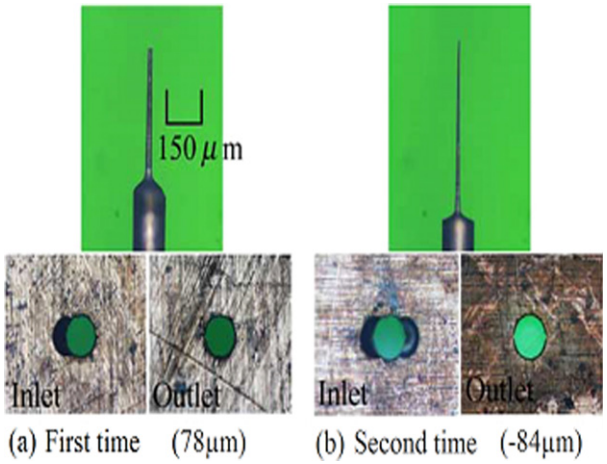


Figure 52 Image of microelectrodes obtained by double forming (110 V, 100 pF, 2 μm s^{-1}, and 5 min): (a) first time (78 μm) and (b) second time (− 84 μm).[105]

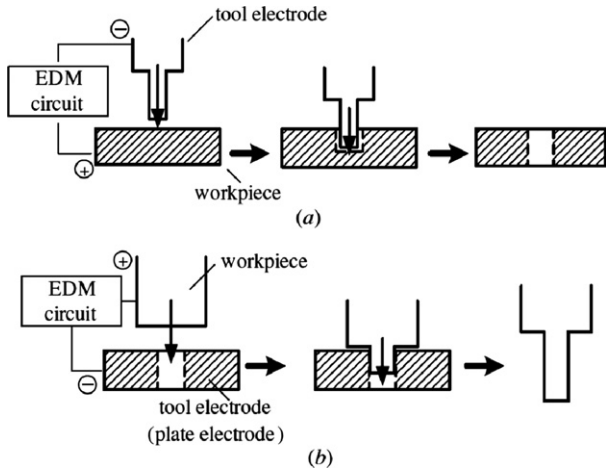


Figure 54 (a) Normal EDM and (b) REDM (reverse EDM).[106]

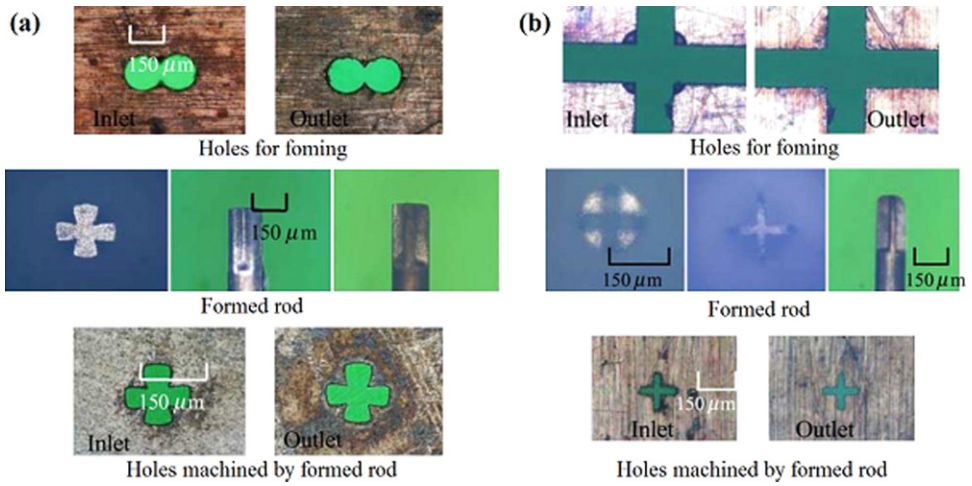


Figure 53 Image of microelectrodes were fabricated by various holes for forming and holes obtained by cross-shaped section (110 V, 100 pF, and 2 μm s^{-1}).[105]

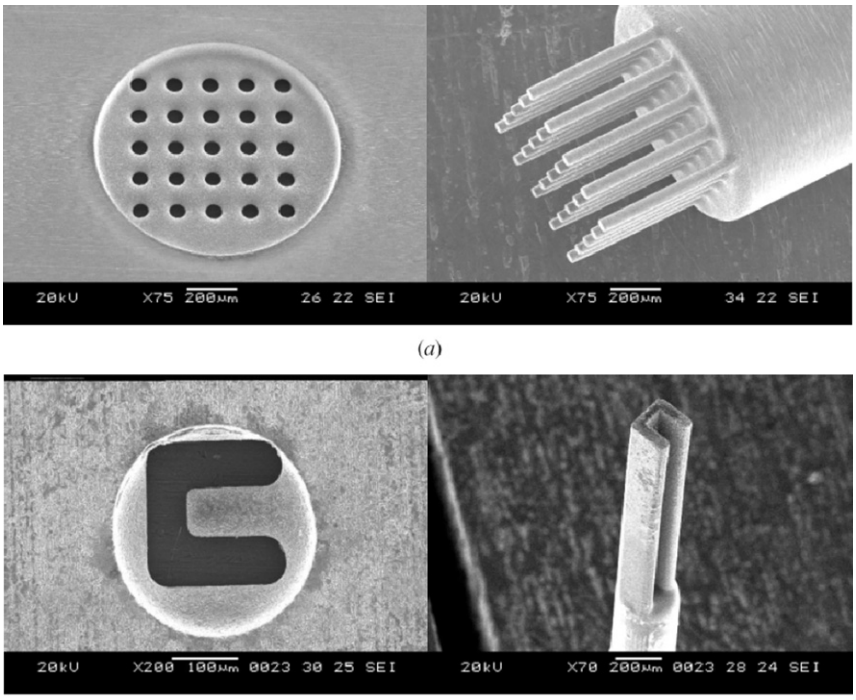


Figure 55 Plate electrodes for REDM and microelectrodes fabricated by REDM: (a) 25 multiple microelectrodes and (b) U-shape microelectrode.[106]

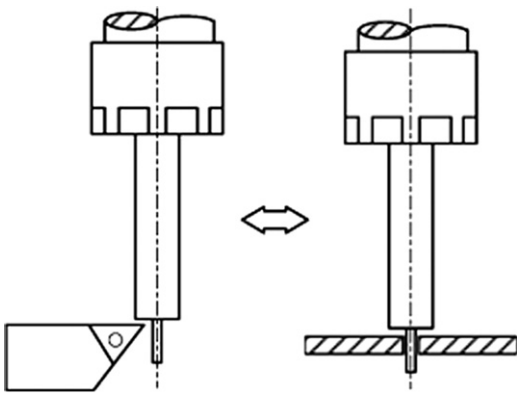


Figure 56 Concept of hybrid process for micro-EDM.[4]

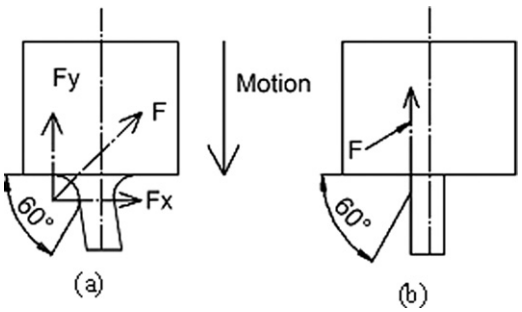


Figure 57 Cutting force components in (a) a larger nose radius tool and (b) a sharp cutting edge tool.[3]

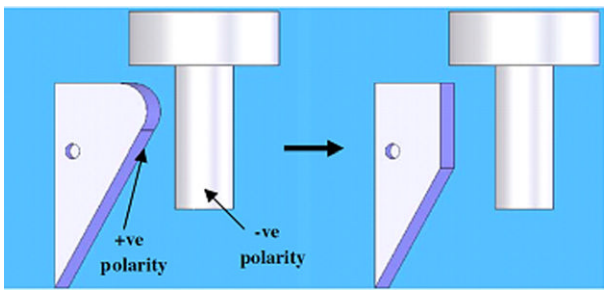


Figure 58 Image on the left illustrates the EDG process on the tool tip and the image on the right illustrates modified PCD tool after EDG process.[3]

Table 8 Parameters for the fabrication of turning insert

Cutting conditions	*Capacitance (pF)*	*Voltage (V)*	*Spindle (rpm)*	*Machined depth (µm)*
Roughing	4700	120	1000	100
Finishing	100	80	1000	5

1.10.4.3.8.3 Continuous machining process of array micro-holes

To gain high consistency accuracy of array micro-holes and to avoid the negative effects of low rigidity of long microelectrode, a continuous machining process is presented according to the TF-WEDG method. **Figure 63** demonstrates the continuous machining process of array micro-holes. After the implement of the self-drilled holes process (**Figure 62**), the microelectrode is machined with a larger diameter D and an

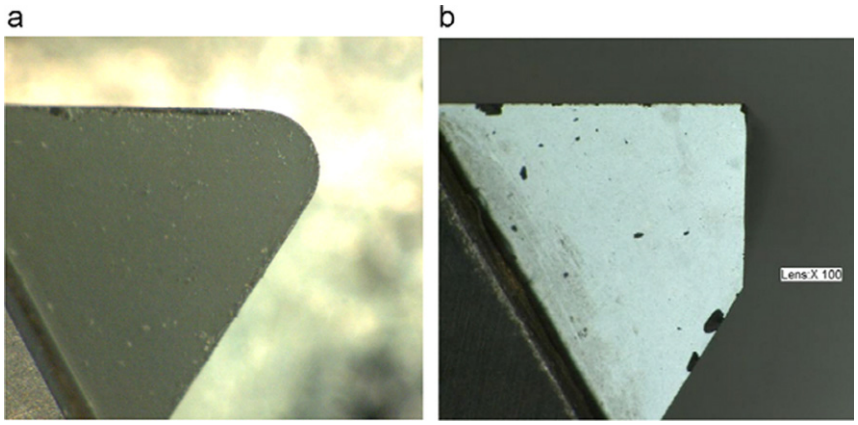


Figure 59 (a) Commercial tool and (b) modified PCD tool.[3]

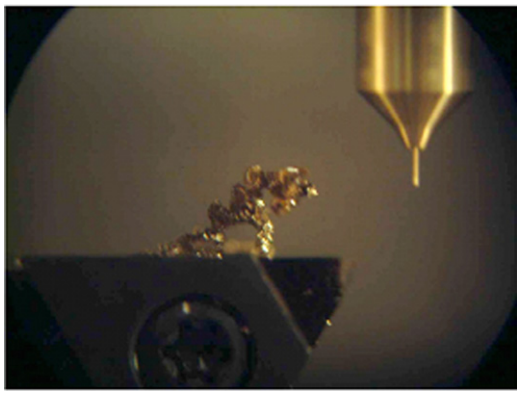


Figure 60 The 2 mm long microelectrode fabricated using modified PCD tool and observed under tool scope.[4]

effective length L. The diameter D guarantees the rigidity of the electrode with the length L. As shown in Figure 63(a), firstly the microelectrode with the desired diameter d and proper aspect ratio of length $L1$ is machined by TF-WEDG. The aspect ratio guarantees enough rigidity of the microelectrode. The desired aspect ratio between d and $L1$ guarantees enough rigidity of the microelectrode. Secondly, the microelectrode is utilized for micro-hole EDM drilling (Figure 63(b)). The microelectrode becomes shorter (wear length ΔL) after micro-EDM drilling the expected number of holes because of electrode wear during micro-EDM. When the microelectrode becomes too short after micro-hole EDM drilling (Figure 63(c)). The remained part of the microelectrode with diameter D is re-machined by TF-WEDG to produce again the microelectrode with diameter d and length $L1$. The procedures are repeated (Figures 63(a)–63(c)) are repeatedly performed until all designed holes are produced (Figure 63(d)). Array micro-holes can be produced by the circulation process.[99]

Based on the continuous machining process, 5×5 array micro-holes were produced through 5 times microelectrodes machining by TF-WEDG and 5 times micro-hole machining with 5 micro-holes each time. The consistency accuracy of micro-holes is evaluated by measuring the magnified images of 25 micro-holes. The experimental results of the micro-holes and the used microelectrodes are presented in Figures 64(a) and 64(b) respectively. The results revealed that the consistency accuracy of 25 micro-holes of $\Phi 73\ \mu m$ is ± 1.1 m, and the drilling time of single micro-hole is 1 min 10 s on the 200 μm thick stainless steel plate.[99]

1.10.4.3.8.4 LIGA–micro-EDM hybrid machining process

The flow of the LIGA process is shown in Figure 65. The LIGA process (step 1–5) which was developed by the University of Wisconsin at Madison[107] fabricates the electroplated electrodes for the micro-EDM. The electrodes that are produced on a silicon substrate are basically negative-type microstructures with ultrafine designs. An electroplated metal plate is used to form many microelectrodes. In the step 5, the metal plate that has the electrodes is released from the substrate as step 5 as the negative-type electrodes are self-supporting. The electrode position in the metal plate is very accurate as photolithographic methods are used for electrode fabrication.[108]

Step 6 shows a positive type of patterned structure is fabricated by feeding the WC–Co workpiece into one of the electrodes using micro-EDM. During this step the shape of the electrode is deformed due its wear. To achieve a uniform cross section along the workpiece length, the electrode has to be replaced before its deformation takes place throughout the thickness. Such deformed electrodes can be replaced with a new electrode by X-Y position between the workpiece and each of the electrodes. This can be done with a high precision as the accurate position of the electrodes as in the step 7. A patterned microstructure with high aspect ratio is achieved after repeating the machining and replacing process.[108]

In the LIGA method an array of nickel electrodes with a negative type gear pattern with 200 μm outside diameter was machined as illustrated in Figure 66. The height of the structure is 300 μm. The primary shape of the nickel electrode is illustrated on the left side of Figure 67. It is deformed by metal wear as illustrated on the right side of Figure 67. Deformation occurs when the WC–Co workpiece with 300 μm diameter is fed to the electrode about 400 μm by using micro-EDM. Though the length of the EDMed structure is confined to the amount of feed depth in single machining, much larger height can be fabricated be repeating the machining and replacing the worn electrode with a new one at X-Y position.[108]

Figure 68 illustrates a positive-type WC–Co microstructure having a 1 mm length fabricated by using three different electrodes of the serial micro-EDM. However, much higher aspect ratio

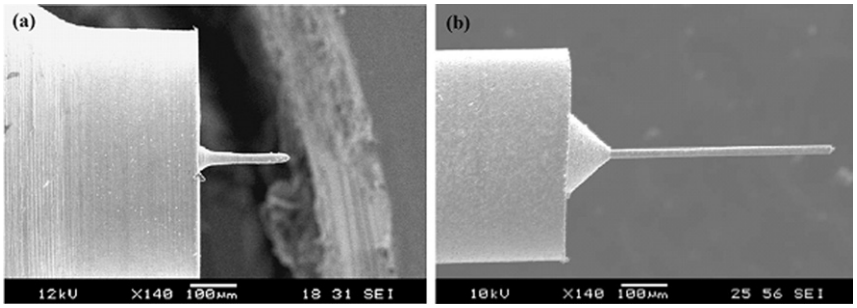


Figure 61 (a) A 22 μm brass electrode fabricated by micro-turning process and used for machining 10 micro-holes on 100 μm thick stainless steel plate, showing some wear.[3,4] (b) A 19 μm graphite micro-microelectrode of 0.5 mm length fabricated by micro-turning process.[3]

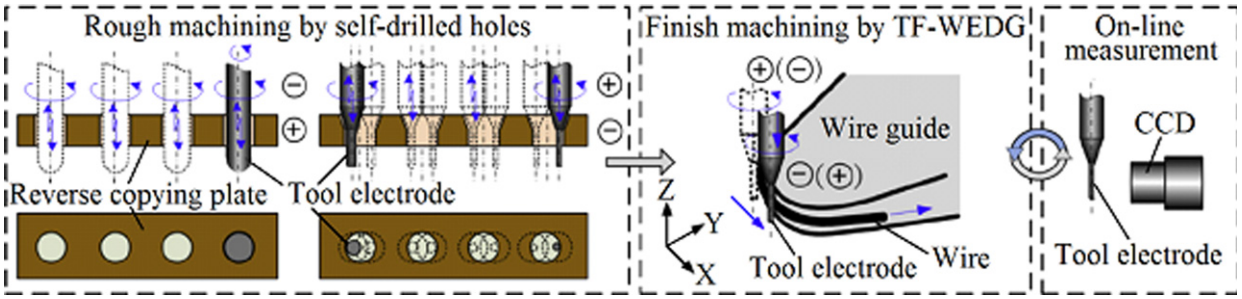


Figure 62 Schematic diagram of hybrid machining process (self-drilled holes and TF-WEDG).[99]

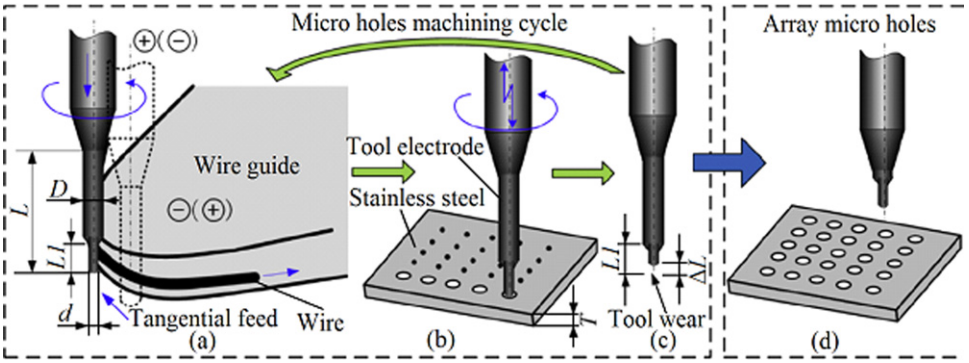


Figure 63 Continuous process for array micro-holes.[99]

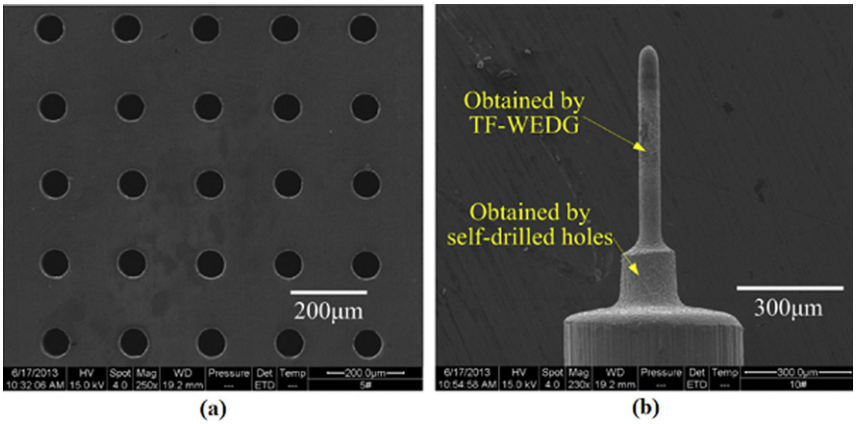


Figure 64 (a) Experimental result of array micro-holes. (b) Microelectrode after machining micro-holes.[99]

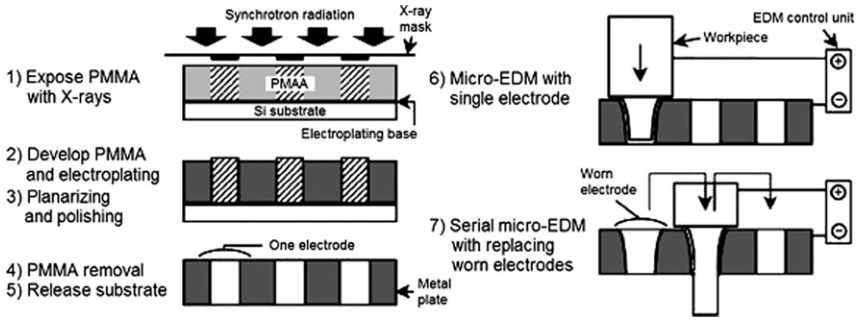


Figure 65 Flow of new microfabrication process combining LIGA (step 1–5) and micro-EDM (step 6–7).[108]

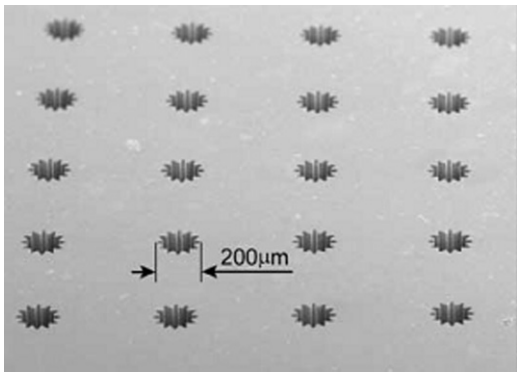


Figure 66 Array of negative-type nickel electrodes by the LIGA.[108]

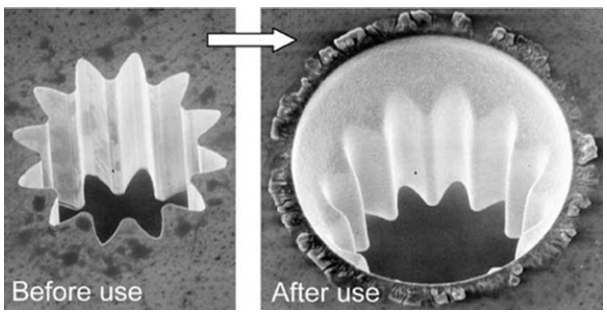


Figure 67 Initial shape of patterned negative-type electrode and deformed one after use.[108]

structure with over 1 mm length can be fabricated by increasing the replacement cycles. The variation in the outside diameter of the 1 mm long structure along its length is measured and the result is illustrated in Figure 69. The provided graph depicts this particular gear length varies by an amount of about 4 μm in the outside diameter along its length. The results illustrate this process has capability to produce high aspect ratio microstructures from various bulk materials as well as WC–Co.[108]

1.10.5 Prospective on Process Selection

A micro-mold cavity is needed, when the mass production of various micro-components is involved.[5] Micro-holes are required in micro-dies and micro-molds.[109] Moreover, hard materials are used for micro-injection-mold, which requires

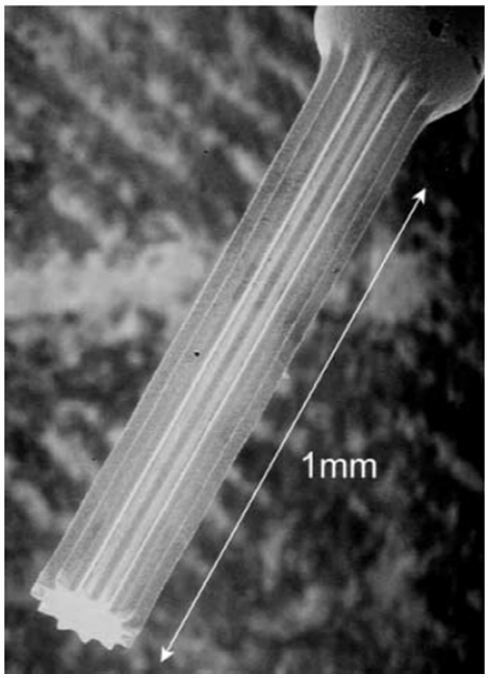


Figure 68 1 mm long WC–Co microstructure with gear pattern produce by micro-EDM.[108]

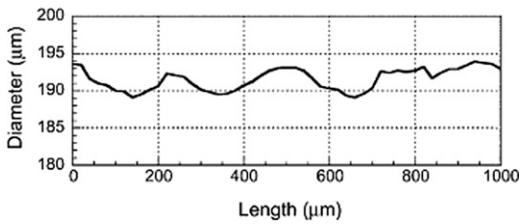


Figure 69 Variation of outside diameter of 1 mm long gear in Figure 68.[108]

very accurate machining of complex and three dimensional shapes in micron range.[5]

Tungsten carbide (WC) and composite of tungsten carbide (WC–Co) are employed for producing cutting tools, dies, other special tools and components owing to high hardness, strength, wear and corrosion resistance of WC and WC-Co over a wide range of temperatures;[72,73] therefore, machining of WC plays a

remarkable roles in recent trend of manufacturing.[110] EDM and electro-chemical machining (ECM) are the only feasible processes for the modern machining of WC–Co.[73] Investigation of Watson and Freer[111] revealed that due to a resistant oxide layer generation on the surface, MRR is very slow during ECM of WC–Co. In fact, more the percentage of cobalt in the alloy increases, the amount of MRR decreases more with it. Singh[112] reported that, the EDM machining process is more suitable for the machining of carbides and other refractory materials.

In the EDM process, conductive materials are removed according to the thermal energy (melting and partial vaporization of the workpiece) produced by series of sparks occurring between the electrode and electrical workpiece.[113] EDM is a useful process in industry for machining conductive materials with accurate dimensions regardless of hardness, strength, and toughness.[114,115] Adding aluminum powder to the dielectric leads to increased MRR and improved surface roughness during EDM.[27,91] The chain formation among powder particles in the dielectric helps bridge the gap between electrode and workpiece that can cause an early explosion. Therefore, faster sparking within discharge and faster erosion of the workpiece surface take place.[90] Micro-EDM and EDM have the same characteristics, with the only differences being the electrode size, discharge energy, and axis movement resolution at the micron level in micro-EDM.[6] Micro-mold making, production of dies and cavities, and producing of the complex three-dimensional shapes at the micro-level are the major functions of micro-EDM.[38] In EDM and micro-EDM, no direct contact and negligible force between the workpiece and tool cause the elimination of tool deformation, chatter, mechanical stress, and vibration errors during machining.[6,39,40] Therefore, micro-EDM is one of the most effective methods of machining of ECM (WC).[43,57]

Jahan *et al.*[57] used AgW, CuW, and W microelectrodes for machining of WC-10wt.%Co. The highest MRR was obtained with the CuW electrode. Also, Jameson[34] stated that "copper tungsten is often used for machining of tungsten carbide." Electrode polarity produces a re-sticky effect during EDM of tungsten carbide.[116] It was reported that the WC workpiece surface does not have any re-sticky regions after finishing with positive electrode polarity in the EDM process.[116] On the other hand, negative electrode polarity for micro-EDM of WC is more suitable as it provides higher MRR, lower electrode wear, better surface roughness, and controlled performance.[117] Jahan *et al.*[43,55] investigated the micro-EDM parameters effects on WC (micro-hole quality) using a transistor and RC-type pulse generator. The results indicated that micro-EDM performance relies on the discharge energy. It has been reported that controlling the performance of RC-type micro-EDM is easier as the electrical discharge energy is determined by voltage and capacitance only. In RC-type micro-EDM, Jahan *et al.*[55,57] used voltage and capacitance (capacitor) as parameters during micro-EDM of WC–10%Co and 0.6% others. Moreover, in transistor-type micro-EDM, they applied voltage, resistance, pulse-ON time, pulse-OFF time,[55,117] and electrode rotational speed[117] as parameters during micro-EDM of WC–10%Co and 0.6% others.[55,117]

The thermal stress during EDM of tungsten carbide creates micro-cracks on the machined surface, as tungsten carbide has low thermal conductivity and brittleness.[118–124] This is especially true during EDM of WC–Co composite, since WC and Co are two quite different phases.[121] Micro-cracks and micropores on the machined surface severely deteriorate the service life, reliability, and machining precision of tungsten carbide tool or mold.[122] Suitable machining parameters during EDM of WC reduce the damage caused by the micro-cracks on the machined surface.[122] It has also been reported that the EDM process has no effect on the microstructure of the bulk workpiece material (WC). This means that EDM causes damage only on the machined surface (surface layer) within a certain depth.[121] Hence, a complimentary finishing operation might become necessary to remove micro-cracks on the machined surface and to produce good surface quality when utilizing the EDM process.[73] On the other hand, the depth of the damaged layer and the average length, width, and number of micro-cracks reportedly increase with increasing current and pulse-ON time.[121] The micro-cracks are more visible when the spark energy (electrical discharge energy) is set to a higher level. Moreover, the machined surface becomes smoother as the spark energy is set at a lower level.[121,122]

Moreover, micro-EDM possess a significant place in the field of micromachining. Because of its non-contact nature, a very long and thin electrodes can be used in micro-EDM.[5] Main disadvantages of micro-EDM are EWR and low MRR. Electrode wear can be balanced by changing the microelectrode, preparing a longer microelectrode from the earlier stage or manufacturing the microelectrode *in situ* for further machining.[4] Also, changing the microelectrode during machining causes decreased accuracy due to changing the setup or microelectrode re-clamping. Thus, An on-machine microelectrode fabrication can eliminate clamping error in the micro-EDM process.[4]

The microelectrode production procedures explained have a number of benefits. For one, the BEDG method setup is simple and the rotating sacrificial disk can be used to fabricate microelectrodes with smooth surface.[5] The block electrode can fabricate cylindrical, triangular, or square microelectrodes at low cost.[125] Moreover, the moving BEDG process has all the advantages of the rotating sacrificial disk and BEDG method. Therefore, moving BEDG can be utilized to manufacture non-tapered cylindrical or non-cylindrical microelectrodes with smooth surface and accurate shapes at low cost using a simple setup.[3,4]

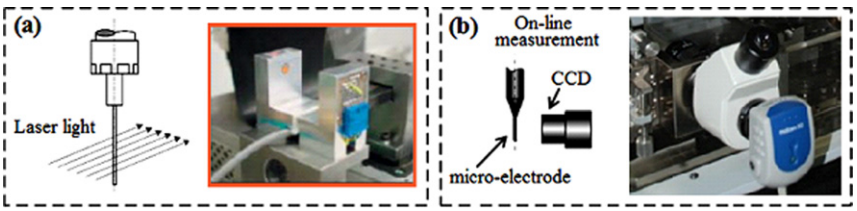


Figure 70 Online measurement (a) Laser light[3–5] and (b) charge coupled device.[99]

Nonetheless, the microelectrode fabrication procedures addressed have some disadvantages as well. For instance, deflection occurs during thin microelectrode fabrication with the micro-turning process.[4] Also, the microelectrode produced with a micro-turning machine needs to be transferred and clamped to the micro-EDM or EDM machine. The fabricated microelectrode cannot be aligned on the micro-EDM or EDM machine, which causes reduced accuracy. The self-drilling hole method usually produces tapered microelectrodes.[99] In addition, tapered or uneven microelectrode diameters are produced with the BEDG process.[5] The rotating sacrificial disk method produces microelectrodes with better surface roughness than the WEDG (guided running wire) process.[5] Moreover, WEDG requires special equipment and high investment. Rotating sacrificial disk setup is relatively complicated. Hybrid machining requires special equipment and high investment. It can be easily outsourced through other workshop. Using a rotating sacrificial disk involves a rather complex setup.[3] Hybrid machining requires special equipment and high investment. Besides, it cannot be easily obtained from all workshops.



Figure 71 AG40L Sodick electrical discharge machine.

Moreover, on-machine measurement is needed to achieve the desired and accurate microelectrode because of estimation of the microelectrode diameter is very difficult. Thus, optical measurement and CCD were applied for the microelectrode measurements, as shown in Figure 70.[3–5,99]

In this research, EDM machine is used instead of micro-EDM and hybrid machines, because the EDM machine is cheaper and more widely available in workshops. CuW is selected as microelectrode to produce the micro-holes in WC–16%Co. There is less information about the effects of micro-EDM parameters (voltage, current, pulse-ON time,

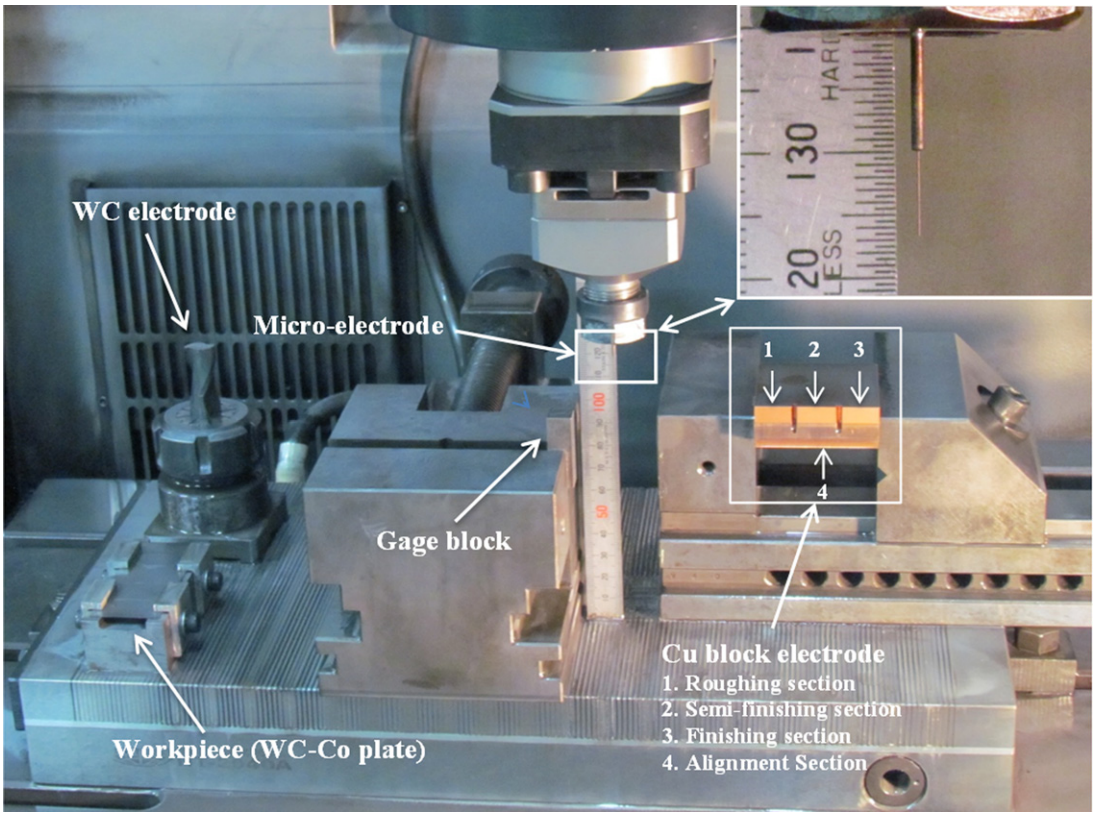


Figure 72 Experimental setup design for the on-machine fabrication and measurement techniques of microelectrodes and micro-EDM drilling.

pulse-OFF time, rotating speed, and capacitor) on micro-EDM drilling of WC–16%Co using an ordinary EDM machine. This research is carried out to investigate the effects of micro-EDM parameters on MRR, EWR, surface roughness, micro-cracks, migration of material to the workpiece, and overcut during micro-EDM drilling of WC–Co using an EDM machine.

Table 9 Table properties of CuW microelectrode

Kind	*Ingredient*	*Specific gravity*	*Conductivity %IACS*	*Solidity*
CuW	30Cu + 70 W	14.3	28.0	HRB93

Table 10 Properties of WC–Co (typical nominal properties)

Grade	*Percent cobalt*	*Grain structure*	*Rockwell hardness*	*Transvers rupture*	*Density (gm cc^{-1})*
HC-13.82	US16	16	Sub-micron	90.8	500

1.10.6 Methodology

1.10.6.1 Experimental Setup

In this research, an AG40L Sodick electrical discharge machine was used to replace the micro-EDM machine, as shown in **Figure 71**. This EDM machine has 0.0001 mm (0.1 μm) movement resolution on each axis and the amount of discharge energy can be controlled toward lower energy. **Figure 72** shows the experimental setup for fabricating microelectrodes and measuring microelectrodes diameter, electrode wear, and micro-holes EDM drilling. CuW material (30%Cu + 70%W) with 1 mm diameter was selected as the raw material for the microelectrode and WC–16%Co (HS-US16 plate with 0.331 mm thickness) was chosen as the workpiece. **Tables 9** and **10** illustrate the properties of the CuW electrode and WC–16%Co. The copper block electrode was used to manufacture the microelectrodes as shown in **Figure 72**.[60] A WC electrode was utilized to dress the tapered microelectrode after micro-holes EDM drilling in order to produce a straight electrode.[96] The polarity of the microelectrode during fabrication and electrode dressing was positive, while negative polarity

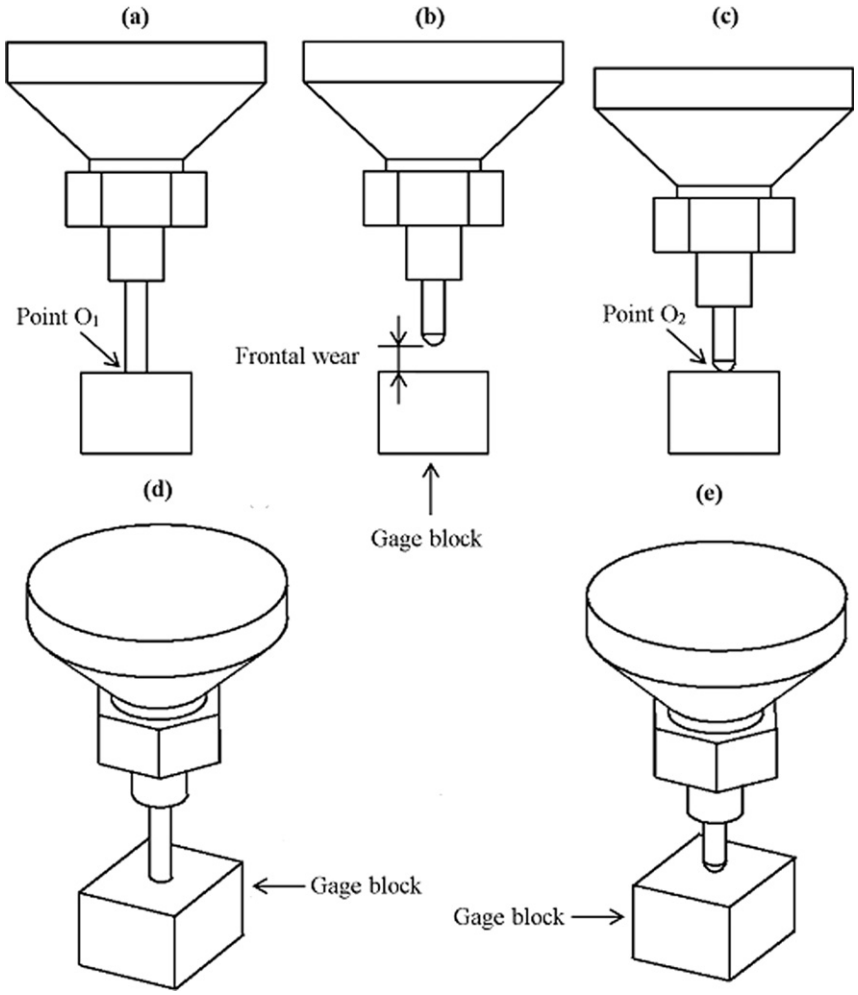


Figure 73 Measuring frontal wear of microelectrode (a) microelectrode before micro-hole EDM drilling touches gage block, (b) microelectrode after micro-hole EDM drilling, (c) microelectrode after micro-hole EDM drilling touches gage block, (d) 3D shape of section a, and (e) 3D shape of section c.

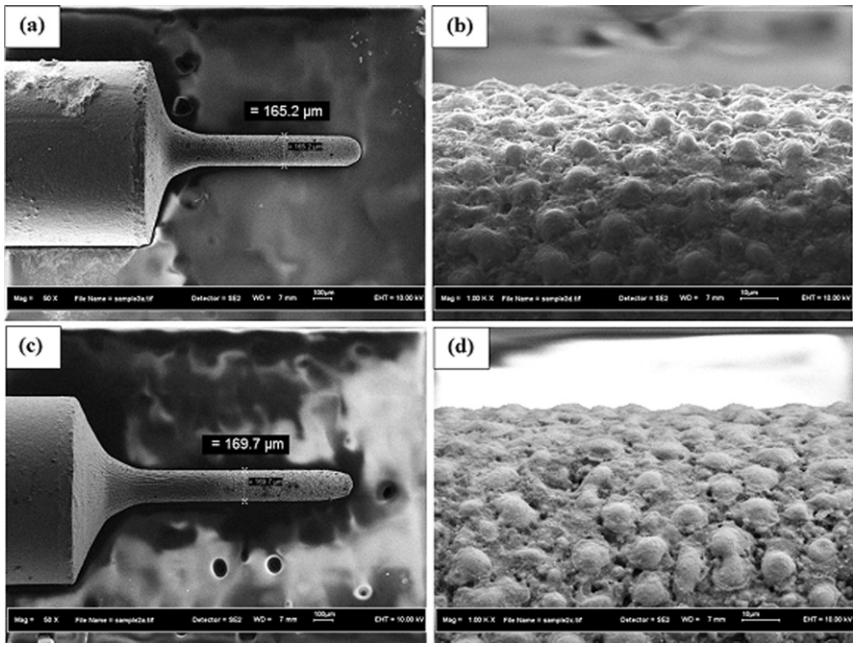


Figure 74 (a) Microelectrodes with 165.2 μm diameter. (b) Surface of microelectrodes with 165.2 μm diameter. (c) Microelectrodes with 169.7 μm diameter. (d) Surface of microelectrodes with 165.2 μm diameter.

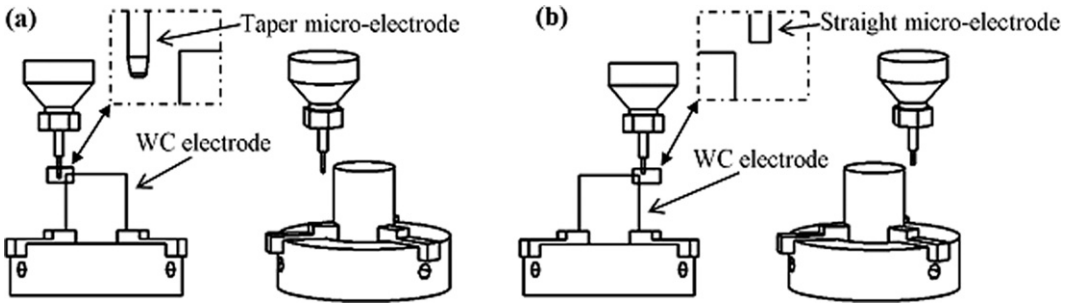


Figure 75 Dressing process. (a) Taper part of microelectrode after machining micro-hole and before dressing process. (b) Straight microelectrode after dressing process.

helped produce the micro-holes.[96] Oil-based dielectric fluid mixed with aluminum powder (PGM WHITE 3) at 1.5 g l^{-1}[126] was also used as it is recommended by Sodick company[126] and the excitation of the aluminum powder in dielectric can help increase MRR and improve the surface quality during EDM.[27,91] A 10 mm thick gage block was used to measure the frontal wear of the microelectrode. The gage block and copper block electrode were aligned with a dial test indicator with 2 μm accuracy.

The frontal electrode wear was measured in the steps shown in Figure 73 and eqn [14]. First, the microelectrode touches the top surface of the gage block at point O_1 before micro-hole EDM drilling (Figures 73(a) and 73(d)), then it will be touch again the top surface of the gage block O_2 after machining the micro-hole (Figures 73(c) and 73(e)). The difference between these positions shows frontal electrode wear (Figure 73(b)).

$$\text{Front wear} = |O_2 - O_1| \qquad [14]$$

1.10.6.2 Micro-EDM of WC–Co

Two CuW microelectrodes with 165.2 and 169.7 μm diameter and around 6.8 mm initial lengths (Figure 74) were utilized for producing micro-holes. These two electrodes were fabricated on-machine by moving BEDG process as described in our previous paper[127] and carried out according to the experimental setup shown in Figure 72. As described before, the polarity of the microelectrode during fabrication and electrode dressing was positive while negative polarity was used for producing micro-hole. Through holes were produced on WC–16%Co plate with 0.331 mm thickness. After micro-EDM drilling of every hole, the microelectrode becomes tapered. The dressing process serves to remove the taper of the microelectrode and produce a straight microelectrode for the next micro-hole EDM drilling based on Figure 75 and using setup shown in Figure 72. Voltage, current, pulse-ON time, pulse-OFF time, rotating speed, and capacitor were adopted as the

parameters to analyze MRR, EWR, surface roughness, microcrack, migration of material to the workpiece, and over cut during micro-EDM drilling of WC–Co using EDM machine. MRR, EWR, and overcut were calculated by following eqns [8, 9, and 11], respectively (the geometry is shown in **Figure 13** and **Figure 73**).[96] **Table 11** demonstrates the machining parameter levels and symbols.

The experiments were designed with 2^{6-2}_{IV} fractional factorial design and 3 center points consisting of 19 runs including 16 ($=2^{6-2}$) and 3 center points. These (resolution IV designs) are designs in which no main effect is aliased with any other main effect or with any two-factor interactions, but two-factor interactions are aliased with each other. The factorial effects defining contrast are I=ABEF=ACDF=BCDE. The alias relationships are as follows:

A=BEF=CDF
B=AEF=CDE
C=ADF=BDE
D=ACF=BCE
E=ABF=BCD
F=ABE=ACD
AB=EF
AC=DF
AD=CF
AE=BF
AF=BE=CD
BC=DE
BD=CE
ABC=ADE=BDF=CEF
ABD=ACE=BCF=DEF

The three-, four-, five-, and six-factor interactions are considered errors. Therefore, the aliased of two-factor interactions are important in this case.

Table 11 The levels of machining parameters

Symbol	*Parameters*	*Unit*	*Level*		
			Low	*Center*	*High*
A	Voltage (*V*)	*V*	50	70	90
B	Current (I_p)	*A*	0.4	2.7	5
C	Pulse-on time (t_{on})	μs	1	3	5
D	Pulse-OFF time (t_{off})	%	1	5	9
E	Rotating speed (*R*)	rpm	0	10	20
F	Capacitor (*C*)	μF	0	0.05	0.1

1.10.7 Results and Discussions

1.10.7.1 Analysis of Results on Micro-EDM of WC–Co

Table 12 shows the experimental design and results. Moreover, **Figure 76** demonstrates the effects of the micro-EDM parameters on the holes' diameters and shapes. As can be seen in **Figure 76**, various machining parameters produced microholes with different diameters and shapes. The micro-hole's diameters depend on microelectrode's diameter, overcut, and electrode wear.

1.10.7.1.1 Overcut

Figure 77 illustrates the amount of overcut in various machining conditions. It is clear that overcut varied from 0.0155 to 0.039225 mm. Most of the overcut at different parameter values was around 0.025 mm and below. The minimum overcuts were achieved during machining hole 6 (0.0155 mm) (90 V voltage, 0.4 A current, 5 μs pulse-ON time, 1 μs pulse-OFF time, 20 rpm rotating speed, and without capacitor) and hole 5 (0.015775 mm) (50 V voltage, 0.4 A current, 5 μs pulse-ON time, 9 μs pulse-OFF time, and without spindle rotation and capacitor). The maximum overcut was reached when machining hole 1 (0.039225 mm) (50 V voltage, 0.4 A current, 1 μs pulse-ON time, 9 μs pulse-OFF time, 20 rpm rotating speed, and 0.1 μF capacitor).

Table 12 Experimental design and results

STD	V	I_p	t_{ON}	t_{OFF}	R	C	*MRR*	*EWR*
1	50	0.40	1	9	20	0.1	0.0927687	24.73173
2	90	0.40	1	1	0	0.1	0.0424533	25.94548
3	50	5	1	1	20	0	0.0177225	31.58372
4	90	5	1	9	0	0	0.0249439	19.69877
5	50	0.40	5	9	0	0	0.00593853	46.49713
6	90	0.40	5	1	20	0	0.00430031	56.43734
7	50	5	5	1	0	0.1	0.0771423	41.79489
8	90	5	5	9	20	0.1	0.0771382	47.81725
9	90	5	5	1	0	0	0.0155904	54.00696
10	50	5	5	9	20	0	0.0203297	35.20764
11	90	0.40	5	9	0	0.1	0.0345459	29.93017
12	50	0.40	5	1	20	0.1	0.0708279	28.98942
13	90	5	1	1	20	0.1	0.0861362	40.07686
14	50	5	1	9	0	0.1	0.0831022	33.78316
15	90	0.40	1	9	20	0	0.00747033	20.04386
16	50	0.40	1	1	0	0	0.00761251	29.15251
17	70	2.70	3	5	10	0.05	0.0429182	28.73914
18	70	2.70	3	5	10	0.05	0.0406649	27.34764
19	70	2.70	3	5	10	0.05	0.0423782	27.16618

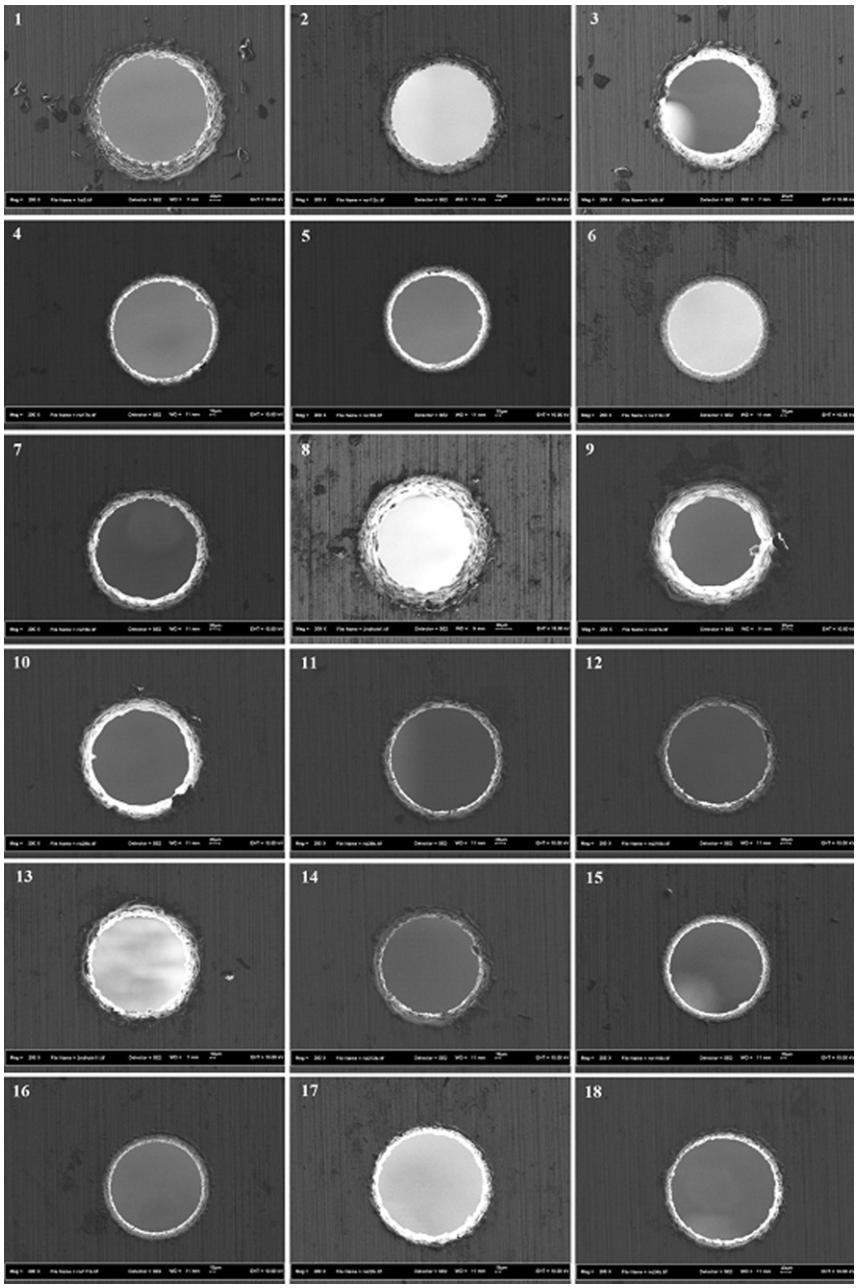


Figure 76 Micro-holes.

In the micro-EDM process, the micro-hole is very small and low amounts of energy for material removal causes to produce small overcut. So the chips cannot be removed easily from the sparking gap (between the microelectrode and workpiece) inside the micro-hole. The remaining chips inside the micro-hole are passed on to the workpiece by the spark electricity force. The remaining chips are re-machined with spark energy into smaller than normal amounts of removed material from the workpiece material, as described in Figure 78. This leads to inefficient EDM. The smaller chips can be removed more easily. Also, the chips collected in the sparking gap create unstable servo operation, which further deteriorates machining efficiency due to the electrode-to-workpiece voltage variation with the free movement of chips. The machine's servo system advances and holds the position or retracts the electrode from the workpiece by comparing the electrode-to-workpiece voltage to a reference voltage. The electrode moves forward and reverses, increasing the chip movement on the surface.[34]

1.10.7.1.2 MRR and EWR

Design-Expert software was used to analyze the experimental outcomes for MRR and EWR. Analysis of variance (ANOVA) was conducted to test the significance of the models, individual

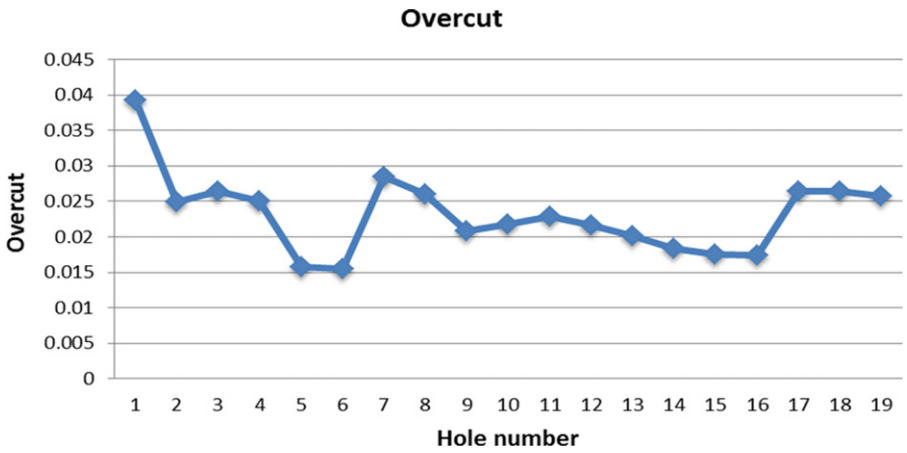


Figure 77 Amount of overcut during various machining conditions.

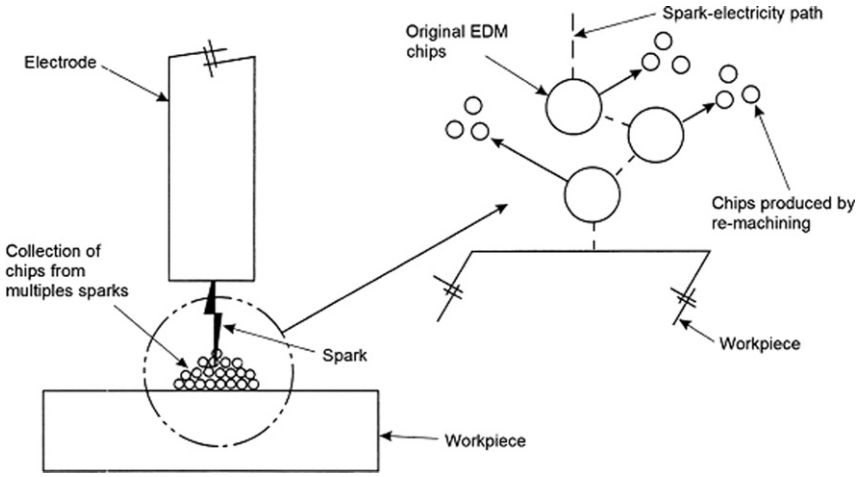


Figure 78 Chip collection and re-machining in sparking gap.[34]

Table 13 ANOVA table for MRR

Source	*Sum of squares*	*d.f.*	*Mean square*	*F-value*	*Prob > F*	*Status*
Model	0.11	7	0.016	152.44	< 0.0001	Significant
A-Voltage	0.001998	1	0.001998	18.72	0.0015	
B-Current	0.011	1	0.011	101.71	< 0.0001	
C-Pulse-ON time	0.001217	1	0.001217	11.40	0.0070	
E-Rotating speed	0.001694	1	0.001694	15.87	0.0026	
F-Capacitor	0.094	1	0.094	878.59	< 0.0001	
AB	0.002586	1	0.002586	24.22	0.0006	
AF	0.001772	1	0.001772	16.60	0.0022	
Curvature	0.0009097	1	0.0009.097	8.52	0.0153	Significant
Residual	0.001068	10	0.0001068			
Lack of Fit	0.001051	8	0.0001314	15.84	0.0607	Not significant
Pure error	0.00001659	2	0.000008294			
Cor total	0.12	18				
R-Squared	0.9907	Adj R-Squared		0.9842		
Pred R-Squared	0.9634	Adeq precision		31.929		

Table 14 ANOVA table for EWR

Source	*Sum of squares*	*d.f.*	*Mean square*	*F-Value*	*Prob > F*	*Status*
Model	1843.23	8	230.40	20.75	<0.0001	Significant
A-Voltage	30.85	1	30.85	2.78	0.1299	
B-Current	111.52	1	111.52	10.05	0.0114	
C-Pulse-ON time	836.15	1	836.15	75.32	<0.0001	
D-Pulse-OFF time	157.99	1	157.99	14.23	0.0044	
E-Rotating speed	1.04	1	1.04	0.094	0.7665	
AC	151.22	1	151.22	13.62	0.0050	
AD	286.25	1	286.25	25.79	0.0007	
AE	268.22	1	268.22	24.16	0.0008	
Curvature	146.11	1	146.11	13.16	0.0055	Significant
Residual	99.91	9	11.10			
Lack of Fit	98.43	7	14.06	18.99	0.0509	Not significant
Pure error	1.48	2	0.74			
Cor total	2089.26	18				
R-Squared	0.9486	Adj R-Squared		0.9029		
Pred R-Squared	0.7523	Adeq precision		16.039		

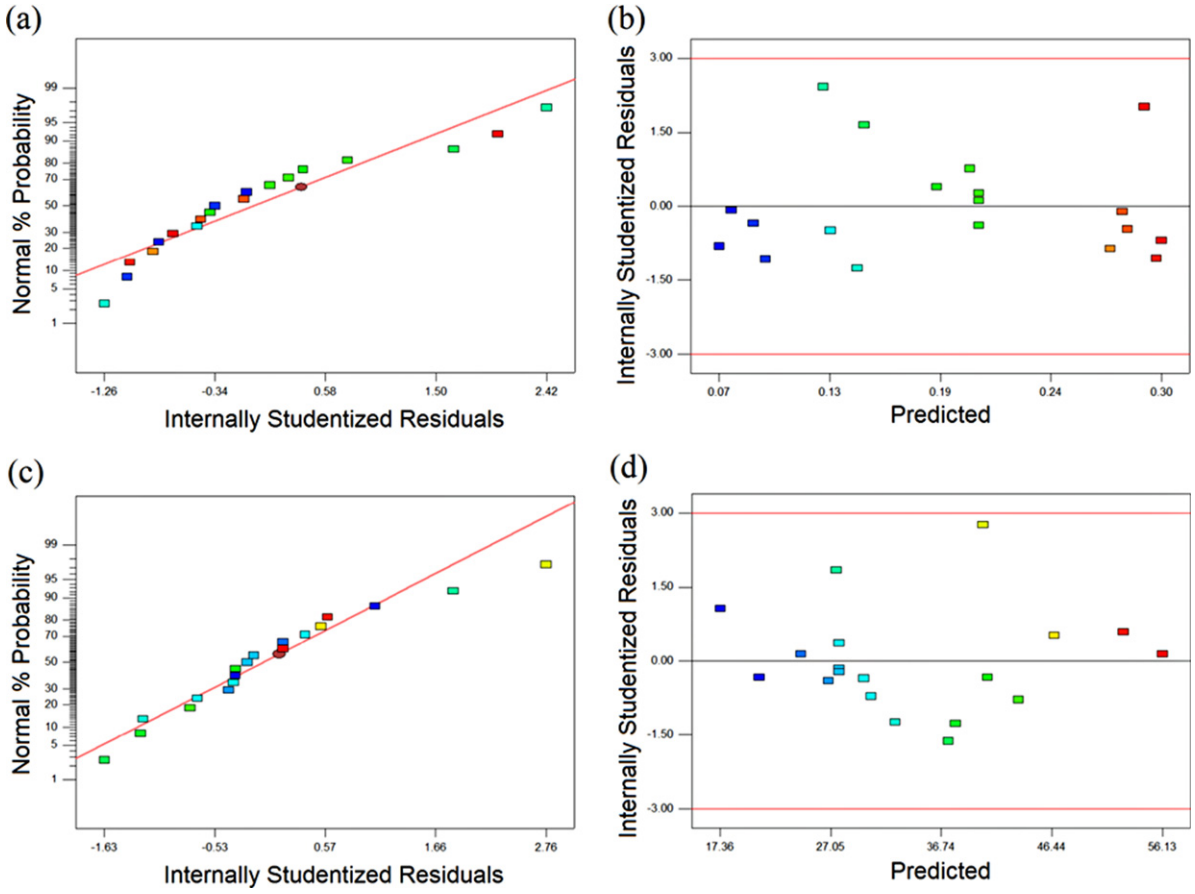


Figure 79 (a) Normal plot of residuals for MRR. (b) Residuals versus predicted for MRR. (c) Normal plot of residuals for EWR, and (d) Residuals versus predicted for EWR.

model terms and lack-of-fit. Square root transformation was applied on the MRR response for ANOVA validation, while EWR did not require any transformation.

Tables 13 and 14 demonstrate the ANOVA tables for MRR and EWR. If the 'Prob > F' value is less than 0.05, it is significant.[95] In this research, A, B, C, E, F, AB, and AF were

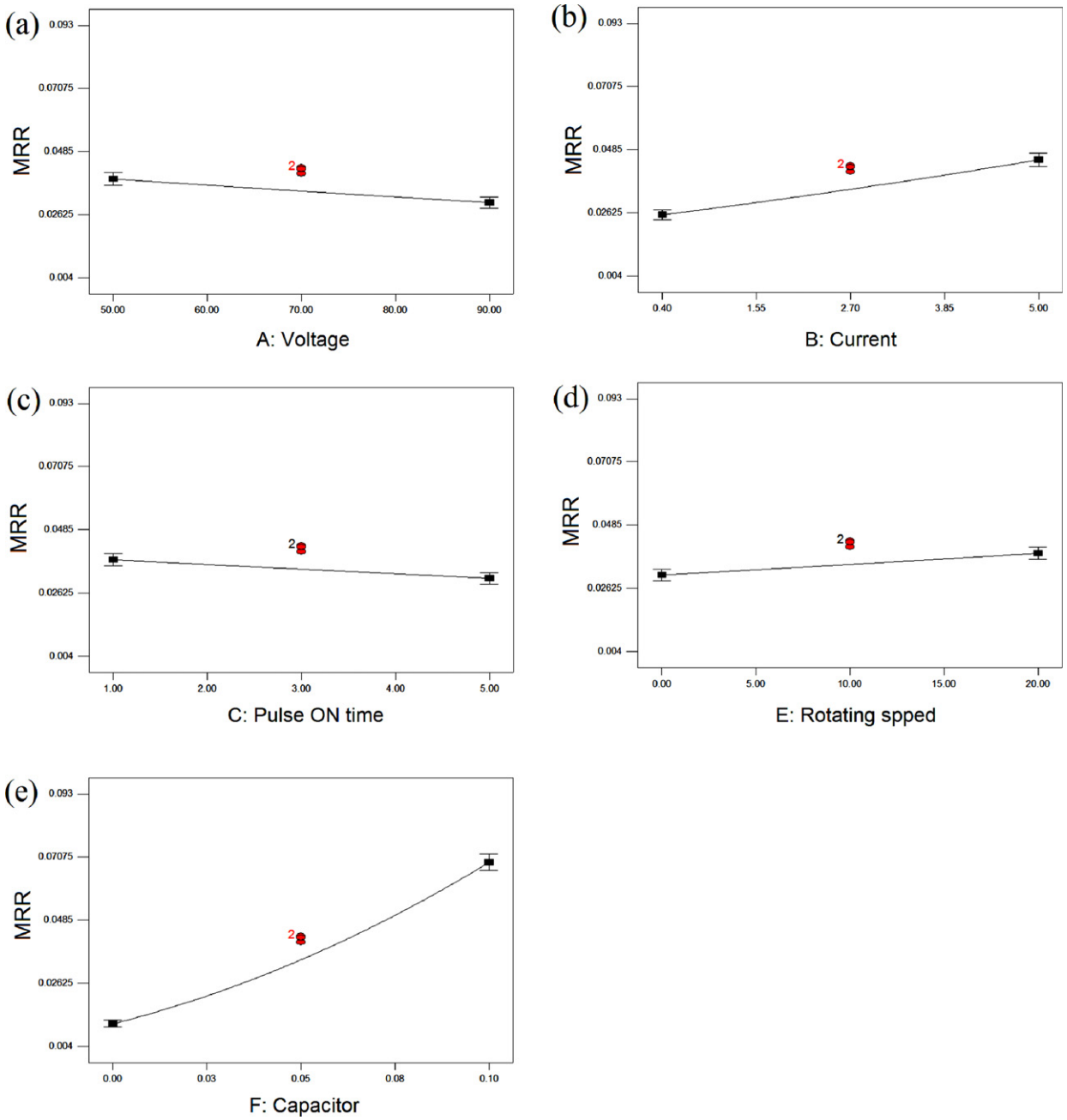


Figure 80 Response graphs for MRR vs. (a) voltage, (b) current, (c) pulse-ON time, (d) rotating speed, and (e) capacitor.

significant model terms for MRR response. Moreover, B and F were the most significant factors. But AB, EF, AF, BE, and CD were possibly significant due to aliase. The ANOVA table results for EWR response depict that B, C, D, AC, AD, and AE were significant. In addition, C was the most significant factor, while AC, DF, AD, CF, AE, and BF were possibly significant.

Insignificant lack-of-fit is desirable for MRR and EWR responses. The outcomes for both MRR and EWR illustrate that an R-Squared value approaching one is desirable. In addition, there were minor differences between Adj. R-Squared and Pred. R-Squared, meaning that the models had acceptable transaction between the input and output parameters. Furthermore, Adeq. Precision greater than four is desirable, as it measures the signal-to-noise ratio.[95]

Residuals must have normal distribution and constant variance. Figure 79 depicts that a normal probability plot of residuals mapped the residuals versus the predicted response for MRR and EWR after the square root transformation was performed only on MRR. Figures 79(a) and 79(c) reveal small departures from the straight line in the normal probability plot of residuals for MRR and EWR, which are common.

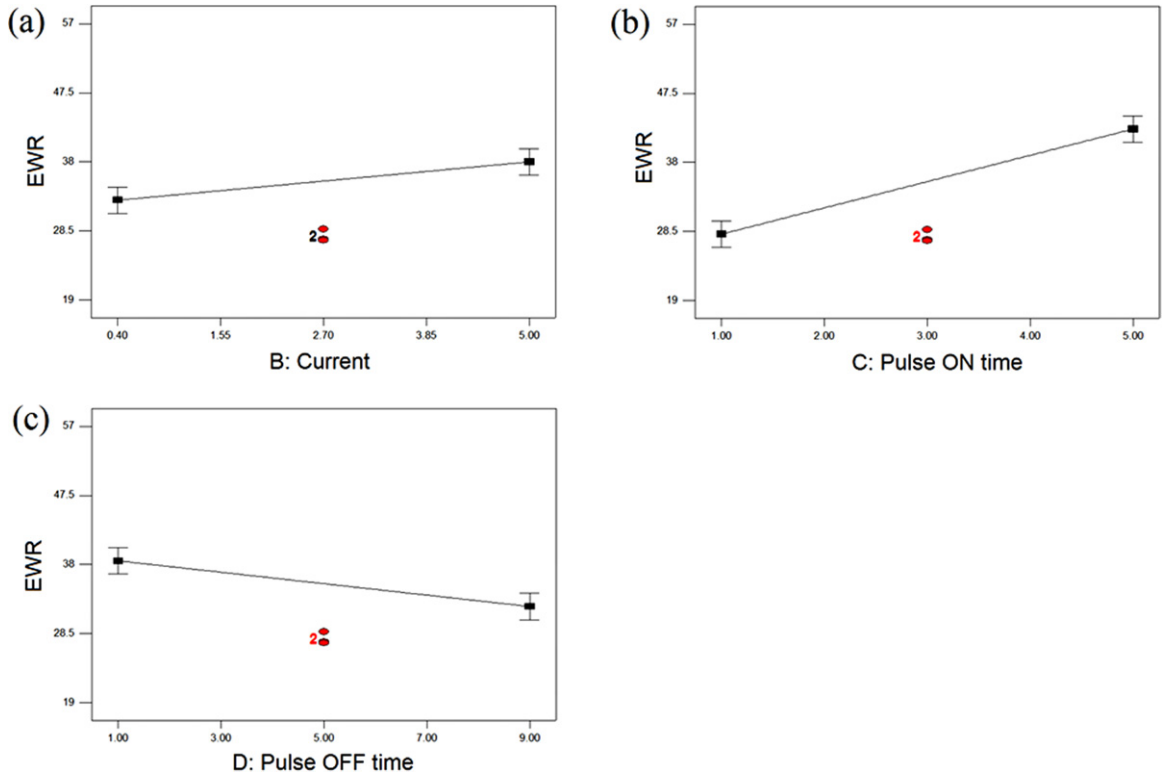


Figure 81 Response graphs for EWR vs. (a) current, (b) pulse-ON time, and (c) pulse-OFF time.

Figures 79(b) and 79(d) depict unusual scatter and patterns. Based on these plots, it can be concluded that the residuals had normal distribution and constant variance after using the square root transformation to analyze and model MRR response.

Figure 80 illustrates the response graph for MRR. According to Figure 80, MRR increased with amplifying current, rotating speed and capacitor, and decreasing voltage and pulse-ON time. The current and capacitor were the most significant factors; however, the effect of the capacitor was greater than the current. The voltage controls the discharge gap between the microelectrode and workpiece, and increasing the voltage increases the discharge gap.[128] Suitable voltage according to current, pulse-ON time, pulse-OFF time, capacitor, and rotating speed results in improved MRR. Figure 80(a) demonstrates that the amount of MRR decreased with voltage greater than 50 V because the discharge gap was larger than the suitable range[95] for low amounts of energy in micro-EDM (current (0.4–5 A), pulse-ON time (1–5 μs), and capacitor (0–0.1 μF) are low). Based on Figure 80(b), MRR increased with current amplification due to the rising amount of heat and energy transmitted to the workpiece for melting and vaporization. Figure 80(c) shows the effect of pulse-ON time on MRR. Sparks occurred during pulse-ON time. Increasing pulse-ON time causes an increase in the amount of energy.[34] During long pulse-ON time, sparks initially take place between the microelectrode and workpiece, after which some of the sparks take place between the microelectrode and chip and some between the microelectrode and workpiece owing to the difficulty in removing chips between the microelectrode and workpiece. The occurring sparks between the microelectrode and chips cause the chip size to decrease. Thus, machining efficiency is reduced.[34] Another reason for the further decrease in machining efficiency is that chips collected inside the micro-hole produced unstable servo operation. As a result, MRR deteriorated with increasing pulse-ON time (Figure 80(c)). Figure 80(d) shows that MRR improved by amplifying the rotating speed, because higher rotating speed helped remove chips from the distance between the workpiece and microelectrode. Figure 80(e) shows that the capacitor was the most significant factor on MRR. MRR increased with increasing capacitor due to the amplified electrical discharge energy transmitted to the workpiece.

Figure 81 illustrates the EWR response graph. Figures 81(a) and 81(b) show that EWR increased with increasing current and pulse-ON time due to the rising amount of heat and energy transmitted to the workpiece for melting and vaporizing that caused microelectrode melting or vaporizing as well.[34] Another reason for the EWR amplification with pulse-ON time is that in micro-EDM, the micro-hole is very small and the low amount of energy for removing material causes overcut, as described in Section 1.10.7.1.1. Hence, the chips cannot be easily removed inside the hole between the microelectrode and workpiece. Some of the sparks took place between these chip and microelectrode that caused to augment wear of the microelectrode.[34] Moreover, the collection of chips inside the micro-hole produces unstable servo operation, which further decreases machining efficiency and increases EWR.[34] During

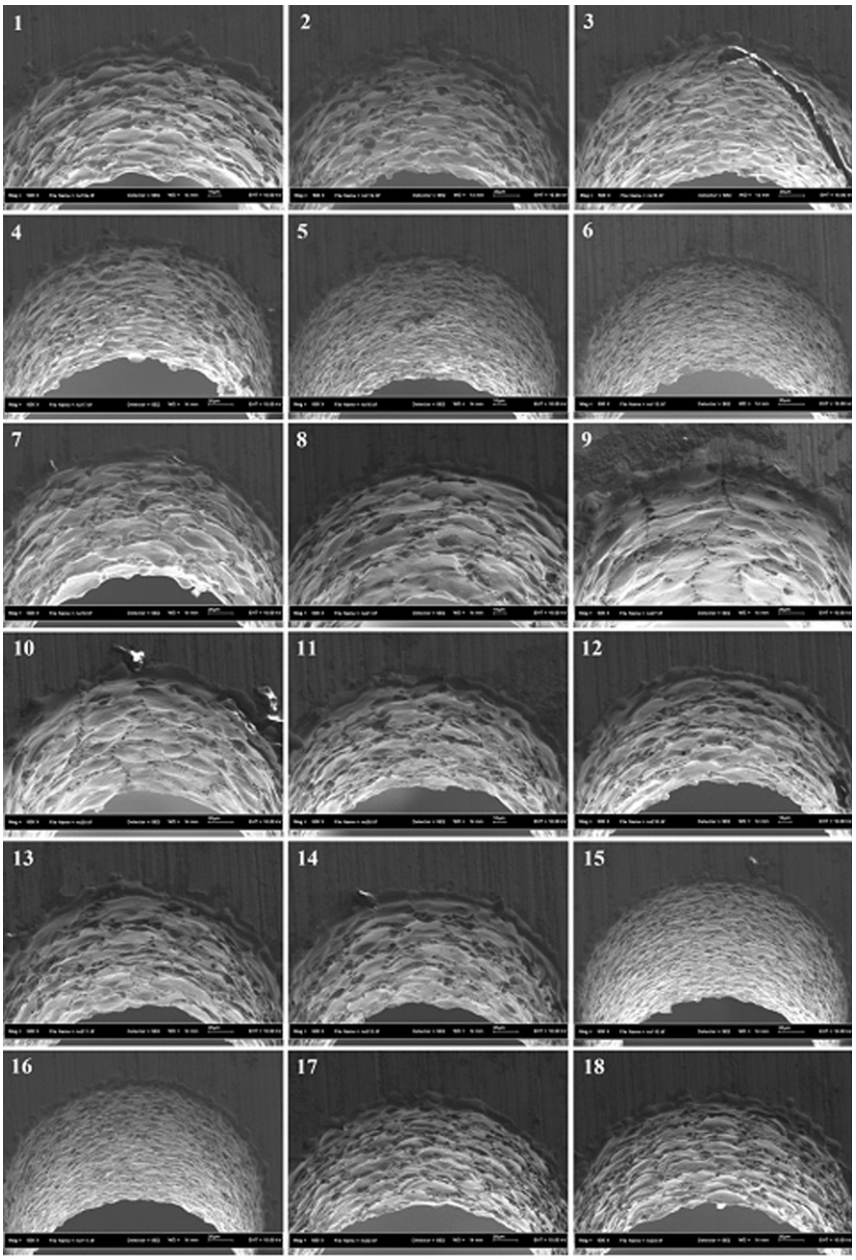


Figure 82 Comparison of surface quality at the rim of the micro-holes at deferent conditions.

pulse-OFF time, sparks did not occur, so melted and vaporized material solidified to the EDM chips, allowing the chips to be removed from the distance between the microelectrode and workpiece. Increasing pulse-OFF time caused more chips to be removed from the distance between the microelectrode and workpiece. This decreased the amount of sparks that occurred between the microelectrode and chips and increased the amount of sparks between the microelectrode and workpiece. Thus, EWR was reduced by increasing pulse-OFF time (Figure 81(c)). Based on Figure 81, the effect of pulse-ON time on EWR seemed more significant than the other parameters.

1.10.7.1.3 Surface roughness

Figure 82 demonstrates FESEM images presenting the surface quality at the rim (wall) of the micro-holes attained in WC–16%Co composite in different EDM conditions. These pictures were taken by rotating the WC–Co plate inside the FESEM. It was found that there are direct relationships between the micro-hole surface finish, burr-like recast layer at the top surface and MRR, based on observations in Figure 82 and Table 12 surface roughness enhanced by decreasing the MRR, but it deteriorated by increasing the MRR. The amount of burr-like recast layer at the top surface decreased when the surface roughness enhanced. It can be concluded that the surface

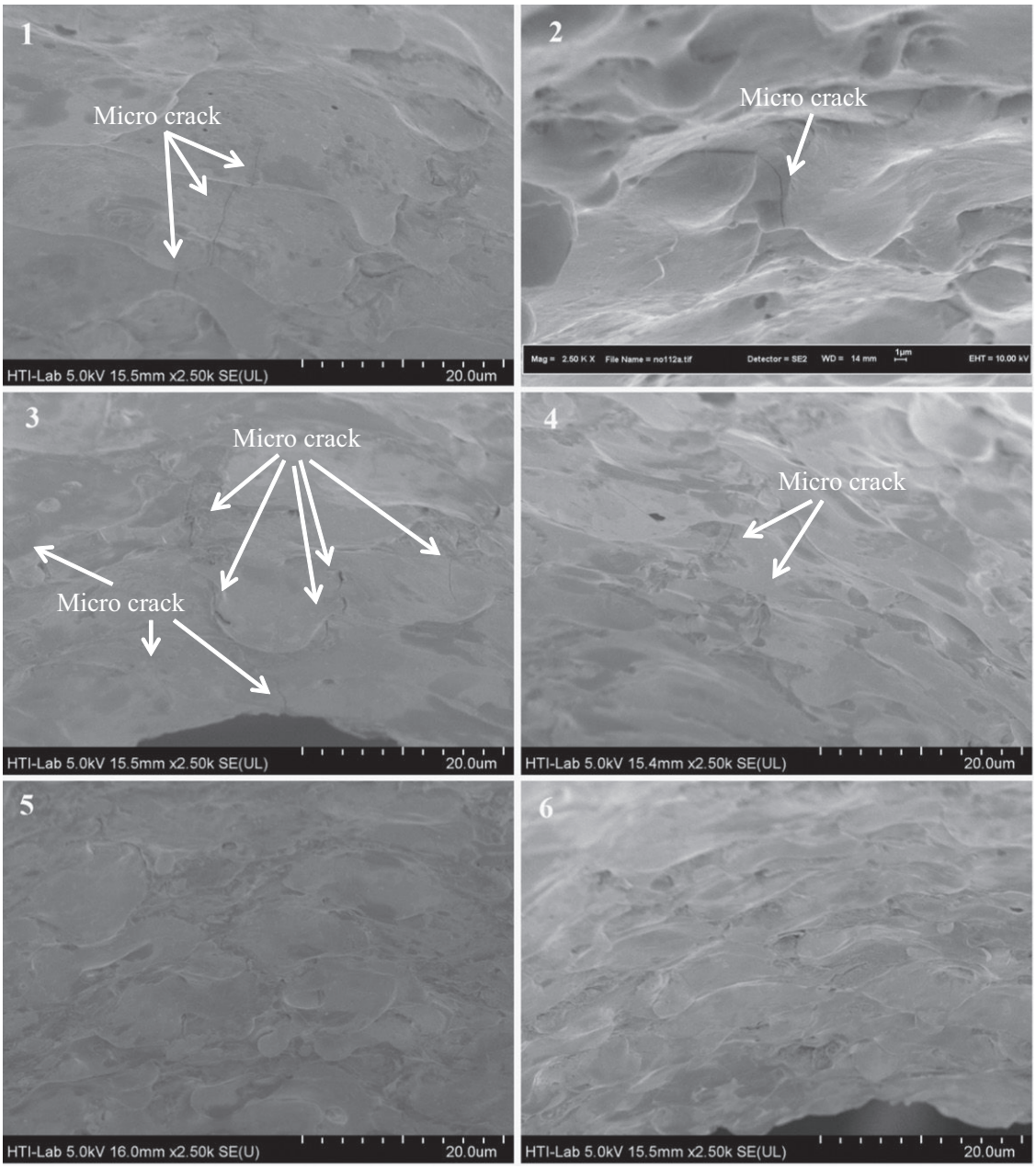


Figure 83 Micro-cracks at various machining conditions (holes 1–18).

roughness improved and the burr-like recast layer at the top surface decreased with decreasing current, rotating speed, and capacitor and increasing voltage and pulse-ON time because of decreasing MRR. Current and capacitor were the most significant factors; however, the effect of the capacitor was more prominent than current.

1.10.7.1.4 Micro-crack

The electrical discharge energy increases with the amplification of voltage, current, pulse-ON time, and capacitor, while pulse-OFF time and rotating speed have no effect on the electrical discharge energy according to the formula for calculating electrical energy ($E=VI_{\mathrm{p}}t_{\mathrm{on}}$[34] and $E=(1/2)CV^2$ [45,59]). Moreover, the voltage controls the discharge gap between electrode and workpiece. Increasing the voltage will increase the discharge gap.[95] Suitable voltage according to current, pulse-ON time, pulse-OFF time, rotating speed, and capacitor results in better MRR and helps the thermal energy reach the workpiece. When current and pulse-ON time are high, MRR increase with amplifying voltage up to a desired value due to the increased discharge gap and because the chips and debris can easily be removed from this area. Subsequently, the amount of MRR decreases with voltage above the desired value because the discharge gap is larger than the suitable range and less energy reaches the workpiece.[95]

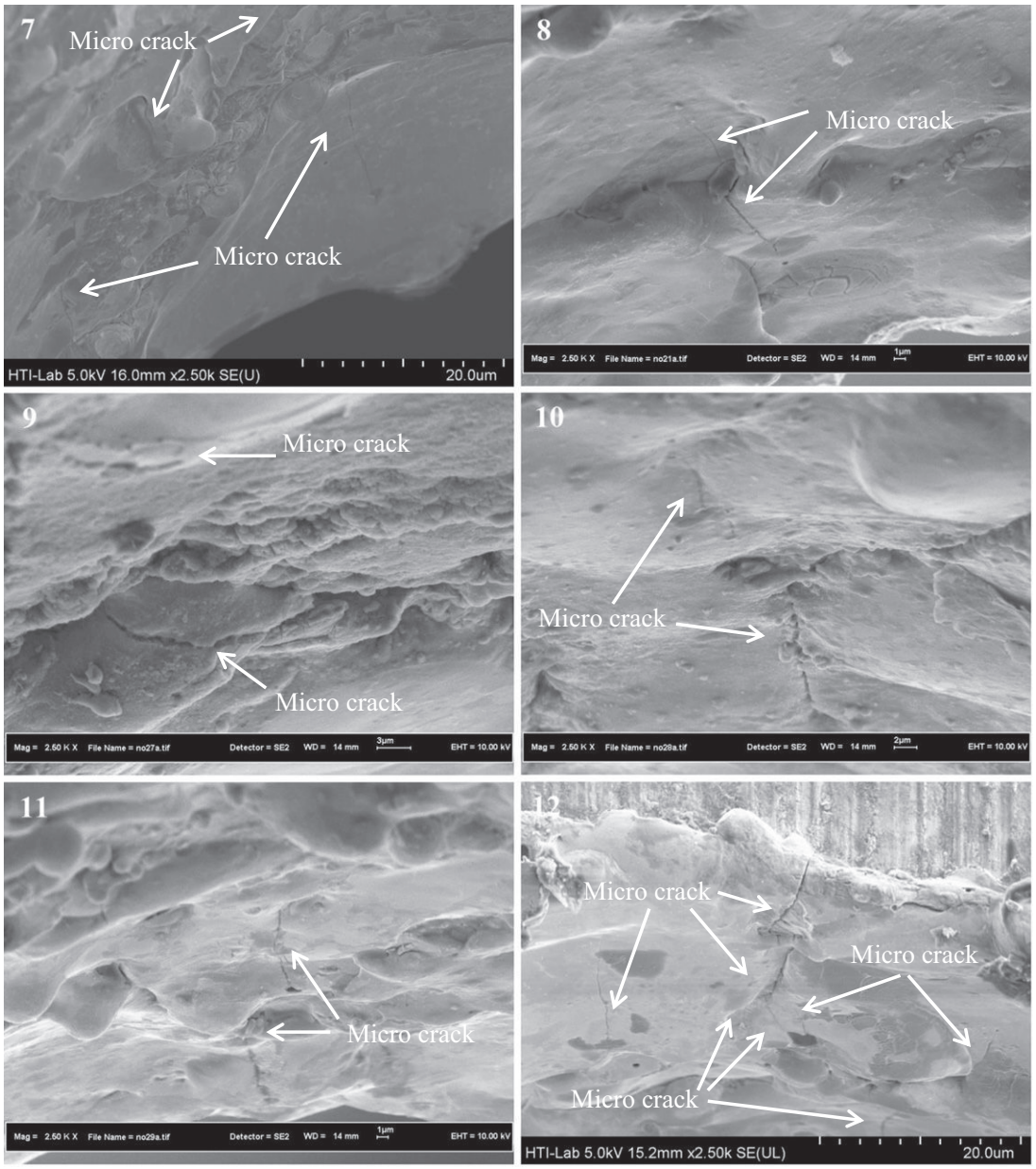


Figure 83 (Continued)

FESES served for taking pictures with 2500 magnification. Figure 83 shows that the amounts of micro-cracks were on the surface in different machining conditions for holes 1–16. Figure 83 demonstrates that pulse-OFF time and rotating speed had no effect on the amount of micro-cracks, because they had no effect on electrical discharge energy. It is clear that the amounts of micro-cracks on holes 5, 6, 15, and 16 were less than on other holes. Larger pictures of these holes (at the end of Figure 83) show the distribution of micro-cracks. Comparing low pulse-ON time (holes 15 and 16) with high pulse-ON time (5 and 6) indicates that pulse-ON time had less effect on changing the amount of micro-cracks because the deference between low and high pulse-ON time (1 and 5 μs) is short. Analyzing low voltage (holes 1 and 3) and high voltage (holes 2 and 4) depicts that voltage was one of the most significant factors on the amount of micro-cracks. Investigating low current (holes 15 and 16) and high current (holes 3 and 4) demonstrates that current was another significant factor affecting the amount of micro-cracks. Studying low capacitor (holes 15 and 16) and high capacitor (holes 1 and 2) represents that the capacitor was another factor determining the amount of micro-cracks. Evidently, the highest amount of micro-cracks appeared in hole 7 (low voltage, low current, high current, high pulse-ON time, and high capacitor), hole 12 (low voltage, low current, high pulse-ON time, and high capacitor), and hole 14 (low voltage, high current, low pulse-ON time, and high capacitor). The least micro-cracks appeared on hole 15 at 90 V voltage, 0.4 A current, 1 μs pulse-ON time,

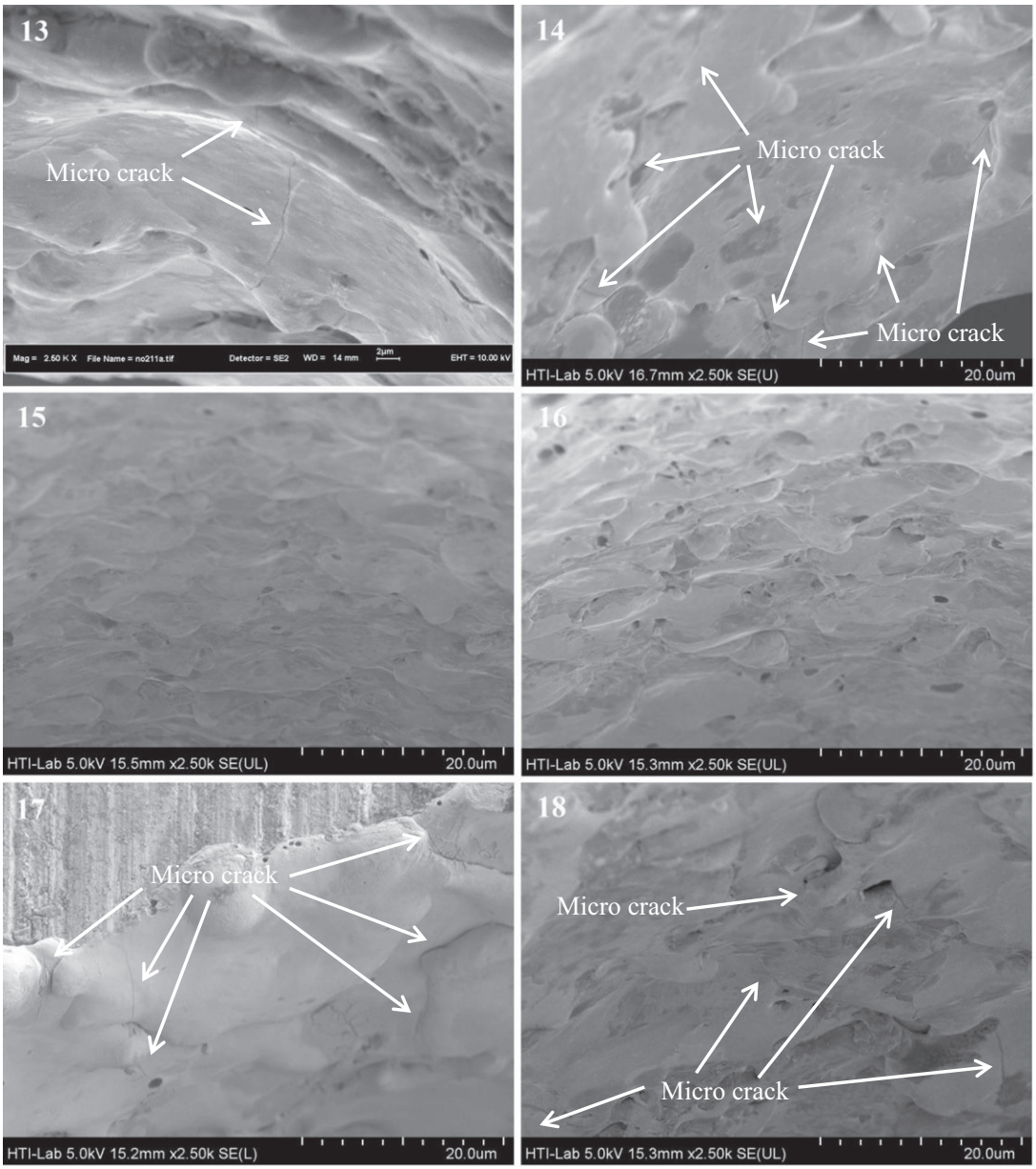
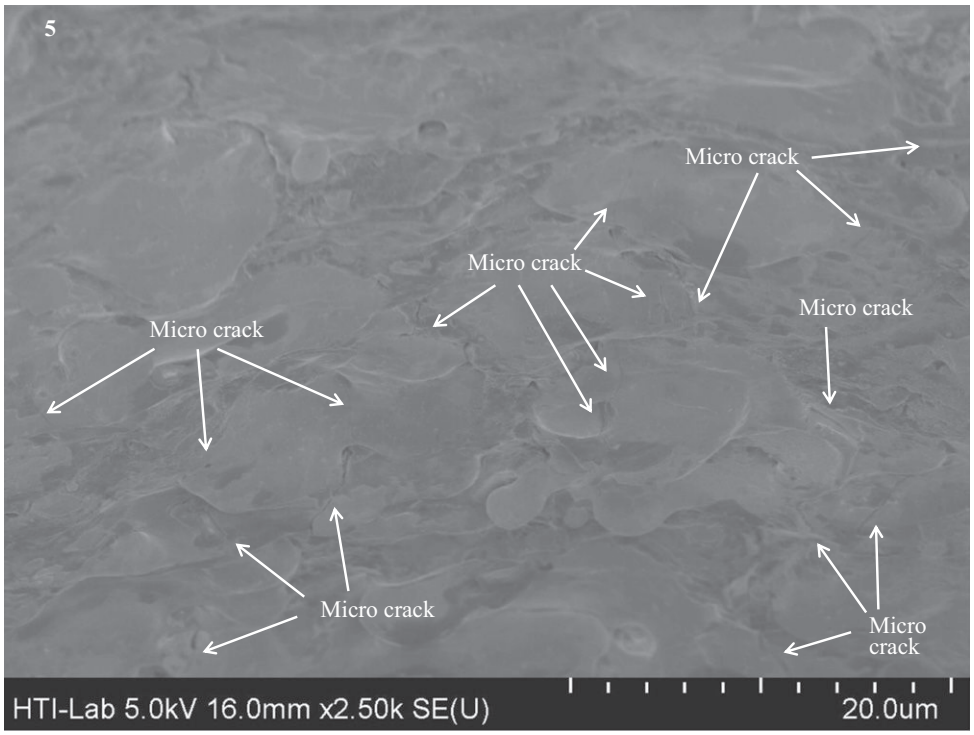


Figure 83 (Continued)

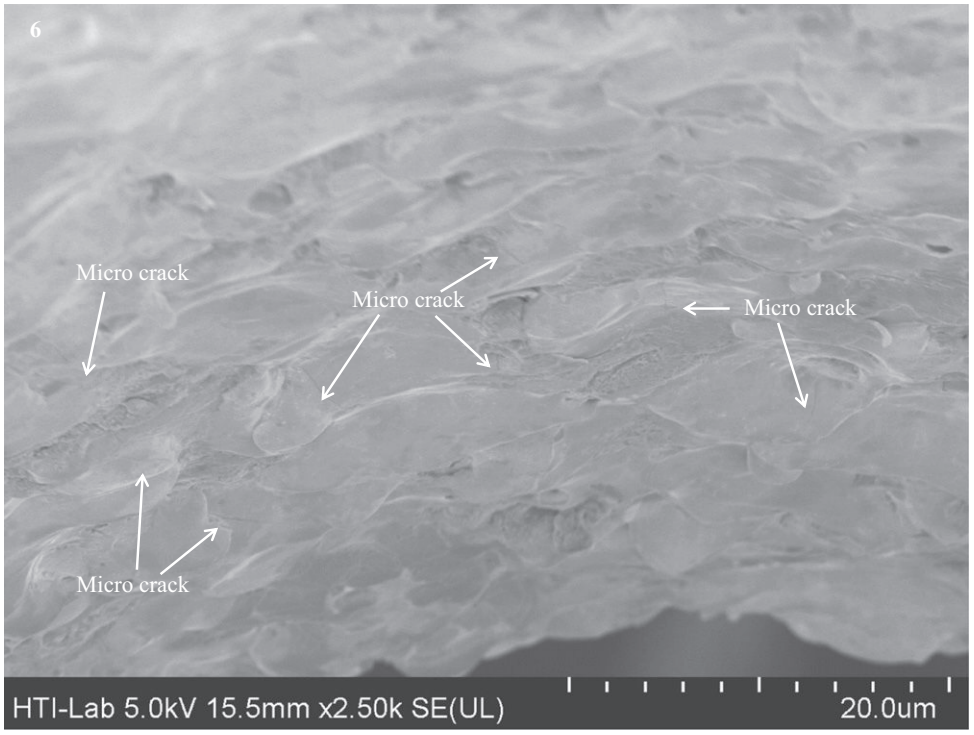
9 μs pulse-OFF time, 20 rpm rotating speed, and 0 μF capacitor. It is clearly observed that more micro-cracks formed when the current, pulse-ON time, and capacitor were at high levels, due to high electrical discharge energy and low thermal conductivity and brittleness of the cemented tungsten carbide. Besides, the amount of micro-cracks decreased when current, pulse-ON time, and capacitor were adjusted to low levels. As described before, the MRR diminished by increasing the voltage because the voltage increases to the more suitable current range of 0.4–5 A, pulse-ON time range of 1–5 μs, pulse-OFF time range of 1–9 μs, rotating speed range of 0–20 rpm and capacitor range of 0–0.1 μF.[95] This caused the workpiece to receive less energy at the high level voltage. It can be concluded that voltage, current, pulse-ON time, and capacitor were the most significant factors contributing to the amount of micro-cracks. The effects of voltage, current, and capacitor were greater than pulse-ON time according to these machining parameter levels.

1.10.7.1.5 Material migration

EDX spectrum analysis was performed to analyze the elemental composition of the raw material and recast layer at the wall of the holes. Figure 84 shows the EDX spectrum analysis of the raw material surface and recast layer at the wall of hole 11 as an example. Moreover, Figure 85 demonstrates the elemental composition and percentage of each element for the material and the entire hole's wall. As seen in Figure 85, W, Co, C, and O elements were present in the workpiece's raw

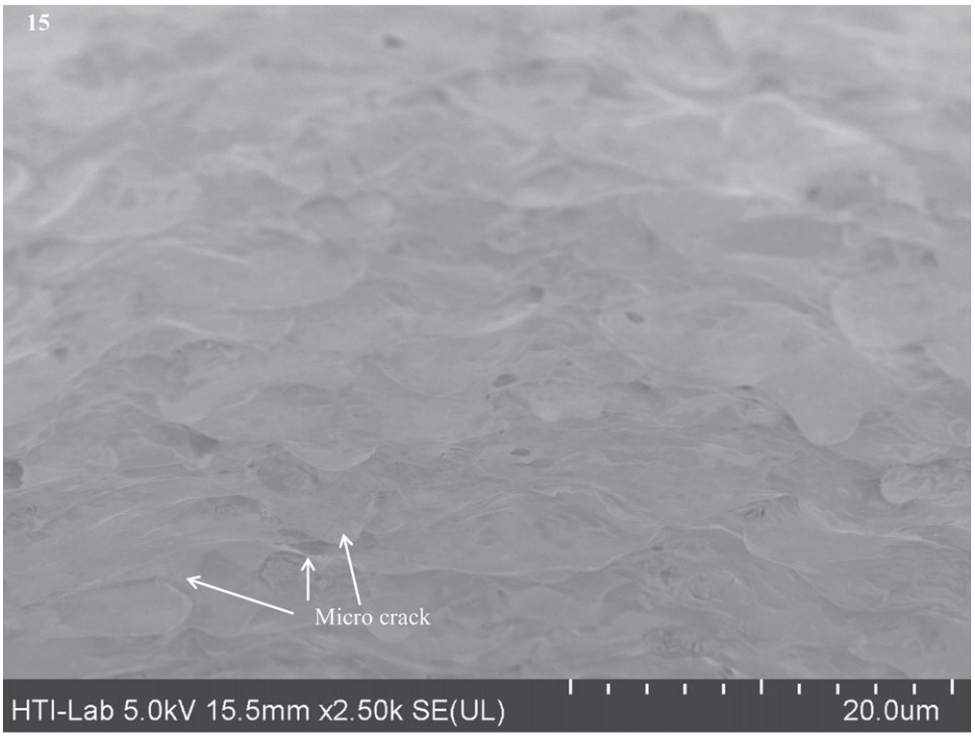


Enlargement of picture of hole 5

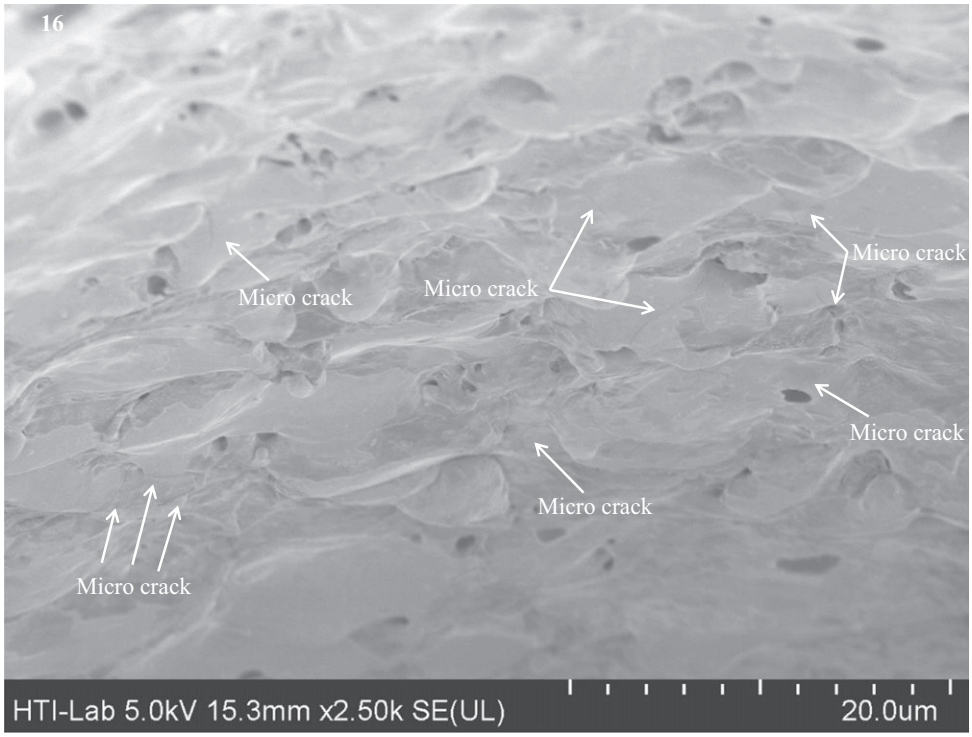


Enlargement of picture of hole 6

Figure 83 (Continued)



Enlargement of picture of hole 15



Enlargement of picture of hole 16

Figure 83 (Continued)

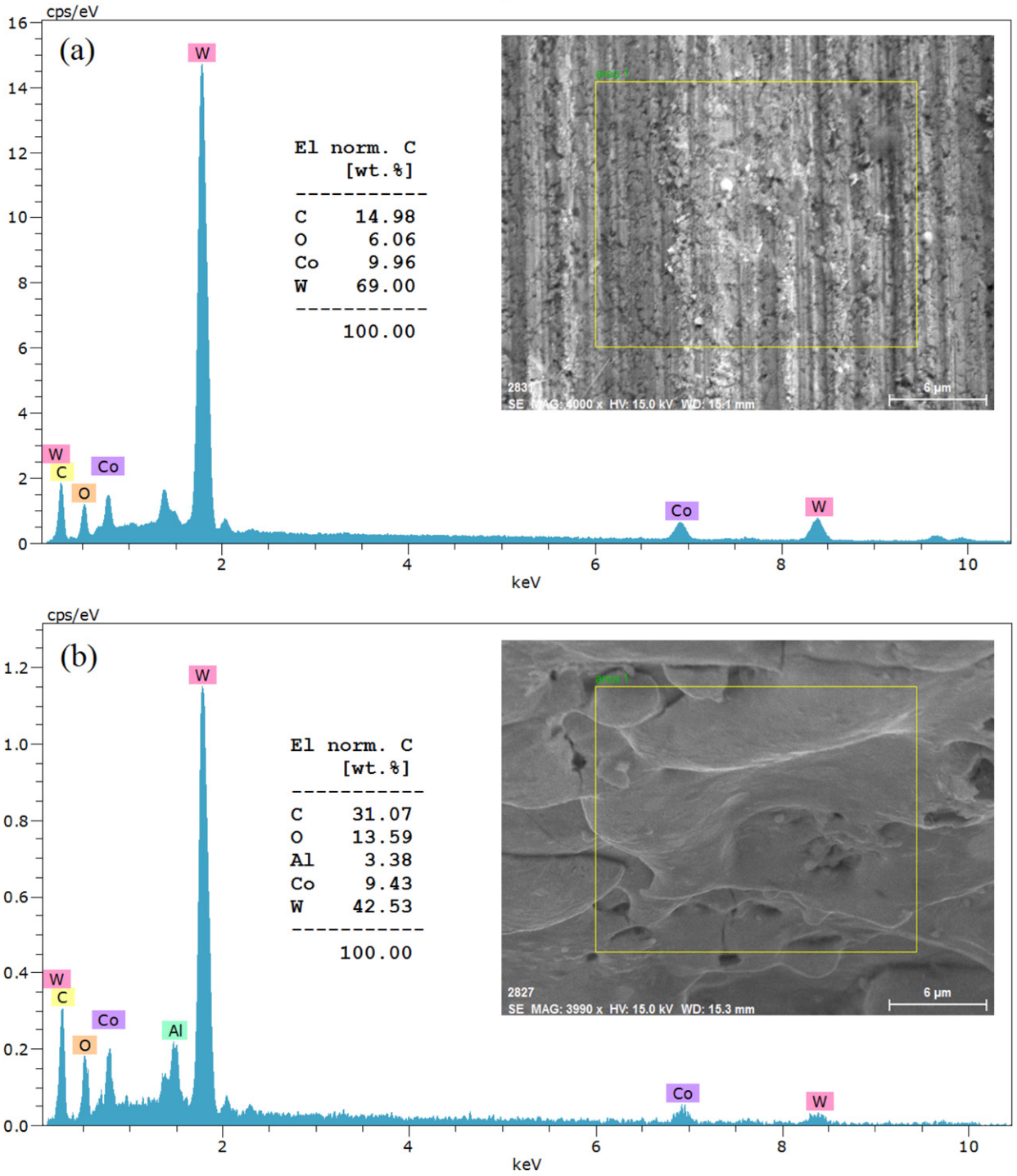


Figure 84 EDX spectrum analysis of the surface on (a) the raw material and (b) the recast layer at the wall of hole 11 as an example.

material, while W, Co, C, O, and Al W elements were present in the recast layer at the wall of the micro-holes. Al was added to the recast layer at the wall of the micro-holes, because aluminum powder was used in the dielectric and aluminum migrated to the machined surface and recast layer. The amount of C and O in the recast layer increased when oil-based dielectric was used. On the other hand, the amount of W and Co decreased due to increasing C and O. Moreover, the percentage of W decreased sharply. The lowest percentage of W, approximately the lowest percentage of Co and the highest percentage of C appeared in the recast layer at the wall of hole 9. As a result, it is suggested to use powder with greater elemental composition similarity to the workpiece in the dielectric.

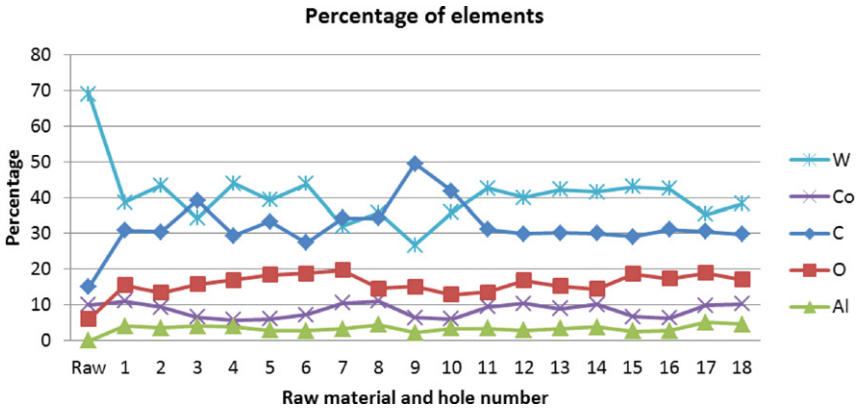


Figure 85 Percentage of elements.

1.10.8 Conclusions

This work describes EDM and micro-EDM comprehensively and compares the types of pulse generators, electrodes and methods for calculating MRR, EWR, overcut, and surface roughness for these methods. Various fabrication and measurement processes of microelectrode are explained as well. Moreover, this research work was carried out to characterize the effects of micro-EDM drilling of WC–16%Co with a CuW microelectrode by using EDM machine. The results show that:

- Various machining conditions produced different amounts of overcut.
- ANOVA analysis illustrated that MRR increased with amplifying current, rotating speed and capacitor, and decreasing voltage and pulse-ON time. The current and capacitor were the most significant factors, but the effect of the capacitor was greater than current. It can be concluded that the capacitor had the greatest impact on improving MRR. Moreover, EWR increased by increasing current and pulse-ON time and decreasing pulse-OFF time. The effect of pulse-ON time on EWR was more prominent than other parameters.
- It was found there were direct relationships between the surface finish of micro-holes, burr-like recast layer at the top surfaces and MRR. It can be concluded that surface roughness enhanced and the amount of burr-like recast layer at the top surfaces decreased with decreasing current, rotating speed and capacitor, and increasing voltage and pulse-ON time. The current and capacitor were the most significant factors; however, the effect of the capacitor was greater than current.
- Pulse-OFF time and rotating speed had no effect on the amount of micro-cracks due to the insignificant effect on electrical discharge energy. On the other hand, the electrical discharge energy depends on the voltage, current, pulse-ON time, and capacitor. It can be concluded that amount of the micro-cracks decrease with increasing voltage and decreasing current, pulse-ON time and capacitor. The voltage, current, pulse-ON time, and capacitor were significant factors contributing to the amount of micro-cracks. However, the effects of voltage, current, and capacitor were stronger than pulse-ON time.
- Al was added to the recast layer at the wall of the micro-holes, and because aluminum powder was used in the dielectric, aluminum migrated to the machined surface and recast layer. The amount of C and O in the recast layer increased because oil-based dielectric was used. As a result, it is suggested to use powder that is more similar in terms of elemental composition to the workpiece in dielectric. Finally, various machining conditions produced different amounts of overcut.
- In conclusion, EDM can be used confidently for producing micro-holes.

Acknowledgment

The authors would like to acknowledge the University of Malaya for providing the necessary facilities and resources for this research. This research was funded by the University of Malaya Research Grant (UMRG) Program No. RP039B-15AET and Postgraduate Research Grant (PPP) Program No. PG027-2015A.

See also: 1.7 Techniques to Improve EDM Capabilities: A Review

References

1. Masuzawa, T.; Tönshoff, H. Three-Dimensional Micromachining by Machine Tools. *CIRP Ann.-Manuf. Techn.* **1997**, *46*, 621–628.
2. Goda, J.; Mitsui, K. Development of an Integrated Apparatus of Micro-EDM and Micro-CMM. *Measurement* **2013**, *46*, 552–562.
3. Rahman, M.; Asad, A.; Masaki, T.; Saleh, T.; Wong, Y.; Senthil Kumar, A. A Multiprocess Machine Tool for Compound Micromachining. *Int. J. Mach. Tool Manu.* **2010**, *50*, 344–356.
4. Asad, A.; Masaki, T.; Rahman, M.; Lim, H.; Wong, Y. Tool-Based Micro-Machining. *J. Mater. Process. Tech.* **2007**, *192*, 204–211.
5. Lim, H.; Wong, Y.; Rahman, M.; Lee, M. E. A Study on the Machining of High-Aspect Ratio Micro-Structures Using Micro-EDM. *J. Mater. Process. Tech.* **2003**, *140*, 318–325.
6. Masuzawa, T. State of the Art of Micromachining. *CIRP Ann.-Manuf. Techn.* **2000**, *49*, 473–488.
7. Weller, E. J. *Nontraditional Machining Process*; Society of Manufacturing Engineers: Dearborn, MI, 1984.

8. Lu, Z.; Yoneyama, T. Micro Cutting in the Micro Lathe Turning System. *Int. J. Mach. Tool Manu.* **1999**, *39*, 1171–1183.
9. Rahman, M.; Senthil Kumar, A.; Prakash, J. Micro Milling of Pure Copper. *J. Mater. Process. Tech.* **2001**, *116*, 39–43.
10. Jagadesh, T.; Samuel, G. Investigations into Cutting Forces and Surface Roughness in Micro Turning of Titanium Alloy Using Coated Carbide Tool. *Procedia Mater. Sci.* **2014**, *5*, 2450–2457.
11. Vazquez, E.; Gomar, J.; Ciurana, J.; Rodríguez, C. A. Analyzing Effects of Cooling and Lubrication Conditions in Micromilling of Ti6Al4V. *J. Clean. Prod.* **2015**, *87*, 906–913.
12. Cheng, J.; Gong, Y. Experimental Study of Surface Generation and Force Modeling in Micro-Grinding of Single Crystal Silicon Considering Crystallographic Effects. *Int. J. Mach. Tool Manu.* **2014**, *77*, 1–15.
13. Cheng, J.; Wang, C.; Wen, X.; Gong, Y. Modeling and Experimental Study on Micro-Fracture Behavior and Restraining Technology in Micro-Grinding of Glass. *Int. J. Mach. Tool Manu.* **2014**, *85*, 36–48.
14. Snoeys, R.; Staelens, F.; Dekeyser, W. Current Trends in Non-Conventional Material Removal Processes. *CIRP Ann.-Manuf. Techn.* **1986**, *35*, 467–480.
15. Matsui, S.; Kaito, T.; Fujita, J.; Komuro, M.; Kanda, K.; Haruyama, Y. Three-Dimensional Nanostructure Fabrication by Focused-Ion-Beam Chemical Vapor Deposition. *J. Vac. Sci. Technol. B Microelectron Nanometer Struct.* **2000**, *18*, 3181–3184.
16. Okuyama, H.; Takada, H. Micromachining with SR and FEL. *Nucl. Instrum. Meth. B* **1998**, *144*, 58–65.
17. Biswas, R.; Kuar, A.; Mitra, S. Multi-Objective Optimization of Hole Characteristics During Pulsed Nd: YAG Laser Microdrilling of Gamma-Titanium–Aluminide Alloy Sheet. *Opt. Laser. Eng.* **2014**, *60*, 1–11.
18. Zhou, W.; Deng, W.; Lu, L.; *et al.* Laser Micro-Milling of Microchannel on Copper Sheet as Catalyst Support used in Microreactor for Hydrogen Production. *Int. J. hydrogen. Energ.* **2014**, *39*, 4884–4894.
19. Ha, K. H.; Lee, S. W.; Kim, J.; Jee, W. Y.; Chu, C. N. Fabrication of a Micro-Hole Array on Metal Foil by Nanosecond Pulsed Laser Beam Machining Using a Cover Plate. *J. Micromech. Microeng.* **2015**, *25*, 027001.
20. Saxena, I.; Ehmann, K.; Cao, J. High Throughput Microfabrication Using Laser Induced Plasma in Saline Aqueous Medium. *J. Mater. Process. Tech.* **2015**, *217*, 77–87.
21. Utlaut, M. Focused Ion Beams for Nano-Machining and Imaging. In *Nanolithography: The Art of Fabricating Nanoelectronic and Nanophotonic Devices and Systems*; Feldman, M., Ed.; Woodhead Publishing: Philadelphia, PA, 2014; pp. 116–157.
22. Toyoda, N.; Houzumi, S.; Mashita, T.; Mitamura, T.; Mochiji, K.; Yamada, I. Novel Precision Machining Using Gas Cluster Ion Beams. *Surf. Coat. Tech.* **2007**, *201*, 8624–8627.
23. Rahman, M. A.; Rahman, M.; Kumar, A. S.; Lim, H.; Asad, A. Development of Micropin Fabrication Process Using Tool Based Micromachining. *Int. J. Adv. Manuf. Tech.* **2006**, *27*, 939–944.
24. Schoth, A.; Förster, R.; Menz, W. Micro Wire EDM for High Aspect Ratio 3D Microstructuring of Ceramics and Metals. *Microsyst. Technol.* **2005**, *11*, 250–253.
25. Yu, Z.; Masuzawa, T.; Fujino, M. Micro-EDM for Three-Dimensional Cavities-Development of Uniform Wear Method. *CIRP Ann.-Manuf. Techn.* **1998**, *47*, 169–172.
26. Zhao, W.; Yang, Y.; Wang, Z.; Zhang, Y. A CAD/CAM System for Micro-ED-Milling of Small 3D Freeform Cavity. *J. Mater. Process. Tech.* **2004**, *149*, 573–578.
27. Kung, K.-Y.; Horng, J.-T.; Chiang, K.-T. Material Removal Rate and Electrode Wear Ratio Study on the Powder Mixed Electrical Discharge Machining of Cobalt-Bonded Tungsten Carbide. *Int. J. Adv. Manuf. Tech.* **2009**, *40*, 95–104.
28. Liu, H.; Tarng, Y. Monitoring of the Electrical Discharge Machining Process by Abductive Networks. *Int. J. Adv. Manuf. Tech.* **1997**, *13*, 264–270.
29. Tang, L.; Guo, Y. Electrical Discharge Precision Machining Parameters Optimization investigation on S-03 Special Stainless Steel. *Int. J. Adv. Manuf. Tech.* **2014**, *70*, 1369–1376.
30. Teimouri, R.; Baseri, H. Experimental Study of Rotary Magnetic Field-Assisted Dry EDM with Ultrasonic Vibration of Workpiece. *Int. J. Adv. Manuf. Tech.* **2013**, *67*, 1371–1384.
31. Keskin, Y.; Halkacı, H. S.; Kizil, M. An experimental study for determination of the effects of Machining Parameters on Surface Roughness in Electrical Discharge Machining (EDM). *Int. J. Adv. Manuf. Tech.* **2006**, *28*, 1118–1121.
32. Sidhu, S. S.; Batish, A.; Kumar, S. EDM of Metal Matrix Composite for Parameter Design Using Lexicographic Goal Programming. *Mater. Manuf. Process.* **2013**, *28*, 495–500.
33. Yan, B. H.; Wang, C. C.; Liu, W.; Huang, F. Y. Machining Characteristics of Al_2O_3/6061Al Composite Using Rotary EDM with a Disklike Electrode. *Int. J. Adv. Manuf. Tech.* **2000**, *16*, 322–333.
34. Jameson, E. C. *Electrical Discharge Machining*; Society of Manufacturing Engineers: Dearbern, MI, 2001.
35. Allen, D. M.; Lecheheb, A. Micro Electro-Discharge Machining of Ink Jet Nozzles: Optimum Selection of Material and Machining Parameters. *J. Mater. Process. Tech.* **1996**, *58*, 53–66.
36. Kunieda, M.; Lauwers, B.; Rajurkar, K.; Schumacher, B. Advancing EDM through Fundamental Insight into the Process. *CIRP Ann.-Manuf. Techn.* **2005**, *54*, 64–87.
37. Rajurkar, K.; Levy, G.; Malshe, A.; *et al.* Micro and Nano Machining by Electro-Physical and Chemical Processes. *CIRP Ann.-Manuf. Techn.* **2006**, *55*, 643–666.
38. Alting, L.; Kimura, F.; Hansen, H. N.; Bissacco, G. Micro Engineering. *CIRP Ann.-Manuf. Techn.* **2003**, *52*, 635–657.
39. Ho, K.; Newman, S. State of the Art Electrical Discharge Machining (EDM). *Int. J. Mach. Tool Manu.* **2003**, *43*, 1287–1300.
40. Tsai, Y. Y.; Masuzawa, T. An Index to Evaluate the Wear Resistance of the Electrode in Micro-EDM. *J. Mater. Process. Tech.* **2004**, *149*, 304–309.
41. Chen, S.; Yan, B.; Huang, F. Influence of Kerosene and Distilled Water as Dielectrics on the Electric Discharge Machining Characteristics of Ti–6A1–4V. *J. Mater. Process. Tech.* **1999**, *87*, 107–111.
42. Uhlmann, E.; Piltz, S.; Doll, U. Machining of Micro/Miniature Dies and Moulds by Electrical Discharge Machining – Recent Development. *J. Mater. Process. Tech.* **2005**, *167*, 488–493.
43. Jahan, M.; Rahman, M.; Wong, Y. A Review on the Conventional and Microelectrodischarge Machining of Tungsten Carbide. *Int. J. Mach. Tool Manu.* **2011**, *51*, 837–858.
44. Bleys, P.; Kruth, J. P.; Lauwers, B. Sensing and Compensation of Tool Wear in Milling EDM. *J. Mater. Process. Tech.* **2004**, *149*, 139–146.
45. Jahan, M. P.; Asad, A.; Md, A. B.; Rahman, M.; Wong, Y. S.; Masaki, T. Micro-Electro Discharge Machining (μEDM). *Micro-Manufacturing: Design and Manufacturing of Micro-Products* **2011**, 301–346.
46. Masaki, T.; Kawata, K.; Masuzawa, T. Micro Electro-Discharge Machining and Its Applications, Micro Electro Mechanical Systems, 1990. In *Proceedings, An Investigation of Micro Structures, Sensors, Actuators, Machines and Robots*, IEEE, 1990; pp. 21–26.
47. Masaki, T.; Mizutani, T.; Yonemaochi, K.; Tanaka, A. Electric discharge machining method and apparatus for machining a microshaft, Google Patents; 1990.
48. Han, F.; Wachi, S.; Kunieda, M. Improvement of Machining Characteristics of Micro-EDM Using Transistor Type Isopulse Generator and Servo feed Control. *Precis. Eng.* **2004**, *28*, 378–385.
49. Rajurkar, K.; Yu, Z. 3d Micro-Edm Using Cad/Cam. *CIRP Ann.-Manuf. Techn.* **2000**, *49*, 127–130.
50. Rahman, M.; Asad, A.; Masaki, T.; Wong, Y.; Lim, H. Integrated Hybrid Micro/Nano-Machining. In *ASME 2007 International Manufacturing Science and Engineering Conference*; American Society of Mechanical Engineers, 2007; pp. 197–209.
51. Wong, Y.; Rahman, M.; Lim, H.; Han, H.; Ravi, N. Investigation of Micro-EDM Material Removal Characteristics Using Single RC-pulse Discharges. *J. Mater. Process. Tech.* **2003**, *140*, 303–307.
52. Kumar, S.; Singh, R.; Singh, T.; Sethi, B. Surface Modification by Electrical Discharge Machining: A Review. *J. Mater. Process. Tech.* **2009**, *209*, 3675–3687.
53. De Bruyn, H. Slope Control: A Great Improvement in Spark Erosion. *Ann. of the CIRP* **1968**, *16*, 183–191.
54. Jahan, M.; Anwar, M.; Wong, Y.; Rahman, M. Nanofinishing of Hard Materials Using Microelectrodischarge Machining. *P. I. Mech. Eng. B-J. Eng.* **2009**, *223*, 1127–1142.
55. Jahan, M.; Wong, Y.; Rahman, M. A Study on the Quality Micro-Hole Machining of Tungsten Carbide by Micro-EDM process Using Transistor and RC-type Pulse Generator. *J. Mater. Process. Tech.* **2009**, *209*, 1706–1716.
56. Jahan, M. P.; Saleh, T.; Mustafizur, R.; Wong, Y. S. Study of Micro-EDM of Tungsten Carbide with Workpiece Vibration. *Adv. Mat. Res.* **2011**, *264*, 1056–1061.
57. Jahan, M. P.; Wong, Y. S.; Rahman, M. A Study on the Fine-Finish Die-Sinking Micro-EDM of Tungsten Carbide Using Different Electrode Materials. *J. Mater. Process. Tech.* **2009**, *209*, 3956–3967.
58. McGeough, J. A. *Advanced Methods of Machining*; Springer Science & Business Media: New York, 1988.

59. Masuzawa, T. *Micro EDM Proceedings of the 13th International Symposium for Electro-Machining (ISEM)*, 2001; pp. 3–9.
60. Wang, C. C.; Lin, Y. C. Feasibility Study of Electrical Discharge Machining for W/Cu Composite. *Int. J. Refract. Metals. Hard. Mater.* **2009**, *27*, 872–882.
61. Che Haron, C.; Deros, B. M.; Ginting, A.; Fauziah, M. Investigation on the Influence of Machining Parameters when Machining Tool Steel Using EDM. *J. Mater. Process. Tech.* **2001**, *116*, 84–87.
62. Raghu, T.; Sundaresan, R.; Ramakrishnan, P.; Rama Mohan, T. Synthesis of Nanocrystalline Copper–Tungsten Alloys by Mechanical Alloying. *Mater. Sci. Eng.: A* **2001**, *304*, 438–441.
63. Smid, I.; Akiba, M.; Vieider, G.; Plöchl, L. Development of Tungsten Armor and Bonding to Copper for Plasma-Interactive Components. *J. Nucl. Mater.* **1998**, *258*, 160–172.
64. Das, J.; Chakraborty, A.; Bagchi, T.; Sarma, B. Improvement of Machinability of Tungsten by Copper Infiltration Technique. *Int. J. Refract. Metals. Hard. Mater.* **2008**, *26*, 530–539.
65. Ho, P.; Li, Q.; Fuh, J. Evaluation of W–Cu Metal Matrix Composites Produced by Powder Injection Molding and Liquid Infiltration. *Mater. Sci. Eng.: A* **2008**, *485*, 657–663.
66. Ibrahim, A.; Abdallah, M.; Mostafa, S.; Hegazy, A. A. An Experimental Investigation on the W–Cu Composites. *Mater. Design* **2009**, *30*, 1398–1403.
67. Davis, J. R. *Copper and Copper Alloys*; ASM International: Materials Park, OH, 2001.
68. Lee, S. H.; Li, X. P. Study of the Effect of Machining Parameters on the Machining Characteristics in Electrical Discharge Machining of Tungsten Carbide. *J. Mater. Process. Tech.* **2001**, *115*, 344–358.
69. Soni, J.; Chakraverti, G. Experimental Investigation on Migration of Material During EDM of Die Steel (T215 Cr12). *J. Mater. Process. Tech.* **1996**, *56*, 439–451.
70. Porter, F. C. *Corrosion Resistance of Zinc and Zinc Alloys*; CRC Press: Boca Raton, FL, 1994.
71. Kern, R. Sinker Electro Material Selection, EDM Today, 2008.
72. Kumar Sahoo, A.; Sahoo, B. Performance Studies of Multilayer Hard Surface Coatings (TiN/TiCN/Al_2O_3/TiN) of Indexable Carbide Inserts in Hard Machining: Part-II (RSM, Grey Relational and Techno Economical Approach). *Measurement* **2013**, *46*, 2868–2884.
73. Mahdavinejad, R.; Mahdavinejad, A. ED Machining of WC–Co. *J. Mater. Process. Tech.* **2005**, *162*, 637–643.
74. Jahan, M.; Rahman, M.; Wong, Y.; Fuhua, L. On-Machine Fabrication of High-Aspect-Ratio Microelectrodes and Application in Vibration-Assisted Microelectrodischarge Drilling of Tungsten Carbide. *P. I. Mech. Eng. B-J. Eng.* **2010**, *224*, 795–814.
75. Zhengui, Y.; Stiglich, J. J.; Sudarshan, T. S. *Nano-Grained Tungsten Carbide–Cobalt (WC/Co)*; Materials Modification, Inc.: Fairfax, VA, 1999; pp. 1–27.
76. Tristo, G.; Bissacco, G.; Lebar, A.; Valentinčič, J. Real time Power Consumption Monitoring for Energy Efficiency Analysis in Micro EDM Milling. *Int. J. Adv. Manuf. Tech.* **2015**, 1–11.
77. Al-Ahmari, A.; Rasheed, M. S.; Mohammed, M. K.; Saleh, T. A Hybrid Machining Process Combining Micro-EDM and Laser Beam Machining of Nickel–Titanium-Based Shape Memory Alloy. *Mater. Manuf. Process.* **2015**, *31* (4), 447–455.
78. Kuriachen, B.; Varghese, A.; Somashekhar, K.; Panda, S.; Mathew, J. Three-Dimensional Numerical Simulation of Microelectric Discharge Machining of Ti–6Al–4V. *Int. J. Adv. Manuf. Tech.* **2015**, 1–14.
79. Kuriachen, B.; Mathew, J. Effect of Powder Mixed Dielectric on Material Removal and Surface Modification in Microelectric Discharge Machining of Ti-6Al-4V. *Mater. Manuf. Process.* **2016**, *31*, 439–446.
80. Imran, M.; Mativenga, P.; Gholinia, A.; Withers, P. Assessment of Surface Integrity of Ni Superalloy after Electrical-Discharge, Laser and Mechanical Micro-Drilling Processes. *Int. J. Adv. Manuf. Tech.* **2015**, *79*, 1303–1303.
81. Liew, P. J.; Yan, J.; Kuriyagawa, T. Fabrication of Deep Micro-Holes in Reaction-Bonded SiC by Ultrasonic Cavitation Assisted Micro-EDM. *Int. J. Mach. Tool Manu.* **2014**, *76*, 13–20.
82. Wong, Y.; Lim, L.; Lee, L. Effects of Flushing on Electro-Discharge Machined Surfaces. *J. Mater. Process. Tech.* **1995**, *48*, 299–305.
83. Sommer, C. *Non-Traditional Machining Handbook*; Advance Publishing: Houston, TX, 2000.
84. Maskiell, E. C.; Galbraith, W. *Machine Shop Technology*; McGraw-Hill Book Company: Melbourne, 1985.
85. Chakraborty, S.; Dey, V.; Ghosh, S. K. A Review on the Use of Dielectric Fluids and Their Effects in Electrical Discharge Machining Characteristics. *Precis. Eng.* **2015**, *40*, 1–6.
86. Zhang, Q.; Du, R.; Zhang, J.; Zhang, Q. An Investigation of Ultrasonic-Assisted Electrical Discharge Machining in Gas. *Int. J. Mach. Tool Manu.* **2006**, *46*, 1582–1588.
87. Abbas, N. M.; Solomon, D. G.; Bahari, M. F. A Review on Current Research Trends in Electrical Discharge Machining (EDM). *Int. J. Mach. Tool Manu.* **2007**, *47*, 1214–1228.
88. Leão, F. N.; Pashby, I. R. A Review on the Use of Environmentally-Friendly Dielectric Fluids in Electrical Discharge Machining. *J. Mater. Process. Tech.* **2004**, *149*, 341–346.
89. Furutania, K.; Saneto, A.; Takezawa, H.; Mohri, N.; Miyake, H. Accretion of Titanium Carbide by Electrical Discharge Machining with Powder Suspended in Working Fluid. *Precis. Eng.* **2001**, *25*, 138–144.
90. Garg, R.; Singh, K.; Sachdeva, A.; Sharma, V. S.; Ojha, K.; Singh, S. Review of Research Work in Sinking EDM and WEDM on Metal Matrix Composite Materials. *Int. J. Adv. Manuf. Tech.* **2010**, *50*, 611–624.
91. Assarzadeh, S.; Ghoreishi, M. A Dual Response Surface-Desirability Approach to Process Modeling and Optimization of Al_2O_3 Powder-Mixed Electrical Discharge Machining (PMEDM) Parameters. *Int. J. Adv. Manuf. Tech.* **2013**, *64*, 1459–1477.
92. Jeswani, M. Effect of the Addition of Graphite Powder to Kerosene used as the Dielectric Fluid in Electrical Discharge Machining. *Wear* **1981**, *70*, 133–139.
93. Singh, S.; Bhardwaj, A. Review to EDM by Using Water and Powder-Mixed Dielectric Fluid. *J. Mineral. Mater. Charact. Eng.* **2011**, *10*, 199–230.
94. Luis, C. J.; Puertas, I.; Villa, G. Material Removal Rate and Electrode Wear Study on the EDM of Silicon Carbide. *J. Mater. Process. Tech.* **2005**, *164–165*, 889–896.
95. Hourmand, M.; Farahany, S.; Sarhan, A. A.; Noordin, M. Y. Investigating the Electrical Discharge Machining (EDM) Parameter Effects on Al-Mg_2Si Metal Matrix Composite (MMC) for High Material Removal Rate (MRR) and Less EWR–RSM Approach. *Int. J. Adv. Manuf. Tech.* **2014**, 1–8.
96. Jahan, M. P.; San Wong, Y.; Rahman, M. A Comparative Experimental Investigation of Deep-Hole Micro-EDM Drilling Capability for Cemented Carbide (WC-Co) Against Austenitic Stainless Steel (SUS 304). *Int. J. Adv. Manuf. Tech.* **2010**, *46*, 1145–1160.
97. Yan, B.; Huang, F.; Chow, H.; Tsai, J. Micro-Hole Machining of Carbide by Electric Discharge Machining. *J. Mater. Process. Tech.* **1999**, *87*, 139–145.
98. Machado, A.; Wallbank, J. Machining of Titanium and Its Alloys – A Review. *P. I. Mech. Eng. B-J. Eng.* **1990**, *204*, 53–60.
99. Zhang, L.; Tong, H.; Li, Y. Precision Machining of Micro Tool Electrodes in Micro EDM for Drilling Array Micro Holes. *Precis. Eng.* **2015**, *39*, 100–106.
100. Sheu, D.-Y. High-Speed Micro Electrode Tool Fabrication by a Twin-Wire EDM System. *J. Micromech. Microeng.* **2008**, *18*, 105014.
101. Egashira, K.; Mizutani, K.; Nagao, T. Ultrasonic Vibration Drilling of Microholes in Glass. *CIRP Ann.-Manuf. Techn.* **2002**, *51*, 339–342.
102. Chen, S.-T. A High-Efficiency Approach for Fabricating Mass Micro Holes by Batch Micro EDM. *J. Micromech. Microeng.* **2007**, *17*, 1961.
103. Rakwal, D.; Heamawatanachai, S.; Tathireddy, P.; Solzbacher, F.; Bamberg, E. Fabrication of Compliant High Aspect Ratio Silicon Microelectrode Arrays Using Micro-Wire Electrical Discharge Machining. *Microsyst. Technol.* **2009**, *15*, 789–797.
104. Kuo, C.-L.; Huang, J.-D. Fabrication of Series-Pattern Micro-Disk Electrode and its Application in Machining Micro-Slit of Less than 10 μm. *Int. J. Mach. Tool Manu.* **2004**, *44*, 545–553.
105. Yamazaki, M.; Suzuki, T.; Mori, N.; Kunieda, M. EDM of Micro-Rods by Self-Drilled Holes. *J. Mater. Process. Tech.* **2004**, *149*, 134–138.
106. Kim, B. H.; Park, B. J.; Chu, C. N. Fabrication of Multiple Electrodes by Reverse EDM and their Application in Micro ECM. *J. Micromech. Microeng.* **2006**, *16*, 843.
107. Guckel, H.; Christenson, T.; Skrobis K.; *et al. Deep X-Ray and UV Lithographies for Micromechanics, Solid-State Sensor and Actuator Workshop*, 1990, 4th Technical Digest., IEEE, 1990; pp. 118–122.
108. Takahata, K.; Shibaike, N.; Guckel, H. High-aspect-ratio WC–Co Microstructure Produced by the Combination of LIGA and Micro-EDM. *Microsyst. Technol.* **2000**, *6*, 175–178.
109. Mark, B.; Toshihiko, M.; Teruaki, M.; Kazushi, T. Micro-Hole Punching Using Multi-Point Punch and Die Made by EDM. *J. Adv. Manuf. Tech.* **2009**, *3*, 73–86.
110. Jangra, K.; Grover, S.; Aggarwal, A. Optimization of Multi Machining Characteristics in WEDM of WC-5.3% Co Composite Using Integrated Approach of Taguchi, GRA and Entropy Method. *Front. Mech. Eng.* **2012**, 1–12.

111. Watson, S.; Freer, H. A Comparative Study of Electro-Chemical and Electro Discharge Machining of a Tungsten Carbide 25% Cobalt alloy. In *Proceedings of 6th Symposium for Electro-Machining*, ISEM VI, 1980; pp. 150–154.
112. Singh, M. K. *Introduction of Unconventional Manufacturing Process, Unconventional Manufacturing Process*; New Age International: New Delhi, 2007; pp. 6–7 (Chapter 1).
113. Puhan, D.; Mahapatra, S. S.; Sahu, J.; Das, L. A Hybrid Approach for Multi-Response Optimization of Non-Conventional Machining on AlSiC$_p$ MMC. *Measurement* **2013**, *46*, 3581–3592.
114. Gopalakannan, S.; Senthilvelan, T. Application of Response Surface Method on Machining of Al–SiC Nano-Composites. *Measurement* **2013**, *46*, 2705–2715.
115. Puertas, I.; Luis, C.; Alvarez, L. Analysis of the Influence of EDM Parameters on Surface Quality, MRR and EW of WC–Co. *J. Mater. Process. Tech.* **2004**, *153*, 1026–1032.
116. Chou, S.-H.; Wang, A.-C. Investigating and Removing the Re-sticky Debris on Tungsten Carbide in Electrical Discharge Machining. *Int. J. Adv. Manuf. Tech.* **2014**, *71*, 1151–1158.
117. Jahan, M. P.; Wong, Y. S.; Rahman, M. Experimental Investigations into the Influence of Major Operating Parameters During Microelectro Discharge Drilling of Cemented Carbide. *Mach. Sci. Technol.* **2012**, *16*, 131–156.
118. Endo, H.; Ueki, M.; Kubo, H. Microstructure and Mechanical Properties of Hot-Pressed SiC–TiC Composites. *J. Mater. Sci.* **1991**, *26*, 3769–3774.
119. Lee, L.; Lim, L.; Narayanan, V.; Venkatesh, V. Quantification of Surface Damage of Tool Steels after EDM. *Int. J. Mach. Tool Manu.* **1988**, *28*, 359–372.
120. Lee, L.; Lim, L.; Wong, Y.; Fong, H. Crack Susceptibility of Electro-Discharge Machined Surfaces. *J. Mater. Process. Tech.* **1992**, *29*, 213–221.
121. Lee, S. H.; Li, X. Study of the Surface Integrity of the Machined Workpiece in the EDM of Tungsten Carbide. *J. Mater. Process. Tech.* **2003**, *139*, 315–321.
122. Lin, Y.-C.; Hwang, L.-R.; Cheng, C.-H.; Su, P.-L. Effects of Electrical Discharge Energy on Machining Performance and Bending Strength of Cemented Tungsten Carbides. *J. Mater. Process. Tech.* **2008**, *206*, 491–499.
123. Nakamura, M.; Shigematsu, I.; Kanayama, K.; Hirai, Y. Surface Damage in ZrB_2-Based Composite Ceramics Induced by Electro-Discharge Machining. *J. Mater. Sci.* **1991**, *26*, 6078–6082.
124. Ramulu, M.; Garbini, J. EDM Surface Characterization of a Ceramic Composite TiB2/SiC. *J. Eng. Mater. Technol.* **1991**, *113*, 437–442.
125. Ravi, N.; Chuan, S. X. The Effects of Electro-Discharge Machining Block Electrode Method for Microelectrode Machining. *J. Micromech. Microeng.* **2002**, *12*, 532.
126. Instruction Manual. Sodick Wire-Cut EDM PGM WHITE 3 AG Series (Version 2.0).
127. Hourmand, M.; Noordin, M. Y. Microelectrode Fabrication Process Using EDM. *Adv. Mat. Res.* **2014**, *845*, 980–984.
128. Egashira, K.; Matsugasako, A.; Tsuchiya, H.; Miyazaki, M. Electrical Discharge Machining with Ultralow Discharge Energy. *Precis. Eng.* **2006**, *30*, 414–420.

1.11 Micromachining

MY Ali, International Islamic University Malaysia, Kuala Lumpur, Malaysia
WNP Hung, Texas A&M University, College Station, TX, USA

© 2017 Elsevier Inc. All rights reserved.

1.11.1	**Introduction**	322
1.11.2	**Tool Based Micromachining**	323
1.11.2.1	Micromilling	323
1.11.2.1.1	Surface roughness	323
1.11.2.1.2	Vibration	323
1.11.2.2	Microdrilling	324
1.11.2.3	MQL	324
1.11.2.4	Ductile Regime Machining	325
1.11.2.5	Tooling	326
1.11.3	**Silicon Micromachining**	329
1.11.3.1	Bulk Micromachining	329
1.11.3.2	Surface Micromachining	330
1.11.4	**Energy Beam Micromachining**	330
1.11.4.1	Laser Micromachining	330
1.11.4.2	Focused Ion Beam Micromachining	331
1.11.4.2.1	Deposition	331
1.11.4.2.2	Sputtering	331
1.11.4.3	Electron Beam Micromachining	332
1.11.5	**Electrical Discharged Micromachining**	332
1.11.5.1	Electrical Discharged Micromilling	333
1.11.5.2	Micro Wire EDM	333
1.11.5.3	Micro-EDM of Nonconductive Ceramics	334
1.11.5.3.1	Assisting electrode	334
1.11.5.3.2	Dielectric fluid	334
1.11.5.3.3	Mechanism of material removal	335
1.11.5.3.4	Recast layer	337
1.11.6	**ECM**	338
1.11.6.1	Micromachining	338
1.11.6.2	Micro/Nano Polishing	339
1.11.6.3	Deburring	339
1.11.7	**Summary**	340
References		340
Relevant Websites		343

1.11.1 Introduction

Micromachining is an advanced technology that enables micro components with dimensions in the range of 1–500 μm to be fabricated using micro fabrication techniques. Micromachined components are important for the advancement of micro/nano electromechanical systems (MEMS/NEMS), microelectronics such as semiconductor devices and integrated circuit technology and nanotechnology.[1–3] Different manufacturing processes such as Lithographie Galvanoformung Abformung (LIGA), micromachining of silicon and similar semiconducting materials, and tool based micromachining are the applications of micromachining that are used to fabricate small precision components and micro structured parts.[4]

In modern manufacturing industries, the product miniaturization becomes significantly important due to demanding market trend for a more compact device with ever increasing features. The field of application of conventional mechanical machining processes has been extended to micromachining after a significant technological effort worldwide. These processes have been enhanced for small series and single piece production due to their flexibility and effectiveness concerning the producible geometries, material spectrum, removal rates, and achievable surface topographies.[4,5] However, scaling down of parameters or process modeling from macroscale to micromachining cannot be simply applied due to size effect, workpiece material inhomogeneity, minimum chip thickness, cutting forces, brittle and ductile mode machining, surface quality, and lack of suitable microcutting tools.[5]

The size effect in traditional machining occurs due to the relative dimensions of uncut chip thickness and tool edge radius. An undesirable ploughing of workpiece material rather than chip shearing happens when these dimensions are approximately the same. Microstructure of workpiece material can also have major influence on the cutting mechanism. The workpiece materials behave homogeneously and isotropically

in macromachining but then act differently in micromachining. In homogeneity, microstructural defects, grain size, grain boundaries, inclusions, local hardness, and elastic recovery all contribute to the complexity of micro/nano machining. Micromachining processes are influenced by the ratio of the depth of cut to the cutting edge radius which determines how chip is formed, and quality of the machined surface. Although low cutting forces in some micromachining processes, such as diamond turning, can reduce tool deflection and tool wear, delay tool failure, and narrow the workpiece tolerance limits[5]; such relative low cutting forces, however, can be detrimental in other processes such as microdrilling and micromilling when the resulting high stresses can lead to catastrophic breakage of fragile microcutting tools.

Size effect must also be considered for nontraditional micromachining processes. Tiny electrodes for electrical discharge micromachining may not last due to repeating high energy sparks, or may be deflected due to flow of dielectric fluid. Similarly, when the size of an electrode for electrochemical micromachining (ECM) is comparable with the workpiece grain size, then the resulting material removal rate (MRR) would be different from grain to grain and contributes to poor surface quality. This chapter provides background information for readers to (1) understand the fundamentals of traditional and nontraditional micromachining and (2) present key challenges and advantages for each technique.

1.11.2 Tool Based Micromachining

Micromachining with mechanical cutting tool also known as tool based micromachining is capable of producing high profile accuracy, surface finish quality, and acceptable subsurface integrity at a reasonable cost. It is the primary choices amongst various manufacturing processes in fabricating micro components.[6,7] However, unreliable tool life and early tool failure are the most common problems when employing micro tools for micromachining applications. Many contributions have been made toward the development and investigation of microtools.[8] Examples of the tool based micromachining are discussed in the following subsections.

1.11.2.1 Micromilling

Micromilling is a type of micromachining with mechanical cutting tool that is capable of fabricating microfeatures (Figure 1) with high-accuracy and high-surface quality at a reasonable cost. It is known as a microcutting method which removes workpiece material by mechanical forces via chip shearing or brittle breakage. Most of the workpiece materials, either metals or plastics, can be machined by micromilling with the exception of very hard and brittle materials.[6,9] Although micromilling technique can be similar to conventional macromilling technique including the kinematics process,[10–12] the cutting and surface generation mechanisms involved in the process do change when it comes to micromilling operation. It is due to the different cutting mechanics brought by the scaling relationship between the tool geometry, workpiece microstructure, and cutting geometry.[12] The ratio of feed per tooth to tool edge radius for micromilling is much

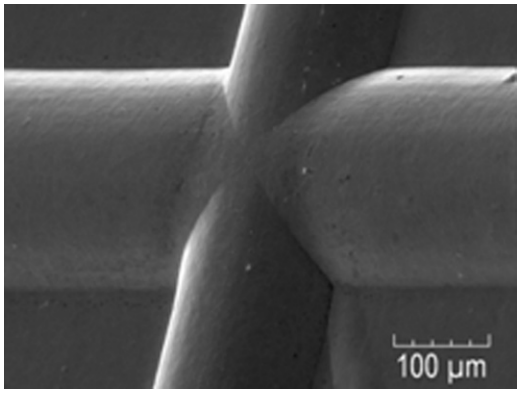


Figure 1 SEM image of milled and polished microchannels on 316L stainless steel.

larger compared to the conventional macromilling in order to maintain productivity. The stresses on a tiny microtool are substantially higher compared to those on a macrotool, and they can effectively shorten the tool life of fragile microtools.[10,11] This technique is related with sudden tool failure because of its highly unpredictable cutting action, and the wear in the tool is not obvious.[13–17] In micromilling, the chip formation depends on the minimum chip thickness and chip does not constantly form whenever the tool and work material is engaged.[13–16,18] The size effect and ploughing forces are vital for surface integrity and force generation in micromilling when chip load is small compared to the cutting edge radius.[16,18,19] Two of the main issues of micromilled structure are discussed in the following subsections.

1.11.2.1.1 Surface roughness

Surface roughness R_a is commonly used to indicate the level of surface roughness. In order to get good surface finish and high accuracy in micromilling operation, it is essential to cut at a low-chip load. This feed per tooth and the cutting depth should be maintained less than 1 μm, if machining tolerance is desired to be less than 1 μm. An important ploughing phenomenon will emerge when the ratio of chip load and tool edge radius is less than a critical value.[17,19–21] Chip load is the most influential factor that affects surface roughness since surface roughness deteriorates with the increase of chip load.[22] However, due to dynamic behavior (low vibration), surface roughness decreases when high feed and depth of cut are used.[23] A micromilled surface roughness reduces with chip load until embedded built-up-edges (BUEs) become significant.[24]

1.11.2.1.2 Vibration

Vibration is frequently caused by the dynamic forces in machines due to lack of a rigid setup, or rotation of imbalanced, misaligned, or worn machine components. A repeating force is capable in producing small resonance which is initiated by the motion of the machine components. This mild repetition is the beginning of the vibration that can lead to brisk and severe damage. Vibration can affect the stability of the machining operation, reduce the dimensional accuracy, deteriorate the surface roughness, and also limit the productivity of machining operation. In order to limit the cutting stability, tool breakage, and machine tool damage, forced and

self-excited vibrations can be used.[25–27] Vibration adversely affects the surface roughness of the machined components and the tool life of micromilling. A higher feed rate enables vibration which eventually has resulted in poor surface quality.[28] Contradictory results are reported when a vibration is rapidly increased when chip loads increases from 0.2 to 0.4 μm per tooth, but vibration decrease rapidly when chip load increases from 1.2 to 1.6 μm per tooth.[23] The difference trends, perhaps, are due to the different natural frequency of each machining system and rigidity of specific set up.[20,25]

1.11.2.2 Microdrilling

Microdrilling has the potential to achieve superior roundness, smoother surfaces, and better lead times. Although similar to macroscale drilling, microdrilling poses a greater challenge than macrodrilling in many aspects:

- A slight lateral skidding motion during initial penetration into the workpiece can bend and fracture a long microdrill.
- Heat dissipation and chip removal from deep microholes is a major issue.
- The process parameters for microdrilling cannot be extrapolated from macrodrilling data.
- Both drill edge sharpness and crystalline orientation of workpiece grains affect microdrill performance.

Microdrill failure is caused by gradual wear of cutting edge or too high-cutting temperature. However, majority of the failure is due to excessive cutting force at the tip of the tool causing it to fail suddenly by brittle fracture.[29] Drill life can be randomly distributed from 1–100 holes depending on different approaches.[30] Monitoring of drilling force and torque is a challenge due to their small magnitudes; perhaps this is the reason why a correlation between drill wear and drilling force is yet to be established. Drill wandering is minimized by predrilling to form a pilot hole,[31] or by changing drilling parameters depending on drilling thrust force and torque.[32] Wandering of a microdrill could be improved by lowering the ratio of drilling speed and feed rate at the beginning. This ratio then can be increased after the tool penetrates below the surface; however, both thrust force and torque increase with drilling depth for continuous drilling due to accumulation of chips in a hole. Peck-drilling helps clearing chips from the bottom of a deep hole, but this practice increases cycle time and slows down the production rate.

Some investigators study microdrilling at low rotational speeds in the range 45–6000 rpm, but most researchers utilize rigid machines with high rotational speeds in the range 50 000–150 000 rpm to achieve a reasonable surface cutting speeds on a microdrill. Process parameters and tool geometries are examined from both analytical and experimental approaches to study microdrilling and its size effect. Chip load should be small enough for low thrust force and torque, but is high enough compared to the drill edge sharpness so that ploughing and work hardening below the workpiece surface can be minimized.[32] A high-drilling speed increases the tool chip temperature, softens the material, and decreases thrust force. However, a very high-drilling speed facilitates BUE formation contrary to macrodrilling practice. Using oil mist for minimum quantity lubrication (MQL) provides the best approach

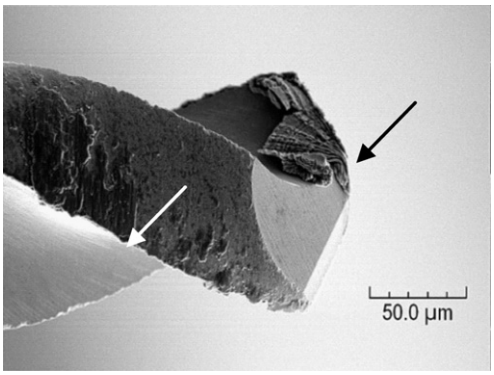


Figure 2 Titanium built-up edges (at arrows) on a microdrill. Speed 14 m min^{-1}, 0.05 μm chipload.

since it reduces drilling force, torque, and cutting temperature. The drilling temperature is lowest when MQL is applied internally through a drill in macrodrilling. When applying MQL externally in microdriling, the temperature is highest for uncoated drill and is lower but about the same for microdrills with different coatings.

Kudla[33] compared different microdrill geometries (twist drill, spade drill, and D-shape drill) to study the behavior of microdrills in bending, compression and torsion under static and dynamic conditions. Buckling of a drill is possible since a microdrill is long and slender. In the beginning when a drill engages to a workpiece surface, it is supported in a shallow spot and its condition is like that of a pin-ended strut. After drilling deeper into a hole, the boundary condition for buckling changes from pin-end to built-in end condition. Buckling load of 6.2–33.7 N is expected for a 0.5 mm twist drill based on Euler formula for column buckling. A high speed steel (HSS) drill deforms more than a carbide drill before fracture. An Ø200 μm HSS drill can be twisted 90° before failure but a carbide drill fails about 28° in a torsion test. Twist drill outperforms the spade drill and D-shape drills since the former would take a higher torque and greater angle of twist to fail. The author also measured both torque and thrust force when drilling various ferrous alloys to confirm the failure mechanisms of microdrills.

Built-up-edges are the main concern in microdrilling (Figure 2). These BUEs worsen hole quality while shortening drill life since a lubricant cannot penetrate to the drill/chip interface in high-aspect-ratio drilling of microsize holes. The problem can be solved with progressive peck drilling in MQL.[34] Thin TiAlN coated microdrills can minimize BUEs, reduce drill wandering 115%, and decrease diametric variation from 0.11% per mm for uncoated drills to 0.003% per mm for coated drills.

1.11.2.3 MQL

MQL is gaining acceptance in metal processing industries because of overall cost saving while enhancing part quality. Conflicting information in published literature on how MQL effect machining probably due to different setting of MQL parameters in each study. The objective of this chapter is to present required conditions of MQL setup for effective machining in high-speed machining.

Marksberry and Jawahir[35] turned high strength low alloy steel (equivalent to SAE 070Y) at 3.2 mm depth, 4 m s^{-1} speed, and 0.3 mm per rev feed in MQL using straight oil, water soluble, semi synthetic, and synthetic fluids. Minimum tool wear was obtained when machining at the highest volumetric flow rate of 160 mL h^{-1}. They found that the synthetic fluid improved tool life by 402% while the straight oil improved 102% over dry machining. When applying vegetable oil mist particles of 3.7 μm to mill Ti 6Al 4 V at 0.67 m s^{-1}, Sun *et al.*[36] reported that MQL improved tool life 800% over dry milling, while flood coolant improved 50% over dry milling. The total cutting force magnitude reduced from 417 N in dry milling to 344 N for milling with flood coolant, and then further reduced to 115 N when machining with MQL. Cutting tools under MQL conditions resulted in the least flank wear when the coolant rate was as low as 6 mL h^{-1}. However, it was postulated that the oil droplets could not reach and wet the cutting edge of a tool moving at a speed within 1.6–2.1 m s^{-1} (96–126 m min^{-1}).[37] In another study, Park *et al.*[38] proposed an imaging technique to reconstruct microdroplet profiles. The authors measured the accumulative mass of Coolube 2210 oil at different distances from a nozzle at nozzle air pressure of 14–55 kPa (2–8 psi). Although very fine droplets were formed at higher air pressure, the accumulative mass was 50% less at 300 mm away from the nozzle. The study stated that the average airborne microdroplet diameter of 10 μm and recommended a working distance less than 50 mm.

The application of MQL is particularly beneficial at high cutting speeds or high rotational speed in micromilling.[39,40] Tool flank wear was reduced ~50% when MQL was used. Poor wetting of emulsion coolant on a cutting tool was due to the slower coolant flowing speed (6.4 m s^{-1}) as compared to the higher cutting speed of the tool (15 m s^{-1}). The much higher speed of air after leaving a nozzle (120 m s^{-1}) allowed MQL microdroplets to reach and efficiently lubricate the cutting tool. However, Rahman *et al.*[41] concluded that MQL was effective at cutting speed lower than 75 m min^{-1}, but it provided no significant effect at cutting speeds above 125 m min^{-1}.

Tool failure mechanisms were studied by Liao *et al.*[42] when they milled NAK80 hardened steel at 150–250 m min^{-1}. Water-soluble flood coolant at 1200 L h^{-1} was applied while MQL was set at 10 mL h^{-1} and 450 kPa air pressure. The study concluded that flood cooling caused thermal crack on tools, while MQL reduced the tool temperature when cutting at 250 m min^{-1}. The surface finish, a 50% improvement compared to that after flood cooling, was due to delay chip welding on cutting tool when wetting with MQL.

Characterization of microdroplet flow in air was presented by Diakodimitris *et al.*[43] The study combined particle image velocimetry (PIV), particle dynamics analysis (PDA), and computational fluid dynamics (CFD) to analyze MQL microdroplets in an air jet. An asymmetric profile of velocity field was found: air flowed at higher speed above the nozzle axis, and the difference of 60 m s^{-1} was observed. The maximum speed location was 4 mm above the nozzle axis and 40 mm away from the nozzle when the air mass flowrate was set to 6.2×10^{-4} kg s^{-1}. When considering different combinations of air mass flow rates (5–6.2×10^{-4} kg s^{-1}) and oil mass flow rates (1.66–2.92×10^{-4} kg s^{-1}), the maximum velocity of microdroplets along the nozzle axis was measured about ~27 m s^{-1} (1620 m min^{-1}) at a distance 40 mm away from the nozzle. In another finite element analysis of air flow near a cutting tool in orthogonal machining, Kamata *et al.*[44] simulated high speed machining in the range 2–5 m s^{-1} (120–300 m min^{-1}) and concluded that high air speed at 300 m s^{-1} can provide an effective mist supply of 15% at 1 mm away from the cutting edge. Although cutting speed reduced the effective mist supply ~2%, this reduction was made up with increasing mist supply due to a low pressure zone at the flank face. This low pressure zone was formed by the suction of boundary layer around a moving workpiece in addition to the dropping of air pressure when flowing into a narrow channel between the flank face and workpiece surface.

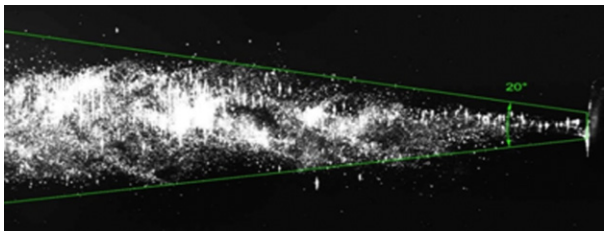


Figure 3 Micromist flow in front of a nozzle by particle image velocimetry. Coolube 2210, 483 kPa (70 psi) input air pressure, nozzle speed 154 m s^{-1}, 8 strokes min^{-1}.

Literature review indicates that when the supply of MQL is inadequate, the lubrication and cooling effect diminishes and degrades machinability. Li *et al.*[45] concluded that the droplet size and its velocity must be in the optimal range so it can acquire an adequate momentum to reach and wet the surface of moving tool and workpiece. Air speed in front of a nozzle can be as high as 10 000 m min^{-1}. A high nozzle speed produces small droplets in front of the coaxial nozzle as shown in Figure 3. The droplets then coalesce to form larger droplets 3–11 μm depending on the exiting air speed. The system can produce nozzle air speed more than 10 000 m min^{-1} for effective high speed machining. The distance between tool and workpiece should be less than 50 mm and the tool size should be less than 17 mm. Multiple nozzles should be used for a larger cutting tool.

1.11.2.4 Ductile Regime Machining

The concept of ductile-regime machining has been investigated since 1960s for amorphous brittle materials such as glasses. Silicon, germanium, and glasses have become strategic materials that are widely used to fabricate intricate components in microelectronics, optical, defense industries, and recently as micro optical-electrical-mechanical systems. Silicon and other brittle materials are known for their low machinability unless they are machined in the ductile-regime conditions. When utilized at the optimal machining conditions, only minimum effort is required for the subsequent etching, grinding, or polishing to remove the damaged subsurface. The mechanism of ductile-regime machining has been studied by many researchers. Using fracture mechanics approach, it can be shown that there is a threshold below which ductile regime prevailed.

A shallow depth of cut, therefore, would energetically promote plastic flow rather than brittle fracture in the substrate and the chips. Table 1 enlisted properties of some brittle materials and their experimental critical depths of cut.

$$d_c = \frac{\text{plastic flow energy}}{\text{fracture energy}} = A\left(\frac{E}{H}\right)\left(\frac{K_c}{H}\right)^2 \quad [1]$$

where,

d_c: critical depth of cut (m, in)
A: constant
E: Young modulus (Pa, psi)
K_C: surface fracture toughness (Pa $m^{0.5}$, psi $in^{0.5}$)
H: surface microhardness (Pa, psi)

The constant A in eqn [1] varies in the range 0.1–0.6 due to measuring uncertainty of surface toughness K_c, elastic modulus E, and microhardness H in a testing environment. These properties depend on crystalline orientation of the materials, surface conditions, and tool geometry.

The critical resolved shear stress, on a crystalline plane due to the cutting action, is directly proportional to the Schmid factor cos ϕ cos λ, where ϕ and λ are the orientations of the slip plane and slip direction. An ideal ductile mode machining would happen when the cutting shear stress is parallel to both the slip plane and the slip direction, otherwise a pseudo ductile mode with micro cleavages occurs. True ductile-regime machining happens only along certain crystalline orientation, but brittle machining occurs at other crystalline orientation. This explains why micromachining a crystalline specimen at the same speed, depth of cut, and coolant produces ductile machined surfaces in one direction (Figure 4) but brittle machined surfaces on others.

Cutting fluid changes the surface properties of materials (Kc, E, and H) and affects conditions for ductile regime micromachining. When micromachining the (100) germanium using a single crystalline diamond (SCD) tool, the critical depth of cut changes from 0.13 μm with distilled water as cutting fluid to 0.29 μm in dry machining.

Tool geometry also affects the results. Ploughing and fracture of material occurs when depth of cut is less than approximately half of the tool cutting edge radius. Tool with negative top rake angle is usually utilized since a negative rake causes compressive zone in the workpiece ahead and below the tool and suppresses microcrack formation.

Table 1 Selected properties of some brittle materials

Materials	*Young modulus (GPa)*	*Fracture toughness (MPa $m^{0.5}$)*	*Knoop hardness (GPa)*	*Critical depth of cut (μm)*
α-Al_2O_3	275–393	3.85–5.90	19.6–20.1	1.0
SiC	382–475	2.50–3.50	24.5–25.0	0.2
Silicon	168	0.6	10	0.5

1.11.2.5 Tooling

Success of micromachining depends on tool quality and precision of a machine tool. Machine spindle runout, tool concentricity and tool positioning accuracy must be in the neighborhood of 1/100 of drill diameter or less for successful operation. Tolerance stack up for spindle runout, tool eccentricity, and wandering of a microdrill cause cyclic bending of a tool that lead to catastrophic failure. At a low rotating speed, the displacement of a spindle can be monitored with a sensitive mechanical indicator. However, this option is not applicable for machines that operates at few thousands rpm or above. Other noncontact techniques using capacitance, magnetism, or light would be more appropriate. An example of spindle runout measurement is shown below. A laser beam is pointed on a rotating precision plug gage. The spindle displacement is then recorded on a computer for further analysis

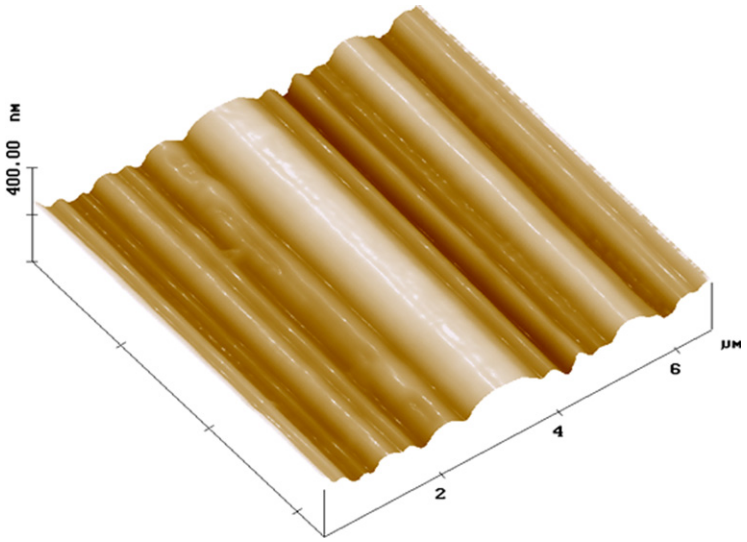


Figure 4 Perfect ductile regime machining of (001) plane of silicon along [$\bar{1}$10] direction. Speed 75 m min^{-1}, feed 2.5 μm rev^{-1}; depth 0.5 μm; SCD tool (5°, 0°, 0°, 5°, 5°, 30°, 0°, 0.5 mm,10–40 nm).

and display in either frequency or time domain. Commercial laser systems can provide displacement reading to ± 0.1 μm resolution or even lower. Figure 5 below shows the frequency spectrum during micromilling. As expected, we have two dominating peaks: one from the spindle frequency of 466.3 Hz when rotating at 27 238 rpm, and one from tool passing frequency of 932.6 Hz from a two-flute micromill.

Tool stiffness and tool edge sharpness are crucial to micromachining success. It is relatively easy to have a rigid turning or facing microtool, but it is requires careful planning to maintain rigidity of a micromill or a microdrill. Geometries of macroscale and microscale drilling/milling tools are the same: tool diameter, number of cutting flutes, point included angle for microdrill, helix angle, web thickness, clearance angle, flute length, shank diameter, and overall length. A careful selection of microtools must consider the intended machined features and highest possible tool stiffness. The two most important geometries that affect the microtool stiffness are the tool diameter and flute length assuming the number of flutes have been chosen. It can be shown that the torsional stiffness of a mill/drill is proportional to (tool diameter)^4 and (flute length)$^{-2}$. For a specific mill/drill tool dimension, we must adjust the milling/drilling strategy accordingly to avoid tool breakage.

The tool edge radius is critical in micromachining. Figure 6 shows two scenarios for a same microcutting tools with edge radius r. The tool can be either a turning, facing, or boring microtool that linearly engages a workpiece material at a certain depth of cut. A similar tool can move in a circular path as a microdrill or micromill, and engages a workpiece at a certain chip load (feed per tooth). If the depth of cut (or chip load) is too shallow, the tool simply plows the material and pushes

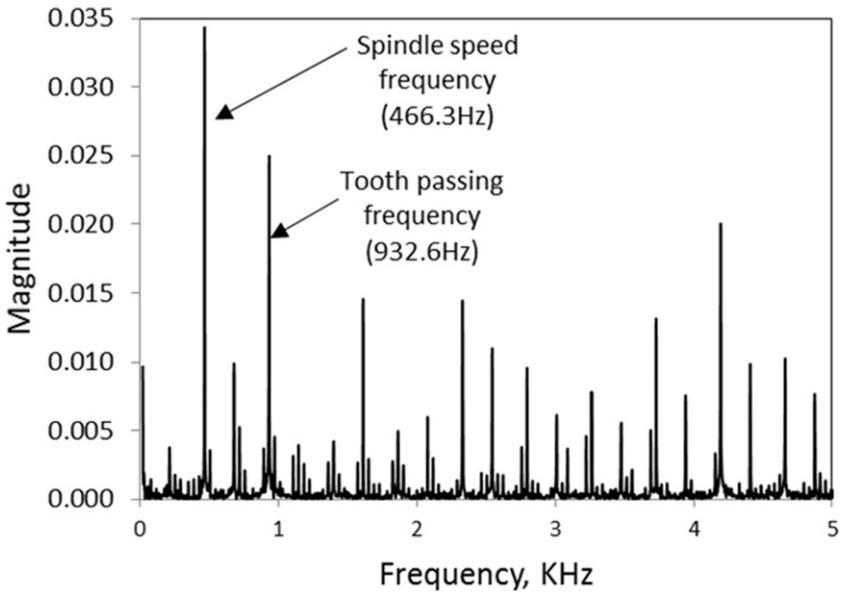


Figure 5 Frequency spectrum of tool and spindle runout. Milling CP Titanium, Ball End Mill ϕ0.152 mm, spindle speed 27 238 rpm, feed rate 2.7 mm min^{-1}, depth of cut 76 μm, MQL.[46]

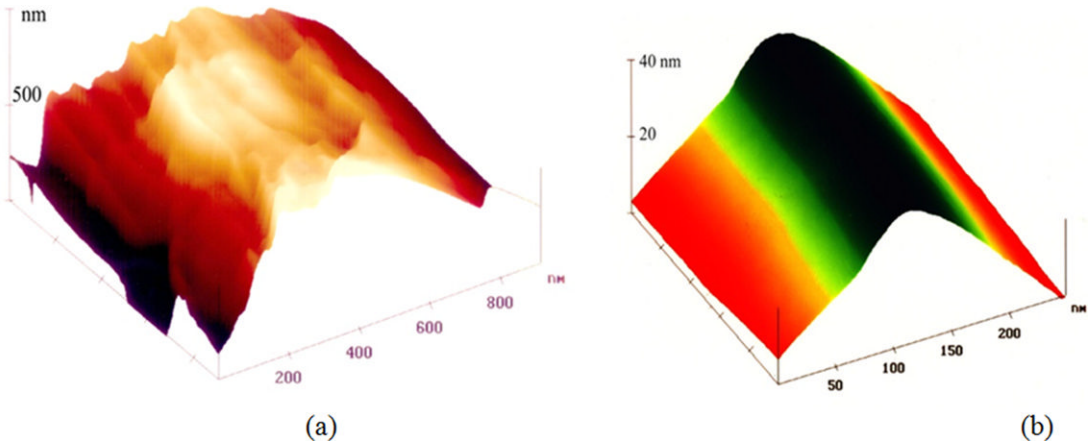


Figure 6 Tool edge measurement by scanning probe microscopy (a) new polycrystalline diamond tool with 750 nm edge radius, and (b) new single crystalline diamond tool with 10 nm edge radius. Note the different vertical and horizontal scales.

it away elastically. This elastic material layer just springs back after the tool passing by. If the depth of cut (or chip load) is substantial, then a chip is formed and a new machined surface is generated.

Typical fine grain carbide tools are first sintered from submicron carbide particles in a cobalt matrix, and then ground and lapped to final geometry. Optimal edge radii of 1–4 μm are typically designed for sintered tools to balance edge sharpness and edge strength. Only SCD tools can be ground and lapped to edge radii within nanometer range.

The threshold depth has been investigated theoretically and verified experimentally by many researchers. It varies from 5–40% of the tool edge radius depending on the workpiece material and original rake angles. A depth of cut or chip load, therefore, can be conservatively set to be 50% of the tool edge radius. When machining below this threshold, a microtool just rubs the surface and deforms it elastically during the first pass. When machining with depth of cut below the critical level, the material is plowed with negative effective rake angle. This results in high cutting force, high specific energy, fast tool wear, rough surface finish, and significant burrs. In subsequent passes when the cumulative depth is above the critical depth of cut, then a tool can remove materials as chips and the cycle repeats.

It is crucial to verify the tool edge radius before deciding on cutting parameters. Measuring of tool edge radius, however, is not trivial. A tool edge radius can be estimated from a scanning electron microscopic picture when the cutting edge is parallel to the electron beam, or scanning probe microscopic picture using a probe to scan the neighborhood of a cutting edge, or by scanning the edge on an optical microscope profiler in different views to reconstruct a 3D image of an tool edge before finding its radius.

Having the right microtool is essential for micromachining. A microtool that successfully drills through holes on a plastic printed circuit board does not necessarily be able to drill deep blind holes on titanium alloys. Understand the requirement and select the right microtool for each condition would save time, money, and frustration.

It has been theoretically derived and experimentally proven that the smaller is the chip, then the higher is the stress to remove it. Microcutting tools, therefore, have to be designed for higher stress with extreme geometrical constraints. When depth of cut is smaller than the average grain size of a workpiece, each grain generates different stress on a cutting edge and eventually fatigues the tool.

Microtools as small as 25 μm are commercially available. Common tool materials are HSS, cermet, carbide, cubic boron nitride (CBN), polycrystalline diamond (PCD), and SCD. The HSS is commonly not used in micromachining of metal since it does not have required hardness and strength to resist plastic deformation. A SCD tool is available for microturning, but not for microdrilling or micromilling. Carbide and cermet, having properties between HSS and diamond, are most suitable for microcutting tools. They are sintered from random abrasive grains in either cobalt or nickel binder with a small addition of molybdenum or chromium. A higher binder content increases the tool toughness and crack resistance, but reduces the tool bulk hardness. Having ultrafine grain (submicron size) abrasives in a lesser amount of binder is the optimal solution since a tool with a submicron carbide grains can maintain a high hardness while improving its crack resistance against chattering, interrupted cut, or cyclic deflection due to spindle runout.

Microtool failure modes include shearing, chipping, and wear. To minimize shearing and catastrophic tool failure, a tool should be made from a high hardness substrate and its geometry would be suitable for micromachining, i.e., large included angle and sharp cutting edge. A tool with smaller than minimum included angle will be deformed and fractured in service.

Coating of microtool is still a technical challenge due to conflicting constraints for tool performance. Chemical or physical vapor deposition (CVD or PVD) techniques have been developed to coat cutting tools with mono/multiple layers of intermetallic or ceramic compounds (**Table 2**). Criteria for acceptable tool coating are numerous: uniformity, high hardness, high toughness, low friction, high wear resistance, surface smoothness, high chemical/diffusion resistance, and high temperature stability at a reasonable cost. Although a coating thickness of 2–4 μm (79–118 μin) is acceptable for a macrotool, coating thickness on a microtool should be thinner to minimize fracture and peeling of the coating. Both CVD and PVD processes not only add the coating thickness to an edge radius, but they also increase the radius due to extra coating at a sharp corner. This is unfortunate since the thicker coating reduces the tool sharpness by enlarging the tool edge radius and causes an unfavorable plowing effect with negative effective rake angle. An uncoated microtool might perform satisfactorily, but the same machining parameter can be devastating to an over-coated microtool. A thin coating less than 1.5 μm following by an edge sharpening process would improve the tool performance, however, at the expense of higher tool cost. Published data indicate that micrograin carbide tools with 1.5 μm-TiN coating is the best for micromilling of H13 tool steel hardened to 45 HRc.

Table 2 Commercial coating for microtools

Coating	*Structure*	*Hardness (GPa)*	*Coefficient of friction*	*Coating (μm)*	*Coating (°C)*
TiN	Monolayer	24	0.55	1–5	600
TiCN	Gradient	37	0.20	1–4	400
TiAlCN	Gradient	28	0.30	1–4	500
TiAlN	Multilayer	28	0.60	1–4	700
AlTiN	Gradient	38	0.70	1–3	900
ZrN	Monolayer	20	0.40	1–4	550

Source: Machinery Handbook, 29th ed., Industrial Press, 2011.

1.11.3 Silicon Micromachining

Silicon micromachining technique is used to fabricate micromechanical structures in silicon using micromachining processes. Gears and spiral springs with dimensions of 50–200 μm are examples for movable structures that are successfully fabricated using this method.[47] Two crucial types of silicon micromachining processes are bulk micromachining and surface micromachining.[48] Although the following discussion is limited to silicon, the process can be applied to other semiconducting materials with subtle modifications.

1.11.3.1 Bulk Micromachining

Bulk micromachining (Figure 7(a)) is a process where a bulk of materials such as silicon and glass is shaped by treatment with either orientation dependent or orientation independent etchants. In bulk micromachining, structures are produced inside a substrate. It is widely used to fabricate 'undercut' structures like membranes, beams, holes, grooves, and other microfeatures.[49–51] Due to the inherent process limitation, bonding methods are used to join thin and two-dimensional components into a complex three-dimensional (3D) and thicker structure. The most common bulk micromachining are wet and dry etching.[49,52,53] These techniques can be distinguished based on the phase of the reactants. Wet etchant refers to the aqueous chemical phase while dry etchants refers to the vapor and plasma phases.[51]

Wet etching (Figure 7(b)) bases on the immersion of workpiece in an aggressive liquid solution. It is a process where isotropic or anisotropic etchant can be adopted, while doping or etch stop methods are used to control machining depth in silicon wafers. Wet etching is commonly used for silicon and glass.[49,52] The geometries of etched features are isotropic if the etching rate is uniform in all directions, and anisotropic if the etching rates depend on the material crystalline orientations. The nature of the chemical reactions, the diffusion of reactants and products, and shapes of the masks

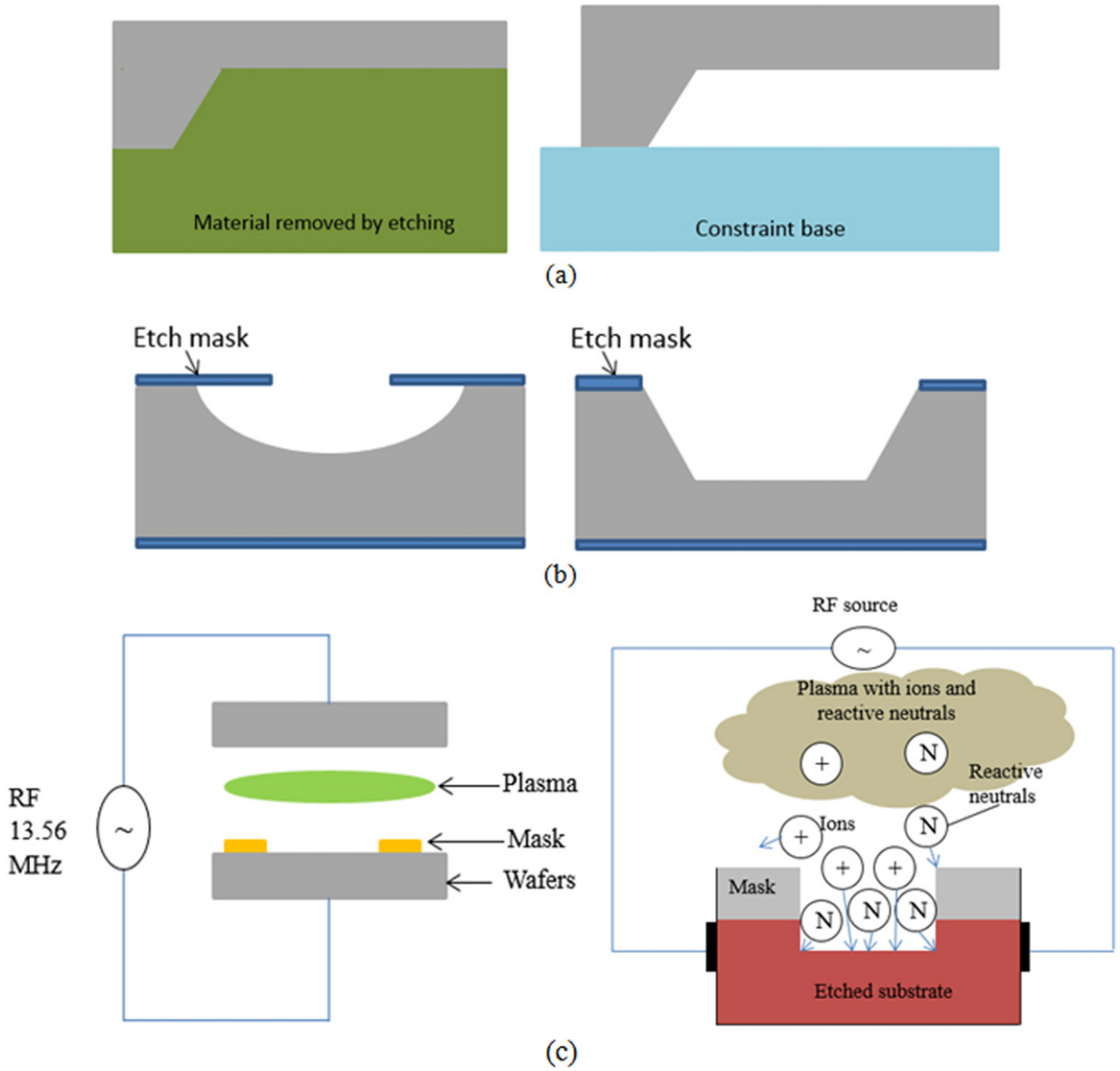


Figure 7 (a) Bulk micromachining, (b) isotopic (left), anisotropic (right) wet etching, and (c) deep RIE.

used to define the etched regions are among the factors that defines the shapes and productivity of final products.[51,54]

As for dry etching, there are a few different processes involve such as physical, chemical, and combinations of physical and chemical etch processes. Sputtering and ion milling are the examples for the physical processes while reactive ion etching (RIE), deep RIE (Figure 7(c)) and reactive ion beam etching are examples of physical and chemical synergy. While wet etching uses unique chemicals for specific material, dry etching can be applied on a variety of metals, ceramics, and plastics. Dry etching is applied in a controlled chamber where ions are accelerated to scan specific areas and remove affected atoms. This process is more expensive compared to the wet etching due to slower MRR, but it is the preferred choice when high-aspect-ratio vertical structures or thin layer machining must be obtained.[49,52]

1.11.3.2 Surface Micromachining

Surface micromachining is a process that relies on deposition of structural thin films on a sacrificial layer. It can produce smaller components compared to those from bulk micromachining. When the sacrificial layer is etched away, an undercut and freely suspended or a movable micromechanical structures are produced.[49,55] The common sacrificial layers are inorganic materials such as silica (SiO_2) and organic polymers such as polymethyl methacrylate (PMMA); acidic etchants such as hydrofluoric acid (HF) are common etching solutions.[56] This procedure typically includes (Figure 8(a)):

- Growing a sacrificial layer and patterning it on a silicon substrate,
- Depositing a structural material by either physical or chemical depositing techniques on top of the sacrificial layer,
- Shaping the this structural materials by appropriate lithography or etching techniques,
- Removing the sacrificial layer by a suitable etchant leaving behind the desired microstructures.

One of the advantages of this process is that the final structural and spacer features can be as small as 10 μm. A surfaced micromachined device (1) has smaller footprint than the that of bulk micromachining devices, (2) can be designed with tighter tolerance compared to the bulk micromachining devices, and (3) is easier to integrate into electronic microstructures. However, the main disadvantage of this technique is the vulnerability of surface microstructures when handling and integrating during manufacturing.[58] An example of microsystem with components fabricated by surface micromachining is shown in Figure 8(b).

1.11.4 Energy Beam Micromachining

Energy beam refers to collection of energetic particles such as photons, ions, or electron. A beam can be scanned or focused for desired material removal process.

1.11.4.1 Laser Micromachining

Light Amplification by Stimulated Emission of Radiation (LASER) is used for metal cutting since 1965. Laser light is collimated, coherent, and monochromatic; and because of its high power density, it can be used to process metals, ceramics, polymers, and even composites. Machining using laser is mainly due to the thermal action where rapid rise in temperature in a limited area caused the irradiation of substrate material by Yttrium Aluminum Garnet (YAG) laser or CO_2

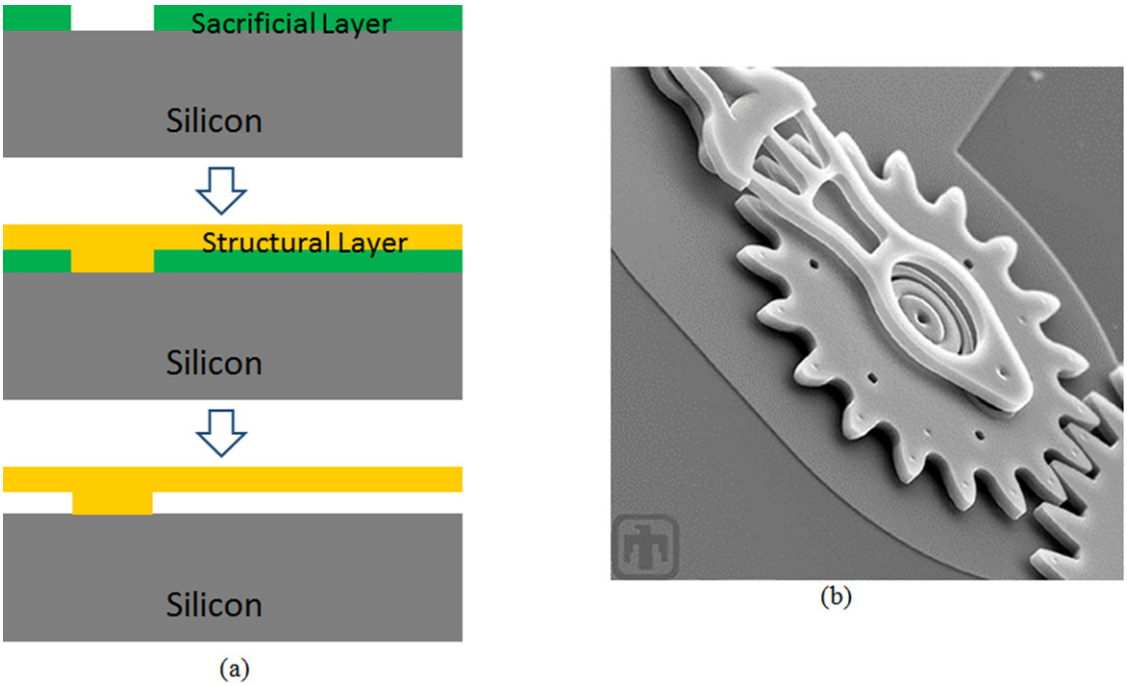


Figure 8 (a) Basic surface micromachining process and (b) An example of microsystem.[57]

laser. With the advances of laser in the recent years, it is also used for microdrilling, micromilling, and other microsurgery. Excimer laser, nanosecond laser and femtosecond laser are the example of many lasers that are used in micromachining. A simplified view of laser machining and an example of microdrilling (marking) are shown in Figure 9.

A short-pulse laser is capable of generating light pulses that last only a few micro/nano/femto-seconds. Short pulse machining process is so rapid that there is little time for heat to diffuse away from the focal spot. It directly changes solid matter into plasma and results not HAZ, microcracks, shock wave, delamination, recast layer, and damage to adjacent structures. This short-pulse laser generally performs micromachining with high accuracy and resolution. Micromachining quality depends on the amount of heat deposited in the workpiece and the amount of heat that is left behind in the material can cause damage. The main advantages of short-pulse laser are as follows:

- The laser energy does not have time to leak away from the micromachining spot.
- Huge amount of energy deposits so fast that the material is forced into a state of plasma which expands away from the material and taking away almost all the heat.
- Very low damage such as microcracks, resolidification of debris.
- The interaction of ultrashort laser pulses with matter is highly reproducible, shot-after-shot.

Laser assisted machining (LAM) is a machining operation that uses laser as a heat source with the beam focused on the surface of the workpiece and immediately in front of a cutting tool. Ductile deformation occurs during the cutting process when the heats soften the surface layer. The power requirement depends on the material and the nature of the machining operation. It is capable of cutting non-reflective materials. Minimum burr and little heat affected zone, resulting from a precise cut with high speed are among the advantages of the LAM process. Moreover, it has the ability to reduce cutting force and lower dynamic forces, producing less segmented chip generation, resulting in a smoother surface finish. Nevertheless, the drawback of this machining operation is that it requires high energy, involves high cost, and must be conducted in special conditions.[59]

1.11.4.2 Focused Ion Beam Micromachining

Focused ion beam (FIB) is a micro/nano machining technique that can produce miniaturized 3D features to form a mold for subsequent replication process. Combination of FIB micromachining and micromolding is an alternative to LIGA process for low aspect ratio component and flexibility when using software-generated masks. A FIB system can be an invaluable tool for micromachining electronic components (IC repair, modification, etc.), failure analysis by microsectioning and secondary ion mass spectrometry (SIMS), and fabrication of non-silicon microcomponents for MEMS (microgear, microneedle, microchannel, micromilling tool, etc.). Two main categories of FIB micromachining are sputtering and deposition.[7,60–62]

1.11.4.2.1 Deposition

Other than FIB sputtering, FIB is the catalyst for depositing materials on the surface of the substrate (Figure 10(a)). In example of deposition a tungsten thin film, a precursor gas such as tungsten hexacarbonyl is used in the FIB system. An injector of precursor needle is directly positioned near the substrate. Upon interacting with incoming ions of a FIB, the gas molecules are decomposed into a thin tungsten layer on top of the machining surface while releasing a volatile compound which is exhausted into a vacuum system.[63] Such FIB deposition is commonly used in microelectronic failure analysis or micro structural modification.[64]

1.11.4.2.2 Sputtering

The FIB sputtering is a technique for maskless micro fabrication where incident ions transfer momentum to the substrate and release atoms through cascades of collisions (Figure 10(b)). There are two types of FIB sputtering which are dry etching/sputtering and gas assisted etching (GAE). The GAE is known for its very complex phenomenon since the material removal is occurred due to the chemical action of the gas, the physical action of energetic ion, and the combination action of the gas and energetic ions. As for the dry sputtering or more commonly known as sputtering for FIB micromachining has become more crucial compared to GAE because it is

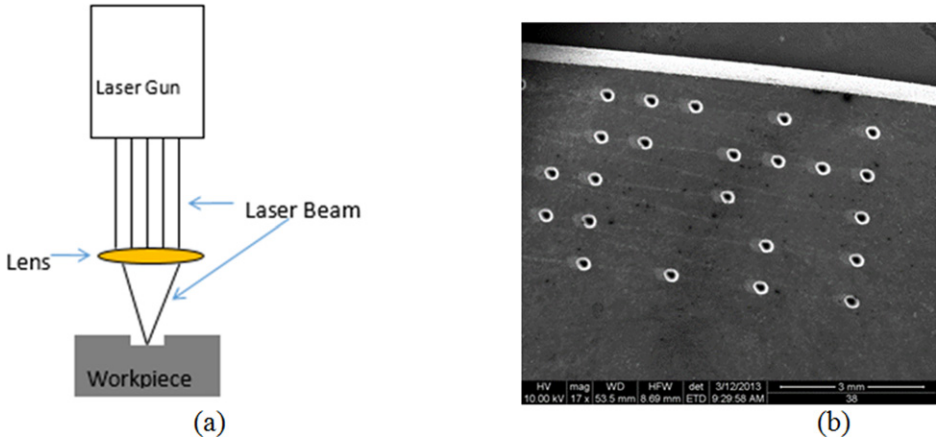


Figure 9 (a) Schemtic diagram of laser machining and (b) Femto laser marking on a turbine component.

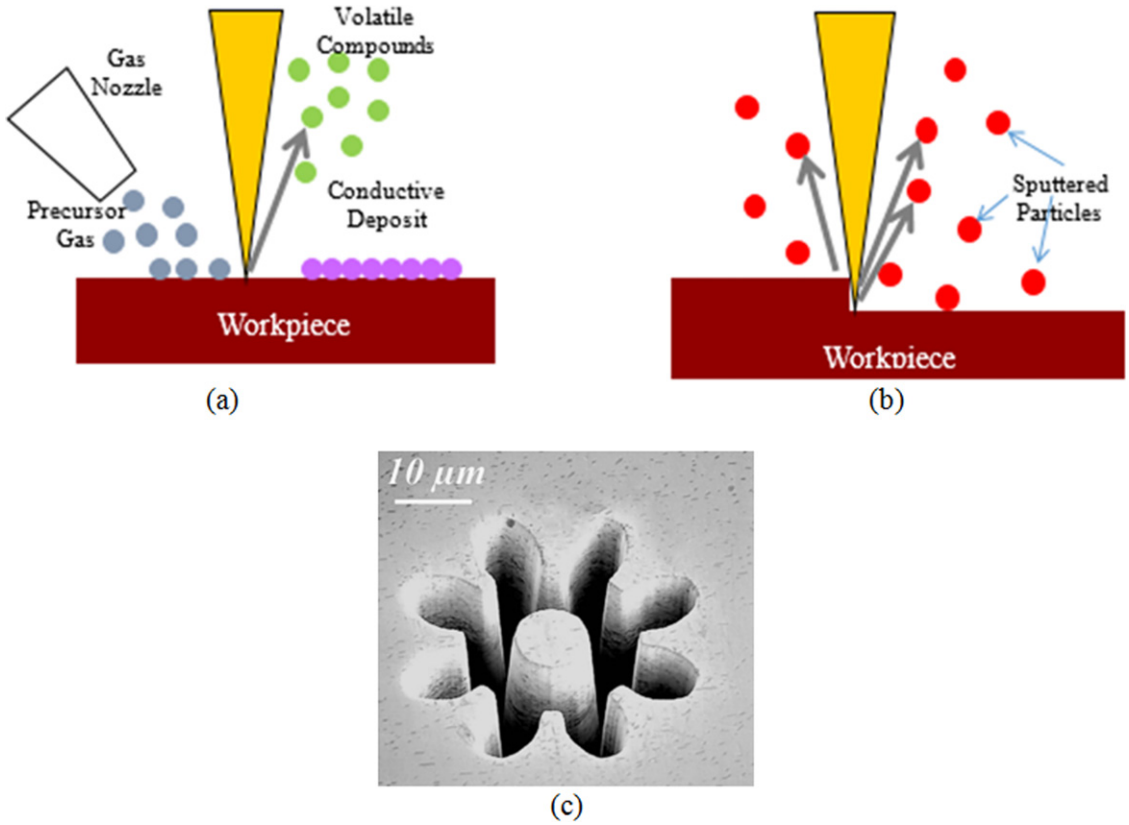


Figure 10 Schematic diagram of (a) FIB assisted deposition, (b) FIB sputtering, and (c) a micromold fabricated by FIB micromachining.

widely used for application in micro/nano engineering and various microscopic techniques.[7] A metallic mold with micromold cavity fabricated by FIB sputtering is shown in Figure 10(c).

1.11.4.3 Electron Beam Micromachining

The principle of electron beam machining (EBM) is similar to that of ion beam machining. Both techniques utilize energetic particles to strike a target so that a substrate is machined or a layer is deposited in presence of an assisted gas. Both techniques, either focused ion beam or focused electron beam, are sometimes cost prohibitive due to the high cost of equipment and maintenance while a small workpiece must be enclosed in vacuum.

The smaller size of electrons makes electron easier to manipulate, but less effective in machining compared to an ion beam. The low momentum of an electron would transfer its kinetic energy to thermal energy for material removal by melting and evaporating rather than sputtering. A small electron would scatter and bounce among substrate atoms and generate a larger heat affected zone, therefore, a microhole drilled by electron beam is typically deep but not precise. Holes with diameters in the range 50–1000 μm can be drilled through 10 mm plates at an astonishing rate of 3000 holes s^{-1}.[65] An electron beam with 1.1 nm spot size drills a much larger hole ~100 nm on a silicon nitrate membrane due to the scattered electrons.[66]

1.11.5 Electrical Discharged Micromachining

The nontraditional electrical discharge machining (EDM) process is commonly used in mold-and-die manufacturing industries due to its capability in removal of difficult-to-cut and brittle conductive materials.[67–69] It is one of the machining alternatives used in fabricating microparts with low cost and less time consuming compared to FIB, LIGA, and other lithography based techniques.[70] It is also used in aerospace and automotive industry as well as in making surgical components.[71] The workpiece machined by EDM depends on the thermal conductivity, electrical conductivity, and melting points of the materials.[72–74] The noncontact nature of the process with nearly force free machining allows soft electrode materials to machine a very hard, fragile, or thin workpiece.[75–77] The inherent noncontact nature of EDM, therefore, minimizes mechanical stresses, chatter, and vibration problems during machining[78]; however, other issues may emerge due to cyclic pumping pressure of dielectric fluids on an electrode and a workpiece.

A workpiece can be either positive or negative relative to the electrode. A negative workpiece would have higher material rate but rougher surface, but a positive workpiece causes high wear rate on the negative electrode. Polarity is a vital factor in this machining operation as electrical sparks are produced between the workpiece and electrode.[74] In this process electrical spark is created by electrical energy and materials are removed by thermal energy of the spark.[79] The series of electrical sparks or

discharges occur rapidly in a short span of time within a constant spark gap between the electrode and workpiece material. The nature of the sparks is repetitive and discrete. The tool and the workpiece are immersed in a dielectric medium, such as kerosene, deionised water, pure water, or any other suitable dielectric fluid.[68,80–82] The gap between the electrode and workpiece are small enough to produce voltage that ionizes the dielectric fluid.[74]

Micro-EDM follows the similar principle of macro EDM technology. But, there are some differences between these two machining in terms of circuitry. A macro EDM system commonly uses resistance capacitance relaxation (RC-relaxation) circuit meanwhile a micro-EDM system utilizes RC-pulse circuit. The RC-pulse circuit type produces a lower MRR due to its very small discharging energy. Micro-EDM is useful to manufacture component less than 1 mm with high precision and high accuracy.[83–86]

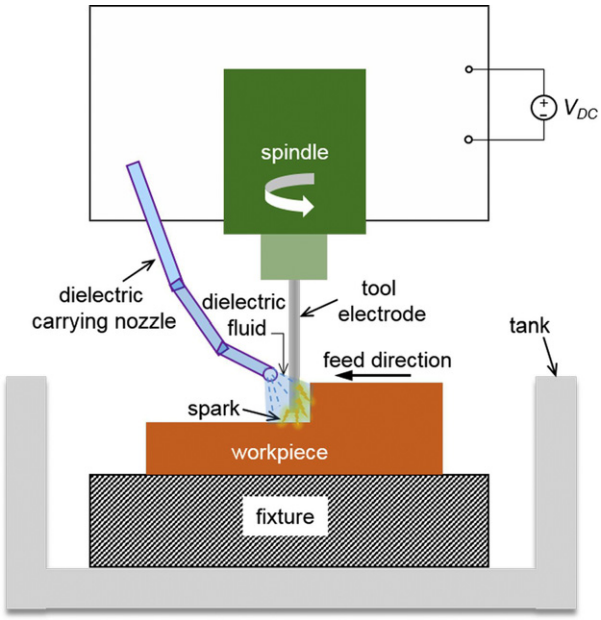


Figure 11 Schematic diagram of a 3-axis micro ED micromilling.[87]

1.11.5.1 Electrical Discharged Micromilling

Electrical discharge (ED) micromilling is a branch of the micro-EDM. It has the specialty in fabricating microfeatures with complex 3D geometries. It is an effective way to fabricate complex contour micromold and microtool for hot embossing. The mechanism of ED micromilling is same as the micro-EDM where the material is eroded by noncontact thermoelectrical process. Typical ED micromilling utilizes 5-axis system to move a rotating electrode into a workpiece. The electrode movement is controlled numerically in order to achieve the desired shape and accuracy of the micro parts.[9,87] The schematic diagram of the micro ED milling operation is shown in Figure 11.

1.11.5.2 Micro Wire EDM

Micro wire EDM (micro-WEDM) technique is a micro version of macro wire EDM. Still, sometimes the macro WEDM is 'stretched' to fabricate microcomponents because of high demand of microparts and less availability of miniaturized machine tools. This process uses thin wire (typically 100 μm) as an electrode to cut the workpiece into desired shapes which is controlled by a computer numerical control (CNC) system. Micro-WEDM (Figure 12(a)) is a machining process that can fabricate microfeatures with nanometric surface finish and submicron accuracy. A gear machined by micro-WEDM is shown in Figure 12(b). The surface quality would get worse with ripples, cracks, and recast layer if higher electrical energy is used. Besides, the debris that is not washed away can cause a short circuit and results in poor surface finish. However, regarding the surface finish, further investigation should be done since the fabricated microparts are usually used as a mold to replicate polymer microstructures.[7,88]

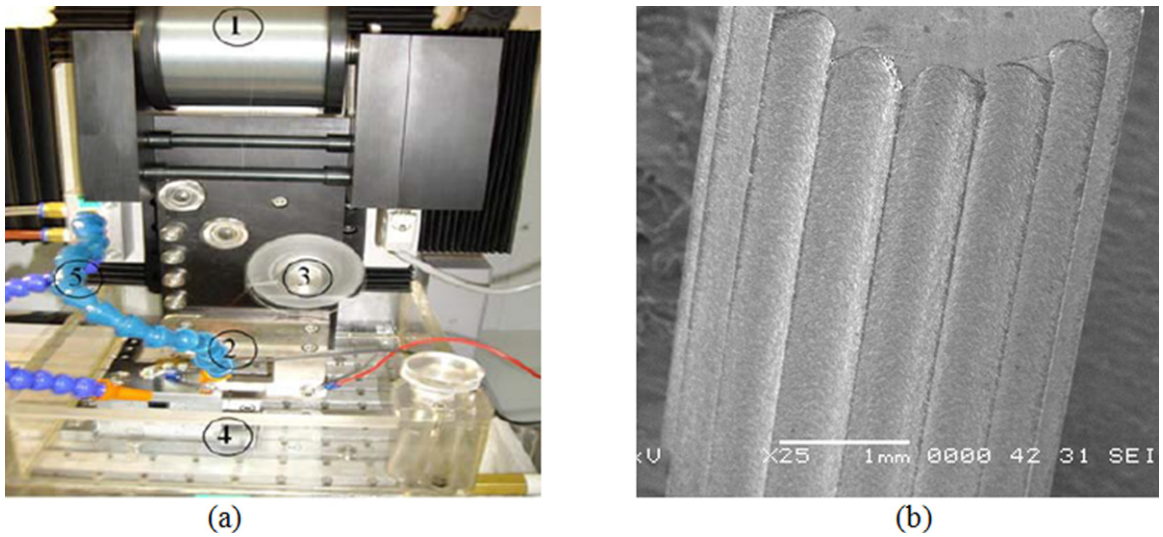


Figure 12 (a) Experimental setup of micro-WEDM (Legend: 1. wire electrode supply spool; 2. workpiece and clamping device; 3. used wire collector spool; 4. dielectric tank; and 5. dielectric supply nozzle) and (b) A spur gear produced by micro WEDM.[7]

1.11.5.3 Micro-EDM of Nonconductive Ceramics

Ceramic materials are commonly used in many applications such as machine tools, molds and dies, vehicle systems, electronic devices, semiconductor systems, and in biomedical field. This is due to their material properties which include:

400–1465 MPa strength,[89,90]
1000–2500 Hv Vickers hardness,[90]
900–1200 MPa bending strength,[91–93]
2050–2720 °C melting temperature,[94,95]
High chemical inertness,[96–98]
Biocompatibility of some ceramics,[84]
Excellent dielectric strength,[68]
Outstanding corrosion resistance,[68] and
Good wear resistance.[96–98]

Aluminum oxide, also known as alumina (Al_2O_3) and zirconium dioxide, also known as zirconia (ZrO_2) are commonly used as advanced technical ceramic materials. Yet these materials are difficult to machine due to high brittleness, hardness, and nonelectrical conductivity.[68,84,94,96–99] In addition to conductive material, nonconductive materials can also be machined using the EDM. Examples of the latter includes:

Oxides[59]: Zirconia (ZrO_2)[68,75,91,92,100] and Alumina (Al_2O_3).[96,101,102]

Non-oxides[59]: Sialon ceramic or Silicon Nitride (Si_3N_4)[79,103,104] and Boron Carbide (B_4C).[105]

Composites[59]: Siliconised Silicon Carbide (SiSiC)[78,105] and Cobalt-bonded Tungsten Carbide (WC–Co).[105]

The common method used to process zirconia is laser scanning followed by milling process to enlarge the shape of the framework and finally ends with sintering to full density for two hours at 1350 °C.[106,107] Materials with a minimum electrical conductivity of 0.1 S cm^{-1} can be processed using EDM. So, conductive materials are capable to undergo this process.[91,92,108] But, the main problem occurs when EDM'ing ceramic materials with electrical conductivity between 0.01 and 3.333×10^{-3} S cm^{-1} (electrical resistivity between 100 and 300 Ωcm).[105] Besides, these materials are hard to shape by cutting techniques or laser ablation due to their material characteristics. Currently they are roughly shaped with diamond tools and then polishing with diamond suspensions; these approaches are time consuming and costly, however.[91,92,96,103]

Despite of above problems, ceramics have been machined with EDM since these materials are difficult to machine using other techniques.[67,79,104,109] Since the ceramics need to be conductive for EDM'ing, one solution is to (1) create a composite with dopants such as titanium nitride (TiN) or tungsten carbide (WC) onto the ceramic, (2) create a conductive compound by embedding the ceramic particles in a metal matrix, or (3) apply ultrasonic assisted spark erosion. The ultrasonic energy can assist in creating spark erosion and lead to crack formation that causes spalling. Nonetheless, the main disadvantage of these methods is that the ceramic's properties are affected. Moreover, material removal of ceramics during the spark erosion is different from metal erosion. This is due to difference in melting, evaporation, spalling, oxidation, and decomposition mechanism.[73,91,92,99] Thus, to avoid this problem, nonconductive ceramics have been successfully machined by EDM using the assisting electrode method (AEM) with some process modifications.[68,101,110–112]

1.11.5.3.1 Assisting electrode

In this method, a conductive layer is applied on top of the nonconductive ceramic in order to produce sparks between the workpiece and the electrode. Assisting electrode (AE) can be metal plates, foils or meshes as long as they are mechanically fixed on the ceramic surface.[68,91,92,96,99,110,113] During the erosion process, AE will be eroded. High temperature that occurs around the dielectric fluid will degenerate the polymer chains and creates carbon elements from decomposed polymer chains. These carbon elements, with combination of conductive debris cover the ceramic surface in order to sustain the conductivity during the erosion process. The spark erosion process for nonconductive ceramic is shown in **Figure 13**. Hence, oil based dielectric fluid such as kerosene is suggested to be used in order to continue the process after the conductive layer has relapse.[68,91,92,101,102,114]

Carbon can also be added into the dielectric fluid in order to support the formation of conductive debris. The thermal load of the discharged spark penetrates the ceramic which leads to stresses that stimulates cracks. Therefore, the ceramic is removed by spalling process which is explained in subsection of mechanism of material removal.[92] A study on EDM of high purity nonconductive ZrO_2 was investigated using two different types of adhesive foils as AE. Adhesive copper foil, known to have excellent thermal conductivity, gives optimum values for MRR, electrode wear rate, and surface roughness.[68] In another study, ceramic specimens were coated via doctor knife and screen printing with thickness of 800 and 30 μm respectively. Both techniques are suitable for machining process, yet screen printing technique is more favorable for thinner layer and better accuracy.[92]

1.11.5.3.2 Dielectric fluid

Closed flushing system and workpiece vibration unit can be added to die sinking micro-EDM to enhance the process. The flushing system varied by modifying the vibration frequency. The vibration frequencies used were in the range of 50–1000 Hz at 1–10 μm amplitudes in feed direction onto the workpiece. It is recommended that silver-based varnish as AE with vibration frequency of 440 Hz in carbon hydride based

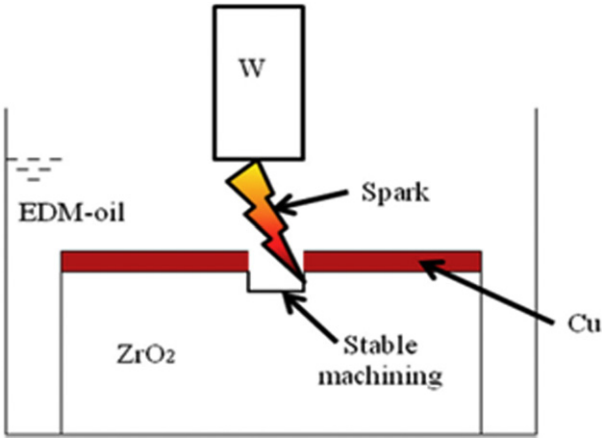


Figure 13 Principle of spark erosion in EDM with copper (Cu) as assisting electrode on nonconductive zirconia ceramic with tungsten (W) electrode.[99]

(IME-82) fluid can reach a stable process.[67] Ultrasonic vibration enables successful micro-EDM of nonconductive ZrO_2 ceramic. The machining was done using silver varnish as the AE with the thickness of 20 μm. The proposed experimental setup was completed by adding a peristaltic pump for flushing and filtering of the medium independent from the main dielectric circulation. Besides that, an active workpiece clamping unit with low-frequency vibration up to 1000 Hz at an amplitude of 20 μm peak to peak was added. The result showed that micro-EDM process with direct vibration gives higher aspect ratio structures with improved process speed. The direct ultrasonic vibration enabled the machining of complex structures with very high aspect ratios.[75] Micro-EDM of ZrO_2 with tungsten electrode and EDM-3 synthetic oil as the dielectric fluid was done in another study. Selection of AE, polarity, feed rate, and flushing type are the major factors that were considered in the process development of this machining process. The results showed that stable machining operation can be achieved with copper adhesive as AE, positive workpiece polarity, 3 μm s^{-1} feed rate, and workpiece submerged in dielectric fluid with one-way circulation.[99]

1.11.5.3.3 Mechanism of material removal

MRR has become one of the main concerns to remove bulk of the materials. Many researchers have attempted to develop empirical models to estimate MRR. The MRR depends on the amount of pulsed current in each discharge, frequency of the discharge, electrode material, workpiece material, polarity, and dielectric flushing condition.[74,115,116]

The MRR is low when the workpiece is connected to positive polarity. This is explained by the tendency of the dissociated carbon elements in dielectric fluid to remain at anode and formed a recast layer.[117] However, in order to obtain high MRR in ceramic, high power should be provided and the workpiece should be positive polarity.[59,96,99,118] This is preferred since more carbon elements are generated, forming a conductive layer that covered the ceramic surface during the EDM process.[99,118] Therefore, MRR is determined by the electrode and workpiece material, current density, and pulse length.[119]

There is a research done on ED-milling whereby the AE was stored in a bobbin and was continuously fed toward the electrode along the surface of the insulating Al_2O_3 ceramic workpiece using the actuating wheel. MRR of the insulating Al_2O_3 ceramic depended on the polarity, the rotational speed, and addition of suitable chemical additives in dielectric fluid. MRR was high when the electrode was positive with high rotational speed. The speed enhanced the flow velocity of the dielectric fluid at the discharge gap and led AE closer to the workpiece surface. The stability and electrical discharge energy acting on the workpiece surface increased and improved the MRR. Water-based emulsion was suggested to be used as the dielectric fluid since there was no production of harmful gases and the equipment was not corroded.[97,98] Since the ceramic took the longest machining time, the machining conditions were highly unstable. The shortest machining time and more stable machining conditions were found for ZrO_2 ceramic. The MRR increased when the thickness of AE was increased. Moreover, ceramics with low thermal conductivity give higher MRR values.[95]

Flushing system and rotation of the electrode are two factors crucial in machining of nonconductive ceramics. It showed that machining rate of nonconductive ceramics decreased without the utilization of flushing system or rotation of electrode. Both of these factors affected the machining rate at high discharge current.[73] Different dielectric fluids have different properties, which play important role in flushing away the debris from the machining gap. The breakdown resistance, conductivity, viscosity, flash point, health, and safety factors of dielectric fluids can all affect the MRR and the tool wear. Rotating electrode can provide an effective gap flushing technique and sparking efficiency that helps in improving the MRR and tool wear.[78] Still, with the increasing of the speed, the centrifugal force will be generated, causing more debris to escape from the machining zone.[117]

Different types of electrodes give different machining effects on the ceramic surface. A research proved this by using Cu, graphite (Poco EDM-3), and copper-infiltrated-graphite (Poco EDM-C3) as electrodes. Conductive layer was formed on the EDMed surface of alumina by all of the electrodes. The thickness of the conductive layer plays a vital role in EDM process since it has the ability to affect the MRR results. Thicker conductive layer give rise to a better MRR results. Semi-sintered electrode material can generate thicker conductive layer such as EDM-C3 and EDM-3.[101]

Another study on micro-EDM of insulating silicon nitride (Si_3N_4) using three different electrodes; Cu, copper tungsten (CuW), and silver tungsten (AgW) were carried out. MRR depends on the dielectric fluid breakdown which is usually initiated by low voltage and also by the electrical and thermal properties of the materials. Based on the investigation, Cu had the higher electrode wear rate than AgW and the later had the highest breakdown voltage compared to Cu since tungsten (W) has higher atomic mass and hardness. High melting and evaporation point together with high thermal conductivity are the basic requirements in choosing an electrode material. Electrode wear rate is also verified to be inversely proportional to melting point of electrode material.[79] Mechanisms of material removal occurring in nonconductive ceramics by EDM process are briefly explained below:

Melting and evaporation. Thermal removal of ceramic is induced by melting of the coated conductive layer. **Figure 14** shows the topography of droplets left on the micro-EDMed surface which probably indicates melting and evaporation. The droplets depend on the material properties such as melting point and thermal conductivity. Micro-cracks can form on the machined surface since ceramics have lower resistance against tensile stresses. This mechanism happens at the central region of the discharge where materials are removed depending on the ceramic material.[120,77,96]

Spalling. Small volumes of material from the base material are dropped out due to the surrounding micro-cracks generated during EDM (**Figure 15**). The formation of micro-cracks depends on the material properties such as thermal conductivity, melting point, and fracture toughness.[68,120] This process happens when large amount of energy is directly discharged into the discharge gap during machining process. The ceramic will encourage the formation of a steep-temperature gradient and high-thermal stress level at the interaction point. If the level of the thermal stress exceeds the maximum tensile

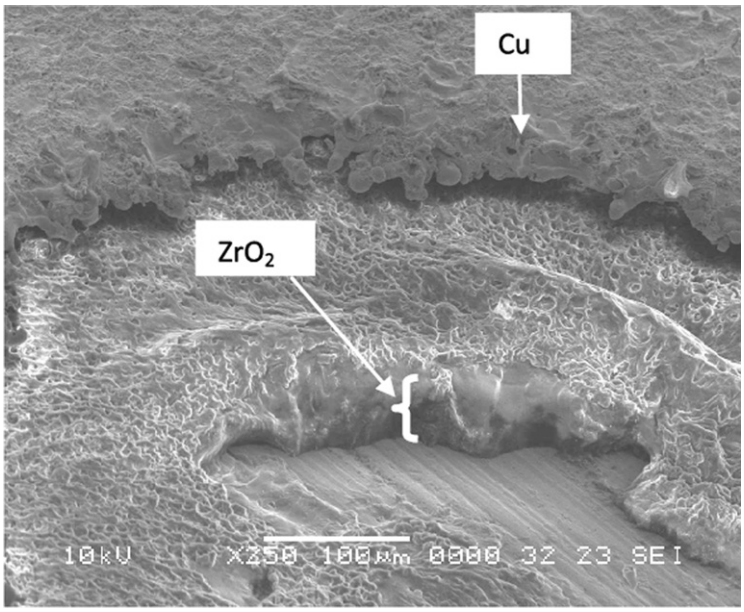


Figure 14 Melting and evaporation at the machined area of zirconia by micro-EDM using EDM-3 synthetic oil as dielectric fluid.

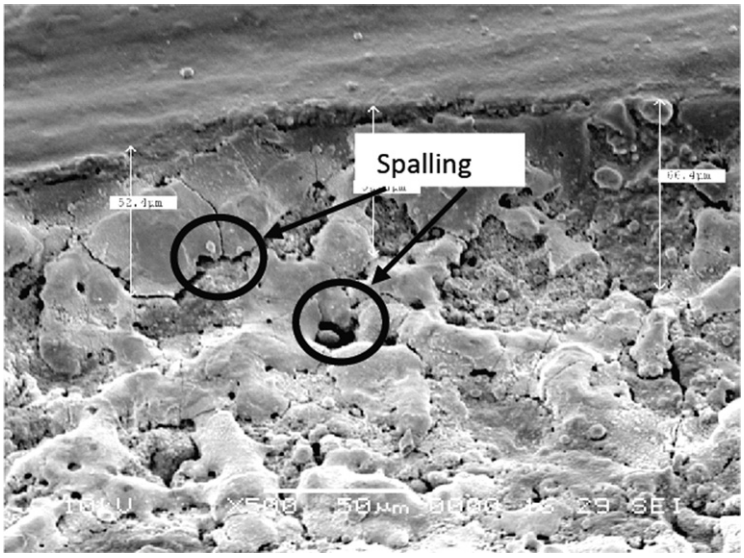


Figure 15 Spalling at the machined area of zirconia by micro-EDM using EDM-3 synthetic oil as dielectric fluid.

strength of the ceramic, it will lead to cracks and removal of the material by spalling.[96,99]

Oxidation and decomposition. After the spalling mechanism, oxidation and decomposition occur due to the thermal energy of the EDM process. **Figure 16** shows formation of foamy and porous layer on the surface of Si_3N_4–TiN, machined by WEDM in de-ionized water. This structure is caused by generation of many gas bubbles during the machining process. The visible bubbles and smell of ammonia are symptoms of oxidation and decomposition mechanism. This mechanism generates a large amount of gas, leading the porous structure of the machined surface as well as increase in MRR. On the contrary, if the machining is performed in oil, the formed droplets and craters produce a smoother recast layer with better machining surface.[120] Even though EDM is capable of machining complex shape with high precision and accuracy, it generates unwanted recast layer and HAZ.[121] Normally three layers are identified on top of the machined surface. The top surface layer is formed with spherical molten metal and electrode material. The next layer is the recast layer forming by resoludified materials, or white layer, and lastly the HAZ or annealed layer (**Figure 17**).[78] The EDM'ed surface is subjected to a very sharp temperature gradient during the machining, and resulting a high thermal residual stresses. Electrode material, dielectric fluid, and discharge condition are factors that can affect the profile of the temperature gradient. Since some of the molten metal cannot be excluded; it will be quenched rapidly by dielectric fluid, forming a recast

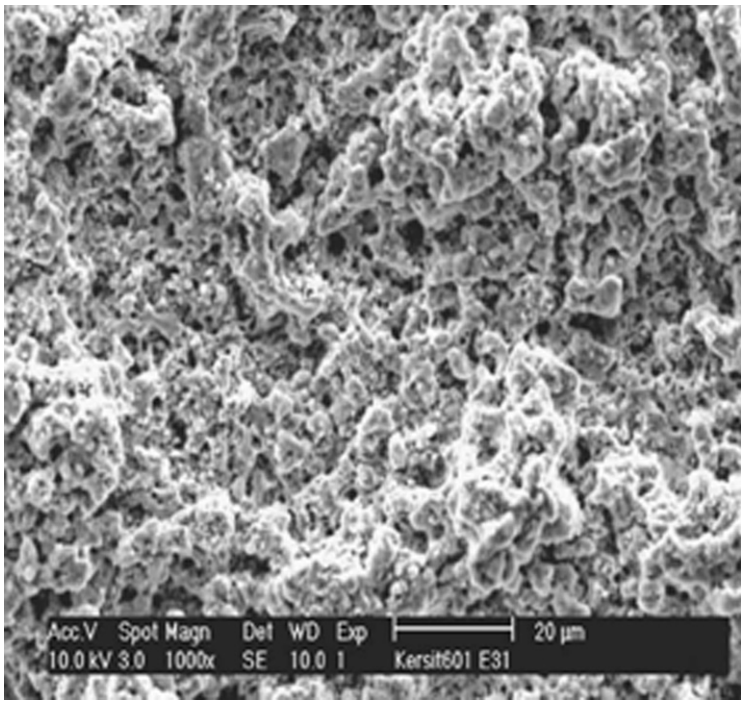


Figure 16 Topography of Si_3N_4–TiN by wire EDM in deionized water.[120]

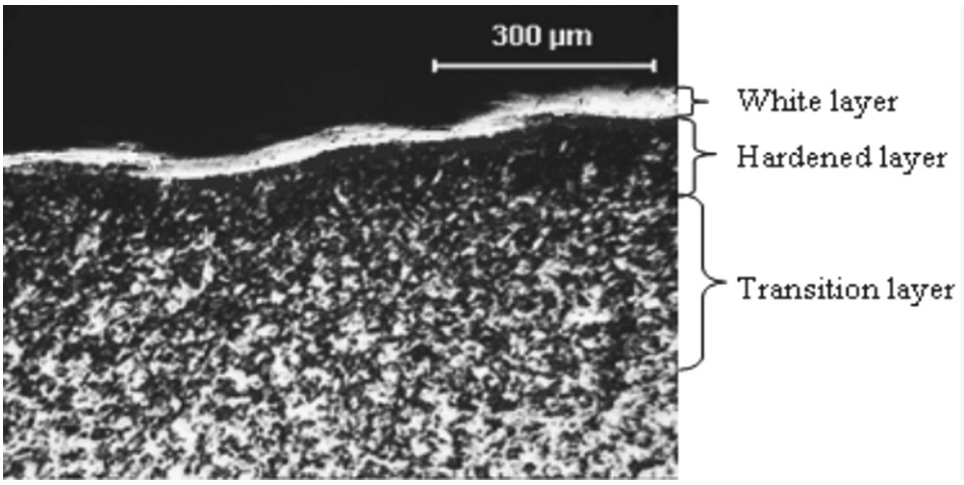


Figure 17 Layers produced on EDMed surface.[129]

layer.[78,114,122,123] Usually, the recast layer consists of craters, micro-cracks, bubbles, and high tensile residual stresses (Figure 18). This can cause deterioration of the surface finish, reduce wear resistance, cause premature part failure, stress cracking, and shorten the part's fine surface finish.[121,122,124–126] Surface quality such as tensile stress, strain, intensity, stiffness, and residual stress can also be affected by the formation of the recast layer.[114,127,128]

1.11.5.3.4 Recast layer

High microhardness of EDMed surface is reported due to the migration of carbon from the oil dielectric fluid to the workpiece surface and formation of recast layer with hard iron carbides. Frequency, polarity, pulse shape, machining gap, and dielectric fluid temperature affect the concentration of these carbides on surface layer of the workpiece. Besides that, recast layer and crack density are also influenced by the flushing rate. Yet, they can be minimized by using the optimal flushing rate.[78] Recast layer created in EDM process has different properties depending on the electrical energy that consist of voltage, current, time of pulse, and pulse interval. The electrode and dielectric fluid properties have a significant role in determining the surface layer properties. Chemical changes on the surface of the workpiece occur due to reactions with the dielectric fluid and the wear of the electrode. It is observed that when electrode is made of Cu in the combination of other

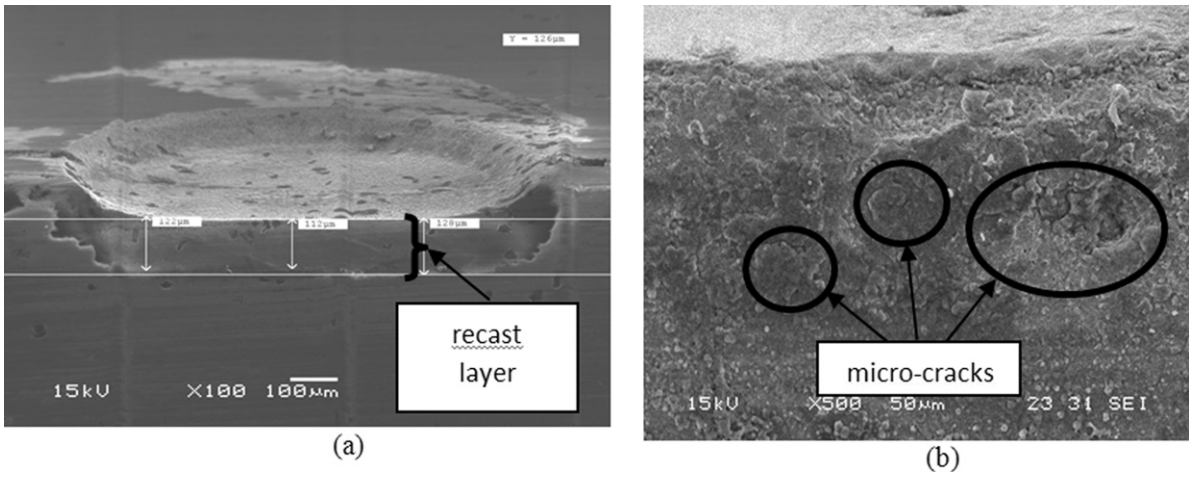


Figure 18 SEM images of (a) recast layer for machined area of zirconia due to micro-EDM and (b) micro-cracks for machined area of zirconia due to micro-EDM.

material for steel workpieces, the average Cu concentration was about 10% with diffusion up to 20 µm. The carbon percentage also increases because of the reactions with carbonic dielectric.[130,131]

Cracks are observed in the recast layer. During the cooling process, melted materials are being contracted rapidly and cracks are formed when the stress on the surface exceeds the material's ultimate tensile strength. It is seen that cracking increased with the increase of pulse energy and the crack density was inversely proportional to the thermal conductivity of the workpiece material. Surface crack intensity increased rapidly with the increase of carbon within the recast layer.[132] Peak current and pulse-on duration have been found as the influential parameters on EDMed surface integrity. Mathematical models were formulated based on the response surface methodology for correlating the influences of peak current and pulse-on time on surface integrity of M2 Die Steel after EDM process. The optimal parametric combinations were found for minimum surface roughness, recast layer thickness, and surface crack density. At peak current, 3.5 A and pulse-on duration, 20 µs, all the three criteria of surface integrity were found to be minimum.[133,122]

Influence of machining parameters on EDM of steels shows that the thickness of the recast layer varied with the change of current, duty factor, and pulse on time. Recast layer thickness increases with the increase in current due to the availability of more power for altering the metallurgical composition of the parent material. Similar results were seen when the duty factor is increased. In contrast, recast layer thickness decreased with the increase of pulse-on-time, contributed by the fact that less amount of heat is generated on the surface of the workpiece during the machining process.[122] Powder mixed dielectric has positive effect on the reduction of white-layer thickness. The effects of titanium carbide (TiC) and Al_2O_3 powder in kerosene on the EDM'ed surface shows that the recast layer thickness and the cracks increase with the increase of current. Higher layer thickness was observed when Al_2O_3 powder was used instead of TiC powder. However, when utilizing TiC powder, higher hardness was found than that of Al_2O_3 powder, besides the increase in electrode material and carbon depositions on the workpiece surface.[134]

1.11.6 ECM

1.11.6.1 Micromachining

ECM is another material removing technique for any conductive material. This anodic dissolution process uses direct current (DC), or pulsed DC, and electrochemical reaction to remove material in micro or nanoscales. Since the process is independent of the workpiece mechanical properties and can maintain the electrode dimension, it is suitable for machining, polishing, or forming intricate features on die and mold for subsequent mass replication, or shaping the difficult to be machined alloys for applications in aerospace, chemical, oil and gas, or medical industries.

While complicated contour of a macrocomponent can be formed by moving a specially shaped electrode on a controlled path, micro patterns can be fabricated using though-mask ECM technique. Rosset and Landolt[135] experimented with through-mask ECM on 304 stainless steel and Phynox cobalt alloy. A 6M $NaNO_3$ electrolyte was used with DC current density between 0.5 and 15 A cm^{-2}. The undercut underneath a mask was measured to be a linear function with feature depth. The undercut to depth ratio (etch factor) was 0.7 and proximity effect was experimentally found. The highest MRR was for the area with the lowest density of mask opening. This proximity effect was reduced and more uniform etching was obtained by integrating a thin cathodic layer on an insulating mask. Although minimum undercut was obtained, the elliptical profile of etched feature was far from an ideal anisotropic profile with straight walls and flat bottom.

An ECM simulation using moving boundary numerical technique was reported.[136] The study investigated shape evolution of a thin metal film sandwiched between a photoresist mask and an insulating support. Diffusion controlled ion transport prevailed in this case and the profile started as an ellipsoid then approached shape of a hemisphere for a round opening or hemicylinder for a slot opening on the mask. Mass transfer mechanism dominated in a very thin resist opening. With a resist thickness of 8% of an opening, the etched profile varied along the center to underneath a mask and the deepest

part was found near the mask edge due to the highest current distribution location. The etch factor varied from 1.45–1.8 depending on the mask opening. Experimental data for 304 stainless steel etched with a DC current density of 3 A cm^{-2} agreed with the simulation data. Similar semi spherical profiles were reported when ECM of titanium in NaBr, HF solutions, or mixture of H_2SO_4 and methanol solution using DC voltages in the range 2–8 V.[137]

Few researchers used high-frequency pulsed DC instead of DC current to investigate the ECM profiles. Kenney and Hwang[138] modeled an ECM cell as RC circuit to study the current response and distribution when using ultrashort pulses (50 ns on-time, 450 ns off-time). The polarization voltage was constant under the electrode, but then tapered away from the edge as predicted due to the exponential decay as seen in the Tafel equation. Assuming a Ø10 μm cylindrical tool advancing into the workpiece, an electrolyte with resistivity of 70 Ωcm, and a substrate double layer capacity of 10 μF cm^{-2}, the simulated hole profile was flat at the bottom, but with tapered side walls and rounded corners at the entrance and bottom. Pulsed DC was also applied to form micro arrays on 304 stainless steel.[139] Square pulses (50–500 kHz, 50% duty cycles) were applied to the system to produce currents in the range 100–400 mA. The cylindrical electrode was surrounded and submerged in a column of electrolyte (30 g L^{-1} or 0.35 M $NaNO_3$) flowing at a constant flow rate of 143 mL min^{-1}. The undercut (under a mask) was significant below the electrode center, but its magnitude reduced linearly and practically none at a distance of three electrode radius away. Kozak *et al.*[140] applied ultrashort pulses of 0.005 ms–5 ns (0.2 MHz–0.2 GHz) on tool steel and 440 stainless steel under 10% $NaNO_3$ electrolyte. Profiles of ECM micro slots, holes, grooves were affected not only by the electrical parameters but also the flow direction of electrolyte. Since the profile slope was proportional to current density of the electrode, a low voltage (resulting in low current and current density) and small electrode gap were recommended for sharper profiles. Similar results were also experimentally verified, i.e., high-frequency ECM improved the profile shapes and surface finish but at lower MRRs.[141,142]

1.11.6.2 Micro/Nano Polishing

The ECM process can be modified to polish a surface. Such electrochemical polishing (ECP) technique was demonstrated to effectively polish channels that were micromilled on 316L and titanium plates. Mirror-like microchannels were resulted from polishing in an alcohol-based electrolyte at two-level current densities. The differences in crystalline orientations, etching rates on each grain, and impurities in grain boundaries contributed to variance in surface finish data; the average surface finish of polished specimens was about 300 nm on a large polycrystalline surface, and few nanometers within a single grain.[143] **Figure 19** below shows the grain boundary between two adjacent titanium grains after ECP. It is obvious that the polishing rate depends on crystalline orientation on each grain.

1.11.6.3 Deburring

Deburring is another application of ECM. Consider a string of burr along the edge of a machined surface, a burr is modeled as an absolute sine wave. The total volume of burr can be shown to be:

$$V_L = \frac{bL}{D}\frac{\pi h^2}{2}\int_0^{P/2}\sin^2\left(\frac{2\pi x}{P}\right)dx \qquad [2]$$

where

V_L: burr volume along a length L,
b: number of burrs under the tool,
D: electrode diameter,
h: maximum burr height,
P: burr period.

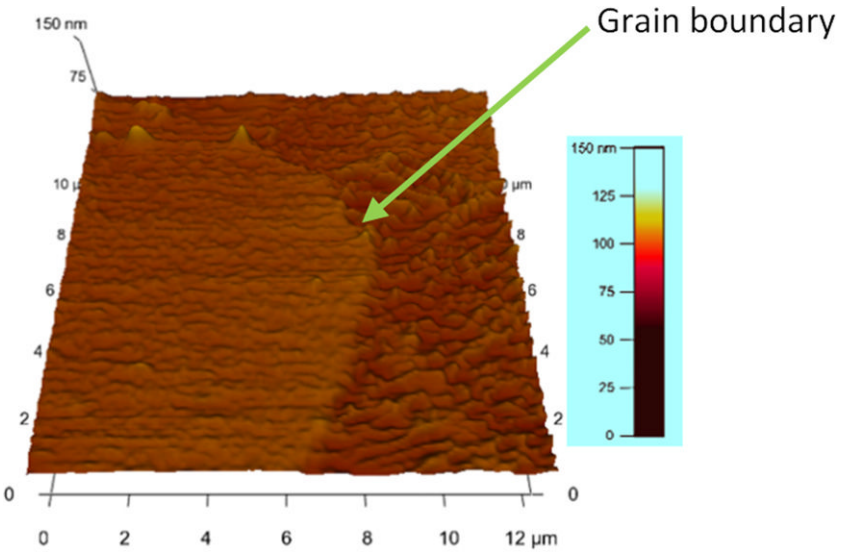


Figure 19 Atomic force microscopic image of adjacent polished titanium grains. 12 × 12 μm area, surface finish 42 nm R_{rms} across grains, and 1–10 nm R_{rms} within a grain.[143]

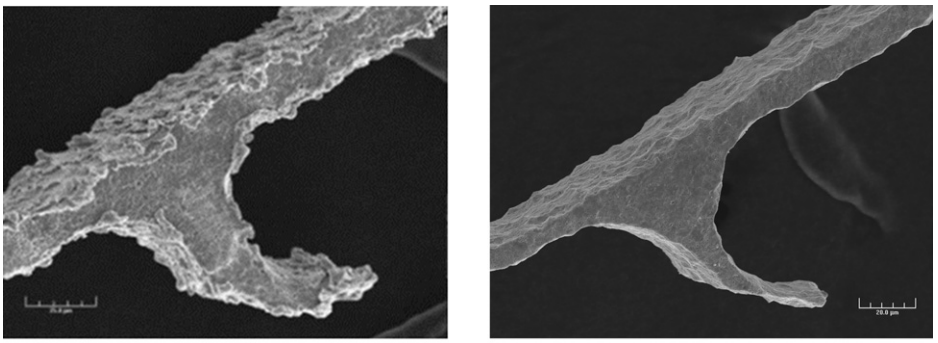


Figure 20 Copper alloy microcomponent (a) after EDM and before ECM, and (b) after ECM deburring using 0.5 mm diameter electrode, 50 KHz, and sodium based electrolyte.

The ECM process removes a volume of material in a single pulse according to Faraday's and Ohm's laws:

$$V_u = \int_0^{\tau} \frac{CEA\mathrm{d}t}{gr} \quad [3]$$

$$C = \frac{100}{F\sum_i \left(\frac{x_i z_i}{A_i}\right) \frac{100}{\sum_i \left(\frac{x_i}{\rho_i}\right)}} \quad [4]$$

where

V_u: volume of burr removed by a single pulse,
F: Faraday's constant = 96,500 C mol $^{-1}$,
E: voltage,
A: electrode area,
A_i : atomic weight of element i,
t: time,
g: interelectrode gap,
r: electrolyte resistivity,
x_i: element percentage,
ρ_i: density of element i,
τ: pulse on-time.

MRR for each pulse is simply:

$$MRR = \frac{V_u}{\tau} \quad [5]$$

Polishing time can be estimated by calculating the number of pulses and pulse frequency. The number of pulses to remove burrs along a distance L is:

$$N = \frac{V_L}{V_u} \quad [6]$$

Figure 20 compares a micropart before and after deburring by ECM. In fact, ECM is the only technique that can effectively remove burrs on micropart. It would be a challenge, however, when the part has internal burr that cannot be accessed with an electrode.

1.11.7 Summary

Micromachining techniques play an important role in product miniaturization. This chapter presents common micromachining techniques for semiconducting materials (bulk and surface micromachining) and for engineering materials (traditional and nontraditional micromachining).

The bulk micromachining can produce structures inside a substrate while surface micromachining can fabricate structural thin films on a sacrificial layer for semiconducting industry.

The tool based traditional processes (micromilling and microdrilling) and nontraditional processes (micro EDM, micro ECM, ion/electron/laser beam), degenerated from macroscale machining processes, are more popular to produce microcomponents in aerospace, transportation, oil & gas, and medical industries. The combination of these techniques not only allows fabrication of a single component, but also fabrication of microtools, microscale mold/die for mass producing of other microcomponents.

Although micromachining methods have been developed, a rapid implementation of micromanufacturing techniques, however, is hindered by lack of metrology and assembling techniques to effectively provide feedback to the fabrication line.

See also: 1.5 Robotic Polishing and Deburring. 1.9 Effect of Electrical Discharge Energy on White Layer Thickness of WEDM Process

References

1. Aramcharoen, A.; Mativenga, P. T.; Yang, S.; Cooke, K. E.; Teer, D. G. Evaluation and Selection of Hard Coatings for Micromilling of Hardened Tool Steel. *Int. J. Mach. Tool. Manuf.* **2008**, *48* (14), 1578–1584.
2. Venugopal, G.; Saini, S.; Kim, S. J. Focused Ion Beam Based Three-Dimensional Nano-Machining. In *Micromachining Techniques for Fabrication of Micro and Nano Structures*; Mojtaba Kahrizi, Ed.; InTech: Rijeka, Croatia, 2012; pp. 1–16 (Open access book), ISBN: 978-953-307-906-6.
3. Huo, D.; Cheng, K. Overview of Microcutting. *Micro-Cutting: Fundamentals and Applications*; John Wiley & Sons: Chichester, 2013; pp. 1–17.
4. Brinksmeier, E.; Glabe, R.; Riemer, O.; Twardy, S. Potentials of Presicion Machining Processes for the Manufacture of Micro Forming Molds. *Microsyst. Technol.* **2008**, *14* (12), 1983–1987.
5. Piljek, P.; Keran, Z.; Math, M. Micromachining – Review of Literature from 1980 to 2010. *Interdiscipl. Descr. Complex Syst.* **2014**, *12* (1), 1–27.
6. Fang, F. Z.; Liu, K.; Kurfess, T. R.; Lim, G. C. Tool-Based Micromachining and Applications in MEMS. In *MEMS/NEMS Handbook Techniques and Applications*; Leondes, C. T., Ed.; Springer: New York, NY, 2006; pp. 678–740, ISBN: 978-0-387-25786-0.

7. Ali, M. Y.; Karim, A. N. M.; Adesta, E. Y. T.; Ismail, A. F.; Abdullah, A. A.; Idris, M. N. Comparative Study of Conventional and Micro WEDM Based on Machining of Meso/Microsized Spur Gear. *Int. J. Precis. Eng. Manuf.* **2010**, *11* (5), 779–984.
8. Chern, G. L.; Wu, Y. J. E.; Cheng, J. C.; Yao, J. C. Study on Burr Formation in Micro-Machining Using Micro-Tools Fabricated by Micro-EDM. *Precis. Eng.* **2007**, *31* (2), 122–129.
9. Ali, M. Y. Fabrication of Microfluidic Channel Using Micro End Milling and Micro Electrical Discharge Milling. *Int. J. Mech. Mater. Eng.* **2009**, *4* (1), 93–97.
10. Popov, K.; Dimov, S.; Pham, D. T.; Ivanov, A. Micromilling Strategies for Machining Thin Features. *Proc. Inst. Mech. Eng., Part C: J. Mech. Eng. Sci.* **2006**, *220* (11), 1677–1684.
11. Araujo, A. C.; Mougo, A. L.; Campos, F. O. Micromilling Cutting Force on Machining Aluminium Alloy. In *8th International Conference Micromanufacturing* (*ICOMM 2013*), March, 2013.
12. Dornfeld, D.; Min, S.; Takeuchi, Y. Recent Advances in Mechanical Micromachining. *CIRP Ann. – Manuf. Technol.* **2006**, *55* (2), 745–768.
13. Bao, W. Y.; Tensel, I. N. Modeling Micro-End-Milling Operations Part I: Analytical Cutting Force Model. *Int. J. Mach. Tool. Manuf.* **2000**, *40* (15), 2155–2173.
14. Bao, W. Y.; Tensel, I. N. Modeling Micro-End-Milling Operations Part II: Tool Run-Out. *Int. J. Mach. Tool. Manuf.* **2000**, *40* (15), 2175–2192.
15. Bao, W. Y.; Tensel, I. N. Modeling Micro-End-Milling Operations Part III: Influence of Tool Wear. *Int. J. Mach. Tool. Manuf.* **2000**, *40* (15), 2193–2211.
16. Dhanoker, A.; Ozel, T. Meso/Micro Scale Milling for Micro-Manufacturing. *Int. J. Mechatron. Manuf. Syst.* **2008**, *1* (1), 23–42.
17. Ali, M. Y.; Khan, A. A.; Asharaf, A. B. M.; Wahab, A. A. Prediction of Minimum Chip Thickness in Tool Based Micro End Milling. *Int. J. Integr. Eng.* **2012**, *4* (1), 6–10.
18. Cardoso, P.; Davim, J. P. A Brief Review on Micromachining of Materials. *Rev. Adv. Mater. Sci.* **2012**, *30*, 98–102.
19. Vogler, M. P.; DeVor, R. E.; Kapoor, S. G. On the Modeling and Analysis of Machining Performance in Micro-Endmilling, Part I: Surface Generation. *J. Manuf. Sci. Eng.* **2004**, *126* (4), 685–694.
20. Ali, M. Y.; Mohamed, A. R.; Asfana, B.; Lutfi, M.; Fahmi, M. I. Investigation of Vibration and Surface Roughness in Micromilling of PMMA. *Appl. Mech. Mater.* **2012**, *217–219*, 2187–2193.
21. Miao, J. C.; Chen, G. L.; Lai, X. M.; Li, H. T.; Li, C. F. Review of Dynamic Issues in Micro-End-Milling. *Int. J. Adv. Manuf. Technol.* **2007**, *31* (9–10), 897–904.
22. Mehfuz, R.; Ali, M. Y. Surface Roughness Analysis of Beryllium–Copper Alloy in Micro End Milling. In *Proceedings of 7th International Conference on Mechanical Engineering ICME07-AM-07*, Dhaka, Bangladesh, December 29–31, 2007.
23. Liu, X.; Jun, M. B. G.; DeVor, R. E.; Kapoor, S. G. Cutting Mechanisms and Their Influence on Dynamic Forces, Vibrations and Stability in Micro-End-Milling. In *Proceedings of the ASME International Mechanical Engineering Congress and Exposition* (*IMECHE 2004*); Anaheim, CA: ASME Manufacturing Engineering Division, 2004.
24. Berestovskyi, D.; Hung, N. P.; Lomeli, P. Surface Finish of Ball-End Milled Microchannels. *J. Micro Nano-Manuf.* **2014**, *2*, 0411005.1–0411005.10.
25. Ali, M. Y.; Mohamed, A. R.; Khan, A. A.; Asfana, B.; Lutfi, M.; Fahmi, M. I. Empirical Modelling of Vibration in Micro End Milling of PMMA. *World Appl. Sci. J. (Math. Appl. Eng.)* **2013**, *21*, 73–78.
26. Filiz, S.; Ozdoganlar, O. B. A Three-Dimensional Model for the Dynamics of Micro-Endmills Including Bending, Torsional and Axial Vibrations. *Precis. Eng.* **2011**, *35* (1), 24–37.
27. Hsieh, W. H.; Lu, M. C.; Chiou, S. J. Application of Backpropagation Neural Network for Spindle Vibration-Based Tool Wear Monitoring in Micro-Milling. *Int. J. Adv. Manuf. Technol.* **2012**, *61* (1–4), 53–61.
28. Kim, C. J. *Mechanisms of Chip Formation and Cutting Dynamics in the Micro-Scale Milling Process* (Ph.D dissertation); Ann Arbor, MI: University of Michigan, 2004.
29. Ueng, H. Y.; Guo, C. T.; Dittrich, K. H. Development of a Hybrid Coating Process for Deposition of Diamond-Like Carbon Films on Microdrills. *Surf. Coat. Technol.* **2006**, *200* (9), 2900–2908.
30. Tansel, I. N. Monitoring Micro-Drilling Operations Using Neural Networks. *Key Eng. Mater.* **1998**, *138–140*, 575–592.
31. Imran, M.; Mativenga, P.; Kannan, S.; Novovic, D. An Experimental Investigation of Deep-Hole Microdrilling Capability for a Nickel-Based Superalloy. *J. Eng. Manuf.* **2008**, *222* (12), 1589–1596.
32. Cheong, M. S.; Cho, D. W.; Ehmann, K. F. Identification and Control for Micro-Drilling Control and Productivity Enhancement. *J. Mach. Tool. Manuf.* **1999**, *39* (1), 1539–1561.
33. Kudla, L. A. Fracture Phenomena of Microdrills in Static and Dynamic Conditions. *Eng. Fract. Mech.* **2011**, *78* (1), 1–12.
34. Mohanty, S.; Wells S.; Hung N. P. Microdrilling of Biocompatible Materials. In *Proceedings of International Mechanical Engineering Congress & Exposition* (*IMECE2012–87523*), Houston, TX; 2012.
35. Marksberry, P. W.; Jawahir, L. S. A Comprehensive Tool-Wear/Tool-Life Performance Model in the Evaluation of NDM (Near Dry Machining) for Sustainable Manufacturing. *J. Mach. Tool. Manuf.* **2008**, *48* (7–8), 878–886.
36. Sun, J.; Wong, Y. S.; Rahman, M.; Wang, Z. G.; Neo, K. S. Effects of Coolant Supply Methods and Cutting Conditions on Tool Life in End Milling Titanium Alloy. *Mach. Sci. Technol.* **2006**, *10* (3), 335–370.
37. Rahman, M.; Kumar, A. S.; Salam, M. U. Evaluation of Minimal Quantities of Lubricant in End Milling. *Int. J. Adv. Manuf. Technol.* **2001**, *18* (4), 235–241.
38. Park, K. H.; Olortegui-Yume, J.; Yoon, M. C.; Kwon, P. A Study on Droplets and Their Distribution for Minimum Quantity Lubrication. *J. Mach. Tool. Manuf.* **2010**, *50* (9), 824–833.
39. Kajaria, S.; Chittipolu, S.; Adera, S.; Hung, N. P. Micromilling in Minimum Quantity Lubrication. *Mach. Sci. Technol.* **2012**, *16* (4), 524–546.
40. Lunardelli, A.; Wentz, J. E. Computational Fluid Dynamic Analysis of Eccentric Atomization Spray Cooling Nozzle Designs for Micromachining. *J. Micro Nano-Manuf.* **2014**, *2*, 1–10.
41. Rahman, M.; Senthil, K. A.; Salam, M. U. Experimental Evaluation on the Effect of Minimal Quantities of Lubricant in Milling. *J. Mach. Tool. Manuf.* **2002**, *42* (5), 539–547.
42. Liao, Y. S.; Lin, H. M.; Chen, Y. C. Feasibility Study of the Minimum Quantity Lubrication in High-Speed End Milling of NAK80 Hardened Steel by Coated Carbide Tool. *J. Mach. Tool. Manuf.* **2007**, *47* (11), 1167–1676.
43. Diakodimitris, C.; Iskandar, Y.; Hendrick, P.; Slangen, P. New Approach of Gas–Liquid Computational Fluid Dynamics Simulations for the Study of Minimum Quantity Cooling with Airblast Plain-Jet Injectors. *J. Manuf. Sci. Eng.* **2013**, *135*, 041009.1–041009.9.
44. Kamata, Y.; Obikawa, T.; Shinozuka, J. Analysis of Mist Flow in MQL Cutting. *Key Eng. Mater.* **2004**, *257–258*, 339–344.
45. Li, Q.; Krell, J.; Alvarado, J.; Lerma, I.; Edinbarough, I.; Hung, W. N. P. Characterization of Micromist for Effective Machining. In *Proceedings of International Mechanical Engineering Congress and Exposition, IMECE2015–53632*; Houston, TX: ASME, 2015.
46. Berestovskyi, D. V. *Surface Finish Modeling in Micromilling of Biocompatible Materials* (Thesis); Texas: Texas A&M University, 2013.
47. McGrath, W. R.; Walker, C.; Yap, M.; Tai, T. C. Silicon Micromachined Waveguides for Milimeter-Wave and Submilimeter-Wave Frequencies. *IEEE Microw. Guided Wave Lett.* **1993**, *3* (3), 61–63.
48. Kahrizi, M., Ed. *Micromachining Techniques for Fabrication of Micro and Nano Structures*; InTech: Rijeka, Croatia, 2012 (Open access book).
49. Ziaie, B.; Baldi, A.; Atashbar, M. Z. Introduction to Micro-/Nanofabrication. *Springer Handbook of Nanotechnology*; Springer: Berlin, Heidelberg, 2010; pp. 231–269.
50. Hoffmann, M.; Voges, E. Bulk Silicon Micromachining for MEMS in Optical Communication Systems. *J. Micromech. Microeng.* **2002**, *12* (4), 349–360.
51. Kovacs, G. T.; Maluf, N. I.; Petersen, K. E. Bulk Micromachining of Silicon. *Proc. IEEE* **1998**, *86* (8), 1536–1551.
52. Gentili, E.; Tabaglio, L.; Aggogeri, F. Review on Micromachining Techniques. Springer: Vienna, 2005; pp. 387–396.
53. Hubbard, T. J. *MEMS Design: The Geometry of Silicon Micromachining* (Ph.D Dissertation), Pasadena, CA: California Institute of Technology, 1994.
54. Dennis, J. O.; Ahmad, F.; Khir, M. H. CMOS Compatible Bulk Micromachining. In *Advances in Micro/Nano Electromechanical Systems and Fabrication Technologies*; Takahata, Kenichi, Ed.; InTech: Rijeka, Croatia, 2013; pp. 119–138 (Open access book), ISBN: 978-953-51-1085-9.
55. Akin, T. Silicon Micromachining and Microfabrication Techniques for Integrated Sensor and Actuator Systems. In *Electrotechnical Conference, Proceedings of 7th Mediterranean*; IEEE, April 1994; pp. 529–532.
56. Linder, V.; Gates, B. D.; Ryan, D.; Parviz, B. A.; Whitesides, G. M. Water-Soluble Sacrificial Layers for Surface Micromachining. *Small* **2005**, *1* (7), 730–736.
57. Sandia. Sandia National Laboratories. Available from: http://www.sandia.gov/media/NewsRel/NR1999/layer.htm, 2015. (accessed August 4, 2015).
58. Fedder, G. K. MEMS Fabrication. In *Proceedings of the IEEE International Test Conference* (*ITC'03*), Charlotte, NC, September, 2003.

59. Ting, H. T.; Abou-El-Hossein, K. A.; Chua, H. B. Review of Micromachining of Ceramics by Etching. *Trans. Nonferr. Metals Soc.* **2009**, *19*, s1–s16.
60. Atiqah, N.; Jaafar, I. H.; Ali, M. Y.; Asfana, B. Application of Focused Ion Beam Micromachining: A Review. *Adv. Mater. Res.* **2012**, *576*, 507–510.
61. Ali, M. Y.; Loo, Y. W. Geometrical Integrity of Micromold Cavity Sputtered by FIB using Multilayer Slicing Approach. *Microsyst. Technol.* **2007**, *13*, 103–107.
62. Hajar, N.; Ali, M. Y. Investigation of Microholes Produced by Focused Ion Beam Micromachining. *Adv. Mater. Res.* **2011**, *264–265*, 1346–1351.
63. Stevie, F. A.; Giannuzzi, L. A.; Prenitzer, B. I. The focused Ion Beam Instrument. In *Introduction of Focused Ion Beams*; Giannuzzi, L. A., Stevie, F. A., Eds.; Springer: New York, NY, 2005; pp. 1–12.
64. Kaito, T. Three Dimensional Nanofabrication Using Focused Ion Beams. In *Introduction to Focused Ion Beam*; Giannuzzi, L. A., Stevie, F. A., Eds.; Springer: New York, NY, 2005; pp. 73–86.
65. Karl-Heinz, L.; Koch, H.; Otto, A.; Maaz, A.; Löwer, T.; Schmidt, M. Numerical Simulation of Drilling with Pulsed Beams. *Phys. Procedia* **2012**, *39*, 881–892.
66. Spinney, P. S.; Howitt, D. G.; Smith, R. L.; Collins, S. D. Nanopore Formation by Low-Energy Focused Electron Beam Machining. *Nanotechnology* **2010**, *21*, 1–7, 375301.
67. Schubert, A.; Zeidler, H. Machining of Nonconductive ZrO_2 Ceramics with Micro-EDM. In *Proceedings of the 9th International Conference of the European Society for Precision Engineering and Nanotechnology*; Van Brussel, H.; Brinksmeier, E.; Spaan, H., Eds; Euspen: Cranfield, 2009; pp. 6–9. ISBN: 978-0-9553082-6-0.
68. Chen, Y. F.; Lin, Y. C.; Chen, S. L.; Hsu, L. R. Optimization of Electrodischarge Machining Parameters on ZrO_2 Ceramic Using the Taguchi Method. *J. Eng. Manuf.* **2009**, *224*, 195–205.
69. Chung, D. K.; Shin, H. S.; Park, M. S.; Chu, C. N. Machining Characteristics of Micro EDM in Water Using High Frequency Bipolar Pulse. *Int. J. Precis. Eng. Manuf.* **2011**, *12* (2), 195–201.
70. Ali, M. Y.; Hung, W.; Yongqi, F. A Review of Focused Ion Beam Sputtering. *Int. J. Precis. Eng. Manuf.* **2010**, *11* (1), 157–170.
71. Abbas, N. M.; Solomon, D. G.; Bahari, M. F. A Review on Current Research Trends in Electrical Discharge Machining (EDM). *Int. J. Mach. Tool. Manuf.* **2006**, *47*, 1214–1228.
72. Mohri, N.; Fukusima, Y.; Fukuzawa, Y.; Tani, T.; Sato, N. Layer Generation Process on Work-Piece in Electrical Discharge Machining. *CIRP Ann. – Manuf. Technol.* **2003**, *52* (1), 157–160.
73. Mohri, N.; Fukuzawa, Y.; Tani., T.; Saito, N.; Furutani, K. Assisting Electrode Method for Machining Insulating Ceramics. *Ann. CIRP* **1996**, *45*, 201–204.
74. Mahardika, M.; Tsujimoto, T.; Mitsui, K. A New Approach on the Determination of Ease of Machining by EDM Processes. *Int. J. Mach. Tool. Manuf.* **2008**, *48*, 746–760.
75. Schubert, A.; Zeidler, H.; Hackert, M.; Schneider, J.; Hahn, M. Enhancing Micro-Edm using Ultrasonic Vibration and Approaches for Machining of Nonconducting Ceramics. *J. Mech. Eng.* **2013**, *59* (3), 156–164.
76. Jahan, M. P.; Wong, Y. S.; Rahman, M. A Study on the Quality Micro-Hole Machining of Tungsten Carbide by Micro-EDM Process using Transistor and RC-Type Pulse Generator. *J. Mater. Process. Technol.* **2009**, *209*, 1706–1716.
77. Masuzawa, T. State of the Art of Micromachining. *CIRP Ann. – Manuf. Technol.* **2000**, *49* (2), 473–488.
78. Ho, K. H.; Newman, S. T. State of the Art Electrical Discharge Machining (EDM). *Int. J. Mach. Tool. Manuf.* **2003**, *43*, 1287–1300.
79. Muttamara, A.; Janmanee, P.; Fukuzawa, Y. A Study of Micro-EDM on Silicon Nitride Using Electrode Materials. *Int. Trans. J. Eng., Manag. Appl. Sci. Technol.* **2010**, *1* (1), 001–007.
80. Singh, S.; Bhardwaj, A. Review to EDM by Using Water and Powder-Mixed Dielectric Fluid. *J. Min. Mater. Charact. Eng.* **2011**, *10* (2), 199–230.
81. Chow, H. M.; Yang, L. D.; Lin, C. T.; Chen, Y. F. The Use of Sic Powder in Water as Dielectric for Micro-Slit EDM Machining. *J. Mater. Process. Technol.* **2008**, *195* (1–3), 160–170.
82. Khan, A. A. Role of Heat Transfer on Process Characteristics During Electrical Discharge Machining. In *Developments in Heat Transfer*; dos Santos Bernandes, Marco Aurelio, Ed.; InTech: Rijeka, Croatia, 2011; pp. 417–436 (Open access book), ISBN: 978-953-307-569-3.
83. Pecas, P.; Henriques, E. Electrical Discharge Machining using Simple and Powder-Mixed Dielectric: The Effect of the Electrode Area in the Surface Roughness and Topography. *J. Mater. Process. Technol.* **2008**, *200*, 250–258.
84. Schubert, A.; Ziedler, H.; Wolf, N.; Hackert, M. Micro Electro Discharge Machining of Electrically Nonconductive Ceramics. *AIP Conf. Proc.* **2011**, *1353* (1), 1303–1308.
85. Das, S.; Joshi, S. S. Modeling of Spark Erosion Rate in Microwire-EDM. *Int. J. Adv. Manuf. Technol.* **2010**, *48* (5–8), 581–596.
86. Dhanik, S.; Joshi, S. S. Modelling of a Single Resistance Capacitance Pulse Discharge in Micro-Electro Discharge Machining. *J. Manuf. Sci. Eng.* **2005**, *127* (4), 759–767.
87. Mehfuz, R.; Ali, M. Y. Investigation of Machining Parameters for the Multiple-Response Optimization of Micro Electrodischarge Milling. *Int. J. Adv. Manuf. Technol.* **2009**, *43*, 264–275.
88. Ali, M. Y.; Mohammad, A. S. Experimental Study of Conventional Wire Electrical Discharge Machining for Microfabrication. *Mater. Manuf. Proc.* **2008**, *23*, 641–645.
89. Carden, R. A. A Changing Direction in Dentistry: Full-Countour Zirconia. *J. Dent. Technol.* **2011**, 14–16.
90. Chevalier, J.; Gremillard, L. Ceramics for Medical Applications: A Picture for the Next 20 Years. *J. Eur. Ceram. Soc.* **2009**, *29*, 1245–1255.
91. Hosel, T.; Cvancara, T.; Ganz, T.; Muller, C.; Reinecke, H. Characterization of High Aspect Ratio Non-Conductive Ceramic Microstructures Made by Spark Erosion. *Microsyst. Technol.* **2011**, *17*, 313–318.
92. Hosel, T.; Muller, C.; Reinecke, H. Spark Erosive Structuring of Electrically Nonconductive Zirconia with an Assisting Electrode. *CIRP J. Manuf. Sci. Technol.* **2011**, *4*, 357–361.
93. Mehta, D.; Shetty, R. Bonding to Zirconia: Elucidating the Confusion. *Int. Dent. SA* **2010**, *12* (2), 46–52.
94. Mohri, N.; Fukuzawa, Y.; Tani, T.; Sata, T. Some Considerations to Machining Characteristics of Insulating Ceramics – Towards Practical Use in Industry. *Ann. CIRP* **1991**, *51* (1), 161–164.
95. Kucukturk, G.; Cogun, C. A New Method for Machining of Electrically Nonconductive Workpieces Using Electrical Discharge Machining Technique. *Mach. Sci. Technol.* **2010**, *14*, 189–207.
96. Ji, R; Liu, Y; Zhang, Y; Wang, F.; Chen, Z.; Dong, X. Study on Single-Discharge Machining Characteristics of Non-Conductive Engineering Ceramics in Emulsion with High Open Voltage and Large Capacitor. *J. Eng. Manuf.* **2011**, *225* (10), 1888–1898.
97. Liu, Y. H.; Ji, R. J.; Li, X. P.; Yu, L. L.; Zhang, H. F.; Li, Q. Y. Effect of Machining Fluid on the Process Performance of Electric Discharge Milling of Insulating Al_2O_3 Ceramic. *Int. J. Mach. Tool. Manuf.* **2008**, *48* (9), 1030–1035.
98. Liu, Y. H.; Li, X. P.; Ji, R. J.; Yu, L. L.; Zhang, H. F.; Li, Q. Y. Effect of Technological Parameter on the Process Performance for Electric Discharge Milling of Insulating Al_2O_3 Ceramic. *J. Mater. Process. Technol.* **2008**, *208*, 245–250.
99. Banu, A.; Ali, M. Y.; Rahman, M. A. Micro-Electro Discharge Machining of Non-Conductive Zirconia Ceramic: Investigation of MRR and Recast Layer. *Int. J. Adv. Manuf. Technol.* **2014**, *75*, 257–267.
100. Guo, Y. F.; Deng, G. Q.; Bai, J. C.; Lu, Z. S. Electrical Discharge Machining (EDM) Phenomena of Insulating ZrO_2 Ceramics with Assisting Electrode. *Key Eng. Mater.* **2008**, *375–376*, 313–317.
101. Muttamara, A.; Fukuzawa, Y.; Mohri, N.; Tani, T. Effect of Electrode Material on Electrical Discharge Machining of Alumina. *J. Mater. Process. Technol.* **2009**, *209*, 2545–2552.
102. Fukuzawa, Y.; Mohri, N.; Tani, T.; Muttamara, A. Electrical Discharge Machining Properties of Noble Crystals. *J. Mater. Process. Technol.* **2004**, *149*, 393–397.
103. Muttamara, A.; Fukuzawa, Y.; Mohri, N.; Tani, T. Probability of Precision Micro-Machining of Insulating Si_3N_4 Ceramics by EDM. *J. Mater. Process. Technol.* **2003**, *140*, 243–247.
104. Tani, T.; Fukuzawa, Y.; Mohri, N.; Saito, N.; Okada, M. Machining Phenomena in WEDM of Insulating Ceramics. *J. Mater. Process. Technol.* **2004**, *149*, 124–128.
105. Puertas, I.; Luis, C. J. A Study on the Electrical Discharge Machining of Conductive Ceramics. *J. Mater. Process. Technol.* **2004**, *153–154*, 1033–1038.
106. Yilmaz, H.; Aydin, C.; Gul, B. E. Flexural Strength and Fracture Toughness of Dental Core Ceramics. *J. Prosthet. Dent.* **2007**, *98* (2), 120–128.
107. Komine, F.; Blatz, M. B.; Matsumura, H. Current Status of Zirconia-Based Fixed Restorations. *J. Oral Sci.* **2010**, *52* (4), 531–539.
108. Sabur, A.; Moudood, A.; Ali, M. Y.; Maleque, M. A. Effect of Micro-EDM Parameters on Material Removal Rate of Nonconductive ZrO_2 Ceramic. *Appl. Mech. Mater.* **2014**, *465–466*, 1329–1333.
109. Salonitis, K.; Stournaras, A.; Stavropoulos, P.; Chryssolouris, G. Thermal Modelling of the Material Removal Rate and Surface Roughness for Die-Sinking EDM. *Int. J. Adv. Manuf. Technol.* **2009**, *40*, 316–323.

110. Moudood, M. A.; Sabur, A.; Ali, M. Y.; Jaafar, I. H. Effect of Peak Current on Material Removal Rate for Electrical Discharge Machining of Non-Conductive Al_2O_3 Ceramic. *Adv. Mater. Res.* **2014**, *845*, 730–734.
111. Sabur, A.; Ali, M. Y.; Maleque, M. A. Modelling of Material Removal Rate in EDM of Nonconductive ZrO_2 Ceramic by Taguchi Method. *Appl. Mech. Mater.* **2013**, *393*, 246–252.
112. Sabur, A.; Ali, M. Y.; Maleque, M. A.; Khan, A. A. Investigation of Material Removal Characteristics in EDM of Nonconductive ZrO_2 Ceramic. *Procedia Eng.* **2013**, *56*, 696–701.
113. Fukuzawa, Y.; Mohri, N.; Gotoh, H.; Tani, T. Three-Dimensional Machining of Insulating Ceramics Materials with Electrical Discharge Machining. *Trans. Nonferr. Metal. Soc.* **2009**, *19*, s150–s156.
114. Mohamed, A. R.; Asfana, B.; Ali, M. Y. Investigation of Recast Layer of Non-Conductive Ceramic Due to Micro-EDM. *Adv. Mater. Res.* **2014**, *845*, 857–861.
115. Somashekhar, K. P.; Ramachandran, N.; Mathew, J. Optimization of Material Removal Rate in Micro-EDM using Artificial Neural Network and Genetic Algorithms. *Mater. Manuf. Process* **2010**, *25*, 467–475.
116. Dave, H. K.; Desai, K. P.; Raval, H. K. Modelling and Analysis of Material Removal Rate During Electro Discharge Machining of Inconel 718 Under Orbital Tool Movement. *Int. J. Manuf. Syst.* **2012**, *2* (1), 12–20.
117. Pandey, A.; Singh, S. Current Research Trends in Variants of Electrical Discharge Machining: A Review. *Int. J. Eng. Sci. Technol.* **2010**, *2* (6), 2172–2191.
118. Muttamara, A.; Fukuzawa, Y.; Aursatitwong, K. Feasibility Study for Slit Machining Using EDM on Silicon Nitride. In *2nd International Conference on Mechanical, Production and Automobile Engineering* (*ICMPAE 2012*), Singapore, 2012.
119. Khan, D. A.; Hameedullah, M. Effect of Tool Polarity on the Machining Characteristics in Electrical Discharge Machining of Silver Steel and Statistical Modelling of the Process. *Int. J. Eng. Sci. Technol. (IJEST)* **2011**, *3* (6), 5001–5010.
120. Lauwers, B.; Kruth, J. P.; Liu, W.; Eeraerts, W.; Schacht, B.; Bleys, P. Investigation of Material Removal Mechanisms in EDM of Composite Ceramic Materials. *J. Mater. Process. Technol.* **2004**, *149*, 347–352.
121. Qu, J.; Shih, A. J.; Scattergood, R. O.; Luo, J. Abrasive Micro-Blasting to Improve Surface Integrity of Electrical Discharge Machined WC–Co Composite. *J. Mater. Process. Technol.* **2005**, *166*, 440–448.
122. Rao, G. K. M.; Satyanarayana, S.; Praveen, M. Influence of Machining Parameters on Electric Discharge Machining of Maraging Steels – An Experimental Investigation. In *Proceedings of the World Congress on Engineering, WCE-2008, Vol II*; 2008.
123. Cho, D. H.; Lee, S. A.; Lee, Y. Z. Mechanical Properties and Wear Behaviour of the White Layer. *Tribol. Lett.* **2012**, *45*, 123–129.
124. Ramasawmy, H.; Blunt, L. Effect of EDM Process Parameters on 3D Surface Topography. *J. Mater. Process. Technol.* **2004**, *148*, 155–164.
125. Bonny, K.; De Baets, P.; Vleugels, J.; *et al.* EDM Machinability and Frictional Behaviour of ZrO_2–WC Composites. *Int. J. Adv. Manuf. Technol.* **2009**, *41*, 1085–1093.
126. Iqbal, A. K. M. A.; Khan, A. A. Influence of Process Parameters on Electrical Discharge Machined Job Surface Integrity. *Am. J Eng. Appl. Sci.* **2010**, *3* (2), 396–402.
127. Sommer, C.; Sommer, S. Understanding the Wire EDM Process. In *Complete EDM Handbook*; Advance Publishing: Houston, TX, 2005; pp. 69–81, ISBN: 978-1-57537-302-7.
128. Zeng, Z.; Wang, Y.; Wang, Z.; Shan, D.; He, X. A Study of Micro-EDM and Micro-ECM Combined for 3D Metallic Micro-Structures. *Precis. Eng.* **2012**, *36*, 500–509.
129. Boujelbene, M.; Bayraktar, E.; Tebni, W.; Ben Salem, S. Influence of Machining Parameters on the Surface Integrity in Electrical Discharge Machining. *Arch. Mater. Sci. Eng.* **2009**, *37* (2), 110–116.
130. Grzesik, W.; Kruszynski, B.; Ruszaj, A. Surface Integrity of Machined Surfaces. In *Surface Integrity in Machining*; Paulo Davim, J, Ed.; Springer: London, 2010; pp. 143–179.
131. Mehta, S.; Rajurkar, A.; Chauhan, J. A Review on Current Research Trends in Die-Sinking Electrical Discharge Machining of Conductive Ceramics. *Int. J. Recent Trends Eng.* **2009**, *1* (5), 100–104.
132. Ekmekc, B. White Layer Composition, Heat Treatment, and Crack Formation in Electric Discharge Machining Process. *Metall. Mater. Trans. B* **2009**, *40* (1), 70–81.
133. Bhattacharyya, B.; Gangopadhyay, S.; Sarkar, B. R. Modelling and Analysis of EDMED Job Surface Integrity. *J. Mater. Process. Technol.* **2007**, *189* (1–3), 169–177.
134. Khan, A. A.; Mohammed, B. N.; Zain, Z. M.; Jamaludin, M. F.; Patthi, U. Surface Modification using Electric Discharge Machining (EDM) with Powder Addition. In *2nd International Conference on Mechanical, Industrial, and Manufacturing Technologies* (*MIMT 2011)*, Singapore, February 26–28, 2011a.
135. Rosset, E.; Landolt, D. Experimental Investigation of Shape Changes in Electrochemical Micromachining Through Photoresist Masks. *Precis. Eng.* **1989**, *11* (2), 79–82.
136. West, A. C. Shape Changes During Though-Mask Electrochemical Micromachining of Thin Metal Films. *J. Electrochem.* **1992**, *139* (2), 499–506.
137. Landolt, D.; Chauvy, P. F.; Zinger, O. Electrochemical Micromachining, Polishing and Surface Structuring of Metals: Fundamental Aspects and New Developments. *Electrochim. Acta* **2003**, *48* (20), 3185–3201.
138. Kenney, J. A.; Hwang, G. S. Two-Dimensional Computational Model for Electrochemical Micromachining with Ultrashort Voltage Pulses. *Appl. Phys. Lett.* **2004**, *84* (19), 3774–3776.
139. Hung, N. P.; Viswanatham, L.; Powers, M. Profile of Electrochemically Machined Microcomponents. *J. Min. Met. Mater. Soc. (Supp. Proc.)* **2011**, *3*, 325–332.
140. Kozak, J.; Rajurkar, K. P.; Makkar, Y. Selected Problems of Micro-Electrochemical Machining. *J. Mater. Process. Technol.* **2004**, *149*, 426–431.
141. Ozkeskin F.; Hung, N. P. Automatic Control of High Frequency Electrochemical Microsystem. In *Proceedings of 54th International Instrumentation Symposium*, Pensacola, FL, 2008.
142. Sundarram, S.; Powers, M.; Ozkeskin, F.; Manríquez, J.; Godínez, L.; Hung, N. P. Electrochemical Micromachining of Cu 2Be Alloy and 316L Stainless Steel. In *Proceedings SME, Micro/Nano Manufacturing Conference*, Massachusetts, 2008.
143. Hung, N. P.; Brock, D.; Xiao, H.; Lomeli, P.; Granda, E. Micromachining and Electrochemical Nanopolishing of Titanium Microchannels. *J. Manuf. Des. Sci.* **2015**, *2* (1), 1–10.

Relevant Websites

https://www.makino.com/machining-process/micromachining-process/
Makino.

http://www.mmsonline.com/zones/micro
Modern Machine Shop.

http://etidweb.tamu.edu/faculty/hung/index.html
Texas A&M University.

1.12 Laser Machining Processes

BS Yilbas, King Fahd University for Petroleum and Minerals, Dhahran, Saudi Arabia

© 2017 Elsevier Inc. All rights reserved.

1.12.1	**Introduction**	344
1.12.2	**Laser Drilling**	345
1.12.2.1	Experimental Method	347
1.12.2.2	Hole Quality Assessment	347
1.12.2.2.1	Evaluation of hole geometric features	347
1.12.2.2.2	Factorial analysis	348
1.12.2.2.2.1	Qualitative analysis	348
1.12.2.2.2.2	Quantitative analysis	348
1.12.3	**Laser Cutting Process**	348
1.12.3.1	Experimental Method	349
1.12.3.1.1	Thermal analysis	349
1.12.3.2	Lump Parameter Analysis for Kerf Size	351
1.12.3.3	Cut Quality Assessment	351
1.12.3.3.1	Evaluation of cut quality	351
1.12.3.3.2	Factorial analysis	351
1.12.4	**Laser Bending**	352
1.12.4.1	Experimental	352
1.12.4.2	Mathematical Analysis	352
1.12.5	**Results and Discussions**	354
1.12.5.1	Laser Drilling	354
1.12.5.1.1	Qualitative analysis	355
1.12.5.1.2	Quantitative analysis	357
1.12.5.2	Laser Cutting	357
1.12.5.3	Laser Bending	359
1.12.6	**Concluding Remarks**	362
Acknowledgments		363
References		363
Relevant Website		363

1.12.1 Introduction

Laser machining processes are the demanding focus areas of the materials and manufacturing disciplines. Lasers are considered to be the advanced material processing tools filling the gap in the advanced manufacturing systems because of their precision, low cost, localized processing, and high speed of operation. In laser machining applications, a laser beam is used as a heat source increasing temperature rapidly to the melting and evaporation temperature of the substrate material. Since the arrangements of the optical setting for the laser beam are very precise, the localized heating can be controlled easily. With recent advancement in laser technology and computations power, laser machining application has become almost an integral part of the aerospace, power, electronics, and sheet metal forming industries. However, in laser machining operations, the physical processes are complicated and they require deep understanding of process to secure improved end product quality.

Laser machining can be categorized into two groups based on the type of processing associated with the machining such as drilling, cutting, welding, alloying, and others. The laser processing can be involved with pre or posttreatment operations such as duplex treatment for coatings and scribing after coatings. In laser processing, material removal from the irradiated substrate material is critical to define the machining operation. For example, in laser drilling and cutting processes material removal from the irradiated region is essential to complete machining operation. On the other hand, laser-induced bending and laser annealing processes, control melting takes over the mass removal from the irradiated surface. However, laser welding falls in between these categories. Material removal is essential for deep penetration welding while control melting is necessary for thin substrate welding. In general, material removal and melting processes are involved with high intensity laser irradiation. Interaction of high intensity laser beam with solid surfaces results in evaporation at the surface. If the laser beam diameter at the irradiated surface is smaller than the thickness of the workpiece and the peak intensity is the highest at the irradiated spot center, one dimensional analysis for the surface evaporation becomes possible. In this case, the assumption of energy balance at the surface yields the steady analysis of the heating process, which provides useful information on temperature rise and the recession front velocity. On the other hand, the transient analysis gives detailed information on temperature raise in the irradiated region.

 doi:10.1016/B978-0-12-803581-8.09157-8

In machining applications, laser–workpiece interaction is involved with phase change at the irradiated surface; in which case, the substrate material undergoes a solid heating, melting, and subsequent evaporation at the surface. In the case of high intensity heating with short pulse durations, irradiated surface solid heating and melting takes place in a short duration and evaporation becomes the main phase change process at the surface. In addition, latent heat of melting is much smaller than enthalpy of evaporation, evaporation can be considered to be the major phase change mechanism at the irradiated surface. Allowance of existing of a vaporizing front requires that the temperature gradient at the surface be positive. Phase change process at the surface can be modeled analytically after considering the equilibrium heating situation at which the Fourier heating law is applicable. Laser-induced evaporation process is examined for different laser pulse types and they are given under the appropriate headings.

In order to optimize the laser machining process and reduce the experimental time and cost, the model studies receive considerable attention. In addition, the model studies give insight into the physical processes that take place during the heating process and being easier to accomplish as compared to experimental studies. The measurement of physical properties during laser–workpiece interaction is difficult and costly since, the process is involved with high temperature, short duration, and localized heating. From the modeling point of view, the laser machining can be classified into two categories: (1) laser conduction limited heating and (2) laser nonconduction limited heating. In the laser conduction limited heating situation, substrate surface is heated up to the melting temperature of the substrate material; in this case, substrate remains in the solid state during the process. One of the laser conduction limited applications is the laser quenching of the surfaces. In the laser nonconduction limited heating situation, substrate surface undergoes a phase change during the processing, i.e., melting and subsequent evaporation is resulted. The laser drilling, cutting, and welding are typical examples of laser nonconduction limited heating situation.

Laser drilling, cutting, welding, bending, and surface treatment processes have made significant headway into the well-established area of sheet metal industry. This is due to its low operational cost and high precision. When a high intensity laser is directed onto a metal surface, heating, melting, and evaporation of the substance occur, therefore, conduction, phase change, and convection processes are resulted. To enhance understanding of laser–workpiece interaction mechanism, the study into laser-induced heating and subsequent material removal initiating the laser drilling process is necessary. In industrial application of laser machining, the quality of machined parts is the important factor. The quality of the laser machined parts can be judged by geometric features of the machined sections such as internal form, taper, striations, dross attachments, and heat-affected zone. Consequently, the levels of the machining parameters resulting in geometries with small asperities, such as less taper, parallel-sided walls, small out of flatness, without forming striations, are needed to be identified. The laser and workpiece material parameters affecting the laser machining include laser output energy, pulse length and frequency, focus setting of focusing lens, ambient pressure, scanning speed, and workpiece thickness. The optimum performance in laser machining depends on the proper selection of these factors. However, with many variables and incomplete information of the relationship between them, a statistical method is fruitful to design an experiment and analyze the results accordingly. In addition, factorial experimental design methods are more secure basis and make the identification of controlling factors and interactions possible with reasonable accuracy.

In this chapter, in-depth understanding of laser machining processes, advantages, and limitations of the process parameters are to be presented. The main focus of laser machining is to cover the laser drilling, cutting, welding, and bending processes. Each of the processes is treated under the appropriate subheadings and the findings discussed in line with the previous studies.[1–7]

1.12.2 Laser Drilling

One of the important laser applications is the laser drilling. Laser drilling involves with solid heating, phase change (melting and subsequent evaporation), plasma formation, and vapor/melt ejection from the irradiated region. In laser drilling, laser pulses with millisecond pulse lengths are favorable because of the melt ejection from the irradiated surface. As the laser pulse reduces, melt ejection replaces with the surface evaporation and ablation. This is the case when the required drilled hole size becomes small and hole depth is shallow. In the present section, laser drilling into steel sheet is to be presented in line with the previous study.[1–3]

In laser drilling process one of the concerns is to reduce the drilling duration and minimize the geometric defects associated with the hole geometry. This situation was investigated by Yilbas.[9] He demonstrated that the increasing laser energy and locating the focus position slightly above the workpiece surface increased the mean hole diameter. Taneko *et al.*[8] examined laser hole drilling into electronic components and the findings revealed that the use of high peak pulsed CO_2 laser improved the drilling quality. The parametric analysis based on the statistical assessment of laser drilled hole quality was carried out by Yilbas.[9] He showed that main effects of laser drilling parameters and their interactions had significant effects on the hole geometry. A comprehensive study for the beam waist position and the hole formation in laser drilling process was introduced by Yilbas and Sami.[10] They demonstrated that altering the beam waist position resulted in converging and diverging hole walls for negative and positive positions, respectively. Furthermore, Yilbas[11] investigated the laser hole drilling into various metals. He showed that the parameter, almost for all cases, the most affecting parameter was the workpiece thickness.

In laser hole drilling process, thermal analysis provides useful information on the physical insight into the process. Since the heating is involved with melting and evaporation, the heat transfer analysis employing a phase change process in the region irradiated by a laser beam needs to be considered. However, when the laser–workpiece interaction time is comparable to the heating time of the substrate material (10 ps), the nonequilibrium energy transport dominates the heating process. The Fourier heating model over-estimates the lattice site temperature rise during the short interaction period. On

the other hand, as the duration of heating extends to nanoseconds or milliseconds, the equilibrium energy transport occurs inside the metallic substrates during the heating period. Consequently, the Fourier heating model becomes appropriate to describe the physical process that takes place during the nanosecond heating durations.

In most of the laser drilling applications, the laser beam power intensity can be approximated to a Gaussian profile. Therefore, in the analysis, a Gaussian power intensity distribution of a laser beam with its spot center at the center of the coordinate system is considered. This gives rise to an axisymmetric heating of the substrate material. As the temperature reaches the phase change temperatures of the substrate material during the heating process, the phase change is considered i.e., melting and subsequent evaporation of solid substrate should be introduced in the governing equation of heat transport with appropriate boundary conditions. During the solid heating (prior to the phase change), the conduction heating of the solid substrate with insulated boundary condition at the surface can be considered. This consideration minimizes the complication involved with the analysis. Therefore, the transient heat transfer equation for a solid substrate irradiated by a laser beam with a Gaussian intensity profile can be written as:

$$\rho_s Cp_s \frac{\partial T}{\partial t} = k_s \frac{\partial^2 T}{\partial z^2} + \frac{k_s}{r}\frac{\partial}{\partial r}\left(r\frac{\partial T}{\partial r}\right) + I_o(1-r_f)\delta \exp(-\delta z)\exp\left(-\frac{r^2}{a^2}\right) \quad [1]$$

where, I_o, δ, r_f, and 'a' are the laser peak power intensity, absorption coefficient, reflectivity, and the Gaussian parameter, respectively. The initial condition is:

At time $t \to 0$ $T(r,z,0) = T_o$ (specified)

The boundary conditions are

$$z = \infty \to T(r,\infty,t) = T_o$$
$$r = \infty \to T(\infty,z,t) = T_o$$
$$r = 0 \to \frac{\partial T(0,z,t)}{\partial r} = 0$$
$$z = 0 \to \frac{\partial T(r,0,t)}{\partial z} = 0$$

During the phase change process, it is assumed that the substrate material has single melting and boiling temperatures, i.e., when the substrate material reaches the melting or evaporation temperatures, the phase change takes place at a constant temperature. To describe the energy transfer during a phase change process, an energy or enthalpy methods can be used. In the case of enthalpy method, the governing equation of energy transport can be written in terms of enthalpy equation. Moreover, once the phase change occurs, a mushy zone (partially solid and partially liquid or partially liquid and partially vapor) is generated across the region where the phase change takes place. Consequently, when formulating the phase change problem, consideration is given for the generation of a mushy zone. In this case, during the phase change process, temperature of the substrate material remains same, but it's enthalpy changes. In order to formulate the problem the following approach is introduced, namely the energy method. Consider a differential element in a substrate material, which is subjected to a melting process and let x_m be the mass fraction of liquid present in the element, then the energy content ΔU of the differential element with volume ΔV at melting temperature T_m can be written as:

$$\Delta U = \rho_m \Delta V[x_m(L_m + Cp_m(T_m - T_{ref})) + Cp_s(1-x_m)(T_m - T_{ref})] \quad [2]$$

where

$$x_m = \frac{m_m}{m_m + m_s}$$

T_{ref}, x_m, m_m, m_s are reference temperature for enthalpy, quality of liquid, mass of liquid, and mass of solid in the element, respectively. After assuming specific heat of melt is the same as solid at melting temperature ($Cp_s = Cp_m$ at $T = T_m$), then above equation reduces to:

$$\Delta U = \rho_m \Delta V[x_m L_m + Cp_m(T_m - T_{ref})] \quad [3]$$

For a unit volume, it reduces to:

$$\frac{\Delta U}{\Delta V} = \Delta u = \rho_m\left[x_m L_m + Cp_m(T_m - T_{ref})\right] \quad [4]$$

Differentiation with time yields:

$$\frac{\partial u}{\partial t} = \rho_m L_m \frac{\partial x_m}{\partial t} \quad [5]$$

since $Cp_m(T_m - T_{ref})$ is constant.

Substituting eqn [5] into eqn [1] gives the energy equation for the differential element subjected to a phase change process:

$$\rho_m L_m \frac{\partial x}{\partial t} = k_m \frac{\partial^2 T}{\partial z^2} + \frac{k_m}{r}\frac{\partial}{\partial r}\left(r\frac{\partial T}{\partial r}\right) + I_o(1-r_f)\delta \exp(-\delta z)\exp\left(-\frac{r^2}{a^2}\right) \quad [6]$$

Equation [6] is applicable for the differential elements (cells defined by nodes in the substrate material) when temperature becomes the same as the melting temperature of the substrate material ($T = T_m$) and $x_m \le 1$, i.e., a mushy zone. Consequently, temperature of the cells with $0 \le x_m \le 1$ is set to the melting temperature ($T = T_m$). When the value of x_m exits 1 ($x_m > 1$) eqn [6] is not applicable for the differential element under consideration. In this case, eqn [1] is used to determine the temperature rise in the liquid heating with the liquid thermal properties employed, i.e., the liquid heating initiates and continues until the boiling point is reached.

When the boiling point is reached, the mushy zone consideration needs to be implemented. In this case, eqn [6] can be modified for a differential element, which is subjected to boiling, i.e.:

$$\rho_b L_b \frac{\partial x}{\partial t} = k_b \frac{\partial^2 T}{\partial z^2} + \frac{k_b}{r}\frac{\partial}{\partial r}\left(r\frac{\partial T}{\partial r}\right) + I_o(1-r_f)\delta \exp(-\delta z)\exp\left(-\frac{r^2}{a^2}\right) \quad [7]$$

Equation [7] is applicable for the range $T=T_b$ and $0\le x_b\le 1$ in the mushy zone (partially liquid partially vapor zone). Consequently, temperature of the cells with $0\le x_b\le 1$ is set to boiling temperature ($T=T_b$). It should be noted that x_m is replaced with x_b, which represents the fraction of vapor phase in the differential element.

The boundary condition at the evaporating surface is introduced in relation to eqn [7]. In this case, the temperature along the evaporated surface is kept at boiling temperature, i.e., the cells in the evaporated region are kept at boiling temperature, i.e.:

$$z=z_b\rightarrow T(r,z_b,t)=T_b$$

where z_b represents the axial location at the evaporated surface.

Equations [6] and [7] determine the relative position of solid–liquid and liquid–vapor interface in the substrate material. The liquid–vapor interface determines the shape and size of cavity generated after the evaporation process.

Equations [1], [6], and [7] can be made nondimensional through introducing the following dimensionless parameters:

$$r^*=r\delta : z^*=z\delta : a^*=a\delta; t^*=\alpha_i\delta^2 t : T^*=\frac{Tk_o\delta}{I_o}$$

where k_o represents the thermal conductivity at standard temperature. After introducing the dimensionless parameters, eqns [1], [6], and [7] yield:

$$\frac{\partial T^*}{\partial t^*}=\frac{\partial^2 T^*}{\partial z^{*2}}+\frac{\partial}{\partial r^*}\left(r^*\frac{\partial T^*}{\partial r^*}\right)+\exp(-z^*)\,\exp\left(-\frac{r^{*2}}{a^{*2}}\right) \quad [8]$$

$$\frac{\alpha_m\delta\rho_m L_m}{I_o}\frac{\partial x_m}{\partial t^*}=\frac{\partial^2 T^*}{\partial z^{*2}}+\frac{\partial}{\partial r^*}\left(r^*\frac{\partial T^*}{\partial r^*}\right)+\exp(-z^*)\,\exp\left(-\frac{r^{*2}}{a^{*2}}\right) \quad [9]$$

$$\frac{\alpha_b\delta\rho_b L_b}{I_o}\frac{\partial x_b}{\partial t^*}=\frac{\partial^2 T^*}{\partial z^2}+\frac{\partial}{\partial r^*}\left(r^*\frac{\partial T^*}{\partial r^*}\right)+\exp(-z^*)\,\exp\left(-\frac{r^{*2}}{a^{*2}}\right) \quad [10]$$

The initial and boundary conditions for eqns [8]–[10] are also nondimensionalized in a similar fashion.

Temperature distribution inside the substrate material is obtained solving the eqns [8]–[10] with the appropriate temperature ranges and boundary conditions.

1.12.2.1 Experimental Method

An Nd: YAG laser delivering energies in between 10–21 J within 1.48 ms pulses was used to irradiate the workpiece while nominal focal length of 51 mm lens was used to focus the laser beam on to the workpiece surface. The mode of laser beam was TEM_{00} and small variation in temporal distribution of the laser power intensity was observed after the each pulses. A vacuum cell was designed and was built to locate the workpiece and regulate the assisting ambient gas pressure during drilling. The optical microscopy and scanning electron microscopes are used to assess the geometry of the hole.

1.12.2.2 Hole Quality Assessment

The affecting parameters considered are laser output energy, focus setting of focusing lens, pressure of drilling ambient, and the workpiece thickness. The hole quality is assessed on the basis of rating the relevant features of the hole geometry. In this case, the hole geometry with minimum geometrical imperfections has received the highest score in the ranking scheme. A statistical analysis based on factorial design is introduced to determine the most effective parameters and level of their effects, i.e., factorial analysis for the quality assessment of the hole geometry.

1.12.2.2.1 Evaluation of hole geometric features

A schematic view of a typical laser drilled hole cross-section is shown in **Figure 1**. The hole geometry was described on the basis of seven features and judged overall by assigning to each feature a mark scored out of weighted maxima, and summing these scores. The features of the hole geometry and the marking scheme are listed below:

Resolidified material: Marks are assigned out of 10 according to the fraction of resolidified material to hole size, i.e., a score of 10 represents no solidification around the hole and 1 corresponds to resolidified material almost block the hole.
Taper: The taper angle, as shown in **Figure 1**, is measured without considering the inlet and exit cone angles. A mark of 0 indicates taper of 90° and 4 corresponds to a parallel-sided hole.
Barreling: The marks are assigned in between 0–4. A mark of 4 represents a straight hole while 0 indicates an even hole.
Inlet cone angle: It is measured as ratio of cone angle to 180°. A mark of 1 indicates no inlet cone and 0 corresponds to a cone angle of 180°.
Exit cone angle: In general, the exit cone is small in size and difficult to measure with accuracy. Therefore, marks are given through visual inspection and mark of 1 indicates no exit cone while 0 represents a large cone angle.

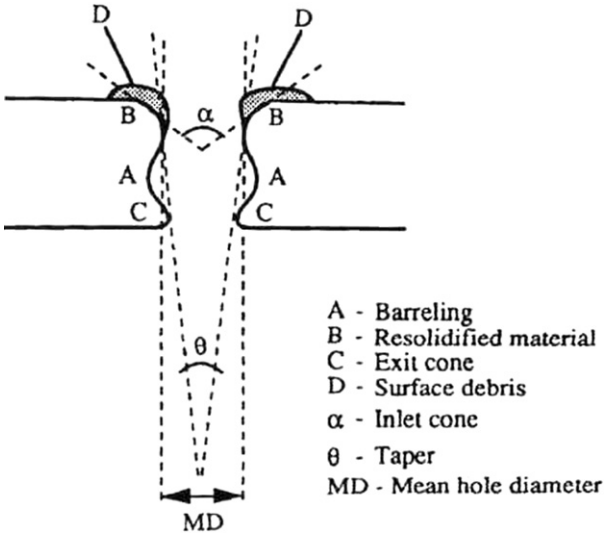


Figure 1 A schematic view of hole drilled.

Surface debris: This is assessed according to the amount of material resolidified at the surface of the workpiece near to the hole circumference. A mark of 1 is given with no or very small amount of surface debris and mark of 0 is assigned with large amount of surface debris.
Mean hole diameter: The mean hole diameter is measured under the microscope and the maximum value of mean hole diameter among all holes is considered and a mark of 3 is assigned. The minimum hole diameter is given a mark of 1.
Overall quality: The overall quality of the drilled hole is obtained summing the all marks assigned each hole feature, i.e.:

$$q = \mathrm{Re} + Ta + Ba + Ec + Ic + Sd \quad [11]$$

where q, Re, Ta, Ba, Ec, Ic, and Sd are marks of overall quality, resolidification, taper, barreling, exit cone, inlet cone, and surface debris, respectively. Moreover, for blank holes a mark of 3 is subtracted from the overall quality.

1.12.2.2.2 Factorial analysis

The qualitative and quantitative analyses are carried out. Four factors at four levels are considered, which are given in **Table 1**. The results and discussion related to the factorial analysis are given under the appropriate headings.

1.12.2.2.2.1 Qualitative analysis

The mathematical expression representing the factorial design can be expressed as:

$$X_{i,j,k,l} = P_i - F_j - E_k - T_l - P_iF_j - P_iE_k - P_iT_l - F_jE_k - F_jT_l - E_kT_l - P_iE_kF_j - P_iE_kT_l - F_jE_kT_l - \varepsilon_{ijkl} \quad [12]$$

where X_{ijkl} is the response (value given to the hole features), P_i, F_j, E_k, T_k are the main effects of pressure, focus settings, laser output energy, and workpiece thickness, P_iF_j, P_jE_k, P_iT_l, F_jE_k, F_jT_l, E_kT_l, $P_iE_kF_j$, $P_iE_kT_l$, $F_jE_kT_l$ are the first and second order interactions of selected factors, and ε_{ijkl} is the random error in the experiment provided that i, j, k, l represent the levels of pressure, focus settings, laser output energy, and thickness respectively. It should be noted that:

$$P_ixF_j = F_jxP_i$$
$$P_ixF_jxE_k = F_jxP_ixE_k$$

The above argument is valid for all the other interactions.

To calculate the main effects of each factor and the effects of interaction, it is necessary to determine the mean corrected sum of squares of response at all levels of factors. However, the mathematical arrangements of qualitative analysis are not given here, but it is referred to Ref.[12]

Table 1 Parameters and their levels employed in the experiment

Pressure (mm Hg)	*Focus setting (mm)*	*Laser output energy (J)*	*Thickness (mm)*
150	50	15	0.6
250	50.5	17	0.8
350	51	19	1.0
760	51.5	21	1.2

The significance of the effect of factors and interactions is tested by making the initial hypothesis that the mean squares of the effects or interactions are from the same populations as the error mean square, which is that all the mean squares are on a comparable basis with respect to error variance. It should be noted that the mean squares of effects and interactions are linear functions of observation. Since there are no repeats, the remainder mean square are representing the higher order interactions being used as an estimate of the error variance to test the significance of the effects calculated by means of the *F*-test.[12] The mean square of the effects is determined by dividing the corrected sum of squares by an appropriate number of degrees of freedom. In this case the variance ratio is:

$$F_{r,s} = \frac{\text{Mean sum of squares}}{\text{Error mean sum of squares}} \quad [13]$$

where r and s are the degrees of freedom of the mean sum of squares and the error mean sum of squares, respectively.

If the calculated variance ratio of any effect exists in the value in the *F*-test table[12] at corresponding r and s degrees of freedom, the effect is significant at that level.

1.12.2.2.2.2 Quantitative analysis

A quantitative factor is a factor for which the levels may be represented in terms of continuous points. The effect of such a factor is a mathematical function of the levels of the factor. This can be written in a polynomial form[12] as:

$$X = a_o\gamma + a_1\gamma^2 + a_2\gamma^3 + \ldots\ldots\ldots\ldots + a_n\gamma^{n+1} \quad [14]$$

where X is the response, γ is the level of factor, and n is the number of levels selected. The coefficients in the polynomial equation are estimated by the least square technique. Since four levels were selected, the values of the orthogonal coefficients are given in **Table 2** where η and γ are the sum of squares of the coefficients and a scale factor, respectively. The actual values of the constants in the orthogonal form of the polynomial are derived from $\Sigma\beta'X$, $\Sigma\gamma'X$, $\Sigma\delta'X$ multiplying the corresponding quantity of η/γ.[12] However, during the calculations of the variances, it is convenient to drop the multiplier γ/η, which is needed only to be introduced when the actual numerical values of the constants are required.

1.12.3 Laser Cutting Process

High power lasers are widely used to cut and shape the sheet metals with desired sizes. However, laser cutting process requires proper selection of cutting parameters such that the process parameters are adjusted and tuned to provide the quality of cut desired. However, this consumes considerable

Table 2 Orthogonal coefficients of polynomial equations

	Y_1	Y_2	Y_3	Y_4	η	γ
Linear	−3	−1	1	3	20	2
Quad.	1	−1	−1	1	4	1
Cubic	−1	3	−3	1	20	10/3

amount of time and effort, and still the optimal cutting parameters may not be found. If a different substance is used for cutting, all these parameters may require readjustment. This has been recognized as a major shortcoming, and this problem of optimized process planning is currently been addressed.[13] Deficiencies in the cutting quality may be related to the slow process drifts and disturbances. The main reasons for this drift to occur may include velocity fluctuations, variation in power and spatial intensity distribution, and optical integrity perturbations. The formation of striations has received considerable attention, since it is closely related to the laser cutting quality.[13–15] Explanations given on striation are, in general, quantitative and some little work has been carried out on classification of striation patterns. In the model introduced by Schuocker,[16] an attempt was made to calculate the striation frequency, but the predictions are limited in its use for characterizing and predicting surface roughness or a striation depth, which is considered as an important parameter in judging the laser cut quality. However, the results predicted for striation frequency agreed well with the experimental data. Study into striation process was also carried out by Olsen.[17] Some explanation of striation and prediction of striation frequency was given in his study.

The preceding sections thermal analysis of laser cutting process and the quality assessment of cut sections are presented. The formulations and the findings are discussed in line with the previous studies.[4–6]

1.12.3.1 Experimental Method

The experiment was carried out to investigate the affecting parameters on the kerf width size during CO_2 laser cutting of mild steel. A CO_2 laser delivering a nominal output power of 2000 W was used. Oxygen as assisting gas was introduced coaxially with the laser beam through a nozzle. The oxygen pressure was set to 200 kPa.

After completion of the cutting process, the widths of resulting cut were measured and SEM microphotography of the cut surfaces was carried out. To measure the striation depths and widths, the surface roughness measurement was carried out using a Bendix stylus instrument.

1.12.3.1.1 Thermal analysis

The energy balance due to absorption of the incident beam results in localized heating in the region of the substrate surface. In laser beam cutting process, some fraction of the beam is reflected and transmitted, and the rest of the beam intensity is absorbed by the substance. Since the heating situation is slow, the consideration of the Fourier law is appropriate to formulate the thermal analysis in the heated region. In this case, a moving heat source supplied along the z axis and the source travels along the x axis at a velocity u, the energy equation can be written as:

$$U\frac{\partial T}{\partial x}+\frac{\partial^2 T}{\partial x^2}+\frac{\partial^2 T}{\partial y^2}+\frac{\partial^2 T}{\partial z^2}=2\lambda\frac{\partial T}{\partial t} \qquad [15]$$

After assuming no heat convection at the surface, then the boundary conditions yield:

$$\frac{\partial T}{\partial x}=0 \quad \text{as} \quad x=\pm\infty$$
$$\frac{\partial T}{\partial y}=0 \quad \text{as} \quad y=\pm\infty$$

This may be rearranged with the source at the origin by making the transformation $\xi=x-Ut$ for the wave front travel in the positive x direction and $2\lambda=1/\alpha$ is used for convenience. On substitution gives:

$$\frac{\partial^2 T}{\partial \xi^2}+\frac{\partial^2 T}{\partial y^2}+\frac{\partial^2 T}{\partial z^2}=-2\lambda u\frac{\partial T}{\partial \xi}+2\lambda\frac{\partial T}{\partial t} \qquad [16]$$

If the solid is of sufficient length, the temperature distribution around the heat source becomes constant, i.e., $\partial T/\partial t=0$. Therefore:

$$\frac{\partial^2 T}{\partial \xi^2}+\frac{\partial^2 T}{\partial y^2}+\frac{\partial^2 T}{\partial z^2}=-2\lambda U\frac{\partial T}{\partial \xi} \qquad [17]$$

The solution of eqn [17] is straight forward[18] and it gives the solution of the temperature distribution in an infinite solid due to continuous line source of q (energy per unit length) is:

$$T=\frac{q}{2\pi kD}e^{\frac{ux}{2\alpha}}K_o\left(\frac{Ur}{2\alpha}\right) \qquad [18]$$

where r is the radial distance to the point being considered (satisfying $r^2=x^2+y^2$), k is the thermal conductivity, D is the thickness of the workpiece, and K_o is the modified Bessel function of second kind zero order. When laser heating is considered the heat flux per unit time becomes:

$$q_{laser}=(1-R_f)I_o \qquad [19]$$

where R_f is the surface reflectivity and I_o is the laser incident power intensity.

In the case of a gas assisted laser cutting process the contribution of exothermic chemical reactions to the heat transfer taking place at the liquid surface may be written as:[15]

$$q_{chem}=\rho_e u_e C_{H_c}\Delta I\left\{1+\left[\frac{C_{H_d}}{C_{H_c}}-1\right]\frac{h_c}{\Delta I}-\frac{B_3}{\Delta I}\right\} \qquad [20]$$

where

$$\Delta I=(I_f)_e-(I_f)_g+h_c$$

and $[(I_f)_e-(I_f)_g]$ is the enthalpy change at the interface due to the assisting gas and h_c is the total chemical reaction enthalpy which is defined as:

$$h_c=\sum_{i\neq E}(h_i)_g[(C_i)_g-(1+B_2)(C_i)_g]+(h_E)_g[B_2-(1+B_2)(C_E)_g] \qquad [21]$$

where B_2 and B_3 are:

$$B_2=B_3\frac{C_{H_c}}{C_{H_d}}$$

and

$$B_3 = \frac{(\rho u)_g}{\rho_e u_e C_{H_c}}$$

Equation [18] gives the heat transfer to the liquid metal due to chemical reactions and mass transfer occurring at the assisted gas–liquid interface when a reacting turbulent flow occurs over the liquid molten metal. The total heat flux available at the surface becomes:

$$q_{tot} = q_{laser} + q_{chem} \quad [22]$$

When the temperature of the surface reaches the melting temperature, melting isotherm develops at the surface, then the temperature of the melting isotherm can be obtained by rearranging eqn [16], i.e.:

$$T_m = \frac{q_{tot}}{4\pi kD} e^{\frac{ux}{2\alpha}} K_o\left(\frac{ur}{2\alpha}\right) \quad [23]$$

Introducing dimensionless coordinates as:

$$X = \frac{ux}{2\alpha}; \quad R = \frac{ur}{2\alpha}$$

Equation [23] yields:

$$T_m = \frac{q_{tot}}{2\pi kD} e^{X} K_o(R) \quad [24]$$

To determine the maximum melt width, rearrangement of eqn [20] is necessary. Using the previously introduced technique,[19] the resulting $X = \frac{ux}{2\alpha}$ for the maximum melt width becomes:

$$X = \frac{RK_o[R]}{K_1[R]} \quad [25]$$

where

$$K_o[R] = \frac{2\pi kDT_m}{q_{tot}} e^{\left[-\frac{RK_o(R)}{K_1(R)}\right]}$$

and $K_1[R]$ is the modified Bessel function of second kind first order.

Solution of eqn [25] gives the values of R for the cut width. Consequently, the maximum melt width ($Y_{\max}$) can be found from:

$$Y_{\max} = RSin\phi \quad [26]$$

where

$$\phi = Cos^{-1}\left[\frac{K_o(R)}{K_1(R)}\right]$$

To determine the area ratio of the total melted area to focused spot area, a geometric description of the focused spot and melted area should be considered (**Figure 2**). Assume that the maximum width of the melting isotherm lies outside of the focused spot. The total area of the focused spot removed is the shaded zone in **Figure 2**, which may be expressed as:

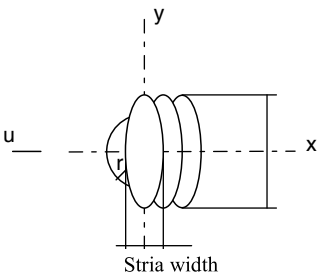


Figure 2 Laser cutting situation and stria width.

$$S_{tot} = S_1 + S_2 = r^2\phi + \frac{r^2 Sin\phi}{2} + 2\int_{X_1}^{X_2} Y\,dx \quad [27]$$

where

$$X_2 = \ln\left\{\frac{2\pi kDT_m}{q_{tot}} K_o[R]\right\}$$

and

$$\phi = Cos^{-1}\left(\frac{X_2}{r}\right)$$

Since,

$$Y = \sqrt{R^2 - X^2} = \left\{R^2 - \ln\left[\frac{2\pi kDT_m}{q_{tot}} K_o[R]\right]^2\right\}^{1/2} \quad [28]$$

and

$$dX = \frac{K_1[R]}{K_o[R]} dR$$

After rearranging eqn [28], it yields:

$$S = \frac{\phi}{\pi} - \frac{Sin2\phi}{2\pi} + \frac{2}{\pi r^2}\int_{X_1}^{r}\left\{R^2 - \left[\frac{2\pi kDT_m}{q_{tot}} K_o[R]\right]^2\right\}^{1/2} \frac{K_1[R]}{K_o[R]} dR \quad [29]$$

Consider **Figure 2**, the melted area may be approximated as an elliptic shape. Therefore, the striation width (w_k) can be calculated from:

$$w_k = \frac{S_{tot}}{2\pi\gamma_{\max}} \quad [30]$$

Consider the speed of melting isotherms penetrating into the workpiece; in this case assuming attainment of steady state at the surface and omitting the surface evaporation, the penetration speed can be written as:

$$v = \frac{q_{tot}}{\rho(L + CpT_m)} \quad [31]$$

The cutting parameters including nondimensional maximum cut width, area ratio, striation width, and penetration speed can be computed incorporating appropriate thermophysical properties of the workpiece.

1.12.3.2 Lump Parameter Analysis for Kerf Size

The overall energy balance in laser cutting process was simplified through introducing lumped parameter technique by Kar *et al.*[20] The simple scaling law states that the relationship is existed among the laser energy absorbed in a unit depth, convection, and conduction contributions of heat transfer and phase change. This yields the relation:[20]

$$\frac{P}{d} = \frac{vw_k + A_3\sqrt{vw_k}}{A_o} \quad [32]$$

where:

$$A_o = \frac{A}{a_o};\ A_3 = \frac{1}{a_o}\frac{(w_k + 2wk(T_mT_o))}{2\sqrt{\alpha w w_k}} \quad \text{and} \quad a_a = \rho[Cp(T_m - T_o) + L_m + \beta L_b]$$

The term 'A_o' is related to energy transfer rate to the workpiece at the surface during laser–workpiece interaction. 'A' is the effective energy coupling factor at the workpiece surface, and 'A_3' is related to energy loss due to conduction in the solid. β is the fraction of evaporation contribution at the workpiece surface.

Using the scale law, the kerf width can be written in a simplified form for a circular laser beam with a beam waist size of w as:[20]

$$w_k = \frac{1}{v}\frac{\left[2.51\sqrt{\frac{\alpha}{w}}\frac{2A\eta_u}{k(T_m - T_o)}P\sqrt{v}\right]}{\left[1 + 3.08\times 10^8 \frac{A_o}{A_3\sqrt{f}}\frac{\rho\rho_g\sigma^2\alpha}{M_w P_g f\sqrt{w}}P\sqrt{v}\right]} \quad [33]$$

where 'f' is the fraction of the pressure drop in the kerf, σ is the molecular diameter (Angstrom unit), M_w is the molecular weight (gr mol^{-1} unit) of the assisting gas, P_g and ρ_g are the pressure and density of the assisting gas, and η_u is the superheating factor in the melt pool.

Equation [33] is used to determine the kerf width while energy coupling factor (A), laser power (P), and cutting speed (v) are considered as variables in eqn [33]. The material properties in the computations are given in **Table 3**.

Table 3 Properties of the workpiece used in the computations

Properties	*Values*	*Units*
Boiling temperature	3133	K
Density of assisting gas	1.97	Kg m^{-3}
Density of workpiece	7880	Kg m^{-3}
Fraction of evaporation contribution ($0<\beta<1$)	0.1	–
Fraction of pressure drop ($0<f<1$)	0.1	–
Latent heat of melting	2.72×10^5	J kg^{-1}
Latent heat of boiling	6.10×10^6	J kg^{-1}
Melting temperature	1809	K
Molecular diameter of oxygen	6	Angstrom
Specific heat capacity	460	J kg^{-1} K^{-1}
Super heating factor	0.02	–
Thermal conductivity	80.3	W m^{-1} K^{-1}
Thermal diffusivity	2.21×10^{-5}	m^2 s^{-1}

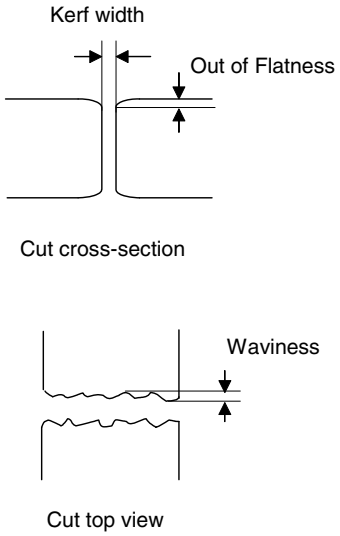


Figure 3 A schematic view of laser cut edges.

1.12.3.3 Cut Quality Assessment

The cut quality assessment is based on the factorial analysis. The analyses pertinent to cut quality assessment are given under the appropriate subheadings.

1.12.3.3.1 Evaluation of cut quality

The cut quality may successfully be evaluated in terms of waviness, flatness (**Figure 3**), and metallurgical changes at cut surface and overall quality provided that the assessment for the cut quality is based on the international standards for thermal cuts (DIN2310). Height of waviness and flatness were measured with a reading microscope in mm units while elemental analysis at the cut edge was carried out using EDS technique. To determine the overall quality of cut, scores are assigned to waviness, flatness, and metallurgical changes. The scoring scheme includes:

1. Waviness (D): $D\leq30$ μm score of 3; $30\leq D\leq60$ μm score of 2; $D\geq60$ μm score of 1 are assigned.
2. Flatness (F): $F\leq20$ μm score of 3; $20\leq F\leq40$ μm score of 2; $F\geq40$ μm score of 1 are assigned.
3. Metallurgical changes (Mm): When no degradation and/or degradation of less than 1% is resulted in any element at the cut surface a score of 1 is assigned or/else a score of 0 is assigned.

The overall quality is then defined as:

$$Q_{\text{overall}} = D + F + Mm \quad [34]$$

1.12.3.3.2 Factorial analysis

To determine the significance levels of the cutting parameters a statistical analysis was carried out. To analyze the effect of laser cutting parameters on the resulting cut quality (measurable variables of waviness, flatness, metallurgical changes at cut surface, and overall quality), it was necessary to design an experiment in such a way that the influence of each parameter

could be examined individually and an interaction. This required a complete factorial design in which selected factors are varied at appropriately selected levels. It should be noted that in qualitative analysis, main effects are zero order effects, i.e., independent of each other. However, first order interactions demonstrate that the effects of the interacted factors on observation are dependent on each other.[12]

The factors affecting the cut quality may include cutting speed, assisting gas pressure, workpiece thickness, and laser pulsing frequency. An *F*-test was conducted to identify the significant effects of the parameters and their interactions on the various observations describing the cut quality. The terms most significant, very significant, and significant refer to minimum correlation levels of 0.99, 0.99 to 0.95, and 0.95 to 0.90 of the factors, respectively.

1.12.4 Laser Bending

One of the laser machining applications can be considered as the laser bending. The bending process differs slightly from the laser welding such that laser forming requires shallow depth of phase change at the surface while laser welding requires deep penetration of the laser beam into the substrate material. From the heating point of view, the irradiated surface undergoes solid heating and melting following the solidification for the forming process. Since laser heating and phase change process is almost rapid, the high cooling rates is resulted during the solidification of the melted regions. This causes attainment of high temperature gradients across the irradiated zone while increasing the thermal strain in this region. Depending on the magnitude and the nature of the residual stress generated, compressive or tensile, bending of irradiated substrate takes place toward or opposite to the irradiated surface of the workpiece. Since the laser heating and cooling processes are rapid, the size of the heat affected zone becomes narrow, which in turn provides advantages of the local treatment by a laser beam. In some cases, the formation of high residual stress results in crack formations in the bended region while limiting the practical use of the bended parts.

Jamil and Sheikh[21] studied laser bending of sheet metals and effect of laser beam geometries on the bending angles. They demonstrated that temperature dependent properties of the sheet metal were more crucial than the laser beam geometry in terms of the resulting bending angles. The simulation study for laser bending angle of sheet metals was carried out by Peng and Hongwei.[22] They showed that dimensional analysis was an effective method for predicting the bending angle accurately. The laser bending of preloaded sheet metals was investigated by Yanjin *et al.*[23] They indicated that the bending angle of the sheet metal increased considerably with the increased of the preloading. Laser bending of sheet metals was examined by Shichun and Jinsong.[24] They demonstrated that there was significant influence of the sheet thickness on the bending angle. Laser bending of circular sheet metal was examined by Nadeem and Na.[25] They introduced the scheme to achieve the geometrical transition from rectangular to ring shapes via laser controlled heating. The residual stresses development in laser bending of stainless steel sheet metal was studied by Gheorghies *et al.*[26] They indicated that the effect of multiple scans was difficult to simulate due to the complications involved when incorporating the material annealing during forming. Laser forming and bending processes were investigated by Yongxiang *et al.*[27] They demonstrated that a continuous decrease in bending angle from concave to convex took place with increasing workpiece thickness.

In this section, some aspects of laser bending are to be provided and the findings are discussed in line with the previous study.[28]

1.12.4.1 Experimental

The CO_2 laser (LC-ALPHAIII) delivering nominal output power of 2 kW is used to irradiate the workpiece surface. The nominal focal length of the focusing lens is 127 mm. Nitrogen assisting gas emerging from the conical nozzle and coaxially with the laser beam is used. The use of nitrogen as an assisting gas is due to its cost and higher specific heat capacity as compared to that of argon. The laser treatment conditions are given in **Table 4**.

The workpiece used is AISI 304 steel sheet at 1 mm in thicknesses. The morphological changes at the kerf surfaces were examined using Jeol 6460 electron microscopy. The XRD analysis was carried out incorporating Bruker D8 Advanced XRD unit with having Cu–Kα radiation. A typical setting of XRD was 40 kV and 30 mA. The parabolically-shaped Göbel Mirror was used in Bruker D8 Advanced, which provided the highly-parallel X-ray beams. The parallel beams from it removed the traditional limitations of the Bragg–Brentano geometry for powder diffraction and thin film investigations.

1.12.4.2 Mathematical Analysis

Laser heating situation is involved with a moving volumetric heat source scanning the workpiece surface as depicted in **Figure 4**.

In the numerical solution, the user subroutine DFLUX in ABAQUS[14] is used to introduce the volume flux described by eqn [1]. The subroutine first calculates the position of the laser beam according to the scanning time, *t*, and then computes the heat flux, *Q*, at each integration point. The Gauss parameter '*a*' is taken as 0.0003 m and velocity of 10 cm s^{-1} is used in line with the experimental conditions.

In the thermal analysis, the solid body heat conduction and phase change with temperature-dependent conductivity, internal energy (including latent heat effects), and convection and radiation boundary conditions are considered. The Fourier heat transfer equation for the laser heating process can be written as:

$$\rho \frac{DE}{Dt} = (\nabla(k\nabla T)) \qquad [35]$$

where E is the energy gain of the substrate material, ρ is the material density, and k is the thermal conductivity. In the case of a moving heat source along x-axis of the sheet with a constant velocity U, energy gain of the substrate material yields:

$$\rho \frac{DE}{Dt} = \rho \frac{\partial E}{\partial t} + \rho U \frac{\partial E}{\partial x} \qquad [36]$$

Table 4 Laser processing conditions used in the experiment

Welding speed (cm s^{-1})	*Peak power (W)*	*Laser peak intensity $\times 10^{12}$ (W m^{-2})*	*Frequency (Hz)*	*Nozzle gap (mm)*	*Nozzle diameter (mm)*	*Focus setting (mm)*	*N_2 gas pressure (kPa)*
10	2000	2.7	1500	1.5	1.5	127	600

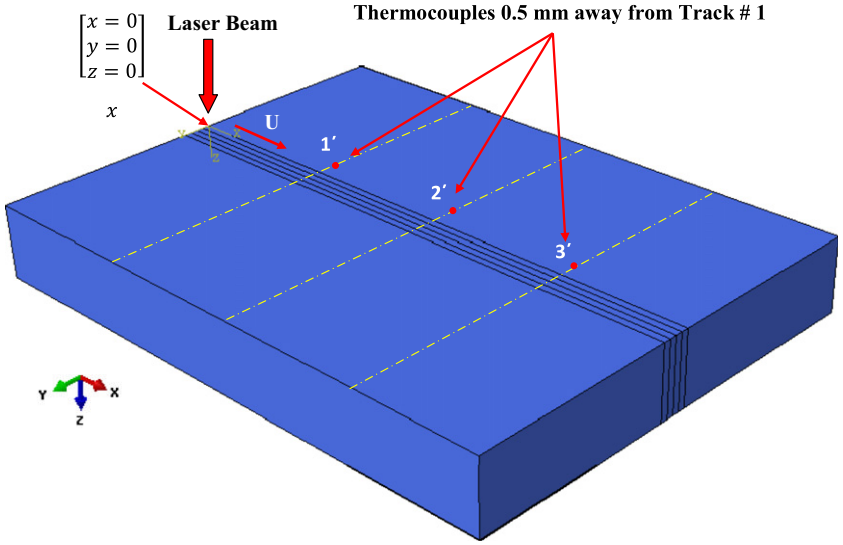


Figure 4 Schematic view of laser heating situation and the coordinate system.

or

$$\rho\frac{\mathrm{D}E}{\mathrm{D}t}=\rho\frac{\partial(C_pT)}{\partial t}+\rho U\frac{\partial(C_pT)}{\partial x} \quad [37]$$

Combining eqns [1] and [3] yields:

$$\rho\frac{\partial(C_pT)}{\partial t}=(\nabla(k\nabla T))+\rho U\frac{\partial(C_pT)}{\partial x} \quad [38]$$

where C_p is the specific heat. To analyze the phase change problem, the enthalpy method is used.[29] The specific heat is associated with the internal energy gain of the substrate material. However, the internal energy gain during the phase change is associated with the latent heat of fusion, which is given separately in terms of solidus and liquidus temperatures (**Table 5**) and the total internal energy associated with the phase change, called the latent heat. Since the primary interest is the stress field developed in the cutting section, the flow field generated in the liquid phase at the kerf surface during the laser cutting process is omitted.

The convective and radiation boundary conditions are considered at the free surface of the workpiece. Therefore, the corresponding boundary conditions are:

At the irradiated surface:

$$\frac{\partial T}{\partial z}=-\frac{I_{\max}}{k}(1-r_f)e^{\left(-\frac{x^2+y^2}{a^2}\right)}+\frac{h_f}{k}(T_s-T_{amb})+\frac{\varepsilon\sigma}{k}(T_s^4-T_{amb}^4) \quad [39]$$

where, $I_{\max}$ is laser power peak density, a is the Gaussian parameter, r_f is the surface reflectivity, x, y, and z are the axes, and $h_f=3000\ \mathrm{W\ m^{-2}\ K}$[30] is the forced convection heat transfer coefficient due to the assisting gas.

At the rear side of the surface:

$$\frac{\partial T}{\partial y}=\frac{h}{k}(T_s-T_{amb})+\frac{\varepsilon\sigma}{k}(T_s^4-T_{amb}^4) \quad \text{and}$$

$$\frac{\partial T}{\partial z}=\frac{h}{k}(T_s-T_{amb})+\frac{\varepsilon\sigma}{k}(T_s^4-T_{amb}^4) \quad [40]$$

where $h=20\ \mathrm{W\ m^{-2}}$ is the heat transfer coefficient due to natural convection, and T_s and T_{amb} are the surface and ambient temperatures, respectively, ε is the emissivity ($\varepsilon=0.9$ is considered), σ is the Stefan–Boltzmann constant ($\sigma=5.67\times10^{-8}\ \mathrm{W\ m^{-2}\ K^4}$). Initially (prior to laser heating), the substrate material is assumed to be at constant ambient temperature, i.e., $T=T_{amb}$, which is considered as constant ($T_{amb}=300$ K).

Equation [38] is solved numerically with the appropriate boundary conditions to predict the temperature field in the substrate material and the properties used in the simulations are given in **Table 5**.[31]

The thermal model consisted of two steps. The first step, which lasts 0.409 s, simulates the response of the sheet under a moving laser heat flux along five tracks each of length 8 mm. The distance between the centers of the spots during any two adjoining tracks were kept as 0.1 mm which resulted in an overlapping ration of 60%. The second step, which lasts for 300 s, simulated the continuous cooling in the model. Cooling was allowed to continue until the sheet reaches the initial temperature (room temperature). The temperature–time

Table 5 Properties used in the simulations

Temperature (K)	*Thermal conductivity ($W\,m^{-1}\,K^{-1}$)*	*Specific heat ($J\,kg^{-1}\,K^{-1}$)*	*Modulus of elasticity, $E \times 10^{11}$ (Pa)*	*Expansion coefficient $\times 10^{-5}$ ($1\,K^{-1}$)*
300	14	456	1.95	1.6
473	15	532	1.83	1.67
673	17.5	557	1.71	1.76
873	21	599	1.52	1.83
1073	25	620	1.33	2.0
1273	28	645	1.24	2.1

Density = 8030 kg m^{-3}; Latent heat = 300 000 J kg^{-1}; Solidus temperature = 1673 K; Liquidus temperature = 1728 K; Poisson's ratio = 0.3; Strength coefficient = 1.4 GPa and $n = 0.44$.

history resulting from the thermal analysis is used as input to the thermal stress analysis.

Solidification involves small strain, so the assumption of small strain is adopted in this work. The thermal strains which dominate thermo-mechanical behavior during solidification are on the order of only a few percent as confirmed by several previous solidification models.[32] In the stress analysis, displacements are stored at the nodal positions as a solution variable, and loads are defined as prescribed displacements and forces. Employing the interpolation functions, it is possible to calculate the strain and stress increments at any point within the element using the compatibility and constitutive equations. ABAQUS[29] transforms the mechanical equilibrium equations into a set of simultaneous equations, such that the nodal displacements and forces are related to each other through the elemental stiffness matrix. However, ABAQUS uses a temperature-dependent total thermal strain coefficient, $\alpha'(T)$. It is considered that the thermal stress field is almost zero (hydrodynamic pressures are present only) in the molten surface. The solid and liquid interface in the kerf vicinity remains at a solidus temperature, and the elastic module reduces at elevated temperatures, which is given in **Table 5**. The material is modeled as a von Mises elastic-plastic material with isotropic hardening. To account for the effects of material melting and resolidification and annealing the ABAQUS command *ANNEAL TEMPERATURE was used. This command causes a point in the material to lose its hardening history by setting the equivalent plastic strain at that point to zero if it exceeds a certain temperature. The annealing temperature used was 1728 K. To avoid computational difficulty, the yielding stress is limited to its value at the annealing temperature.

The mesh is generated after the identification of the critical regions in the geometry. The critical regions are considered as the regions where high temperature gradient and strain occur during the laser multitrack scanning (5 tracks in the present case). These regions are the material volumes around the laser beam path and the heat-affected zone. These regions are estimated experimentally from the bended samples which found to extend in a zone of width equal to about five times of the laser beam diameter. A refined mesh is selected in this region in order to capture the temperature and stress fields with high resolution. In addition, the convergence tests are carried out to ensure the mesh density independency of the predictions.

Sequentially coupled thermo-mechanical analysis is used to describe the laser bending analysis, which means that deformations during bending depend on temperatures but temperatures are independent of deformation. Therefore, the thermal analysis is first solved to obtain the temperature field throughout the specimen as a function of time which is then provided as an input for the stress analysis, to determine the thermal stress fields in the laser irradiated section. Continuum, three-dimensional 6-node linear heat transfer elements (DC3D6) are used in the thermal analysis whereas for stress analysis, three-dimensional 6-node linear stress elements (C3D6) are used. The mesh comprises of 33 520 elements and 23 991 nodes.

1.12.5 Results and Discussions

Laser machining process in general, involves with multiphysics and can be categorized in many different ways. However, main focus are of research in laser machining and extends to include drilling, cutting, bending, and welding. In this chapter, laser drilling and quality assessment is given in line with the previous studies,[28] laser cutting of thin metal sheets and quality assessments is provided in line with the previous studies, and laser bending of steel sheet is explored in line with the previous studies.[28] The findings and discussions are given according to the appropriate subheadings.

1.12.5.1 Laser Drilling

Laser drilling is one of the important applications of the laser machining. The findings of the temperature distribution and statistical analysis are discussed according to the previous studies.[1–3] The nondimensional temperature profiles are predicted for variable properties, which are given in **Table 6** while the pulse parameters employed in the temperature simulations are given **Table 7**.

Figure 5 shows the contour plot of dimensionless temperature profiles inside the substrate material while **Figure 6** shows dimensionless temperature distribution inside the substrate material along the z-axis at different heating periods. Temperature profiles terminate at some depth below the surface depending on the heating period, e.g., for $t^* = 3.05$, the corresponding depth is $z^* = 7.5$. This is because of the cavity formation after the evaporation process. Thus, the depth of cavity depends on the heating duration. Moreover, two regions

Table 6 Properties of the substrate material used in the computation

	δ (1 m^{-1})	ρ (kg s^{-1})	Cp ($J\,kg^{-1}\,K^{-1}$)	K ($W\,m^{-1}\,K^{-1}$)	T_m (K)
Const. Prop.	6.16×10^6	7836	330	52	1810
Var. Prop.	6.16×10^6	7836	$24.558 + 1.223 \times T - 0.37693 \times 10^{-3} \times T^2$	$64.102 - 0.04803 \times T + 1.518 \times 10^{-5} \times T^2$	1810
L_m (J kg^{-1})	L_b (J kg^{-1})	T_b (K)			
2.4×10^{12}	6.26×10^6	3030			

Table 7 Pulse properties used in the computation

Laser peak power intensity ($W\,m^{-2}$)	Gaussian parameter (m)	Heating period
7×10^{12}	3.06×10^{-4}	0–8

in the temperature profiles are evident because of the phase change process. In the first region, a solid heating occurs $T^* < 0.07$, while liquid phase heating is dominant in the second region ($0.07 < T^* < 0.126$). The depth of cavity exceeds the absorption depth of the substrate material for the heating periods shown in Figure 6. Consequently, energy transport due to diffusion dominates the heat transfer process during the heating periods considered. The slope of the liquid heating changes sharply after the initiation of melting process, i.e., in the region of the melt the slope of temperature curves changes sharply. This is because of the mushy zone introduced in the analysis, i.e., some of the substrate material is partially melted at constant temperature. Since the laser input intensity is high and the interaction duration is short, the size of the mushy zone is small.

1.12.5.1.1 Qualitative analysis

Table 8 gives the *F*-test results for the parameters pressure (P), focus settings (F), laser output energy (E), and workpiece thickness (T). The discussion for the test results are given under the headings relevant to the geometric features of the hole drilled.

Resolidified material: The main effect of pressure is significant, the first order interactions of pressure–thickness is most significant, pressure–focus setting and pressure–thickness are significant, and second order interaction of pressure–focus setting-energy is significant. This indicates that the ambient pressure has a significant effect on the resolidified material. In this case, reducing ambient pressure generates a pressure differential across the evaporated front and its surroundings. Consequently, the material removal rate increases from the cavity in the initial stage of the hole formation. Once the hole is drilled in the workpiece, the pressure in the cavity drops considerably. Despite the low pressure in the cavity, the low ambient pressure results in molten metal to drag toward the hole inlet. The molten metal, then, solidifies as soon as the laser pulse ceases. Therefore, the molten metal forms the resolidification at the hole exit. The first order interaction between the pressure-thickness has most significant effect on the resolidified material.

Taper: The main effects of all the parameters are found to be most significant for taper, except energy, which has only significant effect on taper. Almost all the first order interactions have most significant effect on taper while the second order interaction of pressure–focus setting–thickness has significant effect on taper. Therefore, taper increases as ambient pressure reduces, in which case the rate of mass removal from the cavity increases. In addition, the focus setting and thickness have similar effect on the taper. In this case, energy available at the workpiece surface varies as the focus setting changes. This influences the energy coupling at the workpiece surface. Therefore, the pressure generated due to superheating of liquid becomes considerably high, which in turn accelerates the mass removal from the cavity and enhances the liquid surface propagation into the workpiece. Consequently, high rate of material removal from the workpiece results in large taper. The first order interaction indicates that the coupling effects of pressure and thickness, pressure and focus setting, and thickness and focus setting are significant. Therefore, the formation of taper depends on the individual parameters as well as their interactions.

Inlet cone angle: Focus setting and thickness are found to be most significant parameters while pressure and energy are significant parameters in the case of inlet cone angle. Inlet cone angle is, in general, related to focus setting since the larger beam waist at the workpiece surface generates large inlet cone angles. The pressure inside the cavity before the through hole formation is also important. The pressure in the cavity increases as thickness of the workpiece increases. In addition, the differential pressure across the evaporating front and its surroundings increases due to subatmospheric ambient conditions, i.e., the mass removed from the cavity erodes thermally the exiting section of the cavity, which in turn results in large inlet cone angle. Therefore, the coupling effect of pressure and focus setting influences the inlet cone angle formation considerably.

Barreling: The focus setting and thickness have most significant effect on the barreling. The main effects of pressure and energy are found to be significant. Barreling defines the how parallel-sided the hole drilled. Thickness and focus setting contributions are more than pressure and energy contributions for barreling formation. This suggests that formation of parallel-sided hole is related to the pressure rise inside the cavity before through hole formation rather than the mass removal rate, i.e., the regulated mass removal rate results in improved barreling than the fast rate of mass removal. The first order interaction between pressure and focus setting shows that there exists a coupling effect of these parameters on barreling as the combinations of focus settings and pressure vary.

Exit cone: The focus setting and thickness have the most significant effect while pressure and energy have significant

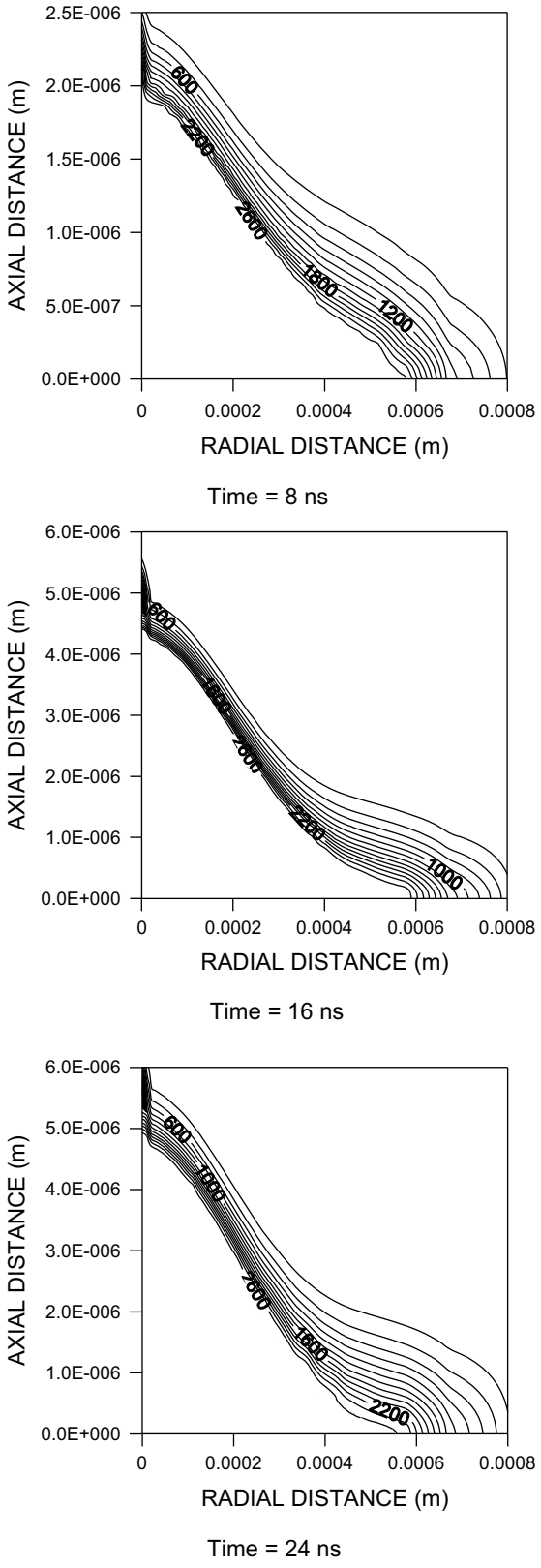


Figure 5 Contour plots of temperature at different heating periods.

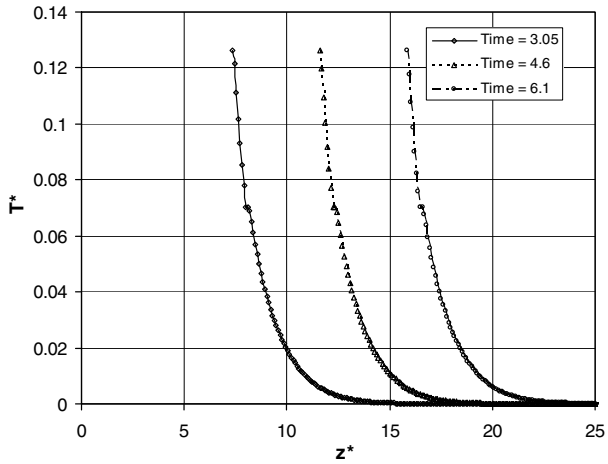


Figure 6 Variation in dimensionless temperature along dimensionless axial distance at different heating periods.

effect on the exit cone. The first order interactions of focus setting–thickness, and focus setting–energy are the most significant. This finding indicates that thickness, focus setting, and energy have significant contribution to the exit cone formation. In this case, the thick workpiece results in large pressure development in the cavity during the hole formation. This is effected by the beam waist position and laser output energy such that large exit cone is resulted for thick workpieces. In addition, the exit cone becomes small for some combinations of these parameters.

Surface debris: Surface debris is a measure of amount of material at the surface around the hole circumference. In almost all cases, the surface debris is not observed. This is because the low ambient pressure. In this case, the material leaving the hole inlet and exit is accelerated due to the pressure differential. This results in less or no debris at the workpiece surface. The first order interaction of pressure and focus setting has a significant effect on the surface debris.

Mean hole diameter: The main effects of all the parameters are found to be most significant. The effects of first order interactions of pressure–thickness, and focus setting–thickness are most significant. The size of the mean hole diameter depends on the amount and the rate of mass removal from the cavity during the hole formation. In this case, increase in pressure in the cavity and low ambient pressure enhance the amount of mass removed and its rate. In addition, the energy coupling at the workpiece surface alters the rate of mass removal, i.e., improved energy coupling at the workpiece surface accelerates the mass removal rate. Moreover, the effects of pressure and focus setting vary with thickness, since the first order interactions of these parameters are most significant.

Overall quality: Overall quality is effected by all parameters provided that the main effects of focus setting and thickness are the most significant while pressure and energy are significant parameters. The first order interaction of focus setting–thickness is very significant while pressure–focus setting is significant. This indicates that overall quality is not only effected by each parameter, but the combinations of

Table 8 Qualitative analysis results (> represents the parameter is not significant)

	Resolid material	*Taper*	*Barrel*	*Inlet cone angle*	*Exit cone angle*	*Surface debris*	*Mean hole diam*	*Overall quality*
P	0.90	0.99	0.90	0.90	>0.9	>0.90	0.99	0.90
F	>0.9	0.99	0.99	0.99	0.99	>0.90	0.99	0.99
E	>0.90	0.90	0.90	0.90	>0.90	>0.90	0.99	0.90
T	>0.90	0.99	0.99	0.99	0.99	>0.90	0.99	0.99
PF	>0.90	0.99	0.90	>0.90	0.90	0.90	>0.90	0.95
PE	>0.90	>0.90	>0.90	0.90	>0.90	>0.90	>0.90	>0.90
PT	0.99	0.99	>0.90	0.99	>0.90	>0.90	0.99	0.95
FE	>0.90	>0.90	0.95	0.95	>0.90	>0.90	>0.90	0.90
FT	>0.90	0.95	>0.90	0.99	0.99	>0.90	0.99	0.95
ET	>0.90	0.95	>0.90	0.95	0.99	>0.90	>0.90	0.90
PFE	>0.90	>0.90	>0.90	>0.90	>0.90	>0.90	>0.90	>0.90
PFT	0.90	0.90	<0.90	0.90	0.99	>0.90	0.95	0.95
PET	>0.90	>0.90	>0.90	>0.90	>0.90	>0.90	>0.90	>0.90
FET	>0.90	0.95	>0.90	>0.90	>0.90	>0.90	>0.90	>0.90

Table 9 Quantitative analysis results (> represents the parameter is not significant)

		Resolid material	*Taper*	*Barrel*	*Inlet cone angle*	*Exit cone angle*	*Surface debris*	*Mean hole diam*	*Overall quality*
P	Linear	>0.90	>0.90	0.95	0.90	>0.90	>0.90`	0.99	0.90
	Quad.	>0.90	0.99	>0.90	0.95	>0.90	>0.90	0.99	>0.90
	Cubic	0.95	>0.90	>0.90	>0.90	>0.90	>0.90	0.90	>0.90
F	Linear	>0.90	0.99	0.99	0.99	0.99	0.90	0.99	0.99
	Quad.	>0.90	>0.90	>0.90	>0.90	>0.90	>0.90	>0.90	>0.90
	Cubic	0.95	>0.90	0.90	>0.90	0.90	>0.90	>0.90	>0.90
E	Linear	>0.90	>0.90	>0.90	0.99	>0.90	>0.90	0.99	>0.90
	Quad.	>0.90	0.95	>0.90	>0.90	>0.90	>0.90	>0.90	0.90
	Cubic	>0.90	>0.90	>0.90	>0.90	>0.90	>0.90	>0.90	>0.90
T	Linear	0.95	0.99	0.99	0.99	0.90	>0.90	0.99	0.99
	Quad.	>0.90	0.99	>0.90	>0.90	>0.90	>0.90	0.99	0.90
	Cubic	>0.90	0.90	0.95	>0.90	>0.90	0.90	0.90	>0.90

pressure–focus setting, and focus setting–thickness also alter the overall quality.

1.12.5.1.2 Quantitative analysis

The quantitative analysis gives the functional relation between the affecting parameters and the response (geometric features of the hole drilled). Table 9 gives the quantitative analysis results. The relation for each parameter is given below.

Pressure: The linear effect of pressure found to be most significant for mean hole diameter, very significant for barreling, and significant for inlet cone. The quadratic effect of pressure is most significant for taper, very significant for inlet cone. The cubic effect of pressure is very significant for resolidified material and it is significant for mean hole diameter. This suggests that taper and inlet cone vary quadratically with pressure while barreling varies linearly with pressure. The cubic relation exists between the resolidified material and pressure.

Focus setting: The linear effect of focus setting is very significant for all hole geometric features, except surface debris. In this case, the linear relation exists between the resolidified material, taper, barreling, inlet cone, exit cone, mean hole diameter, and overall quality with focus setting, i.e., small variation in focus setting results in small variation in features of hole geometry, since the relation between the hole features and focus setting is linear.

Laser output energy: The linear effect of energy is most significant for inlet cone and mean hole diameter. The cubic effect of energy is significant for taper. Consequently, as energy varies, the inlet cone and mean hole diameter change with energy at almost same rate.

Thickness: The linear effect of thickness is most significant for all the features of hole geometry, except surface debris, which varies in cubic form with thickness. Some of quadratic and cubic effects of thickness are also found to be most significant for some hole features. This suggests that although the linear effect of thickness is dominant, but as far as the interactions are concerned this effect may not be linear.

1.12.5.2 Laser Cutting

The energy coupling at the workpiece surface plays an important role in laser cutting process. When the high power laser beam is absorbed by the workpiece material, the solid state heating, melting, and evaporation of the workpiece material are resulted. The melted and the evaporated material with existing of oxygen, due to impinging gas initiate high temperature exothermic reactions. This ionizes the evaporation

Table 10 Affecting process parameters and their levels

Variables	*P (W)*	*A*	*V (cm s^{-1})*
Levels	500 and 1500	0.3 and 0.6	1 and 4

front slightly and generates partially ionized surface plasma, which scatters the laser beam and modifies the focusing conditions of the incident laser beam. In addition, partially ionized surface plasma acts as a heat source enlarging the size of the melt in the kerf. Moreover, when the incident beam partially blocked by the surface plasma, less incident laser energy reaches the workpiece. This reduces the mass removal rate and the size of the surface plasma reduces which in turn results in more laser energy reaching the workpiece surface. This, later, accelerates the mass removal rate. Consequently, the high temperature oxidation reaction, in most cases, results in transiently varying energy coupling mechanism at the workpiece surface. Therefore, the energy coupling needs to be considered as one of the affecting parameters in the analysis. Two levels of each affecting parameter are considered, which are given in **Table 10**. The findings are presented in the light of the previous studies.[4–6]

In the analysis, the difference of kerf width size (Δw_k) due to each affecting parameter is also considered. The difference of kerf width size is determined from:

$$\Delta w_k = (w_k)_{P_n} - (w_k)_{P_{(n+1)}}$$

where P_n is the any affecting parameter at nth level. The variation of Δw_k due to percentage change of affecting parameters is also considered. In this case, any of the affecting parameter is increased gradually and the corresponding kerf width change is determined. Then, the amount of increment is normalized by the magnitude of the affecting parameter, i.e., $\Delta P_n/P_n$, where ΔP_n is the increment in the parameter at nth level and P_n is the parameter at nth level. This arrangement enables to identify the change in Δw_k due to certain percent of change in the parameter. If the laser processing parameters (affecting parameters) vary slightly during the cutting process, the striation is formed on kerf surface. This is because the change of Δw_k during the cutting process, i.e., variation of affecting parameters results in varying kerf width. Moreover, variation of kerf size due to variation of any affecting parameter identifies the significance of the parameter in the striation formation.

Figures 7(a) and **7(b)** show the kerf width with the cutting speed, and Δw_k with the percentage of cutting speed variation (dv_n/v_n). In general, kerf width reduces with increasing cutting speed. The high laser power results in small size of kerf width provided that the decrease in the kerf width is nonlinear with the cutting speed. When comparing the experimental results with the present predictions, they are in reasonably good agreement. In the case of Δw_k, high laser power with high energy coupling factor results in large Δw_k. Moreover, 5% variation in dv_n/v_n results in 2–4% variations in the kerf width for the condition of 1500 W laser power and 0.6 energy coupling factor. As dv_n/v_n increases Δw_k increases considerably. During the laser cutting process, if the cutting speed varies without regulating the laser output power, the size of the striation amplifies. This is especially true when odd-shaped curves or sharp corners are subjected to the laser cutting.

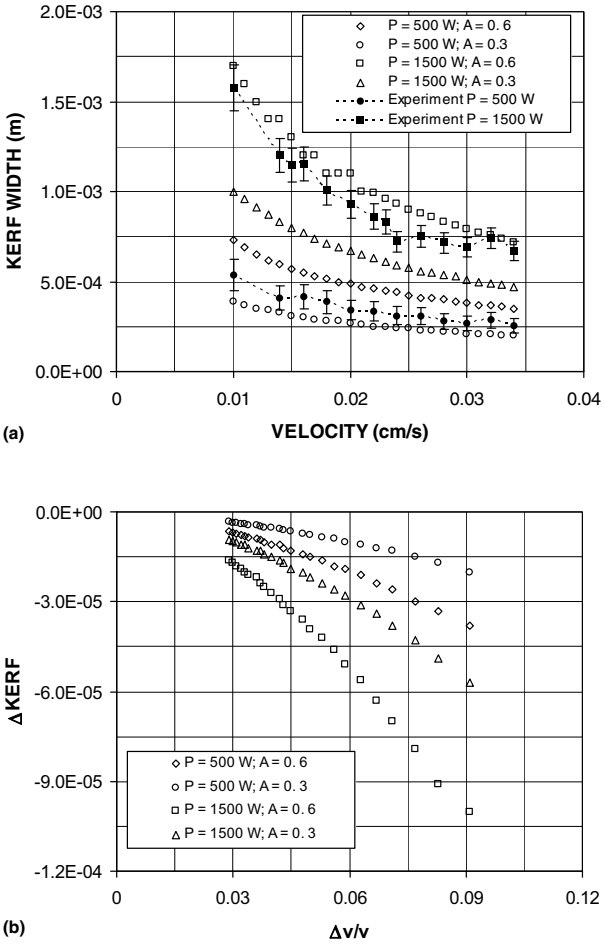


Figure 7 (a) Kerf width with cutting speed for different energy coupling factors and laser powers. (b) Variation in kerf width with cutting speed variation for different energy coupling factors and laser powers.

Figures 8(a) and **8(b)** show the kerf width with laser output power, and Δw_k with percentage of laser output power variation (dP_n/P_n). The kerf width increases with increasing laser output power for all combination of the affecting parameters. The increase in the kerf width is more pronounced as the cutting speed reduces while the energy coupling factor increases. When comparing the kerf width predicted from the present and previous studies,[23] and the experimental results, both predictions and the experimental results are in good agreement for cutting speed of 4 cm s^{-1} and $a = 0.3$. However, the present model over predicts the kerf width for the condition at which the cutting speed is 1 cm s^{-1} and $a = 0.6$. This may occur due to one or all of the following reasons: (1) the energy coupling at the workpiece changes as the cutting speed changes; in this case, the energy coupling improves at low cutting speed, but worsens at high cutting speed. Therefore, the energy-coupling factor should be greater than 0.3 at 4 cm s^{-1} cutting speed, and (2) the simplified model used at present predicts the kerf width with some error when the extreme cutting conditions are introduced. Nevertheless, the trends of

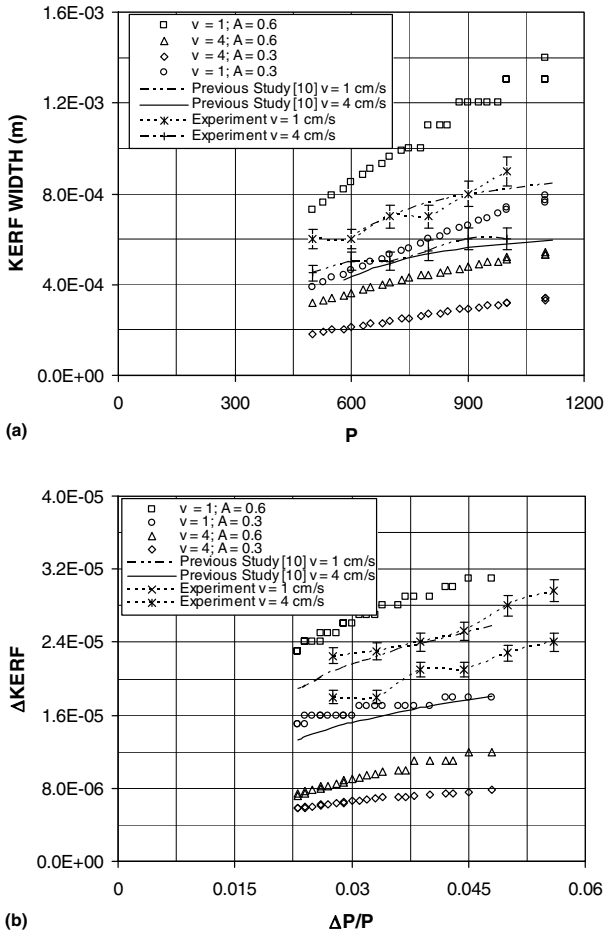


Figure 8 (a) Kerf width with laser power for different cutting speeds and energy coupling factors. (b) Variation in kerf width with laser power variation for different cutting speeds and energy coupling factors.

the predictions and the experimental results are similar. In the case of Δw_k (Figure 8(b)), Δw_k rises with increasing dP_n/P_n. The rate of increase in Δw_k is more pronounced for cutting velocity 1 cm s^{-1} and energy-coupling factor 0.6. Δw_k predicted from the present study agrees well with the previous and experimental results for the affecting parameters of cutting speed 4 cm s^{-1} and energy coupling factor 0.3. However, the present predictions slightly over estimate Δw_k for the cutting speed 4 cm s^{-1} and energy coupling 0.6 as compared to experimental findings. This suggests that the energy-coupling factor of 0.6 may not represent the actual case and it is on the high side. Moreover, it is observed that variation in laser output power modifies the size of the kerf considerably. In this case, the kerf size increases substantially.

1.12.5.3 Laser Bending

Thermal strain developed in the laser heated region results in elasto-plastic thermal deformation of the substrate material. This in turn causes thermal displacement and bending in the laser treated section. The findings and discussions related to the laser bending are provided in line with the previous findings.[28]

Figure 9 shows the geometric arrangements of paths and points at the workpiece. Figure 10 shows the temperature variation along the y-axis (along the line 1–2) as shown in Figure 9 for the time corresponding to the tracks ends. Temperature increases in the region where the laser spot is located. It should be noted that the laser beam intensity is considered to be Gaussian at the surface in the simulations in line with the experimental conditions. Temperature decay is gradual at the irradiated spot center and it becomes sharp as the distance from the laser scan tracks increases toward the workpiece edges. This behavior is attributed to laser beam intensity distribution at the surface, which is Gaussian and the volumetric absorption of the laser beam in the substrate material. However, in the neighborhood of the irradiated spot edge, temperature gradient becomes large because of the low substrate bulk temperature. Thermal diffusion from the irradiated spot increases toward the bulk of the substrate material due to the high temperature gradient in this region. As the number of laser scanning tracks increases, the peak temperature increases. This is attributed to the heating of the substrate material by the initially formed laser scan tracks. Thermal diffusion from the initially laser scanning track enhances the internal energy gain in its neighborhood so that temperature attains high values, despite the high cooling rates from the surface. It should be noted that convection boundary is assumed at the surface resembling the cooling effect of the assisting gas at the irradiated surface. Moreover, the location of the peak temperature changes along the y-axis as the number of laser tracks increases. This is because of the geometric location of the irradiated spot, which is along the line 1–2 (Figure 10) for the first track. However, this point shifts with an amount equal to the laser scanning track width along the y-axis for the following track. Although phase change due to melting is incorporated in the analysis, no mushy zone is observed, where temperature remains constant between the solidus and liquidus temperatures, along temperature profile. This indicates that the mush-zone generated along and above the solidus temperature is considerably narrow at the irradiated surface.

Figure 11 shows von Mises stress variation along the y-axis (along the line 1–2) as shown in Figure 9 for the time corresponding to the tracks ends. The time settings for von Mises stress variation are similar to those shown in Figure 10. The von Mises stress attains high values in the region where the temperature gradient is high, which occurs in the neighborhood of the irradiated spot edges, which is more pronounced for the first laser scanning track. Since the location of the laser irradiated spot center along the each tracks changes, von Mises stress behaves differently for each laser scanning tracks. In this case, von Mises stress attains the highest value for the end of the last scanning track. The self-annealing effect of the initially formed tracks is only effective in the close region of the tracks, since the self-annealing effect lowers stress levels in the region close to the laser scanning track. von Mises stress attains low value across the laser scanning tracks width for scanning track numbers 3–6, which is because of the self-annealing effect of the initially formed laser scanning tracks on the stress field.

Figure 12 shows thermal displacement along the circumference of the mid-plane of the laser scanned workpiece

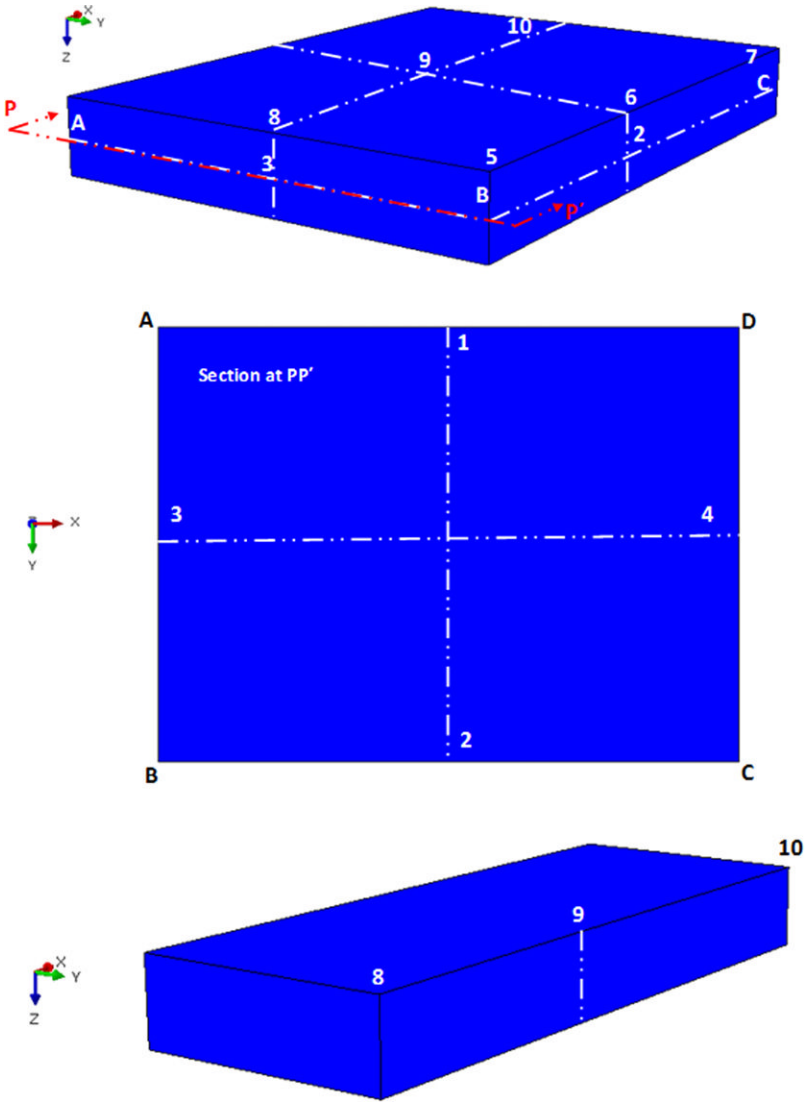


Figure 9 Geometric arrangements of paths and locations at the workpiece.[7]

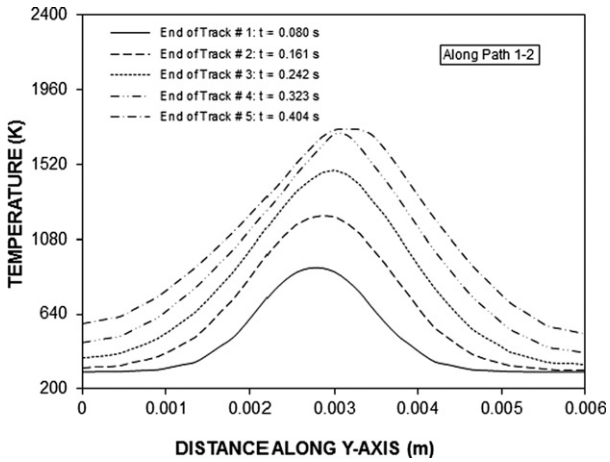


Figure 10 Temperature variation along the *y*-axis for different times corresponding to end of tracks and along path 1–2 (Figure 9).[7]

(Figure 9) for the times when the laser scanning track ends. Thermal displacement attains higher values in the region where the laser scanning takes place. The displacement takes the negative values due to the compression. Since the substrate material is not free to expand at the mid-plane, compressive stress is formed along this plane. The bending takes place under the compressive stress and the magnitude of displacement superimposes with increasing number of laser scanning tracks despite the fact that von Mises stress reduces along the scanning tracks with progressing number of laser scans. The thermal diffusion form the heated region toward the neighborhood of the laser scanning tracks reduces the thermal displacement in this region. Consequently, the region where the thermal displacement is effective by self-annealing is limited within the close region of the laser scanned tracks. This, in turn, causes sharp bending rather than forming a curvature through gradual bending in the vicinity of the laser scanning tracks. Therefore, the narrow

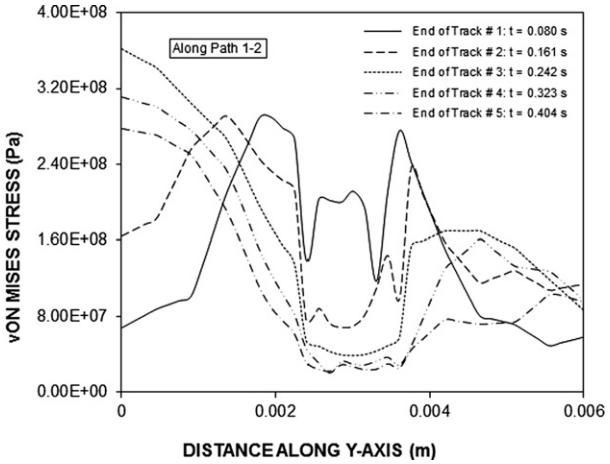


Figure 11 von Mises stress variation along the *y*-axis for different times corresponding to end of tracks and along path 1–2 (Figure 9).[7]

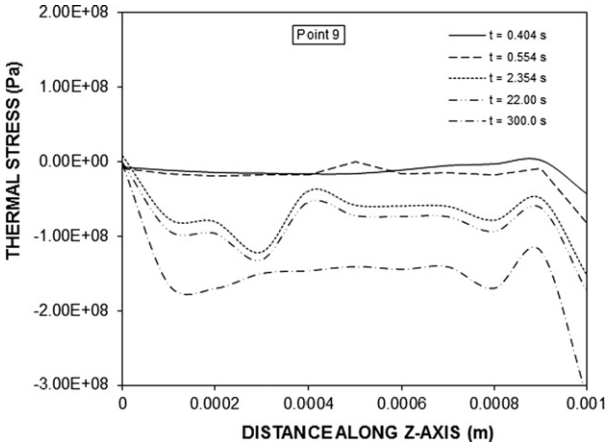


Figure 13 Residual stress variation along *z*-axis at location # 9 (Figure 9).[7]

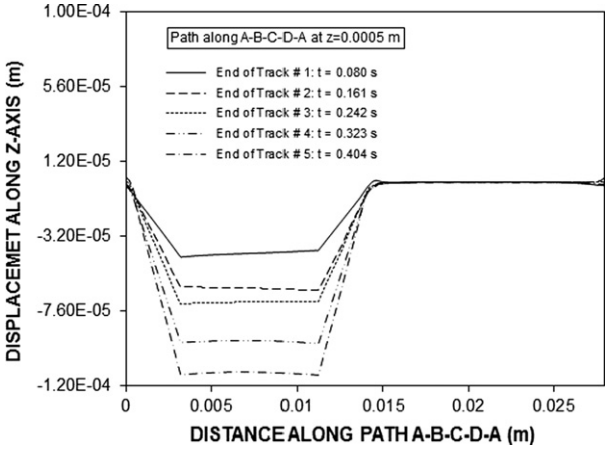
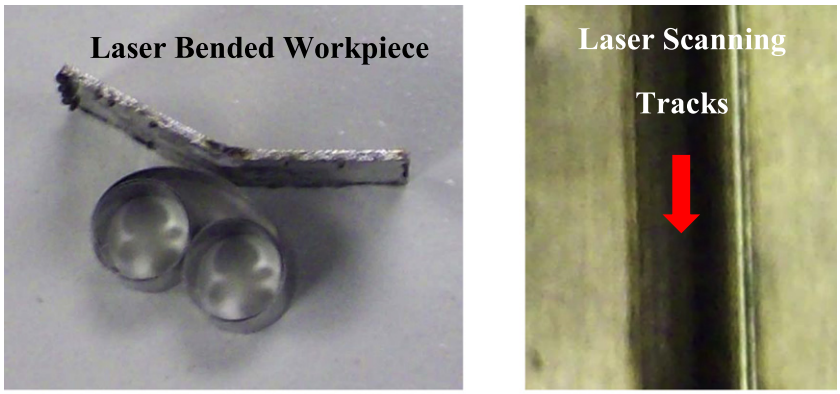


Figure 12 Displacement along the circumference of the workpiece and *z*-axis location is the mid-height of the workpiece (Figure 9).[7]

heat affected zone due to the occurrence of the sharp temperature gradient in this region is responsible for the sharp bending in this region.

Figure 13 shows residual stress distribution along the *z*-axis at location #9 for different times. It should be noted that the location # 9 corresponds to the middle point of the plate (Figure 9). In general, residual stress is compressive, which is more pronounced at the end of 300 s when the cooling period ends. In the early heating period where the laser scanning tracks are formed, residual stress is low, which is associated with the self-annealing effect of the previously formed laser scanning tracks. As the cooling period progresses after forming the laser tracks ($t > 0.404$ s), residual stress along the *z*-axis build up because of bending. This is more pronounced as the depth below the surface increases toward the bottom of the plate along the *z*-axis. The maximum magnitude of the residual stress is on the order of -300 MPa, which occurs at the bottom of the steel plate. The attainment of high residual stress is attributed to the relatively larger displacement at the bottom of the steel plate (Figure 10) as compared to that corresponding to the mid-plane Figure 9.

Figure 14 shows optical photographs and SEM micrographs of top surface of the laser scanned tracks. Optical photograph of laser bended section shows that bending angle is sharp and there is no evidence of geometric curvature in the bend section. This is associated with the high rate of strain formed under the high temperature gradients in the vicinity of the laser scanning tracks. The similar behavior is observed from the displacement simulations (Figure 12); in which case, displacement reduces sharply in the region of the bended section. The laser scan tracks are straight and parallel without showing large scale thermal defects at the scanned surface. This is also observed from the SEM micrograph. However, the closed examination of the laser scanning tracks reveals that few small cavities are formed at the surface. This is associated with the local evaporation at the surface, despite the fact that the laser parameters are selected to avoid the evaporation at the surface. It should be noted that in order to achieve deep penetration of melt layer, the laser power intensity is kept high at the surface. In addition, presence of oxygen in the treated section triggers high temperature oxidation reactions taking place at the surface, which contributes to the cavity formation through excessive heating at the surface. Although nitrogen at high pressure is used to avoid oxidation reactions, presence of small amount of oxygen is sufficient to initiate the exothermic reactions at the scanned surface. Since the laser scans the surface at high frequency repetitive pulses (1500 Hz) (Table 4), the overlapping of laser spots along the laser scanning tracks is notable and the overlapping ratio is of the order of 85%. The high overlapping ratio results in continuous melting along the laser scanning tracks at the surface. However, no excessive melting across the tracks is observed. In addition, self-annealing effect of the recently formed tracks results in crack free structure at the surface despite the fact that the cooling rate is high at the surface. It should be noted that the heat conduction from the recently formed tracks toward the initially formed tracks causes self-annealing effect on the microstructure at the surface.



Optical Photographs

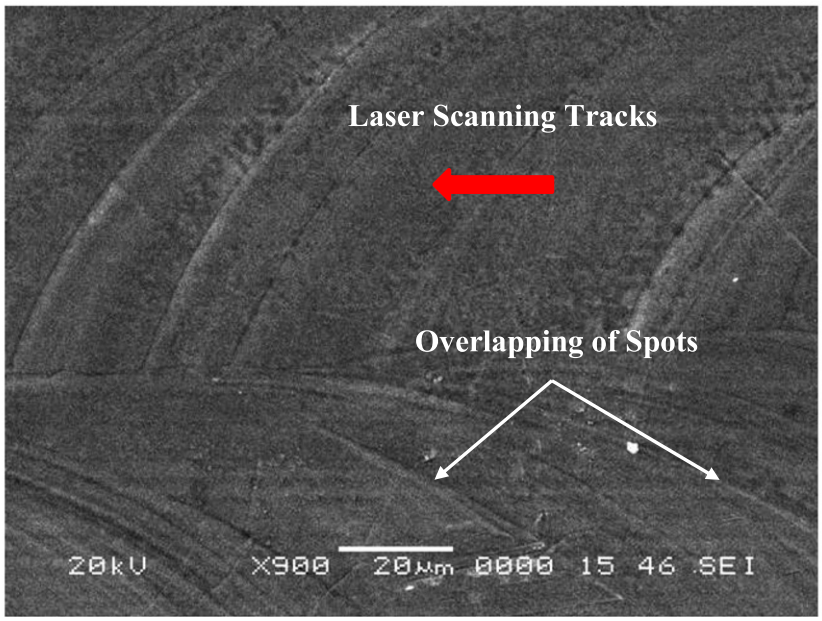


Figure 14 Optical photographs of laser bended workpiece and SEM micrograph of laser scanned surface.[7]

1.12.6 Concluding Remarks

Laser machining is one of the thermal processing techniques, which can be used effectively in sheet metal industries. Since the process is involved with the high temperature phenomena, a care must be taken to minimize the thermally induced defects around the machined parts. This can be possible with proper selection of laser machining properties, which requires prior knowledge about the physical insight into the machining process. Consequently, statistical, numerical, and experimental studies associated with laser machining process become essential to develop such detailed database to achieve the required end product quality. In this chapter, laser drilling, laser cutting, and laser bending are presented in the light of the previous studies. The concluding remarks are given below according to the laser machining processes involved.

In laser drilling, all the factors considered have significant effect on the resulting features of the hole geometry. However, the effects of thickness, focus setting, and ambient pressure are identified as the most significant parameters. The effects of thickness and focus setting are most significant for overall quality of the hole drilled. From the qualitative analysis, the effect of each parameter on the hole geometry varies almost linearly, except thickness and focus setting which vary quadratic or cubic forms. This indicates that small variation of pressure and energy result in small changes in hole geometry, but this change amplifies once the thickness and focus setting vary.

In laser cutting process, increase in laser power, energy coupling factor, and reducing cutting speed result in increased kerf width. The kerf width size varies considerably as the velocity, laser power, and energy coupling factor changes slightly; in which case, striation size increases. The effect of laser power on the kerf width is highly significant, since small variation in laser power alters the kerf size considerably. The laser output power and the energy-coupling factor have a

coupling effect on the resulting kerf size. In this case, as the laser power and the energy coupling factor increase, the kerf width size increases substantially. Consequently, in laser cutting operation, small variation in laser power results in large variation in the kerf size.

In laser bending process, temperature remains high in the region of the laser irradiated spot, which, in turn, results in high temperature gradients in the neighborhood of the laser scanning tracks. The high temperature gradients cause the development of high stress levels in this region. The self-annealing effect of the recently formed tracks influences the stress levels in the heated region; in which case, von Mises stress reduces along the previously formed laser scanning tracks. The displacement along the *z*-axis is high because of the bending of the workpiece. The sharp change of displacement across the laser scanning tracks and the untreated substrate material indicates that the bending is sharp and the curvature bending does not take place in the substrate material. Laser scanned surfaces are free from large size defects and asperities, provided that few scattered shallow cavities are formed at the surface.

Acknowledgments

The authors acknowledge the support of King Fahd University of Petroleum and Minerals, Dhahran, Saudi Arabia for this work.

See also: 1.14 Laser Peening of Metallic Materials

References

1. Yilbas, B. S. Parametric Study to Improve Laser Hole Drilling Process. *J. Mater. Process. Technol.* **1997**, *70* (1–3), 264–273.
2. Yilbas, B. S. Parametric Study for Laser Hole Drilling of Inconel 617 Alloy. *Lasers Eng.* **2002**, *12*, 1–16.
3. Al-Sulaiman, F.; Yilbas, B. S.; Ahsan, M.; Mansoor, S. B. Laser Hole Drilling into Composites and Steel Workpieces. *Lasers Eng.* **2006**, *16* (1–2), 105–120.
4. Yilbas, B. S. The Analysis of CO_2 Laser Cutting. *Proc. Inst. Mech. Eng. Part B* **1996**, *211*, 223–232.
5. Yilbas, B. S. Effect of Process Parameters on the Kerf Width during the Laser Cutting Process. *Proc. Inst. Mech. Eng. Part C: J. Eng. Manuf.* **2001**, *215*, 1357–1365.
6. Yilbas, B. S.; Karatas, C.; Keles, O.; *et al.* Laser Cutting of Corners: Assessment of Cutting Quality. *Lasers Eng.* **2006**, *16* (1–2), 157–171.
7. Yilbas, B. S.; Akhtar, S. S. Laser Bending of Metal Sheet and Thermal Stress Analysis. *Opt. Laser Technol.* **2014**, *61*, 34–44.
8. Taneko, S.; Massahura, M.; Seigo, H. Laser Drilling by Peak Pulsed CO_2 Laser. In *Proceedings of ICALEO' 90, Laser Material Processing*, Orlando; 1990.
9. Yilbas, B. S. The Examination of Optimal Focus Setting with Material Thickness at Atmospheric Pressures of Air and Oxygen in Laser Drilling of Metals. *Proc. Inst. Mech. Eng. Part B: J. Eng. Manuf.* **1988**, *202*, 123–127.
10. Yilbas, B. S.; Sami, M. Study into the Effect of Beam Waist Position on Hole Formation in the Laser Drilling Process. *Proc. Inst. Mech. Eng. Part B: J. Eng. Manuf.* **1996**, *210*, 271–277.
11. Yilbas, B. S. Study of Affecting Parameters in Laser Hole Drilling of Sheet Metals. *ASME J. Eng. Mater. Technol.* **1987**, *109*, 283–287.
12. Davies, O. L. *The Design and Analysis of Industrial Experiments*; 2nd ed.; Longman Group Limited: New York, NY, 1978.
13. Yilbas, B. S.; Yilbas, Z. Effects of Plasma on CO_2 Laser Cutting Quality. *Opt. Lasers Eng.* **1988**, *9*, 1–12.
14. Yilbas, B. S.; Sahin, A. Z. Oxygen Assisted Laser Cutting Mechanism – A Laminar Boundary Layer Approach Including the Combustion Process. *Opt. Laser Technol.* **1995**, *27*, 175–184.
15. Yilbas, B. S.; Sahin, A. Z. Turbulent Boundary Layer Approach Allowing Chemical Reactions for CO_2 Laser Oxygen-Assisted Cutting Process. *Proc. Inst. Mech. Eng. Part C: J. Mech. Eng. Sci.* **1994**, *208*, 275–284.
16. Schuocker, D.; Muller, P. Dynamic Effects in Laser Cutting and Formation of Periodic Striation. *SPIE Proc.* **1987**, *801*, 258–264.
17. Olsen, F. O. Cutting Front Formation in Laser Cutting. *CIRP Ann. – Manuf. Technol.* **1989**, *38*, 215–218.
18. Yilbas, B. S.; Yilbas, Z. An Optical Method to Measure the Pulsed Laser Output Power Intensity Distribution in the Focal Region. *Meas., J. Int. Meas. Confed.* **1996**, *17* (3), 161–172.
19. Gonsalves, J. N.; Duley, W. W. Cutting Thin Metals with the CW CO_2 Laser. *J. Appl. Phys.* **1972**, *43*, 4684–4687.
20. Kar, A.; Rothenflue, J. A.; Latham, W. P. Scaling Laws for Thick-Section Cutting with a Chemical Oxygen-Iodine Laser. *J. Laser Appl.* **1997**, *9*, 279–286.
21. Che Jamil, M. S.; Sheikh, M. A.; Li, L. A Study of the Effect of Laser Beam Geometries on Laser Bending of Sheet Metal by Buckling Mechanism. *Opt. Laser Technol.* **2011**, *43*, 183–193.
22. Peng, Z.; Hongwei, L. Simulation and Control Models of Laser Bending Angle of Sheet Metals. *Key Eng. Mater.* **2010**, *431–432*, 118–121.
23. Yanjin, G.; Sheng, S.; Guoqun, Z.; Yiguo, L. Finite Element Modeling of Laser Bending of Pre-Loaded Sheet Metals. *J. Mater. Process. Technol.* **2003**, *142*, 400–407.
24. Shichun, W.; Jinsong, Z. Experimental Study of Laser Bending for Sheet Metals. *J. Mater. Process. Technol.* **2001**, *110*, 160–163.
25. Nadeem, Q.; Na, S. J. Deformation Behavior of Laser Bending of Circular Sheet Metal. *Chin. Opt. Lett.* **2011**, *9* (5), Article number: 051402.
26. Gheorghies, C.; Nicoara, D.; Paunoiu, V.; Quadrini, F.; Santo, L.; Squeo, E. A. Numerical Prediction of Residual Stresses in Laser Bending of Stainless Steel Sheet Metals. *Key Eng. Mater.* **2009**, *410–411*, 629–640.
27. Yongxiang, H.; Yefei, H.; Zhenqiang, Y.; Jun, H. Three-Dimensional Numerical Simulation and Experimental Study of Sheet Metal Bending by Laser Peen Forming. *J. Manuf. Sci. Eng.* **2010**, *132*, 061001–061011.
28. Yilbas, B. S.; Khaled, M.; Akhtar, S.; Karatas, C. Laser Bending of Steel Sheets: Corrosion Testing of Bended Sections. *Ind. Lubr. Tribol.* **2011**, *63*, 367–372.
29. ABAQUS. *ABAQUS Theory Manual, Version 6.2*, ABAQUS Inc.: Pawtucket, RI.
30. Shuja, S. Z.; Yilbas, B. S. The Influence of Gas Jet Velocity in Laser Heating – A Moving Workpiece Case. *Proc. Inst. Mech. Eng. Part C: J. Mech. Eng. Sci.* **2000**, *214*, 1059–1078.
31. Risso, J. M.; Huespe, A. E.; Cardona, A. Thermal Stress Evaluation in the Steel Continuous Casting Process. *Int. J. Numer. Methods Eng.* **2006**, *65* (9), 1355–1377.
32. Mase, G. E.; Mase, G. T. *Continuum Mechanics for Engineers*; 2nd ed.; CRC Press: New York, 1999.

Relevant Website

www.kfupm.edu.sa
King Fahd University of Petroleum & Minerals.

1.13 ELID Grinding and EDM for Finish Machining

T Saleh and R Bahar, International Islamic University Malaysia, Kuala Lumpur, Malaysia

© 2017 Elsevier Inc. All rights reserved.

1.13.1	**Introduction**	364
1.13.2	**Background of ELID Grinding**	365
1.13.3	**Classifications of ELID Grinding**	368
1.13.3.1	Electrolytic In-Process Dressing (ELID I)	368
1.13.3.2	Electrolytic Interval Dressing (ELID II)	369
1.13.3.3	Electrode-Less ELID (ELID III)	369
1.13.3.4	Electrode-Less ELID (ELID IIIA)	370
1.13.3.5	Ion Shot ELID (ELID IV)	370
1.13.4	**ELID Grinding for Nano Surface Finish**	370
1.13.4.1	ELID Grinding for Ceramics	370
1.13.4.2	ELID Grinding for Coated Film	373
1.13.4.3	ELID Grinding for Metal	374
1.13.4.4	ELID Grinding for Optical Glasses	377
1.13.4.5	ELID on Silicon Wafer	380
1.13.5	**Summary on ELID Grinding**	383
1.13.6	**Background of EDM**	383
1.13.7	**Major Categories of EDM**	384
1.13.8	**EDM Process Performance and Parameters**	388
1.13.8.1	Discharge Voltage	388
1.13.8.2	Peak Current	389
1.13.8.3	Pulse Duration and Pulse Interval	389
1.13.8.4	Pulse Waveform	390
1.13.8.5	Polarity	390
1.13.8.6	Electrode/Workpiece Material	390
1.13.8.7	Dielectric Fluid	390
1.13.8.8	Rotational Motion of Electrode/Workpiece	390
1.13.9	**EDM Applications**	390
1.13.9.1	EDM for Heat-Treated Materials	390
1.13.9.2	EDM for Nonconductive Ceramic	390
1.13.9.3	Modern Semiconductor/Composite Materials	390
1.13.10	**EDM and Its Effect on Workpiece Surface Finish**	390
1.13.10.1	Surface Modification Using EDM	392
1.13.10.1.1	Surface modification by conventional electrode materials	392
1.13.10.1.2	Surface alloying using composite (PM) electrode	395
1.13.10.1.3	Surface modification by dielectric	396
1.13.10.1.4	Ball burnish machining for EDM surface	398
1.13.10.1.5	Special applications	400
1.13.10.2	Surface Modification Using Wire EDM	404
1.13.11	**Summary on EDMed SQ**	404
1.13.12	**Conclusion**	405
References		406

1.13.1 Introduction

Machining is a subtractive manufacturing process that is used for removing material controllably from a piece of raw material. The objective of this process is to produce final product with proper shape and controlled dimension from the workpiece (raw material). In order to manufacture product with accurate dimension, proper tolerance and acceptable surface finish, several things need to be considered during machining such as, tool material, workpiece material, type of machining process, etc. Relative motion between the tool and workpiece is the primary reason behind all machining process that causes material to be removed from the workpiece, however, tool shape and tool penetration into the workpiece are also responsible for this. Relative motion between the tool and workpiece is achieved by the combined action of the primary motion called 'cutting speed' and secondary motion called 'feed speed.' Modern days' machining process is mostly carried out by computer numerical control (CNC) machine in which software based automatic control

 doi:10.1016/B978-0-12-803581-8.09158-X

system carries out the movement and operation of the machine tools.

Machining processes can be divided into mainly two groups 'conventional machining processes' and 'non-conventional machining processes.' Turning, boring, milling, shaping, broaching, slotting, grinding. etc., fall under the category of conventional machining process. Similarly there are several examples of non-conventional machining such as abrasive jet machining (AJM), electro-discharge machining (EDM), electrochemical machining (ECM), and ultrasonic machining (USM), etc. In conventional machining usually harder material is used as tool for changing the shape of a workpiece by cutting operation. Machining hard metals and alloys using conventional methods involves longer time and higher energy, and therefore, an increase in costs. Conventional machining may also higher tool wear and deteriorated quality in the product owing to induced residual stresses during manufacturing. Conventional machining can be defined as a process of using mechanical (motion) energy. On the other hand, most non-conventional machining has no direct contact between the tool and the workpiece. It has several other features and the three main forms of energy that are used in these processes are thermal energy, chemical energy, and electrical energy. If one asks why we need the non-conventional machine? The simple answer is, in several industries, hard and brittle materials like tungsten carbide (used for making cutting tools), high speed steels (used for making gear cutters, drills, milling cutters), stainless steels, ceramics, etc., are often used. If such materials are machined with the help of conventional machining processes, either the tool undergoes extreme wear (in case of hard materials) or the workpiece material is damaged (in case of brittle materials). This is because, in conventional machining, there is a direct contact between the tool and the workpiece. Large cutting forces are involved, and material, are removed in the form of chips. A huge amount of heat is produced in the workpiece. This induces residual stresses, which degrades the life and quality of the workpiece material. To overcome all these drawbacks, non-conventional machining processes are used to machine hard and brittle materials. As well as to machine soft materials, in order to get better dimensional accuracy (DA). The best way to give a clear vision of these two machining groups (conventional and non-conventional) is to introduce a comparison between them. In conventional processes generally macroscopic chip formation by shear deformation. While material removal may occur with chip formation or even no chip formation may take place in non-conventional processes. For example, in an AJM, material removal occurs due to electrochemical dissolution at atomic level. Back to conventional processes, there is a physical tool present such as a cutting tool in a reamer machine. While there may not be a physical tool present in non-conventional processes such as in laser jet machining.

Again in conventional machining the tool should be harder than the workpiece under the machining conditions. While as mentioned in the above, there may not be a physical tool present in non-conventional machining. Tool life in the conventional might be less than the non-conventional (e.g., ECM) due to high surface contact and wear. In the conventional, there are always noisy operations that cause sound pollutions whereas in non-conventional machining sound pollutions is at minimal level. Conventional machining (unlike the non-conventional machining) requires lower capital cost and simple setup of equipment. Skilled or un-skilled operator can run the conventional machining, while only skilled operator can run the non-conventional that generally operates using automated processes. This chapter will be discussing in detail two manufacturing processes namely electrolytic in-process dressing (ELID) grinding (a conventional machining process to attain smooth surface) and EDM (a non-conventional machining process for conductive materials), and their implication in finish machining.

1.13.2 Background of ELID Grinding

In most of conventional rough machining like milling, turning are followed by finishing processes like grinding, polishing, and lapping. Grinding is a finish machining process to obtain a high degree of DA and surface finish on a part. This process uses microscopic abrasive particles for cutting. Grinding is a subset of cutting where each grain of abrasive functions as a microscopic single-point cutting edge with high negative rake angle. Rapid progress in electronic and optical devices (such as IC chips, MEMS, smart sensors, lenses) with the increasing requirement of their performance, demand of ultra-precision surface finish of the specialized glass, silicon wafer in nano-scale is growing. Conventional grinding cannot produce such surfaces with precise form accuracy; therefore, conventional grinding is still considered to be a preliminary finishing process. Typical ways for achieving final finishing of different materials are lapping and polishing. Though these methods have disadvantages like poor grind ability, waste water problem, mechanical damages, etc.[1] Chemical–mechanical polishing (also known as CMP) is another final finishing process for silicon wafer preparation in the IC industries. Some of the disadvantages associated with the CMP process[2] are:

1. Low efficiency due to low removal rates,
2. Non-uniform wafer surface due to the variation in relative cutting speed across the wafer surface, and
3. Relatively high cost involved in this process.

In order to overcome all these drawbacks associated with the conventional finishing processes, demand for nano surface generation by grinding (using super abrasives) to replace the polishing, lapping, etc., have been growing stronger and stronger in the manufacture of optical and electrical parts. In order to achieve ultra-precision surface finish by grinding two issues are needed to be addressed, first the abrasive of the grinding wheel has to be superfine and second the dressing of the grinding wheel needs to be in-process to maintain DA of the finished product. ELID grinding has been proven to be the most potent candidate technology in this regard. In ELID grinding super abrasive grinding wheel is dressed in-process by electrochemical method that employs the electrochemical machining principle to dress the wheel. In this case metal bonded grinding wheel is set as an anode and another metal electrode is set as a cathode.[3] Electrolytic dressing of the wheel applies the basic mechanism of electrolysis. This process converts electrical energy to chemical energy in an electrolytic solution in the presence of two electrodes (anode and cathode)

as shown in Figure 1. An electrical power supply is used to energize anode positively and cathode negatively. As the electric energy is applied ionic dissolutions occurs in the electrolytic solution and the negative and positive ions in the solution move to the positive and negative electrodes, respectively. This will cause anodic metal dissolution and formation of anodic oxide.

The mathematical form of metallic dissolution rate is governed by Faraday's law of electrolysis, which concludes that dissolution from anode material is directly proportional to the integration of current supplied to the electrolytic cell. The mathematical form of anodic dissolution can be written as follows,

$$m = \frac{\int_0^T i\mathrm{d}t}{F} \cdot \frac{M}{z} \tag{1}$$

where m is the mass of the substance altered from anode, i is the electric current passed through the cell, F is the Faraday constant, M is the molar mass of the substance, and z is the valence number of ions of the substance (electrons transferred per ion).

Basic elements of ELID grinding and its mechanism are shown in Figure 2. ELID cell consists of a metal bonded grinding wheel, a cathode electrode, a pulsed DC power supply and electrolyte. The wheel is connected to the positive terminal of the DC power supply thru a carbon brush whereas the electrode is connected to the negative pole of the power supply. Usually, alkaline liquids are used as both electrolytes and coolant for grinding. A nozzle is used to inject the electrolyte into the gap between wheel and electrode. The gap is usually maintained to be approximately 0.1–0.3 mm. An anodic oxide layer is formed on the circumference of the grinding wheel as a result of electrochemical reaction. The formation of this oxide layer is very crucial for the success of ELID grinding. It is soft and brittle in nature as compared to the original metal bond and gets easily worn off because of the excessive grinding force.

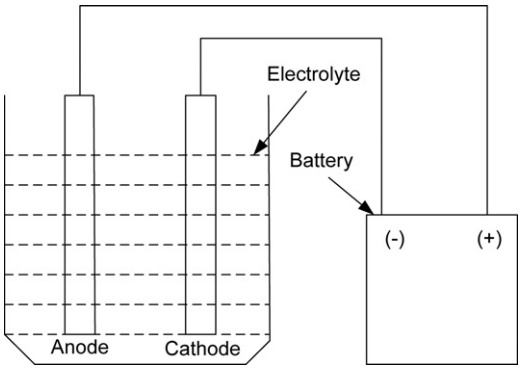


Figure 1 Basic principle of electrolysis.

The basic mechanism of ELID grinding has been explained in the zoom in section of Figure 2. After truing (Figure 2(a)), the grains and bonding material (metal) of the wheel surface are flattened. It is necessary for the trued wheel to be electrically pre-dressed to protrude the grains on the wheel surface and the dressing continues during the grinding operation as well. When pre-dressing starts (Figure 2(b)), the bonding material flows out from the grinding wheel and an insulating layer composed of the oxidized bonding material is formed on the wheel surface (Figure 2(c)) as explained in Figure 1. This insulating layer reduces the electrical conductivity of the wheel surface and prevents excessive flow-out of the bonding material from the wheel. At this moment the grits are held by both the bonding material and the oxide layer. It is important to note that the insulating oxide layer is soft and brittle in nature and wears off very easily as it comes in contact with workpiece during grinding operation (Figure 2(d)). Continuous grinding will cause wearing out of the diamond grains as a result cutting force increases. This excessive cutting force will cause falling off of the blunt grits, which is now mostly held by the brittle insulating material (Figure 2(e)). As a result of breakage of insulating layer, the electrical conductivity of the wheel surface increases and the electrolytic dressing restarts with the flow-out of bonding material from grinding wheel. The protrusion of new diamond grains from the grinding wheel therefore remains constant. This cycle is repeated during the grinding process to achieve stable grinding. There are few terminology widely used for ELID grinding which are used in this book chapters are as follows,

Peak voltage (V_p): This is the maximum voltage applied to the ELID cell by pulsed voltage supply.

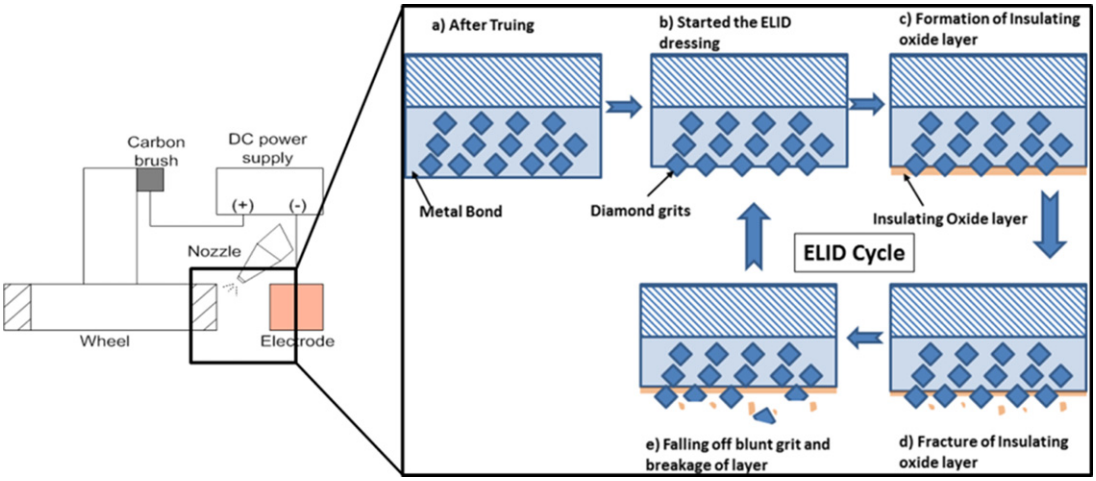


Figure 2 Components of ELID grinding and its mechanism.

Peak current (I_p): Maximum current drawn by the ELID cell when the peak voltage is applied.

T_{ON}: This is the pulse ON time and T_{OFF} is the pulse OFF time.

Duty ratio (R_c): Duty ratio is the % of ON time for one cycle of operation and can be calculated as follows

$$R_c = \frac{T_{ON}}{T_{OFF} + T_{ON}} \times 100\% \quad (2)$$

Considerable number of researches have been carried out and still continuing on various aspects of ELID grinding. This chapter will discuss in detail about different researches about ELID grinding in the subsequent sections.

Murata *et al.*[4] introduced ELID grinding technology in 1985 for structural ceramics as they were difficult for grinding because of their hard and brittle nature. Conventionally, softer grade wheels are used for grinding hard and brittle material which has problem of maintaining desirable form accuracy because of their higher tool wear. In order to cater this problem Murata *et al.*[4] performed ELID grinding operation on the above mentioned ceramics metal bonded grinding wheels with grit size of #80, #100, #150, and #400. Constant protrusion of sharp grits was maintained because of the ELID cycle as described in **Figure 2**. The experimental setup used by Murata *et al.*[4] is shown in **Figure 3**. This shows that ELID is being taken place in one side of the wheel continuously and grinding is being taken place on the other side. ELID has an inherent self-control mechanism that causes proper use of the grits till their life and protrusion of new grits as they are worn out, which is explained in **Figure 2**. This ELID principle ensures significant lower grinding force as observed by Murata *et al.*[4] (**Figure 4**) for grinding ceramics while compared to conventional grinding. In conventional grinding there is no in-process dressing mechanism that may cause the sharpening of the grinding wheel as the grits become dull, that is why the grinding force becomes high as grinding progresses. Further the surface roughness (SR) of the finished product was also found to be much improved when ELID grinding was used for the same underlying reason.

ELID grinding process was further investigated by Ohmori *et al.*[5] while he was experimenting to achieve mirror surface finish by grinding on silicon wafer. **Figure 5** describes the experimental setup that shows cast iron fiber bonded (CIFB) wheel as anode and copper/graphite as cathode. Pulsed DC voltage was used as the power source with grinding fluid as the electrolyte. Necessary isolation between the grinding wheel and machine structure was arranged during the ELID grinding experiment. Application of the pulsed voltage caused higher anodic current flow as shown in **Figure 6**. Eventually, the current decreases as the formation of insulating anodic oxide on the grinding wheel surface. As a result the working voltage also reaches to open circuit voltage gradually as explained in the I–V characteristic shown in **Figure 6**. Few notable issues were highlighted Ohmori *et al.*[5] in this paper,

1. ELID grinding doesn't require any special equipment. Conventional grinding machine can be used. Further die-sinking EDM power supply can be used as ELID power supply as well.
2. ELID produces highly stable and lower grinding force compared to conventional grinding because of continuous protrusion of sharp grits, this also ensures there will be no heat-affected area (caused by rubbing action of the dull grits) commonly known as grinding burn in the case of ELID grinding.

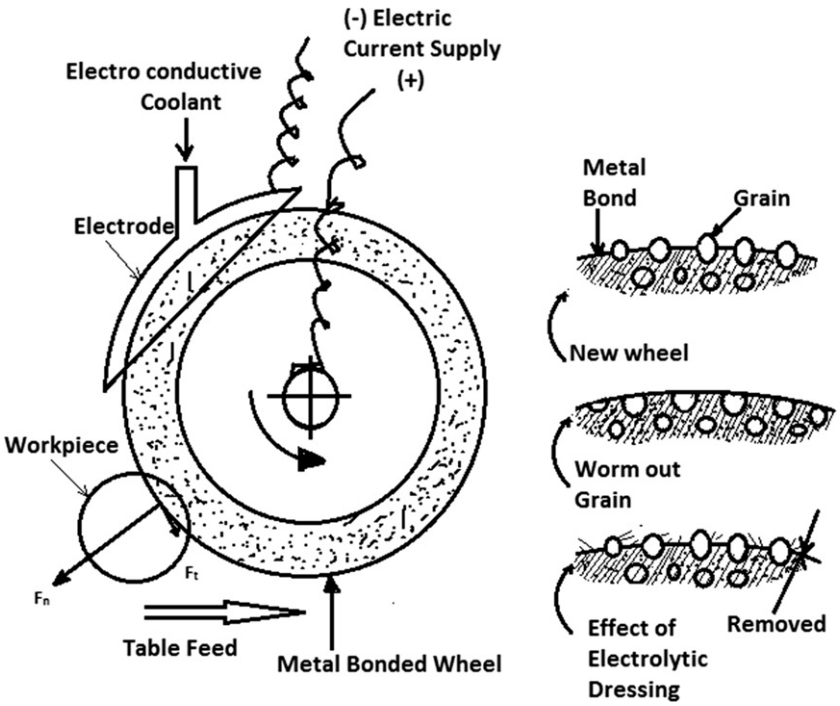


Figure 3 ELID grinding setup proposed by Murata *et al.*[4]

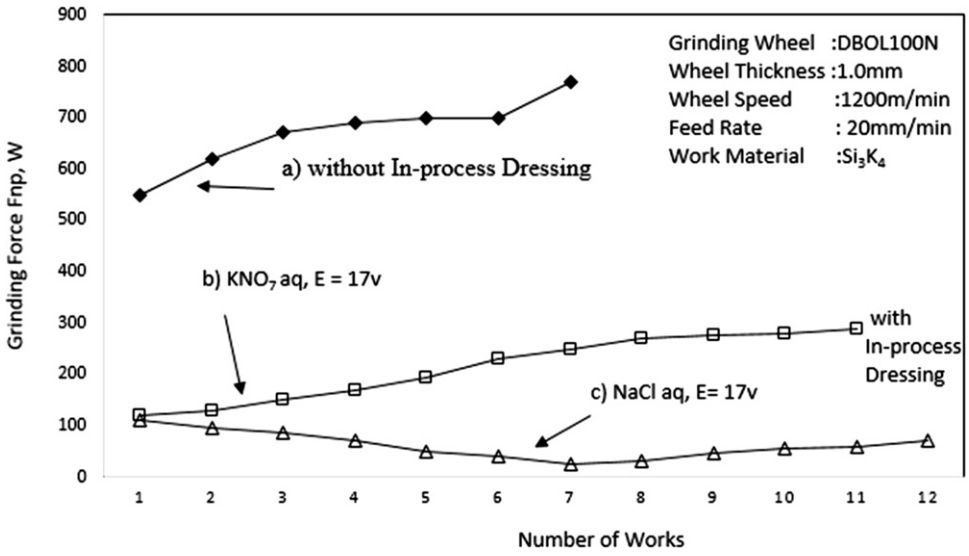


Figure 4 Significant reduction of grinding force when in-process dressing (ELID) is used.[4]

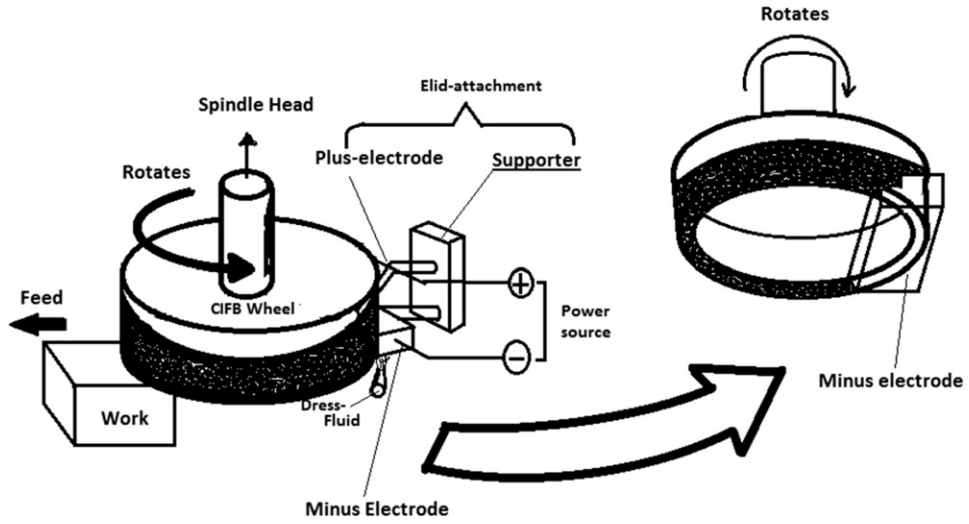


Figure 5 Experimental setup for ELID grinding of silicon wafer, proposed by Ohmori *et al.*[5]

3. As the advantageous effect of *b*, mirror surface can be achieved by ELID grinding without further processing method hence elimination of subsequent finishing process like polishing and lapping can be attained by introducing ELID.
4. ELID grinding can be applied for variety of machining system such as vertical/horizontal grinding machine, planner surface, or cylindrical surface grinding, etc., without any notable modification of the machine.

1.13.3 Classifications of ELID Grinding

Researchers' continued to investigate various aspects of ELID grinding in 1990s. Eventually, they divided ELID grinding into three major types, based on the materials to be ground and application method. However, the basic principle of dressing of the wheel remains the same which is the anodic dissolution metal bonded grinding wheel for in-process dressing. In order to have better understanding about various types of ELID grinding, section below discusses basic methodology of different ELID grinding system.

1.13.3.1 Electrolytic In-Process Dressing (ELID I)

This is the most widely used ELID grinding method used by manufacturing practitioners. In this case the wheel is dressed continuously in-process at one side and grinding is being taken place on the other side. Figure 7 explains the basic mechanism of ELID I method for peripheral grinding. A cathode electrode covers usually 1/4th to 1/6th of the cutting edges of the wheel whereas the other exposed portion of the wheel takes part in the grinding action. The gap between the electrode and the wheel is usually maintained to be 0.1–0.3 mm.

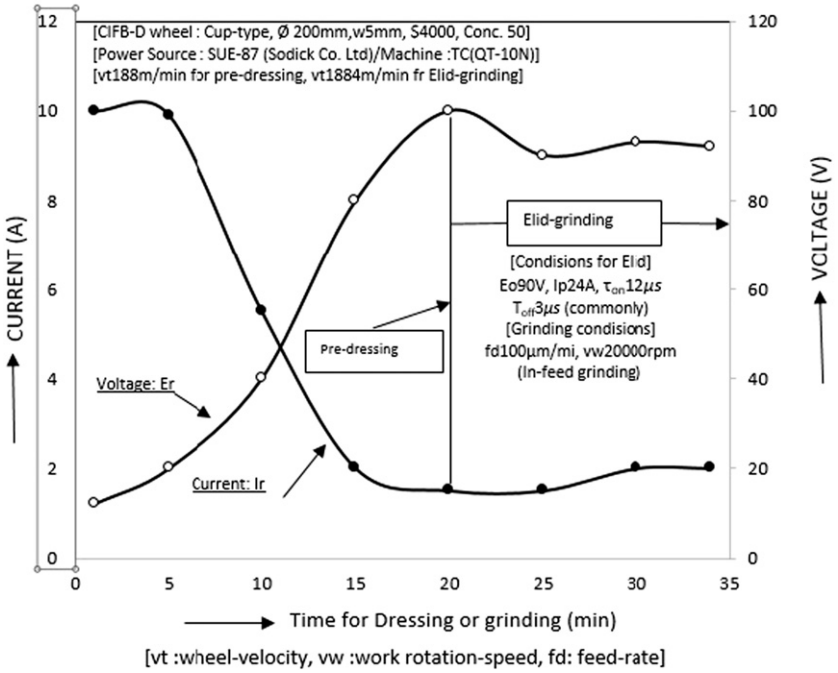


Figure 6 I–V characteristic for dressing of the wheel by ELID shows reduction of dressing current due to the formation of insulating layer.[5]

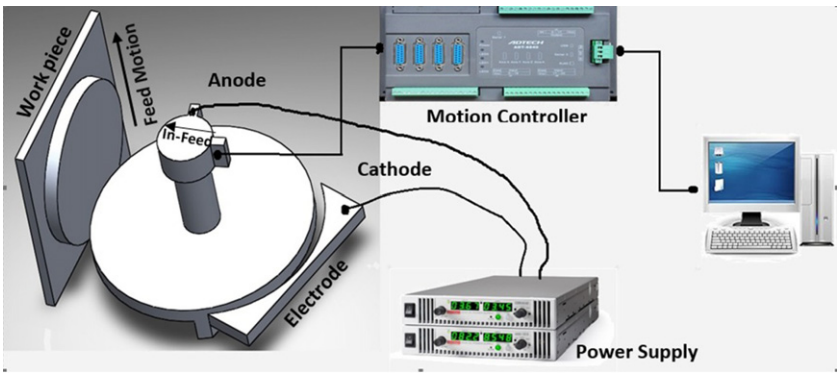


Figure 7 ELID I grinding system.

1.13.3.2 Electrolytic Interval Dressing (ELID II)

In the case of internal grinding of cylindrical surface ELID I method is mostly inapplicable as it is difficult to integrate cathode electrode with the grinding wheel especially for small holes. In order to cater this problem and to carry out precision grinding on the small holes on ceramic materials Zhang *et al.*[6] introduced ELID II method. In this method the dressing of the grinding wheel is carried out intermittently in contrast to ELID I method. In ELID I method wheel is dressed without any process condition monitoring, however, there is inherent self-controlling mechanism in the process that saves the wheel from excessive dressing as described in Section 1.13.2. On the contrary ELID II is an intermittent process and interval time between two successive dressings is set by the user. Therefore, it is necessary to monitor the grinding process, in order to select the interval time. Grinding force is a good choice as it indicates the attritions wear of the grits, thus in ELID II system interval time is set mostly based on pre-decided grinding force limit and sometimes by monitoring other grinding conditions. Figure 8 shows the schematic illustration of the interval ELID dressing and grinding. In this time of arrangement production time will be compromised as the wheel does not take part in the grinding action during dressing.

1.13.3.3 Electrode-Less ELID (ELID III)

The problem of ELID II method is absence of in-process dressing. It can be understood from Figure 8 that during dressing of the wheel no grinding action is being taken place. Therefore, the production time will be compromised when

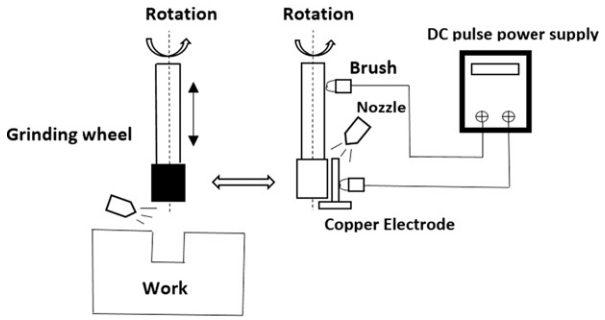


Figure 8 ELID II grinding principle.[6]

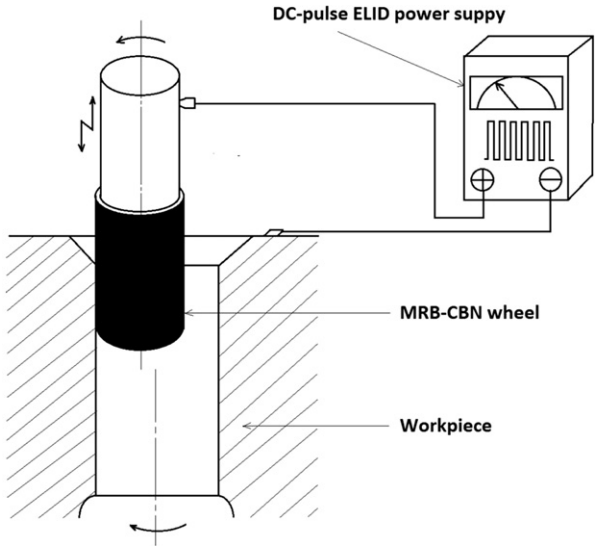


Figure 9 Electrode-less ELID grinding (ELID III).[7]

ELID II method is used. In order to tackle higher production time associated with ELID II system Qian *et al.*[7] introduced ELID III system. In ELID III system the cathode electrode is removed by the workpiece itself as explained in Figure 9. By doing this in-process dressing of the grinding wheel can be achieved and anodic dissolution will be taken place only on the metal bond of the wheel and not on the workpiece. However, this method is limited for grinding of conductive material only. Moreover, as all electrolytes has some degrees of dielectric property this process may introduce unwanted spark between the workpiece and the grinding wheel when pulsed DC power is applied between anode wheel and cathode workpiece (a similar concept of EDM). This may lead to unwanted micro/macrocavities on the wheel. Hence the wheel life will be reduced.

1.13.3.4 Electrode-Less ELID (ELID IIIA)

It is mentioned in the earlier Section 1.13.3.3 is that ELID III has a problem of initiation of unwanted spark that may damage the grinding wheel locally. In order to address this problem an alternating current (AC) power supply was introduced instead of pulsed DC power supply for ELID grinding. This causes the workpiece to become anode during half cycle of the current and cathode during other half cycle of the current. Therefore, anodic dissolution and formation of oxide film occurs not only on the grinding wheel but also on the workpiece material. This method is known as ELID IIIA and was proposed by Lim.[8] The principle of this type of ELID grinding is explained in Figure 10. This version of ELID will cause to create a thick oxide layer (passivation film) on the workpiece as shown in Figure 10(c) to prevent direct contact between the wheel and the workpiece, hence the electrical discharges.

1.13.3.5 Ion Shot ELID (ELID IV)

Ohmori *et al.*[9] developed a new ELID technique where the nozzles have two plates connected to the ELID power supply as shown in Figure 11. When the electrolyte hits the wheels it is already ionized and oxidation of metal bond (of the grinding wheel) can take place. However, it is also true that electrolyte will lose some ionization as it leaves the electrode gap, therefore, this technique is useful for fine grinding technique.

A comparison between various methods of ELID grinding is described in Table 1.

1.13.4 ELID Grinding for Nano Surface Finish

Researchers have been investigating the feasibility of ELID grinding for various types of hard and brittle materials to achieve nanometric surface finish. These include ceramics, optical glass, hardened steel, silicon, etc. The outcomes of these researches are very promising and indicate that ELID grinding can eliminate final finishing process like polishing and lapping. This section discusses research activities related to the applications of ELID grinding on various materials.

1.13.4.1 ELID Grinding for Ceramics

Ohmori *et al.*[10] carried out an experimental study to investigate the performance of ELID grinding on structural ceramics particularly for silicon nitrides. Two different types of silicon nitrides were used in this purpose namely a sintered reaction-bonded silicon nitride (SRBSN), and a cast-and-sintered silicon nitride (Si_3N_4). The effects of cutting speed, feed rate, and grit size on the surface finish of the product were investigated. The findings of the study are summarized in Table 2.

Figure 12 shows the effect of different mesh size of the wheel on surface roughness of Si_3N_4 (a) and sintered reaction-bonded silicon nitride (SRBSN) (b). It can be observed from Figure 12 that both cases sub-20 nm R_a surface finish be achieved, which is considered to be optical quality surface finish by ELID grinding without further material processing technique like lapping and polishing.

Bandyopadhyay *et al.*[11] studied the application of ELID technique for rough grinding operation with high material removal rate (MRR) and compared it with conventional grinding. The workpiece material was silicon nitride. It was observed for conventional grinding that the cutting force increases continuously as the volume of material removed increases; this is because the grinding grits become blunt as the

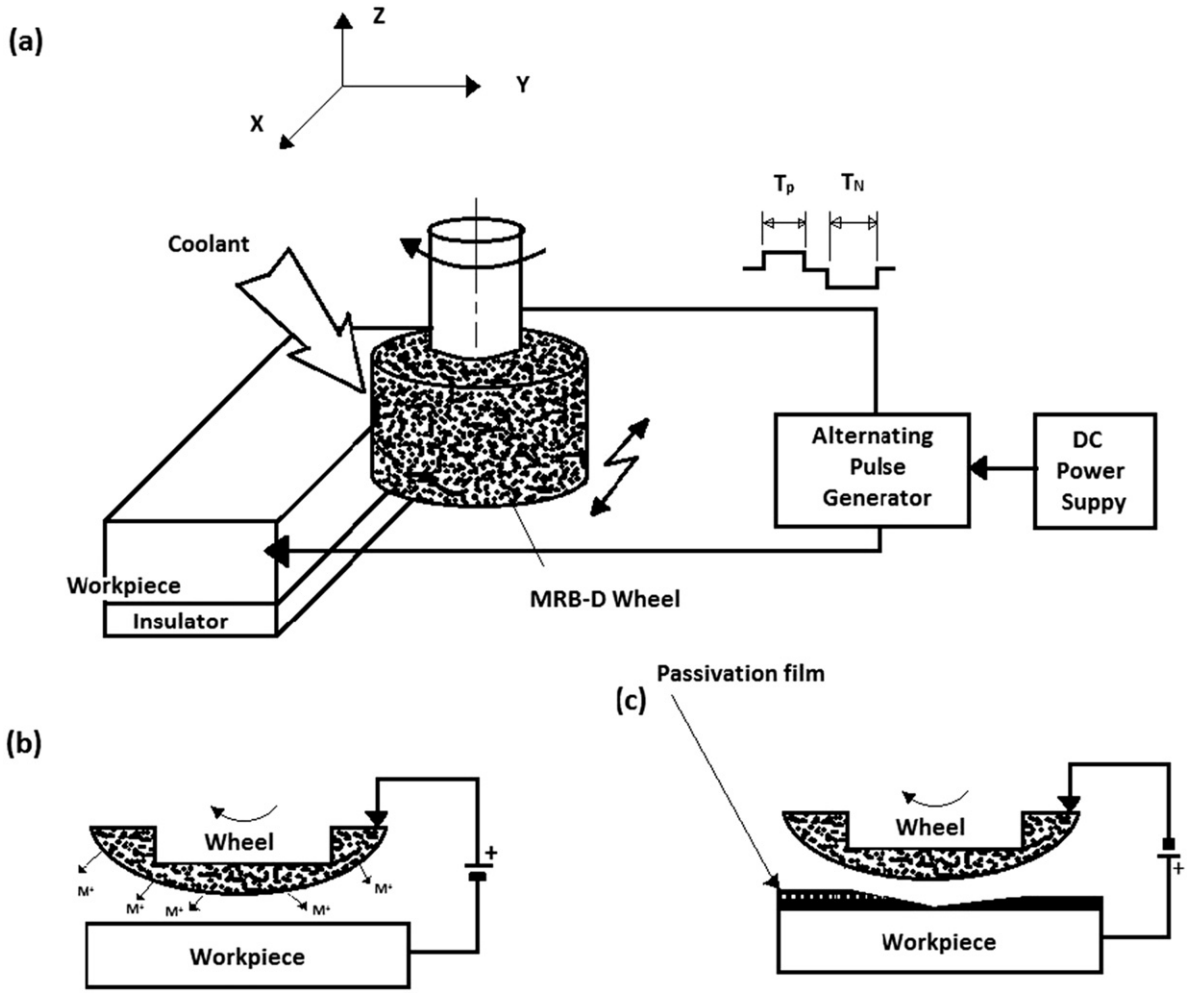


Figure 10 Schematic diagram of ELID IIIA. (a) ELID IIIA machining system with alternating current. (b) ELID without electrode. (c) Electrolysis of workpiece.[8]

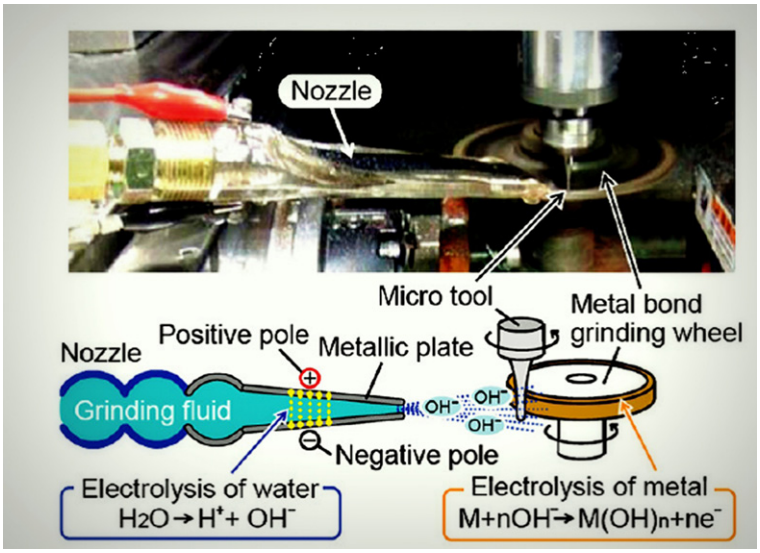


Figure 11 Principle of ELID IV grinding.[9]

Table 1 Comparison between different types of ELID grinding

Attributes	*Electrolytic n-process dressing (ELID I)*	*Electrolytic interval dressing (ELID II)*	*Electrode-less ELID (ELID III)*	*Electrode-less ELID (ELID IIIA)*	*Ion shot ELID (ELID IV)*
Dressing interval	Continuous	Intermittent	Continuous	Continuous	Continuous
Separate electrode	Yes	Yes	No (workpiece is cathode)	No (workpiece is cathode)	No
Dressing current	Pulsed DC	Pulsed DC	Pulsed DC	Alternating current	Pulsed DC
Electrolyte property	Initially deionized	Initially deionized	Initially deionized	Initially deionized	Ionized

Table 2 Summarized result of the study[10]

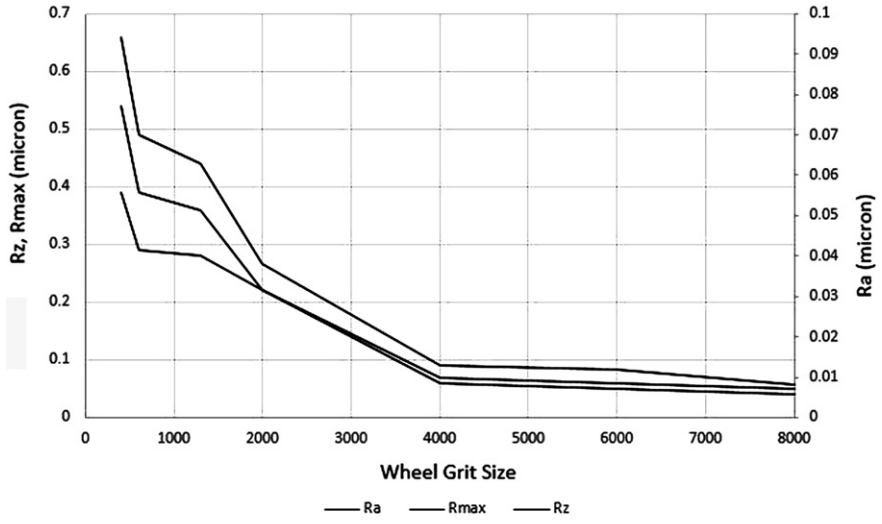
Variable	*Material SRBSN*	*Material Si_3N_4*
Grit size	Higher mesh size wheel produces better surface and #4000 no wheel can produce mirror surface	Same trend was observed as SRBSN. Surface finish achieved by rougher wheel (#320) on Si_3N_4 is worse than that was achieved on SRBSN material, however, for finer wheel equivalent surface can be produced on both materials
Cutting speed	No significant effect on the surface finish of the material	Same as SRBSN
Feed speed	Rough wheel produces bad surface finish at higher feed rate, finer wheel has no significant effect	Similar trend was observed as SRBSN

grinding progresses as there is no in-process dressing for conventional grinding. On the contrary, ELID grinding shows significant reduction of normal force was observed under same cutting condition. The obvious reason behind this is the constant protrusion of new sharp grits during the whole-grinding process because of ELID operation. This also helped to improve the average SR by ~16% for ELID grinding as compared to conventional grinding. The variation of normal grinding force is shown from **Figure 13**. An interesting point to note from **Figure 13** is that higher normal force at the beginning of the cutting stable and low cutting force is achievable after 6000 mm^3 of material removal. The reason behind this is because at the beginning sharp grits are not exposed and electrolysis process is not fast enough to help the sharp grits to be protruded out. In order to address this problem authors proposed two solutions, first one is to use of dummy material for first few cutting cycle before the start of actual workpiece machining. The second solution which is more convincing is to introduce ELID pre-dressing. The pre-dressing condition was different from actual ELID grinding. It was performed in two stages before ELID grinding. In the first stage, the ELID dressing was performed with 90 V for 30 min. The oxide layer produces during ELID dressing was removed mechanically by an aluminum oxide stick. Then the second dressing was performed also with 90 V for 30 min. The ELID grinding was then performed with 60 V, by applying modified ELID dressing as explained above, a stable and low grinding force (almost 5 × lower) can be achieved from the beginning of the grinding operation which can be noticed **Figure 14**.

Katahira *et al.*[12] investigated the surface modifying effect caused by ELID grinding on AlN ceramics and identified the grit size that governs the transition between ductile mode cutting and brittle cutting. This is a very important finding as grit size plays a significant role in achieving nanometric SR on hard and brittle materials by ELID grinding. It was observed that ELID grinding technology can produce extremely smooth surface with nanometric roughness of only $R_a = 8$ nm. If the mesh size of the wheel is greater than #4000 a regular ductile surface with no cracks can be achieved with ELID grinding and the transition between ductile and brittle machining occurs between mesh size #2000 and #4000. **Figure 15(a)** shows the effect of wheel mesh size on the average SR of the material and **Figure 15(b)** explains the transition from brittle mode machining to ductile mode machining. Surface properties were also found to be greatly improved by ELID grinding. It was observed that ELID ground workpiece have better surface characteristics like higher hardness, less friction coefficient, etc., over the conventionally polished workpiece. The authors' investigation suggests that oxygen is diffused into the workpiece when ELID grinding is used for the finishing operation and they identified this diffusion phenomenon as the cause of the improvement of the surface characteristics of the ELID ground samples.

Yang *et al.*[13] developed a new control strategy for ELID grinding and applied it for grinding silicon nitride ceramics. Authors viewed grinding parameters to be constant for particular material with specific requirements, thus cannot be altered. On the other hand, authors concluded that oxide layer states are not the same under different dressing currents as the dynamic behavior of electrolysis and mechanical wearing of oxide layer play roles in ELID grinding. In order to maintain stable dressing current (hence the oxide layer) authors developed an ON-OFF control mechanism which monitors the dressing current and switches the supply of electrical power accordingly. By applying this researchers achieved more uniform dressing current (as shown in **Figure 16**) throughout the grinding process and mirror surface with $R_a = 12$ nm.

Xie *et al.*[14] studied the effects of elliptical torus-shaped diamond wheel for freeform axial-feed grinding of Si ceramics.



(a)



(b)

Figure 12 Effect of grit size on surface finish of Si_3N_4 (a) and SRBSN (b) with constant cutting speed, feed rate, and depth of cut.[10]

The wheel was developed by carrying out form truing of a non-elliptical in an elliptical interpolation paths. The objective of the research was is to understand how the ductile mode mirror grinding can be realized on hard and brittle material using this new wheel profile. It was found that elliptical wheel-profile produces larger wheel working area and more active diamond grains than the arc wheel-profile even in axial-feed grinding of steep freeform surface. This causes reduction in grain cutting depth to a lesser value than critical depth of cut (DOC) without having nanometric positioning capability. This leads more efficient ductile mode cutting. The experimental results confirmed reduction of brittle micro-crack and SR to ductile mode mirror grinding state with the increase of elliptical torus eccentricity as shown in **Figure 17**. Finally, authors concluded that accurate and mirror freeform grinding of hard and brittle material may be achieved by using an elliptical wheel-profile along with valid grain protrusion and suitable grinding variables.

1.13.4.2 ELID Grinding for Coated Film

Katahira *et al.*[15] investigated ELID grinding on TiAlN films. Authors in this research work compared ELID grinding with other finishing process. ELID grinding can produce a mirror surface with an average SR of 2.4 nm whereas other finishing process can only achieve an average roughness of 56.2 nm. Energy-dispersive x-ray spectroscopy revealed that ELID process creates an oxide layer on TiAlN film because of high reactivity of Ti, Al. However, this thin oxide layer enhances surface properties of the TiAlN film. The friction coefficient of the ELID-ground TiAlN film was found to be approximately two-thirds that of the non-ELID-ground TiAlN film (**Figure 18**) as studied in the ball on disk experiments conducted by the researchers.[15] The wear rate of the ELID-ground TiAlN film (disk specimen) also improved by 50% as compared to the non-ELID-ground TiAlN film; and the wear rate against of Al_2O_3 ball for ELID-ground TiAlN film is approximately one-tenth of

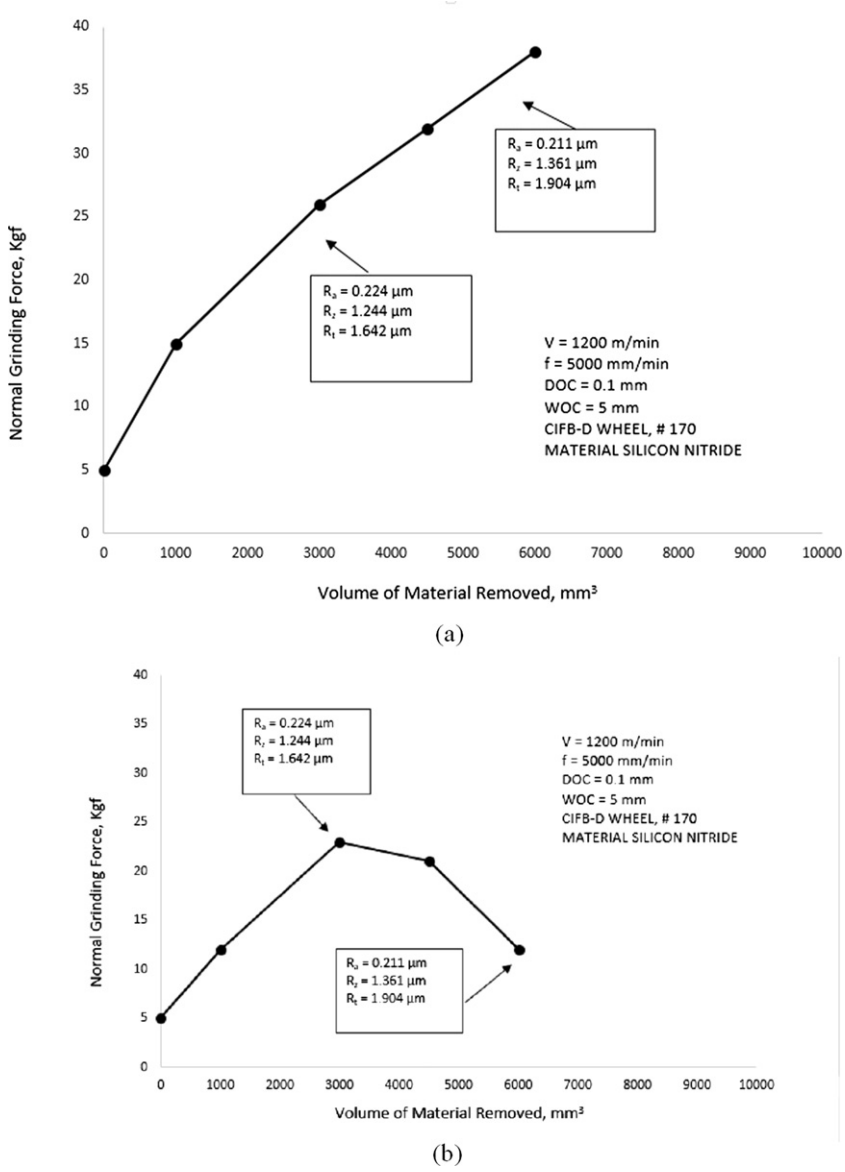


Figure 13 Variation of normal grinding force with volume of material removed (a) conventional grinding, (b) for ELID grinding.[11]

that for non-ELID-ground TiAlN film. The result is shown in Figure 19. The underlying reason behind these improvements in the tribological behavior of ELID ground samples is the diffusion of oxygen into the TiAlN film, which was confirmed by energy-dispersed x-ray diffraction system (EDX) study conducted by the authors (Figure 20).

Zhang *et al.*[16,17] compared ELID grinding with ordinary grinding where the cast iron bonded diamond wheel was dressed mechanically by abrasive stone. It was observed that ELID produces soft oxide layer which holds partially/fully the grits. On the other hand, in mechanical dressing case grits are only held by hard cast iron bond. This caused the ELID grinding to be more stable than conventional grinding and the SR of the ground samples was found to be better in quality in the case of ELID ground samples as described in Figure 21.

Moreover, the morphological study of the samples suggested that in ELID grinding ductile regime machining is the predominant mode of machining (with less pits and fractures) whereas in ordinary grinding both ductile regime and brittle facture machining occurs equally as explained in Figure 22. Therefore, the authors concluded that ELID grinding is a better choice in ultra-precision grinding to achieve nano surface.

1.13.4.3 ELID Grinding for Metal

Qian *et al.*[18] experimented and compared several finishing operation for bearing steel including ELID grinding (Figure 23). Traverse mode and plunge grinding were studied. Moreover, ELID grinding was compared with other finishing process like honing and electro-finishing methods. Experimental findings showed ELID grinding produces better surface finish on the

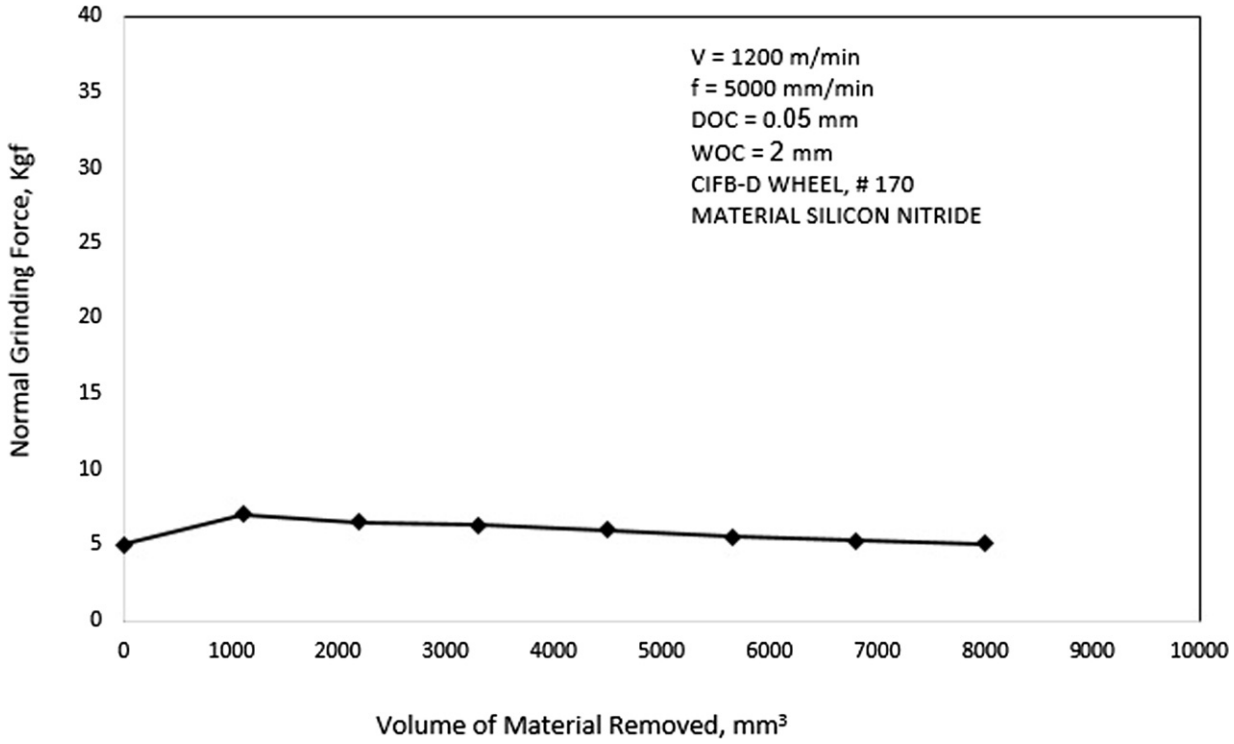


Figure 14 Stable and low grinding force after applying modified ELID grinding as explained in the text.[11]

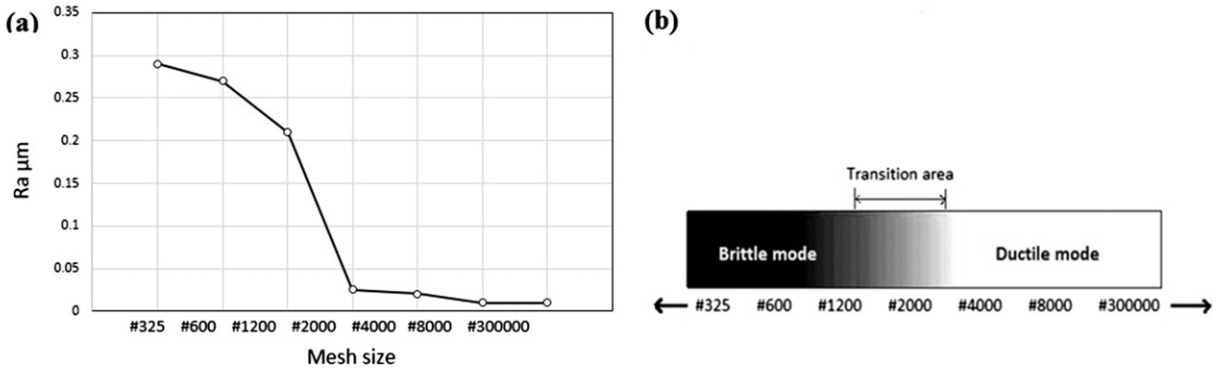


Figure 15 (a) Variation of surface roughness with wheel mesh size. (b) Brittle/Ductile mode transition.[12]

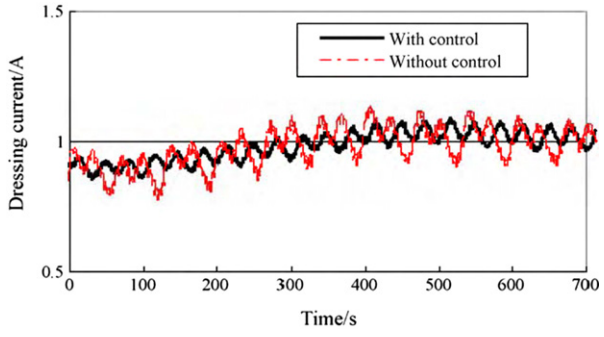


Figure 16 Variation of dressing current as observed by Yang *et al.*[13]

workpiece while comparing with other finishing processes as explained in Table 3.

Qian *et al.*[18] found that in ELID grinding of bearing steel traverse mode generated better surface quality (SQ) than plunge mode grinding, especially when coarser wheels were used. Similar observation was made for waviness of the finished product. Authors carried out metrological study of the samples and found similar degree of waviness on samples processed by ELID grinding honing and electro-finishing method as shown in Figure 24(a). Further, residual stress on the ELID ground sample was also found to be very low (Figure 24(b)). Only negative thing for ELID grinding was longer cycle time as compared to honing and electro-finishing

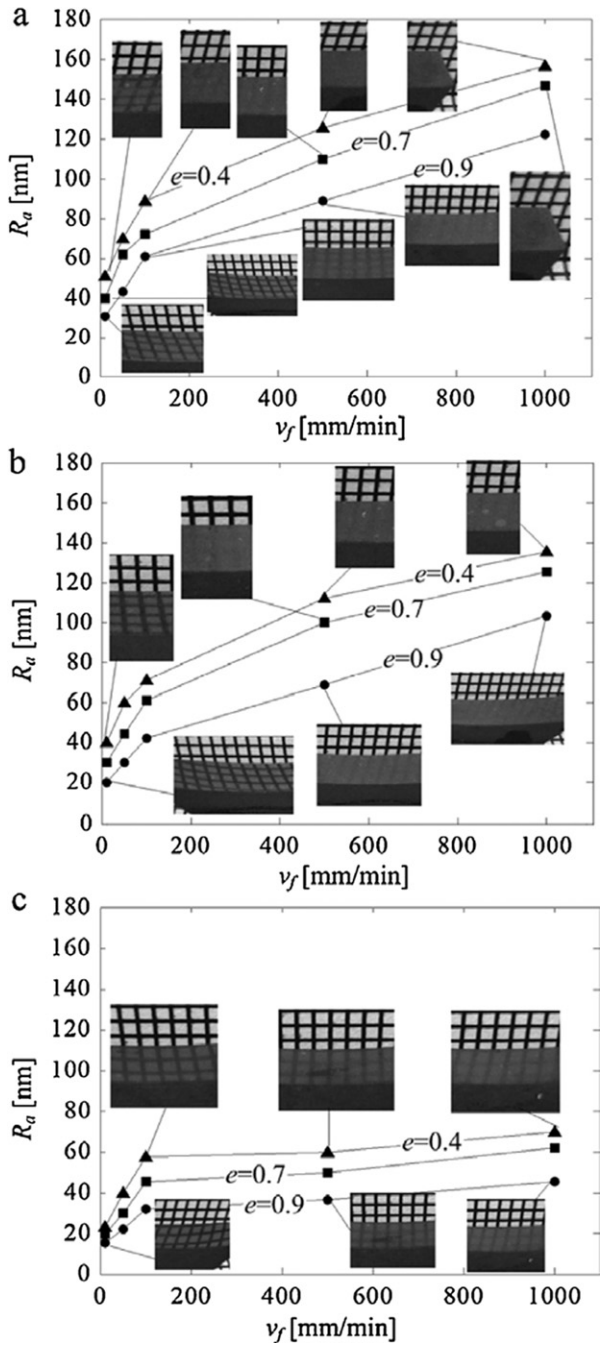


Figure 17 Surface roughness R_a versus elliptical torus eccentricity e and feed rate v_f: (a) wheel speed, v_w=16 m s^{-1}, (b) wheel speed, v_w=24 m s^{-1}, and (c) wheel speed, v_w=32 m s^{-1}.[14]

processes (Figure 24(c)), which indicates that technology should be used for small batch production situations.

Zhang *et al.*[19,20] investigated a similar approach described by Yang *et al.*[13] to carry out internal precision grinding of bearing steel. A similar on-off control mechanism was implemented to realize uniform dressing current and oxide layer thickness. The characteristics of the dressing current is shown in Figure 25, which reports the stability of the real time dressing current as the active control mechanism is applied.

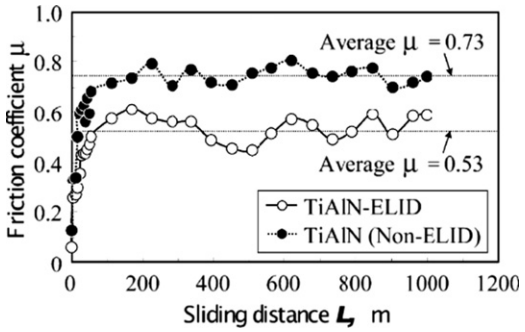


Figure 18 Friction coefficient obtained by ball and disk experiment for ELID-ground TiAlN and non-ELID finished TiAlN film.[15]

Finally, authors concluded that ELID grinding with active control could acquire almost equal SQ, MRR, and grinding force than that with the traditional ELID grinding. Moreover, the dressing current is more stable and in dynamic equilibrium, therefore the attainment of desired SQ would be faster in the proposed new method.

Lens mold requires ultrafine surface finish with high form accuracy. ELID grinding is a potent technology to cater these high end requirements for lens mold fabrication. Saito *et al.*[21] tested and compared the performance of ELID grinding with conventional finishing process like polishing for cemented carbide lens mold fabrication. They also investigated the effect of bond material (namely Cr bond and Cu bond) on the performance of ELID grinding. Authors' finding showed Cr bonded wheel produces better SQ as compared to ELID ground sample with Cu bonded wheel and polished samples (Figure 26). In most of the case of ELID grinding a soft insulating oxide layer is formed which somehow partially retards the protrusion of sharp grits, however, in case of Cr bonded wheel no visible oxide layer is formed on the wheel that causes more protrusion of sharp cutting grits hence better SQ. Moreover, higher oxygen diffusion to the workpiece material in case of Cr bonded wheel also enhances the SQ which is similar to that of Katahira *et al.*[15]

It was reported by other researchers that diffusion of oxygen into the work material during ELID grinding improves the surface property of the work material.[15,21] This inspired Ohmori *et al.*[22] to propose application of a weak positive potential at the workpiece as to control oxide layer formation during ELID grinding of stainless steel. The concept is described in Figure 27. Three different types of abrasive particles (diamond, alumina, silicon dioxide) were tested and compared. It was found that types of abrasive particles do not significantly affect the SR as all of them produced an average SR of 8–10 nm on the ground sample. When compared with conventional polishing it was found that ground samples showed superior surface properties including hardness, tribological and fatigue properties, corrosion and high-temperature oxidation resistances, and adhesive strength with coating films over conventionally polished samples. It was further observed that a stable oxide layer was formed on the ELID ground sample as anticipated by the researchers that enhances the surface characteristics of the ground sample. In addition, it was found very interestingly that the wettability of the processed surface varies with different method and wheel grit

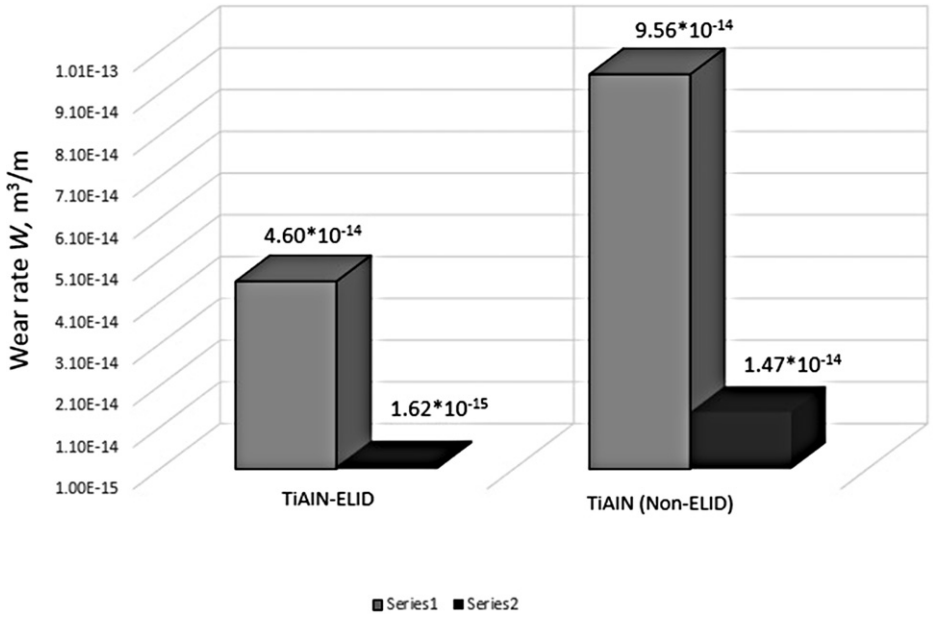


Figure 19 Wear rate of disk and ball specimens.[15]

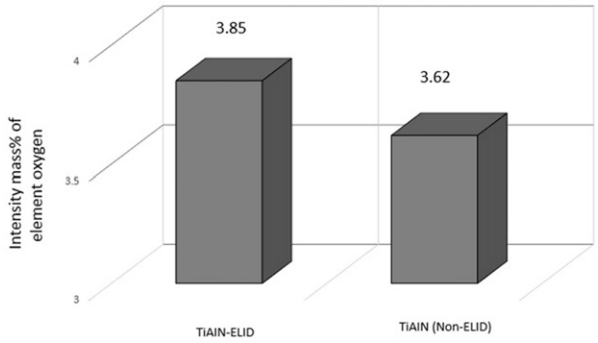


Figure 20 Analytical results of intensity of mass obtained by use of energy-dispersed x-ray diffraction system.[15]

materials. Therefore, researchers proposed that by varying the processing conditions and grinding wheel one can possibly control the surface behavior including hydrophilicity of the surfaces.

Raffles *et al.*[23] investigated different ELID technique (as discussed in Section 1.13.3) for finishing operation of bearing balls using metal-resin bonded CBN wheel. It was observed that a #12 000 series wheel can achieve 2 nm R_a (average SR) with ELID I technique, which is significantly better than balls produced by polishing. Moreover, without ELID MRB-CBN wheel was proven to ineffective for grinding operation as the wheel becomes glazed quickly. However, it was found that ELID I ($R_a = 2$ nm) is better than ELID II ($R_a \leq 10$ nm) because of continuous dressing. On the other hand, ELID III was observed to be unstable.

1.13.4.4 ELID Grinding for Optical Glasses

Optical glass is one of the materials on which ELID grinding technique has been tested for finishing operation. Ohmori *et al.*[24] used ELID grinding to process spherical glass lens. ELID grinding was proven to be more effective than ordinary grinding as it can achieve a SR of 18 nm compared to 138 nm by ordinary grinding method. This was an improvement of 10× times. The ELID ground sample had a very good shape accuracy of submicron range. The variation of the SR with different wheel mesh size is shown in **Figure 28**. Morphological study of the samples also confirmed that ELID grinding can produce much smoother surface than conventional grinding method.

Finishing operation by ELID grinding for BK7 glass was investigated by Kumar *et al.*[25] Kumar *et al.*[25] reported in their work that current duty ratio is one of the key elements to play a major role on the ELID grinding performance and resultant surface finish of the product. It was observed that grinding force was reduced and surface finish was improved as the duty ratio increases as explained in **Figure 29**. The main reason behind this is that higher duty ration dresses the wheel more, therefore renewal of sharp grits are more frequent that causes the improvement in the grinding performance. However, this comes with the price of the grinding wheel life. Higher duty ratio pumps in more dressing current that softens the wheel and eventually reduces its life. Authors also observed that #4000 series wheel with proper grinding condition can generate a flawless ductile surface with sub-10 nm average SR on BK7 glass.

Saleh *et al.*[26,27] developed an intelligent ELID grinding system to conduct nano finishing operation on hard and brittle material like BK7 glass. They first introduced a dedicated ELID grinding machine equipped with several sensory mechanisms with intelligent control. The performance test of the machine was conducted for vertical groove grinding on BK7 workpiece. Vertical grooves with optical SQ were machined using the developed ELID grinding machine. The best SR of 17 nm was achieved at 125 mm min^{-1} feed speed with 3 μm DOC.

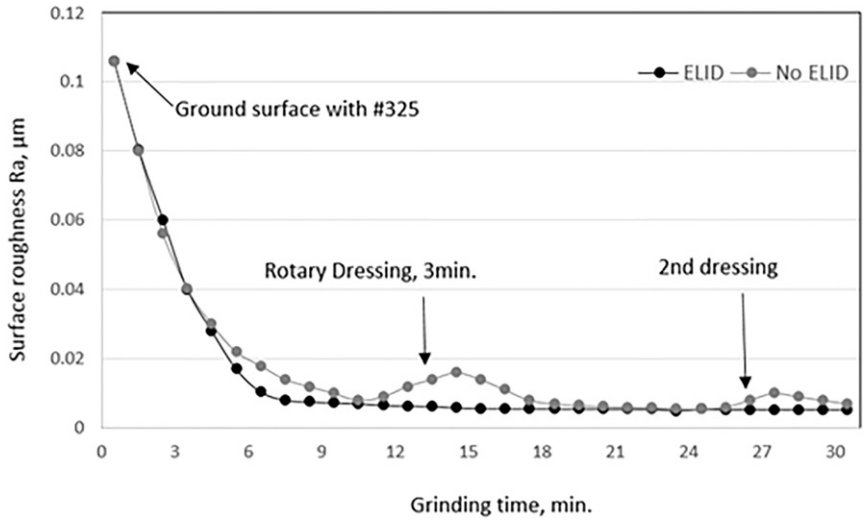


Figure 21 Variation of surface roughness R_a over grinding time.[17]

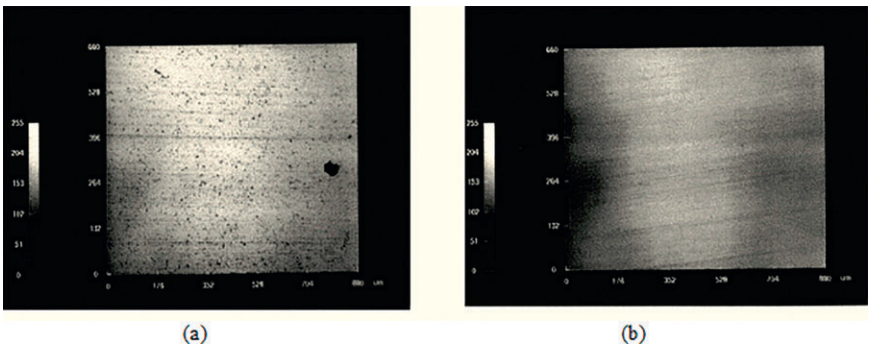


Figure 22 Topography of ground surface of CVD-SiC film (a) ordinary grinding method and (b) ELID grinding method.[16]

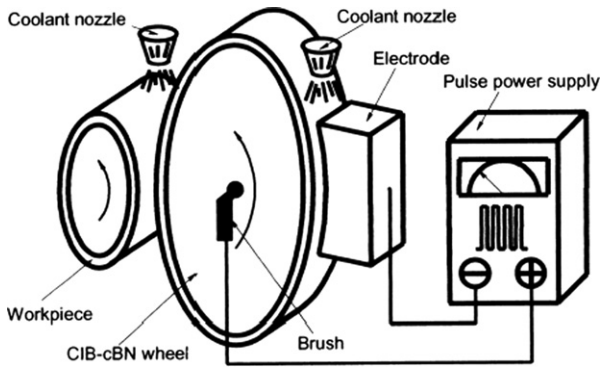


Figure 23 Cylindrical ELID I grinding for bearing steel.[18]

Table 3 Effect of finishing operation on bearing steel[18]

Finishing method	R_a (µm)	R_z (µm)	*Skew risk*	*Delta* q
Honing	0.06	0.5	− 1.1	0.95
Electric polishing	0.04	0.3	− 0.6	0.47
ELID grinding	0.02	0.2	0	0.2

Table 4 shows the effect of DOC/in-feed and feed speed on the SR.

From the table it can be understood that the best surface finish can be achieved at a certain DOC whereas lower feed rate gives better surface finish. It is known that there are three types of material deformation as a grain interacts with the workpiece during grinding: rubbing, plowing, and cutting. In rubbing mode of deformation the material removal is negligible though friction is apparent, which may even cause workpiece burn. Plowing occurs as the depth of penetration is increased; however, the chips are yet to form. With further penetration (the cutting stage) of the grits the actual chip formation occurs, which is desirable for grinding. Again too low in-feed/DOC produces bad quality surface which is due to the reason that rubbing takes place rather than cutting at a very low indentation of the grits as explained earlier. However, at a too high in-feed/DOC the cutting occurs in brittle mode rather than in ductile mode. This explains the trend of the variation of R_a with different DOC. Also lower feed rate produces better surface at a constant DOC/in-feed, as explained in Table 4, because higher the feed rate higher the probability to occur brittle mode cutting.

Overall the performance test of the machine revealed that it can produce an average SR of sub-20 nm, which is of optical

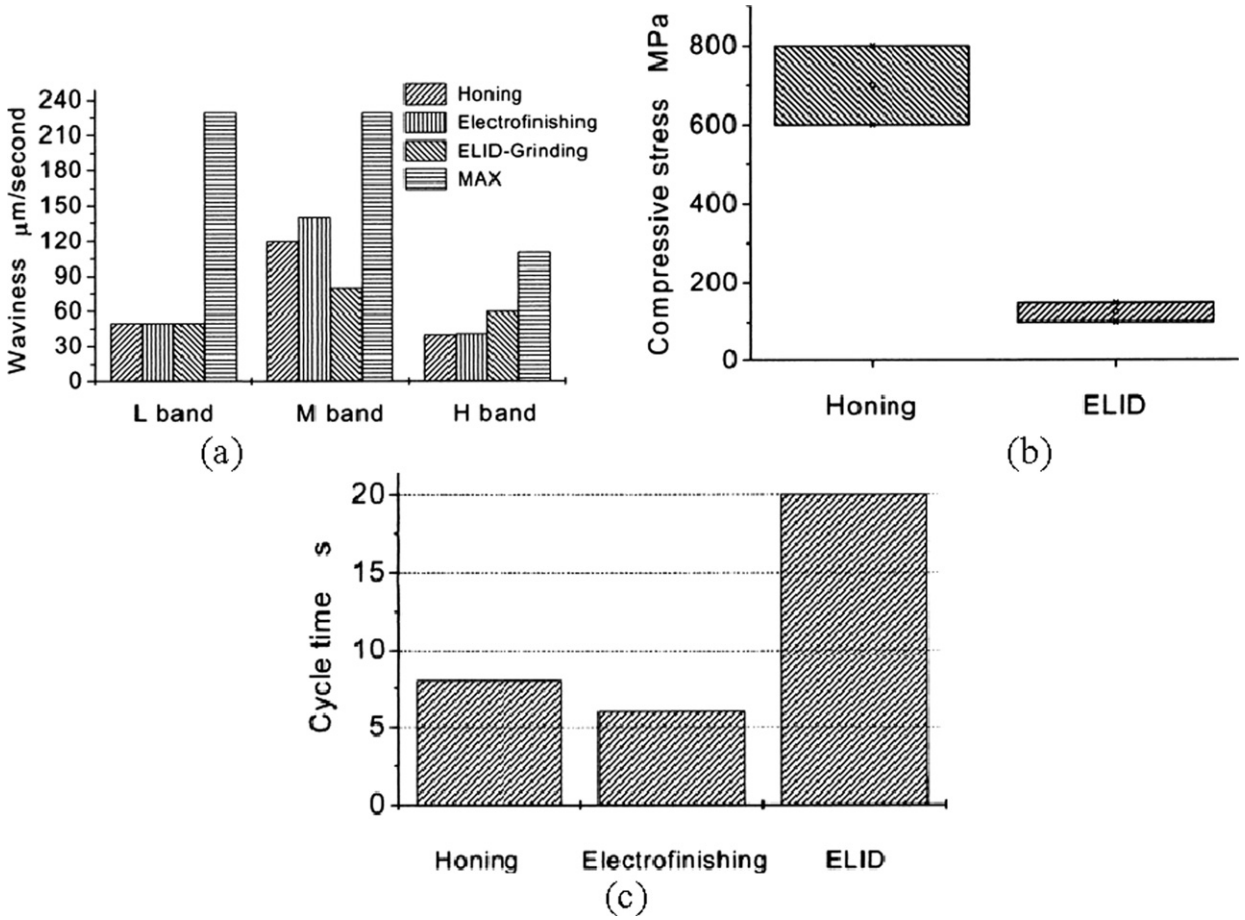


Figure 24 Comparison of ELID performance with different finishing processes for bearing steel (a) surface waviness; here MAX mean maximum allowable limit, (b) surface residual stress, and (c) cycle time of the process.[18]

quality with proper grinding parameters. In ELID grinding operation grinding wheel is dressed continuously therefore the diameter of the tool also changes during one grinding operation, which affects the form accuracy of the finished product especially for curved surfaces. In order to address this issue Saleh *et al.*[26,27] developed a tool wear compensation algorithm. According to this algorithm tool path for spherical lens grinding is generated by considering grinding wheel diameter and desired diameter of the glass lens. Once the lens is fabricated the diameter is measured using a touch probe based on machine measurement system. If the diameter of the lens is found to be offset the lens is reground using a new toolpath which is derived by considering the grinding wheel wear. This algorithm increased the form accuracy significantly as described in **Table 5**. The fabricated lens was found to be of optical quality with $R_a = 15$ nm as shown in **Figure 30**.

In another study Saleh *et al.*[28] developed a dressing control system by periodically observing the grinding wheel wear. Grinding wheel wear was gauged by measuring ratio of normal grinding force over tangential grinding force. When grinding force ratio exceeded a predetermined threshold value ELID power supply was turned on for dressing otherwise it was turned off to save the wheel from excessive dressing. The proposed system dressed the grinding wheel less than conventional ELID grinding because the dressing power is varied according to the change in the force ratio of grinding as explained earlier; however, it was found that the grinding force ratio was still under the critical value. It was also found that SQ obtained by conventional ELID grinding and proposed grinding was comparable. Based on these findings author concluded that dressing current profile over the whole-grinding cycle is much more uniform for the proposed methodology of wheel dressing. The tool wear was found to be only 48% of conventional ELID grinding for equal volume of material removal. However, the ground SQ was not sacrificed as mentioned earlier.

Wheel truing is different from wheel dressing; however, it is very important to maintain the form accuracy of the finished product. In conventional ELID grinding wheel truing is carried out separately by another method such as electrical discharge. Saleh *et al.*[29] proposed a pulse width control of the ELID power supply to carry out truing of the ELID simultaneously during electrolytic dressing. In the study conducted by Saleh *et al.*[29] a pulse width controllable power supply was developed for the in-process truing of the grinding wheel by monitoring the wheel profile on machine using an inductive sensor. The wheel roundness and the wheel workpiece contact were found to be improved significantly after implementing this power supply. Hence authors concluded that ELID is not only meant for wheel dressing alone, but in addition a controlled dressing

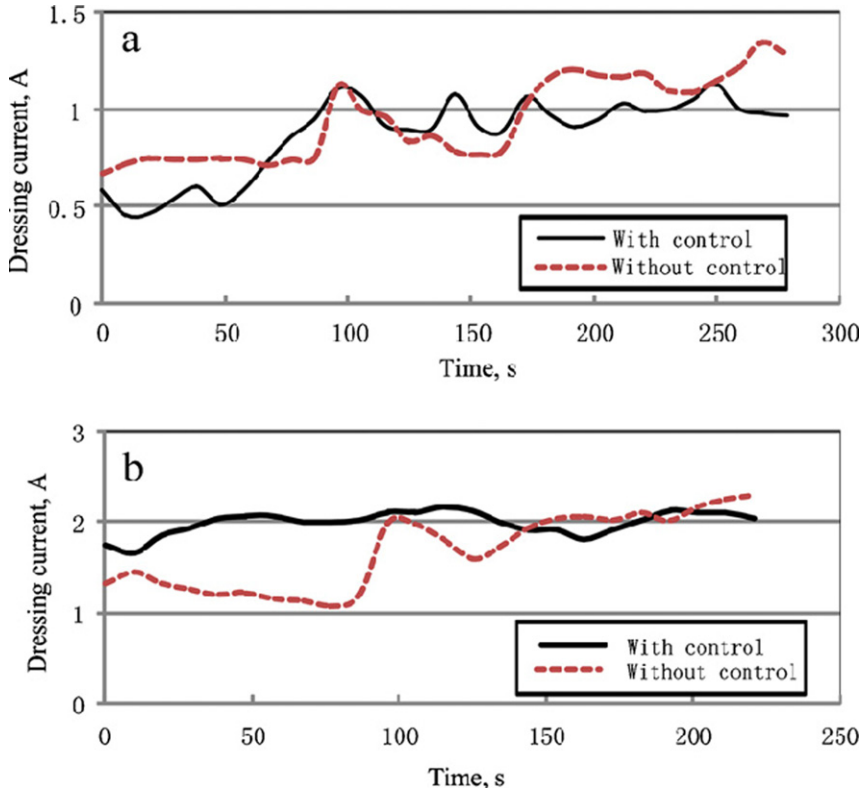


Figure 25 Dressing current change in internal cylindrical ELID grinding: (a) set value of 1 A and (b) set value of 2 A.[19,20]

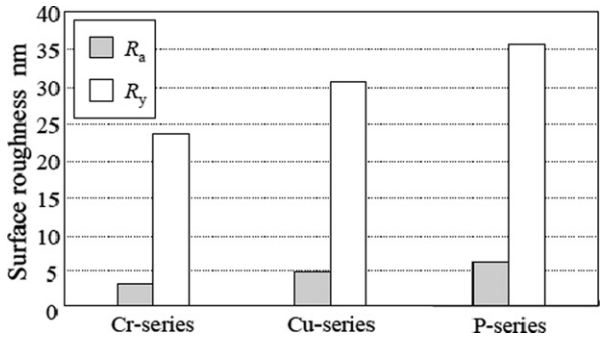


Figure 26 Comparison of surface roughness for wheels with different bond material (wheel mesh size #8000).[21]

can be applied to achieve the uniformity of the wheel thus a the need of separate system for wheel truing can be eliminated.

Studies conducted by Yin *et al.*[30] showed ELID grinding technique can produce a nano surface finish on Zerodur glass with an average SR of 5–10 nm when #4000 series wheels were used. The reason behind achieving such finish by ELID grinding is the ductile mode cutting, which was confirmed by the AFM study of the ground surfaces as described in Figure 31(a). It was found higher feed rate causes high grinding force (Figure 31(b)) that leads to more thermal damages to the surface. Ideal DOC to achieve ductile mode grinding for Zerodur glass was 0.4 μm. In another study conducted by Yin *et al.*[31] further developed a new grinding process and system for the fabrication of large non axisymmetric aspheric surface of fused silica (Figure 32), which is similar to the system described by Saleh *et al.*[26,27] in order to compensate the tool wear for ELID grinding. Notable improvement in form accuracy was observed after introducing compensation scheme as shown in Figures 33 and 34.

1.13.4.5 ELID on Silicon Wafer

Finishing of Si wafer by ELID grinding was investigated by Chao *et al.*[32] using metal and compared the grinding performance that uses resin bonded wheel. Amorphous layer, nanocrystals, polycrystals, dislocations, and microcracks were investigated in both cases. Grinding with resin bonded wheel was found to be superior in many aspects as compared to ELID grinding. ELID grounding was observed to be sensitive to grinding parameter selection and true optimized parameters were difficult to obtain and maintain. On the other hand, ground surface characteristics were less dependent to the machining conditions. Theoretically, formation of oxide layer in the case of ELID grinding weakens the rigidity of the bond material; hence dull grits held by oxide layer are expected to be fallen off by excessive grinding force. However in reality, there are still chances for some protruding grains getting excess attritious wear before it is pulled out in ELID grinding. This might cause unstable grinding condition and subsurface damage of the sample. However, in the case of resin bonded wheel self-sharpening effect of the lowers this chance. Further, in the case of resin bond wheel, except when feed rate is very low (say 2 μm min^{-1}) or wheel is loaded, the amorphous layer generated were normally thinner than

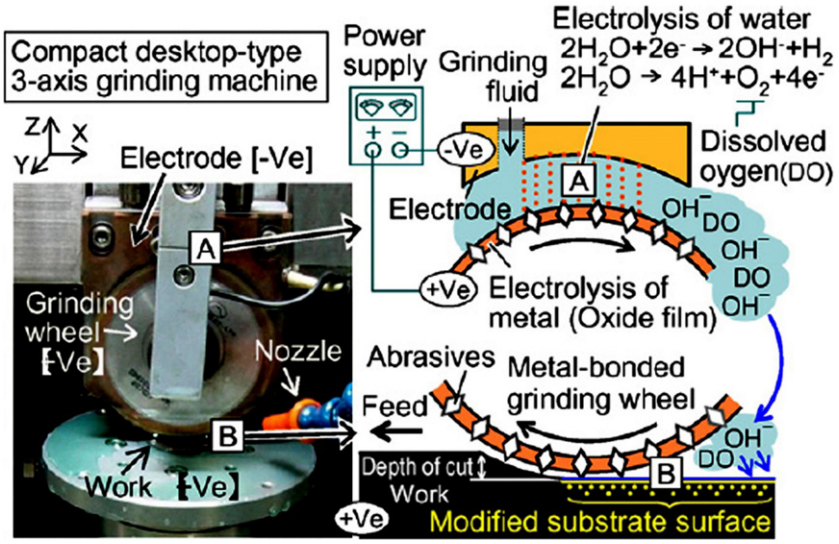


Figure 27 Overview of the proposed grinding system and a schematic illustration of surface modification reactions.[22]

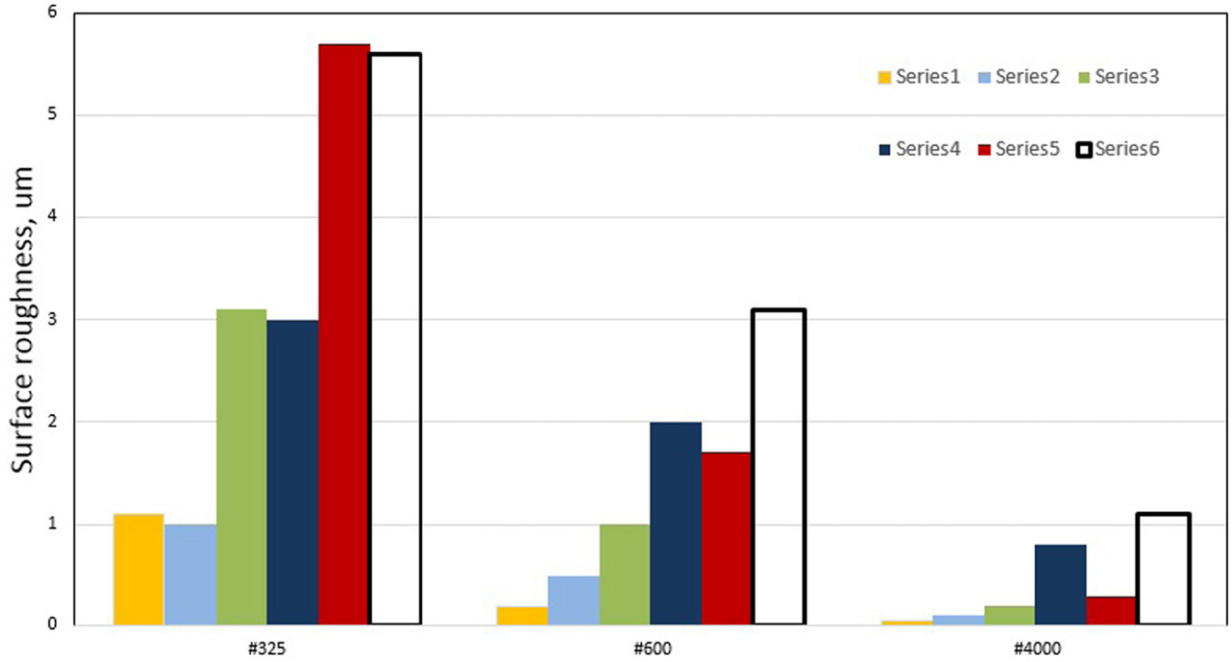
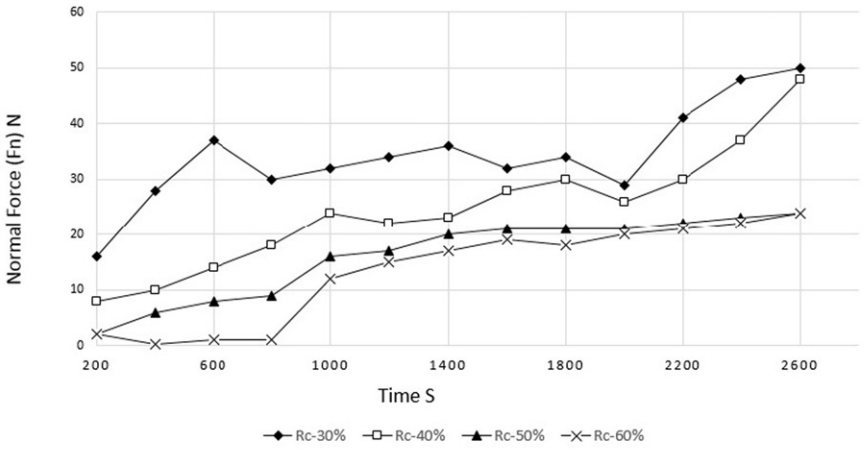


Figure 28 Variation of surface roughness of fabricated lens with wheel mesh number.[24]

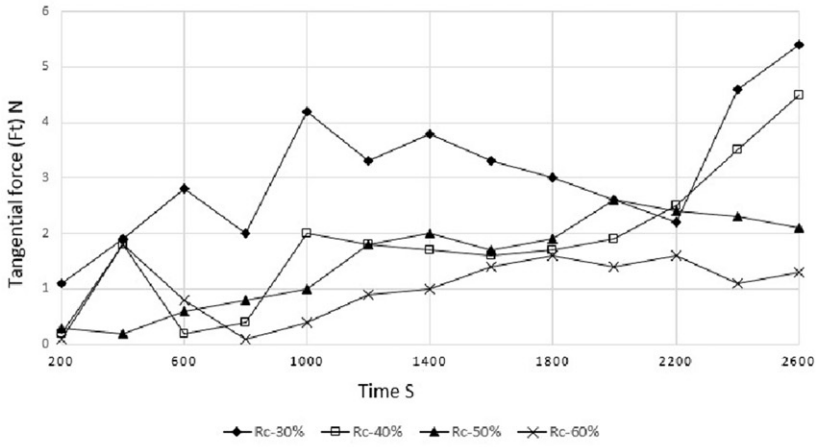
those generated by ELID grinding under the same grinding conditions.

Study on ELID lap grinding for Si wafer was performed by Itoh *et al.*[33] Stable grinding was performed using #8000–#3 000 000 series wheels. Ultrafine surface (sub-nano SR) with average SR of R_a=0.38 nm was obtained using #3 000 000 wheel whereas conventional lap grinding can generate SR R_a=0.47 nm. Another parameter of significant importance is the peak to valley roughness for Si wafer. ELID grinding improved peak to valley SR from 5.05 to 2.8 nm (**Figure 35**) as compared polishing. Moreover, morphological study of the ground samples with SEM and AFM also confirmed effectiveness of ELID grinding of Si wafer.

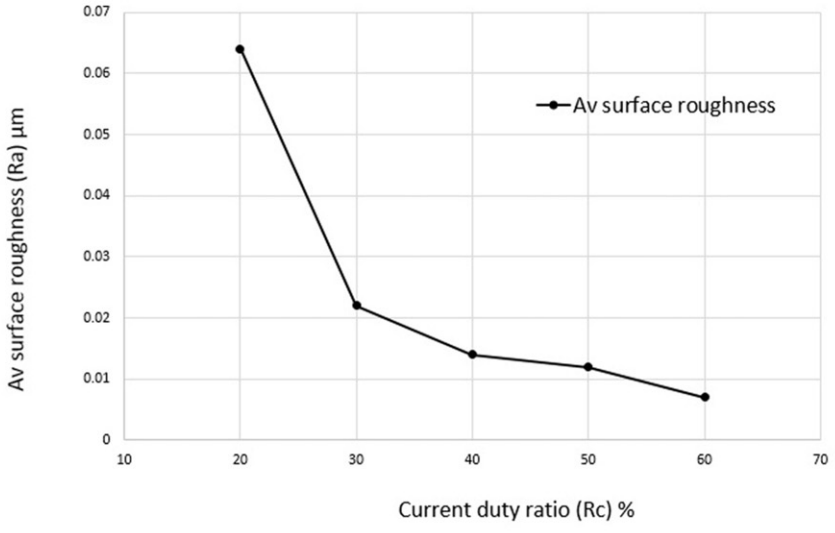
In conventional ELID grinding electrolyte fluid is supplied into the ELID cell by tangential flushing. Islam *et al.*[34] proposed a new idea of injection electrode (IE) in ELID grinding for thinning of silicon wafer. The concept of the system is described in **Figure 36**. This new technique enhances electrolyte filling between electrode-grinding wheel gap than conventional ELID flushing system. Because of this IE ensures better wheel dressing hence lower grinding force as compared to conventional ELID, which is described in **Figure 37**. With the help of IE assisted ELID grinding Islam *et al.*[34] successfully thinned down the silicon wafer from 750 μm to approximately 70 μm with sub-ten nano surface finish and without any visible cracking, pilling, and chipping.



(a)



(b)



(c)

Figure 29 (a) Normal grinding force variation for different dressing duty ratio. (b) Tangential grinding force variation for different dressing duty ratio. (c) Surface roughness for different ELID duty ratio.[25]

Table 4 ELID grinding results obtained by Saleh *et al.*[26,27]

Experiment No.	*Feed speed (mm min^{-1})*	*DOC (μm)*	R_a *(nm)*
1	500	1	34
2	500	2	27
3	500	3	25
4	500	4	31
5	250	1	26
6	250	2	21
7	250	3	18
8	250	4	20
9	125	1	–
10	125	2	19
11	125	3	17
12	125	4	18

Table 5 Comparison of profile accuracy with and without[26,27]

Experimental condition	*Desired profile radius (mm)*	*Actual profile radius (mm)*	*Deviation (%)*
With compensation	100	99.96	0.04
Without compensation	100	98.17	2.83



Figure 30 A spherical lens is ground by ELID grinding with a surface roughness of R_a=15 nm.[26,27]

Islam *et al.*[35] further characterized the ELID lapping process for machining. In this study authors found that rate of formation of oxide layer is dependent on the current duty ration, however, not the total thickness of the layer. It was observed interestingly that intermediate range of current duty ratio and grinding parameter (feed rate) showed better wheel surface condition; as described in Figure 38. Higher current duty ratio is not favorable as it produces hard and thick oxide layer and dull grits do not fall by acting grinding force. This causes excessive grinding force and bad SQ. In the case of grinding parameter such as feed rate, authors found that excessive low feed speed makes the wheel to grind same area repeatedly which may cause excessive attrition wear of the grits resulting poor surface finish. ELID grinding process was found to be better than conventional grinding process for silicon wafer as it exhibited stable grinding forces with low magnitude. Moreover, the subsurface damages exhibited on the samples are significantly lower for ELID grinding process than conventional grinding. The ELID grinding process was able to achieve superior ground wafer SQ with R_a=4 nm. Under all experimental conditions, the ELID grinding process performs better compared to the conventional grinding process.

Researchers also studied the effect of diamond grain size on different aspects of Silicon wafer machining by ELID grinding such as SR, subsurface damage, and material removal.[36] The results are shown in Figure 39. It is clear from the result that smaller grain size improves the SR and reduces the depth of the subsurface cracks. However, MRR is much lower for superfine abrasive wheels. Therefore, it is recommended to use ultrafine abrasive wheel for final finishing operation.

1.13.5 Summary on ELID Grinding

In-process dressing of grinding wheel has been under research interest for several years in order achieve ground surface with better SR and form accuracy. This may eliminate the need for further finishing operation like polishing and/or lapping. Significant studies were carried out by many researchers on this subject area. ELID is proven to be the most effective method of in-process dressing. A lot of researches have been carried out by different researchers since its invention back in 1990s. Continuous anodic dissolution and formation of soft insulating anodic oxide layer ensures more protrusion of sharp cutting grits and lower grinding force than conventional grinding. Sub-10 nm average SR is achievable on hard and brittle materials like optical glasses, silicon wafer, ceramics, bearing steels, etc., by ELID grinding. However, wheel wear rate in ELID grinding is considerably high because of continuous anodic dissolution of metallic bond of the grinding wheel. This leads to low grinding ratio and wheel life. Further, it hampers the form accuracy of the finished products especially for aspheric or curved surface. Researchers proposed tool wear compensation scheme to overcome this problem. One very interesting thing about ELID grinding is that it can be implemented easily to the existing grinding without much modification. However, researchers also tried to develop dedicated intelligent ELID grinding system. Researchers also proved that pulse width control of the dressing current can make ELID grinding useful for in-process trueing of the grinding wheel. In a nutshell it can be concluded that ELID grinding is a promising technology to achieve nano metric surface finish on hard and brittle material and has the potential to eliminate final finishing process like polishing.

1.13.6 Background of EDM

Developed in the late 1940, EDM also called electro-discharge or spark-erosion machining has gained its popularity over the

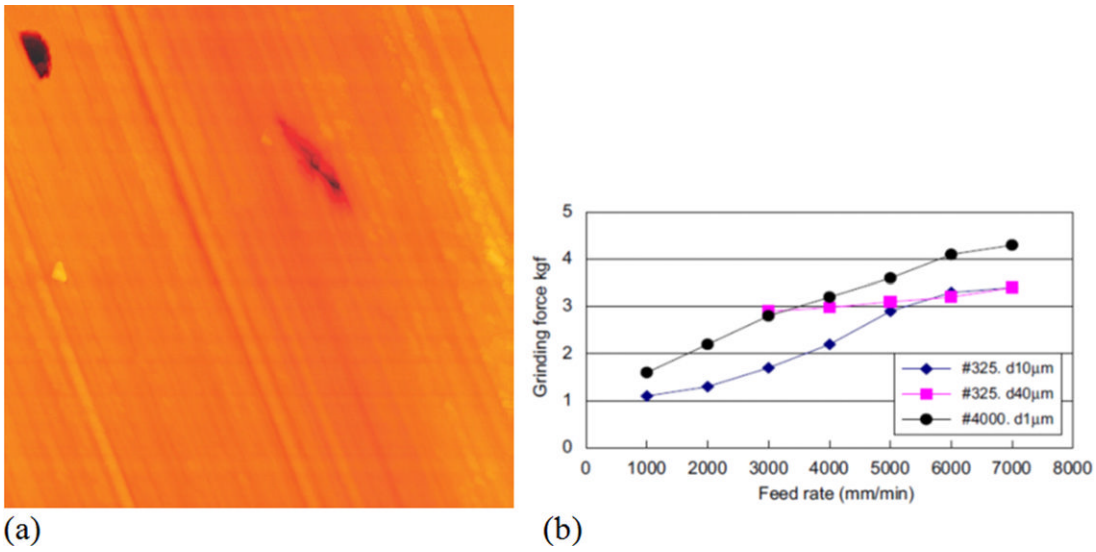


Figure 31 (a) AFM images of surfaces ground by #4000 wheel. (b) Effects of feed rate on grinding force.[30]

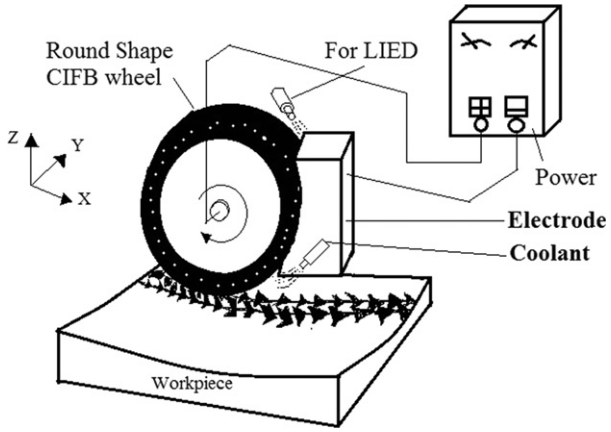


Figure 32 ELID grinding for 3-D arc enveloping grinding.[31]

years as a non-traditional machining method in the tool, die and mold making industries. The origin of EDM dates back to 1770 when British Scientist Joseph Priestly discovered the erosive effect of electrical discharges. EDM is the process of machining electrically conductive materials by using controlled sparks between an electrode and a workpiece in the presence of a dielectric fluid. The electrode usually is considered the cutting tool. The process works under principle of eroding conductive material by a series of discrete spark discharges, that is, only one spark occurs at any instant. Sparking occurs in a frequency range from 2000 to 500 000 sparks per second causing it to appear that many sparks are occurring simultaneously. The basic EDM system consists of a tool (electrode) and the workpiece, placed in nonconducting dielectric fluid. Dielectric fluid used in EDM machines are used for the following advantages: (1) controlling the sparking-gap spacing between the electrode and the workpiece; (2) cooling the heated material to form the EDM chip; and (3) removing EDM chips from the sparking area.[37] When the potential difference between the tool and the workpiece becomes high enough, the dielectric breaks down and a transient spark discharges through the fluid, causing the removal of very small portion of the workpiece surface. An overall EDM process is illustrated in Figure 40(a), while Figure 40(b) shows the discharge and metal removal.

The discharge occurs between the closest points of the two surfaces. The dielectric fluid provides a path for the discharge by being ionized. The erosion of the workpiece is achieved due to the localized melting and removal of the work surface caused by high temperature, which may go as high as 8000 °C.[39] The new flow of dielectric enters the inter electrode volume and flushes away the debris (chip) resulting from the machining.

The EDM process can be used on any material that is an electrical conductor. The melting point and the latent heat of melting are important physical properties that determine the volume of metal removed per discharge.[40]

1.13.7 Major Categories of EDM

To cope with advanced machining demands in the industries, EDM have been evolved based on the basic configurations. In general, we may classify EDM in two major categories, namely: (1) die sink (DS) EDM and (2) wire-cut (WC) EDM. DS EDM is the general process that was introduced in the early 1940 while WC EDM came up in the later years for the purpose of making tools (dies) from hardened steel. It uses a thin wire feeding through the workpiece by a micro-processor eliminating the need for elaborate pre-shaped electrodes, which are required in the EDM.[41] Die-sinker EDM machines are normally used for producing three-dimensional shapes while wire-cut EDM machines are always used for through-hole machining, since the electrode wire must pass through the workpiece being machined. The wires for wire EDM is made of brass, copper, tungsten, and molybdenum. Zinc or brass coated wires are also used extensively in this process. The wire used in this process should possess high tensile strength and good electrical conductivity. Wire EDM can also employ to cut

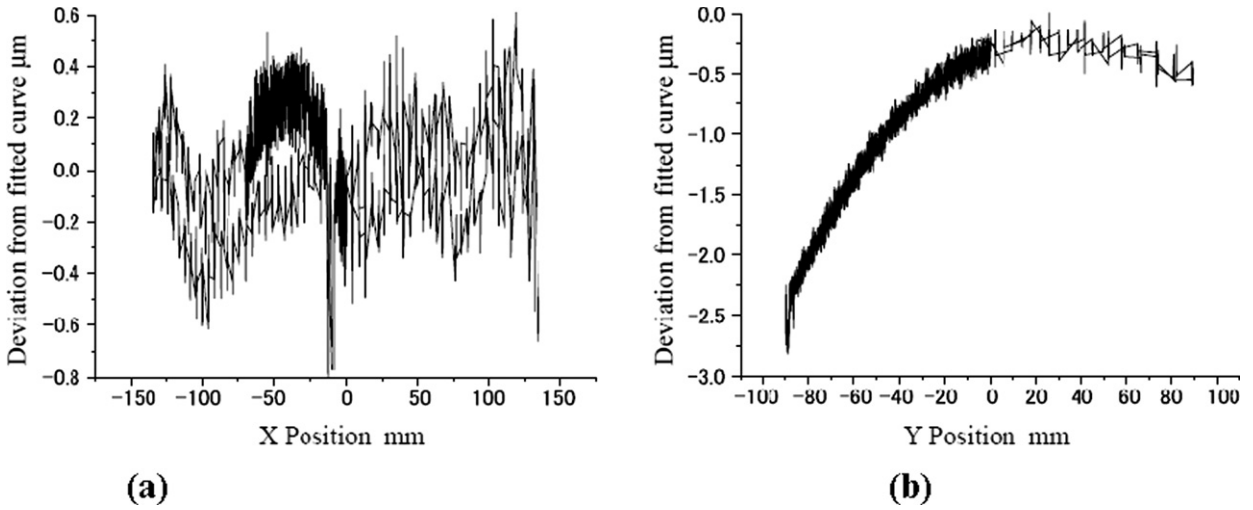


Figure 33 Form deviation profile before compensating form error (a) in X direction and (b) in Y direction.[31]

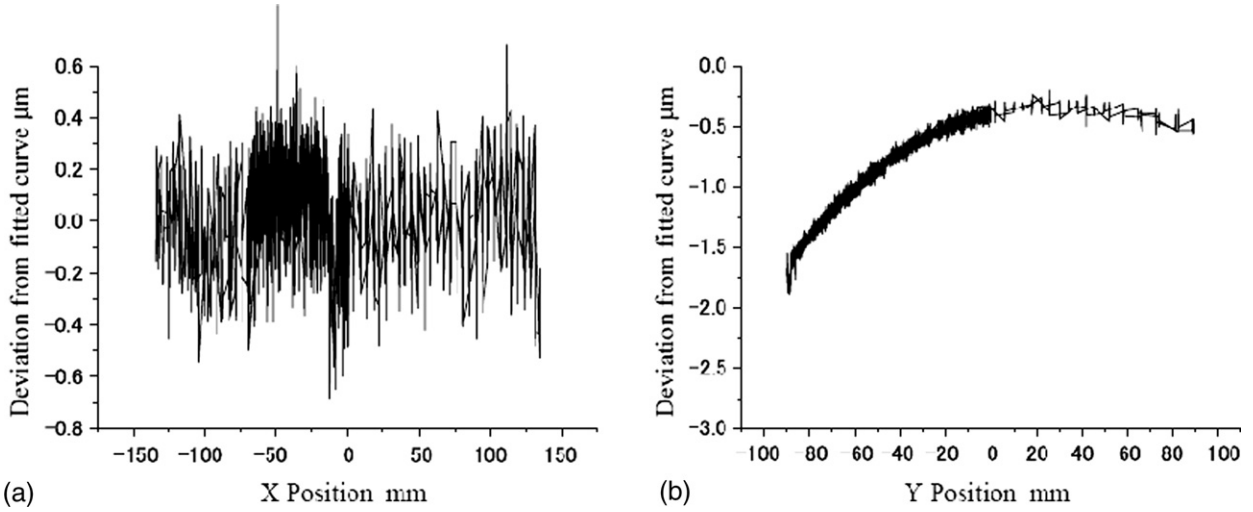


Figure 34 Form deviation profile after compensating form error (a) in X direction and (b) in Y direction.[31]

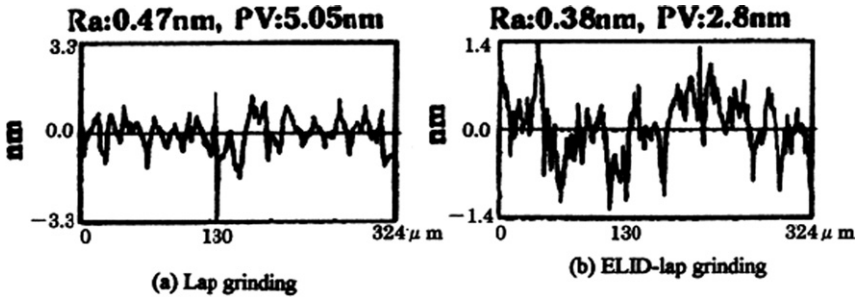


Figure 35 Comparison of surface roughness for Silicon workpiece. (a) Conventional lap grinding. (b) ELID lap grinding.[33]

cylindrical objects with high precision. A wire drive system constantly presents fresh wire to the work so electrode wear (EW) is not a problem. Typical wire diameters range from 0.002 to 0.013 in. Figure 41 shows the wire EDM process.

Besides these two, EDM process can also be directed into drilling by using a rotating electrode and basically performs the same functions as a drill press, far better in quality and finish than what any drill press can produce. These holes may

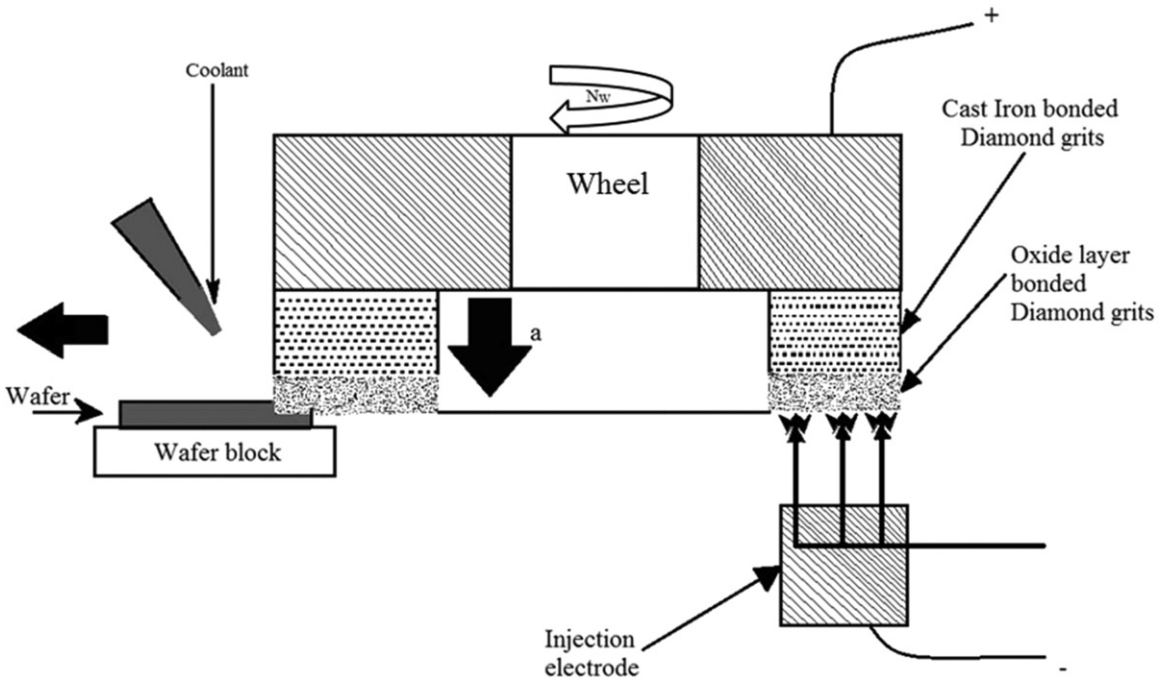


Figure 36 Injection electrode ELID grinding system (IE) for silicon wafer thinning process.[34]

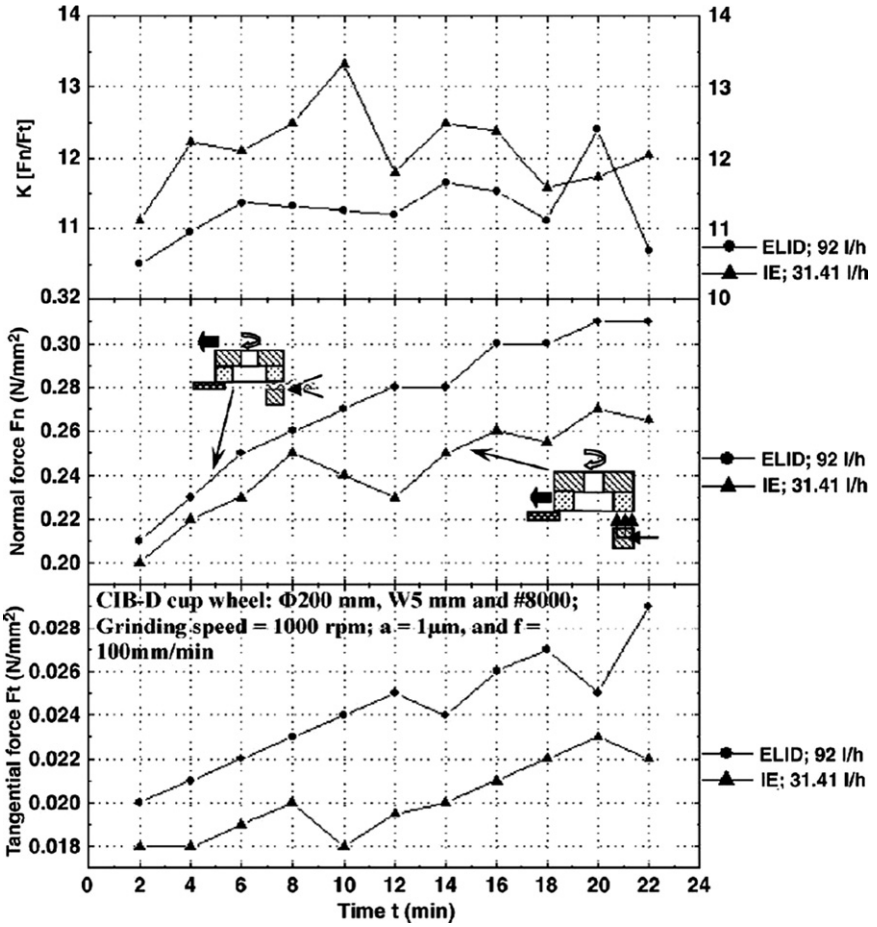


Figure 37 Comparison of grinding force and force ratio between injection electrode ELID grinding system (injection electrode) and conventional ELID grinding system.[34]

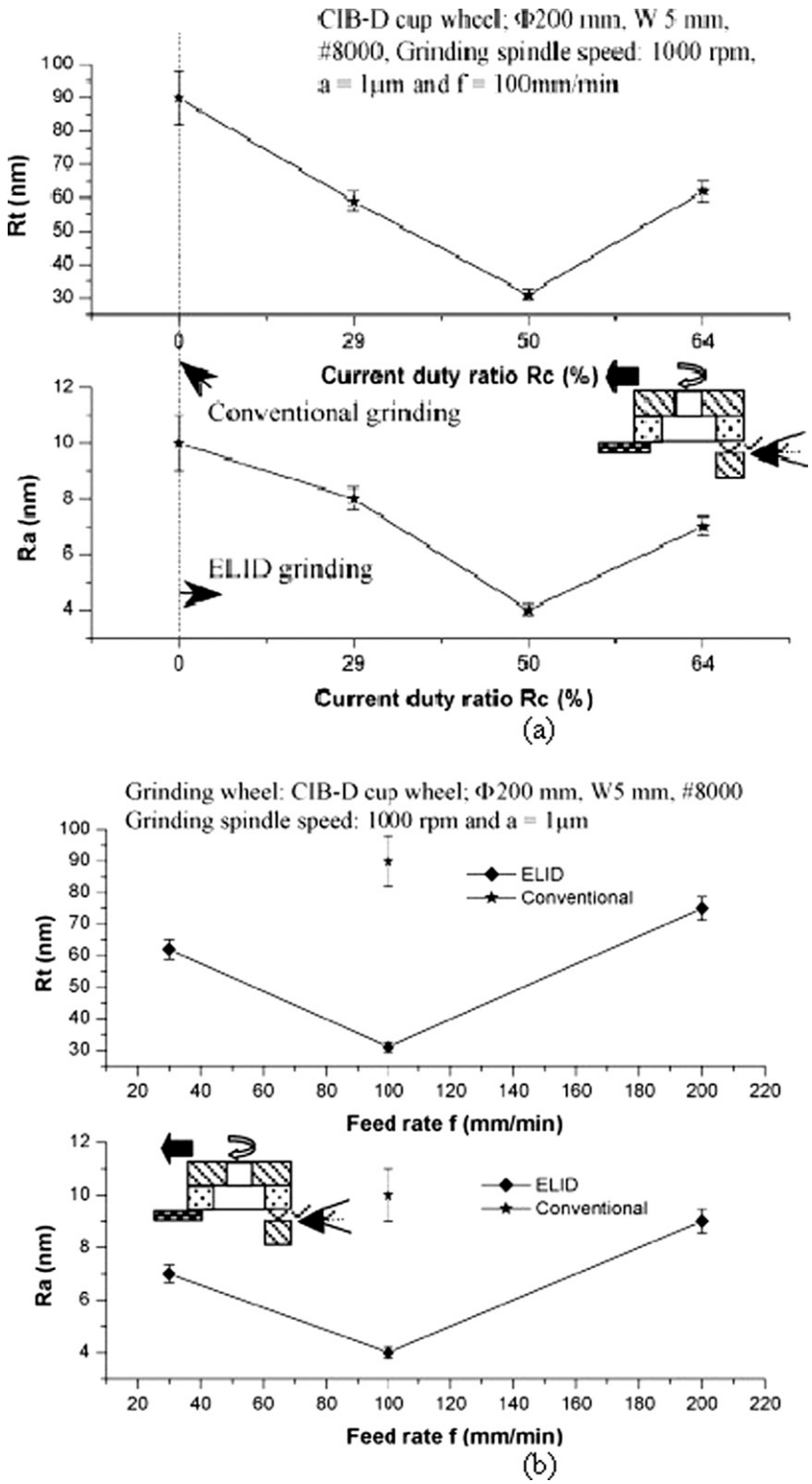


Figure 38 Variation of ground surface roughness of silicon wafer by ELID grinding (a) effect of current duty ratio and (b) effect of feed rate.[35]

have a depth-to-diameter ratio of 30 to 1 or higher.[37] However, with recent advancement in micro-manufacturing, the demand for micro-EDM (μEDM) has also been raised. Micro-EDM possesses various properties that are advantageous over other machining process. Micro-EDM can machine complex shapes that would be difficult to perform it with conventional cutting tools. Extremely hard material can be machined to very close tolerances. Very small workpiece can be machined using

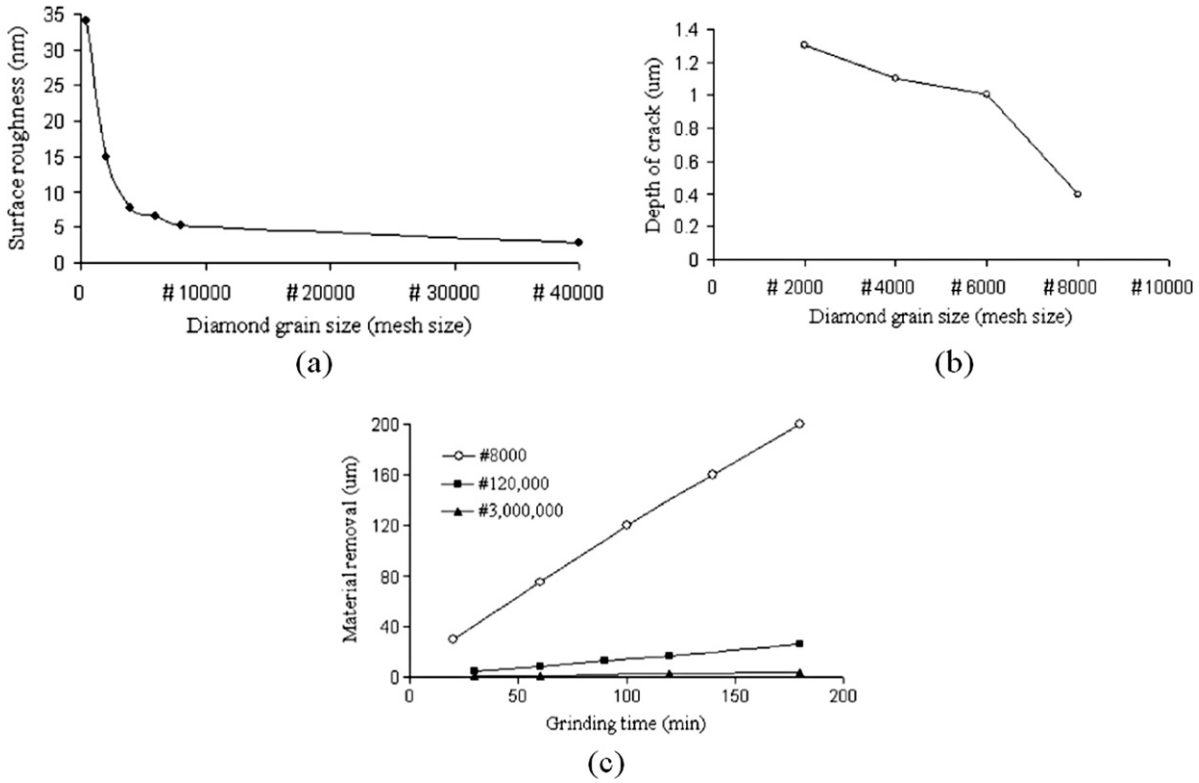


Figure 39 Effect of grain size for ELID grinding of silicon wafer (a) on surface roughness, (b) subsurface crack, and (c) material removal rate.[36]

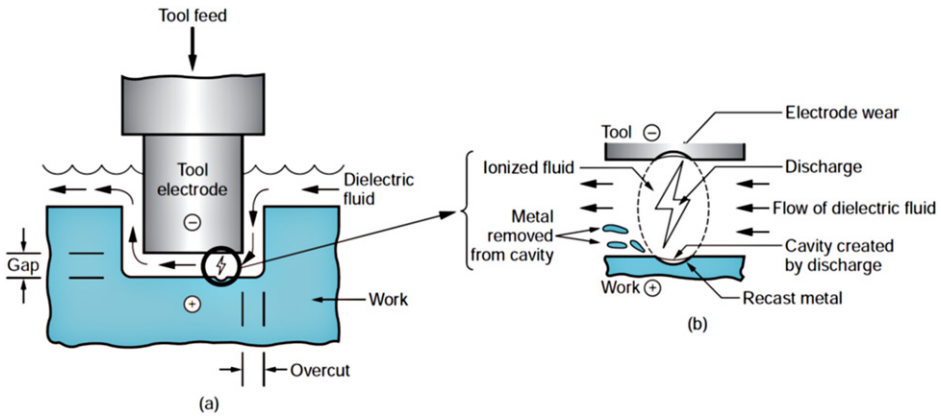


Figure 40 (a) Basic EDM process and (b)close-up of the spark gap.[38]

μEDM where conventional machining tools may damage the workpiece. When there is no direct contact between the tool and the workpiece, small parts and weak materials can be machined without any distortion. The disadvantages of μEDM are it will take a long time to finish the process. It is also very costly machining type. Micro-EDM is capable of machining not only micro-holes and micro-shafts as small as 5 μm in diameter but also complex three-dimensional (3D) microcavities.[42]

1.13.8 EDM Process Performance and Parameters

The EDM process performance is determined by MRR, EW, SR, SQ, and DA. The process parameters play an important role in affecting the performance and they have been classified by in eight major categories: (1) discharge voltage, (2) peak current, (3) pulse duration and pulse interval, (4) pulse waveform, (5) polarity, (6) electrode material, (7) type of dielectric flushing, and (8) rotary motion of electrode/workpiece. Effect of these process parameters influences the MRR and SQ. A brief discussion on the process parameters will be helpful for the readers to understand the extent of the EDMed SQ.

1.13.8.1 Discharge Voltage

Discharge voltage in EDM is related to the spark gap and breakdown strength of the dielectric.[43] The preset voltage is

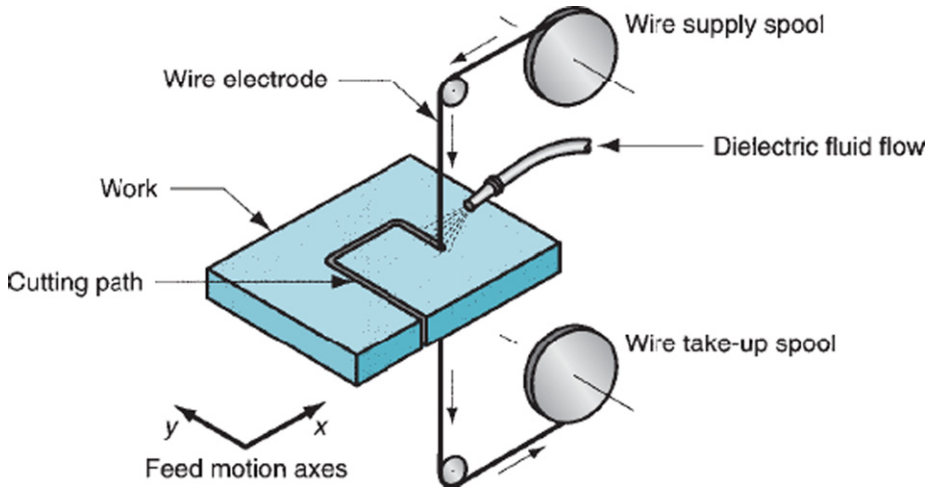


Figure 41 Wire EDM process.[38]

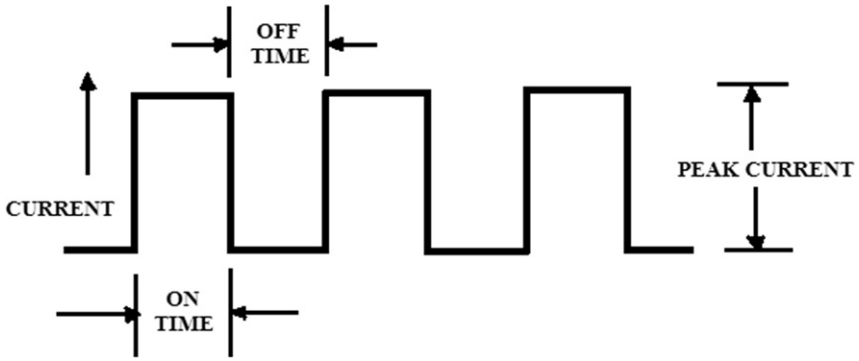


Figure 42 Pulse waveform of controlled pulse generator.[44]

the determining factor for width of the spark gap between the leading edge of the electrode and workpiece. The gap is increased by higher voltage settings, and it improves the flushing conditions thus stabilizes the cut. MRR, tool wear rate (TWR), and SR increases, by increasing open circuit voltage, as a result of increment in electric field strength. However, the impact of changing open circuit voltage on surface hardness after machining has been found to be only marginal.[44]

1.13.8.2 Peak Current

The most important machining parameter in EDM is peak current. The current increases gradually during the 'on' time pulse and reach a maximum value, which is called peak current as seen in Figure 42.

In both die-sinking and wire EDM applications, the maximum amount of current amperage is governed by the surface area of the cut. Higher amperage is used in roughing operations and in cavities or with large surface areas. Higher currents will improve MRR, and SR is also affected by current and frequency, as shown in Figure 43.

The best surface finish is obtained in EDM by operating at high frequencies and low discharge currents.

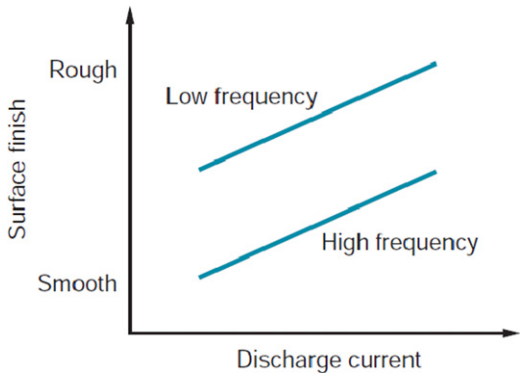


Figure 43 Surface finish in EDM as a function of discharge current and frequency of discharges.[38]

1.13.8.3 Pulse Duration and Pulse Interval

As seen in Figure 42, each cycle in EDM has an on-time followed by off-time that is expressed in units of microseconds. As all the energy is applied during on-time; the duration of these pulses and the number of cycles per second (frequency) are important to control the MRR. The total energy is controlled by the peak current and the duration of the on-time.

Pulse on-time is commonly referred to as pulse duration and pulse off-time is called pulse interval. With longer pulse duration, more workpiece material will be melted away. The resulting crater will be broader and deeper than a crater produced by shorter pulse duration. These large craters will create a rougher surface finish.[44]

1.13.8.4 Pulse Waveform

The pulse shape is generally rectangular but other shapes have been tried and a trapezoidal one could contribute to reduced tool wear.[45]

1.13.8.5 Polarity

The polarity of the electrode can be either positive or negative. It is recommended by Naveen and Pungotra[46] to use +ve polarity to obtain maximum MRR and minimum TWR whereas −ve polarity is recommended for minimum SR.

1.13.8.6 Electrode/Workpiece Material

The hardness and strength of the work material are not factors in EDM, because the process is not a contest of hardness between tool and work. The melting point of the work material is an important property, and metal removal rate can be related to melting point.[38] The high spark temperatures that melt the work and the tool at the same time, creating a small cavity in the surface opposite the cavity produced in the work. Electrodes materials commonly used are graphite, copper, brass, copper tungsten, silver tungsten, and other materials. The selection depends on the type of power supply circuit available on the EDM machine, the type of work material that is to be machined, and whether roughing or finishing is to be done. The prime requirement of any electrode material is that it must be electrically conductive and maintain less EW. In principle, the materials best suited should have a very high melting point and a very low resistance to electricity.[47]

Graphite is preferred for many applications because of its high melting. In fact, graphite does not melt. It vaporizes at very high temperatures, and the cavity created by the spark is generally smaller than for most other EDM electrode materials.[38]

1.13.8.7 Dielectric Fluid

Dielectric fluids used in EDM include hydrocarbon oils, kerosene, and distilled or deionized water. The dielectric fluid serves as an insulator in the gap except when ionization occurs in the presence of a spark. Its other functions are to flush debris out of the gap and remove heat from tool and workpart.[38] Performance improvement using powder-mixed dielectric fluid has been reported by Pecas and Henriques,[48] while the same researcher showed that the presence of powder particles in dielectric fluid and the concentration of powder creates conditions suitable for achieving a better SQ in the machined area.[49]

1.13.8.8 Rotational Motion of Electrode/Workpiece

Both cases of rotational motion applied to tool and workpiece have been investigated. Guu and Hocheng[50] provided a workpiece rotary motion to improve the circulation of the dielectric fluid in the spark gap and temperature distribution of the workpiece yielding better MRR and SR. On the other hand, the rotary motion of the electrode showed improvement in the performance of the EDM process which significantly improved the MRR and SR due to better gap flushing.[51]

1.13.9 EDM Applications

The EDM process has the ability to machine hard, difficult-to-machine materials. Parts with complex, precise and irregular shapes for forging, press tools, extrusion dies, difficult internal shapes for aerospace, and medical applications can be made by EDM process. Based on different materials, EDM applications can be classified in three broad categories as described below.

1.13.9.1 EDM for Heat-Treated Materials

EDM is a more suitable machining choice for heat-treated tool steels. The hardness limit for such steels for ordinary milling ranges up to HRC of 35.[52] However, with EDM, the metal can be fully hardened and still can be machined with secured dimensional stability.

1.13.9.2 EDM for Nonconductive Ceramic

Nonconductive ceramics cannot be machined by traditional metallic tools because of their high brittleness and hardness. EDM is a known process for producing structures from electrically conductive materials with high DA and good surface finish. Most of the engineering ceramics such as Al_2O_3, ZrO_2, Si_3N_4, and SiC are electrically nonconductive.[53] In EDM of conductive materials, material is removed mostly by melting and evaporation, but the main material removal mechanism in EDM of nonconductive ceramics is spalling which occurs due to the alternating thermal load of the electrical sparks.[54,55] In the recent years, either assisted electrode (EDM of ceramic/carbon nanostructure composites[56] or doping/adding with conductive particles to make the ceramic conductive enough are being practised.[57]

1.13.9.3 Modern Semiconductor/Composite Materials

The extensive usage of composites in the modern living has led to an expansion of EDM applications into the area of composite materials. The feasibility of machining ceramic–metal composite steel plate coated with WC–Co (tungsten carbide–cobalt) using plasma spraying was also examined.[58] Same goes with the machining of silicon semiconductor with wire electrodischarge machining (WEDM).[59]

1.13.10 EDM and Its Effect on Workpiece Surface Finish

The EDMed surface may become different in properties than the base material after machining. Due to the high-temperature

generated during machining the upper layer goes through heat treatment naturally. The thermal nature of EDM imparts a heat-affected layer on the machined surface. Generally, the thickness of the heat damaged zone is related to the amount of applied energy.[60] The following **Figure 44(a)** shows the different layer of the EDMed surface,[39] while **Figure 44(b)** provides a more detail about the different temperature zones on the surface layer.[37]

As seen in **Figure 44(b)**, zone A is the surface that faces directly the spark electricity. The temperature at this zone vaporizes the workpiece material, some portion of electrode and dielectric fluid. Temperature zone B is a part of zone A and consists of spherical-shaped projections that extend from the zone A surface. These small projections are named as globules and usually attached loosely to the zone A surface. The temperature at zone C is causes the workpiece surface to melt, but does not separate it from the spark cavity surface while in temperature zone D the heat is less than the heat at a melting point. Material in temperature zone E may be considered as the parent material since it is far enough away from the surface of the spark cavity that any temperature increase will not affect the workpiece material characteristics. The heat-affected zone (HAZ) consists of the total spark cavity surface area that has been changed due to the spark heating (zone A–D).

In many cases, EDM surface finish may be used without additional finishing operations, such as in plastic-injection molds or in press tooling to hold lubricant. EDM manufacturers provide data regarding spark-ON time and peak amperes to produce surface finishes that are acceptable for different applications. For EDMing of high-temperature materials that are highly stressed in their end use, it is necessary to define upto what extent the EDM surface conditions are acceptable. In some instances, the surface must be completely removed. A typical specification for this type of application could include the following items[37]:

i. A total thickness of the re-deposited and re-solidified layers: 0.001 in. (0.025 mm).
ii. A total thickness of the re-deposited, re-solidified, and changed material characteristic layers: 0.002 in. (0.05 mm).
iii. Electrode material present in re-deposited layer: none
iv. Cracks in re-deposited and re-solidified layers: acceptable (depending on the end use).
v. Cracks in parent material: not acceptable.

The reason for being cautious about presence of cracks in high-temperature materials to be used for high-stress applications is that the cracks will propagate and cause part failure. EDM for machine press die tooling is capable of producing very sharp corners in the die opening. As piece-part material is pressed through the die opening, considerable force is applied to the die-opening sidewalls therefore, any sharp corners can become highly stressed and cause failure.

It is found from the preliminary metallurgical studies of the EDMed surface that the changes arise mainly from the rapid cooling of the molten material which solidifies epitaxially on the crater bases.[62] The amount of molten material with each discharge is in the region of 8–10 times the final crater volume.[63] At the end of the discharge and erosion phases only about 10–15 per cent of the total molten material is removed while the remainder resolidifies on the surface to form the recast layer. Lee *et al.* focused on the recast layer's effect on surface crack formation for tool steels, according to their work.[64] The type of recast has been found to be related to the likelihood of the occurrence of cracks. The multi-layer type is most prone to cracks while the thin featureless is generally more crack-free. Cracks tend also to be more prevalent in or around humps on the work surface. The type of recast has been found to be related to the likelihood of the occurrence of cracks where the thickness of the recast layer has a major influence on the type of recast. In general, the three broad categories are the multi-layer, single layer, and featureless types. Lee *et al.* indicated in their studies that thermal conductivity of workpiece and occurrence of cracks are inversely related. The drawing of heat through the base of the workpiece has been shown to be able to reduce the susceptibility of the recast layer to cracks and also to reduce that thickness of the recast layer The multi-layer type is most prone to cracks while the thin featureless is generally more crack-free. Cracks tend also to be more prevalent in or around humps on the work surface. Prior to this work, Lee *et al.* focused on the surface transformation and damage for tool steels.[60]

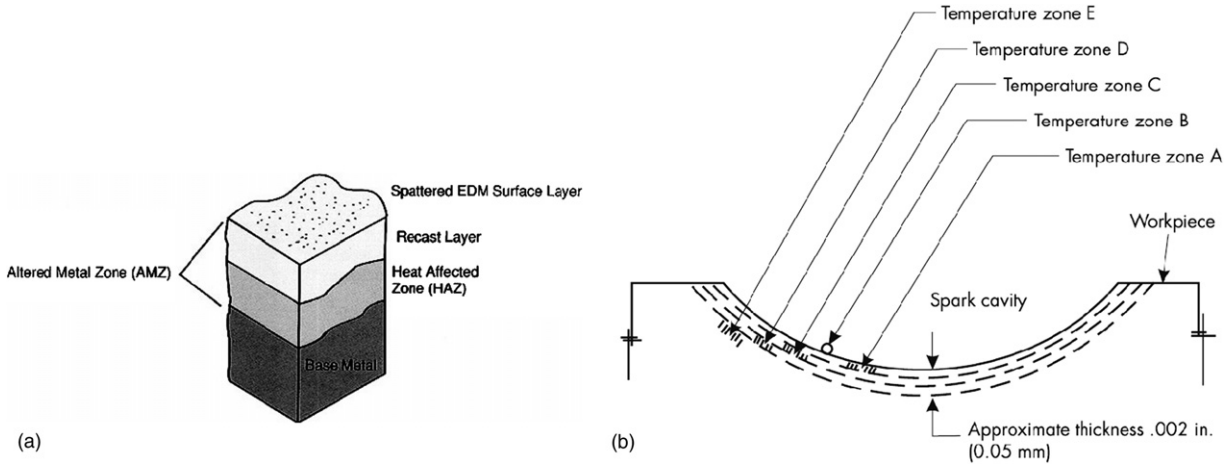


Figure 44 (a) Surface layers after electrical discharge machining.[61] (b) Temperature-range zones in the spark cavity.[37]

Attempts were made to quantify the depth of white (or damaged) layer with respect to the process parameters and SR after EDM. It is found that with a fixed dielectric and flushing condition, the damaged layer correlates well with the pulse energy irrespective of the tool steel material. In general, at low discharge energy, the craters are shallow and the density of global appendages and pockmarks is low. Whereas at higher discharge energy, the craters are deeper and global appendages are most evident. These global appendages are molten metals which were expelled randomly during the discharge and later solidified on the workpiece surfaces. As seen in **Figure 45** that the edge of some of the pockmarks are thin and sharp (arrowed), suggesting that the molten metal must have solidified at an extremely high rate. Otherwise the surface tension of the molten metal would have caused the sharp edges to be rounded off. The microstructure of the EDMed surface varies greatly from its parent metal.

Their work also revealed that under identical discharge conditions, the SRs of all the steels are quite similar. Their values, however, depend on both the pulse energy and current in a complex manner. By and large, at a given pulse energy, a poorer surface finish is obtained with a higher pulse current. This implies that the pulse current has a more dominant effect on the SR compared to the pulse-on duration. It is possible that a higher pulse current (or input power) may cause more frequent cracking of the dielectric, giving rise to more frequent melt expulsion. This in turn will result in a higher density of global appendages and poorer surface finish. Similar performance have been reported by Torres *et al.*[65] for machining on Inconel surface. According to them, current intensity and pulse time are the most influential factors for SR. Increasing current intensity leads to deeper craters but at the same time with greater diameter (lower number of peaks per cm). Minimum R_a (1.11 μm) is reached at 2 A and 50 μs. R_a values obtained with negative polarity are lower compared with the positive one, but the surface is more damaged because more pronounced microcracks appear.

1.13.10.1 Surface Modification Using EDM

Besides the natural heat treatment of the EDMed surface, researchers are trying to improve the EDMed surface in terms of roughness, strength, and residual stresses. Some widely used methods and their applications will be discussed in this section. In general, the surface modification have been tried by manipulating (1) conventional electrode materials, (2) composite electrode, (3) additives in dielectric, and (4) ball burnish machining.

1.13.10.1.1 Surface modification by conventional electrode materials

Playing with different electrode materials to obtain modified EDMed surface has been in practice for the last five decades. The very initial study on the electrode material conducted by Barash and Kahlon[66] revealed that the deposition of metals with a lower melting point on to those with a higher melting point progresses at a much lower rate than vice versa. So, whereas the deposition of tungsten carbide on to steel is fairly fast, the deposition of copper on to steel progresses extremely slowly. They also indicated from their experiments that when mild steel was eroded in liquid medium paraffin using copper electrode, the workpiece was coated with a very hard layer.

Over the years many other attempts have been taken to study the effect of electrode material on the workpiece surface properties. Jahan *et al.*[67] presented their work using different electrode materials and their effect on the fine finish of hard to machine tungsten carbide (WC) during μEDM. Three different materials, namely tungsten (W), copper tungsten (CuW), and silver tungsten (AgW) were used for electrode. It was found that the surface characteristics were dependent mostly on the

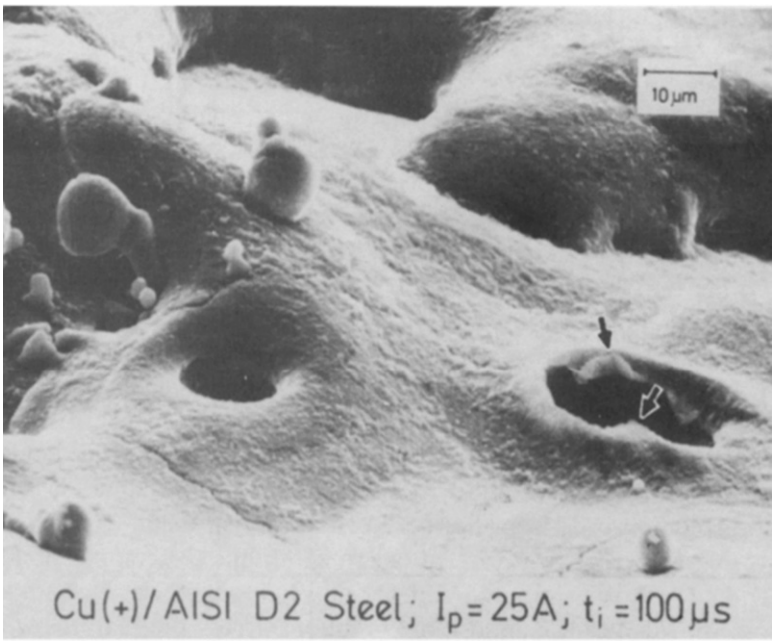


Figure 45 The surface of an AISI D2 tool steel specimen showing craters, global appendages, pockmarks, and cracks.[60]

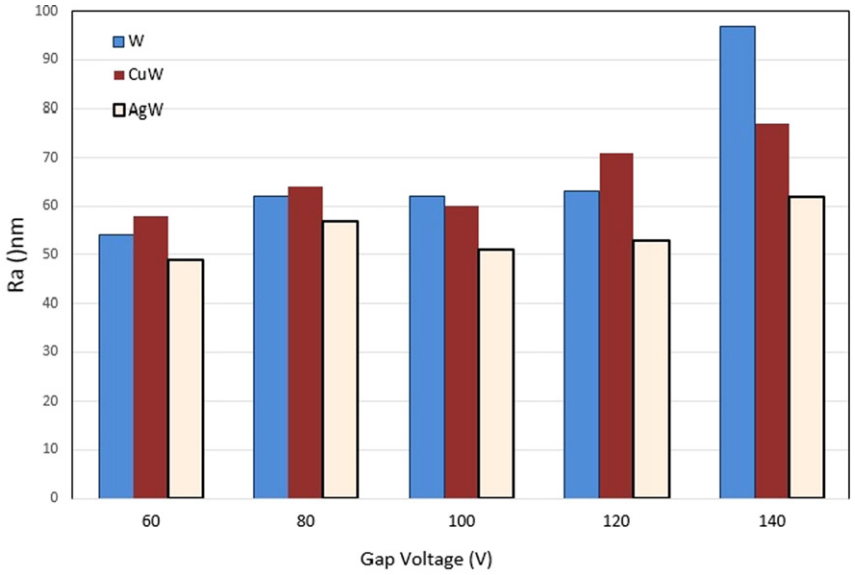


Figure 46 Variation of average surface roughness (R_a) of micro-EDMed WC with gap voltage.[67]

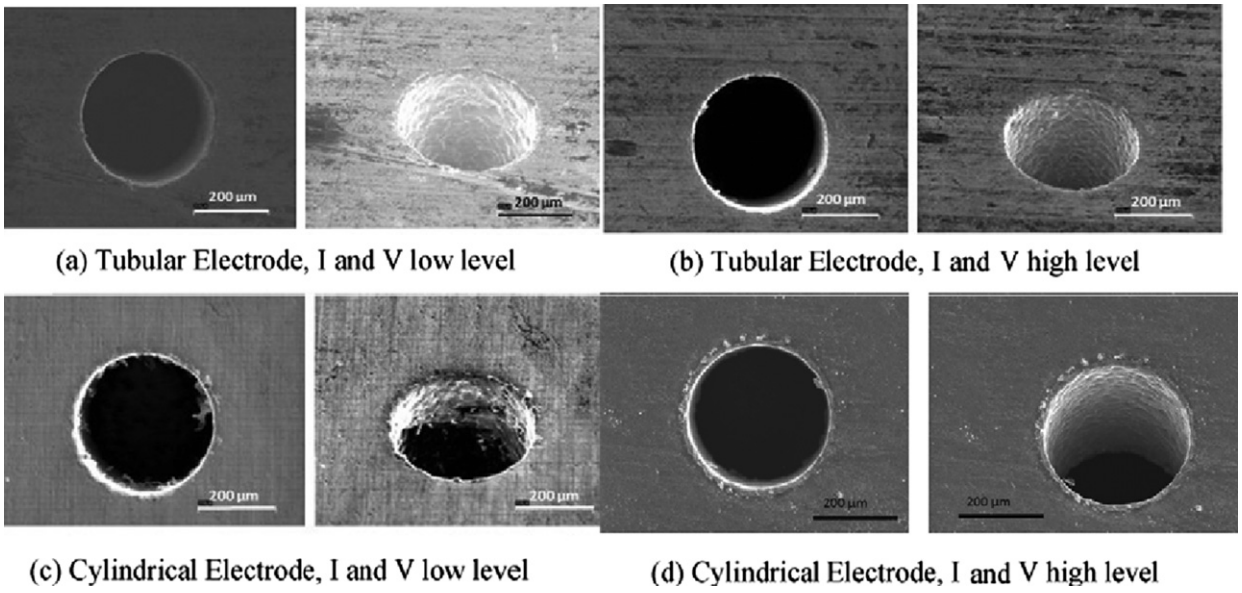


Figure 47 Micro-holes surface finishing for low and high level of peak current/voltage carried out with tubular and cylindrical electrodes.[68]

discharge energy during machining. A detailed experimental investigation was carried out on the finishing μEDM of WC using RC generator due to very small amount of discharge energy. As seen from **Figure 46**, with increased gap voltage, the SR value increased, while using AgW electrode always provided the smoothest surface among the three electrode materials.

It was also noticed that no traces of Ag were found on the workpiece surface, which is a better sign of a clean and shiny surface. Moreover, the percentage of parent material, i.e., W, is higher on the surface using the AgW electrode compared to that on the surface obtained by the W and CuW electrodes. Thus, using AgW electrodes, the properties of the WC after the μEDM process are expected to change very little compared to that when using W and CuW for better surface finish.

D'Urso and Merla[68] highlighted material variation for electrode and workpiece for a micro-drilling experience. The influence of four different workpiece materials (stainless steel, titanium, magnesium, and brass), three electrode materials (copper, brass, and tungsten carbide), and two different electrode shapes (cylindrical and tubular) was investigated.

A total amount of 160 through micro-holes were drilled on thin plates of different materials. **Figure 47** shows the micro-holes drilled using different electrode geometry and peak voltage and current settings while **Figure 48** shows micro-holes surface using different electrodes. In **Figure 47** where the electrode geometry was compared with changing peak current and voltage, it revealed that there was no significant difference in the SQ of the micro-holes made using tubular

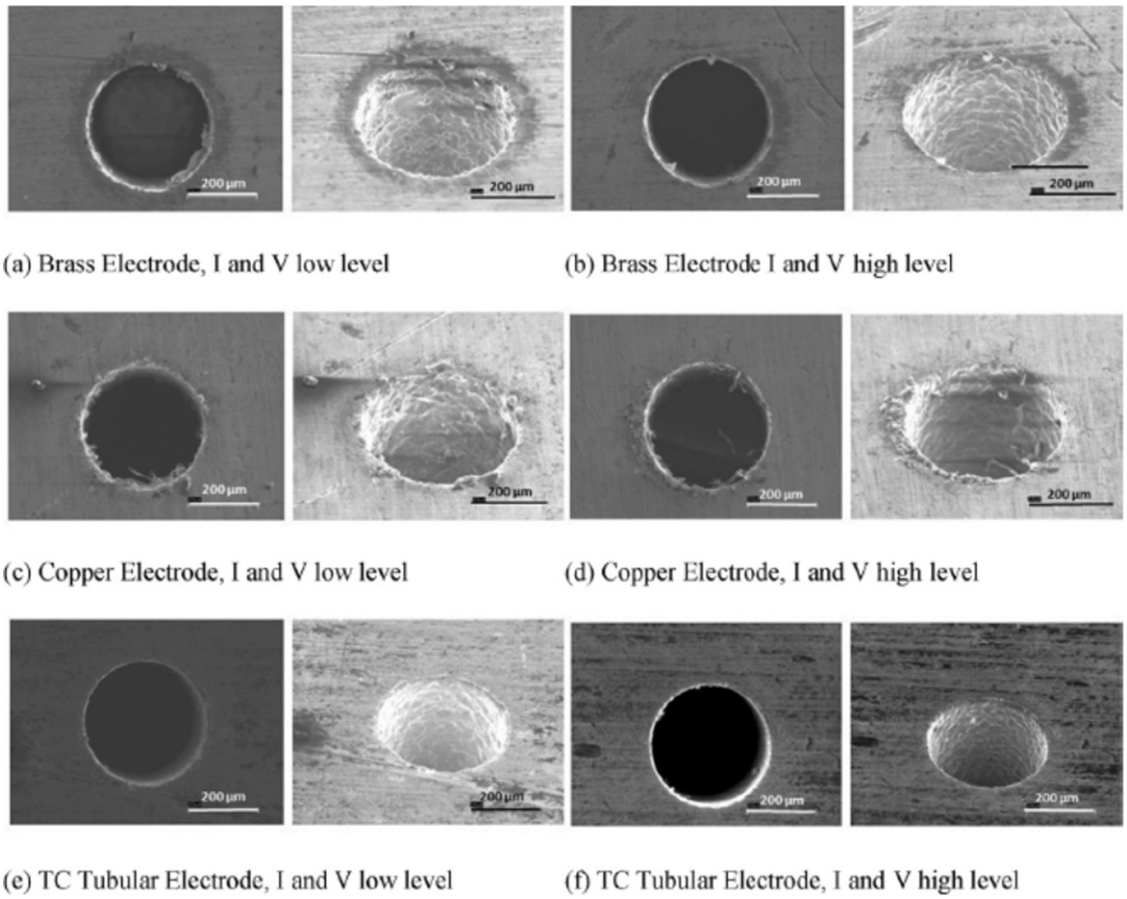


Figure 48 Micro-holes surface characteristics for brass tubular electrode with low and high level of peak current/voltage parameter (a, b); for copper tubular electrode with low and high level of peak current/voltage parameter (c, d), and for WC (tungsten carbide) electrode with low and high level of peak current/voltage parameter (e, f).[68]

electrode: both surfaces were almost burr-free. On the contrary, for the cylindrical electrode, the higher level of the peak current/voltage provided better quality of the surface of the hole. In general, it was concluded that the cylindrical electrode resulted in a surface with a larger amount of burrs if compared with the tubular one.

When considering electrode material, it became clear from **Figure 48** that the poorest SQ of the micro-holes was obtained for using copper electrode which with significant amount of irregularities and debris. Similar observation was found for the brass electrode. Also in this case the surface of the micro-holes was irregular and characterized by a considerable amount of burrs. On the other hand, for the WC (TC) electrode, the surface obtained was more regular and without absence of burrs. Moreover, for brass and copper electrode materials, the higher level of the peak current/voltage parameter resulted in a worse SQ. This could be due to the more aggressive parameter combination adopted for the machining.

The better performance in terms of surface finishing and burr-free surfaces are obtained when working magnesium and titanium workpiece. Copper electrode was used in both cases and the surfaces found were completely free from burrs and re-solidified material on the edge of the micro-holes.

A more recent work by Younis *et al.* showed the performance of two different graphite electrode on different types of workpiece material.[69] The effect of electrode material was studied to investigate improvement issues related to residual stresses, SR, and cracks during EDM. The electrode materials chosen were Dura graphite 11 and Poco graphite EDMC-3. Two grades of tool steels were used as workpiece materials: DIN 1.2080 and DIN 1.237. Machining mode had three categories: rough, medium, and soft. After the EDM process the test materials were examined using scanning electron microscope to observe the surface cracks, roughness, and then x-ray diffraction to examine the residual stresses generated after the three machining conditions. It was found that Dura graphite exhibited higher SR for DIN 1.2080 surface during all machining conditions caused by its easily eroding compressed graphite powder, and also due to the higher carbon content in DIN 1.2080 which solidified upon the surface during solidification and not flushed away.

Figure 49 shows the surface roughness obtained for the overall experimental variables.

Younis *et al.* concluded their results stating that rough EDM machining exhibited more microcracks as a result of higher pulse current while the most significant parameter affecting residual stresses occurred during EDM machining were the electrode material and machining condition.

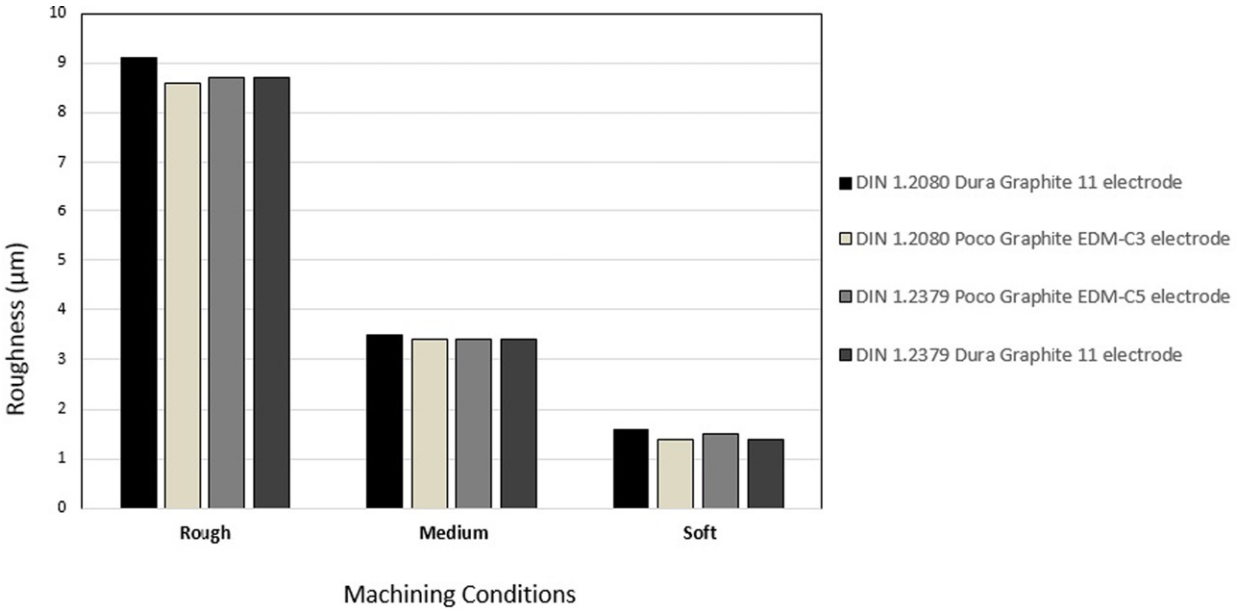


Figure 49 Surface roughness observations.[69]

1.13.10.1.2 Surface alloying using composite (PM) electrode

The composite electrode is also referred to as the green compact, sintered, or powder metallurgy (PM) electrode. Use of powders has propagated in recent years as it increases productivity and reduces workpiece SR/associated microcracks, because of greater electrical conductivity in the spark gap/reduction in the breakdown voltage and higher discharge frequency. A wide range of powders with alternative compositions can be used for the manufacture of tool electrodes. These tend to be materials which can form/transfer hard particles such as carbides and may incorporate a secondary binder phase, for example, WC/Co, TiC/WC/Co, W/CrC/Cu, etc. By using electrodes made from different materials, the possibility exists to 'engineer' one or more alloyed layers (which may be functionally graded) with different mechanical properties.[70] It has low thermal conductivity allowing the composite material to disintegrate from the electrode and alloy onto the workpiece surface producing less cracks, high corrosion, and wear resistance.[41]

PM electrode was applied as an alloying method by Ho *et al.*[71] The pulse generator employed a higher than standard open circuit voltage of 270 V with selectable peak currents of 0.1–2.9 A. The workpiece material was annealed Ti–6Al–4V cut into rectangular pieces 18 mm × 14 mm × 10 mm. The tool electrodes comprised solid HCHP copper bar and Ø10 mm PM copper slugs/buttons soldered on copper rods. The result revealed that PM electrodes produced greater alloying than the solid electrode and PM electrodes used with positive polarity produced thicker recast layers. On the other hand, under negative polarity, recast/alloyed workpiece hardness was in general of lower or of comparable hardness to the bulk material.

Wang *et al.*[72] worked on the electrical discharge coating (EDC) using EDM principle for surface modification of carbon steel. By using an ordinary EDM tool and kerosene, a layer of TiC ceramic about 20 µm thickness is created on the workpiece successfully with a Ti powder green compact electrode in a very short time. In general, the forms of electrodes are green powder compressed, or sintered, and so on. The powder green compact electrode has low thermal conductivity and rapid wearing speed that made it suitable for easy deposition. The resultant surface's lowest hardness achieved was four or five times higher than that of the base material. Ratio of Fe is reduced gradually from the base metal to the surface, and almost to zero at the end, while the ratio of Ti is increased gradually upto the surface. It can also be seen that there is no clear boundary between the layer and the base metal and this is how the EDC layer adheres strongly to the base metal.

Simao *et al.*[70] presented their experimental results on the surface alloying of AISI H13 hot work tool steel during a die sink operation using partially sintered WC/Co electrodes operating in a hydrocarbon oil dielectric. Die-sink surface alloying tests were performed using hydrocarbon oil dielectric BP 180 as the dielectric. The cylindrical PM tool electrodes were made from WC/6 wt.% Co binder in a partially sintered state. Experiments planned with Taguchi method showed the use of partially sintered electrodes made from WC/Co resulted in the formation of a uniform alloyed/modified surface layer with relatively few microcracks and an average thickness of up to 30 µm. Results from the confirmation experiment showed an increase in workpiece surface microhardness from ~640 HK(0.025) to 1319 HK(0.025). **Figure 50** presents the recast layer after Taguchi confirmation test.

The surface hardness value of the recast surface alloyed layer was substantially higher than either that of the hardened AISI H13 steel (~600–640 HK(0.025)) or the typical recast layer hardness (~600 HK(0.025)) when using 'conventional' graphite or copper tool electrodes. This increased value compares extremely favorably with hard chromium surfaces, typically applied by electroplating.

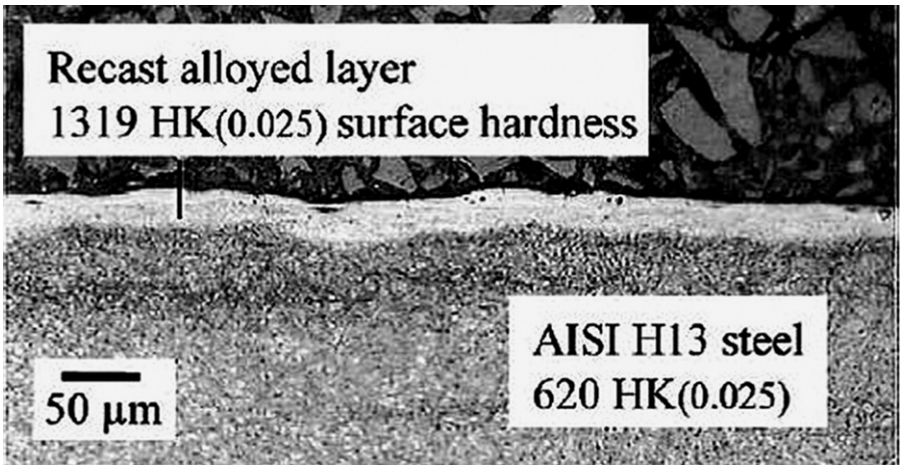


Figure 50 Cross-section of die sink surface machined using a partially sintered WC/Co tool electrode (Taguchi confirmation test).[70]

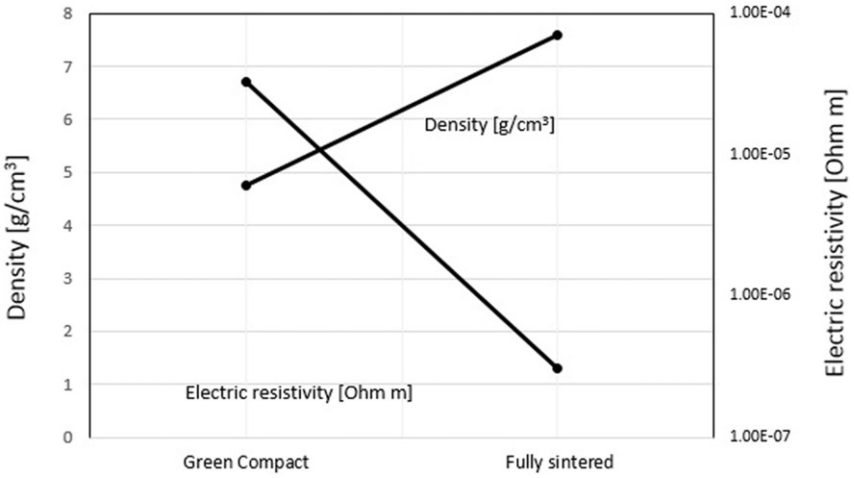


Figure 51 Variation of electrical resistivity (Ω m) with green density (g cm^{-3}) of the PM tool electrodes.[73]

Simao *et al.*[73] presented in their later work using two types of electrodes for electrical discharge texturing (EDT) of hardened AISI D2 Sendzimir rolls, used for the production of stainless steel strip. For moderate size cluster mills, EDT has been tested as an alternative to physical vapor deposition (PVD) method for improvement of the surface. Roll rotation direction (anticlockwise viewed from the tailstock end of the workpiece), roll surface speed (6 m min^{-1}) and electrode axial-feed rate (0.44 mm rev^{-1}) were kept constant throughout the tests, as was the servo gain (5/32). PM electrodes used for the tests were prepared under different compacting and sintering conditions and their properties evaluated, for example, density and electrical resistivity. EDT trials were performed using TiC/WC/Co and WC/Co tool electrodes, both in the green compact and fully sintered states. **Figure 51** shows the comparison in properties between two electrodes.

The use of high sintering temperatures increased the bonding between particles and hence erosion resistance, while electrodes sintered at lower temperatures were subject to rapid wear due to the weak bonding between particles and loosely bonded particles were detached leading to excessive gap contamination. The average SR R_a was much improved for the roll textured using powder sintered TiC/WC/Co electrodes when compared to the 'conventional' EDT roll. Microhardness measurements of roll cross-section samples made before rolling indicated a significantly higher roll white layer hardness of up to 950 HK using the sintered TiC/WC/Co tool electrodes.

1.13.10.1.3 Surface modification by dielectric

Usage of different dielectric materials has been investigated to obtain a better EDMed surface. Currently used dielectrics can be classified basically into three major groups. Moreover, the recent trend is to use nano-particles to the dielectric fluid and it has been reported that adding particles to the dielectric gives better MRR with lower TWR and improves the sparking efficiency.[74]

Jeswani,[75] Mohri *et al.*,[76] and Kunieda *et al.*[77] introduced the concept of using gas instead of liquid as dielectric medium. Later Xu *et al.*[78] applied ultrasonic vibration assisted EDM in gas experimentally with a copper electrode copper and

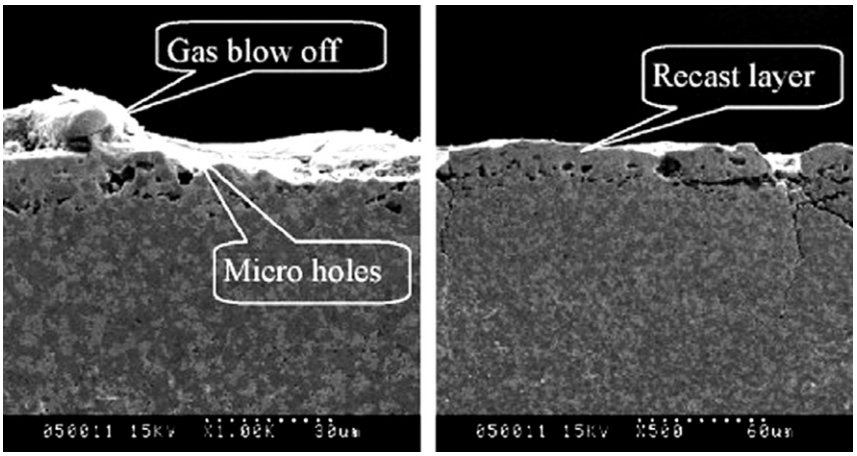


Figure 52 Cross-section of cemented carbide machined by UEDM in gas.

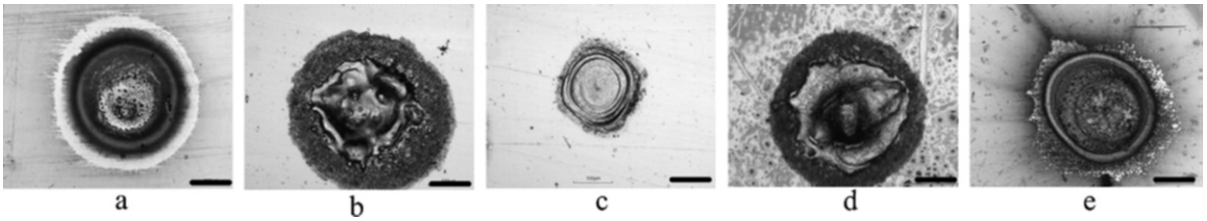


Figure 53 Comparison of the external appearances of craters formed in (a) air; (b) kerosene; (c) deionized water; (d) W/O emulsion; and (e) oxygen. Pulse duration = 105 μs (the length of the scale bar was 100 μm).

workpiece material used was YT15 cemented carbide. It was expected that the high pressure and velocity gas supplied through the internal hole of the electrode would flow over the discharging gap, which could enhance the removal of molten and evaporated workpiece material. In addition, it cooled and solidified the removed material and prevented them from adhering onto the surface of the tool electrode. Also, during the pulse-off time, the gas with a high velocity blew off the plasma formed by the previous discharge ensuring the recovery of the dielectric strength of the gap, and decreased the temperature of the discharge spot on the tool electrode and the workpiece due to heat transfer.

As can be seen from **Figure 52** that the material was melted first and then blown by gas medium with high pressure and velocity. Also, the recast layer is thin and full with many micro-holes and microcracks.

Chung *et al.*[79] studied effect of deionized water as a dielectric for EDM and for electrochemical dissolution for finishing process of micro-hole surfaces processed by μEDM. Thus, the total process is achieved by sequential process without working fluid change. The effects of finishing conditions such as the resistivity of deionized water, the voltage, the tool rotation and the finishing time on the SQ and accuracy of the shape were investigated. The inner surface of the hole was finished successfully via electrochemical dissolution in deionized water. Usage of water was considered as environment friendly dielectric and as there was no contamination of the work-tank by acid or by a neutral salt solution, continuous multiple holes machining including μEDM and finishing was carried out easily. Deionized water was used to remove a thin layer of the inner surface of μEDM hole, its higher resistivity was utilized to complete the finishing process without shape distortions. Considering the surface finishing is based on an electrochemical process, the resistivity of deionized water had an effect on the quality of the surface and the accuracy of the shape.

Zhang *et al.*[80] presented a rather comprehensive study by using five different dielectrics namely air and oxygen, deionized water, kerosene, and water-in-oil (W/O) emulsion. The whole geometry parameters of the craters, including the recast material in the craters, were precisely determined by metallographic method. Their previous study proved that surface with different characteristics can be obtained with different dielectric.

Their experimental work showed that different crater formation was obtained from five different dielectrics (**Figure 53**).

It was found that there was a huge difference of the geometry shape of the craters formed in different dielectrics even with the same experiments conditions. In kerosene, less volume of material was melted compared to other dielectrics.

For dispersion of powder in dielectrics, Mohri *et al.*[76] pioneered in order to break through the limit of roughness in finish EDM as silicon powder was suspended in working fluid at the stage of finish EDM. The powder in working fluid promoted the dispersion of discharging in finish EDM. A series of automatic die manufacturing processes was carried out on trial. A free-form shape with glossy surface was machined without any manual works. Kerosene was used as working fluid, while the electrode was made of copper and the

workpiece was steel, for finish EDM they summarized the effect of powder in dielectric as

i. Powder suspension enlarges the gap distance between electrode and work surface more than several times than that by conventional fluid.
ii. Powder suspension disperses discharges all over the gap region.
iii. Powder suspension decreases finish machining extremely.
iv. The machined roughness with powder suspended working fluid does not depend strongly on the working area.
v. Work surface by powder suspended fluid has strong corrosion resistance.

Jahan *et al.*[81] observed that the presence of semi-conductive graphite nano-powders in the dielectric can significantly improve the surface finish and they reported to have average SR of nano meter scale. For sinking and milling μEDM, added nano-powder lowered the breakdown strength. They also reported that for a fixed powder material and particle size, all the performance parameters varied significantly with powder concentration. Powder-mixed milling μEDM provided smoother and defect-free surface compared to sinking μEDM. The lowest value of R_a (38 nm) and R_{max} (0.17 μm) was obtained for an optimum concentration of 0.2 g l^{-1}.

Zhao *et al.*[82] presented a comprehensive study on powder-mixed EDM (PMEDM). PMEDM is capable of acheiveing machined surface with evenly distributed and large and shadow shaped etched cavities within the same discharge energy level, and eventually can obtain mirror effects in the finish machining phase. They presented their experimental works for rough EDM condition with red copper electrode, 45# steel workpiece. EDM special working fluid from Mobil was used for conventional EDM machining, and self-made powder-mixed working fluid was used for powder-mixed dielectric EDM (PMDEDM) machining the powder of which is aluminum powder 10 μm in granularity and 40 g l^{-1} in density.

Figure 54 shows the comparison between PEDMed and EDMed surface for rough cut. For PEDMed machining, the discharge breakdown was easier and it enlarged the discharge gaps and widened the discharge passage. Because of much loss of discharge energy in the discharge gaps and reduction of the ejecting force on the molten workpiece metal, the SR was smaller in PMEDM machining in comparison with conventional EDM machining.

Hu *et al.*[83] presented their study of surface property on a composite using powder based dielectric. The workpiece material used was SiC particle reinforced Al matrix composites (SiCp/Al). Conventional EDM and PMEDM were compared and surface micro-topography and wear resistance were analyzed. Copper electrode was used and the aluminum powder dispersed in working fluid (kerosene) had concentration of 35 g l^{-1} with Al particle sizes <2 μm. The comparison between two surfaces obtained from the conventional EDM and PMEDM is shown in Figure 55.

On an average, the PMEDM SR decreases about 31.5% with better corrosion resistance and wear resistance is twice of EDM. Besides, the variation range of the roughness was found to be smaller.

1.13.10.1.4 Ball burnish machining for EDM surface

Improvement of workpiece surface integrity has been tried using EDM with ball burnish machining (BEDM). BEDM uses hard smooth balls attached to the electrode to form a plastic deformation layer on the workpiece surface during sparking yielding a hardened and modified surface microstructure.[41] In a study by Yan *et al.*,[84] rotary EDM with ball burnishing for inspecting the machinability of Al_2O_3/6061Al composite was explored. Three ZrO_2 balls were attached as additional components with the rotating electrode tool to provide immediate burnishing following EDM (BEDM). Experimental results were observed for machining rate, SR and improvement of SR. The machining parameters considered were: categorized into two groups: (1) electrical parameters, i.e., peak current, pulse duration, and non-load voltage; and (2) non-electrical parameters, i.e., flushing pressure of dielectric, rotational speed of electrode, and residual height of hump. For the experimental steps, a hollow-tube electrode ($f=19$ mm, thickness 3 mm) was used to drill through the workpiece followed by an electrode tool of BEDM was used to machine through the workpiece to obtain a finer surface effect. The electrode tool developed for this purpose is seen in Figure 56.

The percentage improvement of surface roughness (ISR) was calculated by comparing the SR obtained from EDM with that from BEDM. In solving the Taguchi method, the observed values of MRR, SR, and ISR were set to maximum, minimum

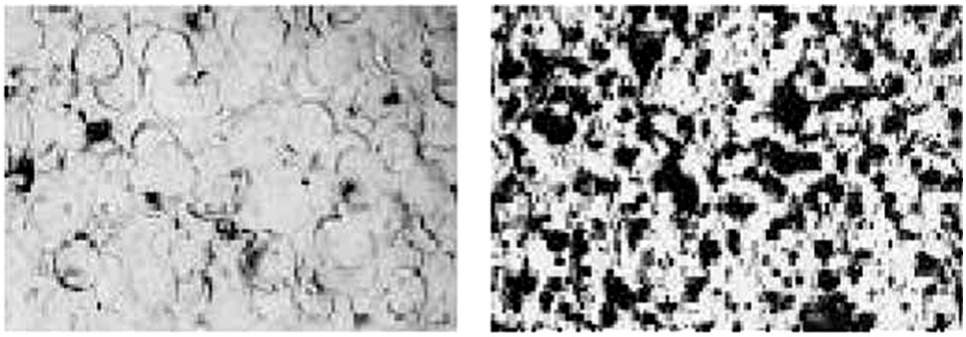


Figure 54 Surface obtained from PEDM and conventional EDM.

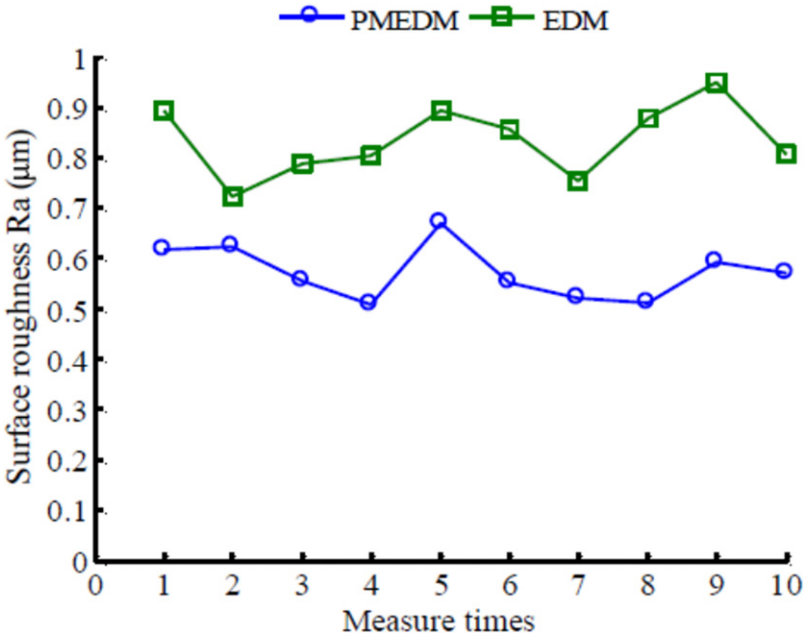


Figure 55 Roughness of the two kinds of surfaces.[83]

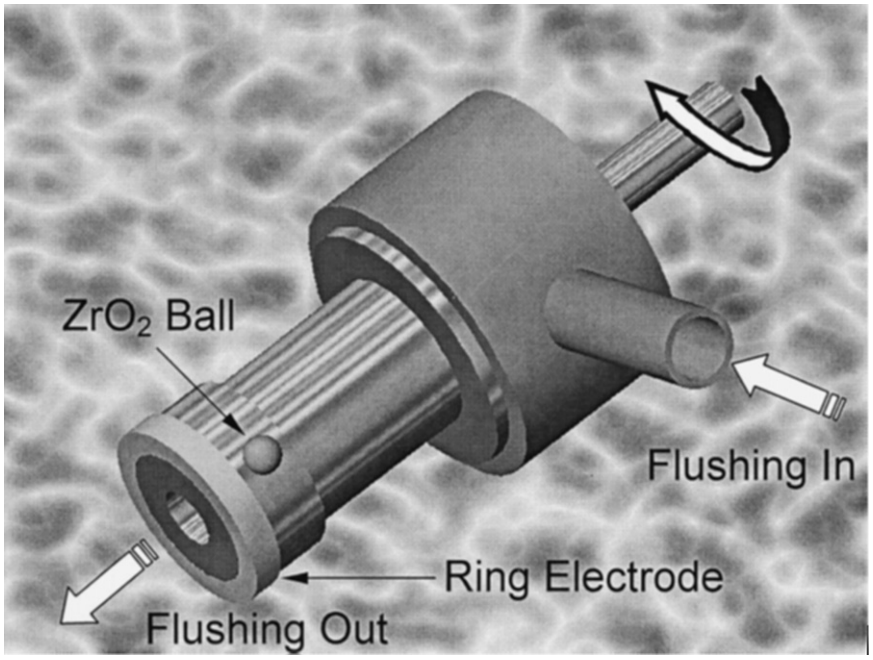


Figure 56 A newly developed electrode tool of BEDM.

and maximum, respectively. Figure 57 presents a comparison between the EDM and BEDM surface generated.

It was observed from results that the ISR increased from 55 up to 92% with various combinations of experimental parameters applying Taguchi method. It was also found that the BEDM process approaches both a higher machining rate and a finer SR. The machining rate was significantly affected by the peak current and non-load voltage parameters significantly affect the machining rate for the BEDM process. In contrast, the experimental parameters play only a minor role in evaluating the SR and the improvement of SR for the BEDM process.

In the later years, Yan and Lim[85] presented their study on surface modification of Al–Zn–Mg alloy by combined EDM with ball burnish machining (BBM). Machining parameters of the combined process, including machining polarity, peak current, power supply voltage, and the protruding of ZrO_2, are chosen to determine their effects on MRR, SR, and the

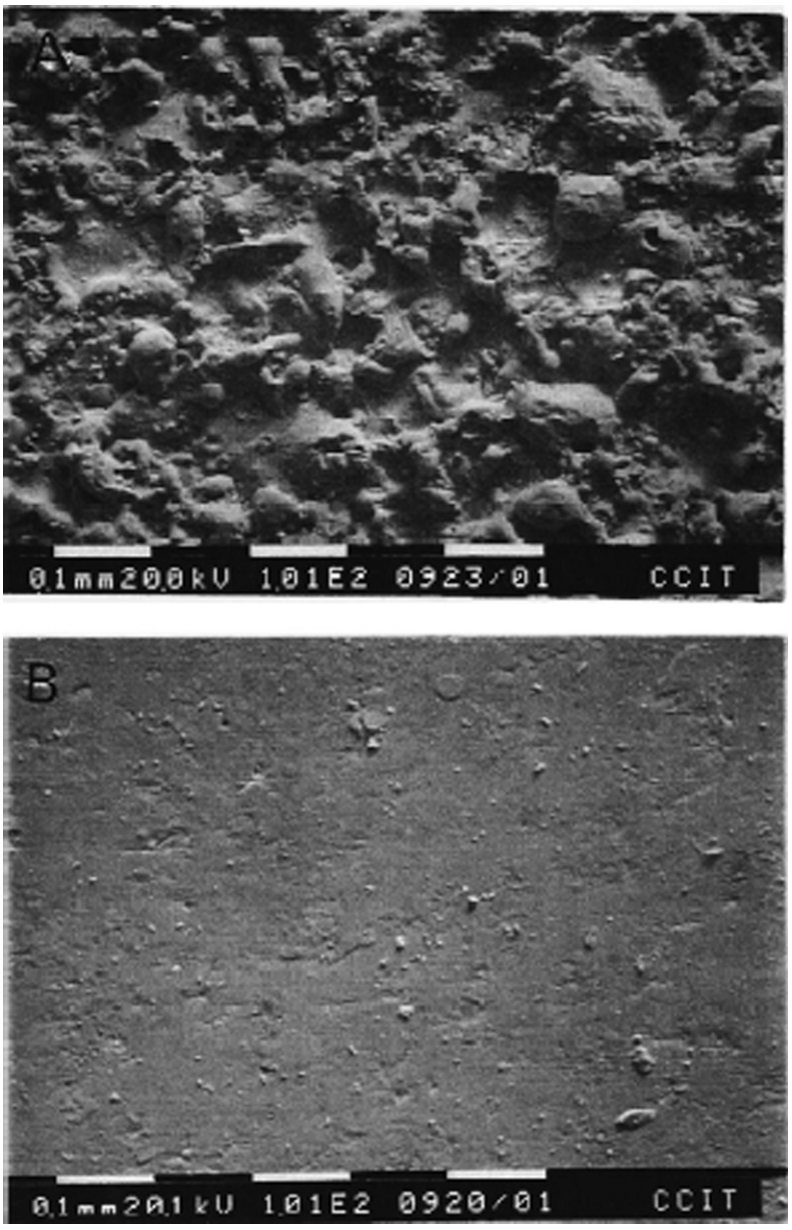


Figure 57 SEM photographs of the machined surface for (A) a surface that has been produced by EDM, (B) a surface that has undergone BEDM with the optimal combination of experimental parameters.

improvement ratio of SR (IRSR). The calculation of IRSR used the formula: $IRSR = (SR_{EDM} - SR_{EDM+BBM})/SR_{EDM} \times 100\%$; SREDM is the SR obtained by conventional EDM (μm R_a); $SR_{EDM+BBM}$ is the SR obtained by combined EDM with BBM (μm R_a). The electrode material was a ring-shaped copper material in which the outer and inner diameters were 32 and 24 mm, respectively, and the thickness of copper electrode was 5.0–4.75 mm to control a situation in which the protruding distance of ZrO_2 balls was fixed at 0–0.25 mm from the electrode surface. Their results showed that the surface integrity produced by the combined process was flatter and finer than that of the conventional EDM under various peak currents. Besides, increasing the peak current would not only cause the SR of conventional EDM to become coarser but also induce the SR of combined EDM with BBM to be rougher. While evaluating the cross-section of the machined surface, it was found that the microcracks and pores with various dimensions distributed on the conventional EDM surface, as caused by an electrical discharge inducing thermal stress and extreme heat, were eliminated by the smooth ZrO_2 balls burnishing to generate plastic deformation on the machined surface. Therefore, the surface integrity became a fine-finishing one. **Figure 58** shows the improved surface with combined EDM and BBM.

1.13.10.1.5 Special applications

Besides these widely used surface modification processes, researchers now a days are interested to broaden their experience in EDM by approaching new method. With rapid progress in

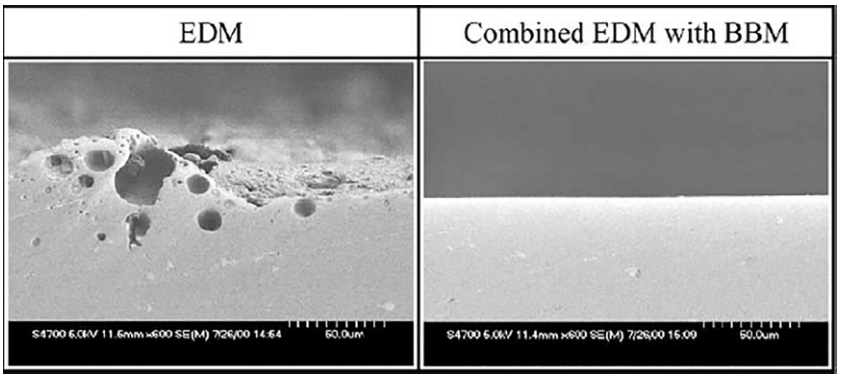


Figure 58 Improvement of combined process for eliminating the micropores and cracks (polarity: (+), peak current: 5 A, power supply voltage: 60 V).[85]

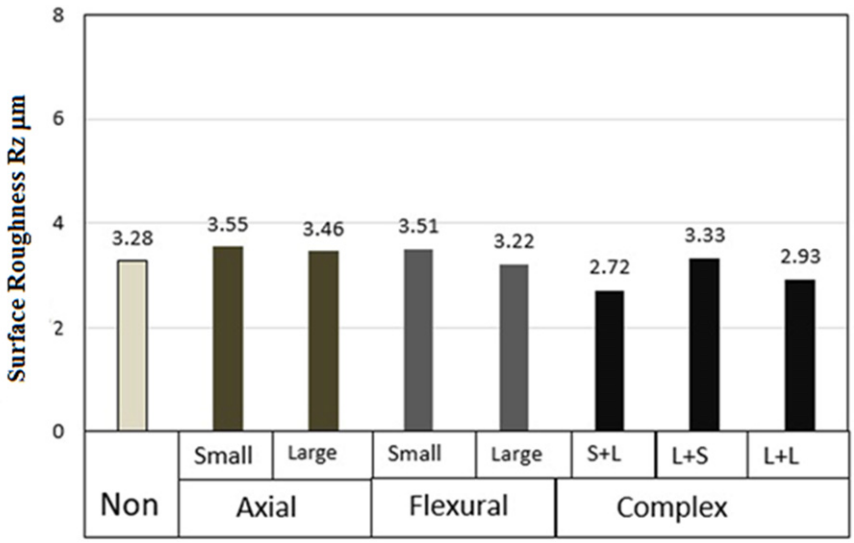


Figure 59 Workpiece surface roughness with and without vibration for EDM on PCD.[89]

polymer development over the years, conductive polymer are being used as electrode or workpiece. Ultrasonic vibrations are also applied to obtain superior quality machined surface. Some of these works will be presented in this section.

Anwar[86] reported micro-patterning of polypyrrole based conductive polymer on μEDM. The patterning feasibility is investigated using air and EDM oil as the dielectric media for the process. When air as dielectric medium, the patterned structures exhibited surface damages including microcracks in both drilling and milling processed structures. It was experimentally shown that stable, high-precision micro-machining of the material could be performed using wet μEDM in commercially available EDM oil instead of dry μEDM in air. Polymer electrode was tried out by Curodeau *et al.*[87] for a standard die-sinking EDM process, where a thermoplastic composite electrode, instead of solid graphite, is used to perform fine EDM finishing with air as dielectric medium. A proof of concept has demonstrated that the process can be used to reduce a 44 µm R_a surface finish down to a 36 µm R_a with three electrodes forming iterations using constant EDM settings. Curodeau *et al.*[88] in their later works tried EDM polishing and texturing process with conductive polymer electrodes. To carry out these new EDM processes, an electrically conductive polymer electrode made of styrene-carbonaceous composite was used and design of experiments was utilized to minimize its electrical resistivity (0.08 Ω cm) and maximize its thermal conductivity. Water was used as dielectric in the projected EDM processes. Micrographs of the electrode and workpiece confirmed that SR peeks can be effectively flatten to 0.21 mm PV, by a replicate electrode of the mold geometry. It was also shown that a fine graphite grade and positive polarity current impulses are contributing to improve the workpiece surface finish.

EDM machinability of PCD was investigated by Iwai *et al.*[89] They used a copper electrode giving ultrasonic vibrations in three modes (axial vibration, flexural vibration, and complex vibration). It was found that EDM efficiency became three times higher than the ordinary EDM without vibration. Reported SR is seen in **Figure 59**. The maximum height of the machined surface R_z was in the range of 2.72–3.55 µm in any experimental conditions, and no big difference was observed.

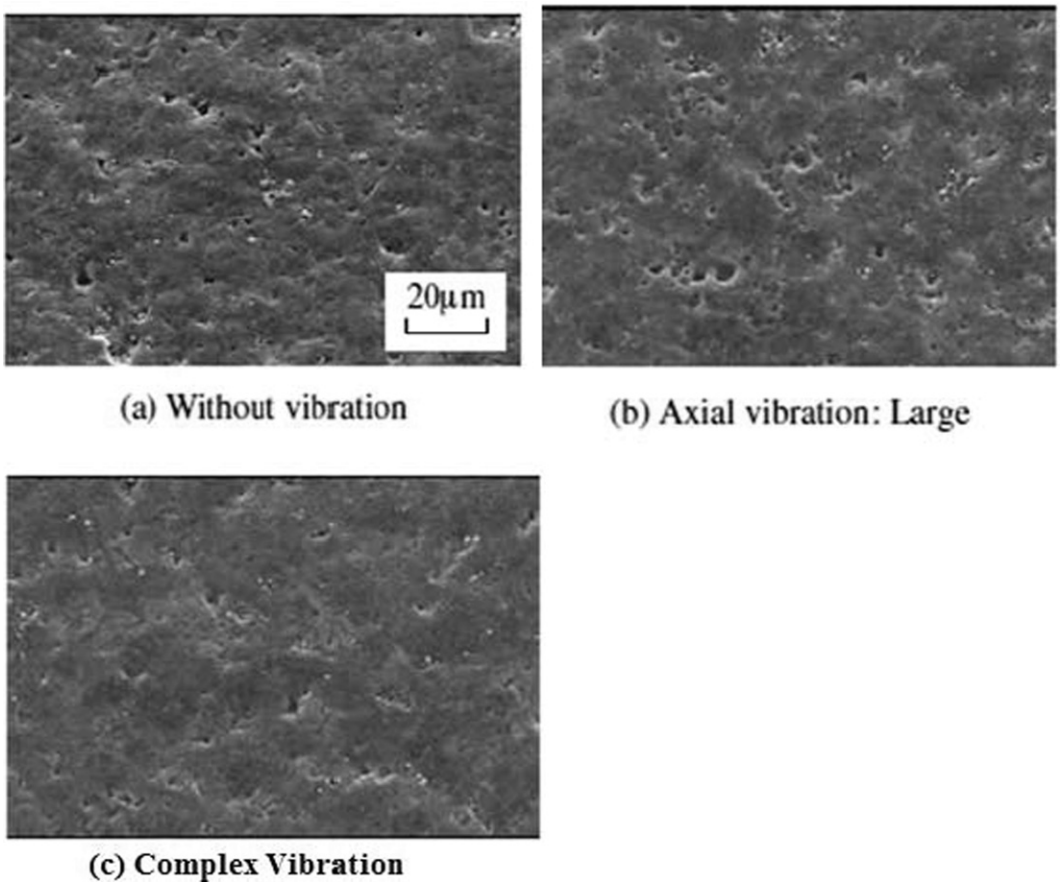


Figure 60 SEM observation results of the surface condition of the worked PCD under different vibration conditions.[89]

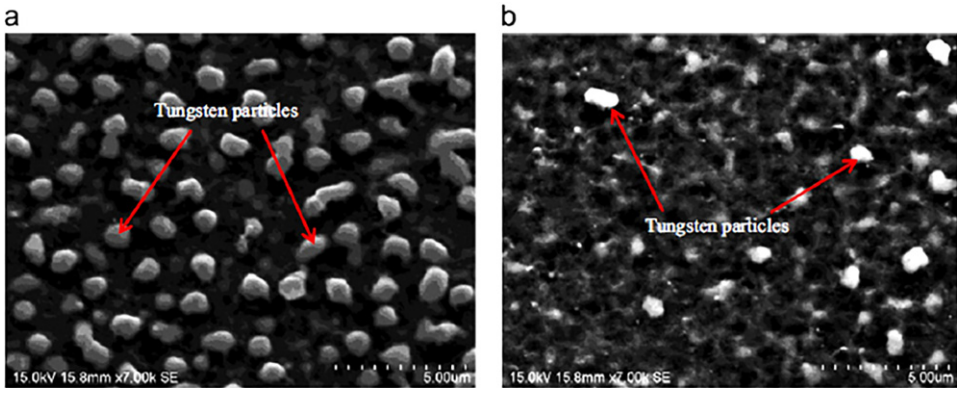


Figure 61 SEM micrograph of surface machined with carbon nanofibers addition (a) without ultrasonic cavitation and (b) with ultrasonic cavitation.[90]

Further investigation on SQ showed no deep discharge mark was found and the worked surface exhibited relatively good condition in any experimental conditions. **Figure 60** shows the SEM of surfaces under different condition.

Liew *et al.*[90] presented their work on μEDM of deep micro-holes in ceramic materials. Results show that ultrasonic vibration not only induced stirring effect but also caused cloud cavitation, which is helpful for removing debris and preventing tool material deposition on machined surface. The machining characteristics are strongly affected by the vibration amplitude, and the best machining performance is obtained when carbon nanofibers are added into the vibrated dielectric fluid. An important ceramic mold material, RB-SiC was used as workpiece while the tool electrode used was tungsten. Commercially available EDM oil was used as dielectric fluid. It has been shown in **Figure 61** the effect of adding of carbon nano fibers in dielectric fluid with/without ultrasonic vibration.

Without ultrasonic cavitation, many tungsten particles are deposited on the workpiece surface. In contrast, with ultrasonic

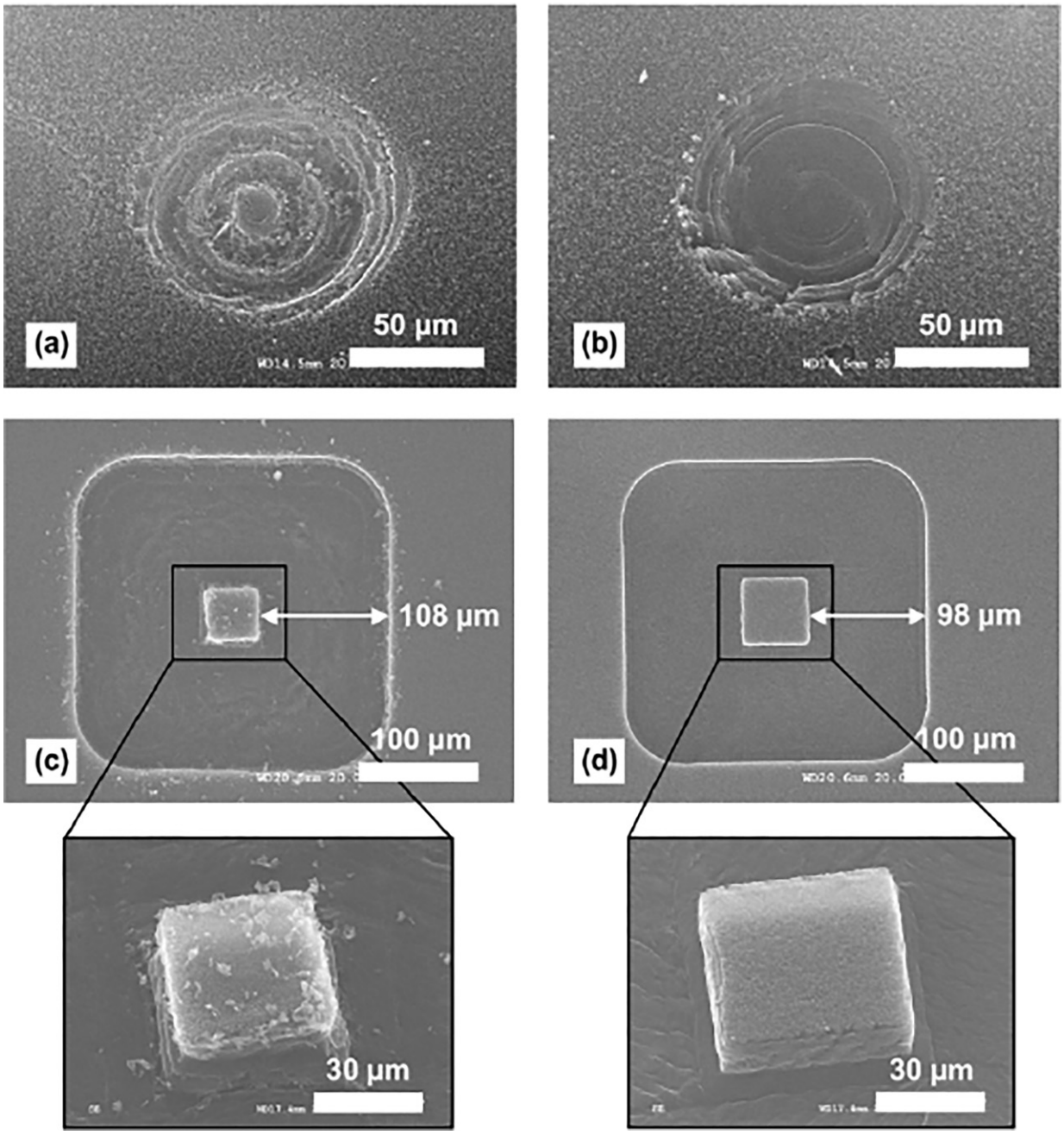


Figure 62 The upper two SEM images show shallow cavities machined in a CNT forest using 20 V and 10 pF with (a) normal polarity and (b) reverse polarity. The lower two SEM images show micropatterns machined in a CNT forest using 10 V and 10 pF with (c) normal polarity, and (d) reverse polarity, for a depth of 40 μm with 1-μm-step electrode feeding in the Z direction. The images in (c) and (d) also show close-up views of the microstructures created in the cavities.[91]

cavitation the tungsten particle deposition is reduced significantly, as seen in Figure 61.

Recently patterning of advanced material like vertically aligned carbon nanotubes (VACNTs) also commonly known as CNT forest has been carried out by several researchers. Saleh *et al.*[91] investigated reversed polarity μEDM of CNT forest and reported its several advantages over conventional μEDM of VACNTs. CNTs are known to be better field emitters; hence discharge sparks can be generated at low applied potentials. Based on this hypothesis, Saleh *et al.*[91] carried out their study and it was observed that the process with the reverse-polarity condition increased the discharge current, because of the enhanced field-emission properties of CNTs that served as the cathode in reversed μEDM. At higher voltage reversed μEDM was found to be detrimental as it generated uncontrolled sparks with bad SQ on the resultant patterns. However, as the operating voltage was lowered this concept was proven to be much better as it could produce more precise structure with good SQ as shown in Figure 62.

Thus authors[91] concluded that the structures machined with reverse μEDM at low voltages can produce higher precision and smoother and cleaner surfaces with almost no debris compared with those produced using conventional, normal-polarity processing. Reverse μEDM was also found to enable more stable and faster machining of the forests. Raman and EDX analyses revealed that reverse μEDM did not cause significant crystalline defects in the processed CNTs and contamination of the forest surfaces with the electrode element, respectively.

Laser machining is also used for micro-machining, however, it is has a disadvantage of producing inferior SQ because of HAZ. On the other hand, μEDM has a great advantage of producing superior SQ on the finished product but its processing time significantly slower as compared to laser machining. Ahmari *et al.*[92] combined the advantage of faster machining time of laser processing and smoother finish of μEDM to propose a hybrid machining technique based on laser processing and μEDM operation. They[92] investigated the process on Ni–Ti based shape memory alloy and found it to be very effective. In their study they conducted the experiments only for drilling operations. It was found that the proposed hybrid machining process resulted in 50–65% reduction in machining time without affecting the quality of micro-holes as compared to the standard μEDM process.

1.13.10.2 Surface Modification Using Wire EDM

In the 1970s with the development of CNC machining wire-cut EDM became a practical machining system. The basic difference between the brief summary about surface finish controlling factors for wire EDM will be discussed in this section. The surface characteristics of the wire-cut machine are very similar to those of the die-sinker machine. Both die-sinker and wire-cut machines use sparking to remove electrically conductive material. However, they do not normally use the same kind of dielectric fluids or electrodes. Therefore, its visual appearance is different due to the deionized water that is used as the dielectric fluid. Since water does not have carbon as a by-product as it breaks down in the sparking process, the machined surface remains clean and the chance of DC arcing is minimized due to the deionized water that is used as the dielectric fluid.[37]

Gupta *et al.*[93] highlighted about analysis and optimization of SR parameters (i.e., average roughness R_a and maximum roughness R_t) of wire electrical discharge machined fine-pitch miniature spur gears. The material used was brass. Experimental effects of four EDM machining parameters (i.e., voltage, pulse-on time, pulse-off time, and wire feed rate) on the SR parameters were observed and it is reported from their studies that the SR increased with higher voltage and longer pulse-on time and decreased with longer pulse-off time and higher wire feed rate.

Huang and Chen[94] presented experimental studies on WEDM to identify the significant factors affecting SR. The controlling factors considered were: type of pulse generating circuit (PS), conductivity of the dielectric (K), resistance in the circuit (R), capacitance in the circuit (C), applied voltage (V), feed rate of the table (F), and pulse-off time (T_{off}). Taguchi quality design was adopted to select appropriate number of experiments. After analyzing the effect of each relevant factor on SR, appropriate values of all parameters are chosen and a fine surface of roughness R_a equals to 0.22 μm was achieved.

Kurian and Yeldose[95] investigated effect of wire EDM parameters on SR of stainless steel. The steel workpiece used was 15-5 PH stainless steel, which was martensitic, precipitation hardening stainless steel. It has excellent strength, transverse toughness and ductility widely used in corrosive as well as high-pressure environments. SR (R_a) were considered for optimizing machining parameters. The surface finish value (in μm) was obtained by measuring the mean absolute deviation, R_a (SR). The minimum value of R_a found from their work was 0.5037 μm.

Saleh *et al.*[59] proposed an improved μ-WEDM and μEDM of silicon (Si) by temporarily coating Si with a high conductive metal (gold in this study). Micro-WEDM process stability was found to be improved ($\sim 100\times$ for different machining condition) if coated Si wafer is used as compared to uncoated Si workpiece. In this research, a p-type pre polished (mirror quality) silicon wafer of 650 μm thickness was used. The wafer was coated with conductive material (Au in this research) using ion spattering machine on the both sides before the start of the actual μ-WEDMing/EDMing process. Three types of samples were prepared for the machining experiment. The first group of samples was silicon (Si) without any coating, the second and third groups were Si coated for 5 min (Si(1)) and 10 min (Si(2)). The resultant surfaces for three different coating are shown in **Figure 63**.

It is seen that machined surface for uncoated Si wafer was rough with visible bumps, whereas machined surface for coated Si wafer (10 min) is remarkably smooth. And the SQ of Si(1) falls in between. Stability of machining could be one reason for enhanced SQ for WEDMed surface for gold-coated Si. Further, during machining, gold-coated Si spark generation was consistent, which led to smoother SQ; on the other hand, inconsistent spark generation for uncoated Si made the machined surface rough with visible bumps.

1.13.11 Summary on EDMed SQ

The surface produced by EDM sparking is non-directional and nonreflective and is made up of many spherical cavities because EDM works under the principle of molten metal removal. Many attempts have been reported in the chapter to focus on the recent improvements in EDMed surfaces. We may summarize few salient points regarding surface generated in EDM, its possible improvements and parameters affecting the SQ:

- Higher spark energy has adverse effect on EDMed surface. The more the spark energy is available, more volume is removed by the process ending up in a coarser surface.
- Electrode material plays an important role on the EDMed surface as sometimes part of it may be associated with the workpart surface. Therefore, the electrode materials thermal conductivity and melting point have significant influence on the EDMed surface besides electrical conductivity.
- Use of a PM or composite electrode has been proved to be a viable alternative to expensive surface coating processes.

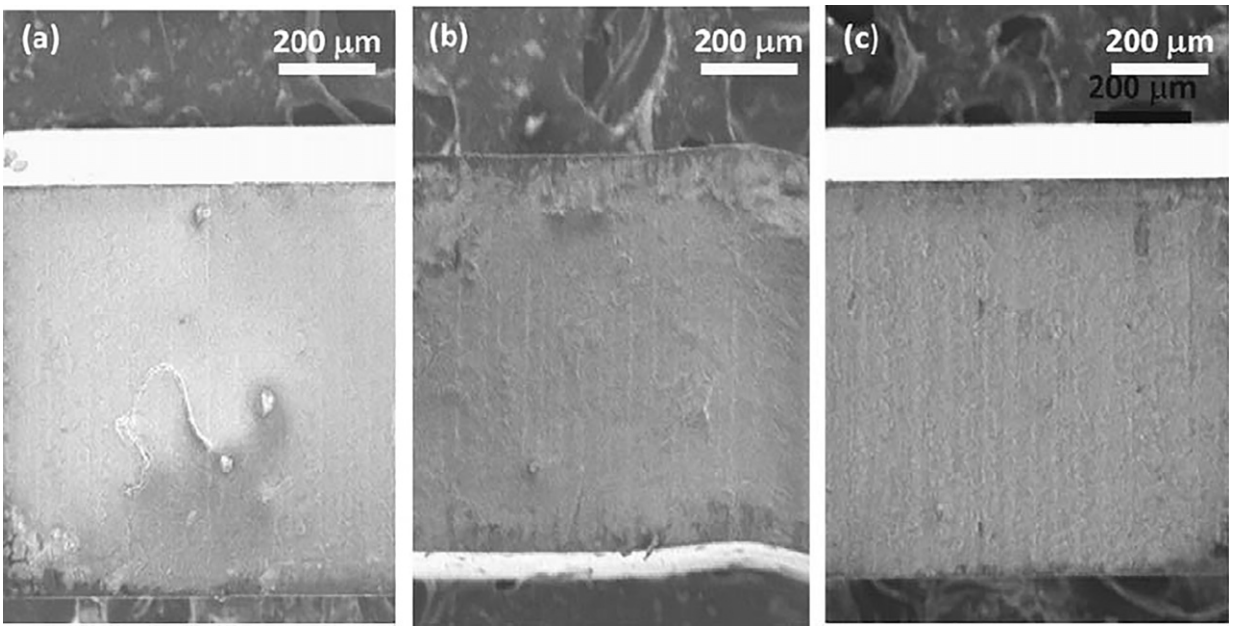


Figure 63 SEM image of the cut surface of the machined slots by μ-WEDM process with machining condition of 95 V and 1 nF for (a) uncoated Si, (b) Si(1), and (c) Si(2).[59]

Table 6 Comparison between ELID grinding and electro-discharge machining

Attributes	*ELID grinding*	*EDM*
Machining type	Conventional grinding	Non-conventional machining
Speciality	Grinding tool is dressed in-process by electrolytic reactions	Machining is taken place by controlled electrical sparks between tool and workpiece
Work materials	Hard and brittle materials can be glass, ceramics, Si wafers, bearing steels, etc.	Difficult to cut materials and conductive metals, carbon nano tubes, conductive polymers, etc.
Machining fluid	Electrolytes	Dielectric
Machining domain	Mostly macro	Macro to micro
Machining arrangement	Planner grinding, lapping grinding, traverse grinding, parallel grinding, cylindrical grinding, etc.	Die-sinking EDM, milling EDM, wire EDM, etc.
Attainable surface roughness	Average surface roughness ranges from sub-nanometers to 10s of nanometers	Minimum, average surface roughness achieved was 30s of nanometers in micro-EDM

- Dielectric is also a determining factor for surface finish. Dielectric with conductive nano-particles dispersed in it has resulted in excellent surface finish for μEDM.
- Ball milling or burnishing can be a good combination to be used with EDM electrode for a better surface finish.
- EDM with conductive electrode, powder associated dielectric combined with ultrasonic vibration, EDM on different conductive polymer have shown promising applications. Further research outcomes are expected from such applications.

1.13.12 Conclusion

ELID grinding and EDM are two subtractive manufacturing processes discussed in this chapter. In ELID grinding actual machining action is conventional; however, dressing of the grinding wheel is taken place by electrolytic reaction. ELID grinding is under research interest for last two decades and has evolved considerably since. On the other hand, EDM is a non-conventional machining process that removes material from the workpiece by controlled and repetitive electric sparks without any physical contact between tool and work materials. Table 6 shows a comparative study between these two machining technologies.

It can be understood from Table 6 EDM is mostly applicable for conductive material in both macro and micro-domain. On the other hand, ELID can be used for both conductive and nonconductive material mostly in macro domain. Sub-10 nm average SR is very common on the product finished by ELID grinding however, best SR achieved in EDM is in several 10s of nanometer and micro-domain. It can be concluded that EDM as the finish machining has the strength to be used in both macro and micro-domain with a capability to produce complicated features, whereas ELID grinding is promising to

achieve mirror surface finish on hard and brittle materials which may potentially eliminate subsequent finishing process such as polishing.

See also: 1.11 Micromachining

References

1. Seok Han, L.; Fathima, K.; Kumar, A. S.; Rahman, M. A Fundamental Study on the Mechanism of Electrolytic In-Process Dressing (ELID) Grinding. *Int. J. Mach. Tool. Manuf.* **2002**, *42* (8), 935–943.
2. Rahman, M.; Lim, H. S.; Neo, K. S.; *et al.* Tool-Based Nanofinishing and Micromachining. *J. Mater. Process. Technol.* **2007**, *185* (1–3), 2–16.
3. Schöpf, M.; Beltrami, I.; Boccadoro, M.; Kramer, D.; Schumacher, B. ECDM (Electro Chemical Discharge Machining), a New Method for Trueing and Dressing of Metal Bonded Diamond Grinding Tools. *CIRP Ann. – Manuf. Technol.* **2001**, *50* (1), 125–128.
4. Rahman, M.; Kumar, A. S.; Biswas, I. A Review of Electrolytic In-Process Dressing (ELID) Grinding. *Key Eng. Mater.* **2009**, *404*, 45–59.
5. Ohmori, H.; Nakagawa, T. Mirror Surface Grinding of Silicon Wafers with Electrolytic In-Process Dressing. *CIRP Ann. – Manuf. Technol.* **1990**, *39* (1), 329–332.
6. Zhang, C.; Ohmori, H.; Li, W. Small-Hole Machining of Ceramic Material with Electrolytic Interval-Dressing (ELID-II) Grinding. *J. Mater. Process. Technol.* **2000**, *105* (3), 284–293.
7. Qian, J.; Ohmori, H.; Lin, W. Internal Mirror Grinding with a Metal/Metal-Resin Bonded Abrasive Wheel. *Int. J. Mach. Tool. Manuf.* **2001**, *41* (2), 193–208.
8. Rahman, M.; Kumar, A. S.; Lim, H. S.; Fatima, K. Nano Finish Grinding of Brittle Materials Using Electrolytic In-Process Dressing (ELID) Technique. *Sadhana* **2003**, *28* (5), 957–974.
9. Ohmori, H.; Katahira, K.; Naruse, T.; *et al.* Microscopic Grinding Effects on Fabrication of Ultra-fine Micro Tools. *CIRP Ann. – Manuf. Technol.* **2007**, *56* (1), 569–572.
10. Ohmori, H.; Takahashi, I.; Bandyopadhyay, B. P. Ultra-Precision Grinding of Structural Ceramics by Electrolytic In-Process Dressing (ELID) Grinding. *J. Mater. Process. Technol.* **1996**, *57* (3–4), 272–277. Available from: http://dx.doi.org/10.1016/0924-0136(95)02079-9 (http://www.sciencedirect.com/science/article/pii/0924013695020799).
11. Bandyopadhyay, B. P.; Ohmori, H.; Takahashi, I. Efficient and Stable Grinding of Ceramics by Electrolytic In-Process Dressing (ELID). *J. Mater. Process. Technol.* **1997**, *66* (1–3), 18–24.
12. Katahira, K.; Ohmori, H.; Uehara, Y.; Azuma, M. ELID Grinding Characteristics and Surface Modifying Effects of Aluminum Nitride (AlN) Ceramics. *Int. J. Mach. Tool. Manuf.* **2005**, *45* (7–8), 891–896.
13. Yang, L.; Ren, C.; Jin, X. Experimental Study of ELID Grinding Based on the Active Control of Oxide Layer. *J. Mater. Process. Technol.* **2010**, *210* (13), 1748–1753.
14. Xie, J.; Li, Q.; Sun, J. X.; Li, Y. H. Study on Ductile-Mode Mirror Grinding of SiC Ceramic Freeform Surface Using an Elliptical Torus-Shaped Diamond Wheel. *J. Mater. Process. Technol.* **2015**, *222*, 422–433.
15. Katahira, K.; Watanabe, Y.; Ohmori, H.; Kato, T. ELID Grinding and Tribological Characteristics of TiAlN Film. *Int. J. Mach. Tool. Manuf.* **2002**, *42* (12), 1307–1313.
16. Zhang, C.; Kato, T.; Li, W.; Ohmori, H. Comparative Study: Surface Characteristics of CVD-SiC Ground with Cast Iron Bond Diamond Wheel. *Int. J. Mach. Tool. Manuf.* **2000**, *40* (4), 527–537.
17. Zhanga, C.; Ohmori, H.; Kato, T.; Morita, N. Evaluation of Surface Characteristics of Ground CVD-SiC Using Cast Iron Bond Diamond Wheels. *Precis. Eng.* **2001**, *25* (1), 56–62.
18. Qian, J.; Li, W.; Ohmori, H. Cylindrical Grinding of Bearing Steel with Electrolytic In-Process Dressing. *Precis. Eng.* **2000**, *24* (2), 153–159.
19. Zhang, K.; Ren, C.; Yang, L.; Li, Q.; Jin, X. Precision Internal Grinding of Bearing Steel Based on the State Control of Oxide Layer with Electrolytic In-Process Dressing. *J. Mater. Process. Technol.* **2012**, *212* (7), 1611–1621.
20. Zhang, K.; Yu, Y.; Wang, W.; Li, H. Experimental Study on Internal Cylindrical Grinding of Bearing Steel with Electrolytic In-Process Dressing Grinding. *Int. J. Adv. Manuf. Technol.* **2015**, *81* (5), 1175–1185.
21. Saito, T.; Katahira, K.; Ohmori, H.; Komotori, J.; Mizutani, M.; Nemoto, A. Fabrication of High-Quality Surfaces on Precise Lens Mold Materials by a New ELID Grinding Wheel. In *Towards Synthesis of Micro-/Nano-Systems. The 11th International Conference on Precision Engineering (ICPE)*, Tokyo, Japan, August 16–18, 2006; Springer: London; pp. 315–318. DOI: 10.1007/1-84628-559-3_55.
22. Ohmori, H.; Katahira, K.; Komotori, J.; Mizutani, M. Functionalization of Stainless Steel Surface Through Mirror-Quality Finish Grinding. *CIRP Ann. – Manuf. Technol.* **2008**, *57* (1), 545–549.
23. Raffles, M. H.; Stephenson, D. J.; Shore, P.; Jin, T. Electrolytic In-Process Dressing Superfinishing of Spherical Bearings Using Metal-Resin Bond Ultra-Fine CBN Wheels. *Proc. Inst. Mech. Eng. Part B J. Eng. Manuf.* **2011**, *225* (1), 112–122.
24. Ohmori, H.; Lin, W.; Moriyasu, S.; Yamagata, Y. *Microspherical Lens Fabrication by Cup Grinding Wheels Applying ELID Grinding* **2001**, *34* (34), 5–7.
25. Kumar, A. S.; Lim, H. S.; Rahman, M.; Fathima, K. A Study on the Grinding of Glass Using Electrolytic In-Process Dressing. *J. Electron. Mater.* **2002**, *31* (10), 1039–1046.
26. Saleh, T.; Rahman, M. S.; Lim, H. S.; Rahman, M. Development and Performance Evaluation of an Ultra Precision ELID Grinding Machine. *J. Mater. Process. Technol.* **2007**, *192–193*, 287–291.
27. Sazedur Rahman, M.; Saleh, T.; Lim, H. S.; Son, S. M.; Rahman, M. Development of an On-Machine Profile Measurement System in ELID Grinding for Machining Aspheric Surface with Software Compensation. *Int. J. Mach. Tool. Manuf.* **2008**, *48* (7–8), 887–895.
28. Saleh, T.; Biswas, I.; Rahman, M. Efficient Dressing of the Wheel in ELID Grinding by Controllable Voltage with Force Feed Back. *Int. J. Adv. Manuf. Technol.* **2010**, *46* (1), 123–130.
29. Saleh, T.; Rahman, M. In-Process Truing for ELID (Electrolytic In-Process Dressing) Grinding by Pulsewidth Control. *IEEE Trans. Autom. Sci. Eng.* **2011**, *8* (2), 338–346.
30. Yin, S.; Ohmori, H.; Dai, Y.; *et al.* ELID Grinding Characteristics of Glass-Ceramic Materials. *Int. J. Mach. Tool. Manuf.* **2009**, *49* (3–4), 333–338.
31. Yin, S.; Morita, S. Y.; Ohmori, H.; *et al.* ELID Precision Grinding of Large Special Schmidt Plate for Fibre Multi-Object Spectrograph for 8.2 m Subaru Telescope. *Int. J. Mach. Tool. Manuf.* **2005**, *45* (14), 1598–1604.
32. Chao, C. L.; Liu, D.S.; Sheu, S.C.; Lin, Y.S.; Lin, H.Y. *A Study on the Surface Integrity of Single Crystal Silicon Ground by CIFB-Diamond Wheels (ELID) and Resin-Bonded Diamond*; Springer: New York; pp. **1999**, 1–5.
33. Itoh, N.; Ohmori, H.; Moriyasu, S.; *et al.* Finishing Characteristics of Brittle Materials by ELID-Lap Grinding Using Metal-Resin Bonded Wheels. *Int. J. Mach. Tool. Manuf.* **1998**, *38*, 747–762.
34. Islam, M. M.; Senthil Kumar, A.; Balakumar, S.; Lim, H. S.; Rahman, M. Performance Evaluation of a Newly Developed Electrolytic System for Stable Thinning of Silicon Wafers. *Thin Solid Films* **2006**, *504* (1–2), 15–19.
35. Islam, M. M.; Kumar, A. S.; Balakumar, S.; Lim, H. S.; Rahman, M. Characterization of ELID Grinding Process for Machining Silicon Wafers. *J. Mater. Process. Technol.* **2008**, *198* (1–3), 281–290.
36. Liu, J. H.; Pei, Z. J.; Fisher, G. R. ELID Grinding of Silicon Wafers: A Literature Review. *Int. J. Mach. Tool. Manuf.* **2007**, *47* (3–4), 529–536.
37. Jameson, E. C. *Electrical Discharge Machining*, Vol. 75, no. 1; Society of Manufacturing Engineers: Dearborn, MI, 2001.
38. Groover, M. *Fundamentals of Modern Manufacturing*, 4th ed.; Wiley: Oxford, 2010.
39. Bhattacharya, A.; Batish, A.; Singh, G.; Singla, V. K. Optimal Parameter Settings for Rough and Finish Machining of Die Steels in Powder-Mixed EDM. *Int. J. Adv. Manuf. Technol.* **2012**, *61* (5–8), 537–548.
40. Serope Kalpakjian, S. R. S. *Manufacturing Engineering and Technology*, 4th ed.; Prentice Hall: New York, 2009.
41. Ho, K. H.; Newman, S. T. State of the Art Electrical Discharge Machining (EDM). *Int. J. Mach. Tool. Manuf.* **2003**, *43* (13), 1287–1300.
42. Rujurkar, K. P.; Yu, Z. Y. 3D Micro-EDM Using CAD/CAM. *CIRP Ann. – Manuf. Technol.* **2000**, *49* (1), 127–130.
43. Kansal, H. K.; Singh, S.; Kumar, P. Application of Taguchi Method for Optimisation of Powder Mixed Electrical Discharge Machining. *Int. J. Manuf. Technol. Manag.* **2005**, *7* (2–4), 329.
44. Kumar, S.; Singh, R.; Singh, T. P.; Sethi, B. L. Surface Modification by Electrical Discharge Machining: A Review. *J. Mater. Process. Technol.* **2009**, *209* (8), 3675–3687.
45. Bruyn, H. E. D. Slope Control: A Great Improvement in Spark Erosion. *CIRP Ann. – Manuf. Technol.* **1968**, *16*, 183–186.
46. Naveen Beri, A.K.; Pungotra, H. To Study the Effect of Polarity and Current During Electric Discharge Machining of Inconel 718 with CuW Powder Metallurgy Electrode, In: *Proceedings of the National Conference on Trends and Advances in Mechanical Engineering*; 2012.

47. Gopalakannan, S.; Senthilvelan, T. Effect of Electrode Materials on Electric Discharge Machining of 316 L and 17–4 PH Stainless Steels. *J. Miner. Mater. Charact. Eng.* **2012**, *11* (7), 685–690.
48. Peças, P.; Henriques, E. Influence of Silicon Powder-Mixed Dielectric on Conventional Electrical Discharge Machining. *Int. J. Mach. Tool. Manuf.* **2003**, *43* (14), 1465–1471.
49. Peças, P.; Henriques, E. Effect of the Powder Concentration and Dielectric Flow in the Surface Morphology in Electrical Discharge Machining with Powder-Mixed Dielectric (PMD-EDM). *Int. J. Adv. Manuf. Technol.* **2008**, *37* (11–12), 1120–1132.
50. Guu, Y. H.; Hocheng, H. Effects of Workpiece Rotation on Machinability During Electrical-Discharge Machining. *Mater. Manuf. Process.* **2001**, *16* (1), 91–101.
51. Sato, T.; Mizutani, T.; Yonemochi, K.; Kawata, K. The Development of an Electrodischarge Machine for Micro-Hole Boring. *Precis. Eng.* **1986**, *8* (3), 163–168.
52. Bayramoglu, M.; Duffill, A. W. Systematic Investigation on the Use of Cylindrical Tools for the Production of 3D Complex Shapes on CNC EDM Machines. *Int. J. Mach. Tool. Manuf.* **1994**, *34* (3), 327–339.
53. Sabur, A.; Ali, M. Y.; Maleque, M. A.; Khan, A. A. Investigation of Material Removal Characteristics in EDM of Nonconductive ZrO_2 Ceramic. *Procedia Eng.* **2013**, *56*, 696–701.
54. Ji, R.; Liu, Y.; Zhang, Y.; Wang, F.; Chen, Z.; Dong, X. Study on Single-Discharge Machining Characteristics of Non-Conductive Engineering Ceramics in Emulsion with High Open Voltage and Large Capacitor. *Proc. Inst. Mech. Eng. Part B J. Eng. Manuf.* **2011**, *225* (10), 1888–1898.
55. Lauwers, B.; Kruth, J. P.; Liu, W.; *et al.* Investigation of Material Removal Mechanisms in EDM of Composite Ceramic Materials. *J. Mater. Process. Technol.* **2004**, *149* (1–3), 347–352.
56. Hanaoka, D.; Fukuzawa, Y.; Ramirez, C.; *et al.* Electrical Discharge Machining of Ceramic/Carbon Nanostructure Composites. *Procedia CIRP* **2013**, *6*, 95–100.
57. Román-Manso, B.; Domingues, E.; Figueiredo, F. M.; Belmonte, M.; Miranzo, P. Enhanced Electrical Conductivity of Silicon Carbide Ceramics by Addition of Graphene Nanoplatelets. *J. Eur. Ceram. Soc.* **2015**, *35* (10), 2723–2731.
58. Mamalis, A. G.; Vaxevanidis, N. M.; Pantelis, D. I. On the Electrodischarge Machining of Ceramic Plasma-Sprayed Steel Plates. *CIRP Ann. – Manuf. Technol.* **1992**, *41* (1), 235–238.
59. Saleh, T.; Rasheed, A. N.; Muthalif, A. G. A. Experimental Study on Improving μ-WEDM and μ-EDM of Doped Silicon by Temporary Metallic Coating. *Int. J. Adv. Manuf. Technol.* **2015**, *78* (9–12), 1651–1663.
60. Lee, L. C.; Lim, L. C.; Narayanan, V.; Venkatesh, V. C. Quantification of Surface Damage of Tool Steels After EDM. *Int. J. Mach. Tool. Manuf.* **1988**, *28* (4), 359–372.
61. Kruth, B.; Stevens, J. P.; Froyen, L.; Lauwers, L. Study on the White Layer of a Surface Machined by Die Sinking Electro-Discharge Machining. *Ann. CIRP* **1995**, *44* (1), 169–172.
62. Lloyd., H. K.; Warren, R. H. Metallurgy of Spark-Machined Surfaces. *J. Iron Steel Inst.* **1965**, *203*, 238–247.
63. Erden, A.; Kaftanoğlu, B. Thermo-Mathematical Modelling and Optimization of Energy Pulse Forms in Electric Discharge Machining (EDM). *Int. J. Mach. Tool Des. Res.* **1981**, *21* (1), 11–22.
64. Lee, L. C.; Lim, L. C.; Wong, Y. S.; Lu, H. H. Towards a Better Understanding of the Surface Features of Electro-Discharge Machined Tool Steels. *J. Mater. Process. Technol.* **1990**, *24*, 513–523.
65. Torres, A.; Luis, C. J.; Puertas, I. Analysis of the Influence of EDM Parameters on Surface Finish, Material Removal Rate, and Electrode Wear of an INCONEL 600 Alloy. *Int. J. Adv. Manuf. Technol.* **2015**, *80* (1), 123–140.
66. Barash, M. M.; Kahlon, C. S. Experiments with Electric Spark Toughening. *Int. J. Mach. Tool Des. Res.* **1964**, *4* (1), 1–8.
67. Jahan, M. P.; Wong, Y. S.; Rahman, M. A Study on the Fine-Finish Die-Sinking Micro-EDM of Tungsten Carbide Using Different Electrode Materials. *J. Mater. Process. Technol.* **2009**, *209* (8), 3956–3967.
68. D'Urso, G.; Merla, C. Workpiece and Electrode Influence on Micro-EDM Drilling Performance. *Precis. Eng.* **2014**, *38* (4), 903–914.
69. Younis, E. M. A. Effect of Electrode Material on Electrical Discharge Machining of DIN 1.2379 and DIN 1.2080 Surface. *J. Mater. Sci. Eng.* **2012**, *1* (2), 111.
70. Simao, J.; Lee, H.; Aspinwall, D.; Dewes, R.; Aspinwall, E. Workpiece Surface Modification Using Electrical Discharge Machining. *Int. J. Mach. Tool. Manuf.* **2003**, *43* (2), 121–128.
71. Ho, S. K.; Aspinwall, D. K.; Voice, W. Use of Powder Metallurgy (PM) Compacted Electrodes for Electrical Discharge Surface Alloying/Modification of Ti–6Al–4V Alloy. *J. Mater. Process. Technol.* **2007**, *191* (1–3), 123–126.
72. Wang, Z. L.; Fang, Y.; Wu, P. N.; Zhao, W. S.; Cheng, K. Surface Modification Process by Electrical Discharge Machining with a Ti Powder Green Compact Electrode. *J. Mater. Process. Technol.* **2002**, *129* (1–3), 139–142.
73. Simão, J.; Aspinwall, D.; El-Menshawy, F.; Meadows, K. Surface Alloying Using PM Composite Electrode Materials when Electrical Discharge Texturing Hardened AISI D2. *J. Mater. Process. Technol.* **2002**, *127* (2), 211–216.
74. Tzeng, Y. F.; Lee, C. Y. Effects of Powder Characteristics on Electrodischarge Machining Efficiency. *Int. J. Adv. Manuf. Technol.* **2001**, *17* (8), 586–592.
75. Jeswani, M. L. Effect of the Addition of Graphite Powder to Kerosene Used as the Dielectric Fluid in Electrical Discharge Machining. *Wear* **1981**, *70* (2), 133–139.
76. Mohri, N.; Saito, N.; Higashi, M.; Kinoshita, N. A New Process of Finish Machining on Free Surface by EDM Methods. *CIRP Ann. – Manuf. Technol.* **1991**, *40* (1), 207–210.
77. Kunieda, M.; Yoshida, M.; Taniguchi, N. Electrical Discharge Machining in Gas. *CIRP Ann. – Manuf. Technol.* **1997**, *46* (1), 143–146.
78. Xu, M. G.; Zhang, J. H.; Li, Y.; Zhang, Q. H.; Ren, S. F. Material Removal Mechanisms of Cemented Carbides Machined by Ultrasonic Vibration Assisted EDM in Gas Medium. *J. Mater. Process. Technol.* **2009**, *209* (4), 1742–1746.
79. Chung, D. K.; Shin, H. S.; Kim, B. H.; Park, M. S.; Chu, C. N. Surface Finishing of Micro-EDM Holes Using Deionized Water. *J. Micromech. Microeng.* **2009**, *19* (4), 045025.
80. Zhang, Y.; Liu, Y.; Shen, Y.; *et al.* Investigation on the Influence of the Dielectrics on the Material Removal Characteristics of EDM. *J. Mater. Process. Technol.* **2014**, *214* (5), 1052–1061.
81. Jahan, M. P.; Rahman, M.; Wong, Y. S. Study on the Nano-Powder-Mixed Sinking and Milling Micro-EDM of WC-Co. *Int. J. Adv. Manuf. Technol.* **2011**, *53* (1–4), 167–180.
82. Zhao, W. S.; Meng, Q. G.; Wang, Z. L. The Application of Research on Powder Mixed EDM in Rough Machining. *J. Mater. Process. Technol.* **2002**, *129* (1–3), 30–33.
83. Hu, F. Q.; Cao, F. Y.; Song, B. Y.; *et al.* Surface Properties of SiCp/Al Composite by Powder-Mixed EDM. *Procedia CIRP* **2013**, *6*, 101–106.
84. Yan, B. H.; Wang, C. C.; Chow, H. M.; Lin, Y. C. Feasibility Study of Rotary Electrical Discharge Machining with Ball Burnishing for Al_2O_3/6061Al Composite. *Int. J. Mach. Tool. Manuf.* **2000**, *40* (10), 1403–1421.
85. Yan, F. Y. H. B. H.; Lin, Y. C. Surface Modification of Al–Zn–Mg Alloy by Combined Electrical Discharge Machining with Ball Burnish Machining. *Int. J. Mach. Tool. Manuf.* **2002**, *42* (8), 925–934.
86. Anwar, M. M. *A Study on Micro-Patterning of Polypyrrole Using Micro-Electro-Discharge Machining*; The University of British: Columbia, 2012.
87. Curodeau, A.; Richard, M.; Frohn-Villeneuve, L. Molds Surface Finishing with New EDM Process in Air with Thermoplastic Composite Electrodes. *J. Mater. Process. Technol.* **2004**, *149* (1–3), 278–283.
88. Curodeau, J. L. A.; Marceau, L. F.; Richard, M. New EDM Polishing and Texturing Process with Conductive Polymer Electrodes. *J. Mater. Process. Technol.* **2005**, *159*, 17–26.
89. Iwai, M.; Ninomiya, S.; Suzuki, K. Improvement of EDM Properties of PCD with Electrode Vibrated by Ultrasonic Transducer. *Procedia CIRP* **2013**, *6*, 146–150.
90. Liew, P. J.; Yan, J.; Kuriyagawa, T. Fabrication of Deep Micro-Holes in Reaction-Bonded SiC by Ultrasonic Cavitation Assisted Micro-EDM. *Int. J. Mach. Tool. Manuf.* **2014**, *76*, 13–20.
91. Saleh, T.; Dahmardeh, M.; Bsoul, A.; Nojeh, A.; Takahata, K. Field-Emission-Assisted Approach to Dry Micro-Electro-Discharge Machining of Carbon-Nanotube Forests Field-Emission-Assisted Approach to Dry Micro-Electro-Discharge Machining of Carbon-Nanotube Forests. *J. Appl. Phys.* **2011**, *110*, 103305.
92. Al-Ahmari, A.; Rasheed, M. S.; Mohammed, M. K.; Saleh, T. A Hybrid Machining Process Combining Micro-EDM and Laser Beam Machining of Nickel–Titanium Based Shape Memory Alloy. *Mater. Manuf. Process.* **2016**, *31* (4).
93. Kapil Gupta, N. K. J. Analysis and Optimization of Surface Finish of Wire Electrical Discharge Machined Miniature Gears. *J. Eng. Manuf.* **2014**, *228*, 673–681.
94. Liao, Y. S.; Huang, J. T.; Chen, Y. H. A Study to Achieve a Fine Surface Finish in Wire-EDM. *J. Mater. Process. Technol.* **2004**, *149* (1–3), 165–171.
95. Anoop Mathew Kurian, E. M. M.; Yeldose, Binu C. Effect of Wire EDM Parameters on Surface Roughness of Stainless Steel 15–5 PH. *Int. J. Eng. Innov. Technol.* **2014**, *4* (2).

1.14 Laser Peening of Metallic Materials

S Gencalp Irizalp and N Saklakoglu, Celal Bayar University, Manisa, Turkey

© 2017 Elsevier Inc. All rights reserved.

1.14.1	**Introduction**	408
1.14.1.1	Conventional Shot Peening	409
1.14.1.2	Laser Peening	409
1.14.1.3	Laser Peening versus Shot Peening	410
1.14.2	**Fundamentals and Physical Mechanisms of Laser Peening**	411
1.14.2.1	Laser Systems for Laser Peening	411
1.14.2.2	Shock Wave Formation	411
1.14.2.3	Residual Stresses Induced by Laser Peening	413
1.14.2.3.1	Generation of residual stresses	413
1.14.2.3.2	Measurement of residual stresses	414
1.14.2.3.2.1	XRD method	414
1.14.2.3.2.2	Hole-drilling method	415
1.14.2.3.2.3	XRD method versus hole-drilling method	416
1.14.2.4	Crystallite Size and Micro-Strain	417
1.14.2.5	Laser Peening Advantages and Disadvantages and Applications	418
1.14.3	**Mechanical and Metallurgical Effects by Laser Peening**	419
1.14.3.1	Metallurgical Modifications During Laser Peening	419
1.14.3.2	Fatigue Properties	422
1.14.3.3	Tensile Properties and Deformation Mechanism	425
1.14.3.4	Corrosion Properties	427
1.14.3.5	Welded Joints Subjected to Laser Peening	429
1.14.4	**Relaxation Behavior of Laser-Peened Materials**	431
1.14.4.1	Mechanical Relaxation of Residual Stress	431
1.14.4.2	Thermal Relaxation of Residual Stress	432
1.14.5	**Future Trends**	435
1.14.6	**Concluding Remarks**	435
References		436

1.14.1 Introduction

Laser surface modification in engineering materials has attracted wide attention due to rapid growth in the applications of lasers. The modification changes not only the surface composition but also the microstructure of material to give desired properties. Laser surface modifications enabled by the development of a high-power laser are: (1) laser surface heat treatment; (2) laser surface melting (or glazing); (3) laser direct metal deposition (cladding, alloying, coating); (4) laser physical vapor deposition; and (5) laser peening. Of these, laser peening is a new surface modification technology made possible by the development of high laser power density and very short-pulsed laser beams.

Several techniques have been developed to introduce compressive stresses in the substrate material. Some of these include shot peening, sand blasting, and surface rolling. However, the efficiency of the process and the magnitude of compressive stress are limited for these techniques. In recent years, laser-aided manufacturing and materials synthesis techniques have been developed. Laser peening is one of these recent developments. It is a promising surface treatment technique that is an alternative to conventional treatments and has been very effective in strengthening metals that are irradiated by very short pulsed and high-power lasers. Laser peening has many advantages over conventional methods, such as nonmechanical contact between the laser source and the metallic material, local treatment, and precision of operation. Laser peening can produce a layer of residual compressive stress in the surface region that is four-times deeper than that attainable from conventional shot peening techniques. Besides providing higher compressive stress with metallurgical properties, such as dislocations, twins, and stacking faults (SFs), and producing favorable surface integrity, laser peening can also be used to fabricate various micro-surface structures such as dent arrays or thin sections with high accuracy using an automatic x–y positioning system. A higher dislocation density results in plastically affected zones and higher surface hardness and strength development in the materials. Deeper levels of compressive stress in laser peening provide greater resistance to potential fatigue and corrosion failures. The laser peening process increases component life and reduces maintenance costs. The process strengthens designs that are structurally vulnerable without adding metal and weight.

The process had been discovered in the early 1960s, and the investigations mainly focused on process development, understanding the mechanisms, use of high laser intensity, progress in physical models, and determining the optimum

 doi:10.1016/B978-0-12-803581-8.09160-8

shock conditions and mechanical effects. The irradiated surfaces are exposed to a shock wave, which generates compressive residual stresses beneath the treated surface of the metallic materials.

Laser peening has many applications in various fields such as aircraft engines, turbomachinery, medical implants, specialized gears, and components with notches and holes. The process involves recoil pressure acting on the surface by avoiding heating effects. These conditions make the process a good candidate for surface treatment of metallic materials.

1.14.1.1 Conventional Shot Peening

Shot peening is a conventional surface treatment technique, and this technique has been used in industry since the 1940s. Metal or ceramic balls act as small, rounded hammers, and every shot strike creates a dimple in the affected region of a metal surface (**Figure 1**). Compressive volume under the dimpled regions is generated. A thin layer is created in shot-peened metal by overlapped dimples. This layer can be resistant to corrosion and crack initiation and propagation. During the shot peening process, an elastically deformed layer around the plastically deformed layer is produced. The plastically deformed layer tends to expand and the adjacent elastically responding material prevents this from occurring.[1,2] As a result of this, the surface layer up to a certain depth is exposed to permanent residual stresses. The shot peening process has some advantages: it is relatively inexpensive[3]; enduring process equipment is used in this process; and it can be easily used for large surface areas. However, this process has some disadvantages: the process is semiquantitative, especially in estimating shot peening intensity[4]; the compressive residual stress is restricted in depth, generally in soft alloys such as aluminum alloy, and does not exceed in 0.25 mm (in hard metals it is even less); it is unsuitable for treating local areas and small surface areas; and it can generally result in a rough component surface, especially in soft alloys such as aluminum. The rough layer is generally removed for industrial applications; therefore, the compressive residual stress layer can also be removed. The actual depth of compressive residual stresses, which are induced during laser peening, is generally in the range of 0.5–1 mm or more,[5] depending on material properties and processing conditions, which could be four-times deeper than that of shot peening.[6] In addition, shot peening can lead to distortion of thin sections, but laser-peened surfaces do not normally lose any dimensional accuracy.[7] Residual stresses are 'confined' stresses in a component. Residual stresses play an important role in fatigue of engineering materials because fatigue crack initiations occur due to tensile stresses, and these are decreased by residual stress.[8]

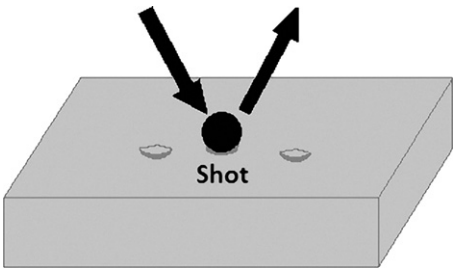


Figure 1 Schematic view of shot peening.

1.14.1.2 Laser Peening

Laser peening is an innovative surface treatment technique that is generally used to improve the material properties of the substrate such as fatigue, wear, corrosion, and strength and hardness.[9–13] Fatigue strength and fatigue life are considerably improved by compressive residual stress that is induced in laser-peened material. Strength and hardness of the material are increased by high-density and tangled dislocations and sub-grain formation, which are developed under the high strain rate of laser peening deformation. Moreover, nano-grains and nano-twins near the surface region are formed by increasing the misorientation of nano-sub-grains under laser shock loading.[14,15]

It was discovered in the early 1960s that an ns-level pulsed laser beam could create an effective shock wave in the metallic materials.[16] Laser peening studies began in US Battele Columbus Laboratories in the United States of America in 1968,[17,18] and studies on improvements continued until 1981.[19] First, the effects of unconfined surfaces were investigated and reported between 1963 and 1968.[16,20,21] Later, the confined ablation mode was reported by Anderholm in 1970, in which gigapascal-level pressures were obtained on confined surfaces. The 'direct ablation' mode is a laser–material interaction with freely expanding plasma; the 'confined ablation' mode is confinement of the plasma arising from laser–material interactions, and this mode enables the magnitude of generated plasma to be substantially increased during its expansion.[22] Further studies also investigated confinement of the plasma, and different transparent overlays were investigated by O'Keefe *et al.* and Yang.[23,24] Significantly increased peak pressures during the confined ablation mode were researched and developed in detail.[25,26] The first laser peening patent was granted to Mallozi and Fairand in 1974.[27] By improvements in laser peening and following the first patent, several patents were granted relating to major modifications in material properties due to the process.[28–30] Laser peening can be used in various metallic materials, stainless steels, aluminum alloys, titanium alloys, and, frequently, super alloys.[31–34]

Laser peening has various commercial trade names and may also be frequently referred to as laser shock processing, laser peening, or laser shot peening. A schematic view of laser peening is shown in **Figure 2**. A target material is irradiated by a short ns-laser pulse at high intensities. The heated zone is vaporized, the vapor continues absorbing laser energy so temperatures reach in excess of 10 000 °C, and it is transformed into plasma due to ionization. The plasma absorbs laser energy until the end of the laser pulse length. Rapid expansion of plasma is confined by transparent overlay (such as water, glass, quartz), which is called 'confined ablation.' The irradiated surface is generally coated with an opaque overlay like a metallic foil tape, dielectric black tape, or plastic paint to avoid heating effects on the metallic surface. High pressure (GPa) is generated at the evaporated surface. Because the process is very short and the magnitude of pressure is very high, the pressure causes shock waves to propagate in the target material and confining medium. Plastic deformation occurs to a depth

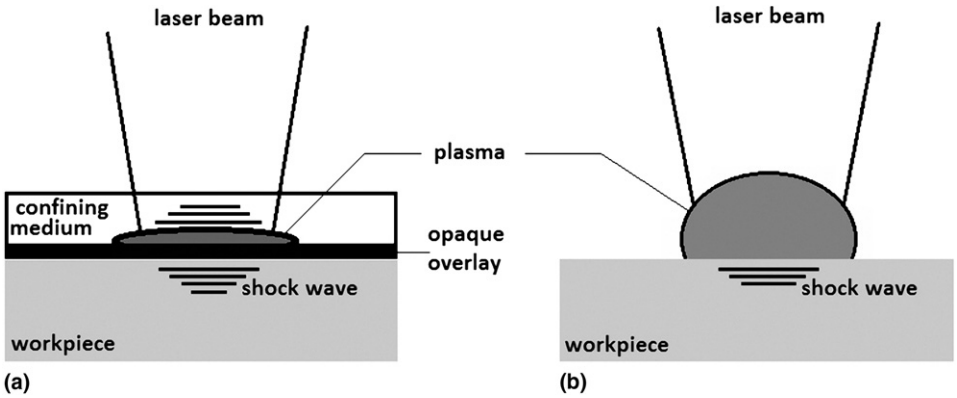


Figure 2 Schematic view of laser peening illustrating the laser beam irradiating the material surface: (a) confined ablation and (b) direct ablation.

where peak pressure exceeds the Hugoniot elastic limit (HEL) of metal and residual stress develops in the plastically affected depth. In the laser peening process, high pressure and short-duration shock waves can offer desirable mechanical and metallurgical results.

The physics of the laser peening process can be used to harden surfaces and strengthen thin sections. Moreover, laser peening has a broad range of applications, especially in the aerospace industry. It is used for many products, including turbine blades, fan blades, compressor blades, rotor components, bearing components, and gear shafts. Also, it can be applied in welded joints, fastener holes, and stop holes in aircraft structures.[5,35–38] Laser peening is an effective surface treatment technique in critical areas that have risks in terms of crack initiation and preexisting notch configurations. It is also preferred for general industrial applications such as land vehicles and weapon systems as well as for the aircraft industry. Furthermore, automotive parts, orthopedic implants, dies, and tooling are potential applications of this process.

1.14.1.3 Laser Peening versus Shot Peening

The residual stress produced by shot peening may be adequate for the intended use for some applications. Laser peening offers different surface enhancement technology and is sufficient for specific applications.

Shot peening intensity is insufficient to generate enough compressive residual stresses and therefore cannot prevent some critical parts from failing. The residual stress distribution below the peened surface is much deeper for laser peening than it is for shot peening.[5] Much higher shot peening intensity is necessary to achieve deeper stresses with shot peening, and achieving deeper stresses causes surface deterioration. Laser peening does not result in a significant alteration of the surface topography.[3] Laser peening usually produces the highest compressive residual stress just below the surface. The deep compressive stresses are due to the shock pressure being maintained above the dynamic yield strength to greater depths than with shot peening.

Laser peening treatment brings about better pitting resistance, and shot peening is also a beneficial influence of mechanical surface treatments that demonstrates localized corrosion properties.[39] Shot peening treatment leads to a dimpled surface finish; however, laser peening treatment produces the smoothest finish.[40] A deleterious material surface induced by shot peening can counterbalance the beneficial effect of residual stress by activating the pitting. A reduction in the passive current density occurs on laser-peened surfaces, and this indicates the increase in corrosion resistance.[39]

Laser peening enhances notched fatigue strength and provides resistance to fatigue cracking. Laser peening appears to be more successful in increasing the fatigue life than shot peening. Hatamleh *et al.*[41] investigated the influence of shot peening and laser peening treatment on the fatigue crack growth of friction stir-welded 7075-T7351 aluminum alloy joints. The laser-peened specimens showed a significant reduction in fatigue crack growth and striation spacing. This situation is attributed to the deeper compressive residual stress induced by laser peening. The improvement in shot-peened specimens is negligible or only minor for crack growth rates in 7075-T7351 aluminum alloy.[42] Gao *et al.*[43] determined the fatigue strength for 1×10^7 cycles of 7050-T7451 aluminum alloy for unpeened, laser-peened, and shot-peened specimens. The results showed that a deeper compressive residual stress layer was obtained for a laser-peened specimen, and that laser peening induced better surface finish; therefore, fatigue properties improved more efficiently. There are many thin metal components that are induced by the two-sided 'peening' process in military airplanes and space vehicles. In thin sections, the use of the shot peening method is not practical due to the potential damage. Laser peening is more suitable for thin sections.[7] Laser peening has the capability of local treatment and process control; for example, laser peening can be applied only to selected regions of a component because the process has the ability to precisely dictate the position of the laser.[44] Therefore, this process can be easily applied to fastener, fastener holes, and weld joints. Laser peening is used in numerous applications, especially airframe structures to combat fatigue, fretting fatigue, and stress corrosion cracking (SCC). The plastic strain induced by the shock wave during laser peening extends much deeper than that during conventional shot peening, and therefore produced a much deeper compressive zone.[45] Compressive residual stress extends to a depth of between five- and ten-times greater than is possible with shot peening.[35]

1.14.2 Fundamentals and Physical Mechanisms of Laser Peening

1.14.2.1 Laser Systems for Laser Peening

Selection of a suitable laser system is necessary to fulfill the steps required for the laser peening process; otherwise, obtaining the effective material properties is not possible. The Q-switched laser system is used in many laser peening studies. Q-switched systems have an electro-optic switch to attain a pulsed output beam. Therefore, a pulsed laser can be obtained in fast switching time during laser peening. Laser beams are commonly produced by neodymium-doped glass (Nd:Glass) or neodymium-doped yttrium aluminum garnet (Nd:YAG) crystal lasing rod. The efficiency of laser peening can be increased by a high repetition rate of laser pulse and a suitable laser wavelength in metallic components. The production of recoil pressures by vaporizing metal surfaces requires irradiation with a short (tenths of nanoseconds), intense (more than 1 GW cm^{-2}), focused laser pulse. The output of the laser with an average power level of several hundred watts to kilowatts and a short nanosecond pulse has been used during progression of laser peening. The common laser system for laser peening is high-energy with a wavelength of 1064 nm. Recently, low-power laser and visible wavelength were found to be favorable in laser systems. **Table 1** shows some typical laser systems used in the laser peening process in the open literature.

The plasma pressure pulse induced by laser peening is a function of laser intensity (laser power density). An increase in the laser intensity increases the magnitude of pressure pulse on the target material. Accordingly, the laser intensity is the most critical parameter in laser peening. A small laser beam spot size ($\sim$1 mm) is preferred to obtain higher laser intensity from a laser system that has lower laser pulse energy (a level of several hundred millijoule). High peak pressure (in GPa levels) can be generated in laser systems with low pulse energy through a small laser beam spot size. Relatively low laser energy is used (50–750 mJ) because low-cost laser systems are commercially applicable.[8]

Three wavelengths are most commonly used in laser peening. These are ultraviolet (355 nm), green (532 nm), and near-infrared (IR) (1064 nm) wavelengths. A water confinement regime is generally performed in IR at a wavelength of 1064 nm. Near-IR wavelength has a good absorption coefficient in the water confinement regime. Short laser wavelengths have a detrimental effect on the water breakdown of plasma. However, the laser interaction in the confined regime is more efficient in ultraviolet irradiation than in IR irradiation.[64] Also, the decrease in wavelength from IR to UV can increase the photon–metal interaction, which provides shock wave generation, although metals are highly reflective.[7] With the photoelectric effect, energy absorption results from electromagnetic radiation of very short wavelengths such as visible or UV radiation.

1.14.2.2 Shock Wave Formation

When a laser beam at high laser intensity with a pulse duration of a few nanoseconds is irradiated at the target material, the surface instantaneously vaporizes and the vapor generates high pressure plasma (in the GPa range) by continuing to absorb the laser energy. In blowing off, the plasma pressure level increases as a consequence of confining medium by inducing a mechanical impulse in the solid. A shock wave is propagated through both the metallic target and the confining medium.[65,66] **Figure 3** presents the geometry for the confined ablation process with relevant parameters used in analytical modelization. The geometry is composed of a bulk material and a transparent confining medium. In the confined ablation mode, the pressure generation depending on shock wave occurs in a three steps:

1. The laser energy is absorbed until the end of the laser is switched off, and the plasma generates at the interface and creates pressure that induces two shock waves (with velocities D_1 and D_2). This pressure propagates in the bulk material and the confining medium. Therefore, an opening of the interface (L) between the two media is defined by the fluid motion and thickness of the interface increases.
2. In the second step, when the laser pulse is switched off, the plasma proceeds to adiabatic cooling and subsequently decreases, but the shock pressure is maintained due to the increase of the plasma interface.
3. Finally, after the complete recombination of the plasma, the projectile like expansion of the plasma in the interface adds further mechanical momentum to the target.[65,67]

The pressure generated by the plasma is adequately strong to drive shock waves. Thus, the displacement of interfaces derives from fluid motion of two shock waves.[26] In eqns [1–3], P is the pulse pressure, L is the length of interface, and V is the expansion velocity between the material surface and the confining medium; u_i ($i=1,2$) is the fluid velocity and Z_i the shock impedance.

$$L(t) = \int [u_1(t) + u_2(t)]\mathrm{d}t_1 \quad [1]$$

$$I(t) = P(t)\frac{\mathrm{d}L(t)}{\mathrm{d}t} + \frac{3}{2\alpha}\frac{\mathrm{d}}{\mathrm{d}t}[P(t)L(t)] \quad [2]$$

$$V(t) = \frac{\mathrm{d}L(t)}{\mathrm{d}t} = \left(\frac{1}{Z_1} + \frac{1}{Z_2}\right)P(t) \quad [3]$$

Pressure (P) is estimated by Fabbro *et al.*[26] as follows:

$$P(\mathrm{GPa}) = 0.01\sqrt{\frac{\alpha}{2\alpha+3}}\sqrt{Z(\mathrm{g\ cm^{-2}\ s^2})}\sqrt{I_0(\mathrm{GW\ cm^{-2}})} \quad [4]$$

Peyre *et al.*[68] established a physical method to predict the peak pressure for a water confinement mode. In this kind of configuration, eqn [4] gives:

$$P(\mathrm{GPa}) = 1.02\sqrt{I_0(\mathrm{GW\ cm^{-2}})} \quad [5]$$

According to eqn [5], it can be said that the peak pressure is directly proportional to the square root of laser intensity in the water confinement mode.

The change of momentum between the evaporating front and solid surface results in recoil pressure formation at the interface.[69] The magnitude of recoil pressure depends on the

Table 1 Typical laser systems used in the laser peening process

Processed materials/targets	*Confining medium*	*Opaque overlay*	*Lasers and beam properties*	*References*
Cu (diameter 4 mm, thickness 1–10 mm)	BK7 glass (6 mm) with vacuum grease (10 μm)		Nd:Glass, 1.06 and 0.53 μm, 100 J and 0.6–3 ns and 170 J and 25–30 ns, spot 6 mm	Fabbro *et al.*[26]
35CD4 steel XC38 steel	Glass foil	Black paint	Nd:Glass, 1.06 μm, 80 J and 0.6 ns, 100 J and 3 ns, 150 J and 30 ns, spot 100 μm	Fournier *et al.*[46]
Fe–Ni alloy	Vacuum		4 kJ, 0.53 μm, 1 ns, spot 4.3 and 25 mm, 10^{11} and 10^{13} W cm^{-2}	Grevey *et al.*[47]
Hadfield manganese steel	Vacuum	Black paint (40–50 μm)	Nd:Glass, 1.054 μm, 0.6 ns, 100 J, spot 3–3.5 mm, 2.4×10^{12}W cm^{-2}	Chu *et al.*[48]
Al (457 μm foil) or Al (200 μm foil)	Tap water (3–4 mm) or transparent glass (5 mm)		Nd:Glass, 1.064 μm, 25–30 ns, 40 J, spot 3 mm, up to 25 GW cm^{-2}	Berthe *et al.*[49]
Al	Water		Nd:Glass, 1.064 μm, 3 ns and 15 ns, 1 and 20 GW cm^{-2}	Berthe *et al.*[50]
2011-T3 alloy (thickness 10 mm)	Flowing water (1–3 mm)	Al foil tape (thickness 0.1 mm)	Q-switched, 1064 nm, 40 ns, 6–8 J, spot 2–4 mm, 2.5 and 5 GW cm^{-2}	Montross *et al.*[51]
Cu (90 μm foil)	High vacuum grease (10 μm)	Al foil (16 μm)	Nd:YAG, 50 ns, beam diameter 12 μm, 160–240 μJ, 2.83–4.24 GW cm^{-2}	Zhang *et al.*[52]
12% Cr martensitic stainless steel, 7075-T7351 aluminum alloy			2–25 ns, 8–20 GW cm^{-2} , and 1, 2, and 3 impacts (FEM-simulation)	Peyre *et al.*[53]
316 Stainless steel	A glass (0.1 mm)		Nd:YAG, 355 nm, 450 mJ, 8 ns, spot 2.5 mm	Yilbas *et al.*[54]
2024 Aluminum, 6061-T6 aluminum	Purified water		Q-switched Nd:YAG, 1064 nm, 1.2 J cm^{-2}, 8 ns, spot 0.8 and 1.5 mm, 5000 pulses cm^{-2} (2024 Al alloy), and 2500 pulses cm^{-2} (6061-T6 Al alloy)	Gomez-Rosas *et al.*[55]
JIS SKD61 tool steel, SUS316L austenitic stainless steel, Ti6Al4V titanium alloy, AC4CH cast aluminum alloy	Water	–	Q-switched Nd:Glass and Nd:YAG, 100 J and 40–250 mJ, 1.05 μm and 532 nm, spot 10 and 1.2 mm, 100 and 10 ns	Sano *et al.*[56]
7075-T6 aluminum alloy	Flowing water (∼1 mm)	Aluminum tape (0.2 mm)	4 GW cm^{-2}, 18 ns, 1 μm	Hatamleh *et al.*[41]
AISI 321 stainless steel	–	–	Ruby laser, 0.3–0.5 GW cm^{-2}, 20–30 ns, spot 3.5 mm, overlapping rate 50%	Mordyuk *et al.*[57]
Aluminum bicrystal	Vacuum grease	Polycrystalline aluminum foil (16 μm)	Q-switched Nd:YAG, 355 nm, spot 12 μm, 50 ns, 320 μJ	Vukelić *et al.*[58]
LY2 aluminum alloy	Water (2 mm)	Aluminum foil (50 μm)	Q-switched laser, 1064 nm, 20 ns, spot 3 mm, 5 J, 9.7 GW cm^{-2}	Luo *et al.*[59]
00Cr12 alloy	Water	Aluminum foil (0.1 mm)	Q-switched high power Nd:Glass, 1.054 μm, 20 ns, 1.54 GW cm^{-2}, spot 6 mm, overlapping rate 50%	Ren *et al.*[60]
6082-T6 aluminum alloy	Flowing water	–	Nd:YAG, 1064 nm, 2.8 J, 9 ns, spot 1.5 mm, overlapping 625 peens on cm^2	Ivetic *et al.*[37]
7050-T7451 aluminum alloy	Water (2 mm)	Thin aluminum foil adhesive tape	Q-switched high power Nd:Glass, 1.054 μm, 20 ns, 2.91 GW cm^{-2}, spot 3 mm	Ren *et al.*[61]

(*Continued*)

Table 1 Continued

Processed materials/targets	*Confining medium*	*Opaque overlay*	*Lasers and beam properties*	*References*
6061-T6 aluminum alloy	Water (2 mm)	Black tape (130 μm)	Q-switched Nd:YAG, 1064 nm, 6 ns, spot 1 and 2 mm, 750 mJ, overlapping 50%	Gencalp Irizalp *et al.*[62]
AISI 316 L stainless steel	Water jet	–	Q-switched Nd:YAG, 9 ns, 1064 nm, 2.4 J pulse^{-1}, spot 1.5 mm	Correa *et al.*[31]
Iron GH2036 alloy	Flowing water	Aluminum foil	Q-switched Nd:Glass, 10 J, spot 3.5 mm, 25 ns	Ren *et al.*[63]

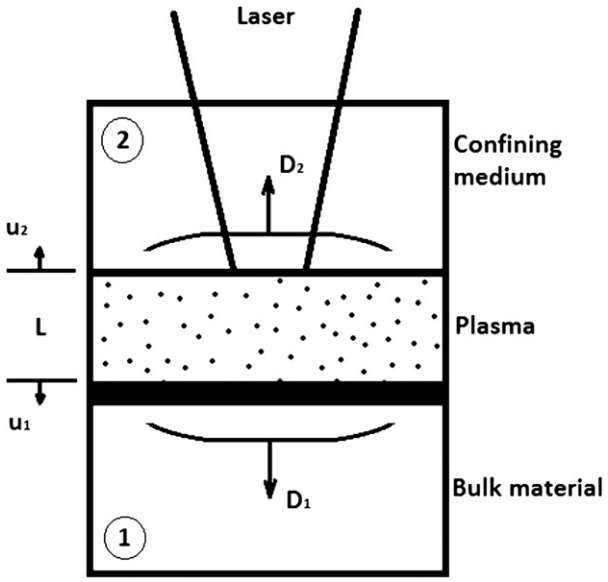


Figure 3 Scheme of the confined ablation process.

laser intensity and pulse duration. The recoil pressure that can be attained is approximately tens of gigapascal. In the confining medium, expansion of the generated plasma is restricted, and thus higher pressures than in the direct ablation mode are generated. In comparison with the direct ablation mode (without any confining medium), pressure of approximately 5 GPa can be easily generated; therefore, magnitude of the pressure is greater than direct ablation for the same laser intensity, and the generated pressure is two- to three-times longer than the laser pulse duration.[65]

Berthe *et al.*[70] studied parasitic plasma and pressure measurement in laser peening by using velocimetry interferometer system for any reflector (VISAR) and a fast camera. They experimentally found that the pressure is a function of laser intensity. The experimental data, which give the relation between pressure and laser intensity, revealed that an increase in pressure occurs when the laser intensity is increased from 1 to 10 GW cm^{-2} and the corresponding pressure is scattered or saturated. This saturation is attributed to a confining water-breakdown phenomenon. The parasitic effect of the water breakdown is questionable beyond 11–13 GW cm^{-2}.

The pressure pulse depends on the magnitude of laser intensity, and other variables produce plastic deformation near the surface of the metal. As the shock wave moves down to the bottom of workpiece, the magnitude of the shock wave decreases. Past a certain depth, the shock wave is below the proportional limit and the waves become purely elastic. The final outcome of the process is a compressive residual stress in the component.[71,72]

In general, investigation of the stress propagation in nonlinear medium is extremely difficult. The material behaves differently in various strain rates. During laser shock loading, the strain rate reaches approximately 10^6 s^{-1} typically, and this rate is much higher than conventional strain rates ($\sim 10^{-6}$ s^{-1}). This ultra-high strain rate is attributed to a shock wave or impact loading. Materials behave differently in static loading (or low strain rates) and dynamic loading (or high strain rates $>10^3$ s^{-1}). Higher stress is necessary to reach the yield strength in impact loading than in the case of slow loading.[71] If the peak stress of the generated shock wave is above the dynamic yield strength of the material, then the material plastically deforms. If the HEL of the material is exceeded, then a shock wave propagates into the material after the elastic stress wave. HEL is defined as the maximum stress sustainable by a solid in one-dimensional shock compression without irreversible deformation taking place at the shock front.[73] When the magnitude of the shock wave exceeds the HEL of the substrate material, plastic deformation takes place, and modification of the microstructure, properties, and state of stress levels of the specimen in the region where the shock wave is effective occurs.[62]

1.14.2.3 Residual Stresses Induced by Laser Peening

1.14.2.3.1 Generation of residual stresses

According to previous discussions, when a laser pulse (high laser intensity $\sim$1–30 GW cm^{-2} and short pulse duration $\sim$1–30 ns) is irradiated on a confined target (confined ablation mode), a plasma is produced.[67] Compressive pressure and shock wave systems result in local plastic strain in the material. A local laser-induced stress wave interacts with a metal and generates mechanical effects. The mechanical effects mainly depend on whether the target is covered with a protective overlay or not covered. Without any protective overlay, thermal effects dominate and tensile stresses develop due to partial melting on the metallic surface. The opaque overlay absorbs the laser energy and protects the metallic surface from the thermal effect. Thus, a pure mechanical effect is created inside the metallic target.

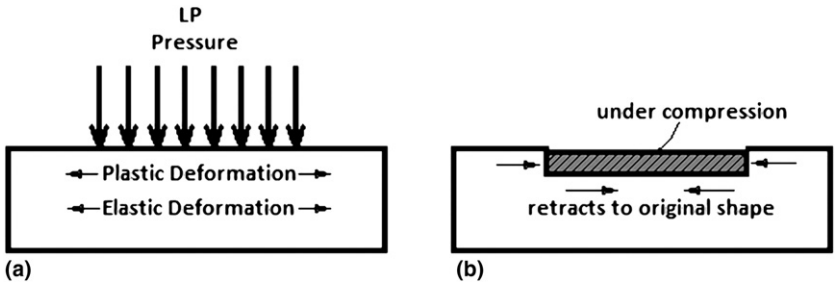


Figure 4 Schematic of compressive residual stress generation: (a) during interaction and (b) after the switch-off the laser pulse.

During shock wave propagation and interaction, the volume affected by the shock wave is plastically strained, whereas the deformation in the surrounding regions is nearly purely elastic (Figure 4). After the switch-off of the laser, the surrounding material responds to the plastically affected volume, so it is opposed to this straining. Whereas the elastically deformed region attempts to return back, plastic deformation is permanent. Thus, the surrounding material induces compressive residual stress in the irradiated region.[65,67]

Detailed analysis of mechanical effects introduced by laser peening was performed by Ballard *et al.*[74] by considering shock wave propagation into an elastic perfectly plastic body. They considered the shock waves to be longitudinal and planar, and considered the pressure pulse to be uniform on the impacted area.[67] A laser-peened metallic target is considered in a biaxial condition. It obeys the von Mises yielding criterion. The model assumed that the plastic deformation occurs when the peak pressure exceeds HEL:

$$\mathrm{HEL} = \left(1 + \frac{\lambda}{2\mu}\right)\sigma_y \qquad [6]$$

σ_y is the uniaxial elastic limit of the target, and λ and μ are the elastic Lame's constants of the target. Plastic deformation increases between HEL and 2HEL. It is assumed to reach its maximum above 2HEL. Above 2.52HEL, surface release waves occur[67] and amplify from the edges of the impacts; therefore, the residual stress field is modified regardless of the impact shape (Figure 5).[4] L_P is plastically affected depth and σ_{sur} is surface residual stress:

$$L_P = \frac{C_{el}C_{pl}\tau}{(C_{el} - C_{pl})}\ \frac{P}{\mathrm{HEL}} \qquad [7]$$

$$\sigma_{sur} = \mu\varepsilon_P\left(\frac{1+\nu}{1-\nu}\right)\left[1 - 4\frac{\sqrt{2}}{\pi}(1+\nu)\frac{L_P}{a}\right] \qquad [8]$$

C_{el} and C_{pl} are elastic and plastic shock wave velocities, respectively. P is shock wave pressure, ε_P is plastic surface strain, μ is pulse duration, ν is Poisson's ratio, and a is side of square impact. If we substitute the equations:

$$\sigma_{sur} = \frac{P}{2\left(1 + \frac{\lambda}{2\mu}\right)}\left[1 - \frac{4\sqrt{2}}{\pi r}(1+\nu)\frac{C_{el}C_{pl}\tau}{(C_{el} - C_{pl})}\right] \qquad [9]$$

r is the radius of the impact.

These equations are considered valid only when P is greater than twice the material's HEL.[4] Consequently, if the shock conditions exceed 2.52HEL, then an inhomogeneous stress field can be produced that can lead to detrimental reverse strains.

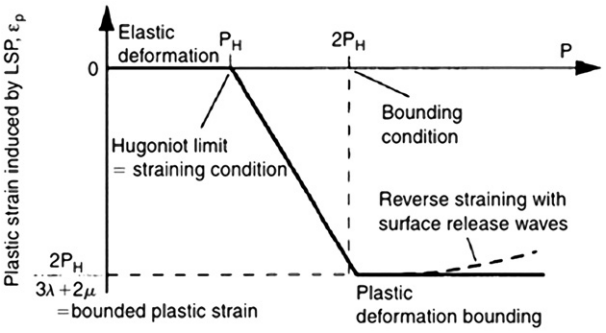


Figure 5 Plastic deformation induced by laser peening as a function of peak pressure.[75]

The magnitude of residual stress and the depth of modification depend on a few process parameters that determine the pressure pulse profile. The depth of compressive residual stress is related to the depth of the plastically affected region. The laser peening parameters can be optimized to generate a higher residual stress magnitude and a higher compressive stress volume.[71] These parameters are laser intensity, pulse duration, pulse shape, spot size, overlapping rate, number of impact, protective coating type, transparent overlay, and others. Residual stress magnitude and depth influence the mechanical properties of impacted material.

1.14.2.3.2 Measurement of residual stresses

There are several residual stress measurement methods. X-ray diffraction (XRD) and hole-drilling techniques attract the most attention. XRD has become one of the standard methods for residual stress measurement over the past few decades. The term stress measurement is a bit misleading, because stress is an extrinsic feature and it is not directly measurable. What is measurable is the strain. All methods of stress determination require measurement of the intrinsic property and the calculation of the associated stress.[76]

1.14.2.3.2.1 XRD method

XRD measures the strain by determining shifts in diffraction peaks due to external stress or residual stress. The measured strains are transformed into the stress via Hooke's law.[76,77] Measurable volume depends on X-ray penetration depth. The penetration depth of X-rays is managed by the linear absorption

coefficient of the material by depending on radiation.[76] For aluminum-based alloys in all of the X-ray sources, more than 70% of the diffracted radiation comes from approximately 100 μm of the top of the material. The penetration depth depends on radiation. For example, Cu-Kα radiation, Co-Kα radiation, and Cr-Kα radiation are various types of radiation used in laboratory settings.

The XRD technique is generally preferred to measure residual stress generated in the surface due to restricted penetration depth. However, via destructive etch/layer removal, the residual stress gradients in metals have typically been measured using XRD.

The strain measurement in material from XRD is performed using Bragg's law, $n\lambda = 2d\sin\theta$, where λ is the wavelength, 2θ is the diffraction angle, and d is the lattice spacing of crystal planes. The choice of the diffraction peak considerably influences the precision of stress measurement. The greater diffraction angle (2θ) brings about the greater sensitivity of residual strain measurements and the greater precision of stress calculations; therefore, in general, the largest diffraction angle (2θ) should be used for certain radiation if possible.[78] Any change in the lattice spacing, d, results in a shift in the diffraction angle, 2θ[76] (**Figure 6**). The sample is rotated by a ψ-angle of the sample's normal during analysis. Initially, when $\psi = 0$, it is known that d_0 is the interplanar lattice spacing and is the d-spacing. d_ψ is the interplanar spacing of the lattice when the sample is rotated ψ-angle from the normal, N. If d-spacing changes, then the diffraction angle, 2θ, will be changed as the sample is rotated from $\psi = 0$ to $\psi = \psi$. Measurement of the strain (the change of d-spacing) by using XRD is a basic principle.[78] In practice, the diffraction angle, 2θ, chosen is required to be higher than 120°.[76,79] If the surface is under compression, then the d-spacing decreases and the diffraction angle increases as a result of the tilt.[80]

Higher speed and more convenience measurements can be gained by making a few key assumptions about the nature of the stress in the surface of crystalline materials. Assuming a plane stress distribution, which has a zero component in the z direction of the strain, leads to simplification of eqn [10]. This approach is well known as the 'd *vs.* $\sin^2\psi$' technique. And it has been beneficial for the determination of biaxial stresses for more than 60 years. When there is zero in-plane shear stress, eqn [10a] is applied. Equation [10b] also calculates for any in-plane shear stress.[78]

$$\frac{d_{\phi\psi} - d_0}{d_0} = \frac{1+\nu}{E}\sigma_\phi \sin^2\psi - \frac{\nu}{E}(\sigma_{11} + \sigma_{22}) \quad [10]$$

$$\sigma_\phi = \sigma_{11}\cos^2\phi + \sigma_{22}\sin^2\phi \quad [10a]$$

$$\sigma_\phi = \sigma_{11}\cos^2\phi + \sigma_{12}\sin 2\phi + \sigma_{22}\sin^2\phi \quad [10b]$$

σ_ϕ is the stress in a given S_ϕ direction (S is the incident beam) and d_0 is known as unstressed plane spacing.[81] σ_{11} and σ_{22} are the principle stresses. d_0 cannot be known in most instances, but it can be replaced by the lattice spacing measured at $\psi = 0$.[78]

Equation [10] can be modified as eqn [6]:

$$d_{\phi\psi} = d_0\frac{1+\nu}{E}\sigma_\phi \sin^2\psi - d_0\frac{\nu}{E}(\sigma_{11} + \sigma_{22}) + d_0 \quad [11]$$

In eqn [11], the multiplier of the term $\sin^2\psi$ is the slope of d versus $\sin^2\psi$ plot. Equation [11] can be rearranged for slope m.

$$m = d_0\frac{1+\nu}{E}\sigma_\phi \quad [12]$$

Equation 12 can be further modified to obtain the stress, σ_ϕ. Therefore, the very simple eqn [13] gives the residual stress.

$$\sigma_\phi = \frac{m}{d_0}\left(\frac{E}{1+\nu}\right) \quad [13]$$

The advantages of the XRD residual stress technique are multidirectional, commonly used, have a wide material range, and are portable. The advantages of this technique include fundamental measurements, laboratory-based systems, and favorable for small components.

1.14.2.3.2.2 Hole-drilling method

The hole-drilling technique is based on drilling a small hole in a stress field. This technique measures the strain released around the drilled hole; therefore, the released strain can be measured to calculate initial residual stress. Electronic speckle pattern interferometer (ESPI) is a system that is adapted to the hole-drilling method to measure the residual stress. The ESPI technique is used to convert the measured deformation around the hole to a value of in-plane residual stress. The ESPI/hole-drilling technique is faster than the strain gage hole-drilling method, can be used in a wider range of materials and surfaces, and provides much more detailed information about the strains that develop as a result of drilling the hole.

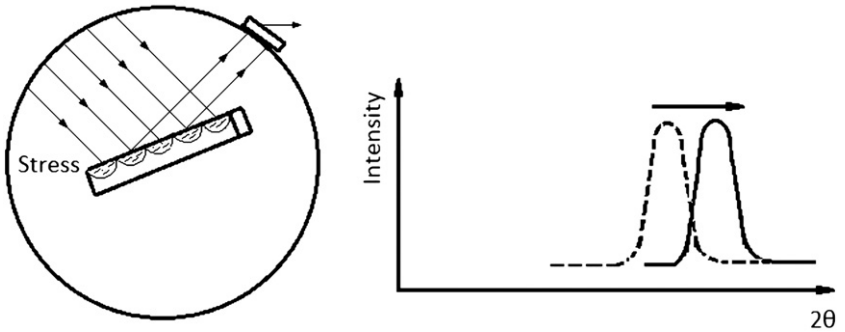


Figure 6 When the sample is tilted, diffraction will take place from other grains but from the same planes (that satisfy Bragg's law). The peak takes place at higher values of 2θ.[80]

Krempazsky *et al.*[82] reported that the strain gage hole-drilling method gives a relative error of approximately 10% and the ESPI/hole-drilling method gives a relative error of approximately 5%. ESPI produces data regarding the displacements in the target surface by mathematically associating the interferograms that are saved as digital before and after the deformation. This method does not need any surface preparation of the materials and is also applicable to rough and inclined surfaces. The main disadvantage of this method is the necessity to isolate the system from vibrations to obtain a fringe pattern with good contrast.[83]

Hole drilling removes a volume of the material. If the volume has residual stress, then drilling will cause distortion around the hole. ESPI directly measures the surface displacement. During the ESPI technique, the image sets before and after the drilling is analyzed by software and transformed into displacement and then correlated with the stress on the surface plane by using elastic properties of the material. For multiple depth measurements, the displacements after each drilling are analyzed together and the depth profile is also completed.[84]

1.14.2.3.2.3 XRD method versus hole-drilling method

Rickert[84] obtained the case depth dependence of the residual stress from ESPI/hole-drilling and XRD methods in shot-peened StE355, X45NiCrMo16, and an aluminum alloy and compared the results. The materials were removed from the surface by electro-polishing each layer to measure the residual stress dependent on the depth with XRD. It was stated that XRD measurements in the aluminum specimen were affected by relatively coarse grains; however, the measurements at and near the surface were acceptable in the regions with a fine-grained structure due to high deformation. Regarding depth, StE355 steel showed a similar trend in both ESPI and XRD data. However, the magnitude of stresses, which was obtained by ESPI measurement, was higher (maximum 35%) than that found with the XRD measurement, and X45NiCrMo16 steel also has similar trend. However, there was less difference between the two methods for StE355 (maximum 15%), and even less for aluminum alloy (maximum 5%).[84] Peyre *et al.*[68] investigated the residual stress generation in laser-peened 7075 aluminum alloy and A356 and Al12Si aluminum alloys. In the study, the residual stress measurement was performed by XRD in 7075 alloy and by hole drilling in A356 and Al12Si alloys. The hole-drilling method was applied on cast A356 and Al12Si alloys because of grain size coarsening up to 300 μm, which is detrimental for XRD measurements.

In laser peening applications, the distribution of the residual stress is investigated. Laser peening appears to achieve a much greater depth of residual stress than shot peening. After laser peening, the residual stress is usually highest at the surface and decreases gradually with distance below the surface. Maawad *et al.*[85] revealed that compressive residual stress in surface layers was much deeper than that caused by shot peening. They investigated the fatigue performance of titanium alloys. The depth profiles of near-surface stresses were deduced by XRD. The effect of laser shock without coating on residual stress was examined in the scanning direction of the laser beam (x direction) and perpendicular to the scanning direction (y direction). The results are showed in **Figure 7**.

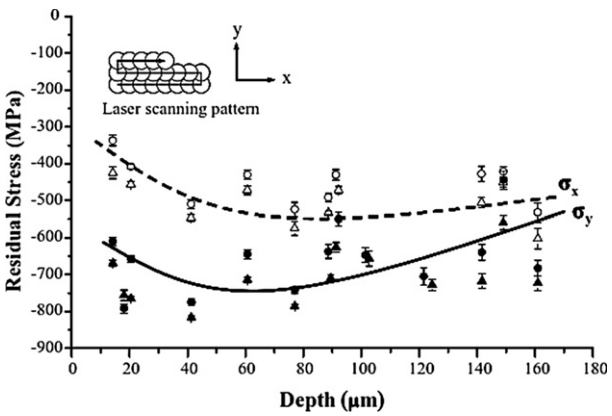


Figure 7 Residual stress distribution in x direction and y direction induced by laser peening without coating.[85]

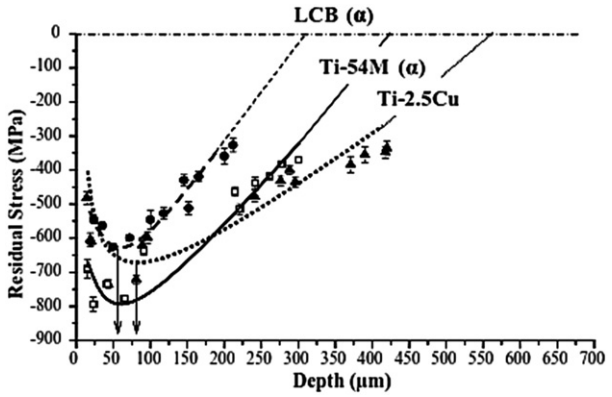


Figure 8 Residual stress distribution in y direction in the alpha phase of Ti–2.5Cu, Ti–54M, and LCB induced by laser peening without coating.[85]

The magnitude of residual stress in y direction after laser peening without coating (LPWC) was larger than in x direction. As shown in **Figure 8**, the residual stresses (σ_y) in the LCB (α), Ti–54M (α), and Ti–2.5Cu alloys were compared. The difference of the residual stress among titanium alloys was explained by the difference in the yield strength.

Saklakoglu *et al.*[32] investigated near-surface modification of 6061-T6 alloy induced by laser peening. The residual stress variation throughout the depth of the workpiece was determined by the ESPI/hole-drilling technique. Residual stress was measured perpendicular to the laser peening direction. Maximum compressive stress measured at a depth of 20 μm was -465 MPa in two laser peening impacts (**Figure 9**).

Montross *et al.*[4] found that compressive stresses could be generated deeper below the surface by applying successive shocks. Saklakoglu *et al.*[32] reported that the depth of compressive residual stress did not change significantly with the increase in laser impact number. The depth of the plastic deformation layer was almost independent of the laser impacts because the plastic deformation near the laser peening-affected region could be saturated. Sathyajith *et al.*[86] investigated the effect of LPWC on 6061-T6 alloy with a low-energy Nd:YAG laser. They measured the surface stress by XRD along the x direction and y direction of the laser-peened area.

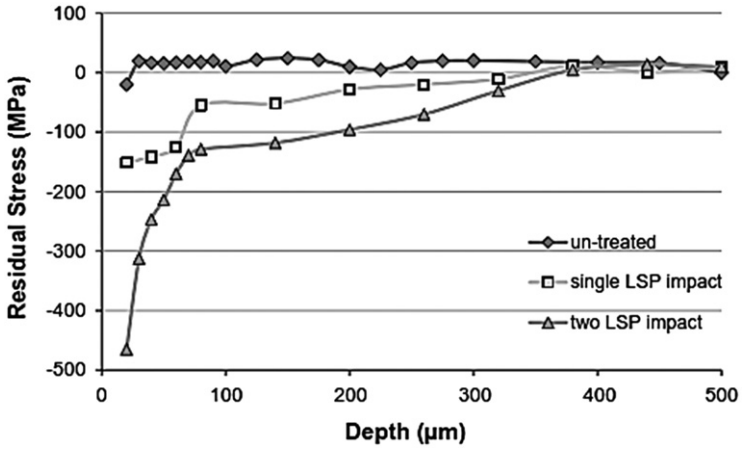


Figure 9 Residual stress-depth profiles of laser peening-treated and untreated material.[32]

A maximum compressive stress of -276.9 MPa was observed in the y direction and -38.8 MPa was found in the x direction. The value of residual stress showed an anisotropic behavior between the x and y directions. Sathyajith *et al.*[86] asserted that lower pulse density introduced lesser anisotropy. Gencalp Irizalp *et al.*[87] studied effects of laser peening on residual stress that were measured by the $\sin^2\psi$ method from the surface after single laser shot and double laser shot. Residual stress measurements were performed at $\varphi = 0^\circ$, 45°, and 90°. Although the residual stress in the direction of 90° is more than 45% with respect to the residual stress in the direction 0° for single-shot laser peening, it is more than 58% for double-shot laser peening. 0° is the main direction and 90° is the perpendicular direction to the laser peening. These results showed that the increasing laser shots increased both compressive stress and anisotropy. Hfaiedh *et al.*[88] discussed that σ_y stresses perpendicular to the laser peening direction are higher than σ_x stresses. They also found that more homogenous stress fields during laser peening can be obtained by increasing the overlapping. Luo *et al.*[89] reported that a single laser peening impact generated the plastic deformation layer approximately 900 μm in the AISI 304 stainless steel. Maximum residual stress of -305 MPa was located at the surface after laser peening. Residual stress distribution was determined by XRD with the $\sin^2\psi$ method.

1.14.2.4 Crystallite Size and Micro-Strain

XRD used for determining the crystallite size and lattice strain in a material is called X-ray line profile analysis (XLPA). XLPA is an effective and nondestructive method for the characterization of the microstructure in crystalline materials. XLPA determines the size and shape of diffracting crystallites. In addition, the method helps to determine the lattice defects.

Intensity of the diffracted beam is measured by a diffractometer detector and results in a diffraction peak. Ideal peak shape is without any widening (i.e., a line). The broadening of the diffraction peak comprises the source of determination of the crystallite size and lattice micro-strain in a material. In general, the width of a peak is measured as half of the intensity's maximum value. Peak broadening can depend on three factors: instrumental effects, crystallite size, and lattice micro-strain.[90,91] Instrumental effects can vary with each diffractometer and occur by imperfect measurement capabilities, such as focused beams and unresolved α_1 and α_2 peaks.[92] Crystallite size and lattice micro-strain contribute to the peak broadening. Lattice micro-strain comprises a combination of mechanical deformation, chemical composition, defects, and SFs.[91] Primarily, the instrumental effect should be quantified to identify the crystallite size and lattice micro-strain on the peak broadening. The XRD pattern of a standard calibration crystal is used to determine the instrumental effect. By subtracting the instrumental broadening effect from the diffraction pattern, the remaining diffraction peak broadening is attributed to small crystallite size and lattice micro-strain.[92]

The peak broadening due to crystallite size is expressed by the Scherrer equation[90,91]:

$$\beta(2\theta) = \frac{K\lambda}{L\cos\theta} \qquad [14]$$

$$\beta = C\varepsilon\frac{\sin\theta}{\cos\theta} \qquad [15]$$

In eqn [14], $\beta(2\theta)$ is the width of the diffraction peak (rad), L is the crystallite size, K is the Scherrer constant, and λ is the wavelength. The aforementioned width of the diffraction peak is expressed in terms of the angle of full width at half maximum of the peaks on the XRD pattern. In eqn [15], the width of the diffraction peak also refers to the lattice micro-strain; ε is the micro-strain and C is a constant.

Plastic deformation modifies lattice structure in target material during laser peening. Woo *et al.*[93] and Mordyuk *et al.*[57] reported that the diffraction broadening resulted in an increase in lattice micro-strain and a decrease in crystallite size of strain-hardened materials. When the target material was exposed to severe deformation, the plastic deformation in the crystal lattice and nonuniform strain led to broadening in the full width at half maximum (FWHM) value of the diffraction peak.

The slope of the Williamson–Hall plot is shown in the micro-strain component ($C\varepsilon$). The Williamson–Hall plot ($\beta\cos\theta$ vs. $\sin\theta$) is obtained from XRD results. As the laser impact increases, the slope of the Williamson–Hall plot

increases.[62,94,95] Due to strain hardening, the width of the diffraction peak increases as a result of the increase in lattice micro-strain and the decrease in crystallite size. The shock wave induced by laser peening produces plastic deformation in the surface layer of the target material. During multiple laser impacts, the superposition of the deformation zone occurs in the laser-irradiated layer. Gencalp Irizalp *et al.*[62] stated that multiple laser impacts are more effective in terms of reducing crystallite size and increasing micro-strain. Sathyajith *et al.*[86] studied the effect of laser peening hardened aluminum alloy in terms of microstructures and mechanical properties. They stated that the laser-peened specimen with lower pulse density exhibited lesser anisotropy broadening in different crystal planes. Saklakoglu *et al.*[32] determined the crystallite size by XRD in laser peening-treated 6061-T6 alloy. A very short interaction time and high plasma pressure during the process could separate the crystalline grains into several coherently diffracting domains. They characterized the crystallite size and dislocation density by using a Williamson–Hall plot obtained from XRD analysis. The crystallite size noticeably decreased by approximately 38% due to the formation of secondary grains in the laser peening-treated region. Also, higher dislocation density resulted from multiple laser peening impacts.

However, transmission electron microscopy (TEM) is another way to determine the crystallite size. However, it is a general observation that grain size or sub-grain size obtained by TEM is much higher than crystallite size determined by XRD analysis. This phenomenon was discussed in light of several studies. Marmy *et al.*[96] investigated the microstructure of ferritic/martensitic steel by TEM. It was found that the dislocation density results obtained from XLPA are relatively high according to TEM. Zhilyaev *et al.*[97] investigated severely plastically deformed Al, Al3%Mg, and Ni. They discovered that grain size obtained from TEM is four-times to six-times higher than the crystallite size determined by XLPA.

The sub-grains and/or dislocation cells in the materials produced by severe plastic deformation (SPD) can be observed by TEM investigations, which can be distinguished by means of low-angle grain boundaries. The crystallite size in severe plastic-deformed metals determined by XRD is equivalent to the mean size domains that coherently scatter X-rays. XRDs recognize the dislocation cells separated from each other by small differences in orientation, typically less than 1°–2°. TEM investigations of severe plastic-deformed metals (by visual observations, in general) provide the size of high-angle grain boundaries. As a consequence, TEM grain size is higher than the dislocation cell size obtained by XLPA. A similar inference for the titanium produced by ECAP was reported by Zhu *et al.*[98] The mean cell size obtained from XLPA is in the range of 30–70 nm. The grain size observed in TEM is higher, at approximately 270 nm. The main mechanism in grain refinement during SPD is dislocation multiplication and rearrangement in the cell to minimize the strain energy. Dislocation cells have low-angle grain boundaries. The orientation difference between the cells is lower (1°–2°), and thus there is no measurable contrast difference between them in TEM micrographs. They can be observed separately by high-resolution TEM investigations.[99] It is more appropriate that primary particle size can be evaluated by TEM and crystallite size can be evaluated by high-resolution TEM.[100] Anand Kumar *et al.*[101] investigated the influence of laser peening on the microstructure of Ti–6Al–4V. They stated that the process generated a large amount of dislocation and the nanocrystallites formed in the material. The formation of nanocrystallites is caused by annihilation and recombination of dislocations to accommodate a high rate of plastic strain generated during SPD. The crystallite size from TEM investigations was obtained in the range of 20–50 nm. However, they found that this result contradicted with XRD observations. In X-ray observations, the diffracted peak has no broadening effect on the laser-peened surface. They asserted that this situation may be because the foils for the TEM investigation were prepared with a thickness of 5 μm and the penetration depth of XRD was approximately 10 μm. Mordyuk *et al.*[57] also characterized laser shock-peened surface layers of AISI 321 stainless steel. They found that cell size in the surface layer was approximately 500 nm in TEM. They measured the physical broadening of refractions, and the relation between the physical broadening, β, and the diffraction angle, θ, was analyzed to characterize the crystallite size. The crystallite size, which is obtained from FWHM values in the study, is approximately 77 nm. XRD crystallite size is lower than TEM cell size.

1.14.2.5 Laser Peening Advantages and Disadvantages and Applications

Laser peening has many advantages such as easy operation, local treatment, and short processing duration.[11,102–104] However, this process induces deeper compressive residual stress, lower surface roughness, and better controllability compared with conventional methods.[105] It requires very little in terms of area accessibility. Laser peening treatment includes precision operation and fast processing time as well as low process cost.[106] During the process, the laser pulse generates a high-amplitude shock wave that propagates into the material. An opaque overlay and transparent overlay prevent the thermal effect and provide effective shock pressure. As a consequence, the material is cold-worked or plastically deformed at the surface. In the confined ablation mode, laser peening produces surface compressive residual stresses at a depth of ~1 mm (four-times deeper than shot peening). There is no surface melting or other heat effects because of the opaque overlay used in laser peening. The optimization of laser peening parameters is considered to generate significantly compressive residual stresses beneath the metallic material surface.[7] Laser peening rarely requires complete surface processing. This process is fully controllable and repeatable; therefore, the benefits of laser peening depend on the processing parameters as well as the specimen geometry and materials. Laser peening can be used to treat various kinds of metallic materials such as titanium alloys, steels, stainless steels, aluminum alloys, nickel alloys, and carburized and nitride steels, among others.

All of these advantages have a wide field of applications: engine components for the Air Force, fatigue-critical components such as F-16 bulk heads, wing attachments, flight control mechanisms, wheels, breaks and landing gear, welded aging aircraft parts for improved reliability, welded aluminum and titanium components for improved reliability, fasteners and

fastener holes to combat fatigue, fretting fatigue, and SCC. However, laser peening is suitable for Army applications, especially those used in fatigue-prone helicopter parts such as transmission gears and other drive train components. The laser treatment can improve the performance and reliability of rapid cycling firearms, artillery on top of vehicle components, and support systems in tanks and armored vehicles. Other potential applications are stress relief of nuclear propulsion system parts for improved SCC resistance. In addition to these, the reliability of automotive and truck parts such as transmission gears and engine parts and the reliability of medical applications such as orthopedic implants (hip, knee replacement joints, spinal fixation devices) are increased by applying laser peening.[107]

Laser peening has existed as a process for nearly 40 years. The General Electric Infrastructure Aviation (GEA) has worked since the early 1990s. One laser peening application that GEA has developed involves the processing of the leading edge and tips of airfoils to abate fatigue failures and produces significant foreign object damage tolerance. The use of laser peening on an existing component increases serviceable limits without the need for airfoil redesign, thus maintaining the aerodynamic performance of the component. To date, GEA has produced in excess of 100 000 laser peening airfoils for US Air Force (USAF) applications such as stage 1 fan blades in the F101-GE-102- (B-1B Lancer) and F110-GE-100-, and -129 turbofans (F-16 Falcon, F-15 Strike Eagle).[108] Rolls-Royce adopted a laser peening system to ensure the safe lifetime of Trent engine fan blades. It is now used to treat all Trent 500, Trent 800, Trent 1000, and XWB blades. The Rolls-Royce Trent engine design is widely used in commercial aircraft, including the latest designs such as Boeing's 787 Dreamliner as well as the Airbus A350 and A380. Sales of 1200 treated Trent XWB engines alone are worth more than £60 billion. In the early 2000s, two high-capacity laser peening systems and peening cells were built at LSP Technologies Inc.'s facility to handle a variety of aerospace components. In 2003, LSP Technologies Inc. began producing laser peening on Pratt & Whitney's F-119 fourth stage IBR for the Air Force's F-22 Raptor.

Some investigations[109–114] propose that laser peening treatment may induce near-surface microstructures and residual stress states that exhibit higher mechanical or thermal stability than those induced from conventional mechanical surface treatments, such as shot peening or deep rolling (DR) treatments. GEA has performed extensive thermal relaxation tests on the high-pressure compressors in which temperatures can exceed 1000 °F. The results indicate that because laser peening imparts deep compressive stress, thermal relaxation is not an issue of the same magnitude as shot peening. In fact, it has been shown that the laser peening fatigue strength is reduced approximately 15% on titanium alloys when thermally cycled at more than 1000 °F for more than 200 h. This simulates the worst case allowable engine temperatures in the compressor.

Because of these advantages, laser peening becomes more and more popular as an innovative technique in surface treatment technology. The disadvantages of the laser peening method are as follows.

Laser peening equipment requires high capital loss, and a clean room environment is necessary for this process. For multiple laser peening processes, repeated coating with opaque overlay requires avoiding thermal effects. Control of the processing variables can be difficult due to complex laser equipment; therefore, process quality control can be slow. Even when the laser power is precisely controlled, variation in the thickness of the water layer (transparent overlay) can vary due to splashing.

1.14.3 Mechanical and Metallurgical Effects by Laser Peening

1.14.3.1 Metallurgical Modifications During Laser Peening

The laser peening causes plastic deformation of the near-surface material and induces beneficial microstructural changes in the affected layer of the material and thus modifies the microstructure and properties of material that induced the shock wave. Various studies have been conducted to observe the microstructure changes. These observations generally indicate the microstructural defects, especially dislocations and SFs. Microstructural analysis has usually been performed via TEM. High-pressure laser shock waves induce grain refinement mechanism.

The generated shock wave can induce SPD in the laser peening-treated region. The microstructure of laser-peened Al–Mg–Si alloy with laser pulse energy of 2.8 J is presented in **Figure 10** by the TEM image.[114] The TEM micrograph shows the high-density dislocations in heavily tangled arrangements. The dislocation density was determined by the

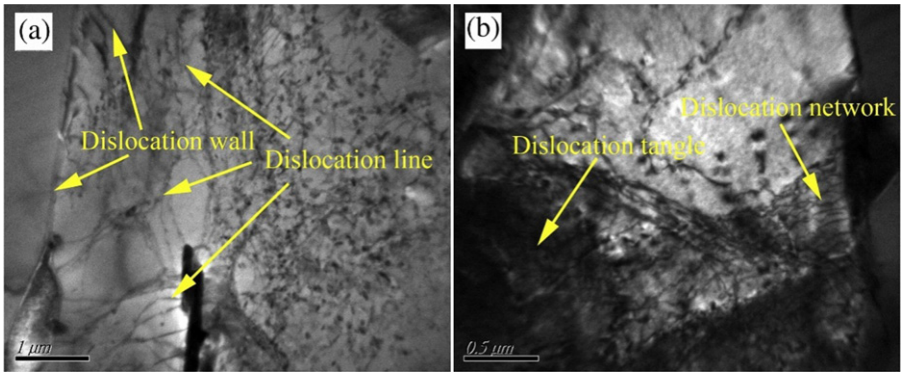


Figure 10 TEM micrographs of 6061-T651 aluminum alloy after laser peening: (a) and (b).[114]

Smith–Guttman linear intercept technique. An example of the procedure for dislocation density measurements is seen in Figure 11.[115] The dislocation density of untreated material is 12×10^{13} m^{-2}; the dislocation density of laser-peened material is in the range of 29×10^{13} m^{-2}. The similar increasing trends in dislocation density in metallic materials exposed to laser peening are also observed in various studies.[4,116,117] In general, the dislocation distribution is not uniform, and heavily tangled dislocation structures attract the attention.[118–120] High-density dislocation tangles (DTs) are randomly rearranged and create new sub-grains. The sub-grains, which are separated with dislocation walls, are also presented in Figure 10.[114]

With the increase of shock wave pressure, high-density dislocations are transformed into dislocation cells by slip, accumulation, and interaction. The schematic illustration in Figure 12 shows how the microstructure is modified as the laser-induced shock wave is propagated into the material.[121] These different microstructures along the depth are related to the shock pressure. Nanocrystalline structure can be developed in the near-surface microstructure due to SPD during laser peening. During SPD, the misorientation of cell boundaries can increase and grain refinement can decrease into the nanometer range. High strain rate deformation can activate more slip systems,[122] and therefore a nanocrystalline structure develops. Also, SFs and deformation twins can induce during SPD. SPD is generated under the influence of high shock wave pressure. Therefore, change in crystal orientation, lattice distortion, dislocation multiplication, dislocation slippage, twins, and other crystal defects can occur as a result of laser peening. These microstructural transformations are characterized by TEM. Figure 13 presents the original TiAl alloy and laser-peened TiAl alloy with a laser pulse of 9 J. However, after laser peening, the microstructure involves heavily tangled dislocations, dislocation walls, and refined grains. TEM examination

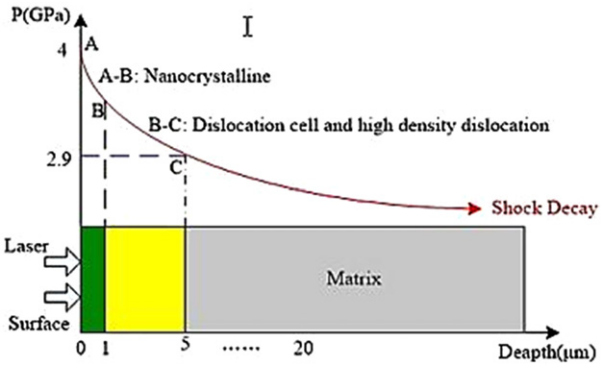


Figure 12 The laser-induced shock decay inside the material. The regions of A–B and B–C along the shock decay represent the typical corresponding microstructures at different depths. The severe plastic deformation is induced by laser shock wave.[121]

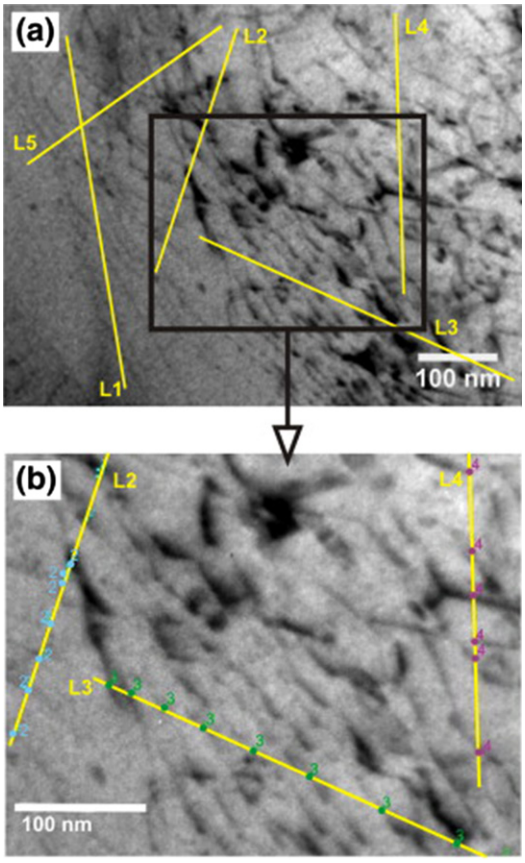


Figure 11 Example of the procedure for dislocation density measurements: (a) placement of five random lines on a TEM image and (b) marks denoting each point where a dislocation intersects a line.[115]

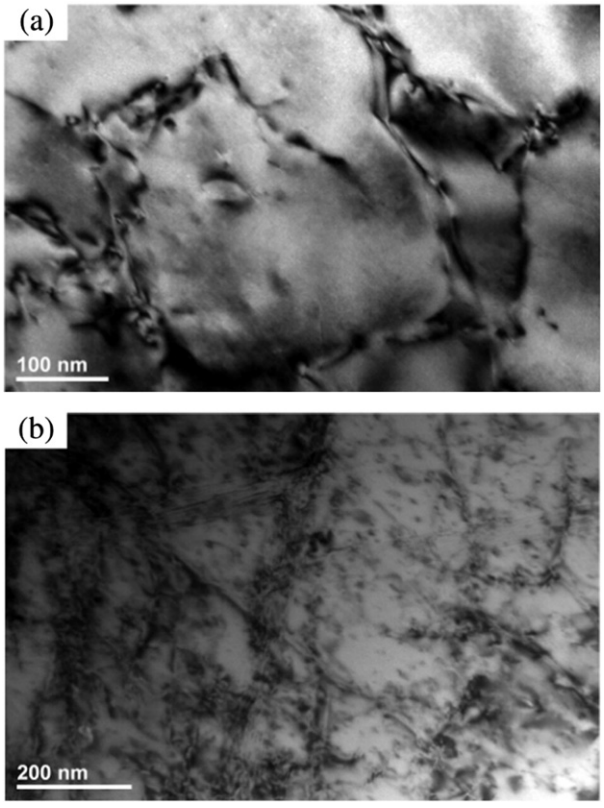


Figure 13 Brightfield TEM image of original and laser-peened samples. (a) Without laser peening and (b) laser peening with 9 J.[123]

also shows that sub-boundaries are produced on the surface of TiAl alloy and the grain size is reduced in the nanometer scale (~120 nm).[123]

TEM images in Figure 14 present NiTi shape memory alloy after laser peening.[124] Figure 14 shows the amorphous and crystalline phases in the laser-peened alloy. The amorphous structure is a result of severe lattice distortion. Lattice structure can be locally disordered by high and short laser pulse pressure. The SFs and nano-twins can form after being processed via severe plastic deformation.

Figure 15 is the TEM image of the laser-peened Al–Mg–Si alloy that irradiated without coating in 2.8 J pulse energy.[115] The presence of SFs in the vicinity of the grain boundary is shown in Figure 15(a). It is well known that the materials with high stacking fault energy (SFE) do not exhibit SFs and twinnings, but SF can form in high SFE metals and alloys with the effects of SPD during laser peening. It can also be seen that the dislocation accumulation contributes to the formation of nano-sized grains (Figure 15(c)). TEM observations have significant importance in laser peening studies.

When no protective opaque overlay is used on the material surface or when multiple laser peening procedures with protective opaque overlay is applied on the material surface, the surface melting and vaporization on the material surface can occur. The surface morphology of laser-peened materials has been investigated by scanning electron microscopy (SEM) observations, atomic force microscopy (AFM) observations, and roughness measurements. The resulting changes in microstructure after laser peening place emphasis on systematic investigations. The surface morphology of laser-peened 6061-T6 aluminum alloy is significantly influenced by peening parameters.[62] The opaque overlay is still present on the treated surface of one laser impact, so melting does not occur on the metallic surface. For multiple laser impacts, the opaque overlay disappeared from the surface and partial melting took place on the metallic surface according to SEM observations (Figure 16).

Without a protective overlay, surface ablation leads to surface melting and therefore the treatment becomes thermo-mechanical. For thermo-mechanical conditions, the combination of ablation and melting of surface layers reveals ablation craters, micro-cracks, and dimples as well as an oxide layer. SEM observation at higher magnification shows these surface defects in Figure 17.[125]

The failure of the structural component can start at the deterioration of surface quality. The surface integrity of

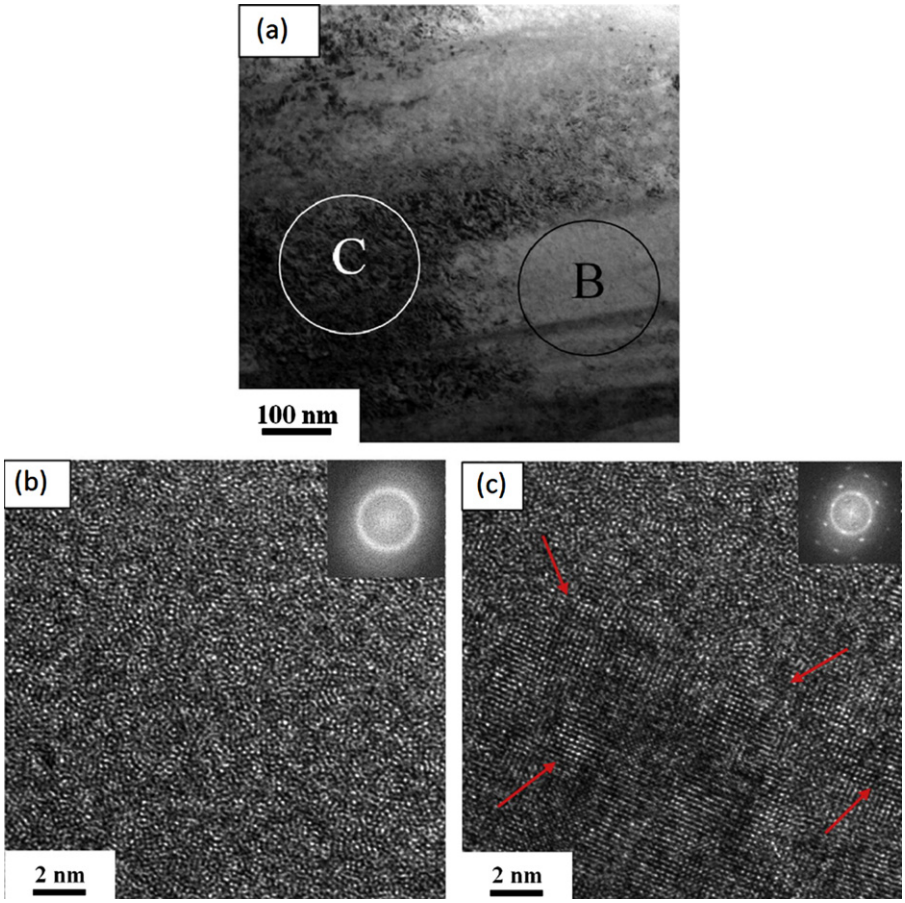


Figure 14 Microstructure after LP: (a) transmission electron microscopy (TEM) images after laser peening showing amorphous and crystalline phase; (b) representative high-resolution TEM images from region B and the corresponding fast Fourier transform (FFT); and (c) representative high-resolution TEM images (the arrows point to the crystalline phase) from region C and the corresponding FFT showing the amorphous halo rings and the bcc[99] direction.[124]

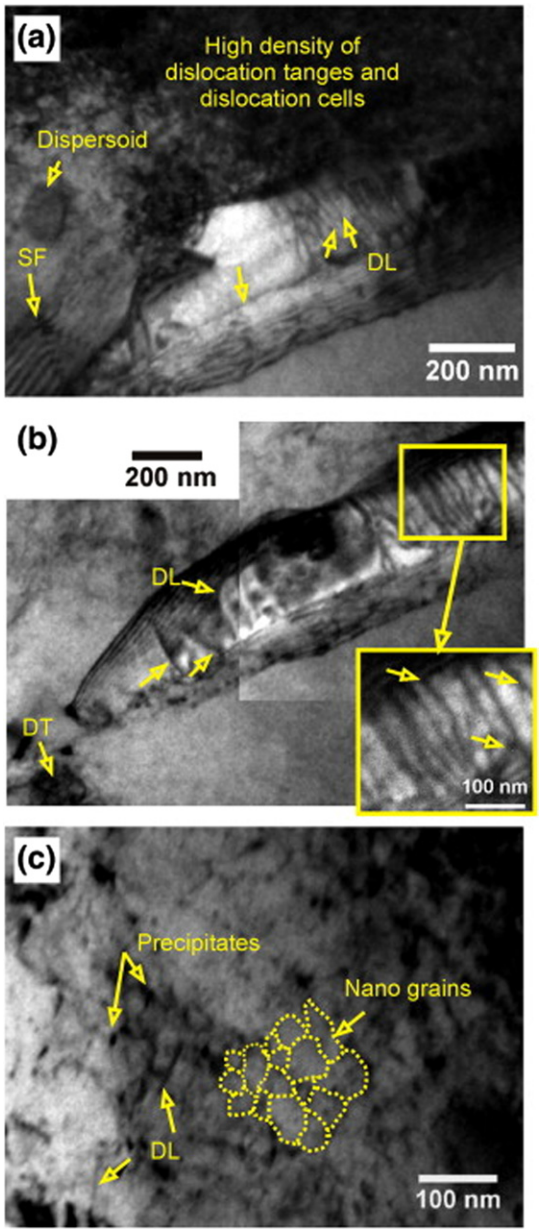


Figure 15 TEM images of laser peening without coating specimen (a) and (b), high density of dislocation tangles (DT), dislocation lines (DL), and dislocation cells (SF = stacking faults), and (c) just below the surface of the nano-grain structure in the proximity of the precipitates.[115]

laser-peened specimens should be analyzed in terms of surface topography and roughness.[86] **Figure 18** shows AFM surface topography of specimens that were both un-peened and laser-peened without coating. The surface roughness increases without the protective coating during laser peening.

1.14.3.2 Fatigue Properties

Laser peening is an innovative technique for a novel industrial treatment to improve fatigue properties of metals.[126,127] A shock wave occurs on irradiating the surface with a pulsed laser. When the pressure of the shock wave exceeds the dynamic yield strength of the metal, plastic deformation occurs, thus imparting residual stresses to the surface.[128] It is similar to shot peening, which uses very small metal or ceramic balls to bombard the surface of a metal object. It is a cold work process used to finish metal parts to prevent fatigue and stress corrosion failures and prolong product life for the part. This technique is considered to be a potential substitute for the conventional shot peening process because the residual compressive stresses from laser peening extend deeper below the surface than those from shot peening, usually resulting in a significantly greater benefit in fatigue resistance after laser shocking.[129]

Peyre *et al.*[68] performed a series experiment on 7075 aluminum alloy's fatigue behavior after laser peening and shot peening. As shown in **Figure 19**, the fatigue limits increased to approximately +22% for laser-impacted specimens and only to +10% for shot-peened specimens. Peyre *et al.*[68] explained that laser peening generated general depression of the material with no roughness changes; shot peening strongly affected the surface and created potential initiation sites.

Zhang *et al.*[126] indicated that laser peening decreased the surface roughness. The micro-indents at the surface of the specimen would be generated after laser peening. However, the surface roughness of the micro-indents was relatively lower than that of the untreated specimen. They found laser peening increased fatigue life at least twofold. It is well known that during the fatigue testing, the local stress concentrations will be generated due to the high surface roughness, resulting in the initiation and growth of the fatigue cracks. Hence, the decrement of the surface roughness after laser peening may lead to the increment of the fatigue life of the specimens.

One of the most important effects of laser peening is the generation of residual stresses. The waves produced during laser peening plastically deform the surface and compressive stresses are extended into the subsurface. These dynamic compressive stresses are highest on the surface and decrease with depth into the material.[67,129] Laser peening produces deeper penetration of compressive residual stresses and therefore may produce better fatigue resistance than shot peening.[130,131] Luong and Hill[132] indicated that laser peening produced a layer of compressive residual stress three-times deeper than that of the shot peening for 7050-T7451 Al alloy.

Laser peening has a higher effect on compressive stress than four-pass ECAP (**Figure 11**).[133] As shown in **Figure 20**, although the maximum compressive residual stress is located at the subsurface after shot peening, it is much deeper in laser peening.

Srinivasan *et al.*[128] showed that residual stress after laser peening extents to 1 mm depth of Ti–6Al–4V and large spots with high intensities yielded higher residual stress (**Figure 21**).

The pulse swept direction is one of the important parameters affecting the magnitude of the compressive stress component. Rubio-González *et al.*[134] found that, as seen in **Figure 22**, the compressive stress component perpendicular to the swept direction was much higher than that parallel to that direction (S_2 is the compressive residual stress perpendicular to the pulse swept direction and S_1 is parallel to the pulse swept direction).

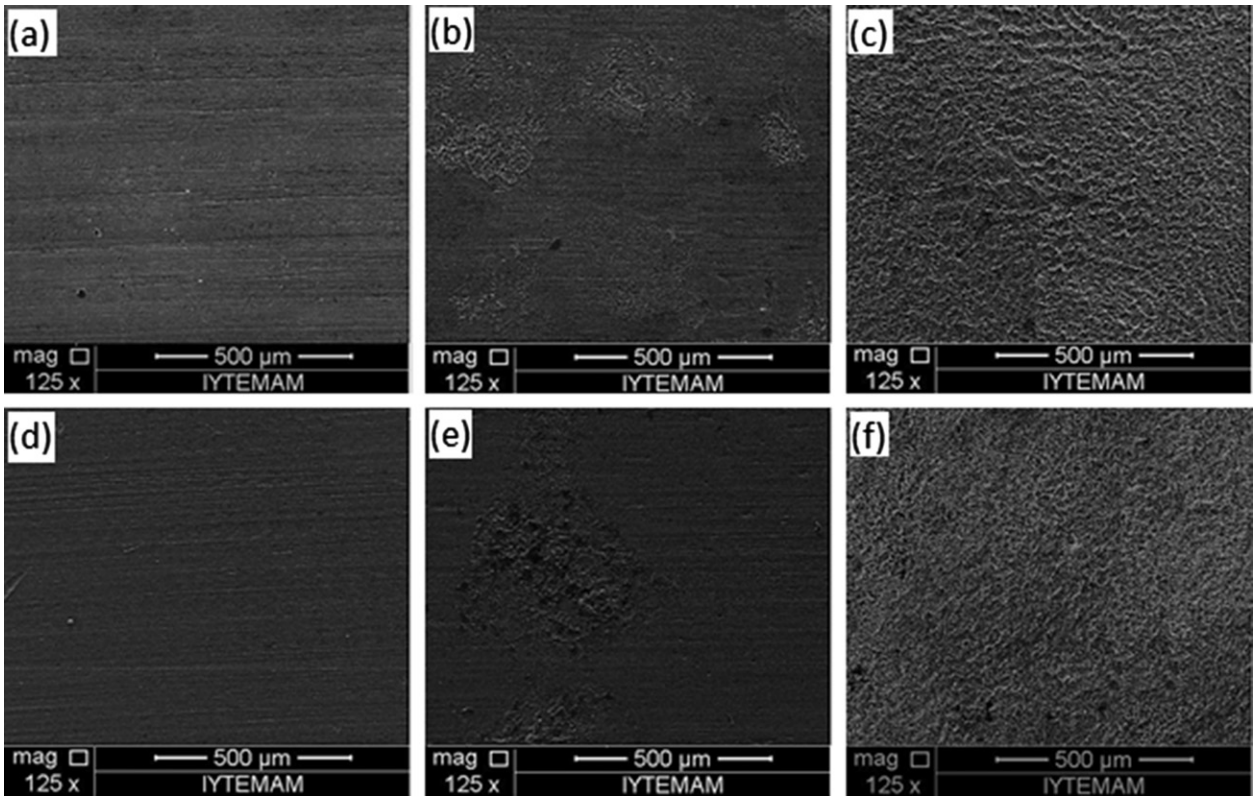


Figure 16 SEM photographs of laser-peened surfaces: (a) 1 shot-1 mm; (b) 2 shot-1 mm; (c) 3 shot-1 mm; (d) 1 shot-2 mm; (e) 2 shot-2 mm; and (f) 3 shot-2 mm.[62]

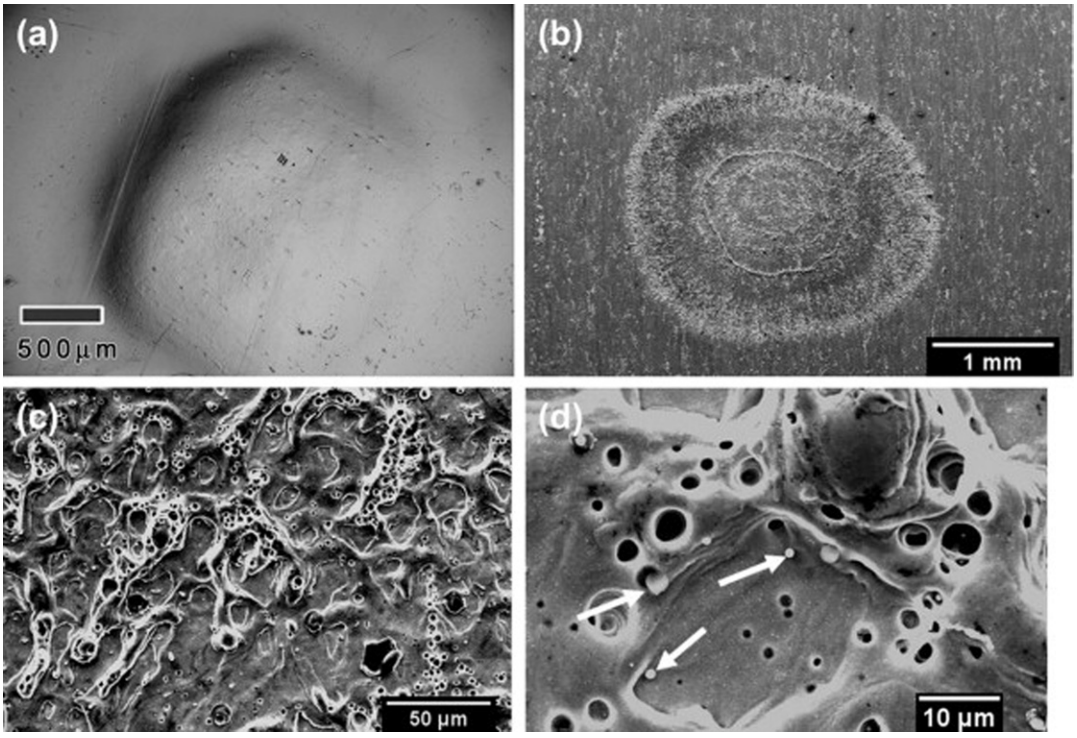


Figure 17 Representative SEM micrograph of the Inconel 718 surface after laser peening: (a) single dimple with overlay and (b), (c), and (d) without protective overlay.[125]

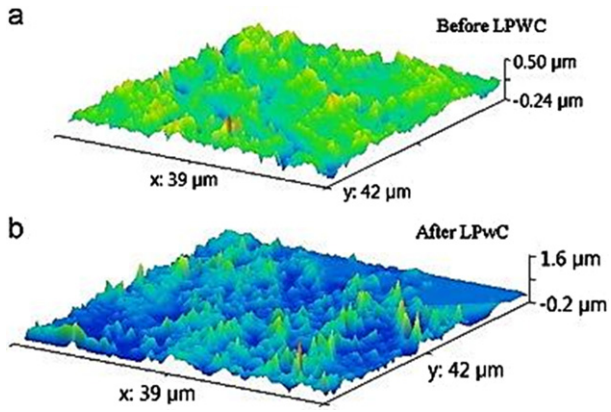


Figure 18 AFM surface topography: (a) unpeened and (b) after laser peening without coating (LPWC).[86]

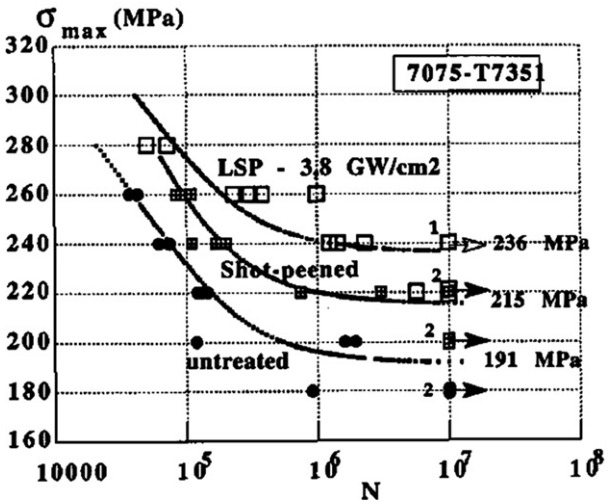


Figure 19 σ_{max}–N curves for unshocked, shot-peened, and laser-shocked 7075 alloy.[68]

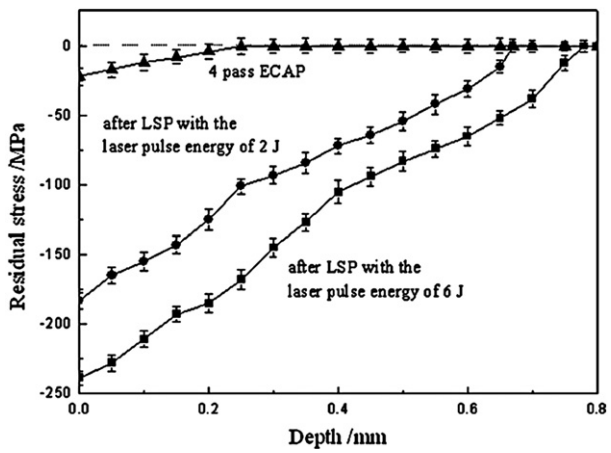


Figure 20 Residual stress profiles of the samples before and after different laser peening pulse.[133]

However, the number of shocks has an important influence on the magnitudes of the residual stresses in the laser-shocked region that has a significant effect on fatigue resistance. When

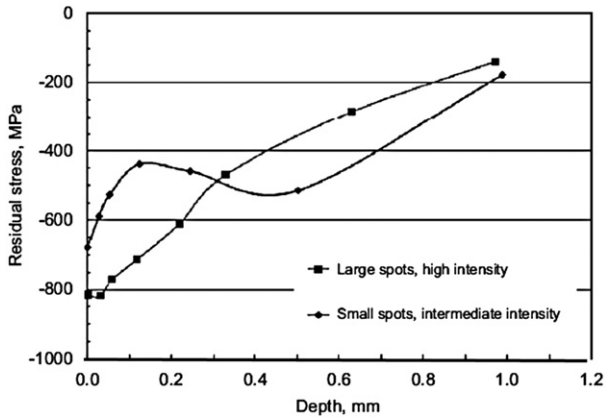


Figure 21 Representative residual stress profiles for two of the laser peening conditions used.[128]

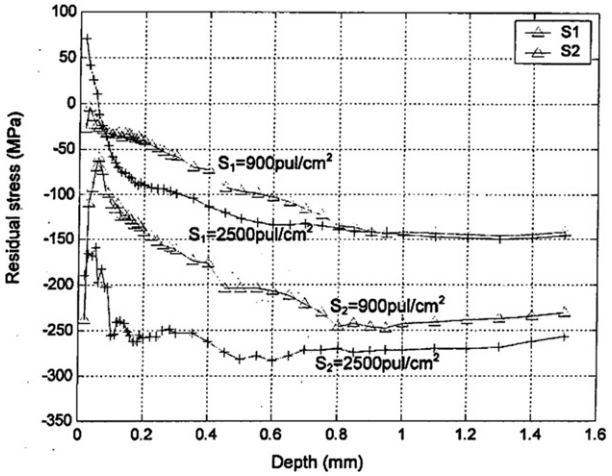


Figure 22 Residual stress distribution induced by laser peening.[134]

the number of laser shocks increased from one to two, the maximum residual stress located at the center increased from 340 to 420 MPa (**Figure 23**). Hence, Zhang *et al.*[135] proposed that the repeated shocks have a beneficial effect on the compressive residual stress levels on the surface. An increment of residual stress developed the microhardness and fatigue life.

Laser peening is considered a promising techniques in terms of its ability to repair or strengthen of the materials after service. Ganesh *et al.*[136] studied a laser peening-treated spring of partly fatigue-damaged in-service spring steel components (~50%) and compared the fatigue life with that of untreated specimens. In that study, laser peening-rejuvenated specimens remained unfailing until $5.2–6.6 \times 10^6$ cycles, whereas the specimen suffered failure after enduring 3×10^6 cycles. Ren *et al.*[61] investigated the effects of laser peening on fatigue crack behavior and residual stresses of the hole on 7050-T7451 aluminum alloy. The results revealed that laser peening resulted in restrained distance between fatigue striations and increased the number of striations. Therefore, the crack expansion distance was reduced, which means that laser peening has a restraint effect on the material fatigue crack initiation and expansion. In another interesting study, the effect of laser peening on the fatigue

behavior of the fastener hole was investigated by Zhang *et al.*[137] As seen in Figure 24, although the initial axial displacement of the unshocked specimen was approximately 0.27 mm and its ultimate fatigue life was 77 720 cycles, it was 0.122 mm and 275 420 cycles for the laser-shocked specimen. The results showed that the final fatigue life was approximately 350% longer than that of untreated case, which revealed that the laser peening treatment appeared to be an effective approach to increase the fatigue life of the fastener hole. Fracture morphologies (Figure 25) obviously showed that laser peening resulted in lower spacing between fatigue striations and higher density of the fracture striations.

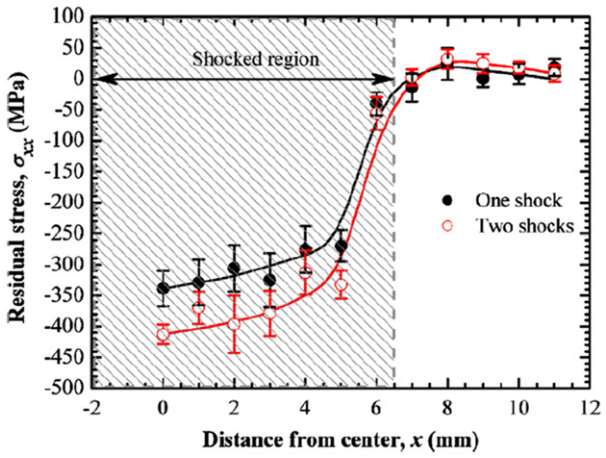


Figure 23 Residual stress profiles at the surfaces of the laser-peened specimens with different numbers of shocks along the distance from the center overlapped.[135]

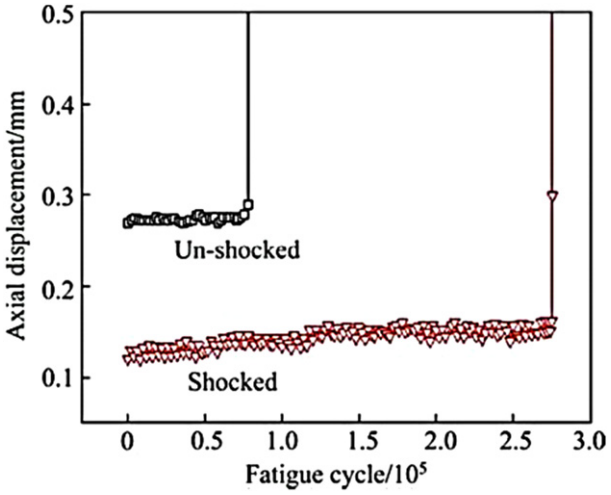


Figure 24 Axial displacement vs. fatigue cycle index in fatigue experiment.[137]

1.14.3.3 Tensile Properties and Deformation Mechanism

Shock waves generated during laser peening in the nanosecond or sub-nanosecond range with power density typically greater than 10^9 W cm^{-2} alter the surface microstructure and mechanical properties of materials, such as hardness and fatigue strength.[138,139]

During laser peening, the peak pressure of the shock wave reaches several gigapascal levels.[73,121,123] Under this peak pressure (approximately several GPa and only tens of nanoseconds),[7,52,65,68] plastic deformation occurs in the material just beneath the laser-shocked area. Therefore, SPD is induced in the material by laser shock wave. The plastic deformation layer revealed by laser peening is composed of the SPD layer and the minor plastic deformation (MPD) layer.[118] Lu *et al.*[118] also pointed out the grain refinement on the plastic deformation (SPD) layer.

There are many articles[11,60] that investigated the mechanical properties of metallic materials subjected to laser peening. All of them explain the increment of mechanical properties depending on plastic deformation mechanisms and grain refinement.

Lu *et al.*[11] experimentally investigated laser peening-treated LY2 Al alloy. It was found that laser peening could develop the UTS, the flow stress, and the elongation of the laser peening-treated samples due to grain refinement. TEM investigations revealed that although the grain size was approximately 100–200 nm at the top surface, the size of the original grain was approximately 8–10 μm.

Trdan *et al.*[115] proposed the grain refinement mechanism schematically (Figure 26) in the following sequence:

1. The first phase: the high-energy plasma and shock waves propagate formation of dislocation lines (DL) and dislocation movements within the original grains.
2. The second phase: repeated plastic deformation increases strain and strain rate on the material yielding to the

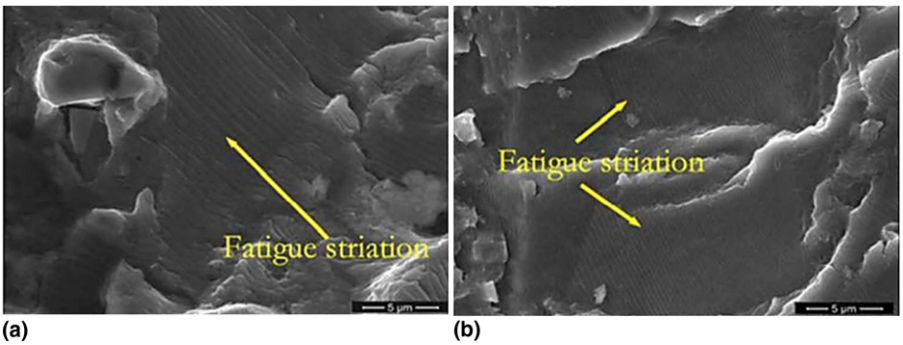


Figure 25 Morphologies of the fatigue crack growth region on LY12CZ specimens: (a) without laser peening and (b) with laser peening.[137]

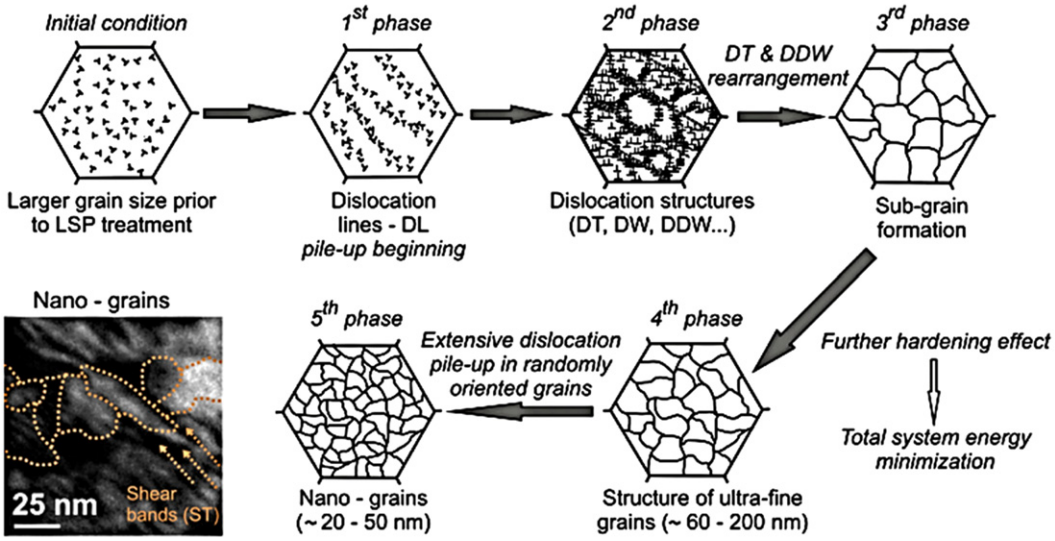


Figure 26 Proposed schematic presentation of the grain refinement mechanism of laser peening without coating of processed 6082-T651 Al alloy.[115]

dislocation movements along the dislocation planes and cross-slips, so high-density dislocations occur. This produces complex/completely random dislocation structures in the form of DT, dense dislocation walls (DDW), and dislocation cells. This type of dislocation has an important blocking effect during slipping at higher strains.

3. The third phase: as plastic deformation increases, the amount of strain increases, resulting in subdivision of original coarse grains into sub-grains with DTs and DWs.
4. The fourth phase: the total energy due to repeated shock waves is minimized by the dislocation annihilation by the formation of multiple shear bands (SB), which further divide sub-grains (formed in the third phase) into ultra-fine grains with high-angle grain boundaries.
5. The fifth phase: extensive amounts of ultra-high strains propagate the sub-grain boundaries, causing nano-grained structures. Dynamic recrystallization (DRX) may have taken place in the final grain refinement process, resulting in the formation of a nano-structured surface layer practically free from dislocations.

In brief, the grain refinement during laser peening involves[140]: formation of high-density dislocation; grain subdivision; and evolution of ultra-fine grain crystalline structure.

Lu *et al.*[118] confirmed three typical deformation-induced microstructure features: DLs, DTs, and DDWs. Laser peening can improve the high-temperature mechanical properties. Ren *et al.*[60] studied laser peening-treated 00Cr12 alloy's mechanical properties at high temperatures. They showed that laser peening successfully enhances the yield strength and tensile strength at high temperatures. It was proposed that the residual compressive stress would counterbalance the tensile stress partially in the stretch process, which was equivalent to reducing the load of the material, so the tensile strength was improved.

Laser peening can enhance the mechanical properties with more impact times.[141] The UTS can make the material withstand being stretched or pulled before necking, when the material cross-section starts to significantly stretch. Lu *et al.*[141] proposed that the UTS of the treated sample with one laser peening impact was close to that of the nonlaser-peened sample, indicating that one laser peening impact could not clearly improve the UTS of AISI 304 stainless steel in the aforementioned strain rate range. The treated sample with two laser peening impacts has the biggest UTS and exhibits excellent UTS resistance. Xiong *et al.*[133] also showed that after four laser peening impacts the ferrite grain size was approximately 150 nm. Another interesting result is that the lattice parameter of α-Fe increased with the laser pulse energy, which indicated that the cementite dissolution increased.

Some researchers expressed the improvement of mechanical properties, such as hardness and yield stress in terms of microstructure, such as dislocation density, SFs, and twins. Chu *et al.*[142] observed the dislocation substructure in the low-carbon steel after laser peening. Liucheng *et al.*[143] explained that as the deviatoric elastic reaches a critical level, dislocations occurred. When the shocks are applied on the surface of the material repeatedly, the shock wave propagates. Therefore, the stress wave caused by shock wave provides an energy for the dislocation movement and an increment. Chen *et al.*[144] indicated that high-density SFs, dislocation loops, and deformation twins occurred on austenitic stainless steel 2Cr13Mn9Ni4 under ultra-fast strain rate by laser peening. Moreover, the density of the SF was greatly increased by the repeated laser shocks and extended to three orientations. It showed that SFs were formed when large amounts of perfect dislocations were dissolved into partial ones. Schneider *et al.*[145] performed some experiments on Cu–2%Al and Cu6%Al to investigate the effect of the laser shock compression. They found that the SF width was 250 nm on average and the spacing was 300 nm. Luo *et al.* denoted[89] that the original grains were subdivided by mechanical twins (MTs) into thin twin–matrix (T–M) ranges from 40 to 400 nm, and the MT width was approximately 50 nm on the laser peening-treated ANSI 304 austenitic stainless steel. Chu *et al.*[142] signified a considerable amount of twin

formations during laser peening. Clauer *et al.*[146] observed the twin formation in Fe–3 wt.%Si alloys at a relatively low shock pressure (0.9 GPa).

A disruption of the long-range stacking sequence can produce two other common types of crystal defects: a SF and a twin region. A change in the stacking sequence over a few atomic spacings produces a SF, whereas a change over many atomic spacings produces a twin region. SFs are commonly produced in face-centered cubic metals (fcc) during treatments such as irradiation, aging after quenching, and deformation.[147] The SFE plays a critical role in the deformation properties of fcc metals and alloys. The SFE influences important phenomena such as the formation of partial dislocations, the ability of a dislocation to cross-slip, and the formation of twin boundaries; all of these have an effect on yield behavior. Fcc metals with SFE such as Al and Cu deform predominantly by slip. However, at low temperatures or high strain rates, deformation twinning can occur even in SFE fcc metals.[148] In fcc metals with low stacking energies such as α-brass, stainless steels, and MP35N (nickel–cobalt–chromium–molybdenum alloy), twinning serves as an important mode of plastic deformation Deformation twinning is one of the major plastic deformation modes in metals and alloys. Under extreme conditions such as shock-wave loading, the material deforms at a very high strain rate and twinning may play an important role.[148] Ye *et al.*[149] affirmed that the location of existing SFs yielded potential for forming new partial dislocation. There was also potential for forming new SFs around the location of the old SFs. Ultimately, old SFs transformed into twins through successively sweeping the partial dislocation on different lattice plane, as seen in **Figure 27**. In **Figure 28**, twin and SF formations on polycrystalline copper treated by laser peening are shown.

The effect of laser peening was characterized depending on the distance from the surface to depth by Lu *et al.*[118] The characteristic of dislocation or grain refinement of the hardening layer from the cross-section is illustrated in **Figure 29**. The change of the dislocation structure can be clearly seen at different layers, that is, it varies from DLs to DTs and DDWs and from sub-grains to refined grains as functions of the distance from the top surface.

Many researchers reported and debated the combination of high strength and high ductility resulting from SPD. Therefore, laser peening can be an alternative method to SPD for thin-sectioned metals. It has been reported that ultra-fine grain and nano-twins in material lead to a combination of high strength and ductility.[150–159] Gencalp Irizalp *et al.*[87] affirmed that laser peening could improve the uniform elongation as much as tensile strength. It is well known that when conventional deformation methods such as rolling, extrusion, or drawing are applied, strength of materials can be significantly increased and ductility decreases. According to Gencalp Irizalp *et al.*[81] this high-strength and high-ductility paradox is related to ultra-fine grain formation on top of the microstructure in the metal after laser peening. Wang *et al.*[155] reviewed and concluded the high-strength and high-ductility mechanism in nanocrystalline materials. According to this argument, partial dislocation emission from grain boundaries in metals with medium-to-high stacking fault energies plays a major role in the deformation of fcc metals with grain sizes of a few tens of nanometers. This consequently produces deformation twins in nanocrystalline fcc metals. Such twins are effective in increasing the dislocation storage capacity, which may be used to improve the ductility. These fcc metals usually do not twin when deformed at room temperature at low strain rates in their coarse-grained states because conventional dislocation sources, such as Frank–Read sources, operate in the interiors of the large grains. It is concluded that nanotwinned metals exhibit an unusual combination of ultra-high yield strength and high ductility.[160,161] Compared with twin boundary (TB), SF, as one other kind of defect in nanocrystal, seems to draw much lower attention to mechanical properties. According to the strengthening mechanism of TB, it still remains unknown whether the SF would strengthen the fcc metals in a similar way. Song showed when the SF spacing is rather fine, the SF acts as strong barrier like TB.[162]

In brief, it is obvious that laser peening results in grain refinement in nanocrystalline sizes and deformation-induced microstructure features such as DL, DT, and DDWs that increase strength. Moreover, laser peening produces unusual deformation mechanism such as TB and SF, and this creates an unusual combination of ultra-high yield strength and high ductility.

1.14.3.4 Corrosion Properties

Many studies have examined the effects of laser peening on the corrosion resistance of austenitic stainless steel.[10,15,32,39,163] Sano *et al.*[163] investigated laser peening without protective coating on SUS304 (type 304) and SUS316L (type 316L) austenitic stainless steels for SCC susceptibility. Typical results

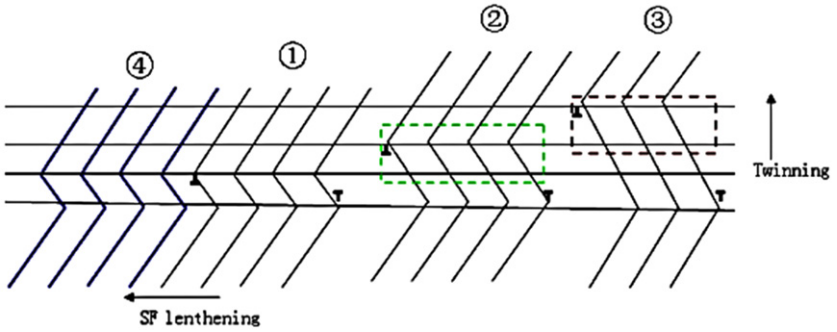


Figure 27 Schematic diagram of partial dislocations sweeping to form twins and lengthen stacking faults (SF).[149]

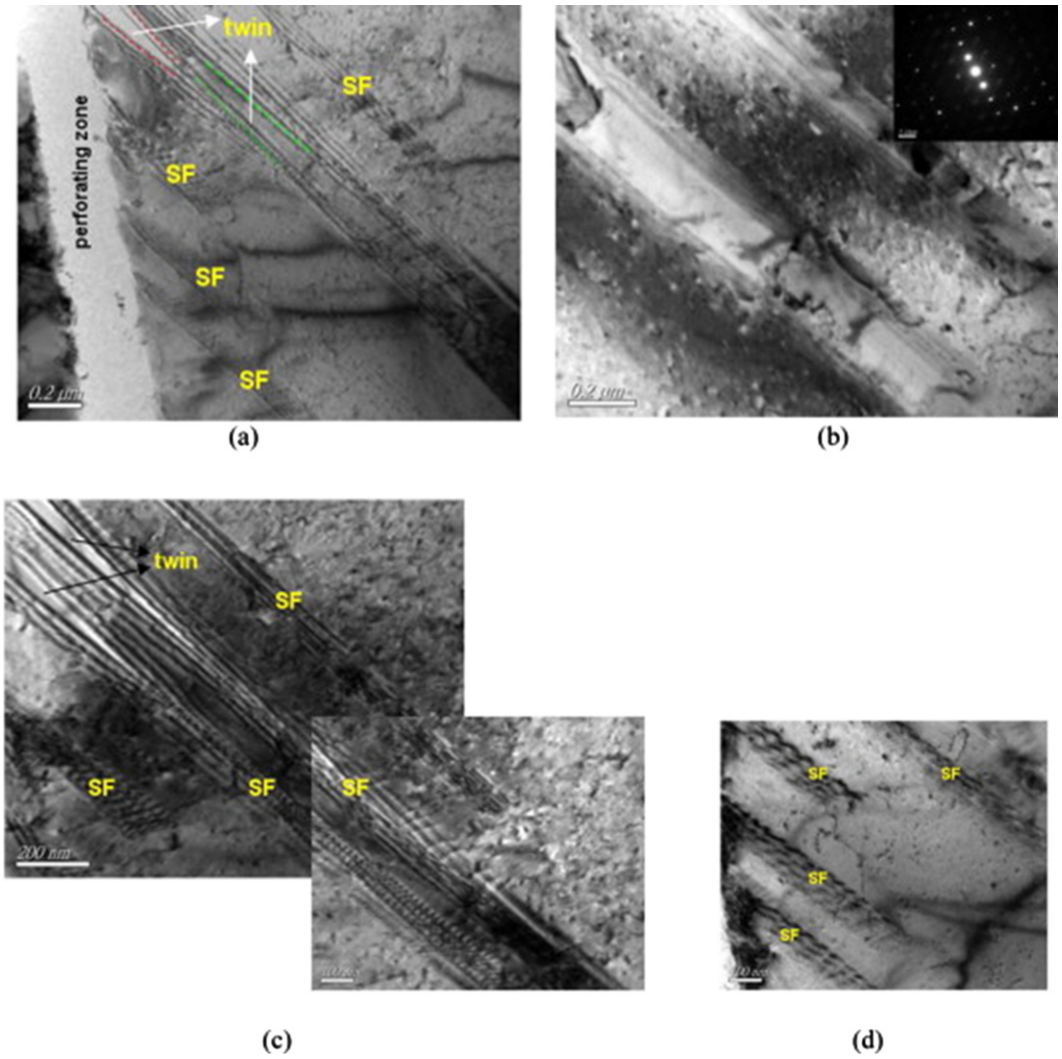


Figure 28 TEM images of the twins and stacking faults obtained through two instances of femtosecond laser shock.[149]

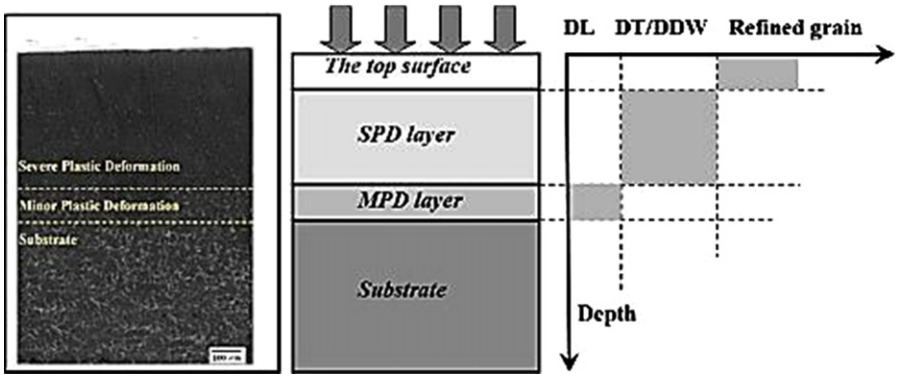


Figure 29 Schematic illustrations of microstructure characteristics along the depth direction in the hardening layer subjected to three laser peening impacts.[118]

are given in Figure 30. Laser peening without protective coating with a Q-switched and frequency-doubled Nd:YAG laser was conducted for SUS304 (type 304) and SUS316L (type 316L) austenitic stainless steels. Regarding the effects on SCC susceptibility, although SCC occurred in all the samples without laser peening without protective coating, there were no cracks in the shocked samples. This means that laser peening without protective coating completely prevented the

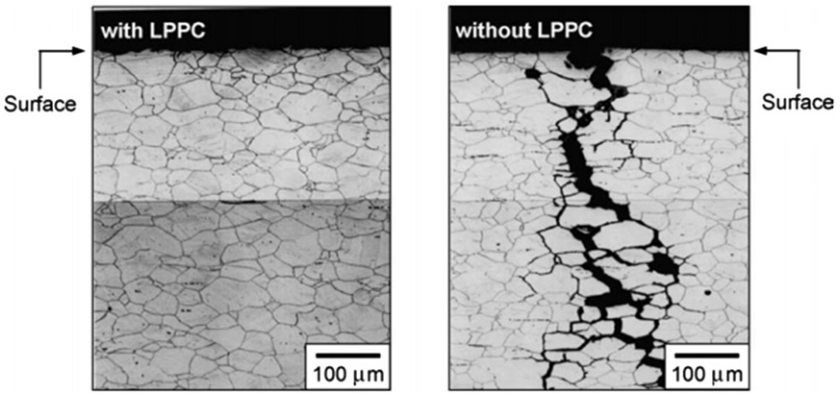


Figure 30 Stress corrosion cracking test results of SUS304.[163]

SCC initiation and propagation of small pre-cracks in high-temperature 42% $MgCl_2$ solution.

Peyre *et al.*[164] presented and evaluated the SCC behavior of 316L steel and uniform corrosion behavior of G41400 steels after laser peening. Their results revealed a 30–120% reduction of G41400 corrosion current in acid medium. They suggested a mechanochemical effect possibly due to a modification of the hydrogen–metal interaction after laser peening. It is obvious that mechanical surface states such as compressive stresses can lead to an inhibiting effect on dissolution rates. Kalainathan *et al.*[165] exhibited the effects of LPWC on the electrochemical corrosion behavior. Laser peening on 316L steel demonstrated that the laser-peened specimen exhibited a nominal increase of current density and, hence, an increase in corrosion rate. However, the corrosion potential (Ecorr) showed that the LPWC specimen had less susceptibility to corrosion and reduced pit growth.

It was reported[10,166,167] that the improvement of the SCC resistance of AISI 304 stainless steel was caused by compressive residual stress and grain refinement during the laser peening process. Although Lu *et al.*[10] found a number of eroding pits with a size of approximately 2 –5 μm for the as-machined specimen, it was reduced up to 0.2–1 μm for the laser-peened specimens. Amar *et al.* revealed[168] that no intergranular corrosion developed in the matrix, pitting potential increased, and the matrix remained passive after laser peening.

Saklakoglu *et al.*[32] observed that laser peening led to a reduction in number of pits in 6061-T6 aluminum alloy that was immersed in 1 g NaOH–1 ml HCl–50 ml water, as seen in Figure 31. It is believed that a work-hardened region resulting from laser peening became more noble and more resistant to pit initiation and that a mechanical state affects surface reactivity.[12,50,51] It is presumed that the pits are composed of dissolved inclusions.[32] Peyre *et al.*[125] proposed that laser peening reduced the potential gap between inclusions and the surrounding matrix; therefore, local galvanic couplings reduced and so did pit initiation. A passive film of 316L stainless steel after laser peening became thinner but more compact and more resistant because of high recoil pressure.[125] Consequently, work-hardening resulting from both SPD and high residual stress level can reduce the pit initiation. Davis *et al.*[169] proposed that pits preferentially occur on some orientations. They found that the (111) crystal face showed the highest number of pit formation, whereas (110) had the least number of pits. Vukelić *et al.*[58] performed a series of experimental and numerical studies using an aluminum bicrystal under laser peening. They revealed that crystallographic orientation was changed as a consequence of lattice rotation. Buggayev *et al.*[170,171] studied laser peening-treated Inconel 600 alloy and 316L stainless steel in a water confinement layer. They found that a column like microstructure was tilted in the direction of laser spot scanning. Chen *et al.*[172] performed lattice rotation of laser shock-induced Al and Cu materials and performed measurements using the electron backscatter diffraction (EBSD) method; they found that maximum in-plane rotation was approximately 3° in Al and approximately 2° in Cu, and the measured rotation distributions were compared with numerical simulations. Toppo *et al.* also point out that the crystallite refinement resulting from laser peening develops the passive film stability by making it more adherent. The high density of grain boundaries, sub-grain boundaries, and twin boundaries can restrict the movement of metal ions from the metal surface to the solution; therefore, passive film is stronger and diminishes pit formation.[172]

As a result, it is believed that laser peening alters the pitting potential as follows: formation of a more passive aluminum surface because of plastic work and compressive residual stress state; reduction of the potential difference between inclusions and the surrounding aluminum; and changing of crystallographic orientation due to nonuniform strain that can occur from different local deviations of the lattice planes.

1.14.3.5 Welded Joints Subjected to Laser Peening

The mechanical properties of the welded joints can significantly decrease compared with the base metal because of the weld and fusion zone structure. The weld zone and fusion zone become the weakest areas.[173] Safety and reliability requirements of producing welded components have attracted increasing attention. Residual stresses and microstructure are very important factors because they seriously affect the strength and service life of welded components.[174] Tensile residual stresses in welded zone reduce the tensile strength and fatigue life.[175] Dendritic microstructure and tensile residual stress that can develop after welding treatment significantly affect the mechanical properties. These residual stresses can seriously influence the service performance of welded materials by facilitating the fatigue crack growth process, SCC, and the lowering of fatigue life by affecting crack nucleation.[50]

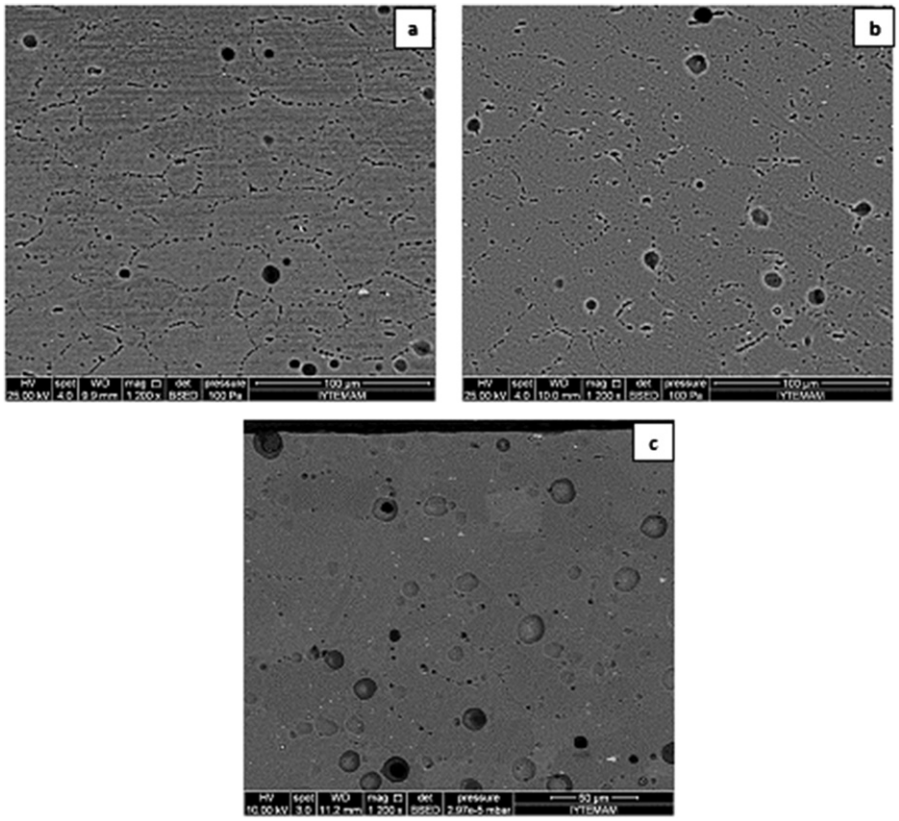


Figure 31 The pits at two different magnifications of 6061-T6 alloy: (a) single laser peening impact; (b) two laser peening impacts; and (c) untreated.[32]

Postweld heat treatment can improve the weld strength, but this is not always an option in welded joints. Welding technology has potential significant applications in various fields, including the aerospace and automotive industries.[176]

Laser peening is beneficial to rapid development of material properties due to its fast and efficient surface application to harden selected areas in complex structures.[174] Accordingly, laser peening can be successfully used for core parts and weld seams. Postweld innovative treatments, such as shot peening, laser peening, or ultrasonic peening, should be performed to improve the structure of the weld joint and to reduce the stress concentration. There are limited availability studies in the literature. Shot peening, laser peening, or LPWC and ultrasonic peening techniques have been applied to welded joints of various metals and alloys.[38,175,177,178]

Laser peening applied to welded joints that are commonly conducted with a friction stir-welding technique has been applied most commonly to aluminum alloys. Friction stir welding is a promising solid-state process that is used to weld the high-strength aerospace aluminum alloys. The use of friction stir welding is becoming more popular due to the advantages according to other conventional fusion welding techniques. However, laser peening has also been utilized in laser-welded and gas metal arc-welded joints. Friction stir welding was invented by the Welding Institute in England in 1991.[179] Friction stir welding has emerged as a promising solid-state process, and this technique has the potential for welding of hardened aluminum alloys.[180] Friction stir welding utilizes a nonconsumable cylindrical pin rotating at high speeds and plunges into butting edges of the workpiece. The friction heating occurs and the metals transform into a plastic state along the joining line, and then the workpiece is welded under pressure.[173,180] The problems resulting from melting temperatures associated with fusion welding are eliminated. However, the residual stresses developed in the weld zone can significantly degrade the material performance of the welds.[180] Five distinct microstructural zones produced during the friction stir welding process can create potential discontinuities in strength and fatigue volume properties.[177]

Laser welding has some advantages, such as smaller deformation of the workpiece and heat-affected zone, narrower fusion zone, lower weld distortion, and higher degree of automation. However, the porosity and crack initiation can be generated in the weld zone requiring laser welding. The strength of the welding joint can decrease due to the volatilization of the elements during melting.[181] The materials may be deformed due to thermal effects during welding processes. Laser peening is a useful way to improve its mechanical properties. Laser peening is a technique with the capability of inducing the residual compressive stresses.[50] Moreover, laser peening becomes attractive for welded joint applications because the process has local surface treatment capabilities.

For instance, LPWC has been applied to friction stir-welded A6061-T6 aluminum alloy. Effects of laser peening on the fatigue performance and mechanical properties have been investigated. As a result, the fatigue strength of friction stir welding

plus laser peening increased. The LPWC induced compressive residual stresses on the friction stir-welded joints.[178] The laser-welded ANSI 304 stainless steel joint treated by laser peening was investigated and the results demonstrated that laser peening could enhance tensile strength and yield strength.[38] The effects of laser and shot peening on tribological properties of friction stir-welded 2195 aluminum alloy joints were investigated, and long-term friction was found to be lowest for samples with no peening treatment.[181] Fatigue crack growth in friction stir-welded 7075-T7351 aluminum alloy joints subjected to laser and shot peening was investigated. The fatigue striation spacings for the laser-peened specimens were assessed and found to be small compared with unpeened and shot-peened samples. Therefore, slower fatigue crack growth rate emerged from laser peening.[41] The laser peening effect on SCC of the friction stir welding joints was investigated on the basis of slow strain rate and tensile tests were performed in an aggressive medium. Laser peening affecting the overall mechanical behavior of the friction stir welding joint induced a surface hardening affect. Also, laser peening positively influenced the overall friction stir welding joint plastic deformation.[182]

1.14.4 Relaxation Behavior of Laser-Peened Materials

Various mechanical surface treatment technologies (shot peening, laser peening, DR, low plasticity burnishing) have been developed for the purpose of improving fatigue performance of metallic materials.[111] These techniques have the beneficial effect of delaying the propensity for fatigue initiation or growth by inducing compressive stresses on the surface and near-surface regions.[183] Laser peening is a surface treatment technique whereby a solid-state laser beam is pulsed on a metallic surface, producing a planar shock wave that travels through the material.[184] It propagates into the material, causing plastic deformation and residual stress.[183]

Numerous studies[112,183,185–187] of steels, titanium, and nickel-based superalloys have shown that residual stresses were generated via surface treatment relaxation when subjected to elevated temperature exposure or mechanical loading. In service, metals experience severe mechanical and thermal loading conditions, particularly high-cycle and low-cycle fatigue cycles resulting from high-frequency vibrations or variable loads. This mechanical or thermal loading can provoke relaxation of residual stresses. The relaxation of residual stress implies the reduction of beneficial effects produced by various techniques decreasing fatigue life.[63] The residual stress relaxation can be categorized as mechanical relaxation of residual stress or thermal relaxation of residual stress. In brief, mechanical relaxation of residual stress occurs when the superposition of applied stress and residual stress reach the yield strength of material. Thermal relaxation of residual stress is a thermal recovery process in which elevated temperature accelerates the rapid annihilation of crystalline defects.[188] Research into relaxation of residual stresses subject to mechanical loading has followed a much different path than thermal relaxation. For thermal relaxation, temperature and exposure time are the primary parameters, whereas for mechanical loading the important factors are temperature, maximum and minimum applied stress, loading frequency, hold time, waveform shape, and number of applied cycles.[189] Residual stress relaxation consists of three different stages, as explained by Holzapfel *et al.*[190] relaxation due to specimen heating; relaxation during the first cycle; and relaxation with the logarithm of cycle count. According to Cao *et al.*[191] thermomechanical relaxation takes place in a two-stage process: the first stage is shakedown of the initial residual stresses described by a monotonic stress–strain law, and the second stage, which is slower, is described by a cyclic softening related to the logarithm of the number of the applied cycles.

1.14.4.1 Mechanical Relaxation of Residual Stress

Fatigue is a failure mechanism arising from cyclic loading. Crack initiation and propagation both involve the concept of cyclic accumulated damage. Monotonic stress–strain relationship controls simple deformation and ultimately fracture, whereas the cyclic relationship controls the finite life fatigue process.[192]

The compressive residual stresses can be beneficial for fatigue durability provided that they are stable. Kodama[193,194] first reported the residual stress relaxation behavior in shot-peened mild steel under uniaxial cyclic loading and suggested a logarithm linear relationship between residual stress and number of cycles. According to the results, residual stress decreased with an increasing applied number of fatigue cycles, and the major residual stress relaxation occurred during the first load cycle.

It is well known that the residual stress relaxation via mechanical processes is a complex phenomenon that may depend on interaction of several factors such as amplitude of the applied cyclic stress, loading mode, number of cycles, actual material and its microstructure, strength properties, and the surface finishing process.[187,195] The main residual stress relaxation normally takes place in the first cycles, followed by further gradual relaxation during the lifetime. Quasi-static loading occurs in the first cycle, resulting in relaxation when the superposition of the applied and residual stresses exceeds the monotonic yield strength of the material in tension and compression. Relaxation during successive cycles is related to the cyclic yield strength. The latter is the most difficult and has attracted the attention of several researchers by using experimental and numerical approaches.[187] Monotonic and cyclic relaxations are the reasons why residual stresses are not stable at high cyclic loads.

Cyclic yield strength is yield strength measured during cyclic loading. In many cases, cyclic yield strength is determined at the same 0.2% offset as static or monotonic tensile strength.[196] This was first observed by Bauschinger. The experiments indicated the yield strength in tension or compression is reduced after applying a load of the opposite sign that caused inelastic deformation. In previous studies, Quadfasel *et al.*[197] extended the phenomenological description of stress relaxation in the Hart–Solomon relationship.[198] Deviations from the Hart–Solomon relationship were also reported.[197]

In the literature, studies of mechanical relaxation of mechanical treated metals focus on shot peening.[185,193,195,199–204] A few studies cover the effect of laser peening.[205,206]

1.14.4.2 Thermal Relaxation of Residual Stress

Some studies focused on thermal relaxation mechanism, which is related to the thermal stability of residual stress that is mainly contributed by the applied thermal loads. Nickel alloys are preferred for high temperatures, as in turbine engine components, due to their outstanding mechanical property, corrosion resistance, and welding characteristics. Thermal relaxation induced by high engine temperatures is one of the primary mechanisms causing significant loss of the protective compressive layer of residual stress on the surface of high-temperature components such as Ni alloys used in turbine engine components. Therefore, the stability of high-temperature alloys during mechanical or thermal cycles is of great importance for the design of components.[183,185] Ti–6Al–4V alloy is also a material commonly used in components of gas turbine engines, and its maximum usage temperature is approximately 275 °C. In a recent study,[207] shot-peened Ti–6Al–4V showed longer fretting fatigue life than unpeened Ti–6Al–4V at room temperature; however, this increase in fatigue life was significantly reduced at elevated temperature, and the difference in fatigue life between shot-peened and unpeened Ti–6Al–4V became negligible at 260 °C.

The beneficial effect of surface treatment arises from the compressive residual stress at and near the surface region; understanding the thermomechanical stability of the residual stress in the service stage is critically important in the prediction of the life of component alloys.[206] Many investigations[4,184,208] show that laser peening results in a higher fatigue life compared with shot peening due to much deeper effective penetration in the material, compressive stress fields much further from the surface, and lower surface roughness. The benefit of high-temperature fatigue resistance from the mechanical surface treatments is thought to be primarily associated with the formation of a near-surface work-hardened layer with a nano-scale microstructure that is stable during thermal exposure or fatigue cycling at high temperatures.[3,111] Some investigations[109–113] propose that laser peening treatment may exhibit highly work-hardened nanoscale surface microstructures and eventually make material have higher thermal stability than those induced from conventional mechanical surface treatments, such as shot peening or DR treatments. Therefore, material surface after laser peening would be expected to be suitable under the high-temperature fatigue conditions.

The stability of residual stress, microstructures, and fatigue resistance in the temperature range of 25–600 °C of laser peening and untreated ASTM: 410L 00Cr12 steel were investigated by Ren *et al.*[113] The ASTM: 410L 00Cr12 steel is one kind of heat-resistant steel with good thermostable susceptibility and organization stability and is usually utilized at elevated temperatures. They found that compressive residual stresses up to 1 mm were approximately 400 MPa after laser peening; laser peening enhanced fatigue life approximately 53.8% in the low-cycle regime at 10^5 cycles at elevated temperatures up to 600 °C; laser peening resulted in more stable near-surface microstructures, deformation-induced martensite, and higher dislocation densities; and the pinning effect, which means surface grain refinement induced by laser peening, is the main reason for prolonging the fatigue life at high temperatures.

Ren *et al.*[114] investigated the influences of laser peening on residual stress relaxation and metallographic structure evolution of 6061-T651 aluminum alloy at elevated temperatures (up to 500 °C). They found that the affected layer of 6061-T651 aluminum alloy by laser peening has a higher magnitude of residual compressive stress between 25 and 300 °C, and laser peening still has a beneficial effect on residual stress at temperatures above 300 °C. The grain size began to enlarge, and the number of precipitated phases tended to grow at the temperature of 400 °C. The primitive grain was phagocytized by the new grain, and the DRX had been completed at 500 °C. Prevey *et al.*[109,209] compared the thermal stress relaxation of the compressive layer produced by shot peening, gravity peening, and laser peening in Ti6Al4V and IN718. They found that both the magnitude and rate of relaxation depended primarily on the degree of cold working (plastic deformation) developed during processing. Initial thermal relaxation of highly cold-worked surfaces can be extremely rapid in both alloys and can result in 50% loss in less than 10 min, even at moderate engine temperatures. However, for laser-peened coupons, only a small relaxation near the surface occurred in Ti6Al4V, and no thermal stress relaxation was found in IN718 at even the highest temperatures (670 °C), which was due to the fact that little cold working of the surface was produced by laser peening.

Nalla *et al.*[3] compared thermal relaxation of residual stresses in Ti–6Al–4V induced by DR and laser peening at 25, 250, and 450 °C. As shown (**Figure 32**), although laser peening resulted in an improvement in fatigue strength, DR was found to be more effective for the process parameters investigated. In this study, for the process parameters used, DR was found to induce the larger near-surface compressive residual stresses and degree of work hardening as compared with laser peening. Moreover, DR was observed to remarkably reduce the surface roughness. In a previous work,[111] similar results were reported. It was found that the residual stress state and work hardening induced by laser peening were less stable under isothermal cyclic loading at elevated temperatures as compared to the deep-rolled condition. However, DR is restricted to certain component geometries. Finally, it can be said that this beneficial effect of both DR and laser peening processes persists in

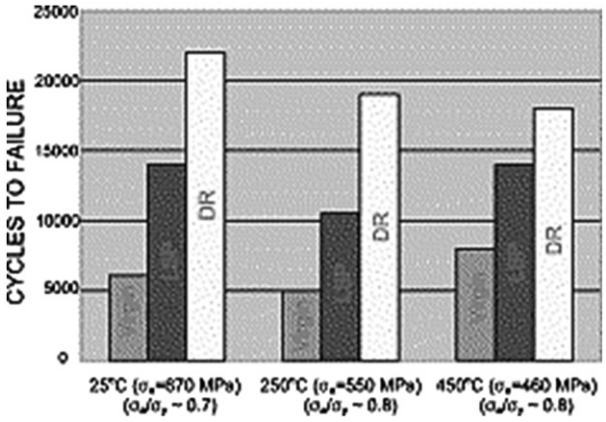


Figure 32 Enhancement in fatigue lifetimes following deep rolling (DR) and laser peening for test temperatures of 25, 250, and 450 °C and stress amplitudes of 670, 550, and 460 MPa, respectively.[3]

Ti6Al4V at temperatures as high as 43% of the melting temperature.

Researchers have found that temperature, exposure time, and initial cold hardening are the primary influencing factors for residual stress relaxation. Aghdam *et al.*[210] studied the time-independent thermomechanical residual stress relaxation around cold-expanded fastener holes in aluminum alloy 7075-T6 and suggested that higher temperatures caused more relaxation of residual stress. Ren *et al.*[63] studied the thermal relaxation of residual stresses in laser-peened iron GH2036 alloy exposed to different temperatures. As shown in **Figure 33**, the applied temperature and exposure time of annealing had significant effects on the magnitude of thermal relaxation. As the temperature increased, the thermal relaxation magnitude increased. The surface residual stress released much more easily than the subsurface. Moreover, the highest relaxation occurred at the depth of maximum compressive residual stress. They indicated that the primary mechanism of thermal relaxation was the mechanism involving rearrangement and annihilation of dislocation.

The relaxation is related to dislocation movement and plastic strain accumulation.[187] Ren *et al.*[63] proposed a mechanism of stress thermal relaxation that involves the evolution of dislocation density and morphology. As shown in **Figure 34(a)**, laser peening propagates formation of high-density dislocations in the specimen, and the dislocations have the majority of storage energy obtained from laser peening. It is known as work hardening. However, this part of the energy is a thermodynamic instability state, and the metal has a spontaneous tendency to return to the steady state of lowest free enthalpy. As temperature increases, the following processes occur, causing thermal relaxation:

1. The self-diffusion activation energy decreases and dislocations are activated and start to slip and climb. During this time, unlike dislocations meet and counterbalance, so that the dislocation density in the sample decreases. However, the pinning effect of precipitated phases delays the movement of dislocations and causes the formation of dislocation walls and dislocation cells (**Figure 34(b)**).
2. Unlike dislocations, the dislocation cells continue to counterbalance, which causes diminishing of the dislocation density (**Figure 34(c)**).
3. Edge dislocations gather at the cell walls, the cell walls become thinner, and sub-grain boundaries form gradually (**Figure 34(d)**).
4. Dislocations on the sub-grain boundaries transfer to the adjacent boundaries through climbing and slipping. Then, the primary grain boundaries disappear and a large-angle sub-grain is formed (**Figure 34(e)** and **34(f)**). The entire process consumes the majority of dislocation density, which means residual stresses release quickly during this period. Moreover, metastable crystalline defects induced by the peening process will reorganize and creep-controlled dislocation will rearrange, resulting in material softening at elevated temperatures.[206] After that, sub-grains rotate and move inside the crystals, releasing the storage energy in the metal. Residual stresses continue to release, but slowly.

Another interesting point is that the residual stress relaxation occurs not only during material softening at elevated temperatures but also during nonuniform distribution of compressive residual stress. As a result, the initial value of residual stress will accelerate the visco-plastic flow, leading to the relaxation of residual stress.[63]

The residual stress and work hardening induced by laser peening are more stable at elevated temperatures, compared with the untreated state. The effect of the work-hardened layer is to reduce the plastic strain amplitude, which acts to lessen the driving force for fatigue damage.[114] Ren *et al.*[113] studied ASTM: 410L 00Cr12 to reveal the effects of laser peening on microstructures and fatigue resistance in the temperature range of 25–600 °C. The results showed significant fatigue strength at the elevated temperatures. They pointed out that the formation of high-density dislocation and the pinning effect at the high temperatures results in stronger surface, lower residual stress relaxation, and a more stable dislocation arrangement. The residual stresses in laser-peened Inconel 718 Ni-based superalloy and their thermal relaxation behavior were investigated by Zhou *et al.*[206] They observed that stress

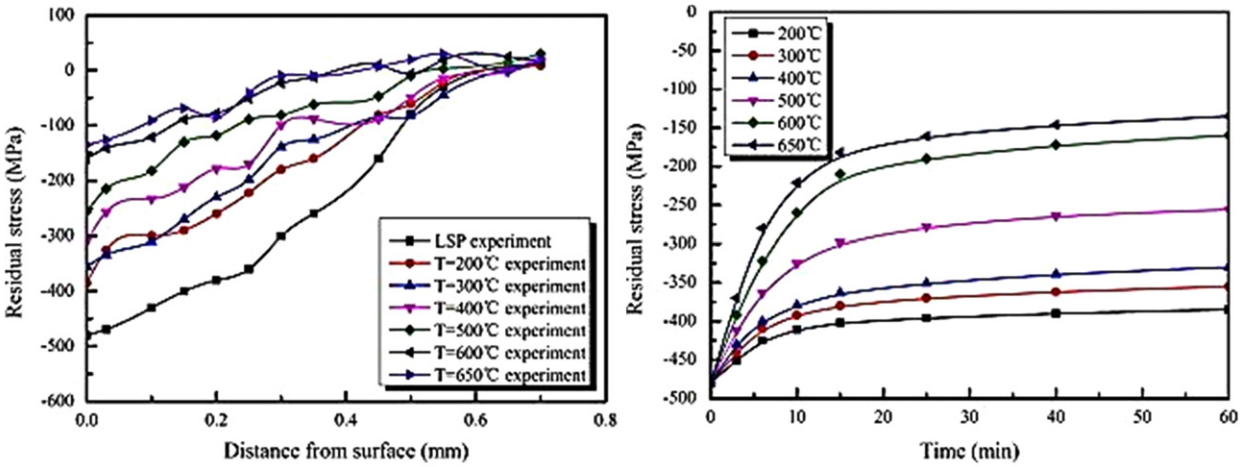


Figure 33 The residual stress distribution along with the depth at elevated temperatures and stress relaxation at different exposure times with annealing temperatures.[63]

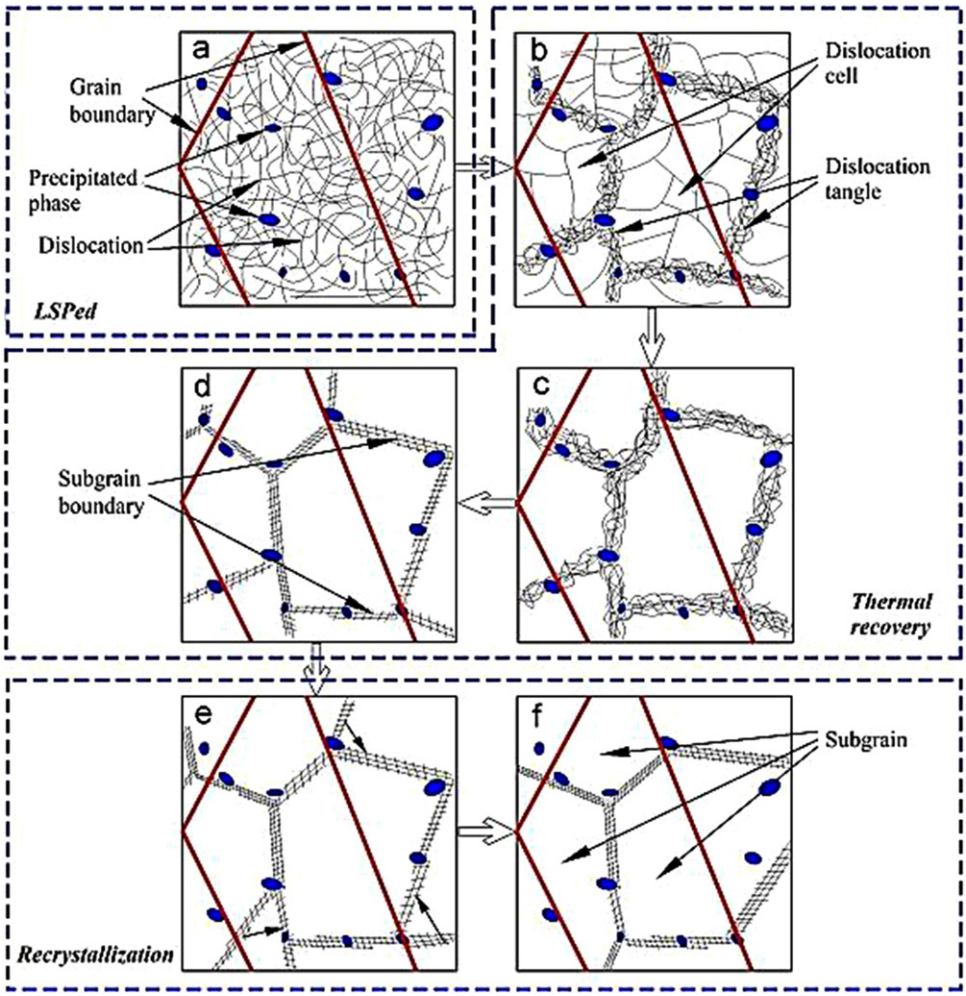


Figure 34 Schematic of grain and dislocation evolution during isothermal annealing: (a) high-density dislocation induced by laser peening; (b) dislocation slip and climb; (c) dislocation counterbalance in cells; (d) sub-grain boundary forming; (e) sub-grain boundary moving; and (f) sub-grain growth and coalescence.[63]

relaxation mainly occurs during the initial period of exposure, and the relaxation amplitude increases with the increase of applied temperature and as-peened plastic deformation. Laamouri *et al.*[187] and Zhou *et al.*[206] showed similar results. Laser peening induced residual stresses in Ti–6Al–4V, and their thermal relaxation due to short-term exposure at elevated temperatures were investigated by Zhou *et al.*[206] They observed that maximal relaxation occurred at the depth of maximum compressive residual stress, and lower initial stress was subjected to less stress relaxation.

The effects of applied temperature and exposure time on thermal relaxation are controlled by a thermally activated mechanism. The residual stresses decrease with increasing annealing time and temperature. According to previous research, thermal relaxation of residual stress can be described by using the Zener–Wert–Avrami function[63,206,211,212]:

$$\frac{\sigma^{RS}}{\sigma_0^{RS}} = \exp[-(At_a)^m] \quad [16]$$

where σ_0^{RS} is the initial stress before annealing, σ^{RS} is the residual stress at a given time, t_a, and temperature, T_a, m is the numerical parameter depending on the dominant relaxation mechanism, and A is the function associated with material properties and temperature.

The function is given as:

$$A = B\exp\left[-\frac{\Delta H}{kT_a}\right] \quad [17]$$

where B is the material constant with the value of 2.05×10^{12} min^{-1}, k is the Boltzmann constant and the value is 8.617343×10^{-5} eV K^{-1}, ΔH is the activation enthalpy of material for the relaxation process, and T_a is the annealing temperature.

Equation [16] can be deduced as

$$\ln\left[\ln\left(\sigma_0^{RS}/\sigma^{RS}\right)\right] = m\ln A + m\ln t_a \quad [18]$$

The process of residual stress relaxation of GH2036 at elevated temperatures was investigated and the plot of $\ln\left[\ln\left(\sigma_0^{RS}/\sigma^{RS}\right)\right]$ versus $\ln t_a$ at a given annealing temperature, T_a, according to experimental data and simulation results was drawn by Ren *et al.*[63] As shown in **Figure 35**, the relationship

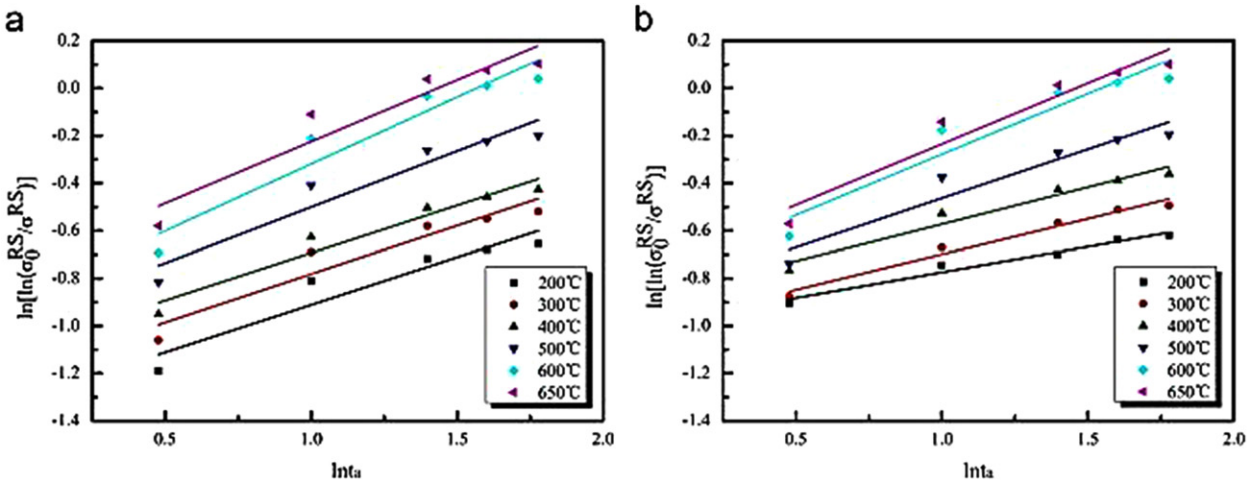


Figure 35 Influence of exposure time on the thermal relaxation of laser peening GH2036 at 200, 300, 400, 500, 600, and 650 °C: (a) experimental data and (b) simulated results.[63]

between $\ln\left[\ln\left(\sigma_0^{RS}/\sigma^{RS}\right)\right]$ and $\ln t_a$ is an approximate linear relationship at a constant annealing temperature and the slope of straight line is m. The value of m is determined by the mean value of these slopes. According to eqn [17], the activation enthalpy ΔH of the relaxation process can be determined. Ren *et al.* determined that while the mean value of m was 0.46 according to the experimental data and the calculated activation enthalpy ΔH was approximately 1.86 eV, the values based on the simulated data were 0.38, and 1.88 eV, respectively.

Similar conclusions were shown by Zhou *et al.*[206] They found that the activation enthalpy ΔH of the relaxation process in laser peening-treated Ti–6Al–4V was calculated in the range of 0.71–1.37 eV, which is close to values reported for self-diffusion of Ti and other solutes in titanium alloys.

1.14.5 Future Trends

Laser peening studies focused on aluminum alloy,[9,11,17,32] titanium alloy,[33,54,67,76] stainless steel[10,31,38,89] and some other steels,[213] and a few metallic glass or ceramics[214] to develop their mechanical properties such as fatigue, tensile, microhardness, and corrosion properties. One of the other potential applications for laser peening is biodegradable materials. Recently, a number of biodegradable metallic alloys have been introduced as implants with the ability of absorption. These biodegradable implants have mechanical strengths similar to that of bones, thereby reducing bone asthenia and helping to hold the clamp implant screw.[215] Laser peening has the potential for corrosion reduction by improving compressive residual stress on a biodegradable metallic implant surface. A few studies have been conducted involving biodegradable materials.[215,216] Laser peening of a biodegradable Mg–Ca alloy has been initiated to improve corrosion performance of orthopedic implants, creating superior surface integrity.[216] In addition to this, selective peening can be performed precisely and the peening of tiny workpieces such as biodegradable cardiovascular stents would now be possible.[215] There are also a few studies about improving welded materials that show a beneficial effect of laser peening.[182,217–219] Iordachescu *et al.*[182] proposed that laser peening can positively affect the welded materials in the uniform elongation zone and delay its failure beyond the ultimate tensile strength.

Another prospective industry for laser peening is fastener holes, which are used in airplane skin to joint skin parts into the whole body with rivets or bolts.[137,220] Zhang *et al.*[220] indicated worthwhile effects of the compressive residual stresses generated due to laser processing on the stress intensity factor. Ivetic *et al.*[37] determined that laser peening treatment increased the fatigue performance of open-hole aluminum specimens. They indicated that laser peening can be a good solution for 'in production' applications with open holes to be drilled after laser peening treatment.

1.14.6 Concluding Remarks

The main points affecting the magnitude of enhancement of material properties after laser peening include the laser spot size, power density, confine layer, pulse swept direction, the number of shocks, the subjected materials, and others. These parameters have a great influence on the residual stress, dislocation density, and, thus, on the morphology and microstructure of the laser-peened area. It is well known that laser peening can improve the fatigue life, strength, and corrosion resistance of materials, and also it has a great potential to improve the mechanical properties of metallic materials. According to the theoretical and experimental results, laser peening can be a powerful tool to supply a reliable design of structural components for the enhancement of mechanical properties like fatigue resistance and SCC resistance.

One of the advantages of laser peening is that the laser system can have direct integration into manufacturing production lines with a high degree of automation using an automatic x–y positioning system for treatment of localized fatigue critical areas without masking. Laser peening also has a high ability to make design changes that would not be

possible using alternative methods for increasing fatigue resistance. The manufacture of blades, disks, and vanes for aircraft gas turbine engines, of gears, connecting rods, and crankshafts for automotive engines, and of medical implants are among the applications that have been identified.

Laser peening has significant advantages for processing thin surface layers of different materials. As the laser technology progresses and high-power laser systems develop, laser peening will have extensive application areas.

See also: 1.8 Natural Fiber-Reinforced Composites: Types, Development, Manufacturing Process, and Measurement

References

1. Shen, S.; Atluri, S. N. An Analytical Model for Shot-Peening Induced Residual Stresses. *Comput. Mater. Contin.* **2006**, *4*, 75–85.
2. Zhan, K.; Jiang, C. H.; Ji, V. Uniformity of Residual Stress Distribution on the Surface of S30432 Austenitic Stainless Steel by Different Shot Peening Processes. *Mater. Lett.* **2013**, *99*, 61–64.
3. Nalla, R. K.; Altenberger, I.; Noster, U.; Liu, G. Y.; Scholtes, B.; Ritchie, R. O. On the Influence of Mechanical Surface Treatments-Deep Rolling and Laser Shock Peening-on the Fatigue Behavior of Ti–6Al0–4V at Ambient and Elevated Temperatures. *Mater. Sci. Eng. A* **2003**, *355*, 216–230.
4. Montross, C. S.; Wei, T.; Ye, L.; Clark, G.; Mai, Y. Laser Shock Processing and Its Effects on Microstructure and Properties of Metal Alloys: A Review. *Int. J. Fatigue* **2002**, *24*, 1021–1036.
5. Clauer, A. H. Laser Shock Peening for Fatigue Resistance. In *Surface Performance of Titanium Alloys*; Gregory, J. K., Rack, H. J., Eylon, D., Eds.; TMS: Warrendale, PA, 1997; pp. 217–230.
6. Kopp, R.; Schulz, J. Optimising the Double-Sided Simultaneous Shot Peen Forming. In *Shot Peening*; Wagner, L., Ed.; Wiley-VCH Verlag GmbH & Co. KGaA: Weinheim, 2003, pp. 227–233.
7. Ding, K.; Ye, L. *Laser Shock Peening Performance and Process Simulation*; Woodhead Publishing: Cambridge, 2006.
8. Lu, J. *Handbook of Measurement of Residual Stresses*; Society For Experimental Mechanics; Prentice-Hall, Inc.: Upper Saddle River, NJ, 1996, pp. 162–219.
9. Ren, X. D.; Zhang, Y. K.; Zhang, T.; *et al.* Comparison of the Simulation and Experimental Fatigue Crack Behaviors in the Nanoseconds Laser Shocked Aluminum alloy. *Mater. Des.* **2011**, *32*, 1138–1143.
10. Lu, J. Z.; Qi, H.; Luo, K. Y.; Luo, M.; Cheng, X. N. Corrosion Behaviour of AISI 304 Stainless Steel Subjected to Massive Laser Shock Peening Impacts with Different Pulse Energies. *Corros. Sci.* **2014**, *80*, 53–59.
11. Lu, J. Z.; Luo, K. Y.; Zhang, Y. K.; *et al.* Effects of Laser Shock Processing and Strain Rate on Tensile Property of LY2 Aluminum Alloy. *Mater. Sci. Eng. A* **2010**, *528*, 730–735.
12. Lu, J. Z.; Zhang, L.; Feng, A. X.; Jiang, Y. F.; Cheng, G. G. Effects of Laser Shock Processing on Mechanical Properties of Fe–Ni Alloy. *Mater. Des.* **2009**, *30*, 3673–3678.
13. Lu, J. Z.; Luo, K. Y.; Dai, F. Z.; *et al.* Effects of Multiple Laser Shock Processing (LSP) Impacts on Mechanical Properties and Wear Behaviors of AISI 8620 Steel. *Mater. Sci. Eng. A* **2012**, *536*, 57–63.
14. Oda, E.; Fujiwara, H.; Ameyama, K. Nano Grain Formation in Tungsten by Severe Plastic Deformation-Mechanical Milling Process. *Mater. Trans.* **2008**, *49*, 54–57.
15. Trdan, U.; Grum, J. SEM/EDS Characterization of Laser Shock Peening Effect on Localized Corrosion of Al Alloy in a Near Natural Chloride Environment. *Corros. Sci.* **2014**, *82*, 328–338.
16. White, R. M. Generation of Elastic Waves by Transient Surface Heating. *J. Appl. Phys.* **1963**, *34*, 3559–3567.
17. Fairand, B. P.; Wilcox, B. A.; Gallagher, W. J.; Williams, D. N. Laser Shock-Induced Microstructural and Mechanical Property Changes in 7075 Aluminum. *J. Appl. Phys.* **1972**, *43*, 3893–3895.
18. Clauer, A. H.; Fairand, B. P. Interaction of Laser-Induced Stress Waves with Metals. In: *ASM Conference Applications of Laser in Material Processing*, Washington, DC; ASM International: Material Park, OH, 1979; pp. 1–22.
19. Clauer, A. H.; Holbrook, J. H.; Fairand, B. P. Effects of Laser Induced Shock Waves on Metals. In *Proceedings of the Society of Photo-Optical Instrumentation Engineers*; Plenum Press: New York, NY, 1981; pp. 675–702.
20. Gregg, D. W.; Thomas, S. J. Momentum Transfer Produced by Focused Laser Giant Pulses. *J. Appl. Phys.* **1966**, *37*, 2787–2789.
21. Skeen, C. H.; York, C. M. Laser-Induced 'Blow-Off' Phenomena. *Appl. Phys. Lett.* **1968**, *12*, 369–371.
22. Anderholm, N. C. Laser Generated Stress Waves. *Appl. Phys. Lett.* **1970**, *16*, 113–115.
23. O'Keefe, J. D.; Skeen, C. H.; York, C. M. Laser-Induced Deformation Modes in Thin Metal Targets. *J. Appl. Phys.* **1973**, *44*, 4622–4626.
24. Yang, L. C. Stress Waves Generated in Thin Metallic Films by a Q-switched Ruby Laser. *J. Appl. Phys.* **1974**, *45*, 2601–2608.
25. Fournier, J.; Fabbro, R.; Fabre, E. Experimental Study of Shock Waves Generated by a High-energy Pulsed Laser. *Academie des Sciences Paris Comptes Rendus Serie Sciences Mathematiques* **1987**, *304*, 1051–1054.
26. Fabbro, R.; Fournier, J.; Ballard, P.; Devaux, D.; Virmont, J. Physical Study of Laser-Produced Plasma in Confined Geometry. *J. Appl. Phys.* **1990**, *68*, 775–784.
27. Mallozi, P. I.; Fairand, B. P. *Altering Material Properties*. US Patent 3 850 698; 1974; Industrial Materials Limited.
28. Mannava, S.; Ferrigno, S. J. *Laser Shock Peening for Gas Turbine Engine Vane Repair*. US Patent 5 675 892; 1997; General Electric Company.
29. Mannava, S.; Mcdaniel, A. E.; Cowie, W. D.; Halila, H.; Rhoda, J. E.; Gutknecht, J. E. *Laser Shock Peened Gas Turbine Engine Fan Blade Edges*. US Patent 5 591 009; 1997; General Electric Company.
30. Ferrigno, S. J.; Cowie, W. D.; Mannava, S. *Laser Shock Peening for Gas Turbine Engine Weld Repair*. US Patent 5 846 057; 1998; General Electric Company.
31. Correa, C.; Ruiz de Lara, L.; Díaz, M.; Gil-Santos, A.; Porro, J. A.; Ocaña, J. L. Effect of Advancing Direction on Fatigue Life of 316L Stainless Steel Specimens Treated by Double-Sided Laser Shock Peening. *Int. J. Fatigue* **2015**, *79*, 1–9.
32. Saklakoglu, N.; Gencalp Irizalp, S.; Akman, E.; Demir, A. Near Surface Modification of Aluminum Alloy Induced by Laser Shock Processing. *Opt. Laser Technol.* **2014**, *64*, 235–241.
33. Nie, X.; He, W.; Zang, S.; Wang, X.; Zhao, J. Effect Study and Application to Improve High Cycle Fatigue Resistance of TC11 Titanium Alloy by Laser Shock Peening with Multiple Impacts. *Surf. Coat. Technol.* **2014**, *253*, 68–75.
34. Forget, P.; Jeandin, M.; Lyoret, A. Determination of Laser Shock Treatment Conditions for Fatigue Testing of Ni-Based Superalloys. *Le Journal de Physique IV* **1993**, *3*, 921–926.
35. Hammersley, G.; Hackel, L. A.; Harris, F. Surface Prestressing to Improve Fatigue Strength of Components by Laser Shot Peening. *Opt. Lasers Eng.* **2000**, *34*, 327–337.
36. Qin, M.; Ju, D. Y.; Oba, R. Investigation of the Influence of Incidence Angle on the Process Capability of Water Cavitation Peening. *Surf. Coat. Technol.* **2006**, *201*, 1409–1413.
37. Ivetic, G.; Meneghin, I.; Troiani, E.; *et al.* Fatigue in Laser Shock Peened Open-Hole Thin Aluminium Specimens. *Mater. Sci. Eng. A* **2012**, *534*, 573–579.
38. Zhang, L.; Luo, K. Y.; Lu, J. Z.; Zhang, Y. K.; Dai, F. Z.; Zhong, J. W. Effects of Laser Shock Processing with Different Shocked Paths on Mechanical Properties of Laser Welded ANSI 304 Stainless Steel Joint. *Mater. Sci. Eng. A* **2011**, *528*, 4652–4657.
39. Peyre, P.; Scherpereel, X.; Berthe, L.; *et al.* Surface Modifications Induced in 316L Steel by Laser Peening and Shot-Peening. Influence on Pitting Corrosion Resistance. *Mater. Sci. Eng. A* **2000**, *280*, 294–302.
40. Turski, M.; Clitheroe, S.; Evans, A. D.; Rodopoulos, C.; Hughes, D. J.; Withers, P. J. Engineering the Residual Stress State and Microstructure of Stainless Steel with Mechanical Surface Treatments. *Appl. Phys. A* **2010**, *99*, 549–556.
41. Hatamleh, O.; Lyons, J.; Forman, R. Laser and Shot Peening Effects on Fatigue Crack Growth in Friction Stir Welded 7075-T7351 Aluminum Alloy Joints. *Int. J. Fatigue* **2007**, *29*, 421–434.
42. Honda, T.; Ramulu, M.; Kobayashi, A. S. Effect of Shot Peening on Fatigue Crack Growth in 7075-T7351. *J. ASTM Int.* **2005**, *2*, 1–14.
43. Gao, Y. K. Improvement of Fatigue Property in 7050-T7451 Aluminum Alloy by Laser Peening and Shot Peening. *Mater. Sci. Eng. A* **2011**, *528*, 3823–3828.
44. Chen, H.; Kysar, J. W.; Yao, Y. L. Characterization of Plastic Deformation Induced by Microscale Laser Shock Peening. *J. Appl. Mech.* **2004**, *71*, 713–723.

45. King, A.; Steuwer, A.; Woodward, C.; Withers, P. J. Effects of Fatigue and Fretting on Residual Stresses Introduced by Laser Shock Peening. *Mater. Sci. Eng. A* **2006**, *435*, 12–18.
46. Fournier, J.; Ballard, P.; Merrien, P.; Barralis, J.; Castex, L.; Fabbro, R. Mechanical Effects Induced by Shock Waves Generated by High Energy Laser Pulses. *Journal de Physique III* **1991**, *1*, 1467–1480.
47. Grevey, D.; Maiffredy, L.; Vannes, A. B. Laser Shock on a TRIP Alloy: Mechanical and Metallurgical Consequences. *J. Mater. Sci.* **1992**, *27*, 2110–2116.
48. Chu, J. P.; Rigsbee, J. M.; Banaś, G.; Lawrence, F. V.; Elsayed-Ali, H. E. Effects of Laser-Shock Processing on the Microstructure and Surface Mechanical Properties of Hadfield Manganese Steel. *Metall. Mater. Trans. A* **1995**, *26*, 1507–1517.
49. Berthe, L.; Fabbro, R.; Peyre, P.; Bartnicki, E. Laser shock Processing of Materials: Experimental Study of Breakdown Plasma Effects at the Surface of Confining Water. In *Proceedings of the SPIE, Lasers and Optics in Manufacturing III*, International Society for Optics and Photonics, 1997; pp. 570–575.
50. Berthe, L.; Sollier, A.; Peyre, P.; Carboni, C.; Bartnicki, E.; Fabbro, R. Physics of Shock-Wave Generation by Laser Plasma in Water Confinement Regime. In *Proceedings of the SPIE, High-Power Laser Ablation*, International Society for Optics and Photonics, 2000; pp. 511–520.
51. Montross, C. S.; Florea, V.; Swain, M. V. The Influence of Coatings on Subsurface Mechanical Properties of Laser Peened 2011-T3 Aluminum. *J. Mater. Sci.* **2001**, *36*, 1801–1807.
52. Zhang, W.; Yao, Y. L. Micro Scale Laser Shock Processing of Metallic Components. *J. Manuf. Sci. Eng.* **2002**, *124*, 369–378.
53. Peyre, P.; Sollier, A.; Chaieb, I.; *et al.* FEM Simulation of Residual Stresses Induced by Laser Peening. *Eur. Phys. J. Appl. Phys.* **2003**, *23*, 83–88.
54. Yilbas, B. S.; Arif, A. F. M.; Shuja, S. Z.; Gondal, M. A.; Shirokof, J. Investigation into Laser Shock Processing. *J. Mater. Eng. Perform.* **2004**, *13*, 47–54.
55. Gomez-Rosas, G.; Rubio-Gonzalez, C.; Ocana, J. L.; *et al.* High Level Compressive Residual Stresses Produced in Aluminum Alloys by Laser Shock Processing. *Appl. Surf. Sci.* **2005**, *252*, 883–887.
56. Sano, Y.; Akita, K.; Masaki, K.; Ochi, Y.; Altenberger, I.; Scholtes, B. Laser Peening without Coating as a Surface Enhancement Technology. *J. Laser Micro/Nanoeng.* **2006**, *1*, 161–166.
57. Mordyuk, B. N.; Milman, Y. V.; Lefimov, M. O.; *et al.* Characterization of Ultrasonically Peened and Laser-shock Peened Surface Layers of AISI 321 Stainless Steel. *Surf. Coat. Technol.* **2008**, *202*, 4875–4883.
58. Vukelić, S.; Kysar, J. W.; Yao, Y. L. Grain Boundary Response of Aluminum Bicrystal Under Micro Scale Laser Shock Peening. *Int. J. Solids Struct.* **2009**, *46*, 3323–3335.
59. Luo, K. Y.; Lu, J. Z.; Zhang, L. F.; Zhong, J. W.; Guan, H. B.; Qian, X. M. The Microstructural Mechanism for Mechanical Property of LY2 Aluminum Alloy After Laser Shock Processing. *Mater. Des.* **2010**, *31*, 2599–2603.
60. Ren, X. D.; Zhang, T.; Zhang, Y. K.; *et al.* Mechanical Properties and Residual Stresses Changing on 00Cr12 Alloy by Nanoseconds Laser Shock Processing at High Temperatures. *Mater. Sci. Eng. A* **2011**, *528*, 1949–1953.
61. Ren, X. D.; Zhan, Q. B.; Yang, H. M.; *et al.* The Effects of Residual Stress on Fatigue Behavior and Crack Propagation from Laser Shock Processing-Worked Hole. *Mater. Des.* **2013**, *44*, 149–154.
62. Gencalp Irizalp, S.; Saklakoglu, N.; Yilbas, B. S. Characterization of Microplastic Deformation Produced in 6061-T6 by Using Laser Shock Processing. *Int. J. Adv. Manuf. Technol.* **2014**, *71*, 109–115.
63. Ren, X. D.; Zhou, W. F.; Xu, S. D.; *et al.* Iron GH2036 Alloy Residual Stress Thermal Relaxation Behavior in Laser Shock Processing. *Opt. Laser Technol.* **2015**, *74*, 29–35.
64. Berthe, L.; Fabbro, R.; Peyre, P.; Bartnicki, E. Wavelength Dependent of Laser Shock-Wave Generation in the Water-Confinement Regime. *J. Appl. Phys.* **1999**, *85*, 7552–7555.
65. Peyre, P.; Fabbro, R. Laser Shock Processing: A Review of the Physics and Applications. *Opt. Quant. Electron.* **1995**, *27*, 1213–1229.
66. Peyre, P.; Fabbro, R. Electromagnetic Gauge Study of Laser-induced Shock Waves in Aluminium Alloys. *Journal de Physique III* **1995**, *5*, 1953–1964.
67. Dahotre, N. B.; Harimkar, S. P. *Laser Fabrication and Machining of Materials*; Springer: New York, NY, 2008.
68. Peyre, P.; Fabbro, R.; Merrien, P.; Lieurade, H. P. Laser Shock Processing of Aluminium Alloys. Application to High Cycle Fatigue Behavior. *Mater. Sci. Eng. A* **1996**, *210*, 102–113.
69. Yilbas, B. S.; Shuja, S. Z.; Arif, A.; Gondal, M. A. Laser-Shock Processing of Steel. *J. Mater. Process. Technol.* **2003**, *135*, 6–17.
70. Berthe, L.; Fabbro, R.; Peyre, P.; Tollier, L.; Bartnicki, E. Shock Waves from a Water-Confined Laser-Generated Plasma. *J. Appl. Phys.* **1997**, *82*, 2826–2832.
71. Singh, G. *Effective Simulation and Optimization of a Laser Peening Process* (Doctor of Philosophy Thesis); Dayton, OH: Wright State University, 2009.
72. Cellard, C.; Retraint, D.; François, M.; Rouhaud, E.; Le Saunier, D. Laser Shock Peening of Ti-17 Titanium Alloy: Influence of Process Parameters. *Mater. Sci. Eng. A* **2012**, *532*, 362–372.
73. Asay, J. R., Shahinpoor, M., Eds. *High-Pressure Shock Compression of Solids*; Springer Science & Business Media: New York, NY, 2012.
74. Ballard, P.; Fournier, J.; Fabbro, R.; Frelat, J. Residual Stresses Induced by Laser-Shocks. *Le Journal de Physique IV* **1991**, *1*, 487–494.
75. Kruusing, A. *Handbook of Liquids-Assisted Laser Processing*; Elsevier: Oxford, 2008.
76. Prevey, P. S. X-Ray Diffraction Residual Stress Techniques. In *ASM Handbook: Materials Characterization*, vol. 10; Whan, R. E., Ed.; ASM International: Metal Park, OH, 1986, pp. 380–392.
77. Martinez, S. A.; Sathish, S.; Blodgett, M. P.; Shepard, M. J. Residual Stress Distribution on Surface-Treated Ti–6Al–4V by X-Ray Diffraction. *Exp. Mech.* **2003**, *43*, 141–147.
78. Banazwski, B. J. *Using X-Ray Diffraction to Assess Residual Stresses in Laser Peened and Welded Aluminum* (Master of Science Thesis); California: Naval Postgraduate School Monterey, 2011.
79. Küçükyılmaz, A. *Experimental Investgation of Residual Stresses Introduced via shot Peening and their Effect on Fatigue Life of Ball Bearings* (Master of Science Thesis); Ankara: Middle East Technical University, 2010.
80. Anderoglu, O. *Residual Stress Measurement Using X-Ray Diffraction* (Master of Science Thesis); Texas: Texas A&M University, 2004.
81. Noyan, C.; Cohen, J. B. *Residual Stress Measurement by Diffraction and Interpretation*; Springer-Verlag: New York, NY, 1987.
82. Steinzig, M.; Ponslet, E. Residual Stress Measurement Using the Hole Drilling Method and Laser Speckle Interferometry: Part 1. *Exp. Tech.* **2003**, 27 (3), 43–46.
83. Barile, C.; Casavola, C.; Pappalettera, G.; Pappalettere, C. Residual Stress Measurement by Electronic Speckle Pattern Interferometry: A Study of the Influence of Geometrical Parameters. *Struct. Integr. Life* **2011**, *17*, 177–182.
84. Rickert, T. J. ESPI Residual Stress Determination in Shot-Peened Aluminum and Steels. In *Proceedings of the SEM Annual Conference*; Albuquerque, New Mexico, 2009.
85. Maawad, E.; Sano, Y.; Wagner, L.; Brokmeier, H. G.; Genzel, C. Investigation of Laser Shock Peening Effects on Residual Stress State and Fatigue Performance of Titanium Alloys. *Mater. Sci. Eng. A* **2012**, *536*, 82–91.
86. Sathyajith, S.; Kalainathan, S.; Swaroop, S. Laser Peening Without Coating on Aluminum Alloy Al-6061-T6 Using Low Energy Nd: YAG Laser. *Opt. Laser Technol.* **2013**, *45*, 389–394.
87. Gencalp Irizalp, S.; Saklakoglu, N.; Akman, E.; Demir, A. Pulsed Nd: YAG Laser Shock Processing Effects on Mechanical Properties of 6061-T6 Alloy. *Opt. Laser Technol.* **2014**, *56*, 273–277.
88. Hfaiedh, N.; Peyre, P.; Popa, I.; Vignal, V.; Seiler, W.; Ji, V. Experimental and Numerical Analysis of the Distribution of Residual Stresses Induced by Laser Shock Peening in a 2050-T8 Aluminium Alloy. *Mater. Sci. Forum* **2011**, *681*, 296–302.
89. Luo, K. Y.; Lu, J. Z.; Zhang, Y. K.; *et al.* Effects of Laser Shock Processing on Mechanical Properties and Micro-Structure of ANSI 304 Austenitic Stainless Steel. *Mater. Sci. Eng. A* **2011**, *528*, 4783–4788.
90. Cullity, B. D.; Stock, S. R. *Elements of X-Ray Diffraction*, 3rd ed.; Prentice Hall: Upper Saddle River, NJ, 2001.
91. Suryanarayana, C.; Norton, M. G. *X-Ray Diffraction: A Practical Approach*; Springer Science & Business Media: New York, NY, 1998.
92. Maisano, A. J. *Cryomilling of Aluminum-Based and Magnesium-Based Metal Powders* (Master of Science Thesis); Virginia: Virginia Tech Blacksburg, 2006.
93. Woo, W.; Balogh, L.; Ungár, T.; Choo, H.; Feng, Z. Grain Structure and Dislocation Density Measurements in a Friction-Stir Welded Aluminum Alloy Using X-Ray Peak Profile Analysis. *Mater. Sci. Eng. A* **2008**, *498*, 308–313.
94. Pant, B. K.; Sundar, R.; Kumar, H.; *et al.* Studies Towards Development of Laser Peening Technology for Martensitic Stainless Steel and Titanium Alloys for Steam Turbine Applications. *Mater. Sci. Eng. A* **2013**, *587*, 352–358.
95. Sathyajith, S.; Kalainathan, S. Effect of Laser shot Peening on Precipitation Hardened Aluminum Alloy 6061-T6 Using Low Energy Laser. *Opt. Lasers Eng.* **2012**, *50*, 345–348.
96. Marmy, P.; Yuzhen, R.; Victoria, M. J. The Tensile and Fatigue Properties of Type-1.4914 Ferritic Steel for Fusion Reactor Applications. *J. Nucl. Mater.* **1991**, *179*, 697–701.

97. Zhilyaev, A. P.; Gubicza, J.; Nurislamova, G.; *et al.* Microstructural Characterization of Ultrafine-Grained Nickel. *Phys. Status Solidi A* **2003**, *198*, 263–271.
98. Zhu, Y. T.; Huang, J. Y.; Gubicza, J.; *et al.* Nanostructures in Ti Processed by Severe Plastic Deformation. *J. Mater. Res.* **2003**, *18*, 1908–1917.
99. Ungár, T.; Tichy, G.; Gubicza, J.; Hellmig, R. J. Correlation between Subgrains and Coherently Scattering Domains. *Powder Diffr.* **2005**, *20*, 366–375.
100. Che, M., Védrine, J. C., Eds. *Characterization of Solid Materials and Heterogeneous Catalysts: From Structure to Surface Reactivity*; Wiley-VCH: Weinheim, 2012
101. Anand Kumar, S.; Sundar, R.; Raman, S. G. S.; *et al.* Influence of Laser Peening on Microstructure and Fatigue Lives of Ti–6Al–4V. *Trans. Nonferr. Metals Soc. China* **2014**, *24*, 3111–3117.
102. Yilbas, B. S.; Arif, A. F. M. Laser Shock Processing of Aluminium: Model and Experimental Study. *J. Phys. D Appl. Phys.* **2007**, *40*, 6740–6747.
103. Fang, Y.; Li, Y.; He, W.; Lu, Y.; Li, P. Numerical Simulation of Residual Stresses Fields of DD6 Blade during Laser Shock Processing. *Mater. Des.* **2013**, *43*, 170–176.
104. Lu, J. Z.; Luo, K. Y.; Zhang, L.; Zhong, J. W.; Cui, X. G.; Zhang, Y. K. Effect of Strain-Rate on the Fracture Morphology of LY2 Aluminum Alloy by Laser Shock Processing. *Key Eng. Mater.* **2011**, *464*, 677–680.
105. Nie, X.; Li, Y.; He, W.; Zhou, L. Optimization and Fracture Mechanism Analysis of TC17 Titanium Alloy Simulated-Blade with Two-Sided Laser Shock Processing. In *Proceedings of the International Congress Recent Advances in Structural Integrity Analysis-Proceedings of the International Congress*; Woodhead Publishing, UK, 2015.
106. Yilbas, B. S.; Arif, A. F. M.; Karatas, C. Laser Treatment of Silicon at Nitrogen Ambient: Thermal Stress Analysis. *Surf. Eng.* **2011**, *27*, 436–444.
107. Tenaglia, R. D.; Lahrman, D. E. Preventing Fatigue Failures with Laser Peening. *Amptiac Q.* **2003**, *7*, 3–7.
108. Rockstroh, T. J.; Bailey, M. S.; Ash, C. A.; Ulanski, W. Laser Shock Processing of Aircraft Engine Components. In *First International Conference on Laser Peening*, Houston-Texas, USA; 2008.
109. Prevéy, P. S. *The Effect of Cold Work on the Thermal Stability of Residual Compression in Surface Enhanced IN718*; Lambda Research: Cincinnati, OH, 2000.
110. Prevéy, P. S.; Shepard, M. J.; Smith, P. R. *The effect of Low Plasticity Burnishing (LPB) on the HCF Performance and FOD Resistance of Ti–6Al–4V*; Materials and Manufacturing Directorate, Air Force Research Lab: Wright-Patterson AFB, OH, 2001.
111. Nikitin, I.; Altenberger, I. Comparison of the Fatigue Behavior and Residual Stress Stability of Laser-Shock Peened and Deep Rolled Austenitic Stainless Steel AISI 304 in the Temperature Range 25–600 °C. *Mater. Sci. Eng. A* **2007**, *465*, 176–182.
112. Altenberger, I.; Nalla, R. K.; Sano, Y.; Wagner, L.; Ritchie, R. O. On the Effect of Deep-Rolling and Laser-Peening on the Stress-Controlled Low-and High-Cycle Fatigue Behavior of Ti–6Al–4V at Elevated Temperatures up to 550 °C. *Int. J. Fatigue* **2012**, *44*, 292–302.
113. Ren, N. F.; Yang, H. M.; Yuan, S. Q.; *et al.* High Temperature Mechanical Properties and Surface Fatigue Behavior Improving of Steel Alloy Via Laser Shock Peening. *Mater. Des.* **2014**, *53*, 452–456.
114. Ren, X. D.; Ruan, L.; Yuan, S. Q.; *et al.* Metallographic Structure Evolution of 6061-T651 Aluminum Alloy Processed by Laser Shock Peening: Effect of Tempering at the Elevated Temperatures. *Surf. Coat. Technol.* **2013**, *221*, 111–117.
115. Trdan, U.; Skarba, M.; Grum, J. Laser Shock Peening Effect on the Dislocation Transitions and Grain Refinement of Al–Mg–Si Alloy. *Mater. Charact.* **2014**, *97*, 57–68.
116. Chen, X.; Wang, J.; Fang, Y.; Madigan, B.; Xu, G.; Zhou, J. Investigation of Microstructures and Residual Stresses in Laser Peened Incoloy 800H Weldments. *Opt. Laser Technol.* **2014**, *57*, 159–164.
117. Gill, A.; Telang, A.; Mannava, S. R.; *et al.* Comparison of Mechanisms of Advanced Mechanical Surface Treatments in Nickel-Based Superalloy. *Mater. Sci. Eng. A* **2013**, *576*, 346–355.
118. Lu, J. Z.; Luo, K. Y.; Zhang, Y. K.; *et al.* Grain Refinement of LY2 Aluminum Alloy Induced by Ultra-high Plastic Strain during Multiple Laser Shock Processing Impacts. *Acta Mater.* **2010**, *58*, 3984–3994.
119. Jia, W.; Hong, Q.; Zhao, H.; Li, L.; Han, D. Effect of Laser Shock Peening on the Mechanical Properties of a Near-α Titanium Alloy. *Mater. Sci. Eng. A* **2014**, *606*, 354–359.
120. Ren, X. D.; Ruan, L.; Yuan, S. Q.; *et al.* Dislocation Polymorphism Transformation of 6061-T651 Aluminum Alloy Processed by Laser Shock Processing: Effect of Tempering at the Elevated Temperatures. *Mater. Sci. Eng. A* **2013**, *578*, 96–102.
121. Zhou, L.; Li, Y.; He, W.; *et al.* Deforming TC6 Titanium Alloys at Ultrahigh Strain Rates during Multiple Laser Shock Peening. *Mater. Sci. Eng. A* **2013**, *578*, 181–186.
122. Mishra, R. S.; Stolyarov, V. V.; Echer, C.; Valiev, R. Z.; Mukherjee, A. K. Mechanical Behavior and Superplasticity of a Severe Plastic Deformation Processed Nanocrystalline Ti–6Al–4V alloy. *Mater. Sci. Eng. A* **2001**, *298*, 44–50.
123. Qiao, H.; Zhao, J.; Zhang, G.; Gao, Y. Effects of Laser Peening on Microstructure and Residual Stress Evolution in Ti–45Al–2Cr–2Nb–2B Alloy. *Surf. Coat. Technol.* **2015**, *276*, 145–151.
124. Ye, C.; Suslov, S.; Fei, X.; Cheng, G. J. Bimodal Nanocrystallization of NiTi Shape Memory Alloy by Laser Shock Peening and Post-Deformation Annealing. *Acta Mater.* **2011**, *59*, 7219–7227.
125. Gill, A. S.; Telang, A.; Vasudevan, V. K. Characteristics of Surface Layers Formed on Inconel718 by Laser Shock Peening with and Without a Protective Coating. *J. Mater. Process. Technol.* **2015**, *225*, 463–472.
126. Zhang, Y. K.; Lu, J. Z.; Ren, X. D.; Yao, H. B.; Yao, H. X. Effect of Laser Shock Processing on the Mechanical Properties and Fatigue Lives of the Turbojet Engine Blades Manufactured by LY2 Aluminum Alloy. *Mater. Des.* **2009**, *30*, 1697–1703.
127. Zhang, L.; Lu, J. Z.; Zhang, Y. K.; *et al.* Effects of Different Shocked Paths on Fatigue Property of 7050-T7451 Aluminum Alloy during Two-Sided Laser Shock Processing. *Mater. Des.* **2011**, *32*, 480–486.
128. Srinivasan, S.; Garcia, D. B.; Gean, M. C.; Murthy, H.; Farris, T. N. Fretting Fatigue of Laser Shock Peened Ti–6Al–4V. *Tribol. Int.* **2009**, *42*, 1324–1329.
129. Gujba, A. K.; Medraj, M. Laser Peening Process and Its Impact on Materials Properties in Comparison with Shot Peening and Ultrasonic Impact Peening. *Materials* **2014**, *7*, 7925–7974.
130. Matthews, W. T. *The Effects of Shot and Laser Peening on Fatigue Life and Crack Growth in 2024 Aluminum Alloy and 4340 Steel*; National Aeronautics and Space Administration, Langley Research Center: Hampton, VA, 2001.
131. Hill, M.; Dewald, A.; Demma, A.; *et al.* Laser Peening Technology. *Adv. Mater. Process.* **2003**, *161*, 65–67.
132. Luong, H.; Hill, M. R. The Effects of Laser Peening and Shot Peening on High Cycle Fatigue in 7050-T7451 Aluminum Alloy. *Mater. Sci. Eng. A* **2010**, *527*, 699–707.
133. Xiong, Y.; He, T.; Guo, Z.; He, H.; Ren, F.; Volinsky, A. A. Effects of Laser Shock Processing on Surface Microstructure and Mechanical Properties of Ultrafine-Grained High Carbon Steel. *Mater. Sci. Eng. A* **2013**, *570*, 82–86.
134. Rubio-González, C.; Ocana, J. L.; Gomez-Rosas, G.; *et al.* Effect of Laser Shock Processing on Fatigue Crack Growth and Fracture Toughness of 6061-T6 Aluminum Alloy. *Mater. Sci. Eng. A* **2004**, *386*, 291–295.
135. Zhang, X. C.; Zhang, Y. K.; Lu, J. Z.; Xuan, F. Z.; Wang, Z. D.; Tu, S. T. Improvement of Fatigue Life of Ti–6Al–4V Alloy by Laser Shock Peening. *Mater. Sci. Eng. A* **2010**, *527*, 3411–3415.
136. Ganesh, P.; Sundar, R.; Kumar, H.; *et al.* Studies on Fatigue Life Enhancement of Pre-Fatigued Spring Steel Specimens Using Laser Shock Peening. *Mater. Des.* **2014**, *54*, 734–741.
137. Zhang, X. Q.; Chen, L. S.; Yu, X. L.; Zuo, L. S.; Yu, Z. H. O. U. Effect of Laser Shock Processing on Fatigue Life of Fastener Hole. *Trans. Nonferr. Metals Soc. China* **2014**, *24*, 969–974.
138. Xiong, Y.; He, T. T.; Ren, F. Z.; Li, P. Y.; Chen, L. F.; Volinsky, A. A. Microstructure Evolution and Microhardness of Ultrafine-Grained High Carbon Steel during Multiple Laser Shock Processing. *J. Iron Steel Res. Int.* **2015**, *22*, 55–59.
139. Hu, Y. X.; Yao, Z. Q.; Wang, F.; Hu, J. Study on Residual Stress of Laser Shock Processing Based on Numerical Simulation and Orthogonal Experimental Design. *Surf. Eng.* **2007**, *23*, 470–478.
140. Prakash, N. A.; Gnanamoorthy, R.; Kamaraj, M. Microstructural Evolution and Mechanical Properties of Oil Jet Peened Aluminium Alloy, AA6063-T6. *Mater. Des.* **2010**, *31*, 4066–4075.
141. Lu, J. Z.; Zhong, J. S.; Luo, K. Y.; *et al.* Strain Rate Correspondence of Fracture Surface Features and Tensile Properties in AISI304 Stainless Steel Under Different LSP Impact Time. *Surf. Coat. Technol.* **2013**, *221*, 88–93.
142. Chu, J. P.; Rigsbee, J. M.; Banaś, G.; Elsayed-Ali, H. E. Laser-Shock Processing Effects on Surface Microstructure and Mechanical Properties of Low Carbon Steel. *Mater. Sci. Eng. A* **1999**, *260*, 260–268.
143. Liucheng, Z.; Yinghong, L.; Weifeng, H.; Donglin, C.; Xiangfan, N. Effect of Multiple Laser Shock Processing on Microstructure and Mechanical Properties of Ti–5Al–4Mo–4Cr–2Sn–2Zr Titanium Alloy. *Rare Metal Mater. Eng.* **2014**, *43*, 1067–1072.

144. Chen, K.; Zheng, C.; Yuan, Z.; Lu, J.; Ren, X.; Luo, X. Deformation Microstructures of Austenitic Stainless Steel 2Cr13Mn9Ni4 Under Ultrafast Strain Rate by Laser Shock Processing. *Mater. Sci. Eng. A* **2013**, *587*, 244–249.
145. Schneider, M. S.; Kad, B.; Kalantar, D. H.; *et al.* Laser Shock Compression of Copper and Copper–aluminum Alloys. *Int. J. Impact Eng.* **2005**, *32* (1), 473–507.
146. Clauer, A. H.; Fairand, B. P.; Wilcox, B. A. Pulsed Laser Induced Deformation in an Fe-3 Wt Pct Si Alloy. *Metall. Trans. A* **1977**, *8*, 119–125.
147. Osetsky, Y. N.; Stoller, R. E.; Rodney, D.; Bacon, D. J. Atomic-Scale Details of Dislocation–Stacking Fault Tetrahedra Interaction. *Mater. Sci. Eng. A* **2005**, *400*, 370–373.
148. Xu, D. S.; Chang, J. P.; Li, J.; Yang, R.; Li, D.; Yip, S. Dislocation Slip or Deformation Twinning: Confining Pressure Makes a Difference. *Mater. Sci. Eng. A* **2004**, *387*, 840–844.
149. Ye, Y. X.; Feng, Y. Y.; Lian, Z. C.; Hua, Y. Q. Plastic Deformation Mechanism of Polycrystalline Copper Foil Shocked with Femtosecond Laser. *Appl. Surf. Sci.* **2014**, *309*, 240–249.
150. Ma, E. Eight Routes to Improve the Tensile Ductility of Bulk Nanostructured Metals and Alloys. *JOM* **2006**, *58*, 49–53.
151. Kumar, K. S.; Van Swygenhoven, H.; Suresh, S. Mechanical Behavior of Nanocrystalline Metals and Alloys. *Acta Mater.* **2003**, *51*, 5743–5774.
152. Youssef, K. M.; Scattergood, R. O.; Murty, K. L.; Koch, C. C. Nanocrystalline Al–Mg Alloy with Ultrahigh Strength and Good Ductility. *Scr. Mater.* **2006**, *54*, 251–256.
153. Valiev, R. Z.; Alexandrov, I. V.; Zhu, Y. T.; Lowe, T. C. Paradox of Strength and Ductility in Metals Processed by Severe Plastic Deformation. *J. Mater. Res.* **2002**, *17*, 5–8.
154. Koch, C. C.; Youssef, K. M.; Scattergood, R. O.; Murty, K. L. Breakthroughs in Optimization of Mechanical Properties of Nanostructured Metals and Alloys. *Adv. Eng. Mater.* **2005**, *7*, 787–794.
155. Wang, Z. W.; Wang, Y. B.; Liao, X. Z.; *et al.* Influence of Stacking Fault Energy on Deformation Mechanism and Dislocation Storage Capacity in Ultrafine-Grained Materials. *Scr. Mater.* **2009**, *60*, 52–55.
156. Zhao, Y. H.; Liao, X. Z.; Horita, Z.; Langdon, T. G.; Zhu, Y. T. Determining the Optimal Stacking Fault Energy for Achieving High Ductility in Ultrafine-Grained Cu–Zn Alloys. *Mater. Sci. Eng. A* **2008**, *493*, 123–129.
157. Zhao, Y. H.; Zhu, Y. T.; Liao, X. Z.; Horita, Z.; Langdon, T. G. Tailoring Stacking Fault Energy for High Ductility and High Strength in Ultrafine Grained Cu and its Alloy. *Appl. Phys. Lett.* **2006**, *89*, 121906.
158. Cao, Y.; Ahlström, J.; Karlsson, B. The Influence of Temperatures and Strain Rates on the Mechanical Behavior of Dual Phase Steel in Different Conditions. *J. Mater. Res. Technol.* **2015**, *4*, 68–74.
159. Xue, P.; Xiao, B. L.; Ma, Z. Y. High Tensile Ductility via Enhanced Strain Hardening in Ultrafine-Grained Cu. *Mater. Sci. Eng. A* **2012**, *532*, 106–110.
160. Pei, L.; Lu, C.; Tieu, K.; *et al.* Brittle versus Ductile Fracture Behaviour in Nanotwinned FCC Crystals. *Mater. Lett.* **2015**, *152*, 65–67.
161. Zhu, T.; Gao, H. Plastic Deformation Mechanism in Nanotwinned Metals: An Insight from Molecular Dynamics and Mechanistic Modeling. *Scr. Mater.* **2012**, *66*, 843–848.
162. Song, H. Y.; Sun, Y. Effect of Coherent twin Boundary and Stacking Fault on Deformation Behaviors of Copper Nanowires. *Comput. Mater. Sci.* **2015**, *104*, 46–51.
163. Sano, Y.; Obata, M.; Kubo, T.; *et al.* Retardation of Crack Initiation and Growth in Austenitic Stainless Steels by Laser Peening Without Protective Coating. *Mater. Sci. Eng. A* **2006**, *417*, 334–340.
164. Peyre, P.; Berthe, L.; Fabbro, R.; Braham, C.; Lédion, J. Corrosion Reactivity of Laser-Peened Steel Surfaces. *J. Mater. Eng. Perform.* **2000**, *9*, 656–662.
165. Kalainathan, S.; Sathyajith, S.; Swaroop, S. Effect of Laser Shot Peening Without Coating on the Surface Properties and Corrosion Behavior of 316L Steel. *Opt. Lasers Eng.* **2012**, *50*, 1740–1745.
166. Lu, J. Z.; Luo, K. Y.; Yang, D. K.; *et al.* Effects of Laser Peening on Stress Corrosion Cracking (SCC) of ANSI 304 Austenitic Stainless Steel. *Corros. Sci.* **2012**, *60*, 145–152.
167. Zhang, L.; Zhang, Y. K.; Lu, J. Z.; *et al.* Effects of Laser Shock Processing on Electrochemical Corrosion Resistance of ANSI 304 Stainless Steel Weldments After Cavitation Erosion. *Corros. Sci.* **2013**, *66*, 5–13.
168. Amar, H.; Vignal, V.; Krawiec, H.; *et al.* Influence of the Microstructure and Laser Shock Processing (LSP) on the Corrosion Behaviour of the AA2050-T8 Aluminium Alloy. *Corros. Sci.* **2011**, *53*, 3215–3221.
169. Davis, B. W.; Moran, P. J.; Natishan, P. M. Metastable Pitting Behavior of Aluminum Single Crystals. *Corros. Sci.* **2000**, *42*, 2187–2192.
170. Bugayev, A. A.; Gupta, M. C.; Orr, J.; Levesque, S.; Payne, R. Laser Shot Peening of Inconel 600 and Surface Morphology Characterization. In *Proceedings of Materials Research Society Symposium, MM2–4*, Vol. 830, Cambridge University Press, 2004; pp. 123–127.
171. Bugayev, A. A.; Gupta, M. C.; Payne, R. Laser Processing of Inconel 600 and Surface Structure. *Opt. Lasers Eng.* **2006**, *44*, 102–111.
172. Fard, S. B.; Guagliano, M. Effects of Surfaces Nanocrystallization Induced by Shot Peening on Material Properties: A Review. *Frattura ed Integrità Strutturale* **2009**, *7*, 3–16.
173. Hatamleh, O. A Comprehensive Investigation on the Effects of Laser and Shot Peening on Fatigue Crack Growth in Friction Stir Welded AA 2195 Joints. *Int. J. Fatigue* **2009**, *31*, 974–988.
174. Chen, X.; Wang, J.; Fang, Y.; Madigan, B.; Xu, G.; Zhou, J. Investigation of Microstructures and Residual Stresses in Laser Peened Incoloy 800H Weldments. *Opt. Laser Technol.* **2014**, *57*, 159–164.
175. Abdullah, A.; Malaki, M.; Eskandari, A. Strength Enhancement of the Welded Structures by Ultrasonic Peening. *Mater. Des.* **2012**, *38*, 7–18.
176. Hatamleh, O. Effects of Peening on Mechanical Properties in Friction Stir Welded 2195 Aluminum Alloy Joints. *Mater. Sci. Eng. A* **2008**, *492*, 168–176.
177. Ali, A.; An, X.; Rodopoulos, C. A.; *et al.* The Effect of Controlled Shot Peening on the Fatigue Behaviour of 2024-T3 Aluminium Friction Stir Welds. *Int. J. Fatigue* **2007**, *29*, 1531–1545.
178. Sano, Y.; Masaki, K.; Gushi, T.; Sano, T. Improvement in Fatigue Performance of Friction Stir Welded A6061-T6 Aluminum Alloy by Laser Peening Without Coating. *Mater. Des.* **2012**, *36*, 809–814.
179. Thomas, W. M.; Nicholas, E. D.; Needham, J. C.; Murch, M. G.; Temple-Smith, P.; Dawes, C. J. International Patent Application PCT/GB92/02203 and GB Patent Application 9125978.8. UK Patent Office, London, December 6, 1991.
180. Pao, P. S.; Gill, S. J.; Feng, C. R.; Sankaran, K. K. Corrosion–fatigue Crack Growth in Friction Stir Welded Al 7050. *Scr. Mater.* **2001**, *45*, 605–612.
181. Zhang, Y.; Lu, J.; Luo, K. *Laser Shock Processing of FCC Metals: Mechanical Properties and Micro-Structural Strengthening Mechanism*; Springer Science & Business Media, Springer-Verlag: Berlin; Heidelberg, 2013.
182. Iordachescu, M.; Valiente, A.; Caballero, L.; Iordachescu, D.; Ocana, J. L.; Porro, J. A. Laser Shock Processing Influence on Local Properties and Overall Tensile Behavior of Friction Stir Welded Joints. *Surf. Coat. Technol.* **2012**, *206*, 2422–2429.
183. Zhou, Z.; Gill, A. S.; Qian, D.; *et al.* A Finite Element Study of Thermal Relaxation of Residual Stress in Laser Shock Peened IN718 Superalloy. *Int. J. Impact Eng.* **2011**, *38*, 590–596.
184. Chahardehi, A.; Brennan, F. P.; Steuwer, A. The Effect of Residual Stresses Arising from Laser Shock Peening on Fatigue Crack Growth. *Eng. Fract. Mech.* **2010**, *77*, 2033–2039.
185. Kim, J. C.; Cheong, S. K.; Noguchi, H. Residual Stress Relaxation and Low- and High-Cycle Fatigue Behavior of Shot-Peened Medium-Carbon Steel. *Int. J. Fatigue* **2013**, *56*, 114–122.
186. Vázquez, J.; Navarro, C.; Domínguez, J. Experimental Results in Fretting Fatigue with Shot and Laser Peened Al 7075-T651 Specimens. *Int. J. Fatigue* **2012**, *40*, 143–153.
187. Laamouri, A.; Sidhom, H.; Braham, C. Evaluation of Residual Stress Relaxation and Its Effect on Fatigue Strength of AISI 316L Stainless Steel Ground Surfaces: Experimental and Numerical Approaches. *Int. J. Fatigue* **2013**, *48*, 109–121.
188. Lee, H.; Mall, S. Stress Relaxation Behavior of Shot-Peened Ti–6Al–4V Under Fretting Fatigue at Elevated Temperature. *Mater. Sci. Eng. A* **2004**, *366*, 412–420.
189. Buchanan, D. J.; John, R.; Brockman, R. A. Relaxation of Shot-Peened Residual Stresses Under Creep Loading. *J. Eng. Mater. Technol.* **2009**, *131*, 031008.
190. Holzapfel, H.; Schulze, V.; Vöhringer, O.; Macherauch, E. Residual Stress Relaxation in an AISI 4140 Steel due to Quasistatic and Cyclic Loading at Higher Temperatures. *Mater. Sci. Eng. A* **1998**, *248*, 9–18.
191. Cao, W.; Khadhraoui, M.; Brenier, B.; Guédou, J. Y.; Castex, L. Thermomechanical Relaxation of Residual Stress in Shot Peened Nickel Base Superalloy. *Mater. Sci. Technol.* **1994**, *10*, 947–954.
192. Hussain, K. Monotonic and Cyclic Stress–Strain Behaviour of a High Strenght Steel. *Metall. Sci. Technol.* **1993**, *11*, 2–30.
193. Kodama, S. The Behavior of Residual Stress during Fatigue Stress Cycles. In *Proceedings of the International Conference on Mechanical Behavior of Metals II*, Vol. 2, Kyoto, Society of Material Science, 1972; pp. 111–118.
194. Kodama, S., The Behaviour of Residual Stress during Fatigue Stress Cycles. In *Proceedings of the International Conference on Mechanical Behaviour of Materials*, Kyoto, 1971; pp. 337–339.

195. Dalaei, K.; Karlsson, B.; Svensson, L. E. Stability of Shot Peening Induced Residual Stresses and their Influence on Fatigue Lifetime. *Mater. Sci. Eng. A* **2011**, *528*, 1008–1015.
196. ASM. *Materials Properties Database Committee, ASM Ready Reference: Properties and Units for Engineering Alloys*; ASM International: Materials Park, OH, 1997.
197. Quadfasel, U.; Mecking, H.; Estrin, Y. Continuous and Cyclic Stress Relaxation in Aluminium. *Mater. Sci. Eng. A* **1991**, *149*, 29–39.
198. Hart, E. W.; Solomon, H. D. Load Relaxation Studies of Polycrystalline High Purity Aluminium. *Acta Metall.* **1973**, *21*, 295–307.
199. Meguid, S. A.; Shagal, G.; Stranart, J. C. 3D FE Analysis of Peening of Strain-rate Sensitive Materials Using Multiple Impingement Model. *Int. J. Impact Eng.* **2002**, *27*, 119–134.
200. Ochi, Y.; Masaki, K.; Matsumura, T.; Sekino, T. Effect of Shot-Peening Treatment on High Cycle Fatigue Property of Ductile Cast Iron. *Int. J. Fatigue* **2001**, *23*, 441–448.
201. De Los Rios, E. R.; Walley, A.; Milan, M. T.; Hammersley, G. Fatigue Crack Initiation and Propagation on Shot-Peened Surfaces in A316 Stainless Steel. *Int. J. Fatigue* **1995**, *17*, 493–499.
202. Sridhar, B. R.; Nafde, W. G.; Padmanabhan, K. A. Effect of Shot Peening on the Residual Stress Distribution in Two Commercial Titanium Alloys. *J. Mater. Sci.* **1992**, *27*, 5783–5788.
203. Torres, M. A. S.; Voorwald, H. J. C. An Evaluation of Shot Peening, Residual Stress and Stress Relaxation on the Fatigue Life of AISI 4340 Steel. *Int. J. Fatigue* **2002**, *24*, 877–886.
204. Luan, W.; Jiang, C.; Ji, V. Residual Stress Relaxation in Shot Peened Surface Layer on TiB2/Al Composite under Applied Loading. *Mater. Trans.* **2009**, *50*, 158–160.
205. Miyashita, D.; Takeda, K.; Ohya, S. I.; Sano, Y.; Saito, T.; Akita, K. Relaxation Behaviour of Laser Peening Residual Stress due to Mechanical Loading on Aluminum Alloy. *J. Soc. Mater. Sci.* **2011**, *60*, 617–623.
206. Zhou, Z.; Bhamare, S.; Ramakrishnan, G.; *et al.* Thermal Relaxation of Residual Stress in Laser Shock Peened Ti–6Al–4V Alloy. *Surf. Coat. Technol.* **2012**, *206*, 4619–4627.
207. Lee, H.; Jin, O.; Mall, S. Fretting Fatigue Behaviour of Shot-Peened Ti–6Al–4V at Room and Elevated Temperatures. *Fatigue Fract. Eng. Mater. Struct.* **2003**, *26*, 778.
208. Peyre, P.; Fabbro, R.; Merrien, P.; Lieurade, H. P. Laser Shock Processing of Aluminium Alloys. Application to High Cycle Fatigue Behaviour. *Mater. Sci. Eng. A* **1996**, *210*, 102–113.
209. Prevey, P.; Hornbach, D.; Mason, P., Thermal Residual Stress Relaxation and Distortion in Surface Enhanced Gas Turbine Engine Components. In *Proceedings of the 17th Heat Treating Society Conference and Exposition and the 1st International Induction Heat Treating Symposium*; Milam, D.L.M.; Poteet, D.A., Jr., Pfaffmann, G.D.; Rudnev, V.; Muehlbauer, A., Albert, W.B., Eds; ASM Materials: Materials Park, OH; 1998; pp. 3–12.
210. Aghdam, A. B.; Chakherlou, T. N.; Saeedi, K.; An, F. E. Analysis for Assessing the Effect of Short-Term Exposure to Elevated Temperature on Residual Stresses Around Cold Expanded Fastener Holes in Aluminum Alloy 7075-T6. *Mater. Des.* **2010**, *31*, 500–507.
211. Wang, Z.; Chen, Y.; Jiang, C. Thermal Relaxation Behavior of Residual Stress in Laser Hardened 17-4PH Steel After Shot Peening Treatment. *Appl. Surf. Sci.* **2011**, *257*, 9830–9835.
212. Fu, P.; Jiang, C. Residual Stress Relaxation and Micro-Structural Development of the Surface Layer of 18CrNiMo7-6 Steel After Shot Peening during Isothermal Annealing. *Mater. Des.* **2014**, *56*, 1034–1038.
213. Xiong, Y.; He, T. T.; Ren, F. Z.; Li, P. Y.; Chen, L. F.; Volinsky, A. A. Microstructure Evolution and Microhardness of Ultrafine-Grained High Carbon Steel during Multiple Laser Shock Processing. *J. Iron Steel Res., Int.* **2015**, *22*, 55–59.
214. Fu, J.; Zhu, Y.; Zheng, C.; Liu, R.; Ji, Z. Effect of Laser Shock Peening on Mechanical Properties of Zr-Based Bulk Metallic Glass. *Appl. Surf. Sci.* **2014**, *313*, 692–697.
215. Kamkarrad, H.; Narayanswamy, S.; Tao, X. S. Feasibility Study of High-repetition Rate Laser Shock Peening of Biodegradable Magnesium Alloys. *Int. J. Adv. Manuf. Technol.* **2014**, *74*, 1237–1245.
216. Sealy, M. P.; Guo, Y. B. Surface Integrity and Process Mechanics of Laser Shock Peening of Novel Biodegradable Magnesium–Calcium (Mg–Ca) Alloy. *J. Mech. Behav. Biomed. Mater.* **2010**, *3*, 488–496.
217. Kong, D. J.; Long, D.; Wu, Y. Z.; Zhou, C. Z. Effects of Laser Shock Processing on Stress Corrosion of X80 Pipeline Steel Welded joInts. *J. Build. Mater.* **2012**, *15*, 484.
218. Chen, X.; Fang, Y.; Zhang, S.; Kelleher, J. F.; Zhou, J. Effects of LSP on Micro-Structures and Residual Stresses in a 4 mm CLAM Steel Weld Joints. *Fusion Eng. and Des.* **2015**, *94*, 54–60.
219. Zhang, Y.; Zhang, L.; Luo, K.; *et al.* Effects of Laser Shock Processing on Mechanical Properties of Laser Welded ANSI 304 Stainless Steel Joint. *Chin. J. Mech. Eng.* **2012**, *25*, 285–292.
220. Zhang, Y.; Ren, X.; Zhou, J. Z.; Lu, J. Z.; Zhou, L. C. Investigation of the Stress Intensity Factor Changing on the Hole Crack Subject to Laser Shock Processing. *Mater. Des.* **2009**, *30*, 2769–2773.

1.15 Micro Plastic Part Filling Capabilities through Simulation and Experiment: A Case Study on Micro Gear Shape

M Azuddin, University of Malaya, Kuala Lumpur, Malaysia
Z Taha, University Malaysia Pahang, Pekan, Malaysia
IA Choudhury, University of Malaya, Kuala Lumpur, Malaysia

© 2017 Elsevier Inc. All rights reserved.

1.15.1 Introduction 442
1.15.2 Micro Plastic Injection Molding 442
1.15.2.1 Machine for Micro Injection Molding 443
1.15.2.2 Flow Observation 444
1.15.2.3 Flow Model 444
1.15.2.3.1 Macro flow model 444
1.15.2.3.2 Micro flow model 444
1.15.2.3.3 Macro – micro flow model 445
1.15.2.3.4 Viscosity model 445
1.15.2.3.5 Viscosity for micro injection molding 446
1.15.2.4 Factors Affecting Micro Injection Molding 446
1.15.2.4.1 Temperature 446
1.15.2.4.2 Pressure 446
1.15.2.4.3 Micro flow model factors 447
1.15.2.4.4 Size 447
1.15.2.4.5 Viscosity in micro molding 447
1.15.2.5 Summary of Literature Reviews 447
1.15.3 Custom-Made Vertical Injection Molding Machine 447
1.15.3.1 Plasticizing Unit and Injection Mechanism 447
1.15.3.2 Injection Mechanism 448
1.15.3.3 Mold Design 448
1.15.4 Study of Straight, Reverse 'T' and Cross '+' Micro Channel Flow 448
1.15.4.1 Mathematical Flow Model 449
1.15.4.1.1 MoldFlow flow model 450
1.15.4.1.2 ANSYS CFX flow model 450
1.15.4.1.3 Suggestion non-Newtonian viscosity model 451
1.15.4.2 Micro Channel Fabrication and Experimental Design 451
1.15.4.2.1 Micro channels mold fabrication 451
1.15.4.2.2 Experimental design 452
1.15.4.3 Experiments and Simulation for Straight Channel 452
1.15.4.3.1 0.8 mm straight micro channel 452
1.15.4.3.2 Discussion on straight micro channel 452
1.15.4.3.3 Modified cross viscosity model for straight micro channels 454
1.15.4.4 Experiments and Simulation for Reverse 'T' Shape Micro Channel 454
1.15.4.4.1 M05 ⊥ S05 reverse 'T' micro channel 454
1.15.4.4.2 Discussion on reverse 'T' micro channel 454
1.15.4.4.3 Modified cross viscosity model for reverse 'T' micro channels 455
1.15.4.5 Experiments and Simulation for Cross '+' Micro Channel 455
1.15.4.5.1 M08+S05 cross '+' micro channel 456
1.15.4.5.2 Discussion on cross '+' micro channel 456
1.15.4.5.3 Modified cross viscosity model for cross '+' micro channel 457
1.15.5 Study on Macro and Micro Gear Shape Molding 457
1.15.5.1 Macro Gear Shape 458
1.15.5.2 Micro Gear Shape 461
1.15.5.2.1 Gear shape with 1.0 mm teeth 461
1.15.5.2.2 Gear shape with 0.5 mm teeth 461
1.15.5.2.3 Gear shape with 0.3 mm teeth 462
1.15.6 Conclusions 463
References 463
Relevant Websites 465

List of Symbols and Abbreviations

a micro channel radius
a numerical parameter
A_i constants in Moldflow second order model
A rate constant
b_i data-fitted coefficients
B viscosity model fitting constants
c constant
c_P heat capacity, j kg^{-1} K^{-1}
C constant
C_i viscosity model fitting constants
C_P specific heat of material
d_o original distance
D_i constants
D an external characteristic length
h average value defined in equation
h_a heat transfer coefficients of air
h_t the heat transfer coefficient
h_w heat transfer coefficients of mold wall
k constant
k thermal conductivity, W m^{-1} K^{-1}
k_m the thermal conductivity of the plastic melt
m constants in power law model
m mass, kg
M_α interfacial force acting on phase α due to presence of other phase
n constants in power law index
P pressure, MPa
P_a pressure of gas/air, kN m^{-2} or kPa
P_o pressure at point O, MPa
P_{total} total pressure, MPa
P_{static} static pressure, MPa
Q flow rate
R universal gas constant, Nm kgK^{-1}
r radius along the radial direction
S_o the filling length. At the instant of time
s length along the channel direction
S_E Energy source, kg m^{-1} k^{-3}
S_M Momentum source, kg m^{-2} K^{-2}
$S_{M\alpha}$ momentum source due to body source
$S_{MS\alpha}$ user specified mass sources
t time, sec
t^i discrete time domain
T temperature, Kelvin
T_W temperature of the mold wall, K
T_s mean temperature, K
T_m melt temperature, K
v Velocity, m s^{-1}
v_s velocity along the micro channel, m s^{-1}
V volume, m^3
V_0 specific volume at zero gage pressure
X direction in the thickness of the main cavity
γ_o distance from the flow front to the point o

Greek letter

η viscosity, Pa s (N s m^{-2})
η_0 viscosity at zero shear rate, Pa s (N s m^{-2})
η_∞ the viscosity at infinite shear rate
η_b the macroscopic viscosity
λ time constant
$\dot{\gamma}$ Shear rate, (s^{-1})
ξ nondimensional constant
ρ density, kilogram per cubic meter, kg m^{-3}
e Specific total energy, kJ kg^{-1}
υ specific volume, m^3
τ Shear stress, N m^{-2}
μ Dynamic viscosity, kg m^{-1} s
α the thermal diffusivity (m^2 s^{-1}),
β subscript to indicate that the quantity applied to air
τ^* Tau, Pa
ω Thermal expansion coefficient, K^{-1}
Γ Diffusivity, (s^{-1})
$\Gamma_{\alpha\beta}$ mass flow rate per unit volume from α phase to β phase

1.15.1 Introduction

Injection molding is one of widely used plastic processing techniques for the plastic products manufacture. It is well suited for mass production because the raw material conversion into a final product usually requires only a single operation. Moreover, minor or no finishing process is required. The process is capable of producing very complicated part geometries with tight specifications. Due to high productivity and flexibility, injection molding applications have grown rapidly in various industries. The process starts with applying heat to solid plastic material, changing solid plastic to liquid state and delivering with high velocity into mold cavity through injection mechanism. As the high injection speed is applied to plastic melt, flow front will pass through runner, gate, and finally flow into the mold cavity. High injection pressure used to compensate the plastic shrinkage and ensuring complete mold cavity filling. This phase is called filling phase, where a plastic melt fills an empty mold cavity. During the filling phase, hot plastic melt makes contact with the wall, and a solidified layer occurs on the mold wall. Once the mold cavity is filled, plastic melt is cooled and the packing phase takes place. The heat is conducted from plastic melt to the mold and then to the cooling line, where the heat transfer is by convection through the coolant circulation. Solidified part is ejected from the mold as soon as the plastic has sufficiently solidified and the cycle repeats. Injection-molded parts are commonly used in automotive, hydraulics, pneumatics, aerospace, packaging, home appliances, optics, medical, electronics, telecommunication, and toy manufacturing.

1.15.2 Micro Plastic Injection Molding

With the recent development in micro engineering technologies there is an increasing demand toward product

miniaturization. Micro part fabrication is an important issue in broadening the use of injection molding. Micro injection molding is one of the important technologies for micro manufacture because of large production quantities, high accuracy, and low production cost. This technology will bring improvements in complexity, reliability, efficiency, and lead to advanced applications in various engineering fields. Micro molding parts accelerate the rapid development of mechanical, electronic, automobile, medical applications, and also have great potential in MEMS sectors.

The micro injection molding is not simply a scaling down of the conventional injection process, rather it requires some radical changes in methods and practices. The capabilities of this process have to be studied consistently in order to identify the process constraints. In micro molding, the ability for the plastic melt to flow into the micro component is a crucial factor for successful molding. It depends greatly on their size, aspect ratio, and cavity surface quality. The travel distance of the plastic melt into the micro structure also depends on the flow rate, which is a function of the geometric dimensions. Micro part has high surface-to-volume ratio which makes the plastic melt fill freeze or solidifies much faster compared with conventional injection molding and leads to an incomplete filling. The achievable aspect ratios and high surface quality also constitute a major fabrication constraint in applying injection molding in a range of microscale applications. The precision requirements for micro plastic parts are around micron and the surface roughness requirements may exceed submicron. To improve the micro molded quality, many research groups investigated different factors that affect micro injection molding process. In particular, these include works in process optimization, material rheology, numerical simulation, and tooling technologies.

The micro injection molding is a material processing technique to produce microscale plastic components.[1] Micro molding is a subset of injection molding process, where a plastic melt is forced into micro cavity, allowed to cool and then removed. Micro injection molding is attracting more attention and showing great commercial potential nowadays.[2] Recent advances in microtechnology are devices with a huge range of applications in the sensors, medical equipment, telecommunications, biomedical, and automotive sectors. Many micro devices, such as micro heat exchangers,[3] biochips,[4] and optical elements[5] have been successfully produced by injection molding.

Micro molding implies that parts produced have various types of parameters on the micron scale, but the term has taken on a relatively liberal definition. There are several definitions for a micro injection-molded parts. Kukla *et al.*[6] defined the micro plastic parts as:

1. Micro weight, parts with few milligrams masses, but not necessarily the size in micrometer scale.
2. Micro structured regions, part with local micro-features.
3. Micro precision dimensions, part size tolerances in the range of micrometer.

1.15.2.1 Machine for Micro Injection Molding

The machine used to mold plastic part can be classified according to their type, tonnage capacity, barrel size, maximum temperature, maximum injection pressure, and overall size. The common machines classifications are horizontal and vertical injection molding machine. There are also machine used for specific application such as rotary injection molding and two color component molding.

The development of molding machines for micro parts fabrications have always been a challenge for machine fabricator. Although, it uses a heating and pressure devices, researchers still are working to find out the best method to fabricate a micro plastic part. Currently, many researchers used Battenfeld Microsystem 50 in their studies on micro plastic part fabrication.[7,8] Other than Battenfeld Microsystem 50, there are few injections molding machines available in the market with capability to produce complex plastic parts. Giboz *et al.*[9] listed the machines that are capable of producing micro plastic parts.

Currently, many researchers introduce their ideas to control, monitor, and even fabricate new machine to make it more fascinating. Processing plastic for microtechnology applications requires high precision process and injection dynamics. Producing plastic part with small production volume does not require expensive machine. Therefore a low cost machine with capability to produce same part quality is more preferable. By using basic principles of plastic injection molding, researchers designed and fabricated their own machine for specific plastic part fabrications. This was due to higher price of commercial micro injection molding machines available in the market.

Michaeli and Spennemann[10] and Michaeli *et al.*[11] had developed an injection molding machine with two stage plungers to analyze the molding properties of micro parts. The injection plunger diameter was 2.0 mm, while the plasticizing plunger had a 5.0 mm diameter. The shot size was 0.01 g at each time and used CO_2 liquid for mold cooling. Spennemann[12] also fabricated a micro injection molding machine for smallest plastic volume. Chang *et al.*[13] developed an external module for thermoplastic molding. The system consisted of two modules; hot runner plunger-type and reciprocating screw-type. From the experimental analysis, performance of the external molding module was comparable with the two stage screw–plunger injection molding machine.

Huang[14] molded the nano-features using a custom-made injection machine. This machine consisted of clamping, melting, and injection units. The clamping unit moved forward and backward using hydraulic press device. The melt unit with hot runner heaters provided energy for the plastic melting. Injection unit consisted of 2.0 mm injection plunger and hydraulic piston, which was used to deliver the plastic melt into the cavity. The maximum recorded injection pressure and shot were 0.7 MPa and 120 mm^3, respectively. The maximum allowed mold and melt temperature were 200–300 °C. With the same machine, Huang[15] investigated the plastic part moldability with nano-ceramic added materials. In the investigation, parts with micro-features have been successfully molded.

Another micro molding machine used to produce micro parts was developed by Quadrini *et al.*[16] This machine was capable of molding three different plastic materials: HDPE, PS, and ABS. Yang *et al.*[17] designed and fabricated a hot runner micro injection molding module and installed in an injection molding machine reciprocating screw device. The performance

of this module was tested with two stage reciprocating screw- and plunger-type micro injection molding machine.

1.15.2.2 Flow Observation

The observation in plastic melt flow can be divided into two categories, during melt flow and after it solidifies. The plastic flow behavior inside mold cavity during filling phase is necessary for earlier quality prediction of molded plastic parts. Ability to monitor and control plastic flow will benefit in designing a mold cavity for complex plastic shapes. There are lots of works done on investigating the plastic flow behavior inside the mold cavity during filling phase.[18] The transparent inserts are embedded into the mold and the moving melt inside the cavity can be observed.[19–21] This method required usage of optical elements and a high speed camera to capture the fast cavity filling. Dvorak *et al.*[22] fabricated a mold with clear glass window for observing the melt flow during injection phase for ceramic injection molding process. An injection molding experiment was conducted to monitor the filling behavior. They also studied the gate size effect and jetting problem with various injection process parameters. Liu and Wu[23] studied the phenomenon of filling-assisted injection molding techniques using fluid dynamics visualization. A thick glass was mounted on the mold base for melt flow visualization. A high speed video camera was used to record the rectangular cavities filling phenomena with different channel geometries.

Yang and Yokoi[24] demonstrated a flow behavior in plastic sandwich molding using dynamic visualization technique. The setup of visualization experiment included 'glass-inserted mold' and in-line high speed camera in the cavity flow. Sato and Yokoi[25] also developed a mold visualization technique with a glass-inserted structure which enabled plastic melt observation behavior inside the cavity along its thickness direction. The visualization window was made from quartz glass for high durability. The melt front profile and surface behavior were observed using a high speed video system and then analyzed with image processing software.

Yokoi *et al.*[26] developed a system which can dynamically measure the flow front position. The system allowed flow front speed measurement at velocities up to 350 mm s^{-1}. The high speed video camera was attached in the driving unit which moved together. In addition to flow marks problem, the system was also capable to capture pictures of the silver streaks formation for the first time. The results of system can be used as a tool for exploring fountain flow formation and detection of molding defects.

Video camcorder with 25 fps capabilities was used by Özdemir *et al.*[27] to record the flow behavior of melt thermoplastic materials. The captured images were transformed to photo capture program for analysis. With same molding parameters, melt flow front profile results were compared with those of analysis software. Although the experiment melt front profiles were similar to the Moldflow results, but the filling times were different. Bociga and Jaruga[18] observed the cavity filling by looking at a specially created flow lines pattern. The flow lines can be used to diagnose the problems during cavity filling. The molded part surface was observed in reflected light using the optical microscope. The experimental results were comparable with Moldflow plastics insight analysis software.

1.15.2.3 Flow Model

1.15.2.3.1 Macro flow model

Improving the knowledge of injection molding technology by trial and error method to produce high quality parts is no longer viable. Many researchers have successfully developed various mathematical models to predict the flow and correct any problems even before actual part being molded. This approach has led to improvements and innovations in molded part quality. Since early nineteenth century, the governing equations of conventional flow for a viscous fluid were developed based on three equations[28]:

1. The continuity equation, plastic deformation accompanying the flow during the filling process while mass is conserved.
2. The equations of momentum, Newton's second law derived momentum (acceleration condition) or the balance of force generated by the plastic flow.
3. The energy equation, which is a system of energy conservation and the law of conservation of flow material in an incompressible fluid.

The basic form of the equations remained unchanged and researchers have been modeling the melt flow for specific needs and solving techniques. This is done by including nonlinearity aspects such as heat transfer, compressibility, scaling effect, rheological, and non-Newtonian characteristics. Hele-Shaw flow formulation originated from simplified creeping-flow lubrication model merged the continuity and momentum equations into a single Poisson-like equation in pressure and fluidity terms. Even though the equations and geometry has been simplified, the Hele-Shaw flow model is successfully applied to the nonelastic liquid, non-Newtonian with non-isothermal conditions in conventional injection molding.

Since then, many researchers modeled the plastic flow based on Hele-Shaw flow approximation. For 30 years, the CAE software for mold cavity filling has been developed based on Hele-Shaw model.[29–31] However, the Hele-Shaw model also has some limitations. It cannot capture physical phenomena when simplifying the equations.[32] In addition, this approach is not capable of representing regions with complex kinematics flow front. A simpler version of this phenomenon is addressed by many researchers through experimental, analytical, and numerical methods. This leads to a model of basic flow kinematics without solving the complex three dimensional (3D) flows.

1.15.2.3.2 Micro flow model

Shen *et al.*[33] and Huang *et al.*[34] stated that the CAE packages have become an accepted tool in mold design. Prediction of micro flow using numerical simulation also received an interest among researchers.[1,33,35–39] The generalized Hele-Shaw flow model proposed by Hieber and Shen[40] simplified the equations for non-isothermal viscous fluid as used by most injection molding analysis software. This model is considered

fully developed, but compressibility, inertia and gap-wise distance is ignored for plastic melt flow in thin cavities. As a result, 3D flow regions cannot be used in Hele-Shaw model. Therefore, only the 3D analyses based on Naiver–Stokes equations are capable to simulate the real situations.[33,34]

1.15.2.3.3 Macro – micro flow model

The plastic melts traveling from macro to micro size is an interesting area to discover. It is not as simple as reducing the plastic melt size to micro, but other factors such as viscosity and friction on the wall will have a significant effect. Feigl and Tanner[40] developed and evaluated micro–macro algorithm for the plastic melt flow. The model employed momentum and mass conservation equations for continuum mechanics, including the plastic stress microscopic-based rheological model. For a macro algorithm, velocity, and pressure fields were generated by solving mass and momentum equations using the finite elements method (FEM). In the micro part algorithm, the updated velocity field was used to compute and update the plastic stress from rheological model.

A fully implicit time integration scheme was carried out for solving time-dependent micro–macro viscoelastic flow using brown fields configuration. Plastic melts micro–macro simulations of momentum and mass conservation equations at macroscopic level using differential equation was presented by Jourdain *et al.*[41] The equations were discretized by a FEM coupled with a Monte Carlo method. The solution method was applicable for a one dimensional (1D), and might be applied to two dimentional (2D), and 3D cases.

1.15.2.3.4 Viscosity model

The viscosity model represents the plastic melt behavior. Using suitable viscosity model, reliable results of injection molding numerical simulation can be achieved. Koszkul and Nabialek[42] presented viscosity functions for modeling an injection molding process. Common viscosity functions available are:

1. Power law models.
2. Moldflow second order model.
3. Cross viscosity model.
4. Carreau viscosity model.
5. Castro Macosko viscosity.
6. Carreau–Yasuda viscosity model.
7. Cross-Exponential Macosko viscosity model.

The well-known Power law model also is given by

$$\eta = m\dot{\gamma}^{n-1} \qquad [1]$$

When $m=\mu$ and $n=1$ the relationship for a Newtonian fluid is obtained. For plastic melts, the constant n lies between 0 and 1. Taking natural logarithms of both sides,

$$\ln\eta = (n-1)\ln(\dot{\gamma}) + \ln(m) \qquad [2]$$

Temperature dependence is usually included by multiplying eqn [1] by an exponential term. That is,

$$\eta = m\dot{\gamma}^{n-1}(\exp cT) \qquad [3]$$

Equation [3] is the first order viscosity model available in Moldflow flow analysis software. The Moldflow second order model is given by

$$\ln\eta = A_0 + A_1\ln\dot{\gamma} + A_2T + A_3(\ln\dot{\gamma})^2 + A_4T\ln\dot{\gamma} + A_5T^2 \qquad [4]$$

The first and second order MoldFlow models were based on empirical observations. The first order model fits experimental data and the second order model is able to characterize the plastic melts behavior.

The cross viscosity model is

$$\eta = \frac{\eta_0}{1+(\lambda\dot{\gamma})^n} \qquad [5]$$

The η_0, can be modeled using the widely accepted seven-constant cross model where

$$\eta_0 = D_1\exp - \left\{\frac{A_1[T-(D_2+D_3p)]}{\tilde{A}_2 + D_3p + [T-(D_2+D_3p)]}\right\} \qquad [6]$$

Another viscosity model, Carreau viscosity model is define as

$$\frac{\eta-\eta_\infty}{\eta_0-\eta_\infty} = \left[1+(\lambda\dot{\gamma})^2\right]^{(n-1)/2} \qquad [7]$$

Anturkar[42] used a Petrov–Galerkin finite element method for computing flow front position, velocity, pressure, and temperature distributions during mold filling with adoption of Castro Macosko viscosity function. A good agreement was found between the numerical and experimental results in the flow front region. The Castro Macosko viscosity function which depend on the temperature is given by

$$\eta(X,T) = \eta(X)\cdot\eta(T) = A_\eta\exp\left(\frac{E_\eta}{RT}\right)\left(\frac{X_g}{X_g-X}\right)^{(A+BX)} \qquad [8]$$

Chen *et al.*[29] used a modified cross model with Arrhenius temperature dependence as viscosity function incorporating numerical algorithm to simulate the filling stage of injection-compression molding process. Modified cross model with Arrhenius temperature dependence viscosity function represent a non-Newtonian characteristics of plastic melt viscosity[43]:

$$\eta(X,\gamma) = \frac{\eta_0(T)}{1+(\eta_0\gamma/\tau^*)^{1-n}} \quad \text{with} \quad \eta_0(T) = B\exp\left(\frac{T_b}{T}\right) \qquad [9]$$

This flow model was based on Marrucci–Greco–Lanniruberto model with the effects of viscoelasticity. The Carreau–Yasuda viscosity model or generalized Newtonian models based only on shear-thinning behavior without elastic properties were developed by Bird *et al.*[44] the viscosity model is given by

$$\eta = \eta_0(1+[\lambda I_2]^a)^{(n-1)/a} \qquad [10]$$

where I_2 is the second invariant of the rate-of-strain tensor $d=(\kappa+\kappa^T)/2$. Moon *et al.*[44] performed 3D-numerical simulations to study the flow characteristics during the injection molding of die stacked package using cross-exponential Macosko

viscosity model. The cross-exponential Macosko viscosity model is for the non-Newtonian viscosity behavior of the plastic melt and described by following equation

$$\eta = \frac{\eta_0(T)}{1+\left(\frac{\eta_0(T)\dot{\gamma}}{\tau^*}\right)^{1-n}} \cdot \left(\frac{\alpha_g}{\alpha_g-\alpha}\right)^{(C_1+C_2)} \quad \text{with} \quad \eta_0(T) = B\exp\left(\frac{T_b}{T}\right) \qquad [11]$$

This simulation showed that the increased mold gap clearance and a decrease in melt viscosity can help achieve a more uniform flow front.

1.15.2.3.5 Viscosity for micro injection molding

Xu *et al.*[45] and Rosenbaum and Hatzikiriakos,[46] reported that the micro flow behavior was opposed to the macro flow. The viscosity increased as the channel size decreased below the 10 μm. Plastic melt slipped over the wall as the channel size dropped below 1 μm. From micro-features experiments and numerical simulations done by Yu *et al.*[47] the microscale geometry and surface tension had a significant influence on the melt flow. Cavity surface roughness, wall slip or even the heat transfer behavior in microscale were another characteristics that might have influence. Young[1] analyzed a filling distance in cylindrical micro-features without considering viscosity and wall slip effect on the channel. Griffiths *et al.*[7] explained the melt temperature and injection speed effects on viscosity in micro injection molding. Increasing the melt temperature improved the plastic flow by reduction of viscosity. A high injection speed can improve the filling of micro cavities by delaying the premature freezing in thin walled sections. This effect can reduce the viscosity of the material and help in the filling process.

Su *et al.*[39] used an analytical solution to investigate the impact of microscale phenomena in the wall slip and surface tension during micro channels filling. They simulated the micro channels filling process for polymeric materials using the viscosity model proposed by Eringen and Okada.[48] The viscosity model introduced a nonlocal continuum theory with the molecular orientation effects. Therefore, the equation for viscosity was:

$$\eta = \eta_b\left[1+\xi(g/D)^2\right] \qquad [12]$$

where η_b is the macroscopic viscosity from eqn [5]. The macroscopic viscosity is corrected to microscopic viscosity using a micro size factor following the Eringen–Okada equation which is represented by

$$\eta(\dot{\gamma},T,p) = \Phi(z)\eta_b(\dot{\gamma},T,p) = \left(1+\xi\frac{g^2}{z^2}\right)\eta_b(\dot{\gamma},T,p) \qquad [13]$$

1.15.2.4 Factors Affecting Micro Injection Molding

A successful good quality macro plastic parts fabrication is highly dependent on the mold, machine and processing condition. The development in understanding the plastic and its relation to the processing factors are undertaken by focusing on the molding parameter such as mold temperature, melt temperature, injection pressure, holding pressure and clamping force.[35,48–50] The question is, whether changes in processing condition to archive quality molded parts can be applied to micro plastic parts. Generally, a good quality micro molded part is achieved by increasing the flow rate and velocity. This can be done by increasing the mold temperature, melt temperature and injection pressure. But, the clamping force and viscosity have to be reduced for better result. The cavity sizes also will affect the selected processing conditions. Therefore, researches plays with these factors to find the best processing condition for micro molded parts. The major molding parameters investigated by researchers are melt temperature, mold temperature, injection speed and injection pressure due to their direct effects on the melt flow property in micro injection molding.[35,38,39,51] Mönkkönen *et al.*[50] Zhao *et al.*[52] and Yu *et al.*[48] found that the injection speed, melt temperature and holding pressure were the most influential factors in micro injection molding.

Differences in their results can be explained by different plastic materials used and different test structures. Although high settings of molding parameters can improve the melt flow, this also have a negative effect on micro molded parts. For example, high mold temperature can lead to temperature-induced defects, increased cycle time and processing costs. On the other hand, the high melt and mold temperatures and high injection speed has a positive effect on the flow of plastic melt into a micro cavity.

1.15.2.4.1 Temperature

D'Amore *et al.*[53] and Whiteside *et al.*[54] found that the mold temperature was a key parameter for the micro parts fabrication. Therefore they suggested to increase the mold temperature to be the same or higher than the plastic softening temperature. As a result, more aspect ratio can be achieved. Shen *et al.*[36] Shen and Wu[35] suggested that a high mold temperature above the glass transition temperature or close to melt temperature, improved the micro filling capabilities.

Sha *et al.*[55,56] studied the effects of melt temperature, mold temperature, injection speed, injection pressure, clamping pressures, and cooling time to achieve high aspect ratios. They found that melt temperature, mold temperature and injection speeds were the most influential factors affecting the micro-features aspect ratios.

1.15.2.4.2 Pressure

The pressures used in the micro injection molding can reach more than 200 MPa, however conventional injection pressures are generally ten times lower. Sub-milligram products are highly sensitive to changes in injection pressure.[54,57] The injection pressure has to be increased in order to increase the injection speed to have successful filling.[58] According to several researchers,[59] Despa *et al.*[60] Yu *et al.*[48] higher injection speeds increases the mold cavity filling by reducing the plastic viscosity. Therefore, total injection cycles time is reduced. These conditions also can be achieved by taking consideration of runners and gate design.

1.15.2.4.3 Micro flow model factors

Currently, the plastic melts flow behaviors in micro cavities are not fully understood. Flow problem in micro parts are governed by their sizes, wall slip behavior, surface tension, viscosity, forces and thermos-physical property. Because of large surface-to-volume ratio, surface effects will dominate the flow behavior at the microscale. A number of researches indicated that microflows were different from macroflows.[61]

1.15.2.4.4 Size

Besides common injection molding parameters, the geometric configuration of parts is also a factor affecting plastic melt flow in micro molding. For example, Yu *et al.*[48] studied the distance effect between micro cavity and the gate. The result showed that micro cavity near the flow end would be better filled. Also, the study by Mönkkönen *et al.*[50] showed that the angle of micro-features could result in different filling depth. These studies provided useful information for mold design that incorporates micro-features. Geometric configurations showed different responses to changes of molding parameter in micro injection molding. Thus, it is very important to study the combined effects of relevant factors. Yao and Kim[62] investigated the effects of microscale phenomena such as viscosity, wall slip and surface tension on the filling process of plastic materials into micro channels. The results indicated the importance of employing size-dependent viscosity and wall slip to predict micro filling behaviors. But, the surface tension effect was not important in micro molding. Despa *et al.*[63] used available injection molding simulation packages to predict the moldability of micro-features. Micro channels experiment with dimensions of 10 μm have shown that, the viscosity close to the channel wall is higher than the bulk fluid viscosity.[61]

1.15.2.4.5 Viscosity in micro molding

Xu *et al.*[46] and Rosenbaum and Hatzikiriakos[47] reported that the flow in the microscale was different from macroscale. The plastic melt was found to slip over the wall surface as the channel size was down below about a micrometer. Roughness of cavity surface, wall slip conditions and the heat transfer behaviors in the microscale had an influence. For analysis simplification, Young[1] analyzed a filling distance in cylindrical micro-features for micro injection molding without considering viscosity and wall slip effect. Yao and Kim[62] used simulation to study the consequences of size-dependent viscosity on the micro channels filling process. Griffiths *et al.*[7] studied the effect of viscosity on melt temperature and injection speed in micro injection molding. An increase of melt temperature improved the plastic flow due to viscosity and shear stress reduction. Also, some plastics may show shear rate increment at a higher melt temperature. This effect can reduce the viscosity of the material and thus assist the process of filling.

1.15.2.5 Summary of Literature Reviews

There is a need to explore more on micro injection molding in the areas of micro parts, molding machine, and micro melt flow analysis. With current classification on micro parts, analysis, and fabrication of micro parts are the main challenge. As tight specifications are required, controlling injection molding parameters with appropriate viscosity model are highly useful for successful micro molding. This study will design, fabricate, and validate a custom-made injection molding machine suitable for micro molding application. A special mold incorporating viewing window will be designed for the purpose of melt flow observation. Study of micro melt flow starts with straight micro channel and continues with more complex shapes including variable molding parameters. A dedicated micro gear shape case study will be conducted in order to verify the findings in simple and complex micro channel shapes with variable sizes.

1.15.3 Custom-Made Vertical Injection Molding Machine

A custom-made vertical injection molding machine was designed, built, and tested based on the basic principles of plastic injection molding, which was heating a solid plastic into liquid state and injecting to mold cavity and finally ejecting from mold cavity after solidification. The machine consisted of melting chamber, plunger, temperature, and pressure controllers. The overall view of custom-made vertical injection molding machine which consists of vertical injection structure, injection mechanism, plasticizing unit, and custom-made mold are shown in **Figure 1**. The system can be considered as bench top or desktop injection molding machine. There are four solid rods of 25.4 mm diameter and 370 mm length which are used to connect top and bottom plate in vertical arrangement. The top plate is used to support pneumatic cylinder and bottom plate is used as table for the mounted mold. The sizes of both plates are 150 mm × 150 mm × 25 mm. The overall structure is very rigid and strong enough to absorb pressure from pneumatic cylinder during vertical injection operation. To increase the rigidity during operation, the structure is mounted on a working table.

1.15.3.1 Plasticizing Unit and Injection Mechanism

The plasticizing unit consists of melting chamber, nozzle, heating element, and thermocouple. The inner size of melting

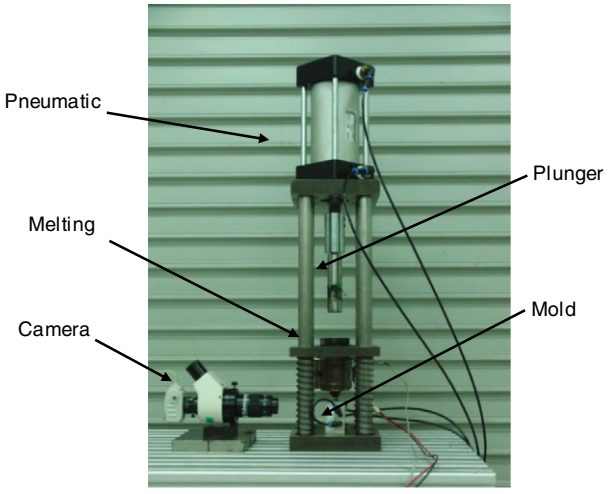


Figure 1 Detail structure of custom-made vertical injection molding machine.

chamber is 30 mm in diameter and 50 mm in length, while outer diameter is 50 mm and covered by heater band and type *K* thermocouple for its feedback system. The thermocouple is attached to the bottom of the heater location. The maximum shot volume that can be held inside melting chamber is 2100 mm^3. The power requirement for heater band is 240 V and produces heat equivalent to 300 W. The heating rate used was 10 $^{\circ}C\,min^{-1}$. Plunger with diameter 30 mm and maximum 100 mm stroke length is connected to pneumatic piston. Compression spring mechanism is used to return melting chamber back to its original position. The compression spring has wire diameter 2.5 mm, outer diameter 22 mm, total length 93.70 mm, and number of free turn equal to 13. After testing with various loads for compression, the stiffness of this compression was 3.9.

1.15.3.2 Injection Mechanism

The plunger for injection motion was powered up by a pneumatic cylinder. The pneumatic cylinder was placed at the top plate and connected to the injection plunger through reduced size coupling. There are two ways to control injection speed: by controlling the input compressed air or by changing the pneumatic cylinder sizes which are 25, 40, and 80 mm in diameter. The movement of piston can be controlled manually by push start button on the control panel or automatically by push start timer. Using manual control, user has to press the start button for downward movement and again press release button for upward piston movement. For automatic piston controller, user is able to set the time for downward and upward piston movement. Therefore, injecting and holding time can be controlled.

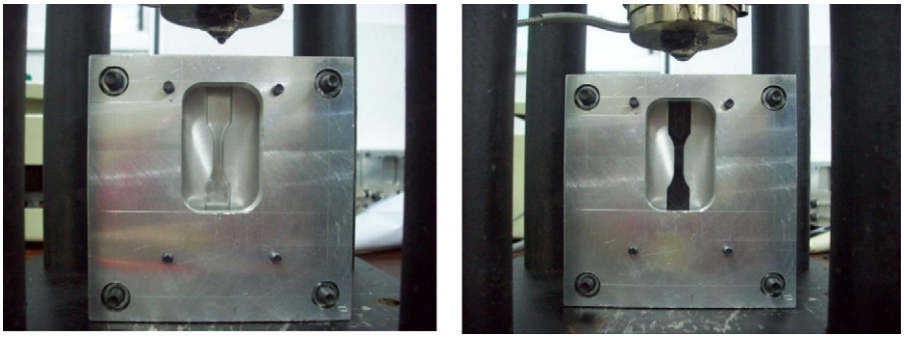
1.15.3.3 Mold Design

The standard molds available in the market are unable to be used with this machine due to machine size and simplicity of the system. Therefore a mold has to be designed and fabricated to meet the specific machine requirement. The custom-made molds also have visualization capabilities which are able to track the plastic melt flow. For specific machine requirement, the maximum size of each mold in length, width, and thickness was 100 mm × 100 mm × 20 mm, respectively. The opening and closing of the mold have to be done manually with screw and nut mechanism. Definitely, it will increase the setup and opening time. The clamping forces are controlled by tightening the screw using torque wrench. The aluminum mold with polymethyl methacrylate (PMMA) transparent window allows user to see the plastic melt flow inside the mold cavity during filling phase. The term 'seeing is believing' was employed to understand the plastic melt flow behavior. Flow visualization technique is compared to quantitative data. Because human mind is designed to rapidly process an incredible amount of information with visualization. A timeline visualization method was used to track the plastic melt flow front during filling phase. Capability of this type of mold to visualize the flow behavior when plastic melts enters entire mold cavity will help user to understand more on the plastic part fabrication during injection phase. This will help in detecting molding problem through filling phase. The viewing window gives the user to capture the end of filling and starting of holding phase. But, aluminum/PMMA mold is not suitable for mass plastic parts production due to its inability to withstand the repeatable higher injection force and processing temperature in each cycle. By using a high speed video camera in-line with PMMA window, a melt flow through the mold cavity was observed. Figures 2(a) and 2(b) show aluminum mold with PMMA window before and after polypropylene (PP) was injected using the custom-made vertical injection molding machine.

1.15.4 Study of Straight, Reverse 'T' and Cross '+' Micro Channel Flow

This section will provide a detailed description of the mathematical fluid flow model and experiments of various shapes and sizes of micro channels. The section starts with the formulation of an analytical plastic flow model for fast and quick filling distance and analysis of results for various sizes of micro channel. The governing equations used in MoldFlow Part Advisor in solving plastic injection molding problems are discussed. Also, the governing equations used in ANSYS CFX software are discussed.

The investigations continue with fabrication of micro channels with straight, reverse 'T' and cross '+' shape with various mold cavity sizes. These mold cavities will be filled



(a) (b)

Figure 2 Aluminum/PMMA Mold (a) before injection and (b) after injection.

with PP using custom-made vertical injection molding machine. A study on the effect mold and melt temperatures on micro channel filling distance will be presented. The experimental objectives were to explore the flow behavior during simulation and actual injection process. Also, the effects of molding parameters on the micro channel filling distance are investigated. A MoldFlow, ANSYS CFX, and experimental results for each channel shape and sizes will be discussed thoroughly. The formation of plastic channel in different sizes with understanding the flow behavior requires specific mathematical model. Before any calculations can be done, replication of flow behavior in specific parts into mathematical model is mandatory. Mathematical modeling is an indispensable tool that gives constant demand for a better product quality. This generates interest in the analysis and the prediction of physical properties of the product.[63]

1.15.4.1 Mathematical Flow Model

As an introduction to this section, the conservation of mass principles on fluid flow modeling will be explained. The conservation of mass principle for a control volume is defined as the net mass transfer to or from a control volume during a time interval Δt. This is equal to the net change in the total mass within the control volume during finite time interval Δt. The equation is given by

$$\dot{m}_{\text{in}} - \dot{m}_{\text{out}} = \Delta m_{\text{CV}} = \frac{\mathrm{d}m_{\text{CV}}}{\mathrm{d}t} \quad [14]$$

where, $\dot{m}_{\text{in}}$ and $\dot{m}_{\text{out}}$ are the total rates of mass flow in and out of the control volume and $\frac{\mathrm{d}m_{\text{CV}}}{\mathrm{d}t}$ is the rate of change of mass within the control volume boundaries.

The mass flow rate $\dot{m}$ is the amount of mass flowing through a cross section per unit time is defined as

$$\dot{m} = \rho v_{\text{avg}} A_{\text{c}} = \rho \dot{v} = \frac{\dot{v}}{v} \quad [15]$$

where, v_{avg} is the average speed through the cross section and in integral form is

$$v_{\text{avg}} = \frac{1}{A_{\text{c}}} \int_{A_{\text{c}}} v_n \mathrm{d}A_{\text{c}} \quad [16]$$

The volume flow rate, $\dot{v}$ is the volume of fluid flowing through the cross section per unit time and expressed as

$$\dot{v} = \int_{A_{\text{c}}} V_n \mathrm{d}A_{\text{c}} = v_{\text{avg}} A_{\text{c}} = v A_{\text{c}} \quad [17]$$

The mass balance equations is applicable to control volume undergoing any fluid flow model.

$$\mathrm{d}m = \rho \mathrm{d}V \quad [18]$$

Therefore, the total mass within control volume

$$m_{\text{CV}} = \int_{\text{CV}} \rho \mathrm{d}V \quad [19]$$

For an incompressible steady flow, the $\frac{\mathrm{d}m}{\mathrm{d}t}$ term in the conservation of mass equation is equal to zero. In other words, 'What goes in must come out' or

$$\sum_{\text{outlets}} \dot{m} = \sum_{\text{inlets}} \dot{m} \quad [20]$$

As the flow is incompressible, the density is constant,

$$\dot{m} = \int_{\text{surface}} \rho V \bullet n \mathrm{d}A \quad \rho \int_{\text{surface}} V \bullet n \mathrm{d}A \quad [21]$$

The integral term of eqn [21] becomes volume flow rate, Q, therefore

$$\dot{m} = \rho Q \quad [22]$$

so the conservation of mass equation becomes:

$$\sum_{\text{outlets}} Q = \sum_{\text{inlets}} Q \quad [23]$$

Thus, $Q_{\text{out}} = VA$. Therefore, at an inlet $\dot{m}_{\text{in}} = \rho VA$ and $Q_{\text{in}} = VA$. The conservation of mass equation with simplification,

$$\sum_{\text{outlets}} \dot{m} - \sum_{\text{inlets}} \dot{m} = 0 \quad [24]$$

The formulation of eqns [14]–[24] will be used to explain the flow front position and behavior in reverse 'T' and cross '+' micro channels.

Another important parameter when working with non-Newtonian fluid is the viscosity. For clarity, the viscosity formulation is explained with an example of straight channel. The basic melt flow viscosity in a straight channel can be explained using drag flow in order to identify the shear stress τ and shear rate $\dot{\gamma}$.

Movement of plastic melt flow at each layer as shown in Figure 3 is sustained by the motion of the left side while the right side remained stationary. A force, F is required to maintain the motion while the right side moves at velocity, v.

The shear stress, τ is given by

$$\tau = \frac{F}{A} \quad [25]$$

the shear rate is proportional to the velocity gradient,

$$\dot{\gamma} = \frac{\mathrm{d}v}{\mathrm{d}x} \quad [26]$$

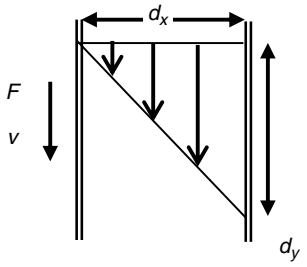


Figure 3 Plastic melt flow at each layer.

For plastic melt, assuming the shear rate proportional to the strain rate, $\tau = -\eta\dot{\gamma}$, where η is Power Law viscosity model from eqn [1].

1.15.4.1.1 MoldFlow flow model

The Moldflow Part Advisor filling simulations is to formulate from Generalized Hele-Shaw (GHS) flow model for a viscous plastic melt under non-isothermal conditions, non-Newtonian and inelastic flows as stated by Kennedy.[64] This model was used by several researchers[29,62] to simulate the plastic flow behavior in plastic injection molding. They used this approach to model polymer melt flow in the 3D thin cavities. Due to complicated 3D configurations and plastic melt rheological behavior, Su[38] simplified the flow model with the following assumptions:

1. Smaller cavity thickness compared to other dimensions.
2. Velocity component in thickness direction is zero.
3. A fully developed Hele-Shaw flows regions.

In this way, the GHS flow model significantly simplified the equations to 2D fluid flow problems. This approach also can be applied to power law fluid, Cross-Carreau and modified cross fluid flow model. It also applies to no isothermal flow in which the hot plastic melts freezes on the cold mold wall. Fluid flow problems involve solution of the equations that express conservation of mass, momentum, and energy. The conservation equations[64] are

$$\text{Mass}: \quad \frac{\partial \rho}{\partial t} + (\nabla \cdot \rho v) = 0 \qquad [27]$$

$$\text{Momentum}: \quad \rho \frac{\partial v}{\partial t} = -\nabla \rho + \left[\nabla \cdot \eta \underline{\dot{\gamma}}\right] - \rho[v \cdot \nabla v] \qquad [28]$$

$$\text{Energy}: \quad \rho c_P \left(\frac{\partial T}{\partial t} + v \cdot \nabla T\right) = \beta T \left(\frac{\partial p}{\partial t} + v \cdot \nabla T\right) + \eta\dot{\gamma}^2 + \nabla \cdot (k \nabla T) \qquad [29]$$

The viscosity of plastic is dependent on temperature, pressure and shear rate, therefore the sevent-constants cross-WLF viscosity model is used in MoldFlow simulation. The relationship of the variables is described in eqns [5] and [6]. An extra complexity in injection molding simulation is the need to incorporate a density variation as a function of temperature and pressure. The equation relates the material specific volume, pressure, and temperature are referred to as the material's pressure volume temperature (PVT) characteristic. It is complex equations and varies depending on the type of material.[64] The specific volume approach in MoldFlow is represented by the modified Tait equation.

The modified two-domain Tait PVT model has 13 constants which capture the effects of temperature and pressure on density. The modified two-domain Tait PVT model is given by the following equations:

$$V(T,P) = V_0(T)\left[1 - C\ln\left(1 + \frac{P}{B(T)}\right) + V_t(T,P)\right] \qquad [30]$$

For the upper temperature region ($T > T_t$), the V_0, $B(T)$ $V_t(T, P)$ parameters for eqn [30] can be described by following equations:

$$V_0 = b_{1m} + b_{2m}(T - b_5) \qquad [31]$$

$$B(T) = b_{3m}\exp[-b_{4m}(T - b_5)] \qquad [32]$$

$$V_t(T,P) = 0 \qquad [33]$$

For the lower temperature region ($T < T_t$), the V_0, $B(T)$, $V_t(T,P)$ parameter for eqn [30] can be described by following equations:

$$V_0 = b_{1s} + b_{2s}(T - b_5) \qquad [34]$$

$$B(T) = b_{3s}\ \exp[-b_{4s}(T - b_5)] \qquad [35]$$

$$V_t(T,P) = b_7\exp[(b_8(T - b_5)) - (b_6 P)] \qquad [36]$$

Also, the effect of T_t on pressure can be described by the equation:

$$T_t(P) = b_5 + b_6 P \qquad [37]$$

From PVT diagram in MoldFlow database for PP, the transition temperature varies between 75 and 125 °C for specific pressure and volume.

1.15.4.1.2 ANSYS CFX flow model

The ANSYS CFX software has more flexibility in modeling a plastic flow by allowing user to modify lot of flow model parameters compared to Moldflow part advisor. The software also enables user to modify or add an equation to the flow model which can give better correlation between simulation and experimental results. Even though Moldflow part advisor is better in producing faster result, ANSYS CFX is more reliable in analyzing a micro plastic flow problem. In formulating a plastic flow model using ANSYS CFX, the mold cavity is assumed to be filled by air. The plastic melts pushes the air from cavity and replaces it with plastic. Therefore, a multiphase approach or two phases flow is suitable to model this plastic flow problem.

The governing equations required to solve the plastic flow problem are multiphase continuity equation, momentum, and energy conservation equations. The governing equations are solved with rheological characteristic of the selected material. The ANSYS CFX solves the governing equations using Cartesian spatial coordinates and velocity components. The multiphase linear momentum equation is:

$$\frac{\partial}{\partial t}(r_\alpha \rho_\alpha v_\alpha) + \nabla.(r_\alpha(\rho_\alpha v_\alpha . v_\alpha)) = -r_\alpha \nabla P_\alpha + \nabla.\left(r_\alpha \mu_\alpha \left(\nabla v_\alpha + (\nabla v_\alpha)^T\right)\right) + \sum_{\beta=1}^{N_\alpha}\left(\Gamma^+_{\alpha\beta} v_\beta - \Gamma^+_{\beta\alpha} v_\alpha\right) + S_{M\alpha} + M_\alpha \qquad [38]$$

The $\left(\Gamma^{+}_{\alpha\beta}v_{\beta} - \Gamma^{+}_{\beta\alpha}v_{\alpha}\right)$ term represents momentum transfer by interphase mass transfer.

The continuity equation for multiphase problem is defined as:

$$\frac{\partial}{\partial t}(r_{\alpha}\rho_{\alpha}) + \nabla.(r_{\alpha}\rho_{\alpha}v_{\alpha}) = S_{\mathrm{MS}\alpha} + \sum_{\beta=1}^{N_{\alpha}}\Gamma_{\alpha\beta} \qquad [39]$$

A transient simulation is selected for simulating the filling process of the plastic melt. In order to generate the free surface of the plastic melt at every time step, the melt front was tracked using a volume of fluid method. The volume of fluid equation is:

$$\sum_{\alpha}\frac{1}{\rho_{\alpha}}\left(\frac{\partial}{\partial t}(r_{\alpha}\rho_{\alpha}) + \nabla.(r_{\alpha}\rho_{\alpha}v_{\alpha})\right) = \sum_{\alpha}\frac{1}{\rho_{\alpha}}\left(S_{\mathrm{MS}\alpha} + \sum_{\beta=1}^{N_{\mathrm{P}}}\Gamma_{\alpha\beta}\right) \qquad [40]$$

Instead of energy conservation equation, the thermal energy also considers the plastic melt viscous dissipation during mold filling. The thermal energy equation is:

$$\frac{\partial(\rho e)}{\partial t} + \nabla\cdot(\rho U e) = \nabla\cdot(\lambda\nabla T) - P\nabla\cdot U + \tau:\nabla v + S_{\mathrm{E}} \qquad [41]$$

The term $\tau{:}\nabla v$ is always positive and called the viscous dissipation
where

$$e = h - \frac{P}{\rho}$$

h is the internal energy.

1.15.4.1.3 Suggestion non-Newtonian viscosity model

Using ANSYS CFX simulation package, a proposed modified cross viscosity model was included in the plastic melt flow modeling. The non-Newtonian cross viscosity model used in ANSYS CFX package was

$$\eta = \frac{\eta_0}{1 + (\lambda\dot{\gamma})^{n}} \qquad [42]$$

where the η_0 is defined as

$$\eta_0 = D_1\exp\left[-\frac{A_1(T - D_2)}{A_2 + (T - D_2)}\right] \qquad [43]$$

where n, D_1, D_2, D_3, A_1 and A_2 are the constants specific for plastic material. The respective values for PP at melt temperature 240 °C were 0.275 1, 24 200 Pa, 4.66e + 012 Pa s, 263.15, 0 K Pa^{-1}, 26.12, and 51.6 K.[65] Yao and Kim[62] used eqn [13] proposed by Eringen and Okada[61] to model micro plastic flow incorporating micro functions relating size, travel length, cross section area, etc. The η_0 will be

$$\eta_0 = D_1\exp\left[\frac{-A_1(T - D_2)}{A_2 + (T - D_2)}\right] \times f_{(\mathrm{microscopic})} \qquad [44]$$

In order to identify the $f_{(\mathrm{microscopic})}$, experiments on various micro channel sizes will be conducted. Also the effect of melt and mold temperature will be considered.

1.15.4.2 Micro Channel Fabrication and Experimental Design

Many researchers investigated the effect of molding parameters on the flow behavior and filling distance. Sha *et al.*[66] fabricated various sizes of micro channels to identify injection molding factors that affect the achievable aspect ratios. The factor included barrel temperature, mold temperature, injection speed, holding pressure, the air evacuation, and the micro feature sizes. Yao and Kim[62] fabricated a micro channel to investigate the microscale phenomena on the micro channels filling process. The finding indicated that the micro channel cavities were filled almost isothermally by using microscale viscosity and wall slip effect. Young[67] also fabricated a micro channel mold to find the effect of mold temperature, injection rate, and micro channel sizes on the filling distance. A simplified flow model was developed to estimate the filling distance into the micro channels from the main channel. The filling distance increased with respect to the increment of the channel sizes, mold temperature, and injection rate.

1.15.4.2.1 Micro channels mold fabrication

An aluminum mold with visualization windows was used in this experiment. Each channel was milled using DT110 multipurpose micro machine, which was suitable for micro channel fabrication on aluminum mold. In order to understand the melt plastic flow behavior in macro, transition from macro to micro and micro size, and the channel sizes fabricated were 1.0, 0.8, 0.5, 0.4, and 0.3 mm. Three types of micro channels namely straight, reverse 'T' and cross '+' shape channel as shown in Figure 4 were studied.

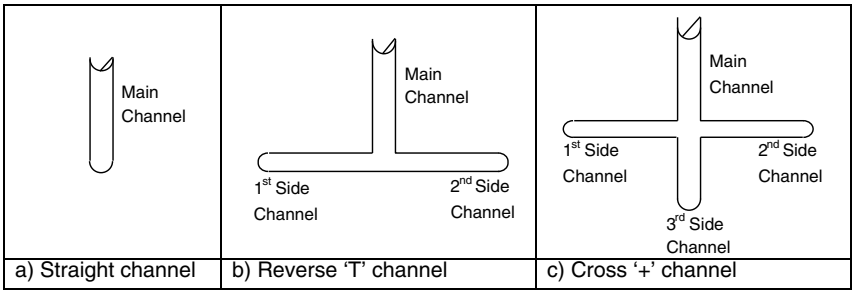


Figure 4 Shape of straight, reverse 'T' and cross '+' shape channel.

Table 1 Reverse 'T' and cross '+' shape channel size combination

			Main channel (mm)		
			1.0	*0.8*	*0.5*
Side channel (mm)	Reverse 'T'	1.0	X		
		0.8	X	X	
		0.5	X	X	X
	Cross '+'	1.0	X		
		0.8	X	X	
		0.5	X	X	X

The combination of main and side channel for reverse 'T' and cross '+' shape channel is shown in Table 1. In total, 17 molds were fabricated for straight, reverse 'T', and cross '+' shape channels.

1.15.4.2.2 Experimental design

The experiments were designed to evaluate the flow behavior and filling capabilities at different mold and melt temperatures. Then performance of software analysis simulation was compared with the actual injection process. The comparison was based on the micro channel size and shape. PP was selected as the molding material. The injection molding parameter used in this experiment was mold and melt temperatures. The custom-made vertical injection molding machine can be operated up to 0.8 MPa of compressed air input. The compressed air supply to pneumatic piston was 0.8 MPa and the piston size was 80 mm. The minimum mold temperature suggested for PP is the room temperature and maximum of 60 °C. For the experiments, three levels of mold temperature were selected, which were 25 (room temperature), 35, and 50 °C. Allowable melt temperature for PP was between 240 and 260 °C. Therefore, 240, 250, and 260 °C were chosen as melt temperature variables. A high speed video camera with capability of 210 fps was used to capture the melt flow from starting position at macro section to micro section until its solidified at some distance of travel.

Each micro channel experiment was repeated three times and the filling distance was measured using digital microscope. The same experimental procedures were applied to reverse 'T' and cross '+' micro channel shapes. The flow behavior of reverse 'T' and '+' shape micro channel with different sizes will be explained through conservation of mass and energy, then compared with visualization of flow from actual experiments. Each shape and size with various mold and melt temperature will be discussed with regard to filling capability aspects.

The experiments on the effect of mold and melt temperature on micro channel filling distance were conducted and verified with analytical, MoldFlow software, and ANSYS CFX simulation results. The increment of mold or melt temperature should increase the filling distance. This study was extended to utilize the ANSYS CFX which used governing equations with more flow constant and complex parameters including viscosity model. ANSYS CFX allowed user to include suitable equation to make the flow simulation close to experimental results. In order to predict simulation result close to experiment results, the cross viscosity model was embedded with micro function in ANSYS CFX flow model as explained in Section 1.15.4.2. The micro function used in the cross viscosity model will be developed through experimental work on various sizes of micro channel.

1.15.4.3 Experiments and Simulation for Straight Channel

This section describes the analytical, MoldFlow, ANSYS CFX, and experimental filling results of straight micro channel in various sizes. The filling time results are also presented in all the three cases. For the purpose of comparison with experimental results, only filling distance and time results will be presented. The filling distance capabilities in each straight micro channel at various combinations of mold and melt temperature will be discussed. In each straight micro channel result, an example figure of MoldFlow, ANSYS CFX, and experiment are shown to explain the cavity pressure distribution and filling capabilities. Specific η_0 value used in ANSYS CFX simulation is highlighted and used in the formulation of a modified cross viscosity model for specific straight micro channel size.

1.15.4.3.1 0.8 mm straight micro channel

Figure 5 shows filling distance and pressure distribution of MoldFlow, ANSYS CFX, and experiment when mold temperature was 35 °C and melt temperature was 240 °C. The MoldFlow filling distance prediction was less compared to ANSYS CFX and actual experiment. The maximum pressure achieved in MoldFlow analysis was 3.13 MPa and in ANCYS CFX, it was 1.433 MPa with η_0 value equal to 346.53 Pa s.

A very close filling distance was found between ANSYS CFX and experiment compared to MoldFlow prediction as shown in Figure 6. It shows that, to achieve longer filling distance, modification of temperature can be made either with mold or melt temperature. But, in experiment, there is no need to increase the melt temperature to achieve the same filling distance result when the mold temperature was 25 °C. There is an unrealistic result shown when mold was heated at 35 °C and melting temperatures were 240 and 260 °C. The percentage difference in mold filling distance recorded in ANSYS CFX when compared to experiment was 1–3%, whit it was between 10 and 15% when compared with MoldFlow results. On the other hand, MoldFlow shows much close prediction with ANSYS CFX and experiment at mold temperature 25 °C and melt temperatures of 240 and 250 °C.

1.15.4.3.2 Discussion on straight micro channel

For 1.0–0.8 mm straight micro channels, analytical, experimental, ANSYS CFX, and MoldFlow showed almost similar mold filling distance trend. For the 0.5, 0.4, and 0.3 mm straight micro channels, MoldFlow results showed inconsistent filling trend as expected, which was incremental filling distance as the mold and melt temperature increased. Figure 7 shows an average percentage difference in filling distance for various sizes of straight micro channels. The percentage difference of MoldFlow result when compare with experiments was in between 10 and 60%. The percentage difference in filling distance for analytical result was in between 5 and 22%. It is considered higher, but it was due to simplification and

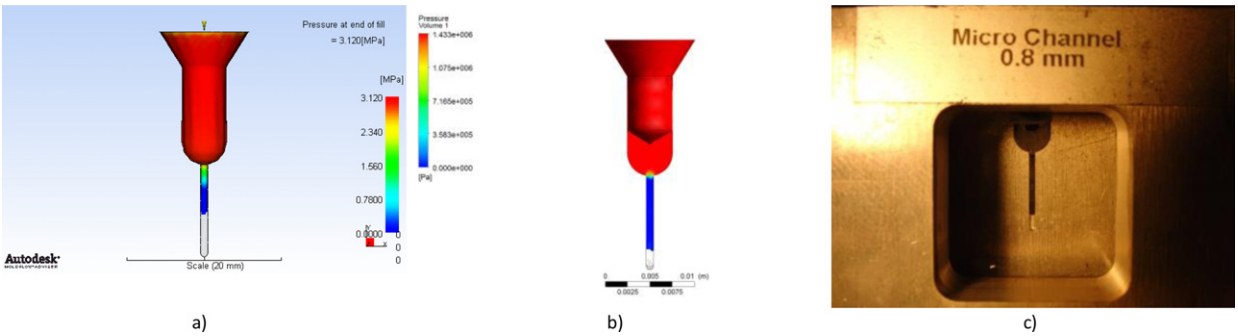


Figure 5 Example of pressure distribution and filling capability for 0.8 mm micro channel at 35 °C mold temperature and 240 °C melt temperature (a) MoldFlow, (b) ANSYS CFX, and (c) experimental.

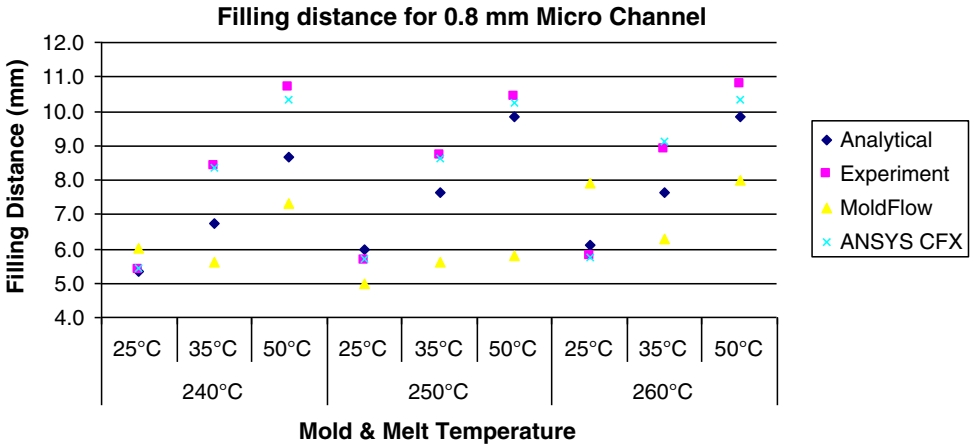


Figure 6 Filling distance for 0.8 mm micro channel with various mold and melt temperature combinations.

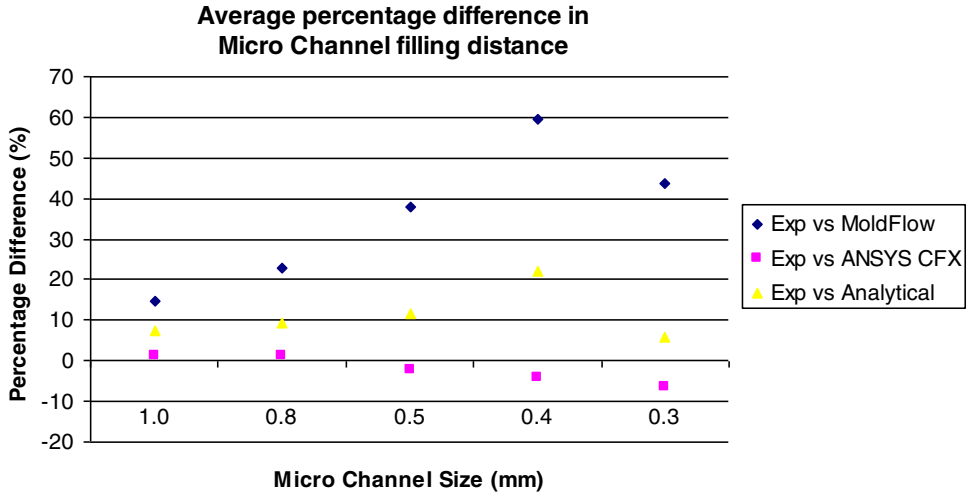


Figure 7 Average percentage differences in mold filling distance for various sizes of straight micro channel.

assumption during equations formulation. With proper modification of cross viscosity model used in ANSYS CFX, the percentage difference recorded was less than 10% for all micro channel sizes at various mold and melt temperatures.

As reported by Shen *et al.*[35,36] a mold temperature above the glass transition temperature of plastic is the most important factor for improving the replication capability of micro injection molding. Also, increment in melt temperature will

increase the filling distance. However, from analysis and experiments, it was not applicable for 0.5, 0.4, and 0.3 straight micro channels. Therefore another molding factor has to be considered for micro channel smaller than 0.5 mm.

1.15.4.3.3 Modified cross viscosity model for straight micro channels

After finalizing the average value of η_0 for each micro channel size, the suggestion for cross viscosity model is explained in this section. From eqns [42], [43], and [44], formulation of the proposed cross viscosity model is explained in Table 2. The acceptable η_0 value for each micro channel is based on maximum pressure recorded for both MoldFlow and ANSYS CFX simulation.

From Table 1, the proposed cross viscosity model formulation from the analysis of eqn [44] becomes

$$\eta_0 = D_1 \exp\left[\frac{-A_1(T-D_2)}{A_2+(T-D_2)}\right] \times C\left[\frac{\pi j^2}{2}\right] \quad [45]$$

where C is a constant between 0.7 and 0.8, except for 0.4 mm micro channel. Therefore

$$f_{(\text{microscopic})} = CA_{\text{cross section}} \quad [46]$$

1.15.4.4 Experiments and Simulation for Reverse 'T' Shape Micro Channel

This section explains the filling capabilities of a reverse 'T' shape micro channel at various mold and melt temperature. As the side channel is symmetrical, the filling distance result is only presented at its first side channel only. Examples of filling capabilities results from MoldFlow, ANSYS CFX simulation, and experiments are presented. A suitable η_0 value for cross viscosity model was used by comparing pressure result from MoldFlow simulation. Small percentage difference between MoldFlow and ANSYS CFX pressure results is acceptable in defining the value of η_0. Each micro channel size combination will be discussed based on the filling distance under the effect of mold and melt temperatures.

Table 2 Formulation of constant, C, for various micro channel sizes

Micro channel size	*η_0 (without microscopic)*	*η_0 (with microscopic)*	*$f_{(\text{microscopic})}$*	*Cross sectional area/2*	*Constant*
1.0	1846.53	546.53	0.295 9	0.392 8	0.753 6
0.8	1846.53	346.53	0.187 6	0.251 4	0.746 6
0.5	1846.53	146.53	0.079 3	0.098 2	0.808 2
0.4	1846.53	46.53	0.025 2	0.062 9	0.400 9
0.3	1846.53	46.53	0.025 2	0.035 3	0.712 9

1.15.4.4.1 M05⊥S05 reverse 'T' micro channel

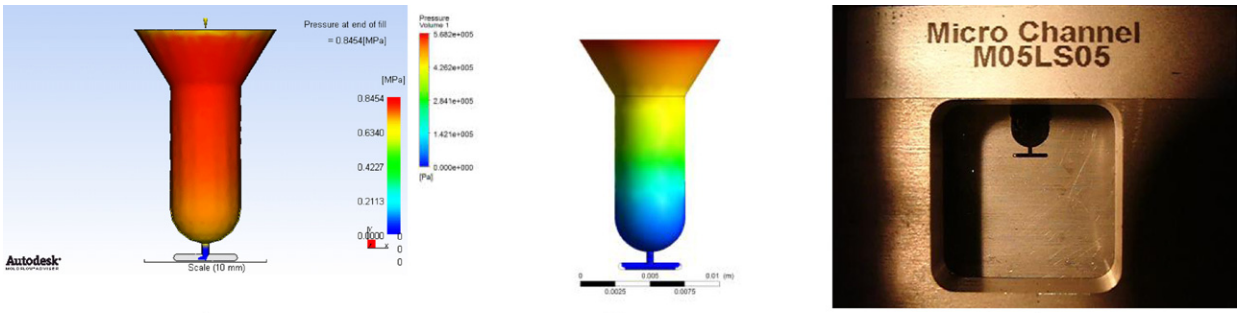
The MoldFlow, ANSYS CFX, and experiment results for M05⊥S05 with micro channel at 35 and 240 °C of mold and melt temperatures respectively are shown in Figure 8. The maximum pressure achieved in MoldFlow analysis was 0.8454 MPa and 0.5588 MPa in ANSYS CFX with η_0 value equal to 36.53 Pa s. The ANSYS CFX result shows almost similar filling capabilities as that of experiment.

The capabilities of flow front to travel at maximum side channel for M05⊥S05 micro channel at various mold and melt temperatures are shown in Figure 9. From the figure, MoldFlow result shows very small mold filling distance at various molds and melts temperature combinations. The 2.0 mm filling distance is maximum distance at each side channel. ANSYS CFX was capable to fill-up all cavities at 50 °C mold temperature and at all melt temperatures. While, the experimental result shows complete filling when melt temperature was 260 °C.

1.15.4.4.2 Discussion on reverse 'T' micro channel

With proposed η_0 for each reverse 'T' micro channel, the ANSYS CFX was able to predict more accurate result close to experimental results compared to MoldFlow simulation for M10⊥S10, M10⊥S08, and M08⊥S08 reverse 'T' micro channels. For reverse 'T' micro channel which has side channel less than 0.8 mm, the MoldFlow was unable to predict the filling distance any closer to experiments results.

With the aim to reduce viscosity in micro channel, it will not be able to help the flow front travel to the end of the cavity. It has to incorporate other factors such as surface roughness and area to travel length ratio. Longer length in the side channel will increase travel length to area ratio and it will also increase the heat loss during its travel to the end of cavity length. Figure 10 shows the average percentage difference in reverse 'T' micro channel filling



a) b) c)

Figure 8 Example of pressure distribution and filling capability for M05⊥S05 micro channel at 35 °C mold temperature and 240 °C melt temperature (a) MoldFlow, (b) ANSYS CFX, and (c) experimental.

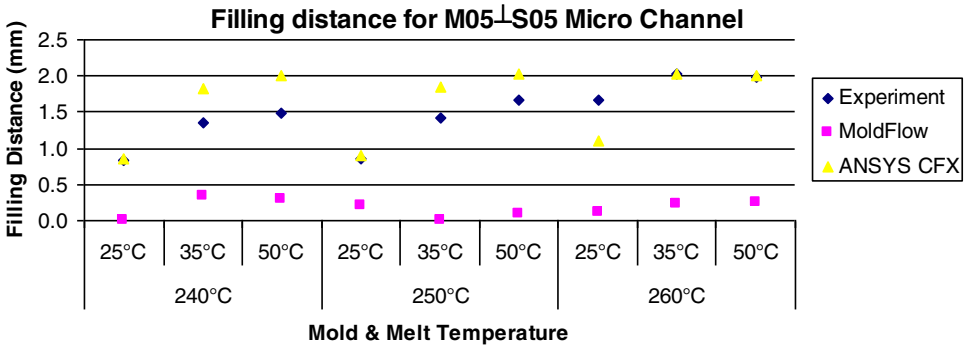


Figure 9 Filling distance for M05⊥S05 micro channel with various mold and melt temperature.

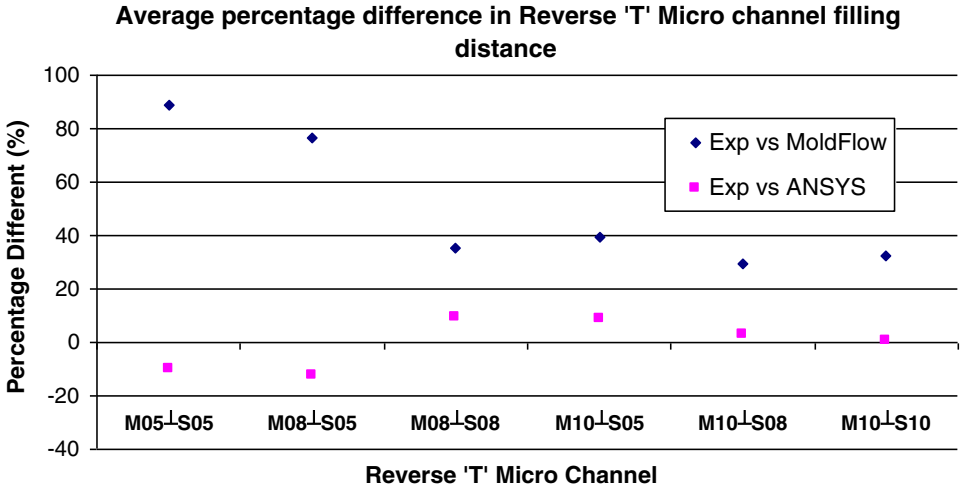


Figure 10 Average percentage differences in filling distance for various sizes combination of reverse 'T' micro channel.

distance with various sizes and combinations. Overall, the percentage difference recorded for ANSYS CFX when compared to experimental result showed a difference less than 20%. On the other hand, MoldFlow simulation showed much higher percentage difference which was between 20 and 90%.

1.15.4.4.3 Modified cross viscosity model for reverse 'T' micro channels

After finalizing the value of η_0 for each micro channel size combination with ANSYS CFX software, the suggestion for extended cross viscosity model is explained in this section. From eqns [42], [43], and [44], formulation of the analysis extended η_0 value for reverse 'T' micro channel and is shown in Table 3.

From Table 3, the proposed cross viscosity model formulation from eqn [44] becomes

$$\eta_0 = D_1 \exp\left[\frac{-A_1(T-D_2)}{A_2+(T-D_2)}\right] \times C\left[\frac{A_1+A_2+A_3}{3}\right] \quad [47]$$

where, CA_1 is the cross sectional area for main channel, CA_2 is the cross sectional area for first side channel and CA_3 is the cross sectional area for second side channel. From Table 2, C is the constant (0.1–0.3). Therefore the proposed η_0 for cross viscosity model formulation from eqn [47] becomes

$$\eta_0 = D_1 \exp\left[\frac{-A_1(T-D_2)}{A_2+(T-D_2)}\right] \times C\left[\frac{\left(\frac{\pi j_m^2}{2}\right)+\left(\frac{\pi j_1^2}{2}\right)+\left(\frac{\pi j_3^2}{2}\right)}{3}\right] \quad [48]$$

1.15.4.5 Experiments and Simulation for Cross '+' Micro Channel

This section present the experimental, MoldFlow, and ANSYS CFX results on pressure distribution and filling distance for cross '+' micro channel with various mold and melt temperature combinations. It starts with explaining the flow front position at specific location using mass flow rate, followed by cross '+' micro channel pressure distribution, and filling capability examples. Then it continues with filling distance capabilities for each micro channel size combinations. Modified cross viscosity model suitable for cross '+' micro channel was formulated through results from ANSYS CFX simulation which was based on pressure distribution results from MoldFlow analysis.

Table 3 Formulation of constant, *C*, for reverse 'T' micro channel

Main	*First side*	*Second side*	*η_0 (without microscopic)*	*η_0 (with microscopic)*	*$f_{(microscopic)}$*	*Area at main*	*Area at first side*	*Area at second side*	*Total area*	*Constant*
1	1	1	1846.53	146.53	0.079 4	0.392 8	0.392 8	0.392 8	0.392 8	0.202 0
1	0.8	0.8	1846.53	146.53	0.079 4	0.392 8	0.251 4	0.251 4	0.298 5	0.265 9
1	0.5	0.5	1846.53	79.53	0.043 1	0.392 8	0.098 2	0.098 2	0.196 4	0.219 3
0.8	0.8	0.8	1846.53	79.53	0.043 1	0.251 4	0.251 4	0.251 4	0.251 4	0.171 3
0.8	0.5	0.5	1846.53	39.53	0.021 4	0.251 4	0.098 2	0.098 2	0.149 2	0.143 4
0.5	0.5	0.5	1846.53	36.53	0.098 2	0.098 2	0.098 2	0.098 2	0.098 2	0.201 5

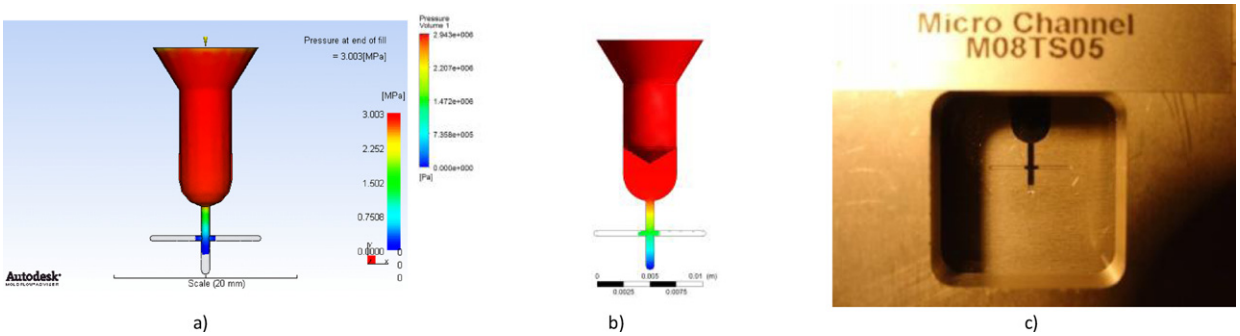


Figure 11 Example of pressure distribution and filling capability for M08 + S05 micro channel at 25 °C mold temperature and 240 °C melt temperature (a) MoldFlow, (b) ANSYS CFX, and (c) experimental.

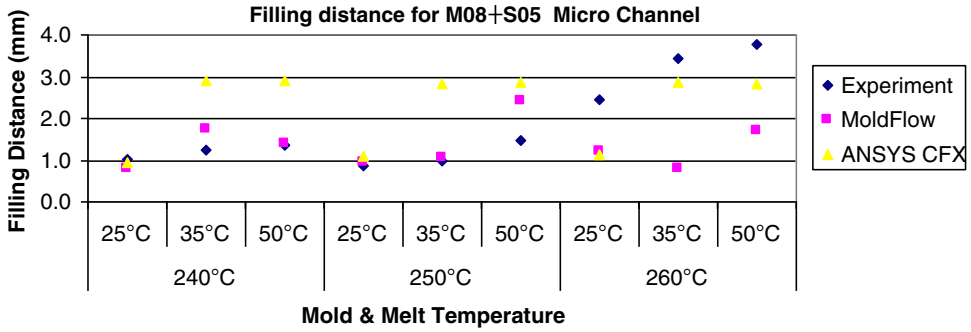


Figure 12 Filling distance for M08 + 05 micro channel with various mold and melt temperature.

1.15.4.5.1 M08+S05 cross '+' micro channel

Figure 11 shows a M08 + S05 micro channel experimental filling capabilities, MoldFlow, and ANSYS CFX pressure distribution results. Mold temperature of 25 and 240 °C melt temperature were applied during the testing. MoldFlow and experimental results showed incomplete filling in third side channel but ANSYS CFX simulation showed better filling capabilities. A 39.53 Pa s was applied for η_0 value in ANSYS CFX cross viscosity model. A 3.003 MPa of maximum pressure was recorded in MoldFlow but ANSYS CFX simulation yielded only 2.643 MPa and showed a complete filling in third side channel.

The maximum filling distance recorded for M08 + S05 micro channel with various mold and melt temperature combinations is shown in Figure 12. A 4.0 mm filling distance is considered as full filling in first and second side channel. The filling distance increased with the increase of mold and melt temperatures. When mold temperature was heated at 35 and 50 °C, ANSYS CFX simulation showed filling distance reaching 3.0 mm for all three melt temperatures. MoldFlow did not show a large filling distance increment even with increment of mold and melt temperatures. The percentage difference between experiment and ANSYS CFX was 2–5%. However the difference was 6–12% when compared with MoldFlow results.

1.15.4.5.2 Discussion on cross '+' micro channel

With suitable η_0 value used in each size and combination of cross '+'micro channel, the ANSYS CFX are capable to predict

filling distance in one of its side channel with low percentage difference when compared to actual experimental results. Filling distance recorded for M10 < S10 and M10 < S05 micro channels showed a complete cavity filling for both ANSYS CFX and experimental results when the mold was heated at 50 °C and melt temperature was set at all three levels.

There are unique flow front behavior recorded when flow was observed at each time interval for M10 + S05 and M08 + S05 micro channels. MoldFlow result showed flow front splitting into three directions when reaching a junction and the filling distance almost equal at each direction. But, experimental flow front results showed the filling distance in third side channel was much longer compared to first and second side channels. The same results were observed in ANSYS CFX simulations. The main and third channel flow direction was in vertical, while the first and second sides were in horizontal directions. As the first and second side channels were smaller than main and third side channel, the flow front traveled easily to bigger channel compared to the smaller channel. After the flow front reached the end of third side channel, the flow front was still in liquid condition. Therefore the flow front was filling more to this side channel.

For M05 + S05, ANSYS CFX result showed a complete cavity filling at third side channel identical to that produced in experiments. But, MoldFlow was unable to simulate the flow capabilities after the flow front leaving the junction. Experimental result at 50 °C mold temperature and 260 °C melt temperature gave longer filling distance in their third side compared to ANSYS CFX result.

For a cross '+' micro channel with the same main and side channel sizes, experimental result showed a better filling distance capability when compared to various filling sizes in each channel as shown in M10 + S10 and M05 + S05 results. The average percentage difference in cross '+' micro channel filling distance with various sizes and combination is shown in **Figure 13**. For the same channel size of main and side channel, there was a very small percentage of difference except for M05 + S05.

1.15.4.5.3 Modified cross viscosity model for cross '+' micro channel

After finalizing the value of η_0 for each micro channel size combination with ANSYS CFX software, the suggestion for extended cross viscosity model is explained in this section. From eqns [42]–[44], η_0 values for cross '+'micro channel is shown in **Table 4**.

From **Table 4**, the proposed cross viscosity model formulation from eqn [44] becomes

$$\eta_0 = D_1 \exp\left[\frac{-A_1(T-D_2)}{A_2+(T-D_2)}\right] \times C\left[\frac{A_1+A_2+A_3+A_4}{4}\right] \quad [49]$$

where CA_1 is the cross sectional area for main channel, CA_2 is the cross sectional area for first side channel, CA_3 is the cross sectional area for second side channel, and CA_4 is the cross sectional area for third side channel. From **Table 4**, C is the constant (0.1–0.3). Therefore the proposed η_o for cross viscosity model formulation from eqn [49] becomes

$$\eta_0 = D_1 \exp\left[\frac{-A_1(T-D_2)}{A_2+(T-D_2)}\right] \times C\left[\frac{\left(\frac{\pi j_m^2}{2}\right)+\left(\frac{\pi j_1^2}{2}\right)+\left(\frac{\pi j_3^2}{2}\right)+\left(\frac{\pi j_4^2}{2}\right)}{4}\right] \quad [50]$$

1.15.5 Study on Macro and Micro Gear Shape Molding

This section describes the case study conducted in MoldFlow, ANSYS CFX, and experiments. Gear shape was selected as a case study. Gear shape resembles various micro channel sizes and flow front splitting. A gear is a toothed wheel designed to transmit torque to another gear or toothed component. Section 1.15.5.1 will discuss on the observation of flow orientation for macro gear shape with the purpose to track the flow front direction using MoldFlow and compare to real time experiments.

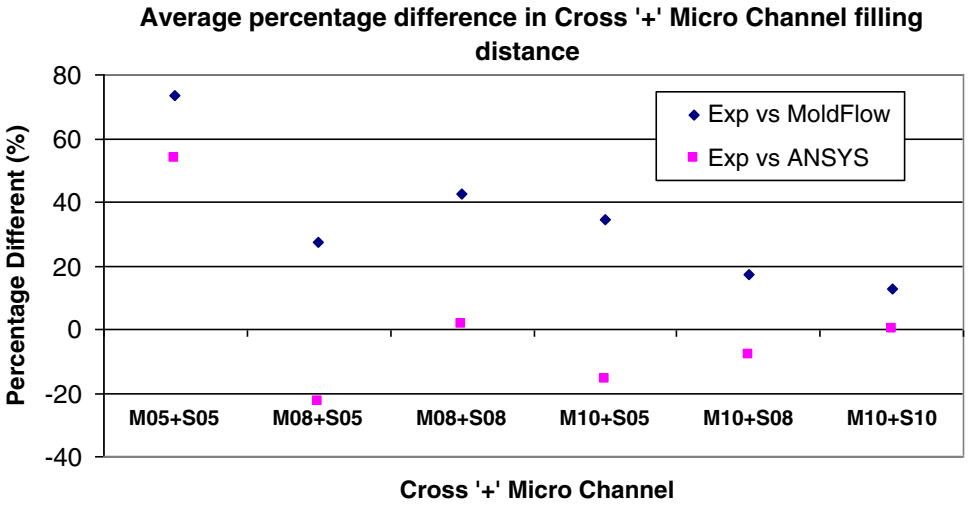
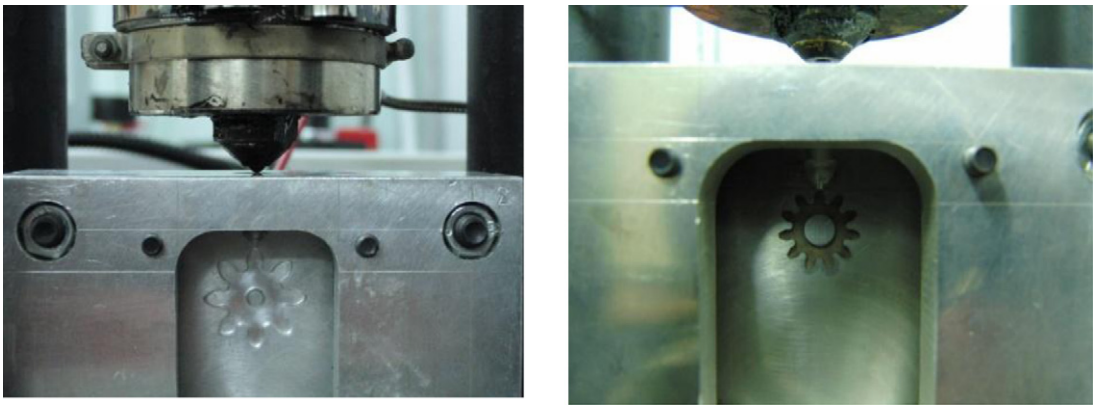


Figure 13 Average percentage differences in filling distance for various sizes combination of cross '+' micro channel.

Table 4 Formulation of constant, C, for cross '+' micro channel

Main	*First side*	*Second side*	*Third side*	η_0 *(without microscopic)*	η_0 *(with microscopic)*	$f_{(microscopic)}$	*Area at main*	*Area at first side*	*Area at second side*	*Area at third side*	*Total area*	*Constant*
1.0	1.0	1.0	1.0	1846.53	146.53	0.079 3	0.392 7	0.392 8	0.392 8	0.392 8	0.392 8	0.202 0
1.0	0.8	0.8	1.0	1846.53	146.53	0.079 3	0.392 7	0.251 4	0.251 4	0.392 8	0.322 1	0.246 4
1.0	0.5	0.5	1.0	1846.53	79.53	0.043 0	0.392 7	0.098 2	0.098 2	0.392 8	0.245 5	0.175 4
0.8	0.8	0.8	0.8	1846.53	59.53	0.032 2	0.251 3	0.251 4	0.251 2	0.251 4	0.251 3	0.128 3
0.8	0.5	0.5	0.8	1846.53	39.53	0.021 4	0.251 3	0.098 2	0.098 2	0.251 4	0.174 8	0.122 5
0.5	0.5	0.5	0.5	1846.53	13.53	0.007 3	0.098 2	0.098 9	0.098 2	0.098 2	0.098 2	0.074 6



a) b)

Figure 14 Gear shape cavity fabricate on aluminum mold with PMMA window. (a) Cavity with macro teeth, (b) Cavity with micro teeth.

The case study components used in this section can be analyzed by MoldFlow software, therefore there is no need to use ANSYS CFX analysis. Section 1.15.5.2 describes the capabilities of plastic melt to fill-up all cavity section in micro gear shape with various sizes of teeth. The teeth was 1.0, 0.5, and 0.3 mm. Extending from full cavity filling, the behavior of flow front direction on each teeth size also will be discussed. Various combinations of mold and melt temperature were used during experiment ranging from 25 to 50 °C and 240 to 260 °C, respectively. For the purpose of this case study, only selected figures will be discussed and explained. Modified cross viscosity models were embedded in ANSYS CFX result as obtained from Sections 1.15.4.3, 1.15.4.4, and 1.15.4.5.

1.15.5.1 Macro Gear Shape

Two gear shapes of with macro and micro structure regions were selected and replicated on the mold cavities using the EDM technique as shown in Figure 14. A Sodick-EDM machine was used to replicate the gear shape to mold cavity.

The aim of these simulation was to examine the flow of plastic melt during filling phase, and then to compare them with the actual melt flow results. The comparison was done to evaluate the capability of MoldFlow for miniature products. MoldFlow was able to generate fill time result report, showing the flow path of the plastic through the mold cavity by plotting contours, which join regions filling at the same time. The fill time result is important because it can be used to predict the flow path inside the mold cavity. Figure 15(a) shows the melt front situation of macro gear shape during the filling stage of MoldFlow simulation and actual plastic injection experimentally. The filling time predicted by MoldFlow was 0.745 5 s, while in actual injection process, the filling time was 1.828 5 s. The variation could be due to the effect of shear resistance on the cavity wall which was neglected in MoldFlow filling model.

The flow front travels as a semicircle moving away from the gate. The semicircle flow front, right from the gate enters the cavity which happens to be the first gear tooth. After filling the first tooth cavity, the melt flows downward and fills the two teeth cavities located sideways. As the melt flows further downward, its meets a circular obstacle where the flows front separates and meets each other again after the obstacle. From this point, the melts flows downward and fills the remaining teeth cavities. An identical flow behavior has been observed in actual injection process as shown in Figures 15(b), 15(d), and 15(e).

The comparison between actual injection and flow simulation by MoldFlow for the micro gear shape can be seen in Figure 16. The filling time predicted by MoldFlow simulation was 0.5266 s, while the actual injection process was 3.742 8 s. Generally, the result of melt flow front from simulation and actual injection showed a similar pattern even though the total time taken in actual injection to fill-up all cavities was large. On the other hand, plastic melt can fill the micro gear shape cavity with lower velocity due to friction of the mold cavity wall and higher melt flow viscosity. The melt front viscosity increased at the smaller cavity which reduced the melt front temperature.

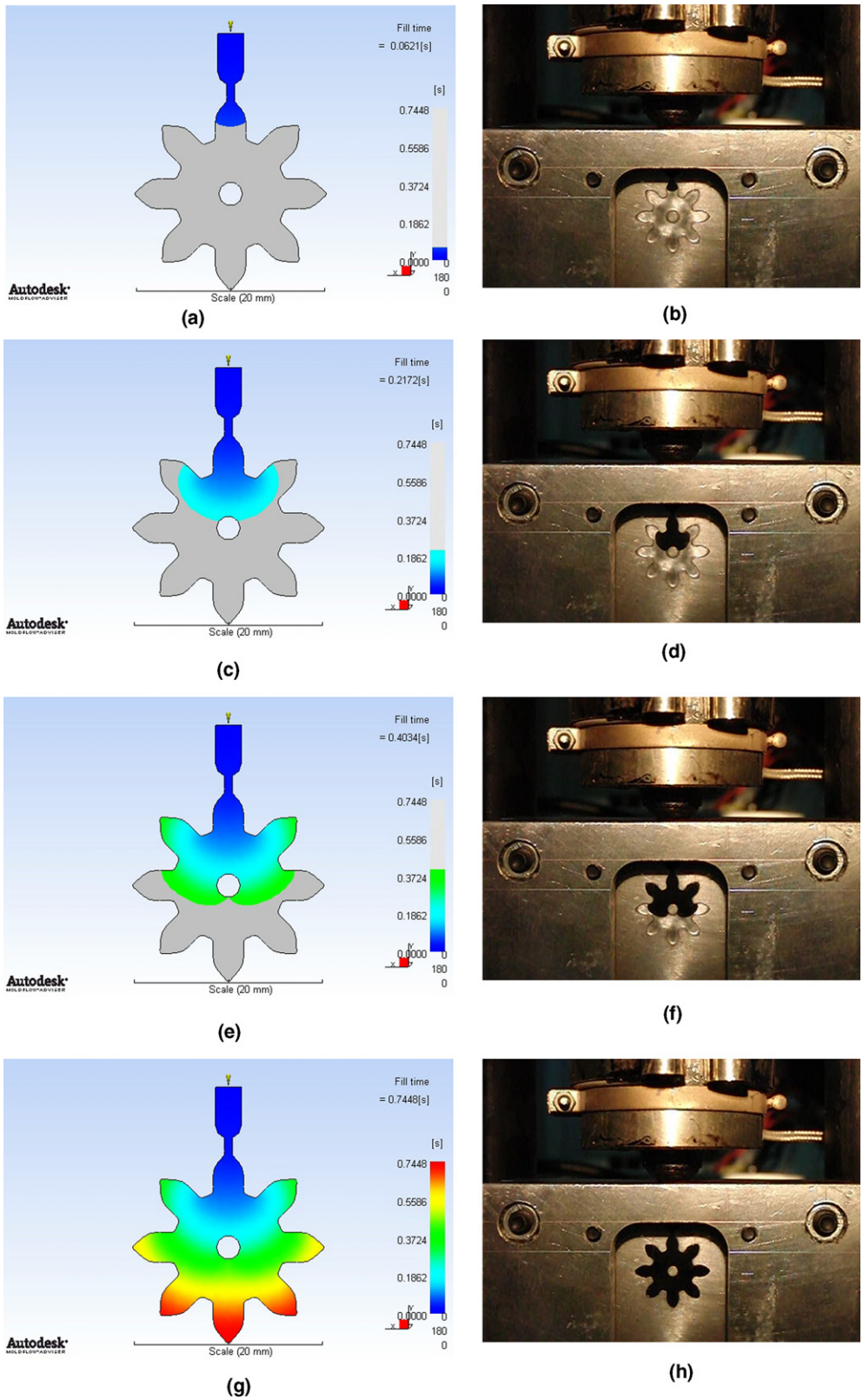


Figure 15 Result of macro plastic gear shape injection from MoldFlow simulation and actual plastic injection.

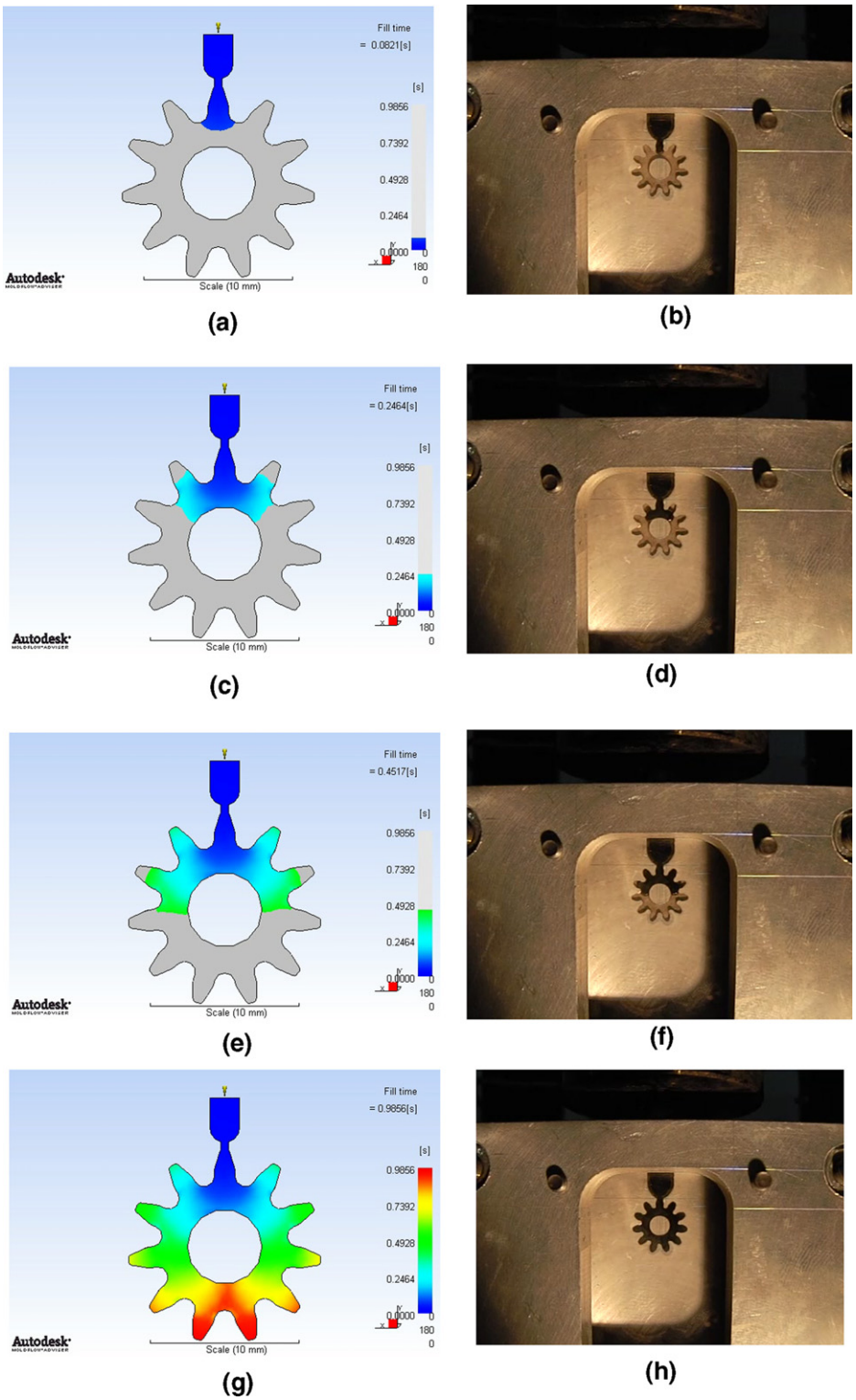


Figure 16 Result of macro and micro plastic gear shape injection from MoldFlow simulation and actual plastic injection.

The results presented here have shown that the prediction of melt flow front by MoldFlow was consistently similar with the actual injection process. But, the time taken to fill the cavities was much longer in actual plastic injection process. This can be explained by the viscosity and PVT model of the melt affecting the flow rate. The PVT model is given by eqn [30].

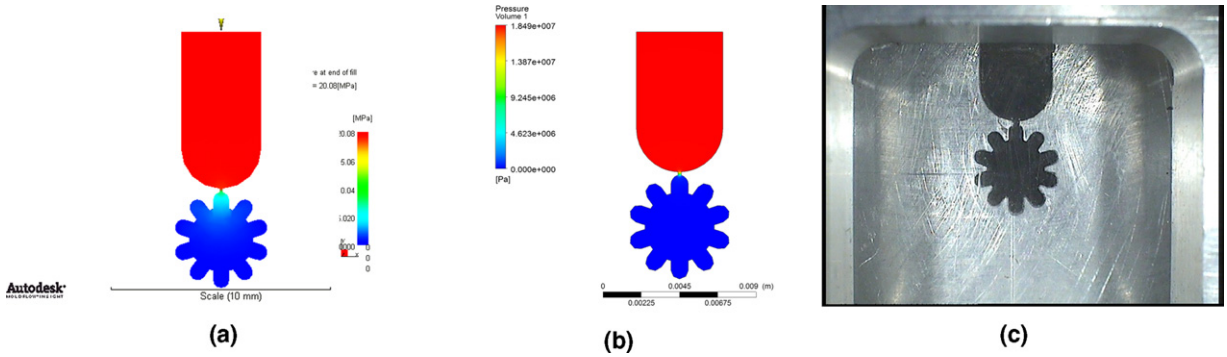


Figure 17 Pressure distribution and filling capabilities for gear shape with 1.0 mm teeth at 35 °C mold temperature and 240 °C melt temperature (a) MoldFlow, (b) ANSYS CFX, and (c) experimental.

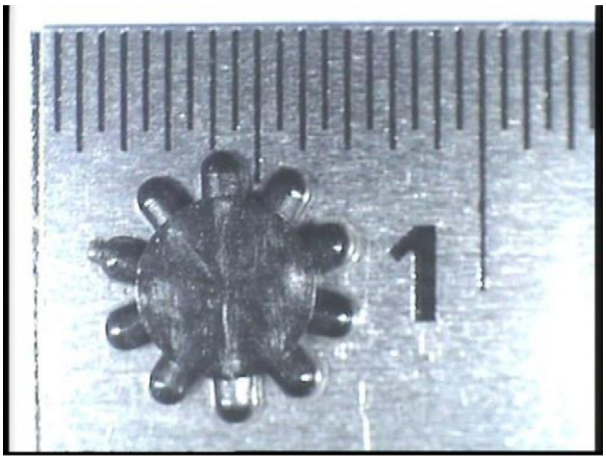


Figure 18 Gear shape with 1.0 mm teeth after solidification.

Table 5 Complete and incomplete cavity filling of gear shape with 1.0 mm teeth for various molds and melts temperature combination

		Melt temperature		
		240 °C	*250 °C*	*260 °C*
Mold temperature	25 °C	X	√	√
	35 °C	√	√	√
	50 °C	√	√	√

Higher viscosity will have higher resistance to melt flow, which will increase the total fill time. Higher viscosity of melt increases the total fill time as flow resistance increases with viscosity. The viscosity of the melt increases as the flow temperature decreases as soon as the melt comes in contact with the mold cavity wall. The fill time and flow path have been affected by viscosity and shear rate.

From this study of both macro and micro gear shapes, it can be concluded that the MoldFlow can simulate very well the filling phase. However there is a huge difference in the filling time of both simulation and actual injection. For macro cavity, the filling time for actual plastic injection increased by 145%, while for micro cavity it increased to 610%. Changes in the melt viscosity while passing through a small cross sectional area have increased the mold cavity filling time. The results also showed that the flow front starts as a semicircle moving away from the gate.

1.15.5.2 Micro Gear Shape

The capability of plastic melt to fill a gear shape cavity with various micro teeth sizes is presented in this section. Each gear shape will be analyzed using MoldFlow and ANSYS CFX simulations followed by actual experiments at various mold and melt temperatures. A suitable η_0 value obtained from study conducted in Sections 1.15.4.3, 1.15.4.4, and 1.15.4.5 will be embedded into cross viscosity model before running the ANSYS CFX analysis.

1.15.5.2.1 Gear shape with 1.0 mm teeth

The MoldFlow, ANSYS CFX and experiment results for gear shape with 1.0 mm teeth are shown in Figure 17. The mold cavity was heated at 35 °C and the melt temperature was set at 240 °C. Both MoldFlow and ANSYS CFX simulation predicted a complete cavity filling which were same as produced by experiments. The ANSYS CFX simulation used 222.53 as η_0 value in cross viscosity model. MoldFlow yielded pressure to fill the cavity equal to 20.29 MPa while that in ANSYS CFX was 18.49 MPa.

Figure 18 shows a gear shape with 1.0 mm teeth after plastic filling the cavity region was completed, solidified, and removed from mold cavity. Attach with 1 cm scale, complete gear shape solidified without any flash defects on its teeth.

Table 5 shows an incomplete and complete cavity filling for 1.0 mm teeth gear shape with various mold and melt temperature combinations. Only 240 and 25 °C of melt and mold temperature combination was not capable of full cavity filling. Others combination gave complete cavity filling.

1.15.5.2.2 Gear shape with 0.5 mm teeth

Figure 19 shows a pressure distribution and filling capabilities for gear shape with 0.5 mm teet size at 50 °C mold

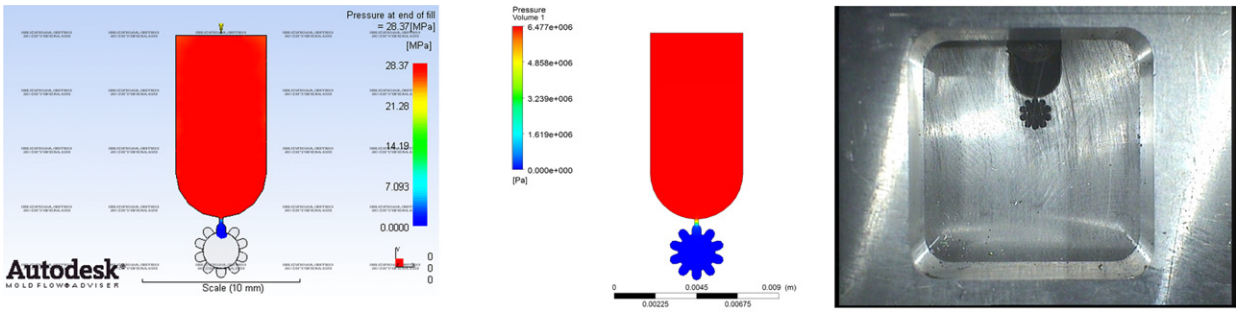


Figure 19 Pressure distribution and filling capabilities for gear shape with 0.5 mm teeth at 50 °C mold temperature and 250 °C melt temperature (a) MoldFlow, (b) ANSYS CFX, and (c) experimental.

temperature and 260 °C melt temperature. Analysis using MoldFlow showed the plastic melt filled the main channel, gate, and one gear tooth only. The remaining teeth were unfilled. However, the ANSYS CFX simulation showed a complete cavity filling same as that produced by actual experiments. This result was due to 32.53 Pa s as η_0 value used in the ANSYS CFX simulation. The maximum pressure recorded by MoldFlow was 6.2 MPa while that in ANSYS CFX was 6.5 MPa. At mold temperature 50 °C and melt temperature set at 250 °C, MoldFlow was unable to predict full cavity filling incidentally identical with experimental result. From Section 1.16.4.4, simulating the filling plastic melt into 0.5 mm micro channel was not possible using MoldFlow.

Figure 20 shows a complete plastic gear shape with 0.5 mm teeth after being removed from its cavity. The gear shape was molded without any flashing problem occurring along its teeth at 50 and 250 °C of mold and melt temperature, respectively.

At 260 °C melt temperature and 35, 50 °C of mold temperatures, the cavity filled completely as shown in Table 6. The combination of remaining melt and mold temperatures did not produce filling of the entire mold cavity.

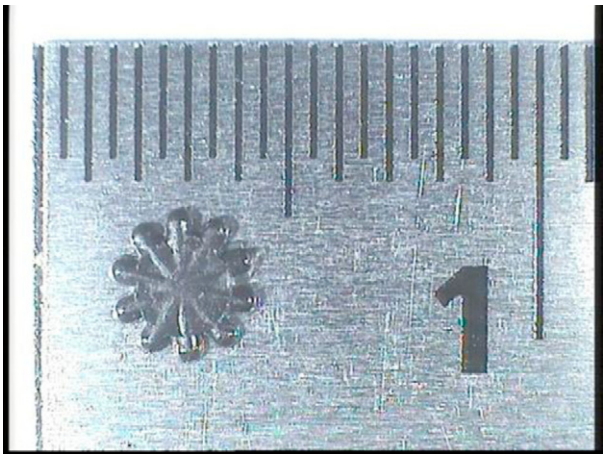


Figure 20 Gear shape with 0.5 mm teeth after solidification.

Table 6 Complete and incomplete cavity filling of gear shape with 0.5 mm teeth for various molds and melts temperature combinations

		Melt temperature		
		240 °C	*250 °C*	*260 °C*
Mold temperature	25 °C	X	X	X
	35 °C	X	X	√
	50 °C	X	√	√

1.15.5.2.3 Gear shape with 0.3 mm teeth

A simulation pressure distribution result from MoldFlow and ANSYS CFX simulations for gear shape of 0.3 mm teeth are shown in Figure 21. Also, a complete experimental injection process was done at 50 °C mold temperature and 260 °C melt temperature. Figure 21(b) shows a full cavity filling obtained from ANSYS CFX with 52.53 Pa s as η_0 value in the cross viscosity model. The maximum pressure in MoldFlow was 5.73 MPa, while ANSYS CFX recorded much higher pressure 12.72 MPa. But, ANSYS CFX was capable to simulate a complete filling compared to MoldFlow. MoldFlow showed the plastic melt filling only one teeth of gear cavity. With the combination of this mold and melt temperatures, MoldFlow was unable to simulate the plastic melt flow into the gear shape with 0.3 mm teeth. On the other hand, ANSYS CFX was capable of predicting full cavity filling identical with actual experiment.

Figure 22 shows a solidified gear shape with 0.3 mm teeth after it been removed from the mold. The gear shape had small flash problem occurring at its teeth. This was due to 50 °C of mold temperature and 260 °C melt temperature used as molding condition. At higher mold and melt temperatures, plastic melt viscosity is reduced and ability to fill micro cavity increases. There was a possibility of plastic melt filling the parting line which caused the flash problem.

Table 7 shows an incomplete and complete cavity filling for 0.3 mm teeth gear shape at various mold and melt temperature combinations. When mold was heated at 35 and 50 °C with 260 °C of melt temperature, the full cavity filling can be achieved. Others mold and melt temperature combinations gave incomplete cavity filling. As micro areas to be filled, mold and melt temperature have significant effect on the filling capability.

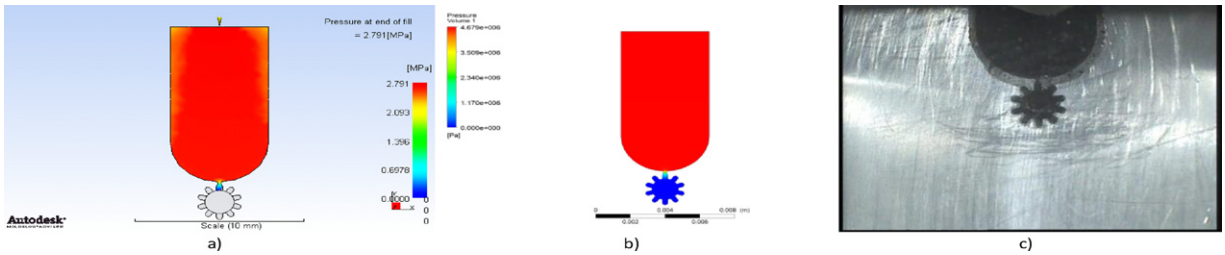


Figure 21 Pressure distribution and filling capabilities for gear shape with 0.3 mm teeth at 50 °C mold temperature and 260 °C melt temperature (a) MoldFlow, (b) ANSYS CFX, and (c) experimental.

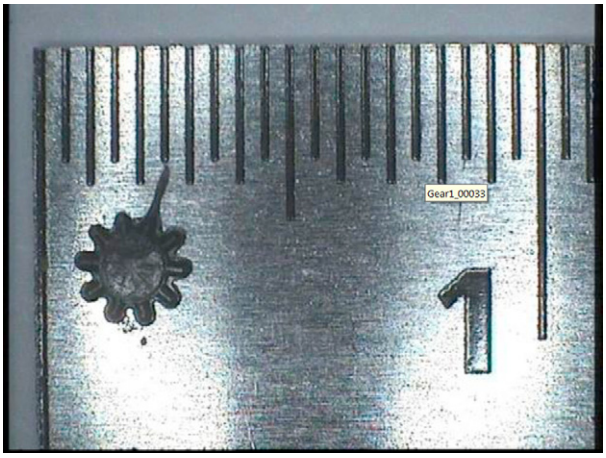


Figure 22 Gear shape with 0.3 mm teeth after solidification.

Table 7 Complete and incomplete cavity filling of gear shape with 0.3 mm teeth for various molds and melts temperature combination

		Melt temperature		
		240 °C	*250 °C*	*260 °C*
Mold temperature	25 °C	X	X	X
	35 °C	X	X	√
	50 °C	X	X	√

1.15.6 Conclusions

Molding of micro plastic parts require specific machine which must be capable of delivering small amount of melt plastic into micro cavity. The developed machine was embedded with controller for controlling pressure, mold, and melt temperatures during cavity filling process. Testing the machine capability with standard Tensile and Izod specimens is required for their reliability. Verification of the heat transfer behavior along flow direction with acceptable heat transfer model was an added value for the developed injection molding machine. A special mold embedded with visualization windows was developed which enables user to track the flow front position, time, and also the direction of flow. Comparison of experimental results with simulation from software showed a very good agreement for macro molding applications.

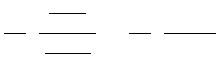
Filling of micro part or micro structure region began with exploring the filling capability of plastic melt in the micro channels with 1.0, 0.8, 0.5, 0.4, and 0.3 mm in diameter. At three levels of mold and melt temperatures applied to PP, experiments was designed to incorporate various micro straight channel sizes. Analytical straight filling capability was formulated with simple 1D direction flow for faster filling capability. Together with MoldFlow and ANSYS CFX analysis software, experiments results were compared to find the most suitable method in predicting micro straight channel filling capability. Generally, MoldFlow shows good filling capability predictions with experiments for micro channel size larger than 0.5 mm. ANSYS CFX embedded with modified cross viscosity model is able to predict filling distance compared to MoldFlow and analytical results.

Fabrications of macro gear and micro gear shape with micro teeth shows the custom-made vertical injection molding machine capabilities in delivering the plastic melt into the entire cavity without any serious molding defects. For macro gear shape fabrication, MoldFlow produced almost the same flow front direction as shown by experiments. But, filling time difference recorded for both methods was more than 100%. This was due to the simplification in equations used in MoldFlow, without considering the cavity roughness, air vent location, and dynamic viscosity due to micro size. Considering application to micro teeth cavity filling, MoldFlow is unable to predict well as produced in the actual experiments for gear shape with teeth sizes of 0.5 and 0.3 mm. Therefore, ANSYS CFX analysis with modified viscosity model was used to simulate almost similar plastic melt behavior as shown by experiments. ANSYS CFX embedded with modified cross viscosity model gives realistic plastic melt flow behavior when compared with experiments.

See also: 1.4 Review of Gear Finishing Processes

References

1. Young, W. B. Analysis of Filling Distance in Cylindrical Microfeatures for Microinjection Molding. *Appl. Math. Model.* **2007**, *31* (9), 1798–1806.
2. Chien, R. D.; Jong, W. R.; Chen, S. C. Study on Rheological Behavior of Polymer Melt Flowing through Micro-Channels Considering the Wall-Slip Effect. *J. Micromech. Microeng.* **2005**, *15*, 1389–1396.
3. Harris, C.; Despa, M.; Kelly, K. Design and Fabrication of a Cross Flow Micro Heat Exchanger. *J. Microelectromech. Syst.* **2000**, *9* (4), 502–508.



controlling of these parameters enhance part quality, but some are more critical.

1.16.3.2.3 Critical factors influencing part quality in IM

The choices of IMM, feedstock material selection, process condition, mold, and part design are critical factors that influence molded part quality in injection molding.[70] According to Surace *et al.*,[71] researchers investigated the optimum processing conditions for microfabrication of various parts. The following process parameters were found to affect part quality in μIM: mold temperature, melt temperature, injection speed, injection pressure, holding time, holding pressure, and cooling time. Therefore, application of optimization techniques to μIM processes will enhance molded part quality and lead to less scrap, efficient cycle times, and improved productivity.

1.16.3.3 Debinding Process

This is the process of binder removal. It is described as the most complex, difficult, expensive, and time-consuming stage, and it depends on processing conditions. In line with the formulation of the binder constituent, the minor binder components (such as plasticizers, surfactants, and lubricants) are usually removed first and the backbone binder component is removed last. In practice the debinding techniques adopted are solvent debinding,[72–73] thermal debinding,[74–75] catalytic debinding,[76] and wicking debinding,[77] respectively.

A multi-step debinding technique is now practiced, whereby the green part is processed via solvent medium (such as hexane and heptane) and then followed by thermal debinding. The multistep technique is preferred as a result of defects associated with direct thermal debinding such as cracking, slumping, porosity, and blistering.[78,79] Combining solvent and thermal debinding techniques reduces processing time; the parameters are presented in **Table 10**.

The fundamental principles of the solvent and thermal debinding techniques are discussed next.

1.16.3.3.1 Solvent debinding

This is a technique that removes the binder constituent of the feedstock using solvent. The green part is immersed in the solvent (such as water, hexane, heptain, acetone, ethanol, and other alcohols). At specified temperatures, binder constituent is dissolved in liquid at low temperatures and a network of interconnected porosity is formed in the part while being immersed in the solvent. However, most of available solvents used are dangerous to the environment if necessary precautions and measures are not observed. Meanwhile, water is identified as a safe solvent that is environmentally friendly. Solvent debinding requires a longer time to remove binder constituent relative to other techniques, such as catalytic and thermal debinding processes. Cost and environmental challenges are much lower, especially when water is used.

Table 10 Some process parameters of solvent and thermal debinding technique

Debinding technique	*Process parameters*
Thermal	Heating rate, holding temperature, holding time, cooling rate
Solvent	Immersion time, immersion temperature, dissolving medium

1.16.3.3.2 Thermal debinding

The polymeric constituent of the binder system can be eliminated by heating the green part to temperatures that cause the main polymers to decompose or degrade. The temperature could be up to 800 °C, but it strongly depends on the binder system. Meanwhile, the thermal binder burnout requires times longer than for catalytic debinding. To reduce the processing time, a combination of solvent and thermal debinding is usually adopted. Herranz *et al.*[80] used a PE-based binder system and demonstrated the successful application of the double-cycle debinding process involving solvent (heptane solvent) debinding and thermal debinding.

The use of a thermal debinding technique is widely practiced due to its high efficiency in binder burnout, but the occurrence of part defects has limited the practice as a standalone method. Therefore, the double-stage method, which involves solvent and thermal energy, is mostly practiced. The process is simple and similar to the sintering process. Therefore, it is widely accepted and used. Typically, the burnout of the polymeric constituent from the green part involves chemical and physical mechanisms.

The chemical mechanisms occur because of thermal degradation of polymers into volatile species, called pyrolysis. The physical mechanisms involve diffusion of the volatile species to the surface and changes in the polymer distribution within the green body. Depending on the material properties, such as thermal conductivity, porosity, pore size, and related features, it is possible for mass diffusion or thermal diffusion to be controlling steps. As a further complication, component heating depends on heat transfer and the reaction enthalpies associated with pyrolysis events, leading to thermal–kinetic effects that couple to the chemical–physical aspects.

1.16.3.3.3 Other debinding techniques

Apart from the solvent and thermal debinding methods, other techniques such as catalytic debinding and wicking debinding are practiced. The uses of other techniques, other solvents, and thermal debinding arise as a result of the requirements of the binder formulation or composite such as polyacetal. The polyacetal binder systems require debinding in a gaseous acid environment (usually highly concentrated nitric or oxalic acid) at a temperature of approximately 120 °C (a temperature slightly lower than that for softening the binder system). The nitric or oxalic acid used served as a catalyzer in the degradation of the polyacetal constituent of the binder system.

1.16.3.3.4 Development of master decomposition curve

The design and optimization of the debinding process are enhanced through effective investigation and development of the master decomposition curve (MDC) for the polymeric binder component of the feedstock. This is an essential tool used for the prediction of part behavior at the debinding step, a process that is viewed to be a challenging task for PIM. This is due to the fact that several researchers have reported that the process of binder removal from the green part is expensive and

time-consuming, and is sometimes viewed as a limitation for PIM processing. According to Aggarwal *et al.*,[81] the feedstock of PIM consists of multiple components that can be categorized into two groups according to their molecular weight as:

- Low-molecular-weight polymers, such as solvents and plasticizers, that can either be evaporated or are decomposed at low temperatures.
- High-molecular-weight polymers, such as polymers possessing higher thermal stability, that are pyrolyzed at relatively high temperatures.

Therefore, the need for the kinetic investigation of the binder components of the molded part during debinding is paramount and monitored through weight loss. The TGA and differential thermal analysis are used extensively for the determination of weight loss of the binder component as a function of time and temperature. **Figure 9** illustrates a typical TGA plot of the binder components at various rates in an argon atmosphere.

The concept of the master sintering curve (MSC), developed by Su and Johnson,[82] successfully extended to include binder behavior during solvent extraction and wicking process of debinding, respectively.[72] The MDC was developed for single-step and multistep burnout of the polymeric binder and is presented in the next section.

1.16.3.3.4.1 Single-step burnout process

Depolymerization of polymeric binders can be described by first-order reaction kinetics. The remaining weight fraction of a polymer, α, is expressed as[83,84]:

$$\frac{d\alpha}{dt} = -K\alpha \qquad [26]$$

where t is the time and K is the rate constant for degradation and relate to the Arrhenius eqn [27]:

$$K = K_0 \exp\left(\frac{-E}{RT}\right) \qquad [27]$$

where K_o is the specific rate constant, E is the apparent activation energy for thermal degradation, R is the gas constant, and T is the absolute temperature. Combining eqns [26] and [27] provides the following:

$$-\int_1^{\alpha} \frac{d\alpha}{\alpha} = -\ln \alpha \qquad [28]$$

$$-\ln \alpha = \int_0^t K_0 \exp\left[-\frac{E}{RT}\right] dt = K_0\Theta \qquad [29]$$

Where the decomposition (ψ) is expressed as:

$$\Theta(t, T; Q) = \int_0^t K_0 \exp\left[-\frac{E}{RT}\right] dt \qquad [30]$$

$$\alpha(\Theta; K_0) = \exp[-K_0\Theta] \qquad [31]$$

Equation [30] defines the MDC, where the decomposition curves for a given polymer with any decomposition cycle uses the concept of work of decomposition, Θ.

In addition, Enneti *et al.*[72] proposed a modification to the MSC by incorporation of the shape factor. The modified MSC is capable of estimating activation energy without further dependency on solvent extraction rate to the square of the length of the part as previously practiced. The fundamental MSC model is expressed as eqn [31], whereas the modified MSC for the prediction of activation energy during solvent extraction and wicking process is given by eqn [32].[72]

$$\Phi(\rho) = \theta(t, T) = \int_0^t \frac{1}{T} \exp\left(\frac{-E}{RT}\right) dt \qquad [32]$$

$$\Phi(\rho) = \theta(t, T) = \left(\tfrac{1}{\psi^2}\right) \int_0^t \frac{1}{T} \exp\left(\frac{-E}{RT}\right) dt \qquad [33]$$

where $\Phi(\rho)$ is the densification, ψ is the shape factor, t is the time, T is the absolute temperature, E is the apparent activation energy, and R is the universal gas constant.

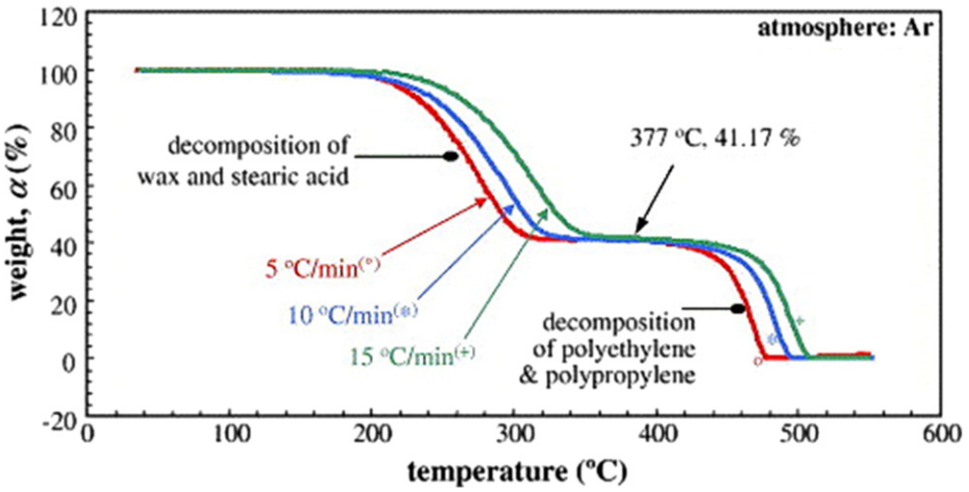


Figure 9 A typical thermogravimetric analysis plot of binder components at various rates. Aggarwal, G.; Smid, I.; Park, S. J.; German, R. M. Development of Niobium Powder Injection Molding. Part II: Debinding and Sintering. *Int. J. Refract. Metals Hard Mater.* **2007**, *35*, 226–236.

1.16.3.3.4.2 Evaluation of apparent activation energy

To evaluate the decomposition (Θ) from eqn [30], the apparent activation energy (E) needs to be determined. The activation energy for polymeric binder decomposition can be determined from TGA data using the Kissinger method. The temperature (T_{max}) at which the maximum rate of weight loss occurs at various heating rates is used for the determination as follows:

$$\frac{d}{dt}\left(-\frac{d\alpha}{dt}\right)=0 \text{ and } T=T_{max} \quad [34]$$

considering constant heating rate (r) and then

$$\frac{dT}{dt}=r \quad [35]$$

$$\frac{rE}{RT_{max}^2}=K_0 \exp\left(\frac{-E}{RT_{max}}\right) \text{ at } T=T_{max} \quad [36]$$

Equation [36] is simplified in linear form and expressed as:

$$\ln\left[\frac{r}{T_{max}^2}\right]=E\left(-\frac{1}{RT_{max}}\right)-\ln\left[\frac{E}{K_0R}\right] \text{ at } T=T_{max} \quad [37]$$

The apparent activation energy E of the reaction represents the slope from a plot of $\ln\left(\frac{r}{T_{max}^2}\right)$ and $\left(-\frac{1}{RT_{max}}\right)$, which are determined from the TGA experiments with several constant heating rates.

However, Aggarwal *et al.*[84] proposed a statistical approach for the determination of the apparent activation energy based on the MDC concept. The idea is to minimize the mean residual (MR) while varying the activation energy. MR is mathematically defined as follows:

$$MR=\sqrt{\int_t^0\left[\frac{\sum_{i=1}^{N}\left(\frac{\Theta_i}{\Theta_{avg}-1}\right)^2}{N}\right]d\alpha} \quad [38]$$

where N is the number of TGA experiments, i is the running index for the TGA experiment label, Θ_i is the work of decomposition calculated from TGA experiments with the label of i, and Θ_{avg} is the average work of decomposition calculated from all TGA experiments, respectively. This alternative method is simple because it does not attach any condition to the TGA experiments. The two methods are derived from the same fundamental equations.

1.16.3.3.4.3 Multistep burnout process

Typical TGA curves of polymer degradation follow a single sigmoidal path. However, multicomponent binder systems may have two or more sigmoids due to the different molecular weights, bonding groups, and degradation paths for each polymer constituents. Then, each sigmoid describes a rate-controlling step whose activation energy differs from those of other controlling steps. It is then important to remember that powder–binder systems in PIM often consist of several components. Typically, the binder components can be categorized into two groups based on molecular weight of the constituents: high-molecular-weight (HMW) and low-molecular-weight (LMW). The LMW ones are additives such as solvents and plasticizers, which either evaporate or decompose at low temperatures. Whereas the HMW polymers are characterized as possessing higher thermal stability and decomposing at high temperatures relative to the LMW. Therefore, the difference in molecular weight of the PIM binder system is responsible for the TGA curve with multiple sigmoids. Superposition of several sigmoids may be observed when the constituents have similar activation energy. Sigmoids typically represent a distinct reaction step with sufficiently different activation energy. A sigmoid is described by three kinetic parameters in reference to the Arrhenius equation. The frequency factor, activation energy, and reaction order are used for distinguishing each sigmoid that represents each powder. However, some powders may have catalytic effects on the pyrolysis rate; however, the shape of the pyrolysis curve with powders is similar to that without powders.

Therefore, the mathematical form of polymer pyrolysis can still be applied. Two polymers of the binder system used in this study are decomposed during the thermal debinding process:

$$\alpha=\omega\alpha_1+(1-\omega)\alpha_2 \quad [39]$$

where α is the mass ratio of the initial masses of two polymers, α_1 is the ratio of mass to initial mass of the low-molecular-weight polymer, α_2 is the ratio of mass to the initial mass of the high-molecular-weight polymer, and ω is the ratio of the initial mass of the low-molecular-weight polymer to the initial mass of the two polymers.

The mathematical form that is generally applied to the TGA curve of a polymer is modified to describe the TGA curve of organic pyrolysis with powders. In the present analysis, we assume that the kinetics are solely controlled by the temperature:

$$-\frac{1}{k_0\beta^n}d\alpha=\exp\left[-\frac{E}{RT}\left(\frac{1}{T}-\frac{1}{T_t}\right)\right]dt$$

$$\text{if } T\geq T_t(\text{or } \alpha\geq\omega),\ \alpha=\omega\alpha_1+(1-\omega),$$

$$\beta=\frac{\alpha+(\omega-1)}{\omega},\ n=n_1\ K_0=K_{01},\ E=E_1$$

$$\text{if } T>T_t(\text{or } \alpha<\omega),\ \alpha=(1-\omega)\alpha_2,$$

$$\beta=\frac{\alpha}{(1-\omega)},\ n=n_2\ K_0=K_{02},\ E=E_2 \quad [40]$$

where T_t is the transition temperature between the first and second sigmoids, and subscripts 1 and 2 that appear along with a, E, and K_0 represent the low- and high-temperature degradation, respectively. In addition, it is possible to evaluate a decomposition kinetic curve with more than two sigmoids using the concept described. Meanwhile, the Kissinger method is applied to estimate the activation energy, as described in Section 1.16.3.3.4.2.

Splitting eqn [40] and integrating each side separately is expressed as the left side of eqn [40] as a function of the mass ratio α and material properties K_0, yielding:

$$\Phi(\alpha; k_0) = \int_1^{\alpha} \frac{1}{K_0 \beta^n} \mathrm{d}\alpha \qquad [41]$$

Likewise, integrating the right side of eqn [40] is expressed as a function that depends on t, T, E, and T_t:

$$\Theta(t, T; E, T_t) = \int_0^t \exp\left[-\frac{E}{R}\left(\frac{1}{T} - \frac{1}{T_t}\right)\right] \mathrm{d}t \qquad [42]$$

where $\Phi(\alpha)$ is considered a characteristic that quantifies the effect of binder components on the decomposition kinetics. Therefore, the relationship between the mass ratio (α) and Φ (α) is defined as the MDC. MDC is unique for each powder and binder system, as described previously. **Figure 10**[84] is typical illustration of MDC developed for PIM feedstock based on intrinsic kinetics of polymer pyrolysis. In addition, Enneti *et al.*[74] presents a detailed review article on major progress of the thermal debinding process in particulate materials processing. This study includes progress made in understanding various phenomena during polymer burnout from PIM molded parts, focusing on a substantial reduction in thermal debinding time.

1.16.3.4 Sintering Process

In PIM, sintering is the fourth and final processing step. It is used to produce high-density parts with good mechanical properties. According to German,[85] sintering is a thermal treatment for bonding particles into a coherent, predominantly solid structure via mass transport events that often occur on the atomic scale. In addition, depending on the formulation and design of the binder system, the likely residues after the debinding process and pores left in the brown part are completely removed at this stage. Less attention is given to the debinding residues, which could be a serious issue for structural and/or magnetic effects of the finished part. The sintering process is identified as the processing stage that influences mechanical properties and other quality characteristics of the finished part.[77] At this stage, approximately 17–22% of shrinkage as well as other processing part defects become visible and pronounced. Therefore, it is important to handle the process with a robust design of experiment (DOE) to determine the optimum operating conditions. An optimum cooling rate of 10 °C min^{-1} was determined for both the mechanical properties and corrosion resistance of the sintered 316L stainless steel part, considering temperature, time, heating rate, and cooling rate as processing parmeters.[86] However, it is important to note that hardness and strength are the two mechanical properties commonly used to track finished part quality.

Typical processing parameters of the sintering operation are temperature, particle size, time, and pressure; the degree depends on the material properties. Although it is important to note that many materials densify as part of sintering, not all sintering involves densification. The process is characterized as pressure-assisted or pressureless sintering techniques.[85] Also, during the debinding (thermal debinding) and sintering processes, the green and brown parts are subjected to subsequent heat treatments, as depicted in **Figure 11**.[87]

The capability of PIM as a net-shaped microfabrication technique to produce parts with shiny and high surface finish values gives the technology a unique feature and makes it stand out among other microfabrication processes. This advantage is achieved through a number of factors: high density must be achieved and the metal surface must be free from reaction with sintering atmospheres to avoid the formation of oxides, nitrides, or other products. Consequently, the oxygen content or dew point in the atmosphere must be sufficiently low, and the amount of hydrogen or the degree of vacuum must be sufficiently high to reduce the metal oxides on micrometal parts surfaces. All these factors are considered to produce defect-free parts. Postprocessing of the finished part is implemented, but this strongly depends on target application. **Figure 12** illustrates tensile specimen parts at various processing stages of niobium powder injection molding, which depicts the advantages of multistep debinding techniques.

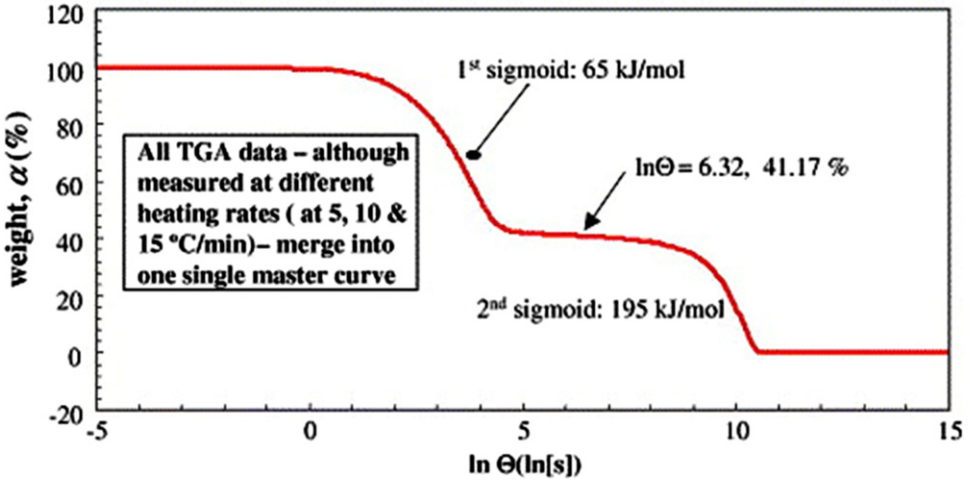


Figure 10 MDC of 57 vol.% of Nb solid loading feedstock. Aggarwal, G.; Smid, I.; Park, S. J.; German, R. M. Development of Niobium Powder Injection Molding. Part II: Debinding and Sintering. *Int. J. Refract. Metals Hard Mater.* **2007**, *35*, 226–236.

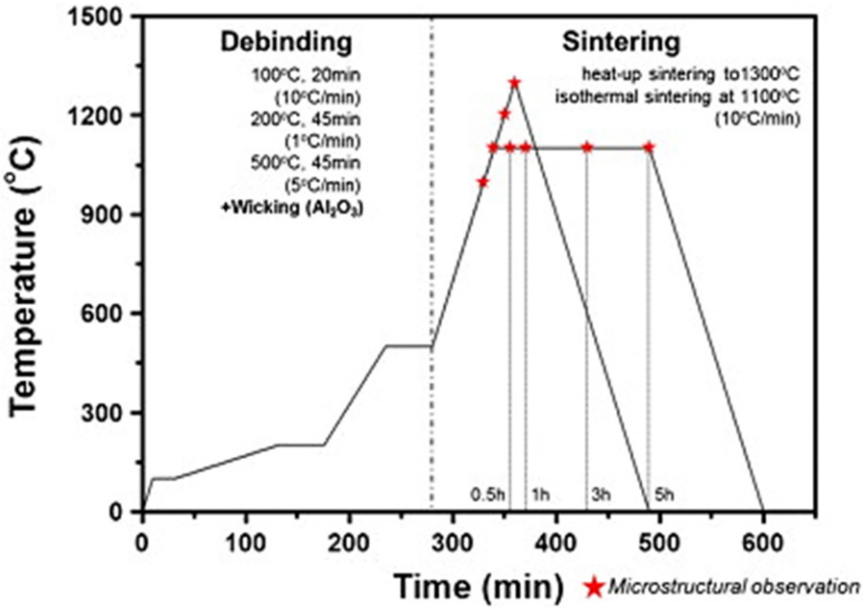


Figure 11 Typical heat treatment cycle during debinding and sintering processes of the molded part. Choi, J.-P.; Lee, G.-Y.; Song, J.-I.; Lee, W.-S.; Lee, J.-S. Sintering Behavior of 316l Stainless Steel Micro–Nanopowder Compact Fabricated by Powder Injection Molding. *Powder Technol.* **2015**, *279*, 196–202.

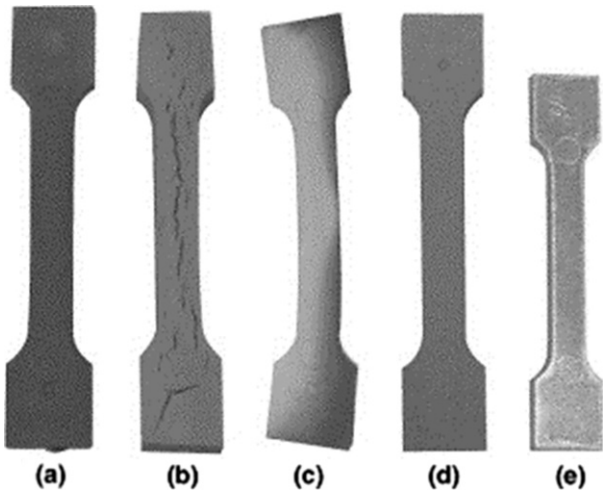


Figure 12 Niobium powder injection molding of tensile specimen and various processing products: (a) green part; (b) brown part by thermal debinding only; (c) brown part by solvent debinding followed by thermal debinding in nitrogen atmosphere; (d) brown part by solvent debinding followed by thermal debinding in argon atmosphere; and (e) defect-free finished part after sintering. Aggarwal, G.; Smid, I.; Park, S.J.; German, R. M. Development of Niobium Powder Injection Molding. Part II: Debinding and Sintering. *Int. J. Refract. Metals Hard Mater.* **2007**, *25*, 226–236.

1.16.4 Optimization and Simulation of Microinjection Molding Process

Product quality is improved by the application of optimization techniques to the manufacturing processes. These optimization techniques were developed based on global search process, statistical, and mathematical approximation. A broad classification of optimization techniques applied by researchers to injection molding process is presented in **Figure 13**.

A survey of literature as depicted in **Figure 13** shows that optimization techniques applied in injection molding process are classified as: intelligent algorithms,[88–91] iterative,[88,92–95] and noniterative[96–98] methods. In addition, a simulation-based classification of optimization techniques for IM is presented in **Figure 14**.[53] This consists of two broad categories: the direct discrete optimization and metamodel-based optimization methods. The metamodel-based method is further classified as response surface methodology (RSM), radial basis function, artificial neural network (ANN), and Kriging.

However, numerical simulations are sometimes integrated with DOE as optimization techniques to enhance product quality. The DOE approach is implemented to study the impact of processing parameters on quality characteristics such as strength, surface finish, part weight, shrinkage, and warpage of the finished part. These quality characteristics have been investigated to determine the optimum processing conditions of the microinjection molding process for different materials using the DOE approach. Zhao *et al.*[10] used DOE and considered the effect of five processing parameters on the microinjection molding process and quality of microgears. Various investigations based on DOE were performed to focus on determining optimal operating conditions[99–101] and quality characteristics of molded parts.[102–104] It is important to identify and control some key parameters that influence finished part quality in injection molding processes.

1.16.4.1 Parameter Control in Injection Molding Processes

It is important to control and monitor the injection molding process. IM is a repetitive process that requires close monitoring of many variables and parameters. Production consistency and

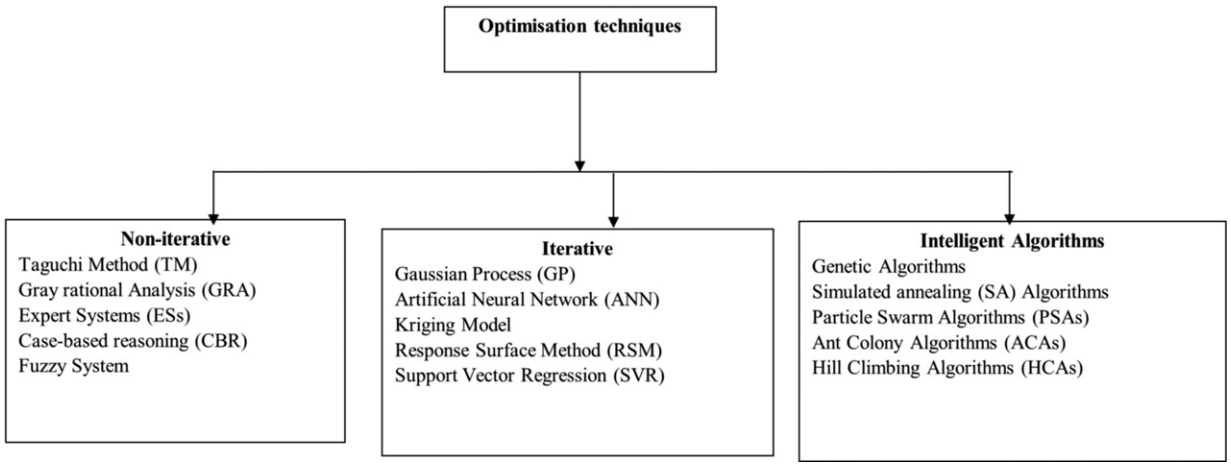


Figure 13 Optimization techniques used for IM process.

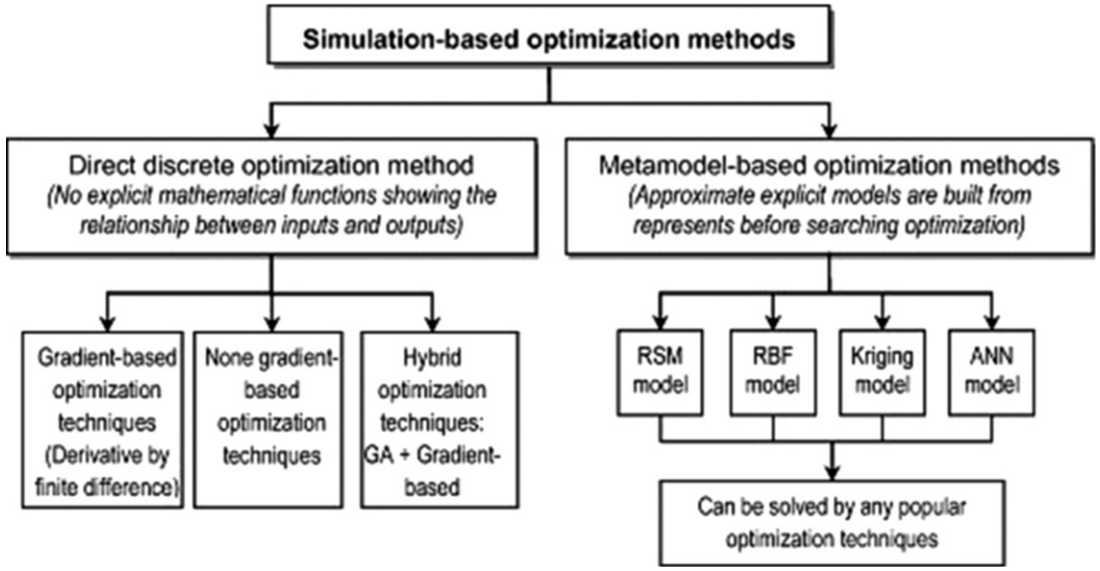


Figure 14 Simulation-based optimization techniques for IM. Dang, X.-P. General Frameworks for Optimization of Plastic Injection Molding Process Parameters. *Simul. Model. Pract. Th.* **2014**, *41*, 15–27.

part quality in IM are enhanced through control and monitoring of process parameters and conditions. IM is a very complex process that involves a high degree of interaction between feedstock material, machine, and process conditions. Therefore, the optimal performance of the IMM is characterized by production consistency and repeatability of the mold cycle. Therefore, precise control and monitoring of the processing conditions are necessary for efficient performance of IMM. However, not all parameters can be controlled and monitored at the same time. Some important parameters are linked directly to molded part quality. A typical control system in the modern injection molding process has the following main functions:

- manipulation of machine operational sequence control
- control of process and/or machine variables
- monitoring of process and performance evaluation status of the machine
- quality control of product to ensure consistency.

The sequence control ensures the molding machine operates according to the predetermined order and implements defined logic to provide target functions based on the circuit or tasks as specified in the software. This is an important function, but it does not directly influence product quality. The consistency of part quality from one production batch to another is a serious challenge in the IM process. In fact, sometimes the problem is experienced within batch production from one cycle to another, especially when manually operated or controlled. Then, process control and automation of machine operations become necessary to maintain

production consistency of parts. It is necessary to outline some important factors or key variables of the process, including process variables, material variables, and mold design variables, as presented in Table 11.

Therefore, the extent of the variability encountered by the machine output during operations is an indication of the level of inherent stability of the production. Hence, the smaller the variation, the more consistent and stable is the process.

Control and monitoring of the IM process provide continual support toward achieving a higher level of technology implementation to meet performance demands at the lowest cost. The control systems for the IM process available at present include closed loop (feedback) control, open load control, learning control, and advanced control. In addition, monitoring of the IM process is focused on statistical process control, multivariate statistics, and multiphase statistical process control. The functions of the control in injection molding are manipulation of machine sequence/mold cycle, control of machine variables, monitoring of process status and performance, and quality control of product/molded part. In addition, the control system is a useful tool for performing supervisory functions, process monitoring, and online evaluation of process variables statistically that can be used to alert the operator of any potential problems.

Table 11 Some processing variables of injection molding

Variable	*Factor/properties*	*Parameter*
Operating variables	Temperature	Melt temperatures Barrel temperature Nozzle temperature Mold temperature Cooling medium temperature
	Pressure	Injection pressure Holding/packing pressure Hydraulic back pressure Nozzle pressure Mold clamping pressure/force
	Time	Injection time Holding/packing time Pause (dwell) time Cycle time Cooling time
	Speed	Mold opening and closing mechanism speed Screw/ram speed Screw/ram recovery speed Component retraction spee
Material variables	Physical properties	Shear rate Shear stress Thermal conductivity Thermal diffusivity Specific volume Specific heat Viscosity Density
	Mechanical properties	Tensile strength Tensile modulus Elongation Compressive strength Compressive modulus Flexural strength Flexural modulus Impact strength Hardness Tensile creep Flexural creep Tensile fatigue Flexural fatigue
Mold design variables	Mold cavity measurements/ dimensions	Part dimensions and tolerances Cooling channel size Venting channel size Gate(s) location and size Runner system design

Some key variables that are often controlled in the IM process that allow optimum machine output are enumerated as temperature, pressure, injection velocity, and screw speed control. A typical experimental setup for monitoring and control of variables such as melt temperature, barrel temperature, nozzle temperature, and screw speed is illustrated in Figure 15.[105]

Figure 15 is a typical example of experimental setup of the control structure featuring SM25 IMM by Jhen-Syong Company, as reported by Lin and Lian.[105] Multiple sensors are used for data acquisition systems during operation to monitor various changes of both processing parameters and quality of the molded part. Many researchers have investigated the injection molding process by using sensors for measured variables such as injection pressure, cavity pressure, displacements and velocity of the injection pin, mold temperature, clamping, and demolding force.

1.16.4.2 Optimization Methods

The application of optimization methods in the injection molding process has become popular among researchers as they explore ways to improve quality of molded parts. The quality of molded parts is described in terms of quality characteristics, including physical and mechanical properties of dimensional conformity, surface finish, strength, hardness, and microstructure morphology. Part quality is affected by many variables and factors that are influenced by the process conditions of injection molding. This, in turn, gives rise to many processing parameters of injection molding that need to be monitored and controlled to achieve the desired molded part quality. Then, the need for selecting appropriate input variables and response factors becomes necessary. Based on this requirement, researchers applied the method of trial and error to investigate the effect of process parameters on the quality of characteristics. This involves choosing one parameter at a time and observing its effect on molded part quality characteristics of interest.

However, this technique is useful but not economical; it wastes time and materials. Due to this shortcoming, there was a shift to the DOE. The DOE technique considered the effect of more than one parameter at a time on specified quality characteristic of the molded part. This approach is widely accepted and adopted for investigation of processing parameters in microinjection molding. Table 12 presents a summary of the DOE technique as applied to microinjection molding process investigations and corresponding statements of the research findings for various materials.[101,106]

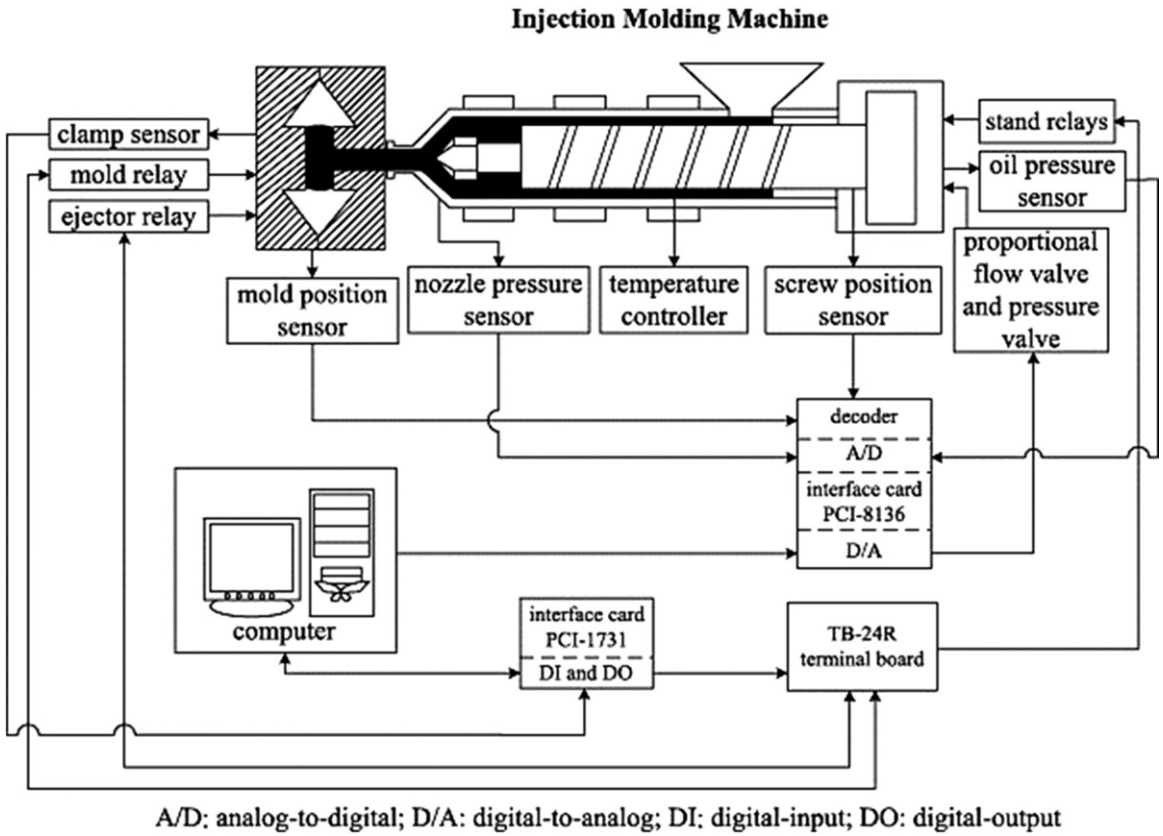


Figure 15 Experimental setup of control system for IMM. Lin, J.; Lian, R.-J. Self-Organizing Fuzzy Controller for Injection Molding Machines. *J. Process. Contr.* **2010**, *20* (5), 585–595.

The approach of DOE is most suitable for consideration of a few variables. However, as the number of variables increased, the techniques became cumbersome and the need for a more robust experiment design became required. Therefore, the method of optimization is then used for investigation of the processing conditions and the response factor(s).

The intelligent algorithms are optimization methods that are based on a global search process in a given design window. Meanwhile, long computational times are required for the simulations, which are based on black-box software. Likewise, the iterative methods are based on the approximate mathematical function obtained by a surrogate model constructed by running a simulation code. The most well-known surrogate models are the RSM, Kriging model, Gaussian process, ANN, and support vector regression. The third category is the non-iterative, with techniques that involve searching for optimum process conditions. This category includes the expert systems, gray relational analysis, fuzzy systems, case-based reasoning, and Taguchi method. In terms of product quality, the Taguchi method is widely used; therefore, some details of this method are outlined here. The Taguchi method is based on a robust design that requires the minimum cost of material and time for experiments and/or simulations.

In recent years, application of the Taguchi method has been proven to be efficient for product quality improvement.[100] However, the Taguchi method is outstanding because it centers on improvement of quality characteristics and integrates engineering and statistical methods to provide high-quality products at minimum cost. The method is based on robust DOE and is implemented by orthogonal array (OA), signal-to-noise (S/N) ratio, and analysis of variance.

The uniqueness of the Taguchi method is the design of OA. The OA responses are obtained via running the simulation code or performing corresponding experiments. OA can be divided into several classes: full level, two levels, and three levels; it is expressed as $L_n(x^y)$, where n is number of runs and x and y represent the level and number of factors considered. **Table 13** is an illustration of the OA design that features $L_9(3^4)$.

Empirical data are evaluated based on three criteria for optimized quality: the more nominal the better; the smaller the better; and the higher the better; the quality characteristics are continuous for engineering analysis. The mean-square deviation for these three quality characteristics can be expressed as:[107]

The more nominal the better:

$$\mathrm{MSD} = \frac{\bar{y}^2}{S^2} \qquad [43]$$

The smaller the better:

$$\mathrm{MSD} = \left(\frac{1}{n}\sum_{i=1}^{n} y_i^2\right) \qquad [44]$$

Table 12 Application of design of experiment for the investigation of molded part quality

Materials[a]	*Number of variables*	*Factors*		*Finding*
		Controlled	*Response*	
PC, SBS, MABS, COC, and PMMA	6	Melt temperature, injection pressure, holding pressure, injection speed, and mold temperature	Filling quality of microfeatured channels	Melt temperature and mold temperature are most significant parameters
PS, PC, and PMMA	5	Injection time, injection pressure, injection temperature, and mold temperature	3D numerical simulation of part filling	The mold temperature is the most important parameter; it must be higher than material T_g
PC and POM	6	Injection speed, holding pressure time, metering size, melt temperature, and mold temperature	Part weight and dimensions	Metering size and holding pressure are most significant; the interaction between both is also important
PS and PC	5	Injection speed, mold temperature, melt temperature, and holding pressure	Complete filling of donut-shaped parts	Injection speed and holding pressure are the most influential, whereas melt temperature and mold temperature have less influence
PP, POM, and ABS	7	Melt temperature, mold temperature, injection speed, holding pressure, air evacuation, and the size of features	Complete filling of high-aspect-ratio rods	Melt temperature and injection speed are key factors for PP and ABS; mold temperature is also significant in case of POM
PC	6	Injection speed, shot size, vacuum, holding pressure, piston diameter	Microfeature height	The diameter of the piston, shot size, injection speed, and mold temperature are significant parameters
PP, POM, and ABS	5	Melt temperature, mold temperature, injection speed, and distance between microfeatures	Complete filling of microstructures	Injection speed and melt temperature are influential in cases of POM and ABS with some side effects; mold temperature improves filling for some shapes; distance between microfeatures is not influential
PP, ABS, and PC	5	Melt temperature, mold temperature, injection speed, and surface finish	Flow length along a micro-channel into a flat cavity	The high levels of all processing parameters result in better filling; surface finish is related to level of turbulence in melt flow
PS	5	Melt temperature, mold temperature, injection speed, and holding pressure	Weld-line formation	Injection speed and mold temperature have the main effect on weld-line placement and orientation
PP	5	Injection pressure, melt temperature, mold temperature, and flow ratio	Flow length	Melt temperature and injection pressure are the most significant factors
COC	4	Holding pressure, filling flow rate, and mold temperature	Filled volume fraction of microfilters	Flow rate found to be the most important processing parameter

[a]Polycarbonate (PC); styrene-butadiene-styrene (SBS); methylmethacrylate acrylonitrile-butadiene-styrene (MABS); cyclic olefin copolymer (COC); polymethylmethacrylate (PMMA); polyoxymethylene (POM); acrylonitrile-butadiene-styrene (ABS); polypropylene (PP); polystyrene (PS).

Source: Modified from Attia, U.; Marson, S.; Alcock, J. Micro-Injection Moulding of Polymer Microfluidic Devices. *Microfluidics and Nanofluidics* **2009**, *7* (1), 1–28; From Attia, U. M.; Alcock, J. R. Optimising Process Conditions for Multiple Quality Criteria in Micro-Injection Moulding. *International Journal of Advanced Manufacturing Technology* **2010**, *50* (5–8), 533–542.

The higher the better:

$$\mathrm{MSD} = \left(\frac{1}{n}\sum_{i=1}^{n}\frac{1}{y_i^2}\right) \quad [45]$$

where $\bar{y}$ is the mean of the sample, S is the standard deviation, y_i is the response value for the specified problem in the ith test, and n is the number of replications in each test trial. Regardless of the category of the quality characteristics, a higher algebraic value of the S/N ratio corresponds to better quality characteristic, such as the smaller variance of the output characteristic around the desired (target) value. The S/N ratio for either of these mentioned criteria is evaluated using eqn [46] with a unit of dB.

$$\eta = S/N = -10\log(\text{MSD}) \quad [46]$$

Therefore, the application of the Taguchi[108,109] optimization method based on multiple quality characteristics of IM continues to emerge as the approach to minimize cost, time, and variation of production processes. This has increased performance and productivity of a given process or system, and improves part quality. Figure 16 illustrates the flow sequence of the Taguchi method.

1.16.4.3 Application of Computer Modeling in Injection Molding Processes

Simulation of the MIM process is quite complex and involves nonisothermal, non-Newtonian flow of shear-thinning of the two-phase fluid flow. The principles were adopted from early developments made in plastic injection molding simulation codes and software based on the Hele–Shaw model. These software solutions are implemented by discretization methods such as finite difference method (FDM), finite volume method (FVM), and finite element modeling (FEM) methods. Newer methods such as the mesh-free method have been developed to eliminate issues with mesh and element grids.

The process design of microinjection molding involves the determination of a number of processing parameters such as pressure (injection, holding, and melt), temperature (coolant, nozzle, barrel, melt, and mold), time (fill, holding, cooling, and cycle), clamping force, injection speed, and injection stroke. In such process, due to the irregular geometry in microscale and the complex thermo-mechanical history during the injection molding cycle, it is generally necessary to resort to numerical simulation methods to properly simulate the molding process and develop the capability of predicting the final configuration of the molded part. The target goals of adopting simulations in the injection molding process by researchers are summarized under the following heading[71, 106]:

i. Flow visualization and prediction of the mold cavity filling during injection molding process. The focus is on the material properties of the melt and tooling geometry on flow and the filling of mold cavity. The objective includes monitoring incomplete filling of the mold cavity and determination of part defects such as weld line and voids, which depend on the runners and gate location of the mold design.
ii. Parametric design analysis and optimization of the part and mold cavity design. This includes the virtual geometry analysis of the mold cavity in relation to the shape of the parts to be produced. This eliminates cost of reconstruction and early identification of a likely problem if trial-and-error methods were used. In addition, the technique will determine and establish optimum mold design and operating conditions.

Table 13 $L_9(3^4)$ Taguchi orthogonal array

Run	*P_1*	*P_2*	*P_3*	*P_4*
1	1	1	1	1
2	1	2	2	2
3	1	3	3	3
4	2	1	2	3
5	2	2	3	1
6	2	3	1	2
7	3	1	3	2
8	3	2	1	3
9	3	3	2	1

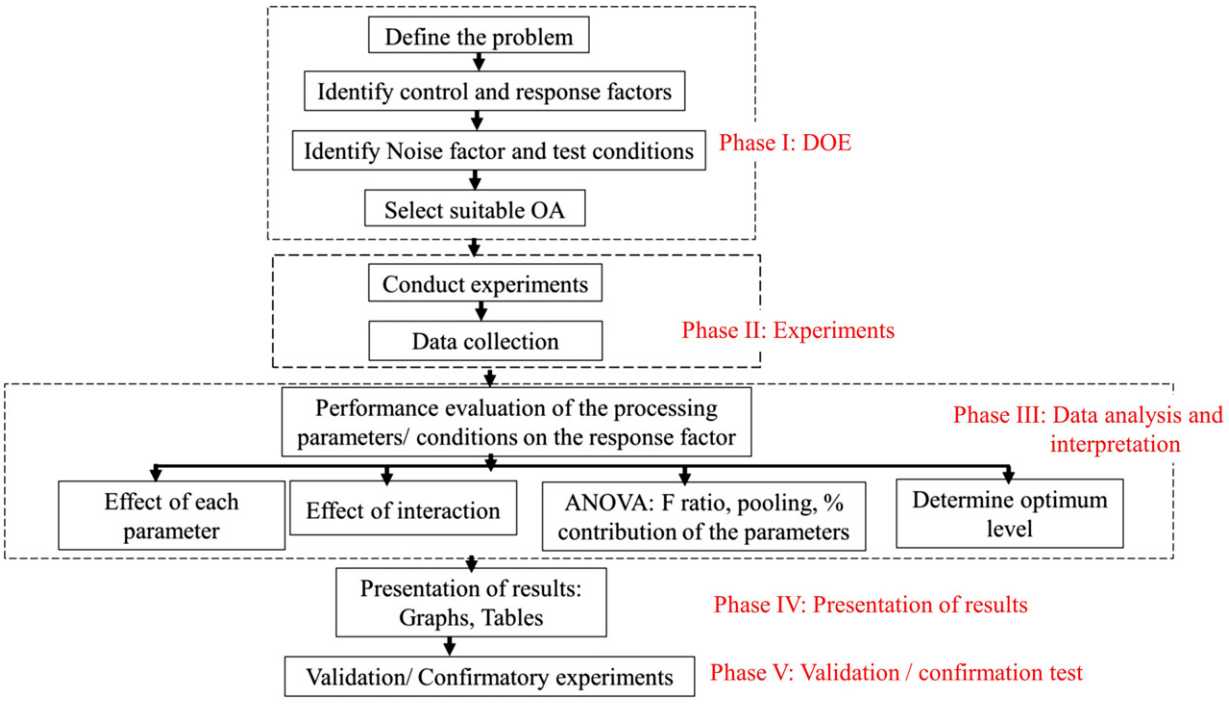


Figure 16 Operational sequence of the Taguchi method.

iii. Modeling of the material properties such as thermal, residual stresses, specific heat coefficient, and processing conditions of melt flow during filling and cooling, which would be useful in estimating the cycle time and determining the critical processing variables and factors.
iv. To identify postprocessing properties and factors, which influence finished part quality characteristics such as shrinkage, warpage, weight, density, and surface finish.
v. To measure and validate empirical data such as warpage and volumetric shrinkage of the part, which are not easily determined experimentally. These quality characteristics are monitored through computer simulation, some of which influenced quality of the finished part.

Despite success of the simulation techniques in micro-injection molding, several factors affect the accuracy of model results.[71] Peter and Rong[110] generalized the complications as:

i. the nature of injection molding, particularly the basic physics of the process
ii. the properties of the material
iii. the geometric complexity of the mold.

1.16.4.3.1 Developments in the simulation of injection molding process

There are several milestones in the history of computer aided engineering (CAE) applications for injection molding. The history of simulation and computer software development are described in detail by Peter and Rong,[110] Zheng *et al.*,[111] and Zhou.[112]

According to Liu *et al.*,[41] computer simulation is used to reduce the design-to-manufacture cycle time through optimization of both design and process parameters. A survey of literature indicates that melt temperature, mold temperature, holding pressure, injection pressure, and injection speed were mostly investigated; these parameters directly influenced part quality.[113] Other factors such as material properties, powder loading, and surface finish of the mold may influence part quality. Therefore, software and codes are developed to predict quality characteristics of products in IM. For some quality characteristics, properties and/or factors are not easily measurable experimentally.[105,114] Several commercial software programs such as ANSYS CFX, PIMSolver, SIGMASOFT, CMOLD, Moldex3D, Moldflow, Solidworks plastics, and others are widely used for injection molding simulations.[115] Some of these software programs were originally developed to handle convectional injection molding and other applications. With little modification to the simulation setup, the software is found to very useful for the prediction of quality characteristics of μIM molded parts.

1.16.4.3.2 Computer simulation and molded part quality enhancement

Computer simulation has significantly supported the development of μPIM, starting from the use of applications and codes developed for plastic injection molding. Many studies have been conducted and various findings reveal a better understanding of the technology. The simulation is used for the determination of optimum operating conditions of the process, the inter-relationships, and correlation among parameters. A survey of the literature indicates that application of computer modeling for enhancement of molded part quality in μIM could be categorized into three phases: simulation, optimization, and process control and monitoring, as depicted in Figure 17.

Today, computer applications in PIM are used extensively beginning from part drafting, which involves computer-aided drafting, and sometimes the process is implemented in CAE. CAE is a very wide field of computer applications including finite element analysis, computational fluid dynamics (CFD), multibody dynamics (MBD), and optimization. In addition, optimization in μIM includes both the design and process, as shown in Figure 17. The design aspect of the optimization is the parametric analysis of the virtual part to be produced to determine appropriate part dimensions, shrinkage factors, and other design variables considered. The application of various optimization techniques to determine optimum operating conditions from the process variables is also considered. This aspect has been described in Section 1.16.4.2. Then, the control and monitoring of defect-free parts is to ensure quality variables through the process of machine execution. This is connected to monitoring and control of finished part quality characteristics.

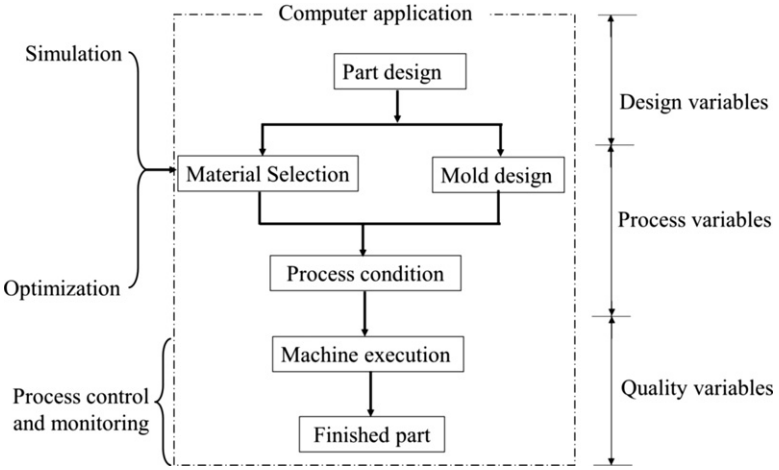


Figure 17 Application of computer modeling for quality enhancement of molded parts in μIM.

However, it is important to investigate the process condition and to establish the influence of process parameters on the quality characteristics of the molded or finished part in μIM. Prior to experimental setup, researchers used computer simulation to investigate the material properties, melt flow into mold cavities (runners and gate). The simulation analysis includes three phases (the filling, packing/holding, and cooling phase) of μIM process.

1.16.4.3.3 Modeling of injection molding process

The success of a defect-free part in μIM depends strongly on the ability of the feedstock melt to flow into the mold cavity for microstructures and nanostructures.[116] Lin *et al.*[117] examined the effects of the processing parameters on the filling of nano feature components through the development of analytical models that were verified and validated experimentally. Their finding indicates that nanoscale filling requires higher mold temperatures. However, whenever the filling aspect ratio is more than 1, the mold temperature should be raised near or above the glass transition temperature of the polymer. The suitability of analytical methods diminishes as the complexity of the microfeature/molded part increases, thus giving rise to the use of numerical methods. Modeling and mathematical derivations have been implemented by the application of suitable numerical methods to solve the governing equations developed or formulated for injection molding simulation.[118–121] These governing equations are formulated to consider the operational condition as well as the material properties of the feedstock.

1.16.4.3.3.1 Feedstock properties and mixing simulation

The material properties of the feedstock considered for injection molding simulation depend on many factors and processing conditions. Thus, rheological investigations of the feedstock are essentially studied for the analysis of melt flow behavior during mixing and injection (filling, packing, and cooling phase) of molded part modeling. Some of these properties considered are viscosity, shear modulus, specific heat capacity, elastic modulus, thermal conductivity, and pressure–volume–temperature (PVT), among others. A general rule-of-mixtures model for some of these properties is presented in Section 1.16.3.1.3. Due to the importance of viscosity and availability of models, it is further discussed here. For the model injection molding process, a viscosity model (function) is required to predict the fluid flow behavior. The viscosity curves of most thermoplastics and polymeric binders used in the PIM process have the same dependence on shear rates. The viscosity hardly changes when the rate of shear is very low or very high; at this time, pseudoplastic fluid acts similar to a Newtonian fluid. At least four parameters are required to reflect this relationship between viscosity and shear rate.

Modeling of viscosity has attained remarkable landmarks by models proposed by Cross[122] in 1965 and Carreau[123] in 1972, respectively. These models are believed to be better than the others in terms of representation of characteristics of the thermoplastic polymer investigated. In addition, the Sisko model[124] proposed by Sisko in 1958 combined the characteristics of Bingham plastics and the power law model. Models such as the Prandtl–Eyring model, Ellis model, Casson model, and fractional exponential model are developed for other specific applications. Currently, the power law and the cross model are widely used in injection molding to describe the viscosity function.[125] Therefore, an overview of these models and the mathematical relationship is presented.

1.16.4.3.3.1.1 Power law model

This is a well-known viscosity model that is often used in most injection molding simulations. de Waele in 1923 and Ostwald in 1925 proposed the power law model,[122] also known as the Ostwald–de Waele relationship, which has been used successfully to predict the shear thinning region. This model has the following form:

$$\eta = \eta_0 |\dot{\gamma}|^{n-1} \quad [47]$$

$$\eta_0 = B\left(\frac{T_b}{T}\right) \quad [48]$$

where η_0 is the Newtonian viscosity or zero shear rate viscosity, which is defined as the viscosity at zero shear rate, B is a constant called the consistency index, T_b is a constant showing the temperature sensitivity of this material, T is the melting temperature, and n is the power law index with a value between $0 < n \geq 1$ for polymer melts. The natural logarithms of the eqn [48] give:

$$\ln(\eta) = (n-1)\ln(\dot{\gamma}) + \ln(\eta_0) \quad [49]$$

Flow behaviors of a power law fluid depend on the value of n[126] for:

$n < 1$, the fluid exhibits shear-thinning properties;
$n = 1$, the fluid shows Newtonian behavior;
$n > 1$, the fluid shows shear-thickening behavior.

According to Thavanayagam *et al.*,[37] feedstocks that exhibit shear thinning ($n < 1$) are suitable for PIM. Feedstock with dilatant flow behavior ($n > 1$) is not suitable for PIM because powder and binder separation can occur under a high shear rate. Therefore, rheological properties should be assessed over a wide range of shear rates.

Equation [49] is termed the first-order viscosity model and used in Moldflow software for flow analysis of the injection molding process. To improve the modeling of viscosity in the low shear rate region, the second-order model was developed by Moldflow and expressed as:

$$\ln \eta = A_0 + A_1 \ln \dot{\gamma} A_2 T + A_3 (\ln \dot{\gamma})^2 + A_4 T \ln \dot{\gamma} + A_5 T^2 \quad [50]$$

where A_i are constants and T is temperature. According to Koszkul and Nabialek,[127], this model has been criticized on the grounds that it is based on empirical observations. This is of little relevance for our purposes. What is required is a model that fits the experimental data as closely as possible, and the second-order model is able to characterize the observed behavior of polymer melts. In particular, the second-order model can model the following features of polymer melts:

a. convergence of iso-shear rate curves with increasing temperature,
b. convergence of isotherms with increasing shear rate,

c. the increasing rate at which viscosity decreases as shear rate is increased,
d. the increasing rate at which viscosity decreases with increasing temperature.

In general, the literature demonstrates that the power law represents the behavior of polymer melts in the high shear rate region, and it is also quite easy to fit experimental data for the model and determine the constants η_0 and n. In the Moldflow simulation software, the first is developed based on empirical data. The second model is used to characterize the behavior of the melts. However, the main disadvantage of the model is in the low shear rate range. Despite this shortcoming, the model has been widely used for modeling flow in injection molding. It is important to consider the phase of the process under consideration independently. For instance, particularly in the filling phase, shear rates are frequently high enough to justify the use of the first-order model. Shear rates are often low in the packing phase. Also, it is possible to have low shear rates in the filling phase when the filling pattern is unbalanced.

1.16.4.3.3.1.2 Cross Model

The cross viscosity model is expressed as:

$$\eta = \frac{\eta_0}{1 + \left(\frac{\eta_0|\dot{\gamma}|}{\tau^*}\right)^{n-1}} \quad [51]$$

where τ^* is the shear stress at the transition between Newtonian and power law behavior, which can be modeled using the widely accepted seventh constant cross model

$$\eta_0 = D_1 \exp\left[-\frac{A_1(T - T^*)}{A_2 + (T - T^*)}\right], \quad A_2 = A_3 + D_3 P, \quad \text{and} \quad T^* = D_2 + D_3 p \quad [52]$$

where η_0, n, τ^*, and $\dot{\gamma}$ denote the zero heat rate viscosity, the power law index, the critical stress level at the transition to shear thinning, and the shear rate. T^* is the glass transition temperature, p is the pressure, and A_1, A_2, A_3, D_1, D_2, and D_3 are data-fitted coefficients.

Compared to plastic injection molding, PIM is more prone to IM defects such as jetting and nonuniform flows, and both PIMSolver and Moldflow are useful simulation software for predicting injection molding filling defects. However, a follow-up with experiments is highly recommended, especially for PIM. Concentrated powder/binder mixtures have a peculiar nature of yield stress with shear-thinning viscous behavior. To be able to simulate these natures, the modified cross model for viscosity as a function of the effective shear rate and temperature is used for PIMSolver.

$$\eta(\dot{\gamma}, T) = \frac{\eta_0}{1 + C(\eta_0\dot{\gamma})^{1-n}} + \tau_y\dot{\gamma} \quad [53]$$

where η_0, n, τ^*, and Tb denote the zero shear rate viscosity, the power law exponent, the transition shear stress, the constant amplitude, and the reference temperature in absolute scale for the Arrhenius temperature dependence of the viscosity. A new term τ_y is added to the modified cross model in eqn [53] for the yield stress.[128,129] Equation [56] is a viscosity model developed by PIM specialists for PIMSolver software.

1.16.4.3.3.1.3 Carreau model

The Carreau model has the form:

$$\frac{\eta - \eta_\infty}{\eta_0 - \eta_\infty} = [1 + (\lambda\dot{\gamma})]^{(n-1)/a} \quad [54]$$

where η_∞ is the viscosity at infinite shear rate, η_0 is the viscosity at zero shear rate, n is a dimensionless constant with the same interpretation as the power law model eqn [47], and K is a material time constant parameter. The Bird–Carreau model is given by $a=2$. For many shear thinning fluids, $a \approx 2$.

1.16.4.3.3.1.4 Ellis Model

The Ellis model presents the viscosity as a function of shear stress τ, mathematically represented as:

$$\frac{\eta_0}{\eta} = 1 + \left(\frac{\tau}{\tau_{1/2}}\right)^{\alpha-1} \quad [55]$$

where $\tau_{1/2}$ is the value of shear stress for which $\eta=\eta_{0/2}$ and $\alpha - 1$ is the slope of the graph $\ln[(\eta_0/\eta) - 1]$ versus $\ln(\tau/\tau_{1/2})$.

However, the research effort is still ongoing for a more suitable model for different material. Recently, Hidalgo *et al.*[35] proposed a generalized rheological model that involves the following parameters: shear rate (γ), temperature (T), solid loading (Φ), and particle size (PS). The model is expressed as:

$$\eta(\dot{\gamma}, T, \phi, \mathrm{PS}) = \frac{C_u}{d_{50}} \cdot \exp\left(\frac{E_a}{\mathrm{RT}}\right) \cdot \left(\frac{\tau}{\dot{\gamma}} + \left(\frac{\eta_0}{1 + K\dot{\gamma}^n}\right)\right) \cdot \left(\frac{\phi_{\mathrm{crit}}}{\phi_{\mathrm{crit}} - \phi}\right)^m \quad [56]$$

Having fully understood the properties of the metal powder, valuable information will be obtained from simulation of the mixing process.

1.16.4.3.3.1.5 Modeling of feedstock mixing

In practice, distributive mixing of feedstock constituents is investigated without concern for molecular diffusion. Although the behavior of melt during preparation is analyzed by fluid flow governing equations for specific mixer geometry for given material properties and operating conditions. Finite element method (FEM) is used mostly for the analysis of the governing fluid flow equation. According to Huang and Kuo,[130] computer simulation is a numerical tool that is more cost-effective than performing experiments in complex systems. This establishes a basis for design optimization, scale-up, and control of the system. Nevertheless, there are two common numerical approaches for studying particle mixing: the discrete approach and the continuum approach. The Monte Carlo method, cellular automata, and discrete element method (DEM) were developed based the on discrete approach. In addition, researchers now prefer to analyze granular flow with CFD because the continuum approach does not account for a system size relative to DEM. The flow pattern of mixing particles can be described as either dispersive or distributive mixing,[131] as illustrated in **Figure 18**.

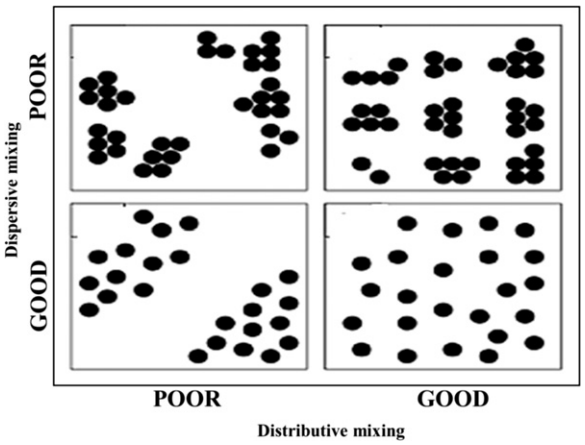


Figure 18 An illustration of dispersive and distributive mixing.

Therefore, the governing equations for the analysis of the feedstock melt during mixing are as follows:

$$\nabla \cdot \vec{V} = 0 \quad [57]$$

where $\vec{V}$ is the local velocity of the moving part

$$H(v - \vec{V}) + (1 - H)\left[\nabla \cdot \vec{\tau} - \nabla p + \rho\left(\frac{\partial v}{\partial t} + v \cdot \nabla \vec{V}\right)\right] = 0 \quad [58]$$

where H is a step function equal to 0 for fluid field and 1 for inner moving parts, v is the fluid velocity, $\vec{\tau}$ is the strain rate tensor, P is the fluid pressure, ρ is the fluid density, and t is the time.

$$\rho C(T)\left(\frac{\partial T}{\partial t} + v \cdot \nabla T\right) = T \cdot \nabla v + r - \nabla \cdot q \quad [59]$$

where $C(T)$ is the heat capacity as a function of temperature, r is volumetric heat source, and q is the heat flux.

Equation [57] is the continuity equation, eqn [58] is the momentum, and eqn [59] is the energy equation. The stress tensor and the shear rate are defined by eqn [60] and expressed as:

$$\vec{\tau} = 2\eta(\dot{\gamma}, T)\vec{D} \quad [60]$$

$$\dot{\gamma} = \sqrt{2\vec{D} : \vec{D}} \quad [61]$$

Suitable viscosity model is selected or developed from empirical data to describe the material behavior of the feedstock.

The equations formulated are solved by the numerical method, but the FEM is dominantly used. The particle tracking method has been successfully applied. Analysis of feedstock mixing by the particle tracking scheme involved three steps:

- flow analysis to obtain a velocity field of a mixing device;
- particle tracking step to obtain distribution of particles at the end of the mixer;
- quantification of mixing from the obtained particle distribution.

Then, to track the relative position of particles within a specified domain, the solution of the physical model involved is an ordinary differential equation (ODE):

$$\frac{dx}{dt} = u \quad [62]$$

where x is the particle position vector, u is the particle velocity, and t is the time. The numerical method is used for the solution of the 3D problem. These equations are sometimes simplified to 2D to save time and resources. The fourth-order Runge–Kutta method is widely used for solving eqns [62].

The homogeneity of the powder-binder mixture is evaluated by the mixing uniformity to achieve the required distribution of the particles. A proper measure of mixing is the uniformity of the particle distribution as well as information on material properties such as the entropy of the particles at any given cross-section within the mixing domain based on tracking method. The characterization of the mixing progress requires first the division of the mixer cross-section into a number of cells. Then, for a certain particle configuration, the mixing entropy S is defined as a sum of the information entropy of individual cells constituting the cross-sectional area, defined by:

$$S = -\sum_{i=1}^{N} n_i \log n_i \quad [63]$$

where N is the number of cells and n_i is the particle number density at the ith cell. Instead of directly using the information entropy in the mixing analysis, we use a normalized entropy. Increased S^* as a measure of mixing is given by:

$$S^* = \frac{S - S_0}{S_{max} - S_0} \quad [64]$$

where S_0 is the entropy at the inlet and S_{max} is the maximum possible entropy, defined by log$N$, which is the ideal case with a uniform distribution of the particles, such as $n_i = 1/N$.

1.16.4.3.3.2 Fundamentals of governing equations and boundary conditions

The governing equations are a set relationship describing the physical model or system. In typical fluid flow, the conservation equation of mass, momentum, and energy are expressed in a similar form. The mathematical representations of these equations are based on fundamental physical principles, on which all fluid flow is derived. However, formulation or choice of a suitable equation for the analysis of the fluid flow is very important and fundamental for CFD. When obtaining the basic equations of fluid dynamics, the following philosophy is always followed:

(1) The governing equations are derived from the fundamental physical concepts of physics, namely:
   - mass is conserved
   - conservation of momentum F = ma (Newton's second law)
   - energy is conserved.

(2) The fundamental physical concepts are applied to a suitable model to describe the fluid.

(3) Mathematical modeling for the fluid.

A suitable boundary condition is imposed on the ODE or partial differential equation (PDE). These conditions (such as slip, inertia, isothermal, isobaric, etc.) and specified values for the independent variable(s) such as temperature, pressure, and velocity over a range at which the solution being analytical or numerical is expected to converge.

1.16.4.3.3.3 Melt flow behavior in micro-size channel

The actual design of the runner is usually trapezoidal in the cross-section, which allows easy ejection of the part from the mold. However, most 2.5D mold-filling simulation software programs approximate the geometry of the channel to the circular cross-section runner. The graphical user interface of the software may provide various alternatives, but usually the black-box evaluation of the software approximates to an equivalent circular cross-section. This approach is not a satisfactory approximation and may introduce an appreciable error in computational results of the software. Therefore, there is a need for analytical modeling or in-house code to study the melt front flow behavior in microcavity filling of μIM.

The flow and filling analysis of the mold cavity during μIM by the feedstock melt has been investigated. In this analysis, a single point injection of melt is considered through the runner channel to the mold cavity. **Figure 19** is a schematic representation of the runner channel. It is important to note that some assumptions were made. The injection flow rate is considered to be constant during the filling process of the cavity and locally filled. Likewise, the volume in the part required is far smaller as compared to the main cavity. The amount of melt flow rate in the main cavity is assumed to be the same as the injection rate. For one-dimensional viscous flow, the momentum equation can be expressed as:

$$\frac{dp}{dx} = \frac{d}{d\gamma}\left(\eta \frac{du}{d\gamma}\right) \quad [65]$$

where η is the viscosity and, for a power law fluid, can be written as

$$\eta = m_x \dot{\gamma}^{n-1} \quad [66]$$

where $\dot{\gamma}$ represents the shear rate, m_x is the flow consistency index, and n is the power law index. The microinjection molded cavity feature is filled within a short period of time. Then, the temperature of the melt within the thickness (h) of the main flow path is assumed to be constant. The consistency index (m_x) can be expressed as:

$$m_x = m_o e^{-a_0(T_m - T_0)} \quad [67]$$

where T_m is the melting temperature at the main cavity, and m_o, a_o, and T_o are material constants. To solve for the velocity of the flow (u), eqns [66] and [67] are substituted into eqn [65] and expressed as:

$$u = \left(\frac{1}{m_x}\right)^{\frac{1}{n}} \left(\frac{n}{n+1}\right) \left|\frac{dp}{dx}\right|^{\frac{1}{n}} \left[\left(\frac{h}{2}\right)^{\frac{n+1}{n}} - \gamma^{\frac{n+1}{n}}\right] \quad [68]$$

and the injection flow rate (Q) across the cross-section of the flow channel is given by:

$$Q = \left(\frac{1}{m_x}\right)^{\frac{1}{n}} \left(\frac{2nw}{2n+1}\right) \left|\frac{dp}{dx}\right|^{\frac{1}{n}} \left(\frac{h}{2}\right)^{\frac{2n+1}{n}} \quad [69]$$

Also, the pressure (P_o) at point o, as indicated in **Figure 19**, depends on the melt filled distance (x_o) from the point to the flow front, which is assumed to be constant across the thickness of the main cavity and expressed as:

$$P_o = \frac{2^{n+1}(2n+1)^n}{n^n} \frac{m_x x_o}{w^n h^{2n+1}} Q^n \quad [70]$$

The melt velocity (V_x) along the flow path of the main cavity is expressed as:

$$V_x = \frac{dx}{dt}$$
$$\frac{dx}{dt} = \frac{Q_x}{wh} \approx \frac{Q}{wh} \quad [71]$$

where w is the width of the channel and h represents the depth of the micro-size channel. It is assumed that the amount of melt into the channel is quite small, and Q_x represents the flow rate at the main cavity. Also, Q_x is approximately the same as the injection flow rate, Q. Then, evaluating eqn [71] to estimate the flow front from point o is expressed as:

$$x_o = \frac{Qt}{wh} \quad [72]$$

From eqn [68], pressure drop can be estimated and evaluated using:

$$\frac{dp}{dx} = m_x \left(\frac{2nw}{2n+1}\right)^{-n} \left(\frac{h}{2}\right)^{-(2n+1)} Q^n \quad [73]$$

Then, substituting for m_x in eqn [73], the pressure drop can be expressed as a function of both the melt flow filled distance x_0 and the temperature.

$$\frac{dp}{dx} = \left(\frac{2n+1}{nw}\right)^n \left(\frac{h}{2}\right)^{-(2n+1)} Q^n m_o e^{-a_0(T_m - T_0)} \quad [74]$$

Integrating eqn [74] or substituting for m_x in eqn [70] yields an expression for pressure in terms of the material properties and as a function of the temperature.

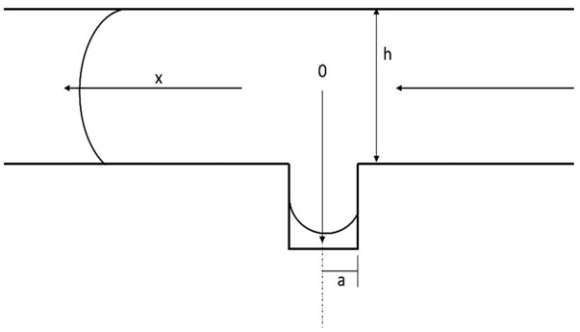


Figure 19 Schematics of the physical model for μIM flow channel.

$$p(x_0, T_0) = \left(\frac{2n+1}{nw}\right)^n \left(\frac{h}{2}\right)^{-(2n+1)} Q^n x_0 m_o e^{-a_0(T_m - T_0)} \quad [75]$$

Total pressure drop is a summation of the losses across the sprue, runner, and gate, as well as the within the mold cavity.

$$\Delta p = \Delta p_{\text{Pipe}} + \Delta p_{\text{cavity}} \quad [76]$$

Lin and Young[116] derived an analytical model for the estimation of pressure drop in the mold cavity as well as in the pipe. The combined effect of the pressure drop in the sprue, runner, and gate is referred to as Δp_{pipe} and expressed as:

$$\Delta p_{\text{Pipe}} = \left[\frac{2m_x(3n+1)^n \Delta x}{n^n \pi} R^{-(3n+1)}\right] Q^n = \overline{R}_{\text{pipe}} Q^n \quad [77]$$

where $\overline{R}_{\text{pipe}}$ is the hydraulic radius of the sprue, runner, and/or gate.

1.16.4.3.3.4 Filling phase of injection molding

The filling phase of injection molding is a very complex process. Its analysis is based on the generalized Hele-Shaw model with incompressible, generalized, non-Newtonian fluid under nonisothermal conditions. The governing equations of the feedstock melt are expressed as follows.

The continuity equation is expressed as:

$$\frac{\partial v_x}{\partial x} + \frac{\partial v_y}{\partial y} + \frac{\partial v_z}{\partial z} = 0 \quad [78]$$

The momentum equations are expressed as:

$$\frac{\partial p}{\partial x} = \frac{\partial}{\partial x}\left(\eta \frac{\partial u}{\partial z}\right) \quad [79]$$

$$\frac{\partial p}{\partial y} = \frac{\partial}{\partial y}\left(\eta \frac{\partial v}{\partial z}\right) \quad [80]$$

$$\frac{\partial p}{\partial z} = 0 \quad [81]$$

From eqn [78], V_x, V_y, and V_z represent velocity function along the x, y, and z axes, respectively, whereas p is the pressure and η is the viscosity. Most textbooks use u, v, and w for V_x, V_y, and V_z; these are only used for clarity. Then, combining eqns [78], [69], and [80] and integrating them along the z-direction (thickness direction) gives the fluid flow governing equation for the filling stage, expressed as:

$$\frac{\partial}{\partial x}\left(s\frac{\partial p}{\partial x}\right) + \frac{\partial}{\partial y}\left(s\frac{\partial p}{\partial y}\right) = 0 \quad [82]$$

$$s = \int_{-b}^{b} \frac{z^2}{\eta}\, dz \quad [83]$$

Based on the lubrication and Hele–Shaw approximations, the energy equation governing the mold cavity filling stage during injection molding by the melt is express as:

$$\rho C_p \left(\frac{\partial T}{\partial t} + V_x \frac{\partial T}{\partial x} + V_y \frac{\partial T}{\partial x}\right) = K \frac{\partial^2 T}{\partial x^2} + \eta \dot{\gamma}^2 \quad [84]$$

the shear rate $(\dot{\gamma})$ is express as:

$$\dot{\gamma} = \left[\left(\frac{\partial v_x}{\partial z}\right)^2 + \left(\frac{\partial v_y}{\partial z}\right)^2\right]^{\frac{1}{2}} \quad [85]$$

From eqn [69], the absolute temperature (T), time (t), melt density (ρ), specific heat of the feedstock (C_p), and K represent thermal conductivity of feedstock. The energy equation for the solid phase is expressed as:

$$\rho_s C_{p_s} \frac{\partial T_s}{\partial t} = K \frac{\partial^2 T_s}{\partial {z_s}^2} \quad [86]$$

where the subscript s represents the solid phase referring to the ceramic or metal powder constituent of the feedstock. Once the governing equations are derived from the continuum-based conservation laws and the constitutive relations, the next task is boundary conditions. A boundary condition for the governing equations involves specification of parameter value(s) and conditions for the filling stage, typically:

Flow equation: melt flow rate at injection point; slip/no slip at cavity wall; free surface at melt front.
Energy equation: melt/injection; temperature at injection point; mold wall temperature; free surface at melt-front.

Note that the boundary conditions are required to solve the governing equation. Therefore, the initial values of the flow rate and injection temperature at the injection node are required. Jiang *et al.*[132] analyzed the feedstock melt and solid phase considering basic assumptions of non-Newtonian and nonisothermal fluid flow.

1.16.4.3.3.5 Packing phase of injection molding

As illustrated in **Figure 8** in Section 1.16.3.2, as the mold cavity filling is nearly completed, the packing phase began. A switchover is experienced as the ram/screw control strategy of the IMM changes from velocity control to pressure control.

Pressure control is required to ensure full filling of the mold cavity and to provide the needed pressure by the filled cavity prior to freezing of the gate. It is important to note that the packing pressure is used to compensate for the anticipated shrinkage in the cooling stage.

In the analysis of the packing stage, it is important to include the effect of melt compressibility. The melt compressibility is dependent on the specific volume of pressure and temperature; this leads to a feedstock-specific PVT relationship/equation state.

Then, suitable PVT and viscosity models are required for the analysis of the packing stage based on the continuum approach; the governing equations are presented as follows.

Mass conservation of the feedstock is expressed as:

$$\frac{\partial \rho}{\partial t} + \frac{\partial(\rho V_x)}{\partial x} + \frac{\partial(\rho V_y)}{\partial y} + \frac{\partial(\rho V_z)}{\partial z} = 0 \quad [87]$$

Assuming that pressure convection terms are ignored in the packing stage, then eqn [87] becomes:

$$K\frac{\partial \rho}{\partial t} - \beta\left(\frac{\partial T}{\partial t} + V_x\frac{\partial T}{\partial x} + V_y\frac{\partial T}{\partial y}\right) + \left(\frac{\partial V_x}{\partial x} + \frac{\partial V_y}{\partial y}\right) = 0 \qquad [88]$$

Where K is the isothermal compressibility coefficient of the material. The energy equation for this processing stage is expressed as:

$$\rho C_p\left(\frac{\partial T}{\partial t} + V_x\frac{\partial T}{\partial x} + V_y\frac{\partial T}{\partial y}\right) = K\frac{\partial^2 T}{\partial x^2} + \eta\dot{\gamma}^2 + \beta T\frac{\partial P}{\partial t} \qquad [89]$$

To replicate the physical model, the same value of shear rate is used for both packing and mold cavity filling, respectively. Typical boundary and initial conditions for the packing analysis stage of IM is presented as follows:

- mass and momentum conservations: specified pressure at injection point, slip condition at cavity wall, and free surface at melt-front.
- energy equation: specified temperature at injection point, mold wall temperature condition at the cavity wall, and free surface at melt-front.
- initial conditions: pressure, velocity, temperature, and density from the results of the filling stage analysis are used.

1.16.4.3.3.6 Cooling phase of injection molding

Mold filling and other preceding processes significantly contribute to the quality of the molded part, but the successful completion of the cooling stage enhances the productivity and the quality of the final component. Cooling starts immediately upon injection of the melt into the mold cavity; theoretically, cooling time is referred to as the period that elapses between when the gate freezes and part ejection.

In the cooling analysis of the mold, the main focus is on the temperature profile at the cavity walls as well as on surface of the mold. The boundary condition will be guided by the melt or filling/injection temperature and the packing phase. When the injection molding process is in the steady state, the mold temperature will fluctuate periodically over time due to the interaction between the hot melt and cavity surface supported by the activities of the cooling medium. Therefore, analysis of the cooling phenomena is investigated to determine the effect of the variant temperature on the molded part. A 3D cycle-averaged approach is adopted for the determination of the cycle-averaged temperature field and its effects on the molded part. This method is chosen to reduce the computation time for the transient component of the thermal analysis of the process. The governing equations of the heat transfer for the injection mold cooling stage based on the cycle-averaged concept is expressed as:

$$\nabla^2\overline{T} = 0 \qquad [90]$$

$$\rho C_p\frac{\partial T}{\partial t} = K\frac{\partial^2 T}{\partial z^2} \qquad [91]$$

Next, specifications of the initial and boundary conditions for the solution of the governing equations are presented. Typically, the initial and boundary conditions for the cooling stage of injection molding are:

- process condition used or specified during packing stage analysis is maintained as initial conditions
- considerations for convective heat transfer associated with the cooling medium, natural convection heat transfer with air, and material properties of the melt and mold.

1.16.4.4 Analytical and Numerical Methods for Injection Molding Simulations

The governing equations are solved using analytical methods, but as the physics of the problem becomes more complex, the use of numerical methods and/or software is implemented. However, FDM, FVM, and FEM[133–135] methods were mostly used for the analysis of melt flow with variant conditions such as isothermal, nonisothermal,[136] and non-Newtonian.[137] Due to the challenges of handling mesh or elements in the aforementioned methods, the use of mesh-free methods[133,138] for the injection molding process is now being investigated. Kim and Turng[139] present a comprehensive review of the developments of 3D CAE simulation for injection molding. The study is aimed at providing insights into the emerging 3D CAE tools to facilitate judicious application and further developments for the design and manufacturing of complex injection molded parts.

1.16.4.5 Process Simulation and Quality Characteristics for Defect-Free Parts in PIM

Process simulations are performed to evaluate quality characteristics of the products at various processing stage of PIM. Simulations are implemented to gain a better understanding of the relationship between processing conditions and part quality, which may be possible by experience alone. This has been the main reason for the development of injection molding simulation. The target goal of setting up simulations in injection molding is outlined in Section 1.16.4.3.

Specifically, simulations are set-up to evaluate the effect of processing conditions on quality characteristics of the product. Some of these response factors or quality characteristics tested are homogeneity of feedstock, mold cavity filling, dimensional, mechanical, surface-finished and microstructural morphological, optical thermal, and electrical properties. Attention is always directed toward finished part quality, which can be broadly classified into two groups: internal properties and external properties. The internal properties that characterized the microstructure of a molded part are the internal stress, molecular weight, degree of crystallization, orientation, spherulite size, and the distribution of fillers and reinforcements. The external properties are the dimension, shape, surface, electrical, optical, and mechanical properties. However, research themes and literature on molded part quality are mostly concerned with the external properties and less on the internal properties of the injection molded parts. Molded part quality is critically influenced by material properties, IMM, part/mold cavity design, and processing conditions. Therefore, research interests are focused on the effects of processing parameters and conditions for improved molded parts. These

investigations include modeling and experimental validation of the simulation and predicted results. Simulation and modeling of microinjection molding have been presented in this chapter. However, it is important to remember that debinding of the polymeric binder is critical and requires extra caution for successful PIM. Therefore, several efforts have been put forth to model and predict the decomposition of the polymeric binder during the debinding process to improve production of defect-free parts. Based on the free decomposition model, the depolymerization of polymeric binder components can be described by first-order reaction kinetics. Shi *et al.*[83] proposed a diffusion-controlled model for predicting the remaining weight fraction of the polymeric binder (h), assuming a linear heating rate (z) is expressed as:

$$h = \exp\left\{\frac{K_0 RT^2 \exp[-E/(RT)]}{ZE}\left[1 - \frac{2RT}{E} + \frac{6(RT)^2}{E^2}\right]\right\} \cdot (t \le t_{\mathrm{db}}) \quad [92]$$

When heating rate is high and temperature is uniform, then the polymeric decomposition within the period is relatively small, especially for metal powders, which are good conductors. An estimate of the remaining polymeric weight fraction (h_{db}) at the debinding temperature (T_{db}) is obtained by substituting T_{db} for T in eqn [92]. However, when ($t > t_{db}$), the remaining weight fraction of the polymer is expressed as:

$$h = h_{\mathrm{db}} \exp\left[-K_0 (t - t_{\mathrm{db}}) \exp\left(-\frac{E}{RT_{\mathrm{db}}}\right)\right] \quad [93]$$

The monomer production rate $\dot{Q}$ based on the volume of the polymer particle is estimated from the relationship:

$$\dot{Q} = \frac{V_p}{V_2}\frac{\mathrm{d}(1-h)}{\mathrm{d}t} = \frac{V_p}{V_2} Kh \quad [94]$$

alternatively expressed as:

$$\dot{Q} = \rho_p V_p K_0 \exp\left(-\frac{E}{RT}\right) \exp\left\{\frac{K_0 RT^2 \exp[-E/(RT)]}{ZE}\left[1 - \frac{2RT}{E} + \frac{6(RT)^2}{E^2}\right]\right\} \quad [95]$$

where ρ_p is the density of the polymer, V_P is the polymer volume fraction, K_o is the specific rate constant, Z is the heating rate, E is the activation energy for thermal degradation, and T is the absolute temperature.

Considering diffusion-controlled decomposition situations, the free decomposition model assumes that the monomer pressure in the polymer has no effect on the decomposition kinetics. Therefore, $\dot{Q}$ is expressed as:

$$\dot{Q} = \frac{V_p}{V_2} Khf = \frac{V_p}{V_2} K(1 - W_1)(1 - a_1) \quad [96]$$

where f is the limiting factor that depends on the activities of the monomer and expressed as:

$$f = 1 - \frac{a_1}{a_e} \quad [97]$$

This expression indicates that the limiting factor depends on the ratio of the activity of the monomer (a_1) to the equilibrium activity, and the depolymerization will go to completion at the debinding temperature even in the presence of monomers. The monomer activity in the aforementioned equation can be calculated using the Flory–Huggins relation expressed as:

$$a_1 = \theta_1 \exp\left[(1 - \theta_1) + x(1 - \theta_1)^2\right] \quad [98]$$

where θ is the volume fraction of monomers in the polymer–monomer solution, and x is an interaction parameter for the polymer–monomer system which also appears later in the free volume theory of diffusion. Alternatively, if the monomer vapor pressure over the polymer–monomer solution, P_1, is known, then the activity of the monomer can be obtained as:

$$a_1 = \frac{P_1}{P_1^0} \quad [99]$$

where P_1^0 is the monomer vapor pressure and can be estimated by the Clausius–Claperon relation expressed as:

$$\ln P_1^0 = -\frac{\Delta H_{\mathrm{vap}}}{RT} + I \quad [100]$$

where H_{vap} is the enthalpy of vaporization, I is a constant, and its value depends on the pressure unit used.

Therefore, the monomer concentration (C) within the undegraded core is estimated by the PDE

$$\frac{\partial C}{\partial t} = \frac{1}{r}\frac{\partial}{\partial r}\left(rD\frac{\partial C}{\partial r}\right) + \dot{Q} \quad [101]$$

where r is the radial distance and D is the diffusion coefficient of the monomer through the powder–polymer suspension. Considering two-phase medium containing polymer and particle, the D is estimated by:

$$D = \left(1 - \frac{3V_c}{\partial r}\right) D_p \quad [102]$$

$$D_p = D_{01}(1 - \theta_1)^2(1 - 2x\theta_1) \exp\left[\frac{W_1 V_1(0) + \zeta(1 - W_1)V_2(0)}{V_{Fh}/\omega}\right] \quad [103]$$

$$D_{01} = D_0 \exp\left(-\frac{E_d}{RT}\right) \quad [104]$$

where D_{01} is the pre-exponential factor, D_0 is a constant, and E_d is the activation energy for monomer diffusion. The subscripts 1 and 2 in eqn [103] denote monomer and polymer, respectively. x is the ratio of critical molar volumes of hopping units of the monomer and the polymer. The average hole free volume per unit mass (V_{FH}) is defined in terms of an overlap factor for free volume (ω), K_{11}, K_{12}, K_{21}, and K_{22} represent free volume parameters, and $(T_g)_1$ and $(T_g)_2$ are the glass transition temperatures of the composites materials, expressed as:

$$\frac{V_{FH}}{\omega} = \frac{K_{11}}{\omega} W_1 \left[K_{21} + T - (T_g)_1\right] + \frac{K_{12}}{\omega}(-W_1)\left[K_{22} + T - (T_g)_2\right] \quad [105]$$

1.16.5 PIM Part Fabrication and Applications

Microfabrication of parts and components can be categorized under three main types: microprecision parts, micropatterned parts, and single microparts.[68] These categories are based on precision, scale, and tolerance limits of the components and fabrication capabilities of the techniques.

1.16.5.1 Fabrication Capabilities of μMIM

Fabrication of 3D hollow[140,141] and movable[142] parts by μMIM is now possible. Attia *et al.*[142] developed a novel framework for fabrication of a moving interface by a powder micromolding process. The fundamental principles and techniques of μMIM machines are utilized in pharmaceutical industries for the production of drugs.[143]

1.16.5.2 Inspection and quality control of MIM products

Application of inspection and quality control techniques to products in MIM enhanced finished part quality and productivity. In general, quality control evaluation techniques can be either destructive or nondestructive.[144] These measures are taken to control product defects at various processing stages of MIM and are supported by statistical quality control.[145] This is to correct production inconsistency and product defects such as short shot, shrinkage, distortion, void, sink mark, weld line, and cracks. MIM involved many processing parameters that are interrelated to one another; hence, the defect identified can be handled in multiple ways. **Table 14** illustrates some common defects, causes, and remedies to improve finished part quality. However, finished part quality is enhanced through effective control and monitoring of the process conditions at different stages.[146] Quality characteristics include homogeneity of the

Table 14 Potential causes and remedies of common defects in MIM

Defects	*Potential causes*	*Remedies*
Flash	Viscosity issue	Increasing feedstock solids loading to improve melt viscosity; introduce high-molecular-weight polymers to improve viscosity of the melt
	Low clamp tonage	Decrease injection pressure as well as pack pressure; use higher tonage machine
	Misalignment of parting line, tooling issue	Ensure tooling is appropriately positioned and clamped, parting line
Incomplete fill	Deficient of molten feedstock into mold cavity	Increase pack pressure, injection speed, melt temperature, mold temperature, and shot size; in addition, increase venting
	Material feeding problem	Decrease back pressure and size of feedstock and regrind; if hygroscopic material is involved, ensure that it dried
Sink mark	Poorly filled part	Increase pack pressure, melt temperature, mold temperature, and back pressure for screw recovery; in addition, increase venting and gate size
Voids	Trapped gas and moisture issue	Increase holding pressure and mold temperature and decrease injection speed; in addition, increase gate size
Weld line and/or wrinkle	Premature solidification of molten feedstock (material)	Increase injection speed, melt temperature, pressure for switchover to pack control
	Gas entrapment	Decrease injection speed and increase venting on runner and part
Shrinkage and/or warpage	Part or component distorts during ejection	Decrease mold temperature and increase cool time; in addition, use improved cooling tools and means
	Pressure gradient in component	Decrease hold pressure
Crack	Part cracking during ejection	Decrease pack pressure and melt temperature and increase mold temperature; in addition polish tool
	Cracking after solvent debinding due to stress	Increase venting and mold temperature, then anneal the finished part

Table 15 Comparison of PIM and other manufacturing process

Characteristics	*PIM*	*Sintering*	*Investment casting*	*Machining*
Density[a] (%)	98	86	100	100
Magnetic force[a] (%)	100	70	95	100
Stress[a] (%)	100	70	100	100
Surface finish (μm)	0.8	1.6	3.2	1.6
Weight (g)	0.1–100	5–2000	30–4500	No limit
Wall thickness (mm)	≥0.3–30	≥1.4	≥2	≥2
Design flexibility	High	Medium	Medium	Low
Shape complexity	High	Low	Medium	High
Production rate	High	High	Low	Medium
Material range	High	High	High	Medium
Dimensional tolerance	Close	Poor	Poor	Poor

[a]These quantities are expressed as a percentage of the actual measurement of the quantity.

feedstock test as well as physical and mechanical properties and microstructure of the molded parts.

Despite part defects encountered during the production process of PIM, the technology still stands out and compares favorably with other processes. Table 15 is a comparison of PIM with sintering, investment casting, and machining based on some selected characteristics.

1.16.5.3 Applications and Market Trend of PIM Products

Increased consumer demand and manufacturing for complex, intricate miniature parts and microdevices were catered to by MIM. Application of injection molding to parts and components fabrication has changed product design significantly across all sectors. PIM has applications in many fields of human life, including electronics industry, mechanical parts, armaments industry, household products, medical appliances, automotive parts, tooling, sporting goods, and many more. Table 16 presents an outline of industries and areas of PIM applications, but the technique still faces some challenges, just like other manufacturing processes. Despite these challenges, there is a brighter indication for PIM application in electronic devices and medical implants.[147]

German [148] conducted a survey of available MIM products by region (North America, Europe, Asia, and the rest of the world [ROW]) for various applications. Findings indicated applications that lead in these regions are medical in North America, automotive in Europe, electronics in Asia, and firearms in ROW. Available records have indicated that MIM is heading toward high-volume production of medical, automotive, electronics, and consumer goods for larger and more sophisticated microproducts.[149]

Table 16 Industrial sectors and areas of PIM applications

Industry	*Applications: parts/components*
Electronics	Printer components Digital cameras Disk drive components Heat sinks Mobile SIM card connectors PIN connectors for mobile phone Mobile phone components
Medical	Orthodontic bracket Orthopedic implants Forceps Surgical equipment Sensor housing implantables Aseptic expandable precision blade
Mechanical	Weaving machine components Welding nozzles Mechanical heat engine components Small transmission parts Lock mechanism Gear wheel for microgear Microfluidic devices
Armaments	Rifle sights Magazine catch Trigger and trigger guard Tocket guidance components Projectile stabilizer fin
Tools	Investment casting core Drill bit inserts Wood cutting bit Machining tools
Automotive	Valves Injection nozzles Transmission parts Airbag components Seat worm gear
Consumer	Jewelry Electric toothbrush microgears Watch components Tea and coffee cups Hair-cutting shears
Sports	Golf club heads Spikes/cleats Bicycle parts Ski bindings

1.16.6 Future Research Outlook

Process development is achieved through systematic innovations, and research investigations of injection molding processes over the years have witnessed remarkable achievements. The process of μ-PIM has been developed in recent years with the objective of making ceramics, metals, and its alloys available through mass production of microparts, components, and microdevices. Competing manufacturing technologies such as sintering, investment casting, or micromachining are often limited concerning processable materials and/or large-scale production capability. The process allows introducing new materials (feedstock) with additional properties such as high-temperature stability, strength, toughness, high precision, and surface finishing, as well as heat conductivity and magnetic properties when subject to life applications. Moreover, comparable to microinjection molding of plastics, biomaterial processing has been developed for μPIM to allow in-process joining of two different metallic materials during the injection molding process and within injection machines.

Process development involved all the processing steps of PIM, from powder selection and feedstock preparation to adjustment of injection molding parameters, debinding, and co-sintering conditions of the metal powders. However, more research is needed to enhance both process and part quality. Therefore, the future research outlook of injection molding can be summarized as follows:

i. Developments and investigations of new feedstock moldability in terms of the binder composition and the metal powder. Also, the successful implementation of the PIM process, especially the debinding and sintering processes.
ii. Further development of related manufacturing techniques such as two-component micrometal injection molding (2C-μ-MIM), bicomponent, biomaterial, and multimaterial, among many other new processing techniques of injection molding in terms of tooling and quality part are being

investigated. This produces net-shape parts with solid interfaces of either different colors or different materials obtained.

iii. Process integration and development to enhance capability and wider application. This could be integration of mixing mechanism and injection process via rapid prototyping and/or additive manufacturing techniques with μMIM.

iv. Development of improved microinjection system with high precision and control capability over the present custom-made μMIM machine in terms of enhanced speeds and control, and process monitoring for producing defect-free parts.

v. To investigate process conditions as they affect molded part quality. A robust design and formulation of multiobjective optimization frameworks allow multiple quality criteria for μIM. The development of these frameworks is to establish a relationship between process parameters and quality characteristics such as part dimensions, surface finish, and mechanical properties as they affect part quality.

vi. Modeling and simulation have improved microinjection molding processes over the years but are still hindered by a number of challenges. Therefore, development of new suitable software or improvement of the existing software, especially for PIM, is highly recommended.

1.16.7 Conclusions

Modern manufacturing processes adopt nearly net-shape techniques for fabrication of parts and components, which requires a minimum number of processing steps and cost. Micrometal PIM technology as a net-shape microfabrication technique has been widely adopted in the manufacturing of various consumer products and medical and electronics components. In general, μPIM has achieved this over the years due to its advantages, such as:

i. suitability for mass production of various products with minimum production cost and short cycle times;

ii. process and product development of the technology has been improving over the years, with the capability of producing two-material/two-color and movable parts;

iii. ability to process various materials such as polymers, ceramics, and metal powders.

Although μPIM technology has been described as a net-shape microfabrication technique, some challenges are encountered at various processing stages. Powder–binder segregation, short shot, void, sink mark, weld line, cracks, shrinkage, and warpage are some of the defects. Furthermore, difficulties in measuring some material properties and factors, which cannot be easily determined experimentally, are now being investigated by modeling, optimization, and process control to improve the quality of molded parts. Therefore, application of computer simulation has improved the quality of molded parts.

Multimedia

Overview of the production process of fabricating net-shape microparts by the metal injection molding (MIM) technique is illustrated in four video tracks. These video files illustrate the processing steps of the MIM showing powder-binder mixing, injection molding, debinding, and sintering processes (Videos 1–4).

Acknowledgments

The authors acknowledge the financial support of the University of Malaya, 50603 Kuala Lumpur, Malaysia, through the University of Malaya Research Grants (UMRG) (RP020–2012A) and (RP020–2012B). Also worthy of appreciation are the provision of facilities and technical contributions by the faculty members in Engineering at the University of Malaya, as well as the editorial team.

See also: 1.15 Micro Plastic Part Filling Capabilities through Simulation and Experiment: A Case Study on Micro Gear Shape

References

1. Lenz, J.; Enneti, R. K.; Onbattuvelli, V.; Kate, K.; Martin, R.; Atre, S. Powder Injection Molding of Ceramic Engine Components for Transportation. *JOM* **2012**, *64* (3), 388–392.
2. Attia, U. M.; Alcock, J. R. A Review of Micro-Powder Injection Moulding as a Microfabrication Technique. *J. Micromech. Microeng.* **2011**, *21* (4), 043001.
3. Piotter, V.; Bauer, W.; Knitter, R.; Mueller, M.; Mueller, T.; Plewa, K. Powder Injection Moulding of Metallic and Ceramic Micro Parts. *Microsyst. Technol.* **2011**, *17* (2), 251–263.
4. Piotter, V.; Mueller, T.; Plewa, K.; Ritzhaupt-Kleissl, H. J.; Ruh, A.; Hausselt, J. One- and Two-Component Micro Powder Injection Moulding Derived from Thermoplastic Microreplication. *Plastics, Rubber, and Composites* **2010**, *39* (7), 287–292.
5. Ruprecht, R.; Gietzelt, T.; Müller, K.; Piotter, V.; Haußelt, J. Injection Molding of Microstructured Components from Plastics, Metals and Ceramics. *Microsyst. Technol.* **2002**, *8* (4–5), 351–358.
6. Rajabi, J.; Muhamad, N.; Sulong, A. B. Effect of Nano-Sized Powders on Powder Injection Molding: A Review. *Microsyst. Technol.-Micro-and Nanosyst.-Inf. Storage and Process. Syst.* **2012**, *18*, 1941–1961.
7. Pantani, R.; Coccorullo, I.; Speranza, V.; Titomanlio, G. Morphology Evolution During Injection Molding: Effect of Packing Pressure. *Polymer* **2007**, *48* (9), 2778–2790.
8. Sha, B.; Dimov, S.; Griffiths, C.; Packianather, M. S. Micro-Injection Moulding: Factors Affecting the Achievable Aspect Ratios. *Int. J. Adv. Manuf. Technol.* **2006**, *33* (1–2), 147–156.
9. Pantani, R.; Coccorullo, I.; Speranza, V.; Titomanlio, G. Modeling of Morphology Evolution in the Injection Molding Process of Thermoplastic Polymers. *Prog. Polym. Sci.* **2005**, *30* (12), 1185–1222.
10. Zhao, J.; Mayes, R. H.; Chen, G.; Xie, H.; Chan, P. S. Effects of Process Parameters on the Micro Molding Process. *Polym. Eng. Sci.* **2003**, *43* (9), 1542–1554.
11. Rosato, D. V.; Rosato, M. G. *Injection Molding Handbook*; Springer Science & Business Media: New York, NY, 2012.
12. Chang, P.-C.; Hwang, S.-J.; Lee, H.-H.; Huang, D.-Y. Development of an External-Type Microinjection Molding Module for Thermoplastic Polymer. *J. Mater. Process. Technol.* **2007**, *184* (1–3), 163–172.
13. Galomb, D. E. Hand Operated Injection Molding Apparatus; US Patent 8616871 B2, December 31, 2013.
14. Galomb, D. E. Injection Molding Apparatus and Method of Constructing the Injection Molding Apparatus; US Patent 2012/0076879 A1; March 29, 2012.
15. Galomb, D. E. Injection Molding Apparatus and Method of Constructing the Injection Molding Apparatus; US Patent 8,070,469 B2; December 6, 2011.
16. Galomb, D. E. Injection Molding Machine Apparatus and Method of Constructing the Same; US Patent 2008/0031995 A1; February 7, 2008.

17. Pracilio, F. P. Hand Operated Injection Molding Instructional Device; US Patent 213 87; April 23, 1974.
18. Azuddin, M.; Choudhury, I. A.; Taha, Z. Development and Performance Evaluation of a Low-Cost Custom-Made Vertical Injection Molding Machine. *J. Braz. Soc. Mech. Sci. & Eng.* **2015**, *37* (1), 79–86.
19. Michaeli, W.; Spennemann, A. A New Injection Molding Technology for Micro Parts. *J. Polym. Eng.* **2001**, *21* (2–3), 87–98.
20. Michaeli, W.; Spennemann, A.; Gärtner, R. New Plastification Concepts for Micro Injection Moulding. *Microsyst. Technol.* **2002**, *8* (1), 55–57.
21. Enneti, R. K.; Onbattuvelli, V. P.; Atre, S. V. 4 – Powder Binder Formulation and Compound Manufacture in Metal Injection Molding (MIM). In *Handbook of Metal Injection Molding*; Heaney, D. F., Ed.; Woodhead Publishing: Cambridge; Philadelphia, PA; New Delhi, 2012; pp. 64–92.
22. González-Gutiérrez, J.; Stringari, G. B.; Emri, I. Powder Injection Molding of Metal and Ceramic Parts. In *Some Critical Issues for Injection Molding*; Wang, J., Ed.; INTECH Open Access Publisher: Zagreb, 2012; pp. 65–88.
23. Sakai, T.; Kikugawa, K. Part II: Injection Molding Machinery and Systems: Injection Molding Machines, Tools, and Processes. In *Injection Molding*; Kamal, M. R., Isayev, A. L., Shih-Jung Liu, Eds.; Hanser: Berlin, 2009; pp. 71–131.
24. Verbraak, C. P. J. M.; Meijer, H. E. H. Screw Design in Injection Molding. *Polym. Eng. Sci.* **1989**, *29* (7), 479–487.
25. Pessoles, X.; Tournier, C. Automatic Polishing Process of Plastic Injection Molds on a 5-Axis Milling Center. *J. Mater. Process. Technol.* **2009**, *209* (7), 3665–3673.
26. Grandguillaume, L.; Lavernhe, S.; Quinsat, Y.; Tournier, C. Mold Manufacturing Optimization: A Global Approach of Milling and Polishing Processes. *Procedia CIRP* **2015**, *31*, 13–18.
27. Hocheng, H.; Kuo, K. L. Fundamental Study of Ultrasonic Polishing of Mold Steel. *Int. J. Mach. Tool. Manu.* **2002**, *42* (1), 7–13.
28. Choi, J. Y.; Jeong, H. D. A Study on Polishing of Molds using Hydrophilic Fixed Abrasive Pad. *Int. J. Mach. Tool. Manu.* **2004**, *44* (11), 1163–1169.
29. Giboz, J.; Copponnex, T.; Mélé, P. Microinjection Molding of Thermoplastic Polymers: A Review. *J. Micromech. Microeng.* **2007**, *17* (6), R96–R109.
30. Smarslok, B.; German, R. M. Identification of Design Parameters in Metal Powder Injection Molding. *J. Adv. Mater.* **2005**, *37* (4), 3–11.
31. Petzoldt, F. Micro Powder Injection Moulding-Challenges and Opportunities. *Powder Inject. Mould. Int.* **2008**, *2* (1), 37–42.
32. EPMA. *Metal Injection Moulding – A Manufacturing Process for Precision Engineering Components*, 3rd ed.; European Powder Metallurgy Association (EPMA): Shrewsbury, 2013.
33. Heaney, D. F. 3 – Powders for Metal Injection Molding (MIM). In *Handbook of Metal Injection Molding*; Heaney, D. F., Ed.; Woodhead Publishing: Cambridge, 2012; pp. 50–63.
34. Heaney, D.; Zauner, R.; Binet, C.; Cowan, K.; Piemme, J. Variability of Powder Characteristics and Their Effect on Dimensional Variability of Powder Injection Moulded Components. *Powder Metall.* **2004**, *47* (2), 144–149.
35. Hidalgo, J.; Jiménez-Morales, A.; Barriere, T.; Gelin, J. C.; Torralba, J. M. Capillary Rheology Studies of Invar 36 Feedstocks for Powder Injection Moulding. *Powder Technol.* **2015**, *273*, 1–7.
36. Wen, G. A.; Cao, P.; Gabbitas, B.; Zhang, D.; Edmonds, N. Development and Design of Binder Systems for Titanium Metal Injection Molding: An Overview. *Metall. Mater. Trans. A* **2013**, *44A* (3), 1530–1547.
37. Thavanayagam, G.; Pickering, K. L.; Swan, J. E.; Cao, P. Analysis of Rheological Behaviour of Titanium Feedstocks Formulated with a Water-Soluble Binder System for Powder Injection Moulding. *Powder Technol.* **2015**, *269*, 227–232.
38. Bakan, H. I. Injection Moulding of Alumina with Partially Water Soluble Binder System and Solvent Debinding Kinetics. *Mater. Sci. Tech.* **2007**, *23* (7), 787–791.
39. Azmirruddin, M.; Johari, N.; Jabir, M.; Ibrahim, R.; Talib, A. R. A. Analysis of the Rheological Behavior and Stability of Inconel 718 Powder Injection Molding (PIM) Feedstock. *Adv. Mater. Conf. (Amc 2012)* **2014**, *879*, 63–72.
40. Abdoos, H.; Khorsand, H.; Yousefi, A. A. Torque Rheometry and Rheological Analysis of Powder-Polymer Mixture for Aluminum Powder Injection Molding. *Mairan. Polym. J.* **2014**, 745–755.
41. Liu, Z. Y.; Loh, N. H.; Tor, S. B.; Khor, K. A. Characterization of Powder Injection Molding Feedstock. *Mater. Charact.* **2003**, *49* (4), 313–320.
42. Rajabi, J.; Muhamad, N.; Sulong, A. B.; Fayyaz, A.; Raza, M. R. The Effect of Nano-Sized Stainless Steel Powder Addition on Mechanical and Physical Properties of Micro Powder Injection Molded Part. *Mater. Des.* **2014**, *63*, 223–232.
43. Abolhasani, H.; Muhamad, N. A New Starch-Based Binder for Metal Injection Molding. *J. Mater. Process. Technol.* **2010**, 961–968.
44. Setasuwon, P.; Bunchavimonchet, A.; Danchaivijit, S. The Effects of Binder Components in Wax/Oil Systems for Metal Injection Molding. *J. Mater. Process. Technol.* **2008**, *196* (1–3), 94–100.
45. Supriadi, S.; Baek, E. R.; Choi, C. J.; Lee, B. T. Binder System For STS 316 Nanopowder Feedstocks in Micro-Metal Injection Molding. *J. Mater. Process. Technol.* **2007**, 270–273.
46. Shimizu, T.; Kitazima, A.; Nose, M.; Fuchizawa, S.; Sano, T. Production of Large Size Parts by MIM Process. *J. Mater. Process. Technol.* **2001**, *119* (1–3), 199–202.
47. Li, Y.-m.; Liu, X.-q.; Luo, F.-h.; Yue, J.-l. Effects of Surfactant on Properties of MIM Feedstock. *T. Nonferr. Metal. Soc.* **2007**, *17* (1), 1–8.
48. Ani, S. M.; Muchtar, A.; Muhamad, N.; Ghani, J. A. Fabrication of Zirconia-Toughened Alumina Parts by Powder Injection Molding Process: Optimized Processing Parameters. *Ceram. Int.* **2014**, 273–280.
49. Dobrzański, L. A.; Matula, G.; Herranz, G.; Várez, A.; Levenfeld, B.; Torralba, J. M. Metal Injection Moulding of HS12–1–5–5 High-Speed Steel Using a PW-HDPE Based Binder. *J. Mater. Process. Technol.* **2006**, *175* (1–3), 173–178.
50. Moballegh, L.; Morshedian, J.; Esfandeh, M. Copper Injection Molding Using a Thermoplastic Binder Based on Paraffin Wax. *Mater. Lett.* **2005**, *59* (22), 2832–2837.
51. Huang, B.; Liang, S.; Qu, X. The Rheology of Metal Injection Molding. *J. Mater. Process. Technol.* **2003**, *137* (1–3), 132–137.
52. Lin, K.-H. Wear Behavior and Mechanical Performance of Metal Injection Molded Fe–2Ni Sintered Components. *Mater. Des.* **2011**, *32* (3), 1273–1282.
53. Dang, X.-P. General Frameworks for Optimization of Plastic Injection Molding Process Parameters. *Simul. Model. Pract. Th.* **2014**, *41*, 15–27.
54. Lenz, J.; Enneti, R. K.; Park, S. J.; Atre, S. V. Powder Injection Molding Process Design for UAV Engine Components Using Nanoscale Silicon Nitride Powders. *Ceram. Int.* **2014**, *40* (1), 893–900.
55. Sun, S.-H.; Tsai, L.-Z. Development of Virtual Training Platform of Injection Molding Machine Based on VR Technology. *Int. J. Adv. Manuf. Technol.* **2012**, *63* (5–8), 609–620.
56. Zhang, N.; Chu, J. S.; Gilcharist, M. D. In Micro Injection Molding: Characterization of Cavity Filling Process. In *SPE Annual Technical Conference*; Society of Plastics Engineering: Boston, MA, 2011; pp. 2085–2091.
57. Liu, L.; Loh, N. H.; Tay, B. Y.; Tor, S. B.; Yin, H. Q.; Qu, X. H. Preparation and Characterization of Micro Components Fabricated by Micro Powder Injection Molding. *Mater. Charact.* **2011**, *62* (6), 615–620.
58. Li, D.; Hou, H.; Liang, L.; Lee, K. Powder Injection Molding 440c Stainless Steel. *Int. J. Adv. Manuf. Technol.* **2010**, *49* (1–4), 105–110.
59. Okubo, K.; Tanaka, S.; Ito, H. Molding Technology for Improvement on Dimensional Accuracy in Micro Metal Injection Molding. *Microsyst. Technol.* **2009**, *15* (6), 887–892.
60. Demers, V.; Turenne, S.; Scalzo, O. Segregation Measurement of Powder Injection Molding Feedstock Using Thermogravimetric Analysis, Pycnometer Density and Differential Scanning Calorimetry Techniques. *Adv. Powder Technol.* **2015**, *26* (3), 997–1004.
61. Hidalgo, J.; Jiménez-Morales, A.; Barriere, T.; Gelin, J. C.; Torralba, J. M. Water Soluble Invar 36 Feedstock Development For μPIM. *J. Mater. Process. Technol.* **2014**, *214* (2), 436–444.
62. Hanemann, T.; Weber, O. Polymethylmethacrylate/Polyethyleneglycol-Based Partially Water Soluble Binder System for Micro Ceramic Injection Moulding. *Microsyst. Technol.-Micro-and Nanosystems-Information Storage and Processing Systems* **2014**, *20* (1), 51–58.
63. Lobo, H. 8 – Characterization of Feedstock in Metal Injection Molding (MIM). In *Handbook of Metal Injection Molding*; Heaney, D. F., Ed.; Woodhead Publishing: Cambridge, 2012; pp. 183–196.
64. Huang, B. Y.; Liang, S. Q.; Qu, X. H. The Rheology of Metal Injection Molding. *J. Mater. Process. Technol.* **2003**, *137* (1–3), 132–137.
65. Kate, K. H.; Enneti, R. K.; Park, S.-J.; German, R. M.; Atre, S. V. Predicting Powder-Polymer Mixture Properties for PIM Design. *Crit. Rev. Solid. State.* **2014**, *39* (3), 197–214.
66. Xie, L.; Shen, L.; Jiang, B. Modelling and Simulation for Micro Injection Molding Process. In *Computational Fluid Dynamics Technologies and Applications*; Minin, I., Ed.; INTECH Open Access Publisher: Croatia, 2011; pp. 317–332.
67. Piotter, V.; Benzler, T.; Gietzelt, T.; Ruprecht, R.; Hausselt, J. Micro Powder Injection Molding. *Adv. Eng. Mater.* **2000**, *2* (10), 639–642.
68. Ruprecht, R.; Finnah, G.; Piotter, V. Microinjection Molding-Principles and Challenges. In *Microengineering of Metals and Ceramics: Part I: Design,*

Tooling and Injection Molding; Baltes, H., Brand, O., Fedder, G. K., Hierold, C., Korvink, J., Tabata, O., Eds.; WILEY-VCH: Germany, 2005; pp. 253–287.
69. Fu, G.; Loh, N. H.; Tor, S. B.; Tay, B. Y.; Murakoshi, Y.; Maeda, R. A Variotherm Mold for Micro Metal Injection Molding. *Microsyst. Technol.-Micro-and Nanosystems-Information Storage and Processing Systems* **2005**, *11* (12), 1267–1271.
70. Kulkarni, S. *Robust Process Development and Scientific Molding: Theory and Practice*; Hanser Publications: Cincinnati, OH, 2010.
71. Surace, R.; Trotta, G.; Fassi, I.; Bellantone, V. The Micro Injection Moulding Process for Polymeric Components Manufacturing. In *New Technologies – Trends, Innovations and Research*; Volosencu, C., Ed.; INTECH Open Access Publisher: Croatia, 2012; pp. 65–90.
72. Enneti, R. K.; Shivashankar, T. S.; Park, S.-J.; German, R. M.; Atre, S. V. Master Debinding Curves for Solvent Extraction of Binders in Powder Injection Molding. *Powder Technol.* **2012**, *228*, 14–17.
73. Krauss, V. A.; Oliveira, A. A. M.; Klein, A. N.; Al-Qureshi, H. A.; Fredel, M. C. A Model for PEG Removal from Alumina Injection Moulded Parts by Solvent Debinding. *J. Mater. Process. Technol.* **2007**, *182* (1–3), 268–273.
74. Enneti, R. K.; Park, S. J.; German, R. M.; Atre, S. V. Review: Thermal Debinding Process in Particulate Materials Processing. *Materials and Manufacturing Processes* **2012**, *27* (2), 103–118.
75. Shengjie, Y.; Lam, Y. C.; Yu, S. C. M.; Tam, K. C. Thermal Debinding Modeling of Mass Transport and Deformation in Powder-Injection Molding Compact. *Metall. Mater. Trans. B* **2002**, *33* (3), 477–488.
76. Li, S. G.; Fu, G.; Reading, I.; *et al.* Dimensional Variation in Production of High-Aspect-Ratio Micro-Pillars Array by Micro Powder Injection Molding. *Appl. Phys. A* **2007**, *89* (3), 721–728.
77. Gorjan, L.; Kosmač, T.; Dakskobler, A. Single-Step Wick-Debinding and Sintering for Powder Injection Molding. *Ceram. Int.* **2014**, *40* (1), 887–891.
78. Md Ani, S.; Muchtar, A.; Muhamad, N.; Ghani, J. A. Binder Removal via a Two-Stage Debinding Process for Ceramic Injection Molding Parts. *Ceram. Int.* **2014**, *40* (2), 2819–2824.
79. Wongpanit, P.; Khanthsri, S.; Puengboonsri, S.; Manonukul, A. Effects of Acrylic Acid-Grafted Hdpe in Hdpe-Based Binder on Properties After Injection and Debinding in Metal Injection Molding. *Mater. Chem. Phys.* **2014**, *147* (1–2), 238–246.
80. Herranz, G.; Levenfeld, B.; Várez, A.; Torralba, J. Development of New Feedstock Formulation Based on High Density Polyethylene for MIM of M2 High Speed Steels. *Powder Metall.* **2005**, *48* (2), 134–138.
81. Aggarwal, G.; Smid, I.; Park, S. J.; German, R. M. Development of Niobium Powder Injection Molding. Part II: Debinding and Sintering. *Int. J. Refract. Metals Hard Mater.* **2007**, *25*, 226–236.
82. Su, H.; Johnson, D. L. Master Sintering Curve: A Practical Approach to Sintering. *J. Am. Ceram. Soc.* **1996**, *79* (12), 3211–3217.
83. Shi, Z.; Guo, Z. X.; Song, J. H. A Diffusion-Controlled Kinetic Model for Binder Burnout in a Powder Compact. *Acta Mater.* **2002**, *50* (8), 1937–1950.
84. Aggarwal, G.; Park, S. J.; Smid, I.; German, R. M. Master Decomposition Curve for Binders Used in Powder Injection Molding. *Metall. Mater. Trans. A* **2007**, *38a* (3), 606–614.
85. German, R. M. *Sintering: From Empirical Observations to Scientific Principles*; Butterworth-Heinemann: New York, NY, 2014.
86. Raza, M. R.; Ahmad, F.; Omar, M. A.; German, R. M. Effects of Cooling Rate on Mechanical Properties and Corrosion Resistance of Vacuum Sintered Powder Injection Molded 316l Stainless Steel. *J. Mater. Process. Technol.* **2012**, *212* (1), 164–170.
87. Choi, J.-P.; Lee, G.-Y.; Song, J.-I.; Lee, W.-S.; Lee, J.-S. Sintering Behavior Of 316l Stainless Steel Micro–Nanopowder Compact Fabricated by Powder Injection Molding. *Powder Technol.* **2015**, *279* (0), 196–202.
88. Shen, C.; Wang, L.; Li, Q. Optimization of Injection Molding Process Parameters Using Combination of Artificial Neural Network and Genetic Algorithm Method. *J. Mater. Process. Technol.* **2007**, *183* (2–3), 412–418.
89. Kurtaran, H.; Erzurumlu, T. Efficient Warpage Optimization of Thin Shell Plastic Parts Using Response Surface Methodology and Genetic Algorithm. *Int. J. Adv. Manuf. Technol.* **2005**, *27* (5–6), 468–472.
90. Yin, F.; Mao, H.; Hua, L. A Hybrid of Back Propagation Neural Network and Genetic Algorithm for Optimization of Injection Molding Process Parameters. *Mater. Des.* **2011**, *32* (6), 3457–3464.
91. Wu, C.-Y.; Ku, C.-C.; Pai, H.-Y. Injection Molding Optimization with Weld Line Design Constraint Using Distributed Multi-Population Genetic Algorithm. *Int. J. Adv. Manuf. Technol.* **2010**, *52* (1–4), 131–141.
92. Shi, H.; Xie, S.; Wang, X. A Warpage Optimization Method for Injection Molding Using Artificial Neural Network with Parametric Sampling Evaluation Strategy. *Int. J. Adv. Manuf. Technol.* **2013**, *65* (1–4), 343–353.
93. Tzeng, C.-J.; Yang, Y.-K.; Lin, Y.-H.; Tsai, C.-H. A Study of Optimization of Injection Molding Process Parameters for SGF and PTFE Reinforced PC Composites Using Neural Network and Response Surface Methodology. *Int. J. Adv. Manuf. Technol.* **2012**, *63* (5–8), 691–704.
94. Shi, H.; Gao, Y.; Wang, X. Optimization of Injection Molding Process Parameters Using Integrated Artificial Neural Network Model and Expected Improvement Function Method. *Int. J. Adv. Manuf. Technol.* **2010**, *48* (9–12), 955–962.
95. Yarlagadda, P. K. D. V. Development of an Integrated Neural Network System for Prediction oProcess Parameters in Metal Injection Moulding. *J. Mater. Process. Technol.* **2002**, *130–131* (0), 315–320.
96. Urval, R.; Lee, S.; Atre, S. V.; Park, S. J.; German, R. M. Optimisation of Process Conditions in Powder Injection Moulding of Microsystem Components Using a Robust Design Method: Part I. Primary Design Parameters. *Powder Metall.* **2008**, *51* (2), 133–142.
97. Khan, Z. A.; Kamaruddin, S.; Siddiquee, A. N. Feasibility Study of Use of Recycled High Density Polyethylene and Multi Response Optimization of Injection Moulding Parameters Using Combined Grey Relational and Principal Component Analyses. *Mater. Des.* **2010**, *31* (6), 2925–2931.
98. Ozcelik, B. Optimization of Injection Parameters for Mechanical Properties of Specimens with Weld Line of Polypropylene Using Taguchi Method. *Int. Commun. Heat. Mass.* **2011**, *38* (8), 1067–1072.
99. Attia, U. M.; Alcock, J. R. Evaluating and Controlling Process Variability in Micro-Injection Moulding. *Int. J. Adv. Manuf. Technol.* **2010**, *52* (1–4), 183–194.
100. Fei, N. C.; Mehat, N. M.; Kamaruddin, S. Practical Applications of Taguchi Method for Optimization of Processing Parameters for Plastic Injection Moulding: A Retrospective Review. *ISRN Ind. Eng.* **2013**, *2013*, 1–11.
101. Attia, U. M.; Alcock, J. R. Optimising Process Conditions for Multiple Quality Criteria in Micro-Injection Moulding. *Int. J. Adv. Manuf. Technol.* **2010**, *50* (5–8), 533–542.
102. Wang, Y.-q.; Kim, J.-g.; Song, J.-i. Optimization of Plastic Injection Molding Process Parameters for Manufacturing a Brake Booster Valve Body. *Mater. Des.* **2014**, *56*, 313–317.
103. Panahi, A. K.; Mianajiy, H.; Miandoabchi, E.; Fareed, M. H. Optimization of the Powder Injection Molding Process Parameters Using the Sequential Simplex Algorithm and Sensitivity Analysis. *J. Manuf. Sci. E-T ASME* **2013**, *135* (1), 1–7.
104. Annicchiarico, D.; Attia, U. M.; Alcock, J. R. A Methodology for Shrinkage Measurement in Micro-Injection Moulding. *Polym. Test.* **2013**, *32* (4), 769–777.
105. Lin, J.; Lian, R.-J. Self-Organizing Fuzzy Controller for Injection Molding Machines. *J. Process. Contr.* **2010**, *20* (5), 585–595.
106. Attia, U.; Marson, S.; Alcock, J. Micro-Injection Moulding of Polymer Microfluidic Devices. *Microfluid. Nanofluid.* **2009**, *7* (1), 1–28.
107. Zhao, P.; Gao, Y.; Zhou, H.; Turng, L. S. Noniterative Optimization Methods. In *Computer Modeling for Injection Molding: Simulation, Optimization, and Control*; Zhou, H., Ed.; John Wiley & Sons: Singapore, 2013; pp. 255–282.
108. Chen, W. C.; Kurniawan, D. Process Parameters Optimization for Multiple Quality Characteristics in Plastic Injection Molding Using Taguchi Method, BPNN, GA, and Hybrid PSO-GA. *Int. J. Precis. Eng. Man.* **2014**, *15* (8), 1583–1593.
109. Mehat, N. M.; Kamaruddin, S. Multi-Response Optimization of Injection Moulding Processing Parameters Using the Taguchi Method. *Polym.-Plast. Technol.* **2011**, *50* (15), 1519–1526.
110. Peter, K.; Rong, Z., *Flow Analysis of Injection Molds*, 2nd ed.; Carl Hanser Verlag GmbH & Co. KG: München, 2013.
111. Zheng, R.; Fan, X.-J.; Tanner, R. I. Injection Molding Integration of Theory and Modeling Methods; Springer Science & Business Media: Germany, 2011.
112. Zhou, H. *Computer Modeling for Injection Molding: Simulation, Optimization, and Control*; John Wiley & Sons: Singapore, 2013.
113. Xie, L.; Ziegmann, G. Influence of Processing Parameters on Micro Injection Molded Weld Line Mechanical Properties of Polypropylene (PP). *Microsyst. Technol.* **2009**, *15* (9), 1427–1435.
114. Gou, G.; Xie, P.; Yang, W.; Ding, Y. Online Measurement of Rheological Properties of Polypropylene Based on an Injection Molding Machine to Simulate the Injection-Molding Process. *Polym. Test.* **2011**, *30* (8), 826–832.
115. Tsai, M.-H.; Ou, K.-L.; Huang, C.-F.; *et al.* Study on Micro-Injection Molding of Light Guiding Plate by Numerical Simulation. *Int. Commun. Heat. Mass.* **2008**, *35* (9), 1097–1100.
116. Lin, H.-Y.; Young, W.-B. Analysis of the Filling Capability to the Microstructures in Micro-Injection Molding. *Appl. Math. Model.* **2009**, *33* (9), 3746–3755.

117. Lin, H.-Y.; Chang, C.-H.; Young, W.-B. Experimental and Analytical Study on Filling of Nano Structures in Micro Injection Molding. *Int. Commun. Heat Mass.* **2010**, *37* (10), 1477–1486.
118. Alexandra, R. New Approaches for the Mathematical Model of Injection Technology Processes. *Analele Universitatii Maritime Constanta* **2012**, *13* (18), 159–162.
119. Wang, W.; Li, X.; Han, X. Numerical Simulation and Experimental Verification of the Filling Stage in Injection Molding. *Polym. Eng. Sci.* **2012**, *52* (1), 42–51.
120. Binet, C.; Heaney, D. F.; Spina, R.; Tricarico, L. Experimental and Numerical Analysis of Metal Injection Molded Products. *J. Mater. Process. Technol.* **2005**, *164–165* (0), 1160–1166.
121. Zauner, R.; Binet, C.; Heaney, D. F.; Piemme, J. Variability of Feedstock Viscosity and Its Correlation with Dimensional Variability of Green Powder Injection Moulded Components. *Powder Metall.* **2004**, *47* (2), 151–156.
122. Cross, M. M. Rheology of Non-Newtonian Fluids: A New Flow Equation for Pseudoplastic Systems. *J. Colloid Sci.* **1965**, *20* (5), 417–437.
123. Carreau, P. J. Rheological Equations from Molecular Network Theories. *Trans. Soc. Rheol. (1957–1977)* **1972**, *16* (1), 99–127.
124. Sisko, A. The Flow of Lubricating Greases. *Ind. Eng. Chem.* **1958**, *50* (12), 1789–1792.
125. El Otmani, R.; Zinet, M.; Benhadid, H. Numerical Simulation and Thermal Analysis of the Filling Stage in the Injection Molding Process: Role of the Mold-Polymer Interface. *J. Appl. Polym. Sci* **2011**, *121* (3), 1579–1592.
126. Chhabra, R. P.; Richardson, J. F. *Chapter 1 – Non-Newtonian Fluid Behaviour*; Butterworth-Heinemann: Oxford, 2008. pp. 1–55.
127. Koszkul, J.; Nabialek, J. Viscosity Models in Simulation of the Filling Stage of the Injection Molding Process. *J. Mater. Process. Technol.* **2004**, *157–158*, 183–187.
128. Kim, J.; Ahn, S.; Atre, S. V.; Park, S. J.; Kang, T. G.; German, R. M. Imbalance Filling of Multi-Cavity Tooling during Powder Injection Molding. *Powder Technol.* **2014**, *257*, 124–131.
129. Ahn, S.; Park, S. J.; Lee, S.; Atre, S. V.; German, R. M. Effect of Powders and Binders on Material Properties and Molding Parameters in Iron and Stainless Steel Powder Injection Molding Process. *Powder Technol.* **2009**, 162–169.
130. Huang, A. N.; Kuo, H. P. Developments in the Tools for the Investigation of Mixing in Particulate Systems – A Review. *Adv. Powder Technol.* **2014**, 163–173.
131. Combarros, M.; Feise, H. J.; Zetzener, H.; Kwade, A. Segregation of Particulate Solids: Experiments and DEM Simulations. *Particuology* **2014**, 25–32.
132. Jiang, B.-y.; Zhong, J.; Huang, B.-y.; Qu, X.-h.; Li, Y.-m. Element Modeling of Fem on the Pressure Field in the Powder Injection Mold Filling Process. *J. Mater. Process. Technol.* **2003**, *137* (1–3), 74–77.
133. Liu, Y. J.; Li, X. G.; Huang, Y. G.; Wei, S. S.; Zeng, G. S. Comparison of Rheological Analytic Model with Numerical Simulation in Powder Injection Molding Filling Process. *J. Cent. South. Univ. T.* **2008**, *15*, 51–56.
134. Jiang, S.; Wang, Z.; Zhou, G.; Yang, W. An Implicit Control-Volume Finite Element Method and Its Time Step Strategies for Injection Molding Simulation. *Comput. Chem. Eng.* **2007**, *31* (11), 1407–1418.
135. Hwang, C. J.; Kwon, T. H. A Full 3D Finite Element Analysis of the Powder Injection Molding Filling Process Including Slip Phenomena. *Polym. Eng. Sci.* **2002**, *42* (1), 33–50.
136. Yang, B.; Ouyang, J.; Liu, C.; Li, Q. Simulation of Non-Isothermal Injection Molding for a Non-Newtonian Fluid by Level Set Method. *Chinese J. Chem. Eng.* **2010**, *18* (4), 600–608.
137. Wang, X.; Li, X. Numerical Simulation of Three Dimensional Non-Newtonian Free Surface Flows in Injection Molding Using ALE Finite Element Method. *Finite Elem. Anal. Des.* **2010**, *46* (7), 551–562.
138. Shamekhi, A.; Sadeghy, K. Cavity Flow Simulation of Carreau–Yasuda Non-Newtonian Fluids Using PIM Meshfree Method. *Appl. Math. Model* **2009**, *33* (11), 4131–4145.
139. Kim, S.-W.; Turng, L.-S. Developments of Three-Dimensional Computer-Aided Engineering Simulation for Injection Moulding. *Model. Simul. Mater. SC* **2004**, *12*, S151–S173.
140. Attia, U. M.; Alcock, J. R. Fabrication of Hollow, 3D, Micro-Scale Metallic Structures by Micro-Powder Injection Moulding. *J. Mater. Process. Technol.* **2012**, *212* (10), 2148–2153.
141. Attia, U. M.; Alcock, J. R. Fabrication of Ceramic Micro-Scale Hollow Components by Micro-Powder Injection Moulding. *J. Eur. Ceram. Soc.* **2012**, *32* (6), 1199–1204.
142. Attia, U. M.; Hauata, M.; Walton, I.; Annicchiarico, D.; Alcock, J. R. Creating Movable Interfaces by Micro-Powder Injection Moulding. *J. Mater. Process. Technol.* **2014**, *214* (2), 295–303.
143. Zema, L.; Loreti, G.; Melocchi, A.; Maroni, A.; Gazzaniga, A. Injection Molding and Its Application to Drug Delivery. *J. Control. Release* **2012**, *159* (3), 324–331.
144. Zhao, P.; Zhou, H.; He, Y.; Cai, K.; Fu, J. A Nondestructive Online Method for Monitoring the Injection Molding Process by Collecting and Analyzing Machine Running Data. *Int. J. Adv. Manuf. Technol.* **2014**, *72* (5–8), 765–777.
145. Gasparin, S.; Tosello, G.; Hansen, H. N.; Islam, A. Quality Control and Process Capability Assessment for Injection-Moulded Micro Mechanical Parts. *Int. J. Adv. Manuf. Technol.* **2012**, *66* (9–12), 1295–1303.
146. Barriere, T.; Liu, B.; Gelin, J. C. Determination of the Optimal Process Parameters in Metal Injection Molding from Experiments and Numerical Modeling. *J. Mater. Process. Technol.* **2003**, *143–144*, 636–644.
147. Tuncer, N.; Bram, M.; Laptev, A.; Beck, T.; Moser, A.; Buchkremer, H. P. Study of Metal Injection Molding of Highly Porous Titanium by Physical Modeling and Direct Experiments. *J. Mater. Process. Technol.* **2014**, *214* (7), 1352–1360.
148. German, R. M. Markets Applications, and Financial Aspects of Global Metal Powder Injection Moulding (MIM) Technologies. *Met. Powder Rep.* **2012**, *67* (1), 18–26.
149. German, R. M. PIM Breaks the $1 bn Barrier. *Met. Powder Rep.* **2008**, *63* (3), 8–10.

Relevant Websites

http://www.advancedpowderproducts.com
Advanced Powder Products, Inc. (APP).
http://www.epma.com/
European Powder Metallurgy Association.
http://www.fimmtech.com
Frontier Injection Molding & Material Technologies.
http://www.pim-international.com/
Magazine for the MIM and CIM Industries.
http://www.mimaweb.org/
Metal Injection Molding Association.
http://www.designforpm.net
Resource for designers and engineers about Powder metallurgy & MIM.
http://www.injectionworld.com/
The Global Magazine for Injection Molders.

1.17 Review of Miniature Gear Manufacturing

NK Jain and SK Chaubey, Indian Institute of Technology Indore, Indore, India

© 2017 Elsevier Inc. All rights reserved.

1.17.1	**Introduction**	505
1.17.1.1	Classification of Gears	506
1.17.1.2	Gear Materials	506
1.17.1.3	Quality of Gears and Its Standards	507
1.17.1.4	Miniature Gear Manufacturing Processes	508
1.17.2	**Subtractive Process of Miniature Gear Manufacturing**	508
1.17.2.1	Gear Hobbing	508
1.17.2.1.1	Types	510
1.17.2.1.2	Advantages	510
1.17.2.1.3	Limitations	510
1.17.2.1.4	Applications	511
1.17.3	**Additive Process for Miniature Gear Manufacturing**	511
1.17.3.1	P/M Process	511
1.17.3.1.1	Advantages	513
1.17.3.1.2	Limitations	513
1.17.3.1.3	Applications	513
1.17.3.2	Die Casting	514
1.17.3.2.1	Types	514
1.17.3.2.1.1	Hot chamber die casting process	514
1.17.3.2.1.2	Cold chamber die casting process	514
1.17.3.2.2	Advantages	514
1.17.3.2.3	Limitations	516
1.17.3.2.4	Applications	516
1.17.3.3	MIM	516
1.17.3.3.1	Process capabilities	517
1.17.3.3.2	Advantages	518
1.17.3.3.3	Limitations	518
1.17.3.3.4	Applications	518
1.17.3.4	ICM	518
1.17.3.4.1	Advantages	518
1.17.3.4.2	Limitations	519
1.17.3.4.3	Applications	519
1.17.3.5	μ-PIM	519
1.17.3.5.1	Advantages	520
1.17.3.5.2	Limitations	521
1.17.3.5.3	Applications	521
1.17.3.6	LIGA	521
1.17.3.6.1	Advantages	522
1.17.3.6.2	Limitations	522
1.17.3.6.3	Applications	522
1.17.4	**Deformative Processes for Miniature Gear Manufacturing**	522
1.17.4.1	Stamping	522
1.17.4.1.1	Advantages	523
1.17.4.1.2	Limitations	523
1.17.4.1.3	Applications	524
1.17.4.2	Extrusion	524
1.17.4.2.1	Advantages	524
1.17.4.2.2	Limitations	524
1.17.4.2.3	Applications	525
1.17.4.3	Forging	525
1.17.4.3.1	Types	525
1.17.4.3.2	Advantages	525
1.17.4.3.3	Limitations	525
1.17.4.3.4	Applications	526
1.17.4.4	Hot Embossing	526

 doi:10.1016/B978-0-12-803581-8.09159-1

1.17.4.4.1	Advantages	526
1.17.4.4.2	Limitations	527
1.17.4.4.3	Applications	527
1.17.5	**Miniature Gear Manufacturing by Spark-Erosion-Based Processes**	527
1.17.5.1	EDM	527
1.17.5.1.1	μ-EDM	529
1.17.5.1.2	Advantages	529
1.17.5.1.3	Limitations	529
1.17.5.1.4	Applications	529
1.17.5.2	WEDM	530
1.17.5.2.1	μ-WEDM	530
1.17.5.2.2	Advantages	531
1.17.5.2.3	Limitations	532
1.17.5.2.4	WEDM Applications	533
1.17.6	**Comparative Evaluation**	534
1.17.7	**Summary**	533
References		537

1.17.1 Introduction

Miniaturization and demands of miniaturized components, devices and products are increasing at a very fast rate in modern manufacturing industries due to the reduction in the physical scale of machines and electronic components to micro- or even to nano-scale with their dimensions ranging from tens of nanometers/micrometers to a few millimeters. Micro-components and devices are extensively used in various micro-products and micro-systems such as micro/nano electromechanical systems (MEMS/NEMS) and micro-systems. Most of these micro-systems use miniature gears for the purpose of motion and/or power transmission. Figure 1 shows different applications of the miniature gears which are used as important actuating elements in MEMS and NEMS and are extensively used in various medical, aerospace, automotive, communication, and military/defense



Figure 1 Various applications of the miniature gears.

applications.[1] With continuously increasing demands for MEMS, NEM and micro-products necessity to manufacture high quality of fine pitched miniature gears is ever growing. The functional characteristics and performance of these devices mainly depend on the micro-geometry, macro-geometry and surface quality and surface integrity of the miniature gears. Therefore, miniature gear manufacturing process should be highly precise and accurate because service life and operating performance of miniature gears primarily depend on the manufacturing quality of the gear tooth profile.[2] The miniature gear tooth profile should be accurate in form and burr-free to ensure satisfactory, smooth, and noiseless operation.

1.17.1.1 Classification of Gears

Gear is a modified form of a wheel having teeth uniformly spaced around its circumference. Gear is the one of most important and widely used mechanical element to transmit power and/or motion from one shaft to another through successive engagement of teeth without slipping and connected shafts rotate at constant speed and velocity ratio. Basic requirements of gears are noiseless, accurate and efficient transmission of motion and/or power transmission, higher torque transfer capability, better operating performance without wear and tear, and longer service life. To fulfill these requirements, gears should have accurate dimension and form, better surface finish, and wear resistance at their tooth flanks.

Various types of gears are used in different industrial, commercial, domestic, scientific, entertainment, and other applications. **Table 1** presents classification of gears according to different criteria whereas **Figure 2** depicts different types of gears. According to the outside diameter, gears are classified into two categories namely miniature gears and macro-gears as shown in **Figure 3**. Gears having outside diameter in a range from 0.1 to 10 mm are known as 'miniature gears.' Gears having outside diameter greater than 10 mm are known as 'macro-gears.' Miniature gears are further classified as 'micro-gears' (having outside diameter in the range from 0.1 to 1.0 mm) and 'meso-gears' (having outside diameter in the range from 1.0 to 10 mm). Main advantages of using miniature gears include compactness, higher precision and accuracy, higher efficiency, better operating performance, longer operating life, zero backlash, and sustaining their performance characteristics at extreme environmental conditions.[2,3]

1.17.1.2 Gear Materials

Gears can be made of different materials which are generally classified as metallic and nonmetallic materials as shown in **Figure 4**. Metallic materials are further classified as ferrous and nonferrous materials. Nonmetallic gear materials mainly include different types of plastics. Ferrous materials are used for low speed and high load application while nonferrous materials are preferred for high speed and no-load to low-load

Table 1 Classification of gears according to different criteria[4,5]

Criteria of classification	*Type of gears*	
According to the position of axes of the shafts	1. Parallel shaft	• Spur gear • Helical gear
	2. Intersecting shaft	• Miter gear • Straight bevel gear • Spiral bevel gear
	3. Nonparallel and nonintersecting shafts	• Worm and worm wheel • Screw gear
According to the peripheral velocity of gears	1. Low velocity (<3 m s^{-1}) 2. Medium velocity (3–15 m s^{-1}) 3. High velocity (>15 m s^{-1})	
According to the type of gearing	1. External gearing 2. Internal gearing 3. Rack and pinion	
According to the position of the shaft on gear surface	1. Straight 2. Inclined 3. Curved	
According to the operation	1. Motion transfer gear 2. Power transfer gear 3. Precision gear (used in the scientific instruments)	
According to the form of tooth profile	1. Standard gear 2. Profile shifted gear • Positive profile shifted gear • Negative profile shifted gear	



Figure 2 Various types of gears.

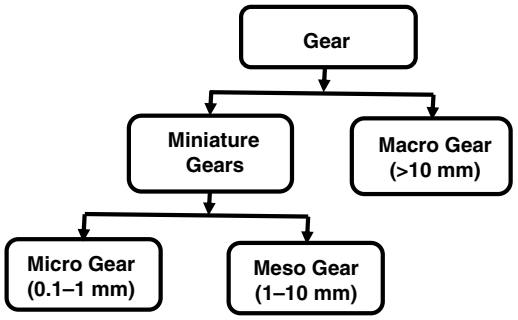


Figure 3 Classification of gears according to the outside diameter.

applications. Nonferrous materials are generally used for noiseless operation at high speed at no-load application. Selection of gear materials depends on various factors such as cost of materials, characteristics, strength, and type of application. Table 2 presents summary of different gear materials, their characteristics, features, and applications.[6]

1.17.1.3 Quality of Gears and Its Standards

Quality of a gear indicates accuracy in its micro-geometry (deviations in form, i.e., lead and profile, and deviation in location, i.e., pitch and runout), macro-geometry, (deviations in span, outside diameter, chordal tooth thickness) and topography of gear tooth flank surface. Gear quality is determined by gear manufacturing, gear finishing, and surface treatment processes. Poor gear quality leads to vibrations, noise, poor transmission characteristics, and less operating life thus giving overall poor operating performance. Therefore, level of gear quality is used to classify suitability of a gear for different applications. Following standards are available to indicate gear quality:

- American Gear Manufacturers Association (AGMA) standard
- Deutsches Instut fur Normung or German institute for standardization (DIN) standard
- British Standards Institute (BSI) standard
- French Gear standard
- Italian Gear standard
- Australian Gear standard
- Japanese Industrial Standards (JIS) gear standard
- Japanese Gear Manufacturing Association (JGMA) standard
- Indian Standard Specifications (ISS)
- International Organization for Standardization (ISO) gear standard.

Out of these gear standards, AGMA, DIN and JIS are the most commonly used gear standards. Gear quality is classified into 12 categories in DIN and BSI gear standards; into 15 categories in AGMA gear standard; and into 10 categories in ISS. Higher value in AGMA standard and lower value in DIN standard indicate better gear quality. Table 3 presents details of AGMA, DIN, JIS, ISO, BSI, and ISS gear standards.

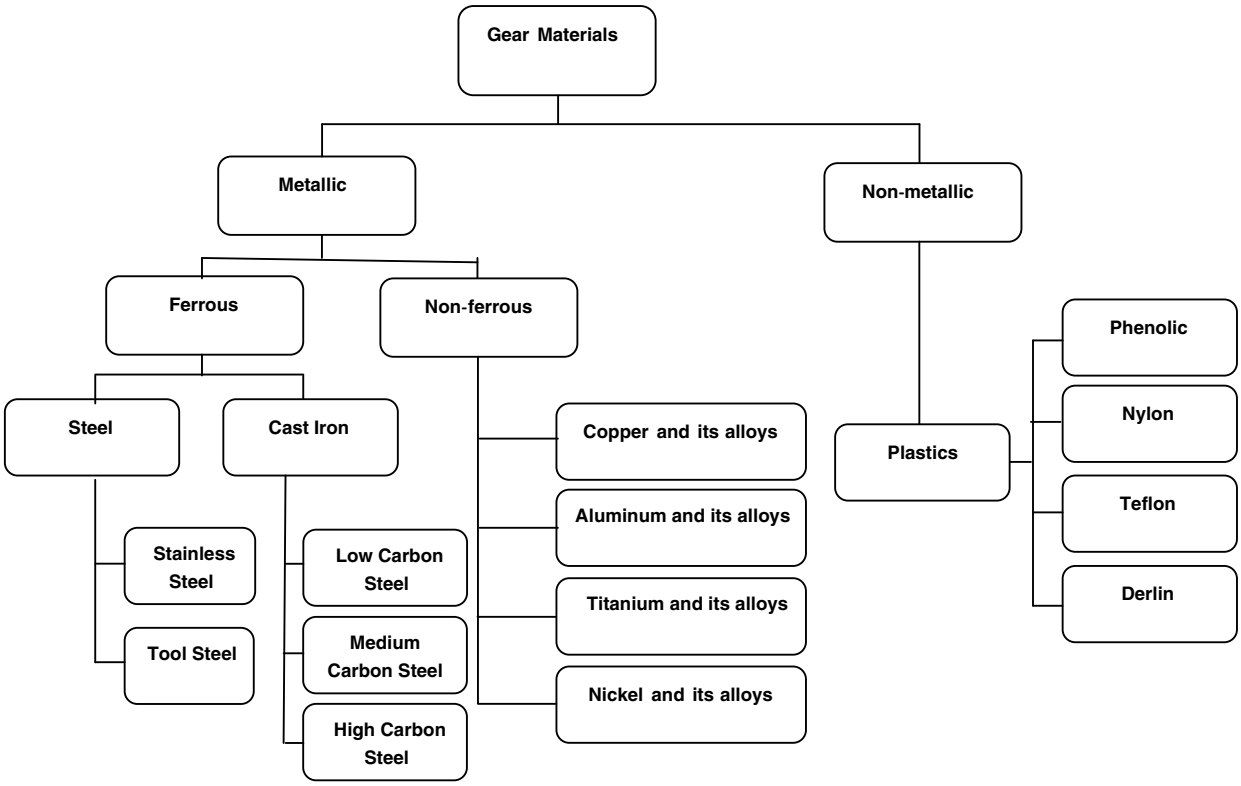


Figure 4 Classification of different gear materials.

1.17.1.4 Miniature Gear Manufacturing Processes

Miniature gears can be manufactured by conventional and unconventional or advanced processes. Table 4 presents different processes used for manufacturing miniature gears. Conventional manufacturing processes give poor quality (DIN standard 9–12) of miniature gears. Moreover, secondary finishing and treatment operations are required to achieve the desired quality of the miniature gears. To overcome the limitations of conventional processes, spark-erosion-based processes such as electric discharge machining (EDM), wire electric discharge machining (WEDM), and their micro versions have been explored for near net-shape manufacturing of high quality fine pitched miniature gears with better dimensional accuracy and surface quality. WEDM has been reported to achieve gear quality up to 6 DIN standard.[3]

1.17.2 Subtractive Process of Miniature Gear Manufacturing

Subtractive type manufacturing process, referred as machining, is the only process by which all types of gears can be manufactured in all sizes. Machining still is unsurpassed for those gears that must have very high accuracy. Gear machining processes can be divided broadly into form cutting and generating processes. In the 'form cutting,' the gear tooth profile is obtained by using a form cutting tool which may be a multiple-point cutter as used in a gear milling and broaching process or a single-point tool as used in a shaping machine. In the gear 'generating process,' the gear tooth profile is obtained by a tool that simulates one or more teeth of an imaginary generating gear. A relative rolling motion of the tool with the gear blank generates the gear tooth surface. This method is used in gear hobbing, gear shaping, and gear milling processes for manufacturing spur and helical gears and in the face milling and face hobbing of bevel gears. Out of different gear machining processes, only gear hobbing is used for manufacturing miniature gears.

1.17.2.1 Gear Hobbing

Hobbing is a generating type gear machining process in which both the cutting tool (known as hob) and the workpiece (i.e., gear blank) revolve in a constant relative motion as the hob is being fed across the face width of the gear blank as schematically illustrated in Figure 5. Hob is similar to a fluted worm in appearance and has form-relieved cutting edges. It rotates about an axis normal to that of the gear blank per forming teeth cutting on a rotating gear blank in succession each time cutting in a slightly different position. Tilting of the hob is maintained according to the hob thread angle and helix angle of the gear teeth. The hob travels radially to the desired depth of the teeth a little clear from the blank and then feeds axially along the width of the gear teeth. The gear teeth are generated progressively by a series of cuts.[8,9] It is widely used for cutting involute teeth on gears with hob having essentially straight sides at the given pressure angle. In this process gear blank and hob rotate in a definite relationship that depends on the number of teeth on the hob and the number of teeth to be on the gear blank. The index-change gears formula for hobbing

Table 2 Summary of different gear materials, their characteristics, features, and applications[7]

Material type	*Characteristics*	*Features and applications*
(A) Ferrous materials		
Cast irons	Low cost, good machinability, and high internal damping	For large-sized gears, moderate power rating, and for commercial applications
Cast steels	Low cost and high strength	For power gears, medium power rating, and for commercial applications
Plain-carbon steels	Good machinability and heat treatable	For power gears, medium power rating, and for commercial to medium precision applications
Alloy steels	Very high strength, heat treatable, and durability	For very high power requirement and for precision and high-precision applications
Stainless steel (300 series)	High corrosion resistance, nonmagnetic, and non-hardenable	Low power rating and for precision applications
Stainless steel (400 series)	Moderate corrosion resistance, magnetic, and hardenable	Low to medium power rating and for high-precision applications
(B) Nonferrous materials		
Aluminum alloys	Lightweight, noncorrosive, and excellent machinability	For extremely light-duty instrument gears and for high-precision applications
Brass alloys	Low cost, noncorrosive, and excellent machinability	For low-cost commercial equipment and for medium precision applications
Bronze alloys	Excellent machinability, low friction, and good compatibility with steel gears	Mating gears for steel power gears and for high-precision applications
Magnesium alloys	Extreme lightweight and poor corrosion resistance	For low-load applications and for medium precision applications
Nickel alloys	Low thermal expansion coefficient and poor machinability	For special thermal applications and for commercial applications
Titanium alloys	Higher strength to weight ratio and corrosion resistant	For lightweight strength applications and for medium precision applications
Die cast alloys	Low cost, low precision, and low strength	Higher production rate, low quality, and for low-grade commercial applications
Sintered powdered alloys	Low cost, low quality, and moderate strength	Higher production rate, low quality, and for commercial applications
Nonmetallic materials		
Delrin	Wear resistant, longer life, and low water absorption	Less noise, low loads, and for commercial applications
Phenolic laminates	Quiet operation and highest strength plastic	Medium loads and for commercial applications
Nylons	Low friction, less noise, and no lubricant	Longer life and for low-load commercial applications
Teflon	Low friction and no lubricant	For low friction commercial applications

Table 3 Details of most commonly used gear standards

Details	*Name of gear standard*		
	AGMA	*DIN*	*JIS*
Number of gear quality categories and range	15 (1–15)	12 (1–12)	8 (0–8)
Category for the worst quality (coarse gears)	1	12	8
Category for the best quality (high-precision gears)	15	1	0
Equivalence between different gear standards	13	4	0
	12	5	1
	11	6	2
	10	7	3
	9	8	4
	8	9	5

process as given below[4]:

$$\text{For spur gears,}\quad \text{Index gear ratio} = \frac{KT}{N} \qquad [1]$$

$$\text{For helical gears,}\quad \text{Index gear ratio} = \frac{KCT}{(CN) \pm 1} \qquad [2]$$

where, K is machine index constant, C is constant, T is number of threads on hub, and N is number of teeth on gear.

For the helical gear hobbing, differential change gears are calculated by formula which is given below to satisfy the relationship between the axial feed screw and the gear blank table rotation.[4]

$$\text{Differential change gears} = \text{Revolution of axial feed screw} \times \text{Lead of axial feed screw} \qquad [3]$$

The time required to manufacture a gear by hobbing can be calculated by following formula[5]:

$$\text{Hobbing time (min)} = \frac{\text{number of teeth to be cut (face + gap)}}{\text{number of hob teeth} \times \text{hob feed rate} \times \text{rpm}} \qquad [4]$$

Figure 6 shows manufacturing of miniature gear by the hobbing process and **Figure 7** depicts mini-hob cutter used in this process. Surface finish of the hobbed gear teeth is

Table 4 Different manufacturing processes for miniature gear

Type	*Basic nature*	*Process name*
Conventional processes	Subtractive	• Hobbing
	Additive or accretion	• Powder metallurgy • Die casting • Metal injection molding • Injection compression molding • Micro-powder injection molding • Lithography, electroforming and molding process
	Deformative	• Stamping • Extrusion • Forging • Hot embossing
Advanced or unconventionalprocesses	Controlled spark-erosion	• Electric discharge machining and micro-electric discharge machining • Wire electric discharge machining and micro-wire electric discharge machining

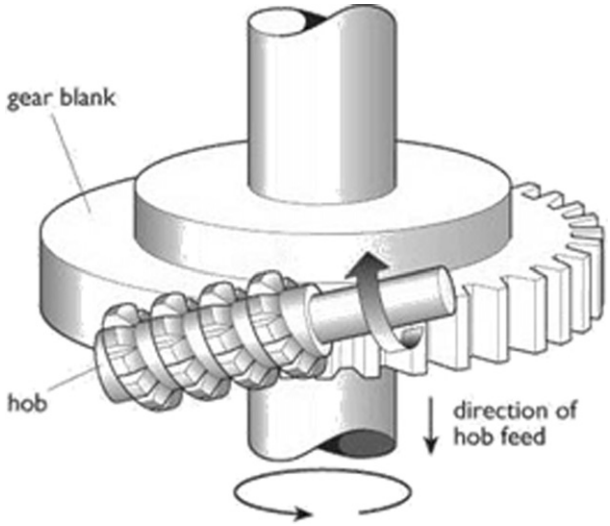


Figure 5 Working principle of gear hobbing process.

significantly dependent on the accuracy, rigidity, and feed rate of the hob cutter. Hobbed gears can have AGMA gear quality standard number 12. A very fine surface finish about 0.4 μm on gear tooth profiles can be achieved with proper tooling and small amount of feed. Using coarse feed, 4 μm surface finish can be achieved in roughing operation. Shaving or grinding operation is required for the semifinished hobbed gears.

1.17.2.1.1 Types

Following are three versions of the gear hobbing process according to relative position of the gear blank and hob and feed direction of the hob.[11]

- Hobbing with axial feed: this method is mainly used for cutting spur or helical gears. Firstly the gear blank is brought toward the hob to get the desired tooth depth and then the gear hob is fed against gear blank along the face of the gear blank and parallel to its axis. Gear cutting by with axial hobbing is obtained by 'climb noting' or 'conventional hobbing.'
- Hobbing with radial feed: this method of hobbing is generally used for cutting worm wheels. In this method the hob and gear blank are set with their axis normal to each other. The gear blank is continuously rotated at a set speed about its vertical axis and the rotating hob is given a feed against the gear blank in the radial direction or perpendicular to the axis of gear blank. The feed of hob is stopped when the required depth of tooth is obtained.
- Hobbing with tangential feed: this method is also used for cutting worm wheel teeth on gear blank. In this method, the hob is held at right angle to the axis of the gear blank but on horizontal axis. The hob is set at full depth of the tooth and then fed forward axially. The front part of the hob is tapered up to a certain length and fed in tangential to the face of gear blank and therefore it is known as 'tangential hobbing.'[11]

1.17.2.1.2 Advantages

The hobbing process offers following advantages:

- fast, accurate, and economical method for manufacturing external gears,
- higher production rate,
- excellent surface finish,
- close tolerances,
- less tool wear,
- economical production cost, and
- low tooling cost as compared to broaching and shear cutting.

1.17.2.1.3 Limitations

Following are the limitations of the hobbing process:

- cannot be used for manufacturing conical and internal gears;
- tool marks left on the gear teeth;

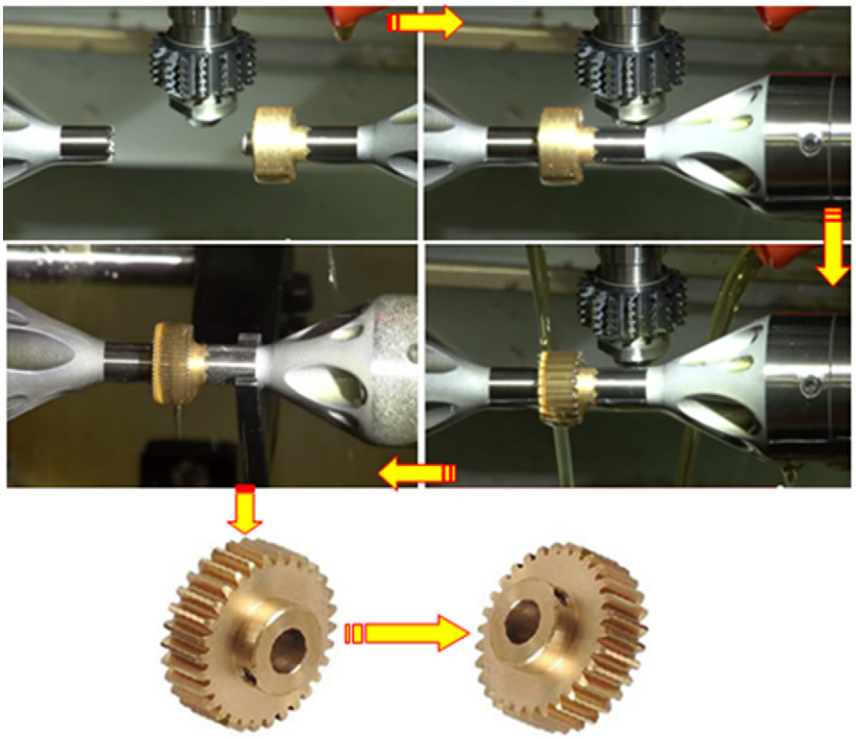


Figure 6 Manufacturing of a miniature gear by the hobbing process.

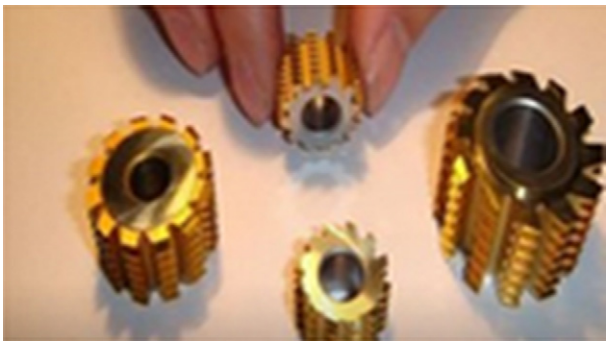


Figure 7 Mini-hob cutters used in manufacturing miniature gears by hobbing.[10]

- poor micro-geometry, i.e., hobbed gears require subsequent finishing operation to achieve desired gear quality; and
- longer setup time.

1.17.2.1.4 Applications

Gear hobbing is the most productive process for all type of gears such as spur gears, helical gears, herringbone gears, worms, worm wheels, splines, gear sprockets, and many special forms in all types of materials. Gears from ferrous, nonferrous, and nonmetallic materials are cut by high speed TiN coated steel hobs. Carbide tip hob is used to cut steel gears for automobile applications. It is most suitable for medium to high volume production but easily adaptable to small-lot production also.[4]

1.17.3 Additive Process for Miniature Gear Manufacturing

Additive or accretion type processes for manufacturing the miniature include: powder metallurgy (P/M) process, die casting, metal injection molding (MIM), injection compression molding (ICM), micro-powder injection molding (μ-PIM), and Lithography, electroforming and molding (LIGA). They are described in the following section.

1.17.3.1 P/M Process

P/M has been used since 1930s to manufacture various types of parts and components from the raw materials in the powdered form.[4] The first P/M gear was used in an oil pump in 1938. The size of P/M gears ranges from few millimeters to 300 mm in diameter depending on the available press size. It consists of the following five major steps as shown in **Figure 8** along with the processes that are used to perform every step of P/M.

- Production of powder: The P/M process begins with preparation of product material in the powder form which may be pure metal or combination of different metals. Metallic powder can be prepared by various processes such as atomization, chemical reduction, electrolytic dissolution, granulation process, mechanical pulverization, and ball milling. Nickel steels are used to produce gears with high strength, high impact properties, and excellent wear properties.
- Blending of powders in a mold/die: After powder preparation, the powder is blended with lubricants and

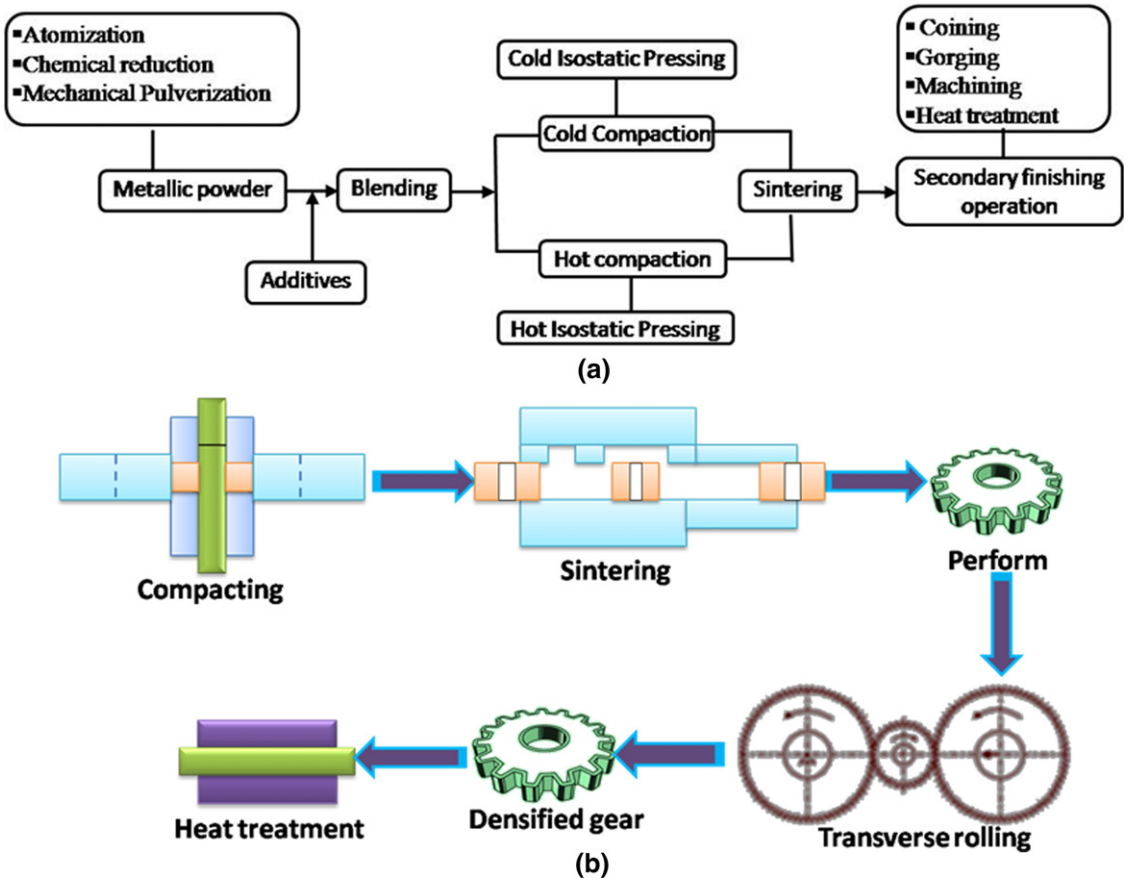


Figure 8 (a) Five major steps involved in the powder metallurgy (P/M) process and (b) processing sequence to manufacture gears by the P/M process.

suitable binders to form a homogenous mixture. Binder improves the 'green strength' of green compact. Both binder and lubricant burns off during the sintering process.

- Compacting of powders in the mold/die: After proper mixing, the powder is poured into a die cavity and compressed with a punch having its cross-section and geometry corresponding to the die on a press. Compacting is generally performed at room temperature and at high pressure and compacted powder is known as 'green part.' In conventional pressing, the pressure is applied uniaxially which limits the part geometry because metallic powders do not readily flow in the directions perpendicular to the applied pressure and leads to density variation in the compact after pressing. Whereas, in isostatic pressing (cold and hot isostatic pressing), pressure is applied from all the directions against the powders by using hydraulic pressure to achieve the compaction. In the 'cold isostatic pressing (CIP)' process, compaction water or oil is used to compress the powder into mold cavity by the hydrostatic pressure and carried out at room temperature. Mold is made of either rubber or some other elastomer and is oversized to compensate for shrinkage. The CIP process provides uniform compaction giving uniform density with less expensive tooling within shorter production runs. 'Hot isostatic pressing (HIP)' is carried out at higher temperatures and pressures combining pressing and sintering in single step using a gas such as argon or helium as the compression medium. Despite this apparent advantage, it is a relatively expensive process and its applications seem to be concentrated in the aerospace industry. P/M parts with high density (porosity near zero), thorough interparticle bonding, and good mechanical strength are achieved by HIP.[12] **Figure 9** shows the compaction of powders to manufacture a gear.
- Sintering: after pressing, sintering is performed in which green compact is heated to a temperature below the melting point of powdered material to bind its particles so as to increase the strength of the final product. Binding among the powder particles takes places in three ways: (1) melting of minor constituents in the powder particles, (2) diffusion between the powder particles, and (3) mechanical bonding. Sintering is usually done at an elevated temperature but at atmospheric pressure. **Figure 10** shows sequence of sintering process on the microscopic scale showing initiation of particle bonding at contact points (**Figure 10(a)**); formation of necks (**Figure 10(b)**); reduction in interparticle distance (**Figure 10(c)**); and formation of green boundaries between particles at the points of the necks (**Figure 10(d)**). Tolerances of P/M gears are determined by the compaction tooling, compaction process, sintering process, and the gear material. Dimensional control is difficult during sintering if density variations during compaction exceed 0.2 g cm^{-3}.

- Finishing operation: after sintering, some finishing operation such as re-pressing, coining, forging, machining, infiltration, and plating may be needed to achieve the desired dimensional accuracy and quality of the product. The P/M process is capable of manufacturing high strength and precision gears with high repeatability at reasonable low cost per piece and giving gear quality value in a range from 6 to 9 in AGMA standard.[6] Re-pressing and coining operation after sintering are required to achieve the AGMA gear quality value 9 while, a value of 6 can be achieved after sintering operation also. Repressed gears exhibit excellent surface finish while conventional sintered gears have sufficient porosity gears and can be vacuum-impregnated with oils for longer lubrication duration.[9]

1.17.3.1.1 Advantages

Following are the major advantages of the P/M process:

- capability to manufacture the gears with multifunctional features such as bosses, notches, collars, keyways, projections, and other irregular shapes without additional operations which reduces the manufacturing cost;
- minimized secondary finishing operations by producing near net-shaped gears;
- improved surface finish on gear tooth by elimination tool marks;
- higher density or porosity to suit a particular application;
- excellent repeatability and uniformity of part features;
- production of light-weight gear;
- tight tolerances;
- lower energy consumption;
- higher production rate; and
- economical in mass production.

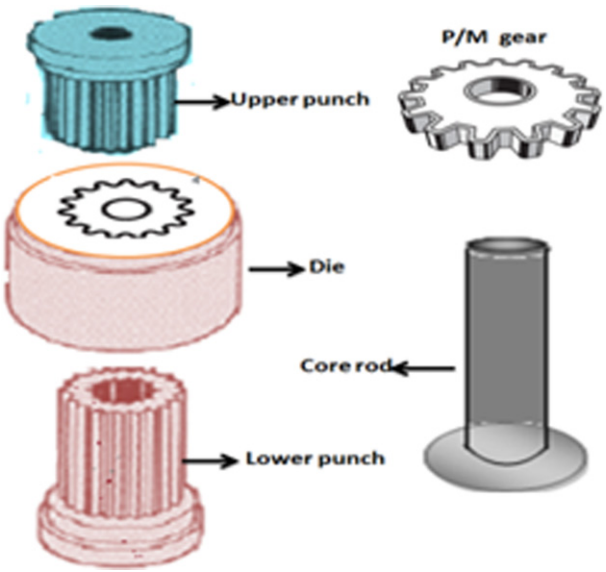


Figure 9 Compaction of powders to manufacture a gear.

1.17.3.1.2 Limitations

P/M process has following limitations:

- higher cost of preparing metallic powders;
- difficulty in storage of the fine metallic powders;
- difficulty in removal of part from the mold/die;
- variations in material density throughout the part, especially for complex part geometries;
- higher porosity which decreases mechanical properties of the P/M components;
- gears are subjected to re-pressing or coining after sintering;
- intricate designs are difficult to produce;
- lower material utilization;
- size of a part is limited by the press capacity;
- higher tooling and equipment cost; and
- longer processing cycle time.

1.17.3.1.3 Applications

The P/M process is used to make components and products used in many applications. Some applications worth mentioning are:

- Automotive applications: brake pads gear parts, connecting rods, planetary carriers, sintered engine bearings, etc.
- Aerospace applications: light-weight aluminum-based structural materials, high temperature composite materials, etc.
- Medical applications: dental implants, surgical instruments, etc.
- Applications in atomic energy: fuel elements, control rod systems, etc.
- Applications in electrical, electronic and computer parts: permanent magnets, electrical contacts, electric light bulbs, fluorescent lamps, radio valves, oscillator valves, etc.

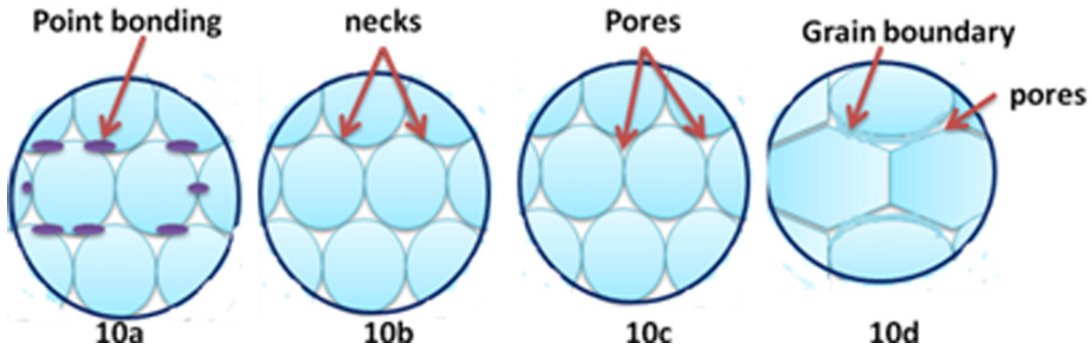


Figure 10 Sintering process on microscopic scale; (a) particle bonding initiated at contact points; (b) formation of necks; (c) reduction in interparticle distance; and (d) formation of grain boundaries between particles at the points of necks.

- Applications in cutting and machine tools: hard metals, diamond containing materials, master gear electrodes for EDM process, various parts of lathes, drilling, threaded guides, grinding and polishing wheels, and disks.

The P/M process can be used to manufacture spur gear, helical gear (with maximum helix angle 35°), bevel gear, face gear and hypoid gears, eccentric gear, reduction gears, powder forged internal ring gear, etc. Gear with fine pitches up to 64 can be produced by the P/M process. Fine pitch P/M gears are used for power tools, small appliances and fractional horse power electric motors while, coarse pitch P/M gears are widely used for heavy appliances, automotive equipment and agricultural equipment.[4] It is an effective and economical process for manufacturing powdered metal gear in large quantities due to the high tooling cost. **Figure 11** depicts different gears manufactured by the P/M process.

1.17.3.2 Die Casting

Die casting is a precision, high volume manufacturing process that was developed in the early 1900s. Traditional die casting process is also known as 'high pressure die casting process (HPDCP).' It is similar to plastic injection molding in which molten material is used instead of plastic. In this process molten material is injected into a mold cavity with high velocity and under high pressure in a range from 20 to 200 bar maintained till solidification stage. The mold cavity is formed by using two blocks of hardened, heat resistant tool steel which is machined to net-shape or near net-shape of the die cast parts along with the parting line. Fine vents are provided to allow the air to escape from them old cavity during pouring of molten material in it. Otherwise, air is trapped into the molten material and form blow holes and porosity in the die cast product.

1.17.3.2.1 Types

There are two types of the die casting process namely (1) hot chamber die casting process and (2) cold chamber die casting process. Size and materials of the gears are two important factors on which proper selection of die casting process depend. For example, cold chamber process is a more efficient choice for the aluminum than the hot chamber method.

1.17.3.2.1.1 Hot chamber die casting process

Hot chamber die casting process is also known as 'gooseneck casting.' In this process melting unit is an integral part of the machine which primarily consists of a hot chamber and a gooseneck type cast iron container as shown in **Figure 12**. The cylinder chamber of the injection system is completely submerged in the molten material bath. The die is split into two halves. The front half is known as cover die and is mounted on the stationary platen and is aligned with the gooseneck channel. Other half of the die is known as the ejector die and it is mounted on the movable die platen. The molten material from the container is injected into die cavity under high pressure by a hydraulically operated plunger submerged in the molten material. When the plunger moves upward, the molten material comes and fills the cylinder which is then forced into the die cavity through a nozzle in the gooseneck of the container during downward motion of the plunger. Injection pressure can range from 69 to 345 bar. Alloys with high melting temperature and having tendency to dissolve iron and steel cannot be used in this process since they would react with plunger and cylinder. Therefore, this process is suitable only for the low melting temperature metals and alloys such as zinc, tin, and lead-based alloys. The advantage of this process is short cycle time (around 15 cycles min^{-1}) as molten material is not transported from separate furnace.

1.17.3.2.1.2 Cold chamber die casting process

The cold chamber die casting is a permanent mold casting process. The melting unit is not an integral part of the machine for this process. Therefore, material is melted in a separate furnace, and then ladled, either by hand or with mechanical ladle, into a cold chamber where it is fed into an unheated shot chamber or injection cylinder as shown in **Figure 13**. Then the molten material is forced into the desired mold cavity by a hydraulically or mechanically operated plunger maintaining the pressure till solidification stage. The process is completed into following four steps:

- pouring of the molten material in the cold chamber and placing the moveable platen and cores in position;
- injecting the molten material into the mold cavity under high pressure by the plunger;
- removing cores and dies; and
- ejecting casting from movable dies platen.

This process mainly focuses on minimizing machine corrosion than production efficiency. Major disadvantage of this process is slower cycle time due to transfer of molten material from furnace to the cold chamber. This process is better suited for high melting temperature alloys such as aluminum, brass, and magnesium.

1.17.3.2.2 Advantages

Following are the major advantages of the die casting process:

- Ability to manufacture gears having dense and homogeneous microstructure without any impurities.



Figure 11 Different types of gears manufactured by powder metallurgy process.

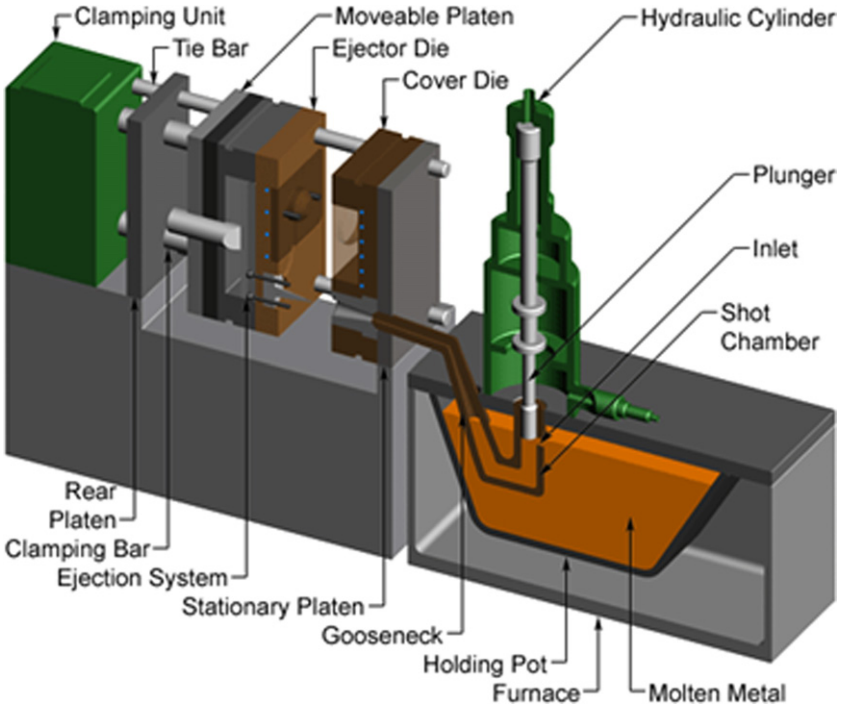


Figure 12 Hot chamber die casting process.[13]

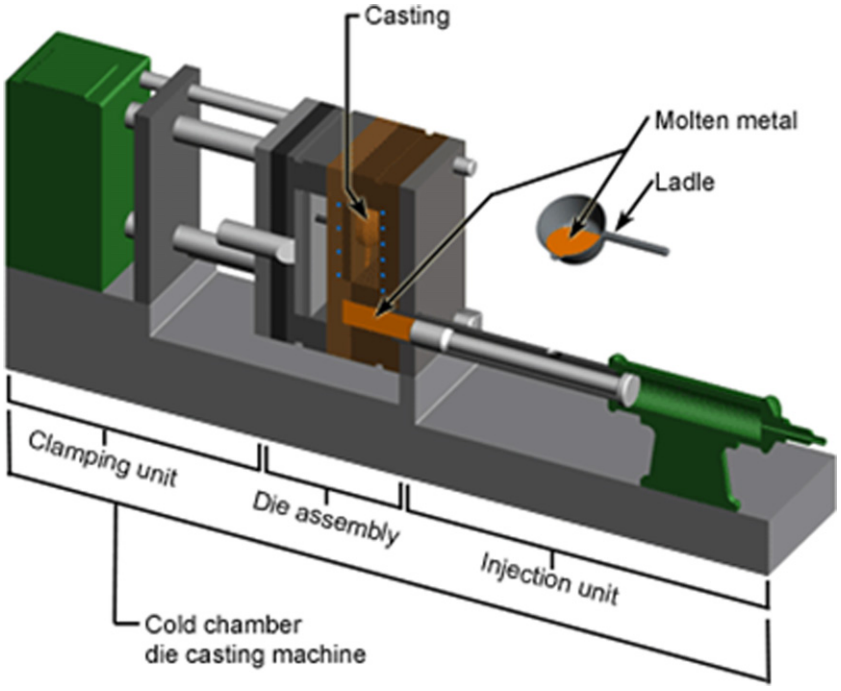


Figure 13 Cold chamber die casting process.[13]

- It can manufacture different types of gears such as spur, helical worm, clusters, and bevel gears and also with multifunctional features.
- Higher dimensional accuracy (tooth spacing and concentricity), better surface finish and stability.
- Die cast gears are stronger and light in weight than the injection molded gears of same dimensions.
- No or very little post-manufacturing finishing is required.
- Gears of AGMA quality value 8 can be produced by die casting process.

- Higher operating performance, repeatability, wear resistance, and production rate.
- Capability to produce fine surface texture with tight tolerance.
- Ability to manufacture thin-wall parts with uniform thickness.
- Low manufacturing and labor cost.
- Faster production rate.
- Economical and cost-effective process for mass production of the miniature gears.

1.17.3.2.3 Limitations

Die casting process has following limitations:

- not suitable for gear manufacturing for high speed and high load applications;
- limited to nonferrous materials having high fluidity and low melting-point temperature;
- cannot be used where high accuracy is needed;
- suitable for high volume production only;
- a certain amount of porosity is common;
- requires secondary finishing operations after gear manufacturing; and
- higher capital and tooling costs.

1.17.3.2.4 Applications

Die casting process is mainly used for nonferrous materials with high fluidity and low fusion temperature such as zinc and its alloys, copper, aluminum, brass, magnesium, and tin-based alloys. Approximately 50% of gears made of zinc-based alloys are manufactured by the die casting process.[14] Die cast gears are used in various industries and appliances such as automobile, aerospace, machine and power tool, instruments, cameras, business machines, washing machines, gear pumps, small speed reducers, lawn movers, and household appliances.[4] This process allows manufacturing of gears with high degree of accuracy and repeatability. Figure 14 depicts the different types of miniature gears made of zinc and manufacture by die casting process.

1.17.3.3 MIM

MIM process was developed by Raymond Wiech of the USA in the 1970s for the processing the metallic powders. This process is a combination of injection molding and P/M for net-shape or near net-shape manufacturing of complex and small components. It is also referred as PIM process because it uses fine metallic powders with organic binder injected into a die under high pressure instead of allowing to flow under gravity. It is a cost-effective alternative process to the many conventional processes such as investment casting, P/M, and stamping. It consists of the following five major steps[15] as shown in Figure 15:

- Feedstock preparation: the MIM process begins with blending of fine metallic powders (having particle size less than 20 μm) with organic binder (polymer and wax) in a ratio of 60:40 for preparation of a moldable powder. This blend is placed in special mixing equipment and heated to a temperature causing the binders to melt. Subsequently, it is mixed mechanically until the powder particles are uniformly coated with the binders. Then it is cooled and granulated into free flowing pellets termed as feedstock which can be accepted by the injection molding machine.
- Injection molding process: plastic injection molding is used to shape the feedstock into the desired shape. The pelletized feedstock is fed through hopper by gravity to the barrel of a conventional plastic injection molding machine where heater melts the binder at 200 °C. Then the feedstock injected under high pressure by reciprocating screw of the plastic injection molding machine into a two-part die or desired mold cavity trough the opening called gates. The molded part is known as 'green part' which is approximately 20% larger than the final product size to compensate for shrinkage of the green part during sintering. Shrinkage allowance depends on type of the material.
- Debinding: it removes the binders from the green part. About 80% binders are removed either by closed loop solvent or catalyst process or by heating process or combination of them. Time required for debinding is directly related to wall thickness. A debound part is called a 'brown part' which is semi-porous and fragile with no change in size. Remaining binders are removed during the sintering process.
- Sintering: sintering is performed by heating the brown part in a vacuum furnace at an elevated temperature but below the melting point of its material so that the particles fuse together to eliminate the void space between the particles. This achieves high dimensional accuracy and shrinkage, about 15–25%. The sintered part density is normally 95–99% of the theoretical density for most of the materials.



Figure 14 Different types of miniature gears manufactured by die casting.

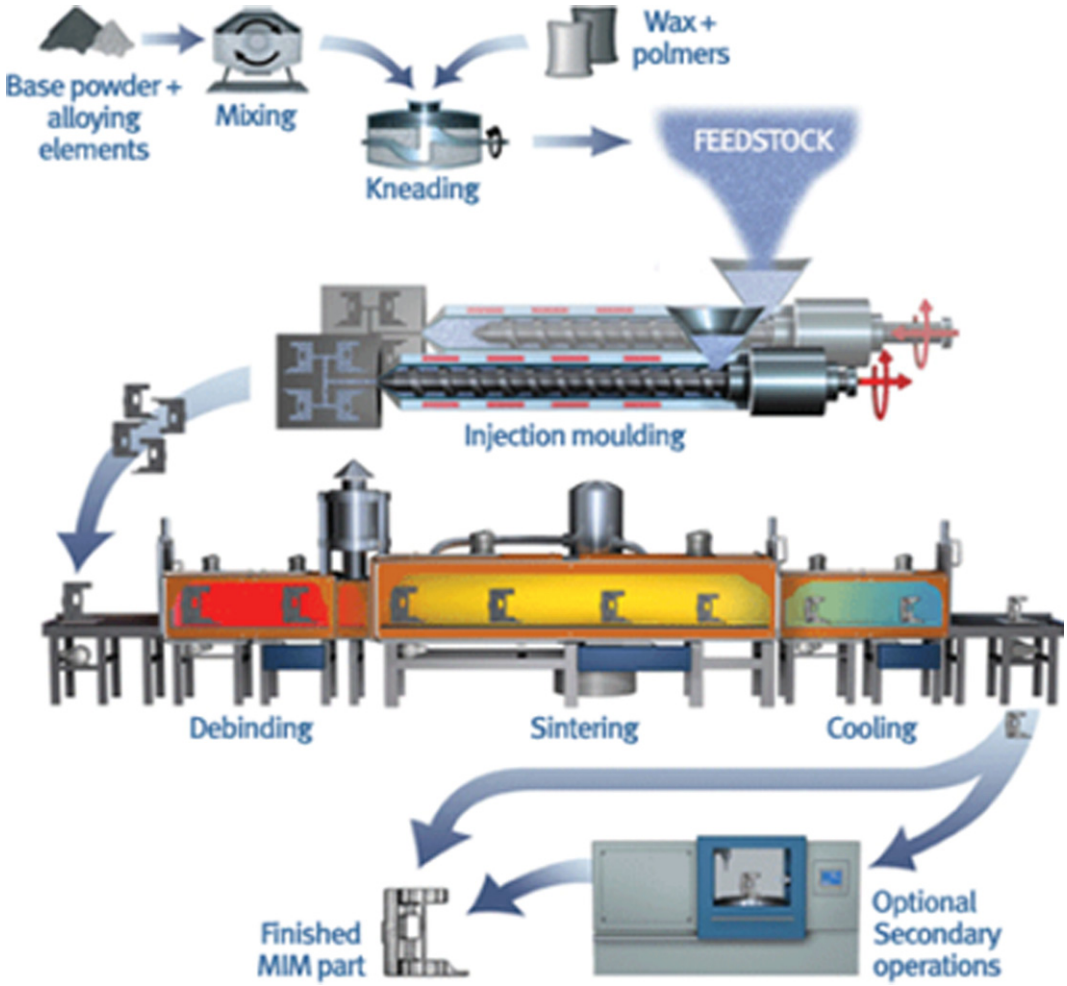


Figure 15 Major steps involved in metal injection molding process.[15]

Properties of the sintered parts are similar to the wrought product. The entire cycle including debinding generally takes 24–36 h.

- Post sintering process: the physical characteristics and properties of final MIM components can be further improved according to requirement of the final product using a wide range of secondary operations such as heat treatment, coating, plating, cold working, etc.

1.17.3.3.1 Process capabilities

MIM process possess following capabilities that make it a versatile process[16]:

- Complexity: MIM provides three-dimensional (3-D) design freedoms with excellent material properties similar to plastic injection molding which gives almost unlimited shape production capability. MIM is cost-effective process as compared to conventional process for production of multifunctional components.
- Precision: MIM is a precision manufacturing process to produce net-shape or near net-shape components with tolerance from ± 0.3 to $\pm 0.5\%$ of the dimension. Certain features can be made net-shape to $\pm 0.3\%$. Tolerances that cannot be achieved by MIM alone can be achieved through various finishing processes. This makes this process more competitive than investment casting and machining process.[17]
- Materials: MIM process is capable to produce small and complex components from variety of materials including ferrous alloys, super alloys, titanium alloys, copper alloys, refractory metals, cemented carbides, ceramics and metal matrix composites.[18] Nonferrous alloys such as aluminum and brass can be also used as powder material for MIM process.
- Weight and size: very small and micro-sized parts having weight less than 0.1 g can be easily manufactured by MIM process. This is effective and economical process for parts having weights less than 100 g. However, part weight up to 250 g can also be processed.
- Section thickness: the MIM process is suitable for components with wall sections of less than 6 mm; however, thicker sections can also be process easily.
- Production volume: MIM is a highly scalable process. Low volume of several thousand parts annually up to millions of parts can be economically achieved. A tooling and engineering investment is necessary for the MIM process

similar to casting or plastics, which will normally drive the decision process for low volume products.
- Manufacturing cost: manufacturing cost of products manufactured by MIM is 50% less than investment casting and CNC machining.
- Applications assistance: MIM provides comprehensive assistance for materials selection and in product design and development such as industrial product design, rapid prototyping finite element analysis, and laser scanning.

1.17.3.3.2 Advantages

Following are the major advantages of the MIM process:

- Net-shape or near net-shape manufacturing of metallic, small, and complex geometrical features such as internal and external threads, profiled holes and knurling.
- Capability to produce multiple components simultaneously thus reducing part and assembly costs.
- Capability to produce features such as small holes, thin walls, and fine surface that cannot be achieved by conventional methods such as investment casting and P/M.
- Higher repeatability, excellent surface quality, higher density components, tight tolerances.
- Less material wastage and overall product cost.
- Eliminate secondary machining operation.
- Reduced production cycle time as compare to investment casting.
- Economical and cost-effective process for complex and small components in high volume.

1.17.3.3.3 Limitations

Following are the limitations of the MIM process:

- suitable for manufacturing small components only;
- lead time is higher than the injection molding;
- materials shrinkage about 25–30% during sintering;
- due to multiple steps, the processing costs are more expensive than injection;
- higher material and mold cost.

1.17.3.3.4 Applications

MIM is an additive manufacturing process used to produce 3-D small, complex, intricate and precision parts and components with tight tolerances from a variety of materials without needing any secondary machining operation.[19] Micro-gears are manufactured by μ-MIM process.[20] MIM manufactured components are widely used in various industrial and commercial applications such automobile, military, aerospace, medical and surgical, food processing, lock and armature, consumer appliances, measurement and control systems, precision engineering equipment, tool engineering, domestic appliances, power hand tools, cellular phones, sporting equipment, electronics (connectors, hard drives, housings), implants for orthopedic and dental applications, laparoscopic instruments for grasping tissue and cutting, micro-wheel and impeller, micro-gears, etc.[19–22]

1.17.3.4 ICM

ICM process is modified form of the injection molding process with an additional compression system thus combining the techniques of the rapid charging of the injection molding and uniform compression of the compression molding process. This combination increases the production rate by eliminating manual cutting and placement of sheet molding compound (SMC) because raw material is injected through a gate during injection phase. It is also called coining, stamping, compressive-fill, or hybrid molding. **Figure 16** schematically depicts working principle of the ICM process showing major steps which involves (1) bringing the mold close to compression gap; (2) filling the mold cavity with molten plastic by injection process; (3) complete filling and packing of the mold by compressing the molten plastic into the mold cavity by compression process; and (4) cooling, opening, and ejection of the molded part.[23] Entire process sequence occurs in phases, i.e., injection phase and compression phase, therefore ICM process is considerably more complex and difficult to simulate than the compression molding process.[24]

- Injection phase: in this phase, thickness of the target part is designed to be smaller than the mold cavity thickness to ensure easy flow of the molten plastic under low pressure and stress to the extreme corners of the mold cavity. The mold is initially kept partially open so that the plastic material within the mold is either partially stressed or completely unstressed. This helps to reduce the flow resistance by providing high porosity in fibrous medium. The filling process begins by injecting a required amount of catalyzed plastic material into the mold through inlet gates. After completion of the injection phase, all inlet gates are closed and the filling stage is finished by compressing the mold to the final configuration of the part.
- Compression phase: during this phase, a compressive force reduces the part thickness by forcing the plastic material to the unfilled portions of the mold cavity. It produces more uniform packing pressure across the mold cavity and the plastic material is set to the final part geometry. Consequently, ICM process gives more homogeneous physical properties with less molding stresses as compared to conventional injection molding process.[25]

1.17.3.4.1 Advantages

Various advantages of ICM process include[26]:

- capability to manufacture large, complex and low tension plastic components;
- higher dimensional accuracy due to uniform distribution of the raw material;
- less molding pressure, injection pressure, variation in density and residual stress;
- easy and fast mold filling with improved venting;
- uniform packing and filling permits overfilling of the mold cavity;
- compensates uneven shrinkage by compressing the melt through the clamping movement;
- high dimensional stability by eliminating warpage;
- requires less clamping force during compression;
- minimizes holding pressure time, shortens cycle times;
- minimum molecular orientation and alignment during injection;
- eliminates sink mark with thicker wall section;

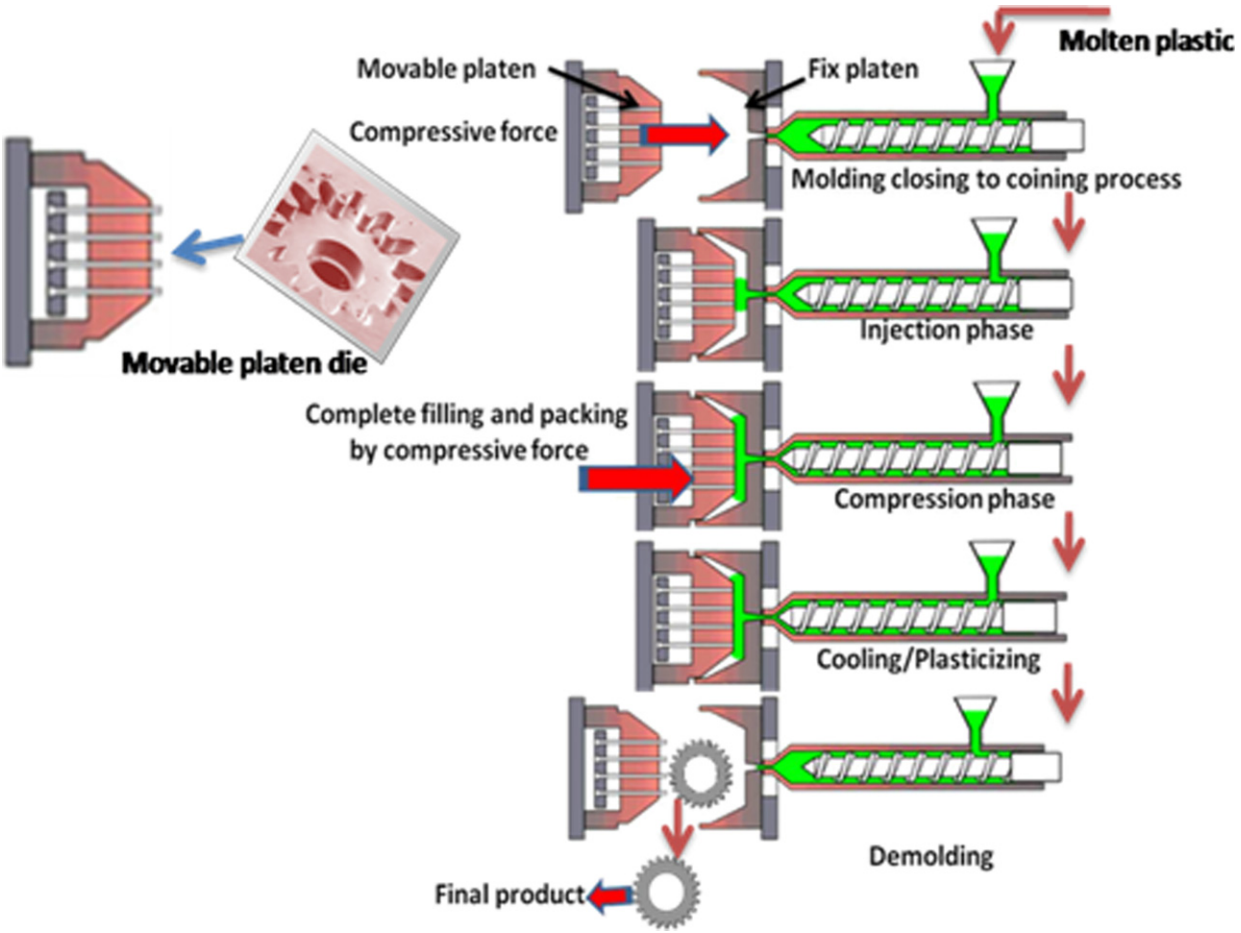


Figure 16 Working principle of injection compression molding process for manufacturing miniature gears.

- reduces film stresses in direct back injection for decorative parts;
- produces low stress, thick-walled components with high contour accuracy;
- minimizes birefringence;
- improved mechanical properties by reducing fiber degradation in long-fiber-reinforced thermoplastics (LFTs) parts; and
- improved optical properties for parts made of transparent material.

1.17.3.4.2 Limitations

Limitations of the ICM process are as follows:

- not suitable for parts having higher depth toward injection;
- material wastage due to mold overfilling;
- higher cost of machine and mold;
- slower process;
- difficulty in flash control;
- complex process control; and
- contamination.

1.17.3.4.3 Applications

ICM process is capable of producing parts which are relatively stress-free and dimensionally stable using low clamping force. It is generally used to produce high volume of plastic components with features and qualities that cannot be produced by the conventional injection molding process.[27] It is widely used to manufacture strong, lightweight, stiff, and high quality mechanical and auto components made of fiber reinforced plastics for automobile applications such as gears. Other major applications of ICM process are[26]:

- manufacturing of various optical parts, foamed parts, decorative parts, thin-wall packaging parts;
- finely textured surfaces;
- cell phone cover, notebook cover;
- fuel cell bipolar plate, sd card, etc.

1.17.3.5 μ-PIM

μ-PIM is combination of micro-injection molding and P/M and was developed at Forschungszentrum Karlsruhe. It is an additive process of manufacturing the micro-components with feature size less than 50 μm for micro-system devices and has become a reliable process to manufacture ceramic micro-gears. Ceramic powders are readily available in submicron size and are easier to handle as compared to the metallic powders which often become pyropheric when powder particle size is reduced to nano-level thus posing safety risks and making

their handling difficult.[28] The μ-PIM process is performed at higher injection pressure as compared to low pressure injection molding process. It involves following steps[29] as shown in Figure 17:

- Feedstock preparation: by mixing the micro- or nano-sized metallic or ceramic powder with an organic binder and then pelletizing the mixture to an appropriate shape in equipment such as extruder or mixer. The binder acts as a carrier medium for the powders and removed in a subsequent step when a part is molded. Use of feedstock powder at submicron or nano-level is required to utilize the complete potential of μ-PIM process for better shape retention and flow behavior. Variotherm process is often used to avoid freezing risk of the feedstock as thermal conductivity of the feedstock is very high but dimensions of the cavity are very small and the mold is heated during the injection process and then cooled down to room temperature before ejecting the part.
- MIM: it involves feeding the feedstock to the mold cavity to produce the desired shaped 'green part.' This step similar to conventional plastic injection molding with some changes to take care of compressibility and viscosity of the feedstock. Shrinkage during sintering is controlled by using oversized mold.
- Debinding: removing the binder from the molded green part and the resulting part is referred as the 'brown part.' It can be performed in three ways, i.e., (1) debinding by thermal degradation and elimination of the organic components of the binder using organic solvents or water; (2) debinding by using supercritical carbon dioxide in an autoclave which normally operates at temperature more than 57 °C and 300 bar pressure; and (3) debinding using a solvent or catalyst.[30]
- Sintering: sintering is performed to obtain good mechanical properties of the 'brown part' and carried out in a tube furnace having 88 mm diameter and 600 mm height. Air supply is used for sintering of the ceramic micro-parts while a reducing H_2 atmosphere is used for the metallic micro-parts to prevent their oxidation. Approximately 20–30% shrinkage take place during the sintering process which depends on the proportion of the powders in the feedstock.[31] Properties of final component are similar to that of the base material.

1.17.3.5.1 Advantages

The μ-PIM process offers following advantages[32]:

- It is a net-shape or near net-shape and cost-effective process to manufacture complex metallic and ceramics micro-components with high precision, dimensional accuracy, and replication.
- It combines design flexibility of the injection molding process and the advantage of P/M for nearly unrestricted variety of materials.
- It overcomes various difficulties the MIM process while manufacturing the micro-components such as incomplete filling of narrow cavities, failure in removal of the fragile green compacts, deformation in debinding and sintering processes.
- It can manufacture 3-D micro-components of complex shapes with good accuracy and replication.
- Higher material utilization.
- Economical and cost-effective for mass production.

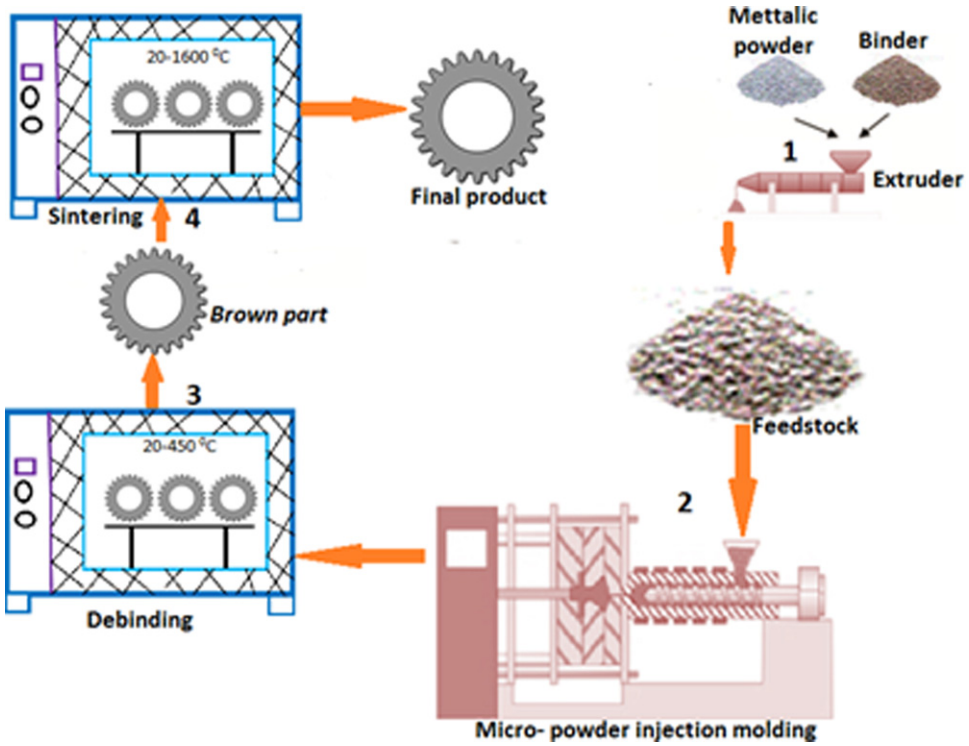


Figure 17 Steps of manufacturing of micro-gears by the micro-powder injection molding process.

- Low-pressure PIM (L-PIM) can be used for small size and prototyping where pressure values are limited to 1–10 bar and low-viscosity paraffin or wax is used instead of a high viscosity polymeric binder.

1.17.3.5.2 Limitations

Following are the limitations of the μ-PIM process:

- Surface roughness and minimum size of micro-components depend on the powder particle size.
- Can be used for fine powder size (less than 5 μm) only.
- Grain growth during sintering and presence of porosity may adversely affect the mechanical properties of the manufactured micro-products.
- Higher investment cost particularly for mold fabrication.
- Long processing time due to time consumed in debinding and sintering.
- Considerable amount of the feedstock could be scrapped as the size of the runner system become large relative to the size of the micro-product.

1.17.3.5.3 Applications

The μ-PIM process can be used for manufacturing the micro-components used in following applications:

- Micro-mechanical components: micro-gearbox, steeped gear wheel structures, micro-mold inserts, μ-EDM electrodes, micro-components for camera, operating cams, and weights for clock parts.
- Micro-system components: ceramic nozzle structures, components for communication devices, optical-electronic systems, data storage devices, and automotive systems such as airbag components.
- Micro-fluidics: micro-fluidic devices for chemical and medical applications such as micro-mixers and micro-heaters.
- Micro-reaction technologies: reactors for highly corrosive media, and high temperature gas phase reactors.
- Medical applications: surgical tools, dental equipment, micro-needles, small substitute bones, pharmaceutical powder inhalers, hearing aids, cranium reconstruction, tiny endoscopes, biopsy forceps, and sensors.

Figure 18 shows the micro-gears manufactured by μ-PIM process: a micro-gear having 1 mm outside diameter and 1 mm face width (Figure 18(a)), scanning electron microscope (SEM) micrograph showing distribution of powder and binder at the gear tooth (Figure 18(b)), and SEM micrograph of a double gear (Figure 18(c)).

1.17.3.6 LIGA

LIGA is an acronym for the German terms lithography (X-ray lithography), galvanoformung (i.e., electrodeposition) and abformung (i.e., molding).[35] It was developed at the Karlsruhe nuclear research centre in Karlsruhe (Germany) to manufacture nozzle for uranium enrichment process in 1990s.[36] Combination of electrodeposition and X-ray lithography process was first used by Romankiw and co-workers at IBM in 1975.[37] Figure 19 illustrates the processes and their sequence to manufacture micro-gear by LIGA process. It involves the following steps:

- Preparation of X-ray mask: a thin film of gold on beryllium is used as the X-ray mask which prevents transmission of X-rays to the photoresist material other than the patterned area.
- Substrate preparation: LIGA process uses collimated deep X-ray lithography (DXL) which illuminates and develops the desired patterns on thick film of an X-ray sensitive photoresist material such as polymethyl methacrylate (PMMA) or acrylic glass or plexiglass, polycarbonate, epoxy phenol resin, ploy vinylidene fluoride (PVDF), polysulfones, and polyether ketones. The substrate material used in the LIGA process should have (1) high resistance to dry and wet etching; (2) thermal stability up to 1400 °C; (3) exhibit excellent adhesion tendency to the substrate during electroplating; and (4) the unexposed resist must be absolutely insoluble during development. Suitable size of photoresist material is chosen to make substrate then it is cleaned properly to remove foreign material from its top surface. This is placed on a base material. Base material in LIGA process can be electrically conductive or insulator coated with an electrically conductive material in order to facilitate the subsequent electroplating over photoresist mold. Austenitic steel, titanium, nickel, silicon wafers with thin titanium and copper plated with gold are used as substrate materials. Sometimes, glass plates with thin metallic coating can also be used as base material.[38]
- Pattern transfer or exposure of the substrate: the prepared substrate is placed beneath the X-ray mask then it is exposed to synchrotron X-ray radiations of short wavelength. It provides deeper penetration into the photoresist material which is necessary for high resolution and high aspect ratio. It also results in formation of the desired pattern having sharp,

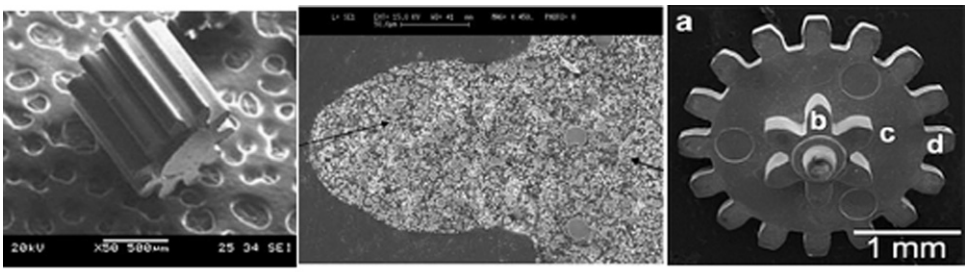


Figure 18 Micro-gears manufactured by μ-PIM process: (a) micro-gear having 1 mm outside diameter. Reprinted with permission from Ref. [33]. © Elsevier 2009; (b) scanning electron microscope (SEM) micrograph showing distribution of powder and binder at the gear tooth; and (c) SEM micrograph of a double gear. (b) and (c) reprinted with permission from Ref. [34]. © Elsevier 2012.

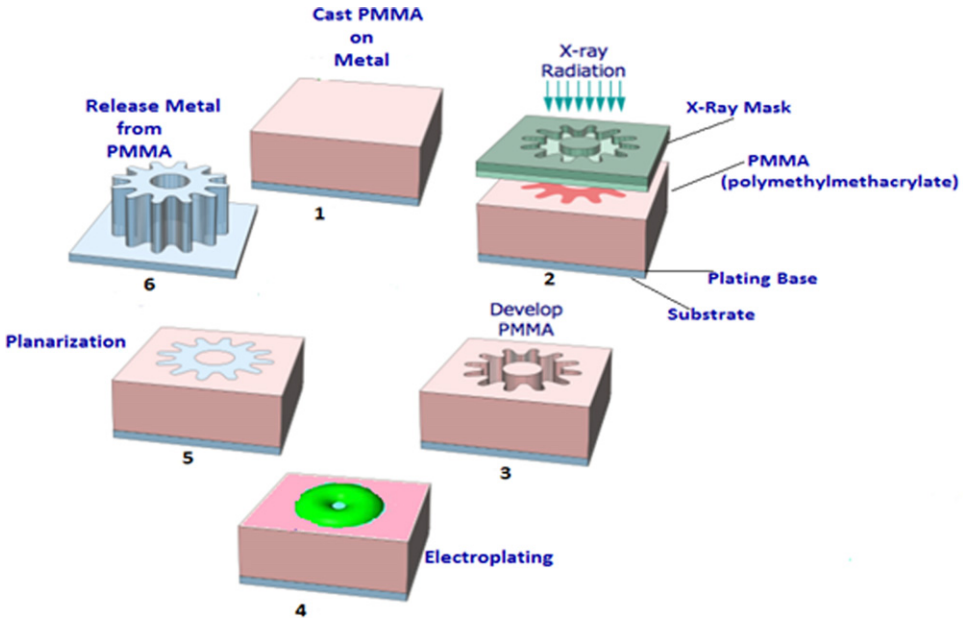


Figure 19 Processes and their sequence to manufacture micro-gear by the lithography, electroforming and molding process.[40]

thin, and deep cavities on the photoresist material. Line width of 0.2 μm and aspect ratio of 100 can be achieved by using short wavelength X-ray.

- Development of mold in the exposed substrate: the photoresist material, present in the exposed geometry corresponding to pattern image, gets melted due to its exposure to the X-ray radiations. This material is removed to develop the mold cavity in the photoresist material.
- Electrodeposition of the work material in the mold: the patterned photoresist material is placed in an electroplating bath in which mold cavities are filled with the material of the product by electrodeposition process. The final product can also be used as mold to manufacture thousands of similar products by hot plastic embossing and injection molding.[39]
- Planarization: it involves removal of excess eletrodeposited material from the top surface of the patterned mold so that top surface of the final product is perfectly flat.
- Release or separation of the final product: it involves removal or stripping of the surrounding photoresist material from the final product.

1.17.3.6.1 Advantages

The LIGA process offers following advantages:

- capability to manufacture high-precision metallic and plastic micro-parts;
- flexibility in configuration and geometry of the micro-parts;
- ability to manufacture high aspect ratio micro-parts;
- higher dimensional accuracy (<1 μm) and better surface finish (<50 nm);
- high-precision metallic parts without edge formation;
- suitable for mass production; and
- no thermal distortion.

1.17.3.6.2 Limitations

Following are the limitations of the μ-PIM process:

- Complex process because it requires multiple steps.
- Requires X-ray generation source, preparation of mask, substrate, and development of the mold.
- Requires special protection for the operator against exposure to X-ray radiations.
- Difficulty in maintaining tight tolerances in the pattern design.
- Very expensive process due to high equipment cost.

1.17.3.6.3 Applications

LIGA is an additive manufacturing process which is used to manufacture complex and intricate 3-D micro-parts having submicron size and high aspect ratio. It is used for following applications:

- Micro-mechanical parts: micro-gears, micro-motors, micro-actuators, and micro-nozzles for variety of application.
- Micro-opto-electro-mechanical systems (MOEMS) and communication: micro-sensors.
- Micro-fluidics: micro-valves, micro-channels, and micro-pumps.

Figure 20 shows SEM image of a high aspect ratio micro-gear manufactured by the LIGA process.

1.17.4 Deformative Processes for Miniature Gear Manufacturing

Deformative processes used for manufacturing the miniature gears are stamping, extrusion, forging, and hot embossing process. They are described in the following sections.

1.17.4.1 Stamping

Stamping is a fast and cost-effective process of manufacturing small gears from a thin metallic sheet. Thickness of metallic

sheet depends on the coarseness of stamped gears teeth and ranges from 0.25 to 3 mm.[6] **Table 5** presents recommended thickness of sheet for different ranges of the gear pitches. Before stamping, the metallic sheet is passed through a roll straightener which flattens the sheet. Gears from a thin sheet are cut by placing it between an upper die (or punch) and lower die and shearing it by the punch under very high pressure supplied by a hand operated press or a hydraulic press. **Figure 21** shows die set used in the gear stamping process. When upper punch comes into contact with sheet then sheet enters into lower die with upper punch and shearing action take place which produces gears of similar shape that of the upper punch die to a mating hole attached to the lower die. High speed press operating at speed of 200 strokes min^{-1} has capability to produce 400 gears min^{-1}. The press is equipped with a set of stamping dies in which toothed gear elements are formed to produce net-shape or near net-shape gears. The stamping die is designed by considering the various aspects of gear tooth such as backlash, whole depth, and corrected tooth thickness. Generally, an additional allowance is provided to the whole depth of gear stamping die to compensate for the die wear. 'Drawdown' is a phenomenon in stamping process by which teeth and outside periphery of gear is rounded due to shearing action. Usually, shaving operation is performed to reduce the drawdown and achieve close tolerance and accuracy of gears.

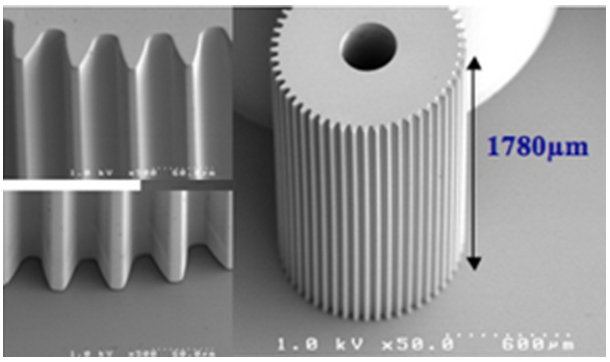


Figure 20 SEM images of the high aspect ratio micro-gear manufactured by the lithography, electroforming and molding process.

Table 5 Recommended sheet thickness for stamping of gears[4,6]

Pitch range	*Sheet thickness (mm)*
20–36	0.51–1.98
38–60	0.38–1.57
62–72	0.25–1.02
74–90	0.25–0.89
92–120	0.25–0.64

1.17.4.1.1 Advantages

Main advantages of stamping process include:

- Capability to manufacture light-weight stamped gears made of brass, full hard aluminum, high carbon steel, and AISI 1010 steel at high production rate without special die requirement.
- Gears of AGMA quality value 9 can be manufactured.
- Uniform dimensional accuracy and quality of the manufactured gear; and
- Ability of manufacturing gears of different materials.
- Economical and efficient process for manufacturing of small, light-weight gears in large quantity.
- Higher production rate, i.e., can manufacture 35–200 gears min^{-1}.
- Easy to automate.

1.17.4.1.2 Limitations

Following are disadvantages of the stamping process:

- can manufacture gear having face width up to 3 mm only;
- size of stamped gears ranging from 20 to 120 diametral pitch;

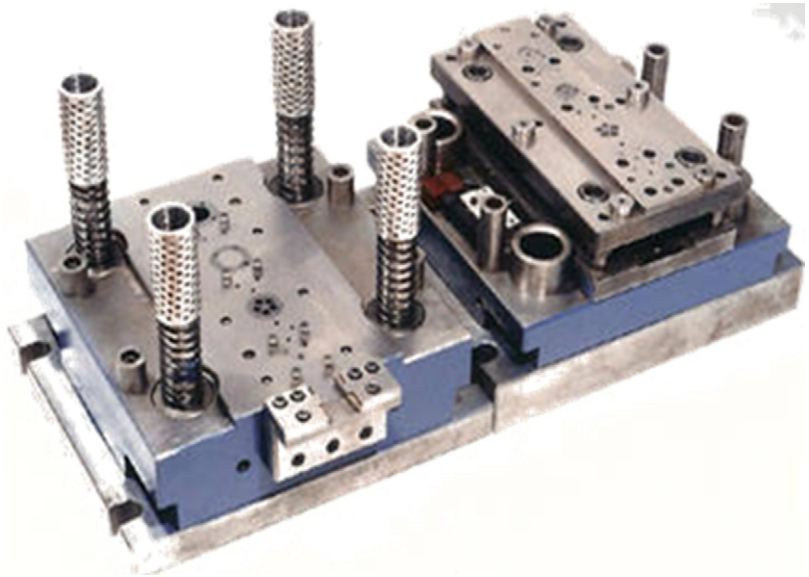


Figure 21 Die set used in stamping process for manufacturing thin gears.[41]

- particular die can perform a particular specific operation;
- applicable for no-load to medium-duty gears only;
- poor surface finish and accuracy;
- requires shaving operation after stamping;
- longer tooling time;
- fabrication of die and punch are difficult and complex; and
- higher equipment and die cost.

1.17.4.1.3 Applications

tamping is used to manufacture spur gears having face width (or sheet thickness) less than 3 mm. Stamped gears are widely used in toys, clocks, watches, timer mechanism, water and electric meters, in small appliances such as mixers, blenders, toasters, can openers, in larger appliances such as washers, dryers, and hand operated machine gears for slow speed mechanism.[4,6]

1.17.4.2 Extrusion

In extrusion process, a long round bar of 3–3.7 m long and approximately 6 mm in diameter is used to form the desired gear teeth on its entire length. The process begins with pre-heating of the metallic bar known as 'ingot or billet' to the plastic stage then placing it into a chamber known as 'container' in which hydraulically operated ram forces the material through a series of several dies to form the desired tooth form on entire length of the bar. Generally 5–7 dies in progression are used in this process. The first die has a similar shape of the desired pinion but larger in size so that material can easily pass through this die. After each pass, the metallic bar is annealed for next pass and with each succeeding pass bar assumes a shape close to the final shape. The bar comes into final shape after last pass. The time required to produce teeth on round bar is the time required to pull the metallic bar through series of dies.[5] Gear of desired thickness is cut-off from the extruded bar as shown in **Figure 22(a)**. The cut-off time depends on the extruded bar and the gear diameter. Various allowances are provided to the die to compensate the backlash, whole depth, and corrected tooth thickness in the final gear tooth shape. An additional whole depth is provided to compensate for the tool error at the root of gear tooth.[4,6] **Figure 22(b)** depicts the extrusion die set for spur gear.

Extruded gear should have number teeth in range of 15–24. Gear module may range from 0.25 to 1 mm with 20° pressure angle. The tooth contour should have a full radius root fillet and a full radius at the outside diameter with sufficient addendum to avoid undercut. Since, the material is displaced by pressure the outside surfaces of the extruded gears are quite hardened and smooth.[4] Material flow during extrusion depends on various factors such as material properties during preheating, billet–container interface and metal–die interface friction, and extrusion ratio.[43]

1.17.4.2.1 Advantages

Advantages of gear extrusion process include:

- Any desired gear tooth form can be produced by this process.
- Gear quality of AGMA 6 standard can be achieved by extrusion process.
- Better utilization of material and energy.
- Minimum or no loss of the gear material.
- Enhanced mechanical properties.
- Clean and porosity-free edges.
- Dense structure and higher strength of gear.
- Good surface finish and work-hardened surface of the extruded gears
- Requires least tool expenditure for mass production of spur gears.
- Higher production rate.

1.17.4.2.2 Limitations

Following are limitations of the gear extrusion process:

- surface cracking occurs;
- suitable for nonferrous materials having good drawing property such as aluminum and cooper;

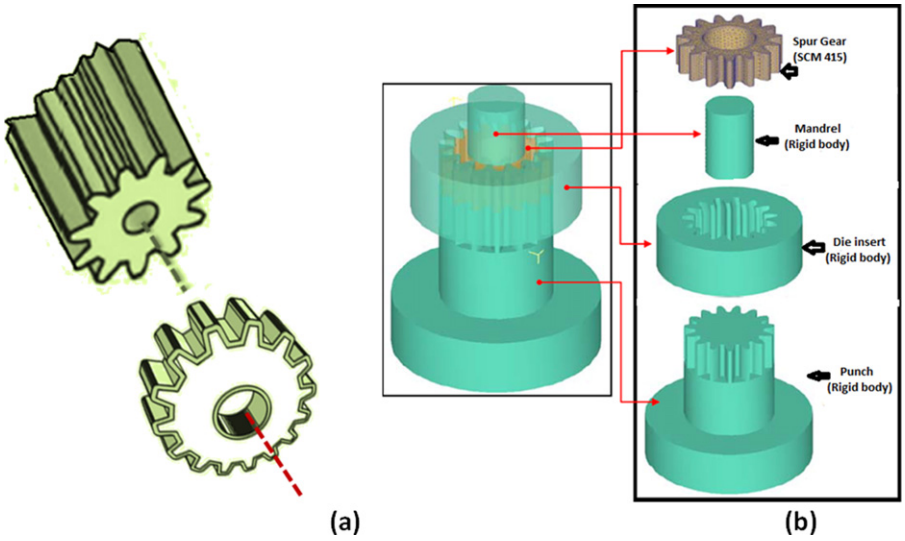


Figure 22 (a) Gear cut from an extruded bar; (b) die set for extrusion of a spur gear. Reprinted from Ref. [42] with kind permission from Springer Science and Business Media.

- secondary drawing operation is required after extrusion to improve the gear accuracy; and
- excessive wear of the extrusion die.

1.17.4.2.3 Applications

Gears and pinions manufactured by extrusion process are used in variety of commercial applications such as watches, electric clocks, spring-wound clocks, instruments, typewriters, multigraph machines, motion picture machines, carburetors, small motors, switch apparatus, taximeters, cameras, slot machines, mechanical toys, and other appliances.[6] Figure 23 shows the gears manufactured by the extrusion process: micro-gear made of 7075 aluminum (Figure 23(a)), extruded spur gear (Figure 23(b)), and helical gear manufactured by extrusion process (Figure 23(c)).

1.17.4.3 Forging

Forging is a net-shape or near net-shape metal forming process which can be used to manufacture gears by compressing their heated blanks in the forging dies by applying compressive forces manually or through power press. Gear forging involves an additional step as compared to the conventional forging process. Gear blanks are prepared from a billet by reducing it to the required size and shape by turning process, removing sharp corners by centerless grinding, improving surface finish by polishing, heat treating in an electric induction furnace, and cutting into exact weight and width for rough and finish forging. The gear blank is placed between upper and lower die and forced into the lower die cavities to form the shape of finished gear. The forged gears are manufactured in a single blow. The forged gear is air cooled to the ambient temperature. Controlled cooling is necessary to reduce the thermal distortion in forging. For effective cooling, a rotating cooling table is used to ensure the uniform distribution of the air around the forged gear. A scale is formed on forged gears after cooling which is removed by shot blasting before heat treating or finishing the forged gear. An envelope of excess material (or stock allowance) is formed around the forged gear tooth profile which is subsequently removed by grinding or finishing operation. Generally, forging dies are manufactured by EDM process.

1.17.4.3.1 Types

Forging process can be performed in different ways. Following are its variants[8,45]:

- Open die or flat die forging: in this process, the desired shape is obtained by repeated blows of powered flat-faced hammer reducing height of the billet and increasing its area of cross-section. This process can be computer controlled to obtain high accuracy of the final product. It is widely used for production of rough or near net-shaped gears.
- Closed die or impression forging: it is also known as hot stamping. In this process, two die halves are used to form an enclosed cavity corresponding to the desired shape of the product. The upper die attached to the drop hammer is allowed to fall freely on lower die by means of pneumatic or mechanical pressure and gear blank is deformed to fill the die cavities. Trimming operation is used to remove the surplus material known as 'flash' from the edges of forged part.
- Hot upset forging: in this process hot material fills the die cavity to form the desired product. Excess material squeezes out around the cavity in the form of flash which is trimmed off by a trimming die. The portion of billet which is not upset, is clamped by a clamping die and process is performed either as open or closed die forging process.
- Precision forging: precision forging is used to manufacture highly stressed net-shape, near net-shape or flashless forged products reducing the post-forging finishing processes. The net forged products do not require any further secondary finishing process while minimum finishing is required for near net-shape forged products. Only about 0.015 in of material on each side of the gear tooth is required for finishing the near net-shaped forged gears.
- Flashless forging: in this process no excess material (or flash) is squeezed between the die halves thus eliminating any post-forging process such as cutting or grinding. Figure 24 depicts the sequences of flashless die forging of a pinion gear.

1.17.4.3.2 Advantages

Main advantages of the forging process are:

- net-shape or near net-shape gear manufacturing;
- most suitable for straight bevel gears and face gears;
- forged gear have greater load carrying capacity;
- forged gears are stronger than cast or machined gear;
- refines the structure of the gear material;
- high strength to weight ratio;
- minimum or no material loss during forging of gears; and
- low manufacturing cost as compared to gear machining.

1.17.4.3.3 Limitations

Following are limitations of the forging process:

- requires high forging force;
- sometimes cracking and distortion of the material occurs;

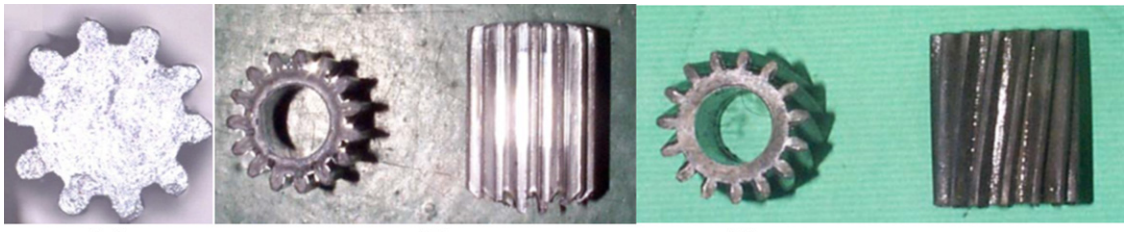


Figure 23 (a) Micro-gear made of 7075 aluminum. Reprinted with permission from Ref. [44]. © Elsevier 2015; (b) extruded spur gear; and (c) extruded helical gear. (b) and (c) reprinted with kind permission from Ref. [42].

- not suitable for spur gear due to short die life;
- short life of the forging die due to excessive wear; and
- higher initial cost.

1.17.4.3.4 Applications

Precision forged gears are commonly used in automotives, axle and differential of heavy trucks, aerospace, helicopter, railroad, marine applications, agriculture, material handling equipment, energy, and mining applications.[4,6] Figure 26 shows the different types of gears manufactured by the forging process: different types of forged gears (Figure 25(a)), and spiral bevel gear manufacture by forging process (Figure 25(b)).

1.17.4.4 Hot Embossing

Hot embossing process was developed by a group of researchers from RCA laboratories in Princeton, New Jersy (USA) in 1970s.[47] It is one of the most productive and extensively used techniques for the parallel replication of precise micro- or nano-features on thermoplastic substrates at elevated temperature by applying high pressure (approximately 10 bar) over a very small area.[48] A master die or stamp is pressed into a thermoplastic material to form the desired microstructure pattern on the substrates. Identical structures such as arrays of holes, dots, wires, and ring transistors can be reproduced on substrates using a single master die. Micro-gears are manufactured by micro-hot embossing process.[49] Hot embossing involves following four major steps[47,50] as depicted schematically in Figure 26:

- Preparation: a micro- or nano-structured mold is placed above the polymer substrate to form a stack. This stack is placed on the lower heating plate which contains cooling channel in which high heat capacity oil is circulated that allows isothermal heating and cooling of both the mold and the substrate.
- Hot embossing: the lower heating plate is moved upwards so that the stack is heated and pressed by upper and lower heating plates under a certain pressure applied by a pneumatic or hydraulic cylinder for a few minutes to ensure full replication of microstructure on the substrate. In order to transfer mold pattern completely on the substrate, mold and substrate are heated above the glass transition temperature of the substrate material to soften it and to minimize the force required for the material to flow into the desired mold cavities.
- Cooling: cooling of embossed or molded parts by the cooling plates to the demolding temperature while maintaining the pressure.
- Demolding: separating the mold and part from each other.

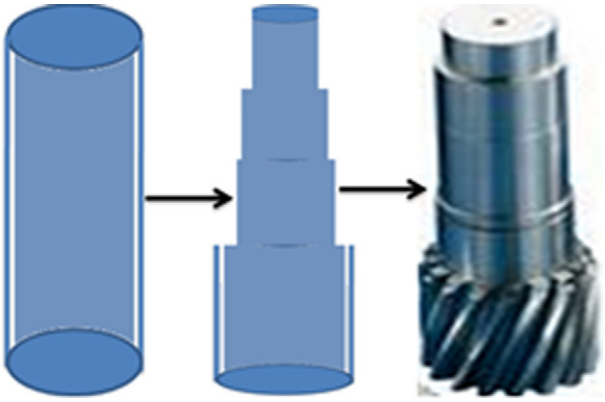


Figure 24 Steps involved in flashless forging to manufacture a pinion shaft.

1.17.4.4.1 Advantages

Hot embossing is the best replication process for micro- and nano-structures due to requirement of simple setup and short lead time for implementation. Other advantages of the hot embossing process include:

- higher dimensional accuracy;
- suitability for high aspect ratio features;
- easy manufacturability;
- mold can be used more than a thousand times;
- low shear stress;
- cost-effective process for high volume production; and
- lower gear manufacturing cost.

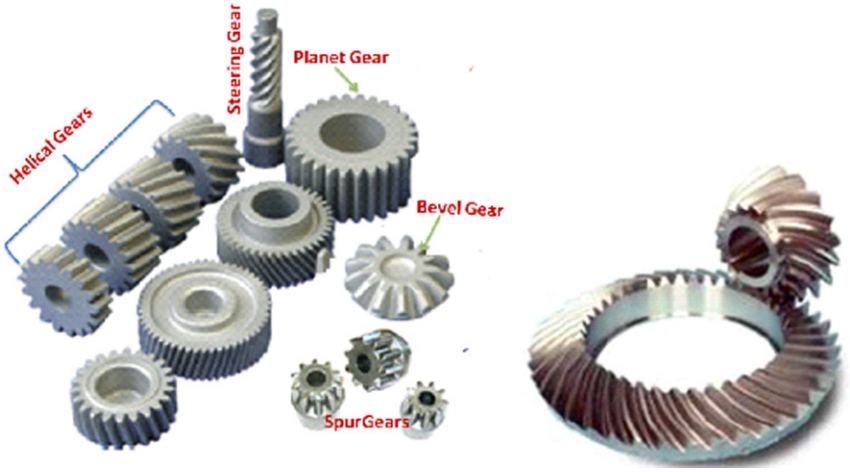


Figure 25 Different gears manufactured by the precision forging process.[46]

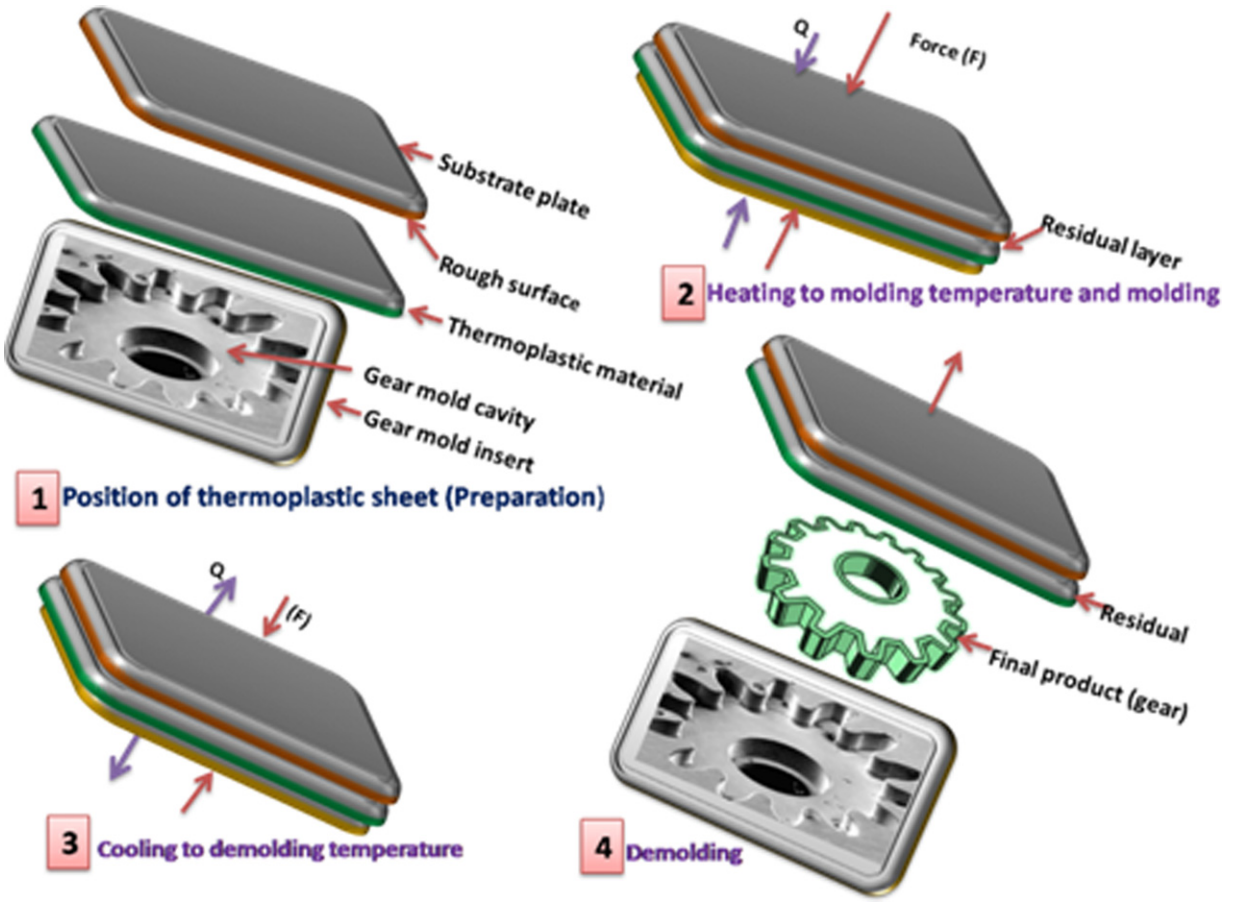


Figure 26 Major steps involved in the hot embossing process.

1.17.4.4.2 Limitations

Following are the limitations of the hot embossing process:

- suitable for thermoplastic materials only;
- slower process (requires four steps);
- difficulty in attaining high embossing pressure; and
- complex and expensive mold and equipment.

1.17.4.4.3 Applications

Hot embossing can fabricate a variety of materials but it is most suitable for thermoplastics. An amorphous and semi-crystalline thermoplastic can be hot embossed but amorphous materials can also easily be embossed due to process flexibility which allows its application for a wide range of embossing temperature. It is used for following applications[51]:

- Micro-optical applications: compact disk, optical lenses, wave guides, and switches.
- Micro-fluidics: lab-on-chip analysis devices, valves, pressure sensors, and flow sensors.
- Micro-electrical applications: acceleration sensors, electrical switches, and combo drives.
- Micro-mechanical applications: micro-gears for MEMS devices.
- Biomedical applications: biosensors and bio-MEMS devices, micro-total analysis system (μ-TAS), rapid prototyping, and patterned media.

Figure 27 Shows the SEM image of the micro-gears and molds manufactured by the hot embossing process: PMMA gear (Figure 27(a)), and gear on etched silicon wafer (Figure 27(b))

1.17.5 Miniature Gear Manufacturing by Spark-Erosion-Based Processes

EDM, WEDM and their micro-versions namely μ-EDM, and μ-WEDM processes are the spark-erosion-based processes which are used for manufacturing the miniature gears. Gupta *et al.*[54] have critically reviewed the spark-erosion-based processes from application aspect of miniature gear manufacturing. These processes are described in the following sections.

1.17.5.1 EDM

An English scientist, Sir Joseph Priestly was discovered the phenomenon of material removal by electrical sparks in 1768. But, this could not be used for machining purpose till 1943 when two Russians scientists B.R. Lazarenko and N.I. Lazarenko developed a circuit to supply pulse power required for material removal by the controlled spark-erosion phenomenon. A computer numerical controlled (CNC) machine for EDM process was developed in the USA in 1980s.[55] EDM is an unconventional machining process which approximately reproduces complimentary image of an electrically conducting tool on an

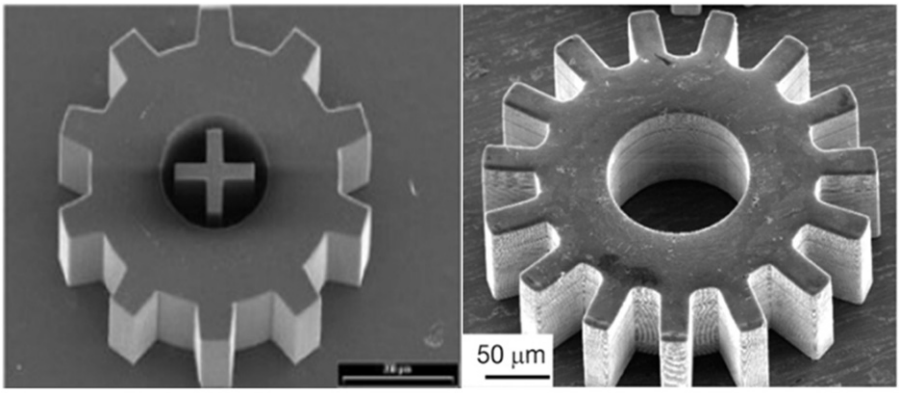


Figure 27 Scanning electron microscope images of the micro-gears manufactured by the hot embossing process and micro-gear mold insert for micro-hot embossing: (a) polymethyl methacrylate gear[52] and (b) gear on etched silicon wafer.[53]

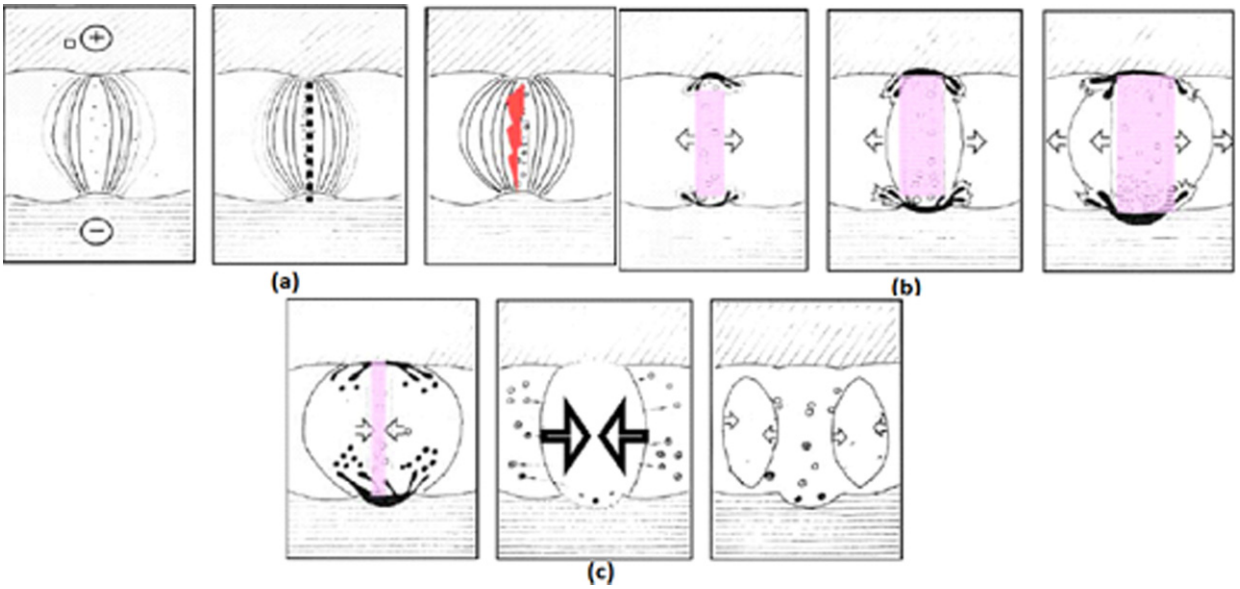


Figure 28 Different phases of spark generation in the EDM process. (a) Preparation phase, (b) discharge phase, and (c) interval phase. Reprinted with permission from Ref. [59]. © Elsevier 2004.

electrically conducting workpiece by a series of sparks occurring in the tool-workpiece gap (or interelectrode gap, IEG) in the presence of a suitable dielectric. Figure 29 depicts the generation of spark phenomenon in EDM process: preparation phase (Figure 28(a)), discharge phase (Figure 28(b)), and interval phase (Figure 28(c)). Generally, workpiece and tool are connected to positive (i.e., anode) and negative (i.e., cathode) terminals of a direct current (DC) pulsed power supply provided a pulse generator system. Constant value of IEG (approximately 0.01–0.5 mm) is maintained by a servo-system. DC voltage in the range of 80–200 V having pulse frequency in some kilohertz is supplied between the two electrodes with and IEG is flooded with a suitable dielectric. During the pulse-on time, electrons emitted from the cathode move toward the anode and ions toward the cathode. When the supplied voltage becomes more than the breakdown voltage of the dielectric then dielectric molecules also ionize releasing secondary electrons. This results in forming a high conductivity channel at a point where IEG has minimum value. In this channel, electrons continuously strike the anode and the ions strike the cathode converting their kinetic energy into heat energy. This causes momentary impulse resulting in a generation of a short duration spark at the point of minimum IEG increasing temperature to a very high value which is sufficient to melt and even vaporize the electrode materials. This causes spark-erosion of both the electrodes but erosion of cathode is very less as compared to anode because the velocity of the electron is higher than the ions. Most of molten workpiece material is ejected with a pressure forming a crater on the workpiece surface thus changing the value IEG at this location. During the pulse-off time, the eroded material is flushed away from the IEG by the flow of the dielectric. Same cycle of events occur at the next location where IEG is minimum. Thus, spark keeps occurring throughout the IEG. Some of the molten material is redeposited on the workpiece surface

forming a very hard layer known as 'recast layer.' The EDM-manufactured components have better wear resistance and improved fatigue strength.[56] The technology and applications of EDM process has matured and spread significantly from 1950 onwards to an extent that most of EDM machines are CNC machines and it is no longer considered as an unconventional or nontraditional process.

1.17.5.1.1 μ-EDM

EDM process is the variant of EDM for micro-machining applications including manufacturing the miniature gears and other micro-parts. The physical characteristics and working principle of μ-EDM is similar to the EDM process except the size of the electrode, the power supply, (current, voltage, and pulse frequency) and the resolution of the *X*, *Y*, and *Z*-axes.[57] **Table 6** presents the comparison between EDM and μ-EDM.[58]

Main objective in μ-EDM is to minimize the erosion of workpiece in a single discharge while EDM maximizes the erosion of workpiece so as to minimize machining time. Generally, μ-EDM process uses deionized water as dielectric to avoid the formation of the white or recast layer which usually occurs with a mineral oil such as kerosene. The pulse generator used in μ-EDM process produces very small pulses of few microseconds or nanoseconds duration enabling μ-EDM to use low discharge energies to remove small volumes of the material making possible manufacturing of micro-gears, micro-dies, micro-holes, micro-slot, etc. Low setup cost, high aspect ratio, improved precision, and improved design freedom are other advantages of μ-EDM process.[57] Limitations of μ-EDM include low MRR, high tool wear rate per spark and formation of the heat affected layer. Tool wear leads to poor dimensional accuracy. The μ-EDM process is extensively used for various applications in MEMS, biomedical devices, automotive industry, and defense industry. **Figure 29** illustrates the machine for μ-EDM process.

1.17.5.1.2 Advantages

EDM and μ-EDM processes have following advantages:

- It can machine any electrically conducting material irrespective of their melting points, hardness, toughness, brittleness, and microstructure.
- Capability to produce micro-parts having complex and intricate shapes.
- Capability to produce micro-holes with high aspect ratio.
- Capability to machine very thin fragile materials and brittle materials.
- No direct contact between tool and workpiece.
- Minimum tool wear and no tool breakage.
- Tool material need not be harder than work material.
- Easy to automate and requires little attention from machine operator.
- Burr-free process, thus eliminates the secondary finishing operation.
- Low operating fixtures and tooling cost.

1.17.5.1.3 Limitations

Following are the limitations of the EDM and μ-EDM processes:

- Both tool and workpiece material should be electrically conductive.
- Fabrication of master tool electrodes for gear is complex and difficult.
- Gear cutting rate is slow as compared to the conventional process.
- Not suitable for mass production of gears.
- Not applicable for very large gears.
- Chances of formation of recast layer.
- Higher capital cost.

1.17.5.1.4 Applications

EDM process is used for machining electrically conducting but difficult-to-machine materials such as superalloys, Ti-based alloys, tool steels, alloy steels, refractory materials, metal matrix composites, tungsten carbides, etc. It is used for two-dimensional (2-D) profiling, 3-D contouring, making dies having complicated profile, stamping of tool dies, making blind complex cavities, drilling of various hole shapes including noncircular holes, drilling of micro-holes for nozzles and aerofoil blades, drilling of inclined holes (hole axis having inclination with the top surface as low as 20°), through cutting of noncircular holes,

Table 6 Comparison between electric discharge machining (EDM) and micro-electric discharge machining (μ-EDM)

Parameter	*EDM*	*μ-EDM*
Current	0.5–400 A	0.1–10 mA
Voltage	40–400 V	60–120 V
Pulse duration	User defined: 0.5 μs–8 ms	Not constant: nano- to micro-seconds
Interelectrode gap	10 μm	1–5 μm
Current and gap voltage	Mechanism for constant gap voltage and current during spark	Single capacitive discharge, gap voltage, and current are variable
Effect of gap voltage on machining	Significant	Negligible effect
Dielectric	Mineral oil	Mineral oil, deionized water
Dielectric flushing	External and internal flushing	Internal flushing
Tool material	Copper/graphite	Tungsten
Pulse generator	Switch circuit	RC circuit
Electrode wear ratio	1–5%	1.5–100%
Surface roughness	0.8–3.1 μm	0.07–1 μm
Efficiency of process	Low	High
Typical applications	Automotive, defense, aerospace, prototype production, coin and die making, etc.	Fabrication of micro-nozzles, micro-gears, micro-punches, micro-holes, micro-slots, ink jet nozzle, etc.

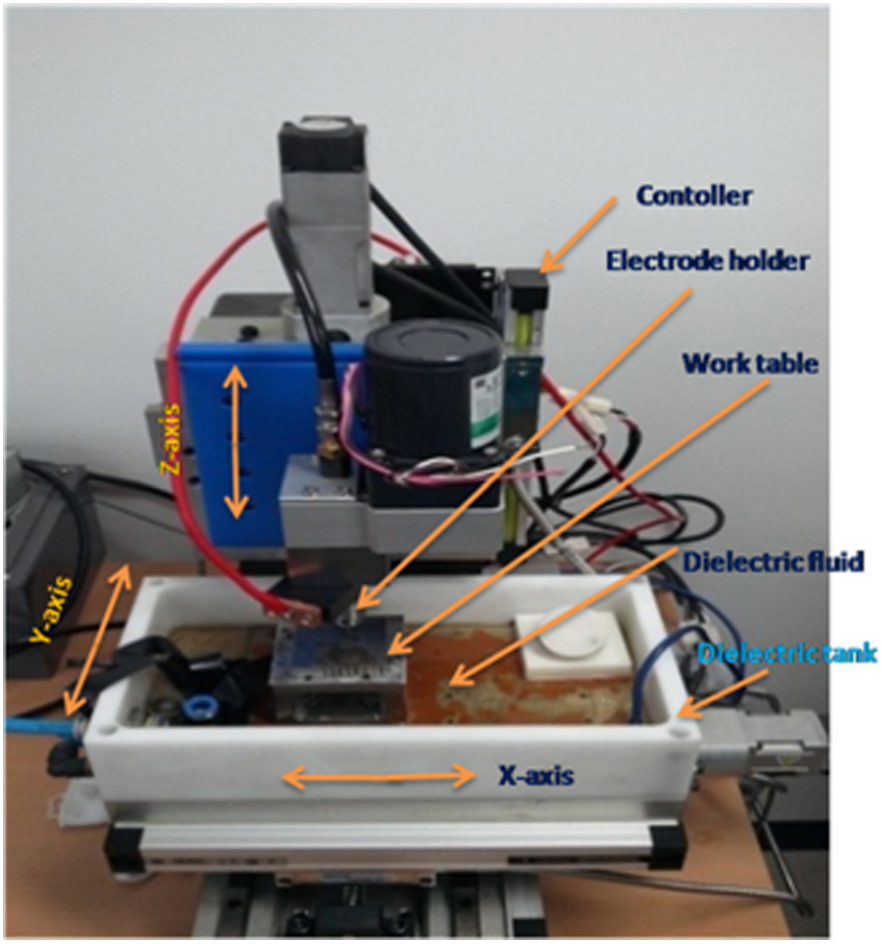


Figure 29 Machine for the micro-electric discharge machining process.[60]

cutting of narrow slots, etc. Main applications of μ-EDM process include manufacturing of micro-holes for different nozzles, narrow slots, high aspect ratio (i.e., deep) micro-holes, non-circular micro-holes, blind complex micro-cavities, turbine blades, high quality miniature gears, etc.

1.17.5.2 WEDM

Manufacturing the tool is the most challenging aspect in EDM. This problem is overcome by using a very fine wire having diameter in the range from 0.05 to 0.3 mm, as the tool in the derived version of EDM process which known as WEDM process. This process is similar to band saw in which a small diameter wire continuously fed under tension, acts as 'saw' for cutting as illustrated schematically in Figure 30. Commonly used wire materials are brass, copper, molybdenum, tungsten, and zinc coated wire. Wire and workpiece are separated by a very small IEG and deionized water is used as dielectric supplying it coaxially with wire feeding resulting in localized dielectric flushing. Use of very thin wire as tool necessitates use of small value of voltage, IEG (in the range of 0.025–0.05 mm), pulse-on time and pulse-off time, i.e., very high pulse frequency in the order of megahertz, in the WEDM process. Constant value of IEG between the wire and workpiece is maintained by a servo-system. The mechanism of material removal in WEDM is the same as that of EDM. Workpiece material ahead of the continuously moving wire is eroded by rapidly occurring discrete electric sparks in the kerf (profile generated by the travel of the wire as shown Figure 30). The material removal rate determines the economics of machining and rate of production where the kerf governs the degree of precision. WEDM is a very slow process and material removal rate is slower than the EDM and other machining processes.[61]

1.17.5.2.1 μ-WEDM

μ-WEDM is a variant of WEDM process and became one of the most popular and versatile micro-machining processes to manufacture complex micro-parts from electrically conductive material of any hardness. The process principle of μ-WEDM is similar to WEDM except the size of wire, voltage, and current. μ-WEDM uses a micro-wire made of copper, brass, tungsten, and molybdenum and having diameter in a range from 0.02 to 0.1 mm as the tool. Consequently, even smaller amount of material than WEDM is removed by the sparks generated in the IEG. Figure 31 illustrates the machine for μ-WEDM process. It is an effective machining technique used for machining of micro-components from difficult-to-machine materials using micro-wire as tool with advantages of high machining efficiency and precision. It is extensively used in various applications in different industries such as automotive,

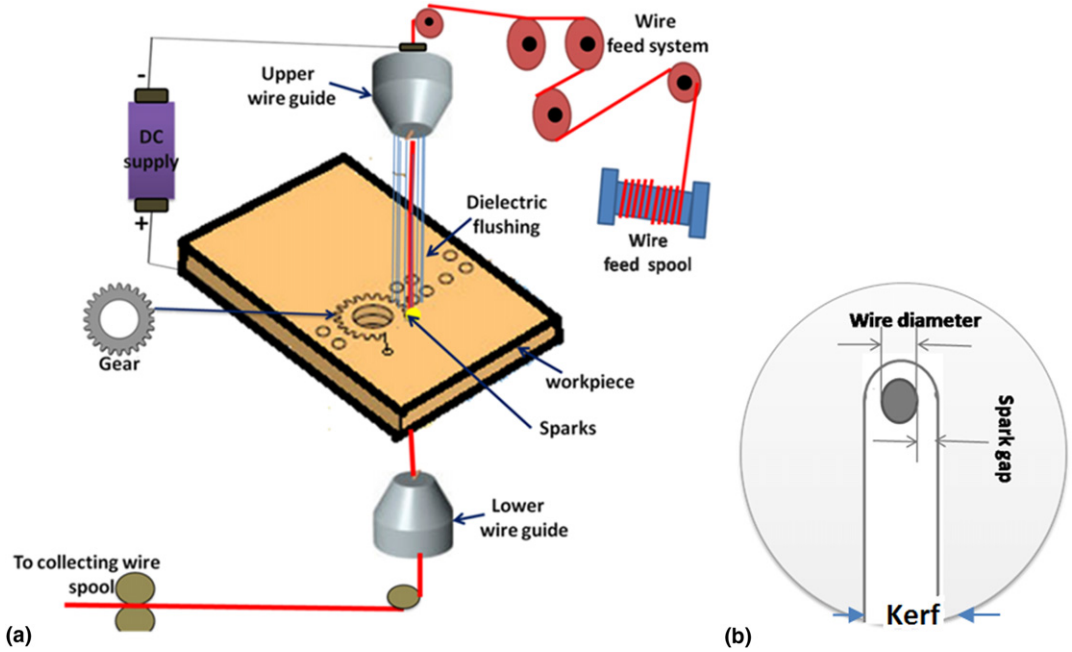


Figure 30 Schematic diagram of miniature gear manufacturing by the wire electric discharge machining process.

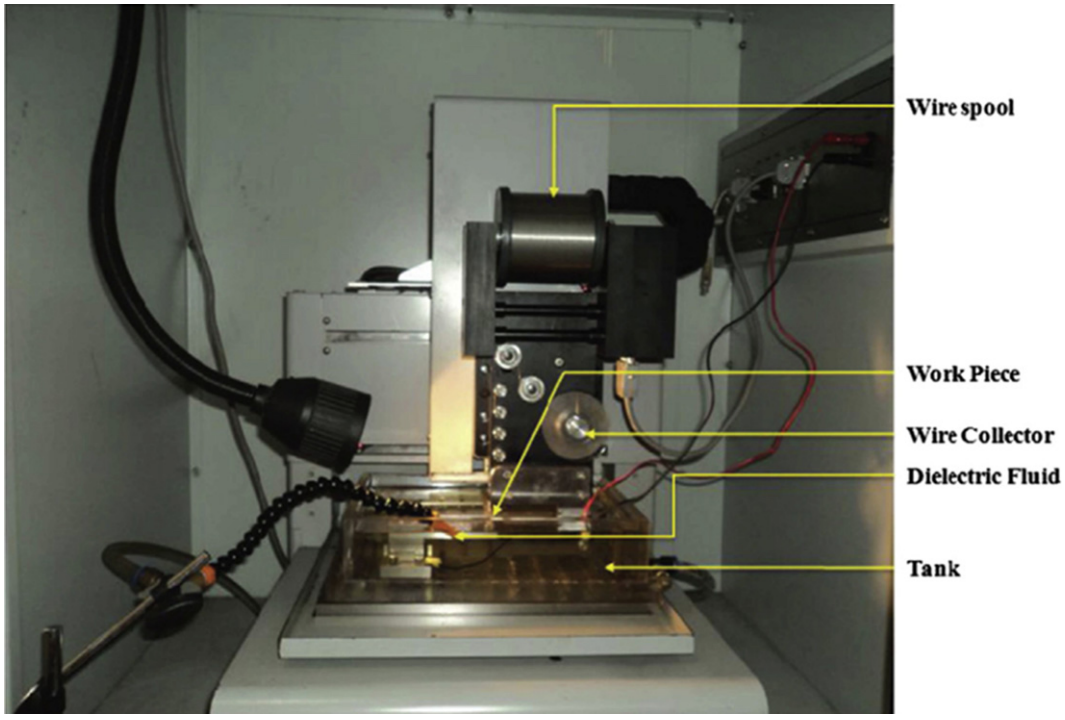


Figure 31 Machine for micro-wire electric discharge machining process. Reprinted with permission from Ref. [62]. © Elsevier 2014.

aerospace, defense, electronics, telecommunications, healthcare, environmental, industrial, and consumer products, etc. having micro-features requiring nano-finishing and nano-level dimensional accuracy.

1.17.5.2.2 Advantages

The main advantages of WEDM and μ-WEDM processes are:

- does not require design and fabrication of a special tool;
- can machine any electrically conductive material irrespective of its hardness and other mechanical properties;
- can manufacture 2-D and 3-D complex and intricate shapes;
- μ-WEDM process can easily machine very thin and fragile sections;

- high degree of accuracy and surface finish and excellent repeatability;
- burr-free process thus eliminate secondary finishing operation;
- unattended gear manufacturing for a long period; and
- no mechanical stresses and tool marks.

1.17.5.2.3 Limitations

Following are the limitations of WEDM and μ-WEDM processes:

- Suitable for electrically conductive materials only.
- Suitable for through cut only.
- Not suitable for mass production.

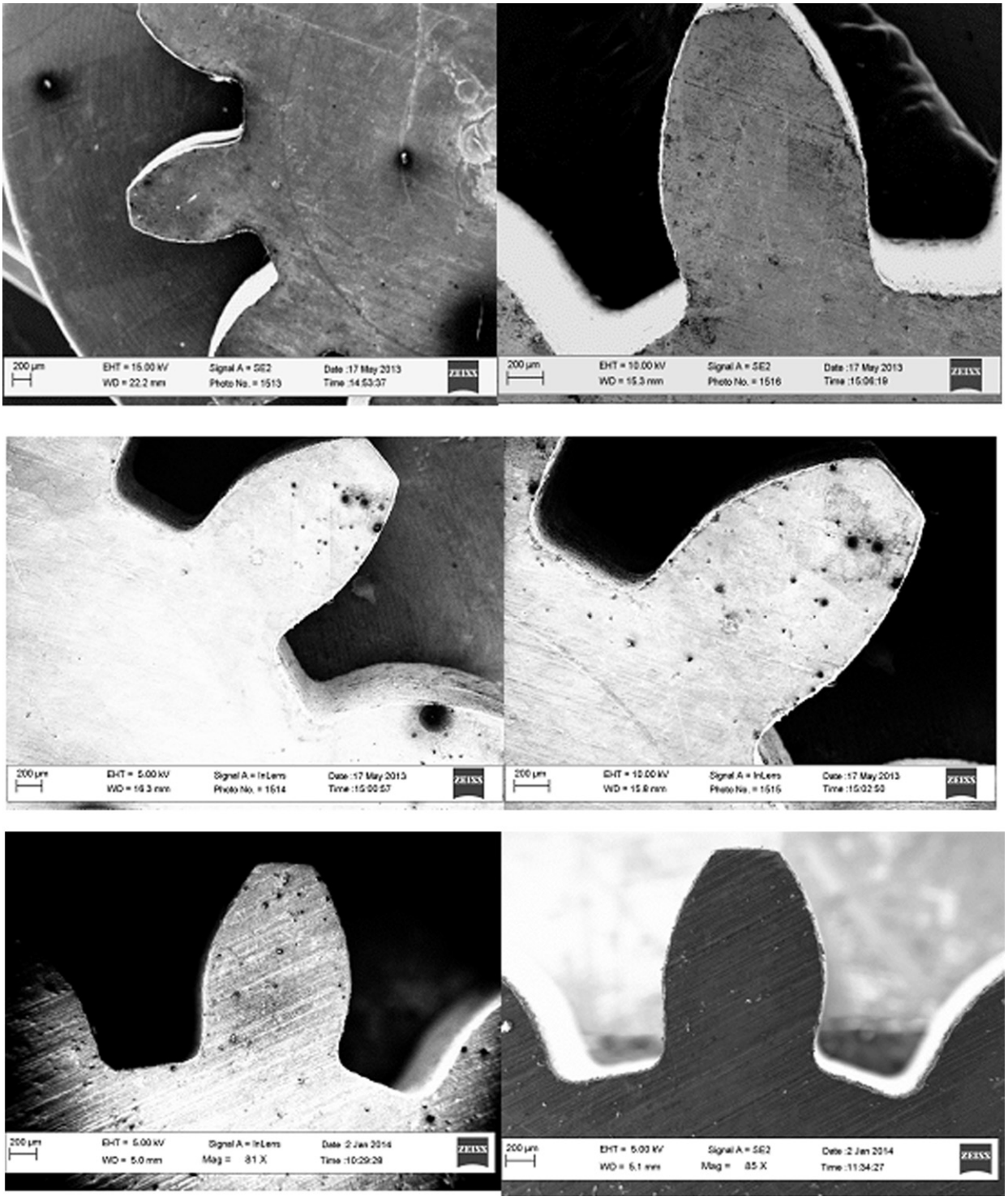


Figure 32 Scanning electron microscope images of the best quality brass miniature spur gear manufactured by wire electric discharge machining. Reprinted from Ref. [54] with kind permission from Springer Science and Business Media.

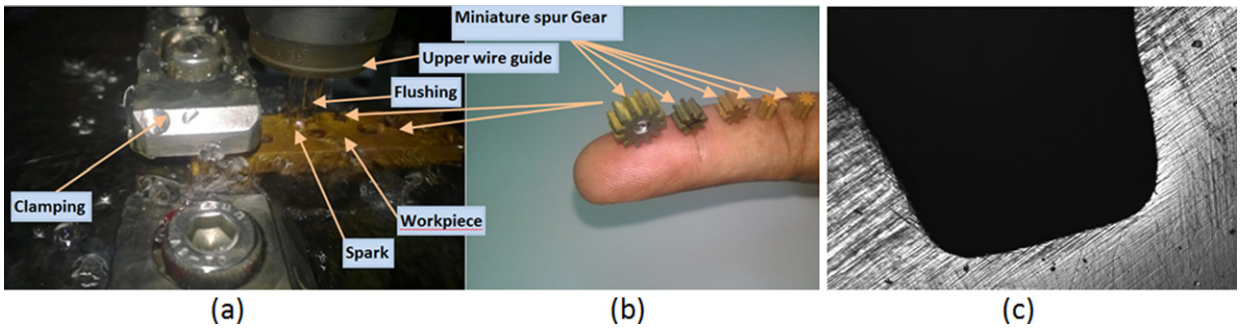


Figure 33 Manufacturing of miniature spur gears by wire electric discharge machining at IIT Indore: (a) photograph of the actual process; (b) photograph of manufactured miniature gears of different size and different materials; and (c) microscopic images of gear tooth profile of SS 304 miniature spur gear.

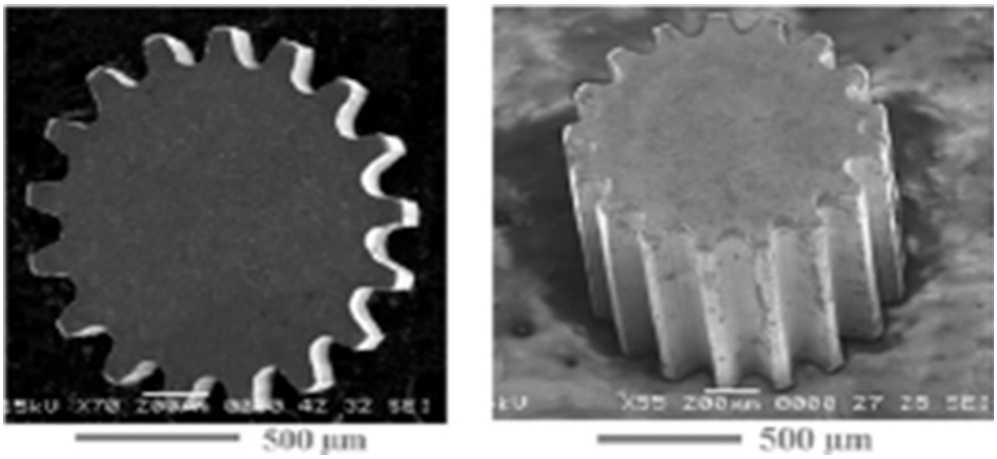


Figure 34 Scanning electron microscope images of micro spur gear manufactured by micro-wire electric discharge machining process. Reprinted from Ref. [66] with kind permission from Springer Science and Business Media.

- Material removal rate is low as compared to conventional processes.
- Requires precise and uniform wire fed under constant tension.
- Wire breakage causes interruption in the process.
- Formation of recast layer.
- Not efficient and economical for a very large-size gears.
- High capital and operating cost.

1.17.5.2.4 WEDM Applications

WEDM process is used to manufacture complex and intricate 2-D and 3-D components from an electrically conductive material regardless of its hardness and other mechanical properties just using a simple thin wire. It is routinely used for manufacturing various dies and molds, EDM tools, complex profiles, accessories and equipment used automotive, aerospace, electronics, medical and surgical applications, parting-off applications, miniature gears, etc. Gupta and Jain have worked extensively in establishing WEDM process for net-shape manufacturing of miniature spur gears made of brass; investigating and optimizing the micro-geometry,[63] surface finish[64] and surface integrity[65] of the manufactured miniature gears. They have reported that though WEDMed miniature spur gears have better micro-geometry and surface integrity than hobbed miniature gears but hobbed gears have better surface finish.[2] Figure 32 depicts SEM images of the best quality miniature spur gear (having outside diameter 9.8 mm; module 0.7 mm; and number of teeth 12 manufactured by WEDM process.[54] Figure 33 depicts some results of ongoing research work on manufacturing of different types of miniature gears (i.e., spur, helical, and bevel gears) of different materials and different sizes by WEDM process at IIT Indore showing photograph of actual process (Figure 33(a)) manufacturing miniature spur gears, manufactured miniature gears of different size and different materials (Figure 33(b)), and microscopic images of stainless steel (SS 304) miniature spur gear showing gear tooth profile (Figure 33(c)).

μ-WEDM process is commonly used for manufacturing micro-components, making micro-features, micro-holes, cutting micro-profiles in any electrically conducting material in general and in high strength, high corrosion, and wear resistant materials in particular. Figure 34 shows SEM images of a micro spur gear manufactured by μ-WEDM process.

1.17.6 Comparative Evaluation

Manufacturing process	*Capabilities*	*Limitations*	*AGMA gear quality*	*Material*	*Applications*
Hobbing	• Fast and continuous process • Higher production rate • Excellent surface finish • Close tolerances • Economical production cost • Minimum tool wear	• Cannot be used for manufacturing conical and internal gears also • Tool marks left on gear teeth • Poor micro-geometry, i.e., hobbed gears require subsequent finishing operation to achieve desired gear quality • Longer setup time	8–13	Ferrous and nonferrous	Instruments, cameras, automatic transmission systems, and high speed machineries
P/M	• Multilevel gears production • Higher repeatability • Higher production rate • Lower energy consumption • Tight tolerances • Minimize secondary finishing operations by producing near net-shaped gears	• Arrangement and storage of fine metallic powder of all type is difficult • Higher cost of metallic powders • More porosity which decreases mechanical properties of P/M components • Gears are subjected to re-pressing or coining after sintering • Removal of part from mould is difficult	6–9	Metallic and Nonmetallic material	Hand tools, pumps, clocks, slow speed machineries, and various appliances
Die casting	• Higher production rate • Can be used for manufacturing any type of gear, i.e., spur, bevel, helical, worm, and spiral • Economical process for high volume production of miniature gear	• Higher initial cost • Limited to high-fluidity materials only • A certain amount of porosity is common • Suitable for gear manufacturing for light load application • Cannot be used where extreme accuracy is needed • Requires of finishing operation after gear manufacturing	5–8	Nonferrous material	Toys, washing machines, hand tools, cameras, business machines, small appliances, etc.
MIM process	• Net-shape or near net-shape gear manufacturing with minimal material waste	• Higher tooling costs and lead time • Higher process cost due to multiple steps	6–7	Nonferrous	Small appliances, clocks, small motors, toys, instruments, small tools, etc.

	• Requires minimum finishing operations	• Shrinkage of injected material in sintering • Requires sintering after metal injection process			
ICM	• Higher dimensional accuracy of gear due to uniform distribution of materials • Eliminates shrinkage marks, stresses and warpage	• Higher cost of machine and mould • Slower process • Control of flash is difficult • Material wastage due to mould overfilling • Contamination • Complicated process control	4–8	Plastic	Micro-motors, toys, instruments, communication devices, etc.
μ-PIM	• Can be used for manufacturing of micro gear of different metallic materials and ceramics • Higher dimensional accuracy of micro-gears	• Requires the micro-mold • Need of vacuum prior to injection • Risk of freezing of feed stock during injection molding • Complex process parameters for micro-injection molding	Not available	Plastic	Surgical and dental instruments, Miro-motors, and other appliances
LIGA	• Higher dimensional accuracy (<1 μm) • Better surface finish (<50 nm) • High Aspect ratio	• Very expensive process • Complex process (requires multiple steps) • Requires mask, resist and X-ray source • Tight tolerance for pattern overlay	Not available	Metallic, alloys and polymer	Micro-pump, Micro-motor, and watches
Stamping	• Uniform dimensional accuracy and quality of gear • Higher production rate • Lower labor cost • Easy to automate • Ability of manufacturing gear of different materials	• Can manufacture gear up to 3 mm thickness only • Applicable for no-load to medium-duty gears only • Requires shaving operation after stamping • Higher tooling cost (both equipment and die) • Poor accuracy due to higher tolerances • Longer tooling time	6–9	Sheet metal	Toys, timer mechanism, watches, mixers, and other appliances
Extrusion	• Good surface finish with clean edge and porosity-free edges with dense structure	• Surface cracking occurs • Suitable for nonferrous	4–6	Aluminum, copper, naval brass, architectural	Watches, Electric clocks, spring-wound clocks, typewriters, small

	and higher strength of gear • Higher production rate	materials such as aluminum and copper alloys • Secondary drawing operation is required after extrusion to improve the gear accuracy • Excessive wear of extrusion die		bronze, and phosphor bronze	motors, cameras, etc.
Forging	• Net-shape or near net-shape gear manufacturing • Greater load carrying capacity of forged gear	• Requires high forging force • Short life of the forging die due to excessive wear	Not available	Ferrous	Marine, stern drives, differential, etc.
Hot embossing	• Higher dimensional accuracy • Lower gear manufacturing cost	• Suitable for polymers only • Slower process (requires four steps) • Difficulty in attaining high embossing pressure	Not available	Polymer	Toys, instruments, micro motor, and small appliances
EDM and μ-EDM	• High dimensional accuracy and surface finish • Less material loss • Gear can be cut from thin and fragile material • No mechanical stresses and burr-free process	• Suitable for only electrically conductive material • Slower process • Not suitable for mass production • Fabrication of tool electrodes are difficult and complex • Chances of formation of recast layer	Not available	Electric conductive material	Aerospace, micro pump, micro motor, medical and dental instruments, etc.
WEDM and μ-WEDM	• High dimensional accuracy and surface finish • Gear DIN quality standard upto 6 can be produced • Gear can be cut from thin and fragile material • No mechanical stresses and burr-free process • No secondary finishing operation is required	• Limited to electrically conductive material only • Requirement of precise, accurate and uniform diameter wire • Slower process • Not suitable for mass production • Fabrication of tool electrodes are difficult and complex • Chances of formation of recast layer		Electric conductive	Master die gears for EDM, aerospace, micro pump, micro motor, medical and dental instruments, etc.

Abbreviations: P/M, powder metallurgy; MIM, metal injection molding; ICM, Injection compression molding; μ-PIM, micro-powder injection molding; LIGA, lithography, electro-forming and molding; EDM, electric discharge machining; μ-EDM, micro-electric discharge machining; WEDM, wire electric discharge machining; and μ-WEDM, micro-wire electric discharge machining.

1.17.7 Summary

Manufacturing of miniature gears is a complex and challenging task which should be highly precise and accurate because performance and functional characteristics of devices are highly dependent on the quality of the miniature gears. The various conventional and nonconventional manufacturing processes are used to manufacture miniature gears. Most of the conventional miniature gears manufacturing processes produce miniature gears quality ranging between 9 and 12 DIN standard and require secondary finishing process to achieve the desired gear quality, i.e., they are not net-shape miniature gear manufacturing processes. Spark-erosion-based processes can achieve gear quality up to DIN standard 6 thus eliminating requirement of any secondary finishing operations. WEDM and μ-WEDM processes have the potential to be established as net-shape manufacturing process for high quality meso- and micro-gears respectively. Sustained research is in progress at the author's institute to establish WEDM for net-shape manufacturing of high quality meso-gears of different types and of different materials. Following conclusions can be drawn from review of miniature gear manufacturing processes:

- Miniature gears are extensively used in MEMS, aerospace, medical, defense, precision instruments, automobile, toys, and other appliances.
- Hobbing process produces miniature gears with high surface finish, but micro-geometry is poor as compared to those manufactured by the spark-erosion-based processes.
- Conical and internal gears cannot be manufactured by Hobbing process.
- ICM and LIGA processes can be used for polymer materials only.
- High aspect ratio miniature gears are manufactured by μ-PIM, LIGA, and hot embossing process.
- Stamping is suitable for thin sheet up to 3 mm thickness only.
- Die casting, extrusion and MIM processes are limited to high fluidity, nonferrous materials only.
- MIM, extrusion, and forging near net-shape gear manufacturing processes.
- Spark-erosion-based processes are net-shape miniature gear manufacturing processes and their performance does not depend on gear material hardness and other mechanical properties. These processes manufacture miniature gears of very good quality, but they can be used only for electrically conductive materials

See also: 1.4 Review of Gear Finishing Processes

References

1. Gupta, K.; Jain, N. K. Deviations in Geometry of Miniature Gears Fabricated by Wire Electrical Discharge Machining. In *Proceedings of International Mechanical Engineering Congress and Exposition of ASME*, San Diego, California, USA, November 15–21, 2013.
2. Gupta, K.; Jain, N. K. Comparative Study of Wire-EDM and Hobbing for Manufacturing High-Quality Miniature Gears. *Mater. Manuf. Process.* **2014**, *29* (10), 1470–1476.
3. Gupta, K.; Chaubey, S. K.; Jain, N. K. Exploring Wire-EDM for Manufacturing the High Quality Meso-Gears. *Proc. Mater. Sci.* **2014**, *5*, 1755–1760.
4. Townsend, D. P. *Dudley's Gear Handbook*, 2nd ed.; Tata McGraw-Hill Publishing Company: New Delhi, 2011.
5. Radzevich, S. P. *Dudley's Handbook of Practical Gear Design and Manufacture*, 2nd ed.; CRC Press: New York, NY, 2012.
6. Davis, J. R., Ed. *Gear Materials, Properties and Manufacture*, 1st ed.; ASM International: Materials Park, OH, 2005.
7. University of Massachusetts. Available from: www.ecs.umass.edu/mie/labs/mda/dlib/machine/gear/gear_mat.html (accessed 18 February 2016).
8. Bralla, J. G. *Design for Manufacturability Handbook*, 2nd ed.; McGraw Hill Inc.: New York, NY, 1998.
9. Groover, M. P. *Fundamentals of Modern Manufacturing: Materials, Process and Systems*, 4th ed.; John Wiley & Sons, Inc.: New York, NY, 2010.
10. ZGCLW. Available from: www.m.zgclw.org/Product/d?id=105 (accessed 18 February 2016).
11. Bhardwaj, B. P. *Production of Automobile Components & Allied Products*; NPCS: New Delhi, 2014.
12. GKN Sinter Metals. Available from: www.gkn.com/sintermetals/capabilities/surface-densified-pm/process/Pages/default.aspx (accessed 18 February 2016).
13. Custompart. Available from: www.custompartnet.com/wu/die-casting#process_cycle (accessed 17 February 2016).
14. Industrialmetalcastings. Available from: www.industrialmetalcastings.com/application_casting_gears.html (accessed 18 February 2016).
15. INDO-MIM. Available from: www.indo-mim.com/howMimWorks.html (accessed 17 February 2016).
16. GKN Sinter Metals. Available from: www.gkn.com/sintermetals/capabilities/MIM/process/Pages/default.aspx (accessed 18 February 2016).
17. Tandon, R. Metal Injection Molding. In *Encyclopedia of Materials: Science and Technology*; Jürgen Buschow, K. H., Cahn, R. W., Flemings, M. C., Ilschner, B., Eds.; Elsevier: Oxford, 2001; pp. 5439–5442.
18. Divya, P.; Singhal, A.; Pattanayak, D. K.; Mohan, T. R. R. Injection Molding of Titanium Metal and AW–PMMA Composite Powders. *Trends Biomater. Artif. Organs* **2005**, *18* (2), 247–253.
19. INDO-MIM. Available from: www.indo-mim.com/applicationsGuidelines.html (accessed 18 February 2016).
20. Imgrund, P.; Rota, A.; Kramer, L. Processing and Properties of Bi-Material Parts by Micro Metal Injection Moulding. In *Proceedings of the 1st International Conference on Multi-Material Micro Manufacture*, Forschungszentrum Karlsruhe, Karlsruhe, Germany, 29 June–1 July, 2005; pp. 131–134.
21. European Powder Metallurgy Association (EPMA). *Metal Injection Moulding – A Manufacturing Process for Precision Engineering Components*, 3rd ed.; EPMA: Shrewsbury, UK, 2013.
22. Schunk Sinter metalltechnik GmbH. *Powder Metallurgical Injection Moulding MIM – Metal Injection Moulding*, pp. 1–8. Available from: http://www.schunk-group.com/uploads/tx_rmsschunktest/SST_Powder-metallurgical-injection-moulding_05.pdf (accessed 11 April 2016).
23. Jenoptik. Available from: http://www.moldex3d.com/en/can-moldex3d/process/icm (accessed 11 April 2016).
24. Davis, B. A.; Theriault, R. P.; Osswald, T. M. Optimization of Compression (Injection/Compression) Molding Process Using Numerical Simulation. In *Proceedings of ASME Conference*, 1997.
25. Shojaei, A. A Numerical Study of Filling Process Through Multilayer Performs in Resin Injection/Compression Molding. *Compos. Sci. Technol.* **2006**, *66*, 1546–1557.
26. Sumitomo (SHI) Demag. Available from: www.sumitomoshidemag.eu/uploads/tx_braindownloads/%20071120_tb_spritzpraegen_en.pdf (accessed 18 February 2016).
27. Autodesk. Available from: knowledge.autodesk.com/support/moldflow-flex/learn-explore/caas/CloudHelp/cloudhelp/2015/ENU/MoldflowInsight360/files/GUID-081F4AE0-4B43-4DA3-B1F5-01D04D9C837C-htm.html (accessed 18 February 2016).
28. Piotter, V.; Gietzelt, T.; Merz, L. Micro Powder Injection Moulding of Metals and Ceramics. *Sadhana* **2003**, *28* (1–2), 299–306.
29. Attia, U. M.; Alcock, J. R. A Review of Micro-Powder Injection Moulding As a Microfabrication Technique. *J. Micromech. Microeng.* **2011**, *21* (4), 1–41.
30. Gutierrez, J. G.; Stringari, G. B.; Emri, I. Powder Injection Molding of Metal and Ceramics Parts. In *Some Critical Issues for Injection Molding*; Wang, J., Ed.; InTech: Croatia, 2012; Vol. 3; pp. 65–88.
31. Zauner, R. Micro Powder Injection Moulding. *Microelectron. Eng.* **2006**, *83* (4–9), 1442–1444.
32. Nishiyabu, K. Micro Metal Powder Injection Molding. In *Some Critical Issues for Injection Molding*; Wang, J., Ed.; InTech: Croatia, 2012; Vol. 5; pp. 105–130.

33. Tay, B. Y.; Loh, N. H.; Tor, S. B.; Ng, F. L.; Fu, G.; Lu, X. H. Characterization of Micro Gears Produced by Micro Powder Injection Moulding. *Powder Technol.* **2009**, *188*, 179–182.
34. You, W. K.; Choi, J. P.; Yoon, S. M.; Lee, J. S. Low Temperature Powder Injection Molding of Iron Micro-Nano Powder Mixture. *Powder Technol.* **2012**, *228*, 199–205.
35. Saile, V. Introduction: LIGA and its Applications. In *LIGA and Its Applications. Advanced Micro and Nanosystems Series*; Saile, V., Wallrabe, U., Tabata, O., Korvink, J. G., Eds.; Vol. 7; Wiley-VCH Verlag GmBH and Co. KGaA: Weinheim, 2009; pp. 1–10 (Chapter 1).
36. Southwest Center for Microsystems Education (SCME). *MEMS Micromachining Overview, MEMS, Micromachining Primary Knowledge (PK) Unit*, **2010**; pp. 2–32.
37. Kreith, F.; Mahajan, R. *MEMS Design and Fabrication*, 2nd ed.; CRC Press: New York, NY, 2006.
38. Hsu, T. R. *MEMS and Microsytems: Design and Manufacture*, 20th ed.; McGraw Hill Education Private Limited: New Delhi, 2002.
39. Mahalik, N. P. *MEMS*, 13th ed.; McGraw Hill Education Private Limited: New Delhi, 2013.
40. MEMS & Nanotechnology Exchange. Available from: www.mems-exchange.org/MEMS/fabrication.html (accessed 18 February 2016).
41. HOKY. Available from: www.szhoky.com/En/ProductView.asp?ID=2 (accessed 18 February 2016).
42. Jung, S. Y.; Kang, M. C.; Kim, C.; Kim, C. H.; Chang, Y. J.; Han, S. M. A Study on the Extrusion by a Two-Step Process for Manufacturing Helical Gear. *Int. J. Adv. Manuf. Technol.* **2009**, *41*, 684–693.
43. Saha, P. K. *Aluminum Extrusion Technology*, 1st ed.; ASM International: Materials Park, OH, 2000.
44. Dong, X.; Chen, F.; Chen, S.; *et al.* Microstructure and Microhardness of Hot Extruded 7075 Aluminum Alloy Micro-Gear. *J. Mater. Process. Technol.* **2015**, *219*, 199–208.
45. Rathi, M. G.; Jakhade, N. A. An Overview of Forging Processes with Their Defects. *Int. J. Sci. Res. Publ.* **2014**, *4* (6), 1–7.
46. POLIMAK. Available from: www.polimak.com/Gear_Gearbox.htm (accessed 18 February 2016).
47. Liu, Y.; Liu, W.; Zhang, Y.; Wu, D.; Wang, X. A Novel Extrusion Microns Embossing Method of Polymer Film. *Mod. Mech. Eng.* **2012**, *2*, 35–40.
48. Cheng, C. C.; Yang, S. Y.; Lee, D. Novel Real-Time Temperature Diagnosis of Conventional Hot-Embossing Process Using an Ultrasonic Transducer. *Sensors* **2014**, *14*, 19493–19506.
49. Kuo, C. C.; Zhuang, B. C. A Simple and Low-Cost Method to the Development of a Micro-Featured Mold Insert for Micro-Hot Embossing. *Indian J. Eng. Mater. Sci.* **2014**, *21*, 487–494.
50. Worgull, M. *Hot Embossing: Theory and Technology of Micro-Replication* (Series Editor J. Ramsden), 1st ed.; William Andrew Elsevier: Oxford, 2009; pp. 137–177.
51. Omar, F. *Hot Embossing Process Parameters: Simulation and Experimental Studies* (Ph.D. Thesis); Cardiff, Wales, UK: Institute of Mechanical and Manufacturing Engineering, Cardiff School of Engineering, Cardiff University, 2013.
52. MEMS & Nanotechnology Exchange. Available from: www.mems-exchange.org/capabilities/embossing (accessed 18 February 2016).
53. Kumar, G.; Tang, H. X.; Schroers, J. Nanomoulding With Amorphous Metals. *Nature* **2009**, *457*, 868–872.
54. Gupta, K.; Jain, N. K.; Laubscher, R. F. Spark Erosion Machining of Miniature Gears: A Critical Review. *Int. J. Adv. Manuf. Technol.* **2015**, *80* (9), 1863–1877. doi:10.1007/s00170-015-7130-2.
55. Pandey, P. C.; Shan, H. S. *Modern Machining Process*; Tata McGraw Hill Education Pvt. Ltd. Publication: New Delhi, 2013.
56. Jain, V. K. *Advanced Machining Processes*, 2nd ed.; Allied Publishers Pvt. Ltd: New Delhi, 2014.
57. Gurule, N. B.; Pansare, S. A. Potentials of Micro-EDM. In *Proceedings of 2nd National Conference on Recent Developments in Mechanical Engineering, Journal of Mechanical and Civil Engineering* (IOSR-JMCE); pp. 50–55.
58. Joshi, S. S. Micro-Electrical Discharge Micromachining. In *Introduction to Micromachining*, 2nd ed.; Jain, V. K., Ed.; Narosa Publishing House Ltd.: New Delhi, 2014.
59. Schumacher, B. M. After 60 Years of EDM the Discharge Process Remains Still Disputed. *J. Mater. Process. Technol.* **2004**, *149* (1–3), 376–381.
60. CAD/CAM. Available from: www.cadcam708.blogspot.in/2012/07/micro-edm-machine.html (accessed 18 February 2016).
61. Benedict, G. F. *Nontraditional Manufacturing Processes*; Marcel Dekker Inc.: New York, NY, 1987.
62. Sivaprakasham, P.; Hariharan, P.; Gowri, S. Modeling and Analysis of Micro-WEDM Process of Titanium Alloy (Ti6Al4V) using Response Surface Approach. *Eng. Sci. Technol.: Int. J.* **2014**, *17*, 227–235.
63. Gupta, K.; Jain, N. K. Analysis and Optimization of Micro-Geometry of Miniature Spur Gears Manufactured by Wire Electric Discharge Machining. *Precis. Eng.* **2014**, *38* (4), 728–737.
64. Gupta, K.; Jain, N. K. Analysis and Optimization of the Surface Finish of the Wire Electrical Discharge Machined Miniature Gears. *Proc. IMechE, Part B: J. Eng. Manuf.* **2014**, *228* (5), 673–681.
65. Gupta, K.; Jain, N. K. On Surface Integrity of Miniature Spur Gears Manufactured by Wire Electrical Discharge Machining. *Int. J. Adv. Manuf. Technol.* **2014**, *72* (9–12), 1735–1745.
66. Ali, M. Y.; Karim, A. N. M.; Adesta, E. Y. T.; Ismail, A. F.; Abdullah, A. A.; Idris, M. N. Comparative Study of Conventional and Micro-WEDM Based on Machining of Meso/Micro Sized Spur Gear. *Int. J. Precis. Eng. Manuf.* **2010**, *11* (5), 779–784.

COMPREHENSIVE MATERIALS FINISHING

COMPREHENSIVE MATERIALS FINISHING

EDITOR-IN-CHIEF

MSJ HASHMI

Dublin City University, Dublin, Ireland

VOLUME 2

SURFACE AND HEAT TREATMENT PROCESSES

VOLUME EDITOR

SHAHJAHAN MRIDHA

University of Strathclyde, Glasgow, United Kingdom



ELSEVIER

Amsterdam • Boston • Heildelberg • London • New York • Oxford
Paris • San Diego • San Francisco • Singapore • Sydney • Tokyo

Elsevier
The Boulevard, Langford Lane, Kidlington, Oxford OX5 1GB
225 Wyman Street, Waltham MA 02451

Copyright © 2017 Elsevier Inc. All rights reserved

No part of this publication may be reproduced or transmitted in any form or by any means, electronic or mechanical, including photocopying, recording, or any information storage and retrieval system, without permission in writing from the publisher. Details on how to seek permission, further information about the Publisher's permissions policies and our arrangements with organizations such as the Copyright Clearance Center and the Copyright Licensing Agency, can be found at our website: www.elsevier.com/permissions.

This book and the individual contributions contained in it are protected under copyright by the Publisher (other than as may be noted herein).

Notices
Knowledge and best practice in this field are constantly changing. As new research and experience broaden our understanding, changes in research methods, professional practices, or medical treatment may become necessary.

Practitioners and researchers may always rely on their own experience and knowledge in evaluating and using any information, methods, compounds, or experiments described herein. In using such information or methods they should be mindful of their own safety and the safety of others, including parties for whom they have a professional responsibility.

To the fullest extent of the law, neither the Publisher nor the authors, contributors, or editors, assume any liability for any injury and/or damage to persons or property as a matter of products liability, negligence or otherwise, or from any use or operation of any methods, products, instructions, or ideas contained in the material herein.

Library of Congress Cataloging-in-Publication Data
A catalog record for this book is available from the Library of Congress

British Library Cataloguing-in-Publication Data
A catalogue record for this book is available from the British Library

ISBN 978-0-12-803249-7

For information on all publications visit our website at http://store.elsevier.com



Publisher: Oliver Walter
Acquisition Editor: Ruth Ireland
Content Project Manager: Gemma Tomalin
Associate Content Project Manager: Joanne Williams
Designer: Matthew Limbert

Printed and bound in Canada

EDITOR-IN-CHIEF



Saleem Hashmi is emeritus professor in the School of Mechanical & Manufacturing Engineering at Dublin City University, Ireland. He founded the School in January 1987, in addition to setting up the Materials Processing Research Centre (MPRC), a research centre of excellence in the field of materials processing.

In 1990, Professor Hashmi established Advances in Materials and Processing Technologies (AMPT), a much-needed international conference in materials processing. He continues to be the chairperson of the steering committee for this series of conferences. In 1998 he was appointed as editor-in-chief of Elsevier's *Journal of Materials Processing Technology* and continued in this role until 2008.

In 1995, Professor Hashmi was awarded the higher doctorate degree of DSc, by the University of Manchester, the highest academic degree any university in the UK can award.

Professor Hashmi has supervised or co-supervised 112 PhD and 55 MEng research students to successful completion. Over the years he has also acted as an external examiner and expert assessor for PhD candidates and engineering departments with universities in Ireland, the UK, India, Pakistan, Bangladesh, Hong Kong, Canada, Australia, and Malaysia. He has published in excess of 460 papers and 25 books so far.

Professor Hashmi was the editor-in-chief for Elsevier's 13-volume major reference work *Comprehensive Materials Processing* which was published in 2014.

He has been appointed as the editor-in-chief for Elsevier's *Materials Science and Materials Engineering Reference Module*, a 14-section online resource comprising around 3500 reviewed articles. This launched in December, 2015 and is constantly being updated.

VOLUME EDITORS



Imtiaz Ahmed Choudhury is currently a professor at the Department of Mechanical Engineering, University of Malaya (UM), and has been with UM since 1996. He received his Bachelor degree in Mechanical Engineering from Bangladesh University of Engineering and Technology (BUET), MEng from Asian Institute of Technology (AIT), Thailand, and MSc in Mechanical Engineering from Arizona State University, USA. He obtained his PhD from Dublin City University. He started his career as an assistant engineer in a gas transmission and distribution company, Dhaka, Bangladesh. He worked as a maintenance engineer in a power station for 3 years in Libya. He started his academic career in 1982 as an assistant professor in an engineering college, Bangladesh. Since then, he has been working in academia. Imtiaz's research interests include traditional/nontraditional machining with vegetable oil-based lubricant, tool condition monitoring, machining difficult-to-cut and high strength materials, injection molding and application and use of solar energy. He has been a member of a panel of judges for the SME innovation award 2011–2013, Malaysia, under the category of "Manufacturing Sector." He was a Senate member of the University of Malaya. He has authored and coauthored about 100 papers in referred journals, more than 60 conference papers and some book chapters published in Elsevier works. He has also been a reviewer of various international journals. Imtiaz is a Fellow of Institution of Mechanical Engineers, UK (IMechE), and a life Fellow of Institution of Engineers, Bangladesh (IEB). He is a chartered engineer, UK (CEng).



Professor Shahjahan Mridha was born in Bangladesh and obtained his BSc and MSc in Metallurgical Engineering at the Bangladesh University of Engineering & Technology (BUET), Dhaka, and PhD at the University of Leeds in UK (1980) on Gas Nitriding of Low Alloy Steels. Since 1972 he has worked at the Department of Metallurgical Engineering, BUET for 20 years as a faculty member except for 1986–1987 where he was a Commonwealth Academic Staff member at the University of Birmingham, UK, working on Plasma Nitriding.

Professor Mridha was a senior research fellow at the University of Strathclyde, UK from 1989–1994 and worked on laser processing of aerospace materials in collaboration with UK Ministry of Defence. In late 1994 he moved to Nanyang Technological University (NTU) in Singapore where he was employed as an associate professor until 2001, working on semiconductor materials, composite and intermetallic coatings.

In January 2002 he joined the International Islamic University Malaysia (IIUM) as professor, later assuming the position of Head of the Department of Manufacturing and Materials Engineering. He left IIUM in July 2012 to join the Department of Mechanical and Aerospace Engineering at the University of Strathclyde (UK) as a Leverhulme Trust Professor, and remains there presently as visiting professor.

Professor Mridha has published more than 150 journal and conference papers. His research contributions are primarily on microstructure–properties relationships, semiconductor materials and surface modification of light alloys and steel using high power laser and TIG torch melting technology. He is the pioneer of TIG torch techniques for surface coating applications. Professor Mridha is subject editor of the *Metallic Materials* section in Elsevier's *Reference Module in Materials Science and Materials Engineering* launched in December 2015.

In addition to his academic career, Professor Mridha worked as an international consultant for the United Nations Industrial Development Organization (UNIDO) from 2001 until 2007, delivering expert advice and training to engineers working in manufacturing industries in the Indian and African continents.



Bekir Sami Yilbas is a distinguished professor in the Mechanical Engineering Department, King Fahd University of Petroleum and Minerals, Saudi Arabia. He received his PhD in Mechanical Engineering from Birmingham University, and was awarded a doctorate of Engineering at Birmingham in 2005 due to his significant contribution to his field of study. He has received numerous awards as recognition of his research work. Some of these include President of India's Prize for 1988 by Indian Royal Engineering Society, Technology Prize for 1990 by Science and Technology Foundation in Turkey, Best Research Award for 1997, 2002, 2007 by King Fahd University of Petroleum and Minerals, Silver Jubilee Medal by Silesian University of Technology, Donald Julius Groen Prize for 2007 by Institution of Mechanical Engineers (IMechE), Distinguished University Professor award at King Fahd University of Petroleum and Minerals, 2008 – present by King Fahd University of Petroleum and Minerals, Professor W. Johnson International Gold Medal for 2008 by Advances in Materials and Processing Technologies (AMPT) Steering Committee, Professor Fryderyk Staub Golden Owl Award by World Academy of Metals and Manufacturing, Almarai's Distinguished Scholar Prize by King Abdulaziz City of Science and Technology.

Bekir Sami Yilbas has published 720 journal papers in reputable international journals and presented over 100 papers at international conferences. He has 12 patents issued and is the subject editor of *Arabian Journal of Science and Engineering* and editor of *Journal of Fluids*. He has served as an editorial board member of international journals, including the *International Journal of Machine Tool and Manufacture Design, Research and Application, International Journal of Subsurface Sensing Technologies and Applications, Journal of Materials Processing Technology, Journal of Achievements in Materials and Manufacturing Engineering, International Journal of Nanomanufacturing*, and *Archives of Materials Science and Engineering*, and has received numerous awards as recognition of his research work.

CONTRIBUTORS TO VOLUME 2

Q Ahsan
University Teknikal Malaysia Melaka (UTeM), Melaka, Malaysia

NR Bandyopadhyay
Indian Institute of Engineering Science and Technology, Howrah, India

MK Banerjee
Malaviya National Institute of Technology, Jaipur, India

CA Barbosa
CAB Consulting, Campinas, Brazil

J Barglik
Silesian University of Technology, Katowice, Poland

AKM Bazlur Rashid
Bangladesh University of Engineering and Technology, Dhaka, Bangladesh

MMA Bepari
Bangladesh University of Engineering and Technology, Dhaka, Bangladesh

AK Bhargava
Malaviya National Institute of Technology, Jaipur, India

I Chakrabarty
Indian Institute of Technology (Banaras Hindu University), Varanasi, India

A Edrisy
University of Windsor, Windsor, ON, Canada

K Farokhzadeh
University of Windsor, Windsor, ON, Canada

ASMA Haseeb
University of Malaya, Kuala Lumpur, Malaysia

S Ismail
University Teknikal Malaysia Melaka (UTeM), Melaka, Malaysia

AR Machado
Federal University of Uberlandia, Uberlândia, Brazil and Pontifícia Universidade Católica do Paraná – PUC-PR, Curitiba, Brazil

RA Mesquita
RAF Consult, Ann Arbor, MI, USA

G Quan
Southwest Jiaotong University, Chengdu, PR China

HMMA Rashed
Bangladesh University of Engineering and Technology, Dhaka, Bangladesh

L Ren
Southwest Jiaotong University, Chengdu, PR China

S Sanyal
Indian Institute of Engineering Science and Technology, Howrah, India

A Sinha
Indian Institute of Engineering Science and Technology, Howrah, India

T Slatter
The University of Sheffield, Sheffield, UK

A Smalcerz
Silesian University of Technology, Katowice, Poland

R Thornton
University of Leicester, Leicester, UK

BS Yilbas
King Fahd University of Petroleum and Minerals, Dhahran, Saudi Arabia

M Zhou
Southwest Jiaotong University, Chengdu, PR China

CONTENTS OF VOLUME 2

Preface xiii

Introduction to Surface and Heat Treatment Processes xv

VOLUME 2 – Surface and Heat Treatment Processes

2.1 Fundamentals of Heat Treating Metals and Alloys *MK Banerjee* 1

2.2 Hardenability of Steel *AK Bhargava and MK Banerjee* 50

2.3 Carburizing: A Method of Case Hardening of Steel *MMA Bepari* 71

2.4 Surface Hardening by Gas Nitriding *K Farokhzadeh and A Edrisy* 107

2.5 Laser Beam Processing for Surface Modifications *BS Yilbas* 137

2.6 Surface Induction Hardening *J Barglik and A Smalcerz* 154

2.7 Recent Advances in Mechanical Surface Treatment *S Ismail, Q Ahsan, and ASMA Haseeb* 171

2.8 Heat Treatment of Commercial Steels for Engineering Applications *MK Banerjee* 180

2.9 Heat Treatment of Tool Steels *RA Mesquita, CA Barbosa, and AR Machado* 214

2.10 Heat Treatment of Cast Irons *I Chakrabarty* 246

2.11 Thermal Treatment for Strengthening Titanium Alloys *A Sinha, S Sanyal, and NR Bandyopadhyay* 288

2.12 Heat Treatment of Aluminum Alloys *HMMA Rashed and AKM Bazlur Rashid* 337

2.13 Solutionizing and Age Hardening of Aluminum Alloys *G Quan, L Ren, and M Zhou* 372

2.14 Heat-Treating Copper and Nickel Alloys *AK Bhargava and MK Banerjee* 398

2.15 Cryogenic Treatment of Engineering Materials *T Slatter and R Thornton* 421

PREFACE

Finish manufacturing processes are final stage processing techniques which are deployed to bring products to a stage where they are ready for marketing and putting in service. Over recent decades, a number of finish manufacturing processes have been developed by researchers and technologists. Some of these new processes have been documented and illustrated both individually and collectively in relation to application in specific areas. The advancement of tools of physics has resulted in considerable changes to these processes, and the precision with which they can be applied. The reporting of these developments are sometimes fragmentary, and this reference work provides a more connected and thorough review of these processes.

Comprehensive Materials Finishing is the primary reference source for researchers at different levels and stages in their career both in academia and industry. This reference work encompasses the knowledge and understanding of many experts into a single, comprehensive work. Containing a combination of review articles, case studies, and research findings resulting from research and development activities in both industrial and academic domains, this reference work focuses on how some of these finish manufacturing processes are advantageous for a broad range of technologies. These include applicability, energy and technological costs, and practicability of implementation. A wide range of materials such as ferrous, nonferrous, and polymeric materials are covered.

This work details the three foremost and distinct types of finishing processes: surface treatment, finish machining processes, and surface coating processes. Surface treatment refers to properties of a material being modified without otherwise changing the physical dimensions of the surface. Finish machining processes involve a small layer of material being removed from the surface by various machining type processes to render improved surface characteristics. Surface coating processes are where the surface properties are improved by adding fine layer(s) of materials with superior surface characteristics to improve the service life of the surface being coated. Each primary surface finishing process is presented in a separate volume, comprising chapters on many of the following relevant specific processes as follows:

Volume 1: Finish Machining and Net-Shape Forming: developments in conventional finish machining processes (honing, lapping, polishing, burnishing, and deburring), fine grinding, free EDM, laser finishing, electrical discharge grinding (EDG), electro-chemical honing (ECH), electrochemical discharge grinding (ECDG), electrochemical grinding (ECG), electrochemical turning (ECT), micro-machining process, and high-speed machining.
Volume 2: Surface and Heat Treatment Processes: This contains aspects of heat treatments, stress relieving, annealing, normalizing, hardening, tempering, austempering, martempering, carburizing (pack, liquid, gas, and post carburizing treatments), nitriding (gas and plasma), salt bath (boriding, chromizing, cyaniding, and carbonitriding), phase transformation of the outer surface (induction, flame, laser, electron beam, and anodizing).
Volume 3: Surface Coating Processes: Plating (electroplating, alloys (bronze/brass and others), chromium, dense chromium, copper and tin, gold, silver and other precious metals, zinc and nickel, electroforming, electroless nickel, hot dip galvanizing, selective/brush plating, surface finish coatings, air spray painting, and chemical vapor deposition (CVD)).

Finishing processes are at the core of successful production of marketable products and address recent progress in materials finishing technologies and science as well as covering recent developments in specific manufacturing processes involved with finishing of products for applications in all areas of engineering, biomedical, environmental, health and safety, and monitoring and control. The in-depth study of these finishing processes as presented in these volumes will assist scientists and engineers in the selection, design, and usage of materials, whether required in small- or large-scale uses across industries.

The initiations for this project began in 2014 and by January, 2015, I had selected the volume editors – Bekir Yilbas, Imtiaz Choudhury, and Shahjahan Mridha and we met with Gemma Tomalin, Joanne Williams, and Graham Nisbet at the Elsevier office in Oxford to finalize the table of contents and plan the project. Throughout 2015, the volume editors and I worked resolutely to select topics to be covered, invite authors, and review their manuscripts, eventually getting all content ready for production by the end of 2015. In 2016, authors returned their proof corrections and final files were produced. To create a work of this scale, the most in-depth reference ever published on materials finishing processes and surface engineering, relies on a collaboration of authors, editors, and the team at Elsevier. I would like to thank the many dedicated authors, whose contributions will be an essential reference for materials scientists and engineers. Each chapter has been reviewed by one of the volume editors, leading experts in their fields, whose knowledge and expertise have proved invaluable. I am indebted to each volume editor and their dedication to making their volume an exhaustive and relevant resource for the scientific community for many years to come. Finally, on behalf of myself and the volume editors, I would like to thank Gemma Tomalin and Joanne Williams at Elsevier for their support, cooperation, and good humor throughout this project – from the first meeting in early 2015, to the publication mid-2016.

MSJ Hashmi
Editor-in-Chief
Dublin City University, Dublin, Ireland

INTRODUCTION TO SURFACE AND HEAT TREATMENT PROCESSES

This volume on Surface and Heat Treatment Processes is one of three volumes in Comprehensive Materials Finishing and comprises of 15 chapters of which 5 chapters are focused on Surface Treatments, while the remaining chapters are on Bulk Heat Treatment Processes. The chapters on surface treatments are limited to surface hardening by structural modification of a surface layer. Although surface treatment is a part of heat treatment processes, for convenience of the readers the title of the volume is spelled out as surface and heat treatment processes.

In metallurgical practice, heat treatment represents a whole class of techniques – involving thermal, mechanical and chemical treatments – by which the desired properties of structural materials are obtained to suit the variety of applications. The properties influence the performance of a material in service. The modification and transformation of crystalline structures can be achieved by employing mechanical and thermal treatments or by infusion of new elements. Within close composition limits, the processing of a material to the finished product controls the microstructure and so the properties. Depending on the various processing parameters, transformed products may be of different phases. Presence of these phases and morphology of the products decide the resultant properties of metals. Heat treatments change the microstructure and make the materials hard or soft. Surface treatments harden the surface layer by infusion of new elements, phase transformation, plastic deformation or surface melting; in all these processes the core microstructures mostly remain unchanged.

The first chapter (2.1) introduces the fundamental principles involved in heat treatment processes applied to metallic components. This chapter provides sufficient information to be of use to metallurgists, researchers and engineers seeking to understand the importance of different thermal treatments to attain material properties required for specific applications. The readers will realize the fundamental importance of the internal structure of the metals; they will also be familiar with the typical features of such structures and understand how they are produced during heat treatments. The second chapter (2.2) on hardenability of steels describes basic aspects on the range and degree of hardening of steels, which are very important in the material selection and design of heat treatment processes in order to achieve properties of specific service requirements.

Chapters 2.3 and 2.4 describe how infusion of carbon (carburizing) and nitrogen (nitriding) using thermochemical treatments modifies the surface microstructures and properties of steels. While chapter 2.5 details the laser treatment that changes surface structures and properties upon resolidification of a melted thin surface layer. Chapter 2.6 is on induction treatment, which relates to the surface transformation hardening technique for steels of close composition limits without significantly modifying bulk properties. Chapter 2.7 contains mechanical treatments at the localized surface areas that create stain hardening by micro-deformation rather than phase transformation.

Heat treatments of important commercials steels, tool steels and cast irons are dealt with in chapters 2.8, 2.9 and 2.10, respectively. Details of microstructural changes related to properties under different heat treatment processes are outlined in these chapters. Each of these chapters gives a comprehensive treatise encompassing treatment, properties and application of all the main groups of steels used in engineering practice. The readers will be able to differentiate processes suitable for developing specific properties in these ferrous materials.

Heat treatments applied to important nonferrous materials are presented in chapters 2.11–2.14. Chapter 2.11 describes heat treatments of titanium alloys. Chapter 2.12 contains general heat treatments of aluminum alloys, while chapter 2.13 on specific processes dealt with solutionizing and aging treatments for strengthening of aluminum alloys. Heat treatments of copper and nickel alloys are given in chapter 2.14. Chapter 2.15 concentrates on cryogenic treatments or cryo-treatments, which refer to a range of subzero heat treatments that are applied to materials with the aim of causing permanent microstructural changes and corresponding changes in mechanical properties and behaviors.

Acknowledgements

I would like to thank all authors for their hard work, and editors, especially the editor-in-chief for inspiration and successful guidance in preparation of the volume. Finally, I am grateful to the Elsevier team particularly Gemma Tomalin and Joanne Williams who continuously supported me with appropriate information and necessary facilities at every stage of this work.

Shahjahan Mridha
University of Strathclyde, Glasgow, United Kingdom

2.1 Fundamentals of Heat Treating Metals and Alloys

MK Banerjee, Malaviya National Institute of Technology, Jaipur, India

© 2017 Elsevier Inc. All rights reserved.

2.1.1	**Introduction**	2
2.1.1.1	Stages of Heat Treatment	2
2.1.1.2	Heating Step	2
2.1.1.2.1	Heating rate	3
2.1.1.2.2	Heating temperature	3
2.1.1.3	Soaking Stage	4
2.1.2	**Heat Treatment of Steel**	4
2.1.2.1	Production of Homogeneous Austenite	8
2.1.2.2	Effect of Excess Heating Beyond Homogenization	8
2.1.2.3	Common Heat Treating Processes	9
2.1.3	**Heat Treatment Process Variables**	9
2.1.3.1	Austenitization	10
2.1.4	**Introduction of Alloying**	11
2.1.4.1	Classification of Alloying Elements	11
2.1.4.2	Effect of Alloying Elements	12
2.1.4.2.1	Effect of individual alloying elements in summarized form	14
2.1.4.3	Effect of Alloying Elements on TTT and CCT Curves	15
2.1.5	**Annealing**	20
2.1.5.1	Full Annealing	20
2.1.5.2	Isothermal Annealing	20
2.1.5.2.1	Patenting	21
2.1.5.3	Incomplete Annealing or Intercritical Annealing	22
2.1.5.4	Spheroidizing Annealing	23
2.1.5.5	Homogenization or Diffusion Annealing	24
2.1.5.6	Recrystallization Annealing	24
2.1.5.7	Subcritical Annealing	27
2.1.6	**Normalizing**	27
2.1.6.1	Distinctions between Annealing and Normalizing Purpose	28
2.1.7	**Hardening**	29
2.1.7.1	Factors Influencing Hardening Process	31
2.1.7.1.1	Adequate carbon content to produce hardening	31
2.1.7.1.2	Austenite decomposition to produce pearlite, bainite, and martensite structures	31
2.1.7.1.3	Temperature of heating, rate of heating, and the time of holding	32
2.1.7.1.3.1	Temperature	32
2.1.7.1.3.2	Heating rate and soaking time	32
2.1.8	**Heat Treatment Fundamentals of Nonferrous Alloys**	32
2.1.8.1	Age-Hardening Treatment	32
2.1.8.2	Annealing of Nonferrous Alloys	34
2.1.8.3	Martesite Formation in Nonferrous Alloys	34
2.1.8.3.1	Heat-treat principles of nonferrous alloys exhibiting polymorphic transition	35
2.1.8.3.2	Application of heat treatment principles in Mg-alloys	36
2.1.9	**Quenching and Quenching Medium**	36
2.1.10	**Tempering**	39
2.1.10.1	Stages of Tempering	40
2.1.10.2	Formation of Bainite in Steels	42
2.1.10.2.1	Mechanism of bainite formation	42
2.1.10.3	Martempering	43
2.1.10.4	Austempering	44
2.1.11	**Retained Austenite**	45
2.1.11.1	Subzero Treatment	46
2.1.12	**Heat Treatment Defects**	47
2.1.12.1	Quench Cracks	47
2.1.12.2	Overheating	48

References 48
Further Reading 49
Relevant Website 49

2.1.1 Introduction

Heat treatment is essentially a process of heating and cooling a material to achieve a desired set of physical and mechanical properties. The properties of materials are dependent upon their structural aspects. The structures may be of different scales of magnitude viz. macrostructure, microstructure, nanostructure, crystal structure, or atomic structure. In general, heat treatment of metals and alloys concerns the change in microstructure. Planned thermal treatment may affect desired changes in the defects structure of metallic crystals; this in turn alters the mechanical properties of the metals and alloys. During the course of heat treatment, the metals and alloys may undergo change in crystal structure (polymorphic transformation), change in chemical composition and change in the degree of order; depending upon the system, these changes may take place either singularly or in combination. However these changes have direct bearing on the final properties of the material. Also it will be seen that without any of the above three changes, heat treatment may enable to obtain desired properties of materials by way of changing its substructure. In a nutshell, heat treatment of metals and alloys envisages:

- Polymorphic change with or without change in local composition with in a system. The average composition however remains the same. This type of change is very common and Fe–C system is a classic example.
- Overall change in chemical composition at the surface of a component followed by above mentioned polymorphic change as stated above. This type of change is realized in surface hardening of metals and alloys.
- Change in local composition at a very fine scale of magnitude. Age hardening in alloy exemplifies such incidence.
- Dissolution of unwanted second phase particles, and formation of clean single phase alloy.
- Grain refinement of a pure metal or a single phase alloy which is previously subjected to mechanical working at a low temperature.

It is to be understood that changes stated above are brought about by previously chosen thermal treatment with an eye to achieving a predefined set of properties. Thus the purposes of heat treatment of metals and alloys are:

- To improve strength, hardness, and wear resistance properties.
- To increase toughness and ductility.
- To obtain fine grain size.
- To remove internal stresses induced by differential deformation by cold working, nonuniform cooling from high temperature during casting and welding.
- To improve machineability.
- To improve cutting properties of tool steels.
- To improve surface properties of materials especially in respect of wear and corrosion resistance.
- To improve physical properties viz. electrical and magnetic properties.
- To induce such other unique material functionalities as are possible due to specific phase transformation; some examples are transformation induced plasticity, metamagnetic shape memory effect, etc.

2.1.1.1 Stages of Heat Treatment

The heat treatment as a process is accomplished in the following three stages:

- Heating to a high temperature to obtain homogeneous single phase. In a multiphase alloy system, the homogeneous single phase can be obtained at high temperatures only with special care, as described later.
- Holding at the high temperature for preselected time period.
- Cooling the object under treatment to room temperature or below.

Again, it may be required to repeat the same three stages with different process parameters. It is necessary to know, how to select the heating temperature. Equally important is to acquire the knowledge about the criteria of selecting the rate of heating to reach the selected temperature and the duration of time one needs to spend at the heating temperature. During cooling operation knowledge about the cooling rate to use is also required. If the cooling rate is very slow, equilibrium microstructure in accordance with the prediction of phase diagram of the concerned system is possible to achieve. It is pertinent to remember that, attainment of equilibrium during cooling of a multicomponent system undergoing phase changes may be possible only if infinitesimal rate of cooling is practiced; it is very difficult to impose such a slow cooling rate in practice, although it is not impossible in today's technological scenario. The practice of heat treatment at such slowest possible cooling rate to aim at achieving the equilibrium microstructure is called annealing.

If an iron–carbon alloy contains equilibrium phases in its microstructure, the alloy is said to reach its softest state. This is why annealing of iron–carbon alloy is quite often considered as a softening process, whereas all other processes leading to deviation from equilibrium structures may be looked as hardening process. However this behavior is not generic and is not authenticated in many alloy systems, where the nonequilibrium phase is softer than its equilibrium counterpart. One such example is Cu–Zn–Al alloy, which when rapidly cooled from a high temperature is seen to produce softer phase than that present in annealed condition.

2.1.1.2 Heating Step

One of the main objectives in the heating stage is to obtain a homogeneous single phase unless otherwise dictates of compulsions are there; for example, hypereutectoid steels are

deliberately heated to a two-phase region for accruing certain specific benefits, as narrated in later sections. Another target of heating stage is to attain uniform temperature throughout the cross-section of the object being heat treated. Rapid heating may allow one part of the object to expand faster than another and as a result distortion or warpage may take place. However the heating rate depends on several factors. One important factor is the heat conductivity of the component. A metal with a high-heat conductivity heats at a faster rate than one with a low conductivity. The size of the stock to heat treat and its initial structural condition determine the rate at which it should be heated. A slower heating helps to get rid of thermal shock due to differential heating at surface and at the center. A component with higher cross-sectional area should be subjected to a slower heating rate in order to minimize the difference in temperature between surface and center of the stock. This helps to minimize the chance of warpage and distortion. Parts with nonuniform cross-sections experience uneven temperature rise across the section and hence a slower heating rate must be used to avoid cracking or warpage.

2.1.1.2.1 Heating rate

Whenever there is a phase transformation involving a change in crystal structure, volume change ought to occur. In a heat treatment process, the heating step comes across two different types of stresses: one is the thermal stress due to the existence of temperature differential between surface and center of the object being heat treated. This stress is consequential to thermal expansion of the material.

The other type of stress originates from the volume change accompanying the phase transformation. These two stresses make the component vulnerable to distortion or warpage. In extreme cases cracking may also occur for an otherwise intricate geometry. Difference in magnitude of thermal expansion at the surface and the center of the component depends upon the difference in temperature between the two at any instant of heating. This temperature difference is further dependent on the thermal conductivity, specific heat, and the section size of the object. The rate of heating is therefore decided by both the thermal and the transformational stresses. As previously mentioned, thermal stresses may be managed by a slower heating rate, whereas magnitude of transformational stresses is fixed for a definite phase transformation. However phase transformation takes place within specific range of temperature and so special care is taken in heating the material through this range of temperature. Quite often at temperature near to, where phase transformation is likely to occur, a short holding time is recommended. The purpose of this holding time is to equalize the temperatures at the surface and center of the stock. Thus there is no thermal stress, only the transformation stress is to be taken care.

There are a number of constraints to come across during heating. These are:

- Thermal properties of the material are functions of temperature and these are not accurately known for all metal and alloys under all conditions of heating. This leads to the problem of unpredictable and nonuniform thermal stresses to take care by manipulation of heating cycle.
- The flow stress of the material decreases at elevated temperature and if a phase transformation takes place at a high temperature with appreciable volume change, the stress due to transformation may lead to plastic deformation of the component being heated. Thus distortion or warpage becomes inevitable. In such cases manipulation in heating rate is of little use.
- Beyond the temperature of transformation only thermal stress is important and a slower rate of heating might appear to be a solution. However, it is certainly not because a slower heating implies a higher time to reach the soaking temperature. In many alloy systems there is ample chance of chemical degradation due to heating at high temperature. A slower rate of heating leaves a greater scope for chemical degradation, as the total residence time at the elevated temperature is quite high. So, it is desirable to employ a higher heating rate to reach the soaking temperature as soon as possible. The chemical degradation may be due to reaction with aerial gases in the furnace environment (as in titanium alloys), internal oxidation by entrapped oxygen in aluminium alloys, etc. Further a fast heating across the transformation temperature will raise the transformation temperature due to hysteresis effect and this results in higher degree of superheat and enhancement of driving energies for transformation. A controlled soaking time and temperature envisage the formation of fine-grained single phase alloy. However for cases of heating to subcritical temperature for specific heat treatment types (stress relieving, second stage graphitization in cast iron), a slower heating rate is preferred.

2.1.1.2.2 Heating temperature

The microstructure of the heat-treated component may follow from the dictates of equilibrium phase diagrams; sufficient time at the transformation temperature is available for diffusion processes to take place. Near-equilibrium state is normally attained in case of extremely slow cooling. With increasing cooling rate, availability of time to attain equilibrium at each stage of transformation is a constraint. This leads to a non-equilibrium situation. Thus quantitative estimation of phases by the usual technique of applying lever rule is not tenable. Even under deviation from equilibrium a system may undergo diffusional transformation, and can form phases qualitatively similar to what are predicted by the phase diagrams.

However, the phases so formed will increasingly differ in composition, morphology, and amounts with increasing cooling rate. This aspect is quite prevalent in case of iron–carbon system where normal cooling in air called normalizing, leads to significant difference in structure and property of the alloy. Faster cooling leads to a lower transformation temperature as compared to that of the annealed samples. In such cases it is prudent to study the isothermal transformation behavior of the samples at lower transformation temperatures. However diffusional transformation in solid state is limited by certain critical cooling rate (CCR), beyond which the system can no longer undergo diffusional transformation; rather it tends to produce supersaturated solid solution. Depending upon the system, where polymorphic transformation is unavoidable, crystal structure of the product phase changes through diffusionless shear transformation, where large-scale atomic movement is not required. Such kind of transformation is called martensitic transformation and it is observed in

rapidly cooled iron–carbon alloy. On the contrary, there are many systems, like a number of aluminum alloys, where there is no possibility of polymorphic transition and hence rapid cooling simply produces supersaturated solid solutions. In either case super saturation may be relieved by gently heating the supersaturated solid solution above room temperature so that the solute atoms gather appreciable mobility. Such process of getting rid of supersaturation through rejection of solute-rich phase is called precipitation.

2.1.1.3 Soaking Stage

When the preselected temperature is reached the component undergoing heat treatment is required to be kept at that temperature until the desired degree of structural homogenization take place. This process is generally termed 'Soaking.' The length of time the object is kept at the soaking temperature is known as 'Soaking period.' The soaking period depends upon the chemical composition of the material being heat treated, its thermal history, initial microstructure, maximum section size, and the weight of the component. In parts having different cross-sections the soaking period is decided by the largest cross-sectional area. As mentioned earlier, the temperature at the center of finite-sized workpiece lags behind the temperature at its surface.

Therefore the center of the stock will reach the soaking temperature at a later time than the surface. Hence the soaking time has two components: one is the time required for equalization of temperature at the surface and the center while the other one is the time for the structural homogenization to take place. The homogenization process may be simple dissolution of solute-rich phase into the matrix phase or a combination of both phase transformation with crystal structure change and second phase dissolution.

Figure 1 qualitatively shows the temperature differential to exist between surface and center of the heat treating stock. In most of the practical and industrial operation a time of 15 min is considered sufficient to make the temperature uniform across the section. Taking homogenization time in consideration, a thumb rule of 1 h per 25 mm of section size is normally employed for soaking at the high temperature. However in an industrial situation when a number of components are to be heated together, the thumb rule of 1 h per 25 mm thickness may not work out. In every such case, it is needed to understand the temperature profile within a furnace, and based on this knowledge, the time to be taken for all the items to attain the heat treatment temperature need to be deduced. However the general approach must be to keep the holding time to its minimum possible value. Too high a holding time may lead to grain coarsening and chemical degradation, whereas an inadequate soaking time may not yield homogeneous single phase everywhere within the workpiece.

As shown in Figure 2, sometimes the metal is brought from room temperature to the soaking temperature in more than one step; the workpiece is first heated slowly to a temperature where phase transformation is likely to take place and then it is held at that temperature for some predefined period of time so that the temperature of the workpiece is equalized throughout its cross section. This action is called 'preheating.' Following preheating the workpiece should be finally heated to the required heating temperature at a faster rate.

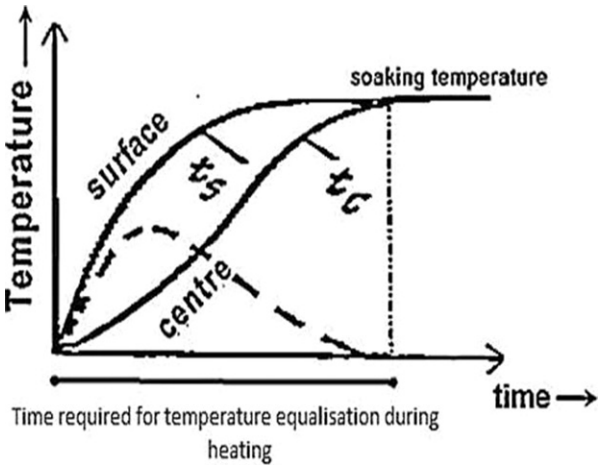


Figure 1 Temperature differential between surface and center.

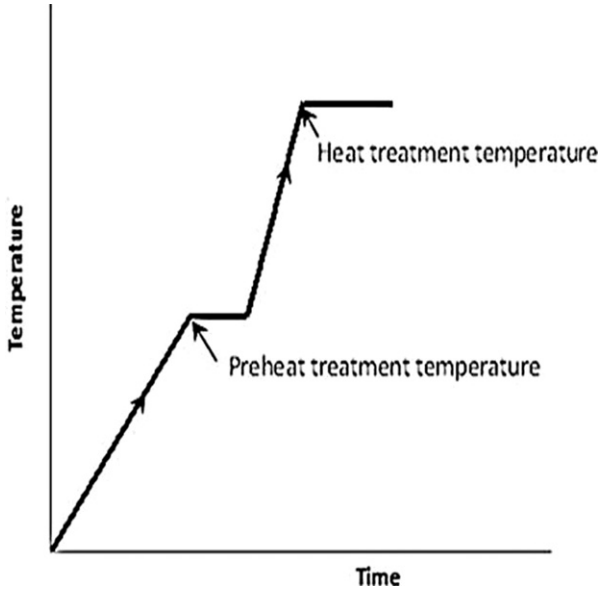


Figure 2 A complex heat cycle.

Different types of heat treatment processes applicable to various material systems are shown in Figure 3.

Majority of the aforementioned heat treatment practices are implemented in different types of steel. Therefore to elucidate the fundamentals of these heat treatment processes, the following discussion is made with reference to steel panel of iron–carbon alloys.

2.1.2 Heat Treatment of Steel

The steel is an alloy of iron and carbon with a maximum carbon content of 2 wt.%. The steel panel of Fe–C phase diagram as shown in Figure 4 is extended up to the extremum of eutectic isotherm.

The present discussion is confined to the metastable phase diagram of the system, because of the obvious reason that

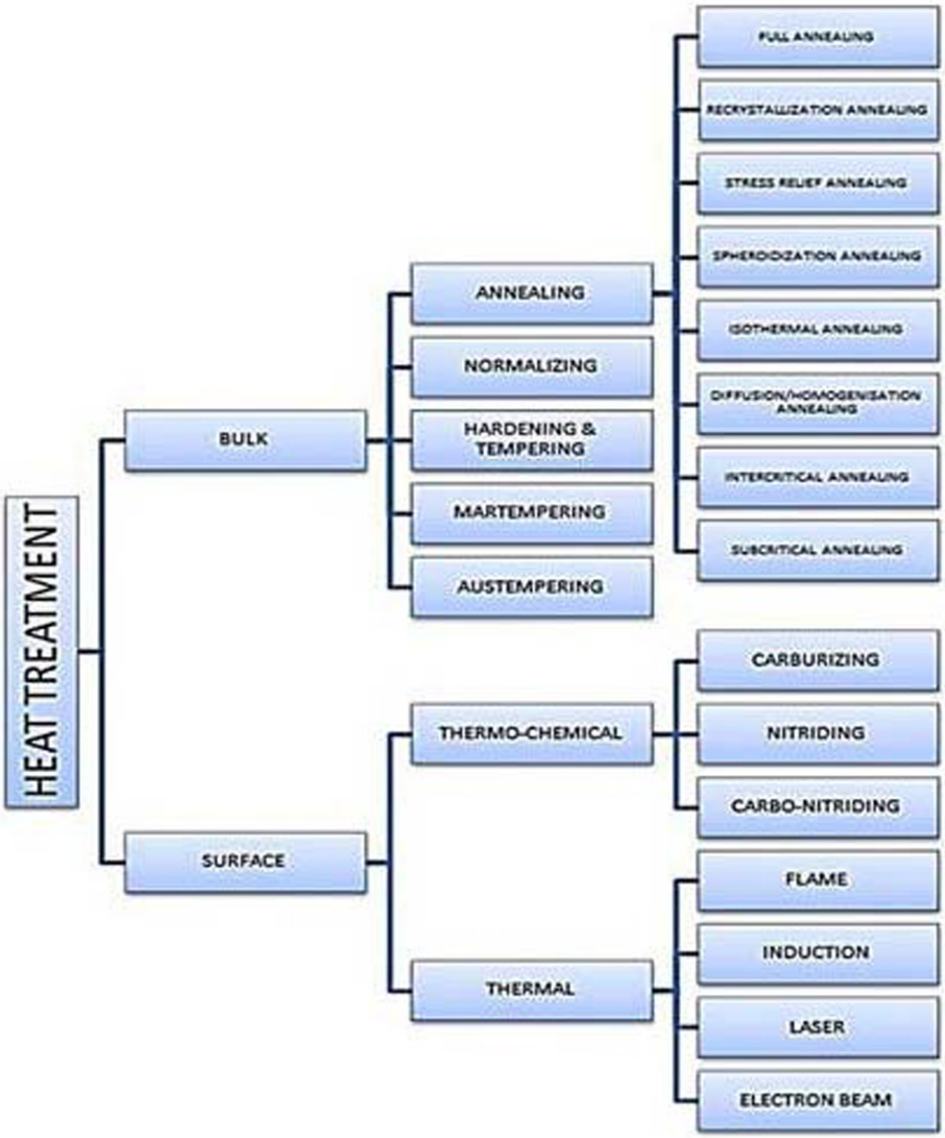


Figure 3 Different types of heat treatment processes.

a very long time is taken by the system to attain the stable state. The information about the different phases present at different temperature–composition combination may be obtained from the above equilibrium diagram. It may be noted that, A_1, the lower critical temperature denotes the minimum temperature up to which austenite(γ) can be present; A_3, is the upper critical temperature describing the equilibrium between γ and ferrite(α); whereas A_{cm}, is the line describing the solubility of carbon in γ. Quite often the suffixes c, e, and r are used with the critical temperatures. For example, Ac_1 denotes the temperature at which γ forms from ferrite during heating. Its equilibrium counterpart is written as Ae_1, whereas Ar_1 stands for γ to ferrite transformation during cooling. Similar meanings are assigned to Ac_3, Ae_3, Ar_3, Ac_{cm}, Ae_{cm}, and Ar_{cm}. Addition of alloying elements tend to alter the position of A_1 and A_3 lines; at the same time it changes the eutectoid composition which is 0.8 wt.%C in pure binary Fe–C alloy. The alloying elements added in iron–carbon system are classified broadly in to two types:

One group of alloying elements is known to stabilize ferrite; these alloying elements are called ferrite stabilizers and in general the crystal structure of ferrite stabilizing elements is body centered cubic (BCC). Cr, Mo, W, Nb, etc. are some examples of ferrite stabilizer.

Similarly, the elements stabilizing austenite are called austenite stabilizer. The austenite stabilizers are mainly those with face centered cubic (FCC) crystal structure; Cu, Mn, Ni, C, etc. are austenite stabilizers.

If ferrite stabilizing elements are added to steel, there will be rise in A_1 and A_3 temperatures, which restrict the austenite phase field; on the other hand the addition of γ stabilizing elements will depress A_3 and A_1 lines in the equilibrium diagram. The effect of commonly used alloying elements on A_1 temperature and eutectoid carbon content is shown in Figure 5.

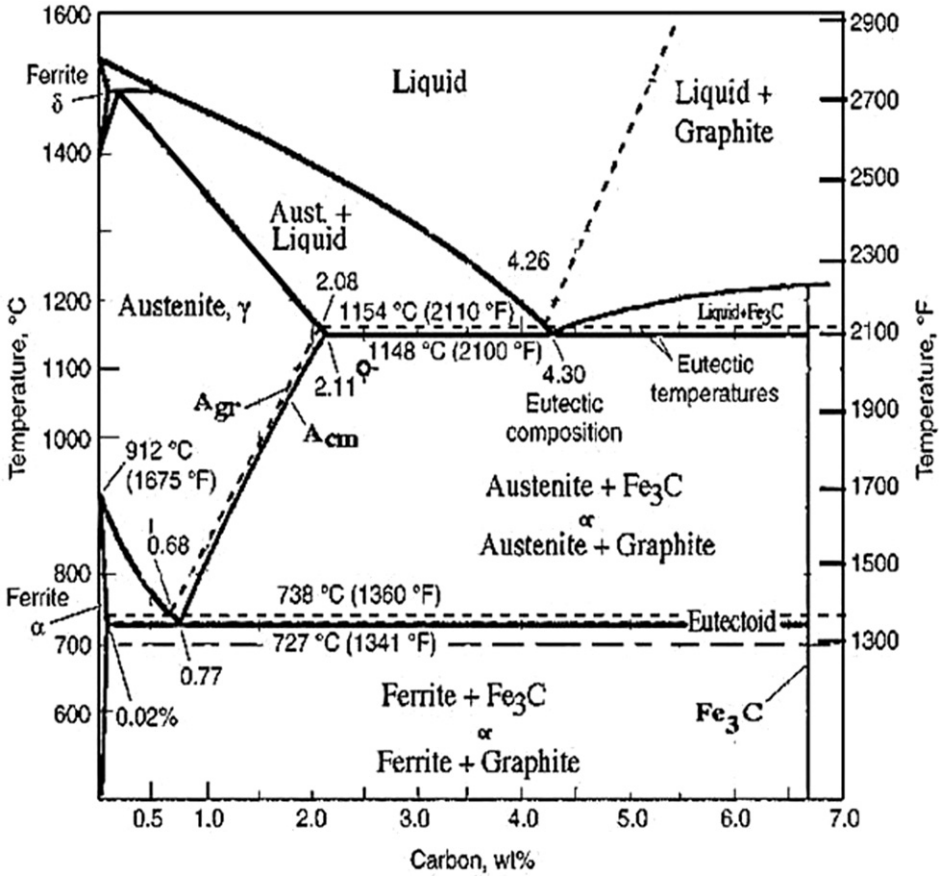


Figure 4 Combined iron–graphite and Fe–Fe_3C phase diagram showing steel panel up to 2.11 wt.% carbon.

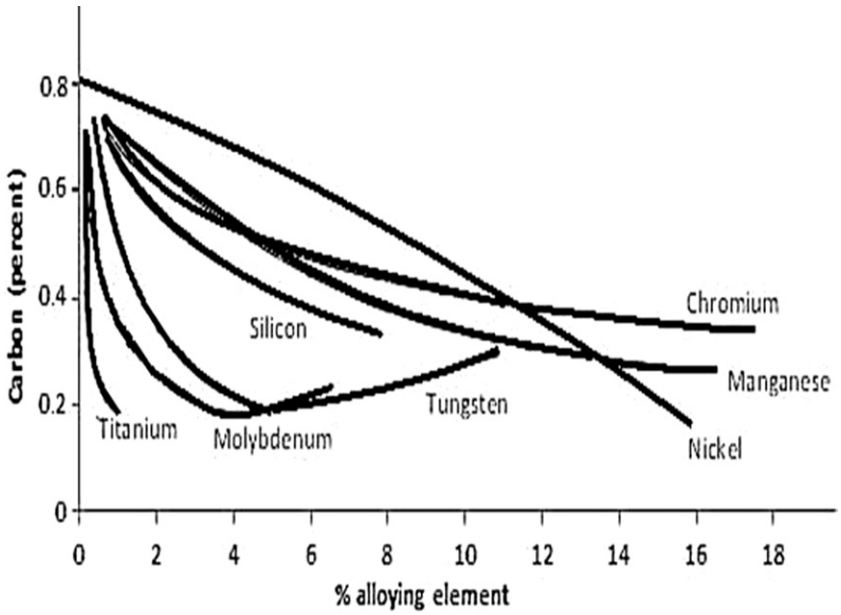


Figure 5 Effect of alloying element on the carbon content of the eutectoid composition.

As stated earlier the prediction of equilibrium phase diagram is of limited use in practical heat treatment processes except for annealing, which attempts to achieve equilibrium microconstituents. The heat treatment practices in general take resort to finite cooling rate causing deviation from equilibrium. As discussed previously that up to a certain degree of

rapid cooling, it is possible to effect diffusional transformation and thus realizing the microconstituents qualitatively similar to what are presented in the corresponding equilibrium diagram. To understand this situation it is important to review the isothermal transformation behavior of steel at temperature below the equilibrium isotherm. This isothermal transformation behavior is described by time–temperature–transformation (TTT) diagram as shown in **Figure 6**.

It is clear from the diagram that for transformation of steel at any temperature less than the equilibrium one needs some time to start the diffusional transformation and this gets completed after some more time as seen in the TTT diagram. The nature of TTT diagram is generic and is applicable for any diffusional transformation. As can be seen from the diagram, it is a C-shaped curve. As the transformation temperature is lower:

- the driving energy for phase transformation, i.e., diffusional decomposition of austenite to ferrite and carbide (pearlite) increases;
- the diffusional transformation of γ is due to nucleation and growth mechanism (readers may consult any text book of physical metallurgy of steel for details of diffusional decomposition of austenite); and
- the increase in driving force for phase transformation tends to lower the critical nucleus size and energy of nucleation.

Thus a higher number of nuclei are formed at lower transformation temperature. This phenomenon accelerates the overall transformation kinetics so long as the growth rate due to lowering of transformation temperature is not reduced to any objectionable value. It is for this reason, the time required to start the transformation called 'incubation period' decreases with decreasing transformation temperature, i.e., with increasing degree of undercooling. The reduction in incubation time continues till a particular temperature is reached. Below this critical temperature, the time required to start the diffusional transformation is seen to increase. This retardation of transformation kinetics below a critical transformation temperature describes the overriding influence of the diminution of rate of growth of the product phase. The growth of a nucleus is accomplished by continuous attachment of the atoms through long-range migration. The mobility or the diffusivity of atoms are strongly dependent on the temperature. Below a certain critical value of temperature, the diffusivity of atoms becomes so low as to stop the growth of nuclei; as a result there is a net increase in the time to start transformation, thereby making the TTT diagram C-shaped.

This is supported by the curve in **Figure 7**, which shows the variation of rate of nucleation and rate of growth with temperature.

The point, at which incubation period is minimum, is known as the nose of TTT diagram. Incidentally, the portion of the curve below the nose of TTT diagram of 0.8 wt.%C steel does not represent same type of transformation as it is above the nose of the curve. It is evident from the equilibrium diagram shown in **Figure 4** that austenite of 0.8 wt.%C completely transforms to pearlite below the eutectoid isotherm. Taking this steel as a reference, the transformation of γ till the nose of TTT diagram represent the transformation of austenite to pearlite and below the nose of plain 0.8 wt.%C steel, austenite decomposes to the aggregate of ferrite and carbide through a different mode of phase transformation known as 'bainitic transformation' (please refer to book *Physical Metallurgy Principles* authored by Robert E. Reed-Hill or any other text book).[1] The TTT diagram of a plain carbon 0.8 wt.%C steel is continuous, and so it is difficult to distinguish the exact point of transition from a pearlitic reaction to a mechanistically different bainitic reaction. It is quite certain that above the nose of TTT diagram, at about 550 °C, only pearlitic reaction takes place; it is also clear that transformation at any temperature below 450 °C austenite undergoes bainitic transformation. It is presumed that from around 550 °C till 450 °C both pearlite and bainite reaction may take place. Isothermal transformation of

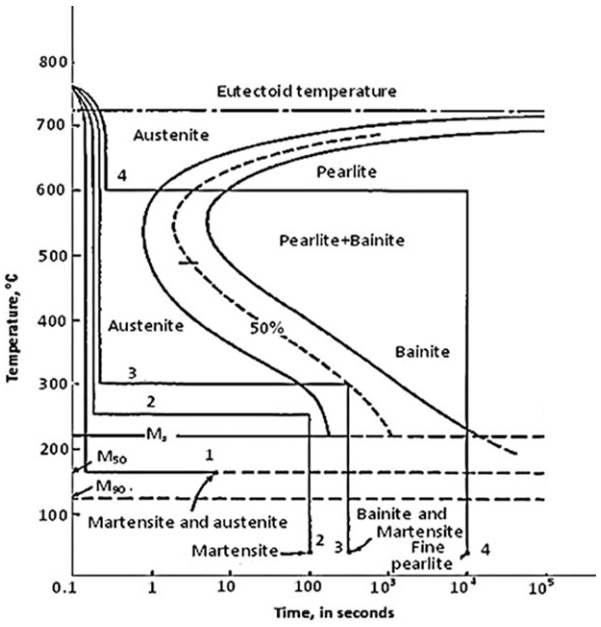


Figure 6 Hypothetical cooling path on isothermal transformation of eutectoid steel.

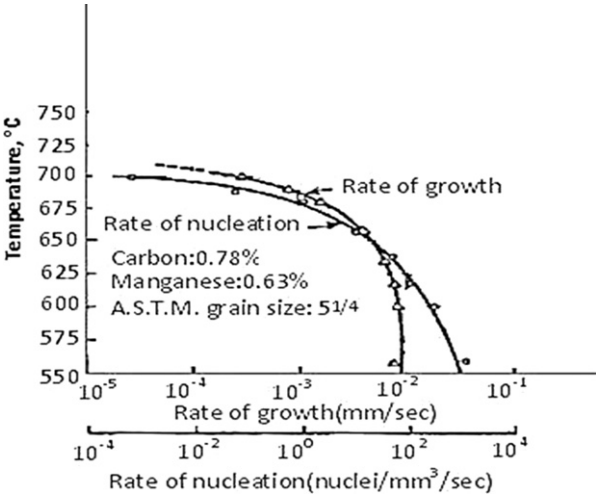


Figure 7 Variation of nucleation and growth rate for eutectoid steel with temperature. Mehl, R. F.; Dube, A. *Phase Transformation in Solids*; John Wiley and Sons, Inc.: New York, NY, 1951; p. 545. © 1951.

austenite indicates several important aspects of phase transformation in steel. It describes the transformation of austenite to pearlite above the nose of TTT diagram; it also helps to understand the bainitic reaction in plain C-steel below the nose of TTT diagram. It is obvious that continuous cooling cannot give rise to the formation of bainite in plain C-steel. If cooling rate is such high, as to bypass the nose of TTT diagram, neither pearlite nor bainite can form; instead, metastable austenite transforms by diffusionless shear mechanism to form a supersaturated solid solution of BCT structure called 'martensite.' In this context it is important to note that equilibrium diagram is of limited use in actual heat treatment operation, as it cannot provide any information about the product of transformation when in industrial heat treatment the cooling rate deviates from equilibrium.

In case of annealing a steel, care is taken to effect the decomposition of austenite at a low supercooling such that the transformation takes place in near-equilibrium condition. Since austenite decomposition envisages diffusion of participating atom species, the alloy steel with higher stability of austenite is required to be annealed at a considerably slower cooling rate, 10 °C h^{-1}. The cooling rate can be effectively controlled at a low value by providing suitable means of power input marginally less than what is required during the soaking period to maintain the constancy of temperature. Incidentally annealing of chromium bearing steels encounters the probability of embrittlement at a temperature around 550 °C. Therefore after transformation of austenite to ferrite and carbide as near to equilibrium temperature as possible, the steel is cooled rapidly to avoid the precipitation of chromium carbide. Whenever stress relieving during annealing is an important issue as is the case of intricate shaped casting, the slow cooling should continue till room temperature.

2.1.2.1 Production of Homogeneous Austenite

As a first step of heat treatment the workpiece is required to be heated to a temperature high enough to produce a homogenous single phase alloy. However there are exceptions like hypereutectoid steel where heating is carried out quite often to a temperature having a two-phase microstructure. In all cases, the final temperature is selected on the basis of information provided by the equilibrium diagram of the concerned system. In many cases (as in steels), achieving a single phase at high temperatures involves both polymorphic transformation and dissolution of the second phase constituent. In such cases, the first formed single phase alloy is compositionally inhomogeneous requiring a special attention to make the system homogeneous. In some other cases the initial microstructure may be of multiphase structure, needing dissolution of solute reach second phase without any phase transformation undergoing in between. In those cases heating temperature is to be decided by the equilibrium diagram which shows the temperature at which a single phase solid solution may be obtained. Only in case of subcritical heating, the kinetic aspect of the target activity is to be paid attention to. For an example, when second stage graphitization is envisaged, that is, when the pearlitic cementite is required to decompose into graphite, temperature of heating is decided by the kinetics of the process.

The fixing of ideal soaking temperature is a critical job. The soaking temperature is always fixed above the critical temperature describing the formation of single phase. For an example, temperature above Ac_3 line in iron cementite diagram. Increasing the soaking temperature has the advantage of making the system homogenous at an earlier time and thereby saving time and energy in the process. But unlimited enhancement of the soaking temperature to take advantage of achievable higher productivity is constrained by the chance of grain coarsening. Many systems require a dissolution of solute rich second phase and subsequent homogenization of these high temperature phases. This is essentially a thermally activated process and is time dependent. Higher is the temperature, shorter is the time requirement to achieve identical result. However large reduction in soaking time is restricted due to the fact that soaking temperature is limited by its greater vulnerability to chemical degradation and higher chance of grain coarsening. Hence optimization of heating temperature is very important. Normally the temperature of soaking is kept 50–75 °C higher than the equilibrium temperature.

2.1.2.2 Effect of Excess Heating Beyond Homogenization

Grain coarsening takes place if heating temperature is made excessively high. Coarsening of grains also results if holding time is unnecessarily prolonged even when homogeneous austenite has been formed. The initial grain size of austenite depends upon the number of nuclei formed due to superheating.

The grain coarsening is a thermally activated process and requires movement of grain boundaries. So long as there are constraints for grain boundary movement in presence of precipitates or compositional heterogeneity, the grain boundary movement is restricted; under such circumstances, once homogenized such barriers are no longer existent.

Any further holding at high temperature will cause, grain coarsening to set in, because coarse grains are thermodynamically stable. Grain coarsening leads to reduction in grain boundary area and thus the surface free energy and hence the total energy of system decreases. It may be noted that there are grains which are inherently fine and can remain so, even if heated to as high as 1000 °C or more. Rapid grain growth in these steels can take place only upon heating to 1050 °C or beyond. In contrast inherently coarse-grained steels exhibit rapid grain growth much earlier. The different tendency for grain growth is ascribed to the internal deoxidation practice. The air melted aluminum-killed steels are known to produce aluminum nitrides which are uniformly distributed within the matrix. These fine precipitates of aluminum nitride inhibit grain coarsening. Likewise many alloying elements, viz. titanium, vanadium, niobium, or other strong carbide formers, retard grain growth till they are not completely dissolved during austenitization. However inherently fine-grained steels do not mean that their grain sizes will always be less than those of the inherently coarse-grained steels; as shown in **Figure 8**, the initial rate of grain growth in inherently fine-grained steel is much slow as compared to that of the inherently coarse-grained steels which start growing appreciably quite early in the heating stage with a nearly constant rate of grain growth.

The inherently fine-grained steels experience an initial slow grain growth, which becomes much rapid at higher temperature and the ultimate grain size can be higher than its inherently coarse-grained counterpart. Quite often alloy steels containing strong carbide forming tendency are required to be austenitized at much higher temperature due the fact the alloy carbides do not go in solution so easily and take longer time or higher temperature to completely dissolve. As a result, they behave as inherently fine-grained steels because grain coarsening can take place only after complete dissolution of all the carbide particles which finally remove the barriers to grain boundaries movement. It is pertinent to remember the importance of achieving small grain size after heat treatment. Hall–Petch relation is given by

$$\sigma_y = \sigma_o + \frac{k_y}{\sqrt{d}}$$

where,

σ_y = yield stress,
σ_o = material constant for starting stress for dislocation movement,
k_y = strengthening coefficient, and
d = average grain diameter.

In accordance with above, yield strength of a single phase alloy is enhanced by its decreasing grain size. In general, structural fineness of a material gives rise to higher strength and toughness of the same; therefore wherever structural fineness is described by grain size, the prediction of Hall–Petch relationship holds good. In order to gain more insight into it, the readers may consult the text book *Mechanical Metallurgy* authored by Dieter.[2]

2.1.2.3 Common Heat Treating Processes

The heat treating practices most commonly employed for commercially important metals and alloys are cited below:

Age hardening is the process where a supersaturated solid solution is formed by heating the material in single phase region and holding there for sufficient time to make up a homogeneous solid solution. Following this, the alloy is rapidly cooled to produce the supersaturated solution. This supersaturated solid solution is heated in a controlled manner; super saturation of solid solution is relieved by precipitation of solute reach phase. If α is the solid solution of B in A and β is a B-rich phase age-hardening process is described by:

$$\alpha_{\text{saturated at high temperature}} \xrightarrow[\text{quench}]{} \alpha_{\text{supersaturated}} \xrightarrow[\text{aging (controlled heating)}]{} \alpha_{\text{saturated at room temperature}} + \beta$$

Annealing is generally a softening process in which the metals are heated to form the equilibrium high temperature phase and then allowed to cool very slowly. The purpose of annealing is to obtain the equilibrium microstructure; it aims to improve machinability, formability, and sometimes magnetic properties.

Normalizing is a process of natural cooling in still air from a preselected high temperature where the required single phase is formed. This results in increase in strength with a little reduction in ductility. Its purpose is to refine grain structure, to improve mechanical properties, and to relieve internal and surface stresses.

Stress relieving is a process of heating to a relatively low temperature to reduce the level of residual stresses in a material.

Quenching is a process of rapid cooling of a material from its homogeneous state at high temperature. The different media may be used to quench the material; it may vary from forced air, oil, water with or without addition of salt, and polymers. Steel is hardened by heating to austenitic phase and then quenching it to room temperature; this results in the formation of martensite which is a very hard and brittle constituent in iron–carbon system.

Tempering involves gentle heating of hardened steel and allowing it to cool slowly so that brittleness of the hardened material is reduced. Tempering of steel refers to softening by decomposition of iron–carbon martensite which is very hard and brittle. Tempering of martensites in steel leads to relieve of its supersaturation through various structural changes as described in later section. Also for nonferrous alloys, tempering brings about precipitation of different phases intragranularly at the internal faults within martensites and also in intercrystalline manner at the lath/plate boundaries of martensite crystals.

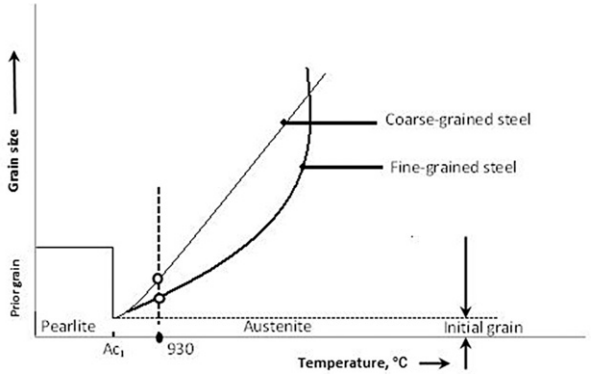


Figure 8 Austenitic grain growth in inherently fine- and coarse-grained steels.

2.1.3 Heat Treatment Process Variables

On the basis of previous discussion it is evident that the major process parameters influencing the quality of heat treatments are holding temperature, holding time, and rate of heating and cooling. The required magnitudes of these variables are decided by the chemical composition, size, and shape of the object along with the desired properties in the metals/alloys. If the chemical composition of the alloy to be heat treated is such that the material is highly prone to oxidation or is inherently coarse-grained material having a high tendency toward grain growth, the heat treatment of the same may result in poor mechanical properties unless special precautions are taken.

In order to minimize the problem of oxidation or grain growth, two salt bath heat treatment furnaces are sometimes employed. In one furnace, the object is heated to a temperature up to which there is no appreciable oxidation or grain growth. The object is then transferred to the second furnace, heated rapidly for a short time, and maintained at heat treatment temperature for minimum period. This practice reduces the total time of holding at the higher heat treatment temperature and thus the above mentioned problems are reduced. The temperature–time relationship for such a heating cycle is shown in Figure 2.

In addition to the mode of heating up to heat treatment temperature, the rate of heating is also of significance. The heating rate depends on the size and shape of the object and the thermal conductivity of the alloy. Almost all metallic alloys have good thermal conductivity and thus, in general, these parameters play only a marginal role. However, in the case of alloys like stainless steels, thermal conductivity is an important factor to consider while deciding the employable rate of heating. Secondly, low heating rates ensure better homogeneity of the structure and reduce the holding time at the heat treatment temperature. Complicated shapes, sharp cornered objects, and objects with variable sections are also heated slowly. Some alloys, such as high carbon steels and austenitic stainless steels, are subjected to slow heating rates. Smaller and simple shaped objects can be heated with higher heating rates and homogeneity of the structure can be ensured in such cases by increasing the holding time. Also, for the alloys that are prone to oxidation at high temperatures of heat treatment, faster rates of heating are recommended at high temperature range. Heat treatment temperature is governed mainly by chemical composition of the alloy, prior heat treatment, if any, and the final properties required. Heat treatment of steel is accomplished by heating it above upper critical temperature (Ac_3). This is known as austenitizing temperature, and can be determined from the iron–carbon equilibrium diagram. For plain carbon steel, Ac_3 temperature decreases with increasing carbon content. During heating, actual austenitizing temperature is raised above the equilibrium temperature. Similarly upon cooling the transformation temperature is depressed. Hence, during heat treatment practice, temperatures in excess of equilibrium temperature are employed. The austenite produced at these temperatures is homogeneous. In case of alloy steel, some alloying elements or their compounds do not dissolve easily in austenite and so they need to be austenitized for longer time at higher temperature. Unlike cementite which dissolves readily in austenite, the dissolution of alloy carbides is rather slow. For an object having variable section size, the soaking time is determined on the basis of largest section size. Lowering of heat treatment temperature has the implication of higher holding time. Generally soaking time of alloy steels is kept higher than plain carbon steels of low carbon content and the thinly enriched alloys. Heavy sections, complicated shapes, objects with variable section thickness, and highly enriched alloys should be cooled slowly. Extremely slow cooling results in the development of a structure as evident from the equilibrium diagram. The size, shape, distribution, and relative proportions of microconstituents can be controlled over a wide range by way of varying the cooling rates. Up to a certain limits, higher cooling rate results in a structure which is qualitatively similar to that in the equilibrium diagram. By increasing the cooling rate beyond this limit, structures produced will consist of either nonequilibrium transformation products or the high temperature phases retained by sudden quenching.

2.1.3.1 Austenitization

Austenitization is the first step of heat treatment of steel. Avoidance of microstructural gradient in the heat-treated part is very much necessary; else the final property will be different in different portion of the heat-treated part. The same strategy as discussed in the preceding section is applied during austenitization process. Formation of austenite from the initial microstructure of ferrite and cementite is a nucleation and growth process. It may be recalled that the austenitization process involves a polymorphic transition of BCC-ferrite to FCC-austenite and subsequent dissolution of cementite in austenite. The initial composition of austenite is the weighted average of those of ferrite and austenite in the intercritical region and the entire austenitization process is controlled by diffusion. The first nucleus of austenite will form above A_1 temperature at the high energy interphase boundaries (like ferrite–ferrite and ferrite–cementite) as available within the initial structural configuration. If the initial microstructure is lamellar pearlitic, the formation of austenite is quite rapid. Its nucleation will start at the ferrite–cementite boundaries as shown in the Figure 9.

On the contrary if initial microstructure contains globular cementite embedded in the ferritic matrix, nucleation of austenite will generally takes place in ferrite–ferrite boundaries, although cementite–ferrite interfaces are not excluded from being the potential nucleation sites. Evidently such situations of dispersed cementite within the ferrite matrix will take a longer time for the formation of homogenous austenite.

Figure 9 demonstrates the stages of formation of austenite from pearlite upon isothermal holding at a particular temperature. The time–temperature plot for such process is shown in Figure 10.

It is evident from the above isothermal transformation diagram that initiation of austenite formation from pearlite takes a definite incubation time which is a function of temperature. Upon formation of initial nuclei of austenite on ferrite boundary, the nuclei of austenite will gradually grow; concurrently cementite will dissolve in newly formed austenite as a demand of equilibrium. However equilibrium is not attained and dissolution of cementite lags behind the formation of austenite by polymorphic change of ferrite. A stage may be visualized when partially transformed austenite coexist

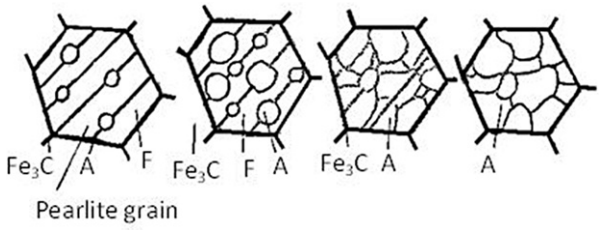


Figure 9 Stages in austenitization.

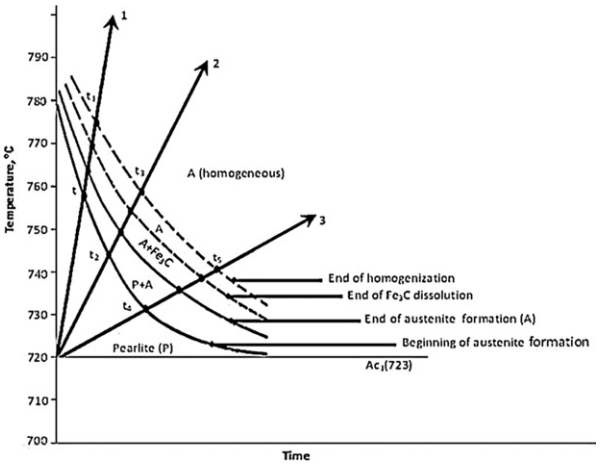


Figure 10 Time–temperature relationship in forming homogeneous austenite.

with pearlite. Upon further holding at the transformation temperature the entire pearlitic ferrite is converted to austenite with some cementite still remaining to dissolve in austenite. This cementite dissolution is a diffusional process and it takes some time to produce 100% austenite in the microstructure. However even after completion of austenite formation it does not immediately become homogenous. This is because the regions where the dissolution of cementite took place last will be of higher carbon concentration than elsewhere. Further holding for some more time will produce homogenous austenite, ready for subsequent heat treatment steps.

This process of achieving a homogenous single phase alloy is generic in the sense that for any initial multiphase microstructure, the sequence described above is followed by other systems, as for example, solutionizing of age hardenable alloy at elevated temperature.

2.1.4 Introduction of Alloying

Plain carbon steels are of limited use because of its deficiencies on many counts. They are unsuitable for applications where considerably higher strength and toughness properties are required. These steels are incapable to withstand highly corrosive environment, neither they are useful for high temperature or cryogenic applications. Plain carbon steels can be hardened only to a limited section and exhibit a marked tendency for softening at higher temperature. The above limitations of plain carbon steel are overcome by alloying steels with other elements. By definition, the elements that are deliberately added to achieve desirable properties in a metallic system are called alloying elements, whereas those elements that are inevitably present in steel without any deliberate intention to serve additional purposes are known as impurities. For example, the steel making operation cannot fully remove sulfur and therefore some amount of sulfur is always present in steel. Sulfur in such situation is called an impurity. Again the same sulfur when present in appreciable amount has the capacity to make chips brittle during machining. A particular variety of steel, known as free-cutting steel contains deliberately added sulfur. In this case sulfur, is an alloying element, even though in majority of cases sulfur is considered an unwanted element in steel due to its adverse effect on the properties of steel, for example, inducing hot-shortness to steel. Steels containing alloying element are called alloy steels. So long as the total alloying element content is less than 5 wt.%, the steels are considered as low alloy steels whereas the steels with alloying elements in excess of 5 wt.% is called high alloy steels.

2.1.4.1 Classification of Alloying Elements

The alloying elements in steel are classified in to two broad types. Some alloying elements stabilize the higher temperature phase austenite, which is of FCC crystal structure. The crystal structure of these austenite stabilizing elements is FCC. The other class of alloying elements is those which stabilize ferrite phase. These ferrite stabilizing elements are in general of BCC crystal structure. The majority of ferrite stabilizers are seen to be strong carbide formers. However at room temperature any alloying element in steel has to be present either in solution in ferrite or in carbide. The austenite formers do not in general form carbides. It is to be recalled that any element added to steel is partitioned between the two phases, carbide and ferrite. The austenite formers which partition to ferrite are not generally found in carbide. The austenite stabilizing elements are appreciably soluble in austenite by being of FCC crystal structure; these elements delay austenite to ferrite transformation, i.e., the basic lattice transformation in Fe–C system. However when austenite to ferrite transformation takes place, an austenite stabilizer can have altogether two options: either it goes in solution within ferrite or it gets precipitated in elemental form. Whether the austenite stabilizing alloying element will remain in solution within ferrite will depend upon how the concerned solute obeys the other rules of alloying. In the case of nickel, it is observed that nickel partitions to ferrite. The atomic radius of iron and nickel are very near to each other, as a result nickel goes in solution in ferrite at ease. On the contrary, one would find that copper with FCC structure is not soluble in ferrite. Moreover it is not carbide former; hence it is left with the lone option of being precipitated in element form. The precipitates of copper lead to hardening of steel.

Majority of austenite formers being non carbide formers are either present in ferrite or get precipitated depending upon the solubility of the concerned element in BCC ferrite. Manganese is the exceptional austenite stabilizer, which forms isomorphous carbide with cementite. Thus manganese gets partitioned between ferried and carbide, forming $(Fe,Mn)_3C$ type of carbide.

On the contrary, the ferrite stabilizers like Cr, Mo, Nb, etc. are generally carbide formers. In steel containing more than one carbide formers, the formation of carbides and partitioning between ferrite and carbide depend upon their relative affinities for carbon and solubility in ferrite.

The alloying elements have significant influence on the phase transformation behavior of steels. All the alloying elements influence the decomposition behavior of austenite and in the process, the alloying elements exert their characteristics effects on the equilibrium phase diagram, TTT or continuous cooling transformation (CCT) diagrams.

Some of the important purposes of alloying are:

1. To enhance strength and toughness at room temperature.
2. To improve strength, ductility, and impact properties at high as well as very low temperature.
3. To improve resistance to degradation under aggressive service condition.
4. To develop wear resistant steel for employment at ambient and elevated temperatures.
5. To develop magnetic properties with minimum hysteresis loss.
6. To improve the strength of steel without aid of quenching.

However, alloying elements cannot change the structure insensitive properties like stiffness of the steel. The stiffness is dependent on the elastic modulus, which is the slope of true stress–true strain (σ–ε) curve within elastic limit. Although alloying elements can improve elastic limit, it cannot appreciably change the modulus of elasticity which is a structure insensitive properties.

2.1.4.2 Effect of Alloying Elements

Alloying elements bring about changes in the Fe–Fe_3C equilibrium diagram. It is to be understood that by the addition of alloying elements, it is possible to alter the composition and properties of phases, without giving rise to the formation of entirely new phases in general. Since alloying elements are responsible for change in transformation temperature and the rate of decomposition of austenite, the properties of plain C-steel can be modified by alloying.

Addition of alloying elements changes the free energy of participating phases in phase transformation, either diffusional or diffusionless. Therefore the transformation temperature of austenite is changed by the addition of alloying elements.

The diffusional decomposition of alloyed austenite necessitates adequate movement of the atoms of alloying elements. Since such movement is generally sluggish the alloying element influences the kinetics of diffusional decomposition.

Solubility of C in austenite as well as in ferrite is modified by the addition of alloying elements. This is because the alloying elements dissolved in austenite or ferrite tend to induce lattice strain due to difference in size of solvent and solute; this directly influences the solubility of C in austenite as well as in ferrite.

The diffusionless shear transformation proceeds through stacking shifts of atoms on the habit planes. The presence of alloying elements changes the strain field distribution on the habit plane and thus influences the stacking shifts required for martensitic transformation. This leads to the stabilization of either the parent or the product phase and is characterized by depression or elevation of the characteristic transformation temperature. The general microstructure of steel at room temperature is comprised of ferrite and carbides. Alloying elements like Ni, Si, Al, Zr, P, S, and Cu dissolve at ease in austenite and also in ferrite at different degrees. Some of these elements like Si, Al, and Zr may form oxides and be present in steel in the form of nonmetallic inclusions. Similarly Mn and Zr may form sulfide inclusions. These elements however do not have appreciable tendency toward formation of carbides. The other elements like Cr, W, V, Mo, Ti, Nb, and Mn have tendencies for forming carbides. In the absence of carbon to react with, these elements should be in a ferrite solution. The increasing order of carbide forming tendency is Mn, Cr, W, Mo, V, and Ti. The alloying elements dissolved in ferrite increase the hardness due to solid solution effect and it is schematically shown in **Figure 11**.

As stated earlier, addition of alloying elements not only modifies the transformation temperature of austenite to ferrite, but also the eutectoid point. Thus both A_1 and A_3 temperatures are altered due to the addition of alloying elements. **Figure 12** shows the effect of alloying addition on the eutectoid transformation temperature. From the diagram, it can be seen that those alloying elements that are known to stabilize austenite would lower the A_1 temperature. Whenever ferrite stabilizers are added by a large amount, the austenite loop gradually becomes narrower due to the increase in upper critical temperature; beyond some specific concentration of ferrite stabilizers like Cr, the austenite may not form at all and the steel remains ferritic at both elevated and room temperature.

All the alloying elements except cobalt shift the TTT- and CCT-diagrams toward right. Austenite forming elements stabilize the metastable austenite and delay its diffusional decomposition. Therefore it is easy to understand that all

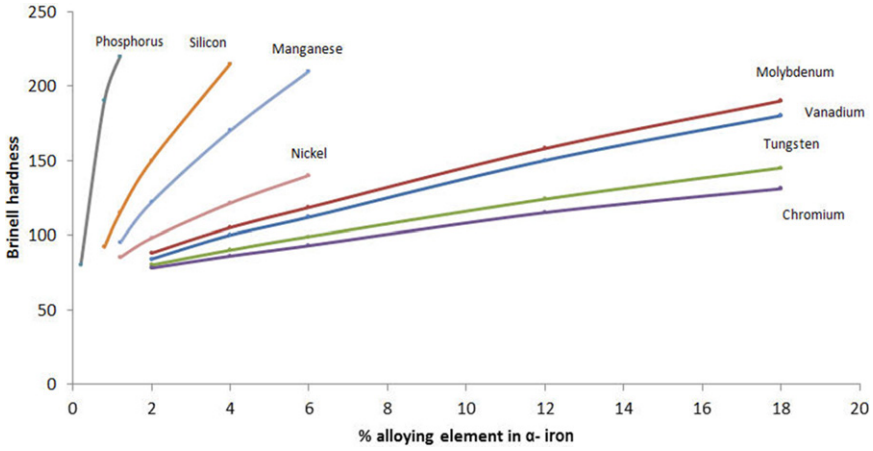


Figure 11 Effects of various alloying elements on hardness of steel.

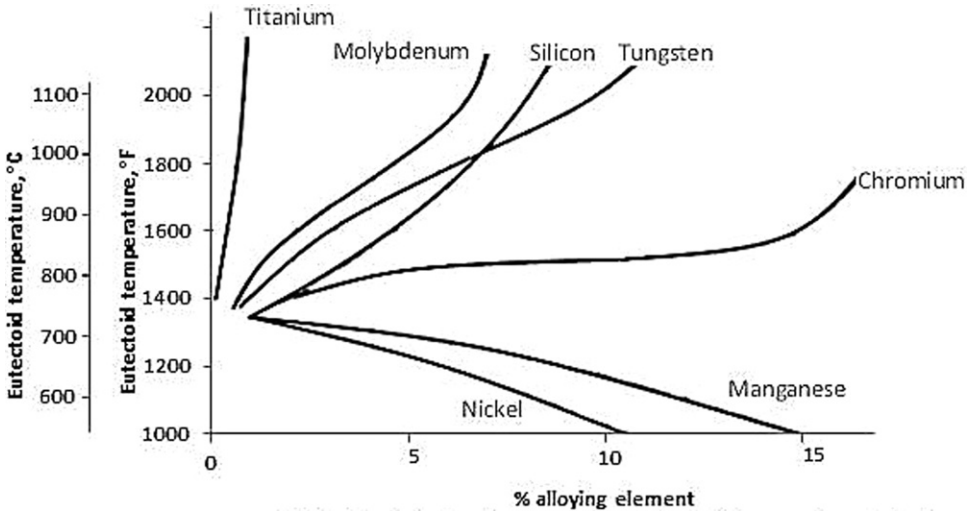


Figure 12 Effect of alloying element on eutectoid temperature of steel.

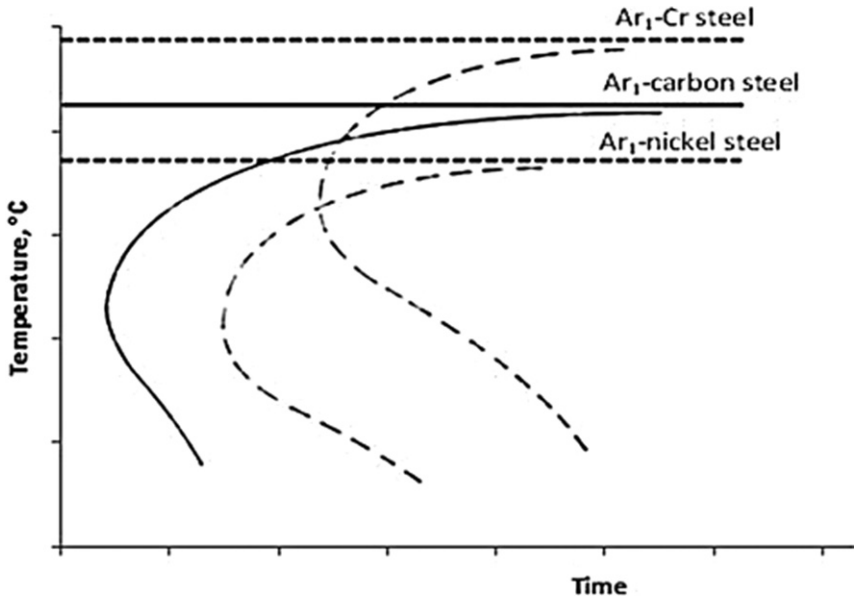


Figure 13 Diagram showing shift of TTT diagram due to alloying with nickel and chromium.

austenite stabilizers should cause a rightward shift of TTT- or CCT-diagrams. The ferrite stabilizers are in general carbide formers. It is known that nucleation of pearlite from austenite is initialized by the formation of Fe_3C. In the presence of strong carbide formers, the formation of Fe_3C at prior grain boundaries becomes more difficult. Strong carbide formers prefer to neighbor the C-atoms in austenite; the formation of cementite requires free C-atoms to react with iron. However getting away from the attraction of the neighboring atoms of carbide formers is a thermally activated process and hence time dependent. Thus more time is required for the carbon atoms to make them available for iron atoms to form cementite. This implies a shift of CCT- or TTT-diagrams toward right. The shift of TTT and CCT due to Ni and Cr is shown in Figure 13.

It is clear that diffusional decomposition of austenite is delayed due to the addition of alloying elements. The alloying elements influence the kinetics of both pearlitic and bainitic transformation. Any specific alloying element is liable to shift pearlitic reaction and bainitic reaction to larger times but by different magnitudes. A carbide forming element is expected to shift the pearlitic reaction to a larger extent than the bainitic reaction due to difference in the mechanism of these two transformations.

As seen from Figure 13 both nickel and chromium shift the TTT diagram toward right, but to different extent. If equal amount of chromium and nickel are added, it is expected that the shift of TTT diagram will be more toward right; the magnitude of shift may appear to be additive. However the actual shift of TTT diagram is more than the summed up shifts due to addition of either elements. This effect is called 'Synergism.' Chromium and nickel are known to shift TTT and CCT diagram synergistically toward right. Several such synergisms are

observed in Fe–C system and examples may be cited of molybdenum–boron and copper–boron, which depress the austenite to ferrite transformation temperature synergestically. However effect of each element on pearlitic and bainitic reaction is different and so the pearlitic and bainitic bays get retarded differently due to addition of alloying elements.

2.1.4.2.1 Effect of individual alloying elements in summarized form

- Manganese (Mn): manganese has got very high solubility in austenite because of its FCC structure, but its solubility in BCC-iron is less than 3%. Manganese is a medium carbide former, forming isomorphous $(Fe, Mn)_3C$ carbides. Manganese is a very good hardenability raiser, and is of highest multiplying factor in determining the hardenability of steels. It reduces hot-shortness by binding sulfur as MnS. Manganese is an austenite stabilizer.
- Molybdenum (Mo): it is a ferrite stabilizer, and is extremely soluble in BCC-iron, having solubility greater than 35% whereas it is soluble only up to 3 wt.% in FCC-iron. The solubility of Mo in FCC-iron is increased if carbon is added to the system. It forms intermetallic compound with iron and therefore causes precipitation hardening in Mo–Fe system. It is a strong hardenability raiser, stronger than most of other alloying elements. It gives rise to appreciable secondary hardening. As the dissolution of molybdenum carbide in austenite is a slow process, the grain coarsening temperature of austenite is significantly increased by molybdenum. It increases the high temperature strength and red hardness of steel. Molybdenum imparts resistance to pitting corrosion in stainless steels; further molybdenum increases abrasion resistance by forming hard molybdenum carbide particles in ferrite matrix. Molybdenum reduces temper embrittlement in a chromium bearing steel. It is not capable to inhibit the formation of chromium carbides, but slows down the kinetics of precipitation of chromium carbide, thereby putting a constraint to embrittlement.
- Nickel (Ni): nickel with FCC structure is an austenite stabilizer, with unlimited solubility in FCC-iron. Its solubility in BCC-iron is limited to 10 wt.%, irrespective of whether there is any carbon or not. Nickel strengthens and toughens iron by solid solution hardening. It is a moderate hardenability raiser but in combination with Cr and Mo, it increases hardenability significantly. Nickel is not carbide former but is a weak graphitizer. Nickel does not increase tempering resistance of steel to any appreciable extent. Nickel promotes grain coarsening at elevated temperature.
- Cobalt (Co): cobalt is soluble in FCC-iron, with unlimited solubility. It is extensively soluble in BCC-iron with the limit of solubility being 75 wt.%. It improves hardness of iron by solid solution hardening and is a significant contributor to raise hardness by way of hardening ferrite. Its carbide forming tendency is similar to that of iron and is the only alloying element which decreases the hardenability when dissolved in iron.
- Chromium (Cr): chromium is a ferrite stabilizer and has got unlimited solid solubility in BCC-iron. Limit of its solubility in FCC-iron is about 13 wt.%; however, this may be extended up to 20 wt.% with addition of carbon up to 0.5%. It is a strong carbide former; its carbide forming tendency is greater than Mn but less than W. Chromium increases the resistance to oxidation by forming a very thin layer of chromium oxide. Chromium is a moderate hardenability raiser; however, Cr and Ni increase the hardenability of steel synergistically. It imparts very good abrasion and wear resistance by forming chromium carbide in the microstructure.
- Silicon (Si): silicon is least soluble in FCC-iron, with solubility up to 2 wt.%. Silicon increases the activity of C in ferrite. Its solubility in BCC-iron is about 18 wt.%. Silicon hardens steels with loss in plasticity. Silicon is a very strong oxidizing element. Silicon segregates at basal plane of graphite crystal to prohibit inherent growth form of graphite. Thus silicon leads to the formation of graphite flakes. It increases the hardenability but quite moderately. Silicon influences tempering in low carbon steels through solid solution hardening. Silicon is generally used as a deoxidizer; however silicon as an alloying element up to 4 wt.% is capable of grain orientation. This makes the steel useful for transformers. Silicon improves the oxidation resistance of steel.
- Titanium (Ti): titanium is mildly soluble in austenite, with solubility less than 1%. However its solubility in BCC-iron is higher and around 6 wt.%. It is a hardenability raiser but it is generally added to steel in very low concentration for the formation of titanium carbide which enhances the material properties during thermo-mechanical treatment. It prevents formation of austenite containing high amount of chromium. It also inhibits sensitization in austenitic stainless steel by way of forming distributed titanium carbide.
- Vanadium (V): vanadium is very little soluble in FCC-iron, with solubility up to 1 wt.% whereas its solubility in BCC-iron is unlimited. It acts as hardenability raiser. It is strong carbide former but its carbide forming tendency is less than titanium and niobium. Vanadium is excellent in giving rise to secondary hardening. Similar to molybdenum, vanadium enhances the grain coarsening temperature of austenite, because the dissolution of vanadium carbide in austenite takes a longer time.
- Tungsten (W): tungsten is weakly soluble in FCC-iron; however its solubility in BCC-iron is quite high, around 33 wt.%. Tungsten is a strong hardenability raiser, and is also strong carbide former. Tungsten is capable of providing secondary hardening during tempering. Tungsten is able to provide very high wear resistance due to formation of hard particles of carbide in microstructure. It also improves the elevated temperature strength property of steel.
- Phosphorous (P): phosphorus is very weakly soluble in austenite (Avner),[3] whereas it is around 3 wt.% in alpha iron (maximum solubility in α iron at 950 °C). Phosphorus leads to hardening of steel by solid solution strengthening. It is also known to improve hardenability. It improves machinability of free-cutting steels, by way of making the chip brittle. It also improves corrosion resistance.
- Aluminum (Al): aluminum is extremely soluble in BCC-iron up to 36 wt.%, whereas its solubility in FCC-iron is around 1 wt.% (Avner).[3] It strengthens ferrite by solid

solution hardening. However it is a graphitizer. Aluminum is a very good grain refiner by way of dispersing its oxides and nitrides throughout the matrix of ferrite. Aluminum is alloyed in steels to be subjected to nitriding, because strengthening of nitrided steel is realized by the formation of aluminum nitride.

2.1.4.3 Effect of Alloying Elements on TTT and CCT Curves

Shift of pearlite reaction curve and that of bainite reaction curve are different due to addition of a single alloying element. This is because the pearlitic and bainitic reactions are mechanistically different; hence the same alloying element should be responsive to two reactions in different ways. Taking the instance of addition of a strong carbide former like molybdenum, it is recognized that initiation of pearlitic reaction is conditioned by carbon atom being freed from the influence of molybdenum atoms, which have high affinity for carbon atoms. Since this depends upon diffusion of molybdenum atoms and also since such movement is quite sluggish, the reaction is shifted to longer times. The same element will delay upper bainitic reaction in a different way. Upper bainite formation is conditioned by taking away carbon atom from the vicinity of iron atoms, so that the carbon-depleted austenite transforms martensitically to bainitic ferrite. The presence of molybdenum itself aids to this as it removes some carbon atoms from the influence of iron atoms by way of neighboring the carbon atoms it has affinity with.

Thus iron atoms populated regions, relatively free of carbon atoms, are now made available. So martensitic transformation of austenite to upper bainitic ferrite is accentuated. Therefore the addition of such alloying elements brings about differential shifts in pearlitic and bainitic bays, thereby separating the two bays; hence the alloy systems become amenable to bainitic transformation by continuous cooling. This is not possible for a plain carbon steel, where TTT curve is continuous with superimposition of pearlitic and bainitic bay as shown in Figure 14.

However, when the cooling rate is so fast as to bypass the nose of CCT diagram, neither pearlite nor bainite is possible to form; rather a diffusionless martensitic reaction takes place, else the metastable austenite phase remains as it is.

It is to be recalled that austenite undergoes phase transition only when it attains a finite degree of metastability. This means that stable austenite above A_3 or above A_1 for eutectoid steel does not undergo any transformation.

Supercooling of austenite below equilibrium temperature makes it metastable; this then acquires driving energy for transformation to product phase (for elaborate understanding any text book of physical metallurgy may be consulted).

In normal circumstances, finite cooling rate is applied to gain sufficient driving force for transformation to takes place. Thus as previously mentioned, the equilibrium phase diagram is of limited use in practical heat treatment. Equilibrium cooling is not generally practiced; nevertheless knowledge of equilibrium diagram of a system is extremely important to understand its heat treatment behavior. Equilibrium diagram

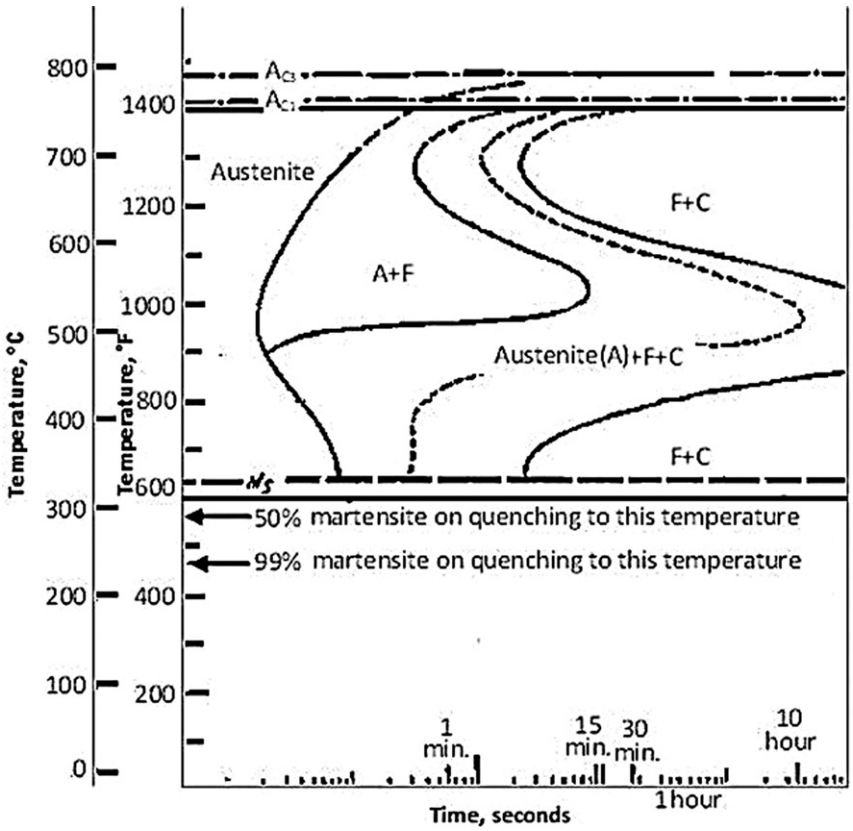


Figure 14 T–T diagram of a 0.33 wt.% carbon, 0.45 wt.% manganese, and 1.97 wt.% chromium steel (Austenitized at 870 °C).

provides information about which phase is stable at what temperature–composition combination.

From the information one can decide the temperature of heating to get a single phase alloy at higher temperature.

Equilibrium diagram denotes the stability of different phases at various temperature–composition combinations. It provides information of possible polymorphic transition, limit of solubility of a solute in a solvent as a function of temperature and also the amount of different phases present in an alloy at any particular temperature. However all these information are true only if equilibrium state exists all through. In practice equilibrium is not maintained in most of the time; at any finite cooling rate there is factually a deviation from equilibrium. A fast cooling puts constraints to attainment of equilibrium in a diffusional transformation which depends upon time. So, transformation must take place at temperature lower than the equilibrium temperature. It is also known that a phase transformation takes place only with a finite undercooling; the number of nuclei available for transformation depends upon the degree of supercooling and hence the temperature at which transformation is given to take place. This information however is not available from equilibrium diagram. Hence it is very important to get the information about the transformation characteristics at temperature lower than the equilibrium one. This necessitates the construction of isothermal transformation diagram; these are essentially temperature–time plot for various amounts of transformation, say transformation start, its finish or any other percentage of transformation. Such diagram for eutectoid steel is shown in **Figure 6**. It is found that pearlite and bainite transformation overlap and from the nose of the TTT curve at about 550 °C upward, pearlitic reaction takes place; below 450 °C, bainitic transformation is certain. From the very nature of TTT diagram it is apparent that if cooling rate is such that the time required to reach the temperature of the nose is less than or equal to its incubation time, diffusional decomposition of austenite is completely suppressed.

The time required to start the transformation at a temperature is the incubation time required by the system to overcome the activation barrier of the concerned diffusional transformation.

The TTT diagram of hypoeutectoid steel shows its similarity with that of eutectoid steel in the sense that:

1. The curves are 'C' shaped characterizing diffusional transformation.
2. Being asymptotic to the critical temperatures at long time, hint that undercooling is must for transformation to take place, else infinite time will be required to effect a transformation which is impossible.

However the dissimilarity between the two is the presence of a line 'ab' lying above and to the left of lines describing the austenite to pearlite transformation. This line 'ab' is asymptotic to A_3 temperature at infinite time and defines the formation of proeutectoid ferrite. From the cooling paths imposed on the TTT diagram of hypoeutectoid steel, it is apparent for path 1 that the proeutectoid ferrite forms between A_3 and A_1 temperature and holding for a long time it simply equilibrates to produce ferrite and unreacted austenite. However for path 2, the proeutectoid ferrite formation is followed by the complete transformation of remaining austenite to pearlite. In contrast cooling path 3 passes through the lines of TTT diagram below its nose and leads to the formation of bainite. Although isothermal transformation behavior is understandable by following the cooling paths drawn in **Figure 15**, these cooling paths are not possible to be realized in practice.

Superimposition of cooling curves on to an isothermal transformation diagram may be made to avoid the imaginary cooling path envisaged in the preceding paragraph. Cooling

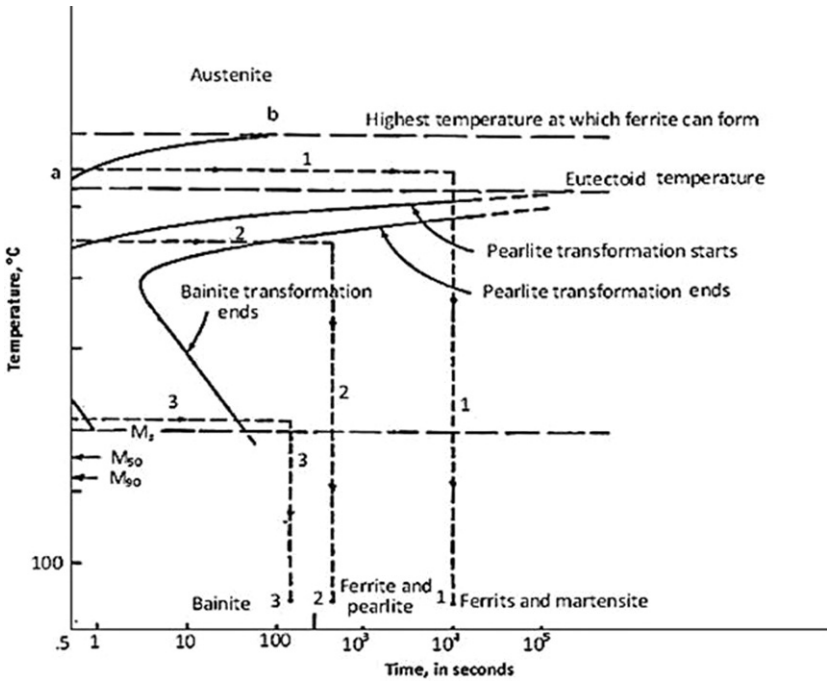


Figure 15 Arbitrary time–temperature paths on the isothermal diagram of a hypoeutectoid steel.[1]

curves are essentially a temperature–time recording continuous change of temperature of a cooling object with time. This superimposition is demonstrated in Figure 16. For a very slow cooling rate aiming to resemble full annealing, it is found that transformation is completed within a narrow temperature band just below the critical temperature A_1; the microstructure simulates that of annealed steel and consists of pearlite of large interlamellar spacing. The cooling path is however the one that demonstrates the entire transformation to take place at constant temperature due to isothermal holding for sufficient period of time. Relatively faster cooling rate (as in cooling path 3) has led to transformation occurring at lower temperature to yield fine pearlite. Cooling path 4 represents the CCR which when employed disallows diffusional transformation of austenite to pearlite. Any rate of cooling higher than the CCR will retain metastable austenite till a different mechanism of phase transformation without the aid of diffusion is realized by the system. A diffusionless shear transformation has to take place unless the metastability of austenite is enhanced so much so by alloying, that the temperature of martensite formation, M_s, goes below room temperature (readers may check up with text books on phase transformation). In that case metastable austenite will remain at room temperature as in the case with austenitic stainless steel.

Unfortunately superimposition of continuous cooling curve on a TTT diagram is not scientifically justified, although it gives a rough estimate of phase transformation in steel under nonequilibrium cooling (Figure 17).

That is why TTT diagram cannot be directly used for describing the transformation of austenite in practical situation. For this purpose CCT diagrams are needed to be constructed. Incidentally it is possible to derive the CCT diagram from the corresponding TTT diagram.

As evident from Figure 18 the supercooled austenite under a state of continuous cooling transforms over a range temperature. On the contrary TTT diagrams are drawn by monitoring time dependent austenite decomposition at constant temperatures.

The approximate CCR from a TTT diagram is obtainable by the use of Grange–Kiefer formula:

$$\mathrm{CCR} = (\mathrm{A}_1 - T_{\mathrm{nose}})/1.5t_{\mathrm{min}}$$

where, t_{min} = minimum incubation period at the nose of the TTT diagram, T_{nose} = temperature at the nose where incubation period is minimum.

Moreover commercial heat treatment is hardly accomplished isothermally at constant temperature. Therefore one needs to understand the difference between TTT and CCT diagram. From Figure 18, it is noticed that continuous cooling from a temperature above eutectoid temperature reaches the line for austenite–pearlite transformation after a time say t_1 second. Let it be taken that after a lapse of t_1 second while cooling the stock at the cooling rate C_1, the temperature attained by the stock is T_1°C. It may now be presumed that entire stock had been at T_1°C for a time of t_1 second with in

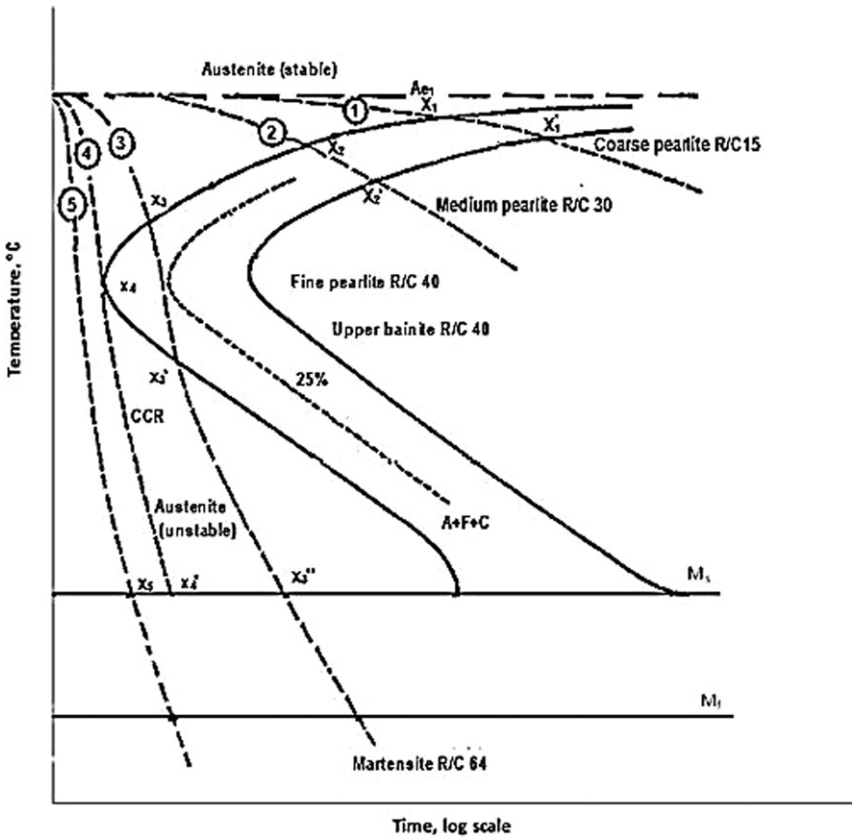


Figure 16 Superimposed cooling curve on TTT diagram.

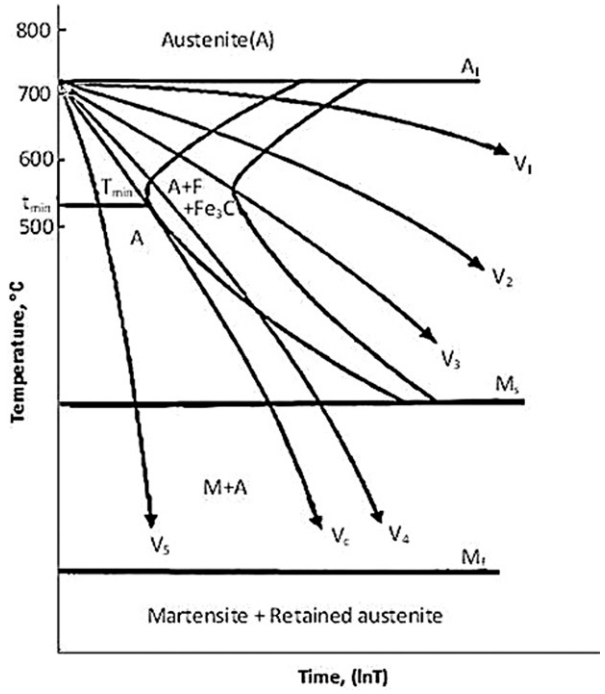


Figure 17 Superimposition of cooling curves on a TTT curve (austenite decomposition). Cooling rates $V_1 < V_2 < V_3 < V_4 < V_5$.

the metastable austenite region. This is as tenable as at any temperature higher than T_1°C; the stock requires more than t_1 second to reach the line for pearlite start temperature. The continuously cooled sample is not ready to form pearlite after t_1 seconds, rather it will take a slightly higher time to initiate the reaction. Thus the point '*a*' is shifted toward right. Again higher time implies a greater drop in temperature. This means the actual position of pearlite start point '*b*' is toward right of '*a*' as well as depressed. Similarly at the γ-pearlite finish point may be found lie at '*d*' to mean that the '*c*' point on TTT diagram is shifted toward right and downward.

TTT diagram is therefore quite useful in predicting the cooling rate required to avoid soft pearlitic transformation of austenite. From the foregoing discussion it is very clear that if a rate of cooling is faster than the CCR in accordance with TTT diagram, it is certain that in actual case of prediction made on the basis of corresponding CCT diagram, the same cooling rate will always give rise to non-diffusional products of transformation.

CCT diagram can be obtained quite accurately by a number of techniques. Differential dilatometric technique is generally employed to construct the CCT diagram of any steel under preprogramed cooling schedule. **Figure 19** shows the CCT diagram drawn in Gleeble machine which makes use of dilatometry to accomplish the task.

From the curve in **Figure 19**, it is clear that transformation under continuous cooling takes place over a range of temperature. Since structure and morphology of phases formed

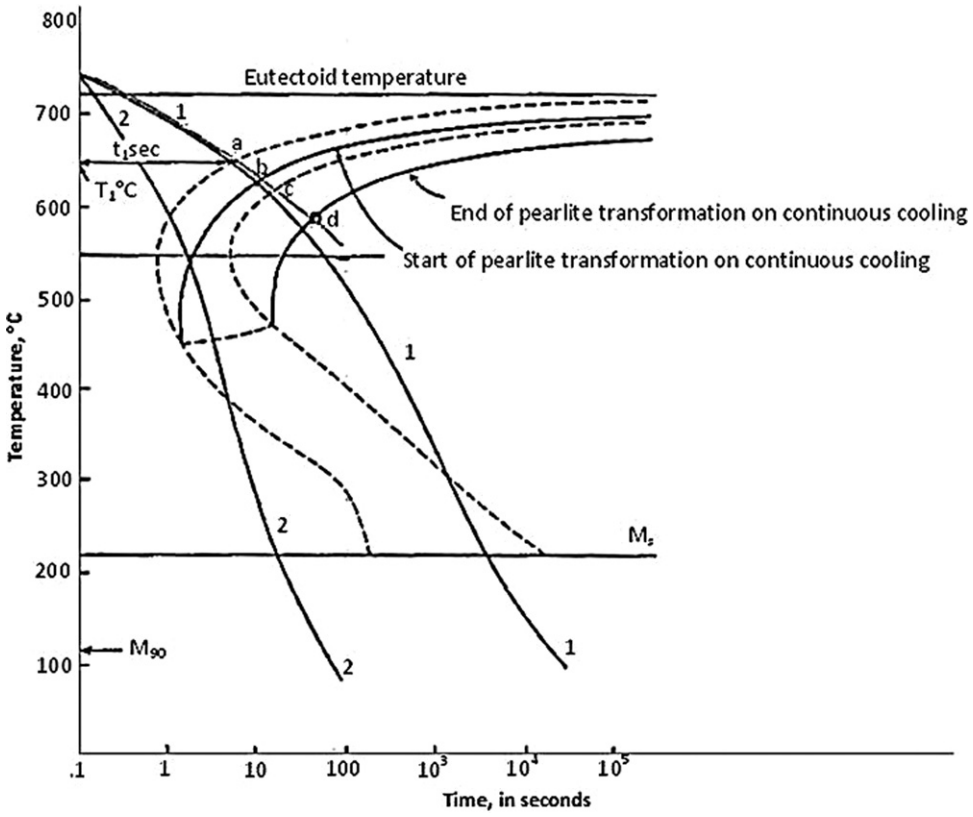


Figure 18 The relationship of the continuous cooling diagram to the isothermal diagram for an eutectoid steel (schematic). After Atlas of Isothermal Transformation Diagram; United States Steel Corporation: Pittsburgh, 1951.

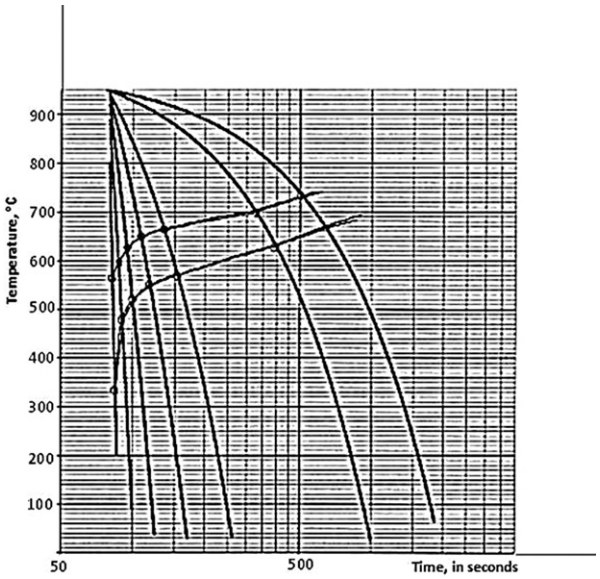


Figure 19 Continuous cooling transformation diagram of a low carbon steels constructed by dilatometric method.

due to phase transformation depend upon the transformation temperature, it is imperative that there will be a structural gradient in steels cooled continuously. Moreover it is pertinent to remember that phase transformation in many steels is mechanistically transient over a range of temperature, the complete transformation of parent phase takes place. This is particularly important for low carbon steels, where the mechanisms of austenite to ferrite transformation are different at different temperatures. Thus quite often a multiphase microstructure is obtained by continuous cooling of low carbon steels. However microstructural gradient is not desirable in respect of deriving uniform properties in the heat treating object. The shape of the CCT diagram determines if there will be uniformity of microstructure. In some alloy steel it is possible to get flat CCT diagram in both cases of transformation start and finish, which represent low carbon bainite and hence chances of microstructural gradient is least in this case. Whenever a decomposition of austenite takes place under continuous cooling, a number of mechanisms are operative for austenite to ferrite transformation depending upon the temperatures of transformation. For example, in low carbon high strength low alloy steel (HSLA) steel, progressively decreasing transformation temperature or equivalently the increasing cooling rate, envisages the transformation of austenite in the following sequence.

$$\text{Austenite}(\gamma) \rightarrow \text{Equiaxed ferrite}(\alpha_P) \rightarrow \text{Quasipolygonal ferrite}(\alpha_q) \rightarrow \text{Widmanstatten ferrite}(\alpha_w) \rightarrow \text{Massive ferrite}(\alpha_{\text{massive}}) \rightarrow \text{Granular bainite}(\alpha^0 B) \rightarrow \text{Acicular bainite}(\alpha_B) \rightarrow \text{Martensite}(\alpha_M)$$

However in the regime of CCT diagram where acicular bainite or martensites are formed, the transformation mechanism is practically same at all transformation temperatures, viz. martensitic transformation. This situation of microstructural gradient is of much greater concern for finite-sized samples. Whenever a finite sized sample is cooled from the austenite state to effect

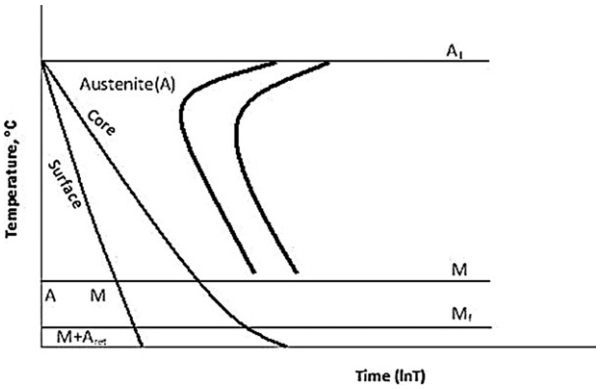


Figure 20 Diagram showing different cooling rates at surface and center of the workpiece.

phase transformation, the cooling rate at the surface and at the center of the sample ought to differ as shown in Figure 20.

The temperature difference at each time during cooling is dependent upon two important factors. One is the material and other is the external media used to cool the object. For the same material, cooling from the same austenitizing temperature but in different media like water and oil will result in different temperature differential between surface and center of the sample. So whenever it is required to avoid the nose of a TTT or CCT diagram in a heat treatment process, it is required to decide the cooling media for the same due to following reasons:

1. Different cooling media has different heat extracting ability from a specific stock of definite size, that is different quenching media have different severity of quench; it is further important to note that the cooling rate achievable from a quenching medium varies with the changing temperature of the sample during cooling. Thus severity of quench is a sole property of the quenching medium.
2. By virtue of heat transfer ability, different materials exhibit different responses to cooling in various quenching media. Also each material has its characteristic section sensitivity (i.e., variation of cooling rate at different places at any time). This implies that there is a sole material property which defines the ability of a material to avoid diffusional decomposition of the metastable parent phase. To get a reach to this material property, it is necessary to remove the effect of cooling rate on the ability of material to avoid the nose of TTT diagram of a material.

This inherent property of steel is called hardenability which describes the depth up to which a steel component is able to avoid soft pearlite transformation. The term hardenability originates from the fact that avoidance of the nose of CCT curve by a cooling rate higher than the CCR leads to the hardest possible phase in steel, which is martensite. This definition of hardenability is not universal. The idea of increasing the hardness of a material by avoidance of diffusional decomposition of high temperature parent phase is not generic. It is true that if a metastable solid solution is not allowed to undergo its due decomposition by way of diffusional means at relatively high temperatures, the solid solution will take chance to form more thermodynamically feasible alternative phase, through diffusionless shear transformation

mechanism. This type of transformation, martensitic transformation, takes place in a number of systems. For steel, the martensites are extremely hard. There are many systems like Cu–Zn–Al, Cu–Al–Ni, Ni–Ti, In–Th, where the martensite phase is very soft. The high hardness of iron–carbon martensites is ascribed to (1) solid solution hardening due to it being a supersaturated solid solution of carbon in body centered tetragonal structure, (2) dispersion hardening due to fine-scale precipitation of carbide due to auto tempering, (3) dislocation hardening due to martensite being internally faulted with dislocations, (4) hardening due to interaction between dislocations and distortion dipole produced in martensite due to asymmetric alignment of carbon atoms in the unit cell and finally due to fine crystal size. The suppression of solid state diffusional transformation by fast quenching is quite common in many systems; it is true that a rapid cooling to bypass the diffusional transformation (hence the nose of corresponding CCT diagram) results in the formation of a supersaturated solid solution. The supersaturated solid solution in iron–carbon system is hardest and hence this process is called hardening heat treatment. In other systems, the supersaturated solid solution may not be the hardest (e.g., Al–4 wt.%Cu) constituent, but this may give rise to hardening when heated to slightly higher temperature and held for preselected period of time.

However hardening of hypoeutectoid steel is carried out 50 °C above A_3 temperature and then it is soaked there for sufficient period of time as discussed earlier. The homogeneous austenite is then rapidly cooled with the aim to produce 100% martensite in the structure. In case of eutectoid steel, the steel requires a temperature of 780–800 °C for production of homogeneous austenite and then it is quenched.

An empirical relationship between the M_s temperature and alloying element content may be written as,

$$M_s(^\circ C) = 561 - 474(\text{wt. \%C}) - 33(\text{wt. \%Mn}) - 21(\text{wt. \%Mo}) - 17(\text{wt. \%Ni}) - 17(\text{wt. \%Cr}) \quad [1]$$

It is evident that carbon has the maximum effect to lower the M_s temperature. Thus for high carbon austenite in hypereutectoid steel, the depression of M_f temperature below room temperature will always yield some retained austenite in the quenched microstructure. This retained austenite will make the material softer at specific location, thereby rendering it to an inferior quality material.

2.1.5 Annealing

Annealing is the process of heating the object to single phase field followed by equilibrium cooling to aim at achieving equilibrium microstructures. Depending upon the purpose, various annealing types are carried out at different temperature. The temperatures used for various types of annealing operation are shown in Figure 21.

2.1.5.1 Full Annealing

Full annealing is carried out to achieve a microstructure predicted by the equilibrium phase diagram of the alloy system. Full annealing process involves heating hypoeutectoid and eutectoid steels 50 °C above Ac_3 and Ac_1 temperatures, respectively. The

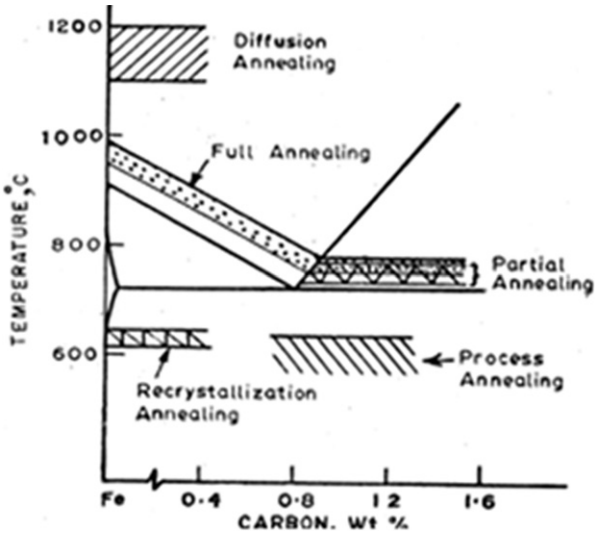


Figure 21 Diagram showing temperature ranges of different annealing process.

component is held for 1 h per 25 mm of section size and then subjected to very slow cooling. The rate of cooling should be as slow as possible and an example of industrially acceptable cooling rate to obtain near-equilibrium structure is 50 °C h^{-1}. Again, care must be taken to avoid decarburization especially in case of annealing high carbon steels. The aim of full annealing is to effect diffusional decomposition of parent phase, viz. austenite in case of steel, at as low an undercooling as is possible to be provided by the furnace. The microstructure in annealed hypoeutectoid steel consists of proeutectoid ferrite and pearlite whereas it is full pearlite in eutectoid steel (Figures 22(a) and 22(b)). Hypereutectoid steels are not ordinarily put to full annealing. The A_{cm} line is quite steep and full annealing of hypereutectoid steel attempting to produce completely homogeneous austenite necessitates heating the steel to a very high temperature, with associated risk of grain coarsening and decarburization. However full annealing of hypereutectoid steel is required if prior hot working is done at a very high temperature causing overheating and gain coarsening. Under such situation a judicious full annealing may result in partially refined grain structure. If cooling rate is high, network of proeutectoid constituents around the grain boundaries is likely to form; a slower cooling on the other hand may lead to the formation of separate ferrite regions in full annealed hypoeutectoid steel.

2.1.5.2 Isothermal Annealing

In case of isothermal annealing, steel is heated in the same manner as that in the case of full annealing. After austenitization the steel is rapidly cooled at a predetermined temperature and it is held there for sufficient period of time so that transformation of austenite becomes complete. A prior knowledge of TTT diagram enables to determine the time of holding at the isothermal annealing temperature. Isothermal annealing is advantageous as the total heat treatment time is considerably reduced yet obtaining comparable microstructure and properties. Isothermal annealing is particularly suitable for alloy steels which otherwise require at extremely slow

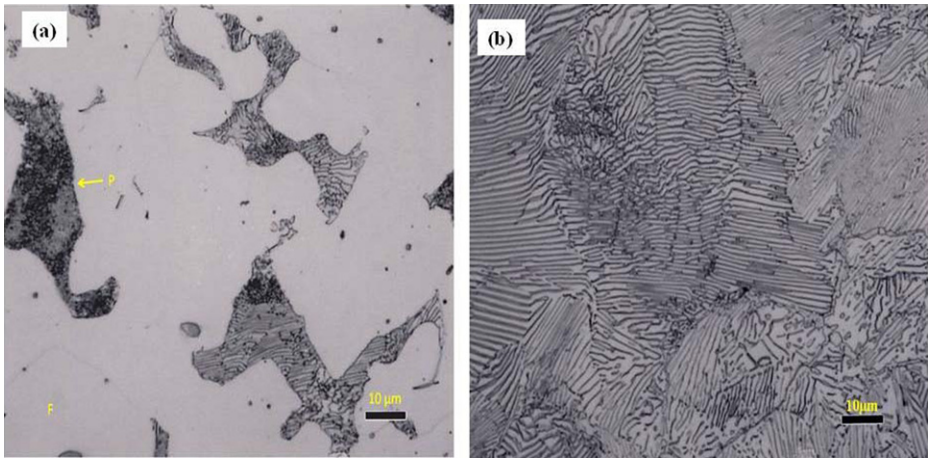


Figure 22 (a) Ferrite–pearlite microstructure of 1018 carbon steel annealed at 900 °C, (b) fully pearlitic microstructure of 1095 carbon steel annealed at 900 °C. Courtesy of George Vander Voort, USA.

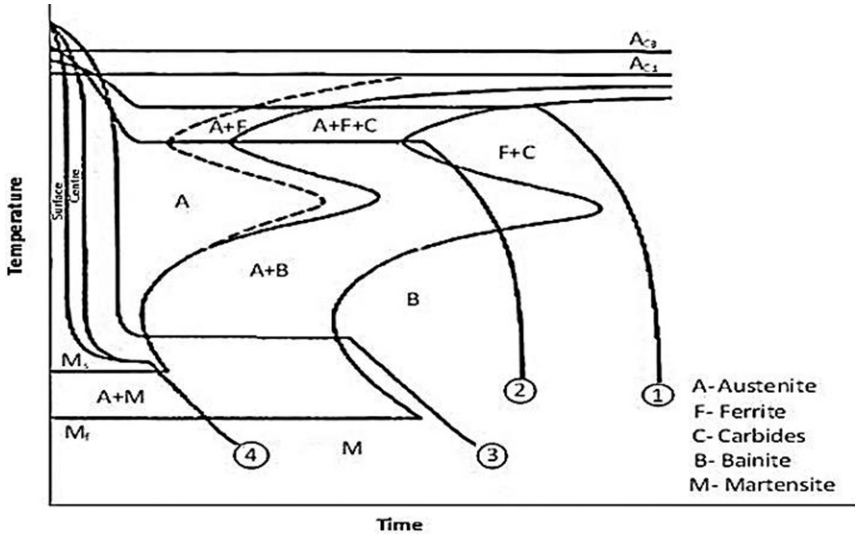


Figure 23 Isothermal annealing of alloy steel.

cooling in order to effect transformation involving the long range of migration of slowly moving atoms of the alloying elements. As evident from the **Figure 23**, object being heat treated is cooled rapidly after austenite is completely transformed to the desired phase that is pearlite.

Patenting is a specific isothermal annealing where the transformation of metastable austenite is effected just at the nose of the TTT diagram of the material under heat treatment. Normally patenting is carried to impart high strength to musical wires. A high carbon steel of nearly eutectoid composition is austenitized 15 °C above Ac_3 for hypoeutectoid and above Ac_1 for eutectoid composition (0.65–0.80). After producing homogeneous austenite rapid cooling is done in a salt bath kept at about 450–550 °C and held for complete transformation of austenite to fine ferrite–carbide aggregate. In accordance with the possible mechanism of transformation of austenite to fine ferrite–carbide aggregate, the microstructure may comprise of either fine pearlite or a mixture of fine pearlite and upper bainite. The patented rod is cold drawn to fine wire, to be used in musical instrument as combined microstructural and strain-hardening results in a very high strength of the wire.

2.1.5.2.1 Patenting

'Patenting' is a process of annealing which is generally employed in wire and rod manufacturing process. Patenting is normally carried out when extra toughening is required in steels containing 0.5 wt.% or higher amount of carbon. The annealing process in the name of patenting involves isothermal annealing of steels in a suitable salt bath at temperature near the nose of the TTT diagram. After austentizing the steel is cooled rapidly to the isothermal holding temperature viz. 550 °C. The object is kept at that temperature for sufficiently time so that complete transformation of austenite to fine pearlite is possible.[4] The objective of patenting is to produce very fine pearlite in the microstructure (**Figure 24**); since smaller inter lamellar spacing of pearlite envisages high toughness of steel it is applied to medium- and higher-carbon grades of steel, rod, or wire products.[5]



Figure 24 1080 steel isothermally annealed at 482 °C (patenting). Courtesy of George Vander Voort, USA.

Sometimes drawing and patenting steps are successively repeated for obtaining the desired size and strength level. Appropriate tailoring of composition may enable complete transformation of austenite to fine pearlite by air cooling; this alleviates with the use of salt bath or molten lead bath which is health hazardous. Air patenting is less expensive than lead patenting but results in pearlite of varying inter lamellar spacing which is not desirable. For a less, hardenable steel possibility of formation of proeutectoid ferrite may not even be precluded.

The steels to be used for manufacturing suspension bridge wires demand extra strengthening after patenting; for this hypereutectoid steel with minor addition of chromium ~0.5 wt. % is now a day's employed. Chromium induces a higher degree of refinement in interlamellar spacing of pearlite in hypereutectoid chromium bearing steel, even down to 70 nm.[6–8] Also the carbide lamella becomes shorter and discontinuous. When steel with such fine pearlitic microstructure is subjected to heavy deformation during wire drawing cementite particles decompose. The ferrite crystals get supersaturated with carbon. Complete decomposition of cementite is envisaged in chromium bearing hypereutectoid steel. Excess carbon precipitated on dislocations within the resulting ferrite not only increases the strength of the steels but also its work hardening rate quite significantly. This aids in suppression of delamination. Heavy drawing of such steels reportedly leads to a super saturation of ferrite up to 0.5 wt.% carbon with consequent UTS being about 1500 MPa. The degree of decomposition of cementite depends upon the rise in temperature during wire drawing; the adiabatic heating in heavily drawn wire causes decomposition of cementite with concurrent deposition of carbon atoms at the dislocations which are pinned by the carbon atoms; as a result of consequential strain aging effect yield strength of the steel is significantly increased. The microstructure of a 1080 carbon steel is in Figure 24.

The decomposition of cementite phase, θ during heavy drawing has been ascribed to elastic interaction between dislocations and C-atoms.[4,8] It is postulated by one school of thought that heavy deformation during wiredrawing leads to refinement of cementite. Upon continued deformation, the slip steps is formed in θ; these two events lead to increase in interfacial areas and hence the surface free energy. The dictates of Gibbs–Thomson effect in respect of urge to lower surface energy results in ultimate decomposition of cementite. The state of C-atoms in α, may provide clues to such decomposition of cementite; if carbon is present at dislocations, strain aging effect will enhance the yield strength quite significantly. On the contrary, if carbon is assumed to cause super saturation of ferrite solid solution hardening shall be the chief hardening mechanism with concurrent change in the lattice parameter. Equally the other proposals that carbon segregates at the prior α–θ interfaces,[5] or that carbon precipitates out in the form of carbide on to the dislocations[9] have grounds to attract due attention. The observation that no significant change in lattice parameter in noted in the process may cast doubt on the ferrite super saturation model.

There are reports[10] that heavy deformation during forging of white cast iron led to collapse of cementite lattice and that elemental carbon released in huge quantity leads to graphitization. High carbon steel for wire drawing contains much less proeutectoid cementite as compared to ledeburitic cementite in white cast iron grown further in size due to precipitation of proeutectoid cementite. The author hypothesizes that heavy deformation during wire drawing leads to collapse of cementite and the concurrent diffusion of carbon atoms from cementite–ferrite boundary to intragranular dislocations in ferrite takes place at high temperature due to local adiabatic heating. However, being energetically cheaper, the carbon atoms prefer to segregate at the dislocations in the form of metastable cementite and not in elemental form. In this case one will find that carbon content of ferrite is high without tangible rise in lattice parameter. All observations made so far are also compatible to the hypothesis. Nevertheless it is of paramount importance to study the nature of particles present at the dislocations within ferrite; the possibility of formation of ε-carbide and/or chromium bearing carbide of higher carbon content must not be ruled out especially in situation of high strain rate deformation.

2.1.5.3 Incomplete Annealing or Intercritical Annealing

Incomplete annealing aims at relieving internal stresses thereby improving machinability of the steel. Normally this type of annealing is carried out by heating the stock just above Ac_1 and then holding there for sufficient time. Finally it is cooled slowly within the furnace. It must be understood that this type of annealing does not eliminate proeutectoid ferrite or cementite from the microstructure at the annealing temperature. Mainly incomplete annealing of such type is applied to hyper eutectoid steel. Annealing of hypereutectoid steel produces the microstructure with cementite network enclosing the pearlitic region. Whenever incomplete annealing is carried out in eutectoid steel, the effect of full annealing is realized because the annealing temperature lies in the austenite phase field.

Intercritical annealing of hypoeutectoid steel followed by rapid cooling gives rise to a duplex ferrite–martensite structure. This type of heat treatment for low carbon micro-alloyed steel is quite popular in recent years. The steel is held at a convenient intercritical temperature till the time it is equilibrated between higher carbon austenite of low volume fraction and low carbon ferrite. Upon rapid cooling from the intercritical



Figure 25 (a) Microstructure of intercritcally annealed 4140 alloy steel showing ferrite and martensite (Courtesy of George Vander Voort, USA) and (b) microstructure of hypereutectoid steel annealed above A_{cm} temperature followed by slow cooling.

annealing temperature, austenite transforms to martensite. This biphasic structure, where martensitic island are interspersed with in soft ferrite matrix strengthens the material significantly. Figure 25(a) delineates ferrite–martensite structure in 4140 steel intercritically annealed at 775 °C within $\gamma + \alpha$ phase field followed by water quenching.

The yield–tensile ratio of this steel is about ~0.5; this HSLAs possess excellent deep drawability and is considered to be a very good automotive material.

Again annealing of hypereutectoid steel is essentially an intercritical annealing as it is austenitized above A_1 temperature in the two-phase field γ + cementite and then furnace cooled. This makes the proeutectoid cementite agglomerated or spheroidized. On the contrary if it is annealed by austenitizing at temperature above A_{cm} and then slow cooled to room temperature, proeutectoid cementite forms a network along prior austenite grain boundaries. These types of microstructures promote intercrystalline fracture and thus make it brittle (Figure 25(b)). Annealing of hypereutectoid steel in two-phase field breaks the continuous cementite network by agglomeration into spherical carbide particles. The associated reduction in austenite–cementite interfacial area acts as the driving force for the process.

2.1.5.4 Spheroidizing Annealing

Spheroidizing annealing is meant for obtaining granular cementite in a ferrite matrix. The lamellar pearlite of high carbon steel is converted to granular morphology by way of heating the steel just above the critical temperature, 740–750 °C and then holding at that temperature for considerable period of time. This is followed by a slow cooling of the order of 25 °C per hour down to a temperature of 600 °C. To obtain granular cementite the annealing temperature should not be too high above Ac_1 and cooling rate should be so slow as to allow decomposition of austenite to be completed at a low degree of supercooling. This enables the cementite particles to attain globular morpohology. High carbon steels are conducive to such spheroidizing annealing temperature when heat treatment is carried at a temperature slightly above Ac_1 temperature; however spherodization of cementite particles is also aimed in relatively lower carbon containing alloy steels as a pretreatment for facilitating production of homogeneous austenite during the subsequent autenetization. Instead of holding the steel just above Ac_1 temperature, thermal cycling across Ac_1 temperature for a number of times may also give rise to spheroidization of carbides. During thermal cycling across Ac_1 the steel is held at a temperature just below Ac_1 for predetermined period of time followed by gentle heating. Repetition of isothermal cycles will produce the desired spheroidized morphology. In the heating stage of thermal cycling carbides tend to dissolve but reappear in the following cooling cycles. Attempts to effect phase transformation with such a low driving energy entices the system to assume spheroidal morphology; spheroidization diminishes the specific surface area and thus overcome the constraint due to surface free energy term in the target phase transformation. Implicitly the spheroidal structures are softer with good machinability. As stated earlier a microstructure with spheroidal cementite aids in production of homogeneous austenite. Figure 26 exhibits spheroidized cementite in hypereutectoid steel containing 1.05 wt.% carbon steel.



Figure 26 Microstructure of steel after spheroidizing annealing. Courtesy of George Vander Voort, USA.

Inter critical annealing of hypereutectoid steel gives rise to globular cementite and thus leads to the formation of granular

pearlite. Within the intercritical region, undissolved cementite particles tend to globularise due to prolonged heating at the annealing temperature. Spheroidization of particles held at elevated temperature is a natural event. Spheres have minimum specific surface area as compared to other shapes and hence spherodization of a micro-constituent leads to the diminution of its surface free energy. Thus the process of spherodization enables the system to lower its overall energy. At the temperature of inter critical annealing diffusion is not a constraint; this favors the kinetics of spheroidization. During slow cooling the carbon content of austenite will gradually decrease down the A_{cm} line. So rejection of carbon in the form of cementite may take place on to the existing cementite particles as this will reduce the requirement of supply of energy for nucleation of new phase. When austenite is cooled just below the Ac_1 line, austenite needs to undergo eutectoid reaction which is essentially a discontinuous precipitation where cementite is the leading nucleating phase.

Eutectoidal cementite will form mostly through deposition on the existing cementite particles although nucleation of new cementite on the prior austenitic grain boundaries is not excluded. In any case this cementite will have a better scope of equiaxed growth and hence the overall microstructure will consist of globular pearlite.

Spheroidization is also carried out by holding the object under heat treatment just below A_1 temperature. Prolonged holding at this temperature effects spheroidization of cementite particles, embedded in ferrite matrix. However this method of spheroidization is rather slow. It is not out of place to mention than the equilibrium shape of the particle is not strictly spheroid but ellipsoidal. Particles assume spheroidal morphology due to the urge to attain low energy state is reasoned out by the fact that in solid state transformation strain energy is equally important.

Maximum reduction in strain energy is not concurrent with spheroidal growth of the particle. Rather growth of particles along specific direction reduces the lattice disregistry, and hence the strain energy. However continued nonspherical growth to reduce strain energy is in opposition toward attainment of stability in a system; this is because the nonspherical growth increases the surface area and hence the surface free energy. Thus a situation comes, when urge to reduce surface energy takes over and a spheroidization process sets in. This continues till strain energy term prohibits spherical growth and thus the aspect ratio of the particle swings across a value near to but less than unity.

2.1.5.5 Homogenization or Diffusion Annealing

Homogenization or diffusion annealing is usually carried out for heavy and intricate castings which are prone to significant intercrystalline segregation. Homogenization annealing is carried out to remove the inevitably occurring chemical inhomogeneity in heavy alloy steel casting. In reality most of steel casting produced under moderate cooling rate as in sand molds experience segregation of alloying elements along the cell boundary of the cellular dendritic structure. To ensure microstructural homogeneity diffusion annealing is carried out at high temperature as 1150 °C so that appreciable diffusion of atoms of the alloying elements takes place easily. This entails the possibility of achieving austenite of uniform composition. However homogenization annealing as demanded to be carried out at such a high temperature is liable to produce coarse-grained microstructure along with formation of scales at the surface of the casting. Therefore homogenization annealing is followed by subsequent heat treatment process to incorporate the desired set of properties in the steel castings. These heat treatments may be conventional full annealing, normalizing or normalizing followed by tempering depending upon the specified property requirement.

2.1.5.6 Recrystallization Annealing

Recrystallization annealing is a process of heating cold-worked steel above the recrystallization temperature, holding at that temperature for a predetermined time and then followed by normal air cooling. Recrystallization annealing is carried out for removing strain-hardening effect of multipass cold-working operation. In such case, recrystallization annealing is an intermediate process to facilitate further deformation by cold working. On the contrary, recrystallization annealing is also employed as a final heat treatment where removal of cold-working effect with replacement by fine equiaxed strain-free grains is derived. Proper selection of time and temperature of annealing enables to achieve fine-grained uniform microstructure comprised of recrystallization. Sometimes a cold-worked structure is subjected to annealing at a temperature less than the recrystallization temperature with the purpose of rearranging dislocations to some low energy configurations. This is known as a recovery process and is accomplished by suitable annealing process.

When metals and alloys are cold worked, that is when these are subjected to plastic deformation at a low temperature, say, less than 0.4 T_m (T_m is the melting point of the concerned metal or alloy in degree Kelvin), a portion of energy spent for cold-working remains stored within the material in the form of crystal defects. The amount of stored energy ranges from a low value to around 10% of the total energy spent in a deformation process. The work of deformation leads to generation of point defects and dislocations. These crystal defects are associated with strain energy and the creation of crystal defects during deformation is the manifestation of stored energy in cold-worked materials. Obviously the magnitudes of stored energy increases with increasing amount of deformation up to a certain saturation value which is different for different materials and deformation condition; however in most practical cases, the maximum of stored energy does not exceed 15% of the energy spent in cold working and the rest energy is dissipated in the form of heat.

The above stated stored energy drives the relaxation processes during subsequent annealing. Upon annealing, the stored energy is released through different recovery processes which may occur in steps. The process involved during the release of stored energy is called recovery, recrystallization, and grain growth. During recovery process the point defects viz. vacancies are annihilated at the sinks like grain boundaries, or it may annihilate at edge dislocation affecting its climb. The reduction in density of point defects due to recovery process leads to reduction in resistivity of the metals and alloys. Resistivity is due to incoherent scattering of electrons at the

scattering centers like point defects. Also during recovery process, the dislocations generated by cold working either get annihilated or reorganize themselves into low energy arrays. Annihilation of dislocations takes place where dislocations of opposite sign come together either through slip or through climb. Normally the dislocations remaining in excess after annihilation would try to reorganize themselves into low energy array for the purpose of lowering the overall energy of the system. One example of such process is what is termed as polygonization. When a crystal is bent, the excess positive edge dislocation may lie along the active slip planes in disorderly fashion. When a row of edge dislocation lie on a specific plane, its total strain field in quite high; if the dislocations lying on different vertical planes are arranged in disorderly fashion, the overall strain energy due to dislocations in bent crystal becomes quite high. However, if the bent crystal is heated, the dislocation climb is possible and a regular arrangement as shown in Figure 27 is realized.

When the dislocations are rearranged in the manner as shown in Figure 27, the tensile and compressive component of strain field due to adjacent dislocations will tend to cancel each other; as a result total strain energy of the system will be reduced. The region of crystal in between any two lines of dislocations is essentially devoid of dislocations and thus becomes a strain-free region. These strain-free regions within the crystal are bound by thin arrays of dislocations, describing a small degree of misorientation across the regions; considered as boundary, it is called a sub grain boundary. During recovery of cold-worked crystals, mechanical and physical properties are changed. The resistivity decreases with increase in time or temperature till a saturation value is attained (Figure 28).

A typical microstructure containing sub grain boundaries is shown in Figure 29.

When annealing is carried out at temperatures above 0.4 T_m a different recovery process takes place. During this process, highly strained grain within cold-worked material (characterized by high dislocation densities) is replaced by the strain-free grains. This process of relaxation is called recrystallization. Recrystallization is a nucleation and growth type process as initiated by the formation of nuclei of strain-free grains which, subsequently, grow by migration of its high angle boundaries. The growth of strain-free crystals continues in all directions until there is impingement from the surrounding crystals. Being a thermally activated process, recrystallization is temperature and time dependent; also the process is influenced by

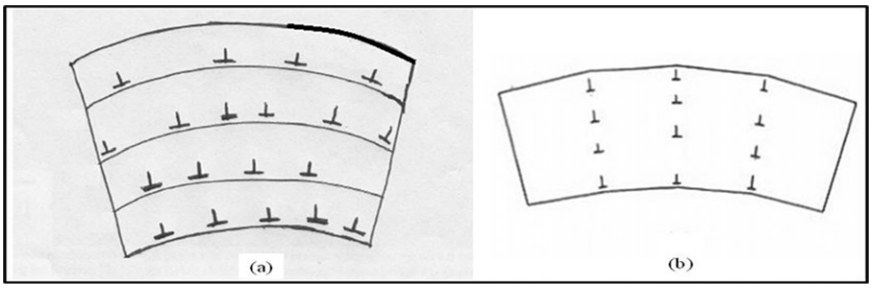


Figure 27 Recovery of crystal showing rearrangement of dislocations in bent crystal (polygonization); (a) shows irregular arrangement of dislocations and (b) shows rearrangement to low energy array.

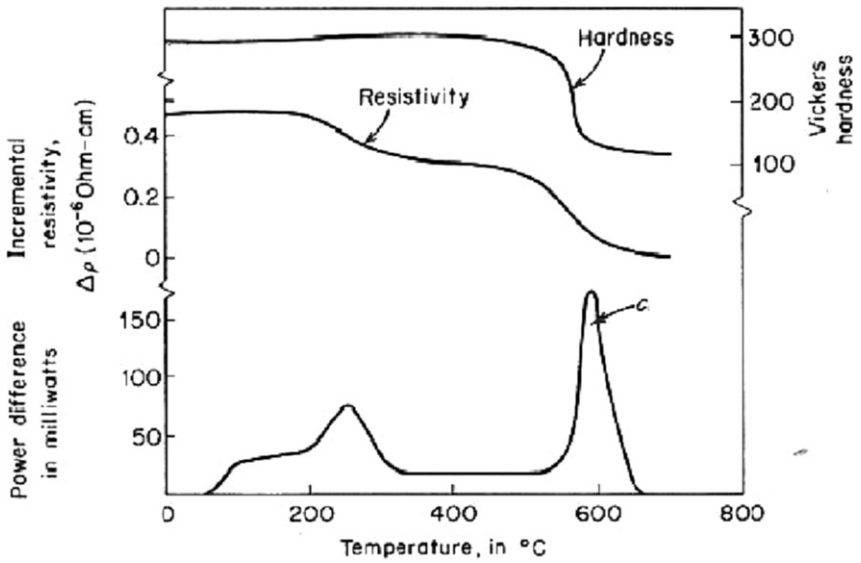


Figure 28 Variation of properties for cold-worked nickel due to recovery annealing. Courtesey of J.E. Indacochea University of Illinois at Chicago, USA.

the amount of deformation. The following observations can be made in any recrystallization process.

1. A minimum amount of deformation is required to effect recrystallization at a particular temperature.
2. Time required to complete recrystallization increases as the temperature of recrystallization is lowered.
3. With increasing deformation percent, the temperature to start recrystallization is decreased.
4. Recrystallized grain size becomes smaller with larger percentage of deformation at a particular temperature.
5. New strain-free grains don't grow into deformed grains.
6. A metal or alloy with fine initial grain produces smaller recrystallized grain.

The recrystallization kinetics in metals and alloys shows typical sigmoidal behavior as shown in **Figure 30**.

The same figure demonstrates that increase in recrystallization temperature reduces the time to complete recrystallization. It also takes less time to initiate the process of recrystallization.

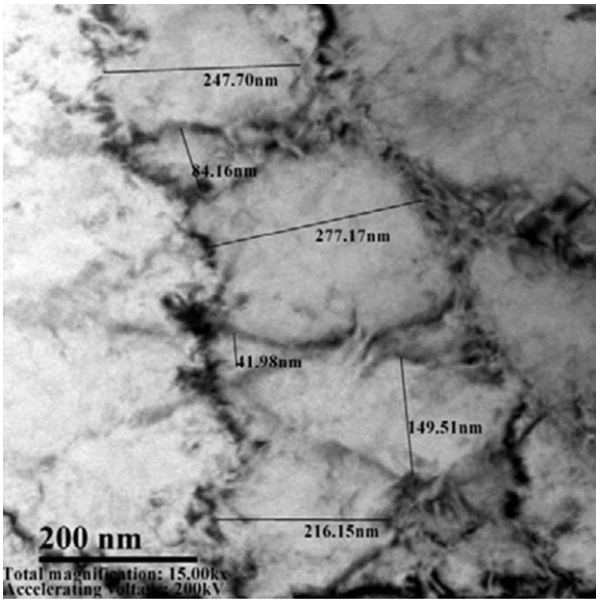


Figure 29 TEM of 0.05C–1.5Cu–1.5Mn steel showing subgrain boundaries. Courtesy of Material Research Centre, MNIT Jaipur, India.

Several mechanisms of recrystallization are proposed. There can be different dislocation density across a grain boundary; the grain boundary is not strictly planar but it is perturbed with transient wavy character. A small bulged-type region at grain boundary may move into region of high dislocation density. Grain boundary acts as sinks for dislocations and annihilates them; the creation of such small dislocation free region lowers the local free energy and hence becomes a stable nucleus. The nucleus then grows to form a strain-free grain (**Figure 31**).

The other mechanism of recrystallization is the coalescence of sub grains to form a region bound by high angle boundary and hence a strain-free grain is formed under the driving force of lowering of strain energy due to replacement of a number of sub grain boundaries by a single boundary of large misorientation.

While recovery process reduces the electrical resistivity, recrystallization leads to reduction of hardness values with progressive diminution of dislocation density. For a fine recrystallized grain structure both strength and ductility are simultaneously improved. The change in properties of a heavily cold-worked metal subjected to isothermal annealing above recrystallization temperature is shown in **Figure 32**.

Further annealing at still higher temperature leads to grain growth. The driving force for grain growth is lowering of

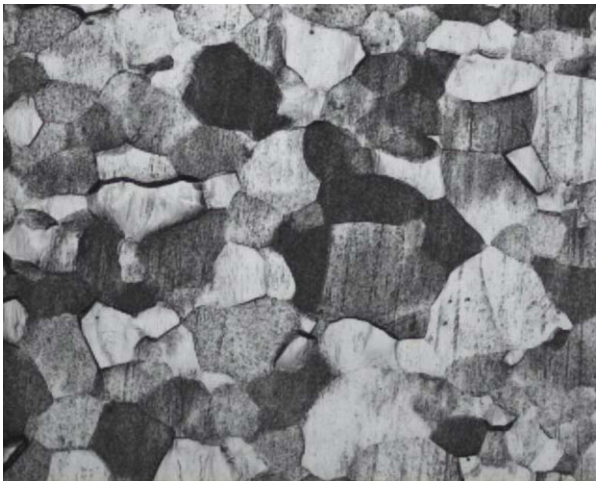


Figure 31 Recrystallized structure of IF steel. Courtesy of Material Research Centre, MNIT Jaipur, India.

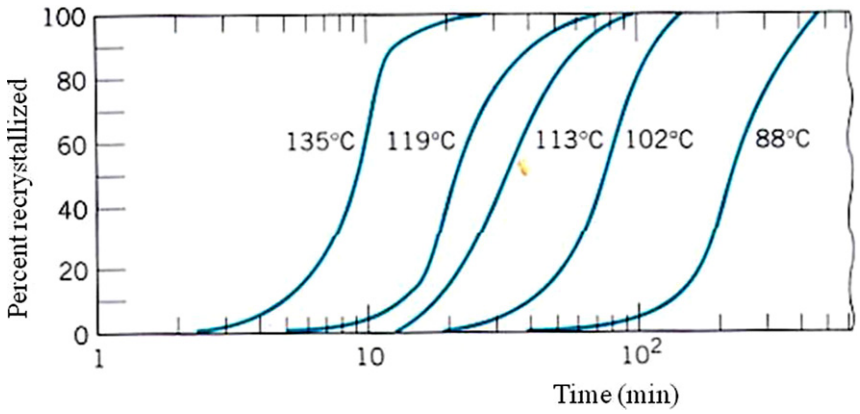


Figure 30 Sigmoidal curves to show recrystallization kinetics. Courtesey of J.E. Indacochea University of Illinois at Chicago, USA.

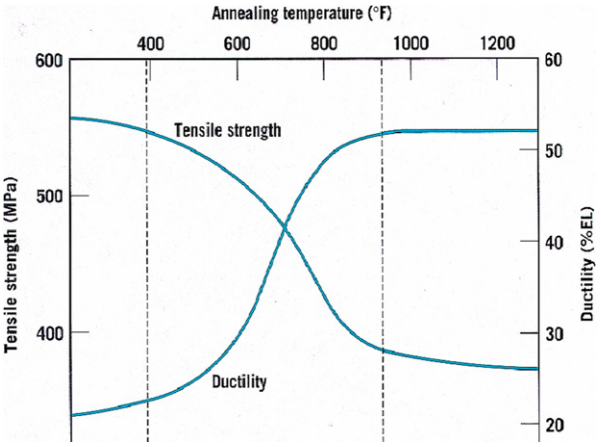


Figure 32 Variation of mechanical properties during recrystallization. Courtesy of J.E. Indacochea University of Illinois at Chicago, USA.

surface free energy. Anything which aids grain boundary movement shall accelerate grain coarsening.

During recrystallization annealing proper control of recrystallization temperature and time is required. After the completion of recrystallization, the process must be stopped; else grain coarsening will set in.

2.1.5.7 Subcritical Annealing

Subcritical annealing is generally carried out at a temperature below the lower critical temperature, A_1. There are a number of purposes for which subcritical annealing is considered to be a useful heat treatment operation. Apparently subcritical annealing is not liable to cause any phase transformation. However it will be demonstrated in the following discussion that in certain cases phase transformation may be realized in subcritical annealing.

1. Indirect second stage graphitization of cast iron is a subcritical annealing process, where cast iron with pearlitic matrix is heated to an elevated temperature below A_1 temperature. Upon holding for a prolonged time, the pearlitic cementite may undergo decomposition to form graphite, leaving behind ferrite in the matrix. Thus complete second stage graphitization will lead to the formation of ferritic cast iron, which is a cast iron where graphite particles (flakes or other shapes) are contained in a ferrite matrix; this makes the cast iron soft and ductile.
2. Subcritical annealing is carried out in large and intricate castings to get rid of internal stresses. It is also carried out after welding of some steels where there is a chance of formation of martensite at the heat affected zone. The welded joints are subjected to both thermal stress and stress due to volume change accompanying martensite transformation.

Subcritical annealing relieves the thermal stress by dislocation annihilation at the grain boundaries and as well it removes transformational stress by way of tempering martensite to make it decompose to fine ferrite–carbide aggregate. The microstructure of 0.10C–2Mn steel subjected to subcritical annealing at 710 °C is shown in **Figure 33**.

Sometimes subcritical annealing is employed to drive away the dissolved harmful gases within the steel component. For example, in cases where hydrogen is known to remain dissolved in steel in excess of limit of tolerance, subcritical annealing at 400 °C is carried out. Diffusivity of hydrogen is quite high at this temperature, and so it diffuses out quite easily; thus chances of hydrogen embrittlement is greatly reduced.

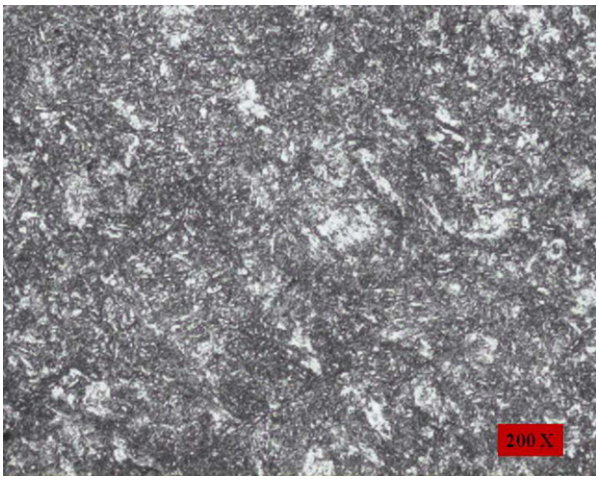


Figure 33 Microstructure of subcritically annealed steel. Courtesy of George Vander Voort, USA.

In certain cases subcritical annealing or high temperature tempering just below the lower critical temperature is employed to improve upon the sub-ambient impact strength.

2.1.6 Normalizing

Normalizing is the heat treatment process, which consists of heating the object to the austenitization temperature, holding it to produce homogeneous austenite and then allowing to be cooled in still air. Normalizing tends to imply a normal cooling of austenite to produce stronger steel in much shorter time than what can be obtained by full annealing. Due to the fact that normalizing refines the microstructure of the steel thereby improving its toughness, it is quite often employed as the final heat treatment. Normalizing is carried at a temperature 50 °C above upper critical temperatures (A_3 and A_{cm}). Being austenitized at higher temperature (20 °C) than annealing, normalizing produces greater homogeneity of austenite but at a lower temperature than homogenizing annealing and in shorter time. Quite often grain size becomes rather large after hot working; normalizing of such coarse-grained hot work material gives rise to formation of fine-grained austenite which upon air cooling produces small ferrite grains and fine pearlite in the microstructure of hypoeutectoid steels. This type of microstructures of greater uniformity helps to achieve superior mechanical properties. For example, when medium carbon steels are forged high temperature like 1100 °C, the size of recrystallized austenite grains is quite large due to adiabatic heating; the final microstructure is also very coarse (**Figure 34(b)**). Moreover distribution of pearlite and ferrite in its microstructures is nonuniform and thus the forged steel may not possess good and uniform mechanical properties. Hence it is imperative to suitably heat treat the forged product for refinement of its microstructure;

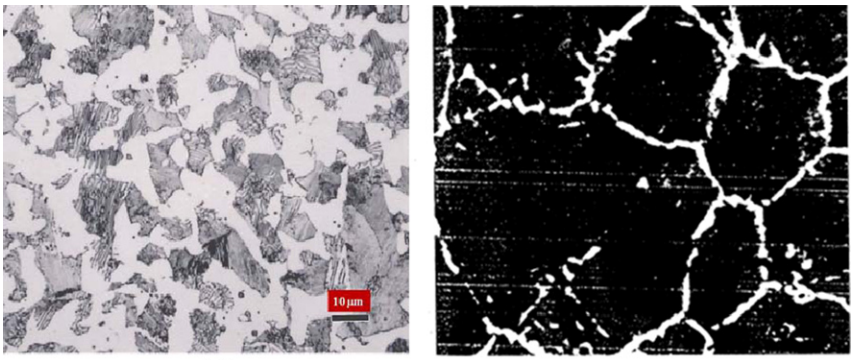


Figure 34 Microstructure of (a) 0.4 C–0.6Mn steel under normalized condition (Courtesy of George Vander Voort, USA) and (b) microstructure of 0.5 wt.%C steel forged at 1100 °C and cooled in air.

normalizing of forged steel can lead to desired structural refinement thereby enabling to produce fine uniform ferrite–pearlite structure. Due to relatively rapid cooling, the transformation of austenite takes place at a lower temperature, around 600 °C. The cooling rates superimposed on a CCT diagram of eutectoid steel qualitatively describe the difference in transformation behavior between annealing and normalizing. The properties of the steel casting are made improved by normalizing operation. It is used to remove micro-segregation in steel castings producing thereby a homogeneous structure. In hypereutectoid steel normalizing is carried out above A_{cm} temperature; this insures dissolution of carbides which aids in removal of carbide network which might have developed in prior processing. Normalized structure is highly responsive to spheroidizing treatment. Quite often normalizing is used as a preceding treatment to hardening operation, which requires a uniformly homogeneous structure without any structural gradient. If there is a structural gradient in steel before being subjected to hardening operation, the hardened steel will yield nonuniform hardness consisting of localized soft and hard spots. Well-normalized steel enables to overcome this difficulty. Air cooling is faster than furnace cooling and so normalizing heat treatment envisages austenite decomposition at a lower temperature. The resultant microstructure is significantly different from that obtained by full annealing. A lower temperature of transformation during normalizing reduces the critical nucleus size and the energy of nucleation of proeutectoid ferrite. So grain size of ferrite formed due to normalizing is smaller than the annealed steel. Again due to faster cooling formation of equilibrium amount of ferrite is not tenable. Thus the amount of proeutectoid ferrite is less than its annealed counterpart. In contrast with furnace cooling, equilibrium is not attained at any stage of air cooling during normalizing. So ferrite contains carbon in excess of equilibrium amount. Similar reasoning applies to austenite to pearlite transformation. Lower transformation temperature envisages higher density of operating nuclei for pearlitic transformation. This leads to decrease in the size of pearlite colonies. At the same time the interlamellar spacing of pearlite is reduced due to lower transformation temperature. Since amount of proeutectoid ferrite is reduced, the amount of pearlite is correspondingly increased as a consequence of shift of eutectoid point toward left upon faster cooling. Thus when compared with the achievable microstructure by annealing hypoeutectoid steel, normalizing results in decrease of ferrite grain size, increase of carbon content of ferrite, decrease in its amount. All these factors increase the hardness and strength of the steel. Again normalizing is liable to produce higher amount of pearlite with smaller colony size and interlamellar spacing. All these increases strength and hardness of the steel. Thus normalized steel is structurally finer than annealed steel and is stronger than the annealed variety. Strengthening of hypoeutectoid steel due to normalizing improves the machinability. The microstructure of normalized 1045 carbon steel is shown in Figure 34.

Low carbon mild steel is quite soft and ductile in the annealed state. Therefore chips of this ductile material get adhered to the tool tip making the machining quite difficult. Higher becomes the depth of cut, more would be the removal of material and the chances of tool tip jamming with adherent ductile chip will increase. On the contrary, normalizing makes the steel strong and relatively less ductile; this entails the scope of relatively brittle chip formation and chips can easily get away from tool tip. This ultimately improves machinability. Steel compositions may be suitably tailored so that normalized itself can harden the steel or can even alleviate with the conventional hardening and tempering heat treatment, yet achieving equivalent or better mechanical properties. For the advantages which can be accrued from normalizing steel the recent efforts to make use of normalizing as the final heat treatment process of new generation steels is noteworthy.[11–13]

2.1.6.1 Distinctions between Annealing and Normalizing Purpose

Annealing is a widely used heat treatment operation and is generally carried to refine the microstructure of materials and hence to improve its ductility. Annealing also aims to relieve internal stress, to eliminate micro-segregation in cast material for obtaining uniform grain structure, and to suitably modify the microstructure when needed for a subsequent heat treatment processes.

In case of annealing, cooling rate is extremely slow and almost equilibrium microstructure is obtained. In contrast, normalizing heat treatment employs air cooling which also produces near-equilibrium microstructure but of a smaller grain

size compared to annealing. Thus for the same composition of steel, normalizing produces stronger and tougher steel than what can be obtained by annealing. In certain cases of high hardenability steels, normalizing may lead to the formation of nonequilibrium martensite phase and in that case, the steel is said to have been air hardened.

Annealing serves identical purposes for both ferrous and nonferrous metals and alloys. Air cooling may be done in nonferrous metals and alloys to avoid the possibility of grain coarsening due to slow cooling in annealing operation; however, air cooling of nonferrous materials is not termed normalizing. Air cooling may be carried out in nonferrous alloys only when there is no chance of precipitation of solute-rich phase. If an alloy contains high amount of solute dissolved at elevated temperature, and if the solubility of solute is appreciably lower at room temperature, the alloy ought to be cooled quite fast after annealing; this is because, the slow cooling say in air may lead to precipitation at the grain boundaries of matrix alloy; these grain boundary precipitates, enriched with solute make the alloy vulnerable to premature intercrystalline failure.

In case of annealing the cooling rate is extremely slow and the rate of cooling may be same at all points across various section of the component under heat treatment. This implies that annealed material is structurally isotropic. This insures better uniformity in mechanical properties in annealed components. On the contrary, in normalizing the nonequilibrium cooling rate is experienced and hence in this case, microstructure may be different at different locations of the same component. This in turn results in nonuniformity in mechanical properties across various sections of the same component. Annealing employs a slower cooling rate; this implies higher residence time of the components at higher temperatures. Therefore the chances of grain coarsening is rather high during annealing; however, chances of grain coarsening is relatively less in normalizing due to its higher cooling rate which insures that less time is available for grain growth. Hardness of normalized components is higher than its annealed counterpart; this aids in improving machinability for very low carbon steel. However medium and high carbon steels have better machinability in annealed conditions. Due to discontinuous chip formation in normalized low carbon steel, the surface finish after machining of normalized component is better than when it is annealed. In a nutshell the similarity and difference between annealing and normalizing is summarized as:

Similarities

- Both the process are carried out in fully austenite state for hypoeutectoid and eutectoid steel.
- Heating rate and soaking time for both the process are identically selected.
- Microstructures consist of diffusional transformation product of austenite but finer in normalized steel.

Differences

- For hypereutectoid steel complete austenitization is needed in normalizing treatment whereas its annealing requires holding within $A_1 - A_{cm}$ but for which cementite network may form around austenite grain boundary making the steel very brittle.
- Annealing employs equilibrium cooling whereas cooling due to normalizing is nonequilibrium.
- Normalizing temperature of hypoeutectoid and eutectoid steel is 20 °C higher than the corresponding annealing temperature; this insures structural fineness and compositional uniformity in normalized steels.

Moreover, the microstructural distinction between normalized and annealed plain carbon steels reveals the difference between mechanical properties achievable in them.

It is understood that when hypo eutectoid steel of low carbon content, say 0.20 wt.%, is annealed, its microstructure consists of about 25% pearlite and 75% ferrite; as evident from equilibrium diagram, the carbon content of ferrite is very small. When the same steel is subjected to normalizing the following microstructural changes take place.

1. The grain size of ferrite becomes smaller due to lower temperature of transformation of austenite. This results in higher magnitude of undercooling; hence less critical nucleus size is envisaged. This leads to the formation of higher number of effective nuclei and hence fine-grained ferrite is achieved in its microstructure.
2. The carbon content of ferrite will be higher than that in the annealed samples. This is due to the fact that a fast cooling provides less time for diffusion of carbon. Hence equilibrium is not attained. This retains more carbon in ferrite.
3. The amount of ferrite is less than that in the annealed sample owing principally to less time available for the formation of proeutectoid ferrite, which is a diffusional process and is time dependent.
4. The amount of pearlite is higher than the annealed sample.
5. The colony size of pearlite is less than that in annealed sample because a lower transformation temperature aids in formation of higher number of pearlite nuclei.
6. The interlameller spacing of pearlite is smaller in normalized steel sample than that in annealed sample. The changes in the microstructures are shown in **Figures 35(a)** and **35(b)**.

Each of the above changes in microstructure is brought about by faster cooling in normalizing; this results in enhancement of strength and toughness. Thus normalized component is always stronger and tougher than the annealed component. The difference between the properties of annealed and normalized steels are furnished in **Table 1**.

2.1.7 Hardening

Hardening is the heat treatment process by which the hardness and hence the strength of a material is increased. Different types of hardening processes are employed in different situations. There are cases of age hardening where the material is heated to get a homogeneous single phase solid solution which is cooled very fast from the high temperature and in the process a supersaturated solid solution is obtained. The super saturation is relieved by precipitation of solute-rich phase mostly in certain sequences where coherent GP zone formation is followed by a series of precipitate formation; the precipitates in their initial stages of formation are either coherent or semicoherent with the matrix. Equilibrium incoherent precipitate is

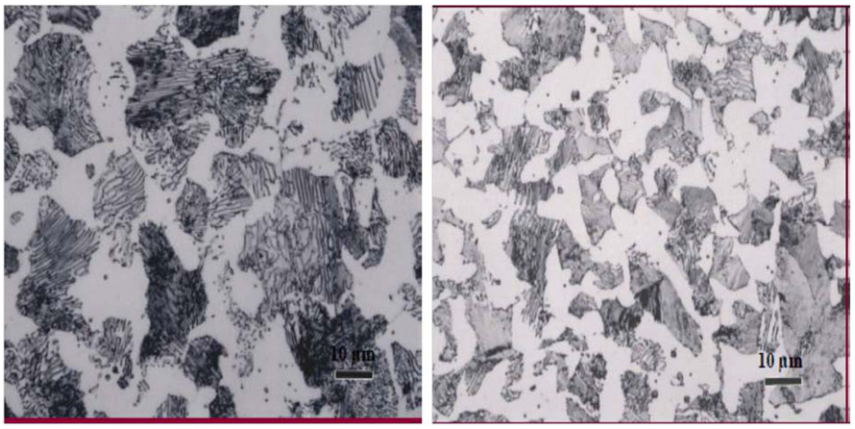


Figure 35 (a) 1045 Steel annealed from 900 °C and (b) 1045 steel normalized from 900 °C. Courtesy of George Vander Voort, USA.

Table 1 Comparison of mechanical properties of annealed and normalized steel

Carbon %	*Yield point*	*Tensile strength*	*Elongation*	*Reduction in area*
	MPa	*MPa*	*%*	*%*
Normalized				
0.01	179	310	45	71
0.20	310	441	35	60
0.40	351	586	27	43
0.60	413	751	19	28
0.80	482	923	13	18
1.00	689	1048	7	11
1.20	689	1054	3	6
1.40	661	1020	1	3
Annealed				
0.01	124	324	47	71
0.20	248	255	37	64
0.40	303	206	30	48
0.60	337	158	23	33
0.80	358	103	15	22
1.00	351	151	22	26
1.20	344	165	24	39

Source: Taken from Brick, R. M.; Gordon, R. B.; Phillips, A. *The Structure and Properties of Alloys*, 3rd ed.; McGraw-Hill Book Company: New York, NY, 1965.

formed only at later stages. The process is halted before that and the coherent or semi-coherent metastable phases give rise to precipitation hardening through dislocation particle interaction. Many aluminum alloys harden by such age-hardening treatment. So hardening in such situation is a quench-aging process. There are many single phase systems like austenitic stainless or aluminum magnesium alloys which cannot be hardened by any method other than cold working where dislocation density created due to cold working without recrystallization hardens the material. This is a typical work hardening process. More discussion on the heat treatment of nonferrous systems are narrated in later section.

However in case of steels, hardening is possible by quench-hardening means; in this case rapid cooling of homogeneous

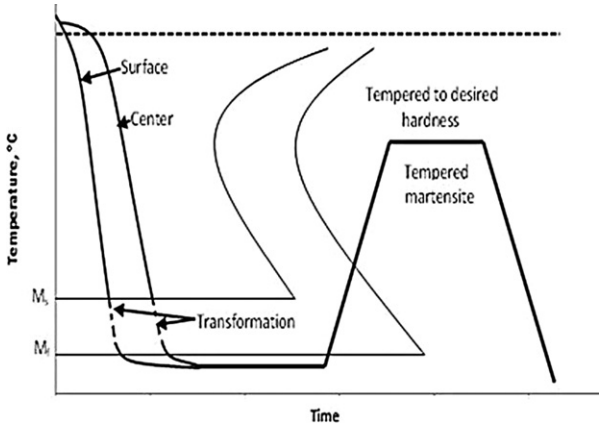


Figure 36 Diagram showing the hardening and tempering of euctectoid steel.

austenite leads to the formation of martensites as discussed earlier. This martensite is very hard in steel. So hardening in steel is a typical quench-hardening process. In this process the steel is heated to austenitization temperature; the temperature up to which the steel is to be heated is also decided by whether a homogeneous austenite can be achieved in reasonable period of holding or not. Normally, for hypoeutectoid steel the heating temperature is 50 °C above A_3 temperature and that for eutectoid steel it is 50 °C above A_1 temperature. From this high holding temperature, the steel sample is quenched at a rapid rate. The rate of cooling which is to be applied without formation of quench crack is judiciously decided as it is dependent on the composition of the steel. The severity of quench of individual cooling medium is different and the steel under hardening is cooled from high temperature in water, oil, air, or molten salt baths. The process of hardening is schematically shown in **Figure 36**.

The hardening process thus consists of three steps: First step is the production of homogeneous austenite in hypoeutectoid and eutectoid steel while austenite plus undissolved carbide in case of hypereutectoid steel. The heating temperature may range from a very high magnitude for alloy steel ~1200 °C to quite a low value like 750 °C for hypereutectoid steel. For hypoeutectoid and eutectoid carbon steels it varies between

780 and 880 °C. The heating is followed by holding for predetermined time for dissolution of carbide and production of homogeneous austenite; in case of hypereutectoid steel, however, undissolved carbide is deliberately kept in the microstructures for reasons stated earlier. Finally, the workpiece is cooled at a cooling rate that produces martensitic structure with minimum residual stress. The heat treatment is required to be carried out in a protective atmosphere so that chemical degradation due to decarburization can be avoided as far as practicable. Cooling is performed in different media viz. water, saline water, hardening oils, polymers, salt bath, and nitrogen or argon gas. Individual cooling medium has its own characteristic advantages and disadvantages; however, salt bath quenching reduces chemical degradation as well as minimizes the chance of warpage due to fact that the objects immersed in liquid bath experiences Pascal pressure which is same along all directions. Moreover the inert gas quenching like nitrogen or argon minimizes oxidation and decarburization. The hardened steel is extremely brittle and cannot be put to use unless it is toughened suitably.

Thus the salient features of hardening of steels are:

1. Selection of proper quenching medium should be made so that thermal stresses can be kept to minimum.
2. Alloy steels having high hardenability and low CCR should be subjected to air cooling to avoid warpage or cracking.
3. High carbon steels have slightly higher CCR and has to be hardened by oil quenching.
4. Medium carbon steels with relatively high CCR may require judicious selection of quenching medium; many a time oil quenching or polymer quenching is preferred to avoid heat treatment defects.

2.1.7.1 Factors Influencing Hardening Process

The hardening process of steel is appreciably influenced by the following:

2.1.7.1.1 Adequate carbon content to produce hardening

As stated earlier the alloying elements with the exception of Co and Al depress the martensite reaction temperatures and carbon exerts the strongest effect to lower both M_s and M_f temperatures. As shown in Figure 37, carbon in excess of 0.7 wt.%C lowers the M_f temperature to below room temperature and so, higher carbon steels quenched into water often contain appreciable amounts of retained austenite in the microstructure.

2.1.7.1.2 Austenite decomposition to produce pearlite, bainite, and martensite structures

Steels must have adequate hardenability to avoid soft pearlitic transformation for producing fully martensitic structure throughout the section. For this purpose, the alloying elements having good ability to shift TTT or CCT diagrams toward right are often added in steels, meant for quench hardening. The microstructure of hardened steel containing martensite and some retained austenite is shown in Figure 38. During martensitic transformation some austenite remains untransformed. The amount of retained austenite depends upon the chemical composition, cooling rate, and mechanical treatment. Stabilization of austenite in quenched steel is discussed in subsequent section.

Another way of forming martensite is by fast cooling in the softer region, i.e., the pearlitic and the bainitic region and then



Figure 38 Microstructure showing martensite.

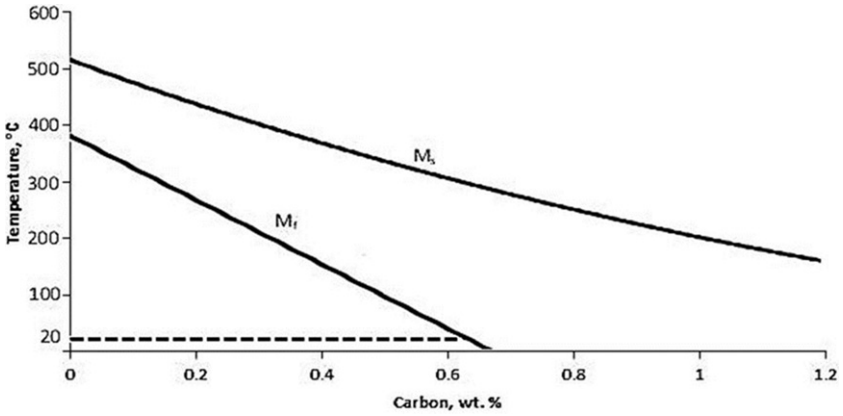


Figure 37 Carbon content vs. martensite start (M_s) and martensite finish (M_f) temperatures in unalloyed steels.

a comparatively slow cooling rate can be employed to produce martensite.

2.1.7.1.3 Temperature of heating, rate of heating, and the time of holding

2.1.7.1.3.1 Temperature

Proper selection of temperature is essential for successful hardening operation. For hypereutectoid steels the heating is done below the A_{cm} line, has the unique benefit of retention of undissolved cementite in the microstructure which apart from inhibiting grain growth provides high wear resistance to the heat-treated parts.

2.1.7.1.3.2 Heating rate and soaking time

The heating rate is so selected that there should not be any decarburization or grain growth. For this the heating is done in steps. For an example heating to 800 °C and soaking for some time to homogenize the structure and then heating the material rapidly to the peak temperature; this process necessitates a low soaking period at the high austenitizing temperature. This leads to complete homogenization of austenite without appreciable grain growth. The soaking period and heating rate depend on the size and shape of the part being heat treated.

In order to avoid defects due to hardening of steels the following guidelines are useful:

- The properties required in the heat-treated part are obtained without the parts being distorted beyond acceptable limits.
- The ideal design for a heat treatable part should be such as to attain the same temperature at its every point with minimal chances of abrupt change in thermal stresses. This necessitates the avoidance of abrupt change in the section sizes.
- Long thin parts like connecting rods should be as symmetrical as possible to reduce stresses.
- The holes in a part should be kept centered such that metallic mass around these holes are nearly same; this insures balanced mass around and hence less chance of cracking.
- The internal corners in a part should be provided sufficient fillets and regions prone to lead to stress concentration should be avoided.

2.1.8 Heat Treatment Fundamentals of Nonferrous Alloys

A variety of heat treatment processes are practiced to control the structure and properties of nonferrous alloys. Most of these processes have their characteristics features that are common to the alloys undergoing such treatment; the general principles of individual processes adopted for heat treating nonferrous alloys are briefly reviewed in this section.

2.1.8.1 Age-Hardening Treatment

A number of nonferrous alloys exhibit sloping solvus in their phase diagrams. This makes the concerned alloys amenable to age hardening; age hardening is the heat treatment that envisages formation of a single phase by heating the alloy to a high temperature which insures complete dissolution of second phase particles. Upon being quenched to room temperature the solid becomes supersaturated with respect to solute concentration. Supersaturation is a state of thermodynamic instability and hence the system becomes prone to be relieved of supersaturation through what is called precipitation.

However a homogenous solid solution becomes heterogeneous if it is cooled rapidly from a high temperature to the room temperature. All quenched alloys contain vacancies in excess of equilibrium number. The presence of excess vacancies entices the solute atoms for small-scale migration. This has the implication that perceptible chemical heterogeneity is created in a local scale. If the composition of the alloy lies within its spinodal points, the alloy decomposes spontaneously without regard to chemical potential barrier. This fine scale solute-rich region created within the system is known zone, more customarily Guinier–Preston (GP) zones. The aging sequence in age-hardening alloys can be obtained in text books on light alloys and in *ASM Metal Hand Book Volume 4*.[14]

Quite often the heat treatment cycle is so designed as to maximize the density of GP zones by a low temperature aging treatment just after solutionizing followed by quenching. Following this, a second step of aging treatment is carried out at a high temperature. The preexisting GP zones dissolve (above GP solvus) and give way to the formation of a series intermediate precipitates which are mostly coherent or semicoherent with the matrix. The first step of aging at low temperature (below GP solvus) is called natural aging and the aging at temperatures above GP solvus is known as artificial aging. The overall aging process is referred to as duplex aging; duplex aging has the advantage of achieving precipitates of varying sizes which when suitably designed may lead to the formation of duplex precipitate structure which is extremely beneficial in simultaneous improvement of both yield strength and fracture toughness of the heat-treated alloy. It is to be noted that during artificial aging a series of metastable phases are formed and the formation of equilibrium precipitate may not even occurs in many cases.

A few nonferrous alloys exhibit precipitation hardening behavior due to the formation of fine coherent precipitates of the intermetallics during aging. In this way it resembles aging in maraging steel where coherent precipitates of types Ni_3Mo, Ni_3Al are formed. Cu–7.5Ni–1.5Si–1.2Cr is one such alloy in which the quenched-aged microstructure exhibits nanometer scale precipitates of β-Ni_3Si and δ-Ni_2Si.[15] However it may be noted that when transition metals like chromium is alloyed with a full metal like copper, the as solidified alloys are normally heterogeneous with preferential segregation of chromium.[16] In conventionally cast alloys the microstructure exhibits large chromium rich phases. The segregation of chromium in as cast condition is ascribed to high Chromium–Chromium coordination in the liquid state due to differential mobility of the solute and solvent atoms at the conventional temperature of molten alloy.[16] This type of micro-segregation is the main reason why these alloys containing appreciable amount of chromium is solution treated for as long a time as 10 h at high temperatures like 970 °C. In this connection special mention must be made of nickel-based superalloys like Inconel, Hastalloy, Nimonic, Udimet, and Waspalloy which are subjected to quench and aging heat treatment, where diffusion of solute atoms plays a vital role. These superalloys need to possess high creep resistance and hence its microstructure should be such

that it is not only very hard at room temperature but also can retain its hardness at high temperature. Hard refractory compounds embedded in strong and tough matrix enable the material to attain good high temperature strength. Thus all the superalloys are dispersion-strengthened and or precipitation-hardened alloy. Since these superalloys contains refractory elements like Mo, W, Cr along with some carbon and alloying elements the hardened phase are generally intermetallic compounds and carbides of refractory material.[17–19] The diffusion of these high melting refractory metals are very sluggish at the average tempering temperature of 600–700 °C unless it is aged for a prolonged period of time. A long holding time at the aging temperature makes it possible to precipitate all the solute atoms in the form of refractory intermetallics or carbides.

A sloping solvus in equilibrium diagram of a system is a necessary but not sufficient condition for any alloy system to be age hardenable. Example may be cited of Al–Mg system which possesses a sloping solvus in its equilibrium diagram, but does not exhibit age hardening. It is postulated that GP zones are not formed in Al–6Mg alloy due to GP solvus lying below room temperature and that the alloy in solidified condition contains coarse Mg_2Al_3-type intermetallic. However it is found that trace additions of different elements in several nonferrous alloys impact their aging response quite significantly.[20–23] Different trace element additions exert different types of effects. Some trace additions in some systems stimulate formation of GP zones; for example, addition of silver in Al–Mg alloy leads to formation of GP zones in the alloy; it is not certain if these zones are magnesium atom dominated zones or are of the same type of zones as is known to form in binary Al–Ag alloys. Al–Ag alloy forms spherical GP zones; hence the possibility that stimulation in GP zone formation in Al–Mg alloy is due to silver rich GP zone formation cannot be over ruled. On the contrary minor addition of scandium leads to very prominent age-hardening effect in Al–6Mg alloy.[24,25] Scandium in aluminum forms Al_3Sc precipitates and strengthens the alloy. Recent investigation through position annihilation and coincidence Doppler boundary spectroscopy has confirmed that GP zones are not formed in Al–Mg (Sc) alloy even though it shows excellent age-hardening behavior.[26,27] It implies that for precipitation hardening to take place, the formation of GP zone is not mandatory (**Figure 39**).

Moreover, the observation that scandium treated Al–Mg alloys age harden but do not form GP zones while silver added Al–Mg alloy records GP zone formation, raises a doubt on the common belief that binary Al–Mg alloy does not exhibit age hardening because its GP solvus lies below room temperature. There is another class of alloys which have the sloping solvus in their phase diagrams but are nonresponsive to age hardening due to quench sensitiveness. The ideal example of this class is aluminum – transition metal alloys viz. Al–Cr alloy which is highly quench sensitive. These alloys are highly prone to form coarse intermetallics in microstructure and do not exhibit age hardening in general.[28] It is surmised that density difference between solvent and solute leads to prevalence of biased neighboring of like atoms. Treating these alloys with rare earth elements makes the liquid alloy more homogenous and as a result homogenous supersaturated solid solution is likely to form after solutionizing treatment followed by rapid quenching. It is further demonstrated that the alloys which

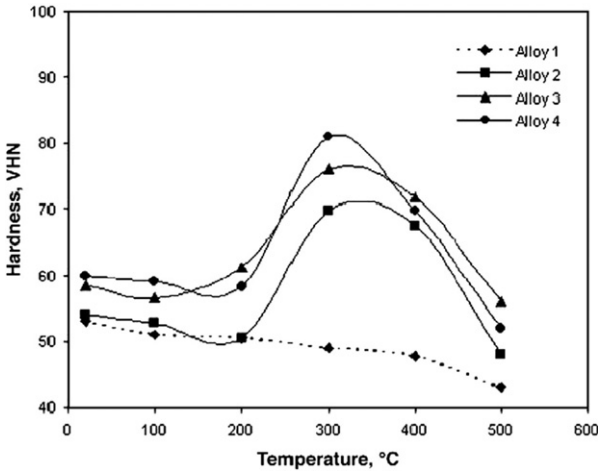


Figure 39 Age-hardening curves of Al–6Mg alloy containing 0.2, 0.4, 0.6 wt.%Sc. Dotted curve is for the base alloy.[19]

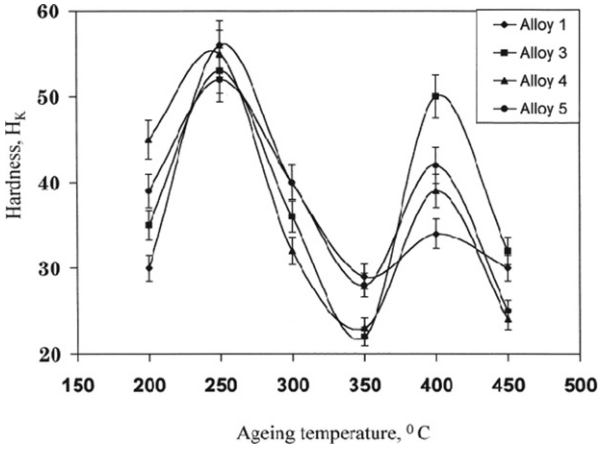


Figure 40 Variation of hardness with aging temperature for cold-worked Al–Cr (Zr) with trace rare earth addition.[23]

become responsive to age hardening due to trace addition are those for which cold-working accentuates age hardening. The aging curves in **Figure 40** demonstrate that cold-worked Al–Cr alloy is highly age hardenable even though it is otherwise a quench sensitive alloy. It is described earlier[28] that the first peak is due to the formation of $CrAl_7$ phase which is the chief hardening phase. At high temperature the $CrAl_7$ phase dissolves and the new precipitate of Cr_2Al_{11} appears. The volume fraction of this precipitate is less due to paucity of flux of chromium atoms against the need to form higher aluminizes, Cr_2Al_{11}. Also recrystallization takes place partially due to high temperature aging and so, the number of dislocations available as nucleation sites for Cr_2Al_{11} becomes quite low. As a result the extent of age hardening is less after geeing at 350 °C.

Quench-sensitive alloy contains coarse insoluble in its quenched state (**Figure 41**). The incoherent insoluble – matrix interface acts as the sink for vacancy annihilation. As a result, availability of vacancy in its quenched structure is limited. So solute diffusion becomes restricted; neither GP zone formation nor formation of intermetallic precipitate is encouraged.

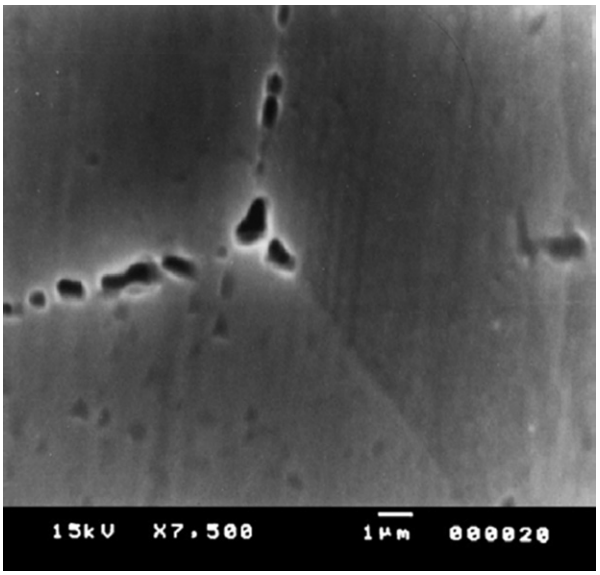


Figure 41 SEM micrograph of Al–6Mg–0.6Sc alloy.[19]

It is known that precipitation phenomenon involves long-range transport of atoms. Cold-worked alloy provides dislocations as the nucleation sites for precipitates and punched out vacancies from dislocations also make solute diffusion easy thereby aiding in precipitate formation in many quench sensitive systems.[29] However dislocation-induced precipitation is not generic of age-hardening alloy systems. Vacancy solute atom complex formation and its easy transportation to nucleation sites is the chief controlling factor of precipitation of Al_3Sc in Al–6Mg (Sc) alloy. This alloy does show any benefit in aging response after cold working following quenching.

2.1.8.2 Annealing of Nonferrous Alloys

The other common heat treatment processes applied to nonferrous alloys are homogenizing, conventional annealing and stress reliving. For example, many copper alloys are single phase solid solution and therefore can be heat treated only by the above mentioned processes.

In general the alloy castings are subjected to homogenization annealing heat treatment by heating the cast alloys to a high temperature where rapid diffusion of substitutional solute atoms is possible. The selected temperature should not be so high as to promote unwarranted grain growth. The alloy like Cu–Sn which shows a wide gap between solidus and liquidus temperature is prone to coring or micro-segregation. These alloys are normally homogenized at high temperature.

In order to relieve internal stresses and to restore the original structure and properties that are affected during cold working, the nonferrous alloys are subjected to recrystallization annealing as usual. High solute alloy like α brass are recrystallization annealed appreciably above the recrystallization temperature to assist diffusion of solute atoms. Stress relieving annealing treatment of nonferrous alloys is carried out as usual to relieve internal residual stresses those are introduced during the welding, brazing, casting, machining, or the fabrication processes. Stress relieving treatment may also be carried out for the purpose of securing partial recovery in cold drawn alloys. When extremely deformed alloys are subjected to low temperature annealing treatment, point defects are eliminated in particular and the excess lattice defects in general. Such stress equalizing treatment as it is called, is commonly practiced in the case of cold-worked Monel alloys by annealing it at 300 °C. Sometimes propensity to stress corrosion cracking as in the season cracking of α brass (>15 wt.%Zn) is minimized by annealing the cold-worked material below recrystallization temperature. This retains strain-hardening effect with some loss in hardness. In this condition, the strain-hardened components do not get softened. However some hardness drop inevitably accompanies this process.



Figure 42 Self accommodating thermoelastic martensite in Cu–Zn–Al alloy.[27]

2.1.8.3 Martesite Formation in Nonferrous Alloys

Although many nonferrous alloys including α–β brass are strengthened by precipitation hardening, copper zinc alloys are not always meant for precipitation hardening. Ternary addition of aluminum in Cu–Zn alloys produces thermoelastic martensite,[30–33] capable of exhibiting shape memory effect (Figure 42). If the alloy is deformed in martensitic state to assume a different shape, the high temperature shape can be regained by the original article upon being heated beyond a certain temperature, called recovery temperature.

When Cu–xZn–yAl or Cu–xAl–yNi is quenched from high temperature in β-phase field, martensites are formed. These martensites are very soft and are amenable to shape change with the application of small force.

The volume change 'ΔV' accompanying martensitic transformation is quite small and the lattice invariant deformation mode is either twin or stacking faults (Figure 43).

The reversible internal faults enable the reverse transformation of martensite to parent phase to take the same path as that of the forward transformation (β-M). The inherent reversibility characteristics of martensitic transformation in Cu–Zn–Al and Cu–Al–Ni alloy are envisaged due to low thermal hysteresis.[34–37]

The repetitive use of these shape memory alloys exhibit degradation in shape memory behavior due to cumulative

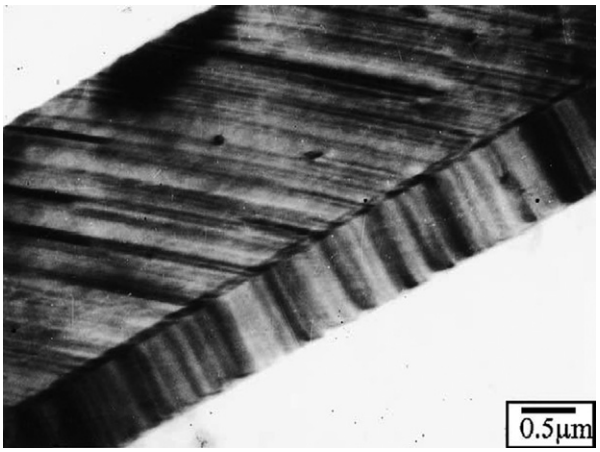


Figure 43 Internal twins in Cu–Zn–Al shape memory alloy with trace Zr add.[26]

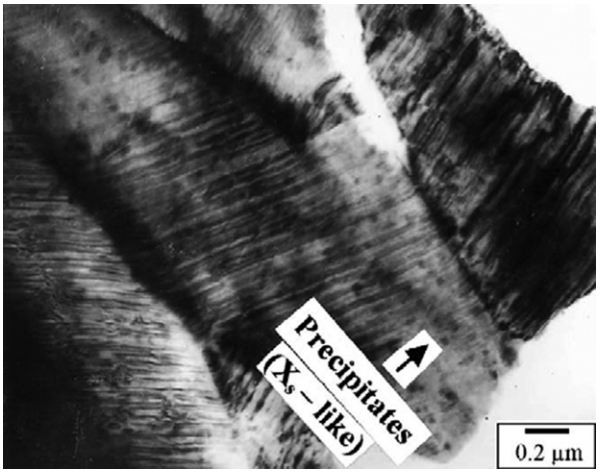


Figure 44 Microstructure of Cu–Zn–Al (Ti) alloy showing fine precipitates after repeated shape memory cycling.[32]

aging effect. Repetitive shape recovery cycling leads to precipitation of inter metallic compounds on to the twin boundaries and make them immobile. Thus de-twinning during reverse transformation is inhibited thereby, resulting in a loss of shape memory effect.[38,39] The effect of aging precipitates on the SME is elaborately studied elsewhere.[40,41] Excepting a few cases, formation of precipitates due to aging, in general degrade shape memory behavior, with concurrent rise in hardness (**Figure 44**).

In view of apparent differences in heat treatment of some technologically important nonferrous systems, a brief review of fundamentals underlying principles of heat treating a few such systems is done in the following paragraphs.

2.1.8.3.1 Heat-treat principles of nonferrous alloys exhibiting polymorphic transition

Unlike aluminum, copper or nickel, titanium undergoes polymorphic transition at 882.5 °C; high temperature β-phase is BCC and this phase undergoes phase transition through formation of hcp α below the transition temperature. This makes it possible to produce α, β, or $\alpha+\beta$ alloy of titanium. Therefore evolution of different kinds of phases due to various types phase transformations accompanying heat treatment of titanium alloys is noticed. This enables to achieve specified set of properties in titanium alloys suiting the needs of target applications.[42–45] Being low temperature single phase system, α-alloys are generally cold worked and annealed to achieve grain refinement while it is in fully α-phase state. However if fully 'α' alloy is quenched from β-phase field, α' martensite may form, with very little change in properties. Similar to many ferrous and nonferrous systems a relatively slower cooling from β-phase field (say air cooling) produces Widmanstatten α with a consequent deterioration in fatigue strength. If α-alloy of approximate composition, Ti–11Sn–2.25Al–5Zr–1Mo–0.2Si is equilibrated at temperature within $\alpha+\beta$-phase field, evolution of microstructure takes place in the same way as in duplex ferrite–martensite steel. When the alloy is annealed at 900 °C within $\alpha+\beta$-phase field and then cooled fast, the β-phase transforms to α' martensite; on the contrary a relatively slow cooling like air cooling produces fine equiaxed primary α and Widmanstatten α obtained from β.

In α/β-alloys several heat treatment processes may be adopted. The most common α/β-alloy is Ti–6Al–4V alloy. In such α/β-alloy 4–6% β-stabilizing (V) elements are added to retain some β even after quenching from β- or $\alpha+\beta$-phase.[46–48] Annealing of the alloy can be done from β-phase field as well as from $\alpha+\beta$-phase field. When it is annealed at β-phase and then cooled to room temperature, Widmanstatten 'α' is formed in a β-matrix or β may partially or wholly transform to α' martensite depending upon the cooling rate. When annealed from $\alpha+\beta$-phase field the microstructure consists of equiaxed α and transformed β. Transformed β may be Widmanstatten 'α' or α'. The strength of annealed alloy increases with increasing alloy content.

β-quenching: the α/β-alloy may be betatised at elevated temperature, where single phase β is present. The β-phase is then quenched. In case of dilute alloy, β may convert to α' (hcp) martensite; α' martensite may finally convert to lath martensite α'' or twinned martensite α'''. However in a concentrated alloy 'β' phase is retained as metastable 'β' which is then subjected to aging heat treatment as is done in a typical precipitation-hardened stainless steel. In dilute alloys β-phase may directly convert to laths of orthorhombic α' to α'' martensite and face-centered orthorhombic α''' martensite. The transition from α' martensite to α'' martensite takes place with increasing solute content. Thus,

$\beta \rightarrow \alpha''$ with retained β

i.e., $\beta \rightarrow \beta_{(\text{lean})} + \beta_{(\text{rich})} \rightarrow \alpha'' + \beta_{(\text{rich})}$

When the alloy is very rich in β-stabilizing elements, a fast quenching from β-phase field may give rise to metastable β. Aging of metastable β decomposes differently at different temperature regime.

In a medium alloy aged within 100–500 °C $\beta_{(\text{metastable})} \rightarrow \beta + \omega \rightarrow \beta + \alpha$

In concentrated alloy β metastable $\rightarrow \beta + \beta_1 \rightarrow \beta + \alpha$

ω-phase leads to severe embrittlement of the alloys. Formation of ω-phase takes place through displacive mode of transformation; ω particles are cuboidal and maintain specific orientation relationship with β-phase.

Within the group of β-alloys, a relatively lean solute content produces metastable 'β' upon fast cooling; whereas above a critical value of the concentration of β-stabilizers stable 'β' remains present in the microstructure. The alloys are cold formed and aged to secure high strength.

2.1.8.3.2 Application of heat treatment principles in Mg-alloys

In view of recent interest in commercial use of magnesium alloys due to its advantage of low specific weight, more elaborate discussion is made to know about the heat treatment of Mg-alloys. Cast magnesium alloys are quite often subjected to solutionizing followed by aging. The solutionizing is carried out to attain a single phase from where it is cooled fast to form supersaturated solid solution. The cast alloys show microsegregation and quite often cast magnesium alloys contain intermetallic precipitates of the form AB, AB_2 (laves phase), or CaF_2 (BCC) in the microstructures. Mg–(8–10)Al–0.5Zn–0.3Mn alloys are subjected to natural aging after solutionizing or first solutionizing and then artificial aging to effect intra granular precipitation of magnesium aluminides. On the contrary Mg–(4–6)Zn–0.7Zr (RE) is directly subjected to T_5 tempering, that is artificial aging[49]; this leads to the formation of Mg_2Zn type precipitates. In general, magnesium alloys form three different types of precipitates. These precipitates form at grain boundaries if the alloys are cooled at moderate cooling rate as in sand casting. In order to improve strength and corrosion behavior of magnesium alloys, it is required that these intergranular precipitates are dissolved during solutionizing heat treatment. Subsequent aging to form intragranular precipitates of intermetallic phases gives rise to significant improvement in mechanical and mechano-chemical properties. A large number of magnesium alloys are precipitation hardenable; the precipitate phases forming in different magnesium alloys with their precipitation sequences in furnished in the **Table 2**.

In observance of the aging sequence in important magnesium alloys, it may be understood that most of these alloys are subjected to age-hardening heat treatment and in most of the cases combined T_4 and T_6 is recommended so that a duplex precipitates structure may result in the microstructure. In Mg–RE system, maximum strengthening is obtained due to the formation of β'' phase which exhibits DO_{19} ordering. But aging at higher temperature till 250 °C leads to loss of coherency and the semi-coherent β'-phase with hcp structure forms, mainly on to the existing dislocation. This drastically reduces creep resistance. Solution treatment temperature for this alloy is judiciously selected and is normally around 420–450 °C for most of the commercially important alloys because it can avoid both grain coarsening and chemical degradation.

2.1.9 Quenching and Quenching Medium

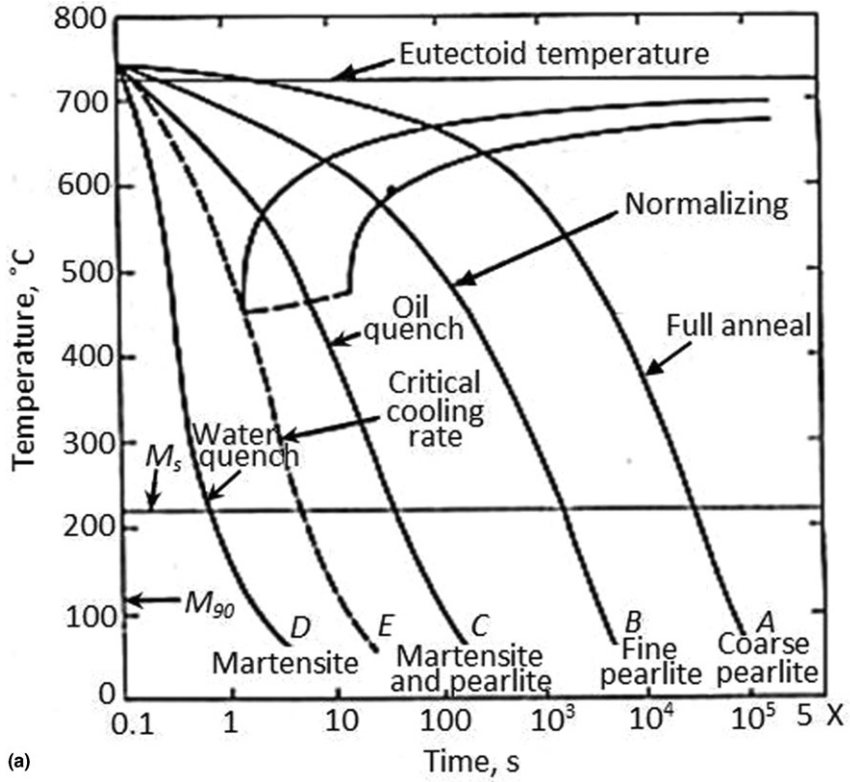
In case of age hardening the supersaturation is relieved by fine-scale precipitation through a definite sequence. However the alloy becomes hardest at particular time and temperature of aging. As stated earlier in case of the Fe–Fe_3C system the supersaturated solid solution is the strongest phase but is extremely brittle. Heating it to some elevated temperature below A_1 temperature decomposes the supersaturated solid solution leading to ductilization of the alloy. As in contrast with the previously stated age-hardening phenomena, the decomposition of the alloy leads to toughening of the alloy. As described earlier hardening of steel is conditioned by a CCR as defined earlier. It is to be further noted that whether the cooling rate offered by a particular cooling medium is able to give rise to the formation of 100% martensite throughout the section or not depends upon the section size of the stock being cooled.

Figure 45(a) shows the effect of various cooling medium on a round-eutectoid steel bar. It is apparent that water having more severity of quench can bypass the nose of CCT diagram up to a greater depth then oil and air of lower severity of quench. Hence to gain idea about the inherent ability of a material to avoid soft pearlitic transformation, it is required to alleviate with the influence of severity of quench while determining the achievable depth of hardening. This is done by imagining an ideal quenching medium with infinite severity of quench.

By definition the ideal quenching medium will take away the heat from the surface at the same rate as it flows to the surface from inside the bar which is being quenched. The cooling efficiency of the usual quenching media such as water, oil, brine, etc., relates with that of the ideal quenching medium. If round bars of varying diameters are quenched in a medium from an austenitizing temperature, there will be a particular diameter of which 50% martensite and 50% pearlite will be formed at the center. Conventionally this diameter is called critical diameter and is usually taken as the measure of hardenability. It must be noted that reckoning hardenability of steel on the basis of existence of 50% martensite and 50% pearlite in the structure is not mandatory. Depending upon the design requirement of steel, on the basis of strength and toughness parameter, it is possible to describe hardenability as the depth up to which 100% martensite is formed; however the classical definition of hardenability, as the depth up to which 50% martensite and 50% pearlite is formed, owes its origin to the easy identification of a structure with 50% martensite and 50% pearlite. The fracture of such a material will show a transition from ductile to brittle type and a plot of hardness versus the depth from the center shows a point of

Table 2 Heat treatment of Mg-alloys

System	*Precipitates process*
Mg–Al	SSSS → BCC equilibrium precipitate $Mg_{17}Al_{12}$ (β-phase) with $(011)_\beta$//(0002)Mg and faceted with lath morphology
Mg–Zn–(Cu)	SSSS → GP zone (coherent, disk) → $MgZn_2$ (rods, coherent) → $MgZn_2$ (disk, semi-coherent) → Mg_2Zn_3 (incoherent)
Mg–RE	SSSS → GP zone (coherent, disk) → β'' Mg_xNd ($x>1$) (Do_{19} ordered) → β' Mg_3Nd (semi-coherent) → $Mg_{12}Nd$ (incoherent)
Mg–Y–Nd	SSSS → β'', Mg_3Nd, GP zone rods coherent Do_{19} → β' $Mg_{12}NdY$ globular + β_1 (plates) $Mg_3(NdY)$ FCC → incoherent $Mg_{14}Nd_2Y$ FCC
Mg–Th	SSSS → β'', Mg_3Th coherent (disk) Do_{19} → β'_1 hcp, β'_2 FCC semi-coherent → β $Mg_{23}Th_6$ FCC incoherent



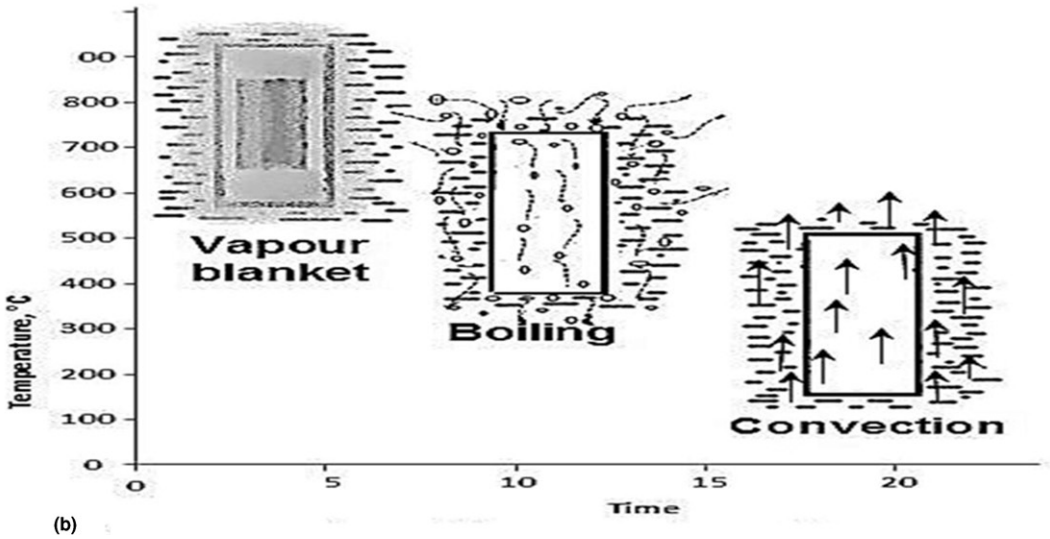


Figure 45 (a) Effect of cooling medium on microstructure evolution in eutectoid steel and (b) different stages in quenching.

inflexion denoting the change in curvature from positive to negative. As stated earlier hardenability is an inherent material property measuring the depth up to which the material can be hardened with a predefined percentage of martensite in the microstructure. The critical diameter of steel for a definite quenching medium of a particular H-value can be made co-related to the ideal critical diameter quenched in an ideal quenching medium (the details of hardenability of steel and methods for its determination can be obtained from physical metallurgy books of steel).

Once hardenability is defined as the depth to which a definite percentage of martensite can be formed, it becomes obvious that all the factors which delay the diffusional decomposition of austenite will improve hardenability. If austenite grain size is large, the nucleation sites for pearlite formation will decrease and hence CCT diagram will shift more toward right, thereby increasing the hardenability. Likewise all alloying elements except cobalt shift the CCT diagram to right and improve hardenability. However individual alloying elements has characteristic influence on degree

of shift of CCT diagram and so a multiplying factor is assigned for each alloying elements to describe the quantitative effect of individual element in increasing the hardenability of steel. From the forgoing discussion it is clear that the microstructure in continuously cooled steel depends on the cooling media employed for the concerned material.

During the cooling operation, a hot object is immersed in a quenching medium – this is a complex process consisting of two major stages:

- Stage 1: vapor blanket stage

  The temperature at the surface of the stock is initially very high and so the cooling medium gets vaporized and forms a thin layer of vapor around the immersed part. Under such circumstances the mode of heat transfer is radiation through vapor blanket which acts as insulating layer. This insulating layer puts a restraint to rapid flow of heat and hence cooling of the object. Thickness of vapor blanket around the object is determined by the quenching efficiency of the medium. The duration up to which this vapor blanket stage prevails around the object is different for different quenching medium. It further depends upon the ratio of the weight of object being heat treated and that of the quenching medium being used. Further the specific surface area and the distance between any two object put inside the quenching media also influence the vapor blanket stage. **Figure 45(b)** shows the formation of vapor blanket around the bar.
- Stage 2: the boiling stage

  In the course of cooling, the temperature at the surface of the stock becomes low enough to reduce the rate of radiation, resulting in the loss of vapor blanket stability. The disappearance of vapor blanket at any region around the object will immediately supply liquid to come in contact with the hot surface of the object. The liquid start boiling and the bubbles emanated thereof create turbulence near to the metal surface; this enhances the rate of heat extraction. Since the quenching media have high latent heat of vaporization, the boiling stage experiences the fastest cooling of the object. After the lapse of some more time with continued heat extraction from the surface of the stock, the temperature at the surface goes down below the boiling temperature of the quenching media. Boiling stops and the mode of heat transfer at this stage becomes only convection. Thus the rate of cooling continues to reduce with falling temperature of the quenching medium. It is important to note that the progressive lowering of temperature of the heat-treated stock and hence that of the liquid surrounding the object leads to increase in the viscosity of cooling medium; this reduces the rate of convection and hence the cooling rate. These stages of quenching are shown in **Figure 45(b)**.

Because of the fact that the thermal property of the liquid is a function of temperature, rate of cooling by any quenching medium would automatically depend upon its temperature dependent thermal properties. Qualitative information on commonly used commercial quenching media is provided in **Figure 46**.

From **Figure 46** it appears that the major feature of water quenching is defined by the extended vapor blanket stage over a wide range of temperature. Its implication is that the cooling rate at the initial stage where diffusional decomposition of austenite is supposed to takes place is rather slow. Thus the formation of diffusional decomposition product takes place with nonuniformity. The cooling capacity is of water at high temperature is sharply reduced and with increase of temperature of water the vapor blanket stage extended. This gives rise to a very nonuniform cooling rate at high temperature region, while quenching in water. The curve further shows that water offers its maximum cooling rate at a temperature between 250 and 300 °C which belongs to the temperature range of martensite transformation in many commercially important steels. The high cooling rates within Ms–M_f range is a great concern for distortion, warpage, and even quench cracks. It may be noted that increasing the temperature of water cannot solve the problem by the way of reducing the rate of cooling during martensite transformation. On the contrary increased

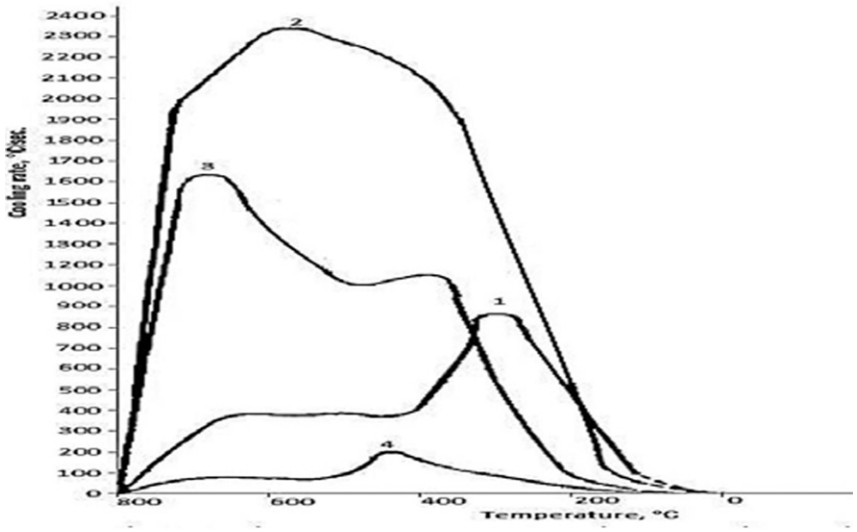


Figure 46 Cooling rate vs. temperature for various quenching media 1-H_2O; 2-H_2O + 10%NaCl; 3-H_2O + 50%NaCl.

water temperature may increase the cooling rate at certain temperature. That is why quench cracks are frequently observed in case of quenching of steel in hot water. In contrast a brine solution containing 10% NaCl in water appreciably changes the situation; the cooling capacity is increased to a high value even with exclusion of first stage of cooling, i.e., the vapor blanket stage. Moreover the cooling by brine solution is found to be uniform, although it is expected to decrease with decrease in temperature. Because of high cooling rate at high temperature where a vapor blanket is expected to form, the temperature of the metal surface decreases fast; this causes the vapor blanket to become unstable and gets destroyed right at the initial stage of cooling. Moreover, the NaCl salt spalling out may accentuate the destruction of vapor blankets. The brine solution is known to be relatively less responsive to heating. Moreover the cooling rate within the M_s–M_f range can be brought down to low value by the use of concentrated brine solution, 40% NaOH in water is a very good quenching medium which greatly minimizes the warpage and ensure a clean surface after heat treatment. Unlike brine solution, NaOH in water is a rapidly degradable quenching medium. This absorbs CO_2 from air and loses its properties within a day or so. The low cooling rate between M_s and M_f range is an important consideration in the evaluation of efficacy of quenching medium. A fast cooling down to M_f temperature induces high thermal stress, also called macro-stress. Micro-stress due to martensite transformation is quite severe and is to be inevitably developed during martensite formation. Therefore a slow cooling rate within the M_s–M_f temperature range is always advantageous in terms of reduction in cumulative stresses developed in the quenched stock. Examples may be cited of a solution of 5% $KMnO_4$ with 3% glycerin in water which decreases the cooling rate in the martensite transformation region to a significant extent. On the average this is around 50 °C s^{-1} as against 600 °C with pure water and 100 °C in water with 50% NaOH.

The other important quenching medium is considered to be mineral oil which has a number of advantages over water as a quenching medium.

- Boiling point of quenching oil is around 250 °C and this mineral oil provides a very low cooling rate within the M_s–M_f range. At a temperature around 200 °C the cooling rate provided by the oil is at least 25% less than that provided by water. As evident from **Figure 46**, the rate of cooling provided by the oil remains more or less unchanged from 150 °C to room temperature.
- However the oil quenching provides a low cooling rate in the intermediate range of transformation temperature, where austenite decomposes in to pearlite. Thus the effective hardenability significantly decreases due to oil quenching.
- Most of the commercial quenching oil is highly inflammable and its flash point is around 128 °C. However oil with higher flash point around 170 °C is also available in the market.
- The cooling rate provided by the oil is rather small at low temperature. Oil preheated to 80 °C provides good fluidity of oil, so that effective convection occurs. Being well below the flash point of oil at 80 °C does not set to fire and continuously provide a slow cooling rate within the M_s–M_f temperature range and thereby reduces the chance of warpages.
- In the recent time, the new generation steels have been developed which are hardenable by cooling in the still air. The air hardening steels are particularly suitable for minimizing the distortion and warpage as the thermal stress induced during quenching is minimum. Also air–water mixtures at a pressure of 2–3 atmospheric pressure is sometimes used for hardening heavy articles made up of alloy steel and are prone to crack on quenching. On examination of the values of severity of quench for air and oil it would appear that air with low moisture contains is able to provide a cooling rate which is nearly same as oil.
- It is possible to increase the efficiency of hardening alloy steels for water quenching is generally prohibitive due to proneness of quench cracking. A leaner alloy steels, which otherwise cannot avoid the nose of CCT diagram for the entire section, may first be subjected to more severe quenching in water down to the level of 450–400 °C (assuming nose to exist between 500 and 550 °C), and then quickly withdrawing the same from water and quenching it in oil which is quite efficient a quenchant within M_s–M_f range. By this technique it is possible to make use of lower alloying element content in steel yet achieving the same strength and toughness properties.
- Apart from what are stated above, proper immersion of the articles in to quenching medium is very important to avoid warpage and cracking due to hardening. The general recommendation in this regard is that longer articles should be immersed with its main axis perpendicular to the surface of quenching bars. Flats and sheets are immersed on their edges. For a better heat transfer it is advisable to create a relative movement between the article and cooling liquid. The lighter articles should normally be moved along the direction in which they are inserted in to the quenching medium. But the heavy stocks may be held stationary and creating agitation in the quenching bath.

2.1.10 Tempering

As stated earlier the hardened steels with full martensite in microstructure cannot be employed for useful purposes because martensite is extremely brittle; martensite formed by quenching produces high internal stresses in the hardened steel. The hardened steel need be heated to higher temperature to reduce its brittleness; this process is called 'Tempering.'

Tempering is generally carried out by heating the hardened steel to temperatures below A_1; it is held there for some preselected period of time and then followed by cooling to room temperature.

The selection of tempering temperature depends upon the composition of the steel and the final properties desired after tempering; this however depends upon the exact microstructure and the hardness of the component at various points across its section. High carbon and high alloy steels are normally tempered at as high temperature range as 550–650 °C (**Figure 47**). In order to achieve good combination of strength and ductility commensurate with the demands of service

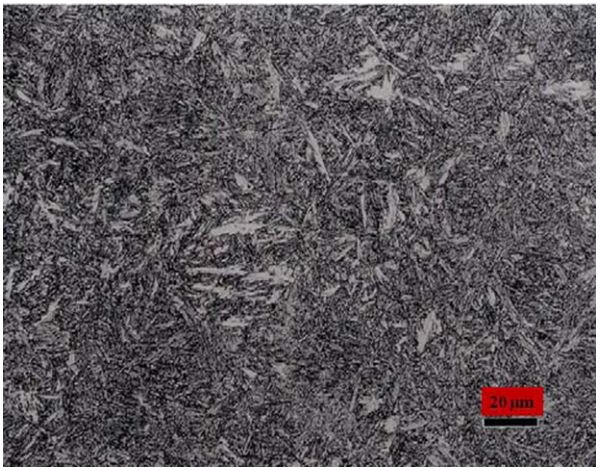


Figure 47 Tempered high carbon plate martensite in 0.9C–0.4Mn steel water quenched from 900 °C and tempered at 538 °C. Courtesy of George Vander Voort, USA.

conditions, proper selection of process parameters for tempering operation is necessary. The concerned process parameters are:

- tempering temperature,
- time to spend at tempering temperature, and
- cooling rate from the tempering temperature.

In some alloy steels, the hardness increases during tempering at high tempering temperature. This is known as secondary hardening. It occurs due to the formation of transition phases which are coherent with the matrix.

Secondary hardening is sometimes termed as fifth stage of tempering as it takes place normally beyond the tempering temperature for globularization of cementite in plain carbon steels. Some workers have termed this process of globularization during tempering as the fourth stage of tempering and so secondary hardening in alloy steels are sometimes referred as fifth stage of tempering. In case of chromium bearing steel the first formed carbide is cementite at low tempering temperature when the diffusion of chromium atoms are very slow. However with increasing tempering temperature the diffusivity of chromium is enhanced and cementite gives way to the formation of alloy carbides. The equilibrium carbide phase forms through the formation of a series of transitional carbide phases. In chromium steel, the sequence is: $Fe_3C \rightarrow Cr_7C_3 \rightarrow Cr_{23}C_6$.[50–52]

The situation becomes more complex in case the steel contains more than single strong carbide formers; in these cases normally more than one carbide may form and the sequence and amount of individual carbide phase depends upon the relative strength in carbide forming ability of the concerned elements.[53–55]

The alloying elements effect carbide formation during tempering at temperatures when their diffusion becomes perceptible. If both molybdenum and tungsten are present, the sequence of carbide formation may be: Fe_3C–M_2C (M ~ Mo&W)–$M_{23}C_6$–M_6C.

Since tempering is the process where the hardened steel is reheated to an intermediate temperature, it must take place in a number of stages that may overlap considerably with characteristics reactions occurring simultaneously as the steel is heated to higher and higher temperatures. The microstructural changes accompanying tempering at different temperatures following hardening of a medium carbon steel may be followed from Figures 48(a)–48(d).

2.1.10.1 Stages of Tempering

During first stage of tempering, formation of transition carbides occur, which can be η carbide (eta carbide) and/or ε carbide (epsilon carbide). The crystal structure of η carbide is orthorhombic and bears composition formula Fe_2C. However no authentic proof about formation of the same has been presented by researchers. The formation of ε carbide of closed pack hexagonal structure with approximate formula $Fe_{2.4}C$ is already ascertained. The first stage of tempering experiences segregation of C atom at the internal fault within martensite. The carbon in excess of 0.2 wt.% is rejected in the form of ε carbide. This converts high carbon martensite to a low carbon matensite of about 0.2%C, with a low tetragonality, as characterized by a c/a ratio of 1.02, against 1.08 of a 0.8%C containing martensite. Formation of low carbon martensite is a softening process, whereas ε-carbide formation is a process of hardening. The opposing action of these two phases results in the hardness of the quenched steel more or less constant (in fact, the reduction in hardness if there is any, is only just marginal).

The second stage of tempering takes place within approximate temperature range of 200–300 °C. During this stage retained austenite is transformed to bainite. However the second stage of tempering is not very important in any ordinary steel, as the quantity of retained austenite present in microstructure is not appreciable. On the contrary in case of alloy steel, retained austenite content is quite large and hence second stage of tempering becomes an important phenomenon. It is associated by rise in hardness as bainite is harder than the austenite.

The third stage of tempering takes place at 300 °C and above; low carbon martensite reduces its tetragonality by way of diffusing out the C-atoms, which further leads to the formation of elliptical ferrite of BCC crystal structure.

The ε carbides dissolve and low carbon martensite loses tetragonality be rejecting carbon. Finally in the third stage of tempering taking place at 300 °C, the microstructure consist of ferrite and cementite; there is an overall contraction in volume because low carbon martensite becomes cubic at extreme rapidity at temperature near 300 °C.

During third stage of tempering the ferrite phase undergoes recovery; dislocations migrate to grain boundaries, resulting in the formation of acicular ferrite structure of low dislocation density. Upon further heating to above 600 °C, acicular ferrite recrystallizes to equiaxed ferrite. However for high carbon concentration, the ferrite boundary may be pinned and thus recrystallization may take place with difficulty. The final microstructure after third stage of tempering consists of equiaxed ferrite with dispersed spheroidal cementite particles.

However it is to be remembered that rapid heating to the third stage tempering temperature range, may allow the changes to take place in the same sequence as described earlier. Due to paucity of time, for example, ε carbide may not even be

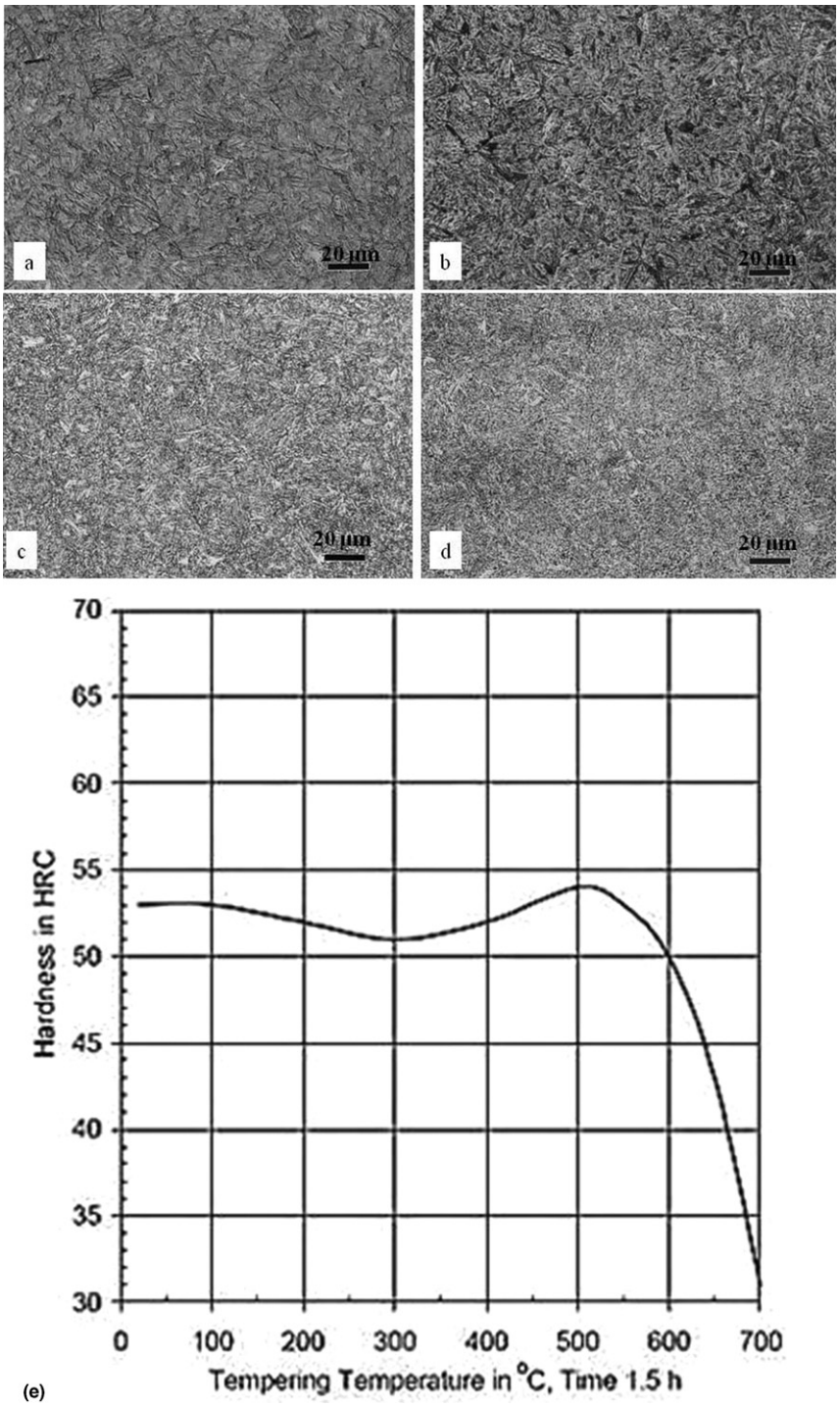


Figure 48 Changes in microstructures and corresponding hardness during tempering of 4140 steel after oil quenching from 870 °C. (a) Quenched (55RC), (b) tempered at 204 °C (53RC), (c) tempered at 427 °C (45RC), (d) tempered at 649 °C (26RC) (Courtesy of George Vander Voort , USA), and (e) tempering curve of AISI H13 steel.

formed and the tempering may result into direct formation of cementite particles.

At the same time it is noted that the retained austenite present in the microstructure may not undergo isothermal transformation to bainite, if the tempering is carried out at temperature 600 °C, by reaching the tempering temperature through rapid heating. If the tempering temperature lies above the nose of CCT diagram, the transformation of austenite to pearlite will occur by diffusional means.

Upon continuation of tempering beyond 600 but below 700 °C, the spheroidal cementite particles grow. The driving force for particle coarsening is the lowering of free energy due

to overall reduction of surface energy. In alloy steel containing elements like Cr, Mo a phenomenon called 'secondary hardening' takes place at higher tempering temperature. If tempering is carried out at a high temperature, where these substitutional alloying elements have sufficient mobility, their carbides are formed at the expense of cementite, which dissolves and supplies the flux of carbon atoms for formation of alloy carbides.

If we follow the tempering curve in Figure 48(e), we observe that during the first stage of tempering there is no significant change in the hardness values due to reasons already stated.

Possible hardening of small magnitude in second stage tempering, due to retained austenite to bainite transformation is masked by the softening due to loss in tetragonality of martensite and so there is a continuous softening during third stage of tempering. Spheroidization followed by coarsening of cementite called fourth stage of tempering also experiences softening.

However as the tempering temperature increases to 600 °C and above, the cementite particles dissolve and alloy carbides start to emerge. The formation of alloy carbides is a sequential event, where a number of transitional carbide phases are formed before the formation of equilibrium carbides.

The transitional carbides are initially coherent with ferrite matrix thereby making the steel stronger through secondary hardening. Secondary hardening is essentially an age-hardening phenomenon where sequential change in precipitation structure and composition occurs; thus secondary hardening follows mechanism of precipitation hardening. In the case of secondary hardening initially formed precipitates are coherent with the matrix and strong interaction between dislocations and coherency strain gives rise to the strengthening.

2.1.10.2 Formation of Bainite in Steels

It is seen that diffusional transformation of austenite produces pearlite whereas transformation of austenite under complete suppression of diffusional process takes place through diffusionless shear transformation mode resulting in supersatured solid solution of carbon in body centered tetragonal ferrite that is martensite. However there can be a situation where the driving energy for martensitic transformation is not available and diffusional mode of transformation of austenite is also improbable due to sluggishness of atomic mobility within the temperature range intermediate to nose of TTT diagram and the martensite start temperature. Under such circumstances a mixed mode of transformation, in the form of bainitic reaction takes place. The character of transformation is partly diffusional and partly shear. Again depending upon the transformation temperature and hence the available driving force the diffusion of solute carbon atoms may take place before or after the FCC–BCC polymorphic transition through shear mechanism. Accordingly the transformation products are called upper or lower bainite.

2.1.10.2.1 Mechanism of bainite formation

Below the nose of TTT diagram, lamellar product of decomposition of austenite is no longer seen to form; rather discrete particles of ferrite and cementite with different morphologies are observed in the microstructure. When austenite is given to transform at various temperatures below the nose of TTT diagram, phase transformation of austenite follows different mechanisms. The evidence of change in the manner of association as well as the composition of carbide and ferrite phases in the microstructures of low carbon steels under situation of continuous cooling, has enticed the scientists to advocate for mechanistically transient character of austenite transformation down to martensite transformation temperature. Study on the isothermal decomposition of austenite in these steels, provides good information about the possible mechanism of phase transformation. It has long been known that below the nose of TTT diagram, broadly two different classes of microstructures are formed. The first one forming just below the nose of TTT diagram and above 300 °C is called upper bainite; upper bainite appears feathery under optical microscope. In contrast, the decomposition product forming below 300 °C looks acicular or needle shaped; this phase mixture is called lower bainite. In upper bainite the sheaves of fine elongated ferrite laths are formed. The cementite particles lie along the boundaries between the laths of ferrite. In case of lower bainite, ferrite becomes more acicular and is appreciably supersaturated with carbon. This needle-shaped ferrite crystals exhibited the presence of intra lath carbide particles. The composition of this carbide phase is also different from that in upper bainite, which is orthorhombic cementite, Fe_3C of 6.67 wt.% carbon. In contrast, the lower bainitic carbide phase contains 8.4 wt.% carbon with a stoichiometric formula $Fe_{2.3}C$. The microstructure of upper bainite in 0.8%C steels is shown in (Figure 49); the transmission electron microstructure gives evidence of bainitic ferrite with carbide at the lath boundaries. A high dislocation density within the ferrite is also noticed. Ferrite lath in upper bainite also shows evidence of dislocations generated presumably due to lattice invariant deformation. Similarly the optical and transmission electron microstructure of lower bainite formed during isothermal transformation of austenite in 0.8%C steel show needle-like ferrite crystals with intra granular carbides (Figure 50).

In case of formation of upper bainite, diffusion of carbon in austenite takes place at relatively higher transformation temperature 400 °C; this leads to creation of the localized carbon-depleted regions within the metastable austenite. The preceding carbon diffusion followed by the creation of the above stated carbon-depleted regions result in rise of M_s temperature and since a highly metastable austenite below the nose of TTT diagram seeks for a suitable mode to undergo rapid transformation for its urge to lower overall free energy of the system, the diffusionless martensitic transformation is called for just when adequate driving energy commensurate with martensite formation temperature becomes available.

This behavior is logically consistent with proposed transformation mechanisms of lower bainite; the low transformation temperature of lower bainite tantamount to a much higher available driving forces and hence austenite can undergo polymorphic transformation without regard to prior diffusion of carbon. However one school of thought has proposed that upper bainitic transformation is entirely diffusional and is nothing more than a nucleation and growth type process where the ferrite crystal grow by ledge mechanism; bainitic ferrite sheaves are formed by sympathetic nucleation of new crystals at the boundary of prior crystals; according to this school of

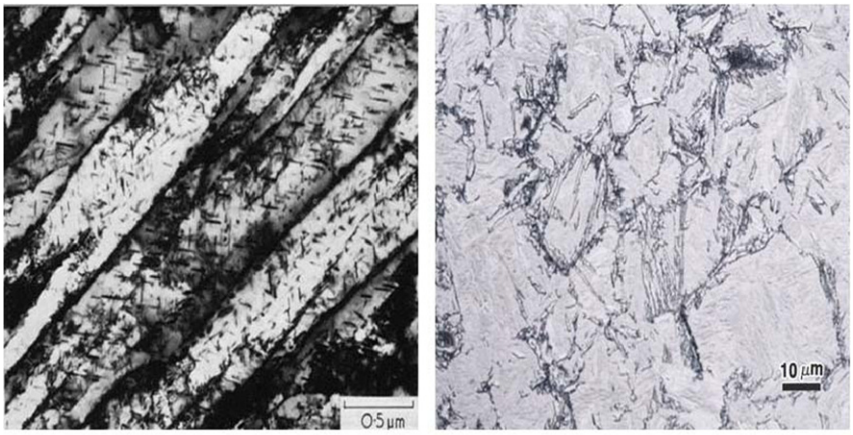


Figure 49 TEM and optical photomicrograph of upper bainite (dark) and martensite (white) in 0.6%C–0.85%Mn–0.25%Si–0.8%Cr steel (austenitized at 830 °C and partially transformed to upper bainite at 530 °C). Courtesy of George Vander Voort, USA. http://cml.postech.ac.kr.

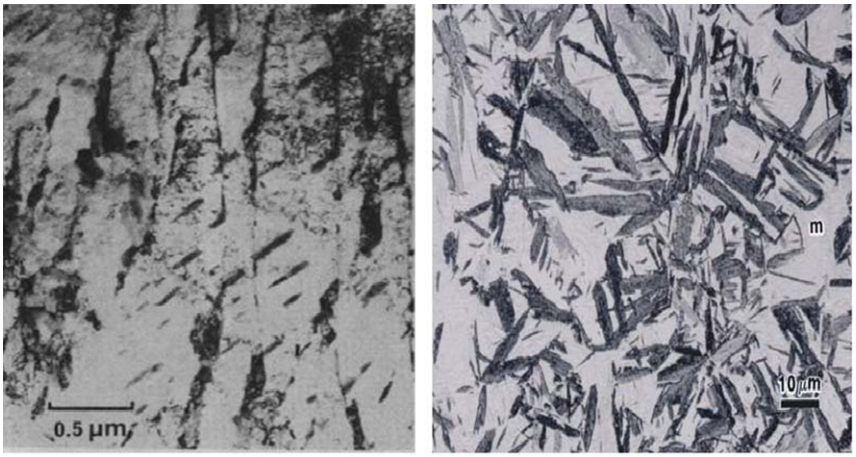


Figure 50 TEM and optical micrograph of lower bainite (dark) and martensite (white) in 0.6%C–0.85%Mn–0.25%Si–0.8%Cr steel (austenitized at 830 °C and partially transformed to lower bainite at 350 °C). Courtesy of George Vander Voort, USA. http://cml.postech.ac.kr.

thought, upper bainite formation can no longer be considered to be a 'partly diffusional and partly diffusion less shear transformation.' In this context it may be recalled that transformation of undercooled austenite is mechanistically transient and different transformation mechanisms operating at various degree of undercooling are distinguishable in continuously cooled low carbon steel. As one increases the degree of under cooling in a pool of transforming austenite, the phase transformation of austenite to ferrite is reported to take place in the sequence: polygonal ferrite–widsmanstatten ferrite–massive ferrite–granular ferrite (bainite)–acicular bainite–martensite. Each transformation type takes place within specific temperature region as decided by the chemical composition and defect structure of the transforming austenite. It has been demonstrated earlier that granular bainite forms by ledge mechanism; there is therefore reasons to believe that for any specific condition of under cooling, the driving force for polymorphic transition of austenite typifies a definite mode of transformation to operate. In extreme circumstances the mechanism of basic transition of austenite to ferrite may be non-diffusional, notwithstanding if diffusion of carbon atoms, required to form bainitic carbides takes place before (upper bainite) or after transformation (lower bainite). Although the proposition of ledge mechanism in formation of some form of bainite must not be reasoned out, it is wiser to dispense with dogmatic documentation in favor of fully diffusional nature of any bainitic transformation. The transient transformation behavior has its origin to the compromise between degree of metastability of austenite and feasibility of any specific transformation mode to operate within the scope of available driving energy with insurance of the most favorable transformation kinetics for FCC austenite to BCC ferrite formation.

2.1.10.3 Martempering

It is stated earlier that hardening of steel gives rise to severe thermal stresses over and above the inevitable transformational

stresses. These two stresses together, quite often lead to warpage or cracking of the heat treating stock. 'Martempering' is a process, which can minimize the chance of cracking during hardening of alloy steels. In this process, the steel after being suitably austenitized, is rapidly quenched in suitable medium, i.e., preferably a salt bath, which is maintained at constant temperature above the M_s temperature and held there for preselected period of time as shown in Figure 51.

Temperature of holding is decided by the M_s temperature of the material being quenched that is the chemical composition of steel. On the contrary, the holding time must commensurate with the time required to equalize the temperatures between the surface and center of the heat treating stock, which further is a function of the geometry of the stock. Too low a holding time will not secure the basic purpose of this process; again too high holding time will bring about decomposition of austenite through diffusional means, which the process of hardening of steel does not aim at. Holding the steel above M_s temperature for sufficient period of time, equalizes the temperature between center and surface of the stock. Thus the thermal stresses generated due to differential volume contraction across the section of the stock are removed; also quenching from low temp to trigger martensite formation will eliminate thermal shock and hence reduce overall thermal stresses. Stresses originated from volume change accompanying martensitic transformation only exist. This leads to minimization of warpage and lessens the chances of formation of quench cracks. Thermal stresses is dependent on section size and if there is sharp change in section size in a component, stress localization may occur at the transition region; failure may initiate from this weak region. A larger section implies a higher magnitude of difference in cooling rate between surface and center; therefore thermal stress becomes quite high. Along with this, rapid change in cross section aggravates the situation and tendency to form quench cracks increases.

2.1.10.4 Austempering

Many medium carbon low alloy structural steels achieve their optimum properties with a microstructure similar to that of lower bainite. This type of structure can be obtained by a heat treatment called 'Austempering.' 'Austempering' is the process of heat treatment where the steel is heated to austenitizing temperature, held there for sufficient period of time to produce homogeneous austenite. The selection of austenitizing temperature and time follows from the same principles as that in the case of conventional quench-hardening process. After austenitization the steel is rapidly cooled to a temperature above M_s temperature and preferably in the region of lower bainite transformation. The severity of quench must be such as to be able to overcome the hardenability constraint if any. A salt bath kept at the quenching temperature say 300 °C, is used for isothermally holding the component for sufficiently long period so that complete decomposition of austenite may take place as shown in Figure 52.

Holding at the austempering temperature eliminates thermal stresses and isothermal transformation of austenite to lower bainite in a salt bath also protects the steel from oxidation due to neutral atmosphere and from distortion due to prevailing situation of hydrostatic pressure. Austempering produces lower bainite which is composed of supersaturated ferrite and ε carbide (Figure 53). Needless to say that after completion of bainitic transformation no other transformation takes place during cooling to room temperature from bainitic reaction temperature.

The low temperature tempering of hardened steel also produces low carbon martensite (i.e., ferrite of low supersaturation) and ε carbide. However strength and toughness properties of austempered material are much better than the hardened and tempered material.

During austempering lower bainitic transformation is envisaged. This means that quenching to austempering temperature leads to the formation of supersaturated ferrite by

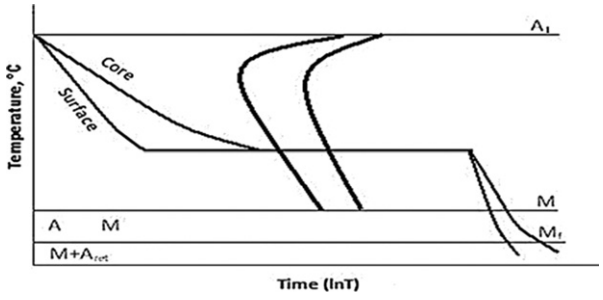


Figure 52 Austempering.

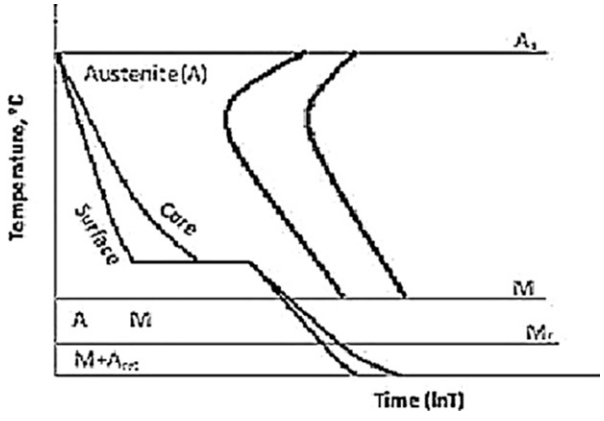


Figure 51 Martempering.

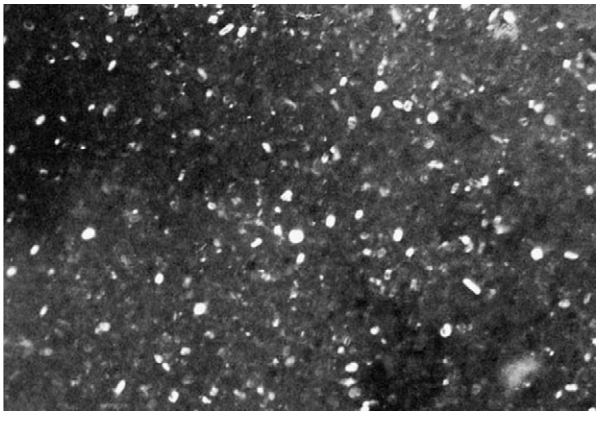


Figure 53 Microstructure showing supersaturated ferrite and ε carbide. Courtesy of George Vander Voort, USA.

diffusionless shear transformation mechanism; but due to the high temperature and also due to great urge for getting relieved from super saturation, the ferrite rejects carbon quite quickly in the form of ε carbide of 8.3 wt.%C (Reed-Hill).[1] Lower bainitic ferrite is much lean in carbon content as compared to the austenite and so excess carbon is rejected by the growing bainitic ferrite crystals ahead of the interface between the product ferrite phase and the parent austenite phase. Thus austenite ahead of bainitic ferrite becomes enriched with carbon; this process of formation of bainitic ferrite and continuous carbon enrichment of austenite ahead of interface continues, till a time is reached when high carbon austenite ahead of growing ferrite crystal cannot give way to the formation of bainite; at this time, growth of bainitic ferrite stops and there remains high carbon austenite, which cannot even transform to martensite during subsequent cooling to room temperature, owing principally to its increased metastability. Such a large amount of austenite retained inevitably due to incomplete bainitic reaction provides adequate ductility to the alloy. Thus austempering enables to achieve a good combination of high strength and high toughness, which otherwise would not have been possible, if the same steel was fully hardened and then tempered at the same austempering temperature (Figure 54). Austempering can harden complicated steel components without causing distortion and cracking. It can impart excellent toughness and ductility in thin sections of plain carbon steel. However, the entire cross section of the steel must be cooled rapidly enough to miss the nose of the IT curve. It is to note that thicker sections (>3 mm) of plain carbon steels are difficult to be austempered because of the short incubation period at the nose of TTT diagram. So, only thin sections are subjected to austempering. However larger sections of alloy steels can be austempered where the time to start the transformation is quite high.

2.1.11 Retained Austenite

In majority of cases the transformation of austenite to martensite does not go to completion. Presence of some untransformed austenite called 'retained austenite' is inevitable although its amount and quality depends upon composition of steel and its initial microstructure. Figure 55, shows that the amount of martensite formed from austenite increases as the transformation temperature is decreased within the M_s–M_f range. Martensite starts to form at M_s and its amount increases with decrease in temperature till the M_f temperature, which denotes completion of transformation. This follows from the typical characteristics of athermal transformation. At this point the transformed phase may contain some retained austenite. Figure 56 gives evidence of retained austenite in 0.9C steel after water quenching from 900 °C

Retained austenite is highly unstable and can be subsequently transformed to bainite or martensite depending upon the parameters of tempering operation. Sometimes a small amount of retained austenite is deliberately kept in the final microstructure. Not only it imparts toughness to the hardened steel but also if it transforms to martensite during post tempering cooling operation, some residual compressive stresses may be developed which is quite helpful to improve fatigue resistance.

Retained austenite is very soft and so if it is present in large quantity, say, by more than 15–20 vol.% in the microstructure, there will be a considerable reduction in the hardness of the quenched steel. As martensite forms, its volume strain is accommodated both by product martensite by lattice invariant deformation and by matrix austenite through plastic deformation. Continued growth of martensite plates lead to small pool of austenite entrapped between adjacent plates of martensite. This austenite contains a high density of crystal imperfection

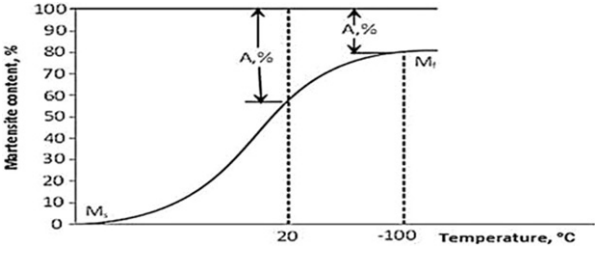


Figure 55 Martensite transformation curve.

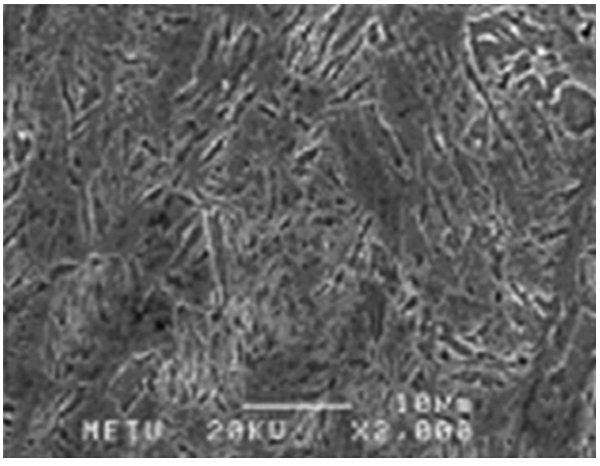


Figure 54 Microstructure of 0.37C–0.48Mn–1.3Cr austempered steel.[56]

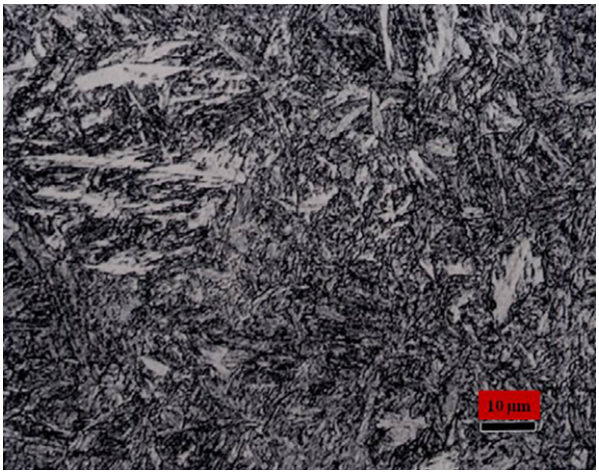


Figure 56 Microstructure showing retained austenite in quenched steel quenched from 900 °C. Courtesy of George Vander Voort, USA.

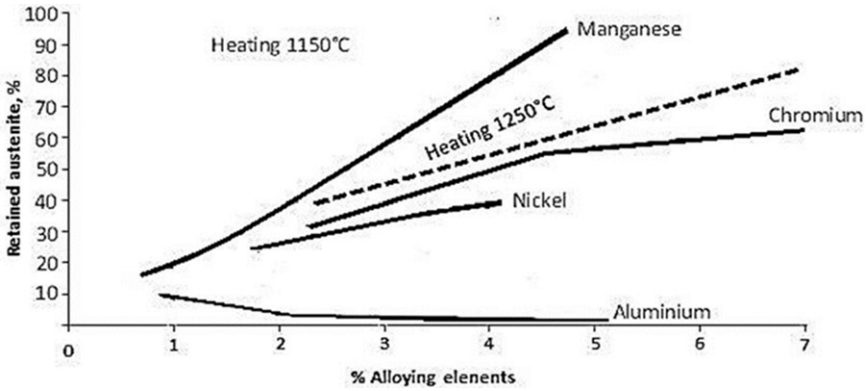


Figure 57 Effect of the alloying elements on the amount of retained austenite in quenched steel (1 wt.%C).

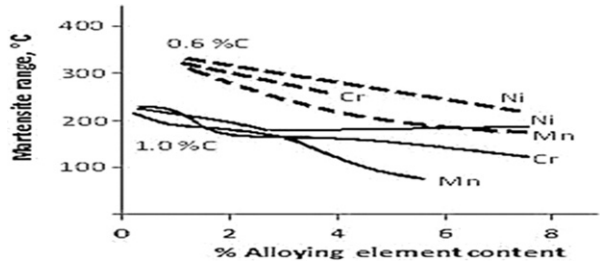


Figure 58 Effect of alloying addition on martensite range.

viz. dislocation and is not amenable to further martensite transformation. So they remain present in the microstructure as retained austenite.

Both M_s and M_f temperature are functions of alloying element content. When M_f goes below room temperature, the amount of retained austenite in the microstructure will expectedly be higher. The amount of austenite to be retained is mainly decided by the M_s–M_f temperature range. The effect of various alloying elements on the amount of retained austenite formed during quenching of steels is shown in Figure 57. The alloying elements which depress the M_s temperature are those which increase the percentage of retained austenite in the microstructure.

In alloy steels, the martensite start point M_s is lowered by most of the alloying elements and the martensite range narrows under the influence of carbon. The influence of carbon on austenite content is stronger than that of other alloying elements as shown in Figure 58.

In addition to the carbon content and alloying elements, the other factor which can influence the amount of retained austenite formed during quenching of steel is the rate of cooling between the martensite start point M_s and the final quenching temperature.

However at temperature just below M_s temperature a slow cooling may affect isothermal transformation of martensite formation. Here a phenomenon called the stabilization of austenite takes place. Holding the transforming austenite after appreciable amount of athermal martensite has formed, makes it prone to stabilization due to, relaxation of stress. Austenite stabilization takes place due to stress relaxation which leads to permanent loss of coherence between parent and product phase. The longer the holding time, the greater would be stress relaxation and thus greater will be stabilization. If martensitic transformation is interrupted between M_s–M_f ranges, then for further transformation to take place, much higher driving force will be required by intensive cooling.

The effect of quenching temperature is linked to the magnitude of thermal stresses due to transformation of austenite to martensite. When steel is heated substaintially above A_3 temperature, grain coarsening of austenite takes place, which further results in the formation of larger martensite plates. This leads to higher volume fraction of retained austenite in the microstructure. Higher austenitizing temperature lowers the martensite start temperatures (M_s), due to complete dissolution of carbide. When hypereutectoid steels are quenched from the region of pure austenite, i.e., after heating the steel above the A_{cm} temperature for complete dissolution of carbides (which is not usual), the quenched microstructure consists of martensite and retained austenite; the hardness is reduced due to high amount of retained austenite. The initial retained austenite amount (after quenching) is dependent on the austenitizing (hardening) temperature to a large extent. The higher the hardening temperature, the greater the amount of retained austenite, but this retained austenite can be made transformed to martensite by subzero treatment.

2.1.11.1 Subzero Treatment

Subzero treatment consist of cooling the metal to a temperature below 0 °C, but in general subzero treatment temperature may range from -130 to -30 °C with holding time around 1 h. In some cases the subzero treatment temperature can be as low as -190 °C in accordance with the M_f temperature of the steel which in turn depends on its chemical composition. If austenite stabilization takes place at room temperature, it will be difficult to transform retained austenite to martensite by subzero treatment.

Subzero treatment should to be done in continuation with the original quenching, without much residence time at room temperature. If we wish to convert retained austenite to martensite at room temperature, it must be heated to higher temperature in a region of metastable austenite. Cooling from that temperature down to room temperature will enable austenite to transform to martensite. Multiple tempering may

effect transformation of retained austenite to martensite during post tempering cooling and repetition of the process may ultimately eliminate the retained austenite from the structure.

Subzero treatment is normally employed in high alloy steels which are prone to form high amount of retained austenite after quenching to room temperature. However in case of industrial scale operation, subzero treated steel is reported to have suffered from a loss in bending strength. There are reports confirming the enhancement of wear resistance in ledeburitic steels. It is also observed that the bending strength of the steel can be recovered by tempering above the secondary hardness peak temperature. Reportedly, the three point bending strength of material undergoing subzero processing is lower than the non-subzero processed one. However the reason for this apparently anomalous behavior requires further investigation.[57] It is further reported that accelerated rate of precipitation due to subzero treatment contributes significantly to the enhancement of wear resistance; the high wear resistance of steel subjected to subzero treatment is ascribed to the formation of carbides of size less than 0.5 μ; also the improvement in wear resistance outweighs the marginal loss in bending strength. Because of the fact that the quenched hardness of the subzero treatment is higher than that of the non-subzero treated steels, a greater latitude in decrement of hardness due to tempering is available. This ensures better mechanical property of subzero-treated steel after low temperature tempering.[58]

2.1.12 Heat Treatment Defects

2.1.12.1 Quench Cracks

When hardening is accomplished with a martensite transformation, evolution of large residual stress is inevitable. Such stress owes its origin to differential thermal contraction of a material cooled rapidly from a high temperature and stress due to transformation.

When the steel sample is quenched rapidly from a high temperature to the room temperature for hardening two types of stresses are developed; one is due to volume change accompanying phase transformation and the other is due to differential coefficient of contraction of different phases present in the material. Also thermal stress due to temperature difference between surface and center of the component is superimposed. When the cumulative value of these stresses becomes large enough, plastic deformation of the steel sample may take place. This plastic deformation may lead to warpage of the component; whenever plastic deformation is unable to take care of all the quench stresses, there would be accumulation of the residual stress which when exceeds the fracture stress of the material will lead to quench crack.

When a round steel bar is quenched, the surface undergoes martensite transformation before the center. It is known that martensite transformation leads to expansion whereas rapid cooling leads to thermal contraction. When expansion at the surface is larger than thermal contraction, the surface will be in a state of tension whereas center is at the state of contraction as shown in Figure 59.

If contraction exceeds expansion at the surface the reverse stress pattern with surface under residual compressive stress and center with tension will prevails. Which of these two will

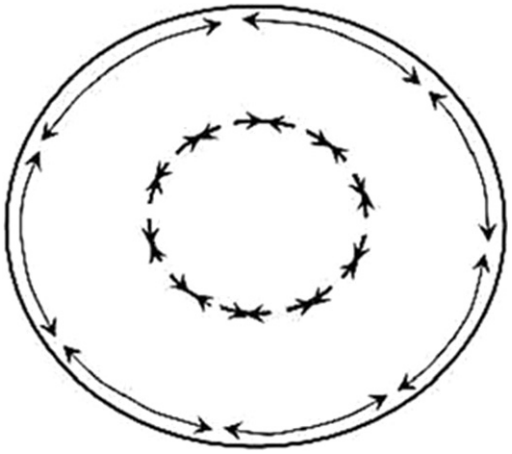


Figure 59 State of stresses due to quenching of a round bar.

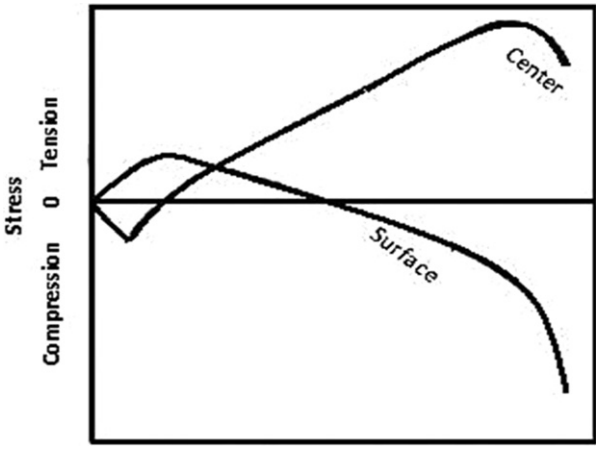


Figure 60 Residual stresses in a steel cylinder quenched to form martensite as computed by Scott. Scott, H. Origin of Quenching Cracks. *Sci. Pap. Bur. Stand.* **1925**, *20*, 399.

actually be present is decided by the relative cooling rate at the surface and at the center of the bar; this is a function of both size of the bar and severity of quench. For large diameter and fast cooling, the surface will form martensite while the center is still at high temperature. Under such circumstances thermal stress will be quite large and it will determine the pattern of volume change. Usually thermal contraction will exceed expansion due to martensite transformation. On the other hand for a thinner object, the difference in cooling rate between surface and center is small the thermal contraction after hardening of surface is still smaller as compared to expansion due to martensite transformation. The variation in stress due to temperature difference between center and surface of the bar is shown in Figure 60.

In many cases the tensile stress persists at the surface. Initially over a large range of specimen diameter tensile stress is seen to increase with cooling rate differentials. Those steel which have high carbon content, transform to martensite with higher degree volume expansion and hence in such case the tensile stress prevails at surface. Since quench crack is formed

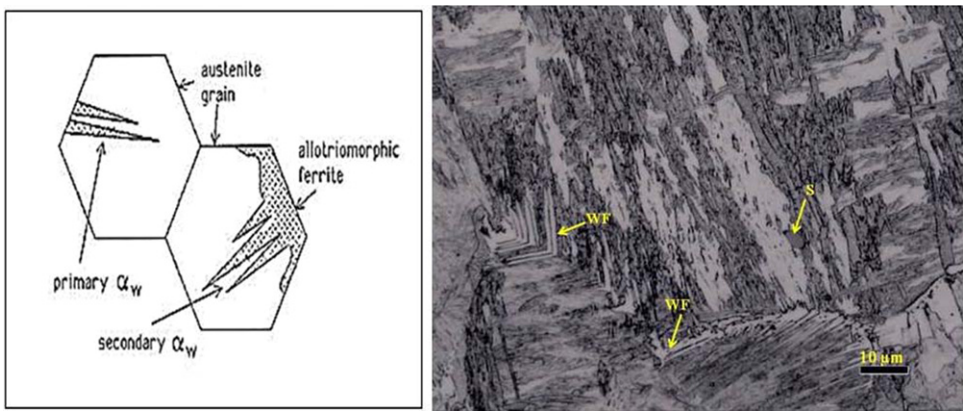


Figure 61 Widmanstatten ferrite in water quenched 1018 steel. Courtesy of George Vander Voort, USA.

as a result of tensile stress high carbon steel with high volume change put to a very fast quenching, results in quench crack.

2.1.12.2 Overheating

If a steel specimen is heated for a very long time far above the stipulated temperature, over heating may occur with the result of getting coarse grains. Structure of the overheated steel sample with Widmanstätten ferrite is shown in **Figure 61**. If a prolonged heating at a temperature is carried out in a furnace where no control of atmosphere is existent or if the material is heated to a temperature near to its melting point, the damage of the specimen is visualized as burning. In this case carbon atoms segregate at the grain boundaries and lead to intercrystalline fracture. A lot of cavities can form including the formation of iron oxide which will be present as inclusion and this leads to stone like fracture at a low ductility level. Quite often in an uncontrolled furnace a high austenitizing temperature leads to decarburization of the surface and the hardness of the surface is decreased, and it misleads the heat treater. Excessive decarburization is associated with the formation of thick scale that acts as an insulating blanket and does not allow heat extraction to desired level. This makes the entire heat treatment process uncertain and undesirable.

See also: 2.8 Heat Treatment of Commercial Steels for Engineering Applications

References

1. Reed-Hill, R. E. *Physical Metallurgy Principles*, 2nd ed.; PWS-Kent Publishing Company: Boston, MA, 1973.
2. Dieter, G. E. *Mechanical Metallurgy*, 3rd ed.; Mc Graw Hill Book Company, 1986.
3. Avner, S. H. *Introduction to Physical Metallurgy*, 2nd ed.; Mc Graw Hill, Education (India) Private Limited: New Delhi, 1974.
4. Tarui, T.; Ohashi, O.; Takahashi, T.; Uemori, R. Microstructure Control and Strengthening of High-Carbon Steel Wires. *Iron Steelmak.* **1994**, *21*, 25.
5. Tarui, T.; Maruyama, N.; Takahashi, J.; Nishida, S.; Tashiro, H. *Microstructure Control and Strengthening of High-Carbon Steel Wires: Nippon Steel Technical Report No. 91,* 2005; pp. 56–61.
6. Languillaume, L.; Kapelski, G.; Baudelet, B. Cementite Dissolution in Heavily Cold Drawn Pearlitic Steel Wires. *Acta Mater.* **1997**, *45*, 1201–1212.
7. Danoix, F.; Julien, D.; Sauvage, X.; Copreaux, J. Formation of Fine Cementite Precipitates in an Ultra-Fine Grained Low Carbon Steel. *Mater. Sci. Eng. A* **1998**, *250*, 8.
8. Hong, M. H.; Reynolds, W. T.; Tarui, T.; Hono, K. Atom Probe and Transmission Electron Microscopy Investigations of Heavily Drawn Pearlitic Steel Wire. *Metall. Mater. Trans. A.* **1999**, *30*, 717.
9. Bargujer, S. S.; Suri, N. M.; Belokar, R. M. Thermo Mechanical Processing of Hypereutectoid Steel Wire Rod in Lead Patenting. *Int. J. Innov. Technol. Explor. Eng.* **2013**, *3* (5), ISSN: 2278-3075.
10. Bandyopadhyay, N. R.; Banerjee, M. K.; Das, P. P. Hot Forging: A Tool to Improve the Structure of White Cast Iron. *Trans. Indian Inst. Met.* **1986**, *39* (5), 486–491.
11. Barbadikar, D. R.; Deshmukh, G. S.; Maddi, L.; *et al.* Effect of Normalizing and Tempering Temperatures on Microstructure and Mechanical Properties of P92 Steel. *Int. J. Pres. Ves. Pip.* **2015**, *132–133*, 97–105.
12. Hui Li; Yun-li Feng; Meng Song; Jing-long Liang; Da-qiang Cang. Effect of Normalizing Cooling Process on Microstructure and Precipitates in Low-Temperature Silicon Steel. *Trans. Nonferr. Metals Soc. China* **2014**, *24* (3), 770–776.
13. Shitong Weia; Shanping Lu. Effects of Multiple Normalizing Processes on the Microstructure and Mechanical Properties of Low Carbon Steel Weld Metal with and without Nb. *Mater. Des.* **2012**, *35*, 43–54.
14. ASM. *ASM Hand Book Volume 4: Heat Treating*; American Society of Metals: Metal Park, OH, 1991.
15. Huei-Sen Wang; Hou-Guang Chen; Jhen-Wang Gu; Cheng-En Hsu; Chung-Yung Wu. Effects of Heat Treatment Processes on Microstructures and Properties of Powder Metallurgy Produced Cu–Ni–Si–Cr Alloy. *Mater. Sci. Eng. A* **2014**, *619*, 221–227.
16. Banerjee, M. K. Effect of Melt Homogeneity on the Age Hardening of Copper–Chromium Alloys. *CastMetals* **1994**, *6*, 204.
17. Gogebakan, M.; Kursun, C.; Gunduz, K. O.; Tarakci, M.; Gencer, Y. Microstructural and Mechanical Properties of Binary Ni – Si Eutectic Alloys. *J. Alloys Compd.* **2015**, *643*, S219–S225.
18. Yun, D. W.; Seo, S. M.; Jeong, H. W.; Kim, I. S.; Yoo, Y. S. Modelling High Temperature Oxidation Behaviour of Ni – Cr – W – Mo Alloys with Bayesian Neural Network. *J. Alloys Compd.* **2014**, *587*, 105–112.
19. Fivel, M. C.; Strudel, J. L.; Chung, H. J. Initial Stage of Creep in Nickel Based Super Alloy, a 3d Discrete Dislocation Dynamics Integration. In *International Workshop on Modeling and Simulation of Super Alloys, Organized by ICMAS, Ruhr-Universitat Bochum*, Germany, Sepember 13 – 17, 2014.
20. Polmear, I. J. Role of Trace Elements in Aged Aluminium Alloys. *Mater. Sci. Forum* **1987**, *13/14*, 195.
21. Mohamed, I. F.; Yonenag, Y.; Lee, S.; Edalati, K.; Horit, Z. Age Hardening and Thermal Stability of Al–Cu Alloy Processed by High-Pressure Torsion. *Mater. Sci. Eng. A* **2015**, *627*, 111–118.
22. Kim, J. H.; Marioara, C. D.; Holmestad, R.; Kobayashi, E.; Sato, T. Effects of Cu and Ag Additions on Age-Hardening Behavior During Multi-Step Aging in Al–Mg–Si Alloys. *Mater. Sci. Eng. A* **2013**, *560*, 154–162.
23. Ding, X. P.; Cui, H.; Zhang, J. X.; *et al.* The Effect of Zn on the Age Hardening Response in an Al–Mg–Si Alloy. *Materi. Des.* **2015**, *65*, 1229–1235.
24. Kaiser, M. S.; Datta, S.; Roychowdhury, A.; Banerjee, M. K. Effect of Scandium on the Microstructure and Ageing Behaviour of Cast Al–6Mg Alloy. *Mater. Charact.* **2008**, *59*, 1661–1666.

25. Kaiser, M. S.; Datta, S.; Roychowdhury, A.; Banerjee, M. K. Effect of Prior Cold Work on Tensile Properties of Al–6Mg Alloy with Minor Scandium Additions. *Can. Metall. Q.* **2014**, *53* (4), 486–493.
26. Kaiser, M. S.; Datta, S.; Bandyopadhyay, P. P.; Guha, A.; Roychowdhury, A. Effect of Grain Refinement through Minor Additions of Scandium and Zirconium on the Machinability of Al–Mg Alloys. *J. Inst. Eng. (India): Ser. D* **2013**, *94* (1), 17–24.
27. Kaiser, M. S.; Nambissan, P. M. G.; Banerjee, M. K.; Sachdeva, A.; Pujari, P. K. Positron Life Time Studies and Co-Incidence Doppler Broadening Spectroscopy of Al–6Mg–xSc(x = 0 to .6 wt%) Alloys. *J. Mater. Sci.* **2007**, *42*, 2618–2629.
28. Banerjee, M. K.; Datta, S. Effect of Cold Work and Trace Rare-Earth Additions on the Aging Behavior of Al–Cr Alloys Containing Zirconium. *Mater. Charact.* **2000**, *44*, 277–284.
29. Banerjee, M. K. Age Hardening in Aluminium–Chromium Alloys. *J. Mat. Sci.* **1997**, *32* (24), 645.
30. Data, S.; Bhunya, A.; Banerjee, M. K. Two Way Shape Memory Loss in Cu–Zn–Al Alloy. *Mater. Sci. Eng. A* **2001**, *300*, 291–298.
31. Bhuniya, A.; Chattopadhyay, P. P.; Datta, S.; Banerjee, M. K. Study on the Effect of Trace Zirconium Addition on the Micro Structural Evolution in Cu–Zn–Al Shape Memory Alloy. *Mater. Sci. Eng. A* **2005**, *391*, 34–42.
32. Chattopadhyay, P. P.; Bhuniya, A. K.; Datta, S.; Banerjee, M. K. Effect of Trace Addition of Ti on the Micro Structural Degradation in Cu–Zn–Al Shape Memory Alloy due to Ageing Effect. *Mater. Sci. Eng. A* **2005**, *393* (1), 125–132.
33. Gomidželović, L.; Požega, E.; Kostov, A.; *et al.* Thermodynamics and Characterization of Shape Memory Cu–Al–Zn Alloys. *Trans. Nonferr. Metals Soc. China* **2015**, *25* (8), 2630–2636.
34. Kadletz, P. M.; Krooß, P.; Chumlyakov, Y. I.; *et al.* Martensite Stabilization in Shape Memory Alloys – Experimental Evidence for Short-Range Ordering. *Mater. Lett.* **2015**, *159*, 16–19.
35. Jia Wen Xu. Effects of Gd Addition on Microstructure and Shape Memory Effect of Cu–Zn–Al Alloy. *J. Alloys Compd.* **2008**, *448* (1–2), 331–335.
36. Asanović, V.; Delijić, K.; Jauković, N. A Study of Transformations of β-Phase in Cu–Zn–Al Shape Memory Alloys. *Scr. Mater.* **2008**, *58* (7), 599–601.
37. Saud, S. N.; Hamzah, E.; Abubakar, T.; Bakhsheshi-Rad, H. R. Correlation of Microstructural and Corrosion Characteristics of Quaternary Shape Memory Alloys Cu–Al–Ni–X (X = Mn or Ti). *Trans. Nonferr. Metals Soc. China* **2015**, *25* (4), 1158–1170.
38. Furlani, A. M.; Stipcich, M.; Romero, R. Phase Decomposition in a β Cu–Zn–Al–Ti–B Shape Memory Alloy. *Mater. Sci. Eng. A* **2005**, *392* (1–2), 386–393.
39. Stalmans, R.; Van Humbeeck, J.; Delaey, L. The Two Way Memory Effect in Copper Based Shaps Memory Alloys Thermodynamics and Mechanisms. *Acta Metall. Mater.* **1992**, *40*, 2921.
40. Bhattacharya, S.; Bhuniya, A.; Banerjee, M. K. Influence of Minor Additions on Characteristics of Cu–Al–Ni Alloy. *Mater. Sci. Technol.* **1993**, *9* (8), 654–658.
41. Rios-Jara, D.; Guenin, G. On the Characterization and Origin of the Dislocation Associated with the Two-Way Memory Effect in Cu–Zn–Al Alloys. *Acta Metall.* **1987**, *35*, 109.
42. Du, Z. X.; Xiao, S. L.; Shen, Y. P.; *et al.* Effect of Hot Rolling and Heat Treatment on Microstructure and Tensile Properties of High Strength Beta Titanium Alloy Sheets. *Rare Metal Mater. Eng.* **2015**, *44* (2), 327–332.
43. Yuhua Li; Chao Yang; Haidong Zhao; Shengguan Qu; Xiaoqiang Li; Yuanyuan Li. New Developments of Ti-Based Alloys for Biomedical Applications. *Materials* **2014**, *7*, 1709–1800. doi:10.3390/ma7031709.
44. Jiangkun Fana; Jinshan Li; Hongchao Kou; Ke Hua; Bin Tang; Yudong Zhang. Influence of Solution Treatment on Microstructure and Mechanical Properties of a Near β Titanium Alloy Ti-7333. *Mater. Des.* **2015**, *83*, 499–507.
45. Gu, Y.; Zeng, F.; Qi, Y.; Xia, C.; Xiong, X. Tensile Creep Behavior of Heat-Treated TC11 Titanium Alloy at 450–550 °C. *Mater Sci. Eng. A* **2013**, *A55*, 74–85.
46. Chao, Q.; Hodgson, P. D.; Beladi, H. Ultrafine Grain Formation in a Ti–6Al–4V Alloy by Thermomechanical Processing of a Martensitic Microstructure. *Metall. Mater. Trans. A* **2014**, *45A*, 2659–2671.
47. Li, C.; Chen, J.; Ren, Y. J.; Li, W.; He, J. J.; Chen, J. H. Effect of Solution Heat Treatment on the Stress-Induced Martensite Transformation in Two New Titanium Alloys. *J. Alloys Compd.* **2015**, *641*, 192–200.
48. Yuyong Chen; Zhaoxin Du; Shulong Xiao; Lijuan Xu; Jing Tian. Effect of Aging Heat Treatment on Microstructure and Tensile Properties of a New β High Strength Titanium Alloy. *J. Alloys Compd.* **2014**, *586*, 588–592.
49. Beladi, H.; Barnett, M. R. Influence of Aging Pre-Treatment on the Compressive Deformation of WE54 Alloy. *Mater. Sci. Eng. A* **2007**, *452–453*, 306–312.
50. Fujita, N.; Bhadeshia, H. K. D. H. Modelling Simultaneous Alloy Carbide Sequence in Power Plant Steels. *ISIJ Int.* **2002**, *42* (7), 760.
51. Baltušnikas, A.; Levinskas, R.; Lukoštūtė, I. Kinetics of Carbide Formation During Ageing of Pearlitic 12X1MΦ Steel. *Mater. Sci.* **2007**, *13* (4), 286–292.
52. Robson, J. D.; Bhadeshia, H. K. D. H. Kinetics of Precipitation in Power Plant Steels. *Calphad* **1996**, *20* (4), 447–460.
53. Zhou, W. H.; Challa, V. S. A.; Guo, H.; Shang, C. J.; Misra, R. D. K. Structure–Mechanical Property Relationship in a Low Carbon Nb–Cu Microalloyed Steel Processed through a Three-Step Heat Treatment: The Effect of Tempering Process. *Mater. Sci. Eng. A* **2015**, *620*, 454–462.
54. Xie, Z. J.; Fang, Y. P.; Han, G.; Guo, H.; Misra, R. D. K.; Shang, C. J. Structure–Property Relationship in a 960 MPa Grade Ultrahigh Strength Low Carbon Niobium–Vanadium Microalloyed Steel: The Significance of High Frequency Induction Tempering. *Mater. Sci. Eng. A* **2014**, *618*, 112–117.
55. Hasan, H. S.; Peet, M. J.; Avettand-Fènoël, M.-N.; Bhadeshia, H. K. D. H. Effect of Tempering Upon the Tensile Properties of a Nanostructured Bainitic Steel. *Mater. Sci. Eng. A* **2014**, *615*, 340–347.
56. Chennakesava, R. A. Effects of Holding Temperature and Time for Austempering on Impact Toughness of Medium Carbon and High Alloy Steel. *Int. J. Comput. Netw. Secur.* **2013**, *3* (1), ISSN: 0975–8283.
57. Jurči, P.; Sobotová, J.; Cejp, J.; Salabová, P.; Prikner, O. Effect of Sub-Zero Treatment on Mechanical Properties of Vanadis 6 PM Ledeburitic Tool Steel. In *Proceedings of the 19th International Metallurgical and Materials Conference (METAL '10)*; Tanger, S. R. O., Ed.; Rožnov pod Radhoštěm, Czech Republic, 2010.
58. Jurči, P.; Dománková, M.; Ptačinová, J.; Hudáková, M. *Phase Constitution of Sub-Zero Treated Vanadis 6 Tool Steel, Metal 2015*, 2015.

Further Reading

Gunn, R. N., Ed. *Duplex Stainless Steels, Microstructural Properties and Applications*; Abington Publishing: Cambridge, 1997.

Lakhtin, Y. *Engineering Physical Metallurgy*; Mir Publishers: Moscow and CBS Publishers and Distributors: India, 1998.

Relevant Website

www.georgevandervoort.com/.../20001270-microstructure-of-ferrous-alloys George Vander Voort.

2.2 Hardenability of Steel

AK Bhargava and MK Banerjee, Malaviya National Institute of Technology, Jaipur, India

© 2017 Elsevier Inc. All rights reserved.

2.2.1	**Introduction**	50
2.2.2	**Hardness versus Hardenability**	52
2.2.3	**Criterion for Measuring Hardenability**	52
2.2.3.1	Mechanism of Heat Removal During Quenching	53
2.2.3.2	Quenching Media	53
2.2.3.2.1	Water	53
2.2.3.2.2	Aqueous solutions	54
2.2.3.2.3	Oils	55
2.2.3.2.4	Polymer quenchants	55
2.2.3.2.4.1	Mechanism of quenching in polymer quenchants	55
2.2.4	**Quantitative Methods of Measuring Hardenability: Grossman's Method**	56
2.2.4.1	Critical Diameter	56
2.2.4.2	Severity of Quench	57
2.2.4.2.1	Experimental evaluation of '*H* of a coolant	57
2.2.4.2.2	Evaluation of critical diameter	59
2.2.4.3	Ideal Critical Diameter	59
2.2.5	**Jominy End-Quench Test**	60
2.2.5.1	Correlation between Jominy Test Distance and Grossmann Method, D_I	61
2.2.5.2	Hardenability Bands	61
2.2.6	**Factors Affecting Hardenability**	62
2.2.6.1	Effect of Grain Size	63
2.2.6.2	Austenitizing Temperature and Time	64
2.2.6.3	Effect of Carbon Content on Hardenability	64
2.2.6.4	Effect of Alloying Elements on Hardenability	65
2.2.7	**Estimation of Hardenability from Chemical Composition and Austenite Grain Size**	66
2.2.8	**Effect of Boron on Hardenability**	67
References		69

2.2.1 Introduction

The term hardenability, as associated with steels, is closely related to hardening by heat treatment. Hardenability of steel is a material property describing the ability of steel to avoid diffusional transformation of austenite to equilibrium products which includes pearlite. Hardening of steels occurs due to the formation of martensite – a nonequilibrium phase formed by diffusionless shear transformation of austenite. For the formation of martensite in steel, the specimen is heated to the single phase austenitic region of Fe–C phase diagram. The steel specimen is held at austenitizing temperature for specified period of time in order to homogenize austenite; homogenization of austenite insures uniformity in chemical composition of austenite at all locations. After homogenization, the specimen is cooled at such a rate that equilibrium phases do not form. Such a cooling rate is generally achieved by immersing the steel sample from austenitizing temperature into water or oil. In order to produce martensite the applied cooling rate must exceed a critical value. This critical value depends upon the composition and other structural features of the steel. Figure 1 illustrates the critical cooling rate.

Any rate of cooling higher than this will produce martensitic structure in steel. In contrast, a cooling rate slower than this will produce pearlite. When a steel specimen of appreciable diameter is immersed in water or oil, the cooling rate at the surface is vastly different from that at the center. This is because of large thermal gradient across the section of the steel section. This difference increases with severity of quench. As soon as the specimen is immersed in the cooling medium from austenitic temperature, cooling starts immediately over the entire surface area surrounded by the coolant. The cooling rate is very high at the surface of the specimen but it decreases toward the center and reaches to minimum there. So long as the cooling rate at any location within the sample is greater than or equal to critical cooling rate, 100% martensite is formed. Thereafter, at increasing depth, the cooling rate remains less than the critical cooling rate and so, equilibrium products such as pearlite or ferrite are formed. At an intermediate cooling rate a mixture of fine pearlite and martensite may form due to split transformation. This effect is demonstrated in Figure 1, where cooling rate curves corresponding to surface and center of a sizable eutectoid steel bar quenched rapidly in a quench medium are superimposed on partial IT curves. In addition, two more cooling rate curves corresponding to critical cooling rate and one at intermediate cooling rate are also shown in the same diagram. The intermediate cooling rate curve is assumed to give a structure

 doi:10.1016/B978-0-12-803581-8.09186-4

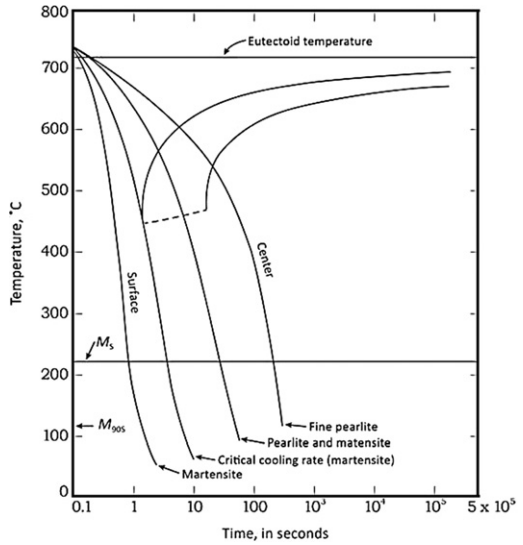


Figure 1 Effect of the difference in the cooling rate at the surface and center of a cylindrical bar of eutectoid steel on resulting microstructures. T_s: Transformation start, T_f: Transformation finish, M_s: Martensite starts, M_f: Martensite finish.[1]

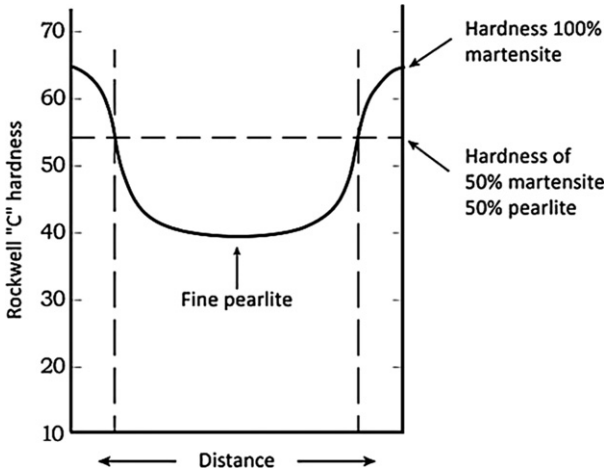


Figure 2 Hardness traverse along a diameter on cross-section of a cylindrical steel specimen from surface toward the center.[1]

comprising of 50% martensite and 50% pearlite. Thus the specimen is expected to have 100% martensite at its surface while 100% pearlite at its center. Since microstructure is varying from surface to core, the corresponding variation in hardness is obvious. The hardness test is performed on the circular cross-section along a diameter at number of locations and the results are plotted as function of distance from center toward the surface of the specimen, as shown in **Figure 2**. The martensite formed at the surface produces high hardness of 65 HRC whereas the pearlite formed at the center gives lowest hardness of 40 HRC. The horizontal line represents the hardness corresponding to 50% martensite and 50% pearlite (which has been estimated from the microscopic measurement. In the microstructure pearlite etches darker than martensite). Surface hardness, depends on the carbon content of

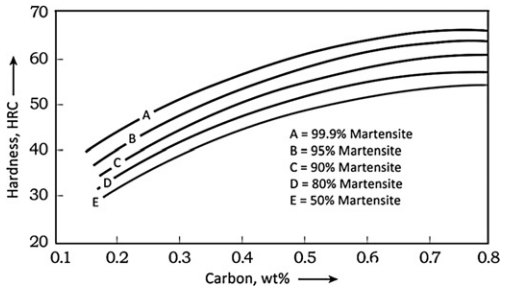


Figure 3 Relationship between hardness, carbon content, and percentage of martensite in steels.[2]

the steel more precisely the carbon content of the transformed martensite. Undissolved carbide, if present in austenite may promote formation of pearlite. The hardness of quenched steel is maximum if all carbon goes into solution in austenite, critical cooling rate is attained during quenching, no austenite is retained after quenching, and no autotempering occurs during quenching. **Figure 3** illustrates the effect of carbon content on hardness of martensite and the amount of martensite formed. It can be noted from this figure that for any percentage of martensite, hardness increases with increasing carbon content.

If the thickness or diameter of the specimen is so small that cooling rate up to its center is greater than the critical cooling rate, martensite will form throughout the specimen. The specimen is said to be fully hardened. The depth up to which the desired hardness in the specimen is achieved is a measure of hardenability of steel. Thus, hardenability of steel can be defined as the depth of hardening achieved in a steel sample after being quenched from the austenitizing temperature. It is the ability of steel to harden (by formation of martensite) throughout its cross-section. Hardenability sometimes is also defined on the basis of microstructure produced by quenching to a certain depth such as 50% martensite and 50% fine pearlite or other equilibrium transformation product. The steels which exhibit hardness to a greater depth below the surface are said to have high hardenability. On the contrary, the steels which harden to a shallow depth are said to possess low hardenability. Plain carbon steels are shallow hardening type. In deep hardening steels, uniform hardening is possible throughout the section depending on its thickness. This is illustrated in **Figure 4** for plain carbon steel 1060 and steel 5160 (an alloy steel containing 0.8% chromium) bars of 25 mm diameter quenched in oil. The hardness at the surface is same for both the steels having same carbon content but the hardness in the central region of 1060 steel is much lower due to formation of pearlite in this region. In contrast, steel 5160 exhibits nearly same hardness from surface to center. The word 'hardenability' does not mean the magnitude of hardness rather it is the depth of useful hardness and the usefulness is a user criterion. The basic purpose of quenching a steel article from austenitic temperature is to attain desired value of hardness up to the required depth. Each grade of steel has its own transformation behavior and therefore its own depth of hardening; hence hardenability is an important factor in the selection of steel for heat treated parts.

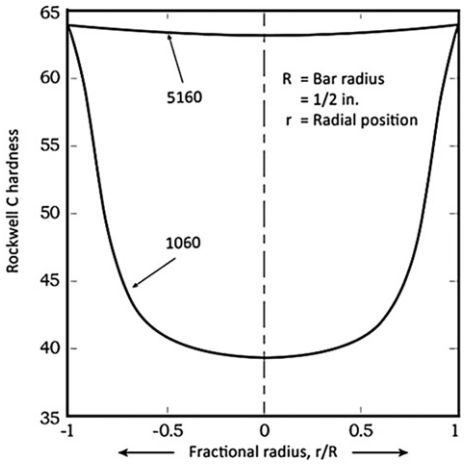


Figure 4 Rockwell hardness as a function of radius of 25 mm diameter bars of oil quenched 1060 and 5160 steels.[3]

2.2.2 Hardness versus Hardenability

Hardness of a material is the resistance offered by it against indentation or penetration of an indenter under a definite load as measured by Brinell, Rockwell, or Vickers tests. Hardness of steel is the maximum hardness that can be developed in it by the formation of martensite which in turn is a function of carbon content. Hardenability, on the other hand, is the depth up to which this hardness is developed from the surface of steel after hardening treatment. The maximum hardness that can be developed in steel depends on several factors stated previously in context of Figure 2. In contrast, carbon content has only minor effect on improvement of hardenability as explained in detail in Section 2.2.6.3. Plain carbon steels are characterized by low hardenability due to short incubation period for diffusional transformation during quenching. Hardenability is principally governed by the presence of alloying elements in steel and its grain size. Moreover, the depth of hardness is affected by the characteristic of the coolant used, the method of quenching, the massiveness of the steel specimen, and the criterion of hardenability set by the user. Hardenability is of considerable significance as it correlates to many of the mechanical properties of steels including yield strength, tensile strength, toughness, and fatigue strength.

2.2.3 Criterion for Measuring Hardenability

One of the most widely accepted criterion of measuring hardenability is the depth from the surface of steel where 50% martensite and 50% pearlite is produced during quenching. It is easy to distinguish a microstructure consisting of 50% martensite and 50% pearlite in a steel sample of finite size, which has been quenched from austenitization temperature. The diameter of the sample must be sufficient to prevent through hardening. The sample is generally fractured in the middle of its length. The visual examination of the as fractured surface shows two distinct regions.[4] The outer region appears smooth, bright, granular, and faceted, characterizing brittle type of fracture due to hard and brittle martensite formed in

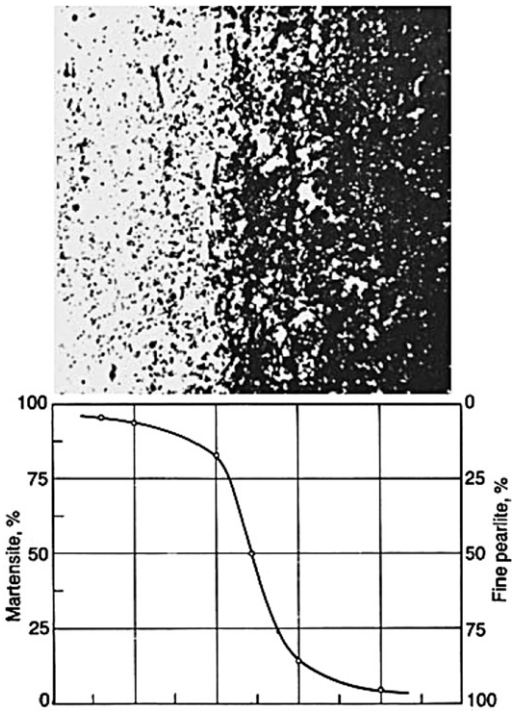


Figure 5 Transition from martensite (top left) to pearlitic (top right) microstructure between hardened and unhardened zones of a quenched steel.[5]

this region. The inner core region appears somewhat rough, fibrous, and dull in color characterizing ductile or tough type of fracture due to soft equilibrium product. The 50% martensitic structure delineates the boundary of two types of fracture. If the fractured surface is polished and etched in nital and examined microscopically, dark and light color regions are delineated. The outer lighter region is due to martensite which etches light whereas the inner region is due to pearlite which etches dark as illustrated in Figure 5. The color change occurs from lighter region to dark at 50% martensite. That is, 50% martensitic structure is the transition of this color change. These findings are generally confirmed from hardness measurement carried out on polished section along with one of the diameters from outer surface toward the inner core. The hardness data are then plotted against distance from surface to center as illustrated in Figure 2. It can be seen from this figure that the hardness is high at the surface and is constant a little up to certain depth where the microstructure 100% martensite. Thereafter, the hardness decreases with distance somewhat rapidly, passes a point of inflection, and then decreases slowly. At the point of inflection the proportion of martensite is 50%. Thus, at 50% martensite, there are abrupt changes in fracture behavior, etching, and also in the curvature of distance versus hardness plots; all the changes are easily detectable. This is why; the depth up to which 50% martensite is present in microstructure of quenched samples is taken as criterion for measuring hardenability.

The foregoing discussions show that the proportion of martensite and the corresponding hardness (Figure 3) at a certain depth below the surface of quenched steel of specific composition is a function of cooling rate (Figure 1) at that

point. However, the cooling rate at any point during quenching from austenitizing temperature may not be the same. It varies with the temperature at that point which in turn depends on severity of quench and section size of the steel sample. The effect of section size on surface hardness of a plain carbon steel quenched in water is shown in Figure 6.

2.2.3.1 Mechanism of Heat Removal During Quenching

To understand the mechanism of heat removal during quenching, consider a typical cooling curve for a small steel cylinder quenched in water as shown in Figure 7. The cooling curve is divided into three stages based on the rate of change of temperature with time.

In Stage I, which is known as Vapor Blanket Stage, the hot metal part immersed in a cooling (quenching) medium, leads to vaporization of liquid and forms a thin uniform film of vapor that is a vapor blanket around the metal. The vapor blanket is maintained for some time because the heat supplied from the interior of the part to its surface exceeds the amount of heat needed for vaporization of the quenching medium. Due to insulating nature of the vapor film, the cooling rate is relatively slow in vapor blanket stage. The vapor blanket formed is continuously washed off by the surrounding layers of the liquid, and this effect is intensified if the viscosity of the liquid is less, i.e., the greater its fluidity.

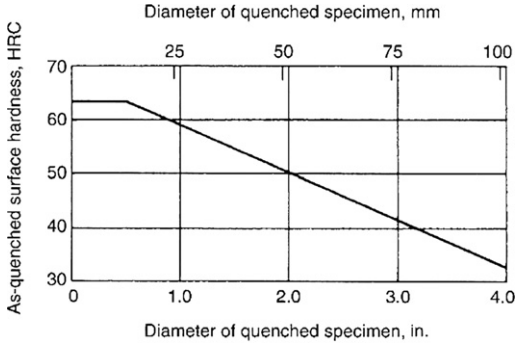


Figure 6 Effect of section size on surface hardness of 0.54% carbon steel quenched in water.[6]

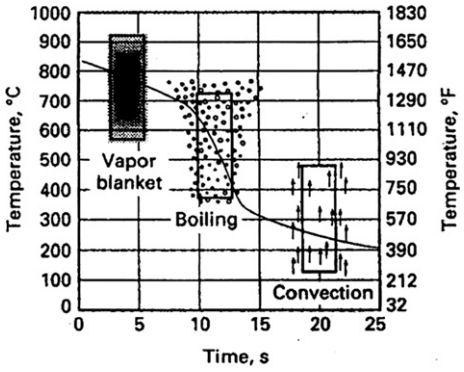


Figure 7 Three stages of heat removal during quenching of a small steel cylinder in water.[7]

Stage II is Vapor-Transport Cooling stage, in this stage as the metal surface cools down, the vapor film becomes unstable and collapse. At this instant the metal surface comes in direct contact with the quenchant and as a consequence, heat extraction from the metal part occurs rapidly and causes violent boiling of quenching medium (Figure 7). Due to this vigorous boiling, the second stage of cooling is also called vapor transport cooling or nucleate boiling stage. Latent heat of vaporization is responsible for rapid heat extraction from the hot metal during the boiling stage.

Third stage of cooling, known as liquid cooling stage, begins when the temperature of the metal is reduced below the boiling point of the quenchant; boiling stops and liquid vapor no longer forms. Cooling occurs by conduction and convection into the liquid quenchant. This stage is also called as convective stage.

If either the quenchant is agitated (e.g., by circulation of the quenchant) or the article is moved relative to quenching medium then mechanical disruption of the vapor blanket takes place which in turn results in faster transition to boiling stage of cooling. Agitation causes cooling of the part more or less uniform and usually produces faster cooling rates in all the three stages of quenching. In the absence of agitation quenching is mostly nonuniform due to uneven heat removal from the metal part, in particular, in the first stage of quenching.

2.2.3.2 Quenching Media

High hardenability is wanted to insure formation of martensite up to a higher depth of a metal part subjected to hardening. In order to obtain martensitic structure in a given steel, quenching medium must be such as to provide a cooling rate faster than the critical cooling rate. This enables to avoid soft diffusional transformation product of austenite, viz. pearlite and ferrite. On the other hand, it is desirable to cool the steel part at a considerably slower rate during martensitic transformation (300–200 °C) so as to minimize residual stresses accompanied structural change. For given steel, the required depth of hardening depends on the quenching medium used. The quenching rate varies vastly in different quenching media. The cooling rates for small specimens of steel in various quenching media are shown in Table 1 and Figure 8 gives cooling curves comparing the cooling characteristics of several quenching media. Some important quenching media are described in the following paragraphs.

2.2.3.2.1 Water

Water, by far, the most popular quenching medium used commercially, principally because of its ease of availability, low price, ease of handling, free of pollution, and produces fast cooling rates. Among all quenching media, water is next to aqueous solutions with regard to quenching rate (Table 1) not only in the metastable austenite region (which is excellent) but also during martensitic transformation temperature range (which is bad). However, drastic quenching during martensitic transformation temperature range, lead to danger of warpage and quench cracks, especially in complex shaped steel articles. Warming of water greatly reduces the cooling rate (Table 1) within the metastable austenite range and has very little effect

on cooling rate in the martensitic transformation range. This suggests that in most cases, preheating of water is not advisable.

Gases dissolved in water also reduce its cooling rate to a considerable extent. This explains why fresh water cools the hot steel part less drastically than already used water which has lost part of the gases dissolved in it. Similarly scum-forming (e.g., soap) drastically reduce the cooling rate. Optimum cooling power is achieved in water when its temperature lies in the range 20–40 °C. Cooling power of water rests in between those of aqueous solutions and oils.

Table 1 Cooling rates for small specimens in various quenching media

Cooling medium	*Cooling rate (°C s^{-1}) in the temperature range*	
	650–550 °C	*300–200 °C*
Water at 18 °C	600	270
Water at 30 °C	500	270
Water at 50 °C	100	270
Water at 75 °C	30	200
10% NaOH aqueous solution	1200	300
10% NaCl aqueous solution	1100	300
10% Na_2CO_3 aqueous solution	800	270
Distilled water	250	200
Water saturated with CO_2	100–200	200
Soap suds	30	200
Oil emulsion in water	70	200
Mineral oils (average)	100–150	20–50
Compresses air	30	10
Still air	3	1

Source: Ref. [9].

Investigation carried out by Mehmet Cakir and Abdullah Özsoy[8] on AISI 1050 steel quenched from austenitizing temperature (860 °C) with air–water mixture in Jominy end-quenched test showed that the cooling rate achieved was surprisingly higher as compared to cooling rate provided by water alone. In the quenching operation, water pressure at 22 mm water column and air mixture (0.40 bar) at about 18 °C (this condition is equivalent to the standard Jominy water pressure at 65 mm water column) was maintained. The reason for improved hardenability is that the air–water mixture spreaded the vapor phase formation and improved heat transfer and thus to enhanced hardenability.

2.2.3.2.2 Aqueous solutions

Aqueous solutions of 10 wt% of NaCl and $CaCl_2$ called brines and 10 wt% NaOH called caustic are widely used in industries. These solutions extract heat from the hot steel part very rapidly. Salts reduce the absorption of atmospheric gases that, in turn reduce the amount of bubbles. The salt elevates the boiling temperature and aid to quick collapse of the vapor blanket formed during stage I. As a result, the solution wets the surface of hot metal and cools it more rapidly than water. The consequent effect is the shortening of stage I (of relatively slow cooling) to appreciable extent. In addition to rapid and uniform cooling, the aqueous solution removes a large percentage of scale if present on the surface of hot metal. These aqueous solutions are of particular use for shallow hardening grade steels. The notable point with these quenching media is that, though the cooling rates are high (highest among all quenching media), the distortion is less severe in contrast to water quenching. Just like water, these solutions are used at room temperature. The disadvantages these solutions offer over water are high price due to the added cost of salts, and these solutions are corrosive in nature.

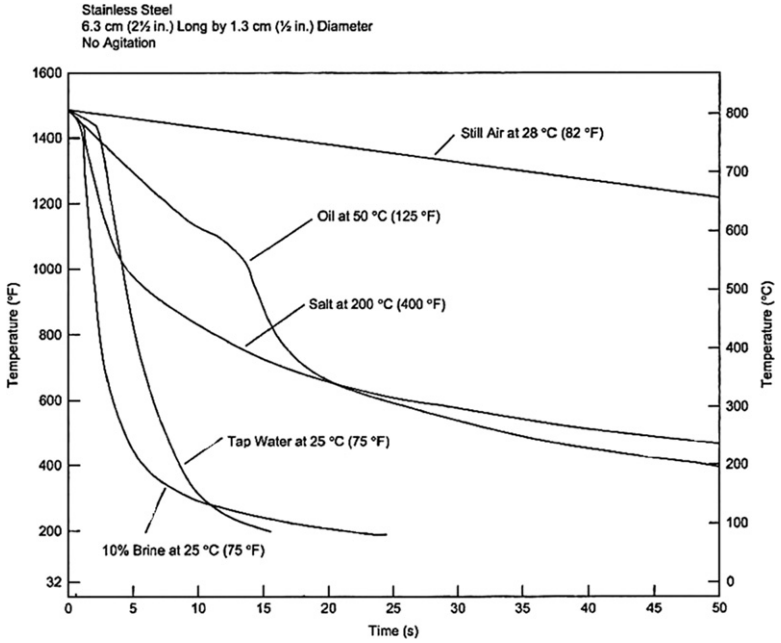


Figure 8 Comparison of some quench media.[7]

2.2.3.2.3 Oils

Oils are classed as an intermediate quench media because they have cooling rates slower than water or brine but faster than air. Oils are widely used as a quenching media in industry because it results in much lower residual stresses, distortion and very little probability of cracking. The cooling rates obtained by oils during first and third stages are much slower to suppress the transformation of austenite in carbon steels into a ferrite–cementite aggregate, as well as within the martensitic transformation range which is considered as a fairly favorable condition. Cooling rates of oils can be controlled by adjusting certain variables such as type of the oil used, bath temperature and degree of bath agitation. Major kind of oils used as quenching media includes animal oils, fish oils, vegetable oils, and mineral oils. The main drawbacks of mineral oils as quenching medium are limited range of cooling rate, water contamination of quenching oil tanks and hazards from smoke, fume and fire.

Molten salt and lead baths are used as quenching media when it is desirable to quench in the temperature range of 150–500 °C. These baths are used in austempering and isothermal treatments.

2.2.3.2.4 Polymer quenchants

Polymer quenchants are used to reduce or eliminate many of the problems encountered with water or oil-based quenchants. These are organic chemicals of high molecular weight and dissolve in water at room temperature to form a solution. The important property of such polymer quenchants is reverse solubility which imparts them a unique cooling mechanism as compared to oil quenchants. As this solution is heated by the immersion of hot metal into the quenching tank, the polymer becomes insoluble at temperatures greater than 70 °C, as the quenching medium cooled again; the polymer goes back into a fully miscible solution.

2.2.3.2.4.1 Mechanism of quenching in polymer quenchants

Cooling in polymer involves three stages:

Stage I: When the hot metal part is immersed into the polymer quenchant, the solution in contact with the metal is heated to above the inverse solubility temperature (65–85 °C). The polymer immediately becomes insoluble in the water and a thin polymer layer is deposited on the surface of the part. This stage is one of slow cooling, similar to the vapor blanket stage in water quenching.
Stage II: After a certain period of time this polymer layer becomes active and the cooling rate increases, equivalent to boiling stage in water quenching. The beginning of stage II depends upon the thickness of the deposited layer.
Stage III: The local temperature falls below the inversion temperature of the polymer, the layer redissolves and the heat is conducted away by the liquid solution. This stage is analogous to that of liquid cooling.

All the above three stages are illustrated by pictures in **Figure 9** for an austenitized steel rod quenched into an aqueous PAG polymer solution.

Cooling rate of a polymer quenchant can be varied by changing the polymer concentration as per the requirement for a particular operation. Many types of polymer quenchants have been developed and are commercially available as replacements for quenching oils to avoid flammability and pollution.

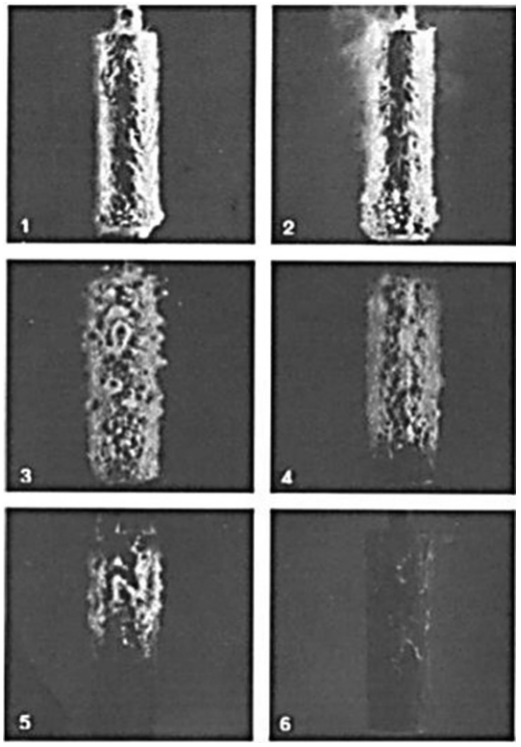


Figure 9 Sequence of photographs of a hot steel rod being quenched in a 25% PAG polymer in water solution. (1) When a rod is immersed, a polymer film forms on its surface, (2) After 15 s, polymer activates and begins to boil, (3) After 25 s, boiling occurs over the entire rod as the cooling rate increases, (4) After 35 s, boiling collapses and the convection stage begins, (5) After 60 s, the polymer starts to redissolve, (6) After 75 s, polymer film has completely redissolved and the heat removal is achieved entirely by convection.[10]

Elimination of smoke or fume during quenching clearly offers improved working conditions. Elimination of fire hazard removes the need for protective equipment.

Three prominent commercially available polymer quenchants are: polyalkylene glycol (PAG), polyvinyl alcohol (PVA) and polysodium acrylate (PA). PVA used to be very popular quenchant in early days and still in use in some countries. Proper PAG quenchant can provide an accelerated wetting so that the cooling rates achieved are faster than water and even approach those of brines. Thus brine like quenching is possible without the problems of hazards and corrosiveness associated with brine or caustic solutions.

Quench severity of aqueous solution of polymer can be controlled by the following parameters:

- Concentration of polymer in water,
- Quenchant temperature, and
- Quenchant agitation.

Higher the concentration of polymer in aqueous solution more is the thickness of the polymer layer formed on the hot metal during quenching and lower is the cooling rate.

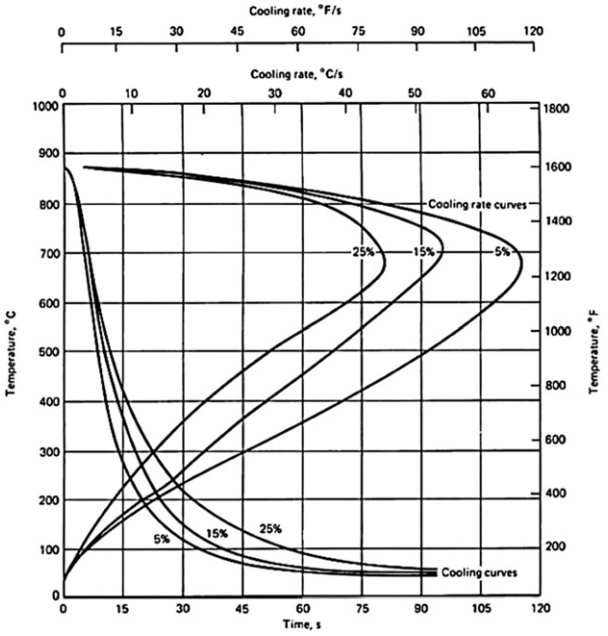


Figure 10 Cooling curves and cooling rate curves for a 25 mm (1″) diameter stainless steel probe quenched 5, 10, and 15% polyalkylene glycol (PAG) at 45 °C that is flowing at 0.25 m s^{-1}.[10]

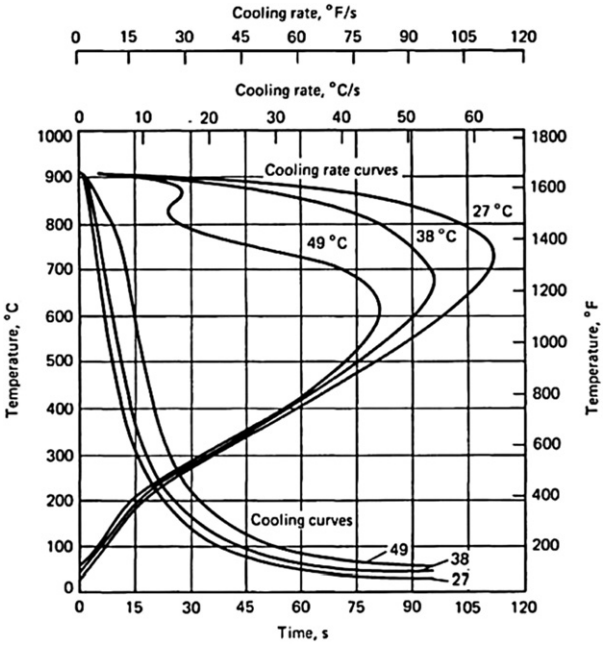


Figure 11 Cooling curves and cooling rate curves for 25 mm (1″) diameter stainless steel probe quenched in 10% PAG at 27, 38, and 49 °C that is flowing at 0.25 m s^{-1}.[10]

Figure 10 is an illustration showing the effect of PAG concentration on cooling rates in a 25 mm diameter steel probe. Any increases of temperature of the polymer quenchant results in a marked decrease in cooling rate of the quenchant. Effect of bath temperature on cooling rate of PAG quenchant is apparent from Figure 11. In general, low to moderate degree of agitation of the polymer quenchant is recommended to ensure adequate replenishment of polymer at the hot metal surface. This also provides uniform heat transfer from hot metal part to the surrounding quenchant. In case of shallow hardening steels it is recommended to use vigorous agitation of polymer quenching bath to avoid formation of undesirable transformation products. The effect of agitation on cooling rate is illustrated in Figure 12.

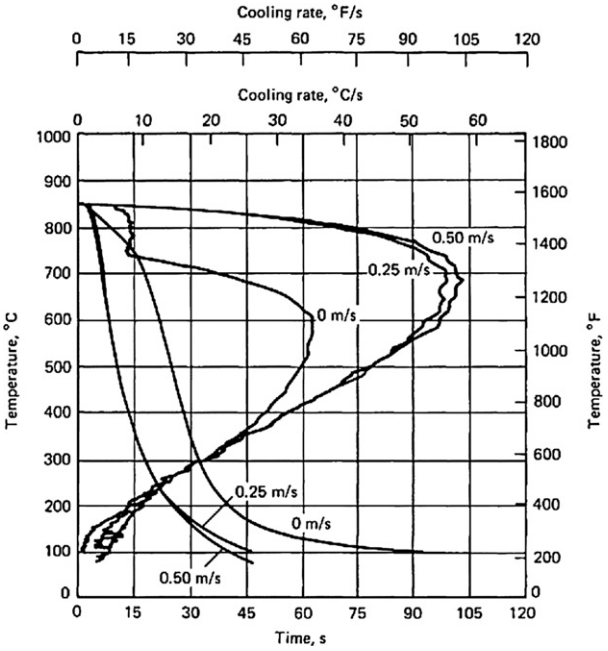


Figure 12 Cooling curves and cooling rate curves for 25 mm (1″) diameter stainless steel probe quenched in 20% PAG at 45 °C that is flowing at 0, 0.25, and 0.50 m s^{-1}.[10]

2.2.4 Quantitative Methods of Measuring Hardenability: Grossman's Method

2.2.4.1 Critical Diameter

It is more convenient and useful to express hardenability as the depth of penetration of hardness. The hardenability of a steel can be obtained by determining the diameter of a bar sample that will just hardened through to the center. M. A. Grossmann has devised a direct method in which hardenability is measured in terms of critical diameter. In this method, several round bar samples of different diameter are heated to austenitizing temperature and quenched rapidly in water or oil. The length of the samples is kept at least five times the diameter to avoid end effects. After quenching the samples are cut in the middle and hardness measurements are made at various depths along a diameter on the cross-section (also called hardness traverse) or etched to reveal the depth of hardening. The hardness is plotted against the depth from the surface from either end of the diameter selected so that perfectly symmetrical curve, as shown in Figure 13 is obtained. This figure shows that the bars having smaller diameters are through hardened. If steel contains 0.8% or more of carbon, a

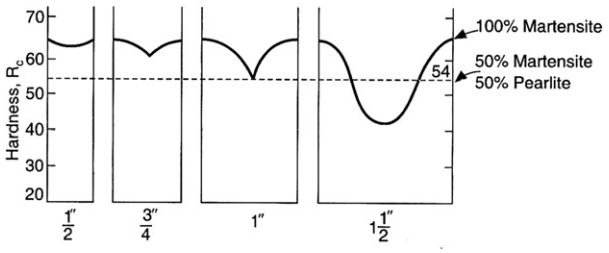


Figure 13 Rods of different diameters hardened to various depths on quenching in a given medium.[1]

hardness of 65 HRC is attained throughout the section. As the diameter increases, under the identical quenching conditions, the cooling rate at the center of steel decreases and resulting in soft core containing pearlite. As a consequence hardness decreases in the core. In 1.5″ diameter bar, the central region contains less than 50% martensite and therefore is called unhardened core. The largest diameter (1.5″) bar shown in **Figure 13** has pearlite at the center. It is notable in this sample that the hardness falls most rapidly at a value of 54 HRC which is the hardness for 50% martensite and 50% pearlite. This point where hardness fall is steepest and is called point of inflection. This inflection point is taken as the transition region between hardened and unhardened portions of the section of the steel bar. The bar sample of 1″ diameter displays 50% martensite and 50% pearlite at its center. This diameter is called 'Critical diameter, D_c.' Critical diameter, D_c, of a steel under a given quenching condition is defined as 'the diameter of the cylindrical bar which hardens up to center, i.e., contains 50% martensite at its center.' The critical diameter can also be determined as the diameter of cylindrical bar at the center of which nature of fracture changes from brittle to ductile under given quenching conditions. Any bar having diameter greater than D_c will not harden throughout, that is, up to the center. It has been observed that with increasing diameter of the bar, surface hardness also decreases (**Figure 6**). The value of critical diameter varies with composition of steel and the severity of quench. Addition of alloying elements increases critical diameter of steel. Similarly, increasing the severity of quench increases the critical diameter of steel. For instance, it has been observed that when the steel 3140 (a nickel–chromium steel with 0.41C–1.2Ni–0.67Cr) when quenched in water and oil, the critical diameter observed for water quench sample is greater (1.83″) than that (1.25″) of the sample of same diameter quenched in oil as illustrated in **Figure 14**. Thus, when hardenability is expressed in term of critical diameter, it is necessary to specify the severity of quench. Ideally, the hardenability of steel should be expressed in terms of ideal quench so as to eliminate the effect of quenching medium.

2.2.4.2 Severity of Quench

The effectiveness of a given cooling medium is expressed by a parameter called 'severity of quench'; this is designated by the symbol '*H*' which is also called coefficient of surface heat transfer between steel and quenchant. '*H*,' in general, is defined as the rate of heat removal by the quenching medium

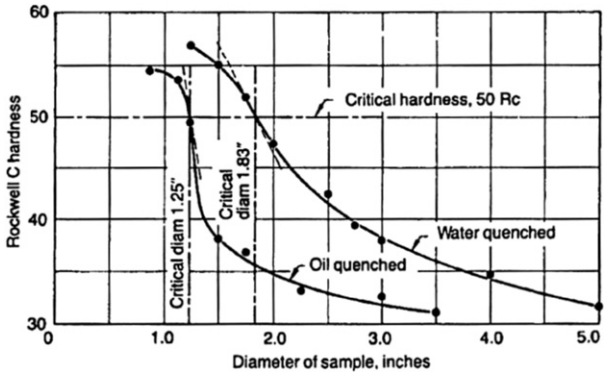


Figure 14 Hardness at the centers of water and oil quenched round bars of 3140 steel of various sizes.[11]

from an object. The cooling rate of austenitized steel when it is subjected to quenching depends on:

1. Thermal diffusivity (α) which is the ratio of thermal conductivity to volume specific heat. Here, thermal conductivity means the ability of the heat to diffuse from the interior of the steel to its surface. Thermal diffusivity increases as does thermal conductivity of the steels with the decrease of temperature.
2. Ability of the quenching medium to remove heat from the surface of the steel.

According to Newton's law of cooling, the rate of heat transfer is proportional to the difference in temperature between the surface of steel (T_s) and the temperature of the coolant (T_c), and thus,

$$Q = P(T_c - T_s) \quad [1]$$

where Q is the rate of heat transfer per unit surface area, P is the proportionality constant and denotes heat transfer coefficient across the metal–coolant interface. Severity of quench, '*H*,' is expressed in terms of rate of heat transfer coefficient (P) and thermal conductivity, K according to the relation:

$$H = \frac{P}{K} \quad [2]$$

where H has units of $(\text{length})^{-1}$, and the thermal conductivity, K has the units J m^{-1} s^{-1} $^{\circ}C^{-1}$ or W m^{-1} $^{\circ}C^{-1}$.

2.2.4.2.1 Experimental evaluation of 'H' of a coolant

Experimentally H is determined by heating a series of round bars of hardenable steel (such as steel 3140) of varying diameters to austenitizing temperature and subsequently quenching in two different media, namely, water and oil. The bars are cross-sectioned and etched to delineate the soft core and hard outer rim or case. The results are schematically represented in **Figure 15**. The cross-hatched areas represent the unhardened (or soft) core produced in various rounds. The unhardened region is assumed to have less than 50% martensite. The notable point here is that the larger the diameter, D of the bar, the greater the unhardened diameter (D_u) as is apparent from the hatched areas. Moreover, as the diameter of

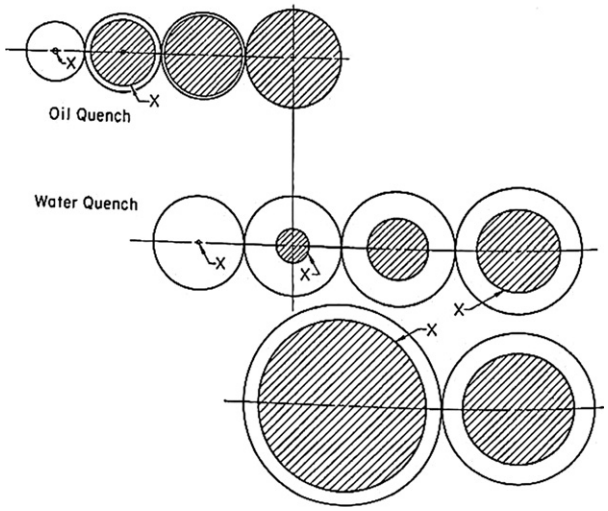


Figure 15 Etched cross-sections of SAE 3140 steel quenched in water and oil.[5]

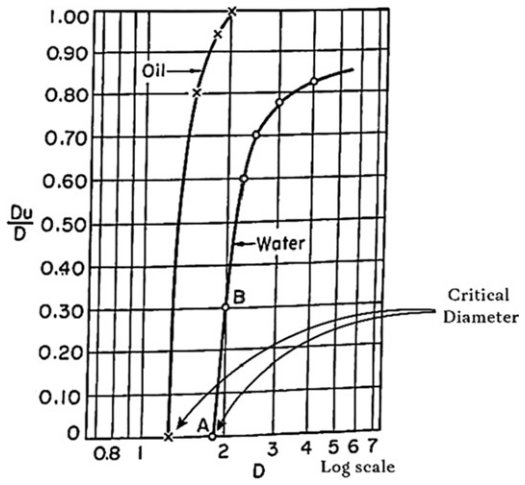


Figure 16 Plot of experimental D_u/D against D. Left curve, oil quench and right curve, water quench.[11]

bar increased beyond the critical, the proportion of unhardened core increased more rapidly in oil quench and much less rapidly in water quench. In other words, as the diameter of the bar is increased, the hardened case soon disappears in oil quench (e.g., when $D_u = D$) whereas it still exists in water quench though it is thinned down. The experimental results shown in **Figure 15**, that is, all the proportions of unhardened diameters, are plotted against the bar diameters as D_u/D versus log D for both the water- and oil-quenched series as shown in **Figure 16**. It can be noted from **Figure 10**, that the curve corresponding to oil-quench is quite steep whereas that for water-quenching bends markedly to the right. The steepness of oil-quench curve suggests the reduced power of quenching of oil so that hardening is not produced in larger sections. **Figure 16** is the basis of estimating severity of quench. A comparison of both these curves also suggests that when a bar of steel of large diameter is quenched in a milder quenching medium, hard case may not form at the surface. This is the situation when D_u equals D (**Figure 15**) for oil quenched sample. It also proves that for a steel of given hardenability greater is the severity of quench greater will be the critical diameter or for a given severity of quench, the greater the hardenability of steel the larger the critical diameter exhibited by the steel.

In order to determine H, each of the curves shown in **Figure 16** is matched with one of the large number of calculated curves available for a wide range of quench severities. The matching is generally performed by plotting D_u/D versus log D (**Figure 16**) on a tracing paper and finding the best correspondence to a theoretical D_u/D versus log HD curves shown in **Figure 17**. The matching gives HD value on x-axis.

When this HD value is divided by corresponding D value, H value can be computed. This is explained by taking an example. Considering point A (**Figure 16**) which corresponds to the critical diameter 1.83 for water quenched 3140 steel and following the above procedure to give HD value of 2.6″ H value is found to be $H = (HD)/D = 2.6/1.83 = 1.4$ for water quenched sample.

The 'H' values of commonly used cooling media in different state of agitation are listed in **Table 2**. A quenching medium that is able to extract heat from the surface of a hot steel

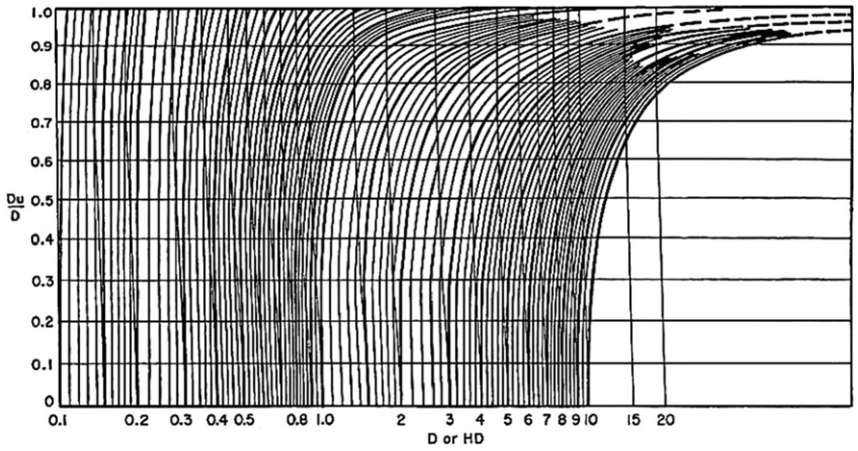


Figure 17 Curves for estimating cooling power (severity of quench) of quenching baths.[11]

Table 2 Severity of quench 'H' for some commonly used quenching media

Quenching condition	H-*values*			
	Air	*Oil*	*Water*	*Brine*
No circulation of fluid/agitation of specimen	0.02	0.25–0.30	0.9–1.0	2.0
Mild circulation/agitation		0.30–0.35	1.0–1.1	2.0–2.2
Moderate circulation/agitation		0.35–0.40	1.2–1.3	
Good circulation/agitation		0.40–0.50	1.4–1.5	
Strong circulation/agitation		0.50–0.80	1.6–2.0	
Violent circulation/agitation	0.05	0.80–1.10	4.0	5.0

Source: Ref. [5].

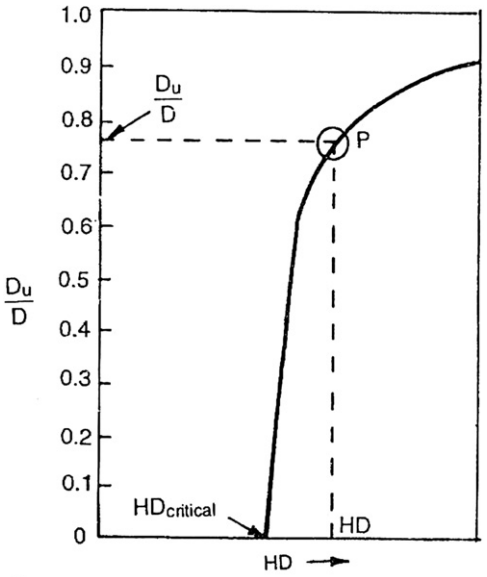


Figure 18 Calculation of D_c in a quenching medium of known '*H*' value.[4]

object extremely fast and enables the object to attain the temperature of the medium instantaneously is called 'ideal quenching medium.' Thus the ideal quenching medium is able to remove the heat from the surface of hot steel as fast as the heat is transferred from interior to the surface and brings down the surface temperature equal to its own temperature. In fact, such a quenching medium can only be imagined. It does not exist in practice. Still an ideal quenching medium is considered for comparison of its severity of quench with other quenching media used in practice. Accordingly, when H tends to infinity the cooling rate is said to very rapid corresponding to that of an ideal quench. 'H' values in practice are much lower than that of ideal quenching medium.

2.2.4.2.2 Evaluation of critical diameter

Having known the severity of quench 'H,' D_u (from experiment) for a particular diameter D of the given steel, one can calculate D_u/D and the product HD. Projections from these values on the diagram shown in **Figure 17** intersect one of the curves at point P as shown in **Figure 18**. It is known previously that at critical diameter, the unhardened region is zero, that is,

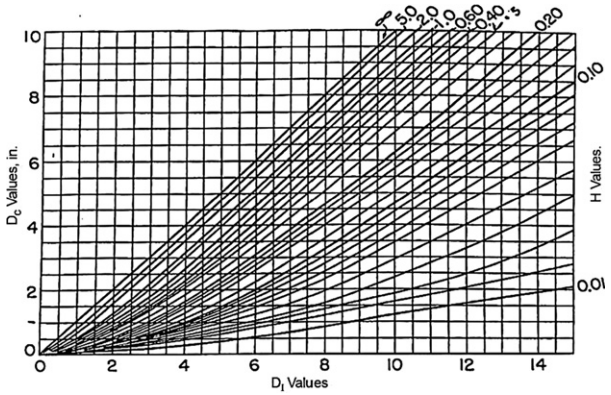


Figure 19 Relationship among experimental critical diameter, D_c, the ideal critical diameter, D_I, and severity of quench, H.[11]

$D_u/D=0$. Corresponding to this, one can obtain the value of the product HD along the curve shown in **Figure 18**. This gives $HD_{critical}$, HD_c. Critical diameter of the steel can be computed by dividing this value by severity of quench 'H.' That is, $D_c=HD_c/H$ is the critical diameter.

2.2.4.3 Ideal Critical Diameter

As illustrated in **Figure 16**, the critical diameter D_c is directly related to severity of quench (H). The higher the quench severity, larger is the critical diameter of steel bar for a given composition. Therefore, just on the basis of critical diameter one cannot compare the hardenabilities of two steels quenched in different quenching media. In order to make critical diameter independent of H, Grossmann proposed a concept based on 'ideal critical diameter.' The ideal critical diameter, D_I, is defined as "the diameter for which the unhardened core just disappears if the bar is subjected to an ideal quench." This means that when a bar of steel is subjected to an ideal quench it would have 50% martensite at its center. The diameter of this bar is then said to be ideal critical diameter. In an 'ideal quench,' 'H' is infinitely large. D_I gives value of inherent hardenability of the steel.

Grossmann has developed a relationship between the critical diameter, D_c, ideal critical diameter D_I, and severity of quench, H in the form of a master graph based on thermodynamic considerations (that is by heat flow analysis). The graph is represented in **Figure 19**. The graph shows a number of curves for various cooling rates. Knowing the value of severity of quench, 'H,' and the value of D_c, the corresponding D_I and hence the hardenability can be found out from the graph. For instance, for D_c assumed to be equal to 1″, and $H=5$ (for agitated brine quench), the ideal critical diameter (i.e., the hardenability) works out to 1.2″ (**Figure 20**). **Figure 19** shows that for D_c (10″)$=D_I$ (10″), $H=\infty$. Accordingly, the ideal quench would produce the maximum possible depth of hardening and the corresponding critical diameter would be the largest attainable which is equal to D_I. **Figure 19** also shows that for a given value of D_c, D_I is always larger than D_c, that is, always $D_c < D_I$, and that H is less than infinity. In practice, ideal quench can never be attained. However, the highest quench attainable in agitated brine quench ($H=5$) falls in close proximity to ideal quench (**Figure 19**).

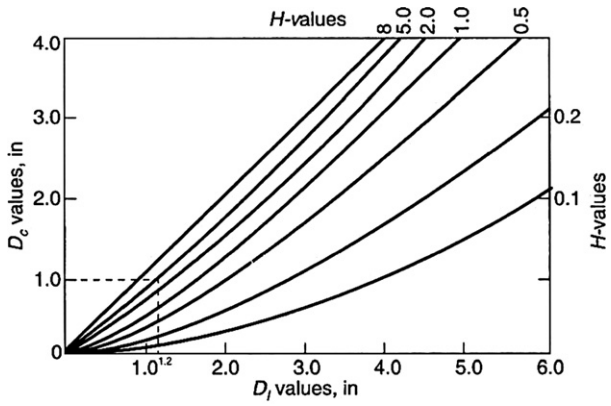


Figure 20 Relationship between D_I, D_c for fully hardened steel bar quenched in a medium with cooling power H.[12]

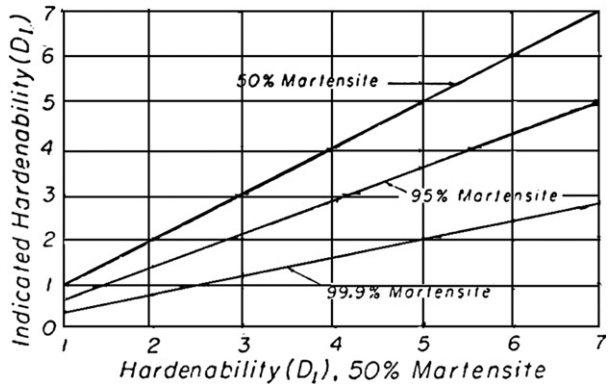


Figure 21 Average relationship between D_I and D_I with 95 and 99.9% martensite.[4]

Sometimes the criterion for hardenability is set by 90% martensite or more. In such case, first D_c can be determined experimentally for 90% or higher percentage of martensite as per requirement, and if H is known, then D_I corresponding to higher percentage of martensite can be obtained by referring Figure 19. Figure 21 gives the average relationship between D_I corresponding to 50% martensite and D_I for higher % of martensite for medium carbon low alloy steels. If D_I for 50% martensite is known, then one can obtain the value of D_I (or hardenability) corresponding to higher percent of martensite using the plot shown in Figure 21.

2.2.5 Jominy End-Quench Test

Though the Grossmann method of quantitative measurement of hardenability in terms of ideal critical diameter, is highly useful in explaining the concept of hardenability and is reproducible too, the method is highly time consuming, complicated, and expensive because it requires a series of round bars of steel to be quenched, sectioned, and tested.

End-quench test (Jominy) is a simple, generally accepted, and most widely used method of evaluating hardenability of carbon and alloy steels. This test provides much useful information to fabricators and designers. In contrast to Grossmann

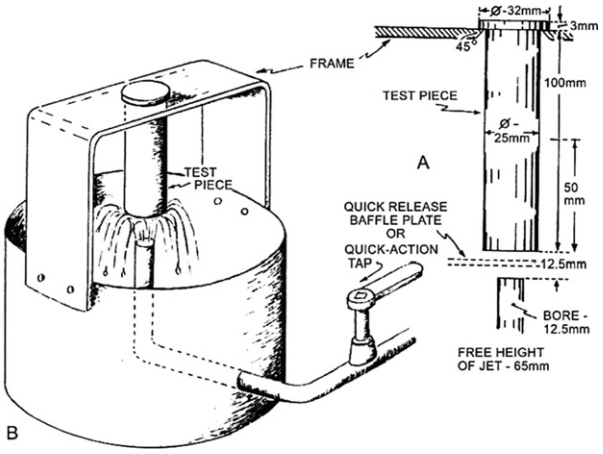


Figure 22 Experimental set-up for Jominy end-quench test.[13]

method where a series of specimens are used to perform test, Jominy end-quench test uses a single specimen to evaluate hardenability. In this method, a standard steel specimen of 1″ (25 mm) diameter and 4″ (100 mm) long with a 1.25″ (32 mm) diameter collar at one of its ends (to facilitate its holding in the quenching jig) is used for testing. The physical set-up of this test is illustrated in Figure 22. In this set up the diameter of nozzle is 0.5″ (12.5 mm). When the specimen is held in the jig, the bottom end of the specimen is kept 0.5″ away from the nozzle. Using a valve, the water flow is so controlled that when no specimen is placed in the jig, the height of unimpinged jet is 2.5″, that is, the free flight of water column is maintained as 2.5″ and that the volume of water striking the end of the specimen must remain constant.

The steel specimen is heated to about 50 °C above the lowest temperature at which full austenitic structure is obtained. The specimen is then immediately transferred to the quenching device and placed in the jig within 5 s and almost simultaneously the water jet is directed against the bottom end of the specimen at constant velocity such that water impinges on the end of the specimen only, then drains away. The cooling rate at the quench end is very rapid but it decreases progressively with distance from the quenched end. The cooling rate is very slow at the opposite end. This results in a wide range of hardness along the length of the specimen. After quenching for 10 min on the fixture, the specimen is removed. Two mutually parallel flat surfaces are ground longitudinally to a depth of 0.015 in. (0.380 mm). These surfaces are etched with 5% nital solution to remove tempered layer due to grinding. Rockwell hardness test on C scale is then performed on ground flat surface along the length at 1/16″ (about 1.6 mm) interval from the quenched end of the bar. Near the quench end, this interval may be reduced to 1/32″ to obtain higher accuracy. The results are expressed as a curve of hardness values versus distance from the quenched end of the Jominy specimen as illustrated in Figure 23. Figure 23 shows that as the distance from the quench end increases hardness decreases; this is due to the decrease of cooling rate which in turn can be correlated to the formation of equilibrium products. The curve shown in Figure 23 is called 'Jominy hardenability curve.' The distance from the quenched end is commonly known as Jominy distance – J such that one Jominy

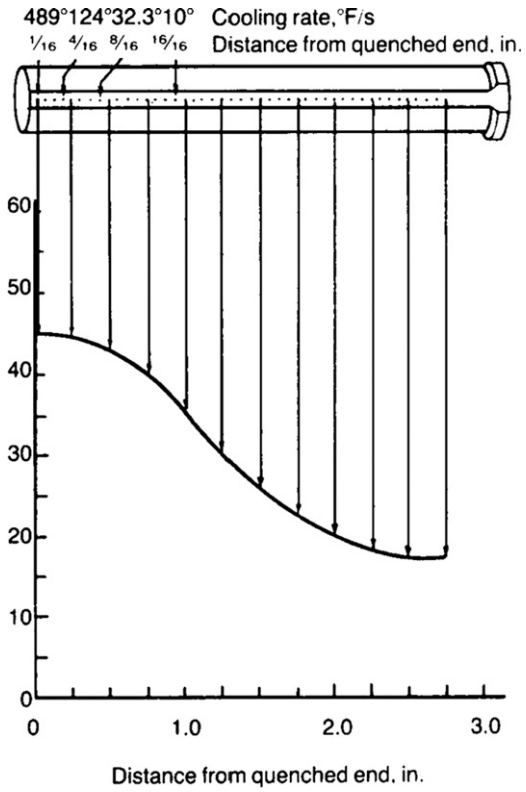


Figure 23 Variation of hardness with distance from the quench-end of Jominy specimen.[6]

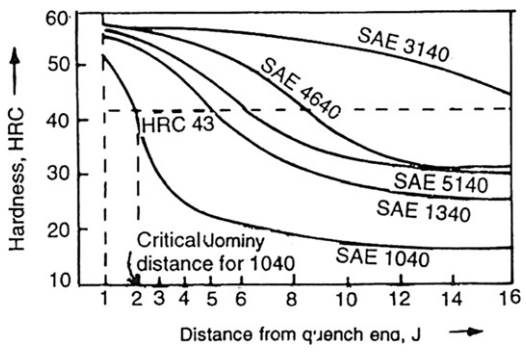


Figure 24 Jominy hardenability curves for some low alloy steels with 0.4% C.[4]

distance is equal to 1/16″ and is designated as J_1. Figure 24 illustrates Jominy hardenability curves for some grades of steels. By comparing these curves the relative hardenability of different grades of steels can be established. At a given distance from the quenched end of the specimen, the harder a steel is, higher is its hardenability than steel having lower hardness at the same distance. Thus a flatter Jominy curve implies higher hardenability. The inflection point on the hardness versus distance curve for SAE 1040 steel shown in Figure 24 generally correlates with 50% martensite and is used to measure the hardenability of steels. This distance is the critical Jominy distance. The hardness corresponding to this point is 43 HRC. This means that for the steel under consideration, 50% martensite in the

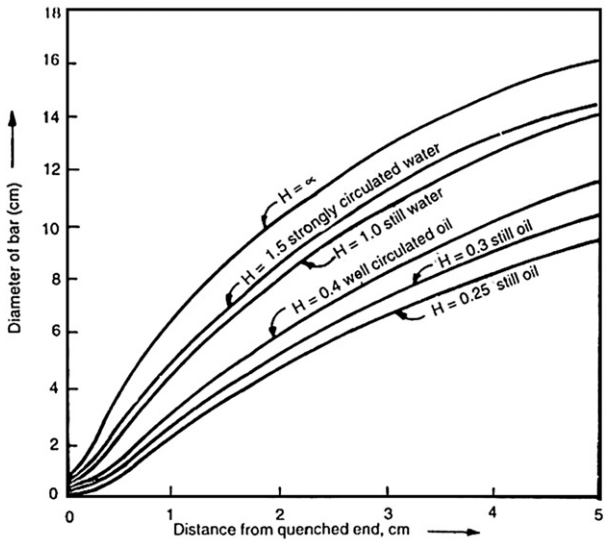


Figure 25 Correlation between Jominy distance and bar diameter, where cooling rate for the center of the bar is same as that for the point in Jominy bar.[4]

structure is represented by a hardness of 43 HRC. Now intersection of a horizontal line drawn at this hardness (Figure 24), with the hardenability curves of different grades of steels gives the critical Jominy distances or the hardenability of these steels.

2.2.5.1 Correlation between Jominy Test Distance and Grossmann Method, D_I

Both Jominy distance (as obtained from the Jominy end-quench test) and ideal critical diameter, D_I as determined from Grossmann's method are measure of hardenability of steel. A correlation between Jominy test distance, J and D_I can be established. This correlation is based on the fundamental relationship between hardness and the rate of cooling. For instance, consider a steel tested for hardenability by end-quench test and Grossmann test. Now consider a point on Jominy test specimen at a distance J from the quench end and a point at the center of the quenched round bar of diameter D_c such that both points have the same hardness. Since both these points display same hardness so cooling rate is also same at both these locations in the samples.

Thus, the critical diameter, D_c can be determined from the Jominy end-quench hardenability. After having D_c determined from Jominy test one can obtain the ideal critical diameter, D_I with the help of Figure 13. Grossmann computed the cooling rate (in terms of half-time) at the center of an ideally quenched round bar of diameter, D_I and at any point on the Jominy test bar at a distance J from the quenched-end. He developed a relationship between D_I (Grossmann) and Jominy distance, J as shown in Figure 25 for a range of cooling baths, i.e., Jominy test can be used to get D_I or D_c from Figure 25.

2.2.5.2 Hardenability Bands

It is well known that a steel producer cannot produce a steel of exact composition specified by a customer. The composition always varies to some extent from heat-to-heat. He can

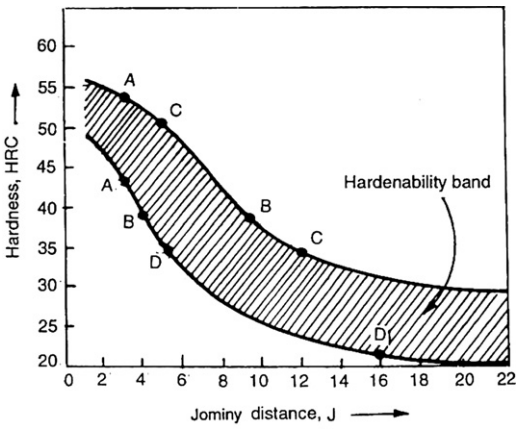


Figure 26 Hardenability band and different method of specifying hardenability.[4]

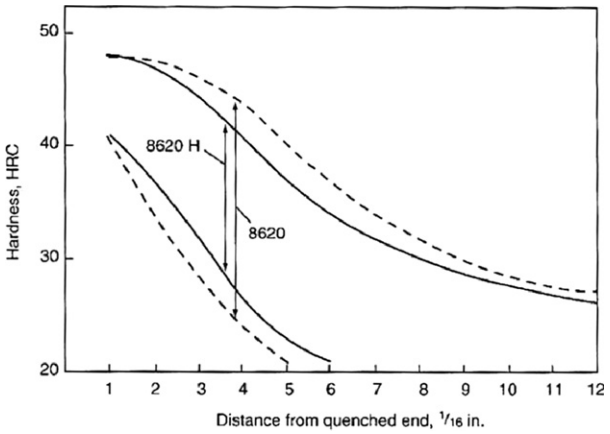


Figure 27 Comparison of Jominy hardenability curves for 8620H and 8620 steels. Chemistry at maximum and minimum of the chemistry range.[6]

produce a steel of composition that falls within the range specified by the customer. This composition range for the given steel results in two Jominy hardenability curves, one on top of the other. The upper curve represents the hardness obtained with the upper limit of elements in composition for the steel while the lower curve is that for composition at the lower limit. The area bounded by these two curves is referred to as a hardenability, or Jominy band as illustrated in Figure 26. The upper and lower curves not only show the possible variation in hardness at the quenched end caused by the allowable carbon range but also the difference in hardenability produced by the alloying elements that fall in the upper and lower side of the prescribed limits. The hardenability bands which include plain carbon steels (such as AISI 1036) and many grades of the frequently used low alloy steels are very useful in selecting alloys for particular application. Therefore, there has been trend that customer orders for steels the hardenability of which falls within the specified limits. Society of Automotive Engineers (SAE) in association with the American Iron and Steel Institute (AISI) devised hardenability bands for many steels, in particular, the low alloy steels. These steels are named H-steels. H-steels are those which are produced and sold with guaranteed hardenability bands. These steels are designated in the same way as standard grades except that numerical parts are followed by the letter H such as in 4140H steel. Thus H-steels are the modifications of the normal standard grade steels with respect to chemical composition. These compositions allow manufacturer to adjust the chemical composition of the steels that have hardenability within the prescribed limits. However, the modifications are so made as not to influence the general characteristics of the original compositions of the steels. Steels are sold either on the basis of 'chemistry only' as per standard grade such as AISI 8620 steel or based on the hardenability requirement as 8620H. A comparison of these steels as shown in Figure 27, clearly shows that the hardenability band for H-steel is narrower than that for the 'chemistry only' steel (i.e., AISI 8620).

For any H-steel, there can be various methods of specifications as illustrated in Figure 26 and listed below:

1. The maximum and minimum hardness at any desired distance on the Jominy end-quenched specimen can be specified, as for instance by points A–A, corresponding to the section size of interest to the user. The point A–A are correspond to HRC54 to HRC43 at $J=3/16''$.
2. The maximum and minimum Jominy distances at which desired hardness is to be attained as at points B–B, can be specified. The corresponding distances are $J=4/16$ to $9/16''$ at HRC39.
3. Two maximum hardness values at two desired Jominy distances can be specified, as at points C–C (HRC50, $J=5/16''$ and HRC34, $J=12/16''$).
4. Two minimum hardness values at two Jominy distances can be specified as illustrated at points D–D (HRC35, $J=5/16''$ and HRC21, $J=16/16''$).

For each steel part to be heat treated, it is essential to determine the minimum hardenability required for proper functioning of the part in specific application. Generally it is not recommended to specify higher than the minimum, as it increases the cost as well as increases the danger of quench cracking. For example,

1. 80% martensite at the center of largest section is normally needed for highly stressed parts, whereas for less highly stressed parts, 50% martensite is sufficient.
2. 80% martensite at the 3/4 radius position is needed for automotive parts where torsional loading predominates.

Hardenability can be increased either by increasing the alloy content of steel or for a specific alloy steel by increasing the carbon content. Increasing alloy content implies increase of cost of steel. Alloy steel can be hardened to a greater depth with minimum distortion or quenching cracks if quenched in oil. But then cost of oil will also be involved. Increasing carbon content deteriorates ductility and toughness of steel. Severity of quench also increases the depth from the surface to which the desired microstructure and hence hardness is achieved.

2.2.6 Factors Affecting Hardenability

Hardenability is a property of steel and this inherent property is influenced by the external factors as discussed in preceding

paragraphs. Apart from the external factors like cooling medium, section sensitivity, hardenability criterion used, there are some materials parameters which make hardenability of one steel different from others; in the design of steels these factors affecting hardenability of steels are of important considerations. All those factors which reduce the critical cooling rate (i.e., increase stability of austenite) increase hardenability. The following factors may be considered to affect the hardenability of steel.

1. Grain size,
2. Austenitizing temperature and time,
3. Carbon content of the steel,
4. Alloying element in steel.

2.2.6.1 Effect of Grain Size

Since hardenability is sometimes defined as the measure of depth below the surface of steel (bar, for instance) up to which 100% (full) martensite is formed, it tantamounts to the ability of steels to avoid pearlite transformation. The diffusional transformation products of austenite are detrimental to hardenability and this transformation takes place heterogeneously at the grain boundaries. As both pearlite and proeutectoid ferrite nucleate along grain boundaries of austenite greater availability of high energy surfaces from grain boundary accentuates diffusional transformation of austenite and hence lower the hardenability. A fine grain steel with ASTM number 7 exhibits four times grain boundary area than a coarse grain steel having ASTM grain size number 3. Higher the grain boundary area higher will be the sites for nucleation of diffusion dependent transformation. A large grain size means reduced grain boundary area per unit volume, and therefore fewer nucleation sites for diffusion dependent phase transformations (i.e., ferrite, and pearlite). Figure 28 illustrates the effect of austenite grain size on time of transformation to pearlite. Nucleation occurs at austenite grain boundary. If it is assumed that the rate of nucleation and growth are constant then it will take more time to complete the transformation to pearlite in large austenite grain than in small grain. This results in lower rate of transformation of the entire structure. The consequent effect is not only shifting the transformation start curves on the IT diagrams to longer times (increase incubation period) but also the nose of the IT diagram (Figure 29) and hence delaying the critical cooling rate. Austenite is stable below the lower critical temperature and thus transformation to martensite occurs at lower temperature accompanied with lower thermal shock. Thus, martensite is able to form even at lower cooling rate prevailing at greater depth from the surface of steel. In other words, martensite is likely to form to a greater depth along the diameter of steel section for a coarse grained austenite. Thus a higher temperature of austenitization, where a coarse grain structure is obtained, may be used in order to achieve complete hardening. The hardenability of carbon steel may increase as much as 50% with an increase of grain size from ASTM 8 (6–10) to ASTM 3 (1–4) and the effect is further intensified if the carbon content is increased. For simple shapes where the probability of quench cracks is less, it appears to be more practical to use coarse-grain steel rather than a fine-grain steel to achieve hardenability. However, from the point of view of improving hardenability, the criterion of coarsening austenite grain size is not recommended. This is because the other properties such as ductility and notch toughness get deteriorated. The martensite formed from coarse austenite grain structure prone to quenching cracks or cracking may result due to thermal shocks.

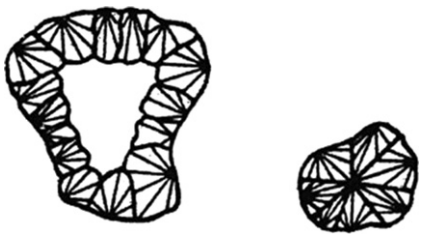


Figure 28 Effect of grain size on time of transformation to pearlite with rate of growth constant.[14]

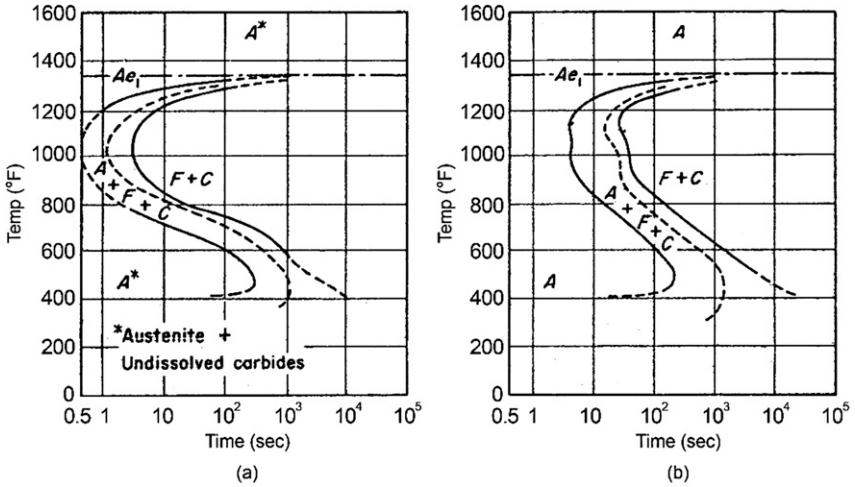


Figure 29 Isothermal transformation diagram. (a) 0.87%C, 0.30%Mn, 0.27%V steel at 815 °C; ASTM grain size 11. (b) Same steel at 1052 °C; grain size 2–3.[14]

2.2.6.2 Austenitizing Temperature and Time

Austenitizing temperature and time at temperature have significant effect on hardenability of steel. The purpose of austenitizing is to dissolve almost all the second phases such as carbides and obtain a homogeneous structure of austenite with uniformly distributed carbon and alloying elements. This is because the hardenability of steel is greatly dependant on chemical composition and grain size of austenite at the onset of quenching. If the carbides remain undissolved in the austenite then neither the carbon nor the alloy content can contribute to hardenability as both are not in the solution. Undissolved carbides, of course resist grain growth at austenitizing temperature. During quenching from austenitizing temperature, the undissolved carbides tend to promote the transformation to diffusional product and thus reduce hardenability. This is especially important in high carbon (0.5–1.1%) and alloy carburizing grade steels which may contain excess carbides at austenitizing temperature. In order to dissolve these carbides completely in austenite a higher temperature of austenitization is required. Even sometimes, the temperature of austenitization is raised to accelerate the formation of homogeneous austenite. A higher temperature may increase the austenite grain size which in turn produces deeper hardening, particularly in plain carbon steels. Iron carbides dissolve much more rapidly in austenite than more complex alloy carbides formed by chromium, molybdenum, etc. Therefore, to obtain complete solution of these complex carbides in austenite, a longer time at temperature or a higher temperature than the normal austenitizing temperature of steels of identical carbon content is necessary. The time required to obtain homogeneous austenite is longer for alloy steels than for plain carbon steels. This is because the alloying elements, in particular carbide forming ones, dissolve much slowly in austenite than simply iron carbides. Carbides of most alloying elements are stable and therefore their dissolution in austenite needs higher temperatures and longer times. Sometimes coarsening of fine-grained steel by heating to a high temperature may not improve hardenability. This may be due to the presence of nonmetallic inclusions which promote the nucleation of equilibrium soft product and thus reduce hardenability. Both higher temperature of austenitization or longer time of austenitization at lower temperature may result in decarburization and oxidation and also tend to promote cracking and distortion. So it is important to keep the temperature as low as possible to reduce the tendency toward cracking and distortion, minimizing oxidation, decarburization, and grain growth and is economic as well. To minimize the time for austenitization, the temperature is generally kept about 50–60 °C above the minimum temperature for formation of 100% austenite. The time is approximately 1 h per 25 mm thickness of steel.

2.2.6.3 Effect of Carbon Content on Hardenability

Carbon in steels serves dual functions: (1) it controls the maximum attainable hardness and (2) contributes to enhancement of hardenability. Higher content of carbon in steel tends to stabilize austenite and act in a way to delay the transformation of austenite into pearlite. The stability of austenite can be judged from the consideration of IT curves for steels with increasing carbon content. This is illustrated in Figure 30 or three plain carbon steels 1021, 1061, and 1080 (AISI designation).

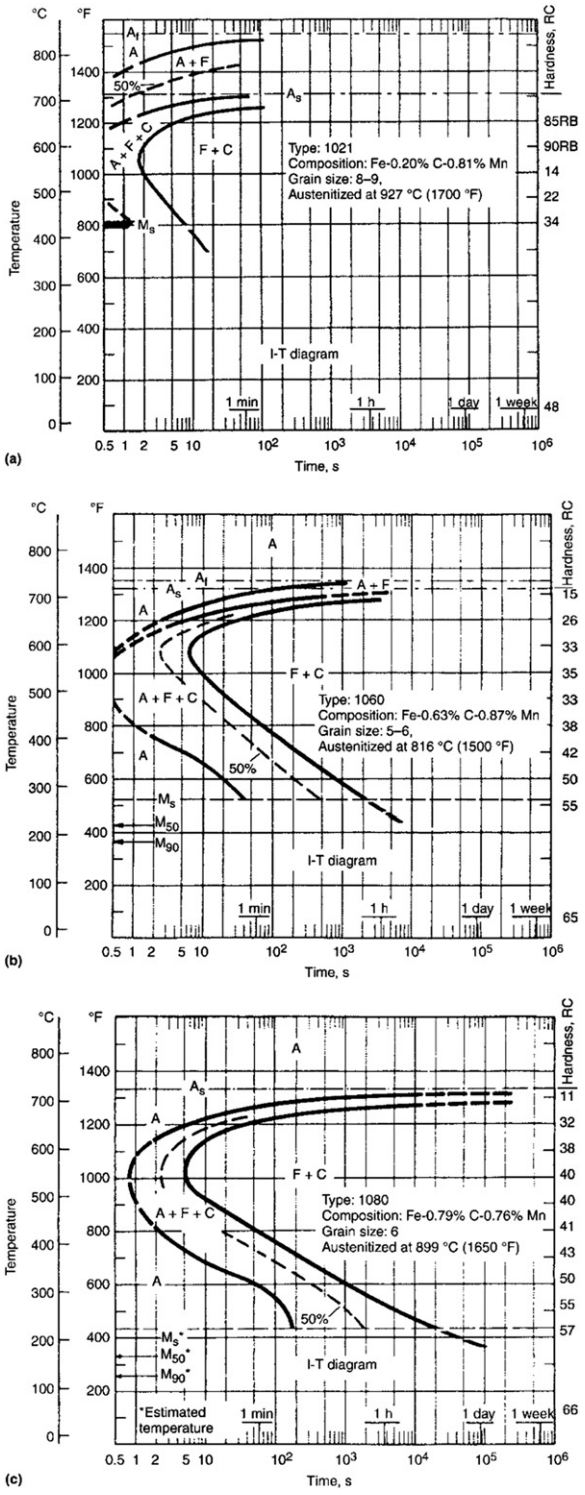


Figure 30 Isothermal transformation diagrams for plain carbon steels AISI 1021, 1060, and 1080 showing the effects of increasing carbon content.[3]

It can be noted from the IT curves of these steels that as percentage of carbon increases, the curves shift to the right, that is, for longer times. The location of the nose is shifted to longer times from below 0.5 s for 1021 and 1060 lower carbon steels to 0.8 s for 1080 eutectoid steel. The shifting of start curves to longer times also makes it difficult for the product pearlite to form from austenite. This shifting of transformation start curves toward longer times with increasing carbon concentration clearly suggests that the hardenability of steels increases with increasing carbon content. Thus it appears that increasing the carbon content of steel is the least expensive approach to improve hardenability. However, the effect of carbon on hardenability is comparatively less. It is true to some extent, but several limitations are there for use of large concentration of carbon in steel:

1. Increasing the carbon content of steel lowers the toughness at room as well as at subzero temperatures. This is because the higher carbon martensite is harder and more brittle than low carbon martensite.
2. The microstructure in the annealed state imparts hardness and wear resistance which makes cold shearing, sawing, machining, and other cold forming processes difficult.
3. Increased amount of carbon makes steel susceptible to hot shortness during hot working.
4. Increasing carbon content also makes steel more susceptible to distortion and cracking after quench hardening.
5. Increasing carbon in steel lowers M_s temperature (**Figure 30**). Steel is less plastic at lower M_s temperature and has less ability to accommodate the large volume change accompanying martensitic transformation.

Because of the above disadvantages, more than 0.6% carbon is rarely used in steels for machine parts where deep hardening is required with exception to springs and bearings. Moreover, the hardenability achieved in steels with up to about 0.8% carbon is not appreciable. Hypereutectoid steels, in practice, are generally hardened by austenitizing at above lower critical temperature where proeutectoid cementite exists. On quenching, proeutectoid cementite particles act as nucleation sites for pearlite formation resulting in lower hardenability.

Effect of carbon content on hardenability of dual phase steel has been studied by Valeria and his coworkers.[15] They observed that hardenability of dual phase steels also increases with increase of carbon content from nominal of about 0.1% to about 0.35%. As the carbon content increased, for the same intercritical temperature of 740 °C, the proportion of martensite has also been found to increase from 23% for 0.1%C to 74% for 0.38% carbon through 50% for 0.2% carbon. Also the hardness of the high carbon content steel was observed to be high. The best combination of mechanical properties was reached for steels with carbon in the range 0.1–0.15% with 50% martensite.

2.2.6.4 Effect of Alloying Elements on Hardenability

When alloying elements are present in steel, these are also nearly uniformly distributed in austenite when steel is heated to austenitic region. Upon cooling, this austenite tends to decompose into a mixture of ferrite and carbide. The carbide forming element prefers to go into cementite (carbide) while non carbide forming element prefers to go into ferrite phase. That is the alloying elements and carbon redistribute between ferrite and cementite. This process of redistribution of alloying elements involves diffusion. Diffusivity of alloying elements is much lower than that of carbon in iron. Therefore, the presence of alloying elements makes austenite difficult to transform to pearlite and shifts the transformation start curves on IT diagrams to longer times. In other words the critical cooling rate is reduced by alloying elements in steel provided these elements are completely dissolved in austenite. Thus the alloying elements which shift the IT curves toward right improve hardenability. **Figure 31** illustrates the shift of transformation start curve toward longer time on IT diagram produced by chromium and nickel. Among the common alloying elements (Mn, Cr, Ni, Si, Mo, Co, etc.) added in steels, cobalt seems to be the only element which decreases hardenability of steel. The presence of cobalt in steel increases both rate of nucleation and rate of growth of pearlite. So steels containing cobalt transform to pearlite in preference to martensite. As previously stated, the alloying elements will be effective in imparting deep hardenability only if they form complete homogeneous solution with austenite. **Figure 32** illustrates the effect of dissolved chromium on hardenability of steel.

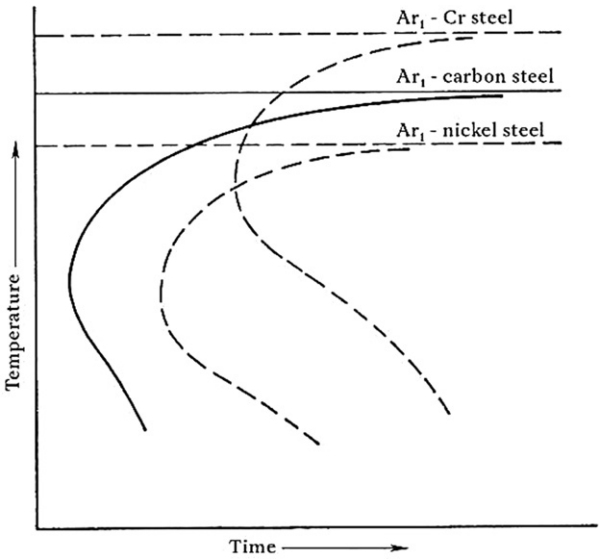


Figure 31 Effect of nickel and chromium on IT diagram.[14]

This figure also shows that hardenability increases with increasing amount of alloying elements. Different alloying elements have different effect on degree of hardenability. The effect of individual alloying elements on hardenability of steel is independent of each other as well as of carbon content. The influence of individual alloying elements is also independent of grain size of austenite.

Hardenability is appreciably enhanced by manganese, chromium, molybdenum, and very small additions of boron (0.001–0.003%). On the contrary, nickel and silicon have mild influence on increase of hardenability of steels. Effect of nickel content on hardenability of dual phase steel has been studied by Demir and Erdogan.[16] This study has shown that nickel content in dual phase steel decreases the critical cooling rate. At any cooling rate from as low as 0.1 °C s^{-1} to as high as

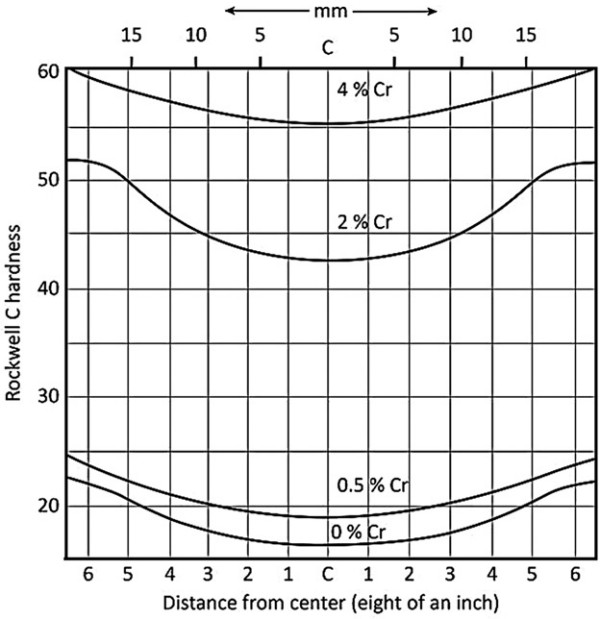


Figure 32 Variation of hardness from end to end of oil quenched 40 mm 0.35% carbon steel bar with different chromium content.[12]

1400 °C s^{-1}, the microstructure of the treated dual phase steel did not show any sign of ferrite cementite aggregate formation. These authors also observed that originally fine grain dual phase steel produced more martensite than coarse grain steel after annealing at low temperature and particularly at low cooling rates. The reason stated is that fine grain structure is more enriched with carbon content than coarse grain structure. The higher proportion of martensite in dual phase steels is correlated to high hardenability.[15,16]

It has been reported that when small amounts of several alloying elements are added, the hardenability of steel is improved significantly. Though a very small amount of boron enhances hardenability of steels to a great extent but its amount is so small that it is not regarded as alloying element in steel from the point of improving hardenability. Therefore, the effect of boron on hardenability of steels is discussed in separate section. Again combined additions of two elements like boron and molybdenum shows synergism while increasing hardenability.

2.2.7 Estimation of Hardenability from Chemical Composition and Austenite Grain Size

Though Grossmann has devised the experimental measurement of hardenability in terms of ideal critical diameter, he also proposed a method of estimating hardenability of steel based on the knowledge of chemical composition and austenite grain size. This method is further based on some facts. The hardening in steel principally arises due to carbon content. As stated earlier hardening effect increases with increasing carbon content (**Figure 3**); also martensitic hardness is not affected by the presence of alloying elements in steel as illustrated in **Figure 4** which demonstrates identical surface hardness of plain carbon steel and alloy steel. However, presence of

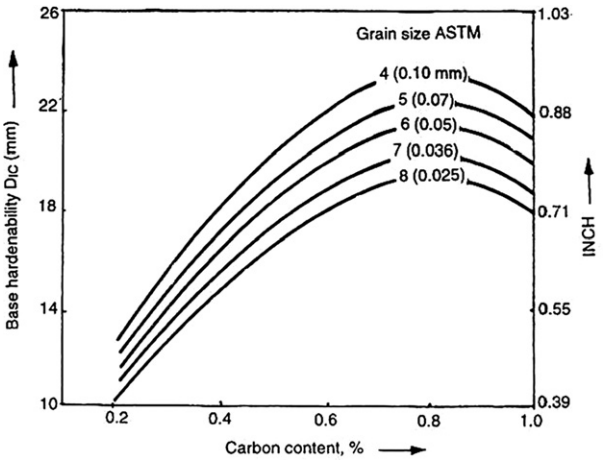


Figure 33 Effect of carbon content and austenite grain size of steel on base hardenability, D_{IC}.[4]

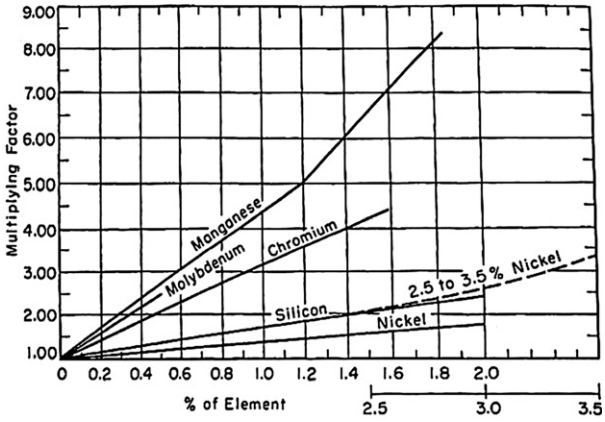


Figure 34 Multiplying factors for ordinary proportions of the common alloying elements.[11]

alloying elements affects the rate of reaction when austenite transforms to product phase during quenching. Thus, every steel has a base hardenability which is governed by its carbon content and austenite grain size before quenching. The effects of individual alloying elements on hardenability of steel are independent of each other as well as of carbon content. The influence of individual alloying elements is also independent of grain size of austenite.

Grossmann expressed the hardenability D_I (the ideal critical diameter) in terms of D_{IC} (the ideal critical diameter corresponding to a particular carbon content),the base hardenability based on carbon content and austenite grain size of steel, and the multiplying factors F_j, for the common alloying elements (other than carbon) present in steel, that is,

$$D_I = D_{IC} \times F_j \qquad [3]$$

The base hardenability, D_{IC} can be obtained from the relationship between base hardenability D_{IC} and percent carbon content as shown in **Figure 33** depending on the austenite grain size (ASTM) and the multiplying factor, F_j can be obtained from **Figure 34**. **Figure 33** is useful for steels

Table 3 Grossmann multiplying factors

Percent of element	*Grain size*			*Mn*	*Si*	*Ni*	*Cr*	*Mo*
	#6	*#7*	*#8*					
0.05	0.0814	0.0750	0.0697	1.167	1.035	1.018	1.1080	1.15
0.10	0.1153	0.1060	0.0995	1.333	1.070	1.036	1.2160	1.30
0.15	0.1413	0.1315	0.1212	1.500	1.105	1.055	1.3240	1.45
0.20	0.1623	0.1509	0.1400	1.667	1.140	1.073	1.4320	1.60
0.25	0.1820	0.1678	0.1560	1.833	1.175	1.091	1.5400	1.75
0.30	0.1991	0.1849	0.1700	2.000	1.210	1.109	1. 6480	1.90
0.35	0.2154	0.2000	0.1842	2.167	1.245	1.128	1.7560	2.05
0.40	0.2300	0.2130	0.1976	2.333	1.280	1.146	1.8640	2.20
0.45	0.2440	0.2259	0.2090	2.500	1.315	1.164	1.9720	2.35
0.50	0.2580	0.2380	0.2200	2.667	1.350	1.182	1.0800	2.50
0.55	0.2730	0.2510	0.2310	2.833	1.385	1.201	2.1880	2.65
0.60	0.2840	0.2620	0.2410	3.000	1.420	1.219	2.2960	2.80
0.65	0.2950	0.2730	0.2510	3.167	1.455	1.237	2.4040	2.95
0.70	0.3060	0.2830	0.2600	3.333	1.490	1.255	2.5120	3.10
0.75	0.3160	0.2930	0.2700	3.500	1.525	1.273	2.6200	3.25
0.80	0.3260	0.3030	0.2780	3.667	1.560	1.291	2.7280	3.40
0.85	0.3360	0.3120	0.2870	3.833	1.595	1.309	2.8360	3.55
0.90	0.3460	0.3210	0.2960	4.000	1.630	1.321	2.9440	3.70
0.95				4.167	1.665	1.345	3.0520	3.55
1.00				4.333	1.700	1.364	3.1600	3.70

Source: Ref. [4].

containing carbon content in the range 0.2 to 1.0% and the grain size in the range ASTM 4 to 8. The Grossmann hardenability multiplying factors corresponding to grain size and specific content of alloying elements including carbon are given in **Table 3**. The multiplying factor is considered unity for an element having no effect on hardenability. For instance, sulfur and phosphorous are considered as impurity in steels and therefore these elements have multiplying factors to be unity.

To illustrate the calculation (or estimation) of hardenability D_I of a steel one can consider a composition[14]: 0.395%C, 0.83%Mn, 0.31%Si, 0.20%Ni, 0.99%Cr, 0.17% Mo,0.018%P, and 0.029%S and ASTM grain size No. 7. The value of the base hardenability, D_{IC} corresponding to 0.395% C and ASTM grain size No.7, obtained from **Figure 33** for the given steel is 0.214″. The multiplying factors for the other elements present in steel are obtained with reference to **Figure 34** and these values are given in **Table 4**.

Using Grossmann eqn [3], hardenability D_I can be estimated as:

$$D_I = 0.214 \times 3.80 \times 1.20 \times 1.07 \times 3.15 \times 1.52 = 5.0''$$

Thus the hardenability of the given steel is 5″ which means that the steel with diameter of 5″ is fully hardenable.

Table 4 Multiplying factors of alloying elements present in the given steel

Percent alloying element	*Multiplying factor, F_j*
0.83 Mn	3.80
0.31 Si	1.20
0.20 Ni	1.07
0.99 Cr	3.15
0.17 Mo	1.52

Source: Ref. [14].

2.2.8 Effect of Boron on Hardenability

Boron forms interstitial solid solution with iron. The solid solubility of boron in iron is very limited due to its size (atomic diameter 0.188 nm) which is largest among the interstitial solid solution forming elements. Its solid solubility in γ-Fe is about 0.001% at 910 °C which increases with temperature to as high as about 0.005% at eutectic temperature. The solubility of boron in α-Fe is essentially zero. Because of its low solid solubility boron is preferentially located in the grain boundaries of austenite.

Boron plays a vital role in enhancing the hardenability of steels, in particular, those of fully deoxidized low carbon steels. In fact boron is mostly added to steels only to enhance their hardenability. Since the cost of boron is very low so it is considered as potent and economical alloying element in steels from the point of view of enhancing hardenability. The unusual features of boron hardenability can be considered in the following respects:

- A very small amount of boron has a substantial effect on hardenability.
- Hardenability effect of boron increases with decreasing the grain size of austenite.
- High temperature treatment reduces the hardenability effect of boron.
- The effect of boron on hardenability is much more in low carbon steels than in high carbon steels.

As little as about 0.001% boron in steels has substantial and optimum effect on hardenability (**Figure 35**) in fully

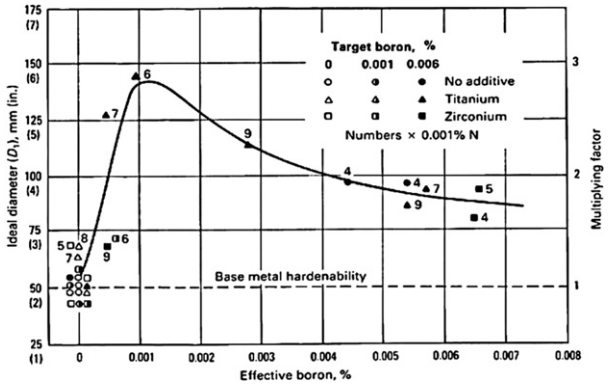
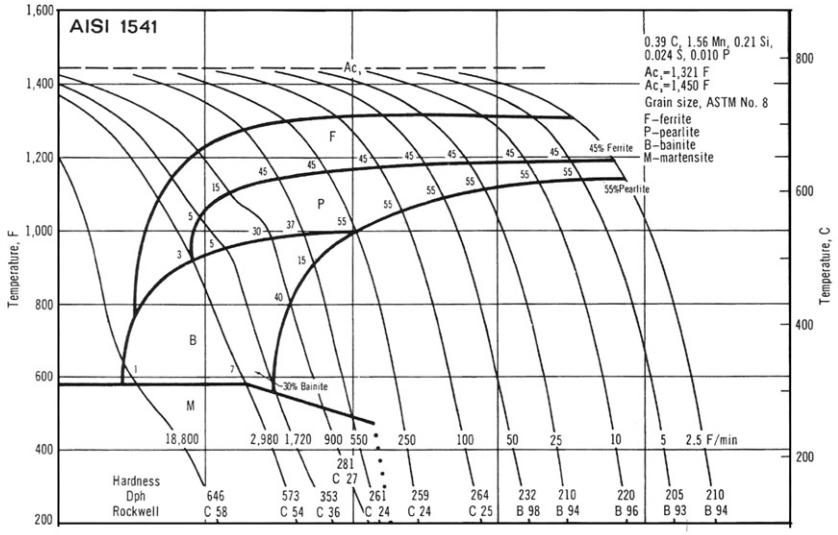


Figure 35 Influence of effective boron (B_{eff}) content on hardenability of AISI 8620 steel. $B_{eff} = B–[(N - 0.002)–Ti/5–Zr/15]$.[2]

deoxidized steels. Boron content greater than about 0.003% reduces the hardenability of steels. Any excess boron tends to form borocarbides $M_{23}(C,B)_6$ at austenite grain boundaries.[4,17] When exceed a critical size these borocarbides act as nucleation sites for proeutectoid ferrite and pearlite. Boron treated commercial steels contain 0.0005–0.005% of boron. Boron distribution, whether it is present as solute atoms or as $M_{23}(C,B)_6$ along the austenite grain boundaries has been found to be affected by cooling rate also as observed by Dong *et al.*[17] for steel containing 0.0021%B, 0.51%Si, 2.0%Mn as the principal elements. This steel when cooled from 900 °C in the cooling rate range of 10–20 °C s^{-1} significant amount of boron segregation along austenite grain boundaries has been observed. This boron in turn has been observed to retard the formation of ferrite during cooling from austenitizing temperature in the cooling rate (CR) range of $10 \leq CR \leq 20$ °C s^{-1}



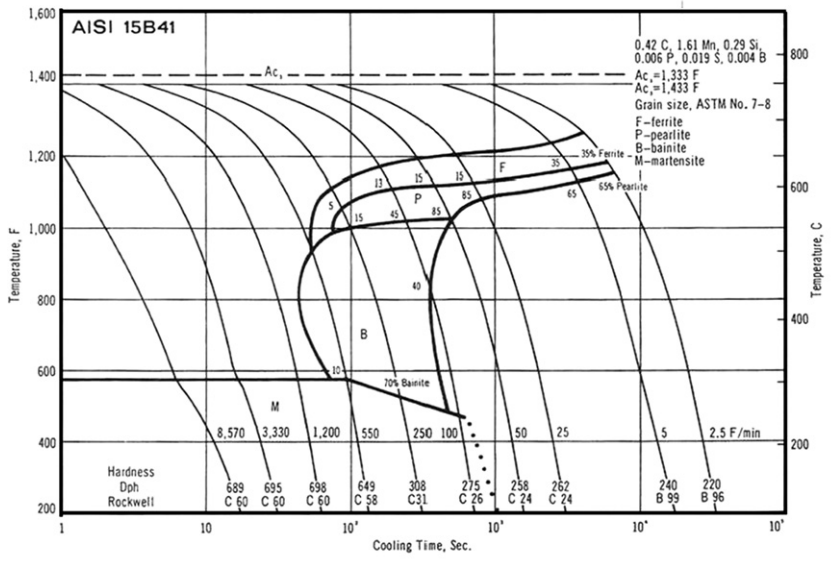


Figure 36 Comparison of CCT diagram of (a) AISI 1541 and (b) AISI 15B41, showing the boron hardenability effect.[18]

and thus improved hardenability of steel. The dramatic effect of addition of boron to a C–Mn steel (in plain carbon steels nominal content of Mn range from 0.60 to 0.90%) can be noted from the comparison of CCT diagrams of AISI 1541 and AISI 15B41 steels (**Figure 36**).

Here 0.004% boron promoted a structure which was entirely martensitic when formed at cooling rates greater than about 9 °C s^{-1} (540 °C min^{-1}). The difference in the rapidity with which transformations occur is quite evident from this figure.

Like other alloying elements, boron is effective in imparting hardenability only when it is in solution of austenite. Any boron which does not enter in austenite solution is ineffective in imparting hardenability to steel. Boron has strong tendency to combine with oxygen and nitrogen and form B_2O_3 and BN, respectively, in their presence during steel making. Once formed, these compounds cannot dissolve in austenite at the highest austenitizing temperatures used. Therefore, hardenability of boron treated steels varied with the state of deoxidation and with nitrogen content. Thus, proper steel melting practice must be used to protect boron from oxidation or nitride formation. This is done by (1) by proper deoxidation practice with the addition of Al, Si, or other deoxidizers, (2) by addition of strong nitride formers, such as Ti or Zr prior to addition of boron, or adding more boron to take care of existing nitrogen. Generally it is desirable to add boron slightly in excess over that required for optimum hardenability effect. Boron is added in steel in the form of ferro-boron alloy containing Al, Mn, Si, Ti, Zr, etc.

Boron in steel is believed to segregate to grain boundaries of austenite and retards the nucleation of proeutectoid ferrite, and thus promoting greater hardenability effect with fine austenite grain size. This means that a fine austenite grain size with large grain boundary area will promote suppression or retardation of nucleation of ferrite during austenite transformation upon quenching. This is in contrast to the effect of grain size on hardenability, i.e., boron diminishing the hardenability effect of grain size. In other words, boron has larger hardenability effect in fine grained steels. This suggests that if the boron level is too small, it is ineffective in imparting high hardenability in fine grain steels or at lower austenitization temperature but is effective to produce marked increase in hardenability in coarse grain steel. Grain size of austenite depends on austenitization temperature. Higher the temperature of austenitization coarser will be the grain structure.

Effect of hot deformation on hardenability of boron bearing low carbon high strength steel has been examined by Dong *et al.*[17] They observed that hot deformation increased the stability of solute boron that segregated to austenite grain boundaries during cooling from austenitizing temperature. This increase occurred because of the increase in boundary area by grain refinement. Hence the hardenability was improved in this steel.

Boron hardenability has been found to be affected by austenitizing temperature. An austenitizing temperature in the range 845 to 985 °C gives maximum boron hardenability but the most commonly used temperature is around 900 °C. However, as the temperature of austenitization increased beyond the above range, boron hardenability decreases with increasing the temperature. This is attributed to greater content

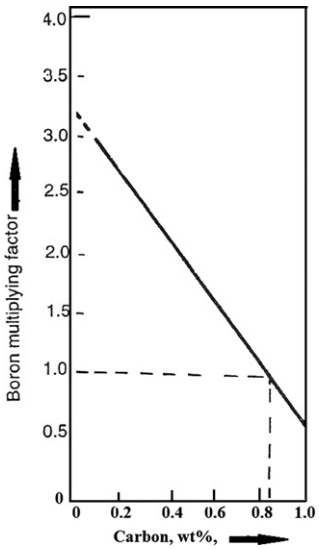


Figure 37 Effect of carbon on boron multiplying factor in 0.8%Mn steel.[4]

of boron dissolved in austenite. This promotes precipitation of borocarbides in advance of austenite transformation and is responsible for lowering the hardenability effect of boron.[17,19] For this reason, case-hardenability of boron treated steels is better if quenched from 925 °C. If the austenitizing temperature is very high, for instance, around 1100 °C, then a phenomenon called boron 'fade' occurs, in particular, in nitride bearing steels. The resultant effect is partial or total loss of boron hardenability and is permanent. The prolonged high temperatures of austenitization break the nitrogen protection provided by the elements Al, V, or Nb faster than if protected by Ti or Zr. The boron in solution is permanently lost to nitrogen resulting in decrease of hardenability.

Effect of boron on hardenability of carbon steels has been found to be more intensive in low to medium carbon steels than in high carbon steels. Even in hypoeutectoid steels, the highest effect of boron on hardenability occurs at low carbon concentration ≈0.10%. With carbon concentration greater than this the boron multiplying factor decreases continuously to unity at ≈0.80%C (**Figure 37**).

An element having multiplying factor of unity has no effect on hardenability. With further increase of carbon in the hypereutectoid range, multiplying factor of boron becomes less than unity. Combined additions two elements like boron and molybdenum shows synergism while increasing hardenability.[20]

See also: 2.1 Fundamentals of Heat Treating Metals and Alloys

References

1. Reed-Hill, R. E. *Physical Metallurgy Principles*; D. Van Nostrand Co., Inc.: NewYork, NY, 1966.
2. *ASM Handbook. Properties and Selection: Iron and Steels and High Performance Alloys*, Vol. 1, 10th ed. of Metals Handbook, second printing; ASM International: Materials Park, OH, 1993.

3. Verhoeven, J. D., Ed. Hardenability of Steel. In *Steel Metallurgy for Non-Metallurgist*; ASM International: Materials Park, OH, 2007 (Chapter 9). DOI: 10.1361/smnm2007p083.
4. Singh, V. *Heat Treatment of Metals*; Standard Publishers Distributors: New Delhi, 1998.
5. Krauss, G., Ed. Hardness and Hardenability. In *Steels: Processing, Structure and Performance*; ASM International: Materials Park, OH, 2005 (Chapter 16). DOI: 10.1361/spsap2005p297.
6. Dossett, J. L., Boyer, H. E., Eds. Hardness and Hardenability. In *Practical Heat Treating*, 2nd ed.; ASM International: Materials Park, OH, 2006 (Chapter 3). DOI: 10.1361/pht2006p027.
7. Campbell, F. C. *Elements of Metallurgy and Engineering Alloys*; ASM International: Materials Park, OH, 2008; pp. 117–199.
8. Cakir, M.; Özsoy, A. Investigation of the Correlation between Thermal Properties and Hardenability of Jominy Bars Quenched with Air–Water Mixture for AISI 1050 Steel. *Mater. Des.* **2011**, *32*, 3099–3105.
9. Zakharov, B. *Heat Treatment of Metals*; Peace Publishers: Moscow, 1962; p. 75.
10. *ASM Handbook. Heat Treating*, Vol. 4; ASM International: Materials Park, OH, 1991.
11. Grossmann, M. A.; Bain, E. C. *Principles of Heat Treatment*; ASM Publication, 1964.
12. Rajan, T. V.; Sharma, C. P.; Sharma, A. *Heat Treatment: Principles and Techniques*, 2nd ed.; PHI Learning Pvt. Ltd.: New Delhi, 2011.
13. Higgins, R. A., *Engineering Metallurgy Part 1: Applied Physical Metallurgy*, 5th ed.; ELBS edition, 1988.
14. Clark, D. S.; Varney, W. R. *Metallurgy for Engineers*; D. Van Nostrand Co. Inc.: NewYork, NY, 1968.
15. de la Concepcion, V. L.; Lorusso, H. N.; Svoboda, H. G. Effect of Carbon Content on Microstructure and Mechanical Properties of Dual Phase Steels. *Proced. Mater. Sci.* **2015**, *8*, 1047–1056.
16. Demir, B.; Erdogan, M. The Hardenability of Austenite with Different Alloy Content and Dispersion in Dual-Phase Steels. *J. Mater. Process. Technol.* **2008**, *208*, 75–84.
17. Dong Jun Mun; Eun Joo Shin; Young Won Choi; Jae Sang Lee; Yang Mo Koo. Effects of Cooling Rate, Austenitizing Temperature and Austenite Deformation on the Transformation Behavior of High-Strength Boron Steel. *Mater. Sci. Eng.* **2012**, *545*, 214–224.
18. ASM. *Source Book on Heat Treating, Vol. II-Production and Engineering Practices*; ASM: Metals Park, OH, 1975; p. 343.
19. Byoungchul Hwang; Dong-Woo Suh; Sung-Joon Kim, Austenitizing Temperature and Hardenability of Low-Carbon Boron Steels. *Scripta Mater.* **2011**, *64*, 1118–1120.
20. Futao Han; Byoungchul Hwang; Dong-Woo Suh; Zuocheng Wang; Duk Lak Lee; Sung-Joon Kim. Effect of Molybdenum and Chromium on Hardenability of Low-Carbon Boron-Added Steels. *Met. Mater. Int.* **2008**, *14* (6), 667–672. DOI: 10.3365/met.mat.2008.12.667.

2.3 Carburizing: A Method of Case Hardening of Steel

MMA Bepari, Bangladesh University of Engineering and Technology, Dhaka, Bangladesh

© 2017 Elsevier Inc. All rights reserved.

2.3.1	**Introduction**	73
2.3.2	**Methods of Carburization**	73
2.3.2.1	Solid or Pack Carburization	73
2.3.2.1.1	Carburizing process	73
2.3.2.1.2	Chemical reactions	74
2.3.2.1.3	Decarburization	74
2.3.2.1.4	Advantages	75
2.3.2.1.5	Disadvantages	76
2.3.2.2	Liquid Carburization	76
2.3.2.2.1	Carburizing Process	76
2.3.2.2.1.1	Low temperature baths	76
2.3.2.2.1.2	High temperature baths	77
2.3.2.2.2	Advantages	77
2.3.2.2.3	Disadvantages	77
2.3.2.2.4	Safety precautions	77
2.3.2.3	Gas Carburization	78
2.3.2.3.1	Carburizing process	78
2.3.2.3.2	Carburizing reactions	78
2.3.2.3.3	Atmospheric conditions for gas carburization	78
2.3.2.3.4	Carrier gases	79
2.3.2.3.5	Carbon potential	79
2.3.2.3.6	Advantages	79
2.3.2.3.7	Disadvantages	79
2.3.2.3.8	Safety measures for gas carburization	79
2.3.2.4	Vacuum Carburizing	80
2.3.2.4.1	Carburizing process	80
2.3.2.4.2	Control of carbon supply and case depth	80
2.3.2.4.3	Advantages	80
2.3.2.4.4	Disadvantages	80
2.3.2.5	Plasma Carburizing	80
2.3.2.5.1	Carburizing process	80
2.3.2.5.2	Control of carbon supply and case depth	81
2.3.2.5.3	Advantages	81
2.3.3	**Theory of Carburization**	81
2.3.3.1	Fick's Laws of Diffusion	81
2.3.3.2	The Equilibrium State for Chemical Reaction	82
2.3.3.3	Controlling Factors of Carburization	82
2.3.3.3.1	The flow of carbon in iron	82
2.3.3.3.2	Flow of carbon from the supply source	85
2.3.4	**Heat Treatment after Carburizing and Properties of Carburized Parts**	86
2.3.4.1	Single Hardening without Core Refinement	87
2.3.4.2	Single Hardening with Core Refinement	87
2.3.4.3	Double Hardening	88
2.3.4.4	Direct Quench Technique	89
2.3.4.5	Quenchants for Carburized Steels	89
2.3.4.6	Heat Treatment of Gas-Carburized Steels	90
2.3.4.7	Subzero Treatment	90
2.3.5	**Microstructures of Carburized Steels**	90
2.3.5.1	Martensite	90
2.3.5.1.1	How martensite forms	90
2.3.5.1.2	Martensite morphologies	91
2.3.5.1.3	Effect of tempering	92

2.3.5.1.4 Role of transition carbides 92
2.3.5.2 Austenite 92
2.3.5.2.1 Characteristic features of austenite 92
2.3.5.2.2 Effect of austenite composition 93
2.3.5.2.3 Excessive retained austenite 93
2.3.5.2.3.1 Effect on properties 93
2.3.5.2.3.2 Major cause 93
2.3.5.2.4 Reducing retained austenite 94
2.3.6 Carburization of Alloy Steels 94
2.3.6.1 Carburization of Low Alloy Steels 94
2.3.6.1.1 Carburization of chromium–nickel steel 94
2.3.6.1.2 Carburization of molybdenum–nickel steel 94
2.3.6.2 Carburization of Microalloyed Steels 97
2.3.6.2.1 Carburization of vanadium-microalloyed steel 97
2.3.6.2.2 Carburization of niobium-microalloyed steel 98
2.3.6.3 Low Temperature Carburization of Austenitic Stainless Steel 99
2.3.6.3.1 Introduction 99
2.3.6.3.2 Activation 99
2.3.6.3.3 Processing temperature ranges 100
2.3.6.3.4 Carburizing atmosphere 101
2.3.6.3.5 Microstructure of the low temperature carburized layer 101
2.3.6.4 Carburization of Tool Steels 101
2.3.6.4.1 Carburization of hot working tool steel 101
2.3.6.4.2 Carburization of cold working tool steel 102
2.3.6.4.3 Carburization of shock resisting tool steel 102
2.3.6.5 Carburization of Mold Steel 102
2.3.7 Problems during Carburization and their Remedy 102
2.3.7.1 Nonuniform Carburizing 103
2.3.7.1.1 Prevention 103
2.3.7.2 Uneven Case Depth 103
2.3.7.2.1 Prevention 103
2.3.7.3 Insufficient Case Depth 103
2.3.7.3.1 Prevention 103
2.3.7.4 Low Hardness 103
2.3.7.4.1 Higher case depth 103
2.3.7.4.2 Prevention 103
2.3.7.4.3 Retained austenite 103
2.3.7.4.4 Prevention 103
2.3.7.4.5 Decarburization 103
2.3.7.4.6 Prevention 103
2.3.7.5 Sooting 103
2.3.7.5.1 Prevention 103
2.3.7.6 Distortion 104
2.3.7.6.1 Release of internal stresses 104
2.3.7.6.2 Prevention 104
2.3.7.6.3 Drastic quenching 104
2.3.7.6.4 Prevention 104
2.3.7.6.5 High temperature hardening 104
2.3.7.6.6 Prevention 104
2.3.7.6.7 Rehardening 104
2.3.7.6.8 Prevention 104
2.3.7.6.9 Uneven heating 104
2.3.7.6.10 Prevention 104
2.3.7.7 Soft Spots 104
2.3.7.7.1 Prevention 104
2.3.7.8 Cracking and Exfoliation 104
2.3.7.8.1 Prevention 104

2.3.7.9 Grinding Cracks 105
2.3.7.9.1 Prevention 105
2.3.8 Recommended Processing Sequence for Carburized Components 105
References 105

2.3.1 Introduction

The service condition of many machine parts of steel such as gears, shafts, cams, pinions, and piston pins demands very hard and wear-resistant surface but with tough and shock-resistant core. Such a combination of properties is not usually possible from the commercial steels. A low carbon steel containing carbon 0.10–0.30% is sufficiently tough while a high carbon steel containing carbon up to 1.00% possesses adequate hardness. By suitable heat treatment the high carbon steel can be made very hard while low carbon steel will develop sufficient toughness. A machine part requiring hard surface but tough core will require a combination of high carbon surface and low carbon core which is developed by heat treatment only.

Carburizing is the most satisfactory and widely used method of surface hardening of low carbon steel. It is a process by which the carbon content of the surface of steel is increased. Since the objective of surface hardening is to obtain a hard, wear-resistant surface called case with a tough interior called core, the first consideration is the selection of low carbon (usually $\leq$0.20%) steel. It is then subjected to carburization to an extent of eutectoid–hypereutectoid composition and by subsequent heat treatment to the desired hardness.

Carburizing is the addition of carbon to the surface of low carbon steels at a temperature between 850 and 950 °C. At this temperature stable austenite structure has higher solubility of carbon which is diffused from the surrounding carburizing environment. Hardening is accomplished when the high carbon surface layer is quenched to form martensite. This produces a high carbon martensite case with good wear and fatigue resisting properties while the low carbon martensite core gives high toughness and shock resisting properties. A Schematic representation of carburizing process is shown in Figure 1.

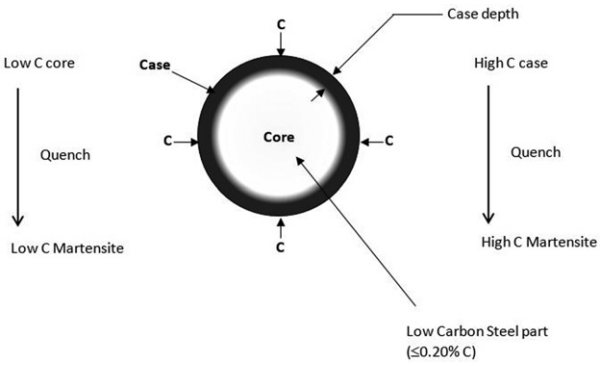


Figure 1 Schematic representation of carburizing process.

2.3.2 Methods of Carburization

There are three general methods of carburization depending on the carburizing medium.

1. Solid or pack carburization – solid medium.
2. Liquid carburization – liquid medium.
3. Gas carburization – gas medium.

Two other specialized methods are plasma carburization and vacuum carburization.

2.3.2.1 Solid or Pack Carburization

2.3.2.1.1 Carburizing process

In solid or pack carburization process parts to be carburized are charged in a heat resisting metallic box with a carburizing mixture (Figure 2). The solid carburizing mixture is of the following proportions:

Hard wood charcoal	53–55 parts
Sized coke	30–32 parts
Barium carbonate	10–12 parts
Calcium carbonate	3–5 parts
Sodium carbonate	2–3 parts

In the preparation of the above carburizing mixture, molasses is commonly used as binder. The carbonates are used as energizers. They are added to the charcoal to accelerate the carburizing process.

Workpieces, which are to be pack carburized, are first cleaned of dirt, scale, and rust. They are then placed in a box. Welded heat resisting steel boxes are generally employed. The

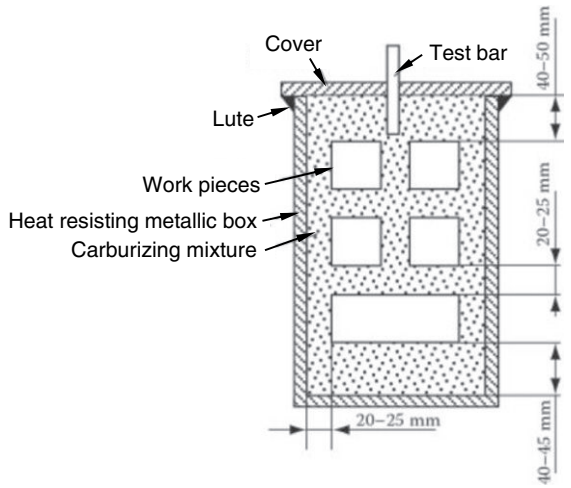


Figure 2 Packing of workpieces (low carbon steel parts) in a box for carburizing.[1]

boxes are usually in rectangular or cylindrical form. It is advisable to employ cylindrical boxes or pots. Packing the work is accomplished by first covering the bottom of the box with a 40–45 mm layer of carburizer (Figure 2). The workpieces to be carburized are placed on this layer with spaces of 20–25 mm between them and the box walls. Then they are covered with a dense layer of carburizer, 20–25 mm thick, which is rammed before laying the next row of workpieces. The upper row is covered with a layer of carburizer 40–50 mm thick. The box is closed with a cover whose edges are luted with fireclay or with mixture of clay and talc with water glass. Packed box is placed in the furnace.

The carburizing compound is in form of coarse particles or lumps, so that when the cover is sealed on the box, sufficient air will be trapped to form carbon monoxide. The box is then heated to the proper temperature (about 900–925 °C) for a required period of time (usually 3–5 h) and cool slowly in the furnace. The box is then withdrawn from the furnace and workpieces are taken out from the box.

The holding time at the carburizing temperature depends on the specified depth of carburized case. The deeper the case required, the longer the holding time should be at the carburizing temperature. The required holding times for various depths of carburized case are given in Table 1.[1]

At carburizing temperature the steel consists of austenite. Carburizing is concerned with the solid solution of carbon in austenite. The limits of carbon content of this phase depend on the temperature and composition of the steel. The maximum amount of carbon that can be dissolved in austenite at the carburizing temperature is indicated on the iron–iron carbide equilibrium diagram at the A_{cm} line (Figure 3). Therefore very quickly a surface layer of high carbon (about 1.2%) is built up. Since the core is of low carbon content, the carbon atoms trying to reach equilibrium will begin to diffuse inward. The rate of diffusion of carbon in austenite at a given temperature is dependent upon the diffusion coefficient and carbon concentration gradient. After the diffusion has taken place for the required amount of time dependent upon the case depth desired, the part is cooled in the furnace and examined microscopically. The carbon gradient will be visible in the gradual change of the structure. At the surface is hypereutectoid zone consisting of pearlite with a white cementite network, followed by the eutectoid zone of only pearlite and finally hypoeutectoid zone of ferrite and pearlite, with amount of ferrite increasing until the core is reached. This is illustrated in the Figure 4. Figure 5 shows carbon concentration gradient in the carburized steel with 0.08 in. total case.

Table 1 Relationship between case depth and holding time (carburizing temperature 930 °C)

Case depth (mm)	*Holding time (hour)*
0.4–0.7	4.5–5.5
0.6–0.9	5.5–6.5
0.8–1.2	6.2–10.0
1.0–1.4	8.0–11.5
1.4–1.8	11.5–16
1.5–1.9	13–18
1.6–2.0	14–19
1.8–2.2	16–22

2.3.2.1.2 Chemical reactions

There is always air present in the carburizing box, even when it is filled with carburizer. At the carburizing temperature, the oxygen in the air reacts with the carbon in the carburizer to produce carbon dioxide gas. This carbon dioxide further reacts with carbon in the carburizer to produce carbon monoxide.

$$C + O_2 \rightarrow CO_2 \quad [I]$$

$$CO_2 + C \rightarrow CO \quad [II]$$

This carbon monoxide is the carrier of carbon and when comes in contact with austenitic iron, iron carbide is formed, which is dissolved in austenite.

$$Fe + CO \rightarrow [C]Fe\ (C\ \text{dissolves in austenite}) + CO_2 \quad [III]$$

Energizers (like $BaCO_3$, $CaCO_3$, and $NaCO_3$) in the carburizing mixture decompose at the carburizing temperature to produce oxides and CO_2 as follows:

$$BaCO_3 \rightarrow BaO + CO_2$$

$$CaCO_3 \rightarrow CaO + CO_2$$

$$Na_2CO_3 \rightarrow NaO + CO_2$$

This ensures enough supply of CO_2 for the reaction [II] to continue, and hence enough supply of CO for the reaction [III]. The reactions cycle will be repeated.

At the initial stage of carburization, the maximum saturation limit of carbon (about 1.2%C) at the surface of the steel is reached. Then carbon begins to diffuse to the interior as shown in Figure 6. The diffusion of carbon depends on the diffusion coefficient $D = D_0\, e^{-Q/RT}$, where Q is the activation energy, R is gas constant, and T temperature in degree kelvin. As D increases, depth of penetration of carbon or case depth increases.

The relation of carburizing time and temperature to case depth is shown in Figure 7. The higher the temperature and longer the period of carburization, the greater is the case depth.

2.3.2.1.3 Decarburization

The carburization equation given previously,

$$Fe + CO \rightarrow [C]Fe\ (C\ \text{dissolves in austenite}) + CO_2$$

is reversible and may proceed to the left, removing carbon from the surface layer if the steel is heated in an atmosphere containing carbon dioxide (CO_2). This is called decarburization.

Other possible decarburization reactions are:

$$Fe_3C + H_2O \rightarrow Fe + CO + H_2$$

$$Fe_3C + O_2 \rightarrow Fe + CO_2$$

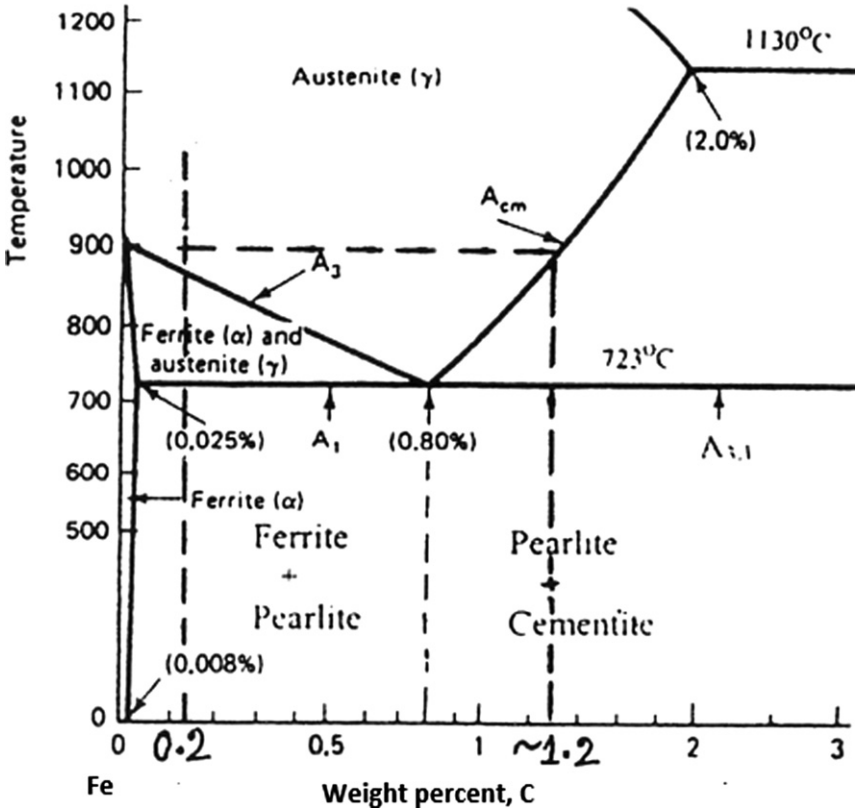


Figure 3 Portion of Iron–Iron Carbide equilibrium diagram.

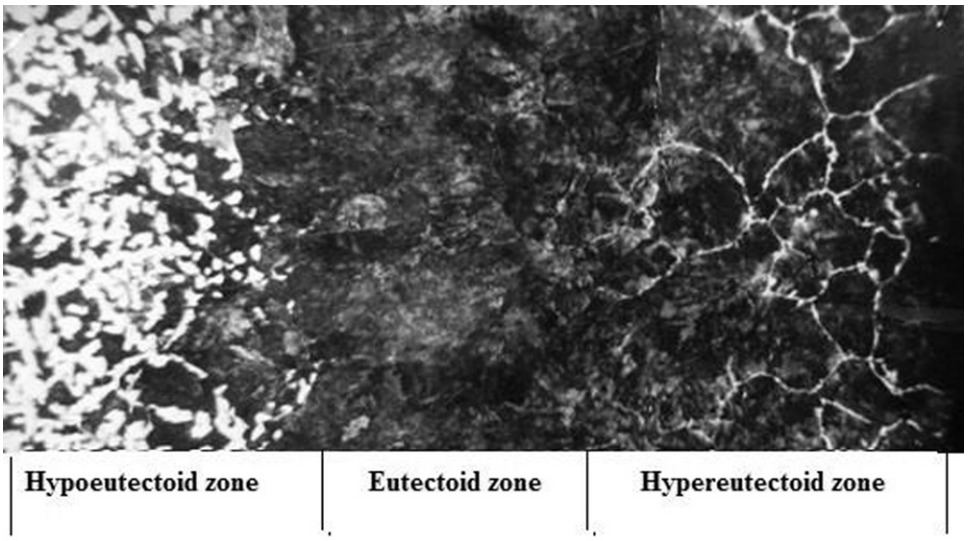


Figure 4 Microstructure of pack carburized and furnace cooled low carbon steel showing different zones from case (right) to core (left), × 400.

Decarburization is a problem primarily with high carbon steel and tool steel.

2.3.2.1.4 Advantages

- Pack carburization is economical and advantageous for small machine parts.
- Special furnaces are not required to heat the carburizing boxes.
- The soft case produced by slow cooling from the carburizing temperature permit additional machining prior to hardening.
- It does not require a controlled atmosphere furnace.

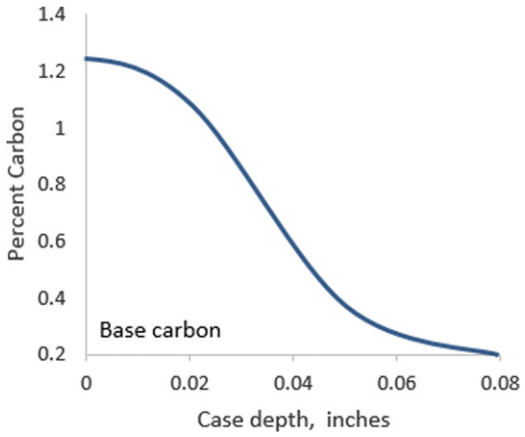


Figure 5 Carbon concentration gradient in a carburized steel with 0.08 in. total case.

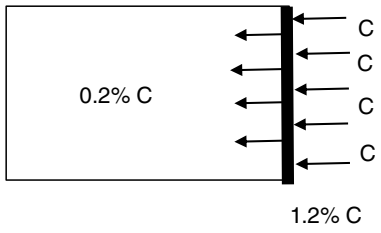


Figure 6 Flow of carbon from high carbon surface to the interior.

- Carburizing compounds give good support to parts, helping to prevent sagging at high temperatures.

2.3.2.1.5 Disadvantages

- Larger and complicated machine parts cannot be carburized effectively.
- There are some limitations in handling larger and complicated machine parts.
- Packed carburized machine parts cannot be hardened directly from the carburizing temperature.
- The box containing the charge when heated gets oxidized and warrants frequent replacement.
- Uniform case depth cannot be obtained in pack carburization.
- The preparation of judicious mixture is a skilled job and is time consuming.

2.3.2.2 Liquid Carburization

2.3.2.2.1 Carburizing Process

The liquid carburization is used for parts requiring thin carburized case. The liquid carburization is suitably practiced for complex machine parts and is carried out by heating them in a liquid bath.

In liquid carburizing, workpieces to be carburized are immersed in molten salt baths maintained at carburizing temperatures as shown in Figure 8. These baths contain sodium cyanide as a carburizing agent. Liquid carburizing

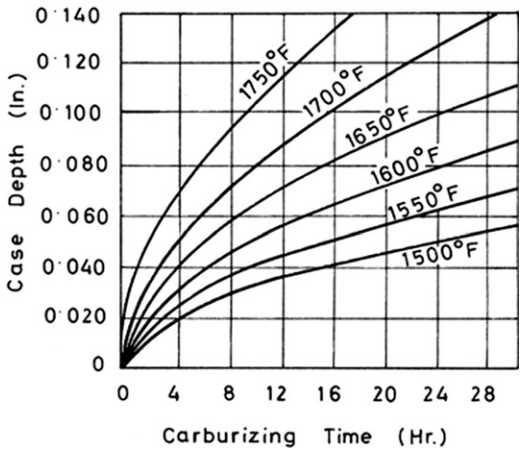


Figure 7 The relation of time and temperature to case depth.[2]

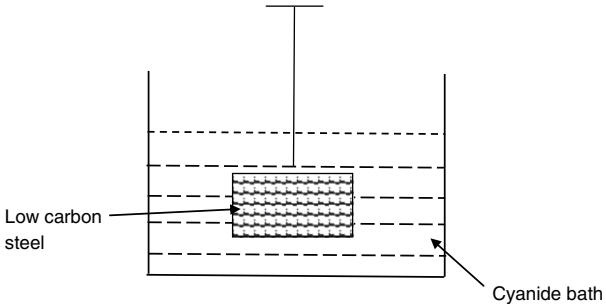


Figure 8 Liquid carburization in cyanide bath.

baths can be divided into two categories: (1) low temperature baths and (2) high temperature baths.

They not only differ with respect to temperatures of carburizing, but the compositions of these baths and the mechanisms (chemistry) of carburizing are also different. Table 2 gives compositions of these baths. Recently some noncyaniding liquid baths have also been developed.

2.3.2.2.1.1 Low temperature baths

These are normally operated at 850–900 °C and are best suited for producing shallow case depths (~0.075–0.75 mm). Typical composition of low temperature carburizing baths is given in Table 2.

Chemistry of carburizing in low temperature baths is rather complex. The main reactions involved are as follow:

$$2NaCN \rightarrow Na_2CN_2 + C \text{ (Cynamide shift)} \quad [IV]$$

and either

$$NaCN + O_2 \rightarrow 2NaNCO \text{ (Cyanate formation)}$$

or

$$NaCN + CO_2 \rightarrow NaNCO + CO \text{ (Cyanate formation)} \quad [V]$$

The cyanate (NaNCO) thus produced, further reacts to give:

$$NaNCO + C \rightarrow NaCN + CO \quad [VI]$$

Table 2 Compositions of liquid carburizing baths (in wt%)

Constituent	*Low temperature baths*	*High temperature baths*
Sodium cyanide	10–23	6–16
Barium chloride	–	30–55
Salts of alkaline earths	0–10	0–10
Potassium chlorides	0–25	0–20
Sodium chlorides	20–40	0–20
Sodium carbonate	40 max.	30 max.
Other accelerators	0–5	0–2
Sodium cyanate	1.0 max.	0.5 max.
Density	1760 kg m^{-3} (at 1173 K)	2000 kg m^{-3} (at 1198 K)

$$4NaNCO + 2O_2 \rightarrow 2Na_2CO_3 + 2CO + 4N \quad [VII]$$

and

$$4NaNCO + 4CO_2 \rightarrow 2Na_2CO_3 + 6CO + 4N \quad [VIII]$$

CO and C produced by above reactions react with Fe at the steel surface to enrich it with carbon as,

$$2CO + Fe \rightarrow C(Fe) + CO_2 \quad [IX]$$

and

$$C + (Fe) \rightarrow C(Fe) \quad [X]$$

Reactions [VII] and [VIII] deplete the activity of the bath and lead to an eventual loss of carburization potential, unless suitable replenishment is done.

2.3.2.2.1.2 High temperature baths

These are normally operated at 900–950 °C. Typical composition of high temperature baths is given in **Table 2**. High temperature baths are used for producing deeper case depths, in the range of 0.5–3.0 mm. Apart from cyanide, these baths contain a major amount of barium chloride.

In liquid carburization the carburizing reaction depends primarily on the sodium cyanide, activated by the presence of alkaline earth salt-usually barium (or calcium) chlorides. The salts (chloride) react with the cyanide to form a cyanide of alkaline earth metal, which then reacts with iron to form Fe_3C.

Although reaction given above for low temperature baths occur here also to some degree, the principle reactions in high temperature baths are:

$$2NaCN + BaCl_2 \leftrightarrow 2NaCl + Ba(CN)_2 (\text{barium cyanide}) \quad [XI]$$

$$2NaCN + CaCl_2 \leftrightarrow 2NaCl + Ca(CN)_2 (\text{calcium cyanide}) \quad [XII]$$

$$Ba(CN)_2 + Fe \rightarrow [C]Fe + BaCN_2 (\text{barium cyanamide}) \quad [XIII]$$

$$Ca(CN)_2 + Fe \rightarrow [C]Fe + CaCN_2 (\text{calcium cyanamide}) \quad [XIV]$$

Carbon content of the case can be controlled by the cyanide content of the bath. Low temperature bath operates at higher cyanide content than high temperature bath. Both high as well as low temperature baths can be operated with varying cyanide content, through which the carbon activity of the bath can be controlled to some extent. **Table 3** gives preferred operating cyanide content at different temperatures. Lower end of the cyanide content range, at a given temperature, would normally produce a hypoeutectoid case, whereas, a hypereutectoid case is obtained with the cyanide content near the upper limit.

Table 3 Sodium cyanide content in liquid carburizing bath at different operating temperature

Temperature (°C)	*Sodium Cyanide (%)*		
	Maximum	*Preferred*	*Minimum*
815	23	18	14
840	20	16	12
870	18	14	11
900	16	12	10
925	14	10	8
955	12	8	6

Reactions [VII] and [VIII] show that, there is also nascent nitrogen present in the carburizing baths to some extent. This nitrogen is also absorbed at the surface of steel and diffuses inwards. However, at cyanide concentrations of carburizing baths, nitrogen activity is relatively low and hence only very little nitrogen diffuses into the steel. Activity of nitrogen is higher at higher end of the cyanide content range at a given temperature.

2.3.2.2.2 Advantages

- Complicated machine parts can be carburized.
- Uniform case depth can be obtained.
- Less distortion and cracking in hardening.
- High output even from a relatively small furnace due to rapid rate of heat transfer.
- Labor costs are reduced, since the operation of the process is simple.
- Surface decarburization is eliminated.
- Time of carburization is reduced compared to pack carburization.

2.3.2.2.3 Disadvantages

- Materials cyanide solution and fumes coming up from the both are poisonous.
- Great care required in disposal of cyanide bearing salts.
- Necessary of removing the salt from the work by special means, such as hot water spray washing, acid dip, etc.
- There is a danger of explosion if moisture is introduced into the salt.
- Separate storage required for keeping the salts under lock and key.
- Exhaust system is required.
- High cost of the carburizing salt.

2.3.2.2.4 Safety precautions

Sodium cyanide is a very poisonous substance and requires great care in its handling and storage. At all stages of the use of sodium cyanide, care must be taken to prevent any body contact so that no cyanide can enter the blood stream

(e.g., via cuts). Adequate protective clothing must be worn. Well-designed eye shields or goggles and well-fitting helmets are essentials in order to protect eyes and head.

2.3.2.3 Gas Carburization

2.3.2.3.1 Carburizing process

In gas carburization, the carbon of the furnace atmosphere is in the form of gaseous hydrocarbon compounds such as methane, ethane, propane, and butane or carbon monoxide. The principal source of carbon in gas carburizing is methane, which is present in manufactured and in natural gas. Gas carburizing is carried out at 900–950 °C and a case depth of up to about 0.4 mm may be obtained after 1 h heating at 900 °C. A case depth of up to 1 mm is commonly produced.

The low carbon ($\leq$0.2%C) steel parts are placed in the carburizing chamber. The air inside the carburizing chamber is then driven out by introducing hydrocarbon gas or carbon monoxide gas. The carburizing chamber is then heated to the temperature (900–925 °C) in the furnace and a continuous gas flow is maintained. A typical gas carburizing process is shown in Figure 9.

At this temperature and environment the low carbon steel part is heated for 2–3 h. At the end of the holding period the temperature of the furnace is reduced to 840–870 °C in order to decrease the grain size. The carburized part is then withdrawn from the chamber and quenched directly in water or oil. As a result the high carbon surface layer transforms into a hard wear-resistant case.

Quenching produces martensite microstructure with high residual stress inside the machine parts. This residual stress is undesirable because it causes cracking and distortion. In order to remove the residual stress, the machine part is tempered at a temperature of 150–180 °C immediately after quenching.

2.3.2.3.2 Carburizing reactions

The reaction involving the actual transfer of carbon occurs at the steel surface (interface) and the reactants, which are carbon compounds (gas), may be considered independently. The interface reactions[3,4] for common carbon compounds may be written:

$$CH_4(g) + 3Fe(steel) \leftrightarrow [C]Fe(in\ austenite) + 2H_2(g) \quad [XV]$$

$$C_2H_6(g) + 9Fe(steel) \leftrightarrow [C]Fe(in\ austenite) + 4H_2(g) \quad [XVI]$$

$$C_3H_8(g) + 9Fe(steel) \leftrightarrow [C]Fe(in\ austenite) + 4H_2(g) \quad [XVII]$$

$$2CO(g) + 3Fe(steel) \leftrightarrow [C]Fe(in\ austenite) + CO_2(g) \quad [XVIII]$$

Reactions that occur for the same compounds, away from the interface (i.e., the reactions for the deposition of carbon)[3,4] are as follows:

$$CH_4(g) \leftrightarrow 2H_2(g) + C(solid\ carbon) \quad [XIX]$$

$$C_2H_6(g) \leftrightarrow 3H_2(g) + C(solid\ carbon) \quad [XX]$$

$$C_3H_8(g) \leftrightarrow 3H_2(g) + C(solid\ carbon) \quad [XXI]$$

$$2CO(g) \leftrightarrow 2H_2(g) + C(solid\ carbon) \quad [XXII]$$

After the required period of carburization the parts are either cooled in the furnace or quenched directly from the furnace.

If water vapor is present in the gas it will act as a decarburizing agent, removing carbon from steel by the reaction[3]:

$$Fe_3C + H_2O \rightarrow Fe + CO(g) + H_2(g) \quad [XXIII]$$

2.3.2.3.3 Atmospheric conditions for gas carburization

Usually the volume of the chamber of gas carburizing furnace is small and it is sealed, which ensure small volume of gas requirement for each shift. For a pit furnace having a working chamber 64 cm in diameter and 90–120 cm deep, the commonly used gas flow rate is 63–118 $cm^3\ s^{-1}$.[5] The rate at which the furnace atmosphere responds to changes in inlet gas composition depends on the mean residence time of the

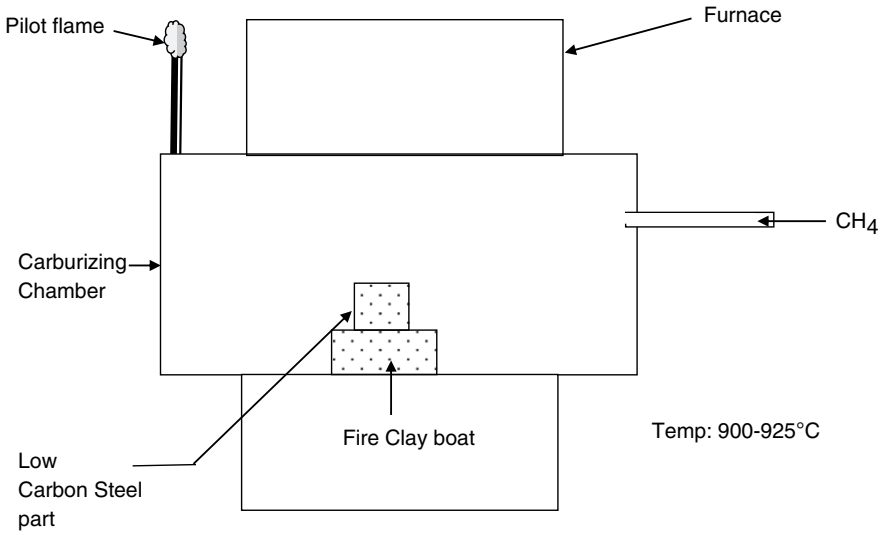


Figure 9 Gas carburizing process.

atmospheric gases in the furnace. The mean residence time (t_{res}) of the gas in the furnace is,[6]

$$t_{res} = V \cdot T_a / F \cdot T_f \quad [1]$$

where V is the chamber volume, T_f is the absolute temperature, and F is the flow rate of gas measured at ambient temperature T_a. Residence time may be from 2 to 15 min.[6] For times of this order the reaction in the furnace chamber are fast enough so that equilibrium gas composition are approached closely for the usual carburizing temperatures.

For natural gas as carburizing medium the possible constituents of the gas carburizing atmosphere are CO, CO_2, H_2, H_2O, CH_4, and C_2H_6 gases. For uniformity of carburizing the above gases have to be well circulated within the chamber and the parts being carburized must be well spaced to get contact of the carburizing gases. A positive pressure in the furnace should be maintained for effective carburization rate and to prevent infiltration of air within the chamber. For gas carburizing a positive furnace pressure of about 12–37 Pa is satisfactory[6] and it is controlled by adjusting the gas flow rate.

2.3.2.3.4 Carrier gases

In gas carburizing, it is found that the amount of carbon available is more than what is required for absorption. This excess carbon precipitates as a heavy soot and deposits on the component surface as well as on the walls of the furnace. Hence, in gas carburizing, it is necessary that the hydrocarbon gases used are diluted with carrier gas to avoid the formation of heavy soot.

Carburizing agent (hydrocarbon gas) is diluted by a carrier gas before it enters the carburizing furnace. The carrier gas itself is normally made by controlled burning of CH_4, or some other hydrocarbon gas. Most commonly used carrier gas is endothermic base, obtained by controlled burning of CH_4 in air, with air-to-gas ratio of 2:5, to give:

$$CH_4 + O_2(\text{air}) \rightarrow 2CO + 4H_2 \quad [XXIV]$$

Endothermic carrier gas, then, contains the remaining nitrogen from air, CO, and H_2 as by-products of above reaction and small amounts of CO_2 and H_2O that may form during the production of carrier gas. Composition of the carrier gas is 39–40% N_2, 20–21% CO, 38–39% H_2 and small amount of CH_4, CO_2, and H_2O (all in vol.%). Sometimes, commercially pure nitrogen is also used as a carrier gas. Ratio of hydrocarbon gas (carburizing agent) to carrier gas in a carburizing gas mixture could vary from about 1:8 to 1:30, depending upon the desired surface carbon content, temperature of carburizing, and other considerations.

2.3.2.3.5 Carbon potential

The carbon potential in a furnace atmosphere at a specified temperature is defined as the carbon content in pure iron that is in thermodynamic equilibrium with the atmosphere. The carbon potential of the furnace atmosphere must be greater than the carbon potential of the surface of the workpiece in order for carburizing to occur. It is the difference in carbon potential that provides the driving force for carbon transfer to the parts. In most systems, the addition of a hydrocarbon gas such as methane is used for the control of carbon potential.

The gases CO and CH_4 are carburizing, whilst H_2, H_2O, and CO_2 are decarburizing agents. In order to control the carbon availability of the atmosphere, i.e., the carbon potential, a hydrocarbon gas is used to enrich the carrier gas, by reducing the H_2O (dew point) according to the reaction:

$$CH_4 + H_2O \rightarrow CO + 3H_2 \quad [XXV]$$

and by reducing the CO_2 according to the reaction:

$$CH_4 + CO_2 \rightarrow 2CO + 2H_2 \quad [XXVI]$$

as well as the following carburizing reaction takes place:

$$CH_4 \rightarrow CFe + 2H_2 \quad [XXVII]$$

in addition to reaction [XXVII], the other main carburizing reactions in a CO–CO_2–H_2–H_2O–CH_4 atmosphere are:

$$CO + H_2 \rightarrow CFe + H_2O \quad [XXVIII]$$

$$2CO \rightarrow CFe + CO_2 \quad [XXIX]$$

(in the gas reactions described CFe is the available carbon, from the atmosphere, for diffusion into the steel surface).

Reactions [XXVIII] and [XXIX] are considered the main equilibrium reactions for the basic method of carbon transfer into the steel surface. The assumption is that the carburizing is taking place as a direct result of the CO content in the atmosphere.

2.3.2.3.6 Advantages

- The complicated machine parts can easily be carburized by the gas.
- Uniform case depth can be obtained by the gas carburizing compared to that by pack carburizing.
- Time–temperature cycles can be determined accurately for close control of the case depth.
- Composition of the carburizing gas can be varied to provide a close control of the carbon content of the cases.
- It is cheaper than pack carburization.
- Hardening by direct quenching from the carburizing temperature is possible in gas carburizing.
- The rate of penetration of carbon is more in gas carburizing as compared to pack carburization.
- Less time is required to attain the carburizing temperature, since there is no need to heat the boxes as in pack carburization.

2.3.2.3.7 Disadvantages

- A gas generator is required to produce carrier gas.
- Partial carburizing cannot be performed which is possible in liquid carburizing.

2.3.2.3.8 Safety measures for gas carburization

The outlet gas from the chamber is very toxic and highly inflammable whether it is mixed or unmixed with air. For this, a safety program is essential to avoid the risks of the operation especially for the personnel under work. As a safety measure, all the gas discharged from the furnace has to be burned to

ensure that poisonous carbon monoxide has been converted into carbon dioxide. Therefore, a pilot flame has to be maintained until carburizing gas flow is continued. For safety measure, it is convenient to have a source of inert gas, such as nitrogen for purging the chamber after completion of the process.

2.3.2.4 Vacuum Carburizing

2.3.2.4.1 Carburizing process

Vacuum carburizing refers to carburizing of steel components in vacuum furnaces with the introduction of controlled amounts of carburizing gaseous mixture, usually a mixture of nitrogen and hydrocarbon gases (normally CH_4 or C_2H_8), at relatively low pressure. Heating steel components in vacuum furnaces provide excellent oxidation and decarburization resistance. A vacuum furnace may be backfilled with a carburizing gas mixture after the load has been heated to the desired carburizing temperature usually 900–1050 °C. Vacuum furnaces are specifically suited for high temperature carburizing. Carburizing gas mixture containing oxygen compounds are not generally used in vacuum carburizing, as CO and H_2O react with the traditional vacuum furnace materials, such as graphite and molybdenum. Hydrocarbons present in the backfilled carburizing gas mixtures crack at the surface of steel and provide carbon to the steel surface.

$$CH_4 \rightarrow 2H_2 + C(Fe) \qquad [XXX]$$

or

$$4C_2H_8 \rightarrow 4H_2 + 2C(Fe) \qquad [XXXI]$$

Carbons produced by these cracking reactions are highly reactive and is easily absorbed at the surface of steel. As a result of cracking of hydrocarbons, the gas mixture in the furnace consists of N_2, CH_4 (or C_2H_8), and H_2. Such atmosphere has tendency to produce soot.

2.3.2.4.2 Control of carbon supply and case depth

With no chemical equilibrium available as a control parameter, the carburizing process during vacuum carburizing is controlled by controlling the process variables, i.e., the partial pressure of hydrocarbon gas in the backfilled gas mixture, and the temperature and the time of carburizing. Shallow cases, that are formed in less than 20–30 min, can be obtained by time control only, i.e., fixed amount of hydrocarbon gas is introduced and carburization is carried out for a predetermined time. For deeper cases and to allow for more accurate surface carbon control, a two-step process consisting of a boost period and a diffusion period is used. During the boost period, sufficient hydrocarbon gas is introduced to obtain saturated carbon level without undue sooting of the furnace or components. Subsequently, the furnace is evacuated of all gases and diffusion is allowed to occur. Under vacuum heating, during the diffusion period, decarburization at surface does not occur. The existing carbon at the surface is redistributed, lowering the surface carbon and increasing the depth of carburizing. Figure 10 shows typical results obtained by a two-step process. The relative durations of boost and diffusion steps depend on the desired surface carbon content and depth of carburizing, and are empirically determined.

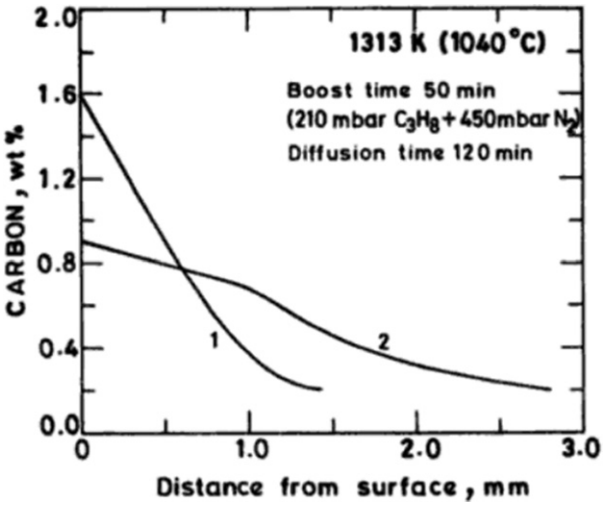


Figure 10 Carbon concentration profiles after (1) boost stage and (2) diffusion stage, in a two-step vacuum carburizing of AISI-1022 steel at 1040 °C.[7]

2.3.2.4.3 Advantages

- Fast carbon transfer.
- No surface oxidation.
- Good case depth uniformity.
- Integration into manufacturing lines.
- Small consumption of carburizing gas.
- No formation of furnace atmosphere.
- High carburizing temperatures possible.

2.3.2.4.4 Disadvantages

- Higher initial capital equipment cost than atmosphere carburizing equipment.
- Empirical process control, which requires processing loads to determine optimal settings or fine tune simulator.
- Formation of soot and tar, which occur due to the type, pressure, and quantity of hydrocarbon gas introduced.

2.3.2.5 Plasma Carburizing

2.3.2.5.1 Carburizing process

In plasma carburizing partial heating of parts and their carburization is carried out in a plasma of low-pressure ionized gases. This method is also known as 'glow discharge' carburizing. The component to be carburized works as cathode of glow discharge, with a suitable d.c voltage impressed between the cathode and anode to support a stable glow as well as to act as carburizing agent. An atmosphere of hydrocarbon gas (like CH_4) at a proper pressure is provided as a conducting atmosphere. Figure 11 schematically shows a plasma carburization chamber.

The chamber is evacuated and then backfilled with a hydrocarbon gas at reduced pressure, generally in the range of 0.1–2.7 kPa. A continuous flow of gas at reduced pressure is maintained during the carburization (boost) cycle. High

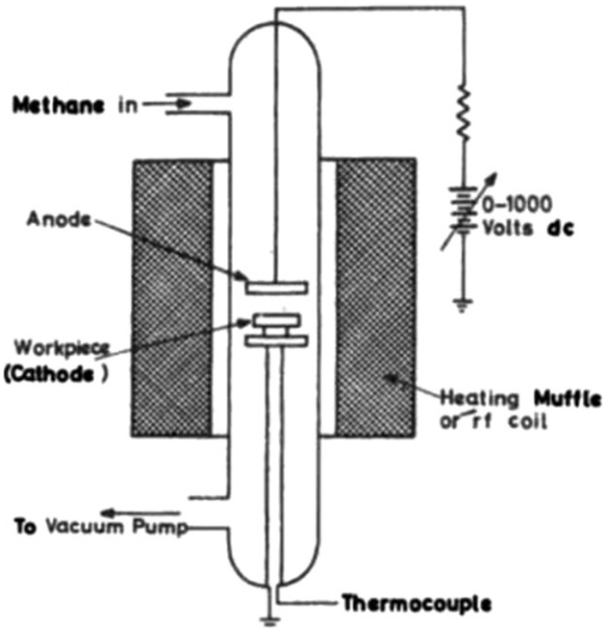


Figure 11 Schematic illustration of plasma carburizing setup.[8]

voltage (500–1000 V) is applied to strike the plasma in a methane atmosphere of ~2.7 kPa. Under these conditions, a thin plasma completely envelops the workpiece and closely follows its contours, even if the surface is quite irregular. Methane is dissociated within this thin plasma envelope and a high carbon potential is established at the workpiece surface, even though the total pressure in the furnace is relatively low.

The plasma consists of ionized gases and electrons. Positively charged ions of the type CH_i^{+n} (i=0–3) accelerate toward the cathode (workpiece) and introduce carbon at the surface, whereas electrons accelerate to the anode. In the process, both anode and cathode also get heated. However, heating the workpiece in plasma process in not sufficient to heat it up to the carburizing temperatures of 900–1050 °C. Thus to keep the workpiece at appropriate carburizing temperature an auxiliary induction or radiation heating source (Figure 11) is used.

2.3.2.5.2 Control of carbon supply and case depth

Rate of carburization in plasma carburizing is higher compared to vacuum or conventional gas carburization. Within the glow discharge gaseous molecules, some chemical reactions may occur, which would not occur under normal thermodynamic equilibrium condition. The electrons in the plasma atmosphere help to break chemical bonds and thereby dissociate methane to provide necessary carbon at the surface. Hydrogen generated by dissociation of CH_4 and ion bombardment of the surface may also dissociate surface oxides, and thus remove potential barrier to quick introduction of carbon at the surface. These factors accelerate uniform introduction of carbon and the attainment of saturation level of carbon at the surface. Like vacuum carburizing, plasma carburizing is normally carried out in two steps. In the first step, carbon is introduced at the surface by methane plasma and the second step is carried out by further heating the workpiece in vacuum to decrease surface carbon to the desired level and to

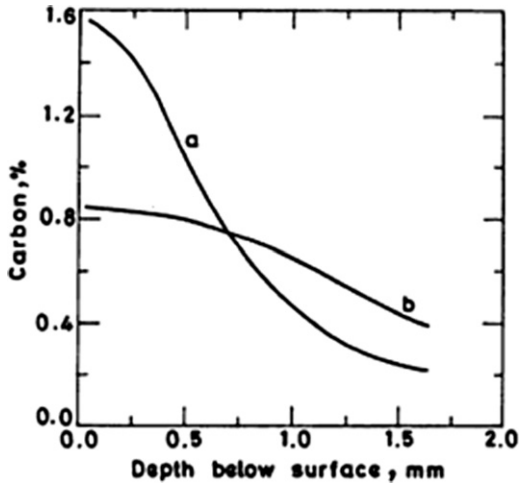


Figure 12 Carbon concentration profiles in AISI-1018 steel, plasma carburized at 1050 °C (a) after plasma carburizing for 10 min; (b) after additional diffusion period of 30 min.[8]

increase the case depth by diffusion processes. As the second step is carried out in vacuum, no decarburization at the surface occurs, only redistribution of carbon by diffusion takes place. Figure 12 shows carbon profiles obtained in AISI-1018 steel in plasma carburizing for 10 min at 1050 °C followed by a diffusion period of 30 min at the same temperature.

2.3.2.5.3 Advantages

- Consumption of gases in plasma carburizing is much less compared to conventional gas carburizing.
- No oxidation takes place at grain boundaries, and the finished surface is clean and glossy.
- Uniform carburized layer is obtained, no sooting is encountered.
- Carburizing of high concentration and the one into the hard-to-carburized materials such as stainless steel and sintered metals can easily be carburized.
- Due to fast carburizing rate and low temperature/short time treatment, no grain growth is observed and residual strain is very little.
- This is a pollution-free and energy-saving processing.

2.3.3 Theory of Carburization

The carburization of steel may be explained on the basis of two fundamental concepts. The first is diffusion, influenced by the properties of the iron, and concerned with the movement of carbon in the iron itself; the second deals with the source supplying the carbon, and with the transfer of carbon to the surface.

These two general concepts may be described briefly:

2.3.3.1 Fick's Laws of Diffusion

Fick's first law[3]: it describes diffusion under equilibrium conditions and is stated mathematically by:

$$J_1 = D_1 \frac{dc_1}{dx} \qquad [2]$$

Where D_1 is the diffusion coefficient and J_1 is the resulting flux gradient.

Fick's second law[3]: it expresses the nonequilibrium condition of diffusion where the concentration, at a point, changes with respect to time.

$$\frac{dc}{dt} = \frac{d}{dx}\left(D_1 \frac{dc_1}{dx}\right) \quad [3]$$

Carburizing is a nonequilibrium process, i.e., the gaseous constituents of the atmosphere are not fully in equilibrium with one another and the atmosphere is not in equilibrium with the steel being carburized.

The value of the diffusion coefficient is critical in any calculation dealing with carburizing or any other diffusion process. The diffusion coefficient D is defined by:

$$D = D_0 e^{-Q/RT} \quad [4]$$

where D_0 and Q are experimentally determined constants. Q is the heat of diffusion (activation energy, i.e., the energy required for one atom to jump to a new position in the lattice); R is the gas constant; and T is the absolute temperature. The greater is the value of Q, the smaller is the value of D at a given temperature and hence the slower is the rate of diffusion.

The diffusion coefficient which describes the diffusion of carbon in austenite varies somewhat with carbon content. The following expression, according to Tibbetts,[9] is a good fit to the experimental data.

$$D = 0.47 \exp(-1.6C)\exp\{-(37000-6600C)/RT\}\text{cm}^2\ \text{s}^{-1} \quad [5]$$

where, C is the carbon concentration in weight percent and T is the temperature in degrees Kelvin.

2.3.3.2 The Equilibrium State for Chemical Reaction

The equilibrium state[3] for chemical reactions may be represented by numerical constants, K_p, derived from the general expression,

$$\log K_p = \frac{A}{T} - B \quad [6]$$

where K_p is termed as the 'equilibrium constant,' which is derived from the values for the concentrations of the reactants and products of a chemical reaction. The subscript p denotes the dependency of the chemical reaction on pressure. T is the absolute temperature at which the reaction takes place. A and B are constants derived for the particular reaction.

2.3.3.3 Controlling Factors of Carburization

Instead of being developed in a formal way from the basic principles, the mechanism of carburization may be analyzed from the view point of carbon flow, by stating the controlling factors.[3] These factors may be divided for discussion into two distinct classifications:

1. Factors that control the of carbon in iron.
2. Factors that influence the transfer of carbon to the iron surface.

The mechanism may by explained as follows:

2.3.3.3.1 The flow of carbon in iron

Iron when heated in presence of carbon makes a solid solution. A solid solution may be described to be a solution of two or more components as solute and solvent sharing their atoms in their initial cells in the solid state. In other words a solution may be defined as any phase of which the composition may vary continuously within certain limits. Carburizing is concerned with the solid solution of carbon in austenite. The limits of carbon content of this phase depend on the temperature. The solid solution of carbon in gamma iron is an interstitial type of solid solution. As is evident from the iron and iron–carbide thermal equilibrium diagram (**Figure 13**), at temperature below about 910 °C (1183 K), pure iron occurs as a body-centered cubic (bcc) structure. Above 910 °C (1183 K) there is a temperature range in which iron has a face-centered cubic (fcc) structure. In fcc lattice, a relatively large unoccupied 'hole' exists in the center of the unit cell.[10] Carbon being an extremely small atom can move into this hole to produce a solid solution of iron and carbon as shown in **Figure 14**. When iron has a bcc structure at lower temperatures, the interstices between the iron atoms become much smaller and consequently the solubility of carbon in bcc iron is relatively small.

The penetration of carbon into the iron forming steel will depend upon the temperature, the time at temperature and the carburizing agent. Since the solubility of carbon in steel is the greatest above the Ac_3 temperature, carburization takes place most readily above this temperature. Furthermore, the higher the temperature, the greater the rate of carbon penetration, since the rate of diffusion is greater. It is customary to select a temperature about 50 °C above the Ac_3 point. The carburizing temperature is an important factor and is usually maintained within 900–925 °C. The depth of carbon penetration depends mostly upon the holding time.

Figure 15(a) shows the carburizing procedure in which a low carbon iron (carbon-free iron) is held for several hours at a high temperature in contact with an atmosphere, such as natural gas, capable of supplying carbon to the metal. The initial carbon content of the iron plate is zero at all distances from the surfaces. As the carbon atoms go into solution at the surface of iron, they are free to diffuse further into the plate. The maximum concentration of carbon atoms in iron at 925 °C can be used from the iron–carbon diagram, and is about 1.3%C.[11] The carburizing atmosphere can build up this carbon concentration at the surface almost immediately, so that the carbon penetration curve shortly after the beginning of carburizing is of the form shown in **Figure 15(b)**. The carbon penetration source that is produced by carburizing for a number of hours at a given temperature (925 °C in this case) is shown in **Figure 15(c)**.

The rate of flow of carbon in austenite depends on values for the diffusion coefficient and characteristics of the concentration gradient. The diffusion coefficient is in turn a function of temperature and carbon concentration. The diffusion of carbon proceeds from the higher concentration, developed from the supply source, to the lower concentration

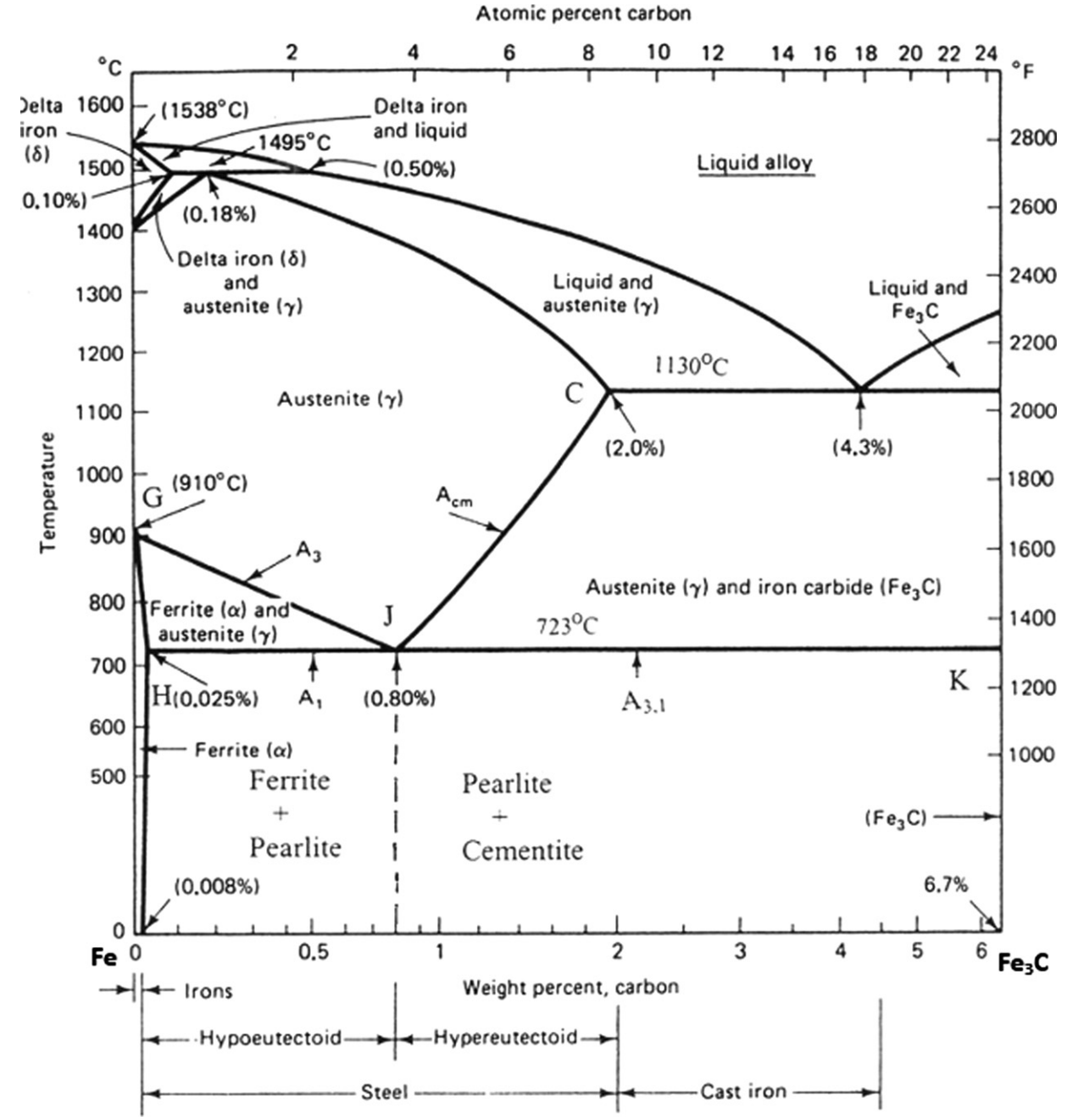


Figure 13 Iron and iron–carbide equilibrium diagram.

of the core when the concentration limits are maintained consistently, the form of the gradient may be predicted for any given and constant temperature of operation.[3]

The general form of the carbon gradient is influenced only by the range of concentration from surface to the core. For a given temperature, the rate of diffusion increases with increasing carbon concentration. For common carburizing steels and practice, the surface concentration limits are from 1.0 to 1.3%C with core concentration usually from 0.12 to 0.25%C.[3] For its attainment, the standard carbon gradient obviously requires a constant temperature of operation and a sufficient supply of carbon to the steel surfaces.

The case depth for a carburized machine parts may be considered to be the extent of carbon concentration which on heat treatment provides the desired uniform mechanical properties. The case depth for carburized steel is a function of process temperature and time. It has already been mentioned that the higher the temperature the greater will be the rate of carbon diffusion and thus deeper will be the case depth. Experiment shows that 40% more[5] will be the rate of diffusion by 50 °C rise of carburizing temperature, say from 875 to 925 °C.

For consistent results in carburizing, it is important that the temperature be uniform. Uniformity in various locations throughout the work load depends on the furnace design,

load density, gas recirculation, and heating rate. For a given density of load the difference in temperature between the outer and inner portions of the load may be high at carburizing temperatures, because the outside of the load is heated primarily by radiation and the rate of heating is rapid to reach to carburizing temperature. For better control of temperature, the thermocouple should be placed as close as possible to the work.

F. E. Harris[5] has developed a formula for the effect of time and temperature on case depth for normal carburizing:

$$\text{Case depth} = \frac{31.6\sqrt{t}}{10^{\left(\frac{6700}{T}\right)}}$$

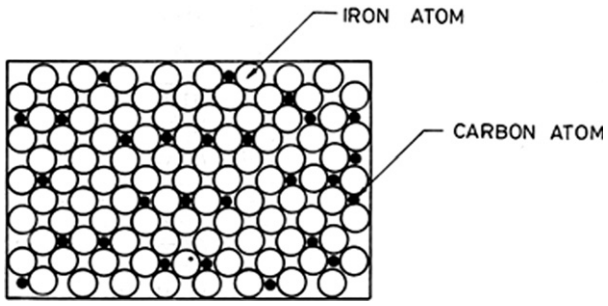


Figure 14 Interstitial solid solution (carbon in face-centered cubic iron).[10]

where case depth is in inches: t is time at temperature, in hours: and T is the absolute temperature, in degree Rankine.

For a specific carburizing temperature, the relationship becomes simply:

$$\begin{aligned}\text{Case depth} &= K\sqrt{t} \\ &= 0.025\sqrt{t} \quad \text{for} \quad 925\ ^\circ\text{C} \\ &= 0.021\sqrt{t} \quad \text{for} \quad 900\ ^\circ\text{C} \\ &= 0.018\sqrt{t} \quad \text{for} \quad 875\ ^\circ\text{C}\end{aligned}$$

When carburizing is purposely controlled to produce surface carbon concentrations somewhat less than saturated austenite, the case depth will be slightly less than the Harris equation shown above. The case depth determined by the equation is total case depth. For case depths in the range of 0.040–0.070 in the case depth corresponds to a point on the carbon gradient where the carbon concentration is about 0.07%C higher than the carbon content of the core.[5]

In addition to the time at carburizing temperature several hours may be required for bringing the work to operating temperature. For work quenched directly from the carburizer, the cycle may be further lengthened to allow time for the work to cool from carburizing temperature to a quenching temperature of perhaps 840 °C. Although some diffusion of carbon from case to core occurs during this time, diffusion is slower than it would be at the carburizing temperature. This period may be used deliberately as a moderate diffusion period to lower the carbon concentration at the surface by

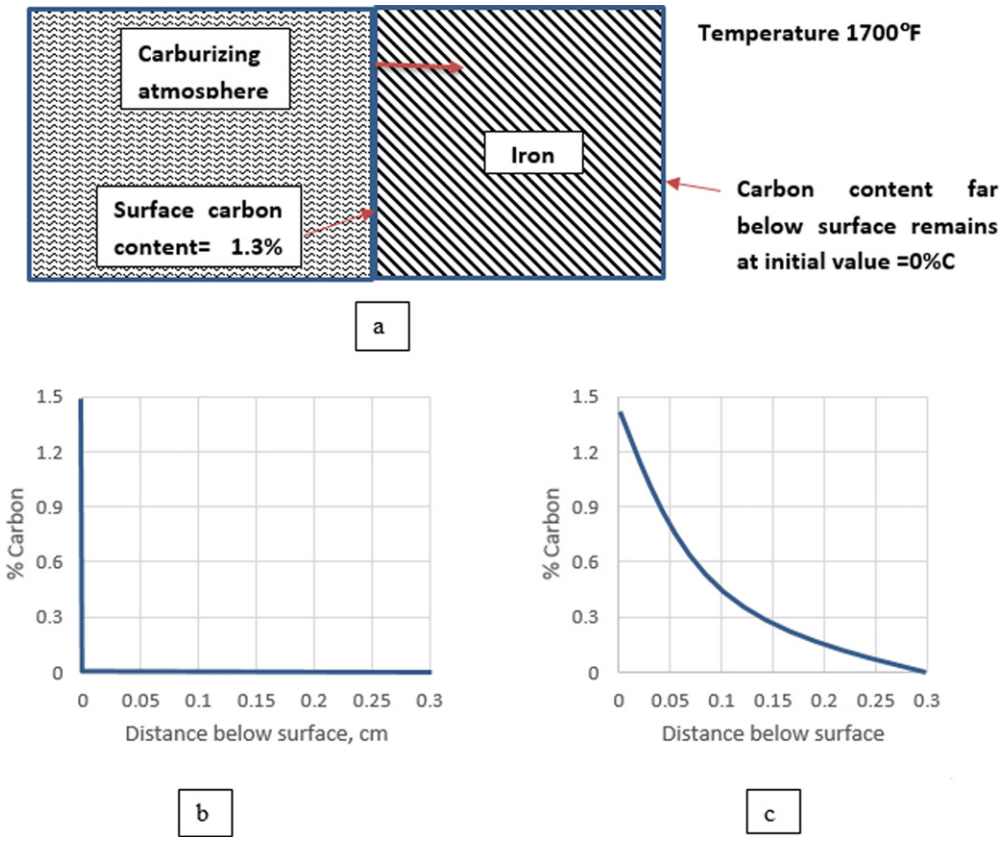


Figure 15 The diffusion of carbon in iron during carburizing. (a) Schematic representation of the procedure used in carburizing an iron plate. (b) Carbon penetration curve near the beginning of the carburizing process, and (c) after 10 h.[11]

maintaining an atmosphere of low carbon potential in contact with the work during this time.[5]

F. E. Harris[5] has also developed a method for calculating the carburizing time and diffusion time to produce a carburized case of predetermined depth and carbon concentration at the surface:

$$\text{Carburizing time} = \text{Total time}\left(\frac{C - C_i}{C_0 - C_i}\right)^2$$

and

$$\text{Diffusion time} = \text{Total time} - \text{carburizing time}$$

Where total time in hours, C is the final desired surface carbon concentration, C_0 is the surface carbon concentration at the end of carburizing cycle, and C_i is the concentration of carbon at the core. Effect of carburizing time and temperature on case depth obtained in gas carburizing is shown in **Figure 7**.

Diffusion coefficient varies with the nature of the solute atoms, with the nature of the solid structure and with changes in temperature. Higher temperatures provide higher diffusion coefficients, because the atoms have higher thermal energies and therefore, greater probabilities of being activated over the energy barrier. Carbon has a higher diffusion coefficient in iron because the carbon atom is small one. Atoms have higher diffusion coefficients in bcc iron than in fcc iron because the former has a lower atomic packing factor.[10]

The diffusion proceeds more rapidly along the grain boundaries because this is a zone of crystal imperfections.[10] At the grain boundaries between two adjacent grains there is a transition zone which is not aligned with either grains as shown in **Figure 16**. The mismatch of the orientation of adjacent grains produce a less efficient packing of the atoms along the boundary. Thus the atoms along the boundary have a higher energy than those within the grains. This higher energy of the boundary atoms is important for the nucleation of polymorphic phase changes and the lower atomic packing along the boundary favors atomic diffusion.

Other crystal imperfections namely point defects facilitate atomic diffusion more rapidly. Interstitials is the most prominent point defect which favors diffusion of carbon in iron and steel. It arises when an extra atom is ledged within a crystal structure particularly if the atomic packing factor is low. Such an imperfection produces atomic distortion as shown in **Figure 17**, unless the interstitial atom is smaller than the rest of the atoms in the crystal.

The interstitial mechanism moves atoms among the neighboring atoms of the crystal structure shown in **Figure 18**.

The interstitial atom of **Figure 18** has an equal probability of moving in the six coordinate directions. If the atoms are to change locations, the 'energy ridges' of **Figure 18** must be overcome. The energy required to overcome them is called the activation energy of diffusion. With interstitial diffusion, energy is required to force the atom into closer contact with neighboring atoms as it moves among them. The activation energy varies with a number of factors. For example, a small atom has a lower activation energy than a larger atom or a molecule. Likewise, interstitial movements require more energy than vacancy movements.[10]

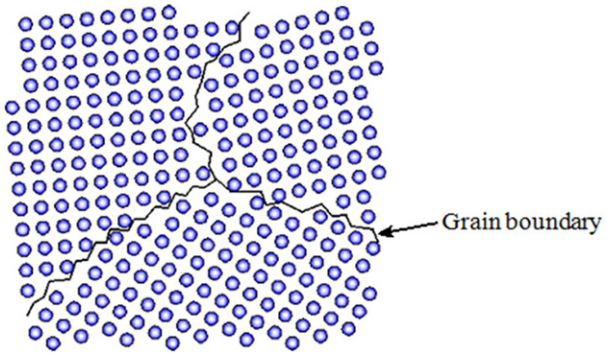


Figure 16 Grain boundaries. Note the area of disorder at the boundary.

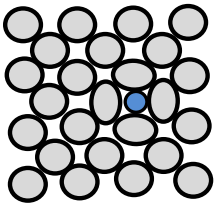


Figure 17 Point defects: interstitialcy.

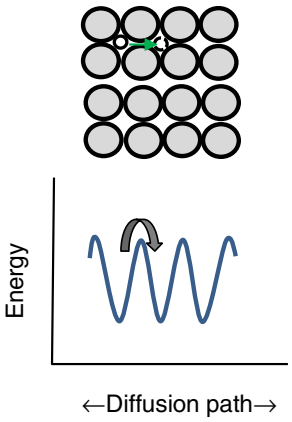


Figure 18 Atom movements: interstitial mechanism.

2.3.3.3.2 Flow of carbon from the supply source

The primary function of carburizing mediums is to furnish an adequate supply of carbon to the steel surface. The transfer of carbon from the source of supply to the steel is involved with reactions occurring at this surface. The carburizing agent responsible for the actual transfer of carbon is a carbon compound. The extent to which various carbon compounds may supply carbon is related to the conditions that determine the equilibrium with the surface carbon of the steel. The equilibrium composition of the reactants and products is a function of temperature and also of the carbon concentration at the surface.

Low carbon steels when heated to the carburizing temperature, will be completely transformed into austenite. At the carburizing temperature austenitic iron is capable of holding

in solid solution an amount of carbon approaching the saturation limit of 1.7%. When a source of carbon, such as carbon monoxide is brought into contact with the steel in this condition, there will be a transfer of carbon from the gas to the steel. There is a difference of opinion[12] as to the exact form of the carbon.

Some feel that there is an interaction of the carbon monoxide and the iron to form iron carbides, which are then absorbed by the steel, others feel that the carbon being brought to the surface of the metal as carbon monoxide will, in the presence of austenite, break down to form atomic carbon, which will diffuse as such in the iron.

In pack carburization the carburizing compound is in reality the gas producer. In other words, the carbon monoxide is the result of the reaction between the carbonaceous compound and the oxygen from the air entrapped with the compound particles. The CO thus formed will give up its carbon to the iron according to the following equations:

$$2CO + 3Fe \rightleftharpoons 2CO_2 + [C]Fe \qquad [XXXII]$$

Without a further supply of CO this reaction between CO, CO_2, and austenite would soon reach equilibrium and carburizing would stop. Herty[12] states the CO:CO_2 ratio must be above 24 for this reaction [XXXII] to proceed and also that the rate of penetration must be about 0.01–0.02 mm h^{-1}.

Since at carburizing temperature, there is always a large amount of incandescent carbon present, the CO_2 will be constantly reduced, so that there will be a continuous supply of CO according to the reaction:

$$2CO_2 + C \rightleftharpoons 2CO \qquad [XXXIII]$$

This cycle continues to repeat itself, and the process of carburizing will continue as long as the proper temperatures are maintained and the CO:CO_2 is kept high enough. In this case the carbon will be absorbed, the concentration of carbon will be built up at the surface and will then move inward according to the simple laws of diffusion of heat or dissolved substances, i.e., from a region of high concentration to one of lower concentration as stated earlier. The carburizing phase of case hardening is, thus, one of absorption at the surface plus inward migration.

Since the usual carburizing compounds have incorporated in them one or more of the carbonates of alkaline or alkaline earth metals, it is generally considered that they may react according to the following equation:

$$MxCO_3 + \text{heat} \rightarrow MxO + CO_2 \qquad [XXXIV]$$

The M is any metal of the alkaline or alkaline earth group. The CO_2 formed will react with hot carbonaceous packing, as in reaction [XXXIII], and will increase the concentration of available CO.

It is also believed that the carbonate reacts with the hot carbon as:

$$MxCO_3 + C \rightarrow MxO + 2CO \qquad [XXXV]$$

and that the oxide thus formed will act as a catalyst between the reaction of the CO and the iron.

In gas carburizing, the carbon of the furnace atmosphere is in the form of gaseous hydrocarbon compounds such as methane, ethane, propane, and butane or carbon monoxide. The principal source of carbon in gas carburizing is methane which is present in manufactured and in natural gas.

The reactions involving the actual transfer of carbon occur at the steel surface (interface) and the reactants, which are carbon compounds, may be considered independently. The interface reactions[3,4] for common carbon compounds may be written as:

$$CH_4(g) + 3Fe(\text{steel}) \rightleftharpoons [C]Fe(\text{in austenite}) + 2H_2(g) \qquad [XXXVI]$$

$$C_2H_6(g) + 9Fe(\text{steel}) \rightleftharpoons 3[C]Fe(\text{in austenite}) + 4H_2(g) \qquad [XXXVII]$$

$$C_3H_8(g) + 9Fe(\text{steel}) \rightleftharpoons 3[C]Fe(\text{in austenite}) + 4H_2(g) \qquad [XXXVIII]$$

$$2CO(g) + 3Fe(\text{steel}) \rightleftharpoons [C]Fe(\text{in austenite}) + CO_2(g) \qquad [XXXIX]$$

Considering the reactions that occur for the same compounds, away from the interface, the reactions for deposition of carbon[3,4] are expressed as:

$$CH_4(g) \rightarrow 2H_2(g) + C(\text{Solid carbon}) \qquad [XXXX]$$

$$C_2H_6(g) \rightarrow 3H_2(g) + 2C(\text{Solid carbon}) \qquad [XXXXI]$$

$$C_3H_8(g) \rightarrow 4H_2(g) + 3C(\text{Solid carbon}) \qquad [XXXXII]$$

$$2CO(g) \rightarrow CO_2(g) + C(\text{Solid carbon}) \qquad [XXXXIII]$$

The reactions [XXXVI] and [XXXIX] are definitely reversible reactions at carburizing temperature. Pure CO_2 would decarburize steel to form CO by reversing reaction [XXXIX] and pure H_2 would decarburize steel by forming CH_4, the reverse of reaction [XXXVI]. If water vapor is present in the gas it will act as a decarburizing agent, removing carbon from steel by the reaction,[3,4]

$$H_2O(g) + Fe_3C(\text{in austenite}) \rightleftharpoons 3Fe(\text{steel}) + H_2(g) + CO(g) \qquad [XXXXIV]$$

2.3.4 Heat Treatment after Carburizing and Properties of Carburized Parts

The purpose of carburization is to develop hard, wear-resistant surface, and a tough core in some moving machine parts. Carburization mainly provides the concentration of carbon on the surface to a case depth of about 1.25–1.50 mm. The case of carburized parts is eutectoid or hypereutectoid steel and the core is a hypoeutectoid steel of initial composition containing from 0.1 to 0.2% carbon. The mechanical properties of the machine part will be obviously different for the case and the core due to differential concentration of carbon and may not be sufficient enough to respond to the desired properties wanted from the carburized machine part. **Figure 19** represents the equilibrium microstructure of a carburized machine part which is furnace cooled after carburizing.

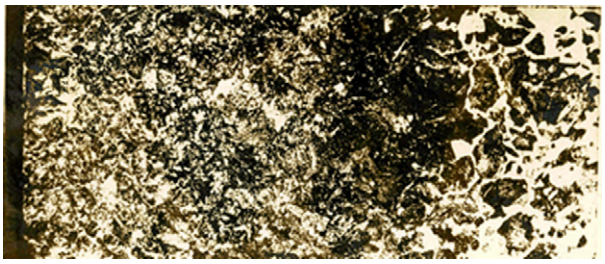


Figure 19 Microstructure of carburized and furnace cooled machine parts (× 100). High carbon case at the left, low carbon core at the right.[2]

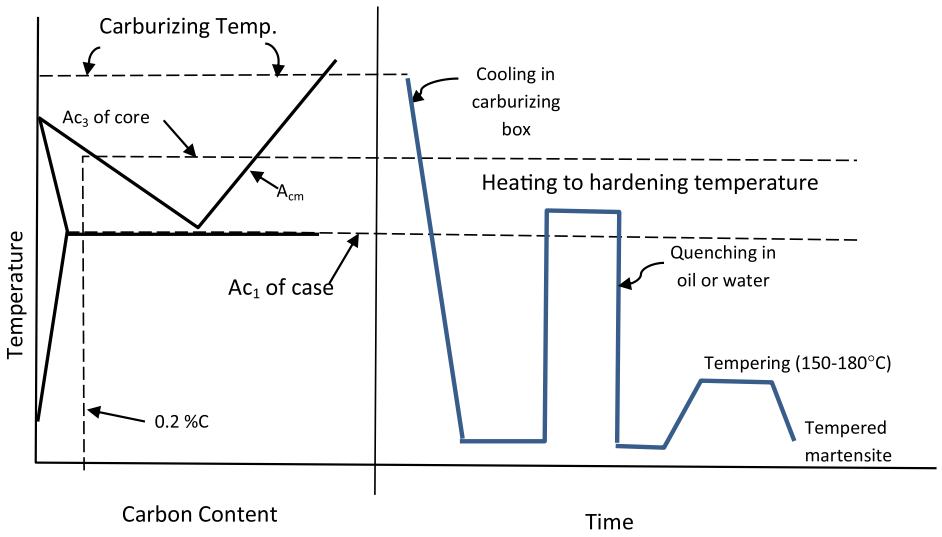


Figure 20 Heat treatment cycle without core refinement of carburized steel.

Hence the carburized machine parts are heat-treated to get higher mechanical properties namely hardness at the surface and toughness at the core.

2.3.4.1 Single Hardening without Core Refinement

Parts which are pack carburized, are first allowed to cool in the box, and then heated to a temperature necessary for hardening. After heating them just above Ac_1 temperature (750–780 °C), they are quenched in water, oil, or salt bath. In quenching from such a temperature, the outer zone will be hardened and the core will be partially refined. This avoids overheating of surface layer and results in reduced distortion. Therefore, this method is more suitable for treatment of complex shaped parts.

This method can also be adopted for parts that are carburized in salt bath, whose case depth exceeds 0.5 mm with 0.8–1.0% carbon potential. If the parts are quenched directly from the carburizing bath, it may lead to lower surface hardness due to presence of retained austenite resulting from higher surface carbon. Quenching from a low temperature results a higher hardness. The amount of retained austenite may be reduced further by subzero treatment. After quenching, the part is tempered at a low temperature of 150–180 °C to relieve stress. The heat treatment cycle is shown in Figure 20.

2.3.4.2 Single Hardening with Core Refinement

In this method, after carburizing the components are cooled slowly to room temperature. They are then reheated to a higher temperature (880–900 °C) for core refinement. Parts quenched from this temperature possess a higher impact and tensile strength. This method is widely used for automobile gears, and the resulting product has a case which secures more support from the hardened core, specially required for heavy duty services. A further advantage is the minimized distortion, since only one quenching treatment is used. The treatment is best adopted for fine-grained steels. If used on steels possessing marked hardening tendencies, the high quenching temperature favors the retention of austenite due to the presence of a relatively high proportion of alloying elements. This may result in some reduction in case hardness. Retention of austenite is undesirable, and it can be reduced by suitable subzero treatment. After quenching, the part is tempered at a low temperature of 150–180 °C to relieve stress. The heat treatment cycle is shown in Figure 21.

Single hardening with core refinement is being increasingly preferred over other methods. It is true that the grain of the surface layer is somewhat coarse, but this is quite often accepted in view of the fact that the mechanical properties of the core are equal to those produced by a double-hardening operation.

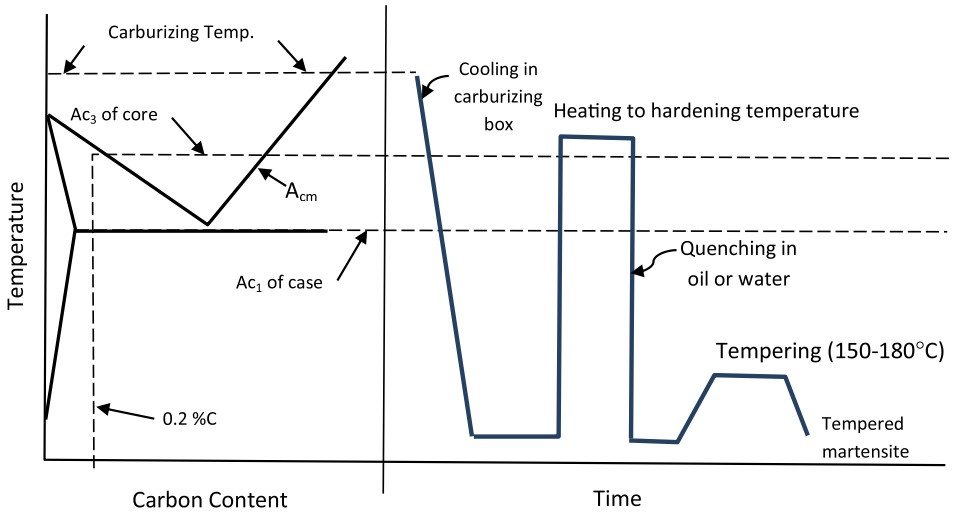


Figure 21 Heat treatment cycle with core refinement of carburized steel.

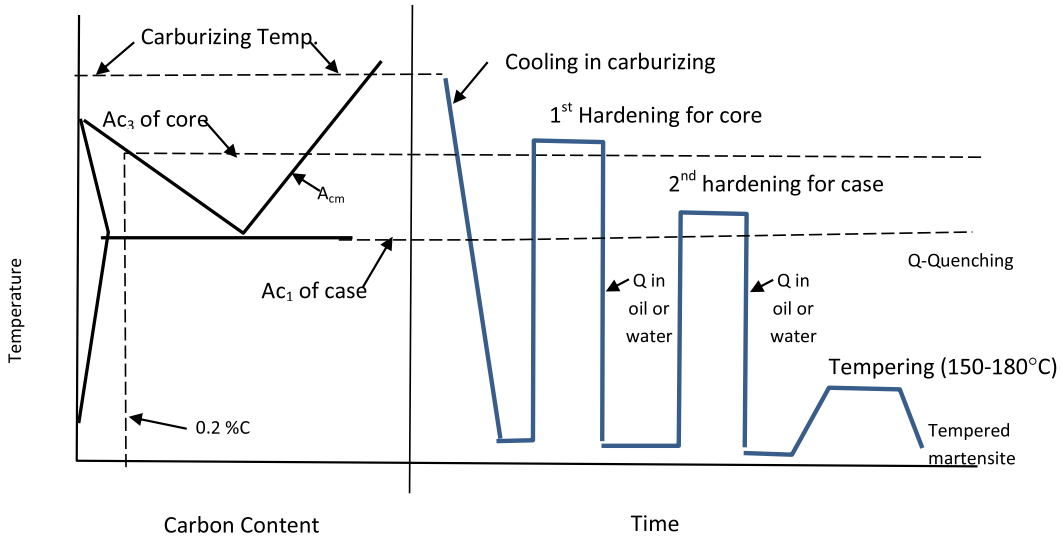


Figure 22 Heat treatment cycle for double-hardening (double heat treatment) process of a carburized steel part.

2.3.4.3 Double Hardening

Parts of carbon steel requiring high mechanical properties, are usually subject to double hardening, followed by tempering, after the carburizing process. The following considerations made double hardening a necessary procedure in these cases.

After carburizing, the work may be considered to consist of two layers: an outer layer, which is a eutectoid or hypereutectoid steels and requires a hardening temperature of 750–780 °C (above point Ac_1), and a core which is a hypoeutectoid steel of initial composition containing from 0.1 to 0.25%C and requiring grain refinement by heating above point Ac_3 (for the core), i.e., 880–900 °C. Thus to improve structure of the core and to impart optimum properties to the surface layers, a single heating to one temperature will evidently be insufficient. Therefore, the first hardening is conducted at temperature of 880–900 °C to improve the core structure of the work which has been overheated in carburization. This heating will also dissolve the cementite network which will not reappearing in quenching. The second hardening operation is conducted at 750–780 °C to eliminate the effects of overheating and to impart a high hardness to the carburized case. A schematic representation of the double heat treatment procedure is shown in Figure 22. Heat treatment is completed by tempering at 150–180 °C. The variation of hardness and toughness properties in relation to carbon contents from surface to the core of the double heat-treated carburized steel are shown in Figure 23.

The chief disadvantages of this heat treatment are the complexity of the procedure, excessive warping of the work, and the possibility of oxidation and decarburization. For these reasons, single hardening at 820–850 °C is extensively used at present for inherently fine-grained carbon steels and alloy

steels. Such procedure will refine the grain in both core and case and, at the same time, warping and decarburization will be considerably reduced.

2.3.4.4 Direct Quench Technique

In direct quenching method, the components are hardened by quenching directly from the carburizing temperature. This method can be employed when the components are carburized by using molten liquid or a gaseous medium. Quenching can be done in water, oil, or in a martempering bath, depending on the type of steel used. For minimum distortion, quenching in a martempering bath may be adopted, followed by air cooling. After water, oil, or martempering bath quenching, the components are tempered at a low temperature of 150–180 °C to relieve stress and hence to minimize cracking and distortion. For this reason direct hardening generally results in the smallest dimensional changes of the components. Figure 24 shows the direct quenching method.

Quenching directly from the carburizing temperature results in the hardening of both case and core. However, quenching directly from the carburizing temperature may leave retained austenite; when high alloy content steels are treated to minimize the retained austenite this technique is not suitable. In steels of high alloy content, it is the usual practice to control the carbon of the case to a somewhat lower level than in low alloy and plain carbon steels.

Such procedure will refine the grain in both core and case and, at the same time, warping and decarburization will be considerably reduced. But for coarse-grained structure at the case and the core, and high proportion of retained austenite is found at the case. Therefore, direct quenching for the furnace is only used when the work is made of an inherently fine-grained steel and where best properties are not required.

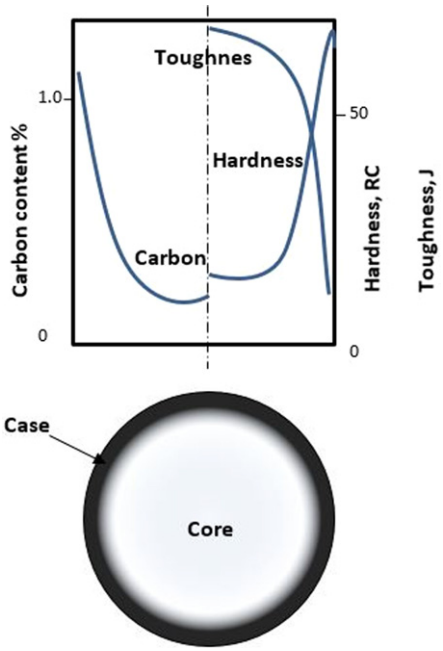


Figure 23 Variation of hardness and toughness from surface to the core of the double heat-treated carburized steel.

2.3.4.5 Quenchants for Carburized Steels

The carburized parts are hardened by quenching into a certain medium known as quenchant. The cooling rate for hardening is controlled by selection of proper quenching medium. There are numerous quenchants such as brine, tap water, salts, soluble oil and water solutions, oil and air, etc. If the part is to be used as heat-treated condition without any finishing operation to control dimensional accuracy marquenching can be used. In marquenching the part is quenched into molten salts or hot oil keeping the quenchants temperature above the M_s temperature of the case, but below the M_s temperature of the core. Consequently, the core transforms while parts are in the quenchant, to a mixed microstructure of martensite, bainite, and ferrite. The case

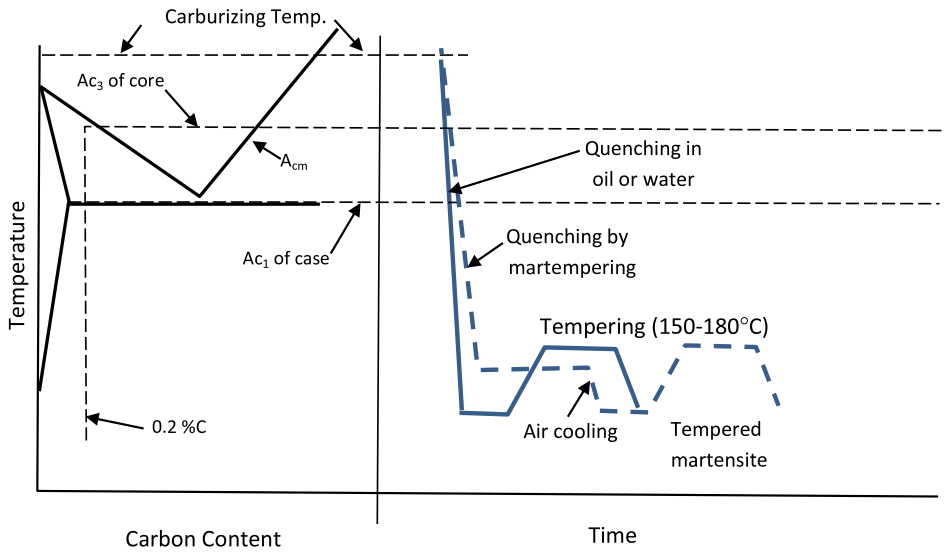


Figure 24 Heat treatment cycle for direct quenching of carburized steel.

transforms to martensite while the parts are cooling in air after leaving the quenchant.

2.3.4.6 Heat Treatment of Gas-Carburized Steels

Direct quenching is applied to gas-carburized parts at the end of carburization. The steel is precooled to 840–860 °C in the carburizing chamber (Figure 25) with the carburizing medium and then quenched in water or oil.

The surface layer, after heat treatment, will have a martensite structure with excess carbides. In cases of quenching direct from the carburizing furnace, the heating temperature of the core will be in the vicinity of Ac_3. In low carbon steels, austenite cannot be supercooled to the martensite point in quenching from this temperature and the core will have a ferrite and bainite structure. After heating austenite in alloy steels to a temperature close to point A_{cm}, it can easily be supercooled, without decomposition, to the martensite point. This core will acquire a low carbon martensite structure possessing high strength and ample toughness. After quenching, subzero treatment is done in liquid nitrogen to transform the retained austenite into martensite. Finally the part is tempered at a low temperature of 150–180 °C to relieve stress.

The microstructure of the carburized case of a low carbon steel after hardening is shown in Figure 26. The normal hardness at the surface of carburized case is usually within the range of RC 59–64.

2.3.4.7 Subzero Treatment

When alloy steels are subjected to single hardening treatment, a large amount of retained austenite will be found in the carburized case. This sharply reduces its hardness. Retained austenite may be eliminated by a subzero treatment which transforms mostly into martensite, thereby substantially increasing the hardness.

2.3.5 Microstructures of Carburized Steels

2.3.5.1 Martensite

The microstructures of hardened carburized steels consist of high carbon martensite at the surface and low carbon martensite in the core. High carbon martensite is gradually replaced by martensite of lower carbon content with increasing distance from the surface. Lightly tempered martensite is the dominant microstructural constituent of properly carburized steel. However, the martensite changes in morphology, amount, and properties as a function of distance from the surface. Other case microstructural constituents may also be present and may significantly affect the performance of carburized parts. These other microstructural features include retained austenite, carbides of various origins, sizes and morphologies; inclusions; prior austenite grain boundaries embrittled by phosphorus segregation; microcracks; and processing-induced surface oxides. Superimposed on the case microstructures are compressive residual stresses produced during quenching. Core microstructures, depending on hardenability, may consist of tempered martensite, bainite, or ferrite and pearlite.

2.3.5.1.1 How martensite forms

Under slow or moderate cooling rate the carbon atoms are able to diffuse out of the austenite structure. The iron atoms then move slightly to become bcc structure. This austenite to ferrite transformation is a diffusion-controlled process. This transformation takes place by a process of nucleation and growth and is time dependent. With still further increase in cooling rate, insufficient time is allowed for carbon to diffuse out of solution and although some movement of iron atoms take place, structure cannot become bcc while the carbon atom is trapped in solution. The resultant microstructure is called martensite. It is formed from austenite by a diffusion-less shear transformation and quenching has the important function of providing cooling rates rapid enough to suppress competitive diffusion-controlled transformations of austenite. Martensite

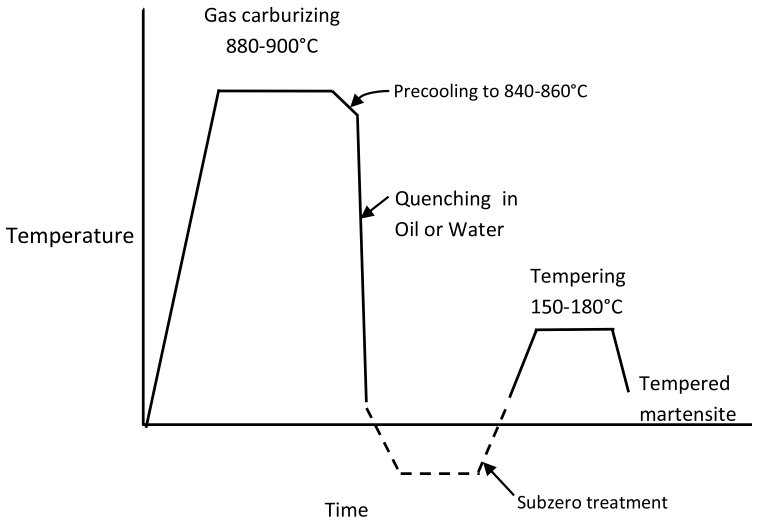


Figure 25 Carburizing cycle of gas carburized steel.

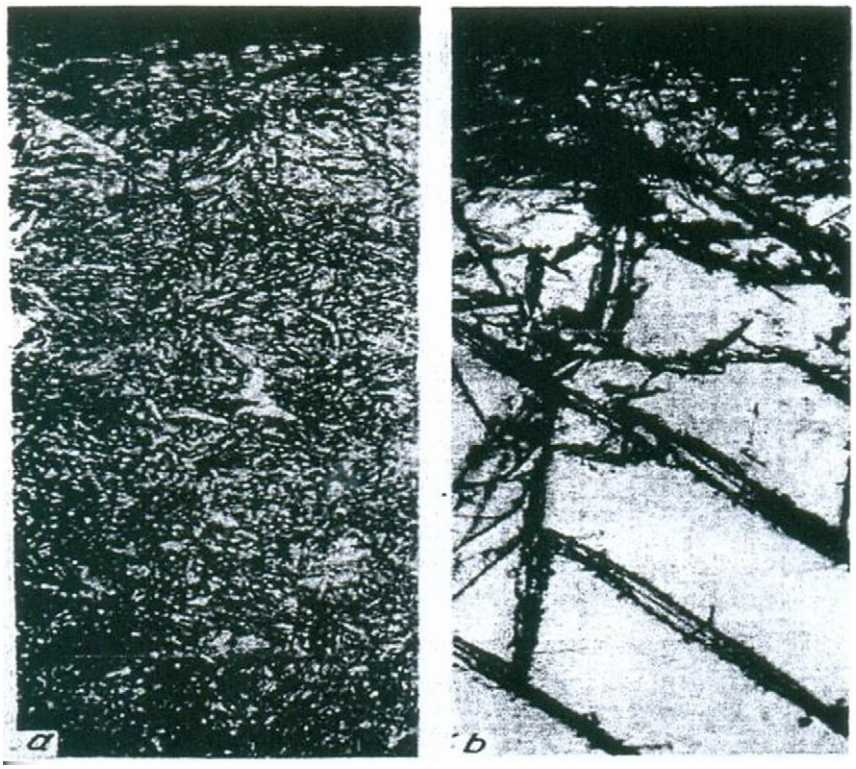


Figure 26 Structure of carburized case of low carbon steel after hardening. (a) normal martensitic microstructure, × 250 and (b) with an increased amount of retained austenite, × 500.[1]

is a supersaturated solid solution of carbon trapped in body center tetragonal (bct) structure. Two dimensions of the unit cell are equal, but the third is slightly expanded due to trapped carbon.

During carburization carbon is introduced into austenite typically at a temperature of around 925 °C. After carburization, martensite is produced by quenching. This martensite is reheated or tempered at low temperature (150–180 °C) to produce low temperature tempered (LTT) martensite. This LTT martensite is the primary component of carburized microstructure that gives the desired properties to carburized steel.

Carburizing is applied to low carbon steels containing typically 0.2 wt%C. The process introduces carbon to the surface of the steel, and the carbon diffuses into the low carbon interior. Depending on atmosphere control and carburizing temperature and time, surface carbon contents of 0.8% or more and carbon gradients over a range of distances, or case depths, into the steel are produced. The carbon gradients have a profound influence on martensitic transformation, morphology and properties. The temperature at which martensite begins to form during the quench is designated as the martensite start temperature, M_s. As carbon content increases, M_s decreases.

2.3.5.1.2 Martensite morphologies

The martensite crystals that form at low M_s temperature have a three-dimensional plate geometry, and hence are called plate martensite. Figure 27 is a micrograph of martensite in the high carbon case of a carburized low carbon Ni steel. Adjacent plates of martensite are nonparallel, and the appearance of the microstructure under the light microscope is that of a zigzag array of needles or acicular shapes. The needlelike shapes are in fact cross sections of martensite plates. The plates etch dark after tempering and are surrounded by white-appearing retained austenite. The amount of martensite that forms is determined only by the amount of cooling below M_s; therefore, the lower the M_s, the smaller the amount of martensite and the larger the amount of retained austenite after cooling to room temperature.

In contrast to high carbon regions, the martensite that forms in austenite of medium or low carbon content assumes a completely different morphology. The martensite crystals appear to have a lath or board-shaped geometry – the crystals are relatively thin and flat with one long dimension and adjacent crystals form parallel to each other in stacks or packets. Figure 28 is a micrograph of martensite in the low carbon core of a carburized steel.

The high M_s temperature of low carbon austenite provides a much wider temperature range over which martensite can form during quenching, and therefore there is little or no retained austenite in low carbon lath martensites cooled to room temperature. With increasing carbon content, the amount of retained austenite in lath martensitic microstructures increases, but the austenite is retained as thin films between the laths and is not resolvable in the light microscope.

The carbon gradients introduced into austenite by carburizing result, after quenching, in a gradient of martensitic microstructure, ranging from plate martensite morphologies with large amounts of retained austenite to lath martensitic microstructures with essentially no retained austenite (Figure 29).



Figure 27 Plate martensite microstructure in the case of a gas-carburized low carbon Ni steel. The 'needles' are cross sections of plates. Retained austenite appears white. Light photomicrograph, nital, × 500.

These gradients in microstructure are related directly to the hardness and strength gradients produced by carburizing. Although features resolvable in the light microscope influence hardness (especially retained austenite, which coexists with plate martensite in the case region), it is the carbon-dependent fine structure of LTT martensite crystals that primarily determines the strength gradients in carburized steels.

2.3.5.1.3 Effect of tempering

When the as-quenched martensite is tempered at low temperatures, very fine carbides precipitate to relieve the carbon supersaturation. Low tempering temperatures of 150–180 °C ensure that the precipitated carbides remain fine. In addition, the retained austenite remains stable at these low temperatures. Consequently, the only microstructural changes produced by tempering occur on a very fine scale within the martensite plates.

The carbides are not cementite, which forms on tempering at higher temperatures, but are transition carbides. These transition carbides have been designated either epsilon carbides or eta carbides, depending on small differences in their crystal structures and diffraction patterns. High densities of dislocations, produced by the deformations that accompany martensitic and subsequent tempering transformations, are also associated with the transition carbides.

2.3.5.1.4 Role of transition carbides

The higher the carbon content of the martensite, the higher the density of the clusters of transition carbides after tempering. These carbide arrays, and the associated dislocation substructures, make deformation by slip or dislocation motion difficult. As a result, the hardness and strength of LTT martensite increases with increasing carbon content. This is illustrated in Figure 30. The figure shows the hardness of as-quenched martensitic microstructures, and LTT martensitic microstructures tempered between 150 and 180 °C. The hardness increase is almost linear up to 0.8%C. At higher carbon contents, the rate of hardness increase falls because of larger amounts of retained austenite. Low temperature tempering lowers the hardness of as-quenched martensite because of the relief of carbon supersaturation and stress relief, but increases toughness.



Figure 28 Lath martensite microstructure in the core of a gas-carburized low carbon steel. Light photomicrograph, nital, × 300.

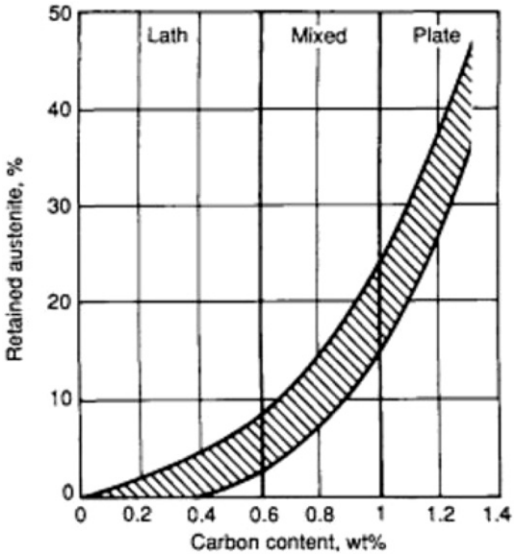


Figure 29 Percent retained austenite as function of carbon content. Vertical lines show carbon ranges in which lath and plate martensites are found in Fe–C alloys.[13]

2.3.5.2 Austenite

Although LTT martensite dominates strengthening in the case regions of carburized steels, case microstructures are actually composites of LTT martensite and retained austenite. Depending on the amount of retained austenite and the loading conditions in service, the austenite may either degrade or enhance performance of the part.

2.3.5.2.1 Characteristic features of austenite

Austenite is essential to the manufacture of carburized steels. It has a high solubility for the carbon introduced into steel by high temperature exposure to carburizing atmospheres. On quenching, the high carbon austenite transforms into high

carbon martensite. This high carbon martensite on tempering, produces high-strength tempered martensite. This high-strength tempered martensite is the backbone of carburized steels.

The parent austenite phase influences the microstructure of carburized steels in several ways. Most important, the chemical composition of the austenite, directly determines M_s temperature and the amount of austenite retained after quenching to room temperature.

Also, the grain structure of the parent austenite affects the martensitic microstructure after quenching, because austenite grain size limits the size of martensite crystals. Thus, fine-grained austenite results in fine distributions of martensite plates and improved mechanical properties.

For this reason, most carburizing grade are aluminum-killed, fine-grain steels. Small amounts of aluminum are added during melting and dissolve in austenite during subsequent high temperature bar rolling or forging. At lower temperatures (about 900 °C), where carburizing is typically performed, the solubility of aluminum in austenite is low, and the aluminum combines with nitrogen to form aluminum nitrides. These fine aluminum nitride particles restrict grain growth during carburizing. At higher carburizing temperature the aluminum nitride particles are coarser and because of higher solubility, are present in lower densities, resulting in coarser austenite grain sizes.

2.3.5.2.2 Effect of austenite composition

Martensite transformation start temperature M_s is a function of chemical composition of austenite. The relation between M_s and chemical composition is given by the following empirical equation[15]:

$$M_s(^\circ C) = 539 - 423C - 30.4Mn - 12.1Cr - 17.7Ni - 7.5Mo \quad [7]$$

where the element amounts are in weight percent. The above equation shows very strong dependence of M_s on carbon content and lesser dependence of M_s on the alloying elements manganese, chromium, nickel, and molybdenum, which are often added to improve hardenability. When the M_s temperature is calculated from the composition of a steel of uniform carbon content, or at a point in a carburized case, the amount of martensite that forms on cooling to a given quench temperature, T_q, can be estimated from[16]:

$$f_m = 1 - \exp^{-(0.011\ \Delta T)} \quad [8]$$

where f_m is the volume fraction of martensite, and ΔT is the undercooling below $M_s(\Delta T = M_s - T_q)$.

Figure 31 shows martensite and retained austenite in the case of a carburized microalloyed steel containing small amounts of niobium. The martensite plates appear dark and the retained austenite appears white between the martensite crystals.

2.3.5.2.3 Excessive retained austenite

2.3.5.2.3.1 Effect on properties

Too much retained austenite, ~40 vol.% or more, may be detrimental to the performance of carburized steels in several ways. Most important, because austenite is of much lower strength than tempered martensite, the hardness, wear resistance, and fatigue resistance of a carburized part may be reduced. Also, high retained austenite content may reduce surface compressive residual stresses and accordingly, contribute to a decrease in fatigue resistance.

2.3.5.2.3.2 Major cause

A very high carbon content is the major cause for excessive retained austenite. Equations [7] and [8] show that M_s and the

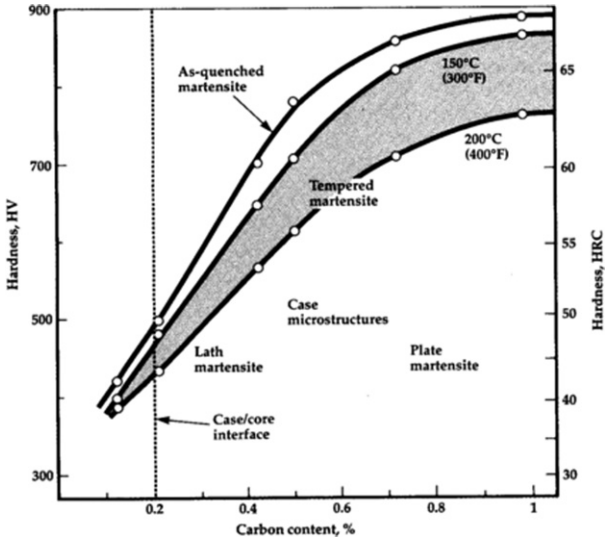


Figure 30 Hardness as a function of carbon content for as-quenched martensite and LTT martensite tempered between 150 and 180 °C. Case martensitic microstructures have similar hardness gradients, with maximum and minimum values determined by surface and core carbon contents, respectively.[14]



Figure 31 Tempered martensite (black) and retained austenite (white) in the case of a carburized Nb-microalloyed steel. Light photomicrograph, nital, × 300.

amounts of martensite formed on cooling are very sensitive to carbon content. If carburizing temperatures are high and if the austenite is allowed to become saturated with carbon, then large amounts of retained austenite can be expected.

However, excessive austenite may be retained even in boost-diffuse carburizing in regions of a part where surfaces meet at included angles of 90° or less. At such corners, carbon diffuses in from the carburizing atmosphere from two surface, but the high carbon content that results has only a limited area through which to diffuse into the interior of the part. The result is that carbon concentration at the corner remains high throughout the diffusion step. Excessive retained austenite at the corner of a gas-carburized low carbon steel specimen is shown in Figure 32(a). Figure 32(b) shows that surface hardness at the corner is considerably lower than that of the plane surface with its more moderate amount of retained austenite. Massive carbides may also be present at corners because of the high carbon concentration.

2.3.5.2.4 Reducing retained austenite

In steels directly quenched after carburizing, excessive retained austenite may be reduced by several methods, such as tempering, refrigeration, or subzero treatment. Process selection depends on the desired performance level of the carburized part.

2.3.6 Carburization of Alloy Steels

2.3.6.1 Carburization of Low Alloy Steels

Low carbon steel is usually used for carburization because of its excellent toughness. For high duty applications alloy steels are also carburized for additional properties of both the case and the core. In alloy steels, the alloying elements remain in the form of various carbide and nitride precipitates. To take precipitates into the solution higher temperature is required. For this reason, comparatively a higher carburization temperature is usually selected for alloy steels. Low carbon steels containing nickel, chromium, manganese, vanadium, molybdenum, etc. singly or in combination usually have sufficient hardenability. From these steels maximum case hardness can be attained by oil quenching and desired core properties up to a tensile strength of 1380 MPa is obtainable with suitable toughness by proper selection of the steel composition.

2.3.6.1.1 Carburization of chromium–nickel steel

Chromium increases the case depth of the carburized steels while nickel decreases it (Figure 33(a)). Chromium (as Cr_3C) and nickel refine the austenite grain size of the carburized case but nickel is more effective than chromium in inhibiting the austenite grain growth (Figure 33(b)). Both chromium and nickel promote the formation of retained austenite but chromium is more effective than nickel in promoting the formation of retained austenite in the case of carburized and hardened steels.[17]

Microhardness measurements have shown that chromium in solution and as Cr_3C increase and nickel in solution decreases the hardness of the case while both of them increase the core hardness although chromium is more effective than nickel as far as core hardness is concerned (Figure 34).

The hardenability increases with the increase of austenite grain size and with the extent of carbon penetration in the case of carburized steels. Nickel and chromium reduce the toughness of the core of low carbon steels in the carburized and hardened condition. Chromium is more detrimental to toughness than nickel.[18]

2.3.6.1.2 Carburization of molybdenum–nickel steel

Both molybdenum and nickel in steel increase the carburized case depth. Nickel is more effective than molybdenum in increasing the case depth. The combined effect of molybdenum and nickel is much greater than that of either molybdenum or nickel alone in increasing case depth (Figure 35(a)).

The undissolved particles of Mo_2C refine the austenite grain size of the carburized case. Nickel in solution does not have any effect in restricting grain growth of austenite. But the presence of nickel enhances the austenite grain size refining effect of molybdenum steel in the carburized case (Figure 35(b)).

Under identical conditions, molybdenum and nickel enhance the formation of retained austenite in the case of carburized and hardened steels but nickel is more effective than molybdenum in enhancing the formation of retained austenite. In the presence of molybdenum this enhancing

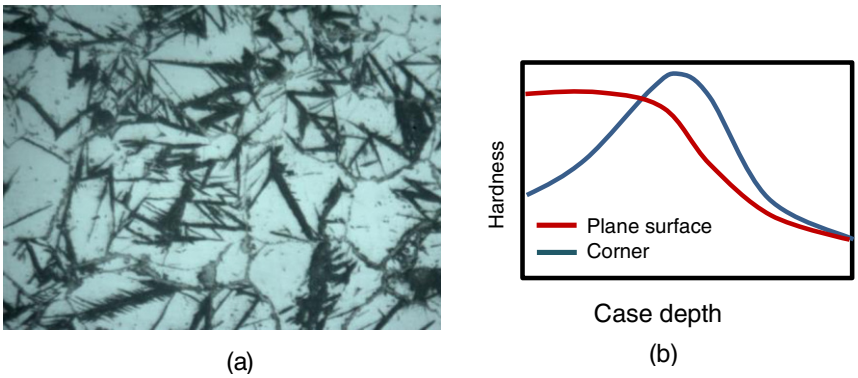


Figure 32 (a) Excessive retained austenite at the corner of a speicmen of low carbon steel. Light photomicrograph, nital, × 500. (b) Schematic representation of variation of hardness as a function of distance from a specimen corner or a specimen surface in the same steel.

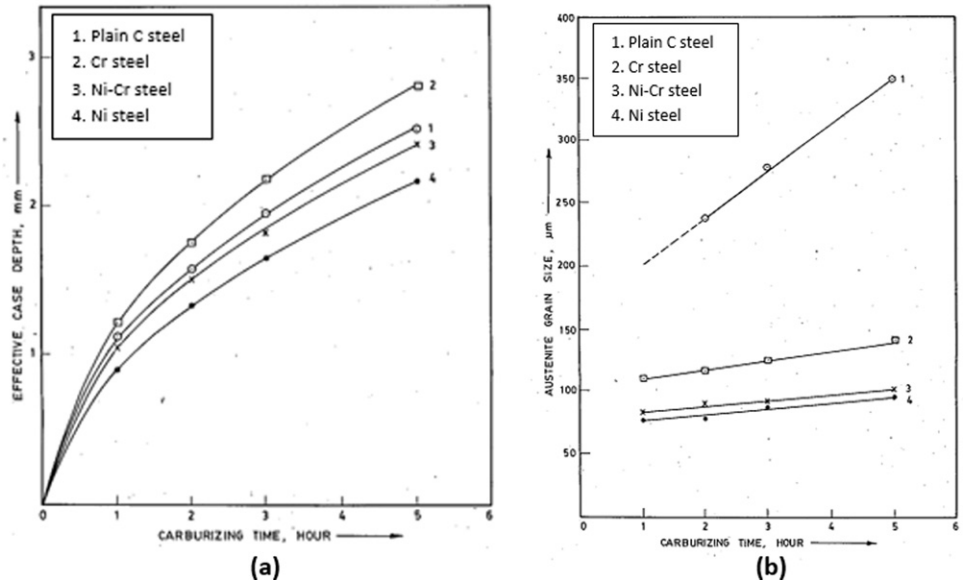


Figure 33 (a) Variation of effective case depth with carburizing time at 950 °C in steels 1–4 and (b) variation of prior austenite grain size with carburizing time at 950 °C in the case of steels 1–4.[17]

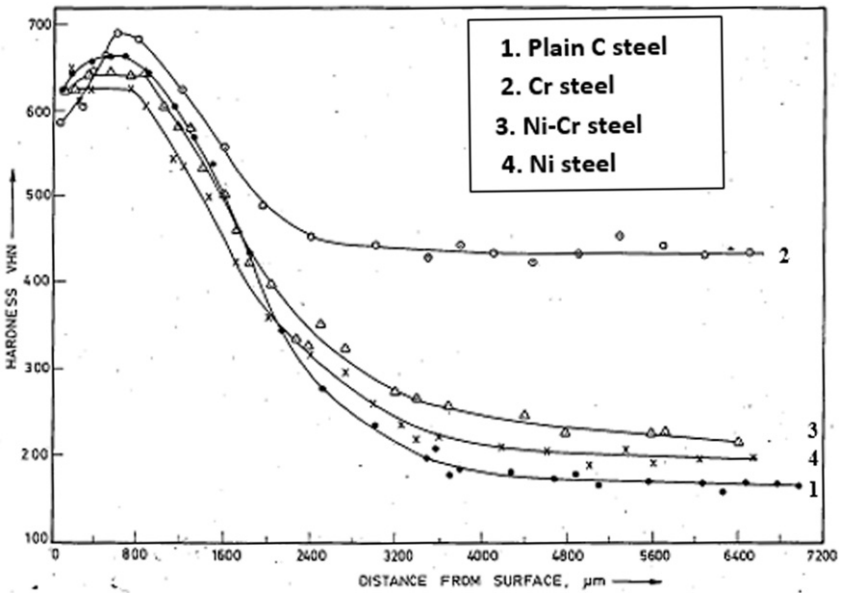


Figure 34 Microhardness profiles of steels 1–4 carburized at 950 °C for 1 h, quenched in 10% brine and tempered at 160 °C.[18]

effect of nickel is increased as shown in Figure 36. Subzero treatment substantially reduces the retained austenite content in the hardened cases of all the steels. Molybdenum and nickel both sluggish the retained austenite transformation to martensite during subzero treatment. Molybdenum is more effective than nickel in sluggishing the transformation of retained austenite to martensite. In the presence of nickel this sluggishing effect of molybdenum reduces.[20]

Molybdenum improves and nickel reduces the maximum case hardness and wear resistance of low carbon steels in the carburized and hardened condition. The presence of nickel decreases the effect of molybdenum in the increment of maximum case hardness. Molybdenum and nickel both increase the core hardness but molybdenum is more effective than nickel. Molybdenum with nickel is more effective in increasing the core hardness than molybdenum without nickel (Figure 37(a)).

Subzero treatment increases the surface hardness and maximum hardness of the carburized low carbon steels in the hardened and tempered condition (Figure 37(b)). The maximum surface hardness values of the carburized, hardened,

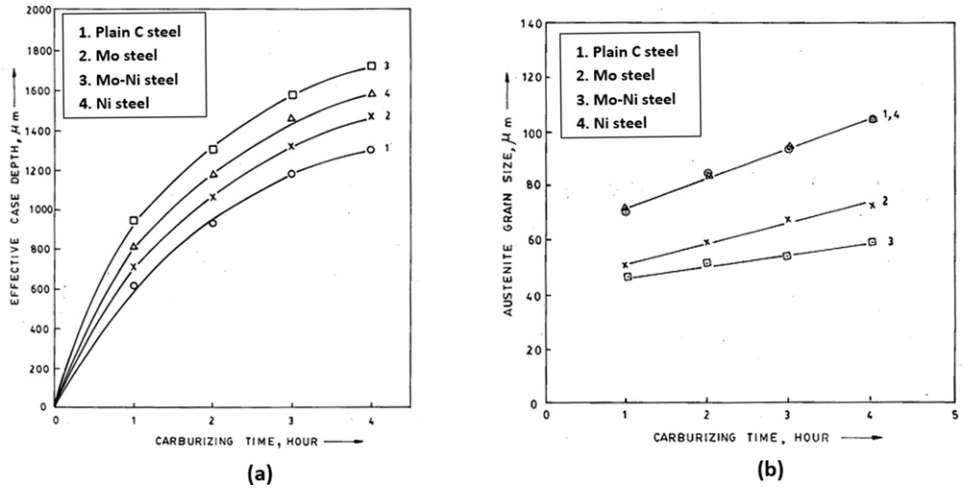


Figure 35 (a) Variation of effective case depth with carburizing time of steels 1–4 carburized at 950 °C and (b) variation of prior austenite grain size with carburizing time of the case of steels 1–4 carburized at 950 °C.[19]

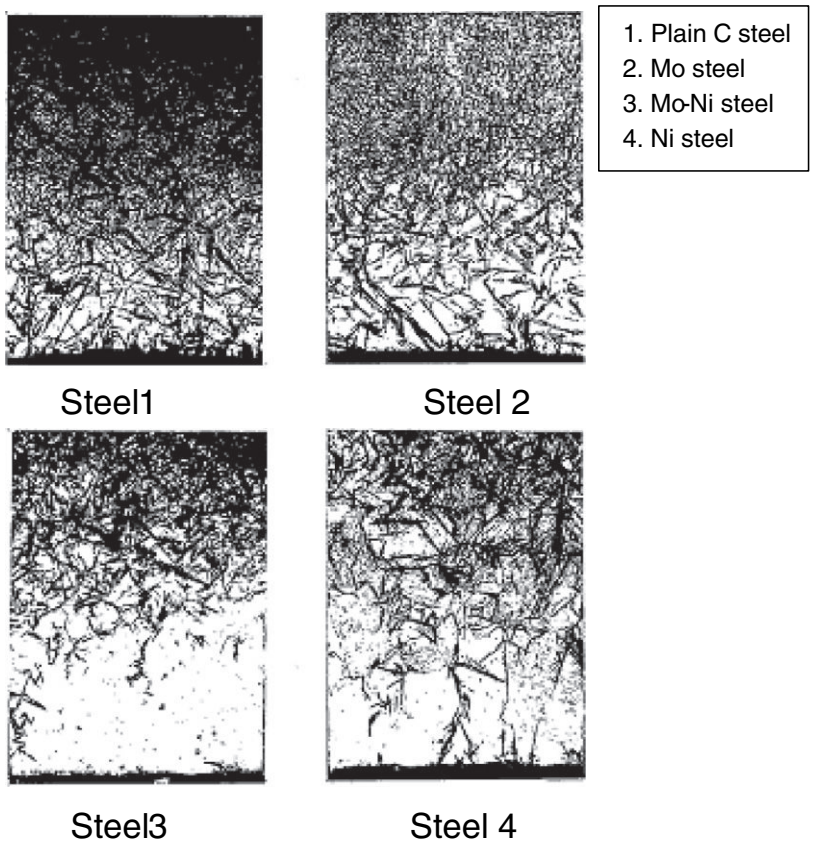


Figure 36 Optical micrographs showing the microstructures in the case of steels 1–4 carburized at 950 °C for 4 h, quenched in 10% brine and tempered at 160 °C, × 300.[20]

and tempered plain carbon, molybdenum and nickel steels are always lower than those of subzero treatment ones (Figure 37). Molybdenum improves and nickel reduces the wear resistance of the carburized case of low carbon steel. Subzero treatment improves the wear resistance of the carburized, hardened, and tempered cases of low carbon steels containing molybdenum and nickel alone and in combination. Molybdenum and nickel both reduce the toughness of the core in the carburized and hardened condition. Nickel is more detrimental to toughness than molybdenum. The combined effect of molybdenum and nickel is greater than that of either molybdenum or nickel alone in reducing toughness.[20]

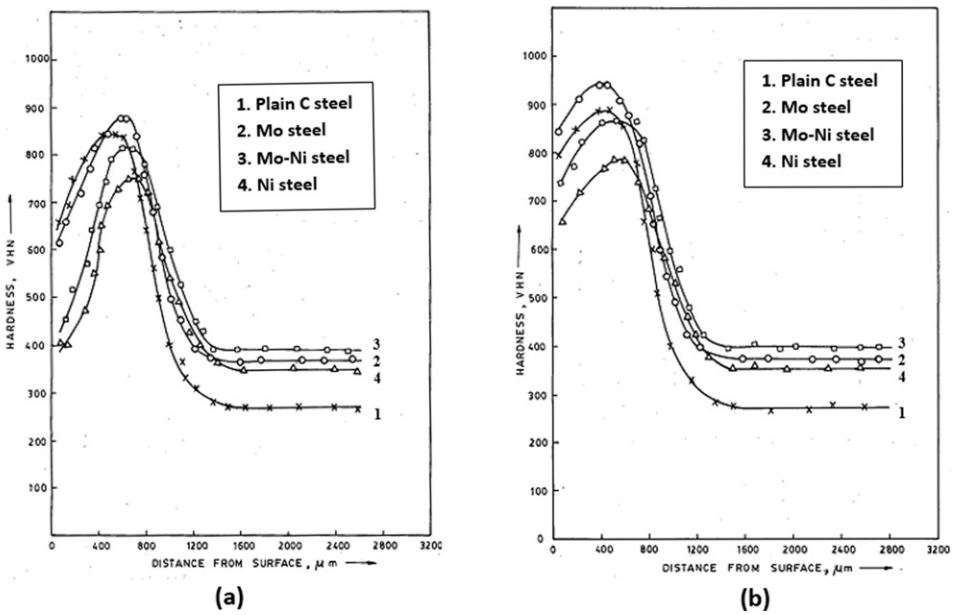


Figure 37 (a) Microhardness profiles of steels 1–4 carburized at 950 °C for 1 h, quenched in 10% brine and tempered at 160 °C and (b) microhardness profiles of steels 1–4 carburized at 950 °C for 1 h,quenched in 10% brine, subzero treated in liquid nitrogen and tempered at 160 °C.[20]

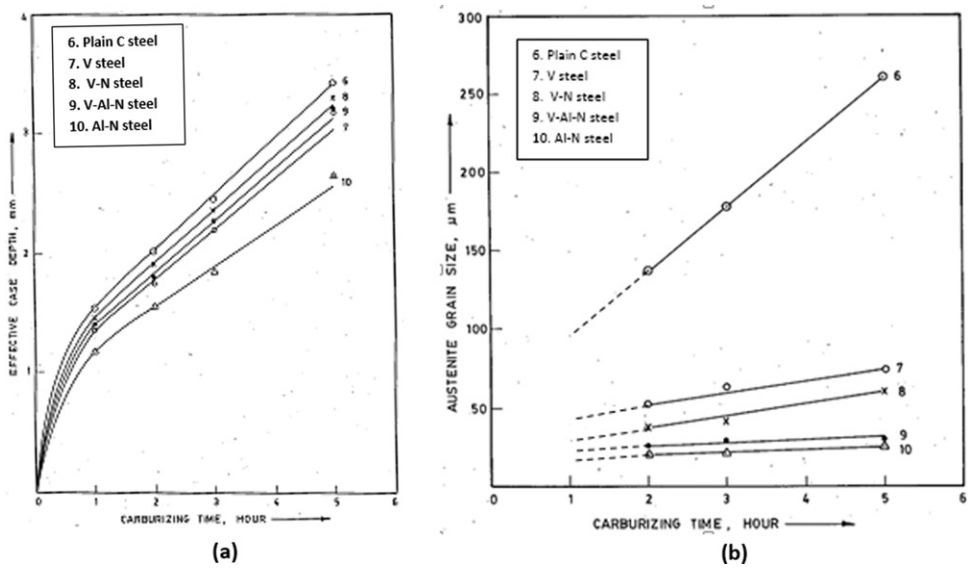


Figure 38 (a) Variation of effective case depth with carburizing time at 950 °C in steels 6–10, and (b) variation of prior austenite grain size with carburizing time at 950 °C in case of steels 6–10.[21]

2.3.6.2 Carburization of Microalloyed Steels

2.3.6.2.1 Carburization of vanadium-microalloyed steel

Microalloying elements such as vanadium with or without nitrogen and aluminum with nitrogen reduce the case depth of the carburized steels. Vanadium without nitrogen is more effective than vanadium with nitrogen in reducing the case depth while aluminum with nitrogen is the most effective of all in reducing the case depth (**Figure 38(a)**).

The undissolved particles of vanadium carbide (VC), vanadium carbonitride, (V(C,N)) and aluminum nitride (AIN) all refine the austenite grain size of the carburized case, but V(C,N) is much more effective than VC; AIN is the most effective in inhibiting the grain growth of austenite in the case of carburized steels (**Figure 38(b)**). Vanadium without nitrogen does not have any effect in the formation of retained austenite while vanadium with nitrogen promotes the formation of retained austenite in the carburized case. Aluminum is the most effective in promoting the formation of retained austenite in the case of carburized steels (**Figure 39**).

The undissolved particles of VC and V(C,N) increase the case and core hardness while AIN reduces the case and core

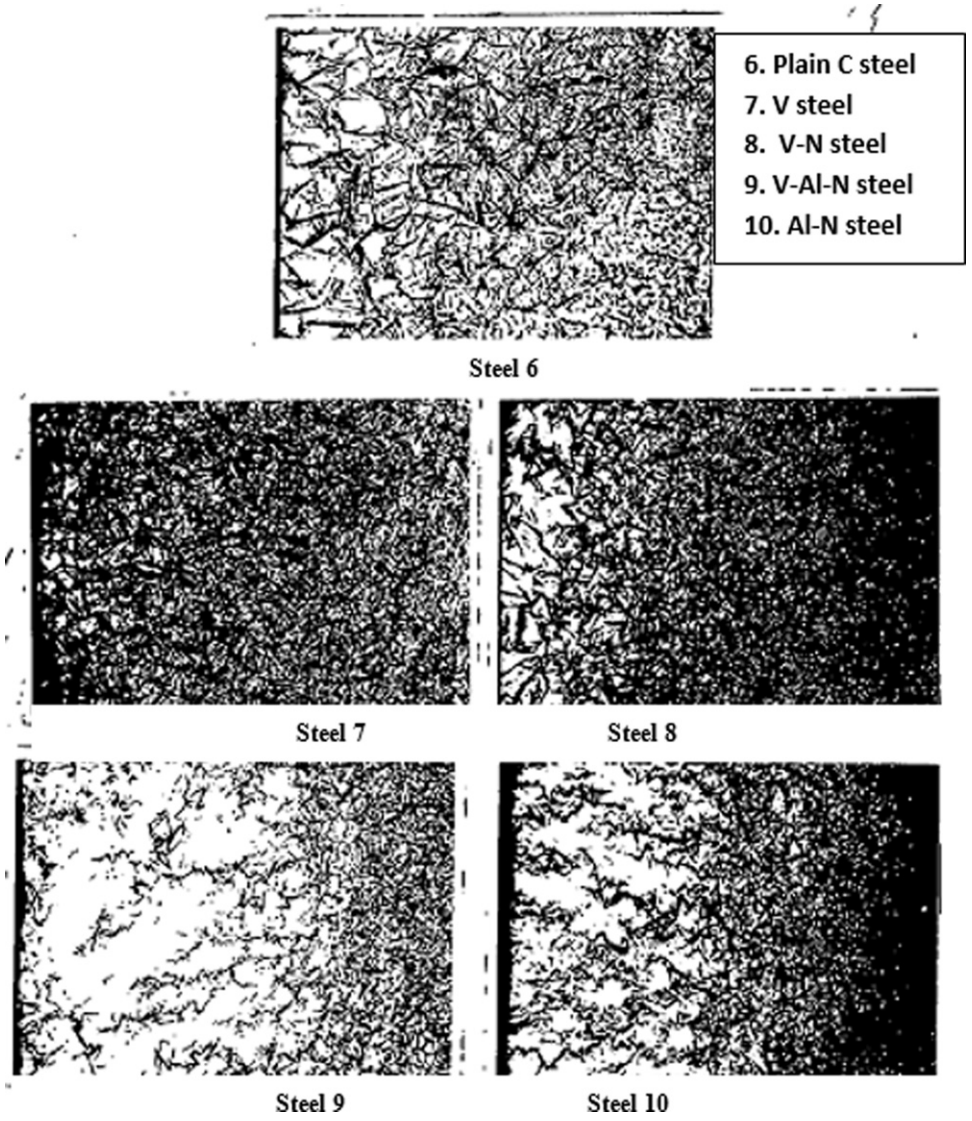


Figure 39 Optical micrographs showing the microstructures of steels 6–10 carburized at 950 °C for 4 h quenched in 10% brine and tempered at 160 °C, × 280.[22]

hardness. V(C,N) is more effective than VC in raising the hardness of the case and core. Vanadium alone and combination with nitrogen increase the case and core hardness (Figure 40) while vanadium alone reduces the toughness, and vanadium with nitrogen improves toughness.[22]

2.3.6.2.2 Carburization of niobium-microalloyed steel

Niobium with or without nitrogen decreases the case depth of the carburized steels. Niobium with nitrogen is more effective than niobium without nitrogen in reducing the case depth (Figure 41(a)). Both the undissolved particles of niobium carbide (NbC) and niobium carbonitride (Nb(C,N)) refine the austenite grain size of the carburized case, but Nb(C,N) is much more effective than NbC in restricting the austenite grain growth Figure 41(b).

Under identical conditions, niobium alone and in combination with nitrogen decrease the formation of retained austenite in the carburized and hardened steels. Niobium with nitrogen is more effective than niobium in reducing the austenite retention (Figure 42). Subzero treatment substantially reduces the retained austenite content in the hardened cases of all the steels.[24]

Niobium improves the surface hardness and maximum hardness of the case and core hardness of low carbon steels in the carburized and hardened conditions (Figure 43(a)). It also improves wear resistance of the carburized and hardened low carbon steel. Niobium in combination with nitrogen causes further improvement in hardness and wear resistance. Subzero treatment again causes further improvement in the case and core hardness of these carburized steels (Figure 43(b)).

Both the NbC and Nb(C,N) particles are detrimental to the toughness of the core of low carbon steels in the carburized and hardened condition, but Nb(C,N) precipitates are less harmful than NbC precipitates.[24]

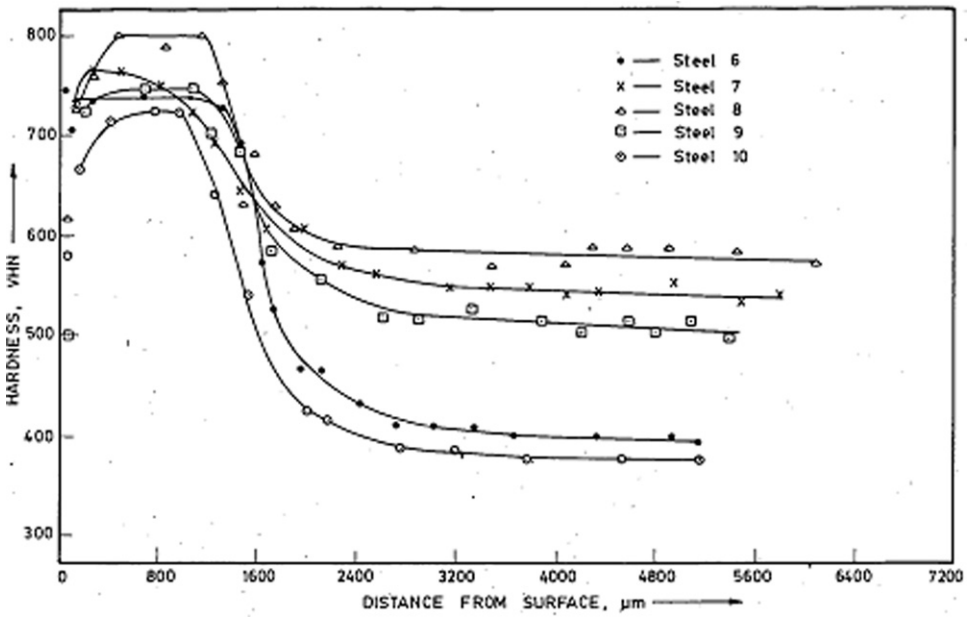


Figure 40 Microhardness profiles of steels 6–10 carburized at 950 °C for 1 h, quenched in 10% brine and tempered at 160 °C.[22]

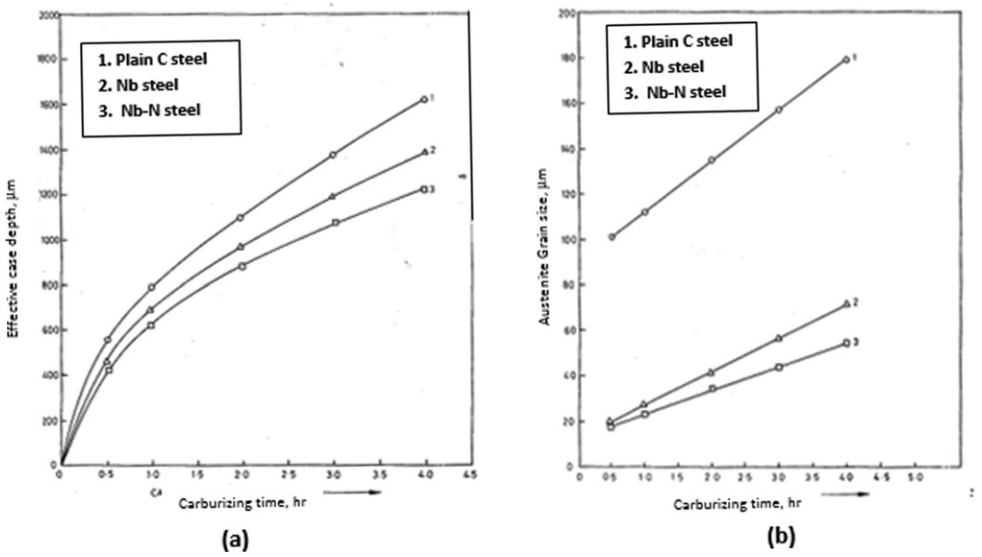


Figure 41 (a) Variation of effective case depth with carburizing time of steels 1–3 carburized at 950 °C and (b) variation of prior austenite grain size with carburizing time of the case of steels 1–3 carburized at 950 °C.[23]

2.3.6.3 Low Temperature Carburization of Austenitic Stainless Steel

2.3.6.3.1 Introduction

Low temperature carburization is a gaseous carburization process performed at atmospheric pressure, at temperatures where the kinetics of substitutional diffusion are very slow. Low temperature (350–550 °C) carburization hardens the surface of austenitic stainless steels through the diffusion of interstitial carbon, without the formation of carbides. The surface must be activated, by modification and removal of the naturally occurring chromia (chromium oxide) layer, for the diffusion process to work. The process results in a hardened diffusional case on the surface, typically 20–35 μm thick, with carbon content at the surface in excess of 10 at% and near-surface hardness of about HV 1200 (over 70 HRC). The case remains austenitic and retains its ductility.

2.3.6.3.2 Activation

Stainless steels and other chromium-containing alloys obtain their 'stainless' characteristic from the chromium-rich oxide that forms on the exposed surface. This oxide layer forms when a fresh surface is exposed to an oxygen containing medium, such as air, and will form after very short time exposures. The chromia layer on the surface of stainless steel constitutes a

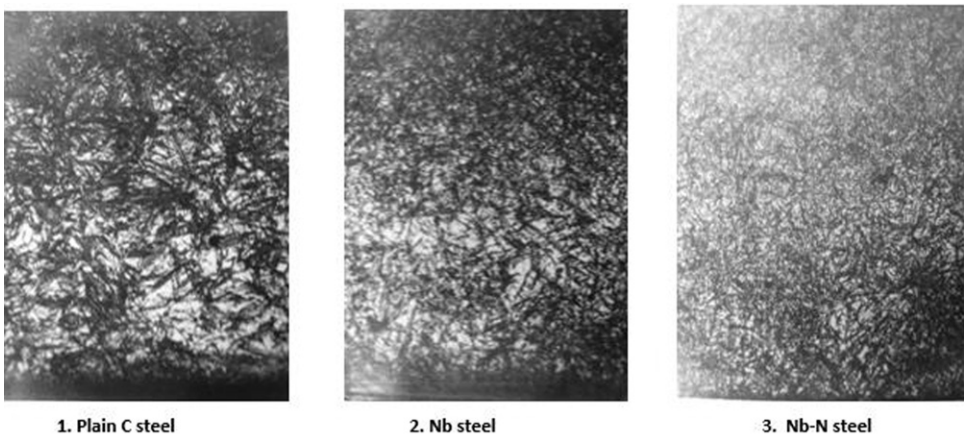


Figure 42 Optical micrographs showing the microstructures in the case of steels 1–3 carburized at 950 °C for 4 h, quenched in 10% brine and tempered at 160 °C, × 300.[24]

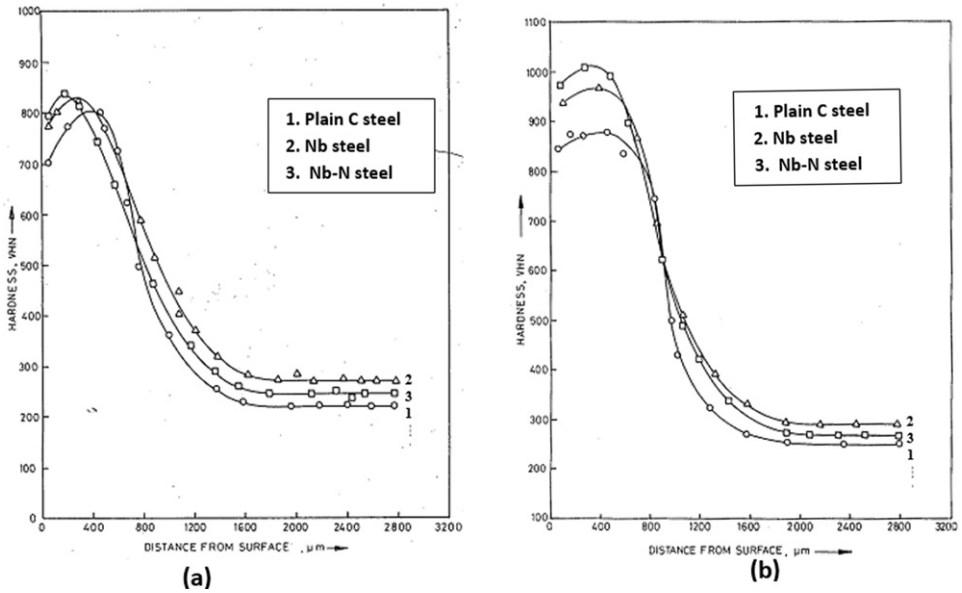


Figure 43 (a) Microhardness profiles of steels 1–3 carburized at 950 °C for 1 h, quenched in 10% brine and tempered at 160 °C. (b) Microhardness profiles of steels 1–3 carburized at 950 °C for 1 h, quenched in 10% brine, subzero treated in liquid nitrogen and tempered at 160 °C.[24]

major barrier to low temperature carburization because it prevents the inward diffusion of carbon. In order to diffuse the carbon atoms into the stainless steel from the surface, the chromium oxide layer must be removed, or at least modified to become carbon-transparent. This step generally is known as surface activation or depassivation.

Several methods have been developed[25–29] that eliminate the inhibiting effects of the oxide and activate the surface for efficient transport of carbon from a conventional carburizing atmosphere into the stainless steel matrix. Some processes, such as plasma or liquid sodium treatments, readily activate a passive stainless steel surface by removing the oxide by sputtering. In commercial production processing, activation can be achieved by exposing the furnace load to a halide-containing gas mixture such as nitrogen trifluoride or hydrogen chloride and nitrogen at atmospheric pressure. Hydrochloric acid is effective as an activating gas for a wide range of chromium-containing corrosion-resistant austenitic alloys, including stainless steels.

2.3.6.3.3 Processing temperature ranges

Low temperature carburization has a limited temperature processing range, usually 350–550 °C. At the lower processing temperature, the process becomes very slow and less economically feasible. Lower temperatures mean longer times for the same case thickness. At the upper end, it becomes increasingly difficult to avoid the formation of carbides, which depend in part on the thermally assisted mobility of substitutional alloying elements, such as chromium, in the iron matrix. Traditionally, carburization is carried out at high temperature to maximize the solubility and the rate of interstitial solute diffusion. On cooling to room temperature, however, a major part of the solute atoms will precipitate as carbide phases. Figure 44 shows the appropriate

time–temperature–transformation (TTT) diagram for the heat treatment of an austenitic stainless steel with conventional carbon contents.[30] After high temperature carburization (T > 950 °C), precipitation of carbides can be avoided only by extremely high cooling rates (path A). Furthermore, it is easy to exceed the solubility limit at these temperatures and form carbides during the carburization process itself. At the cooling rates typical of industrial processes, however, the path will cross the carbide 'nose' and precipitation will occur (path B). Carburization at low temperatures proved capable of hardening the surface of austenitic stainless steel without forming phases that would deplete the matrix of chromium, and thereby degrade corrosion resistance. In this process, the formation of carbides is kinetically suppressed (path C). This results in an extremely high carbon supersaturation, in fact far higher than can be achieved by high temperature carburization.

At moderate temperatures, substitutional solutes such as chromium and nickel diffuse much more slowly in austenitic steels than do interstitial solutes such as carbon. At 450–500 °C, the diffusivity of chromium is on the order of 10^{-21} m^2 s^{-1},[31] whereas the carbon diffusivity at this temperature is in the range 10^{-16}–10^{-17} m^2 s^{-1}.[32–34] This factor of 10^4–10^5 differences in diffusion coefficients enables homogeneous carburization in austenitic stainless steels (and other fcc alloys) under conditions where the formation of chromium-rich carbides is suppressed by insufficient diffusion kinetics for substitutional solutes. In other words, carburization is possible below the nose of the carbide curve on the TTT diagram shown in Figure 44.

2.3.6.3.4 Carburizing atmosphere

Several carburizing gas species will impart carbon to the active surface, with varying levels of efficiency at the processing temperatures required for low temperature carburization. These include acetylene and carbon monoxide, among others. A side effect of the high carbon potential needed for processing can be the generation of soot, which then has to be removed after processing using standard aqueous cleaning methods.

2.3.6.3.5 Microstructure of the low temperature carburized layer

The low temperature carburized layer is a diffusion gradient of carbon in solid solution in the austenite matrix. The structure of the case has been shown to be expanded austenite. The lattice parameter of the austenite expands from 0.360 to 0.372 nm after treatment.[35] However, there is no phase transformation and the layer does not represent a new phase. Expanded austenite is formed when large amounts of either nitrogen or carbon (or both) are dissolved in the surface of an austenitic stainless steel, forming a supersaturated solid solution without the precipitation of chromium-containing nitrides or carbides.

2.3.6.4 Carburization of Tool Steels

Carburization may be employed to retard abrasive and adhesive wear in tool steels with satisfactory case depth and improving hardenability and toughness. Different types of tool steels require relevant carburization technique.

2.3.6.4.1 Carburization of hot working tool steel

Hot working tool steels generally require a combination of high temperature strength (i.e., hot hardness and temper resistance), wear resistance, and toughness. In addition, heat check resistance is also required for applications involving thermal cycling.[36] To obtain desired properties gas carburizing can be employed to extensively increase case hardness by diffusion of carbon into the surface of a component. It is conducted at a temperature generally over 900 °C, followed by quenching and tempering operations. A typical gas carburizing cycle is depicted in Figure 45.

After normal stress relieving annealing treatment, carburization is carried out at around 930 °C followed by quenching in oil bath from 830 to 180 °C. Tempering is conducted at 200 °C for 2 h immediately after quenching. After carburizing, the surface layer is saturated with carbon to a eutectoid or moderately hypereutectoid content. The microstructure of hot working tool steels after quenching consists of high carbon martensite and some amount of carbides (i.e., Fe_3C, M_7C_3, and $M_{23}C_6$).

The determining factors for gas-carburized tool steels include microstructure, grain size, morphology and quantity of carbides, chemical compositions, hardness, and internal oxidation including retained austenite. The effect of retained austenite (softer phase) content has two different schools of thought. The transformation of retained austenite to martensite act to increase the yield stress under compression but reduce viscosity, which is favorable for friction coefficient.[37] The presence of retained austenite, under the effect of the compressive stresses, resulting from abrasion contact, can harden under the effect of

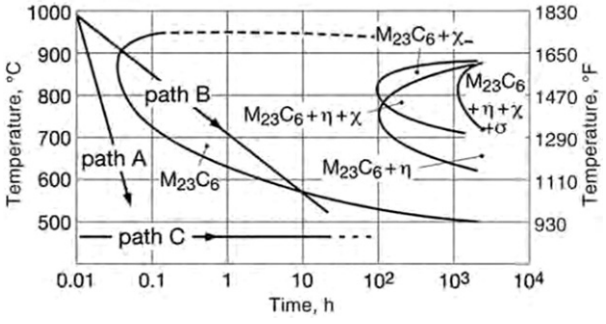


Figure 44 Time–temperature–transformation (TTT) diagram of carbide formation in austenitic stainless steels.[30]

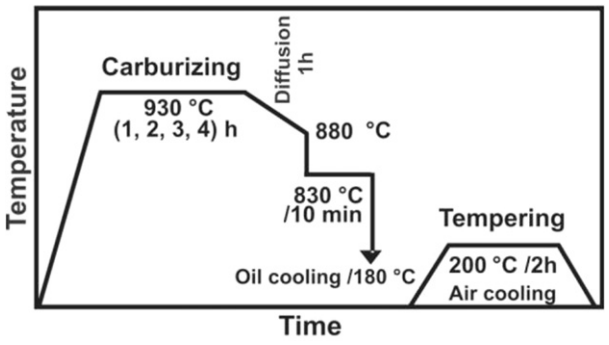


Figure 45 Gas carburizing cycle for hot working tool steels.[36]

induced work hardening, i.e., strain accommodation resulting an improvement in terms of friction.[38,39] In addition, during abrasive test the strain accommodation induces ability of retained austenite to evolve into martensite.[40]

2.3.6.4.2 Carburization of cold working tool steel

Cold work tool steels are designed for operation under the conditions of dry friction. Carburization is carried out on cold work tool steels to modify the surface layer for substantially increasing its abrasive wear resistance thereby increasing the quality of manufactured tools.[41]

Cold work tool steel introduces substantial changes to the surface layer as a result of changes of the carbide phase and the matrix. The carbide phase is responsible for the properties of surface layer. The initial microstructure of cold work tool steel consists of different degree of refinement of ledeburite carbides and dissolved dispersion and spheroidization of dispersion carbides.

After carburizing, the main carbides present in the structure are of M_3C and M_7C types with Fe, Cr, V, and Mo in their composition. Tempering causes carbides of M_3C, M_7C_3, and $M_{23}C_6$ types to precipitate from the oversaturated martensite solution with the carbides of types $M_{23}C_6$ occurring only at a temperature above 550 °C (823 K). The microstructure of matrix phase consists of a complex of austenite, martensite, and tempered martensite.

2.3.6.4.3 Carburization of shock resisting tool steel

To address repetitive impact stresses shock-resistant tool steels are employed. The specific properties to consider are good fracture toughness performance but with low-to-medium wear resistance.[42,43] To improve the surface hardness of shock resisting tool steel the vacuum carburizing surface hardening method can be adopted to obtain high surface carbon content and hardness.[44] The tool steels are generally preheated at 650–700 °C for 30 min carburized at 950 °C for 30 min under a low-pressure acetylene atmosphere followed by a rapid quench in nitrogen gas. The carburized and quenched specimens are tempered at around 300–600 °C.

As carburizing is carried out at high austenitizing temperature, alloying elements are easily dissolved in the solid solution resulting drop in M_s temperature. The microstructure corresponds to twin martensitic structure and retained austenite within the matrix. After tempering, the microstructure consists of needle-shaped tempered martensite inside cementite network.

During tempering, alloying elements, especially Cr, Mo, and V, combined with the high carbon content supplied by the carburizing to form a number of carbides of different sizes and compositions, which strongly influenced the toughness and strength of the steel. Carbide precipitation results in high surface hardness when tool steels are tempered. A typical highest fracture toughness of 80 MPa $m^{-1/2}$ can be obtained for tools steels tempered at 600 °C.

2.3.6.5 Carburization of Mold Steel

The molds made from low carbon steels (P2, P3, P4, P5, P6) in which cavities are formed by hubbing are always carburized before hardening and tempering, and molds made from P20 steel, with its higher carbon content, are frequently carburized when used for plastic molding. It is extremely important that the surfaces of parts to be carburized be as clean as possible, because foreign matter on surfaces may lead to nonuniform carburizing, which in turn leads to polishing difficulties.

Carburizing is a well-established heat-treating technology and can be accomplished by gas carburizing, pack carburizing in solid carbon-containing compounds, liquid carburizing in salt baths, vacuum carburizing, and plasma or ion carburizing. Carburizing temperatures may range from 870 to 995 °C, with carburizing times ranging between 2 and 24 h depending on the desired case depth.

All the low carbon hubbing grades and P20 are typically cooled in air or in the pack after carburizing and are therefore reheated for hardening. Reheating for hardening at temperatures below A_{cm} produces a dispersion of small carbide particles and a fine austenite grain size. This structure then transforms on quenching to a fine martensitic microstructure of high hardness and low susceptibility to intergranular cracking.[45] The carbide particles retained on austenitizing are incorporated into the martensitic structure, and the retained austenite content of reheated and hardened case microstructures is low.

Mold steels with higher hardenability, such as P4, can be hardened by air cooling directly after carburizing, but the retained austenite content may be high and the hardened microstructure will be susceptible to intergranular cracking.[45,46] The retained austenite content can be reduced by refrigeration at subzero temperatures, but reheating, as noted above, may more effectively lower retained austenite and increase hardness.

Austenitizing, quenching, and solution treating of type P21 mold steel are usually done by the tool steel manufacturer. Therefore, the only heat treatment required after machining is relatively low temperature aging between 510 and 540 °C for 20–24 h. No surface protection is necessary during the aging treatment. Type P21 can be simultaneously nitrided and aged in one operation. Once P21 steel is nitrided, it is very difficult to resoften or remove the nitrided case.

Tempering of mold steels requires no special precautions. For plastics molding, a surface hardness near 60 HRC is advantageous for polish ability and wear resistance, while molds for die casting of low-melting alloys are operated satisfactorily at a hardness of about 50 HRC or lower. To ensure structural stability and hardness retention during operation, a tempering temperature close to maximum operating temperature of the mold is desirable, though not always mandatory.

2.3.7 Problems during Carburization and their Remedy

There are a number of problems usually encountered in the carburizing process. The most commonly encountered problems are:

1. Nonuniform carburizing
2. Uneven case depth
3. Insufficient case depth

4. Low hardness
5. Sooting
6. Distortion
7. Soft spots
8. Cracking and exfoliation
9. Grinding cracks.

The above problems are discussed as follows:

2.3.7.1 Nonuniform Carburizing

This is due to improper cleaning of components before carburizing. If the components are dirty, with a greasy work surface or an oxidized surface, it will lead to nonuniform carburizing.

2.3.7.1.1 Prevention

The components are thoroughly cleaned before carburizing, either by degreasing, or sand blasting, or acid cleaning.

2.3.7.2 Uneven Case Depth

In pack carburizing, the uneven case depth may be due to an improper packing or an uneven heating of the container. In gas carburizing, if the free flow of gas all around the surface is prevented, some parts of the components will not be in contact with the gas long enough to be carburized.

2.3.7.2.1 Prevention

1. Thorough mixing of the carburizer.
2. Use of a solution of carbonate and molasses as a binder in the manufacture of the carburizer.
3. Uniform heat soaking of the container.
4. In gas carburizing, a powerful circulating fan together with a suitable baffle system should be used to have a uniform distribution of the gas around the charge.

2.3.7.3 Insufficient Case Depth

Insufficient case depth may be due to the low temperature employed during carburizing. Insufficient case depth may also be due to a weak solid carburizer or an insufficient gas feed in gas carburizing.

2.3.7.3.1 Prevention

1. Carburizing should be repeated with the usual carburizer at a normal temperature between 900 and 930 °C.
2. In gas carburizing, required case depth can be obtained by using a strong carburizer and sufficient feeding of gas.

2.3.7.4 Low Hardness

The common causes of low hardness are mainly due to a higher case depth, presence of retained austenites and decarburization.

2.3.7.4.1 Higher case depth

Higher case depth is produced when the surface of the steel is enriched by higher carbon content (~1.2–1.4% carbon) on carburization. Higher carbon content lowers the M_S and M_f temperatures during quenching. Lower M_s and M_f temperatures enhance the formation of retained austenite which is responsible for low hardness of the carburized case.

2.3.7.4.2 Prevention

This problem may be overcome by subjecting the components to a single quench treatment. That is after cooling from carburizing temperature, the components are heated above the critical temperature (800–830 °C), followed by quenching.

2.3.7.4.3 Retained austenite

Retained austenite occurs mostly in high alloy steels. The presence of carbon and alloying elements in steels prevent the transformation of austenite to martensite during quenching. This untransformed austenite is called the retained austenite. The retained austenite is soft, and hence contributes toward lowering the overall hardness of the components.

2.3.7.4.4 Prevention

This situation generally is avoided in gas carburizing by adopting a two-step process: the first step introduces a high surface carbon content (>1 wt%), while the second is performed at a lower carbon potential, which lowers the surface carbon content by permitting carbon introduced in the first stage to diffuse deeper into the steel. This process is often referred to as boost-diffuse carburizing and if properly controlled, results in reasonable levels of retained austenite.

2.3.7.4.5 Decarburization

In pack carburizing, the decarburization may occur due to slow cooling rate. As a result carbon content of the surface deceases. During quenching, low carbon martensite is formed in the lower carbon surface. This low carbon martensite will cause low hardness in the carburized layer. Decarburization may also occur due to the moisture present in the carburizing mixture.

2.3.7.4.6 Prevention

Carburizing should be repeated at a normal temperature for a short time, followed by cooling of the container in air at a faster rate. The carburizing mixture should be dried in order to make it free from moisture.

2.3.7.5 Sooting

Sooting in gas carburizing spoils the appearance of the work and also interferes with carburizing. Sooting is due to an excessive amount of gas being fed into the furnace, resulting in a free-carbon deposit on the components and in the furnace.

2.3.7.5.1 Prevention

This may be minimized, or prevented, by controlling the carburizing atmosphere, so that the rate of carbon supply to the steel surface does not exceed the rate at which it can be absorbed. Various methods can be adopted, but the use of either a diluted hydrocarbon mixture under controlled flow conditions, or a mixture of gases which will mutually react to give an atmosphere in equilibrium, is generally satisfactory.

2.3.7.6 Distortion

A certain amount of dimensional alteration usually takes place due to the change in microstructure when a part is quenched. The distortion may occur during hardening due to the following reasons:

2.3.7.6.1 Release of internal stresses

Stresses can be caused in steel by carrying out rolling, forging or machining operations before hardening. It is these stresses that will be released during heating to the hardening temperature and cause heavy distortion after hardening.

2.3.7.6.2 Prevention

It is best to release stresses due to rolling or forging by annealing or normalizing before machining.

2.3.7.6.3 Drastic quenching

Distortion may take place due to drastic quenching; the extent depends on the shape of components. Long, slender parts or parts with abrupt and considerable changes of section will always warp to a certain extent after the steel is quenched from the hardening bath.

2.3.7.6.4 Prevention

Distortion will be more if the components are water-quenched, and may be reduced by quenching in oil (60 °C). Further, it may be reduced by quenching in a warm bath maintained at 180–200 °C, and subsequently cooling in air.

2.3.7.6.5 High temperature hardening

When case-hardened mild steel parts of fair size, with only a superficial case, are water-quenched from approximately 900 °C, there is a decided tendency for warpage and expansion.

2.3.7.6.6 Prevention

Distortion may be reduced by hardening from a low (780 °C) or a medium hardening temperature (800–830 °C).

2.3.7.6.7 Rehardening

Sometimes repeated hardening will lead to abnormal dimensional changes in the component, leading to rejection of the component itself.

2.3.7.6.8 Prevention

It is necessary to counter-check the furnace temperature before hardening.

2.3.7.6.9 Uneven heating

Uneven heating is a cause of distortion. It is more common in the 'box' carburizing process, where the portion of the component nearest to the wall of the box gets heated well before the central parts get heated. Also, long shafts which have to be laid horizontally, undergo distortion as the carburizing compound underneath them gets consolidated, resulting in unevenness. Such parts can be hung vertically by using a proper fixture.

2.3.7.6.10 Prevention

The carburizing treatment of such components should be done either by liquid carburizing or gas carburizing to reduce distortion to a minimum.

2.3.7.7 Soft Spots

The causes of soft spots are as follows:

1. The presence of dirt patches or scale on the surface will hinder, or entirely prevent, the penetration of carbon. This may result in soft spots.
2. Unevenness of carburizing may be another cause for soft sports. This is more common in pack carburizing, if the compounds are not properly mixed before packing.
3. Soft sports may also result because of the insufficient time allowed for the center of the pack to attain and remain at the required temperature for a sufficiently long time during carburizing. Even though carburization may have taken place, it may be very thin in some places, and a subsequent grinding may expose the soft core.
4. Another cause for softness may be the development of an excessively high temperature under the grinding wheel.
5. Use of an insufficient quenching media, too warm a condition of quenching media, or improper agitation of the quenchant may also cause soft spots in the case of a heavy charge.

2.3.7.7.1 Prevention

1. Cleaning the components thoroughly before carburizing.
2. Proper mixing and packing of compounds.
3. Avoiding repeated use of used compounds.
4. Using proper coolant during grinding.
5. Control of temperature of quenching media.

2.3.7.8 Cracking and Exfoliation

Cracking and exfoliation occur on the carburized component due to the supersaturation of the case with carbon, leading to the formation of a carbide network. This phenomenon takes place because of too slow heating to the carburizing temperature (mainly in pack carburizing) with a high carbon potential.

In pack carburizing, if the concentration of the carburizing compound is higher, the austenite is supersaturated with carbon, leading to precipitation at the austenite grain boundaries, when the components are subjected to slow cooling from the carburizing temperature. This structure causes brittleness and is responsible for the development of cracking and exfoliation.

2.3.7.8.1 Prevention

1. Maintain appropriate carbon potential in the carrier gas during heating.
2. In pack carburizing, a low activator may be preferred.
3. A faster rate of cooling may be adopted after carburizing.
4. Single or double hardening with case refinement may be adopted during heat treatment.

2.3.7.9 Grinding Cracks

The supersaturated case has a greater tendency to crack during grinding than a eutectoid case. Even a perfect case can crack if an unsuitable wheel, without proper dressing, is used. The process of grinding heavy cuts or insufficient coolant may also cause cracks.

2.3.7.9.1 Prevention

1. Use of proper grinding wheel.
2. Proper dressing.
3. Sufficient coolant, especially with high velocity jets.

2.3.8 Recommended Processing Sequence for Carburized Components

Depending on the type of the component to be manufactured, the following processing sequences may be adopted[47]:

A. Small and medium size components:
   1. forge
   2. normalize
   3. anneal
   4. pre-machine
   5. carburize and harden
   6. temper
   7. finish machine.

B. Small and medium size components with machine operations, such as drilling, broaching, tapping, etc., after hardening:
   1. forge
   2. normalize
   3. anneal
   4. pre-machining
   5. carburize and anneal
   6. machine
   7. harden and temper
   8. finish machine.

C. Big and complicated shape components with machining operations such drilling tapping, etc., after hardening:
   1. forge
   2. normalize
   3. anneal
   4. rough machine
   5. stress relieve
   6. pre-machine
   7. carburize and anneal
   8. machine
   9. harden
   10. temper
   11. finish machine.

See also: 2.6 Surface Induction Hardening

References

1. Lakhtin, Y. *Engineering Physical Metallurgy (Engl. transl.)*; Mir Publisher: Moscow, 1977; p. 247, 257.
2. Clark, D. S.; Varney, W. R. *Physical Metallurgy for Engineers*; 2nd ed.; D. Van Nostrand Company, Inc.: New York, NY, 1962; pp. 150, 253–255.
3. Harris, F. E. The Mechanism of Carburization. In *The Metal Handbook*, 1948 ed.; The American Society for Metal: Cleveland, OH, 1948; pp. 678–680.
4. Leighou, R. B. *Chemistry of Engineering Materials*; 4th ed.; McGraw-Hill Book Company, Inc.: New York, NY; London, 1942; pp. 342–345.
5. Harris, F. E. *Metals Handbook*, Vol. 2, 8th ed.; American Society for Metals: Metals Park, OH, 1971; pp. 93–114.
6. Stickels, C. A. Gas Carburizing. In *ASM Handbook Volume 4: Heat Treating*. American Society of Metals: Metals Park, OH, 1991; pp. 312–324.
7. Luiten, C. H.; Limque, F.; Bless, F. *Heat Treatment '79*; The Metals Society: London, 1979; p. 69.
8. Grube, W. L.; Gay, J. G. High-Rate Carburizing in a Glow Discharge Methane Plasma. *Metall. Trans. A* **1978**, *9A*, 1421.
9. Tibbetts, G. L. Diffusivity of Carbon in Iron and Steels at High Temperatures. *J. Appl. Phys.* **1980**, *51*, 4813–4816.
10. Vlack, V. *Elements of Material Science*; 2nd ed.; Addison-Wesley Publishing Company, Inc.: London, 1964; pp. 86–103, 389.
11. Guy, A. G. *Elements of Physical Metallurgy*; 2nd ed.; Oxford & IBH Publishing Co.: New Delhi, 1967; pp. 406–407.
12. Teichert, E. J.; *Metallography and Heat Treatment of Steel*, Vol. 3, 2nd ed.; McGraw-Hill Book Company, Inc.: New York, NY and London, 1944; pp. 343–345.
13. Stickels, C. A.; *Carburizing, Friction, Lubrication, and Wear Technology, ASM Handbook*, Vol 18; ASM International: Metals Park, OH, 1992; pp. 873–877.
14. Grange, R. A.; Hribal, C. R.; Porten, L. F. Hardness of Tempered Martensite in Carbon and Low-Alloy Steels. *Metall. Trans. A* **1977**, *8*, 1775–1785.
15. Andrews, K. W. Empirical Formulae for the Calculation of Some Transformation Temperatures. *J. Iron Steel Inst.* **1965**, *203*, 721–727.
16. Koistinen, D. P.; Marburger, R. E. A General Equation Prescribing the Extent of the Austenite–Martensite Transformation in Pure Iron–Carbon Alloys and Plain Carbon Steels. *Acta Metall.* **1959**, *7*, 59–60.
17. Haque, M. N.; Bepari, M. M. A. Effects of Chromium and Nickel Additions on the Structure, Depth, and Austenite Grain Size of the Case of Carburized 0.1% Carbon Steels. *J. Inst. Eng. Bangladesh* **1989**, *17* (1), 37–47.
18. Bepari, M. M. A.; Haque, M. N.; Islam, M. S. Effects of Chromium and Nickel Additions on the Structure and Properties of Carburized and Hardened Low Carbon Steels. *J. Trans. Indian Inst. Metals* **2000**, *53* (4–5), 509–518.
19. Shorowordi, K. M.; Bepari, M. M. A. Effects of Molybdenum Additions on the Structure, Depth and Austenite Grain Size of the Case of Carburized 0.13% Carbon Steels. *J. Mater. Eng. Perform.* **2002**, *11* (6), 625–630.
20. Bepari, M. M. A.; Shorowordi, K. M. Effects of Molybdenum and Nickel Additions on the Structure and Properties of Carburized and Hardened Low Carbon Steels. *J. Mater. Process. Technol.* **2004**, *155*, 1972–1979.
21. Haque, M. N.; Bepari, M. M. A. *Effects of Small Additions of Vanadium, Aluminum and Nitrogen on the Structure, Depth and Austenite Grain Size of the Case of Carburized Low Carbon Steels*, To be published.
22. Bepari, M. M. A.; Haque, M. N.; Shorowordi, K. M. The Structure and Properties of Carburized and Hardened Vanadium Microalloyed Steels. *Adv. Mater. Res.* **2010**, *83*, 1270–1281.
23. Islam, M. A.; Bepari, M. M. A. Effects of Niobium Additions on the Structure, Depth, and Austenite Grain Size of the Case of Carburized 0.07%C Steels. *J. Mater. Eng. Perform.* **1996**, *5* (5), 593–597.
24. Islam, M. A.; Bepari, M. M. A. Structure and Properties of Carburized and Hardened Niobium Micro-Alloyed Steels. *J. Mater. Process. Technol.* **1998**, *74* (1), 183–189.
25. Ihara, Y.; Sakiyama, K.; Ohgame, H.; Hashimoto, K. The Corrosion Behavior of Chromium in Hydrogen Chloride Gas and Gas Mixtures of Hydrogen Chloride and Oxygen at High Temperatures. *Corros. Sci.* **1983**, *23* (2), 167–181.
26. Williams, P. C.; Marx, S. V. Selective Case Hardening Processes at Low Temperature. U.S. Patent 6,165,597, 26 December 2000.
27. Williams, P. C.; Marx, S. V. Low Temperature Case Hardening Processes. U.S. Patent 6,093,303, July 25, 2000.
28. Williams, P. C.; Marx, S. V. Low Temperature Case Hardening Processes. U.S. Patent 6,461,448 B1, 8 October 2002.
29. Williams, P. C.; Marx, S. V. Modified Low Temperature Case Hardening Processes. U.S. Patent 6,547,888 B1, 15 April 2003.
30. Weiss, B.; Sticker, R. Phase Instabilities During High Temperature Exposure of 316 Austenitic Stainless Steel. *Met. Trans. A* **1972**, *3* (4), 851–866.
31. Bowen, A. W.; Leak, G. M. Solute Diffusion in Alpha- and Gamma-Iron. *Met. Trans.* **1970**, *1* (6), 1695–1700.

32. Wells, C.; Mehl., R. F. Rate of Diffusion of Carbon in Austenite in Plain Carbon, in Nickel and in Manganese Steels. *Trans. Metal. Soc. AIME* **1940**, *140*, 279.
33. Batz, W.; Mehl, R. F.; Wells, C. Concentration Dependence of Carbon Diffusivity in Iron. *Trans. Metal. Soc. AIME* **1950**, *188*, 553–560.
34. Liu, W. J.; Brimacombe, J. K.; Hawbolt, E. B. Influence of Composition on the Diffusivity of Carbon in Steels – I. Non-Alloyed Austenite. *Acta Metall. Mater.* **1991**, *39* (10), 2373–2380.
35. Cao, Y.; Ernst, F.; Michal, G. M. Colossal Carbon Supersaturation in Austenitic Stainless Steels Carburised at Low Temperature. *Acta Mater.* **2003**, *51*, 4171.
36. Fares, M. L.; Athmani, M.; Abidi, Y. Surface Characteristics Analysis of Gas Carburized New Hot Working Tool Steel. *Surf. Sci. Nanotech.* **2011**, *9*, 430–437.
37. Totten, G. E.; Liang, H. *Surface Modification and Mechanisms: Friction Stress and Reaction Engineering*; CRC Press: Boca Raton, FL, 2004; pp. 625–630.
38. Fares, M. L.; Touhami, M. Z.; Belaid, M.; Bruyas, H. Surface Characteristics Analysis of Nitrocarburized (Tenifer) and Carbonitrided Industrial Steel AISI 02 Types. *Surf. Interface Anal.* **2009**, *41*, 179.
39. Parrich, G. *Carburizing: Microstructure and Properties*; ASM International Metals Handbook: Materials Park, OH, 1999.
40. Silva, V. F.; Canale, L. F.; Spinelli, D. W.; Bose-Filho, W.; Crnkovic, O. R. Influence of Retained Austenite on Short Fatigue Crack Growth and Wear Resistance of Case Carburized Steel. *J. Mater. Eng. Perform.* **1999**, *8*, 543.
41. Wencel, Z.; Budzik, R.; Križanić, R.; Kolmasiak, C. The Synergy of the Surface Layer after Carburizing of Tool Steel as a Measure of Operational Quality. *Metalurgija* **2007**, *46* (4), 255–260.
42. ASM. *Metals Handbook*, Volume 1; ASM International: Materials Park, OH, 1990; p. 766.
43. Chiu, L. H.; Chen, S. S. *Proceeding of Second Asian Conference on Heat Treatment of Materials*, Simane, Japan, 2001; p. 93.
44. Chiu Liu-Ho; Chen Yu-Jen; Wu Chang-Hui; Chang Heng Vacuum Carburizing of AISI S7 Tool Steel. *Solid State Phenom.* **2006**, *118*, 91–96.
45. Krauss, G. *Steels: Heat Treatment and Processing Principles*; ASM International: Materials Park, OH, 1990; pp. 291–305.
46. Apple, C. A.; Krauss, G. Microcracking and Fatigue in a Carburized Steel. *Metall. Trans.* **1973**, *4*, 1195–1200.
47. Prabhudev, K. H. *Handbook of Heat Treatment of Steels*; Tata Mcgraw-Hill Publishing Company: New Delhi, 1988; p. 351.

2.4 Surface Hardening by Gas Nitriding

K Farokhzadeh and A Edrisy, University of Windsor, Windsor, ON, Canada

© 2017 Elsevier Inc. All rights reserved.

2.4.1	**Introduction**	108
2.4.2	**Fundamentals of Gas Nitriding**	109
2.4.2.1	Thermodynamics of Nitriding	109
2.4.2.1.1	Iron–nitrogen system	109
2.4.2.1.2	Lehrer diagrams	110
2.4.2.1.3	Titanium–nitrogen system	112
2.4.2.1.4	Aluminum–nitrogen system	113
2.4.2.2	Nitriding Kinetics	113
2.4.3	**Gas Nitriding Process**	117
2.4.3.1	Pre-Treatment Step	117
2.4.3.2	Gas Nitriding Set-Up	119
2.4.3.3	Post-Treatment Step	119
2.4.3.4	Common Problems in Nitriding: Causes and Remedies	120
2.4.3.4.1	Formation of white layer	120
2.4.3.4.2	Insufficient depth or hardness of the diffusion zone	120
2.4.3.4.3	Oxidation during nitriding	120
2.4.3.4.4	Dimensional changes	120
2.4.3.4.5	Exfoliation and spallation of the compound layer	120
2.4.4	**Gas Nitriding of Structural Alloys**	120
2.4.4.1	Ferrous Alloys	120
2.4.4.1.1	Microstructure and phase composition	120
2.4.4.1.2	Nitriding time and temperature	124
2.4.4.1.3	Nitriding atmosphere	124
2.4.4.1.4	Steel composition and heat treatment history	124
2.4.4.2	Non-ferrous Alloys	125
2.4.4.2.1	Microstructure and phase composition	125
2.4.4.2.2	Nitriding atmosphere	127
2.4.4.2.3	Nitriding time and temperature	127
2.4.4.2.4	Substrate composition	127
2.4.5	**Effect of Gas Nitriding on Mechanical Properties**	127
2.4.5.1	Ferrous alloys	127
2.4.5.2	Titanium Alloys	129
2.4.6	**Effect of Gas Nitriding on Wear and Corrosion Resistance**	131
2.4.6.1	Ferrous Alloys	131
2.4.6.2	Titanium Alloys	131
2.4.7	**Industrial Applications**	131
2.4.8	**Recent Developments in Gas Nitriding**	132
References		132
Relevant Websites		135

List of Abbreviations

BCC Body-centered cubic
BCT Body-centered tetragonal
COF Coefficient of friction
FCC Face-centered cubic
HCP Hexagonal close packed
PVD Physical vapor deposition
SMAT Surface mechanical attrition treatment
TIG Tungsten inert gas

List of Symbols

a_N Activity of nitrogen
at% Atomic percentage
C_0 Initial concentration of nitrogen in the substrate

C_N Concentration of nitrogen
C_s Concentration of nitrogen on the surface
D Diffusion coefficient ($m^2\ s^{-1}$)
E Elastic modulus (GPa)
H Hardness
K Equilibrium constant
K_{IC} Fracture toughness (MPa $m^{-1/2}$)
[N] Dissolved nitrogen in the substrate structure
p_i Partial pressure of gas component i (Pa)
R Universal gas constant (J $mol^{-1}\ K^{-1}$)
R Stress ratio, the ratio of minimum to maximum stress ($\sigma_{min}/\sigma_{max}$) during fatigue tests
r_N Nitriding potential (or K_N in German literature) ($Pa^{-1/2}$)
S-phase Expanded austenite phase
t Time (s)
T Absolute temperature (K)
T_s Absolute solidus temperature (K)
wt% Weight percentage
x Distance from the surface (m)
α-Fe Ferrite, body-centered cubic structure of iron
α-Ti Hexagonal close packed structure of titanium
α' Martensite in Fe–N system with body-centered tetragonal crystal structure
α'' $Fe_{16}N_2$ iron nitride phase with body-centered tetragonal crystal structure
β-Ti Body-centered cubic structure of titanium
γ-Fe Austenite, face centered cubic structure of iron
γ' Fe_4N_{1-x} iron nitride phase with face-centered cubic crystal structure
δ TiN titanium nitride phase with face-centered cubic crystal structure
δ′ $TiN_{0.6}$ titanium nitride phase with tetragonal crystal structure
ΔH_0 Standard enthalpy change (J mol^{-1})
ΔS_0 Standard entropy change (J $mol^{-1}\ K^{-1}$)
ε Fe_2N_{1-z} iron nitride phase with hexagonal crystal structure
ε Ti_2N titanium nitride phase with anti-rutile tetragonal crystal structure
ζ Fe_2N iron nitride phase with orthorhombic crystal structure
σ_γ Yield strength (MPa)

2.4.1 Introduction

Gas nitriding is one of the most common surface modification treatments with extensive industrial applications especially in manufacturing of machine components and tools. It is classified as a diffusion-based surface treatment, distinguished from overlay coating deposition techniques, in which the substrate is exposed to a controlled nitriding atmosphere. Gas nitriding is an industrially established finishing treatment to enhance fatigue, wear, and corrosion resistance of ferrous alloys and with the increasing trend of replacing steels with lightweight alloys, for example, titanium and aluminum alloys; it has also been adopted for wear improvements in non-ferrous alloys. Titanium and aluminum alloys are attractive candidate materials in many industrial applications due to their high strength to weight ratio, corrosion resistance, fatigue resistance, etc., and a variety of surface engineering technologies including gas nitriding have been utilized to improve their wear and corrosion resistance.[1]

Nitriding of steels is usually conducted within the temperature range of 495–565 °C in ammonia or ammonia–hydrogen atmosphere.[2] The nitriding conditions (gas composition, temperature, duration, etc.) and the microstructure and composition of the substrate determine the structure and properties of the nitrided workpieces. The nitrided microstructure is mainly composed of a compound layer predominantly consisting of ε-Fe_2N_{1-z} and γ'-Fe_4N_{1-x} (i.e., white layer) on top of a nitrogen diffusion zone (i.e., case).[3] The compound layer improves the corrosion and wear resistance. However, the compound layer is also susceptible to spallation due to its brittle nature and may cause accelerated wear and seizure, thus in many cases it is removed before service.[4] The diffusion zone consists of interstitial solid solution of nitrogen with a gradient gradually decreasing toward the bulk and iron nitride precipitates (in iron and carbon steels) and/or alloying element nitride precipitates (in steels that contain nitride forming alloying elements such as Al, Cr, V). The development of precipitation hardening and compressive residual stresses in the diffusion zone is responsible for enhancement of high-cycle fatigue strength and wear resistance.[3] Due to the relatively low temperatures practiced in the gas nitriding of steels, this treatment does not promote any adverse effects on the ductility of tempered substrates and the resulting volumetric changes and distortions are relatively small.[4]

Nitriding of non-ferrous alloys (i.e., titanium and aluminum alloys) forms a compound layer composed of TiN and Ti_2N nitrides on titanium surfaces and aluminum nitride (AlN) on aluminum surfaces.[5] In titanium alloys, due to the high solubility of nitrogen in α-Ti (~22 at% at 1050 °C[6]) a diffusion zone strengthened by nitrogen interstitial atoms develops underneath the compound layer. The compound layer increases the surface hardness and wear resistance of titanium surfaces while the diffusion zone increases the load bearing capacity of nitrided Ti surfaces by providing mechanical support for the compound layer.[1,7] Nitriding of aluminum alloys, however, tends to be more challenging due to the insolubility of nitrogen in aluminum, high-thermal expansion mismatch between aluminum and aluminum nitride, and the naturally occurring oxide layer on the surface of aluminum alloys. Furthermore, typical gas nitriding temperature lies within the solution treatment temperature range of titanium alloys (0.55–0.65 T_s) and annealing temperature range of aluminum alloys (0.75–0.85 T_s) and causes detrimental effects on the substrates microstructure and properties.[5b,8] Specifically, nitriding of titanium alloys is associated with adverse

side effects on their fatigue properties and loss of ductility due to substrate over aging and grain growth.[1,9]

Following the Introduction, a brief history of the development of gas nitriding process is given in Section 2.4.2, followed by the description of fundamentals, thermodynamics, and kinetics aspects of gas nitriding. Section 2.4.3 describes an overview of the practical aspects of gas nitriding treatment as well as commonly practiced pre- and post-treatments. Section 2.4.4 discusses the gas nitriding conditions for ferrous and non-ferrous alloys and the effect of nitriding parameters on the microstructural development of the alloys. Subsequently, the effect of gas nitriding on mechanical properties, wear and corrosion resistance of structural alloys are presented in Sections 2.4.5 and 2.4.6. Finally, the industrial applications and recent developments in the gas nitriding technology are presented in Sections 2.4.7 and 2.4.8.

2.4.2 Fundamentals of Gas Nitriding

Gas nitriding treatment was pioneered by parallel work of Machlet[10] (American Gas Company, Elizabeth, NJ) and Fry[11] (Krupp Steel Works, Essen, Germany) in early twentieth century. They discovered that nitrogen promoted hard surface layers in steels that significantly improved corrosion and wear resistance. Fry discovered that alloying elements such as molybdenum, vanadium, tungsten, aluminum, and chromium increase the surface hardness of nitrided steel and he developed the family of 'Nitralloy' steels specifically for nitriding. At the time ammonia was used to provide nascent nitrogen for nitriding but Machlet[10] found that introducing hydrogen as a dilutant gas enhanced the nitrogen activity and controlled the decomposition rate of ammonia and nitrided microstructure.[12] However, the development of gas nitriding in the United States initiated after Fry's work was presented in the 'Society of Manufacturing Engineers' conference in 1927.

Based on the findings of Machlet and Fry, McQuaid and Ketcham[13] (Timken-Detroit Axle Company, Detroit, MI) investigated the effect of process parameters such as time, temperature, cooling rate, and gas composition on the nitriding microstructure. Their findings indicated that nitriding at high temperatures (more than 650 °C) reduced the core hardness of alloy steels and increased the surface susceptibility to early formation and exfoliation due to the formation of nitride networks. Perhaps more importantly, they reported that the formation of compound layer should be avoided due to its brittle nature. They also noted that the possible decarburization of surface layers has a detrimental effect on nitriding as it increases the chances of exfoliation and premature failure of the nitride layer.

The role of alloying elements on the nitriding and carburizing chemistry of steels were reviewed and studied by Sergeson[13] (Central Alloy Steel Corporation, Canton, OH). In agreement with McQuaid and Ketcham,[13] he noted that controlling the nitriding treatment was easier than carburizing. He also investigated the effect of reheating, temperature, gas flow, and decarburization on nitriding chemistry. According to his findings while gas flow rate had little effect on the case hardness and depth, increasing the nitriding temperature resulted in the development of a deeper case and a lower surface hardness. A two-stage nitriding process composed of a first low-temperature step at 510 °C, followed by a high-temperature step at 620–650 °C was also recommended to minimize the surface brittleness.

It should be noted that the nitriding equipment used in the experiments were at their primitive stage of development. The first steps toward advanced nitriding process technology were contributed by Floe[13] (Massachusetts Institute of Technology). His research was focused on the characterization of microstructure and properties of nitrided layers and he developed a nitriding treatment to reduce the compound layer thickness, i.e., the Floe Process (to be discussed in Section 2.4.3). Soon with the advent of process technology such as sensors, computer control systems, flow control devices, and automatic monitoring of dissociation rate, and based on experimentation and theoretical calculations, gas nitriding was conducted under accurately controlled conditions.[14] The nitriding process has been the subject of many studies ever since[15] and modifications have made it applicable for other structural alloys such as stainless steels and titanium alloys[16] and new fabrication technologies such as powder metallurgy.

2.4.2.1 Thermodynamics of Nitriding

2.4.2.1.1 Iron–nitrogen system

Iron–nitrogen (Fe–N) system has been the subject of many studies over the past decades and is one of the most extensively used due to its practical significance.[17] **Figure 1** presents the equilibrium binary Fe–N phase diagram. Due to the lack of experimental data for temperatures above 1200 K, the phase diagram has been constructed by thermodynamic mathematical calculations at high temperatures.[18] Crystal structure, space group, and chemical composition of the most common solid phases in the Fe–N phases are listed in **Table 1**.

Fe–N system consists of two solid solution phases (e.g., α, γ), several nitride compounds (e.g., ε, γ', ζ), and several non-equilibrium phases (e.g., α', α''). The low temperature solid solution, i.e., ferrite (α-Fe), is stable below 912 °C has a limited nitrogen solubility. Austenite (γ-Fe) is stable above 600 °C and over a wide range of compositions. The austenite phase may undergo a martensitic transformation to α' martensite but can be fully retained at room temperature by quenching upon dissolution of 8.6 at% nitrogen.[17d] The main nitride phases in Fe–N system, from the practical point of view, are hexagonal ε-nitride and cubic close packed γ'-nitride. The cubic γ'-nitride has a narrow range of composition but ε-nitride has a wide range of compositions and shows a high ordering of the nitrogen interstitial atoms in the octahedral sites. This phase has a higher probability of formation in steels with high carbon contents. The ε-nitride with nitrogen contents below 27 at% is metastable at room temperature and dissociates into a nitrogen-rich ε phase and γ' (or α'') phase.[19]

In order to predict the nitriding behavior and obtain the desired nitrided microstructure in ferrous alloys, the phase

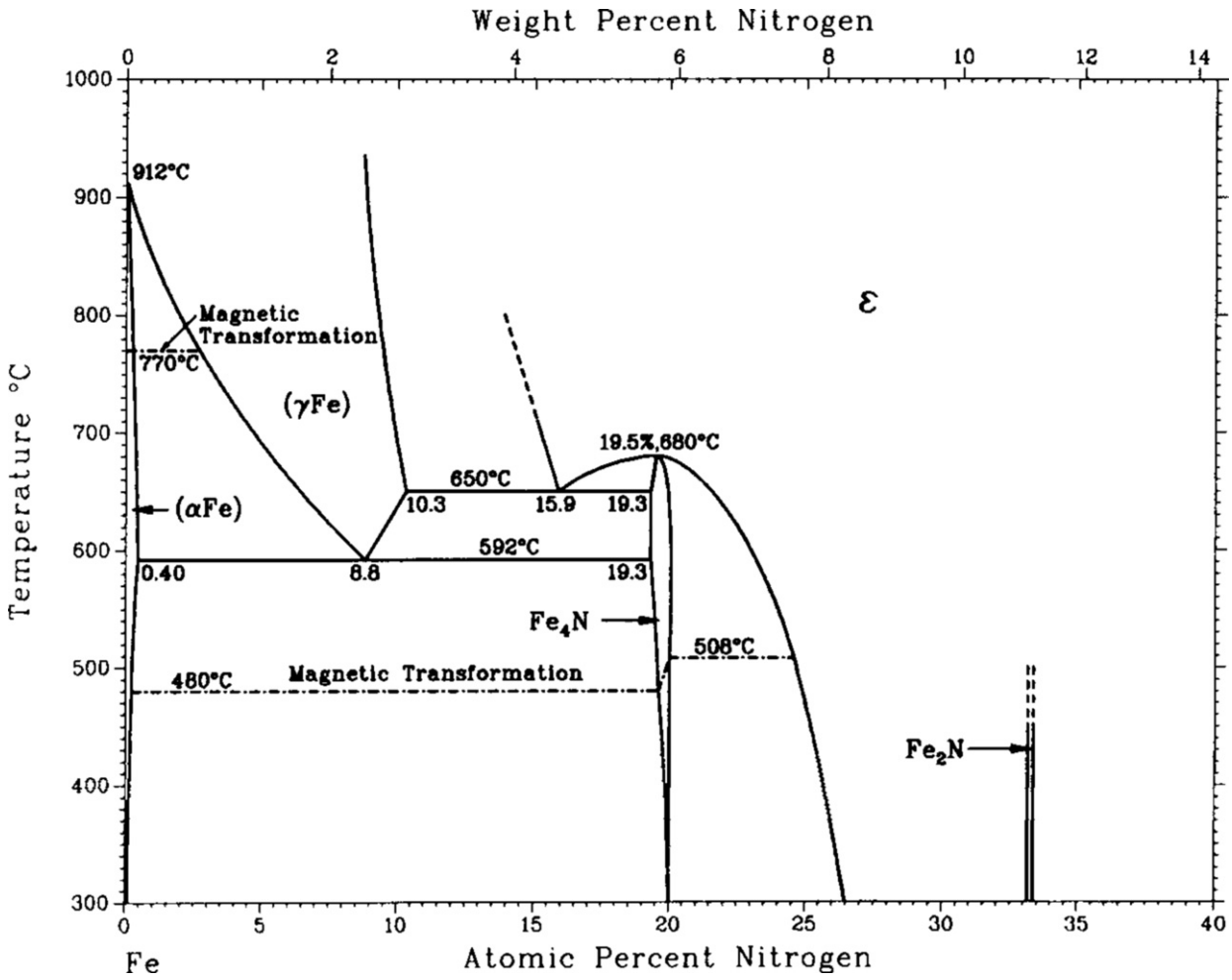


Figure 1 Equilibrium iron–nitrogen binary phase diagram.[17d]

Table 1 Crystal structure, space group, and chemical composition for phases in the iron–nitrogen system

Phase	*Composition*	*Nitrogen content (at%)*	*Crystal structure*	*Space group*	*References*
α (ferrite)	Fe (N)	0–0.4	BCC	$Im\bar{3}m$	3,17d,20
γ (austenite)	Fe (N)	0–10.3	FCC	$Fm\bar{3}m$	3,17d
α'	Fe (N)	0–2.7	BCT	$Im\bar{3}m$	3,17d
α''	$Fe_{16}N_2$	~11.1	BCT	$I4/mmm$	3,17d,20,21
γ'	Fe_4N_{1-x}	19.3–20.0	FCC	$Pm\bar{3}m$ or $P\bar{4}3m$	17d,20,22
ε	Fe_2N_{1-z}	~15–33	Hexagonal	$P6_322$ or $P6_3/mmc$	17d,17g,20,21,22
ζ	Fe_2N	33.2	Orthorhombic	Pbcn	20,23

Source: Shibata, H.; Tokaji, K.; Ogawa, T.; Hori, C. The Effect of gas Nitriding on Fatigue Behaviour in Titanium alloys. *Int. J. Fatigue* **1994**, *16* (6), 370–376.

stabilities of Fe–N system were studied in relation to temperature and nitriding medium. The investigations resulted in the development of Lehrer diagrams for describing the gas nitriding behavior of iron and steels as will be discussed in the following section.

2.4.2.1.2 Lehrer diagrams

The nitriding reaction in NH_3–H_2 atmosphere (Reaction I) can be considered as the sum of two hypothetical reactions: (1) dissociation of ammonia at the surface (Reaction II) and (2) liberation of nascent nitrogen dissolving in the metal surface (Reaction III), as schematically illustrated in **Figure 2**.

$$NH_3 \leftrightarrow [N] + 3/2H_2 \quad [I]$$

$$NH_3 \leftrightarrow 1/2N_2 + 3/2H_2 \quad [II]$$

$$1/2N_2 \leftrightarrow [N] \quad [III]$$

where [N] is the dissolved nitrogen in the substrate structure. Accordingly, the equilibrium constant of Reaction (I), K_I can be written in terms of nitrogen activity (a_N), partial pressure of nitrogen (p_{NH_2}), partial pressure of ammonia (p_{NH_3}), and pressure of gases in the reference state (p^0) according to eqn [1]. The equilibrium constants of Reactions [II] and [III] are K_{II} and K_{III} as presented by eqns [2] and [3], respectively, assuming ideal gas behavior or constant fugacity coefficients of gaseous components. Due to the local equilibrium on the surface, the chemical potential of nitrogen in the nitriding atmosphere is equal to the chemical potential of nitrogen on the nitrided surface and thus in eqn [3], $a_N = \frac{\sqrt{p_{N_2}}}{\sqrt{p^0}}$.

$$K_I = \frac{a_N \cdot p_{H_2}^{3/2}}{\sqrt{p^0} \cdot p_{NH_3}} \quad [1]$$

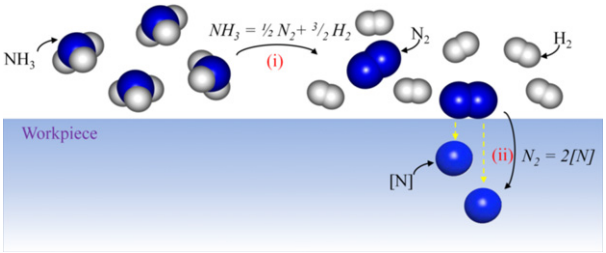


Figure 2 A schematic drawing showing hypothetical surface reactions during gas nitriding in ammonia–hydrogen nitriding atmosphere: (1) ammonia dissociation and (2) liberation of nascent nitrogen in the work surface. ([N] is the solid solution of nitrogen in the substrate structure.) Hosmani, S. S.; Schacherl, R. E.; Mittemeijer, E. J. Compound Layer Formation on Iron-Based Alloys Upon Nitriding; Phase Composition and Pore Formation. *J. Heat Treat. Mater. (HTM Härtereitechnische Mitteilungen)* **2008**, *63* (3), 139–146.

$$K_{II} = \frac{p_{N_2}^{1/2} \cdot p_{H_2}^{3/2}}{p^0 \cdot p_{NH_3}} \quad [2]$$

$$K_{III} = \frac{\sqrt{p_{N_2}}}{\sqrt{p^0} \cdot a_N} \quad [3]$$

It follows that nitrogen activity is proportional to $\frac{p_{NH_3}}{p_{H_2}^{3/2}}$, where p_{NH_3} is the partial pressure of ammonia and p_{H_2} is the partial pressure of hydrogen (eqn [4]). The nitriding potential, r_N (or K_N in German literature), was thus defined based on the partial pressure of ammonia p_{NH_3}, and hydrogen p_{NH_2} to represent the activity of nitrogen (eqn [5]).[24]

$$a_N = \frac{K_{III} \cdot p_{NH_3} \cdot \sqrt{p^0}}{p_{H_2}^{3/2}} = \frac{K_I \cdot p_{NH_3} \cdot \sqrt{p^0}}{p_{H_2}^{3/2}} \quad [4]$$

$$r_N = p_{NH_3} / p_{H_2}^{3/2} \quad [5]$$

A plot of the nitriding potential against temperature provides graphic illustration of possible thermodynamically stable phases in Fe–N system during nitriding (**Figure 3**). This plot is named after 'Lehrer' who constructed it for the first time for pure Fe. As such, a 'Lehrer diagram' can be used to predict the desired nitriding outcome by controlling NH_3–H_2 gas mixture composition and pressure, and thus the chemical potential of nitrogen in the nitriding atmosphere.[3,17a,19b,25]

When the nitriding potential is sufficiently high that the activity of nitrogen dissolved in iron is equal to its equilibrium value in iron nitrides γ' and ε, nitrides precipitate on the surface. However, the thermodynamic equilibrium is established

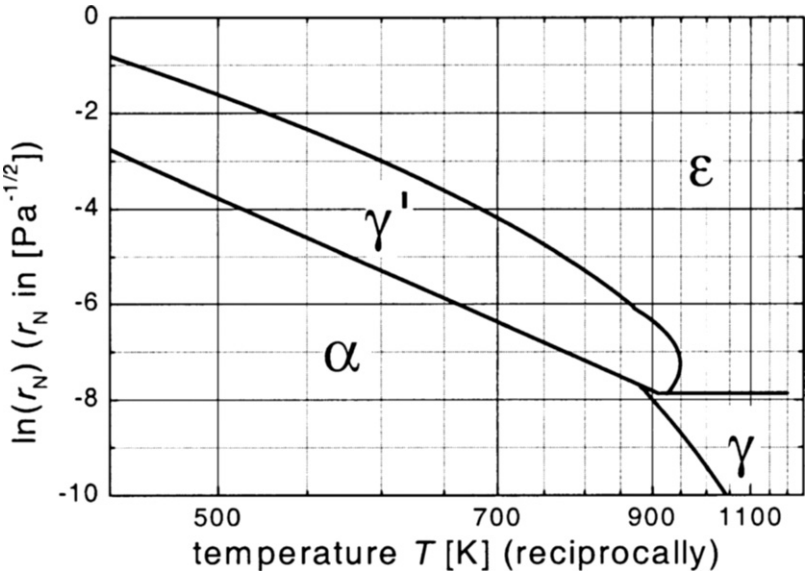


Figure 3 A schematic representation of Lehrer diagram for pure Fe; α and γ are the solid solutions of nitrogen in BCC and FCC iron, γ' and ε are Fe_4N_{1-x} and Fe_2N_{1-z} nitride compounds, respectively.[79]

only at the surface which is in direct contact with the nitriding atmosphere. Thus as the iron nitrides grow and develop a compound layer, the nitride phases that are no longer in contact with the nitriding medium will be thermodynamically unstable. As a result, γ' and ε phases have a strong tendency to dissociate into iron and nitrogen with time. The nitrogen atoms liberated from the decomposition reaction combine to form N_2 molecules at a faster rate than nitrogen escape through the compound layer, and thus N_2-filled pores form in the compound layer.[26] The pores preferentially develop within the ε-Fe_2N_{1-z} phase (mostly at grain boundaries) where the decomposition driving force is higher because it is the oldest part of the nitrided structure and has higher nitrogen concentration. The pores coalesce into channels toward the free surface or blister inside the material.[27]

Although the kinetics of decomposition is slow at low temperatures ($T < 400\ ^\circ C$), at higher temperatures it is inevitable. The decomposition rate nitrides is also faster in austenite compared to ferrite due to the higher solubility limit of nitrogen (10.3 at%) in the former compared with the latter (0.4 at%) and higher temperatures required for austenitization by nitriding. Moreover, the formation of porosity is dependent on nitrogen activity in the nitriding media, a_N, and it is proposed that low nitrogen activities reduce the probability of porous compound layers.[25b]

2.4.2.1.3 Titanium–nitrogen system

Titanium experiences an allotropic phase transformation from HCP crystal structure stable at lower temperatures (α phase) to BCC crystal structure (β phase) at 882 °C (e.g., β-transus temperature). Alloying elements such as Al, O, N, and C increase the β-transus temperature and are α stabilizers, while alloying elements such as V, Mo, Nb, Cr, Fe, and Ni stabilize the β phase through eutectoid formation or decreasing the β-transus temperature. Thus depending on their alloying element content, titanium alloys can be classified as α, $\alpha+\beta$, and β alloys.[28]

Gas nitriding is thoroughly investigated on pure titanium and α-Ti alloys, $\alpha+\beta$ Ti alloys, and β-Ti alloys.[8] The nitriding microstructure evolves according to Ti–N phase diagram (Figure 4). Nitrogen dissolves interstitially in both α- and β-Ti, with high solubility in the former and lower solubility in the latter. Ti–N system also consists of several nitride compounds. TiN_{1-x} (δ phase) has a rock salt crystal structure and is

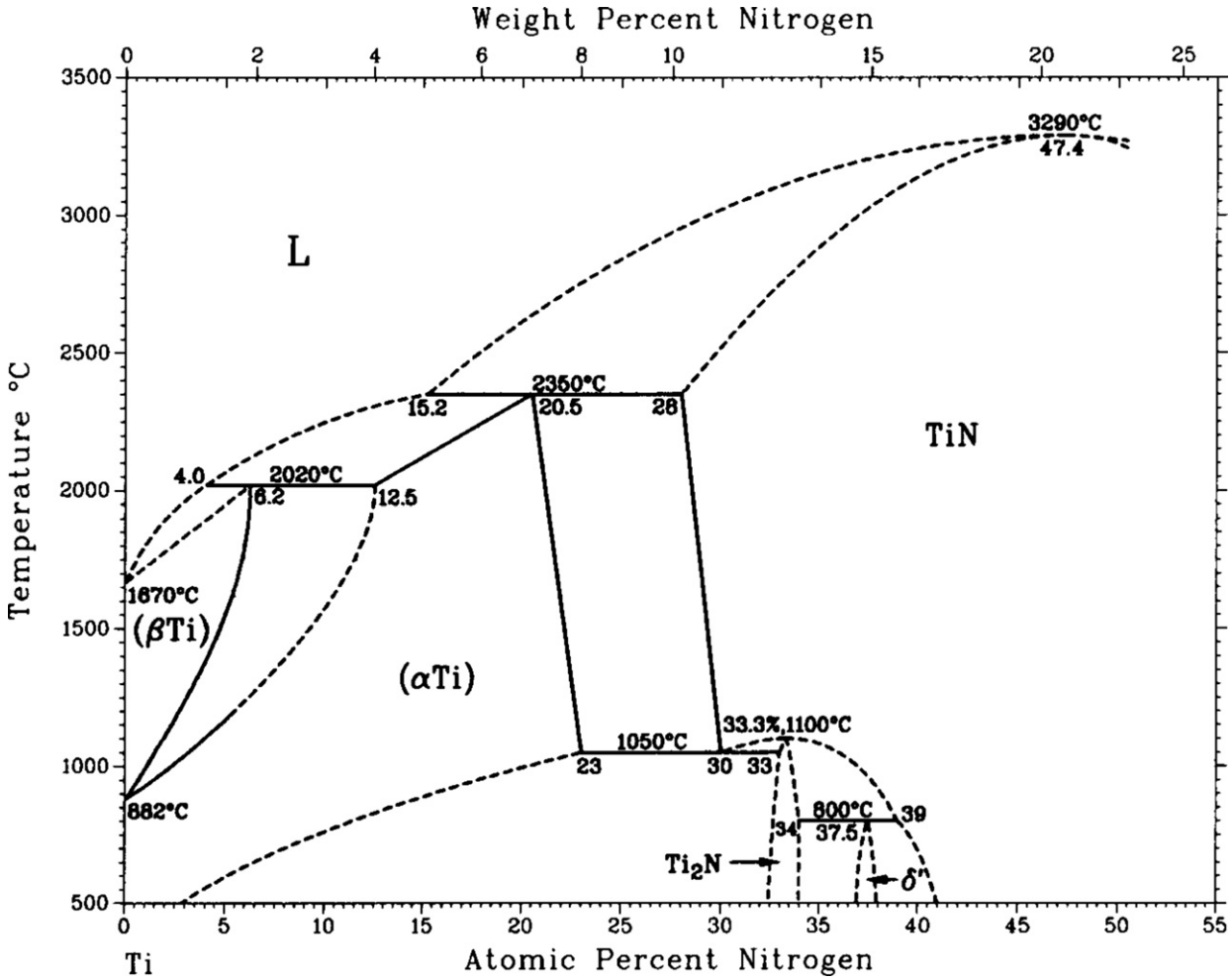


Figure 4 Equilibrium titanium–nitrogen binary phase diagram.[30]

stable over a wide range of compositions. Peritectoid Ti_2N (ε phase) has an anti-rutile tetragonal structure and is stable over a narrow composition with ~33.3 at% N.[6,29] Crystal structure, space group, and chemical composition of the main phases in titanium–nitrogen (Ti–N) system are summarized in Table 2.

2.4.2.1.4 Aluminum–nitrogen system

AlN is known as a refractory compound with high hardness (~1400 HV) and good thermal shock resistance, low coefficient of thermal expansion, high-electrical resistivity, and good corrosion and wear resistance. It has found numerous applications in electronic and semiconductor devices, handling of corrosive and molten metals, etc.[35] Nonetheless, gas nitriding of aluminum alloys is quite challenging. To begin with, aluminum alloys are typically nitrided within the temperature range of 0.8–0.9T_s (T_s is the solidus temperature), which lies above their annealing temperature. This causes severe adverse effects on the microstructure and properties of aluminum substrates. Furthermore, nitrogen does not dissolve in aluminum (Figure 5) and thus the aluminum nitrides formed on the surface do not get any mechanical support from their substrates.[8]

2.4.2.2 Nitriding Kinetics

The thermodynamic studies explained in the previous section predict the formation of nitrided microstructure at the state

Table 2 Crystal structure, space group, and chemical composition for phases in titanium–nitrogen system

Phase	*Composition*	*Nitrogen content (at%)*	*Crystal structure*	*Space group*	*References*
α	Ti (N)	0–22	HCP	$P6_3/mmc$	6
β	Ti (N)	0–6	BCC	$Im\bar{3}m$	6
δ	TiN	30–55	FCC	$Fm\bar{3}m$	6,31
ε	Ti_2N	33.3	Tetragonal	$P4_2/mnm$	6,32
–	$TiN_{0.28}/TiN_{0.3}$	~19–23	HCP	$P6_3/mmc$	33
δ'	$TiN_{0.6}$	38	Tetragonal	$I4_1/amd$	6,34

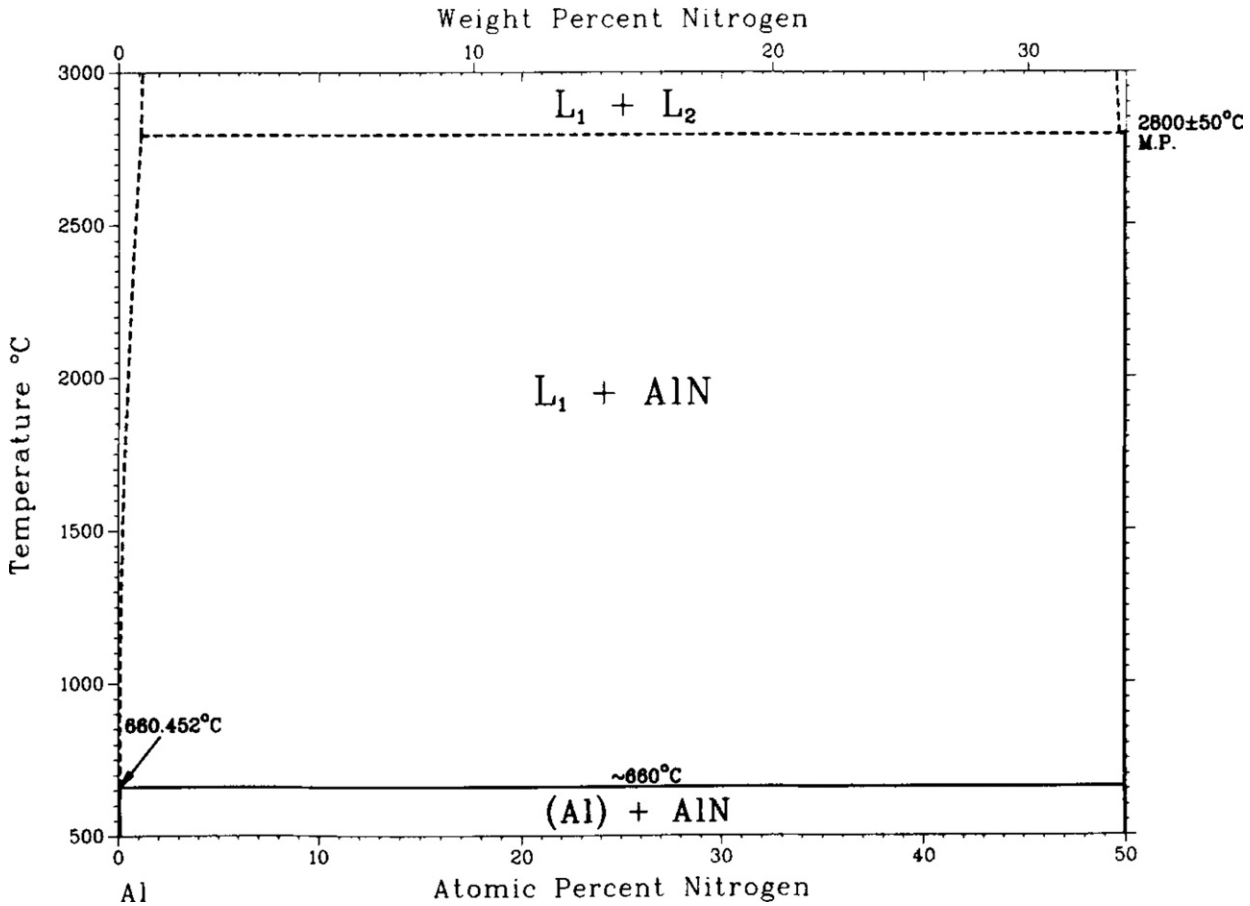


Figure 5 Equilibrium aluminum–nitrogen binary phase diagram.[79]

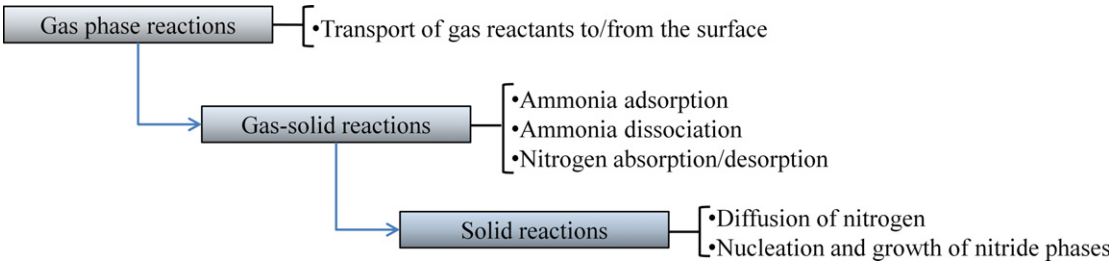


Figure 6 A schematic diagram presenting the main steps involved in the process of gas nitriding including gas-phase reactions (such as nitriding gas transport phenomena), gas–solid reactions (such as adsorption of ammonia on the work surface) and solid-phase reactions (such as nucleation of nitrides on the work surface). The overall gas nitriding rate is controlled by the rate of the slowest step. Mridha, S. Gas Nitriding of En40B Steel with Highest Growth Rate of the Case and Reduced White Layer Formation. *Int. J. Microstruct. Mater. Prop.* **2007**, *2* (1), 54–63.

of equilibrium; however, the actual composition and thickness of the nitrided layers are explained through the nitriding kinetics. The development of nitrided microstructure is the result of several steps including, gas-phase phenomena (e.g., transfer of the nitrogen-containing gas to the surface), gas–solid reactions (e.g., absorption, desorption), chemical reaction (e.g., nitride phase formation), and solid-phase phenomena (e.g., diffusion). The rate of the gas nitriding is controlled by the rate of the slowest step.[36]

Since the majority of literature on the fundamentals of gas nitriding is focused on the nitriding of iron and steels.[24,37] This section covers the concepts of nitriding kinetics for ferrous alloys, non-ferrous alloys will be discussed where applicable. **Figure 6** summarizes some of the main steps during gas nitriding that should be considered in determining the nitriding kinetics, as described below;

i. A minimum gas flow rate is essential in order to transport N-containing medium to the surface (and nitriding products away from the surface) and maintain a controlled, homogeneous nitriding atmosphere.[26]
ii. Ammonia dissociation is a catalytic reaction activated by the work surface and the interior furnace walls. Grabke *et al.*[38] proposed that this step is the result of several subreactions including physical adsorption of ammonia, dissociation of adsorbed ammonia into adsorbed NH_2, NH radicals and N atoms, and the formation of N_2 and H_2 molecules from adsorbed N and H atoms. Many factors contribute to the kinetics of this step such as surface roughness, chemical and phase composition of the surface, crystallographic orientation, etc. According to Slycke and Ericsson,[39] the overall rate is controlled by the rate of formation of nitrogen molecules from adsorbed N atoms.
iii. Inward diffusion of nitrogen atoms and the formation of surface nitrides. As the rate of nitrogen adsorption exceeds that of its inward diffusion, the nitrogen concentration at the surface increases to reach equilibrium with the nitriding atmosphere. At this point, surface nitrides begin to form on the surface possibly through a nucleation and growth mechanism.[40]

Lightfoot[20] introduced a critical flux of nitrogen (controlled by the alloy composition and nitriding potential) for the formation of nitride phases on the surface. He explained that the equilibrium state at the gas/ε-Fe_2N_{1-z}, ε-Fe_2N_{1-z}/Fe_4N, and Fe_4N/ferrite interfaces dictates a nitrogen concentration gradient within the ε-Fe_2N_{1-z} and Fe_4N layers. He stated that the formation of Fe_4N had an incubation time and under conditions of high-nitriding potential, ε-Fe_2N_{1-z} could form on the surface and grow rapidly without leaving time for Fe_4N to nucleate.

Mittemeijer *et al.*[27a,41] proposed that γ'-Fe_4N_{1-x} nitrides nucleate on the gas–solid interface at locations where the concentration of dissolved nitrogen exceeds a critical value, i.e., active centers, after a certain incubation time. The kinetics of nitride layer formation is largely dependent on the number of active centers. Several surface activation pre-treatments have been developed to increase the number of active centers via increasing the defectiveness and roughness, and removal of inherent oxides from the work surface such as cathode sputtering. Both nitrogen and argon have been used as the sputtering gas and significant improvements in the nitriding rate were reported.[42]

Having nucleated on the surface, γ' nitrides consume the dissolved nitrogen in the surrounding matrix to grow (since nitrogen dissolves faster in ferrite than γ'-Fe_4N_{1-x} nitride). At this time ε-Fe_2N_{1-z} may also nucleate on top of γ'-Fe_4N_{1-x}, if the nitriding potential is favorable. A the growth proceeds, a continuous layer of iron nitrides (compound layer) develops on the surface and further growth is then controlled by the diffusion rate of nitrogen through this layer. As discussed in Section 2.4.2.1, the iron nitrides are not at thermodynamic equilibrium as they are no longer in direct contact with the nitriding medium. They tend to decompose into iron and nitrogen, resulting in the evolution of porosity preferentially within/at the grain boundaries of ε-Fe_2N_{1-z} phase. A schematic illustration of this mechanism is presented in **Figure 7**.

Underneath the compound layer, nitrogen dissolves interstitially in the diffusion zone with limited solubility in ferrite and high solubility in austenite (**Table 1**). The inward diffusion rate of nitrogen determines the nitrogen gradient in the diffusion zone. As the nitrogen content at the surface of the ε layer is dependent on the nitriding potential of the nitriding atmosphere, assuming that the composition of surface nitrides are known and change linearly with depth at each layer, the diffusivity of nitrogen in ε phase and γ' phase can be calculated by analytical or numerical methods and verified with

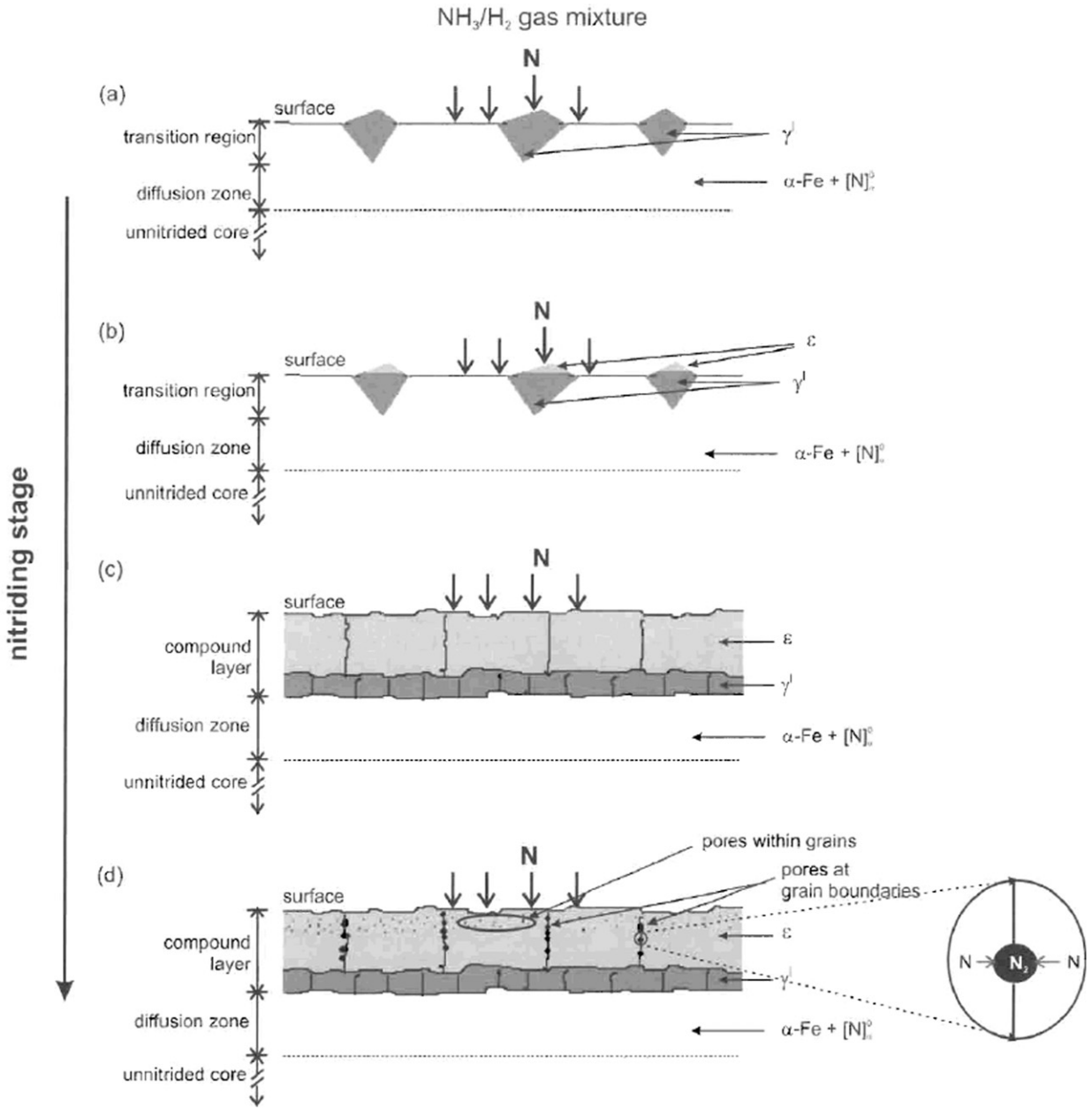


Figure 7 Schematic illustration of the nucleation and growth mechanism of the compound layer during nitriding of (ferritic) iron in NH_3/H_2 mixture. (a) Nucleation of γ' nitrides on the surface and their growth via consuming dissolved nitrogen in the surrounding matrix, (b) nucleation of ε on top of γ' phase (if the nitriding potential is favorable), (c) growth of the nitrided phases and formation of a continuous compound layer covering the entire surface; further growth requires diffusion of nitrogen atoms through this layer, (d) evolution of porosity within the ε phase, more likely at grain boundaries, due to the nitride phase decomposition and generation of N_2 molecules.[41]

experimental results (**Figure 8**).[24] Several researchers have developed mathematical models for nitriding to predict nitride layer growth rate and nitrogen concentration profile. Torchane *et al.*[43] investigated the mechanisms of phase formation and mass transfer at the gas–solid interface and validated their calculations with thermogravimetric experiments and metallurgical observations. Du *et al.*[44] used analytical models and numerical calculations to solve diffusion coefficients for modeling of compound layer growth behavior.

When substitutional alloying elements with high chemical affinity to nitrogen, for example, Ti, V, Al, Mo, Cr, W, are present in the steel composition, coherent submicroscopic nitride precipitates form in the diffusion zone during nitriding. As such, the nitriding kinetics will be affected by the alloying elements content, kinetics and thermodynamics of alloy element nitride precipitation and prior heat treatment of the steel substrate. Lightfoot and Jack[20] explained that the nitriding microstructure depends on the heat of formation (ΔH_f) and

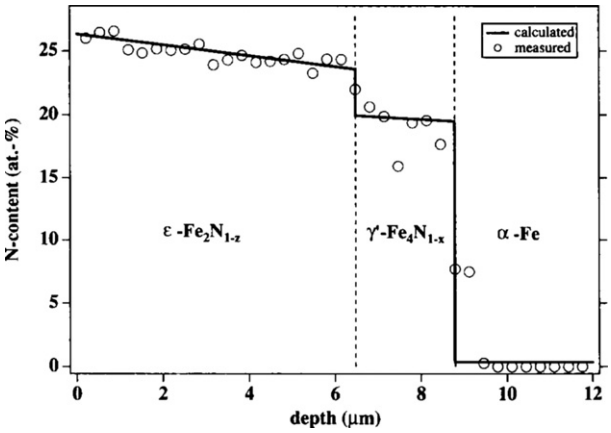


Figure 8 Nitrogen content vs. depth profile of the compound layer ($\varepsilon+\gamma'$) formed by nitriding at 570 °C for 2 h and NH_3–H_2 (56:44) gas mixture. The experimental results were in agreement with the assumption of linear nitrogen content-depth profile in each nitride layer.[41]

ease of nucleation of the alloying element nitrides. They stated that alloying elements of weaker nitride-forming tendency or slower nucleation rate such as molybdenum ($\Delta H_f^{Mo_2N} = -81.6\ kJ\ mol^{-1}$, where $\Delta H_f^{Mo_2N}$ is the heat of formation for molybdenum nitride (Mo_2N)) require large supersaturations for nitride precipitation. The nitriding response is thus controlled by the precipitation rate of nitrides and inward diffusion of nitrogen interstitials. The delayed nitride formation and competition between iron nitrides and alloying element nitrides provides sufficient time for nitrogen atoms to diffuse deeply in the structure (**Figures 9(a)** and **9(b)**). This behavior was also observed in Fe–Al, Fe-1.2 wt% Cr and Fe-5 wt% Mo.[20]

Conversely, fast precipitation rates were predicted for strong nitride-forming elements with easy nucleation such as titanium ($\Delta H_f^{TiN} = -335\ kJ\ mol^{-1}$, where ΔH_f^{TiN} is the heat of formation for titanium nitride (TiN)). A uniform surface layer with high hardness forms on the surface of titanium-containing steels during nitriding over a wide range of temperatures and nitriding potentials (**Figures 9(b)** and **9(c)**). The thickness of the nitrided layer, ξ, can be approximated by eqn [6];

$$\xi^2 = \frac{2}{r}\frac{[N]}{[Ti]}Dt \qquad (6)$$

where r is the ratio of nitrogen to titanium, [N] is the concentration of nitrogen on the surface, [Ti] is the original concentration of titanium in the steel composition, D is the diffusion coefficient of nitrogen, and t is the nitriding duration. The rate-controlling step of the nitriding process in this case is the diffusion of nitrogen from the surface to the non-nitrided interface. Fe–5Cr showed similar nitriding behavior at 500 °C and 18% NH_3 atmosphere.

In case of chromium-containing ($\Delta H_f^{CrN} = -125.5\ kJ\ mol^{-1}$, where ΔH_f^{CrN} is the heat of formation for chromium nitride (CrN)) steels, a hard surface zone forms at the beginning of nitriding with a diffuse interface between the case and the

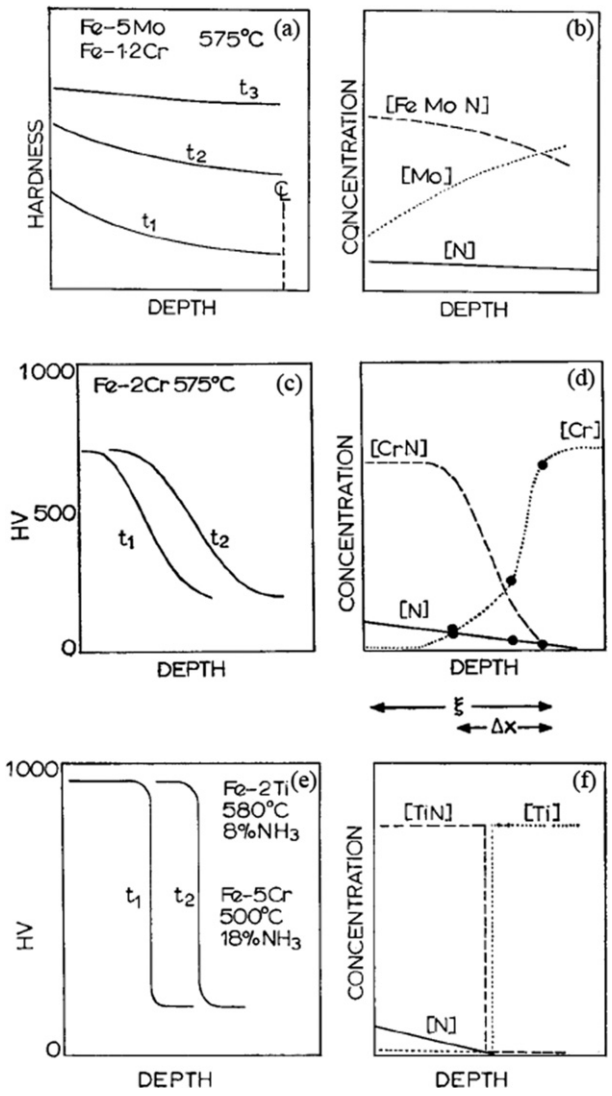


Figure 9 Schematic illustration of hardness and chemical composition profiles against distance from the nitrided surface showing the nitriding behavior of steels containing (a, b) alloying elements with weak interaction with nitrogen or difficult nucleation, (c, d) alloying elements that have strong interaction with nitrogen and easy nitride nucleation behavior, and (e, f) alloying elements that form a diffusion interface between the case and the substrate (core).[20]

substrate (core). The interface morphology depends on the nitriding potential and temperature; a sharper interface is expected for high nitriding potentials and high-chromium contents in the steel substrate (**Figures 9(c)** and **9(d)**). The depth of the nitrided zone, ξ, can be predicted by eqn [7];

$$\xi^2 \propto \frac{[N]}{[Cr]}D_N^{\alpha-Fe}t \qquad [7]$$

where [N] is the concentration of nitrogen on the surface, [Cr] is the initial concentration of chromium in the steel substrate, $D_N^{\alpha-Fe}$ is the diffusion coefficient of nitrogen in ferrite, and t is the duration of nitriding.

In addition to the concentration of substitutional chromium, the nitriding response of chromium-containing steels depends on the carbides in the substrate microstructure. Since the nitride-forming tendency of chromium is higher than that of carbon, fine CrN particles precipitate in the nitrided zone at the expense of chromium-containing cementite $(Fe, Cr)_7C_3$ in the steel substrate. Therefore, the kinetics of hardening is controlled by the decomposition rate of $(Fe, Cr)_7C_3$ carbides. High nitriding temperatures, for example, close to the tempering temperature of the substrate, lead to coarsening of $(Fe, Cr)_7C_3$ carbides which will (1) slow down their decomposition rate and (2) drain substitutional Cr atoms in the matrix that could contribute to precipitation hardening. Thus increasing the nitriding temperature does not necessarily promote higher hardness in the nitrided case of chromium-containing steels.[20]

According to Hosmani *et al.*[41,45] due to the strong interaction of alloying elements such as Ti, Cr, V with nitrogen, precipitation of alloying element nitrides at the surface precedes the formation of iron nitrides. Furthermore, the alloying element nitrides may also be incorporated in the compound layer composition. They stated that the compound layer exhibits a nonuniform thickness; at some locations penetrating deeper into the diffusion zone along the substrate grain boundaries. According to their proposed nitriding mechanism (**Figure 10**), with the progression of nitriding the coherent alloying element precipitates at the surface coarsen and grow to form a lamellar microstructure in the surface vicinity. This is accompanied by the reduction of nitrogen solubility in the surrounding ferrite matrix and liberation of the excess nitrogen in the form of grain boundary nitrides or porosity. The porosity can evolve into cracks that open to the free surface and act as preferential nucleation sites for the formation of iron nitrides. As such iron nitrides develop on the surface and along the grain boundaries and grow to cover the entire grain.

The kinetics and mechanisms of nitrogen interaction with titanium and the nitriding behavior of titanium alloys is well established in the literature.[46] Malinov *et al.*[47] stated that the evolution of nitrided microstructure during gas nitriding of titanium alloys is a diffusion-controlled process when the nitriding temperature is lower than the β-transus temperature. Their model (as schematically shown in **Figure 11**) suggests that after absorption of nitrogen from the nitriding atmosphere, nitrogen atoms diffuse interstitially in the titanium structure forming a nitrogen-rich solid solution (diffusion zone). With the progress of nitriding, the nitrogen concentration on the surface exceeds the solubility limit of α phase leading to the formation of ε-Ti_2N, and subsequently δ-TiN nitrides on the surface.

The kinetics of formation and growth of nitrided layers under different nitriding conditions exhibits a typical diffusion-controlled parabolic time dependency. If the diffusion coefficient of nitrogen in the nitrided layers is known, the inward flux of nitrogen and the rate of layer growth in the surface vicinity can be determined from Fick's equations such as eqn [8]. Both analytical and mathematical models have been utilized to solve the equations.[49] Where, $C_N(x,t)$ is the concentration of nitrogen, C_0 and C_s are the initial concentration of nitrogen and on the surface, x is the distance from the surface, D is the diffusion coefficient, and t is the nitriding duration. The diffusion coefficient has an Arrhenius-type dependence with temperature and its typical values for Ti–N and Fe–N system are given in **Table 3**.

$$C_N(x,t) = C_0 + (C_s - C_0) \cdot erf\left(x/\sqrt{4Dt}\right) \qquad [8]$$

2.4.3 Gas Nitriding Process

2.4.3.1 Pre-Treatment Step

Finishing processes such as cutting, buffing, finish grinding, lapping, and burnishing leave contaminants on the surface that retard nitriding kinetics or lead to surface defects and nonuniform nitriding. Moreover, a very thin layer (1–10 nm) of inherent metal oxide scales or water and hydrophobic agents may also exist on the surface that interferes with the nitrogen transfer during the posterior nitriding treatment. Surfaces may be cleaned by vapor degreasing, industrial cleaning agents, or grit blasting with alumina, garnet, SiC, etc. Ferrous surfaces may also undergo an oxidizing pretreatment, typically performed at 300 °C for 30–45 min, to evaporate hydrocarbons and cleaning agents. The oxidation pretreatment as well as other nucleation pre-treatments also promote the nitriding kinetics by activating the surface for enhanced nucleation and growth of the nitride phase, as explained in Section 2.4.2.[55]

More recently pre-treatments such as surface nanocrystallization have proven beneficial in improving the nitriding kinetics in steels and titanium alloys, facilitating nitriding at lower temperatures for shorter durations. The higher nitriding efficiency is due to the increased density of non-equilibrium defects and grain boundaries introduced by the severe plastic deformation. The nanocrystalline surface layer can be introduced by supersonic fine particle bombarding, shot peening, surface mechanical attrition treatment (SMAT). These pretreatments enhance the nitrogen diffusivity, as evidenced by higher depth and hardness of diffusion zone, and increase surface chemical reactivity due to the high excess stored energy. As a result significant improvements in surface hardness and wear resistance have been reported compared with conventionally nitrided surfaces.[56]

In order to minimize the dimensional and microstructural changes during nitriding (hardenable) steels are quenched and tempered prior to the nitriding treatment. The tempering temperature is 20–30 °C higher than the nitriding temperature[57] (at/above 575 °C[20]) to ensure structural stability at nitriding temperatures. With the exception of steels whose case hardness is affected by the core hardness (such as 4100 and 4300 steels). They can be tempered at lower tempering temperatures to achieve their maximum core hardness.[58]

Nitride forming alloying elements such as Al, V, Cr, Ti (in the solid solution form) lead to the formation of thermally-stable and coherent nitride precipitates (AlN, VN, CrN, TiN) in the surface vicinity. A high hardness is thus achieved in the

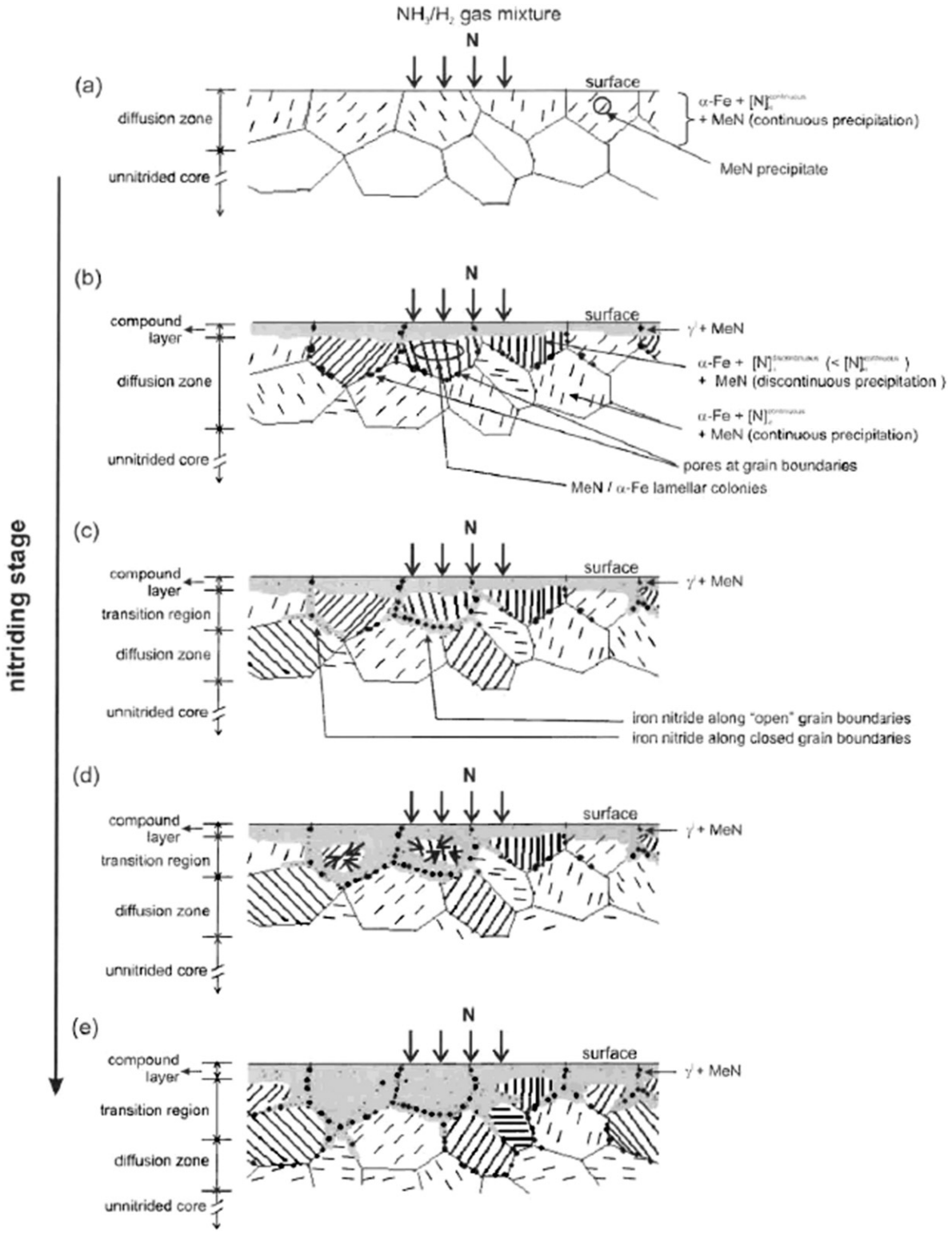


Figure 10 Schematic illustration of the evolution of compound layer on the surface of ferritic alloy steels containing nitride forming alloying elements such as Al, Cr, V in a NH_3–H_2 atmosphere. (a) Diffusion of nitrogen and precipitation of coherent alloying element nitrides in the surface vicinity. (b) Formation of compound layer on the surface and coarsening of the alloying element nitride precipitates; the coarsening of alloying element nitrides reduces solubility of nitrogen in the matrix and segregate as N_2 pores at grain boundaries. (c) Coalescence of pores and crack formation at grain boundaries. (d) Precipitation of iron nitrides along grain boundaries preferably at cracked faces and compound layer growth toward the center of the grains. (e) Full transformation of the ferrite grains to iron nitrides in the surface vicinity, precipitation, and coarsening of alloying element nitrides underneath the compound layer and void formation along the grain boundaries due to the segregation of excess nitrogen.[41]

nitrided layers while exhibiting ductility and high wear resistance. One of the common problems during nitriding of steels with carbide forming elements (Cr, V, Mo) is that carbon atoms diffuse toward the surface and form a carbide-rich region that retards further diffusion of nitrogen. Thus the recommended carbon content for the steel substrate is less than 0.15% (or a decarburization treatment prior to surface alloying).

2.4.3.2 Gas Nitriding Set-Up

Several types of furnaces are used to perform gas nitriding including vertical air-circulating furnaces, horizontal retort furnaces, bell-type movable furnaces, box-type movable furnaces, tube retorts, batch/integral quench furnaces, pusher furnaces, conveyor belt furnaces, and continuous batch-type furnaces. A typical gas nitriding furnace has a means of sealing, inlet/outlet lines for introducing/exhausting gases, heat unit and programmable controllers for temperature, time, gas flows, and a means of circulating atmosphere for uniform temperature distribution.[58,59] Advanced gas analyzers and gas distribution systems enable automatic control of the atmosphere to the desired dissociation rate or nitriding potential.[60]

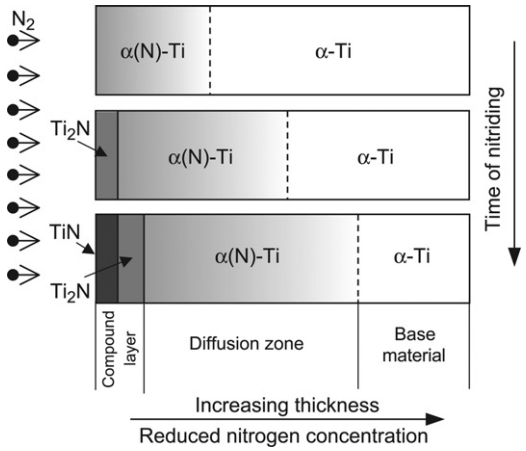


Figure 11 A schematic illustration of the gas nitriding mechanism in titanium resulting in the formation of compound layer ($TiN + Ti_2N$) and diffusion zone.[48]

The parts will be loaded and the air will be purged out using nitrogen or ammonia after sealing the furnace. The furnace will be heated to temperature (Care must be taken to avoid the ignition temperature of flammable gases. Explosion hazards are prevented by using an inert gas flow, or evacuating the chamber before purging.) and a controlled nitriding atmosphere will be sustained for the nitriding duration. In order to ensure the repeatability and reproducibility and achieve the desired metallurgical specifications and microstructures, the process parameters should be accurately selected and controlled. The furnace heating and cooling rates should be optimized for minimum temperature gradients and distortion throughout large and complex parts and maximum production economy.[59a]

2.4.3.3 Post-Treatment Step

Several post-treatment methods have been developed for further improvements in the corrosion and wear resistance of nitrided surfaces such as oxidation post-treatments. A typical oxidation post-treatment is carried out at temperature range of 350–520 °C and results in the formation of a thin (1–3 μm thick) oxide layer consisting of magnetite (Fe_3O_4) and hematite (Fe_2O_3) on top of the compound layer.[61] Investigations by Borgioli *et al.*[62] indicated that when the oxidation post-treatment of the nitrided steels was performed at lower temperatures such (e.g., 350 °C), the oxide layer was mainly composed of magnetite while hematite was detected when the oxidation post-treatments was carried out at higher temperatures (e.g., 500 °C). Their findings indicated that although the

Table 3 The diffusivity of nitrogen is an Arrhenius function of temperature defined by $D = D_0 \cdot \exp(-Q/RT)$

	D_0 ($cm^2\ s^{-1}$)	Q ($J\ mol^{-1}$)	Temperature range (°C)	References
N in α-Fe	0.0042	76120	– 47–911	24
	0.0066	77900	–	50
N in γ-Fe	0.91	168450	831–1394	24
N in ε-Fe_2N_{1-z}	2.1×10^{-4}	93517	–	43
	0.0044	113200	–	43
	0.227	147370	–	43
N in γ′-Fe_4N	3.77×10^{-6}	91400	504–570	24
	1.7×10^{-5}	64000	–	50
N in α-Ti	0.21	223850	450–700	51
	0.8	135080	800–1500	52
	0.012	178000	900–1400	53
	0.012	176900	900–1570	47
	0.96	214700	800–1080	54
N in β-Ti	0.75	147700	800–1080	54
N in δ-TiN	4.4×10^{-5}	152700	800–1080	54
N in ε-Ti_2N	0.0027	149800	800–1080	54

Where D is the diffusion coefficient, D_0 is the diffusion constant, Q is the activation energy for diffusion, and R is the universal gas constant.

corrosion resistance was improved in both cases after oxidation post-treatments, magnetite oxide layers were more protective against corrosion damage. This has been attributed to the partial sealing of the pores in the white layer. Doche *et al.*[63] introduced a final polymer impregnation step after the oxidation post-treatment to seal the porous structure near the surface. They reported a significant reduction in corrosion rates after the polymer impregnation step. In addition to improvements in corrosion resistance, oxidation post-treatment of nitrided steels also offered wear enhancement and reduction of coefficient of friction.[61b]

Oxidation post-treatments of the nitrided titanium surfaces were practiced at 700 °C, resulting in the formation of titanium oxide (TiO_2) with rutile structure and traces of nanocrystalline titanium oxide with anatase structure. The treated surfaces offered enhanced protection against wear-corrosion damage (wear resistance in corrosive media).[64]

2.4.3.4 Common Problems in Nitriding: Causes and Remedies

2.4.3.4.1 Formation of white layer

The formation of white layer is often not desirable during nitriding of ferrous alloys due to its brittle nature and susceptibility to spallation. The white layer is normally removed prior to service at a cost almost equal to that of the nitriding treatment. Several approaches can be taken toward control and elimination of the white layer. One of the conventional methods is grinding/lapping with abrasive papers, which is time-consuming and expensive and may not be suitable for components of complex shapes. Chemical dissolution by soaking in a hot cyanide solution is another alternative, although posing environmental hazards. Perhaps, one of the best approaches is to eliminate/minimize the formation of white layer through continuous and accurate control of the nitriding conditions (ammonia dissociation rate, temperature, etc.). Alternatively, several researchers attempted to exploit the thermodynamic instability of γ' and ε phases to design a post-treatment step for the reduction of white layer in a controlled N_2–H_2 mixture. However, this practice was accompanied by the loss of surface hardness.[65]

2.4.3.4.2 Insufficient depth or hardness of the diffusion zone

This problem may be attributed to the substrate properties and pre-treatment conditions. It is important to ensure that the composition and microstructure of the substrates are suitable for nitriding. For instance, presence of substitutional nitride-forming elements enhances the depth and hardness of nitrided case in ferrous alloys. In some steels, the case hardness is directly proportional to the core hardness and thus increasing the core hardness with prior heat treatments increases the case hardness. In addition, as mentioned in Section 2.4.3.1, surface oxides, contamination and machining residues retard the nitriding kinetics and the surfaces of workpieces are to be properly cleaned and passivated prior to nitriding. Alternatively, improper selection of process parameters is a common cause of low hardness and shallow diffusion zone. The selection of treatment parameters should be carried out accurately to avoid excessively high or low nitriding temperatures, insufficient nitriding duration and nonuniform temperature distribution inside the furnace.[58]

2.4.3.4.3 Oxidation during nitriding

This is usually a result of contamination either on the workpiece or inside the furnace. It can be avoided by ensuring appropriate pre-cleaning of surfaces and absence of leakage on the furnace seals. Any leakage inside the furnace (around pipes, thermocouple, base, etc.) results in the introduction of air, moisture, or oil into the furnace. In ferrous alloys oxidation during nitriding manifests as discoloration of surfaces.

2.4.3.4.4 Dimensional changes

Several factors are responsible for unacceptable dimensional changes in the nitrided parts including complex/unsymmetrical profiles and residual stresses from prior machining/heat treatment history. In addition, finishing treatments after nitriding upset the balance between compressive residual stresses on the surface and tensile stresses in the core and lead to dimensional changes. This can be avoided by preparing the parts close to their desired final dimensions and stress-relieving prior to nitriding.[66] Dimensional changes are generally low during nitriding of ferrous alloys – especially compared to carburizing treatments – due to their low nitriding temperatures.

The arrangement of parts inside the furnace is also an important factor that may contribute to volumetric changes and distortion. The nitriding set-up should be such that the parts see proper support and uniform heating inside the furnace.

2.4.3.4.5 Exfoliation and spallation of the compound layer

Several factors contribute to the formation of compound layers that are prone to spalling and premature failures. Improper nitriding conditions that promote thick and brittle compound layers, design and shape of the workpieces and inappropriate pre-treatment and cleaning prior to nitriding are among the main influential factors.[58] Sharp corners should be avoided in parts as the higher concentration of nitrogen at the corners leads to brittle structures that are susceptible to chipping.

In ferrous alloys, surface decarburization increases the chances of cracking and chipping by formation of nonuniform nitrided cases and brittle nitride phases, often in the form of nitride needles, inside ferritic grains near the surface.[67] This results in an 'orange peel' appearance of surfaces and can be prevented by complete removal of the decarburized layer prior to nitriding.

2.4.4 Gas Nitriding of Structural Alloys

2.4.4.1 Ferrous Alloys

2.4.4.1.1 Microstructure and phase composition

Gas nitriding of ferrous alloys may be carried out as a single-stage or a double-stage process. A single-stage process is typically performed within the temperature range of 495–525 °C and

ammonia dissociation rate of 15–35%. The high-nitriding potential promotes the formation of surface nitrides and the nitrided microstructure consists of a compound layer at the surface of a nitrogen diffusion zone. The compound layer is also referred to as the 'white layer' because it remains unetched in Nital (3% nitric acid + balance ethanol) solution.[68] In the double-stage process, also known as the Floe process,[13] the first nitriding step is followed by a second step at a higher temperature range (550–565 °C) and dissociation rate (75–80%). The main purpose of the Floe process is to reduce the thickness of the white layer, increase the depth of nitrogen diffusion and promote precipitation of fine nitrides in the diffusion zone. The higher depth and hardness of the diffusion zone promote higher fatigue strength in the nitrided alloys.[59a]

The white layer thickness can range from tens to hundreds of micrometers and mainly consists of $\gamma' - Fe_4N_{1-x}$ and $\varepsilon - Fe_2N_{1-z}$ but may also contain Fe_3C-cementite[69] and $\varepsilon - Fe_{2-3}(C,N)$, depending on the nitriding conditions and substrate composition. In irons the white layer is composed of a $\varepsilon - Fe_2N_{1-z}$ layer on top of a $\gamma' - Fe_4N$ layer (**Figure 12**). White layer offers high-corrosion resistance and enhanced lubricability. Nonetheless, due to its brittle nature and accumulation of residual stresses, the white layer is prone to spalling and premature failures and promotes severe abrasive wear in service. While the benefits of a single-phase white layer, for example, hard ε (H = 7.1 GPa) or γ' (H = 6.5 GPa) layer[70] are debatable, the formation of white layer is considered undesirable for industrial applications. In many instances the white layer is eliminated altogether by grinding or chemical treatments prior to service.[20] Moreover, as explained in Section 2.4.2.2, both γ' and ε nitrides are thermodynamically unstable under nitriding conditions and their decomposition generates porosity in the compound layer. The pores preferentially form at the grain boundaries of ε phase

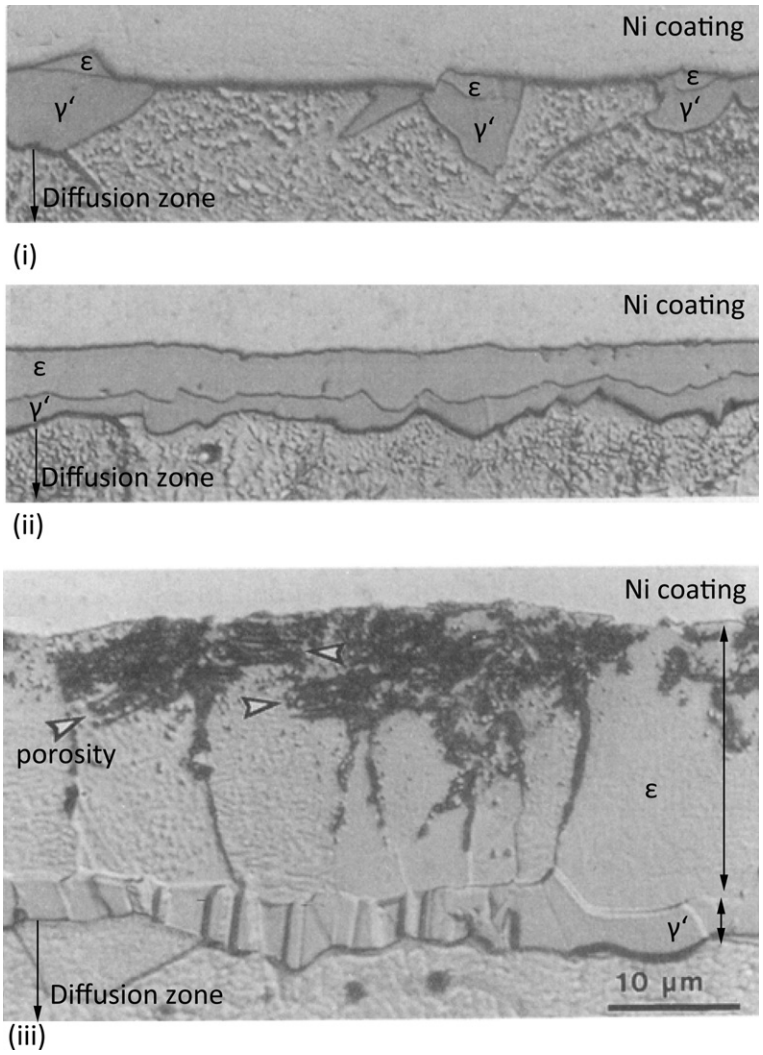


Figure 12 Typical cross-sectional micrographs showing the evolution of microstructure in iron gas nitrided at 570 °C for (i) 15 min; nucleation of ε and γ' nitrides on the surface, (ii) 35 min; growth of the compound layer ($\varepsilon + \gamma'$) into a uniform layer, and (iii) 8 h; the formation of porosity (mostly along ε grain boundaries). (Electroplated Ni coating was used in order to protect the surface against damage during metallography sample preparation.)[24]

and their coalescence channels the grain boundaries to the free surface (Figure 12). Due to the porous structure of the ε phase, the measured hardness values of the white layer are typically less than that of the diffusion zone underneath it.

Typical microstructure of the compound layer formed on the surface of (ferritic) iron is shown in Figures 12 and 13, the iron nitride nuclei grow laterally until the compound layer covers the entire surface with uniform thickness. Figures 14 and 15 show typical nitrided microstructures of steel substrates containing nitride forming alloying elements such as Al, V, Cr. Due to the strong affinity of these elements to nitrogen, precipitation of alloying element nitrides precedes the formation of iron nitrides. The coarsening of the nitrides liberates some of the dissolved nitrogen in the form of porosity or grain boundary nitrides. The voids combine together and channel toward the top surface. The compound layer has a nonuniform thickness; it evolves on the surface and along substrate grain boundaries and then grows toward the center of grains.

Diffusion zone (also known as the 'nitrided zone' or the 'Case') is a region of nitrogen solid solution in Fe structure with a concentration gradient decreasing toward the bulk that may contain iron nitride precipitates (Fe_4N or $Fe_{16}N_2$ in irons and low-alloy steels) or alloying element nitride precipitates (in steels containing Al, Cr, Mo, V, etc.).[72] The hardness and depth of diffusion zone indicate the content of nitride precipitates as well as nitrogen solid solution and depend on the nitriding parameters (temperature, time, etc.) and the material composition.[73] The alloying element nitrides are submicroscopic precipitates, finely dispersed, with coherent boundaries with the matrix. They hinder plastic deformation and slip mechanisms and induce residual compressive elastic strains that strengthen the diffusion zone and reduce the crack propagation rate.[74] In addition to alloying element nitride precipitates in the diffusion zone, several investigations found the presence of cementite precipitates along prior austenite grain boundaries parallel to the nitriding direction. Mridha and Jack[69] clarified that due to the stronger affinity of N to Cr

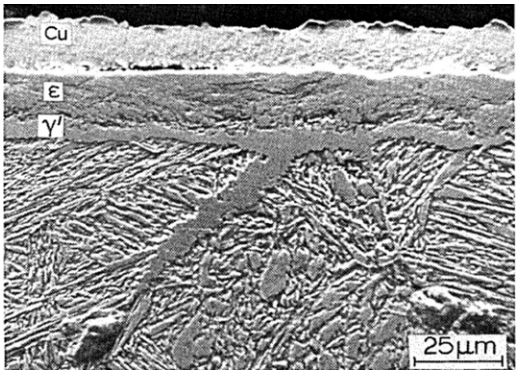


Figure 14 Typical nitrided microstructure of Fe–5Cr–0.2C after nitriding at 500 °C for 48 h in NH_3 atmosphere.[69]

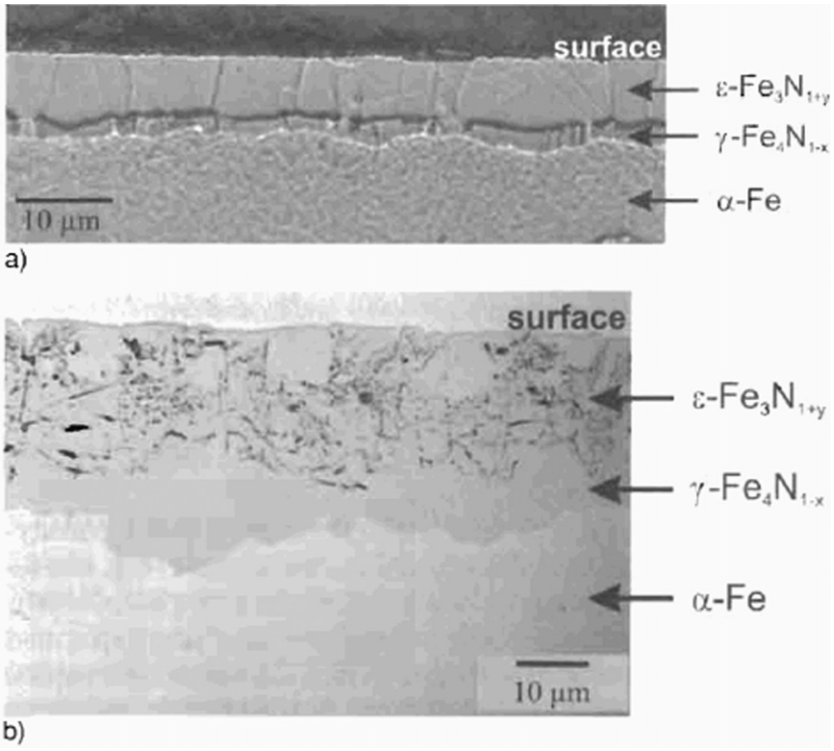


Figure 13 Optical micrographs showing the evolution of compound layer on the surface of nitrided iron. (a) After nitriding at 550 °C for 5 h, a continuous ε layer formed on top of a layer of γ'. (b) After nitriding at 560 °C for 20 h, pores were formed within the ε layer. (Nitriding potential: 2.37 $atm^{-0.5}$, etched in 1 vol.% Nital solution containing 0.1 vol.% HCl.)[41]

compared with C to Cr, chromium nitrides form in the diffusion zone at the expense of dissolution of substrate carbides or their *in-situ* replacement with CrN. The carbon atoms released from this dissolution either diffuse inwards (forming a carbide-rich zone below the diffusion zone) or precipitate along prior austenite grain boundaries in orientations with minimal compressive stress (**Figure 16**).

As such the inward migration of carbon atoms ahead of the nitriding front forms a carbon-rich region (the carbon-rich layer has limited hardening and appears black in Oberhoffer's etching solution) underlying the diffusion zone and may result in decarburization on the surface (in the absence of compound layer). From a thermodynamic point of view, this migration has a chemical (reduction of chemical potential) and a mechanical (strain balance in the tensile stress region) driving force. An uphill diffusion of carbon atoms toward the core in the presence of nitrogen was also reported by other researchers.[75]

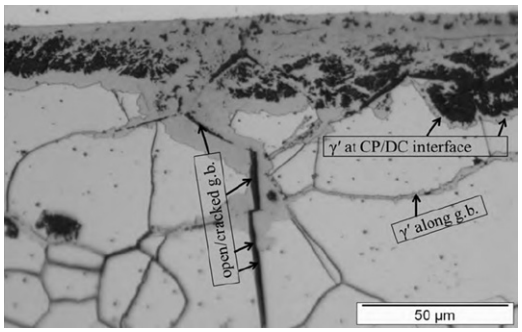


Figure 15 Optical cross-sectional micrograph of nitrided Fe–4V specimen (atomic percent) showing the formation of γ' at the surface and along the grain boundaries (Nitriding potential: 0.8 $atm^{-0.5}$, etched in 2 vol.% Nital, at 580 °C for 4 h).[71]

The limit of the nitrided zone as revealed by the etching does not correspond to any particular hardness since that depends on the nitride forming alloy content, the nitriding temperature and time and the prior tempering treatment of steel. It does mark the limit of alloy nitride formation and the transition from case containing residual compressive stresses to a core containing balancing tensile stresses.

Gas nitriding of stainless steels is relatively challenging as the surface passivity due to high-chromium content affects the nitriding kinetics and microstructure.[76] Stainless steels are nitrided at low temperatures (typically below 440 °C) to avoid precipitation of chromium nitrides and reduction of corrosion resistance. This process does not form a compound layer but promotes the formation of metastable 'expanded austenite' or 'S' phase. The expanded austenite phase is a 20–40 μm deep nitrogen-rich phase with a high hardness (~1800 HV) that does not have any adverse effects on corrosion.[42a,77] Conversely, an 'expanded martensite' region develops during low temperature nitriding of martensitic and ferritic steels. This layer may be in the form of a uniform nitrogen-rich layer or a duplex layer, with a nitrogen-rich outer layer and a carbon-rich inner layer.

The microstructure of nitrided surfaces can be controlled by the nitriding treatment operating parameters (time, temperature, atmosphere composition, and pressure, etc.) and the composition and microstructure of steel substrates (microstructural stability with temperature, ductility, carbon content, alloy element concentration, etc.) as discussed briefly below.

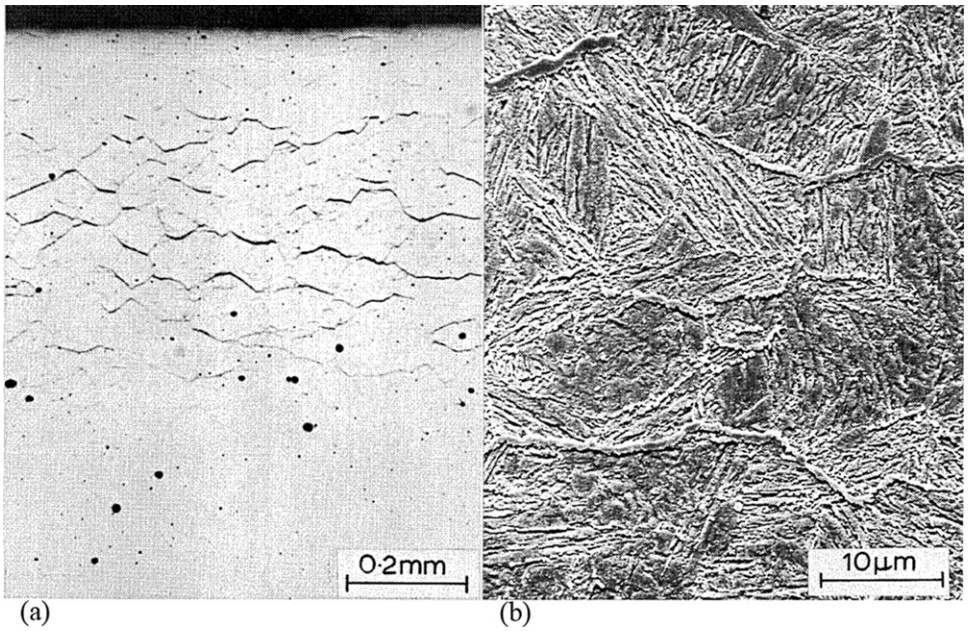


Figure 16 (a) Optical and (b) scanning electron microscopy images of the near surface microstructure (etched in boiled alkaline sodium picrate and 2% natal, respectively) of 3% Cr steel nitrided at 520° in a 30% NH_3 atmosphere for 48 h showing the precipitation of grain boundary cementite in the diffusion zone.[69]

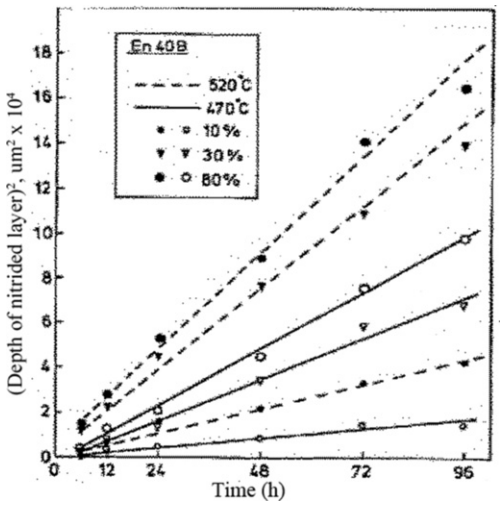


Figure 17 The parabolic relationship between depth of the nitrided layer and time.[79]

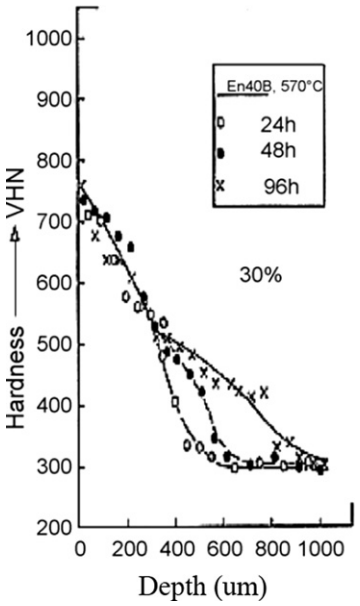


Figure 18 Hardness vs. depth profiles illustrating the evolution of hardness as a function of time in En40B steel (high-chromium nitriding steel) nitrided in 30% NH_3 atmosphere at 570 °C for 24, 48, 96 h.[78]

2.4.4.1.2 Nitriding time and temperature

It is established that the depth of hardening increases parabolically with nitriding time.[4] The nitriding depth also increases with temperature (**Figure 17**). However, in high-chromium carbon steels increasing the temperature may lead to a reduction in the hardness and case depth (especially at higher temperatures). This is due to the coarsening of chromium-rich carbide particles ahead of the nitriding front, leaving less chromium for precipitation of fine chromium nitrides. As such, the depth and hardness reach their maximum at the initial stage of nitriding and further increase in the nitriding duration results in the coarsening of carbide/nitride particles and reduction of hardness (**Figure 18**).[78]

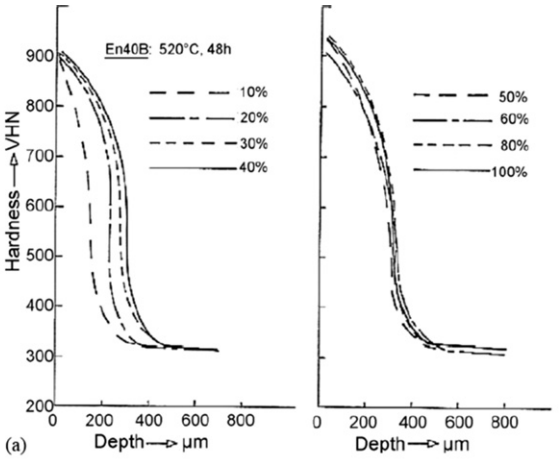
2.4.4.1.3 Nitriding atmosphere

Increasing the pressure of nitriding atmosphere at a constant nitriding potential increases the nitrogen flux, facilitates the evolution of the compound layer and diffusion zone. Conversely, low-pressure nitriding offers a more homogeneous nitriding due to better distribution of nitriding gas.[80] Nitriding under a dilute medium is also similar to low-pressure nitriding, it minimizes the thickness of the compound layer and increases nitrogen diffusivity. Nitriding media normally consist of ammonia and hydrogen. Perez[81] utilized nitrous oxide and a carbon containing gas in addition to ammonia and nitrogen, in the low-pressure nitriding media for ferrous alloys. This method is known for being environmentally friendly and providing better nitriding uniformity and penetration depth. Addition of ammonium chloride to the nitriding mixture is associated with surface activation during gas nitriding of stainless steels.[82]

Mridha and Khan[78] reported that the surface hardness of the 3% Cr steel increased with the nitriding potential but the depth of nitriding was independent of the nitriding potential. Mridha[4,79] clarified that the case depth increases with the nitriding potential before the formation of white layer on the surface and then remains constant for higher nitriding potentials. At low temperatures (e.g., 470 °C) , the growth rate remained constant after the formation of a dense white layer mainly composed of γ' due to its lower diffusivity compared to α-Fe. However, at high temperatures (e.g., 570 °C) the growth of diffusion continues even after the formation of white layer due to the presence of porosity in this zone making nitrogen accessible to the substrate interface (**Figure 19**).

2.4.4.1.4 Steel composition and heat treatment history

Unalloyed carbon steels are not suitable for nitriding because of the limited hardness improvement in the diffusion zone (120–250 HV). Increasing the carbon content increases the depth of diffusion zone and results in smoother hardness gradient within the diffusion zone. Carbon increases nitrogen activity and promotes formation of iron carbonitrides at lower nitriding potentials. Transition metals (aluminum, chromium, vanadium, tungsten, and molybdenum, etc.) as alloy elements increase the nitrogen solubility of the ferrite. These substitutional alloy elements form stable submicroscopic coherent nitride particles at the nitriding temperatures, which effectively strengthen the diffusion zone. During the process of nitriding, Al alloy element diffuses toward the surface and dissolves in the γ' phase and increases the fraction of covalent bonds in the Fe lattice, resulting in higher hardness and low ductility.[83] Alloy elements such as chromium, vanadium, and molybdenum provide deeper cases with higher ductility but comparatively lower hardness.[68] The nitride precipitates tend to coarsen during high temperature nitriding treatments, resulting in a low concentration of fine nitride particles and reduction of hardness.[78] Chromium also increases the surface hardness and



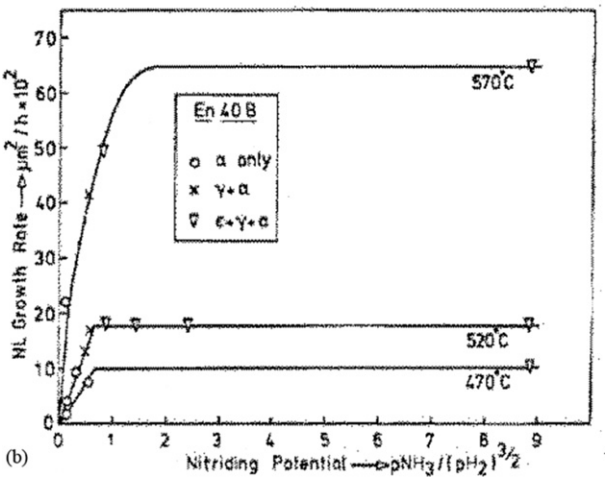


Figure 19 (a) Hardness vs. depth profiles illustrating the evolution of hardness as a function of nitriding potential (En40B steel nitrided at 520 °C for 48 h).[78] (b) The growth rate of nitrided layer against nitriding potential for EN40B commercial steel nitrided at 470, 520, and 570 °C.[79]

has a synergistic effect on Al-containing alloys by enhancing the nucleation of aluminum nitride in the ferrite matrix and the formation of (Cr, Al)N nitrides. Niobium and zirconium restrict the formation of nitride zone and grain refinement, reduce brittleness of the case and increase the hardness of the case.[83] Other alloying elements, such as nickel, copper, silicon, and manganese, do not have any significant influence on the nitriding.[84] While theoretically any type of ferrous alloys can be nitrided, certain steels are particularly suitable for nitriding such as aluminum-containing Nitralloy steels for high-surface hardness, Cr–Mo or Cr–Mo–V steels of 2.5–3.5% Cr with good hardenability, and low-alloy steels.[20]

Mridha and Khan[78] indicated that austenitizing temperature does not affect the surface hardness nor the case depth of 3% Cr steel. Tempering temperature, however, has a strong influence on the evolution of hardness in the surface vicinity. Increasing the tempering temperature results in the coarsening of chromium-rich carbide precipitates. This in turn retards the formation of chromium nitride precipitates due to the slow

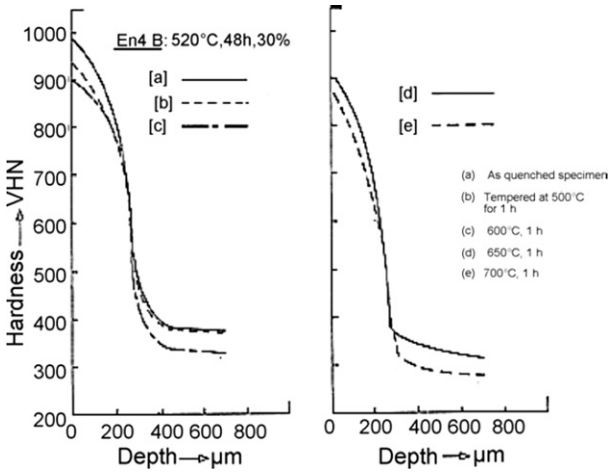


Figure 20 Hardness vs. depth profiles illustrating the evolution of hardness as a function of tempering history (En40B steel nitrided at 520 °C for 48 h).[78]

kinetics of dissolution of large carbide particles. Thus the maximum hardness and the depth of hardenability are inversely related to the tempering temperature (Figure 20).

2.4.4.2 Non-ferrous Alloys

2.4.4.2.1 Microstructure and phase composition

Gas nitriding of aluminum alloys leads to the formation of a hard AlN layer on the surface (~1500 HV). The AlN layer is susceptible to cracking and spallation due to the absence of diffusion zone to mechanically this layer since nitrogen is insoluble in aluminum.[5a] Furthermore, due to the high affinity of aluminum for oxygen and aluminum oxide films that naturally occur on aluminum surfaces hinder the reaction between nitrogen and aluminum substrate.[85] Finally, the evolution of aluminum nitride layer on the surface of aluminum alloys is restricted by the high-thermal expansion difference between AlN and aluminum substrate, which promote undesirable residual stresses in the layer. Extensive research in the field exhibited that nitriding of aluminum alloys is enhanced by surface modification techniques such as plasma-assisted nitriding technologies[86] and ion implantation.[87]

Nitriding of titanium alloys results in the formation of a compound layer composed of δ-TiN_{1-x} and ε-Ti_2N on the surface. Titanium nitrides are generally known as good high temperature materials with thermal shock resistance, high hardness, high abrasion, and wear resistance and good corrosion resistance.[35a] The compound layer may also contain $TiN_{0.3}$ titanium nitride and V_2N vanadium nitride in nitrided $\alpha+\beta$ and β type titanium alloys.[88] Due to the high affinity of titanium for oxygen, a thin layer of TiO_2 titanium oxide has also been reported on the outermost surface of titanium alloys during gas nitriding experiments.[88b,89]

A layer of nitrogen-enriched α titanium (α-Case) forms underneath the compound layer since nitrogen is an α stabilizing element (Figure 21). The α-Case has a brittle nature and usually forms at high nitriding temperatures (at or higher than

800 °C).[90] The α-Case morphology varies from a single-phase layer with preferentially oriented α grains to coarse, columnar α grains growing toward the titanium alloy core.[91] Distinguishing the α-Case is more difficult in α-titanium alloys; however, hydrogen pick up and hydride precipitation in the Ti substrate during nitriding can create contrast against the α-Case.[1] The formation α-Case is known to be detrimental to the mechanical properties of nitrided titanium alloys and is associated with a reduction of fatigue strength, ductility, and fracture toughness. Furthermore, in the presence of aluminum as an alloying element in titanium substrates, the aluminum atoms segregate below the compound layer and form an aluminum-rich region.[85] This has been attribute to the low solubility of aluminum in titanium nitride and may lead to the formation of Ti_3Al phase in this region (**Figure 22**).[92]

Typical gas nitriding temperature range for titanium alloys is $0.55–0.65T_s$ (T_s is the solidus temperature of the alloy), which is clearly higher than the temperature range for ferrous alloys. Unfortunately, the nitriding temperature of titanium alloys falls within the range of their solution treatment (β-transus temperature) and thus induces adverse effects on the microstructure and properties of the substrate.[85]

Unlike steels, nitriding of titanium alloys does not promote precipitation strengthening mechanisms and strengthening of diffusion zone occurs by the interstitial solid solution hardening of titanium with nitrogen.[93] Microstructural evolution of titanium alloys during gas nitriding is dependent on the

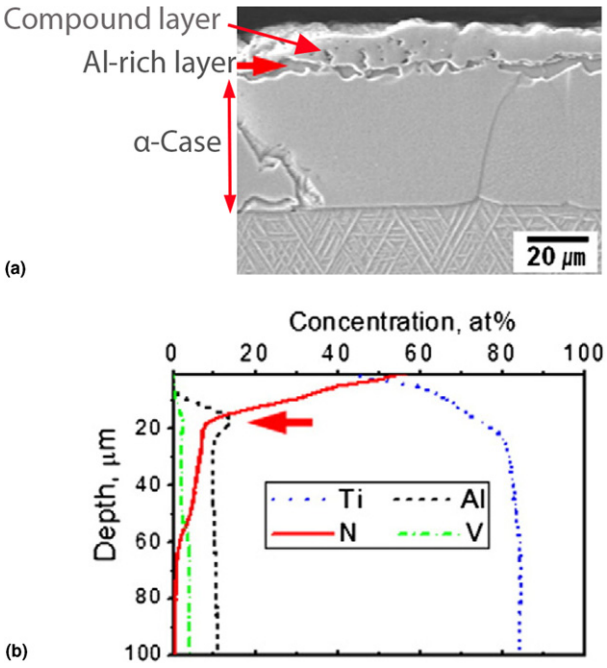


Figure 22 (a) A typical scanning electron microscopy image of the microstructure of Ti–6Al–4V alloy nitrided at 1150 °C for 10 h and (b) corresponding glow discharge spectroscopy (GDS) showing the presence of an aluminum-rich layer underneath the compound layer.[92]

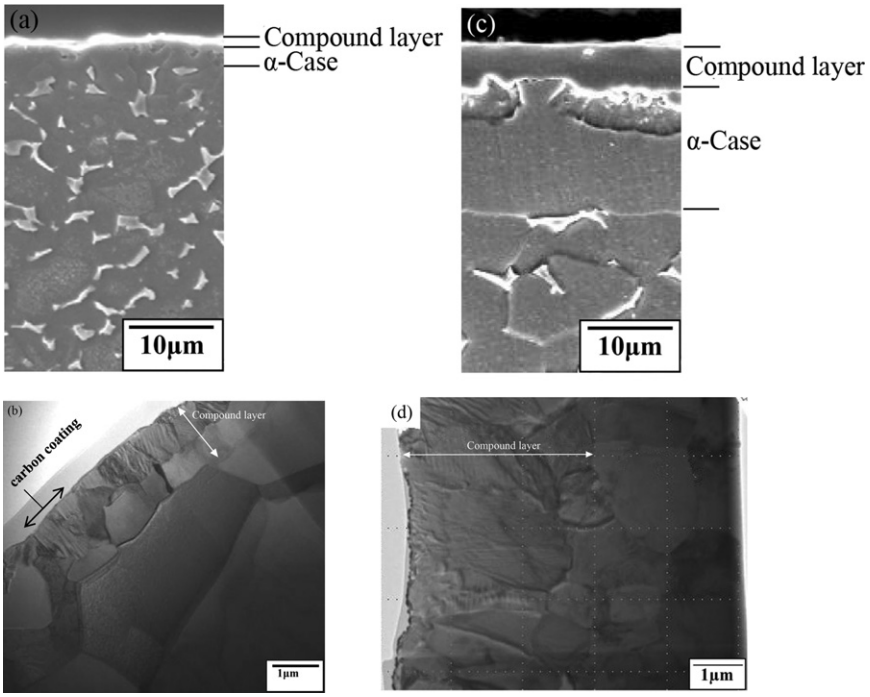


Figure 21 Typical scanning electron microscopy (SEM) and transmission electron microscopy (TEM) images of the gas nitrided microstructure of Ti–6Al–4V. (a, b) SEM and corresponding TEM images after nitriding at 850 °C for 1 h showing formation of a 0.8 μm compound layer and 2.5 μm α-Case. (c, d) SEM and corresponding TEM images of the nitrided microstructure at 850 °C for 12 h showing the formation of a 5 μm compound layer and 14 μm α-Case.[90]

alloy composition as well as nitriding conditions (e.g., time, temperature, atmosphere, etc.) as summarized below.

2.4.4.2.2 Nitriding atmosphere

Several nitriding media have been used for gas nitriding of titanium and titanium alloys including N_2, N_2–H_2, N_2–Ar, or cracked NH_3. Titanium has a high affinity for oxygen, and despite protective measures taken to avoid air/oxygen in the nitriding atmosphere, the presence of TiO_2 has been reported due to the possibility of a small amount of oxygen.[89,91b] The nitriding kinetics is complex and insignificant at low nitriding pressures (<13.3 Pa), and even at 133.3 Pa no technologically useful surface is created in N_2 or NH_3 below 800 °C. At pressures of several 100 Pa, all the absorbed nitrogen dissolves in the titanium surface without significant formation of nitrides.[29a] Treatments at higher pressures, such as 1.2 MPa, yields thicker compound layers and diffusion zones. The high pressure used in the process allows treatment of narrow, deep, blind holes, and intricate details such as fine threads. Nitriding of titanium alloys may be carried out in hot isostatic pressing equipment, where pressures of up to 100 MPa have been used. For the nitrided components in ammonia, a dehydrogenation treatment will be performed in a temperature ranging from 300 to 400 °C at a pressure of 1 Pa.[94]

2.4.4.2.3 Nitriding time and temperature

Due to the diffusion-controlled nature of gas nitriding in titanium alloys, the depth and hardness of nitrided layers increase with the time and temperature of nitriding. Moreover, the possibility of grain growth and phase transformations in the bulk microstructure is higher at higher temperatures and prolonged durations.[47]

2.4.4.2.4 Substrate composition

In titanium alloys, the α and β phases have different potential capacities for nitrogen diffusivity and dissolution. The solubility of nitrogen is higher in α-Ti (HCP structure) compared with β-Ti (BCC structure) by two orders of magnitude. However, the diffusion coefficient of nitrogen in β titanium is two to three orders of magnitude higher than that of the α phase. Therefore, even low contents of the β phase can act as diffusion paths for fast diffusion of nitrogen atoms and accelerate kinetics of the formation of the diffusion zone. As a result the surface concentration of nitrogen decreases but the thickness of the diffusion zone increases with the β phase content.[95]

Furthermore, the severity of microstructural changes during nitriding depends on the β-transus temperature of the titanium alloy. Generally, nitriding treatments performed at temperatures higher than the β-transus temperature of the alloy result in significant phase transformations in the substrate as well as the formation of α-Case, both of which impair the mechanical properties of the alloy.[47,88b,1] The family of β-Ti alloys is more susceptible to bulk microstructural changes during nitriding due to their lower β-transus temperatures compared to α and $\alpha+\beta$ alloys (**Figures 23** and **24**). Therefore, nitriding treatments are normally performed at lower temperatures in β-Ti alloys.[47,96]

2.4.5 Effect of Gas Nitriding on Mechanical Properties

2.4.5.1 Ferrous alloys

It is well established that surface hardening by gas nitriding improves the high-cycle fatigue life of iron-base alloys on account of the hardened diffusion zone and compressive residual stresses developed near the surface. The enhanced surface hardness hinders crack initiation while compressive residual stresses retard the crack propagation. At low stress amplitudes (high-cycle fatigue), the failure initiation site shifts from the surface toward internal defects such as nonmetallic inclusions in the core.[97] In case of smooth samples under rotation bending condition, the internal cracks initiate below the nitrided case, at the case/core interface. With an increase in nitriding depth, a higher bending stress is needed for initiation of subsurface fatigue cracks and thus the fatigue strength increases further. Conversely, at high stress amplitudes (low cycle fatigue) premature crack initiation from the surface due to the lower ductility of the case compared with the core and result in deterioration of low cycle fatigue strength of the alloy.[98] The presence of white layer is detrimental to the fatigue life of nitrided steels due to its brittle nature and is commonly removed by mechanical (honing, fine sand blasting) and chemical treatments (acid pickling) prior to service. Since the white layers produced in a two-stage nitriding have higher ductility compared to those of single-stage treatments, they may not have an adverse effect on fatigue properties.[68]

Even though nitriding affects a thin surface layer (<2 mm) of the total core cross section, it marginally increases the tensile strength and substantially decreases the ductility of the alloy. This has been attributed to the brittle nature of the nitrided layer and the tensile residual stress build up in the substrate.[99] Once the thin layer is broken it acts as a stress raiser. Moreover, the difference between the Poisson's ration of the case (0.3) and bulk (0.5) results in stress triaxiality at the interface as a result the core contracts more than the case and transverse stresses are generated in the radial and circumferential directions. Failure of nitrided tensile samples is normally accompanied by an array of circumferential (secondary) cracks along the gage length. Mencik[100] proposed that these cracks form when the shear stresses at the interface between the case and the core increase the tensile stresses in the case until the case strength is reached. The failure of the case creates a new crack and this phenomenon repeats itself.[100]

Limodin *et al.*[101] investigated the fatigue and tensile properties of gas nitrided AISI 4140 steel under rotation bending and axial fatigue conditions. They reported that the fatigue life of nitrided steel is a competition between surface crack propagation in the presence of compressive residual stresses and initiation and growth of internal cracks, for example, from metallurgical defects. The depth of the nitrided region and the developed compressive residual stress field, affect fatigue crack initiation from the surface; increasing the nitriding depth delayed surface failures and shifted the failure origin to an internal crack. They correlated subsurface failures,

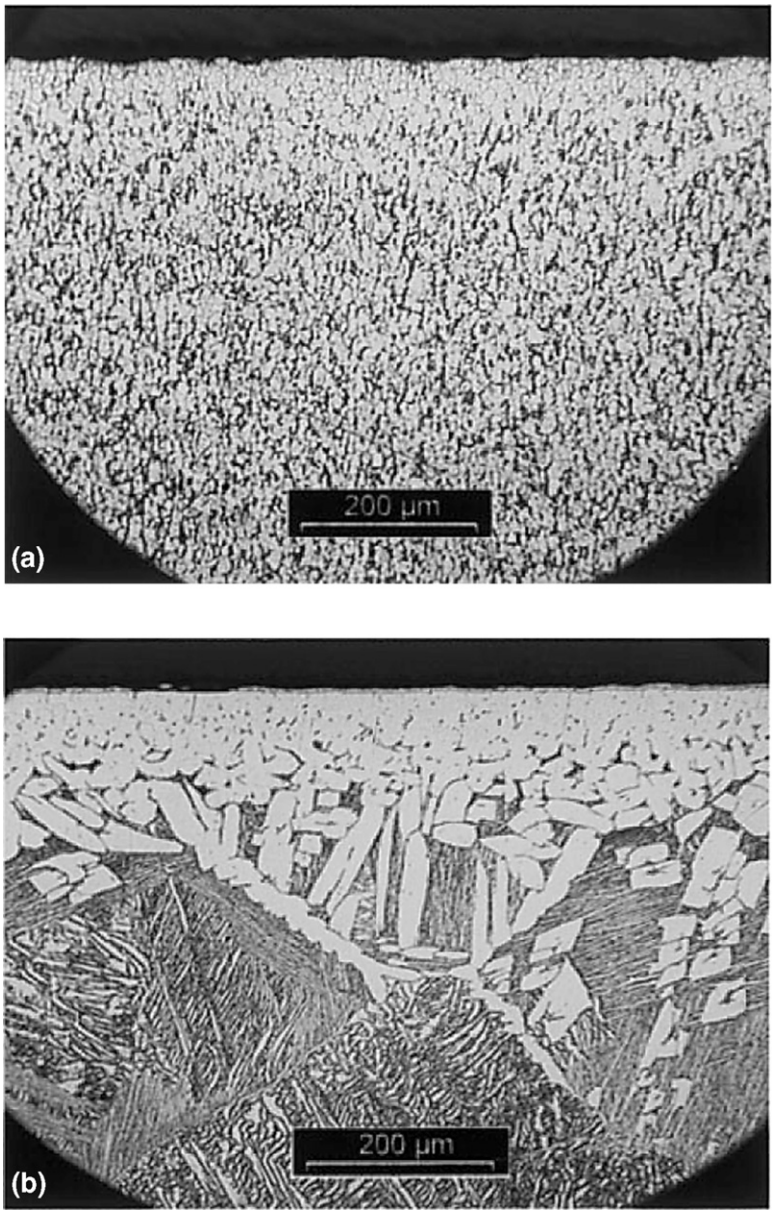


Figure 23 Typical microstructure of near-α Ti–8Al–1Mo–1V titanium alloy after gas nitriding at (a) 950 °C (below the β-transus temperature) for 5 h and (b) 1050 °C (above the β-transus temperature) for 5 h. The nitrided microstructure consisted of a thin compound layer (less than 10 μm thick) on top of a diffusion zone (~350 μm deep). Nitriding above the β-transus temperature resulted in phase transformations in the core and formation of coarse nitrogen-stabilized α-Ti grains underneath the compound layer.[91b]

also known as 'fish-eye' cracks, with the core metallurgical properties especially to the size and distribution of internal defects. Similar observations were reported by Murakami *et al.*[102] They found that the fatigue strength can be predicted by the maximum size of inclusions defined by the square root of the projected area of an inclusion.

Gas nitriding of high strength maraging steels (nitrided at 500 °C, 24 h, 20–30% NH_3 dissociation) was investigated in an early work by Tsyrlin *et al.*[103] They found that compared with the baseline alloy (treated at 500 °C, 24 h, and vacuum), the nitrided alloy had lower ultimate tensile strength, yield strength, and fracture toughness. It was proposed that nitriding reduces the critical defect size, $\left(K_{IC}/\sigma_y\right)^2$, and leads to easier crack propagation. Nonetheless, the tensile and yield strength of the nitrided alloy where similar to those of the untreated material but the fracture toughness decreased considerably after nitriding. This was attributed to the change of stress condition from plane stress to plane strain and easier crack initiation. The load-deflection curves and fractographic observations indicated ductile characteristic of the core confirming that nitriding did not have an adverse effect on the plasticity of the core material.

Hussain *et al.*[104] studied the effect of retained austenite on the properties of gas nitrided maraging steels (nitrided at

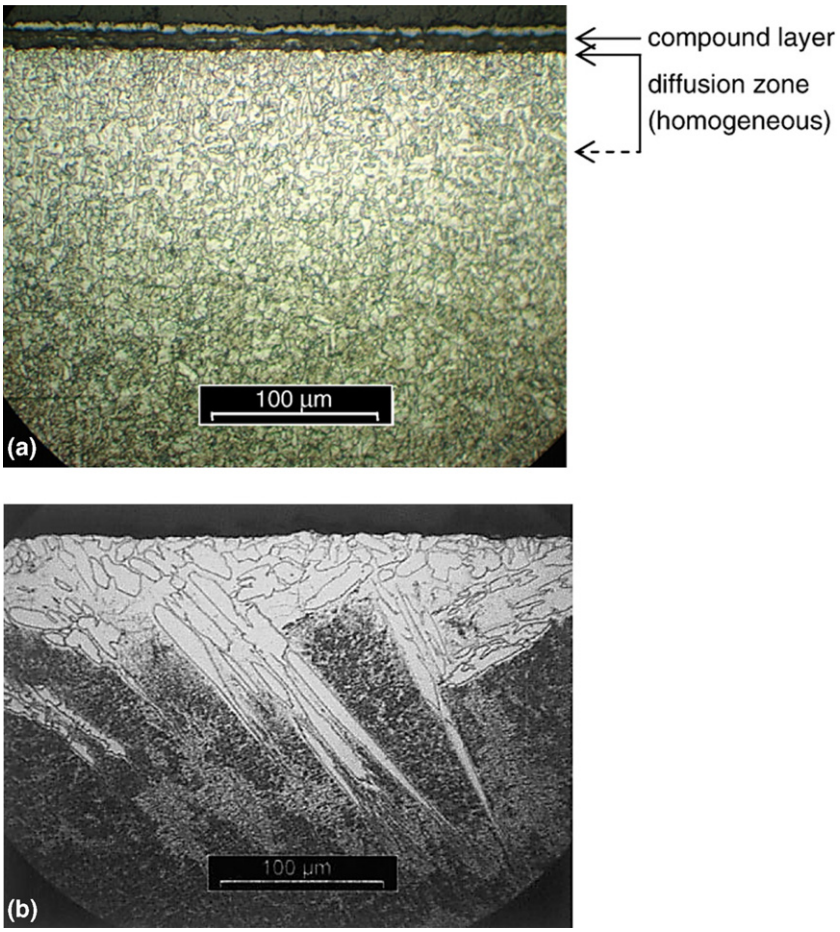


Figure 24 Typical microstructure of near-β Ti–10V–2Fe–3Al titanium alloy after gas nitriding at (a) 750 °C (below the β-transus temperature) for 5 h and (b) 950 °C (above the β-transus temperature) for 5 h. The nitrided microstructure consisted of a thin compound layer on top of a diffusion zone. Nitriding above the β-transus temperature resulted in phase transformations in the core and formation of coarse nitrogen-stabilized α-Ti grains underneath the compound layer.[88b,91b]

450 °C, 8 h in 35% dissociated NH_3 atmosphere). They reported that the surface hardness and case depth were inversely proportional to the retained austenite content of the alloy possibly due to lower diffusivity of nitrogen in austenite. Higher surface hardness and case depth were developed in the nitrided alloy with lower retained austenite content. As a result the fatigue resistance decreased because of higher elastic modulus mismatch between the core and the case.

Guagliano and Vergani[105] studied the fatigue behavior of 42CrMo4 steel nitrided at different conditions (505–530 °C, 5–55 h, 20–70% NH_3 dissociation). They reported that at low stress amplitudes fatigue cracks initiated in the subsurface region underneath the case and nitriding had a beneficial effect on the fatigue strength. However, upon increasing the stress level (low cycle fatigue), the fatigue life of nitrided alloy decreased especially after longer duration treatments. This was attributed to the stiffness mismatch between the case and the core, the case stiffness increased with the nitriding duration, resulting in stress concentration in the case and premature crack formation at the surface.

2.4.5.2 Titanium Alloys

The effect of elevated temperatures involved in the nitriding procedures on the bulk microstructure is an influential factor on the fatigue behavior of titanium alloys.[5] Fairly high nitriding temperatures (>700 °C) are necessary to produce a moderate nitrided depth in titanium alloys, due to the slow kinetics of nitrogen diffusion in titanium. Nitriding of titanium alloys is performed at the temperature range of 750–1000 °C for several hours and cause significant grain growth and over aging of the microstructure.[1]

Investigations by Morita *et al.*[106] indicated that the compound layer formation on the surface and grain growth in the substrate were both responsible for the reduction of fatigue strength after gas nitriding of titanium. Their fractographic observations revealed that the fatigue cracks initiated from the brittle fracture of compound layer. They proposed that the stiffness gradient between the compound layer (E=426 GPa) and the substrate (E=100 GPa) led to stress concentration in former. The developed stress concentration canceled the

positive effect of residual compressive stresses and resulted in brittle fracture at the surface. They also found that the fatigue strength of nitrided titanium had a Hall–Petch relationship with grain size. The effect of grain growth was more pronounced than the brittle compound layer, after a 1 h treatment at 880 °C, however, a 24 h treatment both the low fracture toughness of the compound layer and grain growth had detrimental effects on fatigue strength (Figure 25a). Consequently, they reported promising results by inhibiting grain growth through a low temperature nitriding process (Figure 25b).

Similarly, Tokaji *et al.*[9] reported loss of fatigue strength and endurance limit in Ti–6Al–4V ($\alpha+\beta$ Ti alloy) and Ti–15Mo–5Zr–3Al (β-Ti alloy) after gas nitriding at different temperatures (750–850 °C) and durations (4–60 h). They studied the effect of microstructural changes in the substrate during nitriding on fatigue properties by treating a series of titanium alloys under vacuum. The fatigue limit of nitrided alloys after a 4-h treatment was slightly higher than that of the vacuum treated condition; however, after 15 h of nitriding the fatigue strength was significantly reduced. They discussed that the formation of the compound layer and diffusion zone were both responsible for impaired fatigue properties and confirmed their findings by gradual removal of the nitrided surface layers by electropolishing. Improvements were observed in fatigue life by complete removal of the compound layer and partial removal of the diffusion zone (Figure 26).

Conversely, Steinert *et al.*[107] reported fatigue improvements after nitriding of Ti–6Al–4V alloy at 870 °C for 8 h in a N_2–NH_3 atmosphere (95:5). The nitrided alloy showed a 20% higher fatigue strength compared to a PVD TiN-coated alloy and slightly higher strength compared to the untreated electropolished alloy in the rotation bending fatigue tests. It was found that while fatigue cracks initiated from multiple locations on the surface of gas nitrided alloy, there was a single crack initiation origin on the surface of PVD coated alloy. This was attributed to the steep stiffness gradient between the TiN coating deposited by the PVD process and the titanium substrate. However, for the gas nitrided alloy, the compressive residual stress in the compound layer and diffusion zone suppressed dislocation slip and early crack initiation and resulted in a higher fatigue strength.

Rodriguez *et al.*[108] reported that the low cycle fatigue resistance of Ti–6Al–4V alloy also deteriorated after nitriding. They carried out several nitriding treatments at 850 and 900 °C for 1 and 4 h and noted that the fatigue results of the nitrided samples were similar to – or even slightly better than – those that went through the same treatment under vacuum. Therefore, the reduction of low cycle fatigue resistance was attributed to the substrate microstructural transformations. They proposed that when the imposed strains during cyclic loading were not sufficiently high for compound layer failure, the residual compressive strains on the surface of nitrided samples could slow down the crack nucleation process. However, at high cyclic strains due to the stiffness difference between Ti–6Al–4V and titanium nitrides, cracks nucleated and propagated in the brittle compound layer. Surface roughness was also found to be an influential factor since an increase in the average surface roughness during nitriding leads to stress

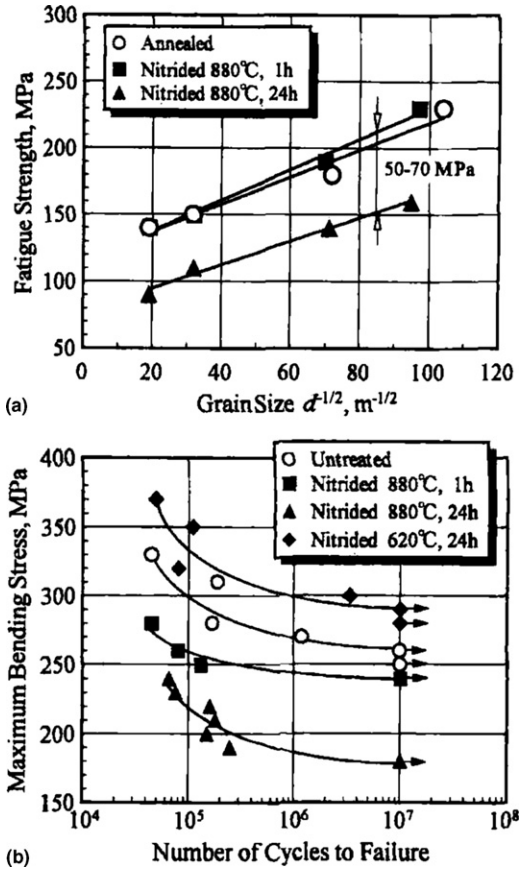


Figure 25 (a) A Hall–Petch type of relationship between the fatigue strength and the grain size in nitrided titanium and (b) typical S–N curves for nitrided titanium showing significant improvements in fatigue strength by low temperature nitriding.[106]

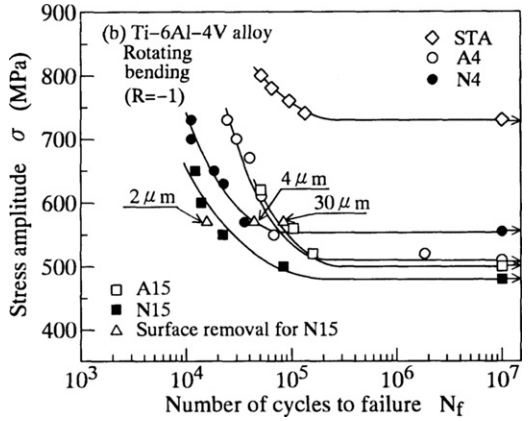


Figure 26 The S–N curve obtained by rotation bending fatigue tests on Ti–6Al–4V alloy. STA: solution treated at 950 °C for 1 h and aged at 540 °C for 4 h; A4 and N4: annealed and nitrided at 850 °C for 4 h; A15, N15: annealed and nitrided at 850 °C for 15 h.[9]

concentration at the surface and promotes early fatigue crack nucleation.[108,109]

2.4.6 Effect of Gas Nitriding on Wear and Corrosion Resistance

2.4.6.1 Ferrous Alloys

Improvements in wear and corrosion resistance after nitriding were correlated to the low coefficient of friction of the compound layer, its chemical resistivity in different media (neutral salt solutions, atmospheric corrosion, chloride irons, liquid metal, etc.), as well as high hardness and improved pitting/crevice resistance of the diffusion zone.[58]

Kato *et al.*[110] identified the responsible wear mechanisms for untreated and gas nitrided EN41B steel (chromium–aluminum–molybdenum nitriding steel) and constructed the corresponding wear maps. They carried out wear investigations over a wide range of applied loads and sliding speeds and observed three distinct wear regimes (mild wear, severe wear, and extremely severe wear) for untreated steel and two different wear regimes (mild wear, severe wear) for gas nitrided steel. For untreated steel, oxidation dominated wear in the mild wear regime characterized by low wear rates, formation of patchy oxides on the surface and generation of fine Fe_2O_3 and Fe_3O_4 debris particles. Severe wear regime was distinguished by high wear rates (one or two orders of magnitude higher than those of the mild regime), plastic deformation, and generation of large metallic wear debris. Adhesion dominated wear in the extremely severe wear regime, characterized by transfer of steel to the counterface and generation of very large metallic debris. Conversely, the nitrided surfaces showed lower wear rates at all tested conditions (between two and four orders of magnitude lower than those of the untreated steel). Gas nitriding also delayed the transition from mild (oxidative) to severe (metallic) regimes and extended the mild wear region toward higher loads and sliding speed. They observed that the compound layer was removed during the initial stages of sliding and thus the enhanced wear performance of nitrided surfaces was attributed to the hardness of the diffusion zone.

Similar results have been reported for stainless steels where gas nitriding resulted in substantial increase in the surface hardness and wear resistance.[111] However, despite improvements in wear resistance and load bearing capacity, gas nitriding can lead to precipitation of dissolved chromium as chromium nitrides and impair the corrosion resistance of stainless steels. In order to inhibit precipitation of chromium nitrides and compound layer formation nitriding of stainless steels is practiced at low temperatures (at or below 450 °C). This results in the development of shallow cases of high hardness. Alternatively, nitriding of stainless steels may be performed at temperatures above 1000 °C (i.e., solution nitriding) to create deep austenitic diffusion zones.[112] According to Spies *et al.*[113] when nitriding temperature was kept below 440 °C, resistance against general corrosion improved in both austenitic and ferritic stainless steels. The pitting corrosion resistance, however, significantly improved in austenitic stainless steels and marginally decreased in ferritic stainless steels.

2.4.6.2 Titanium Alloys

Titanium alloys possess excellent resistance against general corrosion due to the presence of a naturally occurring protective passive film on their surface, mainly composed of TiO_2 (possibly also TiO and Ti_2O_3). This oxide film is highly adherent and due to the high affinity of titanium and oxygen it forms instantaneously on fresh titanium surfaces exposed to air or water.[114] Titanium alloys exhibit corrosion resistance in atmospheric conditions, brines, sea water, and salt solutions (pH level ranging from 3 to 11) such as chlorides, bromides, iodides, sulfites, phosphates, carbonates, etc. Titanium alloys also exhibit corrosion resistance in mildly reducing to highly oxidizing acidic environments. Nonetheless their performance is dependent on the temperature, acid concentration and titanium alloy composition. The influence of gas nitriding on corrosion resistance of titanium alloys is diverse and highly affected by the corrosive environment and test temperature. In an investigation by Sha *et al.* the effects of alloy composition and corrosive media were studied on Ti–8Al–1Mo–1V and Ti–6Al–2Sn–4Zr–2Mo after nitriding at 950 °C for 5 h. Their findings indicated that both untreated and nitrided titanium alloys showed excellent corrosion resistance in NaCl solution (0.5 M concentration). When exposed to very aggressive reducing acid solution environment (HCl solution, 4.9 M concentration), the corrosion rate slightly increased for Ti–8Al–1Mo–1V after nitriding, but for Ti–6Al–2Sn–4Zr–2Mo the corrosion rate was substantially higher after nitriding. In an oxidizing acid solution (H_2SO_4, 1.8 M concentration), regardless of the testing temperature, the corrosion resistance of both alloys decreased after nitriding.[47]

Improvements in the wear resistance of titanium alloys after gas nitriding have been attributed to increased surface hardness due to the formation of titanium nitrides (TiN,Ti_2N) and mechanical support from the nitrogen-strengthened diffusion zone underneath. Wear investigations by Januszewicz and Klimek[80a] on gas nitrided commercially pure (CP) titanium and Ti–6Al–4V alloy indicated that the surfaces treated at a high temperature of 850 °C exhibited higher wear resistance as the nitrided surfaces and were able to withstand relatively high contact pressures due to a deeper hardened diffusion zone. Titanium alloys treated at lower temperatures of 650 and 750 °C experienced high wear rates and third body abrasive wear due to the compound layer failure during early stages of wear testing.

Shashkov *et al.*[115] promising wear results were achieved when nitriding was performed below 900 °C. They reported that nitriding temperatures exceeding 900 °C were accompanied by of the development of thick nitride layers and detrimental microstructural changes in the bulk (e.g., grain coarsening) that led to higher wear rates.

2.4.7 Industrial Applications

Gas nitriding of ferrous alloys has found numerous applications due to its effective role in improving wear, corrosion, and fatigue properties. Furthermore, gas nitriding is a versatile surface hardening process where the nitriding parameters can

be adjusted to achieve the desired properties. It is extensively used in manufacturing of aircraft and automotive components, textile machinery, and turbine generation systems.[58]

The nitriding conditions are adjusted toward the formation of compound layer for applications requiring wear and corrosion resistance, such as automotive and aerospace components subject to sliding, for example, crankshafts, seat screws, components of solenoid actuators, and car window sector.[59b] The components that are subject to high shock loads or very high contact stress levels and need to maintain surface hardness at elevated temperature, such as gears.[68]

For the components where the formation of a brittle compound layer is unfavorable such as cutting tools or fatigue resistance is required such as crankshafts, nitriding will be modified to obtain deep diffusion zone. Gas nitriding is also extensively applied to extrusion tools. The extrusion tools experience high friction at elevated temperatures, which deteriorates their dimensional tolerance and the surface quality of the extruded profiles. Dies and die casting molds are required to possess optimum formability, lubrication properties, and corrosion resistance to molten metal and thus need a combination of compound layer and diffusion zone.[116]

With the recent trend in replacing cast irons and steels with lightweight alloys, gas nitriding of titanium alloys has gained much industrial popularity. Titanium components such as surgical instruments, implant materials, racing engine and racing car components, golf club heads, watch cases, and precision machine parts are frequently nitride.[117] It should be noted that the negative effect of gas nitriding on fatigue life of titanium alloys has posed restrictions on their extensive application.

2.4.8 Recent Developments in Gas Nitriding

An alternative to conventional gas nitriding technologies is solar gas nitriding in which concentrated solar energy provides the energy source for nitriding in a nitrogen-containing atmosphere. Investigations of Olías *et al.*[118] and Rodriguez *et al.*[119] showed a great reduction of nitriding time and greater nitriding rate in titanium alloys using solar gas nitriding technology.

Laser gas-assisted nitriding has also been successfully applied for surface modification of steels and titanium alloys.[120,121] The optimization of laser treatment process to avoid residual tensile stresses on the surface and surface cracking has been the subject of many studies.[122] It has been reported that after process optimization, the laser nitrided surfaces exhibit increased hardness, better corrosion and wear/cavitation erosion resistance.[123]

Several investigations have also been undertaken to produce wear resistant nitrided layers by simultaneous surface melting and nitriding under in nitrogen-rich atmosphere.[124] Hioki *et al.*[124b] achieved significant improvements in the surface hardness (almost four times higher than the bulk) and depth of the hardening ($\sim$0.2 mm) in aluminum by this method. They reported that the nitrided microstructure consisted of AlN and α-Al lamellae. Microstructural investigation of nitrided titanium surfaces by tungsten inert gas torch melting were carried out by Mridha.[124c] He reported a dendritic structure with inhomogeneous distribution within the melt zone on top of a heat affected zone. A high density of fine, interconnected TiN dendrites randomly distributed in the surface vicinity increased the surface hardness to more than 2000 HV. Coarser dendrites of TiN, Ti_2N, and $TiN_{0.3}$, oriented perpendicular to the surface, were observed deeper in the melt zone. The hardening depth exceeded 3 mm from the surface of the melt zone owing to the dissolution of nitrogen atoms and formation of α' martensite phase.

Furthermore, during the past decades many duplex surface engineering techniques have been designed and implemented to exploit the hardening depth of gas nitriding processes as a mechanical support for wear resistant surface coatings such as PVD or CVD nitride coatings and DLC.[125] In one of the earliest investigations Spies *et al.*[126] deposited PVD TiN and Cr_2N coatings on nitrided 31CrMoV9 low-alloy steel and reported that the duplex treatment resulted in considerable improvements in wear and friction of nitrided surfaces without affecting the fatigue limit. They attributed their findings to the presence of compressive residual strains and a deeply strengthened diffusion zone that mitigated the hardness mismatch between TiN coating and steel substrate. Further adhesion improvements were achieved by incorporation of a Ti–TiN_x interlayer at the interface of TiN/nitrided surface[126a] or the deposition CrN PVD coating on the nitrided surface.[127] Nonetheless, the extent of improvements in the surface hardness and wear resistance by duplex treatments, according to Zeghni and Hashmi,[128] is a function of surface roughness, type of PVD coating, and gas nitriding conditions.

References

1. Bell, T.; Bergmann, H. W.; Lanagan, J.; Morton, P. H.; Staines, A. M. Surface Engineering of Titanium with Nitrogen. *Surf. Eng.* **1986**, *2*, 133–143.
2. Knerr, C. H.; Rose, T. C.; Filkowski, J. H. Gas Nitriding. In *ASM Handbook Volume 4: Heat Treating*; ASM International: Materials Park: OH, 1991; pp. 387–409.
3. Mittemeijer, E. J. Fundamentals of Nitriding and Nitrocarburizing. In *ASM Handbook, Vol. 4A: Steel Heat Treating Fundamentals and Processes*; Dossett, J. L., Totten, G. E., Eds.; ASM International: Materials Park, OH, 2013; pp. 619–646.
4. Mridha, S. Growth Kinetics of Hardened Layers Produced During Nitriding in Ammonia Gas Environments. *Mater. Sci. Forum* **2006**, *526*, 109–114.
5. (a) Spies, H.-J. Surface Engineering of Aluminum and Titanium Alloys: An Overview. *Surf. Eng.* **2010**, *26* (1–2), 126–134. (b) Spies, H.-J.; Reinhold, B.; Wilsdorf, K. Gas Nitriding – Process Control and Nitriding Non-ferrous Alloys. *Surf. Eng.* **2001**, *17* (1), 41–54.
6. Wriedt, H. A.; Murray, J. L. The N–Ti (Nitrogen–Titanium) System. *Bull. Alloy Phase Diagr.* **1987**, *8* (4), 378–388.
7. Dong, H. Current Status and Trends in Duplex Surface Engineering of Titanium Alloys, Heat Treating. In *Proceedings of the 20th Conference*; Funatani, K.; Totten, G.E., Eds.; ASM International: Materials Park, OH, 2000; Vol. 1, pp 170–177.
8. Spies, H.-J. Surface Engineering of Aluminium and Titanium alloys: An Overview. *Surf. Eng.* **2010**, *26* (1–2), 126–134.
9. Tokaji, K.; Ogawa, T.; Shibata, H. The Effects of Gas Nitriding on Fatigue Behaviour of Titanium and Titanium Alloys. *JMEPEG* **1999**, *8*, 159–167.
10. Fry, A. Process for Hardening of Steel Alloys. US Patent 1,487,554, 1924.
11. Machlet, A. W. Hardening or Treatment of Steel, Iron, etc. US Patent 1,092,925, 1914.
12. (a) Modylevskii, V. B.; Movchan, P. S.; Klimenko, E. A.; Shramchenko, S. V.; Simoneko, I. S. Gas Nitriding with Automatic Control of Dissociation of

Ammonia. *Met. Sci. Heat Treat.* **1976**, *18* (9), 782–784. (b) Lakhtin, Y. M.; Kogan, Y. D. Controlled Nitriding Processes. *Met. Sci. Heat Treat.* **1978**, *20* (8), 667–671.

13. Floe, C. F. A Study of the Nitriding Process Effect of Ammonia Dissociation on Case Depth and Structure. In *Source Book on Nitriding*; Unterweiser, P. M., Gary, A. G., Eds.; American Society for Metals: Materials Park, OH, 1977; pp. 144–171.
14. Weymer, P. Principles of Gas Nitriding. *Heat Treat. Prog.* **2009**, *9* (4), 12–13.
15. (a) Homerberg, V. O.; Walsted, J. P. A Study of the Nitriding Process – Part I. In *Source Book on Nitriding*; Unterweiser, P. M., Gary, A. G., Eds.; American Society for Metals: Materials Park, OH, 1977; pp. 56–98. (b) Bell, T.; Birch, B. J.; Korotchenko, V.; Evans, S. P. Controlled Nitriding in Ammonia–Hydrogen Mixtures. In *Source Book on Nitriding*; Unterweiser, P. M., Gary, A. G., Eds.; American Society for Metals: Materials Park, OH, 1977; pp. 259–265.
16. Wyatt, J. L.; Grant, N. J. Nitriding of Titanium with Ammonia. *Trans. ASM* **1954**, *46*, 191–218.
17. (a) Du, H. A Reevaluation of the Fe–N and Fe–C–N Systems. *J. Phase Equilib.* **1996**, *14* (6), 682–693. (b) Kardonina, N. I.; Yurovskikh, A. S.; Kolpakov, A. S. Transformations in the Fe–N System. *Met. Sci. Heat Treat.* **2010**, *52* (9–10), 457–467. (c) Slycke, J. T.; Mittemeijer, E. J.; Somers, M. A. J. Thermodynamics and Kinetics of Gas and Gas–Solid Reactions. In *Thermochemical Surface Engineering of Steels*; Mittemeijer, E. J., Somers, M. A. J., Eds.; Woodhead Publishing: Cambridge, 2015; pp. 96–98. (d) Wriedt, H. A.; Gokcen, N. A.; Nafziger, R. H. The Fe–N (Iron–Nitrogen) System. *Bull. Alloy Phase Diagr.* **1987**, *8* (4), 355–377. (e) Hinomura, T.; Nasu, S. A Study of Fe–N Alloy Systems. *Hyperfine Interact.* **1998**, *111*, 221–226. (f) Malinov, S.; Bottger, A. J.; Mittemeijer, E. J.; Pekelharing, M. I.; Somers, M. A. J. Phase Transformations and Phase Equilibria in the Fe–N System at Temperatures below 573 K. *Metall. Mater. Trans. A* **2001**, *32A*, 59–73. (g) Jack, K. H. The Iron–Nitrogen System: The Crystal Structures of ε-Phase Iron Nitrides. *Acta Crystallogr.* **1952**, *5*, 404–411.
18. (a) Frisk, k. A New Assessment of the Fe–N Phase Diagram. *Calphad* **1987**, *11* (2), 127–134. (b) Frisk, K. A Thermodynamic Evaluation of the Cr–N, Fe–N, Mo–N and Cr–Mo–N Systems. *Calphad* **1991**, *15* (1), 79–106.
19. (a) Rochegude, P.; Billon, B. Metastability of ε-FeNx Solid Solution with Low Nitrogen Content. *Scr. Metall.* **1986**, *20* (8), 1095–1098. (b) Somers, M. A. J.; Kooi, B. J.; Maldzinski, L.; *et al.* Thermodynamics and Long-Range Order of Interstitials in an h.c.p. Lattice: Nitrogen in ε-Fe_2N_{1-z}. *Acta Mater.* **1997**, *45* (5), 2013–2025.
20. Lightfoot, B. J.; Jack, D. H. Heat Treatment '73. *Kinetics of Nitriding with and Without White-Layer Formation*; The Metals Society: London, 1973; pp. 59–65.
21. Jack, K. H. The Occurrence and the Crystal Structure of α"-Iron Nitride; A New Type of Interstitial Alloy Formed During the Tempering of Nitrogen–Martensite. *Proc. R. Soc. Lond. A Math. Phys. Sci.* **1951**, *208*, 216–224.
22. Jacobs, H.; Rechenbach, D.; Zachwieja, U. Structure Determination of γ'-Fe_4N and ε-Fe_3N. *J. Alloy. Compd.* **1995**, *227* (1), 10–17.
23. (a) Rechenbach, D.; Jacobs, H. Structure Determination of ζ-Fe_2N by Neutron and Synchrotron Powder Diffraction. *J. Alloy. Compd.* **1996**, *235* (1), 15–22. (b) Jack, K. H. Binary and Ternary Interstitial Alloys. I. The Iron–Nitrogen System: The Structures of Fe_4N and Fe_2N. *Proc. R. Soc. Lond. A Math. Phys. Sci.* **1948**, *195* (1040), 34–40.
24. Somers, M. A. J.; Mittemeijer, E. J. Layer-Growth Kinetics on Gaseous Nitriding of Pure Iron: Evaluation of Diffusion Coefficients for Nitrogen in Iron Nitrides. *Metall. Mater. Trans. A* **1995**, *26A*, 57–74.
25. (a) Kooi, B. J.; Somers, M. A. J.; Mittemeijer, E. J. An Evaluation of the Fe–N Phase Diagram Considering Long-Range Order of N Atoms in γ'-Fe_4N_{1-x} and ε-Fe_2N_{1-z}. *Metall. Mater. Trans. A Phys. Metall. Mater. Sci.* **1996**, *27* (4), 1063–1071. (b) Mittemeijer, E. J.; Slycke, J. T. Chemical Potentials and Activities of Nitrogen and Carbon Imposed by Gaseous Nitriding and Carburising Atmospheres. *Surf. Eng.* **1996**, *12* (2), 152–162.
26. Mittemeijer, E. J.; Somers, M. A. J. Thermodynamics, Kinetics and Process Control of Nitriding. *Surf. Eng.* **1997**, *13*, 483–497.
27. (a) Somers, M. A. J.; Mittemeijer, E. J. Model Discription of Iron–Carbonitride Compound Layer Formation During Gaseous and Salt-Bath Nitrocraburizing. *Mater. Sci. Forum* **1992**, *102–104*, 223–228. (b) Zinchenko, V.; Georgievskaya, B.; Olovyanishnikov, V.; Kuznetsov, V. New Methods of Gas Carburization and Nitriding. *Met. Sci. Heat Treat.* **1984**, *26* (10), 775–780.
28. Lutjering, G.; Williams, J. C. *Titanium*, 2nd ed.; Springer-Verlag: Berlin, 2007.
29. (a) McDonald, N. R.; Wallwork, G. R. The Reaction of Nitrogen with Titanium Between 800 and 1200 °C. *Oxid. Met.* **1970**, *2* (3), 263–283. (b) Anandan, C.; Babu, P. D.; Mohan, L. Effect of Gas Composition on Nitriding and Wear Behavior of Nitrided Titanium Alloy Ti–15V–3Cr–3Al–3Sn. *JMEPEG* **2013**, *22*, 2623–2633.
30. Wriedt, H. A.; Murray, J. L. The N–Ti (Nitrogen–Titanium) System. *Bull. Alloy Phase Diagr.* **1987**, *8* (4), 378–388.
31. Lengauer, W. Properties of bulk δ-TiN_{1-x} Prepared by Nitrogen Diffusion into Titanium Metal. *J. Alloy. Compd.* **1992**, *186* (2), 293–307.
32. Khidirov, I. Revision of the Ti–N Phase Diagram as Probed by Neutron Diffraction. *Russ. J. Inorg. Chem.* **2011**, *56* (2), 298–303.
33. Bars, J.-P.; David, D.; Etchessahar, E.; Debuigne, J. Titanium α-Nitrogen Solid Solution Formed by High Temperature Nitriding: Diffusion of Nitrogen, Hardness, and Crystallographic Parameters. *Metall. Trans. A* **1983**, *14* (8), 1537–1543.
34. Christensen, A. N.; Alamo, A.; Landesman, J. P. Structure of Vacancy-Ordered Titanium Heminitride δ'-Ti_2N by Powder Neutron Diffraction. *Acta Crystallogr.* **1985**, *41*, 1009–1011.
35. (a) Hochman, R. F. Effects of Nitrogen in Metal Surfaces. In *Proceeding of ASM's International Conference on Ion Nitriding/Carburising*. Cleveland, OH, September 15–17, 1986; pp. 23–30; (b) Shahien, M.; Yamada, M.; Yasui, T.; Fukumoto, M. Cubic Aluminum Nitride Coating Through Atmospheric Reactive Plasma Nitriding. *J. Therm. Spray Technol.* **2010**, *19* (3), 635–641.
36. Yang, M. *Nitriding – Fundamentals, Modeling and Process Optimization* (Ph.D. thesis); Worcester, MA: Worcester Polytechnic Institute, 2012.
37. Sun, Y.; Bell, T. Computer Prediction of Threshold Nitriding Potential Curves. *Heat Treat. Met.* **1997**, *24* (2), 43–49.
38. (a) Grabke, H. J. Adsorption, Segregation and Reactions of Non-Metal Atoms on Iron Surfaces. *Mater. Sci. Eng.* **1980**, *42* (C), 91–99. (b) Grabke, H. J. Kinetics of Gas–Solid Interactions. *Mater. Sci. Forum* **1994**, *154*, 69–86.
39. Slycke, J.; Ericsson, T. A Study of Reactions Occurring During the Carbonitriding Process. *J. Heat Treat.* **1981**, *2* (1), 3–19.
40. Slycke, J. T.; Mittemeijer, E. J.; Somers, M. A. J. Thermodynamics and Kinetics of Gas and Gas–Solid Reactions. In *Thermochemical Surface Engineering of Steels*; Mittemeijer, E. J., Somers, M. A. J., Eds.; Woodhead Publishing: Cambridge, 2015; pp. 3–109.
41. Hosmani, S. S.; Schacherl, R. E.; Mittemeijer, E. J. Compound Layer Formation on Iron-Based Alloys Upon Nitriding; Phase Composition and Pore Formation. *J. Heat Treat. Mater. (HTM Härtereitechnische Mitteilungen)* **2008**, *63* (3), 139–146.
42. (a) Baranowska, J. Characteristic of the Nitride Layers on the Stainless Steel at Low Temperature. *Surf. Coat. Technol.* **2004**, *180–181*, 145–149. (b) Baranowska, J.; Szczecinski, K.; Wysiecki, M. Increasing of Gas Nitriding Kinetics via Surface Pre-Treatment. *Surf. Coat. Technol.* **2002**, *151–152*, 534–539.
43. Torchane, L.; Bilger, P.; Dulcy, J.; Gantois, M. Control of Iron Nitride Layers Growth Kinetics in the Binary Fe–N System. *Metall. Mater. Trans. A Phys. Metall. Mater. Sci.* **1996**, *27* (7), 1823–1835.
44. Du, H.; Agren, J. Theoretical Treatment of Nitriding and Nitrocarburizing of Iron. *Metall. Mater. Trans. A* **1996**, *27A*, 1073–1080.
45. Hosmani, S. S.; Schacherl, R. E.; Mittemeijer, E. J. Morphology and Constitution of the Compound Layer Formed on Nitrided Fe-4wt.%V Alloy. *J. Mater. Sci.* **2009**, *44*, 520–527.
46. (a) Strafford, K. N.; Towell, J. M. The Interaction of Titanium and Titanium Alloys with Nitrogen at Elevated Temperatures. I. The Kinetics and Mechanism of the Titanium–Nitrogen Reaction. *Oxid. Met.* **1976**, *10* (1), 41–67. (b) Strafford, K. N.; Towell, J. M. The Interaction of Titanium and Titanium Alloys with Nitrogen at Elevated Temperatures. II. The Nitridation Behavior of Alloys Containing 5 wt% of Aluminum or Chromium. *Oxid. Met.* **1976**, *10* (1), 69–84.
47. Sha, W.; Malinov, S. *Titanium Alloys: Modelling of Microstructure, Properties and Applications*; Woodhead Publishing Ltd. and CRC Press, LLC: Cambridge, 2009.
48. Zhecheva, A.; Sha, W.; Malinov, S.; Long, A. Enhancing the Microstructure and Properties of Titanium Alloys Through Nitriding and Other Surface Engineering Methods. *Surf. Coat. Technol.* **2005**, *200* (7), 2192–2207.
49. (a) Zhecheva, A.; Malinov, S.; Katzarov, I.; Sha, W. Modelling of Kinetics of Nitriding Titanium Alloys. *Surf. Eng.* **2006**, *22* (6), 452–454. (b) Zhecheva, A.; Malinov, S.; Sha, W. Simulation of Microhardness Profiles of Titanium Alloys After Surface Nitriding Using Artificial Neural Network. *Surf. Coat. Technol.* **2005**, *200*, 2332–2342.
50. Sun, Y.; Bell, T. A Numerical Model of Plasma Nitriding of Low Alloy Steels. *Mater. Sci. Eng. A* **1997**, *224*, 33–47.
51. Anttila, A.; Räisänen, J.; Keinonen, J. Diffusion of Nitrogen in α-Ti. *Appl. Phys. Lett.* **1983**, *42*, 498–500.
52. Wood, F. W.; Paasche, O. G. Dubious Details of Nitrogen Diffusion in Nitrided Titanium. *Thin Solid Films* **1977**, *40*, 131–137.

53. Fromm, E. Adsorption of Oxygen and Nitrogen on Clean Surfaces of Transition Metals. In *The 7th International Vacuum Congress*, Vienna, Autria, 1977.
54. Metin, E.; Inal, O. T. Kinetics of Layer Growth and Multiphase Diffusion in Ion-Nitrided Titanium. *Metall. Trans. A* **1989**, *20* (9), 1819–1832.
55. (a) Friehling, P. B.; Somers, M. A. J. On the Effect of Pre-Oxidation on the Nitriding Kinetics. *Surf. Eng.* **2000**, *16*, 103–106. (b) Somers, M. A. J.; Mittemeijer, E. J. Model Description of Iron–Carbonitride Compound-Layer Formation During Gaseous and Salt-Bath Nitrocarburizing. *Mater. Sci. Forum* **1992**, *102–104*, 223–228.
56. (a) Gu, J. F.; Bei, D. H.; Pan, J. S.; Lu, J.; Lu, K. Improved Nitrogen Transport in Surface Nanocrystallized Low-Carbon Steels During Gaseous Nitridation. *Mater. Lett.* **2002**, *55* (5), 340–343. (b) Tong, W. P.; Tao, N. R.; Wang, Z. B.; Lu, J.; Lu, K. Nitriding Iron at Lower Temperatures. *Science* **2003**, *299* (5607), 686–688. (c) Ge, L.; Tian, N.; Lu, Z.; You, C. Influence of the Surface Nanocrystallization on the Gas Nitriding of Ti–6Al–4V Alloy. *Appl. Surf. Sci.* **2013**, *286*, 412–416. (d) Tong, W. P.; Han, Z.; Wang, L. M.; Lu, J.; Lu, K. Low-Temperature Nitriding of 38CrMoAl Steel with a Nanostructured Surface Layer Induced by Surface Mechanical Attrition Treatment. *Surf. Coat. Technol.* **2008**, *202* (20), 4957–4963. (e) Tong, W. P.; Liu, C. Z.; Wang, W.; *et al.* Gaseous Nitriding of Iron with a Nanostructured Surface Layer. *Scr. Mater.* **2007**, *57*, 533–536. (f) Lu, K. Nanocrystalline Metals Crystallized from Amorphous Solids: Nanocrystallization, Structure, and Properties. *Mater. Sci. Eng. Rep.* **1996**, *16* (4), 161–221. (g) Tong, W. P.; Tao, N. R.; Wang, Z. B.; Zhang, H. W.; Lu, J.; Lu, K. The Formation of e-Fe_3–2N Phase in a Nanocrystalline Fe. *Scr. Mater.* **2004**, *50*, 647–650.
57. Kolozsvary, Z. Nitriding Structure and Properties of Nitrided Layers. In *ASM Handbook Vol. 4D: Heat Treating of Irons and Steels*; Dossett, J., Totten, G. E., Eds.; ASM International: Materials Park, OH, 2014; pp. 88–95.
58. Davis, J. R. Nitriding. *Surface Hardening of Steels, Understanding the Basics*; ASM International: Materials Park, OH, 2002; pp. 141–187.
59. (a) Pye, D. *Practical Nitriding and Ferritic Nirocarburizing*; ASM International: Materials Park, OH, 2003. (b) Totten, G. E.; Funatani, K.; Xie, L. *Handbook of Metallurgical Process Design*; Marcel Dekker: New York, NY, 2004.
60. Spies, H.-J.; Thien, H. L.; Biermann, H. B. Nitriding and Carbonitriding of Steels. *Metal Sci. Heat Treat.* **2004**, *46* (7–8), 272–276.
61. (a) Sola, R.; Poli, G.; Veronesi, P.; Giovanardi, R. Effects of Surface Morphology on the Wear and Corrosion Resistance of Post-Treated Nitrided and Nitrocarburized 42$CrMo_4$ Steel. *Metall. Mater. Trans. A Phys. Metall. Mater. Sci.* **2014**, *45* (6), 2827–2833. (b) Alsaran, A.; Altun, H.; Karakan, M.; Çelik, A. Effect of Post-Oxidizing on Tribological and Corrosion Behaviour of Plasma Nitrided AISI 5140 Steel. *Surf. Coat. Technol.* **2004**, *176* (3), 344–348. (c) Mahboubi, F.; Fattah, M. Duplex Treatment of Plasma Nitriding and Plasma Oxidation of Plain Carbon Steel. *Vacuum* **2005**, *79*, 1–6.
62. Borgioli, F.; Galvanetto, E.; Fossati, A.; Bacci, T. Glow-Discharge Nitriding and Post-Oxidising Treatments of AISI H11 Steel. *Surf. Coat. Technol.* **2002**, *162*, 61–66.
63. Doche, M. L.; Meynie, V.; Mazille, H.; Deramaix, C.; Jacquot, P. Improvement of the Corrosion Resistance of Low-Pressure Nitrided and Post-Oxidized Steels by a Polymer Impregnation Final Treatment. *Surf. Coat. Technol.* **2002**, *154* (2–3), 113–123.
64. Fernandes, A. C.; Vaz, F.; Ariza, E.; *et al.* Tribocorrosion Behaviour of Plasma Nitrided and Plasma Nitrided + Oxidised Ti6Al4V Alloy. *Surf. Coat. Technol.* **2006**, *200*, 6218–6224.
65. Clayton, D. B.; Sachs, K. Reduction of 'White Layer' on the Surface of Nitrided Components. In *Source Book on Nitriding*; Unterweiser, P. M., Gary, A. G., Eds.; American Society for Metals: Materials Park, OH, 1977; pp. 242–247.
66. Bever, M. B.; Floe, C. F. Case Hardening of Steel by Nitriding. In *Source Book on Nitriding*; Unterweiser, P. M., Gary, A. G., Eds.; American Society for Metals: Materials Park, OH, 1977; pp. 125–143.
67. Sergeson, R. Investigation in Nitriding. In *Source Book on Nitriding*; Unterweiser, P. M., Gary, A. G., Eds.; American Society for Metals, 1977; pp. 26–55.
68. Davis, J. R. *Gear Materials, Properties, and Manufacture*; ASM International: Materials Park, OH, 2005.
69. Mridha, S.; Jack, D. H. Characterization of Nitrided 3% Chromium Steel. *Met. Sci.* **1982**, *16*, 398–404.
70. Weber, T.; Wit, L. D.; Saris, F. W.; *et al.* Hardness and Corrosion Resistance of Single-Phase Nitride and Carbide on Iron. *Mater. Sci. Eng. A* **1995**, *199* (2), 205–210.
71. Meka, S. R.; Mittemeijer, E. J. Abnormal Nitride Morphologies Upon Nitriding Iron-Based Substrates. *JOM* **2013**, *65*, 769–775.
72. Mridha, S.; Jack, D. H. Etching Techniques for Nitrided Irons and Steels. *Metallography* **1982**, *15*, 163–175.
73. Staines, T. Low Temperature Thermochemical Treatments: Opening Process Widow. *Surf. Eng.* **2010**, *26* (1–2), 97–102.
74. Yang, M.; Sisson, R. Alloy Effects on the Gas Nitriding Process. *J. Mater. Eng. Perform.* **2014**, *23* (12), 4181–4186.
75. (a) Hoffmann, F.T.; Steinbacher, M.; Clausen, B.; Bischoff, S.; Klumper-Westkamp, H.; Zoch, H.-W. New Carbonitriding Processes. In *Proceedings of the 26th ASM Heat Treating Society Conference*, Cincinnati, OH; Ferguson, B. L.; Jones, R.; MacKenzie, D.S.; Weires, D., Eds.; ASM International: Cincinnati, OH, 2011; pp 115–121; (b) Spies, H.-J.; Burlacov, I.; Börner, K.; Biermann, H. Active Screen Plasma Nitriding and Nitrocarburising of Steels: An Overview. *Int. Heat Treat. Surf. Eng.* **2014**, *8* (3), 94–106. (c) Tsujikawa, M.; Yamauchi, N.; Ueda, N.; Sone, T.; Hirose, Y. Behavior of Carbon in Low Temperature Plasma Nitriding Layer of Austenitic Stainless Steel. *Surf. Coat. Technol.* **2005**, *193*, 309–313.
76. Kochmański, P.; Nowacki, J. Influence of Initial Heat Treatment of 17–4 PH Stainless Steel on Gas Nitriding Kinetics. *Surf. Coat. Technol.* **2008**, *202* (19), 4834–4838.
77. Fewell, M. P.; Mitchell, D. R. G.; Priest, J. M.; Short, K. T.; Collins, G. A. The Nature of Expanded Austenite. *Surf. Coat. Technol.* **2000**, *131*, 300–306.
78. Mridha, S.; Khan, A. A. The Effects of Process Variables on the Hardness of Nitrided 3% Chromium Steel. *J. Mater. Process. Technol.* **2008**, *201*, 325–330.
79. Mridha, S. Gas Nitriding of En40B Steel with Highest Growth Rate of the Case and Reduced White Layer Formation. *Int. J. Microstruct. Mater. Prop.* **2007**, *2* (1), 54–63.
80. (a) Januszewicz, B.; Klimek, L. Nitriding of Titanium and Ti6Al4V Alloy in Ammonia Gas Under Low Pressure. *Mater. Sci. Technol.* **2010**, *26* (5), 586–590. (b) Maksimovich, G. G.; Fedirko, V. M.; Pogrelyuk, I. M. Effects of Low Pressures in a Dynamic Nitrogen Atmosphere on Titanium-Alloy Nitriding. *Mater. Sci.* **1990**, *26* (3), 338–340.
81. Perez, G. Low-Pressure Nitriding. *Ind. Heat.* **2006**, *73* (9), 67–70.
82. Kochmański, P.; Nowacki, J. Activated Gas Nitriding of 17–4 PH Stainless Steel. *Surf. Coat. Technol.* **2006**, *200*, 6558–6562.
83. Lakhtin, Y. M. Prospective Developments in Nitriding. *Met. Sci. Heat Treat.* **1980**, *22* (7), 501–509.
84. Lakhtin, Y. M.; Ioffe, G. A.; Tsyrlin, É.S.; Kogan, L. I.; Éntin, R. I. Nitriding Steels of the Low-Carbon Martensitic Type. *Met. Sci. Heat Treat.* **1980**, *22* (3), 167–171.
85. Spies, H.-J.; Reinhold, B.; Wilsdorf, K. Gas Nitriding – Process Control and Nitriding Non-Ferrous Alloys. *Surf. Eng.* **2001**, *17* (1), 41–54.
86. (a) Chen, H.-Y.; Stock, H.-R.; Mayr, P. Plasma-Assisted Nitriding of Aluminum. *Surf. Coat. Technol.* **1994**, *64* (3), 139–147. (b) Stock, H. R.; Jarms, C.; Seidel, F.; Doring, J. E. Fundamental and Applied Aspects of the Plasma-Assisted Nitriding Process for Aluminium and Its Alloys. *Surf. Coat. Technol.* **1997**, *94–95*, 247–254. (c) Meletis, E. I.; Yan, S. Formation of Aluminum Nitride by Intensified Plasma Ion Nitriding. *J. Vac. Sci. Technol. A* **1991**, *9*, 2279–2284.
87. (a) Rauschenbach, B.; Kolitsch, A.; Richter, E. Formation of AlN by Nitrogen Ion Implantation. *Thin Solid Films* **1983**, *109* (1), 37–45. (b) Kanno, I.; Nomoto, K.; Nishijima, S.; *et al.* Tribological Properties of Aluminum Modified with Nitrogen Ion Implantation and Plasma Treatment. *Nucl. Inst. Method. Phys. Res. B* **1991**, *59–60* (2), 920–924. (c) Booske, J. H.; Zhang, L.; Wang, W.; *et al.* Nitrogen Plasma Source Ion Implantation for Corrosion Protection of Aluminum 6061-T4. *J. Mater. Res.* **1997**, *12* (5), 1356–1366.
88. (a) Qian, J.; Farokhzadeh, K.; Edrisy, A. Ion Nitriding of a Near-β Titanium Alloy: Microstructure and Mechanical Properties. *Surf. Coat. Technol.* **2014**, *258*, 134–141. (b) Zhecheva, A.; Malinov, S.; Sha, W. Titanium Alloys After Surface Gas Nitriding. *Surf. Coat. Technol.* **2006**, *201*, 2467–2474.
89. Nakai, M.; Niinomi, M.; Akahori, T.; *et al.* Surface Hardening of Biomedical Ti–29Nb–13Ta–4.6Zr and Ti–6Al–4V ELI by Gas Nitriding. *Mater. Sci. Eng. A* **2008**, *486*, 193–201.
90. Lee, D. B.; Pohrelyuk, I.; Yaskiv, O.; Lee, J. C. Gas Nitriding and Subsequent Oxidation of Ti–6Al–4V Alloys. *Nanoscale Res. Lett.* **2012**, *7* (21), 1–5.
91. (a) Liu, L.; Ernst, F.; Michal, G. M.; Heuer, A. H. Surface Hardening of Ti Alloys by Gas-Phase Nitridation: Kinetic Control of the Nitrogen Surface Activity. *Metall. Mater. Trans. A* **2005**, *36A*, 2429–2434. (b) Malinov, S.; Zhecheva, A.; Sha, W. Nitriding of Titanium and Aluminum Alloys: Relation Between the Microstructure and Properties of Commercial Titanium Alloys and the Parameters of Gas Nitriding. *Met. Sci. Heat Treat.* **2004**, *46* (7–8), 286–293.
92. Lee, H.; Kang, H.; Kim, J.; *et al.* Inward Diffusion of Al and Ti_3Al Compound Formation in the Ti–6Al–4V Alloy During High Temperature Gas Nitriding. *Surf. Coat. Technol.* **2014**, *240*, 221–225.

93. Dearnley, P. A.; Bell, T.; Hombeck, F. Crafting the Surface with Glow Discharge Plasmas. In *Surface Engineering: Processes and Applications*; Strafford, K. N., R.S.C.S., Sare, I., Subramanian, C., Eds.; Technomic Publishing Company, Inc: Lancaster, PA, 1995; pp. 21–47.
94. Marshall, J.; Jacobs, M. H.; Armstrong, G. R.; Rickinson, B. A. The Application of HIP Processing for Rapid Gas Nitriding. In *Proceedings of the International Conference on Hot Isostatic Pressing – HIP '93*; Delaey, L., Tas, H., Eds.; Elsevier: Antwerp, Belgium, April 21–23, 1993; pp. 317–324.
95. Matychak, Y. S.; Pohrelyuk, I. M.; Fedriko, V. M. Kinetic Features of the Process of Nitriding of ($\alpha + \beta$) Titanium Alloys. *Mater. Sci.* **2011**, *46* (5), 660–668.
96. Zhecheva, A.; Malinov, S.; Sha, W. Microstructure and Microhardness of Gas Nitrided Surface Layers in Ti–8Al–1Mo–1V and Ti–10V–2Fe–3Al Alloys. *Surf. Eng.* **2005**, *21* (4), 269–278.
97. Nishijima, S.; Kanazawa, K. Stepwise S–N Curve and "Fish-Eye" Failure in Gigacycle Fatigue. *Fatigue Fract. Eng. Mater. Struct.* **1999**, *22*, 601–607.
98. Qian, J.; Fatemi, A. Cyclic Deformation and Fatigue Behaviour of Ion-Nitrided Steel. *Int. J. Fatigue* **1995**, *17* (1), 15–24.
99. Ebert, L. J.; Krotine, F. T.; Troiano, A. R. Why Case Hardened Components Fracture. *Met. Prog.* **1966**, *90*, 61–64.
100. Mencik, J. Solid Mechanics & Its Applications. *Mechanics of Components with Treated or Coated Surfaces*; Kluwer Academic Publishers: Amsterdam, 1986.
101. Limodin, N.; Verreman, Y.; Tarfa, T. N. Axial Fatigue of a Gas-Nitrided Quenched and Tempered AISI 4140 Steel: Effect of Nitriding Depth. *Fatigue Fract. Eng. Mater. Struct.* **2003**, *26*, 811–820.
102. Murakami, Y.; Usuki, H. Quantitative Evaluation of Effects of Non-Metallic Inclusions on Fatigue Strength of High Strength Steels. II: Fatigue Limit Evaluation Based on Statistics for Extreme Values of Inclusion Size. *Int. J. Fatigue* **1989**, *11* (5), 299–307.
103. Tsyrlin, É.S.; Lakhtin, Y. M.; Blinov, V. M. Effect of Nitriding on the Resistance to Fracture of High-Strength Maraging Steel N18K9M5T. *Met. Sci. Heat Treat.* **1978**, *20* (12), 981–984.
104. (a) Hussain, K.; Tauqir, A.; Haq, A. U.; Khan, A. Q. Influence of Gas Nitriding on Fatigue Resistance of Maraging Steel. *Int. J. Fatigue* **1999**, *21*, 163–168. (b) Hussain, K.; Tauqir, A.; Haq, A. U.; Khan, A. Q. Effect of Retained Austenite on Gas Nitriding of High Strength Steel. *Mater. Sci. Technol.* **1998**, *14* (12), 1218–1220.
105. Guagliano, M.; Vergani, L. Effect of Nitriding on Low-Cycle Fatigue Properties. *Int. J. Fatigue* **1997**, *19* (1), 67–73.
106. Morita, T.; Takahashi, H.; Shimizu, M.; Kawasaki, K. Factors Controlling the Fatigue Strength of Nitrided Titanium. *Fatigue Fract. Eng. Mater.* **1997**, *20* (1), 85–92.
107. Steinert, R.; Lindemann, J.; Leyens, C. Effect of Nitride Coatings on the Wear and Fatigue Behavior of Titanium Alloy Ti–6Al–4V. In *Proceedings of the 12th World Conference on Titanium,* Beijing, China, June 19–24, 2011; Science Press: Beijing, 2011; pp. 858–861.
108. Rodriguez, D.; Manero, J. M.; Gil, F. J.; Panell, J. A. Low Cycle Fatigue Behavior of Ti6Al4V Thermochemically Nitrided for Its Use in Hip Prostheses. *J. Mater. Sci.* **2001**, *12*, 935–937.
109. Farokhzadeh, K.; Edrisy, A. Fatigue Improvement in Low Temperature Plasma Nitrided Ti–6Al–4V Alloy. *Mater. Sci. Eng. A* **2014**, *620*, 435–444.
110. Kato, H.; Eyre, T. S.; Ralph, B. Wear Mechanism Map of Nitrided Steel. *Acta Metall. Mater.* **1994**, *42* (5), 1703–1713.
111. Yang, J.; Liu, Y.; Ye, Z.; Yang, D.; He, S. Microstructure and Tribological Characteristics of Nitrided Layer on 2Cr13 Steel in Air and Vacuum. *Surf. Coat. Technol.* **2009**, *204* (5), 705–712.
112. (a) Peng, D. Q.; Kim, T. H.; Chung, J. H.; Park, J. K. Development of Nitride-Layer of AISI 304 Austenitic Stainless Steel During High-Temperature Ammonia Gas-Nitriding. *Appl. Surf. Sci.* **2010**, *256*, 7522–7529. (b) Christiansen, T. L.; Somers, M. A. J. Low Temperature Gaseous Surface Hardening of Stainless Steel: The Current Status. *Int. J. Mater. Res.* **2009**, *100*, 1361–1377.
113. Spies, H.-J.; Eckstein, C.; Zimdars, H. Structure and Corrosion Behaviour of Stainless Steels After Plasma and Gas Nitriding. *Surf. Eng.* **2002**, *18* (6), 459–461.
114. Donachie, M. J. *Titanium: A Technical Guide*, 2nd ed.; ASM International: Materials Park, OH, 2000.
115. Shashkov, D. P. Effect of Nitriding on Mechanical Properties and Wear Resistance of Titanium Alloys. *Met. Sci. Heat Treat.* **2001**, *43* (5–6), 233–237.
116. (a) Bohmer, S.; Schroter, W.; Lakhtin, Y. M.; Lerche, W.; Kogan, Y. D. Principles of Classification, Control, and Application of Nitriding Processes. *Met. Sci. Heat Treat.* **1979**, *21* (10), 761–766. (b) Gorobets, G. K. Wear Resistance of Dies Hardened by Gas Nitriding. *Sov. Mater. Sci.* **1981**, *16* (5), 480.
117. (a) Tamura, Y.; Yokoyama, A.; Watari, F.; Kawasaki, T. Surface Properties and Biocompatibility of Nitrided Titanium for Abrasion Resistant Implant Materials. *Dent. Mater. J.* **2002**, *21* (4), 355–372. (b) Panjwani, B. Application of Biocompatible Thin Organic Coatings to Improve Tribology of Ti6Al4V Alloy (Master thesis); Singapore: National University of Singapore, 2011.
118. Olías, J. S.; García, I.; Vázquez, A. J. Synthesis of TiN with Solar Energy Concentrated by a Fresnel Lens. *Mater. Lett.* **1999**, *38* (5), 379–385.
119. Rodriguez, G. P.; Herranz, G.; Romero, A. Solar Gas Nitriding of Ti6Al4V Alloy. *Appl. Surf. Sci.* **2013**, *283*, 445–452.
120 Schaaf, P. Laser Nitriding of Metals. *Prog. Mater. Sci.* **2002**, *47*, 1–161.
121. (a) Schaaf, P.; Kaspar, J.; Hoche, D. Laser Machining and Surface Treatment, Laser Gas-Assisted Nitriding of Ti Alloys. In *Comprehensive Materials Processing, Vol. 9*; Hashmi, M. S. J., Ed.; Elsevier Ltd: Italy, 2014; pp. 261–278. (b) Hu, C.; Xin, H.; Watson, L. M.; Baker, T. N. Analysis of the Phases Developed by Laser Nitriding Ti–6Al–4V Alloys. *Acta Mater.* **1997**, *45* (10), 4311–4322.
122. Xue, L.; Islam, M.; Koul, A. K.; Bibby, M.; Wallace, W. Laser Gas Nitriding of Ti–6Al–4V Part 1: Optimization of the Process. *Adv. Perfor. Mater.* **1997**, *4* (1), 25–47.
123. (a) Kaspar, J.; Bretschneider, J.; Jacob, S.; Bonß, S.; Winderlich, B.; Brenner, B. Microstructure, Hardness and Cavitation Erosion Behaviour of Ti–6Al–4V Laser Nitrided Under Different Gas Atmospheres. *Surf. Eng.* **2007**, *23* (2), 99–106. (b) Zhang, C.; Tang, L.; Hu, F.; Zhang, S.; Man, H. Study on Wear and Corrosion Properties of Ti6Al4V Alloy by Laser Gas Nitriding. *Adv. Mater. Res.* **2011**, *299–300*, 188–192.
124. (a) Sohi, M. H.; Ansari, M.; Ghazizadeh, M.; Zebardast, H. Liquid Phase Surface Nitriding of Aluminium Using TIG Process. *Surf. Eng.* **2015**, *31* (8), 598–604. (b) Hioki, S.; Yamada, T.; Hatano, K.; Ibaragi, Y. A Feasibility Study on Nitriding of Aluminum by Surface Melting. *J. Heat Treat.* **1980**, *1* (3), 65–72. (c) Mridha, S. Titanium Nitride Layer Formation by TIG Surface Melting in a Reactive Environment. *J. Mater. Process. Technol.* **2005**, *168*, 471–477.
125. (a) Björk, T.; Westergård, R.; Hogmark, S. Wear of Surface Treated Dies for Aluminium Extrusion – A Case Study. *Wear* **2001**, *249*, 316–323. (b) Kessler, O.; Surm, H.; Hoffmann, F.; Mayr, P. Enhancing Surface Hardness of Titanium Alloy Ti–6Al–4V by Combined Nitriding and CVD Coating. *Surf. Eng.* **2002**, *18* (4), 299–304. (c) Podgornik, B.; Hogmark, S.; Sandberg, O.; Leskovsek, V. Wear Resistance and Anti-Sticking Properties of Duplex Treated Forming Tool Steel. *Wear* **2003**, *254*, 1113–1121.
126. (a) Spies, H.-J.; Larisch, B.; Hock, K.; Broszeit, E.; Schroder, H.-J. Adhesion and Wear Resistance of Nitrided and TiN Coated Low Alloy Steels. *Surf. Coat. Technol.* **1995**, *74–75*, 178–182. (b) Bader, M.; Spies, H.-J.; Hock, K.; Broszeit, E.; Schroder, H.-J. Properties of Duplex Treated (Gas-Nitriding and PVD-TiN, -Cr_2N) Low Alloy Steel. *Surf. Coat. Technol.* **1998**, *98*, 891–896.
127. Walkowicz, J.; Smolik, J.; Tacikowski, J. Optimization of Nitrided Case Structure in Composite Layers Created by Duplex Treatment on the Basis of PVD Coating Adhesion Measurement. *Surf. Coat. Technol.* **1999**, *116–119*, 370–379.
128. Zeghni, A. E.; Hashmi, M. S. J. The Effect of Coating and Nitriding on the Wear Behaviour of Tool Steels. *J. Mater. Process. Technol.* **2004**, *155–156*, 1918–1922.

Relevant Websites

http://www.asminternational.org/web/hts/home
ASM International Heat Treating Society (HTS).

https://www.ferronova.com/international/web/lg/fer/likelgfer.nsf/repositorybyalias/training_nitr/$file/Nitr3.pdf
FERRONOVA Process Support.

http://global-heat-treatment-network.com/en/
Global Heat Treatment Network.

http://www.industrialheating.com/articles/89998-principles-of-gas-nitriding-the-nitriding-process-part-1?v=preview
Industrial Heating.

http://steel.keytometals.com/Articles/Art117.htm
Key to Metals.

http://coursenotes.mcmaster.ca/701-702_Seminars/2005-2006/701_JeromeDarbellay_March_2006.pdf
McMaster University.

http://www.gas-nitriding.com/index.php?p=1_6_Technical-Information
RGB Metallurgical Ltd.
http://standards.sae.org/ams2759/6a/
SAE International.
https://www.secowarwick.com/en/tech-spotlights-/gas-nitriding/
Seco/Warwick.
http://www.struers.com/resources/elements/12/101812/Application%20Notes%20Nitrided%20coatings%20English.pdf
Struers.
http://www.totalmateria.com/page.aspx?ID=CheckArticle&LN=EN&site=kts&NM=117
Total Materia.

2.5 Laser Beam Processing for Surface Modifications

BS Yilbas, King Fahd University of Petroleum and Minerals, Dhahran, Saudi Arabia

© 2017 Elsevier Inc. All rights reserved.

2.5.1	**Introduction**	137
2.5.2	**Experimental Studies**	137
2.5.3	**Background**	139
2.5.3.1	Phosphorous Bronze	139
2.5.3.2	Yttria-Stabilized Zirconia	140
2.5.3.3	Rene 41	140
2.5.4	**Findings and Discussions**	141
2.5.4.1	Phosphorous Bronze	141
2.5.4.2	Yttria-Stabilized Zirconia	144
2.5.4.3	Rene 41	147
2.5.5	**Concluding Remarks**	151
2.5.5.1	Phosphorous Bronze	151
2.5.5.2	Yttria-Stabilized Zirconia	151
2.5.5.3	Rene 41	151
Acknowledgments		151
References		152

2.5.1 Introduction

Lasers are widely used in surface engineering because of their superior processing characteristics. Some of these characteristics include precision of operation, local treatment, fast processing, and low cost. Although laser surface treatment has several advantages, high cooling rates during the processing give rise to development of high stress levels in the treated layer. If the process is not controlled through the proper selection of laser treatment parameters, surface defects including micro-cracks and voids become unavoidable. This lowers the treated surface quality and limits the practical applications of the laser-treated surface. In general, laser beam intensity distribution is Gaussian and the peak intensity occurs at the irradiated spot center. In order to increase the melted region across the irradiated spot, laser intensity remains high at the surface. This gives rise to partial evaporation at the surface, particularly in the region of the irradiated spot center. In some situations, the presence of oxygen in the laser-treated region triggers the exothermic reactions in the treated region. The excess energy released during the exothermic reaction results in increased rate of evaporation in the irradiated region while forming a deep cavity at the surface. Although the use of inert gas, as the assisting gas, during processing prevents the exothermic reactions, high intensity beam at the irradiated center can still cause the formation of the cavity at the surface. The size of the cavity can be controlled through the melt flow from the irradiated region toward the cavity center, however, care must be taken to avoid excessive melting and overflow of the molten material at the surface. The excessive melting and molten flow at the surface increases the surface roughness and modifies the morphological characteristics. In this case, wear resistance or surface hydrophobicity is negatively affected by the overlay of the molten material at the treated surface.

In laser surface treatment process, repetitive pulses with high frequency of repetition is favorable.[1] This is because of the fact that the repetition of the laser pulses results in overlapping of the irradiated spots when the workpiece or laser beam moves at a constant speed during the processing. Therefore, closely spaced scanning tracks are formed during the laser processing. The laser scanning tracks has two-fold effects, which are: (i) regular surface texture can be possibly resulted, and (ii) self-annealing effect can be created, which reduces the thermal stress levels in the irradiated region. In this case, heat conduction from the lately formed laser scanning tracks toward the early formed tracks alters the cooling rates in the laser-treated region. Consequently, this lowers the temperature gradients and thermal strain in the surface region while suppressing high levels of stress formation in this region. On the other hand, assisting gas contributes to the cooling rates through forced convection heat transfer from the irradiated surface. However, it was demonstrated that the heat transfer coefficient at the heated surface under the assisting gas is in the order of $3 \times 10^3\ \mathrm{W\,m^{-2}\,K^{-1}}$, which is relatively low as compared to the irradiated energy.[2] Therefore, the effect of assisting gas on the cooling rates is not significant at the laser-treated surface.

In the present chapter, laser treatment of three different materials including phosphorous bronze, yttria-stabilized zirconia, and Rene 41 is presented in line with the previous studies.[3–5] The background and relevant findings are given in accordance with each material considered.

2.5.2 Experimental Studies

Although theoretical analysis provides useful information on the thermal and stress fields taking place during laser surface treatment process, the experimental studies are necessary to

explore the actual changes in the laser-treated layer. Consequently, in this chapter, the main focus covers the experimental study of the laser surface processing.

A CO_2 laser (LC-ALPHAIII) delivering a nominal output power of 2 kW was used to ablate the workpiece surface. The nominal focal length of the focusing lens was 127 mm. The laser beam diameter focused at the workpiece surface was of the order of 200 μm. Nitrogen assist gas emerging from the conical nozzle and co-axial with the laser beam was used. The laser surface ablation process was carried out with different laser parameters. Therefore, through trial and error, the optimal laser parameters resulting in surface ablation with low surface roughness were selected. The laser melting/ablation parameters are given in **Table 1**. The laser treatment experiments were repeated three times to ensure almost the same topology at the surface under high pressure (600 kPa) nitrogen assisting gas ambient.

Material characterization of the laser ablated surfaces was carried out using SEM, EDS, AFM, and XRD. A Jeol 6460 electron microscope was used for the SEM examination and a Bruker D8 Advanced with CuKα radiation was used for XRD analysis. A typical setting for the XRD system was 40 kV and 30 mA, the scanning angle (2θ) was ranged over 20°–90°. The parabolically-shaped Göbel Mirror was used in the Bruker D8 Advanced; this provided highly-parallel X-ray beams.

A microphotonics digital hardness tester (MP-100TC) was used to obtain Vickers microindentation hardness values at the ablated surface. The standard test method for Vickers indentation hardness of advanced ceramics (ASTM C1327-99) was adopted. Microhardness was measured at the workpiece surface after the laser ablation process. The measurements were repeated five times at each location for the consistency of the results.

A linear micro-scratch tester (MCTX-S/N: 01-04300) was used to determine the friction coefficient of the laser ablated and as-received surfaces. The equipment was set at the contact load of 0.03 N and end load of 5 N. The scanning speed was 5 mm min^{-1} and loading rate was 5 N min^{-1}. The total length for the scratch tests was 5 mm.

The residual stress measurement relied on the stresses in fine grained polycrystalline structure. The position of the diffraction peak exhibited a shift as the specimen was rotated by an angle ψ. The magnitude of the shift was related to the magnitude of the residual stress. The relationship between the peak shift and the residual stress (σ) could be written as:

$$\sigma = \frac{E}{(1+\upsilon)sin^2\psi}\frac{(d_n - d_o)}{d_o} \quad [1]$$

where E is Young's modulus, υ is Poisson's ratio, ψ is the tilt angle, d_n is the d spacing measured at each tilt angle, and d_o is the stress-free lattice spacing. If there are no shear strains present in the specimen, the d spacing changes linearly with $\sin^2\psi$.

The fracture toughness of the surface was measured using the indenter test data for microhardness (Vickers) and crack inhibiting. In this case, the crack length generated due to indentation at the surface was measured. The length (l) measured corresponded to the distance from the crack tip to the indent. The crack lengths were individually summed to obtain $\sum l$ as described in the previous study.[6] The crack length 'c' from the center of the indent was the sum of individual crack lengths ($\sum l$) and half the indent diagonal length '$2a$.' Therefore, $c = a + \sum l$. However, depending upon the ratio of $\frac{c}{a}$, various equations were developed to estimate the fracture toughness (K). However, the equation proposed by Anstis *et al.*[7] has limitations due to nonlinearity of the coefficients for values of $\frac{c}{a} > 2$, which is not appropriate for the silicon carbide (≈ 1.5–2.1). Therefore, the equation proposed by Evans and Charles[6] is used to determine the fracture toughness (K_c), which is applicable for ($0.6 \leq \frac{c}{a} \leq 4.5$), i.e.:

$$K_c = 0.079\left(\frac{P}{a}\right)^{1.5} \cdot \log\left(4.5P\frac{a}{c}\right) \quad [2]$$

where P is the applied load on indenter, c is the crack length, and a is the half indent diagonal length.

The wetting experiment was performed using Kyowa (model – DM 501) contact angle goniometer. A static sessile drop method was considered for the contact angle measurement. The water contact angle between the water droplet and the laser-treated surface was measured with the fluid medium as deionized water. Droplet volume was controlled with an automatic dispensing system having a volume step resolution of 0.1 μl. Still images were captured, and contact angle measurements were performed after 1 s of deposition of water droplet on the surface. The experiments were repeated three times at different locations at the laser-treated and as-received surfaces. In order to determine the surface free energy of the laser-treated surface contact angle measurements are extended to include glycerol and diiodomethane. The analysis related to the surface energy formulation is presented in the light of the previous study.[8] The surface energy of solids and liquids can be divided into components according to Van Oss *et al.*[9–12]; in which case, the surface energy can be written as:

$$\gamma = \gamma^L + \gamma^P \quad [3]$$

Where γ^L is the apolar component due to Lifshitz–van der Waals intermolecular interactions and γ^P is due to electron acceptor and electron donor intermolecular interactions. However, γ^P can be written as[9–12]:

$$\gamma^P = 2\sqrt{\gamma^+ \cdot \gamma^-} \quad [4]$$

where γ^+ and γ^- are the electron acceptor and electron donor parameters of acid–base component of the solid and liquid

Table 1 Laser ablation conditions used in the experiment

Scanning speed (m s^{-1})	*Power (W)*	*Frequency (Hz)*	*Nozzle gap (mm)*	*Nozzle diameter (mm)*	*Focus setting (mm)*	*N_2 pressure (kPa)*
0.1	97	1500	1.5	1.5	127	600

surface free energy, respectively. The interfacial free energy for a solid–liquid system can be written as[9–12]:

$$\gamma_{SL} = \gamma_S + \gamma_L - 2\sqrt{\gamma_S^L \cdot \gamma_L^L} - 2\sqrt{\gamma_S^+ \cdot \gamma_L^-} - 2\sqrt{\gamma_S^- \cdot \gamma_L^+} \quad [5]$$

where subscripts S and L represent solid and liquid phases, respectively. However, the Young's equation for the surface free energy of a solid is[13]:

$$\gamma_L cos\,\theta = \gamma_S - \gamma_{SL} - Pe_L \quad [6]$$

where γ_S is the solid surface free energy, γ_{SL} is the interfacial solid–liquid free energy, γ_L is the liquid surface tension, θ is the contact angle, and Pe_L is the pressure of the liquid film, which is negligibly small and considered to be zero.[14] Combining eqns [5] and [6] and re-arrangements yield:

$$\gamma_L(cos\,\theta + 1) = 2\sqrt{\gamma_S^L \cdot \gamma_L^L} + 2\sqrt{\gamma_S^+ \cdot \gamma_L^-} + 2\sqrt{\gamma_S^- \cdot \gamma_L^+} \quad [7]$$

Equation [7] can be used to determine the values of γ_S^L, γ_S^+, and γ_S^- while incorporating the contact angle data for γ_L^L, γ_L^+, and γ_L^-. However, the data for γ_L^L, γ_L^+, and γ_L^- can be found in the open literature for water, glycerol, and diiodomethane, which are given in **Table 2**.[10,15] Since eqns [7], [4], and [3] are applicable only for smooth surfaces, experiments are repeated at lower power intensity to ensure thin layer of melting in the irradiated region. In this case, surface evaporation is avoided and the surface texture was not formed due to ablation. The contact angle measurements are repeated several times to ensure the repeatability of the contact angle data.

2.5.3 Background

The background and the literature for the surface treatment of the selected materials for the case studies are presented under the relevant subheadings in line with the previous studies[3–5]:

2.5.3.1 Phosphorous Bronze

The relevant literature related to the laser heating of phosphorus bronze is given below in line with the previous study.[3]

Phosphorous bronze finds wide applications in industry due to its good formability, desirable resistance to corrosion in marine environments,[16] and high electrical and thermal conductivities. In general, copper alloys have antimicrobial attributes and several bacteria, known to be human pathogens, die when they come in contact with dry copper and copper alloy surfaces at room temperature. It was demonstrated the amount of live bacteria dropped by several orders of magnitude, to zero in 1–2 h when they were in contact with a copper alloy surface.[17] However, the use of phosphor bronze in antibacterial environments requires special attention to improve the surface properties of the alloy prior to its application in such environments. In this case, improvement of the surface hydrophobicity of the alloy reduces the contact area of bacterial fluid and minimizes the stains left over after the dry-out of the hazardous fluid at the surface. However, phosphor bronze surface is hydrophilic and it is hard to repel the infected fluids from the surface.[18] The surface hydrophobicity can be improved significantly via texturing of the surface while forming a nano/micro size poles and cavities. One of the methods to texture the bronze surface is the laser ablation of the alloy surface in a controlled environment. In addition, laser surface treatment improves tribological properties of the surface such as hardness, wear, and corrosion resistance.[19–21] Although laser treatment improves surface characteristics of bronze, high temperature gradient generated during the process causes thermally induced cracks and limits the practical application of the treated surface. In addition, high thermal conductivity of bronze makes the desired thermal texturing difficult to achieve.

A study on surface properties of gilt-bronze artifacts after Nd:YAG laser cleaning was carried out by Lee *et al.*[22] They demonstrated that chemical cleaning removed corrosion products of copper through dissolution, however, the removal was not uniform at the surface. Microstructure and performance of laser cladding on surface of aluminum bronze was studied by Xu *et al.*[23] They demonstrated that the microstructure of cladding was affected by solidification rate and the microstructure was cellulated crystal at the surface; however, it was dendritic crystal in the middle section of the cladding. Laser surface alloying of a marine propeller bronze using aluminum powder was investigated by Cheng *et al.*[24] They showed that the galvanic effect between the laser-treated and as-received samples was small. Laser processing of nickel–aluminum bronze for improved surface corrosion properties was examined by Cottam *et al.*[25] The findings revealed that laser processing improved the corrosion resistance of the treated surface. Investigation of laser surface melting of a manganese–nickel–aluminum bronze was carried out by Tang *et al.*[26] They indicated that erosion–corrosion synergism constituted a significant contribution to the overall cavitation erosion–corrosion in 3.5 wt% NaCl solution for the treated surface. Mechanical and electrochemical properties of laser surface modified titanium alloy for biomedical applications were examined by Khosroshahi *et al.*[27] They showed that a high value of microhardness was resulted, which could be attributed to grain refinement associated with laser melting and rapid solidification. Laser melt injection of WC particles on aluminum surface was studied by Li *et al.*[28] They demonstrated that the powder should be fed from the back side of the laser beam to achieve appropriate surface enhancement effect and the depth of the melt layer increased first, and then decreased with increasing laser power. Laser processing of TiC reinforced composite layer on Al–Si alloy surface was investigated by Chan *et al.*[29] They demonstrated that unlike bronzes exposed to oxidizing conditions, which developed protective SnO_2 layers, the H_2S (aq)-exposed surface was considerably depleted in Sn.

Table 2 Lifshitz–van der Walls components and electron donor parameters used in the simulation

	γ_L ($mJ\,m^{-2}$)	γ_L^L ($mJ\,m^{-2}$)	γ_L^+ ($mJ\,m^{-2}$)	γ_L^- ($mJ\,m^{-2}$)
Water	72.8	21.8	25.5	25.5
Glycerol	64	34	3.92	57.4
Diiodomethane	50.8	50.8	0.72	0

2.5.3.2 Yttria-Stabilized Zirconia

The background and relevant literature on laser treatment of yttria-stabilized zirconia are given below in line with the previous study.[4]

Stabilized zirconia is widely used in industry due its superior properties such as high wear and temperature resistances, low thermal conductivity, etc. Some of the applications include thermal barrier coating in jet and diesel engines to allow operation at higher temperatures,[30] sensor technologies for oxygen sensing,[31] and fuel cell membranes operating at high temperatures.[32] The surface characteristics of stabilized zirconia, including hardness and hydrophobicity, can be improved further through various surface treatment methods. Since biomimetric characteristics of surfaces received great attention in industry, various methods have been developed in this regard. Some of these methods include phase separation,[33] electrochemical deposition,[34] template method,[35] emulsion,[36] plasma method,[37] crystallization control,[38] chemical vapor deposition,[39] sol–gel processing,[40] lithography,[41] electrospinning,[42] and solution immersion.[43] However, transforming lowsurface-energy materials into textured surfaces is one of the techniques, which can be used to enhance hydrophobicity of the surfaces. Laser surface texturing through a controlled ablation offers considerable advantages over the conventional texturing methods. Some of these advantages include high speed operation, high precision, local treatment, and low cost. However, the presence of the mixed regime of melting and ablation at the surface modifies the surface texture, which alters the wetting state of the surface. In addition, high stress levels are developed in laser-treated region because of the high temperature gradients, which are formed in the irradiated region due to high heating and cooling rates. The fraction toughness of the surface also reduces due to microhardness enhancement at the surface after the treatment process. Consequently, investigation of laser treatment of zirconia surface for improved hydrophobicity and assessment of the residual stress and the fracture toughness in the treated region becomes essential.

Laser surface treatment of partially stabilized zirconia for biomedical applications was presented by Hao and Lawrence.[44] They observed that the thickness of the adsorbed layer decreased as the polar surface energy of partially stabilized zirconia increased. Laser treatment of zirconia surfaces was examined by Chwa and Ohmori.[45] They indicated that the surface roughness of zirconia prior to the laser treatment was important, since the melt depth of the polished coatings was approximately half of the rough coatings when treated at the same power density. Laser surface treatment of plasma-sprayed yttria-stabilized zirconia coatings was investigated by Pinto *et al.*[46] They showed that the microstructure of the treated layer presented a cellular structure which has grown perpendicular to the surface and the micrographs depicted small cracks and absence of porosity. Laser surface nitriding of yttria-stabilized tetragonal zirconia was studied by Kathuria.[47] The findings revealed that the transformation of the t-ZrO_2 exhibited the typical yellow-gold color of ZrN with high hardness at the surface. Laser surface modification of plasma-sprayed yttria-stabilized zirconia coatings was examined by Shankar *et al.*[48] They observed that distinct interface separating fine and coarse grains took place at all scan speeds and the microhardness of the glazed surface improved considerably. Laser treatment of zirconia surface and morphological and microstructural changes in the treated layer was investigated by Daniel *et al.*[49] They showed that the surface morphology closely followed the microperiodic heat treatment provided by the interfering laser beams and the pore size distribution within the periodic surface morphology ranged from a few nanometers to a maximum of half of the periodic line distances. Laser ablation characteristics of yttria-doped zirconia in nanosecond and femtosecond regimes were studied by Heiroth *et al.*[50] They showed that femtosecond pulses prevented the exfoliation of micron-sized fragments, but result invariably in a pronounced ejection of submicron particles. Thermal fatigue properties of laser-treated surfaces were investigated by Aqida *et al.*[51] They observed that carbides and oxide compounds were formed on the laser-treated surface after the thermal fatigue test. Thermal stability of laser-treated die material for semisolid metal forming was examined by Aqida *et al.*[52] The findings revealed that crystallization in glazed zone increased as the annealing temperature increased and the microhardness decreased due to local crystallization at the surface.

Hydrophobicity of the substrate surfaces can be improved through forming fine poles at the surface during laser texturing.[53] The surface energy of zirconia can be modified by a laser heating at the surface,[54] which may further improve surface hydrophobicity.

2.5.3.3 Rene 41

The literature related to the laser treatment of Rene 41 is provided below in line with the previous study.[5]

Rene 41 is one of the nickel-based high-performance alloy, which exhibits excellent mechanical strength and high resistance to creep at high temperatures. It finds applications in the aerospace,[55] industrial gas turbine, and marine turbine industries.[56] Surface characteristics of high-performance alloy, such hardness, can be improved through restructuring of the surface through adopting some techniques while integrating grain refinement and hard particle injections at the surface. One of the methods to achieve improved surface hardness is laser controlled melting and hard particle injection during the process, since laser melting is involved with high heating and cooling rates, which result in grain refinement in the melted region. In addition, the depth of laser melted region is limited to tens of micrometers, which allow imbedding the hard particles, such as carbide particles, during the melting process.[57] However, high heating and cooling rates as well as presence of hard particles give rise to high micro-stress levels in the laser-treated layer, which trigger the formation of defect sites such as micro-cracks and crack networks at the treated surface. This, in turn, limits the practical application of the resulting treated surface. Consequently, investigation of surface characteristics due to laser control melting and presence of hard particles of Rene 41 surface becomes essential.

Effect of heat treatment on microstructure and mechanical properties of laser-treated Rene 41 was investigated by Li *et al.*[58] They showed that extensive precipitation of γ' resulted in high hardness and ductility, and the subsequent alignment and coalescence of γ' precipitates induced low strength in the

laser-treated layer. Microstructure evolution of laser repair welded nickel-based superalloy cast was studied by Wang *et al.*[59] Their findings revealed that, due to suffering from different thermal histories during the multi-pass welding process, microstructures within the weld region formed six distinct zones. In addition, no cracks were formed in the weld fusion zone or in the heat-affected zone when appropriate welding parameters were used. Laser treatment of nickel-based superalloy was examined by Durocher and Richards.[60] They indicated that laser-treated region was free from asperities and laser treatment could be one of the good candidates for repair applications of nickel-based superalloys. Laser treatment of nickel-based superalloys, in relation to repair applications, was studied by Rush *et al.*[61] They showed that cracking was caused primarily by liquation in the laser-treated layer and it was exacerbated by post-weld heat treatment cracking during the process. Influence of heat treatment on microstructure and hot crack susceptibility of laser-treated nickel-based superalloy was studied by Osterle *et al.*[62] They demonstrated that increasing fraction of grain boundaries with densely spaced borides and lack of secondary γ'-particles in matrix channels between the coarse cuboidal γ'-precipitates increased the rate of cracking in the laser-treated layer. Hot cracking in the heat-affected zone of laser-treated nickel-based superalloy was investigated by Matijasevic-Lux *et al.*[63] They showed that laser treatment resulted in different hot crack lengths in the heat-affected zone, which depended on local microstructural configuration in the close region of the treated region.

2.5.4 Findings and Discussions

The findings of the laser surface treatment of selected materials, including phosphorous bronze, zirconia, and Rene 41 are given in line with the previous studies[3–5] under the appropriate subheadings.

2.5.4.1 Phosphorous Bronze

The characteristics of laser-treated phosphorous bronze surface are given below.[3] The phosphor bronze with elemental composition (wt%) of 6% Sn, 0.1% P, and balance of Cu was used in the experiments. The samples were prepared from phosphor bronze sheet within the size of 3 mm in thickness and 20 mm × 20 mm (length × width).

Figure 1 shows SEM micrographs of laser ablated phosphor bronze surface. Laser ablation takes place during the irradiation of repetitive laser pulses along the laser scanning direction.

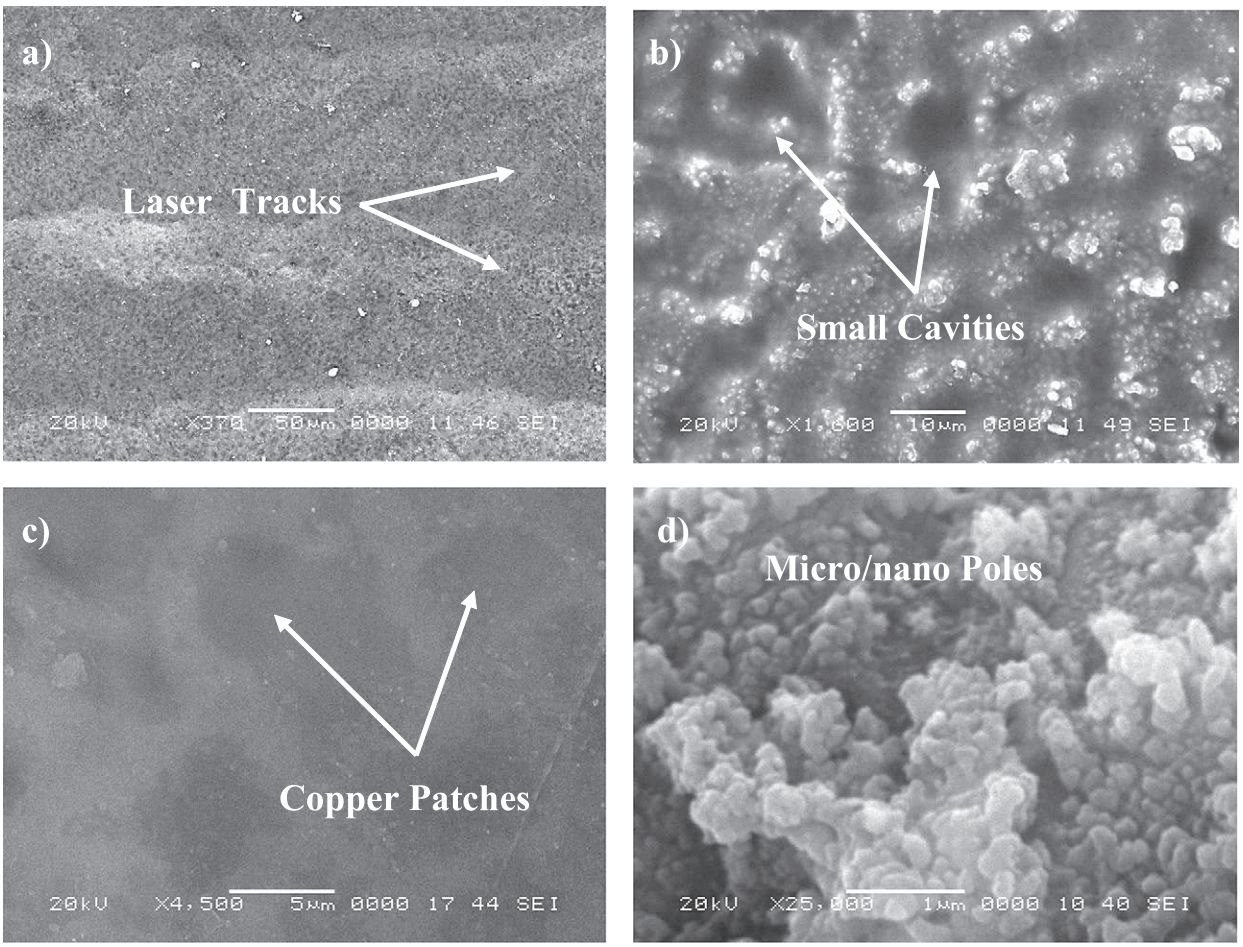


Figure 1 SEM micrographs of laser ablated phosphor bronze surface: (a) regular laser scanning tracks, (b) fine size cavities at ablated surface, (c) mahogany color and scattered Cu_3N dissolved spots, and (d) micro/nano size surface texture.[3]

The overlapping ratio is in the order of 70% at the surface. Laser intensity distribution is Gaussian and the pulse intensity remains high at the irradiated spot center. This in turn, results in surface evaporation in the region limited to the irradiated spot center and the melting takes place in the remaining region of the irradiated spot. The melt flow toward the cavity center from its neighborhood modifies the cavity shape and reduces to the cavity depth. Therefore, surface texture consisting of micro/nano poles and cavities is resulted at the treated surface. However, the close examination of the surface reveals that surface appears a mahogany and the presence of randomly scattered few red spots, which are indications of copper. The mahogany color represents the presence of Cu_3N in the surface region, which is also observed from X-ray diffractogram (Figure 2), i.e., the presence of Cu_3N (100) is associated with the high nitrogen pressure incorporated in the laser treatment process. The presence of few scattered copper spots is due to the dissolution of Cu_3N at elevated temperatures through forming NO_x gases. In this case, in the near region of the cavity, surface melts and solidifies rapidly because of the convection cooling of the nitrogen assisting gas; therefore, the dissolution of Cu_3N does not cover the whole surface. Laser-treated surface composes of submicron grains, which is attributed to the rapid solidification and formation of nitrides at the surface region. In addition, the submicron size of the packed particles indicates that each particle contains many single crystals of Cu_3N as consistent with the early work.[64] Although use of assisting gas increases cooling rates at the surface, no micro-cracks are observed in between the packed grains.

Figure 3(a) shows SEM micrographs of cross-section of the laser ablated layer. A dense structure, consisting of submicron-sized packed particles and extremely fine grains are formed in the surface region (Figure 3(b)). Formation of Cu_3N in the surface region lowers the density and causes volume shrinkage in the dense layer. In addition, the high quench rates in the cooling cycle after laser ablation is responsible for the formation of fine grains in the dense layer. A dendritic structure with elongated grains is observed at some distance below the dense layer (Figure 3(c)). The formation of a dendritic structure indicates the high rate of solidification in this region and the non-uniform cooling is responsible for the formation of the elongated grains. As the distance below the surface increases further, a cellular structure is formed (Figure 3(d)), which is associated with the relatively lower cooling rates as compared that of the surface region. EDS data for the elemental composition of the laser-treated surface are given in Table 3. Although quantification of the light elements in EDS data involves with error, presence of nitrogen is evident, which has a high concentration at the surface. The absence of Sn in some EDS spectrums indicates that Sn was evaporated in the surface region during the laser ablation process. The heat-affected zone is shallow without forming a demarcation line between the heat-affected zone and the base material, which is attributed to the high thermal conductivity of the bronze.

In the case of residual stress calculation, if shear strains are not present in the specimen, the d spacing changes linearly with $\sin^2\psi$. However, d_o is the inter-planar spacing when substrate material is free from stresses. Therefore, the calculations were performed for $Cu_3N(100)$ planes ($2\theta = 23.44^\circ$) with an inter-planar spacing of 0.3844 nm. It should be noted that Cu_3N is identified in accordance with the ICDD 00-055-0308 card. The linear dependence of $d(100)$ results in a slope of $-1.9 \times 10^{-3} \pm 9.12 \times 10^{-5}$ nm and intercept of $0.3844 \pm 4.75 \times 10^{-3}$ nm. The elastic module and Poisson's ratio of phosphor bronze are 96.5 GPa and 0.34,[26] respectively. The residual stress measured is of the order of -350 MPa, which is compressive, and the estimated error is ± 10 MPa, which is 2.4%. It should be noted that the error is estimated based on three repeats of the XRD measurements. Since ablation takes place along the laser scanning tracks, lately ablated regions creates a self-annealing effect on the previously ablated regions. This in turn modifies the cooling rates, particularly, below the surface. However, the self-annealing effect created during the cooling period does not significantly alter the stress levels in the surface vicinity because of the convective cooling of the assisting gas at the surface; therefore, the residual stress remains high in the surface region. It should be noted that the residual stress measured is limited to the surface vicinity, since the penetration depth of the X-ray radiation is of the order of few micrometers. Although the workpiece surface expands freely during the laser ablation process, the surface vicinity is not free to expand and

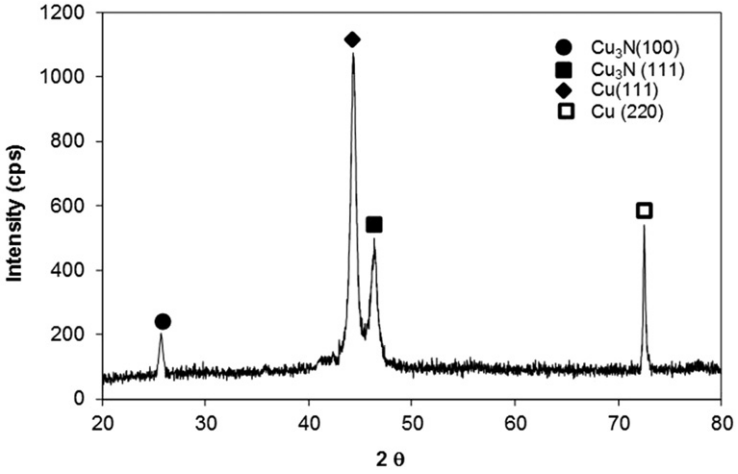


Figure 2 X-ray diffractogram of laser ablated surface for phosphorous bronze.[3]

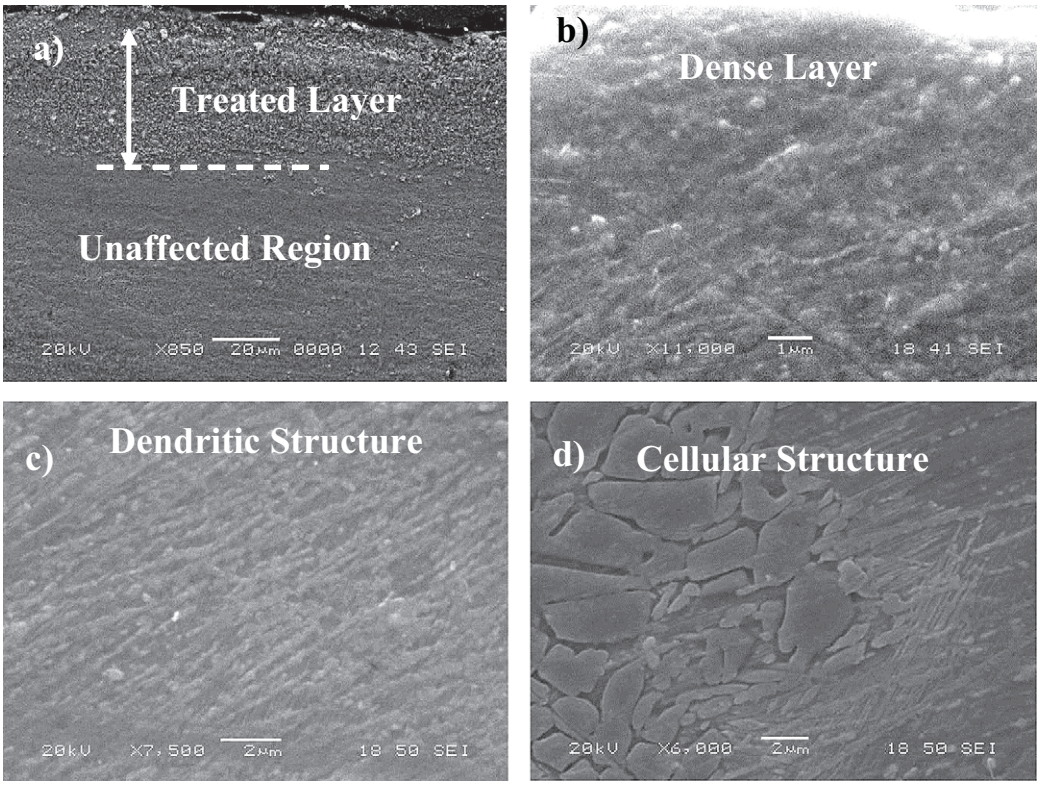


Figure 3 SEM micrographs of cross-section laser ablated layer phosphorous bronze: (a) cross-section, (b) small size grains, (c) dendritic structure, and (d) cellular structure.[3]

Table 3 EDS data and corresponding locations at the laser-treated surface (wt%)

Spectrum	*N*	*P*	*Sn*	*Cu*
Spectrum 1	7	–	5.7	Balance
Spectrum 2	4	0.1	6	Balance
Spectrum 3	6	0.1	5.8	Balance

Table 4 Microhardness and residual in the coating produced using two different wire materials

	Hardness (HV)	*Residual stress (MPa)*
Laser ablated surface	580 (+30/−30)	−350 (+10/−10)
As-received surface	140 (+10/−10)	–

compressive stresses are formed. This behavior is responsible for the attainment of high residual stress in the surface region. The microhardness and residual stress data for the laser ablated surface are given in **Table 4**. The microhardness of the laser ablated surface is high (580 ± 30 HV), which is almost four times hardness of the base material (145 ± 10 HV). This is due to one or all of the following: (i) the dense structure formed in the surface region, and (ii) the formation of Cu_3N compounds in the surface region after the laser ablation process. The residual stress measured by the XRD technique is of the order of -350 ± 10 MPa. **Figure 4** shows the scratch test results used to determine the friction coefficient of the laser ablated and as-received surfaces. The friction coefficient of the laser ablated surface is lower than that corresponding to as-received workpiece surface. This is mainly associated with the microhardness enhancement at the laser ablated surface because of the dense layer formation in the surface region under the high cooling rates and formation of Cu_3N at the surface due to high pressure nitrogen assisting gas. It should be noted that no peeling and delamination of the surface is observed during and after the scratch tests.

Since the laser ablated surface is chemically heterogeneous because of the local nitride formations (Cu_3N) and nitride dissolutions (through NO_x gas formation) at the surface the application of Young's equation[65] is limited to assess the contact angle. Wenzel[66] and Cassie and Baxter[67] proposed a relationship between the contact angle of a liquid droplet and the surface roughness factor to overcome this limitation. **Figure 5** shows optical images of the water droplet on the laser ablated and untreated surfaces while **Table 5** provides the data on the contact angle measurements at different locations at the surfaces. The contact angle varies slightly with the location at the surface, which is attributed to the surface texture variation and the texture composition at the surface.[68] In general, laser-treated surface demonstrates superhydyrophobic behavior and the averaged contact angle of the surface is in the order of 142°. Consequently, the texture of the laser ablated surface, consisting of fine pillars and poles at micro/nano scale, results in large contact angles of the water droplet.

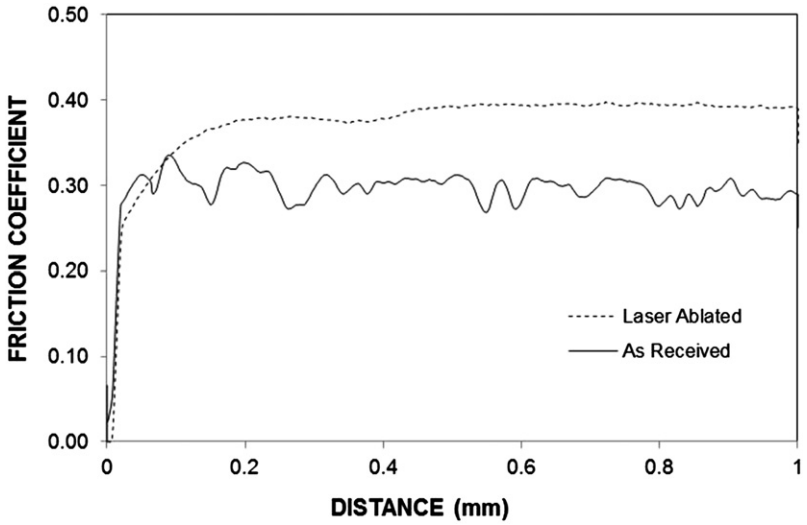


Figure 4 Friction coefficient for laser ablated and as-received phosphorous bronze.[3]

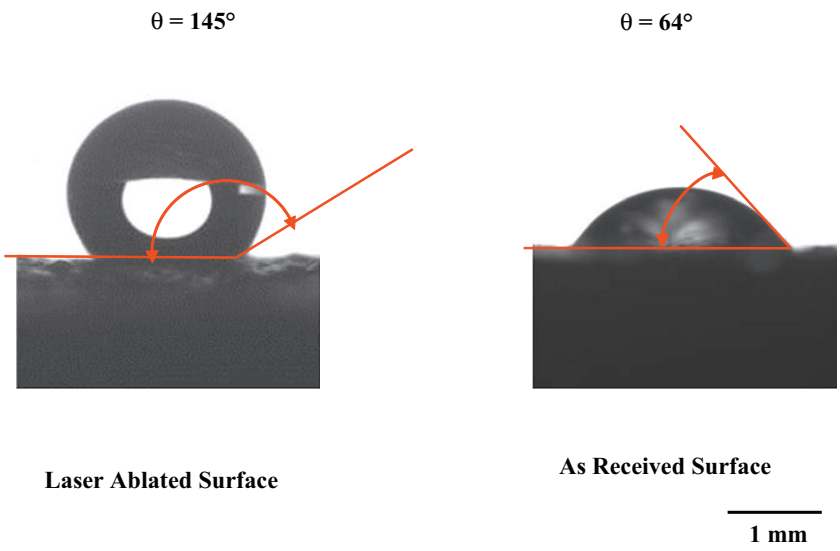


Figure 5 Optical images of water droplets for contact angle measurements for phosphorous bronze.[3]

Table 5 Contact angles measurement results at the surfaces of laser ablated and as-received workpieces

	Contact angle (degrees)	
	Location 1	*Location 2*
Laser ablated surface	148 (+5/−5)	141 (+5/−5)
As-received surface	62 (+5/−5)	63 (+5/−5)

2.5.4.2 Yttria-Stabilized Zirconia

The findings of the laser-treated zirconia surface characteristics are provided in line with the previous study.[4] The zirconia tiles measuring 25 mm × 15 mm × 3 mm were used in the experiments.

Figure 6 shows scanning electron microscope micrographs of the top surface of the treated layer. The laser scanning forms regular ablated/melted tracks at the surface. Due to the repetition of the laser pulses during the processing, laser irradiated spots are overlapped at the surface during the scanning. The overlapping ratio of the spots is in the order of 72%, which provides continuous ablated/melted sites along the tracks. The laser-treated surface is free from large scale asperities such as large scale cracks or crack networks, pores, and cavities. In addition, no melt flow is observed across the laser scanning tracks. The treated surface composes of micron/nano-sized grooves as consistent with the previous work.[69] The surface roughness varies along the laser scanning tracks, which is associated with the ablation of the surface during the scanning. In this case, laser beam partially impinges onto previously formed cavity and partially onto the neighboring untreated

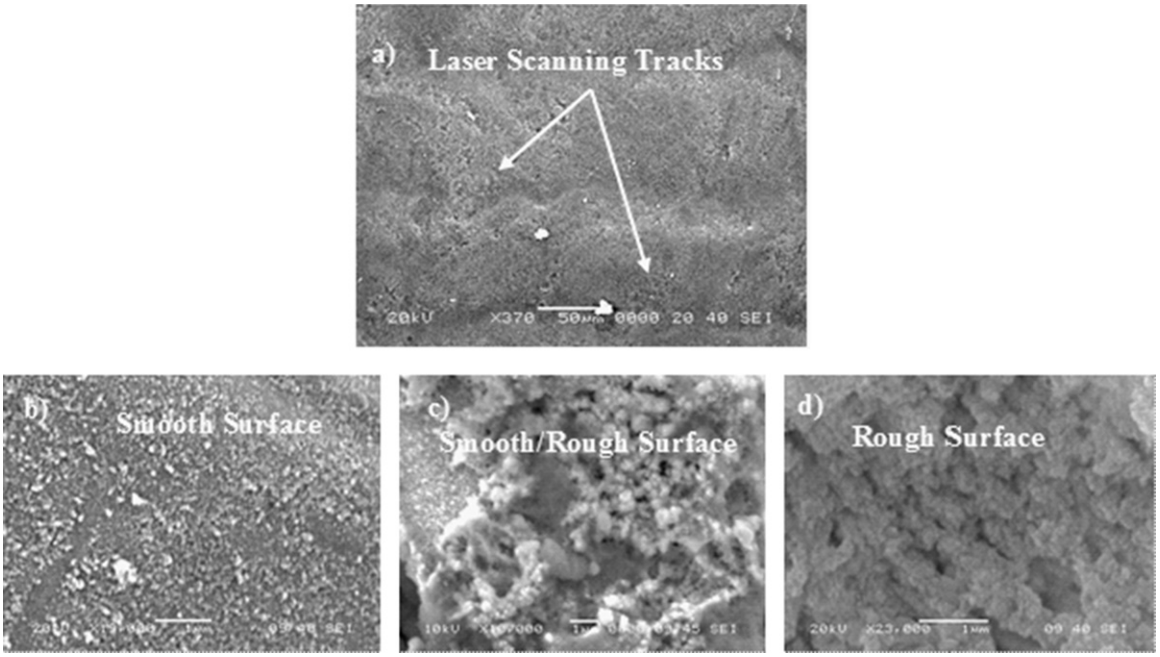


Figure 6 SEM micrographs of laser-treated zirconia surface: (a) laser-treated zirconia surface and presence of scanning tracks, (b) laser-treated zirconia smooth surface, (c) mixture of smooth and rough structures at laser-treated zirconia surface, and (d) laser-treated rough zirconia surface.[4]

surface along the scanning direction. Since the overlapping ratio is high, the area where the laser intensity incident onto the untreated neighboring surface becomes larger than that corresponding to the initially formed cavity surface. Therefore, laser intensity remains high on the untreated neighboring surface than that of the initially formed cavity surface because of the Gaussian intensity distribution of the incident laser beam. Low intensity causes partial melting of the initially formed cavity surface while modifying surface texture and altering the surface roughness along the scanning tracks. The micro-sized cavities are few and they are randomly distributed at the surface. The formation of micro-sized cavities can be explained in terms of the thermal agitation of the surface plasma at the irradiated surface. In this case, evaporated front absorbs the incident laser energy and forms small surface plasma, which is transiently hot.[70] The surface plasma acts like an additional heat source at the surface while increasing the cavity size during the ablation.

Figure 7 shows scanning electron microscope micrographs of the cross-section of the laser-treated layer. Laser treatment results in dense layer at the surface because of the high cooling rates in this region. The dense layer consists of fine grains and closely spaced fine dendrites forming a feathery-like structure in this region. The formation of dense layer is because of high cooling rates at the surface while forming the small grains. The surface layer has higher density than that of the untreated substrate below the dense layer, which causes volume shrinkage in the surface region. The dissolution of ZrN through NO_X formation and volume shrinkage in the dense layer causes some small size voids to be formed below the dense layer. However, the voids are small and few in numbers in the treated layer. As the depth below the surface increases, slightly longer and larger columnar structures are formed. This is attributed to the relatively lower cooling rates taking place in this region as compared to that in the surface region. Microcracks are not observed in the dense layer and in the large columnar region despite the occurrence of high cooling rates at the workpiece surface. This is because of the self-annealing effect of the lately formed laser scanning tracks. In this case, lately formed tracks act as heat source to initially formed tracks while generating a self-annealing effect on the previously formed tracks. The heat-affected zone is not observable at the interface of the laser-treated layer and the base material, which is associated with the low thermal conductivity of zirconia.

Figure 8 shows XRD diffractograms of the laser-treated and as-received surfaces. As-received material comprises of tetragonal ZrO_2 (t-ZrO_2). The presence of ZrN peaks are observed from the diffractogram for the laser-treated surface. The use of nitrogen at pressure is responsible for the formation of ZrN compound at the surface. However, ZrN compound is formed through a two step process. Firstly, the transformation of tetragonal structure of zirconia (t-ZrO_2) into cubic zirconia (c-ZrO_2), which takes place at high temperatures at the surface. Secondly, oxygen release through the dissociation process, which results in formation of zirconium nitride (ZrN). Therefore, the chemical process can be outlined as: $t\text{-}ZrO_2 \rightarrow c\text{-}ZrO_2$ and $2ZrO_2 + N_2 \rightarrow ZrN + O_2$, which occurs at elevated temperatures (above the melting temperature). However, the reactions that take place in the surface vicinity results in formation of vacancies in the zirconia,[71] which alters the surface energy. Elemental composition across the treated surface remains almost uniform, which can be observed from Table 6, in which the EDS data obtained from the laser-treated surface are given. Although the quantification of light elements, such as nitrogen, from the EDS data involves error, the presence of nitrogen is evident from the EDS data. This agrees with the presence of ZrN peaks in the XRD diffractogram. Table 7 gives the microhardness and fracture toughness of the

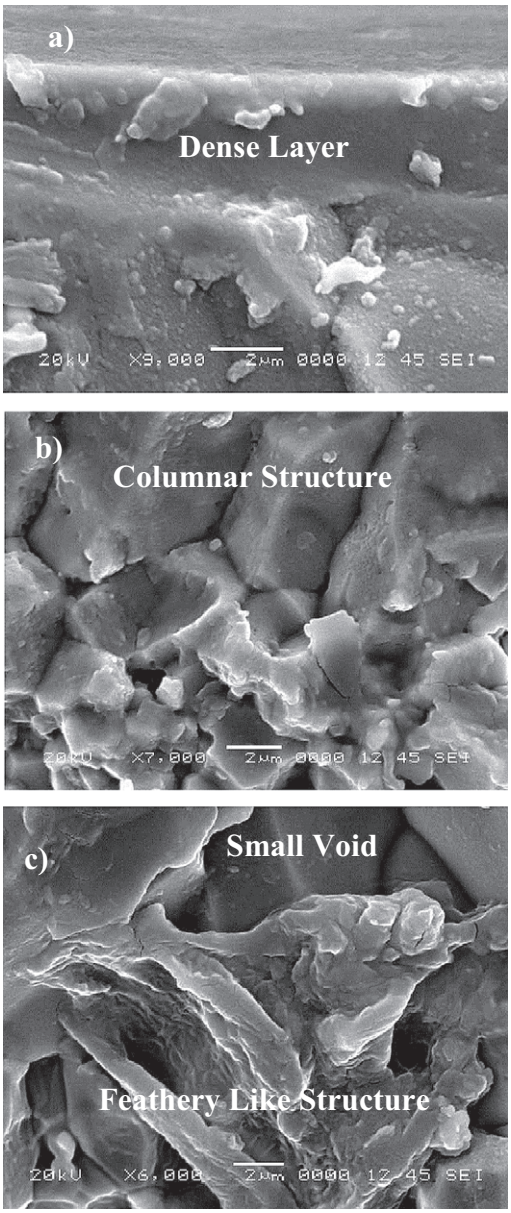


Figure 7 SEM micrographs of cross-section of laser-treated zirconia layer: (a) dense layer formed at the surface vicinity, (b) columnar structure formed below the surface, and (c) feathery-like structure in the treated layer.[4]

laser-treated and as-received surface. It is evident that the laser treatment improves the microhardness at the surface, however, fracture toughness reduces because of the microhardness enhancement at the surface. The formation of a dense layer, feathery-like structures, and presence of ZrN compound in the surface vicinity are responsible for the microhardness enhancement at the surface. The linear dependence of d(113), in nanometer unit, on $\sin^2\psi$ in the region of laser-treated surface can be used to determine the residual stress. The Zr_3O peak takes place at 63.106°, which corresponds to (113) plane with the inter-planar spacing of 0.147 2 nm. The slope of the curve indicates that the in-phase residual stress is compressive. The XRD experiment for the residual stress measurement was repeated five times at four locations at the laser-treated workpiece surface to secure the repeatability of the results. The error related to the measurements is estimated as 3%. The residual stress predicted is compressive and it is in the order of -1.6 ± 0.05 GPa.

Figure 9 shows images obtained from the contact angle measurements and **Table 8** gives the contact angles measured at different locations on the surface. The surface texture and surface energy influence the wetting properties of the surface.[68] Since the surface texture composes of micro/nano grooves, the wetting state varies across the surface. In addition, formation of ZrN at the surface alters the wetting state due to modification of the surface energy; in which case surface energy of laser-treated reduces due to formation of ZrN.[72,14] In the present study, the surface energy of laser-treated workpieces is measured as 49.33 mJ m^{-2}, which is very close to finding of the previous study (52.6 mJ m^{-2}) for ZrN.[15] In addition, the surface energy of as-received (untreated) workpiece is measured as 55.31 mJ m^{-2}, which is in agreement with the data reported in the previous study (56.1 mJ m^{-2}) for zirconia.[72] Consequently, laser treatment reduces the surface energy of the workpiece while contributing to surface hydrophobicity increase. Moreover, the combined wetting states can be explained through the Laplace pressure. In the case of nano-sized texturing, having a heterogeneous interface, confining the water at the air/water interface takes place. However, increasing Laplace pressure allows more air to be trapped in the groove, which in turn prevents the droplet meniscus touching the bottom surface of the groove while causing increased contact angle. The Laplace pressure estimated varies at the laser-treated surface because of combined micro/nano textures. The Laplace pressure estimated is in the range of $0.9 \times 10^4 - 0.1 \times 10^4$ Pa. This indicates the presence of Cassie state,[67] which can also be seen from the images of contact angle measurements. At some locations, where the micro-texturing is dominant, the Laplace pressure calculations lose its meaning and water meniscus touches the treated surface. Wenzel state[66] dominates in this region and the contact angle reduces, which can be seen from the image in **Figure 9**. The composite surface texture with the combination of micro/nano grooves results in two state of hydrophobicity at the treated surface, which can be seen from **Figure 9**. Since the droplet angle measurements repeated at nine locations at the treated surface, seven locations prevails the presence of Cassie state and two locations are in Wenzel state; therefore, Cassie state dominates over Wenzel state. It can also be observed from the photographs that in the first case (rough surface), Wenzel state takes place; therefore, the water droplet penetrates into the grooves and touches the surface without presence of the air gap.

2.5.4.3 Rene 41

The results obtained from laser-treated Rene 41 surfaces are given in line with the previous study.[5] Rene 41 sheets measuring 20 mm × 15 mm × 3 mm (length × width × thickness) are used in the experiments. The water soluble phenolic resin (thermoset viny-phenolic resin) mixed with B_4C and SiC particles are applied to the workpiece surfaces separately.

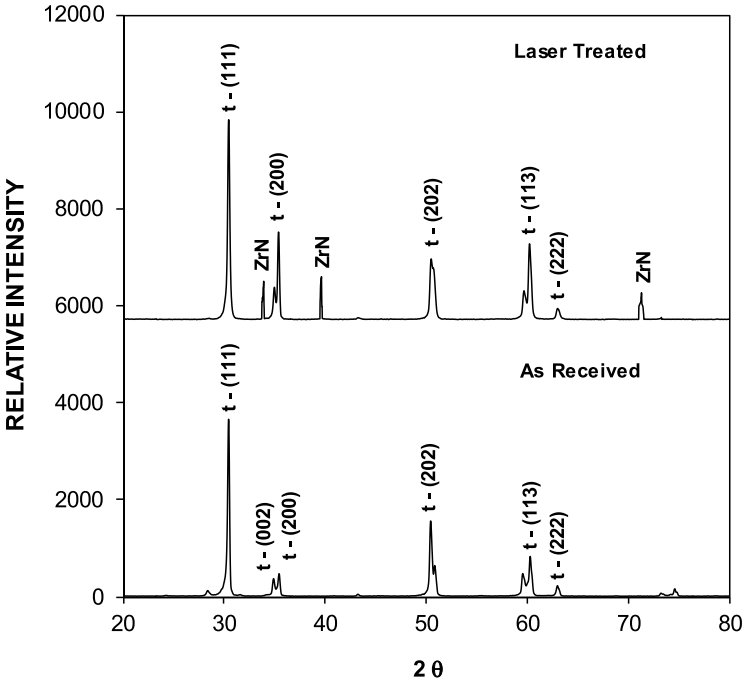


Figure 8 X-ray diffractogram of laser-treated and as-received zirconia surfaces.[4]

Table 6 EDS data for elemental composition of laser-treated workpiece surface (wt%)

Spectrum	*Y*	*N*	*O*	*Zr*
Spectrum 1	5	4	46	Balance
Spectrum 2	6	5	44	Balance
Spectrum 3	6	5	45	Balance

Table 7 Microhardness and fracture toughness and data used for fracture toughness calculations

	Hardness HV (GPa)	*Fracture toughness (MPa $\sqrt{m}$)*	*P (N)*	*a (μm)*	*c (μm)*
As-received surface	15.7 ± 0.06	9.5 ± 0.4	5	20	50
Laser-treated surface	19.2 ± 0.06	7.2 ± 0.4	5	25	50

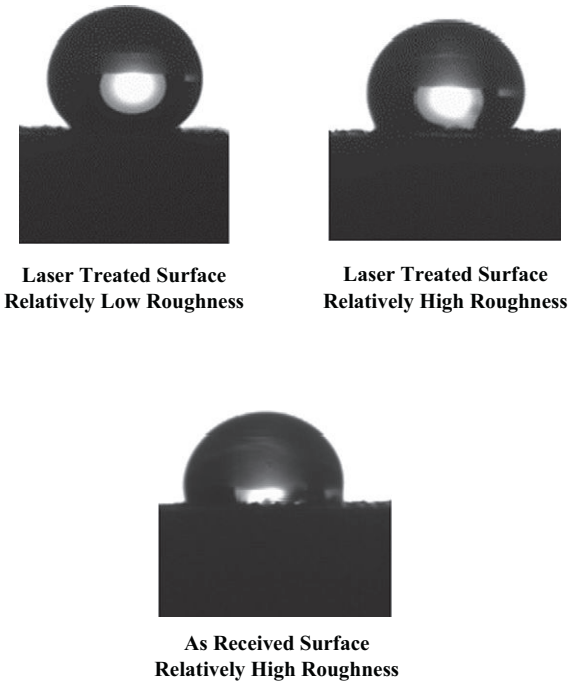


Figure 9 Photographs of water droplet shapes on the zirconia surface.[4]

The samples prepared for B_4C (only) and SiC (only) at the surface are kept at 8 bar argon pressure and 175 °C for 2 h in the furnace. The conversion of the phenolic matrix into carbon layer is ensured through monitoring the density. The average size of the B_4C and SiC particles is in the order of 2 and 4 μm, respectively, and the volume fraction of B_4C and SiC particles inserted into the carbon film is about 5%.

Figure 10 shows SEM micrographs of laser-treated surface. It can be observed that laser-treated surface composes of regular tracks, which are formed during laser scanning at the surface. Since laser pulses at high frequencies (1500 Hz) is used during scanning, overlapping of irradiated laser spots is responsible for the formation of these tracks. The overlapping ratio of laser irradiated spots is estimated as 70%, which in turn results in continuous melting of the surface along the laser scanning track. The close examination of the surface reveals that no melt

Table 8 Contact angles measurement results prior to and after the laser treatment using water, glycerol, and diiodomethane

	Contact angle (degrees)					
	Water		*Glycerol*		*Diiodomethane*	
	Low roughness	*High roughness*	*Low roughness*	*High roughness*	*Low roughness*	*Roughness*
Untreated	51.1±5		36.2±5		20.5±5	
Laser treated	121.4±5	98.8±5	114.6	93.4	41.1	40.2

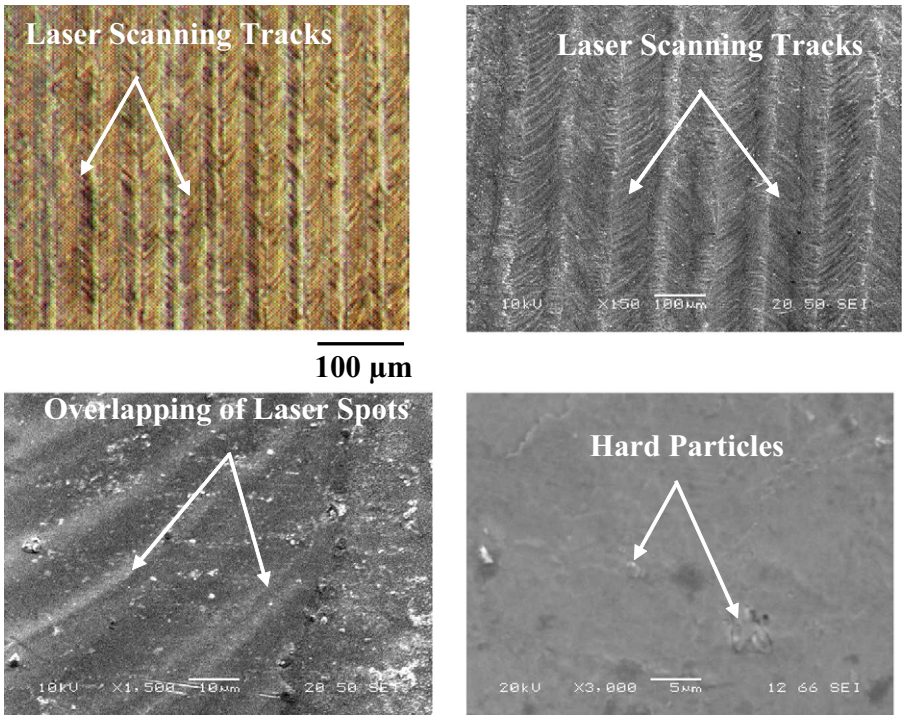


Figure 10 Optical and SEM micrographs of laser-treated Rene 41 surface with presence of B_4C particles.[5]

flow across the tracks and large size cavities are observed at the treated surface. This indicates the proper selection of laser parameters during scanning of the surface. It should be noted that slight increase in laser output power and decrease in scanning speed cause surface evaporation in the irradiated region. This, in turn, results in cavities and melt overflow at the surface while increasing the surface roughness. Surface roughness of the laser-treated workpiece is in the order of 2.3 µm, which is considerably low. Treated surface is free from asperities such as voids and cracks. This is attributed to self-annealing effect of the lately formed laser scanning tracks, which suppress stress levels in the region of the initially formed tracks. In this case, heat conduction from lately formed laser scanning tracks toward initially formed laser scanning tracks suppresses the cooling rates at the treated surface. Moreover, partially imbedded hard particles are evident from SEM micrographs. This is because of the high melting temperature of carbide particles, which remain in solid phase during the treatment process. Although thermal expansion coefficients of hard particles and the base material are different, no micro-cracks or crack networks are observed in the vicinity of the hard particles at the surface. It should be noted that expansion and contraction of hard particles differ from that of the base material; consequently, micro-stresses are formed in the near region of the hard particles after solidification of treated surface. The carbon film at the workpiece, prior to laser treatment, forms carbonic gasses during the high temperature laser processing at the surface. In addition, full wetting of the hard particles is observed at the surface, i.e., no partially wetted particle while causing a void in its near neighborhood is observed. It should be noted that because of the differences in thermal expansion coefficients between the hard particles and the base substrate, wetting state of the particles may change during the solidification process. In this case, the surface tension force, due to melted base material, generated around the hard particle surface overcomes the force created by the differences in thermal contraction between the melted metal and the solid hard particle during the solidification.

Figure 11 shows SEM micrographs of cross-section of laser-treated regions. Laser-treated layer, mainly, composes of three

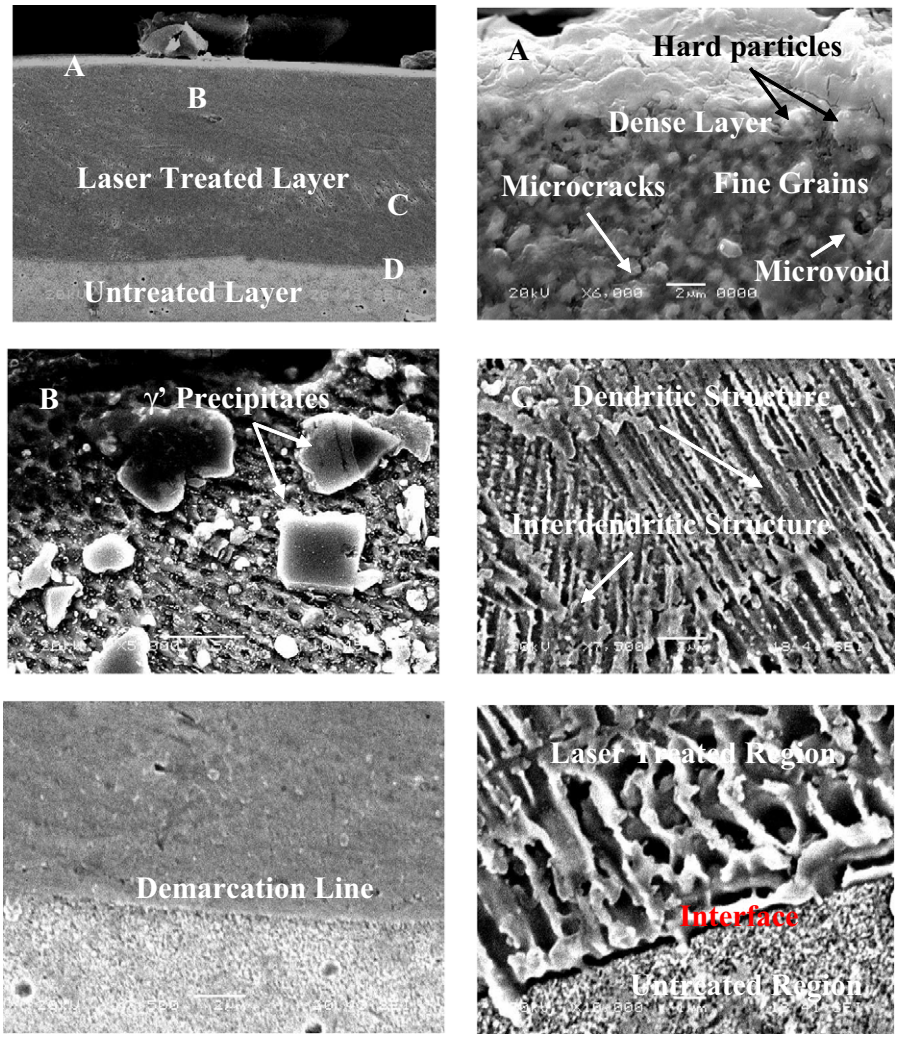


Figure 11 SEM micrographs of laser-treated layer cross-section for Rene 41: (a) Cross-section, (b) Dense layer composes of fine grains and hard B4C particles, (c) γ' phases below the treated surface, (d) dendritic structure and short interdendritic arms, (e) demarcation line at the vicinity of heat-affected zone, and (f) interface between treated layer and the untreated base material of Rene 41.[5]

regions. In the first region, a dense layer is formed, which consists of fine grains and hard particles. This is attributed to high cooling rates at the surface and high melting temperature of hard particles. Convection effect of the assisting gas contributes to cooling rate enhancement at the surface. However, dense layer increases the density of the treated layer while causing volume shrinkage in this region. Therefore, volume shrinkage due to the density mismatched in the treated layer causes increased stress level, particularly in the interface zone of the first region. Moreover, mismatch of thermal expansion coefficients between hard particles and base material contributes to the stress levels in the surface region, which is particularly true for B_4C carbide particles ($12.6 \times 10^{-6}\,K^{-1}$), which have higher thermal expansion coefficient than that of SiC particles ($5.68 \times 10^{-6}\,K^{-1}$).[73] Consequently, few microcracks are observed around B_4C particles in the region close to the surface. These cracks are locally distributed and do not conform a crack network below the surface of laser-treated layer. This is attributed to the stress relaxation after the microcrack formation in the neighborhood of hard particles. In addition, a micro-void next to the hard particle is observed, which is associated with the difference between the contraction rates of hard particles and base material as well as surface texture of hard particles. It should be noted that the wettability state of the surface is highly influenced by the surface texture.[74] Nevertheless, the size of the voids is small and they are few in number, which do not cover a large area in the treated layer. The dendritic structures are formed in the region below the dense layer and locally distributed MC carbides are formed in the interdendritic regions (where M represents Ti and Mo). This is attributed to the interdendritic zones where solidification takes place slowly and liquid phase solidifies lastly. This in turn, results in solute enrichment leading to the formation of MC carbides.[75] The secondary dendrite arms are present because of large dendrites formed below the dense layer, which are attributed to relatively slow cooling rates as compared to that of at the surface. γ' phases of cubic morphology are also observed in this region and their sizes varies. Since small solutes precipitate diffuse to form large ones, the coarsening of γ' phases takes place through minimization of

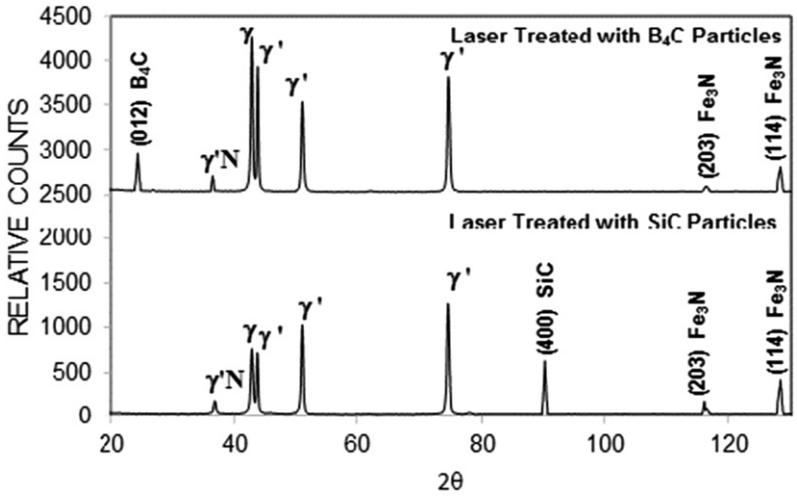


Figure 12 X-ray diffractogram for laser-treated Rene 41 surfaces.[5]

Table 9 EDS data obtained at laser-treated surface with presence of particles (wt%). Each spectrum represents a treated surface with different particles

	Al	*Si*	*B*	*Cr*	*Fe*	*Co*	*N*	*Mo*	*Ni*
Spectrum (including B_4C)	2.1	–	4.8	21	4.1	12.1	5.3	2.1	Balance
Spectrum (including SiC)	1.9	5.1	–	19.7	4.2	11.6	4.2	1.9	Balance

interfacial energy.[76] The presence of heat-affected zone is evident and the demarcation zone is clearly observed between the treated layer and base material.

Figure 12 shows X-ray diffractogram of the laser-treated surface with presence of B_4C and SiC separately at the surface. $\gamma'N$ nitride peak is evident from the diffractogram at the surface, which is subjected to high pressure nitrogen assisting gas during the treatment process. Therefore, high temperature reactions at the surface results in formation of $\gamma'N$ nitride species at the surface. In addition, γ and γ' phases are visible in the diffractogram. The presence of B_4C and SiC peaks reveal the existence of solid phase particles at the surface vicinity. Fe_3N peaks are observed in the diffractogram, which is attributed to a high pressure nitrogen assisting gas impinging at the surface. Due to small volume of intermetallic phases, MC carbides are not observed in the diffractogram. The EDS data (as shown in Table 9) reveals that the elemental composition of laser-treated and untreated surfaces are almost the same. In addition, aluminum reduction does not occur at the treated surface unlike the observation presented in the previous study.[77] The quantification of nitrogen, which is one of the light elements, is involved with an error in energy dispersive spectroscopic analysis, yet its presence is evident from the EDS data.

Indentation test results for microhardness are given in Table 10 for laser-treated and untreated surfaces. The data presented in the previous study for laser induced surface nitriding are also included for the comparison reason. In general, inclusion of hard particles (TiC, SiC, and B_4C) results in higher microhardness at the surface than that corresponding to laser gas assisted nitrided surface. This is associated with the

Table 10 Microhardness data for TiC and laser-treated, laser-treated, and as-received surfaces

	Microhardness (HV)	*Residual stress (MPa)*
As-received surface	390	–
Laser nitrided surface	460	−680
TiC and laser treated	520	−850
SiC and laser treated	500	−720
B_4C and laser treated	610	−890

micro-stress levels developed in the close region of the hard particles at the surface. In addition, laser-treated surface with presence of B_4C particles results in the highest microhardness. This is attributed to thermal expansion and contraction of B_4C particles, which is higher than those of SiC and TiC.[73] Consequently, the micro-stress levels developed in the near region of B_4C particles become higher than those of due to SiC particles. As compared to base material hardness, laser treatment enhances microhardness at the surface, which is because of the formation of fine grains, nitride species, and micro-stresses developed due to presence of hard particles in the surface region.

The (114) reflection from the ε-Fe_3N (ICDD-PDF4 04-007-2962) was used for residual stress measurements. The measurements were carried out normal to the workpiece surface and the linear dependence of d(114) on $\sin^2\psi$ in the region of laser-treated surface was established. The ε-Fe_3N peak takes place at 128.445°, which corresponds to d(114) plane with the inter-planar spacing of 0.8570 Å. The linear dependence of d(114) results in the slope of -5.08×10^{-13} m and the

intercept of 0.8570×10^{-10} m for the laser-treated surface containing B_4C particles. The residual stress, therefore, determined from the XRD technique at the surface vicinity is of the order of -890 ± 30 MPa. The measurements are repeated for the other laser-treated surfaces containing SiC particles. XRD measurements are repeated three times and the error related to the measurements is of the order of 3%. Residual stresses are given in Table 10 for laser-treated with presence of hard particles and laser gas assisted nitrided surfaces. Residual stress increases with presence of hard particles, which is more pronounced for B_4C particles. This is because of high micro-stress levels developed around the hard particles at the surface, particularly in the near region of B_4C particles. In addition, the formation of dense layer in the surface region, due to high cooling rates, causes the volume shrinkage in the surface region, which contributes to residual stress enhancement at the treated surface.

2.5.5 Concluding Remarks

Laser surface treatment offers considerable advantages over the conventional methods. In order to achieve the desired texture and characteristics at the treated surface, the proper selection of the laser treatment parameters are essential. Metallic and nonmetallic material surfaces can be treated with high precision, in which case, surface asperities including micro-cracks, voids, and cavities can be avoided. In addition, the use of high pressure nitrogen assisting gas forms the nitride species at the surface, which improves the microhardness and hydrophobicity of the surface. Laser scanning along the closed spaced tracks at the workpiece surface creates self-annealing effect in the treated region while modifying the cooling rates at the surface. This in turn lowers the thermal strain and stress levels in the laser-treated layer. The conclusions of the case studies are given in line with the previous studies under the appropriate subheadings.

2.5.5.1 Phosphorous Bronze

The laser-treated phosphorous bronze surface consists of micro/nano poles and cavities, which result in superhydrophobic characteristics at the ablated surface. The average contact angle of the surface is 142°, which is well above that corresponding to as-received surface. The use of high pressure nitrogen assisting gas gives rise to the formation of Cu_3N phase at the surface, which contributes to the formation of a dense layer in the vicinity of the ablated surface via volume shrinkage. A dense layer comprises of submicron-sized packed particles and extremely fine grains, which in turn contributes significantly to microhardness enhancement at the surface. Microhardness of the laser ablated surface is four-fold higher than as-received workpiece surface, which in turn lowers the friction coefficient at the surface. The residual stress formed in the surface vicinity is compressive and it is in the order of -350 ± 10 MPa. The findings reveal that laser ablation of phosphor bronze provides superhydrophobic surface, high hardness, reasonably low residual stresses, and low friction coefficient.

2.5.5.2 Yttria-Stabilized Zirconia

The surface of laser-treated zirconia is free from large size cracks and cavities and the surface texture composes of fine grooves. The surface roughness was well-altered by the laser processing with the maximum surface roughness generated to be of the order of 0.35 μm. This in turn, modifies the wetting state of the surface, provided that Cassie state dominates over Wenzel state at the treated surface. In addition, formation of ZrN modifies the surface energy while contributing to the hydrophobicity enhancement at the surface. A dense layer consisting of fine size grains are formed at the surface. The volume shrinkage, because of the dense layer formation at the surface, causes few scattered voids in the dense layer. The treated surface is free from large scale asperities such as micro-cracks and crack networks, and large size pores and cavities. The use of high pressure nitrogen assisting gas during the processing resulted in the formation of ZrN compounds at the surface. Laser treatment increased the microhardness and lowered the fracture toughness of the surface. The measured decrease in the fracture toughness was associated with the microhardness enhancement at the surface. The residual stress measured from the X-ray diffraction data is in the order of -1.6 ± 0.05 GPa, which is compressive.

2.5.5.3 Rene 41

The laser-treated Rene 41 surface is free from large size asperities such as cavities and cracks. High cooling rates results in dense layer formation in the surface region while causing volume shrinkage and contributing to residual stress formation. Use of nitrogen at high pressure as an assisting gas results in formation of nitride species, such as $\gamma'N$ and Fe_3N at the treated surface. These new nitride phases also contribute to microhardness and residual stress enhancement at the treated surface. MC carbides are formed in the interdendritic regions below the dense layer. Due to the mismatch between the thermal expansion coefficients of hard particles and base substrate, micro-stresses are formed in the neighborhood of hard particles, which is more pronounced for B_4C particles. In this case, the wetting characteristics of hard particles vary and few micro-voids are formed adjacent to B_4C particles. In addition, because of high thermal expansion confident of B_4C, few scattered micro-cracks are observed around B_4C particles. Residual stress is the highest for laser-treated surface with presence of B_4C particles, then follows SiC and B_4C particles.[5]

Acknowledgments

The authors acknowledge the financial support of King Fahd University of Petroleum and Minerals (KFUPM) through project number SB131007 to accomplish this work.

References

1. Yilbas, B. S.; Ali, H. Laser Treatment of Alumina Surface with Chemically Distinct Carbide Particles. *Optic. Laser Technol.* **2014**, *64*, 1–6.

2. Yilbas, B. S.; Shuja, S. Z. The Influence of Gas Jet Velocity in Laser Heating – A Moving Workpiece Case. *Proc. Inst. Mech. Eng., Part C: J. Mech. Eng. Sci.* **2000**, *214*, 1059–1078.
3. Yilbas, B. S. Laser Ablation of Phosphor Bronze for Superhydrophobic Surface. *Surf. Eng.* **2015**, Available from: http://dx.doi.org/10.1179/1743294414Y.0000000325 (accessed February 16, 2016).
4. Yilbas, B. S. Laser Treatment of Zirconia Surface for Improved Surface Hydrophobicity. *J. Alloy. Compds.* **2015**, *625* (15), 208–215.
5. Yilbas, B. S. Characterization of Laser Treated Rene 41 Surface Due to B_4C and SiC Particles at Surface Prior to Laser Treatment. *Surf. Int. Anal.* **2014**, *46* (1), 30–35.
6. Evans, A. G.; Charles, E. A. Fracture Toughness Determinations by Indentation. *J. Am. Ceram. Soc.* **1976**, *59* (7–8), 371–372.
7. Anstis, G. R.; Chantikul, P.; Lawin, B. R.; Marshall, D. B. A Critical Evaluation of Indentation Techniques for Measuring Fracture Toughness: I, Direct Crack Measurements. *J. Am. Ceram. Soc.* **1981**, *64*, 533–538.
8. Gonzalez-Martin, M. L.; Labajos-Broncano, L.; Janczuk, B.; Bruquez, J. M. Wettability and Surface Free Energy of Zirconia Ceramics and Their Constituents. *J. Mater Sci.* **1999**, *34*, 5923–5926.
9. Van Oss, C. J.; Good, R. J.; Chaudhury, M. K. Mechanism of DNA (Southern) and Protein (Western) Blotting on Cellulose Nitrate and Other Membranes. *J. Chromatogr.* **1987**, *391*, 53–65.
10. Van Oss, C. J.; Good, R. J.; Busscher, H. J. Estimation of the Polar Surface Tension Parameters of Glycerol and Formamide for Use in Contact Angle Measurements on Polar Solids. *J. Disp. Sci. Technol.* **1990**, *11*, 75–81.
11. Van Oss, C. J.; Chaudhury, M. K.; Good, R. J. Interfacial Lifshitz-van der Waals and Polar Interactions in Macroscopic Systems. *Chem. Rev.* **1988**, *88* (6), 927–941.
12. Zenkiewicz, M. Methods for the Calculation of Surface Free Energy of Solids. *J. Achiev. Mater. Manuf. Eng.* **2007**, *24* (1), 137–145.
13. Adamson, A. W. Physical Chemistry of Surface, 5th ed.; Wiley-Interscience: New York, NY, 1991.
14. Sun, C.-C.; Lee, S.-H.; Hwang, W.-C.; Hwang, J.-S.; Tang, I.-T.; Fu, Y.-S. Surface Free Energy of Alloy Nitride Coatings Deposited Using Closed Field Unbalanced Magnetron Sputter Ion Plating. *Mater. Trans.* **2006**, *47* (10), 2533–2539.
15. Janczuk, B.; Wojcik, W.; Zdziennicka, A. Determination of the Components of the Surface Tension of Some Liquids from Interfacial Liquid–Liquid Tension Measurements. *J. Coll. Int. Sci.* **1993**, *157* (2), 384–393.
16. Han, Z.; He, Y. F.; Lin, H. C.; Zhao, H. Dealloying Characterizations of Cu–Al Alloy in Marine Environment. *J. Mater. Sci. Lett.* **2000**, *19* (5), 393–395.
17. Grass, G.; Rensing, C.; Solioz, M. Metallic Copper As an Antimicrobial Surface. *Appl. Environ. Microbiol.* **2011**, *77* (5), 1541–1547.
18. Shirtcliffe, N. J.; McHale, G.; Newton, M. I.; Perry, C. C. Wetting and Wetting Transitions on Copper-Based Super-Hydrophobic Surfaces. *Langmuir* **2005**, *21* (3), 937–943.
19. Yilbas, B. S.; Toor, I.; Malik, J.; Patel, F.; Karatas, C. Electrochemical Testing of Laser Treated Bronze Surface. *J. Alloy. Compds.* **2013**, *563*, 180–185.
20. Yilbas, B. S.; Akhtar, S.; Karatas, C. Laser Nitriding of the Surface of Phosphor Bronze. *Int. J. Adv. Manuf. Technol.* **2013**, *65* (9–12), 1553–1565.
21. Yilbas, B. S.; Akhtar, S.; Karatas, C.; Chatwin, C. Laser Embedding of TiC Particles into the Surface of Phosphor Bronze. *Surf. Int. Anal.* **2012**, *44* (7), 831–836.
22. Lee, H.; Cho, N.; Lee, J. Study on Surface Properties of Gilt-Bronze Artifacts, After Nd:YAG Laser Cleaning. *Appl. Surf. Sci.* **2013**, *284*, 235–241.
23. Xu, J.-L.; Yang, B.; Gao, W.; *et al.* Microstructure and Performance of Laser Cladding on Surface of Aluminum Bronze. *J. Aeronaut. Mater.* **2009**, *29* (1), 63–67.
24. Cheng, F. T.; Tang, C. H.; Man, H. C. Laser Surface Alloying of a Marine Propeller Bronze Using Aluminium Powder. *Surf. Coat. Technol.* **2006**, *200* (8), 2594–2601.
25. Cottam, R.; Barry, T.; McDonald, D.; *et al.* Laser Processing of Nickel–Aluminum Bronze for Improved Surface Corrosion Properties. *J. Laser Appl.* **2013**, *25* (3), doi:10.2351/1.4799555.
26. Tang, C. H.; Cheng, F. T.; Man, H. C. Effect of Laser Surface Melting on the Corrosion and Cavitation Erosion Behaviors of a Manganese–Nickel–Aluminium Bronze. *Mater. Sci. Eng.: A (Struct. Mater.: Prop., Microstruct. Process.)* **2004**, *A373* (1–2), 195–203.
27. Khosroshahi, M. E.; Mahmoodi, M.; Saeedinasab, H.; Tahriri, M. Evaluation of Mechanical and Electrochemical Properties of Ti_6Al_4V Alloy Surface Modified by Nd:YAG Laser for Biomedical Applications: An *In Vitro* Study. *Surf. Eng.* **2008**, *209*, 24–27.
28. Li, F. Q.; Li, L. Q.; Chen, Y. B. Arc Enhanced Laser Melt Injection WC Particles on Al Surface. *Surf. Eng.* **2013**, *29* (4), 296–299.
29. Chan, M.; Capek, A.; Brill, D. A.; Garrett, S. J. Characterization of the Patina Formed on a Low Tin Bronze Exposed to Aqueous Hydrogen Sulfide. *Sur. Interface Anal.* **2014**, doi:10.1002/sia.5520.
30. Almeida, D. S.; Cairo, C. A. A.; Silva, C. R. M.; Nono, M. C. A. Thermal Barrier Coating by Electron Beam-Physical Vapor Deposition of Zirconia Co-Doped with Yttria and Niobia. *J. Aerosp.Technol. Manag.* **2010**, *2* (2), 195–202.
31. Benammar, B. Design and Assembly of Miniature Zirconia Oxygen Sensors. *IEEE Sens. J.* **2004**, *4* (1), 3–8.
32. Silva, V. S.; Ruffmann, B.; Silva, H.; *et al.* Zirconium Oxide Hybrid Membranes for Direct Methanol Fuel Cells – Evaluation of Transport Properties. *J. Membr. Sci.* **2006**, *284* (1–2), 137–144.
33. Han, J. T.; Xu, X. R.; Cho, K. W. Diverse Access to Artificial Superhydrophobic Surfaces Using Block Co-Polymers. *Langmuir* **2005**, *21* (15), 6662–6665.
34. Shirtcliffe, N. J.; McHale, G.; Newton, M. I.; Chabrol, G.; Perry, C. C. Dual-Scale Roughness Produces Unusually Water-Repellent Surfaces. *Adv. Mater.* **2004**, *16* (21), 1929–1932.
35. Hwang, H. S.; Lee, S. B.; Park, I. Fabrication of Raspberry-Like Superhydrophobic Hollow Silica Particles. *Mater. Lett.* **2010**, *64* (20), 2159–2162.
36. Yang, T.; Tian, H.; Chen, Y. Preparation of Superhydrophobic Silica Films with Honeycomb-Like Structure by Emulsion Method. *J. Sol–Gel Sci. Technol.* **2009**, *49* (2), 243–246.
37. Kinoshita, H.; Ogasahara, A.; Fukuda, Y.; Ohmae, N. Superhydrophobic/Superhydrophilic Micropatterning on a Carbon Nanotube Film Using a Laser Plasma-Type Hyperthermal Atom Beam Facility. *Carbon* **2010**, *48* (15), 4403–4408.
38. Guo, Z. G.; Fang, J.; Hao, J. C.; Liang, Y. M.; Liu, W. M. A Novel Approach to Stable Superhydrophobic Surfaces. *Chem. Phys. Chem.* **2006**, *7* (8), 1674–1677.
39. Lau, K. K.; Bico, J.; Teo, K. B. K.; *et al.* Superhydrophobic Carbon Nanotube Forests. *Nano Lett.* **2003**, *3* (12), 1701–1705.
40. Latthe, S. S.; Imai, H.; Ganesan, V.; Rao, A. V. Superhydrophobic Silica Films by Sol–Gel Co-Precursor Method. *Appl. Surf. Sci.* **2009**, *256* (1), 217–222.
41. Furstner, R.; Barthlott, W.; Neinhuis, C.; Walzel, P. Wetting and Self-Cleaning Properties of Artificial Superhydrophobic Surfaces. *Langmuir* **2005**, *21* (3), 956–961.
42. Ma, M.; Mao, Y.; Gupta, M.; Gleason, K. K.; Rutledge, G. C. Superhydrophobic Fabrics Produced by Electrospinning and Chemical Vapor Deposition. *Macromolecules* **2005**, *38* (23), 9742–9748.
43. Zhang, X.; Guo, Y.; Zhang, P.; Wu, Z.; Zhang, Z. Superhydrophobic CuO:Cu_2S Nanoplate Vertical Arrays on Copper Surfaces. *Materials Lett.* **2010**, *64* (10), 1200–1203.
44. Hao, L.; Lawrence, J. The Adsorption of Human Serum Albumin (HSA) on CO_2 Laser Modified Magnesia Partially Stabilised Zirconia (MgO–PSZ). *Coll. Surf. B: Biointerfaces* **2004**, *34* (2), 87–94.
45. Chwa, S. O.; Ohmori, A. The Influence of Surface Roughness of Sprayed Zirconia Coatings on Laser Treatment. *Surf. Coat. Technol.* **2001**, *148* (1), 88–95.
46. Pinto, M. A.; Osorio, W. R.; Lima, C. R. P.; Garcia, A.; Lerardi, M. C. F. Laser Surface Treatment of Plasma-Sprayed Yttria-Stabilized Zirconia Coatings. *Revis. Metal. (Madrid), Spec.* **2005**, *625*, 154–159.
47. Kathuria, Y. P. Laser Surface Nitriding of Yttria Stabilized Tetragonal Zirconia. *Surf. Coat. Technol.* **2007**, *201* (12), 5865–5869.
48. Shankar, A. R.; Mudali, U. K. Laser Surface Modification of Plasma Sprayed Yttria Stabilised Zirconia Coatings on Type 316L Stainless Steel. *Surf. Eng.* **2009**, *25* (3), 241–248.
49. Daniel, C.; Armstrong, B. L.; Howe, B. J. Y.; Dahotre, N. B. Controlled Evolution of Morphology and Microstructure in Laser Interference-Structured Zirconia. *J. Am. Ceram. Soc.* **2008**, *91*, (7), 2138–2142.
50. Heiroth, S.; Koch, J.; Lippert, T.; Wokaun, A.; Gunther, D.; Garrelie, F.; Guillermin, M. Laser Ablation Characteristics of Yttria-Doped Zirconia in the Nanosecond and Femtosecond Regimes. *J. Appl. Phys.* **2010**, *107* (1), 014908–014918.
51. Aqida, S. N.; Calosso, F.; Brabazon, D.; Naher, S.; Rosso, M. Thermal Fatigue Properties of Laser Treated Steels. *Int. J. Mater. Form.* **2010**, *3* (Suppl. 1), 797–800.
52. Aqida, S. N.; Maurel, M.; Brabazon, D.; Naher, S.; Rosso, M. Thermal Stability of Laser Treated Die Material for Semi-Solid Metal Forming. *Int. J. Mater. Form.* **2009**, *2* (Suppl. 1), 761–764.

53. Yilbas, B. S.; Khaled, M.; Abu-Dheir, N.; Aqeeli, N.; Furquan, S. Z. Laser Texturing of Alumina Surface for Improved Hydrophobicity. *Appl. Surf. Sci.* **2013**, *286*, 161–170.
54. Norouzian, S.; Larijani, M. M.; Afzalzadeh, R. Effect of Nitrogen Flow Ratio on Structure and Properties of Zirconium Nitride Films on Si(100) Prepared by Ion Beam Sputtering. *Bull. Mater. Sci.* **2012**, *35* (5), 885–887.
55. Srinivasan, R.; Zawada, L. P.; Pierce, J. L. Tensile Behavior of SiC/C and Rene 41 Following Isothermal Exposure and Thermal Fatigue. *J. Mater. Sci.* **2000**, *35* (12), 2973–2984.
56. Hamed, A.; Tabakoff, W.; Wenglarz, R. Erosion and Deposition in Turbomachinery. *J. Propul. Power* **2006**, *22* (2), 350–360.
57. Yilbas, B. S.; Matthews, A.; Leyland, A.; Karatas, C.; Akhtar, S. S.; Abdul Aleem, B. J. Laser Surface Modification Treatment of Aluminum Bronze with B_4C. *Appl. Surf. Sci.* **2012**, *263*, 804–809.
58. Li, J.; Wang, H. M.; Tang, H. B. Effect of Heat Treatment on Microstructure and Mechanical Properties of Laser Melting Deposited Ni-Base Superalloy Rene 41. *Mater. Sci. Eng.: A (Struct. Mater.: Prop., Microstruct. Process.)* **2012**, *550*, 97–102.
59. Wang, H.-S.; Huang, C.-Y.; Ho, K.-S.; Deng, S.-J. Microstructure Evolution of Laser Repair Welded Rene 77 Nickel-Based Superalloy Cast. *Mater. Transact.* **2011**, *52* (12), 2197–2204.
60. Durocher, J.; Richards, N. L. Evaluation of the Low Heat Input Process for Weld Repair of Nickel-Base Superalloys. *J. Mater. Eng. Perform.* **2011**, *20* (7), 1294–1303.
61. Rush, M. T.; Colegrove, P. A.; Zhang, Z.; Broad, D. Liquation and Post-Weld Heat Treatment Cracking in Rene 80 Laser Repair Welds. *J. Mater. Process. Technol.* **2012**, *212* (1), 188–197.
62. Osterle, W.; Krause, S.; Moelders, T.; Neidel, A.; Oder, G.; Volker, J. Influence of Heat Treatment on Microstructure and Hot Crack Susceptibility of Laser-Drilled Turbine Blades Made from Rene 80. *Mater. Charact.* **2008**, *59* (11), 1564–1571.
63. Matijasevic-Lux, B.; Neidel, A.; Riesenbeck, S.; Ullrich, T.; Volker, J.; Wallich, S. Hot Cracking in the Heat-Affected Zone of Laser-Drilled Turbine Blades Made from the Nickel-Based Superalloy Rene 80. *Prakt. Metall.* **2007**, *44* (9), 413–429.
64. Khana, Z. A.; Hadfield, M.; Tobe, S.; Wang, Y. Ceramic Rolling Elements with Ring Crack Defects – A Residual Stress Approach. *Mater. Sci. Eng. A* **2005**, *404*, 221–226.
65. Nosonovsky, M.; Bhushan, B. Multiscale Dissipative Mechanisms and Hierarchical Surfaces: Friction, Superhydrophobicity, and Biomimetics. Springer: Heidelberg, 2008.
66. Wenzel, R. N. Resistance of Solid Surfaces to Wetting by Water. *Indust. Eng. Chem.* **1936**, *28*, 988–994.
67. Cassie, A. B. D.; Baxter, S. Wettability of Porous Surfaces. *Trans. Faraday Soc.* **1944**, *40*, 546–551.
68. Zan, H.-W.; Yen, K.-H.; Liu, P.-K.; Ku, K.-H.; Chen, C.-H.; Hwang, J. Low-Voltage Organic Thin Film Transistors with Hydrophobic Aluminum Nitride Film as Gate Insulator. *Org. Electron.* **2007**, *8*, 450–454.
69. Luo, B. H.; Shum, P. W.; Zhou, Z. F.; Li, K. Y. Preparation of Hydrophobic Surface on Steel by Patterning Using Laser Ablation Process. *Surf. Coat. Technol.* **2010**, *204*, 1180–1185.
70. Yilbas, B. S.; Davies, R.; Gorur, A.; *et al.* Investigation into Development of Liquid Layer and Formation of Surface Plasma During Co_2 Laser Cutting Process. *Proc. Inst. Mech. Eng., Part B: J. Eng. Manuf.* **1992**, *206*, 287–298.
71. Xing, H.; Fu, Y.; Margam, C.; Batchelor, A. W. X-ray Imaging of Laser Remelted Plasma Sprayed Zirconia Coating. *J. Mater. Sci. Lett.* **1998**, *17*, 163–165.
72. Noro, A.; Kaneko, M.; Murata, I.; Yoshinari, M. Influence of Surface Topography and Surface Physicochemistry on Wettability of Zirconia (Tetragonal Zirconia Polycrystal). *J. Biomed. Mater. Res. B: Appl. Biomater.* **2012**, *101B*, 1–9.
73. Engberg, C. J.; Zehms, E. H. Thermal Expansion of Al_2O_3, BeO, MgO, B_4C, SiC, and TiC Above 1000°C. *J. Am. Ceram. Soc.* **1959**, *42* (6), 300–305.
74. Koch, K.; Bhushan, B.; Barthlott, W. Diversity of Structure, Morphology and Wetting of Plant Surfaces. *Soft Matter* **2008**, *4* (10), 1943–1963.
75. Wang, H. M.; Zhang, J. H.; Tang, Y. J.; *et al.* Rapidly Solidified MC Carbide Morphologies of a Laser-Glazed Single-Crystal Nickel-Base Superalloy. *Mater. Sci. Eng.: A* **1992**, *156*, 109–116.
76. Safari, J.; Nategh, S. On the Heat Treatment of Rene-80 Nickel-Base Superalloy. *J. Mater. Process. Technol.* **2006**, *176*, 240–250.
77. Yilbas, B. S.; Nickel, J.; Coban, A.; Sami, M.; Shuja, S.; Aleem, A. Laser Melting of Plasma Nitrided Ti–6Al–4V Alloy. *Wear* **1997**, *212*, 140–149.

2.6 Surface Induction Hardening

J Barglik and A Smalcerz, Silesian University of Technology, Katowice, Poland

© 2017 Elsevier Inc. All rights reserved.

2.6.1	Idea of Induction Surface Hardening	154
2.6.2	Mathematical Modeling of Surface Induction Hardening Processes	158
2.6.3	Calculation Example	164
2.6.4	Some General Remarks on Induction Surface Hardening Installations	168
2.6.5	Conclusions	170
Acknowledgment		170
References		170
Relevant Websites		170

2.6.1 Idea of Induction Surface Hardening

Induction hardening in general is such a form of the heat treatment in which a whole metallic workpiece or only its selected part is heated by induction, then kept for a short period of time for a temperature equalization and finally quenched. It is a modern, innovation, environment-friendly, and energy saving heat treatment technology especially frequently used for axi-symmetric and flat steel elements. It is in fact the most popular application of induction heating in industry especially in case of the surface treatment.[1]

The idea of the surface hardening is connected with the hardening of rather thin surface zone only and keeping the internal part of the treated material soft, which means in general remaining of not hardened structure in internal parts of the material. Due to features of the induction heating the surface induction hardening could be realized as stationary or continual. The first solution means induction heating and immediate cooling by spraying or by merging the body into a container with any suitable quenchant. The second solution means simultaneous heating and the consequent immediate cooling of the heated part.

In general the induction surface hardening consists of three consecutive stages:

I. Induction heating. Fast heating of the surface and a thin layer of the material to be hardened provided during a short heating time t_h up to a hardening temperature T_h being bigger than the upper critical temperature A_{c3}. The metallurgical result of the stage should be forming the uniform austenite microstructure,
II. Austenitization. It means holding a temperature of the body during short, but sufficient period of time t_e in order to obtain a structural equilibrium in the hardened zone of the body,
III. Quenching. It means the intensive cooling of the body in order to achieve the more harder, stable martensitic microstructure.

In the surface induction hardening process the austenitization time t_e is often minimized to a technological break between heating and cooling only, necessary to remove the body from the inductor into cooling treatment region.

The main factors influencing on the hardness and the depth of the hardening zone are as follows:

- chemical composition of steel,
- temperature distribution within the body,
- starting microstructure of the material,
- quenching conditions.

Induction surface hardening is realized mostly for steel with the carbon content of about 0.35–0.6%. Content of carbon influences the maximum obtained hardness.[2]

A typical time evolution of temperature within the hardened body is shown in **Figure 1**. The induction heating starts from any initial temperature which could be in general equal to the ambient temperature T_a. In order to obtain the requested uniform austenite microstructure before quenching the final temperature at the surface and in the thin surface layer of the body should be bigger than the upper critical upper temperature A_{c3}

$$T_h = T|_{t_h+t_e} \geq A_{c3} \qquad [1]$$

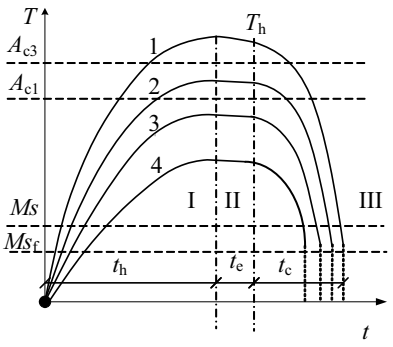


Figure 1 Time evolution of temperature in different zones of the hardened body. I – induction heating, II – austenitization, III – quenching. 1 – curve for zone with expected completely hardened material, 2 – curve for zone with expected incompletely hardened material, 3 and 4 – curves for zones of expected not hardened material, A_{c3} and A_{c1} – upper and lower critical temperature, Ms – martensite start temperature, Ms_f – martensite finish temperature, T_h – hardening temperature, t_h – heating time, t_e – austenitization time, and t_c – quenching time.

 doi:10.1016/B978-0-12-803581-8.09189-X

In order to secure the structural equilibrium of the material the hardening temperature should be sufficiently bigger than the A_{c3} temperature

$$T_h = A_{c3} + (35 \div 50)\ ^\circ C \quad [2]$$

As it is mentioned such a condition is satisfied not only at the surface but also at the thin zone near the surface of the body represented for instance by curve 1 in **Figure 1**. It represents the part of material with the uniform austenite microstructure. We could expect that a complete hardening characterized by the uniform acicular martensitic microstructure and the highest hardness will be noticed there. However, for deeper zones of the material the temperature is smaller than the upper critical temperature A_{c3}, but still higher than the lower critical temperature A_{c1}

$$A_{c3} \geq T|_{t_n+t_e} \geq A_{c1} \quad [3]$$

For such temperatures of the material the austenite begins to form, but the process is not completed. So in this zone of the body represented for instance by the curve 2 in **Figure 1** we obtain the not fully formed austenite microstructure and we may expect here the incomplete hardened material. The resultant hardness is smaller than at the surface of the body and the microstructure contains a mixture of martensite, pearlite, and ferrite. And finally for more deeper layers of the body the material does not reach even the lower critical temperature A_{c1}

$$T|_{t_n+t_e} \leq A_{c1} \quad [4]$$

The austenite microstructure do not start to form and the material remains unchanged. When the temperature before cooling is only slightly smaller than the lower critical temperature A_{c1} we could observe, depending on grade of steel, a tempering phenomenon (see curve 3 in **Figure 1**). If the temperature before cooling is distinctly smaller than the lower critical temperature A_{c1} (see curve 4 in **Figure 1**) the material remains unchanged.

For the dual frequency induction surface hardening of the process if the induction heating stage is divided into two parts (**Figure 2**):

Such a kind of induction surface hardening is applied for instance for gear wheels. It makes possible to obtain the specific contour zone.[3] The first longer period of the induction heating is characterized by a high current of the medium frequency MF and when the average temperature of the body surface reaches a prescribed value, the final part of induction heating realized by a current of lower value and higher frequency HF is provided. A time break between them t_b should be as small as possible. Resulted hardness of the material and its microstructure finally depend on cooling. The classical time temperature cooling (CCT) diagram for a typical plain carbon steel presenting cooling of the material from the hardening temperature T_h being sufficiently bigger than the upper critical temperature A_{c3} is shown in **Figure 3**. The CCT diagram shows the dependence of the resultant hardness on the time of cooling.

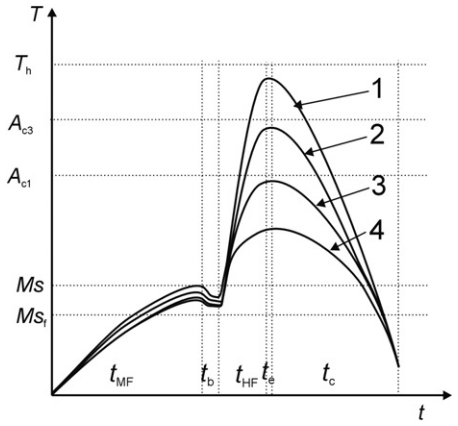


Figure 2 Time evolution of temperature in different zones of the hardened body for the dual frequency induction hardening. MF – medium frequency, HF – high frequency, t_b – time of break between MF and HF heating. Other denotations as in **Figure 1**.

For the surface zone the cooling lines start from the hardening temperature T_h. Its value at the moment when cooling starts

$$T|_{t_n+t_e} \geq A_{c3} \quad [5]$$

is still higher than the upper critical temperature.

When the hardened material reaches *Ms* temperature the transformation from austenite into martensite begins. Cooling should terminates at a temperature lower than the martensite finish temperature Ms_f defined as a temperature when 99% of the austenite transforms into the martensite

$$T|_{t_n+t_e+t_c} < Ms_f \quad [6]$$

The higher velocity of cooling means obtaining the harder microstructure. For the cooling lines from **Figure 3** only three of them pass through the martensite region (M). For them the final temperature of material after heating and cooling satisfy inequalities eqns [5] and [6], respectively, and we obtain the uniform acicular martensitic microstructure. It leads to the complete hardening process for a part of the body which is characterized by such a time evolution of temperature. Resultant hardness of 750, 735, 700 HV, respectively, as well as acicular martensitic microstructure are achieved. It is characteristic that induction surface hardening provides to slightly higher hardness that it would be achieved for the conventional hardening. The phenomenon is sometime referred as a super hardening.[4] The next curves characterized by a lower speed of cooling (located in the right part of **Figure 3**) pass through the areas of the CCT diagram containing bainite (B), pearlite (P), or ferrite (F). It leads to an incomplete hardening process which means the lower hardness and mixed microstructure containing partly martensite with the addition of bainite, pearlite, and ferrite. For the very slow cooling ($v_c = 0.02\ K\ s^{-1}$) the resultant hardness is equal to 263 HV only. The material in this part of the body remains unchanged.

Another problem is connected with a speed of heating. For the induction hardening it is characteristic a big value of the

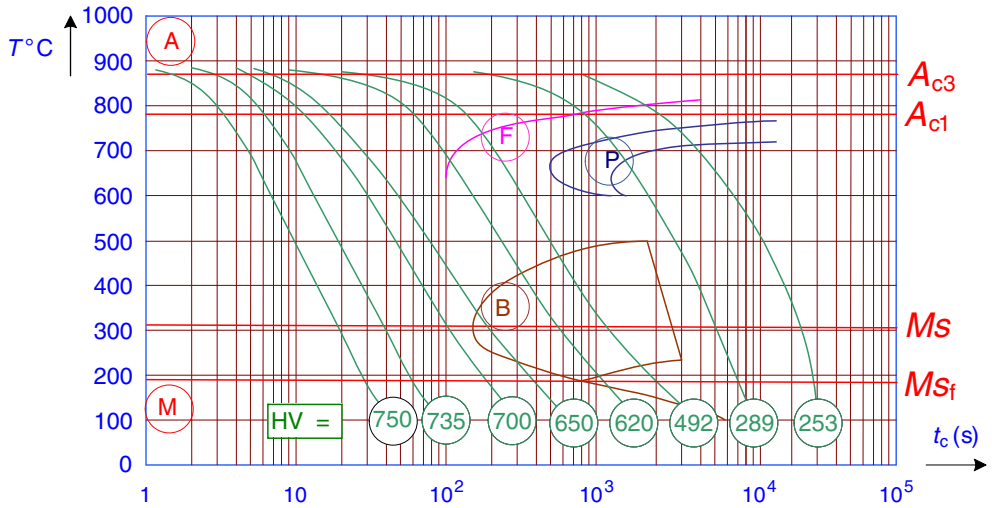


Figure 3 The classical time temperature cooling diagram for a typical plain carbon steel. M – martensite, A – austenite, B – bainite, P – pearlite, F – ferrite, and HV – hardness in Vickers degrees.

heating rate, which could reach in some cases values of about 1000 K s^{-1} or more. It causes a change of critical temperatures. So for such a rapid heating the relation [2] is not valid. In order to obtain the uniform austenite microstructure of the material it is necessary to heat the body till the distinctly bigger hardening temperature T_h. It resulted by increasing the temperature of beginning and termination of austenite transformation in comparison with the classical process and consequently increasing of the hardening temperature T_h

$$T_h = A_{c3} + \Delta T(v_c) \qquad [7]$$

Transformations taking place during austenitization with a big velocity of induction heating could be analyzed based upon the TTA diagrams (Time – Temperature – Austenitization) for the hardened material. As the example let us consider the TTA diagram for the plain steel with carbon content of 0.45%. Speed of pearlite – austenite transformation and criteria temperature increases with increasing speed of heating. In order to analyze this phenomenon some experiments are provided.[5] For classical conditions of conventional austenitization of samples made from the investigated steel the critical temperatures are as follow: $A_{c1} = 736$ °C and $A_{c3} = 801$ °C. The TTA diagram for the rapid induction heating taken from experiments is presented in **Figure 4**.[5]

The TTA diagram confirms that both criteria temperatures A_{c1}, A_{c3} strongly depend on the speed of heating. For example, if the speed of heating $v_h = 97$ K s^{-1} the lower critical temperatures increases to the value of $A_{c1m} = 781$ °C and the upper critical temperature to the value of $A_{c3m} = 879$ °C. In comparison with the determined earlier classical critical temperatures it means the increase of them of about $\Delta T = 50 \div 70$ °C.[5] Details are collected in **Table 1.**

At the highest applied speed of heating ($v_h = 1000 \div 3000$ K s^{-1}) the lower critical temperature A_{c1} increases till (804 ÷ 820) °C, however, the upper critical temperature A_{c3} also increases to (978 ÷ 1074)°C. In comparison with the determined earlier critical temperatures for the conventional hardening the distinct increasing is noticed:

$$A_{c1m} = A_{c1} + \Delta A_{c1}(v_c); \quad \Delta A_{c3} = 70 \div 80 \text{ K} \qquad [8]$$

$$A_{c3m} = A_{c3} + \Delta A_{c3}(v_c); \quad \Delta A_{c3} = 180 \div 270 \text{ K} \qquad [9]$$

For the conventional heat treatment process the hardening temperature $T_h = 840$ °C. It means that for a typical range of the induction heating speed (50 ÷ 1000 K s^{-1}) the hardening temperature T_h should be distinctly higher:

$$T_h \approx 1000 \div 1050°\text{C} \text{ and } \Delta T_h \approx 100 \div 210°\text{C} \qquad [10]$$

Dependence of the hardening temperature on speed of heating is shown in **Figure 5.**

Transformations taking place in samples made from steel with carbon content of 0.45% during fast induction surface hardening characterized by rapid both processes of heating and cooling are presented at the non-conventional TTC$_C$ (Time – Temperature – Cooling continual) diagram (**Figure 6**). It differs from the classical one (the similar classical diagram is shown in **Figure 3**). It is obtained by measurements. The samples of the hardened material are heated with the average speed of $v_h \approx 1000$ K s^{-1} to the hardening temperature $T_h = 1050$°C, then kept for austenitization at the short period of time $t_e = 2$ s and finally cooled by water spraying with an average speed of $v_c = 1 \div 333$ K s^{-1}.

The investigated steel in condition of induction hardening characterized by slightly bigger hardenability in comparison with a classical heat treatment. Martensite microstructure is obtained for samples cooled with a critical speed of $v_c \geq 100$ K s^{-1}. For samples cooled with speed of $v_c \approx 50$ K s^{-1} the microstructure contains not only martensite but also bainite. If the speed of cooling becomes more slower ($10 \text{ K s}^{-1} \leq v_c \leq 35 \text{ K s}^{-1}$) some particles of ferrite are appeared. For the smallest investigated speed of cooling ($0.01 \text{ K s}^{-1} \leq v_c \leq 7 \text{ K s}^{-1}$) the microstructure consists of mixture of martensite, bainite, ferrite, and pearlite.

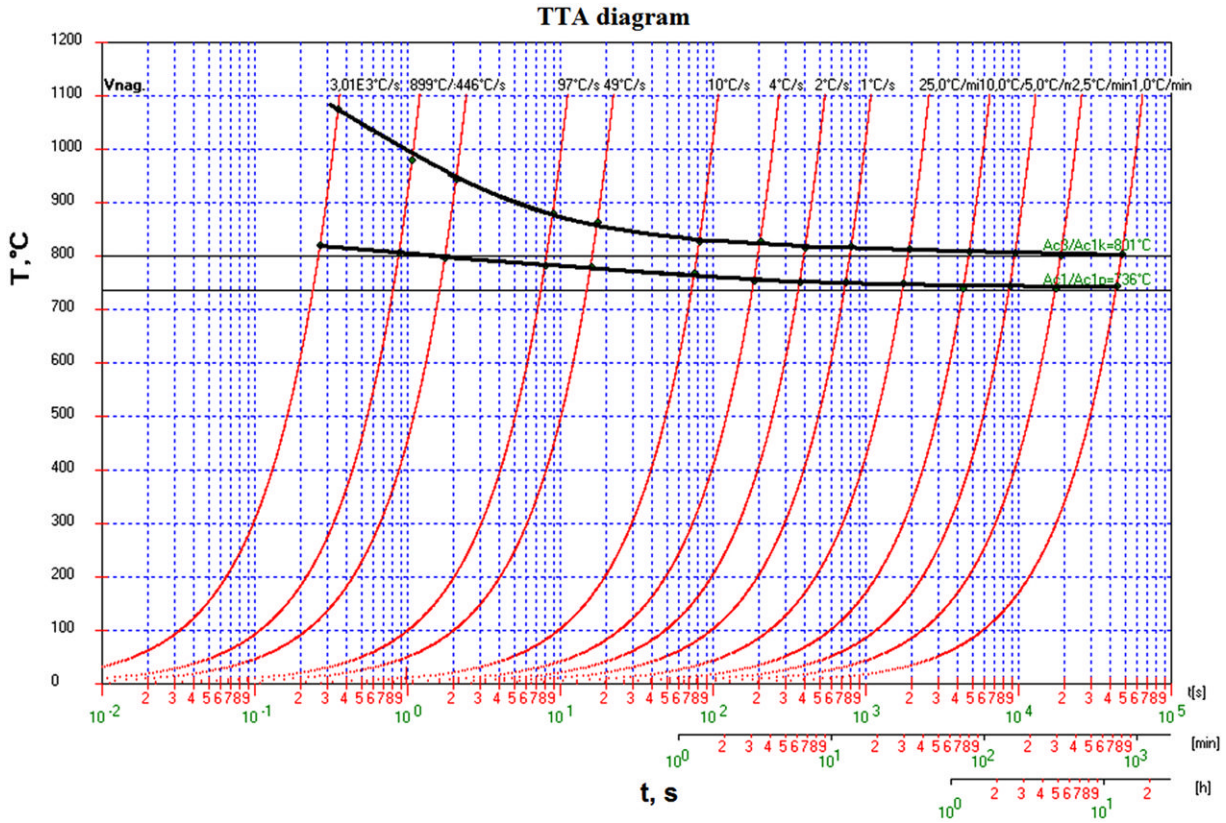


Figure 4 The modified Time – Temperature – Austenitization diagram for steel with a carbon content of 0.45%. Barglik, J.; Smalcerz, A.; Przylucki, R.; Doležel, I. 3D Modeling of Induction Hardening of Gear Wheels. *J. Comput. Appl. Math.* **2014**, *270*, 231–242.

Table 1 Dependence of critical temperatures on speed of heating

v_h	K s^{-1}	0.0078	0.017	0.042	0.083	0.167	0.417	1	2	4	10	49	97	446	900	3088
A_{c1m}	°C	736	743	739	744	737	747	749	750	752	767	779	781	795	804	820
A_{c3m}	°C	801	802	801	804	806	813	817	814	826	827	861	879	942	978	1074

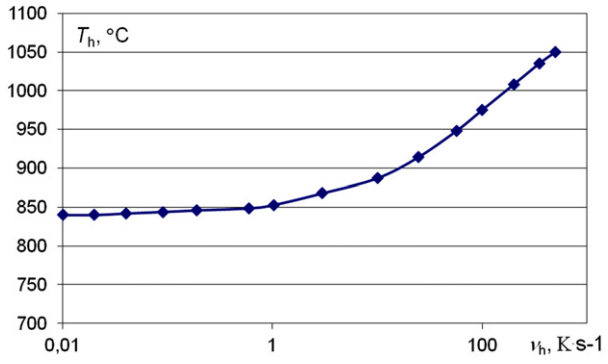


Figure 5 Dependence of the modified upper critical temperature A_{c3m} of the speed of heating.

The induction heating technology seems to be particularly suitable for the realization of this process because of:

- the possibility to locate the heat treatment process exactly within a surface layer of the body facing the inductor, whose thickness depends on many factors like: the field current frequency, the thermal material properties and heat transfer parameters of the body and the total heating time,
- developing very high volumetric power density in the hardened layer making possible to obtain thin hardened zones.

There are no general rules that allow to define the optimal values of:

- the distribution of the induced current in the hardened body,
- the induction heating time and its influence on the upper critical temperature,
- the time interval between the end of the induction heating and the beginning of the quenching,
- the speed of quenching.

All these mentioned above quantities depend on:

- material properties of the treated body,
- the shape of the workpiece and presence of any irregular parts (holes or edges),
- configuration of inductor–body system including thickness of the air-gap between the inductor and the body,
- the required thickness of the hardened layer.

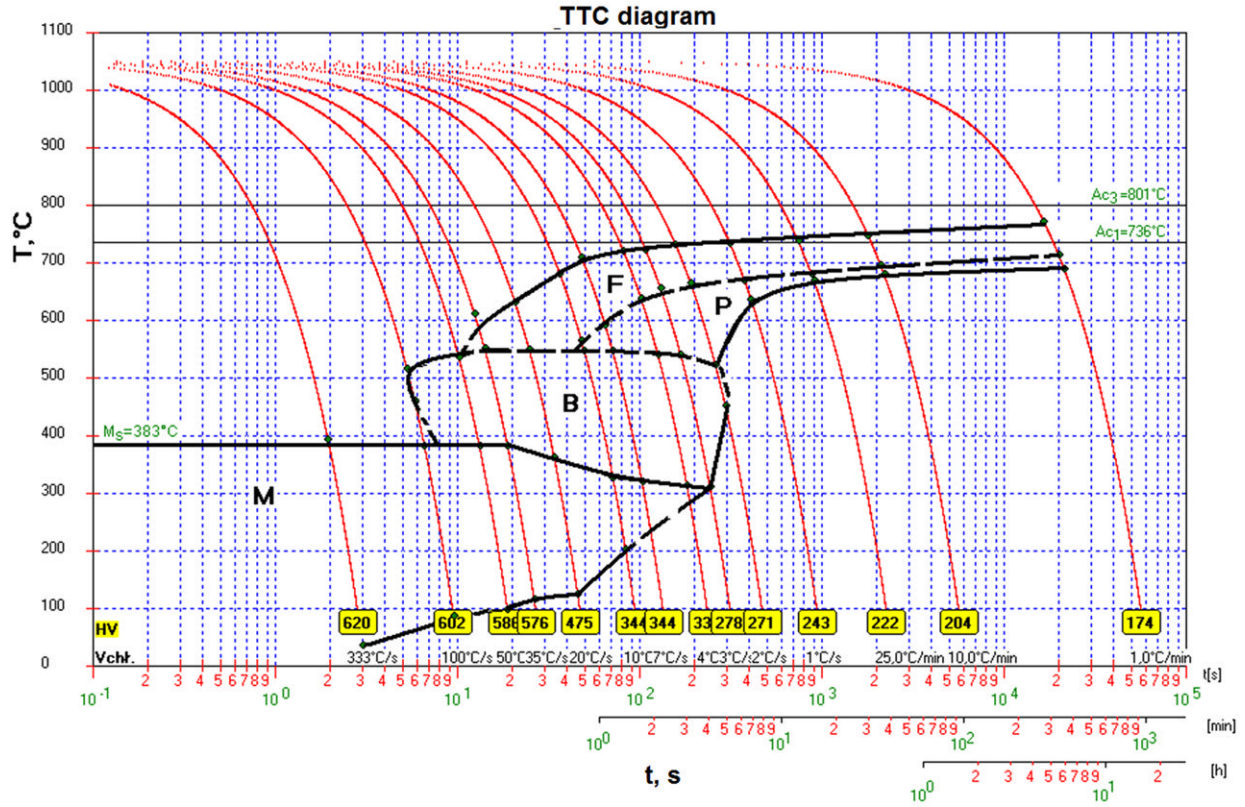


Figure 6 Modified diagram TTCc for steel with carbon of 0.48% obtained by dilatometric measurements.

The depth of hardening Δg is defined as a distance between the surface and any point inside the body where the hardness decreases to 80% of its minimal value at the surface.[4] However, hardness requirements are often more complicated. They of course depend on the particular technology. The requirements are often connected not only with the value of hardness and martensite microstructure at the surface of the body and in the thin surface zone but also with a hardness and microstructure distribution within the whole body. As a good example of such a specific demand the dual induction surface hardening of gear wheels should be shown. Let us consider the gear wheel made of the special quality steel with the carbon content of $0.43 \div 0.5\%$ (Figure 7).

The region of the tooth and its root are divided into four zones with different hardness requirements. The thin contour zone (1) is fully hardened with the acicular martensite microstructure. It is heated to the hardening temperature above A_{c3m}. For the investigated steel its hardness should reach values between $620 \div 720$ HV. For the analyzed case its thickness is $\Delta g = 0.2 \div 0.3$ mm. The transition zone (2) represents a part of incompletely hardened material with a hardness between $500 \div 660$ HV. Its value is lower than that in zone (1). The hardness of the internal zone (3) representing the core of the tooth should be below 500 HV. And finally, the hardness of the zone (4) containing the base material is required to be below 266 HV.

In order to implement the surface induction hardening into industry a numerical simulation is applied as the effective tool.

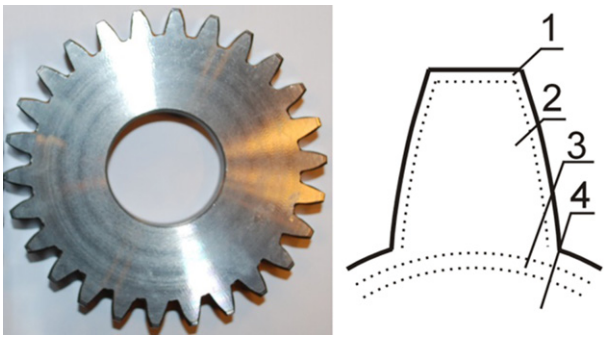


Figure 7 View of gear wheel and its zones with different hardness requirements. 1 – contour zone, 2 – transition zone, 3 – internal zone, 4 – zone of unchanged material.

However, the computations should be realized jointly with a successful experimental verification and adjustment of the inductor in order to achieve the required results.

2.6.2 Mathematical Modeling of Surface Induction Hardening Processes

Induction hardening requires description of interaction of several coupled physical fields: electromagnetic, temperature, heat stress, and metallurgical. They are described by means of

partial differential equations system for the separate fields with the exception for metallurgical field. Hardness and microstructure are mostly described based upon the experimental data. The simplified algorithm for such a computation model is shown in Figure 8.

For electromagnetic field calculations constant values for expected average temperature of the magnetic permeability μ and the electric conductivity γ are taken. Based upon the known distribution of electromagnetic field the volumetric Joule losses p_v released in the body are determined. Then temperature distribution within the body using average values of material properties: heat conduction λ, specific heat at constant pressure c_p, convection and radiation heat transfer coefficients α_{cc} and α_r, respectively, are calculated. If the average temperature of surface of the hardened body reaches prescribed value the induction heating stage terminates. The task is analyzed as the inverse problem using simplified optimization procedures in order to determine parameters of induction heating systems (field current density and its frequency, configuration and dimensions of inductor–hardening body system, heating time, or speed of movement) in order to achieve the required distribution of temperature in the hardened element. Then the distribution of heat stresses are determined. If deformations are too big it would be necessary to modify parameters of the induction heating process. Then temperature distribution at beginning of the intensive cooling is determined. Next the temperature field during intensive cooling in the quenchant is calculated with taking into account non-linear dependence of the convection heat transfer coefficient on temperature $\alpha_{ch}(T)$. Radiation is taken into consideration for the induction heating and the austenitization stages only. Such a simplification is correct for cooling by merging also for cooling by spraying, however, in the second case a radiation through semi-transparent layer may be taken

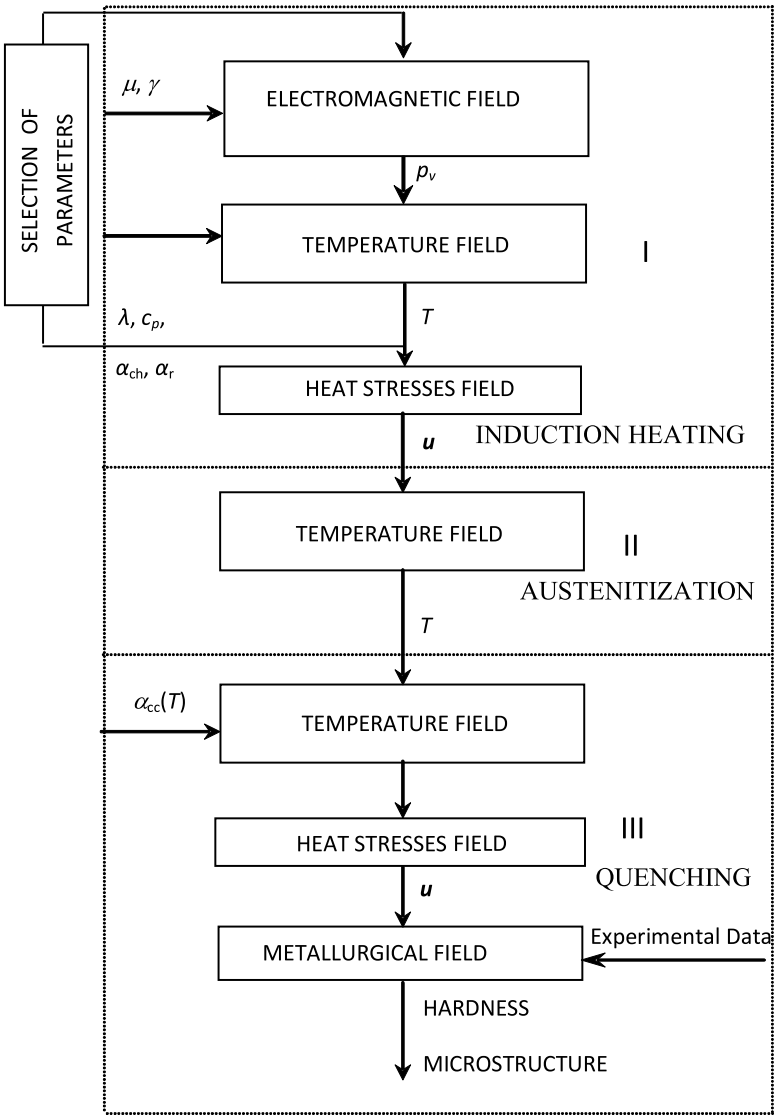


Figure 8 Simplified algorithm of two step coupled electromagnetic, thermal, heat stress, and metallurgical fields for modeling of induction surface hardening.

into consideration. The heat stresses are calculated again. If the final temperature reached the prescribed value (lower than the Ms_f temperature). Then hardness distribution and microstructure of hardened layer are determined. They are based on the experimental data. Such a simplified calculation method may cause significant errors. Its advantage is a simplicity. However, it is especially good in case of systems with complicated geometry like gear wheels. Its main advantage is mostly a relatively short time of computations.

In order to provide more precise calculations a direct coupled model is applied (Figure 9). In the stage I induction heating phenomena are analyzed. For material properties taken at an initial temperature T_i the electromagnetic field is calculated. As a result of these calculations the magnetic flux density

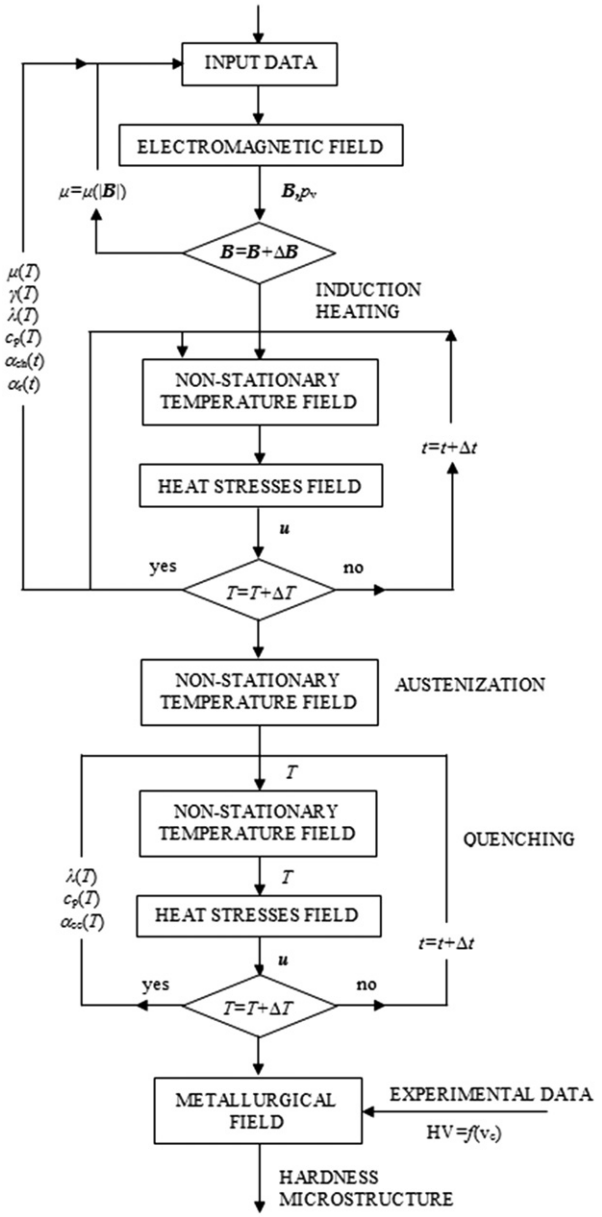


Figure 9 Algorithm of electromagnetic, thermal, heat stress, and metallurgical fields indirect coupled formulation.

$\boldsymbol{B}$ and volumetric Joule losses p_v for particular time are determined. If for any next stage the calculated value of magnetic flux density $\boldsymbol{B}$ differs from the previous one more than as assumed $\Delta\boldsymbol{B}$ the electromagnetic field calculations are repeated for the new value of magnetic permeability $\mu(B)$. Then nonstationary temperature field is calculated. If temperature increases more than of ΔT the material properties (conduction heat, specific heat, and both heat transfer coefficients) of heated body are corrected. Then electromagnetic computations are provided again for corrected values of magnetic permeability μ and electric conductivity γ. Heat stress field is determined in order to check if deformations are not too big.

Then the next cycle of the electromagnetic and temperature calculations is provided for the period of time $t+\Delta t$ until $t=t_n$ (the end of induction heating). Of course for small calculation steps Δt, $\Delta\boldsymbol{B}$, and ΔT a big accuracy could be achieved, but in opposite it causes a longer computation time. Then in the short stage of the austenitization the temperature distribution for time $t=t_n+t_e$ is calculated. The quenching begins with computations of nonstationary temperature field during intensive cooling in a fluid quenchant. Temperature decreasing of ΔT causes correction of material properties λ, c_p, α_{ch}, α_r in the next steps. At the next step the heat stress field is calculated again. Heat stresses and their distribution within the hardened body is a basis for a possible decision to repeat the computations or to continue the heat treatment by tempering. Calculations of quenching terminate at $t=t_n+t_e+t_c$ (see Figure 1) after achieving of selected criteria of the assumed time of intensive cooling or average final temperature being of order of the martensite finish temperature Ms_f. Then based upon the experimental data and registered history of cooling the hardness and microstructure distribution are determined.

Mathematical model of the process is described by a system of differential equations for electromagnetic, thermal, and heat stress fields. The electromagnetic problem is an open boundary task, but it may be considered as a classical closed boundary problem after location of the steel element inside the domain with external borders sufficiently distant to the inductor–body system. Dimensions of the domain is selected based upon some preliminary calculations. For the analyzed task the external border of the domain is selected in a sufficient distance from the inductor–workpiece system being at least seven time bigger than diameter of the hardened element.[6] Electromagnetic field is described by the classical equation for the magnetic vector potential $\boldsymbol{A}$[7]

$$\operatorname{curl}\left(\frac{1}{\mu}\operatorname{curl}\boldsymbol{A}\right)+\gamma\left(\frac{\partial\boldsymbol{A}}{\partial t}+\boldsymbol{v}\times\operatorname{curl}\boldsymbol{A}\right)=\boldsymbol{J}_z \qquad [11]$$

where μ denotes the magnetic permeability, γ is the electric conductivity, $\boldsymbol{v}$ is the velocity of movement, and $\boldsymbol{J}_z$ is the field current density.

For coreless inductor and for the case when the magnetic permeability of hardened element may be considered as constant at each cell of the system the eqn [11] may transform into the Helmholtz equation for the phasor of the magnetic vector potential $\underline{\boldsymbol{A}}$:

$$\operatorname{curl}\operatorname{curl}\underline{\boldsymbol{A}}+\mathrm{j}\omega\mu\sigma\underline{\boldsymbol{A}}-\mu\gamma(\boldsymbol{v}\times\operatorname{curl}\underline{\boldsymbol{A}})=\mu\underline{\boldsymbol{J}}_z \qquad [12]$$

where j denotes the imaginary unit and ω is the angular frequency.

The eqn [12] is simplified by neglecting the third term of the left side. It is possible when the velocity of inductor movement to the workpiece is not very big, which is normally satisfied in typical induction hardening installations. The problem is discussed with more details for instance in ref.[8]

$$\text{curl curl } \boldsymbol{A} + \mathrm{j}\omega\mu\gamma\underline{\boldsymbol{A}} = \mu\boldsymbol{J}_z \quad [13]$$

For surfaces of external borders of the domain:

$$\underline{\boldsymbol{A}} = 0 \quad [14]$$

For the symmetry plane $z=0$

$$\underline{\boldsymbol{A}} \times \boldsymbol{n} = \boldsymbol{0} \quad [15]$$

For 2D arrangement:

$$\frac{\partial \underline{\boldsymbol{A}}}{\partial \boldsymbol{n}} = 0 \quad [16]$$

Hysteressis losses are neglected. Eddy current density $\underline{\boldsymbol{J}}_{\text{ind}}$ and volumetric Joule losses p_{v} are expressed, respectively:

$$\underline{\boldsymbol{J}}_{\text{ind}} = \mathrm{j}\omega\gamma\underline{\boldsymbol{A}}, \quad p_{\text{v}} = \frac{\underline{\boldsymbol{J}} \times \underline{\boldsymbol{J}}^*}{\gamma} \quad [17]$$

Temperature calculations are provided by means of the Kirchhoff-Fourier equation supplemented by internal heat source represented by the volumetric Joule losses taken from electromagnetic calculations[9]

$$\text{div}(\lambda \text{grad} T) - \rho c_p (v \text{grad} T) - \rho c_p \frac{\partial T}{\partial t} = -p_{\text{v}} \quad [18]$$

where λ denotes heat conduction, ρ is the density, and c_p is the specific heat.

On symmetry planes:

$$\frac{\partial T}{\partial n} = 0 \quad [19]$$

At external surfaces of the body the third kind of boundary condition of convection and radiation heat transfer is satisfied[10]

$$-\lambda\frac{\partial T}{\partial n} = \alpha_{\text{ch}}(T - T_{\text{c}}) + \sigma_{\text{o}} \cdot \varepsilon_{\text{p}}\left(T^4 - T_{\text{r}}^4\right) = \alpha_{\text{ch}}(T - T_{\text{c}}) + \alpha_{\text{r}}(T - T_{\text{r}}) - p_{\text{r}} \quad [20]$$

where α_{ch} denotes convection heat transfer coefficient for induction heating, T_{c} is the temperature of convection environment, σ_{o} is the Stefan–Boltzmann constant, ε_{p} is the total emissivity, T_{r} is the temperature of radiation environment, and p_{r} is the component connected with multiple reflection phenomena.

Often we could suppose that $T_{\text{c}} \approx T_{\text{r}} = T_{\text{cr}}$. It is possible as well to neglect multiple reflection phenomena.[11,12] Then we could apply one general heat transfer coefficient α_{g} taking into account convection and radiation heat transfer between steel element and surroundings

$$-\lambda\frac{\partial T}{\partial n} = \alpha_{\text{g}}(T - T_{\text{c}}), \quad \alpha_{\text{g}} = \alpha_{\text{cc}} + \sigma_{\text{o}} \cdot \varepsilon_{\text{p}}\left(T^2 + T_{\text{cr}}^2\right) \cdot (T + T_{\text{cr}}) \quad [21]$$

For surface induction hardening the inductor is often supply by high frequency field current. Volumetric Joule losses are concentrated practically only near the surface. From the numerical point of view it is better to neglect volumetric Joule losses in eqn [18] and introduce to the condition eqn [20], additional term of the surface power density p_{s}. For cylindrical workpiece of diameter R the surface power density p_{s} could be determined based upon assumption that the heat delivered to the elementary surface with length of dz is equal to the heat released due to eddy currents

$$q = p_{\text{s}} \cdot 2\pi R \cdot \text{d}z = \int_0^R p_{\text{v}} \cdot 2\pi r \cdot \text{d}r\text{d}z \quad [22]$$

where q is the heat delivered to the body during unit of time.

So the eqn [18] and boundary condition eqn [20] transform to forms eqns [23] and [24], respectively

$$\text{div}(\lambda \text{grad} T) - \rho c(\boldsymbol{v}\,\text{grad} T) - \rho c\frac{\partial T}{\partial t} = 0 \quad [23]$$

$$-\lambda\frac{\partial T}{\partial n} = \alpha_{\text{c}}(T - T_{\text{c}}) + \alpha_{\text{r}}(T - T_{\text{r}}) - p_{\text{r}} - p_{\text{s}} \quad [24]$$

During induction heating and especially during intensive cooling could appear heat stresses connected with non-uniform temperature distribution within the hardened body. Heat stress field and associated deformations may be described by Lame equations for displacements[14]

$$(\varphi_{\text{u}} + \psi_{\text{u}})\text{grad div } \boldsymbol{u} + \psi_{\text{u}}\nabla^2 u - (3\varphi_{\text{u}} + 2\psi_{\text{u}})\alpha_{\text{T}}\text{grad } T + f_{\text{m}} = 0 \quad [25]$$

where φ_{u} and ψ_{u} coefficients defined by means of relations eqns [26] and [27], respectively, $\boldsymbol{u}$ is the vector of displacements, α_T is the temperature extension coefficient, and f_{m} and volumetric density of the Lorentz force.

$$\varphi_{\text{u}} = \frac{v \cdot E}{(1 + v) \cdot (1 - 2v)} \quad [26]$$

where v is the the kinematic tension coefficient and E is the Young's modulus.

$$\psi_{\text{u}} = \frac{E}{2(1 + v)} \quad [27]$$

$$f_{\text{m}} = \boldsymbol{J}_{\text{ind}} \times \text{curl } \boldsymbol{A} \quad [28]$$

Based upon known distribution of displacements tensors of deformations ε and stresses σ are determined.

$$\left.\begin{aligned}
&\varepsilon_{xx}=\frac{\partial u_x}{\partial x},\quad \varepsilon_{yy}=\frac{\partial u_y}{\partial y},\quad \varepsilon_{zz}=\frac{\partial u_z}{\partial z},\\
&\varepsilon_{xy}=\frac{1}{2}\left(\frac{\partial u_x}{\partial y}-\frac{\partial u_y}{\partial x}\right),\quad \varepsilon_{yz}=\frac{1}{2}\left(\frac{\partial u_y}{\partial z}-\frac{\partial u_z}{\partial y}\right),\\
&\varepsilon_{zx}=\frac{1}{2}\left(\frac{\partial u_z}{\partial x}+\frac{\partial u_x}{\partial z}\right)
\end{aligned}\right\} \quad [29]$$

$$\left.\begin{aligned}
&\sigma_{xx}=\varphi_L\left(\varepsilon_{xx}+\varepsilon_{yy}+\varepsilon_{zz}\right)+2\psi_L\varepsilon_{xx}-(3\varphi_L+2\psi_L)\alpha_T\cdot T,\\
&\sigma_{yy}=\varphi_L\left(\varepsilon_{xx}+\varepsilon_{yy}+\varepsilon_{zz}\right)+2\psi_L\varepsilon_{yy}-(3\varphi_L+2\psi_L)\,\alpha_T\cdot T,\\
&\sigma_{zz}=\varphi_L\left(\varepsilon_{xx}+\varepsilon_{yy}+\varepsilon_{zz}\right)+2\psi_L\varepsilon_{zz}-(3\varphi_L+2\psi_L)\alpha_T\cdot T,\\
&\sigma_{xy}=2\psi_L\varepsilon_{xy},\quad \sigma_{yz}=2\psi_L\varepsilon_{yz},\quad \sigma_{zx}=2\psi_L\varepsilon_{zx}
\end{aligned}\right\} \quad [30]$$

Values of displacements appeared during induction heating is rather small (about 10^{-6} m or less). Only if speed of induction heating is very big they may take into consideration.

The austenitization stage is analyzed based upon eqn [23] and boundary condition eqn [21]. And finally the next stage is intensive cooling of the steel element in quenchant. For this stage the eqn [23] could be applied. The boundary condition has a form of eqn [31]

$$-\lambda\frac{\partial T}{\partial n}=\alpha_{cc}\cdot\left(T-T_q\right) \quad [31]$$

where α_{cc} denotes temperature dependent convection heat transfer coefficient for cooling and T_q is the temperature of quenchant.

For determination of temperature field a key role plays accuracy of heat transfer coefficient α_{cc}. The best way seems to be its determination by measurements of the material sample of a shape similar to the analyzed element.[13]

The basic part of the numerical analysis of induction surface hardening is the directly coupled electromagnetic thermal problem (**Figure 10**). So in further part of the chapter where illustrative example will be present heat stress problems are neglected and the basic interest is concentrated on coupled electromagnetic thermal problem.

Selection of input data is done in a way described previously. Material properties of hardened element and its temperature dependences are measured. In case of the magnetic permeability its dependence on temperature and on module of the magnetic flux density, obtained also from measurements, is taken into consideration. Dependence of the magnetic permeability on field current frequency is neglected. Arrangement of the induction hardening system is selected based upon preliminary calculations and database systems. Electromagnetic and temperature fields are considered by the modified indirect coupled approach, which is different from this one presented in **Figure 9**.[13] Boundary condition for temperature field takes into account radiation with multiple reflection phenomena. The computation of induction heating terminates when the average temperature in the surface zone of the material reached the prescribed value being a range of the hardening temperature. This value is determined by measurements using the modified TTA diagram. Then computations of non-stationary temperature field during austenitization with

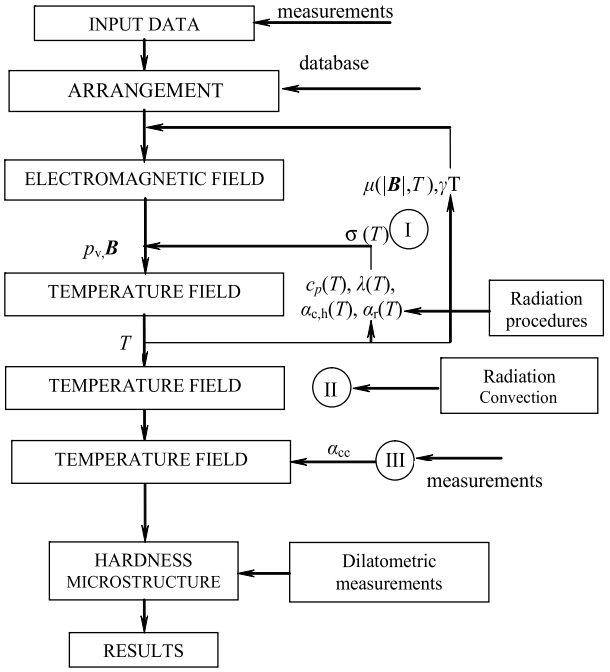


Figure 10 Calculation model of modified indirect coupled electromagnetic and temperature for simultaneous induction surface hardening. I – induction heating, II – austenitization, and III – cooling.

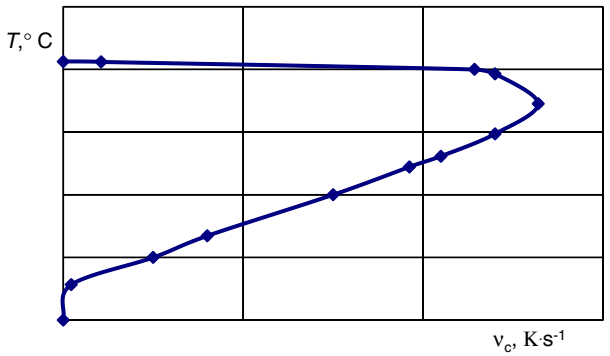


Figure 11 Dependence of temperature on cooling velocity of a cylinder made from the investigated steel in water.

taking into account both convection and radiation are provided. After that nonstationary temperature field with convection only is calculated. The convection heat transfer coefficient α_{cc} is determined by measurements provided at samples of investigated material. Dependence of temperature on cooling velocity (**Figure 11**) and time (**Figure 12**) in water of a cylinder made from the investigated steel are determined by the specialized measuring system.[13]

Based upon curves from **Figures 11** to **12** and the heat balance eqn [32] it is possible to determine the convection heat transfer coefficient and its dependence on temperature (**Figure 13**)

$$q=\rho c_p\cdot V\cdot v_c(t)=\alpha_{cc}(T)\cdot S\cdot\left(T-T_q\right) \quad [32]$$

Determination of $\alpha_{cc}(T)$ for the real hardened element having in general a different shape than the cylindrical sample is realized by means similarity criteria using Nusselt and Reynolds numbers (Holman). Calculation of nonstationary temperature field during cooling terminates when the average temperature at the body surface satisfy eqn [6]. Then based upon obtained from dilatometric measurements the CCT diagram the hardness and microstructure distribution is determined.

The computation algorithm for continual induction surface hardening is presented in **Figure 14**.

Numerical algorithm for computation of the continual induction hardening is based on the assumption that the continual movement is replaced by n small discrete shifts Δl.[15]

$$\Delta l = v \cdot \Delta t \qquad [33]$$

where v is the velocity of movement and Δt is the time step.

The number of shifts n should be sufficiently big in order to achieve the expected accuracy of the modeling. Calculations begin at the starting position of the inductor–sprayer system. The distribution of electromagnetic field in the total area and corresponding volumetric density of the Joule losses in the hardened element are determined. Then the temperature field is calculated. Material properties and heat transfer parameters for heating and cooling are corrected in iteration procedures. During induction heating the convection heat transfer α_{ch} is determined based upon Nusselt criterion Nu

$$\alpha_{ch} = \frac{Nu \cdot \lambda_f}{d} \qquad [34]$$

where λ_f denotes conduction heat of fluid in a layer near surface of the element and d is the characteristic dimension.

Determination of the convection heat transfer α_{cc} for cooling by spraying is more complicated. A way of its determination is described for instance in refs.[11,12] For that case the procedure consists of following steps:

- experimental induction hardening of the steel element made from the same material and having the same shape and based upon known parameters of spraying like flow-rate of quenchant and its pressure,
- measurement of hardness distribution,
- determination of convection heat transfer for the investigated sample based upon known unbalanced phase diagrams for the hardened material,
- usage of criteria of similarity including Nusselt and Reynolds numbers in order to recognize convection heat transfer coefficient for investigated body.

The presented procedure makes it possible to determine average value of the convection heat transfer coefficient for analyzed range of temperature.

Exemplary dependence of the convection heat transfer coefficient during cooling by spraying α_{cc} on temperature is presented in **Figure 15**.

Achieved results for water spraying are about 10 times smaller than for cooling in water by merging. The temperature distribution in the whole hardened element at all time steps is determined. Then inductor–sprayer system is removed for the next position and computations are repeated. If the final position of the inductor–sprayer system is reached, hardness and microstructure distribution is determined.

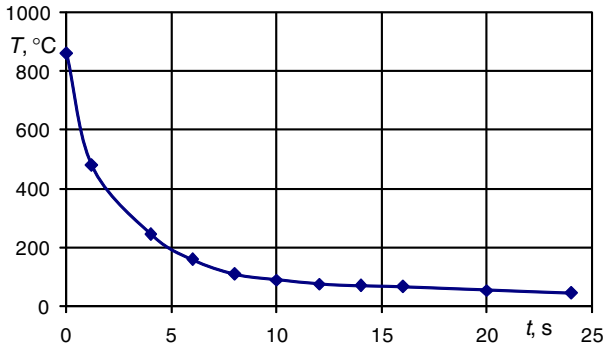


Figure 12 Dependence of temperature on cooling time of a cylinder made from the investigated steel in water.

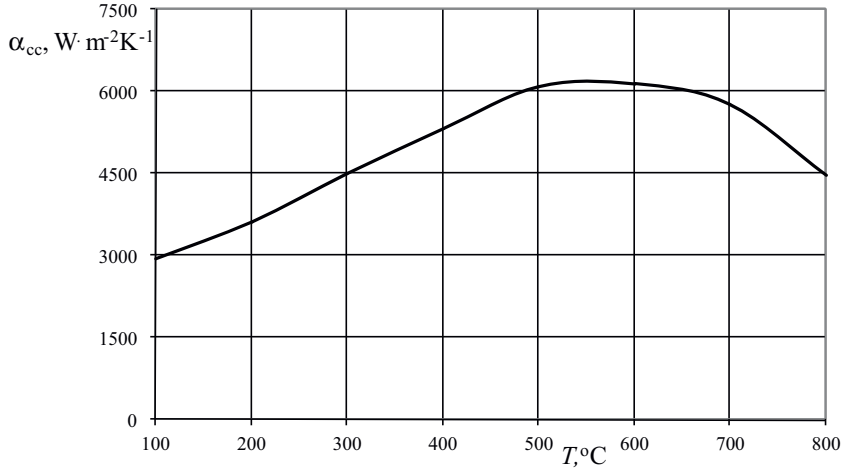


Figure 13 Dependence of convection heat transfer coefficient α_{cc} on temperature during cooling of steel cylinder in water by merging.

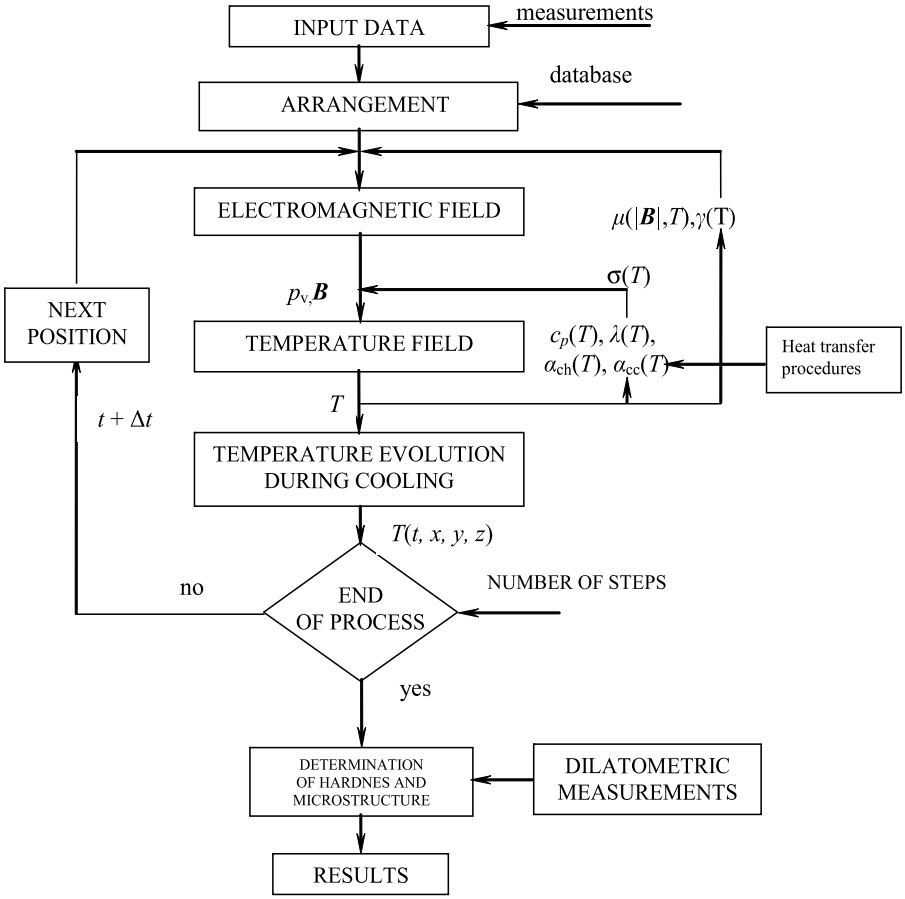


Figure 14 Numerical algorithm for computation of the continual induction hardening.

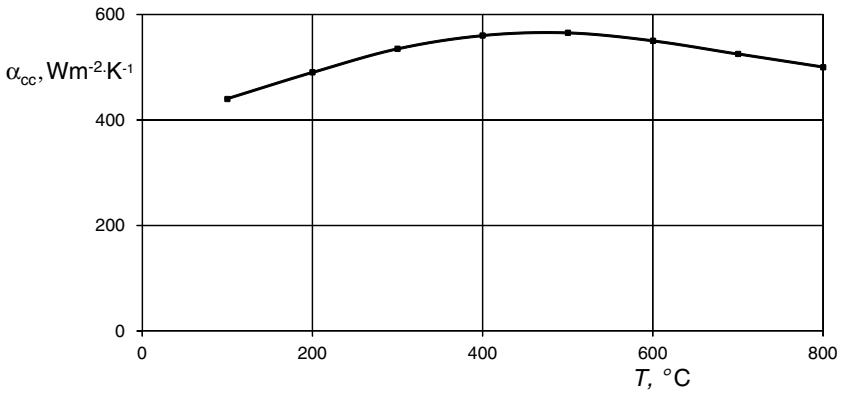


Figure 15 Dependence of convection heat transfer coefficient α_{cc} on temperature during cooling of steel cylinder in water by spraying.

2.6.3 Calculation Example

Let us consider as the illustrative example the induction surface hardening of bending brakes. The arrangement of the hardening system is presented in Figure 16.

Surface of the element which should be fully hardened is depicted in Figure 16 (segments BC, B′C′), however, the segment CD and C′D′ should remain soft. Segment AB, A′B′ may be incompletely hardened. Induction hardening is provided as continual process. Inductor–sprayer system moves along the z axis with a velocity of several millimeter per second. Typically the frequency of the field current is equal to several kHz. It means that currents induced in the hardened body because of movement could be neglected.[10]

There are two reasons making very difficult to solve the problem as nonstationary. The first of them is connected with

a long computation time due to a disproportion between the field current frequency and the time of heating. The second reason requires more detailed explanations. The magnetic permeability of hardened body used for the electromagnetic computations is temperature dependent. However, when we start the electromagnetic distribution of temperature within the hardened body is unknown. So the distribution of the magnetic permeability is also unknown. In order to simplify the computation model and to shorten the computation time the analyzed domain of the element is divided into two parts (Figure 17).

It is assumed that in the first part – thin surface layer the temperature exceeds the temperature of the magnetic transformation and the relative magnetic permeability

$$\mu_r|_{T \geq T_{Curie}} = 1 \quad [35]$$

Dimensions of the thin surface layer are determined based upon estimations.

In all remaining points of the element the temperature does not exceed the temperature of the magnetic transformation and

$$\mu_r|_{T < T_{Curie}} = \mu_r(|H|) \quad [36]$$

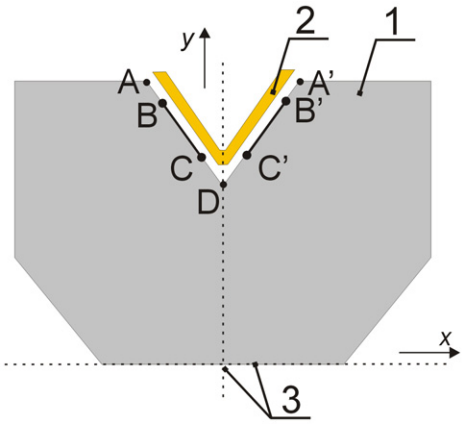


Figure 16 Cross-section of bending brake. 1 – element, 2 – inductor, and 3 – symmetry axes.

The problem is solved for the following parameters of the hardening system:

1) material: steel C50E with a carbon content of about 0.48%,
   a) its critical temperatures $Ms = 325\ ^\circ C$, $A_{c1} = 730\ ^\circ C$, $A_{c3} = 780\ ^\circ C$, $A_{c3m} = 880\ ^\circ C$,
   b) hardening temperature $T_h = 930\ ^\circ C$,
   c) dependence of hardness on velocity of cooling is determined from the CCT diagram, dependence of material properties on temperature are taken into account,
   d) hardness requirements: 600÷720 HV in thin surface zone between points BC, less than 600 HV in thin surface zone between points AB, not hardened material in other points.
2) dimensions: length $l = 0.118$ m, width $b = 0.095$ m, and height $h = 0.0125$ m
3) inductor and its supply parameters:
   a) copper conductor of the rectangular cross-section $3 \times 9 \cdot 10^{-3}$ m,
   b) field current density $J_z = 1.05 \times 10^7$ A m^{-2},
   c) its frequency $f = 10$ kHz,
   d) velocity of inductor–sprayer system movement $v = 2 \times 10^{-3}$ m s^{-1}.
4) heat transfer and cooling parameters:
   a) quenchant: water in spray of temperature $T_q = 10\ ^\circ C$,
   b) generalized heat transfer coefficient for heating $\alpha_{ch} = 20$ W m^{-2} K^{-1},
   c) convection heat transfer coefficient for cooling $\alpha_{cc} = 500$ W m^{-2} K^{-1},
   d) ambient temperature $T_a = 30\ ^\circ C$.

Numerical model for analysis of continual induction surface hardening of the bending brakes steel is presented in Figure 18. At the beginning ($t = 0$) the inductor–sprayer system is located in the initial position (depicted by lower Ω_2 in Figure 18). After some period of time because of continual movement with a small velocity $v = 10^{-3}$ m s^{-1} the system changes its position into the final one (depicted in Figure 18 by the upper Ω_2).

Calculations start with the completion of input data partly based on measurements of material properties. At the beginning the stationary induction heating of the front part of the bending brake is provided. Computation of the quasi-stationary

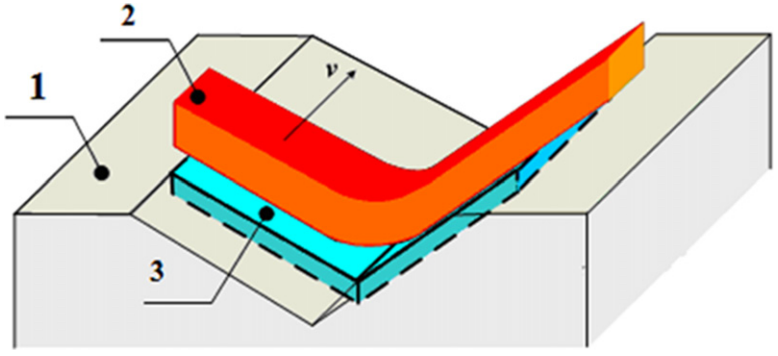


Figure 17 The view of the hardening system. 1 – bending brake, 2 – inductor, 3 – thin part of the element with temperature bigger than the temperature magnetic transformation.

electromagnetic field for the starting position of the inductor–sprayer system is provided. Based upon known value of the volumetric Joule losses the nonstationary temperature field is calculated. After a selected period of time the inductor–sprayer system starts to move. Continual movement of inductor–sprayer system is replaced by a number n of discrete shifts. It means a different configuration of the inductor–sprayer system in each position and time dependent boundary conditions of the temperature field. The time step $\Delta t = 0.5$ s corresponds to the shift $\Delta l = 10^{-3}$ m. For each cycle the dependence of material properties on temperature is taken into consideration. Results of temperature distribution is saved in order to use them for further hardness determination. Then the inductor–sprayer system is shifted to the next position and the computations are repeated. When the final position of inductor–sprayer system is reached the cooling of last part of the bending brake is calculated and then the hardness distribution is determined. The calculations are provided by the FEM based single-owned software prepared in the framework of the Polish–Czech project (Figure 19).[15,16]

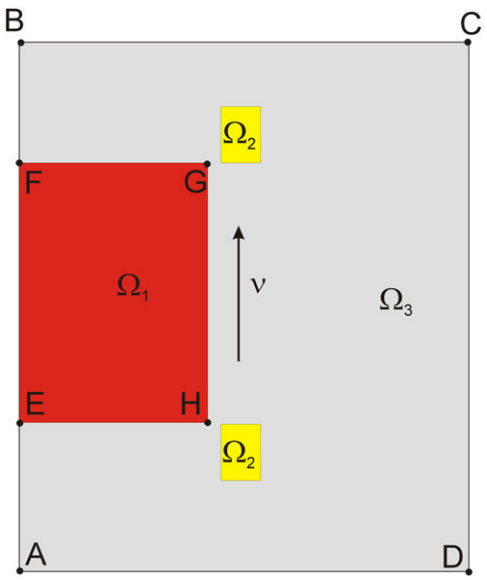


Figure 18 Numerical model for analysis of continual induction surface hardening of steel element Ω_1 – element, Ω_2 – inductor, and Ω_3 – surroundings.

The mesh for electromagnetic field has about 250 000 elements, but for the temperature field contains about 30 000 elements.

The time evolution of temperature during heating and cooling for two points on a line parallel to the axis z passing through a center of BC segment is presented in Figure 20.

The temperature in this zone reaches its maximum of 1000 °C. There are temperature differences before points along this line in a range of not more than 15 °C. However, the lowest value of the maximal temperature (not shown in Figure 20) is noticed in the front part of the body where induction heating

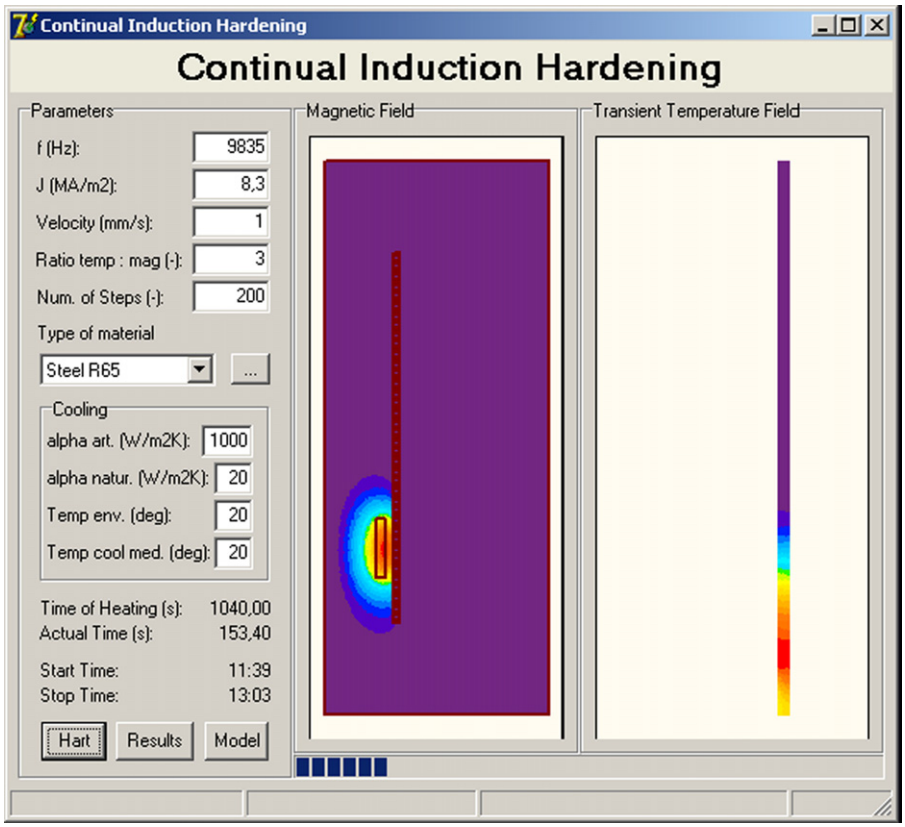


Figure 19 Cover page of the continual induction hardening software.

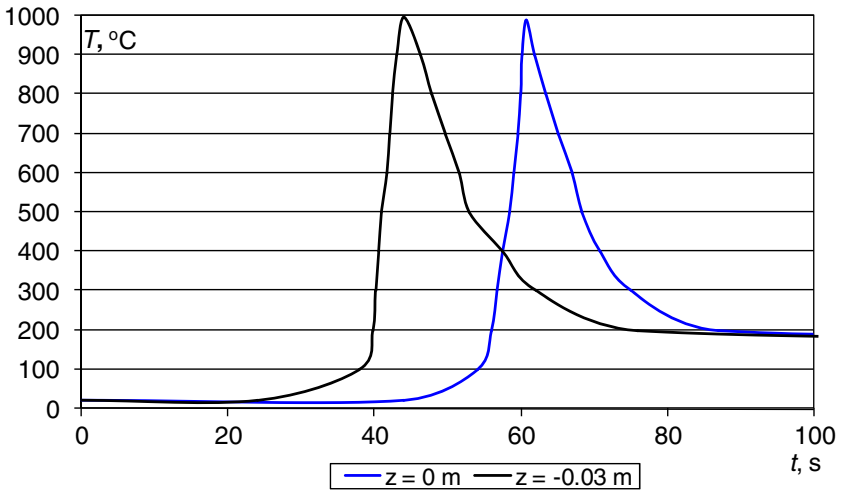


Figure 20 Time evolution of temperature on two selected points of central part of the bending brake in a line parallel to the axis z passing through a center of segment BC.

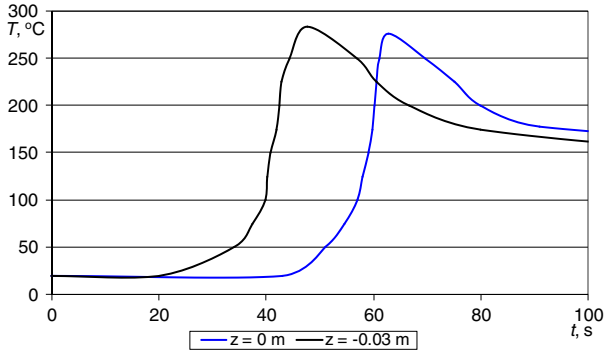


Figure 21 Time evolution of temperature of two selected points of central part of the bending brake in a line parallel to the axis z passing close to point D.

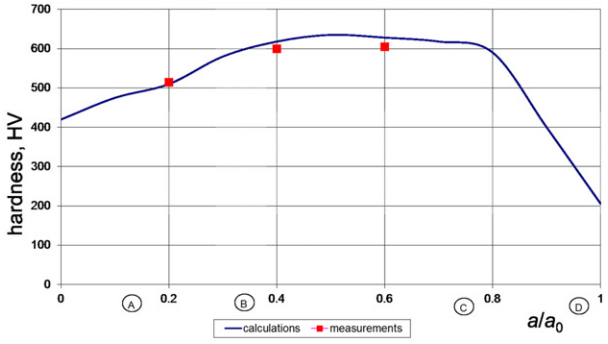


Figure 22 Hardness distribution along the line crossing the working surface of the bending brake. A, B, C, D points depicted in Figure 16.

starts (T=960 °C). Such a temperature evolution secures the complete hardening of the material in this part of the body.

The time evolution of temperature during heating and cooling for two points on a line parallel to the axis z passing through a point located near the point D is presented in Figure 21. According to requirements material in this zone of the bending brake should remain soft. Average value of temperature after induction heating does not exceed 290 °C, however, there are bigger differences between points along this line in comparison with a previous results. They are in a range of 70 °C with the maximum of 330 °C for not depicted in Figure 17 line for $z = -0.059$ m. Such a temperature evolution match the requirements and secures keeping the material soft in the part of the body.

But these calculations were provided with a simplification: without taking into radiation and multiple reflection phenomena. For comparison the similar computations by means of the Ansys package having a built-in special procedure making possible to analyze multiple reflection phenomena are provided. Taking into account both convection and radiation with multiple reflection phenomena increasing of the maximal temperature of about 60 ÷ 100 °C is noticed.

However, in order to optimize the hardening process and to get expected hardness during the whole element including boundary areas the process consists of three parts:

- stationary induction heating without movement t_i=7.5 s,
- continual hardening like described previously,
- stationary cooling of the end of the element without movement t_f=3.5 s.

Calculated and measured hardness distribution along the working surface of the bending brake for such a regime of hardening is presented in Figure 22.

There is a quite good accordance between measurements and computations with a maximal inaccuracy of 28 HV. Also distribution of hardness along the working surface match the requirements. At the upper corner of the hardened body the hardness exceeds 420 HV. It means the incompletely hardened zone. At the central part of the bending brake the hardness exceeds 600 HV. The material is fully hardened there. And finally at the lower part of the body near point D hardness is about 210 HV. It means that material remains soft. Dependence of hardness on distance from the working surface directed into the interior part of the treated material was presented in Figure 23.

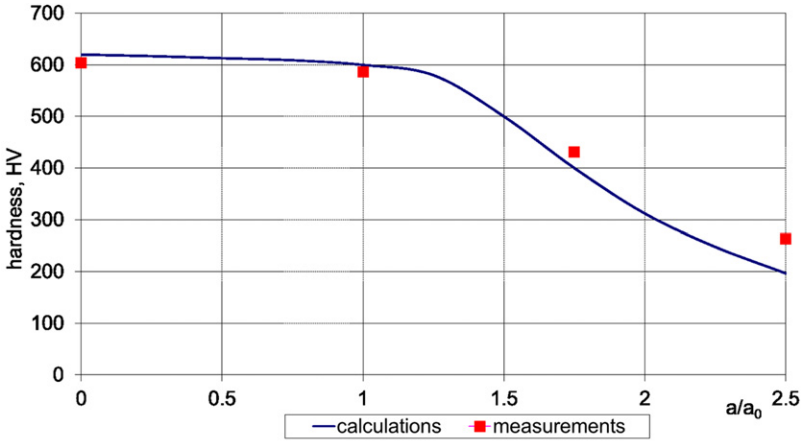


Figure 23 Hardness distribution in a function of distance from the surface.



Figure 24 Microstructure of steel C50E after induction hardening near point B (Figure 16). Acicular martensite with some retained austenite (enlargement $\times 800$).

The thickness of the hardness layer being equal to about 10^{-3} m seems to be reasonable and matching the requirements. The computations were compared with measurements provided on the laboratory stand. Quite good accordance being of order of $1 \div 3\%$ between computations and measurements is achieved. Both computations and measurements have confirmed that the length of the hardened later is acceptable and totally match the technological requirements. Another point seems to be the microstructure of the surface layer. The microstructure at the surface layer between point B and C is presented in Figure 24.

2.6.4 Some General Remarks on Induction Surface Hardening Installations

The design of inductors applied in induction surface hardening installations seem to be a complex problem.[1,4,17–23] Its solving, even with the use of advanced numerical programs, needs unfortunately expensive and time consuming experimental validation. The hardened bodies are often made from materials whose properties and their dependences on temperature are known with a big inaccuracy only. In any case in order to reduce time of experimental works it is necessary to predict the effect produced by a certain type of inductor in the different parts of the workpiece. It means estimation of the total induced power in the hardened body, its distribution within the body and on the treated surface and the inductor impedance of the inductor–body system. For frequently applied axi-symmetrical configuration of the inductor–body systems we can take into account the radial variations of the material properties produced by the temperature distribution necessary for the induction hardening. It is based upon assumption that the cylindrical workpiece can be divided into three zones (layers):

- external nonmagnetic surface layer representing zone with the average temperature exceeded the hardening temperature T_h,
- two internal zones the nonmagnetic layer with average temperature exceeded the Curie temperature and magnetic core with lower temperatures.

The design problem is more complicated for induction surface hardening of steel elements with more complicated shapes like for instance gear wheels.[1,4,5,16–18,23] A typical example of such a heat treatment seems to be the simultaneous induction surface hardening of gear wheels by means of cylindrical inductor. The purpose of the process is to obtain an uniform hardened layer along the whole working surface of the teeth including the tip, the flanks, and the roots. In this case, the choice of the optimal field current frequency has a big importance not only from the temperature distribution view point but also the electrical one. From the electrical viewpoint a good enough electrical efficiency of the inductor–hardened body system η_e defined as the ratio of the power released in the body P_i to the total power of the inductor:

$$\eta_e = \frac{P_i}{\int_V p_v \mathrm{d}V} \qquad [37]$$

has guaranteed requested energy transmission from the inductor to the hardened body. Of course it could be practically realized for gear wheels with the module satisfying inequality eqn [38]

$$m \leq 2 \div 3 \quad [38]$$

The choice of the field current frequency depends on the desired hardness thickness. This leads to the conclusion that the choice of single frequency heating system will be a kind of a compromised solution only. In fact it required the realization of the conditions mentioned above would theoretically require two different frequencies. In the case of the spin induction hardening the entire gear part is brought up to the hardening temperature by means of an inductor surrounding it and is subsequently quenched. The gears are rotated during heating to ensure an even distribution of energy. In doing this it is possible to through harden the gear part down to the tooth root (in the same way as the classical case hardening) or to harden the outer surface at either a uniform or irregular depth from the surface. Although the best pattern is usually an uniform thickness of the hardened layer along the contour, different patterns may be acceptable, or sometimes desirable depending on the application. In particular, breaks in the hardened layer may be accepted on the tips of the teeth where mechanical loading is very low, while on the flanks and roots it must be continuous in order to withstand big contact pressure and tensile stresses from loading. The main parameters playing a dominant role in obtaining the required hardness pattern are:

- geometry of the inductor–hardened body system,
- field current frequency,
- volumetric (surface) power density,
- total heating time,
- quenching conditions.

In particular, contour profile of the hardening layer can be obtained by a single frequency or dual frequency treatments. The single frequency single shot hardening process is a kind of the spin hardening in which all teeth are simultaneously contour hardened by means of a single frequency. It requires the use of high induced power density and short heating time in order to avoid the heat transmission from the surface layer to the core of the material and eliminate the possibility of through hardening of the teeth. Moreover, the process requires a convenient choice of the field current frequency in order to obtain suitable values of the induced power density at the flanks, tips, and roots of the teeth. In order to estimate the optimal value of field current frequency f_{opt} the formula eqn [39] is applied[23]:

$$f_{opt} \approx \frac{3 \cdot 10^5}{m^2} \quad [39]$$

where m denotes module of the gear in m^{-3}.

Often the single frequency induction surface hardening with preheating called also as the pulsing single frequency process has been used.[4] It consists of four consecutive stages:

- slow preheating with a reduced power to the temperature of about 500–700 °C (exact value of temperature is dependent on a grade of steel),
- fast main heating (pulse) to the hardening temperature with the high power density and in a relatively short time,
- immediate quenching,
- low temperature tempering.

Advantage of such a way of hardening seems to be:

- obtaining the correct contour zone with a convenient heated depth at the roots,
- no overheating of gear tips,
- better initial microstructure consisting of homogeneous fine grained tempered martensite,
- reduction of distortions.

Dual frequency induction surface hardening could be applied for gear wheels of rather small diameter ($d \leq 0.25$ m). This limitation is caused by a very short heating time and the corresponding high volumetric power density, which require the use of supply sources with output power of about several hundreds kW. The process is divided into four consecutive stages:

- slow preheating by applying a low power of medium frequency (MF) (3 kHz $\leq f_{MF} \leq$ 20 kHz),
- fast final heating with a big high frequency (HF) power (30 kHz $\leq f_{HF} \leq$ 500 kHz) during a very short heating time,
- immediate quenching,
- low temperature tempering.

The selection of suitable values of the field current frequency, power and time of heating depends on type of gear, its size, kind of material and required hardness pattern. The preheating temperature is usually distinctly below the lower critical temperature.

$$T|_{t = t_{MF}} = A_{c1} - (100 \div 300\ ^\circ\mathrm{C}) \quad [40]$$

The value of preheating temperature depends on type and size of the gear, tooth shape, initial microstructure, required hardness pattern, and expected level of distortions which could be accepted.[4] During the final heating the hardening temperature should be reached very quickly (0.1 s $\leq t_{HF} \leq$ 1.5 s). In order to avoid through heating of the tooth the final heating requires a very precise control of time and power and immediate transfer of the gear from the MF inductor to the HF inductor and also small enough switching speed. The alternative method of the dual frequency hardening is the simultaneous method (SDF). The common inductor is simultaneously supplied with the MF and HF power. The power ratio is given by the formula eqn [41]

$$k_p = \frac{P_{MF}}{P_{HF}} \approx 2 \quad [41]$$

The typical heating time is also given by eqn [40].

The correct choice of the quenchant has the same importance as the selection of the heating system.[1,4,11,23] The most used quenchants are: water, oil, synthetic polymers solutions, aqueous emulsions of oil, solutions of water and salt, air, baths of salt melts, and some metal melts. Numerical modeling of the temperature field during quenching makes possible to choose the requested velocity of cooling in relation to the dimensions, form and material of the hardened body.

Too fast cooling may cause irregular martensitic transformation and induce substantial internal stresses which can cause unexpected deformations. The problem is especially important in case of bodies with a complex shape (like gear wheels) or having any surface defects.[24]

2.6.5 Conclusions

Induction surface hardening belongs to modern technology making possible to apply energy efficient and environment-friendly heat treatment method to a wide sort of steel elements well known for many years. The main factors deciding about efficiency of the induction hardening methods seems to be the elaboration of good but simple computation methods making possible to design induction hardening systems. For calculation of such systems the available professional software supplemented by several singled owned procedures could be applied. The most important factors deciding about effectiveness of the applied methodology are as follows:

- well preparation input data like material properties and their temperature dependencies for the investigated steel and corrected values of the critical temperatures for induction hardening conditions. They should be first based upon well – completed databases or if possible better by especially prepared measurements. In case of the modified critical temperatures their values could be determine by dilatometric measurement done at samples of the material for initially recognized known speed of the induction heating and the intensive cooling,
- formulation of the mathematical model including coupled formulation of several physical fields including some optimization procedures and preparation of experimental-based algorithm describing dependence of hardness on time of cooling. It makes possible to finish the computations with hardness and microstructure distribution,
- experimental verification of the computations.

The induction surface hardening seems to be the innovative especially effective in many high tech applications like:

- contour induction hardening of gear wheels applied in aerospace or automobile or other branches of machinery industry,[17–20,22,23]
- laser assisted induction treatment.[24]

Acknowledgment

Support from the National Centre for Research and Development (project PBS2/A5/41/2014) is gratefully acknowledged.

See also: 2.2 Hardenability of Steel

References

1. Rudnev, V.; Loveless, D.; Cook, R.; Black, M. *Handbook on Induction Heating*; Marcel Dekker Inc.: New York, 2003.
2. Schlesselmann, D.; Nikanorov, A.; Nacke, B.; Galunin, S.; Schon, Z. Numerical Calculation and Comparison of Temperature Profile and Martensite Microstructures in Induction Surface Hardening Processes. In *Proceedings of the International Symposium Heating by Electromagnetic Sources*, Padua, 2013; pp. 127–134.
3. Spezzapria, M.; Dughiero, F.; Forzan, M.; Candeo, A.; Multiphysics, F. E. M. Simulation of Contour Induction Hardening Process on Aeronautic Gears. *J. Iron Steel Res. Int.* **2012**, *19* (1–2), 95–98.
4. Rudnev, V.; Totten, G.; *Induction Heating and Heat Treatment*, Vol. 4C; ASM Handbook: Materials Park, OH, 2014; p. 820.
5. Barglik, J.; Smalcerz, A.; Przylucki, R.; Doležel, I. 3D Modeling of Induction Hardening of Gear Wheels. *J. Comput. Appl. Math.* **2014**, *270*, 231–242.
6. Lupi, S.; Forzan, M.; Alifierov, A. *Induction and Direct Resistance Heating. Theory and Numerical Modelling*; Springer International Publishing: Switzerland, 2015.
7. Wentworth, S.; *Fundamentals of Electromagnetics with Engineering Applications*; Wiley: New York, 2005.
8. Barglik, J.; Doležel, I.; Ulrych, B. Induction Heating of Moving Bodies. In *Proceedings of the International Conference of Electrical Engineering SPETO*, 1999; pp. 167–170.
9. Holman, P. *Heat Transfer*; McGraw Hill Higher Education: New York, 2009.
10. Barglik, J.; Czerwiński, M.; Hering, M.; Wesołowski, M. *Radiation in Modelling of Induction Heating Systems*; IOS Press: Amsterdam; Berlin; Oxford; Tokyo; Washington, DC, 2008; pp. 202–211.
11. Barglik, J.; Ducki, K. Mathematical Modelling of Continual Induction Surface Hardening of Axi-Symmetric Bodies. *Arch. Electr. Eng.* **2005**, *54* (4), 479–497.
12. Barglik J.; Ulrych B.; Doležel I. Determination of Coefficient of Convection Heat Transfer at Continual Induction Hardening of Axi-Symmetric Bodies. Scientific Issues of Łódź Technical University Electrical Engineering, 2003; pp. 9–16.
13. Barglik, J.; Dołęga, D.; *Coupled Problem Solutions in Induction Heating and Heat Treatment*, Vol. 4C; ASM Handbook: Materials Park, OH, 2014; pp. 165–169.
14. Pelleg, J. *Mechanical Properties of Materials*; Springer: Dordrecht, 2013; pp. 36–50.
15. Barglik, J.; Doležel, I.; Karban, P.; Ulrych, B. Modeling of Continual Induction Hardening in Quasi-Coupled Formulation. *COMPEL* **2005**, *24* (1), 251–260.
16. Doležel, I.; Barglik, J.; Ulrych, B. Continual Induction Hardening of Axi-Symmetric Bodies. *J. Mater. Process. Technol.* **2005**, *16*, 269–275.
17. Schwenk, M.; Schwenk, W. Substitution of Case Hardened Gearbox Components in the Automotive as well as Airplane Industry Through Contour True Induction Hardening. In *Proceedings of the International Symposium Heating by Electromagnetic Sources*, Padua, 2007; pp. 175–182.
18. Stiel, H.; Marquis, F. An Overview of Inductive Gear Spin Hardening. In *Proceedings of the International Symposium Heating by Electromagnetic Sources*, Padua, 2007; pp. 183–190.
19. Biasutti, F.; Krause, C. Experimental Investigation of Process Parameters Influence on Contour Induction Hardening of Gear Wheels. In *Proceedings of the International Symposium Heating by Electromagnetic Sources*, Padua, 2010; pp. 189–200.
20. Bocher, P.; Mingardi, D.; Larregain, B.; Brider, F.; Dughiero, F. Simulation of Induction Surface Heating and Comparison with Experimental Full-Field Surface Temperature Measurements. In *Proceedings of the International Symposium Heating by Electromagnetic Sources*, Padua, 2013; pp. 99–109.
21. Jones, K.; Newsome, M.; Carter, M. Gas Carburizing vs Contour Induction Hardening of Bevel Gears. *Gear Solut.* **2010**, *8* (10), 38–54.
22. Candeo, A.; Ducassy, C.; Bocher, P.; Dughiero, F. Multiphysics Modeling of Induction Hardening of Ring Gears for the Aerospace Industry. *IEEE Trans. Magn.* **2011**, *47* (5), 918–921.
23. Barglik, J. *Induction Surface Hardening, Induction Heating Technologies*; Publishing House of ETU: Sankt Petersburg, 2013; pp. 54–81.
24. Mach, M. *Modelling and Application of Induction – Assisted Laser and Laser Hybrid Welding Processes* (Ph.D. thesis); Hannover, 2011; p. 150.

Relevant Websites

http://www.cedrat.com/
CEDRAT – Design Solutions for Electrical Engineering.
http://fluxtrol.com
Fluxtrol – Centre for Induction Technology.
http://www.professorinduction.com/
The Inductotherm Group – Ask Professor Induction.
http://www.uni-hannover.de/
University of Hannover.

2.7 Recent Advances in Mechanical Surface Treatment

S Ismail and Q Ahsan, University Teknikal Malaysia Melaka (UTeM), Melaka, Malaysia
ASMA Haseeb, University of Malaya, Kuala Lumpur, Malaysia

© 2017 Elsevier Inc. All rights reserved.

2.7.1	**Introduction**	171
2.7.2	**Peening**	171
2.7.2.1	Shot Peening	171
2.7.2.1.1	Surface of morphology	172
2.7.2.1.2	Residual stress and microhardness analysis	172
2.7.2.2	Warm Peening	174
2.7.2.2.1	Warm peening procedure	174
2.7.2.2.2	Residual stress in warm peening	174
2.7.2.2.3	Relation between temperature and fatigue life	174
2.7.2.3	Laser Peening	174
2.7.3	**SMAT**	174
2.7.3.1	SMAT Process	175
2.7.3.2	Mechanism of Surface Nanocrystallization by SMAT	176
2.7.3.3	Microstructure Characterization of the SMAT	176
2.7.3.4	Properties of SMAT Surface Layer	176
2.7.4	**Conclusions**	178
References		179

2.7.1 Introduction

The history of mechanical surface treatment dates back to as early as 2700 BC. Evidence suggests that during that time, gold helmets were hammered on the surface to improve their mechanical properties in the city of Ur.[1] During later periods, this technique was applied to enhance the properties of the sword. Mechanical surface treatment evolved into a manufacturing process in the early 1920s and 1930s. Today, it is a well-established process for enhancing the properties of metallic components in wide-ranging industries such as automotive, aerospace, medical, and others.

In mechanical surface treatment, a localized elastic–plastic deformation is introduced near the surface region of metallic components. The deformation leads to intense work hardening, severe breakdown of microstructure, and the formation of a compressive residual stress. The strengthened near-surface region may result in significantly higher resistance to the initiation and early growth of fatigue crack. It can also lead to improved resistance to stress corrosion, corrosion fatigue or fretting fatigue, and wear.

During the mechanical surface treatment process, deformation is usually applied as mechanical pulses by impacting the surface with hard shots. Sometimes a high-pressure water jet is used to induce deformation at the surface layer. In a modern variation of the process, shockwaves created by laser beam incident on the surface are used to achieve the same results. Mechanical surface treatment can also be performed by deep rolling. In this technique, near-surface region is plastically deformed by applying a controlled force using a spherical or cylindrical rolling element. Examples of components that are commonly treated by mechanical surface treatment to improve their properties include helical springs, rockers, welded joints, propeller, blades, transmission shafts, torsion bars, and others.[2]

This chapter is intended to provide an overview of recent research advances in the field of mechanical surface treatment. The first part of the chapter deals with different peening processes. The second part describes recent developments in the area of surface mechanical attrition treatment (SMAT) to create a nanostructured surface layer.

2.7.2 Peening

Peening is defined as the mechanical surface treatment process in which peening media with a specified shape and sufficiently high degree of hardness are accelerated onto the specimen, thereby inducing compressive stresses or relieving tensile stresses already present. Peening can also encourage strain hardening of the surface metal. It is the process of working a metal surface to improve its material properties, usually by mechanical means such as hammer blows, by blasting with shots (shot peening), or blasting high-intensity light beams (laser peening).

2.7.2.1 Shot Peening

In this process, small spherical peening media hit the surface of metal components at high-speed.[3] This process creates large compressive residual stress on the surface and changes the structure and properties of the surface layer.[4] The modified mechanical behavior of the peened components is mainly due to the residual stress field, strain hardening, and grain distortion caused by the multiple impacts of the shot.[5] Impact energy imparted to the surface of the workpiece is able to cause surface plastic deformation.

The shot peening process under normal conditions produces compressive residual stress on the surface of a material without inducing phase transformation. However, the shot peening process produces phase transformation (e.g., nanoferrite layer and metal flow layer) on the surface of carbon steel under intensified peening conditions of high peening velocity and the use of high-hardness shot media.[6] Conventional shot peening can be applied to obtain surface nanocrystallized materials.[7]

Conventional shot peening is performed with two methods. The first method involves the acceleration of shot material with compressed air. Shot material is introduced into a high-velocity air stream that accelerates the shot speed up to 250 ft s^{-1}. The second method involves accelerating the shots with a wheel. The shots get dropped onto the middle of the wheel and are accelerated to the outer edge, where they leave on a tangential path. Normally, there are three main types of shots used in the process: glass or ceramic beads, steel shots, and cut wire shots. Ceramic shots are harder and can be reused. Another issue that needs to be considered during this process is the intensity of shot peening.[8]

Shot peening is already established as being excellent at preventing stress corrosion cracking (SCC). This crack initiates at the surface of the chemical equipment due to the combined effect of tensile stress and corrosion. The mechanism of preventing this cracking is the same as that for preventing fatigue failure. Yoshie[9] explained that by applying shot peening on the chemical processing equipment, the performance and lifetime of the equipment are improved. He described that the intergranular SCC was detected at the vapor zone of a reactor. The intergranular SCC was caused by the sensitization due to the heat effect of the welding. Modification and repair of SCC is performed by welding, and then shot peening is applied to the vapor zone of the reactor. This shot peening process would change the tensile stress of welding at the surface to compressive stress.

2.7.2.1.1 Surface of morphology

Shot peening induces roughness on the surface that is linearly proportional to the velocity/intensity of the shot. As a general rule, larger shot size results in greater roughness at lower velocities,[10] as shown in Figure 1, where a comparison is made between steel shot (ss230, ss110, and s70) and glass beads (100, 50, 35 μm GB). The roughness of the surface is the side effect of the shot peening process. Microstructure observation after the peening process detected defects on the shot peening surface, as seen in Figure 2.

Figure 3 shows the surface morphology of as-received and shot-peened Al–Li alloy.[11,12] Smooth surface and material flow direction can be seen in the as-received sample. On the shot-peened sample, a certain increase in surface roughness, a degree of surface damage, local delamination, and cracked phenomenon around the crater are seen. The average crater size was approximately 100 μm. In addition, the overlap of the impact region of each shot caused the differences in the shape of the crater.

2.7.2.1.2 Residual stress and microhardness analysis

A certain depth of compressive residual stress is generated in the surface layer of the Al–Li alloy after shot peening (Figure 4). The residual stress is seen to gradually decrease

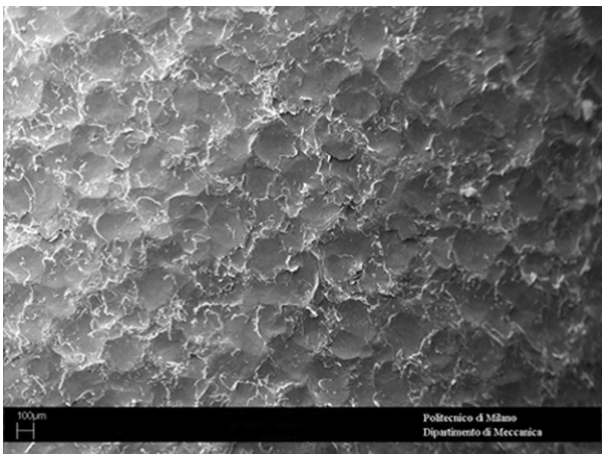


Figure 2 SEM micrograph showing the surface morphology of the SSP (severe shot sample) sample.[7]

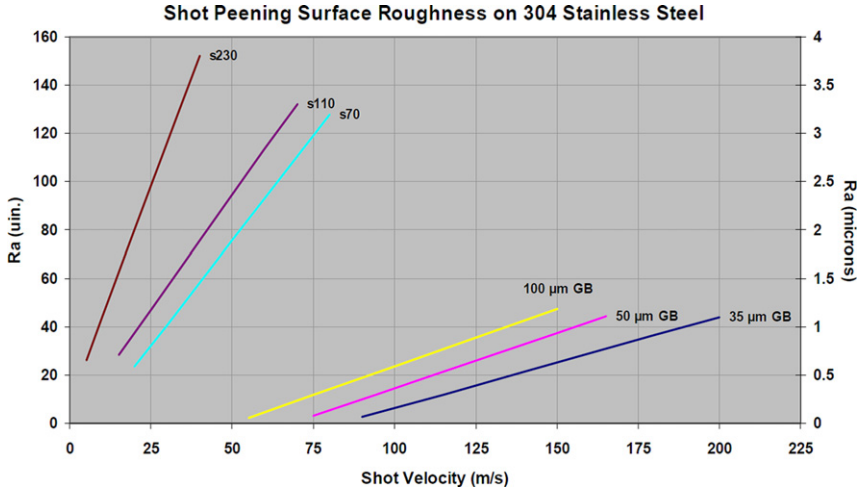


Figure 1 Surface roughness versus shot velocity.[10]

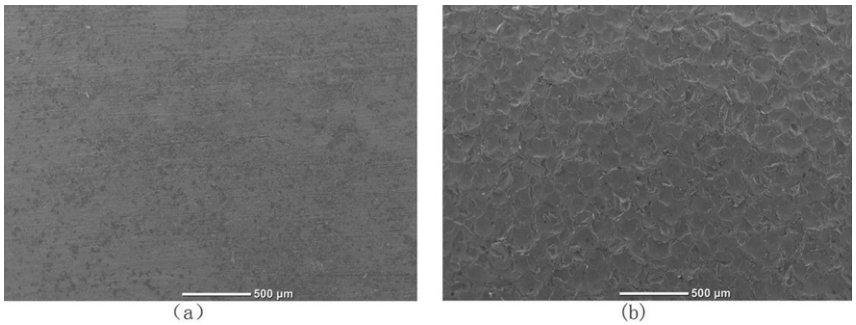


Figure 3 Surface morphology of (a) as-received and (b) shot-peened Al–Li alloy.[12]

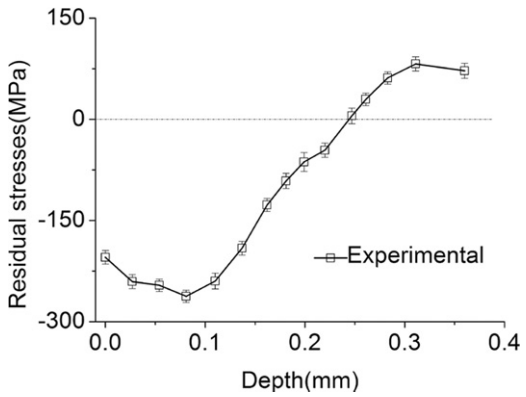


Figure 4 Residual stress distributions of Al–Li alloy.[12]

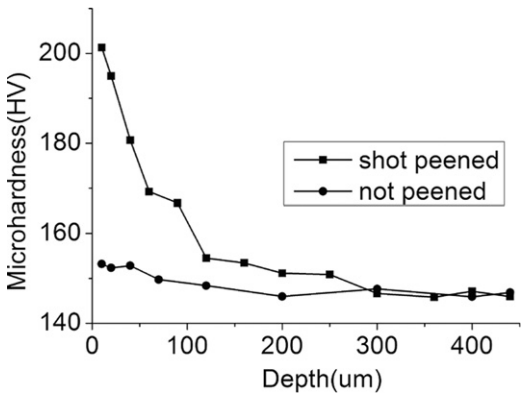


Figure 5 Microhardness profiles of as-received and shot-peened Al–Li alloy samples.[12]

within a few hundred micrometers of the surface. The residual compressive stress of the surface layer can hinder the generation of fatigue cracks, which greatly improves the fatigue resistance of the part.

The microhardness values of as-received and shot-peened specimens of the Al–Li alloy are shown in **Figure 5**. The increase in the microhardness of peening Al–Li at the surface is due to the grain refinement and work-hardening during the peening. As the surface of the workpiece is continuously impacted by the shots, it causes plastic deformation on the

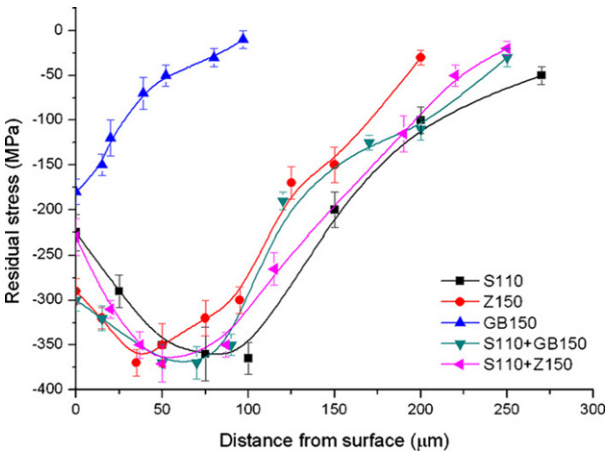


Figure 6 Compressive residual stress field caused by shot peening of 7050–T7451 aluminum alloy using different shots (S110: steel shot; Z150: ceramic bead; and GB150: glass bead).[13]

surface of the specimen. The surface hardening caused by shot peening improves surface hardness and wear resistance.

7050–T7451 aluminum alloy has been treated by the shot-peening technique to improve its fatigue performance. This alloy has been used in the fatigue-critical aircraft components due to its high strength, good stress corrosion cracking property, and high fracture toughness. Gao *et al.*[13] have discussed the effect of different shot peening on the compressive residual stress along the surface layer of 7050–T7451 aluminum alloy. **Figure 6** shows the compressive residual stress distribution along the surface layer for shot-peened samples under different shot materials. The material peened with glass beads (GB150) at an intensity of 0.10 A showed the lowest absolute value and thinnest compressive layer among all peened samples. For both ceramic beads (Z150) and steel shots (S110) with diameters of 0.15 and 0.28 mm, respectively, peening at an intensity of 0.20 A led to higher values of surface residual stress and deeper compressive residual stress fields.

Gao *et al.* also showed that by using double shot-peening, further modification of surface topography and higher surface compressive residual stress can be obtained. This double shot-peening is performed by peening the material first with high-intensity shots, and then a second shot-peening operation at a lower intensity.

2.7.2.2 Warm Peening

Warm peening is a variant of the shot-peening process whereby the workpiece is exposed to an elevated temperature during shot peening. The most common concern regarding this warm peening is that the temperature should not be too high because this would cause the decrease in hardness due to an annealing effect and therefore reduce the benefit of peening. Thus, the active temperature level should occur on the workpiece and the shot only. It was found that the dynamic and static strain aging effect during and after shot peening can stabilize the dislocation structure and therefore contribute to higher stability of the induced residual stress.[14]

2.7.2.2.1 Warm peening procedure

Warm shot peening treatment can be performed using an air blast machine. An air flow heater can be applied to the air blast machine for the warm peening system. Warm shot peening can also be performed in a heat-circulating oven. The appropriate temperature of warm shot peening is between 200 and 350 °C or below the tempering temperature. Residual stress of the specimen is normally determined using an X-ray technique. The depth of the distribution of the residual stress was determined by the iterative electrolytic removal of thin surface layers and subsequent X-ray measurement.[14] The residual stress and the microdeformation state of the material can be characterized by the half width at full maxima of a suitable X-ray diffraction peaks.

2.7.2.2.2 Residual stress in warm peening

Warm-peened samples have higher compressive residual stress compared with samples treated by the conventional peening. However, the stability of the residual stress is improved by peening at elevated temperatures due to the strain aging process.

Compressive residual stress developed in tempered AISI 4140 steel after shot peening at temperatures between 20 and 410 °C is shown in Figure 7.[14] At higher temperatures, thermally induced dislocation movement is possible, leading to rearrangement and annihilation of dislocations. This results in internal stress relaxation and decreased compressive residual stresses.

Warm peening generally increases the quasi-static as well as cyclic yield strength of the material. This is due to optimized peening temperatures resulting from dynamic and static strain aging effects. The strain aging phenomenon substantially contributes to reducing the Bauschinger effect by stabilizing the dislocation structure. The dislocations are locked through diffusion of carbon atoms to preferred edge dislocations and formation of very small carbides. Dislocation movement is restricted and the residual stresses are stabilized.

2.7.2.2.3 Relation between temperature and fatigue life

The increase of surface hardness by warm peening is the reason for the improvement of fatigue life.[15] The temperature involved below the recrystallization temperature allows some hardening to occur. Even though the fatigue life is dependent on many factors, in this process the surface roughness, strain hardening, and residual stresses are the parameters affected by the shot-peening temperature and need to be considered.

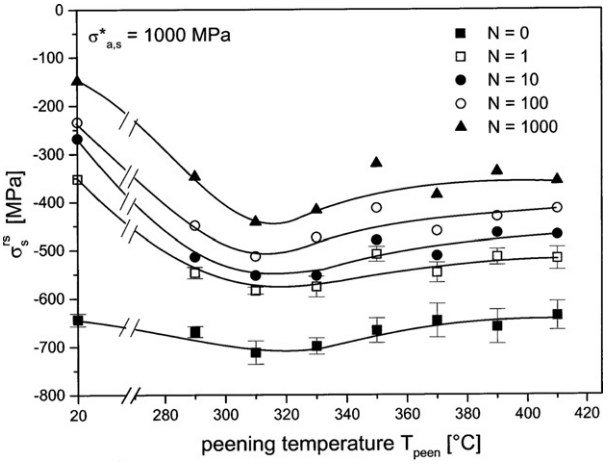


Figure 7 Residual stresses versus peening temperatures after different numbers of cycles of alternating bending load N.[14]

Ruy *et al.* investigated the effect of warm peening on the fatigue performance of spring steel (SAE 5161), in which the increase in fatigue life is due to the strain hardening effect.[16]

2.7.2.3 Laser Peening

Laser peening or laser shock peening is a technique similar to shot peening that imparts compressive residual stresses in materials for improved fatigue resistance. During a laser shock peening event, pressures well above the dynamic yield strength of the material are imparted on the target in a fraction of a microsecond. The severity of the loading causes local plastic deformation that ultimately results in the development of favorable residual stresses.[17] Laser shock treatment is a process whereby the surface of the specimen is exposed to the laser pulse for a certain duration. This method can be applied for the mechanical treatment of the near-surface regions of the workpiece, reaching surface depths of approximately millimeters. Laser shock was proven to generate plastic deformation on metallic targets.[18] This technique can result in significant improvement of metal properties such as wear resistance, resistance to stress corrosion, and fatigue strength of highly stressed metallic components used in a variety of engineering applications.[19] In this process, a thin, opaque overlay, such as a black tape, is placed on the metal surface. A transparent overlay, such as a water layer, is then applied on the black tape. The water layer directs the energy of the shock wave onto the surface. As the laser beam passes through water, it creates a shock wave that deforms the metal up to a depth of a few millimeters.

The process is dependent on the pulse energy or the intensity, as well as the duration of the pulse. In this process, the metal target is subjected to a certain pulse ($\sim$20 ns) of generated laser light (GW cm^{-2}) through a surface plasma.

2.7.3 SMAT

Most failures such as fatigue, wear, and corrosion initiate on the surface of materials. Modification of surface structure and

properties of materials enhance the life of materials by suppressing the initiation of failures. Development of a nanostructured surface is an effective surface modification process that is widely accepted in industrial applications. A nanostructured surface mainly consists of a nanocrystalline structure that improves the overall properties and behavior of the material by enhancing the surface properties without altering the chemical composition. Usually, nanocrystalline structures possess more novel properties in terms of strength and wear fracture as compared to conventional crystalline structures. Usually, nanostructured surfaces can be formed by two techniques, either by coating and deposition of nanoparticles by conventional techniques (Figure 8(a)) such as PVD, CVD, and plasma processes or by grain refinement of the surface layer by the localized plastic deformation (Figure 8(b)) process. The latter one is referred to as smart mechanical attrition (SMAT), which is a recent advancement in surface treatment methods that enables formation of a surface layer of nanostructure materials on the conventional bulk structure.

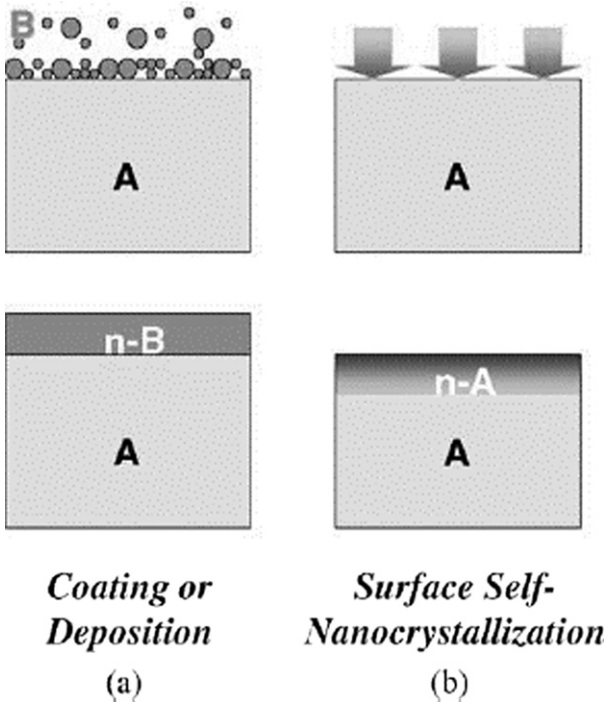


Figure 8 Schematic presentation of nanocrystallized surfaces formed by (a) surface coating or deposition and (b) surface self-nanocrystallization.[20]

The SMAT is a fairly recent surface modification technique in which a large number of metallic balls are vibrated at high frequency by a generator. The vibrating balls are impinged on the surface of the sample, which is fixed at the upper side of the chamber. The high impact of the balls on the sample surface causes severe plastic deformation. These processes will only transform a few micrometers of the surface to nanocrystalline, but the bulk material structure will remain unchanged. Due to severe plastic deformation during SMAT, grain refinement takes place and sub-grain boundaries also form at the submicron level. The parameters that control the nanostructure formation are: the size, weight, speed, and nature of the impacting balls; duration of treatment; and frequency and amplitude of the vibration. The salient features of a surface treated by the SMAT method are improved surface hardness and fatigue strength and increased corrosion resistance. The SMAT method can be successfully applied in various kinds of materials, including pure metals, steels, and alloys.[20]

2.7.3.1 SMAT Process

Usually, SMAT is performed in a chamber containing samples and spherical balls made of steel, glass, or ceramics (Figure 9). The metal balls of different diameters are placed at the bottom of the pot and are used to peen the surface of the tested metal/alloy during SMAT. The samples are fixed at the top and the balls are vibrated by a vibration generator. The distance between the sample and the balls varies. The sample pot is evacuated by a rotary pump before treatment and the low pot pressure is maintained during the treatment. Typically, ball sizes are 1–10 mm in diameter and the vibration frequency of the chamber ranges from 50 Hz to 20 kHz. The sample surface is randomly impacted by a large number of resonated balls at a velocity ranging from 1 to 20 m/s over a short period of

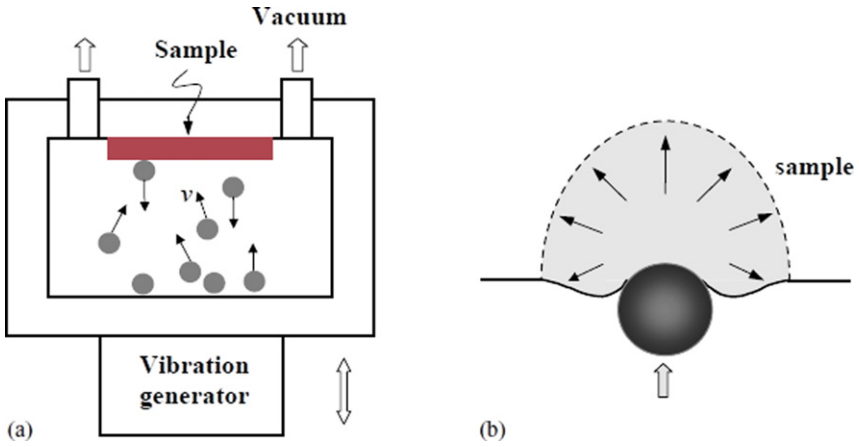


Figure 9 (a) Arrangement of sample and balls on the surface during mechanical attrition treatment and (b) impact of flying balls deforming the surface of the test sample.[25]

time. The time duration of the SMAT process is generally approximately 15 min. During the process, the sample surface encounters repeated impact from the balls, which induce severe plastic deformation and grain refinement. As a result, an increase in temperature is also noted, for example, for an iron sample, it is approximately 50–100°C,[20] depending on the intensity of the impact.

2.7.3.2 Mechanism of Surface Nanocrystallization by SMAT

The severity of deformation in terms of strain and strain rate by SMAT has a gradient from a few nanometers (on the top surface layer) to several micrometers at the subsurface of the sample. The deformation induces grain refinement during plastic deformation and forms nanostructures from the coarse-grained polycrystals through subgrain formation associated with various dislocation activities. The nanostructure formation in metals depends mainly on the lattice structure and the stacking fault energy (SFE). For materials with high SFEs, subgrains are formed by the ease of movement of dislocation walls accumulating strains, and sub-boundaries are formed to subdivide coarse grains. However, for those with low SFEs, the plastic deformation mode may change from the dislocation slip to mechanical twins (especially under high strain rate and/or low temperature).[20] Research has been conducted regarding three metals/alloys with different crystal structures and SFEs to explain the mechanisms of the nanocrystallization process by SMAT treatment. **Table 1** shows the features of the nanocrystal structure of these three metals and alloys.

Pure BCC iron, a structure with the highest SFE, showed a thin surface layer of grain refinement that occurs in three successive three stages: (1) formation of a high volume of dense dislocation walls (DDWs) and dislocation tangles (DTs) originating from plastic deformation; (2) sub-boundaries; and (3) refined subgrains are formed by the relocation of DDWs and DTs.

In copper with medium SFE with FCC structure, after the SMAT treatment, a different grain refinement mechanism occurred compared to BCC iron (Fe), with following sequence: (1) under plastic deformation, a high density of dislocations at different planes formed a cell boundary with equiaxed dislocation cells (DCs) instead of DDWs or DTs as in Fe and (2) a low level of dislocations inside the cell. With further increases in strain, in addition to DCs, mechanical twinning activates in some grains, thus dividing the original coarse grains into ultrafine (sub)grains. Finally, at maximum strains, subgrain boundaries transform into conventional grain boundaries with large misorientations.

With low SFE, AISI 304 stainless steels have different dislocation movements under plastic deformation.[21] The dislocation movements in this austenite phase usually occur at planes, forming regular dislocation grids instead of irregular DCs (as in FCC Al alloy, Cu) or DDWs (as in BCC Fe) due to the restriction of partial dislocations to cross-slip. With increasing strains, twins in different planes intersect with each other, and the formation of the strain-induced martensite phase of different ranges (nanometer to micrometer) at the intersections of the twin is reported. In the top surface layer, similar to other systems, randomly oriented nanocrystallites are formed via grain rotation or other grain boundary activities (motion or sliding) to accommodate the high strains.

2.7.3.3 Microstructure Characterization of the SMAT

In most cases, after SMAT, material phases remain the same but vary in deformation severity: nanostructures to microstructures in terms of nanograins to micrograins are observed from the surface to depths. Unlike steels, some grades of stainless steels undergo phase changes reported in the literature.[22] A scanning electron microscopy study of SMAT for a steel sample is shown in **Figure 15**.[23] A comparison between an original (**Figure 10(a)**) microstructure and the surface layer after SMAT treatment of the same sample (**Figures 10(b)** and **10(c)**) is also presented. Coarse grain structures in the range of 100–200 μm are clearly seen in the untreated surface; after SMAT of the microstructure of the treated surface layer (approximately 30 μm thick), grain structures are significantly refined. The existence of grain refinement can also be validated by studying XRD diffraction patterns of the refined crystal structure.[23]

Figure 11 shows the XRD patterns for the Fe sample before and after SMAT. Grain refinement and microstrain development in SMAT clearly broaden the Bragg reflections relative to the coarse-grain sample. Several quantitative analysis methods, such as the Scherrer–Wilson method, are utilized to estimate the grain size of the surface layer using X-ray diffraction patterns after SMAT. This is because the grain size measurement of the SMAT surface layer by a standard microscopy technique is difficult to obtain.

Investigators also compared[24] the X-ray diffraction peaks of nickel-based alloys with and without SMAT (**Figure 12**). Broadening of the Bragg diffraction peak observed in the sample after SMAT can be attributed to the small crystallite size and microstrain.

2.7.3.4 Properties of SMAT Surface Layer

It has already been mentioned that hardness, strength, fatigue, and wear of the surface layer of SMAT material improved significantly as compared to that of bulk material. Nanoindentation measurements revealed that in the SMAT Fe sample,

Table 1 Typical features of metals/alloys in nanocrystallization

Materials	*Lattice structure*	*Stacking fault energy (mJ m^{-2})*	*Mechanism involved*	*Depth of refinement*	*Grain size at surface*
Fe	BCC	200	Dense dislocation walls (DDW) and dislocation tangles (DT)	60 μm	10–50 nm
Cu	FCC	78	Dislocation cell (DC) and twin	10–100 μm	10–20 nm
AISI 304	FCC	17	Planar dislocation array (PDA) and twin	10–50 μm	10–20 nm

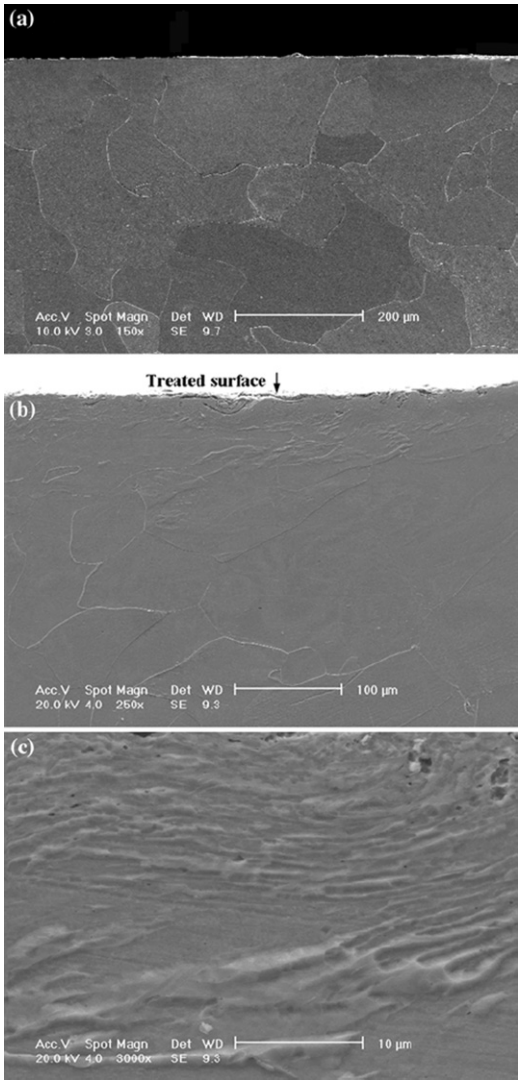


Figure 10 Cross-sectional SEM observations of (a) the original coarse-grained Fe sample (sample A), (b) the SMAT Fe sample (sample B, in which the treated surface is indicated), and (c) local magnification SEM image of the SMAT surface layer.[23]

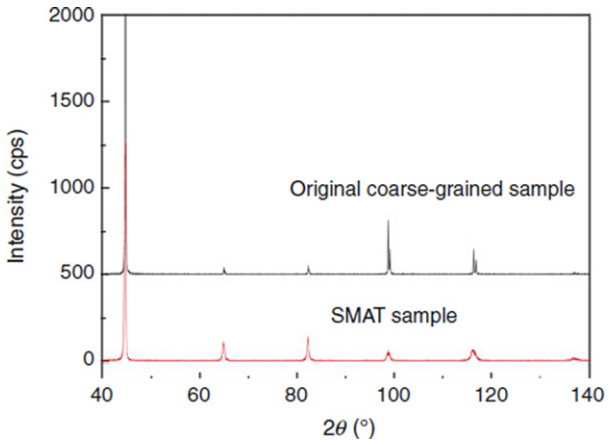


Figure 11 X-ray patterns of the original Fe sample and the SMAT Fe sample.[23]

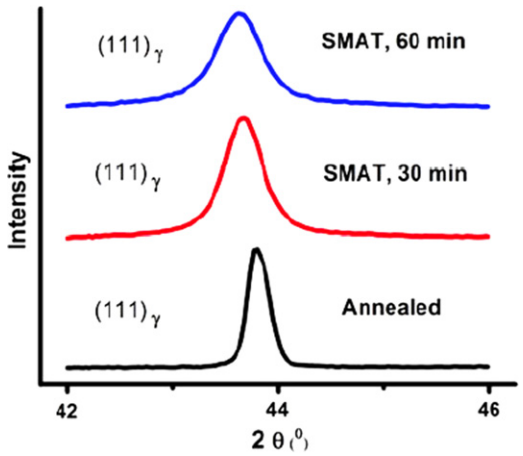


Figure 12 XRD profiles of nickel-based alloy 718 in annealed and SMAT conditions.[24]

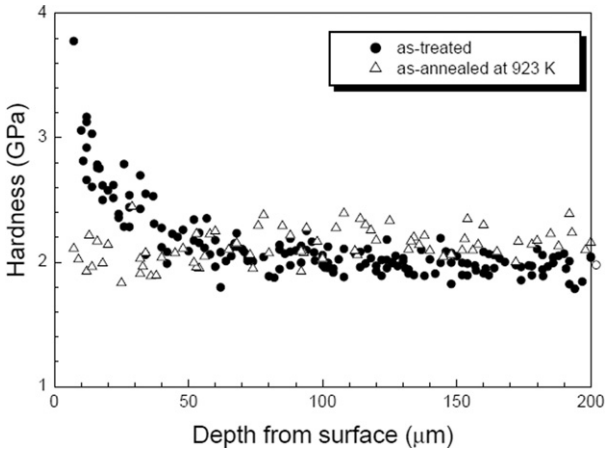


Figure 13 Measured hardness as a function of depth from the top surface for the SMAT Fe sample and for the annealed (at 593 K for 30 min) sample.[20]

treated surface possesses two- to three-times higher hardness compared with untreated coarse grain structure beneath the treated layer (Figure 13).

After SMAT, the sample was stress-relieved and annealed, and the hardness was measured again, but there was no change in hardness profile. This implies that the increment in the surface hardness resulted from refined grain structure, but not from the effect of strain hardening by SMAT. However, after recrystallization annealing for which nanostructures transform to a coarse-grain structure at the surface, the hardness in the surface layer decreases to that of the coarse-grain matrix. In addition, hardness values versus measured grain sizes from the surface to substrate validate the Hall–Petch relation in a wide range of grain sizes (from 10 nm to 50 μm). Strength tests for both low-carbon steel and stainless steel sheet with SMAT clearly showed the enhanced strength of the treated samples as compared to that of untreated samples. Such a strength enhancement can be attributed to the strong

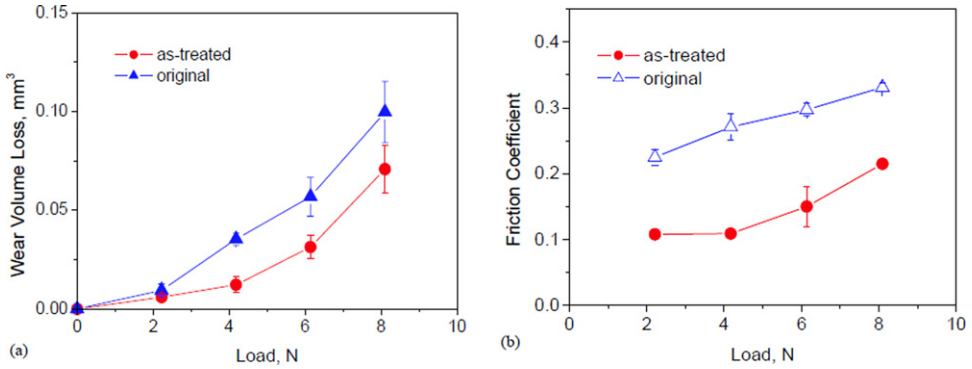


Figure 14 Variations of the wear volume loss with load (a) and variations of the coefficient of friction with load (b) for the SMAT and the original low-carbon steel samples.[20]

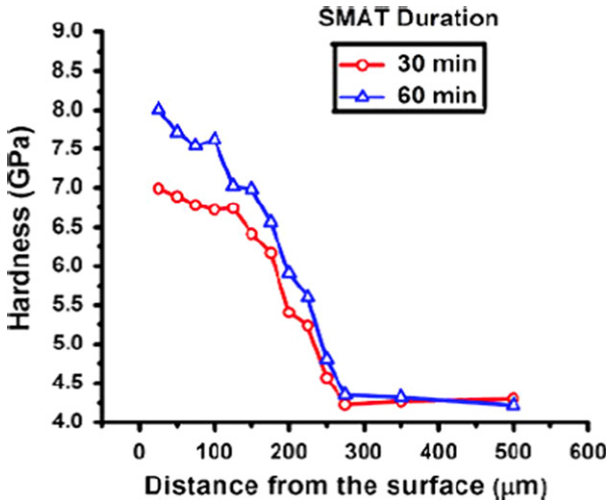


Figure 15 Variation of hardness with distance from surface of nickel-based alloy (718) subjected to SMAT.[24]

nanostructured surface layers on both sides of the sample. The increase in surface hardness and tensile strength is attributed to the grain refinement and strain hardening.

Although a study of wear mechanism was not comprehensively performed, some research results indicate the improvement of wear properties in terms of less wear volume loss and low coefficient of friction. The effects of work hardening, material transfer, and erosion during wear situations result in microstructures of wear surfaces comparable to those observed during mechanical attrition.[20] In particular, during sliding wear, large plastic strains and strain gradients are created near the surface[20] due to grain refinement of the SMAT specimen. As shown in Figure 14, the wear volume loss of the nanostructured surface layer in the SMAT sample is lower than that for the untreated original. The friction coefficient values at different applied loads for the as-treated sample are evidently smaller (approximately half) than those for the original sample. These observations indicate that the friction and wear properties of the low-carbon steel can be improved by means of formation of the nanostructured surface layer. The improved wear and fraction properties can be attributed to the strong surface layer with nanograins and a gradient variation in the microstructure and properties along the depth near the top surface.[20]

The effect of SMAT and its duration on fatigue life of nickel-based alloy 718 has been studied.[24] The SMAT process was performed in a vacuum (-0.1 MPa) with SAE 52100 steel balls with a 5-mm diameter for 30 and 60 min at a vibrating frequency of 50 Hz. SMAT resulted in surface nanocrystallization, higher surface roughness, higher surface hardness, higher compressive residual stress, higher tensile strength, reduced ductility, and superior fatigue lives. The increase in hardness of the alloy after SMAT is due to the increase in grain refinement and strain hardening (Figure 15). The enhancement in the fatigue lives of treated samples can be attributed to the positive influence of nanostructured surface layer, compressive residual stress, and work-hardened layer, which surpassed the negative effect of increased surface roughness.[25]

2.7.4 Conclusions

The development of mechanical surface treatment is one of the most important challenges facing industries such as automotive, aircraft, power plant, and petrochemical. Various surface treatment methods, including mechanical and thermo-mechanical methods, are competing with each other to increase the performance and strength of individual components. Factors required for component design as well as manufacturing conditions control the choice of the optimal surface treatment method. Usually, mechanical surface treatments allow for improving the mechanical and structural properties of metallic material. This study outlines some effective mechanical surface treatment methods, such as shot peening, warm peening, laser peening, and mechanical attrition. Based on their technological details and the associated characteristics of modified surface conditions, fatigue, wear, hardness, and several other properties of materials are explained. In addition, influence of residual stress state, work-hardening state, microstructural changes, and roughness after nanosurface treatment are also highlighted. Currently, most research activities are concentrated to achieve surface modification by generating nanostructured surface layers to improve localized mechanical properties. However, difficulties still exist in fabricating nanostructured layers because the

layers are not free from porosity, contamination, and other defects. Attention is required to develop special processes for increasing the stability of surface layers associated with defect-free structures.

References

1. Schulze, V. *Modern Mechanical Surface Treatment: States, Stability, Effects*; Wiley-VCH Verlag GmbH & Co, KGaA: Weinheim, 2006.
2. Niku-Lari, A. *Advances in Surface Treatments Technology – Applications – Effects*; Pergamon Press: Oxford, 1986.
3. Harrison, J. Controlled Shot Peening: Cold Working to Improve Fatigue Strength. *Heat Treat.* **1987**, *19* (8), 16–18.
4. Marsh, K. J. *Shot Peening: Techniques and Applications*; Engineering Materials Advisory Service Ltd: London, 1993; p. 320.
5. Fu, P.; Zhan, K.; Jiang, C. Micro-Structure and Surface Layer Properties of 18CrNiMo7–6 Steel After Multistep Shot Peening. *Mater. Des.* **2013**, *51*, 309–314.
6. Mano, H.; Kondo, S.; Matsumuro, A. Microstructured Surface Layer Induced by Shot Peening and its Effect on Fatigue Strength. In *IEEE International Symposium on Micro-Nanomechatronics and Human Science*; 2006.
7. Bagherifard, S.; Pariente, I. F.; Ghelichi, R.; Guagliano, M. Fatigue Properties of Nanocrystallized Surfaces Obtained by High Energy Shot Peening. *Procedia Eng.* **2010**, *2* (1), 1683–1690.
8. Kyriacou, S. Shot-Peening Mechanics: A Theoretical Study. In *6th International Conference on Shot Peening (ICSP-6)*, San Francisco, CA, September, 1996.
9. Yoshie, K. Application of Shot Peening to Stress Corrosion Cracking of Chemical Processing Equipment. In *Proceeding of ICSP*, 1990.
10. Champaigne, J. *Shot Peening Overview*; Metal Improvement Company: Mishawaka, IN, 2001.
11. Bagherifard, S.; Ghelichi, R.; Guagliano, M. A Numerical Model of Severe Shot Peening (SSP) to Predict the Generation of a Nanostructured Surface Layer of Material. *Surf. Coat. Technol.* **2010**, *204* (24), 4081–4090.
12. Sun, B. L.; Wang, Y. J.; Xiao, J. Y.; Gao, G. Q.; Qiao, M. J.; Xiao, X. D. Evolution of Microstructure and Properties of 2196 Al–Li Alloy Induced by Shot Peening. *Procedia Eng.* **2014**, *81*, 1043–1048.
13. Gao, Y. Improvement of Fatigue Property in 7050–T7451 Aluminum alloy by Laser Peening and Shot Peening. *Mater. Sci. Eng. A* **2011**, *528* (10), 3823–3828.
14. Menig, R.; Schulze, V.; Vöhringer, O. Optimized Warm Peening of the Quenched and Tempered Steel AISI 4140. *Mater. Sci. Eng. A* **2002**, *335* (1), 198–206.
15. Tange, A.; Koyama, H.; Tsuji, H.; Schaad, J. Study on Warm Shot Peening for Suspension Coil Spring; *SAE Technical Paper*, 1999.
16. Ruy, M.; Tarpani, J.; Milan, M.; Spinelli, D.; Bose, W. 4733 – The Effect of Warm Shot Peening on the Fatigue Performance of A Sae 5160 Spring Steel. In *ICF11, Italy 2005*, 2013.
17. Braisted, W.; Brockman, R. Finite Element Simulation of Laser Shock Peening. *Int. J. Fatigue* **1999**, *21* (7), 719–724.
18. Peyre, P.; Fabbro, R.; Berthe, L.; Dubouchet, C. Laser Shock Processing of Materials, Physical Processes Involved and Examples of Applications. *J. Laser Appl.* **1996**, *8* (3), 135–141.
19. Nalla, R.; Altenberger, I.; Noster, U.; Liu, G.; Scholtes, B.; Ritchie, R. On the Influence of Mechanical Surface Treatments – Deep Rolling and Laser Shock Peening – On the Fatigue Behavior of Ti–6Al–4V at Ambient and Elevated Temperatures. *Mater. Sci. Eng. A* **2003**, *355* (1), 216–230.
20. Lu, K.; Lu, J. Nanostructured Surface Layer on Metallic Materials Induced by Surface Mechanical Attrition Treatment. *Mater. Sci. Eng. A* **2004**, *375*, 38–45.
21. Balusamy, T.; Venkateswarlu, M.; Murthy, K.; Vijayanand, S.; Narayanan, T. S. Effect of Surface Mechanical Attrition Treatment (SMAT) on the Surface and Electrochemical Characteristics of Pb–Sn Alloy. *Int. J. Electrochem. Sci.* **2014**, *9*, 96–108.
22. Zhang, H.; Hei, Z.; Liu, G.; Lu, J.; Lu, K. Formation of Nanostructured Surface Layer on AISI 304 Stainless Steel by Means of Surface Mechanical Attrition Treatment. *Acta Mater.* **2003**, *51* (7), 1871–1881.
23. Zhong, C.; Hu, W.; Jiang, Y.; Deng, B.; Li, J. Lower Temperature Aluminizing and its Effect on Improving Corrosion Resistance of Iron Treated by Surface Mechanical Attrition Treatment. *J. Coat. Technol. Res.* **2011**, *8* (1), 107–116.
24. Anand Kumar, S.; Ganesh Sundara Raman, S.; Sankara Narayanan, T. S. Effect of Surface Mechanical Attrition Treatment on Fatigue Lives of Alloy 718. *Trans. Indian Inst. Met.* **2012**, *65* (5), 473–477.
25. Tao, N.; Wang, Z.; Tong, W.; Sui, M.; Lu, J.; Lu, K. An Investigation of Surface Nanocrystallization Mechanism in Fe Induced by Surface Mechanical Attrition Treatment. *Acta Mater.* **2002**, *50* (18), 4603–4616.

2.8 Heat Treatment of Commercial Steels for Engineering Applications

MK Banerjee, Malaviya National Institute of Technology, Jaipur, India

© 2017 Elsevier Inc. All rights reserved.

2.8.1	**Introduction**	180
2.8.2	**Medium-Carbon Low-Alloy Steels or Plain-Carbon Steel**	181
2.8.2.1	Forging Quality Steel	181
2.8.2.1.1	Annealing	181
2.8.2.1.2	Normalizing	181
2.8.2.2	Precipitation Hardened Martensitic Steels	181
2.8.2.3	Heat Treatment of 9Ni4Co Steel	184
2.8.2.4	Heat Treatment of AF1410 Steel	185
2.8.2.5	Press Hardenable Ultrahigh-Strength Steel	186
2.8.2.6	Nanoscale Precipitations Hardenable Steel	187
2.8.2.7	Medium-Carbon Low-Alloy Steel	188
2.8.2.8	Si-Modified 4340 Steel	188
2.8.2.9	Ni–Cr Structural Steel	189
2.8.2.10	Medium-Carbon Chromium–Vanadium Steel	192
2.8.2.11	Chromium–Molybdenum Steel: Steel for High-Temperature Boiler Application	192
2.8.3	**Spring Steel**	192
2.8.4	**Silicon Steel**	195
2.8.5	**Bearing Steel**	196
2.8.6	**Hadfield Steel**	197
2.8.7	**Stainless Steel**	199
2.8.7.1	Martensitic Stainless Steel	199
2.8.7.2	Ferritic Stainless Steel	200
2.8.7.3	Austenitic Stainless Steel	200
2.8.7.4	Duplex Stainless Steel	204
2.8.7.5	Precipitation Hardenable Stainless Steel	204
2.8.8	**Maraging Steel**	205
2.8.8.1	Heat-Treatment Sequence of Maraging Steels	207
2.8.8.2	Embrittlement in Maraging Steel	207
2.8.9	**Heat Treatment of Transformation Induced Plasticity Steel**	208
2.8.10	**Dual Phase Steels**	208
2.8.10.1	Rapid Heating Producing Ultrafine Grained Dual Phase Steel	210
2.8.10.2	Bake Hardened Dual Phase Steels	211
2.8.11	**Heat Treatment of Steel Casting**	211
References		212
Further Reading		213

2.8.1 Introduction

The steels having common engineering applications are quite often commercially important; sometimes huge requirements of certain class of steels for specific application area make them attractive to manufacturing industries. Paradigm shift of design philosophy has raised the demand for development new and high-performing steels for commercial applications at less cost. In general the commercially important steels may be grouped as structural steels, automotive steels, ultrahigh strength steels for critical applications, abrasion and shock resistance steels, and above all stainless steels; being low-, medium-, or high-alloy steels of varying carbon contents, the above mentioned commercially important steels have posed additional challenges in heat-treatment practices to insure improved mechanical and mechano-chemical properties.

Therefore in the present chapter, attempts are made to discuss the basic principles underlying heat treatment of some important commercial steels. This encompasses discussion of the whole spectrum of commercially important steels ranging from medium carbon commercial steels with low or no alloy contents to the present generation advanced high-strength steel (AHSS). Present trend in development of ultrahigh-strength steels envisages the modification of AF1410 or AerMet 1000 steels. This calls for newer strategy for heat treating these steels. Special attention is also paid in designing the heat treatment of this class of steels. Current interest in development of new generation AHSSs for safe, reliable, and cost-effective application in automotive sectors is also duly regarded while describing the heat-treatment challenges of these steels.

Evolution of microstructure during heat treatment of the steels under consideration is also followed so as to gather a

 doi:10.1016/B978-0-12-803581-8.09190-6

better understanding of their processing–structure–property relationship. Moreover the criticality of phase transformation associated with the heat treatment of maraging steels is elaborated in the current chapter. Heat-treatment processes of different varieties of stainless steels, its limitations, and protocol to develop suitable microstructure are separately discussed. There are always some constraints in industrial heat-treatment practice. Taking example of austenitic manganese steels and other steel castings in general, efforts are made to explain how a heat treater can overcome the difficulty confronting the achievement of ideal microstructures in real life industrial situation.

2.8.2 Medium-Carbon Low-Alloy Steels or Plain-Carbon Steel

2.8.2.1 Forging Quality Steel

It is known that forging quality steels are used in production of gears and tooth wheels in automobile sector. In present scenario the objective of profitable production of above automotive components are to:

1. achieve a very high strength and toughness,
2. adopt shortest possible heat-treatment cycle, and
3. improve damage tolerance.

The commercially important forging quality plain-carbon steels include AISI 1040 and 1045 steels along with other similar ones.

Medium-carbon steels are known to be quite suitable for applications where a good combination of strength, toughness, and wear resistance is required. AISI 1045 is one such medium-carbon steel which is used for manufacturing of forged parts which require sufficient strength and toughness for applications as crank-shafts and couplings. These medium-carbon steels are normally forged from 1250 to 1200 °C, finished forging temperature being 950–1000 °C. However the forging temperature depends upon the geometry and amount of deformation to be given during forging. The forged components are subjected to the following heat treatment.

2.8.2.1.1 Annealing

Full annealing of the forged steel components is accomplished at a temperature between 900 and 850 °C followed by slow cooling at 10 °C h^{-1} till 600 °C; afterward the stock may be air cooled.

2.8.2.1.2 Normalizing

Normalizing of the annealed component is carried out by heating at 870 °C, holding for sufficient time and then cooling the components in still air. A lower temperature around 850 °C is preferred for normalizing in the event, it is the final heat treatment. The normalized stock is then hardened from a temperature of 850 °C; quenching is normally carried out in oil. Depending upon the application of a component, induction hardening is carried out by quickly heating it to the desired case depth and then quenching in water. The induction hardened parts are normally tempered at a low temperature like 150–200 °C to reduce the residual stress without much affecting the hardness at the surface of the component, which is normally kept at R_c 56–58. For the volume hardened material, the tempering temperature ranges between 400 and 675 °C in accordance with the required mechanical properties. Microstructural changes accompanying heat treatment of AISI 1045 steel is shown in Figures 1(a)–1(c).

The low-alloy steel so far used for such components is 42CrMo4, whose composition is shown in Table 1.

Heat-treatment cycle of 42CrMo4 steel is as follows:

1. Normalized from 880 to 900 °C after holding for 1 h per 25 mm thickness.
2. Hardening is done after heating to 860–880 °C; holding is done for sufficient period of time, and finally quenched in oil at 80 °C.
3. Tempering is carried out at suitable temperature between 530 and 680 °C. The exact tempering temperature is determined by final property required.

In general this class of steels is used in quenched and tempered condition; by controlling the heat-treatment process, it is possible to derive the required properties of the steels.[1] The structural changes taking place due to forging of varying amount and post-forging cooling rates is shown in Figure 1(d).

However the recent trend for shortening the process route has led to emergence of ferrite-pearlite precipitation hardenable steel, 38MnVS6. The composition of 38MnVS6 and a modified version of precipitation hardenable ferrite-pearlite steels is shown in Table 1. The microstructure of precipitation hardened ferrite-pearlite steels against quenched and tempered one is shown in Figure 2.

The steel is heated to a temperature around 1150 °C to dissolve all carbides in solution so that a homogenous austenite is available.

After forging the rate of cooling is controlled because it is a very important parameter for control of microstructure in alloy steel. After forging the components are cooled in air. The cooling rate should preferably be within the range of 1–5 °C s^{-1}. This rate of cooling must be continued till the component attains a temperature of 600 °C. The microstructure shows ferrite-pearlite structure with very fine precipitates of vanadium carbide (Figure 2). The high ultimate tensile strength above 900 MPa with impact strength around 20 J is achievable in both 38MnVS6 and the modified version precipitation hardened ferrite-pearlite steels.

2.8.2.2 Precipitation Hardened Martensitic Steels

A class of martensitic steels is strengthened by secondary hardening to impart ultrahigh strength at high-toughness level. AF1410 belongs to this class of steels and contains appreciable amount of nickel and cobalt. Due to high nickel content the steel exhibits a low ductile-to-brittle transition temperature; on the contrary cobalt aids in precipitation hardening and high-temperature strength.[4–6] Another class of steel, AerMet100, is so developed as to impart strength both by precipitation of intermetallic and alloy carbides. Heat treatment of these steels comprises of austenitizing, quenching to room temperature, and then tempering or aging to effect the precipitation of intermetallics and alloy carbides. Alloying elements in these two classes of steel are so chosen that the transformation of austenite may take place at sufficiently low temperatures. The low-temperature transformation products of austenite viz.

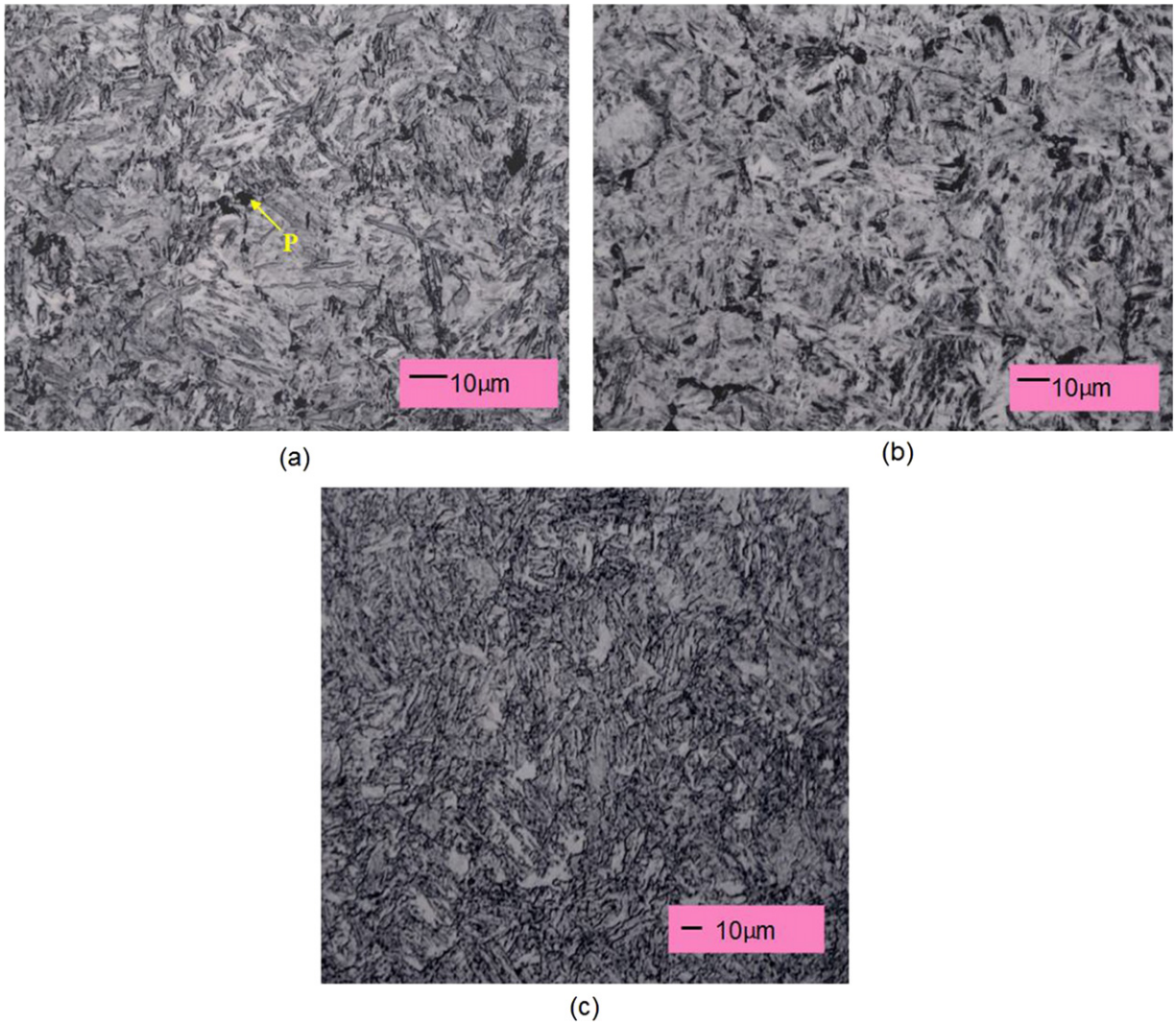


Figure 1 Microstructures of AISI 1045 steel (a) quenched, (b) quenched and tempered at 200 °C, and (c) quenched and tempered at 540 °C. (d) Microstructure of the heat-treatable 42CrMo4 steel for cooling rate 15 Ks^{-1} (left) and 0.07 Ks^{-1} (right); above – without deformation, middle – deformation level 30%, and below – deformation level 60%.[2] Vander Voort, G. F. *Microstructure of Carbon and Low-Alloy Steels*.

lower bainite/martensite are generally produced after quenching of these steels. Aging of these steels are carried out at sufficiently high temperature so that slow diffusing substitutional alloying elements can have adequate mobility to form their carbides or intermetallic compounds with elements other than carbon. The heat treatment of these steels is controlled in such manner that a fine-scale microstructure is achieved to insure higher fracture resistance.

The other steels of this type include HY180 and HP 9–4–20 which led to further development of similar type of steels with improved properties. HY180 steel contains 0.10 wt% carbon, 10 wt% nickel, 8 wt% cobalt, 2 wt% chromium, and 1 wt% molybdenum. After heat treatment, the mechanical property of this steel becomes significantly superior to many high-strength steels.[7–8] A 5 h tempering at 510 °C achieves yield strength of 1250 MPa. The Charpy impact energy of the said steel is found to decrease with increasing tempering temperature above 300 °C till 425 °C; Charpy impact energy attains its minimum value at 425 °C. However tempering at temperatures greater than 425 °C leads to increase in its Charpy impact energy value; its maximum value is attained by tempering the steel at 510 °C. It should be noted that tempering above 425 °C produces intra-lath carbides of type M_2C, which is beneficial to impact strength. Cementite does not form and the needles of these alloy carbide particles are very fine with length being around 10 nm. However multiple heat treatments of HP 9–4–30 steels can lead to further structural refinement with associated improvement in properties. The microstructures of these steels are shown in **Figure 3**.

Cobalt is known to delay recovery processes till a high temperature like 500 °C; the delay in recovery helps to retain the dislocation structure within the material. Thus sites for nucleation of alloy carbides increase many folds and hence numerous fine sized carbides result in the microstructure. Also cobalt increases the activity of carbon in ferrite and thus helps in formation of more carbide. It is also known that higher chromium content in the steels results in more rapid coarsening of the alloy carbides and shifts the secondary hardening

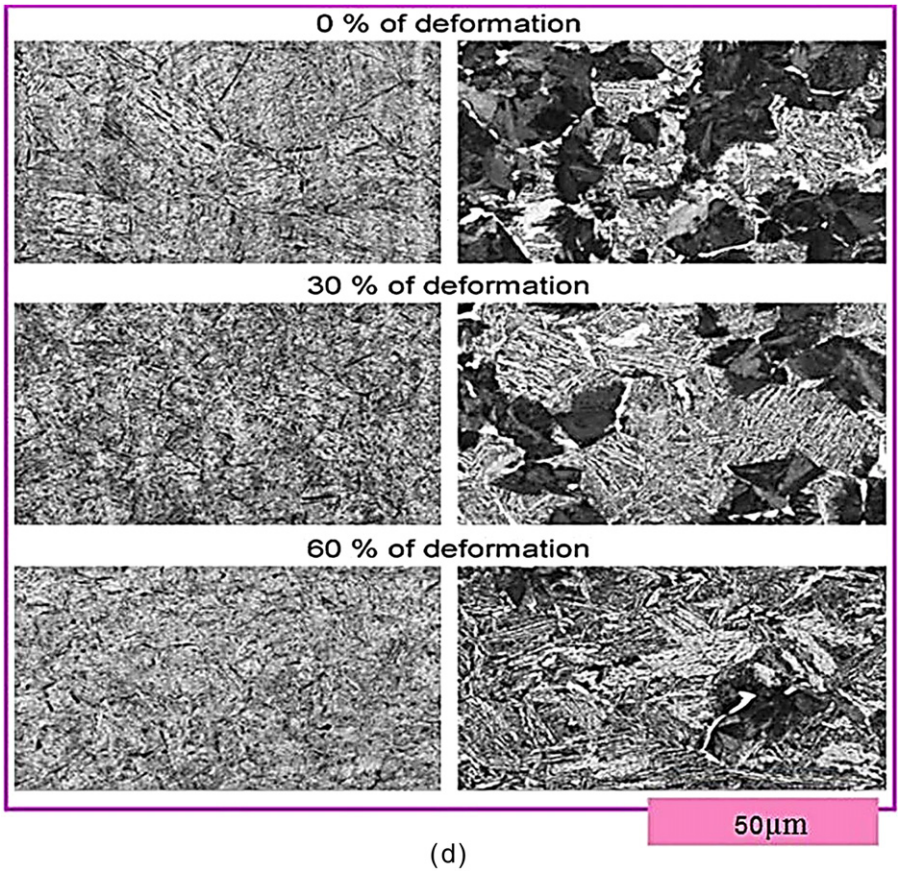


Figure 1 (Continued).

Table 1 Chemical composition of forging quality steel (wt %)

Type	*C*	*Si*	*Mn*	*Cr*	*Mo*	*Nb*	*Ti*	*V*	*Fe*
AISI1045	0.43–0.50	0.15–0.30	0.60–0.90	–	–	–	–	–	Balance
42CrMo4	0.42	0.30	0.80	1	0.20	–	–	–	Balance
38MnVS6	0.38	0.60	1.40	0.04	0.03	–	–	0.10	Balance
PHFP-M	0.36	0.70	1.45	0.15	0.03	0.03	0.02	0.2	Balance

peak to lower tempering temperatures. Increasing the molybdenum content has the opposite effect. This has led to the discovery of AF1410 whose chemical composition approximates 0.16 wt% C, 14 wt% Co, 10 wt% Ni, 2 wt% Cr, and 1 wt% Mo. Alike HY180, AF1410 steel is tempered for 5 h at 510 °C and achieves a yield strength of about 1500 MPa presumably due to higher carbon and cobalt content.

However, AF1410, achieves its maximum yield strength after tempering at 475 °C, not at 510 °C as it is for HY180. This minimum in the toughness as experienced after tempering at 425 °C is ascribed to availability of minimum amount of retained austenite due to its decomposition with the precipitation of cementite. Carpenter Technology developed still higher strength version of this alloy in the name of AerMet100, with a chemical composition of 0.25 wt% C, 13.4 wt% Co, 11.5 wt% Ni, 2.5 wt% Cr, and 1.2 wt% Mo.

Similar to AF1410, the maximum in the yield strength of AerMet100 is obtained after tempering at 475 °C. AerMet100 steel also records the minimum Charpy impact energy on tempering at about 425 °C. AF1410 steel can be strengthened more at higher cobalt content as it ensures higher scope for increasing the carbon content of the steel; it is known that higher carbon content in martensite is responsible for higher hardness of iron–carbon martensite. However the disadvantage of increase in carbon content is realized in having the M_s and M_f temperatures depressed to below room temperature; it is required to elevate these temperature to above room temperature so that one can secure 100% martensite after quenching the steel. Cobalt is an alloying element which, unlike most of the alloying elements in steel, is capable to raise the M_s and M_f temperatures. So cobalt content is increased from 8 to 14% to achieve M_s and M_f temperatures at 327 and 166 °C respectively. Thus a window for increasing the carbon content is now available and this is how AF1410 steel could be modified with composition of 0.17C–10Ni–14Co–2Cr–1Mo with varying amounts of titanium. This gives rise to better

mechanical properties than AF1410 steel which contains 0.13% carbon at 8% cobalt level. The same strategy is employed to design the steel, AerMet100,[9–10] with the chemistry, 0.23C–14Co–12Ni–3Cr–2Mo; here higher carbon content with simultaneous increase in carbide formers can give rise to very high strength upon quenching from 900 to 950 °C followed by tempering at 620–650 °C. The strength of this steel can go as high as 1950 Mpa with K_{Ic} around 126 Mpa $m^{1/2}$.

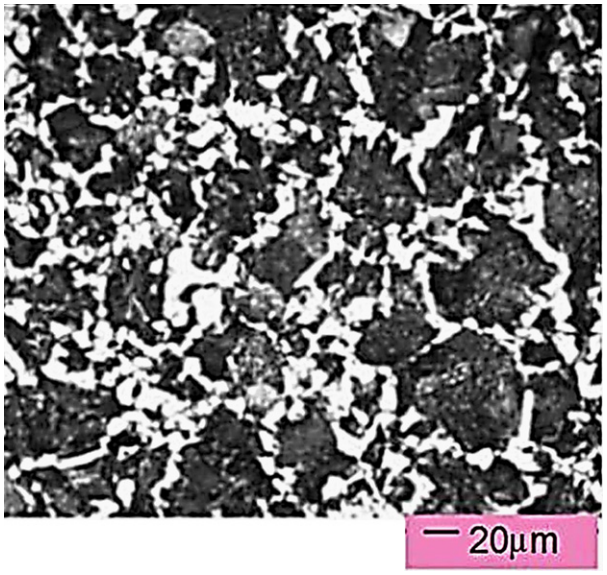


Figure 2 Typical pearlite and ferrite microstructure of air-cooled microalloyed forging steel.[3] Caminaga, C.; Button, S. T. Mechanical Properties of Ausforged 27MnSiVS6 Microalloyed Steel. *Metall. Mater., REM:R.Esc Minas, Ouro Preto* **2013**, *66* (3), 331–338.

2.8.2.3 Heat Treatment of 9Ni4Co Steel

This type of steels has emerged in early 1960s, due to requirement of high fracture toughness at high strength. Commercially known steels under this category are HP 9–4–20 and HP 9–4–30. HP 9–4–20 contains 9% Ni, 4% Co, with 0.20% C; whereas the carbon content is 0.30% in the other variety. These steels possess very high hardenability and presence of 4% Co help to minimize the retained austenite amount in hardened microstructure as cobalt is known to raise the M_s temperature.

The heat-treatment cycle of HP9–4–30 steel is as follows:

- Normalizing is done from 900 °C, after holding at the normalizing temperature for 1 h. per 25 mm thickness.
- Spheroidizing annealing is performed by way of heating to 620 °C and holding it there for 24 h followed by air cooling.
- Alternately multiple annealing from temperature of 700–630 °C with holding time of 4 h at each annealing temperature may be used to produce spheroidized structure. The objective of spheroidizing treatment is that homogenization of austenite for hardening can be facilitated by prior spheroidized microstructure.

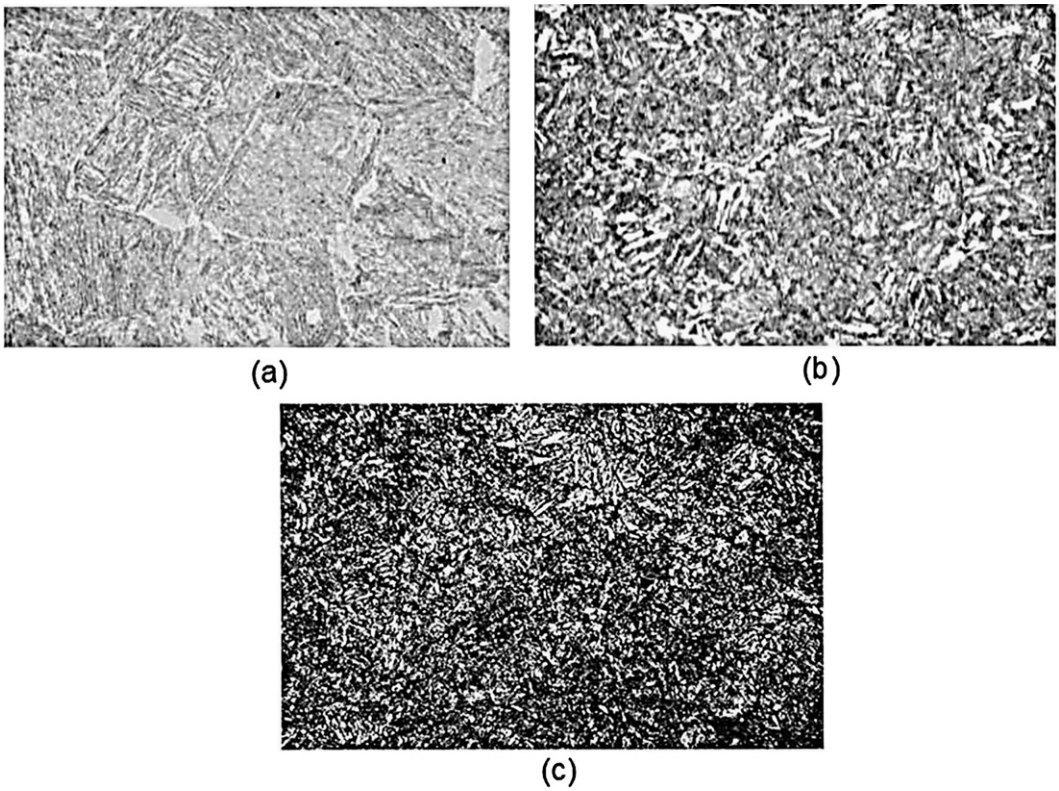


Figure 3 Microstructure of (a) HP 9–4–20 showing tempered martensite, (b) HP 9–4–30 showing tempered martensite, and (c) HP – 9–4–30 grade showing grain refined structure after multiple heat treatment, X400. Rush, H. F. *NASA Technical Memorandum 85816, Grain Refining Heat Treatment to Improve Cryogenic Toughness of High Strength Steel*, 1984.

- For hardening, the steel is austenitized at 850 °C and soaked for 1 h for each 25 mm thickness. This homogenous austenite may be water quenched to ensure complete martensitic transformation. These steels may be subjected to subzero treatment at − 75 °C with a holding time of 1 h and then bringing back to room temperature.
- Tempering is carried out between 300 and 600 °C depending upon the desired strength and ductility property. Most widely used tempering process is a double tempering between 550 and 575 °C, with sufficient hold time at that temperature. Stress relieving at 560 °C for 24 h may be carried out if steel is required to be welded prior to heat treatment. Stress relieving annealing should be carried out by holding for prolonged period of time at elevated temperature and then cooling to room temperature in still air. The micro structures of these steels under various heat-treatment conditions are shown in Figure 3.

2.8.2.4 Heat Treatment of AF1410 Steel

The steel of chemical composition, 0.13–0.17% C; 0.1% Si; 1.8–2.2% Cr; 9.5–10.5% Ni; 0.9–1.1% Mo; 13.5–14.5% Co is described as another variety of ultrahigh strength steels with high fracture toughness and has been developed by US defense for application in submarine structures. The microstructure of this steel consists of lath martensite with dispersed carbides; the general optical microstructure shown in Figure 4 exhibits tempered martensite. The carbide precipitates are formed during tempering and thus give rise to precipitation strengthening. The steel may also subjected to secondary hardening by tempering the workpiece at high temperature above 550 °C which gives rise to the formation of reverted austenite; this improves the impact strength of the steel.

The recommended heat-treatment practice for this steel is as follows:

- Normalizing is carried out as usual to achieve higher machinability. The component is heated in the temperature range 880–900 °C, held there for 1 h per 25 mm thickness of section and then air cooled. Following air cooling the steel can be aged at 650–675 °C for 3–6 h. After machining the stress relieving annealing is carried out at 675 °C, to relieve the mechanical stresses induced due to machining.
- Hardening heat treatment consists of austenitization at temperature of 880 °C where the steel is to be held for 1 h per 25 mm section thickness; then the steel is quenched in oil, if the maximum section size of the article is more than 75 mm. If the maximum section size is 50 mm or less, air quenching can be employed to produce martensite in the hardened steel. The subzero treatment at − 70 °C may be practiced if 100% martensite formation is not possible due to large section size of the heat-treating component.
- Tempering is carried out at 550–570 °C, and holding time at this tempering temperature is normally 5–6 h. It appears from Figure 5 that secondary hardening peak is attained at 480 °C and aging beyond this temperature tends to soften the material with concurrent improvement in impact strength. Also at a temperature of 510 °C maximum improvement in impact property is obtained. This is ascribed to the fact that aging at such high temperature for a prolonged period of time like 6 h leads to the formation of solute rich austenite due to competitive austenite formation. This high solute austenite has a low M_s temperature and therefore after cooling from the tempering temperature to room temperature, the reverted austenite exists in the microstructure. This reverted austenite does not transform to martensite upon cooling from the tempering temperature. The reverted austenite present in the microstructure confers very high-impact strength in these materials. The same features are observed in AerMet 100 steel which contains higher carbon than AF1410. The microstructures of AerMet 100 steel under different heat-treatment conditions (Figures 6 and 7) clearly show that increasing



Figure 4 Tempered martensitic microstructure of AF-1410 ultrahigh-strength steel, tint aged × 100. George F. Vander Voort, Director, Research and Technology, Buehler Ltd in The Microstructure of Ferrous Alloys.

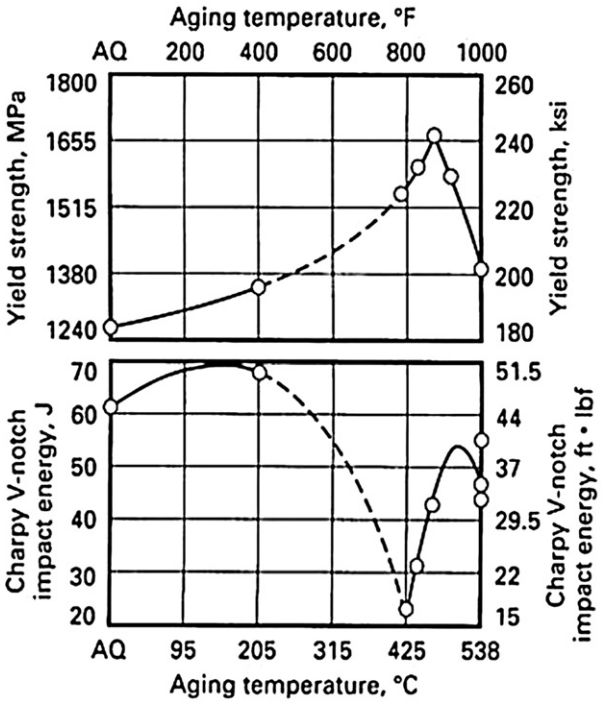


Figure 5 Mechanical properties versus aging temperature of AF1410 Steel. *ASM Handbook*, Vol. 4; p. 522.

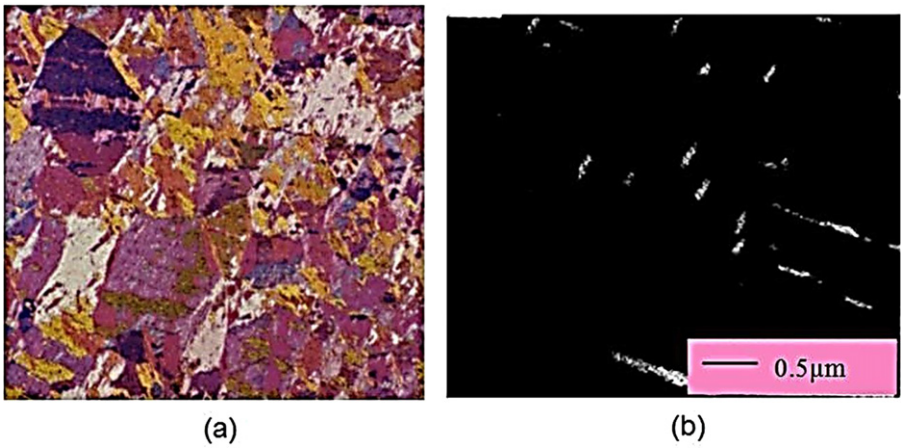


Figure 6 Microstructures of Aer Met 100 steel (a) Austenitized at 1090 °C, air cooled, aged at 675 °C for 5 h, showing lath martensite at × 100 (b) Needle-shaped precipitates of M_2C in Aer Met 100 steel.[11] (a) George F. Vander Voort, Director, Research and Technology Buehler Ltd in 'The Microstructure of Ferrous Alloys'; (b) Wang, L.; Liu, L.; Cheng Xiao; Liu, X.; Chen, C.; Kang, M. Investigation of Transformation for Ultrahigh Strength Steel AerMet 100. *J. Mater. Sci. Tech.* **2000**, *16* (5), 491–494.

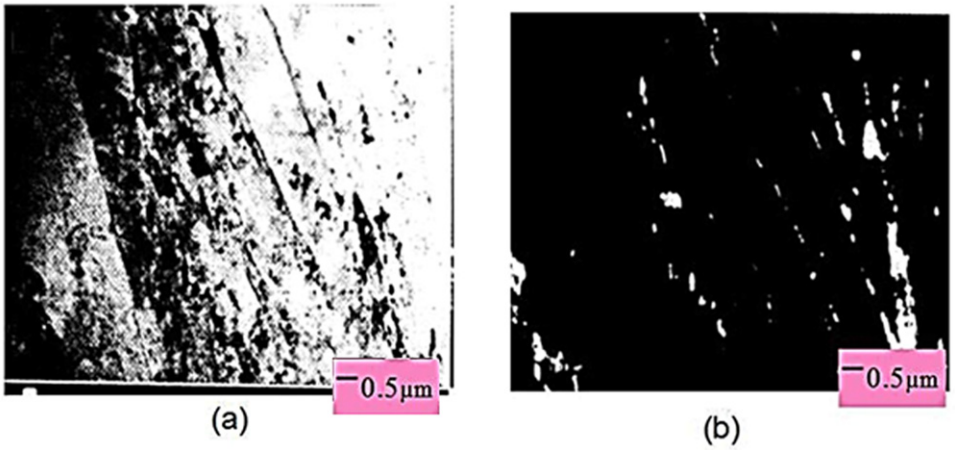


Figure 7 High-temperature tempering of AerMet 100 (530 °C) shows (a) reverted austenite and coarse needles of M_2C, and (b) dark-field image of (a). Wang, L.; Liu, L.; Cheng Xiao; Liu, X.; Chen, C.; Kang, M. Investigation of Transformation for Ultrahigh Strength Steel AerMet 100. *J. Mater. Sci. Tech.* **2000**, *16* (5), 491–494.

tempering temperature leads to the coarsening of needle-shaped M_2C precipitates with concurrent formation of reverted austenite.

The dark-field TEM image in Figure 7(b) gives clear evidence of reverted austenite which is stated to be responsible for high-impact strength of AerMet100 or AF 1410 steel after tempering at high temperatures.

2.8.2.5 Press Hardenable Ultrahigh-Strength Steel

A new-generation martensitic steel of composition, 0.25C–0.40Si–1.40Mn–0.5 (Cr + Mo)–0.005B–0.05Ti–0.05Nb possesses a very high strength. The steel is quenched during pressing and then followed by controlled tempering. The quenched and tempered microstructure showing the presence of martensites is shown in Figure 8. The quenched and tempered steel derives its strength from precipitation hardening along with transformation hardening due to formation of martensite. Molybdenum strengthens the grain boundaries; also it lowers the activity of carbon in ferrite which makes it less susceptible to grain boundary precipitation. Niobium is used for grain refinement of austenite. The fine grained austenite, while being quenched to undergo martensitic transformation, would give rise to smaller martensite packet size. This is highly favorable in imparting extra strength to the steel.

The emerging concept of light-weight technology, has led to the birth of press hardened steel which is invoked recently as a token of new-generation technology in automobile industry.

Addition of Titanium helps to avoid segregation of boron nitride at the grain boundaries. Free boron is now available to segregate at the grain boundaries; thus boron does not leave much space for the nucleation of proeutectoid ferrite and it is how boron may exert its hardenability raising effect. 22MnB5 is the commonly used press hardenable steel. Shift of Bs temperature to longer times and lower temperatures is

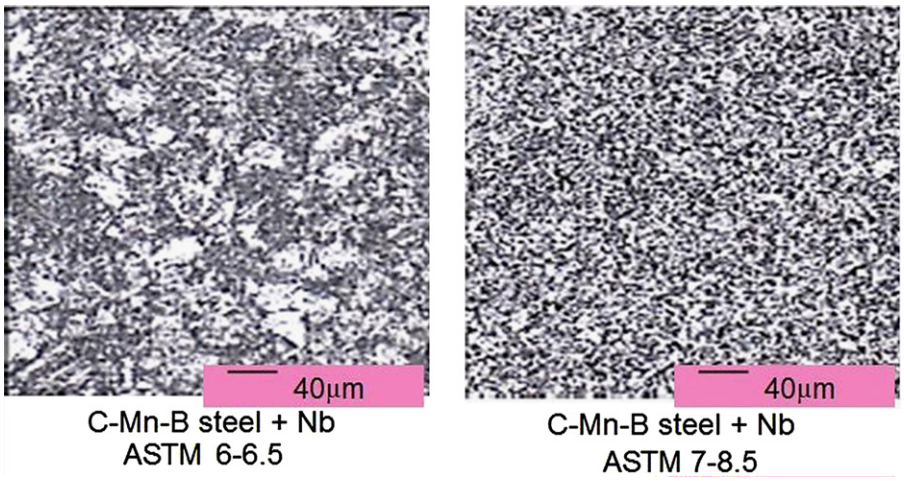


Figure 8 Microstructure showing martensites of fine packet size; prior austenite grain boundary is also revealed in the steel after typical press hardenable steel heat treatment.[12] Bian, J.; Mohrbacher, H. Novel Alloying Design for Press Hardening Steels with Crash Performance. In *International Symposium on New Developments in AHSS*, PR-294–026–2013, USA. Available at: www.niobelcon.com/NiobelCon/publications_files (accessed February 17, 2016).

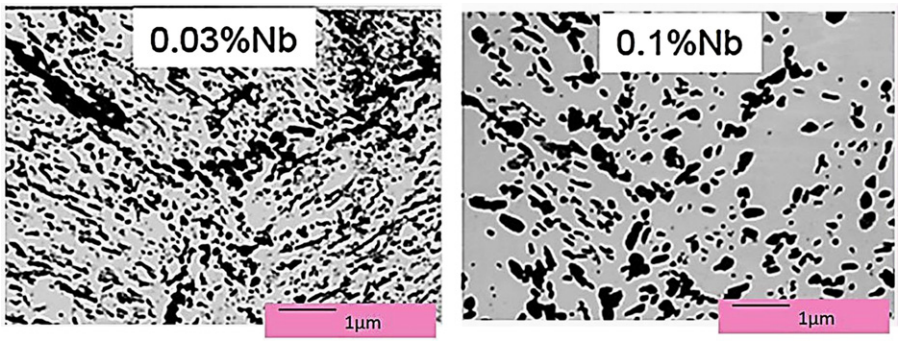


Figure 9 Microstructure of 22MnB5 steel optimized with Nb addition, quenched, and tempered. Microstructure shows distribution and morphology of precipitates in quenched and tempered steel.[12] Bian, J.; Mohrbacher, H. Novel Alloying Design for Press Hardening Steels with Crash Performance. In *International Symposium on New Developments in AHSS*, PR-294–026–2013, USA. Available at: www.niobelcon.com/NiobelCon/publications_files (accessed February 17, 2016).

possible due to addition of elements like C, Mn, Cr, and Mo; thus insurance of martensitic transformation at a slower cooling rate such as, 30 K s^{-1} aids in avoidance of formation of soft diffusinal decomposition product of austenite. This is further accentuated by synergistic effect of Mo and B to delay of austenite to ferrite transformation. All these factors are responsible for production of 100% martensite quite easily after quenching. Moreover the role of microalloys in conferring precipitation strengthening is very important. Microstructure of 22MnB5 steel optimized with Nb addition clearly records a high-population density of nano-sized niobium carbide precipitates distributed uniformly throughout the matrix (**Figure 9**).

2.8.2.6 Nanoscale Precipitations Hardenable Steel

Another ultrahigh-strength steel of 1.9 GPa strength with 10% elongation and 40% reduction in area is developed with newer strengthening strategy accomplished by judicious heat-treatment practice. The chemical composition of the steel is say, Fe–xNi–yAl–1.5Cu–1.5Mo–1.5W–0.07Nb–0.05C–0.01B.[13] The strengthening of this steel is envisaged by co-precipitation of intermetallic like NiAl, and of copper. Both these phases are capable to provide significant precipitation hardening. When the Ni/Cu and Al/Cu ratios are kept at lower level (0.6–1.3 and 0.02–0.5, respectively), precipitation of copper is known to lead the process of co-precipitation. Copper atoms are precipitated first and then the segregation of nickel and aluminum atoms takes place at the interfaces between copper and the matrix; finally the precipitation of NiAl forms at these interfaces upon continued aging at 550 °C. The steel is normally quenched from 900 °C and then it is tempered/aged at the predetermined temperature ~550 °C.

Experienced some shortcomings in respect of its achievable mechanical properties, the magnitudes of Ni/Cu and Al/Cu ratios are now a day increased to 3.3 and 1.3 respectively. This alteration of chemical composition causes nanoscale precipitation of NiAl at first; these precipitates are distributed uniformly throughout the matrix. This is then followed by precipitation of elemental copper at the interface of NiAl and matrix. Thus

co-precipitates (NiAl + Cu) are formed at many locations; however singular precipitates NiAl also remain present at different locations. Both these two types of precipitates confer high strength to the steel.

It is also noted that carbides of the form $Fe_3(Mo,W)C$ and NbC are formed during heat treatment of these steels. These fine carbide particles have significant contribution to the ultimate strength of the material. Therefore it is inferred that martensite matrix of high-dislocation density is infested with numerous highly dispersed nanoscale precipitates of NiAl and co-precipitates of NiAl and copper.[14] As stated, the precipitates of NbC and Fe–Mo–W carbides are also formed in the microstructures. These microstructural constituents make it possible to achieve a very high hardness of around 625HV and ultrahigh strength of 41800 MPa in the above steels.

2.8.2.7 Medium-Carbon Low-Alloy Steel

Medium-carbon low-alloy steels are high-strength, high-toughness steels, the properties of which depends upon the chemical composition and heat treatment. In general these steels contain average carbon of 0.30 or 0.35 wt.%. AISI 4130 or 4140 contains chromium of (0.8–1.1 wt.%) with molybdenum (0.15–0.25 wt.%), whereas AISI 4340 and its modified version are Ni–Cr–Mo steel. In some varieties of this class of steel, vanadium is added to a small amount (0.05–0.1 wt.%). In nickel–chromium steel, the hardenability is quite high as nickel and chromium exhibits synergism in shifting the time temperature transformation (TTT) diagram toward right. In majority of steel of this class the Ni to Cr ratio is maintained at or above 2:1 with Ni ranging from 1.6 to 2 wt%. Commensurate with the application of these steels, machining is required before hardening. For a low-hardenable alloy like AISI4130, 4240, 4330, 4340, and their modified versions, normalizing followed by tempering is required to improve the machinability of steel. Within this class of steels, there are some steels which are of air hardening type. These steels are medium-carbon medium-alloy steel with Cr ~5 wt.%, Mo ~1–3 wt.%, and V ~1.6–1.8 wt.%. The stated compositions are just nominal and may vary according to specification given in the standard hand book. For these steels annealing is preferred before machining. Sometimes severe mechanical working is required and for those situations spheroidization annealing is carried out. These medium-carbon ultrahigh-strength steels contain low to medium alloy contents and are in general hardened and tempered. However before hardening, machining may be required. Normalizing and annealing are the heat-treatment processes preceding the machining operation. Also post-weld stress relieving may be required before hardening and tempering. Some of the steels which have strength higher than 1400 MPa are often exposed to hydrogen during pickling or electro plating. In those cases diffusion annealing to drive out hydrogen is also carried out.

- Normalizing: Whenever normalizing operation is required before machining it is carried out at a temperature 870–900 °C, held there for 1 h 25 mm^{-1} of section size and cooled in steel air. The normalized steels are tempered at 650 °C and then subjected to machining.
- Annealing: Whenever annealing is required it is carried out at a temperature 830–870 °C followed by furnace cooling to about 450 °C at a rate of 10–15 °C per h.

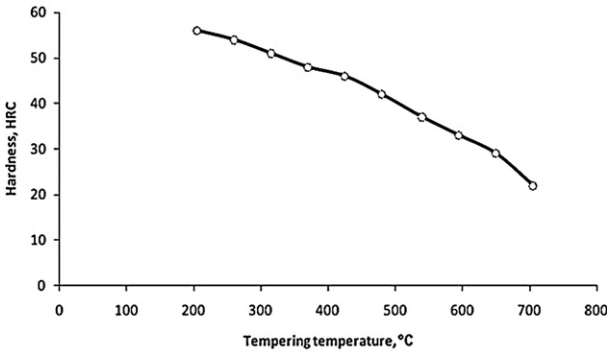


Figure 10 Variation of hardness with tempering temperature. UG Project report, MNIT Jaipur, India after *ASM Handbook*, Vol. 4; p. 506.

- Hardening: The medium-carbon low-alloy steels are generally quenched in oil. The hardening temperature is around 850–880 °C and the soaking time is decided as usual by 1 h 25 mm^{-1} of section thickness. The steel is then quenched in oil bath kept preferably at a temperature 80 °C so as to produce 100% martensite. Following the hardening operation, the tempering is done for sufficient period of time at a temperature ranging from 200 to 650 °C. It may be noted that the tempering temperature is to be decided by the degree of reduction in hardness envisaged to achieve by tempering. A tentative guideline for reaching at a particular hardness value can be obtained from **Figure 10**.
- Spheroidizing: Whenever required, spheroidizing annealing is carried out by heating the steel to 760 °C, holding it there for 12–14 h, and cooling slowly in the furnace.
- Stress relieving annealing: As stated earlier the stress relieving operation is carried out at 650–675 °C if the steel components are welded prior to hardening operation. Whenever the steel is electroplated, the diffusion annealing to drive out hydrogen is carried out by heating it to 200 °C keeping it there for prolonged period of time say 8–10 h depending upon the thickness of the work piece.

However it is to be kept in mind that these annealing operations must not be carried out at a temperature higher than the tempering temperature, if tempering operation is already accomplished. Going above the tempering temperature will lead to degradation of mechanical properties of the steel.

Sometimes polymer quenching such as glycol-based quenchant is used in preference to oil because, it has higher flexibility in adjusting cooling rates and it does not catch fire as easily as oil does. The Microstructural changes accompanying hardening and tempering of AISI 4140 is shown in **Figures 11(a)–11(c)**.

2.8.2.8 Si-Modified 4340 Steel

It is designated as 300 M and contains Si 1.4–1.8 wt%. This steel is normalized by heating to 930 °C, holding there for 30 min per 25 mm of thickness size and then air cooled. If normalizing is a prerequisite for machining, the steel has to be tempered at a temperature of 650 °C. This steel is austenitized at about 860 °C, quenched in oil at 80 °C. Following

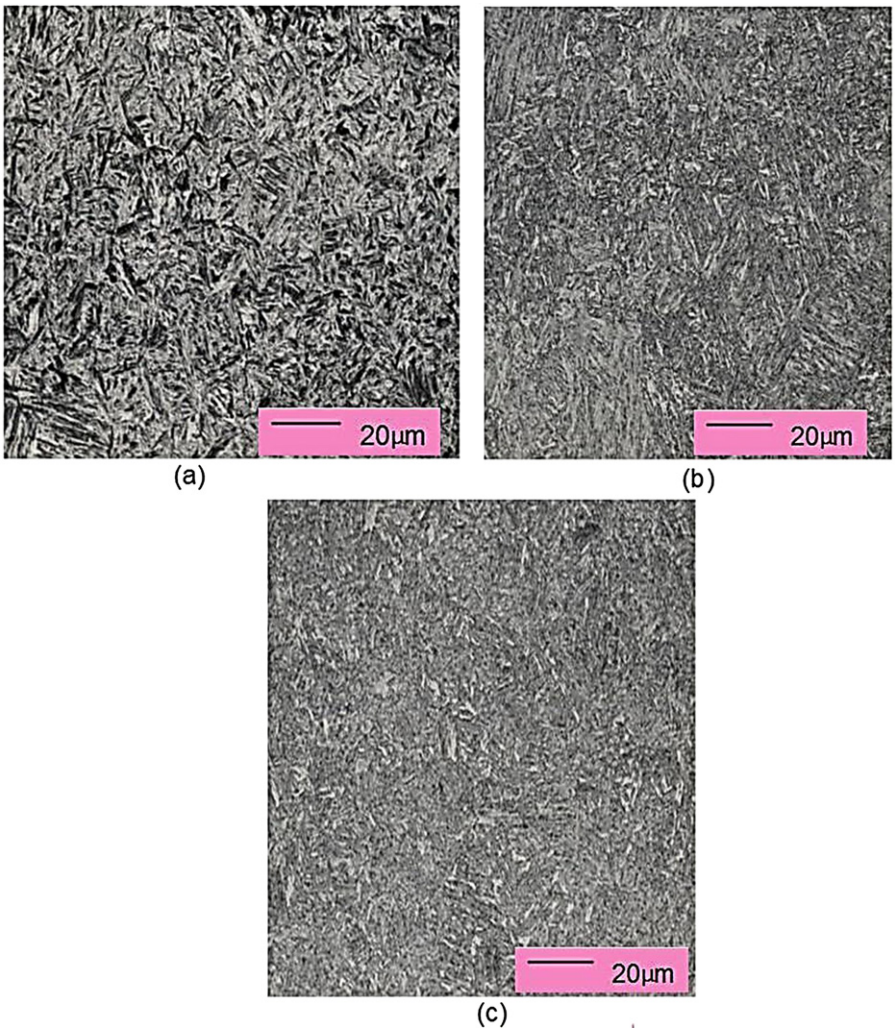


Figure 11 Microstructure of 4140 alloy steel (a) In quenched condition showing martensite, (b) quenched from 900 °C and tempered at 420 °C showing tempered martensitic structure with some acicular product, and (c) tempered at 650 °C showing fully tempered martensitic structure, (all at 20 μ). Courtesy: George F. Vander Voort, Consultant – Struers Inc USA. Vander Voort, G. F. *Understanding Heat Treatment Results using Metallography*. Book on stainless steel; ASM: Metals park, OH, 1935.

quenching operation, tempering is carried out at about 320 °C for 3–4 h. Tempering must be done above 300 °C and the exact temperature is to be decided by final property requirement. Double tempering is recommended for best combination of strength and toughness, because it minimizes the retained austenite content and produces a mixed mode of microstructure comprised of relatively coarse and fine constituent.

2.8.2.9 Ni–Cr Structural Steel

The nickel–chromium steel has wide range of applications. Low carbon chromium–nickel steel is usually subjected to surface hardening treatment to produce a hard and wear resistance surface. These steels are used in heavily loaded gears, shafts, etc. The TTT-diagram of steel containing 0.12% C, 2% Cr, and 4% Ni is shown in the **Figure 12**. After carburizing the composition of the steel at its surface becomes such that M_s–M_f temperatures are considerably lowered due to enhanced stability of austenite caused by alloy addition. When the carburized components are air cooled to room temperature, these are partially hardened. Thus subsequent machining of the parts becomes difficult. So the steels after carburizing must be heated for tempering at a high temperature, viz. 650 °C. Due to presence of high amount of retained austenite the carburized case exhibits a somewhere lower hardness values, RC55.

A single hardening operation is normally carried out for this steel. The steel is heated to 800–830 °C and held for suitable time period. Finally the steel is oil quenched and tempered. Tempering is carried out at such temperature which can give rise to required mechanical properties.

Medium-carbon chromium–nickel steels are often employed for improved structural application. The steel contains 0.37% C, 1.4% Cr, and 3.25% Ni. The hardenability of this steel is quite high and thus this steel is employed for production of heavy forgings, shafts, high-strength crankshafts, etc., without much difficulty in through thickness hardening. It is to be noted that

chromium–nickel steels are highly prone to temper embrittlement, when tempering is carried out at 500 °C followed by slow cooling. Hence after oil quenching these steels are tempered at temperature less than 300 °C (say 230–240 °C). This help to achieve high strength with adequate ductility.

Molybdenum and tungsten further strengthen the steels without loss of ductility. These elements resist softening and lessen the quantum of temper embrittlement. Molybdenum reduces temper embrittlement by delaying the kinetics of precipitation; however this element does not put any thermodynamic constraints to the formation of chromium carbide which are supposedly responsible for temper embrittlement.

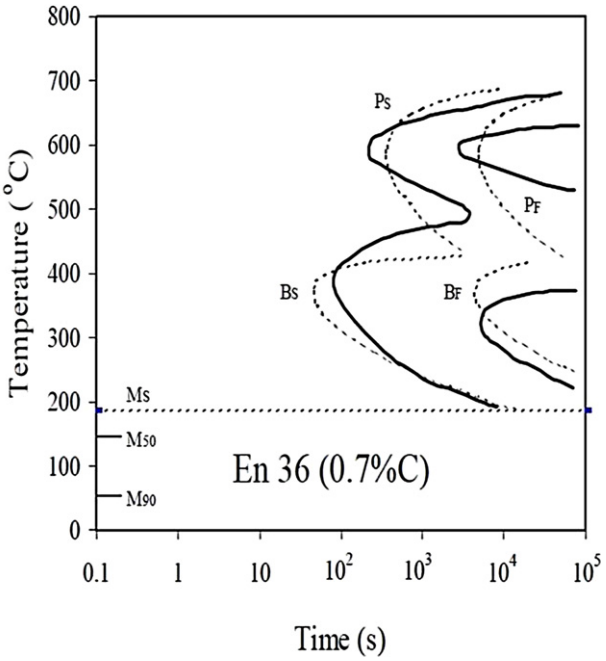


Figure 12 Time temperature transformation diagram for Ni–Cr structural steel.[15] Saunders, N.; Guo, Z.; Li, X.; Miodownik, A. P.; Schille, J. P. *The Calculation of TTT and CCT Diagram of General Steels*. Available from: http://www.sentesoftware.co.uk/media/2540/ttt_cct_steels (accessed July 4, 2011); Atlas of Isothermal Transformation Diagrams of BS En Steels, Special Report No. 56; The Iron and Steel Institute: London, 1956.

Ultrahigh-strength steels (Table 2) containing 5% Cr are known as hot-work die steel. In this category, H_{11} and H_{13} are commercially important.

The chemical compositions of these two steels (H_{11} and H_{13}) are very much similar; hence their heat treatment and ultimate mechanical properties do not vary much. These steels are also known as deep-hardening steel, which imply that they can be hardened by simple air cooling. Air hardening minimizes the thermal stress and thus the chances of distortion or cracking are reduced. The modified H_{11} steel differs from conventional H_{11} steels in respect of carbon content. Both H_{11} and H_{13} are capable to achieve secondary hardening and so the best properties of these steels will be achievable by tempering at temperature higher than 500 °C, that is beyond the secondary hardening peak. The microstructures of these varieties of steel after suitable heat treatments comprise of tempered martensites of desired fineness as shown in Figures 13(a)–13(c). This high-temperature tempering insures stabilization of microstructures. For air-hardening steels like H11 modified or H13, the cooling after forging must be done quite slowly, else there will be considerable martensite transformation, which may lead to crack formation due to high-transformational strain.

Therefore after forging the component should be charged in furnace kept at 800 °C and should be soaked until the equalization of temperature, throughout the section of component is attained. After this the component is cooled very slowly within the furnace.

The heat-treatment schedule for modified H11 is as follows:

- Normalizing: Normally it is not recommended for these steels because these are air hardening steels.
- Annealing: Annealing is carried out after forging. The component is heated to 800 °C in a furnace in controlled atmosphere, and held there for sufficient period to achieve homogeneity of temperature and microstructure. Following soaking the component is cooled slowly within furnace up to a temperature of 450 °C and then rapid cooling to room temperature may be performed. This will ensure freedom from carbide network at grain boundaries.

Table 2 Chemical composition of some ultrahigh-strength steels

Type		*C (wt.%)*	*Mn (wt.%)*	*Si (wt.%)*	*Cr (wt.%)*	*Ni (wt.%)*	*V (wt.%)*	*W (wt.%)*	*Mo (wt.%)*	*Co (wt.%)*	*Al (wt.%)*
Chromium hot-work tool steel											
H10	T20810	0.40	–	–	3.25	–	0.40	–	2.50	–	–
H11	T20811	0.35	–	–	5.00	–	0.40	–	1.50	–	–
H12	T20812	0.35	–	–	5.00	–	0.40	1.50	1.50	–	–
H13	T20813	0.35	–	–	5.00	–	1.00	–	1.50	–	–
H14	T20814	0.40	–	–	5.00	–	–	5.00	–	–	–
H19	T20819	0.40	–	–	4.25	–	2.00	4.25	–	4.25	–
Tungsten hot-work tool steel											
H21	T20821	0.35	–	–	3.50	–	–	9.00	–	–	–
H22	T20822	0.35	–	–	2.00	–	–	11.00	–	–	–
H23	T20823	0.30	–	–	12.00	–	–	12.00	–	–	–
H24	T20824	0.45	–	–	3.00	–	–	15.00	–	–	–
H25	T20825	0.25	–	–	4.00	–	–	15.00	–	–	–
H26	T20826	0.50	–	–	4.00	–	1.00	18.00	–	–	–

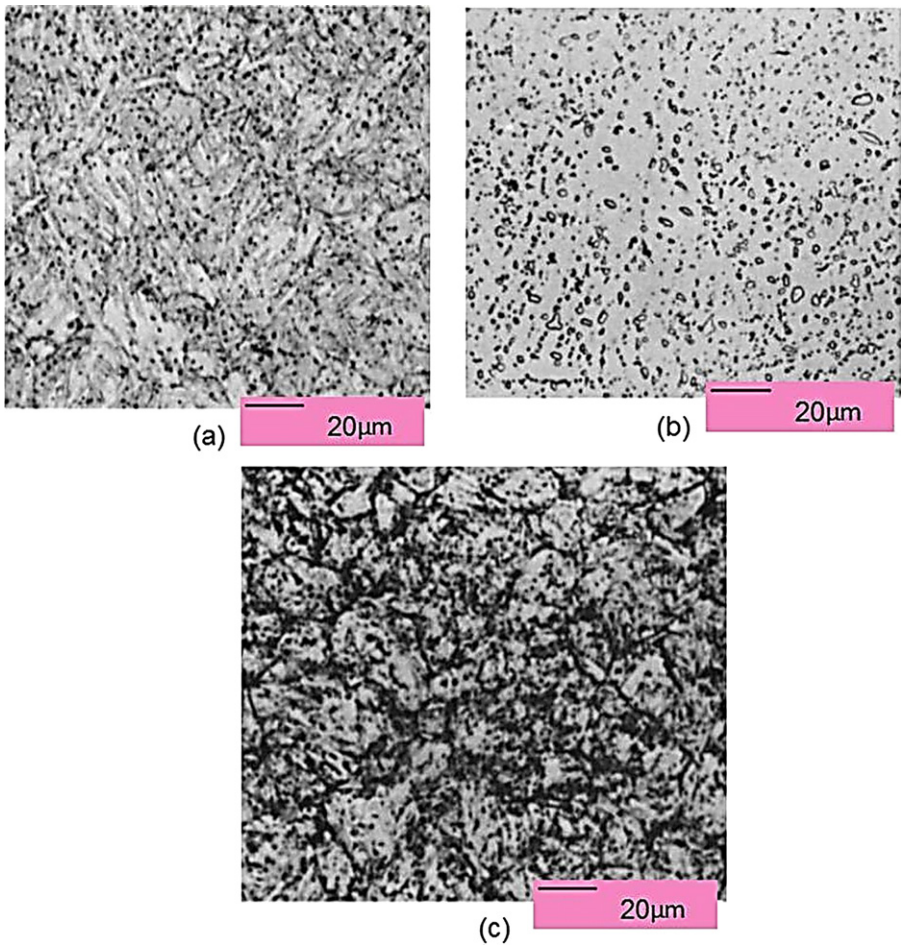


Figure 13 Microstructure of (a) AISI H11 steel austenitized at 1010 °C, air quenched, and double tempered at 510 °C showing fine carbides in martensitic matrix, (b) microstructure of AISI H13 steel, after spheroidizing annealing, and (c) H13 Steel austenitized at 1025 °C, air quenched and double tempered at 595 °C showing small amount of very fine undissolved carbides in a martensitic matrix. *ASM Hand Book*, Vol. 9; p. 1566, 1549, 1567.

- Hardening: For this the components are heated to 760–790 °C at a moderate heating rate of 100 °C per hour, and held there for half an hour until the temperature from surface to center equalizes. This will minimize the thermal stresses in the component. Again, following the preheating treatments the temperature of component may be raised to above 1000 °C, held for about 30 min (however the soaking time is to be suitably adjusted as per the maximum thickness size and total mass of a particular charge in the heat-treatment cycle). After soaking the components are quenched in still air. During air hardening, the distortion due to heat treatment is negligibly small.
- Tempering: Tempering of these steels is carried out at such high temperature where secondary hardening may take place efficiently. In the majority of cases the tempering temperature should be about, 550 °C. At this peak secondary hardening temperature maximization of strength occurs. However tempering the steel at slightly higher temperature beyond the secondary hardening peak is considered to be a better option, because this improves ductility with minimum sacrifice in hardness.

Multiple tempering operations are sometimes carried out in this type of steel. The first tempering is carried out at 550 °C, and held there for 1–2 h depending upon their section size. After this, the component is cooled to room temperature and again heated to tempering temperature which should be 15 °C higher than the previous tempering temperature which means 565 °C and is held there for 2 h, following which the component is again cooled to room temperature. This may be carried out for the third time if it is required to improve ductility to a greater extreme.

- Stress relieving: After rough machining prior to heat-treatment stress relieving anneal is practiced for these steels. Stress relieving is carried out at a temperature of 650 °C for preselected time and then cooled very slowly to room temperature. The stress relieving following rough machining helps to achieve higher dimensional accuracy in the heat treated parts.
- Nitriding: This is often required for achieving high-wear resistance for this variety of steel. In that case the components after finish machining and heat treatment are subjected to nitriding operation. Nitriding is carried out at a

temperature of around 525 °C or at slightly higher temperature, and this treatment may be considered to be second tempering of a double tempering operation.

It serves two purposes:

- double tempering to produce more favorable microstructure and
- formation of nitrides at the surface ensures very high-wear resistance.

Exactly identical heat-treatment schedule with similar requirements will be performed for H13 variety of steel, with only difference is in their tempering temperature. H13 steel is tempered at temperature lower than H11 modified due to existing difference in their composition.

2.8.2.10 Medium-Carbon Chromium–Vanadium Steel

These steels contain above 0.4 wt% carbon with about 1 wt% chromium and are common structural steels, used in automobile sector. However the addition of vanadium by 0.2 wt% is found to increase the resistance to softening upon heating to elevated temperature. This steel is very much suitable for crank shaft, spindle, shaft, etc. Increasing the carbon content to 0.50 wt%, makes the steel become suitable for applications as heavy duty springs.

Heat treatment of medium-carbon chromium–vanadium steel

- A normalizing treatment is carried out by heating the steel to 900 °C, held for suitable time period and then it is cooled in still air.
- Normalizing is followed by hardening process. Hardening is carried by heating at moderate heating rate till 700 °C, holding there for 15 min to relieve thermal stress and then heating at a faster rate, 100–150 °C h^{-1}, to a temperature of 880–890 °C. The steel is held there for 1 h for each 25 mm of maximum section thickness. For heavy duty spring steel with the high carbon content, ($\sim$0.5 wt%); a slightly lower austenitizing temperature is recommended; the temperature of austenitization may be kept at 850–860 °C. The austenitized steel is quenched in oil.
- Following oil quenching, the structural steel for use as crank shaft (0.4 wt%C) is tempered at high temperature just beyond the secondary hardening peak. The tempering temperature for this steel is around 650 °C whereas tempering temperature for heavy duty springs is kept somewhat lower, $\sim$450 °C. The idea of high-temperature tempering for structural steel stems from the requirement of high fracture toughness of the steel at relatively high-strength level. Hence attempt is made to achieve a strength of 900 MPa at 50% reduction in area. For spring steels however the strength requirement is rather high and a low-tempering temperature enables to achieve strength of 1300 MPa.

2.8.2.11 Chromium–Molybdenum Steel: Steel for High-Temperature Boiler Application

Molybdenum bearing steels are generally employed for heat resistance application. Steels containing lower carbon of 0.15 wt% with 0.5 wt% Mo can retain its strength quite satisfactorily till 550 °C. Another variety of the steel containing 0.15 wt% carbon, 0.5 wt%Mo with 1 wt% Cr has excellent weld ability. Its weldability is good because of low carbon content. Since Molybdenum is present in substantial amount, the steel possesses excellent high-temperature properties. Moreover presence of chromium imparts good corrosion resistance. This steel is a good choice for boiler drum, boiler tubes, and super heater pipes. In the present day's boilers, high-temperature steam is in use. The super heater materials of today's boiler plants must have very good high-temperature properties; resistance to deterioration of mechanical properties due to rise in temperature must be quite high in the materials to be used in modern super heater pipes.

Another medium-carbon steel of composition 0.30 wt% carbon, 0.25–0.3 wt% Mo, and 1 wt%Cr is employed for manufacturing of critical components of turbine such as rotor, shaft, etc. Fastening parts of high-temperature boiler are preferentially made from the same type of steel but with a high chromium content, i.e., 1.6–1.8 wt%. The steels belonging to this group are used in hardened and tempered condition.

Heat-treatment schedules of Cr–Mo steel:

- Normalizing from a temperature of 900–925 °C.
- Holding at the austenitizing temperature, 840–880 °C for suitable time, followed by oil quenching with oil temperature at 50–60 °C.
- Tempering is carried out at the preselected temperature; the selection of tempering temperature depends upon the final mechanical strength to achieve.

2.8.3 Spring Steel

To ensure good performance as a spring material, the important factors are the elastic limit, or the proportional limit in tension and that under torsion which must be quite high. If loading is done upto higher stress values, it would result in permanent set and in such case the material will not return to its original state.

Impact loading, rapid cycling, extreme temperature, i.e., where creep is important, adversely affect the spring properties of the steel. The corrosion or stress corrosion is the other issue creating constraints to the performance of spring steel. A typical composition of spring steel is provided in the **Table 3**.

Table 3 Composition of heavy duty spring steel

C (wt%)	*Mn (wt%)*	*P (wt%)*	*S (wt%)*	*Si (wt%)*	*Al (wt%)*	*Cr (wt%)*	*Ni (wt%)*	*V (wt%)*	*Mo (wt%)*	*N_2 (wt%)*
0.50–0.55	0.760	0.010	0.001	0.257	0.034	0.8–1.1	0.016	0.15	0.003	0.005
0.50–0.55	0.75	0.03	0.03	0.25	0.04	0.60–0.70				
							(<0.02)		(<0.004)	(<0.005)

The factors influencing allowable working stress of spring steels are:

- range of working stress,
- frequency of deflection or oscillations that the spring is to undergo, and
- temperature of operation.

If operating temperature of a spring is increased, its load bearing capacity is decreased. This is reflected by the relaxation or load loss as shown in **Figure 14**.

Different types of spring steels used for various applications are plain carbon manganese steels, silicon–manganese steels, and different types of alloy steels including stainless steels. The steels which are capable to release the stored energy responsively are normally used for spring application. It is emphasized that limited use of spring under load does not give up their original dimension; thus for these steels, high-elastic modulus, high-yield strength, and precipitation hardening are preferred. Further, spring steels must have high-fatigue strength as they also experience fluctuating stresses and sometimes overloading. Its plasticity must be sufficiently high so as to enable the manufacturer to form springs of appropriate shape. High-carbon steels with suitable alloying elements are required to be judiciously heat treated in order to achieve above properties.

As stated earlier, the modulus of spring steels should not be less than 21×10^4 MPa, with a modulus of rigidity higher than 8×10^4 MPa. The failure of spring steels is commonly a fatigue failure initiated by stress raisers. Therefore the spring steels must be made up of very hard and strong materials.

In order to get these properties, most spring steels except stainless steel variety, are used in hardened and tempered condition. Schematic heat-treatment schedule for particular spring steel is shown in **Figure 15(a)**.

In the hardened condition the spring steels must achieve 100% martensite at the center of the section. It is important to avoid retained austenite in hardened condition, which creates soft spots and affects the properties of spring. Therefore judicious selection of alloying element is made to design spring steels, so that M_s temperature does not go below room temperature.

However hardenability of spring steels must be sufficiently high to produce 100% martensite at the center. This allows high-carbon steel with suitable alloying elements to compose a good spring material.

The heat treatment of spring steel should be carried out very carefully, because the spring characteristic is inherently dependent on the heat treatment which ensures achieving the desired microstructure.[15–17] Microstructures of the above spring steel are seen to be tempered martensites of varying fineness when oil quenched and tempered at different temperatures (**Figure 15(b)**).

The successful heat treatment of spring steel must envisage:

- Complete absence of non-martensitic product of transformation of austenite in its hardened state; this is possible only if a compositionally homogeneous austenite is produced in the heating stage and sufficiently rapid cooling, commensurate with hardenability of the spring steels is employed.

  If there is any quench delay because of material handling difficulties, the austenite phase in steel may undergo slow air cooling and may reach such a temperature from where it becomes difficult for the inner section of the material to avoid softer components to form. Thus in industrial situation, delay in quenching must be prohibited. The quality achieved by stipulated heat-treatment cycle is equally important and so the hardness testing of hardened material must be checked to ensure if 100% martensite is formed up to center of stock.

  Because the spring steels are generally of high carbon content, extremely high-temperature austenitization is also discouraged. Moreover furnace atmosphere for high austenitization temperature must not be too much oxidizing so as to effect decarburization beyond the level of acceptance.

  Owing to the fact that decarburization takes place at high temperature, there is a chance that fatigue strength of material may be adversely affected. Normally the spring steel requires appropriate shaping by way of hot working at elevated temperature of around 925 °C, preferably in controlled atmosphere. However the exact temperature of working depends upon the chemical composition of steel. Any difficulty during shaping can be taken care by intermediate annealing for softening the material. Sometimes cold working followed by subcritical annealing around temperature of 650 °C, in neutral atmosphere is performed. Permitted by the cold deformability, this kind of recrystallization annealing for softening the material is a better choice because it prohibits decarburization. Silicon present in the steel increases the activity of carbon in iron and therefore a silicon alloy steels is very prone to surface decarburization. In order to take care of this difficulty the silicon bearing steels are annealed for shortest possible time at the lowest possible temperature.

  It is advisable to normalize the spring steel, which are generally exposed to high-working stress during shaping. In fact the steels which are hot worked by forging are always required to be normalized prior to final heat treatment.

  This is because of sudden energy input in such type of metal forming operation which may lead to adiabatic heating

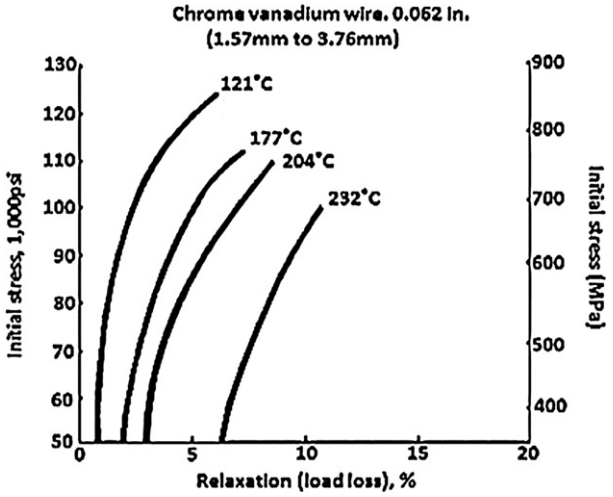


Figure 14 Load loss diagram. www.centuryspring.com.

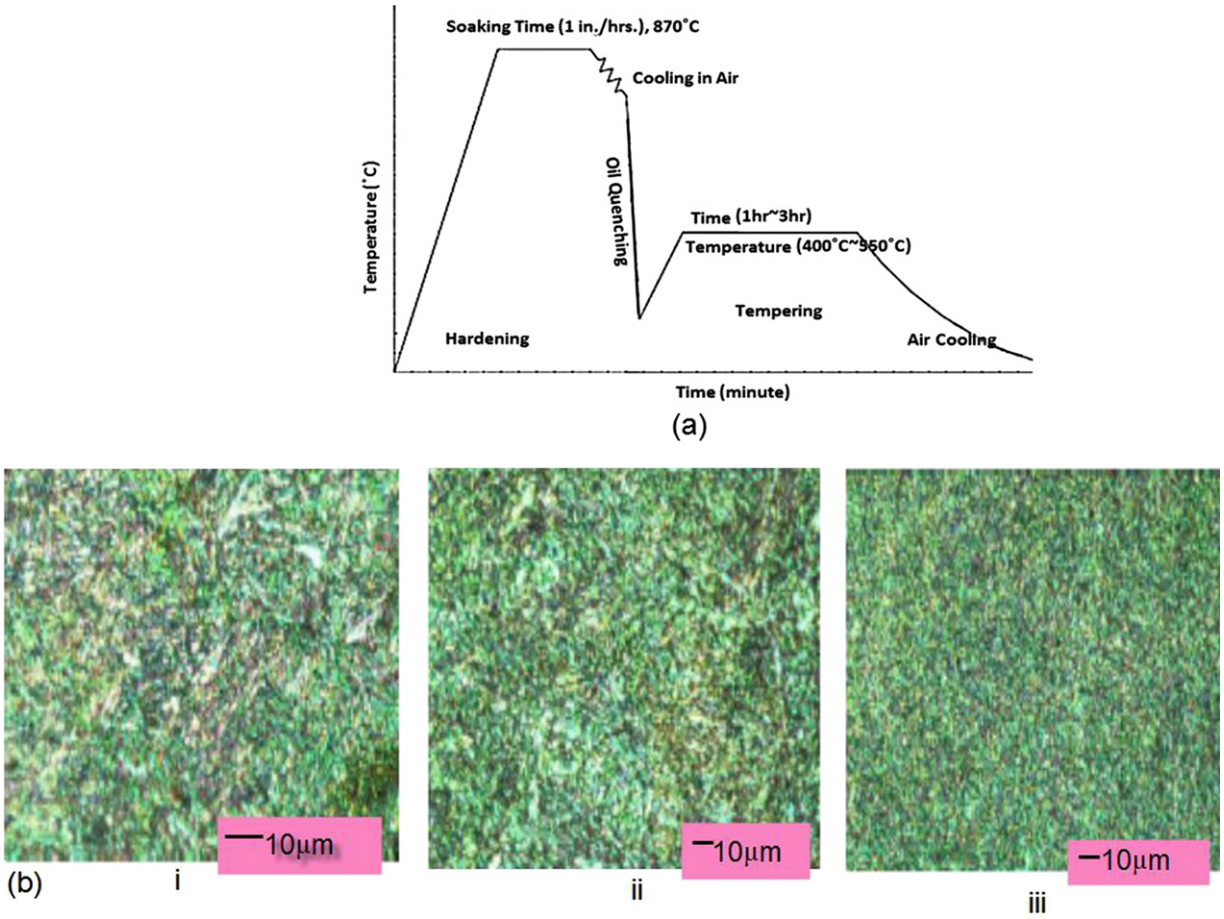


Figure 15 (a) Heat-treatment cycle and (b) The microstructure of spring steel oil quenched and tempered for 2 h at (i) 450 °C, (ii) 500 °C, and (iii) 550 °C.[17] Htun, M. S.; Kyaw, S. T.; Lwin, K. T. Effect of Heat Treatment on Microstructures and Properties of Spring Steel. *J. Min. Met. Mats.* **2008**, *18* (2), 191–197.

thereby leading to the formation of unacceptable structure. Normalizing leads to structural refinement and can be a good starting material for the subsequent heat-treatment operation. In general the steel is heated to a temperature of 850–880 °C, held for certain period of time following the rule of 1 h 25 mm^{-1} section thickness and then cooled in still air.

The hardening operation for the spring steel is extremely critical. Springs are required to be heated quite uniformly throughout the section while attaining the stipulated hardening temperature. It is very important that during heating of steel, there is no change in dimension or shape of the charged material. It is therefore advisable to load the spring within the furnace in horizontal position. Vertically loaded springs for heating may be deformed due to its own weight; when it becomes quite hot during austenitizing the flow stress reduces and the spring deforms. To avoid distortion of long spring, the furnace wall must be plain and smooth without creating any imbalance in load throughout the length of the spring. For a long spring, change in radial dimension is also a concern and it is advisable to insert a mandrel inside the spring. As discussed earlier, holding time depends upon the maximum cross section and also on the total charge placed in a furnace. Springs of smaller dimension are heated to the lower limit of the temperature range for hardening, whereas the upper limit of hardening temperature is normally employed for the springs of larger dimension. It may be recalled that too high a hardening temperature or a prolonged holding time at the hardening temperature gives rise to grain coarsening and excessive decarburization, whereas too low hardening temperature is not desirable as it adversely affect proper hardening.

After holding for suitable period of time at the hardening temperature, the spring is taken off from furnace and then quenched in oil or water depending upon their composition and the final properties required. The temperature of water should be maintained to 30–40 °C so that a slower cooling rate within M_s–M_f can be achieved. The quenching bath must be agitated for improving efficiency of quenching.

For high-carbon high-alloy steels, oil quenching is preferred over water quenching because water quenching leads to the formation of quenching cracks. However the quenching oil should be heated to a temperature of 80 °C, at which it will have adequate fluidity for effective quenching within the M_s–M_f region. Similar to water quenching, the oil quenching bath is also to be subjected to agitation when heat treatable items are put to the quenching medium.

Sometimes very high-hardenable steels are used to impart suitable properties by suitable heat treatment of steels. In

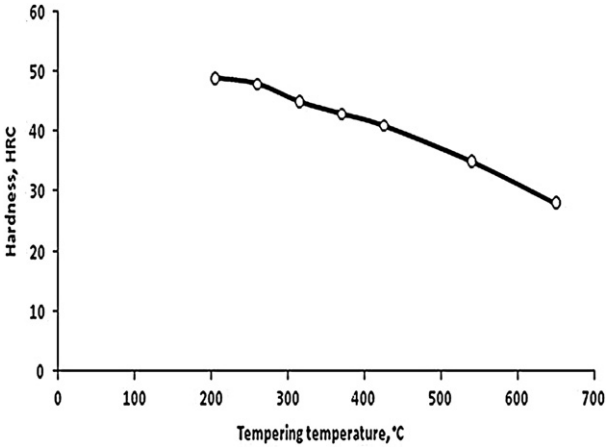


Figure 16 Reduction in hardness due to tempering of spring steel.

this case the work pieces are tempered immediately after quenching as it helps to avoid the quench cracks.

Tempering temperature is decided by the final properties desired in the material. The reduction in hardness due to tempering of a spring steel of different composition at different temperatures is shown in Figure 16. It is experienced in general that beyond a tempering temperature, degree of reduction in hardness value decrease due to increase in temperature. It is apparent from the figure that the reduction in hardness during tempering is a function of tempering temperature for a particular tempering time. It is important to note that the magnitude of reduction in hardness during tempering is a deciding factor of finally achievable toughness properties in the materials. To acquire a good spring characteristics the hardness reduction by tempering must not be less than R_C15. For successful heat treatment of a particular spring steel of similar specification, such type of master curves are to be generated by experimental trials. Sometimes some spring steels are also subjected to patenting operation. Austenitization is carried out at sufficiently high temperature above Ac_3; it is then cooled in molten salt bath kept at fixed temperature near the nose of continuous cooling transformation (CCT) diagram so that a fine pearlitic microstructure or a combination of pearlitic and upper bainitic structure can be produced.

Specific heat-treatment cycles of some common spring steels are given below:

- AISI 1065: (C-0.6–0.7 wt%; Si-0.35 wt% max; Mn-0.60–0.90 wt%; S,P-0.035 wt% max)
  - It is mainly used for light flat spring, for example, seat cushions spring for vehicles.
  - Heat-treatment cycle comprises, of soft annealing at 660 °C, hardening by oil quenching from 825 °C followed by tempering at around 500 °C.
  - Tempered hardness to be achieved is R_C45.
- AISI 1074: (C- 0.7–0.8 wt%; Mn-0.5–0.8 wt%; S, P-0.03 wt% max.)
  - These are used for flat and coiled spring for automobile and vehicles.
  - Soft annealed at 650 °C oil quenching from 800 °C and tempering at 625 °C.
- AISI 1084: (C-0.8–0.9 wt%; Si-0.35 wt%; Mn-0.6–0.9 wt%; S,P-0.04 wt% max.)
  - These are mainly used for flat and coiled spring for automobiles and railways.
  - Heat-treatment cycle comprises, soft annealing at 650 °C, oil quenching from 800 °C, and tempering at 625 °C.
- AC22–76: (C-0.5–0.6 wt%; Si-1.8–2.2 wt%; Mn-0.7–0.95 wt%; S,P-0.035 wt% max.)
  - Silico–manganese steel: Normalizing followed by hardening from 850 °C and then oil quenching with oil at 80 °C, and then tempering at 600–625 °C.
- AISI 1095: (C-0.92–1 wt%; Mn-0.05 wt%)
  - Annealing at 810 °C; Normalizing at 880 °C; Hardening at 800–820 °C.
  - Oil quenching and tempering to RC50.

2.8.4 Silicon Steel

The steel used as the core material of electrical transformers is generally a soft magnetic material viz. grain-oriented silicon steel.[17–18] After due processing, this material exhibits a pronounced Goss texture, i.e., a {110} ⟨001⟩ texture, which is indicative of preferred orientation of grains. High-temperature annealing during the processing of this steel leads to abnormal growth of grains with Goss orientation. Till date universally accepted reasoning is yet to be put forward in respect of the origin of preferred growth of the above Goss grains. It is conjectured that the Goss orientation is inherited since early stages of the production of this material and at later stages of processing it grows at the expense of others, due probably to the strain energy factor.

It is known that the Goss orientation owes its origin to shear deformation during hot rolling. The deformation confined to the surface is responsible for evolution of Goss texture.

The general processing of transformer steels include the production of ultraclean steel with the available technology; the strip is then subjected to first cold rolling to reach to an intermediate thickness. Decarburization re-crystallization annealing is done with cold-rolled strip in continuous annealing furnace. Second cold rolling is done to achieve the final thickness. Then a heat-resistant coating is applied (MgO) and following this, high-temperature batch annealing is accomplished. During this annealing strong Goss texture develops. The microstructure of the annealed steel is shown in Figure 17.

Soft magnetic material possesses minimum coercive force and maximum magnetic permeability. For this, a homogenous single phase microstructure is required. The material must not contain any residual stress which adversely affects the performance of the material. In electrical industries low-carbon silicon steels are widely used as soft magnetic material. Silicon goes in solution in iron and expectedly increases the electrical resistivity. The electrical resistivity is due to the incoherent scattering of electrons at the small-scale irregularities within the crystal. Substitutional Si-atoms are the irregularities of atomic scale of magnitude and hence increase the resistivity. At the same time it reduces the eddy current losses and improves magnetic permeability. The hysteresis loss is minimized in

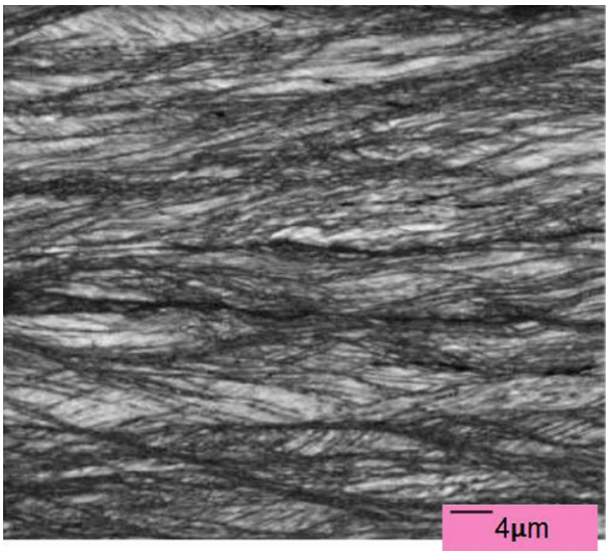


Figure 17 Microstructure of grain-oriented silicon steel after annealing.[19] Dorner, D.; Zaefferer, S.; Lahn, L.; Raabe, D. *Magn, J. Magn. Mater.* **2006**, *304* (2), 183–186.

steel containing 4% Si at a carbon contain below 0.02%. This kind of electrical-sheet steel requires special heat treatment. Batch annealing is carried out in a reducing atmosphere at a very high temperature like 1200 °C. This high-temperature annealing is carried out in inert environment or in vacuum; such a high-temperature annealing for a long period of time, i.e., 15–30 h aims at recrystallization followed by grain coarsening and also deliberate decarburization to burn out carbon at high temperature. The development of a textured material gives a high initial permeability and ensures easy magnetization.

For application as permanent magnet hyper eutectoid chromium steel containing 0.9–1% of carbon with 1.2–1.5 wt% of chromium, is commonly used. Chromium content may be varied up to 3.5 wt% in special cases. Maximum value of coercivity is obtained after hardening of steel. Quenching stresses are relieved by tempering the steel after hardening. The general heat-treatment process for this kind of steel for use as a permanent magnet consists of heating the material to around 850 °C, holding there for 1 h per each 25 mm of maximum section thickness and then quenching in oil or in suitable polymer quenching medium. After hardening, the steel is tempered at a low temperature of 100–120 °C for a prolonged period, even up to 20–25 h; this first stage of tempering stabilizes the microstructure and hence the magnetic properties. Magnetic properties can be improved by alloying the above steel with tungsten by around 5%. It is to be remembered that the steels meant for application as permanent magnet must not be held above Curie temperature for the sake of softening of the steel or as a strategy for preheating before forging, as this will exert a permanent detrimental effect to the microstructure and hence the properties. It should be understood that the ferromagnetic iron requires the favorable alignment of magnetic domains containing parallel spins. This is also possible in a iron–carbon alloy where a single phase exists. Magnetic spoiling due to annealing at 800 °C is ascribed to the coarsening of carbide particles which will not dissolve properly during austenitization. Thus the quenched microstructure is not a single phase and is comprised of carbon depleted martensite and undissolved carbides. These carbides restrict the movement of the domain boundaries required for getting the correct alignments in favorable directions in respect of the externally applied magnetic field.

If the same steel is normalized at a very high temperature like 1200 °C, the carbides go into solution and a single phase microstructure is obtained with the resultant removal of magnetic spoiling. In some cases due to the advantage of cobalt to improve magnetic property (Co is a ferromagnetic material), the steel containing 8–10 wt%Cr and 13–15 wt% Co are used as permanent magnetic material. However Cobalt steels are very prone to magnetic spoiling mainly because the cobalt steels are extremely hard and require a high temperature of 800 °C to get softened. Thus magnetic spoiling is an inevitable consequence of manufacturing of cobalt bearing steel.

The recommended heat treatments for these steels are

- Heating the steel to 1200–1230 °C for austenitization accompanied by complete dissolution of carbides; the steel is held for suitable time at these hardening temperatures.
- Quenching it in air to reduce the thermal stress yet producing a completing single phase martensitic microstructure.
- Tempering the steel at 700–750 °C for 1 h per each 25 mm of section size followed by air cooling.
- Raising the temperature of the steel to around 1050 °C and holding there for a selected period time; the steel in austenitic condition is quenched in oil and finally aged at low temperature, like 100 °C.

Austenitizing for the first hardening leads to complete dissolution of the preexisting carbide particles. Tempering the hardened steel at 750 °C leads to the formation of uniformly distributed fine carbide particle in a matrix of low-carbon martensite. Dissolution of these fine carbide particles in austenite becomes very easy and therefore the second hardening from a low temperature gives rise to the required homogenization effect without the risk of other microstructural damages affecting the magnetic properties.

- The alloy containing 14Ni8Al20Co3Cu is a very good magnetic material. The alloy is extremely hard and so produced by casting. The heat treatment of these alloys is quite complex and is as follows.
  - o Heating to 1300 °C at a very slow rate of the order of 20–30 °C per hour under a magnetic field of intensity 3000 Oe (oersteds).
  - o After this treatment material achieves a very good magnetic property.

2.8.5 Bearing Steel

A bearing is used as a support and allows relative movement to take place between two bodies. In a diesel engine, the principal bearings are those which allow rotation of the crankshaft about its own longitudinal axis in the main engine and those between the connecting rod and crankshaft.

The surface undergoing relative movement, the lubricant to be used and the environment are the deciding factors of property requirements in bearing steel. The steel must have

- resistance to fatigue and crack growth,
- high hardness and strength,
- resistance to hydrogen cracking,
- high corrosion resistance, and
- high toughness.

Types of bearing:

There can be several types of bearings for commercial application depending upon the nature of contact. These are:

- solid contact bearing or journal bearing:
  a) hydro dynamically lubricated bearing
  b) boundary lubricated bearing.
- rolling contact bearing:
  a) ball bearing
  b) roller bearing.

Ball-bearing steels are a special class of steel. The nominal compositions of this variety of steels are given in the Table 4.

In practice the materials of bearing, like the balls, rings, and the rollers are subjected to abrasive wear and corrosion. It is known that chromium in high-carbon steel is introduced to impart aforesaid of the properties. High strength of the material is normally obtained by hardening and tempering.[20–22] This ensures a high fatigue limit, good contact fatigue resistance at high-abrasion resistance. Normally the starting microstructure of this steel is fine pearlite with dispersed cementite particles. The procedure to be adopted for hardening is dependent upon the sizes of the bearing component. The small balls are quenched in oil whereas water quenching may be involved for large sized balls. It is to be recalled that volume expansion due to martensite transformation in a ball will be mostly isotropic and there will be less propensity for cracking even when it is quenched in water. However a polymer quenching with suitable concentration of polymer may be a more reliable quenching medium. The hardened balls are subjected to tempering at relative low temperatures that is around 150–160 °C so that fine low-carbon martensite with dispersed carbide particle constitute the microstructure. However better results can be obtained if the thermal stresses accompanying quenching can be taken care by employing martempering process. The materials austenitized at 850 °C may be quenched in a salt bath maintained at a temperature of 180–190 °C. Formation of matrensite and its first stage of tempering take place simultaneously, with the likelihood of the presence of some retained austenite. The retained austenite present in the oil quenched samples may be reduced by subzero treatment at −50 °C for about an hour. This is then followed by tempering at 160–180 °C for 2 h. The microstructure of ball-bearing steel of type 52 100 is shown in Figure 18.

2.8.6 Hadfield Steel

Hadfield manganese steel is essentially high-carbon high-manganese steel where carbon content is around 1.1–1.4% with 11–14% manganese. The alloy is principally made for high-wear resistance application and its high work hardening ability makes it applicable for various applications including armors. Microstructurally Hadfield manganese steel must be fully austenitic without the presence of any carbide in the microstructure. The compositions of some commercial Hadfield manganese steels are given in Table 5.

Fully austenitic steel is non-magnetic. As stated, the microstructure of Hadfield steel is fully austenitic at all the temperatures; thus there is no scope of structural refinement of these steels through conventional heat treatment. The commercial Hadfield manganese steels are required to have the commonly specified grain size of ASTM-4 or finer. Therefore proper melting techniques are employed to achieve the required grain size.

It is very common that the solidified Hadfield manganese steel contains some carbide particles at the grain boundaries. The precipitated carbides are shown in the Figure 19(a). Slower is the solidification rate, higher will be the amounts of carbides present in the microstructure. These carbides are of the type $(FeMn)_3C$.

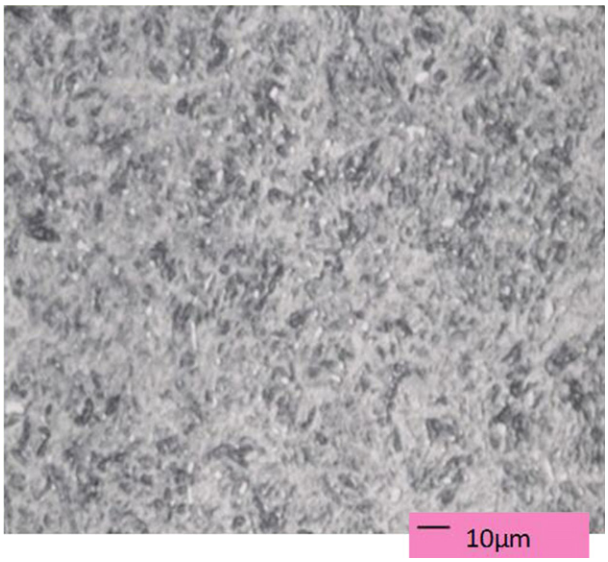


Figure 18 Microstructure of 52 100 type ball-bearing steel showing tempered martensite and undissolved carbide. G.F. Vander Voort *The Microstructure of Ferrous Alloys*.

Table 4 Composition of ball-bearing steel

Sl. no.	*Carbon*	*Chromium*	*Silicon*	*Manganese*	*Sulfur and Phosphorus*
1	1.05–1.15	0.4–0.7	0.15–0.35	0.25–0.45	0.025 max
2	1–1.1	0.9–1.2	–	–	–
3	0.95–1.05	1.3–1.65	–	–	–

Table 5 Chemical compositions of different grades of austenitic manganese steels

Grade	*Carbon*	*Manganese*	*Chromium*	*Molybdenum*	*Nickel*	*Silicon*	*Phosphorous*
	(wt%)	*(wt%)*	*(wt%)*	*(wt%)*	*(wt%)*	*(wt%) max*	*(wt%) max*
A	1.05–1.35	11.0 min	–	–	–	1.00	0.07
B-1	0.90–1.05	11.5–14.5	–	–	–	1.00	0.07
B-2	1.05–1.20	11.5–14.5	–	–	–	1.00	0.07
B-3	1.12–1.28	11.5–14.5	–	–	–	1.00	0.07
B-4	1.20–1.35	11.5–14.5	–	–	–	1.00	0.07
C	1.05–1.35	11.5–14.5	1.5–2.5	–	–	1.00	0.07
D	0.70–1.30	11.5–14.5	–	–	3.0–4.0	1.00	0.07
E-1	0.70–1.30	11.5–14.5	–	0.90–1.20	–	1.00	0.07
E-2	1.05–1.45	11.5–14.5	–	1.80–2.10	–	1.00	0.07
F	1.05–1.35	6.0–8.0	–	0.90–1.20	–	1.00	0.07

Source: *ASM Hand Book*, Vol. 1, p. 1274.

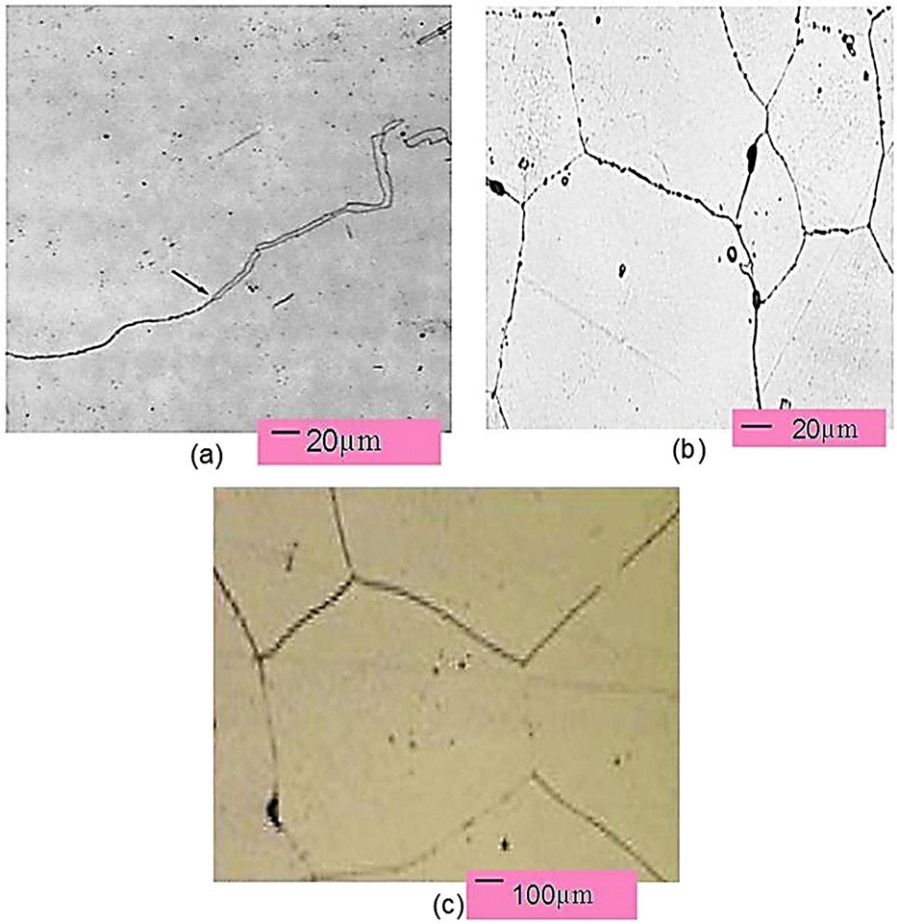


Figure 19 Microstructure of Hadfield steel showing (a) precipitated carbides, (b) undissolved carbide, and (c) clean grain boundaries after heat treatment.[23] (a) and (b) *ASM Hand Book*, Vol. 9; p. 1675, 1678; (c) Hosseini, S.; Limooei, M. B. Optimization of Heat Treatment to Obtain Desired Mechanical Properties of High Carbon Hadfield Steel. *World Appl. Sci. J.* **2011**, *15* (10), 1421–1424.

The heat treatment of Hadfield manganese steel aims at dissolving the precipitated carbides at high temperature and then cooling it very fast to achieve carbide free grains of austenite which is considered to be the ideal microstructure for its commercial application.[23–26] The most commonly stated heat treatment is to heat the steel at a high temperature like 1000 °C, holding it there for preselected time and then quenching it in water. Importantly the complete dissolution of the carbide depends upon judicious selection of heating temperature and the concerned soaking time. The cooling rate is of extreme

importance as a slower cooling rate makes the steel prone to precipitate carbide. So the major points to consider for successful heat treatment of Hadfield manganese steels are:

- Elimination of any undissolved carbide by solutionizing at a high temperature.
- Avoidance of precipitated carbide in the final microstructure.

In industrial situation the control of austenitization temperature and holding time is not so easy in the midst of operational constraints due to inherent difficulty in mechanical handling of the heated objects of heavy weight. From the phase diagram of the steel it may be observed that the formation of carbides is highly probable if the steel is held for sufficient time at temperature below 700 °C. It is for this reason the heating rate at the initial stage is very important. Also this high-alloy steel is very prone to decarburization and demanganization on prolonged holding at high temperature which may lead to compositional degradation and formation of a microstructure that does not secure the desired property of the steel, thereby rendering the component unusable. Thus the suggested strategy of heat treatment may be as follows.

- Heating the component at a very fast rate till a temperature of 750–800 °C is attained by the objects; below this temperature, the probability for formation of $(FeMn)_3C$ is very high. Depending upon the capacity of the furnace, a heating rate of 150–200 °C h^{-1} is also recommendable.
- Because of fast heating there will be thermal shock due to temperature difference between surface and center of stock. However austenite is face-centered cubic (FCC) in structure and is a ductile phase; therefore the chance of cracking due to thermal shock is less. Nevertheless the chance of distortion due to differential volume change at different position of the section cannot be underrated. Therefore the component is held at 750–800 °C for about 30 min. The exact time of holding must be determined through experience of the hardware system and charge quantity of a specified batch under heat treatment in a particular shop.
- The material is then heated to a high temperature like 1050–1075 °C at a moderate heating rate say 75 °C h^{-1}. A slower heating rate is preferred to avoid thermal gradient which may lead to distortion of the material which being austenitic is highly plastic at elevated temperature. On the contrary a slower heating rate implies a higher residence time at a high temperature; this makes the steel liable to decarburization unless the furnace atmosphere is highly controlled. Again the slower heating rate takes a longer time to reach the austenitizing temperature which affects productivity. Therefore proper measures are to be taken while selecting the heating rate.
- The steel is soaked at 1050 °C for 1 h per 25 mm of section size for complete dissolution of carbides. The dissolution of carbides should be completed at a reasonably low temperature but not with prolonged holding time; the idea is to dissolve the carbides rapidly without much chemical degradation at the solutionizing temperature. If solutionizing temperature is too much increased to reduce the socking time, rapid grain coarsening may take place when there is no restrictive agent at the grain boundaries.
- After almost complete dissolution of carbides, the steel is heated as fast as possible up to a temperature of 1100–1150 °C so that
  a) there is insurance of complete carbide dissolution without anything being left to be dissolved,
  b) production of compositionally homogenous austenite is possible,
  c) grain coarsening by unnecessary high-temperature exposure for a long time may be avoided, and
  d) ample provision may be made for inevitable delay in quenching in an industrial situation irrespective of efficacy of material handling system.
- The steel is held at this high temperature for a very short period of time, say for 15–20 min due to above stated reasons. The steel components are then quenched very fast in a circulating bath of water with 4–5% of sodium chloride (NaCl) in it.

A typical microstructure without any carbide is shown in the Figure 19(c).

2.8.7 Stainless Steel

Stainless steels are categorized on the basis of various microstructures. Accordingly different classes of stainless steels are termed as martensitic, austenitic, ferritic, duplex (ferrite with austenite), and precipitation hardening stainless steel. Each variety has a range of composition and within this range a number of steels each with specific designation and different composition from others are available. For example, steels of types 403, 410, 416, 420, 440A, etc., belong to the general class of martensitic stainless steel. Stainless steels are employed in application where corrosion resistance and heat resistance are important. All stainless steels ought to contain chromium as its principal alloying element; the stainlessness is due to the formation of a thin impervious layer of Cr_2O_3 on the surface of the stainless steel component. The passivity of this layer in presence of most of the aggressive environments makes it a versatile corrosion and weather resistant material.

2.8.7.1 Martensitic Stainless Steel

Martensitic variety of stainless steel contains 12–18 wt% of chromium. The composition of some commercially important steels falling under this class is given in Table 6.

Being martensitic, these steels are magnetic and are amenable to cold working at low-carbon concentration; the heat

Table 6 Chemical composition of martensitic stainless steels (in wt %)

Type	*C*	*Cr*	*Ni*	*Si*	*Mn*	*P*	*S*	*Other*
403	0.15	11.5–13	–	0.5	1	0.04	0.03	–
410	0.15	11.5–13.5	–	1	1	0.04	0.03	–
416	0.15	12–14	–	1	1.25	0.06	0.03	0.6Mo
420	0.15	12–14	–	1	1	0.04	0.03	–
440A	0.60–0.75	16–18	–	1	1	0.04	0.03	0.75Mo

Source: ASM Metal Hand Book, Vol. 1.

treatment of martensitic stainless steel envisages the production of martensite from austenitic phase field.[27–29] and therefore the heat-treatment process is similar to those practiced for plain-carbon or low-alloy steels where strength of the steels are required to be obtained from the hardness of martensite that forms due to rapid cooling of high-hardenability austenite.

It is to be noted that stainless steels are high-alloy steels and due to characteristic effect of alloying elements the hardenability of this class of steel is very high; this entails the possibility of formation of martensite even under the ordinary air cooling. However chromium being a strong ferrite stabilizer raises the upper critical temperature by constricting the austenite phase field. The constriction of austenitic loop in the equilibrium diagram of high-chromium steels requires a judicious selection of temperature to produce austenite at a particular carbon level. The cross section of Fe–C–Cr phase diagram at 12% Cr is shown in the diagram in Figure 20. From this diagram it is possible to determine the austenitizing temperature for a martensitic stainless steel of 12% Cr.

Thus martensitic stainless steels are normally heated to a temperature above 1020 °C for austenitizing. However the time at holding temperature must be kept to minimum because at such high austenitizing temperature, there is a great risk of fast grain coarsening just after the dissolution of carbides is completed; at the same time decarburization at the surface of the steel component may take place in martensitic stainless steels which contain appreciable amount of carbon. Following austenitization, the steel is quenched in oil or air. Air quenching, wherever possible, is encouraged due to the potential it bears to minimize thermal stresses. Tempering of the steel follows hardening operation. Tempering of the quenched martensitic stainless steel is carried out at about 580–600 °C so as to take the advantage of secondary hardening. The microstructure of the martensitic stainless steel showing tempered martensite is furnished in Figure 21.

If the carbon content of the martensitic stainless steel is high, tempering must not be carried out too long near 580 °C because it will lead to the precipitation of chromium carbides; consequential formation of chromium depleted matrix will lead to deterioration of corrosion resistance. In the event the carbon content of the martensitic stainless steel is low, the severity of lowering of corrosion resistance property is not so significant as to warrant any special action.

Martensitic stainless steel of high-chromium content with appreciable amount of carbon content must not be tempered within the range of 390–500 °C because there will be significant lowering of impact strength of material. This temper embrittlement is known as 400 °C embrittlement and must be avoided while heat treating martensitic stainless steel.

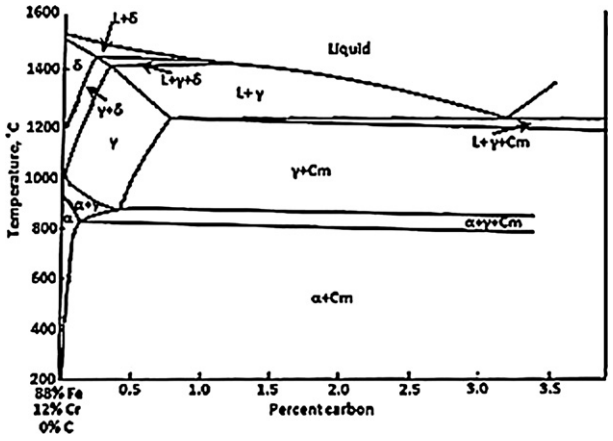


Figure 20 Phase diagram of iron–carbon–chromium alloy for 12 wt% chromium. Thum, E. E. *Book on Stainless Steels*, 2nd ed.; ASM: Metals Park, OH, 1935.

2.8.7.2 Ferritic Stainless Steel

Ferritic stainless steel contains higher chromium content than the martensitic stainless steel. Normally the chromium content of the ferritic stainless steel ranges from 14 to 27 wt%. From the Fe–C–Cr diagram sectioned at 18% chromium, shown in Figure 22, it appears that for a low-carbon level, the austenite is not possible to form until a very high temperature, viz 1200 °C is attained for a carbon content of 0.06%. This implies that the steel of this composition is ferritic from room temperature till 1200 °C and is not amenable to hardening. Ferritic stainless steel may be hardened by only cold working. Microstructure being ferritic, ferritic stainless steel can be readily cold worked and deep drawn. This is why this type of stainless steel is used in food industries and for architectural trims, etc. Annealed steels are very soft and ductile and it possesses a very good formability. In the annealed condition ferritic stainless steels are much stronger then the annealed low-carbon steels and its corrosion resistance is much higher than the martensitic stainless steel. The composition of some ferritic stainless steels is given in Table 7.

Other than annealing, there is no other meaningful heat-treatment practice which may help to improve the properties of ferritic stainless steel. The microstructure of a fully ferritic stainless steel is shown in Figure 23.

However this steel is highly prone to embrittlement if held at temperature within 400–500 °C. This embrittlement leads to sharp deterioration of impact properties and therefore the annealing operation must be carried out at a temperature from above 500 °C till the temperature at which austenite is likely to form. After holding for adequate period of time which is decided by whether there is any carbide phase present in its microstructure and if the carbides can easily go in solution to produce a single phase homogenous ferrite. The steel is then slowly cooled till 500 °C; in any case, long time holding within 400–500 °C is not allowed for the sake of avoiding 400 °C embrittlement. It is advisable to cool the material slowly within the furnace till 500 °C after which a faster cooling must be accomplished to avoid 400 °C embrittlement. The exact cause of 400 °C embrittlement is not known but the recorded observation of enhanced embrittlement with increasing chromium content tends to hint upon that 400 °C embrittlement is related to the formation of harmful carbides while holding the steel at the above temperature region.

2.8.7.3 Austenitic Stainless Steel

In consideration of the means to take care of susceptibility of intergranular corrosion, the austenitic stainless steels are

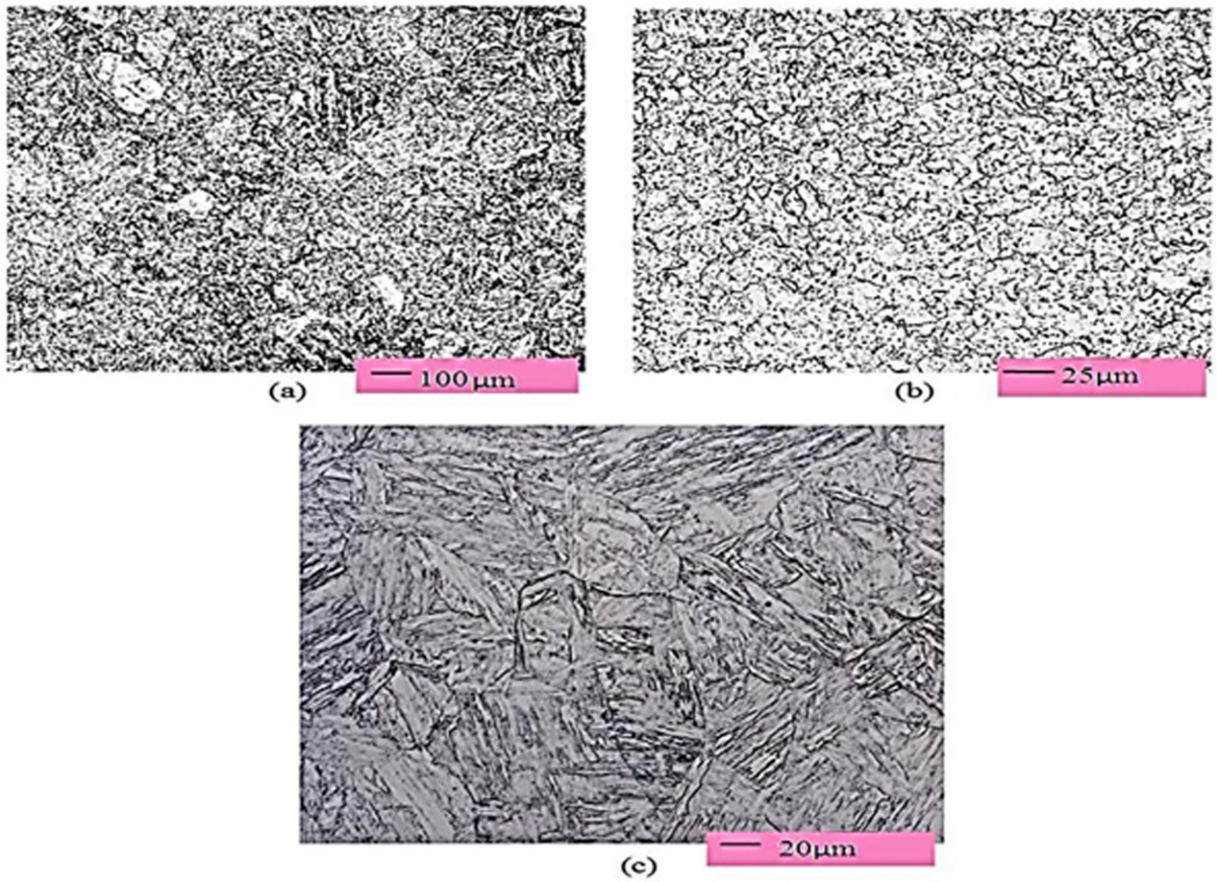


Figure 21 Microstructure of AISI 403 martensitic stainless steel (a) in annealed condition, (b) in quenched and tempered condition showing tempered martensite, and the (c) microstructure of AISI 410, martensitic stainless steel oil quenched from 1040 °C followed by tempering at 650 °C showing tempered martensite. Courtesy: George F. Vander Voort, Director, Research and Technology, Buehler Ltd. Vander Voort, G. F. *The Microstructure of Stainless Steels*.

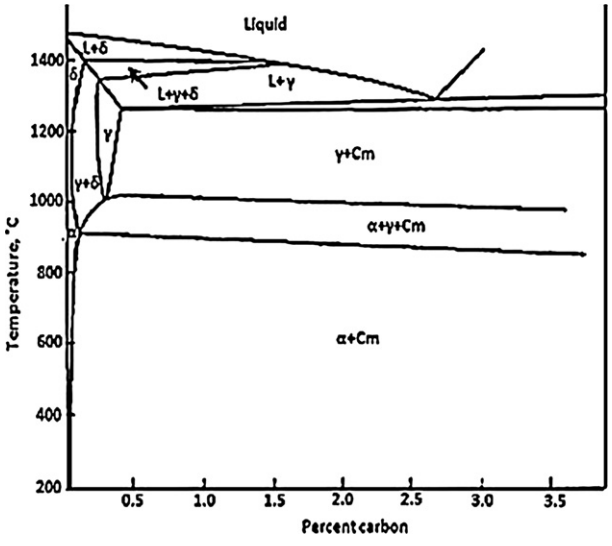


Figure 22 Phase diagram of iron–carbon–chromium alloy with 18 wt% chromium. Thum, E. E. *Book on Stainless Steel*, 2nd ed.; ASM: Metals Park, OH, 1935.

divided into several groups. The conventional austenitic steel contains around 0.15% carbon which in stabilized group is managed by addition of carbide formers. The low carbon variety directly avoids the formation of carbide which is known to be the main cause of intergranular corrosion. There are high-nitrogen steels where nitrogen is employed as austenite stabilizer; however nitrogen also imparts a better surface property. Some of the austenitic stainless steels are alloyed with other alloying elements to incorporate special properties. The general composition of a few commercially important austenitic stainless steels encompassing all the varieties as stated above is furnished in **Table 8**.

The coefficient of thermal expansion of austenitic stainless steel is very high, so extra precaution is to be taken while loading the heat-treatment furnace with a number of components. There should be proper spacing to accommodate thermal expansion between two adjacent components; because austenite is soft and highly deformable, stacking of items must be done judiciously so as to avoid such deformation. The conventional austenitic stainless steels are supposed to be austenitic at all the temperatures, therefore are not amenable to quench hardening. However hardening can be obtained by

Table 7 Composition of some ferritic stainless steels (in wt %)

Type	*C*	*Mn*	*Si*	*Cr*	*Ni*	*P*	*S*	*Other*
405	0.08	1	1	11.5–14.5	–	0.04	0.03	0.01–0.03 Al
430	0.12	1	1	10.5–11.75	–	0.04	0.03	
434	0.12	1	1	16	–	0.04	0.03	
444	0.12	1	1	17.5–19.5	–	0.04	0.03	1.75–1.25 Mo; 5 × %C min 1.10 Ti
446	0.12	1	1	23–27	–	0.04	0.03	

Source: *ASM Hand Book*, Vol. 1.

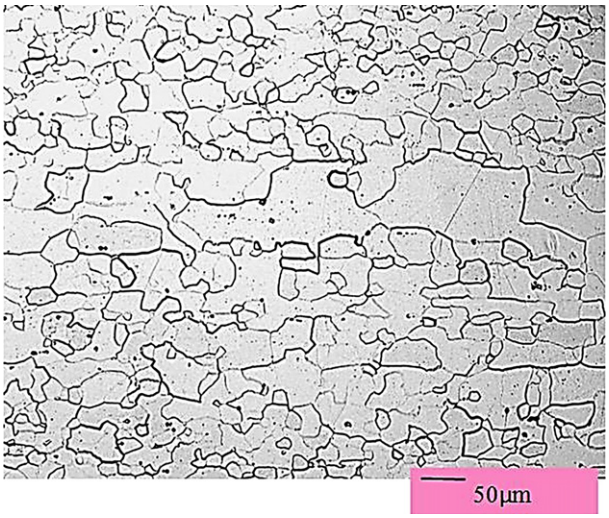


Figure 23 Microstructure of Ferrtic grain AISI409 stainless steel sheet showing fully ferritic structure. Courtesy: George F. Vander Voort, Director, Research and Technology, Buehler Ltd. Vander Voort, G. F. *The Microstructure of Stainless Steels*.

cold working the steel. If welding is done, then the steel must be subjected to heat treatment. In general the conventional austenitic stainless steels are heated to a temperature above 1000 °C, within a preferable range of 1050–1150 °C, held there for sufficient time to dissolve the carbides originally present in the microstructure and then cooling very fast. The annealing temperature may somewhat vary for steels of different compositions and a higher temperature is recommended for those compositions where the chances of presence of carbides in the original microstructure is high. The soaking time to be spent for annealing operation depends upon the section size. However 50–60 min for 25 mm of the section size is the thumb rule which is normally followed to determine the holding time at the annealing temperature. In general water quenching is recommended for achieving maximum amount of corrosion resistance. Although in some variety of steels, oil quenching is also done. Conventional austenitic stainless steel experiences the precipitation of Cr-carbides between 425 and 900 °C if the steel is exposed within this temperature region for a long period of time. Thus the annealing temperature must be considerably above 900 °C so that all the carbides can be fully dissolved in austenite before it is subjected to quenching treatment; moreover the rate of dissolution of chromium carbide being quite sluggish, a high-annealing temperature around 1100 °C is generally recommended for successful implementation of commercial heat treatment of austenitic steel. In order to limit the grain growth to an acceptable limit, the annealing temperature must not be much higher than 1100 °C. The microstructure of AISI 304 steel in Figure 24 exhibits a fully austenitic structure.

As stated earlier the quenching must be done very rapidly; if size, shape, and weight put a concern for distortion due to rapid cooling then quenching in forced air blast may be recommended. In some cases extremely thin sectioned parts cannot withstand a forced air blast without having excessive distortion; in such cases, normal air cooling is recommended. In cases of ultrathin components a slow air cooling may bring down the temperature of the component from annealing temperature of 1100 °C down to room temperature within a very short time. This short duration may not trigger the precipitation of chromium carbides in steels whose carbon content is relatively less to exceed the solubility product of carbon and chromium in FCC austenite. But in cases where the composition is such that this type of air cooling cannot prevent the precipitation of carbides then corrosion resistance is required to be sacrificed. To avoid this situation stabilized grade of austenitic stainless steel or extra low-carbon steels are to be invoked.

In the stabilized grade, the presence of Ti or Nb inhibits intergranular precipitation of chromium carbide and thereby helps to avoid sensitization. Nevertheless these alloys must be annealed to relieve the stresses present in the material and to increase the ductility properties of the same with additional stabilization of austenite.

Normally the steel is heated to a temperature up to 1000–1050 °C followed by a rapid cooling. In this particular case the dissolution of carbide is a greater concern than the precipitation of these carbides during cooling. Thus the annealing temperature and the soaking time are more important for consideration than the cooling rate. Heating temperature must be high enough to dissolve all the carbides in least possible time and with limited grain growth. In this respect a maximum temperature of 1050–1060 °C is reasonably acceptable with a time consideration of 50–60 min per 25 mm thickness. Whenever maximum corrosion resistance from stabilized variety is required to be obtained, the recommendable heat treatment should comprise of heating the material to 1000 °C and holding at this temperature for 5 h and then followed by rapid cooling to room temperature.

The extra low-carbon austenitic stainless steel does not have the problem of sensitization because of the fact that there is no scope for carbide formation and hence unlike non-stabilized grades this variety of steel does not require any rapid quenching from a high temperature (Figure 25). Nevertheless

Table 8 Chemical composition of some austenitic stainless steel (in wt %)

Type	*C*	*Mn*	*Si*	*Cr*	*Ni*	*P*	*S*	*Other*
202	0.15	7.5	1	17	4–6	0.06	0.03	0.25N
302	0.15	2	1	17–19	8–10	0.045	0.03	–
304	0.08	2	1	18–20	8–10.5	0.045	0.03	–
304L	0.03	2	1	18–20	8–12	0.045	0.03	–
310	0.25	2	1.5	24–26	19–22	0.045	0.03	–
308	0.08	2	1	19–21	10–12	0.045	0.03	–
310S	0.08	2	1.5	24–26	19–22	0.045	0.03	–
316	0.08	2	1	16–18	10–14	0.045	0.03	2–3 Mn
316L	0.03	2	1	16–18	10–14	0.045	0.03	2–3 Mo
316LN	0.03	2	1	16–18	10–14	0.045	0.03	2–3Mo; 0.10–0.16N
321	0.08	2	1	17–19	9–12	0.045	0.03	5 × %C min Ti
347	0.08	2	1	17–19	9–13	0.045	0.03	10 × %C min Nb
347H	0.04–0.10	2	1	17–19	9–13	0.045	0.03	8 × %C min to 1.0 max Nb

Source: *ASM Hand Book*, Vol. 1.

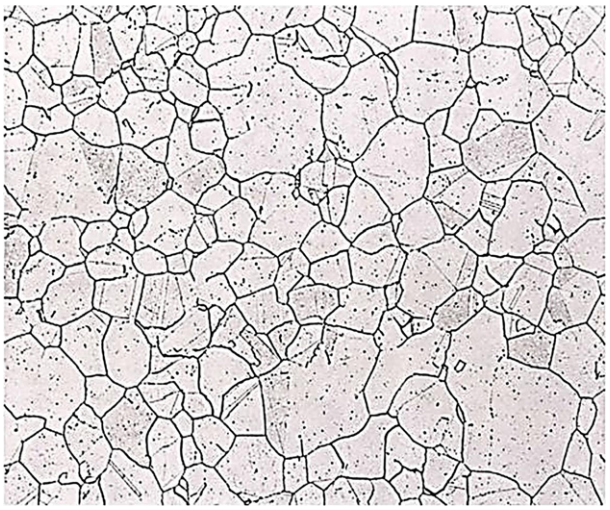


Figure 24 Microstructure of solution annealed AISI 304 austenitic steel revealing austenite grains; annealing twin is also observed X100. Courtesy: George F. Vander Voort, Director, Research and Technology, Buehler Ltd. Vander Voort, G. F. *The Microstructure of Stainless Steels*.

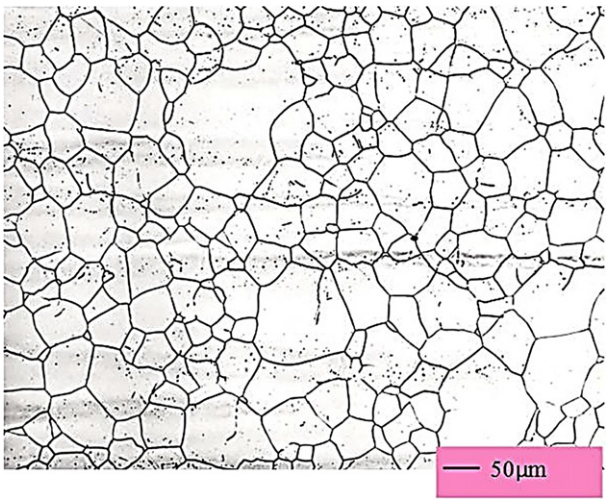


Figure 25 Microstructure of AISI 316L steel Solution annealed at 950 °C showing austenite grains. (In 50 μ). Courtesy: George F. Vander Voort, Director, Research and Technology, Buehler Ltd. Vander Voort, G. F. *The Microstructure of Stainless Steels*.

this steel should not be employed for long-time service within the sensitizing region, 540–760 °C.

Stress relieving of austenitic stainless steel is required if parts made of this steel is exposed to stress-corrosion environment. The steel is then heated to 900 °C or above and a slower cooling is more effective to remove stresses, as the fast water cooling may induce thermal stresses.

Selection of heat-treatment process is quite critical; the processes which aim to avoid sensitization and hence to improve corrosion resistance are those which act in opposition to stress relieving. So stress relieving is to be judiciously applied with an eye to compositional response to such treatment without bringing about sensitization.

The following factors are required to be given consideration during heat treatment of austenitic stainless steel:

- Heating in the range of 470–850 °C envisages carbide precipitation at the austenite grain boundaries. In ferritic stainless steel carbides first form discontinuously within the ferrite grains and then at the grain boundary.
- In high molybdenum-bearing steel σ (sigma) phase form within 550–900 °C. This deteriorates corrosion resistance and ductility.
- Slow cooling of non-stabilized grades may experience sensitization or σ-phase formation or both.
- Heating above 1000–1130 °C enables dissolution of all carbides in austenite.
- Stress relieving may be required only in special situation, and should be practiced only if it is otherwise favorable in respect of retaining corrosion resistance.

Due to presence of molybdenum, 316L and 317L are prone to σ phase embrittlement due to a long-time exposure between 660 and 860 °C; corrosion resistance can however be improved by stabilization annealing at 900 °C for 2–3 h; after this any stress relieving operation at 640–650 °C will not deteriorate the

corrosion properties. Heat treatment of high-nitrogen austenitic steel is exactly similar to conventional austenitic stainless steel as problems encountered due to sensitization and distortion are identical in either case. The steels like 316N or 304N are austenitized at 1020–1100 °C and following holding for 1 h per 25 mm section thickness the jobs are rapidly cooled in water. High alloy grade steels are heated to higher temperature range 1125–1150 °C with a specific purpose. Due to addition of high amount of molybdenum to reduce pitting corrosion and to improve high-temperature resistance, the concerned alloys are produced with very low carbon; nevertheless the steels are prone to δ ferrite formation at a high temperature of austenitization. Again at temperature just below 900 °C, these steels are susceptible to σ phase formation. Therefore neither a low temperature nor a high temperature is convenient for avoidance of property degradation. So austenitization is carried within narrow temperature regime. If stress relieving is to be carried out at a temperature lower than the annealing temperature, holding time must be of minimum possible value.

2.8.7.4 Duplex Stainless Steel

This type of steel is a combination of ferrite and austenite; in some compositions ferrite content is higher and in others austenite content is higher. Also ferrite and austenite contents may balance in some steels. Table 9 gives some typical composition. Duplex steels like 329 are austenitized at temperatures between 925 and 975 °C, held there for predetermined period of time and then cooled quite rapidly but rapidity of cooling must be consistent with limitations of distortion.[30,31] For the molybdenum bearing duplex steels (>6% Mo), the austenitization temperature is kept at higher level say 1000–1050 °C and then the steel in quenched rapidly to room temperature. A typical micrograph of the same steel is shown in Figure 26.

2.8.7.5 Precipitation Hardenable Stainless Steel

Chemical composition of precipitation hardenable stainless steel is given Table 10.

In the heat treatment of precipitation hardenable stainless steels the processes to perform are:

Cleaning: All parts to be heat treated are first subjected to cleaning operation prior to heat treatment. The chemical composition of precipitation hardenable steels is selected very judiciously and therefore it is important that the composition does not alter due to any impurity at the surface. For example, if surface of component contains any lubricants, such as oil, etc., carburization may take place during heat treatment and this will lead to unpredictable product. The cleaning of components is carried out by techniques like abrasive blast cleaning.

Furnace atmosphere: Heat treatment of precipitation hardenable stainless steels cannot be done in any furnace which is fired with oil or natural gas as this will alter the composition of the steel, most commonly carburization. Induction furnaces or gas fired radial tube furnaces are suitable in heat treating this kind of steel. Creating controlled reducing atmosphere either in the form of dissociated ammonia or by any other means bears a risk of nitriding or carburizing, which are detrimental to the final properties of the product. Argon or helium atmosphere may be used for austenite formation at temperature 950 °C or higher. The procedures consisting of full annealing, austenite conditioning, effecting the phase transformation, and finally aging of the steel are narrated below:

- Solutionizing is carried out at temperature of 1050–1070 °C, and held there for 1 h per each 25 mm section for annealing and cooling to room temperature in water.
- Austenite conditioning is generally carried out at a temperature of 900–950 °C for a period of 1 h per 25 mm

Table 9 Chemical composition of type 329 duplex stainless steel (in wt%)

Type	*C*	*Mn*	*Si*	*Cr*	*Ni*	*P*	*S*	*Other*
329	0.20	1	0.75	23–28	2.5–5	0.04	0.03	1–2 Mo

Table 10 Composition of precipitation hardenable stainless steel (in wt%)

Type	*C*	*Mn*	*Si*	*Cr*	*Ni*	*P*	*S*	*Other*
17–7-PH	.09	1	1	16–18	6.5–7.75	0.04	0.04	0.75–1.5 Al

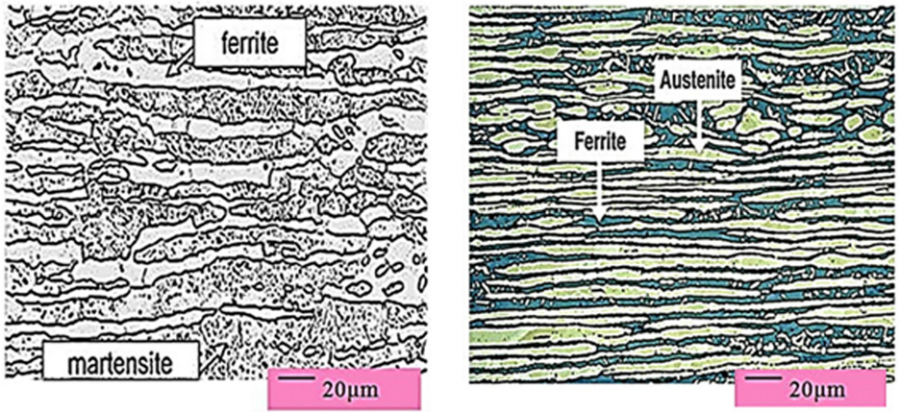


Figure 26 Typical micrographs of duplex stainless steel. International Molybdenum Association, www.imoa.info; Nippon Steel and Sumitomo Metal, www.nssmc.com (public domain).

thickness followed by air cooling or oil quenching for heaviest section.
- The transformation cooling is carried out from the solutionizing temperature by water cooling to room temperature and then cooling to subzero temperature within the range of −70 to −80 °C.
- The aging is carried out at temperature of 520–550 °C for the time period as predetermined by the final properties required, followed by air cooling.

In all cases of heat treatment of this stainless steel, furnace atmosphere must not carburize the steel under any condition. An excessive oxidizing environment is not very welcome; the carbonaceous environment inside the heat-treatment furnace is also prohibited, as this leads to carbon pick up; higher carbon pick up implies greater risk of sensitization.

Due to presence of molybdenum, 316L and 317L are prone to σ phase embrittlement[32] due to a long-time exposure between 660 and 860 °C; corrosion resistance can however be improved by stabilization annealing at 900 °C for 2–3 h; after this any stress relieving operation at 640–650 °C will not deteriorate the corrosion properties.

Heat treatment of high-nitrogen austenitic steel is exactly similar to conventional austenitic stainless steel as problems encountered due to sensitization and distortion are identical in either case. The steels like 316N or 304N are austenitized at 1020–1100 °C and following holding for 1 h per 25 mm section thickness the jobs are rapidly cooled in water.

High-alloy grade steels are heated to higher temperature range 1125–1150 °C with a specific purpose. Due to addition of high amount of molybdenum to reduce pitting corrosion and to improve high-temperature resistance, the concerned alloys are produced with very low carbon; nevertheless the steels are prone to δ ferrite formation at a high temperature of austenitization. Again at temperature just below 900 °C, these steels are susceptible to σ phase formation. Therefore neither a low temperature nor a high temperature is convenient for avoidance of property degradation. So austenitization is carried within narrow temperature regime. If stress relieving is to be carried out at a temperature lower than the annealing temperature, holding time must be of minimum possible value. Figures 27 and 28 show the microstructure of 17–4PH steels under different treatment conditions.

2.8.8 Maraging Steel

Maraging steels are ultrahigh-strength steels containing high amount substitutional alloying element at very low-carbon content. These steels are very much suitable for high-strength high-toughness applications. It is known that carbon steels with or without alloying elements derives its strength and toughness at a balanced amount by first forming martensite which is an extremely hard phase in Fe–C alloy system and is a super saturated solid solution of carbon in body centered tetragonal ferrite, this hard constituent is subsequently tempered where fine scale precipitation of carbide enables

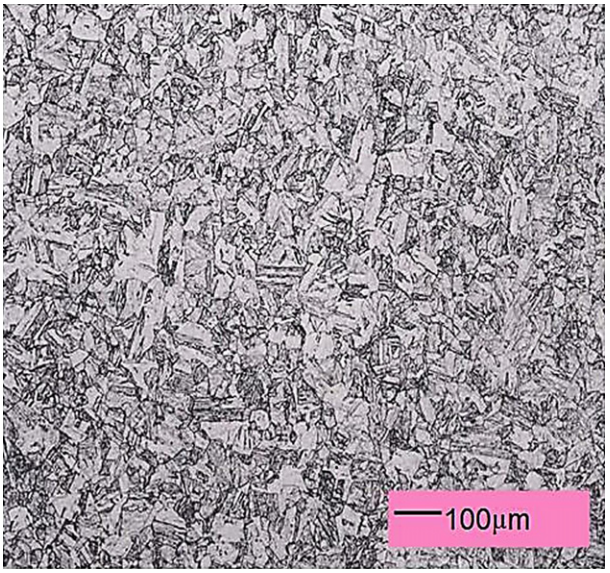


Figure 28 Microstructure of 17–4 PH steel solutionized at 1100 °C oil quenched and followed by aging at 480 °C. Courtesy: George F. Vander Voort, Director, Research and Technology, Buehler Ltd. Vander Voort, G. F. *The Microstructure of Stainless Steels*.

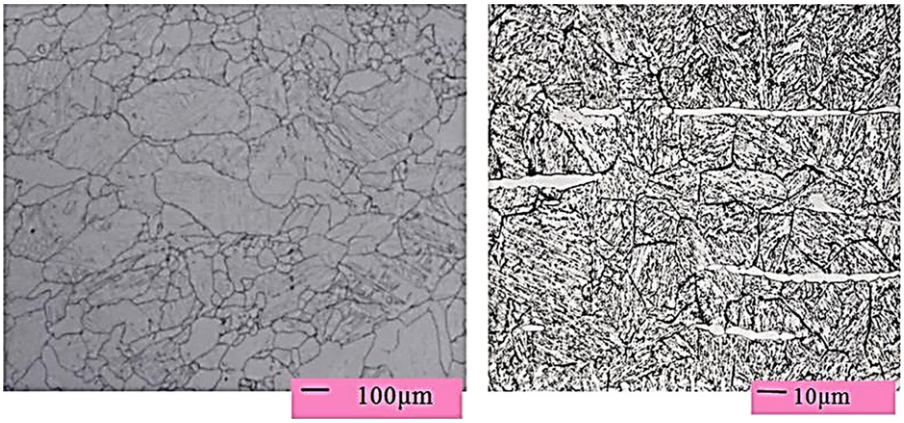


Figure 27 (a) Microstructure of 17–4PH (precipitation hardenable stainless steel) solutionized but unaged, showing austenite grain boundaries, and (b) martensite prior austenite grain boundary and delta ferrite. Courtesy: George F. Vander Voort, Director, Research and Technology, Buehler Ltd. *The Microstructure of Stainless Steels*.

Table 11 Chemical composition and properties after solutionizing at 820 °C

Alloy	*Composition*					*Properties*				
18Ni maraging steel (series)	*Ni*	*Mo*	*Co*	*Ti*	*Al*	*Y.S.*	*Ultimate tensile strength*	*%E*	*RC*	*RA*
200	18	3–3.5	8.5	0.2	0.1	~800	965–1000	17–18	28–30	72–80
250	18	~5	~7.75	0.4	0.1	750–900	1000–1140	8–16	28–35	55–70
300	18	~5	~9	0.6	0.1	760–900	1000–1170	6–15	30–32	45–60
350	18	4	12.5	1.6	0.1					

Note: Carbon content of all the steels are kept below 0.03 wt%.
Source: *ASM Hand Book*, Vol. 4; p. 529.

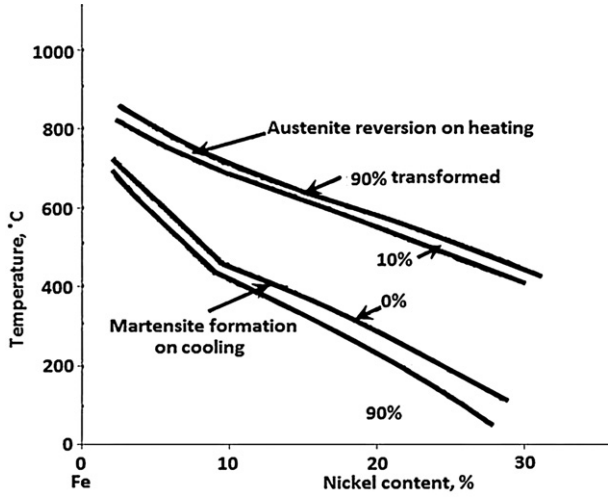


Figure 29 Metastable phase diagram of iron–nickel system. *ASM Hand Book*, Vol. 1; p. 1226.

martensite to get rid of super saturation and intimate mixture of fine ferrite and carbide particles in the microstructure confers a good amount of toughness. In contrast maraging steel produces a very soft martensite. Fe–18Ni alloy produces body centered cubic martensite which is very soft. This soft martensite is strengthened to a very high magnitude by the way of aging the martensite at an elevated temperatures; aging leads to the formation of precipitates of different kinds of thermally stable intermetallics to ensure a very high strength at a high ductility level.[33–35] Ternary or quaternary elements are added to form different intermetallics as the hardening phases.[36] It is quite easy to achieve a very high fracture toughness $\sim 150\ \text{MPa}\sqrt{m}$ at ultrahigh strength level around 1650–1700 Mpa. The nominal composition of some standard commercial maraging steels are given in **Table 11**.

Martensitic reaction is reversible; however due to large thermal hysteresis the reversion from martensite to austenite transformation is considerably delayed. It is for this reason, heating of martensite to about 600–650 °C enables intermetallic precipitates to form; these intermetallic phases are the chief hardening phases in maraging steel.

The martensite in maraging steel is formed after cooling the material from the austenitizing temperature which can be selected from the metastable equilibrium diagram **Figure 29** and the steel is held at the austenitizing temperature for sufficient time so as to make up homogenous austenite phase. This austenite is of FCC crystal structure and after cooling it transforms to BCC martensite through diffusion less shear transformation.

The transformation takes place until M_s temperature is reached and the M_s temperature of most of the varieties of maraging steel ranges between 200 and 300 °C. This implies that maraging steels are fully martensitic at room temperature. These martensites are internally faulted with dislocations due to lattice invariant deformation. The lath martensites in maraging steels do not contain any reversible faults like twins. The alloying elements added to maraging steels influence the M_s temperature but the CCT diagram of the steel would indicate that diffusional decomposition of austenite in this maraging steel is not possible (*ASM Metal Hand Book, Vol.4*). Thus the microstructure of Fe–18%Ni maraging steel is comprised of lath martensite. If nickel percentage is increased beyond 25 wt.%, the martensite becomes internally twinned so as to accommodate macroscopic shape deformation accompanying martensitic transformation.

Most of the maraging steels contain cobalt, which enables the addition of those alloying elements which lowers the M_s temperature but can form intermetallic phases. The main task of strengthening maraging steels is to produce 100% martensite, which upon aging must experience adequate amount of precipitate formation. This leads to age hardening. To assist the formation of different intermetallics, addition of titanium, aluminum, molybdenum etc., are mandatory. However all these elements are known to lower the M_s temperature. Unless M_s temperature is kept at a high level it is not possible to produce 100% martensite; the M_s temperature must be kept around 200–300 °C and cobalt assists in achieving the desired M_s temperature.

Cobalt is the only alloying element, known to raise M_s temperature in maraging steels; so addition of cobalt up to 6–8% nullifies the effect of other elements in depressing the M_s temperature, which otherwise are considered to be very important alloying elements to give rise to precipitation hardening. Since retained austenite is not a concern in most of the commercially available maraging steels, subzero treatment prior to aging is not needed. However if addition of alloying elements like Mo, Ti, and Al are done at a high level, retained austenite may occur in the microstructure and this retained austenite is considered to be a highly unwanted phase in maraging steel.

There are two possibilities during aging of maraging steels, which are:

1. Firstly, the reversible transformation of martensite to austenite, if the selected aging temperature lies above the austenite start temperature.

2. Second, formation of aging precipitates, while the martensite is heated to a temperature below the austenite start temperature.

Aging for a prolonged period of time at a relatively high temperature may lead to formation of high-alloy austenite, known as reverted austenite. This kind of reversion reaction takes place quite significantly, if aging is done at a temperature higher than 550 °C.

Like all other age hardening systems, maraging steels have their own characteristic aging sequences. The elements like Ti and Be act as strong hardeners, whereas the alloying elements like Al, Ni, Mo, Mn, Si, tantalum, tungsten, and niobium leads to moderate hardening. Again there are elements like Co, Cu, and Zr which are known as weak hardeners.[37,38]

In a molybdenum bearing alloy, metastable Ni_3Mo of orthorhombic crystal structure is commonly observed as precipitate phase; this forms on dislocations or at the lath boundaries. In case of titanium containing steels the precipitated phase is identified as Ni_3Ti which has high potential for strengthening the steel.

Cobalt does not directly take part in aging reaction but a phenomenon called Co–Mo interaction lends a definite contribution to the aging effect of maraging steels. Cobalt is known to reduce the solubility of Mo in BCC matrix; as a result higher volume fraction of fine sized Ni_3Mo precipitates are formed in maraging steel containing cobalt and molybdenum. Molybdenum and cobalt exert synergistic effect on strengthening of maraging steels.

2.8.8.1 Heat-Treatment Sequence of Maraging Steels

The different steps followed in the heat treatment of maraging steel is shown schematically in the **Figure 30**.

Solutionizing: As stated earlier the first stage of heat treatment of maraging steels is solution-annealing treatment, carried out at a temperature sufficiently above the austenite finish temperature. In general the commercial variety of maraging steels is solutionized at 815–825 °C for 1 h per each 20 mm thickness of workpiece. It is advisable to have controlled atmosphere furnace and many a times inert gas atmosphere like jet of nitrogen and argon at a positive pressure is considered suitable for the heat treatment of maraging steels; this is because maraging steels are prone to the chemical degradation during heating at a high temperature.

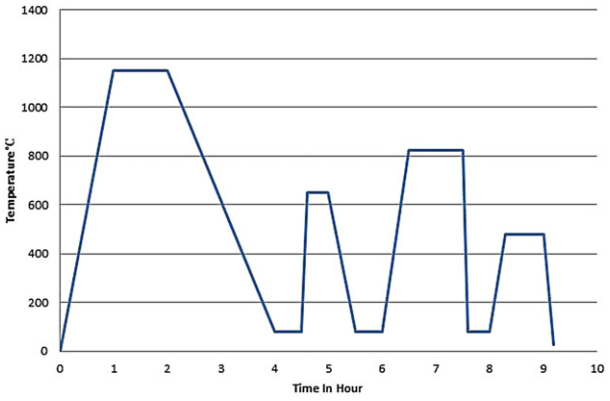


Figure 30 Heat treatment of maraging steel.

Casting of maraging steels are subjected to annealing treatment by heating them to a high temperature like 1150 °C followed by air cooling. Subsequent to this high-temperature treatment the material is reheated to 600 °C held for 1 h and then cooled in air.

The 600 °C heating realizes the formation of reverted austenite which gets distributed throughout the matrix. These reverted austenite particles act as the nucleation sites during the following solutionizing treatment, so that a fine grained austenite can be formed.

After solutionizing, maraging steels are cooled to room temperature. The rate of cooling is of less significance because formation of martensite in maraging steel is inevitable as per dictates of CCT diagram. However it is to be understood that the cooling must be carried out till room temperature, so that 100% martensite formation is envisaged. Because maraging steel is quite strong and the volume change in martensitic transformation of maraging steels is quite small, these steels are not susceptible to quench cracking. Martensite formed after cooling is aged at a temperature between 480 and 500 °C. The microstructure of quenched and aged maraging steel of type of grade 18Ni250 is shown in **Figure 31**. The two microstructures of the same sample at different magnifications essentially demonstrate the presence of martensite phase without any evidence of reverted austenite phase; the presence of precipitates, though hinted in **Figure 31** must require confirmation by high-resolution microscopy. As stated earlier the aging temperature should be kept below 500 °C so as to avoid reversion reaction. By aging at this temperature the commercial maraging steels attain a hardness value of HRc 52–54. The properties of the maraged alloys are shown in the **Table 11**.

2.8.8.2 Embrittlement in Maraging Steel

If maraging steel contains carbon in excess of 0.03 wt% and is alloyed with Ti, there is a great chance of forming precipitates of titanium carbides and titanium carbonitride phases which form at the prior austenite grain boundaries.[39,40] However proper heat treatment can avoid this unwanted precipitation. Nevertheless, embrittlement becomes inevitable due to heating maraging steel at high temperature, i.e., 1180 °C and above, where all carbon atoms in maraging steel go in solution in austenite followed by slow cooling or holding the steel at a temperature region of 750–1050 °C. Precipitation of carbon takes place as grain boundary phase and thus embrittlement results. However if it is required to heat this steel to such a high temperature as in casting, the cooling of the steel from the high temperature must be quite rapid through the temperature region of 1100–750 °C so that the precipitation of carbon at grain boundaries can be avoided and hence the problem of embrittlement can be overcome.

The typical age hardening temperature ranges between 450 and 550 °C with long holding time say 4–12 h; subsequent cooling is done in air. However the time and temperature used for tempering of maraging steels are quite important to determine the final properties of the steel. In initial period of aging the hardening is quite rapid but beyond a definite period

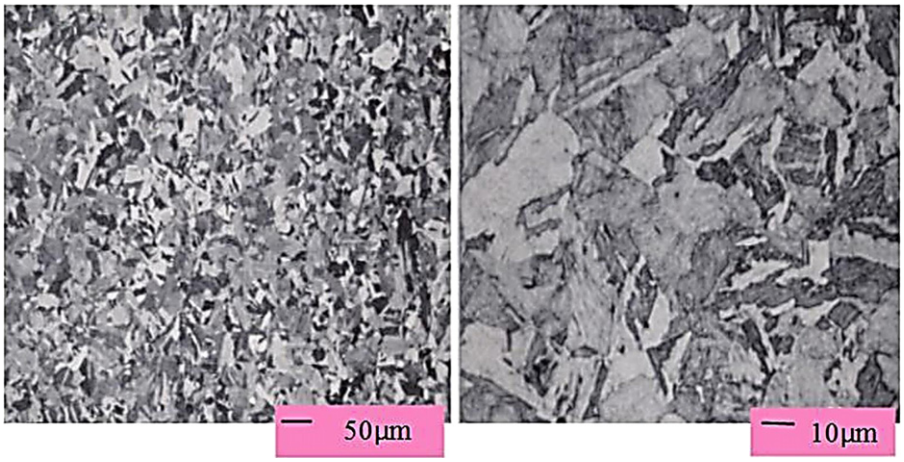


Figure 31 Microstructures of 18Ni250 maraging steel showing martensite after solutioning and aging. Courtesy: George F. Vander Voort, Director, Research and Technology Buehler Ltd. Vander Voort, G. F. *The Microstructure of Ferrous Alloys*.

of aging, particle coarsening takes place and the hardness of the maraging steel reduces. If aging is carried out at a low temperature, the particle coarsening will not be there and age hardening curve may be seen to be a continuous hardening curve. Nevertheless the hardness of the aged martensite must be kept around HR_C 52–53 in order to achieve the desired tensile strength of the order of 2000–2500 MPa.

2.8.9 Heat Treatment of Transformation Induced Plasticity Steel

Transformation induced plasticity (TRIP) steel is a class of steel with ferrite–bainite microstructure and is capable of providing TRIP. Normally these types of ferrite–bainite steels contain a good amount of retained austenite due to incomplete bainitic reaction. These low-carbon steels containing around 0.15% C with silicon of the order of 1.7%, are intercritically annealed so that under equilibrium at the intercritical annealing temperature, a mixed ferrite–austenite microstructure exists. The austenite in the intercritical region is richer in carbon and is given to react isothermally in the bainitic region. The decomposition of austenite to bainite does not go to completion due to formation of low-carbon bainitic ferrite.

The retained austenite is thermally stable due to high solute content, which decreases the M_s temperature to below room temperature.[41,42] However *Md* temperature, the temperature below which martensite transformation may take place by stress induced mode, is very near to room temperature for this kind of steels and any crack propagating through the material will have high-stress concentration ahead of it. If a moving crack comes across a retained austenite particle present in microstructure, the mechanically unstable austenite undergoes stress induced martensitic transformation. These hard martensites are required to be fractured if crack is to propagate through these particles. Since the stress concentration ahead of crack tip is not so high as to be able to fracture the hard martensite, the crack stops propagating. Thus effective plasticity is artificially improved.

The heat treatment of TRIP steel is therefore as follows:

- Normalizing is done by heating the steel to 900 °C and holding there for suitable period of time followed by cooling in still air.
- Heating at intercritical temperature say 750 °C, holding there for specified period of time which depends upon section size. The holding time must be sufficiently high to achieve equilibrium. At this temperature the microstructure of the steel consists of ferrite–austenite mixture of composition as may be deduced from **Figure 32(a)**.
- The steel is then quenched in a bath kept at temperature 350–250 °C; the austenite transforms to bainite (**Figure 32(b)**). Due to incomplete bainitic reaction some high-solute austenite is retained within bainite and this is responsible to impart TRIP. The heat-treatment cycle is shown in **Figure 32(c)**.

2.8.10 Dual Phase Steels

Duplex ferrite martensite steels are first generation AHSSs and are employed in automotive sectors. The composition of a commercial grade dual phase steel, DP500 is given in **Table 12**.

The microstructure of dual phase steel comprises of martensite islands in a matrix of ferrite. The steel is heated to some intercritical temperature, T_i and held there for sufficient time so as to attain equilibrium between two phases, ferrite and austenite. **Figure 32(a)** shows that at temperature T_i, ferrite of composition Z is in equilibrium with austenite of composition Y and after equilibration the steel is rapidly quenched to room temperature.[44,45] High-carbon austenite transforms to martensite and the microstructure is comprised of islands of martensite in the matrix of ferrite as shown in **Figure 33**.

The CCT diagram of this steel along with heat-treatment cycle is shown in **Figure 34**. It is to be understood that the formation of high-carbon martensite is associated with large magnitude of volume change. This volume change is accommodated with the surrounding rigid matrix by way of dislocation, as shown in **Figure 34**.

The transmission electron microstructure is shown in **Figure 35**. It clearly shows huge dislocation in ferrite matrix

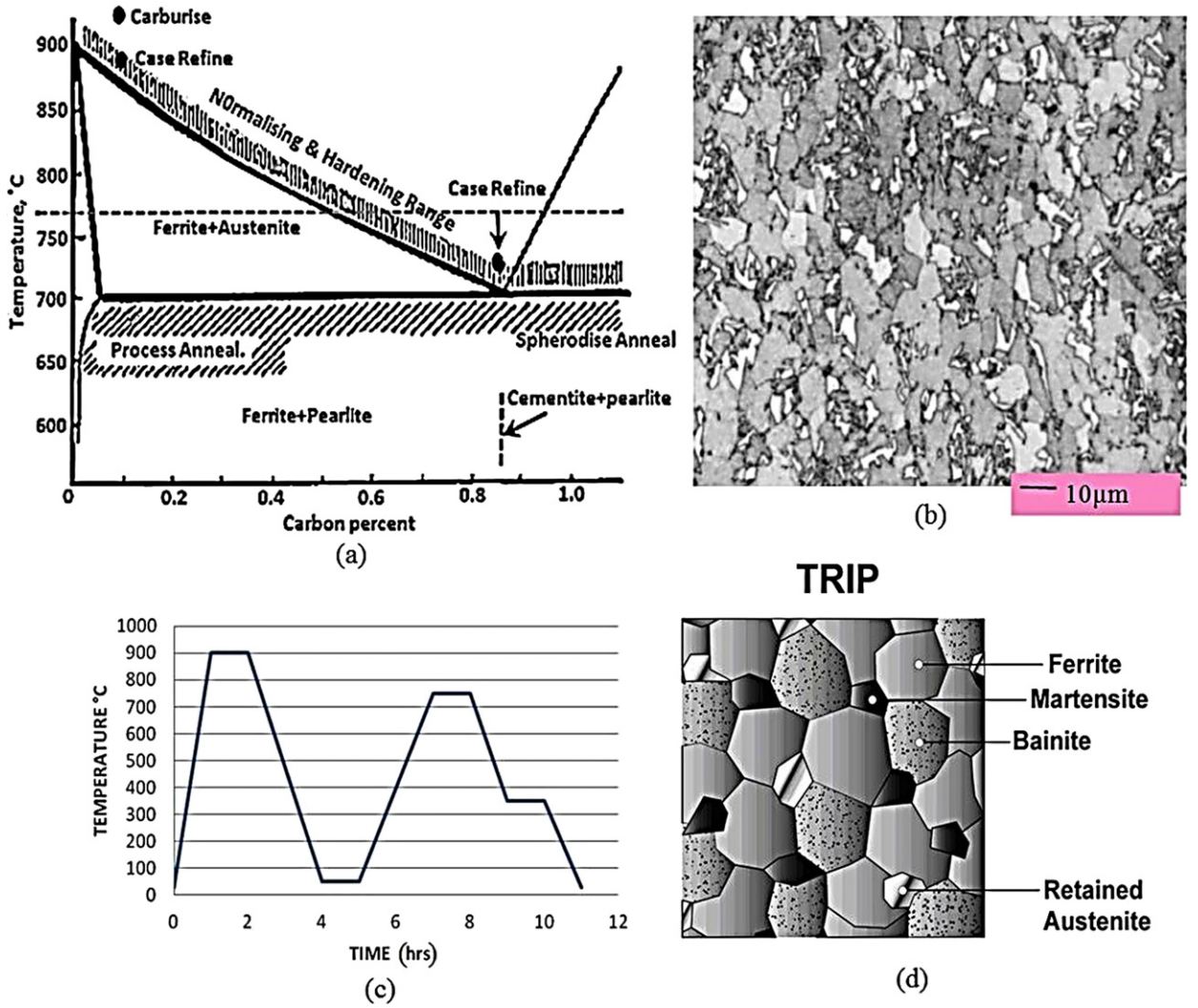


Figure 32 (a) Intercritical annealing temperature shown by a line, (b) Optical photomicrograph of duplex ferrite–bainite TRIP steel,[43] (c) heat-treatment cycle of TRIP steel, and (d) schematic microstructure of TRIP steel. (b) Andrade-Carozzo, V.; Jacques, P. J. Interactions between Recrystallisation and Phase Transformations during Annealing of Cold Rolled Nb-Added TRIP-Aided Steels. *Mater. Sci. Forum* **2007**, *539–543*; 4649; (c), (d) www.worldautosteel.org (public domain).

Table 12 Chemical composition of DP500 Steel (in wt%)

Fe	C	Si	Mn	P	S	N	Cr	Ti	Ni
98.2	0.06	0.308	0.007	0.007	0.005	0.012	0.027	0.002	0.035
V	Sn	Nb	As	Zr	W	Co	Pb	Mo	Al
0.009	0.057	0.057	0.002	<0.010	<0.010	0.005	<0.001	<0.001	0.226

surrounding the martensite crystals. The martensite itself is also highly dislocated due to lattice invariant deformation.

Thus commercial dual phase steel is intercritically annealed and rapidly quenched in water. Due to fast quenching, the ferrite remains supersaturated. These steels are also subjected to another heat treatment called 'Bake hardening.' Bake hardening is a process where the component after being painted is baked at low temperature viz. 160–170 °C. At this temperature the carbon in solution in ferrite becomes more mobile and can migrate to the nearby dislocations if available.

From the heat-treatment schedule of dual phase steel, it appears that the islands of martensite can be made homogeneous and uniformly distributed throughout the matrix. It may lead to a very uniform distribution of dislocations generated around individual martensite particle. The steel is now painted and then baking is carried out by annealing the steel at low temperature of 160 °C. The carbon from supersaturated ferrite starts migrating to dislocations around martensite particles and locks the dislocation. This is typically similar to strain aging and yield strength of steel is improved.[47,48]

2.8.10.1 Rapid Heating Producing Ultrafine Grained Dual Phase Steel

Ultrafine grained duplex ferrite–martensite steels leads to further improvement in properties than the classical dual phase steel. Thermomechanical treatment carried out before intercritical annealing heat treatment has been known to have produced fine grained ferrite in dual phase steels. However through the employment of rapid heating it is also possible to develop very fine microstructures in steels using rapid transformation annealing technique. Steel containing 0.17 wt.% carbon 0.85 wt.% manganese can be subjected to rapid heating technology to produce ultrafine grained ferrite in dual phase steel. The initial microstructure can be fine ferrite – pearlite structure or the tempered martensitic structure. The rapid heating at the rate of 300 C s^{-1} produces austenite at a high degree of superheating; the degree of superheating is the decisive factor in fixing the energy of nucleation ΔG_{max}. Transformation at high superheat reduces the critical nucleus size of austenite as well as the energy of nucleation.[49,50] This leads to formation of ultrafine austenite which upon transformation produces fine microstructure. A low holding time does not allow grain coarsening and so fine structure formation is possible.

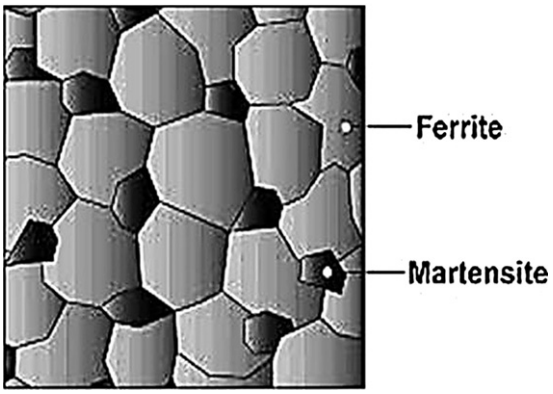


Figure 33 Ferrite–martensite structure in a dual phase steel. www.worldautosteel.org (open).

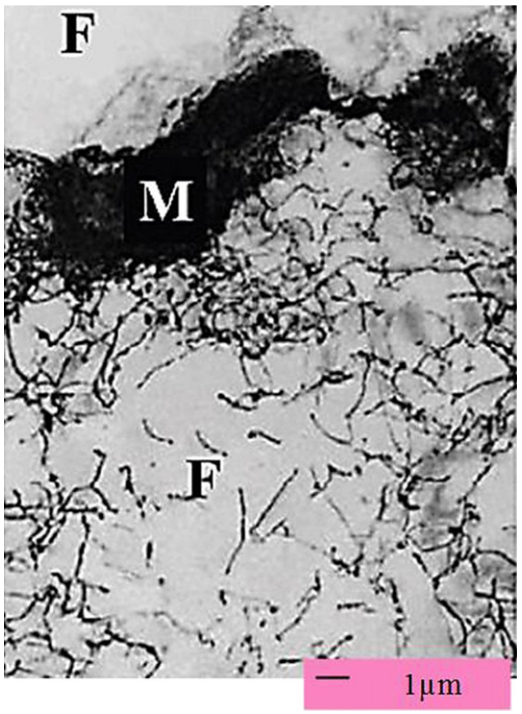


Figure 35 Transmission electron micrograph of dual phase steel showing dislocations around martensite.[46] Chang Peng-Heng. Temper-Aging of Continuously Annealed Low Carbon Dual Phase Steel. *Metall. Trans. A* **1984**, *15.1*; pp. 73–86.

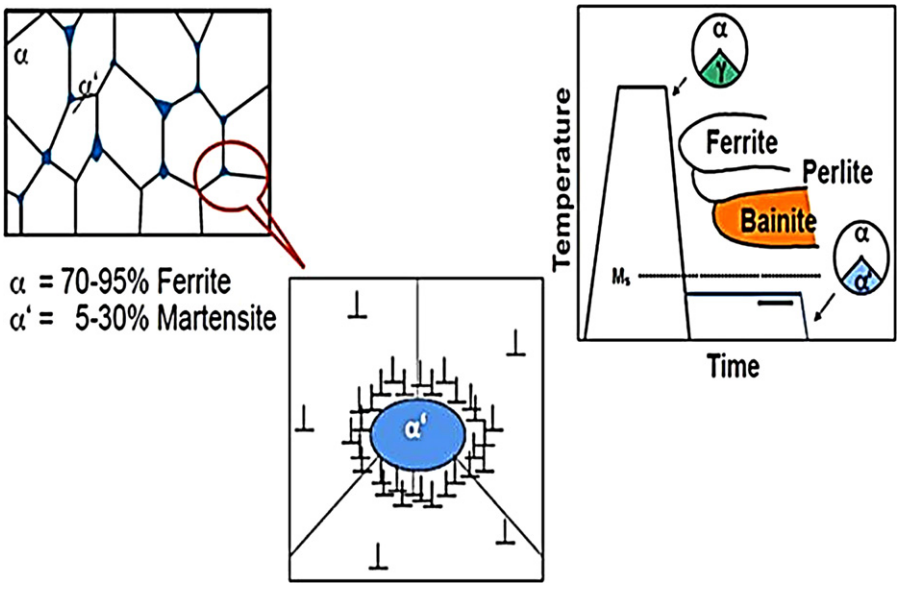


Figure 34 Dual phase steel showing dislocations around martensite particle and time temperature relationship. Presentation by Prof. Bleck on "Dual Phase Steel DP500", Chemistry, Microstructure processing, RWTH AACHEN University.

2.8.10.2 Bake Hardened Dual Phase Steels

Bake hardening has now been recognized as an effective heat treatment to impart extra strengthening in AHSSs. Bake hardening is essentially a strain aging treatment. The stretch formed steel panels are subjected to a small amount of prestrain; this prestrain introduces dislocations. The ferrite in these steels contains 15–20 ppm carbon in solid solution. The prestrained steel panels are painted and then given to bake at 170 °C. At this temperature the carbon atoms in ferrite become more mobile and migrate to the nearby dislocations. The carbon atoms are segregated there and creates Lomer Cottrell atmosphere; the dislocations are anchored by these carbon atoms. Extra stress is therefore required for dislocations to get away from the above Lomer Cottrell barriers and thus the steels experience extra strengthening, known as bake hardening.[51–54] However it is apparent that for bake hardening to be uniformly effective, the dislocation population should be quite high and should be uniform in distribution. In case of dual phase steel, it is possible to have uniform distribution of numerous martensite islands of high carbon content. The volume strain accompanying Bain distortion creates dislocation around martensite particles. Numerous the martensite regions higher is the uniformity in dislocation distribution and thus bake hardening will be more effective. Similar possibility exists in TRIP aided dual phase ferrite bainite steels. In this case it is required to have a uniform distribution of bainitic regions around which one may expect dislocations to be present. So, proper heat treatment to produce ferrite bainite steels with finely divided bainitic regions throughout the matrix envisages efficient bake hardening.

2.8.11 Heat Treatment of Steel Casting

Heat treatment of steel casting is a tricky job as most of the commercial C–Mn steel castings show cellular dendritic segregation of impurity elements along the grain boundary. In order to achieve a uniform property of steel castings a judicious heat-treatment strategy must be adopted.

Let us take the example of heat treatment of steel castings made of the following composition: 0.28–0.32% C; 1.5–1.7% Mn; 0.4–0.6% Si; 0.25–0.3% Mo; and 0.025% S, P maximum. This steel casting is very commonly used in railways. The heat treatment to secure uniform properties in this steel are:

- Homogenization: Since the impurity elements like Si, Mn, etc., are segregated at the grain boundary, the casting must be homogenized to destroy dendritic structure. To get homogenized microstructure in the casting, component must be heated to a very high temperature, where mobility of substitutional alloying element is quite high and the homogeneous composition of austenite is obtained. The heat treatment is carried out in between 1050 and 1100 °C or higher. If the steel is deoxidized by aluminum or if it contains microalloying element like Ti, V, or niobium, the steel will be inherently fine grained and will exhibit resistance to coarsening. The fine precipitation of AlN or Ti(C, N) inhibits grain boundary movement and hence retard tendency for grain coarsening.

However choice of avoidance of grain coarsening and decarburization is not included in the concept of homogenization, especially when major target of the process is to completely eliminate the microsegregation. Sufficient time is allowed for soaking at high-homogenizing temperature and the exact time is to be decided under the perspective of plant condition. The total charge, with spacing between the charges, the weight of individual item will all decide the total time for homogenization. After soaking, the steel casting should be allowed to cool slowly. The cooling rate is to be as slow as possible. Cooling process may be stopped when temperature of charge inside the furnace reaches 400 °C.

- After the homogenization, conventional annealing is done for which the steel castings are heated within the temperature range of 880–900 °C and held there for 1 h per each 25 mm section thickness; following this the castings are cooled in furnace. Where conventional annealing is not required, the casting may be normalized after homogenization annealing. For this the charge is heated to 860–880 °C and held there for 1 h per 25 mm of thickness.

  After soaking at a higher temperature, when the pallet/tray is taken out for quenching, there may be quenching delay irrespective of the efficacy of the available material handling system, unless the entire process is automated through robotics. Heat treater must raise the temperature of the charge by 20–30 °C higher than the stipulated temperature such that the unavoidable delay in quenching can be taken care.
- In normalizing special care must be taken during cooling. If castings are stacked in layers, the cooling of the over lying casting, releases heat which interferes with the cooling of the adjoining casting thereby creating a very complex situation in respect of achieving predictable cooling rate for all the castings put inside the furnace.

  It is wiser to make use of adequate number of cooling fans positioned at different location, which may ensure a better cooling of castings during normalizing. Sometimes forced air quenching is a recommended heat-treatment process.
- After normalizing, tempering is required to be carried out to achieve desired properties. The castings are then put in tempering furnace and tempering is performed normally in the temperature range of 500–550 °C and held there for the preselected period of time. As discussed earlier, the time and the temperature of holding are decided on the basis of final property requirements.

The above example is a generic heat-treatment cycle of steel casting as can be seen in Figure 36. The time, temperature, or

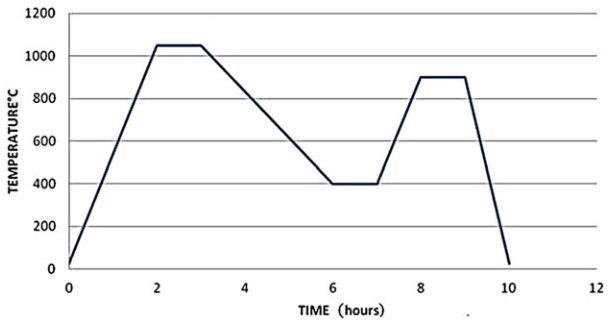


Figure 36 Heat-treatment cycle for steel casting.

the nature of process may be different in cases where different kinds of alloy steels are heat treated. Nevertheless, homogenization at high temperature, conventional full annealing, normalizing, and finally tempering are the basic steps in heat treatment of steel casting.

In industrial situation another major problem is related to material handling.

This particular issue is very critical in case the heat treatment of casting which requires quenching in oil, water, or any other solvent.

See also: 2.1 Fundamentals of Heat Treating Metals and Alloys. 2.2 Hardenability of Steel

References

1. Murugan, V. K.; Koshy Mathews, P. Effect of Tempering Behavior on Heat Treated Medium Carbon (C35 Mn75) Steel. *Int. J. Innov. Res. Sci. Eng. Technol.* **2013**, *2* (4), 945–950.
2. Nürnberger, F.; Grydin, O.; Schaper, M.; Bach, F.-W.; Koczurkiewicz, B.; Milenin, A. Microstructure Transformations in Tempering Steels during Continuous Cooling from Hot Forging Temperatures. *Steel Res. Int.* **2010**, *81* (3), 224–233.
3. Caminaga, C.; Button, S. T. Mechanical Properties of Ausforged 27MnSiVS6 Microalloyed Steel. *Metall. Mater., REM:R.Esc Minas, Ouro Preto* **2013**, *66* (3), 331–338.
4. Magnee, A.; Drapier, J. M.; Dumont, J.; Coutsouradis, D.; Habraken, L. *Cobalt-Containing High-Strength Steels*; Centre d'Information du Cobalt: Brussels, 1974.
5. Handerhan, K. J.; Garrison, W. M., Jr.; Moody, N. R. A Comparison of the Fracture Behavior of Two Heats of the Secondary Hardening Steel AF1410. *Metall. Trans. A* **1989**, *20*, 105–123.
6. Novotny, P. M.; Dahl, J. M. Aermets 100 Alloy for Aerospace Structural Applications. In *Proceedings of the 32nd Mechanical Working and Steel Processing Conference*; Iron and Steel: Society: Warrendale, PA, 1991; pp. 275–281.
7. Bray, J. W.; Maloney, J. L.; Raghavan, K. S.; Garrison, W. M., Jr. A Comparison of the Fracture Behavior of Two Commercially Produced Heats of HY180 Steel Differing in Sulfide Type. *Metall. Trans. A* **1991**, *22*, 2277–2285.
8. Maloney, J. L. The Effect of Primary Void Nuclei on the Fracture Initiation Toughness of Ultra High Strength Steels (Ph.D. thesis); Pittsburgh, PA: Carnegie Mellon University, 1992.
9. Novotny, P. M. An Aging Study of Carpenter Aermets 100 Alloy. In *Speich Symposium Proceedings*; Krauss, G., Repas, P. E., Gilbert, R., Eds.; Iron and Steel Society: Warrendale, PA, 1992; pp. 215–236.
10. Iorio, L. E.; Maloney, J. L.; Garrison Jr., W. M. The Influence of Carbon, Chromium, and Molybdenum Contents on the Tempering Behavior of High Strength 14 Cobalt/10nickel Secondary Hardening Steels. In *Proceedings of the 40th Mechanical Working and Steel Processing Conference*. Iron and Steel Society: Warrendale, PA, 1998; pp. 901–919.
11. Wang, L.; Liu, L.; Cheng Xiao; Liu, X.; Chen, C.; Kang, M. Investigation of Transformation for Ultrahigh Strength Steel AerMet 100. *J. Mater. Sci. Tech.* **2000**, *16* (5), 491–494.
12. Bian, J.; Mohrbacher, H. Novel Alloying Design for Press Hardening Steels with Crash Performance. In *International Symposium on New Developments in AHSS*, PR-294–026–2013, USA. Available at: www.niobelcon.com/NiobelCon/publications_files (accessed February 17, 2016).
13. Jiao, Z. B.; Luan, J. H.; Miller, M. K.; Liu, C. T. Precipitation Mechanism and Mechanical Properties of an Ultra High Strength Steel Hardened by Nano Scale NiAl and Cu Particles. *Acta Mater.* **2015**, *97*, 58–67.
14. Schuller, R.; Fitzka, M.; Irrasch, D.; Tran, D.; Pennings, B.; Mayer, H. VHCF Properties of Nitrided 18Ni Maraging Steel Thin Sheets with Different Co and Ti Content. *Fatigue Fract. Eng. Mater. Struct.* **2015**, *38* (5), 518–527.
15. Saunders, N.; Guo, Z.; Li, X.; Miodownik, A. P.; Schille, J. P. The Calculation of TTT and CCT Diagram of General Steels. Available from: www.sentesoftware.co.uk/media/2540/ttt_cct_steels (accessed July 4, 2011); Atlas of Isothermal Transformation Diagrams of BS En Steels, Special Report No. 56; The Iron and Steel Institute: London, 1956.
16. Sharma, S. S.; Jagannath, K.; Bhat, C. Effect of Heat Treatment on Mechanical Properties of AISI 4147 Spring Steel. In *3rd International Conference on Mechanical, Automotive and Materials Engineering (ICMAME'2013)*, Singapore, April 29–30, 2013; pp. 102–106.
17. Htun, M. S.; Kyaw, S. T.; Lwin, K. T. Effect of Heat Treatment on Microstructures and Properties of Spring Steel. *J. Min. Met. Mats.* **2008**, *18* (2), 191–197.
18. Park, J. T.; Szpunar, J. A. Effect of Initial Grain Size on Texture Evolution and Magnetic Properties in Nonoriented Electrical Steels. *J. Magn. Magn. Mater.* **2009**, *321*, 1928–1932.
19. Dorner, D.; Zaefferer, S.; Lahn, L.; Raabe, D. Overview of Microstructure and Microtexture Development in Grain-Oriented Silicon Steel. *J. Magn. Magn. Mater.* **2006**, *304* (2), 183–186.
20. Ramadan, R.; Ibrahim, S. A.; Farag, M.; Elzatahry, A. A.; Es-Saheb, M. H. Processing Optimization and Characterization of Magnetic Non Oriented Electrical Silicon Steel. *Int. J. Electrochem. Sci.* **2012**, *7*, 3242–3251.
21. Henger, F.; Lucas, G.; Nyberg, B. Mid-Temperature Transformation in Bearing Steel. *HTM* **1974**, *2*, 71–79.
22. Hsu, T. Y.; Chen Yexin; Chen Weiye. Isothermal Martensite Formation in an AISI 52100 Ball Bearing Steel. *Metall Trans A* **1987**, *18.8*, 1389–1394.
23. Hosseini, S.; Limooei, M. B. Optimization of Heat Treatment to obtain desired Mechanical Properties of High Carbon Hadfield Steel. *World Appl. Sci. J.* **2011**, *15* (10), 1421–1424.
24. Burier, H. *ASM Handbook, Vol. 1: Properties and Selection of Iron Steels and High Performance Alloys*; ASM International Handbook Committee: Materials Park, OH, 1987; pp. 380–388.
25. Tęcza, G.; Sobula, S. Effect of Heat Treatment on Change Microstructure of Cast High-Manganese Hadfield Steel with Elevated Chromium Content. *Arch. Foundry Eng.* **2014**, *14*, 67–70.
26. Curiel-Reyna, E.; Contreras, J.; Rangel-Ortis, T.; *et al.* Effect of Carbide Precipitation on the Structure and Hardness in the Heat-Affected Zone of Hadfield Steel After Post-Cooling Treatments. *Mater. Manuf. Process.* **2007**, *23*, 14–20.
27. Isfahany, A. N.; Saghafian, H.; Borhani, G. The Effect of Heat Treatment on Mechanical Properties and Corrosion Behavior of AISI420 Martensitic Stainless Steel. *J. Alloy. Compd.* **2011**, *509* (9), 3931–3936.
28. Leem, D. S.; Lee, Y. D.; Jun, J. H.; Choi, C. S. Amount of Retained Austenite at Room Temperature after Reverse Transformation of Martensiteto Austenite in an Fe–13% Cr–7% Ni–3% Si Martensitic Stainless Steel. *Scr. Mater.* **2001**, *45* (7), 767–772.
29. de Andrés, C. G.; Caruana, G.; Alvare, L. F. Control of M 23 C 6 Carbides in 0.45 C–13Cr Martensitic Stainless Steel by Means of Three Representative Heat Treatment Parameters. *Mater. Sci. Eng.* **1998**, *241*, 211–215.
30. Martins, M.; Casteletti, L. C. Heat Treatment Temperature Influence on ASTM A890 GR 6 A Super Duplex Stainless Steelmicrostructure. *Mater. Charact.* **2005**, *55*, 225–233.
31. Lee, K. M.; Cho, H. S.; Choi, D. C. Effect of Isothermal Treatment of SAF 2205 Duplex Stainless Steel on Migration of δ/γ Interface Boundary and Growth of Austenite. *J. Alloy. Compd.* **1999**, *285*, 156–161.
32. Sieurin, H.; Sandström, R. Sigma Phase Precipitation in Duplex Stainless Steel 2205. *Mater. Sci. Eng.: A* **2007**, *444* (1–2), 271–276.
33. Beiber, C. G. Progress with 25% Nickel Steels for High Strength Applications. *Met. Prog.* **1960**, *78 (* (November), 99–100.
34. Peters, D. T.; Cupp, C. R. The Kinetics of Aging Reactions in 18 pct Ni maraging steels. *Trans. Metall. Soc. AIME* **1966**, *236*, 1420–1429.
35. Floreen, S. The Physical Metallurgy of Maraging Steels. *Metall. Rev.* **1968**, *13*, 115–128.
36. Asayama, Y. Effect of Chromium on the Precipitation Behavior and Notch Toughness of Fe–Ni–Ti Maraging Steels. In *Maraging Steels: Recent Developments and Applications*; Wilson, R. K., Ed.; TMS: Warrendale, PA, 1988; pp. 295–311.
37. Decker, R. F.; Floreen, S. Maraging Steels – The First 30 Years. In *Maraging Steels: Recent Developments and Applications*; Wilson, R. K., Ed.; TMS: Warrendale, 1988; pp. 1–38.
38. Schnitzer, R.; Schober, M.; Zinner, S.; Leitner, H. Effect of Cu on the Evolution of Precipitation in an Fe–Cr–Ni–Al–Ti Managing Steel. *Acta Mater.* **2010**, *58* (10), 3733–3741.
39. Cox, T. B.; Low, J. R. An Investigation of the Plastic Fracture of AISI 4340 and 18 Nickel-200 Grade Maraging Steels. *Metall. Trans.* **1974**, *5*, 1457–1470.
40. Kalish, D.; Rack, H. J. Thermal Embrittlement of 18Ni(350) Maraging Steel. *Metall. Trans.* **1971**, *2*, 2665–2672.

41. Masek, B.; Stankova, H.; Novy, Z.; Meyer, L. W.; Kracik, A. The Influence of Thermomechanical Treatment of TRIP Steel on Its Final Microstructures. *J. Mater. Eng. Perform.* **2009**, *18* (4), 385–389.
42. Sadhukhan, S.; Das, K. P.; Bandyopadhyay, N. R.; Banerjee, M. K. TRIP in Low Silicon High Manganese Boron Treated Duplex Ferrite-Bainite Steel. *J. Inst. Engineers (India), Metall. Mater. Sci. Div. (India)* **2001**, *82*, 65–68.
43. Andrade-Carozzo, V.; Jacques, P. J. Interactions between Recrystallisation and Phase Transformations during Annealing of Cold Rolled Nb-Added TRIP-Aided Steels. *Mater. Sci. Forum* **2007**, *539–543*, 4649.
44. Hansen, S. S.; Pradhan, R. R. Structure–Properties Relationships and Continuous Yielding Behaviour in Dual Phase Steels. In *Fundamental of Dual Phase Steels*; Kot, R. A., Bramfitt, B. L., Eds.; TMS-AIME: Warrendale, USA, 1981; pp. 113–144.
45. Lis, J.; Lis, A. K.; Kolan, C. Processing and Properties of C–Mn Steel with Dual-Phase Microstructure. *J. Mater. Process. Technol.* **2005**, *162*, 350–354.
46. Chang Peng-Heng. Temper-Aging of Continuously Annealed Low Carbon Dual Phase Steel. *Metall. Trans. A* **1984**, *15.1*, 73–86.
47. Lou, S.; Northwood, D. O. Effect of Temperature on the Lower Yield Strength and Static Strain Ageing in Low-Carbon Steels. *J. Mater. Sci.* **1995**, *30.6*, 1434–1438.
48. Davies, R. G. Early Stages of Yielding and Strain Aging of a Vanadium-Containing Dual-Phase Steel. *Metall. Trans. A* **1979**, *10.10*, 1549–1555.
49. Lesch, C.; Álvarez, P.; Bleck, W.; Gil Sevillano, J. Rapid Transformation Annealing: a Novel Method for Grain Refinement of Cold-Rolled Low-Carbon Steels. *Metall. Mater.Trans.* **2007**, *38A*, 1882.
50. Azizi-Alizamini, H.; Militzer, M.; Poole, W. J. Formation of Ultarfine Grained Dual Phase Steel through Rapid Heating. *ISIJ Int.* **2011**, *51* (6), 958–964.
51. Dehghani, K.; Jonas, J. J. Dynamic Bake Hardening of Interstitial-Free Steels. *Metall. Mater. Trans.* **2000**, *31A*, 1375–1384.
52. De, A. K.; Vandeputte, S.; De Cooman, B. C. Bake Hardening in Ultra-Low Carbon Steel. *Scr. Mater.* **2001**, *44*, 695–700.
53. Banerjee, M. K. Microstructural Engineering of Dual Phase Steel to Aid in Bake Hardening. *Adv. Mat. Res.* **2015**, *4* (1), 1–12.
54. Zhao, J. Z.; De, A. K.; De Cooman, B. C. A model for the Cottrell Atmosphere Formation During Ageing of Ultra Low Carbon Bake Hardening Steel. *ISIJ Int.* **2000**, *40* (7), 725–730.

Further Reading

ASM (American Society for Metals) Handbook, Vol. 1; ASM International Handbook Committee: Materials Park, OH, 1991a.
ASM (American Society for Metals) Handbook, Vol. 4: Heat Treating; ASM International Handbook Committee: Materials Park, OH, 1991b.
ASM (American Society for Metals) Handbook, Vol. 9: Metallography and Microstructure; ASM International Handbook Committee: Materials Park, OH, 2004.
Lakthtin, Y. *Engineering Physical Metallurgy*; Mir Publishers: Moscow, 1998.
Robert, G. N. *Duplex Stainless Steel*; Woodhead Publishing Ltd, 1997.
Sydney, A. H. *Introduction to Physical Metallurgy*; Mc Graw Hill Education: India, 1974.

2.9 Heat Treatment of Tool Steels

RA Mesquita, RAF Consult, Ann Arbor, MI, USA
CA Barbosa, CAB Consulting, Campinas, Brazil
AR Machado, Federal University of Uberlandia, Uberlândia, Brazil and Pontifícia Universidade Católica do Paraná – PUC-PR, Curitiba, Brazil

© 2017 Elsevier Inc. All rights reserved.

2.9.1	**Introduction to Tool Steels**	214
2.9.1.1	Definition	214
2.9.1.2	Historical Development of Tool Steels	215
2.9.1.3	Tool Steels – Families and Classification	215
2.9.1.4	Names and Classifications Employed in the World	215
2.9.2	**Tool Steels Families**	215
2.9.2.1	Cold Work Tool Steels	216
2.9.2.2	Hot Work Tool Steels	216
2.9.2.3	Plastic Mold Steels	216
2.9.2.4	HSS	216
2.9.3	**Tool Steels Heat Treatment Concepts**	218
2.9.4	**Physical Metallurgy Principles**	218
2.9.4.1	Iron Allotropy	218
2.9.4.2	Carbon Steels	222
2.9.4.3	Martensitic Transformation	222
2.9.4.4	Austenitization and Quenching	224
2.9.4.5	Tempering	226
2.9.4.6	Secondary Hardness	227
2.9.4.7	Multiple Temperings	228
2.9.5	**Practical Aspects of the Heat Treatment**	231
2.9.5.1	Design, Machining, and Stress Relief	232
2.9.5.2	Heating Furnaces	232
2.9.5.3	Preheating	233
2.9.5.4	Austenitization	233
2.9.5.5	Cooling Mediums for Quenching	233
2.9.5.6	Time and Temperature of Tempering	233
2.9.5.7	Quality of the Heat Treatment	234
2.9.6	**Heat Treatment Troubleshooting**	236
2.9.6.1	The Importance of Heat Treatment in Tool Steels	236
2.9.6.2	Analysis of Several Conditions of Heat Treatment in VF800AT Steel	237
2.9.6.3	Analysis of Several Conditions of Heat Treatment in ISO VH13 Steel	238
2.9.6.4	Case Study – Forging Die with Premature Failure	239
2.9.7	**Examples of Application and Performance of New Hot Work Steels**	240
2.9.7.1	Properties of the TENAX 300 and VHSUPER Steels	241
2.9.7.2	Case Analysis	241
2.9.7.2.1	Warm forging punch – Case 1	242
2.9.7.2.2	Connecting rod hot forging die – Case 2	243
2.9.7.2.3	Hot forging die with complex geometry – Case 3	244
2.9.7.2.4	Aluminum casting die – Case 4	244
References		244

2.9.1 Introduction to Tool Steels

2.9.1.1 Definition

Tool steels are alloys used in the manufacture of tools, dies, and molds that shape or cut other materials including steel, nonferrous metals, and plastics. This tool steel definition has its explanation in steel tools section of the manual of Iron and Steel Society[1]

> "Tool steels are carbon steels, alloy steels and high speed steels capable of being quenched and tempered. Usually they are melted in electric arc furnaces and produced under certain practices to meet particular specifications. They can be used in certain hand tools or mechanical fasteners in cutting and shaping material at room temperature or at elevated temperatures. Tool steels are also used in a wide variety of other applications where resistance or wear, toughness, mechanical strength and other properties are selected for optimum performance."

 doi:10.1016/B978-0-12-803581-8.09191-8

In this definition, in addition to the alloying elements tool steels are considered special for its heat treatment characteristics and manufacturing. In the first aspect, there is no exaggeration to consider that without proper heat treatment tool steels are not different from ordinary carbon steels. Manufacturing is also of particular interest because these materials are typically difficult to be produced, requiring the highest quality at every stage of processing.

Peter Payson, in his book *The Metallurgy of Tool Steels*, published in 1962,[2] reported the importance of processing to support the separation of tool steels and steels of 'mass production':

> "Even tool steels are not perfect, but they are much superior than those denominated "tonnage steels", regarding the absence of porosity, morphology of undesirable non-metallic inclusions, chemical segregation and surface defects. Various physical methods are used for inspection and macro metallographic procedures for micro inspection, to ensure that the tool steel is according to consumers' demands."

2.9.1.2 Historical Development of Tool Steels

The first uses of steel were for tools and weapons, and since high hardness and durability were the valuable properties for such application. The attainment of high hardness was followed by three facts: the ability to produce iron, the introduction of carbon in the iron to form steel, and heating and tempering to produce martensite. Maddin[3] explored the first hardening steel and described a mining pick – the first known example of martensitic steel tool. The pick (**Figure 1**) dates from the late thirteenth century or 12 BC. **Figure 1(b)** shows the microstructure of the hardened martensite. Older objects had previously been documented, but had pearlitic microstructure, indicating that annealing was not yet used.

The first knowledge and skills to produce high performance steels were used in the production of swords in China, Damascus, and Japan. **Table 1** lists the chronological developments in steels, emphasizing the important dates or periods of tool steels technology and high speed steels (HSS).

2.9.1.3 Tool Steels – Families and Classification

The tool steels come in a wide range of compositions and are classified by different rules in different countries. Many manufacturers also have their own compositions and denominations, some developed by themselves or even patented. The result is the existence of a large number of compositions and tool steels names. The ASTM A681-94 Standard[5] presents the steels most used worldwide, including those separated by their denominations.

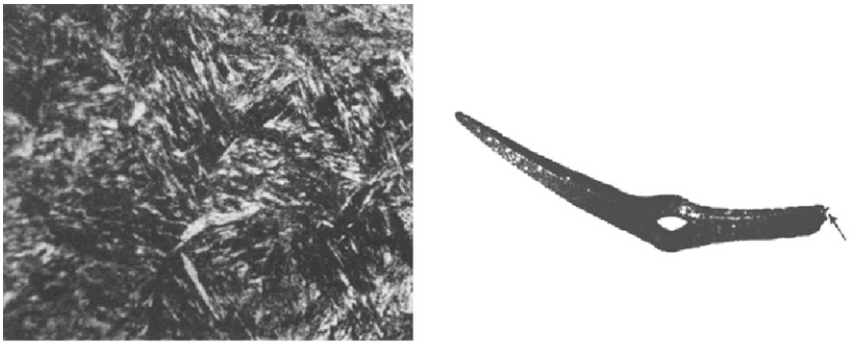
2.9.1.4 Names and Classifications Employed in the World

The most used classification is the one given by American Iron and Steel Institute (AISI)[6–8] and the literature offers the similar products in other standards.[9] Another classification is the German DIN,[10] wherein the numbers are usually employed (W. Nr.). For example, AISI M2 corresponds to W.Nr. DIN 1.3343. The DIN standard is the most used in Europe and was the base for the unified Euronorm where the designation starts with EN. Because of the ease of comprehension and its increased use in many countries, this chapter basically addresses the AISI classification.

AISI classification system arranges tool steels into groups based on prevailing properties, applications, or heat treatment. **Table 2** lists the nine major groups of the AISI. Groups are followed by numbers classifying the steel in question. A list of these steels is given in **Table 2**. In addition to AISI (American) and DIN (German), there are other classifications used worldwide such as the Japanese, British, French, and Swedish (**Table 3**).[9] A cross-reference between them is shown in **Table 4**.

2.9.2 Tool Steels Families

There are several ways of grouping tool steels. One of the AISI has been described in terms of the application or heat treatment. However, for teaching purposes and also focusing on the application, a more interesting way is to classify tool steels according to the branch of application. Thus it can be distinguished into four classes: (1) tool steels for cold working, (2) for hot working, (3) for plastic molds, and (4) HSS. The class of HSS has very peculiar properties and some authors prefer to treat them separately from tool steels. This chapter, however, includes them in tool steels because they have many similarities and these can often be employed in molds or dies



a) b)

Figure 1 (a) Mining pick dated from 13 BC or 12 BC. The arrow shows the sample withdraw point, whose microstructure is shown in (b) martensitic microstructure, obtained by optical microscopy (magnification approximately $\times 500$).[3]

Table 1 Most important developments in the history of tool steels[4]

Date	*Development*
1200 BC	First hardened steel documented
350 BC	Wootz steels in India
500 AC	Layered steel knives produced in Damascus
540 AC	Layered steel knives produced in Japan
Middle ages	Production of steel from iron carburation
1740	Steel production in furnace Crucible: Huntsman
1868	The steel being hardened tungsten air: Mushet
1903	0.76–14W–4CR – prototype of modern high speed steels (HSS)
1904	Adding to 0.4% V alloy
1906	Introduction of fusion in an electric furnace
1910	Introduction of HSS T1: 18W–4CR–1V
1912	Adding 3–5% Cr to give hot hardness tool steels
1923	12% Cr Steel for machining at high speed
1939	Super high-speed steels with high C and high V (M4 and T15)
1940	Start of W replacement for Mo. Rise of M2
1953	Resulfurized HSS
1961	HSS with hardness up to 70 HRC (M40 series)
1970	Introduction of high-alloyed HSS steel by powder metallurgy
1973	High levels of Si and N to increase hardness of the M7
1975	First Nb containing HSS developed
1980	Development of super high-speed steels without Co
1980	Coating tool steels with TiN
1982	HSS modified to Al
1992	8% Cr tool steels with high toughness
2000	Low silicon hot work tool steels

Table 2 Main tool steels families according the AISI classification with letter symbols[10]

Family	*Letter symbol*
Water-hardenable tool steels	W
Shock-resistant tool steels	S
Oil-hardenable cold work tool steels	O
Air-hardenable tool steels, moderately alloyed	A
High-carbon and high-chromium cold work tool steels	D
Plastic mold steels	P
Hot work tool steels alloyed with chromium, molybdenum, or tungsten	H
Tungsten HSS	T
Molybdenum HSS	M

with high demand. In the following sections a brief discussion on these four classes will be presented.

2.9.2.1 Cold Work Tool Steels

This class of tool steel is used in dies for metal forming at temperatures below 200 °C, typically at room temperature. The cold shaped materials are low-carbon steels, mainly used in plates or billets, in coinage operations, stamping, shear cutting, etc. In these applications good properties are required in the tool steel, especially high strength and wear resistance. Examples of cold-formed parts are shown in **Figure 2**.

2.9.2.2 Hot Work Tool Steels

The hot work tool steels are mainly used in metal forming at temperatures above 600 °C. The main processes of hot forming are steel forging and extrusion and casting of nonferrous alloys, especially aluminum alloys. During the work, the dies are simultaneously subjected to mechanical stress and exposure to high temperatures. Thus, the employed tool steels must have properties such as hot strength, toughness (shock resistance), and resistance to thermal and mechanical fatigue. **Figure 3** shows examples of forging dies and casting dies (also known as injection process) and some parts obtained by hot working process.

2.9.2.3 Plastic Mold Steels

The steels of this class are applied to the forming operations of thermoplastic polymers in injection, extrusion, and blow molding. The plastic molds are made of a special class of tool steels, in which the processing characteristics of the steel are crucial. Properties such as machinability, polishability, behavior during texturing, and in some cases, corrosion resistance is usually very important for the proper production of the mold. The application of **Figure 4(a)**, for example, requires perfect polishing of the mold and, therefore, the steel tool must meet a number of special requirements. As shown in **Figure 4(b)**, plastic molds are typically complex and therefore have high costs. Therefore, the use of high-quality steel is critical in order to not compromise the performance of the mold.

2.9.2.4 HSS

The HSS have noticeably different metallurgy from the others tool steels. They are mainly used in cutting tools such as drills, taps, milling cutters, hand saws, etc. Its application in molds and dies is limited, but can be used; especially in cold forming, where high wear resistance is required. The microstructure of HSS produced by conventional metallurgy is composed of a tempered martensite matrix of high hardness, reaching levels above 64 HRC, and undissolved primary carbides, some rich in Mo/W (M_6C type) and others rich in V (MC type) (see **Figure 5**). As shown in **Table 5**, the MC carbides have very high hardness, significantly higher than the carbides of Cr of the type M_7C_3 present in the steels of the D series and even higher than the abrasive particles of alumina. Being harder and being present in a high-toughness matrix promotes high wear resistance.

Some factors limit the application of HSS for cold work. The first is the low toughness of these materials when obtained from bars produced via conventional metallurgy process with diameters above 60 mm, exhibiting relatively coarse microstructure. To minimize this fact, the cold working tools are usually treated to lower hardness than the maximum usually obtained; generally, around 60 HRC. The second factor is economical, because the HSS have high amount of alloying elements and substantially more complex heat treatment (austenitizing temperature of 1200 °C range). **Figure 6** shows examples of tools made of HSS. In some very high demanding situations it is recommended to apply the modern HSS produced via powder metallurgy due to the microstructure

Table 3 Chemical composition of the main AISI tool steels[10]

AISI	UNS No.	Identifying elements (%)								
		C	Mn	Si	Cr	V	W	Mo	Co	Ni
Water-hardening tool steels										
W1	T72301	0.061–1.40[a]	–	–	–	–	–	–	–	–
W2	T72302	0.061–1.40[a]	–	–	–	0.25	–	–	–	–
W5	T72305	1.10	–	–	0.50	–	–	–	–	–
Shock-resisting tool steels										
S1	T41901	0.50	–	–	1.50	–	2.50	–	–	–
S2	T41902	0.50	–	1.00	–	–	–	0.50	–	–
S5	T41905	0.55	0.80	2.00	–	–	–	0.40	–	–
S6	T41906	0.45	0.40	2.25	1.50	–	–	0.40	–	–
S7	T41907	0.50	–	–	3.25	–	–	1.40	–	–
Oil-hardening cold-work tool steels										
O1	T31501	0.09	1.00	–	0.50	–	0.50	–	–	–
O2	T31502	0.09	1.60	–	–	–	–	–	–	–
O6[b]	T31506	1.45	0.80	1.00	–	–	–	0.25	–	–
O7	T31507	1.20	–	–	0.75	–	1.75	–	–	–
Air-hardening, medium-alloy cold-work tool steels										
A2	T30102	1.00	–	–	5.00	–	–	1.00	–	–
A3	T30103	1.25	–	–	5.00	1.00	–	1.00	–	–
A4	T30104	1.00	2.00	–	1.00	–	–	1.00	–	–
A6	T30106	0.70	2.00	–	1.00	–	–	1.25	–	–
A7	T30107	2.25	–	–	5.25	4.75	1.00[c]	1.00	–	–
A8	T30108	0.55	–	–	5.00	–	1.25	1.25	–	–
A9	T30109	0.50	–	–	5.00	1.00	–	1.40	–	1.50
A10[b]	T30110	1.35	1.80	1.25	–	–	–	1.50	–	1.80
High-carbon, high-chromium cold-work steels										
D2	T30402	1.50	–	–	12.00	1.00	–	1.00	–	–
D3	T30403	2.25	–	–	12.00	–	–	–	–	–
D4	T30404	2.25	–	–	12.00	–	–	1.00	–	–
D5	T30405	1.50	–	–	12.00	–	–	1.00	3.00	–
D7	T30407	2.35	–	–	12.00	4.00	–	1.00	–	–
Low-alloy special-purpose tool steels										
L2	T61202	0.05–1.10[a]	–	–	1.00	0.20	–	–	–	–
L6	T61206	0.70	–	–	0.75	–	–	0.25[c]	–	1.50
Mold steels										
P2	T51602	0.07	–	–	2.00	–	–	0.20	–	0.50
P3	T51603	0.10	–	–	0.60	–	–	–	–	1.25
P4	T51604	0.07	–	–	5.00	–	–	0.75	–	–
P5	T51605	0.10	–	–	2.25	–	–	–	–	–
P6	T51606	0.10	–	–	1.50	–	–	–	–	3.50
P20	T51620	0.35	–	–	1.70	–	–	0.40	–	–
P21	T51621	0.20	1.20(Al)	–	–	–	–	–	–	4.00
Chromium hot work tool steels										
H10	T20810	0.40	–	–	3.25	0.40	–	2.50	–	–
H11	T20811	0.35	–	–	5.00	0.40	–	1.50	–	–
H12	T20812	0.35	–	–	5.00	0.40	1.50	1.50	–	–
H13	T20813	0.35	–	–	5.00	1.00	–	1.50	–	–
H14	T20814	0.40	–	–	5.00	–	5.00	–	–	–
H19	T20819	0.40	–	–	4.25	2.00	4.25	–	4.25	–
Tungsten hot work tool steels										
H21	T20821	0.35	–	–	3.50	–	9.00	–	–	–
H22	T20822	0.35	–	–	2.00	–	11.00	–	–	–
H23	T20823	0.30	–	–	12.00	–	12.00	–	–	–
H24	T20824	0.45	–	–	3.00	–	15.00	–	–	–
H25	T20825	0.25	–	–	4.00	–	15.00	–	–	–

(*Continued*)

Table 3 Continued

AISI	UNS No.	Identifying elements (%)								
		C	Mn	Si	Cr	V	W	Mo	Co	Ni
H26	T20826	0.50	–	–	4.00	1.00	18.00	–	–	–
Molybdenum hot work tool steels										
H42	T20842	0.60	–	–	4.00	2.00	6.00	5.00	–	–
Tungsten high-speed tool steels										
T1	T12001	0.75[a]	–	–	4.00	1.00	18.00	–	–	–
T2	T12002	0.80	–	–	4.00	2.00	18.00	–	–	–
T4	T12004	0.75	–	–	4.00	1.00	18.00	–	5.00	–
T5	T12005	0.80	–	–	4.00	2.00	18.00	–	8.00	–
T6	T12006	0.80	–	–	4.50	1.50	20.00	–	12.00	–
T8	T12008	0.75	–	–	4.00	2.00	14.00	–	5.00	–
T15	T12015	1.50	–	–	4.00	5.00	12.00	–	5.00	–
Molybdenum high-speed tool steels										
M1	T11301	0.80[a]	–	–	4.00	1.00	1.50	8.00	–	–
M2	T11302	0.85–1.00[a]	–	–	4.00	2.00	6.00	5.00	–	–
M3, class 1	T11313	1.05	–	–	4.00	2.40	6.00	5.00	–	–
M3, class 2	T11323	1.20	–	–	4.00	3.00	6.00	5.00	–	–
M4	T11304	1.30	–	–	4.00	4.00	5.50	4.50	–	–
M6	T11306	0.80	–	–	4.00	2.00	4.00	5.00	12.00	–
M7	T11307	1.00	–	–	4.00	2.00	1.75	8.75	–	–
M10	T11310	0.85–1.00[a]	–	–	4.00	2.00	–	8.00	–	–
M30	T11330	0.80	–	–	4.00	1.25	2.00	8.00	5.00	–
M33	T11333	0.90	–	–	4.00	1.15	1.50	9.50	800	–
M34	T11334	0.90	–	–	4.00	2.00	2.00	8.00	8.00	–
M36	T11336	0.80	–	–	4.00	2.00	6.00	5.00	8.00	–
Ultrahard high-speed tool steels										
M41	T11341	1.10	–	–	4.25	2.00	6.75	3.75	5.00	–
M42	T11342	1.10	–	–	3.75	1.15	1.50	9.50	8.00	–
M43	T11343	1.20	–	–	3.75	1.60	2.75	8.00	8.25	–
M44	T11344	115	–	–	4.25	2.00	5.25	6.25	12.00	–
M46	T11346	1.25	–	–	4.00	3.20	2.00	8.25	8.25	–
M47	T11347	1.10	–	–	3.75	1.25	1.50	9.50	5.00	–

[a]Available with different carbon contents.
[b]Contains graphite.
[c]Optional.
Source: Ref. [2]

refining obtained in this production route leading to higher toughness.

2.9.3 Tool Steels Heat Treatment Concepts

The heat treatment of tool steels is essential for their good performance. Many low-performance problems and unexpected failures found in practical situations are caused by heat treatment errors. Furthermore, the right properties of the tool steels can only be achieved after heat treatment.

The aim of this chapter is to provide simplified and concise information about heat treatment used in the manufacture of tools. Standard normalizing and annealing treatments will not be covered since the users and toolmakers and mold and die industry usually do not perform them. Rather, these treatments are usually performed in the production plants of tool steels. They are an essential part of the material supply condition because they prepare the microstructure to provide adequate response to the final heat treatment and thus optimal performance. **Figure 7** summarizes the change in microstructure (in terms of L, A, C, and F phases, which are defined in **Figure 7**) as a function of temperature and time during the production of tool steel.

2.9.4 Physical Metallurgy Principles

2.9.4.1 Iron Allotropy

Pure iron in solid state has three equilibrium phases: α, γ, and δ. The δ phase is hardly relevant to tool steels. However, α and γ phases are the basis for all the understanding of the structure and properties of iron and hence the steel. These two phases are stable, depending on the temperature. As shown in **Figure 8**, at low temperatures there is only one stable phase called ferrite or α phase. Above 912 °C, the nature (or more precisely the thermodynamics) of Fe identifies that this phase

Table 4 Similarity (cross-reference) among some international tool steel classification standards[10]

United States of America (AISI)	*Germany (DIN)*[a]	*Japan (JIS)*[b]	*Great Britain (B.S.)*[c]	*France (AFNOR)*[d]	*Sweden (SS_{14})*
Molybdenum high-speed steels (ASTM A600)					
M1	1.3346	–	4569 BM1	A35-590 4441 Z85DCWV08-04-02-01	2715
M2, reg C	1.3341, 1.3343, 1.3345, 1.3553, 1.3554	G4403 SKH51 (SKH9)	4569 BM2	A35-590 4301 Z85WDCV06-05-04-02	2722
M2, high C	1.3340, 1.3342	–	–	A35-590 4302 Z90WDCV06-05-04-02	–
M3, class 1	–	G4403 SKH52	–	–	–
M3, class 2	1.3344	G4403 SKH53	–	A35-590 4360 Z120 WDCV06-05-04-03	(USA M3 class 2)
M4	–	G4403 SKH54	4569 BM4	A35-590 4361 Z130 WDCV06-05-04-04	–
M7	1.3348	G4403 SKH58	–	A35-590 4442 Z100DCWV09-04-02-02	2782
M10, reg C	–	–	–	–	–
M10, high C	–	–	–	–	–
M30	1.3249	–	4569 BM34	–	–
M33	1.3249	–	4569 BM34	–	–
M34	1.3249	–	4569 BM34	–	–
M35	1.3243	G4403 SKH55	–	A35-590 4371 Z85WDKCV06-05-05-04-02 A35-590 4372 Z90WDKCV06-05-05-04-02	–
M36	1.3243	G4403 SKH55, G4403 SKH56	–	A35-590 4371 Z85WDKCV06-05-05-04	2723
M41	1.3245, 1.3246	G4403 SKH55	–	A35-590 4374 Z110WKCDV07-05-04-04	2736
M42	1.3247	G4403 SKH59	4569 BM42	A35-590 4475 Z110DKCWV09-08-04-02	–
M43	–	–	–	A35-590 4475 Z110DKCWV09-08-04-02-01	–
M44	1.3207	G4403 SKH57	4659 (USA M44)	A35-590 4376 Z130KWDCV12-07-06-04-03	–
M46	1.3247	–	–	–	–
M47	1.3247	–	–	–	–
Intermediate high-speed steels					
M50	1.2369, 1.3551	–	–	A35-590 3551 Y80DCV42.16	(USA M50)
M52	–	–	–	–	–
Tungsten high-speed (ASTM A 600)					
T1	1.3355, 1.3558	G4403 SKH2	4659 BT1	A35-590 4201 Z80WCV18-04-01	–
T2	–	–	4659 BT2, 4659 BT20	4203 18-0-2	–
T4	1.3255	G4403 SKH3	4659 BT4	A35-590 4271 Z80WKCV18-05-04-01	–
T5	1.3265	G4403 SKH4	4659 BT5	A35-590 4275 Z80WKCV18-10-04-02	(USA T5)
T6	1.3257	G4403 SKH4B	4659 BT6	–	–
T8	–	–	–	–	–
T15	1.3202	G4403 SKH10	4659 BT15	A35-590 4171 Z160WKVC12-05-05-04	(USA T15)
Chromium hot work steels (ASTM A 681)					
H10	1.2365, 1.2367	G4404 SKD 7	4659 BH10	A35-590 3451 32DCV28	–
H11	1.2343, 1.7783, 1.7784	G4404 SKD 6	4659 BH11	A35-590 3431 FZ38CDV5	–
H12	1.2606	G4404 SKD62	4659 BH12	A35-590 3432 Z35CWDV5	–
H13	1.2344	G4404 SKD61	4659 BH13, 4659 H13	A35-590 3433 Z40CDV5	2242
H14	1.2567	G4404 SKD4	–	3541 Z40WCV5	–

(*Continued*)

Table 4 Continued

United States of America (AISI)	*Germany (DIN)*[a]	*Japan (JIS)*[b]	*Great Britain (B.S.)*[c]	*France (AFNOR)*[d]	*Sweden (SS_{14})*
H19	1.2678	G4404 SKD8	4659 BH19	–	–
Tungsten hot work steels (ASTM A 681)					
H21	1.2581	G4404 SKD5	4659 BH21, 4659 BH21A	A35-590 3543 Z30WCV9	2730
H22	1.2581	G4404 SKD5	–	–	–
H23	1.2625	–	–	–	–
H24	–	–	–	–	–
H25	–	–	–	–	–
H26	–	–	4659 BH26	–	–
Molybdenum hot-work steels (ASTM A 681)					
H42	–	–	–	3548 Z65WDCV6.05	–
Air-hardening, medium-alloy cold-work steels (ASTM A 681)					
A2	1.2363	G4404 SKD12	4659 BA2	A35-590 2231 Z100CDV5	2260
A3	–	–	–	–	–
A4	–	–	–	–	–
A5	–	–	–	–	–
A6	–	–	4659 BA6	–	–
A7	–	–	–	–	–
A8	1.2606	G4404 SKD62	–	3432Z38CDWV5	–
A9	–	–	–	–	–
A10	–	–	–	–	–
High-carbon, high-chromium cold-work steels (ASTM–A–681)					
D2	1.2201, 1.2379, 1.2601	G4404 SKD 11	4659 (USA D2), 4659 BD2 4659 BD2A	A35-590 2235 Z160CDV12	2310
D3	1.2080, 1.2436, 1.2884	G4404 SKD1, G4404 SKD 2	4659 BD3	A35-590 2233 Z200C12	–
D4	1.2436, 1.2884	G4404 SKD2	4659 (USA D4)	A35-590 2234 Z200CD12	2312
D5	1.2880	–	–	A35-590 2236 Z160CKDV12.03	–
D7	1.2378	–	–	2237 Z230CVA12.04	–
Oil-hardening cold-work steels (ASTM A 681)					
O1	1.2510	G4404 SKS21, G4404 SKS3, G4404 SKS93 G4404 SKS94, G4404 SKS95	4659 BO1	A35-590 2212 90 MWCV5	2140
O2	1.2842	–	4659 (USA 02) 4659 BO2	A35-590 2211 90MV8	–
O6	1.2206	–	–	A35-590 2132 130C3	–
O7	1.2414, 1.2419, 1.2442, 1.2516, 1.2519	G4404 SKS2	–	A35-590 2141 105WC13	–
Shocking-resisting steel (ASTM A 681)					
S1	1.2542, 1.2550	G4404 SKS41	4659 BS1	A35-590 2341 55WC20	2710
S2	1.2103	–	4659 BS2	A35-590 2324 Y45SCD6	–
S5	1.2823	–	4659 BS5	–	–

S6	–	–	–	–	–
S7	–	–	–	–	–
Low-alloy special-purpose steels (ASTM A 681)					
L2	1.2235, 1.2241, 1.2242, 1.2243,	G4404 SKT3, G4410SKC11	–	A35-590 3335 55CNDV4	–
L6	1.2713, 1.2714	G4404 SKS51, G4404 SKT4	–	A35-590 3381 55NCDV7	–
Low-carbon mold steels (ASTM A 681)					
P2	–	–	–	–	–
P3	1.5713	–	–	2881 Y10NC6	–
P4	1.2341	–	–	–	(USA P4)
P5	–	–	–	–	–
P6	1.2735, 1.2745	G4410SKC31	–	2882 10NC12	–
P20	1.2311, 1.2328, 1.2330	–	4659 (USA P20)	A35-590 2333 35CMD7	(USA P20)
P21	–	–	–	–	–
Water-hardening steels (ASTM A 686)					
W1	1.1525, 1.1545, 1.1625, 1.1654, 1.1663, 1.1673, 1.1744, 1.1750, 1.1820, 1.1830	G4401 SK1, G4401 SK2, G4401 SK3, G4401 SK4, G4401 SK5, G4401 SK6, G4401 SK7 G4401 SK7, G4410 SKC3	4659 (USA WI), 4659 BW1A 4659 BW1B 4659 B, W1C	A35-590 1102 Y(1) 105, A35-590 1103 Y (1) 90 A35-590 1104 Y (1) 80, A35-590 1105 Y (1) 70 A35-590 1200 Y (2) 140, A35-590 1201 Y (2) 120 A35-596 Y75, A35-596 Y90	–
W2	1.1645, 1.2206, 1.283	G4404 SKS43 G4404 SKS44	4659 BW2	A35-590 1161 Y120V, A35-590 1162 Y 105V A35-590 1163 Y90V, A35-590 1164 Y75V	(USA W2A) (USA W2B) (USA W2C)
W5	1.2002, 1.2004, 1.2056	–	–	A35-590 1230 Y(2) 140C, A35-590 2130 Y100C2 A35-590 1232 Y 105C	–

[a]Deutsche Industrie Normen (German Industrial Standards).
[b]Japanese Industrial Standard.
[c]British Standard.
[d]l'Association Française de Normalisation (French Standards Association).
Source: Ref.[3,4]

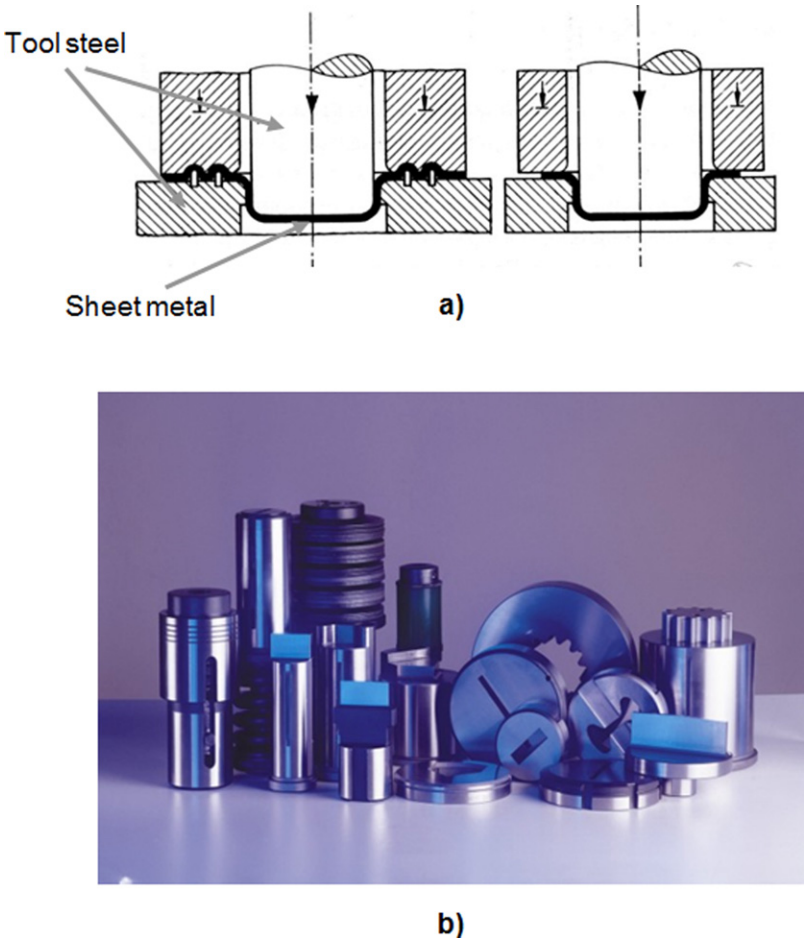


Figure 2 (a) Cold forming scheme (sheet forming) and (b) some examples of cold work tools.

is no longer stable. Therefore a phase transformation begins in the solid state, in which the iron changes its structure from ferrite (α) to austenite (γ).

The crystalline structure of the α and γ phases are shown in Figure 8. The α phase has body centered cubic symmetry and the γ phase is face centered cubic. The arrangement of the Fe atoms in the two phases is significantly different and the transformation from one phase to another involves atoms movement by diffusion, which means that it takes some time to transform. On heating, the α–γ transformation begins to take place with the formation of a small portion of γ (termed nucleus) that grows consuming the α phase. The same occurs when cooling by a nucleation and growth reaction, the austenite is transformed to ferrite.

2.9.4.2 Carbon Steels

In carbon steels, the phases present are provided by the iron–carbon equilibrium diagram (Figure 9). The eutectoid equilibrium line determines the transformation of the austenite to ferrite. However, the introduction of carbon gives rise to the appearance of a new phase – the cementite, with Fe_3C stoichiometry. For steels having less than 0.77% of carbon, the A_1 line determines the dissolution of the cementite and the transformation of a microstructure in which ferrite and cementite ($\alpha + Fe_3C$) coexist to a microstructure containing austenite and ferrite ($\alpha + \gamma$). After the temperature exceeds the A_3 line, the microstructure will contain only the austenitic phase.

Carbon is much more soluble in austenite than in ferrite. As shown in Figure 9, the maximum solubility of carbon in ferrite is only 0.0218% (at 727 °C). However, in the austenite up to 2.11% of carbon can be dissolved (at 1148 °C). For a composition of 0.4% C, for instance, the phases observed at room temperature are $\alpha + Fe_3C$. This is because the carbon cannot remain in solid solution and thus forms Fe_3C carbide with iron. However, above 750 °C, the equilibrium diagram shows only the presence of austenite. All carbon that was not soluble in the ferrite was dissolved in the austenite.

2.9.4.3 Martensitic Transformation

Continuing in the example of the 0.4% C steel, if cooled from 750 °C slowly, the thermodynamics determines that the diagram phases are reversible and, at room temperature, $\alpha + Fe_3C$ will again be formed. These transformations in the solid state occur by nucleation and growth, which in turn require time for the movement of C and Fe atoms for the formation of Fe_3C. In other words, it takes time to occur, and depends on the atomic diffusion process.

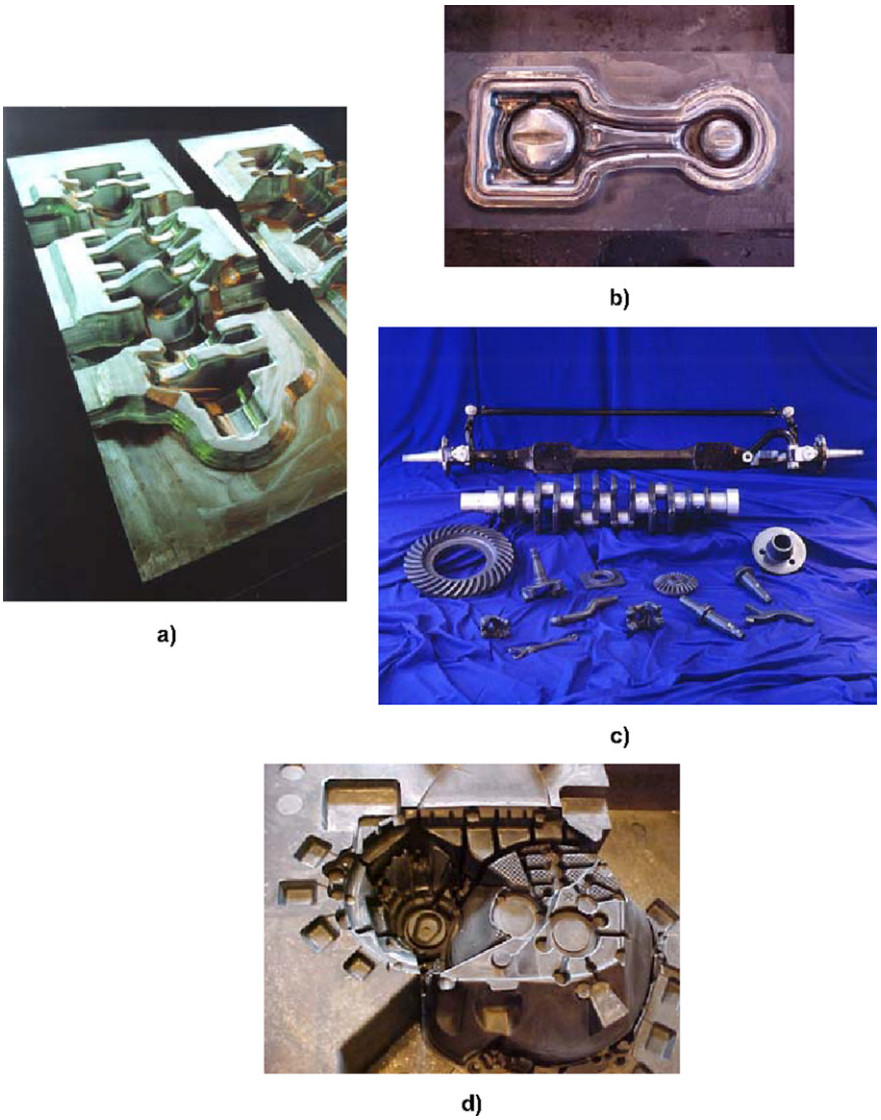


Figure 3 (a) Crankshaft hot forging dies and (b) connecting rods before use, (c) some examples of hot forged parts, and (d) pressure casting die for automotive industry.

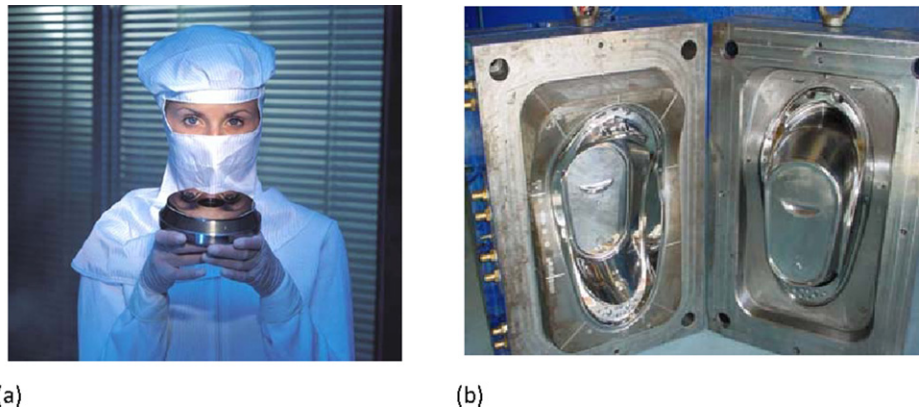


Figure 4 (a) CD's injection mold, showing the absolutely polished internal surfaces and (b) external view of a plastic mold showing its complex shape.

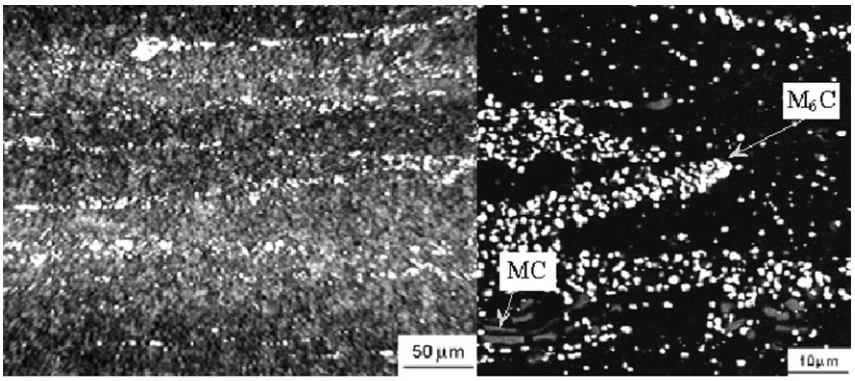


Figure 5 (a) AISI M2 high speed steel ½ radius longitudinal optical microstructure of a 100 mm diameter bar[8] and (b) backscattered electron image differentiating carbides MC type (gray) and M_6C (white).[8]

Table 5 Typical matrix and primary carbides hardness found in tool steels. Approximate values converted from the data of the references[10,11]

Phase	*Composition*	*Hardness (HV)*
Cold work tool steel martensite (60,5HRC)	Varied	700
High-speed steel martensite	Varied	870
M_3C	Rich in Fe	1100
M_7C_3 in cold work tool steel	Rich in Cr	1800
M_6C in high-speed steel	Rich in Mo and/or W	1500
M_2C in high-speed steel	Rich in Mo and/or W	2000
MC in high-speed steel	Rich in V	3000
Alumina abrasive particle	Al_2O_3	2200

Suppose that the same steel is heated, for example at 800 °C, resulting in only one phase – austenite (γ). If this material is quickly cooled from this temperature, for example, in water, there will be no time for all the carbon to get out of the austenite and then the austenite decomposes in the equilibrium phases and Fe_3C. In this situation, the most important transformation of the carbon iron system occurs – the 'martensitic transformation.' This is a kind of transformation that does not need diffusion (it is diffusionless) and thus occurs very quickly.

The martensitic transformation depends only on the temperature to occur. It starts when the steel reaches the temperature of the beginning of martensitic transformation, or M_s line, and ends when the temperature drops down up to the end of martensitic transformation, or M_f line. In some steels M_f temperature is below the room temperature, resulting in not all austenite is transformed into martensite. The portion of untransformed austenite is called 'retained austenite.'

The martensite has next to the ferrite symmetry, but with the *c*-axis bigger than the others (the crystalline structure is characterized by a 'cube' with a side larger than the others and therefore it is no more a cube). It has body-centered tetragonal symmetry and the size of the *c*-axis depends on the carbon content.[14] Due to its structure, martensite has high hardness and also high brittleness. The hardness of the martensite depends on the carbon content, as shown in **Figure 10(a)**. The microstructure of a quenched steel is shown in **Figure 10(b)**.

2.9.4.4 Austenitization and Quenching

Considering the above basis, quenching can be defined as: "the rapid cooling of the steel from a temperature above its critical temperature (A_1 temperature) in a medium such as oil, water, brine or even air."[14] The purpose of quenching is to obtain the martensitic structure and, therefore, the cooling curve must pass on the left elbow of the continuous cooling transformation (CCT) curve, thus preventing the transformation of austenite into ferrite and pearlite.

The CCT curve corresponds to a schematic representation of the phases and morphologies formed as a function of the cooling speed. Obviously, in slow coolings the formed phases are ferrite and carbides, in a spheroidized morphology or pearlite. In rapid coolings, the phase formed is martensite. For intermediate coolings, there are other morphologies, such as bainite and fine pearlite. The alloying elements generally increases the possibility of formation of the martensite, making it possible even at not very rapid coolings; in high-alloy steels, martensite can be obtained even in air cooling. Therefore, it is said that the alloying elements increase the hardenability.

Figure 11 shows two examples of CCT curves for two tool steels, one with low and the other with high alloying elements. For both steels, as the cooling becomes slower martensitic transformation can no longer occur, appearing as pearlite, bainite, ferrite, and carbides. The big difference between the two steels is that for high-alloy steels, this only occurs at much slower cooling rates than for low-alloy steels. In other words, the high-alloy steel does not need rapid coolings such as that for the low-alloy steel in order to obtain martensitic phase.

An important factor to consider in the quenching operation, due to the action it exerts on the final structure of the steel, is the heating temperature, or more specifically the austenitizing temperature. Take the example of a 0.4% C steel

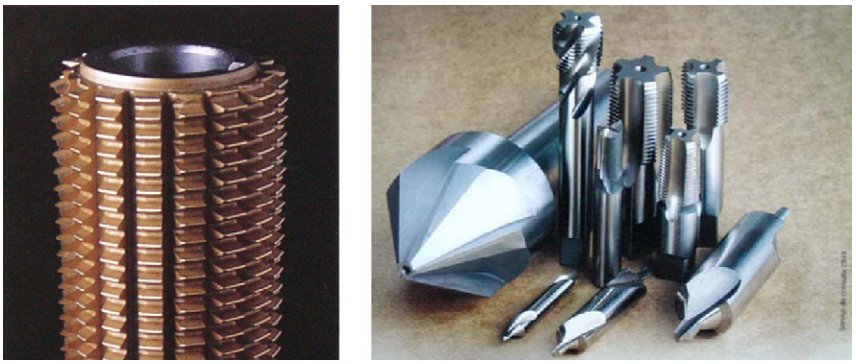


Figure 6 Cutting tools made of high speed steels.

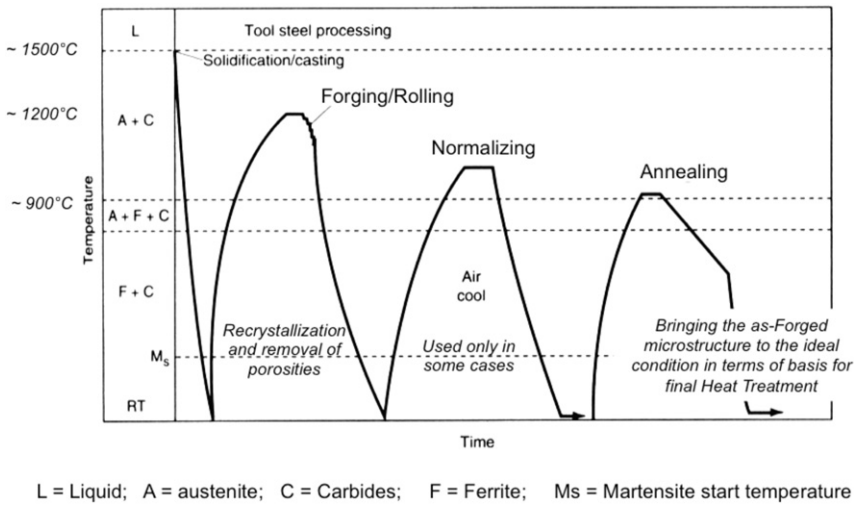


Figure 7 Schematic representation of the transformations that occur in manufacturing of tool steels, from solidification until annealing.[12]

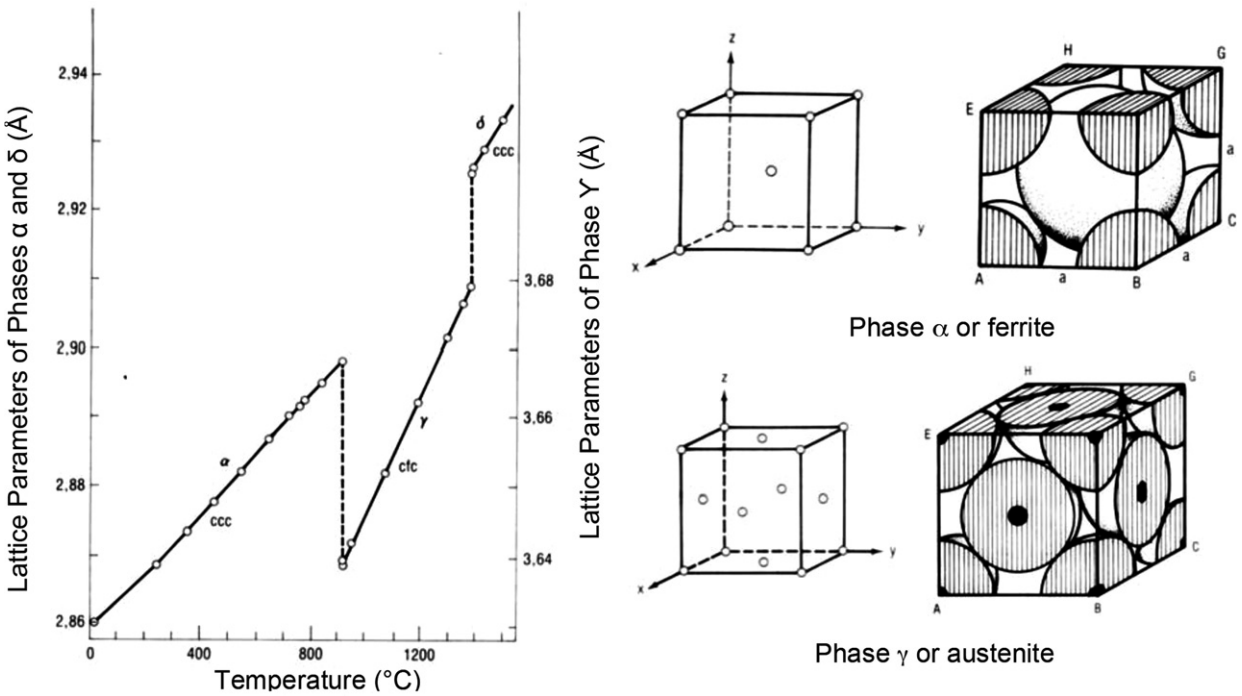


Figure 8 Equilibrium phases of pure iron and their respective crystalline structures.[13]

austenitized at 750 °C (see Figure 9). At this temperature, besides the austenite, ferrite grains will also be present. When quenching in water (assuming a small sample) martensite will be present along with ferrite, because the latter was present during the austenitizing. There is, therefore, incomplete quenching or incomplete hardening. As a result, when heating hipoeutectoide steels for quenching, the temperature must be raised just above the upper limit of the critical zone – A_3 line – and then its structure will consist solely of austenite to be transformed into martensite in the subsequent rapid cooling.

In tool steels, annealed microstructure prior to quenching consists of ferrite and carbides. The austenitizing should promote necessarily the transformation of the whole ferrite into austenite. However, it is not always possible for (and also it is not necessary or desirable) the total dissolution of the carbides in the austenite. The higher the temperature, the greater the fraction of carbides that can be dissolved. However, the austenitizing temperature cannot be too high. This is because the excessive increase in the temperature also promotes strong growth of austenitic grain, which impairs the properties and reduces the toughness of the tool steel. Furthermore, in extreme cases, the use of excessively high temperatures can reach the point of forming liquid, a phenomenon known as overheating or burning. Unlike carbon steels, the austenitizing temperature of tool steel varies considerably between different compositions and types of steel. Adequate temperatures for each steel are provided in books specialized in tool steels and also in tool steel manufacturers catalogs.

In summary, the purpose of austenitizing and quenching is to increase the strength and hardness of the steel. Also resulting from quenching, or rather from the formation of martensite are the reduction of the ductility (low values of elongation and necking),toughness, and appearance of considerable internal stresses. Such drawbacks can be mitigated or eliminated by tempering.

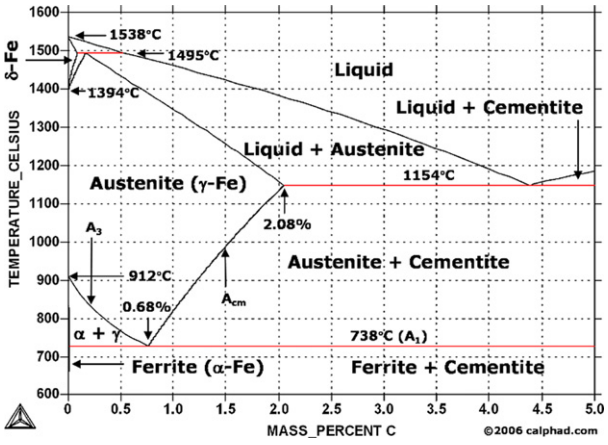


Figure 9 Fe–C equilibrium diagram.

2.9.4.5 Tempering

Tempering is a heat treatment that normally follows the quenching in order to eliminate most of the drawbacks produced by: correcting excessive hardness and brittleness of the material, and increasing its ductility and impact resistance (see Figure 12) in addition to relieving or removing internal stresses.

The heating of martensite allows the reversal of the unstable crystalline lattice to the stable body centered cubic lattice, produces internal adjustments that relieve stresses and also gives rise to precipitation of carbide particles which grow in accordance with temperature and time.

According to the tempering temperature, this heat treatment promotes the following changes, divided into four stages[14]

i. first tempering stage – occurs with the precipitation of iron carbide of epsilon type (ε) with $Fe_{2-3}C$ formula and hexagonal lattice; this carbide may be absent in low-carbon steels and low-alloy steels; Rockwell hardness begins to fall, reaching 60 HRC;
ii. second tempering stage – occurs during transformation of retained austenite into bainite (in carbon steel); Rockwell hardness continues to fall;
iii. third tempering stage – forms a metastable carbide, with Fe_5C_2 formula; when this transformation occurs in

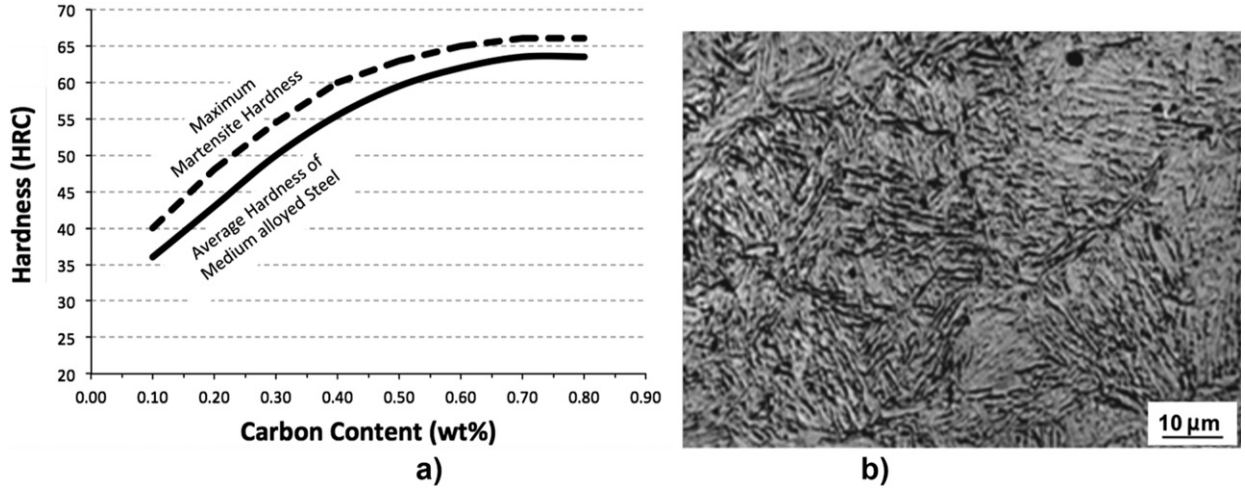


Figure 10 (a) Effect of carbon content on the hardness of the martensite; (b) micrographic aspect of 0.8% C steel quenched: martensite.[14]

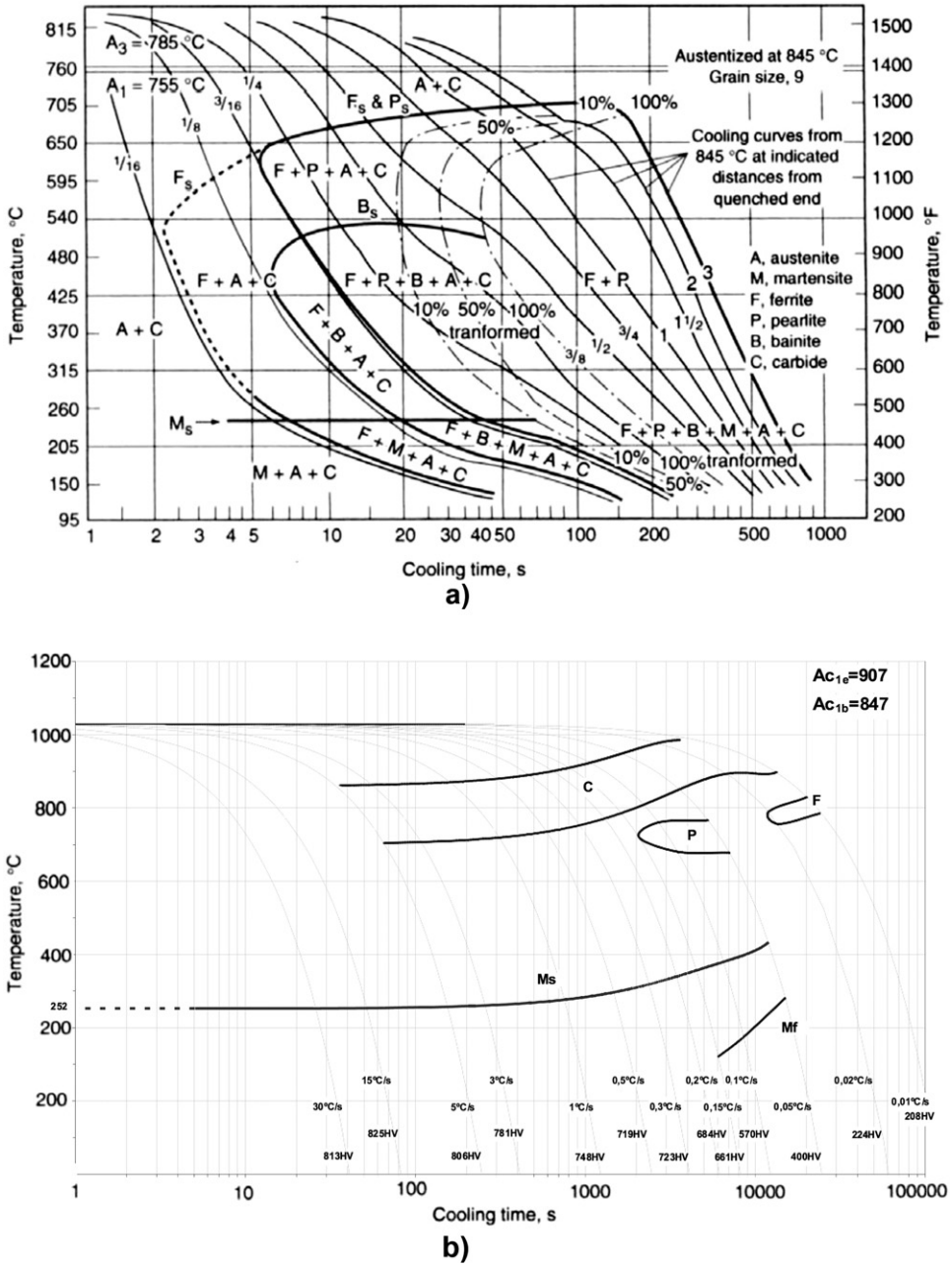


Figure 11 CCT curve of steels (a) low-alloy steel (1.06C–0.33Mn–0.32Si–0.11Ni–1.44Cr–0.3Mo)[15] (b) high-alloy steel – VF800AT (0.85C–0.4Mn–0.90Si–8.5%Cr–2.0Mo–0.6V–0.15 Nb).[16]

high-carbon steel, a dark microscopically visible structure is observed that was called 'troostita' in the past, designation no longer used; Rockwell hardness continues to fall, reaching values slightly greater than 50 HRC; and

iv. fourth tempering stage – between 500 °C and 600 °C only in steels containing Cr, Mo, V, Nb, or W; there is precipitation of alloying carbides and the transformation is called 'secondary hardness' (as discussed in Section 2.9.4.6).

From what has just been exposed, it is noticed that the tempering temperature can be chosen according to the combination of mechanical properties that is wanted in the hardened steel. In this choice, the relationship between hardness–toughness (see **Figure 12**) should be considered in order to meet the application requirements.

2.9.4.6 Secondary Hardness

In the quenched condition, the steels normally consist of martensite, retained austenite, and carbides undissolved during the austenitization. The alloying elements are present either in solid solution in the martensitic matrix or in the form of residual carbides. It is believed that the

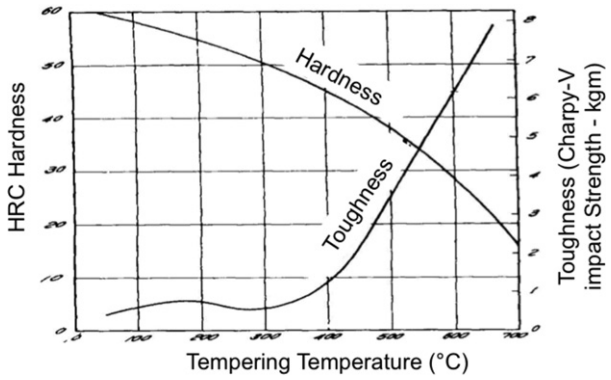


Figure 12 Effect of tempering temperature in the hardness and toughness of a carbon steel.[17]

composition of the retained austenite is the same as martensite, that is, both carbon and alloying elements such as chromium, vanadium, tungsten, and molybdenum are present. When tempering an alloy steel, modifications of its hardness occur which is different from carbon steels, as shown in **Figure 13**.

The dotted curve of **Figure 13(a)** corresponds to a common carbon steel, characterized by the continuous drop of the hardness as a function of tempering temperature due to decomposition of the martensite. The dashed curve is related to the hardening by the precipitation of special carbides (commonly known as secondary carbides), which occurs during the heating for tempering and causes an increase in hardness. The continuous bold line curve refers to a high-alloy tool steel (e.g., a HSS) and is the sum of the two other curves. By examining these curves, the following can be pointed out:

- At lower tempering temperatures, the curve corresponding to HSS is more or less parallel to the common C steel;
- At high temperatures, the HSS curve follows the hardening by the precipitation of secondary carbides.

This 'secondary hardening' or the appearance of a 'secondary hardness' – typical phenomenon of many highly alloyed steels and more pronounced in HSS – which develops mainly in the temperature range of 550–565 °C, is assigned to a combination of two processes: (1) transformation of retained austenite into martensite during cooling and tempering (mainly after the first tempering cycle); (2) precipitation of extremely fine dispersion of carbides of alloying elements mainly containing chromium, vanadium, tungsten, and molybdenum. The contribution of retained austenite is verified by tempering at temperatures between 540 and 590 °C; the contribution due to the precipitation of alloying carbides occurs when the tempering is performed between 480 and 650 °C.

Formation of alloy carbides is slow at low tempering temperature because of 'low diffusion rates.' Diffusion of alloying elements becomes faster with increasing temperature. Tempering alloy steels at a temperature higher than that used in plain carbon steels produces 'fine alloy carbide particles' at a faster rate, so that it gives higher hardness. In other words, the diffusion rate of the alloying element(s) present in these steels is significantly high at higher tempering temperatures (>550 °C) precipitating hard alloy carbides and thus increased hardness is recorded. This type of hardening effect is often called secondary hardening.

The curve that represents carbide precipitation involves two stages, an increase and a decrease in hardness. The increase in hardness is caused by the progressive enhancement of precipitation of carbides, which are extremely small (see **Figure 14(a)**) of nanometer order, i.e., tens of atoms. However, as the temperature increases, these carbides begin to coalesce ('thickening'), as shown in **Figures 14(b)** and **14(c)**, and then the hardness decreases. The coalescence of the carbides occurs by diffusion, depending on the temperature and time. **Figure 13(b)** shows this phenomenon relating the tempering curve as a function of not only the temperature but also a function of time through the tempering parameter, with the formula $T(\log t + 20)$, where 't' is the time in hours and 'T' is the temperature in °F + 460.[12]

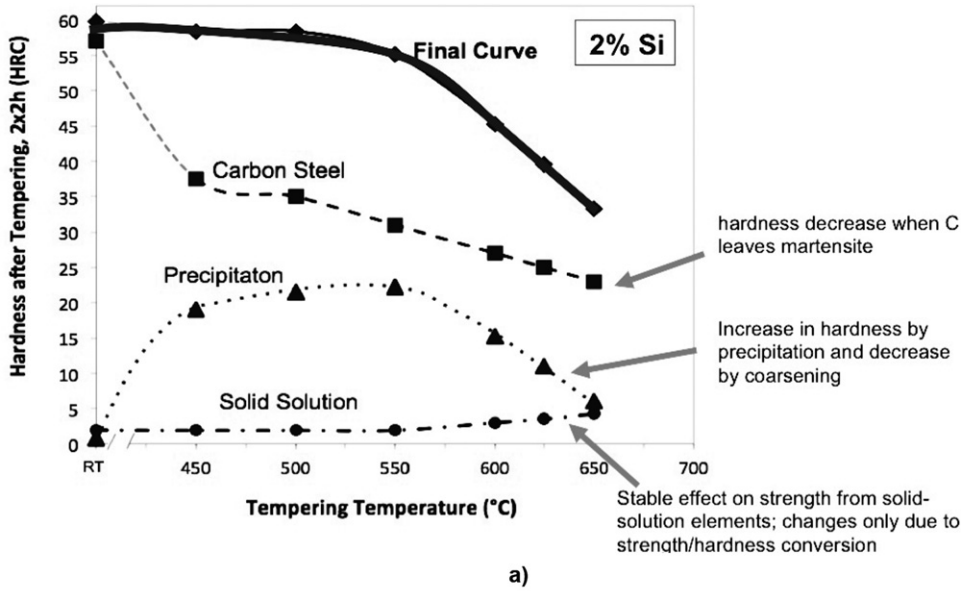
Especially for hot work steels or HSS this reduction in hardness is very important, as these materials are exposed to high temperatures (next to those used in tempering) during use. Therefore, in addition to tempering heat treatment, these materials continue tempering (martensite continues decompose) in their applications. Thus, it is always desirable to have greater resistance to this loss in hardness, normally called as 'resistance to tempering.'

The effects of the alloying elements in the secondary hardening can be seen in **Figure 15**. The chromium carbides are typically of the type M_7C_3 and at high temperatures (>650 °C) they are $M_{23}C_6$ (where 'M' is the metal and 'C' carbon). The Cr has less intense effect and the hardness resulted is sufficient just to promote an adequate level up to ~540 °C. From this temperature the hardness drops sharply. W and Mo form carbides of the same type, M_2C type at low temperatures and M_6C at high temperatures. As the atomic weight of W is approximately twice as that of Mo, the effect of 1% Mo is equivalent to 2% W; it is common to use the equivalent tungsten relation: '$W_{eq} = W + 2Mo$.' Considering this, it is verified that the effects of Mo and W in the fraction of the carbides formed are similar. The tungsten and molybdenum carbides promote high hardness and also high resistance to tempering; for high levels of these elements the drop in hardness is observed only after 650 °C. Vanadium also precipitates carbides (MC type) that provide high hardness and resistance to tempering. It acts more intensely than Mo and W; 2% of V generate more pronounced effect than 5% of Mo. Vanadium, even in low concentrations, is effective in promoting resistance to tempering. For example, the steel with 0.26% of V at 760 °C presents 60 HV harder than the composition without V.

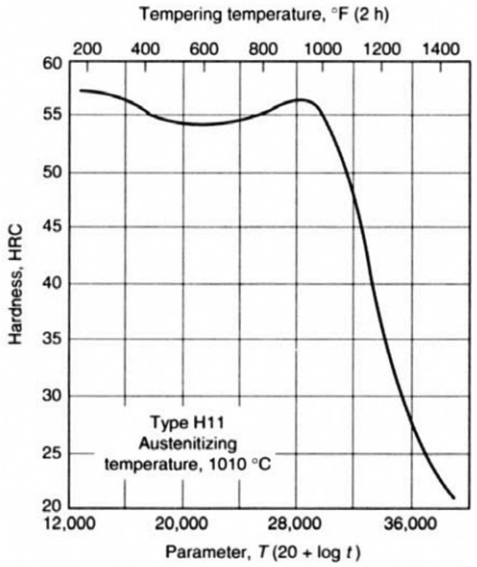
Example of the types of carbides formed in H13 steel is shown in **Figure 16**, along with the chemical composition determined by microanalysis.

2.9.4.7 Multiple Temperings

As seen in the Section 2.9.4.6, the tempering of high-alloy steels generally involves precipitation of carbides of alloying elements, which reduces the content of solid solution elements in the martensite. Such precipitation also occurs in the



a)



b)

Figure 13 (a) Response to tempering of a high alloy steel[18]; (b) response to tempering of H11 steel as function of the tempering parameter: $T(20 + \log t)$, where t=time in hours and T=temperature in °F + 460.[12]

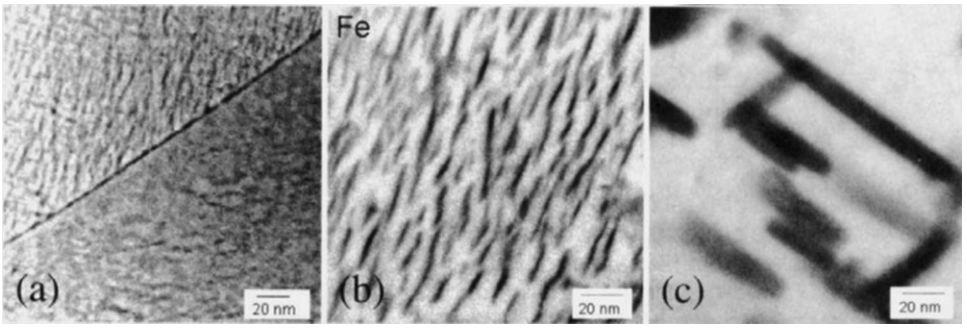


Figure 14 Secondary carbides of the AISI M42 high speed steel after different tempering treatment (austenitized at 1180 °C) (a) 530 °C, triple for 2 h; (b) 590 °C, triple for 2 h; and (c) 680 °C, triple for 2 h.[19] If related to the **Figure 13(a)**, it can be seen that the drop in hardness is accompanied by coalescence ('thickening') of secondary carbides.

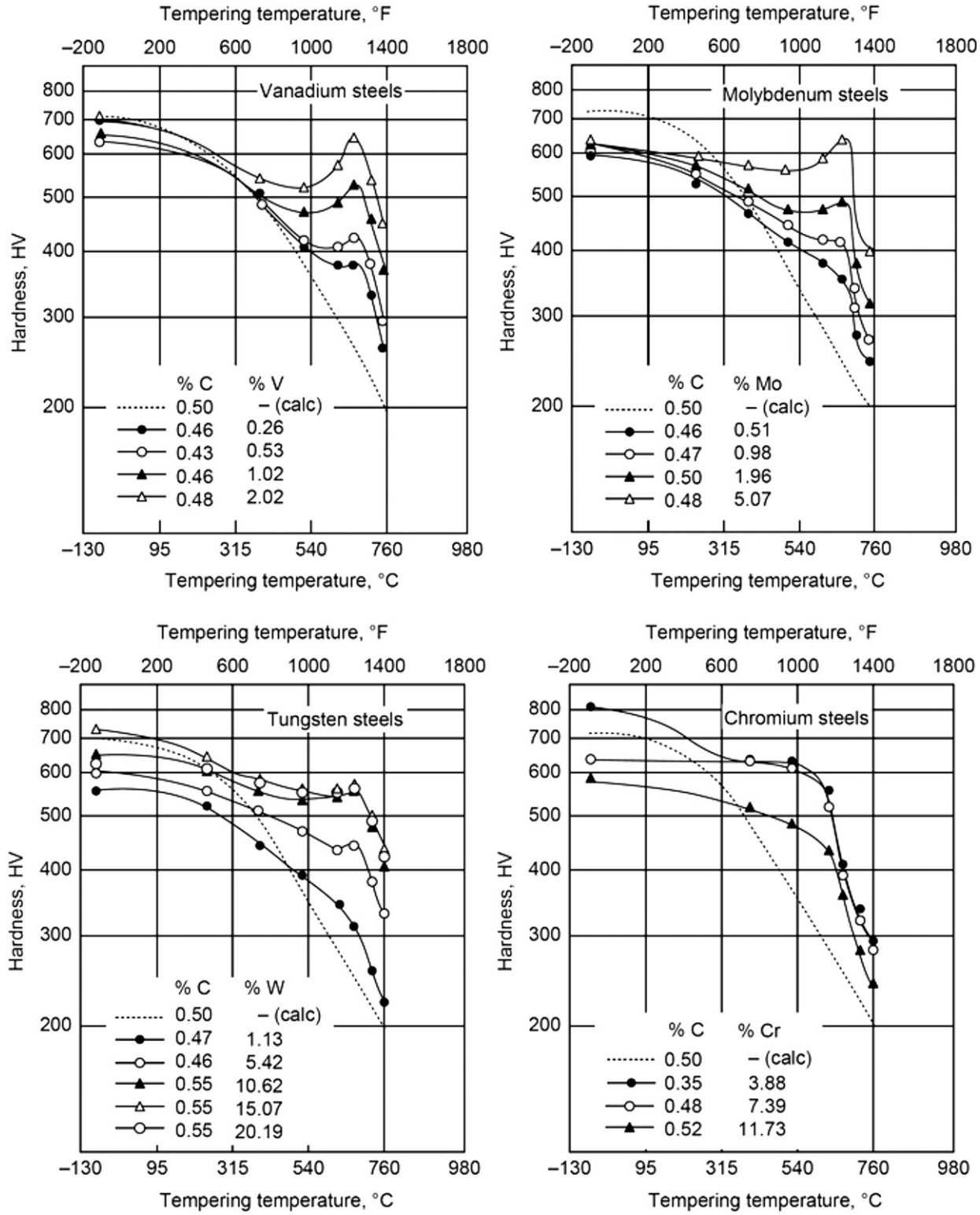
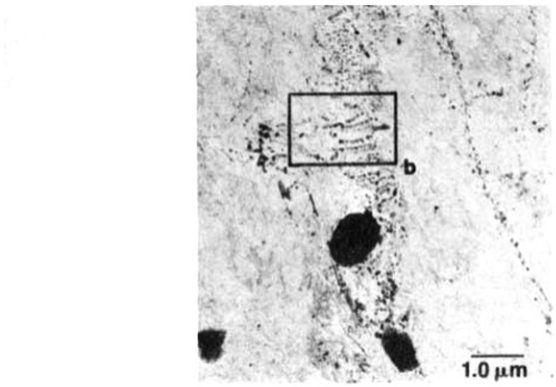
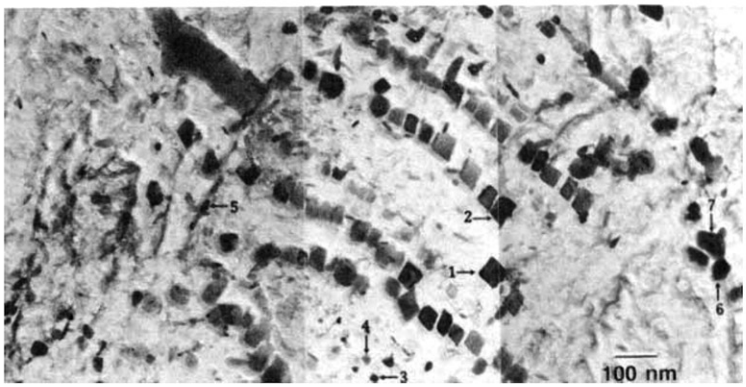


Figure 15 Effect of V, Mo, W, and Cr in the secondary hardness of 0.5% C steel.[20]

retained austenite, making it also poorer in C and alloying elements. The M_s and M_f temperatures depend strongly on the content of elements in solid solution in the austenite. In general, the lower this content the higher are the temperatures of M_s and M_f. Therefore, the precipitation generates rise in the M_s and M_f temperatures.

The most important result is that during the cooling of the tempering, the austenite can transform into martensite (or





Composition of the Metallic Portion of the Carbides Labeled in Figure 18b

Particle I.D.	Type of Carbide	Metal Composition(%) Fe	Mo	Cr	V	Si
1	MC	1	15	11	71	2
2	MC	1	16	15	65	3
3	MC	3	23	27	42	5
4	MC	4	23	24	40	9
5	M_2C	22	15	56	4	3
6	$M_{23}C_6$	28	6	60	4	2
7	$M_{23}C_6$	38	4	54	3	1

* Heat treatment: 1066°C - 80 min., 305 mm rd. simulation, 593°C - 2 hr. + 2 hr., A.C.

+ Analyzed using a Philips 420T TEM/STEM operating in TEM mode with a spot size of 100 nm, E_o = 120 kV, an acquisition time of 300 sec. and a dead time <20%. Specimen was a single stage carbon extraction replica evaluated at 0° tilt.

Figure 16 Secondary carbides analyzed by TEM precipitated in H13 steel after quenching from 1066 °C and double tempering at 593 °C. The chemical analysis and types of carbides identified are presented in the table below the figure.[21]

bainite) as the M_s and M_f temperatures increased. This newly transformed martensite (fresh martensite) has not yet been tempered and therefore is hard and brittle, which may weaken the entire tool. Thus, new tempering should be performed to effectively temper this martensite. Double temperings are needed and it is common in many tool steels. If some retained austenite still remains, the precipitation that occurs in the second tempering may promote its transformation into martensite. Therefore, a new tempering (third) is required. Three temperings are recommended for high-alloyed HSS.

2.9.5 Practical Aspects of the Heat Treatment

Although summarized, the concepts presented in Section 2.9.4 are very important for understanding and for correct application

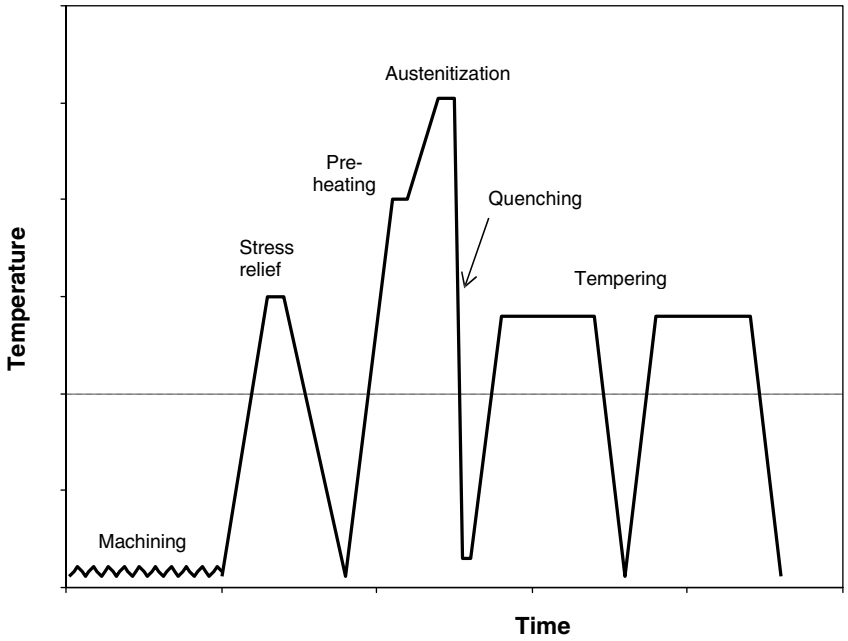


Figure 17 Schematic diagram of the main operations performed by tool steel users in manufacturing of molds, dies, and tools.

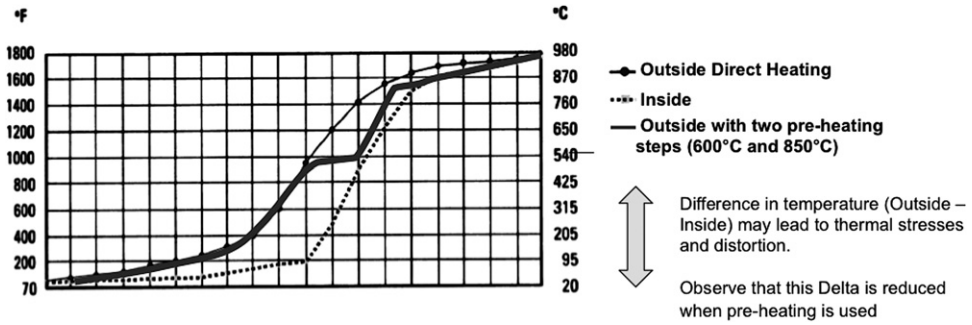


Figure 18 Difference between the temperature of the surface and core of a piece during heating within a furnace.[22]

of heat treatments in tool steels. Following are some important information to obtain desirable results after heat treatment of this kind of steels.

Operations typically performed by the manufacturer of the mold or die steels are shown schematically in Figure 17.

2.9.5.1 Design, Machining, and Stress Relief

The mold or die design is an important part and is closely related to possible problems of the heat treatments. Regions with abrupt variation in the cross-section and sharp corners are points that can lead to cracks or warpage during heating and mainly during quenching. It is not objectified here to describe all design conditions but in project design, all aspects and transformations of heat treatment should be considered.

Despite the finish machining performed after the heat treatment, the prior finish cannot be too rough. Rough machining marks can act as notch and cause fracture of the mold or die during the heat treatment.

In addition to giving shape of a component, machining also introduces stresses in the material. These stresses must be relieved before heat treatment in order to avoid distortion or warpage. This treatment is called stress relief and should be done immediately after machining. Stress relieving is strictly necessary in parts with pictures and profiles, in which the material removal was greater than 30%. The stress relief procedure in tool steels involves slow heating to temperatures between 500 and 600 °C and cooling in the oven until the temperature is 200 °C.

During cutting (work) the tool can also be subject to tensions. In this case, the stress relieving must be carried out at a temperature 50 °C lower than the temperature of the final tempering. The procedure is the same.

2.9.5.2 Heating Furnaces

There are many types of heating furnaces that can be used in treatment of tool steels. Some examples are the muffle furnace,

salt bath furnaces, vacuum furnaces, and fluidized bed furnaces. The description of the types of furnaces falls beyond the objective of this chapter, but can be found in books for this specific topic.

The use of appropriately controlled atmospheres is important to prevent the occurrence of decarburization. This is characterized by the 'loss' of carbon or alloying elements during the treatment, caused by oxidation. It causes decrease in hardness of the surface layer, which needs to be removed by a finishing machining.

An important thing to mention about the heating furnaces is the need of rigorous knowledge and control of the temperature. If the temperature calibration of the furnaces is not properly performed, there may be deviations of hardness and properties in the treated materials. A treatment temperature 15 °C higher or lower can lead to very undesirable consequences, ranging from the low performance to the loss of the mold or die. Moreover, the furnaces used must have adequate capacity to perform the treatment, since the whole piece needs to be treated at the appropriate temperature. There should not be hotter or colder points within the furnaces.

2.9.5.3 Preheating

When ensured that the furnace used is appropriate, heating for quenching can now be realized. However, as shown in **Figure 18**, the surface heats up more rapidly than the core. Considering that the tool steels are treated at relatively high temperatures, this difference can cause distortions.

To avoid these problems, it is recommended to carry out preheating before the austenitization (as shown in **Figure 17**). The time should be sufficient for equalization of the temperature between the surface and the core, usually between 15 and 30 min (assuming that the part is heated with the furnace). The temperature depends on the steel in question, being available in specialized books and tool steel manufacturers catalogs.

2.9.5.4 Austenitization

The temperature and time of austenitization are essential for adequate performance of the tool. As already mentioned, the austenitization is the part of the heat treatment in which ferrite is transformed into austenite, which dissolves the carbides of alloying elements that in turn, will re-precipitate causing hardening. The temperature, therefore, should be high enough to allow these phenomena to occur. Otherwise, the ferrite cannot be completely converted to austenite, and in the end, the required martensite is not formed. Still, if the temperature is too low, there may be low dissolution of carbides, jeopardizing the response to the secondary hardening.

However, the temperature cannot be too high. As shown in **Figure 19**, the austenite consists of grains that grow as the austenitization temperature increases. The excessive grain growth weakens the material and decreases the life of the tools. As already explained in Section 2.9.4.4, very high austenitizing temperatures can cause liquid formation in regions rich in carbides, causing severe embrittlement in the material (burning). This can happen especially in HSS. The austenitizing temperatures also vary widely among tool steels (800–1200 °C). Like temperature, the time of austenitization also cannot be too long or short. Temperatures and times recommended for each steel are given in manufacturer technical brochures.

2.9.5.5 Cooling Mediums for Quenching

Books and tool steel catalogs usually indicate possible mediums of quenching for each steel. The cooling mediums are even used to classify tool steels. It should be stressed that the indicated mediums should be followed as recommended, always taking into consideration the size of the pieces. In case of oil, it must be suitable for quenching and (as in the case of water quenching) be renewed with certain frequency.

For the cases where reduction in distortions is targeted the use of martempering (when possible) is interesting. This treatment makes the equalization of the temperature between the surface and core occur prior to the martensitic transformation, reducing the risk of cracks and distortions.

2.9.5.6 Time and Temperature of Tempering

The tempering temperature should be chosen according to the required hardness for the application, using the correct tempering curve. Contrary to what occurs in carbon steel, the tempering curve of tool steels varies considerably with the austenitizing temperature employed. In this choice, here are some general tips:

- The conditions of austenitization, always use the highest tempering temperature possible. In some steels such as AISI D2 or VF800AT, the tempering curve analysis shows that the hardness of HRC 58 can be obtained by using low temperatures, approximately 200 °C or higher temperatures, 530–560 °C (see tempering curves in the manufactures' catalogs). Higher tempering temperatures are recommended for three reasons: (1) cause elimination of retained austenite, which could transform during operation and cause expansion ('seizure or gripping') and embrittlement of the material; (2) increase in hardness by the secondary hardening, a mechanism that produces tougher pieces (tools) than a little tempered martensite; and (3) make possible the realization of surface treatments such as nitriding, without loss of core hardness.
- When using HSS for cold work with hardness around 60 HRC, keep the tempering near the secondary peak (~560 °C) and get the hardness from reducing the austenitizing temperature. The other possibility would be to use the standard austenitization temperature (~1200 °C) and tempering at high temperature (~610 °C) to obtain the desired hardness. However, using smaller austenitizing temperatures results in lower grain growth, generating higher toughness. Moreover, the adjustment of the austenitizing temperature rather than the tempering provides greater control of the hardness. As shown in **Figure 15**, the hardness rapidly decreases beyond the peak, and an error of 5 or 10 °C can easily modify them in 2–3 points. Other advantages of the smaller austenitizing temperatures

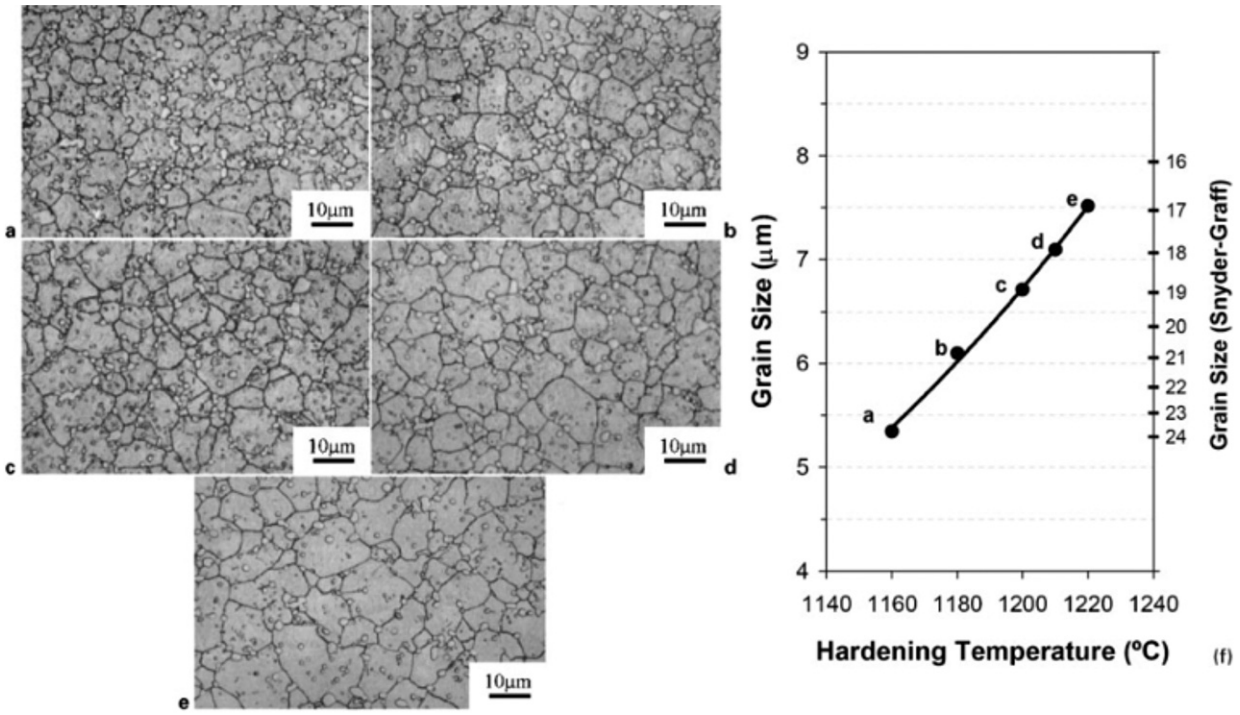


Figure 19 Variation of the austenite grain size of M2 steel as function of the austenitization temperature. Etching: Nital 4% (8 min) and Villela (20 s). Images represent the typical microstructures after hardening (quenching) at: (a) 1160 °C, (b) 1180 °C, (c) 1200 °C, (d) 1210 °C (e) 1220 °C (etching, nital 10% (8 min) and Villela (20 s)), and (f) austenite grain size measured by Snyder–Graff method.[23]

are less deterioration of the furnaces and the lowest energy consumption for heating.

- In steels for hot work, the tempering temperature must always be higher than the temperature of work of the matrix. Explanation: if the tempering temperature is lower than the usage, the material will experience tempering during application, losing hardness in an uncontrolled manner. Moreover, tempering at lower temperatures may not provide the total elimination of the retained austenite, generating the problems already discussed. Lower temperatures are often used on the grounds of promoting greater hardness, and consequently, higher strength and less hot wear (see **Figure 13(b)**). However, this practice is flawed because it must be taken into consideration that the material will work at elevated temperatures. As the hardness of work is the property that determines the hot resistance, there are no direct gains in this practice because the material is tempered again, but this is time uncontrolled (at work), and the hardness will again fall.
- The time for each tempering should be approximately 2 h (at temperature). Unlike austenitizing, there are no problems if the time is a little higher (occurs possibly a slight decrease in hardness). However, if the time is less, the microstructure may not have been sufficiently tempered, causing reduction in properties. This brings an interesting phrase, used routinely, 'hardly the steel can be super-tempered, but can easily be sub-tempered.'[21]
- Another important recommendation is that the tempering should be performed immediately after hardening (quenching), i.e., as soon as the piece reaches approximately 60 °C (this temperature may vary from one steel to another steel). If longer times (more than 1 h) pass before the tempering, stabilization of retained austenite phenomenon will occur. As discussed in Section 2.9.7, the austenite tends to transform again into martensite or bainite after the first tempering. However, if the time between quenching and tempering is excessive, part of the austenite no longer transforms – a phenomenon known as stabilization of the retained austenite. Thus, in practical terms, quenching cannot be performed one day and tempering the day after. It is also important to remember that excessive rush for tempering must be avoided, i.e., tempering cannot be started until the entire piece has cooled. This is because, if the tempering starts above 150 °C for example, great part of the microstructure has not yet been transformed into martensite.

2.9.5.7 Quality of the Heat Treatment

The primary measure of control of the heat treatment is a measure of surface hardness. Although important, however, the hardness can hardly evaluate all aspects of the microstructure. Let's take the example of **Figure 20**, where several microstructures of the VH13 (AISI H13) steel were found, all with similar hardness, between 44 and 46 HRC. In **Figure 20(a)**, the normal microstructure is observed, consisting of tempered martensite and secondary carbides; this is responsible for the high value of toughness identified – 350 J. **Figure 20(b)** shows a typical microstructure of a steel austenitized at too high temperature, showing the high grain size of the austenite. As a result the toughness drops to 42 J, showing that embrittlement has occurred. **Figure 20(c)** presents a steel that was austenitized at very low temperature, which did not

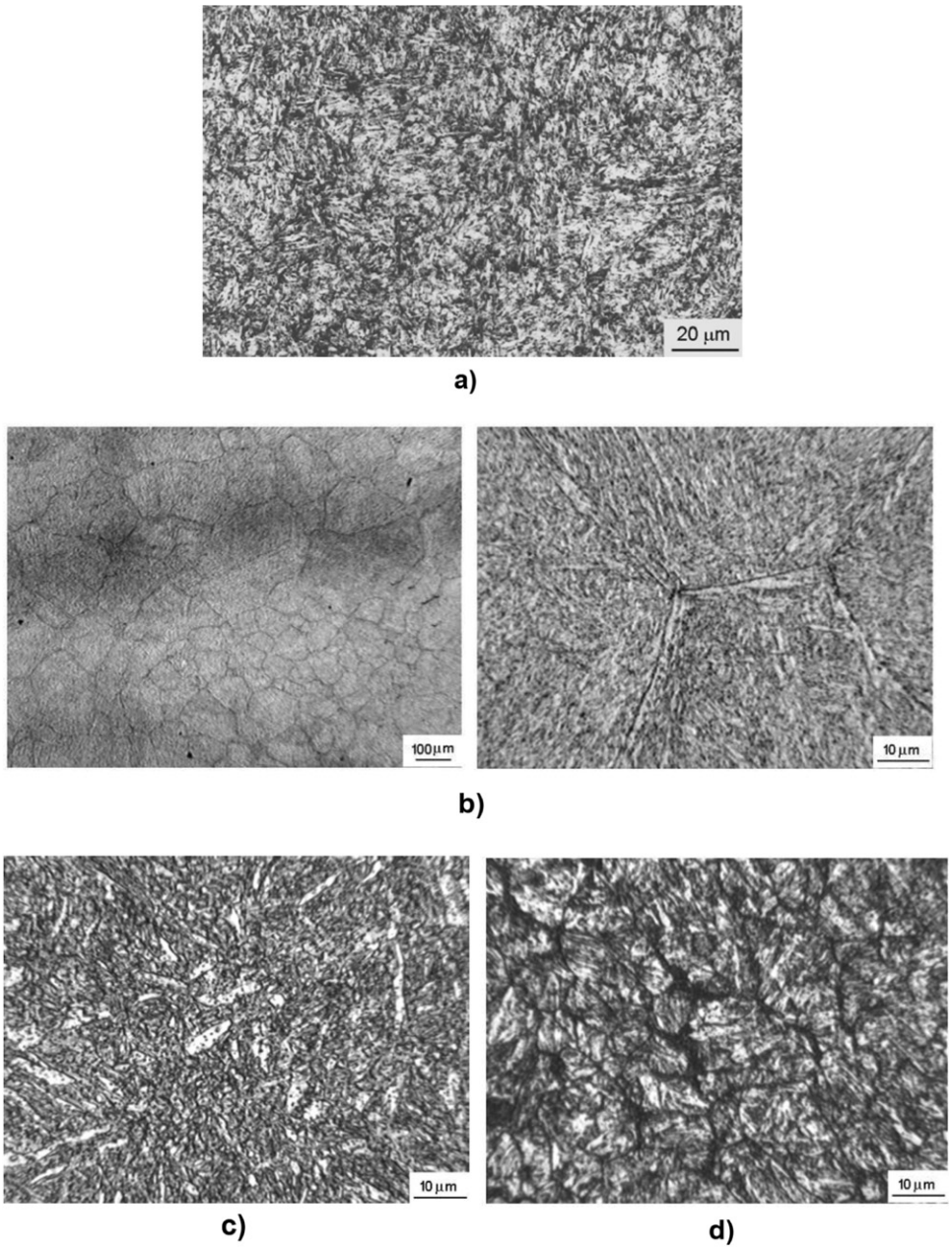


Figure 20 Representative microstructures of the H13 steel, heat treated to a hardness range of 4446 HRC in the following conditions: (a) right condition, austenitization at 1020 °C, quenched in oil and double tempering at 610 °C, impact energy of 350 J and loss in hardness of 0.5 HRC being exposed at 550 °C for 10 h; (b) wrong condition, austenitization at 1150 °C, quenched in oil and double tempering at 630 °C, impact energy of 35 J; (c) wrong condition, austenitization at 890 °C, quenched in oil and double tempering at 250 °C, impact energy of 208 J and loss in hardness of 3 HRC, after being exposed at 550 °C for 10 h; (d) wrong condition, austenitization at 1020 °C, quenched with slow cooling and double tempering at 610 °C, impact energy of 225 J (the darker regions are perlite).

promote total transformation of the ferrite into austenite. The toughness is again lower than expected (210 J). Furthermore, in order to obtain the required hardness, this steel was tempered at low temperature (200 °C). After exposure to 550 °C, a drop of 3 HRC in hardness is observed, although only 0.5 HRC was expected. Thus, the microstructure of **Figure 20(c)**, besides being more brittle, would present poorer hot performance, given its biggest loss in hardness. In **Figure 20(d)**, a microstructure with pearlite traces (dark in the triple points) is seen, confirming an erroneous condition in the cooling for quenching. Again, less toughness is verified.

The microstructures of **Figure 20** can easily be found in practical situations. The situation of **Figure 20(b)** may result from an uncalibrated austenitizing furnace or even an incorrect charge in order to take the load (and temperature!) of a different steel. The microstructures of **Figure 20(c)**, instead, may occur if the furnace temperature is uncalibrated to lower temperatures or occurs even when treated in a furnace with

temperatures not exceeding 1000 °C (which is common). In the case of Figure 20(d), this condition could occur, for example, in a mold or die with large dimension, that instead of quenching in oil as recommended, it was rather cooled in still air.

For the above example it is clear that the hardness is not sufficient condition for an appropriate heat treatment. To be considered an appropriate treatment, their microstructure should be evaluated. However, in practical terms, it is extremely complicated to evaluate the microstructure of a mold or die steel, because it would normally be necessary to destroy the part (e.g., to observe the microstructure of the core). Thus, a good heat treatment can only be guaranteed if all procedures (equipment, temperature, and time) are strictly respected.

It is worth mentioning that different heat treatment routes or when involving thermomechanical processing or processed in a semisolid state[24] the results might be completely different. Cryogenic treatments have also been frequently applied to tool steels either during production (or during the conventional heat treatment)[25,26] or after the conventional heat treatment[27] and on both cases properties enhancement are achieved. Another way to obtain better quality is employing hard coatings[28,29] on them. In this case friction reduction, improved wear and corrosion resistances are usually searched.

2.9.6 Heat Treatment Troubleshooting

2.9.6.1 The Importance of Heat Treatment in Tool Steels

The heat treatment has very important effects on properties, and consequently, on the performance of tool steels. Nevertheless, the vast majority of premature tool failure is a result of an incorrect heat treatment (it is estimated that about 70% of premature tool failure is caused by incorrect heat treatment).

The heat treatment of the tool steel has many peculiarities. For a number of factors, not just metallurgical factors heat treatments of tool steels are very different from heat treatment of plain carbon or low-alloy steels, for example, those applied in large volume parts production. Firstly, there is a high dependence of the final properties of the material with the heat treatment applied. The conditions of temperature, time and heating and cooling rates, the equipment utilized, and finally the entire procedure in most cases will be strongly related to the final performance of the tool. Secondly, the high value of the parts to be treated; in this case, dies and molds in which machining costs and the steel itself are already included. Thirdly, because it is usually one of the last steps of the process. So, if serious problems occur, it will hardly be possible to reset the tool treated within the required procedure. Fourthly, dies and molds are not standardized tools and consequently, the heating time and geometry, and the stress concentrators related to it, are constantly changing. Fifthly, the narrow temperature range, both of austenitizing and tempering as well as the variation of this range between the various types of steels used in tools.

All of these specificities of heat treatment of tool steels, if not well observed, can lead to problems or process failures that consequently cause a low yield of the tool. In terms of failures, it is interesting to divide them into two subgroups. The first are the flaws identified in the process itself, as small or catastrophic cracks, distortions, superficial problems (such as decarburization and oxidation), and other failures visibly observed. Although serious, these failures generally do not compromise the tool life, or at least do not create unexpected results during their use, because they are identified before it enters into operation. The second possibility of deviation in the heat treatment refers to conditions of temperature, time, and cooling rates employed. Quality control of the heat treatment, in most cases, is performed only by hardness measurements on the surface of the tool. This is because normally it is dealt with unique pieces and high values, with no possibility of its destruction for microstructural analysis and determination of properties. Thus, once the hardness is right, it is possible that the heat treatment deviations will hardly be identified before use of the tool and these will only be observed if a smaller tool life is perceived, and the cause of failure can be defined accurately.

Therefore, it is important to have knowledge of possible inaccuracies in the heat treatment. Two types of tool steels and the effect of heat treatment procedures on their properties will be discussed here. The first steel is the VH13ISO, similar to AISI H13, but produced with special manufacturing processes to provide improved toughness and isotropic properties.[30] The second steel, called VF800AT was developed for applications requiring greater toughness than the conventional steel,[31] typically AISI D2 and D6. The compositions of these steels are presented in Table 6.

For both steels studied, VH13ISO and VF800AT, various conditions of quenching and tempering were employed. Some are correct by following the recommended temperatures and times for each steel, and some considered incorrect, for not following these recommendations. The heat treatment conditions used for each steel will be described later, in the results. When not mentioned, the austenitizing times were 30 min and double tempering temperature in 2 h.

To evaluate the toughness, the VH13 steel was analyzed by unnotched impact test, following recommendations of NADCA,[32] because this test relates very well to yield of hot work dies.[30,33] For the VF800AT steel, the four points bending test[34] was used with test samples of 5×7 mm^2, taken in the longitudinal direction. The mechanical results were correlated to the microstructures observed by optical microscopy. For the case study, the failure (fracture surface of impact specimens) of the VHSUPER, another hot work tool steel, was analyzed by scanning electron microscopy.

The following results are described in three parts. In the first one it will be described the simulations of various heat treatments in VF800AT steel. Secondly, the same approach is taken for the VH13 steel. Because of excessive marks of austenite

Table 6 Nominal chemical composition of the steels VH13ISO and VF800AT

	C	*Si*	*Mn*	*Cr*	*Mo*	*V*	*Nb*
VH13ISO	0.40	1.0	0.3	5.2	1.5	0.9	–
VF800AT	0.85	0.9	0.4	8.0	2.0	0.5	0.15

grain boundaries in the latter material its evaluation in laboratory was inaccurate. This would require slow cooling of the sample, but not so slow as in an oven. Being impossible to simulate this slow cooling, it was employed a real case of die failure, held by cooling at too slow quenching. This fact is described in the third part, for a forging die made in VHSUPER steel.

2.9.6.2 Analysis of Several Conditions of Heat Treatment in VF800AT Steel

To study the heat treatment of VF800AT steel, a correct routine was followed as well as an incorrect one. Bending tests of the samples were then carried out. For all materials the hardness was maintained at 60 HRC. The condition A refers to the material treated properly, with 1030 °C quenching and double tempering at 530 °C. All the other conditions refer to incorrect treatments (but would be correct for other materials). Figure 21 shows these results.

The condition B features a double incorrect treatment condition, wherein both the austenitizing and the tempering temperatures were inadequate. Compared to the correct treatment, there is loss in 25% of flexural stress strength and lower rupture energy, indicating less toughness. The condition B is close to the thermal treatment applied to the VC131 (AISI D6) steel, very widespread in cold work applications.

The condition C, on the other hand, has the correct austenitizing temperature, but tempering was applied at a low temperature. This procedure is typical for VD2 (AISI D2) steel, which has higher austenitizing temperature than the VC131, but is tempered at a low temperature, because the secondary peak is not sufficiently intense to promote hardness of 60 HRC. In this case, there is also loss of strength and toughness.

The fourth condition D is typical for heat treating HSS – austenitization at very high temperature and tempering above 550 °C. In this case, the loss in toughness was even more significant.

The above mechanical properties can be understood by analyzing the microstructures obtained in each condition (Figure 22). In the correct condition (A) a microstructure with martensitic matrix and undissolved primary carbides are observed. At that magnification (approximately × 350), the identification of the austenitic grain boundaries is unclear, because they are thin, due to the austenitizing temperature being adequate. It is also observed as a matrix darkened by metallographic etching. This condition of the matrix results from tempering at high temperature, with precipitation of secondary carbides, removing alloying elements from the matrix and providing greater susceptibility for the chemical etching. The mechanical properties are higher, in this case, because the stresses in the matrix, generated by the martensitic transformations, are alleviated and hardness is promoted by secondary precipitations, improving further the mechanical properties.

In the condition B, it is observed that the quenching and tempering at low temperatures are able to promote adequate hardness. However, the microstructure practically consists of crude martensite, i.e., not tempered. In such a condition, the stresses on the microstructural matrix are very high, reducing the strength and toughness of the material.

The condition C is slightly better than the condition B, in terms of mechanical properties. However, the fact of tempering at yet low temperature, promotes better toughness in comparison to the correct treatment (condition A). The microstructure still presents as somewhat less tempered, a fact highlighted by the high resistance of the material to metallographic etching, thus generating low toughness.

In the condition D, on the other hand, the microstructural matrix is more etched by the chemical reagent. However, the obtained toughness is too low because in this case the negative factor refers to the very high austenitizing temperature (typical of HSS). Under these conditions, there is too much grain growth because, unlike HSS, the VF800AT alloy was not designed to withstand as high austenitizing temperatures.

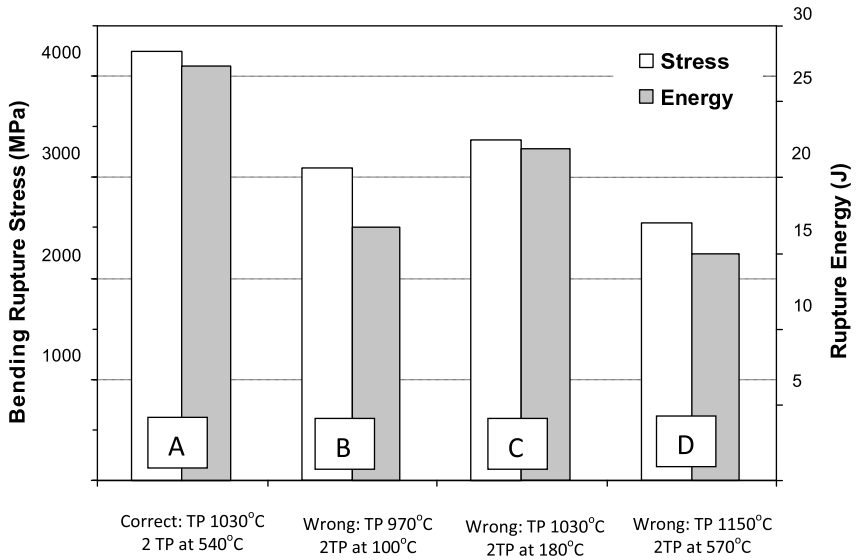


Figure 21 Resistance to bending and rupture energy, for VF800AT steel treated under several conditions, all with 60 HRC. The conditions A–D are described in the text.

The martensite formed during cooling is consequently rough and properties are reduced.

2.9.6.3 Analysis of Several Conditions of Heat Treatment in ISO VH13 Steel

As performed for the VF800AT steel, various heat treatment conditions were also applied to the VH13ISO steel. The conditions are described below and the results of impact are shown in Figure 23.

Condition E: correct heat treatment for the H13 steel, with austenitization at 1020 °C, rapid cooling during quenching, and tempering at high temperature of 610 °C. This condition generates the greatest toughness values.

Condition F: low austenitizing and tempering temperatures. This procedure may be erroneously applied when using low-temperature ovens.

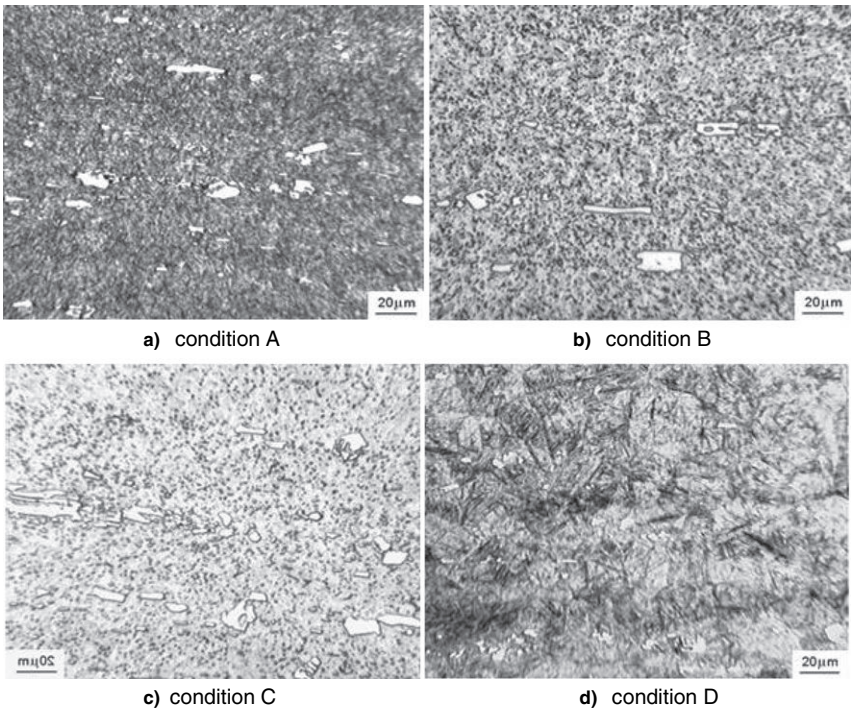


Figure 22 VF800AT steel microstructures resulting from heat treatment under the conditions A–D, described in Figure 21. Magnification of × 350, Villela etching, for 10 s.

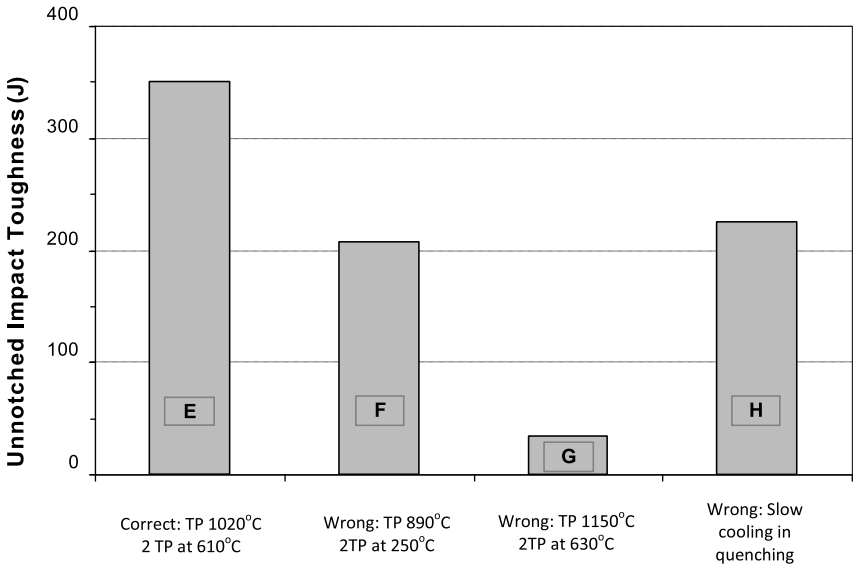
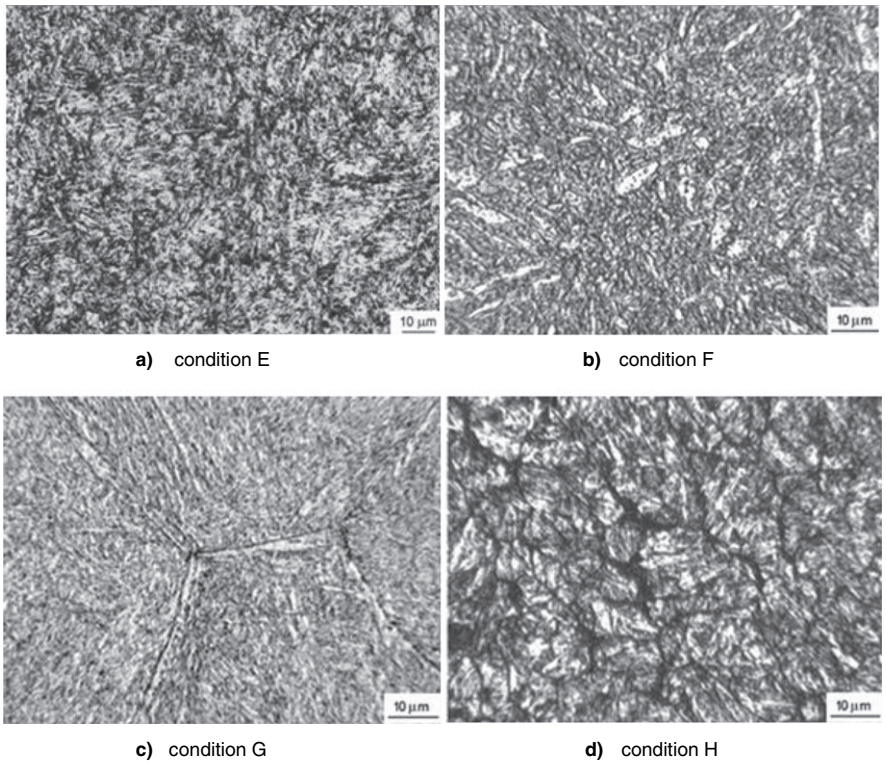


Figure 23 Unnotched impact energy according NADCA[32] for VH13ISO steel treated for various conditions, all 45 HRC. The conditions E–H are described in Section 2.9.6.2 of the text.



a) condition E **b)** condition F

c) condition G **d)** condition H

Figure 24 Microstructures of the VH13ISO steel as a result of the heat treatments under the conditions E–H as described previously (Figure 23). Nital etching (4%).

Condition G: too high austenitizing temperature and tempering temperature slightly higher than usual, to adjust the hardness to the required range.

Condition H: normal austenitizing and tempering temperatures, but the material cooled very slowly to room temperature (approximately 6 °C min^{-1}). This procedure may be caused, for example, due to quenching in poor aggressive cooling medium such as quenching in air.

Figure 24 shows the features of the microstructure of each condition of heat treatment. In Figure 24(a), a typical microstructure is observed consisting of tempered martensite and secondary carbide (condition E); this generates high toughness identified value – 350 J.

In Figure 24(b), condition F, the too low austenitizing temperature did not cause the total transformation of ferrite. The toughness is lower than expected (210 J). Furthermore, in order to obtain the required toughness, the steel is tempered at a low temperature (200 °C). After exposure for 10 h at 550 °C, it has reduced 3 HRC points in hardness where only 0.5 HRC were expected. Thus, this microstructure, besides being more fragile, would cause loss in hot performance, given its biggest loss in hardness.

Figure 24(c) shows the typical microstructure of austenitized steel to too high temperature (condition G), evidencing the high austenite grain size. The result is dramatically lower toughness (42 J), showing that the embrittlement occurred. Just as in the condition D of the VF800AT steel, very high austenitizing temperature promotes the formation of coarse martensite and sharp reduction in toughness.

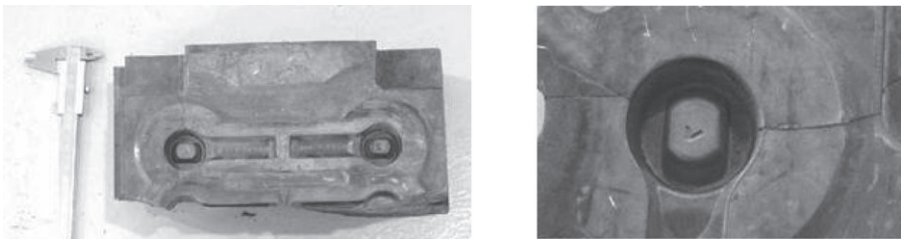
For condition H (Figure 24(d)), the microstructure has traces of pearlite (dark in triple points), showing an erroneous condition in the cooling of quenching. Again, low toughness is observed. Besides the pearlite formation, too slow cooling provides grain boundaries embrittlement, as will be shown in the following item.

2.9.6.4 Case Study – Forging Die with Premature Failure

A practical case of failure similar to the condition H, previously described, was identified in a forging die made of VHSUPER steel. In this case, the matrix had much lower than expected life. The failure occurred by catastrophic cracks, shown in Figure 25.

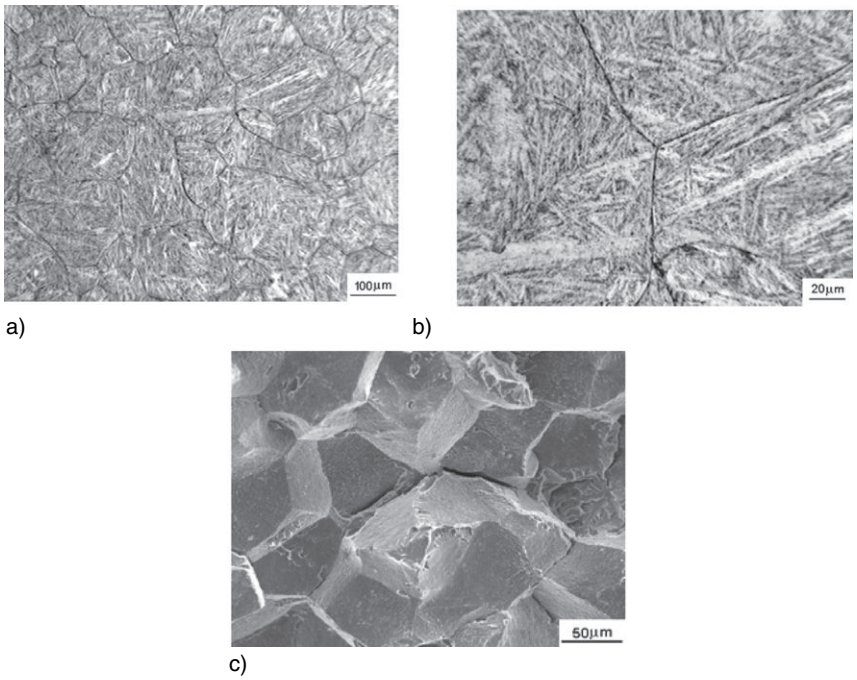
The microstructure of the material, Figure 26, showed strong marking of austenitic grain boundaries. This results from precipitation of carbides during cooling, due to a too slow cooling rate during quenching. It is also observed as coarse austenitic grain, indicating that the heat treatment was performed with excessive austenitizing temperature or times, which facilitates the precipitation of carbides.

To analyze the toughness, impact test specimen's samples were withdrawn from the fractured die. The results found are much lower than expected for the VHSUPER steel. The energy of rupture was 50 J in unnotched specimens, machined according to the recommendations of NADCA, and the expected rupture value for this steel is more than 250 J. The fractured surface, shown in Figure 26(c), made up of predominantly intergranular, evidencing the fragilizing effect of the carbides.



a) b)

Figure 25 Premature failure of a forging die. (a) whole die and (b) details of the cracked regions.



a) b)

c)

Figure 26 Microstructure observed in the cracked die. Austenitic grain in detail at (a) low magnification; (b) high magnification; and (c) fracture of impact test specimens taken from the die, obtained by scanning electron microscopy, secondary electron.

After this result, a sample of the material was taken and an annealing followed by new quenching and tempering was performed, for the same hardness but with cooling in oil during quenching. The rupture energy increased from 50 J to 360 J.

From the previous examples, Sections 2.9.6.3 and 2.9.6.4, it is clear that hardness is not sufficient information for an appropriate heat treatment. To be considered an appropriate treatment, the microstructure and mechanical properties should also be evaluated.

However, in practical terms, it is unfeasible to evaluate the microstructure and properties of a mold or die, because normally it would be necessary to destroy the part (e.g., to observe the microstructure of the core). Thus, appropriate heat treatment can only be guaranteed if all procedures (equipment, temperature and time) are strictly adhered to.

To summarize, the conditions of heat treatment significantly influence the microstructure and properties of the tool steels and consequently, have a strong influence on the life of the mold, matrix, or the tool used. Either for tool steels for cold working or in steels for hot work, heat treatment conditions vary intensely from steel to steel. So the individual conditions of each material in terms of temperature, time, and heating and cooling rates must be respected for proper performance of the tool. Studies in the laboratory have shown the influence of wrong conditions on the final properties of the tool steels. They therefore confirm the need of using a correct procedure, in order to guarantee an appropriate heat treatment.

2.9.7 Examples of Application and Performance of New Hot Work Steels

Hot forming tools are applied in various industries, focused on the production of parts for mechanical applications, especially automobile parts. The variety of methods used can be divided into three basic operations: tools for hot and warm forging, molds and dies for casting of nonferrous alloys, and extrusion dies of nonferrous alloys.

In forging applications, the hot forging of steel, especially of engineering steels applied in automobile parts, is distinguished. In such operations, the forged billet is heated at temperatures above 1100 °C. During the forming, the die surface is heated; the higher the temperature of the billet and the contact time of the workpiece with the tool, the higher is the temperature of the die. In relation to the contact time, this is higher in press forging and lower in the case of hammer forging. If temperatures reach the surface of the matrix, for example, over 550 °C, the tempering mechanisms start to occur in tool steel promoting loss of mechanical strength in such regions. Thus, a key property is the resistance to tempering (i.e., the loss in hardness) of the tool steel.

In extruding nonferrous alloys, the temperatures used are too high, but the billet is heated to lower temperatures in comparison to forging operations. In the aluminum extrusion, for example, the temperature of the billet is in the order of 600 °C. However, the long contact with the billet with constant friction also generate hardness loss in tool steel. In copper alloy extrusion the temperature is higher than that of aluminum, thus requiring steels with high resistance to tempering. In both applications, nitrided tools are often employed, in order to increase the hot wear resistance. However, long time of exposure to heat promotes diffusion of the nitrided layer, requiring re-nitriding of the tool.

In both forging and extrusion, toughness is also an important property. In local stress concentration, lack of toughness can generate coarse cracks, which depending on the size involved may condemn the tool. In forging, such cracks could be catastrophic, immediately suspending the operation, or be caused by mechanical stresses. The toughness is also important in extrusion operations in parts of auxiliary tools to the die, receiving the impact of the billet or having areas of higher stress concentration.

Other application that requires high performance of the tools and special tool steel properties is the casting of nonferrous alloys, especially aluminum alloys. In the press casting process the main solicitation applied to the dies is thermal cycling. As a result, the normal way to determine the end of tool life is the formation of a network of thermal cracks (heat-checking) in such a severe manner that compromises the surface quality of the part being produced.[35] The main property of tool steel related to the formation and propagation of such cracks is toughness. Physical properties such as thermal conductivity and thermal expansion coefficient are also important because they act in the homogenization of the temperature between the surface and the core of the die and in the expansion generated by the heating, respectively. The increase in these properties decreases, however, the fatigue stresses. But the variation of these physical properties is limited in tool steels.

Therefore, the hot strength, more specifically, the resistance to loss in hardness (tempering resistance) and toughness are the most important properties of the tool steels used in hot forming. Depending on the employed forming process, one or other property, or even both, may be more important. Other properties, physical properties such as conductivity and thermal expansion already mentioned, can also be important, but to a lesser degree in most applications. Yet, there are situations in which the machinability and the reduction of alloying elements may also be important, such as in large forging dies.

Each tool steel has a set of properties, depending on the chemical composition and manufacturing process. As shown in previous studies,[36–38] the modification of H13 steel manufacturing process promotes increased unnotched impact energy (from 60 J to more than 200 J). Special processes, including refining by electro-slag remelting (ESR), may also promote even greater improvements.

Thus, the selection of the best steel for each application must involve the combined analysis of all the previously described properties and the influence of the manufacturing process. For this analysis, it is essential to have good knowledge of the application in question in order to determine the primary failure mechanism and the best strategy to slow it down.

The use of new steels is also related to this purpose. Through the knowledge of the main tool failure mode one can select the new material in order to act in the cause of this failure. In the following section the analysis of application of two new tool steels in hot forming will be shown. The failure modes are analyzed and compared with the main properties of the materials, so as to understand the performance improvement achieved.

2.9.7.1 Properties of the TENAX 300 and VHSUPER Steels

The two new materials and modifications that provided their properties have been described in previous papers.[38–40] However, as the knowledge of such properties will be important in subsequent discussions, they are summarized in Figure 27 and compared to the conventional AISI H13 steel. As shown in Figure 27(a), the main improvement of the TENAX 300 steel is the increased toughness characterized by impact energy. However, in Figure 27(b) it is also observed slight improvement in the hot strength of the material. In the same figure a considerable higher heat resistance of the VHSUPER steel can be seen. In these cases, the hot strength is measured by tempering resistance (or resistance to loss in hardness) which is basic in hot conformation applications.

It is also important to note that such improved properties obtained from chemical composition changes only become effective after production in appropriate conditions. As shown in previous studies,[36–38] the routes of the so called ISO® and ISOMAX® contain major process modifications, to produce improvement in isotropy and mechanical properties of the tool steels. In ISO® process, changes refer to secondary refining of molten steel in ladle furnace, the time of homogenization and forging conditions associated with particular annealing, which prevents precipitation of carbides in the grain boundaries. In ISOMAX® process on the top of all these changes, a refining by ESR is added, greatly reducing the amount of inclusions and increasing isotropic properties.

2.9.7.2 Case Analysis

Following are information about four applications of new steels. Two of them concern the use of VHSUPER steel in forging dies and the other two the use of TENAX 300 steel in forging die and die casting die. Besides these tests, other applications were also analyzed. However, data of the following cases are more complete and therefore, they were

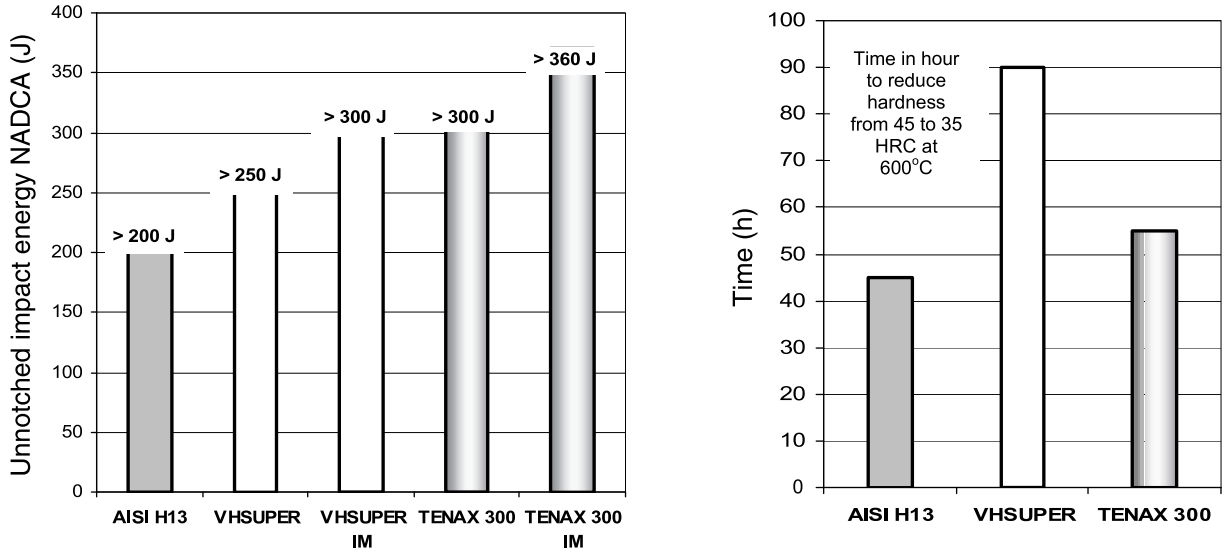


Figure 27 (a) Impact resistance in unnotched specimens for TENAX 300® and VHSUPER® steels, obtained by ISO® processes (not shown) and ISOMAX® (identified by IM). The toughness of H13 steel produced by ISO process is shown for comparison. Test specimens 5×7 mm^2, in the transverse direction, machined and treated to 45 HRC$\pm$1 according to NADCA; (b) resistance to tempering of typical AISI H13 TENAX 300 and VHSUPER, characterized the time necessary for the drop of hardness from 45 to 35 HRC when the materials are subjected to the temperature of 600 °C.

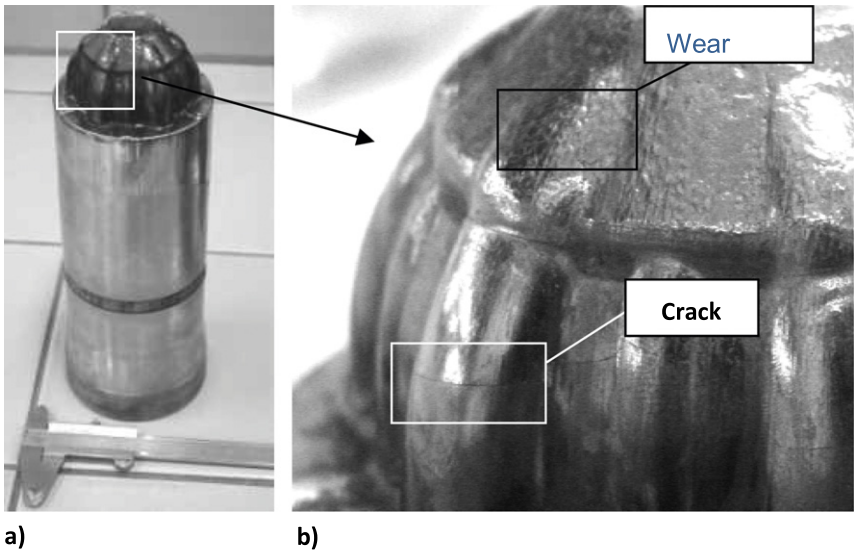


Figure 28 (a) Visual aspect of the punch and (b) detail of the hot worn regions and cracks.

selected to be presented here. In them, the process variables and conditions of use of the tools, including the hardness, were kept approximately constant. Thus, the results can be attributed to the replacement of the steel.

2.9.7.2.1 Warm forging punch – Case 1

The process in question is a high-speed warm forging. Despite the forged billet having a lower temperature than in the usual hot forging, at high speed of the process the contact between the heated billet and the die is bigger, thus heating the surface thereof. The process also employs high cooling, thereby promoting thermal shock in the surface region.

Process data: product: spindle; tool: precision forging punch to warm; forged material: SAE 1045 and modified SAE 1050 steels; billet temperature: 900 °C; cooling: high, with water;

Stroke speed: high; previously tool steel used: AISI H13; tested steel: VHSUPER; gain in tool life obtained by replacement 56%.

Figure 28 shows the punch analyzed at the end of its life. As this type of forging produces parts with high dimensional accuracy (in the order of tenths of a millimeters) deviations compromise the piece produced. Thus, the end of life is caused by wear on the rounded protruding regions and the emergence of thermal cracks (see Figure 28(b)).

In order to get more information, the punch was cut and microhardness tests were performed on the worn area. The results were plotted as a function of distance from the contact surface, as shown in Figure 29. The hardness to depths greater than 1 mm is practically uniform, with the value specified for the material – 53 HRC. However, surface areas, specifically where the wear occurs, the hardness decreases significantly, reaching about 42 HRC. Thus, wear is effectively related to the loss in hardness of the tool during operation and little change in the hardness of the core was observed. The onset of thermal cracking is also related with a loss in hardness because lower hardness regions become more sensitive to thermal crack initiation.[41]

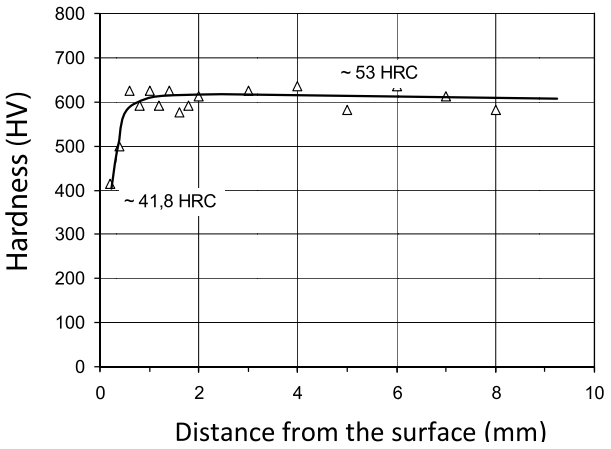


Figure 29 Microhardness measurements of the punch shown in Figure 28, from the working surface downwards to the inner regions in the direction of the die center.

Thus, increasing the tempering resistance of the material becomes essential to promote increased life of this tool. Verified by this fact, the VHSUPER steel was then tested and approved for the application, providing 56% increase of tool life.

The comparative analysis of the tempering curves and the drop in hardness as a function of temperature and time for VHSUPER and H13 steels, Figure 30, allows full understanding of the phenomenon. In both steels there is hardness losses when the steel is subjected to high temperatures. The greater the time and temperature employed the greater is the loss in hardness. However, it can be seen in Figures 30(a) and 30(b) greater stability at high temperature of the VHSUPER steel, as discussed previously. Thus, during the forging process failure will occur after a larger number of strokes, producing the yield gain observed.

2.9.7.2.2 Connecting rod hot forging die – Case 2

The increased hot resistance of the VHSUPER steel was also evaluated in hot forging die for connecting rods, shown in Figure 31(a). In this type of forging, the dimensional requirements

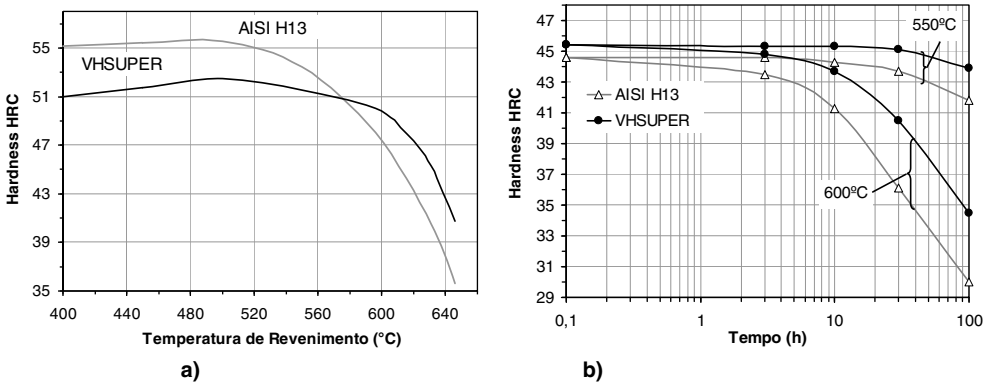


Figure 30 Comparative tempering resistance of the AISI H13 and VHSUPER steels (a) decrease in hardness as a function of temperature, double tempering after 2 h; (b) Hardness versus time in logarithmic scale.

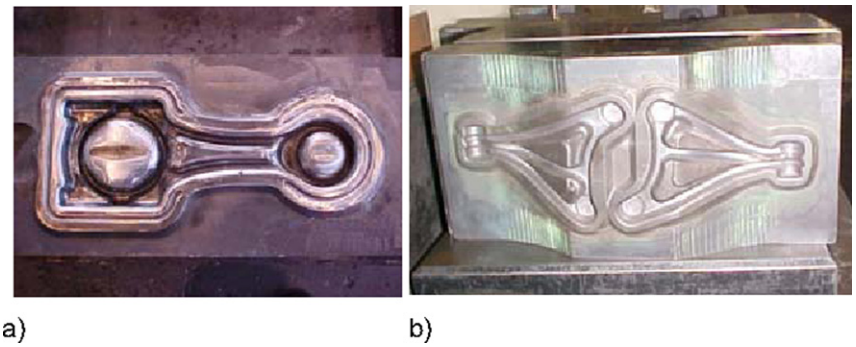


Figure 31 (a) Connecting rod hot forging die, analyzed in case 2, where the steel VHSUPER was tested and (b) engine support hot forging die, where the steel TENAX 300 was tested.

are lower than in the forging described in Section 2.9.7.2.1, but the contact time and the temperature of the forged billet are substantially higher. However, the depth of the surface region of the matrix affected by the heat of the process is worse. Some data indicated that the affected region is about 5 mm and, as shown in **Figure 29**, the hardness of the matrix decreases toward the surface.

Process data: product: forged connecting rod; tool: hot forging preform die; forged material: medium carbon steel; temperature: about 1250 °C; stroke speed: slow, typical of forging press; tool steels previously used: AISI H12 and H13 steels; tested steel: VHSUPER; Gain in lifetime obtained with the substitution: about 50%.

The end of life of the tools is caused by two factors: warm wear associated with the formation of thermal cracks. These cracks have depths greater than those observed in the warm forging punch (**Figure 28(b)**), because of the greater heat and higher temperature of the forged billet, which promotes more intensive thermal shock. The replacement of the AISI H12 and H13 steels by the VHSUPER steel can be understood based on the comparative analysis of resistance to tempering (**Figure 30**) and toughness (**Figure 27(a)**). The improvement in both properties of the VHSUPER promotes reduction in the hot wear. The higher the hardness values the longer is the time of use. Furthermore, the thermal cracks are reduced because of the increased hot hardness and toughness.[35]

2.9.7.2.3 Hot forging die with complex geometry – Case 3

The process analyzed in this case is very similar to that described in Section 2.9.7.2.2. However, the failure mode is quite different, therefore, a different solution has been proposed. It is also about the press hot forging, details of which will be described later. However, the geometric complexity of the die used causes the failure mode be associated with cracks arising due to mechanical fatigue in stress concentration regions (see **Figure 31(b)**). The fundamental property of the tool steel in this case is toughness because it is related to the material resistance to crack propagation when subjected to a stress concentrator. Thus, the use of a high toughness steel is fully consistent with the need of the failure mode.

Process data: product: engine support; tool: hot forging die; forged material: mild carbon steel; stroke speed: slow, typical of forging press; tool steel previously used: AISI H13; tested steel: TENAX 300; life gain with the replacement: approximately 40%.

The application of the TENAX 300 tool steel was suggested by their substantially higher toughness compared to H13 steel, as shown in **Figure 27(a)**. Thus, a useful life gain of 50% was observed.

2.9.7.2.4 Aluminum casting die – Case 4

The end of life mechanism of casting dies is often discussed in the literature[35,38] and is associated with the formation of thermal fatigue cracks, as described in Section 2.9.7.2.1.

The important property of tool steel for this application is the toughness again. Studies show that, for a given hardness, the material's resistance to thermal fatigue damages is greater the higher the toughness, measured by the impact test on unnotched specimens.[41] Consequently, the TENAX 300 steel was applied in an aluminum press casting die. This process is described below. The performance of the die produced with the H13 steel was low because the geometry and the injection process brought many cracks to the die. After application of TENAX 300 IM steel, there was very significant increase in the tool life (greater than 100%!).

Process data: product: engine flange; tool: die cavity of an aluminum press casting die; process: die casting; tool steel previously used: AISI H13; tested steel: TENAX 300; gain in lifetime with the replacement: production of 80 000 shots per die against 200 000 shots.

For this application, the steel produced with ISOMAX process was employed due to the maximum toughness and isotropic properties obtained. So the high toughness of TENAX 300 IM steel, identified by impact energy values greater than 360 J, can be considered the main property responsible for the excellent results obtained in this application.

See also: 2.3 Carburizing – A Method of Case Hardening of Steel. 2.4 Surface Hardening by Gas Nitriding

References

1. Tool Steels. *Steel Products Manual*; Iron and Steel Society: Warrendale, PA, 1988.
2. Payson, P. *The Metallurgy of Tool Steels*; John Wiley & Sons: New York, NY, 1962.
3. Maddin, R. A History of Martensite: Some Thoughts on Early Hardening of Iron. In *Martensite*; Olson, G. B., Owen, W. S., Eds.; ASM International: Materials Park, OH, 1992; pp. 11–19.
4. Roberts, G.; Krauss, G.; Kennedy, R. *Tool Steels*, 5th ed.; ASM International: Materials Park, OH, 1998; pp. 1–6.
5. Norma ASTM A681-94. *Standard Specification for Tool Steel Alloy*, 2004.
6. Norma ASTM A600-92a. *Standard Specification for Tool Steel High Speed*, 2010.
7. Chandler H. Ed., Tool Steels. In *Heat Treaters Guide: Practice and Procedures for Irons and Steels*; ASM International: Materials Park, OH, 1995; pp. 517–669.
8. Gensure, J. G.; Potts, D. L. *International Metallic Materials Cross-Reference*, 3rd ed.; Genium Publishing: Schenectady, NY, 1988.
9. Bringas, J. E., Ed. *Handbook of Comparative World Steel Standards. ASTM DS67B*, 3rd ed.; ASTM International: West Conshohocken, PA, 2004; 669 pp.
10. Norma DIN 17350. *Tool Steels Technical Conditions of Delivery*, 1980.
11. Roberts, G.; Krauss, G.; Kennedy, R. *Tool Steels*, 5th ed.; ASM International: Materials Park, OH, 1998; pp. 7–18.
12. Roberts, G.; Krauss, G.; Kennedy, R. *Tool Steels*, 5th ed.; ASM International: Materials Park, OH, 1998; pp. 68–123.
13. Van Vlack, L. H.; *Princípio de Ciência e Tecnologia dos Materiais*; Elsevier: Rio de Janeiro, Campus, 1985; pp. 85–110.
14. Chiaverini, V. *Aços e Ferros Fundidos*, 6th ed.; ABM: Rio de Janeiro, 1988.
15. Hess, R. C.; Blickwede, D. J. Cooling Transformation Diagrams for AISI 4024 and 52100. *Met. Prog.* **1958**, *74*, 96B.
16. Mesquita, R. A.; Andrijauskas, P. S.; França, L. C.; Barbosa, C. A., Um Novo Aço para Trabalho a Frio de Alta Tenacidade – VF800AT. In *Anais da IV Conferência Nacional de Conformação de Chapas*, Gramado-RS, 2001; pp. 72–79.
17. American Society for Metals. *Metals Handbook*, Vol. 8, 8a ed., ASM International: Metals Park, OH, 1973; pp. 275–276.
18. Mesquita, R. A.; Kestenbach, H. J. Influence of Silicon on Secondary Hardening of 5 wt.% Cr Steels. *Mater. Sci. Eng., A Struct. Mater.: Prop., Microstruct. Process.* **2012**, *566*, 970–973.
19. Ebner, R.; Leitner, H.; Jeglitsch, F.; Caliskanoglu, D. Methods of Property Oriented Tool Steel Design, In *Proceedings of the Anais do 5th International Tooling Conference*, Leoben, Austria, 1999; pp. 3–24.
20. Crafts, W.; Lamont, J. L. *Secondary Hardening of Tempered Martensitic Alloy Steel*, Vol. 180; TMS–AIME: Warrendale, PA, 1949; p. 741.

21. Schmidt, M. L. Effect of Austenitizing Temperature on Laboratory Treated and Large Section Sizes of H-13 Tool Steel. In *Tool Materials for Moulds and Dies*, 1st ed.; Krauss, G., Nordberg, H., Eds.; Colorado School of Mines (CSM) Press Center: Golden, CO, 1987; pp. 118–164.
22. Bryson, B. *Heat Treatment, Selection and Application of Tool Steels*, 1st ed.; Hanser Gardner Publications: Cincinnati, OH, 1997; pp. 29–47.
23. Gonçalves, C. S.; Slaviero, A. L.; Mesquita, R. A.; Tschipchin, A. P.; Haddad, P. T. R. Effect of Cooling Rate During Quenching on the Toughness of High Speed Steels. *J. ASTM Int.* **2011**, *8*, 1–9.
24. Mašek, B.; Aišman, D.; Jirková, H. Microstructure of Tool Steel Upon Combined Semi-Solid Processing and Thermomechanical Treatment. *J. Alloys Compd.* **2014**, *586*, S165–S167. doi:10.1016/j.jallcom.2013.02.168.
25. Ghasemi-Nanesa, H.; Jahazi, M. Alternative Phase Transformation Path in Cryogenically Treated AISI D2 Tool Steel. *Mater. Sci. Eng. A* **2015**, *634*, 32–36. doi:10.1016/j.msea.2015.03.028.
26. Ghasemi-Nanesa, H.; Jahazi, M. Simultaneous Enhancement of Strength and Ductility in Cryogenically Treated AISI D2 Tool Steel. *Mater. Sci. Eng. A* **2014**, *598*, 413–419. doi:10.1016/j.msea.2014.01.065.
27. Da Silva, F. J.; Franco, S. D.; Machado, A. R.; Ezugwu, E. O.; Souza, A. M., Jr. Performance of Cryogenically Treated HSS Tools. *Wear* **2006**, *261*, 674–685. doi:10.1016/j.wear.2006.01.017.
28. Telasang, G.; Dutta Majumdar, J.; Padmanabhamb, G.; Manna, I. Wear and Corrosion Behavior of Laser Surface Engineered AISI H13 Hot Working Tool Steel. *Surf. Coat. Technol.* **2015**, *261*, 69–78. doi:10.1016/j.surfcoat.2014.11.058.
29. Chen, W.; Zheng, J.; Meng, X.; Kwon, S.; Zhang, S. Investigation on Microstructures and Mechanical Properties of AlCrN Coatings Deposited on the Surface of Plasma Nitrocarburized Cool-Work Tool Steels. *Vacuum* **2015**, *121*, 194–201. doi:10.1016/j.vacuum.2015.08.021.
30. Mesquita, R. A.; Barbosa, C. A. Aços Ferramenta De Alto Desempenho Para Matrizes De Fundição Sob Pressão. *Revista Metalurgia & Materiais* **2003**, *59* (539), 17–22 (also at Caderno Tecnológico ABM, Metalurgia de Não Ferrosos, 1).
31. Mesquita, R. A.; Andrijauskas, P. S.; Barbosa, C. A. Desenvolvimento De Um Novo Aço Para Trabalho a Frio De Alta Tenacidade. In *Anais do 56 Congresso Anual da ABM*, Belo Horizonte, Brazil; 2001 (ABM, 2001. 1 CD-ROM).
32. North American Die Casting Association. *Premium Quality H13 Steel Acceptance Criteria for Pressure Die Casting*, *NADCA No. 207/90*, River Grove, IL; 1990.
33. Wilmes, S.; Burns, K. P. Vergleich der Zähigkeit von Warmarbeitsstahl Unterschiedlicher Herstellverfahren im Hinblick auf die Verwendung für Druckgießformen. *Giesserei* **1989**, *76* (24), 835–842.
34. Hoyle, G.; Ineson, E. A Modified Bend Test for Hardened Tool Steels. *J. Iron Steel Inst.* **1959**, *1* (1), 44–55.
35. Benedyk, T. C.; Moracz, D. J.; Wallace, J. F. Thermal Fatigue Behaviour of Die Materials for Aluminum Die Casting. In *Proceedings of the International Die Casting Congress*; Paper No. 111, 1970; pp. 1–20.
36. Costa Neto, A. F.; Barbosa, C. A. Efeito da Refusão ESR nas Propriedades de um Aço para Trabalho a Quente: Qualidades ISO e ISOMAX. In *SENAFOR – Seminário Nacional de Forjamento*, Porto Alegre, Brazil, UFRGS – Centro de Tecnologia, 1996; pp. 40–50.
37. (a) Eliasson, L.; Sandberg, O. Effect of Different Parameter on Heat-Checking Properties of Hot-Work Tool Steels. In *New Materials and Processes for Tooling*; Berns, H., Nordberg, H., Fleischer, H.-J., Eds.; Verlag Schurmann & Klagges KG: Bochum, 1989; pp. 1–7. (b) Roberts, G.; Krauss, G.; Kennedy, R. *Tool Steels*, 5th ed.; ASM International: Metals Park, OH, 1998.
38. Mesquita, R. A.; Barbosa, C. A. Aços Ferramenta de Alto Desempenho para Matrizes de Fundição sob Pressão. *Caderno Tecnológico da Revista Metalurgia & Materiais* **2003**, *59* (539), 17–22.
39. Pinedo, C. E.; Barbosa, C. A. Aços Ferramenta para Trabalho a Quente com Elevada Tenacidade e Isotropia. In *Anais do 49 Congresso Anual da ABM*, São Paulo, ABM, 1994; pp. 517–530.
40. Mesquita, R. A.; França, L. C.; Barbosa, C. A. Desenvolvimento de um Novo Aço Ferramenta para Trabalho a Quente com Tenacidade Otimizada. In *Anais do 57 Congresso Anual da ABM*, São Paulo, ABM, 2002; pp. 444–453.
41. Mesquita, R. A.; Barbosa, C. A. Novos Aços para Trabalho a Quente. In *Anais do 1 Encontro de Integrantes da Cadeia Produtiva de Ferramentas, Moldes e Matrizes*, São Paulo, AMB: Associação Brasileira de Metalurgia e Materiais, 2003; pp. 131–140.

2.10 Heat Treatment of Cast Irons

I Chakrabarty, Indian Institute of Technology (Banaras Hindu University), Varanasi, India

© 2017 Elsevier Inc. All rights reserved.

2.10.1	**Introduction**	247
2.10.1.1	Types of Cast Irons	247
2.10.1.2	Heat Treatment of Cast Irons: General Considerations	248
2.10.1.2.1	Critical temperature ranges	248
2.10.1.2.2	Carbon content in the matrix	248
2.10.1.2.3	Hardenability	249
2.10.1.2.4	Shape and size of the castings	249
2.10.1.2.5	Surface oxidation and decarburization	249
2.10.2	**Heat Treatment of Gray Irons**	249
2.10.2.1	Stress Relieving of Gray Irons	249
2.10.2.1.1	Case studies on stress relieving	250
2.10.2.2	Annealing of Gray Irons	251
2.10.2.2.1	Types of annealing	251
2.10.2.2.1.1	Ferritizing annealing	251
2.10.2.2.1.2	Full annealing	251
2.10.2.2.1.3	Graphitizing annealing	251
2.10.2.2.2	Effects of alloying on annealing soaking time	251
2.10.2.3	Normalizing of Gray Iron	252
2.10.2.4	Through Hardening and Tempering of Gray Iron	252
2.10.2.4.1	Case study on hardening and tempering of gray iron	253
2.10.2.5	Austempering of Gray Iron	253
2.10.2.5.1	Case studies on austempering of gray iron	255
2.10.2.6	Martempering of Gray Iron	255
2.10.2.6.1	Case studies on martempering of gray iron	255
2.10.2.7	Surface Hardening of Gray Iron	256
2.10.3	**Heat Treatment of Malleable Irons**	256
2.10.3.1	Whiteheart Malleable Iron	256
2.10.3.2	Blackheart Malleable Iron	257
2.10.3.3	Hardening and Tempering of Malleable Irons	257
2.10.3.4	Martempering of Malleable Irons	258
2.10.3.5	Bainitic Heat Treatment of Malleable Irons	258
2.10.3.6	Surface Hardening of Pearlitic Malleable Irons	258
2.10.3.6.1	Case studies on surface hardening of malleable irons	259
2.10.4	**Heat Treatment of Ductile Irons**	260
2.10.4.1	Fundamental Considerations for Heat Treatment of Ductile Iron	261
2.10.4.2	Annealing of Ductile Irons	262
2.10.4.3	Normalizing of Ductile Irons	262
2.10.4.4	Hardening and Tempering of Ductile Irons	264
2.10.4.5	Austempering of Ductile Irons	264
2.10.4.5.1	Effect of metallurgical variables on the properties of ADI	264
2.10.4.5.1.1	Effect of metal composition	264
2.10.4.5.1.2	Practical factors affecting successful austempering	266
2.10.4.5.2	Two-step austempering heat treatment	268
2.10.4.6	Surface Hardening of Ductile Irons	269
2.10.4.7	Stress Relieving of Ductile Irons	269
2.10.5	**Heat Treatment of High-Alloy Irons**	269
2.10.5.1	Austenitic Graphitic Irons	270
2.10.5.1.1	Effects of composition on the structure and properties	270
2.10.5.1.2	Heat treatment of austenitic graphitic irons	271
2.10.5.1.2.1	Stress relieving	271
2.10.5.1.2.2	Spheroidizing annealing	271
2.10.5.1.2.3	High temperature stabilization	271
2.10.5.1.2.4	Dimensional stabilization	271
2.10.5.1.2.5	Solution treatment	272

 doi:10.1016/B978-0-12-803581-8.09192-X

2.10.5.1.2.6	Refrigeration and reaustenitization	272
2.10.5.1.3	Case studies on austenitic graphite irons	272
2.10.5.2	Heat Resistant High Silicon Irons	273
2.10.5.2.1	Heat treatment of heat resistant high-silicon irons	273
2.10.5.3	Heat Treatment of Corrosion Resistant High Silicon Irons	275
2.10.5.4	Oxidation Resistant High-Aluminum Irons	276
2.10.5.5	Abrasion Resistant High-Alloy White Irons	276
2.10.5.5.1	Heat treatment of nickel–chromium white irons	277
2.10.5.5.1.1	Stress relieving	278
2.10.5.5.1.2	Destabilization treatment	279
2.10.5.5.1.3	Cryogenic treatment	279
2.10.5.5.1.4	Case study on heat treatment of nickel–chromium iron	279
2.10.5.5.2	Heat treatment of high-chromium white irons	280
2.10.5.5.2.1	Annealing	281
2.10.5.5.2.2	Destabilization treatment	282
2.10.5.5.2.3	Subcritical heat treatment	282
2.10.5.5.2.4	Case studies on failure of high-chromium iron	283
2.10.5.5.2.5	Cryogenic treatment	285
References		286
Relevant Websites		287

2.10.1 Introduction

Cast irons primarily are alloys of iron and carbon, the carbon percentage being 2–6.67% and undergo eutectic solidification. Since, high carbon content produce high brittleness, for most commercial applications the carbon content is restricted to 2.5–4%. However, beside carbon, industrial cast irons invariably contains silicon more than 1% with varying percentages of manganese, sulfur, phosphorus, and other alloying elements occasionally added. Binary Fe–C melt may solidify either by metastable Fe–Fe_3C system or by stable Fe–Graphite system. The solidification either by stable or metastable system depends on factors like graphitization potential, inoculation treatment, and cooling rate. These factors also govern the morphology of the stable graphite during solidification. Apart from the carbon, silicon has a contribution to increase strongly the graphitizing potential.[1,2] Silicon also shifts the eutectic and eutectoid compositions to lower carbon contents and pushes up these transformation temperatures (Figure 1). The ultimate properties of cast iron depend on the form of carbon precipitation and the matrix structure. The graphite form during solidification by Fe–Graphite system cannot be changed further by solid-state transformation by heat treatment. However, the cementite (Fe_3C) and the matrix structure can be changed by a suitable heat treatment to achieve desired properties. Important matrix structures and their characteristics and contributions to the iron properties are summarized in Table 1.

2.10.1.1 Types of Cast Irons

The cast irons are classified mainly according to the conditions and physical forms of the carbon present.[2] As stated earlier the carbon in cast iron may be present as graphite in stable system or as combined form of cementite in metastable system. In

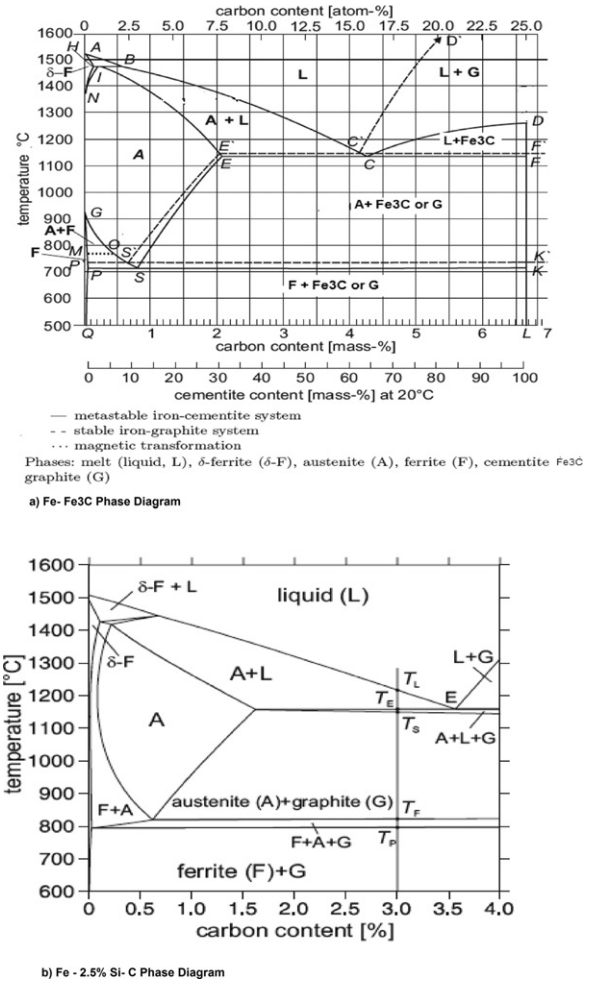


Figure 1 Fe–Carbon phase diagrams. (a) Fe–Fe_3C system and (b) Fe–2.5%Si–C. Modified from Berns, H.; Theisen, W. *Ferrous Materials, Steel and Cast Irons*, 1st. ed.; Springer Berlin; Heidelberg, 2008.

Table 1 Important matrix structures and their characteristics

Matrix structures	*Characteristics*	*Contributions*
Ferrite	Relatively soft, ductile Fe–C solid solution. Other elements viz. Si, Mn, Cu, and Ni may dissolve in the solid solution. Ferrite matrix can be produced either in as-cast condition or by annealing heat treatment	Yields low strength and poor wear resistance but good fracture toughness, thermal conductivity, and machinability
Pearlite	Decomposition product of austenite by eutectoid reaction into alternate lamellae of ferrite and cementite. A relatively hard phase. Carbon content varies depending on the iron composition and cooling rate	Develops moderate toughness, reduced thermal conductivity, and good machinability. The improvements in properties depend on the interlamellar spacing of pearlite
Ferrito–pearlite	A mixture of two phases, ferrite and pearlite	Results in a combination of extreme properties of the constituent phases
Bainite	The structure can be obtained by suitable alloying with Ni and Mo in as-cast condition or by austempering heat treatment	Several mechanical property advantages can be obtained such as combination of strength and toughness, good fatigue resistance, wear resistance, damping capacity, casting properties, formability, and machinability
Austenite	A high percentage of austenite stabilizing elements viz. Ni, Cu, etc., is needed to stabilize the austenite at room temperature	Austenitic matrix yields good toughness and high temperature property up to about 800 °C. Develops heat and corrosion resistance and nonmagnetic properties
Martensite	This hard phase can be produced either in as-cast condition by proper alloying or by heat treatment. Often associated with austenite retained in the microstructure	Martensitic matrix produces high strength and hardness, wear and abrasion resistance

Source: Modified from Elliott, R. *Cast Iron Technology*, 1st ed.; Butterworths: London; Boston, MA, 1988 and Angus, H. T. *Cast Iron: Physical and Engineering Properties*, 2nd ed.; Butterworths: London; Boston, MA, 1976.

stable system graphite may be of different shapes and accordingly the classifications are,

- Gray iron: Graphite is present as flakes and the fracture surface has a grayish appearance and so the name gray cast iron.
- Ductile iron: It is so named because of its good ductility. The graphite is present as spheroid form in which numerous flakes form into ball-like cabbage leaves. It is also known as spheroidal or nodular graphite iron.
- Compacted or vermicular graphite iron: The graphite morphology is intermediate between spheroids and flakes. The graphite phase shows segmented growth features with blunted edges but is interconnected within the eutectic cells.

Other important cast iron categories are:

- White iron: Most of the carbon is in brittle cementite form and the fracture appearance is crystalline whitish.
- Malleable iron: In this type of iron most or all the carbon is in uncombined temper carbon form. The rounded temper carbons are formed by prolonged annealing treatment of white cast iron.
- High-alloy irons: The properties and structure of any of the above types are modified by alloying additions generally over 4%. This class of iron includes wear resistant white irons, the austenitic and ferritic high-alloy heat and corrosion resistant irons.

2.10.1.2 Heat Treatment of Cast Irons: General Considerations

2.10.1.2.1 Critical temperature ranges

The selection of heat treatment temperatures is based on the understanding of the phase diagram and the critical temperature ranges in the phase diagram. In almost all types of heat treatments most important is the selection of austenitizing temperature to develop a single phase austenitic matrix above the critical temperature and below which austenite transforms to ferrite and pearlite /graphite. Silicon, manganese, and phosphorus are the most significant elements which influence the critical temperature of cast irons.[4–6] The location and size of this range is shown in Figure 2. The quantitative effects of various elements on the critical temperature ranges are shown in Table 2.

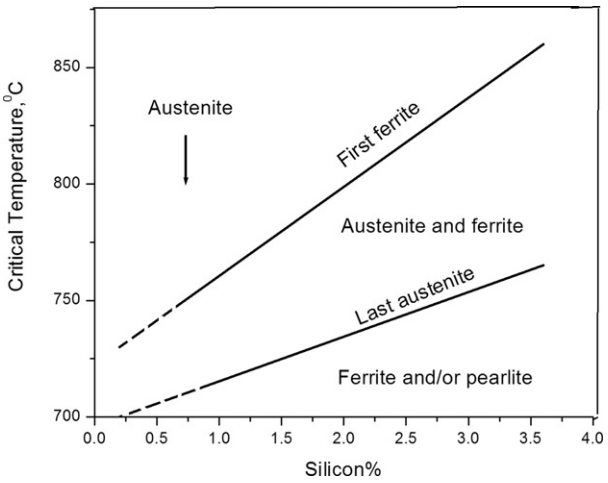


Figure 2 Effect of silicon percent on the critical temperature range of gray, malleable, and ductile irons cooled at 5 °C h^{-1}. Rehder, J. E. Critical Temperature Heat Treatment of Cast Irons. *Foundry*, June 1965; pp. 65–67. American Foundry Society.

2.10.1.2.2 Carbon content in the matrix

The carbon content in the matrix is directly related with the austenitizing temperature, higher the austenitizing temperature

Table 2 Effects of some common elements on the critical temperature ranges

Element (%)	*Upper critical temperature; effect: °C per (%)*	*Lower critical temperature; effect: °C per (%)*
Silicon, 0.3–3.5	37 increase	29 increase
Phosphorus, 0–0.2	220 increase	220 increase
Manganese, 0–1.0	37 increase	130 decrease
Nickel, 0–1.0	17 decrease	24 decrease

Source: Elliott, R. *Cast Iron Technology*, 1st ed.; Butterworths: London; Boston, MA, 1988; Table 4.1, p. 130.

higher will be the carbon content in equilibrium with the austenitic matrix.

2.10.1.2.3 Hardenability

The hardenability is significantly increased by carbon and silicon in conjunction with other alloying elements such as manganese, nickel, molybdenum, copper, etc., which enables cast iron to be quenched in media with low severity of quench viz. air, oil, or a polymer. This is to harden the cast iron to higher strength and hardness. Water as quenching medium with high severity of quench is not commonly employed to avoid distortion or cracks.[2]

2.10.1.2.4 Shape and size of the castings

Heavy and complex shape castings pose difficulties in heat treatment. For homogeneous heating from external surface to the core of the casting the heating rate must be slow enough and steady temperature soaking time must be adequate to avoid any temperature differential. After the soaking the rates of cooling also to be slow enough to avoid any residual stress development.[2] In case of quenched components, immediate tempering treatment is to be followed.

2.10.1.2.5 Surface oxidation and decarburization

Heat treatment furnace atmosphere must be controlled to avoid any surface oxidation and decarburization. Heavily oxidized surface poses machining problem due to the formation of hard oxide scale and hence drastically reduces the cutting tool life.[2] Due to decarburized layer formation proper hardening effect on the surface is not achieved by quenching.

2.10.2 Heat Treatment of Gray Irons

Gray irons are most widely used irons for general engineering applications. As described earlier gray irons undergo solidification as stable Fe + graphite system, the graphite formed are in flaky shape. The chemical composition of this gray iron is usually in the range of 2.5–4.0% carbon, 1–3% silicon, and 0.1–1.2% manganese. The manganese being a carbide stabilizer is kept at lower range for ferritic matrix, while higher range is preferred for pearlitic higher strength matrix. Apart from these, other alloying elements such as nickel, copper, molybdenum, chromium, etc., are added occasionally to achieve desired specific properties.

The most commonly employed heat treatment processes for gray irons include stress relieving and annealing. Through hardening and tempering is occasionally carried out to produce hard martensitic matrix for high strength, hardness, wear, and abrasion resistance. Surface hardening such as flame hardening or induction hardening is often carried out to replace chilled iron or costly alloying.

Other than the stress-relieving treatment, all heat treatments involve phase transformations to improve the properties. As the heat treatment has little or no influence on the graphite flake shape and distribution, matrix phase transformation is responsible for the property improvements. Although the graphite flakes are unchanged, the flake size has influence on the rate of matrix transformation by controlling the rate of diffusion of carbon. Finer the flakes, shorter will be diffusion distance causing a rapid transformation rate.

2.10.2.1 Stress Relieving of Gray Irons

Complex-shaped castings during their solidification may develop residual elastic stresses in the casting due to differential contractions. In contrast, castings with more or less uniform section thickness, the extent of residual stresses are not appreciable. In extreme cases, when the residual stresses are significant it will cause distortion or cracking.[2–4] The extent of residual stress is influenced by the factors like shape and size of the casting, the casting technique, and material properties and composition of the casting.

The residual stresses in castings develop due to following reasons:

- Differential contraction in castings with nonuniform sections.
- Restraint of the free thermal contraction of the casting by the rigid mold.
- Introduction of compressive residual stresses during surface cleaning operations such as shot peening.
- Thermal processes such as welding, through hardening or surface hardening.

The extent of stress relieving by stress-relieving heat treatments depends on various factors[3] such as,

- Initial level of residual stress
- The time–temperature relationship for stress-relieving treatment
- The rate of heating
- The rate of cooling
- The chemical composition and the microstructure.

Higher the initial level of residual stress, the more readily the stress will be relieved. The temperature and holding time at the stress-relieving temperature are two crucial parameters. Generally, the temperature is chosen in the range of 565–650 °C much below the critical temperature.[6–9] Selection of higher temperature requires shorter time of holding but will cause a slight structural change with lowering of hardness and tensile strength. However, the economics of the process definitely favors higher temperature process with shorter times. **Figure 3** indicates the effects of stress relieving at 650 °C for 6 h on the tensile strength and hardness variations in different grades of

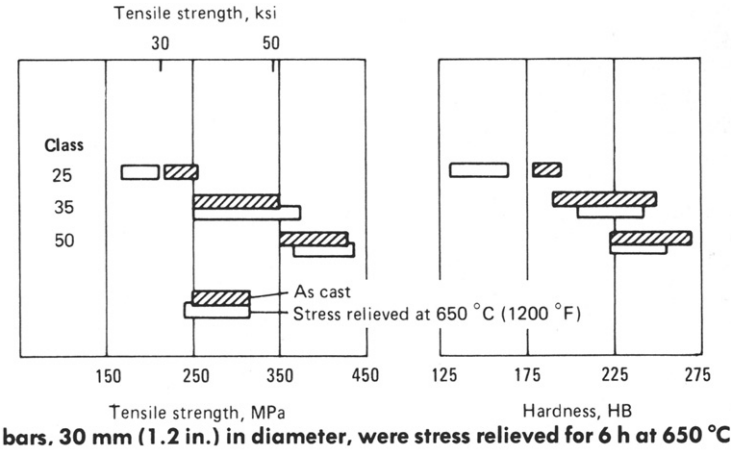
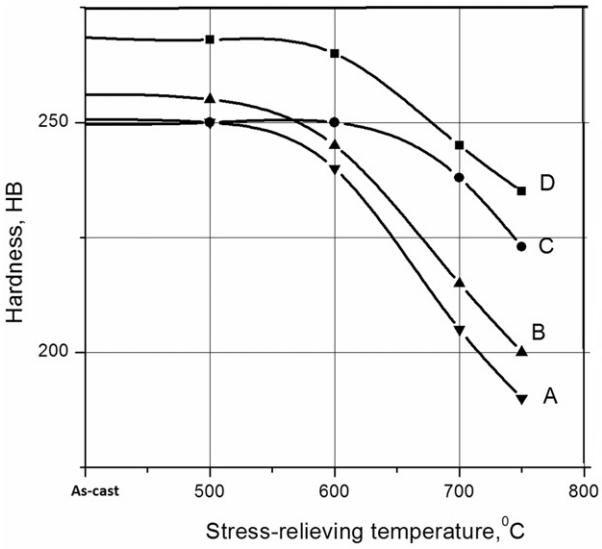


Figure 3 Effect of stress relieving on tensile strength and hardness of gray iron bars (30 mm diameter), stress relieved at 650 °C for 6 h. *ASM Handbook*, Vol. 4, 1991 ed., Heat Treating of Grey Irons; Figure 14, p. 1480.

gray irons. The hardness variations after stress relieving of alloyed and unalloyed gray irons at different temperatures are shown in **Figure 4**. The suitable temperature range as evident from the figure is 540–565 °C with a minimum decomposition of carbides in unalloyed irons. In this temperature range the effects of holding time on the residual stress percentage are depicted in **Figure 5**. Even after 1 h of holding could reduce the residual stress to 75–85%; higher holding times are not very much effective.

Table 3 shows the effects of composition on stress-relieving temperature of unalloyed and high-alloy irons. Alloying elements such as Mn, Cr, and Mo increase the strength at higher temperature range and such alloyed irons need higher stress-relieving temperatures.[10]

The heating and cooling rate of castings are two controlling factors; a slow heating rate of the order of 100–120 °C h^{-1} is optimum to avoid the generation of thermal stress especially for complex large castings. Similarly, a slow cooling rate is desirable after the soaking period at least in the upper range of temperatures. Complex shapes are recommended to cool down in the furnace to about 200 °C and can be subsequently air cooled. In batch type of stress relieving the loading temperature should not exceed 95 °C. A common heat cycle is to heat to 620–650 °C in about 3 h, isothermally soaked at this temperature for 1 h and cooled to 200 °C in 5 h in the furnace and then the castings are allowed to cool in air. In continuous furnace also this type of temperature zones can be adjusted.[6,8]



Iron	Composition, %					
	TC (a)	CC (b)	Si	Cr	Ni	Mo
A	3.20	0.80	2.43	0.13	0.05	0.17
B	3.29	0.79	2.58	0.24	0.10	0.55
C	3.23	0.70	2.55	0.58	0.06	0.12
D	3.02	0.75	2.38	0.40	0.07	0.43

(a) Total carbon; (b) Combined carbon

Figure 4 Effect of stress-relieving temperature on hardness of different alloyed gray iron bars (30 mm diameter) held at respective temperature for 1 h and air cooled. *ASM Handbook*, Vol. 4, 1991 ed., Heat Treating of Grey Irons; Figure 15, p. 1481.

2.10.2.1.1 Case studies on stress relieving

Case 1: As-cast clutch plates made of gray iron of composition 3.4%C (0.7–0.9 combined C), 1.3–1.8% Si, 0.25–0.4%Cr, 0.3–0.4%Mo, and Ni and Cu as required, minimum tensile strength 275 MPa and hardness 207–255 HB, are to machined with a flatness tolerance of 0.1 mm. In as-cast condition the tolerance could not be maintained but when castings were stress relieved at 620 °C for 2 h it became alright.[8]

Case 2: A cast transmission case made of gray iron of composition 3.1–3.4%C, 2.15–2.35%Si, and 0.2–0.4%Cr did not follow the usual procedure of slow cooling in the mold before shake-out and some of the castings were cracked (1.3 mm wide) because of fast shake-out needed for a rush order. Other castings developed cracks not after the machining but during final hot washing operation. The problem was eliminated for the remaining ordered pieces by stress relieving at 620 °C for 2 h. When original shake-out practice was followed, no further crack developed and eliminates the need for stress relieving.[8]

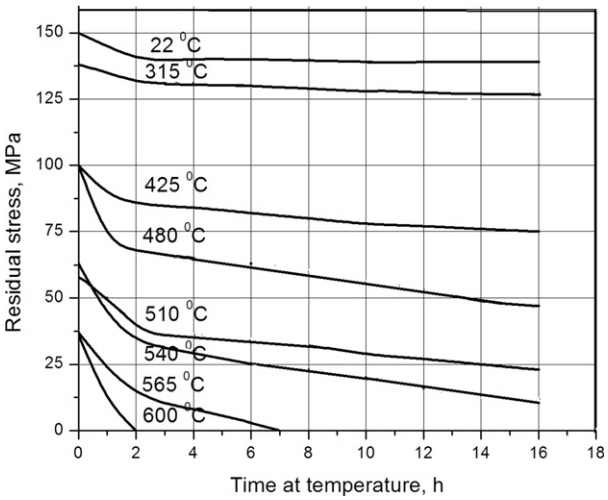


Figure 5 Effect of stress-relieving temperature and time on residual stress in gray iron (Composition: 2.72%C, 1.97% Si, 0.141% P, 0.08% S, 0.51% Mn). *ASM Handbook*, Vol. 4, 1991 ed., Heat Treating of Grey Irons; Figure 17, p. 1482.

Table 3 Recommended stress-relieving temperature for unalloyed and alloyed gray irons

Gray iron type	*Stress-relieving temperature (°C)*
Unalloyed or alloyed without Cr	510–565
0.15–0.30% Cr	595–620
>0.30% Cr	620–650

Source: Dossett, J. L.; White, C. V. *Heat Treating of Gray Irons, Heat Treating of Irons and Steels*; *ASM Handbook*, Vol. 4D; ASM International: Materials Park, OH, 2014; pp. 493–507.

Case 3: Hot tears and out-of-roundness developed in gray iron as-cast rings and also the flat plane is distorted during machining. A modified gating system which equalized the temperature differentials and controlled the shrinkage distribution resulted in the elimination of hot tears and distortion. Further stress-relieving treatment at 370 °C for 2 h eliminated the machining distortion.[8]

2.10.2.2 Annealing of Gray Irons

The main objective of annealing is to soften the iron by decomposition of eutectic carbides or pearlitic carbides into ferrite and graphite by slow cooling through the critical temperature ranges. The structure promotes increase in ductility and machinability of the gray irons. There are several types of annealing processes in practice namely; (1) ferritizing annealing, (2) full annealing, and (3) graphitizing annealing. The processes are differing on the range of annealing temperature employed.

2.10.2.2.1 Types of annealing

2.10.2.2.1.1 Ferritizing annealing

This is to convert the combined carbon in pearlite to ferrite and graphite. The heat treatment involves heating the iron more commonly above 700 °C and up to maximum temperature of 760 °C, the lower critical transformation temperature. Lower the treatment temperature employed longer will be the time of soaking. The recommended soaking time at 760 °C is 1 h per 25 mm section thickness. The exact ferritizing temperature can be determined for a particular composition by annealing at different temperatures in the range of 700–760 °C for a fixed soaking time; most suitable temperature will be with lowest hardness.[3,4]

For simultaneous stress relieving along with ferritizing, the castings after soaking period are to be cooled slowly at the rate of 110–290 °C h^{-1} especially for complex shapes.



Figure 6 Fully ferritic, annealed gray iron (etched with 2% Nital). George Vander Voort. *Metallographic Procedures for Cast Irons*; Vac Aero International Inc. Newsletter; Figure 4.

2.10.2.2.1.2 Full annealing

A full annealing involves two stages of annealing. The first stage is to process above the critical temperature in the range of 790–900 °C.[8] This is aimed to decompose any small quantities of carbides present in the structure and to homogenize the matrix. The holding times may be same as those in ferritizing annealing. After this holding period the second stage involves a slow cooling through 675–790 °C temperature range to promote a ferritic matrix with graphite (**Figure 6**).

2.10.2.2.1.3 Graphitizing annealing

The graphitizing annealing with a higher annealing temperature in the range of 900–955 °C is employed to convert the intercellular massive carbides into pearlite and graphite. Further softening may be accomplished by a ferritizing annealing. The single graphitizing annealing followed by air cooling is employed if maximum strength and wear resistance are to be retained with a pearlitic matrix. On the other hand, double-stage treatment, i.e, graphitizing and ferritizing is suitable for developing ferritic matrix with maximum machinability.[4,8]

2.10.2.2.2 Effects of alloying on annealing soaking time

Alloying elements present in gray iron have pronounced effects on the annealing temperature and soaking time at the annealing temperature. Alloying elements can be grouped as graphite stabilizing and carbide stabilizing. The formers such as carbon and silicon accelerate the decomposition of pearlite and eutectic massive carbides whereas the later such as antimony, tin,

Table 4 Effect of 0.1% additions of various elements on pearlite decomposition time

Elements	*Increase in soaking time (%)*
Manganese	60
Nickel	30
Copper	30
Chromium	200
Phosphorus	30

Source: Dossett, J. L.; White, C. V. *Heat Treating of Gray Irons, Heat Treating of Irons and Steels; ASM Handbook*, Vol. 4D; ASM International: Materials Park, OH, 2014; pp. 493–507.

vanadium, chromium, manganese, phosphorus, nickel, and copper favors pearlite formation and hinder decomposition. For an example, when silicon content is increased from 1.93 to 2.68%, the decomposition time of pearlite is reduced from 45 to 10 min during annealing at 750 °C.[8] The effects of various carbide stabilizers (0.1% additions) on the decomposition times of pearlite are shown in Table 4.

2.10.2.3 Normalizing of Gray Iron

Normalizing for gray irons is employed to enhance the mechanical properties or to restore the as-cast properties which have been changed by the thermal processes. The castings are austenitized in the temperature range of 880–925 °C for a soaking period of 1 h 25 mm^{-1} section thickness and cooled to room temperature in still air.[6] The austenitization temperature has a great influence on the microstructure, hardness, and tensile properties. The most important compositional and microstructural parameters, combined carbon and interlamellar spacing of pearlite dictate the ultimate properties after normalizing (Figure 7). A higher carbon solubility is attained by a higher austenitization temperature which in turn, increases the volume percent of pearlite in the structure. The higher volume percent of pearlite is responsible for improved hardness and strength. The effects of other elements are also important to change the solid solubility of carbon in the austenite. The combined effect can be assessed by carbon equivalent and the effects of manganese, chromium, nickel, and molybdenum contents in the iron. Figure 8 shows the effect of carbon equivalent and %chromium and % nickel of the normalized hardness of the two different irons. As the austenitization temperature is gradually increased from 800 to 980 °C the hardness increases because of the stabilizing effects of alloy contents. Higher hardness can be achieved with lower carbon equivalent and alloying with Cr, Ni, and Mo.[6]

The interlamellar spacing of the resultant pearlite matrix is influenced by the composition and rate of cooling subsequent to austenitization. The composition effect is mainly due to the combined effect on the carbon solubility in the austenite. So far as the cooling rate is concerned, a fast cooling promotes smaller spacing and results in higher strength and hardness. Very high cooling rate combined with high-austenitizing temperature favor martensitic transformation impairing the machinability. The final hardness after normalizing can be partially controlled by the temperature of removal of components from the furnace.

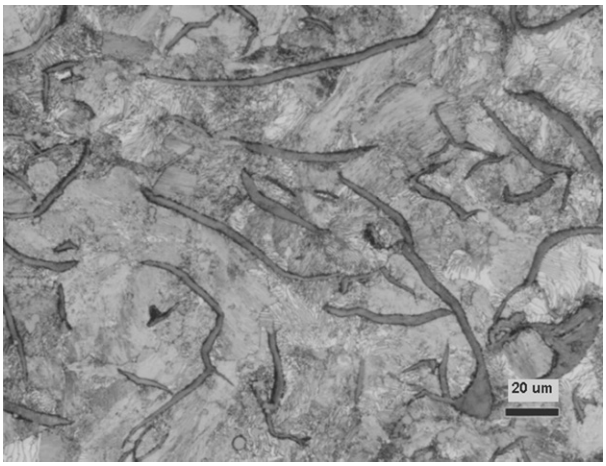


Figure 7 Fine pearlitic gray iron in normalized condition. George Vander Voort. *Metallographic Procedures for Cast Irons*; Vac Aero International Inc. Newsletter; Figure 5.

2.10.2.4 Through Hardening and Tempering of Gray Iron

Objective of the through hardening and tempering treatment is to enhance the mechanical properties particularly the strength and wear resistance. The hardening involves austenitizing above the critical temperature range, soaked at this temperature for adequate time for optimum carbon and alloying elements dissolution in the austenite, followed by quenching in a suitable medium to form martensite (Figure 9).

An optimum austenitization temperature is to be selected to dissolve adequate amount of carbon, a high-carbon austenite on quenching forms high-carbon martensite with high hardness and strength. On the other hand, a very high austenitization temperature causes danger of distortion, cracking, and retention of austenite.[4,6] The minimum austenitizing temperature is about 55 °C above the lower critical temperature A_1 of a particular iron. The A_1 temperature is calculated from the relationship,

$$A_1 = 730 + 28(\%\mathrm{Si}) - 25(\%\mathrm{Mn})$$

The austenitizing time is also an important control parameter. For unalloyed gray irons, the austenitizing time is longer to saturate more carbon in austenite and thus increased quenched hardness is obtained.

The austenitized gray iron castings are quenched in a molten salt or oil or water soluble polymer quenchant. Water quenching is not recommended as quench cracks and distortions are developed. Alloyed gray irons with high hardenability can even be forced air quenched to obtain a high percentage of martensite. Because of the high-thermal and transformation stresses in as-quenched condition, the castings are prone to cracking at room temperature. So, especially complex shape castings are t be withdrawn from the quenching bath in hot condition at about 150 °C and immediately tempered. The as-quenched castings are tempered at an elevated temperature in the subcritical range usually for a time of 1 h 25 mm^{-1} to impart strength, ductility, and toughness. The effect of tempering temperature on the strength, hardness, and impact

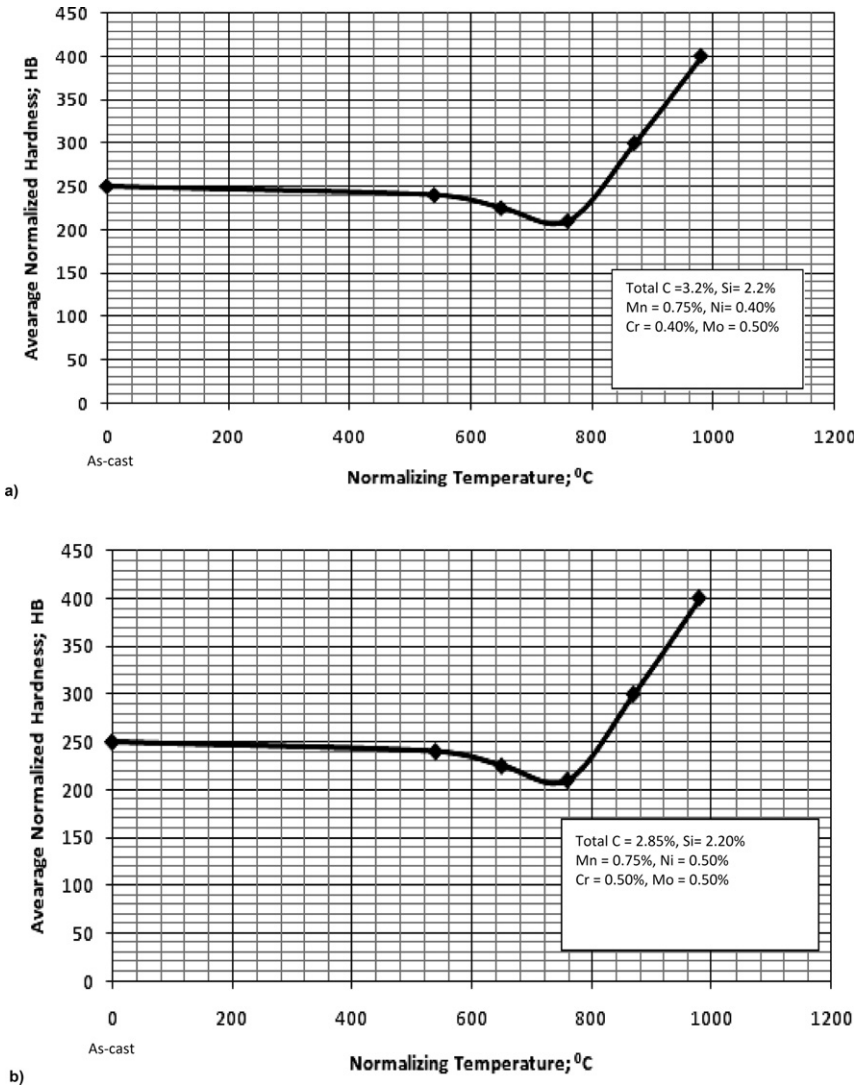


Figure 8 Effect of carbon equivalent (%C and %Si) and alloy contents on the normalized hardness of gray iron. Modified from Davis, J. R. *ASM Specialty Handbook: Cast Iron*; ASM International: Materials Park, OH, 1996; Figure 4, p. 182.

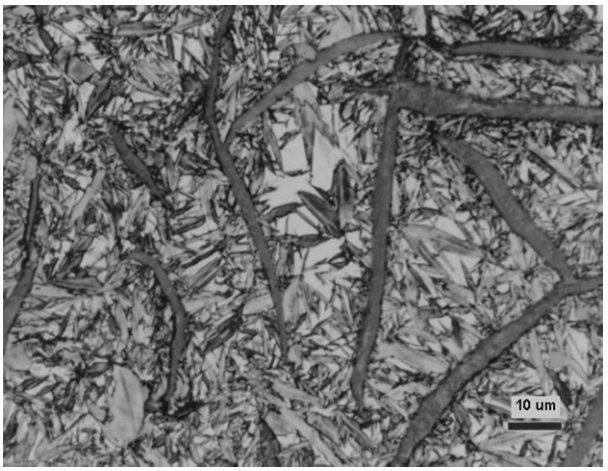


Figure 9 Pearlitic gray iron hardened to form martensite and retained austenite. George Vander Voort. *Metallographic Procedures for Cast Irons*; Vac Aero International Inc. Newsletter; Figure 6.

toughness of low-silicon gray iron are shown in Figure 10. The maximum strength developed depends on alloy content. To achieve high strength for both alloyed and unalloyed gray irons, the usual tempering temperature ranges from 370 to 510 °C.[6]

2.10.2.4.1 Case study on hardening and tempering of gray iron

Case 1: Valve guides made of unalloyed gray iron of which hardness requirement is 30–34 HRC in hardened and tempered condition. To achieve this final hardness the components are austenitized at 885 °C for 1 h followed by quenching in hot oil at temperature of 60 °C. The as-quenched hardness obtained in the range of 45–50 HRC. The quenched valve guides are tempered at 480 °C to achieve the desired final hardness.[6]

2.10.2.5 Austempering of Gray Iron

The austempering is an isothermal tempering process of as-quenched austenite phase in the acicular or bainitic ferrite

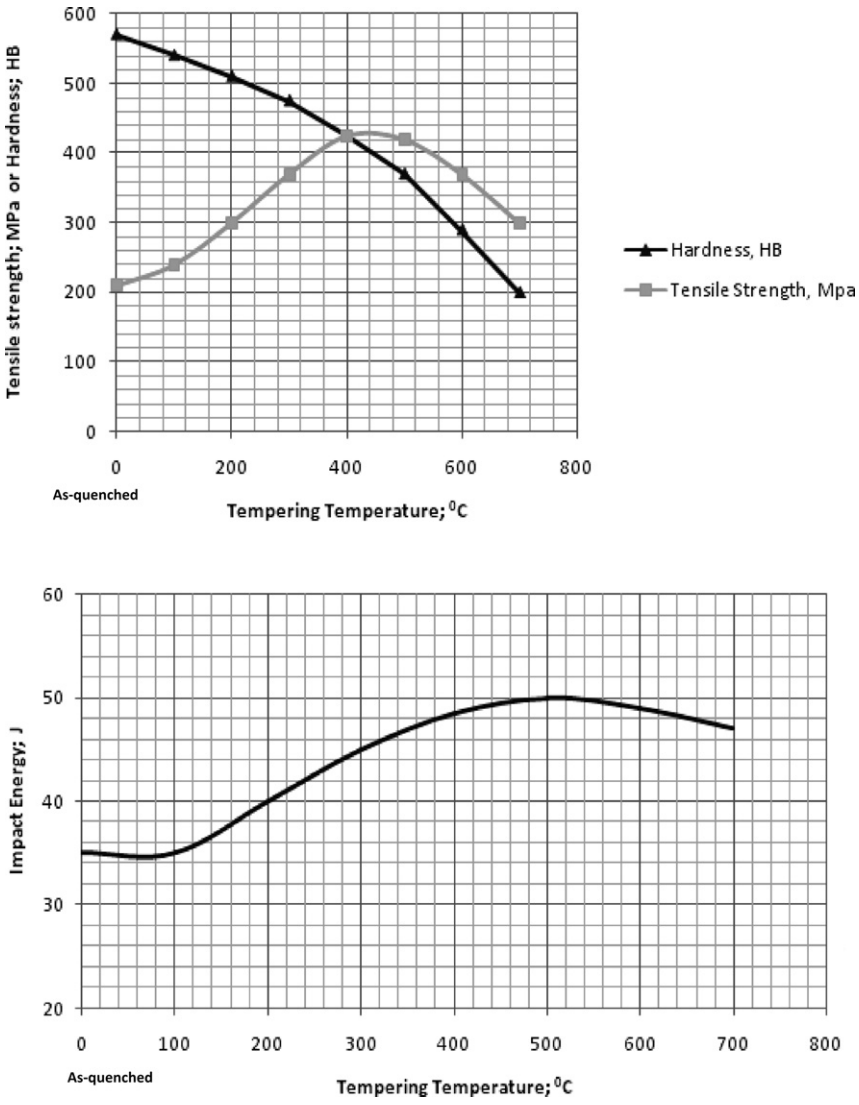


Figure 10 Effect of tempering temperature on the strength, hardness, and impact toughness of low-silicon gray iron. Modified from Davis, J. R. *ASM Specialty Handbook: Cast Iron*; ASM International: Materials Park, OH, 1996; Figure 8, p. 185.

region. The ultimate microstructure is acicular ferrite or bainite with varying percentages of retained austenite (**Figure 11**). The process comprise of austenitizing followed by rapid quenching in an isothermal temperature bath in the range of temperature 250–425 °C and maintained a constant temperature until the austempering transformation is complete. Austempered gray iron components exhibit increased wear resistance, higher strength, and better noise damping properties. **Figure 12** shows the tensile strength of austempered gray iron as a function of hardness for classes 20, 30, and 40 gray irons.

The essential requirement for austempering is to have sufficient hardenability of the iron to avoid the formation of pearlite on quenching to the austempering bath. The section thickness and shape determine the percentages of elements like Ni, Cu, and Mo for sufficient hardenability.[11]

Initial austenitization temperature and time are similar to the conventional hardening temperature and time of holding.

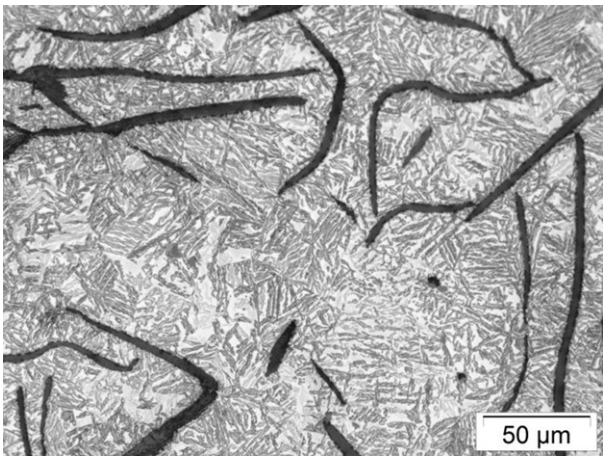


Figure 11 Microstructure of austempered gray iron.

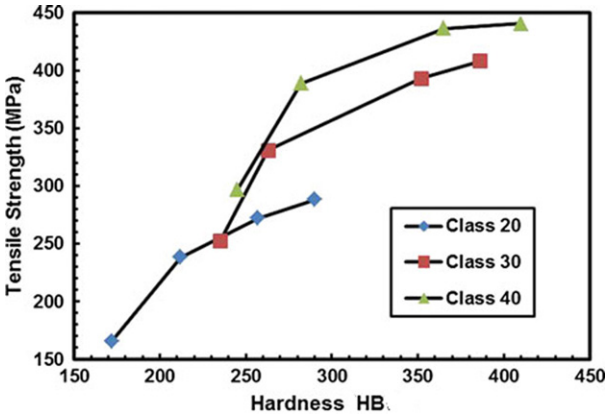


Figure 12 Tensile strength of austempered gray iron as a function of hardness for classes 20, 30, and 40 gray irons. Voigt, R. C.; Loper, C. R., Jr. Austempered Ductile Iron-Process Control and Quality Assurance. *J. Mater. Eng. Perform.* **2013**, *22* (10), 2776–2794.

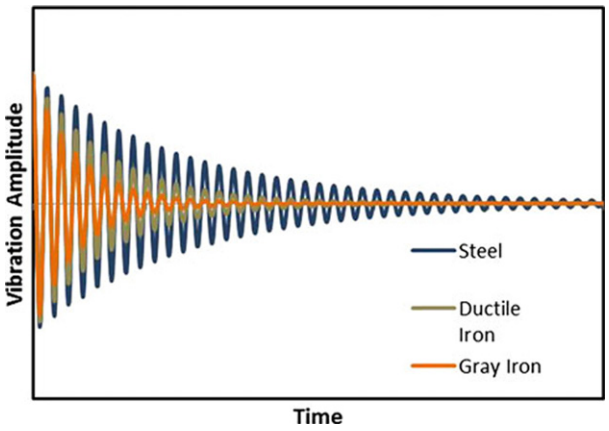


Figure 13 Schematic of vibration characteristics of Gray Iron, Ductile Iron, and Steel. Voigt, R. C.; Loper, C. R., Jr. Austempered Ductile Iron-Process Control and Quality Assurance. *J. Mater. Eng. Perform.* **2013**, *22* (10), 2776–2794.

A suitable temperature range is 840–900 °C for gray cast iron and the holding time is to be determined from chemical composition, size, and complexity of the shape of the casting.

Subsequent to austenitization, the components are usually quenched in salt, oil, or lead baths for austempering. A lower austempering temperature is chosen in the range of 230–290 °C when a high-ultimate hardness is desired. The isothermal holding time is dependent on the bath temperature and composition of the iron. Presence of nickel, chromium, and molybdenum lengthen the transformation kinetics.[11–14]

2.10.2.5.1 Case studies on austempering of gray iron

Case 1: Diesel engine cylinder liners made of gray cast iron are often subjected to austempering to achieve the properties with minimum distortion and cracking as compared to hardening and tempering.[15] The austempering cycle involves in preheating at 650 °C for 5 min and then the temperature is raised to austenitization temperature at 870 °C and held for 8 min. Subsequently quenched in salt bath at 250 °C and isothermally held for 20 min and cooled in air.

Case 2: For power train applications such as gears, shafts, etc., austempered gray iron is a potential material.[15] Along with desirable galling wear resistance, strength, and hardness properties austempered gray iron provides best noise reduction capacity. The vibration damping characteristics of gray iron is increased in austempered condition than its as-cast counterparts. Austempered gray iron with a tensile strength of 414 MPa can have the noise damping capabilities of a fully damped class 20 gray iron with tensile strength of 138 MPa (Figure 13).

2.10.2.6 Martempering of Gray Iron

To overcome the restrictions of conventional quenching and tempering like distortions, cracking tendency etc., martempering is a solution. Martempering involves interrupted quenching – the cooling is stopped at a point above the martensitic start temperature (Ms) to allow sufficient time for homogenization of temperature differential from surface to core of the component to be heat treated. Further cooling is continued through the martensite region of continuous cooling transformation (CCT) diagram followed by the usual tempering to avoid brittleness of the martempered component.

In martempering the casting is initially austenitized above the range of transformation and quenched in salt, oil, or molten lead bath, the temperature of which is maintained just above the martensitic start temperature (Ms). For unalloyed gray iron the martempering temperature is in the range of 200–260 °C. The component is held at this temperature for adequate time to attain the bath temperature and subsequently cooled to room temperature. The holding temperature in the bath depends on the size and complexity of shape of the component.[6]

2.10.2.6.1 Case studies on martempering of gray iron

Case 1: Rey iron cylinder liners or sleeves for engines of chemical composition 3.25–3.50%C, 2.0–2.25% Si, 0.025% P (max.), 0.12% S (max.), 0.55–0.80% Mn, and 0.30–0.40% Cr are subjected to following martempering cycle[6]:

a. Subjected to full annealing in a pusher type continuous furnace at 870 °C, and rough machined.
b. Austenitization for martempering at 870 °C for 1 h in a neutral atmosphere.
c. Quenched in a salt bath of molten nitrate–nitrite at 245 °C for 1 min and air cooled for 30 min.
d. Tempering of cleaned castings at 200 °C for 2 h.

The as-cast sleeves were having flake graphite microstructure with mostly type A graphite flakes and of size 4–6. The matrix dissolves about 0.70%C during the course of austenitization and results in a martensitic matrix after martempering. The bulk hardness in the range of 45–50 HRC with matrix microhardness higher than 60 HRC develops. The martempering reduces the tendency of distortion by 50% of those in conventional oil quenching. Martempering also eliminates the cracking tendency.

2.10.2.7 Surface Hardening of Gray Iron

Surface hardening is an economical method to impart high wear resistance in selected areas of the casting. Most common surface hardening methods include flame and induction hardening.

In flame hardening the form of hardening is due to transformation hardening in which the surface layer is heated above the critical temperature A_1 to austenitize and during subsequent quenching hard martensite is formed. But the inside core temperature being at below the A_1, it is remaining unhardened and so softer.[3,4,6]

For successful flame hardening the combined carbon content is an important parameter. Most suitable range is 0.5–0.7% but a lower combined carbon with 0.4% can even be flame hardened. However, a high combined carbon above about 0.8% is susceptible to cracking. As silicon favors graphite formation it reduces the combined carbon and so a low silicon content (<2.4%) is recommended for flame hardening. A porous and rough surface is generated after flame hardening when the iron contains a high total carbon with coarse graphite flakes. The flakes are burnt out during flame heating.

Because of their higher hardenability alloyed gray irons are better flame hardened with higher surface hardness and depth. Nickel, chromium, and molybdenum additions are often helpful for this purpose. An unalloyed iron containing 3% total carbon, 1.7% Si, 0.6–0.8% Mn develops a maximum hardness of 400–500 HB. In contrast, an average surface hardness of 550 HB can be developed with either 2.5% Ni and 0.5% Cr or 1–1.5% Ni and 0.25% Mo additions.[3]

The surface hardness of flame hardened gray irons is slightly lower than that in the immediate below. This is due to the retention of soft austenite phase at the surface. The surface hardness can be increased by heating at 200–250 °C which also relieves the residual stresses.

Induction hardening is more expensive than flame hardening but it is justified for large number components to be hardened. The hardening is carried out in the range of temperature of 870–925 °C for a short heating cycle. A minimum combined carbon as pearlite ranging from 0.4 to 0.5% is essential for successful hardening. The surface hardness is very much dependent on the carbon equivalent (i.e., %total carbon + %Si), higher the carbon equivalent, more graphite is present in the microstructure causing decrease in the hardness.[3]

2.10.3 Heat Treatment of Malleable Irons

Malleable irons are produced by solid-state phase transformation by annealing of white cast iron components. The metastable iron carbide (Fe_3C) is decomposed to graphitic temper carbon in various matrices such as ferritic, pearlitic, and ferrite–pearlitic depending upon the composition and the type of annealing employed. The starting white iron must be of controlled compositions as various elements have varying response toward malleablizing annealing. Carbon and silicon percentages are so balanced to ensure freedom from graphite formation during solidification. Higher silicon content increases annealing response. Higher silicon content results in rapid annealability and a short-cycle process can be employed.

Table 5 Typical compositions for Whiteheart, Blackheart, and short-cycle Blackheart irons

Element (%)	*Whiteheart malleable iron*	*Blackheart malleable iron*	*Blackheart short cycle*
Total C	3.0–3.7	2.2–3.0	2.35–2.45
Si	0.4–0.9	0.7–1.2	1.5–1.6
Mn	0.2–0.4	0.2–0.5	0.3–0.4
S	0.3 max.	0.05–0.16	0.1–0.15
P	0.1 max.	0.12 max.	0.05 max.
Cr	0.1 max.	0.1 max.	0.1 max.

Source: Elliott, R. *Cast Iron Technology*, 1st ed.; Butterworths: London; Boston, MA, 1988; Table 1.8, p. 14.

Bismuth and tellurium favor white iron solidification while boron and/or aluminum increase the nucleating potency of graphite clusters and increase annealing response. Addition of about 1% manganese promotes pearlitic matrix to develop higher strength. Copper, nickel, and/or molybdenum are often alloyed to improve strength, wear, and corrosion resistances. Certain elements like phosphorus, antimony, tin, and chromium have negative effects on graphitization process and are to be restricted.[3] Typical compositions of various types of malleable irons are shown in **Table 5**.

The malleablizing annealing involves three stages, the initial nucleation of graphitic temper carbon in the first stage of graphitization occur during the holding period at 900–970 °C. In this stage, massive eutectic carbides are decomposed to temper carbon and austenite. Next stage involves rapid cooling to 740 °C and then slow cooling (2–28 °C h^{-1}) through the austenite to pearlite transformation range. Due to very slow cooling the pearlite decomposes to ferrite and temper carbon. This graphitization is known as second stage of graphitization. Faster rate of cooling from annealing temperature such as air cooling produces a pearlitic matrix while oil quenching develops martensitic matrix. There are two types of malleable irons, whiteheart and blackheart, based upon the appearance of the final fracture reflecting the basic difference in their microstructures.

2.10.3.1 Whiteheart Malleable Iron

In the whiteheart malleablizing, the white as-cast iron is decarburized during annealing leaving a structure of iron carbide in a metallic matrix. When fractured the appearance is whitish, giving rise to the name 'whiteheart.' Decarburization is only possible in thin sections; in heavier sections some conversion of carbide to graphite nodules occurs so that the annealed casting has a white rim with core having different structure and mechanical properties. This limits the application to which it can be put.[4]

Malleablizing annealing in this case is a combined decarburization and graphitization process carried out in an oxidizing atmosphere. Originally it was done by packing castings into iron ore mixtures but now it is performed in continuous atmosphere controlled furnaces at about 1070 °C. Small castings may be fully decarburized and are referred to as weldable malleable irons.

Controlled oxidation of carbon in the castings occurs producing a carbon gradient from edge to center. The surface is

deeply decarburized which is fully ferritic but becomes pearlitic further below the surface and the center is pearlitic containing temper carbon (Figure 14). Although, the center of whiteheart castings is normally pearlitic, the presence of decarburized ferritic skin ensures freedom from brittleness and can absorb plastically a considerable amount of energy from a local blow and is freely machinable.[3–5]

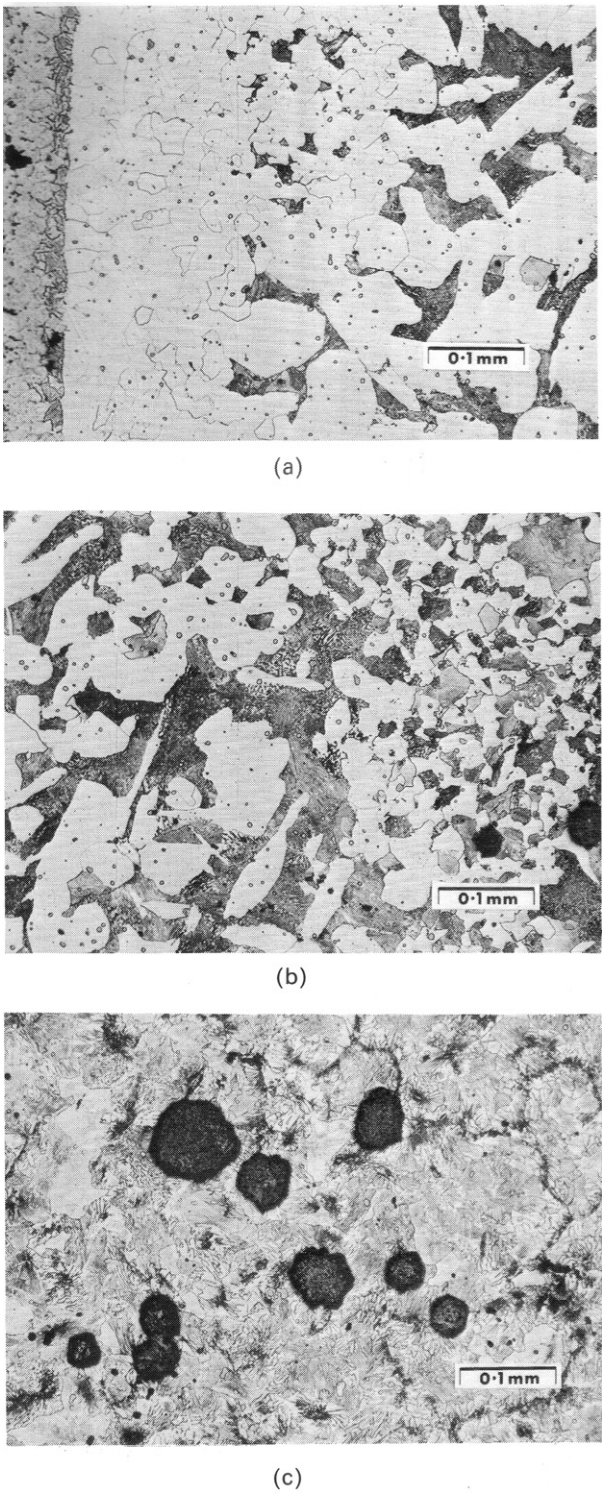


Figure 14 Variation in structure from surface to core (a–c) of a whiteheart malleable iron (3.0%C, 0.75%Si, 0.24%Mn, 0.22%S, 0.06%P). Elliott, R. *Cast Iron Technology*; Butterworths; Figures 6.30 (a),(b),(c), p. 232.

2.10.3.2 Blackheart Malleable Iron

Blackheart malleable irons are produced with lower total carbon content and slightly higher silicon content than whiteheart. Blackheart malleable irons can be with a softer and ductile ferritic matrix or a harder, less ductile pearlitic matrix. Both these matrices are produced by annealing in an inert material like sand or slag packing at 850–950 °C for a prolonged period of 7 days. Alternatively, the annealing is done in a controlled atmosphere furnace with reduced 70 h of soaking. During this soaking period, the first stage of graphitization takes place which is followed by a controlled slow cooling down to 650 °C for second stage of graphitization to occur. As the annealing is performed in neutral atmosphere the chances of decarburization is almost nil (Figure 15) and very slow cooling through the critical temperature range provides the whole of carbon to be deposited as temper carbon and the matrix is ferritic from surface to core. The fracture surface thus appears as blackish in color. Because of its lower hardness, blackheart malleable iron is very freely machinable and with high shock resistance.[3,4]

The higher strength pearlitic malleable irons are produced by (1) increasing the carbide-stabilizing element like manganese to about 1%, (2) by increasing the rate of cooling through the second stage so as to retain the pearlitic matrix, or (3) by annealing, reheating, and air or oil quenching with or without tempering. A wide range of properties can be achieved by transformation of austenite after first stage of graphitization into pearlite, bainite, or martensite.[3,4]

2.10.3.3 Hardening and Tempering of Malleable Irons

The process is most suited in pearlitic malleable iron and involves three consecutive steps, (1) first step is to anneal and air quenching to retain about 0.75% carbon in the matrix; (2) reaustenitization and homogenization of the combined carbon in the matrix at around 885 °C for 1 h, and (3) subsequent quenching in hot agitated oil at temperature of 50–55 °C. A martensitic matrix is developed without any bainite (Figure 16). The selection of austenitization temperature is of utmost importance to obtain the matrix structure (Figure 17). Higher the austenitization temperature and time, more is the amount of dissolved carbon in the matrix and the austenite will be more homogenized. This will result in a homogeneous martensite after quenching but the tendency toward distortion and cracking is increased.[6,16]

The microstructure of air-quenched and tempered malleable iron shows tempered carbon surrounded by ferrite envelops and the pearlites are of broken lamellar pattern. In contrast, the oil-quenched and tempered iron shows matrix of tempered martensite without any ferrite envelop.

The final hardness can be tailored by proper selection of tempering temperature and time in case of pearlitic matrix while for martensitic matrix, temperature is the prime factor

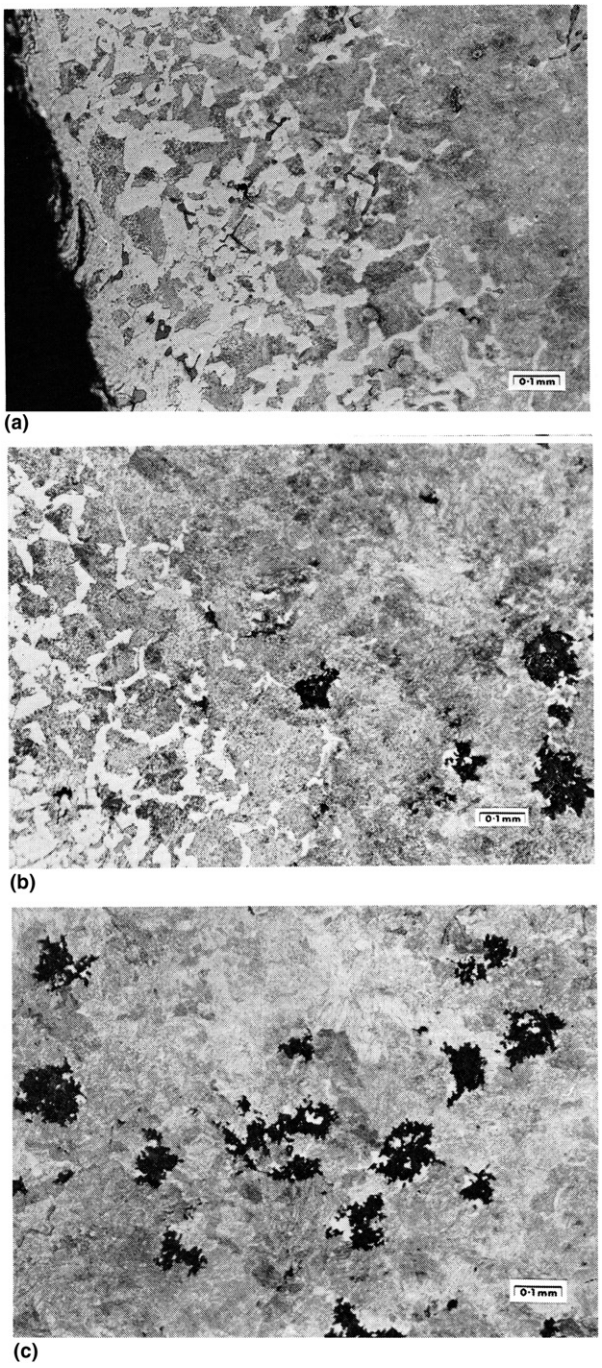


Figure 15 Variation in structure from surface to core (a–c) of a blackheart malleable iron (2.6%C, 1.1%Si, 1.1%Mn, 0.12%S, 0.03% P). Elliott, R. *Cast Iron Technology*; Butterworths; Figures 6.31, 6.32, 6.33, p. 233.

(Figure 18). Tempering times are predetermined on the section thickness and the as-quenched microstructures. Tempering time should be longer than 2 h for uniformity of hardness. The pearlitic structures are tempered at a slower rate than that with martensite. The beneficial effects of alloying on the tempered hardness are shown in (Table 6).

The hardened and tempered malleable irons can also be produced from fully annealed ferritic malleable irons. To obtain a uniform carbon content in the austenite the austenitization temperature and time should be comparatively higher than those in pearlitic malleable iron. During austenitization some of the carbon from the temper carbon is dissolved in the austenite as the initial matrix is carbon-free ferrite. This austenite contains lesser carbon compared to the initial pearlitic malleable iron. Accordingly, the tempering temperature is to be selected at lower range for a desired final hardness.[16]

2.10.3.4 Martempering of Malleable Irons

Pearlitic malleable iron components while subjected to conventional hardening treatment by oil quenching in warm oil are susceptible to quench cracking. These iron components can be martempered to achieve mechanical properties similar to those obtained by oil quenching and tempering typically as, ultimate tensile strength 860 MPa, yield strength 760 MPa, and hardness 300 HB. For martempering, pearlitic malleable irons are first austenitized at 880–900 °C for 1 h and followed by quenching in a molten salt or oil bath maintained at a temperature of 200 °C.[6,16]

2.10.3.5 Bainitic Heat Treatment of Malleable Irons

Isothermal holding subsequent to austenitization of pearlitic malleable iron in the range of bainitic transformation region develop either upper or lower bainite structure depending on the holding temperature. The bainitic structure causes a marked increase in strength and hardness but impairs ductility. For example, a pearlitic malleable iron with 2.6%C, 1.4%Si, 0.5%Mn and 0.11%S when annealed at 930 °C for 16 h, air quenched and tempered at 680 °C for 4 h produced ultimate tensile strength of 650 MPa, yield strength of 460 MPa, elongation of 3.4%, and hardness 217 HB. The iron when austenitized at 900 °C in salt bath for 1 h, quenched in molten salt at 295 °C for 3 h and air cooled produced a much higher tensile strength (995 MPa), yield strength (920 MPa), and hardness (388 HB), but the elongation is only 1%.[16]

2.10.3.6 Surface Hardening of Pearlitic Malleable Irons

For surface hardening by flame or induction hardening, initial pearlitic matrix is most suitable. Ferritic malleable irons respond to the surface hardening provided adequate time is allowed in austenitization for dissolution of carbon from the temper graphitic carbon to the matrix. Response of lamellar pearlitic are more readily, compared to spheroidized structures. For adequate hardenability a minimum 0.5% Mn is effective. A hardness ranging from 55 to 60 HRC can be attained with adequate depth of hardness which can be controlled by the rate of heating and the surface temperature developed. In induction hardening, the controlling factors are power output, operating frequency, heating time, and the alloy content. The heating temperature is critical as the minimum temperature is dictated by austenite homogenization and the maximum temperature is to avoid fusion and burning. A more uniform and deeper case can be obtained with increased

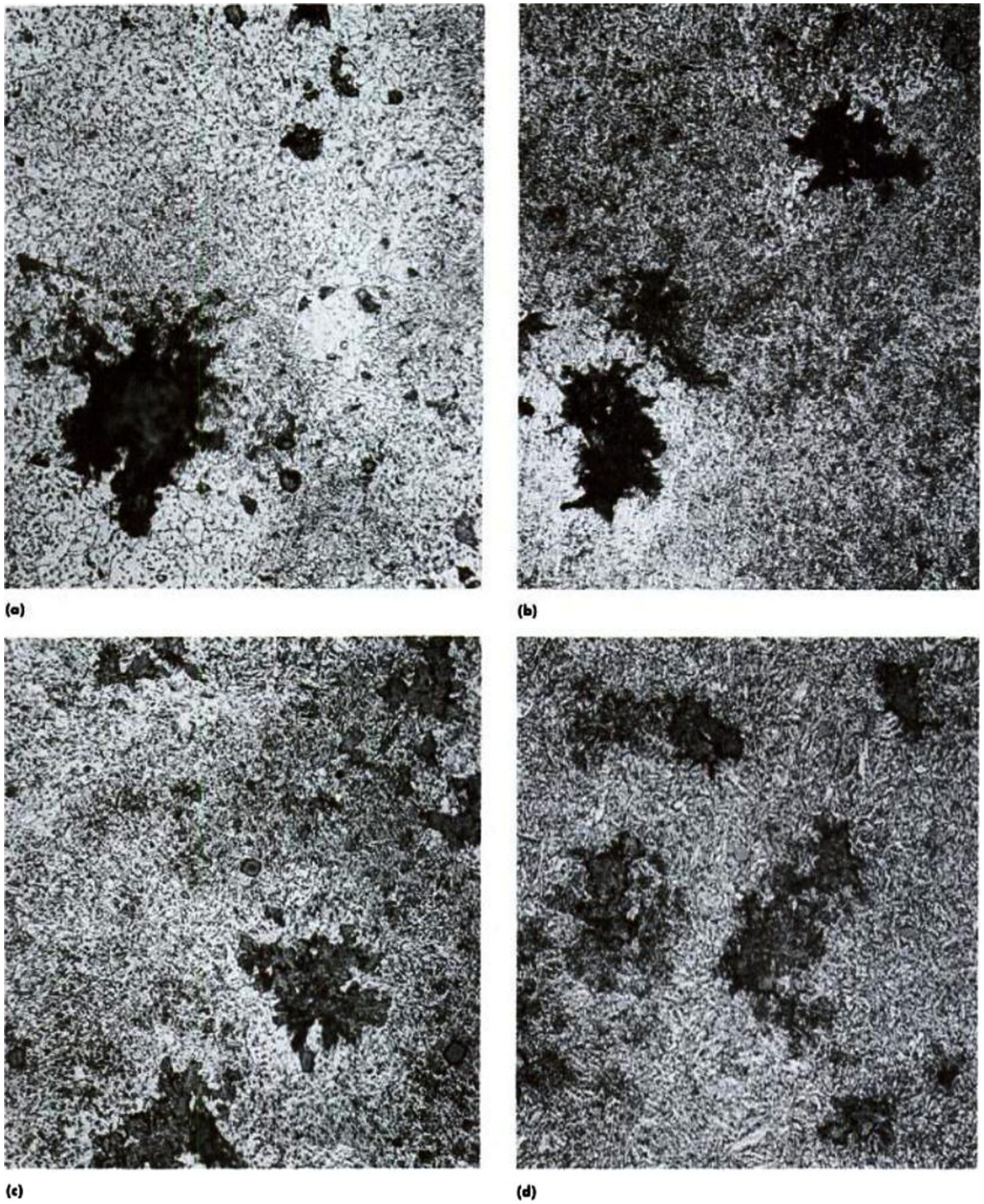


Figure 16 Structure of oil-quenched and tempered martensitic malleable iron, (a) 163 HB, (b) 175 HB, (c) 207 HB, (d) 229 HB. Davis, J. R. *ASM Specialty Handbook: Cast Iron*; ASM International: Materials Park, OH, 1996.

heating time. Generally, quenching in water is necessary to produce high hardness and adequate case depth.[4,6,16]

2.10.3.6.1 Case studies on surface hardening of malleable irons

Case 1: Crimping tool jaws for electrical connectors originally were made of tool steels. Now, it has been possible to replace it by shell mold integral casting made of pearlitic malleable iron (Grade 45010). The intricate contour of the jaws is then surface hardened by induction heating and water quenching to develop required wear resistance. So, the hardening is done in the selected jaw areas and the strength and toughness inherent in grade 45010 are maintained in the arms of the handles.[16]

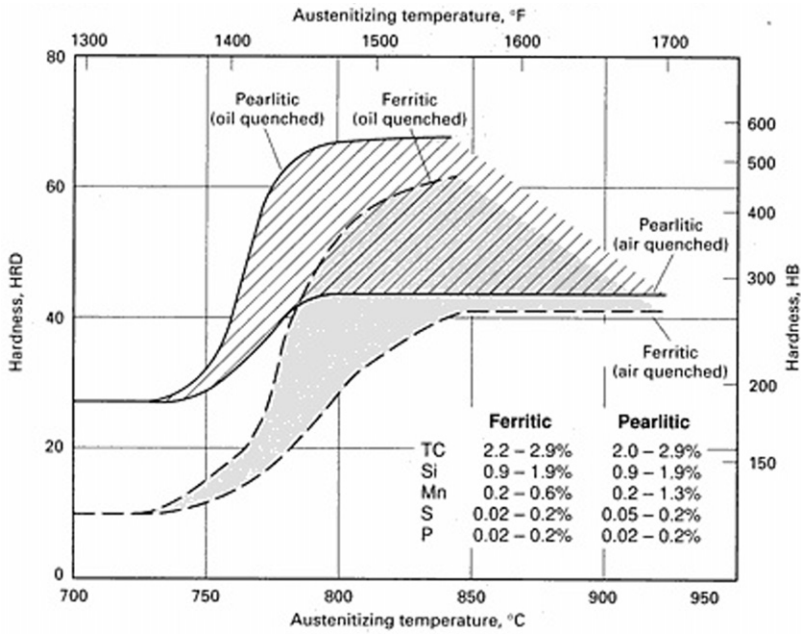


Figure 17 Effects austenitizing temperature and quenching media on the hardness of as-quenched malleable iron. *ASM Handbook*, Vol. 4, 1991 ed., Heat Treating of Malleable Iron; Figure 3, p. 1512.

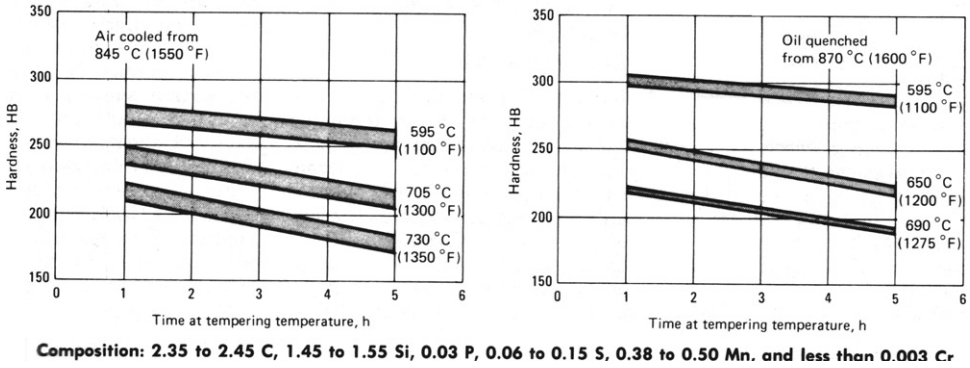


Figure 18 Effects of tempering temperature and time on the hardness of pearlitic malleable iron (composition: 2.35–2.45%C, 1.45–1.55%Si, 0.03%P, 0.06–0.15%S, 0.38–0.50%Mn, <0.003%Cr). *ASM Handbook*, Vol. 4, 1991 ed., Heat Treating of Malleable Iron; Figure 5, p. 1513.

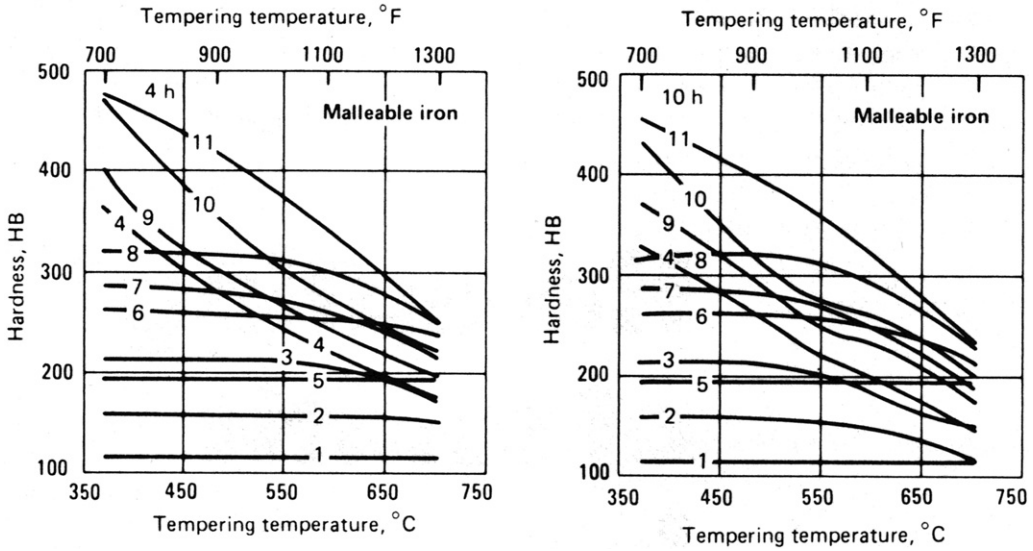
Case 2: Pinion spacers supporting the cups of roller bearings have been made of pearlitic malleable iron and the two ends of the pinion spacers were flame hardened to a hardness above 58 HRC to a depth of about 2.4 mm. It has been possible to eliminate the service failure by this treatment.[16]

2.10.4 Heat Treatment of Ductile Irons

The ductile iron also known as nodular iron or spheroidal graphite iron solidifies as iron-graphite system and the graphite has the spheroid form. Because of its comparable strength and ductility the ductile iron are potential material to replace many structural steels. The as-cast matrix is usually comprise of ferrite, pearlite, or ferrite-pearlite depending on the section size and alloy contents. Although, control of microstructure and properties can be achieved in as-cast condition, the heat treatment is a versatile tool for further extending the range of properties in ductile irons. The most common and important heat treatments and their objectives include[11]:

- Stress relieving at subcritical temperature range to relieve the residual stresses in the castings.
- Annealing to increase the ductility, toughness, and machinability, to decrease hardness and eliminate carbides.
- Normalizing to improve strength with adequate ductility.
- Through hardening and tempering to impart strength and hardness.
- Austempering to develop a microstructure providing high strength and wear resistance and some ductility.

Table 6 Effect of tempering temperature, time, and alloy additions on the hardness



Malleable iron type and conditions	*%TC*[a]	*%Si*	*%S*	*%Mn*	*%Mo*	*Alloying and prior heat treatment*	*Hardness; HB*
Standard ferritic grade 32510	2.4	1.8	0.072	0.3	–	Unalloyed; fully malleablized	116
Pearlitic malleable iron, Grade 45007	2.4	1.8	0.072	0.3	–	Unalloyed; air quenched from 925 °C, tempered 8 h at 695 °C	156
Pearlitic malleable iron, Grade 60003	2.4	1.8	0.072	0.3	–	Unalloyed; oil quenched from 870 °C, tempered 3 h at 650 °C	212
Oil-quenched malleable iron	2.4	1.8	0.072	0.3	–	Unalloyed; oil quenched from 870 °C, not tempered	444
Pearlitic malleable iron, Grade 45010	2.4	1.8	0.076	0.9	–	Alloyed (Mn); air quenched from 940 °C, tempered 34 h at 715 °C	192
Pearlitic malleable iron, Grade 80002	2.4	1.8	0.072	0.9	0.45	Alloyed (Mn and Mo); air quenched from 940 °C, tempered 12 h at 620 °C	262
Air-quenched alloyed malleable iron	2.4	1.8	0.079	0.9	–	Alloyed (Mn); air quenched from 925 °C, not tempered	285
Air-quenched alloyed malleable iron	2.4	1.8	0.076	1.10	–	Alloyed (Mn); air quenched from 925 °C, not tempered	321
Oil-quenched alloyed malleable iron	2.4	1.8	0.079	0.9	–	Alloyed (Mn); oil quenched from 830 °C, not tempered	514
Oil-quenched alloyed malleable iron	2.4	1.8	0.076	1.1	–	Alloyed (Mn); oil quenched from 830 °C, not tempered	578
Air-quenched alloyed malleable iron	2.4	1.8	0.072	0.9	0.45	Alloyed (Mn and Mo); air quenched from 940 °C, not tempered	514

[a] TC = Total Carbon.

Source: Jenkins, L. R. *Heat Treating of Malleable Irons, Heat Treating; ASM Handbook*, Vol. 4; ASM International: Materials Park, OH, 1991; Table 1, p. 1515.

- Surface hardening to impart high surface hardness and wear resistance in some selected areas of the casting.

2.10.4.1 Fundamental Considerations for Heat Treatment of Ductile Iron

The presence of high carbon and silicon causes some specific characteristics of ductile iron toward the response to heat treatment. The high carbon content is advantageous to yield a high hardenability without the necessity for expensive alloying additions. The high carbon, on the other hand, is harmful in respect of quench cracking due to formation of high-carbon martensite and/or retention of metastable austenite. Silicon also has an important role to reduce the solid solubility of carbon in the austenite and favors graphite formation in ferritic matrix during slow cooling. The graphite nodules also play an important role in heat treatment. During austenitization carbon from nodules diffuse in the austenitic matrix causing carbon enrichment while during slow cooling carbon

rejected out from the austenite returns to the nodules as 'sink.' This transfer of excess carbon from nodule to matrix and vice-versa favors the easier heat treatment.[6,17]

In general, different heat-treatment processes involve austenitization and subsequent controlled cooling or isothermal soaking or a combination of the two. As a consequence, the structure developed can be categorized according to the matrix phases; (1) thermodynamically stable ferritic matrix and (2) metastable austenitic matrix.

CCT diagram (Figure 19) and the isothermal transformation (IT) diagram (Figure 20) are two important diagrams to predict the ultimate matrix phase for a particular cooling process. From CCT diagram, it is evident that, slow furnace cooling for annealing will produce a ferritic matrix, air cooling or normalizing will produce pearlitic matrix, and quenching will produce martensitic matrix with some retained austenite.[17–22] The corresponding micrographs are shown in Figure 21.

The process sequence in austempering of ductile iron can be explained by the IT diagram. The austenitized iron is subsequently quenched in salt bath maintained at a steady temperature. Isothermal holding will result in a ausferritic (high-carbon metastable austenite γ_H and plate-like ferrite) or a ferrite–carbide aggregate (bainite) with prolonged holding time. After the required holding time the austempered iron is cooled to room temperature.

The presence of high silicon content prevents the iron carbide formation and the carbon rejected in the first stage of reaction ($\gamma \rightarrow \gamma_H + \alpha$), saturate the austenite and the M_s and M_f temperatures are depressed. Thus, on subsequent cooling, austenite will be stabilized and will not transform to martensite. The austempering time in stage I depends on the alloy content and section size and generally ranging from 1 to 4 h. Prolonged austempering will cause stage II reaction ($\gamma_H \rightarrow \alpha +$ Carbides) producing unwanted bainite which impairs toughness and ductility.[17–22]

Except in case of subcritical treatments like stress relieving, for all other heat treatments an initial austenitization is essential for further treatments to follow. As ductile irons are ternary Fe–C–Si alloys, the critical temperature varies with carbon an silicon contents. The austenitizing temperature must exceed the upper critical temperature. The solubility of carbon in the austenite is dependent on the temperature. So, the selection of a particular austenitizing temperature determines the desired carbon content in the matrix and hence the hardenability or austemperability. Most commonly adopted austenitizing temperature is in the range of 900–950 °C with 1–3 h of holding time.

The range of tensile strength and elongation percentage and hardness values obtained with different types of heat treatments are shown in Figures 22 and 23 respectively.[17]

2.10.4.2 Annealing of Ductile Irons

The objective of annealing is to produce maximum ductility and toughness, reduced strength and hardness, improved machinability, and uniform properties. These properties can be achieved by generating a carbide-free ferritic matrix (Figure 24). Certain elements tend to retard the annealing process which include manganese, phosphorus, chromium, and molybdenum and should be restricted in the casting. Table 7 summarizes the details of various types of annealing processes adopted in practice with their individual purpose.[17,22]

The effect of subcritical ferritizing at 705 °C for various length of time on the hardness of four different grades of ductile irons are shown in the Figure 25.

2.10.4.3 Normalizing of Ductile Irons

The normalizing treatment involves austenitizing and subsequent air cooling to room temperature. The purpose of

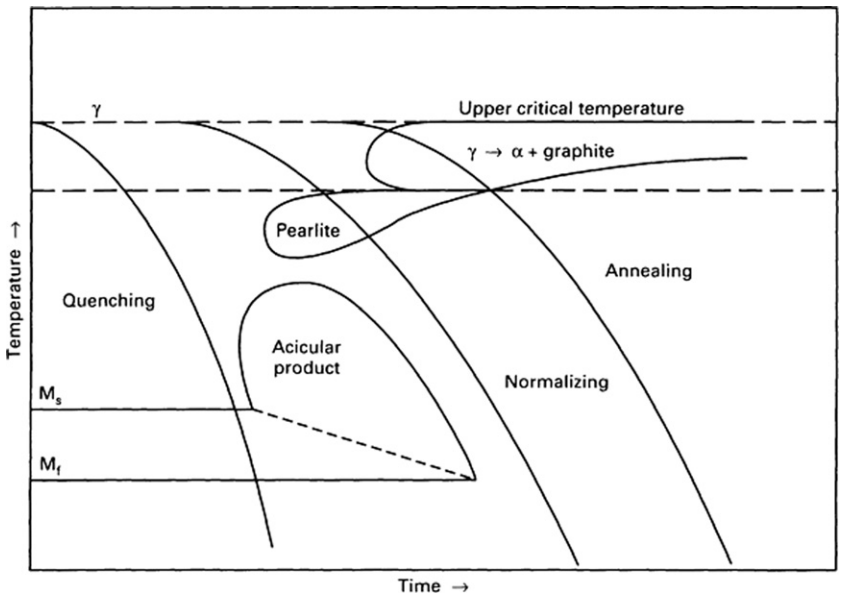


Figure 19 Continuous cooling transformation diagram of ductile irons showing different treatment zones. *ASM Handbook*, Vol. 4, 1991 ed., Heat Treating of Ductile Iron; Figure 1, p. 1487.

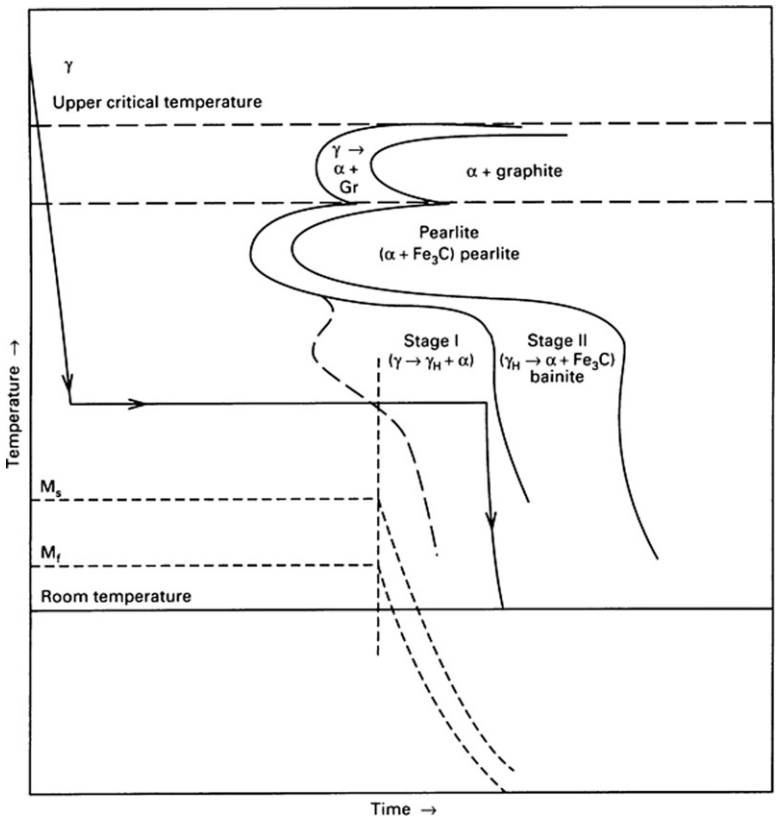


Figure 20 Isothermal transformation diagram of ductile iron showing austempering process sequence. *ASM Handbook*, Vol. 4, 1991 ed., Heat Treating of Ductile Iron; Figure 2, p. 1488.

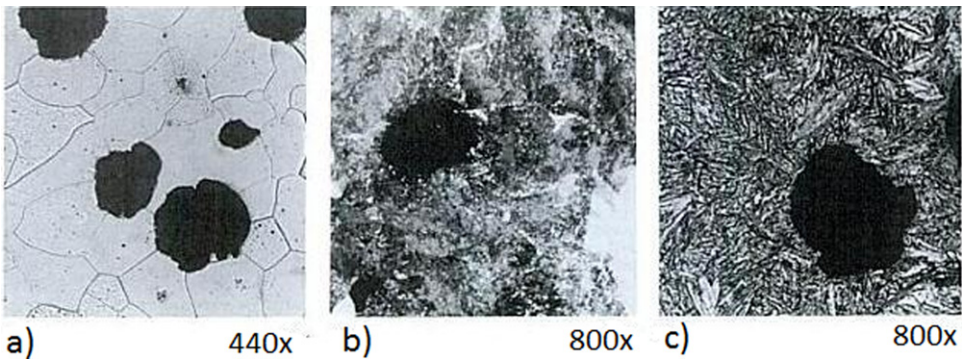


Figure 21 Optical micrographs of ductile iron with different treatments and matrices; (a) ferritic in annealed casting, (b) fine pearlitic in normalized casting, and (c) martensitic in quenched casting. *ASM Handbook*, Vol. 4, 1991 ed., Heat Treating of Ductile Iron; Figure 3, p. 1488.

normalizing is to dissolve eutectic carbides, increase the strength and hardness, and to develop a uniform structure throughout the casting. The microstructure developed in normalizing depends on the composition of the casting and the cooling rate. According to the composition the continuous cooling transformation diagram changes and hence the critical cooling rate. The actual cooling rate is dependent on the mass of the casting, ambient temperature, and air flow in the surrounding. Adequate fast cooling rate should be provided to develop a fine fully pearlitic matrix without any ferrite (**Figure 26**). Alloying additions such as nickel, molybdenum, and additional manganese are to be made to increase the hardenability of heavier castings so that a fully pearlitic structure after normalizing could be achieved.[17]

Figure 27 illustrates the effect of nickel and other alloy content on the hardness of castings with various section thicknesses.

The normalizing temperature is generally selected as 100 °C above the critical temperature range and typically the temperature ranges between 870 and 940 °C. The standard

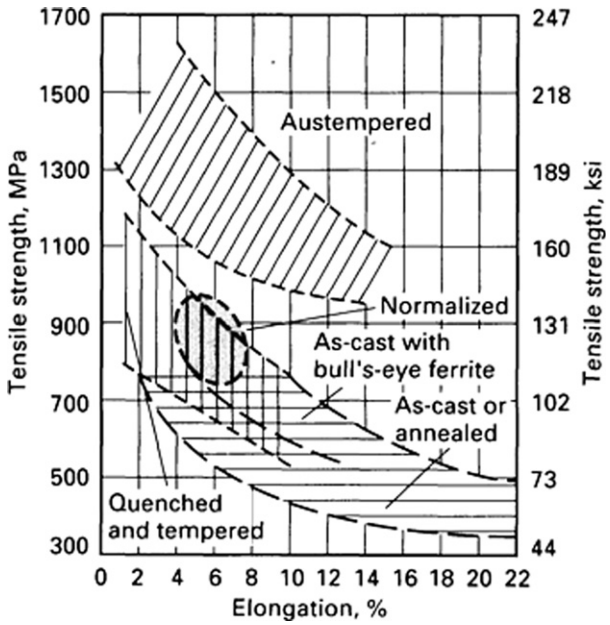


Figure 22 Tensile strength versus elongation percentage of ductile irons with different heat treatments. *ASM Handbook*, Vol. 4, 1991 ed., Heat Treating of Ductile Iron; Figure 4(c), p. 1490.

holding time for unalloyed castings at this temperature range is 1 h plus 1 h 25 mm^{-1} of section thickness.

Sometimes, tempering treatment is subjected to normalized castings to obtain the desired hardness, toughness, and for stress relieving due to differential cooling rates during normalizing. The actual composition and the normalized hardness value dictate the response of tempering on the final tempered hardness (**Figure 28**). Typical tempering temperature ranges from 425 to 650 °C with a holding time of 1 h 25 mm^{-1} section thickness.[17,23]

2.10.4.4 Hardening and Tempering of Ductile Irons

Hardening treatment includes austenitizing followed by quenching, provides maximum hardness resulting from transformation of austenite to martensite (**Figure 29**). The as-quenched hardness depends on the carbon content in the martensite, volume fractions of martensite, and the retained austenite in the microstructure. Austenitizing temperature determines the carbon content in the austenite and hence in the martensite after quenching. An austenitizing temperature of 845–925 °C is the common temperature range to obtain the optimum carbon content and maximum hardness. The effect of austenitizing temperature on the water quenched hardness of a ductile iron is shown in **Figure 30**. It is evident from the figure that, the highest range of hardness is obtained with austenitizing at 845–870 °C. Above 870 °C the greater percentage of retained austenite is stabilized lowering the as-quenched hardness.[17]

The choice of quenching media is also very important so that the maximum as-quenched hardness, minimum chances of residual stresses, and quench cracking tendency result in. The most widely used medium is oil to meet up these requirements. However, water or brine also may be used for simple shapes. For complex-shaped castings hot oil at 80–100 °C is preferred to avoid any distortions and cracking.

The as-quenched castings are immediately tempered in the range of temperature of 425–600 °C for different length of time. The purpose is to reduce residual stresses and chances of cracking, decrease strength and hardness at the cost of increment in ductility and toughness and to improve machinability. Tempering process is influenced by other factors like alloy content, as-quenched microstructure and nodule count. Low alloy martensitic matrix with high nodule count decreases the tempering temperature and/or time. **Figure 31** shows the effect of tempering temperature and time on the tempered hardness of two different ductile irons. The tempering process in this temperature range involves two stages; (1) precipitation of carbides and (2) nucleation and growth of small secondary graphite nodules at the expense of carbides. This secondary graphite formation causes drop in hardness in the second stage and consequently decrease the tensile and fatigue strengths. **Figure 32** illustrates the effect of tempering on the hardness and tensile properties.[17,24]

2.10.4.5 Austempering of Ductile Irons

Austempering of ductile irons produce a unique material with outstanding properties of high strength and good ductility. Austempered ductile iron (ADI) is twice as strong as standard ductile iron grades with comparable toughness. Apart from these, it is responsive to work hardening surface treatments and posses excellent fatigue and wear properties. Compared to forged steel components ADI offers high strength-to-weight ratio, lower production costs of near net shape castings, and good machinability. The austempering treatment involves following steps[6,14,17,25,26,28–33]:

- Austenitizing the casting normally in the range of temperature 845–925 °C for a holding time adequate to saturate the austenite with carbon.
- Austenitizing followed by rapid quenching in a hot bath maintained at temperature of 230–400 °C to avoid pearlite formation. The temperature range of salt bath is above the martensite start temperature (Ms) of the iron.
- Isothermal holding in the hot bath, i.e, austempering for adequate time to produce an ausferritic matrix, a combination of acicular ferrite and high-carbon austenite.
- Subsequent cooling to room temperature after predetermined austempering time.

2.10.4.5.1 Effect of metallurgical variables on the properties of ADI

2.10.4.5.1.1 Effect of metal composition

The selection of composition for both ductile iron as well as ADI is important. Firstly, the elements which adversely affect the spheroid formation or carbide and inclusion formation or propmotion of shrinkage should be restricted. Secondly, control should be exercised to the elements which affect hardenability and the properties of transformed microstructure. The section size of components, the type of quenching media

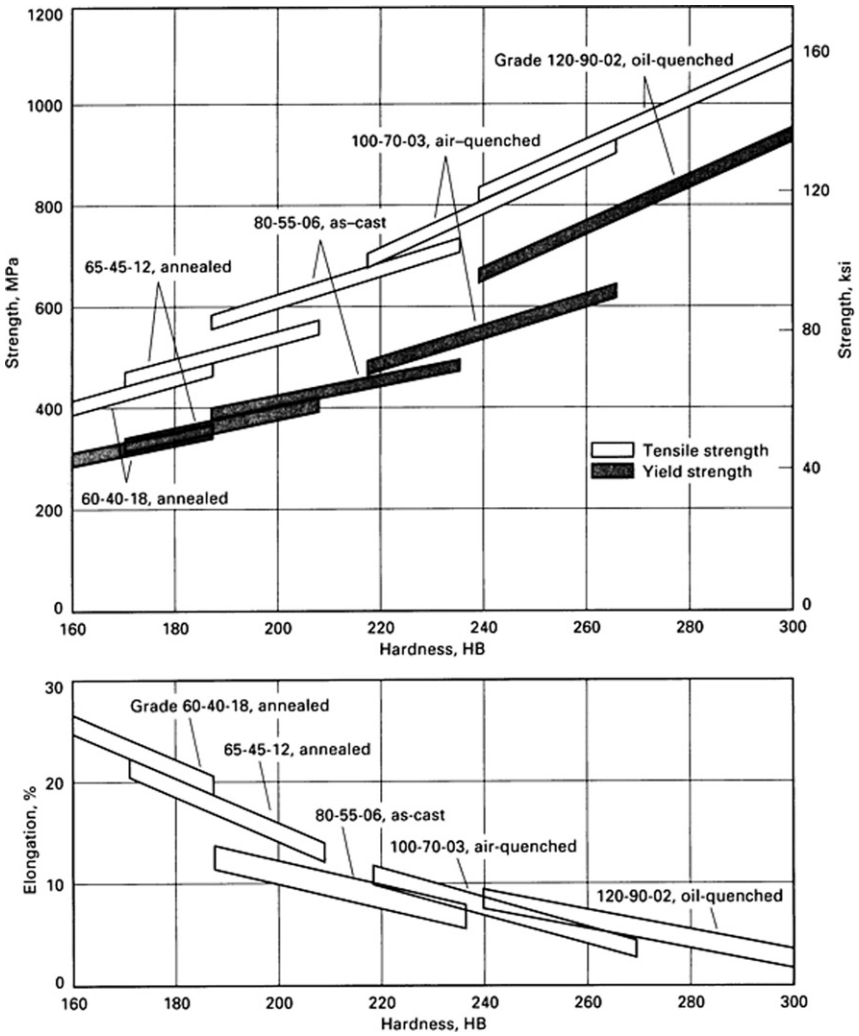


Figure 23 Strength and ductility versus hardness of ductile iron. *ASM Handbook*, Vol. 4, 1991 ed., Heat Treating of Ductile Iron; Figure 5, p. 1491.

and the severity of quench are determining factors for the optimum alloying requirements.[6]

In an agitated molten salt bath quench, section sizes up to about 10 mm of an unalloyed ductile iron can be successfully through hardened without the formation of pearlite. In an agitated austempering bath with water saturation, section sizes up to about 20 mm can be through hardened for unalloyed iron. Proper alloying is needed to through harden and to avoid pearlite formation in the microstructure. Followings are the effects of carbon, silicon, and other alloying elements like manganese, copper, nickel, and molybdenum.

Carbon: Variation of total carbon in a narrow range (~3.6%) will have little effect on the properties of austempered iron. Since equilibrium carbon content in the austenite phase will not be affected much, the IT characteristics will not be changed.
Silicon: Silicon is a graphitizing element and decreases the solubility of carbon in austenite. It raises the eutectoid temperature and inhibits the formation of bainitic carbide. Increasing the silicon content increases the impact energy of the ADI and lowers the ductile–brittle transition temperature. The Si content should be restricted to 2.4–2.8%.
Manganese: Mn is an element which has a strong effect on hardenability but it has a tendency to segregate at cell boundaries and retards the austempering transformation by forming carbides. This segregating tendency is particularly prominent in the castings with lower nodule counts or thick section castings (>20 mm). The high segregation of Mn causes shrinkage, carbides, and unstable austenite. The ultimate effect is deterioration of mechanical properties and poor machinability. In view of this, the Mn content is restricted in austemepered ductile iron to less than 0.3%.
Copper: Copper is also effective in increasing the hardenablity. However, it has no significant on tensile strength but improves ductility when austempered at a temperature below 350 °C.
Nickel: Nickel is also effective in increasing the hardenability but at lower austempering temperature below 350 °C. Nickel has a tendency to decrease the tensile strength but increases the ductility and fracture toughness. Nickel content is restricted to 2% in ADIs.

Molybdenum: It is a very potent element to increase the hardenability (**Figure 33**) and is invariably necessary for heavy section castings to prevent pearlite formation. Like Mn it also has a segregating tendency at cell boundaries and forms carbides. As a result, both tensile strength and ductility decrease with increase in Mo content. Therefore, Mo content is restricted to 0.2% in heavy section castings with an objective to improve the hardenability.

Alloy Combination: Combination of the aforesaid alloying elements are often used to overcome the problems of segregation and degradation of mechanical properties. A judicious use of Mn and Mo for improvement of hardenability and the excess use can be supplemented by either Cu or Ni. A typical iron composition which ensures consistent nodule count and pearlite/ferrite ratio with castings free from shrinkage is shown in the **Table 8**.

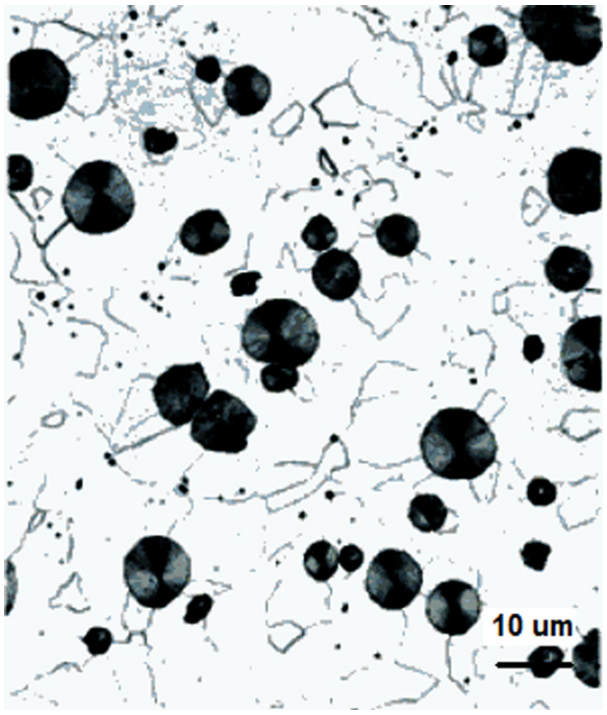


Figure 24 Microstructure of annealed ductile iron featuring a fully annealed ferritic matrix. Davis, J. R. *ASM Specialty Handbook: Cast Iron*; ASM International: Materials Park, OH, 1996; Figure 7, p. 195.

2.10.4.5.1.2 Practical factors affecting successful austempering

In addition to the effect of composition and section thickness of the components, the practical factors like austenitizing temperature and holding time at austempering temperature and time, furnace atmosphere, etc., are of utmost importance.

a. *Austenitization*: As the austempered hardness is high enough, only finish machining is to be carried out after austempering. Care must be taken to avoid surface decarburization and scaling during high-temperature austenitizing. Suitable process includes austenitization in salt bath, controlled atmosphere furnace, fluidized beds, or employing some scale resistant coating on the casting surface. The temperature distribution in the furnace should be homogeneous otherwise failure to austenitization and distortion of the castings are caused. Variation in the temperature can arise from the incorrect stacking of the charge, poor process control, and inadequate furnace design.

   Austenitization is usually carried out within the temperature range of 850–950 °C. As the austenitization temperature is increased the equilibrium carbon content in the austenite will increase and this will ultimately affect the IT characteristics during austempering. With increase in 'C' content the martensite start temperature (Ms) is depressed and the bainite transformation time is delayed particularly at lower austempering temperature. It has been observed that, both tensile strength and yield strength are increased as the austenitization temperature is increased from 850 to 925 °C for 1 h and austempered between 300 and 425 °C. Elongation is not affected by the change in austenitization temperature.[5,6,17,27]

   Austenitizing time should be minimum necessary to homogenize the temperature throughout the cross-section and to saturate the austenite with equilibrium 'C' content. Austenitization time is also affected by the chemical composition, the austenitization temperature, and the nodule count.[5,6,17,27]

b. *Austempering*: The ultimate mechanical properties of austempered iron depends on the microstructural parameters such as the bainite or ausferrite morphology, the volume percentage of retained austenite, and the presence of

Table 7 Details of annealing processes for ductile irons

Annealing processes	*Purpose*	*Temperature of castings*	*Time of soaking*	*Cooling cycle*
Subcritical ferritizing	In absence of carbides to develop a ferritic matrix	700–720 °C	1 h 25 mm^{-1} section thickness	Furnace cooling @ 55 °C h^{-1} to 345 °C, air cooling
Full annealing (for 2–3% Si)	No eutectic carbides. To develop ferritic matrix with maximum low temperature impact toughness	870–900 °C	Same as above	Same as above
Full annealing	With presence of carbides. To develop a ferritic matrix	900–925 °C	2 h minimum; longer time for heavier sections	Furnace cooling @ 110 °C h^{-1} to 700 °C, hold at 700 °C for 2 h, furnace cooling @ 55 °C h^{-1} to 345 °C and air cooled

Source: Modified from Rundman, K. B. Heat Treating of Ductile Irons, Heat Treating; ASM Handbook, Vol. 4; ASM International: Materials Park, OH, 1991; pp. 682–692.

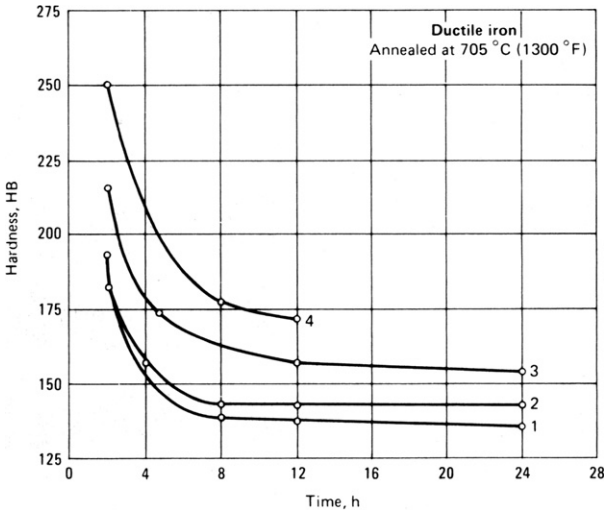


Figure 25 Effect of subcritical annealing time on the hardness of ductile iron. *ASM Handbook*, Vol. 4, 1991 ed., Heat Treating of Ductile Iron; Figure 8, p. 1495.

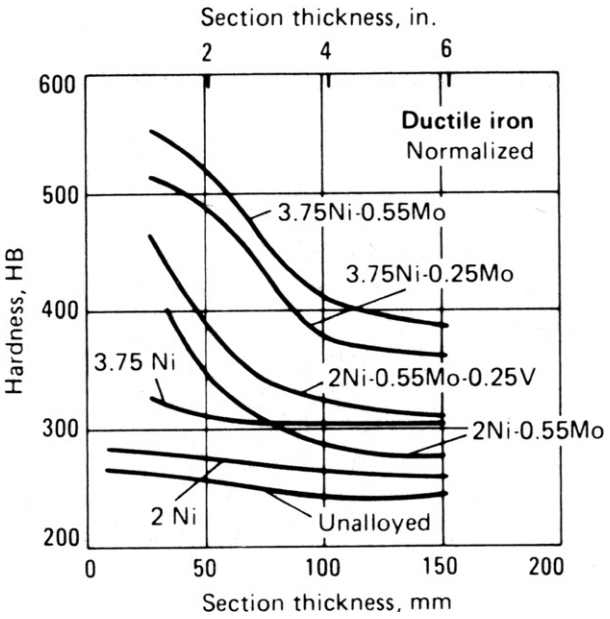


Figure 27 Effect of alloy content and section thickness on the normalized hardness of ductile iron. *ASM Handbook*, Vol. 4, 1991 ed., Heat Treating of Ductile Iron; Figure 13, p. 1499.

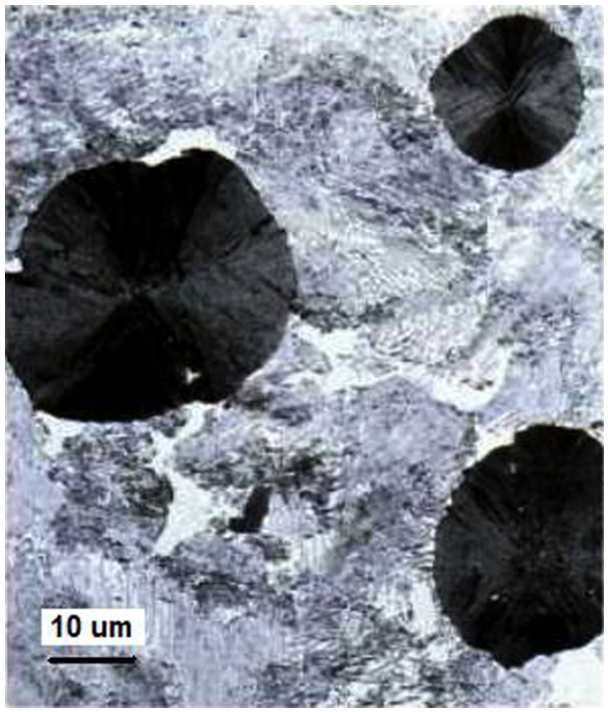


Figure 26 Microstructure of normalized ductile iron showing a pearlitic matrix. Etched in picral. Davis, J. R. *ASM Specialty Handbook: Cast Iron*; ASM International: Materials Park, OH, 1996; Figure 13, p. 196.

martensite. The formation of martensite is accentuated by the low austempering temperature with short holding time.

Irons which have lower bainitic structure (**Figure 34**) yields higher strength and lower ductility than those with upper bainite. Lower bainite is typically formed at austempering temperature below about 330 °C and the transformation kinetics are influenced by chemical composition and the 'C' content in the austenite. The 'C' content in its turn is a function of austenitization temperature and time. Upper bainite is formed at isothermal treatment about 330 °C and below the pearlite formation temperature, i.e., 500 °C. Ductility and toughness of upper bainite structure is much higher compared to lower bainite counterpart (**Figure 35**) but the hardness is lower in the former one. Another microconstituent present after austempering is retained austenite when austempering time ranges 0.5–3 h. The amount of retained austenite is much higher (up to 40%) in the upper bainitic irons than that in lower bainitic irons (less than 10%).

Excessive austempering time can cause the decomposition of ausferrite into ferrite and carbide which results in lower strength, ductility, and fracture toughness.

The attainment of maximum ductility at any selected austempering temperature is a function of austempering time (**Figure 36**). Even with its high strength, ADI shows a remarkable resistance to crack propagation. With a 0.2% proof strength of 1100 MPa K_{IC} values exhibited is 50 MPa. $m^{0.5}$ which is three times greater than those of pearlitic S.G. iron with the yield point of only 500 MPa. Because of the presence of high proportion of retained austenite, there is no obvious ductile to brittle transition temperature in impact toughness.[5,6,17,27]

c. *Surface deformation treatments*: Improved fatigue properties can be achieved by the presence of a compressive residual stress at the surface in the components subjected to fatigue loads. The residual compressive stress can be introduced by shot peening or surface rolling. These cold working can cause an additional benefit to transform the retained austenite in ADI to strain-induced martensite. The strain-induced martensite formation is associated with 4% increase in volume which further cause the increment in

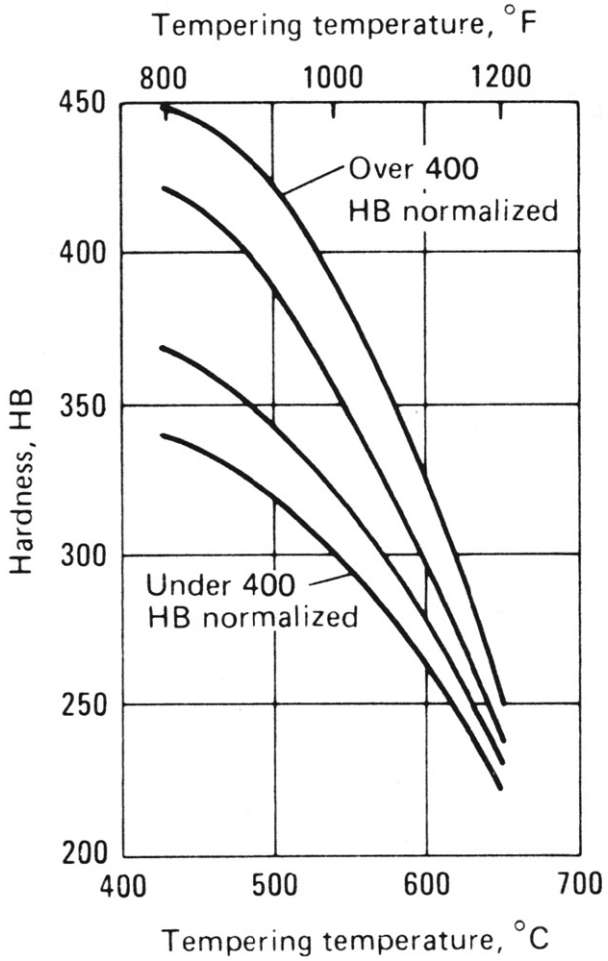


Figure 28 Hardness of normalized and tempered ductile iron at various temperatures. *ASM Handbook*, Vol. 4, 1991 ed., Heat Treating of Ductile Iron; Figure 14, p. 1500.

compressive residual stress. The strain-induced martensite significantly improve the wear resistance.[6,27]

2.10.4.5.2 Two-step austempering heat treatment

To improve further properties of ADI, another two-step austempering heat treatment cycle has been developed. In two-step austempering, the austenitization process is similar to conventional practice.[34,35]

The component is subsequently quenched to a temperature bath in which temperature is increased just after quenching to a final higher temperature (Figure 37). The reason of using that process is to get higher toughness values in combination with high level of strength. Quenching at low temperatures results in finer grains, and consequently, improves the strength. On the other hand, the heating of the salt bath results in faster diffusion of carbon, and this in turn results in higher austenite carbon content, and consequently, higher toughness.

For further improvement of the properties of ADI, it is alloyed with Ni and Mo. In the as-cast form, proper addition of Ni and Mo can improve the properties of ductile cast iron through increasing the pearlite percentage in the structure. While in the ADI, addition of Ni and Mo results in improvement in the

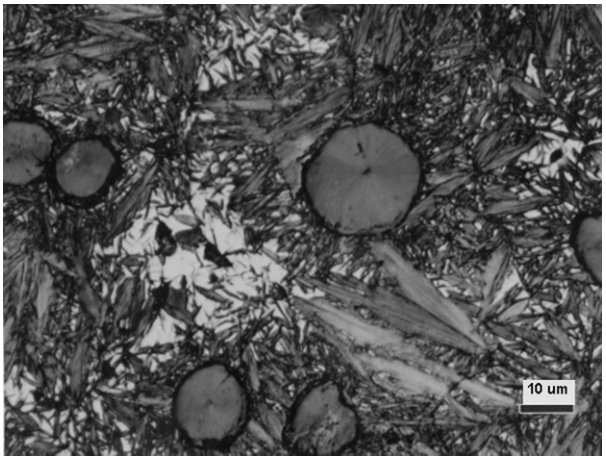


Figure 29 Microstructure of hardened ductile iron. George Vander Voort. *Metallographic Procedures for Cast Irons*; Vac Aero International Inc. Newsletter; Figure 15.

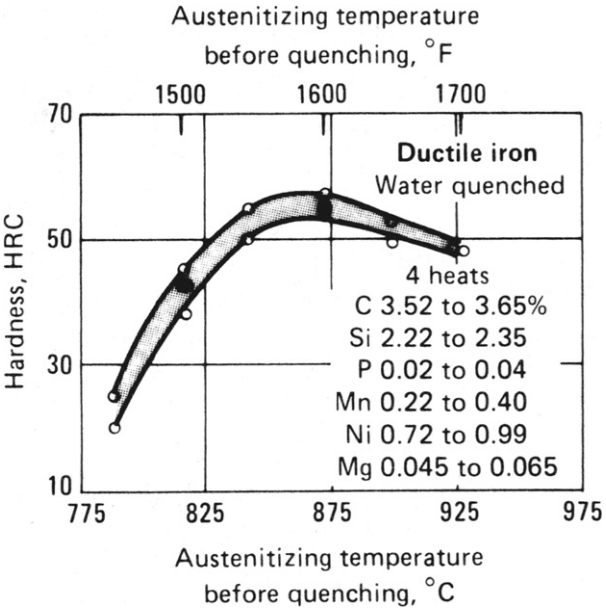


Figure 30 Effect of austenitizing temperature (time 1 h) on as-quenched hardness of ductile iron. *ASM Handbook*, Vol. 4, 1991 ed., Heat Treating of Ductile Iron; Figure 15, p. 1501.

fracture toughness of ADI through their effect on the volume percentage of retained austenite (Figures 38 and 39).

Case study:[37] ADI gears were produced from continuous cast iron bars, heat treated for Grade 3 of ASTM ADI Standard A897M-06 (UTS > 1200 MPa) and compared the performance to carburized steel of AISI 8620 and to induction hardened steel of AISI 4140. The chemical compositions, heat treatment sequences, nodule characteristics of the ADI material and the mechanical properties of the gear materials are shown in Tables 9–12 respectively. Macroscopic images were taken from the gear teeth flank, showing the condition before running-in and after each step of the fatigue tests, so that the damage evolution in the flanks with the loading cycles could be

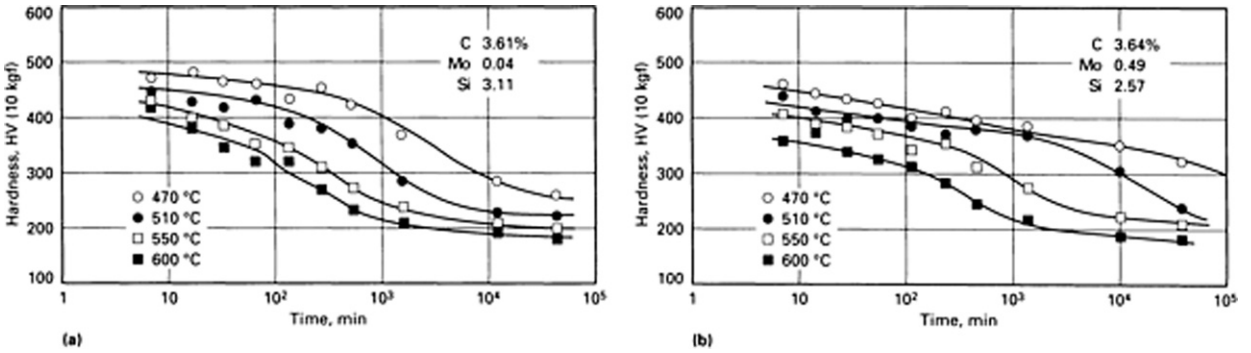


Figure 31 Effect of tempering temperature and time on the tempered hardness of two different ductile irons. Rundman, K. B.; Rouns, T. N. On the Effects of Molybdenum on the Kinetics of Secondary Graphitization in Quenched and Tempered Dutile Irons. *AFS Trans.* **1982**, *90*, 487–497.

observed. These images were used to quantify the pitting area. Tests on gears were made measuring the time for pitting and spalling on the surface of the gears. The results of the total rate of damage (damaged area (*A*%)/number of cycles (*N*)) for all the materials tested are shown in Figure 40.[37]

The ADI with small nodule size showed to be very competitive with wear resistance similar to AISI 4140 induction hardened steel. The nodule size affects the contact fatigue life independently of the ductile iron microstructure. The size and count of nodules affect both the nucleation and propagation of cracks. ADIs with small nodule size has a greater wear resistance.

2.10.4.6 Surface Hardening of Ductile Irons

Ductile irons can be surface hardened by flame, induction, or laser hardening treatments.[17,18,38] As the pearlitic matrix has the less diffusion distances, it can most readily respond to surface hardening treatments. A satisfactory response toward surface hardening is obtained with ferritic matrix. However, a fully ferritic matrix requires higher heating time to be hardened. The hardening temperature is generally ranging from 845 to 900 °C and the surface hardness values range from 35 to 62 HRC depending upon fully ferritic to a mostly pearlitic matrix. The final hardness values depend on various factors such as heating temperature and time, dissolved carbon content in austenite, section size, and rate of quenching. Water quenching develops higher hardness but soluble oil or polymer quenching media are often used to avoid quench cracking.

The response to induction hardening also depends on the amount of pearlite in the matrix and prior condition of the castings. In as-cast condition, the hardening temperature ranges from 955 to 980 °C for 3.5 s depending on the pearlite contents. If the casting contains less than 50% pearlite higher hardening temperature is to be selected and with pearlite content greater than 50%, a lower hardening temperature range 900–925 °C is sufficient. In normalized and tempered condition, the response to hardening is poor with lower pearlite content ($\leq$50%), since during tempering the carbon is diffused from matrix to graphite nodules. The carbon is again absorbed from nodule to matrix during reheating but the extent of migration is not enough due to insufficient time of heating. In this respect the graphite nodule count is also important, higher the nodule count lesser is the diffusion path of carbon resulting in a deeper hardening. Casting having prior quenched and tempered treatment is more responsive even with higher ferrite percentage in the matrix. During tempering the secondary graphite nodules formed are responsible for supplying the adequate carbon to the matrix during induction reheating.

In case of surface hardening by plasma or laser heating a very high local heating is achieved which in turn produce a very small melted area on the surface. This melted area rapidly resolidifies because of self-quenching effect of the casting mass and develop a white iron structure with high hardness and wear resistance. If the source is moved on the surface a sufficient area is possible to be hardened.[17]

2.10.4.7 Stress Relieving of Ductile Irons

Complex-shaped castings which are employed in unheat treated condition should be stress relieved in the subcritical temperature range from 510 to 675 °C. The extent of stress relieving is dependent on factors like severity of initial residual stress, the stress-relieving temperature and time, the heating and cooling rate, and composition and microstructure of the casting.[6,17] The lower temperature of stress relieving is generally used for unalloyed and low-alloyed irons whereas higher ranges are employed for high and austenitic irons. The time of stress relieving depends on the casting shape and the desired extent of stresses relieved (Figure 41). As a common rule, 1 h plus 1 h per 25 mm section thickness is recommended. After soaking, the castings are to be furnace cooled to 290 °C followed by air cooling to room temperature. Austenitic irons are generally uniformly air cooled from stress-relieving temperature.

2.10.5 Heat Treatment of High-Alloy Irons

High-alloy irons are a separate category of irons comprising of alloy content greater than about 4% and intended for use in some specific applications. These specific applications include heat resisting, corrosion resisting, and abrasion resisting. The high-alloy irons can be broadly classified as high-alloy graphitic irons and high-alloy graphite free white irons. The family of these high-alloy irons are shown in Figure 42.

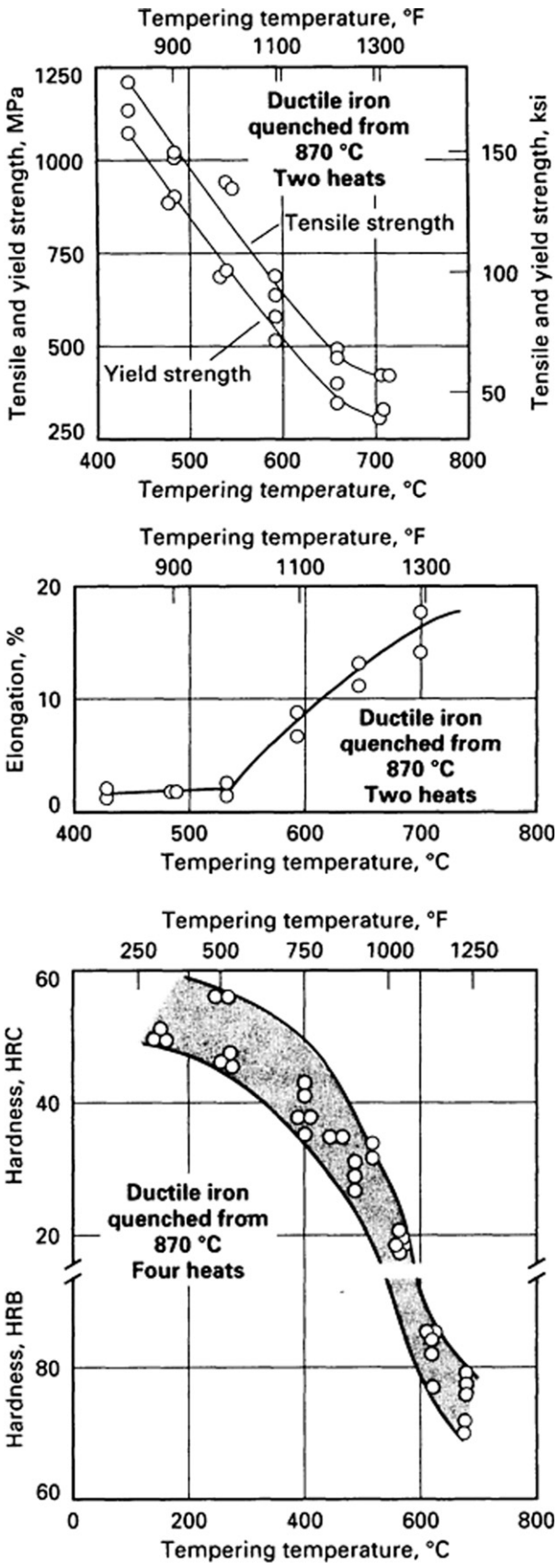


Figure 32 Effect of tempering temperature on the tensile properties and hardness of ductile iron quenched from 870 °C and tempered for 2 h. *ASM Handbook*, Vol. 4, 1991 ed., Heat Treating of Ductile Iron; Figure 17, p. 1502.

2.10.5.1 Austenitic Graphitic Irons

The nickel alloyed austenitic graphitic irons also known as Ni-resist irons may be of flake type or nodular type in an austenitic matrix (**Figures 43** and **44**). The austenite phase is stabilized at room temperature by alloying with austenite stabilizers such as nickel, copper, etc. The spheroidal grades because of higher strength, ductility, and elevated temperature properties are being widely used. The advantages of flake type Ni-resist include lower cost, fewer foundry problems, better machinability, and thermal conductivity.[6,39,40] The standard ASTM flake graphite and austenitic ductile iron compositions are shown in **Tables 13** and **14** respectively.

General characteristics of Austenitic graphitic irons are as follows[40]:

a. Corrosion resistance: The corrosion resistance of this class of irons is much superior to the normal and low-alloy cast irons. Therefore, these irons are employed for corrosion resistant applications such as handling of salt solutions, sea water, mild acids, alkalis, and oil field liquids. These irons degrade by uniform corrosion rather than by localized deterioration.
b. Heat resistance: All Ni-resist irons are heat resistant and relatively low rates of oxidation in air. The adherent oxide layer formed on the surface reduces further oxidation. Among the two types spheroidal graphite Ni-resist has superior elevated temperature properties and can be used at temperature up to about 1050 °C. The flake graphite Ni-resist irons are mostly employed up to 700 °C.
c. Controlled thermal expansion: The thermal expansion of Ni-resist irons ranges from 5.0×10^{-6} to 18.7×10^{-6} cm per cm per °C and because of this low expansion these irons can be employed for producing precision parts.
d. Wear resistance: Austenitic graphitic irons possess excellent galling resistance and so are the potent material for making cylinder liners, piston wear rings, sleeves, bearings, and other metal-to-metal rubbing parts.
e. Erosion resistance: Ni-resist irons are having outstanding corrosion–erosion resistance and are most suitable material for handling slurries, wet stream, and fluids with entrained solids.
f. Magnetic and electrical properties: Because of the non-magnetic nature and high electrical resistance of some Ni-resist irons they are suitable for resistance grids, electric furnace parts, clutches, etc.
g. Machinability: Machinability is similar to higher strength grades of gray cast iron austenitic stainless steel.
h. Castability: Complex-shaped casting which are difficult to be cast in other materials can be economically cast in Ni-resist irons.

2.10.5.1.1 Effects of composition on the structure and properties

Nickel: In Ni-resist irons Ni is the primary element and is responsible for the stable austenite formation. Addition of nickel imparts corrosion and oxidation resistance and mechanical properties required in the high temperature range. Ni is also controlling the co-efficient of thermal expansion of the iron.

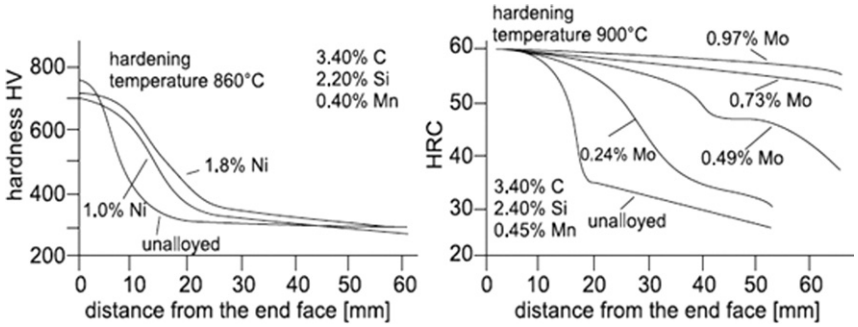


Figure 33 Effect of Ni and Mo on the hardenability of ductile iron. *Duktiles Gusseisen*; Verlag Schiele & Schon: Berlin, 1996; p. 178.

Table 8 Typical iron composition ranges for consistent properties

Carbon*	3.7%	+/−0.2%
Silicon*	2.5%	+/−0.2%
Manganese	0.28%	+/−0.03%
Copper	As required	+/−0.05% up to 0.8% maximum
Nickel	As required	+/−0.10% up to 2.0% maximum
Molybdenum	Only if required	+/−0.03% up to 0.25% maximum

Note: *Carbon and silicon should be controlled to produce the desired carbon equivalent for the section size being produced.
Source: Ductile Iron Data for Design Engineers, Section IV, Alloy Ductile Iron; Ductile Iron Society: Strongsville, OH, 1998.

Chromium: Chromium is responsible for improvement in strength and corrosion resistance at elevated temperature range. The mechanical properties such as hardness, wear, and corrosion–erosion resistance are increased by Cr addition. However, the ductility is deteriorated by the formation of huge amount of hard carbides. High percentage of Cr also tends to form microporosity in the castings.
Copper: It enhances the austenite stabilization effect along with Ni and improves corrosion resistance in mild acidic solution. But it is not suitable in austenitic ductile irons as copper has an adverse effect on Mg treatment.
Carbon: Carbon is the base element for any ferrous alloy. It has the effect to suppress the solidification temperature and improves the melting and pouring behavior. High strength and toughness are developed with lower carbon irons as fewer carbides are formed.
Silicon: Castability of irons especially thin-walled castings is remarkably improved by Si as it enhances the fluidity. The corrosion resistance is also improved by addition of Si. It reduces the extent of chromium carbide formation.
Manganese: Mn is a potent austenite stabilizer and improves low temperature properties of Ni-resist ductile iron D-2M and non-magnetic alloys such as Ni-resist NiMn 13 7. But it has almost no contribution in the improvement of corrosion resistance, high temperature properties, and mechanical properties.
Niobium: It leads to improved weldability of Ni-resist irons. To achieve maximum effect of Nb, the elements like Si, S, and P are to be controlled.
Molybdenum: For improved high temperature strength Mo is sometimes added in a few grades of N-resist irons.[6,39,40]

2.10.5.1.2 Heat treatment of austenitic graphitic irons

The heat treatment processes are similar in both the graphite forms viz. flake graphite and spheroidal graphite.[6,36,39–42] Nominal mechanical properties for flake graphite and spheroidal graphite Ni-resist irons are listed in **Tables 15** and **16** respectively.

2.10.5.1.2.1 Stress relieving

The objective of stress relieving is to remove the residual stresses developed during solidification or machining operation or a combination of both. For heavy thin walled castings mold shake-out is recommended below 315 °C rather than stress-relieving treatment to eliminate the solidification stresses. For other common applications, austenitic cast irons are stress relieved at 620–675 °C for 1 h per 25 mm section thickness followed by furnace cooling. At 675 °C, about 95% of stresses are relieved whereas stress relieving at comparatively lower temperature such as 480 °C with same soaking time will relieve only 60% of the residual stresses.

2.10.5.1.2.2 Spheroidizing annealing

When castings are cooled at fast rates especially thin-walled castings, formation of carbides causes high hardness greater than 200 HB. A spheroidizing annealing in the range of temperature of 980–1040 °C for 0.5 to 5 h softens the casting by either dissolving or spheroidizing the carbides. Only the hardness is lowered without affecting the strength.

2.10.5.1.2.3 High temperature stabilization

Castings intended for high-temperature applications above 480 °C are often subjected to a high-temperature stabilization treatment. The treatment involves heating the casting at 760 °C and soaked for minimum 4 h or alternatively, heated to a higher temperature at 870 °C and soaked for minimum 2 h subsequently furnace cooled to 540 °C and air cooled to room temperature. By this treatment excess carbon from the austenitic matrix and carbides are removed and the microstructure is stabilized which prevents distortion in service. Final machining is to be done after the stabilization treatment.

2.10.5.1.2.4 Dimensional stabilization

Precision castings requiring exact dimensional stability are to be treated for stabilization before employing in service. In this treatment the castings are to be heated to 870 °C and soaked for minimum 2 h and additional 1 h per 25 mm of section thickness followed by furnace cooling to 540 °C at the

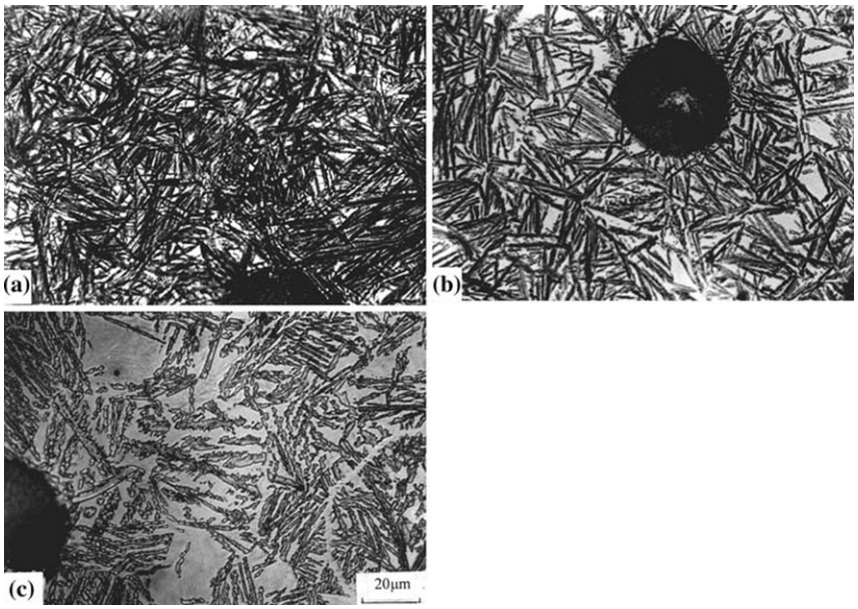


Figure 34 Microstructures of austempered ductile iron (3.5 C, 2.8Si, 0.3Mn, 0.02 S, 0.02 P, 0.04Mg, 0.5Cu, 1.5Ni, 0.3Mo) austempered at (a) 300 °C; (b) 350°; and (c) 400 °C. *J. Mater. Sci.* **2008**, *43*, 359; Figure 2.

maximum rate of 50 °C h^{-1} held at this temperature for 1 h per 25 mm section thickness followed by air cooling to room temperature. Then it is rough machined and reheated to 455–480 °C for a soaking period of 1 h per 25 mm section thickness and cooled to room temperature by air cooling. Finally, finish machining is done and reheated to 260–315 °C followed by uniform air cooling.

2.10.5.1.2.5 Solution treatment

As the name implies, the treatment involves the dissolution of some of the carbons in the austenitic matrix and subsequent rapid quenching suppressing the carbon precipitation. The higher carbon austenite will produce higher strength and hardness than normal conditions. In actual practice, the treatment comprise of heating the casting to 925–1000 °C followed by oil/water quenching. Quench cracking is not likely to take place as no phase transformation occurs.

2.10.5.1.2.6 Refrigeration and reaustenitization

This treatment is given to some specific types of irons viz. type D2 with a purpose to increase the yield strength without affecting magnetic properties and corrosion resistance in sea water or dilute sulfuric acid. Initially, the castings are solution treated at 925 °C followed by cryogenic quenching at − 195 °C. The castings are then reheated to 650–750 °C and air cooled.

2.10.5.1.3 Case studies on austenitic graphite irons

Case 1: Corrosion performance of Ni-resist austenitic irons is excellent in marine environments. Examples are sea-water pumps and valves to combat the corrosion at velocities ranging from no-flow to turbulent conditions. Ni-resist D2 and D2W are preferred. These irons also perform well in aerated and deaerated sea water with increased temperature. The corrosion behavior of pump material at low and high velocities of sea water are shown in **Tables 17** and **18**.[40]

Case 2: The unique combination of corrosion–erosion resistance of Ni-resist irons in sea water as well as petroleum is most suited for applications in oil and gas production.[40] In crude oil and gas containing several gases like hydrogen sulfide, carbon di oxide, and organic acids, the self-protective layer on the surface of these irons causes low corrosion rates. These are shown in **Tables 19** and **20**.

Case 3: The remarkable corrosion resistance of some specific grades of Ni-resist irons such as Ni-resist 3, D3 and D 3A with high nickel content of about 30% makes them suitable for handling of alkalis like sodium hydroxide and other strong caustics (**Tables 21** and **22**). Stress corrosion cracking a common failure observed in other iron-base alloys in such environments can be avoided with stress relieved Ni-resist irons prior to the in-service application.

Case 4: Steam turbine components such as diaphragms, shaft, and control valves are subjected to high steam temperatures where adequate resistance to growth and scaling is required. Ni-resist is potent material to combat these atmospheres.[40] **Table 23** and **Figure 45** show the elevated temperature mechanical properties and short-time tensile properties respectively of some appropriate Ni-resist irons.

Case 5: Cast iron or steel components when subjected to cyclic heating and cooling at elevated temperature range of 675 °C and above the ferrous alloys pass through a critical temperature range. Consequently, cracking and/or distortion results in as the matrix phase alternatively changes between ferrite and austenite. As the Ni-resist iron has a single austenite phase at all temperatures, do not undergo any phase

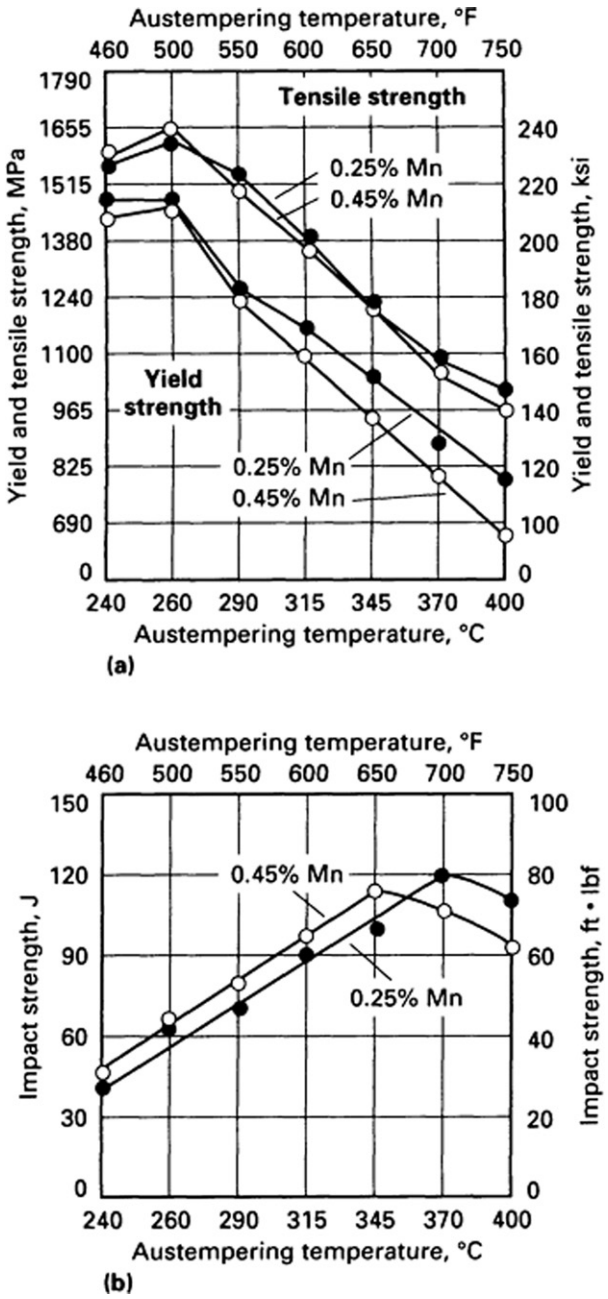


Figure 35 Effect of austempering temperature on the properties of ductile iron; (a) yield and tensile strength versus austempering temperature; (b) impact strength versus austempering temperature. *ASM Handbook*, Vol. 4, 1991 ed., Heat Treating of Ductile Iron; Figure 19, p. 1505.

transformation and so have no sharp volume changes. Even though a high temperature stability heat treatment further improves the problem of cracking and distortion as the excess carbon is dissolved in the austenite.[40]

Case 6: For high temperature oxidation resistance applications, higher strength ductile Ni-resist irons such as D2, D2B, D3, D4, D5B, and D5S provide excellent resistance to oxidation and maintain their mechanical properties up to a temperature of 760 °C. The presence of high-chromium and high-silicon contents form dense, adherent self-protecting surface oxide layers. Under thermal cycling condition, cracking and flaking of oxide protective scale occurs and in such cases low expansion grades such as D4 grade is employed.[40]

2.10.5.2 Heat Resistant High Silicon Irons

Graphitic high silicon irons with 4–6% Si are low-cost group of irons for elevated temperature applications. High silicon irons may be of two types – (1) high-silicon flake graphite gray iron and (2) high-silicon ductile iron. In both these irons the matrix is stable ferritic and up to a temperature of 900 °C. The ferrite does not undergo any phase change. The presence of Si causes to raise the ferrite to austenite transformation temperature of the cast iron. The rate of oxidation at elevated temperature is drastically reduced due to the formation of a dense, adherent iron silicate layer at the surface. The strong ferritizing tendency of Si stabilizes the matrix against the formation of carbides and pearlite, thus reducing the growth associated with the decomposition.[6,39]

The high-silicon gray irons are commonly known as Silal. In this group of irons the matrix consists of stable ferrite along with fine undercooled type D graphite flakes producing a good oxidation resistance. Further improvement in oxidation resistance is achieved by addition of 2% chromium. At room temperature these irons are brittle but are reasonably tough above 250 °C.

High-silicon ductile irons are more widely used oxidation resistant iron as the graphite flakes are replaced by nodules which causes further improvement in oxidation resistance and growth. Higher strength and ductility in this group are added advantages for stringent applications.

With increase in silicon content from 4 to 6% further improvement in the oxidation resistance can be achieved but the impact transition temperature is raised above the room temperature and causes brittleness. The ductility is again restored above 425 °C (**Figure 46**).

Addition of molybdenum of about 0.5% to ferritic ductile iron improves significantly the creep and stress-rupture strengths which are requisites for high-temperature applications. Further improvement in high-temperature tensile, creep, and stress-rupture strengths are observed with an increment of Mo content to 2% (**Tables 24** and **25**). A typical microstructure of Si Mo51 grade ferritic ductile iron is shown in **Figure 47**.

2.10.5.2.1 Heat treatment of heat resistant high-silicon irons

A graphitizing full annealing in the austenitic range is generally adopted to anneal any pearlite and undesirable amounts of carbides present in high-silicon nodular irons. In practice, the casting containing 4–5% silicon are subjected to the full annealing at a minimum temperature of 900 °C for several hours of soaking followed by slow cooling below 700 °C. Higher silicon content (>5%) nodular irons are generally having carbide-free microstructure and if present these are decomposed easily. A subcritical annealing in the range of 720–790 °C for 4 h is sufficient to ferritize the matrix. These subcritically annealed nodular irons develop higher strength but with lower ductility and toughness compared to fully annealed irons.[6,39]

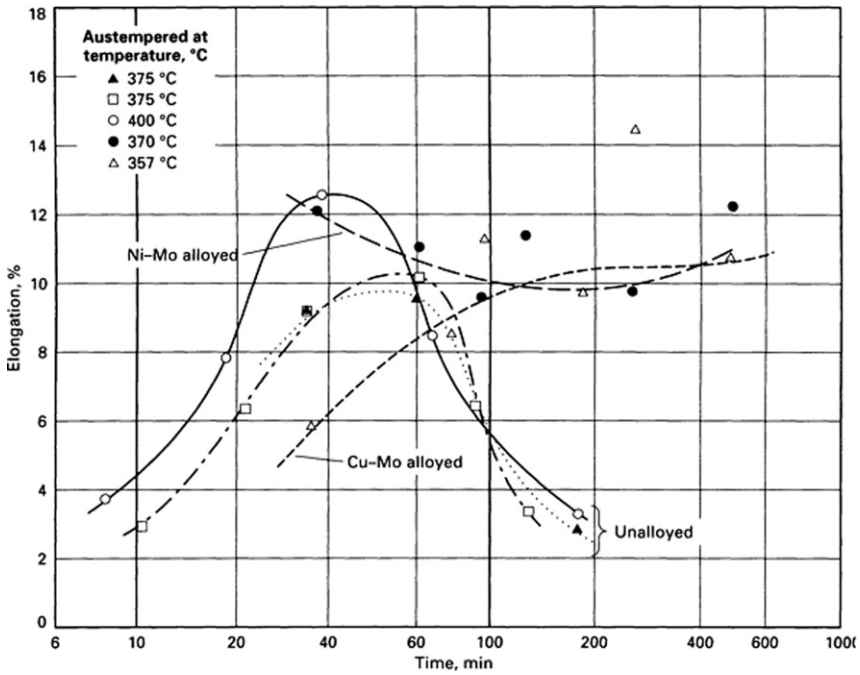


Figure 36 Effect of austempering time on the elongation of alloyed and unalloyed ductile irons. *ASM Handbook*, Vol. 4, Heat Treating of Ductile Iron; Figure 20, p. 1506.

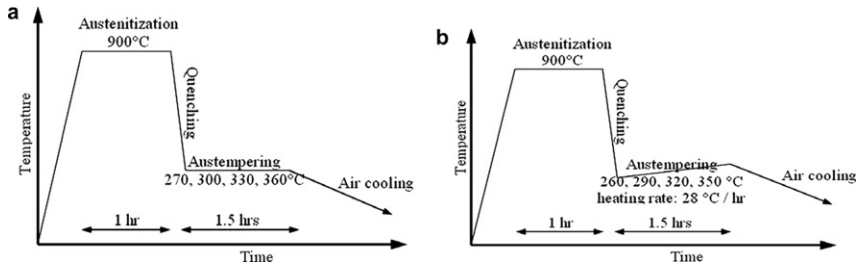


Figure 37 Austempering heat treatment cycle; (a)-single step, (b)-two step. Elsayed, A. H.; Megahed, M. M.; Sadek, A. A.; Abouelela, K. M. Fracture Toughness Characterization of Austempered Ductile Iron Produced Using Both Conventional and Two-Step Austempering Processes. *Mater. Des.* **2009**, *30*, 1866–1877; Figure 1.

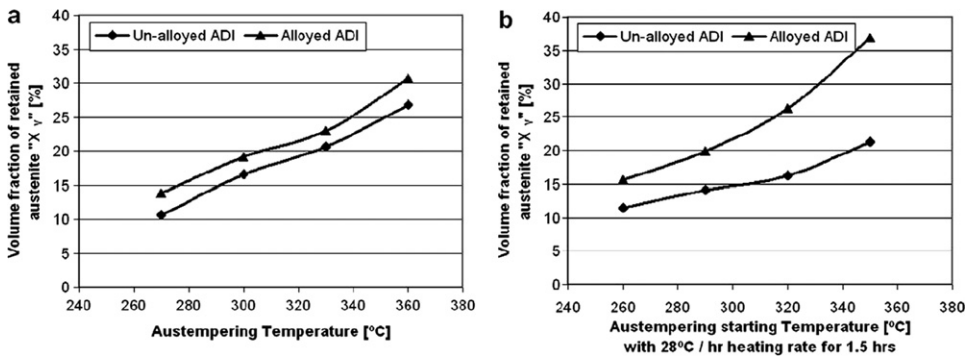


Figure 38 Effect of austempering temperature on volume fraction of retained austenite (a) single-step austempered, (b) two-step austempered. Elsayed, A. H.; Megahed, M. M.; Sadek, A. A.; Abouelela, K. M. Fracture Toughness Characterization of Austempered Ductile Iron Produced Using Both Conventional and Two-Step Austempering Processes. *Mater. Des.* **2009**, *30*, 1866–1877; Figure 9.

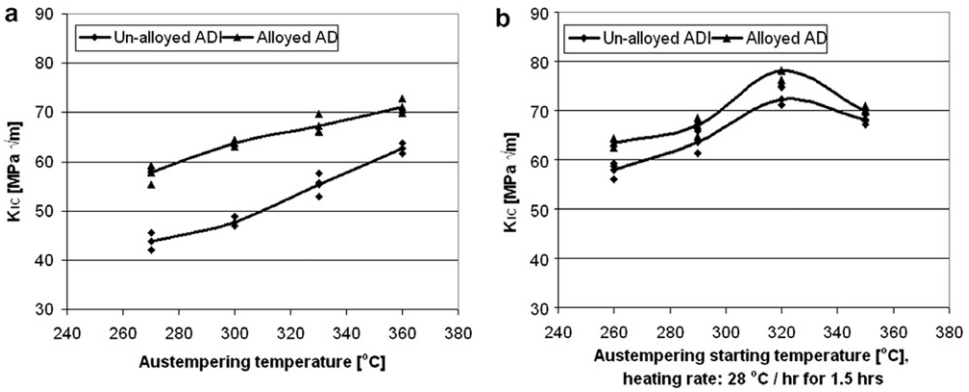


Figure 39 Effect of austempering temperature on fracture toughness (a) single-step austempered and (b) two-step austempered. Elsayed, A. H.; Megahed, M. M.; Sadek, A. A.; Abouelela, K. M. Fracture Toughness Characterization of Austempered Ductile Iron Produced Using Both Conventional and Two-Step Austempering Processes. *Mater. Des.* **2009**, *30*, 1866–1877; Figure 16.

Table 9 Chemical compositions of test alloys

Materials	*C*	*Mn*	*Si*	*Cr*	*Mo*	*Cu*	*Mg*
AISI 4140[a]	0.38–0.43	0.75–1.0	0.15–0.35	0.8–1.1	0.15–0.25	–	–
AISI 8620[a]	0.18–0.23	0.70–0.9	0.15–0.35	0.4–0.6	0.15–0.25	–	–
ADI 1	3.1	0.2	2.3	0.03	0.3	0.7	0.04
ADI 2	2.8	0.4	2.4	0.02	–	0.6	0.03

[a]Standard chemical composition.

Source: Guesser, W. L.; Koda, F.; Blanco Martinez, J. A.; da Silva, C. H. *Austempered Ductile Iron for Gears*; SAE International, 2012. doi:10.4271/2012-36-0305; Table 2.

Table 10 Treatment sequence on the gear materials

Spur material	*Heat and thermochemical treatment*	
AISI 8620	Carburizing	Temperature = 880°C Time = 16 h
	Quenching	Oil temperature = 130°C
	Tempering	Temperature = 200°C Time = 2 h
AISI 4140	Surface hardening	Induction hardening Induction coil method
ADI 1	Austenitization	Temperature = 890°C Time = 2 h
	Austempering	Temperature = 290°C Time = 2 h
ADI 2	Austenitization	Temperature = 900°C Time = 2 h
	Austempering	Temperature = 270°C Time = 2 h (in salt bath)

Source: Guesser, W. L.; Koda, F.; Blanco Martinez, J. A.; da Silva, C. H. *Austempered Ductile Iron for Gears*; SAE International, 2012. doi:10.4271/2012-36-0305; Table 1.

Table 11 Nodule characteristics of the ADI gears

	Form type	*Nodularity (%)*	*Graphite area (%)*	*Nodule count (nod. mm^{-2})*
ADI 1	VI	99	13	196
ADI 2	VI	98	13	532

Source: Guesser, W. L.; Koda, F.; Blanco Martinez, J. A.; da Silva, C. H. *Austempered Ductile Iron for Gears*; SAE International, 2012. doi:10.4271/2012-36-0305; Table 3.

Table 12 Mechanical properties of spur gear materials

Material	*Tensile strength (MPa)*	*Elongation (%)*	*Young modulus (GPa)*	*Hardness (HRc)*	*Charpy energy (Joules)*
AISI 8620	1325[a]	12[a]	205[a]	58	–
AISI 4140	2040[a]	7.6[a]	205[a]	56	4.5
ADI 1	1546	2.1	–	56	–
ADI 2	1273	3.5	186,9	54	5.8

[a]Spur gears materials.

Source: Guesser, W. L.; Koda, F.; Blanco Martinez, J. A.; da Silva, C. H. *Austempered Ductile Iron for Gears*; SAE International, 2012. doi:10.4271/2012-36-0305; Table 4.

2.10.5.3 Heat Treatment of Corrosion Resistant High Silicon Irons

The corrosion–resistant ferritic cast iron group contains high silicon of about 15% and are widely used in chemical processing and corrosive liquid handling.[6,39] Chemical compositions of most common high-silicon irons as per ASTM A 518M specification are shown in **Table 26**.

Because of the presence of high silicon content of about 15%, these irons are very brittle in as-cast condition. Common heat treatments have no significant effects on the corrosion resistance behavior of these irons except stress-relieving treatment. Simple shaped castings can be safely shaken out from

the molds after cooling to ambient temperature. However, to avoid hot cracking complex castings are to be shaken out in hot condition from molds and are subjected to immediate stress-relieving treatment at 870–900 °C followed by furnace cooling to ambient temperature.

2.10.5.4 Oxidation Resistant High-Aluminum Irons

Aluminum in cast iron stabilizes the ferrite phase up to a temperature of 980 °C. It remarkably enhances the oxidation resistance of cast iron at elevated temperatures and forms a dense, adherent self-protecting oxide scale on the surface of the casting and prevent further oxidation. There are two groups of aluminum-alloyed irons- (1) low-alloy group containing 1–7% Al and (2) high-alloy group containing 18–25% Al. As aluminum has a strong graphitizing effect it replaces silicon in the iron. In the low-alloy group as the Al content is increased from 1 to 7% the strength and hardness is increased which is maintained even at higher temperatures. However, in the high-alloy range it is solidified as white iron and very much brittle and as such have no commercial importance.

The commercial productions of aluminum alloyed irons are still limited due to their inherent difficulties in the casting production. As aluminum is highly reactive at molten iron temperature, reacting with air it forms dross and comes in the casting as inclusions. Another problem is cold shut or laps formation in the casting due to viscous nature of the iron.[6]

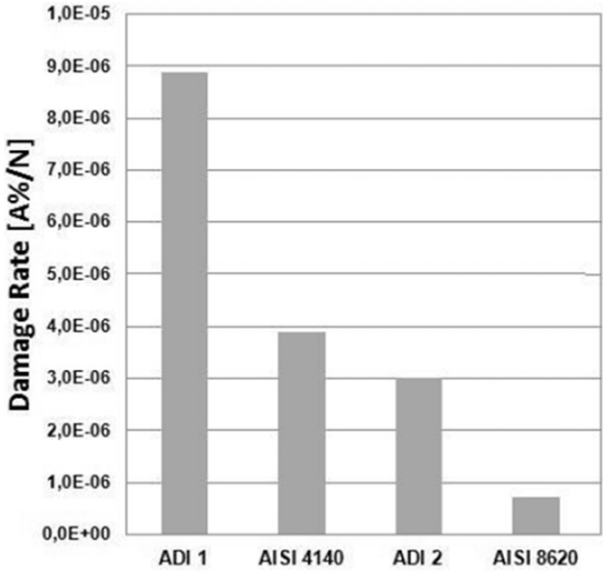


Figure 40 Damage rate of gear materials. Guesser, W. L.; Koda, F.; Blanco Martinez, J. A.; da Silva, C. H. *Austempered Ductile Iron for Gears*; SAE International, 2012. doi:10.4271/2012-36-0305.

2.10.5.5 Abrasion Resistant High-Alloy White Irons

The high-alloy white irons are basically used for abrasion resistant applications such as in mineral processing industries and abrasive materials handling. Both primary eutectic carbides and the secondary carbides produced by heat treatment provide high hardness and wear resistance. The matrix also has vital role to act as a hard and tough holding base for carbides against the wearing and action. Therefore, a suitable composition and heat treatment are to be chosen to develop the desired structure. High-alloy white irons invariably contain chromium, a strong carbide former to stabilize the carbide phase. Other alloying additions such as nickel, molybdenum, and copper are often made to suppress the pearlite transformation and to increase the hardenability and promote martensitic matrix with a range of hardness of 450–800 HB. However, the low-alloy white irons contain pearlitic matrix and possess lower range of hardness of 350–550 HB.[6,39,43–57]

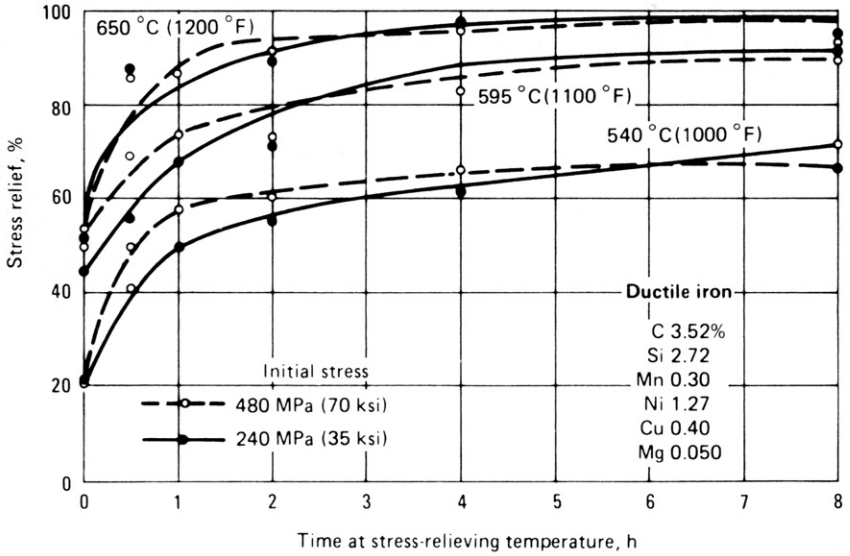


Figure 41 Effect of stress-relieving time on the percent stress relived in ductile iron. *ASM Handbook*, Vol. 4, 1991 ed., Heat Treating of Ductile Iron; Figure 23, p. 1509.

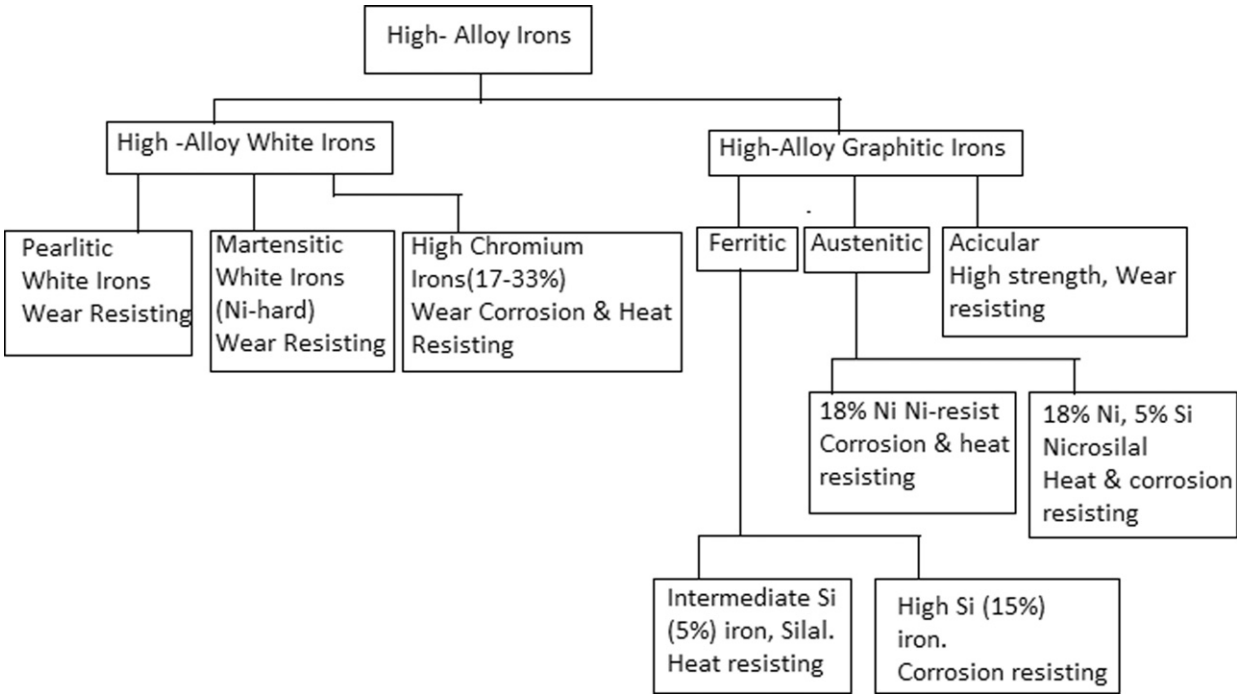


Figure 42 Family of high-alloy irons.

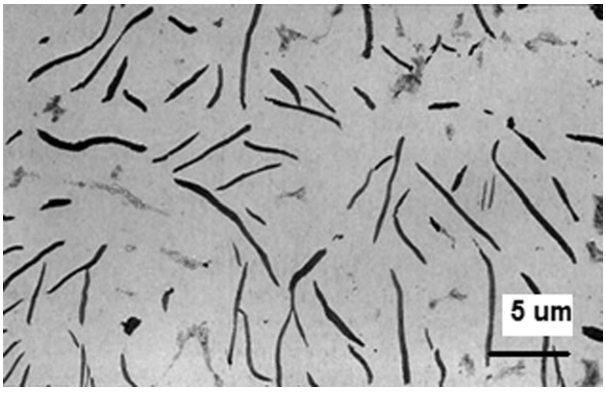


Figure 43 Austenitic flake graphite Ni-resist iron (Ni-resist 1). *Properties and Applications of Ni-Resist and Ductile Ni-Resist Alloys*; Nickel Development Institute. NiDI Publications No. 11018, 1998; Figure 1.

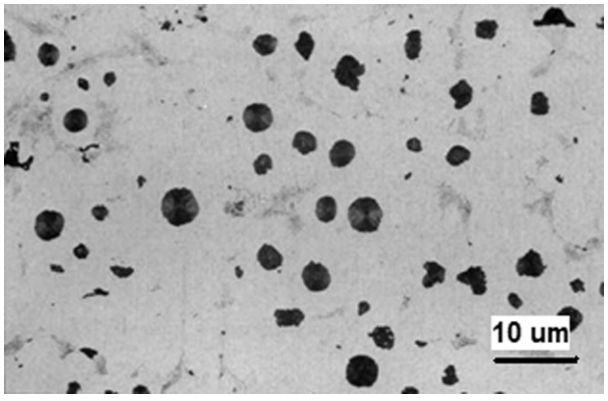


Figure 44 Austenitic spheroidal graphite Ni-resist iron (Ni-resist D 2W). *Properties and Applications of Ni-Resist and Ductile Ni-Resist Alloys*; Nickel Development Institute. NiDI Publications No. 11018, 1998; Figure 2.

The high-alloy white cast irons fall into three broad categories:

a. The nickel–chromium white irons commonly known as Ni-hard irons which are low-chromium alloys containing 1–4% Cr and 3–5% Ni except in one grade contains 7–11% Cr.
b. The Chromium– molybdenum irons containing 11–23% Cr and up to 3% Mo and are sometimes additionally alloyed with elements like Ni or Cu.
c. The 25% Cr to 28%Cr white irons occasionally containing alloying elements like Mo and/or Ni up to 1.5%.

The composition of different grades of high-alloy white irons as per ASTM A 532 are shown in **Table 27**.

2.10.5.5.1 Heat treatment of nickel–chromium white irons

High-alloy nickel–chromium white irons also known as Ni-hard irons are cost effective wear resistant material for mining and mineral processing, cement industries, etc. This class of irons contain 3–5% nickel and 1.4–4% chromium. Nickel promotes a hard martensitic matrix suppressing the pearlitic transformation even on slow cooling in the mold. Chromium is added to form hard eutectic carbides in the structure

Table 13 Compositions of ASTM A 436–84 grades of austenitic flake graphite irons

Type	*UNS No*	*Composition (%)*					
		TC[a]	*Si*	*Mn*	*Ni*	*Cu*	*Cr*
1[b]	F41000	3.0 max.	1.0–2.8	0.5–1.5	13.5–17.5	5.5–7.5	1.5–2.5
1b	F41001	3.0 max.	1.0–2.8	0.5–1.5	13.5–17.5	5.5–7.5	2.5–3.5
2[c]	F41002	3.0 max.	1.0–2.8	0.5–1.5	18.0–22.0	0.5 max.	1.5–2.5
2b	F41003	3.0 max.	1.0–2.8	0.5–1.5	18.0–22.0	0.5 max.	3.0–6.0[d]
3	F41004	2.6 max.	1.0–2.0	0.5–1.5	28.0–32.0	0.5 max.	2.5–3.5
4	F41005	2.6 max.	5.0–6.0	0.5–1.5	29.0–32.0	0.5 max.	4.5–5.5
5	F41006	2.4 max.	1.0–2.0	0.5–1.5	34.0–36.0	0.5 max.	0.1 max.[e]
6[f]	F41007	3.0 max.	1.5–2.5	0.5–1.5	18.0–22.0	3.5–5.5	1.0–2.0

[a]Total carbon.
[b]Type 1 is recommended for applications in which the presence of Cu offers corrosion resistance advantages.
[c]Type 2 is recommended for applications in which copper contamination cannot be tolerated, such as handling of foods or caustics.
[d]Where some machining is required, 3.0–4.0 Cr is recommended.
[e]Where increased hardness, strength, and heat resistance are desired, and where increased expansivity can be tolerated, Cr may be increased to 2.5–3.0%.
[f]Type 6 also contains 1.0% Mo.
Source: *ASM Specialty Handbook-Cast Iron*; p. 126.

Table 14 Compositions of ASTM A 439–83 grades of austenitic nodular graphite irons

Type	*UNS No*	*Compositions (%)*					
		TC[a]	*Si*	*Mn*	*P*	*Ni*	*Cr*
D-2	F43000	3.0 max.	1.5–3.0	0.7–1.25	0.08 max.	18.0–22.0	1.75–2.75
D-2b	F43001	3.0 max.	1.5–3.0	0.7–1.25	0.08 max.	18.0–22.0	2.75–4.0
D-2c	F43002	2.9 max.	1.0–3.0	1.8–2.4	0.08 max.	21.0–24.0	0.5 max.
D-3	F43003	2.6 max.	1.0–2.8	1.0 max.	0.08 max.	28.0–32.0	2.5–3.5
D-3a	F43004	2.6 max.	1.0–2.8	1.0 max.	0.08 max.	28.0–32.0	1.0–1.5
D-4	F43005	2.6 max.	5.0–6.0	1.0 max.	0.08 max.	28.0–32.0	4.5–5.5
D-5	F43006	2.6 max.	1.0–2.8	1.0 max.	0.08 max.	34.0–36.0	0.1 max.
D-5b	F43007	2.4 max.	1.0–2.8	1.0 max.	0.08 max.	34.0–36.0	2.0–3.0
D-5S	–	2.3 max.	4.9–5.5	1.0 max.	0.08 max.	34.0–37.0	1.75–2.25

[a]Total carbon.
Source: *ASM Specialty Handbook-Cast Iron*; p. 126.

Table 15 Mechanical properties of Ni-resist flake graphite irons

Alloy	*Tensile strength (MPa)*	*Compressive strength (MPa)*	*Elongation (%)*	*Modulus of elasticity (MPa × 10^3)*	*Brinell hardness (BHN)*
NiMn 13 7	140–220	630–840	–	70–90	120–150
Ni-Resist 1	170–210	700–840	2	85–105	120–215
Ni-Resist	190–240	860–1100	1–2	98–113	150–250
Ni-Resist 2	170–210	700–840	2–3	85–105	120–215
Ni-Reslst	190–240	860–1100	1–2	98–113	160–250
Nicrosibl	190–280	–	2–3	–	140–250
Ni-Resist 3	190–240	700–910	1–3	98–113	120–215
Ni-Resist 4	170–240	560	–	105	150–210
Ni-Resist 5	120–180	560–700	1–3	74	120–140
Ni-Resist 6	170–210	700–840	–	–	130–180

Source: Properties and Applications of Ni-Resist and Ductile Ni-Resist Alloys; Nickel Development Institute. NiDI Publications No. 11018, 1998; Table V.

(**Figure 48**). Copper and molybdenum are often alloyed to increase the hardenability in heavy sections and to prevent pearlite formation.[6,39,43,44]

2.10.5.5.1.1 Stress relieving

Because martensitic matrix along with some retained austenite is formed even in as-cast condition, the castings are to be

Table 16 Mechanical properties of spheroidal graphite Ni-resist irons

Alloy	*Tensile strength (MPa)*	*Yield strength 0.2% offset (MPa)*	*Elongation (%)*	*Modulus of elasticity (MPa × 10^3)*	*Charpy impact (Kg-m)*	*Brinell hardness*
Ni-Resist D-2	370–480	210–250	7–20	112–130	14–27	140–200
Ni-Resist D-2W	370–480	210–250	8–20	112–130	14–27	140–200
Ni-resist D-2B	390–500	210–260	7–15	112–133	12	150–255
Nicrosilal spheronic	370–440	210–260	10–18	–	–	180–230
Ni-resist D-2C	370–450	170–250	20–40	85–112	21–33	130–170
Ni-resist D-2M	440–480	210–240	25–45	120–140	24–34	150–180
NI-resist D-3A	370–450	210–270	13–18	112–130	16	130–190
Ni-resisl D-3	370–480	210–260	7–18	92–105	8	140–200
Ni-resist D-4A	380–500	210–270	10–20	130–150	10–16	130–170
Ni-resist D-4	390–500	240–310	1–4	91	–	170–250
Ni-resist D-5	370–420	210–240	20–40	112–140	20	130–180
Ni-resist D-5B	370–450	210–290	7–10	112–123	7	140–190
Ni-resist D-5S	370–500	200–290	10–20	110–145	12–19	130–170
Ni-resist D-6	390–470	210–260	15–18	140–150	–	120–150

Source: Properties and Applications of Ni-Resist and Ductile Ni-Resist Alloys; Nickel Development Institute. NiDI Publications No. 11018, 1998; Table VI.

Table 17 Corrosion of cast materials in low velocity sea water

Temperature	Ambient
Duration of test:	3 years
Agitation:	Tidal flow with continuous immersion
Marine fouling:	All specimens completely covered with fouling organisms at time of removal from test
Material	*Corrosion rate cm per year (in per year)*
Ni-Resist 1	0.0053 (0.0021)
Ni-Resist 2	0.0043 (0.0017)
Ni-Resist D-2	0.0041 (0.0016)
Ni-Resist 3	0.0038 (0.0015)
Ductile gray cast iron	0.0246 (0.0097)
Gray cast iron	0.0254 (0.0100)

Source: Properties and Applications of Ni-Resist and Ductile Ni-Resist Alloys; Nickel Development Institute. NiDI Publications No. 11018, 1998; Table IX.

Table 18 Corrosion of pump materials in high velocity sea water

Alloy	*Temperature (°C)*	*Velocity ($m\ sec^{-1}$)*	*Corrosion Rate* ($mm\ year^{-1}$ ($in.\ year^{-1}$))*
Type 316 stainless steel	10	43	0.005 (0.0002)
Ni/Cu alloy 400	11	43	0.010 (0.0004)
Ni-resist 1	27	41	0.990 (0.040)
88Cu/10Sn/2Zn	2	42	1.10 (0.044)
85Cu/5Sn15Zn/5Pb	25	41	1.35 (0.054)
Gray cast iron	20	38	13.5 (0.540)

Source: Properties and Applications of Ni-Resist and Ductile Ni-Resist Alloys; Nickel Development Institute. NiDI Publications No. 11018, 1998; Table X.

invariably stress relieved to reduce the transformation stress for austenite to martensite transformation. A low-temperature tempering treatment at 205–260 °C for at least 4 h of holding are often given to the castings to temper the martensite and to transform some retained austenite. The treatment results in an increase in strength and impact toughness by 50–80% without any reduction in hardness and abrasion resistance.

Precautions must be taken to avoid (1) loading the furnace in hot conditions and (2) fast rate of heating and cooling. These will develop thermal shock in the castings and generate cracks which are particularly important in case of complex and heavy section castings.[43,44]

2.10.5.5.1.2 Destabilization treatment

This hardening treatment is carried out to destabilize the austenite and to form martensite embedded with fine carbides. The castings are austenitized in the temperature range of 750–790 °C with a soaking period of around 8 h. Subsequent air cooling or furnace cooling at rate of 30 °C h^{-1} causes conversion of austenite to martensite. Finally the hardened matrix is tempered to eliminate the residual stress.

2.10.5.5.1.3 Cryogenic treatment

The purpose of this treatment is to convert more amount of retained austenite to martensite to achieve a higher hardness and consequent higher abrasion resistance. The treatment involves in quenching the casting in a cryogenic bath at a temperature between −70 and −180 °C for 0.5–1 h. After cryogenic treatment an increase in as-cast hardness by about 100 HB is observed. Final hardness greater than 650 HB may be developed when the martensite content exceeds 80%. Typical microstructure developed by cryogenic treatment of class I type D nickel–chromium white iron is shown in **Figure 49**.

2.10.5.5.1.4 Case study on heat treatment of nickel–chromium iron

Rolls for coal and cement grinding are generally made of Ni-hard 4 grade with a typical composition of 3.11 C, 1.22Si, 0.6Mn, 8.32Cr, and 5.39Ni. As a result of its high-alloy content, as-cast rolls contains more than 50% retained austenite developing a hardness below 550–600 HV. To increase the hardness to the desired level a more complete transformation of retained austenite to martensitic matrix is required. This is achieved by destabilization above 820–860 °C with a soaking

Table 19 Weight loss in still natural gas with hydrogen sulfide at 80 °C

Alloy	*100h*	*200 h*	*300 h*	*400 h*
	gms lm^{-2} (lbs ft^{-2})			
Ni-resist 1	60 (0.007)	83 (0.010)	83 (0.010)	83 (0.010)
Gray cast Iron	79 (0.010)	189 (0.023)	222 (0.027)	248 (0.030)
Piston ring gray cast iron	157 (0.019)	215 (0.026)	253 (0.031)	295 (0.036)
Plain carbon steel 0.4% carbon	85 (0.010)	218 (0.027)	310 (0.038)	363 (0.044)

Source: Properties and Applications of Ni-Resist and Ductile Ni-Resist Alloys; Nickel Development Institute. NiDI Publications No. 11018, 1998; Table XII.

Table 20 Corrosion tests in sour crude oils

Material	*Corrosion rate cm per year (in per year)*		
	Test 1	*Test 2*	*Test 3*
Ni-resist 1	0.0017 (0.0007)	0.025 (0.010)	0.0023 (0.0009)
Ni-resist 3	–	0.017 (0.007)	–
Gray cast iron	0.0053 (0.0021)	0.113 (0.045)	0.040 (016)
Mild steel	0.0043 (0.0017)	0.130 (0.052)	Consumed
Type 304 stainless steel	<0.0003 (<0001)[a]	0.020 (0.008)[b]	<0.0003 (<0.0001)

[a]010 cm (0.004 in) pitting.
[b]030 cm (0.012 in) pitting.
Source: Properties and Applications of Ni-Resist and Ductile Ni-Resist Alloys; Nickel Development Institute. NiDI Publications No. 11018, 1998; Table XIII.

Table 21 Effect of nickel content on the corrosion rate of cast iron in 50–65% sodium hydroxide

Temperature:	Boiling with vacuum of 66 cm (26 in) of mercury
Duration of test:	81 days
Agitation:	Boiling action only
Percent nickel	*Corrosion rate cm per year (in per year)*
0	212 (0.083)
3.5	0.119 (0.047)
5	0.124 (0.049)
15	0.076 (0.030)
20	0.0084 (0.0033)
20 (2% Cr)	0.0152 (0.0060)
30	0.0010 (0.0004)

Source: Properties and Applications of Ni-Resist and Ductile Ni-Resist Alloys; Nickel Development Institute. NiDI Publications No. 11018, 1998; Table XIV.

Table 22 Plant corrosion tests of various alloys in 74% sodium hydroxide

Temperature:	125 °C (260 °F)
Duration:	Specimens exposed for 20 days in liquid and 12 days in vapor over liquid. Corrosion rates based on 21 days exposure
Agitation:	Stagnant (in storage tank)
Material	*Corrosion rate cm per year (in per year)*
NiCu alloy 400	0023 (0.0009)
Ni-resist 3	0.0064 (0.0025)
Ni-resist D-2	0.0127 (0.0050)
Ni-resist 2	0.0152 (0.0060)
Type 304 stainless steel	0.0381 (0.0150)
Mild steel	0.190 (0.075)
Gray cast iron	0.193 (0.76)

Source: Properties and Applications of Ni-Resist and Ductile Ni-Resist Alloys; Nickel Development Institute. NiDI Publications No. 11018, 1998; Table XV.

time of 10–12 h followed by still air cooling. Martensitic matrix embedded with fine secondary carbides causes higher hardness. The hardenability of Ni-hard four iron is sufficient to allow cooling rates of $<30\ ^{\circ}C\ h^{-1}$ through the temperature range between 600 and 300 °C without pearlite formation. A final tempering is often carried out at 200 and 270 °C to eliminate the residual stresses.[43]

2.10.5.5.2 Heat treatment of high-chromium white irons

High-chromium white irons provide the best combination of abrasion resistance and toughness in alloyed white cast irons. High-chromium martensitic irons generally contain minimum 12% chromium and are often alloyed with molybdenum, nickel, and copper to suppress the pearlite formation and increase the matrix toughness. The presence of high chromium produces a hard and relatively discontinuous M_7C_3 type of eutectic carbides. The as-cast matrix is either fully martensitic or a combination of martensite and austenite. The retained austenite can be transformed to a predominantly martensitic matrix by a suitable heat treatment to achieve maximum abrasion resistance and toughness. However, castings with a mixture of austenite and martensite structure in as-cast condition are also very often employed to avoid the thermal and transformation stress generated in heat treatment. A suitable alloy combination is to be designed to suppress the pearlite transformation.[6,39,45–57] The effective section sizes

Table 23 Elevated temperature mechanical properties of some spheroidal graphite Ni-resist alloys

Property and temperature	*D-2*	*D-2C*	*D-3*	*D-4*	*D-5B*
Tensile strength	*MPa (ksi)*				
Ambient	407 (59)	428 (62)	400 (58)	442 (64)	421 (61)
426 °C (800 °F)	373 (54)	359 (52)	–	–	–
538 °C (1000 °F)	331 (48)	290 (42)	331 (48)	421 (61)	324 (47)
649 °C (1200 °F)	248 (36)	193 (28)	290 (42)	331 (48)	283 (41)
760 °C (1400 °F)	152 (22)	117 (17)	186 (27)	152 (22)	173 (25)
0.2% Yield strength	*MPa (ksi)*				
Ambient	242 (35)	235 (34)	269 (39)	304 (44)	283 (41)
426 °C (800 °F)	193 (28)	179 (26)	–	–	–
538 °C (1000 °F)	193 (28)	159 (23)	193 (28)	283 (41)	179 (26)
649 °C (1200 °F)	173 (25)	166 (24)	186 (27)	235 (34)	166 (24)
760 °C (1400 °F)	117 (17)	117 (17)	104 (15)	131 (19)	131 (19)
Elongation from short-time tensile tests	*Percent*				
Ambient	10.5	25	7.5	3.5	70
426 °C (800 °F)	12	23	–	–	–
538 °C (1000 °F)	10.5	19	7.5	4.0	90
649 °C (1200 °F)	10.5	10	7.0	11	65
760 °C (1400 °F)	15	13	18	30	24.5

Source: Properties and Applications of Ni-Resist and Ductile Ni-Resist Alloys; Nickel Development Institute. NiDI Publications No. 11018, 1998; Table XVI.

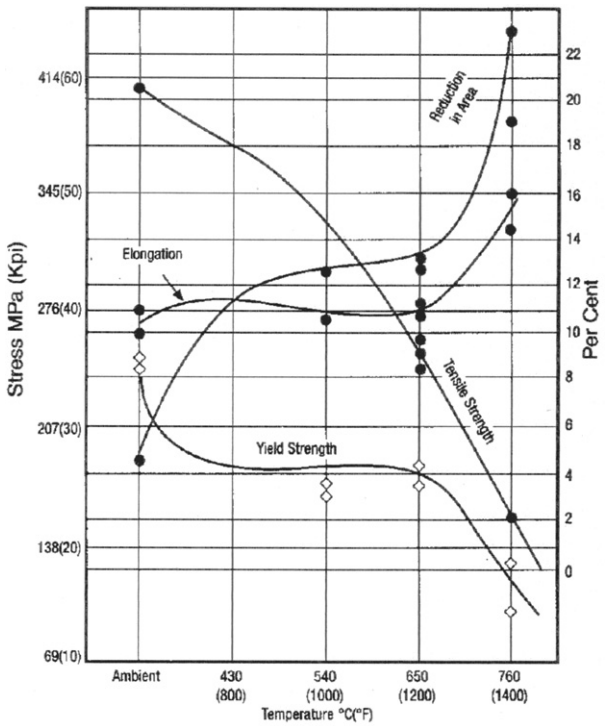


Figure 45 Short-time tensile properties of Ni-resist D2 at elevated temperatures. *Properties and Applications of Ni-Resist and Ductile Ni-Resist Alloys*; Nickel Development Institute. NiDI Publications No. 11018, 1998; Figure 8.

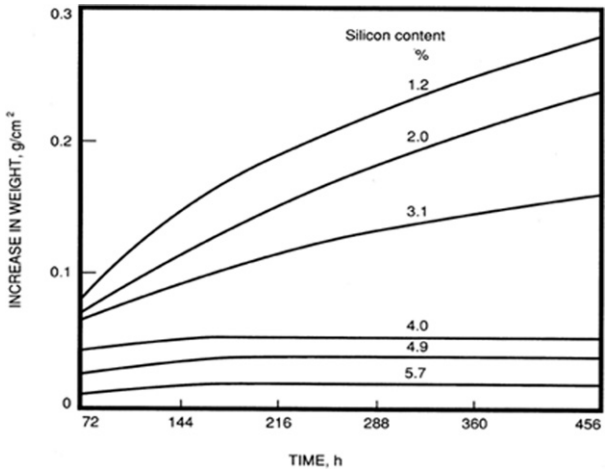


Figure 46 Effect of silicon on the oxidation of ferritic ductile iron in air at 650 °C. *Ductile Iron Data for Design Engineers, Section V, Alloy Ductile Iron*. Ductile Iron Society: Strongsville, OH; Figure 5.2.

without pearlite formation obtained with minimum alloy additions are shown in **Table 28**. Based on the CCT diagrams, the critical cooling rate to avoid pearlite formation for a minimum alloy content have been calculated. **Table 29** indicates the minimum alloy content for air quenching castings of effective section thickness. Ni and Cu promote retained austenite and should be restricted to combined levels of 1.2% max. Mn behaves similarly and should be restricted to 1.0% max.

2.10.5.5.2.1 Annealing

Sometimes, to improve the machinability of the castings either subcritical annealing or a full annealing is adopted. The subcritical annealing involves heating in the range of temperature of 6900–700 °C with a soaking time of 4–12 h. A pearlitic matrix with a hardness range of 400–450 HB is produced. The full annealing is intended for further softening and the castings are heated to 950–1010 °C and subsequently cooled slowly in furnace to a temperature of 760 °C and held at this temperature for 10–50 h depending upon the composition.

Table 24 Effect of silicon and molybdenum on the high-temperature tensile and creep-rupture strengths of ferritic ductile iron

Material	*Tensile strength (MPa)*			*Stress rupture (MPa)*
	425 °C	*540 °C*	*650 °C*	*1000 h @ 540 °C*
Gray Iron	37	25	12	5.9
60–40–18 D.I.	40	25	13	8.3
4% Si D.I.	56	36	13	10
4% Si – 1% Mo D.I.	61	44	19	14
4% Si – 2% Mo D.I.	65	46	20	17

Gray Iron: Unalloyed, stress-relieved. Ductile Irons: Subcritically annealed at 788 °C.
Source: Ductile Iron Data for Design Engineers, Section V, Alloy Ductile Irons; Ductile Iron Society: Strongsville, OH; Table 5.1.

Table 25 Effect of silicon and molybdenum on stress-rupture strength of ferritic ductile irons

Type of iron	*Temperature (°C)*	*Stress to rupture (MPa)*	
		100 h	*1000 h*
2.2% Si	650	40	20
4% Si	650	28	
4% Si 1% Mo	650	43	
4% Si	705	19	12
4% Si 1% Mo	705	33	23
4% Si	815	7	
4% Si 1% Mo	815	9	

Source: Ductile Iron Data for Design Engineers, Section V, Alloy Ductile Irons; Ductile Iron Society: Strongsville, OH; Table 5.2.

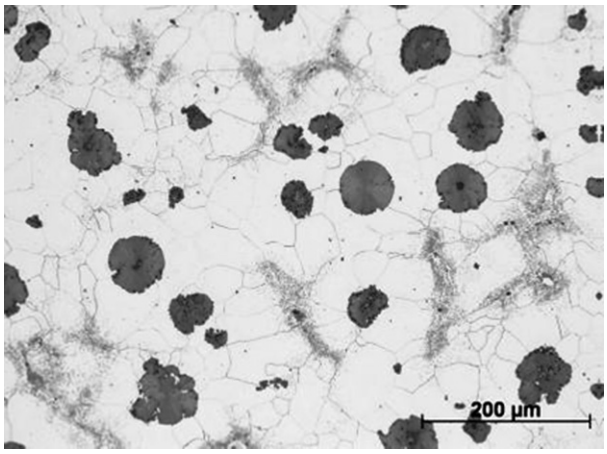


Figure 47 Etched (Nital 2%) microstructure of SiMo51, showing graphite nodules dispersed in ferrite (white) with carbides of M6C-type (M = Fe, Mo, Si), formed in the intercellular regions. Ekström, M. Development of a Ferritic Ductile Cast Iron for Increased Life in Exhaust Applications (Licentiate Thesis); Stockholm, Sweden: Department of Materials Science and Engineering, Division of Mechanical Metallurgy, Royal Institute of Technology, 2013.

2.10.5.5.2.2 Destabilization treatment

To achieve a maximum hardness, toughness, and abrasion resistance by a martensitic matrix structure embedded with fine alloy carbides, destabilization is most suitable treatment and is widely used. The destabilization involves reaustenitization of the castings at 955–1060 °C and held for 3–6 h followed by air cooling. The reaustenitization at just above the upper critical temperature (A_3) causes excess carbon and alloying elements to be rejected out and form very fine secondary M_7C_3 type carbides. The martensite start temperature (M_s) of this alloy depleted austenite is raised and during subsequent air cooling the austenite is transformed to martensite embedded with fine alloy carbides (**Figure 50**). The alloy must have adequate hardenability to allow air hardening.[45–48]

During heating to the austenitization temperature furnace temperature and the rate of heating should not produce any thermal gradients in the castings. Simple shapes can be loaded at 260 °C with a heating rate of 100 °C h^{-1}. On the other hand, complex castings are recommended to load in the cold furnace with slow heating rate of 30 °C h^{-1}. The heating rate can be accelerated once the castings are red hot.

Austenitization temperature and time are selected on the basis of composition and microstructure. A very high austenitizing temperature cause retention of higher amount of austenite and reduces the hardness and abrasion resistance (**Figure 51**). In contrast, lower austenitizing temperature will cause lower amount of dissolved carbon in austenite and produces low-carbon martensite with lower hardness. The austenitizing time can be 3–6 h, shorter times are adopted with as-cast pearlitic matrix whereas longer times are required for predominantly austenitic matrix.

Air quenching from the austenitization temperature preferably by fan cooling to a temperature below the pearlitic transformation range is recommended to produce desired martensitic structure. Below his temperature the cooling rate must be slow enough to minimize the residual stress. Complex and heavy castings are reinserted in the furnace at 550 °C and kept sufficient time to equalize the temperature in the castings following this castings are either furnace cooled or cooled in still air.

The destabilized castings are very often tempered at a low temperature range of 200–230 °C for 2–4 h to improve toughness to some extent and to relieve the residual stress.

The destabilized castings invariably contain 10–30% of retained austenite which are causing failure from spalling. Subcritical tempering in the range of 450–525 °C for a soaking time of 8–12 h reduces the retained austenite content and increases the hardness. Higher treatment temperature and time will cause decrease in hardness as spheroidized ferrite–carbide structure is developed.

2.10.5.5.2.3 Subcritical heat treatment

It has been reported[58] that during such treatments, the highly alloyed metastable austenitic matrix can be decomposed into various combinations of ferritic and secondary carbide phases with the primary M_7C_3 phase being practically unaffected. Wang[50] studied the behavior of a 16Cr–1Mo–1Cu white cast iron during subcritical treatment at 580 °C for different time intervals of processing. A sharp hardness increase was observed between 2 and 10 h, followed by a smooth drop for the next 6 h. Above 16 h of processing, a slight increase was observed. These hardness fluctuations were associated with the different

Table 26 Compositions of high-silicon irons as per ASTM A 518M

Alloy	*Composition (%)*					
	C	*Mn*	*Si*	*Cr*	*Mo*	*Cu*
Grade 1	0.70–1.10	1.50 max.	14.20–14.75	0.50 max.	0.50 max.	0.50 max.
Grade 2	0.75–1.15	1.50 max.	14.20–14.75	3.25–5.00	0.40–0.60	0.50 max.
Grade 3	0.70–1.10	1.50 max.	14.20–14.75	3.25–5.00	0.20 max.	0.50 max.

Source: *ASM Specialty Handbook-Cast Iron*, p. 129.

Table 27 Composition of different grades of high-alloy white irons as per ASTM A 532

Class	*Type*	*UNS No.*	*Designation*	*Composition (wt. %)*					
				C	*Mn*	*Si*	*Ni*	*Cr*	*Mo*
I	A	F45000	Ni–Cr–HC	3.0–3.6	1.3 max.	0.8 max.	3.3–5.0	1.4–4.0	1.0 max.[a]
I	B	F45001	Ni–Cr–LC	2.5–3.0	1.3 max.	0.8 max.	3.3–5.0	1.4–4.0	1.0 max.[a]
I	C	F45002	Ni–Cr–GB	2.9–3.7	1.3 max.	0.8 max.	2.7–4.0	1.1–1.5	1.0 max.[a]
I	D	F45003	Ni–Hi Cr	2.5–3.6	1.3 max.	1.0–2.2	5.0–7.0	7.0–11.0	1.0 max.[b]
II	A	F45004	12%Cr	2.4–2.8	0.5–1.5	1.0 max.	0.5 max.	11.0–14.0	0.5–1.0[c]
II	B	F45005	15% Cr–Mo–LC	2.4–2.8	0.5–1.5	1.0 max.	0.5 max.	14.0–18.0	1.0–3.0[c]
II	C	F45006	15% Cr–Mo–HC	2.8–3.6	0.5–1.5	1.0 max.	0.5 max.	14.0–18.0	2.3–3.5[c]
II	D	F45007	20% Cr–Mo–LC	2.0–2.6	0.5–1.5	1.0 max.	1.5 max.	18.0–23.0	1.5 max.[c]
II	E	F45008	20% Cr–Mo–HC	2.6–3.2	0.5–1.5	1.0 max.	1.5 max.	18.0–23.0	1.0–2.0[c]
III	A	F45009	25% Cr	2.3–3.0	0.5–1.5	1.0 max.	1.5 max.	23.0–28.0	1.5 max.[c]

[a]Maximum: 0.30% P, 0.15% S.
[b]Maximum: 0.10% P, 0.15% S.
[c]Maximum: 0.10% P, 0.06% S, 1.2 Cu.
Source: *ASM Specialty Handbook-Cast Iron*, p. 107.

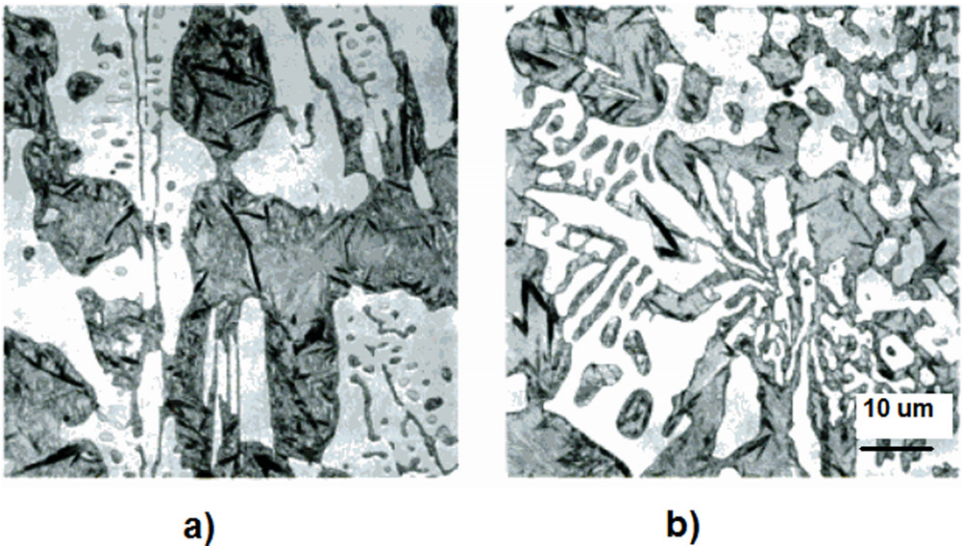


Figure 48 Typical microstructure of (a) Class I type A and (b) Class I type D Nickel–chromium white cast irons. *ASM Handbook*, Vol. 4, 1991 ed., Heat Treating of High-Alloy Iron; Figures 4 and 5, p. 1528.

microstructural features. Wang *et al.*[51] studied the effects of precipitation and transformation of secondary carbides on the hardness of a 15Cr–1Mo–1.5V white cast iron under a sub-critical treatment. Heating at 560 °C led to two hardness peaks, after 10 and 14 h, respectively. The first peak was attributed to martensitic transformation and $M_{23}C_6$ precipitation. The second peak was associated with the presence of MoC, $(Cr, V)_2C$, and $M_{23}C_6$ carbides.

2.10.5.5.2.4 Case studies on failure of high-chromium iron

Case 1:[47] Failure of grinding media ball is a crucial problem due to improper destabilization treatment. The grinding

media are subjected to repeated severe impact causes spalling prior to the failure. The failures have been investigated and the retained austenite contents have been found to be high around 20–70% in the matrix. One of the possible causes of failure is the formation of strain-induced martensite from the retained austenite transformation producing high-transformation stress. The lowering of retained austenite is possible by a subcritical treatment after the destabilization treatment.

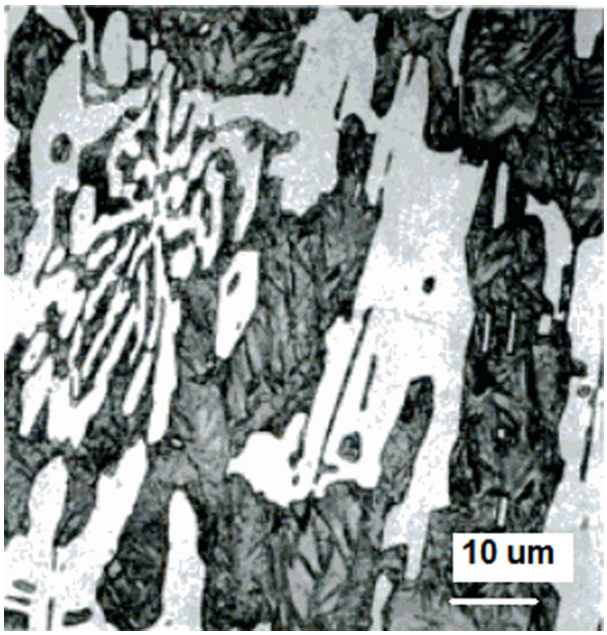


Figure 49 Microstructure of class I type D nickel–chromium white cast iron after cryogenic treatment. *ASM Handbook*, Vol. 4, 1991 ed., Heat Treating of High-Alloy Iron; Figure 6, p. 1530.

The resistance to impact of Fe–Cr–C white irons with high-chromium content is relatively poor, and many researchers have attempted to identify the microstructural features which influence the impact resistance. Some researchers have demonstrated that the austenitic matrix under impact promotes spalling and brittle fracture. Under impact, austenite is thought to transform into martensite in surface regions. The volume expansion associated with martensite formation produces compressive stresses in the surface layers, which, to maintain static equilibrium, are balanced by subsurface tensile stresses. Cracking of the eutectic carbides and carbide matrix interfaces due to these tensile stresses leads to spall formation.[52]

Case 2:[53] High-chromium cast irons (HCCIs) are often used under tribo-corrosive conditions, for example, in slurry transfer pumps. HCCIs possess their appreciable corrosion resistance to the presence of a passive layer that forms on the surface due to a sufficient amount of chromium in solid solution with the iron-based matrix. Hard carbides surrounded by a tough metallic matrix impart a relatively high wear resistance to these alloys. For multiphase alloys like HCCI the galvanic coupling between the matrix and carbides determines the overall corrosion tendency. Therefore, corrosion proceeds

Table 28 Minimum alloy content to avoid pearlite in mold-cooled castings for effective section sizes indicated (plate thickness or radius of rounds)

ASTM A 532 class	*Cr[a] (%)*	*C[a] (%)*	*Plate thickness or radius of rounds*		
			25 mm	*50 mm*	*100 mm*
IIB, C	14–18	2.0	1.0 Mo	1.5 Mo	1.5 Mo + 1.0(Ni + Cu)
		3.5	2.0 Mo	2.5 Mo	2.5 Mo + 1.0(Ni + Cu)
IID, E	18–23	2.0	0.5 Mo	1.0 Mo	1.0 Mo + 1.0(Ni + Cu)
		3.2	1.5 Mo	2.0 Mo	2.0 Mo + 1.0(Ni + Cu)
IIIA	23–28	2.0	–	0.5 Mo	1.0 Mo
		3.0	1.0 Mo	1.5 Mo	1.5 Mo + 1.0(Ni + Cu)

[a]In base irons containing 0.6% Si and 0.8% Mn.
Source: ASM Metals Handbook, Vol. 15, 9th ed., p. 683.

Table 29 Minimum alloy content to avoid pearlite in heat treatment for effective section sizes indicated plate thickness or radius of rounds

ASTM A 532 class	*Cr[a] (%)*	*C[a] (%)*	*Plate thickness or radius of rounds*		
			50 mm	*125 mm*	*150–255 mm*
IIB, C	14–18	2.0	1.5 Mo	1.5 Mo + 0.5(Ni + Cu)	2.0 Mo + 1.0(Ni + Cu)
		3.5	3.0 Mo	2.0 Mo + 1.0(Ni + Cu)	2.5 Mo + 1.2(Ni + Cu)
IID, E	18–23	2.0	1.0 Mo	2.0 Mo	2.0 Mo + 0.5(Ni + Cu)
		3.2	1.5 Mo	2.0 Mo + 0.7(Ni + Cu)	2.0 Mo + 1.2(Ni + Cu)
IIIA	23–28	2.0	0.5 Mo	1.5 Mo	1.5 Mo + 0.5(Ni + Cu)
		3.0	1.5 Mo	1.5 Mo + 0.6(Ni + Cu)	1.5 Mo + 1.2(Ni + Cu)

[a]In base irons containing 0.6% Si and 0.8% Mn.
Source: ASM Metals Handbook, Vol. 15, 9th ed., p. 683.

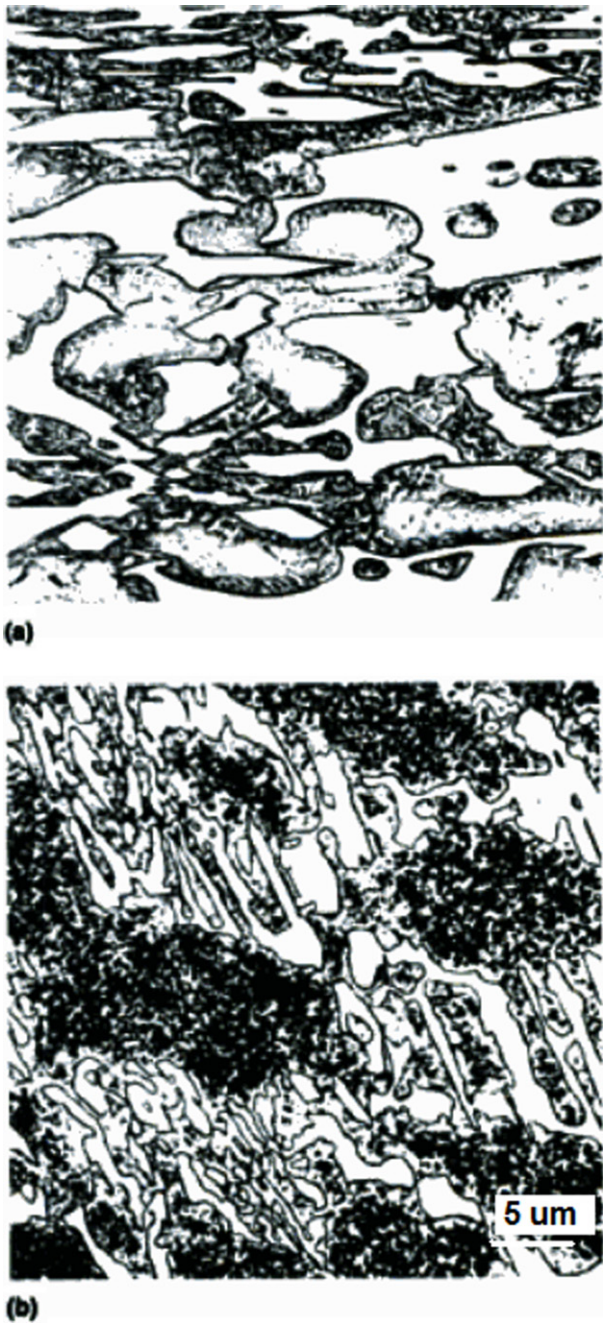


Figure 50 Microstructure of (a) as-cast austenitic matrix and (b) destabilized matrix of high-chromium white iron showing fine M_7C_3 secondary carbides in martensitic matrix. *ASM Handbook*, Vol. 4, 1991 ed., Heat Treating of High-Alloy Iron; Figure 12, p. 1537.

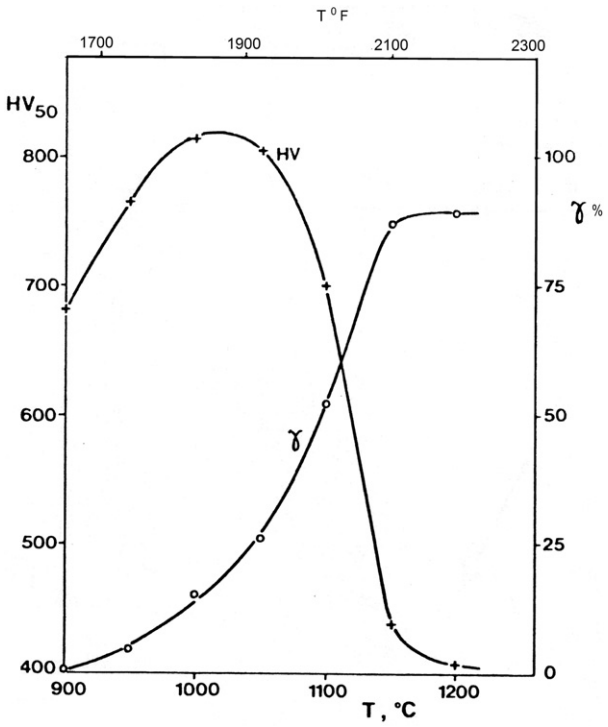


Figure 51 Effect of austenitizing temperature on hardness and retained austenite content in high-chromium white irons. Maratray, F.; Poulalion, A. Austenite Retention in High-Chromium White Irons. *AFS Trans.* **1982**, *90*, 795–804; Figure 1, p. 796.

in a localized manner rather than being uniformly distributed over the surface. Narrow crevices between the carbides and the matrix have been reported as the most susceptible sites where the corrosion process initiates. The electrolyte characteristics (composition, pH, temperature) may significantly alter the severity and mechanism of corrosive attack of HCCIs.

In alkaline media at lower potentials the abrading grits remove both the thin oxidized layer of carbides and the metallic matrix at a similar rate. At noble potentials, the carbide oxidized layer is thicker and the rate of carbide removal is faster than that of the matrix. The matrix is subsequently extruded into the carbide-depleted regions. Presence of aggressive chloride ions in slightly alkaline solution yields localized dissolution of the matrix. In neutral electrolytes, dissolution of the matrix is observed, accelerated by the presence of Cl^- ions. The matrix dissolution that often begins at the matrix/carbide interface leaves behind unsupported carbides. Interaction with abrading grits causes chipping and fracture of carbides.

2.10.5.5.2.5 Cryogenic treatment

Recently, a number of researches have been carried out to establish the effect of cryogenic treatment on the destabilization behavior of HCCIs.[59–63] The purpose is to (1) reduce the retained austenite content after conventional destabilization treatment and (2) increase the volume percentage of secondary ultrafine carbides. Both of these contribute to the increase in hardness and abrasion resistance. For cryogenic treatment the castings are initially austenitized at 900–1150 °C for 0.5 h and quenched in a liquid nitrogen bath at −196 °C and kept immersed for 3 h. The cryogenic treatment causes a reduction in retained austenite to about 10% (with a final hardness of around 62 HRC) compared to 20% in conventional destabilization (Figure 52).

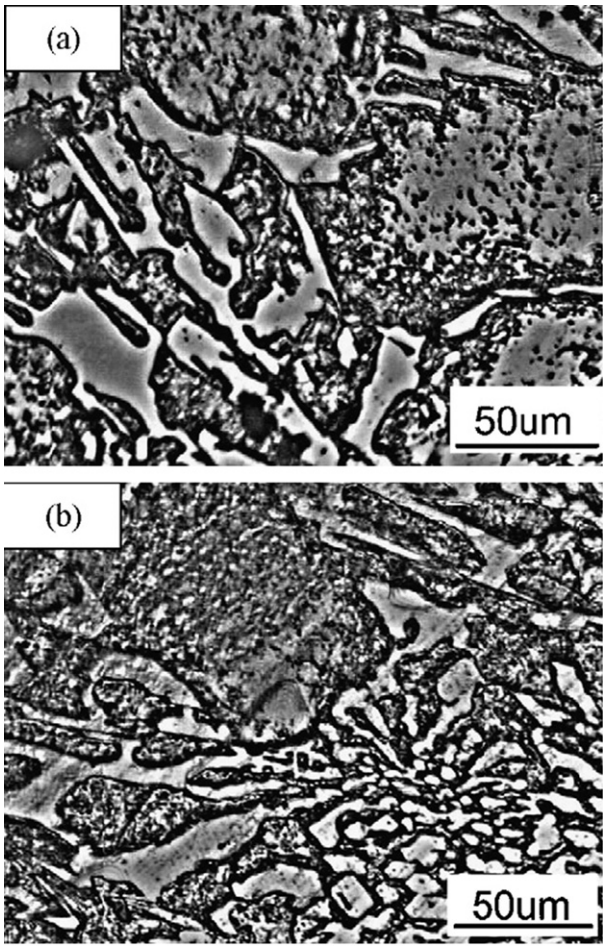


Figure 52 Microstructures of high-chromium iron destabilized at 1000 °C for 0.5 h followed by (a) air cooling, (b) cryogenic treatment. Jum Wang; Ji Xiang; Hongyuan Fan; Hong-Shan Yang; Hao- Huai Liu; Bao-Luo Shen. Effects of High Temperature and Cryogenic Treatment on the Microstructure and Abrasion Resistance of a High Chromium Cast Iron. *J. Mater. Process. Tech.* **2009**, *209*, 3236–3240.

See also: 2.1 Fundamentals of Heat Treating Metals and Alloys

References

1. Goodrich, G. M. *Introduction to Cast Irons, Casting*; *ASM Handbook*, Vol. 15; ASM International: Materials Park, OH, 2008; pp. 785–811.
2. Dossett, J. L.; White, C. V. *Introduction to Cast Iron Heat Treatment, Heat Treating of Irons and Steels*; *ASM Handbook*, Vol. 4D; ASM International: Materials Park, OH, 2014; pp. 483–492.
3. Elliott, R. *Cast Iron Technology*, 1st ed.; Butterworths: London; Boston, MA, 1988.
4. Angus, H. T. *Cast Iron: Physical and Engineering Properties*, 2nd ed.; Butterworths: London; Boston, MA, 1976.
5. Berns, H.; Theisen, W. *Ferrous Materials, Steel and Cast Irons*, 1st ed.; Springer: Berlin; Heidelberg, 2008.
6. Davis, J. R. *ASM Specialty Handbook: Cast Iron*; ASM International: Materials Park, OH, 1996.
7. Rehder, J. E. Critical Temperature Heat Treatment of Cast Irons. *Foundry*, June 1965; pp. 65–67.
8. Dossett, J. L.; White, C. V. *Heat Treating of Gray Irons, Heat Treating of Irons and Steels*; *ASM Handbook*, Vol. 4D; ASM International: Materials Park, OH, 2014; pp. 493–507.
9. Reese, C. H.; Rundman, K. B. Residual Stresses in Gray Cast Iron Brake Rotors. *AFS Trans.* **1998**, *105*.
10. Hallet, M. M.; Wing, P. D. Stress Relief Heat Treatment of Alloy Cast Iron. *Foundry Trade J.* **1949**, *87*, 177–183.
11. Cheng Hsum; Yih-Hsum Shy; Yuan-Hsin Yu; Shen-Chih Lee Effect of Austempering Heat Treatment on Fracture Toughness of Copper Alloyed Grey Iron. *Mater. Chem. Phys.* **2000**, *63* (1), 75–81.
12. Xu, W.; Ferry, M.; Wang, Y. The Effect of Ausferrite Formation on the Mechanical Properties of Grey Iron. *Scripta Mater.* **2004**, *51* (7), 705–709.
13. Balachandran, G.; Vadiraj, A.; Kamraj, M.; Kazuya, E. Mechanical and Wear Behavior of Alloyed Grey Cast Iron in the Quenched and Tempered and Austempered Conditions. *Mater. Des.* **2011**, *32* (7), 4042–4049.
14. Voigt, R. C.; Loper, C. R., Jr. Austempered Ductile Iron-Process Control and Quality Assurance. *J. Mater. Eng. Perform.* **2013**, *22* (10), 2776–2794.
15. Lefevre, J.; Hayrynen, K. L. Austempered Materials for Powertrain Applications. *J. Mater. Eng. Perform.* **2013**, *22* (7), 1914–1922.
16. Jenkins, L. R. *Heat Treating of Malleable Irons, Heat Treating*; *ASM Handbook*, Vol. 4; ASM International: Materials Park, OH, 1991; pp. 693–698.
17. Rundman, K. B. *Heat Treating of Ductile Irons, Heat Treating*; *ASM Handbook*, Vol. 4; ASM International: Materials Park, OH, 1991; pp. 682–692.
18. Rudnev, V. I. Induction Hardening Cast Irons. *Heat Treating Progress*, March 2003; pp. 27–32.
19. Johansson, M. Austenitic–Bainitic Ductile Iron. *AFS Trans.* **1977**, *85*, 117–122.
20. Dorazil, E.; Barta, B.; Munsterova, E.; Stransky, L.; Huvar, A. High Strength Bainitic Ductile Iron. *Int. Cast. Met. J.* **June 1982**, 52–62.
21. Rouns, T. N.; Rundman, K. B. Constitution of Austempered Ductile Iron and Kinetics of Austempering. *AFS Trans.* **1987**, *95*, 851.
22. Walton, C.; Opar, T. *Iron Castings Handbook*; Iron Casting Society, Inc.: Chicago, IL, 1981.
23. Kovacs, B. V. Pearlitic Stabilization in Cast Irons. *AFS Trans.* **1981**, *89*, 79–96.
24. Rundman, K. B.; Rouns, T. N. On the Effects of Molybdenum on the Kinetics of Secondary Graphitization in Quenched and Tempered Dutile Irons. *AFS Trans.* **1982**, *90*, 487–497.
25. Kovacs, B. V. Austempered Ductile Iron: Facts and Fiction. *Mod. Cast.* **1990**, 38–41.
26. Gundlach, R. B.; Janowak, J. F. Austempered Ductile Iron Combines Strength with Toughness and Ductility. *Met. Prog.* **1985**, *128*, 19–26.
27. Blackmore, P. A.; Harding, R. A. The Effects of Metallurgical Process Variables on the Properties of Austempered Ductile Irons. *J. Heat Treat.* **1984**, *3* (4), 310–325.
28. Daber, S.; Prasad Rao, P. Formation of Strain-Induced Martensite in Austempered Ductile Iron. *J. Mater. Sci.* **2008**, *43*, 357–367.
29. El-Baradie, Z. M.; Ibrahim, M. M.; El-Sisy, I. A.; Abd El- Hakeem, A. A. Austempering of Spheroidal Graphite Cast Iron. *Mater. Sci.* **2004**, *40* (4), 523–528.
30. Kumar, K. M.; Hariharan, P.; Venkateshwaran, P.; Tamilarasan, S. Examination of Microstructure and Mechanical Properties of Austempered Ductile Iron as per Austempering Temperature and Time. *Trans. I.I.M.* **2015**, *68* (Suppl. 1), 67–71.
31. Dasgupta, R. K.; Mandal, D. P.; Chakrabarti, A. K. Evolution of Microstructures During Austempering of Ductile Irons Alloyed with Mn and Cu. *Metall. Mater. Trans. A* **2013**, *44* (3), 1376–1387.
32. Ning Zhang; Jiwang Zhang; Liantao Lu; Mintang Zhang; Dongfang Zeng; Qingpeng Song Wear and Friction Behavior of Austempered Ductile Iron as Railway Wheel Material. *Mater. Des.* **2016**, *89* (5), 815–822.
33. Panneerselvam, S.; Martis, C. J.; Putatunda, S. K.; Boileau, J. M. An Investigation on the Stability of Austenite in Austempered Ductile Iron. *J. Mater. Sci. Eng. A* **2015**, *626* (25), 237–246.
34. Jianghuai Yang; Putatunda, S. K. Effect of Microstructure on Abrasion Wear Behavior of Austempered Ductile Iron Processed by a Novel Two-Step Austempering Process. *J. Mater. Sci. Eng. A* **2005**, *406* (1–2), 217–228.
35. Ayman H. Elsayed; Megahed, M. M.; Sadek, A. A.; Abouelela, K. M. Fracture Toughness Characterization of Austempered Ductile Iron Produced Using Both Conventional and Two-Step Austempering Processes. *Mater. Des.* **2009**, (30), 1866–1877.
36. *Ductile Iron Data for Design Engineers, Section IV, Alloy Ductile Iron*; Ductile Iron Society: Strongsville, OH, 1998.
37. Guesser, W. L.; Koda, F.; Blanco Martinez, J. A.; da Silva, C. H. *Austempered Ductile Iron for Gears*; SAE International, 2012. doi:10.4271/2012-36-0305.
38. Burkland, T. L.; Rauch, A. H. Prior Structure Effect on Ductile Iron Response to Induction Hardening. *AFS Trans.* **1962**, *70*, 896–908.

39. Gundlach, R. B.; Doane, D. V. *Heat Treating of High Alloy Irons, Heat Treating*; *ASM Handbook*, Vol. 4; ASM International: Materials Park, OH, 1991; pp. 697–708.
40. *Properties and Applications of Ni-Resist and Ductile Ni-Resist Alloys*; Nickel Development Institute. NiDI Publications No. 11018, 1998.
41. Li, D.; Sloss, C. Heat Treatment of Heat-Resistant Ferrous Cast Alloys. *Int. J. Metal. Cast.* **2015**, *9* (2), 7–20.
42. Alabbasian, F.; Boutorabi, S. M. A.; Kheirandish, S. Effect of Inoculation and Casting Modulus on the Microstructure and Mechanical Properties of Ductile Ni-Resist Cast Iron. *J. Mater. Sci. Eng. A* **2016**, *651* (10), 467–473.
43. *Ni-Hard-Engineering Properties and Applications*; Nickel Development Institute. NiDI Publications No. 70, 1974.
44. Cox, G. J. Development of Abrasion-Resistant Nickel-containing Alloy White Irons of High Hardness. *AFS Trans.* **1989**, *97*, 361–372.
45. Tabrett, C. P.; Sare, I. R.; Ghomashchi, M. R. Microstructure–Property Relationships in High Chromium White Cast Irons Alloys. *Int. Mater. Rev.* **1996**, *41*, 59–82.
46. Dodd, J.; Parks, J. L. Factors Affecting the Production and Performance of Thick-section High Chromium Molybdenum Alloy Iron Castings-Part I: Metallurgical Considerations. *AFS Int. Cast. Metals J.* **1980**, 47–54.
47. Dodd, J.; Parks, J. L. Factors Affecting the Production and Performance of Thick-section High Chromium Molybdenum Alloy Iron Castings-Part II: Production and Performance. *AFS Int. Cast. Metals J.* **1980**, *5* (3), 15.
48. Efremenko, V.; Shinizu, K.; Chabak, Y. Effect of Destabilization Heat Treatment on Solid State Phase Transformation in High Chromium Cast Irons. *Metall. Mater. Trans. A* **2012**, *44* (12), 5434–5446.
49. Karantzalis, A. E.; Lekatou, A.; Kapoglou, A.; Mavros, H.; Dracopoulos, V. Phase Transformations and Microstructural Observations during Subcritical Heat Treatments of a High-Chromium Cast Iron. *J. Mater. Eng. Perform.* **2012**, *21*, 1030–1039.
50. Wang, J. Effects of Secondary Carbides Precipitation and Transformation Abrasion Resistance of the 16Cr–1Mo–1Cu White Iron. *J. Mater. Eng. Perform.* **2006**, *15*, 316–319.
51. Wang, J.; Luo, R. L.; San, Z. P. Influence of Secondary Carbides Precipitation and Transformation of Hardening of a 15Cr–1Mo–1.5V White Iron. *Mater. Charact.* **2005**, *55*, 234–250.
52. Filipovic, M.; Romhanji, E. Strain Hardening of Austenite in Fe–Cr–C–V Alloys under Repeated Impact. *Wear* **2011**, *270*, 800–805.
53. Salasi, M.; Stachowiak, G. B.; Stachowiak, G. W. Three-Body Tribo-Corrosion of High-Chromium Cast Irons in Neutral and Alkaline Environments. *Wear* **2011**, *271*, 1385–1396.
54. Jum Wang; Ji Xiang; Hongyuan Fan; Hong-Shan Yang; Hao-Huai Liu; Bao-Luo Shen. Effects of High Temperature and Cryogenic Treatment on the Microstructure and Abrasion Resistance of a High Chromium Cast Iron. *J. Mater. Process. Tech.* **2009**, *209*, 3236–3240.
55. Zum Gahr, K.-H.; Doane, D. V. Optimizing Fracture Toughness and Abrasion Resistance in White Cast Irons. *Metall. Trans. A* **1980**, *11A*, 613–620.
56. Maratray, F.; Poulalion, A. Austenite Retention in High-Chromium White Irons. *AFS Trans.* **1982**, *90*, 795–804.
57. Cias, W. W. Austenite Transformation Kinetics and Hardenability of Heat Treated 17.5% Cr White Cast Irons. *AFS Trans.* **1974**, *82*, 317–328.
58. Nickel, S. G. *Iron*; NiDI Publications No. 4077 Nickel Development Institute, 1974.
59. Vidyarthi, M. K.; Ghose, A. K.; Chakrabarty, I. Effect of Deep Cryogenic Treatment on the Microstructure and Wear Performance of Cr–Mn–Cu White Cast Iron Grinding Media. *Cryogenics* **2013**, *58*, 85–92.
60. Kumar, P.; Chattopadhyay, K.; Chakrabarty, I. Effect of Sub-critical Tempering and Deep Cryogenic Treatment on Slurry Erosion of Cr–Mn–Cu White Cast Irons. *ISIJ Int.* **2014**, *54* (10), 2294–2301.
61. Jun Wanga; Ji Xionga; Hongyuan Fan; Hong-Shan Yanga; Hao-Huai Liub; Bao-Luo Shenb Effects of High Temperature and Cryogenic Treatment on the Microstructure and Abrasion Resistance of a High Chromium Cast Iron. *J. Mater. Process. Technol.* **2009**, *209*, 3236–3240.
62. Haohuai Liu; Jun Wang; Hongshan Yang; Baoluo Shen Effects of Cryogenic Treatment on Microstructure and Abrasion Resistance of CrMnB High-Chromium Cast Iron Subjected to Sub-Critical Treatment. *Materials Science and Engineering A* **2008**, *478*, 324–328.
63. Hao-huai Liu; Jun Wang; Bao-luo Shen; Hong-shan Yang; Sheng-ji Gao; Si-jiu Huang Effects of Deep Cryogenic Treatment on Property of 3Cr13Mo1V1.5 High Chromium Cast Iron. *Mater. Des.* **2007**, *28*, 1059–1064.

Relevant Websites

http://www.ductile.org/didata/section5
Ductile Iron Society.
http://www.ductile.org/didata/section4
Ductile Iron Society.
http://www.ductile.org/didata/section7
Ductile Iron Society.
http://ispatguru.com
Ispat Guru.
http://www.keytometals.com
Key to Metals.

2.11 Thermal Treatment for Strengthening Titanium Alloys

A Sinha, S Sanyal, and NR Bandyopadhyay, Indian Institute of Engineering Science and Technology, Howrah, India

© 2017 Elsevier Inc. All rights reserved.

2.11.1	**Introduction**	288
2.11.2	**Production of Ti**	289
2.11.2.1	Casting Route	289
2.11.2.2	Powder Metallurgy Route	289
2.11.3	**Alloying System of Ti Alloys**	290
2.11.3.1	α Stabilizers	290
2.11.3.2	β Stabilizers	290
2.11.3.2.1	ω Phase	290
2.11.3.3	Neutral Elements	290
2.11.4	**Classification of Ti Alloys**	290
2.11.4.1	α Alloys	290
2.11.4.1.1	Fully α-Ti alloys	290
2.11.4.1.2	Near α-Ti alloys	291
2.11.4.2	α/β Alloys	291
2.11.4.3	β Alloys	292
2.11.5	**Heat Treatment of Ti alloys**	292
2.11.5.1	Heat Treatment in α-Ti Alloys	292
2.11.5.1.1	Heat treatment in CP Ti and α-Ti alloys	292
2.11.5.1.2	Heat treatment in near α-Ti Alloys	293
2.11.5.2	Heat Treatment in α/β-Ti Alloys	301
2.11.5.2.1	Annealing	305
2.11.5.2.2	Normalizing	305
2.11.5.2.3	Quenching	305
2.11.5.2.4	Tempering	306
2.11.5.2.5	Decomposition of metastable β	306
2.11.5.2.5.1	Formation of ω phase	306
2.11.5.2.5.2	Separation of β phase	306
2.11.5.2.5.3	Formation of equilibrium α phase	306
2.11.5.2.6	A case study on the effect of thermal treatment on an α/β-Ti alloy	306
2.11.5.2.6.1	Composition of the alloy	306
2.11.5.2.6.2	Process of manufacture	306
2.11.5.2.6.3	Observations	307
2.11.5.2.6.3.1	Clearance criteria followed for the fastener material (observations of the input material)	307
2.11.5.2.6.3.1.1	Mechanical properties	307
2.11.5.2.6.3.1.2	Metallurgical analysis	307
2.11.5.2.6.3.1.3	Acceptance test on the fasteners	307
2.11.5.2.6.3.2	Observations on failed bolt	307
2.11.5.2.6.3.2.1	Visual inspection	307
2.11.5.2.6.3.2.2	Metallurgical analysis	308
2.11.5.2.6.4	Results and discussion	309
2.11.5.2.6.5	Conclusions	311
2.11.5.3	Heat Treatment in β-Ti Alloys	311
2.11.5.3.1	Deformation in the β-phase field	313
2.11.5.3.2	Deformation in the $\alpha + \beta$-phase field	317
2.11.5.3.3	Shape memory alloys	321
2.11.5.3.3.1	Phase diagram	322
2.11.5.3.3.2	Martensitic transformation in Ti–Ni alloys	322
2.11.5.3.3.3	Precipitation in Ti–Ni alloys	324
2.11.5.3.3.3.1	Effect of thermomechanical treatment	325
2.11.5.3.3.3.2	Effect of cold rolling	326
2.11.5.3.3.3.3	Effect of aging treatment	328
References		333
Relevant Websites		336

2.11.1 Introduction

Titanium is named after the Titans, the powerful sons of the earth in Greek mythology. Titanium (Ti) is the fourth most abundant metal on Earth's crust (~0.86%) after aluminum (Al), iron (Fe), and magnesium (Mg). It is not found in its free state. The pure metal forms in nature as oxides such as ilmenite ($FeTiO_3$) and rutile (TiO_2). It has almost similar strength as steel, but with a weight nearly half that of steel. Aerospace industries require materials with high strength-to-weight ratios at elevated temperatures. Initially, the stimulus for the development of Ti alloys during the past 40 years came from the critical need for such materials. Ti has a high melting point of approximately 1678 °C, which was taken as an indicator of good creep strength over a wide temperature range. However, thorough investigations revealed that this temperature range was narrower than expected. Nevertheless, Ti alloys are now featured as essential materials in the aerospace industries. Recently, chemical industries have recognized the importance of Ti and its alloys for its excellent corrosion resistivity. This metal is also utilized by medical industries, with Ti and its alloys used for prosthetic and implant materials in the human body.

Ti was produced in the late 1940s, when its relatively low density and high melting point made it uniquely attractive as a potential replacement for Al in the aerospace industries. The high specific strength of Ti alloys when compared with other light alloys, steels, and nickel alloys is presented in Figure 1.[1] The fact that this advantage is maintained to approximately 500 °C has led to the universal acceptance of certain Ti alloys for the components of gas turbine heat exchangers. Ti alloys have also found increasing demand for their use in critical structural components in aircraft as well as in the chemical and power generation industries due to outstanding corrosion resistance.

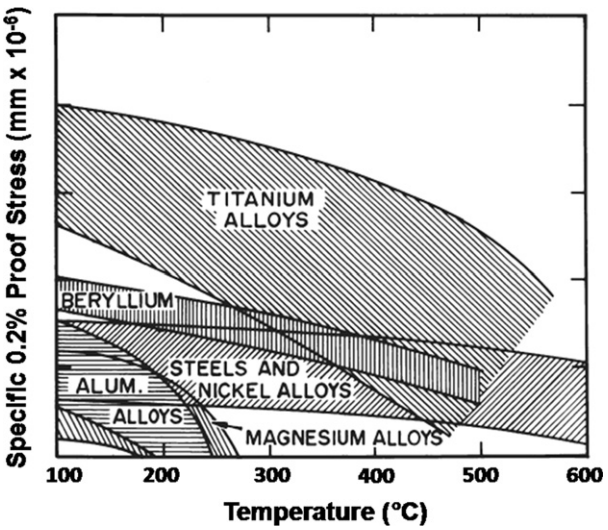
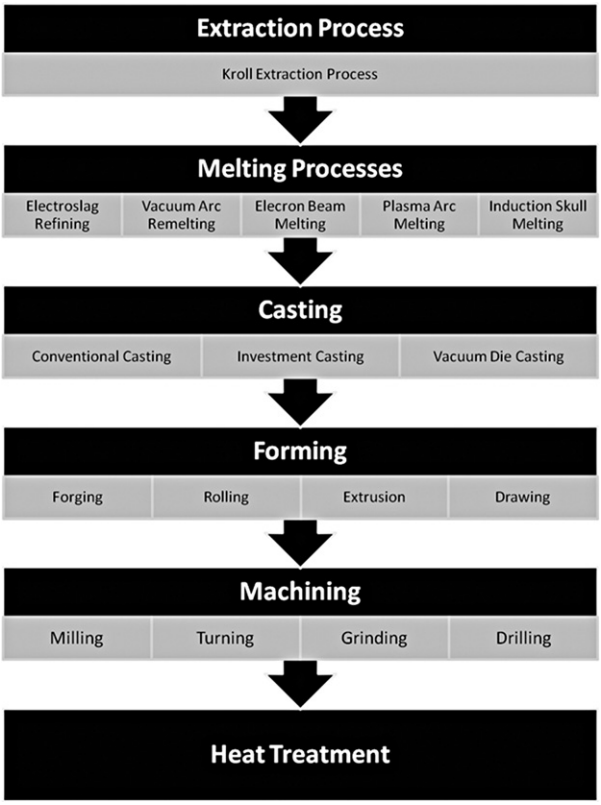


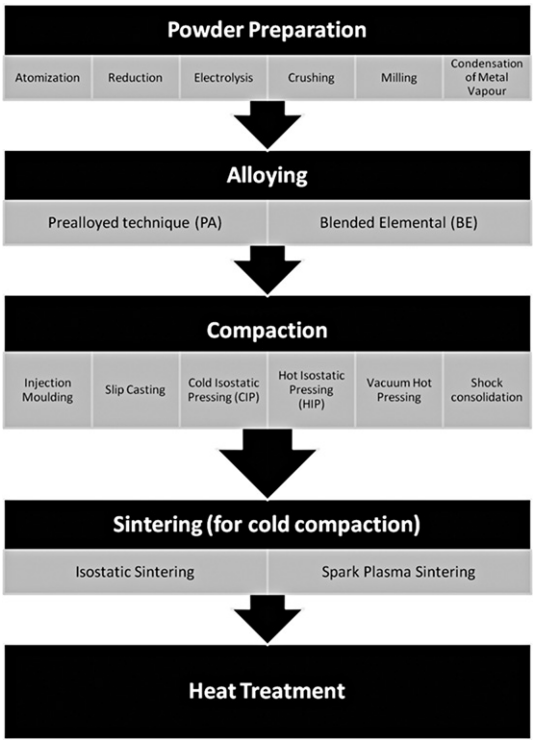
Figure 1 Relationship of specific 0.2% proof stress (ratio of proof stress to relative density) with temperature for light alloys, steels, and nickel alloys.[1]

2.11.2 Production of Ti

2.11.2.1 Casting Route



2.11.2.2 Powder Metallurgy Route



2.11.3 Alloying System of Ti Alloys

Ti is a transition element that has a conversion temperature of 882.3 °C, at which a transformation between the two stable phases of Ti occurs. These two phases are the α phase and the β phase.[2] Apart from these two phases, there is a third phase that is metastable in nature, which is called the ω phase.

2.11.3.1 α Stabilizers

The α phase of Ti has its atoms arranged in a hexagonal close-packed (hcp) structure. The hcp structure results in very high strength and modulus. It is the room temperature phase of Ti. The elements that stabilize the α phase are Al, O, N, C, Ga, Ge, Ce, La, and others. These elements promote the formation of the α phase in Ti, thereby suppressing the formation of other phases. Elements that dissolve preferentially in the α phase expand the α field in the phase diagram, which raise the α/β transus. Among the comparatively few elements that behave in this way, Al and oxygen (O) are the most important.[2]

2.11.3.2 β Stabilizers

The β phase of Ti consists of atoms arranged in a body-centered cubic (bcc) crystal structure. The strength and the modulus are lower than that of the α-Ti alloys. Being the high temperature phase of Ti, this type of alloy requires β-stabilizing elements in adequate amounts to stabilize the phase at room temperature. From a purely β-phase Ti alloy, a combination of α/β phases is noticed by varying amounts of alloying elements. Elements that decrease the α/β transus and stabilize the β phase may be classified in two groups: those that form binary systems of the β-isomorphous type and those that favor formation of a β-eutectoid. It should be noted, however, that the eutectoid reactions, in a number of alloys, are very sluggish and, in practice, the alloys tend to behave as if this reaction did not occur. Examples are the binary systems Ti–Fe and Ti–Mn, and these alloys behave as if they conformed to the β-isomorphous phase diagram. Examples of β-isomorphous stabilizers are V, Mo, Nb, Ta, W, Re, and others. The β-eutectoid stabilizing elements are Cr, Fe, Mn, Cu, Ni, Co, H, Ag, Au, Pb, and others.[2]

2.11.3.2.1 ω Phase

The ω phase is a metastable phase that forms in Ti alloys with elements that tend to stabilize the high-temperature β phase. The formation of this phase can be either during quenching from high temperatures (β phase region) or during aging of the quenched materials, depending on the conditions.[3] This phase provides the alloy strength, but it also increases brittleness. Addition of elements like Al (α stabilizer), zirconium (Zr), or tin (Sn) (neutral, but acts as an α stabilizer in the presence of other α stabilizers) suppress the formation of the ω phase to promote formation of the α phase.[2]

2.11.3.3 Neutral Elements

Neutral elements are those that do not promote any of the α or β phases of Ti. Elements like Zr, Sn, Si, and Hf are neutral to the phases of Ti. They are generally used for purposes other than modification of phases, like strengthening and processing.

2.11.4 Classification of Ti Alloys

Ti alloys are classified according to the constituent phases. The presence of α, β, or their combination dictates the properties and hence, the classification of these alloys. These alloys are mainly classified as:

1. α alloys,
2. α/β alloys, and
3. β alloys.

2.11.4.1 α Alloys

The α stabilizing elements (Al, O, and others) and some of the neutral elements (Sn, Zr, and others) dissolve in the α phase of Ti and help to retain it in low temperatures and also increase its strength by solid solution hardening. O and N (generally present as impurities) promote interstitial hardening. Controlled amounts of O in Ti produce the commercial purity titanium (CP Ti), which may also contain some other alloying elements to produce different grades of CP Ti with different mechanical properties.

The α alloys are further classified into two main categories:

- Fully α-Ti alloys.
- Near α-Ti alloys.

Practically, there is a limit (approximately 9%) to the amount of α-stabilizing elements that may be added to Ti because the alloys tend to embrittle because of an ordering reaction that occurs when the aluminum equivalent exceeds 9%. This quantity of α-stabilizing elements is calculated empirically from by summing the weight percentage as follows:

$$\text{Al Eq} = \text{Al} + 1/3(\text{Sn}) + 1/6(\text{Zr}) + 10(\text{O} + \text{C} + 2\text{N})$$

A finely dispersed, ordered phase (α_2), which is coherent with the lattice of the α phase over a wide temperature range, may form during artificial aging (at elevated temperatures) of alloys with Al content higher than 5–6%. This phase α_2 coarsens gradually when subjected to prolonged aging. In α alloys such as Ti–Sn, and in more complex compositions, there is a larger misfit between α and α_2, which makes the heterogeneous nucleation of α_2 more difficult. This nonuniform dispersion has a less deleterious effect on ductility.[1]

2.11.4.1.1 Fully α-Ti alloys

The several grades of CP Ti (which are, in effect, Ti–O alloys) and the ternary composition Ti–5Al–2.5Sn are the commonly used fully α alloys of Ti. The alloys are of single phase and have tensile strengths that are relatively low, although their high thermal stability leads to reasonable creep strengths in the upper temperature range. Good low-temperature ductility and

weldability are some of the highlighting features of these alloys. Hot working of the alloys at temperatures below α/β transus limits their formability because of their hexagonal crystal structure, causing them to exhibit a high rate of strain hardening. This is the reason why Ti–5Al–2.5Sn has tended to be replaced by the age-hardenable Ti–Cu alloy, which can be more easily fabricated after solution treatment but prior to aging, when it is relatively soft.

CP Ti is the second most used Ti alloy, with applications in the aerospace, architectural, chemical, and process engineering industries. Four commonly available grades, which have increasing levels of oxygen and room temperature tensile strengths ranging from 240 to 740 MPa, are:

- Grade 1 (0.18O–0.2Fe) has the lowest strength and displays excellent cold formability so that it can be deeply drawn.
- Grade 2 has a tensile strength between 390 and 540 MPa and is the most widely used CP Ti alloy. Examples of applications are skin panels and fire walls in aircraft and tubing in heat exchangers.
- Grade 3 (0.40O–0.5Fe) is confined mainly to pressure vessels.
- In addition, a composition containing 0.2% palladium (IMI 260) has been developed that has a particularly high resistance to corrosion.

Use of the alloy Ti–5Al–2.5Sn has declined in recent years because alloys with better forming properties and higher creep resistance have become available. However, there has been one continuing application in cryogenic storage tanks for which the relatively high strength of Ti alloys at low temperatures is attractive. A special grade that is low in interstitial elements (designated extra low interstitials (ELI)) has been developed in the United States of America to increase the toughness of the alloy, and it has been used to store liquid hydrogen ($-253\ ^{\circ}C$). Ti alloy pressure vessels, overtaking the lightweight aluminum and the high-strength stainless steel, have become standard for fuel storage in a number of space vehicles because their specific strengths are approximately double at such temperatures.[1]

2.11.4.1.2 Near α-Ti alloys

Demands for higher operating temperatures in the compressor section of aircraft gas turbine engines, as part of the continuing quest for improved performance and efficiency, made way for development of this class of forging alloys. They possess higher tensile strength at room temperature than do the fully α alloys, and they show the greatest creep resistance of all Ti alloys at temperatures above approximately $400\ ^{\circ}C$. The American composition Ti-8-1-1 and the British alloy IMI 685, which were used for the forged gas turbine compressor disk or wheel, are a few of the early developed near α-Ti alloys. Bomberger has produced an empirical expression to denote those compositions providing maximum creep strength:

$$36 - 2.6(\%\mathrm{Al}) - 1.1(\%\mathrm{Sn}) - 0.7(\%\mathrm{Zr}) - 27(\%\mathrm{Si}) - 3(\%\ \text{Mo equivalent}) \leq 10$$

where

$$\%\ \text{Mo equivalent} = 1.0(\%\mathrm{Mo}) + 0.67(\%\mathrm{V}) + 0.44(\%\mathrm{W}) + 0.28(\%\mathrm{Nb}) + 0.22(\%\mathrm{Ta}) + 2.9(\%\mathrm{Fe}) + 1.6(\%\mathrm{Cr}) + 1.0(\%\mathrm{Al})$$

To introduce small amounts of β phase into the microstructure and improve forgeability, the near α alloys are prepared with up to 2% of β-stabilizing elements. However, normal strengthening through the decomposition of retained β is insignificantly small because these additions of β-stabilizing elements are normally too small. The improvement in mechanical properties in these alloys arises mainly from the formation of martensitic α' and from the manipulation of α/α' microstructures.

Most near α alloys are forged and heat-treated in the $\alpha+\beta$ phase field to ensure presence of primary α grains in the microstructure. More recently, improved creep performance has been achieved in special compositions by performing these operations at higher temperatures, which places the alloys in the β-phase field and results in a change in the microstructure. The two alloys that show the highest creep resistances (maximum operating temperature 590–600 °C) are IMI834 and Ti 1100, and they are forged in the $\alpha+\beta$- and β-phase fields, respectively.[1]

2.11.4.2 α/β Alloys

There are limitations in strength that can be developed in the fully α alloys because of the ordering reaction occurring at higher solute contents. Also, these alloys are difficult to hot-form. These drawbacks led to the early investigation of compositions containing both the α phases and the β phases. Currently, these α/β alloys have the greatest commercial importance with one composition, IMI 318, comprising more than half the sales of Ti alloys both in Europe and the United States of America. IMI 318, also known as Ti64 (i.e., Ti–6Al–4V), offers the prospect of relatively high tensile strength and improved formability with some sacrifice in creep strength (higher than 400 °C) and weldability. The principal use of this alloy is for forged components, such as in the fan blades of jet engines and as bulkheads in the new Lockheed/Boeing F22 military aircraft. This alloy is currently the most popular choice in the case of both bioprosthetic and implant materials because of its excellent corrosion resistance property.

Most α/β alloys contain α-stabilizing elements to stabilize and strengthen the α phase, together with 4–6% of β-stabilizing elements that allow substantial amounts of β phase to be retained on quenching from the β- or $\alpha+\beta$-phase fields. The β phase commonly undergoes solid solution strengthening, although to a relatively small extent. Subsequent tempering or aging treatments can be utilized to improve the strength properties of α/β alloys to achieve as much as 1400 MPa tensile strength at room temperature. However, hardenability effects on quenching, aggravated by the low thermal conductivity of Ti, restrict most of the compositions from sustaining these levels of strength in thick sections.

As mentioned, the most commonly used α/β-Ti alloy is Ti–6Al–4V, which has many applications as a general purpose

alloy used in the annealed condition. For applications such as fasteners that require higher strength, the alloy is solution-treated high in the $\alpha+\beta$-phase field, quenched, and aged or annealed at approximately 700 °C, which results in a structure comprising equiaxed α grains in a matrix of fully transformed β. The alloy combines a minimum tensile strength of approximately 960 MPa with good creep resistance up to 380 °C. It is particularly used in forgings, but it is also available in plate, sheet, rod, or wire forms.

A number of other α/β forging alloys with greater strengths have been developed for applications such as aircraft engine mounting brackets and undercarriage components. The heat treatment potential of the alloys are explored more; in general, the content of stabilizing elements has been increased so that the M_s temperature is decreased well below room temperature, and significant amounts of β are retained, such as the alloys Ti–6Al–6V–2Zr–0.7 (Fe, Cu) (Ti-662), Ti–6Al–2Sn–4Zr–6Mo (Ti-6246), Ti–4Al–4Sn–4Mo–0.5Si (IMI 551), and Ti–4.5Al–5Mo–1.5Cr (Corona-5). Solution treating in the $\alpha+\beta$-phase field, quenching, and aging are performed to transform the retained β to obtain full strengthening. However, fracture toughness is higher if the alloys are first cooled from the β-phase field. For example, the alloy Corona-5 has plane-strain fracture toughness as high as 155 MPa $m^{-1/2}$, with a tensile strength of 950 MPa, if it is first annealed in the β-phase field. This value for fracture toughness is double than that normally obtained with Ti–6Al–4V and is again attributed to the slower rate of crack propagation through the microstructure containing elongated Widmanstätten laths of the α phase.

2.11.4.3 β Alloys

The β-Ti alloys are defined as those containing enough total alloying elements that enable the β phase to be retained in either a metastable or a stable condition after cooling to room temperature during heat treatment (Figure 2).[1] Alloy compositions that place them between the critical minimum level (β_c) of these stabilizing elements (i.e., where the M_s line intersects the room temperature axis) and the similar intersection point of the β-transus line (β_s) are commonly referred to as metastable β-Ti alloys because they will precipitate a second phase (usually α) upon aging. Stable β alloys have more highly alloyed compositions to the right of β_s and could not be hardened by heat treatment.

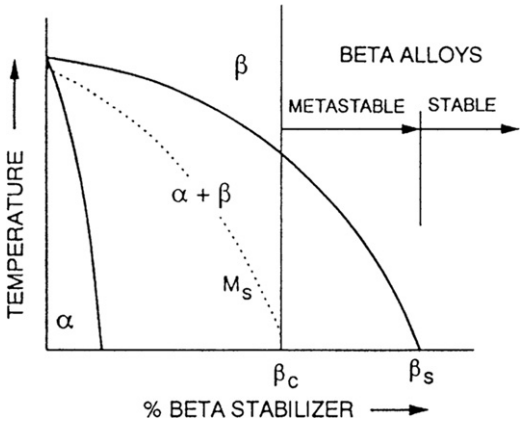


Figure 2 Pseudo-binary β-isomorphous phase diagram showing locations of metastable and stable β-Ti alloys.[1]

Molybdenum (Mo) is a well-known β-stabilizing element. The general class of β alloys has been arbitrarily defined as those having a Mo equivalent content ≥ 10. A formula for calculating the Mo equivalent value was shown in Section 2.11.4.1.2. In its application to β-Ti alloys, the Al content is subtracted to reflect the opposite effect of this element in stabilizing the α-Ti phase. In addition to Mo, those most widely used in β-Ti alloys are V, Cr, and Fe (Figure 3).[4]

The superior forming characteristics anticipated from the bcc structure attracted attention to the β-Ti alloys. Moreover, the prospect of cold-forming in a relatively soft condition and then strengthening by age-hardening is a very useful processing characteristic for any material because a combination of both flowability and strength can be imparted in the alloy. The presence of a high content of solute elements increases hardenability, which may allow the through hardening of thick sections during heat treatment. Such high contents of β stabilizing elements did, however, cause problems with ingot segregation and tend to increase density.

The first commercially used alloy was the composition Ti–13V–11Cr–3Al, which may be solution-treated, quenched, cold-formed, and aged at 480 °C to give a tensile strength as high as 1300 MPa. Strengthening is mainly due to a combination of solid solution hardening of the β phase and precipitation hardening, achieved by precipitation of a fine dispersion of the β phase in the α matrix. Due to formation of the ω phase in the heat-affected zones, the weldability of the alloy is somewhat poor. Moreover, it is proven to be unstable if exposed for long durations at temperatures higher that 200 °C because such treatment causes precipitation of the compound $TiCr_2$, thus reducing the toughness of the alloy. Another relatively early β alloy was the medium-strength British composition Ti–15Mo (IMI 205), which has found applications in the chemical industry.

2.11.5 Heat Treatment of Ti alloys

Heat treatment of any material is dependent entirely on the desired microstructure, properties, and constituents. The heat treatment of Ti alloys is mainly dependent on the desired phases of the alloy: whether α or β or $\alpha+\beta$ or any of these with retained ω phase. Generally, the α alloys are nonheat-treatable. Heat treatment of the α alloy (e.g., CP Ti) from the β-phase region results in a microstructure that contains other phases along with the hcp α phase.

2.11.5.1 Heat Treatment in α-Ti Alloys

2.11.5.1.1 Heat treatment in CP Ti and α-Ti alloys

In CP Ti and α-Ti alloys, which have single-phase microstructures, the tensile strengths are relatively low. However, their high thermal stability leads to reasonable creep resistance and toughness. The α alloys contain stabilizing elements such as Al, Sn, Zr, and O. These alloying elements give rise to substantial solid solution hardening, thereby increasing tensile

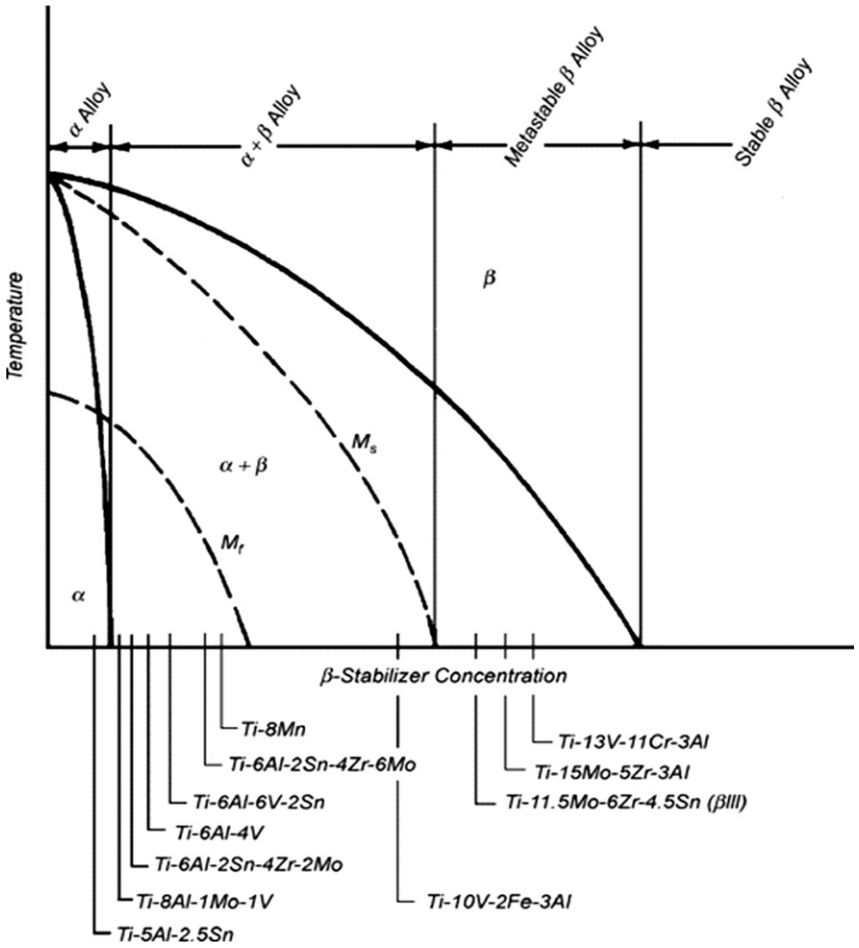


Figure 3 Ti and β-Ti stabilizers phase diagram with positions of some common alloys.[4]

strengths by increments of 35–70 MPa for each percent of the added element.[5] Examples of such alloys are: CP Ti grade 1, Ti–0.5Fe–0.4O–0.05N–0.08C–0.015H; CP Ti grade 2, Ti–0.25Fe–0.08C–0.2O–0.03N–0.015H; CP Ti grade 3, Ti–0.03Fe–0.2O–0.05N–0.08C–0.015H; and CP Ti grade 4, Ti–0.2Fe–0.15O–0.08C–0.015H.[6]

For heat treatment, the alloys are heated to the β-phase field (**Figure 3**) and then cooled by various means as follows:

- Annealing from the β-phase field in CP Ti produces an equiaxed hcp α-phase microstructure.
- Quenching from the same region changes the hcp α phase to martensitic hexagonal α' phase and remaining β grains.
- Air cooling of CP Ti from the β-phase field forms Widmanstätten α plates (**Figure 4**).

2.11.5.1.2 Heat treatment in near α-Ti Alloys

The additions of small amounts of β-stabilizing elements extend the $\alpha + \beta$ temperature range sufficiently to allow both α/β and β hot working.[7] Although these alloys contain some β phase in the microstructure, they behave more like α alloys than α/β alloys. The higher strength of these alloys in comparison to the α alloys arises mainly from the formation of the α' (martensitic) phase or α/α' microstructures during heat treatment. Many near α alloys are thermomechanically processed in the $\alpha + \beta$-phase field, such as those usually found for Ti–2.25Al–11Sn–5Zr–1Mo–0.2Si (IMI 679) and Ti–8Al–1Mo–1V (Ti-8-1-1). To improve creep performance, some alloys such as Ti–6Al–5Zr–0.5Mo–0.25Si (IMI 685), Ti–5.5Al–3.5Sn–3Zr–0.25Mo–1Nb–0.3Si (IMI 829), and Ti–6Al–2.75Sn–4Zr–0.4Mo–0.45Si (Ti-1100) are hot-worked and heat-treated in the β-phase field. Silicon (Si) (an element that dissolves in the α phase and forms silicides as well) is frequently added to increase the strength and creep resistance of these alloys.[8]

Heat treatment of near α-Ti alloys can be classified in two broad categories according to the temperature of heating of the alloy:

- the alloys can be heated to the $\alpha + \beta$-phase field, and
- the alloys can be heated to the β-phase field.

Heat treatment from the $\alpha + \beta$-phase field is possible when the alloys have sufficient amount of α stabilizers without severe loss of ductility. Small amounts of β stabilizers (Mo, V, etc.) are added to promote the response to heat treatment. The alloy is heated to a temperature to obtain an equal amount of α and β phases. Normalizing from this temperature produces equiaxed primary hcp α phase and Widmanstätten α formed by nucleation and growth from the β phase. Quenching from that temperature transforms β into a martensitic hexagonal α'

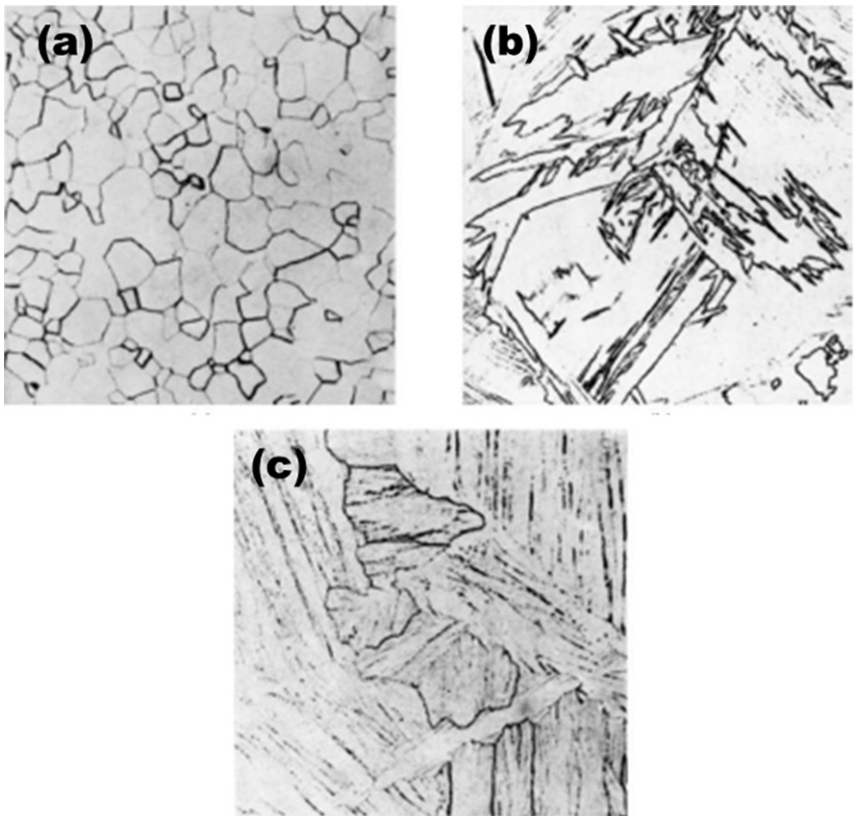


Figure 4 Microstructure of CP Ti: (a) annealed from the β-phase field showing equiaxed hcp α phase, (b) quenched from the β-phase field to obtain martensitic hexagonal α' phase, and (c) air-cooled from the β-phase field forming Widmanstätten α plates.[1]

phase, which gives higher strength. The high-temperature flow curves of CP Ti grade 2,[9] Ti–5Al–2.5Sn,[10] Ti–6Al–5Zr–0.5Mo–0.25Si (IMI 685),[11] and Ti–5.8Al–4Zr–4Sn–1Nb–0.5Mo–0.35Si (IMI 834)[12] are shown in **Figures 5–8**, respectively. It is evident that all the flow curves show an initial work-hardening region followed by a regime of near steady-state flow. Higher peak stresses are observed at higher strain rates and lower temperatures, as shown for CP Ti in **Figure 9**.[13] Comparison of the properties of CP Ti grade 2 and several α alloys (**Figure 10**) reveals that the flow stress at a given temperature increases with the Al equivalent.[14] The increased steady-state stress of α-Ti with Al addition is shown in **Figure 11**.[15] Similar behavior is also observed when the flow stress data are presented in terms of T-T_β, where T is the deformation temperature. For example, Ti–5.8Al–4Zr–4Sn–1Nb–0.5Mo–0.35Si (IMI834) has a total of approximately 15 wt% alloying elements and displays a much higher flow stress than CP Ti grade 2 with only approximately 0.6 wt% additions (**Figure 12**).[14] This increase in flow stress is mainly associated with an increase in substitutional solute strengthening.

Deformation below the β transus is typical of material undergoing dynamic recovery in which the rate of hardening by multiplication of dislocations is balanced by the rate of softening due to dislocations annihilation, thus resulting in the constant flow stress deformation.[16,17] This is very similar to the flow behavior of α-Zr, for which an initial period of hardening followed by steady-state flow is also frequently observed.[18] The apparent activation energy for the deformation of α-Ti alloys has been found to be in the range 200–360 kJ mol^{-1},[18] which is similar to that for creep, as determined over a wide range of strain rates, but is somewhat higher than the activation energy ($\sim$150 kJ mol^{-1}) for self-diffusion in α-Ti.[19] The α-phase flow stress is dependent on strain rate through a power law with an exponent of approximately 4.5 (**Figure 13**).[20] Furthermore, the high-temperature steady-state deformation behavior of α-Ti can be represented by the Dorn equation (eqn [1]),[15] provided that the temperature dependence of the shear modulus is taken into account. The equation gives creep rate as:

$$\dot{\varepsilon} = 8.0 \times 10^4 D \left(\frac{Gb}{kT}\right)\left(\frac{\sigma}{G}\right)^{4.1} \qquad [1]$$

where D is the diffusivity depending on the mechanism of creep, G is the shear modulus, σ is the stress involved, T is the temperature, b is the Burger vector, and k is the Boltzmann constant.

The dependence of the normalized steady-state stress (s) on the normalized strain rate ($\dot{\varepsilon}$) for deformation in the temperature range of 600–850 °C for material with fine α (0.1 mm) or coarse α (1 mm) grains is shown in **Figure 14**.[21] The α-Ti alloys were previously classified as CP Ti, α alloys, and near-α alloys. It is important to emphasize that for CP and α alloys, hot deformation below the β transus occurs in the α-phase field. However, for near α alloys, sub-transus hot deformation takes place in the $\alpha + \beta$-phase field.

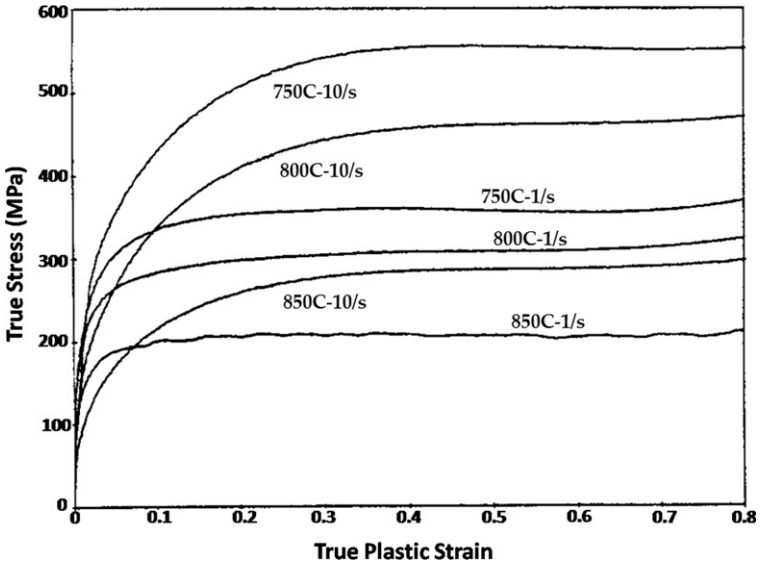


Figure 5 Flow curves for CP Ti grade 2 at various sub-transus temperatures and strain rates.[9]

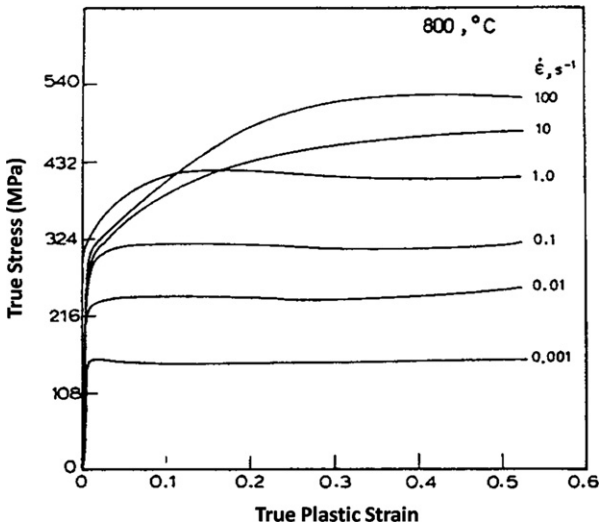


Figure 6 Flow curves for Ti–5Al–2.5Sn at 800 °C and various strain rates.[10]

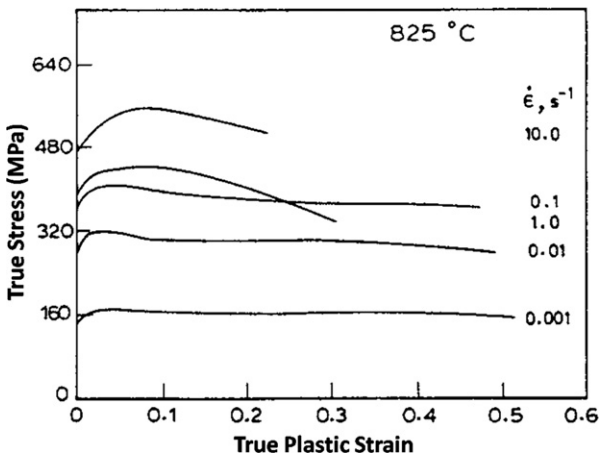


Figure 7 Flow curves for IMI 685 at 825 °C and various strain rates.[11]

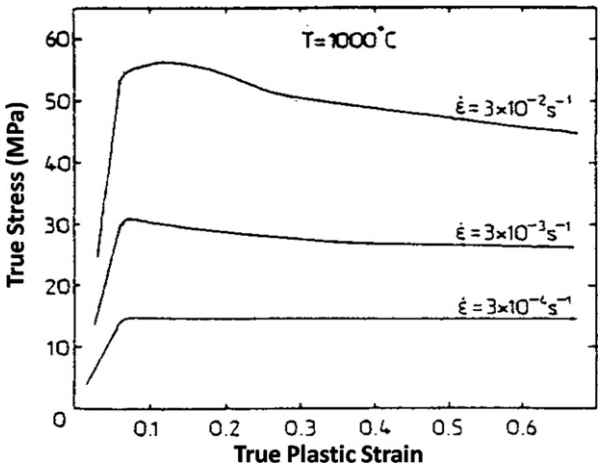


Figure 8 Flow curves for IMI 834 at 1000 °C and various strain rates.[12]

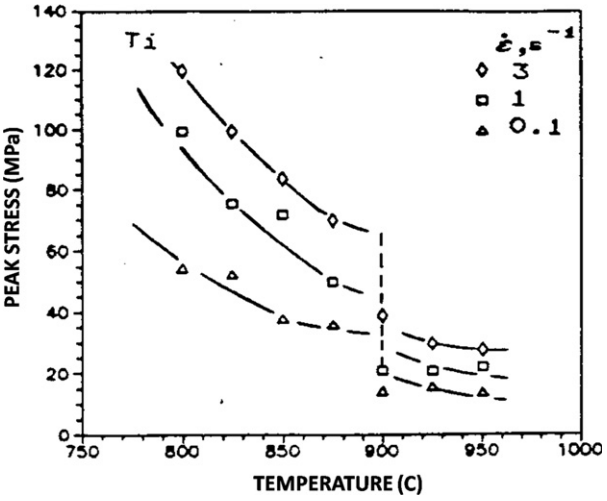


Figure 9 Peak flow stress as a function of strain rate and temperature for CP Ti grade 2.[13]

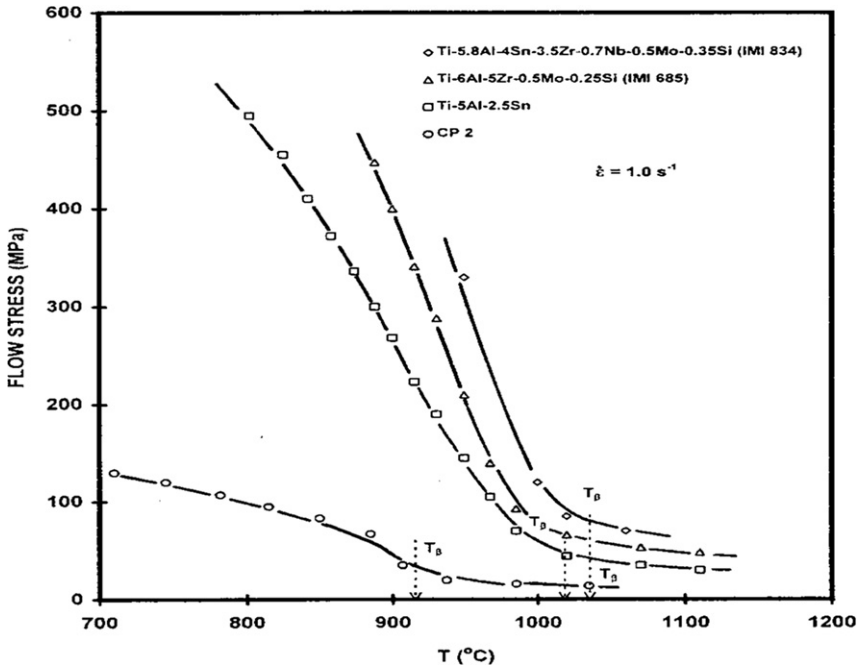


Figure 10 Flow stress of various α and near α-Ti alloys as a function of temperature for a strain rate of 1 s^{-1}.[14]

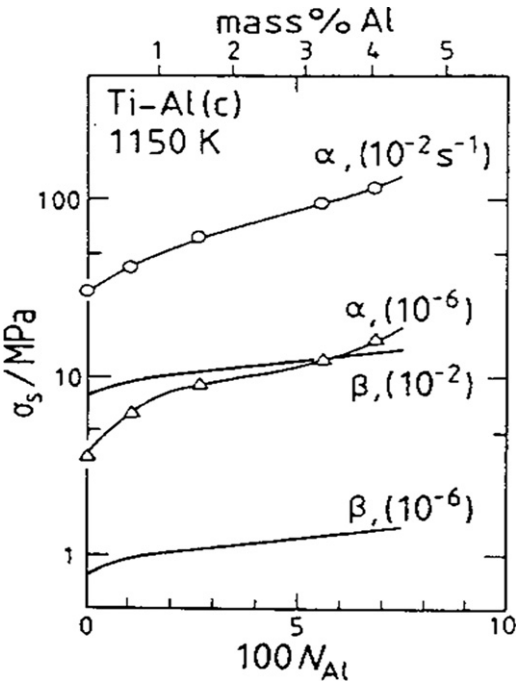


Figure 11 Steady-state stress of α and β Ti–Al solid solutions as a function of solute concentrations at 875 °C.[15]

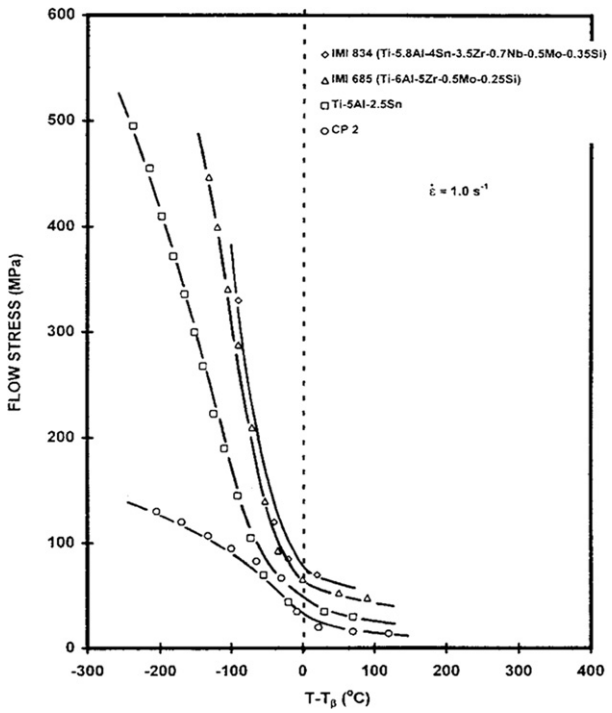


Figure 12 Flow stress of various α and near α-Ti alloys as a function of T–T_β at a strain rate of 1 s^{-1}.[14]

Typical microstructures after hot deformation are shown in Figure 15[11,13] for CP Ti grade 2 and IMI 685 alloys, respectively. The elongated grains observed in Figure 15 are the result of deformation of alloy with an initially equiaxed microstructure at 800 °C and a strain rate of 0.1 s^{-1} to a strain of approximately 0.7.[13] Similarly, the IMI 685 alloy with an initially acicular microstructure deformed at 975 °C, and a strain rate of 10^{-3} s^{-1} to a strain of approximately 0.5 also developed an elongated α grain structure containing the lamellar and equiaxed α phase morphology shown in Figure 16.[11] The α-Ti alloys deformed by slip on basal and prismatic planes give rise to sub-grain structures, which are less recovered than those found in β-Ti alloys.[14] For example, Figures 17 and 18

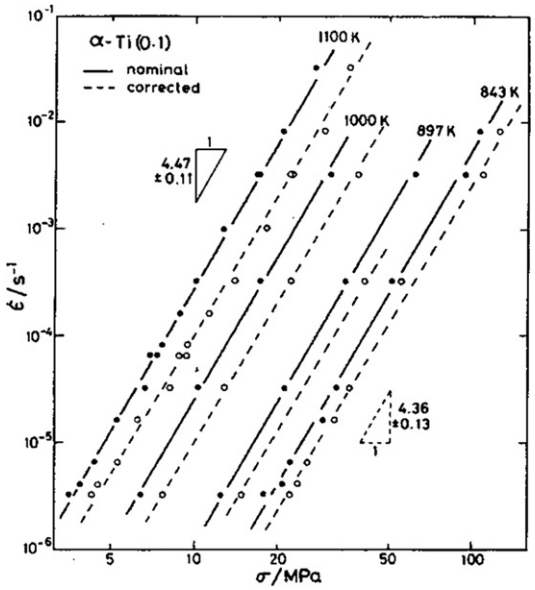


Figure 13 The maximum stress (broken line) and the steady-state stress (solid line) as functions of strain rate for fine-grain α-Ti.[20]

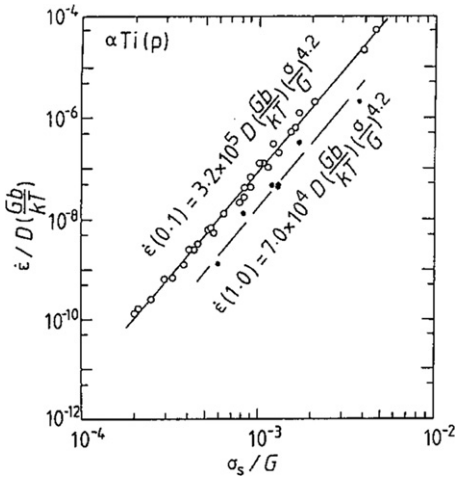


Figure 14 Relationship between the normalized steady-state stress and the normalized strain rate of α-Ti. Solid marks represent coarse-grain samples and open marks represent fine-grain material.[21]

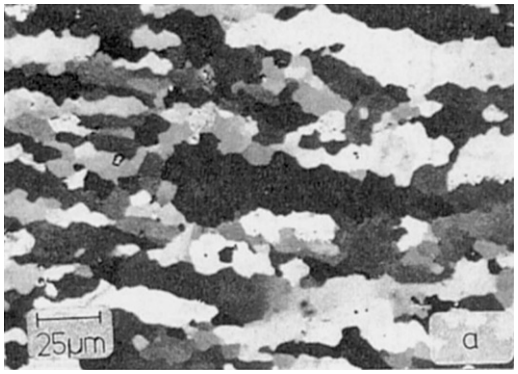


Figure 15 Microstructure of CP Ti grade 2 after hot compression at 800 °C, 0.1 s^{-1} to a strain of 0.7.[13]



Figure 16 Microstructure of IMI 685 after hot compression at 975 °C and 10^{-3} s^{-1} to a strain of 0.5.[11]

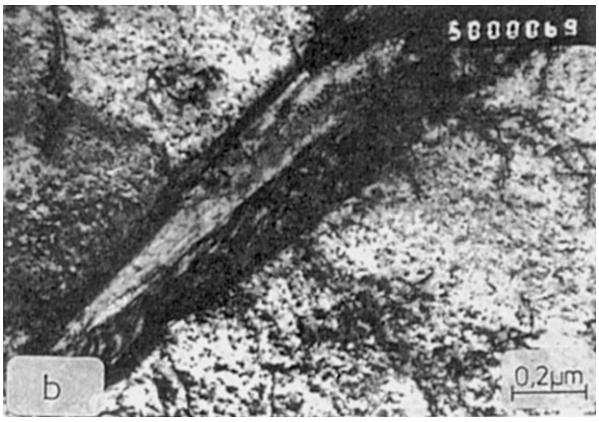


Figure 17 Substructure formed in CP Ti grade 2 after hot compression at 800 °C and 0.1 s^{-1} to a strain of 0.7.[13]



Figure 18 Substructure formed in the α phase of IMI 685 after hot compression at 975 °C and 10^{3} s^{-1} to a strain of 0.5.[11]

show the dislocation substructures in CP Ti[13] and IMI 685[11] alloys, respectively. Sub-grain formation is more pronounced in the α phase of IMI 685.

The control of microstructure and deformation uniformity is of great importance in optimizing final mechanical properties. The selection of process parameters such as deformation temperature, strain rate, and deformation rate to avoid

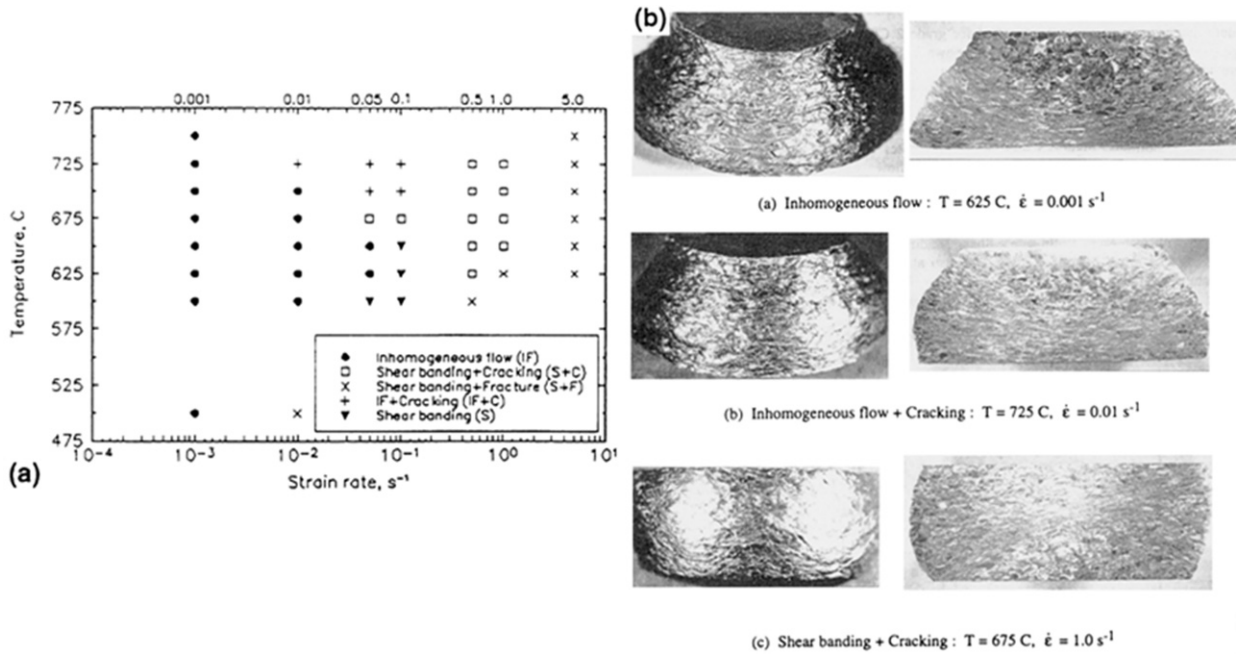


Figure 19 (a) Processing map and (b) corresponding macrographs of the cylindrical surface and the macro-etched longitudinal section of the hot compression samples used to establish the processing map for CP Ti grade 2 magnification of 4.[22]

nonuniform microstructure, strain localization, and failure may be aided by the utilization of processing maps shown in Figure 19.[22] The development of this processing map for α-Ti alloys was based on the appearance of deformed compression samples and the identification of temperature and strain rate conditions that lead to macroscopically uniform deformation. Different deformation modes are identified, including inhomogeneous flow, shear banding, and cracking (Figure 19(b)), which can lead to material failure. The corresponding map for CP Ti grade 2 (Figure 19(a)) delineates these failure modes and identifies those processing parameters that result in uniform deformation. In addition to deformation temperature, strain rate, and total strain, the material starting microstructure can have an important effect on flow stability, workability, and failure.[23] For example, CP Ti grade 2 (0.12 w% O, 0.03 w% Fe) with an acicular starting microstructure exhibits high flow stresses and flow softening during high-temperature deformation (Figure 20).[24] However, CP Ti grade 3 (0.28 w% O, 0.2 w% Fe) with an equiaxed starting microstructure shows lower flow stresses and work hardening during deformation (Figure 20). When CP Ti grade 3 with an equiaxed microstructure is heat-treated to produce a Widmanstätten microstructure, the flow stress increases and slight flow softening is detected (Figure 20).

The near-α alloy IMI 834 was developed to meet the need for a material with a good blend of fatigue and creep properties that could be processed readily.[25–27] This property combination is obtained by α–β processing to produce a microstructure of 7.5–15% equiaxed α in a matrix of transformed β. The small amount of α pins the β-grain boundaries during hot working or heat treatment in the higher region of α + β-phase field. This yields a fine β-grain structure that minimizes the loss of fatigue properties in the presence of a colony of Widmanstätten α microstructures desirable for creep

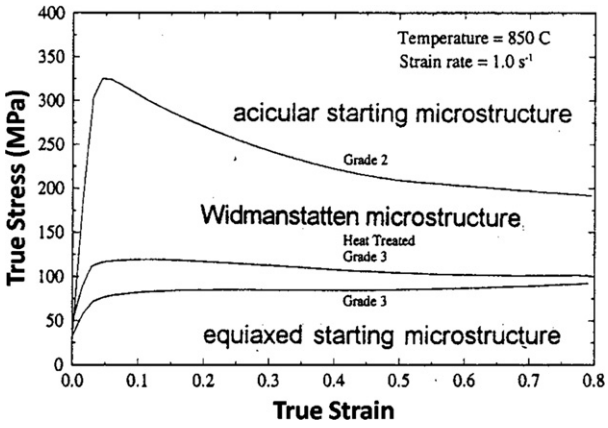


Figure 20 Flow curves of grade 2, grade 3, and heat-treated grade 3 CP Ti at 850 °C and 1 s^{-1}.[24]

performance. Unlike other near-α alloy, IMI 834 has a shallow β-approach curve (Figure 21),[26] an attribute that enhances the ability to control the volume fraction of α near the β transus under typical production conditions. Such a β-approach curve is obtained through an intentional carbon addition to the alloy; the carbon also provides an increase in strength, much like oxygen.

When the alloy is heated to the β-phase field, then different microstructures are obtained depending on the cooling rate. Quenching from the β-phase field produces laths of the martensitic α′ phase, which are delineated by thin films of β phase. Normalizing from the β-phase field gives rise to a 'basket-weave' structure of Widmanstätten α phase delineated by β phase. Aging causes precipitation hardening by precipitation of the α-phase dispersion. Flow curves of CP Ti grade 2,[9] Ti–5Al–2.5Sn,[10] Ti–6Al–5Zr–0.5Mo–0.25Si (IMI 685),[11] and IMI

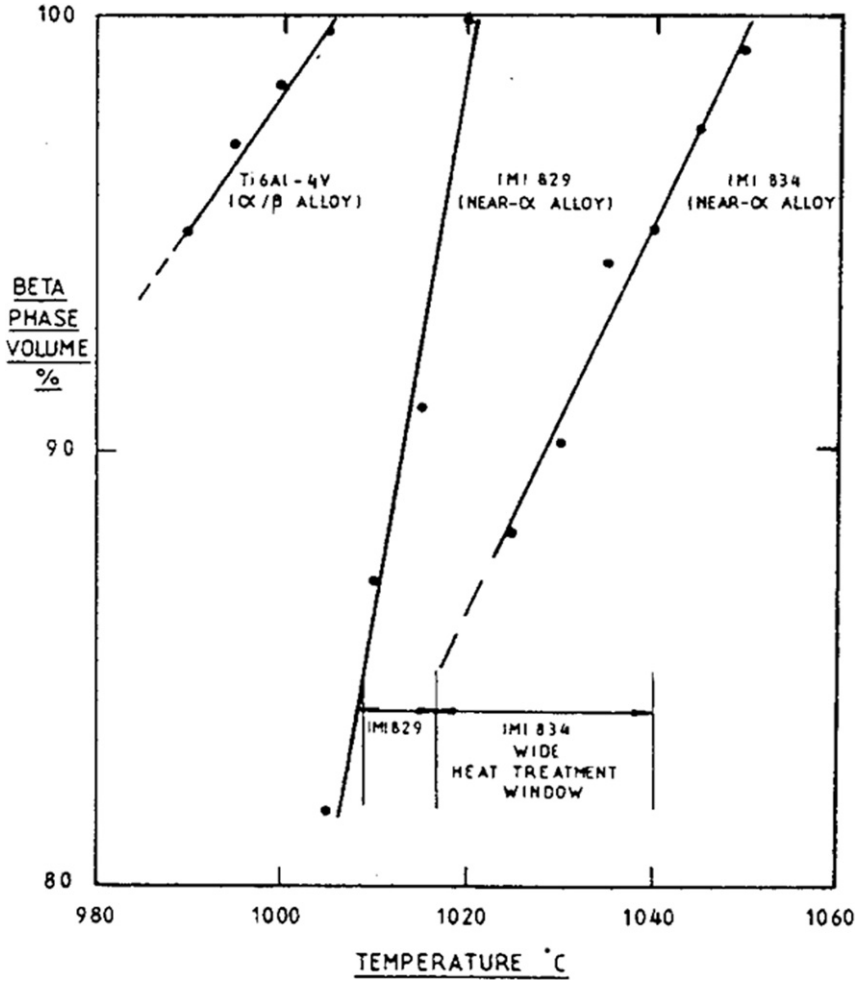


Figure 21 β-Approach curves for IMI 834, IMI 829, and Ti–6Al–4V.[26]

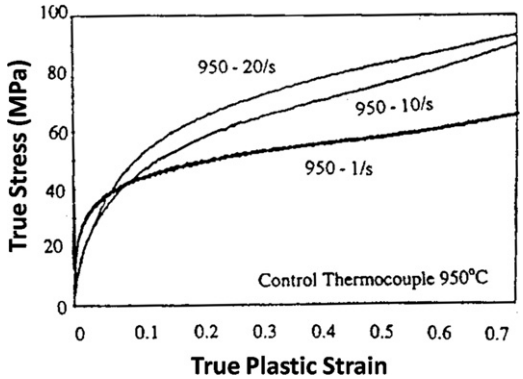


Figure 22 Flow curves for CP Ti grade 2 measured above the β-transus temperature.[9]

834[12] at super-transus temperatures are shown in Figures 22–25, respectively. After yielding, a substantial amount of work hardening is observed, especially for CP Ti. The work-hardening period is followed by steady-state flow at high strains, particularly for high-temperature and low-strain rate conditions. The deformation in the β-phase field is typical of

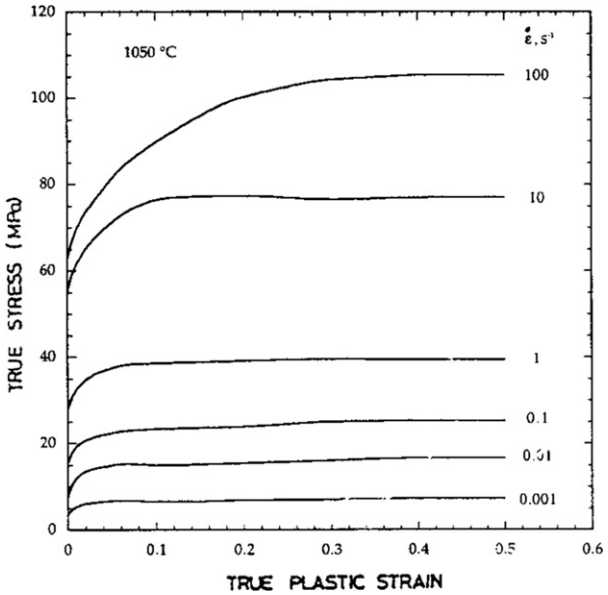


Figure 23 Flow curves for Ti–5Al–2.5Sn measured above the β-transus temperature.[10]

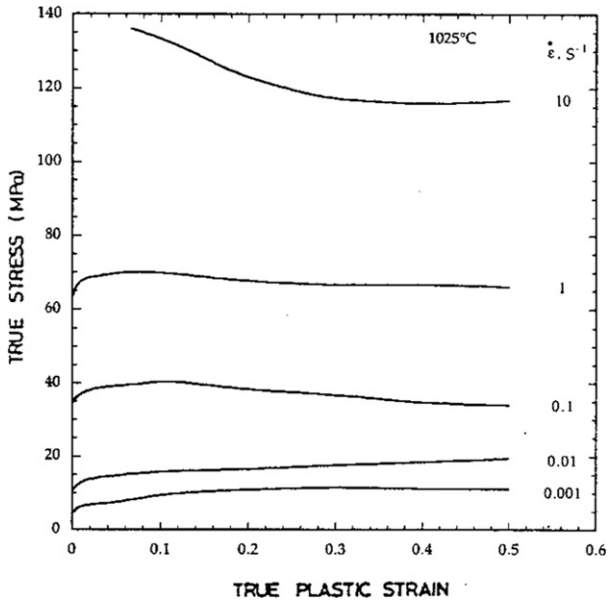


Figure 24 Flow curves for IMI 685 measured above the β-transus temperature.[11]

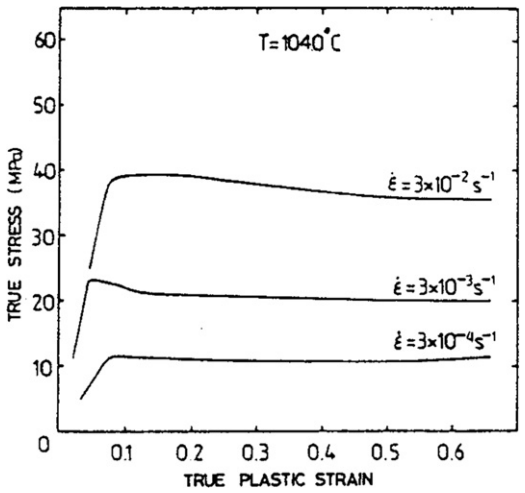


Figure 25 Flow curves for IMI 834 at 1040 °C.[12]

that in material undergoing dynamic recovery, which gives rise to well-developed sub-grains. Under some conditions, flow softening is also observed (**Figures 24** and **25**). Although the bulk of the flow softening observed at high strain rates probably results from deformation heating, some of it may also be ascribed to texture softening of the β phase.

The high-temperature steady-state deformation behavior of CP Ti in the β-phase field can also be represented by the generalized Dorn equation, as given in eqn [1] in Section 2.11.5.1.2,[15] as long as the temperature dependence of the shear modulus is taken into account (**Figure 26**).[21] At high temperatures ($T>0.6T_M$), plastic deformation can be rationalized in a similar way that creep deformation is analyzed, especially in the deformation range where power law creep is operating. At very high temperatures above $0.8T_M$, dynamic recrystallization has also been observed to occur, resulting in

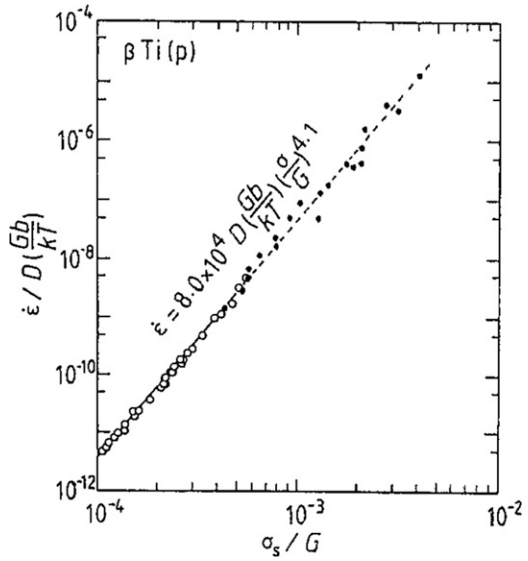


Figure 26 Relationship between the normalized steady-state stress and the normalized strain rate of CP Ti.[21]

the formation of recrystallized grains along the deformed β-grain boundaries (**Figure 27**).[28] Hot deformation in the β-phase field yields apparent activation energy in the range of 180–220 kJ mol^{-1}, which is close to the activation energy for self-diffusion in β Ti (i.e., 153 kJ mol^{-1}).[19,29]

A variation of Ti–6Al–2Sn–4Zr–2Mo–0.1Si, Ti-1100 (Ti–6Al–2.75Sn–4Zr–0.4Mo–0.45Si) is an alloy designed to provide enhanced creep resistance to a temperature of approximately 600 °C. This is accomplished through alloying (increased silicon and thus silicides) and thermomechanical processing in the β-phase field to produce a colony of Widmanstätten α microstructure on cooling. The alloy has a β-transus temperature close to 1015 °C and silicide solvus at 1040 °C. Previous work[30,31] has shown that the creep resistance and post-creep ductility of Ti-1100 were not too sensitive to β-forging temperature and cooling rate following forging, provided that forging was performed above the silicide solvus. In addition, β-forging plus direct stabilization aging provided better post-creep ductility than β-forging plus β-annealing plus aging. Subsequent efforts[32] have shown that fan cooling or oil quenching following β-forging may be required to obtain optimal properties in thick-section forgings. Most recently, it has also been found that sub-transus hot working of Ti-1100 followed by solution heat treatment at temperatures between the β transus and silicide solvus may provide the optimal combination of strength, creep, and fatigue properties.[33] In this processing route, the presence of silicides during β-solution heat treatment restricts β-grain growth and therefore minimizes the concomitant loss of strength, ductility, and high cycle fatigue properties associated with the development of coarse β grains during thermomechanical processing above the silicide solvus.

There are two typical annealing treatments for the near α-Ti alloys: (1) mill annealing and (2) duplex annealing. Mill annealing is a general purpose treatment given to all mill products. It is not a full anneal and can leave traces of cold or warm working in the microstructure of heavily worked

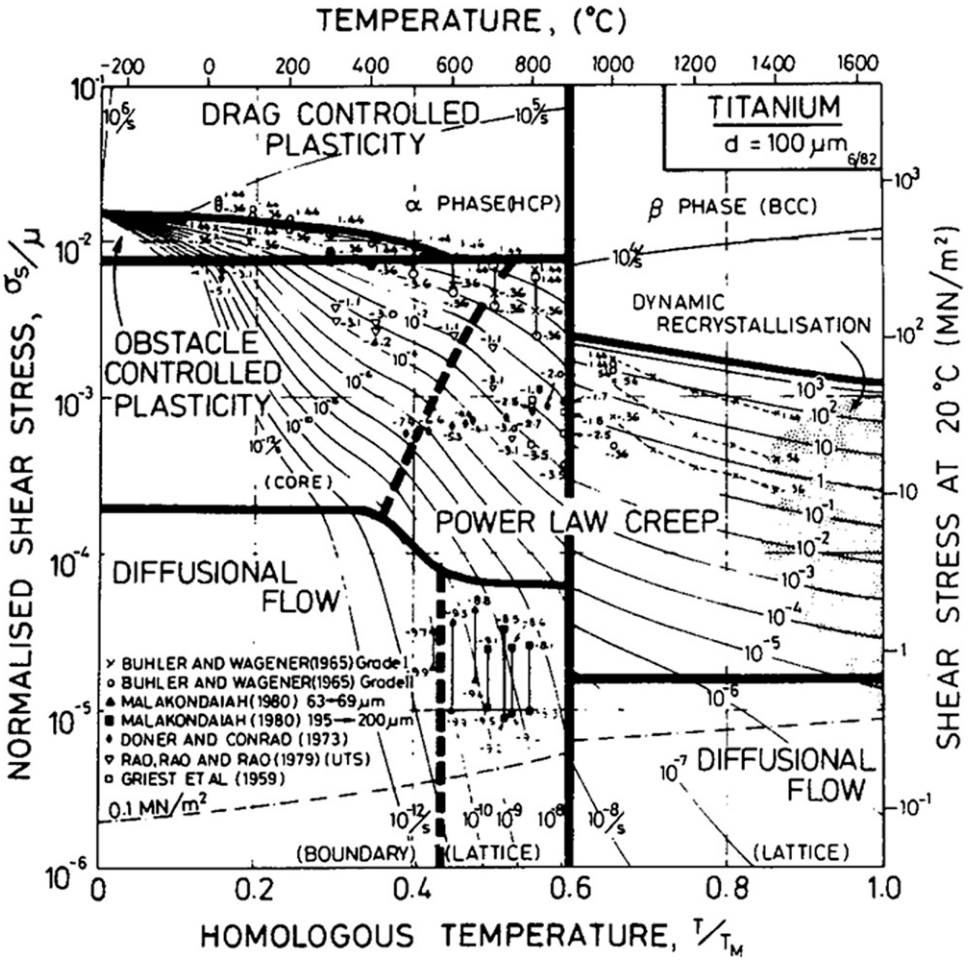


Figure 27 A stress–temperature map for Ti with grain size of 100 mm.[28]

products (particularly sheet). Duplex annealing is an example of the multiple annealing processes that sometimes are specified. This modifies the shapes, sizes, and distributions of phases as required for improved creep resistance and/or fracture toughness. For example, in the duplex annealing of the Corona 5 alloy, the first anneal is near the β transus to globularize the deformed α and to minimize its volume fraction, followed by a second lower-temperature annealing to precipitate new lenticular (acicular) α between the globular α particles. This formation of acicular α is associated with improvements in creep strength and fracture toughness.[6]

2.11.5.2 Heat Treatment in α/β-Ti Alloys

In α/β-Ti alloys, heat treatment can be achieved with incorporation of thermomechanical processes to achieve the desired microstructure and hence, desired properties. These alloys can be strengthened by a series of heat treatment, solution treatment and aging (STA). Ti–6Al–4V, the most popular α/β alloy, is not an exception, and its tensile strength level is raised from 900–1000 MPa in the annealed state to 1100–1200 MPa.[34] Ti–Al–Fe-based α/β alloys such as Ti–5Al–2.5Fe,[35] TIMETAL 62S,[36] and Ti–5.5Al–1Fe,[37] all of which have been developed in the past 15 years, have also been subjected to STA[35,38] in an attempt to increase the strength level. Ti–5.5Al–1Fe has been developed as a low-cost substitute for Ti–6Al–4V[33,34] and has almost the same strength level, β-transus, and M_s temperature as Ti–6Al–4V. The phase transformation of this alloy during STA was examined and compared to that of Ti–6Al–4V.

The STA process is more effective for alloys with an equiaxed microstructure than those with the Widmanstätten structure because strengthening by STA is accompanied by a decrease of ductility, and an equiaxed microstructure exhibits sufficiently higher ductility, unlike Widmanstätten structure. In this respect, near-net shape (NNS) products manufactured by powder metallurgy or casting are not always effectively strengthened by STA because they usually have the Widmanstätten structure. For NNS products, thermochemical processing, in which hydrogen is used as a temporary alloying element, is considered to be effective for the improvement of mechanical properties through microstructural refinement.[39] However, this process generally involves a large amount of hydrogen, and thus hydrogen embrittlement results in the increase of the production cost, which may be one of the reasons hampering its application on an industrial scale. Thus, a new and less costly thermochemical process is introduced based on the previous work[40] on the phase transformation of the hydrogen-added Ti–6Al–4V.

For Ti–6Al–4V, solution treatment at 955 °C followed by water quenching and aging at 538 °C for 4–8 h is used as the standard STA condition.[34] On quenching from the solution treatment temperature, almost all of the β-phase transforms to the α' lath martensite or the fine lath α plates.[34,41] Aging stabilizes those phases to the stable fine acicular α/β structure.[34] For Ti–5.5Al–1Fe, the best relationship between strength and ductility can be obtained by solution treatment at 940 °C, followed by water quenching and aging at 500 °C for 4–8 h.[38]

Tensile properties are shown in Figure 28.[42] The 0.2% proof stress of the as-solution treated alloys was lower than that of the annealed one. However, by following aging at 500 °C for 4–8 h, 0.2% proof stress and tensile strength increased by approximately 100 MPa and 50 MPa, respectively. Aging for 8 h or longer led to overaging, resulting in the decrease of strength level.

The evolution of the phases after different heat treatment schedules is presented in Figure 29.[42] Peaks corresponding to α and β phases appear in the specimen after annealing. In the solution-treated specimen, the diffracted X-ray intensity of the β phase was decreased, whereas the intensity was increased at both sides of the (110) β peak, which corresponds to the (020) and (111) planes of orthorhombic α'' martensite. In fact, the α'' phase was confirmed by transmission electron microscopy (TEM) analyses as shown (Figure 30).[42] Aging at 500 °C for 4 h reduced the intensity of the β phase. Although a clear (110) β peak did not appear, a small amount of the β phase was detected by TEM (Figure 31).[42] The intensity of the β phase was further reduced in the specimen aged at 500 °C for 8 h, whereas there was a strong peak corresponding to FeTi compound in place of the β.

Figure 30 shows the microstructures of the solution-treated specimen. The transformed β phase is composed of the fine acicular α'' martensite (orthorhombic) and the retained β phase (bcc). The microstructures of the aged specimen are shown in Figure 31. It is noticeable that there are two kinds of transformed

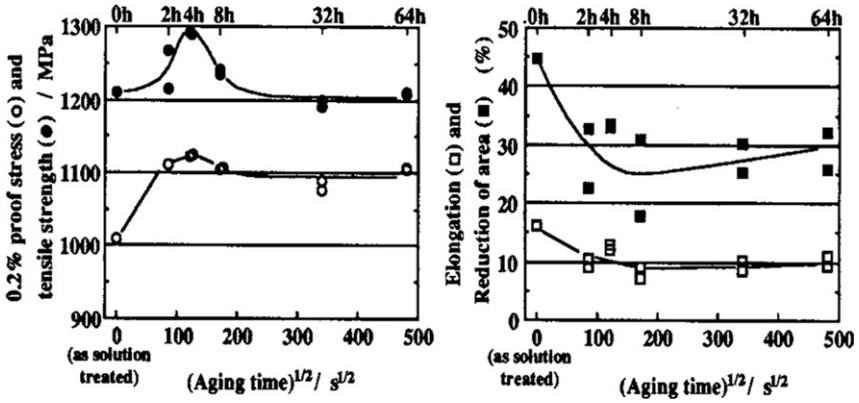


Figure 28 Tensile properties of Ti–5.5Al–1Fe solution treated at 940 °C followed by water quenching and aged at 500 °C for 2–64 h.[42]

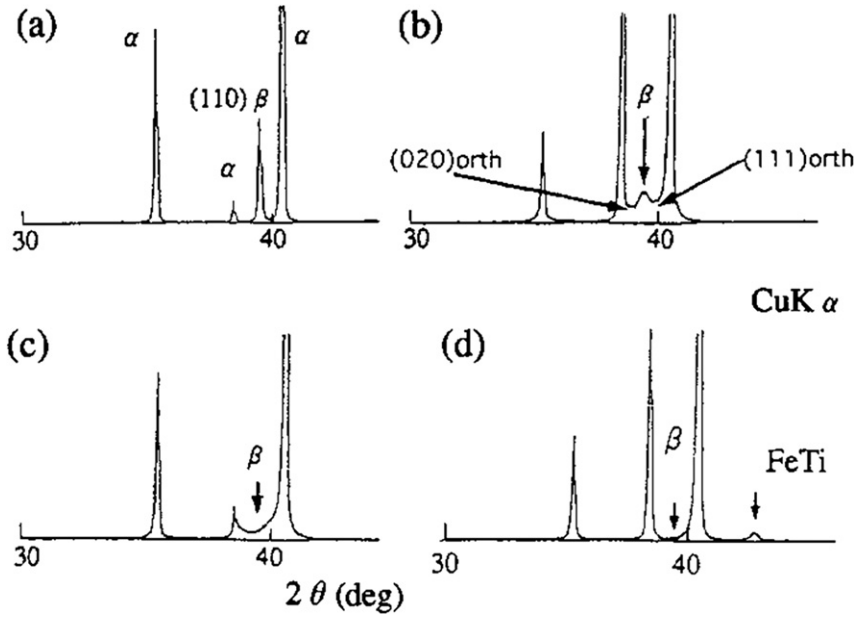


Figure 29 X-ray diffraction analyses for the specimens (a) annealed at 750 °C for 1 h, (b) solution-treated at 940 °C followed by water quenching, plus (c) aged at 500 °C for 4 h, and (d) aged at 500 °C for 8 h.[42]

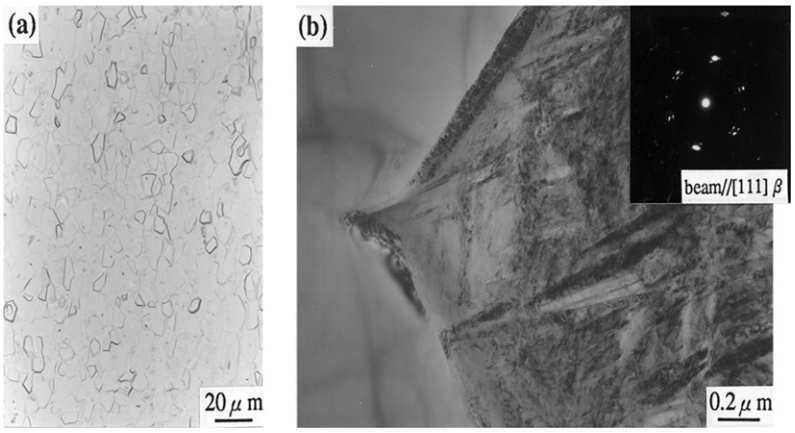


Figure 30 (a) Optical and (b) transmission electron microscopy microstructures of the solution-treated specimen.[42]

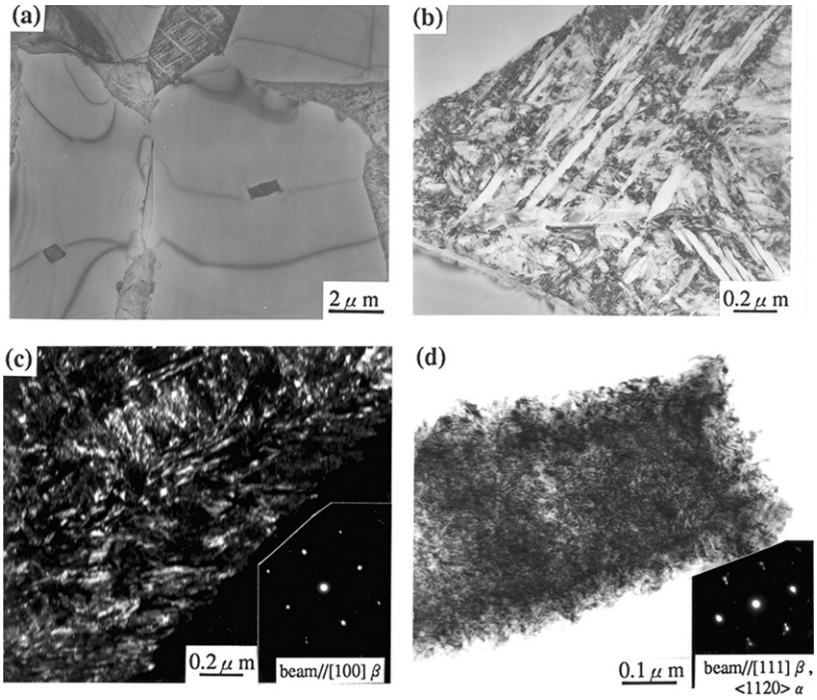


Figure 31 Transmission electron microscopy microstructures of the solution-treated specimen: (a) transformed β phase, which is located between the α grains; (b) transformed β phase, which is located between the fine acicular α phase; (c) the dark field image of the β phase in the transformed β phase in Figure 31(a); and (d) the fine α precipitation in the isolated β phase in the α grain.[42]

β phases. One is the commonly observed transformed β phase, which is located between the α grains (Figure 31(a)), in which a small amount of the β phase is contained as shown in the dark field image (Figure 31(c)) as well as the fine acicular α phase (Figure 31(b)) with similar morphology and size to those of the α'' in the as-solution treated specimen. The other is the isolated β phase existing inside the α grains, in which much finer α particles exist (Figure 31(d)).

The main transformation route that contributes to strengthening is the same in both Ti–6Al–4V and Ti–5.5Al–1Fe, that is, the formation of fine transformation products in the transformed β phase during quenching from the solution treatment temperature and the stabilization of the same, which includes the tempering process. However, there exist few differences between the two alloys.

- First is the morphological difference of the transformation products in the solution-treated alloys; the lath type of the α' or α plates in Ti–6Al–4V and the acicular α'' in Ti–5.5Al–1Fe. The formation of the lath plates is accompanied by the diffusion of the alloying elements and the acicular α'' is formed by complete diffusionless transformation. This indicates that the hardenability of the β phase at the solution treatment temperatures is higher in the Ti–5.5Al–1Fe.

- Second is the larger amount of the retained β phase in the solution-treated Ti–5.5Al–1Fe, which is shown by the relatively strong intensity peak of the diffracted X-ray from (110) β (Figure 29) and a TEM micrograph (Figure 30(b)). This is probably the cause of lower 0.2% proof stress in the solution-treated specimen as a result of the deformation-induced martensite transformation.
- Third is the drastic decrease of the β phase in Ti–5.5Al–1Fe during aging, as shown in Figure 29. The fine martensite is probably converted to the α phase or acts as a nucleation site for the α phase, followed by growth during aging. Although Ti–5.5Al–1Fe is basically an α/β alloy, the aged alloy is liken the α type, which mostly consists of the α phase.
- Fourth is the FeTi formation when the solution-treated alloy is aged at 500 °C for more than 32 h. Although conspicuous deterioration is not detected in tensile properties, unnecessarily longer aging times should be avoided from the viewpoints of fatigue properties and corrosion resistance. The FeTi formation is reportedly very sluggish, and it takes 500–1000 h of exposure at approximately 500 °C in a binary Ti–Fe system.[43] However, the addition of the α stabilizer seems to accelerate it. The faster FeTi formation is also reported in the annealed alloy when exposed at 450 °C for 64 h or longer[37,38] and in Ti–Fe–O–N systems.[43]
- Fifth is the isolated β phase inside the α grains. Such morphology is not seen in Ti–6Al–4V, and it may be a feature of Ti–Fe-based alloys. The fine α particles in this β are probably the trace of the ω phase, which precipitates prior to the α formation at the early stage of aging because they are quite similar to the previously observed ones as a result of the direct transformation from the ω particles.[44] The composition of this Fe-enriched β phase is considered to be in the compositional range in which the ω phase easily forms.

Kerr[45] reported that the addition of more than 0.5 (mass %) hydrogen to Ti–6Al–4V generates the hydride phase below the eutectoid temperature. The author has also confirmed that the three-phase region containing α, β, and hydride does not appear in Ti–6Al–4V with 0.4 (mass %) hydrogen even at temperatures lower than 500 °C.[40] Figure 32[40] is the continuous cooling transformation (CCT) diagram of Ti–6Al–4V + 0.4H (mass %).[40] The β transus is 780 °C and the α'' martensite forms at 480 °C (M_s temperature) when the alloy is cooled at cooling rates higher than 30 °C s^{-1}.[40] The martensite phase is quite large in this case and does not contribute to the microstructural refinement. When the alloys are cooled at cooling rates lower than 0.3 °C s^{-1}, the coarse grain boundary α and the sideplate α phase form.[40] Meanwhile, at the intermediate cooling rates from 0.3 to 30 °C s^{-1}, the extremely fine α precipitation occurs in the β grains and the grain boundary α phase rarely appears.[40]

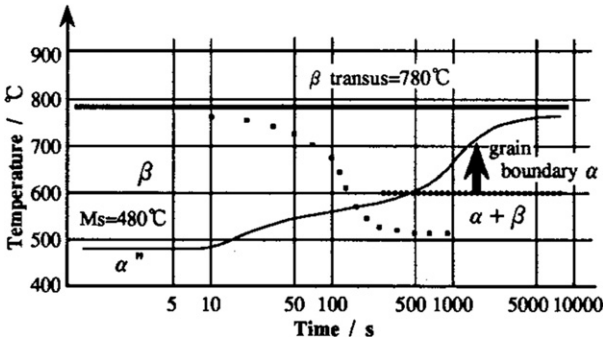


Figure 32 Continuous cooling transformation diagram of Ti–6Al–4V + 0.4 mass % H.[40]

Figure 33[42] shows the microstructural changes that occur during the process. The initial coarse microstructure containing the grain boundary α phase (Figure 33(a)) was converted, by hydrogenation, solution treatment and direct aging, to such a fine microstructure that each α phase could not be distinguished in the optical micrograph (Figure 33(b)) and the fine acicular configuration was made clear by TEM (Figure 33(c)). Another microstructural feature in this specimen is that there is absence of α phase on the grain boundary. No distinct difference was observed between the specimens aged for 1 and 6 h. The microstructure was slightly coarsened and the grain boundary α phase reappeared on a few former β grain boundaries during dehydrogenation at 750 °C for 10 h (Figures 33(d) and 33(e)). However, it is still fine compared with the initial one and no grain boundary α phase was recognized on most of the former β grain boundaries. Mechanical properties of the material aged for 6 h and dehydrogenated are shown in Table 1[46] along with those of the specimens manufactured by the blended elemental powder metallurgy (BE/PM), which generally have a coarse Widmanstätten structure.[46] Tensile strength and fatigue strength were approximately 70 and 90 MPa, respectively, higher in the material processed by the new method, although fatigue strength seems to be lower than that by the conventional process that utilizes hydride.

The α phase is generally coarser in α/β alloys than in β alloys because the precipitation occurs at higher temperature just below the β transus in α/β alloys, whereas the precipitation at lower temperatures is possible in β alloys. In the new process, the α/β alloy is converted to a β alloy temporarily by hydrogen addition and the devised heat treatment pattern to attain the fine α precipitation. The addition of hydrogen lowers the M_s temperature and increases hardenability. However, the amount of hydrogen is not sufficient to lower the M_s temperature below room temperature in Ti–6Al–4V with 0.4 (mass %) hydrogen and to convert the alloy to α/β alloy. Therefore, the heat treatment pattern that consists of solution treatment, relatively rapid cooling to the aging temperature, and direct aging is required in this process. In fact, the aged microstructure shown in Figure 33(c) is quite similar to that of β alloy.[47] Coarsening and reappearance of the grain boundary α phase on a few former β grain boundaries during dehydrogenation may be improved by dehydrogenation at lower temperatures, whereby more improvement of mechanical properties is expected. A few processes that were conducted by Kerr[45] (0.43 and 0.46 mass % hydrogen, solution-treated at 870 °C, followed by air cooling and directly aged at 540 °C for 2 h) are probably the same as the present one, although the exact cooling rate from the solution treatment temperature and the aged microstructure are not shown in their study.

The major advantages of this process are considered to be as follows:

1. The total amount of hydrogen used is low and the time needed for hydrogenation is short compared to the conventional method.

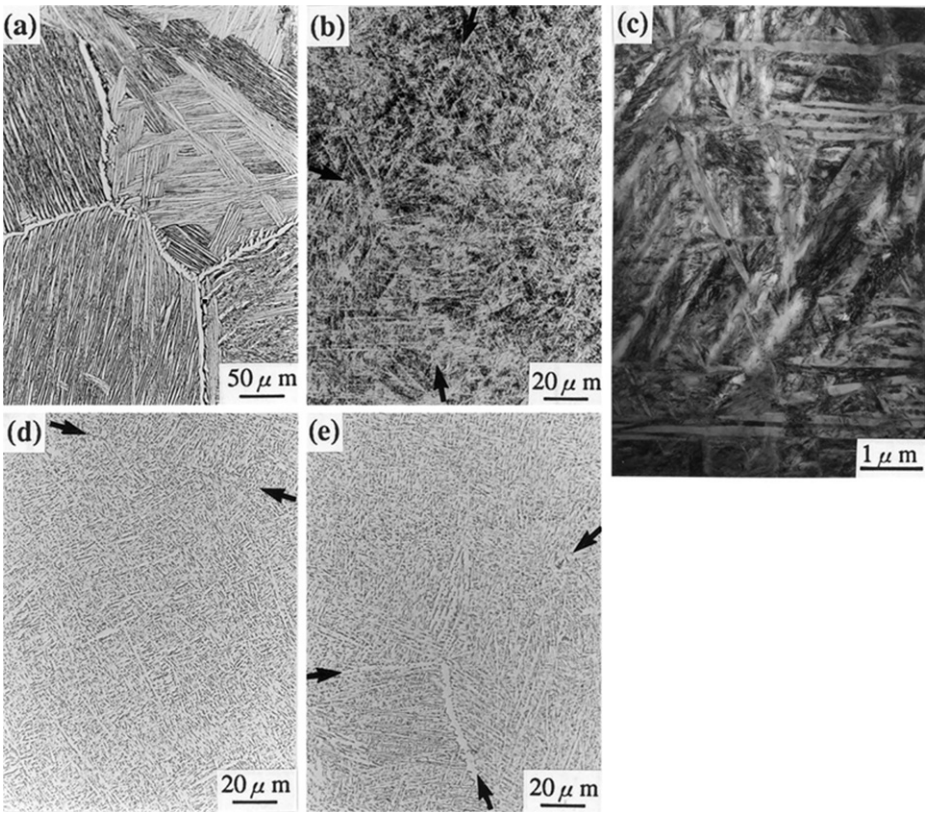


Figure 33 Change of the microstructures during the thermochemical process. (a) Starting microstructure (β-annealed), (b) and (c) 0.4% hydrogenated, solution-treated and directly aged at 500 °C for 1 h, respectively, (d) and (e) plus dehydrogenated at 750 °C for 10 h in vacuum, and (c) is a transmission electron microscopy micrograph. Arrows indicate the former β grain boundaries.[42]

Table 1 Mechanical properties of the materials processed by the new process of the thermochemical process (TCP) and by blended elemental powder metallurgy (BE/PM)[46]

	0.2% Proof stress (MPa)	*Tensile strength (MPa)*	*Elongation (%)*	*Reduction of area (%)*	*Fatigue strength[a] (MPa)*
TCP	952	1042	12.5	21.4	490
BE/PM[b]	862	969	15.1	36.9	392

[a]Rotational bending (R = −1) at 10^7.
[b]Oxygen content is 0.15 mass %, HIPed.

2. Extremely brittle hydride is not needed throughout the process and the handling of intermediate products is much easier.

Both advantages lead to cost reduction. However, fatigue strength is not as high as that by the conventional method at present.

The heat treatment of the α/β-Ti alloys can also be categorized depending on whether it was heated to the $\alpha+\beta$-phase field or to the β-phase field. Depending on the cooling rate, different microstructures can be obtained.

2.11.5.2.1 Annealing

Annealing from the $\alpha+\beta$-phase field produces microstructures approaching equilibrium equiaxed hcp α phase surrounded by the retained β phase.

Annealing from the β-phase field causes a transformation from the β to α microstructure containing the lamellar microstructure of a similar crystal orientation.

2.11.5.2.2 Normalizing

Normalizing from the $\alpha+\beta$-phase field provides equiaxed primary hcp α phase in a matrix of the transformed acicular β phase.

Normalizing from the β-phase field produces fine acicular α, which is transformed from the β phase by nucleation and growth.

2.11.5.2.3 Quenching

When the alloy is quenched from a region, which is below the β transus but above the martensitic start temperature (M_s), the

microstructure obtained consists of the primary α phase embedded in the transformed β phase (α′ martensite).

But when the alloy is quenched from a region that is below the M_s yet above the α transus, then the microstructure obtained consists of the primary α phase and a small amount of retained (untransformed) β phase.

2.11.5.2.4 Tempering

When a quenched alloy is subjected to subsequent elevated temperature treatments, the martensitic microstructure decomposes depending on the martensitic crystal structure and alloy composition. The reactions may be complex and the various types are shown here. These reactions lead to a wide range of microstructures. In the β-isomorphous alloys, α′ decomposes directly to α of equilibrium composition at the tempering temperature and β forms as a fine precipitate, nucleating heterogeneously either at martensite plate boundaries or at internal substructures such as twins. In β-eutectoid alloys, α′ may decompose directly into the α-phase and an intermetallic compound formed in several stages. However, in systems such as Ti–Mn, where the normal eutectoid reaction is sluggish, the martensite tempers first by forming α with precipitates of β, with the intermetallic compound appearing slowly at a later stage.

Tempering of α″ martensite may occur by two mechanisms:

- In alloy compositions in which M_s (α″) occurs at a relatively high temperature, α″ decomposes first by the formation of a fine and uniformly dispersed α-phase in the α″ matrix. Further aging causes both the coarsening of these particles and the nucleation of a cellular reaction at the prior β-grain boundaries, leading to the growth of a lamellar structure of α + β. Growth of these lamellar cells then occurs at the expense of the other regions.
- In alloys with an M_s (α″) temperature near room temperature, the α″ reverts to the β phase, which then decomposes by a mechanism that is characteristic of the particular tempering temperature. Decomposition of the β-phase is discussed in Section 2.11.5.2.5.

α′ Martensite		
β-Isomorphous alloys		$\alpha' \rightarrow \alpha + \beta$
β-Eutectoid alloys	Alloys with slow eutectoid reactions, for example, Ti–Mn	$\alpha' \rightarrow \alpha + \beta \rightarrow \alpha +$ Compound
	Alloys with fast eutectoid reactions, for example, Ti–Cu	$\alpha' \rightarrow \alpha +$ Compound (may form in several stages)
α″ Martensite		
	Alloys with high M_s(α″) temperature	$\alpha'' \rightarrow \alpha'' + \alpha \rightarrow \alpha'' + \alpha + (\alpha + \beta) \rightarrow \alpha + \beta$
	Alloys with low M_s(α″) temperature	$\alpha'' \rightarrow \beta \rightarrow$ Products

2.11.5.2.5 Decomposition of metastable β

The retained β obtained after quenching decomposes when subjected to aging at elevated temperatures, inducing high-tensile strength in the alloy. The metastable β phase is transformed into equilibrium α phase at high aging temperatures due to difficulty in nucleating hcp α phase on the bcc β matrix. Three types of reactions are possible during the decomposition.

2.11.5.2.5.1 Formation of ω phase

The ω phase induces high strength, but it also causes embrittlement. This phase appears as fine dispersion particles after metastable β is isothermally aged at 100–500 °C. This phase can be avoided by controlling the aging conditions, temperature, and composition of the alloy.

2.11.5.2.5.2 Separation of β phase

The β phase may be separated into two bcc phases: $\beta \rightarrow \beta_{(enriched)} + \beta_{1(depleted)}$. This reaction occurs in high-β stabilizer-containing alloy and prevents formation of the ω phase. With time, this β phase slowly transforms into the equilibrium α phase.

2.11.5.2.5.3 Formation of equilibrium α phase

Equilibrium α phase can form directly from the β phase or indirectly from the ω or the β_1 phase.

2.11.5.2.6 A case study on the effect of thermal treatment on an α/β-Ti alloy

A case study of the failure analysis and optimization of thermo-mechanical process parameters of titanium alloy (Ti–6Al–4V) fasteners for aerospace applications is presented here.[48] Ti–6Al–4V is currently the most useful of all the titanium alloys used in aerospace applications because of their high strength-to-weight ratio, good corrosion resistance, excellent fracture toughness, and other attractive mechanical properties. It contains Al as the α-phase stabilizer and V as the β-phase stabilizer at room temperature. Depending on the chemical composition, processing history, and thermal treatment procedures, the alloy shows different microstructures and properties. The objective of the presented study was to perform metallurgical analysis of the failed bolt, fractography study to find out the root cause of the failure, and optimization of processing (i.e., thermal treatment) parameters for fastener manufacturing.

2.11.5.2.6.1 Composition of the alloy

The chemical composition of the alloy studied is given in **Table 2**.

2.11.5.2.6.2 Process of manufacture

The input rod with a 9.0-mm diameter was processed by hot rolling at 955 °C, followed by annealing at 700 °C for 1 h with air cooling. The rods were further reduced to 5.6 mm in diameter by hot swaging. Finally, centerless grinding was applied to achieve a diameter of 4.5 mm.

The rods were head-forged by flame-heating the head portion of feed stock, followed by swagging on the dies. The head-forged feed stock was solution-treated at 940 ± 10 °C

Table 2 Chemical composition of Ti–6Al–4V (by % weight)[48]

Alloy	*C*	*Al*	*V*	*Fe*	*O*	*N*	*H*	*Ti*
Ti–6Al–4V	0.01	6.28	4.03	0.03	0.169	0.008	0.006	Balance

Table 3 Mechanical properties in annealed and solution treatment and aging (STA) condition[48]

Heat treatment condition	*Yield strength (MPa)*	*Ultimate tensile strength (MPa)*	*% Elongation*
Annealed	950	1069	16
STA	1143	1240	15

with a soaking period of 45 min, followed by water quenching. Further, aging was performed at $535 \pm 10\ ^{\circ}C$ for 5 h with air cooling. The socket head was punched by cold working. Threads were processed on the heat-treated head-forged feed stock by thread rolling.

2.11.5.2.6.3 Observations

2.11.5.2.6.3.1 Clearance criteria followed for the fastener material (observations of the input material)

2.11.5.2.6.3.1.1 Mechanical properties

The details of mechanical properties of the input feedstock material in annealed and STA conditions are illustrated in **Table 3**.

2.11.5.2.6.3.1.2 Metallurgical analysis

Metallurgical analysis was performed using light microscopy. The specimens were prepared by grinding with 1000 grit SIC paper and fine polishing with 1 mm diamond paste, followed by etching with kroll (10 ml $HF + 30$ ml HNO_3) reagent in annealed condition.

2.11.5.2.6.3.1.3 Acceptance test on the fasteners

1. Mechanical test on the fasteners was conducted and withstood a specified load of 9.6 kN, further allowing testing up to the breaking load of 10.43 kN.
2. Torque test was conducted at 3.0 N m for five cycles and was found to be satisfactory.
3. Metallurgical analysis was performed on the finished fastener. The β structure in the head portion and $\alpha + \beta$ structure in the shank portion of the fastener in were revealed in the STA condition.
4. Another 100% dimensional inspection was performed as per NFL22-220 with acceptance criteria of 6 g.

2.11.5.2.6.3.2 Observations on failed bolt

To qualify as a bolt for flight assembly, the bolt assembly must have undergone proof pressure testing at 2.4 MPa, vibration testing at a frequency range of 20–100 Hz at ± 3 dB oct^{-1} for 120 s in both lateral and longitudinal directions, and flight acceptance testing. During routine visual inspection before electrical check, it was observed in one of the three fasteners that the head of the bolt had gotten sheared off the shank portion of the bolt. Further, a failure analysis was performed on the failed bolt.



Figure 34 Good fasteners.[48]

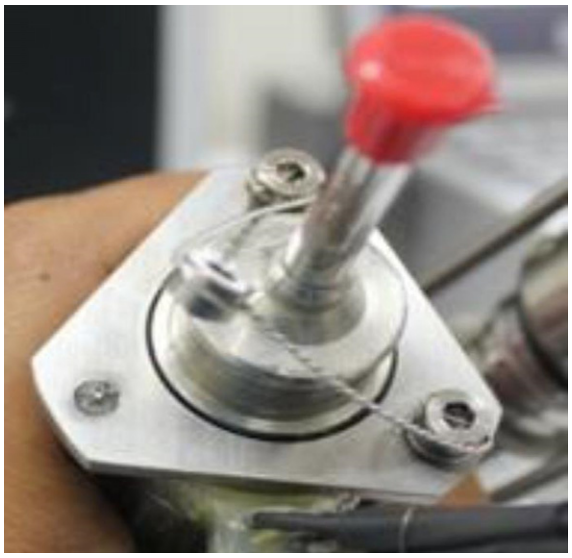


Figure 35 Assembly of the bolt.[48]

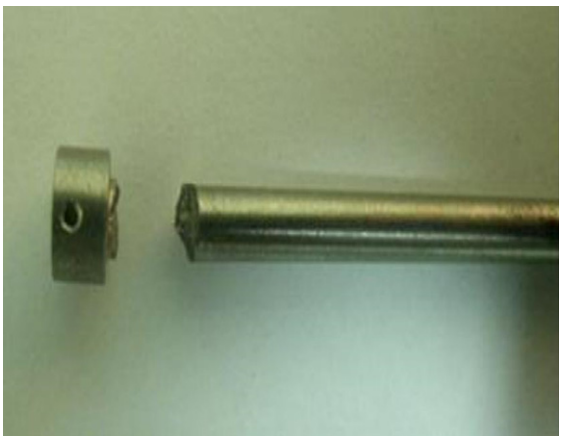


Figure 36 Fracture portion of the bolt.[48]

2.11.5.2.6.3.2.1 Visual inspection

The used bolt had a 25-mm-long thread portion and a 75-mm plain shank portion, as shown in **Figure 34**. It had a bolt assembly with valve housing, as shown in **Figure 35**. Failure occurred at the head–shank junction (**Figures 36** and **37**).



Figure 37 Head region.[48]



Figure 39 Crack at head region.[48]



Figure 38 Hole pierced in the head.[48]

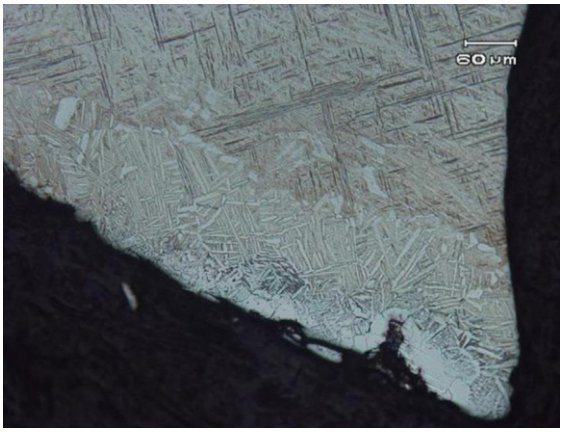


Figure 40 Edge of the failure zone.[48]

Further, stereo zoom microscopic analysis of the crack portion of the head and shank portion was performed. It was observed that a hole was pierced into the shank, as shown in **Figure 38**. Dye penetration test performed on the fresh bolts as per ASTM E165 detected the presence of circumferential cracks at the bottom of the head and some cracks extending to the shank side.

2.11.5.2.6.3.2.2 Metallurgical analysis

The head portion, failure zone, and shank portion of the bolt were subjected to metallurgical analysis. In the head portion, a crack was observed adjacent to one corner of bolt. The micrographs revealed a fine lamellar structure with β grains at the head portion but coarse lamellar with β grains at the portion adjacent to crack region (**Figures 39–42**). It is evident from **Figure 43** that in the shank portion of the failure zone, a crack branched from the cracked region. Microstructure (**Figure 44**) of the same revealed a coarse lamellar structure near the crack region and fine lamellar structure slightly away from the failure zone.

Microstructures of the shank portion of the bolt, as shown in **Figures 45** and **46**, revealed the grain boundary α-phase at prior β-grain boundaries and the martensitic α-structure, respectively. Fractography of the fracture surface of the failed bolt under scanning electron microscope (SCM) indicated a shift in the socket head hole from the center along with machining marks of a pierced hole of the socket head into the shank (**Figures 47** and **48**). At the head location, the nucleation of cracks started at the notch zone and further propagated to the outer periphery, as shown in **Figure 49**. At the shank portion, cracks were confined to a circular hole, as shown in

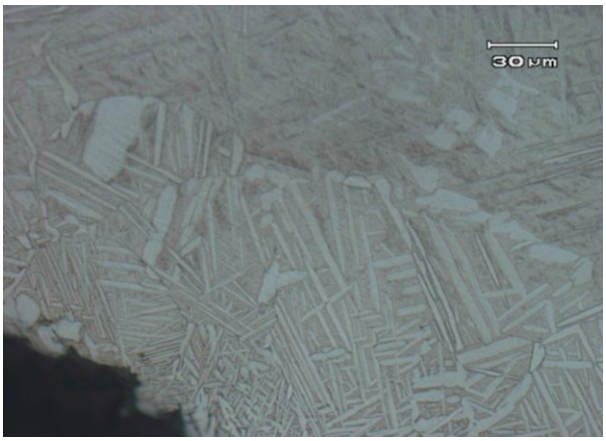


Figure 41 Coarse lamellar structure in β grains.[48]

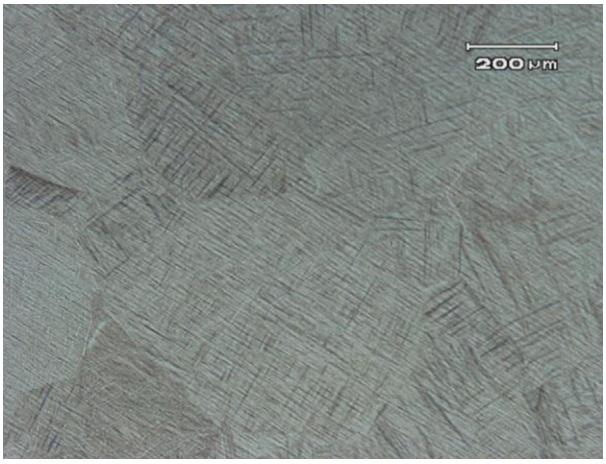


Figure 42 Fine lamellar structure in β grains.[48]

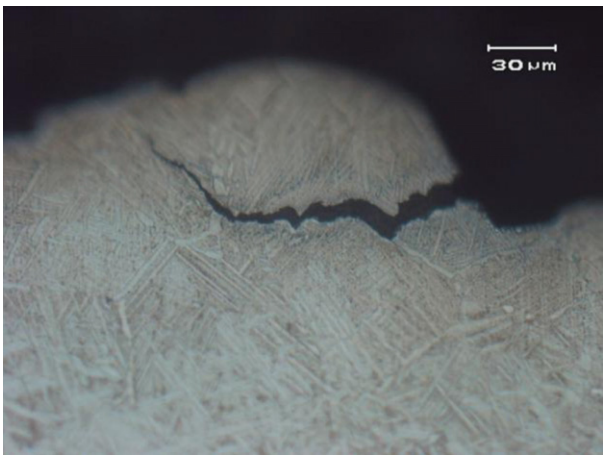


Figure 43 Branching of crack from cracked zone.[48]

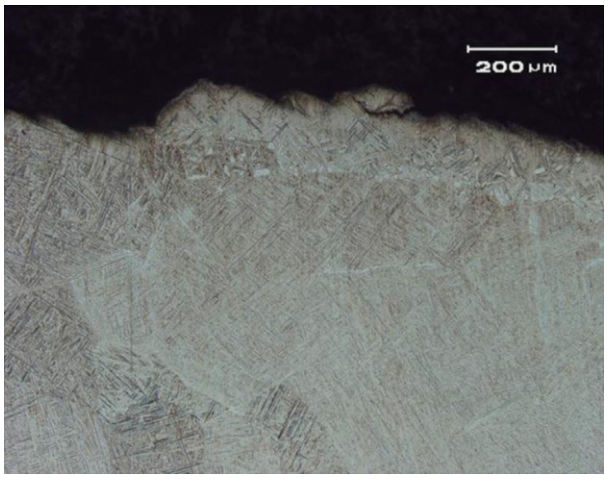


Figure 44 Coarse and fine lamellar structure in β grains.[48]

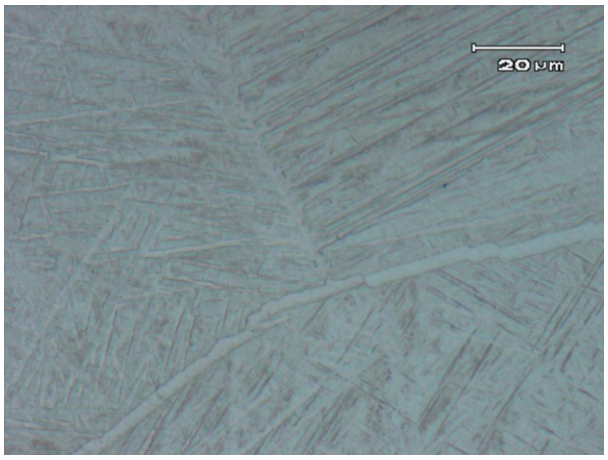


Figure 45 Grain boundary α.[48]



Figure 46 Martensitic α structure.[48]

Figure 50. In addition, fracture surface had fatigue striations, as shown in Figures 51–53, occurred due to vibration loads on the bolts. A dimple type of zone at the periphery of the bolt that was observed is shown in Figure 54.

2.11.5.2.6.4 Results and discussion

Generally, failure in mechanical fasteners occurs due to overload of static loading, such as tension, shear, bending, or

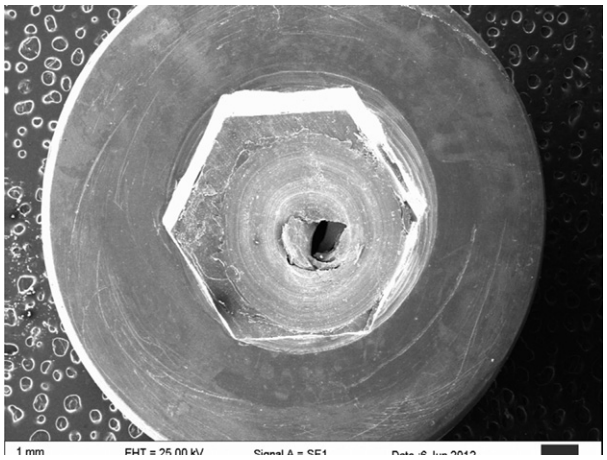


Figure 47 Shift in socket head hole from the center.[48]



Figure 48 Pierced zone of hole in the shank.[48]

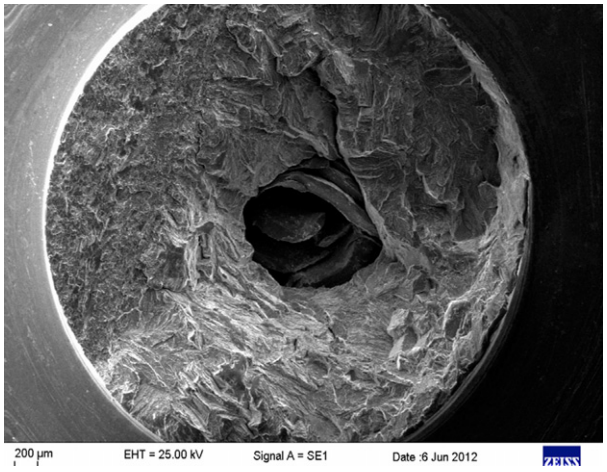


Figure 49 Nucleation crack in head.[48]



Figure 50 Propagation crack in shank.[48]

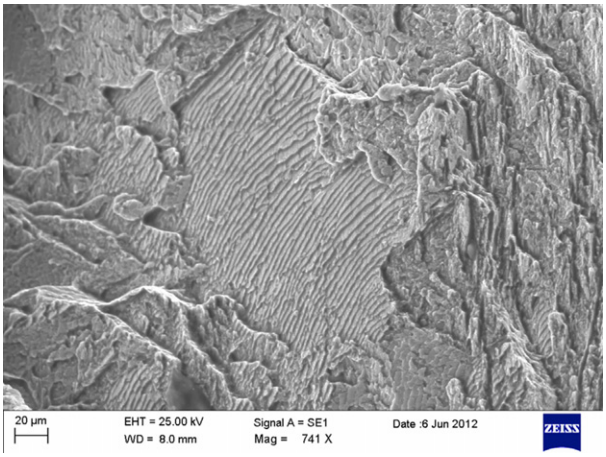


Figure 51 Striations due to fatigue loading at $\times 750$.[48]

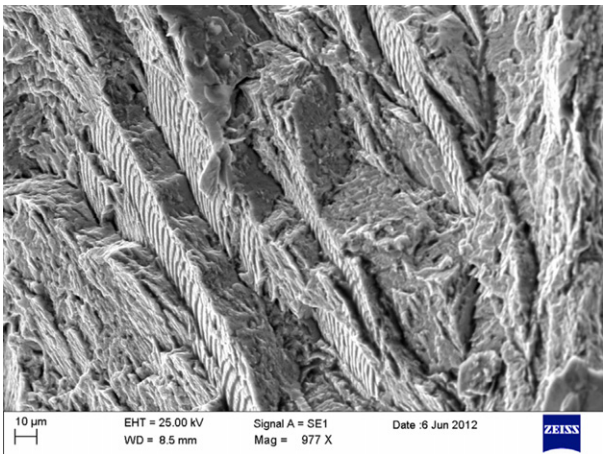


Figure 52 Striations due to fatigue loading at $\times 900$.[48]

torsion and dynamic forces resulting from impact loading and cyclic fatigue loading, including vibration loads. Other common causes of failure include environmental effects, manufacturing discrepancies, improper use, and incorrect installation. However, for the case presented, the primary reason for failure was a socket head hole. The shank portion

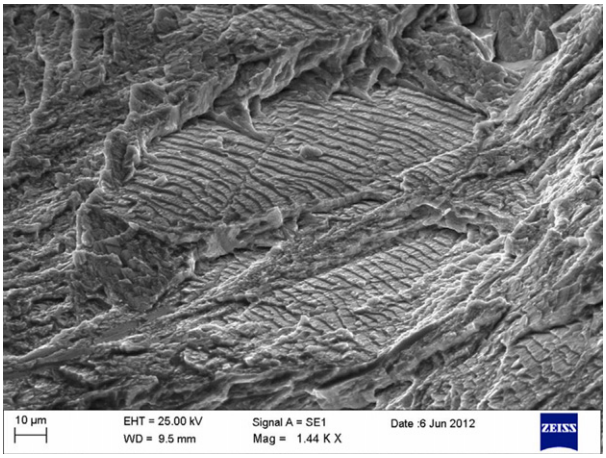


Figure 53 Striations due to fatigue loading at ×1400.[48]

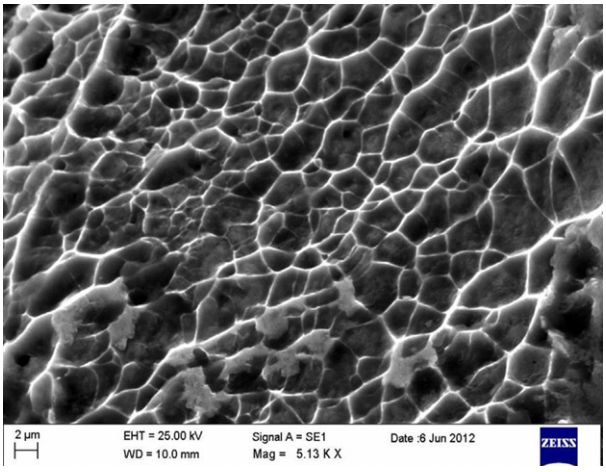


Figure 54 Dimple type of fracture zones observed at ×5000.[48]

became pierced, thus reducing the effective load-bearing area. This allowed more stress concentration zones at the interface zone. The cracks started the interface region as the pierced zone acted as a notch, and this region experienced dynamic loads due to vibration testing. Surface cracks present in the interface region were due to uncontrolled-process parameters that followed head forging and socket head hole punching.

Heterogeneity in microstructures is observed from microstructure analysis of the bolt from the head to shank. A localized increase in temperature during head formation is indicated by absence of primary α in the head portion and coarse lamellar structure in the failed zone. Presence of fine and coarse lamellar structures is also visible in the interface zone. This is credited to transformation decomposition of the high-temperature β phase. Microstructure of the shank portion reveals martensitic α and grain boundary α, with prior grain boundaries occurring because of improper processing after heating to the β field. Improper processing of Ti–6Al–4V after heating to the β field can result in the preferential α phase along the prior β grains. Extensive hot work is required to break up such structures; because cracks tend to propagate in or near interfaces, this type of structure can provide loci for initiation and propagation of cracks, thereby leading to premature failure.

Fatigue performance is greatly influenced by the forging temperature. Forging Ti–6Al–4V just below the phase transition temperature produces a microstructure that has a fatigue limit higher than that of the microstructure obtained by forging above the β_t temperature. It can be finally concluded that the bolt has failed due to fatigue, which transpired due to manufacturing discrepancies of head forging and socket hole. Further, heterogeneity in the microstructure facilitated the propagation of cracks.

The failure analysis was utilized to study the process parameters followed for manufacturing of the fasteners. Possible microstructures during thermo-mechanical processing with different temperatures and cooling mediums are illustrated in **Figure 55**.[48] It was concluded that localized heating (using torch flame) and lack of temperature control during head forging of the bolt caused manufacturing discrepancies. The strain rates followed for head forging are very high (i.e., approximately 10^{-1}–10^{-2} s^{-1}). Finalized process parameters were obtained only after repeated experiments were conducted on head forging. The details of process parameters for manufacturing fasteners are given in **Table 4**.

Head forging was performed by controlled heating below the β-transus temperature (<950 °C) in a furnace. Forging was performed at a strain rate of 10^{-2}–10^{-3} s^{-1} by removing the counter weight of 256 kg.

Dye-penetration test results were obtained and the interface region was found to be free of surface cracks. Radiography suggested no significant discontinuities. Further, metallurgical analysis was performed on the head portion, interface region, and shank area but found no evidence of heterogeneity in the microstructure. Also, the socket hole is removed from the design and the plain hexagonal socket head bolt is recommended for future applications.

2.11.5.2.6.5 Conclusions

The following conclusions can be drawn from the aforementioned case study:

- Failure analysis of Ti–6Al–4V fasteners was performed and the failure was attributed to fatigue damage. This damage occurred due to piercing of the socket head hole into the shank.
- Heterogeneity in the microstructure is confirmed by metallurgical analysis. This is a result of the uncontrolled process parameters that were followed during fastener manufacturing.
- An experimental study was conducted to optimize process parameters. The strain rates during head forging were optimized as 10^{-2}–10^{-3} s^{-1}, and heating was performed in a controlled furnace at 900 °C. Metallurgical analysis of the fasteners produced by optimum process parameters revealed no evidence of heterogeneity in microstructure.

2.11.5.3 Heat Treatment in β-Ti Alloys

The β-Ti alloys form one of the most versatile classes of materials with respect to processing, microstructure, and

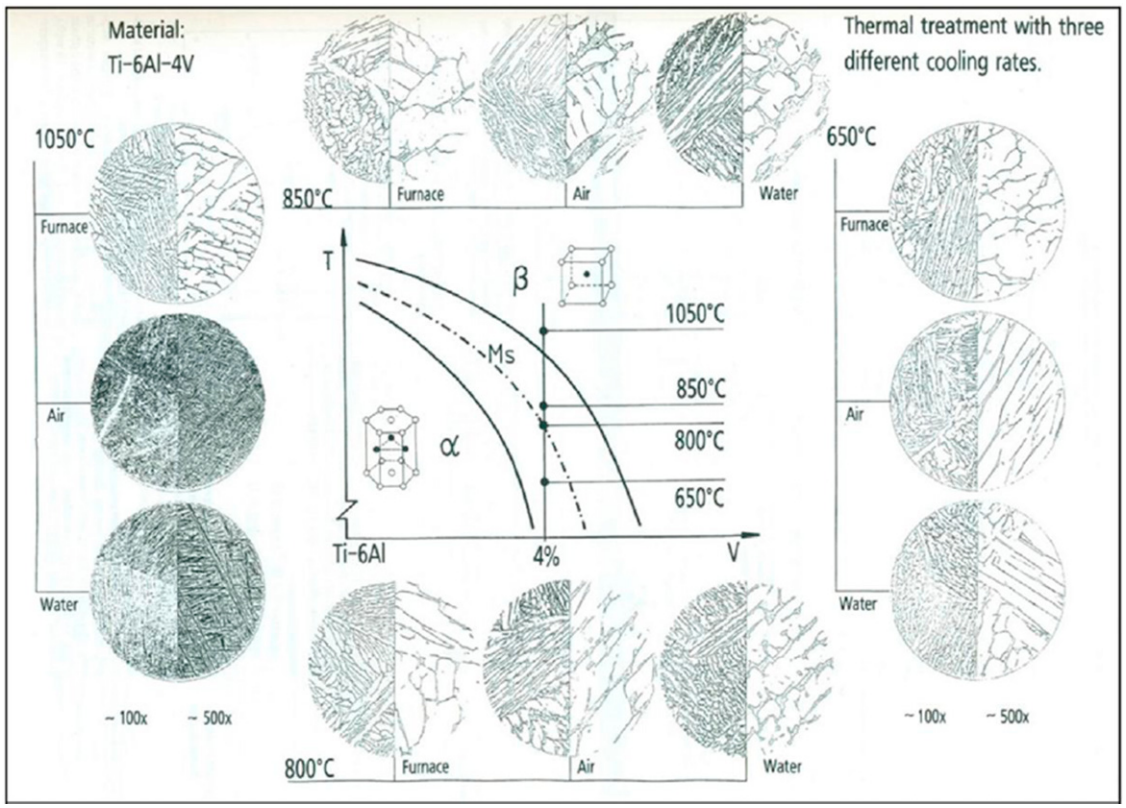


Figure 55 Microstructure of Ti–6Al–4V during thermo-mechanical processing.[48]

Table 4 Process parameters of manufacturing of fastener[48]

Process of manufacture	*Process parameters*
Hot rolling	Hot-rolled to the size F9.0 mm at temperature of 9558 °C
Annealing	700 °C, 1 h, air cooling
Swaging	Reduced to 4.5 mm diameter by hot-swaging
Head forging	Heated to 9008 C, forged at strain rate of 102–103 s^{-1}
Solution treatment and aging	Solution treatment at 895 °C for 1 h, water quenched, aging at 520 °C for 4 h, air cooling
Thread rolling	One single-pass thread-rolling

mechanical properties. These alloys include stable β, metastable β, and β-rich α/β alloys. They offer an attractive alternative to the α/β alloys due to their increased heat treatability, wide and unique range of strength-to-weight ratios, deep hardening potential, and inherent ductility that is the result of their bcc structure. In addition, they possess superior fatigue resistance as compared to α/β alloys. These alloys can be found in aerospace, power plant, sporting good, automotive, orthopedic implant, and down-hole service applications.

Generally, the β-transus temperature (T_β) tends to decrease as the Mo equivalent (Mo eq) (see Section 2.11.4.1.2) increases (**Figure 56**).[49] Higher values of the Mo Eq indicate heavily stabilized alloys, such as Ti–13V–11Cr–3Al (B120VCA) or Ti–35V–15Cr (alloy C). β Alloys were developed in the early 1950s, when the B120VCA alloy was introduced. Later, β alloys such as Ti–1Al–8V–5Fe (Ti-1-8-5), Ti–8V–8Mo–2Fe–3Al (Ti-8-8-2-3), and Ti–11.5Mo–6Zr–4.5Sn (*B* III) were formulated. Three important alloys were commercialized between 1969 and 1978, which are Ti–3Al–8V–4Mo–4Zr (*B* C), Ti–10V–2Fe–3Al (Ti-10-2-3), and Ti–15V–3Cr–3Sn–3Al (Ti-15-3). Newer β alloys such as Timetal® 21S, Timetal® LCB, *B*-CEZ, SP-700, and Ti–13Nb–13Zr were introduced in the 1990s. A more complete description of alloy composition, category, application, source, and year of introduction is provided in **Table 5**[50] for the major β alloys.

The high-temperature flow curves of Ti–10V–2Fe–3Al,[51] Ti–15V–3Cr–3Sn–3Al,[52] and *B* CEZ[53] are shown in **Figures 57–59**, respectively. It is apparent that all the stress–strain curves exhibit a sharp initial peak stress (discontinuous yielding) followed by almost constant stress deformation. Discontinuous yielding has been observed in a large number of β-Ti alloys such as Ti–9.4Mn, Ti–13Mn, Ti–14.8V,[54,55] Ti–8Mn, Ti–15Mo, Ti–13Cr–11V–3Al,[56] Ti–11Mo–6Zr–4.5Sn–0.035Fe, Ti–10V–2Fe–3Al, Ti–3Al–8V–6Cr–4Mo–4Zr,[57] Ti–15V–3Cr–3Sn–3Al,[52,58,59] and Ti–5Al–2Sn–2Cr–4Mo–4Zr–1Fe.[53] Discontinuous yielding has not been observed in CP Ti, Ti–5Al–2.5Sn (α alloy), and Ti–6Al–4V (α/β alloy) hot-deformed above the transus temperature.

This discontinuous yielding phenomenon has been related to the rapid generation of mobile dislocations from grain boundary sources, which leads to hot deformation proceeding from the grain boundary region inward. The magnitude of the peak stress decreases with increasing temperature, decreasing strain rate, and increasing grain size.[60] Following the peak

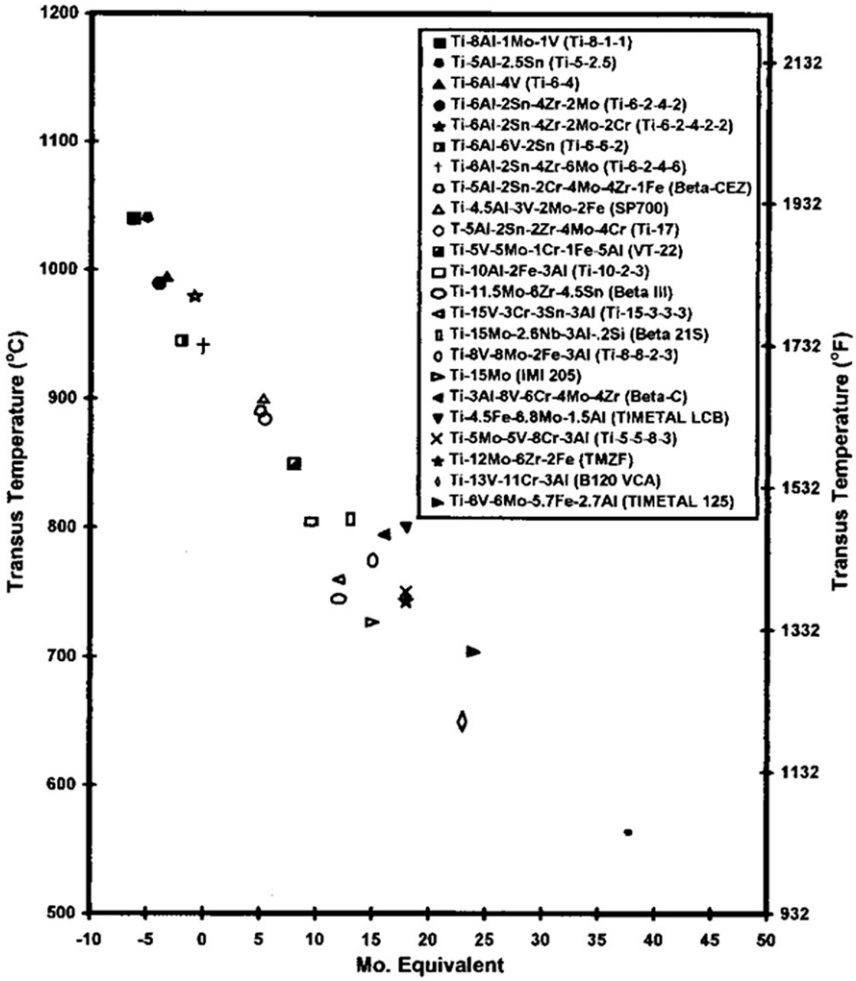


Figure 56 Variation in β-transus temperature with 'moly equivalent.'[49]

stress, a domain of near steady-state flow is usually observed (Figures 57–59). Higher steady-state flow stresses are observed at higher strain rates and lower deformation temperatures, as shown in Figures 60 and 61(a).[61,62] It is evident from the comparison of the flow stresses of several metastable β alloys and Ti–6Al–4V deformed at different temperatures that the flow stress of Ti–6Al–4V is the highest (Figures 60 and 61(a)). However, when the flow stress data are presented in terms of T–T_β (where T is the deformation temperature and T_β is the β-transus temperature), alloys with the highest concentration of alloying elements exhibit the highest flow stresses. For example, Ti–15V–3Cr–3Sn–3Al has a total of 24 wt% alloying elements and displays a much higher flow stress than Ti–6A–4V, with only 10 wt% additions (Figure 61(b)). This increase in flow stress is mainly attributed to an increase in solute strengthening.

2.11.5.3.1 Deformation in the β-phase field

Deformation in the β-phase field is similar to that for alloys undergoing dynamic recovery in which the rate of hardening by generation of dislocations is balanced by the rate of softening due to dislocation annihilation, thus resulting in the constant flow stress deformation noted.[16,17] The apparent activation energy for the deformation of β-Ti alloys has been found to be in the range of 130–175 kJ mol^{-1},[18] which is very close to the activation energy for self-diffusion in β Ti (i.e., 153 kJ mol^{-1}).[53] Table 6[49] contains some deformation parameters for several metastable β and β-rich alloys hot-deformed in the β-phase field. A typical hot deformation microstructure is shown in Figure 62(a)[63] for Ti–10V–2Fe–3Al forged to a 65% reduction at 1230 °C. Deformed β grains with increasingly (during deformation) serrated boundaries are observed. Small recrystallized grains appear in the vicinity of the deformed grain boundaries, when a strain of approximately 1.0 or more is induced. These grains, which are of the size of sub-cells, result from continuous recrystallization.[63] This type of recrystallization can also be considered as a special case of dynamic recrystallization. It is sometimes referred to as necklace recrystallization.[64] Under static annealing of this alloy, nucleation of new recrystallized grains occurs by the bulging mechanism.[65] As shown in Figure 62(b),[63] once nucleated, they grow to consume the recovered regions at a rate controlled by the amount of prior deformation as well as the annealing temperature and time.[17,66]

Details of microstructure and substructure formation, which characterize the dynamic recovery process, can be

Table 5 Composition, category, transus temperature, source, and year of introduction of major β titanium alloys, listed in descending order of their molybdenum (Mo) equivalency[50]

Alloy composition	*Commercial name*	*Category (Mo equivalent)*	*T_β (°C)*	*Actual and potential applications*	*Year introduced (company)*
Ti–35V–15Cr	Alloy C	Beta (47)		Burn-resistant alloy	1990 (P&W)
Ti–40Mo		Beta (40)		Corrosion resistance	1952 (RemCru)
Ti–30Mo		Beta (30)		Corrosion resistance	1952 (RemCru)
Ti–6V–6Mo–5.7Fe–2.7Al	TIMETAL 125	Metastab (24)	704	High-strength aircraft fasteners	1990 (TIMET)
Ti–13V–11Cr–3Al	B120 VCA	Metastab (23)	650	Airframe, landing gear, springs	1952 (RemCru)
Ti–1Al–8V–5Fe	1-8-5	Metastab (19)	825	Fasteners	1957 (RMI)
Ti–12Mo–6Zr–2Fe	TMZF	Metastab (18)	743	Orthopedic implants	1992 (Howmedica)
Ti–4.5Fe–6.8Mo–1.5Al	TIMETAL LCB	Metastab (18)	800	Low-cost, high-strength alloy	1990 (TIMET)
Ti–15V–3Cr–1Mo–0.5Nb–3Al–3Sn–0.5Zr	VT35	Metastab (16)		High-strength airframe castings	n.a. (Russian)
Ti–3Al–8V–6Cr–4Mo–4Zr	Beta-C	Metastab (16)	795	Oil fields, springs, fasteners	1969 (RMI)
Ti–15Mo	IMI 205	Metastab (15)	727	Corrosion resistance	1958 (IMI)
Ti–8V–8Mo–2Fe–3Al	8-8-2-3	Metastab (15)	775	High-strength forgings	1969 (TIMET)
Ti–15Mo–2.6Nb–3Al–0.2Si	Beta 21S	Metastab (13)	807	Oxidation/corrosion resistance, MMC	1989 (TIMET)
Ti–15V–3Cr–3Sn–3Al	15-3	Metastab (12)	760	Sheet, plate airframe castings	1978 (USAF)
Ti–11.5Mo–6Zr–4.5Sn	Beta III	Metastab (12)	745	High strength	1969 (Crucible)
Ti–10V–2Fe–3Al	10-2-3	Metastab (9.5)	800	High-strength forgings	1971 (TIMET)
Ti–5V–5Mo–1Cr–1Fe–5Al	VT22	Metastab (8)	850	High-strength forgings	n.a. (Russian)
Ti–5Al–2Sn–2Zr–4Mo–4Cr	Ti-17	Beta-rich (5.4)	885	High strength, medium temperature	1968 (GEAE)
Ti–4.5Al–3V–2Mo–2Fe	SP700	Beta-rich (5.3)	900	High strength, SPF	1989 (NKK)
Ti–5Al–2Sn–2Cr–4Mo–4Zr–1Fe	Beta CEZ	Beta-rich (5.1)	890	High strength, medium temperature	1990 (CEZUS)
Ti–13Nb–13Zr		Beta-rich (3.6)		Orthopedic implants	1992 (Smith & Neph)

Abbreviation: n.a., Not available.

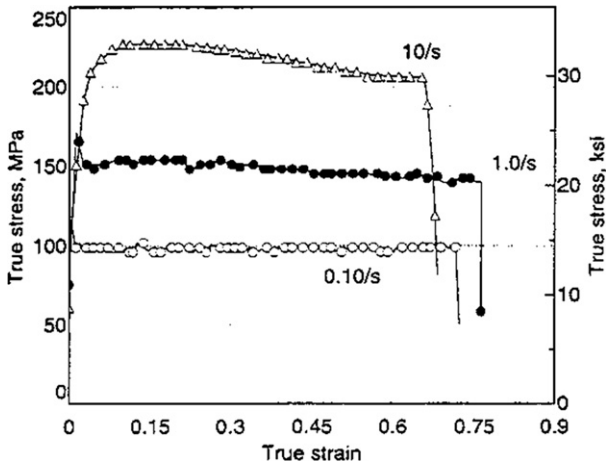


Figure 57 Flow curves of Ti–10V–2Fe–3Al alloy deformed above transus.[51]

obtained from observations for Ti–15V–3Cr–3Sn–3Al[52] and β-CEZ[64] (**Figures 63** and **64**). For some deformation conditions (low temperatures and high strain rates) of coarse grain alloys, such as cast alloys, an inhomogeneous substructure is observed (**Figure 65**).[52] Under these conditions, a finer and denser dislocation structure is developed along deformed grain boundaries. A coarser and less dense substructure is produced in the grain interiors as observed in cast Ti–15V–3Cr–3Sn–3Al deformed at 790 °C to a true strain of 1.05 (**Figures 64(a)** and **64(b)**).

Substructure evolution in the β phase has been quantified by microtexture analysis of β-CEZ samples deformed to strains of 0.25 and 1.0.[64] In this work, substructure misorientations were revealed qualitatively by orientation contrast scanning microscopy, as shown in **Figures 64(a)** and **64(b)**. Quantitative microtexture analysis was also performed on all sub-grains present in two or three adjoining grains (**Figures 66** and **67**).[64] During the initial deformation, it was observed that dynamic recovery produces a large proportion of low-angle sub-boundaries ($\Delta\theta \leq 12^\circ$). At a total strain of 0.25, these sub-boundaries are 97% of the total sub-boundaries measured (**Figure 67(a)**), whereas at a higher strain (approximately 1.0) the proportion of low-angle sub-boundaries is reduced to approximately 54% (even though their density has increased appreciably), and new medium-angle ($13^\circ \leq \Delta\theta \leq 25^\circ$) and high-angle boundaries ($\Delta\theta > 25^\circ$) are formed (**Figure 67(b)**). Measurements of sub-boundary misorientations at intermediate strains indicated that the development of medium-angle and high-angle boundaries is a continuous process that is controlled by dynamic recovery during hot deformation. However, the

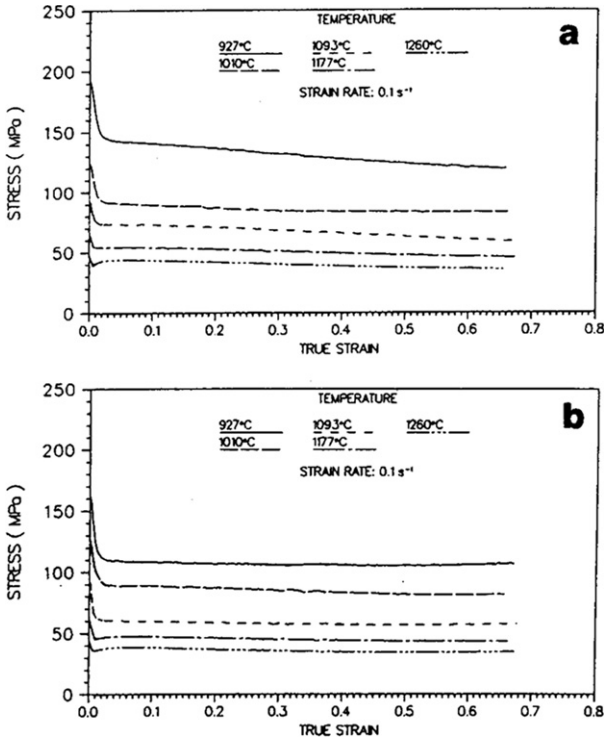


Figure 58 Flow curves of (a) as-cast and (b) recrystallized Ti–15V–3Sn–3Cr–3Al deformed in the range of 927–1260 °C at a strain rate of 0.1 s^{-1}.[52]

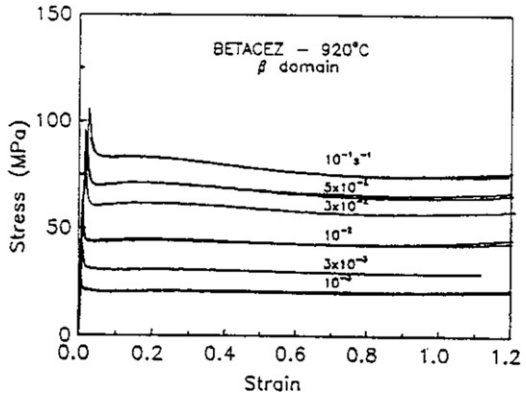


Figure 59 Flow curves of Ti–5Al–2Sn–2Cr–4Mo–4Zr–1Fe (β-CEZ) deformed above transus.[53]

growth process of these high-angle boundaries during or after deformation is similar to meta-dynamic recrystallization; in fact, it is evident that the recrystallization process for the β-Ti phase is not typical dynamic recrystallization whereby nucleation and growth of new recrystallized grains are occurring during hot deformation of low-stacking fault materials.[17]

The control of grain size, shape, and uniformity is very significant for secondary processing and to optimize final mechanical properties. Working in the β-phase region sometimes leads to the formation of a mixed grain structure containing large as well as small grains.[66–68] Such nonuniform microstructures are the result of selective recrystallization in regions of high strain along β-grain boundaries and the

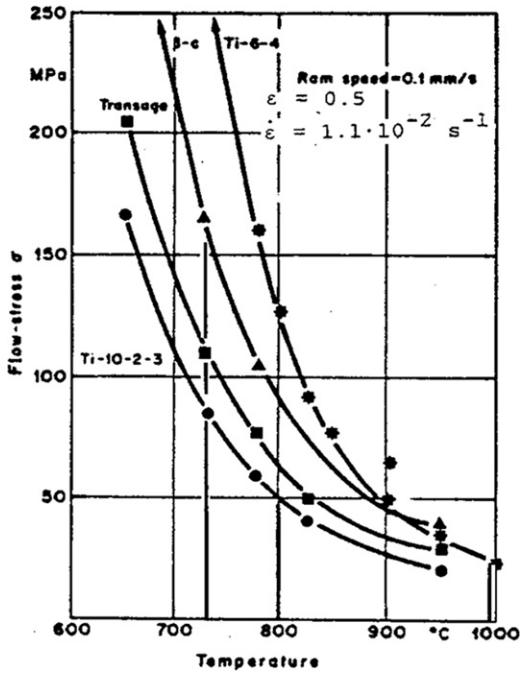


Figure 60 Flow stresses of different titanium alloys at a strain of 0.5.[61]

reduced driving force for recrystallization in the grain interiors, where dynamic recovery dominates. Once introduced, it is impossible to remove the mixed grain structure by heat treatment alone.[67]

Selection of the proper choice of process parameters such as deformation temperature, amount of deformation, and subsequent annealing temperature and time to avoid mixed grain structures may be aided by utilization of processing maps, as shown in **Figures 68** and **69**.[69] The nature of processing maps and the associated 'processing windows' are rationalized in terms of the occurrence of deformation localization at low deformation temperatures, and the formation of coarse and stable substructures are rationalized in terms of the occurrence of deformation localization at high deformation temperatures (**Figure 70**).[68] In addition to deformation and annealing conditions, the chemical composition of the alloy being hot-worked (**Figure 71**)[69] and its initial grain shape and size (**Figure 72**)[69] also affect the extent of the processing window. When processed through the processing window, fine-recrystallized grains can be obtained (**Figure 73**).[69] **Figures 73(a)–73(c)** shows the effects of variation of deformation temperatures prior to annealing treatment at a high temperature, whereas **Figures 73(d)–73(f)** and **Figures 73(g)–73(i)** show the effects of similar variation only for intermediate and low annealing temperatures. However, the effects of variation of the annealing temperature are clear when the microstructures are observed column-wise. **Figure 73(a)** reveals fine grain formed due to low deformation temperatures with a tendency of polygonization at high annealing temperatures. **Figure 73(c)** shows a tendency toward grain coarsening because of both high temperature of deformation and annealing. In **Figure 73(g)**, the grains are fine as well as elongated because of the low deformation temperature and low annealing temperature. **Figure 73(i)** shows distorted

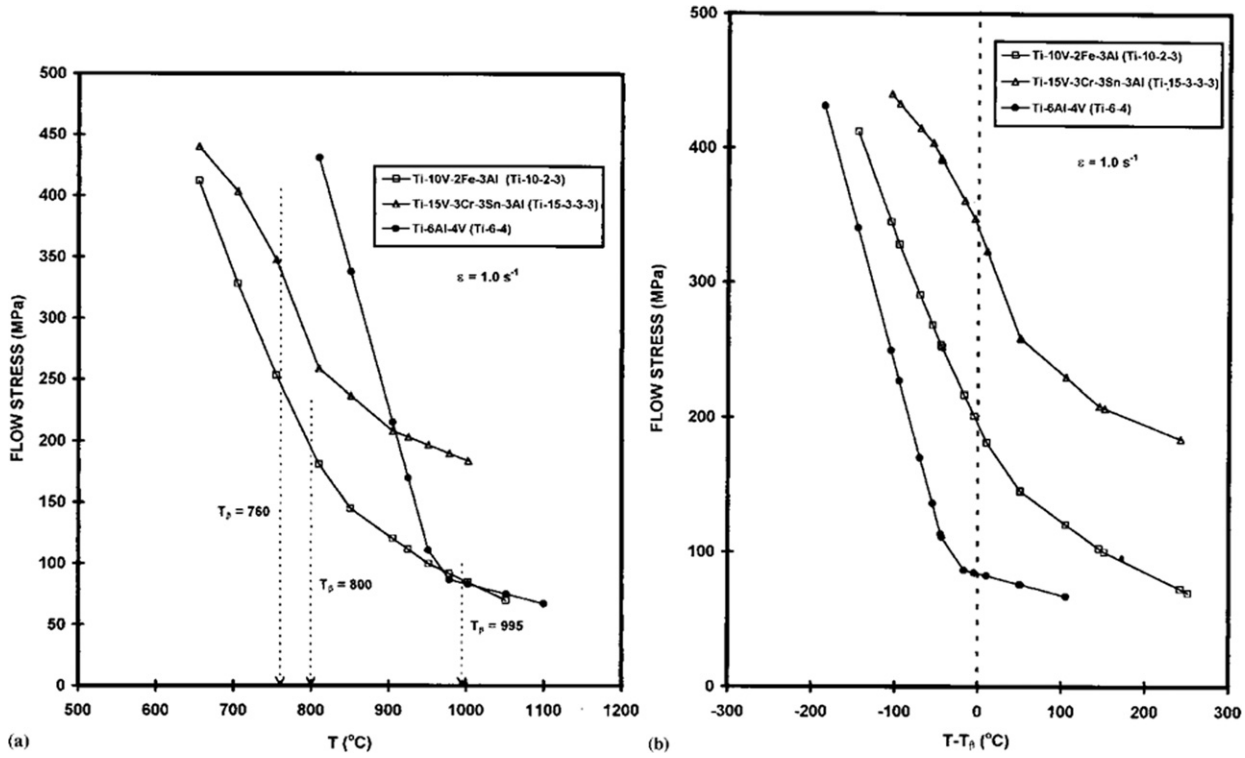


Figure 61 (a) Flow stress as a function of temperature for several titanium alloys deformed at an average strain rate of 1 s^{-1}.[62] (b) Flow stress as a function of $T–T_\beta$ for several titanium alloys deformed at an average strain rate of 1 s^{-1}.[62]

Table 6 Deformation parameters for several metastable β and β-rich alloys hot-deformed in the β-phase field[49]

Alloy	*Temperature range (°C)*	*Strain rate range (s^{-1})*	*Strain rate sensitivity (m)*	*Activation energy for deformation, Q_D (kJ mol^{-1})*
Ti–6Al–4V (Ti-6-4)	1120	5×10^{-3}–5	0.20	300
Ti–10V–2Fe–3Al (Ti-10-2-3)	820	10^{-3}–10^{-1}	0.33	169
Ti–15V–3Cr–3Sn–3Al (Ti-15-3-3-3)	800–900	5×10^{-3}–0.8	0.33	166–174
Ti–5Al–2Sn–2Zr–4Mo–4Cr (Ti-17)	905–950	10^{-3}–10^{0}		161
Ti–5Al–2Sn–2Cr–4Mo–4Zr–1Fe (Beta-CEZ)	890–1000	10^{-2}–10^{-1}	0.33	175

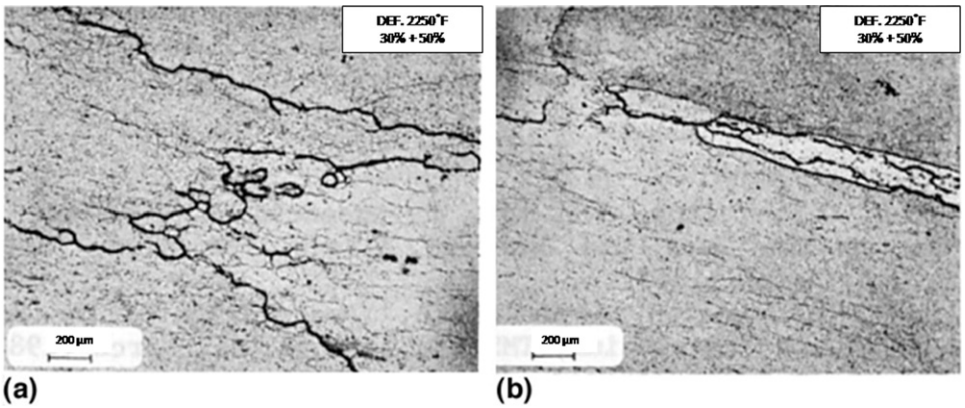


Figure 62 (a) Deformation substructure after forging to a 65% reduction at 1230 °C.[63] (b) Nucleation and growth of recrystallized grains following forging to a 65% reduction and annealing at 1035 °C for a short time.[63]

grain, which is the result of low annealing temperature but is coarser in nature due to high deformation temperature. From these figures it is evident that the grain refinement phenomenon is dominated by the temperature of deformation, whereas distortions of grains are more dependent on annealing temperature. Reheating and annealing times should be controlled and

optimized to eliminate excessive grain growth (Figure 74)[70] to preserve this microstructure.

2.11.5.3.2 Deformation in the $\alpha + \beta$-phase field

The high-temperature flow curves of Ti–10V–2Fe–3Al and Ti–5Al–2Sn–4Mo–4Zr–2Cr–1Fe (β-CEZ)[53] at sub-transus temperatures, as shown in Figures 75 and 76,[49,53] respectively, indicate that after yielding and a very short period of work hardening, a noticeable amount of flow softening takes place, whose magnitude is greatest at low temperatures (Figure 75)[49] and high strain rates (Figure 76).[53] The flow softening is followed by steady-state flow at high strains, particularly for high-temperature and low-strain-rate conditions. Although some of the flow softening observed at high strain rates results from deformation heating, most of it can be credited to dynamic microstructure or texture changes in the α phase. The sub-transus flow stress data also reveal that the β-preform microstructure (produced by β annealing and water quenching) is somewhat stronger than the α/β preform microstructure. However, at large strains, the flow curves for the two microstructures approach each other, and this behavior is similar to the trend observed in α/β alloys. A comparison of the sub-transus flow stresses of different β and α/β alloys with an α/β microstructure indicates that the flow stress of the Ti–6Al–4V alloy is the highest. However, if corrected for the different transus temperatures, the alloy with the highest solute level (Ti-17) exhibits the highest flow stress, as shown in Figure 77.[71]

Hot deformation in the $\alpha + \beta$-phase field yields relatively high apparent activation energy in the range of 400–700 kJ mol^{-1}, which is much higher than the apparent activation energy for self-diffusion in the β phase (153 kJ mol^{-1}).[53] The physical interpretation of the activation energy for sub-transus hot working is complicated by the variation of the α phase volume fraction with deformation temperature (Figure 78).[70] Table 7[49] lists some deformation parameters for several metastable β and β-rich alloys deformed in the

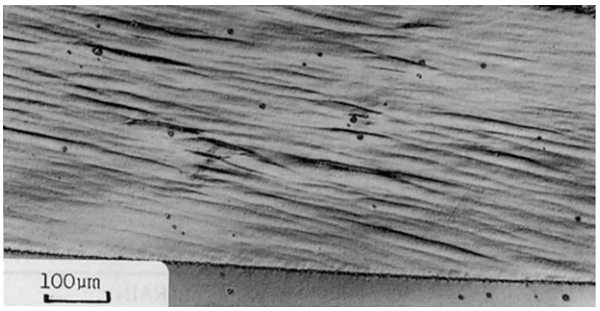


Figure 63 Substructure in as-cast Ti–15V–3Sn–3Cr–3Al deformed at 790 °C to a true strain of 1.05.[52]

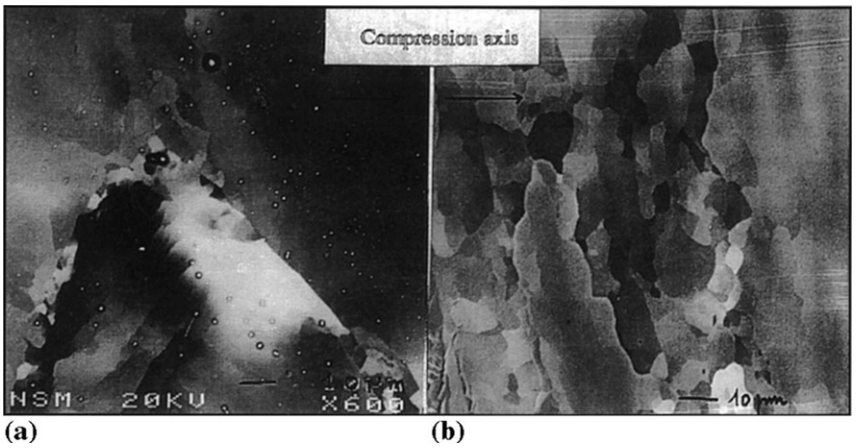


Figure 64 Scanning electron microscope orientation contrast images of substructure at strain of (a) 0.25 and (b) 1.0.[64]

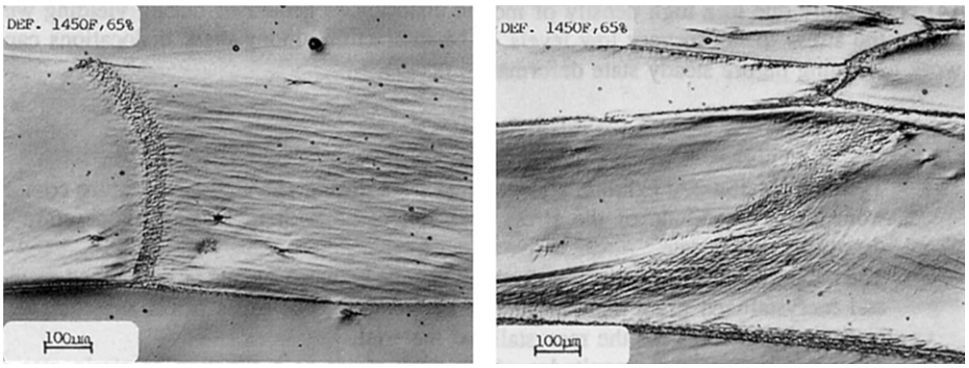


Figure 65 Nonhomogeneous substructure in the vicinity of a grain boundary in as-cast Ti–15V–3Sn–3Cr–3Al deformed at 790 °C to a strain of 1.05.[52]

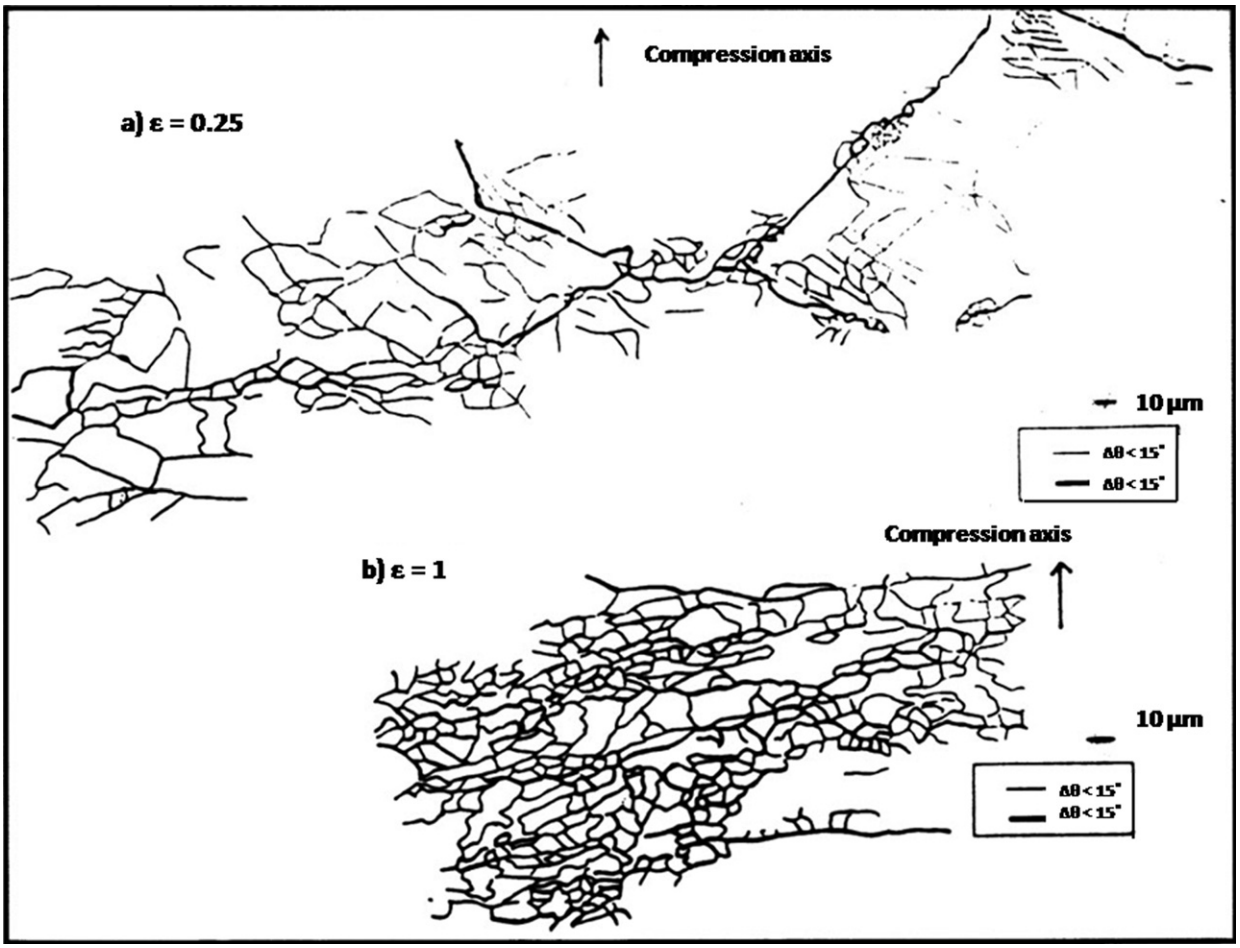


Figure 66 Sub-boundary formation in β-CEZ deformed to strains of (a) 0.25 and (b) 1.0.[64]

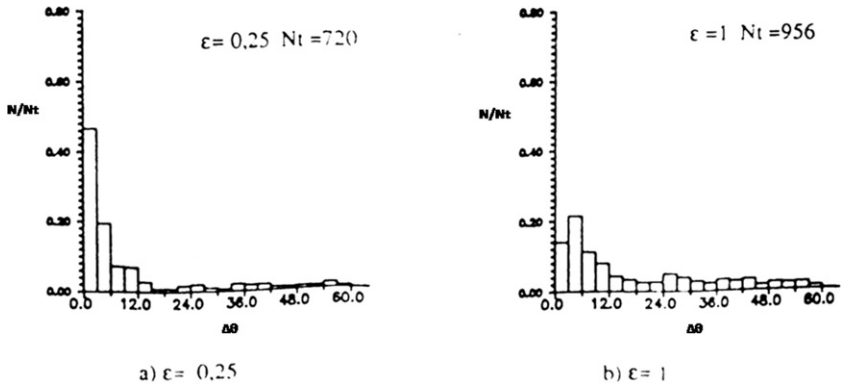


Figure 67 Sub-grain misorientation distribution in β-CEZ deformed to strains of (a) 0.25 and (b) 1.0.[64]

$\alpha+\beta$-phase field. Hot-working temperatures of metastable β and β-rich alloys associated with α/β processing are typically (T_β-100 °C) or higher, at which the volume fraction of the primary α phase is less than 30% (Figure 78).

The effect of microstructure on flow is further explained in Figure 79.[72] Higher flow stresses are displayed by an acicular α morphology microstructure (Figure 79(b)) as compared to those for equiaxed α morphology (Figure 79(a)). It has been observed that the strain rate in the α phase (which is less than the average strain rate) is higher for an acicular or elongated grain morphology and lower for globular grain morphology.[72] Consequently, higher flow stresses are expected for acicular microstructures.

The presence of α grain also affects microstructure and substructure evolution during sub-transus hot working. The α phase is considerably harder than the β phase, and it behaves like a dispersion of hard particles in a soft matrix (Figure 80).[73] Figure 81[53] shows that the strain in the α phase is approximately three-tenths of the nominal strain, thus preventing the α phase from

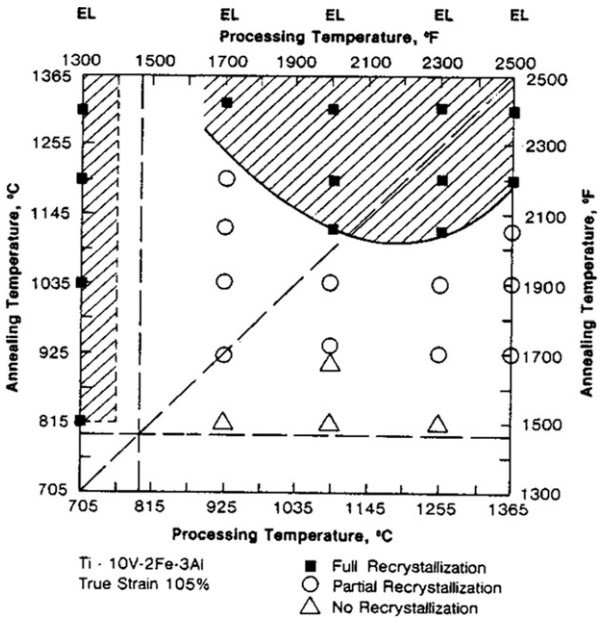


Figure 68 The effect of processing and annealing of Ti–10V–2Fe–3Al alloy forged to 65% reduction.[69]

converting into a more equiaxed morphology. The same effect has been observed in other alloys (Figure 82).[74] Because the α phase deforms less than the β phase, development of strain concentrations in the softer β phase is a necessity in the vicinity of the α phase, leading to the formation of smaller highly misoriented sub-grains in comparison to the sub-grains produced in the remainder of the β matrix (Figure 83).[74] At higher strains, sub-boundaries develop in the α phase, followed by cusp formation and β-phase penetration along the α/α sub-boundaries, resulting in a more equiaxed morphology α phase (Figure 84).[70] Similar features have also been observed in α/β alloys (Figure 85).[75] The softer β matrix also undergoes microstructural changes associated with grain elongation and formation of sub-boundaries, increasing their misorientation continuously, thereby creating small-recrystallized grains surrounded by high-angle boundaries in the vicinity of the highly deformed β grain boundaries.

Control of the size and morphology of the α and β phases can be achieved by selecting the proper hot-working parameters (temperatures and amount of deformation). Along with the volume fraction of the α phase (Figure 86(a)),[73] the size of the α phase can also be modified by changing the deformation temperature, as shown in Figure 86(b).[73] Further control of the α size and morphology can be obtained by fast-cooling β-processed material producing the acicular α morphology (Figure 87)[76]

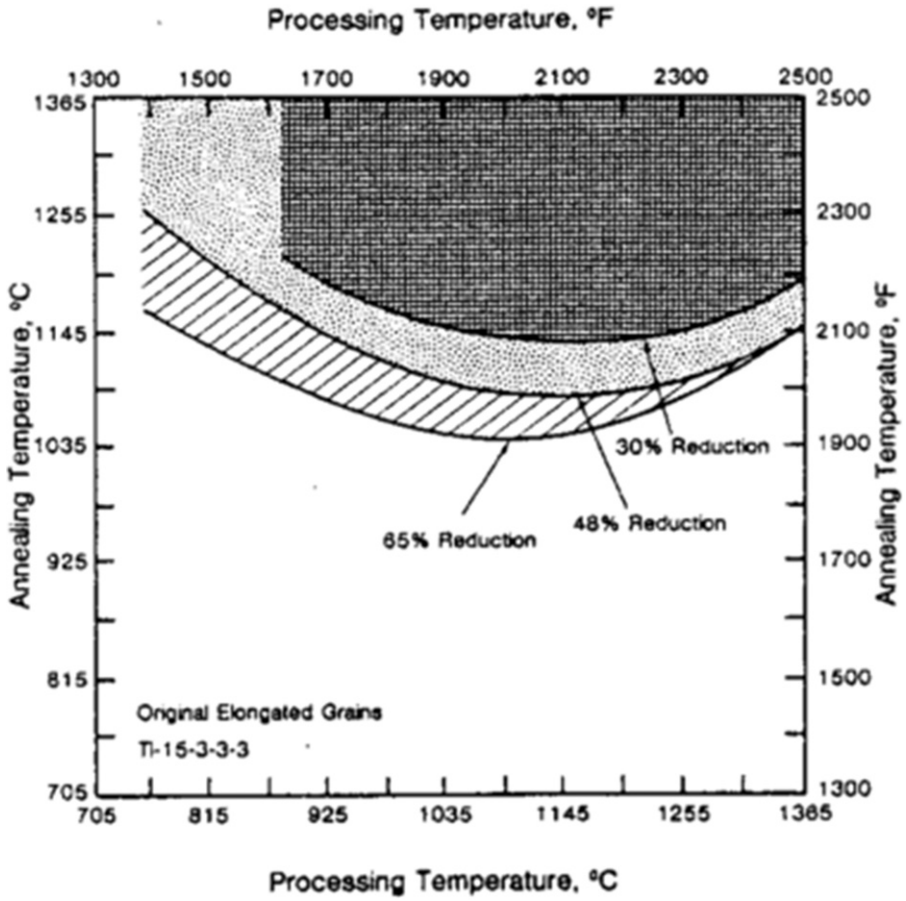


Figure 69 Effect of forging reduction on the processing map for Ti–15V–3Sn–3Cr–3Al alloy.[69]

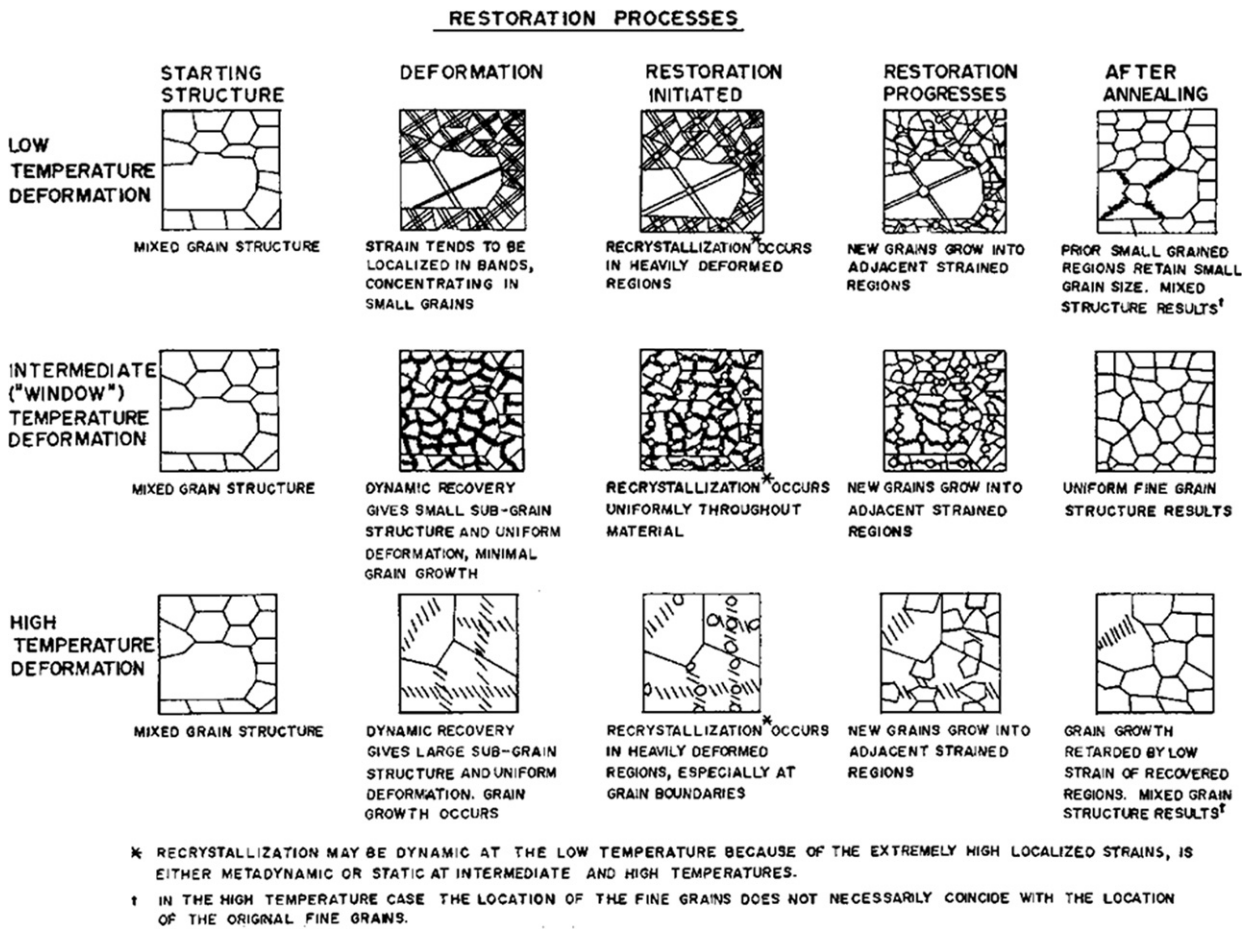


Figure 70 Schematic representation of the sequence of events during restoration process.[68]

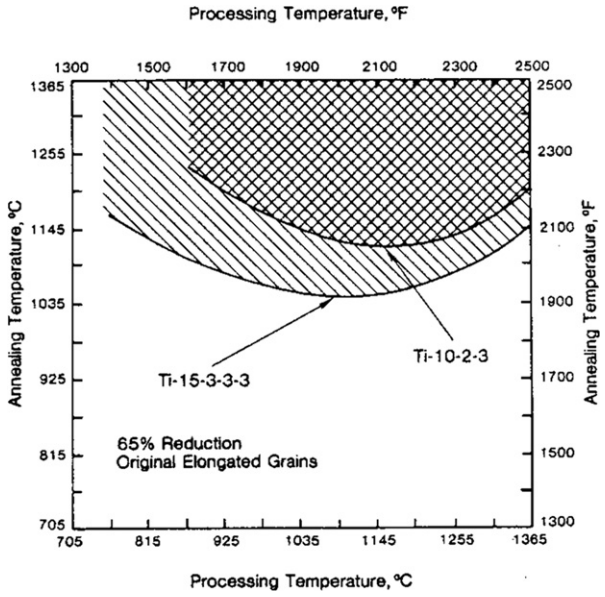


Figure 71 Effect of chemical composition on the processing map of Ti–15V–3Sn–3Cr–3Al alloy forged to 65% reduction.[69]

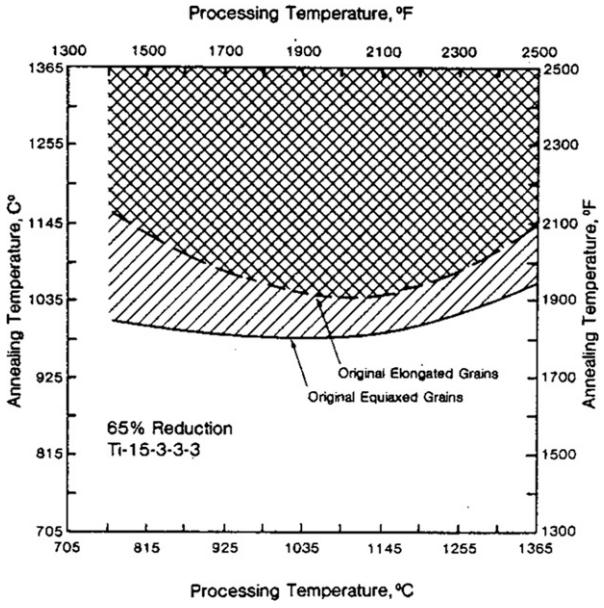


Figure 72 The combined effect of original grain shape and annealing and processing temperatures on the microstructure of Ti–15V–3Sn–3Cr–3Al alloy forged to 65% reduction.[69]

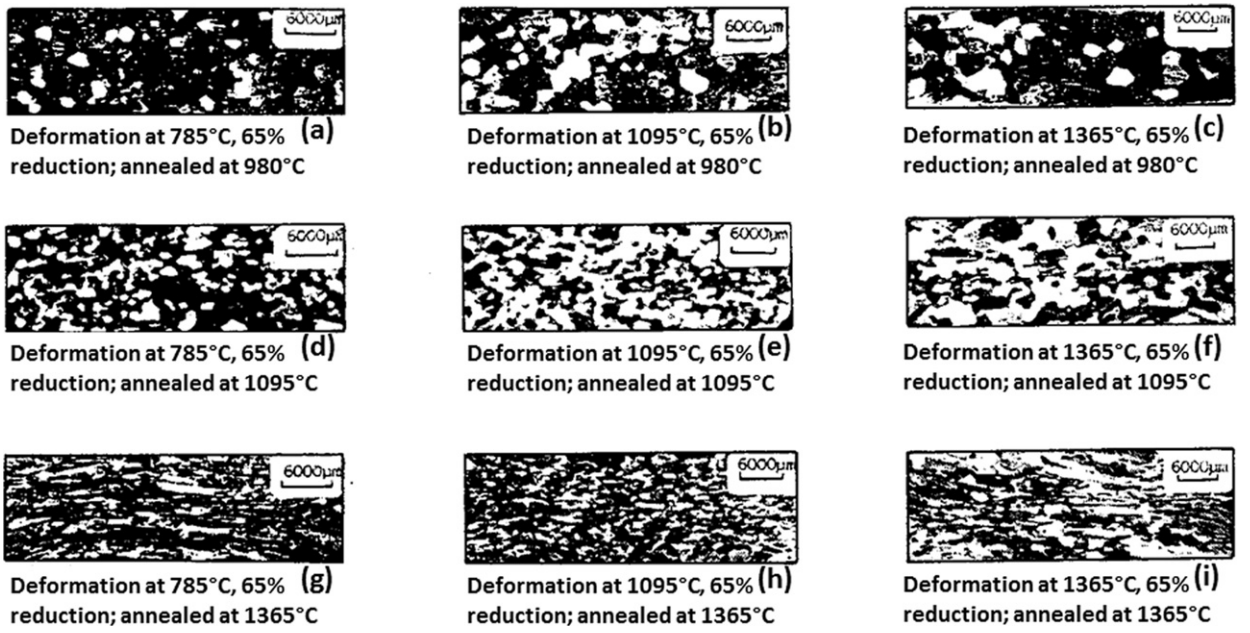


Figure 73 Microstructure of samples forged to 65% reduction at 785, 1095, and 1365 °C and subsequently annealed at 980, 1095, and 1255 °C. For this material, the processing window is defined by deformation and annealing temperature of 1095 °C.[69]

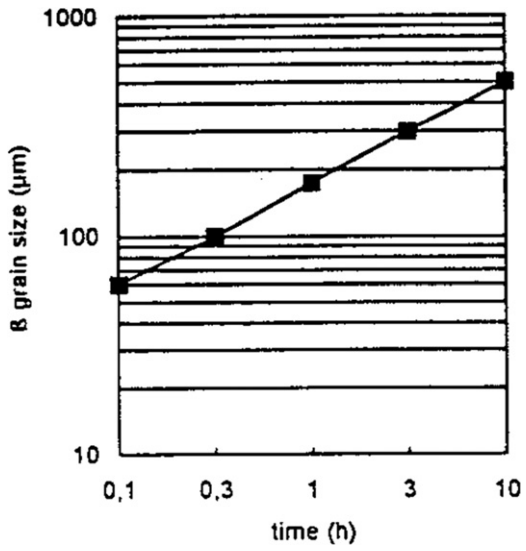


Figure 74 Grain coarsening in the β-phase field.[70]

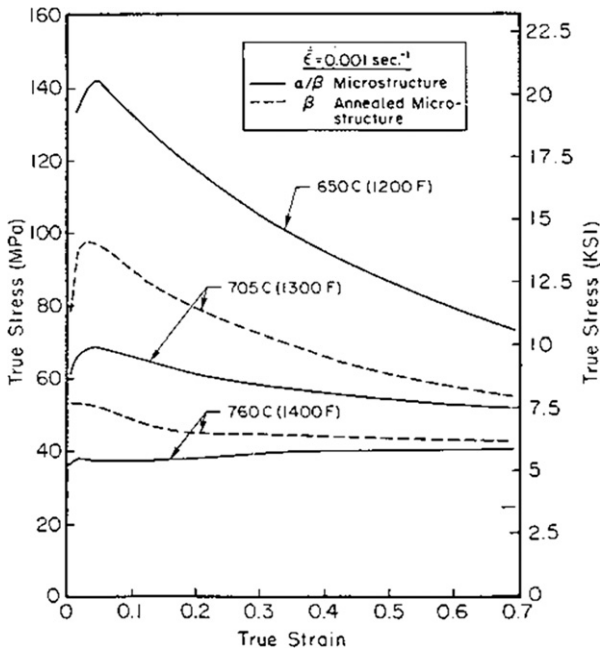


Figure 75 Flow curves of Ti–10V–2Fe–3Al alloy deformed at a strain rate of 0.001 s^{-1}.[49]

followed by α/β deformation and sub-transus annealing (Figure 88).[76] To preserve a fine-grain microstructure, excessive grain growth and, consequently, inferior mechanical properties should be eliminated by controlling and optimizing reheating and annealing parameters (Figure 89).[72]

2.11.5.3.3 Shape memory alloys

The unique shape memory effect (SME) in an equiatomic Ti–Ni alloy was first found by Buehler *et al.*[76] in 1963 at a naval ordnance laboratory. The name of the alloy, nitinol, was derived with the objective of incorporating the chemistry of the alloy and the place of invention. Although the SME was found in Au–47.5 at% Cd[77] and In–Tl[78] alloys previously, it attracted limited attention from researchers. In contrast, the TiNi alloy earned its popularity soon after its discovery, mainly due to its good mechanical properties, which were found to be suitable for various applications. Although Ti–Ni-based alloys exhibited many common characteristics with other shape memory alloys (SMAs) like SME, superelasticity (SE), two-way shape memory effect (TWSME), and others, they also exhibited

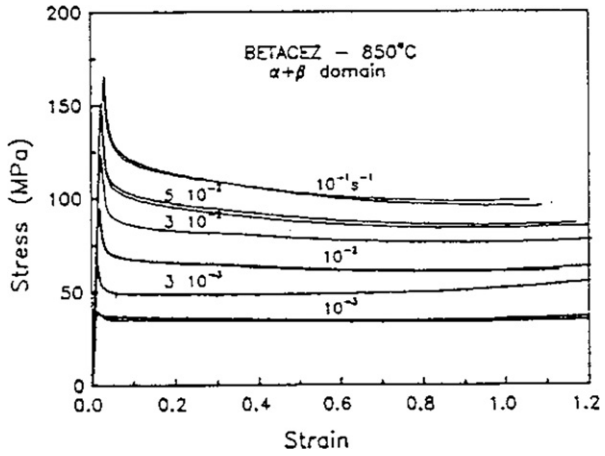


Figure 76 Flow curves of Ti–5Al–2Sn–2Cr–4Mo–4Zr–1Fe (β-CEZ) deformed at 850 °C.[53]

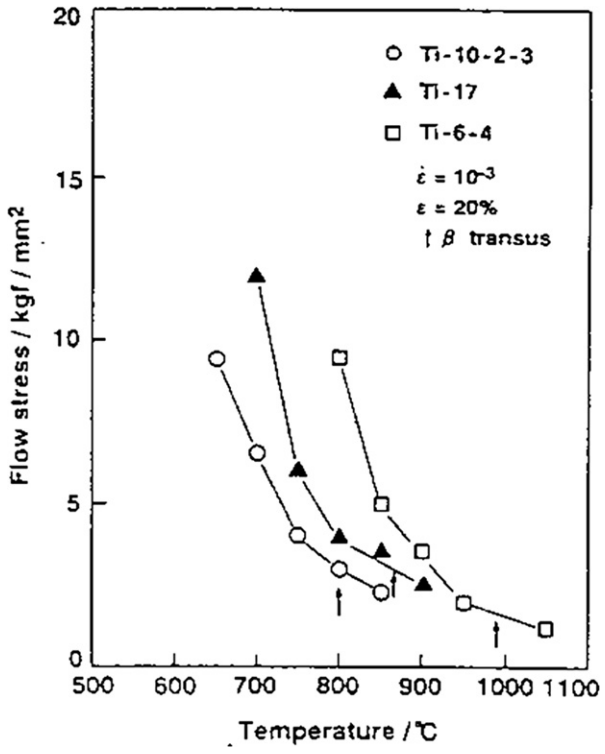


Figure 77 Flow stresses of different titanium alloys at a strain of 0.2.[71]

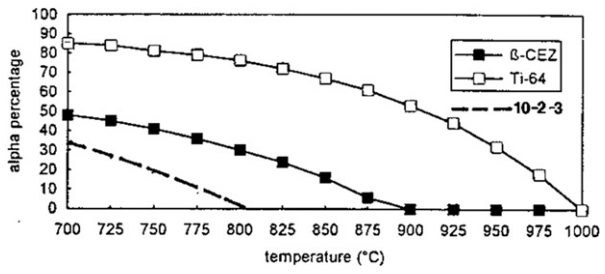


Figure 78 Variation of α-phase percentage with temperature.[70]

some additional characteristics that are quite unique compared to other SMAs. They exhibit low elastic anisotropy, as low as nearly 2, in comparison with other SMAs exhibiting a value of approximately 10 or more.[79]

Although, Ti–Ni is an intermetallics compound, it is quite ductile under certain conditions. The composition of nickel plays a vital role in deciding the transformation temperatures.[2] The austenite start temperature (A_s) for nitinol can vary from −50 to 166 °C through variation in Ni content (wt%) from 53.5 to 56.5%.[80]

2.11.5.3.3.1 Phase diagram

Figure 90 shows the phase diagram of a Ti–Ni alloy system.[81,82] The research interests related to shape memory are focused on the central portion bounded by the $NiTi_2$ and Ni_3Ti phases. The single-phase 'Ti–Ni' appears near the equiatomic composition, which is responsible for the SME. **Figure 90** also shows metastable phase equilibrium between the Ti–Ni and Ti_3Ni_4 phases, which is very useful in adjusting transformation temperatures and in designing the heat treatments schedules.[79]

The Ti–Ni phase has a B2 (CsCl) type of ordered structure with a lattice constant of 0.3015 nm at room temperature.[83] The B2 phase is retained upon quenching or slow cooling to room temperature. This is the phase that plays the essential role in the martensitic transformation (MT) and the associated SME.[79] The boundary of the Ti–Ni phase region is almost vertical on the Ti-rich side, but there is some solubility on the Ni-rich side at high temperatures. The Ti–Ni phase region becomes very narrow at temperatures below 650 °C.

2.11.5.3.3.2 Martensitic transformation in Ti–Ni alloys

The unique behavior of Ti–Ni is based on the temperature-dependent austenite–martensite phase transformation on an atomic scale, which is also called thermo-elastic MT. The thermo-elastic MT causing the shape recovery is driven due to the need of the crystal lattice structure to attain the minimum energy state at a given temperature. In Ti–Ni, the relative symmetries between the two phases lead to a highly ordered transformation in which it is possible to predict the displacements of individual atoms. The transformation eventually leads to a shape change on a macroscopic scale. The crystal structure of martensite is relatively less symmetric compared to that of the parent phase.[79]

Generally, Ti-Ni alloys show a one-stage B2 → B19′ transformation during quenching from high temperatures.[83–87] The vertical boundary in the Ti-rich side of the Ti–Ni phase region makes it difficult to get supersaturated Ti in a Ti–Ni matrix. Therefore, Ti-rich alloys have a relatively consistent matrix because equiatomic alloy and similar transformation behavior are expected. However, on the Ni-rich side, a 1 at% increase in Ni content can change the transformation temperature by more than 100 °C.

Apart from the direct transformation from B2 → B19′, there is a second type of intermediate transformation known as R-phase transformation.[79] There are usually three ways to introduce the R-phase transformation prior to the transformation to B19′ phase,[86] such that the Ti–Ni alloy transforms

Table 7 Deformation parameters for several metastable β and β-rich alloys deformed in the $\alpha + \beta$-phase field[49]

Alloy	*Temperature range (°C)*	*Strain Rate range (s^{-1})*	*Strain rate sensitivity (m)*	*Activation energy for deformation, Q_D (kJ mol^{-1})*
Ti–6Al–4V (Ti-6-4)	850	10^{-3}–10^{-1}	0.18	470–572
Ti–10V–2Fe–3Al (Ti-10-2-3)	650–790	10^{-3}–10^{-1}	0.21	255–480
Ti–5Al–2Sn–2Zr–4Mo–4Cr (Ti-17)	805–845	10^{-3}–10^{0}	0.22	437
Ti–5Al–2Sn–2Cr–4Mo–4Zr–1Fe (Beta-CEZ)	800–850	10^{-2}–10^{1}	0.27	400

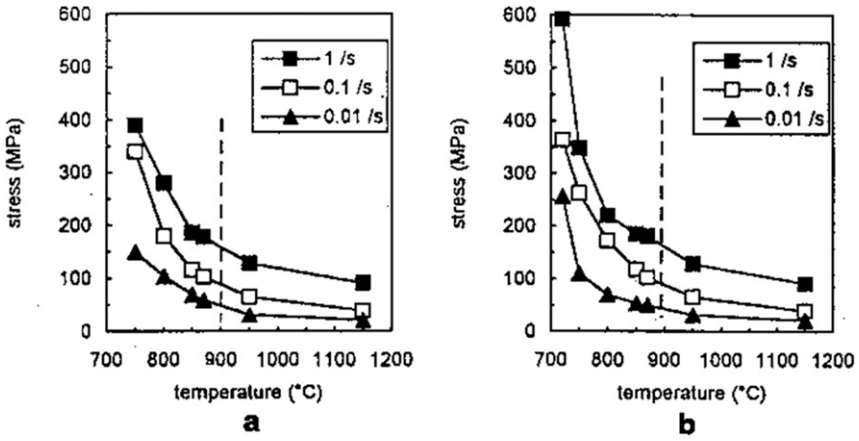


Figure 79 Flow stresses of Ti–5Al–2Sn–2Cr–4Mo–4Zr–1Fe (β-CEZ) with (a) acicular morphology and (b) equiaxed morphology.[72]

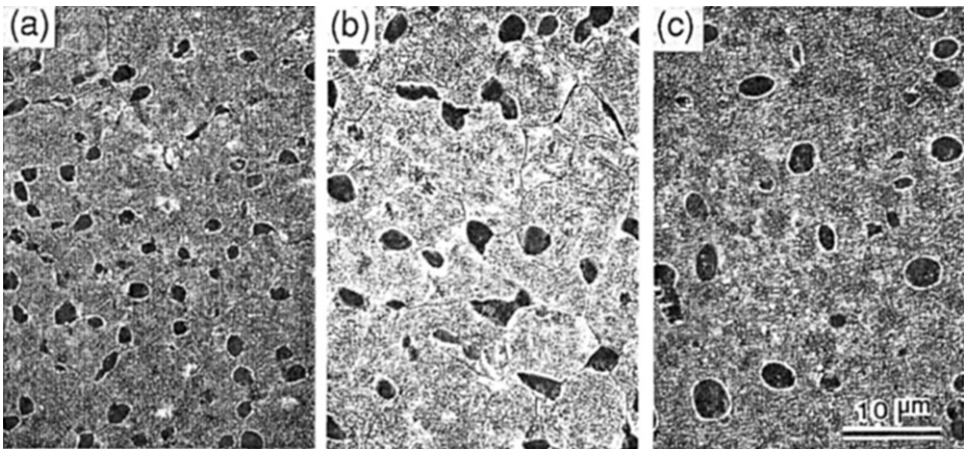


Figure 80 Microstructure of Ti–10V–2Fe–3Al following deformation at 700, 750, and 770 °C.[73]

in two-steps (i.e., B2 → R → B19′): (1) by substitution of a few percent of Ni in Ti–50 at% Ni alloy by Fe or Al; (2) by aging Ni-rich Ti–Ni alloys at proper temperatures (e.g., 400 °C) to cause the precipitation of Ti_3Ni phase; and (3) heat treatment of Ti–Ni alloys after cold-working with the aim of creating rearranged dislocation structures. In these cases, formation of both the R-phase and B19′ phase are affected by: (1) the third element (Fe or Al); (2) stress field of precipitates; and (3) stress field of dislocations. However, the effect for the B19′ phase is larger than that for the R-phase, thus making the transformation temperatures of both phases separable.

The two-step transformation also depends on the applied external stress.[88] For lower stress, the R-phase transformation temperature is higher than the B19′ transformation temperature, but it exhibits smaller stress dependence. Therefore, with increasing stress, the B19′ transformation temperature eventually exceeds the R-phase transformation temperature, and this leads to one-stage transformation.

Figure 91[79] shows the three-different possibilities of transformations in Ni–Ti-based alloys. In the schematic representation it is clearly revealed that all the alloys have a tendency to transform from B2 to B19′ martensite in

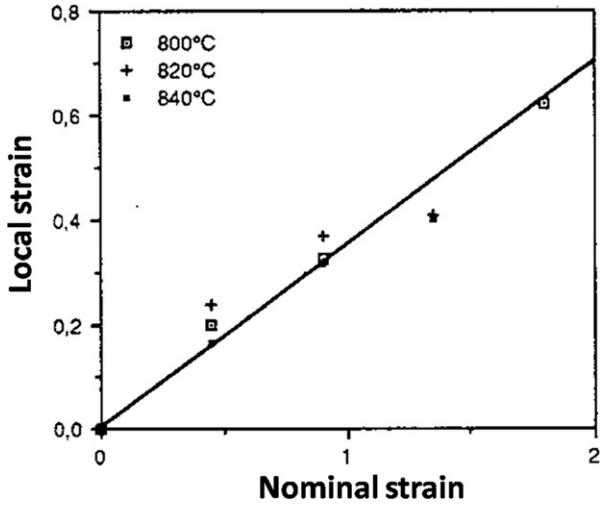


Figure 81 Strain in the α phase for different nominal strains.[53]

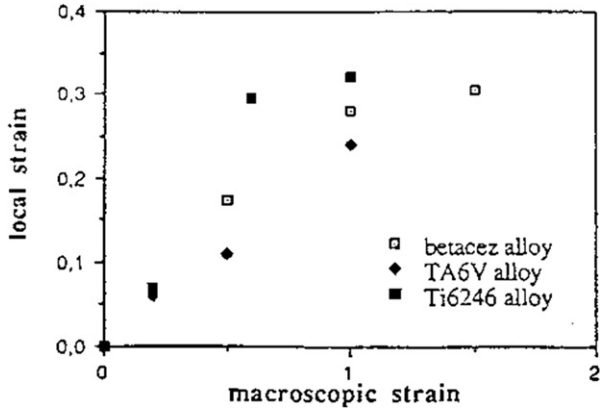


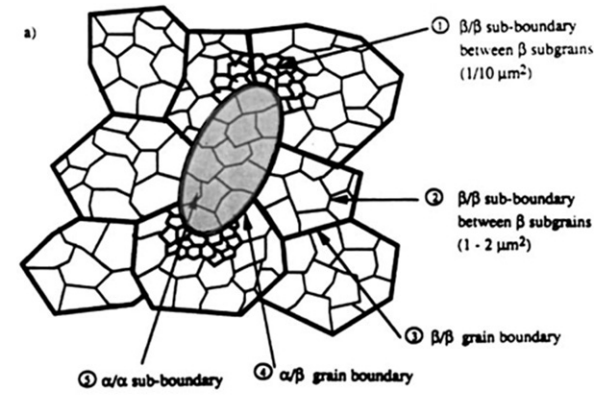
Figure 82 Strain in the α phase as a function of nominal strain for different titanium alloys.[74]

Ni-Ti-based alloys; in fact, for the solution-treated binary Ni–Ti alloys, the transformation occurs from B2 to B19′ directly, whereas for the uppercases and lowercases two successive transformations occur on continuous cooling. However, depending on the composition and heat treatment, only the first transformation may occur and the second one may be lost, because the possible transformation temperatures for the second one become too low (i.e., below 0 K) in that case.[79]

2.11.5.3.3.3 Precipitation in Ti–Ni alloys

Shape memory characteristics of the binary Ti–Ni alloy can be improved by the following treatments:

- specific thermo-mechanical treatments (TMTs), such as annealing following cold working (Ni < 50.5 at% practically),[83,89–91]
- thermal and/or stress cycling,[92–95] and
- aging after solution treatment (Ni > 50.5 at%, practically).[83,86,89,96]



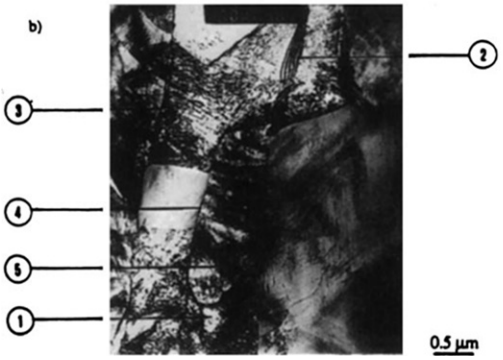


Figure 83 Formation of substructure in the α and β phases during deformation of Ti–5Al–2Sn–2Cr–4Mo–4Zr–1Fe (β-CEZ) at a temperature of 840 °C and strain rate of 0.3 s^{-1}.[74]

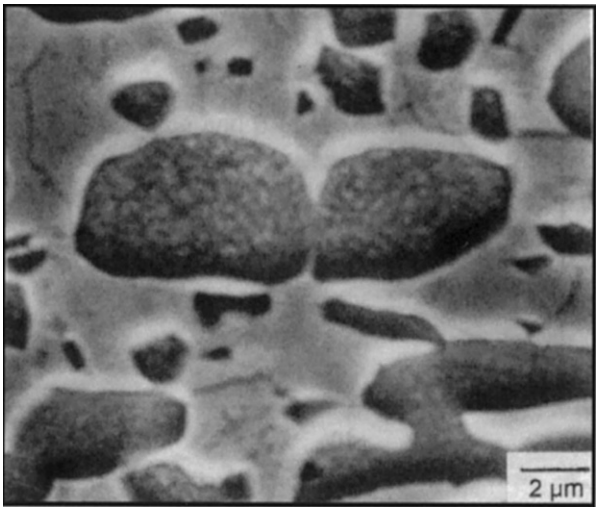


Figure 84 Formation of cusp and β-phase penetration along α/α sub-boundary.[70]

Among these treatments, the aging treatment has been found to be the most effective method for improving the shape recovery and mechanical properties of Ti-Ni-based alloys.

It is important to mention here that studies on the thermomechanical behavior of the Ti-rich Ti–Ni alloys[93,97,98] are

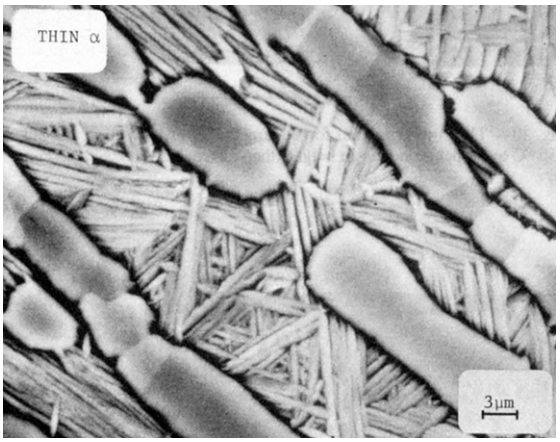


Figure 85 Channeling contrast scanning electron microscope of α-plate material deformed 20%, followed by annealing at 925 °C.[75]

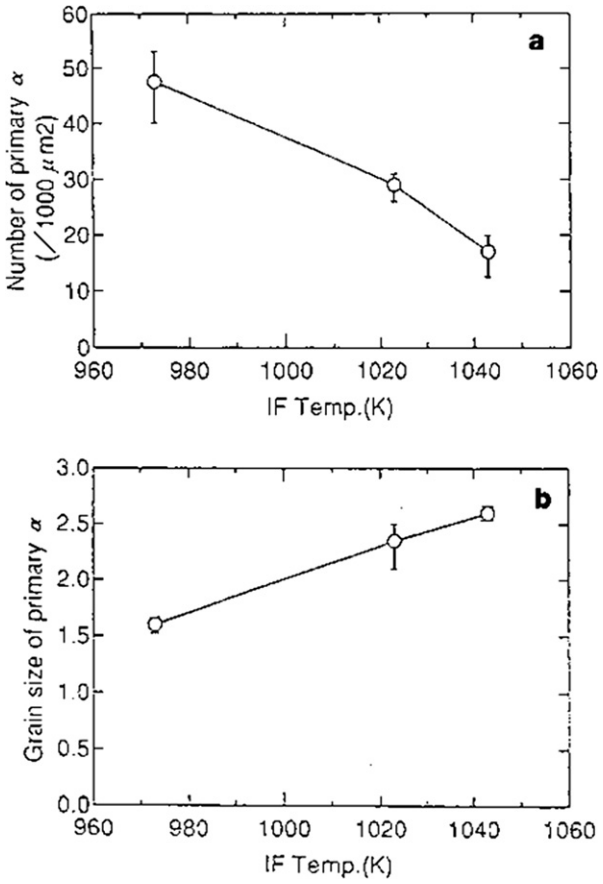


Figure 86 Effect of deformation below transus on (a) volume fraction of primary α phase and (b) size of primary α phase.[73]

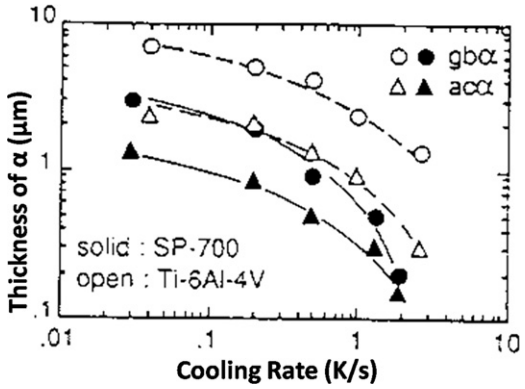


Figure 87 Thickness of grain boundary and matrix α phase for different cooling rates from the β phase.[76]

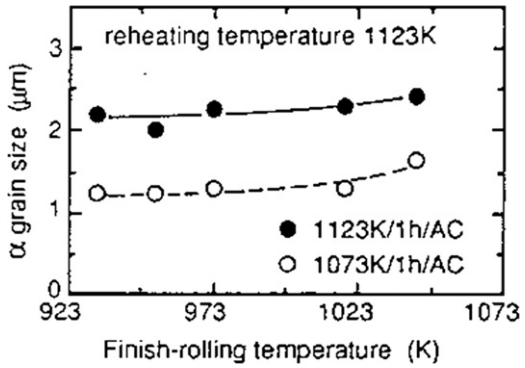


Figure 88 Effect of finish-rolling temperature on the size of the α phase.[76]

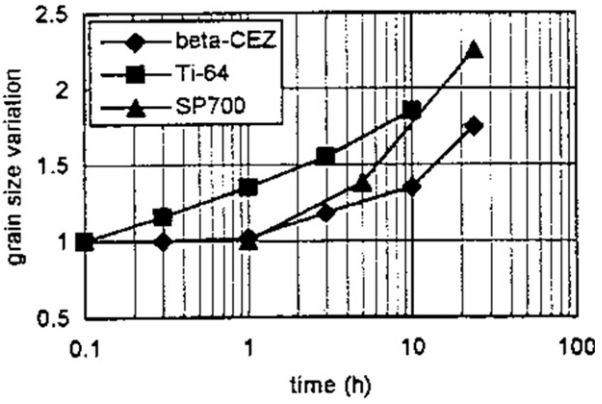


Figure 89 α-phase coarsening at 850 °C for an initial α size ranging from 2 to 5 mm for different alloys.[72]

limited in number, although Pelosin *et al.*[99] reported a detailed investigation on the premartensitic (R-phase) and the MT in the case of Ti–49.6 at% Ni alloy. It has been established that the R phase is formed by annealing of the Ti-rich Ti–Ni thin films.[100,101] Nam *et al.*[102] reported that the R-phase is also induced by rapid solidification of Ni–51Ti alloy ribbons. Both treatments form coherent Ti_2Ni particles that suppress the MT and induce the R phase. Zhang *et al.*[103] reported the effect of the equilibrium Ti_2Ni precipitate phase on the MT and shape memory behavior in the case of Ti–49 at% Ni alloy. The Ti_2Ni phase has been found to be responsible for the possible R-phase formation in this alloy.

2.11.5.3.3.3.1 Effect of thermomechanical treatment

The properties of Ti–Ni alloys are significantly affected by TMTs, which are essential to control the transformation temperatures, mechanical properties, and monotonic and cyclic

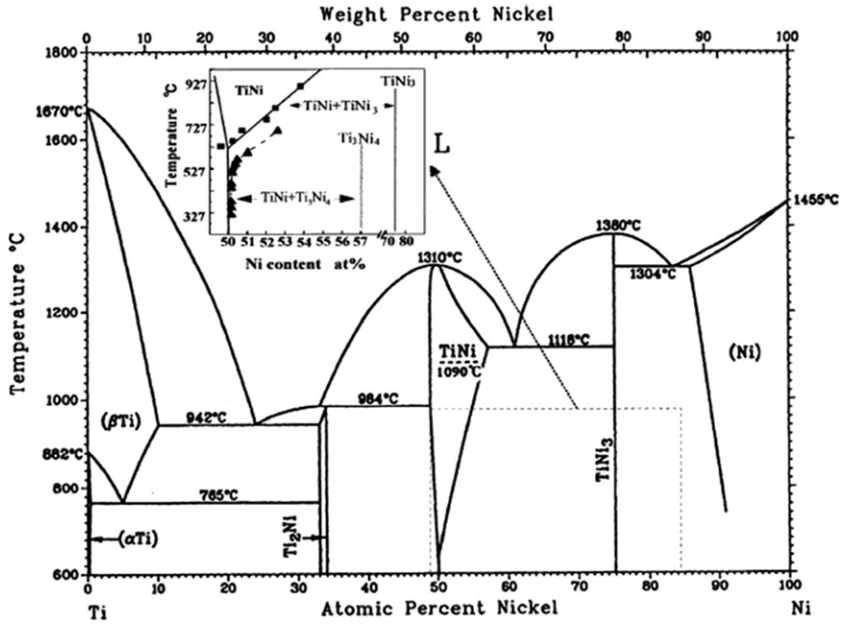


Figure 90 Phase diagram of Ti–Ni,[81] to which the phase equilibrium between the B2 and Ti_3Ni_4 is added (inset).[82]

responses. The common thermomechanical treatments are ausforming[104–106] and marforming,[106,107] in which defects are introduced into the austenitic and martensitic structures, respectively. The purposes of both ausforming and marforming are to improve the characteristic SME and pseudoelasticity (PE) by suppressing the irreversible slip deformation during the martensite reorientation (MR) and stress-induced martensitic transformation (SIMT) by raising the critical shear stress for slip.[89,104,108,109] In particular, the objectives of these thermomechanical processes are: (1) to control transformation temperatures with the aim of achieving the desired transformation path (thermally induced or stress-induced transformation at a given temperature); (2) to increase the transformation stress of the stress-induced parent-to-martensite transformation while the SME and/or PE are expected to be preserved; and (3) to enhance thermomechanical fatigue resistance.[107] Apart from the effects of marforming and ausforming, the thermomechanical treatment of Ti–Ni alloys has been reported in studies related to cold rolling and annealing[110,111] and severe plastic deformation of the SMAs.[105,107,112–114]

2.11.5.3.3.3.2 Effect of cold rolling

The reversible transformation and the concerned microstructural evolution in Ti-rich alloys are critically sensitive to the chemistry of the alloy and thermomechanical treatment to which the alloys are subjected. Phase diagram of Ti–Ni alloy exhibits that at near equiatomic composition, the parent (austenite) phase is a stoichiometric ordered phase with B2 structure. However, on the Ti-rich side, the alloy is amenable to precipitation of the Ti_2Ni phase under favorable conditions. The brittle intermetallic phase acts as the nucleation site of martensite (B19′) that, in turn, alters the composition of the matrix and volume fraction of B2 and B19′ components at room temperature in the microstructure. Such variations are critically manifested in the shape memory behavior.

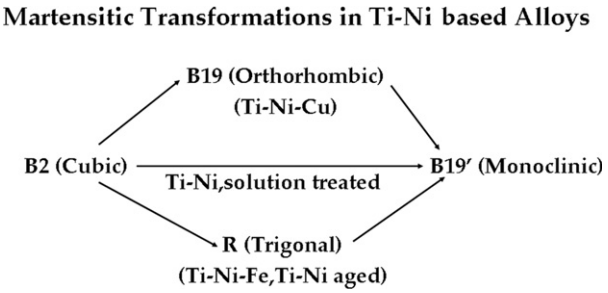


Figure 91 Three-transformation paths of Ti–Ni-based alloys.[79]

The effect of deformation is also significant regarding evolution of the microstructure. Part of the deformation energy may result in the elevation of temperature of the alloy giving rise to transformation of some B19′ back to B2.[115] Simultaneously, some part of the B2 phase may undergo deformation-induced transformation to transform into B19′ phase.[99,116] Plastic deformation of martensite that is present in the matrix also stabilizes the same against reversible transformation on withdrawal of the load. Another issue of concern is the mechanism that governs the deformation of the low-symmetry monoclinic B19′ phase.

- X-ray diffraction: **Figure 92(a)**[117] shows the room temperature X-ray diffraction (XRD) pattern of the homogenized samples quenched in the ice–water mixture. The pattern shows the presence of both austenitic (B2) and martensitic phases (B19′) in the sample. The identity of the phases has been more clearly demonstrated by deconvolution of the relevant portion of the angular (2θ) range (i.e., from 36° to 46°, as appended in the figure). The de-convoluted pattern reveals the sharp intense peak ($2\theta = 42.7°$) corresponding to (110) reflection of the austenite (B2) along with the adjacent peaks corresponding to

(101), (−111), (020), and (111) reflections of the martensite (B19′). Figure 92(b) shows the increase in volume fraction of martensite compared to Figure 92(a). Therefore, an increase in the volume fraction of the martensite in the case of samples deformed at temperatures close to 0 °C substantiates the deformation-induced transformation of the austenite into martensite. It is also apparent that the presence of B2 and B19′ phases, with remarkable differences in the inflow behavior, resulted in the inhomogeneous deformation pattern during rolling. The inhomogeneous deformation pattern is delineated by the formation of bands of martensite.

- TEM: Figure 93(a)[117] shows the finer features of the microstructure in the case of a homogenized and quenched (HQ) sample observed during TEM investigation. Figure 93(a) reveals the presence of internal twins within the martensite plates. Figure 93(b) reveals the deformed microstructure of the cold-rolled or cold-worked (CW) samples quenched in ice water. Figure 93(b) reveals the accommodation variants with evidence of coalescence and detwinning. The microstructure does not reveal any perceptible presence of twinning in the microstructure.[118]
- Tensile property: Figure 94[117] shows the tensile plots obtained from the homogenized samples quenched in ice water and subjected to rolling at temperatures close to 0 °C. In the case of homogenized and quenched samples, the plot exhibits four distinctly different stages identified in accordance with the variation of slopes. Stage I (2% strain), stage II (2–7% strain), stage III (7–15% strain), and stage IV (>15% strain) correspond to the initial elastic deformation, deformation concerning recovery strain, uniform elastic deformation of reoriented martensite, and plastic deformation of martensite, respectively. In contrast to the homogenized and quenched samples, the tensile plots of the deformed samples do not reveal the prominent iso-stress plateau region corresponding to the stage II deformation.

The absence of iso-stress plateau[91,119,120] in the tensile plots of the deformed samples may be attributed to the fact that in the deformed samples, the process related to the recoverable strain like martensite reorientation, variants coalescence, and detwinning have partially occurred prior to cold deformation. After the initial elastic yielding, plastic deformation of the oriented martensite sets in and overlaps with the mechanisms related to the recoverable strain associated with the remaining misaligned martensite. This results in plastic deformation with steeper slopes of work hardening, as evident from the stress–strain plots (Figure 94).

The increasing slope observed in the case of deformed samples in stage II of the tensile curves implies the necessity of the increase in stress with the increase in strain for martensite reorientation and variant coalescence in stage II of tensile deformation. The necessity of increasing stress may be explained in terms of the varying size of the martensite plates present in the microstructure, which lead to

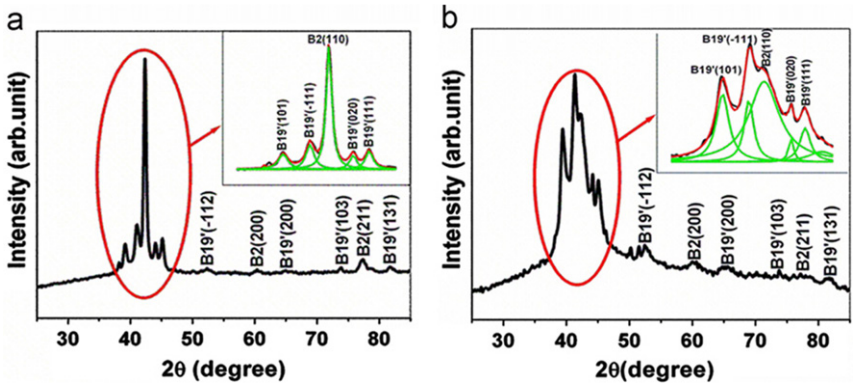


Figure 92 Room temperature X-ray diffraction patterns of the (a) homogenized and quenched (HQ) and (b) cold-rolled (CW) samples (the angular range (2θ) from 36° to 46° in the patterns is de-convoluted and shown as insets).[117]

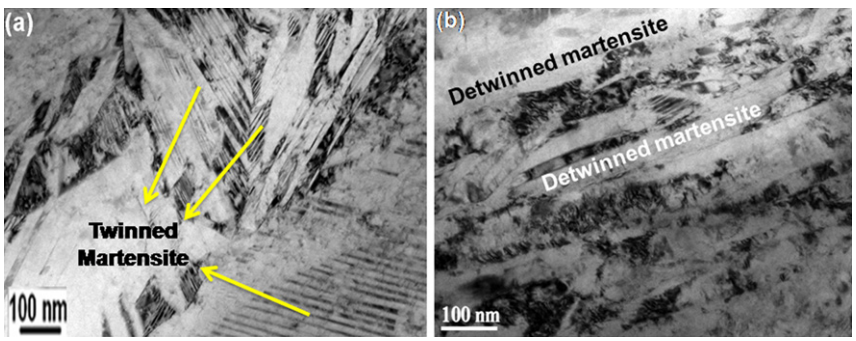


Figure 93 TEM images of (a) homogenized and quenched (HQ) and (b) cold-rolled (CW) samples without aging treatment.[117]

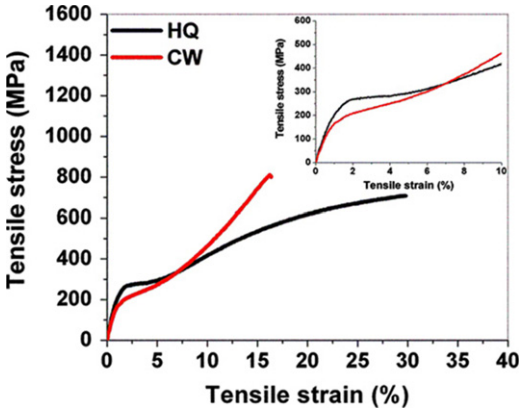


Figure 94 Tensile plots of homogenized and quenched (HQ) samples and cold-rolled (CW) samples.[117]

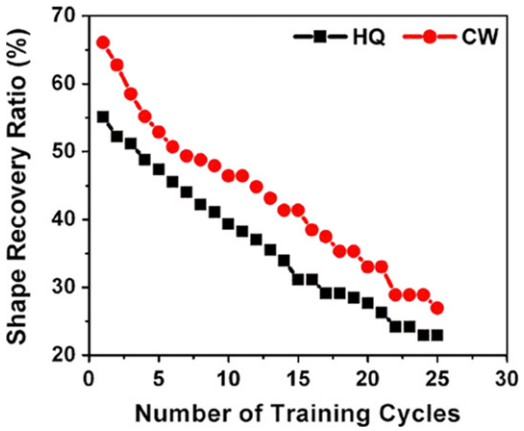


Figure 95 Recovery ratio (%) vs. number of training cycles of the homogenized and quenched (HQ) and cold-rolled (CW) samples.[117]

the microscopic heterogeneity in the process of microstructural transformation. In fact, plates of different sizes necessitate different levels of strain for undergoing the microstructural transformation associated with stage II straining. During the course of subsequent plastic straining, dislocation multiplication, slip, and dislocation pile-ups at twin interfaces are the dominant mode of plastic deformation.[115] However, as the martensite structure becomes heavily deformed, localization of the plastic deformation is expected to give rise to plastic incompatibilities, limiting the further deformation.

In the case of Ti-rich or equiatomic Ti–Ni alloy, the improvement in SME for the cold-deformed samples can be explained in terms of additional strengthening effects, as evident from the tensile plots shown in **Figure 94**.[117] Strengthening by cold working essentially increases the critical resolved shear stress (CRSS) for slip deformation in martensite. With the increase in CRSS, the onset of permanent plastic strain is delayed, favoring the extension of the region of recoverable strain. However, continuous thermal cycling of the martensite under bending strain greater than the recoverable strain introduces more and more permanent strain in martensite and results in the reduced SME.

- Shape recovery: **Figure 95**[117] shows the variation of the shape recovery ratio as the function of the number of training cycles. It is seen that shape recovery is perceptibly higher in the case of the deformed sample as compared to the homogenized and quenched sample. The difference in shape recovery is maintained over the chosen range of the training cycle. The shape recovery experiment indicated improved shape recovery ratio in the case of the deformed samples. Moreover, in the case of the present samples, the thermally activated slip-controlled mode is not the favored mode under the low-temperature deformation condition. The low-temperature strain accommodation like twinning is not as effective as slip to exert hindrance for the martensite reorientation and reversible transformation during thermal cycling. Therefore, the improvement may be attributed to the increase in CRSS due to the formation of finer martensite plates and the consequent delay in the onset of plastic straining during the shape deformation, resulting in improved recovery behavior.

2.11.5.3.3.3.3 Effect of aging treatment

It is well established that the shape memory characteristics of the binary Ti–Ni alloys can be improved by the following treatments: (1) cold working followed by annealing[83,89–91]; (2) aging treatment in Ni-rich alloys[83,85,86,90,92]; (3) thermal and/or stress cycling[92,94,95]; and (4) the addition of third elements.[121] In the case of treatment (1), the binary Ti–Ni alloys were first deformed below the recrystallization temperature and then subjected to annealing heat treatment. In the second type of treatment (2), the Ni-rich Ni–Ti alloys were first solutionized and then aged at different time–temperature combinations. The third treatment (3) involves heating and subsequent rapid cooling cyclically over a range of temperatures and/or implementation of the loading–unloading cycle in the austenitic state of the alloy. Regarding the last case (4), the addition of a third element in the Ti–Ni binary system influences the martensitic transition temperature and results in the formation of 'premartensitic' R phase, which affects the SME and PE. These treatments have focused mainly on the equiatomic Ti–Ni[122,123] or Ni-rich alloys.[88] Very few studies are concerned with similar attempts in the case of Ti-rich Ti-Ni alloys.[97,98,103] Among the aforementioned treatments, the aging treatment has been found to be the most effective method to improve the shape memory characteristics and mechanical properties of the binary Ti–Ni alloys. The potential of the aging treatment is attributed to the formation of fine precipitates, which act as effective obstacles for the movement of dislocations, thereby increasing the CRSS for slip.[104,108,109] In the case of Ti-rich Ti–Ni alloy, the Ti_2Ni precipitate phase formed under the favorable process schedules acts as the nucleation site of the martensite (B19′).[115] As the precipitation reaction proceeds, formation of Ti-rich precipitate is accompanied by the lowering of the Ti content in the Ti–Ni matrix. Therefore, the transformation temperature tends to decrease upon aging.[103] The size and coherency of the precipitates affect the transformation and the mechanical strength of the alloy. The CRSS for slip also increases due to the precipitation hardening. Further, continuation of the aging treatment results

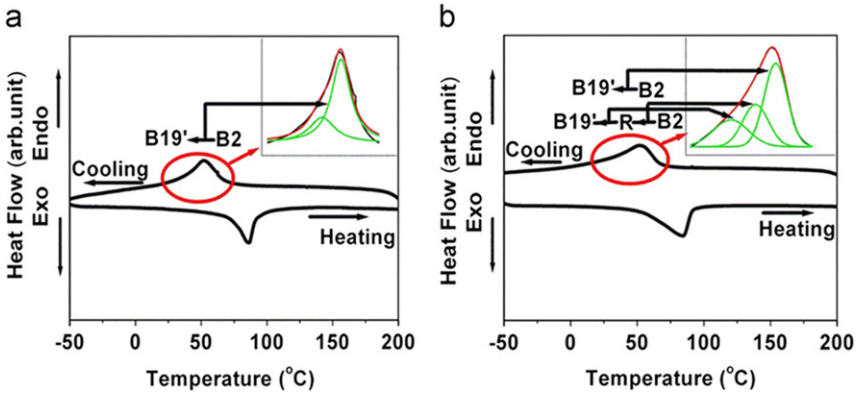


Figure 96 Differential scanning calorimetry thermograms of (a) homogenized and quenched (HQ) and cold-rolled (CW) samples at a heating/cooling rate of 10 °C min^{-1} (the one-stage and two-stage transformations are demonstrated by de-convolution of the appropriate temperature range in the cooling curve).[126]

in an increase in the size of the precipitates and consequent deterioration of mechanical strength. It is well accepted that the interaction of the coherent Ti_2Ni precipitate phase formed during aging with the dislocation substructures formed during thermomechanical processing (i.e., combination of aging treatment and deformation below recrystallization temperature) evolves into a microstructure that favors the formation of the R phase prior to the formation of the B19′ phase.[124] The stress field around the coherent precipitates exerts strong resistance to the formation of B19′[125] because it is associated with a large lattice deformation. On the contrary, the premartensitic R-phase transformation involving smaller lattice deformation is less affected by the presence of precipitate. Thus, the aged Ti-rich Ti–Ni alloys usually undergo a two-stage B2→R→B19′ transformation on cooling from the B2 regime, which is related to the interaction of the Ti_2Ni phase and the dislocation substructures formed during thermomechanical treatments with moving martensite/austenite boundaries.[114,115]

- Differential scanning calorimetry: The reversible transformation behavior of the homogenized sample with and without the subsequent deformation (HQ and CW samples) has been investigated by conducting the differential scanning calorimetric measurements. **Figures 96(a)** and **96(b)**[126] shows the differential scanning calorimetry (DSC) thermograms of the samples at a heating/cooling rate of 10 °C min^{-1}. In the case of HQ samples, one-stage transformation (B2→B19′) takes place during cooling and is depicted by the de-convoluted heat flow profiles of the concerned temperature range in the cooling curve, as appended in the inset of **Figure 96(a)**. Similarly conducted de-convolution in the case of the CW (**Figure 96(b)**) samples exhibits one-stage (B2→B19′) and two-stage (B2→R→B19′) transformations during cooling.

  Table 8[126] presents the enthalpy changes (heat of transformation) related to the one-stage transformations for HQ samples and the multiple stages (both one and two stages) of transformation in the case of CW sample. The heat of transformations decreases because of the prior deformation in the case of the CW sample as compared to the HQ samples.[127]

Table 8 Heat of transformation ΔH (J g^{-1}) of homogenized and quenched (HQ) and cold-rolled (CW) samples at a cooling rate of 10 °C min^{-1}[126]

Sample	*Transformation*	*Heat of transformation ΔH (J g^{-1})*	*Heat of transformation ΔH (J g^{-1}) (from literature)*
HQ	B2→B19′	42.33	33.8±2
	B2→B19′	21.49	25.22
CW	B2→R	7.39	6.36
	R→B19′	8.99	18.18

- High-temperature XRD: The XRD patterns of the HQ and CW samples recorded at different temperatures as shown in **Figures 97(a)** and **97(b)**[126] depict the reversion behavior of B19′ to B2 during heating. The diffraction patterns for the HQ samples recorded at 100 °C reveal the presence of both the B2 and B19′ phases. With increasing temperature, the amount of B19′ is gradually reduced and only the peaks corresponding to (110) and (211) reflections of the B2 phase appear in the pattern recorded at 200 °C. During cooling from 200 °C to room temperature at a rate of 10 °C min^{-1}, the B19′ appears along with the B2 phase. In the case of the CW sample, the diffraction patterns obtained at 100 °C reveal the dominant presence of the B19 phase along with nominal intensity of the B2 phase. With increase in temperature to 200 °C, the intense and sharp B2 peak corresponding to (110) reflection appears in the pattern more prominently. However, in contrast to the HQ sample, presence of the B19′ phase is evident in the XRD pattern of the CW sample recorded at 200 °C. Complete transformation of the B19′ phase to the B2 phase is evidenced in the XRD pattern recorded at 300 °C. After cooling from 300 °C to room temperature at a rate of 10 °C min^{-1}, the peak corresponding to (020) reflection of the B19′ phase and that of the B2 phase appear in the XRD pattern.

  Therefore, the XRD analysis conducted at different temperatures indicates that the plastic strain accumulated in the CW sample effectively stabilizes B19′ and B2 phases during heating and cooling experiments, respectively. The results

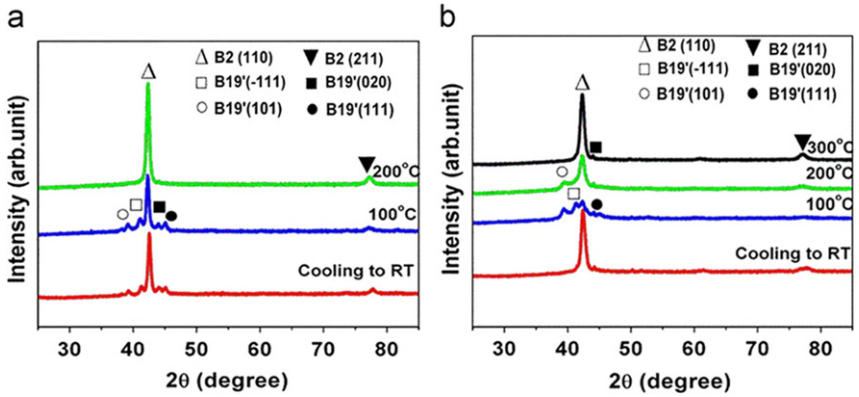


Figure 97 Temperature-dependent X-ray diffraction patterns of the (a) homogenized and quenched (HQ) and (b) cold-rolled (CW) samples.[126]

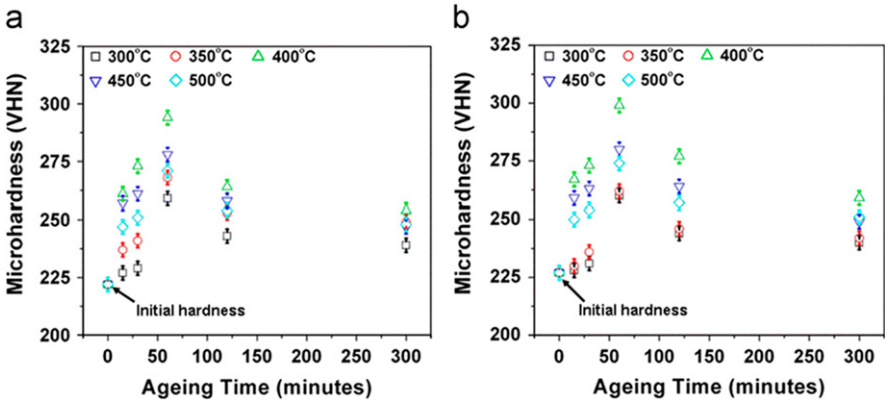


Figure 98 Variation in microhardness (VHN) with aging time at different aging temperatures in the case of (a) homogenized and quenched (HQ) and (b) cold-rolled (CW) samples.[126]

also indicate the effective aging response of the samples, particularly for the deformed ones, at temperature higher than 300 °C.

In view of the results presented in **Figures 96** and **97**, age-hardening behavior of the present samples was studied at selected temperatures in the range of 300–500 °C for different isothermal holding times.

- Microhardness: **Figures 98(a)** and **98(b)**[126] show the variation of hardness (VHN) with aging time at different aging temperatures for HQ and CW samples at a load of 300 gf. Comparison of the hardness results indicates that for all the samples, the maximum hardness values have been achieved for aging treatment conducted at 400 °C for 60 min. Moreover, **Figure 98** shows that the maximum hardness has been achieved after increasing the aging time from 30 to 60 min, beyond which the variation is marginal. Therefore, the results presented in **Figure 98** suggest the combination of 400 °C temperature and 60 min duration as the favorable aging conditions for the present alloy.
- Room temperature XRD: **Figures 99(a)** and **99(b)** shows the room temperature XRD patterns of the HQ and CW samples after aging at 400 °C for 60 min followed by quenching in ice-water solution. The XRD patterns reveal the presence of austenite (B2) and martensite (B19′) phases in all the samples. The angular range (2θ) from 36° to 46° in the patterns is de-convoluted and appended as the insets in **Figures 99(a)** and **99(b)**. In the case of aged HQ samples, the presence of the Ti-rich Ti_2Ni precipitate phase is evident, as well as the presence of B2 and B19′ phases. The deformed samples after aging treatment have yielded a higher volume fraction of martensite in the quenched microstructure as demonstrated by the XRD pattern shown in **Figure 99(b)**. This may be attributed to the role of the plastic strain in refinement of the B2 microstructure during the aging treatment, which, in turn, facilitates the MT. Moreover, the XRD patterns of the deformed samples prior to the aging treatment also show the presence of perceptible amounts of premartensite in the R phase.[128] The Ti_2Ni phase along with the B2 and B19′ phases are also evident.
- SEM: **Figures 100(a)** and **100(b)**[126] shows the SEM images of the homogenized (900 °C) and quenched (in ice water) samples that were aged at 400 °C for 60 min followed by ice-water quenching. It is apparent that the microstructures mainly constitute martensite plates, as revealed in **Figure 100(a)**. It is apparent from **Figure 100(b)** that in several locations, the plates have formed around the coarser precipitates, giving rise to a star-like feature, and such plates have grown to larger sizes relative to the martensitic plates formed elsewhere. Therefore, the coarser precipitates act as the preferential site for martensite

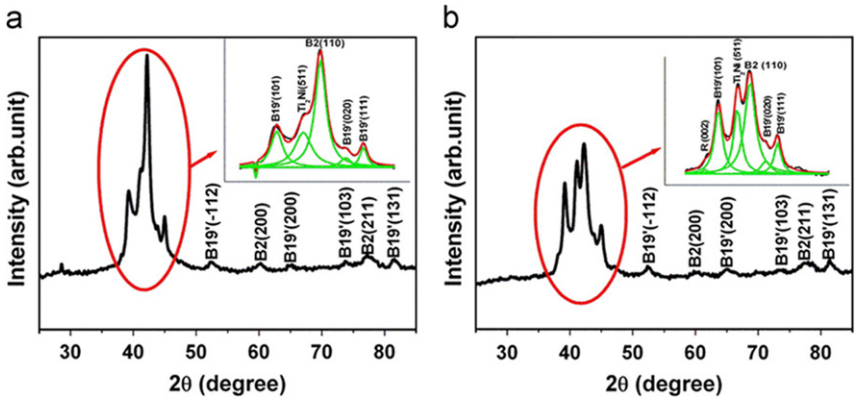


Figure 99 Room temperature X-ray diffraction patterns of the (a) homogenized and quenched (HQ) and (b) cold-rolled (CW) samples followed by aging treatment at 400 °C for 60 min (the angular range (2θ) from 36° to 46° in the patterns is de-convoluted and shown as insets).[126]

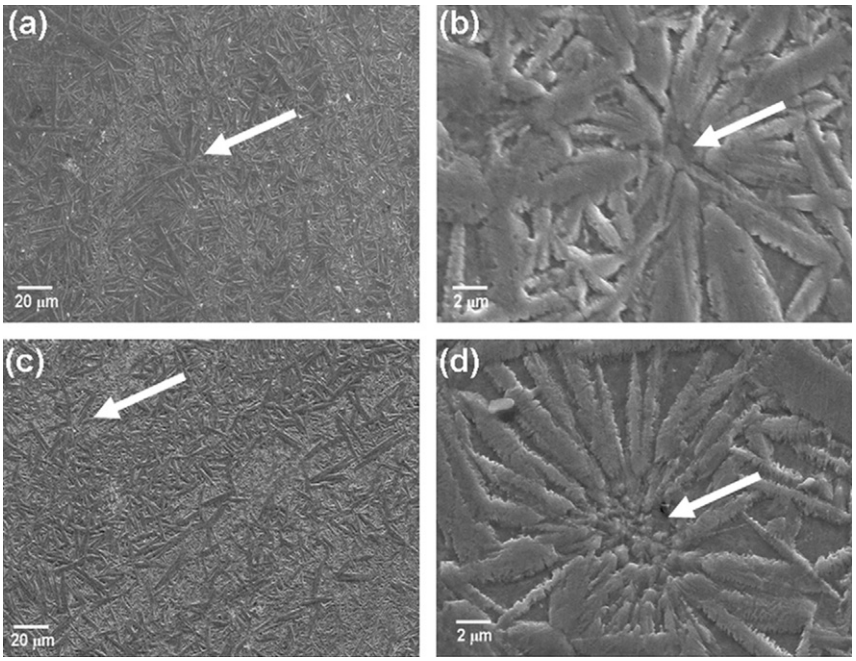


Figure 100 Scanning electron microscope (SEM) images of homogenized and quenched (HQ) sample aged at 400 °C for 60 min showing (a) distribution and (b) morphology of the martensite plates. SEM images of cold-rolled (CW) sample aged at 400 °C for 60 min showing (c) distribution and (d) morphology of the martensite plates (preferential sites for the martensite nucleation are suitably marked by arrows).[126]

nucleation, which has also been reported in previous studies.[115] **Figures 100(c)** and **100(d)** shows the SEM images of the CW (30%) samples aged at 400 °C for 60 min followed by quenching in ice water. The microstructures reveal the random distribution of martensites plates with finer and coarser size scales. The micrographs also reveal significant reduction in the tendency for banding, as observed in the deformed samples, prior to aging treatment.[129] Therefore, it is apparent that the aging treatment has significantly reduced the effect of strain concentration along the shear direction and results in the formation of favorable volume fraction of uniformly distributed martensite. Occasionally, martensites are nucleated from the preferred sites, as revealed in **Figure 100(d)**.

- TEM: **Figure 101(a)**[126] shows the microstructural features observed during TEM studies of the HQ samples subjected to the aging treatment followed by ice-water quenching. **Figure 101(a)** shows the presence of Ti-rich precipitate phase (Ti_2Ni) formed during the aging treatment. **Figure 101(b)** shows the precipitate distribution in the case of CW samples subjected to the aging treatment followed by ice-water quenching. It is evident from the microstructure that the maximum size of the precipitate is less than 50 nm.
- Tensile property: **Figures 102(a)** and **102(b)**[126] presents the tensile plots obtained at different strain rates (4×10^{-2}, 4×10^{-3}, 4×10^{-4} s^{-1}) for HQ and CW samples subjected to the aging treatment. It is evident that with the increase in the strain rate, the plateau region concerning stage II of

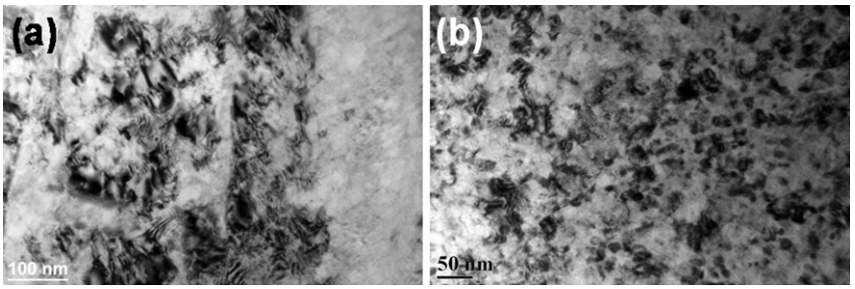


Figure 101 (a) Transmission electron microscopy (TEM) images of homogenized and quenched (HQ) sample after aging at 400 °C for 60 min show the presence of the Ti_2Ni precipitate phase and the B19′ phase. (b) TEM images of cold-rolled (CW) sample after aging at 400 °C for 60 min show the presence of the Ti_2Ni precipitate phase.[126]

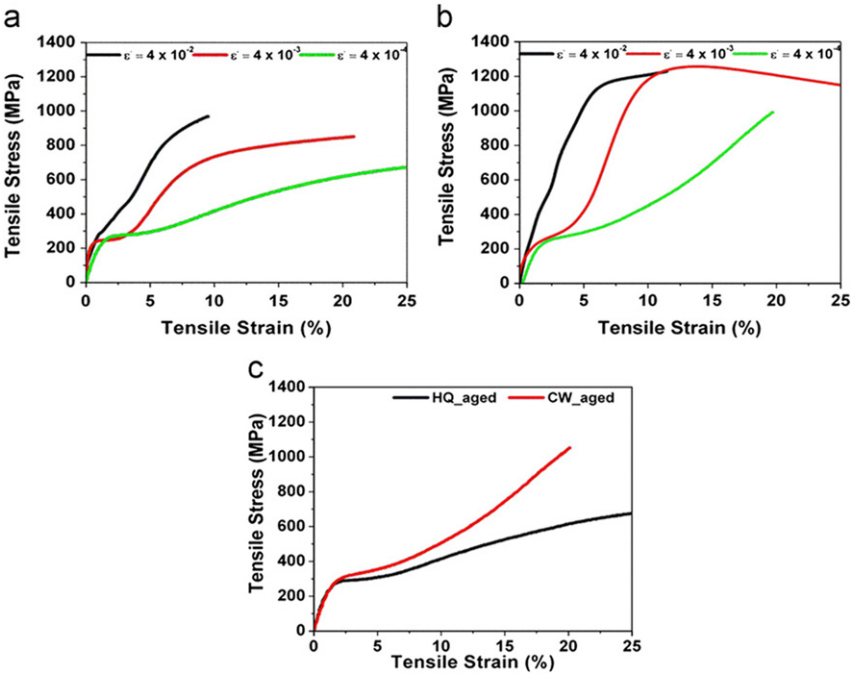


Figure 102 Tensile stress vs. strain plots of (a) homogenized and quenched (HQ) and (b) cold-rolled (CW) samples followed by aging treatment at 400 °C for 60 min at strain rates of 4×10^{-2}, 4×10^{-3}, and 4×10^{-4} s^{-1}. (c) Tensile stress vs. strain plots of HQ and CW samples followed by aging treatment at 400 °C for 60 min at a strain rate of 4×10^{-4} s^{-1}.[126]

deformation is gradually diminished and almost completely disappears at a strain rate of 4×10^{-2} s^{-1} for all the tensile plots. The strain hardening has remarkably increased with the increase in the strain rate in stage III of deformation. It is also interesting to note that the tendency of necking is evident in the case of deformed samples at the intermediate strain rate value of 4×10^{-3} s^{-1}. The results clearly establish the strain rate sensitivity of the samples not only in stages III and IV but also in stage II. The response is most prominent in the case of deformed samples. Figure 102(c)[126] compares the tensile plots of the samples subjected to different processing routes at the strain rate of 4×10^{-4} s^{-1}. It is evident that the CW samples exhibit more pronounced work hardening than the HQ samples.

- Shape recovery: Figure 103(a)[126] shows the variation in the shape recovery ratio with aging time and the aging temperature of 400 °C for HQ and CW samples. It is evident that with increases in aging time, the shape recovery ratio increases up to 60 min and then decreases. Continuation of aging up to 120 min results in a sharp decrease in the shape recovery ratio value. After prolonged aging beyond 120 min, the shape recovery ratio reaches a plateau. Comparisons of the variations in microhardness (Figures 98(a) and 98(b)) and shape recovery ratio (Figure 103(a)) values as functions of aging time reveal a unique agreement, corroborating that the shape recovery behavior of the present alloy critically depends on the aging condition and is maximized at the peak aging condition.

  Figures 103(b) and 103(d)[126] shows the variation of shape recovery ratio as a function of the number of training cycles for HQ and CW samples for durations of 15, 60, and 300 min. It is seen that with all aging conditions, shape recovery is higher in the case of CW samples compared to

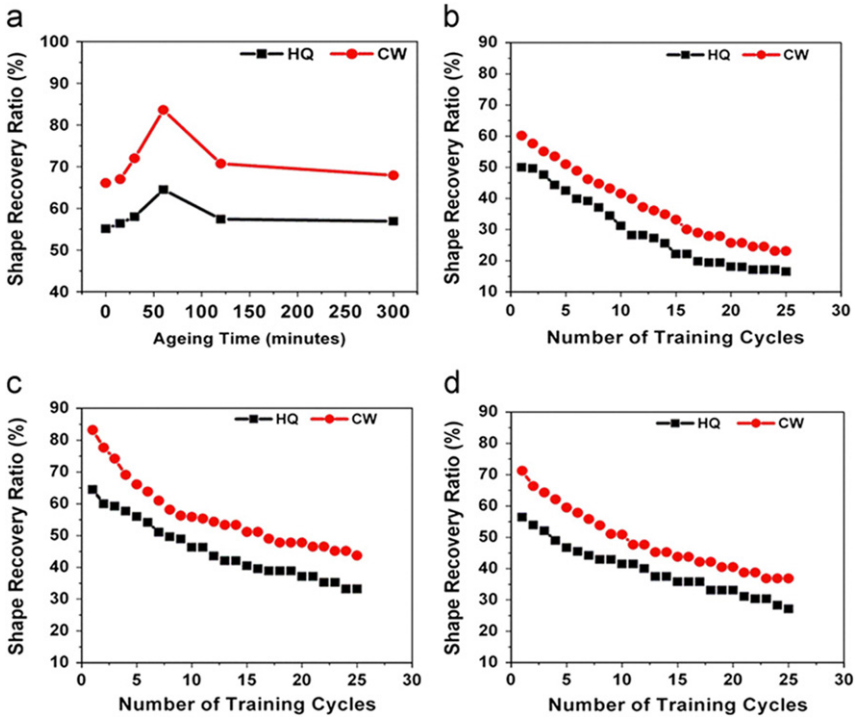


Figure 103 (a) Variation of the shape recovery ratio (%) with aging time at 400 °C for homogenized and quenched (HQ) and cold-rolled (CW) samples and plots of the shape recovery ratio (%) vs. number of training cycles of HQ and CW samples aged at 400 °C for durations of (b) 15 min, (c) 60 min, and (d) 300 min.[126]

the HQ samples. Such a difference in shape recovery is maintained over the range of the training cycles. The maximum shape recovery ratio for different samples has been obtained at 60 min of holding time (**Figure 103(c)**).[126] It is also evident that the degradation in the shape recovery ratio is less pronounced in the case of CW samples, as depicted in **Figures 103(b)** and **103(d)**.

References

1. Polmear, I. J. *Light Alloys from Traditional Alloys to Nanocrystals*, 4th ed.; Butterworth-Heinemann (Elsevier): Oxford, 2006. (first published 1981).
2. Polmear, I. J. Overview: Recent Developments in Light Alloys. *Mater. Trans. JIM* **1996**, *37* (1), 12–31.
3. Hickman, B. S. The Formation of Omega Phase in Titanium and Zirconium Alloys: A Review. *J. Mater. Sci.* **1969**, *4*, 554–563.
4. Zhecheva, A.; Sha, W.; Malinov, S.; Long, A. Enhancing the Microstructure and Properties of Titanium Alloys through Nitriding and Other Surface Engineering Methods. *Surf. Coat. Technol.* **2005**, *200*, 2192–2207.
5. Polmear, I. J. *Light Alloys-Metallurgy of the Light Metals*, 3rd ed.; Edward Arnold: London, 1981; pp. 167–175.
6. Donachie, M. J., Jr. *Titanium – A Technical Guide*, 2nd ed.; ASM International: Materials Park, OH, 1988; pp. 353–365.
7. Flower, H. M. Microstructural Development in Relation to Hot Working of Titanium Alloys. *Mater. Sci. Technol.* **1990**, *6* (11), 1082–1092.
8. Neal, D. F. Alloy Development. In *Titanium '95, Science and Technology, Birmingham, 1995*; Blenkinsop, P. A., Evans, W. J., Flower, E. M., Eds.; The Institute of Materials, Cambridge University Press: London, 1996; pp. 2195–2204.
9. Ray, K.; Poole, W. J.; Mitchell, A.; Hawbolt, E. B. In *Advances in the Science and Technology of Titanium Alloy Processing*; Weiss, I., Srinivasan, R., Bania, P., Eylon, D., Semiatin, S. L., Eds.; TMS: Warrendale, PA, 1997; pp. 201–208.
10. Prasad, Y. V. R. K.; Sasidhara, S. *Hot Working Guide – A Compendium of Processing Maps*; ASM International: Materials Park, OH, 1997; pp. 459–461.
11. Krishna, V. G.; Prasad, Y. V. R. K.; Birla, N. C.; Rao, G. S. Processing Map for the Hot Working of Near-α-Titanium Alloy 685. *J. Mater. Process. Technol.* **1997**, *71* (3), 377–383.
12. Bate, P. S.; Blackwell, P. L.; Brooks, J. W. In *Proceedings of the Sixth World Conference on Ti*; Lacombe, P., Tricot, R., Be'ranger, G., Eds.; Societe Francaise de Metallurgie: Les UlisCedex, 1988; pp. 287–292.
13. Barbosa, R. A. N. M.; Braga, H. C.; Breme, J. Hot Strength of Ti and Ti Alloys Deformed in Axial Compression. In *Titanium '92 Science and Technology*; Froes, F. H., Caplan, I. L., Eds.; TMS: Warrendale, PA, 1993; pp. 1701–1708.
14. Tricot, R. In *Proceeding of the Sixth World Conference on Ti*; Lacombe, P., Tricot, R., Be'ranger, G., Eds.; Societe Francaise de Metallurgie: Les Ulis Cedex, 1988; pp. 23–30.
15. Oikawa, H. In *Metallurgy and Technology of Practical Titanium Alloys*; Fujishiro, S., Eylon, D., Kishi, T., Eds.; TMS: Warrendale, PA, 1994; pp. 93–100.
16. Bourell, D. L.; McQueen, H. J. Thermomechanical Processing of Iron, Titanium, and Zirconium Alloys in the BCC Structure. *J. Mater. Shaping Technol.* **1987**, *5*, 53–73.
17. McQueen, H. J.; Jonas, J. J. Treatise on Material Science and Technology. In *Plastic Deformation of Materials*; Arsenault, R. J., Ed.; Academic Press: New York, NY, 1975; Vol. 6; pp. 393–493.
18. McQueen, H. J.; Bourell, D. L. In *Formability and Metallurgical Structure*; Sachdev, A. K., Embury, J. D., Eds.; TMS: Warrendale, PA, 1987; pp. 341–368.
19. Dyment, F.; Libanati, C. M. Self-Diffusion of Ti, Zr, and Hf in their hcp Phases, and Diffusion of Nb^{95} in hcp Zr. *J. Mater. Sci.* **1968**, *3* (4), 349–359.
20. Oikawa, H.; Cui, M. X. In *Strength of Metals and Alloys, ICSMA7*; McQueen, H. J., Bailon, J. P., Dickson, J., Jonas, J., Akben, M., Eds.; Pergamon Press: Oxford, 1986; Vol. 1; pp. 601–606.
21. Sastry, S. M. L.; Pao, P. S.; Sankaran, K. K. In *Titanium '80 Science and Technology*; Kimura, H., Izumi, O., Eds.; TMS: Warrendale, PA, 1980; pp. 873–879.
22. Thirukkonda, M.; Chaudhury, P. K.; Zhao, K.; Valencia, J. J. In *Microstructure: Property Relationships of Titanium Alloys*; Ankem, S., Hall, J. A., Eds.; TMS: Warrendale, PA, 1994; pp. 17–26.

23. Semiatin, S. L.; Jonas, J. J. *Formability and Workability of Metals – Plastic Instability and Flow Localization. ASM Series in Metal Processing,* 1st ed., Vol. 2; ASM: Metals Park, OH, 1984; p. 43.
24. Guillard, S.; Thirukkonda, M.; Chaudhury, P. K. In *Advances in the Science and Technology of Titanium Alloy Processing*; Weiss, I., Srinivasan, R., Bania, P., Eylon, D., Semiatin, S. L., Eds.; TMS: Warrendale, PA, 1997; pp. 93–100.
25. Neal, D. F. In *Titanium '84: Science and Technology*; Lutjering, G., Zwicker, U., Bunk, W., Eds.; Deutsche Gesellschaft fur Metallkundee. V: Oberursel, 1985; pp. 2419–2424.
26. Neal, D. F. In *Proceedings of the Sixth World Conference on Ti*; Lacombe, P., Tricot, R., Beranger, G., Eds.; Societe Francaise de Metallurgie: Les Ulis Cedex, 1988; pp. 253–258.
27. Daeubler, M. A.; Helm, D.; Neal, D. F. *Proceeding of the 1990 International Conference on Products and Applications*, Titanium Development Association, Denver, 1990; pp. 78–87.
28. Sargent, P. M.; Ashby, M. F. Deformation Maps for Titanium and Zirconium. *Scr. Metall.* **1982**, *16* (12), 1415–1422.
29. Walsoe de Reca, N. E.; Libanati, C. M. Self-Diffusion in β-Titanium and β-Hafnium. *Acta Metall.* **1968**, *16* (10), 1297–1305.
30. Bania, P. J. In *Proceedings of the Sixth World Conference on Ti*; Lacombe, P., Tricot, R., Beranger, G., Eds.; Societe Francaise de Metallurgie: Les Ulis Cedex, 1988; pp. 826–830.
31. O'Connell, T. E.; Bania, P. J. *Proceedings of the 1990 International Conference on Titanium Products and Applications*, Titanium Development Association, Denver, 1990; pp. 794–803.
32. Boyer, R., Welsch, G., Collings, E. W., Eds. *Materials Properties Handbook: Titanium Alloys*; ASM International: Materials Park, OH, 1994; pp. 411–414.
33. Weinem, D.; Kumpfert, J.; Peters, M.; Kaysser, W. A. Processing Window of the Near-α-Titanium Alloy TIMETAL-1100 to Produce a Fine-Grained β-Structure. *Mater. Sci. Eng. A* **1996**, *206* (1), 55–62.
34. Boyer, R., Welsch, G., Collings, E. W., Eds. *Materials Properties Handbook: Titanium Alloys*; ASM International: Materials Park, OH, 1994; pp. 483–636.
35. Borowy, K. H.; Kramer, K. H. On the Properties of a New Titanium Alloy (TiAl5Fe2.5) as Implant Material. In *Titanium '84: Science and Technology*; Lutjering, G., Zwicker, U., Bunk, W., Eds.; Deutsche Gesellschaft fur Metallkundee. V: Oberursel, 1985; pp. 1381–1386.
36. Bania, P. J.; Hutt, A. J.; Adams, R. E.; Parris, W. M. A New Low Cost Titanium Alloy. In *Titanium '92 Science and Technology*; Froes, F. H., Caplan, I. L., Eds.; TMS: Warrendale, PA, 1993; pp. 2787–2794.
37. Fujii, H.; Takahashi, K.; Soeda, S. Development of High-Performance Ti–Al–Fe Alloy Series. In *Titanium '95, Science and Technology, Birmingham, 1995*; Blenkinsop, P. A., Evans, W. J., Flower, E. M., Eds.; The Institute of Materials, Cambridge University Press: London, 1996; pp. 2539–2546.
38. Fujii, H.; Takahashi, K.; Soeda, S. Development of High-Performance Ti–Al–Fe Alloy Series (in Japanese). *CAMP-ISIJ* **1995**, *8*, 642.
39. Froes, F. H.; Eliezer, D.; Nelson, H. G. Hydrogen Effects in Titanium. In *Proceedings of the 5th International Conference on the Effect of Hydrogen on the Behavior of Materials*; Thompson, A. W., Moody, N. R., Eds.; TMS: Warrendale, PA, 1996; pp. 719–733.
40. Fujii, H.; *et al.* Effect of Cooling Rate on the β-Heat Treated Microstructure of Ti–6Al–4V with 0.4 mass % Hydrogen (in Japanese). *JIM* **1991** (Abstracts of 109th Meeting).
41. Sridhar, G.; Gopalan, R.; Sarma, D. A microstructural Characterization of Solution-Treated Titaniumalloy Ti–6Al–4V. *Metallography* **1987**, *20* (3), 291–310.
42. Fujii, H. Strengthening of $\alpha + \beta$-Titanium Alloys by Thermomechanical Processing. *Mater. Sci. Eng. A* **1998**, *243*, 103–108.
43. Van Thyne, R. J.; Kessler, H. D.; Hansen, M. The Systems Ti–Chromium and Ti–Iron. *Trans. Am. Soc. Metals* **1952**, *44*, 974–989.
44. Williams, J. C. Kinetics and Phase Transformation. In *Titanium Science and Technology*; Jaffee, R. I., Burte, H. M., Eds.; AIME: New York, NY, 1973; pp. 1433–1494.
45. Kerr, W. R. The Effect of Hydrogen as a Temporary Alloying Element on the Microstructure and Tensile Properties of Ti–6Al–4V. *Metall. Trans. A* **1985**, *16*, 1077–1087.
46. Fujii, H.; Takahashi, K.; Fujisawa, K.; Takahisa, N.; Yamazaki, T.; Horiya, T. Low Cost Process of Blended Elemental Powder Metallurgy. In *Titanium '95, Science and Technology, Birmingham, 1995*; Blenkinsop, P. A., Evans, W. J., Flower, E. M., Eds.; The Institute of Materials, Cambridge University Press: London, 1996; pp. 2547–2554.
47. Fujii, H.; Suzuki, H. G. Effect of Quenched-in Vacancies on Aged Microstructures in Ti–15V–3Cr–3Sn–3Al. *Materi. Trans. Jpn. Inst. Metals Mater.* **1993**, *34* (4), 382–388.
48. Venkateswarlu, V.; Tripathy, D.; Rajagopal, K.; Thomas Tharian, K.; Venkitakrishnan, P. V. Failure Analysis and Optimization of Thermo-Mechanical Process Parameters of Titanium Alloy (Ti–6Al–4V) Fasteners for Aerospace Applications,. *Case Stud. Eng. Fail. Anal.* **2013**, *1*, 49–60.
49. Weiss, I.; Semiatin, S. L. Thermomechanical Properties of β Titanium Alloys – An Overview. *Mater. Sci. Eng. A* **1998**, *243*, 46–65.
50. Eylon, D. In *Metallurgy and Technology of Practical Titanium Alloys*; Fujishiro, S., Eylon, D., Kishi, T., Eds.; TMS: Warrendale, PA, 1994; pp. 29–34.
51. Kuhlman, G. W.; Chakrabarti, A. K.; Pishko, R.; Nelson, J. W.; Terlinde, G. In *Sixth World Conference on Ti*; Lacombe, P., Tricot, R., Beranger, G., Eds.; Societe Francaise de Metallurgie: Les Ulis Cedex, 1988; pp. 1269–1275.
52. Srinivasan, R.; Weiss, I. In *β Titanium Alloys in the 1990s*; Eylon, D., Boyer, R. R., Koss, D. A., Eds.; TMS: Warrendale, PA, 1993; pp. 283–295.
53. Montheillet, F.; Dajno, D.; Come, N.; *et al.* In *Titanium '92: Science and Technology*; Froes, F. H., Caplan, I., Eds.; TMS: Warrendale, PA, 1993; pp. 1347–1354.
54. Vijayshankar, M. N.; Ankem, S. High Temperature Tensile Deformation Behavior of β-Titanium Alloys. *Mater. Sci. Eng. A* **1990**, *129* (2), 229–237.
55. Vijayshankar, M. N.; Ankem, S. In *Titanium '92: Science and Technology*; Froes, F. H., Caplan, I., Eds.; TMS: Warrendale, PA, 1993; pp. 1733–1740.
56. Griffiths, P.; Hammond, C. Superplasticity in Large Grained Materials. *Acta Metall.* **1972**, *20* (7), 935–945.
57. Morgan, G. C.; Hammond, C. Superplastic Deformation Properties of β-Titanium Alloys. *Mater. Sci. Eng.* **1987**, *86*, 159–177.
58. Srinivasan, R. Yield Points during the High Temperature Deformation of Ti–15V–3Al–3Cr–3Sn Alloy. *Scripta Metall. Mater.* **1992**, *27* (7), 925–930.
59. Paton, N. E. In *Titanium 1984: Science and Technology*; Lutjering, G., Zwicker, U., Bunk, W., Eds.; Deutsche Gesellschaft fur Metallkundee.V: Oberursel, 1985; pp. 649–672.
60. Long, M.; Rack, H. J. In *Titanium '95, Science and Technology, Birmingham, 1995*; Blenkinsop, P. A., Evans, W. J., Flower, E. M., Eds.; The Institute of Materials, Cambridge University Press, 1996; pp. 316–323.
61. Schroder, G.; Duerig, T. W. In *Titanium 1984: Science and Technology*; Lutjering, G., Zwicker, U., Bunk, W., Eds.; Deutsche Gesellschaft fur Metallkundee.V: Oberursel, 1985; pp. 585–592.
62. Vandecastele, B.; Rizzi, N.; Wadier, I. F. In *Proceedings of the Sixth World Conference on Ti*; Lacombe, P., Tricot, R., Be'ranger, G., Eds.; Societe Francaise de Metallurgie: Les Ulis Cedex, 1988; pp. 1325–1337.
63. Weiss, I.; Froes, F. H. In *Titanium '84: Science and Technology*; Lutjering, G., Zwicker, U., Bunk, W., Eds.; Deutsche Gesellschaft fur Metallkundee.V.: Oberursel, 1985; pp. 499–506.
64. Chaussy, F.; Driver, J. H. In *β Titanium Alloys*; Vassel, A., Eylon, D., Combres, Y., Eds.; Editions de la Revue de Metallurgie: Paris, 1994; pp. 57–64.
65. Bailey, J. E.; Hirsch, P. B. The Recrystallization Process in Some Polycrystalline Metals. *Proc. R. Soc. Lond. A* **1962**, *267* (1328), 11.
66. Froes, F. H.; Yolton, C. F.; Hirth, J. P. In *β Titanium Alloys in the 80's*; Boyer, R. R., Rosenberg, H. W., Eds.; TMS: Warrendale, PA, 1984; pp. 185–207.
67. Hall, J. A. In *β Titanium Alloys in the 80's*; Boyer, R. R., Rosenberg, H. W., Eds.; TMS: Warrendale, PA, 1984; pp. 129–143.
68. Froes, F. H.; Yolton, C. F.; Hirth, J. P.; Ondercim, R.; Moracz, D. In *β Titanium Alloys in the 80's*; Boyer, R. R., Rosenberg, H. W., Eds.; TMS: Warrendale, PA, 1984; pp. 161–184.
69. Weiss, I.; Srinivasan, R.; Froes, F. H. In *Recrystallization '90*; Chandra, T., Ed.; TMS: Warrendale, PA, 1990; pp. 609–616.
70. Combres, Y.; Champin, B. In *β Titanium Alloys in the 1990s*; Eylon, D., Boyer, R. R., Koss, D. A., Eds.; TMS: Warrendale, PA, 1993; pp. 27–38.
71. Takemura, A.; Ashida, Y.; Ohyama, H.; *et al.* In *Titanium '92: Science and Technology*; Froes, F. H., Caplan, I., Eds.; TMS: Warrendale, PA, 1993; pp. 2673–2680.
72. Combres, Y.; Champin, B. In *Metallurgy and Technology of Practical Titanium Alloys*; Fujishiro, S., Eylon, D., Kishi, T., Eds.; TMS: Warrendale, PA, 1994; pp. 247–254.
73. Maeda, T.; Okada, M. In *Titanium '95, Science and Technology, Birmingham, 1995*; Blenkinsop, P. A., Evans, W. J., Flower, E. M., Eds.; The Institute of Materials, Cambridge University Press: London, 1996; pp. 948–955.

74. Chaze, A. M.; Montheillet, F. In *β Titanium Alloys*; Vassel, A., Eylon, D., Combres, Y., Eds.; Editions de la Revue de Metallurgie: Paris, 1994; pp. 41–48.
75. Weiss, I.; Froes, F. H.; Eylon, D.; Welsch, G. E. Modification of α Morphology in Ti–6Al–4V by Thermomechanical Processing. *Metall. Trans. A* **1986**, *17* (11), 1935–1947.
76. Ouchi, C. In *Metallurgy and Technology of Practical Titanium Alloys*; Fujishiro, S., Eylon, D., Kishi, T., Eds.; TMS: Warrendale, PA, 1994; pp. 37–44.
77. Otsuka, K.; Wayman, C. M. Mechanism of Shape Memory Effect and Superelasticity. In *Shape Memory Materials*; Otsuka, K., Wayman, C. M., Eds.; Cambridge University Press: Cambridge, 1998; p. 27.
78. Burkart, M. W.; Read, T. A. Diffusionless Phase Change in the Indium–Thallium System. *Trans. AIME* **1953**, *197*, 1516–1524.
79. Otsuka, K.; Ren, X. Physical Metallurgy of Ti–Ni-based Shape Memory Alloys. *Prog. Mater. Sci.* **2005**, *50* (5), 511–678.
80. Jackson, C. M.; Wagner, H. J.; Wasilewski, V. *55-Nitinol-the Alloy with a Memory: Its Physical Metallurgy, Properties and Applications*, *Technical Report*, *NASA SP 5110,* 1972.
81. Massalski, T. B.; Okamoto, H.; Subramanian, P. R.; Kacprzak, L. *Binary Alloy Phase Diagrams*, 2nd ed., Vol. 3; ASM International: Materials Park, OH, 1990; p. 2874.
82. Philip, T. V.; Beck, P. A. CsCl-Type Ordered Structures in Binary Alloys of Transition Elements. *Trans. AIME* **1957**, *209*, 1269–1271.
83. Miyazaki, S.; Ohmi, Y.; Otsuka, K.; Suzuki, Y. Characteristics of Deformation and Transformation Pseudoelasticity in Ti–Ni Alloys. *Journal de Physique Colloques* **1982**, *43*, 255–260.
84. Melton, K. N.; Mercier, O. The Mechanical Properties of NiTi-based Shape Memory Alloys. *Acta Metall.* **1981**, *29* (2), 393–398.
85. Miyazaki, S.; Otsuka, K.; Suzuki, Y. Transformation Pseudoelasticity and Deformation Behavior in a Ti–50.6at%Ni Alloy. *Scr. Metall.* **1981**, *15* (3), 287–292.
86. Miyazaki, S.; Otsuka, K. Deformation and Transition Behavior Associated with the R-phase in Ti–Ni Alloys. *Metall. Trans. A* **1986**, *17* (1), 53–63.
87. Nishida, M.; Wayman, C. M.; Honma, T. Precipitation Processes in Near-Equiatomic TiNi Shape Memory alloys. *Metall. Trans. A* **1986**, *17* (9), 1505–1515.
88. Stachowiak, G. B.; McCormick, P. G. Shape Memory Behaviour Associated with the R and Martensitic Transformations in a NiTi Alloy. *Acta Metall.* **1988**, *36* (2), 291–297.
89. Wurzel, D. Marforming and Tempering of Binary Ni–Ti Alloys Including Precipitation Effects. *Mater. Sci. Eng. A* **1999**, *273–275*, 638–643.
90. Miyazaki, S. In *Engineering Aspects of Shape Memory Alloys*; Duerig, T. W., Melton, K. N., Stockel, D., Wayman, C. M., Eds.; Butterworth-Heinemann: Guildford, 1990; pp. 394–413.
91. Lin, H. C.; Wu, S. K. The Tensile Behavior of a Cold-Rolled and Reverse-Transformed Equiatomic TiNi Alloy. *Acta Metall. Mater.* **1994**, *42* (5), 1623–1630.
92. Miyakazi, S.; Imai, T.; Igo, Y.; Otsuka, K. Effect of Cyclic Deformation on the Pseudoelasticity Characteristics of Ti–Ni Alloys. *Metall. Mater. Trans. A* **1986**, *17* (1), 115–120.
93. Miyakazi, S.; Igo, Y.; Otsuka, K. Effect of Thermal Cycling on the Transformation Temperatures of Ti–Ni Alloys. *Acta Metall.* **1986**, *34* (10), 2045.
94. Stroz, D.; Bojarski, Z.; Iiczuk, J.; Lekston, Z.; Morawiec, H. Effect of Thermal Cycling on As-Quenched and Aged Nickel-Rich Ni–Ti Alloy. *J. Mater. Sci.* **1991**, *26* (7), 1741–1748.
95. Tadaki, T.; Nakata, Y.; Shimizu, K. Thermal Cycling Effects in an Aged Ni-Rich Ti–Ni Shape Memory Alloy. *Mater. Trans. Jpn. Inst. Metals Mater.* **1987**, *28* (11), 883–890.
96. Miyakazi, S.; Otsuka, K. Development of Shape Memory Alloys. *ISIJ Int.* **1989**, *29* (5), 353–377.
97. Michal, G. M.; Moine, P.; Sinclair, R. Characterization of the Lattice Displacement Waves in Premartensitic TiNi. *Acta Metall.* **1982**, *30* (1), 125–138.
98. Ling, H. C.; Kaplow, R. Phase Transitions and Shape Memory in NiTi. *Metall. Mater. Trans. A* **1980**, *11* (1), 77–83.
99. Pelosin, V.; Riviere, A. Effect of Thermal Cycling on the R-Phase and Martensitic Transformations in a Ti-Rich NiTi Alloy. *Metall. Mater. Trans. A* **1998**, *29* (4), 1175–1180.
100. Gyobu, A.; Kawamura, Y.; Horikawa, H.; Saburi, T. Martensitic Transformations in Sputter-Deposited Shape Memory Ti–Ni Films. *Mater. Trans. Jpn. Inst. Metals Mater.* **1996**, *37* (4), 697–702.
101. Kajiwara, S.; Ogawa, K.; Kikuchi, T.; Matsunaga, T.; Miyazaki, S. Formation of Nanocrystals with an Identical Orientation in Sputter-Deposited Ti–Ni Thin Films. *Philos. Mag. Lett.* **1996**, *74* (6), 395–406.
102. Nam, T. H.; Kim, J. H.; Choi, M. S.; *et al.* Effect of Alloy Compositions on the R Phase Transformation in Ti–Ni Alloy Ribbons Fabricated by Rapid Solidification. *J. Mater. Sci. Lett.* **2002**, *21* (10), 799–801.
103. Zhang, L.; Xie, C.; Wu, J. Martensitic Transformation and Shape Memory Effect of Ti–49 at.% Ni Alloys. *Mater. Sci. Eng. A* **2006**, *438–440*, 905–910.
104. Hornbogen, E. Ausforming of NiTi. *J. Mater. Sci.* **1999**, *34* (3), 599–606.
105. Kockar, B.; Karaman, I.; Kulkarni, A.; Chumlyakov, Y.; Kireeva, I. V. Effect of Severe Ausforming via Equal Channel Angular Extrusion on the Shape Memory Response of a NiTi Alloy. *J. Nucl. Mater.* **2007**, *361* (2–3), 298–305.
106. Paula, A. S.; Mahesh, K. K.; dos Santos, C. M. L.; Braz Fernandes, F. M.; da Costa Viana, C. S. Thermomechanical Behavior of Ti-Rich NiTi Shape Memory Alloys. *Mater. Sci. Eng. A* **2008**, *481–482*, 146–150.
107. Karaman, I.; Ersin Karaca, H.; Luo, Z. P.; Maier, H. J. The Effect of Severe Marforming on Shape Memory Characteristics of a Ti-Rich NiTi Alloy Processed Using Equal Channel Angular Extrusion. *Metall. Mater. Trans. A* **2003**, *34* (11), 2527–2539.
108. Hornbogen, E. A Comparative Study of Ausforming of Shape Memory Alloys with A2 and B2 Structures. *Mater. Sci. Eng. A* **1999**, *273–275*, 630–633.
109. Hornbogen, E.; Mertinger, V.; Wurzel, D. Microstructure and Tensile Properties of Two Binary NiTi-Alloys. *Scr. Mater.* **2001**, *44* (1), 171–178.
110. Kurita, T.; Matsumoto, H.; Abe, H. Transformation Behavior in Rolled NiTi. *J. Alloys Compd. 381 (1–2)* **2004**, 158–161.
111. Sadrnezhaad, S. K.; Mirabolghasemi, S. H. Optimum Temperature for Recovery and Recrystallization of 52Ni48Ti Shape Memory Alloy. *Mater. Des.* **2007**, *28* (6), 1945–1948.
112. Prokoshkin, S. D.; Khmelevskaya, I. Yu.; Dobatkin, S. V.; *et al.* Alloy Composition, Deformation Temperature, Pressure and Post-Deformation Annealing Effects in Severely Deformed Ti–Ni Based Shape Memory Alloys. *Acta Mater.* **2005**, *53* (9), 2703–2714.
113. Pushin, V. G.; Valiev, R. Z.; Zhu, Y. T.; *et al.* Effect of Severe Plastic Deformation on the Behavior of Ti–Ni Shape Memory Alloys. *Mater. Trans. Jpn. Inst. Metals Mater.* **2006**, *47* (3), 694–697.
114. Sergueeva, A. V.; Song, C.; Valiev, R. Z.; Mukherjee, A. K. Structure and Properties of Amorphous and Nanocrystalline NiTi Prepared by Severe Plastic Deformation and Annealing. *Mater. Sci. Eng. A* **2003**, *339* (1–2), 159–165.
115. Lopez, H. F.; Salinas, A.; Calderon, H. Plastic Straining Effects on the Microstructure of a Ti-Rich NiTi Shape Memory Alloy. *Metall. Mater. Trans. A* **2001**, *32* (3), 717–729.
116. Tan, G.; Liu, Y. Comparative Study of Deformation-Induced Martensite Stabilization via Martensite Reorientation and Stress-Induced Martensitic Transformation in NiTi. *Intermetallics* **2004**, *12* (4), 373–381.
117. Sinha, A.; Mondal, B. N.; Chattopadhyay, P. P. Mechanical Properties of Ti-(∼49 at%) Ni Shape Memory Alloy: Part I. Effect of Cold Deformation. *Mater. Sci. Eng. A* **2013**, *561*, 338–343.
118. Chen, J. H.; Sun, W.; Wang, G. Z. Investigation on the Fracture Behavior of Shape Memory Alloy NiTi. *Metall. Mater. Trans.* **2005**, *A36* (4), 941–955.
119. Mitwally, M. E.; Farag, M. Effect of Cold Work and Annealing on the Structure and Characteristics of NiTi Alloy. *Mater. Sci. Eng. A* **2009**, *519* (1–2), 155–166.
120. Sittner, P.; Liu, Y.; Novak, V. On the Origin of Lüders-Like Deformation of NiTi Shape Memory Alloys. *J. Mech. Phys. Solids* **2005**, *53* (8), 1719–1746.
121. Hwang, C. M.; Wayman, C. M. Electron Microscopy Studies of Martensitic Transformations in Ternary TiNiAl Alloys. *Scr. Metall.* **1983**, *17*, 1449–1453.
122. Ling, H. C.; Kaplow, R. Stress-Induced Shape Changes and Shape Memory in the R and Martensite Transformations in Equiatomic NiTi. *Metall. Mater. Trans. A* **1981**, *12* (12), 2101–2111.
123. Liu, Y.; Chen, X.; McCormick, P. G. Effect of Low Temperature Ageing on the Transformation Behaviour of Near-Equiatomic NiTi. *J. Mater. Sci.* **1997**, *32* (22), 5979–5984.
124. Corroll, M. C.; Somsen, Ch.; Eggeler, G. Multiple-Step Martensitic Transformations in Ni-Rich NiTi Shape Memory Alloys. *Scr. Mater.* **2004**, *50* (2), 187–192.
125. Ren, X.; Miura, N.; Zhang, J.; *et al.* A Comparative Study of Elastic Constants of Ti–Ni-Based Alloys Prior to Martensitic Transformation. *Mater. Sci. Eng. A* **2001**, *312* (1–2), 196–206.

126. Sinha, A.; Mondal, B. N.; Chattopadhyay, P. P. Mechanical Properties of Ti-(∼49 at%) Ni Shape Memory Alloy, Part II: Effect of Ageing Treatment. *Mater. Sci. Eng. A* **2013**, *561*, 344–351.
127. Liu, Y.; Tan, G. S. Effect of Deformation by Stress-Induced Martensitic Transformation on the Transformation Behaviour of NiTi. *Intermetallics* **2000**, *8* (1), 67–75.
128. Urbina, C.; De la Flor, S.; Gispert-Guirado, F.; Ferrando, F. Quantitative XRD Analysis of the Evolution of the TiNi Phase Transformation Behaviour in Relation to Thermal Treatments. *Intermetallics* **2010**, *18* (8), 1632–1641.
129. Sinha, A. *A Study on the Effect of Deformation on the Performance of Ti-(∼49 at%) Ni Alloy* (Ph.D. Thesis); Bengal Engineering and Science University, Shibpur, Howrah, India, 2011; pp. 69–72.

Relevant Websites

http://asm.matweb.com/
ASM Aerospace Specification Metals, Inc.
http://www.elsevier.co.in/web/default.aspx
Elsevier.
http://www.sciencedirect.com/
ScienceDirect.
http://www.springer.com/gp/
Springer.

2.12 Heat Treatment of Aluminum Alloys

HMMA Rashed and AKM Bazlur Rashid, Bangladesh University of Engineering and Technology, Dhaka, Bangladesh

© 2017 Elsevier Inc. All rights reserved.

2.12.1	**Introduction**	337
2.12.1.1	Designation System of Aluminum Alloys	337
2.12.1.2	Temper Designations	338
2.12.1.2.1	Basic temper designations	339
2.12.1.2.2	Subdivisions of basic tempers	340
2.12.1.2.2.1	Subdivision of H temper: Strain-hardened	340
2.12.1.2.2.2	Subdivision of T temper: Thermally treated	340
2.12.1.2.2.3	Variation of O temper: Annealed	340
2.12.1.2.2.4	Variation of H temper	340
2.12.1.2.2.5	Variation of T temper	340
2.12.1.3	Classification of Aluminum Alloys	340
2.12.1.3.1	Wrought and cast alloys	340
2.12.1.3.2	Heat-treatable and nonheat-treatable alloys	341
2.12.2	**Heat Treatment of Aluminum Alloys**	341
2.12.2.1	Heat Treatment Furnaces	341
2.12.2.2	Strengthening by Heat Treatment	347
2.12.2.2.1	SHT	347
2.12.2.2.2	Quenching	350
2.12.2.2.2.1	Quenched-in vacancies	352
2.12.2.2.3	Aging	353
2.12.2.2.3.1	Natural aging	354
2.12.2.2.3.2	Artificial aging	356
2.12.2.3	Heat Treatment Scheme for Wrought Alloys	357
2.12.2.4	Heat Treatment Scheme for Cast Alloys	358
2.12.2.5	Stress Relief	363
2.12.2.6	Annealing	368
2.12.2.7	Dimensional Changes during Heat Treatment	368
2.12.3	**Inspection and Quality Assurance**	368
2.12.4	**Concluding Remarks**	369
References		369

2.12.1 Introduction

Aluminum is the third-most abundant element (behind oxygen and silicon), comprising 8.1% of the Earth's crust. Alumina is the second-most plentiful compound (behind silica), comprising 15.9% of the Earth's crust. In its pure form, aluminum is a lighter and softer metal with limited strength. It has only one-third the density of ordinary steel. Electrolytic pure commercial aluminum contains much less than 1.0 % impurity. For applications requiring greater mechanical strength, aluminum is alloyed with elements such as copper, magnesium, manganese, and zinc, usually in combinations of two or more of these elements together with silicon and iron.[1]

The properties of aluminum alloys depend on a complex interaction of chemical composition and the microstructural features developed during solidification and then modified by thermal treatment and/or deformation processing. Heat treatment plays a significant role in developing the desired properties of commercial aluminum alloys. In this chapter, some of the most practical aspects of heat treatment of aluminum alloys are discussed.

2.12.1.1 Designation System of Aluminum Alloys

The specifications and designations of widely varied wrought aluminum alloys have differed from country to country. This is why it is important for the secondary fabricators and users of aluminum to have a working knowledge of the aluminum alloys and their temper designation system.

The selection of aluminum alloys for engineering applications is difficult because an impressive number of commercially available aluminum alloys have been developed to meet specific requirements. Aluminum alloys are divided into two major categories, namely those to be fabricated into wrought form and those used for castings. A further division of each category is made based on the primary mechanism of property enhancement. The chemical composition and mechanical properties of the principal alloys are covered in different national and international standards.

The most commonly used alloy designation system is covered by American National Standards Institute (ANSI) standard H35.1 and is registered by the Aluminum Association (AA) of the United States.[2] This system is also adopted by the

International Alloy Development System (IADS) and by most of the countries in the world.

ANSI 35.1 standard uses a four-digit number for each wrought aluminum alloy, and the first of the four digits is assigned for the major alloying element of the alloy within the group (Table 1). Therefore, we have the 1xxx series alloys, which are unalloyed and contain a minimum of 99% aluminum. For the 2xxx through 7xxx series, the alloy group is determined by the alloying element present in the greatest mean percentage. Series 6xxx is an exception in which the proportions of magnesium and silicon to form Mg_2Si are predominant. Another exception is considered for modified alloy of a previously registered alloy. If the greatest mean percentage is the same for more than one element, then the following sequence will be used to determine the group: copper, manganese, silicon, magnesium, magnesium silicide, zinc, or others.

The second digit indicates impurity level or alloy modifications. A zero second-digit indicates unalloyed varieties. Integers 1 through 9 (assigned consecutively if needed) indicate special control of one or more individual impurities in the 1xxx series and specific alloy modification in all other aluminum alloys.

The third and fourth digits are significant in the 1xxx series, but not in other alloys. In the 1xxx series, the last two digits indicate the minimum purity level of aluminum. Thus, alloy 1100 has a minimum purity of 99.00%, whereas alloys 1150 and 1199 have minimum purity levels of 99.45 and 99.99%, respectively. For all other aluminum alloys, the third and fourth digits have no special significance and serve only to identify the different alloys in the series. Thus, alloys 3003, 3004, and 3005 are distinctly different Al–Mn alloys, just as alloys 6061 and 6063 denote two different types of Al–Mg–Si alloys.

A prefix X is often used to denote that the alloy is at an experimental state of its development.

No internationally accepted system of nomenclature similar to wrought aluminum alloys is available for identifying aluminum and aluminum alloys in the form of castings and foundry ingots. However, the AA of the United States has introduced a revised four-digit system of its previous three-digit system, and this has some similarity to that adopted for wrought alloys.

The first digit in this four-digit system indicates the alloy group, determined by the alloying element present in the greatest mean percentage (Table 1). For modified alloy of a previously registered alloy, if the greatest mean percentage is the same for more than one element, then the alloy group is determined by the element that comes first in the sequence.

For the 1xx.x group, the second and third digits indicate the minimum percentage of aluminum in the alloy. Thus, alloy 150.x indicates a composition containing a minimum of 99.50% aluminum. The last digit after the decimal point indicates the product form: 0 indicates castings and 1 indicates ingots.

For the 2xx.x to 9xx.x alloys groups, the second and third digits have no special significance and serve only to identify the different alloys in the series. The last digit after the decimal point again indicates the product form.

A serial letter is included before the numerical designation when there is a modification to the original alloy or to the normal impurity limits. These serial letters are assigned in alphabetical sequence starting with A, but omitting I, O, Q, and X. Like wrought alloys designations, the letter X is reserved for experimental alloys.

2.12.1.2 Temper Designations

A system of temper nomenclature has been adopted for all forms of wrought and cast aluminum alloys (with the exception of ingots) to specify the mechanical properties of an alloy and the treatments, either thermal or chemical or both, used to achieve these properties. This takes the form of letters and digits and is added as suffixes to the alloy number, with the two being separated by a hyphen. Basic temper designations consist of letters, whereas the subdivision of basic tempers

Table 1 Wrought alloys and cast alloys nomenclatures

Four-digit system for wrought alloys		*Three-digit system followed by a decimal value for cast alloys*	
Aluminum of 99.0% minimum purity	1xxx	Aluminum of 99.0% minimum purity	1xx.x
Aluminum alloys, grouped by major alloying element(s):		Aluminum alloys, grouped by major alloying element(s):	
Copper	2xxx	Copper	2xx.x
Manganese	3xxx	Silicon with copper and/or magnesium	3xx.x
Silicon	4xxx	Silicon	4xx.x
Magnesium	5xxx	Magnesium	5xx.x
Magnesium and silicon	6xxx	Zinc	7xx.x
Zinc	7xxx	Tin	8xx.x
Other elements (e.g., tin, lithium)	8xxx	Unused series	6xx.x
Unused series	9xxx	Unused series	9xx.x
• In the 1xxx group, series 10xx is used for unalloyed compositions, with natural impurities. The last two digits indicate the minimum aluminum percentage		• In the 1xx.x group, the second two digits indicate aluminum purity. In the 2xx.x–8xx.x groups, the second two digits indicate alloy content. The last digit separated by decimal indicates product form (0, castings; 1 and 2, ingots)	
• In the 2xxx–8xxx groups, the second digit indicates alloy modification (0, unmodified; 1–9, modified)		• An alphabetic number in front of the numerical designation indicates alloy modification or impurity limits in unalloyed aluminum	

based on strain-hardening or heat treatment are indicated by one or more digits following the letter used for the basic temper. The system deals separately with the nonheat-treatable and heat-treatable alloys. The temper designation system for aluminum alloys indicated in the ANSI 35.1 standard is briefly discussed in the following sections and given in summarized form in Figure 1. Following Figure 1, alloy 5456-H39 refers to commercial aluminum–magnesium alloy heavily worked and hardened. It is noteworthy that yield strength of this alloy is approximately 500 MPa. Also, 7079-T6 would refer to an aluminum–zinc–magnesium–copper alloy, which is solution-treated and quenched, followed by age hardening.

2.12.1.2.1 Basic temper designations

F *As-fabricated*. Applied to the products shaped by cold/hot working or casting, with no special control over thermal conditions or strain hardening.

O *Annealed*. Applied to wrought products, which are annealed to obtain lowest strength and to cast products that are

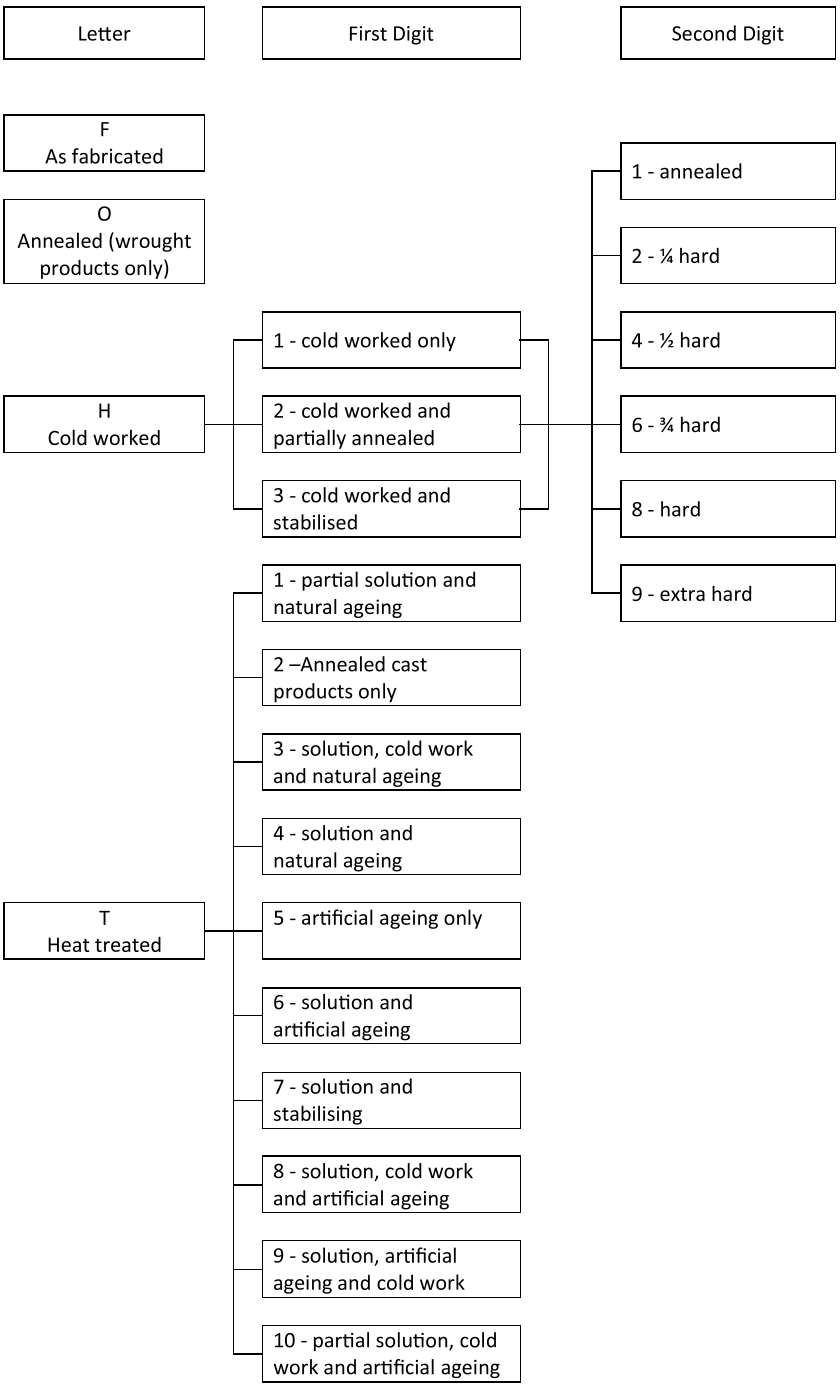


Figure 1 Temper designation system for aluminum alloys.

annealed to improve ductility and dimensional stability; may be followed by a digit other than zero.

H *Strained hardened (for wrought product only)*. Applied to products that have strengthened by strain hardening, with or without thermal treatment; usually followed by two or more digits.

W *Solution heat-treated*. This is applicable to alloys whose strength is unstable and naturally changes at room temperature (RT) over a duration of months or years after solution treatment.

T *Solution heat-treated*. This is applicable to alloys whose strength is stable within a few weeks of solution treatment; always followed by one or more digits.

2.12.1.2.2 Subdivisions of basic tempers

2.12.1.2.2.1 Subdivision of H temper: Strain-hardened

H1 *Strain-hardened only*. Applies to products that are strengthened by strain hardening; digits following H1 indicate the degree of strain hardening.

H2 *Strain-hardened and partially annealed*. Strain-hardened more than the desired final amount and then reduced in strength to the desired level by partial annealing; digits following H2 indicate the degree of strain hardening remaining after annealing.

H3 *Strained-hardened and stabilized*. Products that are strained-hardened and the mechanical properties are stabilized (to improve ductility) by a low-temperature thermal treatment or heat introduced during fabrication; digits following H3 indicate the degree of strain hardening remaining after annealing.

2.12.1.2.2.2 Subdivision of T temper: Thermally treated

T1 *Cooled from high-temperature (HT) shaping process and naturally aged*. Products are not cold-worked after HT shaping process (e.g., casting, extrusion) and mechanical properties are stabilized by natural aging.

T2 *Cooled from HT shaping process, cold-worked, and naturally aged*. Products are cold-worked to improve strength after HT shaping process (e.g., rolling, extrusion) and mechanical properties are stabilized by natural aging.

T3 *Solution-treated, cold-worked, and naturally aged*. Products are cold-worked to improve strength after solution heat treatment (SHT) and mechanical properties are stabilized by natural aging.

T4 *Solution-treated and naturally aged*. Products are not cold-worked after SHT and mechanical properties are stabilized by natural aging.

T5 *Cooled from HT shaping process and artificially aged*. Products are not cold-worked after HT shaping process (e.g., casting, extrusion) and mechanical properties are substantially improved by precipitation heat treatment.

T6 *Solution-treated and artificially aged*. Products are not cold-worked after SHT and mechanical properties and/or dimensional stability are substantially improved by precipitation heat treatment.

T7 *Solution-treated and overaged or stabilized*. Applied to wrought products that are precipitation heat-treated beyond the point of maximum strength to provide special characteristics, such as enhanced resistance to stress-corrosion cracking (SCC).

T8 *Solution-treated, cold-worked, and artificially aged*. Products are cold-worked to improve strength after SHT and mechanical properties and/or dimensional stability are substantially improved by precipitation heat treatment.

T9 *Solution-treated, artificially aged, and cold-worked*. Products are cold-worked specifically to improve strength after SHT and precipitation heat treatment.

T10 *Cooled from HT shaping process, cold-worked, and artificially aged*. Products are not cold-worked specifically to improve strength after HT shaping process (e.g., rolling, extrusion) and mechanical properties are substantially improved by precipitation heat treatment.

2.12.1.2.2.3 Variation of O temper: Annealed

A digit following the O is often used to indicate a product in annealed conditions with special characteristics. For example, O1 indicates a wrought product that has been heat treated at approximately the same time and temperature required for SHT and then slow-cooled to RT, whereas O2 indicates a wrought product laboratory test material that has been furnace-annealed from F temper to determine the minimum limits to which H temper designations are assigned.

2.12.1.2.2.4 Variation of H temper

There are a few H tempers consisting of three digits.[3]

H111 Temper. This is used when alloy is less hardened compared to H11.
H121 Temper. This is used when alloy is less hardened compared to H12.
H311 Temper. This is used when alloy is less hardened compared to H31.
H321 Temper. This is used when alloy is less hardened compared to H32.

2.12.1.2.2.5 Variation of T temper

There are a few T tempers consisting of three to four digits.[3]

T42 Temper. This indicates solution treated from O or F temper, quenched, and naturally aged.
T62 Temper. This indicates solution treated from O or F temper, quenched, and artificially aged.
Tx51 Temper. This indicates stress is relieved by stretching. Permanent deformation can vary from 0.5 to 3%. X denotes 3, 4, 6, or 8.
Tx52 Temper. This indicates stress is relieved by compression. X denotes 3, 4, 6, or 8.
Tx53 Temper. This indicates stress is relieved by thermal treatment. X denotes 3, 4, 6, or 8.
Tx54 Temper. This indicates stress is relieved by both stretching and compression. X denotes 3, 4, 6, or 8.

2.12.1.3 Classification of Aluminum Alloys

2.12.1.3.1 Wrought and cast alloys

In general, the lion share of wrought aluminum products is used in the form of plates (more than 6 mm thickness), sheets (0.15–6 mm), foils (<0.15 mm), extrusions, tubes, rods, bars, and wires. These are produced from cast ingots and the final

structure is developed after various working and thermal treatments.

Aluminum foundry alloys are one of the most versatile and commonly used foundry alloys because of their low melting points and negligible solubility for all gases (except hydrogen), and usually result in good surface finish in the final products. Most alloys also show high fluidity, and a wide variety of compositions can be selected with solidification ranges suitable for particular applications. The most commonly used processes are sand casting, permanent mold (gravity die) casting, and high-pressure die casting.

The heat-treatable and nonheat-treatable wrought and casting aluminum alloys series are reported in **Table 2**. The designation and the chemical composition of commonly used wrought and casting alloys are given in **Tables 3–6**, whereas those of commercial lithium-containing aluminum alloys are given in **Table 7**.

2.12.1.3.2 Heat-treatable and nonheat-treatable alloys

Aluminum alloys with limited solid solubility in the solid state are heat-treatable and normally recognized as the precipitation hardenable alloys. In addition, the other requirements include the possibility of retaining single-phase supersaturated solid solution by quenching and precipitation of coherent or partially coherent solid phase by decomposition of the supersaturated solid solution with time. Alloys containing copper (2xxx and 2xx.x series), silicon and magnesium (6xxx and 3xx.x series), zinc and magnesium (7xxx and 7xx.x series), and lithium (8xxx series) are the most important heat-treatable aluminum alloys.

Binary aluminum alloys of Mg, Si, Zn, Cr, and Mn show little change from thermal treatment whether the solute is completely in solution, partially precipitated, or substantially precipitated. Although these alloys show a decrease in solid solubility in the phase diagrams that is necessary for precipitation hardening, they rarely show any change in the mechanical properties after heat treatment because of their inability to form coherent or partially coherent clusters of solute atoms, either by natural aging or artificial aging.

Alloy compositions that cannot be strengthened by heat treatment are commonly regarded as the nonheat-treatable alloys. They consist of a homogeneous solid solution with or without noncoherent precipitate(s) and show low strength and high ductility. Strength in these alloys is developed by *strain hardening* by cold rolling, drawing, or stretching during manufacturing, *solid solution hardening*, strengthening from *second-phase microstructural constituents* (due to the presence of predominantly second-phase constituents such as iron, nickel, titanium, manganese, and chromium), and *grain refinement* with dispersed precipitates.

Nonheat-treatable wrought alloys mainly comprise the various grades of pure aluminum (1xxx series) and aluminum alloys with manganese or magnesium as the major additions, either singly or in combination (3xxx and 5xxx series). Binary aluminum alloys with silicon (4xx.x series) or magnesium (5xx.x series), however, are the most important nonheat-treatable cast alloys. Further discussions on nonheat-treatable alloys are beyond the scope of this chapter and are not discussed further.

2.12.2 Heat Treatment of Aluminum Alloys

Heat treatment typically indicates an event of thermal practices that invokes microstructural changes leading to desired mechanical properties. In practice, heat treatment can increase hardness, improve wear resistance, modify strength and other mechanical properties, and relieve residual stresses. In ferrous material, heat treatment covers a vast field. However, in aluminum alloys, heat treatment, in particular, refers to strengthening of parts by precipitation hardening. Other strengthening mechanisms of aluminum alloys include hardened by working for a few nonheat-treatable alloys, softening (annealing), solution treatment, and/or quenching processes for a few alloys under specific conditions.

2.12.2.1 Heat Treatment Furnaces

The choice of heating medium depends on the procedure of heat treatment for a particular alloy and parts complexity. To induce thermal environment, molten baths or furnaces are used. Molten baths are usually salts baths, and furnaces are simple air-chamber furnace. Oil or gas-fired furnaces are rarely used for this purpose because the work surface comes in contact with combustion products, leading to severe HT oxidation. Salt baths are not involved with this HT oxidation

Table 2 Heat-treatable and nonheat-treatable wrought alloys and cast aluminum alloys

Wrought alloys series		*Cast alloys series*	
Heat-treatable alloys		*Heat-treatable alloys*	
Al–Cu and Al–Cu–Mg alloys	2xxx	A–Cu alloys	2xx.x
Al–Mg–Si alloys	6xxx	Al–Si–Cu, Al–Si–Mg and Al–Si–Cu–Mg alloys	3xx.x
Al–Zn–Mg and Al–Zn–Mg–Cu alloys	7xxx	Al–Zn, Al–Zn–Mg and Al–Zn–Mg–Cu alloys	7xx.x
Al–Li, Al–Cu–Li, Al–Li–Mg, Al–Li–Cu–Mg, and Al–Li–Cu–Mg–Ag alloys	8xxx		
Nonheat-treatable alloys		*Nonheat-treatable alloys*	
Pure aluminum	1xxx	Al–Si alloys	4xx.x
Al–Mn alloys	3xxx	Al–Mg alloys	5xx.x
Al–Si alloys	4xxx		
Al–Mn–Mg alloys	5xxx		
Miscellaneous alloys	8xxx		

Table 3 Composition of selected heat-treatable wrought aluminum alloys

AA Number	*Si*	*Fe*	*Cu*	*Mn*	*Mg*	*Zn*	*Cr*	*Ti*	*Other*
2002	0.35–0.80	0.30	1.50–2.50	0.20	0.50–1.00	–	–	0.20	–
2618	0.10–0.25	0.90–1.30	1.90–2.70	–	1.30–1.80	0.10	–	0.04–0.10	0.90–1.20 Ni
2117	0.80	0.70	2.20–3.00	0.20	0.20–0.50	–	–	–	–
2048	0.15	0.20	2.80–3.80	0.20–0.60	1.20–1.80	0.25	–	0.10	–
2017	0.20–0.80	0.70	3.50–4.50	0.40–1.00	0.40–0.80	0.25	0.10	0.15	0.20 Zr + Ti
2024	0.50	0.50	3.80–4.90	0.30–0.90	1.20–1.80	0.25	0.10	0.15	0.20 Zr + Ti
2124	0.20	0.30	3.80–4.00	0.39–0.90	1.20–1.80	0.25	0.10	0.15	0.20 Zr + Ti
2014	0.50–1.20	0.70	3.90–5.00	0.40–1.20	0.20–0.80	0.25	0.10	0.15	0.20 Zr + Ti
2011	0.40	0.70	5.00–6.00	–	–	0.30	–	–	0.20–0.60 Bi, 0.20–0.60 Pb
2219	0.20	0.30	5.80–6.80	0.20–0.40	0.02	0.10	–	0.02–0.10	0.05–0.15 V, 0.10–0.25 Zr
6060	0.30–0.60	0.10–0.30	0.10	0.10	0.30–0.60	0.10	0.05	0.10	–
6351	0.70–1.30	0.50	0.10	0.40–0.80	0.20	–	0.20	–	–
6063	0.20–0.60	0.35	0.10	0.10	0.45–0.90	0.10	0.10	0.10	–
6463	0.20–0.60	0.15	0.20	0.05	0.45–0.90	0.05	–	–	–
6081	0.70–1.10	0.50	0.10	0.10–0.45	0.60–1.00	0.20	0.10	0.15	–
6061	0.40–0.80	0.70	0.15–0.40	0.15	0.80–1.20	0.25	0.04–0.35	0.15	–
6003	0.35–1.00	0.60	0.10	0.80	0.80–1.50	0.20	0.35	0.10	–
7072	0.70 Si + Fe		0.10	0.10	0.10	0.80–1.30	–	–	–
7039	0.30	0.40	0.10	0.10–0.40	2.30–3.30	3.50–4.50	0.15–0.25	0.10	–
7020	0.35	0.40	0.20	0.05–0.50	1.00–1.40	4.00–5.00	0.10–0.35	0.08–0.25 Ti + Zr, 0.08–0.20 Zr	
7075	0.40	0.50	1.20–2.00	0.30	2.10–2.90	5.10–6.10	0.18–0.28	0.20	0.25 Zr + Ti
7009	0.20	0.20	0.60–1.30	0.10	2.10–2.90	5.50–6.50	0.10–0.25	0.20	0.25–0.40 Ag
7475	0.10	0.12	1.20–1.90	0.06	1.90–2.60	5.20–6.20	0.18–0.25	0.06	–
7050	0.12	0.15	2.00–2.60	0.10	1.90–2.60	5.70–6.70	0.04	0.06	0.08–0.15 Zr
7010	0.10	0.15	1.50–2.00	0.30	2.20–2.70	5.70–6.70	0.05	–	0.11–0.17 Zr
7178	0.40	0.50	1.60–2.40	0.30	2.40–3.10	6.30–7.30	0.18–0.35	0.20	–
7001	0.35	0.04	1.60–2.60	0.20	2.60–3.40	6.80–8.00	0.18–0.35	0.20	–
7049	0.25	0.35	1.20–1.90	0.20	2.00–2.90	7.20–8.20	0.10–0.22	0.10	–

Note: Compositions are in % maximum by weight unless shown as a range or a maximum.

Source: Adapted from Ref. [3,4], used with permission.

Table 4 Composition of selected nonheat-treatable wrought aluminum alloys

AA Number	*Si*	*Fe*	*Cu*	*Mn*	*Mg*	*Zn*	*Cr*	*Ti*	*Other*
1100	0.95 Si + Fe		0.05–0.20	0.05	–	0.10	–	–	Al min 99.00
1200	1.00 Si + Fe		0.05	0.05	–	0.10	–	0.05	Al min 99.00
1150	0.25	0.40	0.05	0.05	0.05	0.05	–	0.03	Al min 99.45
1199	0.006	0.006	0.006	0.002	0.006	0.006	–	0.002	Al min 99.99
3105	0.60	0.70	0.30	0.30–0.80	0.20–0.80	0.40	0.20	0.10	–
3103	0.50	0.70	0.10	0.90–1.50	0.30	0.20	0.10	0.05	0.10 Ti + Zr
3003	0.60	0.70	0.05–0.20	1.00–1.50	–	0.10	–	–	–
3005	0.60	0.70	0.30	1.00–1.50	0.20–0.60	0.25	0.10	–	–
3004	0.30	0.70	0.25	1.00–1.50	0.80–1.30	0.25	–	–	–
3009	1.00–1.80	0.70	0.10	1.20–1.80	0.01	0.05	0.05	0.10	0.05 Ni, 0.10 Zr
5005	0.30	0.70	0.20	0.20	0.50–1.10	0.25	0.10	–	–
5050	0.40	0.70	0.20	0.10	1.10–1.80	0.25	0.10	–	–
5251	0.40	0.50	0.15	0.10–0.50	1.70–2.40	0.25	0.15	0.15	–
5052	0.25	0.40	0.10	0.10	2.20–2.80	0.10	0.15–0.35	–	–
5454	0.25	0.40	0.10	0.50–1.00	2.40–3.00	0.25	0.05–0.20	0.20	–
5154	0.25	0.40	0.10	0.10	3.10–3.90	0.25	0.15–0.35	0.20	–
5086	0.40	0.50	0.10	0.20–0.70	3.50–4.50	0.25	0.05–0.25	0.15	–
5083	0.40	0.40	0.10	0.40–1.00	4.00–4.90	0.25	0.05–0.25	0.15	–
5056	0.30	0.40	0.10	0.05–0.20	4.50–5.60	0.10	0.05–0.20	–	–
5456	0.25	0.40	0.10	0.50–1.00	4.70–5.50	0.25	0.05–0.20	0.20	–
8001	0.17	0.45–0.70	0.15	–	–	–	0.05	–	0.09–1.30 Ni
8004	0.15	0.15	0.03	0.02	–	–	–	0.30–0.70	–
8011	0.50–0.90	0.60–1.00	0.10	0.10	0.05	0.10	0.05	0.08	–
8008	0.60	0.90–1.60	0.20	0.50–1.00	–	0.10	–	0.10	–
8280	0.07	0.70	0.70–1.30	0.10	–	0.05	–	0.10	18.00–22.00 Sn
8081	1.00–2.00	0.70	0.70–1.30	0.10	–	0.05	–	–	5.50–7.00 Sn, 0.20–0.70 Ni

Note: Compositions are in % maximum by weight unless shown as a range or a maximum.

Source: Adapted from Ref. [3,4], used with permission.

Table 5 Composition of selected cast aluminum alloys

AA number	*Casting process*	*Si*	*Fe*	*Cu*	*Mn*	*Mg*	*Cr*	*Ni*	*Zn*	*Ti*	*Other*
150.1	Ingot	Fe:Si ratio 2:1 min		0.10	–	–	–	–	0.05	–	Al min. 99.50
208.0	S	2.50–3.50	1.20	3.50–4.50	0.50	0.10	–	0.35	1.00	0.25	–
242.0	S and PM	0.70	1.00	3.50–4.50	0.35	0.15–0.35	0.25	1.70–2.30	0.35	0.35	–
295.0	S	0.70–1.50	1.00	4.00–5.00	0.35	0.03	–	–	0.35	0.25	–
201.0	S	0.10	0.15	4.00–5.20	0.20–0.50	0.15–0.55	–	–	–	0.15–0.35	0.40–1.00 Ag
204.0	S	0.30	0.35	4.20–5.00	0.10	0.15–0.35	–	0.10	0.10	0.05–0.35	–
213.0	PM	1.00–3.00	1.20	6.00–8.00	0.60	0.10	–	0.35	2.50	0.25	–
238.0	PM	3.50–4.50	1.50	9.00–11.0	0.60	0.15–3.50	–	1.00	1.50	0.25	–
305.0	S	4.50–5.50	0.60	1.00–1.50	0.50	0.40–0.60	–	0.25	0.10	0.25	–
355.0	S and PM	4.50–5.50	0.60[a]	1.00–1.50	0.50[a]	0.40–0.60	0.25	–	0.35	0.25	–
308.0	PM	5.00–6.00	1.00	4.00–5.00	0.50	0.10	–	–	1.00	0.25	–
319.0	S and PM	5.50–6.50	1.00	3.00–4.00	0.50	0.10	–	0.35	1.00	0.25	–
356.0	S and PM	6.50–7.50	0.60	0.25	0.35	0.20–0.40	–	–	0.35	0.25	–
A356.0	S and PM	6.50–7.50	0.20	0.20	0.10	0.20–0.40	–	–	0.10	0.20	–
357.0	S and PM	6.50–7.50	0.20	0.10	0.10	0.45–0.65	–	0.05	0.10	0.10–0.20	–
A357.0	S and PM	6.50–7.50	0.20	0.10	0.10	0.45–0.65	–	0.05	0.10	0.10–0.20	–
324.0	PM	6.00–8.00	1.00	1.50	0.60	0.20–0.50	–	0.30	0.50	–	–
328.0	S	7.50–8.50	1.00	1.00–2.00	0.20–0.60	0.20–0.60	0.35	0.25	1.50	0.25	–
380.0	D	7.50–9.50	2.00	3.00–4.00	0.50	0.10	–	0.50	3.00	–	–
359.0	S and PM	8.50–9.50	0.20	0.20	0.10	0.50–0.70	–	–	0.10	0.20	–
A380.0	D	7.50–9.50	1.30	3.00–4.00	0.50	0.10	–	0.50	3.00	–	–
354.0	PM	8.60–9.40	0.20	1.60–2.00	0.10	0.40–0.60	–	–	0.10	0.20	–
360.0	D	9.00–10.0	2.00	0.60	0.35	0.40–0.60	–	0.50	0.50	–	–
361.0	D	9.50–10.5	1.10	0.50	0.25	0.40–0.60	0.20–0.30	0.20–0.30	0.20	0.50	–
A332.0	PM	11.0–13.0	1.20	0.50–1.50	0.35	0.70–1.30	–	2.00–3.00	0.35	0.25	–
390.0	D	16.0–18.0	1.30	4.00–5.00	0.10	0.45–0.65	–	–	0.10	0.20	–

443.0	S	4.50–6.50	0.80	0.60	0.50	0.05	0.25	–	0.50	0.25	–
408.0	D	8.50–9.50	0.60–1.30	0.10	0.10	–	–	–	0.10	0.10	–
413.0	D	11.0–13.0	2.00	1.00	0.35	0.10	–	0.50	0.50	–	–
515.0	D	0.50–1.00	1.30	0.20	0.40–0.60	2.50–4.00	–	–	0.10	0.25	
513.0	PM	0.30	0.40	0.10	0.30	3.50–4.50	–	–	1.40–2.20	0.20	–
514.0	S	0.35	0.50	0.15	0.35	3.50–4.50	–	–	0.15	0.25	–
518.0	D	0.35	1.80	0.25	0.35	7.50–8.50	–	0.15	0.15	–	–
535.0	S	0.15	0.15	0.05	0.10–0.25	6.20–7.50	–	–	–	0.10–0.35	–
520.0	S	0.25	0.30	0.25	0.15	9.50–10.6	–	–	0.15	0.25	–
705.0	S and PM	0.20	0.80	0.20	0.40–0.60	1.40–1.80	0.20–0.40	–	2.70–3.30	0.25	–
707.0	S and PM	0.20	0.60	0.20	0.40–0.60	1.40–1.80	0.20–0.40	–	4.00–4.50	0.25	–
712.0	PM	0.15	0.50	0.25	0.10	0.50–0.65	0.40–0.60	–	5.00–6.50	0.10–0.25	–
710.0	S	0.15	0.50	0.35–0.65	0.05	0.60–0.80	–	–	6.00–7.00	0.25	–
711.0	P	0.30	0.70–1.40	0.35–0.65	0.05	0.25–0.45	–	–	6.00–7.00	0.20	–
771.0	S	0.15	0.15	0.10	0.10	0.80–1.00	0.006–0.20	–	6.50–7.50	0.10–0.20	–
713.0	S and PM	0.25	1.18	0.40–1.00	0.60	0.20–0.50	0.35	0.15	7.00–8.00	0.25	–
850.0	S and PM	0.70	0.70	0.70–1.30	0.10	0.10	–	0.70–1.30	–	0.20	5.50–7.00 Sn
851.0	S and PM	2.00–3.00	0.70	0.70–1.30	0.10	0.10	–	0.30–0.70	–	0.20	5.50–7.00 Sn
852.0	S and PM	0.40	0.70	1.70–2.30	0.10	0.60–0.90	–	0.90–1.50	–	0.20	5.50–7.00 Sn
853.0	S and PM	5.50–6.50	0.70	3.00–4.00	0.50	–	–	–	–	0.20	5.50–7.00 Sn

[a]If iron exceeds 0.45%, then manganese content must be less than one-half the iron content.

Abbreviation: D, pressure die casting; PM, permanent mold (gravity die) casting; S, sand casting.

Note: Compositions are in % maximum by weight unless shown as a range.

Source: Adapted from Refs. [3–5], used with permission.

Table 6 Designation and composition of selected cast aluminum alloys according to BS 1490

Designation	*Casting process*[a]	*Si*	*Fe*	*Cu*	*Mn*	*Mg*	*Cr*	*Zn*	*Ti*	*Ni*	*Other*
LM 0[b]	–	0.03	0.40	0.03	0.03	0.03	–	0.07	–	0.03	0.03 Pb, 0.03 Sn
LM 2	P	9.00–11.5	1.0	0.70–2.50	0.50	0.30	–	2.00	0.20	0.50	0.30 Pb, 0.20 Sn
LM 4	S and P	4.00–6.00	0.80	2.00–4.00	0.20–0.60	0.15	–	0.50	0.20	0.30	0.10 Pb, 0.10 Sn
LM 5	S and P	0.30	0.60	0.10	0.30–0.70	3.00–6.00	–	0.10	0.20	0.10	0.05 Pb, 0.05 Sn
LM 6	S and P	10.0–13.0	0.60	0.10	0.50	0.10	–	0.10	0.20	0.10	0.10 Pb, 0.05 Sn
LM 9	S and P	10.0–13.0	0.60	0.10	0.30–0.70	0.20–0.60	–	0.10	0.20	0.10	0.05 Pb, 0.05 Sn
LM 10	S and P	0.25	0.35	0.10	0.10	9.50–11.0	–	0.10	0.20	0.10	0.05 Pb, 0.05 Sn
LM 12	P	2.50	1.00	9.00–11.0	0.60	0.20–0.40	–	0.80	0.20	0.50	0.10 Pb, 0.10 Sn
LM 13	S and P	10.0–12.0	1.00	0.70–1.50	0.50	0.80–1.50	–	0.50	0.20	1.50	0.10 Pb, 0.10 Sn
LM 16	S and P	4.50–5.50	0.60	1.00–1.50	0.50	0.40–0.60	–	0.10	0.20	0.25	0.10 Pb, 0.05 Sn
LM 18	S and P	4.50–6.00	0.60	0.10	0.50	0.10	–	0.10	0.20	0.10	0.10 Pb, 0.05 Sn
LM 20	S and P	10.0–13.0	1.00	0.40	0.50	0.20	–	0.20	0.20	0.10	0.10 Pb, 0.10 Sn
LM 21	S and P	5.00–7.00	1.00	3.00–5.00	0.20–0.60	0.10–0.30	–	2.00	0.20	0.30	0.10 Pb, 0.10 Sn
LM 22	S and P	4.00–6.00	0.60	2.80–3.80	0.20–0.60	0.05	–	0.15	0.20	0.15	0.10 Pb, 0.05 Sn
LM 24	P	7.50–9.50	1.30	3.00–4.00	0.50	0.10	–	3.00	0.20	0.50	0.30 Pb, 0.20 Sn
LM 25	S and P	6.50–7.50	0.50	0.10	0.30	0.20–0.45	–	0.10	0.20	0.10	0.10 Pb, 0.05 Sn
LM 26	P	8.50–10.5	1.20	2.00–4.00	0.50	0.50–1.50	–	1.00	0.20	1.00	0.20 Pb, 0.10 Sn
LM 27	S and P	6.0–8.0	0.80	1.50–2.50	0.20–0.60	0.30	–	1.00	0.20	0.30	0.20 Pb, 0.10 Sn
LM 28	S and P	17.0–20.0	0.70	1.30–1.80	0.60	0.80–1.50	0.60	0.20	0.20	0.80–1.50	0.1 Pb, 0.1 Sn, 0.5 Co
LM 29	S and P	22.0–25.0	0.70	0.80–1.30	0.60	0.80–1.30	0.60	0.20	0.20	0.80–1.30	0.1 Pb, 0.1 Sn, 0.5 Co
LM 30	P	16.0–18.0	1.10	4.00–5.00	0.30	0.40–0.70	–	0.20	0.20	0.10	0.10 Pb, 0.10 Sn

[a]S, Sand casting; P, Permanent mold (gravity die, chill) casting.
[b]Rotor aluminum; minimum purity Al 99.5%.
Source: Adapted from Ref. [4], used with permission.

problem. Induction heating appears to be a good choice in terms of possibility of high heating rates; however, such a high rate may cause nonequilibrium melting followed by a microstructure containing a small portion of eutectics.

Among the choices of heating medium, salt baths appear to be more suitable in terms of soaking time required, dimensional stability during treatment, and interrupted supply of parts. In this medium, parts are heated by conduction of heat from the molten bath. Heat is transferred quickly from the surface to the interior of the parts and uniform heating is thus achieved. Any dimensional distortion is apparently avoided because heating is gradual and uniform, and buoyancy support is obtained from the bath. A suitable salt must be chosen depending on heat treatment schedule and its affinity toward moisture. Instead of molten salt baths, lead baths, oil baths, or fluidized beds can also be used for heat treatment. It should be remembered that exposure to molten baths may possess health hazards, and there may be a small chance of explosion. Therefore, bath concentration generally varies depending on alloy composition, and surface cleaning of parts prior to dipping into baths may be required.

In contrast, air-chamber furnaces perform better because these risks are not encountered and use of different temperatures in regular intervals is possible; therefore, they are more economical than salt baths, especially for complex-shaped parts. Atmosphere of the furnace must be controlled to prevent any blistering of the surface. High-strength 2xxx and 7xxx series alloys are prone to such adverse effects. However, it should be borne in mind that surface discoloration is a common phenomenon during heat treatment (especially SHT) of aluminum alloys, and this should not be considered as damage during heat treatment.

2.12.2.2 Strengthening by Heat Treatment

2.12.2.2.1 SHT

The first stage of heat treatment is to dissolve the maximum possible alloying elements into the solid solution before trapping them by quenching prior to aging to allow them to precipitate as particles to improve hardening. This first stage is known as SHT.

SHT for aluminum alloys is performed in the single-phase region, above the solvus line of the equilibrium phase diagram, to keep all the alloying elements in the solid solution.[6] Before the start of SHT, the solutes are concentrated in different phases or in solution, as shown in **Figure 2(a)**.[7] During heating, these phases/particles start to dissolve into the matrix by diffusion throughout the microstructure (**Figures 2(b)** and **2(c)**). Consequently, dislocation motion is less restricted during deformation and ductility is somewhat improved.[8]

SHT temperature has pronounced effects on expected mechanical properties and microstructure. For example, in **Figure 3(a)**, an aluminum–zinc phase diagram is shown. Prior to any precipitation hardening by aging treatment, the alloy needs to be heated at a suitable temperature in the α-region (here, a single-phase region) so that foreign elements can come back into the solution of the aluminum matrix. In **Figure 3(b)**, an aluminum–magnesium phase diagram is shown. As expected, the SHT temperature range here is in the single-phase field, (Mg) phase. For example, for an Al–10Mg alloy (LM-10 alloy), the temperature range is 425–435 °C. This is clearly depicted in the phase diagram. Typically, the temperature is selected as close as possible to the solidus line.[9] However, utmost care should be taken so that the chosen

Table 7 Composition of commercial lithium containing alloys

AA number	*Li*	*Cu*	*Mg*	*Zr*	*Other*
2020	1.30	4.50	–	–	0.50 Mg, 0.25 Cd
2090	2.20	2.70	–	0.12	–
2091	2.00	2.10	1.50	0.10	–
8090	2.40	1.30	0.90	0.10	–
8091	2.60	1.90	0.90	0.12	–
9092	2.40	0.65	1.20	0.12	–
CP276	2.20	2.70	0.50	0.12	–
X2094	1.30	4.50	0.40	0.14	0.40 Ag
X2095	1.10	4.20	0.40	0.14	0.40 Ag

Source: Adapted from Ref. [3,5], used with permission.

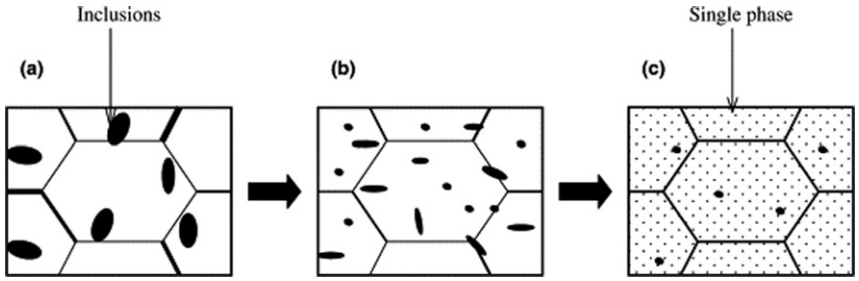


Figure 2 Schematic diagram showing the microstructure evolution for the material. (a) At the beginning of solution heat treatment (SHT). The solutes are concentrated in different phases or in solution. (b) Intermediate SHT. These phases/particles start to dissolve into the matrix. (c) Close to finishing SHT. Dissolving into the matrix is almost complete by traveling throughout the microstructure. Adapted from Ref. [7], used with permission.

temperature does not result in overheating or underheating. If overheating occurs, especially by exceeding the solidus temperature line of the phase diagram, then local melting or liquation of solids at grain boundary regions may occur. This, in turn, will result in loss of tensile properties and fracture toughness. Such incipient melting can effectively be detected by X-ray microtomography methods. In Figure 4, incipient melting, characterized by small irregular regions with smooth surfaces, is seen at 551 °C (824 K) immediately after the start of SHT for an Al–Si–Cu alloy.[10]

In addition, if induction heating is used or if high heating rate is considered, then nonequilibrium heating conditions

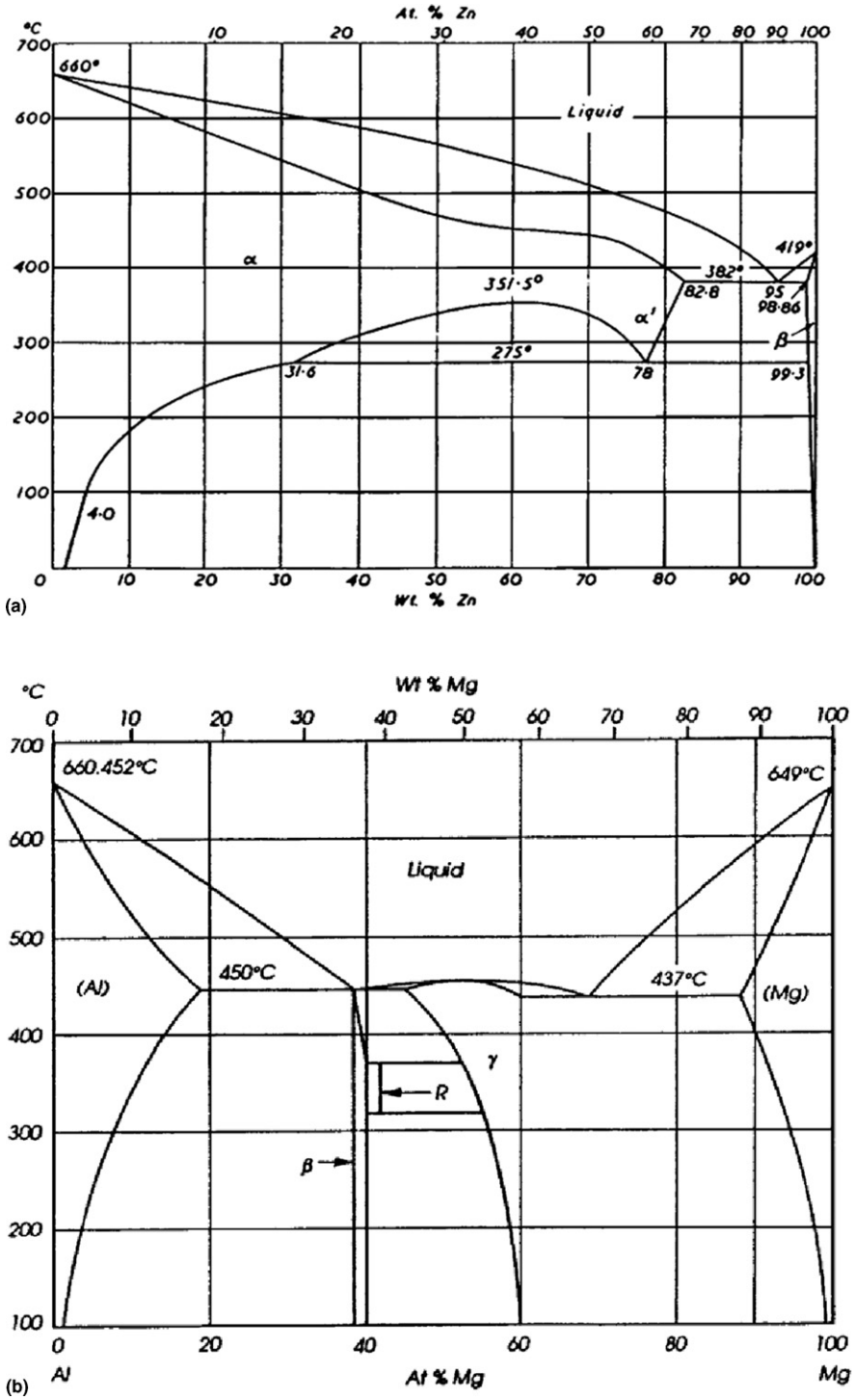


Figure 3 (a) Aluminum–zinc equilibrium phase diagram. (b) Aluminum–magnesium equilibrium phase diagram. Adapted from Ref. [11], used with permission.

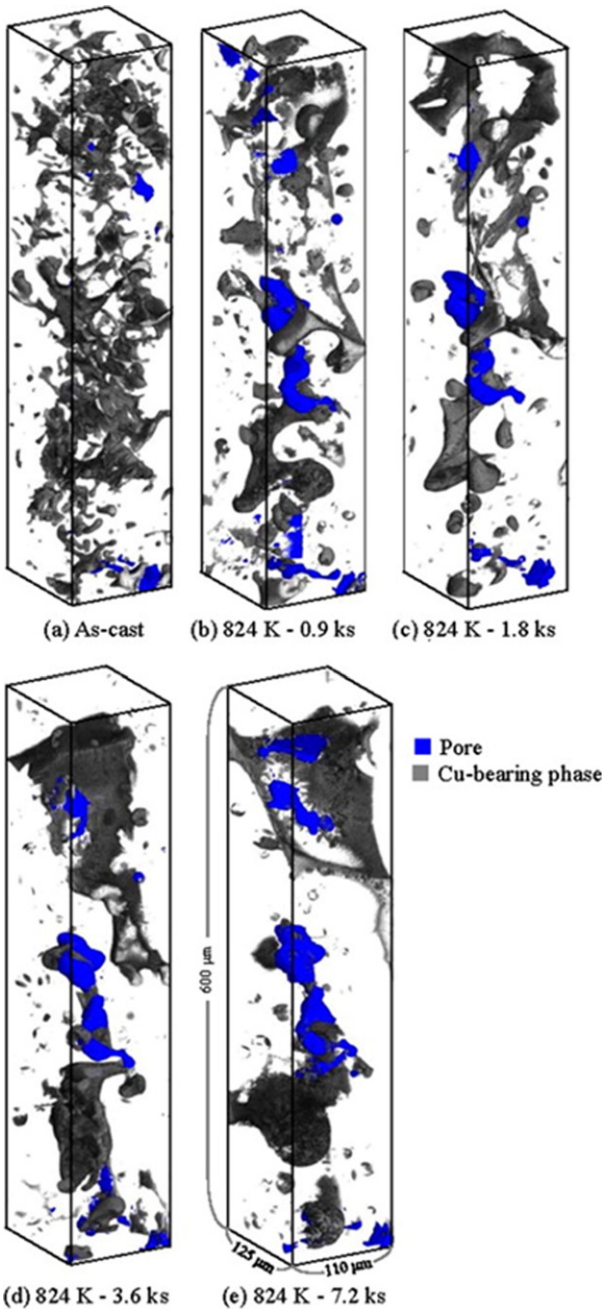


Figure 4 3D perspective views of pores and copper-bearing phase. Solution treatment temperature was 824 K. Incipient melting is clearly seen immediately after the commencement of heating. Large, irregularly shaped regions with smooth surfaces and small spherical regions are the proof of this local melting. These spherical regions disappeared over time, whereas irregular regions were coalesced together with time. Adapted from Ref. [10], used with permission.

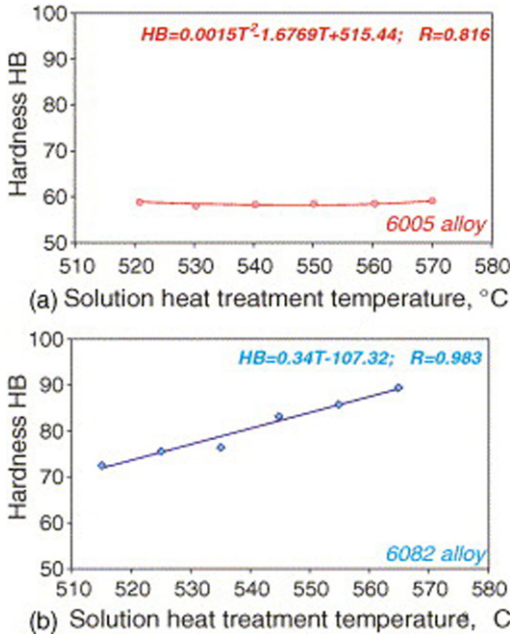


Figure 5 Influence of the solution heat treatment temperature on hardness of: (a) 6005 alloy and (b) 6082 alloy. The mechanical properties of 6005 alloy is not dependent on solution treatment temperature. In contrast, in 6082 alloy a strong dependency is observed. This is due to the difference in magnesium, silicon, and manganese amount in both alloys. More Mg_2Si (β) phase was nucleated when the solution temperature was increased. This explained the improvement of hardness. Adapted from Ref. [12], used with permission.

would prevail, indicating vertical movement of the solidus line, and leading to further liquation. When underheating occurs, expected mechanical properties may not be achieved. In aluminum alloys, solvus lines are typically shallow, and a small decrease in temperature may affect the desired level of trapped solutes by attaining unexpected strengths after aging. For a 6082 alloy, hardness values were observed to increase with SHT temperature.[12] It was experimentally found that the amount of trapped magnesium and silicon in the solid solution required for the formation of Mg_2Si particles (responsible for strengthening) increased when the SHT temperature was moved upward, following corresponding phase diagram. However, it should be kept in mind that increasing SHT temperature only cannot always result in improvement of properties (**Figure 5(a)**); the amount of alloying elements present in the alloy is also of prime concern. In **Figure 5(b)**, the same SHT treatment applied for a 6082 alloy had significantly improved hardness compared to a 6005 alloy, which had a lower concentration of magnesium and silicon. It is noteworthy that in commercial aluminum alloys, obtaining a well-distributed solute atom concentration is a rare event due to nonequilibrium solidification, and formation of eutectic phases with a low melting point from these segregations is unavoidable. Therefore, a very high SHT temperature beyond which these eutectics were solidified can lead to local melting, as mentioned. Unfortunately, such low melting can even occur without any segregation, as seen in Al–Mg–Si[13] and Al–Zn–Mg[14] alloys. Therefore, a slightly lower SHT temperature is industrially preferred.

The time for SHT (soaking time) must be adequate to allow dissolution of phases present and homogenous distribution of solutes,[15] and hence a more formable material. A properly selected soaking time helps to reduce irregular precipitates and residual stresses. A longer time generally helps coarsening of hard particles, which may not dissolve at low SHT temperature.

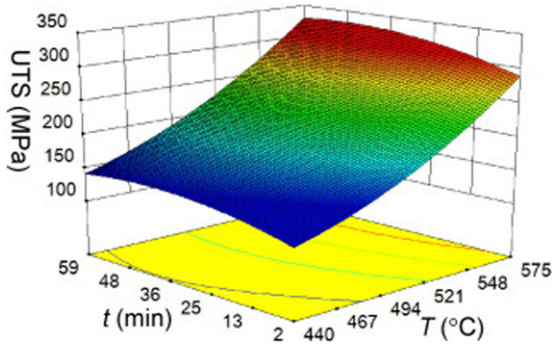


Figure 6 Effect of solution heat treatment temperature (T) and time (t) on ultimate tensile test for an AA6082 alloy sheet with thickness of 1.50 mm. Adapted from Ref. [18], used with permission.

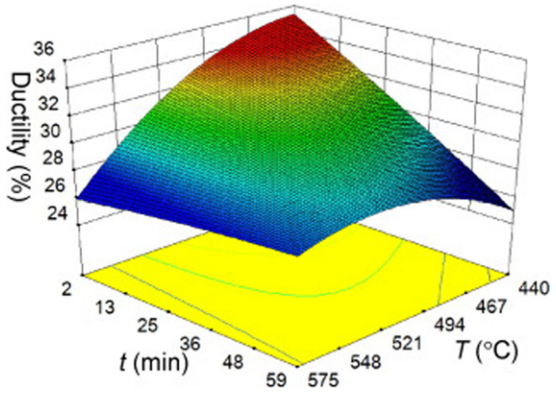


Figure 7 Effects of solution heat treatment temperature (T) and time (t) on ductility for an AA6082 alloy sheet with thickness of 1.50 mm. Adapted from Ref. [18], used with permission.

This spheroidizing ultimately contributes to ductility during flow of materials.[16] The soaking time is generally shorter for investment, sand, and permanent mold castings, in progressive order.[17] The time can vary from a few seconds for very thin sheets to approximately a day for large and complex castings. Soaking time is calculated differently for different heating mediums. In molten salt baths, soaking time is estimated as soon as the parts are immersed and the temperature is still on its way to the scheduled temperature. In contrast, in air-chamber furnaces, soaking time is calculated after the chamber reaches its scheduled temperature on machine readings.

The effects of SHT temperature and soaking time are clearly demonstrated in the surface model, as shown in **Figure 6**. Ma *et al.*[18] showed that for an AA6082 aluminum alloy sheet with a thickness of 1.5 mm, ultimate tensile strength (UTS) was increased with SHT temperature and soaking time. For any particular soaking time, increasing SHT temperature raised UTS significantly, consistent with previous observation with hardness data. Low SHT temperature (above solvus line) may not be sufficient to dissolve a large number of solute atoms, even if the soaking time is reasonably longest. Similarly, the effects of SHT temperature and soaking time on ductility are shown in **Figure 7**. Ductility was enhanced at both shorter soaking time and SHT temperature. Interestingly, the effect of soaking time on ductility was more pronounced at lower SHT temperatures compared to higher SHT temperatures. In a different approach, the strength effects can be considered based on particle coarsening. Strengthening by precipitated particles occur either by shearing of particles or by Orowan loop formation. For large particles, yield strength can be increased by the first method or decreased by the second method. Longer soaking time eventually increases the particle size, because the diameter of $Al_3(Sc,Zr)$ particles of an SSA108 alloy was found to increase significantly during longer soaking time.[19] With an increase in particle diameter, the yield strength was decreased and it was claimed that the Orowan loop mechanism was responsible for this decrease in strength.

It is now obvious that it is possible to depict a limiting range of temperature for solution treatment. As shown in **Figure 8**, for the binary aluminum–copper system, the solution treatment temperature range is carefully chosen slightly below the eutectic temperature for that alloy system.

2.12.2.2.2 Quenching

Quenching is considered one of the most critical thermal processes. It involves heating of the workpiece to a certain temperature and then rapid cooling, usually to RT. The aim of this treatment is to trap maximum possible solute atoms in the solid solution, keeping the minimum residual stresses. Large thermal gradients can cause inhomogeneous plastic deformation, leading to the development of large residual stresses. If the quenching is accomplished in cold water, then forged AA7449 alloy induces biaxial compressive stress of a magnitude of 250–300 MPa at the surface and 350 MPa tensile stress in the core.[20] Quenching also helps to keep a sufficient number of vacancies in solid state to permit diffusion at lower temperatures. Quenching eventually produces a supersaturated solid solution, which is a favorable condition for aging. However, maintaining dimensional stability is a challenge that deals with appropriate quenching medium and quenching duration.

It is believed that quenching heat treatment alters properties, and that tensile properties including ductility are generally improved compared to the as-cast (F) condition. This quenching treatment is designated as T4 (see Section 2.12.1.2.2.2), which denotes SHT followed by quenching and natural aging. However, commercially, this condition is not attractive because artificial aging can improve mechanical properties significantly.

As a quenching medium, water is most commonly used for aluminum alloys. Generally, boiling water, warm water (65 °C), or RT water is used as a quenchant. When selecting a quenchant, factors affecting the cooling rate such as formation of a vapor blanket, heat of vaporization, specific heat, and conductivity become vital,[21] and different alloys require different choices. Further changes in cooling rate can be obtained by coating the part or by adding polymers in the quenchant.

Total quenching duration should be kept as short as possible. Otherwise, there is a possibility of random precipitation, which eventually does not contribute to strengthening and protection from corrosion. To reduce susceptibility of such precipitation, quench delay, such as time to transfer parts from the furnace area to the quenching area of the plant, should be kept as short as possible because such interruption can lead to

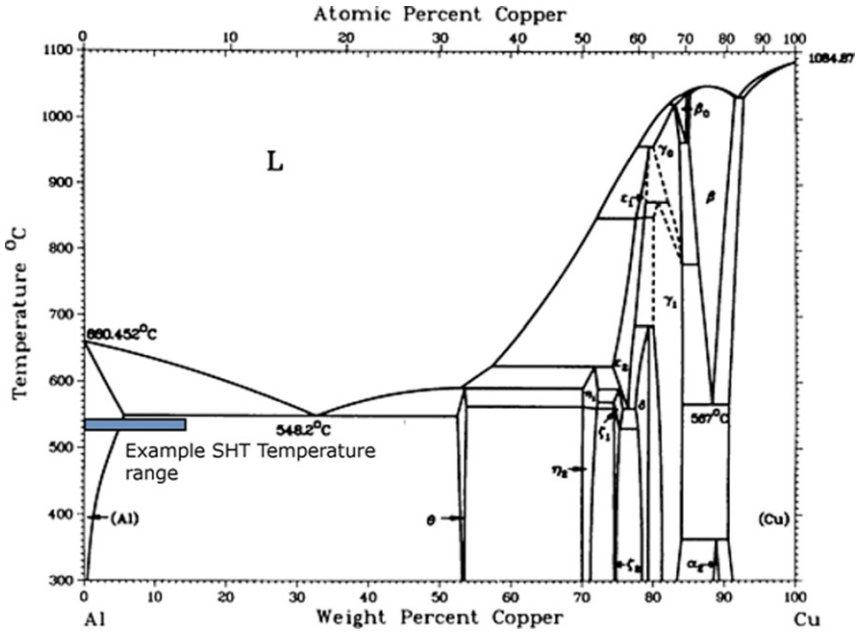


Figure 8 Aluminum–copper binary equilibrium phase diagram. Temperature range for solution heat treatment is shown by highlighting just below the eutectic temperature line. Adapted from Ref. [11], used with permission.

a certain degree of precooling. Also, to prevent any extent of reheating or disruption of cooling during quenching (which can also promote precipitation), the flow of the quench medium should be closely monitored.

Cooling rate affects total strengthening obtainable from quenching and is a crucial factor for microstructural distribution.[22] For example, for a nonstrontium-modified Al–Si–Cu–Mg alloy, a rapid cooling rate was found to improve hardness values.[23] It partly controls aluminum dendrite size, eutectic silicon size (if present), and the size, shape, and distribution of phases and porosity. As mentioned, it is essential to retain all soluble elements in the solid solution of aluminum. Therefore, the rate must be high enough (without any interruption) to ensure greater initial soaking temperature for the estimated duration of quenching to dissolve everything into solution, and at the same time to prevent formation of particles in the grain boundary. Any interruptions (known as quench delay) during quick transfer of job parts from the furnace to the quenching medium would lead to rapid precooling and formation of particles depending on alloy composition and soaking temperature.

If particles are precipitated during quenching, then the total number of formable particles during aging is reduced, and corrosion resistance and mechanical properties are somewhat compromised. A rapid cooling rate also increases total number of excess vacancies in the lattice structure to create an environment favorable for diffusion and ultimately promoting precipitation during aging. Nevertheless, increasing the cooling rate causes greater thermal gradients, resulting in higher internal thermal stresses and instability in dimensions of job parts. To minimize thermal stresses, the quenching medium plays an important role. Warm baths are sometimes suggested to prevent development of residual stresses. Otherwise, job parts are treated by immersion in cold water or by spraying with high-velocity cold water.

It is well established that cooling rate depends on alloy composition and can be denoted by quench sensitivity – minimum cooling rate applicable without substantial precipitation during cooling. Quench sensitivity is defined as a relative measure of removal of solute atoms from solid solution in the form of precipitation.[24] Commercial alloys containing a variety of micro-alloying elements for specific applications and fine precipitates are considered more quench sensitive because they can promote heterogeneous nucleation during the cooling schedule. However, there are disputes about the large impact of alloy composition on residual stresses. Also, quenching response of cast and wrought alloys are different. Robinson *et al.*[25] insisted that both AA7010 and AA1075 alloys had shown a closely similar pattern of residual stresses despite the differences in quench sensitivity due to wide variation in alloy chemistry. Alloys from the 2xxx, 6xxx, and 7xxx series are cooled at higher quench rates because they are more susceptible to precipitate during cooling. For example, alloy AA7050 is an aerospace alloy combining strength, SCC resistance, and toughness, and it is less quench-sensitive compared to most competitors. This alloy is heavily used as plate in fuselage frames and bulkheads within a thickness range of 75–150 mm. Recently, modifications in major alloying elements, in the form of the Zn/Mg/Cu ratio, of these alloys have led to the development of AA7085 – used in Airbus A380. For a 413-type Al–Si cast alloy, it was observed that a warm water bath (60 °C) was preferable to ambient air to improve alloy strength.[26] Also, according to Gauthier and co-workers,[27] for an as-cast 319.2 alloy, the best combination of strength and elongation to failure was found by quenching in warm water at 60 °C prior to artificial aging. In an AA7055 alloy, more grain boundary particles containing greater amounts of zinc and magnesium were precipitated at a slow quench rate. Consequently, these electrochemically active

particles and precipitate-free zones (PFZs) near grain boundaries that accelerate corrosion are more electrochemically active and tend to accelerate corrosion. It is noteworthy that PFZs become wider in slowly quenched alloys. It is obvious from **Figure 9** that the greater the cooling rate, the smaller the PFZ and grain boundary particles.[28] Also, slow quench rate increases volume fraction and spacing of particles.

For a commercial AA7108 alloy, different quenching rates were used to understand the effects of cooling velocity on microstructures.[29] It was found that precipitation of the η-phase was promoted during cooling below the solvus line. At a rapid cooling rate, such a phase was small and needle-shaped compared to the microstructure of a similar alloy quenched at a much slower rate (**Figure 10**). The large and largely spaced needles are distinguishably visible in the microstructure. Also, PFZs around particles are readily identifiable after a slow cooling rate.

For an AA6063 alloy, it was experimentally found that quench holding time had a pronounced effect on age treatment and mechanical properties.[15] The alloy was solution-treated at 535 °C for 1 h, quenched in a salt bath, and held there isothermally for a predetermined time prior to aging at 180 °C for 4 h. It is certain that with the increase of holding time in the quench bath, there was a marked decrease in hardness after aging (**Figure 11**). Also, the number density of particles decreased after coarser particle formation. Guinier–Preston (GP) zones (see Section 2.12.2.2.3) and needle-shaped β' phase, in the Al–Mg–Si alloy system, are responsible for strengthening during aging. With the increase of holding time, the needle-shaped β' phase becomes coarser, which means the number density of this phase is reduced. Consequently, the equilibrium β phase formed at the latter stage is coarser and incoherent but is not an effective barrier for dislocation motion. As more magnesium and silicon atoms are taken by this equilibrium phase, fewer atoms remain for strengthening by β'' particles. Therefore, the contribution of this microstructure to strengthening is negligible.

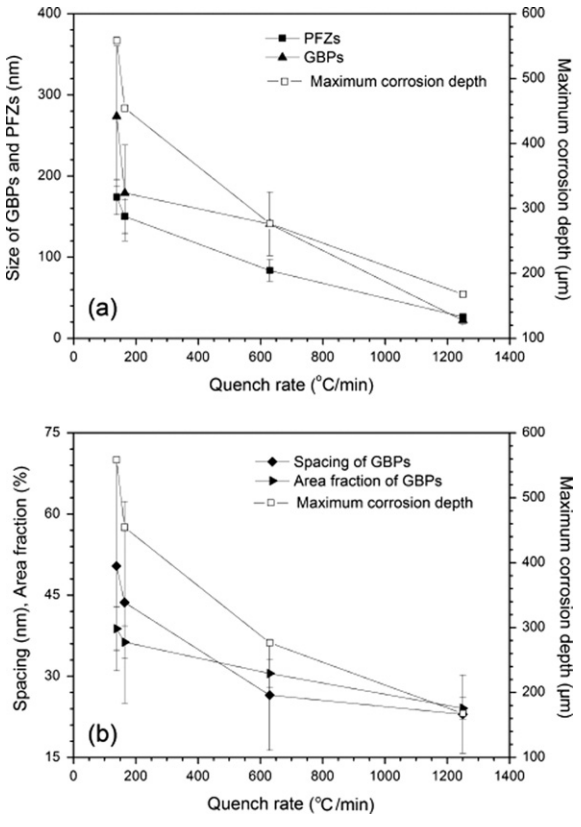


Figure 9 For an AA7055 alloy, the effect of the quench rate on grain boundary microstructures (a) size of precipitate-free zones (PFZs), grain boundary particles (GBPs), and (b) spacing and area fraction of GBPs. The maximum corrosion depth is also given. It is clear that as the quench rate is decreased, the size, spacing, and area fraction of GBPs increase. Also, it is interesting to note that the widths of PFZs near grain boundaries become larger. Adapted from Ref. [28], used with permission.

2.12.2.2.2.1 Quenched-in vacancies

Quenched-in vacancies in the supersaturated solid solution play an important role in further strengthening processes, such as aging.[30] The number of vacancies in equilibrium increases with temperature exponentially. It is therefore expected that at the SHT temperature, the total number of vacancies will be very high. Now, quenching is performed very rapidly, leaving no room for reaching equilibrium conditions, so that equilibrium concentration of vacancies can be rearranged. Consequently, there are many vacancies from the high SHT temperature that become trapped-in – or quenched-in – at RT (quenching temperature). With time, excess vacancies will be annealed out. Vacancies will coalesce to form clusters. Some of these clusters can interact with dislocation loops and grow further, either by adding more vacancies to the cluster or by increase of dislocations. Consequently, these vacancies act as heterogeneous nucleation sites. In addition, vacancies play another vital role. These excess quenched-in vacancies help to accelerate the rate of diffusion of atoms during aging. It is claimed to be the only way the GP zones are formed initially at the very low aging temperature (or RT).[31] As discussed later (see Section 2.12.2.2.3.1), natural aging is accomplished at RT without any stimulation from the outside. Therefore, formation of GP zones by diffusion of atoms can only be explained with the guidance from quenched-in vacancies. If an alloy is solution-treated at different temperatures and then aged after quenching, the rate of GP zone formation is highest for the alloy soaked at the highest temperature. This is proof that quenched-in vacancies increase the rate of diffusion because higher solution temperature means higher concentration of vacancies awaiting being trapped-in. Interestingly, it was found that larger solute atoms would exert stronger affinity for binding with vacancies.[32]

These vacancies are also responsible for formation of PFZ adjacent to grain boundaries. Generally, grain boundaries themselves and the interior of grains contain abundant particles. However, there are some regions very close to boundaries that hardly have any particles. Such a difference in chemical potential can invoke intergranular corrosion. Vacancies with high diffusivity migrate quickly toward grain boundaries as boundaries act as a sink for vacancies. Far-off boundaries and the concentration of vacancies are reduced. As a consequence, precipitation becomes limited due to lack of nucleation sites, because a critical value of supersaturation of vacancies must be

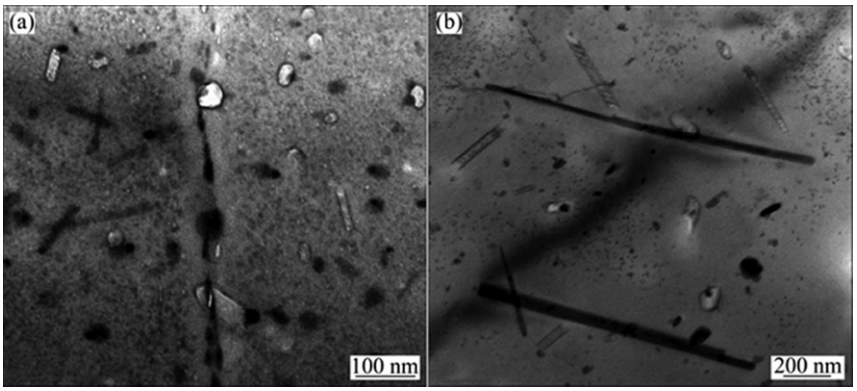


Figure 10 For an AA7108 alloy, TEM bright field micrographs of samples after aging showing microstructure of material continuously cooled from 480 to 200 °C within (a) 10 and (b) 120 min. The microstructure in (a) contains a mixture of η', η, and notable precipitate-free zone (PFZ). Some of the precipitates are needle-shaped. After a longer time, as in (b), η formation is unavoidable in the earlier state, leaving only a subtle amount of solutes for the nucleating η' phase. PFZs are also seen around particles. Adapted from Ref. [29], used with permission.

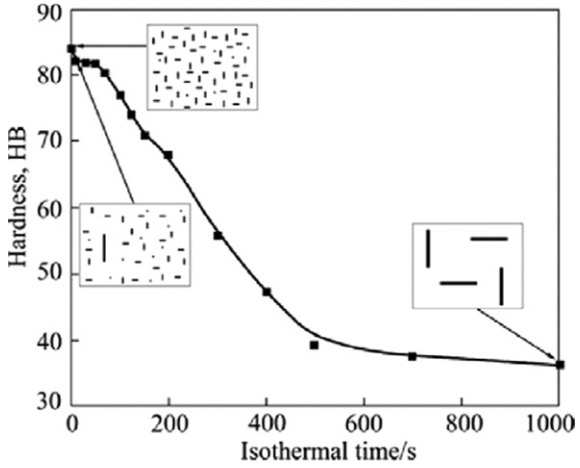


Figure 11 Relationship between precipitate distribution and hardness of aged specimens held at 370 °C for different times for AA6063 alloy. As more magnesium and silicon atoms are taken by the equilibrium β phase, fewer atoms remain for strengthening by needle-shaped β'' particles. Also, the β'' phase becomes coarsened over time. Therefore, the contribution of this microstructure to strengthening is negligible. Adapted from Ref. [15], used with permission.

exceeded for nucleation to occur. It is important to note that solute content in the aluminum matrix in these zones is not affected by this zone formation. Using 3D atom probe tomography techniques, PFZ formation can be visualized.[33] After quenching, excess quenched-in vacancies and different types of solutes are distributed randomly in the aluminum matrix. Now, at the beginning of aging, nanocrystals are formed (**Figure 12(a)**). However, as boundaries act as a sink for vacancies, the number of nanocrystals is comparatively less near the boundaries. As aging continues, these nanocrystals transform into GP zones or intermediate precipitates at grain boundaries and grain interiors, with a limited number of small nanocrystals remaining in areas close to boundaries. These are PFZs. To prevent PFZs from forming, silver may be added as a micro-alloying element. Silver atoms take the nanocrystals as prisoners, and depletion of vacancies in adjacent areas of boundaries is prevented (**Figure 12(b)**). Therefore, a PFZ with a very narrow width is formed. PFZ was reported to form in many aluminum alloys, including Al–Li aerospace alloys,[34] Al–Si cast alloys,[35] and Al–Zn–Mg alloys.[36] There is another mechanical formation of PFZs. At the high-energy grain boundaries, precipitates are formed and grown during quenching from the SHT temperature. This causes a flux of solutes from areas adjacent to grain boundaries. PFZ can deteriorate mechanical properties of alloys.[37] However, it was claimed to have some beneficial effect in damage tolerance by desensitizing the material to the breaking of particles.[38] To prevent formation of PFZs, a higher solution temperature and faster quenching rate are sometimes suggested.

2.12.2.2.3 Aging

Age hardening or precipitation hardening is the final step of three steps of strengthening by the heat treatment process for aluminum alloys. Hardening by aging can be accomplished either at RT (nature aging) or at elevated temperature for a predetermined period of time (artificial aging). Aging involves decomposition of metastable supersaturated solid solution formed during the second step of heat treatment. This decomposition leads to precipitation of a new phase. Interactions between these decomposition products and dislocations play the key role of strengthening by aging. As mentioned, SHT is accomplished at a temperature in the single-phase region and quenching is ended at a temperature in the two-phase region. During aging, precipitation starts with the formation of coherent gathering of solute-rich atoms into the matrix aluminum. These gatherings are called GP zones. The GP zone is the first step of formation of equilibrium precipitates during aging. The next step is semi-coherent intermediate precipitates, which are larger than GP zones. These precipitates can be nucleated at GP zones or at crystalline defects such as dislocations. The final precipitate is incoherent and largest in size. This final phase rarely contributes to strengthening. Maximum strength is obtained from fine dispersion of GP zones and intermediate precipitates. It is important to note that solute clusters and co-clusters of different solute atoms are also observed prior to GP zone

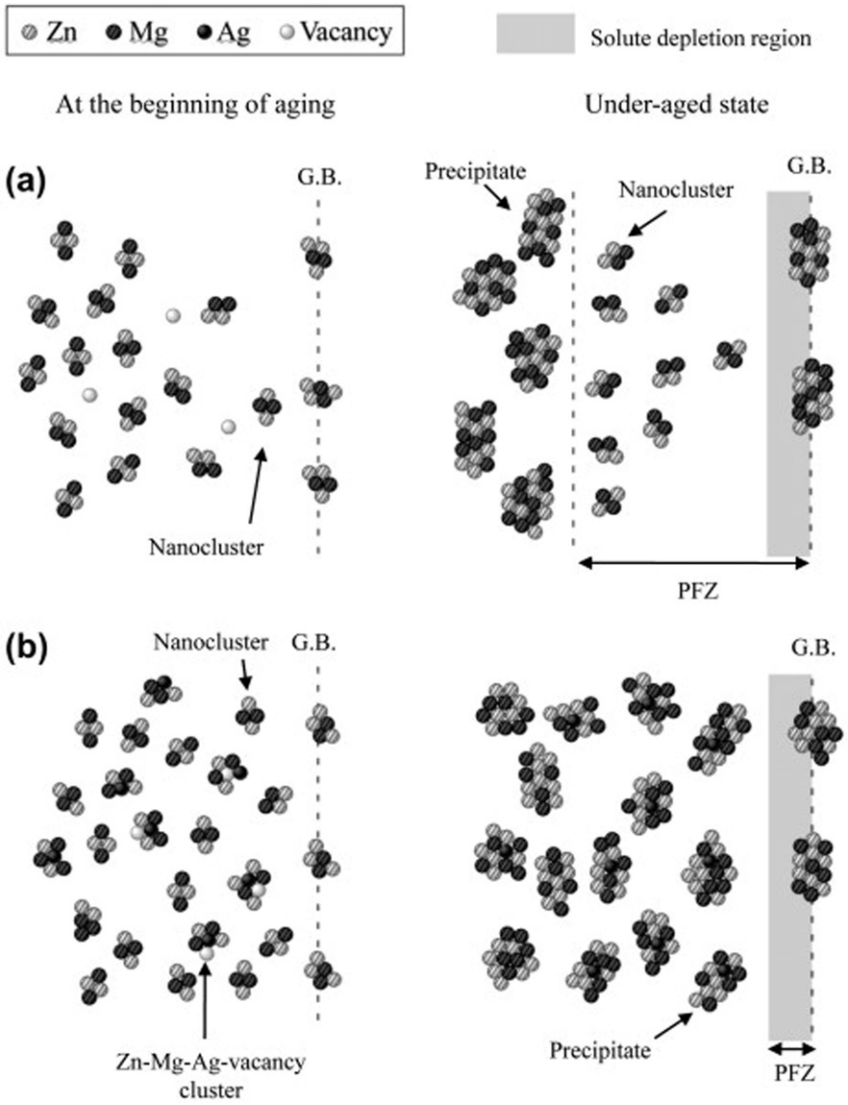


Figure 12 Schematic diagrams of the proposed precipitation processes in the vicinity of grain boundaries during aging in the (a) Al–Zn–Mg ternary and (b) Ag-containing alloys. Left figures are at the beginning of aging, whereas right figures are in an underage state. Adapted from Ref. [33], used with permission.

formation for many aluminum alloys. These clusters are merely regions of concentrated solute atoms. The formation of these clusters was studied using Monte Carlo step (MCS) simulation by Sato and co-workers.[39] **Figure 13(a)** shows that vacancies can be entrapped by solute atoms (here, magnesium). This phenomenon eventually reduces the number of mobile vacancies and restricted diffusion of solute atoms (here, copper). These copper atoms intend to form clusters with magnesium–vacancy complexes, ultimately forming magnesium–vacancy–copper complex co-clusters (**Figure 13 (b)**). These co-clusters act as heterogeneous nucleation sites for GP zones.[40]

For some alloys, especially 2xxx alloys, cold working is performed prior to aging to increase the number of dislocations by dislocation interactions. These forest dislocations provide nucleation sites of the intermediate precipitate to assist in hardening.

2.12.2.2.3.1 Natural aging

Heat-treatable aluminum alloys generally experience at least a small degree of aging at RT. This is termed natural aging. The 2xxx alloys generally reach maximum attainable strength values by 5 days in T3 or T4 temper conditions. On the contrary, a few 6xxx and 7xxx alloys appear to be unstable at ambient temperatures, and precipitation may continue over the course of a year, for example, AA6016 alloy.[41] However, as an exception, AA6014 alloy was observed to attain peak hardness after a few hours of natural aging following T4 treatment, and hardness values were found to decrease after 1 day.[42] Among cast alloys, A356.0 and C355.0 alloys are aged within 48 h, and further changes after this time are negligible. However, T4 tempered 520.0 alloy age hardens over the course of a year.

Composition plays an important role in natural aging. A small addition of gold as an alloying element can restrict the

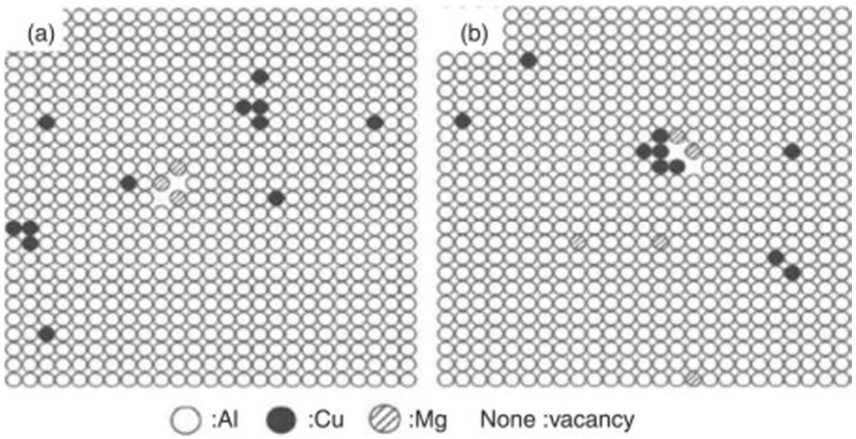


Figure 13 Examples of atom arrangements on the (001) plane simulated for 5X106 Monte Carlo step at 273 K: (a) vacancy trapping and (b) Cu–Mg–vacancy complex clusters. Adapted from Ref. [40], used with permission.

natural aging of Al–Cu alloys due to interaction of quenched-in vacancies with gold atoms.[43] Without the presence of micro-alloying gold, this role is played by copper. The role of quenched-in vacancies is important. They can form complexes with solutes during quenching. These complexes can transport solutes to the solute clusters.[44] Effects similar to the addition of gold are obtained if magnesium is added as a micro-alloying element in Al–Cu systems; the natural aging response is accelerated.[40] However, the formation of solute clusters, which do not interact well in the precipitation reaction sequence, hinder formation of GP zones.[45] In Al–Li–Cu alloys, lithium is generally considered to bind with vacancies and restrict the natural aging response.[46] This is inevitable as the increasing lithium content accelerates formation of intermediate precipitates, sacrificing GP zones due to changes in misfit strain energy by trapping of quenched-in vacancies. However, in the presence of magnesium, lithium–vacancy complexes favor the precipitation sequence (i.e., formation of GP zones).[47]

Cuniberti and co-workers[48] conducted a tensile test on AA6082 alloy sheets in four conditions: SHT and quenched conditions (SS), natural aged conditions (NA), natural aging followed by artificial aging conditions (AA/NA), and artificial aged conditions (AA). It was found that natural aging improved tensile strength, but with loss of ductility. Interestingly the stress–strain curves were serrated for the samples tested in SHT and quenched conditions, and the serration effect was diminished with time during natural aging. It was claimed that solute atoms, in as-quenched conditions, were randomly distributed in the matrix, and their repeated interactions with dislocations occurred during deformation (a well-known Cottrell atmosphere phenomenon), leading to serrated conditions, with profound support from quenched-in vacancies. During natural aging (**Figure 14(a)**), clusters containing solute atoms of Mg/Si in this Al–Mg–Si alloy and quenched-in vacancies were formed, resulting in reduced solutes from the solution and less pronounced serration. In contrast, in AA conditions (**Figure 14(b)**), strength was largest and was found to decrease with samples with a history of AA/NA. This can be understood by observing the microstructural features at different conditions. A few samples were aged at 180 °C for

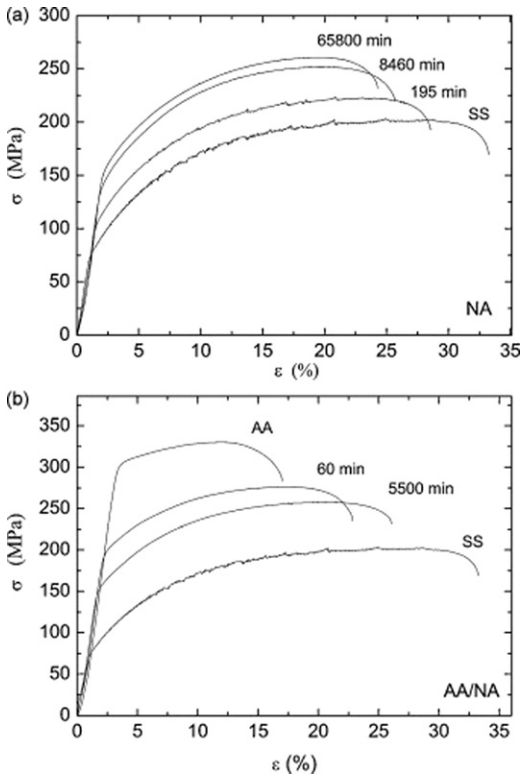


Figure 14 An AW6082 alloy was tensile-tested after aging in different conditions. (a) Stress–strain curves obtained for samples naturally aged (NA) for different durations. (b) Stress–strain curves obtained for samples artificially aged 30 min at 180 °C, with previous natural aging for the duration mentioned (AA/NA). Here, SS denotes as-quenched conditions and AA indicates 180 °C for 30 min of aging with no room temperature pre-aging. Adapted from Ref. [48], used with permission.

30 min (**Figure 15**). If the sample had no history of natural aging, then coherent β'' (Mg_5Si_6) precipitates were formed. However, the lack of these precipitates in naturally aged samples indicates that solute clusters might not be the ideal candidate for heterogeneous nucleation of this phase for this

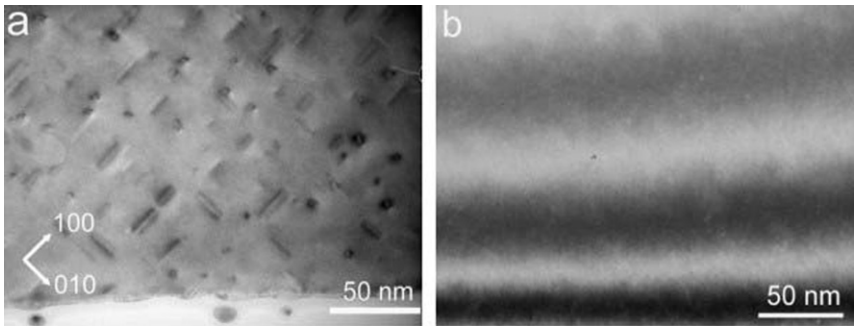


Figure 15 For an AW6082 alloy, TEM images corresponding to 30 min of artificial aging at 180 °C, (a) with no natural aging and (b) with 7 previous days of natural aging. It is clear that after artificial aging for 30 min, immediately after quenching, high number density of needle-shaped β'' precipitates is observed. However, no such precipitates are found if the alloys are naturally aged for 7 days. Adapted from Ref. [48], used with permission.

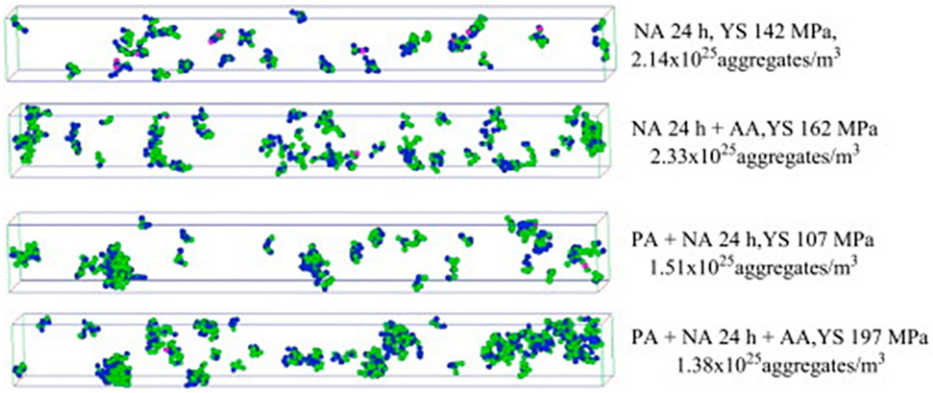


Figure 16 For a 6181A alloy, atom maps were constructed by 3DAP atom probe analysis in different heat treatment conditions. Green, blue, and pink dots represent Mg, Si, and Cu atoms, respectively. To compare visually, the sizes of the boxes were kept the same. The yield strength and overall number density of solute aggregates for each condition are given. AA, artificial aging conditions; NA, natural aging; PA, pre-aging; YS, yield strength. Adapted from Ref. [50], used with permission.

alloy. For an AA6111 alloy undergoing treatment of (1) natural aging for a long time and then artificially aged, and for one undergoing (2) artificial aging immediately after quenching, similar results were found.[49] Flow stress was studied to gradually increase for type (1) – treated specimens. This was attributed to the formation of GP zones, providing effective hardening. It is noteworthy that natural aging prior to artificial aging is typically effective for short aging time.[42]

From a different point of view, pre-aged (PA) AA6181A alloy at 200 °C for 20 s in a salt bath immediately after quenching was found to impede clustering of solutes (atoms of magnesium, silicon, and copper) during subsequent natural aging due to formation of large solute aggregates prior to formation of GP zones.[50] As shown by 3DAP atom probe analysis in **Figure 16**, naturally aged (NA) samples showed small solute aggregates and moderately high yield strength. If this sample is artificially aged (AA), then an expected number of aggregates as well as yield strength will increase. Now, if this alloy is pre-aged in this condition and naturally aged, then the aggregate density is reduced and larger aggregates are observed with a significant decrease in yield strength. Now, if this sample is artificially aged, then a distinct increase in strength is obtained due to the contribution of much larger aggregates – the known β'' phase. Also, solute clusters formed during natural aging can become spherical or elongated, and contribute to strengthening.[51]

2.12.2.2.3.2 Artificial aging

Most of the heat-treatable commercial aluminum alloys are artificially aged at an elevated temperature for a predefined period of time to obtain desired mechanical properties. For the reasons discussed, natural aging is typically avoided prior to artificial aging to minimize any deteriorating effects on properties. For example, Al–Mg–Si alloys containing lower amounts of magnesium and silicon show positive responses toward natural aging prior to artificial aging.[52] However, most commercial alloys of the 6xxx series yield an adverse effect if natural aging occurs. Several explanations are provided in the literature for explaining this behavior. The increase of critical nucleus size for the precipitation of β'' particles by a decrease in vacancy concentration during natural aging or small co-clusters formed may not be efficient enough for nucleation of β'' particles.[53] However, natural aging is sometime unavoidable due to the variety of logistic supports, such as transportation or shifting of parts for aging, present in heat treatment plants. Temperature range for artificial aging generally varies between 100 and 190 °C, and time can be 5 to 48 h, depending on alloy composition and application of the corresponding

alloy. Effects of time and temperature on aging are comparatively less critical than SHT and quenching treatments. However, these two parameters are of paramount importance. Longer time and/or unnecessary higher temperature can lead to low numbers of large lumps of precipitates, ineffective for hardening. T5 to T10 tempers include artificial aging.

Precipitation sequence of artificially aged Al–Mg–Si alloy AA6061 was examined and described by Edwards *et al.*[54] as follows:

Al supersaturated solid solution → Clusters of Si atoms; Clusters of Mg atoms → Dissolution of Mg clusters → Formation of Si/Mg co-clusters → Small precipitates of unknown clusters (GP-I Zone) → β'' Mg_5Si_6 (GP-II Zone) precipitates → β'' and β' precipitates → β Mg_2Si precipitates.

The sequences were observed experimentally using atom probe tomography (**Figure 17**).

Aging of this type of alloy is governed by the number density of mobile vacancies.[56] Number of vacancies present in the quenched condition is controls the rate of advancing the precipitation sequence, irrespective of aging temperature. Aging temperature varies depending on requirement. For example, in the T6 condition, ultimate strength is obtained with negligible hampering of other properties. The same alloy can be aged under T7 conditions, where the temperature is slightly higher and the alloy becomes overaged. Strength is reduced but dimensional stability may be improved or residual stress can be reduced. This AA6061 alloy shows negative responses if naturally aged prior to artificially aging. This phenomenon for this alloy can be explained by the trapping of vacancies by co-clusters of magnesium and silicon.[57] As a consequence, naturally aged AA6061 alloy yields a negative response during artificial aging in standard 170 °C T6 conditions.[55] However, there exists some debate about the efficiency of silicon-rich clusters in aging behavior because it was recently claimed that these clusters might not react to intermediate β'' phases effectively and might remain small during artificial aging.[58] These clusters might be the reason for hardness drop during subsequent artificial aging. Nevertheless, vacancies are again released from the trapping-in co-clusters at higher temperatures; therefore, aging at temperatures above 210 °C results in a marked increase in hardness. To avoid detrimental effects of natural aging, tin can be added as a micro-alloying element. The high affinity of tin for vacancies can avoid formation of clustering to some extent by forming tin–vacancy pairs,[59] and thus the adverse effect of natural aging is minimized. For example, AA6061 alloy was aged between 210 and 250 °C after micro-alloying with 100 ppm tin.[60] An excellent improvement in hardness was noticed immediately. It was assumed that tin might act as heterogeneous nucleation sites and provide guided diffusion of solute atoms, in addition to the trapping effect.

In a few aluminum alloys experiencing T3, T8, and T9 tempers, hardening is improved due to deformation. Cold working results in nucleation of more precipitate particles from increased numbers of dislocations. Alloys such as AA2014 and AA2124 undergoing T8 treatment achieve excellent strength due to cold working after SHT. S phase in AA2139 alloy was reported to nucleate heterogeneously at dislocations.[61]

2.12.2.3 Heat Treatment Scheme for Wrought Alloys

As discussed, wrought alloys can be heat-treatable or nonheat-treatable. Heat-treatable wrought alloys belong to the 2xxx (Al–Cu; Al–Cu–Mg), 6xxx (Al–Mg–Si), and 7xxx (Al–Zn–Mg; Al–Zn–Mg–Cu; Al–Zn–Mg–Cu–Zr) classes. Precipitation hardening type heat treatment is generally used for these alloys for strengthening purposes. Precipitation hardening involves solution treatment, quenching, and aging. Other classes of wrought aluminum alloys show little response toward strengthening by precipitation hardening. These alloys are known as nonheat-treatable wrought alloys. Commonly alloys from the 1xxx (controlled pure aluminum), 3xxx (Al–Mn; Al–Mn–Mg), and 5xxx (Al–Mg) classes are considered nonheat-treatable alloys. Nonheat-treatable alloys are hardened by strain hardening during working (See Section 2.12.1.3.2).

2xxx series alloys (Al–Cu and Al–Cu–Mg systems). These alloys have found their usage in airframes.[62] These alloys experience hardening by precipitation of the Al_2Cu phase. Addition of other micro-alloying elements can modify the precipitation

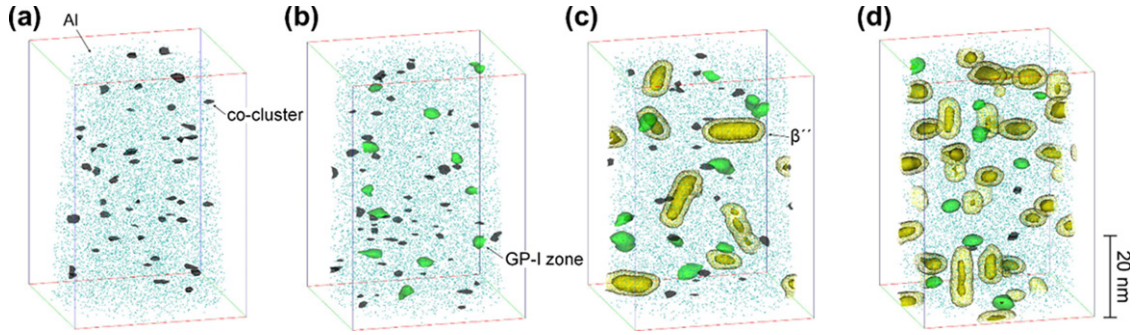


Figure 17 For an AA6061 alloy, atom probe analysis (3DAP) reconstructed for an aluminum matrix for (a) long-term natural aging, (b) 3.6 ks aging, and (c) 28.8 ks aging after quenching and a certain period of storage, and (d) 28.8 ks aging at 170 °C immediately after quenching. Magnesium-rich regions are clearly seen in (a). Due to the tendency to form co-clusters with silicon, black regions (voxels) indicate these co-cluster. The green regions in (b) show the Guinier–Preston (GP) zone (I). These zones are more spherical and rich in solute than co-clusters from natural aging conditions. After longer aging, needle-shaped β'' precipitates are evident in (c). In (d), the microstructure is completely different because it was aged right after quenching. More β'' phase, GP zone (I), and a few co-clusters are observed. Adapted from Ref. [55], used with permission.

reaction, and new precipitates can also be formed. In AA2014 and AA2044, magnesium is added and the Al_2CuMg phase is precipitated simultaneously with Al_2Cu phase. At temperature higher than 100 °C during aging, GP zones are transformed into θ'' (GP zone II), followed by θ' (tetragonal Al_2Cu). Finally, the incoherent equilibrium θ (BCC Al_2Cu) phase is formed. If the alloy contains magnesium, then individual clusters of copper and magnesium are first to nucleate; they can significantly contribute to hardening. Rod-shaped GP zones (magnesium/copper containing GPB zones, i.e., Guinier–Preston–Bagariastkij zones) are then formed,[63] probably heterogeneously on the clusters. Then, the lath-shaped semi-coherent orthorhombic S′ (Al_2CuMg) phase is nucleated at dislocations. Finally, the orthorhombic S phase, equilibrium and incoherent, is developed. Also, the Al_2Cu phase is nucleated and grown depending on Cu:Mg ratio.

6xxx series alloys (Al–Mg–Si system). These alloys are generally aged at 170 °C. From the supersaturated solid solution, individual clusters and co-clusters of magnesium and silicon atoms are formed. These clusters have negligible effects on hardening. Then, spherical GP zones are formed. From the GP zones, needle-shaped coherent monoclinic β'' (approximately MgSi) are nucleated. These precipitates are responsible for hardening in these alloys. As aging continues, the hexagonal β' (Mg1.7Si) phase is formed, which is semi-coherent. At the same time, the semi-coherent hexagonal B′ (MgSi) phase is also precipitated. Finally, the coherent equilibrium FCC β (Mg_2Si) phase is formed from β'.

7xxx series alloys (Al–Zn–Mg systems). These are the most potential alloys. They are high-strength alloys extensively used in aerospace industries. During aging in these alloy systems, at first two types of GP zones (spherical GP I and disc-shaped GP II) are formed. From these GP zones, a disc-shaped hexagonal semi-coherent η' (MgZn) phase is developed. From this η' phase, hexagonal η phase ($MgZn_2$) is formed. It should be noted that if the Mg:Zn ratio is very high, then instead of the η phase, the T′ phase can be formed. This is also a hexagonal semi-coherent phase with a chemical formula of $Mg_{32}(Al, Zn)_{49}$. Ultimately, equilibrium and cubic T phase is nucleated from either η phase or T′ phase. Its chemical formula is $Mg_{32}(Al, Zn)_{49}$. To improve the aging response, copper is added to this alloy system. However, care must be taken to ensure precipitation of large Al_2CuMg phase limiting to a certain amount. For recent alloys, such as 7075, a combined heat treatment procedure is used. It involves T6 treatment and reheating for a short time at a temperature slightly above the aging temperature, followed by cold-water quenching. Then, the alloy is re-aged. The advantages of this are mechanical properties up to the satisfactory level are obtained from T6 temper and resistance to SCC obtainable from T73 temper. This heat treatment is known as retrogression and re-aging (RRA).[3]

Al–Li alloy system. This alloy system belongs to several groups, including 2xxx and 8xxx. Strengthening of these alloys comes from solid solution hardening by lithium and precipitation hardening. During aging, meta-stable spherical cubic and coherent δ' (Al_3Li) phases are precipitated and are responsible for hardening. Note that δ' is an ordered structure of the Cu_3Au ($L1_2$) superlattice type. Finally, the equilibrium noncoherent cubic δ (AlLi) phase is formed. If copper and/or magnesium is added, then the precipitation sequence is altered. Copper promotes θ' and T_1 phase (Al_2CuLi) formation. The crystal structure of the T_1 phase is still a matter of debate.[34] Firm evidence regarding its structure has yet to be obtained. In the presence of magnesium, the rod-shaped Al_2LiMg phase is formed in addition to the δ' phase. The Θ' phase is observed when Cu:Li ratio is greater than 1:3. Also, S′ and S phases can be nucleated if copper and magnesium are present in large amounts. In this alloy system, no direct evidence of presence of GP zones has been reported. Also, presence of the T_1 phase is important for strengthening at an acceptable range. Formation of this phase is facilitated by the presence of copper, magnesium, and silver. T8 temper provides favorable conditions for the nucleation of this phase.

Table 8 shows the heat treatment schedule for common commercial wrought aluminum alloys. After solution treatment, parts should be quenched rapidly without further delay from logistics. Quenching in water in general should be performed with water at RT.

Maximum soaking time and quench delay for solution treatment of wrought aluminum alloys can be related with part thickness. **Table 9** shows the thickness of parts and corresponding required soaking time for both air furnace and molten salt bath and maximum quenched delay.

2.12.2.4 Heat Treatment Scheme for Cast Alloys

Heat treatments for foundry-grade alloys are slightly different from those for wrought alloys. Both types undergo similar procedures of heat treatment but with different limits of parameters. A major difference lies in SHT. Temperature and soaking (holding) time are generally higher in cast alloys due to the presence of larger microconstituents, which take longer to go back into solution. Quenching time is also another parameter that needs proper attention. Casting parts are generally more complex in shape and the quenching process has to be performed carefully to keep residual stresses at a minimum state. For this reason, quenching is often performed in boiling water or similar medium. T6 temper is the most common treatment applied to cast alloys. In addition, T5 and T7 tempers are used in industry. In T5, a slight improvement may occur in hardness. For example, materials of pistons and other machine parts are tempered in T5 conditions to obtain better dimensional stability and strength at elevated temperatures.[64] Sometimes, a combination of toughness and strength is required by sacrificing extra hardness, which can be achieved by using T7 temper. Achievable hardness is not very impressive but toughness is improved.

In high-pressure die casting parts, trapped gases in pores cannot be solution-treated at temperatures (e.g., 540 °C for 8 h) like other alloys. Swelling and/or surface blistering may occur.[65] A360 alloy was solution-treated at different temperatures and time and compared with as-cast conditions (**Figure 18**). The experiment was designed in the following way to compare different specimens: as-cast specimen was indicated by 'a'; sample 'b' was solution-treated for 16 h at 545 °C; in sample 'c,' the time was reduced to 0.25 h (15 min); and SHT temperature was further reduced by 10 °C for samples d, e, f, and g, successively, and soaking time was kept at 15 min. It can be seen that the highest SHT temperature and time

Table 8 Heat treatment schedule for wrought aluminum alloys

Alloy designation	*Product form*	*Solution heat treatment*		*Precipitation heat treatment*		
		Temperature (°C)	*Temper designation*	*Temperature (°C)*	*Time (h)*	*Temper designation*
2011	Rolled or cold-finished rod and bar	525	T3	160	14	T8
		525	T4	–	–	–
		525	T451	–	–	–
2025	Die forgings	515	T4	170	10	T6
2219	Flat sheet	535	T31	175	18	T81
		535	T37	165	24	T87
		535	T42	190	36	T62
	Plate	535	T31	175	18	T81
		535	T37	175	18	T87
		535	T351	175	18	T851
		535	T42	190	36	T62
	Rolled or cold-finished wire, rod, and bar	535	T351	190	18	T851
	Extruded rod, bar, shapes, and tube	535	T31	190	18	T81
		535	T3510	190	18	T8510
		535	T3511	190	18	T8511
		535	T42	190	36	T62
	Die forgings and rolled rings	535	T4	190	26	T6
	Hand forgings	535	T4	190	26	T6
		535	T352	175	18	T852
2018	Die forgings	510	T4	170	10	T61
2024	Flat sheet	495	T3	190	12	T81
		495	T361	190	8	T861
		495	T42	190	9	T62
		495	T42	190	16	T72
	Coiled sheet	495	T4	–	–	–
		495	T42	190	9	T62
		495	T42	190	16	T72
	Plate	495	T351	190	12	T851
		495	T361	190	9	T861
		495	T42	190	9	T62
	Rolled or cold-finished wire, rod, and bar	495	T4	190	12	T6
		495	T351	190	12	T851
		495	T36	190	8	T86
		495	T42	190	16	T62
	Drawn tube	495	T3	–	–	–
		495	T42	–	–	–
2036	Sheet	500	T4			
2038	Sheet	540	T4	205	2	T6
2218	Die forgings	510	T4	170	10	T61
		510	T41	240	6	T72
2008	Sheet	510	T4	205	1	T62
2014	Flat sheet	500	T3	160	18	T62
		500	T42	160	18	T6
	Coiled sheet	500	T4	160	18	T6
		500	T42	160	18	T62
	Plate	500	T42	160	18	T62
		500	T451	160	18	T651
	Rolled or cold-finished wire, rod, and bar	500	T4	160	18	T6
		500	T42	160	18	T62
		500	T451	160	18	T651
	Extruded rod, bar, shapes, and tube	500	T4	160	18	T6
		500	T42	160	18	T62
		500	T4510	160	18	T6510
	Drawn tube	500	T4	160	18	T6
		500	T42	160	18	T62
	Die Forgings	500	T4	170	10	T6

(*Continued*)

Table 8 Continued

Alloy designation	*Product form*	*Solution heat treatment*		*Precipitation heat treatment*		
		Temperature (°C)	*Temper designation*	*Temperature (°C)*	*Time (h)*	*Temper designation*
2017	Rolled or cold-finished wire, rod, and bar	500	T4	–	–	–
		500	T42	–	–	–
2117	Rolled or cold-finished wire and rod	500	T4	–	–	–
		500	T42	–	–	–
2618	Forgings and rolled rings	530	T4	200	20	T61
4032	Die forgings	510	T4	170	10	T6
2090	Sheet	540	T3	165	24	T83
2091	Sheet	530	T3	120	24	T84
	Extruded bar	530	T3	190	12	Peak aged
8090	Extruded bar	530	T3	190	12	Peak aged
CP276	Extruded bar	540	T3	190	12–15	Peak aged
6005	Extruded rod, bar, shapes, and tube	530	T1	175	8	T5
6009	Sheet	555	T4	205	1	T6
6010	Sheet	565	T4	205	1	T6
6053	Sheet	530	T4	160	18	T6
		530	T42	160	18	T62
	Plate	530	T4	160	18	T6
		530	T42	160	18	T62
		530	T451	160	18	T651
	Rolled or cold-finished wire, rod, and bar	530	T4	160	18	T6
		530	T4	160	18	T89
		530	T4	160	18	T93
		530	T4	160	18	T913
		530	T4	160	18	T94
		530	T42	160	18	T62
		530	T451	160	18	T651
	Extruded rod, bar, shapes, and tube	530	T4	175	8	T6
		530	T4510	175	8	T6510
		530	T4511	175	8	T6511
		530	T42	175	8	T62
	Drawn tube	530	T4	160	18	T6
		530	T42	160	18	T62
	Die and hand forgings	530	T4	175	8	T6
	Rolled rings	530	T4	175	8	T6
		530	T452	175	8	T652
	Drawn tube	520	T4	175	8	T6
		520	T4	175	8	T83
		520	T4	175	8	T831
		520	T4	175	8	T832
		520	T42	175	8	T62
6013	Sheet	570	W	190	4	T6
	Plate	570	W	190	4	T651
6066	Extruded rod, bar, shapes, and tube	530	T4	175	8	T6
		530	T42	175	8	T62
		530	T4510	175	8	T6510
		530	T4511	175	8	T6511
	Drawn tube	530	T4	175	8	T6
		530	T42	175	8	T62
	Die forgings	530	T4	175	8	T6
6070	Extruded rod, bar, shapes, and tube	545	T4	160	18	T6
		545	T42	160	18	T62
6111	Sheet	560	T4	175	8	T6
6151	Die forgings	515	T4	170	10	T6
	Rolled rings	515	T4	170	10	T6
		515	T452	170	10	T652
6262	Rolled or cold-finished wire, rod, and bar	540	T4	170	8	T6
		540	T4	170	12	T9

(*Continued*)

Table 8 Continued

Alloy designation	Product form	Solution heat treatment		Precipitation heat treatment		
		Temperature (°C)	Temper designation	Temperature (°C)	Time (h)	Temper designation
		540	T451	170	8	T651
		540	T42	170	8	T62
	Extruded rod, bar, shapes, and tube	540	T4	175	12	T6
		540	T4510	175	12	T6510
		540	T42	175	12	T62
	Drawn tube	540	T4	170	8	T6
		540	T4	170	8	T9
		540	T42	170	8	T62
6463	Extruded rod, bar, shapes, and tube	–	T1	205	1	T5
		520	T4	175	8	T6
		520	T42	175	8	T62
6951	Sheet	530	T4	160	18	T6
		530	T4	160	18	T62
7001	Extruded rod, bar, shapes, and tube	465	W	120	24	T6
		465	W	120	24	T62
		465	W510	120	24	T6510
		465	W511	120	24	T6511
7005	Extruded rod, bar, and shapes	–	–	–	–	T53
7050	Plate	475	W51	–	–	T7651
		475	W51	–	–	T7451
	Extrusion	475	W510	–	–	T6510
		475	W511	–	–	T6511
	Die and hand forgings	475	W	–	–	T74
		475	W52	–	–	T7452
7075	Sheet	480	W	120	24	T6
		480	W	120	24	T62
		480	W	–	–	T76
		480	W	–	–	T73
	Plate	480	W	120	24	T62
		480	W51	–	–	T7351
		480	W51	120	24	T651
		480	W51	–	–	T7651
	Rolled or cold-finished wire, rod, and bar	490	W	120	24	T6
		490	W	120	24	T62
		490	W	–	–	T73
		490	W51	120	24	T651
		490	W51	–	–	T7351
	Extruded rod, bar, shapes, and tube	465	W	120	24	T6
		465	W	120	24	T62
		465	W	–	–	T73
		465	W	–	–	T76
		465	W510	120	24	T6510
		465	W510	–	–	T73510
		465	W510	–	–	T76510
		465	W511	120	24	T6511
		465	W511	–	–	T73511
		465	W511	–	–	T76511
	Drawn tube	465	W	120	24	T6
		465	W	120	24	T62
		465	W	–	–	T73
	Die forgings	470	W	120	24	T6
		470	W	–	–	T73
		470	W52	–	–	T7352
	Hand forgings	470	W	120	24	T6
		470	W	–	–	T73
		470	W52	120	24	T652

(*Continued*)

Table 8 Continued

Alloy designation	*Product form*	*Solution heat treatment*		*Precipitation heat treatment*		
		Temperature (°C)	*Temper designation*	*Temperature (°C)*	*Time (h)*	*Temper designation*
		470	W52	–	–	T7352
	Rolled rings	470	W	120	24	T6
7175	Die forgings	–	W	–	–	T66
		–	W	–	–	T74
		–	W52	–	–	T7452
	Hand forgings	–	W	–	–	T74
		–	W52	–	–	T7452
7475	Sheet	515	W	120	3	–
		515	W	155	3	T61
		515	W	–	–	T761
	Plate	510	W51	120	24	T651
		510	W51	–	–	T7651
		510	W51	–	–	T7351
Alclad 7475	Sheet	495	W	120	3	–
		495	W	155	3	T61
		495	W	–	–	T761

Source: Adapted from Ref. [64], used with permission.

Table 9 Soaking time required for aluminum alloys with different thicknesses for different quenchants and maximum allowable quench delay

Thickness (mm)	*Soaking time (min)*				*Maximum quench delay (s)*
	Air furnace		*Salt bath*		
	Min	*Max*	*Min*	*Max*	
0.41 or under	20	25	10	15	5
0.42–0.51	20	30	10	20	7
0.52–0.64	25	35	15	25	7
0.65–0.81	25	35	15	25	7
0.82–1.02	30	40	20	30	10
1.03–1.27	30	40	20	30	10
1.28–1.35	30	40	20	30	10
1.36–1.80	35	45	25	35	10
1.81–2.03	35	45	25	35	10
2.04–2.29	35	45	25	35	10
2.30–2.54	40	55	30	45	15
2.55–3.18	40	55	30	45	15
3.19–4.06	50	60	35	45	15
4.07–4.57	50	60	35	45	15
4.58–6.35	55	65	35	45	15
For each additional 12.7 or fraction	+30	+30	+20	+20	5

Source: Adapted from Ref. [64], used with permission.

(sample b) resulted in extreme surface blistering and discoloration. Swelling was also evident to some extent, thus questioning its ability regarding dimensional stability. However, soaking time is shortened at the same SHT temperature (sample c), and the detrimental effects on surface and microstructure are eliminated slightly. These effects were almost diminished when temperature was reduced widely (compare sample c with sample g). Therefore, it can be concluded that to minimize porosity and blistering effects, shorter soaking time and lower SHT temperature are required.

Composition, in addition to SHT parameters, plays an important role in mechanical property determination. Lumley and co-workers[67] investigated nine Al–Si–Cu die cast alloys (see **Table 10** for composition) in different temper conditions. Samples that were only solution-treated and quenched showed an increase in percent elongation values, yielding lower strength. T4 temper increased hardness after natural aging, as expected. T6 temper containing official aging improved strength to a very satisfactory level, with a sharp decline in percent elongation values. By adding more copper and magnesium into the alloy (alloy 1 and alloy 5), the 0.2% proof stress was significantly improved. Adding more copper or magnesium (beyond alloy 5) showed no significant increase in strength properties (see **Figure 19**).

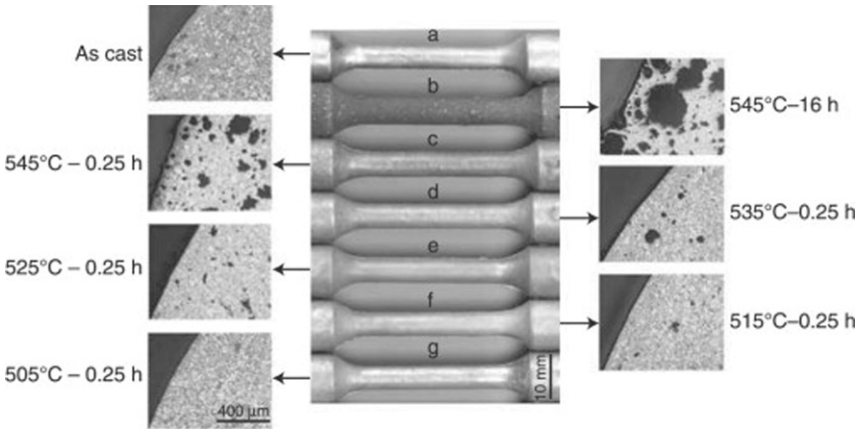


Figure 18 Comparisons of the surfaces and internal microstructures of an A360 alloy solution treated under different conditions. Adapted from Ref. [66], used with permission.

Table 10 Compositions of the nine examined alloys

Alloy	*Figure 19 legend*	*Al*	*Si*	*Cu*	*Mg*	*Zn*	*Fe*	*Mn*	*Other*
1 (base)	▲	Balance	9	3.1	0.1	0.53	0.86	0.16	<0.2
2	◆	Balance	9.1	3.18	0.29	0.6	0.86	0.14	<0.2
3	◊	Balance	9.2	3.11	0.09	2.9	0.9	0.16	<0.2
4	■	Balance	8.6	3.6	0.1	0.53	0.93	0.18	<0.2
5	+	Balance	8.6	3.6	0.3	0.53	1.0	0.2	<0.2
6	○	Balance	8.5	4.9	0.1	0.51	0.97	0.2	<0.2
7	*	Balance	8.7	4.9	0.27	0.51	1.0	0.21	<0.2
8	□	Balance	9.1	4.2	0.22	1.2	1.3	0.2	<0.2
9	△	Balance	8.8	4.0	0.7	0.56	1.1	0.19	<0.2

Source: Adapted from Ref. [67], used with permission.

It is noteworthy that if Al–Si–Cu alloys contain magnesium, then SHT temperature needs to be modified.[68] However, higher SHT temperature may result in local melting of copper-containing phases and less spheroidization of silicon phases.[69] To resolve this, a two-stage SHT can be a good choice. A319 alloy was heat-treated with a two-stage SHT (495 °C for 8 h and 520 °C for 2 h) and good mechanical properties were achieved.[70] The first stage of SHT allowed all copper to dissolve in solution; during HTs of the second stage, most elements were diffused into the solution.

Spheroidization of silicon phases is achieved during SHT. This is important because a good number of commercial cast alloys contain silicon, and sharp edges of silicon reduce toughness and fatigue properties. SHT temperature and time need to be chosen carefully. The parameters can be varied from 540 °C for 3 min for Sr-modified A356 alloy[71] to 40 °C for 30 min for Al–7Si–0.3Mg alloy.[72] In general, therefore, soaking time changes depending on alloy composition and casting condition. If the microconstituents are smaller, as expected progressively in investment, sand, and permanent mold casting, then short time is desirable. Moreover, if silicon modifiers are used, as shown, then soaking time can be shortened significantly because less time is required to spheroidize.

Table 11 shows the heat treatment schedule for common commercial cast aluminum alloys. After solution treatment, parts should be quenched rapidly without further delay due to logistics. Quenching in water in general should be performed with water temperature at 65–100 °C.

2.12.2.5 Stress Relief

Quenching is inevitable for hardening in most commercial aluminum alloys. Fast cooling is preferred in most cases for better mechanical properties. Unfortunately, rapid cooling can introduce residual stresses in parts by inhomogeneous plastic flow (inelastic strains) due to severe thermal gradients.[73] These residual stresses can lead to warping during quenching, degradation of dimensional stability during machining, and reduced fatigue life during service.[74] The aftermath of residual stress is distortion. For example, during machining, in a part with residual stress, the equilibrium state of stress is distorted and a new equilibrium results; local plastic deformation is then unavoidable.

The level of residual stress depends on properties such as elastic modules and the thermal expansion coefficient of the materials involved. Also, the thermal gradient between the surface and the interior of the part is important because the surface is cooled much faster than the interior, inducing tensile stresses at the surface; obviously, compressive stress would develop in the interior (**Figure 20(a)**).[75] Because the surface temperature is still high enough, it remains plastic and can accommodate any stresses that develop. As a result, no residual stress develops. In the second stage, the outer layer is cooler

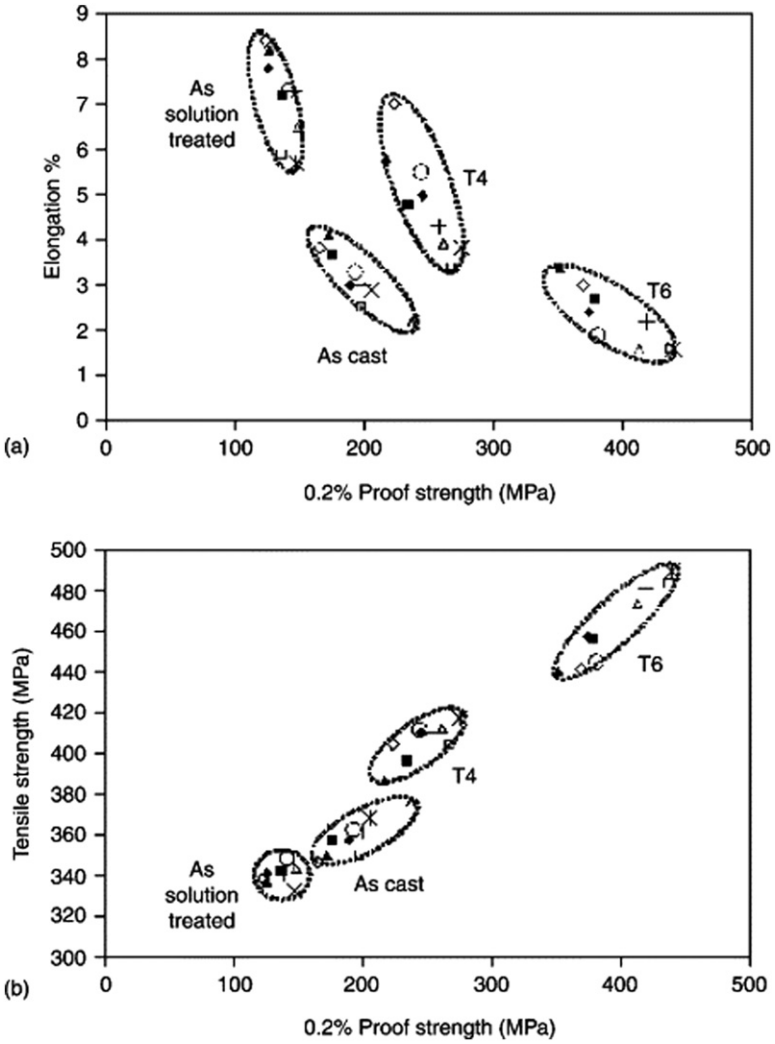


Figure 19 The mechanical properties of HPDC alloys based on Al–Si–Cu showing: (a) elongation as a function of the average 0.2% proof strength and (b) tensile strength as a function of the average 0.2% proof strength for the as-cast solution-treated T4 and T6 tempers. Five samples per condition were tested. Alloy specimens for tensile testing were cylindrical and had a total length of 100 mm, with a central parallel gauge length of 33 mm and a diameter of 5.55 ± 0.1 mm. Adapted from Ref. [66], used with permission.

than the interior and regains strength. Accordingly, the elastic surface can resist any plastic deformation in the interior (**Figure 20(b)**). No residual stress is developed. As the temperature gradient further increases, the cooling rate of the core becomes greater than at the surface; consequently, the elastic interior would try to change its dimension. However, this will be constrained by the elastic surface. As a result, the interior would try to pull the surface inward. That is, tensile stress develops at the core and compressive stress forms at the surface (**Figure 20(c)**). This balanced stress is residual stress.

Residual stresses can be relieved by thermal methods or mechanical methods.

Thermal methods include modifications in the heat treatment schedule by changing temperature, and cooling times are used to reduce stresses. For example, using T7 temper (overaging) for casting causes loss of properties compared to T6 temper, but such a sacrifice is vital compared to the gain in mechanical properties. Also, to reduce the magnitude of residual stress, a less severe quenching method can be applied. For example, as a quenchant, boiling water or organic quenchant can be applied. However, because these quenchants slow the cooling rate, the final mechanical properties may not be to a desired level[76] because microstructural development would be disturbed. This intuitively suggests interrupted quenching by different quenchants. However, there has been some work on it that reduces stresses.[77]

The mechanical method involves stretching or compression of heat-treated parts, which allows a small and controlled amount of plastic deformation at RT or elevated temperature. It is noteworthy that temper designation is slightly different for alloys, diminishing residual stresses by plastic deformation. For example, if residual stress is removed by applying stretching, then temper designation becomes Tx51 (x refers to standard temper digit). Similarly, Tx52 is used when residual stress is removed by compression. For AA7010 aerospace alloy, it was observed that 1% cold compression could relieve most of the residual stress developed during quenching.[78] However, this could not diminish tensile stresses from the core, and

Table 11 Heat treatment schedule for cast aluminum alloys

Alloy designation	*Temper*	*Type of casting*	*Solution heat treatment*		*Aging treatment*	
			Temperature (°C)	*Time (h)*	*Temperature (°C)*	*Time (h)*
201.0	T4	S or P	490–500	2	–	–
	T4	S or P	+525–530	14–20	Minimum of 5 days at room temperature (RT)	
	T6	S	510–515	2	–	–
	T6	S	+525–530	14–20	155	20
	T7	S	510–515	2	–	–
	T7	S	+525–530	14–20	190	5
	T43	–	525	20	24 h at RT + 30 min to 1 h at 160 °C	
	T71	–	490–500	2	–	–
	T71	–	+525–530	14–20	200	4
204.0	T4	S or P	490–500	2	–	–
	T4	S or P	+525–530	14–20	Minimum of 5 days at RT	
	T6	S or P	490–500	2	–	–
	T6	S or P	+525–530	14–20	155	12–24
	T7	S or P	490–500	2	–	–
	T7	S or P	+525–530	14–20	200	4
	T72	S or P	490–500	2	–	–
	T72	S or P	+525–530	14–20	243–248	–
208.0	T55	S	–	–	155	16
222.0	O	S	–	–	315	3
	T61	S	510	12	155	11
	T551	P	–	–	170	16–22
	T65	–	510	4–12	170	7–9
242.0	O	S	–	–	345	3
	T571	S	–	–	205	8
	T571	P	–	–	165–170	22–26
	T77	S	515	5	330–355	2 (Minimum)
	T61	S or P	515	4–12	205–230	3–5
295.0	T4	S	515	12	–	–
	T6	S	515	12	155	3–6
	T62	S	515	12	155	12–24
	T7	S	515	12	260	4–6
296.0	T4	P	510	8	–	–
	T6	P	510	8	155	1–8
	T7	P	510	8	260	4–6
319.0	T5	S	–	–	205	8
	T6	S	505	12	155	2–5
	T6	P	505	4–12	155	2–5
328.0	T6	S	515	12	155	2–5
332.0	T5	P	–	–	205	7–9
333.0	T5	P	–	–	205	7–9
	T6	P	505	6–12	155	2–5
	T7	P	505	6–12	260	4–6
336.0	T551	P	–	–	205	7–9
	T65	P	515	8	205	7–9
354.0	–	–	525–535	10–12	–	–
355.0	T51	S or P	–	–	225	7–9
	T6	S	525	12	155	3–5
	T6	P	525	4–12	155	2–5
	T62	P	525	4–12	170	14–18
	T7	S	525	12	225	3–5
	T7	P	525	4–12	225	3–9
	T71	S	525	12	245	4–6
	T71	P	525	4–12	245	3–6
C355.0	T6	S	525	12	155	3–5
	T61	P	525	6–12	RT	8 (minimum)
	T61	P	525	6–12	155	10–12
356.0	T51	S or P	–	–	225	7–9
	T6	S	540	12	155	3–5

(*Continued*)

Table 11 Continued

Alloy designation	*Temper*	*Type of casting*	*Solution heat treatment*		*Aging treatment*	
			Temperature (°C)	*Time (h)*	*Temperature (°C)*	*Time (h)*
	T6	P	540	4–12	155	2–5
	T7	S	540	12	205	3–5
	T7	P	540	4–12	225	7–9
	T71	S	540	10–12	245	3
	T71	P	540	4–12	245	3–6
A356.0	T6	S	540	12	155	3–5
	T61	P	540	6–12	RT	8 (Minimum)
	T61	P	540	6–12	155	6–12
357.0	T6	P	540	8	175	6
	T61	S	540	10–12	155	10–12
A357.0	–	–	540	8–12	–	–
359.0	–	–	540	10–14	–	–
A444.0	T4	P	540	8–12	–	–
520.0	T4	S	430	18	–	–
535.0	T5	S	400	5	–	–
705.0	T5	S	–	–	RT	21 days
	T5	S	–	–	100	8
	T5	P	–	–	RT	21 days
	T5	P	–	–	100	10
707.0	T5	S	–	–	155	3–5
	T5	P	–	–	RT	21 days
	T5	P	–	–	100	8
	T7	S	530	8–16	175	4–10
	T7	P	530	4–8	175	4–10
710.0	T5	S	–	–	RT	21 days
711.0	T1	P	–	–	RT	21 days
712.0	T5	S	–	–	RT	21 days
	T5	S	–	–	155	6–8
713.0	T5	S or P	–	–	RT	21 days
	T5	S or P	–	–	120	16
771.0	T53	S	415	5	180	4
	T5	S	–	–	180	3–5
	T51	S	–	–	205	6
	T52	S	–	–	–	–
	T6	S	590	6	130	3
	T71	S	590	6	140	15
850.0	T5	S or P	–	–	220	7–9
	T6	P	480	6	220	4
852.0	T5	S or P	–	–	220	7–9

Note: Here, S means sand mold and P means permanent mold.
Source: Adapted from Ref. [64], used with permission.

susceptibility of SSC remains. Another 2% of cold compression ultimately removed most of the residual stresses, and compressive stress was developed in the interior of the part. However, the mechanical method is not suitable for most cast products because cast products are generally complex in shape. Therefore, relaxation of residual stress by compression would require special dies. Stretching may not be suitable at all for cast products.

Residual stress can also be reduced by sub-zero treatment and stabilization. This merely involves experiencing the parts to temperatures below and above RT after solution treatment. To reach temperatures below RT, dry ice mixed with alcohol can be used to reach up to $-70\,^{\circ}C$. Also, several cycles of quenching the parts at sub-zero temperatures and then heating in boiling water are engaged. One such technique is known as the uphill quenching method.[79] This process involves first quenching the part in boiling water quenchant for a predefined period of time and then in liquid nitrogen for a certain period of time. After removing from liquid nitrogen tank, the part is sprayed by either boiling water or water vapor, or it is dipped into the boiling water tank again. After, the natural aging or artificial aging process is applied. It has been used for several 6xxx and 7xxx alloys. The uphill quenching process is schematically shown in **Figure 21**. The figure shows its differences compared to the conventional quenching processes. The temperature gradient is eventually small in the uphill quenching process. For example, for an Al–Si–Mg alloy, the temperature difference between solution treatment temperature and quenching is $472.50\,^{\circ}C$ (SHT $538\,^{\circ}C$ to warm water $65.50\,^{\circ}C$).[75] On the contrary, in uphill quenching the temperature difference is $295.50\,^{\circ}C$ ($100\,^{\circ}C$ boiling water to $-195.50\,^{\circ}C$ liquid nitrogen). It should be noted that the residual stress pattern as obtained in the conventional

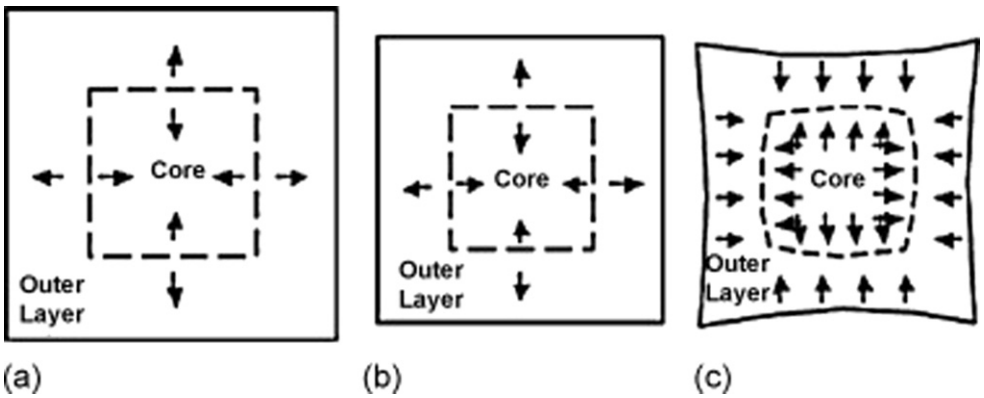


Figure 20 Simplified diagram showing the stress evolution in the specimen during quenching (the arrows represent the forces acting on each section). (a) Step 1: both the outer layer and the core are in the plastic state. (b) Step 2: the outer layer is in the elastic state but the core is still in the plastic state. (c) Step 3: both the outer layer and the core are in the elastic state. Adapted from Ref. [75], used with permission.

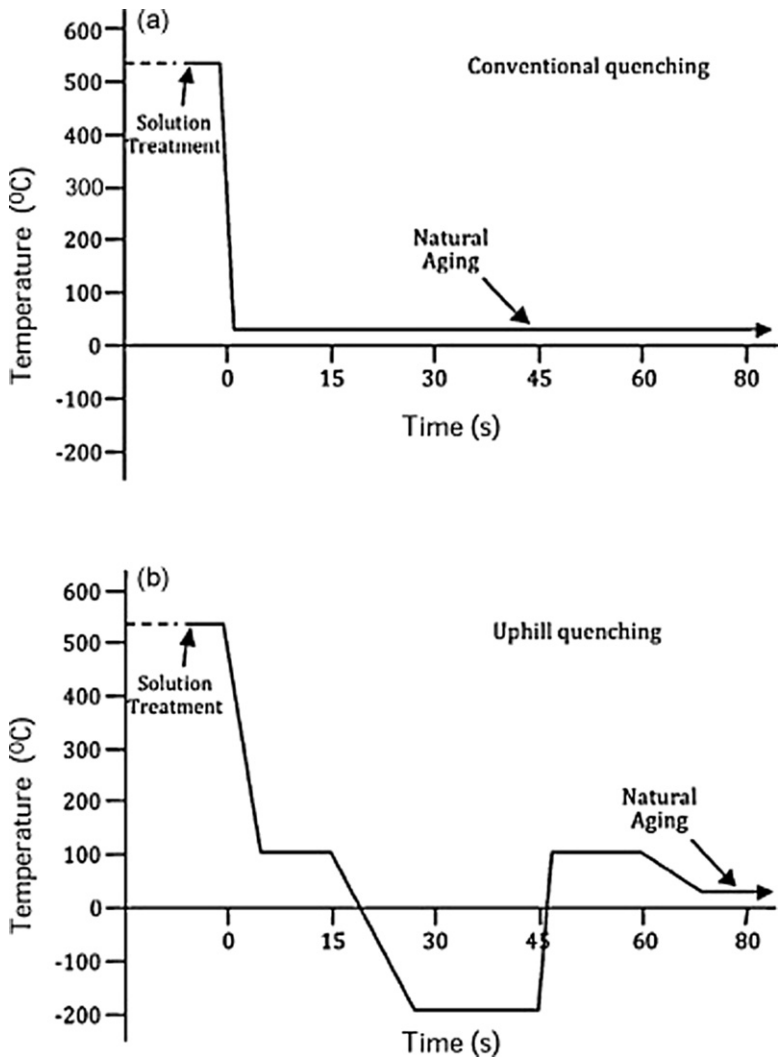


Figure 21 Temperature versus time diagram for (a) conventional and (b) uphill quenching processes. Adapted from Ref. [75], used with permission.

Table 12 Annealing temperatures and soaking times for different groups of aluminum alloys

	Alloy	*Annealing temperature (°C)*	*Soaking time (min)*	*Comment*
Alloys hardened by cold work	1080A	360	20	
	1050	360	20	
	1200	360	20	
	5251	360	20	
	3103	400–425	20	
	3105	400–425	20	
	5154A	360	20	
	5454	360	20	
	5083	360	20	
Heat-treatable alloys (not heat-treated)	–	360 ± 10	60	Cool in air
Heat-treatable alloys (heat-treated)	–	400–425	60	Cool at 15 °C h^{-1} to 300 °C
	Al–Zn–Mg	400–425	60	Air cooling and reheat to 225 °C for 2–4 h

Source: Adapted from Ref. [11], used with permission.

quenching process is reversed in the uphill quenching method. Therefore, careful assessment must be performed before usage.

2.12.2.6 Annealing

The annealing state generally depicts a soft, tougher, dimensionally stable, and low residual stress condition in aluminum alloy parts. However, this also resembles lower strength and poor machinability. Different types of annealing treatments are used for aluminum alloys.

Partial annealing is applied for nonheat-treatable wrought aluminum alloys to soften cold-worked structure. The temperature for this type of annealing is chosen carefully and is below recrystallization temperature so that partial recovery is accomplished by removal of dislocation tangles. The goal is to obtain a sub-cell structure.

Wrought aluminum alloys, to relieve strain hardening effects, are subjected to stress-relief annealing. Any cold-working effect can be diminished by recovering and recrystallization of structures containing dislocation tangles and minimizing store energy of the material. For an AA3003 alloy, up to 400 °C can be used.[64]

A full annealing process is used when soft and workable aluminum alloy parts are required. Unlike partial annealing, the structure involves dislocation-free recrystallized grains. However, the hot-worked structure may not change during full annealing. For heat-treatable and nonheat-treatable alloys, the outcome of full annealing is slightly different. Nonheat-treatable alloys are worked to achieve strength, and softening can be acquired by full recrystallization of the structure. For heat-treatable alloys, the chance of precipitation is low because the alloy has already undergone aging treatment. A temperature chosen from the range of 260–440 °C is generally used for full annealing.[64] To obtain the advantages of full annealing, a long soaking time is preferred to ensure homogeneous temperature distribution throughout the part.

Cast alloys are soaked for a short time (2–4 h) and temperature involved is a minimum of 340 °C.[17] Because cast parts are more complex, special care should be taken so that new residual stresses are not developed during cooling after the annealing temperature.

Table 12 gives a list of annealing temperature for a few alloys.[11]

2.12.2.7 Dimensional Changes during Heat Treatment

There exists a fine line between dimensional changes and dimensional stability. Dimension changes are dealt with by the manufacturers, and stability is of major concern for the end users. During heat treatment, dimensional changes are sometimes unavoidable. Dimensional changes evolve from thermal contraction and expansion, or they may have mechanical or metallurgical origins. Changes obtained by thermal contraction and expansion are reversible and depend on the thermal coefficient of the alloys. Changes due to mechanical origin arise due to plastic deformation or different states of residual stresses. Similarly, dimensional changes may occur by microstructural alternation. To maintain dimensional stability, overaging is used for some aluminum alloys used for engines in transportation industries.[80] However, strength is fairly compromised, but better dimensional stability is obtained by precipitation of more particles at higher temperatures. If better accuracy is required, then an additional heat treatment can be suggested. This treatment includes repeated heating for a few hours at generally 177–204 °C during machining or cycling sub-zero cooling and heating. It is typically claimed that the most stable condition is obtained in the order of: annealing, overaging, aging, and as-cast condition.[17] During heating at HTs and quenching at an appreciably high rate, plastic deformation may occur, leading to residual stresses. This will have adverse effect on properties by changing the balance of the stress state. As a consequence, dimensional stability can be disturbed.

2.12.3 Inspection and Quality Assurance

After heat treatment, proper testing has to be conducted to ensure the quality of products, and these inspections yield

evidence for conformity of quality. Mechanical tests including tensile and hardness tests should be performed in regular intervals. These properties will determine acceptability of the material in the first instance. However, hardness tests are important in ferrous materials. For aluminum alloys, the tensile test is a more convincing method for comparing results and modification of the heat treatment schedule. Because aluminum alloys are strengthened principally by precipitation hardening, an intergranular corrosion test should be performed. For 7xxx series alloys, a fracture toughness test might be required.

Sometimes it is not surprising to achieve results far below the satisfactory level. This can happen because of several factors. The first thing to consider is examination of the composition of the material. Although there are ranges of composition for any alloy, such a variation in range might result in different precipitation kinetics and microstructure, resulting in degraded mechanical properties. Also, segregation, refinement of grains, and shapes of eutectic phases can be responsible for unacceptable properties. For assessment of root causes, proper maintenance of records is essential. After solution treatment, local eutectic incipient melting and development of porosity may occur. Microscopic observation should be performed to find any possible porosity and partial melting. Eutectic melting can be evidenced by rosettes or eutectic structures at three grain boundary points. Morphology of eutectic phases, such as silicon, should be checked for alloys containing silicon. Morphology should match the heat treatment. After solution treatment, if the silicon morphology appears to be like F temper, then there are some problems with the heat treatment procedure.

2.12.4 Concluding Remarks

Aluminum alloys play an important role in the transportation industry because they contribute to fuel economy, and thus to the environment. Although magnesium is considered the lightest structural material, the use of magnesium has yet reach to the level of aluminum. The extraction, casting, forming, and recycling science of aluminum is much more well established. The heat treatment schedules are well written for commercially important alloys. Similar to working with plain carbon steel, industries and foundries confidently work with aluminum. Introduction of the advanced polymer matrix composites in vehicles and aircrafts has resulted in the threat of a decline in aluminum usage over the past few decades, even though aluminum has high specific strength, good formability, excellent crashworthiness, and impressive corrosion resistance. However, use of large amounts of aluminum in recent aircrafts, such as Airbus 380, and the continuous development of advanced aluminum alloys ensures that aluminum technology will dominate in these sectors in the long term.

See also: 2.13 Solutionizing and Age Hardening of Aluminum Alloys

References

1. King, F. *Aluminium and Its Alloys*; Ellis Horwood: Chichester, 1987.
2. ANSI H35.1/H35.1(M). *American National Standard Alloy and Temper Designation Systems or Aluminium*. The Aluminum Association, Inc.: Arlington, VA, 2013.
3. Polmear, I. J. *Light Alloys: From Traditional Alloys to Nanocrystals*, 4th ed.; Butterworth-Heinemann: Oxford, 2006.
4. Hufnagel, W. *Key to Aluminium Alloys. Designations, Compositions, Trade Names of Aluminium Materials*; Aluminium-verlag: Dusseldorf, 1982.
5. Davis, J. R., Ed. *Aluminum and Aluminum Alloys*; ASM international: Materials Park, OH, 1993.
6. Yan, X. Y.; Chang, Y. A.; Xie, F. Y.; Chen, S. L.; Zhang, F.; Daniel, S. Calculated Phase Diagrams of Aluminum Alloys from Binary Al–Cu to Multicomponent Commercial Alloys. *Journal of Alloys and Compounds* **2001**, *320* (2), 151–160.
7. Garrett, R. P.; Lin, J.; Dean, T. A. An Investigation of the Effects of Solution Heat Treatment on Mechanical Properties for AA 6xxx Alloys: Experimentation and Modelling. *International Journal of Plasticity* **2005**, *21* (8), 1640–1657.
8. Gelin, J. C. Modelling of Damage in Metal Forming Processes. *Journal of Materials Processing Technology* **1998**, *80–81*, 24–32.
9. Varley, P. C. *The Technology of Aluminium and Its Alloys*, 1st ed.; Newnes–Butterworths: London, 1970.
10. Toda, H.; Nishimura, T.; Uesugi, K.; Suzuki, Y.; Kobayashi, M. Influence of High-Temperature Solution Treatments on Mechanical Properties of an Al–Si–Cu Aluminum Alloy. *Acta Materialia* **2010**, *58* (6), 2014–2025.
11. Brandes, E.; Brook, G. *Smithells Light Metals Handbook*, 1st ed.; Butterworth-Heinemann: Oxford, 1998.
12. Mrówka-Nowotnik, G.; Sieniawski, J. Influence of Heat Treatment on the Microstructure and Mechanical Properties of 6005 and 6082 Aluminium Alloys. *Journal of Materials Processing Technology* **2005**, *162–163* (Special Issue), 367–372.
13. Reiso, O.; Ryum, N.; Strid, J. Melting of Secondary-Phase Particles in Al–Mg–Si Alloys. *Metallurgical and Materials Transactions A* **1993**, *24* (12), 2629–2641.
14. Droenen, P. E.; Ryum, N. Local Melting in Al–Mg–Zn-Alloys. *Metallurgical and Materials Transactions A* **1994**, *25* (3), 521–530.
15. Li, H.-y.; Zeng, C.-t.; Han, M.-s.; Liu, J.-j.; Lu, X.-c. Time–Temperature–Property Curves for Quench Sensitivity of 6063 Aluminum Alloy. *Transactions of Nonferrous Metals Society of China* **2013**, *23* (1), 38–45.
16. (a) Dons, A. L. The Alstruc Homogenization Model for Industrial Aluminum Alloys. *Journal of Light Metals* **2001**, *1* (2), 133–149. (b) Engler, O.; Hirsch, J. Texture Control by Thermomechanical Processing of AA6xxx Al–Mg–Si Sheet Alloys for Automotive Applications – A Review. *Materials Science and Engineering: A* **2002**, *336* (1–2), 249–262.
17. Kaufman, J. G.; Rooy, E. L. *Aluminum Alloy Castings*; American Foundry Society: Columbus, OH, 2004.
18. Ma, W.; Wang, B.; Yang, L.; Tang, X.; Xiao, W.; Zhou, J. Influence of Solution Heat Treatment on Mechanical Response and Fracture Behaviour of Aluminium Alloy Sheets: An Experimental Study. *Materials & Design* **2015**, *88*, 1119–1126.
19. Senkov, O. N.; Shagiev, M. R.; Senkova, S. V.; Miracle, D. B. Precipitation of $Al_3(Sc,Zr)$ Particles in an Al–Zn–Mg–Cu–Sc–Zr Alloy During Conventional Solution Heat Treatment and its Effect on Tensile Properties. *Acta Materialia* **2008**, *56* (15), 3723–3738.
20. Robinson, J. S.; Hossain, S.; Truman, C. E.; *et al.* Residual Stress in 7449 Aluminium Alloy Forgings. *Materials Science and Engineering: A* **2010**, *527* (10–11), 2603–2612.
21. Bates, C. E. Selecting Quenchants to Maximize Tensile Properties and Minimize Distortion in Aluminum Parts. *Journal of Heat Treating* **1987**, *5* (1), 27–40.
22. Samuel, A.; Samuel, F. Porosity Factor in Quality Aluminum Castings. *American Foundry Society Transactions* **1992**, *100*, 657–666.
23. Ibrahim, M. F.; Samuel, E.; Samuel, A. M.; Al-Ahmari, A. M. A.; Samuel, F. H. Metallurgical Parameters Controlling the Microstructure and Hardness of Al–Si–Cu–Mg Base Alloys. *Materials & Design* **2011**, *32* (4), 2130–2142.
24. Staley, J. T. Quench Factor Analysis of Aluminium Alloys. *Materials Science and Technology* **1987**, *3* (11), 923–935.
25. Robinson, J. S.; Tanner, D. A.; Truman, C. E.; Paradowska, A. M.; Wimpory, R. C. The Influence of Quench Sensitivity on Residual Stresses in the Aluminium Alloys 7010 and 7075. *Materials Characterization* **2012**, *65*, 73–85.
26. Ammar, H. R.; Moreau, C.; Samuel, A. M.; Samuel, F. H.; Doty, H. W. Influences of Alloying Elements, Solution Treatment Time and Quenching Media

on Quality Indices of 413-type Al–Si Casting Alloys. *Materials Science and Engineering: A* **2008**, *489* (1–2), 426–438.
27. Gauthier, J.; Louchez, P.; Samuel, F. Heat Treatment of 319.2 Aluminium Automotive Alloy Part 1, Solution Heat Treatment. *Cast Metals* **1995**, *8*, 91–106.
28. Liu, S. D.; Chen, B.; Li, C. B.; Dai, Y.; Deng, Y. L.; Zhang, X. M. Mechanism of Low Exfoliation Corrosion Resistance due to Slow Quenching in High Strength Aluminium Alloy. *Corrosion Science* **2015**, *91*, 203–212.
29. Westermann, I.; Haugstad, A. L.; Langsrud, Y.; Marthinsen, K. Effect of Quenching Rate on Microstructure and Mechanical Properties of Commercial AA7108 Aluminium Alloy. *Transactions of Nonferrous Metals Society of China* **2012**, *22* (8), 1872–1877.
30. Somoza, A.; Dupasquier, A. 14 – Vacancies in Aluminium and Solute-Vacancy Interactions in Aluminium Alloys. In *Fundamentals of Aluminium Metallurgy*; Lumley, R., Ed.; Woodhead Publishing: Cambridge, 2011; pp. 386–421.
31. Porter, D. A.; Easterling, K. E. *Phase Transformations in Metals and Alloys*, 2nd ed.; Chapman & Hall: London, 1992.
32. Wolverton, C. Solute–Vacancy Binding in Aluminum. *Acta Materialia* **2007**, *55* (17), 5867–5872.
33. Ogura, T.; Hirosawa, S.; Cerezo, A.; Sato, T. Atom Probe Tomography of Nanoscale Microstructures within Precipitate Free Zones in Al–Zn–Mg(–Ag) Alloys. *Acta Materialia* **2010**, *58* (17), 5714–5723.
34. Prasad, N. E.; Gokhale, A.; Wanhill, R. *Aluminum–Lithium Alloys: Processing, Properties, and Applications*; Butterworth-Heinemann: Oxford, 2013.
35. Ran, G.; Zhou, J. E.; Wang, Q. G. Precipitates and Tensile Fracture Mechanism in a Sand Cast A356 Aluminum Alloy. *Journal of Materials Processing Technology* **2008**, *207* (1–3), 46–52.
36. Unwin, P. N. T.; Lorimer, G. W.; Nicholson, R. B. The Origin of the Grain Boundary Precipitate Free Zone. *Acta Metallurgica* **1969**, *17* (11), 1363–1377.
37. (a) Ryum, N. Ageing and Plastic Deformation of an Al–Mg–Zn Alloy. *Acta Metallurgica* **1969**, *17* (7), 821–830. (b) Morgeneyer, T. F.; Starink, M. J.; Wang, S. C.; Sinclair, I. Quench Sensitivity of Toughness in an Al Alloy: Direct Observation and Analysis of Failure Initiation at the Precipitate-Free Zone. *Acta Materialia* **2008**, *56* (12), 2872–2884.
38. Starink, M. J. Reduced Fracturing of Intermetallic Particles During Crack Propagation in Age Hardening Al-Based Alloys due to PFZs. *Materials Science and Engineering: A* **2005**, *390* (1–2), 260–264.
39. Sato, T. Early Stage Phenomena and Role of Microalloying Elements in Phase Decomposition of Aluminum Alloys. *Mater. Sci. Forum* **2000**, *331–337*, 85–96.
40. Sato, T.; Hirosawa, S.; Hirose, K.; Maeguchi, T. Roles of Microalloying Elements on the Cluster Formation in the Initial Stage of Phase Decomposition of Al-Based Alloys. *Metallurgical and Materials Transactions A* **2003**, *34* (12), 2745–2755.
41. Engler, O.; Schäfer, C.; Myhr, O. R. Effect of Natural Ageing and Pre-Straining on Strength and Anisotropy in Aluminium Alloy AA 6016. *Materials Science and Engineering: A* **2015**, *639*, 65–74.
42. Ramesh, R.; Bhattacharya, R.; Williams, G. Effect of Ageing on the Mechanical Behaviour of a Novel Automotive Grade Al–Mg–Si Alloy. *Materials Science and Engineering: A* **2012**, *541*, 128–134.
43. Klobes, B.; Balarisi, O.; Liu, M.; Staab, T. E. M.; Maier, K. The Effect of Microalloying Additions of Au on the Natural Ageing of Al–Cu. *Acta Materialia* **2010**, *58* (19), 6379–6384.
44. Liu, M.; Čížek, J.; Chang, C. S. T.; Banhart, J. Early Stages of Solute Clustering in an Al–Mg–Si Alloy. *Acta Materialia* **2015**, *91*, 355–364.
45. Marioara, C. D.; Andersen, S. J.; Jansen, J.; Zandbergen, H. W. The Influence of Temperature and Storage Time at RT on Nucleation of the β'' Phase in a 6082 Al–Mg–Si Alloy. *Acta Materialia* **2003**, *51* (3), 789–796.
46. Raman, K. S. Resistometric Studies of Solute–Vacancy Interactions and Clustering Kinetics in an FCC Matrix [AlZn Alloy with Ag, Ce, Dy, Li, Nb, Pt, Sb, Y, or Yb]. *Scripta Metallurgica* **1971**, *5* (9), 791–793.
47. Kumar, K. S.; Heubaum, F. H. The Effect of Li Content on the Natural Aging Response of Al–Cu–Li–Mg–Ag–Zr Alloys. *Acta Materialia* **1997**, *45* (6), 2317–2327.
48. Cuniberti, A.; Tolley, A.; Riglos, M. V. C.; Giovachini, R. Influence of Natural Aging on the Precipitation Hardening of an AlMgSi Alloy. *Materials Science and Engineering: A* **2010**, *527* (20), 5307–5311.
49. Poole, W. J.; Lloyd, D. J.; Embury, J. D. The Effect of Natural Ageing on the Evolution of Yield Strength during Artificial Ageing for Al–Mg–Si–Cu Alloys. *Materials Science and Engineering: A* **1997**, *234–236*, 306–309.
50. Cao, L.; Rometsch, P. A.; Couper, M. J. Effect of Pre-Ageing and Natural Ageing on the Paint Bake Response of Alloy AA6181A. *Materials Science and Engineering: A* **2013**, *571*, 77–82.
51. Zandbergen, M. W.; Xu, Q.; Cerezo, A.; Smith, G. D. W. Study of Precipitation in Al–Mg–Si Alloys by Atom Probe Tomography I. Microstructural Changes as a Function of Ageing Temperature. *Acta Materialia* **2015**, *101*, 136–148.
52. Kovaćs, I.; Lendvai, J.; Nagy, E. The Mechanism of Clustering in Supersaturated Solid Solutions of A1-Mg_2Si Alloys. *Acta Metallurgica* **1972**, *20* (7), 975–983.
53. Murayama, M.; Hono, K.; Saga, M.; Kikuchi, M. Atom Probe Studies on the Early Stages of Precipitation in Al–Mg–Si Alloys. *Materials Science and Engineering: A* **1998**, *250* (1), 127–132.
54. Edwards, G. A.; Stiller, K.; Dunlop, G. L.; Couper, M. J. The Precipitation Sequence in Al–Mg–Si Alloys. *Acta Materialia* **1998**, *46* (11), 3893–3904.
55. Pogatscher, S.; Antrekowitsch, H.; Leitner, H.; Ebner, T.; Uggowitzer, P. J. Mechanisms Controlling the Artificial Aging of Al–Mg–Si Alloys. *Acta Materialia* **2011**, *59* (9), 3352–3363.
56. Pogatscher, S.; Antrekowitsch, H.; Leitner, H.; Pöschmann, D.; Zhang, Z. L.; Uggowitzer, P. J. Influence of Interrupted Quenching on Artificial Aging of Al–Mg–Si Alloys. *Acta Materialia* **2012**, *60* (11), 4496–4505.
57. Esmaeili, S.; Lloyd, D. J.; Poole, W. J. Modeling of Precipitation Hardening for the Naturally Aged Al–Mg–Si–Cu Alloy AA6111. *Acta Materialia* **2003**, *51* (12), 3467–3481.
58. Aruga, Y.; Kozuka, M.; Takaki, Y.; Sato, T. Formation and Reversion of Clusters During Natural Aging and Subsequent Artificial Aging in an Al–Mg–Si Alloy. *Materials Science and Engineering: A* **2015**, *631*, 86–96.
59. Werinos, M.; Antrekowitsch, H.; Fragner, W.; Ebner, T.; Uggowitzer, P. J.; Pogatscher, S. Influence of Temperature on Natural Aging Kinetics of AA6061 Modified with Sn. In *Light Metals*; Hyland, M., Ed.; John Wiley & Sons, Inc.: Hoboken, NJ, 2015; pp. 367–371. DOI: 10.1002/9781119093435.ch61.
60. Werinos, M.; Antrekowitsch, H.; Kozeschnik, E.; *et al.* Ultrafast Artificial Aging of Al–Mg–Si Alloys. *Scripta Materialia* **2016**, *112*, 148–151.
61. Bakavos, D.; Prangnell, P. B.; Bes, B.; Eberl, F. The Effect of Silver on Microstructural Evolution in Two 2xxx Series Al-Alloys with a High Cu:Mg Ratio during Ageing to a T8 Temper. *Materials Science and Engineering: A* **2008**, *491* (1–2), 214–223.
62. Dursun, T.; Soutis, C. Recent Developments in Advanced Aircraft Aluminium Alloys. *Materials & Design* **2014**, *56*, 862–871.
63. Abis, S.; Massazza, M.; Mengucci, P.; Riontino, G. Early Ageing Mechanisms in a High-Copper AlCuMg Alloy. *Scripta Materialia* **2001**, *45* (6), 685–691.
64. *ASM Handbook, Heat Treating of Aluminum Alloys, in Vol. 4 Heat Treating*; ASM International: Materials Park, OH, 1991.
65. Lumley, R. N.; Odonnell, R. G.; Gunasegaram, D. R.; Givord, M. Heat Treatment of High-Pressure Die Castings. *Metallurgical and Materials Transactions A: Physical Metallurgy and Materials Science* **2007**, *38* (10), 2564–2574.
66. Lumley, R. N. 10 – Progress on the Heat Treatment of High Pressure Die Castings. In *Fundamentals of Aluminium Metallurgy*; Lumley, R., Ed.; Woodhead Publishing: Cambridge, 2011; pp. 262–303.
67. Lumley, R. N.; Gunasegaram, D. R.; Gershenzon, M.; O'Donnell, R. G. The Effect of Alloy Composition on the Heat Treatment of Aluminium High Pressure Diecastings. In *Proceedings of the 111th Metalcasting Congress Conference*; NADCA, 2007; pp. T07–T013.
68. Samuel, F. H. Incipient Melting of $Al_5Mg_8Si_6Cu_2$ and Al_2Cu Intermetallics in Unmodified and Strontium-Modified Al–Si–Cu–Mg (319) Alloys During Solution Heat Treatment. *Journal of Materials Science* **1998**, *33* (9), 2283–2297.
69. Sjölander, E.; Seifeddine, S. The Heat Treatment of Al–Si–Cu–Mg Casting Alloys. *Journal of Materials Processing Technology* **2010**, *210* (10), 1249–1259.
70. Sokolowski, J. H.; Sun, X. C.; Byczynski, G.; *et al.* The removal of Copper-Phase Segregation and the Subsequent Improvement in Mechanical Properties of Cast 319 Aluminium Alloys by a Two-Stage Solution Heat Treatment. *Journal of Materials Processing Tech.* **1995**, *53* (1–2), 385–392.
71. Ogris, E.; Wahlen, A.; Lüchinger, H.; Uggowitzer, P. J. On the Silicon Spheroidization in Al–Si Alloys. *Journal of Light Metals* **2002**, *2* (4), 263–269.
72. Zhang, D. L.; Zheng, L. H.; StJohn, D. H. Effect of a Short Solution Treatment Time on Microstructure and Mechanical Properties of Modified Al-7wt.%Si-0.3wt.%Mg Alloy. *Journal of Light Metals* **2002**, *2* (1), 27–36.
73. Becker, R.; Karabin, M. E.; Liu, J. C.; Smelser, R. E. Distortion and Residual Stress in Quenched Aluminum Bars. *Journal of Applied Mechanics* **1996**, *63* (3), 699–705.
74. Dolan, G. P.; Robinson, J. S. Residual Stress Reduction in 7175-T73, 6061-T6 and 2017A-T4 Aluminium Alloys Using Quench Factor Analysis. *Journal of Materials Processing Technology* **2004**, *153–154*, 346–351.

75. Lados, D. A.; Apelian, D.; Wang, L. Minimization of Residual Stress in Heat-Treated Al–Si–Mg Cast Alloys Using Uphill Quenching: Mechanisms and Effects on Static and Dynamic Properties. *Materials Science and Engineering: A* **2010**, *527* (13–14), 3159–3165.
76. Tanner, D. A.; Robinson, J. S. Reducing Residual Stress in 2014 Aluminium Alloy Die Forgings. *Materials & Design* **2008**, *29* (7), 1489–1496.
77. Nicol, J.; Seaton, E.; Kuhlman, G.; Yu, H.; Pishko, R. New Quenchant for Aluminum. *Advanced Materials & Processes* **1996**, *149* (4), 40S–40V.
78. Tanner, D. A.; Robinson, J. S. Modelling Stress Reduction Techniques of Cold Compression and Stretching in Wrought Aluminium Alloy Products. *Finite Elements in Analysis and Design* **2003**, *39* (5–6), 369–386.
79. Croucher, T. Uphill Quenching of Aluminum: Rebirth of a Little-Known Process. *Journal of Heat Treating* **1983**, *October*, 30–34.
80. Hunsicker, H. Y. Dimensional Changes in Heat Treating Aluminum Alloys. *Metallurgical and Materials Transactions A* **1980**, *11* (5), 759–773.

2.13 Solutionizing and Age Hardening of Aluminum Alloys

G Quan, L Ren, and M Zhou, Southwest Jiaotong University, Chengdu, PR China

© 2017 Elsevier Inc. All rights reserved.

2.13.1	**Classification of Heat Treatment of Al Alloys**	373
2.13.1.1	General Classification	373
2.13.1.2	Sub-Classification of Solutionizing and Aging	373
2.13.2	**Purpose and Principles of Aluminum Alloy Heat Treatment**	374
2.13.2.1	Purpose of Heat Treatment of All-Purpose Aluminum Alloys	374
2.13.2.2	Principles of Heat Treatment of Aluminum Alloys	374
2.13.2.2.1	SS and equilibrium precipitation	374
2.13.2.2.2	Case study 1: The equilibrium precipitation process of liquid solution and SS	375
2.13.2.2.3	Precipitation sequence and aging process	377
2.13.2.2.4	Case study 2: Al–4Cu alloy and its solutionizing and aging process	378
2.13.2.2.5	Over-aging	380
2.13.2.2.6	Dispersion hardening and dislocation mechanisms	381
2.13.2.2.7	Regression treatment	382
2.13.3	**Tempers Nomenclature of Aluminum Alloy Heat Treatment**	382
2.13.3.1	Tempers for Hot Forged/Extruded Profiles	382
2.13.3.2	Tempers for Hot and Cold Rolled Sheets/Plates	383
2.13.3.3	Tempers for Cast and Forged Aluminum Alloy Parts	383
2.13.4	**Technological Characteristics of Solution Treatment**	383
2.13.4.1	Criterion and Standard	383
2.13.4.2	Heating Rate and Circulation of Furnace Gas	384
2.13.4.2.1	Heating temperature	384
2.13.4.2.2	Heating rate and circulation of furnace gas	384
2.13.4.3	Heat Preservation: Time and Protection	385
2.13.4.4	Cooling Process: Medium, Cooling Rate, and Temperature Range	386
2.13.4.4.1	Medium	386
2.13.4.4.2	Cooling rate	386
2.13.4.4.3	Temperature range	387
2.13.4.5	Cooling Technology: Graded Cooling, Alternative Rate Cooling	387
2.13.4.6	Quenching Faults	387
2.13.5	**Processes of Aging Treatment**	387
2.13.5.1	Pre-Conditions and Property Requirements	388
2.13.5.1.1	Material condition before aging	388
2.13.5.1.2	Determination of aging process	388
2.13.5.2	Aging Processes	389
2.13.5.2.1	Aging parameters	389
2.13.5.2.2	Aging process	389
2.13.5.2.3	Stress aging	389
2.13.5.3	Aging Quality Control	390
2.13.5.3.1	Factors that impact aging process and the properties of aluminum alloys	390
2.13.5.3.1.1	The composition of the alloy	390
2.13.5.3.1.2	Solutionizing treatment system	390
2.13.5.3.1.3	The temperature of the aging	390
2.13.5.3.1.4	Plastic deformation	390
2.13.5.3.1.5	Others	390
2.13.5.3.2	Key points of the operation of aging	390
2.13.6	**Progress in Heat Treatment of Aluminum Alloys**	390
2.13.6.1	Novel Techniques in Aluminum Heat Treatment	390
2.13.6.1.1	New short T6 heat treatment for semi-solid forming	390
2.13.6.1.2	Water–air spray cooling	391
2.13.6.1.3	Digital modeling	391
2.13.6.1.4	Thermo-mechanical treatment	391
2.13.6.1.5	Thermo-mechanical treatment for non-ferrous alloy	392
2.13.6.1.6	A novel multi-stage solutionizing	392

 doi:10.1016/B978-0-12-803581-8.09195-5

2.13.6.2 The Influence of Multi-Heat Treatment on the Performance of Aluminum 394
2.13.6.3 Heat Treatment of Aluminum Matrix Composites 395
2.13.7 Conclusions 396
References 396

2.13.1 Classification of Heat Treatment of Al Alloys

2.13.1.1 General Classification

Al alloys are used in various industrial fabrication fields from digital camera frames and legs to the skin and trusses of aeroplane, and from cast automobile parts to welded high speed train car body, so that the category of heat treatment of Al alloys are also numerous for different alloy systems and different applications. In discussing situation in this chapter the Al alloy is in solid solution (SS) state. Generally, the heat treatment of Al alloy could be classified into three types (refer to Table 5):

- Free status. In this state the parts or ingots are not required to have specific property or other special quality. So it need not any heat treatment.
- Annealed status. This is a state that the parts or products of Al alloy are subjected to heating, heat preservation, slow cooling processes. Usually it is applied to some high precision of size and shape, high corrosion resistance as well, high uniformity of chemical composition and even homogeneous grain structure, and low internal residual stress as well, but not requiring high mechanical property.
- Solutionizing and aging treatment. This is a state that the parts or products need specified mechanical property, or particular physical property. For example, for an application that the parts need very high hardness, a solutionizing plus peak aging process (this is called T6 temper, refer to Table 8) should be applied to the parts. If the application needs not only high hardness and strength, but also good ductility, and high corrosion resistance, a T72 temper (refer to Table 1).

2.13.1.2 Sub-Classification of Solutionizing and Aging

In this chapter, the third type of heat treatment of Al alloys, as mentioned above, will describe in details. Solutionizing and aging treatment as on the word phase is composed by two procedures in general.

First procedure: solutionizing is a heat treatment process that is off course built up by three inseparable steps.

Step 1: heat the parts or products from ambient temperature to specified temperature, which is determined from the solidus of the alloy and the requirement of the application.
Step 2: heat preservation. After the first step the temperature of the furnace gas as well as the parts or products approaches the specified one with some acceptable scatter, then keep the temperature to a given time. The general objective of the heat preservation is to dissolve the secondary phases and alloy elements into the α-Al matrix to get uniform SS.

Step 3: cooling the parts or products to lower temperature, usually room temperature (RT). This is a key procedure for solutionizing process. The cooling rate in general should be high enough to avoid precipitating process during the cooling period. In such a way the parts or products of the Al alloy can be ensured to get a supersaturated solid solution (SSS) at lower temperature.

Second procedure: aging is necessary process for most of parts or products with high mechanical property that is built up by various steps. The sub-classification mainly is due to this procedure. There are four sub-categories of aging process.

(1) One step aging: usually it is called natural aging, that means the parts or products are put on some substrate and kept for specified time, and then get used in service. Before natural aging (one step aging) the parts or products of Al alloys might be cast, cold machined, heat treated somehow, the subsequent aging could ensure the parts or products moderate mechanical property, stable size and shape, low residual stress, etc.
(2) Three step aging: ordinarily also called as artificial aging. This is a normally full aging process including three basic steps: heating the parts or products to specified

Table 1 TXX and TXXX state code and instructions

Code	*Instructions and application*
T42	Apply to O or F state after solution heat treatment, natural aging to steady state, can also be applied to any state of processed products after heat treatment, to achieve good mechanical properties
T62	Apply to O or F state after solution heat treatment, artificial aging products, can also be applied to any state of processed products after heat treatment, to achieve good mechanical performance
T73	Suitable for the products after solution heat treatment, and it can achieve the required mechanical properties and resistance to stress corrosion after aging
T74	The same as the T73's definition but at the state the tensile strength is greater than T73 condition and less than T76 state
T76	The same as the T73's definition, but at the state the tensile strength is higher than T73 and T74 state, stress corrosion cracking resistance lower than T73 and T74 state, respectively. But the exfoliation corrosion resistance is better than them
T7X2	Suitable for O or F state. After solutionizing, carry out artificial aging for good balance between mechanical property and corrosion resistance, make sure they are comparative with T7 state
T81	After solutionizing, subject 1% cold deformation, then artificial, or natural aging

temperature, heat preservation for a specified time, and cooling to (RT). Two key parameters in the second step are very important: aging temperature and keeping time.

(3) Four step aging/grading aging: this aging procedure is constituted by heating the parts or products to a first temperature and keeping a specified time, and then putting them in another temperature (lower or higher than the first temperature), and keeping a time (longer or shorter than the first temperature). This type of aging is usually used in exceptive application, for example, very high mechanical strength.

Complex aging/multi-step aging: this is the variety process and full of alteration. These processes include following variety:

- Cold plastic deformation or forming in some degree, and then artificial/natural aging without previously solutionizing treatment and any other heat treatment.
- Cold plastic deformation in some degree after solutionizing, and then artificial/natural aging. The cold plastic deformation can be compressing or stretching, but the degree is specified.
- Artificial/natural aging just after thermal deformation and cooled down. The thermal deformation could be hot extrusion, forging, rolling, etc.

It must be emphasized that the solutionizing usually is applied for a pre-process of aging, it is an inseparable steps for a full heat treatment of parts or products of Al alloys. Occasionally solutionizing process is used alone, without subsequent aging. In solutionizing state the materials have relatively low mechanical strength, whereas aging processes can endow high mechanical strength.

2.13.2 Purpose and Principles of Aluminum Alloy Heat Treatment

Aluminum alloys are so widely used in industry of nearly all fields from machinery bed to the skin and trusses of aircrafts, and also in articles for daily use from aluminum foil of barbecue to clothes hanger. Both the utilization and processing of aluminum alloys require some regulation of property and status. The most efficient regulating method is heat treatment.

2.13.2.1 Purpose of Heat Treatment of All-Purpose Aluminum Alloys

Heat treatment means that a thermodynamic approach is applied to the products of aluminum alloys to obtain desired property and/or structure. The components or parts can be aluminum alloy ingot, cast machine parts, worked machine parts, even infrastructures, i.e., heat the products in an appropriate rate in a furnace, hold for some time to the solutionizing temperature, and then cool at a designated cooling rate. Through such a process the microstructure of the products will be changed to improve the service performance in the aspect of mechanical properties, corrosion resistance, workability, dimensional stability, and so on. Figure 1 shows the concerning fields of the technologies.

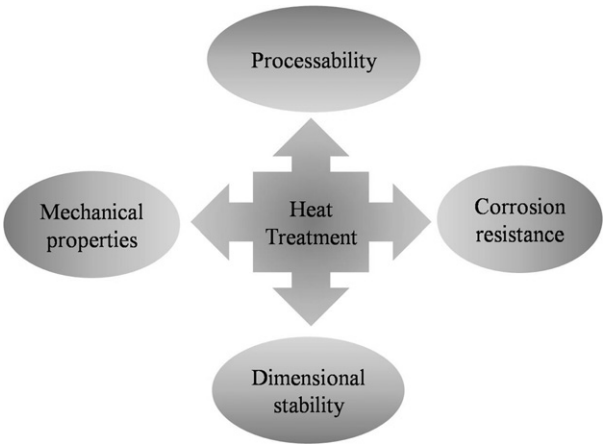


Figure 1 The influence of heat treatment in service performance of aluminum alloys.[1]

In Figure 1 there lists four application fields of heat treatment of Al alloys. The processability is so important that the Al alloys as a type of metallic materials, which must be processed into machine parts (industrial or domestic products) so that the materials get their value. Heat treatment can change or improve processability of Al alloys. For example, by annealing treatment one can improve the punching property of Al alloy: one uses less pressure, less time, and get better products. By T6 (a useful temper code, refer to Table 8) treatment one can make AA2024 (a typical type of Al–Cu–Mg–Mn alloy) very good mechanical property, such as high hardness and high strength, to be used in aeroplane structures. By regression and re-aging (RRA) treatment (another heat treatment code, refer to Table 10) one can get both excellent mechanical property and corrosion resistance. If someone carries out an artificial aging process to a cold worked Al alloy part with proper parameters he will obtain a dimensional stable part in his precise machine.

So you can see, improving processability, improving mechanical property, enhancing corrosion resistance, and increasing the dimensional stability, all need heat treatment.

2.13.2.2 Principles of Heat Treatment of Aluminum Alloys

2.13.2.2.1 SS and equilibrium precipitation

Heat the parts or products of a specific Al alloys to a temperature between the solvus and solidus temperatures and holding for some time to make the intermetallic compounds composed of base aluminum and alloying elements dissolve into base aluminum matrix, and then cool them in an appropriate rate to a lower temperature to get SSS.

The solutionizing involves heating of an alloy to a particular temperature for sufficient time so that the alloying elements go into SS from intermetallic compounds and form a single-phase SS. On quenching (fast cooling) the alloy forms an SSS.

If this SSS is heated at an elevated temperature then precipitation of particle of the secondary phase occurs. In a dispersion state this secondary phase increases the hardness of the alloy and it is called precipitation hardening. The heat treatment which produces the secondary phase is also called aging

treatment. The hardness after solutionizing is comparatively low. The maximum hardness and strength develop by precipitation of very fine dispersed secondary phase particles during aging at a suitable temperature and sufficient time.

2.13.2.2.2 Case study 1: The equilibrium precipitation process of liquid solution and SS[2]

Figure 2 demonstrate the principle why such a process of dissolution-precipitation can happen. Figure 2(a) is an equilibrium phase diagram of ordinary brine (salt water, i.e., you put 60 g solid NaCl powder into 100 ml water and stir and heat the mixture for a while, then you get brine without any solid salt particles), in which the solid line is the solidus, also called as solubility curve, over the line (the space at left side of the curve) the salt is in dissolved state, i.e., in this moment the solid salt NaCl changed into separate Na^+ (basic ion) and Cl^- (negative ion), swimming freely in the water, so you cannot see them. This solution is called unsaturated liquid solution. Under the line (the space right side of the solubility curve, that means decreasing temperature, or increasing the salt content) the solution is called saturated liquid solution. There is solid salt precipitating zone. In the figure the state point moves from X to S point. And the brine's concentration is changed from X to S%. S% is called solubility and the solution at S point is called saturated liquid solution. The precipitating is a nucleation and growth process. Nucleation happens by the accumulation of sufficient number of NaCl molecules which are composed from the basic and negative ions:

$$Na_L^+ + Cl_L^- = NaCl_s \qquad [1]$$

Then you can see the salt particles. As the temperature is low than S point, for example, at T, the concentration of the solution is Q%, and some amount of salt (Na^+ and Cl^- ions) precipitate out of solution, deposited as solid salt particle at the cup bottom. With the temperature decreasing further more and more salt particles precipitate and pile up on the cup bottom. The more salt dissolved out from the salt water because the solubility is decreased with the decreasing temperature. At temperature R the solubility of the salt water is changed into Y%, so in the same cup more solid salt particles precipitated. The concentration now does be the solubility Y%. You now get undissolved salt. Nevertheless the total amount of salt is still the original one, keeping constant.

Figure 2(b) shows a situation of metal alloy. Element A is the solvent (in the above example, water) and element B is the solute (in the above example, salt). The solid line is the solubility curve, here it has a new name: solvus. X_1 is the concentration of the SS, X_2 (in the upper insertion) is the segregated concentration at grain boundary, usually $X_2 > X_1$. S_1 is the solubility at S_1 temperature. At T_1 the SS is located under the solvus and for thermodynamic equilibrium there a number of precipitates occurred from the solution. The concentration of the matrix (α phase) reached to Q_1. The

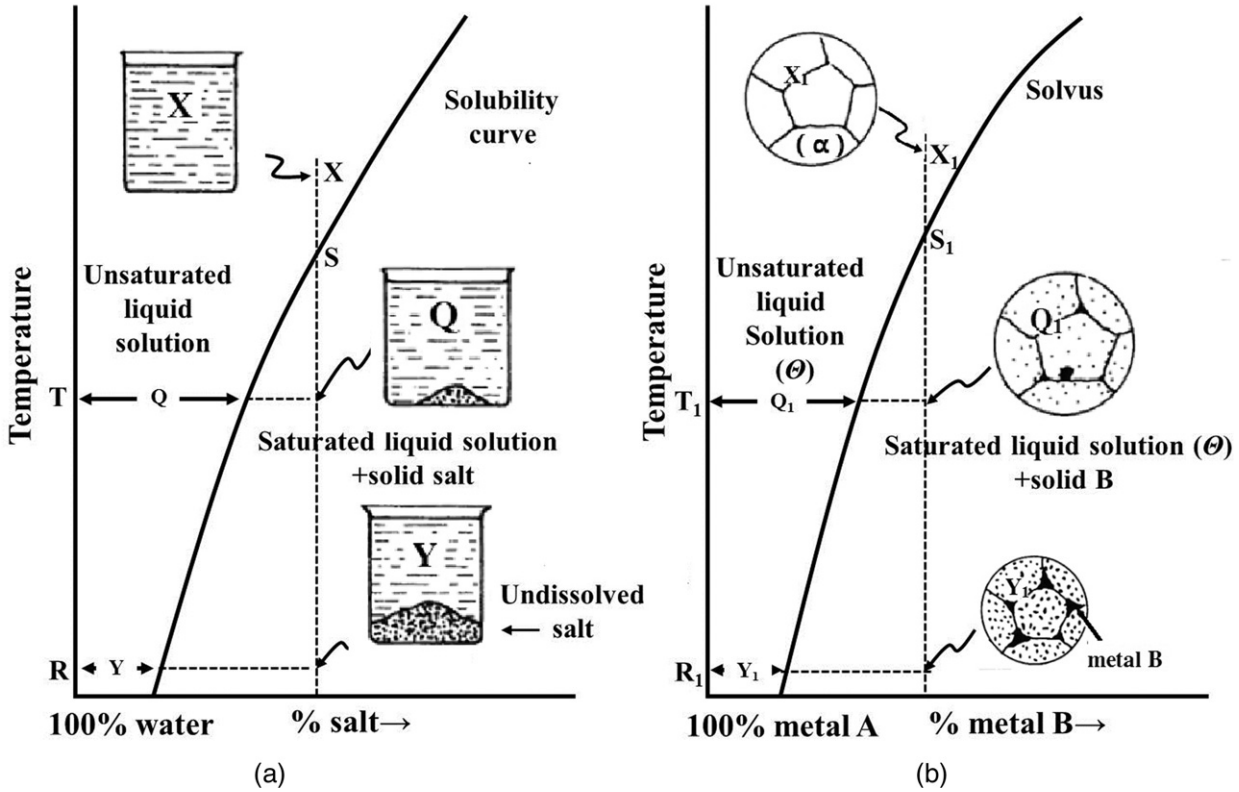


Figure 2 An analogy between the liquid solubility of salt in water and the partial solid solubility of one metal in another. (a) Example of liquid solution and (b) example of solid solution of metal alloy.

precipitated secondary phase is B. B metal exists in two patterns: dispersed particles, located within the grain, and the segregated concentrated at the grain boundary in a continuous net-like deposits. At T_1 the matrix solution is a saturated one. At temperature R_1 there is more B phase precipitated from the matrix, and the concentration of the matrix is Y_1. At this temperature the secondary phase B exists still in two patterns: dispersed particles but much coarse, thicker net-like deposits in grain boundary.

Heat treatable aluminum alloys contain one or more other elements, such as silicon, copper, zinc, and magnesium, etc. The content of these elements can be more than the solubility at low or intermediate temperature, even the maximum solid solubility at eutectic temperature. **Figure 3** is the typical binary phase diagram in aluminum alloys.

The equilibrium microstructure consists of $\alpha+\beta$ phases when the $\omega(B)=C_0$ in which the α phase is the matrix SS based Al, and the β phase is the secondary phase dispersed in α phase. Once the alloy is heated to T_2, the β phase will be dissolved in the matrix and a single α SS phase remained,

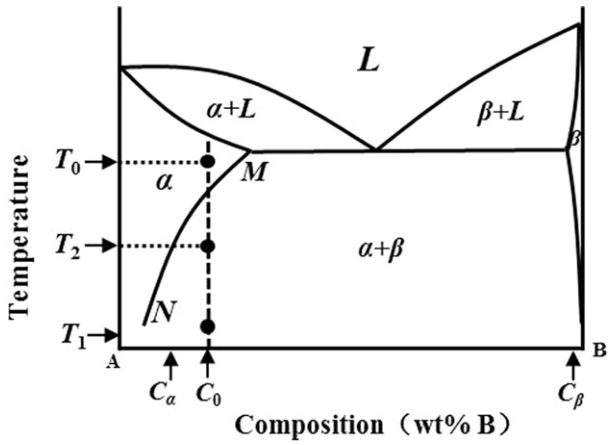


Figure 3 The solubility at different temperature. T_0, T_1, and T_2 should be the specified ones for particular purpose.[2]

which we called solutionizing. If the C_0 alloy is cooled down at a considerable rate from T_2 point, the diffusion and redistribution of solute atom do not have time to take place, leading to little nucleation and growth of β phase in α SS matrix. Moreover, the polytypism shift will not happen in SS matrix in cooling process, the ambient structure is the supersaturated single α SS in which the composition is C_0. This is the solutionizing process, consisting of heat preservation in a given time at specified temperature, and then cooled in an appropriate rate, for example, quenching in water or oil, or air blow.

It should be noted that the SSS mentioned above is not only to the solute atoms, but also to the vacancy, another point crystal defect, that is also supersaturated state. The aging treatment after solutionizing is a diffusion and precipitating process (that will be described in Section 2.13.2.2.2). The existence of vacancies provides an essential condition for atom diffusion in which the interaction between the solute atoms and vacancy concentration can obviously influence the aging precipitation dynamics.

In a binary phase alloy system, the equilibrium phase diagram coupled with the microstructure morphology is presented in **Figure 4**. The upper side of the diagram there is the liquid phase zone, the metal alloy with a B element concentration of X must suffer from full liquid, liquid + α solid phase zone, and then single α phase zone. At lower temperature the alloy goes into another two phase zone: $\alpha+\beta$ two phase zone. The solid curve PQ is the solvus, and under temperature of T_P, but over T_S, the alloy is located in single α phase zone. A little bit lower than T_P, the T_U is specified by the ensuring the alloy not to be remelted, because liquid would occur firstly at grain boundary, that will make some microstructure damage, such as grain boundary cracks or getting oxidized by the oxygen fast diffusion along liquefied grain crevices.

At the interval of T_S and T_U the microstructure of the alloy (parts or products) is single α phase. The solute element atoms are located particular sites separately and uniformly. The SS is unsaturated SS. At the temperature lower than T_S with cooling

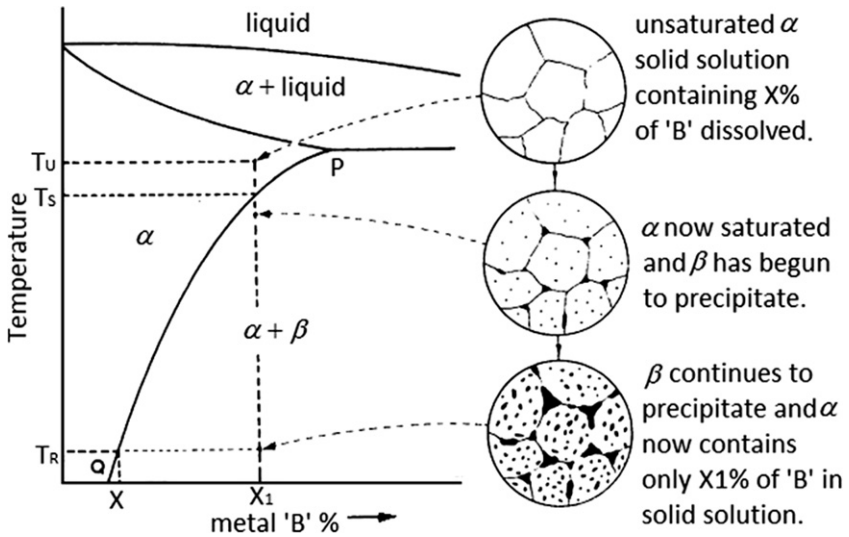


Figure 4 Changes in partial solid solubility with temperature.[2]

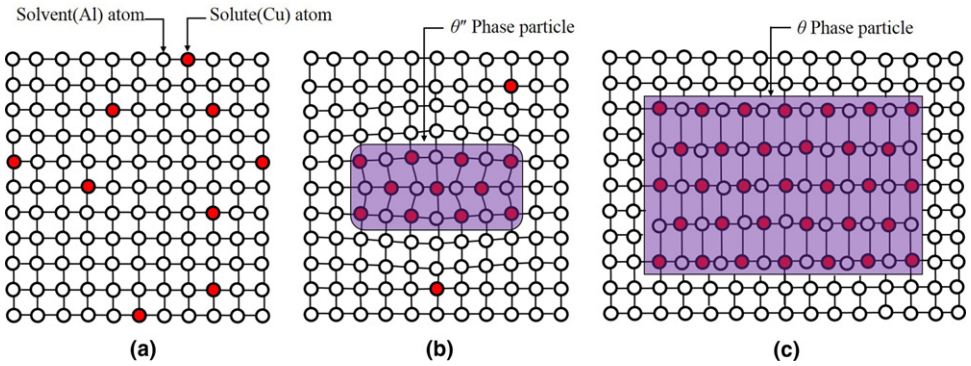


Figure 5 Schematic depiction of several stages in the formation of the equilibrium precipitate (θ) phase. (a) A supersaturated α solid solution. (b) A transition, θ'', precipitate phase. (c) The equilibrium θ phase, within the α matrix phase. Actual phase particle sizes are much larger than shown here.[1]

process, because of the solubility decreased and lower than X %, the solution now changed into SSS, and driven by thermodynamic force the overfull solute B element atoms tend to collect together and changed new β phase.

The solution treatment and precipitation treatment is carried out in those alloys where the solubility of an alloying element increases with increasing temperature. The phase diagram given in **Figure 4** shows that solubility of B element in A increases with increase of temperature and it is maximum at point P. Take an alloy of composition X, which is a two phase structure at RT. On heating at a temperature T_1 the alloy transform to a saturated single-phase SS (α) and on heating at temperature T it becomes unsaturated SS of α-phase. This treatment is solution treatment. Rapid cooling of this SS to RT will maintain single-phase SS, but it is now SSS. Now if this SSS is heated at temperature T_2, the secondary β phase will precipitate out of the SS solution and these particles are extremely fine and precipitate in coherence with the α phase. These particles are responsible for hardening action. However, the aging treatment that produces these hard precipitates is called precipitation treatment.

2.13.2.2.3 Precipitation sequence and aging process

Decomposition of the SSS usually needs to experience at least four distinct stages during aging process, which can be expressed by the following sequence, and the schematic crystal structure evolution is shown in **Figure 5**.

$$\text{SSS} \rightarrow \text{GP 1 zones} \rightarrow \text{GP 2 zones } (\theta'') \rightarrow \theta' \rightarrow \theta \qquad [2]$$

where GP 1 zones are such type of zones that the solute atoms are distributed in clusters, among the clusters the concentration of solute atoms is nearly the equilibrium one. The size of the clusters is very small. In the clusters the solute atoms are short-range ordered. The GP zones are named by the names of two discoverers of such metallurgical phenomenon.[3] GP 2 zones are also solute atom clusters but larger than GP 1 zones, and not so densely distributed. In the GP 2 zones the solute atoms are longer-range ordered, and close to somehow regular crystal lattice, so that they are also designated as θ'' phase. Because they are not regular crystal lattice and much closer to clusters of solute atoms. The transformation from GP 1 zones to GP 2 zones are considered not by merging the GP 1 zones

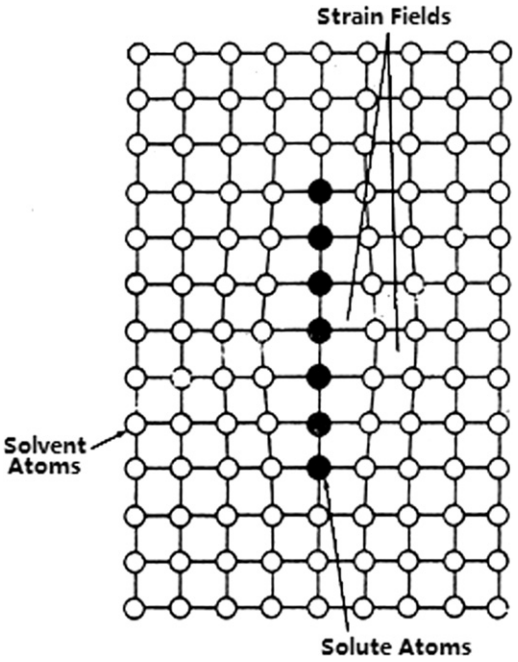


Figure 6 Coherency strains associated with presence of solute atoms having larger radial than solvent atoms.[1]

but by nucleation new cores with GP 2 zones' structure and GP 1 zones dissolving. **Figure 6** shows a schematic of GP 1 zones. θ'' (GP 2 zones) can also be seen as a sub phase and the boundary with the α-phase is coherent. Afterwards with the aging progressing the new phase θ' nucleates, and the GP 2 zones dissolved at the same time. θ' phase is a metastable phase with particular crystal lattice, and the interface between the surrounding matrix (α-phase) is much clearer, not like that between GP zones and α-phase which is blurry even there is not a real interface. The morphology of θ' phase may be particle in shape of dot, needle, sphere, and platelet. Their size (diameter, thickness, or length) is much larger than θ'' clusters. The interface of θ' and α-phase is semi-coherent, i.e., the lattice parameters of θ' in the boundary are very close to that of the matrix (α-phase). So the constraint of coordinate plastic deformation is strong that the hardness and strength of this alloy in this state is higher (refer to **Figures 7** and **8**).

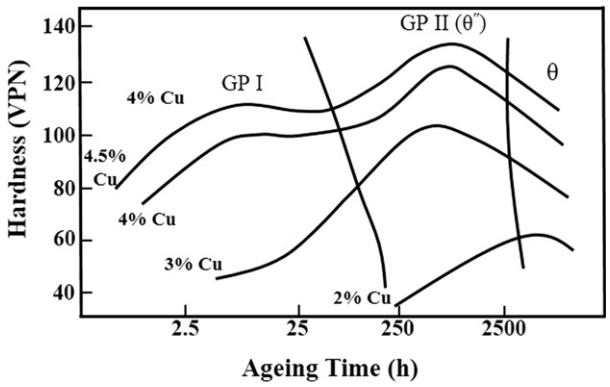


Figure 7 Aging curves for a set of aluminum–copper alloys aged at 130 °C.[1,3]

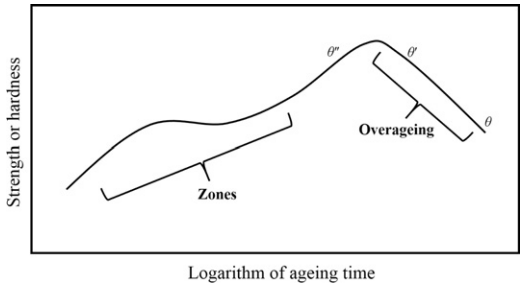


Figure 8 Schematic of full aging dynamic curve.[1]

Late on the equilibrium secondary phase θ nucleates, and the θ' phase dissolved at the same time, too. Usually the new phase θ occurs in the new sites which are not the same as θ'. The morphology of θ phase may also be particulate, in shape of needle, platelet, or sphere. Their size (diameter, thickness, or length) is larger than that of θ' phase. The interface of θ phase and the matrix (α-phase) is incoherent. Thus the constraint of plastic deformation is weaker than that of θ' phase and the alloy demonstrates lower hardness. The atom order of these clusters and metastable phases can be shown in **Figure 5**.

2.13.2.2.4 Case study 2: Al–4Cu alloy and its solutionizing and aging process

Al–4Cu alloy is a typical heat treatable alloy in which the content of copper is about 4 wt.%.[2] The equilibrium phase diagram is presented in **Figure 9**. The eutectic temperature is 548 °C and the maximum solubility is 5.65 wt.% in α phase. The β phase actually is an intermetallic compound $CuAl_2$, Cu content is 54 wt.%. At RT (about 25 °C, 298 K) the solubility of Cu in α phase is about 0.05 wt.%. So if you heat a part or product of the alloy to 540 °C and holding enough time (that would be specified with the size and shape, the heating method as well. For example, you have a piece of Al–4Cu alloy, 10 mm in thickness, 20 mm in width, and 100 mm in length, and you use an electric resistance furnace with gas circulation, and the temperature of the furnace gas is 540°C at the beginning you put you sample, now you can estimate the holding time is 30 min.

Usually experiential method can be used here: the heating through time is about 3 mm (thickness)/minute, namely, the required holding time $= 10\ \text{mm} \times 3\ \text{min mm}^{-1} = 30\ \text{min}$. If your sample shape is complex and with thicker wall somewhere and somewhere else with thinner wall, you can calculate with an average thickness, all Cu atoms should dissolved into the matrix α phase, then you get a single phase.

Solutionizing and aging are the basic heat treatment and then various microstructure and mechanical property can be obtained. At first you heat the parts or products of Al–4Cu alloy into a furnace with gas circulation to a temperature of about 540 ± 5 °C and holding specified time as calculated. Afterwards you take the part out of the furnace and put it into water or carbon dioxide ice to cool it down, i.e., quench the part. The time you transfer the part from the solutionizing furnace to immersing cooling agency is called transferring time. This time should be controlled the shorter the better. For Al–4Cu alloy part, transferring time should not over 15 s, otherwise the part will go through enough time at higher temperature, therefore unexpected precipitation will happen that would use up some solute atoms, and the precipitates at high temperature are not fine enough to bring good hardening effect. Quenching is so important that the fast cooling can ensure to keep the state of the single-phase SS to RT or lower, avoiding unexpected precipitation, then you get SSS, thus the next aging process can produce better fine precipitates. If you cool the parts or products of Al–4Cu alloy slowly, for example, cooled in open air in laboratory, the tensile strength (TS) is 150 MPa, and the microstructure is mainly composed by $\alpha + \beta$, and the morphology of β phase looks as dot-like in grain and net-like in grain boundary. After quenching the alloy has a higher strength of 200 MPa. The part or product with single-phase SSS would be then transferred to another furnace for aging at different temperature. This transferring process here is called parking. Parking effect is fundamental for aging and it is the shorter the better. The greater the supersaturation, the shorter the parking should be. For Al–4Cu alloy of SSS, parking must not exceed 30 min.

In the first stage of aging is the formation of solute-rich (Cu in case of Al–Cu alloy) clusters of atoms within the parent lattice of the SSS. The clusters fit in the crystal structure of the parent (Al) lattice and are completely coherent with it. The clusters are GP (Guinier–Preston) zones and are of 100 Å diameter and three atoms thick (GP 1 zone). These clusters grow to 1500 Å diameter and 150 A thick (GP 2 zone). Another metastable precipitate θ'' forms before the stable θ is observed. When stable θ' forms, the alloy is said to be over-aged and the strength decreases. These precipitation stages are summarized below in sequence (refer to eqn [2]): $\alpha_{sss} \rightarrow \alpha + \text{GP}\ 1 \rightarrow \alpha + \theta''(\text{GP}\ \ 2) \rightarrow \alpha + \theta' \rightarrow \alpha + \theta$. The fine transition precipitates so formed within matrix lead to local distortions and strain fields which restrict dislocation motion. In **Figure 6** the solute atoms distribute into clusters, beside the clusters the internal micro strain fields formed, these strain fields react with dislocations to hinder dislocation movements, and then the plastic deformation force is increased, thus the hardness and strength of the alloy are improved.

With the precipitation from GP 1 zones to GP 2 zones, the internal strain beside them affects larger area, hindering more dislocations to move, therefore the hardness increased. Further

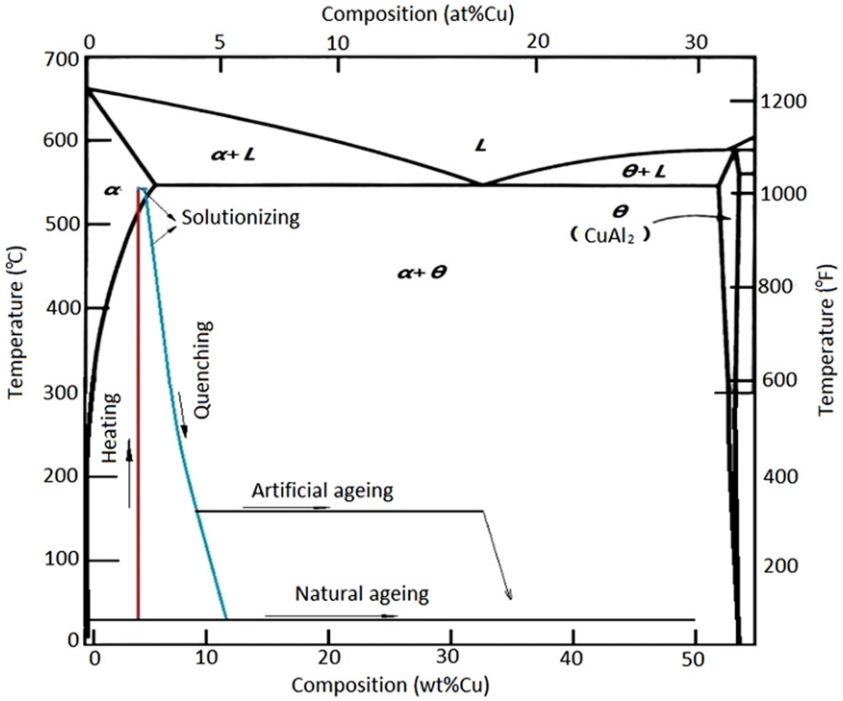


Figure 9 Al–Cu phase diagram and schematic of solutionizing, aging process.[2]

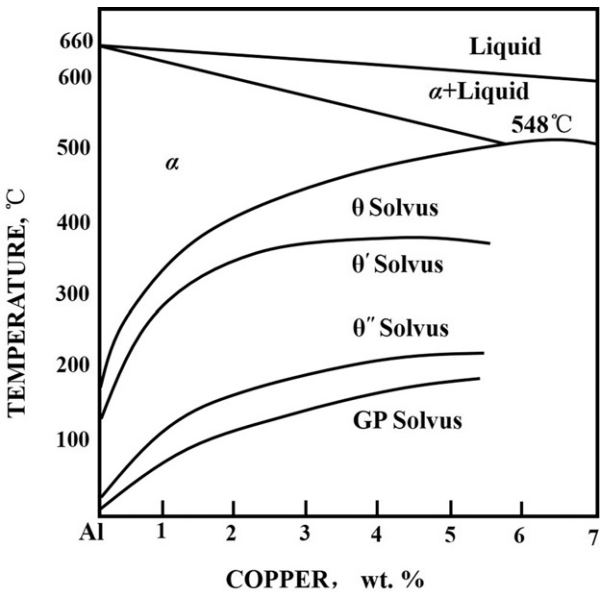


Figure 10 Aluminum–copper phase diagram along with metastable phase boundaries at aluminum end.[4]

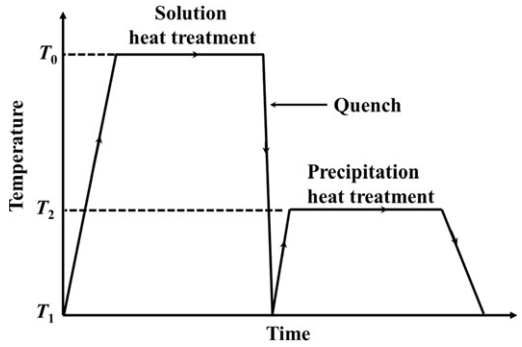


Figure 11 Schematic of solutionizing and aging process.[1]

on the θ' precipitates make much larger internal strain fields, that leads to higher hardness, refer to **Figure 7**.

In **Figure 10** the precipitating temperature of GP zones, θ'', θ', and θ phase are different and depends on the concentration of Cu in the matrix phase. With the increasing in Cu content in matrix, the precipitating temperature increases.

Compare three pictures in **Figure 5**, one can find that in the saturated solid solution (**Figure 5(a)**) the solute atoms (Cu) are randomly distributed in the matrix lattice, and in the metastable phase the solute atoms are located in some specific positions. These positions in θ' (**Figure 5(b)**) and θ (**Figure 5(c)**) phase are different, too. In θ phase the positions in a long-range order.

Figure 11 shows the full solutionizing and aging processes. Where in the figure the solution heat treatment + quenching is solutionizing, and precipitation heat treatment is aging. Temperature T_0, is the solutionizing temperature, T_2 the artificial aging temperature, and T_1 the RT, namely, natural aging temperature.

In **Figure 8** it is illustrated the dependence of aging time at specified temperature on strength or hardness. One can see clearly in different aging period there is corresponding hardness or strength. This is foundation of materials and process design in industry.

The corresponding microstructure of the alloy in different aging period are shown in **Figure 12** analyzed by transmission

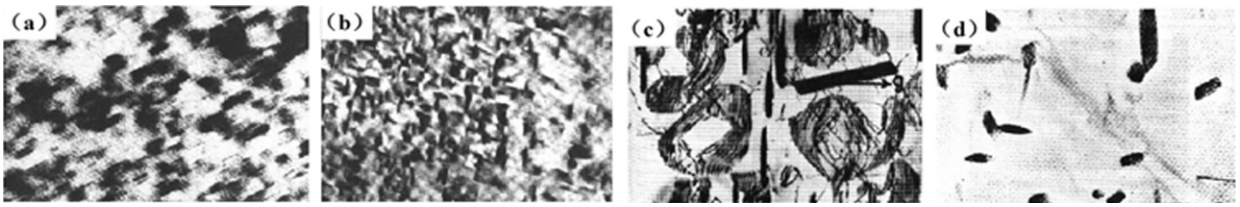


Figure 12 Microstructure evolution during aging by transmission electronics microscope. (a) GP zone; (b) θ''; (c) θ'; (d) θ.[4]

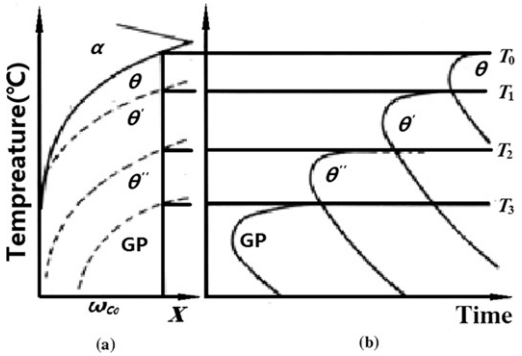


Figure 13 The effect of aging temperature on the sequence of precipitates.[4]

electronics microscope. It is clearly seen that the microstructure is very different for GP zone, θ'', θ', and θ states.

Aging temperature and aging time are the important factors that affect the aging process. The effect of aging temperature on the sequence of precipitates is illustrated by a schematic diagram in **Figure 13**:

(1) When $T<T_3$ the main precipitate is GP zone with the prolonging of aging time, the consequence of precipitates is GP zone $\rightarrow\theta''\rightarrow\theta'\rightarrow\theta$.
(2) When $T_3<T<T_2$ GP zone disappears entirely with the prolonging of aging time, the consequence of precipitates is $\theta''\rightarrow\theta'\rightarrow\theta$.
(3) When $T_2<T<T_1$ both of GP zone and θ'' disappear entirely, with the prolonging of aging time, the consequence of precipitates is $\theta'\rightarrow\theta$.
(4) When $T_1<T<T_0$ the only precipitate that is possible is θ.

So, the full sequence of GP zones and transition precipitates is only possible when the alloy is aged at a temperature below the solvus of GP zones.

Table 2 shows the precipitation sequence in several aluminum alloys series, usually the general precipitation sequence is as follows:

$$\text{Supersaturated solid solutions}\rightarrow\text{GP1 zones}\rightarrow\text{GP2 zones }(\vartheta'')\rightarrow\vartheta'\rightarrow\vartheta$$

In Al–Cu alloys, for example, when the alloys are aged at 130 °C, the formation of GP zone causes the hardness to increase as shown in **Figure 14**. With the prolonging of aging time, GP zone dissolves and θ'' the semi-equilibrium phase forms, leading to further increase of the hardness. And then the hardness begins to decrease with the further increase of aging time, due to dissolution of θ'' which is totally translated into θ', and the overaged phenomenon occurs. But there is no GP zone even at the beginning of the aging process, when the aging temperature is increased to 190 °C.

Table 2 The precipitation sequence in some aluminum alloys[1]

Alloy series	*Precipitation sequence*	*Equilibrium precipitate phase*
Al–Cu	GP zone (Disk)→ϑ'' (Disk)→ϑ'→	ϑ ($CuAl_2$)
Al–Ag	GP zone (Sphere)→γ' (plate)→	γ (Ag_2Al)
Al–Zn–Mg	GP zone (Disk)→ η (plate)→ T'→	η ($MgZn_2$), T ($Mg_3Zn_3Al_2$)
Al–Mg–Si	GP zone (Bar)→β'→	β (Mg_2Si)
Al–Cu–Mg	GP zone (Bar or sphere) → S' →	S (Al_2CuMg)

The aging can be divided into two types according to different aging temperatures, namely cold aging and warm aging. In Al–Ag alloys,[5] for example, as shown in **Figure 15** when the alloy is aged by cold aging (aging at low temperature), the main precipitate is GP zone, and the hardness increases rapidly at the beginning of the aging process, then reach a certain value and keep constant with the prolonging of aging time. And the higher the aging temperature, the faster the increasing in hardness, and the higher the peak hardness as well. So the aging time can be shortened by increasing the aging temperature.

2.13.2.2.5 Over-aging

However, the warm aging is conducted at higher temperature, and the main precipitates are transition phase and equilibrium phase. There is an incubation period at the beginning, and then the hardness increases rapidly up to a maximum value, after that the hardness decreases with time, which is called over-aging. And the higher the aging temperature, the higher the increasing speed of the hardness. But increasing the aging temperature will decrease the maximum hardness value and increase the probability of over-aging.

The essential feature in age hardening of aluminum alloys is the change of solubility with the temperature, i.e., the solubility increases with the increase in temperature. Most of the heat treatable aluminum alloys abide by this condition. The purpose of aging treatment is to create a dense and fine dispersion of precipitated particles in the matrix. The precipitated particles act as obstacles to dislocation movement and thereby strengthen the alloys, and also as a distorted area in crystal structure by the coherent and/or semi-coherent connection with lattice of the matrix.

Table 3 shows the shape of the GP zone in several aluminum alloys series.

The aging hardening of aluminum alloys is quite a complicated process, It not only depends on the composition and

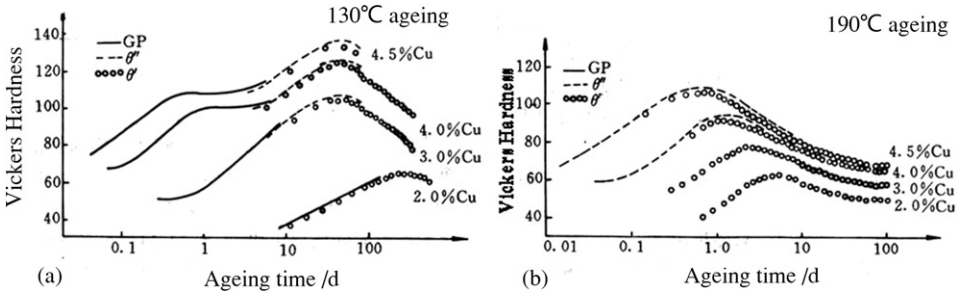


Figure 14 The aging kinetics in Al–Cu alloys at the temperature of 130 and 190 °C.[1]

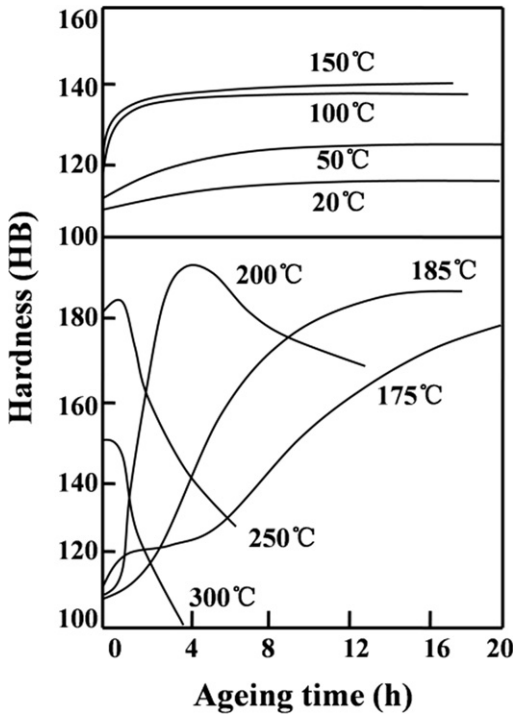


Figure 15 The cold aging and warm aging in Al–Ag alloys.[1]

Table 3 The shape of GP zone in aluminum alloys[1]

Shape of GP zone	*Alloys series*	*Ratio[a] of the majority atom diameters (%)*
Sphere	Al–Ag	+0.7
	Al–Zn	−1.9
	Al–Zn–Mg	+2.6
Disk	Al–Cu	−11.8
Needle	Al–Mg–Si	+2.5
	Al–Cu–Si	−6.5

[a]Ratio of the majority atom diameters is defined as a ratio of atom diameter of the alloying element and that of the base element (Al).

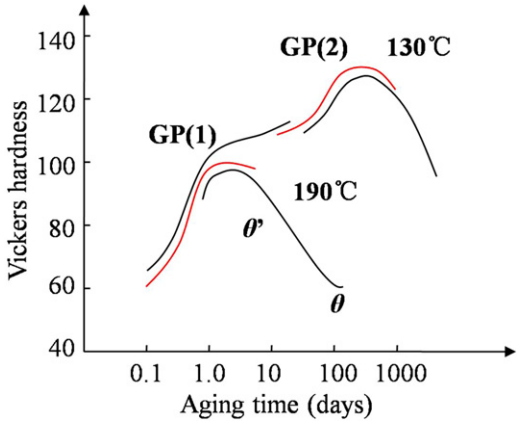


Figure 16 Correlation of structures and hardness of Al–4% Cu alloy aged at 130 and 190 °C.[6]

the aging process, but also the crystal defects, like the amount and/or the distribution of vacancy, the dislocation density, etc. Generally, the aging hardening is a result of the aged zone formation induced by segregation of solute atoms and precipitation. Figure 16 shows hardness change in Al–4% Cu alloy aged at different temperatures.

The vacancies are formed during the solutionizing process, then quench the aluminum at very short time, the cooling rate is so fast that the vacancies will not have enough time to diffuse and vanish. These vacancies remained in the SSS combining with the solute atoms. This is a metastable state in thermodynamics. The metastable thermodynamic state of the SSS must change itself into an equilibrium state at a proper condition. The existence of vacancies accelerates the diffusion rate of solute atoms and also promotes the segregation at the same time and then, the precipitation process emerges.

The size and the number of the precipitates mostly depend on the solutionizing temperature and cooling rate. Higher quenching temperature will give rise to the higher vacancy concentration and afterwards more hardened zone, as well as more precipitation, meanwhile, the decrease in size of hardened zone.

2.13.2.2.6 Dispersion hardening and dislocation mechanisms

Because the clusters are embedded in the crystal structure of the parent metal and because of the atomic size difference between solute and solvent atoms, the coherent structure induces a lot of strain on the lattice. This is referred to as coherency strains and is reflected in an increase in hardness and strength. The strengthening comes from the particles acting as obstacles to dislocation motion.

Dislocation theory explains the actual hardening mechanism. The precipitated particles or zones interact with dislocations. The strain fields associated with the dislocations interact with the strain fields created around the precipitates or zones. Fine particles which are closely spaced hinder the movement of dislocations in the matrix. Moving dislocations can overcome the obstacle either by cutting through the precipitated particles or by bending and by-passing them.

The cutting mechanism is operative when the precipitate particles are small (less than 50 A in size) and are coherent with respect to the matrix. Figure 17 shows the cutting steps. Coupled with this, other surface imperfections such as stacking faults are also created within the particles by cutting mechanism. Both these factors result in increased resistance to dislocation motion.

With larger particles (100–150 Å), the second mechanism, namely, bending of dislocation around the particles and their subsequent by-passing becomes operative. This is explained in Figure 18. The mechanism of by-passing resembles the Frank-read source. The stress needed for bending at dislocation is inversely proportional to average inter particle spacing. Hence when the particles are fine and are closely spaced, there is considerable increase in the level of stress required for bending and by-passing of dislocations. This condition is satisfied when the precipitation hardenable alloy has been aged to optimum level. When the alloy is overaged, particles become coarse (>1000 A); correspondingly, the dislocations are able to bypass them with ease at low stress levels.

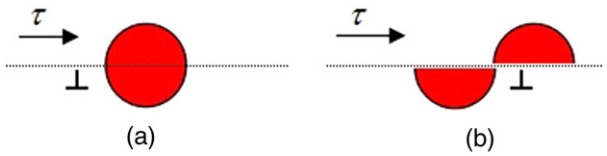


Figure 17 Dislocation cut through the precipitate particles. (a) A dislocation encountering a spherical particle. (b) The dislocation has cut the particle and separated the particle into two parts.

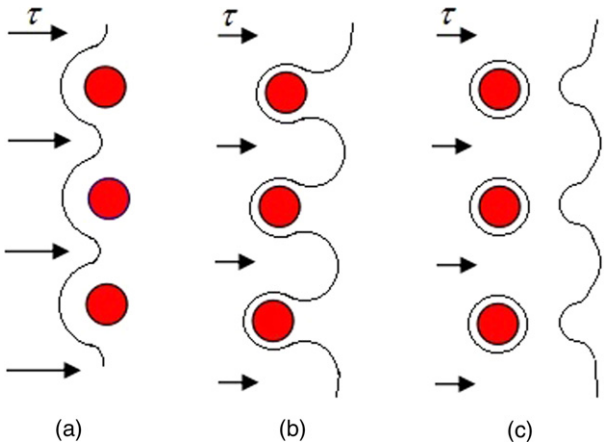


Figure 18 Dislocation bows around the particles. (a) A dislocation encounters a row particles and bent. (b) The dislocation halflings wound the particles and the rest between particles moved forwards. (c) The wound piece of the dislocation surrounded the particles, and the passed-by pieces came across and relinked to a crooked line and went forwards again.[7]

2.13.2.2.7 Regression treatment

For some unexpected mechanical property or microstructure after heat treatment, such as solutionizing and aging process, the property and microstructure can be recovered by another heat treatment, that is regression. Regression is one of the annealing process referring to some changes in the aspects of mechanical properties, physical properties, and intragranular substructure in wrought metals. Usually for higher hardness or better mechanical property, the regression temperature is somehow higher than the normal aging temperature, and then aging in a proper set of aging parameters.[8] For better corrosion resistance and better toughness the regression temperature should even higher. At these higher temperature the regression process is mainly the resolution of partially dissolved precipitates, which makes an unexpected property. In low temperature, regression is dominated by the motion of point defects, while the microscopic structure (i.e., cellular structure) remains steady. In a little higher temperature regime, the main mechanism of regression changes to the movement and interaction of dislocations, as well as the polygonization of subgrain or cellular substructure transformation.

The regression would also happen in cold deformed metals when the annealing temperature is lower and the holding time is shorter. The activation energy for different defects motion is also different. There are various regression mechanisms during the annealing process at different temperatures as show in Table 4.

Schematic diagram of regression annealing dynamics is shown in Figure 19 and the dynamics features of regression is summarized as follows:

1. When annealing at a certain temperature, there are no incubation period in regression, the process is fast at the beginning and then decreases gradually. The properties will tend to steady state after treated for a long time.
2. In a certain temperature, there exist a limit value for a specific properties.
3. The higher the annealing temperature, the closer the properties approach to natural properties P_0, that means the faster the annealing process, the shorter time will be need for arriving the limit value.

2.13.3 Tempers Nomenclature of Aluminum Alloy Heat Treatment

The heat treatment of aluminum alloys has an appointed standard nomination system for all the heat treated conditions. From free machining status to solutionizing and aging, the tempers are listed in Table 5.

2.13.3.1 Tempers for Hot Forged/Extruded Profiles

The eliminating stress heat treatment is often used for forged or extruded aluminum alloys. Add '51,' '510,' '511,' or '54,' etc., after the essential state code 'TX,' 'TXX,' or 'TXXX' to express the status of products which have been treated by eliminating stress heat treatment. The general tempers are listed in Table 6.

Table 4 Three typical regression annealing[1]

Regression process	T_r/T_m	*Mechanism*	*Characteristic*
Low temperature regression	0.1–0.3	Point defects motion	Vacancies or interstitial atoms disappear at grain boundaries or dislocations, together to vacancies couples/group. The point defects concentration decrease while the mechanical properties have almost no change
Mediate temperature regression	0.3–0.5	Dislocation slip, the growth and regulation in subgrain/grain boundary; precipitation resolving and/or growth	The activity of atoms increase with the increasing temperature, dislocation slip or cross slip on slip plane, opposite sign dislocation counteract each other, and the tangle dislocation will redistribute and group with the growth and regulation in subgrain
High temperature regression	>0.5	Grain/subgrain boundary movement, precipitation resolution	With the temperature further increase, the activity of atoms also increase and the grain/subgrain boundary movement

Note: T_r/T_m: T_r regression temperature and T_m melting temperature of the alloys.

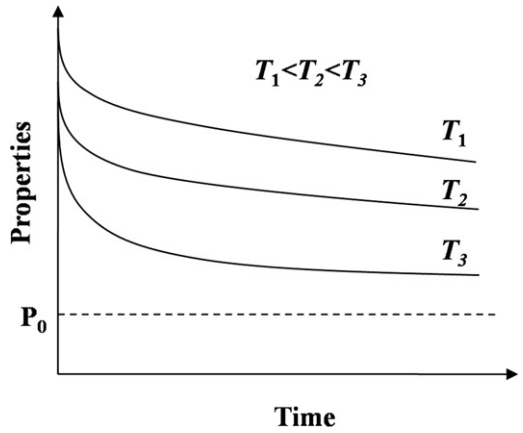


Figure 19 Schematic diagram of regression annealing dynamic.[1]

2.13.3.2 Tempers for Hot and Cold Rolled Sheets/Plates

Hot and cold rolling is a fundamental process of aluminum alloys sheet and plates. The thermodynamic status is designated to H (work hardening). The letter H plus two Arabic numerals (called HXX status), or three digits (called HXXX state), called H subdivision state, listed in Table 7.

2.13.3.3 Tempers for Cast and Forged Aluminum Alloy Parts

The final temper state of heat treated aluminum alloys is divided into 11 categories, coded with T0–T10. Different temper number designates particular tempering technology. Table 8 lists the code, designation, and the instructions of the 11 codes.

For detailed designation of the tempers in sub-steps, the sub-code number of the temper is used. To add a new number after the first category state code TX, becomes TXX and TXXX state (except for eliminating residual stress), namely behind the TX state code to add a one-dimensional Arabic numerals (called a TXX status), or add two Arabic numerals (called TXXX state), said after the obvious change product features (such as mechanical properties, corrosion resistance, etc.) of the specific process condition.

Table 5 Heat treatment status code and instructions

	Code Instructions and application	*Name*
F	Free machining status	Apply to the forming process, no special requirements of work hardening and heat treatment and no requirements for mechanical property in this state
O	Annealed status	Apply to the fully annealed products to obtain the minimum hardness and best corrosion resistance
H	Work hardened status	Apply to the products improving the strength and hardness by work hardening, the softening must be carried out by post-heat treatment
W	Natural aging status	An unsteady status, only apply to the ambient temperature natural aged alloys after hot forging and/or solutionizing treatment
T	Solutionizing and aging status	The alloys achieve to steady status via or not via work hardening after heat treatment

2.13.4 Technological Characteristics of Solution Treatment

2.13.4.1 Criterion and Standard

The solutionizing and quenching process is the most important and rigorous step in the heat treatment. The object of this step is to prepare a SSS for further aging hardening process. There are at least four key factors, like the proper heating temperature, holding time, heating facility, and the cooling method in the design of solutionizing process.

To develop the aging hardening potential of the alloys, heat treated aluminum alloys must be solutionizing treated before the final aging strengthening treatment. The purpose of the solutionizing is to make elements in the SS dissolved well into the matrix to obtain supersaturated alloys, and some good property as well. At the same time, the grains size and shape

Table 6 The state code and instructions for eliminate stress

Code	*Instructions and application*
TX51 TXX51 TXXX51	Apply to the specified amount of tensile plate, cold finishing bars or die forgings and rolling rings after solutionizing or cold formed at the high temperature. The permanent strain for thick plate is 1.5–3%. Rolling or cold finishing rod is 1–3%. The permanent strain of die forgings, rolling rings is 1–5%
TX510 TXX510 TXXX510	Apply to the specified amount of stretched pipes, extruded rods, profiles, and drawn pipes after solutionizing or cooling from the high temperature in high temperature of forming. These products need no longer straightening. The permanent strain of extruded bar, pipe is 1–3% and 1.5–3% for drawn pipe
TX511 TXX511 TXXX511	Apply to the specified amount of stretched pipes, extruded rods, profiles, and drawn pipes after solutionizing or cooling from the high temperature of forming. The permanent strain of extruded bar, pipe is 1–3%, and 1.5–3% for drawn pipe
TX52 TXX52 TXXX52	Eliminate the stress by compression the product to a strain of 1–5% after solutionizing or cooling from the high temperature of forming
TX54 TXX54 TXXX54	Apply to final die forging process, eliminate stress in forged products by cold plastic forming

must be controlled. The factors that influence the solutionizing are heating speed, holding time, quenching transfer time, cooling speed of the quenching, and parking effect (time between quenching and aging). On the other hand, the size of the workpiece, deformation degree, grain size, aluminum clad, quenching stress are also considering factors. When establishing the temperature of solutionizing, firstly, the lowest melting temperature of intermetallic compound phase and the relation between heat treatment parameters and mechanical properties must be measured/calculated, and then the solutionizing system can be decided based on the technical index.

2.13.4.2 Heating Rate and Circulation of Furnace Gas

2.13.4.2.1 Heating temperature

The basic principles to choose solutionizing temperature is to make sure that the SS elements can dissolve fully at as high temperature as possible. However, the precondition is to prevent over burning, inner oxidation in grain boundaries, grain coarsening, and aluminum clad polluted as well. The heating temperature of aluminum alloys is mainly based on the lowest melting point of the eutectic phase in the alloy. When heating, the more the dissolution of the secondary phase, the better the mechanical properties of the alloys are after aging. In general, the process completes faster in higher heating temperature.

But if the temperature is too high, the grains will be coarsened, even the workpiece will melt to be scarped. Therefore the solutionizing temperature range of aluminum alloys is narrow, i.e., the heating temperature deviation must be as small as possible, generally within $\pm 5\ ^{\circ}C$. In such condition, the mechanical properties and microstructure can be ensured.

Table 7 Work hardening state code and instructions

Code	*Instructions and application*
H1	Pure state of strain hardening
H2	Work hardening and incomplete annealing condition
H3	State of work hardening and stabilizing treatment
H4	Work hardening and protuberant processing status
HX1	Tensile strength is limited between O and HX2 state
HX2	Tensile strength is limited between O and HX4 state
HX3	Tensile strength is limited between HX2 and HX4 state
HX4	Tensile strength is limited between O and HX8 state
HX5	Tensile strength is limited between HX4 and HX6 state
H111	Moderate amount of work hardening after final annealing process, work hardening degree not as good as H11 state
H112	Suitable for hot formed products. Require the mechanical properties of products in this state
H116	Apply especially five XXX series alloy when $\omega(Mg) \geq 4.0\%$. These products require mechanical properties and exfoliation corrosion resistance

Figure 20 is a simple binary phase diagram. Firstly, heating temperature should be higher than that of solid solubility temperature to make sure SS elements can dissolve fully in the matrix. Secondly, the heating temperature must be lower than the melting temperature of eutectic phase in the condition of equilibrium and non-equilibrium, or the metal will melt locally, which is called over burning.

2.13.4.2.2 Heating rate and circulation of furnace gas

To determine the heating temperature, following aspects should be considered:

1. Heating rate can influence the recrystallized grain size. The secondary phase dissolution is advantageous to the nucleation of recrystallization. Recrystallization process begins before the secondary phase dissolves at higher temperature, which leads to fine grains after recrystallization.
2. Improving the production efficiency. Speeding up the heating rate can shorten solutionizing time, which is to save energy and improve production efficiency.
3. Controlling the heating rate. When the workpiece is in such condition, such as large size, complex shape or different wall thickness, if the heating rate is too high, because of the big thermal difference between the surface and center, the workpiece would be unevenly heated.
4. In the process of single SS (high temperature solutionizing) of super-high strength aluminum alloy, heating temperature should be controlled. Generally, the process is to heat to 460–470 $^{\circ}C$ within the rate of 60 $^{\circ}C\,h^{-1}$, then increase the temperature to 480 $^{\circ}C$ The aim is particularly to make sure secondary phases in Al–Zn–Mg–Cu alloys dissolved completely first, at the same time, S-phase can be dissolved well. The process can protect the alloy from over burning as well.
5. The installation of furnace air circulation is effective to avoid local overheating and instability of the microstructure after heat treatment.

Table 8 TX state code and instructions

Code	*Designation*	*Instructions and application*
T0	Solutionizing treatment and natural aging	Apply to the product that the strength is improved by cold working
T1	Artificial aging	In metal or green sand mold casting alloy, due to the cooling speed, has been a certain degree of supersaturated solid solution, which is part of the solutionizing effect. Further artificial aging, de-solution strengthening, can increase the hardness and mechanical strength, improve machinability. It is effective to improve the strength quality of ZL104($AlSi_9Mg$), ZL105($AlSi_5Cu_1Mg$) alloys
T2	Annealing	The main aim of T2 is to eliminate internal stress by casting, and size stability of casts, Si and Al–Si-based alloy, to improve its ductility. For Al–Si-based alloy the T2 effect is more obvious, the temperature is 280–300 °C, heat preservation 2–4 h
T3	Solutionizing treatment	Apply to the products after cold working or straightening. Solutionizing at 350–450 °C and holding 2–4 h
T4	Solutionizing treatment and natural aging	By heat insulation, make the soluble phase resolved, and then quenching, to make a large amount of solutionizing strengthening, get the supersaturated solid solution, in order to improve the hardness and strength and the corrosion resistance of the alloy. For Al–Mg alloy as the final heat treatment, an artificial aging is usually employed
T5	Solutionizing treatment and incomplete artificial aging	Used to get higher strength and plasticity, but will decrease the resistance to corrosion, especially the intergranular corrosion sensitivity would be increased. Low aging temperature with shorter holding time is a better way. The aging temperature is about 150–170 °C, heat preservation for 3–5 h
T6	Solutionizing treatment and completely artificial aging	Used to get the highest strength, but the corrosion resistance and plasticity would be reduce. At higher temperature and longer time. It is suitable for the requirement of high load parts, aging temperature is about 175–175 °C, holding time more than 5 h
T7	Solutionizing treatment and stabilizing tempering	Used to stabilize the size and the microstructure of the casts and improve the ability to corrosion resistance (especially the resistance to stress corrosion cracking), and keep high mechanical properties. Suitable for high temperature worked parts below 300 °C, tempering temperature is 190–230 °C, holding time 4–9 h
T8	Solutionizing treatment and soften the tempering	Make solid solution sufficiently decomposed, the precipitates transfer to glomerate, to stabilize the size of casts, improve plasticity, but the tensile strength decreased. Suitable for high the plastic casts, tempering temperature is about 230–250 °C, holding time of 3–6 h
T9	Circulation processing	To further stabilize the size of the casts shape. The repeated heating and cooling, temperature and cycle times are designed according to the parts work conditions, and the required properties. Suitable for size and shape of the parts are required very precise and stable
T10	Cooling after hot forming, cold working, and artificial aging	Suitable for the product that the strength improved by cold working or straightening and leveling

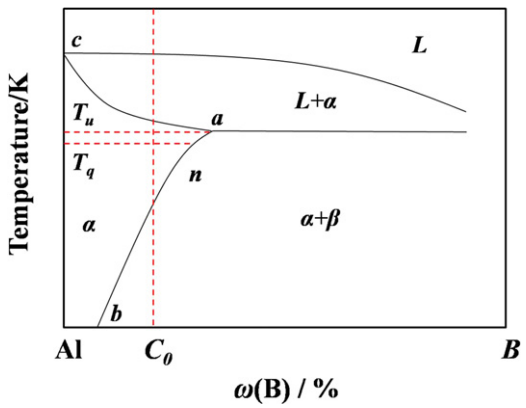


Figure 20 The relationship between solutionizing temperature and composition (T_e – eutectic temperature, T_q – solutionizing temperature).[1]

2.13.4.3 Heat Preservation: Time and Protection

When the temperature of the burden is increased to solutionizing temperature, and then holding for some time to make sure the alloy elements dissolved well. In a continuous production furnace, the speed of the production coming through the work zone should be appropriately deigned, to make sure the holding time meet the requirement of the applicable standard. In industry, the recommended holding time of the wrought aluminum alloy is shown in **Figure 21**. When the burden contains products which has different thickness cross section, the recommended holding time is confirmed according to the cross section of largest thickness.

Choose quenching transfer time is a technological process, too. Quenching transfer time is defined to be the time from the moment metal is out of solutionizing furnace or salt bath to that the work piece is immersed into the quenching medium to be cooled. Quenching transfer time has important effects on the metal properties. When the metal is taken out of the furnace and come into contact with cold air, the temperature at the edges and surface area of the parts falls rapidly, if this fore cooling in air is over too long time, some supersaturated effect would diminishes and the final quenching cooling afterwards will not get the desired effect because of the lower supersaturation. That is why the effect of quenching transfer time and reducing the average cooling rate is alike. In order to prevent the fore local decomposition and precipitation of SSS, which would reduce the effect of solutionizing and aging,

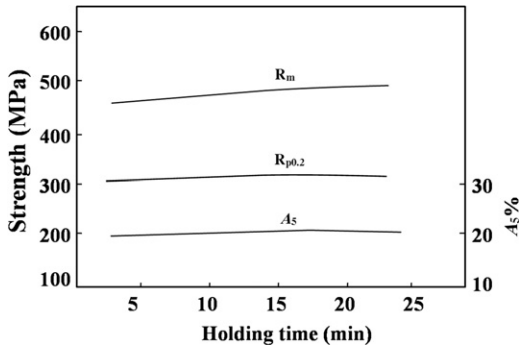


Figure 21 The influence of solutionizing holding time on the mechanical properties for 2A12 alloys (thickness: 1.0 mm, salt bath heating, solutionizing temperature: 500 °C, natural aging).[1]

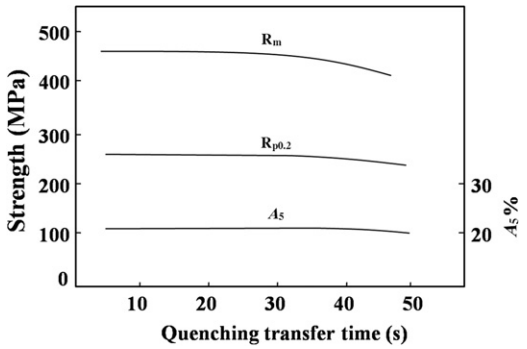


Figure 22 The influence of quenching transfer time on the tensile strength for 2A12 alloy (thickness: 1.0 mm, salt bath heating, solutionizing temperature: 500 °C , natural aging).[1]

quenching transfer time should be as short as possible. The length of quenching transfer time affects the mechanical properties, corrosion resistance, and fracture toughness of high and super-high strength aluminum alloys which are sensitive to quenching speed. To such alloys more strict measure should be taken to control the quenching transfer time. Figure 22 shows a test results for 2A12 alloy.

As for Al–Mg–Si alloys as 6A01, there is a little influence of quenching transfer time on the mechanical properties and corrosion resistance.

2.13.4.4 Cooling Process: Medium, Cooling Rate, and Temperature Range

2.13.4.4.1 Medium

The quenching medium is an important factor to ensure the achievement of the purpose or effect for various heat treatments. The higher the cooling capacity of the quenching medium is, the faster the cooling rate will be got in cast ingot which leading to a higher supersaturation of α SS and reach a good mechanical performance, because many of the alloying elements has been dissolved in the matrix attributing to a strong solutionizing strengthening. The quenching cooling rate in different quenching medium is ranked as follows:

Mixture of dry ice and acetone (−68 °C) > ice water > ambient water > warm water (80–90 °C) > hot water (100 °C) > water spray > vegetable oil > mineral oil (heated to 200–220 °C) > air.

Because the water has some capacity like high heat of vaporization, viscosity, heat capacity, strong cooling ability, and less cost. It is often used as a common quenching medium in industrial production. While its shortcomings are also very distinct: the cooling capacity decrease rapidly once it is heated to boiling. Generally, the cooling process in water can be divided into three stages:

1. Film boiling stage.
   When the hot product contact the cold water, the heterogeneous superheated steam film can be formed and grew upon the surface, it is tightly clinging to the surface and make the cooling rate decrease rapidly because of its poor thermal conductivity of the vapor coat.
2. Bubbling stage.
   Once the steam film is broken, strong heat exchange will happen near the region of surface combing with the boiling and bubbling.
3. Thermal exchange stage.
   Forced cold water circulation or the product motion in the water to break the steam film, accelerate the heat exchange at the interface of ingots and water so increasing the cooling rate.

When the ingots is cooled at boiling water, the cooling process can be divided into two stages:

1. Once put the ingot into water, severe thermal exchange happen at the beginning with a larger cooling rate.
2. The cooling rate turn down accompanying by the formation of lot of bubbles.

2.13.4.4.2 Cooling rate

The object of quenching is to make the alloy cool rapidly to a low temperature to achieve SSS, which contains most both solute elements and vacancies. Preparing the SSS plays a decisive role in the aging aluminum alloys. Faster cooling rate can generally provide a good comprehensive performance of higher strength, toughness, and fine corrosion resistance. That means the improvement of cooling rate is the key factor to ensure the good mechanical property or corrosion resistance.

The cooling rate in the quenching process mainly depends on stability of the SSS. There exist a critical cooling rate v_c, which is tangent to the 'C' curves when the alloy quenching at different cooling rate, shows in Figure 23, v_c is the minimum cooling rate to ensure to obtain the SSS. When the cooling rate in the center of product is higher than the critical v_c, the high temperature microstructure state can be fixed at each part of the product, that is called through hardening.

The cooling rate of quenching influences on the residual stress in the products; the increase in product thickness will turn the cooling rate down.

The lower limit of cooling rate is depended on the corrosion resistance of alloys for most aluminum alloys. For example, 2A11, 2A12, and 7A04 aluminum alloys is most sensitive to slow cooling. To get a higher strength and good corrosion resistance, in 7A04 alloys, the cooling rate in 2A11

and 2A12 needs be over 170 °C s^{-1}, while the cooling rate sensitivity of Al–Mg–Si series is lower.

2.13.4.4.3 Temperature range

The precipitation kinetics often is analyzed using TTT (temperature, time, transformation diagram) curves. In aluminum alloys, the isothermal precipitation kinetics curves is 'C' type which is similar to other solid state phase transformation in cool-down segment. The 'C' type curves is drawn based on the critical time point where the strength decreases to a certain level or the corrosion behavior turns from the pitting corrosion to intergranular corrosion with the precipitation process.

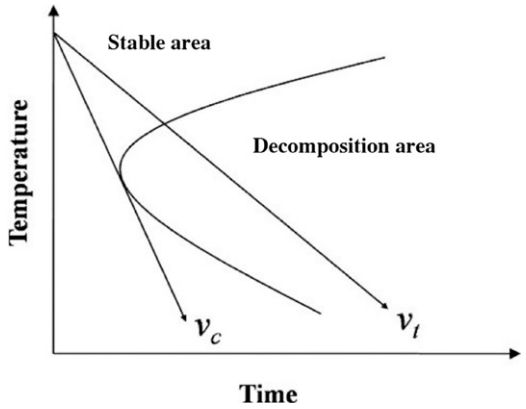


Figure 23 The critical cooling rate, the supersaturation stable area and the supersaturation decomposition area.[1]

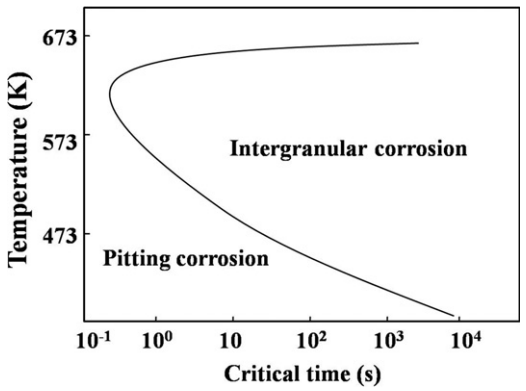


Figure 24 'C' curve of corrosion characteristics of 2A12 alloys after natural aging.[1]

Figure 24 shows the 'C' curve of 2A12 alloys characterized by pitting and intergranular corrosion after natural aging treatment. The fastest precipitate rate happens in the area near the tip region, the corresponding temperature region is called critical temperature region.

2.13.4.5 Cooling Technology: Graded Cooling, Alternative Rate Cooling

The two typical cooling techniques of quenching are shown in Figure 25. Figure 25(a) shows 'isothermal quenching,' namely cooling the products directly to a natural aging temperature. Figure 25(b) shows 'step-quenching' method, i.e., firstly cooling the products to an intermediate temperature of 160–200 °C (the medium may be salt bath or oil), and then after specific time cooling the products again to lower temperature for aging.

Decrease the temperature gradient by designing the temperature of quenching medium can obviously reduce the residual stress after quenching. For the forged product, the water temperature is 10–30 °C, not more than 40 °C, if the product have complex shape and a great differences in thickness, the solutionizing temperature should be a little higher: 40–50 °C, even more than 60–80 °C. The water temperature would be used for more complex small forgings. The isothermal quenching and step quenching can obviously reduce the residual stress and deformation/distortion at the cost of strength, toughness, and the intergranular corrosion resistance.

2.13.4.6 Quenching Faults

Because of the high thermal expansion coefficient of Al alloys and the actual size and shape of the products, the cooling process of the quenching has great effect on the quality of the products. Too faster cooling always makes severe defects, for example, deformation, distortion, warped, twist, etc., even cracks. Table 9 enumerates the main faults and analysis.

2.13.5 Processes of Aging Treatment

Aging treatment, also known as low temperature tempering, is a process in which the solutionized aluminum alloy castings/forgings are heated to a certain lower temperature, held a certain time and then cooled to RT, with the decomposition of SSS and the microstructure more stable.

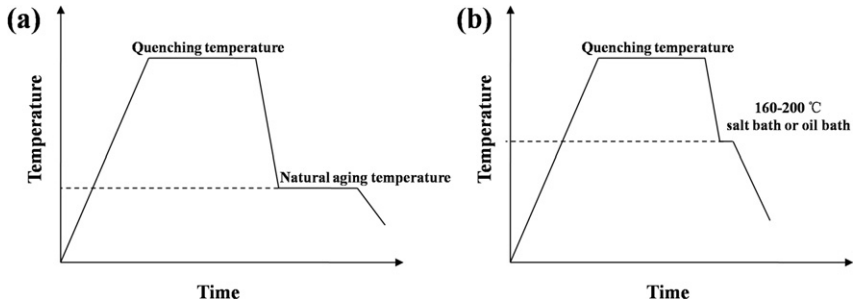


Figure 25 Isothermal quenching and step quenching process in aluminum alloys. (a) Isothermal quenching and (b) step quenching.[1,4,5]

Table 9 The common quenching faults and precautions

Name	*Characteristics*	*Analysis*	*Elimination and precautions*
Deformed, warped	The dimension or shape is changed during the heat treatment	• The heat rate or the cool rate is too fast • Quenching temperature is too high • A complex design of the ingot/forging • Incorrect placing direction in quenching	• Slow down the heating rate and increase the temperature of quenching medium • Thicken the insulation coatings or paint on the quenching sensitive position on the product • Use anti-deformation fixture • Correct the little deformation position directly after quenching
Crack	Macroscopic cracks on ingot/forging surface; the crack is winding and dark gray	• The heating rate or the cooling rate is too fast • Solutionizing temperature is too high • Inhomogeneous temperature distribution in the parts	• Slow down the heating rate or use the isothermal quenching process • Use anti-crack fixture • Thicken the insulation coatings or paint on the quenching sensitive position in the product
Surface corrosion	The casting surface is marked or blocked with spot different color to surface of the aluminum alloy castings	• Not completely cleaning before and after nitrate bath • Nitrate liquid chlorine content is overweight ($>0.5\%$)	• Shorten the transfer time from furnace to quenching bath • Test the chloride content in the nitrate; if it is extensive, make it reduce • Cleaning the ingots using warm water or cold water completely once upon taking it form the nitrate bath
Non-uniform quenching	The hardness and ductility is low in the thick parts and high in the thin positions	• Exist heterogeneity in heating and quenching process • The cooling rate is a little slow in the thick positions, diathermancy of the parts/burden in the furnace is poor	• Do heat treatment again, reduce the heating rate and extend the time of heat preservation • Thicken the insulation coatings or paint on the quenching sensitive position in the product • Make each part of the product quench at the same time, put thick position firstly • Change the quenching medium to organic solvent to reduce the cooling rate

Aging process can be divided into two basic types: natural aging treatment and artificial aging treatment. Natural aging treatment refers to aging strengthening under RT. Artificial aging process is conducted at a higher temperature than room one, which can again be divided into three kinds: incomplete artificial aging (under-aging), full artificial aging (peak aging), and over-aging.

1. Incomplete artificial aging: the casting/forging is heated to 150–170 °C for 3–5 h, so that a better combination of TS, ductility, and toughness can be obtained, but corrosion resistance is lower.
2. Full artificial aging: the casting/forging is heated to 175–185 °C for 5–24 h, so that the highest hardness and TS but lower ductility can be obtained.
3. Over-aging: the casting/forging is heated to 190–230 °C for 4–9 h to lower the strength and improve the ductility, especially to get better anti-stress corrosion cracking and anti-corrosion property can be obtained. It is also known as the stabilization tempering.

The aluminum alloy casting/forging is cooled to a temperature below zero (such as −50, −70, −195 °C) and held for a certain time. Then the casting/forging is heated to a temperature below 350 °C, and the crystal lattice of the SS repeatedly expands and contracts with some little displacement of the grain of each phase, so that the particles in both the alloying atom clustering area and the intermetallic compound area are in a more stable state. In this way, the products size and volume can be more stable. This repeated heating and cooling heat treatment process is called cyclic process. This process is suitable for the products with very sophisticated requirements and stable size (such as some parts on the electronic detecting instrument). Normal casting/forging does not need such treatment.

2.13.5.1 Pre-Conditions and Property Requirements

2.13.5.1.1 Material condition before aging

To realize the potential of age hardening effects, strengthening solution treatment must be carried out before aging for heat treatable alloys, so that the alloying elements could dissolve in the matrix adequately under the non-over burning condition. After the solutionizing treatment, the alloy should be solutionized to make the matrix supersaturated and avoid the second phase precipitation, providing the microstructure basis for the following aging precipitation strengthening. Meanwhile, the grain size and morphology should be controlled in the solution process to ensure the performance of the alloy.

2.13.5.1.2 Determination of aging process

The parameters of aging process are determined on the constituent of alloy, the service performance, such as strength, hardness, toughness and corrosion resistance, and the dimensional stability. If the alloys need high strength and

hardness but moderate ductility, the complete artificial aging (peak aging) would be used. If the alloys require high ductility and toughness and do not require so high strength and hardness, the incomplete artificial aging (under-aging) would be chosen. If the corrosion resistant performance and dimensional stability play more important roles, the aging process with longer aging time and/or higher temperature would be carried out, i.e., over-aging would be conducted. If the alloys need high integrated performance, the multi-stage aging would be used. If the alloy need both high strength and corrosion resistance, the RRA would be chosen.

2.13.5.2 Aging Processes

2.13.5.2.1 Aging parameters

Aging temperature. Aging temperature is one of the most important aging parameters in aging processes. Aluminum alloys with different compositions have different aging temperatures at which they can obtain best aging effect. Statistic results of best aging temperature of all kinds of aluminum alloys show that their best aging temperature is closely related to their melting point, which can be expressed by the following equation:

$$T_a = 0.5 \sim 0.6T_m \quad [3]$$

where T_a and T_m play with degree Kelvin ($T(\mathrm{K}) = T(^\circ\mathrm{C})) + 273.15$ K).

Aging time. For a certain aluminum alloy, **Figure 26** shows the relationship between the hardness and aging time. At lower temperature, the hardening effect increases with the increase in temperature, but the hardness cannot reach the highest value. When the aging temperature reaches a certain value, there is a maximum hardness in the curve, and the alloy can obtain the best hardening effect. Further increasing the aging temperature, the softening (over-aging process) will occur earlier, and the hardening effect decreases with the increase of the aging temperature. Besides, the best hardening effect cannot be obtained.

2.13.5.2.2 Aging process

According to the properties of aluminum alloys and application requirements, different aging process can be adopted, mainly including single-stage aging, step aging, RRA, and deformed aging.

A. Single-stage aging: only aging treatment once after quenching, either natural aging or artificial aging is suitable, and the purpose of single-stage is to obtain aging hardness peak in most cases. Sometimes, over-aging can be used to eliminate residual stress, stabilize microstructure, maintain dimensional stability, or improve the corrosion resistance.

B. Step aging: as-quenched workpieces are heated in two or more times at different temperatures. According to the functions, step aging can be divided into two stages: the pre-aging (also known as nucleation aging) and final aging. The temperature of pre-aging is much lower compared with final aging, due to their different purposes. The purpose of the former is to form high density of GP zone and nuclei of intermetallic compound phase in alloys, but the latter is to promote the continuous growth of the nuclei formed in the pre-aging stage, which can obtain higher density of intermetallic compound and transition phases, and achieve expected performance by adjusting the structure and the dispersion degree of the intermetallic compound phases.

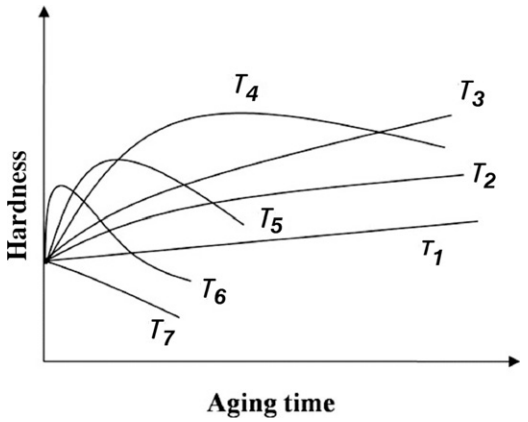


Figure 26 The relationship between the hardness and aging time of aluminum alloys at different aging temperatures ($T_7 > T_6 > T_5 > T_4 > T_3 > T_2 > T_1$).[1]

C. RRA: aluminum alloys after aging are held at higher temperature, leading to decreasing the hardness and strength to a level close to solutionized state, and then aging treatment will be carried out again to achieve required strength of the artificial aging and stress corrosion resistance by step aging. The basic steps include: (1) normal state of solutionizing; (2) peak aging as T6 state; (3) regression process (heated at the temperature that is between T6 aging and solutionizing for a few minutes, then cooled down immediately; (4) T6 aging again.

D. Deformation aging: it is also called thermo-mechanical treatment, which is a new heat treatment method combined aging hardening with work hardening. The purpose is to improve distribution of transition phase and refining the structure in the alloy, in order to obtain high strength, toughness, and corrosion resistance. This method can be applied to plates, thick plates, forged, or extruded components with simple shapes. The deformation degree is usually between 1.5 and 3.5%, a little bit over the general yield strain.

2.13.5.2.3 Stress aging

Stress aging means that the stress lower than the yield stress (YS) is introduced into the casting/forging during the aging, to change the precipitation process of reinforcing phases with coupling effect of stress and temperature, so as to achieve fine, regularly distributed precipitation phases of the type, quantity, morphology, size, and orientation. In 1970s, Hosford and Agrawal[9] studied the effect of stress aging on aluminum alloy, they revealed that the alloys precipitate obvious preferred orientation. Zhu and Starke[10,11] carry out a series of experiments and simulation to study Al–xCu binary alloys in detail, it shows that the factors, such as alloy composition, aging temperature, applied stress amplitude and direction, aging time, have influence on precipitates' orientation. Wang *et al.* find that, in 2E12 alloy, stress aging can prevent continuous precipitation at grain boundary.[12]

2.13.5.3 Aging Quality Control

2.13.5.3.1 Factors that impact aging process and the properties of aluminum alloys

2.13.5.3.1.1 The composition of the alloy

In binary alloys, the major composition of the alloy has a critical concentration and a limited concentration. If the concentration of the major composition is below the critical concentration, aging process is not likely to occur; if the concentration is between these two limits, the growth of hardness of the alloy after aging process increases with the concentration; if the concentration is above the limited concentration, the development of hardness after aging process decreases while the concentration increases (the influence of the composition in ternary alloys is similar to that in binary alloys). The minor composition and the impurity of the alloy, although the contents of which are few, sometimes have an acute impact on the decomposition dynamics of the SSS and the structure and property of the alloys.

2.13.5.3.1.2 Solutionizing treatment system

Higher supersaturated vacancy concentration and degree of supersaturation can be obtained after quenching, so that the diffusion process and dissolution process can be accelerated and higher strength and hardness can be gained. Also the cooling rate of the solutionizing process has a huge impact on the aging. The stability of different SSS differs, so the critical cooling rate, which is meant to restrain the decomposition of the solution in the cooling process, differs too.

The time of the aging. Usually, with the increase in aging time, the tensile stress, YS and hardness of the alloy increase consistently. If the temperature is high enough, these properties will decrease after reaching the maximum, which means the alloy is on the over-aging stage.

2.13.5.3.1.3 The temperature of the aging

When the temperature of the aging increases, the strength of the alloy will decrease after reaching the maximum. If the temperature is high enough, the strength of some alloy is less than as-solutionized state.

2.13.5.3.1.4 Plastic deformation

Usually, aluminum alloys are deformed on some level before aging and after solutionized. The cold deformation before aging of the alloys depending on GP zone and sub-equilibrium precipitating strengthening, can increase the dislocation density, and the vacancies are more likely to enter the dislocation and disappear, which will slow down the generation of GP zone and is against the aging strengthening. On the contrary, the cold deformation, before aging the alloys mainly depending on the disperse and transition phase strengthening, will contribute to the nucleation of the transition phase and the equilibrium phase, thus increasing the strengthening effect.

2.13.5.3.1.5 Others

Ultrasonic can accelerate the dissolution of the SSS and also increase the degree of the disperse of the dissolution, which contributes to the high hardness of the alloy. In addition, irradiation can increase the excessive vacancies, accelerate the dissolution speed and increase the peak value of the hardness.

2.13.5.3.2 Key points of the operation of aging

1. Check if the heat treatment, instruments are functioning properly and the furnace temperature is uniform within the prescribed range ($\pm 5\ ^{\circ}C$).
2. The products are supposed to take grit blasting or get washed, in order to remove oils, dirt, and mud. Do not mix up the alloys with different trademarks.
3. Products whose shapes can be easily changed should be placed on specific plates or brackets, and no parts of the products are supposed to be impending.
4. During the process of heat preserving, the temperatures of everywhere in the furnace should be checked and adjusted at all time, in order to prevent the alloys from being over burnt or even melting.
5. If the furnace is powered off for a long time, the heat preserving state products should be quenched immediately and when later the furnace is working properly, repeat the steps above and continue the heat treatment.
6. Products should be washed and dried to eliminate the rest of the nitrate immediately after have been quenched in nitrate bath.
7. If the products deform after being quenched, the products should be adjusted in time.
8. The products should take aging treatments within half an hour (parking time) after being quenched if they are required to.
9. If the properties of the products after heat treatment are found to be unqualified, repeated heat treatment can be experimented on the same products but no more than twice.
10. The parameters of the heat treatment should be determined by the shapes, sizes, and features of the alloys.

2.13.6 Progress in Heat Treatment of Aluminum Alloys

2.13.6.1 Novel Techniques in Aluminum Heat Treatment

2.13.6.1.1 New short T6 heat treatment for semi-solid forming

The solutionizing treatment is an important part of the heat treatment of aluminum alloys. In this stage, the SSS or the metastable transition microstructure at RT can be obtained, which offers alloying element distribution and microstructure basis for subsequent aging strengthening. For traditional casting aluminum alloys, solutionizing treatment should held for a long time, which limits the efficiency of aluminum alloy heat treatment. However, if the solution time is too short, the secondary phase cannot dissolve in the matrix completely, which is hard to provide ideal microstructure for subsequent aging hardening. Compared with the conventional casting methods, semi-solid forming process has higher cooling rate, which can obtain more homogeneous microstructure and finer intermetallic compounds, which are located next to the eutectic constituent, surrounded by α-phase globules with smaller size. In such a circumstance the diffusion distance of alloying element atoms is quite small and the composition homogeneous time must be shorter. These homogeneous and

finer microstructure existing in components manufactured in semi-solid state can significantly reduce the solution time of T6 heat treatment, leading to a significant increase in productivity and decrease of manufacturing cost. Researches show that the optimal parameters of conventional cast aluminum alloys heat treatment are not applicable to semi-solid processing components, due to their different microstructure and solidification history.[13,14] Menargues *et al.* studied heat treatment characteristics of semi-solid processed A356 and A357 casting alloys, and found that heat treatment, conducted at the solutionizing temperature 540 °C for 30 min, enabled the complete magnesium dissolution, while inhibiting the grain growth of the α-phase and the eutectic silicon.[15]

2.13.6.1.2 Water–air spray cooling

In the heat treatment processes of aluminum alloys, quenching might be the most strict and difficult process to be controlled . Its purpose is to obtain the SSS of solute and vacancies. Therefore, cooling rate of quenching should be fast enough to guarantee the SSS fixed. In general, the highest quenching cooling rate can lead to highest hardness and the best combination of strength and toughness, and obtain the good corrosion resistance, so in order to get good mechanical properties and corrosion resistance, high cooling rate might be adopted. However, with the increase of cooling rate, warping and distortion of the products and the value of residual stress will also increase, thus it is hard to straight and maintain dimension stability when the cooling rate is too high. A novel cooling method which can realize high cooling rate and resist warping and distortion of products should be developed. Water–air spray cooling is such a way (as shown in **Figure 27**). Nowak *et al.* contributed a cooling characteristic of EN AW-6082 aluminum alloy using water–air spray cooling method during extrusion.[16] Their research showed that this method can achieve a high cooling rate, and it can also adjust the final temperature over a wide range and minimize the temperature gradients in the cross section of complex profiles, which can make the products obtain good mechanical properties and deduce profile distortions.

2.13.6.1.3 Digital modeling

With the development of computer technology, digital modeling based on finite element method (FEM), artificial neural network method, etc., is becoming more and more widely applied in materials science and engineering. Digital modeling and simulation can reduce time and costs of laboratory, and greatly improve the efficiency because it does not need to undertake the actual experiments, which makes it a promising material preparation and processing method, even can make some more precise and elaborate work for designing and planning of heat treatment preparation. In the field of heat treatment, digital modeling can be used for preliminary exploration and optimization of technical parameters, which can reduce the costs of production and improve the quality and productivity. However, in order to realistically model different stages of a heat treatment process, it is necessary to prepare sufficient materials data and understand the physical laws that describe the thermal, mechanical behavior of a material during different stage. A commercialized example is Visual Heat Treatment program developed by the company ESI Group. It is based on the interaction of five modules (namely thermal and metallurgical analysis, electromagnetism, diffusion, the formation of secondary phases, analysis of mechanical properties), and then designed to solve problems concerning the heat treatment of materials, such as steels and aluminum alloys. Molotov *et al.* simulated the heat treatment of Al–Mg–Si alloy using the Visual Heat Treatment program, and found that simulation based on FEM could accurately predict mechanical properties of alloy after heat treatment when comparing with the actual experimental results.[17]

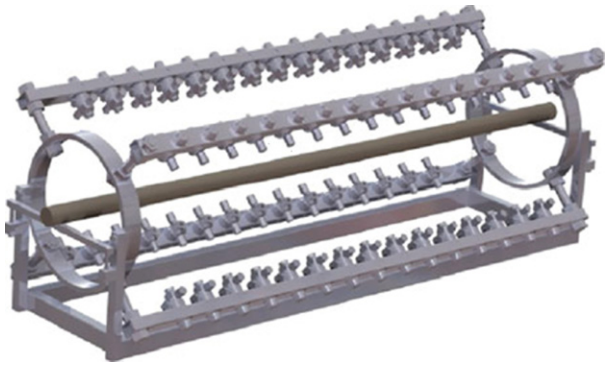


Figure 27 Schematic configuration of the spray cooling device and applied nozzle position.[16]

2.13.6.1.4 Thermo-mechanical treatment

Thermal-mechanical treatment is deforming the metals or alloys at first, and then take heat treatment, usually aging, subsequently. The deformation here is to increase the density and change the distribution of the crystal defects such as dislocation and vacancy, which could increase the driving force for the precipitation and improve the distribution of precipitates. The precipitated phase could pin the dislocation, grain boundary and other defects, and block their motion. After the following treatment, the defects in the metal materials could be stable and refine the microstructure to increase the strength and ductility. The thermal-mechanical treatment on aluminum alloy could be classified into two types by Di Russo *et al.*,[18] and they are intermediate thermal-mechanical treatment (ITMT) and final thermal-mechanical treatment (FTMT). The criterion for dividing categories is that the aging of aluminum alloy under different temperature leads to diverse precipitations. If the precipitation acts as auxiliary particles to induce or hinder the recrystallization, the corresponding process is defined as ITMT. If the precipitation does not effect as auxiliary particles, but a strengthening secondary phase under the aging strengthening process, this kind of thermal-mechanical treatment is FTMT. In the ITMT, the large precipitates impede the dislocation and refine the grains, and they are dissolved in the matrix by solutionizing and quenching in the following recrystallization process. The mechanical property of the aluminum alloys is improved by subsequently aging treatment. The purpose of FTMT is to promote the precipitation of the nano-scale secondary phase to accelerate the aging process. The amount of deformation is always 50% at most. The ITMT has an advantage in improving the ductility on short transverse direction and refining the grains to increase the high-temperature superplasticity.

The FTMT plays a role in increasing the strength of aluminum alloys, accelerating precipitation in the aging process and improving the fatigue performance, corrosion resistance, and toughness.

2.13.6.1.5 Thermo-mechanical treatment for non-ferrous alloy

Used for age-hardenable alloys. Deformation followed by aging treatment. Al, Cu, and Ni-base precipitation hardenable alloys are subjected to TMT. TS increases many times that of conventional quenching and aging treatment.

Two groups:

LT TMT (low temperature thermo-mechanical treatment).

HT TMT (high temperature thermo-mechanical treatment).

In LT TMT heat to single-phase quench (SSS) – deform cold – age at RT or increased temperature (Figure 28(b)). Increased deformation will increase TS, YS, and hardness (after solution treatment and aging).

Mechanism of increased properties: strain hardening and interaction between crystal defects and precipitation of particles. Certain work hardening remains after aging (low temperature). Deformation below recrystallization temperature is cold working. Cold deformation increases defect sites which will increase the rate of precipitated particles transformation from SSS and also increase volume fraction of precipitated particles.

HT TMT (deform – quench) (Figure 28(c)) will increase dislocation and other crystal defects. Increased strength is due to uniform precipitated particles and fine grain size.

In age hardening treatment, the secondary precipitation of fine intermetallic particles develops greater strength and hardness. Because of plastic deformation a large number of defect sites are created. During aging treatment, the supersaturated solute will precipitate out as a secondary phase in the form of a large number of smaller particles at the defect sites, enhanced by deformation. This larger number of smaller particles is responsible for the better mechanical properties achieved by TMT than by conventional aging treatment, which produces less dispersed particles.

In TMT the age hardening alloy is heated to a temperature range where a single SS is formed (Figure 28), the alloy is then plastically deformed at this temperature to a finished shape. And by this deformation a large number of defects are induced in the grain structure. After that it is quenched from this temperature to get a SSS. The deformation may also be carried out after solutionizing and quenching operation. However, the deformed component is then aged at a lower temperature where solute atoms will precipitate out as a secondary phase in a larger number of smaller particles at the defect sites.

2.13.6.1.6 A novel multi-stage solutionizing

Solution strengthening can allow the final solution temperature higher than T_{im} (T_{im} is the onset temperature of incipient melting during solution heat treatment) without producing burnt or coarsened microstructure, leading to improvement of solution degree of solute alloying atoms and final mechanical properties. The solution process includes two stages: in the first stage, low conventional solutionizing temperature (below T_{im})

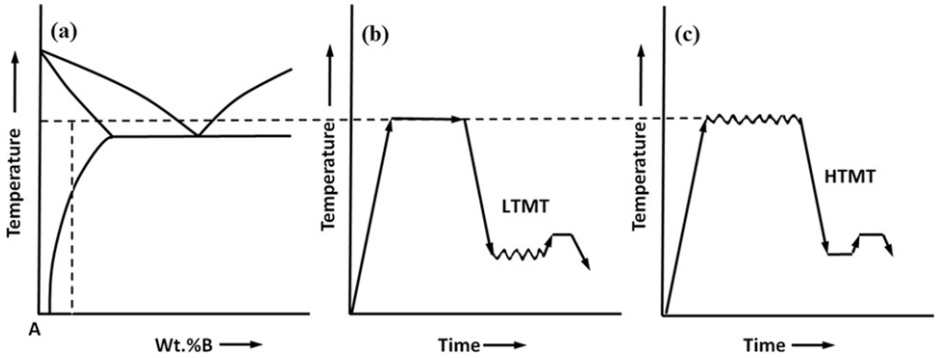


Figure 28 Low temperature thermo-mechanical treatment and high temperature thermo-mechanical treatment cycle for an age hardening alloy.[4]

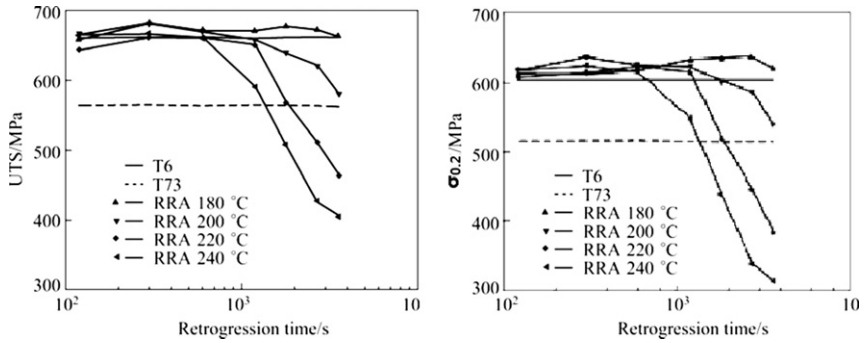


Figure 29 The influence of regression time on the ultimate tensile strength and yield strength in AA7094.[20]

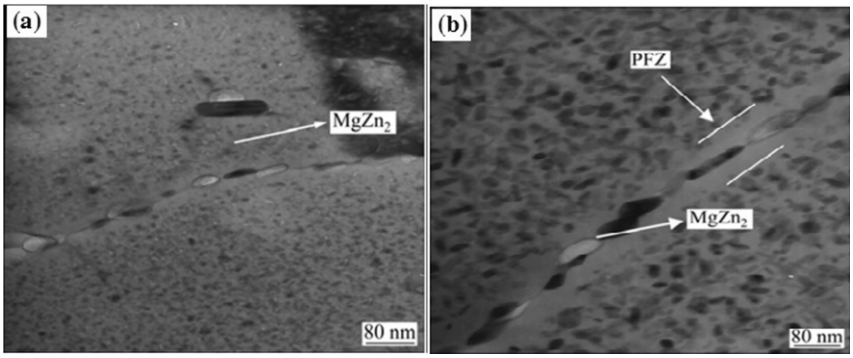


Figure 30 (a) Transmission electronics microscope (TEM) image of alloy in overaged T73 temper; (b) TEM image of alloy after regression and re-aging at 240 °C for 60 min.[20]

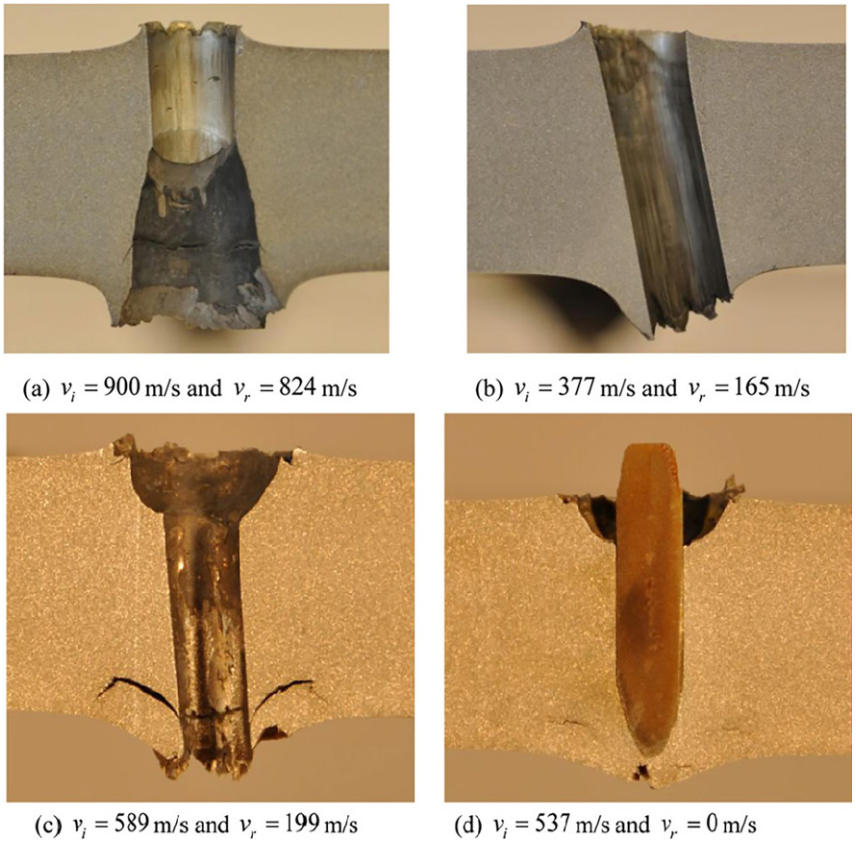


Figure 31 Cross-sectioned morphology of shot targets of 20 mm thick target plates of AA6070 in different tempers. (a) and (b) temper O, (c) and (d) temper T6. The targets were perforated by APM2 bullets at various impact velocities. v_i and v_r are the initial and rear speed of the bullet, respectively.[21]

is used, while in the second stage a much higher temperature is set, and the heating rate should be low from the first stage to the second stage so that the low melting eutectics can dissolve and improve the solid solubility of solute atoms without over burning. By doing this, a more sufficient precipitation strengthening effect can be obtained.

However, Aguilera Luna and colleagues improved the tensile properties of an Al–Si–Cu–Mg aluminum industrial alloy by using multi-stage solution heat treatments.[19] An inverse sequence compared with the sequence used in strengthening solution process is used in their contribution. Namely, the hold temperature of the first stage was always above T_{im}, while the isothermal treatment of the second stage was conducted at a temperature below T_{im}. The results showed that similar or better tensile properties with shorter treatment time than the conventional one can be obtained with the proposed solution treatment.

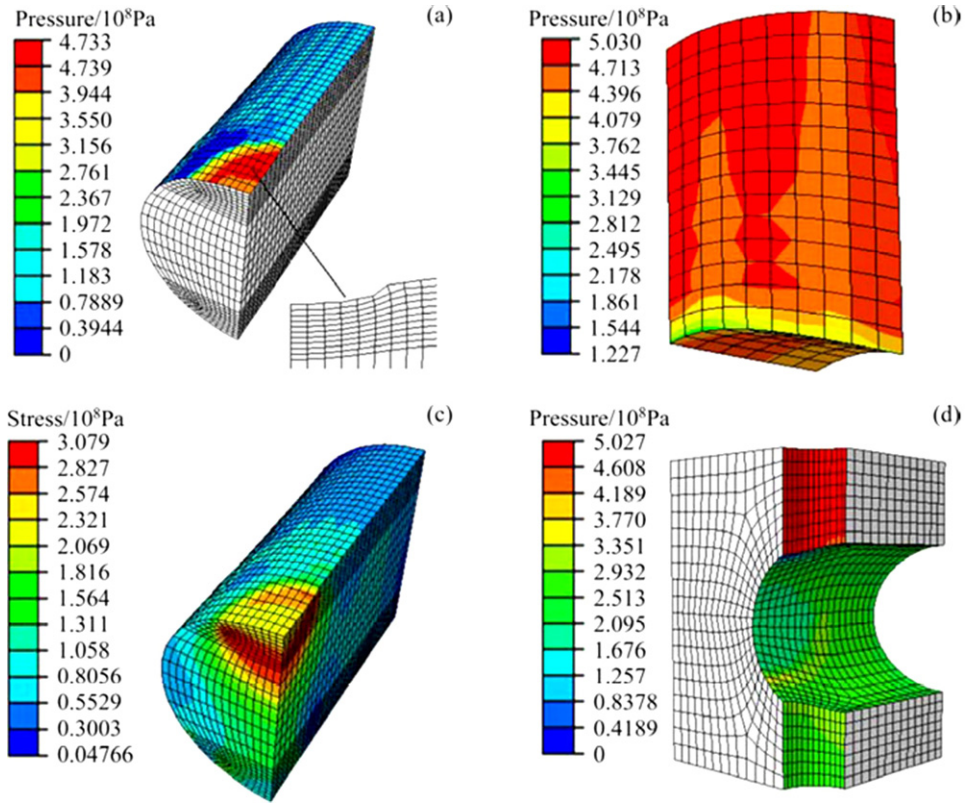


Figure 32 Distribution of heat-induced pressure and stress: (a) heat-induced pressure of cylindrical pin; (b) heat-induced pressure of 2024 alloy; (c) Mises stress of cylindrical pin; (d) heat-induced pressure of mold.[22]

2.13.6.2 The Influence of Multi-Heat Treatment on the Performance of Aluminum

The RRA treat has been proposed in AA7049 alloys.[20] As a multi-stage heat treatment, the RRA is a trade-off between strength in T6 temper and corrosion resistance in T73 temper. This process consists of double aging with an intermediate regression step. The first aging corresponds to the T6 temper, and the regression consists of partial annealing at temperature usually between 180 and 240 °C for a short time ranging from 2 to 60 min, followed by water quenching. Finally, the alloy is re-aged similar to T6 temper. **Figure 29** shows the influence of regression time on the ultimate tensile strength and YS.

Both of T73 temper and RRA can produce a fine distribution of η' precipitates, but the precipitates in RRA is more coarse than that by T73, just shows in **Figure 30**.

Aluminum alloy AA6070 in different tempers are studied to obtain higher integrated property,[21] using target plates of 20 mm thickness in tempers O (annealed), T4 (naturally aged), T6 (peak strengthened), and T7 (overaged). The result (**Figure 31**) shows that the T6 temper leads to an excellent behavior in ballistic properties comparing to O state. **Figure 31** demonstrates that in (a), (b), and (c) the bullet has penetrated the plate and held some velocity to fly more. In (c) the bullet is stopped in the plate, the plate armor exerts the protecting effect. From these test results one can know that the bullet had shot through the target for the velocity of shooting bullet from 900 to 589 m s^{-1}, and the O temper provides worse blocking capacity, whereas the block velocity is larger than 537 m s^{-1} for T6 temper. That means the alloy in different temper has quite different target capacity: T6 temper endows the materials with much better armoring capacity.

Table 10 Heat treatment on 7085 alloys in the experiment[23]

Temper	*Heat treatment*
T6	120 °C/24 h
T74	110 °C/6 h + 160 °C/10 h
RRA	120 °C/24 h + 180 °C/0.5 h + 120 °C/24 h
DRRA	120 °C/24 h + 180 °C/0.5 h + 120 °C/12 h + 180 °C/0.5 h + 120 °C/24 h
HLA	200 °C/5 min + 120 °C/24 h

Abbreviations: DRRR, dual-regression and re-aging; HLA, high-temperature and the subsequent low-temperature aging; RRA, regression and re-aging.

Heat treatment of metals under high pressure can endue different properties. The heat treatment of AA2024 under heat-induced pressure during restricting expansion-deformation has been calculated by ABAQUS platform.[22] The experimental results indicate that high heat-induced pressure can be generated on 2024 products, which is approximately 503 MPa at 500 °C when 42CrMo is used as the mold material. Moreover, the pressure distributions on both the bottom and lateral sides are relatively uniform, the result is shown as **Figure 32**.

The influence of tempers T6, T74, RRA, Dual RRA, high-temperature and the subsequent low-temperature aging (HLA)

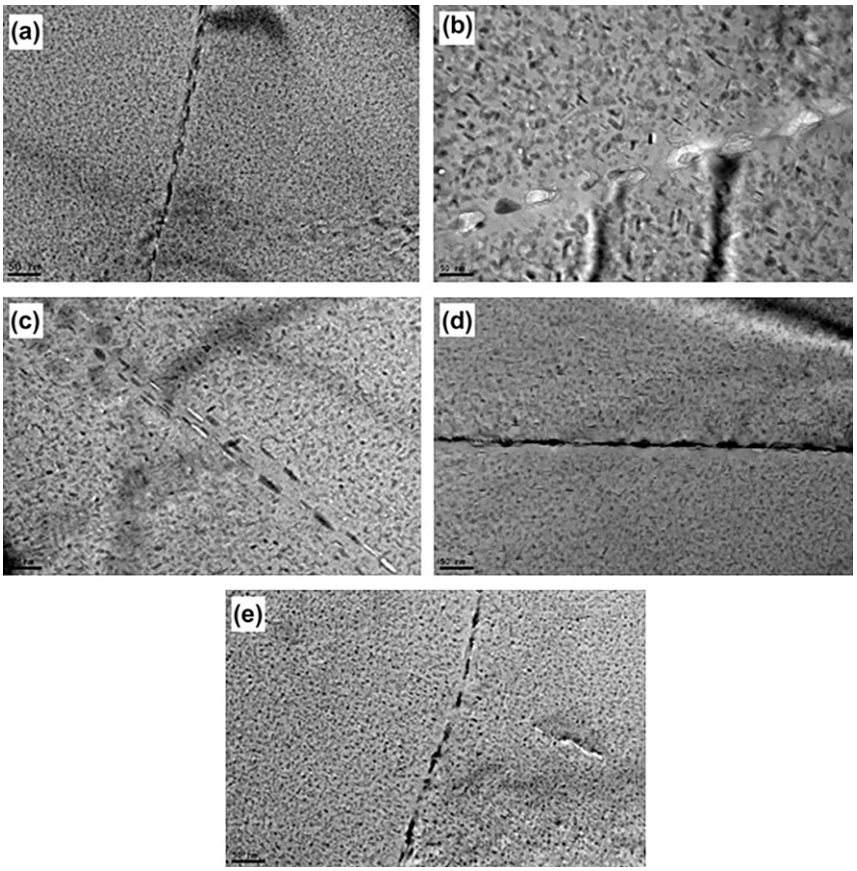


Figure 33 Transmission electronics microscope microstructure of the AA7085 alloy under different heat treatment (a) T6; (b) T74; (c) regression and re-aging; (d) dual RRA; (e) high-temperature and the subsequent low-temperature aging.[23]

on exfoliation corrosion of AA7085 aluminum alloy has been investigated.[23] The heat treatment process is shown in Table 10. The results show that RRA improved exfoliation corrosion resistance without sacrificing the strength compared to T6 temper. DRRA improved exfoliation corrosion resistance equivalent to T74 temper and maintained the strength similar to RRA. The HLA decreased the strength and corrosion resistance compared to the T6 temper. Figure 33 shows the corrosion result after different heat treatment.

The grain boundary corrosion is inhibited in (b), (c), (d) tempers from these microphotographs, compared with other tempers. It is seen that the precipitates both inside grains and in grain boundary neighborhood are changed from longer bars to shorter bars, even dotted distribution by T74 and RRA tempers, which improve the binding capacity of the grain boundaries. The RRA regression treatment changed the precipitates in grain boundary much more effective, the DRRA leads to a spherical precipitates (Figure 33(c)). That is clear that for Al–Zn–Mg–Cu alloys the HRRD treatment could improve the microstructure nearby grain boundary very much, therefore the ductility, toughness, and corrosion resistance as well are improved under the precondition of keeping high strength. HLA, namely, double aging treatment, optimized the precipitates with more uniform distribution and size. Also, the grain boundary precipitates are improved as well (Figure 33(e)).

Table 11 The impact of solutionizing treatment temperature on the composite performance[24]

Composition of composites	*Solutionizing*	*R_m (MPa)*	*A5 (%)*
15% SiC_p (5 μm)/2024Al	495 °C, 40'	416.1	2.63
	500 °C, 1 h	478.5	0.92
	520 °C, 1 h	546.6	1.26
15% Al_2O_{3p} (10 μm)/2024Al	500 °C, 1 h	461.1	1.64
	520 °C, 1 h	492.9	1.20
3.6% CF (chopped)/2024Al	500 °C, 1 h	419.4	9.2
	520 °C, 1 h	465.6	5.8
10% SiC_p (10 μm)/2024Al (Cast and hot extruded with a ratio of 16)	520 °C, 1 h	$R_p0.2$: 400.9	
	550 °C, 1 h	$R_p0.2$: 416.0	

2.13.6.3 Heat Treatment of Aluminum Matrix Composites

Aluminum matrix composites, especially short fiber and particulate reinforced aluminum matrix composites (PRAMC), with high specific strength, specific stiffness, good high temperature properties and wear resistance, are widely used in the aerospace, automotive, and electronics fields. Therefore, the study of the effect of heat treatment on the improvement of mechanical properties of PRAMC is of great significance. In

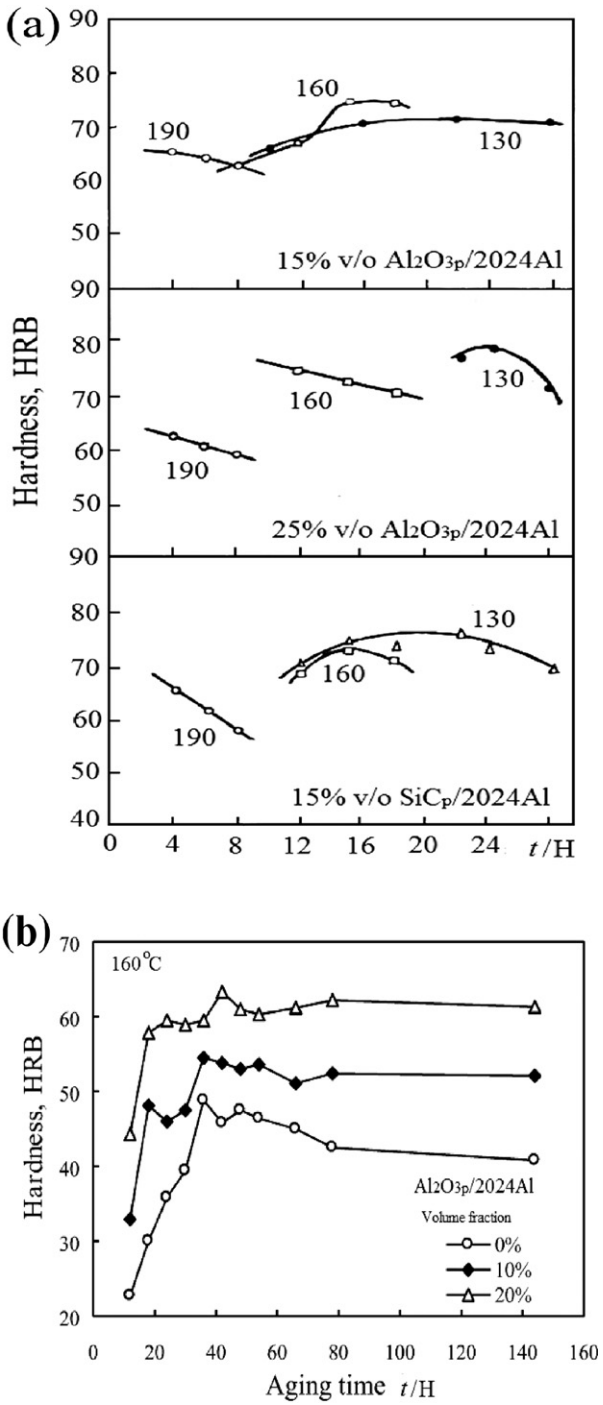


Figure 34 The aging behavior of particulate reinforced aluminum matrix composites by (a) powder metallurgy; (b) cast.[24]

view of this, a series of study are carried out on the effect of heat treatment process on the mechanical properties of PRAMC. The results were as shown in **Table 11** and **Figure 34**.

As shows in **Table 11**, with the increase of the solutionizing treatment temperature in a certain range, the strength of the PRAMC is improved, however, the failure elongation decreases slightly. From **Figures 34(a)** and **34(b)**, it can be drawn a conclusion that aging process which can obtain best properties of the composites varies from the fraction and type of reinforcements, the aging temperature and aging time, which can obtain best properties both decrease obviously.[24]

2.13.7 Conclusions

1. Heat treatment is a particular thermodynamic approach to improve the mechanical properties, corrosion resistance, workability, dimensional stability, and some other characteristics of metal materials especially of aluminum alloys.
2. Solutionizing can make the aluminum alloy products a SSS and a more homogeneous distribution of alloying elements in the aluminum matrix, preparing for the next aging process to obtain better property.
3. Aging process can endow the products with fine precipitation in the microstructure and higher hardness, the temperature – time scheduling can provide various property change for different purpose, such as peak aging makes higher hardness, but over-aging makes better corrosion resistance.
4. In processes of heating, temperature holding, cooling, the defects/faults could occur due to heterogeneous heating and cooling, complex structure, etc. The protective measures for various situation are described.
5. Heat treatment in restricted frames can provide more precise size and shape stability for complex castings/forgings with various compositions.
6. Multi-step heating and cooling process gives the heat treated parts much better property, even better resistance to corrosion, exfoliation, and corrosion cracking as well.
7. The PRAMC have stronger sensitivity to solutionizing and aging temperature and time, usually the temperature is lower, and the time is shorter at peak aging property.

See also: 2.12 Heat Treatment of Aluminum Alloys

References

1. Niankui Li; Gao Ling; Bo Nie; Jingan Liu. *The Aluminium Alloys and Its Heat Treatment Technology*; Metallurgical Industry Press: Beijing, 2012.
2. Deke Shi. *Fundamentals of Materials Science*, 2nd ed.; China Machine Press: Beijing, 2003.
3. Perston, G. D. The Diffraction of X-Rays by an Age-Hardening Alloy of Aluminium and Copper. The Structure of an Intermediate Phase. *Lond. Edinb. Dublin Philos. Mag. J. Sci.* **1938**, *26* (178), 855–871.
4. Xing Lu; Zhengfeng Qi; Chuanya Wang. *Fundamentals of Heat Treatment Engineering*; Metallurgical Industry Press: Beijing, 2007.
5. Ohta Mutsuo. On the Aging and Precipitation of Al–Ag and Al–Zn Alloys. *Mem. Sch. Eng. Okayama Univ.* **1966**, *1* (1), 134–137.
6. Silcock, J. M.; Heal, T. J.; Hardy, H. K. In *Aluminium*; Van Horn, K. R., Ed.; American Society for Metals: Materials Park, OH, 1967; Vol. 1, p. 123.
7. Naiqing Zhao; Genshun Ji; Gaofeng Quan; Hongyan Zhai. *Principle and Process of Heat Treatment*; Metallurgical Industry Press: Beijing, 2011.
8. Zhihui Li; Baiqing Xiong; Yongan Zhang; Baohong Zhu; Feng Wang; Hongwei Liu. Improvements in Strength and Electrical Conductivity in 7B04 Aluminum Alloy Pre-Stretched Thick Plates via Low-Temperature Retrogression and Re-Ageing Heat Treatments. *Mater. Sci. Forum* **2007**, *561*, 139–142.

9. Hosford, W. F.; Agrawal, S. P. Effect of Stress During Aging on the Precipitation of θ' in Al-4 wt pct Cu. *Metall. Trans. A* **1975**, *6* (3), 487–491.
10. Zhu, A. W.; Starke, E. A., Jr. Stress Aging of Al–xCu Alloys: Experiments. *Acta Mater.* **2001**, *49* (12), 2285–2295.
11. Zhu, A. W.; Starke, E. A., Jr. Stress Aging of Al–Cu Alloys: Computer Modeling. *Acta Mater.* **2001**, *49* (15), 3063–3069.
12. Hongwei Wang; Danqing Yi; Jinling Cai; Bin Wang. Effect of Stress Aging on Mechanical Properties and Microstructures of 2E12 Aluminum Alloy. *Chin. J. Nonferr. Met.* **2011**, *12*, 005.
13. Dewhirst, B. A. *Optimization of the Heat Treatment of Semi Solid Processed A356 Aluminum Alloy* (Master thesis); Worcester: Worcester Polytechnic Institute, 2005. Available from: http://www.wpi.edu/ (accessed 30 March 2016).
14. Heinrich, M. *Optimisation of the Heat Treatment Cycles of CSIR Semi-Solid Metal Processed Al–7Si–Mg Alloys A356/7* (Ph.D. thesis); Pretoria: University of Pretoria, 2011.
15. Menargues, S.; Martín, E.; Baile, M. T.; Picas, J. A. New Short T6 Heat Treatments for Aluminium Silicon Alloys Obtained by Semisolid Forming. *Mater. Sci. Eng. A* **2015**, *621*, 236–242.
16. Nowak, M.; Golovko, O.; Nürnberger, F.; Frolov, I.; Schaper, M. Water–Air Spray Cooling of Extruded Profiles: Process Integrated Heat Treatment of the Alloy EN AW-6082. *J. Mater. Eng. Perform.* **2013**, *22* (9), 2580–2587.
17. Kotov, V. V.; Sergeeva, K. I.; Troyanov, V. A.; Belikov, S. V. Use of Mathematical Modeling in Selecting a Heat-Treatment Regime. *Metallurgist* **2015**, *58* (11–12), 1011–1018.
18. Di Russo, E.; Conserva, M.; Gatto, F.; Markus, H. Thermomechanical Treatments on High Strength Al–Zn–Mg(–Cu) Alloys. *Metall. Mater. Trans. B* **1973**, *4* (4), 1133–1144.
19. Rahimi, B.; Khosravi, H.; Haddad-Sabzevar, M. Microstructural Characteristics and Mechanical Properties of Al-2024 Alloy Processed via a Rheocasting Route. *Int. J. Miner. Metall. Mater.* **2015**, *22* (1), 59–67.
20. Ranganatha, R.; Kumar, V. A.; Nandi, V. S.; Bhat, R. R.; Muralidhara, B. K. Multi-Stage Heat Treatment of Aluminum Alloy AA7049. *Trans. Nonferr. Met. Soc. China* **2013**, *23* (6), 1570–1575.
21. Holmen, J. K.; Johnsen, J.; Jupp, S.; Hopperstad, O. S.; Børvik, T. Effects of Heat Treatment on the Ballistic Properties of AA6070 Aluminium Alloy. *Int. J. Impact Eng.* **2013**, *57*, 119–133.
22. Na Zhao; Yanqing Yang; Ming Han; *et al.* Finite Element Analysis of Pressure on 2024 Aluminum Alloy Created During Restricting Expansion-Deformation Heat-Treatment. *Trans. Nonferr. Met. Soc. China* **2012**, *22* (9), 2226–2232.
23. Songyi Chen; Kanghua Chen; Guosheng Peng; Le Jia; Pengxuan Dong. Effect of Heat Treatment on Strength, Exfoliation Corrosion and Electrochemical Behavior of 7085 Aluminum Alloy. *Mater. Des.* **2012**, *35*, 93–98.
24. Gaofeng Quan. *Design and Fabrication of Metal Matrix Composites*, 1st ed.; Science Press: Beijing, 2015.

2.14 Heat-Treating Copper and Nickel Alloys

AK Bhargava and MK Banerjee, Malaviya National Institute of Technology, Jaipur, India

© 2017 Elsevier Inc. All rights reserved.

2.14.1	**Introduction**	398
2.14.2	**Copper and Copper Alloys**	398
2.14.2.1	Copper Alloys	399
2.14.2.2	Homogenization	400
2.14.2.3	Annealing	401
2.14.2.4	Stress Relieving Treatment	405
2.14.3	**Heat Treatment of Copper**	405
2.14.3.1	Heat Treatment of Brasses	406
2.14.3.2	Heat treatment of Bronzes	409
2.14.3.2.1	Tin bronzes	409
2.14.3.2.2	Aluminum bronzes	409
2.14.3.2.3	Beryllium bronzes	410
2.14.3.2.4	Silicon bronze	414
2.14.3.3	Cupronickels	414
2.14.3.4	Chromium Coppers	414
2.14.3.5	Zirconium–Copper Alloys	414
2.14.3.6	Copper–Chromium–Zirconium Alloys	415
2.14.3.7	Copper–Nickel–Silicon–Chromium Alloy	415
2.14.3.8	Copper-Base Shape Memory Alloys	415
2.14.4	**Heat Treatment of Nickel Alloys**	416
2.14.4.1	Annealing	416
2.14.4.2	Solution Annealing	417
2.14.4.3	Stress Relieving	417
2.14.4.4	Stress Equalizing	417
2.14.4.5	Precipitation Hardening	417
2.14.4.6	Nickel-Base Superalloys	418
References		419

2.14.1 Introduction

Various heat treatment practices are employed for different copper alloys. In case of single-phase copper alloys, cold working is followed by recrystallization annealing for improvement of properties. However heat treatment of copper alloys is quite often critical. There are alloys like bronzes where microsegregation attracts special attention to the heat treater. Due to wide gap between liquidus and solidus lines the solidification of alloys like tin bronzes exhibits coring and so under such circumstances the homogenization treatment is called for. Again there are important duplex alloys like alpha–beta brass which may be subjected to hardening treatment. Annealing as a final heat treatment or as a means for stress relieving is not uncommon in copper alloys. Several copper alloys like copper–aluminum, copper–zinc–aluminum, and copper–aluminum–nickel show martensitic transformation. Also there are possibilities of formation of precipitates of intermetallics in many of these martensitic alloys; hence heat treatment of these alloys is judiciously decided depending upon the target microstructures and thus the properties. For example, in a shape memory alloy aging precipitate formation is not welcome in many cases whereas aging precipitates in similar alloys are made to be formed deliberately under demand of situations. So a wide variety of heat treatments are employable in copper alloys of different compositions and property requirements. It is for this reason, a detailed analysis of heat treatment practice, principles behind the evolution of microstructures, and the purpose thereof are presented in this chapter.

Nickel alloys, in general, contain alloying elements like copper, iron, chromium, etc. The single-phase alloys are subjected to recrystallization annealing following cold working. On the other hand solution treatment followed by aging is a very common heat treatment for important alloys like Monel, Inconel, Hastelloy, and others. In each case, there are specific criticalities with respect to proper microstructure achievement through heat treatment and a thorough understanding of the phenomenological issues concerning the above is required. It is for this reason the present chapter has dealt with the heat treatment practices of nickel alloys, the anticipated difficulties, and the required precautions to achieve the desired set of properties. Also the heat treatment of nickel-base superalloys are highlighted.

2.14.2 Copper and Copper Alloys

Copper is well known for its outstanding electrical conductivity which is just next to silver. Copper and its alloys possess excellent corrosion resistance and ease of forming and

 doi:10.1016/B978-0-12-803581-8.09196-7

finishing. Its face-centered cubic (f.c.c) structure accounts for its good ductility. Other distinguishing properties exhibited by copper include very good thermal conductivity and non-magnetic properties. The heat treatment and consequent changes in properties of copper and its alloys are elaborately discussed in subsequent sections. The major commercial grades of copper are:

- oxygen free high conductivity copper (OFHC);
- tough pitch copper; and
- phosphorous deoxidized copper.

'OFHC' is the highest purity copper with at least 99.98% purity. Its electrical conductivity is equivalent to 101% International Annealed Copper Standard (IACS). It is also called as electrolytic tough pitch copper with oxygen content of 0.02–0.05% as Cu_2O. **Figure 1** is the microstructure of cast wire bar of tough pitch electrolytic copper (99.95% Cu; 0.03% O_2) showing the presence of Cu_2O in the interdendritic region. Because of its high purity,electrolytic tough pitch copper is the most expensive among all grades of copper and therefore its applications are limited to electrical industries.

'Tough pitch copper' is produced by the process of fire refining. It contains about 0.04–0.08% oxygen in the form of Cu_2O (0.4–0.8% Cu_2O). Its electrical conductivity is equivalent to 100% IACS conductivity. This copper is tough. The lower the oxygen content of this copper, the higher the so-called 'pitch' and vice versa, hence the term 'tough pitch.' Tough pitch copper is susceptible to hydrogen embrittlement.

'Phosphorous deoxidized copper' is another grade of fire refined copper which is deoxidized by phosphorous. As small as 0.04% phosphorous is retained in this copper which lowers the conductivity of copper to 85% IACS. This grade of copper has good hot and cold workability and is not susceptible to hydrogen embrittlement.

The other grades of copper include silver-bearing copper (7–30 oz t^{-1} of silver), arsenical copper (about 0.3% As) and free cutting copper (about 0.6% tellurium).

2.14.2.1 Copper Alloys

The major copper alloys are the following:

1. Brass:
   A. Single-phase alpha brasses (up to 36% Zn). There are two categories of alpha brasses namely; red brass (5–20% Zn) and yellow brass (20–36% Zn).
   B. Two phase α–β brasses (54–62% Zn).
2. Bronzes:
   A. tin bronze,
   B. silicon bronze,
   C. aluminum bronze, and
   D. beryllium bronze.
3. Cupronickel.
4. Nickel–silver alloys – these are also called nickel brasses. These are the alloys containing copper, nickel, and zinc. Though they do not contain silver, they have an attractive silver luster and therefore termed as nickel–silver alloys. They have moderately high strength and good corrosion resistance.

The term bronze is used to any alloy of copper containing principal alloying element (up to 12%) other than zinc or nickel. The term was originally applied to those copper alloys which contained tin as the sole or principal alloying element. Commercial bronzes are principally the alloys of copper with tin, silicon, aluminum, or beryllium as alloying element.

The commonly employed heat treatment processes to copper and its alloys are:

- homogenizing,
- annealing,
- stress relieving, and
- precipitation hardening.

Most of the copper alloys are single-phase solid solutions and are non hardenable by heat treatment. Therefore first three heat treating processes are used for these alloys as the case may

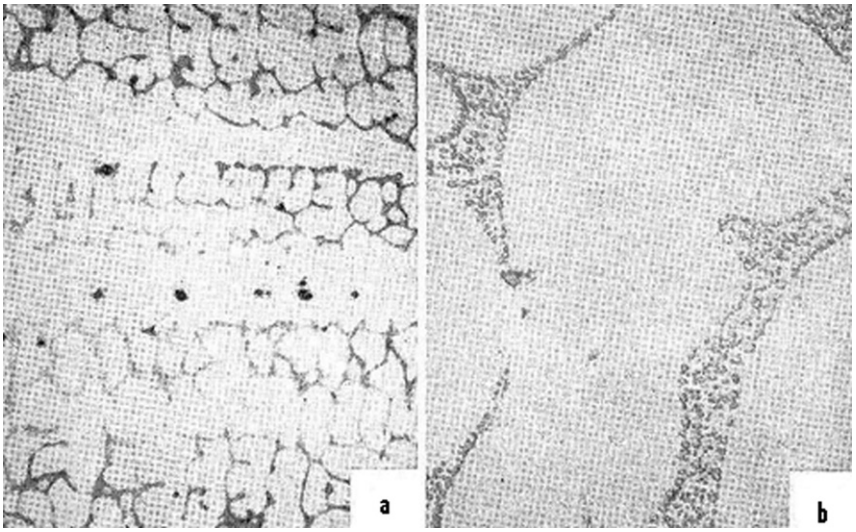


Figure 1 Microstructure of cast tough pitch electrolytic copper showing (a) cells of dendrites (the intersections of dendritic arms with surface of polish) and Cu_2O particles outlining the dendritic cells. The black spots are pores or holes in the cast metal; $\times$ 50, (b) same as in (a) at higher magnification ($\times$ 500). Cu_2O particles are resolved clearly and are seen to be of globular morphology.[1]

be. A brief account of these heat treatments in context with copper alloys is given in the subsequent sections with reference to the corresponding phase diagrams.

2.14.2.2 Homogenization

Homogenization treatment is very commonly applied to castings and cast billets of copper alloys. In this treatment, the cast alloy is heated to a temperature high enough so that diffusion of atoms within the alloy is relatively rapid, but still safely below the nonequilibrium solidus, so that burning of the alloy does not occur. The nonequilibrium solidus temperature depends on the composition of the alloy, its nature, so on. If burning occurs, the shape of the casting is impaired and physical properties also deteriorate. The alloy is held at this temperature for a long period of time depending on the freezing range of the alloy and massiveness of the casting so that the micro-segregation or the so-called coring is eliminated or at least reduced to a great extent. The alloys having wide freezing ranges such as tin (phosphor) bronzes, silicon bronzes, and copper–nickel alloys are invariably cored after solidification under industrial practice. Though commercial copper-base alloys such as α-brasses, α-aluminum bronzes, and beryllium bronzes are also cored, the degree of microsegregation is less. In these alloys, coring is generally eliminated during primary mill processing followed by normal annealing process. Formation of a cored dendritic structure during solidification of castings under nonequilibrium conditions, as in industrial practice, is very common in solid solution alloys. Solid solution crystals usually grow as dendrites. There is large concentration gradient of alloying elements from interior of the dendrite (called core which forms at higher temperature) to its surface which is lastly solidified at lower temperature. This results in coring. The core is enriched with respect to high melting constituent that raises the solidus point while the surface of the dendrite is richer in low melting constituent of the alloy that lowers the solidus point. That is, during nonequilibrium cooling solidification range is widened. Because of the large difference in composition of alloy constituents these portions tend to etch differently and an etched microsection may reveal inhomogeneous composition within a dendrite or grain. **Figure 2** is the microstructure of as-cast 70:30 brass (cartridge brass) showing cored crystals of alpha-solid solution throughout. Apart from segregation of low melting alloy constituent in interdendritic region, a brittle excess phase may also appear which is a characteristic defect commonly associated with cast alloys. This inhomogeneity in composition increases with increasing cooling rate and it also depends on freezing range of the alloy. Such an inhomogeneous cast structure lowers several properties, viz., mechanical, physical, and chemical properties of the alloy. This structure leads to poor ductility and toughness due to frequent brittle phase formation in the interdendritic region. A concentration gradient between dendritic core and dendritic surface leads to the formation of galvanic microcouples which make the many commercial castings susceptible to intergranular corrosion. Because of the nonuniformity of composition across the casting, properties are also nonuniform. Coring can be eliminated by homogenization treatment during which the composition of the alloy is



Figure 2 Microstructure of as cast 70:30 brass; cored crystals of α-solid solution throughout.[2]

equilibrated and thus ductility, toughness, and corrosion resistance are improved. Also properties become uniform across the section of the casting.

The process of homogenization involves diffusion of atoms across concentration gradient. Diffusion of atoms occurs in both the directions, that is, from core to surface of dendrite and vice versa. Diffusion of atoms is thermally activated process and it increases exponentially with increasing temperature. Higher the temperature less will be the time of homogenization. Since diffusivity of atoms varies from alloy-to-alloy, the time and temperature required for homogenization also vary with the type of alloy. In addition, both these parameters vary with degree of segregation and grain size of the casting. High tin–bronzes (above 8% Sn) are well known for extreme segregation. Diffusion and homogenization are both slower and rather difficult in tin (phosphor) bronzes, silicon bronzes and copper–nickel alloys as compared to most other copper alloys. Therefore these alloys are usually subjected to prolonged homogenization treatment. In these alloys, temperatures of homogenization are generally kept about 50 °C below the solidus temperature (**Figure 3**) and the soaking time varies from 3–10 h or even more.

Figure 4 illustrates the effect of homogenization temperature on ductility, tensile strength (T.S.), and yield strength (Y.S.) of phosphor bronze containing 92 wt% Cu, 8% tin, and small amount of phosphorous and traces of other elements. The improvement of ductility with increasing temperature is apparent from this figure. Being a thermally activated process, the progress of homogenization is a function of both temperature and time. This effect has been illustrated by taking an example of another as cast copper alloy namely, 85% Cu–15% Ni in **Figure 5**.

The microstructure of the chill-cast 85% Cu–15% Ni alloy presented in **Figure 5** is composed of dendrites of single-phase α-solid solution. The dendritic coring is apparent in this

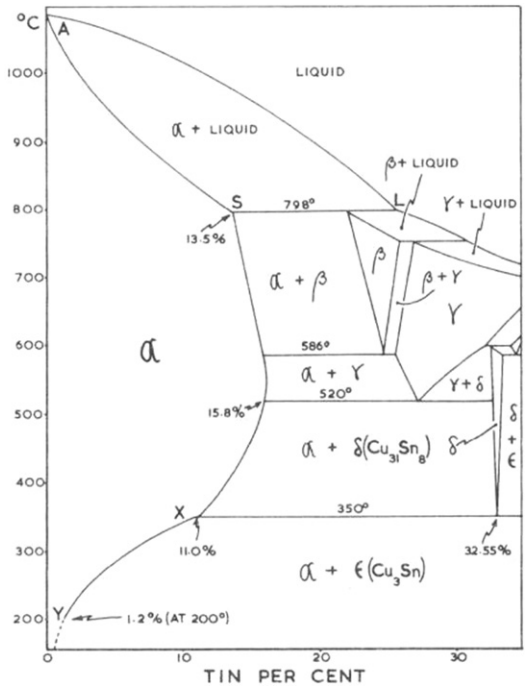


Figure 3 Copper-rich end of the copper–tin phase diagram.[2]

microstructure. When this alloy is homogenized at 750 °C for 3 h only a slight change in cored dendritic structure took place as shown in Figure 5. During annealing, the counter diffusion of atoms of nickel and copper between the nickel-rich cores and copper-rich surfaces of dendrites results in decrease of composition differences to some extent and thus slightly reduced the height of the hills and depth of the valleys. When both the temperature and time of homogenization of the above alloy increased to 950 °C and 9 h, a remarkable change in microstructure occurred as shown in Figure 5(c). The as cast dendritic structure is completely eliminated and a homogeneous grain structure has been developed. Grain boundaries are irregular in shape and are frequently encountered in the cast and homogenized solid solutions. Dark particles are inclusions of copper oxide or nickel oxide.

An initial cold work treatment is often given to cast ingot or billet. This helps in speeding up the homogenization process. Table 1 gives the schedule of homogenization treatment for some typical copper-base alloys.

2.14.2.3 Annealing

The principal heat treatment applied to pure copper and solid solution copper alloys is the recrystallization annealing following the cold working. Cold working is generally carried out

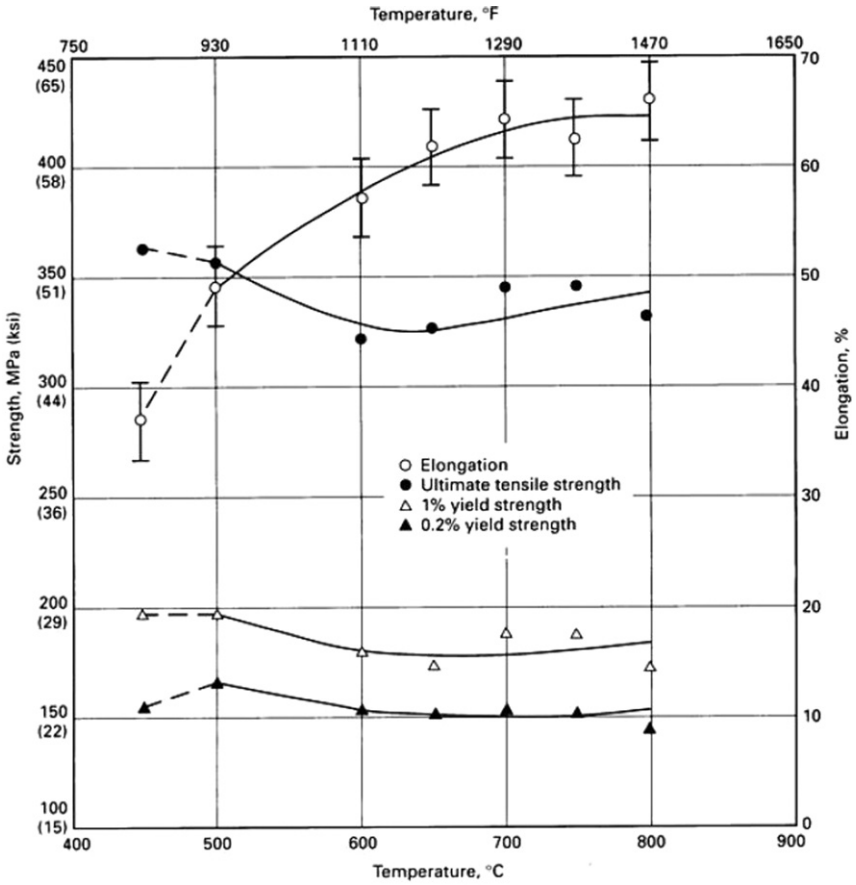


Figure 4 Effect of homogenization temperature on mechanical properties of C52100 (phosphor bronze, 92% Cu–8% Sn) alloy annealed for 4 h.[3]

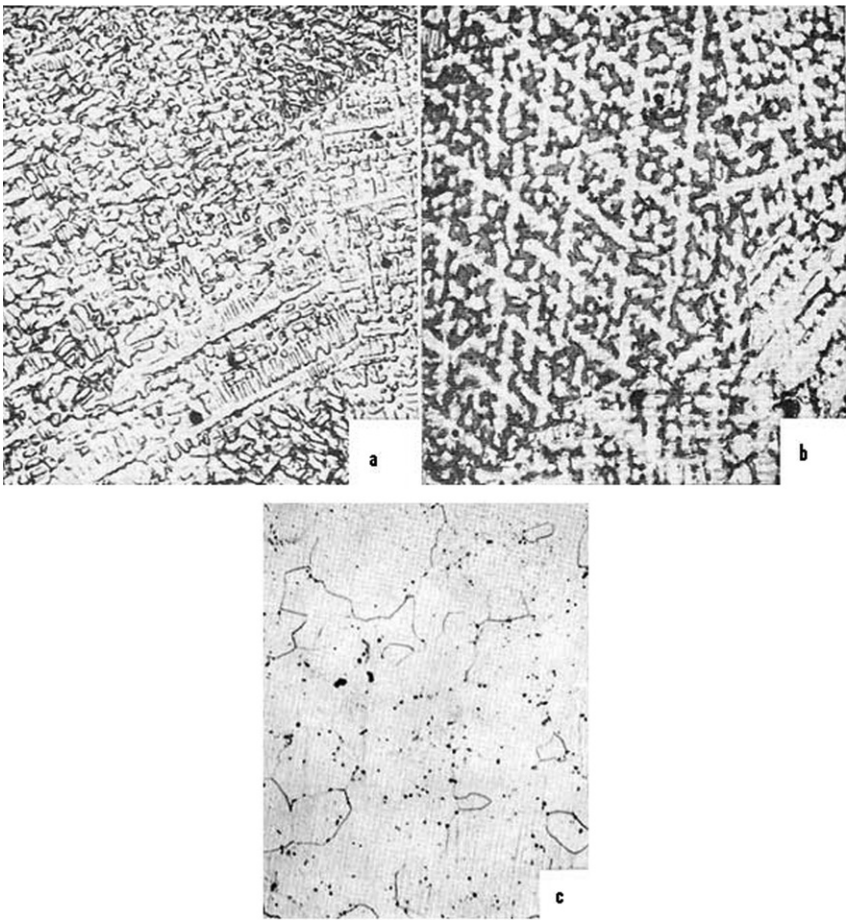


Figure 5 Copper–15% Ni alloy (a) chill cast; × 50, (b) same alloy heated for 3 h at 750 °C; × 50, and (c) heated for 9 h at 950 °C.[1]

Table 1 Schedule of homogenizing treatment for some copper alloys

Material	*Temperature (°C)*	*Time (h)*	*Remarks*
Copper–nickel–chromium alloy billets (alloy C71900) to prevent cracks, seams, etc.	1040–1065	4–9	To prevent cracks and seams
Phosphor bronzes (8–10% Sn) C52100 and C52400	775	5	To reduce embrittlement in billets and slabs that are to be cold formed
Cast cupronickels (70:30 Cu:Ni) C96400	1000	2	Protective atmosphere is to be used. The alloy is cooled to 400 °C in furnace and then in air

Source: Ref. [3].

below $0.4T_m$, where T_m is the melting temperature of the metal or alloy in Kelvin. Plastic deformation of polycrystalline metallic material not only causes a permanent change in its external shape but also brings about changes in internal structure. The internal structural change may be a change in shape and size of grains, generation of lattice imperfections, and development of a texture and so on. The principal kind of lattice imperfections generated during cold working are the dislocations. Of the lattice imperfections generated, dislocations are of great concern. Dislocation density is increased from as low as $10^{10}\,m^{-2}$ in annealed state to as high as $10^{16}\,m^{-2}$ in heavily deformed crystals.[4] All these imperfections produce a lot of lattice distortion and raise the internal energy of the metal or alloy. The type of distortion produced may vary with the type of deformation process such as rolling, swaging, forging, etc. Of the total energy expended in cold working, about 10% remains stored within the crystalline metal and the remaining is lost as heat. The major contributor to the stored energy (called inherent energy) is increased dislocation density. All these imperfections give rise to internal stresses. The increased internal energy makes the metal thermodynamically unstable at any temperature. The free energy of such a metal is higher than it is in as-annealed state. The change in size and shape of individual crystals (or grains) occurs through processes called slip and twinning. The principal process of plastic deformation is slip. Multiplication of dislocations on several slip systems upon plastic deformation leads to their interaction with each other and this restricts their

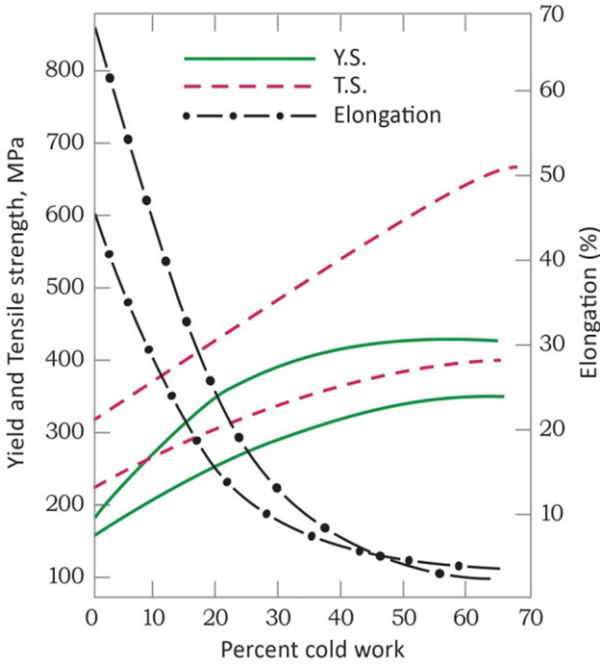


Figure 6 Effect of cold work on strength and ductility of copper and brass. The lower curves are for copper and the upper ones are for brass.

motion. The consequent effect is that for further plastic deformation to take place, higher magnitude of load or stress is required. The material is said to be work (or strain) hardened. Thus cold working results in increase of hardness, Y.S., T.S. but also reduction in ductility (or % elongation) and toughness of a ductile material. **Figure 6** illustrates the effect of percent cold work on strength and ductility of copper and brass. It also increases electrical resistivity because the increasing number of point and line defects incoherently scatters the movement of free electrons. In addition, the chemical reactivity also increases due to cold working.

In order to relieve internal stresses and to improve properties by way of microstructural refinement, the metal or alloy is subjected to annealing heat treatment. Stored internal energy is the driving force for a cold worked metallic material to undergo structural changes and to restore strain-free grains due to annealing heat treatment. Once the metal or alloy is annealed it becomes soft and ductile and is capable of deforming further if so required. When a series of cold reductions are needed, intermittent annealing processes are also required. One or more number of intermittent annealing may be required depending on the extent of reductions needed. Annealing may be a final heat treatment for the concerned metal or alloy in the final product form. When series of cold reductions are required, the first intermittent annealing is preferred to carry out at a temperature well above the recrystallization temperature to cause grain growth and achieve extra softness so that less work is required in the next cycle of cold reduction. But in such case, the temperature of subsequent annealing must decrease to attain a fine grain structure after last annealing process. For copper and brass mill alloys, grain size is the standard means of evaluating a recrystallization annealing.

The basic purpose of annealing is to soften and improve ductility of the copper and its alloys which has been work hardened so that further deformation can be facilitated. The process involves heating the cold worked metal to a temperature that produces recrystallization. Recrystallization temperature generally ranges from 0.3 to $0.6T_m$, where T_m is the melting temperature in Kelvin. Generally recrystallization process is carried out at about $0.4T_m$ or higher where migration of high-angle grain boundaries is possible. The factor $0.3T_m$ is common for pure metals after considerable amount of deformation. Recrystallization temperature is an indicator of the temperature at which a metal must be annealed to get the desired softness. This temperature depends principally on degree of prior cold working. Higher the degree of cold working, lower is the temperature of recrystallization. As the degree of cold working increases, the number of lattice defects also increases which in turn makes the metal thermodynamically more unstable as mentioned earlier. Hence recrystallization occurs at a lower temperature and in shorter time. **Figure 7** illustrates the effect of prior cold work on annealing behavior of pure copper. If the degree of cold working is less than about 10%, recrystallization generally does not occur. The recrystallization temperature is high if the degree of cold working falls in between 10 and 20%. A minimum of 20% cold reduction is normally required for recrystallization. In many instances a high degree of cold working is desirable to achieve a fine grain structure after final annealing. Since the rate of diffusivity of atoms increases with increasing annealing temperature, a shorter annealing time (t) is required for a given degree of cold working at higher annealing temperature (T). The incubation period is also shorter at higher annealing temperature and high degree of cold working. This time t of recrystallization is expressed as[5]:

$$t = t_0 \exp(Q/RT) \quad [1]$$

where t_0 is a constant, Q is activation energy for recrystallization and R is universal gas constant. Both t_0 and Q vary with temperature. During recrystallization, strain-free new crystals are formed at the expense of distorted grain structure. The process comprises of two steps, namely, nucleation and growth. Nucleation of new crystals takes place preferentially at grain boundaries and twin boundaries. Higher the degree of cold working higher will be the rate of nucleation (N) and less will be the rate of growth (G) of new nuclei. Hence finer will be the grain size. Similarly a higher rate of heating results in higher N and therefore favors the formation of fine grain size after recrystallization gets over. After recrystallization, a uniform grain structure is obtained. Grain size is the standard means of evaluating a recrystallization anneal in copper and brass mill alloys. This process of recrystallization is often called primary recrystallization.

The presence of impurities also affects recrystallization temperature. Very pure metals have a lower recrystallization temperature than impure metals.[4] Even a very small concentration of solute atoms raises the recrystallization temperature, the degree of rise being dependent significantly on the nature and concentration of solute atoms. As the solute concentration increases, recrystallization temperature rises to a maximum at certain value of solute content. With further

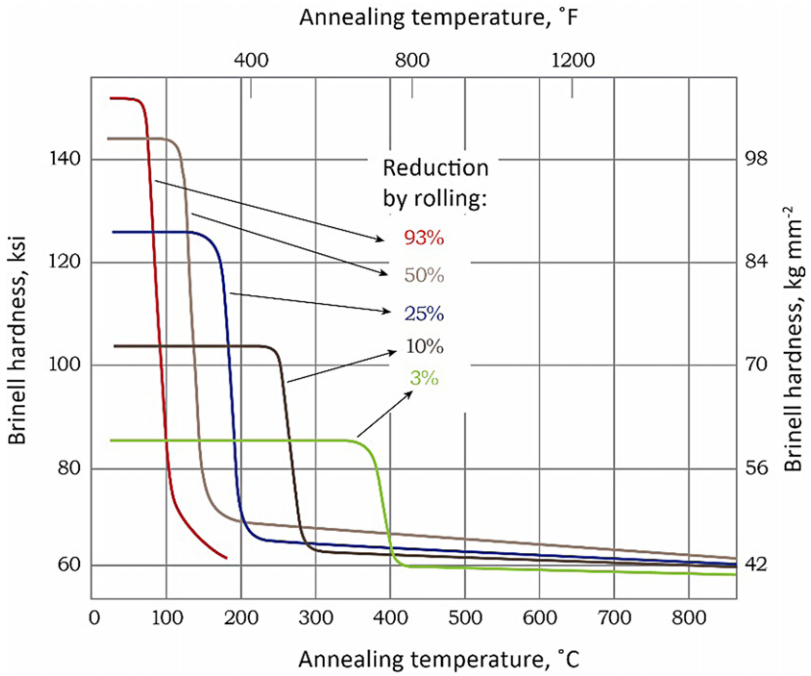


Figure 7 Effect of degree of cold working on the annealing process of pure copper.[3]

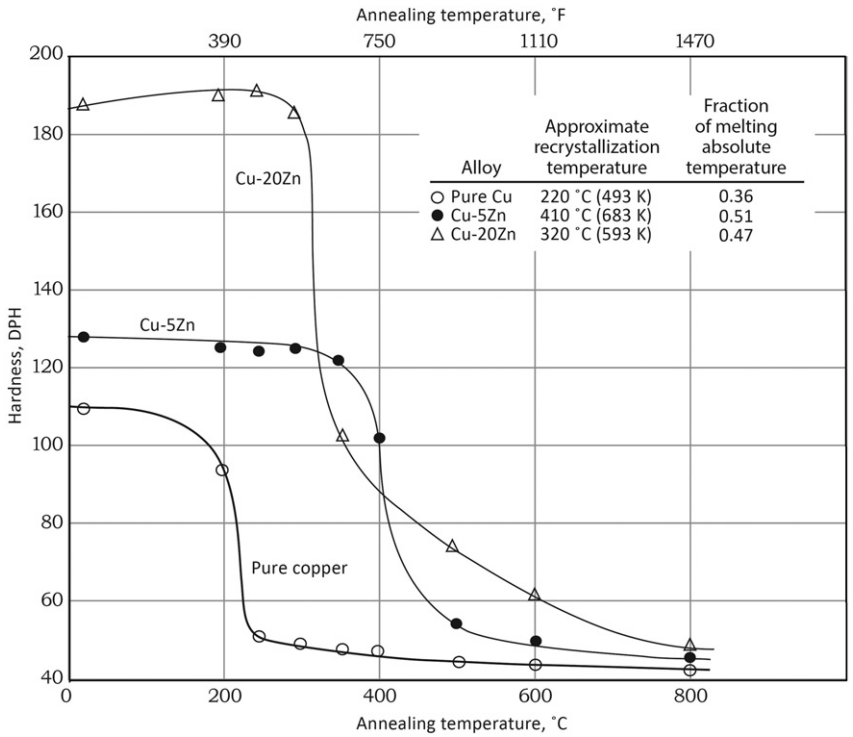


Figure 8 Illustration of effect of zinc content in copper on annealing process. The alloys were cold worked to 60% reduction in thickness at 25 °C.[3]

increase of solute concentration, the recrystallization temperature decreases. This is illustrated in Figure 8. It can be noted from this figure that as the concentration of zinc exceeded about 10%, recrystallization temperature decreased. The increase in recrystallization temperature at lower solute content is believed to be due to strain aging effect.

At low concentration, solute atoms form Cottrell atmospheres around dislocations. These atmospheres restrict the

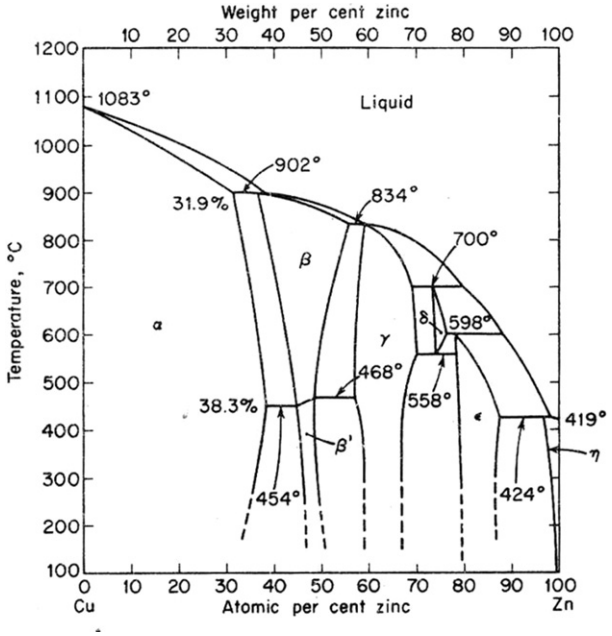


Figure 9 Copper–zinc phase diagram.[1]

movement and rearrangement of dislocations, which is required for the formation of recrystallization nuclei. Solute atoms are also attracted toward grain boundaries. Atoms at grain boundaries also retard their movement and thereby retard nucleation and growth of recrystallization nuclei. When solute concentration increases, saturation occurs at these sites and further increase of recrystallization temperature becomes improbable. Melting temperature of Cu–Zn alloys decreases with increasing concentration of zinc (**Figure 9**). This is the reason for lowering of recrystallization temperature of brasses when zinc content exceeds about 20%. Thus a small concentration of solute atoms is able to raise recrystallization temperature. For instance, an addition of 0.05% silver to copper is able to raise the recrystallization of temperature of pure copper from 140 °C to about 340 °C. In case of copper–zinc alloys, addition of zinc up to about 10% raises the activation energy for mobility of solute atoms and thereafter it decreases as its concentration is increased up to 20% in copper.

2.14.2.4 Stress Relieving Treatment

As the name implies, stress relieving treatment is applied to shaped articles in which the stresses are introduced during fabrication processes. These stresses called residual stresses are frequently tensile in nature and may be introduced during machining, cutting, welding, brazing, casting, or mechanical shaping processes of fabrication. In context of copper and its alloys, this treatment is very commonly used for relieving residual stress of cold formed parts. Cold forming is done to improve strength and hardness of the part or component due to strain hardening effect but at the same time ductility is reduced. Since cold forming is associated with generation of host of crystal imperfections, in particular, the dislocations, the elastic strain, and residual stresses are left in the part after forming operation. If these residual stresses are tensile in

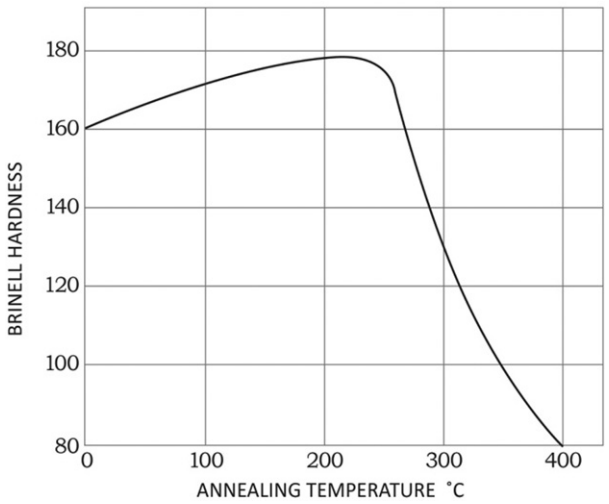


Figure 10 The relationship between hardness and annealing temperature for cartridge brass.[2]

nature and are of sufficient magnitude, these may cause stress corrosion cracking while the parts are stored in warehouse for relatively long periods of time or otherwise exposed to specific environments during service.

For instance, in brasses containing more than 15% zinc, stress corrosion cracking (also popularly known as season cracking) can occur if sufficient magnitude of residual tensile stresses is left from the previous cold forming operation and if the part is exposed to an environment containing traces of ammonia. The problem of season cracking is more pronounced with the cold formed brass parts such as caps, cartridge cases for rifles, caps for incandescent lamps, pipes for air-coolers, etc. Stress relieving heat treatments are carried out by heating the parts, generally, to below the annealing temperature that do not cause recrystallization and hence softening of metal. The properties that are derived due to cold working should not be affected significantly following stress relieving treatment. For this, the temperature of the stress relieving treatment must be kept low but then time must be prolonged to achieve relief of residual stresses. In fact lower temperature stress relieving treatment (generally up to the partial recovery stage of annealing during which excessive point imperfections are eliminated) causes a slight improvement of hardness and strength of heavily deformed alloy. This is illustrated for cold worked 70:30 brass in **Figure 10**. Seemingly, this is due to strain aging effect. Percentage elongation remains unaffected. Stress relieving treatment allows higher external loads to be applied, increases fatigue resistance and impact strength, lowers the susceptibility to brittle fracture, intercrystalline corrosion, and prevents warpage.

2.14.3 Heat Treatment of Copper

The principal heat treatment applied to pure copper is recrystallization annealing following the cold working. Though recrystallization temperature of pure copper is taken as 270 °C ($0.4T_m$), in practice the recrystallization of pure copper is carried out at much higher temperature. The

principal reason is to reduce the time of recrystallization and hence to economize the process. In practice, most recrystallization treatments of pure copper are carried out in air in the temperature range of 375–700 °C. The intermediate temperature, that is 600 °C, is very common. The temperatures used for annealing various grades of cold worked copper are given in Table 2. In the annealed state electrolytic tough pitch copper (C11000) possesses Y.S. of 69 MPa, T.S. of 220 MPa and percent elongation of 45 (in 50 mm gage length of specimen).[6]

However, time and temperature must be controlled to avoid danger of grain growth. A temperature greater than 700 °C is avoided to prevent excessive oxidation of copper (Figure 11). Once recrystallization gets over, copper is quenched in cold water such that the oxide scales formed at the surface may completely flake off, leaving behind a very clean shiny surface of pure reddish copper. In case of annealing oxygen bearing copper, hydrogen in the furnace atmosphere must be maintained to a minimum value to avoid any embrittlement. For instance, when annealing temperature is less than about 480 °C the hydrogen content of the atmosphere should not exceed 1%.

2.14.3.1 Heat Treatment of Brasses

Like pure copper, single-phase alpha brasses are frequently subjected to recrystallization annealing treatment. In fact a single-phase alloy does not undergo any phase transformation; therefore structural refinement through recrystallization of cold worked alloy remains the only means of toughening. Controlled degree of recrystallization or recovery fixes the magnitude of hardening by cold working. It is to be understood that intensive strengthening of single-phase alloy can lead to work softening and to avoid this, low temperature annealing is carried out. Since alloying elements raise the recrystallization temperature, cold worked alpha brasses are generally recrystallized in the temperature range of 700–730 °C. In case the temperature of recrystallization annealing exceeds 700 °C, the furnace atmosphere must be controlled to overcome the problem of excessive oxidation as well as discoloration of the surface. The recrystallization annealing temperatures of some representative brasses (wrought) are given in Table 3. Figure 12 illustrates the microstructural

Table 2 Annealing temperatures for various grades of cold worked copper

Wrought copper	*Common name*	*Temperature (°C)*
C10100–C10300	Oxygen free high conductivity copper (99.9% Cu)	375–650
C10400–C10700	Oxygen free silver-bearing copper	475–750
C10800	Oxygen free low phosphorous copper	375–650
C11000	Electrolytic tough pitch copper	250–650
C11100	Electrolytic tough pitch, anneal-resistant copper	475–750
C11300, C11400, C11500, and C11600	Silver-bearing tough pitch copper	400–475
C12000	Phosphorous deoxidized copper, low residual copper	375–650
C12200	Phosphorous deoxidized copper, high residual copper	375–650
C12500, C12700, and C1300	Fire refined, tough pitch copper with silver	400–650
C14500	Phosphorous deoxidized, tellurium copper	425–650
C14700	Sulfur copper	425–650

Source: Ref. [3].

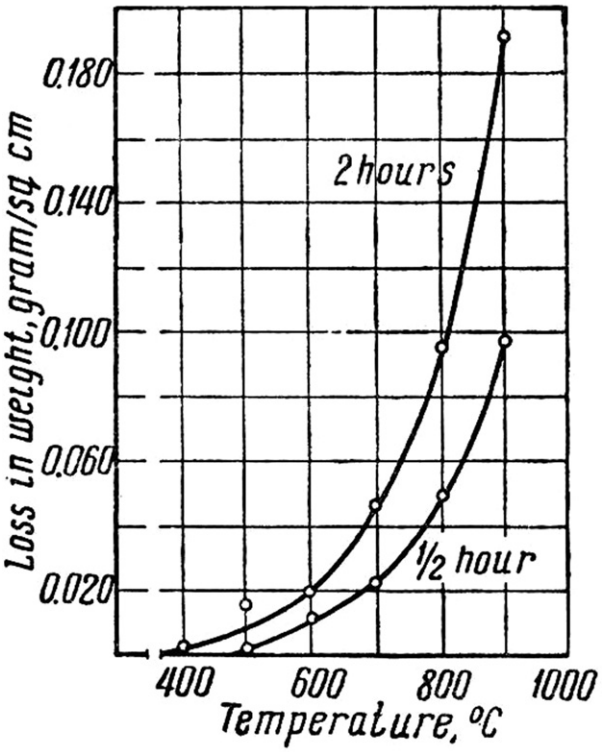


Figure 11 Effect of annealing temperature upon oxidation of copper.[7]

Table 3 Annealing temperatures for some representative cold worked brasses

Alloy	*Temperature (°C)*
Gilding metal (95Cu–5Zn): C21000	425–800
Commercial bronze (90Cu–10Zn): C22000	425–800
Red brass (85Cu–15Zn): C23000	425–725
Low brass (80Cu–20Zn): C24000	425–700
Cartridge brass (70Cu–30Zn): C26000	425–750
Yellow brass (Cu–20–36 Zn): C26800, C27000, and C27400	425–700
Muntz metal (60Cu–40Zn): C28000	425–600
Free cutting brass (61.5Cu–35.5Zn–3Pb): C36000	425–600
Forging brass (60Cu–38Zn–2Pb): C37700	425–600
Naval brass (60Cu–39.25Zn–0.75Sn): C46200, C46400, and C46700	425–600

Source: Ref. [3].

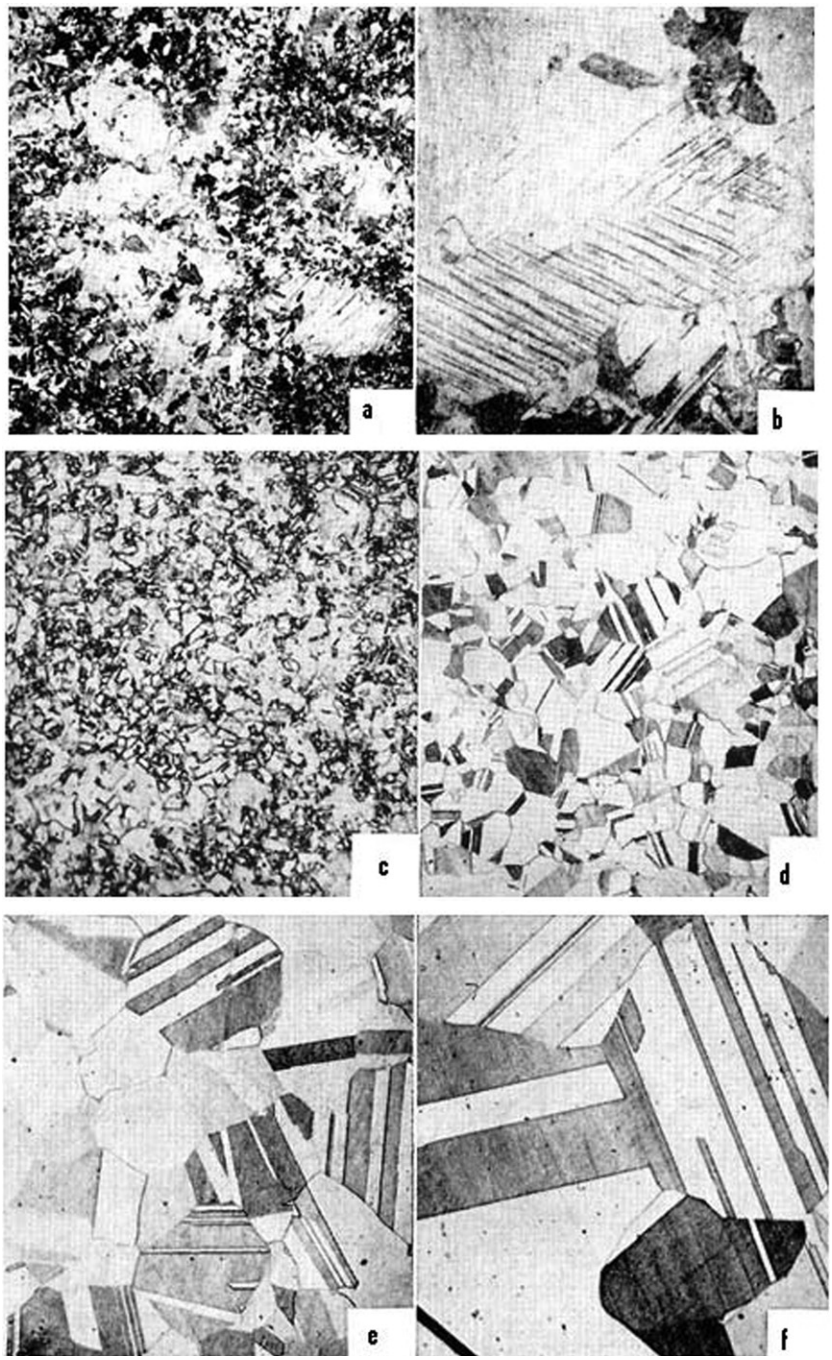


Figure 12 Alpha brass cold-rolled 60% and annealed for 30 min at (a) 300 °C, × 75, (b) same at higher magnification (× 500) where the structure of new crystals is somewhat better resolved, (c), (d), (e), and (f) at 400, 500, 650, and 800 °C, respectively at × 75.[1]

changes that occurred in cold-rolled (60%) α-brass with increasing temperature of annealing for a fixed time of 30 min. It can be noted that recrystallization is almost completed after annealing at 400 °C. Further increasing of temperature of annealing resulted in grain coarsening. Figure 12(a) shows tiny new crystals which are not resolved very well here and some areas of the cold deformed structure containing strain markings are also evident. Figure 12(b) is the same microstructure as in Figure 12(a) with higher magnification (× 500) showing that new crystals resolved somewhat better. The average grain diameter of the new crystals found to be 2 μm. Figure 12(c) is the microstructure of the same specimen reheated for 30 min at 400 °C. At this temperature recrystallization has been completed and some grain growth has occurred. The grain size estimated to be about 20 μm. Same specimen when reheated for 30 min at 500 °C, the microstructure shows an additional grain growth with grain diameter of about 45 μm (Figure12(d)).

On annealing the same specimen at 650 and 800 °C, further grain coarsening is apparent from Figures 12(e) and 12(f). Grain size increased to about 150 and 250 μm, respectively.

Often a low temperature stress relieving annealing treatment is applied to alpha brass articles to relieve internal residual stresses generated during cold forming process. It has been observed that sometimes cold-formed alpha brass articles crack spontaneously without the influence of external stress, as for instance, when such articles are stored in warehouse. Examples of such articles include cartridge cases of rifles, brass caps, aircooler pipes, caps for incandescent lamps, etc. In the cold formed articles or parts, the residual stresses are mostly tensile in nature. When exposed to corrosive atmosphere, in particular, the atmosphere containing small amount of ammonia and sulfur dioxide (as usually found in industrial atmosphere), cracking in brass articles takes place at the grain boundaries. Such type of cracking is called season cracking. Figure 13 exhibits microstructure delineating stress corrosion cracking in an α-brass.

In order to eliminate the problem of season cracking, brass articles are often subjected to stress relieving at low temperature. However, this treatment is frequently accompanied with some reduction of hardness of brass; so the time and temperature of annealing is properly controlled to minimize reduction of hardness.

Dual-phase alpha–beta brasses are generally given a hardening treatment followed by tempering treatment. These alloys consist of 38–46% Zn (Figure 9). These alloys at ambient temperature have two phases namely α and β′. β′ phase is ordered CuZn intermetallic compound characterized by high hardness coupled with brittleness. β-phase, which is high temperature disordered CuZn is soft and allows hot working of the alloy.

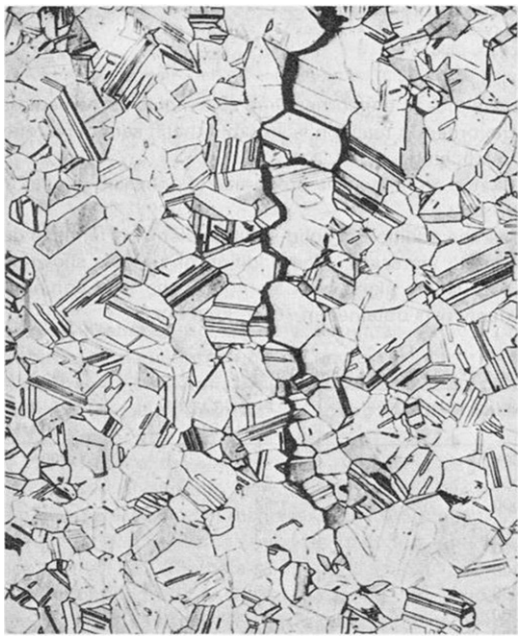


Figure 13 Stress corrosion cracking in alpha brass.[8]

Alpha phase is quite soft and ductile. Most widely used α–β′ brass is well known Muntz metal. Hardening of this alloy involves heating to about 850 °C where single-phase β exists. This is followed by quenching to room temperature. Quenching results in suppression of most of the α-phase while most β-phase is retained as is apparent from the microstructure of water-quenched Muntz metal shown in Figure 14. Subsequent tempering treatment in the temperature range of 100–500 °C results in more of the α-phase precipitated out from the supersaturated solid solution. Tempering curve shows a hardening peak at about 300 °C (Figure 15). Thus it is possible to heat treat alpha–beta brasses.



Figure 14 Microstructure of water-quenched Muntz metal. β′-phase is light and α-phase is dark.[8]

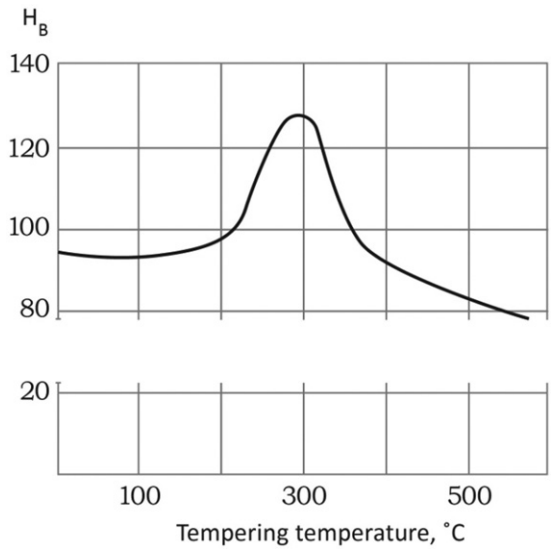


Figure 15 Tempering curve for α–β brass quenched from 850 °C.[7]

2.14.3.2 Heat treatment of Bronzes

2.14.3.2.1 Tin bronzes

Tin bronzes are also called as 'phosphor bronzes' due to the presence of small amount (0.01–0.5%) of phosphorous used as deoxidizer in casting. The wrought alloys usually contain 1–10% tin. Copper containing up to about 6% tin are soft alloys whereas those containing more than 6% tin are hard. The copper-rich end of equilibrium phase diagram of Cu–Sn alloy shown in Figure 3 indicates a long freezing range over useful compositions. When an alloy containing about 6% tin is solidified under normal industrial conditions to ambient temperature, a high degree of coring results. This heavy coring arises due to very low diffusivity of copper and tin into each other. This low diffusivity of copper and tin into each other leads to formation of copper-rich α-dendrites surrounded by small particles of tin-rich δ-phase ($Cu_{31}Sn_8$) which is hard and brittle. The equilibrium ε-phase (Cu_3Sn) is suppressed due to sluggishness of structural changes below about 400 °C. As a result ductility of the casting is greatly reduced. In order to make this alloy amenable to cold working, prolonged homogenization treatment is applied to castings. Phosphor bronzes with 8–10% tin are homogenized in the temperature range of 700–775 °C for a period of 5–6 h to promote diffusion of copper and tin atoms. Eventually the δ-phase is dissolved and uniform α-phase is produced. Subsequent cooling is done quite rapidly to prevent the precipitation of ε-phase (Cu_3Sn). Thus uniform single-phase α is retained at ambient temperature. The homogenized alloys are ductile and therefore can be cold worked. The cold worked tin bronze (C50500) is annealed in the temperature range of 475–675 °C while other phosphor bronzes (C51000, C52100, and C52400) are annealed at 475–675 °C.

2.14.3.2.2 Aluminum bronzes

Like brasses, aluminum bronzes also fall in two categories: single-phase alpha-aluminum bronzes with less than about 8% aluminum and dual-phase alpha–beta aluminum bronzes with aluminum 8–12% plus small amounts of iron (0.5–5.0%), silicon (up to 2%), nickel (up to 5%), and manganese. Both iron and nickel improve strength and hardness and refines the grain but nickel is less effective than iron. Silicon imparts machinability while manganese promotes soundness in the casting. alpha-aluminum bronzes are ductile and therefore are cold workable. Cold working improves strength and hardness. Moreover, these bronzes possess good corrosion resistance against atmosphere and water. Single-phase alpha-aluminum bronzes containing iron up to about 3% are effectively strengthened by cold working. The structure consists of iron-rich particles in alpha phase. Annealing of alpha-bronzes is carried out in the temperature range of 550–870 °C. Iron containing alloys require annealing temperature at higher end of the range. Alloys without iron, are annealed in the temperature range of 595–650 °C. Aluminum bronze castings are annealed at 620–670 °C.

Alpha–beta aluminum bronzes are heat treatable. Their heat treatment can be explained with reference to copper-rich portion of the Cu–Al phase diagram (Figure 16). Consider the slow cooling of Cu–10% aluminum. Slow cooling to ambient temperature yields a dual-phase microconstituent composed of α and γ_2 (Cu_9Al_4). Upon reheating the alloy, the eutectoid $\alpha + \gamma_2$ start transforming to $\alpha + \beta$ above eutectoid temperature of about 565 °C. Further heating results in dissolution of α until at about 910 °C where the structure is composed of completely single-phase β solid solution. Quenching the alloy from this single-phase region from about 960 °C produces a nonequilibrium phase named β' called martensite; Figure 17 micrograph showing needle like martensitic microstructure.

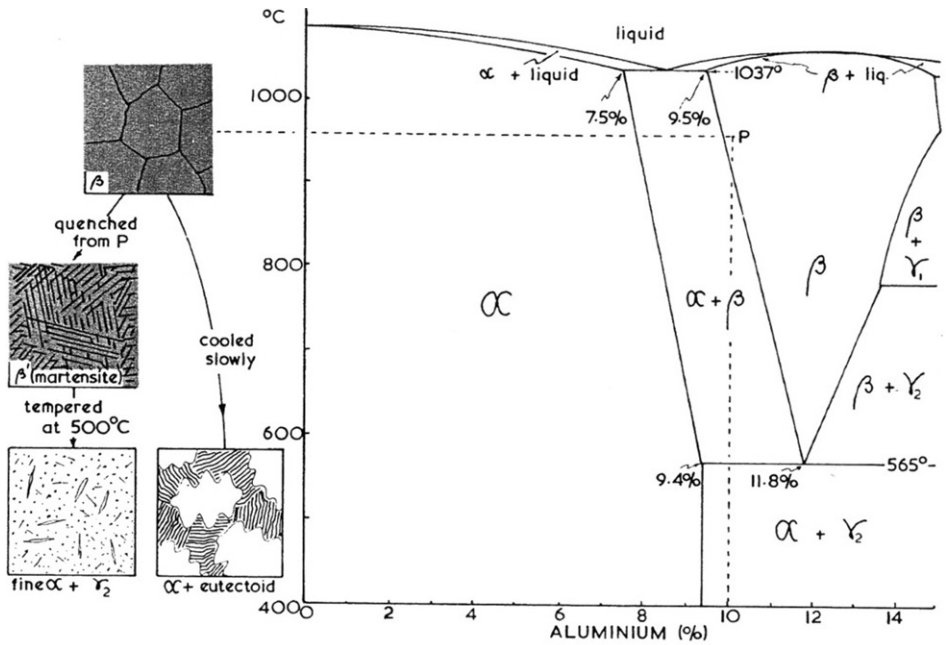


Figure 16 Cu–Al equilibrium phase diagram (copper-rich end). The microstructural sketches indicate the types of structures normally produced commercially.[2]

This martensite is similar to the martensite produced in steel and exhibit similar characteristics. Tempering of β' phase at about 500 °C results in precipitation of a fine aggregate of α and γ_2 phases (Figure 18).

2.14.3.2.3 Beryllium bronzes

The solubility of beryllium in copper decreases from about 2.7% at about 870 °C to about 0.2% at ambient temperature (Figure 19). This suggests that Cu–Be alloy is amenable to precipitation hardening. These alloys are also called beryllium bronzes or beryllium copper. The alloys of copper containing beryllium are perhaps the strongest among the family of copper-base alloys known. The T.S. of these alloys may range from 1300 to 1400 MPa after heat treatment. The high strength together with good electrical conductivity makes copper–beryllium alloys particularly suitable for electrical applications such as electrical contacts and relays. The high strength in these alloys is derived from heat treatment. Heat-treated alloys find wide applications as structural members in spacecraft and aircraft. These alloys are also used as non-sparking tools and springs. Spring properties of Cu–2.25Be–0.25Ni alloy approach those of steel springs together with nonrusting characteristics. Beryllium bronze containing about 2.25% Be are used where high strength is required. The response to precipitation hardening in these alloys is enhanced when a small amount (from 0.5 to about 2%) of nickel or/and cobalt is added to these alloys. The small amounts of elements act as grain refiners and they also increase the stability of the supercooled solid solution. A study carried out on Cu–(0.77–4.0%) Be alloys solution treated at 800 °C and aged at 350 °C for several hours shows that the alloy containing as low as 0.77 % beryllium does not respond to age hardening (Figure 20). On increasing the beryllium concentration a hardening peak is observed only when beryllium content is 2.39% or more. This suggests that copper–beryllium alloys with about 2.25% or more respond to effective age hardening. For this reason most of the commercial beryllium bronzes generally contain about 2% or more of beryllium though a significant hardening has been



Figure 17 Microstructure of 90:10 aluminum bronze water-quenched from 900 °C (showing martensitic β' structure).[2]



Figure 18 Microstructure of the same alloy as in Figure 17 after tempering at 500 °C showing tempered martensite. Martensitic β' transformed to a fine aggregate of $\alpha + \gamma_2$ structure.[2]

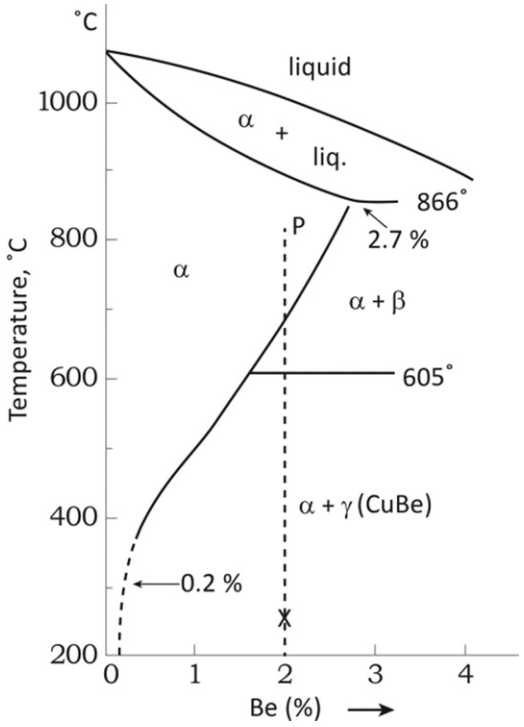


Figure 19 Equilibrium phase diagram of copper–beryllium alloy (copper-rich end).[2]

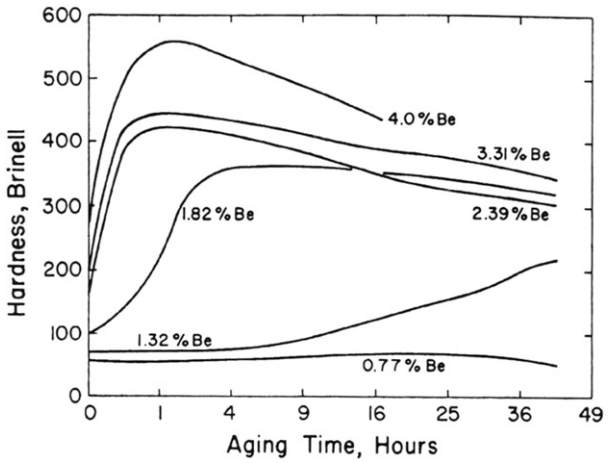


Figure 20 Aging curves of Cu–Beryllium alloys quenched from 800 °C and aged at 350 °C for various times.[9]

shown by Cu–1.82% beryllium after 4 h of aging. Commercially, copper–beryllium alloys are available in two basic classes, namely, high-strength copper beryllium and high-conductivity copper–beryllium alloys. The former alloys develop moderately high strength with good conductivity while the latter alloys develop good ductility with slightly lower level of strength after heat treatment. For high-strength beryllium bronzes, solution treatment is performed at a relatively lower temperature of 790 °C while high-conductivity beryllium bronzes are solution annealed at higher temperature, that is, at about 900 °C. Generally, the minimum specified solutionizing temperature is 700 °C (Figure 21, top). Any temperature less than the minimum specified may result in lower hardness after precipitation hardening treatment; this may be due to incomplete dissolution of alloy content in alpha phase. The alloys containing higher amount of cobalt are solution annealed in the temperature range of 750–950 °C (Figure 21, bottom). An excessive temperature above the upper specified limit may cause grain coarsening in wrought products and overheating in both wrought and cast products. Coarse grain size impairs the formability while overheating introduces brittleness and makes the alloy poor responsive to precipitation hardening. Solution annealing of beryllium copper requires careful control.

Soaking time is also of prime concern as it affects the enrichment of alpha-solid solution with respect to beryllium. Shorter times may result in undissolved beryllium rich phase in the α-solid solution. As a consequence the solid solution will be less enriched with respect to beryllium which in turn lowers the strength and hardness of the alloy after precipitation hardening treatment. Figure 22 is a microstructure of 97.5% Cu, 2.25% Be, and 0.25% Ni alloy quenched from the solution treatment temperature of 800 °C. The presence of undissolved β-constituent is evident in this microstructure. On the contrary, longer times may result in excessive grain growth, in particular, in thin sections of wrought alloys and oxidation as well.

It is recommended to allow a soaking time of 3–5 min for thin sections such as fine wire, 15 min–1 h for thin-walled tubes and small castings. Heavy sections (usually above

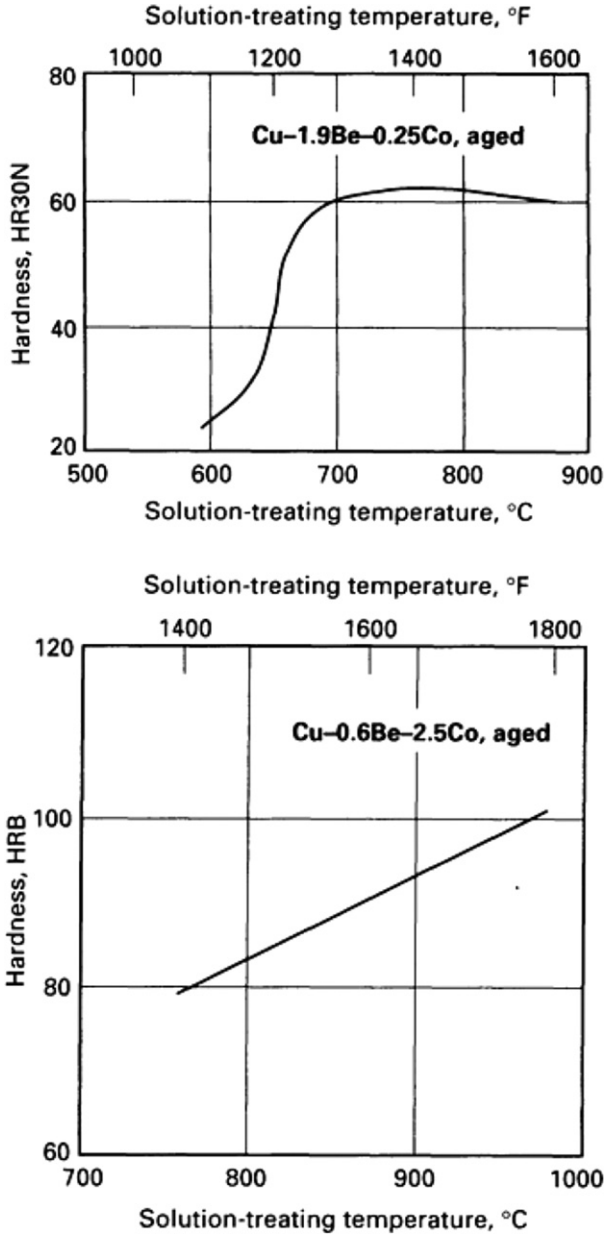


Figure 21 Effect of solution treatment temperature on hardness of C17200 and C17500 alloys after aging.[3]

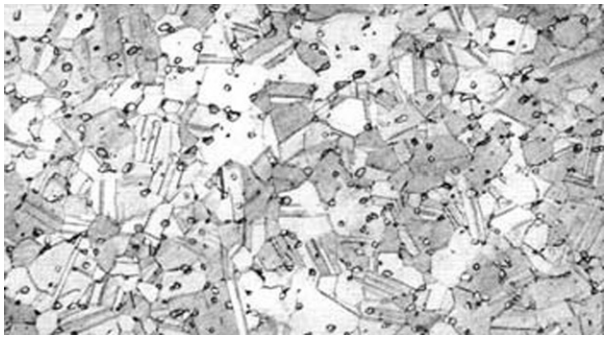


Figure 22 Microstructure of Cu–2.25Be–0.25Ni alloy after quenching showing presence of undissolved β-phase.[1]

about 25 mm) requires a soaking time of 1–3 h at the rate of 1 h duration for each 25 mm section thickness. As the cast structure contains large amounts of micro-segregation within the dendrites a prolonged time may be used for cast products to homogenize the structure. A minimum of 3 h of soaking at solution annealing temperature is recommended for castings. Often a nonoxidizing atmosphere, such as hydrogen, is desirable if solution annealing temperature is 800 °C or more. Under oxidizing atmosphere, oxygen may diffuse inward and oxidize beryllium, thereby cause the surface to remain soft after subsequent aging. The soft surface severely lowers fatigue strength, which is particularly detrimental when the alloy is used for corrosion resistant springs subjected to reversed stresses that are of highest in magnitude at the surface. Thus a careful solution annealing treatment is required to attain a desirable combination of mechanical properties, grain size, and dimensional tolerances without excessive oxidation. The oxide layer formed on the precipitation hardened parts can be removed by chemical treatment or by abrasive cleaning.

Following soaking, quenching operation constitutes the most important part of heat treatment in beryllium bronzes. Once soaking is over, the alloy is quenched immediately without any quench delay. Any delay may lead to partial precipitation. Quenching is recommended to be carried out at the highest possible rate so that there is minimum chance for precipitation of second phase; at the same time quenching must be not so high to cause distortion or warpage of the alloy part. In the as-quenched condition the alloy is supersaturated with respect to alloy content and is soft so that any cold forming (e.g., by forging, swaging, or machining), if needed can be performed at this stage. Most of the commercial beryllium bronzes are supplied in solution annealed or as-annealed and cold worked condition.

The copper–beryllium alloys are finally precipitation hardened by aging to attain the desired combination of mechanical and physical properties. The high-strength beryllium bronzes are generally aged to peak hardening condition. The alloys not aged to maximum strength and hardness are regarded as underaged while the alloys aged beyond the maximum achievable strength and hardness are termed overaged. Under aging (UA) copper–beryllium alloys results in improvement of toughness, uniform elongation, and fatigue strength. Overaging of the alloy increases its electrical and thermal conductivities and dimensional stability as well. Copper–beryllium alloys are not amenable to natural aging even after prolonged holding at room temperature. This is indicative of the fact that either Guinier–Preston (GP) zones are not formed in this alloy or the GP solvus is below room temperature; however further study in this regard is warranted. The allowable time of aging depends on the temperature of the furnace as well as on the requirement of properties. If the motive is to produce maximum hardness, at high aging temperature, a precise control of aging time is essential to avoid overaging. The aging temperatures for high-strength wrought copper–beryllium alloys generally vary from 260 to 370 °C. The time required to reach peak properties is lower at higher aging temperature than at the lower temperature. The time at aging temperature further depends on whether the alloy is only in as solution treated condition or it is cold worked too after solutionizing. The time of aging varies from 2 to 3 h. The lower time is preferred for cold-formed alloys. The standard age hardening cycle for high-strength castings alloys comprises of aging for 3 h at 320–340 °C. The standard precipitation hardening schedule for both wrought and cast high-conductivity beryllium bronzes is 2–3 h of aging at 480 °C. Solution treating and precipitation hardening treatment temperature and time for some beryllium bronzes are given in **Table 4**. All these alloys are rapidly quenched from the solution treating temperature. Thin sections such as strips can be cooled in circulating air. Heavier sections need water quenching. Further, shorter times at solution temperature are desirable to minimize the danger of grain coarsening, in particular for thin sections.

Table 4 Solution treating and precipitation hardening schedule of some beryllium bronzes

Alloy	*Solution treatment*		*Ageing treatment*	
	Temperature (°C)	*Time (h)*	*Temperature (°C)*	*Time (h)*
C17000	775–800	1/2–3	300–330	1–3
C17200	775–800	1/2–3	300–330	1–3
C17300	775–800	1/2–3	300–330	1–3
C17500	900–925	1/2–3	455–480	1–3
C17510	900–925	1/2–3	455–480	1–3

Source: Ref. [3].

The wrought alloys are frequently subjected to cold forming after the solution treatment and quenching. This influences the attainable strength after subsequent precipitation hardening treatment. The final attainable strength further varies with the degree of cold working carried out. The cold-work hard temper produces maximum strengthening effect after aging. **Figure 23** illustrates the aging time required for development of maximum strength in solution annealed, 1/4 hard, 1/2 hard, and hard C17200 (Cu–1.9% Be–0.2% Co + Ni) strip aged at various temperatures in a recirculating air furnace.

Table 5 gives the precipitation treatment and the resulting properties attainable in C17200 flat products. It can be noted that the strength properties of the solution-annealed alloy increases with increasing amount of cold deformation (1/4 hard, 1/2 hard, and hard) and concurrently the ductility property reduces significantly. There is not much decrease of electrical conductivity. The strength properties are superior when the alloy is aged at lower temperature for longer period of time than when aged at higher temperature for shorter times.

The above discussion shows that copper–beryllium alloys containing small amount of cobalt and nickel display a significant precipitation strengthening effect. However, their plasticity and toughness decrease significantly with improvement of strength after aging process, which compromises the safety of these alloys. Under different working conditions, there are often special requirements for the fatigue properties, toughness, formability, creep properties, and other properties of alloys. In order to meet these special requirements, a multistage aging process has been applied to Cu–(1.7–2.0%)Be–(0.2–0.3%)Ni–(0.1–0.2%)Co alloy by Yanchuan Tang *et al.*[6] to obtain multiple precipitation strengthening phases instead of single-stage peak

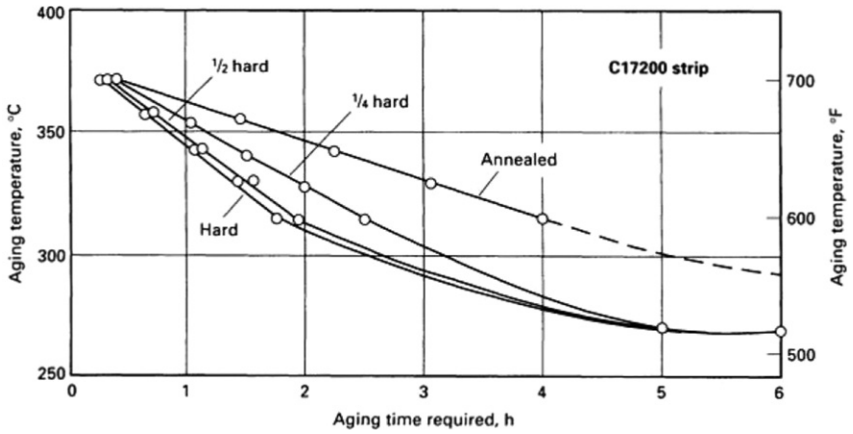


Figure 23 Aging temperature and time relationship for C17200 Cu–Be alloy strip showing aging time required to attain maximum strength in annealed, ¼ hard, ½ hard, and hard C17200 strip aged at various temperatures.[3]

Table 5 Mechanical properties of C17200 flat products after aging treatment

Initial condition	*Standard aging treatment*	*Properties*				
		Tensile strength (MPa)	*Yield strength (MPa)*	*% Elongation*	*Hardness (BHN)*	*Electrical conductivity (% IACS)*
Annealed	None	415–540	195–380	35–60	47–78	17–19
1/4 hard	None	515–605	415–550	10–40	68–90	16–18
1/2 hard	None	585–690	515–655	10–25	88–96	15–17
Hard	None	690–825	620–770	2–8	96–102	15–17
Annealed[d]	3, 315 °C	1140–1345	865–1205	4–10	35–40 HRC	22–25
Annealed	1/2 , 370 °C	1105–1310	895–1205	3–10	34–40 HRC	22–25
1/4 hard	2, 315 °C	1205–1415	1035–1275	3–6	37–42 HRC	22–25
1/4 hard[d]	1/3, 370 °C	1170–1380	965–1275	2–6	36–42 HRC	22–25
1/2 hard[d]	2, 315 °C	1275–1485	1105–1345	2–5	39–44 HRC	22–25
1/2 hard	1/4, 370 °C	1240–1450	1070–1345	2–5	38–44 HRC	22–25
Hard[d]	2, 315 °C	1310–1575	1140–1415	1–4	40–45 HRC	22–25
Hard	1/4, 370 °C	1275–1480	1105–1415	1–4	39–45 HRC	22–25

[d]Heat treatment that provide maximum strength.
Abbreviations: BHN, Brinell hardness number; IACS, International annealed copper standard; HRC, Rockwell C-scale hardness.
Source: Ref. [3].

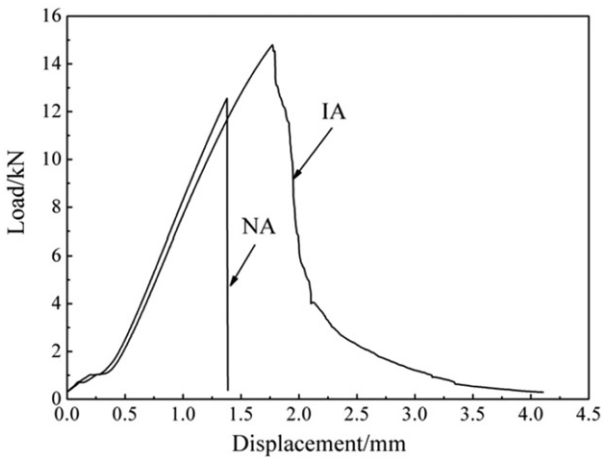


Figure 24 Load–displacement curve for the alloy Cu–Be–Ni–Co in interrupted aging (IA) and normal aging (NA) conditions.[6]

aging process. In this study, they solution annealed the alloy samples at 780 °C for 20 min, quenched in water to room temperature and applied three aging treatments: (1) UA at 320 °C for 30 min and quenched to room temperature, (2) normal aging (NA) at 320 C for 180 min and (3) interrupted aging (IA). Results of the tensile testing showed that the alloy under IA condition exhibited a marked hardening response though the yield and T.S. have been still slightly lower (only about 3%) than those of NA condition. However, the uniform elongation has been found to increase significantly (about 17%) after IA treatment as against the NA condition. The IA condition also increased the tension toughness of the Cu–Be–Ni–Co alloy suggesting its ability to resist crack propagation. Furthermore, the same alloy in the IA-treated condition displayed much superior fracture toughness than in NA condition as can be noted from the load–displacement curves shown in Figure 24.[6] Both the load required for fracture and the total energy absorbed during fracture have been found to increase by about 20% and more.

2.14.3.2.4 Silicon bronze

The solubility of silicon in copper is maximum (that is 5.3%) at about 852 °C and it decreases with decreasing temperature (Figure 25). The eutectoid reaction at about 555 °C is very slow and therefore under normal cooling conditions a single-phase α-solid solution is retained at ambient temperature in copper alloys containing less than 5% silicon. These alloys are termed as silicon bronzes. Being single-phase, these alloys are not susceptible to precipitation hardening. Mechanical properties of these alloys are comparable to those of mild steel and the corrosion resistance exhibited by these alloys is comparable to that of copper. The popular heat treatment applied to silicon bronzes is annealing treatment after cold working which is performed at 475–700 °C.

2.14.3.3 Cupronickels

Cupronickels are binary alloys of copper and nickel. Copper and nickel form a series of solid solutions. Accordingly these are single-phase alloys. Hence they are not susceptible to heat treatment. They can be hardened only by cold working. Commercial cupronickels generally contain up to 30% nickel. Cupronickels have high corrosion resistance together with resistance to corrosion fatigue. They also resist corrosive and erosive actions of rapidly moving seawater. The corrosion resistance of cupronickels increases with increasing nickel content. The electrical resistivity of these alloys also increases with increasing nickel concentration. Cupronickels are moderately hard also but tough and ductile. Cupronickels with 10 and 30% nickel are very commonly employed for condenser, distiller, evaporator, and heat exchanger tubes. The very common heat treatment applied to cupronickels is annealing after cold working. Annealing after cold working of cupronickels containing up to 30% nickel (Alloys C70600, C71000, and C71500) is performed at 600–825 °C.

2.14.3.4 Chromium Coppers

The phase diagram of copper–chromium (Figure 26) shows that the alloys containing chromium from 0.4 to 1.0% are characterized as precipitation hardening alloys.

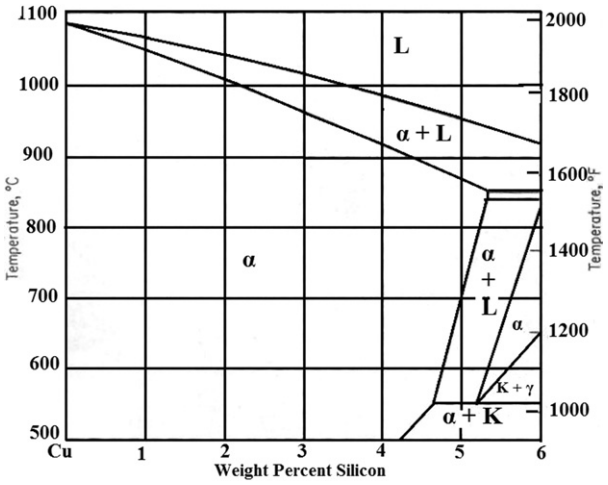


Figure 25 Copper-rich portion of the copper–silicon alloy system.[8]

In the precipitation hardened state these alloys display a reasonably good T.S. coupled with good electrical conductivity (80% IACS). These alloys are solution treated in the temperature range of 950–1010 °C where a single-phase is obtained and cooled rapidly after soaking. However due to differential melting temperatures of copper and chromium, there is a preferred chromium–chromium coordination in the solidified alloy which influences the subsequent aging treatment in a great way. Unless proper care is taken, nonuniform distribution of precipitates may quite often result in the final microstructure. Solution treatment is generally carried out in a controlled atmosphere or in salt bath in order to prevent scaling and internal oxidation. In the solution treated condition the alloys are soft and ductile and therefore can be cold formed if desired. Following this, aging is carried out in the temperature range 400–500 °C for several hours (typically 4 h or even more) depending on the combination of strength and electrical conductivity required. A typical aging cycle is 450 °C, 4 h or more.

2.14.3.5 Zirconium–Copper Alloys

Copper alloys containing 0.13–0.3 % zirconium are solution treated at 900–980 °C and quenched rapidly (as in water). Aging is performed at 500–550 °C for 1–4 h. The strengthening is imparted by coherent Cu_3Zr-type precipitates. It is recommended to minimize the holding time at solution annealing temperature so as to eliminate the danger of excessive grain growth which may occur due to high diffusivity of zirconium at this temperature. Because of the high diffusivity of zirconium at solutionizing temperature, it requires less time for dissolution and hence there is no need for longer soaking time. Moreover, excessive time of soaking may cause internal

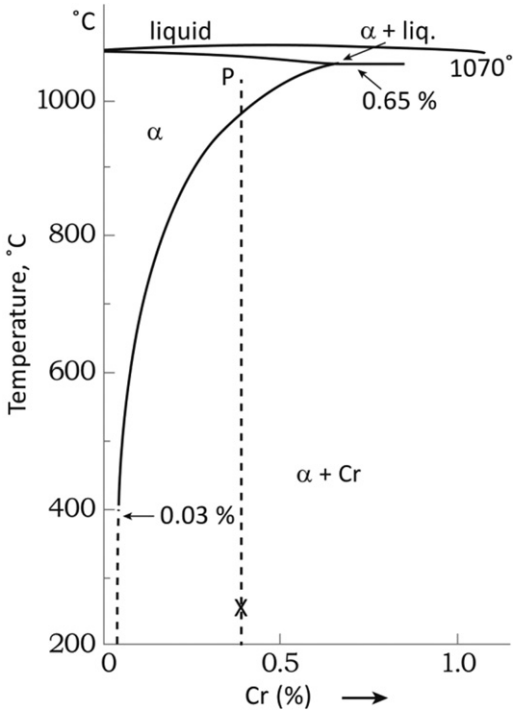


Figure 26 Equilibrium phase diagram of copper–chromium alloy (copper-rich end).[2]

oxidation by reaction of zirconium with the furnace atmosphere. If desired, cold working can be done before aging. In such condition, aging temperature may be reduced to the level between 375 and 475 °C. Prior cold working provides more nucleation sites for precipitation at dislocations and thus accelerates aging.

Other single-phase copper alloys namely cupronickels (10–30% Ni) and nickel–silver alloys are generally annealed after cold working in the temperature range 600–825 °C. Silicon bronzes are annealed at 475–700 °C.

2.14.3.6 Copper–Chromium–Zirconium Alloys

Copper–chromium–zirconium alloys are precipitation hardening alloys developed for high temperature applications where material must meet an optimum combination of mechanical properties coupled with high electrical and thermal conductivities. These alloys derive the best combination of physical and mechanical properties through precipitation hardening treatment. The heat treatment consists of solution treatment followed by rapid quenching (as in water bath), cold working, and aging. The schedules of heat treatment of two Cu–Cr–Zr alloys are given in **Table 6** and the resultant properties are given in **Table 7**. Both these alloys exhibit comparable mechanical property values but the latter alloy displays high electrical conductivity after identical heat treatment. Strengthening in these alloys results due to fine dispersion of Cu_5Zr and chromium precipitates which develop during aging treatment. This microstructure imparts resistance to softening at elevated temperatures. These alloys find applications in resistance welding electrodes, spot welding adaptor shanks, and others where high electrical conductivity and good resistance against softening are required.

Table 6 Schedule of heat treatments of Cu–Cr–Zr alloys

Alloy designation and composition	*Solution annealing treatment*	*Ageing treatment*
ZollernCuCrZr (Cu–0.85Cr–0.09Zr)	970 °C, 20 min/water quench	475 °C, 2 h
KabelmetalCuCrZr (Cu–0.65Cr–0.10Zr)	980 °C, 60 min/water quench	475 °C, 2 h

Source: Ref. [10].

Table 7 Room temperature mechanical properties and electrical conductivity

Alloy and heat treatment	*Yield strength (MPa)*	*Tensile strength (MPa)*	*Elongation at fracture (%)*	*Electrical conductivity*
Zollern CuCrZr				
Solution quenched	118	243	52	35.7% IACS
Solution quenched and aged	310	418	25	76.4% IACS
Kabelmetal CuCrZr				
Solution quenched and aged	316	414	24	83.4% IACS

Abbreviation: IACS, International Annealed Copper Standard.
Source: Ref. [10].

2.14.3.7 Copper–Nickel–Silicon–Chromium Alloy

Apart from the advantageous properties mentioned earlier, beryllium–copper alloys suffer from some drawbacks. Beryllium present in the beryllium bronze is detrimental to human life as well as to environment. The alloys are difficult to recycle after use. In this context, researchers have been studying various other copper alloys as substitute for toxic beryllium bronzes. One such alloy investigated by Huei-Sen Wang *et al.* is Cu–7.4Ni–1.3Si–1.2Cr. This alloy is developed for mold tooling application. When cast conventionally, this alloy exhibits a coarse grain structure (grain size of about 200 μm) embedded with large size precipitates and substantial microsegregation of the alloying elements. Huei-Sen Wang *et al.* processed this alloy through powder metallurgy route. The powder of the alloy was produced by argon atomization process with average size of 25 μm. The powder was consolidated to bulk form by hot pressing followed by sintering to obtain dense mass. The average grain size of the hot pressed and sintered product has been found to be 100 μm. The alloy samples were solution treated at 970 °C for times up to 10 h and subsequently quenched in water. The samples were precipitation hardened at 450 °C for up to 6 h. The best results were observed at 8 h solution treatment at 970 °C followed by 6 h aging at 450 °C. After aging a subgrain structure with grain size less than 30 μm was observed.[11] The alloy was found to exhibit average T.S. of up to 820 MPa and average thermal conductivity of 110 $W\,m^{-1}\,K^{-1}$. The strengthening was produced due to fine dispersion of nanometer size β-Ni_3Si and δ-Ni_2Si precipitates in fine grain size matrix as shown in **Figure 27**. Based on the thermal conductivity and the T.S. developed in the Cu–Ni–Si–Cr alloy Huei-Sen Wang *et al.* suggested the potential application of this alloy for mold tooling.

2.14.3.8 Copper-Base Shape Memory Alloys

Cu–Zn–Al alloys are known to produce thermoelastic martensite. When the alloy is deformed to a different shape in martensitic and then heated to parent state, the original shape is regained; this is called shape memory effect (SME). In general Cu–*x*Zn–*y*Al and Cu–*x*Al–*y*Ni are quenched from high temperature β-phase field to produce martensites. These martensites are soft and can be deformed at a small force. Since volume change 'ΔV' accompanying martensitic transformation is very small these martensites are internally twinned; these reversible defects play important role for SME. The reversible internal faults enable the transformation of martensite to parent phase along the same path as that of the forward transformation (β–M). Influence of a rare earth element, Gd on microstructure on this shape memory alloy has been reported in the literature.[12] Stabilization of martensite is observed in memory alloys.[13] The inherent reversibility

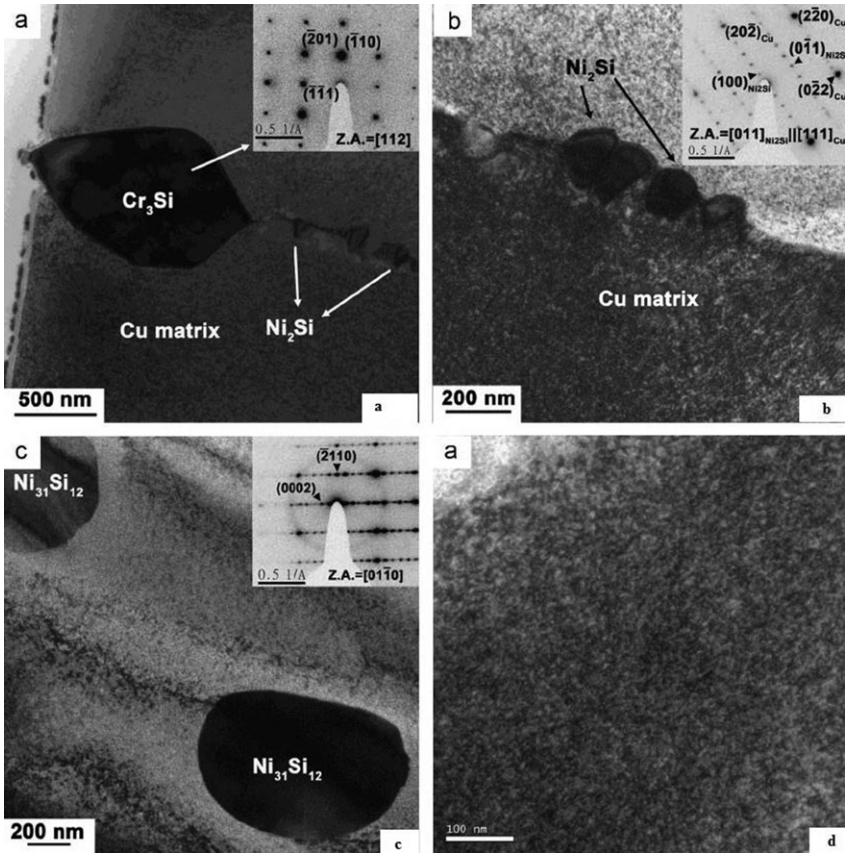


Figure 27 Bright field images of the Cu–Ni–Si–Cr alloy after 6 h aging showing microsize Cr_3Si and Ni_2Si precipitates at the grain boundaries ((a) and (b)), microsize $Ni_{31}Si_{12}$ precipitate within the grain (c), and (d) large number of precipitate particles within copper matrix.[11]

characteristics of martensitic transformation in Cu–Zn–Al and Cu–Al–Ni alloy are envisaged due to low thermal hysteresis. The repetitive use of these shape memory alloys leads to aging effect; this leads to the formation of precipitates of intermetallics which adversely affect the SME. However controlled aging of some shape memory alloys may accentuate SME behavior although in most of the cases chemical degradation is reported to have deteriorated SME in copper alloys.[14–17]

2.14.4 Heat Treatment of Nickel Alloys

Nickel is one of the most important engineering metals. It has FCC structure and does not show any polymorphic changes even up to the melting temperature. It possesses good combination of physical and mechanical properties apart from outstanding corrosion resistance against many corrosive media and good oxidation resistance. However, nickel is prone to attack by sulfur. Sulfur makes nickel embrittled due to the formation of brittle Ni_3S_2 at the grain boundaries.[18] Nickel is principally alloyed with copper, iron, chromium, silicon, and molybdenum. Based on these principal alloying elements, nickel-base alloys are categorized as: nickel–copper alloys, nickel–chromium alloys, nickel–iron alloys, nickel–chromium–molybdenum alloys, nickel–iron–chromium alloys, and so on. Nickel alloys are also popularly known by their trade names given by International Nickel Company (INCO) and these are Monels, Inconels, Nimonics, and Hastelloys.

Since nickel is attacked by sulfur, an important consideration during heat treatment of nickel alloys is the furnace atmosphere which must be free of sulfur. Embrittlement due to sulfur, if occurs, cannot be remedied.

The types of heat treatment applied to nickel alloys are as follows.

2.14.4.1 Annealing

The aim of annealing of cold worked nickel alloys is to make them soft for further cold reduction. This treatment is performed by heating the alloy to a temperature where recrystallization takes place. This temperature for nickel alloys falls in the range of 700–1200 °C depending on the type of alloy and its composition, as well as the degree of cold working. Higher annealing temperature is used where greater softening is desired. The alloy is generally slowly cooled from the annealing temperature. Effects of heat treating temperature on some room temperature mechanical properties of cold drawn Monel 400 alloy are represented in Figure 28. As stated earlier, the heat treatment temperatures for various nickel alloys are also decided by the corresponding phase diagrams. A representative phase diagram of nickel–copper alloy (Monel) is shown in Figure 29 that describes its annealing temperature.

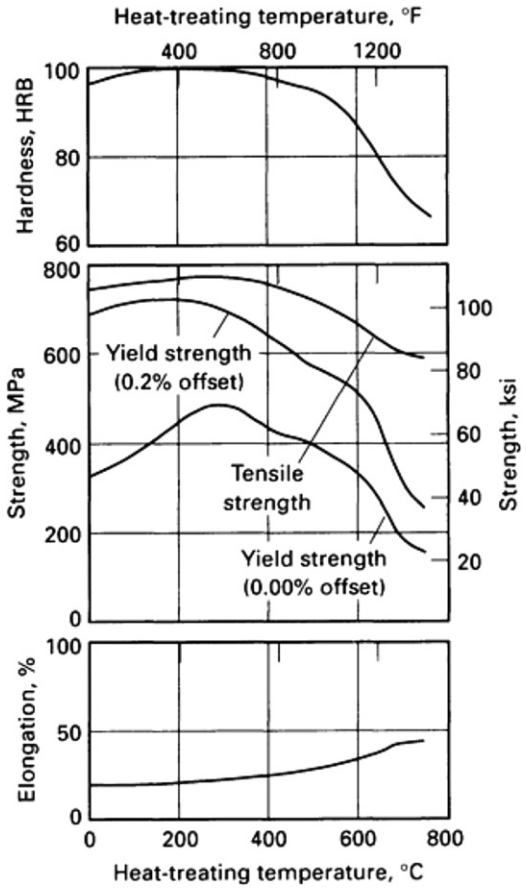


Figure 28 Effect on room temperature properties of cold drawn Monel 400 rod held for 3 h at various temperatures.[3]

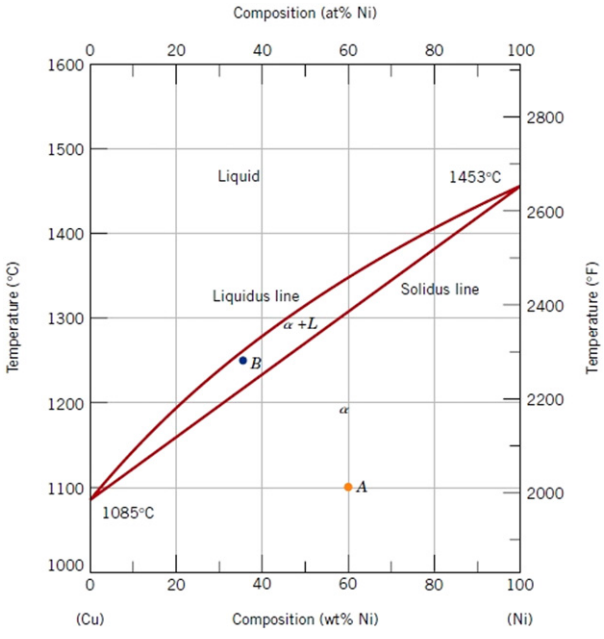


Figure 29 Phase diagram of Cu–Ni system.[19]

The annealing schedule for several nickel and nickel alloys is given in Table 8.

2.14.4.2 Solution Annealing

It is a high temperature annealing treatment applied to some specific nickel alloys so as to bring second phase into solution and cause some grain coarsening which is desirable to improve creep rupture properties. This treatment is applied at a temperature lower than the upper annealing temperature range prior to precipitation hardening. The solution treating temperatures for some nickel alloys are given in Table 9.

2.14.4.3 Stress Relieving

This treatment is applied to cold worked nickel and non-age-hardenable nickel alloys. The alloy is heated to a temperature in the range 425–870 °C and soaked without any recrystallization to occur. Only recovery part of annealing remains effective. The true temperature of annealing depends on the alloy composition and degree of prior cold working. The stress relieving temperatures used for some nickel alloys are given in Table 10.

2.14.4.4 Stress Equalizing

It is a kind of stress relieving treatment performed on cold drawn nickel alloys at lower temperature of annealing so that partial recovery takes place with the elimination of excess lattice defects, in particular, the point imperfections. The consequent effect is the restoration of electrical conductivity while there is no deteriorating effect on improved hardness and strength produced by cold working. The exact temperature of stress equalizing cold drawn alloys depends on their composition and the degree of prior cold reduction. For instance, an optimum temperature range of 230–315 °C is used for cold drawn Monel 400 rod. The applications of stress equalizing include coil springs, wire forms, and flat spring stampings. Table 10 gives the schedule of stress equalizing treatment of Nickel 200, Nickel 201, and Monel 400.

2.14.4.5 Precipitation Hardening

Alloying elements such as Al, Si, Ti, Nb, and others are added in very small concentrations either singly or in combination to make nickel and its alloys susceptible to precipitation hardening. The strength and hardness properties are improved after proper age hardening treatment. Solution treatment is carried out at a temperature where the precipitation hardening constituents dissolve into solid solution and form a single-phase. The temperature at which solution treating is performed varies widely within the temperature interval between 980 and 1315 °C. The upper limit of temperature is preferred when carbides are required to dissolve into solid solution. The time of solution treatment varies from 2 to 4 h. The exact temperature of solutionizing depends on the alloy composition. Subsequently the alloy is cooled rapidly such that supersaturated solid solution is retained at ambient temperature. In this condition the alloy is soft and ductile and it can be fabricated by cold forming

Table 8 Annealing treatment schedule for some representative nickel and nickel alloys

Material with composition	*Temperature (°C)*	*Time*	*Cooling method*
Nickel 200: 99.5 Ni–0.06 C–0.25 Mn–0.15 Fe–0.05 Si–0.05 Cu	705–760 B	2–6 h	AC (air cool)
	815–925 C	1/2–5 min	AC or WQ (water quench)
Nickel 201: 99.5 Ni–0.01 C–0.20 Mn–0.15 Fe–0.05 Si–0.05 Cu	705–760 B	2–6 h	AC
	760–870 C	1/2–5 min	AC or WQ
Monel 400: 66 Ni–0.12 C–0.90 Mn–1.35 Fe–0.15 Si–31.5 Cu	760–815 B	1–3 h	AC
	870–980 C	1/2–15 min	AC or WQ
Monel R-405: 66 Ni–0.18 C–0.90 Mn–1.35 Fe–0.15 Si–31.5 Cu–0.04 S	760–815 B	1–3 h	AC
	870–980 C	1/2–15 min	AC or WQ
Monel K-500: 65 Ni–0.15 C–0.60 Mn–1.00 Fe–0.15 Si–29.50 Cu	870–1040 B	1–3 h	WQ
	870–1040 C	1/2–20 min	WQ
Carpenter nickel–copper 400: (63–70)Cu–0.03 C–2.0 Mn–2.5 (maximum) Fe–0.50 Si–Balance Cu	704–980 870–980 most typical sulfur free atmosphere	1–3 h	–
Inconel 600: 76 Ni–0.04 C–0.20 Mn–7.20 Fe–0.20 Si–0.10 Cu–15.8 Cr	925–980 B	1–3 h	AC
	925–1040 C	1/2–60 min	AC or WQ
Inconel 601: 60.50 Ni–0.05 C–0.50 Mn–14.10 Fe–0.25 Si–23.00 Cr–1.35 Al	1095–1175 B	1–3 h	AC
	1095–1175 C	1/2–60 min	AC or WQ
Inconel 617: 54.00 Ni–0.07 C–22.00 Cr–1.00 Al 9.00 Mo–12.5 Co	1120–1175 B	1–3 h	AC
	1120–1175 C	1/2–60 min	AC or WQ
Inconel 625: 61.00 Ni–0.05 C–0.25 Mn–2.50 Fe–21.50 Cr–1.00 Al–9.00 Mo–3.65 Nb	980–1150 B	1–3 h	AC
	980–1150 C	1/2–60 min	AC or WQ
Inconel 718: 52.50 Ni–0.04 C–0.20 Mn–18.00 Fe–0.20 Si–0.10 Cu–19.00 Cr–0.8 Ti–0.60 Al–3.00 Mo–5.20 Nb	955–1065 B	1–3 h	AC
	955–1065 C	1/2–60 min	AC
Inconel X-750: 73.00 Ni–0.04 C–0.70 Mn–6.75 Fe–0.30 Si–0.05 Cu–15.00 Cr–2.508 Ti–0.80 Al–3.00–0.85 Nb	955–1150 B	1–3 h	AC
	955–1150 C	1/2–60 min	AC
Hastelloy B-2: 69.00 Ni–0.01C–1.00 Fe–28.00 Mo	1095–1175 B	1 h	AC or WQ
	1095–1185 C	5–10 min	AC or WQ
Hastelloy C-276: 57.00 Ni–0.01 C–5.50 Fe–15.50Cr–16.00 Mo	1215 B	1 h	WQ
	1215 C	5–10 min	WQ
Hastelloy X: 48.00 Ni–0.10 C–18.50 Fe–22.00 Cr–9.00 Mo–1.00 Co–0.60 W	1175 B	1 h	AC or WQ
	1175 C	1/2–15 min	AC or WQ

Note: B stands for batch annealing and C stands for continuous annealing. Time given in minutes represent the actual ranges that thin sheet/strip products and heavy cross-sections would receive in continuous furnaces.
Source: Ref. [3].

Table 9 Solution treating and precipitation hardening schedules for some representative nickel alloys

Alloy	*Solution treatment schedule*	*Precipitation hardening schedule*
Monel K-500	980 °C, 1/2–1 h hold, air cool (AC)	Heat to 595 °C, hold 16 h; furnace cool (FC) to 540 °C, hold 6 h; FC to 480 °C; AC
Inconel 718	980–1065 °C, 1 h hold, AC	Heat to 720–760 °C, hold 8 h; FC to 620–650 °C, hold until furnace time for entire precipitation hardening cycle equals 18–20 h; AC
Inconel X-750	1150 °C, 1–2 h hold, AC	Heat to 845 °C, hold 24 h; AC, reheat to 705 °C, hold 20 h; AC
Hastelloy X	1175 °C, 1 h hold, AC	Heat to 760 °C, hold 3 h; AC; reheat 595 °C, hold 6 h; FC to 480 °C; AC
Inconel 901	1095 °C, 2 h hold, WQ	Heat to 790 °C, hold 2 h; AC; reheat 720 °C, hold 24 h; AC
Nimonic 90	1080 °C, 8 h hold, AC	Heat to 705 °C, hold 16 h; AC
Udimet 500	1080 °C, 4 h hold, AC	Heat to 850 °C, hold 24 h; AC; reheat 760 °C, hold 16 h; AC
Waspaloy	1080 °C, 4 h hold, AC	Heat to 845 °C, hold 24 h; AC; reheat 760 °C, hold 16 h; AC

Source: Ref. [3].

process if required. The alloy is finally precipitation hardened at 425–870 °C depending on the alloy type and its composition. Sometimes a double aging treatment is applied. The solution annealing and precipitation hardening cycles of some representative nickel alloys are given in **Table 9**. **Figure 30** is a typical representative microstructure of precipitation hardened alloy Monel K-500 showing fine precipitate of $Ni_3(Al,Ti)$ as black spots.[8]

2.14.4.6 Nickel-Base Superalloys

Nickel-base superalloys have an austenitic matrix structure. Many of these contain molybdenum and/or tungsten, which are soluble in the matrix and act as solid-solution strengtheners. In nickel-base superalloys, γ' and γ'' lead to precipitation strengthening; The γ' phase, is identified as $Ni_3(Al,Ti)$ with its crystal structure as ordered f.c.c of L12-type ordering and is

Table 10 Stress relieving and stress equalizing cycle of heat treatment for some representative nickel and nickel alloys

Material	*Stress relieving*			*Stress equalizing*		
	Temperature (°C)	*Time (min)*	*Cooling method*	*Temperature (°C)*	*Time (h)*	*Cooling method*
Nickel 200	480–705	1/2–120	AC (air cool)	260–480	1–2 h	AC
Nickel 201	480–705	1/2–120	AC	260–480	1–2 h	AC
Monel 400	540–650	1/2–20	AC	230–315	1–3 h	AC
Carpenter nickel–copper 400	540–570	60–120	AC			
Inconel 600	760–870	5–60	AC	–	–	–

Note: Time given in minutes represent the actual ranges that thin sheet/strip products and heavy cross-sections would receive in continuous furnaces.
Source: Ref. [3].

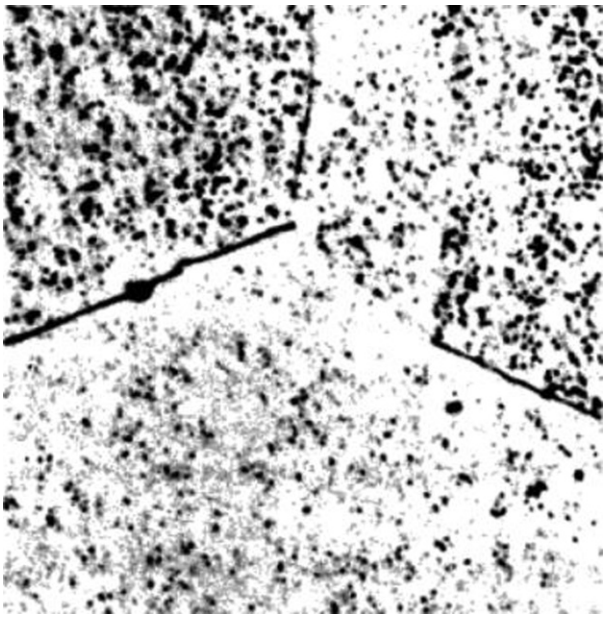


Figure 30 Microstructure of Monel K-500 solution treated at 1200 °C and aged at 700 °C for 4 h.[8]

responsible for antiphase boundary (APB) strengthening. This implies that these superalloys are heat-treated for precipitation hardening by way of solutionizing followed by aging. The strength of γ' phase increases with increasing temperature and so the control of aging temperature is very important.

The γ'' phase is ordered Ni_3Nb phase and of body-centered-tetragonal structure; while γ' is the predominant matrix-strengthening phase in nickel-base superalloys, the γ'' serves as the major strengthening precipitate and it can be stabilized by addition of iron. Compositions of similar type represent INCONEL alloys X-750, 706, and 718. Again η phase in nickel–iron-base superalloys containing Ti and Al is primarily Ni_3Ti and here aluminum does not play any direct role in the precipitation strengthening. Moreover, the stability of both γ' and γ'' phases in Ni–Fe superalloys is enhanced by aluminum. Long-time exposure at about 650–750 °C leads to transformation of the γ' and γ'' phases to η and δ phases, respectively; it therefore appears that compositions of superalloys and factors determining the stability of different strengthening phases are the deciding parameters to design the heat treatment schedule.[17,18] Carbides, nitrides, and carbonitrides such as TiC, TiN, Ti(C, N), M_6C, and $M_{23}C_6$ have also been identified in the structure of many nickel-base alloys. Major type of nickel-base superalloys include Ni–Cr–Fe-based (e.g., Inconels), Ni–Mo–Fe-based (e.g., Hastelloy A and B), and Ni–Cr–Mo–Fe-based (e.g., Hastelloy C and Hastelloy X). Examples of a few nickel-base superalloys along with their heat treatment schedule are given in **Table 9**.

References

1. Brick, R. M.; Philips, A. Structure and Properties of Alloys. In *Metallurgy and Metallugical Engineering Series*; Mehl, R. F., Bever, M. B., Eds.; McGraw-Hill: New York, NY, 1949.
2. Higgins, R. A. *Engineering Metallurgy Part 1: Applied Physical Metallurgy*, 5th ed.; ELBS: London, 1988; pp. 387–416.
3. ASM. *ASM Handbook Volume 4: Heat Treating*; ASM International: Materials Park, OH, 1991; pp. 1960–2009, 2032–2043.
4. Bacon, D.; Dieter, G. E. *Mechanical Metallurgy: SI Metric Edition*; McGraw-Hill Book Company: London, 1988.
5. Gorelik, S. S. *Recrystallization in Metals and Alloys*; Mir Publisher: Moscow, 1981; p. 70.
6. Yanchuan Tang; Yonglin Kang; Lijuan Yue; Xiaoliang Jiao. The Effect of Aging Process on the Microstructure and Mechanical Properties of a Cu–Be–Co–Ni Alloy. *Mater. Des.* **2015**, *85*, 332–341.
7. Zakharov, B. *Heat Treatment of Metals*; Peace Publishers: Moscow, 1962; pp. 294–297.
8. Avner, S. H. *Introduction to Physical Metallurgy*, 2nd ed.; McGraw-Hill Kogakusha Ltd.: Tokyo, 1974; pp. 461–546.
9. Boyer, H. E. Heat Treating of Nonferrous Alloys. *Metallogr. Microstruct. Anal.* **2013**, *2* (3), 190–195.
10. Zinkle, S.J.; Eatherly, W.S. *Effect of Heat Treatments on the Tensile and Electrical Properties of High-Strength, High-Conductivity Copper Alloys*; Fusion Materials Semiannual Progress Report for Period Ending 30 June 1997, DOE/ER-0313/22; Oak Ridge National Laboratory: Oak Ridge, TN, 1997.
11. Huei-Sen Wang; Hou-Guang Chen; Jhen-Wang Gu; Cheng-En Hsu; Chung-Yung Wu. Effects of Heat Treatment Processes on Microstructures and Properties of Powder Metallurgy Produced Cu–Ni–Si–Cr Alloy. *Mater. Sci. Eng. A* **2014**, *619*, 221–227.
12. Jia Wen Xu. Effects of Gd Addition on Microstructure and Shape Memory Effect of Cu–Zn–Al Alloy. *J. Alloys Compd.* **2008**, *448* (1–2), 331–335.
13. Kadletz, P. M.; Krooß, P.; Chumlyakov, Y. I.; *et al.* Martensite Stabilization in Shape Memory Alloys – Experimental Evidence for Short-Range Ordering. *Mater. Lett.* **2015**, *159*, 16–19.
14. Chattopadhyay, P. P.; Bhuniya, A. K.; Datta, S.; Banerjee, M. K. Effect of Trace Addition of Ti on the Micro Structural Degradation in Cu–Zn–Al Shape Memory Alloy due to Ageing Effect. *Mater. Sci. Eng. A* **2005**, *393* (1), 125–132.
15. Datta, S.; Bhunya, A.; Banerjee, M. K. Two Way Shape Memory Loss in Cu–Zn–Al Alloy. *Mater. Sci. Eng.: A* **2001**, *300*, 291–298.
16. Duchao, L. V.; Mc. Allistor, D.; Mills, M.; Wang, Y. Modeling Precipitate Dislocation Interaction in Nickel-Based Superalloys. In *Proceedings of the International Workshop on Modeling and Simulation of Superalloys*, Organized by ICMAS, Ruhr-Universitat Bochum, Germany, September 13–17, 2014.

17. Fivel, M. C.; Strudel, J. L.; Chung, H. J. Initial Stage of Creep in Nickel Base Super Alloy, a 3D Discrete Dislocation Dynamics Integration. In *Proceedings of the International workshop on Modeling and Simulation of Superalloys*, Organized by ICMAS, Ruhr-Universitat Bochum, Germany, September 13–17, 2014 (INSG Secretariat briefing paper, Ni-Based superalloy, April, 2013).
18. Rollason, E. C. *Metallurgy for Engineers*; ELBS: East Sussex, 1973; pp. 300–326.
19. Callister, W. D., Jr. *Materials Science and Engineering: An Introduction*, 4th ed.; John Wiley & Sons Inc.: New York, NY, 1997; pp. 147–177.

2.15 Cryogenic Treatment of Engineering Materials

T Slatter, The University of Sheffield, Sheffield, UK
R Thornton, University of Leicester, Leicester, UK

© 2017 Elsevier Inc. All rights reserved.

2.15.1 Introduction 422
2.15.1.1 Links with Traditional Heat Treatment 422
2.15.1.2 A Brief History of Cryogenic Treatments 422
2.15.1.3 Industrial Context 423
2.15.1.3.1 The cryogenic processing industry 423
2.15.1.3.2 Current uses of CT processes 424
2.15.1.3.3 The future of CT and its applications 424
2.15.1.4 Cryogenic Treatment Processes 424
2.15.1.4.1 CT technology 425
2.15.1.4.2 CT processes 425
2.15.1.4.2.1 Case Study: Optimizing a CT process 426
2.15.2 Cryogenic Processing of Ferrous Alloys 426
2.15.2.1 State of the Art 427
2.15.2.1.1 Mechanical properties 427
2.15.2.1.2 Tribological performance 427
2.15.2.1.3 Mechanisms of microstructural change 429
2.15.2.2 Tool Steels 430
2.15.2.3 Plain Carbon Steels 434
2.15.2.4 Stainless Steels 435
2.15.2.5 Cast Irons and Pearlitic Steels 436
2.15.2.6 Case Studies 437
2.15.2.6.1 Impact wear resistance of low carbon steel and lamellar graphite cast iron 437
2.15.2.6.1.1 Introduction 437
2.15.2.6.1.2 Impact wear 437
2.15.2.6.1.3 Experimental details 437
2.15.2.6.1.4 Results 437
2.15.2.6.1.4.1 Specimen overview and wear scar morphology 437
2.15.2.6.1.4.1.1 Untreated specimens 437
2.15.2.6.1.4.1.2 Cryogenically processed specimens 438
2.15.2.6.1.4.1.3 Wear scar measurement 439
2.15.2.6.1.4.1.4 Estimation of wear scar volume 440
2.15.2.6.1.4.1.5 Comparison with a 'traditional' heat treatment process 441
2.15.2.6.1.5 Summary 442
2.15.2.6.2 Sliding wear resistance of pearlitic brake disk materials 442
2.15.2.6.2.1 Introduction 442
2.15.2.6.2.2 Requirements of brake rotor materials 442
2.15.2.6.2.3 Experimental details 442
2.15.2.6.2.4 Results 443
2.15.2.6.2.4.1 Hardness 443
2.15.2.6.2.4.2 Wear testing 443
2.15.2.6.2.4.3 Microstructural observations 443
2.15.2.6.2.5 Summary 444
2.15.3 Cryogenic Processing of Nonferrous Alloys 445
2.15.3.1 State of the Art 445
2.15.3.2 Aluminum Alloys 447
2.15.3.3 Magnesium Alloys 448
2.15.3.4 Titanium Alloys 448
2.15.3.5 Cobalt-Bonded Tungsten Carbides 449
Acknowledgments 451
References 451
Relevant Websites 453

2.15.1 Introduction

The term 'cryogenic' pertains to something at or causing the creation of very low temperatures (typically < 193 K/-80 °C) and has a wide variety of uses in medical devices, electrical components, and superconductors used in fields such as quantum physics. While low temperatures are indeed involved in both instances, the term 'cryogenic' should not be used when referring to the field of 'cryonics,' which is of course to do with the preservation of living creatures beyond the help of contemporary medicine.

In the context of this chapter, cryogenic processing is taken to refer to a range of subzero heat treatments (cryogenic treatments or cryotreatments (CTs)) that are applied to materials with the aim of causing permanent microstructural changes and corresponding changes in mechanical properties and behaviors.

Closely related fields of interest, but distinct disciplines in their own right, are those that include activities use cryogenic fluids in conjunction with engineering materials and processes. These can be classified into two broad categories:

1. The field of investigating the 'performance of engineering materials at cryogenic temperatures' (e.g., space, electronics, physics research, and indeed the cryogenic processing equipment industry itself when designing the equipment to perform cryogenic processing).
2. The 'use of cryogenic fluids in manufacturing' (e.g., cryogenic machining, cryo-rolling, cryogenic burnishing, and cooling of operating industrial machines).

Both of these areas have crossover with cryogenic processing, for example:

- Studies that consider if materials retain their desired performance at cryogenic temperatures may give insight into what drives any changes observed even if those changes are reversible (i.e., 'disappear') when the materials are returned to ambient temperatures to be used.
- Studies that consider using cryogenic fluids as an alternative to conventional coolant in machining processes may benefit from an understanding of how much coolant could be used for how long a process before the workpiece undergoes unwanted changes.

It is this discipline of cryogenic processing that this chapter considers but links to these complementary fields are noted where necessary. The terms 'cryogenic processing,' 'cryogenic treatment' and 'cryotreatment' are used interchangeably.

This chapter first presents an overview of the development of cryogenic processing before reviewing the current state of the art. Several case studies are presented to illustrate how one might investigate the potential of cryogenic processing for a particular application in more detail.

2.15.1.1 Links with Traditional Heat Treatment

Classical heat treatments, which include bulk heating and cooling (quench hardening, tempering, and aging treatments) as well as surface treatments (such as laser hardening and induction hardening), are used widely throughout engineering to modify the microstructure and the subsequent behavior of metals. All of these methods involve subjecting a component to a controlled cycle of heating and cooling and for classical heat treatments the temperatures are always above 273 K. In ferrous metals, heat treatments are often used to make the materials harder in an attempt to improve their wear characteristics without significantly modifying their bulk properties. There are many applications where this is required to ensure a satisfactory lifetime of components and it is extremely common to treat steel components such as camshafts, crankshafts, and gears.

Less widely used is the extension of 'heat treatment' to cryogenic temperatures. Although routinely considered in the design and manufacture of industrial equipment, especially for use in medicine and the physical sciences, there is a smaller volume of work where cryogenic temperatures are used deliberately to positively modify the microstructure for strength and wear resistance.

CT involves lowering the material to temperatures below 193 K and holding or 'soaking' for a defined period of time before raising the material back to ambient temperature. The objective of CT is therefore to cause permanent changes to the microstructure of a material that enhances desired properties, with minimal or insignificant adverse effects. The process affects the entire cross-section of materials and components and is often considered as a single additional stage to a conventional heat treatment cycle (although, as discussed in Section 2.15.1.3.2, for many tools and components CT is already a part of the 'conventional' process).

By way of a simple example, in hardened steels, cryogenic processing utilizes phase transformations that occur when the material is 'soaked' by being cooled in a liquid nitrogen (LN_2) filled chamber for up to 72 h. It has been observed that the combination of these phenomena give cryogenically processed materials improved wear resistance, stress relief and dimensional stability.[1] The level of these improvements depend on the exact cooling parameters of the processing. In this context, CT can be considered as an extension of a classical heat treatment cycle; extending the effects of quench hardening and preparing steels for further carbide precipitation during subsequent tempering.

Relatively little work has been conducted to investigate the improvements that can, or cannot be made to the mechanical properties of other engineering materials. Similarly there is little information about the ability of materials subjected to the process to resist different types of wear, with the majority of studies to date focusing on the resistance of cryotreated materials to abrasive and adhesive wear, or in use as cutting tools.

2.15.1.2 A Brief History of Cryogenic Treatments

The earliest examples of subzero temperature processing comes from Swiss watchmakers. In the mid-nineteenth century, they used to leave delicate gears and the materials for watch parts buried in snow in mountain caves over the winter, having noticed that this would make gears more durable, and allow parts to be made with more precision as the materials deformed less during machining. This enabled

them to produce more reliable and longer lasting timepieces.[2] During the first half of the twentieth century tool and die-makers began freezing their tooling as they realized they could machine more parts per cutting edge than before. Some aero-engine components and even cutlery started to be treated as well. Although much of the early work has been overlooked in recent years, perhaps due to 'political circumstances' at the time, it is clear that cryogenic treatments were widely used and studied in the USSR in the first half of the twentieth century. In a translation of one of his works on the subject, originally from 1946, Gulyaev[3] clearly describes a number of effects of cryogenic treatments on steels including the martensite transformation, the effects of alloying, stabilization of austenite, and the effects of cryogenic treatments on high-speed steels and carburizing components. Many of these are still the subject of debate amongst the scientific community today.

During the Second World War, cryogenic processing was widely utilized to enhance the wear resistance of mechanical parts in machinery and vehicles, although notable research into its effects were effectively suspended until the 1960s when NASA engineers noticed that spacecraft parts exhibited different properties after returning from space. Shortly afterwards, in the 1970s and 1980s Dr. Randall Barron,[4] along with Charles Mulhern,[5] conducted what are considered the first contemporary research projects into the effects of deep cryogenic processing. In studies using lathe tools and abrasive wear experiments on a range of ferrous alloys, Barron recorded significant increases in wear resistance in some materials (up to 718% in the case of AISI D2 steel) whereas in others (AISI A2, A6, and T2 steels) cryogenic processing appeared to have no effect.

2.15.1.3 Industrial Context

2.15.1.3.1 The cryogenic processing industry

While cryogenic processing has been used as an industrial technique for over 80 years, arguably, a cryogenic processing industry has only existed for around 40 years, as awareness and understanding of cryogenic treatment has grown. While the majority of established companies can be found in the USA and the EU (primarily in the UK), interest in cryogenic treatment is growing in rapidly developing, heavily industrial economies such as India and China.

The oldest of these, 300° Below Cryogenic Tempering Services, Inc. was established in 1966 (as CryoTech), however, the majority of cryogenic treatment companies have started up in the past 30 years. The industry is therefore dominated by small- and medium-sized enterprises (SMEs).

Cryogenic treatment companies offer a range of services, including cryogenic nitrogen and helium treatments, thermal cycling, as well as pre- and post-cryotreatment tempering of finished parts and raw materials. A number of these companies additionally supply cryogenic processing equipment, both to industry and research institutions. **Table 1** summarizes the services offered by some of these companies, indicating typical soaking temperatures (T_s), times (t_s), treatment types, liquid helium (LHe_2) processing capabilities and an overview of the

Table 1 Examples of cryotreatment companies and their advertised service capabilities

Company (location)	*Soaking temperature, $T_{s,min}$ (K)*	*Time, t_s (h)*	*Treatment types*	*Liquid helium treatment*	*Equipment supplied*
300° Below Cryogenic Tempering Services, Inc. (Illinois, USA) Est. 1966	88	72 (total process)	N_2 atmosphere	No	Model 921 processor: electrical and nitrogen cooling, 682 kg capacity, 2.5 kW
Controlled Thermal Processing, Inc. (Illinois, USA) Est. 1980	88	n/a	Air cooled by heat exchange with (liquid temperature) LN_2	Yes	Applied Cryogenics, Inc processors: 0.2–1.2 m^3 capacity, post-cryo tempering, 4.4–11 kW
CryoPlus, Inc. (Ohio, USA) Est. 1994	88	10	Pre-cryo temper; LN_2 spray (vaporizes)	No	n/a
Cryogenic Institute of New England, Inc. (Massachusetts, USA) Est. 2002	88	24	LN_2 immersion	Yes	Batch and continuous cryogenic treatment equipment: 88–878 K range
Cryogenic Treatment Services Ltd. (Nottinghamshire, UK) Est. 2004	78	24	N_2 atmosphere; post-cryo temper	No	n/a
Cryogenics International (Arizona, USA) Est. 1986	78	24–62	N_2 atmosphere	No	Treatment systems up to 0.8 m^3 capacity
Frozen Solid (Cambridgeshire, UK) Est. 1998	78	Material dependent	N_2 atmosphere; post-cryo multi-stage tempering	Yes	n/a

equipment they offer. Given its scarce availability LHe_2 is offered on a limited basis for extremely low-temperature ($-269\ ^{\circ}C$) treatments.

It is interesting to note that the range of services offered by these companies reflects the variety of results highlighted in the published literature. In fact it is possible to relate most of the differences between treatment parameters offered by these companies with the microstructural changes of martensitic steels by association with their temperature- or time-dependence. These changes have been summarized in **Table 2** for reference.

Whereas the elimination of retained austenite is theoretically achieved once a material passes the martensite finish (M_f) temperature, preparation of the material for the development of smaller secondary carbides and nano-carbides is also time-dependent, meaning both lower treatment temperatures and longer soak times may have beneficial effects. In fact, as is subsequently discussed, both these changes have not only been shown to be time-dependent, but intrinsically linked. The issue of pre- or post-cryotreatment tempering is material dependent and related to the initial phase composition of any treated material.

As a result of these factors no cryogenic treatment company should offer a single, 'one-size-fits-all' CT service. CT parameters should be varied to suit the material and degree of microstructural change or performance required. For large and repeated batches of materials or parts to be treated, an optimized CT cycle may represent a significant saving in terms of overheads and reduction in the quantity of cryogenic coolant required. Indeed, for the cryogenic processing industry, it is in this optimization of processes where commercial advantage and valuable intellectual property may lie. However, the extensive materials characterization facilities and high level of expertise required to determine the parameters of these optimal processes have so far prevented acknowledged leaders in commercial cryogenic treatment services from emerging.

Table 2 Summary of the dependence of microstructural changes due to cryogenic treatment in ferrous alloys

Microstructural change	*Parameter dependence*
Conversion of retained austenite to martensite	Temperature only (theoretically)
Precipitation of nano-carbides	Time, temperature
Dispersion and refinement of secondary carbides	Time, temperature

2.15.1.3.2 Current uses of CT processes

Cryogenic treatment companies (such as those mentioned in Section 2.15.1.3.1) are involved in a combination of commercial processing and after-market treatments, with the former becoming increasingly more significant. Although initially CT services were applied almost exclusively to products in their finished forms, it has increasingly become part of larger manufacturing chains; an example of this being the treatment of cutting tool inserts prior to coatings being applied, as CT has been shown to have adverse effects on coatings such as TiN.[6] However, products such as brake disks, sports equipment, and audio cabling are often still treated in their finished forms or after partial disassembly.

Research-led and commercial CT practices differ significantly, as highlighted in **Table 3**. Likely due to the basis of many CT operations on purely anecdotal evidence rather than rigorous analysis, there are a number of examples of 'bad practice' within the commercial cryogenic processing industry, from the point of view of the research community. These include the restriction of cryogenic treatment parameters, the use of anything other than nitrogen atmosphere cooling, and the almost exclusive use of cryogenic treatment as an 'after-market' process.

2.15.1.3.3 The future of CT and its applications

Although ferrous-based alloys feature in the bulk of cryogenic processing research and constitute a significant portion of commercial CT service requirements, a number of other materials have also been shown to benefit from cryogenic treatment. Aerospace materials such as aluminum, titanium, and magnesium alloys represent a developing area for the cryogenic processing industry, while sintered cobalt-bonded tungsten carbide tool materials have also been shown to respond favorably. Perhaps most unexpectedly, cryogenic processing has also been shown to have beneficial effects on nonmetallic composite materials, such as the polytetrafluoroethylene (PTFE)/Kevlar hybrid fabric.[7]

2.15.1.4 Cryogenic Treatment Processes

While subzero treatments of materials have arguably been possible for centuries through the exploitation of naturally occurring environmental conditions, cryogenic treatments have only been practically possible since the liquefaction of a number of important gases (notably nitrogen and helium) was achieved in the late nineteenth century. Following the industrialization of these processes in the first half of the twentieth century cryogenic treatment started to be used on a significant scale in manufacturing. Since then advances in insulation,

Table 3 Summary of differences between research-led and commercial cryotreatment (CT) practices

Research	*Commercial*
Varied CT parameters	Restricted treatment parameters, often only one fixed cycle offered
Wide consensus around use of N_2 atmospheric cooling for best results	Varied cooling practices ((liquid nitrogen) LN_2 immersion, LN_2 spray, N_2 atmosphere, and LN_2 heat exchange with air)
Recognition of need to understand CT holistically within heat treatment cycles	CT typically applied as an 'after-market' process
Small batch sizes	Large batch sizes

temperature sensors, and digital controllers have allowed the development of the efficient cryogenic processors used commercially today.

2.15.1.4.1 CT technology

CT commonly involves a supply of LN_2 into a thermally insulated tank containing the parts or materials to be treated, although specialist treatments are also available using LHe_2. The cryogenic fluid can be used in one of three ways: for direct immersion of parts to perform a 'cryo-quench'; as a working fluid to cool air within the tank; or as a gas that that is circulated by fans, thereby creating a 'dry' atmosphere.

The most common practice is to carry out CT using gaseous nitrogen (N_2) as the cooling medium. Figure 1 shows a schematic diagram for such a setup in which LN_2 is held in an external tank or reservoir, before being vaporized, pumped into an insulated chamber, and blown around the parts to be treated by fans. The flow of nitrogen is controlled by the temperature inside the chamber which is measured by thermocouples. Cooling and heating rates in the chamber typically fall within the range of 0.1–2.0 K/min.

Cryo-quenching (CQ) risks causing thermal shock,[8] where damaging thermal stresses are established by large temperature gradients between the surface and bulk of a material, while cryogenic cooling of air can lead to the build-up of vapor-ice on the surfaces of components, unless all moisture can be removed beforehand. Using N_2 or helium creates a largely inert atmosphere within the tank and has neither of these drawbacks,[9] while allowing for the controlled cooling of parts and materials. Cryogenic treatments using LN_2 and LHe_2 are theoretically able to reach 77 K ($-196\,^{\circ}C$) and 5 K ($-268\,^{\circ}C$) respectively; the temperatures at which they boil. Due to its abundance (making up 78% of the earth's atmosphere) nitrogen is commonly used in CT, whereas helium is reserved for extremely specialized use.

The on-going development of cooling agents has led to the establishment of different classifications of subzero treatments. By soaking temperature these are either cold treatments which can be achieved with dry ice (CT: 273–193 K), shallow cryogenic treatments, (SCT: 193–113 K) or deep cryogenic treatments (DCT: 113–77 K) which both require LN_2.[10]

2.15.1.4.2 CT processes

Figure 2 illustrates the difference between CT cycles involving CQ by LN_2 and cooling or CT by N_2 following on from a regular heat treatment cycle in a typical quench-hardened carbon steel, and preceding a post-treatment tempering cycle. As cryogenic treatments are typically offered as an after-market service, parts and materials are subjected to an indefinite 'transition' period between regular heat treatment and CT. In reality, tempering may have been performed prior to cryogenic treatment, which at best represents wasted process time and in the worst case inhibits the effective application of cryogenic treatment; such as when tempering may cause the decomposition of retained austenite into cementite and ferrite.

The parameters that are typically controlled and varied during CT are: cooling rate, soaking temperature, soaking time, heating rate, and the position of the CT within the overall treatment cycle in cases where materials or components are to be tempered.

Compared to work performed to assess the improvement in performance of cryotreated engineering materials, relatively little work has investigated the influence of varying the parameters of the CT process itself. What work has been performed typically limits the scope of the experiments to a single material, varies either the temperature or duration at which the

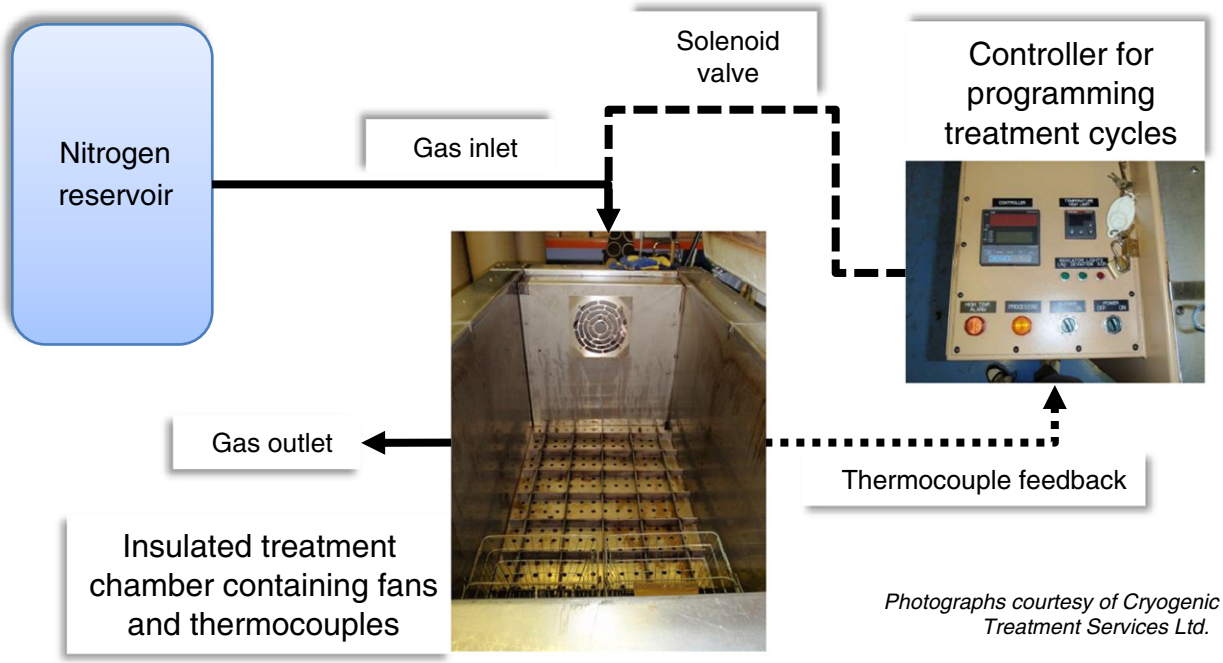


Figure 1 Schematic of equipment for cryotreatment using gaseous nitrogen cooling.

CT is performed and then assesses the improvement, or otherwise, of a mechanical performance parameter.

In their early study on AISI T8 and AISI 1045 steels, Barron and Mulhern[5] determined that the greatest increase in wear resistance for these materials could be achieved by using a low cooling rate (6 K/min), a long soaking time (24 h), and a low-temperature (77 K) soak. More recently, Darwin *et al.*[11] utilized Taguchi design of experimental methods, to determine the significance of parameters in maximizing the wear resistance of a high-chromium martensitic steel through deep cryogenic treatment. They determined that the significance of parameters was as follows: (1) soaking temperature, 72%; (2) soaking time, 24%; (3) rate of cooling, 10%; (4) tempering temperature, 2%; and that the tempering period was statistically insignificant.

One of the key commercial factors supporting the adoption of CT is its relatively low cost, both in terms of the equipment required and running costs per treatment cycle. Although a number of companies treat small batches of finished components for the automotive, aerospace, and manufacturing industries, as well as treating more novel items such as sports equipment. CT is not yet a widely used industrial process despite reported evidence indicating substantial improvements in wear resistance, hardness, and fatigue scatter reduction. The reasons for this lie in the lack of any cohesive understanding of the physical effects of CT on the microstructure and composition of treated materials, although a number of substantial studies have been carried out.[12]

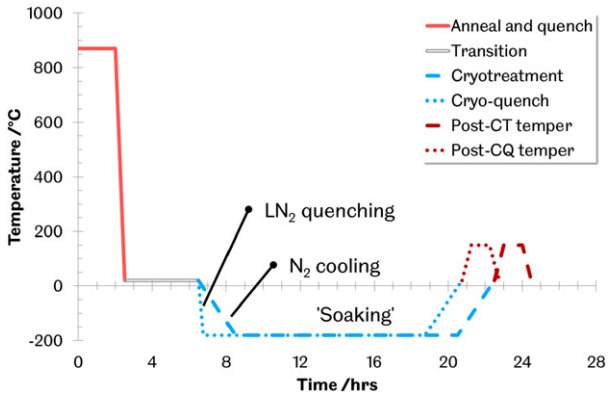


Figure 2 Cryotreatment (CT) cycles illustrating liquid nitrogen quenching and gaseous nitrogen cooling. The 'Transition' line indicates an indefinite period of time for transport and storage prior to CT.

2.15.1.4.2.1 *Case Study: Optimizing a CT process*

In a recent example of this approach,[13] simple rectangular section specimens of a particular tool steel (D2) were treated using a range of different soaking times at the cryogenic temperature. The durations ranged from 0–84 h and all other aspects of the treatment cycle remained uniform across the specimens. These treatment cycles are illustrated in **Figure 3**.

The treated specimens were then subjected to a range of microstructural analyses (e.g., SEM and XRD) and mechanical tests (e.g., hardness, sliding wear) to assess the performance variation as a result of the different process holding durations. In this particular case it was found there was an observable effect of soaking time on the precipitation of secondary carbides during subsequent tempering that lead to an improvement in the hardness and an increase in wear resistance. In all cases it was found that there is an optimum value for the duration at which the specimens were held at the cryogenic temperature.

2.15.2 Cryogenic Processing of Ferrous Alloys

Ever since its inception as a processing technique, ferrous alloys (and in particular, tool steels) have dominated both research and commercial uses of cryogenic treatments. This is due to the responsiveness of hardened steels to cryogenic

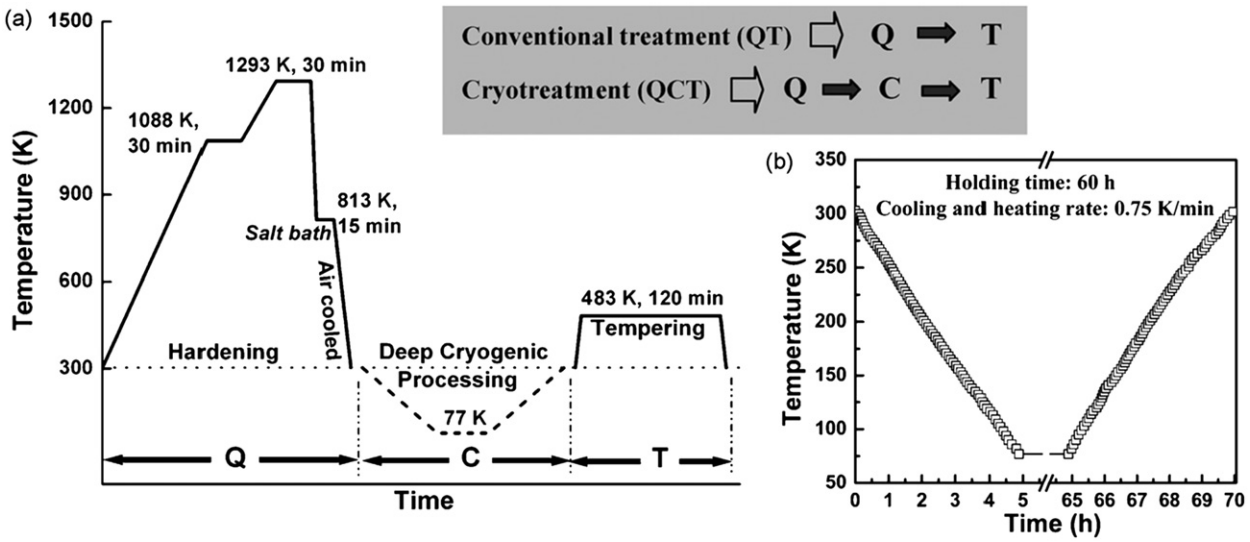


Figure 3 Schematic of (a) full heat treatment cycle, including deep cryogenic treatment, for AISI D2 tool steel and (b) detail of deep cryogenic processing.[13]

treatments that are often able to transform the majority of any retained austenite to martensite. In contrast to the reduction of retained austenite that can be achieved through tempering processes, by forming martensite at cryogenic temperatures better dimensional stability can be achieved.[14] Following hardening and cryogenic treatments it is usually preferable to temper the material to soften the virgin martensite and improve toughness, in line with conventional practice.

Cryogenic treatments have also been shown to cause additional effects in carbon steels. Of greatest focus within the research community has been the influence of cryogenic treatments on the formation of nano-carbide precipitates during tempering that further increase the wear resistance of tool steels. However, further effects have been seen in non-hardened pearlitic steels, cast irons, and stainless steels as well. A chronological summary of the relative changes in the properties and behavior of ferrous alloys due to cryogenic treatments is presented in Table 4. Immediately apparent is the vast range of effects reported in the scientific literature, that in turn, explains the range of different treatment processes on offer by commercial businesses.

This section identifies the state of the art and trends in performance modification that can typically be achieved by subjecting ferrous metals to cryogenic processing. Following this review, a selection of case studies are presented giving specific examples as to the effects cryogenic treatments have on the main ferrous alloy groups.

2.15.2.1 State of the Art

2.15.2.1.1 Mechanical properties

Although, from an engineering design perspective, the rigorous characterization of the influence of cryogenic treatments on the mechanical properties of materials may be desirable, studies that focus on strength, fatigue life, and toughness are few and far between. Hardness is the exception to this rule, with studies reporting changes due to CTs of up to 159%.[38] As hardness is commonly used as a proxy for yield strength, it might be reasonably expected that reported changes in the strength of cryotreated materials may change by similar values. However, this is not the case, with most investigators reporting no change in strength (yield or tensile) against one isolated case where a 16% increase was observed,[38] although it should be noted that very few of the studies surveyed considered strength as a separate parameter.

When it comes to reported values of impact energy (or notch-toughness) and fracture toughness, the results are perhaps surprising. While most investigators report significant decreases in the ability of hardened ferrous alloys to absorb energy following cryogenic treatments, studies involving AISI H13 hot work tool steel goes against this trend, with noticeable increases in fracture toughness reported.[18,43] The reasoning given for this increase is contradictory with previous work demonstrating greater brittle behavior in cryogenically treated AISI D2 tool steel, with both sets of investigators claiming that the fine carbide dispersion that results from cryogenic treatment and tempering is responsible. In their work on AISI D2 tool steel, Das *et al.*[30c] point to evidence of microvoids formed by the decohesion of secondary carbides on fracture surfaces (Figure 4).

2.15.2.1.2 Tribological performance

The majority of research into the effects of CT on the tribological performance of ferrous alloys focuses on their abrasive wear resistance in dry sliding conditions due to its wide relevance to industrial cutting processes and mechanical contacts founding in automotive and manufacturing fields. Beginning this vein of research is arguably the wide-ranging study by Barron, whose abrasive wear tests on 12 tool steels, three stainless steels and four others having been subjected to both shallow cryogenic treatment (SCT: 189 K) and deep cryogenic treatment (DCT: 77 K), illustrated the huge potential, as well as the significant variation, of this technique. Reporting an improvement in sliding wear resistance of 718% (in the case of AISI D2 tool steel after DCT) to the lack of any change in several others (AISI A2, A6, and T2 tool steels), this study by Barron lead to numerous others in which investigators consistently reported extreme performance improvements in some cases and no effect in others, leading Gill *et al.*[12] to comment that 'the reported magnitudes of the enhancement in wear resistance and the proposed governing mechanisms for such enhancement do not provide any unified picture.'

However, since then understanding has developed and it is clear now that the range of reported changes in the tribological performance of cryogenically treated ferrous alloys arises from the different microstructural changes that occur depending on the chemical composition and heat treatment history of the material. The most widely reported of these is the reduction or elimination of retained austenite from hardened steels[44] and its transformation to martensite. Without subsequent tempering this alone may lead to an increase in measured hardness, but a significant decrease in toughness. This effect should be seen in any hardenable steel (>0.3 wt%C) where the hardening process does not result in the complete transformation of austenite to martensite.

Also commonly reported is the appearance of numerous small carbides following cryogenic treatment and tempering.[45] These act to prevent dislocation movement and therefore inhibit local plastic deformation (increasing matrix hardness) while providing greater abrasive wear resistance. The prevalence of these carbides is linked to excess carbon that exists in the matrix following cryogenic treatment and the availability of carbide formers, and hence is seen most clearly in steels that contain significant quantities of alloying elements such as chromium, tungsten, and molybdenum, which are used heavily in cold work (AISI D-type) and high-speed (AISI M-type) steels.

Finally, and least frequently reported, is the effect that cryogenic temperatures have on dislocation density and movement during the thermal deformation that occurs (for a detailed discussion see Gavriljuk *et al.*[46] and Tyshchenko *et al.*[47]). Although not reported on as yet, it could reasonably be theorized that this effect may occur in other multiphase (e.g., ferritic–pearlitic) steels where each phase possesses different thermal expansion coefficients, resulting in additional stresses between them. This is known to be the case in the hardened steels, where the martensite formed during cryogenic treatment has different lattice parameters than that formed during the quenching process.[48] Ultimately, these changes manifest as a change in hardness[18,30a] that increases resistance to abrasion.

The combination of these effects is therefore what causes the wide range of variation reported in the tribological

Table 4 Chronological overview of changes in material properties due to cryogenic treatments (1973–2015). (Need interpretation of data in the fourth column, especially when it is −38%/−38%)

Investigators	*Material*	*Property*	*'Best' change*
Barron[4a]	1) REX-AAA high-speed steel/	Impact energy	1) −38%/
	2) REX-95 high-speed steel		2) −38%
Barron, Mulhern[5]	1) AISI T8 tool steel/	Wear resistance	1) +140%/
	2) AISI 1045 carbon steel		2) +40%
Barron[4b]	AISI D2 tool steel	Wear resistance	+718%
	AISI S7 tool steel		+403%
	AISI O1 tool steel		+172%
	AISI A10 tool steel		+165%
	AISI M1 high-speed steel		+125%
	AISI H13 tool steel		+109%
	AISI T1 tool steel		+76%
	AISI 440 martensitic stainless steel		+21%
	AISI M2 high-speed steel		+20%
	AISI 430 ferritic stainless steel		+20%
	AISI 8620 NiCrMo alloy steel		+12%
	AISI 303 austenitic stainless steel		+11%
	AISI CPM10V tool steel		+31%
	AISI A2 tool steel		+12%
	AISI P20 tool steel		–3%
	AISI 1020 carbon steel		−3%
	AQS Meehanite graphitic cast iron		−4%
Collins and Dormer [15]	AISI D2 tool steel	Hardness	+6%
		Wear resistance	+6%
		Impact energy	−24%
Yun *et al.*[16]	AISI M2 high-speed steel	Hardness	+3%
		Wear resistance	+20%
Mohan Lal *et al.*[17]	1) AISI D3 tool steel/	Wear resistance	1) +175%
	2) AISI M2 high-speed steel		2) +135%
Molinari *et al.*[18]	AISI M2 high-speed steel	Hardness	+8%
		Wear resistance	+51%
Molinari *et al.*[18]	AISI H13 tool steel	Hardness	+7%
		Fracture toughness	+15%
Bensely *et al.*[19]	En 353 (case carburized) steel	Hardness	+3%
		Wear resistance	+372%
Bensely *et al.*[20]	En 353	Hardness	+3%
		Wear resistance	+867%
Liu *et al.*[21]	High-chromium cast irons	Hardness	+57%
		Wear resistance	+15%
Preciado *et al.*[8]	1) 0.18%C case carburized gear steel/	Hardness	1) +17% /
			2) +6%
	2) 0.14%C case carburized gear steel	Wear resistance	1) +25% /
			2) +19%
Yang *et al.*[22]	13Cr2Mn2V white cast iron	Hardness	+9%
		Wear resistance	+9%
Bensely *et al.*[23]	815M17 case carburized steel	Strength	−2%
Firouzdor *et al.* [24]	AISI M2 high-speed steel drills	Tool-life	+126%
Vimal *et al.*[25]	En 31 steel	Hardness	+25%
		Wear resistance	+102%
Dhokey *et al.*[26]	AISI D3 tool steel	Hardness	0%
		Wear resistance	+1257%
Akhbarizadeh *et al.* [27]	AISI D6 tool steel	Hardness	+5%
		Wear resistance	+68%
Wang *et al.*[28]	High-chromium cast iron	Hardness	+15%
		Wear resistance	+19%
Baldissera *et al.*[29]	AISI 302 stainless steel (solubilized and hardened)	Hardness	0%
		Strength	0%
		Fatigue life	+7%
		Corrosion resistance	0%

(*Continued*)

Table 4 Continued

Investigators	*Material*	*Property*	*'Best' change*
Das *et al.*[30]	AISI D2 tool steel	Hardness	+8%
		Wear resistance	+257%
		Fracture toughness	−7%
Li *et al.*[31]	1) Cr8Mo2SiV die steel/	Hardness	1) +5% / 2) +6%
	2) Cr12MoV	Impact energy	1) −42% / 2) −38%
Jaswin *et al.*[32]	1) En52/	Hardness	1) +86% / 2) +12%
	2) 21–4N valve steels	Wear resistance	1) +42% / 2) +24%
Koneshlou *et al.*[33]	AISI H13 tool steel	Hardness	+20%
		Wear resistance	+67%
Slatter *et al.*[34]	1) EN-GJL-250 gray cast iron/ 2) EN 1A mild steel	Wear resistance (impact)	1) +200%/ 1) +400%
Thornton *et al.*[35]	SAE J431 G10 gray cast iron	Hardness	+2%
		Wear resistance	+81%
Amini *et al.*[36]	80CrMo12 5 tool steel	Hardness	+16%
		Wear resistance	+65%
		Impact energy	0%
Gill *et al.*[37]	AISI M2 high-speed steel	Hardness	+8%
		Wear resistance	+58%
Kang *et al.*[38]	$Fe_{75}Ni_{25}$ alloy	Hardness	+159%
		Strength	+16%
		Wear resistance	+56%
Sri Siva *et al.*[39]	100Cr6 bearing steel	Hardness	+18%
		Wear resistance	+37%
Thornton *et al.*[40]	1) EN10083 C50R pearlitic steel/	Hardness	1) +28% / 2) 0% / 3) +4% / 4) +2%
	2) AISI A2 tool steel (annealed)/ 3) AISI D6 tool steel (annealed)/ 4) AISI M2 tool steel (annealed)	Wear resistance	1) +23% / 2) +26% / 3) +30% / 4) +31%
Yan *et al.*[41]	W9Mo3Cr4V high-speed steel	Hardness	+2%
		Wear resistance	+240%
Sri Siva *et al.*[42]	100Cr6 bearing steel	Wear resistance	+52%
Perez *et al.*[43]	AISI H13 tool steel	Hardness	0%
		Strength	0%
		Fracture toughness	+24%

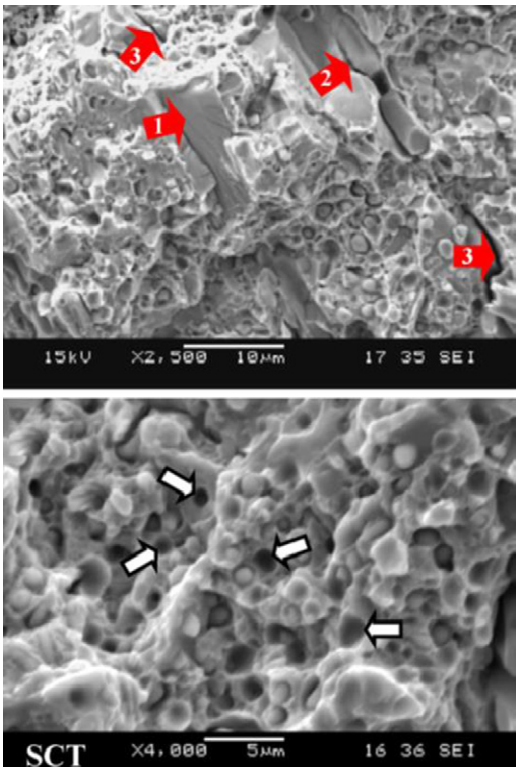
behavior of ferrous alloys following cryogenic treatments. A significant body of work, which is therefore yet to be conducted, is the correlation of chemical and phase composition with pre- and post-cryotreatment heat treatment history with the resulting changes in tribological performance that would enable optimized cryogenic treatment cycles to be developed 'depending on the needs of the application' of the material. This is not a trivial endeavor and will require a concerted and coordinated effort between academic investigators and industrialists.

2.15.2.1.3 Mechanisms of microstructural change

As previously discussed, in ferrous alloys the changes in material properties and behaviors due to cryogenic treatments are thought to result from:

- The transformation of retained austenite to martensite in hardenable steels.[44]
- The precipitation and dispersion of fine carbides in steels with greater excess carbon and strong carbide forming alloying elements.[45]
- The movement and distribution of dislocations during thermal deformation.[46–47]

Higher carbon and higher alloy content steels have lower martensite start and finish temperatures (as illustrated in **Figure 5**), meaning that quenching processes alone cannot convert all of the austenite to martensite. Following quenching, the retained austenite is unstable and can decompose into martensite as a result of the thermal stresses resulting from cryogenic treatments, or the diffusion of excess carbon occurring during tempering.



1. Cleavage facets in primary carbides.
2. Cracking of primary carbides
3. Cracking at the interface between primary carbides and matrix.

White arrows indicate microvoids formed by decohesion of secondary carbides.

Figure 4 SEM micrographs of fracture surfaces of AISI D2 steel as observed by Das *et al.*[30c]

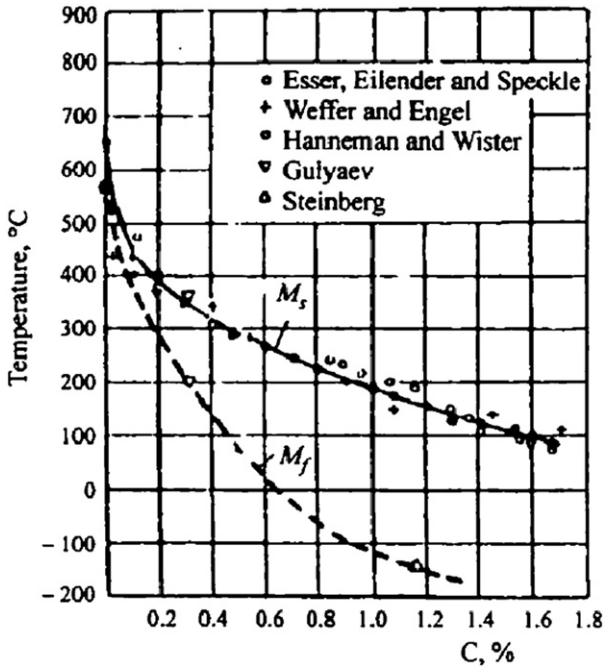


Figure 5 Effect of carbon content in steels on martensite start and finish temperatures.[3]

In their studies, Das *et al.*[30a,45,49] have thoroughly characterized the effects of cryogenic treatment on the microstructure and properties of AISI D2 tool steel, illustrating a marked rise in the proportion of fine carbides following cryogenic treatment and tempering (**Figures 6** and **7**) that is dependent on the cryogenic treatment temperature. This is thought to result from the distortion of the lattice structure, during cryogenic treatment, which leads to dislocation concentrations that carbon atoms may diffuse to during subsequent tempering.[50] The small size of these precipitates is explained by the comparatively low temperatures of tempering, the short time available for diffusion and the local availability of carbide forming elements.

The recent work of Tyshchenko *et al.*[47] and Gavriljuk *et al.*[46] explains the proposed process in more detail. Tyshchenko highlights that carbon atoms at cryogenic temperatures will be effectively immobile and hence unable to form the concentrations necessary for the formation of new precipitates while Gavriljuk suggests that the necessary carbon concentrations are formed by the plastic deformation of martensite at cryogenic temperatures. The transport of carbon atoms is facilitated by the movement of dislocations that underlies this deformation. It is therefore the time-dependent movement of dislocations that causes the relationship between the duration of the cryogenic treatment and the number of fine carbides subsequently precipitated during tempering (and therefore, the extent of change in performance seen in steels with strong carbide forming characteristics).

2.15.2.2 Tool Steels

By a significant margin, the majority of studies involving cryogenic treatments have concerned its application to tool

steels. In this section its effects on these widely used materials are briefly reviewed. Cutting tools are required to machine a wide range of materials including woods, polymers, light alloys, cast irons and steels, hardmetals, and superalloys. The properties of the material to be machined, the desired finish and production rates all impact on the specific properties required of cutting tool materials. As a result the range of materials used to make cutting tools is extensive; however their required properties fall into a manageable number of common categories: strength, hardness, wear resistance, and thermal stability.

Put simply, tool materials must be stronger and harder than the materials they are intended to cut, while their properties must be sustained at the high temperatures they experience during use. For this reason, changes in tool materials due to heat treatments should result in either thermodynamically stable structures or structures that develop beneficially upon heating (e.g., the ability of high-speed steels to 'run the temper').

In the case of a typical orthogonal cutting process (Figure 8), for example, the tool may wear by abrasion (flank face), diffusion (rake face), or by fatigue cracking and impact (which results in notching or chipping of cutting edges). Because of this combination of damage processes, a range of strategies are needed to effectively prevent rapid tool wear. It should therefore be noted that cryogenic treatments, however effective for a particular material, are unlikely to present a solution to all manner of cutting problems in isolation. Therefore exploring coatings and cutting process optimizations are also recommended.

It is often cited that the wear resistance of these classes of materials needs to be improved as cutting and metal forming tools are typically exposed to impact and sliding conditions. Therefore much research effort has been expended in conducting basic dry sliding wear tests in laboratory environments, for which it is easy to obtain specimens, conduct experiments, and provide comparative data with that obtained from industry. However, this also means that there is great variation in the work presented in the literature and released by industry as illustrated by the range of testing conditions highlighted in Table 5. The significance of the tribological conditions (load, sliding speed, and material pairing) applied is typically not considered, even though this may have a significant influence on the results.

Even today, tool steels likely account for the greatest number of cutting tools produced globally. Using the primary strengthening mechanisms of alloying (including chromium, molybdenum, vanadium, and tungsten), control of grain size

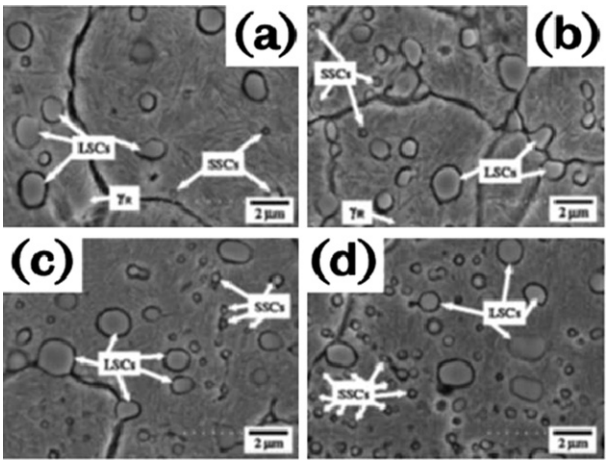


Figure 6 Micrographs showing effects of (a) conventional, (b) 'cold,' (c) shallow cryogenic, and (d) deep cryogenic treatments in AISI D2 tool steel.[30a]

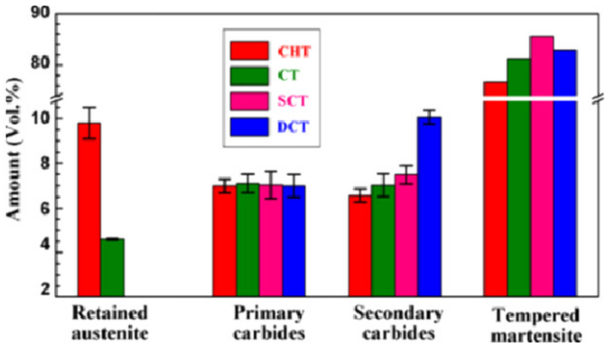


Figure 7 Volume fractions of microstructural constituents following conventional (CHT), 'cold' (CT), shallow cryogenic (SCT), and deep cryogenic treatments (DCT) in AISI D2 tool steel.[30a]

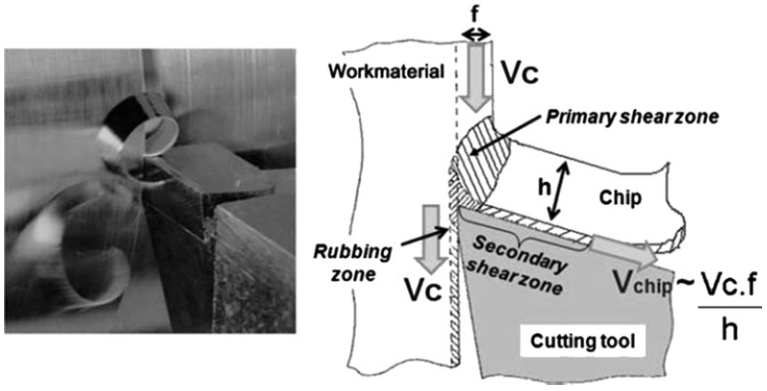


Figure 8 Standard orthogonal cutting model.[51]

(through heat treatment), and due to carbide precipitations these materials can be produced with a hardness up to 8 GPa (815 HV) and thermal stability to 1000 °C.[54]

A typical heat treatment process for a tool steel will involve austenitizing, quenching (rapid cooling by water, oil or gas), and tempering. The quenching process is designed to cause as complete a transformation of austenite to martensite as possible although, as previously highlighted (**Figure 5**), the high alloy content of tool steels can lower the martensite finish temperature to below ambient temperatures. Following quench hardening, tempering serves two purposes. Firstly, to cause the decomposition of retained austenite to martensite by allowing the diffusion of excess carbon and secondly, to allow for the nucleation and growth of carbide precipitates.

Even in the early works of Gulyaev,[3] it had been established that the sooner after quench hardening cryogenic treatment could be applied, the greater the proportion of retained austenite that could be converted to martensite. Yet today, cryogenic treatment is still commonly conducted as an 'after-market' treatment on finished or semifinished components that may have been heat treated hours, days or even months previously, thus limiting the effectiveness of CT in this respect. Furthermore, to avoid austenite stabilization, cooling from the critical temperature to cryogenic temperatures should be continuous.[55]

This is not the complete picture, however, as more recently it has been suggested that there does exist a lower temperature limit below which further transformation will not take place and that a time-dependent isothermal transformation of retained austenite to martensite may continue at cryogenic temperatures. Studying the behavior of X153CrMoV12 powder metallurgy steel using Mössbauer spectroscopy, Gavriljuk *et al.*[46] demonstrated that cooling the material to −196 °C and soaking for 96 h had no effect on martensite content, whereas soaking at −150 °C did cause the transformation of retained austenite. Findings such as these hint at substantial benefits still to be obtained by optimizing CT processes, both in terms of maximizing beneficial properties and minimizing process costs.

By reviewing the three most commonly tested tool steels from the scientific literature (AISI D2, H13 and M2) some further trends can be identified. Their nominal compositions are given in **Table 6**.

Two robust studies of note, concerning the application of cryogenic treatments to AISI D2 tool steel, are those by Collins and Dormer[15] and Das *et al.*[30a,30b] The treatment parameters adopted by these investigators are summarized in **Table 7**.

In their study, Collins and Dormer illustrated two effects influencing wear resistance following cryogenic treatment. Firstly, the complete transformation of retained austenite to martensite and secondly, the precipitation of secondary carbides following CTs. They determined that although a higher austenitizing temperature (and therefore greater retained austenite) leads to a greater hardness attainable with cryogenic treatment, the maximum wear resistance was found following a lower temperature austenitization due to the greater precipitation of secondary carbides during tempering. Lower cryogenic treatment temperatures and longer soaking

Table 5 Wear testing conditions reported in a selection of studies on cryogenic treatments

Investigator(s)	*Sample*		*Counterbody*		*Test parameters*		
	Shape	*Material*	*Shape*	*Material*	*Normal load (N)*	*Sliding velocity ($m\,s^{-1}$)*	*Sliding distance (m)*
Barron[4b]	Pin	M1, M2, T1, T2, H13, D2, A6, A10, O1, P20, S7, etc.	Wheel	Course grit alumina grinding wheel	430	0.48	2160
Collins and Dormer[15]	Block	D2	Wheel	Hardened D2 steel	21	0.50–3.62	200–600
Meng *et al.*[48]	Pin	D2	Disk	WC-coated En 35 steel	49–78	1.50	900
Molinari *et al.*[18]	Disk	M2, H13	Disk	Hardened 100Cr6	150	0.80	5000
Das *et al.*[52]	Pin	M2, D3	Disk	Grinding wheel	20–50	0.18–0.6	324–1080
Rhyim *et al.*[53]	Pin	M2	Disk	Alumina abrasive paper	10	0.11	3.22
Gill *et al.*[37]	Pin	M2	Disk	En 32	49–88	1.5	1800

Source: Adapted from Das, D.; Dutta, A. K.; Ray, K. K. On the Enhancement of Wear Resistance of Tool Steels by Cryogenic Treatment. *Philos. Mag. Lett.* **2008**, *88* (11), 801–811.

Table 6 Compositions of commonly cryotreated AISI tool steels reported in the literature (P, S omitted; balance Fe)

wt.%	*C*	*Si*	*Mn*	*Cr*	*Mo*	*V*	*Other*
AISI D2	1.40–1.60	0.60	0.60	11.00–13.00	0.70–1.20	1.10	1.00Co 0.25Cu
AISI H13	0.32–0.45	0.80–1.20	0.20–0.50	4.75–5.50	1.10–1.75	0.80–1.20	0.25Cu
AISI M2	0.86–0.94	0.45 maximum	0.40 maximum	3.80–4.50	4.70–5.20	1.70–2.10	5.90–6.70 W

Table 7 Heat treatment sequences applied to AISI D2 tool steel in the studies of Collins and Das

	Collins and Dormer[15]	*Das* et al.[30]
Hardening (Q)	(1070, 1040, 1010, 970)°C – N_2-quenched	1024 °C for 30 min – air-quenched
Tempering (T)	200 °C	210 °C for 2 h
Cryotreatment (C)	(−196, −130, −80)°C for 30 min	(−196, −125, −75)°C for 36 h
Treatment order	QCT	QCT

Table 8 Heat treatment sequences applied to AISI H13 tool steel in the studies of Molinari and Koneshlou

	Molinari et al.[18]	*Koneshlou* et al.[33]
Hardening (Q)	1020 °C – vacuum-quenched	1040 °C for 30 min – air-quenched
Tempering (T)	570 °C for 3 h	560 °C for 2 h
Cryotreatment (C)	−196 °C for 35 h	−196 °C for 8 h
Treatment order	QTTC	QTCT

durations were found to be beneficial both in terms of maximizing wear resistance and minimizing loss of toughness.

Subsequently Das *et al.* studied the wear behavior of AISI D2 tool steel in more detail, having observed similar microstructural changes. Under pin-on-disk testing that resulted in severe delamination of the material, they determined that the increased wear resistance of the cryotreated samples was due to their resistance to subsurface plastic deformation and therefore resistance to white layer formation. While a more complete transformation of retained austenite to martensite may result in the highest bulk hardness, the fine carbide precipitates act to limit dislocation movement further and therefore inhibit plastic deformation.

The teams lead by Molinari[18] and Koneshlou[33] have studied the mechanical properties of AISI H13 tool steel in some detail, adopting very similar heat treatment parameters but with different treatment cycle orders (**Table 8**). While Molinari *et al.* applied cryogenic treatment as a final step, Koneshlou *et al.* tempered the material both before and after CT. The difference in material properties developed was significant, with Molinari *et al.* reporting no change in hardness while Koneshlou *et al.* observed a hardness change of 20% (49 HRC–5 HRC) following cryogenic treatment. It seems likely that this marked difference resulted from the quantity and stability of retained austenite remaining prior to cryogenic treatment; in the case of Molinari *et al.* the double tempering cycles will likely have resulted in the decomposition of the austenite.

More recently Perez *et al.*[43] have also studied how cryogenic treatments affect the mechanical properties and fracture behavior of AISI H13 tool steel. Of particular interest in their study was the influence of the rate of the initial cooling, which they varied through the use of different quenching media (**Table 9**). Although the rate of initial cooling did not appear to

Table 9 Heat treatment sequences applied to AISI H13 tool steel in the study of Perez

	Perez et al.[43]		
Hardening (Q)	1020 °C – gas-quenched	1020 °C – oil-quenched	1020 °C – air-quenched
Tempering (T)	590 °C for 2 h		
Cryotreatment (C)	−196 °C for 12 h		
Treatment order	QCTTT		

influence the effectiveness of the cryogenic treatment the application of the subzero treatment had a pronounced effect on fracture toughness, resulting in a greater than 20% improvement. Fractography suggested that the presence of a uniform distribution of fine carbides in the cryotreated samples had resulted in a more 'ductile' fracture behavior, based on the growth and linking of microcavities, in comparison to the brittle fractures that resulted from the stress concentrating effect of more coarse carbides that are otherwise present in the material. The corresponding reduction in carbon content of the martensite, following cryogenic treatment, also contributes to a tougher matrix.

Studies involving AISI M2 high-speed steels present some mixed results. Even as early as the work of Gulyaev, variations in improvements in high-speed steel tool lives following cryogenic treatments had been reported between 40–400%.[3] More recent investigators have reported modest increases in hardness[16,18,37] along with significant improvements in toughness[16,18] and wear resistance.[18,37] In common with other studies involving tool steels, the hardness changes are not proportional to increases in abrasive wear resistance, indicating multiple contributing microstructural factors. However, beyond the conversion of retained austenite to martensite the other changes are less clear.

Treatment cycles adopted by recent investigators have varied widely. Yun *et al.*[16] explored the effects of varied duration and cyclic cryogenic treatments (**Table 10**), as well as its effectiveness after tempering had already been carried out. They determined that cycling cryogenic treatment had a greater effect than simply extending its duration, while CT following tempering still resulted in modest changes in material properties. Hot hardness was found to improve markedly that was argued to result from the formation of sub-nanometer (30–60 Å) carbides on twinning surfaces and other crystallographic defects during cryogenic treatment. Upon heating these carbides were able to grow further and compensate for the thermal effects on the matrix.

By contrast Molinari *et al.*,[18] who also studied whether cryogenic treatment was most effective before or after tempering, and to what degree tempering should be done (**Table 11**), came to different conclusions. While noticeable changes in hardness, strength, toughness, and wear resistance were reported, they observed no change in carbide distributions and even 'tempered martensite de-twinning' following cryogenic treatment. The most effective treatment was deemed to be applying cryogenic treatment following double tempering – based on other studies this would likely have resulted in a tougher material with moderately increased hardness.

Table 10 Heat treatment sequences applied to AISI M2 tool steel in the study of Yun

	Yun et al.[16]			
Hardening (Q)	1250 °C			
Tempering (T)	560 °C			
Cryotreatment (C)	− 196 °C for 24 h	− 196 °C for 48 h	− 196 °C totaling 48 h	− 196 °C for 48 h
Treatment order	QCTTT	QCTTT	QCCCTTT	QTTTC

Table 11 Heat treatment sequences applied to AISI M2 tool steel in the study of Molinari

	Molinari et al.[18]		
Hardening (Q)	1220 °C – vacuum-quenched		
Tempering (T)	550 °C for 2 h		
Cryotreatment (C)	− 196 °C for 35 h		
Treatment order	QTTC	QCT	QCTT

Table 12 Heat treatment sequences applied to AISI M2 tool steel in the study of Gill

	Gill et al.[37]	
Hardening (Q)	Unspecified	
Tempering (T)	150 °C	
Cryotreatment (C)	− 110 °C for 18 h	− 196 °C for 38 h
Treatment order	QCTT	

More recently Gill *et al.*[37] focused on the influence of cryogenic treatment temperature, with only a low-temperature temper applied subsequently (**Table 12**). They determined that hardness was most significantly improved by shallow cryogenic treatment (− 110 °C for 18 h) while wear resistance benefitted substantially from deep cryogenic treatment for a longer period (− 196 °C for 38 h). It was proposed that stresses from the austenite transformation, during cryogenic treatment, result in greater twinning and dislocations; defects to which alloying elements segregate during tempering. The lack of diffusion at cryogenic temperatures results in greater lattice distortion and decreased stability of the martensite, in comparison to that formed through tempering alone. This corresponds closely with the prevailing understanding Gulyaev described at the time.[3]

What is clear from the plethora of studies concerning cryogenic treatment of tool steels is that it can have very substantial (and often substantially beneficial) effects on their properties and in-service performance. However, care needs to be taken to treat tool steels appropriately to maximize the specific qualities required.

For instance, if maximum hardness is required a shallow cryogenic treatment applied immediately following high-temperature austenitization may provide best results. If greatest toughness is needed then perhaps the steel should be first tempered before deep cryogenic treatment to encourage a ultrafine carbide precipitation. As tool-life requires resistance to a combination of wear mechanisms, it may be preferable to perform a medium temperature austenitization followed by quench hardening, multiple deep cryogenic treatment, and tempering cycles.

Defining and expressing the relationships that allow the optimum cycle parameters to be applied, depending on material and application conditions, seems to be the next big challenge in this field.

2.15.2.3 Plain Carbon Steels

In contrast to the wealth of research involving high alloy content tool steels, there is relatively little concerning the effects of cryogenic treatment on 'plain' or low-alloy content carbon steels. As such it is difficult to draw strong correlations from the results and observations reported. Instead, more general findings are highlighted with the compositions of those steels reported in literature given in **Table 13**.

Gulyaev[3] made specific reference to the likely effectiveness of cryogenic treatments on plain carbon steels, suggesting that they would be entirely ineffective on steels with $<0.6\%$C as their martensite finish temperature lies above 0 °C (see **Figure 5**). However, Gulyaev also highlighted that even small amounts of alloying additives can significantly reduce the martensite finish temperature. At the time, cold treatment of carburizing steels was more common than for high-speed steel, as the carburized (higher carbon content) layer retains more austenite during quenching.

In some of their early work, Barron and Mulhern[5] applied varied CTs to AISI 1045 carbon steel, finding that there was no measurable change in hardness but that the retained austenite was almost completely converted to martensite. Modest increases ($\sim 10\%$) were reported in wear resistance but there was no visible carbide formation using optical microscopy. Assuming the wear findings to be accurate, finer precipitates may have developed and been responsible for the change in wear resistance.

The same observations were made by Bensely *et al.*[19] when testing the effect of cryogenic treatments on carburized En 353 low-alloy steel (with notable Cr and Ni, but lower C content). Although the retained austenite was largely converted to martensite through CTs and optical microscopy revealed no change in carbide precipitation, increases in wear resistance of up to 372% were reported. The authors attributed this improvement to fine carbide precipitates that they assumed were present. Although the carburized gear steels used by Preciado *et al.*[8] were very similar in composition, significant hardness increases (up to 17%) in the near surface region were reported alongside much more modest (up to 25%) increases in wear resistance. In this case only a low-temperature (150 °C) temper was conducted. Although the wear testing conditions of each study are difficult to

Table 13 Compositions of plain and low-alloy carbon steels reported in the literature (P, S omitted; balance Fe)

wt.%	*C*	*Si*	*Mn*	*Cr*	*Mo*	*Ni*	*Other*
AISI 1045[5]	0.45	0.20	0.70	0.05	0.01	0.02	0.01Cu
En 353[19]	0.17	0.19	0.92	1.09	0.11	1.05	–
0.18 C steel[8]	0.15–0.21	0.15–0.40	0.60–0.90	0.85–1.15	0.15–0.25	–	–
0.14 C steel[8]	0.11–0.17	0.15–0.40	0.30–0.60	0.80–1.10	0.20–0.30	3.00–3.50	–
En 31[25]	0.96	0.21	0.57	1.09	–	–	–

Table 14 Compositions of stainless steels reported in the literature (P, S omitted; balance Fe)

wt.%	*C*	*Si*	*Mn*	*Cr*	*Mo*	*Ni*	*Other*
AISI 303[4b]	0.08	1.00	2.00	18.00	–	8.00	–
AISI 430[4b]	0.12	1.00	1.00	16.00	–	0.50	–
AISI 440[4b]	0.70	1.00	1.00	17.00	0.75	0.50	–
AISI 304L[56]	0.022	0.35	1.79	18.32	–	8.23	0.40Cu 0.08Co 0.055N
AISI 308L[56]	0.014	0.86	1.73	19.68	0.05	10.15	0.05Cu
AISI 302[29]	0.05–0.15	<2.00	<2.00	16–19	<0.80	6.00–9.50	–

compare (10 N on 6 mm diameter ball in the former and 60–80 N on 10 mm diameter flat-headed pin in the latter), it could be speculated that the higher tempering temperature used by Bensely softened the martensite formed during cryogenic treatment while promoting a more significant fine carbide precipitation. In Preciado's study, the lower temperature tempering may have allowed the martensite to retain its hardness but prevented substantial precipitation of fine carbides.

Vimal *et al.*[25] experimented with a much higher carbon (~1%) low-alloy steel, En 31. Varying the heat treatment process order, with CTs before and after tempering, they obtained the maximum hardness and wear resistance by applying cryogenic treatments immediately after quenching, but before tempering. Observations made suggested the transformation of retained austenite and formation of fine carbides were responsible.

Similarly to studies conducted on tool steels, those (few) conducted on plain carbon or low-alloy steels allow some practical suggestions to be made. Cryogenic treatment can clearly be effective on these materials. However, if a significant increase in hardness is sought, then the composition of the material must be such that the martensite finish temperature is significantly below 0 °C – this may be true in high-carbon steels or those with strong austenite stabilizers such as Cr and Ni. If wear resistance is to be improved then the quenching and CT processes must result in excess carbide formers being present in the microstructure that can then form precipitates during tempering. Therefore low-alloy steels that contain noticeable amounts of Cr or Mo may be suitable for this treatment approach.

2.15.2.4 Stainless Steels

Stainless steels present an interesting 'challenge' when it comes to assessing the effectiveness of cryogenic treatments. While austenitic stainless steels are most common, the fact that they can be produced as ferritic or martensitic materials, with or without significant carbide precipitations arguably means they cannot be treated as a single family of materials. However, the limited quantity of published research involving these materials necessitates a combined approach. Table 14 summarizes the compositions of the stainless steels subsequently discussed. It should be noted that the AISI 3XX stainless steels are austenitic while the AISI 430 stainless is ferritic and the AISI 440 stainless is martensitic.

The earliest application of cryogenic treatments to stainless steels can be found in Barron's wide-ranging wear resistance study[4b] in which, along with a number of other carbon, alloy, and tool steels, AISI 303 (austenitic), 430 (ferritic), and 440 (martensitic) stainless steels were subjected to abrasive wear testing. Although this was an unusual test for materials that are typically not considered for their wear resistance, Barron's study indicated cryogenic treatment could affect any of these materials, with reported increases in wear resistance of 10–20%. In the case of the martensitic stainless steel, transformation of any retained austenite was likely an influencing factor, although with the other two materials it clearly could not have been. This therefore indicates that other microstructural alterations (fine carbide precipitations and/or change in dislocation characteristics) are significant factors.

Despite these seemingly significant findings, very few subsequent studies have involved stainless steels. Singh *et al.*[56] investigated the application of cryogenic treatment in improving the fatigue life of welded joints (AISI 308L) between stainless steel (AISI 304L) plates. Under high-cycle fully-reversed loading conditions, they concluded that the strain-induced martensitic transformation, which occurred during the CT process, resulted in compressive stresses that effectively raised the fatigue limit of the joints; more than doubling their fatigue lives in some cases.

Although this was another seemingly significant finding, the next major study (and by far the most robust to date) was that of Baldissera *et al.*[29] who conducted a full factorial

design of experiments approach to investigate the effects of cryogenic treatments on the hardness, strength, fatigue life and corrosion resistance of AISI 302 stainless steel. Different cryogenic soaking temperatures and times, as well as the effect of solubilization treatments were considered. CTs were found to have no significant effect on the static mechanical properties of the material, or its corrosion resistance under salt-spray. However, deep cryogenic treatment (88 K) was found to significantly improve the fatigue life of the solubilized (but not hardened) samples. Fractographic analyses revealed a number of small secondary cracks in the cryotreated material that could have originated from fine precipitates and acted to absorb energy from the cyclic loading process, increasing the nominal stress intensity required for crack initiation and therefore increasing the toughness of the material.

Studies on stainless steels are too few for strong conclusions to be drawn as to the possible benefits of cryogenic treatments. However, it does appear that subzero treatments may be effective at increasing the fatigue life of stainless steels 'after certain types of treatments.' Aside from being able to convert retained austenite to martensite, if that is what is desired, the changes in mechanical behavior reported to date appear to relate to changes in precipitation behavior, with the possibility of more subtle microstructural changes playing a role as well.

2.15.2.5 Cast Irons and Pearlitic Steels

Two other interesting, overlapping groups when it comes to the application of cryogenic treatments are ferritic and pearlitic cast irons and steels. Although not considered in much of the early work, over the past 10 years investigators have begun to study these alloys more closely. The studies subsequently reviewed involve the alloys summarized in **Table 15**.

There are currently just two groups of work in this field at present. The first, involving the team of Liu,[21] Yang,[22] and Wang[28] *et al.*, have worked extensively to characterize the factors influencing the effectiveness of cryogenic treatments on high-chromium (and therefore austenite retaining and carbide forming) cast irons. More recently the present authors have focused on 'plain' graphitic cast irons[34,35] and pearlitic steels.[40,57]

In their studies, investigators Liu and Yang *et al.* observed that cryogenic treatments following subcritical heat treatments were more effective than air cooling in transforming retained austenite to martensite and promoting the formation of fine secondary $(Fe, Cr)_{23}C_6$ carbides in high-chromium cast irons. While the maximum hardness (+57%) of these materials can be achieved by subcritical heating to around 550 °C before quenching directly in LN_2, the maximum wear resistance (+15%) was obtained by heating to around 600 °C before cryogenic quenching. The reported observations suggested that while the lower temperature treatment resulted in a more complete austenite to martensite transformation, the higher temperature allowed for a greater precipitation and growth of fine secondary carbides, which enhanced the abrasive wear resistance further.

Using a very similar alloy to their colleagues' previous studies, Wang *et al.* further explored the influence of high-temperature treatments on these alloys, with destabilization treatments conducted at 900–1150 °C before air cooling or cryogenic quenching. It was reported that secondary carbides were more uniformly distributed following cryogenic treatment, while the proportion of martensite also increases. In this case both maximum hardness (+15%) and wear resistance (+19%) were found following cryogenic quenching after destabilization treatment at between 1000–1100 °C.

In their recent studies, the present authors have concentrated on characterizing the wear performance of cryogenically treated gray cast irons and pearlitic steels under different dominant wear mechanisms and contact conditions. Investigating the effectiveness of cryogenic treatment on EN-GJL-250 gray cast iron and EN1, a mild steel, Slatter *et al.*[34] recorded 200% and 400% increases, respectively, in their resistance to wear under repetitive hammering impact. Phase transformations were not possible as the low-alloy content and slower cooling (in the case of gray cast iron) prevents austenite being retained; it decomposing to ferrite and cementite instead. No change in precipitation behavior was observed either.

Conducting sliding wear tests on SAE J431 G10 gray cast iron and EN10083 C50R pearlitic steel break disk materials, Thornton *et al.*[35,40] recorded significant increases in the wear resistance of each material. In the case of gray cast iron this was up to +81% at high contact pressures and low sliding speeds, with negligible changes observed at low contact pressures and high sliding speeds. While the hardness of the gray cast iron was not affected by the CT, the hardness of the pearlitic steel was found to have increased by around 20%. This was coupled with a more consistent improvement in wear resistance of 15–20% across all contact pressures tested and visible signs of a shift to a more brittle dominant wear mechanism (with more extensive cracking and pitting visible in cryotreated specimens). As with the previous study by Slatter *et al.*, there were

Table 15 Compositions of cast irons and pearlitic steels reported in the literature (P, S omitted; balance Fe)

wt%	*C*	*Si*	*Mn*	*Cr*	*Mo*	*V*	*Other*
14Cr2Mn2V[21a]	2.76	0.90	1.98	13.72	–	1.6	–
13Cr3Mn1.5V[21b]	2.82	1.24	2.80	13.34	0.70	1.5	–
14Cr4Mn0.5B[21c]	2.92	0.82	3.66	13.86	–	–	0.5B
13Cr2Mn2V[22]	2.76	0.90	1.98	12.62	–	1.6	–
16Cr1Mo1Cu[28]	2.77	0.70	1.90	16.38	1.08	–	0.9Cu
EN-GJL-250[34]	3.25	2.50	0.50	–	–	–	–
SAE J431 G10[35]	3.35–3.60	1.90–2.30	0.60–0.90	–	–	–	–
EN10083 C50R[40]	0.47	0.18	0.75	0.03	<0.01	–	0.03Ni

no obvious microstructural changes to explain these changes. Further analysis of the pearlitic steel using X-ray diffraction, electron-backscatter diffraction, and transmission electron microscopy ruled out the possibility of the presence and transformation of small quantities of retained austenite or fine carbide precipitations resulting from cryogenic treatments.[57]

These findings lead to the conclusion that a more fundamental change in the materials was responsible. It is theorized that a change in dislocation distribution or density due to the cryogenic treatment process could result in a change in the residual stress state and therefore wear behavior of the materials tested. These studies are further elaborated upon as case studies that may provide outline methodologies for assessing the basic tribological performance of cryogenically treated ferrous alloys.

2.15.2.6 Case Studies

2.15.2.6.1 Impact wear resistance of low carbon steel and lamellar graphite cast iron

2.15.2.6.1.1 Introduction

This case study outlines investigations into the influence of cryogenic treatment on the impact wear resistance of low carbon steel and lamellar graphite cast iron. This has been selected because it provides more detailed insight into the types of mechanical performance improvement that can be seen with cryogenic treatment of carbon steels and cast irons, and also because there is very little literature that discusses the impact wear resistance of cryogenically treated engineering materials. It also provides a basic methodology that could be used for assessing the potential using CT in a particular application.

2.15.2.6.1.2 Impact wear

Percussive impact wear mechanisms arise from two or more bodies impinging normally or otherwise to each other. These mechanisms typically involve elements of elastic and plastic deformation, when impact energy is high and depending on the ductility of the materials, and/or fatigue accompanied by wear debris as a result of crack propagation. This mechanism is commonly found in a great many mechanical devices.

Impact wear resistance of materials can be investigated in numerous ways – by firing multiple projectiles being propelled into a stationary target/specimen by gravity, a fluid stream, or magnetic fields and in the case of single impact events a projectile fired by gas propelled barrel. That said, the majority of the previous experimental work conducted in this area has used a reciprocating hammer-type test rig to generate the cyclic percussive impact and it is this type that was used here to subject both untreated and cryogenically treatment specimens to impact. These types of tests rigs are simple to design and construct.

2.15.2.6.1.3 Experimental details

For the purpose of comparing results, it is important to characterize the contact that is produced by the test rig geometry. In this case, the rig impinged a 15 mm chrome steel ball normally to the specimen surface at 10 Hz (impacts per second). The striker had a closing velocity of 0.45 m s^{-1} and an impact energy of 0.22 kJ. Applying analyses demonstrated by Goldsmith[58] and Hertz[59] the contact stress was calculated to be 1.8 GPa. The material specification equivalent to that of the ball is EN 31 or AISI 52100. The hardness of the balls was in the range of 700–900 HV with a maximum surface roughness of 0.125 μm.

The cast iron material used was EN-GJL-250 lamellar graphite cast iron (average hardness of 235 HV) and the low carbon steel used was EN 1A (average hardness of 175 HV).The form of the specimens was circular disks, 50 mm in diameter, cut from an as-cast bar of each material. For simple tests such as these it is useful to keep the geometry of the specimens as simple as possible as this allows isolation of the fundamental material performance, aids comparison at a later date and makes creating a robust dataset easier. Each specimen was cut and ground to be 10 mm thick with a uniform surface finish (0.5 μm).

Two sets of specimens were prepared for each material, one set was cryogenically processed and the other set was left untreated. To the naked eye, the specimens that were cryogenically processed were indistinguishable from those that were left untreated and had similar macro-hardness. When compared to the calculated contact stress of 1.8 GPa the measured hardness values, and therefore the yield strength of the materials tested, indicates that deformation of the material in the contact zone is likely.

Both material types were subjected to identical cryogenic processing using a cryogenic chamber similar to that described in Section 2.15.1.4. All of the specimens were placed in the chamber at room temperature and were then gradually cooled down to $-180\ ^{\circ}C$ over a period of 4 h. The chamber was then held at this temperature for 16 h to ensure uniform transformation in all the specimens. The specimens were then brought back up to room temperature over another period of 4 h. To remove any potential thermal residual stress all the specimens were then subjected to a post-process temper. The specimens were then heated to $170\ ^{\circ}C$ over a period of 2 h. This temperature was held for another 2 h and then was allowed to return to room temperature, again over a period of 2 h.

Five different test lengths were conducted; 4500 impacts, 9000 impacts, 18 000 impacts, 36 000 impacts, and 72 000 impacts. Each test was performed with a new specimen and a new striker and was repeated. The specimens and strikers were cleaned in ethanol prior to testing.

All specimens were examined with a microscope, photographed and measured with a profilometer before and after testing. The total wear was assessed by geometry change due to the very small fraction of the overall specimen mass being removed. Geometry change is also preferred as mass that can be 'moved' via plastic deformation to a position where it can bear little or no load and this is a phenomenon that is undetected by mass difference techniques. Wear scar volumes were estimated by modeling the wear scars as spherical caps and using the recorded scar geometry to calculate an estimated wear scar volume. The form and nature of any visible wear debris was also recorded along with any notable features.

2.15.2.6.1.4 Results

2.15.2.6.1.4.1 Specimen overview and wear scar morphology

2.15.2.6.1.4.1.1 Untreated specimens

The wear scars can be easily seen by the naked eye as roughly circular craters on the surface of the specimens and the wear debris visible varied in size and nature. In general, the wear

debris visible on the low carbon steel specimens can be characterized as small amounts of fine dark colored debris with more metallic particles visible after the longer tests and for the lamellar graphite cast iron large metallic flakes were visible. In all cases a negligible amount of debris was adhered to the ball. Each wear scar was examined under a microscope and any observations regarding the condition and form of the edge and nearby debris were also recorded. In general, the low carbon steel wear scars (**Figure 9**) exhibited smooth, well-defined edges, some scars were slightly oval in shape and there was pitting of the scar surface indicating that there was material removal. The lamellar graphite cast iron wear scars were rougher, but still had well-defined edges. The scars were generally regular in shape with some evidence of cracking around the scar edge as shown in **Figure 10**.

2.15.2.6.1.4.1.2 Cryogenically processed specimens

The low carbon steel specimens had very little visible wear debris, even after the longer tests; whereas there were small amounts of dark, and after the longer tests more metallic looking, debris on the untreated specimens. Again, in all cases a negligible amount of debris was adhered to the ball. The wear scar edge present after the 4500 impact test was very clean and well defined. Longer tests had slightly rougher, cracked edges, but otherwise clean and well-defined wear scar (**Figures 11** and **12**). All the wear scars created had grinding marks (from the surface preparation) clearly visible in the wear scar crater, the number of marks observed to be inversely proportional to test length, indicating a mixture of brittle fracture, and plastic deformation in the impact zone.

After the 4500, 9000, and 18 000 impact tests the cryogenically treated lamellar graphite cast iron specimens all had clearly visible wear scars with grinding marks still distinguishable in the crater too. Each specimen had fine, dark colored ring of wear debris around the edge of the wear scar crater. The specimens subjected to 36 000 and 72 000 impacts had thicker rings of wear debris (**Figures 13** and **14**) and in the case of the 72 000 impact test some of the wear debris were several millimeters away from the impact zone. The predominant feature of the untreated lamellar graphite cast iron was rough, but still well-defined wear scar edges with some evidence of cracking (**Figure 10**). The wear scars created on the untreated specimens also did not leave any evidence of grinding marks in the wear scar craters. The grinding marks

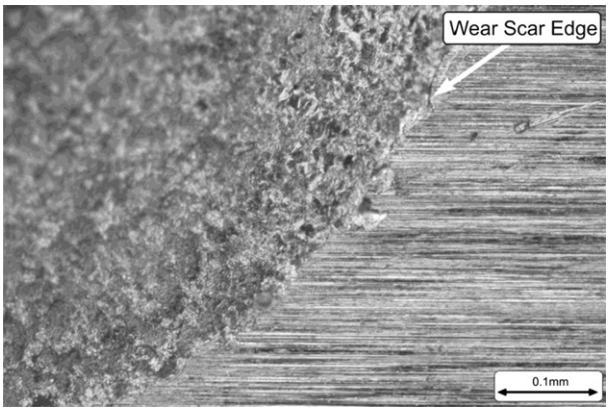


Figure 9 Section of wear scar edge of a low carbon steel specimen subjected to 72 000 impacts.

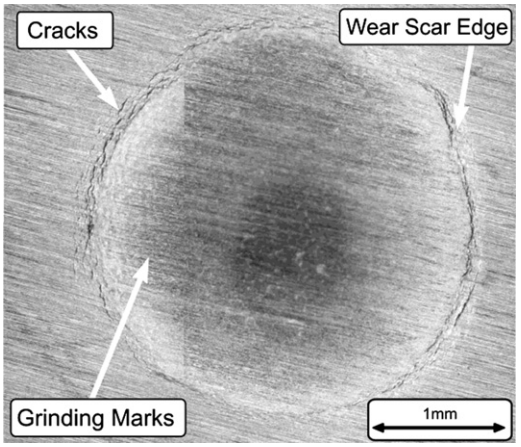


Figure 11 Wear scar on a cryogenically processed low carbon steel specimen subjected to 72 000 impacts.

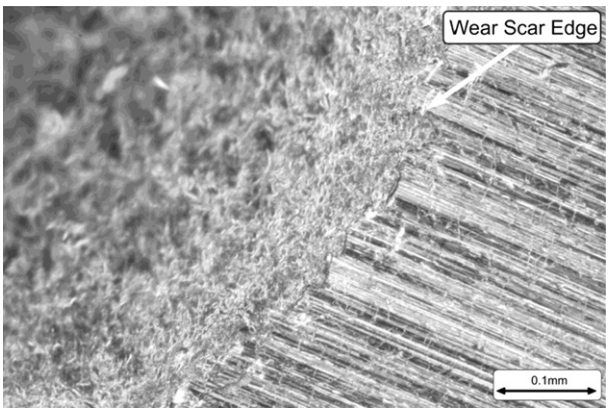


Figure 10 Section of wear scar edge of a lamellar graphite cast iron specimen subjected to 72 000 impacts.

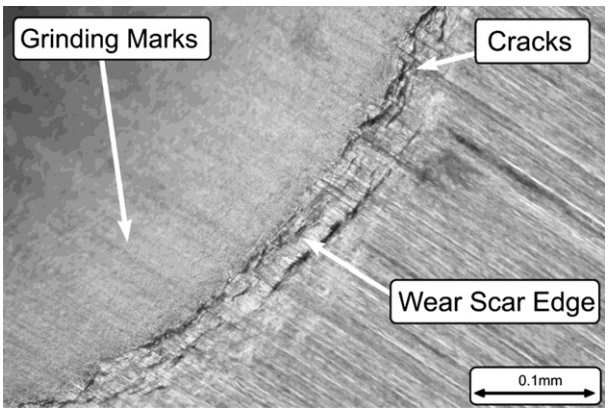


Figure 12 Wear scar edge on a cryogenically processed low carbon steel specimen subjected to 72 000 impacts.

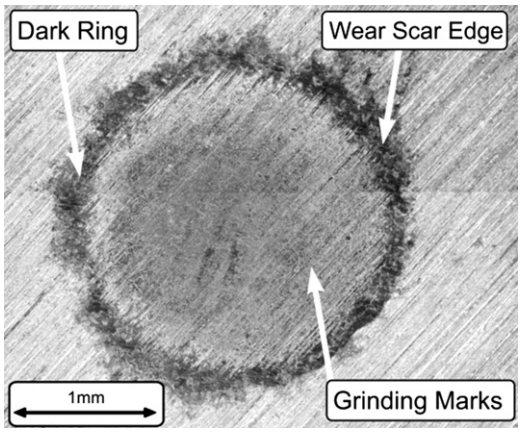


Figure 13 Wear scar from a cryogenically processed lamellar graphite cast iron specimen subjected to 72 000 impacts.

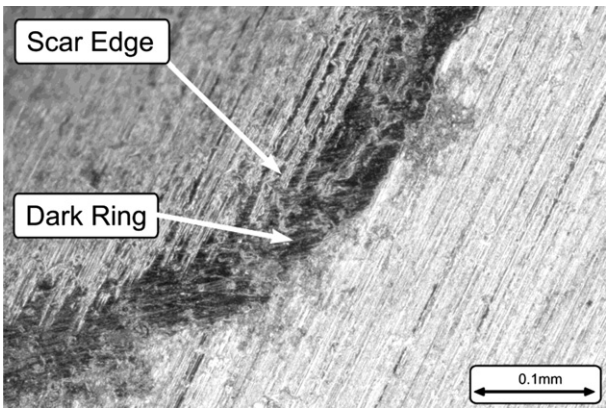


Figure 14 Wear scar edge from a cryogenically processed lamellar graphite cast iron specimen subjected to 72 000 impacts.

visible on the processed specimens after testing (**Figures 9** and **10**) are wider or flatter indicating plastic deformation.

These differences suggest that the cryogenic processing has modified the material properties so that plastic deformation 'wear' is the predominant wear mechanism rather than brittle fracture as was the case with the untreated specimens. The suggestion that the material has been modified is supported by the difference in wear debris that was visible. The untreated specimens produced large metallic flake-like debris whereas cryogenically processed specimens produced much finer darker particles.

2.15.2.6.1.4.1.3 Wear scar measurement

A profilometer was used to confirm the optically measured wear scar diameters and to investigate the nature of wear scar 'shoulders.' Traces were taken across the center of each wear scar and the typical profiles for each of the specimen types after the 72 000 impact tests are shown here.

Three different diametric measurements were taken across the center of the wear scar and the averages of these are shown in **Figure 15**. The maximum and minimum measured values are indicated by the error bars. **Figure 15** clearly shows that the cryogenic processing improves the impact wear resistance of the low carbon steel specimens. For all test lengths the average wear scar diameter of the cryogenically processed specimens is between 55 and 80% that of the corresponding test for an untreated specimen. The results of the lamellar graphite cast iron are less clear cut. It is clear that for the longer tests the cryogenic processing has improved the impact wear resistance of the specimens to a similar extent to that of the low carbon steel. That said, however, for the shorter tests it appears that when considering the wear scar diameter, the cryogenic processing has reduced the ability of the material to resist impact wear.

The profiles shown in **Figure 16** show that the size of the wear scars on the cryogenically processed low carbon steel specimens is clearly smaller, in depth and diameter, than the

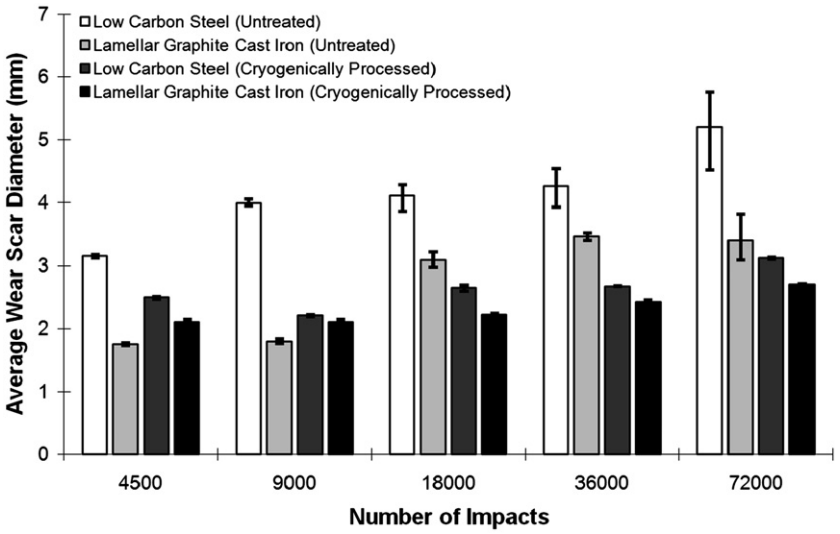


Figure 15 Average wear scar diameter vs. number of impacts for cryogenically processed and untreated low carbon steel and lamellar graphite cast iron specimens.

scar present on the untreated low carbon steel specimens for the same number of impacts. As mentioned previously, the untreated low carbon steel specimens exhibited plastically deformed shoulders and this phenomenon is also present in the cryogenically processed specimens. It is interesting to note that the size of the shoulders has not decreased to the same degree as the overall size of the wear scar. This suggests that the cryogenic processing has not reduced the ductility of the material at the expense of improving the wear resistance. That said however, the level of surface cracking around the wear scar edges has increased on the processed specimens (compare **Figure 9** with **Figure 12**) suggesting that the ductility has actually been reduced as the load on the material has exceeded the plastic limit.

Figure 17 shows the difference in wear scar profile between the untreated and cryogenically processed lamellar graphite cast iron specimens subjected to 72 000 impacts. As with the low carbon steel specimens the wear scar is smaller after processing. The difference in wear scar depth is less than before, but the plastically deformed shoulders are minimal on the cryogenically processed specimens. This suggests that the processing modifies the cast iron in such a way to reduce the ductility of the material. Comparing the images of the wear scar edges supports this statement as the surface cracking visible on the untreated material (**Figure 10**) is not visible on the edges of the processed cast iron (**Figure 14**).

2.15.2.6.1.4.1.4 Estimation of wear scar volume

Using the wear scar profilometry data an estimation of wear scar volume can be made using the spherical cap method (**Figure 18**). Again, the overall trend is that of the results presented so far in this section in that the processed materials

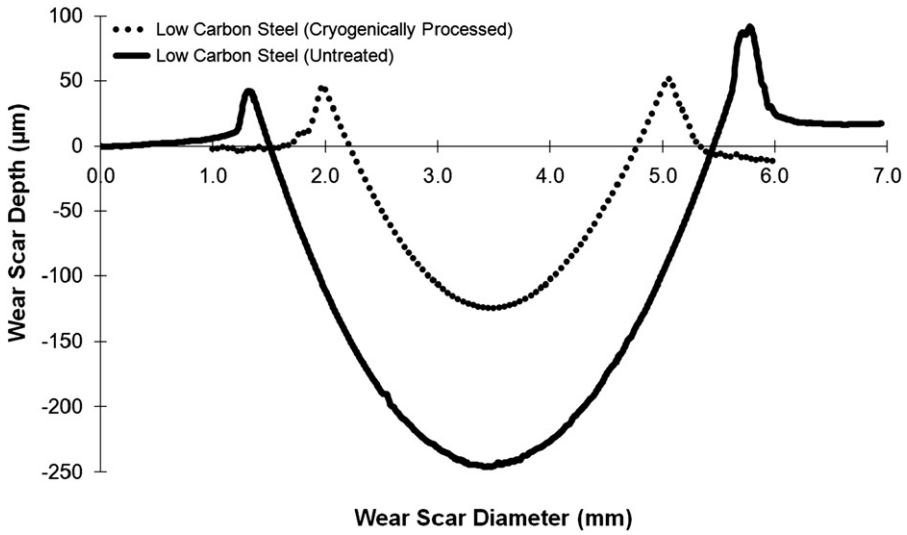


Figure 16 Profiles of wear scar on untreated and cryogenically processed low carbon steel specimens after 72 000 impacts.

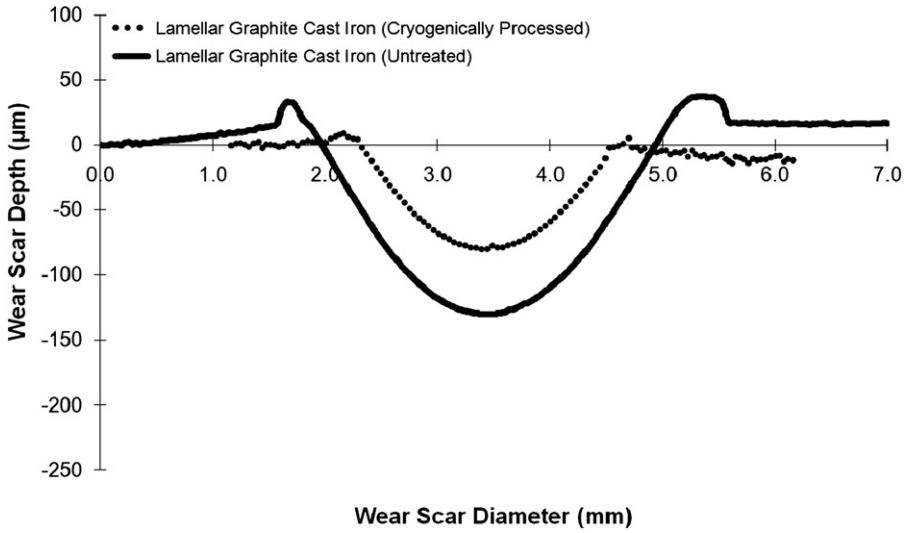


Figure 17 Profiles of wear scars on untreated and cryogenically processed lamellar graphite cast iron specimens after 72 000 impacts.

exhibit improved resistance to impact. The cast iron has the greatest change in wear volume between the untreated and treated specimens. Given the magnitude of measured error for these particular results it seems likely that there is a microstructural reason for this rather than simply experimental variance, however a detailed microstructural analysis would need to be performed.

2.15.2.6.1.4.1.5 Comparison with a 'traditional' heat treatment process

Figure 19 compares the estimated wear scar volumes for the lamellar graphite cast iron specimens presented here with those estimated during work on laser hardening of lamellar graphite cast iron.[19] For clarity, only the results for the 72 000 impact tests are included. As part of that investigation, lamellar graphite cast iron specimens were subjected to laser transformation hardening in an attempt to improve their resistance to impact wear. Several different sets of laser operating parameters, primarily energy density and speed, were used when treating the cast iron specimens and these induced different levels of localized phase transformations in the surface of the material. These specimens were then subjected to identical tests as those described earlier. The best performing laser treated cast iron specimens exhibited similar levels of wear to the best performing cryogenically processed cast iron specimens tested for the work presented here. It appears that the potential of improving the wear resistance of lamellar graphite cast iron is similar to that of more classical heat treatment in the form of the laser hardening process.

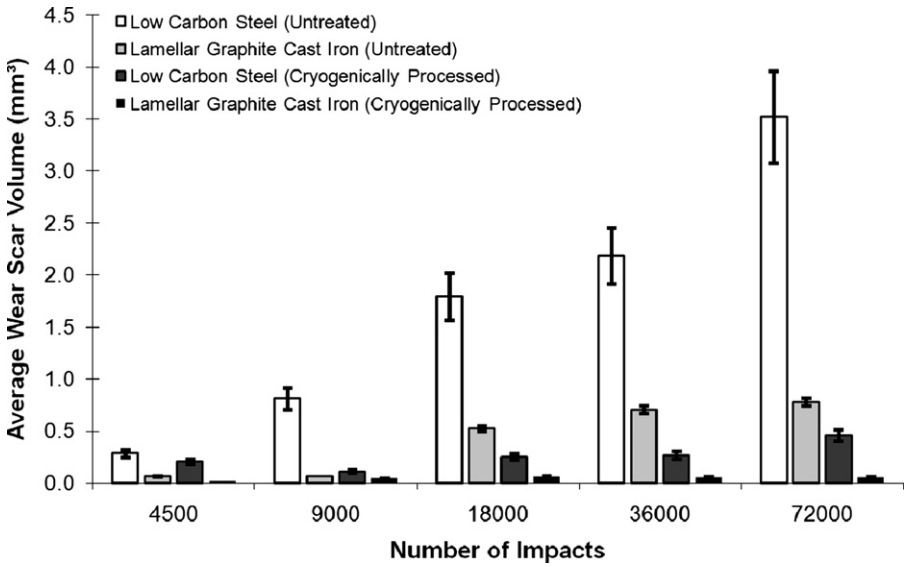


Figure 18 Average wear scar volume vs. number of impacts.

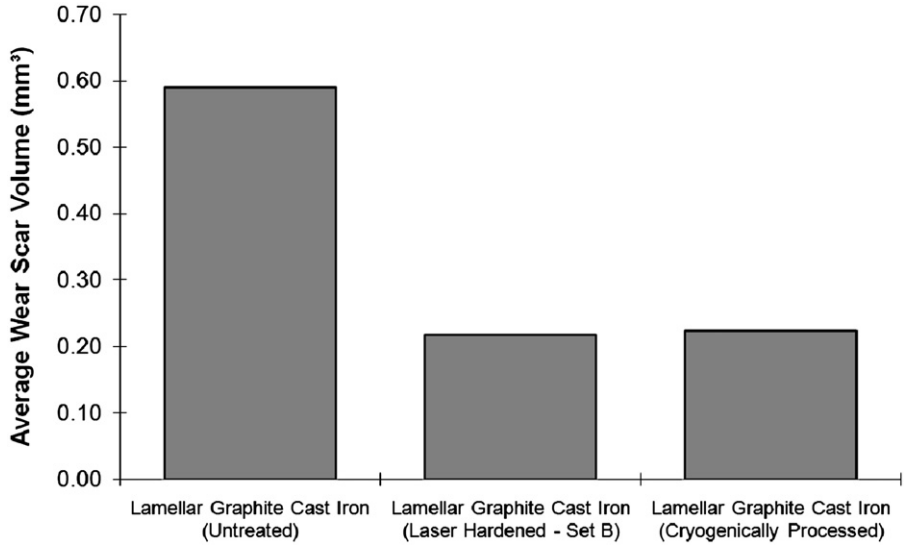


Figure 19 Comparison of wear scar volume for lamellar graphite cast iron specimens subjected to 72 000 impacts.

2.15.2.6.1.5 Summary

This case study shows that cryogenic processing can have a positive effect on the wear resistance of Fe–C alloys. It also demonstrates how relatively similar materials respond differently to the same treatment. The low carbon steel that was tested using the impact wear test rig showed some improvement to its ability to resist impact wear but more investigation would be required to confidently say if the improvement was 'significant' as described in the literature.[1] The lamellar graphite iron also showed improvement in its ability to resist impact wear and the general level of improvement was greater than the low carbon steel.

In general, the wear mechanisms observed in all specimens were as typically found in impact wear studies. Where there is a high impact velocity, which is considered to be the case throughout this work, and therefore high impact energy, if there is a soft material in the contact plastic deformation occurs with ductile extrusion away from the contact. This was observed particularly in the untreated specimens subjected to 72 000 impacts and, as can be seen in **Figure 16**, the low carbon steel specimen exhibits large shoulders as a result of the plastic deformation. The 'softer' material, the steel (**Figure 9**), exhibited smooth wear scar edges that further support the presence of this wear mechanism.

This case study also illustrates one of the difficulties of assessing cryogenically treated materials as it is clear that much more data would need to be collected to have a high level of confidence in the performance improvements seen and their subsequent repeatability. This would reveal any unknown artefacts of the test procedure, such as changes in the loading conditions, even though the measured variance is small. Similarly, small microstructural flaws in the material, coincident to the loading of those particular specimens, could suddenly accelerate the wear process.

2.15.2.6.2 Sliding wear resistance of pearlitic brake disk materials

2.15.2.6.2.1 Introduction

This case study reviews investigations concerning the influence of cryogenic treatments on the sliding wear resistance of hypo-eutectoid pearlitic carbon steel and lamellar graphite pearlitic cast iron brake disk materials.[35,40,57] These have been selected because, although they are commonly commercially cryo-treated components, there is almost no coverage of them in the scientific literature. As anecdotal commercial evidence suggests cryogenic treatments may substantially increase the life of these components, preliminary tribological studies and microstructural observations were conducted in an attempt to provide some scientific verification.

2.15.2.6.2.2 Requirements of brake rotor materials

Brake rotors are invariably required to withstand a range of conditions, which are strongly influenced by their specific applications. In light goods vehicles (LGVs), sports cars, whether used for motor racing, locomotives, or aircraft, brake rotors need to provide consistent performance throughout their design life. Composites and light alloys offer a range of benefits including weight saving and therefore reduced fuel consumption,[60] high performance at extreme loads and temperatures,[61] as well as improved thermal stability.[62]

Nonetheless, traditional materials such as-cast irons and plain carbon steels still dominate markets in terms of volume produced, due to their low cost, ease of manufacture and good machinability, as well as a high heat capacity which lends itself to thermal stability. These factors are crucial as brake disks must absorb the vast majority of the kinetic energy of the vehicle during braking, much of which is inevitably converted to heat. Even in typical LGV applications, brake disk temperatures may reach 700 °C.[63]

Furthermore, the parameters of braking cycles vary significantly. Typical LGV brake rotors may be subjected to longer applications of low braking forces (to gently slow and stop the vehicle) while racing cars will exert very high braking loads for short periods of time on their braking systems. Temperature requirements for motorsports brake rotor materials are therefore substantially higher, hence the wide use of ceramics and composites. Conversely, brake rotors for domestic vehicles are expected to have long fatigue lives (often as long as the life of the whole vehicle); therefore steels and cast irons are still desirable.

2.15.2.6.2.3 Experimental details

The commercial brake disk materials selected for this study were SAE J431 G10 (a lamellar graphite cast iron) and AISI 1050/EN10083 C50R (a medium carbon steel). Material compositions are given in **Table 16**.

The brake disk materials were tested as finished rotors (with modifications made away from the wear track to fit them to the test rig). Their surfaces had a machined finish with a roughness of around 2.5 µm. Both materials had pearlitic–ferritic microstructures while SAE J431 G10 also contained lamellar graphite flakes and sulfide inclusions.

All specimens were subjected to the same deep cryogenic treatment cycle, illustrated in **Figure 20** and summarized as: cooling at 1–2 K min^{-1} to 93 K, soaking for 24 h, heating at 1–2 K min^{-1} back to ambient temperature with a low-temperature stress relief cycle conducted at 60 °C for 1 h.

The testing program involved Vickers macro- and micro-hardness tests (20 kgf/196.2 N and 0.05 kgf/4.905 N, respectively), pin-on-disk sliding wear testing using a Plint TE99 (BICERI/Eyre) Universal Wear Testing Machine (**Figure 21**) 15 mm diameter hardened AISI 52100 chrome steel balls (**Table 17**), volume-loss wear measurements using measurements made with a 2D stylus profilometer (**Figure 22**) and subsurface microstructural observations using optical and

Table 16 Nominal compositions of brake disk materials studied

%wt.	C	Si	Mn	P	S	Cr	Mo	Ni
SAE J431 G10	3.35–3.60	1.90–2.30	0.60–0.90	0.10	0.15	–	–	–
C50R	0.47	0.18	0.75	0.010	0.007	0.03	<0.01	0.03

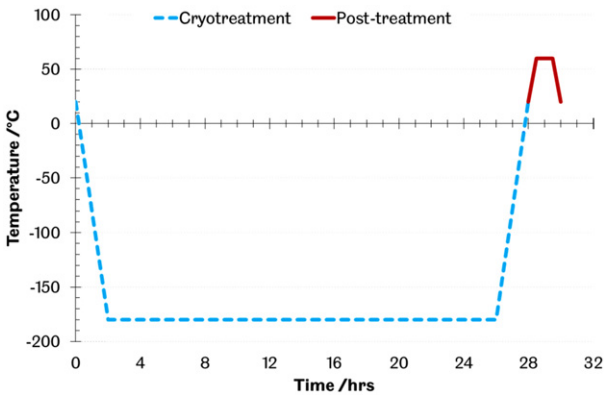


Figure 20 Deep cryogenic treatment cycle applied to specimens used in this study.

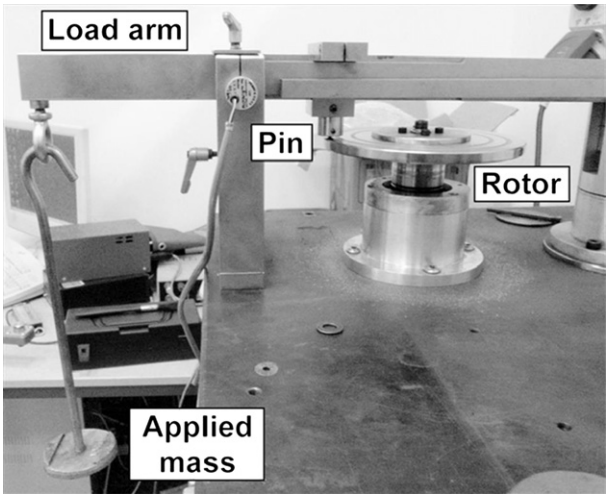


Figure 21 TE99 in pin-on-disk mode as used in this study.

Table 17 Properties of AISI 52100 chrome steel wear pins

Material	*$HV_{98.1N}$ (MPa)*	*R_a,max (μm)*	*Diameter (mm)*
AISI 52100	6878–8829	0.125	15

scanning electron microscopy. Given the changes subsequently reported for the pearlitic carbon steel, additional samples were later prepared for transmission electron microscopy.

Sliding wear tests were conducted over a range of initial Hertzian contact pressures and sliding speeds in each case. As it is difficult to replicate realistic brake cycling conditions in a laboratory environment, these were chosen to provide comparative data when a dominant wear mechanism could be clearly defined. In the case of SAE J431 G10 GCI brake rotors, this involved contact pressures of 375.0, 562.5, and 750.0 MPa and sliding speeds of 1.34, 1.78, and 2.24 m s^{-1}. Similarly, C50R carbon steel rotors were subjected to contact pressures of 1000, 1300, and 1600 MPa at a fixed sliding speed of 1.18 m s^{-1}. Optical and scanning electron micrographs were generated from untreated and cryotreated brake rotors not used in testing, to ensure that the observed microstructures were not affected by thermal or mechanical conditions resulting from wear testing.

2.15.2.6.2.4 Results

2.15.2.6.2.4.1 Hardness

While neither the bulk hardness (**Table 18**) or matrix hardness (**Table 19**) of the gray cast iron (G10) material was substantially affected by the cryogenic treatments, the carbon steel (C50R) was shown to respond significantly, with 28 and 17% increases in hardness determined during macro- and microhardness testing respectively.

2.15.2.6.2.4.2 Wear testing

Similarly to the hardness results, wear tests of the G10 and C50R brake rotors displayed very different results. In the case of the GCI rotors, the changes in measured wear rates following cryogenic treatment were highly variable (**Figure 23**) with a weak trend toward increasing benefits of cryogenic treatments in improving wear resistance under higher contact pressures. When changes in wear rates were considered against overall sliding distance (**Figure 24**) another weak trend with an apparent negative correlation between increased wear resistance and longer sliding distances. Optical microscopy of wear scars revealed no dominant change in wear mechanism from predominantly abrasion and pitting.

By contrast, sliding wear testing of the carbon steel brake rotors showed a consistent, if statistically small, increase in wear resistance following deep cryogenic treatment over all the contact conditions tested (**Figure 25**). The mean reductions in wear rate at initial contact pressures of 1000, 1300, and 1600 MPa were 14.4, 12.1, and 22.7%, respectively. However, observations of the worn surfaces (**Figure 26**) revealed no substantial change in the dominant wear mechanism that was, once again, abrasion and pitting.

2.15.2.6.2.4.3 Microstructural observations

In neither case did optical microscopy reveal any obvious changes in microstructure that may explain the observed changes in mechanical performance of either material. Darkfield optical micrographs (**Figure 27**) revealed a mixture of coarse (A) and fine (B) pearlite was the dominant structure in G10 specimens, along with lamellar graphite flakes (C) and manganese sulfide inclusions (small bright spots). In C50R specimens (**Figure 28**) the microstructure again consisted of coarse (A) and fine (B) pearlite interspersed with a smaller number of ferrite grains (C). Scanning electron microscopy allowed these structures to be resolved further, but again did not reveal any obvious microstructural changes due to CT processes.

Given the consistent changes measured in its hardness and wear resistance, the microstructural characterization was continued for the carbon steel (C50R) using transmission electron microscopy to obtain evidence for any change in nanoprecipitation behavior or dislocation structure that may have occurred due to deep cryogenic treatment. The micrographs generated (**Figure 29**) revealed similar nano-precipitates in both untreated and cryotreated samples. These ranged from 50–150 nm hexagonal, to 10–50 nm spherical and tiny

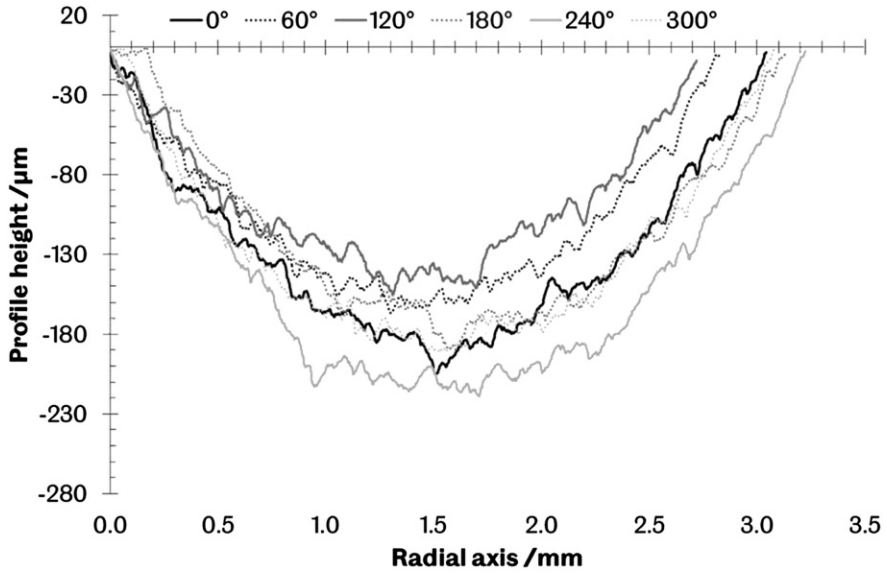


Figure 22 Typical profilometry traces of wear scars used to estimate wear volume in brake disk specimens.

Table 18 Macro-hardness test results from brake disk surfaces

Specimen type	*Treatment*	*$HV_{196.2N}$ (MPa)*	*Coefficient of variation*
SAE J431 G10	As-received	2070	3.5%
	DCT	2109 (+1.9%)	4.9%
C50R	As-received	1622	4.3%
	DCT	2071 (+27.7%)	1.8%

Table 19 Micro-hardness test results from brake disk samples

Specimen type	*Treatment*	*$HV_{0.4905N}$ (MPa)*	*Coefficient of variation*
SAE J431 G10	As-received	3600	17.2%
	DCT	3679 (+2.2%)	11.8%
C50R	As-received	1927	2.6%
	DCT	2244 (+16.5%)	2.0%

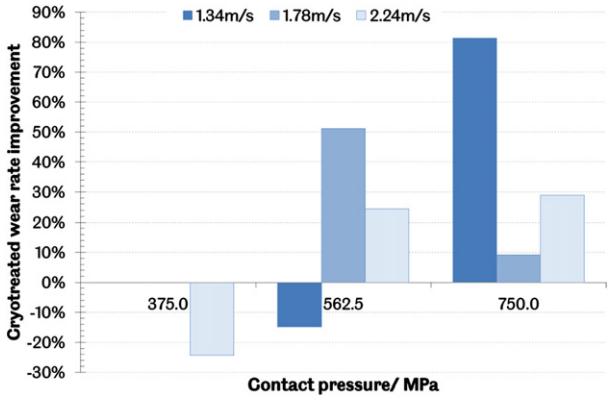


Figure 23 Change in wear rates determined from G10 pin-on-disk tests.

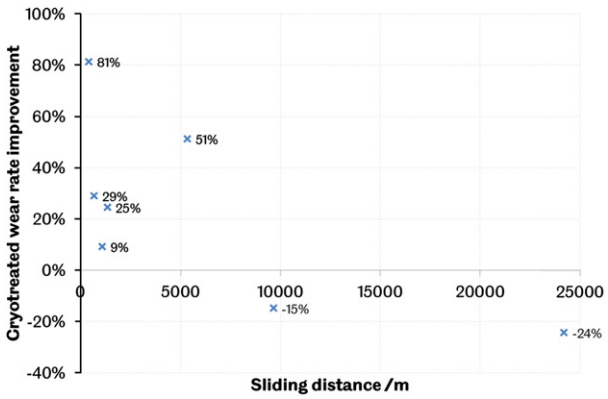


Figure 24 Change in wear rates from G10 pin-on-disk tests normalized by contact pressure and sliding speed.

(<10 nm) rod-like precipitates. Observations made along phase interfaces revealed no evidence of change although, qualitatively, there did appear to be fewer dislocations in the cryogenically treated samples.

2.15.2.6.2.5 Summary

This case study illustrates that cryogenic processing can have a significant positive effect on the wear resistance of pearlitic carbon steels, although its influence over lamellar graphite cast irons remains unclear. It also demonstrates the innate difficulty in identifying the fundamental microstructural changes that are responsible, given the need for nanoscopic investigations that are beyond the reach of most providers or users of cryogenic treatment processes. It is also challenging to make representative observations of microstructures on the basis of commercial components, where geometric factors may influence the homogeneity of the structure produced in different regions during manufacturing.

In the case of the cast iron, the differential between rates of thermal contraction of the graphite flakes and adjacent phases may have resulted in damaging stresses being exerted. This, in turn, may have reduced the self-lubricating properties of GCI[64] that are dependent on the shearing of graphite flakes along precise crystallographic planes.[65]

The increases in hardness (>15%) and wear resistance (>15%) for the pearlitic carbon steel tested are significant and support the need for further study, as there are other microstructural changes that remain to be explored. For instance nano-precipitates may have been obscured, in the present study, along grain boundaries or at phase interfaces, while changes in the distribution of dislocations throughout the material may significantly influence its mechanical performance.

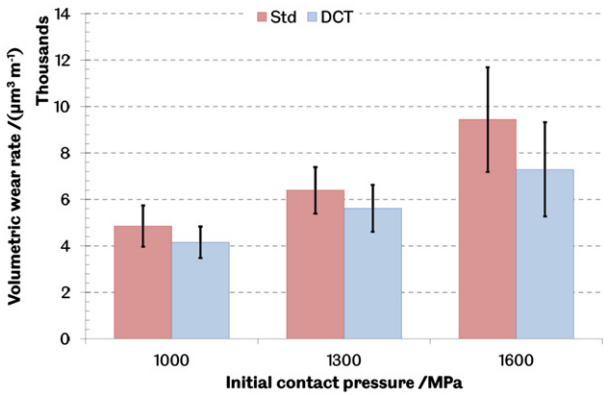


Figure 25 Volumetric wear rates ($\pm 1\sigma$) determined from carbon steel brake pin-on-disk tests.

2.15.3 Cryogenic Processing of Nonferrous Alloys

Considering the wide use of nonferrous metals, particularly in structural applications and machine tools, there is a disproportionate focus on ferrous-based alloys as the target of cryogenic processing research and commercial endeavor. This is probably because much of the early research in this area was driven by tool manufacturers requiring greater wear resistance and the oft-reported 'fact' that cryogenic processing relies on converting the any retained austenite into martensite. That said, light alloys such those based on aluminum, titanium, and magnesium, represent a developing area for cryogenic treatment with a view to minimize the trade-offs that are made in performance at the expense of mass reduction. A much smaller area of focus considers whether cryogenic treatment has potential to be applied to nonmetallic composite materials.

This section identifies the state of the art and trends in performance modification that can typically be achieved by subjecting nonferrous metals to cryogenic processing and then offers a selection of specific examples of its use across the main light alloy families and cobalt-bonded tungsten carbide.

2.15.3.1 State of the Art

When compared to the volume of work conducted to investigate the cryogenic treatments on ferrous materials, the body of work investigating its effect on nonferrous materials is very

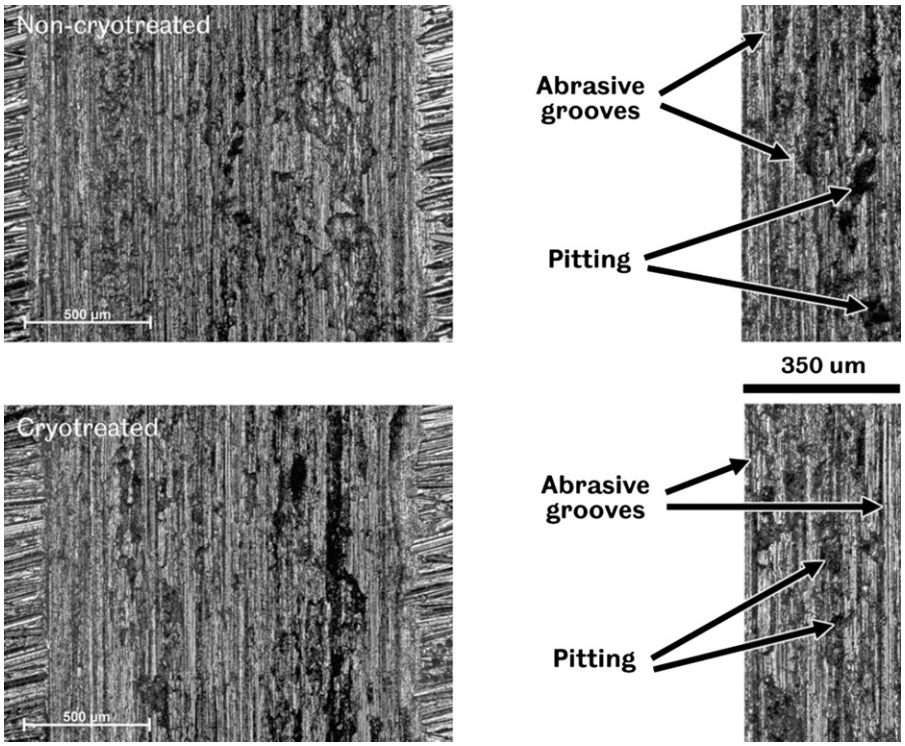


Figure 26 Typical wear scars developed in (top) standard treated and (bottom) cryotreated C50R disks.

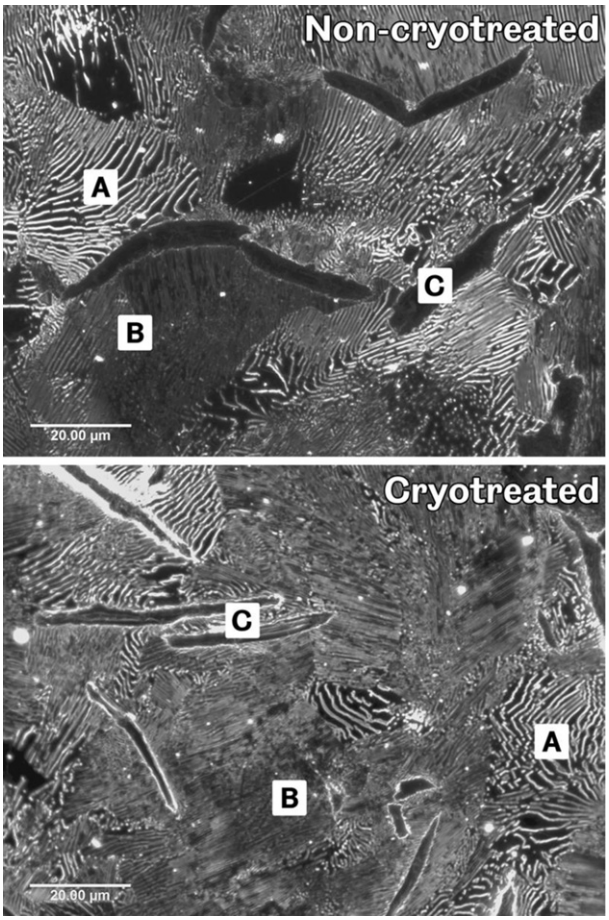


Figure 27 Optical micrographs of non-cryotreated (top) and cryotreated (bottom) SAE J431 G10 material.

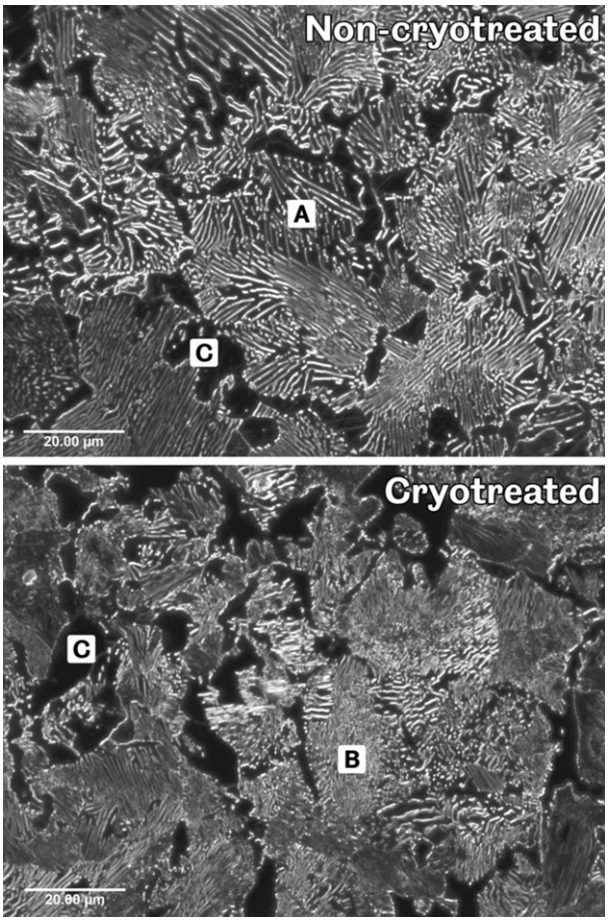


Figure 28 Optical micrographs of non-cryotreated (top) and cryotreated (bottom) C50R material.

small. Much of the effort has been focused on the performance of these classes of materials when used in components that typically operate at cryogenic temperatures (e.g., in space) or their response to being subjected to a manufacturing process that has a cryogenic element to it (e.g., cryogenic machining, rolling, or friction stir welding) rather than a cryogenic treatment process as defined here. The varied but preliminary studies conducted to date clearly demonstrate the need for greater investigations into the effects of cryogenic treatments in light alloys.

The broad approach to investigating the behavior of these materials is similar to that used for ferrous materials; specimens are subjected to a fixed CT process followed by a range of mechanical tests and microstructural analyses.

In the same way that there are common microstructural changes caused by cryogenic treatment to be found across ferrous materials the same is true for nonferrous metals and this is most often described as taking the form of a microstructural refinement of some description. For example, in titanium alloys it appears that cryogenic treatment changes the morphology of β particles which means the now coarse divorced eutectic β phase particles penetrate the matrix and thus strengthen it against crack propagation. Broad observations described as 'refinement of grain size' and 'microstructural stabilization' are also regularly made for many light metal alloys but without conclusive evidence being presented.

These microstructural changes are often presented in attempts to explain changes in the performance of materials subjected to cryogenic treatment that result from common engineering assessments. It is often suggested that the bulk macro-hardness of the material changes and that this is dependent on the parameters of the treatment process, usually the length of the soak at a particular cryogenic temperature. If this is optimized then some materials show potential for an improvement in their hardness, but this is often restricted to an 'apparent hardness increase' reported by users of a treated component rather than a robust laboratory analysis.

Improvement in hardness is often an area of interest because of its role in wear performance. As with ferrous metals, for nonferrous materials to be subjected to contacts across a range of loads and lubrication regimes is an increasingly common occurrence, particularly as component lightweighting becomes more prevalent in the automotive and aerospace industries. The largest gains to date have been seen in magnesium alloys but the process has competition in this area in the form of the much more mature coating technologies. Although the bulk of work carried out to investigate cryogenic processing of nonferrous metals has considered alloys of

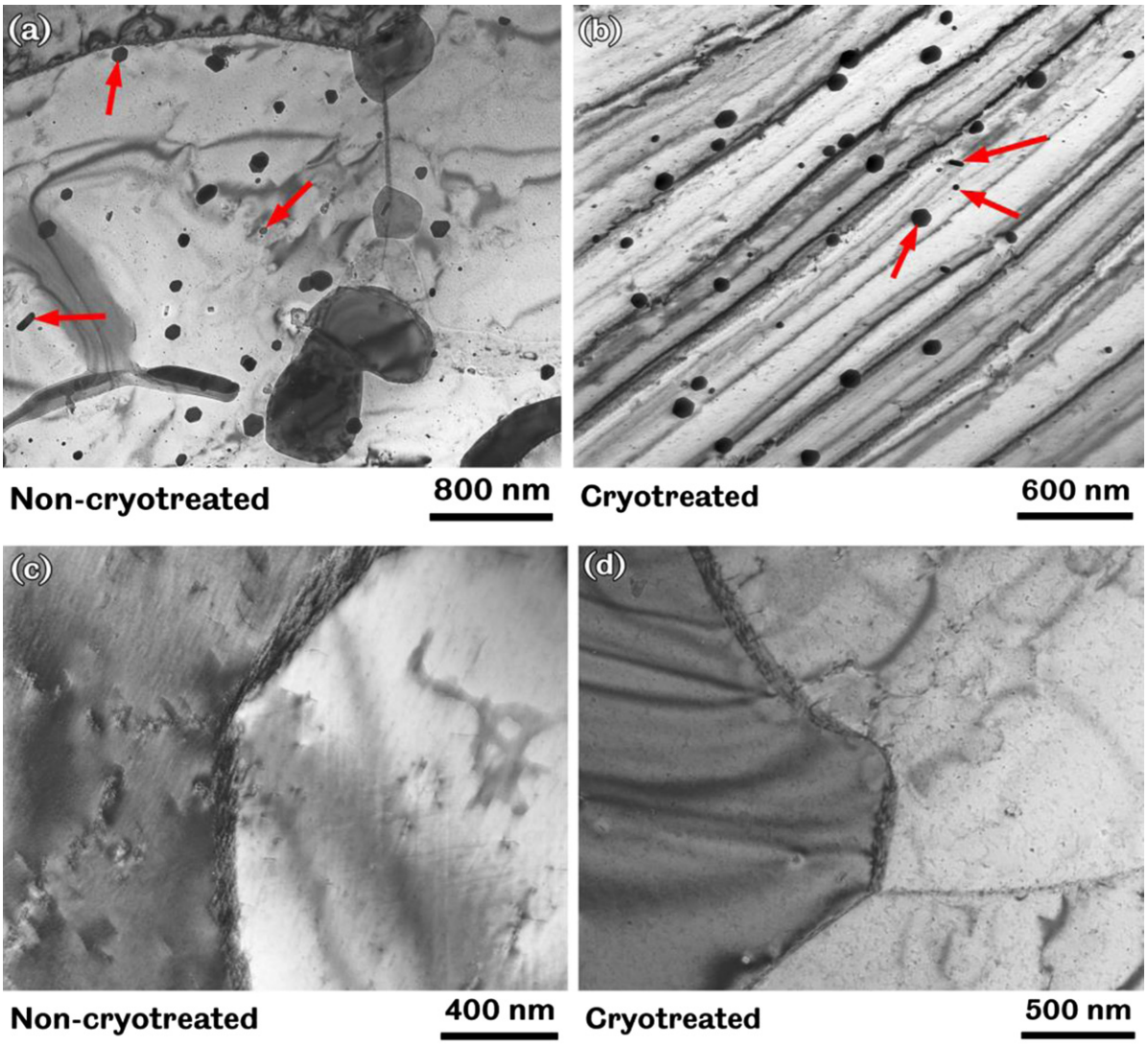


Figure 29 TE micrographs showing: (a) non-cryotreated and (b) cryotreated nano-precipitates in ferrite; (c) non-cryotreated and (d) cryotreated ferrite–ferrite grain boundaries.

aluminum, titanium, and magnesium some consideration has been given to other nonferrous alloys. These studies tend to consider the response of one particular parameter of one particular alloy so therefore it is very difficult to draw any cross-cutting conclusions. Examples of these studies include; the improvement of the thermal conductivity of a proprietary copper alloy[66] and improving electrical discharge machining (EDM) by treating the electrodes.[67] An emerging area is the consideration of cryogenic processing as a suitable treatment for composite materials, particularly those with a metallic component such as metal–matrix–composites (MMCs).[68]

Although a niche area of work, cryogenic processing has also been shown to have beneficial effects on nonmetallic composite materials, such as the PTFE/Kevlar hybrid fabric.[7] Typically used as bearing liner materials due to their tribological properties, PTFE and Kevlar exhibit poor adhesion to the resin binder due to their chemically inert nature. Cryogenic treatment was shown to improve the wear resistance of the hybrid material, with the improvement suggested to be as a result of increased mechanical interlocking of the phenolic resin used, as a result of the fabric roughening at cryogenic temperatures.

2.15.3.2 Aluminum Alloys

As the oft-cited mechanisms behind cryogenic processing are similar to those behind ageing, it seems likely that aluminum alloys that are age-hardenable should also respond to cryogenic processing. Work conducted with a view to investigating this hypothesis on AA6061 discovered that adding a deep cryogenic soak (optimized to be in the range 18–21 h) in between a quenching and ageing treatment had an effect on its performance.[69] When compared to AA6061-T6 the cryogenically processed material had up to three times the hardness and when subjected to a simple milling process showed an improvement in roughness ($1.4R_a$–$0.7R_a$). Both of these effects are attributed to the formation of fine precipitates during the cryogenic

processing. Similarly, AA 6106-T4 subjected to DCT and micro-abrasion tests demonstrated a 26% reduction in wear rate.[70]

Efforts to improve the resistance of aluminum alloys to crack growth, either through fracture or fatigue, have led to attempts to apply cryogenic treatment to these types of materials. A 7075-T651 alloy was cryogenically treated at −196 °C (77 K) caused a 12% increase in the Charpy impact energy, but without any significant change in strength or hardness. It is interesting to note that specimens held at their soak temperature for 2 h showed no significant improvement, whilst those treated for 48 h did, indicating a time-dependent microstructural change is likely responsible.[71]

Research attempting to improve the wear resistance of aluminum overhead conductor suspension clamps recorded a 20% increase in the lifespan of the conductor wire material along with a reduction in damage to the suspension clamps. This was judged to have occurred as a result of an increase in 'ultra-fine distributed precipitates' following cryogenic treatment.[72]

This effect and the inhibiting effect of increased dislocations following cryogenic treatment are discussed by Wang *et al.*[73] in their study on the effects of cryogenic pretreatments on the mechanical performance of friction-stir-welded joints in 2024-T351 aluminum alloy. In testing, they observed improved elongation before fracture in samples having undergone cryogenic treatment.

2.15.3.3 Magnesium Alloys

The recent trend for lightweighting engineering components in the aerospace and automotive sectors has seen a significant increase in the use of magnesium alloys because of their low relative density. In automotive components, where it is beneficial to reduce rotating/moving mass, there are many sliding contacts where wear resistance is critical. As one of the generally cited benefits of CT is to improve wear resistance, it seems worthwhile to attempt to apply it to magnesium alloys. Similarly, although many magnesium alloys have adequate creep resistance at ambient temperatures, their limitations are quickly reached at the elevated temperatures found in automotive powertrain components. As one might expect with its near universal use when a magnesium alloy is specified AZ91, particularly because of its castability, is commonly used as the material to be treated.

Studies investigating the effects of cryogenic treatment on AZ91 magnesium alloy have observed improved wear resistance after DCT at −196 °C (77 K).[74] A >60% reduction in wear rate of an Mg–Zn–Gd alloy following deep cryogenic treatment by direct immersion in LN_2 have also been achieved. Following treatment, the alloy was observed to contain a substantially greater volume fraction of secondary phase particles, to which the increase in wear resistance was attributed, and it had changed from a disordered solid solution to an ordered solid solution.[75]

Efforts to improve the creep resistance of AZ91 magnesium alloy by using a cryogenic treatment have resulted in improved wear resistance after DCT at −196 °C (77 K).[74] The improved creep behavior was attributed to morphological changes which prevented grain boundary sliding at high temperatures.

Tests to determine the tensile properties of an extruded Mg–Gd–Y–Zr(Mn) alloy at cryogenic temperatures have shown a significant increase in tensile strength, yield strength, and elongation before fracture, which is attributed to the precipitation of a large number of 'rod-like, tree-like, and chrysanthemum-like' features within the microstructure. While direct immersion in LN_2, or CQ may lead to thermal shock and brittleness of materials, these investigations seem to show that the microstructural changes due to DCT may have a more significant effect on the performance of a material.[76]

It appears that there is at least some degree of consensus about the mechanism behind observable mechanical improvements that can be made to magnesium alloys using cryogenic processing.

Tests on AZ31 magnesium alloy[77] subjected to range of DCT soak times (2–48 h) using electron microscopy techniques and pole figure analysis suggest that cryogenic processing causes changes in grain orientation. This change is attributed to a frame-like twinning process and results in a reported increase in hardness and tensile strength but this improvement is highly dependent on the length of the soak. This means that any specific application would need optimizing to ensure repeatable results.

Similar work on AZ31, and also ZK60, shows that there are changes to the grain orientation accompanied by second phase precipitate strengthening[78] again resulting in reported improvements in hardness and tensile strength. A more quantitative analysis[79] adds to these findings by stating that for AZ91 the sizes of the precipitates are refined from 8–10 μm to 2–4 μm. It has also been suggested that, in the case of AZ91 in particular, the improvement in hardness is facilitated by the aluminum atoms jumping to defect sites as the material contracts at low temperature[80] and then forming the basis for nucleation of precipitates during the final aging process.

2.15.3.4 Titanium Alloys

There is very little known about the effect that cryogenic processing has on titanium and its alloys. This is due to the general understanding that cryogenic processing is a 'heat' treatment and that commercially available titanium alloys are not amenable to thermal hardening. Some research has attempted to investigate the effect of CT on titanium alloys but the results are inconclusive and are often arrived at obliquely during research not directly considering the problem.

In dentistry, nickel–titanium alloys are commonly used as an alternative material to stainless steel for endodontic tools which are used to remove material during root canal therapy. CT of these types of instruments results in a small increase in measureable micro-hardness, but no apparent 'hardness' improvement when used clinically,[81] or in their wear resistance.[82]

What can be broadly described as 'materials at low temperature' research, such as conducted by the space community, often produces insight that crosses over into cryogenic processing. Mechanical tests performed on a Ti–2.5Cu alloy immersed in LN_2 at temperatures of 77 K found that that both the ductility and low-cycle fatigue life of the alloy was improved.[83] It was concluded that nano-scale precipitates

hinder the movement of dislocations, thereby preventing crack formation.

Commercial alloy grades of titanium, such as Ti–6Al–4V, are commonly used in components where they are subjected to tensile loads. CT has been used to modify the plasticity of Ti–6Al–4V and, when combined with a suitable ageing process, this can be improved by >20% with no change in microhardness but at the expense of some (5%) reduction in tensile strength. It is suggested that this improvement is due to the CT reducing the β phase content of the material thus decreasing the resistance to dislocation movement. The combination of CTs and aging treatments appears to cause the formation and interaction of dislocation networks, resulting in the formation of twins within the microstructure.[84]

Due to their low shear modulus, titanium alloys regularly undergo surface engineering (usually a deposition-type coating) when they are subjected to sliding contacts. Cryogenic processing has potential to be used in lieu of a coating for these applications and it has been reported that DTC can produce a slight increase in hardness, due to grain refinement, giving improved resistance to sliding wear. It has also been reported that the increase in hardness is linear with soak temperature and soaking time.[85]

Due to their reputation as 'difficult to machine' materials titanium alloys have been the focus of a significant proportion of the development of cryogenic machining. There has been a considerably less effort expended investigating the potential of cryogenically processing the material prior to processing using conventional machining techniques (i.e., non-cryogenic machining).

Due to its high electrical resistivity, titanium is difficult to process using EDM techniques. Many avenues (such as ultrasound assisted EDM, dry EDM, and indeed cryogenically cooling the electrode) have been explored to improve the efficiency of EDM for titanium alloys, including cryogenically processing the workpiece prior to machining operations being performed. A 24 h DCT soak has been found[86] to improve the machinability of Ti 6246 by allowing up to 8.5% improvement in material removal rate in an EDM drilling operation. Claims for EDM operations using proprietary titanium alloys producing greater improvements have also been made.[87]

The wear rate of the tool is also a significant consideration in EDM processes and this was reduced by around 30%. The surface roughness measured inside the holes improved by up to 10%. It is suggested that these improvements are as a result of the reduction in electrical resistivity and conductivity (as measured using a standard four probe setup) but it is unknown how the cryogenic processing causes this change in a titanium alloy.[86]

2.15.3.5 Cobalt-Bonded Tungsten Carbides

In the last decade, attention has partly shifted from the application of cryogenic treatments to tool steels, to its application to sintered, cobalt-bonded tungsten carbide tool materials. These materials (often referred to as 'hardmetals' or 'cermets') are inherently harder and more wear resistant, with greater thermal stability, and are therefore commonly used for high volume manufacturing operations. When combined with appropriate coatings they can sometimes be used in high-speed machining and hard machining operations as well.

Although very minimal work has been done to characterize the mechanical properties of cryogenically treated sintered carbides to date, alongside a variety of tool wear and tool-life studies the hardness of these materials has been reported. Summarized in **Table 20**, it can be seen that the hardness changes reported are far more moderate than those reported for tool steels. However, these data suggest that cryogenic treatments may significantly improve the hot hardness[88] of

Table 20 Hardness data reported for cryotreated WC–Co

Investigators	*Material description*	*Temperature (°C)*	*Treatment*	*Hardness (change)*
Seah *et al.*[90]	WC–7Co–1??	Ambient	As-received	89.3 HRA
			Cryoquenched	89,4 (+0.1%)
			Cryotreated	89.4 (+0.1%)
			Cryo + Temper	89.4 (+0.1%)
			Cold treated	89.5 (+0.2%)
			Cold + Temper	89.7 (+0.4%)
Thakur *et al.*[91]	93WC–Co–??	Ambient	Untreated	17760 $HV_{19.6}$
			Cryotreated	17850 (+0.6%)
SreeramaReddy *et al.*[88]	Kennametal P-30	Ambient	Untreated / cryotreated	88.5 / 86.5 HRA (−2.2%)
	WC–17Co–1.4TiC–1.4TaC	100		85.0 / 86.0 (+1.2%)
		200		82.0 / 84.0 (+2.4%)
	Multilayer CVD coating:	300		81.0 / 83.0 (+2.5%)
	TiN: 1.5 μm, TiCN: 12.5 μm,	400		76.5 / 79.8 (+4.3%)
	Al_2O_3: 6 μm, TiN: 5 μm	500		73.0 / 78.0 (+6.8%)
		600		63.0 / 71.8 (+14.0%)
Gill *et al.*[89]	ISO-P25	Ambient	Untreated	88.2 HRA
	WC–6Co–1.4TiC		SCT	92.6 (+5.0%)
			DCT	92.8 (+5.2%)
Thornton *et al.*[92]	SHM H13A	Ambient	Untreated	20740 $HV_{4.905}$
	WC–6Co		DCT	22 640 (+9.2%)

Note: ?? indicates the presence of unknown additional alloying elements.

Table 21 Tool wear data reported for cryotreated WC–Co

Investigators	*Tool material*	*Feed rate (mm rev^{-1})*	*Depth of cut (mm)*	*Cutting speed (m min^{-1})*	*Tool-life changes reported*
Gill *et al.*[94]	Sandvik ISO P-25	0.1	1.0	110	+27–36%
	SPUN 120308			130	+21–27%
	WC–6Co–1.4TiC			150	+19–25%
				180	+13–20%
Gill *et al.*[94b]	Sandvik ISO P-25	0.1	1.0	110	−3.9–+34%
	SPUN 120308			130	+9.8–32%
	WC–6Co–1.4TiC			150	+15–24%
	TiAlN coated			180	+18–21%
SreeramaReddy *et al.*[88]	Kennametal ISO P-30	0.22	1.0		
	WC–17Co–1.4TiC–1.4TaC				
				200	+7.7%
	Multilayer CVD coating:			250	+22%
	iN: 1.5 μm			300	+22%
	TiCN: 12.5 μm			350	+15%
	Al_2O_3: 6 μm				
	TiN: 5 μm				
Thornton *et al.*[92] (Reduction in flank wear values given)	SHM H13A	0.2	0.5	50	0%
	WC–6Co			95	+6%
				140	−5%

complex WC–Co alloys, while only shallow cryogenic treatments (163–193 K) may be required[89] for this to happen.

Due to their prevalence as cutting tools, and the relative difficulty with which laboratory samples can be made from sintered carbide materials, the majority of studies to date have focused on tool-life and tool wear. The results from these have generally indicated benefits to the application of cryogenic treatments, as summarized in **Table 21**. However, as might be expected and supported by observations made by the present authors,[92] increases in hardness and predominantly abrasive wear resistance is typically accompanied by a decrease in toughness. In the case of cutting tools this may lead to more unexpected catastrophic failures if the material properties are not properly characterized and cutting parameters adjusted accordingly.

Generally speaking, it has been reported that cryogenic treatment diminishes the adhesion strength of common tool coatings (such as TiN and (Ti, Al)N) resulting in an overall decrease in tool-life,[93] although cryogenic treatment has consistently been found to improve the tool-life of uncoated carbide tools.[94] The reason for this weakening of the interface between coating and substrate is thought likely to be due to the difference in thermal contraction between the two materials during cryogenic treatment.

During cutting operations, tools are subjected to high temperatures and therefore it is important that any changes as a result of a heat treatment or coating process are stable at those temperatures. A good indicator of this is the relative performance of tools under dry and wet, continuous and interrupted machining processes – the latter conditions leading to greater cooling and lower temperature rises in the tool material.

Based on the studies of Yong *et al.*[95] and Gill *et al.*[96] (**Figure 30**), it appears as though at least some of the changes resulting from cryogenic treatments are not thermodynamically stable. Yong *et al.* reported that the improvement in tool-life due to deep cryogenic treatment could be increased by 10% when milling a medium carbon steel with coolant, as opposed to without. During turning operations, Gill *et al.* observed that

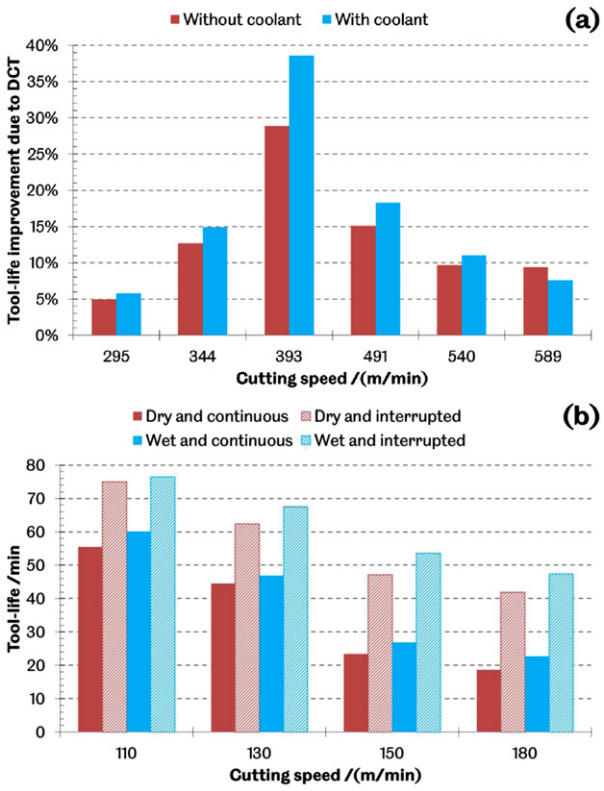


Figure 30 Influence of cutting conditions on performance of cryotreated WC–Co cutting tools[57] based on studies by (a) Yong *et al.*[95] and (b) Gill *et al.*[96]

interrupting the cutting process (disengaging the tool from the workpiece) was more effective in prolonging the life of cryo-treated tungsten carbide inserts than by using coolant.

Numerous process factors influence the properties of WC–Co materials, with the physical effects responsible tending to concern the concentration of cobalt binder or carbon near the surface, compressive stresses induced in the WC phase due to cobalt hardening, and the precipitation of fine eta-phase carbides. Reported microstructural changes due to cryogenic treatments are often not backed up by robust characterization techniques and are sometimes contradictory. For instance the shrinkage/densification of the cobalt binder,[91] enlarging of the carbide grains[88] and resulting in fine eta-phase carbide precipitates[88,90,97] have all been suggested to play a role.

In a particular study of note, Gisip *et al*. performed a series of energy-dispersive X-ray spectroscopic analyses at increasing distances from the edges of flouted router bits used to machine medium-density fiberboard. Their chemical analysis illustrated a significant reduction in the rate of removal of binder phase and carbide grains from the surface following cryogenic treatment. There was also less tendency for high-temperature oxidation and corrosion to occur.

The range of tool-life and tool wear studies available for cobalt-bonded tungsten carbides paints a compelling picture that cryogenic treatments can offer significant benefits. However, to date, the explanation from rigorous microstructural studies are lacking, thus preventing more widespread adoption of the technique.

Acknowledgments

The authors wish to acknowledge the assistance of Cryogenic Treatment Services Ltd. (UK) (http://www.195below.co.uk/) for carrying out the deep cryogenic treatment on the specimens and the Materials Engineering Research Institute (MERI) at Sheffield Hallam University (UK) (http://www.shu.ac.uk/meri) for the use of their facilities to capture a number of the wear scar images used in the case studies presented.

See also: 2.1 Fundamentals of Heat Treating Metals and Alloys

References

1. Reitz, W.; Pendray, J. Cryoprocessing of Materials: A Review of Current Status. *Mater. Manuf. Process.* **2001**, *16* (6), 829–840.
2. Bond, K. Cryogenic Treatment of Gears. *Gear Sol.* **2009**, 6.
3. Gulyaev, A. P. Cold Treatment of Steel. *Vestnik Inzhenerov i Technikov* **1946**, *4–5*, 7.
4. (a) Barron, R. F. Effect of Cryogenic Treatment on Lathe Tool Wear. *Prog. Refrig. Sci. Technol.* **1973**, *1*, 529–533. (b) Barron, R. F. Cryogenic Treatment of Metals to Improve Wear Resistance. *Cryogenics* **1982**, *22* (8), 409–413.
5. Barron, R. F.; Mulhern, C. R. Cryogenic Treatment of AISI-T8 and C1045 Steels. *Adv. Cryog. Eng.* **1981**, *27*, 20.
6. Kumar, M. S.; Lal, D. M.; Renganarayanan, S.; Kalanidhi, A. An Experimental Investigation on the Mechanism of Wear Resistance Improvement in Cryotreated Tool Steels. *Indian J. Eng. Mater. Sci.* **2001**, *8* (4), 198–204.
7. Zhang, Z. Z.; Zhang, H. J.; Guo, F.; Wang, K.; Jiang, W. Enhanced Wear Resistance of Hybrid PTFE/Kevlar Fabric/Phenolic Composite by Cryogenic Treatment. *J. Mater. Sci.* **2009**, *44* (22), 6199–6205.
8. Preciado, M.; Bravo, P. M.; Alegre, J. M. Effect of Low Temperature Tempering Prior Cryogenic Treatment on Carburized Steels. *J. Mater. Process. Technol.* **2006**, *176* (1–3), 41–44.
9. Stratton, P. F. Optimising Nano-Carbide Precipitation in Tool Steels. *Mater. Sci. Eng. A: Struct. Mater. Prop. Microstruct. Process* **2007**, *449*, 809–812.
10. Das, D.; Ray, K. K.; Dutta, A. K. Influence of Temperature of Sub-Zero Treatments on the Wear Behaviour of Die Steel. *Wear* **2009**, *267* (9–10), 1361–1370.
11. Darwin, J. D.; Lal, D. M.; Nagarajan, G. Optimization of Cryogenic Treatment to Maximize the Wear Resistance of 18% Cr Martensitic Stainless Steel by Taguchi Method. *J. Mater. Process. Technol.* **2008**, *195* (1–3), 241–247.
12. Gill, S. S.; Singh, H.; Singh, R.; Singh, J. Cryoprocessing of cutting Tool Materials – A Review. *Int. J. Adv. Manufact. Technol.* **2010**, *48*, 175–192.
13. Das, D.; Dutta, A. K.; Ray, K. K. On the Enhancement of Wear Resistance of Tool Steels by Cryogenic Treatment. *Philos. Mag. Lett.* **2008**, *88* (11), 801–811.
14. Bensely, A.; Paulin, P.; Nagarajan, G.; Lal, D. M. Dimensional Stability in Cryogenic Treatments. *Gear Solutions*, July 2009, p. 6.
15. Collins, D. N.; Dormer, J. Deep Cryogenic Treatment of a D2 Cold-Work Tool Steel. *Heat Treat. Met.* **1997**, *24* (3), 71–74.
16. Yun, D.; Lin, X. P.; Xiao, H. S. Deep Cryogenic Treatment of High-Speed Steel and Its Mechanism. *Heat Treat. Met.* **1998**, *25* (3), 55–59.
17. Lal, D. M.; Renganarayanan, S.; Kalanidhi, A. Cryogenic Treatment to Augment Wear Resistance of Tool and Die Steels. *Cryogenics* **2001**, *41* (3), 149–155.
18. Molinari, A.; Pellizzari, M.; Gialanella, S.; Straffelini, G.; Stiasny, K. H. Effect of Deep Cryogenic Treatment on the Mechanical Properties of Tool Steels. *J. Mater. Process. Technol.* **2001**, *118* (1–3), 350–355.
19. Bensely, A.; Prabhakaran, A.; Lal, D. M.; Nagarajan, G. Enhancing the Wear Resistance of Case Carburized Steel (En 353) by Cryogenic Treatment. *Cryogenics* **2005**, *45* (12), 747–754.
20. Bensely, A.; Venkatesh, S.; Lal, D. M.; Nagarajan, G.; Rajadurai, A.; Boland, J. Determination of Poisson's Ratio of Cryogenically Treated Case Carburised Steel (En 353) by Using Ultrasonic Technique. In *Proceedings of the International Conference on Manufacturing Science and Technology*, Melaka, Malaysia, 2006; p. 4.
21. (a) Liu, H. H.; Wang, J.; Yang, H. S.; Shen, B. L.; Gao, S. J.; Huang, S. J. Effect of Cryogenic Treatment on Property of 14Cr2Mn2V High Chromium Cast Iron Subjected to Subcritical Treatment. *J. Iron Steel Res. Int.* **2006**, *13* (6), 43–48. (b) Liu, H. H.; Wang, J.; Shen, B. L.; Yang, H. S.; Gao, S. J.; Huang, S. J. Effects of Deep Cryogenic Treatment on Property of 3Cr13Mo1V1.5 High Chromium Cast Iron. *Mater. Des.* **2007**, *28* (3), 1059–1064. (c) Liu, H. H.; Wang, J.; Yang, H. S.; Shen, B. L. Effects of Cryogenic Treatment on Microstructure and Abrasion Resistance of CrMnB High-Chromium Cast Iron Subjected to Sub-Critical Treatment. *Mater. Sci. Eng. A: Struct. Mater. Prop. Microstruct. Process* **2008**, *478* (1–2), 324–328.
22. Yang, H. S.; Wang, J.; Shen, B. L.; Liu, H. H.; Gao, S. J.; Huang, S. J. Effect of Cryogenic Treatment on the Matrix Structure and Abrasion Resistance of White Cast Iron Subjected to Destabilization Treatment. *Wear* **2006**, *261* (10), 1150–1154.
23. Bensely, A.; Senthilkumar, D.; Lal, D. M.; Nagarajan, G.; Rajadurai, A. Effect of Cryogenic Treatment on Tensile Behavior of Case Carburized Steel-815M17. *Mater. Charact.* **2007**, *58* (5), 485–491.
24. Firouzdor, V.; Nejati, E.; Khomamizadeh, F. Effect of Deep Cryogenic Treatment on Wear Resistance and Tool Life of M2 HSS Drill. *J. Mater. Process. Technol.* **2008**, *206* (1–3), 467–472.
25. Vimal, A. J.; Bensely, A.; Lal, D. M.; Srinivasan, K. Deep Cryogenic Treatment Improves Wear Resistance of En 31 Steel. *Mater. Manuf. Process.* **2008**, *23* (3–4), 369–376.
26. Dhokey, N. B.; Nirbhavne, S. Dry Sliding Wear of Cryotreated Multiple Tempered D-3 Tool Steel. *J. Mater. Process. Technol.* **2009**, *209* (3), 1484–1490.
27. Akhbarizadeh, A.; Shafyei, A.; Golozar, M. A. Effects of Cryogenic Treatment on Wear Behavior of D6 Tool Steel. *Mater. Des.* **2009**, *30* (8), 3259–3264.
28. Wang, J.; Xiong, J.; Fan, H. Y.; Yang, H. S.; Liu, H. H.; Shen, B. L. Effects of High Temperature and Cryogenic Treatment on the Microstructure and Abrasion Resistance of a High Chromium Cast Iron. *J. Mater. Process. Technol.* **2009**, *209* (7), 3236–3240.
29. (a) Baldissera, P. Deep Cryogenic Treatment of AISI 302 Stainless Steel: Part I – Hardness and Tensile Properties. *Mater. Des.* **2010**, *31* (10), 4725–4730. (b) Baldissera, P.; Delprete, C. Deep cryogenic Treatment of AISI

302 Stainless Steel: Part II – Fatigue and Corrosion. *Mater. Des* **2010**, *31* (10), 4731–4737.
30. (a) Das, D.; Dutta, A. K.; Ray, K. K. Sub-Zero Treatments of AISI D2 Steel: Part I. Microstructure and Hardness. *Mater. Sci. Eng. A: Struct. Mater. Prop. Microstruct. Process.* **2010**, *527* (9), 2182–2193. (b) Das, D.; Dutta, A. K.; Ray, K. K. Sub-Zero Treatments of AISI D2 Steel: Part II. Wear Behavior. *Mater. Sci. Eng. A: -Struct. Mater. Prop. Microstruct. Process* **2010**, *527* (9), 2194–2206. (c) Das, D.; Sarkar, R.; Dutta, A. K.; Ray, K. K. Influence of Sub-Zero Treatments on Fracture Toughness of AISI D2 Steel. *Mater. Sci. Eng. A: Struct. Mater. Prop. Microstruct. Process* **2010**, *528* (2), 589–603.
31. Li, S. H.; Xie, Y. Z.; Wu, X. C. Hardness and Toughness Investigations of Deep Cryogenic Treated Cold Work Die Steel. *Cryogenics* **2010**, *50* (2), 89–92.
32. (a) Jaswin, M. A.; Lal, D. M.; Rajadurai, A. Effect of Cryogenic Treatment on the Microstructure and Wear Resistance of X45Cr9Si3 and X53Cr22Mn9Ni4N Valve Steels. *Tribol. Transact.* **2011**, *54* (3), 341–350. (b) Jaswin, M. A.; Shankar, G. S.; Lal, D. M. Wear Resistance Enhancement in Cryotreated En 52 and 21-4N Valve Steels. *Int. J. Precis. Eng. Manufact.* **2010**, *11* (1), 97–105.
33. Koneshlou, M.; Asl, K. M.; Khomamizadeh, F. Effect of Cryogenic Treatment on Microstructure, Mechanical and Wear Behaviors of AISI H13 Hot Work Tool Steel. *Cryogenics* **2011**, *51* (1), 55–61.
34. Slatter, T.; Lewis, R.; Jones, A. H. The Influence of Cryogenic Processing on Wear on the Impact Wear Resistance of Low Carbon Steel And Lamellar Graphite Cast Iron. *Wear* **2011**, *271* (9–10), 1481–1489.
35. Thornton, R.; Slatter, T.; Jones, A. H.; Lewis, R. The Effects of Cryogenic Processing on the Wear Resistance of Grey Cast Iron Brake Discs. *Wear* **2011**, *271* (9–10), 2386–2395.
36. Amini, K.; Nategh, S.; Shafyei, A.; Rezaeian, A. Effect of Deep Cryogenic Treatment on the Properties of 80CrMo12 5 Tool Steel. *Int. J. Miner. Metall. Mater.* **2012**, *19* (1), 30–37.
37. Gill, S. S.; Singh, J.; Singh, R.; Singh, H. Effect of Cryogenic Treatment on AISI M2 High Speed Steel: Metallurgical and Mechanical Characterization. *J. Mater. Eng. Perform.* **2012**, *21* (7), 1320–1326.
38. Kang, Y.; Yang, J.; Ma, J.; Bi, Q.; Fu, L.; Liu, W. Effects of Cryogenic Treatment on the Mechanical and Dry-Sliding Tribological Behaviour of an Fe75Ni25 alloy. *Proc. Instit. Mech. Eng. Part J: J Eng. Tribol.* **2012**, *226* (J1), 71–78.
39. Siva, R. S.; Jaswin, M. A.; Lal, D. M. Enhancing the Wear Resistance of 100Cr6 Bearing Steel Using Cryogenic Treatment. *Tribol. Transact.* **2012**, *55* (3), 387–393.
40. Thornton, R.; Slatter, T.; Ghadbeigi, H. Effects of Deep Cryogenic Treatment on the Dry Sliding Wear Performance of Ferrous Alloys. *Wear* **2013**, *305* (1–2), 177–191.
41. Yan, X. G.; Li, D. Y. Effects of the Sub-Zero Treatment Condition on Microstructure, Mechanical Behavior and Wear Resistance of W9Mo3Cr4V High Speed Steel. *Wear* **2013**, *302* (1–2), 854–862.
42. Sri Siva, R.; Mohan Lal, D.; Kesavan Nair, P.; Jaswin, M. A. Influence of Cryogenic Treatment on the Wear Characteristics of 100Cr6 Bearing Steel. *Int. J. Miner. Metall. Mater.* **2014**, *21* (1), 46–51.
43. Pérez, M.; Belzunce, F. J. The Effect of Deep Cryogenic Treatments on the Mechanical Properties of an AISI H13 Steel. *Mater. Sci. Eng.: A* **2015**, *624* (0), 32–40.
44. (a) Huang, J. Y.; Zhu, Y. T.; Liao, X. Z.; Beyerlein, I. J.; Bourke, M. A.; Mitchell, T. E. Microstructure of Cryogenic Treated M2 Tool Steel. *Mater. Sci. Eng. A: Struct. Mater. Prop. Microstruct. Process.* **2003**, *339* (1–2), 241–244. (b) Surberg, C. H.; Stratton, P.; Lingenhole, K. The Effect of Some Heat Treatment Parameters on the Dimensional Stability of AISI D2. *Cryogenics* **2008**, *48* (1–2), 42–47.
45. Das, D.; Dutta, A. K.; Ray, K. K. On the Refinement of Carbide Precipitates by Cryotreatment in AISI D2 Steel. *Philos. Mag.* **2009**, *89* (1), 55–76.
46. Gavriljuk, V. G.; Theisen, W.; Sirosh, V. V.; *et al.* Low-Temperature Martensitic Transformation in Tool Steels in Relation to Their Deep Cryogenic Treatment. *Acta Mater.* **2013**, *61* (5), 1705–1715.
47. Tyshchenko, A. I.; Theisen, W.; Oppenkowski, A.; *et al.* Low-temperature Martensitic Transformation and Deep Cryogenic Treatment of a Tool Steel. *Materials Science and Engineering: A* **2010**, *527* (26), 7027–7039.
48. Meng, F.; Tagashira, K.; Azuma, R.; Sohma, H. Role of Eta-Carbide Precipitations in the Wear Resistance Improvements of Fe–12Cr–Mo–V–1.4C Tool Steel by Cryogenic Treatment. *ISIJ Int.* **1994**, *34* (2), 206–210.
49. (a) Das, D.; Dutta, A. K.; Toppo, V.; Ray, K. K. Effect of Deep Cryogenic Treatment on the Carbide Precipitation and Tribological Behavior of D2 Steel. *Mater. Manuf. Process.* **2007**, *22* (4), 474–480. (b) Das, D.; Dutta, A. K.; Ray, K. K. Correlation of Microstructure with Wear Behaviour of Deep Cryogenically Treated AISI D2 Steel. *Wear* **2009**, *267* (9–10), 1371–1380.
50. Collins, D. N. Deep Cryogenic Treatment of Tool Steels: A Review. *Heat Treat. Met* **1996**, *23* (2), 40–42.
51. Zemzemi, F.; Bensalem, W.; Rech, J.; Dogui, A.; Kapsa, P. New Tribometer Designed for the Characterisation of the Friction Properties at the Tool/Chip/Workpiece Interfaces in Machining. *Tribotest* **2008**, *14*, 11–25.
52. Das, D.; Dutta, A. K.; Ray, K. K. Influence of Varied Cryotreatment on the Wear Behavior of AISI D2 Steel. *Wear* **2009**, *266* (1–2), 297–309.
53. Rhyim, Y. M.; Han, S. H.; Na, Y. S.; Lee, J. H. Effect of Deep Cryogenic Treatment on Carbide Precipitation and Mechanical Properties of Tool Steel. In *Heat Treatment of Materials*; Sung, J. H., Lee, C. G., You, Y. Z., Lee, Y. K., Kim, J. Y., Eds.; Trans Tech Publications Ltd: Stafa-Zurich, 2006; Vol. 118; pp. 9–14.
54. Roberts, G. A.; Krauss, G.; Kennedy, R. *Tool Steels*, 5th ed.; ASM International: Materials Park, OH, 1998.
55. Gulyaev, A. P. Improved Methods of Treating High Speed Steels to Improve the Cutting Properties. *Metallurgy* **1937**, *12*, 65.
56. Singh, P. J.; Guha, B.; Achar, D. R. G. Fatigue Life Improvement of AISI 304L Cruciform Welded Joints by Cryogenic Treatment. *Eng. Fail. Anal.* **2003**, *10* (1), 1–12.
57. Thornton, R. *Investigating the Effects of Cryogenic Processing on the Wear Performance and Microstructure of Engineering Materials* (White Rose eTheses Online); Sheffield: The University of Sheffield, 2014.
58. Goldsmith, W. *Impact*; Courier Corporation: Chicago, IL, 2001.
59. Hertz, H. Über die Berührung Fester Elasticher. *Journal für die reine und angewandte Mathematik* **1881**, *92*, 16.
60. Prasad, S. V.; Asthana, R. Aluminum Metal-Matrix Composites for Automotive Applications: Tribological Considerations. *Tribol. Lett.* **2004**, *17* (3), 445–453.
61. Hutton, T. J.; McEnaney, B.; Crelling, J. C. Structural Studies of Wear Debris from Carbon–Carbon Composite Aircraft Brakes. *Carbon* **1999**, *37* (6), 907–916.
62. Jang, G. H.; Cho, K. H.; Park, S. B.; Lee, W. G.; Hong, U. S.; Jang, H. Tribological Properties of C/C–SiC Composites for Brake Discs. *Metal. Mater. Int.* **2010**, *16* (1), 61–66.
63. Breuer, B.; Bill, K. H. *Brake Technology Handbook*, 1st ed.; SAE International: Warrendale, PA, 2008; p. 576.
64. Sugishita, J.; Fujiyoshi, S. The effect of Cast Iron Graphites on Friction and Wear Performance I: Graphite Film Formation on Grey Cast Iron Surfaces. *Wear* **1981**, *66*, 13.
65. Hinrichs, R.; Vasconcellos, M. A. Z.; Österle, W.; Prietzel, C. A TEM Snapshot of Magnetite Formation in Brakes: The Role of the Disc's Cast Iron Graphite Lamellae in Third Body Formation. *Wear* **2011**, *270* (5–6), 365–370.
66. Isaak, C. J.; Reitz, W. The Effects of Cryogenic Treatment on the Thermal Conductivity of GRCop-84. *Mater. Manuf. Process.* **2007**, *23* (1), 82–91.
67. Sundaram, M. M.; Yildiz, Y.; Rajurkar, K. Experimental Study of the Effect of Cryogenic Treatment on the Performance of Electro Discharge Machining, In *ASME 2009 International Manufacturing Science and Engineering Conference*, American Society of Mechanical Engineers, West Lafayette, IN, 2009; pp 215–222.
68. (a) Panchakshari, H. V.; Girish, D. P.; Krishna, M. Investigation on Effect of Cryogenic Parameters on Wear Behavior of Aluminium – Al_2O_3 MMCSS Using Taguchi Method. *Int. J. Soft Comput. Eng.* **2012**, *2* (3), 4. (b) Xun, Z. Effects of Cryogenic Treatment on Microstructure and Properties of Al_2O_3 Particle and Fibre Hybrid Reinforced Aluminum Matrix Composites. *Spec. Cast. Nonferr. Alloy.* **2006**, *3*, 185–187. (c) Hemanth, J. Tribological behavior of cryogenically treated B4Cp/Al–12% Si Composites. *Wear* **2005**, *258* (11–12), 1732–1744.
69. Gogte, C. L.; Likhite, A.; Peshwe, D.; Bhokarikar, A.; Shetty, R. Effect of Cryogenic Processing on Surface Roughness of Age Hardenable AA6061 Alloy. *Mater. Manuf. Process.* **2014**, *29* (6), 710–714.
70. Ashiuchi, E. S.; Steier, V. F.; Silva, C. R. M.; Barbosa, T. D.; Melo, F. O.; Araujo, J. A. Deep Cryogenic Treatment and CrN Coating Effects on Micro-Scale Abrasion of Aluminum Alloy AA 6101-T4. *Adv. Mater. Res.* **2014**, *936*, 9.
71. Lulay, K. E.; Khan, K.; Chaaya, D. The Effect of Cryogenic Treatments on 7075 Aluminum Alloy. *J. Mater. Eng. Perform.* **2002**, *11* (5), 479–480.
72. Steier, V. F.; Badibanga, R. K.; Moreira da Silva, C. R.; Nogueira, M. M.; Araujo, J. A. Effect of Chromium Nitride Coatings and Cryogenic Treatments on Wear and Fretting Fatigue Resistance of Aluminum. *Electr. Power Syst. Res.* **2014**, *116*, 322–329.
73. Wang, J.; Fu, R.; Li, Y.; Zhang, J. Effects of Deep Cryogenic Treatment and Low-Temperature Aging on the Mechanical Properties of Friction-Stir-Welded Joints of 2024-T351 Aluminum Alloy. *Mater. Sci. Eng.: A* **2014**, *609* (0), 147–153.
74. Asl, K. M.; Tari, A.; Khomamizadeh, F. Effect of Deep Cryogenic Treatment on Microstructure, Creep And Wear Behaviors of AZ91 Magnesium Alloy. *Mater.*

Sci. Eng. A: Struct. Mater. Prop. Microstruct. Process. **2009**, *523* (1–2), 27–31.
75. Liu, Y.; Shao, S.; Xu, C. S.; Yang, X. J.; Lu, D. P. Enhancing Wear Resistance of Mg–Zn–Gd alloy by Cryogenic Treatment. *Mater. Lett.* **2012**, *76*, 201–204.
76. Xiong, C. X.; Zhang, X. M.; Deng, Y. L.; Xiao, Y.; Deng, Z. Z.; Chen, B. X. Effects of Cryogenic Treatment on Mechanical Properties of Extruded Mg–Gd–Y–Zr(Mn) Alloys. *J. Cent. South Univ. Technol.* **2007**, *14* (3), 305–309.
77. Jiang, Y.; Chen, D.; Chen, Z.; Liu, J. Effect of Cryogenic Treatment on the Microstructure and Mechanical Properties of AZ31 Magnesium Alloy. *Mater. Manuf. Process.* **2010**, *25* (8), 837–841.
78. (a) Chen, D.; Qiong, J.; Jiang, Y.; Chen, Z. Effect of Deep Cryogenic Treatment on Microstructure and Mechanical Properties of As-Cast ZK60 Magnesium Alloy. *Mater. Mech. Eng.* **2011**, 02. (b) Yang, D.; Wu, Z.; Liu, C. Effects of Cryogenic Treatment on Microstructure and Mechanical Properties of AZ31 Magnesium Alloy Welded Joint. *Heat Treat. Met.* **2012**, *8*, 007.
79. Li, G.-R.; Wang, H.-M.; Cai, Y.; Zhao, Y.-T.; Wang, J.-J.; Gill, S. A. Microstructure and Mechanical Properties of AZ91 Magnesium Alloy Subject to Deep Cryogenic Treatments. *Int. J. Miner. Metall. Mater.* **2013**, *20* (9), 896–901.
80. Amini, K.; Akhbarizadeh, A.; Javadpour, S. Investigating the Effect of Quench Environment and Deep Cryogenic Treatment on the Wear Behavior of AZ91. *Mater. Des.* **2014**, *54*, 154–160.
81. Kim, J. W.; Griggs, J. A.; Regan, J. D.; Ellis, R. A.; Cai, Z. Effect of Cryogenic Treatment on Nickel–Titanium Endodontic Instruments. *Int. Endod. J.* **2005**, *38* (6), 364–371.
82. Vinothkumar, T. S.; Miglani, R.; Lakshminarayananan, L. Influence of Deep Dry Cryogenic Treatment on Cutting Efficiency and Wear Resistance of Nickel–Titanium Rotary Endodontic Instruments. *J. Endod.* **2007**, *33*, 1355–1358.
83. Sun, Q. Y.; Yu, Z. T.; Zhu, R. H.; Gu, H. C. Mechanical Behavior and Deformation Mechanisms of Ti–2.5Cu Alloy Reinforced by Nano-Scale Precipitates at 293 and 77 K. *Mater. Sci. Eng. A: Struct. Mater. Prop. Microstruct. Process.* **2004**, *364* (1–2), 159–165.
84. Gu, K.; Zhang, H.; Zhao, B.; Wang, J.; Zhou, Y.; Li, Z. Effect of Cryogenic Treatment and Aging Treatment on the Tensile Properties and Microstructure of Ti–6Al–4V alloy. *Mater. Sci. Eng.: A* **2013**, *584*, 170–176.
85. Gu, K.; Wang, J.; Zhou, Y. Effect of Cryogenic Treatment on Wear Resistance of Ti–6Al–4V alloy for Biomedical Applications. *J. Mech. Behav. Biomed. Mater.* **2014**, *30*, 131–139.
86. Gill, S. S.; Singh, J. Effect of Deep Cryogenic Treatment on Machinability of Titanium Alloy (Ti-6246) in Electric Discharge Drilling. *Mater. Manuf. Process.* **2010**, *25* (6), 378–385.
87. Singh, R.; Singh, B. Comparison of Cryo-Treatment Effect on Machining Characteristics of Titanium in Electric Discharge Machining. *Int. J. Automot. Mech. Eng.* **2011**, *3*, 239–248.
88. SreeramaReddy, T. V.; Sornakumar, T.; VenkataramaReddy, M.; Venkatram, R. Machinability of C45 Steel with Deep Cryogenic Treated Tungsten Carbide Cutting Tool Inserts. *Int. J. Refract. Metal. Hard Mater.* **2009**, *27* (1), 181–185.
89. Gill, S. S.; Singh, J.; Singh, H.; Singh, R. Metallurgical and Mechanical Characteristics of Cryogenically Treated Tungsten Carbide (WC–Co). *Int. J. Adv. Manuf. Technol.* **2012**, *58* (1–4), 119–131.
90. Seah, K. H. W.; Rahman, M.; Yong, K. H. Performance Evaluation of Cryogenically Treated Tungsten Carbide Cutting Tool Inserts. *Proc. Inst. Mech. Eng. Part B: J. Eng. Manuf.* **2003**, *217* (1), 29–43.
91. Thakur, D.; Ramamoorthy, B.; Vijayaraghavan, L. Influence of Different Post Treatments on Tungsten Carbide–Cobalt Inserts. *Mater. Lett.* **2008**, *62* (28), 4403–4406.
92. Thornton, R.; Slatter, T.; Lewis, R. Effects of Deep Cryogenic Treatment on the Wear Development of H13A Tungsten Carbide Inserts When Machining AISI 1045 Steel. *Prod. Eng. Res. Dev.* **2014**, 1–10.
93. (a) da Silva, F. J.; Franco, S. D.; Machado, A. R.; Ezugwu, E. O.; Souza, A. M. Performance of Cryogenically Treated HSS Tools. *Wear* **2006**, *261* (5–6), 674–685. (b) Gill, S. S.; Singh, J.; Singh, H.; Singh, R. Investigation on Wear Behaviour of Cryogenically Treated TiAlN Coated Tungsten Carbide Inserts in Turning. *Int. J. Mach. Tool. Manuf.* **2011**, *51* (1), 25–33.
94. Gill, S. S.; Singh, H.; Singh, R.; Singh, J. Flank Wear and Machining Performance of Cryogenically Treated Tungsten Carbide Inserts. *Mater. Manuf. Process.* **2011**, *26* (11), 1430–1441.
95. Yong, A. Y. L.; Seah, K. H. W.; Rahman, M. Performance of Cryogenically Treated Tungsten Carbide Tools in Milling Operations. *Int. J. Adv. Manuf. Technol.* **2007**, *32* (7–8), 638–643.
96. Gill, S. S.; Singh, R.; Singh, H.; Singh, J. Wear Behaviour of Cryogenically Treated Tungsten Carbide Inserts Under Dry and Wet Turning Conditions. *Int. J. Mach. Tool. Manuf.* **2009**, *49* (3–4), 256–260.
97. Vadivel, K.; Rudramoorthy, R. Performance Analysis of Cryogenically Treated Coated Carbide Inserts. *Int. J. Adv. Manuf. Technol.* **2009**, *42* (3–4), 222–232.

Relevant Websites

http://www.195below.co.uk/
Cryogenic Treatment Services Ltd.
http://www2.le.ac.uk/departments/engineering/research/mechanics-of-materials
Mechanics of Materials Research Group, University of Leicester.
http://www.leonardocentre.co.uk/
The Leonardo Centre for Tribology, The University of Sheffield.

COMPREHENSIVE MATERIALS FINISHING

COMPREHENSIVE MATERIALS FINISHING

EDITOR-IN-CHIEF

MSJ HASHMI

Dublin City University, Dublin, Ireland

VOLUME 3

SURFACE COATING PROCESSES

VOLUME EDITOR

BEKIR SAMI YILBAS

King Fahd University of Petroleum and Minerals, Dhahran, Saudi Arabia



ELSEVIER

Amsterdam • Boston • Heildelberg • London • New York • Oxford
Paris • San Diego • San Francisco • Singapore • Sydney • Tokyo

Elsevier
The Boulevard, Langford Lane, Kidlington, Oxford OX5 1GB
225 Wyman Street, Waltham MA 02451

Copyright © 2017 Elsevier Inc. All rights reserved

No part of this publication may be reproduced or transmitted in any form or by any means, electronic or mechanical, including photocopying, recording, or any information storage and retrieval system, without permission in writing from the publisher. Details on how to seek permission, further information about the Publisher's permissions policies and our arrangements with organizations such as the Copyright Clearance Center and the Copyright Licensing Agency, can be found at our website: www.elsevier.com/permissions.

This book and the individual contributions contained in it are protected under copyright by the Publisher (other than as may be noted herein).

Notices
Knowledge and best practice in this field are constantly changing. As new research and experience broaden our understanding, changes in research methods, professional practices, or medical treatment may become necessary.

Practitioners and researchers may always rely on their own experience and knowledge in evaluating and using any information, methods, compounds, or experiments described herein. In using such information or methods they should be mindful of their own safety and the safety of others, including parties for whom they have a professional responsibility.

To the fullest extent of the law, neither the Publisher nor the authors, contributors, or editors, assume any liability for any injury and/or damage to persons or property as a matter of products liability, negligence or otherwise, or from any use or operation of any methods, products, instructions, or ideas contained in the material herein.

Library of Congress Cataloging-in-Publication Data
A catalog record for this book is available from the Library of Congress

British Library Cataloguing-in-Publication Data
A catalogue record for this book is available from the British Library

ISBN 978-0-12-803249-7

For information on all publications visit our website at http://store.elsevier.com



Publisher: Oliver Walter
Acquisition Editor: Ruth Ireland
Content Project Manager: Gemma Tomalin
Associate Content Project Manager: Joanne Williams
Designer: Matthew Limbert

Printed and bound in Canada

EDITOR-IN-CHIEF



Saleem Hashmi is emeritus professor in the School of Mechanical & Manufacturing Engineering at Dublin City University, Ireland. He founded the School in January 1987, in addition to setting up the Materials Processing Research Centre (MPRC), a research centre of excellence in the field of materials processing.

In 1990, Professor Hashmi established Advances in Materials and Processing Technologies (AMPT), a much-needed international conference in materials processing. He continues to be the chairperson of the steering committee for this series of conferences. In 1998 he was appointed as editor-in-chief of Elsevier's *Journal of Materials Processing Technology* and continued in this role until 2008.

In 1995, Professor Hashmi was awarded the higher doctorate degree of DSc, by the University of Manchester, the highest academic degree any university in the UK can award.

Professor Hashmi has supervised or co-supervised 112 PhD and 55 MEng research students to successful completion. Over the years he has also acted as an external examiner and expert assessor for PhD candidates and engineering departments with universities in Ireland, the UK, India, Pakistan, Bangladesh, Hong Kong, Canada, Australia, and Malaysia. He has published in excess of 460 papers and 25 books so far.

Professor Hashmi was the editor-in-chief for Elsevier's 13-volume major reference work *Comprehensive Materials Processing* which was published in 2014.

He has been appointed as the editor-in-chief for Elsevier's *Materials Science and Materials Engineering Reference Module*, a 14-section online resource comprising around 3500 reviewed articles. This launched in December, 2015 and is constantly being updated.

VOLUME EDITORS



Imtiaz Ahmed Choudhury is currently a professor at the Department of Mechanical Engineering, University of Malaya (UM), and has been with UM since 1996. He received his Bachelor degree in Mechanical Engineering from Bangladesh University of Engineering and Technology (BUET), MEng from Asian Institute of Technology (AIT), Thailand, and MSc in Mechanical Engineering from Arizona State University, USA. He obtained his PhD from Dublin City University. He started his career as an assistant engineer in a gas transmission and distribution company, Dhaka, Bangladesh. He worked as a maintenance engineer in a power station for 3 years in Libya. He started his academic career in 1982 as an assistant professor in an engineering college, Bangladesh. Since then, he has been working in academia. Imtiaz's research interests include traditional/nontraditional machining with vegetable oil-based lubricant, tool condition monitoring, machining difficult-to-cut and high strength materials, injection molding and application and use of solar energy. He has been a member of a panel of judges for the SME innovation award 2011–2013, Malaysia, under the category of "Manufacturing Sector." He was a Senate member of the University of Malaya. He has authored and coauthored about 100 papers in referred journals, more than 60 conference papers and some book chapters published in Elsevier works. He has also been a reviewer of various international journals. Imtiaz is a Fellow of Institution of Mechanical Engineers, UK (IMechE), and a life Fellow of Institution of Engineers, Bangladesh (IEB). He is a chartered engineer, UK (CEng).



Professor Shahjahan Mridha was born in Bangladesh and obtained his BSc and MSc in Metallurgical Engineering at the Bangladesh University of Engineering & Technology (BUET), Dhaka, and PhD at the University of Leeds in UK (1980) on Gas Nitriding of Low Alloy Steels. Since 1972 he has worked at the Department of Metallurgical Engineering, BUET for 20 years as a faculty member except for 1986–1987 where he was a Commonwealth Academic Staff member at the University of Birmingham, UK, working on Plasma Nitriding.

Professor Mridha was a senior research fellow at the University of Strathclyde, UK from 1989–1994 and worked on laser processing of aerospace materials in collaboration with UK Ministry of Defence. In late 1994 he moved to Nanyang Technological University (NTU) in Singapore where he was employed as an associate professor until 2001, working on semiconductor materials, composite and intermetallic coatings.

In January 2002 he joined the International Islamic University Malaysia (IIUM) as professor, later assuming the position of Head of the Department of Manufacturing and Materials Engineering. He left IIUM in July 2012 to join the Department of Mechanical and Aerospace Engineering at the University of Strathclyde (UK) as a Leverhulme Trust Professor, and remains there presently as visiting professor.

Professor Mridha has published more than 150 journal and conference papers. His research contributions are primarily on microstructure–properties relationships, semiconductor materials and surface modification of light alloys and steel using high power laser and TIG torch melting technology. He is the pioneer of TIG torch techniques for surface coating applications. Professor Mridha is subject editor of the *Metallic Materials* section in Elsevier's *Reference Module in Materials Science and Materials Engineering* launched in December 2015.

In addition to his academic career, Professor Mridha worked as an international consultant for the United Nations Industrial Development Organization (UNIDO) from 2001 until 2007, delivering expert advice and training to engineers working in manufacturing industries in the Indian and African continents.



Bekir Sami Yilbas is a distinguished professor in the Mechanical Engineering Department, King Fahd University of Petroleum and Minerals, Saudi Arabia. He received his PhD in Mechanical Engineering from Birmingham University, and was awarded a doctorate of Engineering at Birmingham in 2005 due to his significant contribution to his field of study. He has received numerous awards as recognition of his research work. Some of these include President of India's Prize for 1988 by Indian Royal Engineering Society, Technology Prize for 1990 by Science and Technology Foundation in Turkey, Best Research Award for 1997, 2002, 2007 by King Fahd University of Petroleum and Minerals, Silver Jubilee Medal by Silesian University of Technology, Donald Julius Groen Prize for 2007 by Institution of Mechanical Engineers (IMechE), Distinguished University Professor award at King Fahd University of Petroleum and Minerals, 2008 – present by King Fahd University of Petroleum and Minerals, Professor W. Johnson International Gold Medal for 2008 by Advances in Materials and Processing Technologies (AMPT) Steering Committee, Professor Fryderyk Staub Golden Owl Award by World Academy of Metals and Manufacturing, Almarai's Distinguished Scholar Prize by King Abdulaziz City of Science and Technology.

Bekir Sami Yilbas has published 720 journal papers in reputable international journals and presented over 100 papers at international conferences. He has 12 patents issued and is the subject editor of *Arabian Journal of Science and Engineering* and editor of *Journal of Fluids*. He has served as an editorial board member of international journals, including the *International Journal of Machine Tool and Manufacture Design, Research and Application, International Journal of Subsurface Sensing Technologies and Applications, Journal of Materials Processing Technology, Journal of Achievements in Materials and Manufacturing Engineering, International Journal of Nanomanufacturing*, and *Archives of Materials Science and Engineering*, and has received numerous awards as recognition of his research work.

CONTRIBUTORS TO VOLUME 3

SS Akhtar
King Fahd University of Petroleum and Minerals, Dhahran, Saudi Arabia

KS Al-Athel
King Fahd University of Petroleum and Minerals, Dhahran, Saudi Arabia

M Aliofkhazraei
Tarbiat Modares University, Tehran, Iran

AFM Arif
King Fahd University of Petroleum and Minerals, Dhahran, Saudi Arabia

MA Azmah Hanim
Universiti Putra Malaysia, Serdang, Malaysia

N Bala
Baba Banda Singh Bahadur Engineering College, Fatehgarh Sahib, India

I Bogrekci
Adnan Menderes University, Aydın, Turkey

ML Bosko
Universidad Nacional del Litoral-CONICET, Santa Fe, Argentina

J Butler
University of Limerick, Limerick, Ireland

H Caliskan
Bartin University, Bartin, Turkey

LM Cornaglia
Universidad Nacional del Litoral-CONICET, Santa Fe, Argentina

SK Das
Jadavpur University, Kolkata, India

P Demircioglu
Adnan Menderes University, Aydın, Turkey

Z Evis
Middle East Technical University, Ankara, Turkey

M Farsari
Foundation for Research and Technology – Hellas (FORTH-IESL), Heraklion, Greece

AA Gandhi
University of Limerick, Limerick, Ireland

P Henshaw
University of Windsor, Windsor, ON, Canada

NK Jain
Indian Institute of Technology Indore, Indore, India

M Jokar
Tarbiat Modares University, Tehran, Iran

M Karimi-Jafari
University of Limerick, Limerick, Ireland

M Kaur
Baba Banda Singh Bahadur Engineering College, Fatehgarh Sahib, India

M Khaled
King Fahd University of Petroleum and Minerals, Dhahran, Saudi Arabia

S Kilic
Ahi Evran University, Kirsehir, Turkey

K Kowal
University of Limerick, Limerick, Ireland

C Kurbanoglu
Istanbul Medeniyet University, Istanbul, Turkey

RH Lara
Universidad Juarez del Estado de Durango, Durango, Mexico

R Manu
Sree Vyasa N.S.S. College, Thrissur, India

K McNamara
University of Limerick, Limerick, Ireland

H Mojiri
Tarbiat Modares University, Tehran, Iran

J Mostaghimi
University of Toronto, Toronto, ON, Canada

A Owais
Beni-Suef University, Beni-Suef, Egypt

F Ozturk
The Petroleum Institute, Abu Dhabi, UAE

P Panjan
Jožef Stefan Institute, Ljubljana, Slovenia

S Pathak
Indian Institute of Technology Indore, Indore, India

J Paulo Davim
University of Aveiro, Aveiro, Portugal

R Ray
University of Windsor, Windsor, ON, Canada

I Romero-Ibarra
Unidad Profesional Interdisciplinaria en Ingeniería y Tecnologías Avanzadas – IPN, Ciudad de México, México

P Sahoo
Jadavpur University, Kolkata, India

A Selimis
Foundation for Research and Technology – Hellas (FORTH-IESL), Heraklion, Greece

SMA Shibli
University of Kerala, Thiruvananthapuram, India

H Singh
Indian Institute of Technology Ropar, Rupnagar, India

FS Sosa-Rodríguez
Universidad Autónoma Metropolitana, México, D.F., Mexico

AM Tarditi
Universidad Nacional del Litoral-CONICET, Santa Fe, Argentina

SAM Tofail
University of Limerick, Limerick, Ireland

E Ul-Haq
University of Limerick, Limerick, Ireland

J Vazquez-Arenas
Universidad Autónoma Metropolitana – Iztapalapa, México, D.F., México

MM Verdian
Islamic Azad University, Najafabad, Iran

BS Yilbas
King Fahd University of Petroleum and Minerals, Dhahran, Saudi Arabia

CONTENTS OF VOLUME 3

Preface xiii

Introduction to Surface Coating Processes xv

VOLUME 3 – Surface Coating Processes

3.1 Electroless Plating of Pd Binary and Ternary Alloys and Surface Characteristics for Application in Hydrogen Separation *AM Tarditi, ML Bosko, and LM Cornaglia* 1

3.2 Tuning of the Microstructure and Surface Topography of Hot-Dip Galvanized Coatings *SMA Shibli and R Manu* 25

3.3 Surface Finish Coatings *P Sahoo, SK Das, and J Paulo Davim* 38

3.4 Residual Stresses in Thermal Spray Coating *AFM Arif, KS Al-Athel, and J Mostaghimi* 56

3.5 Laser Texturing of Materials and Surface Hydrophobicity *BS Yilbas* 71

3.6 Surface Texture Properties of Co–Ni Alloys Formed with Unipolar and Bipolar Plating *J Vazquez-Arenas, I Romero-Ibarra, RH Lara, and FS Sosa-Rodríguez* 86

3.7 HVOF Coating of Nickel Based Alloys: Surface and Mechanical Characteristics *BS Yilbas* 96

3.8 Laser-Based 3D Printing and Surface Texturing *A Selimis and M Farsari* 111

3.9 Hydrophobicity and Surface Finish *A Owais, M Khaled, and BS Yilbas* 137

3.10 Atomizers and Finish Properties of Surface Coatings *R Ray and P Henshaw* 149

3.11 Gas Nitriding of H13 Tool Steel Used for Extrusion Dies: Numerical and Experimental Investigation *SS Akhtar, AFM Arif, and BS Yilbas* 158

3.12 Hot-Dip Galvanizing Process *F Ozturk, Z Evis, and S Kilic* 178

3.13 Finishing and Post-Treatment of Thermal Spray Coatings *MM Verdian* 191

3.14 High Velocity Oxy-Fuel Spraying and Surface Finish *H Singh, M Kaur, and N Bala* 207

3.15 Electroless Plating as Surface Finishing in Electronic Packaging *MA Azmah Hanim* 220

3.16 Hard Coatings on Cutting Tools and Surface Finish *H Caliskan, P Panjan, and C Kurbanoglu* 230

3.17 Topological Evaluation of Surfaces in Relation to Surface Finish *P Demircioglu* 243

3.18 Evaluation of Surface Finish Quality Using Computer Vision Techniques *I Bogrekci and P Demircioglu* 261

3.19 Effect of Surface Roughness on Wetting Properties *H Mojiri and M Aliofkhazraei* 276

3.20 Surface Preparation and Adhesion Tests of Coatings *M Jokar and M Aliofkhazraei* 306

3.21 Powder Metallurgical Processing of NiTi Using Spark Plasma Sintering *K McNamara, J Butler, AA Gandhi, and SAM Tofail* 336

3.22 Spark Plasma Sintering of Lead-Free Ferroelectric Ceramic Layers *M Karimi-Jafari, K Kowal, E Ul-Haq, and SAM Tofail* 347

3.23 Electrochemical Processing and Surface Finish *NK Jain and S Pathak* 358

Index 381

PREFACE

Finish manufacturing processes are final stage processing techniques which are deployed to bring products to a stage where they are ready for marketing and putting in service. Over recent decades, a number of finish manufacturing processes have been developed by researchers and technologists. Some of these new processes have been documented and illustrated both individually and collectively in relation to application in specific areas. The advancement of tools of physics has resulted in considerable changes to these processes, and the precision with which they can be applied. The reporting of these developments are sometimes fragmentary, and this reference work provides a more connected and thorough review of these processes.

Comprehensive Materials Finishing is the primary reference source for researchers at different levels and stages in their career both in academia and industry. This reference work encompasses the knowledge and understanding of many experts into a single, comprehensive work. Containing a combination of review articles, case studies, and research findings resulting from research and development activities in both industrial and academic domains, this reference work focuses on how some of these finish manufacturing processes are advantageous for a broad range of technologies. These include applicability, energy and technological costs, and practicability of implementation. A wide range of materials such as ferrous, nonferrous, and polymeric materials are covered.

This work details the three foremost and distinct types of finishing processes: surface treatment, finish machining processes, and surface coating processes. Surface treatment refers to properties of a material being modified without otherwise changing the physical dimensions of the surface. Finish machining processes involve a small layer of material being removed from the surface by various machining type processes to render improved surface characteristics. Surface coating processes are where the surface properties are improved by adding fine layer(s) of materials with superior surface characteristics to improve the service life of the surface being coated. Each primary surface finishing process is presented in a separate volume, comprising chapters on many of the following relevant specific processes as follows:

Volume 1: Finish Machining and Net-Shape Forming: developments in conventional finish machining processes (honing, lapping, polishing, burnishing, and deburring), fine grinding, free EDM, laser finishing, electrical discharge grinding (EDG), electro-chemical honing (ECH), electrochemical discharge grinding (ECDG), electrochemical grinding (ECG), electrochemical turning (ECT), micro-machining process, and high-speed machining.
Volume 2: Surface and Heat Treatment Processes: This contains aspects of heat treatments, stress relieving, annealing, normalizing, hardening, tempering, austempering, martempering, carburizing (pack, liquid, gas, and post carburizing treatments), nitriding (gas and plasma), salt bath (boriding, chromizing, cyaniding, and carbonitriding), phase transformation of the outer surface (induction, flame, laser, electron beam, and anodizing).
Volume 3: Surface Coating Processes: Plating (electroplating, alloys (bronze/brass and others), chromium, dense chromium, copper and tin, gold, silver and other precious metals, zinc and nickel, electroforming, electroless nickel, hot dip galvanizing, selective/brush plating, surface finish coatings, air spray painting, and chemical vapor deposition (CVD)).

Finishing processes are at the core of successful production of marketable products and address recent progress in materials finishing technologies and science as well as covering recent developments in specific manufacturing processes involved with finishing of products for applications in all areas of engineering, biomedical, environmental, health and safety, and monitoring and control. The in-depth study of these finishing processes as presented in these volumes will assist scientists and engineers in the selection, design, and usage of materials, whether required in small- or large-scale uses across industries.

The initiations for this project began in 2014 and by January, 2015, I had selected the volume editors – Bekir Yilbas, Imtiaz Choudhury, and Shahjahan Mridha and we met with Gemma Tomalin, Joanne Williams, and Graham Nisbet at the Elsevier office in Oxford to finalize the table of contents and plan the project. Throughout 2015, the volume editors and I worked resolutely to select topics to be covered, invite authors, and review their manuscripts, eventually getting all content ready for production by the end of 2015. In 2016, authors returned their proof corrections and final files were produced. To create a work of this scale, the most in-depth reference ever published on materials finishing processes and surface engineering, relies on a collaboration of authors, editors, and the team at Elsevier. I would like to thank the many dedicated authors, whose contributions will be an essential reference for materials scientists and engineers. Each chapter has been reviewed by one of the volume editors, leading experts in their fields, whose knowledge and expertise have proved invaluable. I am indebted to each volume editor and their dedication to making their volume an exhaustive and relevant resource for the scientific community for many years to come. Finally, on behalf of myself and the volume editors, I would like to thank Gemma Tomalin and Joanne Williams at Elsevier for their support, cooperation, and good humor throughout this project – from the first meeting in early 2015, to the publication mid-2016.

MSJ Hashmi
Editor-in-Chief
Dublin City University, Dublin, Ireland

INTRODUCTION TO SURFACE COATING PROCESSES

Surface finish plays a major role in manufacturing processes. A high-quality surface finish is one of the key parameters determining whether the parts being manufactured will be accepted or rejected. In addition, surface finish becomes critically important when many parts are assembled to form a final product. There are several methods to produce the desired surface finish; however, the cost, ease of operation, precision, and local effects are the main concerns for the selection of the processes to achieve the desired surface finish. Although some methods appear to be the only solution to meet the required surface finish criteria, the large-scale production of such surfaces limits the practical applications of these methods. In addition, after effects of the process, such as reduction in fracture toughness, residual stress formation, surface hardness alteration, and nonuniform distribution of elemental composition, are the common concerns during selection of the processes. When surface treatment involves thermal processing, such as high energy beam interaction, formation of high residual stresses becomes unavoidable because of the high temperature gradient formed in the surface vicinity. However, introducing an annealing process to reduce residual stresses may not be applicable for certain surfaces because of alteration of the surface finish, such as highly textured polymeric surfaces; in some cases, it requires state-of-the-art equipment and dedicated human power, which in turn increases the treatment cost. However, electrical and chemical processes involve local alteration of surface chemistry and, in some cases, cause modification of the elemental composition of the surface. Although an electropolished surface is essentially balanced, the local galvanic differences caused by polishing give rise to stress formation in the surface region. In addition, the surface peaks can be dissolved earlier than the valleys of the surface because of the variation in the current concentration over the protrusions. This, in turn, results in rounding of the surface profile. Nevertheless, surface finish and the associated processes are still in progress and require further research studies to meet the desired quality with minimal environmental hazards.

In general, three main characteristics of the surface are considered when measuring the surface finish of the substrate materials: lay (form), surface roughness, and waviness. Although these characteristics are critically important for practical applications, surface roughness and waviness become crucial for reducing friction on the surface. In bearing applications, frictional losses play a major role in energy loss due to heat dissipation. In addition, they have detrimental effects on the bearing potential of the surface once the surface roughness increases due to surface scratches under a dynamic load. In some cases, stick-slip friction can take place during the sliding action of bearings, which also depends on surface finish. Therefore, friction and wear conditions depend greatly on the surface texture parameters. Contact and noncontact methods are used to assess the surface finish of substrate materials. Contact methods use a stylus indenter across the surface while producing surface profiles. Noncontact methods provide texture details of the surface. Depending on the assessment accuracy and nature of the surface, both methods can be utilized to measure the surface profiles. However, the stylus tip gives rise to fine surface scratches, which are not favorable for the assessment of optical surfaces such as lenses and mirrors. Speculative inconsistencies in surface roughness measurements are introduced by different equipment, which result in misunderstandings and confusion in measurement accuracy. In particular, developments in the pharmaceutical and biotechnology industries require new designs of different geometric configurations and sizes of valves and pipes with specific surface finishes. Consequently, a unified description of surface texture assessment and measurement accuracy becomes vital in such industries. In general, various parameters, including grit size, tool load, feed rate, lubricant used, and others, affect the surface finish. However, the surface texture quality of the end product is mainly assessed by the surface roughness average value, which is identified as the centerline average or arithmetic average. The surface roughness value is defined as the average value of the departures from its centerline through a prescribed sampling length and the measured values expressed as the root mean square.

One interesting area of research in surface finish is associated with the enhancement of the hydrophobic characteristics of a surface. Changes in climate result in extreme dust storms, particularly in the Middle East region. Solar energy-harvesting devices, such as photovoltaic panels, are affected by dust accumulation on the protective cover surface. This, in turn, results in operational difficulties in terms of reduced energy-harvesting efficiency and device life cycle. To create a self-cleaning effect on the soiled surfaces, re-engineering of active surfaces of such devices becomes essential, as does mimicking nature (eg, lotus leaves, shark skin, rose petals). In this case, two important features of such surfaces are the focus: micro/nano texturing and reducing surface energy through chemical processing. To improve surface hydrophobicity, several methods have been reported and strategies have been introduced.[1–10] The adopted methods are related to the multi-step procedures and are involved with mostly harsh conditions that require specialized reagents. Some of these methods are associated with phase separation,[1] electrochemical deposition,[2] plasma treatment,[6] sol-gel processing,[7] electrospinning,[8] laser texturing,[9] and solution immersion.[10] The main purpose of these processes is to modify free energy of the surfaces through changing compositions via chemical and physical reactions. However, surface texturing has many challenges, including cost-effective processing, short processing duration, reduced initial capital for equipment, and trained human power requirements. In general, a cost-effective, one-step process of surface texturing is demanding and requires extensive research and development in the area of surface engineering. Crystallization or etching of optical surfaces under controlled environments generates surface textures composing micro/nano structures, which improve surface hydrophobicity significantly.[9] However, due to the molecular distortion and optical scattering of the crystallized/etched surface, optical

transmittance of the textured surface is significantly reduced.[9] This limits the application of the textured surfaces when transmittance of a visible spectrum of light is required. Laser texturing of optical surfaces can also provide improved hydrophobic characteristics at the surface; however, due to high residual stresses, the practical application of the textured surfaces becomes limited.[9] Although reconstruction of surfaces textured by using polydimethylsiloxane (PDMS) has been reported,[11] the process involved and the characteristics of the reproduced surface require further investigation to achieve an exact copy of the surface finish, particularly for surfaces with complicated geometric configurations.

Chapters in This Volume

3.1 Electroless Plating of Pd Binary and Ternary Alloys and Surface Characteristics for Application in Hydrogen Separation
3.2 Tuning of the Microstructure and Surface Topography of Hot-Dip Galvanized Coatings
3.3 Surface Finish Coatings
3.4 Residual Stresses in Thermal Spray Coating
3.5 Laser Texturing of Materials and Surface Hydrophobicity
3.6 Surface Texture Properties of Co–Ni Alloys Formed with Unipolar and Bipolar Plating
3.7 HVOF Coating of Nickel Based Alloys: Surface and Mechanical Characteristics
3.8 Laser-Based 3D Printing and Surface Texturing
3.9 Hydrophobicity and Surface Finish
3.10 Atomizers and Finish Properties of Surface Coatings
3.11 Gas Nitriding of H13 Tool Steel Used for Extrusion Dies: Numerical and Experimental Investigation
3.12 Hot-Dip Galvanizing Process
3.13 Finishing and Post-Treatment of Thermal Spray Coatings
3.14 High Velocity Oxy-Fuel Spraying and Surface Finish
3.15 Electroless Plating as Surface Finishing in Electronic Packaging
3.16 Hard Coatings on Cutting Tools and Surface Finish
3.17 Topological Evaluation of Surfaces in Relation to Surface Finish
3.18 Evaluation of Surface Finish Quality Using Computer Vision Techniques
3.19 Effect of Surface Roughness on Wetting Properties
3.20 Surface Preparation and Adhesion Tests of Coatings
3.21 Powder Metallurgical Processing of NiTi Using Spark Plasma Sintering
3.22 Spark Plasma Sintering of Lead-Free Ferroelectric Ceramic Layers
3.23 Electrochemical Processing and Surface Finish

The materials presented in all the chapters in this volume are sufficient to explain different laser processing techniques and their applications in practice. Six chapters describe surface hydrophobicity and characterization of surface finish, five chapters deal with the various aspects of electroplating and surface finish, and three chapters detail different spraying operations and surface characteristics. The remaining chapters provide insight into the 3D printing and coating evaluations pertinent to the surface finish.

Concluding Remarks

This volume covers the fundamentals, technologies, and recent developments in surface finishing pertinent to scientific and engineering applications. The chapters presented in this volume are self-contained in terms of their descriptions of the physical processes involved and the practical applications in industry. Surface analysis at a micro/nano level, characterizations, and processes involved are presented in detail. The current research associated with surface finishing applications is included in the introduction sections of all chapters, and the future trends in surface finishing technologies are also discussed; these form the guidelines for researchers and engineers in this field. Readers should find this volume to be a great source of pertinent information and relevant literature.

Acknowledgment

The editor expresses his deep appreciation to all the authors and co-authors of the chapters contained in this volume for all their hard work and devotion to preparing their individual chapters. The editor greatly acknowledges the support provided by the Deanship of Scientific Research of King Fahd University of Petroleum and Minerals.

BS Yilbas
King Fahd University of Petroleum and Minerals, Dhahran, Saudi Arabia

References

1. Han, J. T.; Xu, X. R.; Cho, K. W. Diverse Access to Artificial Superhydrophobic Surfaces Using Block Co-Polymers. *Langmuir* **2005**, *21* (15), 6662–6665.
2. Shirtcliffe, N. J.; McHale, G.; Newton, M. I.; Chabrol, G.; Perry, C. C. Dual-Scale Roughness Produces Un-Usually Water-Repellent Surfaces. *Adv. Mater.* **2004**, *16* (21), 1929–1932.
3. Hwang, H. S.; Lee, S. B.; Park, I. Fabrication of Raspberry-Like Superhydrophobic Hollow Silica Particles. *Mater. Lett.* **2010**, *64* (20), 2159–2162.
4. Huang, Y. H.; Wu, J. T.; Yang, S. Y. Direct Fabricating Patterns Using Stamping Transfer Process with PDMS Mold of Hydrophobic Nanostructures on Surface of Micro Cavity. *Microelectron. Eng.* **2011**, *88* (6), 849–854.
5. Yang, T.; Tian, H.; Chen, Y. Preparation of Superhydrophobic Silica Films with Honeycomb-Like Structure by Emulsion Method. *J. Sol-Gel Sci. Technol.* **2009**, *49* (2), 243–246.
6. Kinoshita, H.; Ogasahara, A.; Fukuda, Y.; Ohmae, N. Superhydrophobic/Superhydrophilic Micropatterning on a Carbon Nanotube Film Using a Laser Plasma-Type Hyperthermal Atom Beam Facility. *Carbon* **2010**, *48* (15), 4403–4408.
7. Latthe, S. S.; Imai, H.; Ganesan, V.; Rao, A. V. Super-Hydrophobic Silica Films by sol–gel Co-Precursor Method. *Appl. Surf. Sci.* **2009**, *256* (1), 217–222.
8. Ma, M.; Mao, Y.; Gupta, M.; Gleason, K. K.; Rutledge, G. C. Superhydrophobic Fabrics Produced by Electrospinning and Chemical Vapor Deposition. *Macromolecules* **2005**, *38* (23), 9742–9748.
9. Yilbas, B. S.; Khaled, M.; Abu-Dheir, N.; *et al.* Wetting and Other Physical Characteristics of Polycarbonate Surface Textured Using Laser Ablation. *Appl. Surf. Sci.* **2014**, *320* (30), 21–29.
10. Zhang, X.; Guo, Y.; Zhang, P.; Wu, Z.; Zhang, Z. Superhydrophobic CuO at Cu_2S Nanoplate Vertical Arrays on Copper Surfaces. *Mater. Lett.* **2010**, *64* (10), 1200–1203.
11. Hannibal Madsen, M.; Feidenhans'l, N. A.; Hansen, P.-E.; Garnæs, J.; Dirscher, K. Accounting for PDMS Shrinkage When Replicating Structures. *J. Micromech. Microeng.* **2014**, *24* (12), 127002–127005.

3.1 Electroless Plating of Pd Binary and Ternary Alloys and Surface Characteristics for Application in Hydrogen Separation

AM Tarditi, ML Bosko, and LM Cornaglia, Universidad Nacional del Litoral-CONICET, Santa Fe, Argentina

© 2017 Elsevier Inc. All rights reserved.

3.1.1	**Basic Aspects of Electrochemical Deposition**	1
3.1.1.1	Electroplating	1
3.1.1.1.1	General principles	1
3.1.1.1.2	Main electroplating features	2
3.1.1.2	ELP	2
3.1.1.2.1	General principles	2
3.1.1.2.2	Catalytic aspects	3
3.1.1.2.3	Mechanistic overview	3
3.1.1.2.4	Surface conditioning	4
3.1.1.2.5	Conditions and chemical composition of different metal solutions	4
3.1.2	**Electroless Deposition of Pure Metals**	6
3.1.2.1	Palladium	6
3.1.2.2	Nickel	6
3.1.2.3	Silver	7
3.1.2.4	Copper	7
3.1.3	**Palladium Binary Alloys**	8
3.1.3.1	Sequential and Co-Deposition of PdAg Alloys	8
3.1.3.2	Sequential and Co-Deposition of PdRu Alloys	10
3.1.3.3	Sequential Deposition of PdCu Alloys	10
3.1.3.4	Sequential Deposition of PdAu Alloys	11
3.1.4	**Palladium Ternary Alloys**	11
3.1.4.1	PdAgAu Alloys	12
3.1.4.2	PdAgCu Alloys	13
3.1.4.3	PdCuAu Alloys	13
3.1.5	**Applications in Hydrogen Purification**	14
3.1.5.1	Hydrogen Permeation Properties	15
3.1.5.2	H_2S Treatment: Hydrogen Inhibition Transport and Flux Recovery	17
3.1.6	**Surface Properties of Pd Binary and Ternary Alloys**	19
3.1.6.1	Surface Segregation of Clean Surfaces	19
3.1.6.2	Surface Segregation After of H_2S Exposure	20
3.1.7	**Conclusions**	21
References		22

3.1.1 Basic Aspects of Electrochemical Deposition

The electrochemical deposition technique involves electrodeposition or electroplating, electroless deposition, and displacement deposition; in all cases, a metal layer is deposited on a substrate.[1]

In the electroplating process for electric-conductive material, the deposition of a metallic layer is achieved by the presence of a negative charge on the substrate, which is immersed into a solution that contains a salt of the metal. The substrate is the cathode of an electrolytic cell and the electrons are supplied by an external power supply. The metallic ions of the salt with positive charge are thus attracted to the surface, which provides electrons to reduce the ions depositing the metal on the substrate surface.[2]

Compared with electrodeposition, electroless plating (ELP) can cover all surface types, regardless of size, shape, and electrical conductivity of the substrate. Electroless and displacement depositions have one basic feature in common: no power supply is required to produce the deposition reaction.[3] In the electroless deposition process, the electrons are provided to the support surface by a reducer (Red), which is present in the electroless bath. On the other hand, in the displacement deposition process, the substrate provides the electrons, becoming the electron-donating species.[3]

3.1.1.1 Electroplating

3.1.1.1.1 General principles

The electrodeposition of metals consists of the reduction of metal ions from different electrolyte solutions on top of a surface to be coated.[1] **Figure 1** shows the operation principle of the electroplating process.[2]

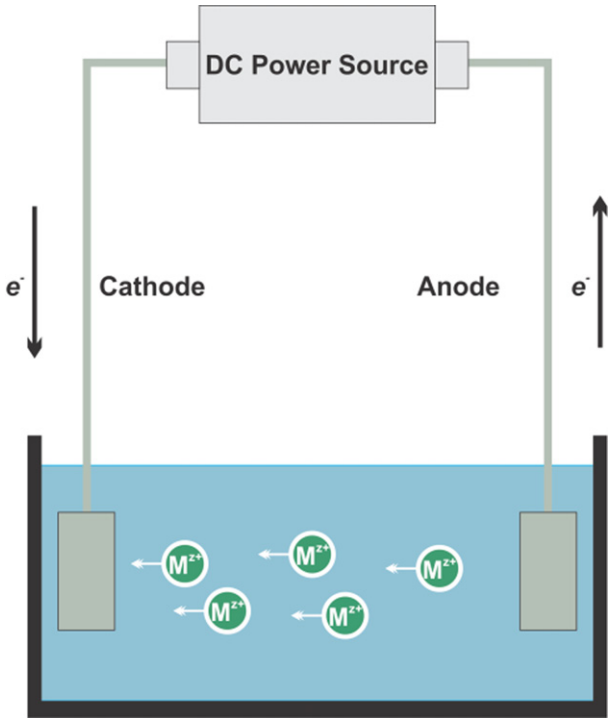


Figure 1 Schematic illustration of electroplating.

This phenomenon is represented by the next reaction [1]:

$$M^{z+}_{solution} + ze^{-} \xrightarrow{Surface} M_{lattice} \quad [1]$$

In this process, z electrons are supplied by an external power supply. However, in a simplified illustration, it is possible to consider that there are immobile metal ions in the metal lattice permeated by a gas of free electrons (reaction [2]).

$$M^{z+}_{solution} \xrightarrow{Surface} M^{z+}_{lattice} \quad [2]$$

According to this equation, a metal ion M^{z+} is transferred from the solution into the ionic metal lattice. This process requires the transfer of z electrons (e^{-}) from an external electron source to the electron gas in the metal M.[1] The equilibrium potential of the electrode (E), associated with the reaction [1] of the metal/metal ion electrode when there is no flowing of current ($I=0$), could be represented by the Nernst equation [3]. Note that this potential is defined with respect to a reference electrode potential.[1]

$$E_{[I=0]} = E^{o} + \frac{RT}{zF}\ln[M^{z+}] \quad [3]$$

where R, T, z, and F are the universal gas constant, absolute temperature, electron numbers, and Faraday's constant, respectively, and $[M^{z+}]$ is the concentration of metallic ions. However, when a current is flowing in an electrochemical cell, the electrode potential differs from eqn [3] and the difference between both potentials is known as 'overpotential.' This 'overpotential' is necessary to overcome the real limitations of the overall electrode reaction.[1]

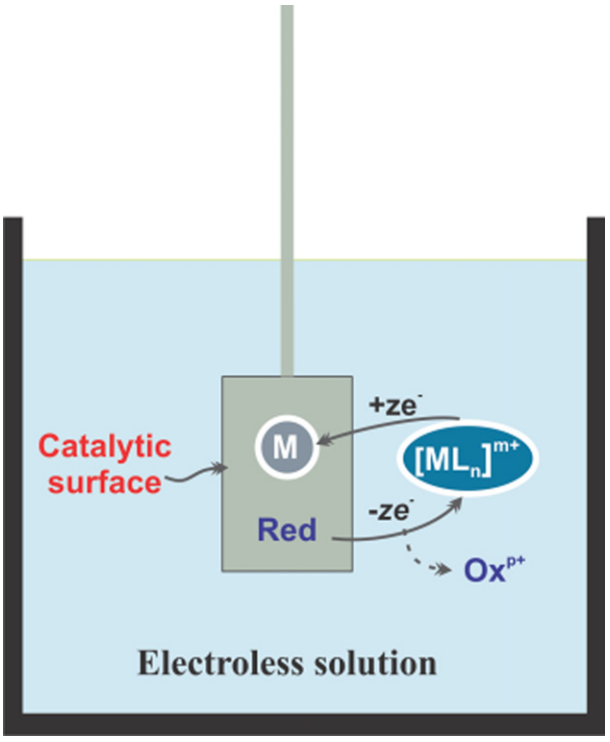


Figure 2 An electrolytic cell for electroless deposition of a metal M from an aqueous solution which contains a reducing agent (Red).

3.1.1.1.2 Main electroplating features

The main features of the deposit are governed by the growth processes of the crystals. The key factors are the composition of electroplating solutions, the current density (current/electrode area), the mass transport and the shape, structure, surface morphology, and metal (or alloy) employed in the electrode.

During the initial step, each nucleus grows independently of each other. However, in the next stages, the overlap between diffusion fields around the growing nucleus can be observed.[1] The growth of the first crystals could be achieved mainly by the lateral spreading of a layer or nucleation–coalescence mechanism. These formation processes affect the deposit features.

On the other hand, the solutions used by the deposition of the metals and alloys contain several inorganic and organic additives. These components (and impurities) could affect the crystal-building processes due to the fact that they can be present as adsorbates on the electrode surface.[1]

3.1.1.2 ELP

3.1.1.2.1 General principles

Unlike electroplating, the electrolytic cell for electroless deposition does not contain power supply, and the anodic/cathodic reactions occur on the surface of the substrate.[1] A scheme of the ELP setup is shown in **Figure 2**. The plating baths used for electroless deposition are more complex and contain a complex compound of the metal to be deposited, a reducing agent, complexing agents, stabilizers, and buffering agents as main components.[1]

The overall reaction of electroless metal deposition could be expressed as:

$$x[ML_n]^{m\pm} + y\text{Red}_{\text{solution}} \xrightarrow{\text{Catalytic Surface}} xM_{\downarrow} + xn\text{L} + y\text{Ox}^{p+}_{\text{solution}} \quad [4]$$

where $[ML_n]^{m\pm}$ is a complex ion of reducible metal, $\text{Red}_{\text{solution}}$ is the reducing agent, M is the metal atom, $\text{Ox}^{p+}_{\text{solution}}$ is the oxidation product of the reducer, and L are the ligands. The catalytic surface may be the substrate itself or the catalytic nuclei of the dispersed metal M that could act as specific surface sites on a non-catalytic substrate surface.[1] In addition, the homogeneous reaction between $[ML_n]^{m\pm}$ and $\text{Red}_{\text{solution}}$ in the bulk solution must be inhibited.

The selection of the L ligands of the central metal should be such that the obtained complex ions $[ML_n]^{m\pm}$ are moderately stable. Otherwise, a strong metal–ligand interaction could inhibit the discharge of the reduced metal on the support surface.[4] The brightness and the good adherence of the coating to the support are the main features of the deposits obtained by ELP. However, if the reaction occurs between the metal ion M^{z+}, not from $[ML_n]^{m\pm}$, and the same reducer, a little amount of powder without adherence could be obtained.[4] In the case of palladium, this powder is black and does not have mechanical resistance.

The metal deposition in ELP could be separated into two electrochemical semi-reactions [5] and [6], of reduction and oxidation[1] that occur at the same electrode–electrolyte interphase. Thus, in the substrate there are two catalytic sites, anodic and cathodic sites.[1]

$$y\text{Red}_{\text{solution}} \xrightarrow{\text{Catalytic Surface}} y\text{Ox}^{p+}_{\text{solution}} + ze^- \quad [5]$$

$$x[ML_n]^{m\pm} + ze^- \xrightarrow{\text{Catalytic Surface}} xM_{\downarrow} + xn\text{L} \quad [6]$$

3.1.1.2.2 Catalytic aspects

From the view point of catalysis, the main reaction in ELP is the oxidation of the reducer. The metal ability to catalyze this reaction allows the deposition of a metal by ELP.[5] However, there is not one unique metal that could act as a good catalyst for the oxidation of all reducing agents at specific reaction conditions.

Cu is an excellent catalyst for H_2CO oxidation but is inactive for hypophosphite and dimethylamine borane (DMAB) oxidation.[5] Ni and Co exhibit activity for different reductants such as NaH_2PO_2, $NaBH_4$, DMAB, and NH_2NH_2; however, these metals are poor catalysts to H_2CO oxidation. Palladium could be considered as the best catalyst for all reducing agents. The combination of its nobility and the resistance to dissolution in an electroless bath has converted Pd in the universal catalyst to start the electroless deposition.

Ohno *et al.*[6] reported the potentials of several reductants when the current density was kept at 1.0×10^{-4} A cm^{-2}. These values are shown in **Figure 3**. The observed tendency could be taken as a starting point for the design of electroless baths. However, it is important to analyze each case, to optimize the catalytic behavior of several metals in different types of ELP solutions.

3.1.1.2.3 Mechanistic overview

Several mechanisms have been proposed for electroless deposition reactions with different reducing agents.[7] Van den Meerakker proposed a mechanism that takes into account both the electrochemical and the catalytic nature of the process.[8] The proposed mechanism represents most of the common features of the metal electroless deposition. However, the mechanism fails to describe it on nonconductive surfaces, and also with metal particles deposition in solution. On the other

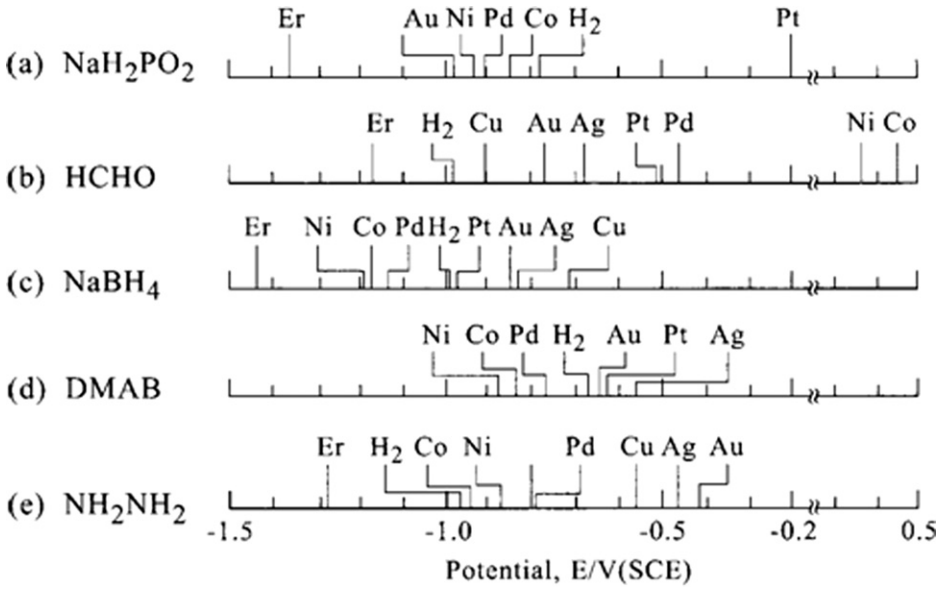


Figure 3 Catalytic activities of metals (as potentials measured at 10^{-4} A cm^{-2}) for anodic oxidation of different reductants. Er, thermodynamic oxidation–reduction potential of reductant; H_2, reversible hydrogen electrode potential in solution used to study oxidation of each reductant.[6] Reprinted from Electrochemical Science and Technology: Ohno, I.; Wakabayashi, O.; Haruyama, S. Anodic Oxidation of Reductants in Electroless Plating. *J. Electrochem. Soc.* **1985,** *132*, 2323–2330. Reproduced with permission from The Electrochemical Society.

hand, some reductants could present different steps and global reactions depending on the bath pH (alkaline and acidic) and the metal to deposit. A more realistic approach would be to look for each specific system with particular conditions and substrates.[8] O'Sullivan claims that this mechanism is a good starting point for the study of a mechanism in a particular metal-reducing agent system.[5]

The universal mechanism was developed according to the following features, which are common to several electroless systems[8]:

1. The electroless deposition processes are produced only on some catalytic metals, which are recognized as effective to hydrogenation–dehydrogenation reactions;
2. The evolution of hydrogen gas is always present;
3. Poisons for hydrogenation–dehydrogenation reactions act as stabilizers in almost all electroless processes; and
4. The deposition rates are normally accelerated by the pH increase.

The unified mechanism could be summarized by the following reaction scheme:

Anodic:

$$\text{Dehydrogenation:}\quad \mathrm{RedH} \longrightarrow \mathrm{Red}^{\bullet}_{ads} + \mathrm{H}^{\bullet}_{ads} \qquad [7]$$

$$\text{Oxidation:}\quad \mathrm{Red}^{\bullet}_{ads} + \mathrm{OH}^{-} \longrightarrow \mathrm{RedOH} + e^{-} \qquad [8]$$

$$\text{Recombination:}\quad \mathrm{H}^{\bullet}_{ads} + \mathrm{H}^{\bullet}_{ads} \longrightarrow \mathrm{H_2}\uparrow \qquad [9]$$

$$\text{Oxidation:}\quad \mathrm{H}^{\bullet}_{ads} + \mathrm{OH}^{-} \longrightarrow \mathrm{H_2O} + e^{-} \qquad [10]$$

Cathodic:

$$\text{Metal deposition:}\quad [\mathrm{ML}_n]^{m\pm} + ze^{-} \longrightarrow \mathrm{M} + n\mathrm{L} \qquad [11]$$

$$\text{Hydrogen evolution:}\quad 2\mathrm{H_2O} + 2e^{-} \longrightarrow \mathrm{H_2}\uparrow + 2\mathrm{OH}^{-} \qquad [12]$$

where, RedH represents the reducing agent, which is adsorbed on the surface of the deposited metal[5,7]; and then it is dissociated to form the radical $\mathrm{Red}^{\bullet}_{ads}$ and atomic hydrogen $\mathrm{H}^{\bullet}_{ads}$(reaction [7]). The electrons that are necessary to reduce the metal ions to the metal are supplied by reactions [8] or [10]. The contribution of each of these two reactions defines the efficiency of the reductant. The formation of gaseous hydrogen could be obtained by both the anodic reaction [9] and cathodic reactions [12].[7]

The evolution of the H_2 gas in electroless deposition systems is a phenomenon that requires to be understood in order to elucidate both the mechanism of deposition and the effect on the deposit morphology through the H inclusion.[5] This H inclusion is produced by the absorption of H in the lattice of the electroless deposit, which was previously an adsorbed H intermediate (reaction [13]).[5]

$$\mathrm{H}^{\bullet}_{ads} \longrightarrow \mathrm{H}^{\bullet}_{bulk} \qquad [13]$$

Avoiding the stress caused by H absorbed in the progress of electroless deposition could allow the application of electroless layers in areas where the metallization of smooth surface is desired.[5]

3.1.1.2.4 Surface conditioning

Several surfaces do not show catalytic activity for ELP, for example, polymers, nonconductors, noncatalytic metals, noncatalytic semiconductors, ceramic, and glass. Thus, these surfaces have to be conditioned prior to the electroless deposition. This process could normally be broken down into three steps: surface preparation, sensitization, and activation.

In order to improve the adhesion and the catalytic nuclei seeding, the surface preparation normally needs an etching process to modify the noncatalytic substrates.[2]

During the sensitization process, the adsorption of the reducing agent takes place, as Sn^{2+} or N_2H_4.[8] Then, the sensitized surfaces are activated by exposure to a solution containing Pd^{2+} and HCl to produce the Pd nuclei.[9]

The overall reaction can be seen in the following equation (eqn [14]).

$$y\mathrm{Red}^{q+}_{\mathrm{solution}} + x\mathrm{Pd}^{2+} \longrightarrow y\mathrm{Ox}^{p+}_{solution} + xPd^{0} \qquad [14]$$

3.1.1.2.5 Conditions and chemical composition of different metal solutions

Normally, ELP solutions include the components shown in **Table 1**. Additives in small quantities are usually employed to improve the solution stability and to achieve the desired physical properties of the deposited film.[7]

The composition of ELP baths for different metals such as Pd, Ag, Cu, Au, Ru, Ni, and Co are displayed in **Table 2**.

Table 2 also includes the pH values employed which normally depend on the selected reducing agent. For example, borohydride is limited to a high alkaline medium; the amineboranes are used from mildly alkaline to mildly acidic baths.[4] However, hydrazine can reduce metal ions under both acidic and basic conditions. In an alkaline medium, it is a strong reducing agent[28] which allows the deposition of thick films when high pHs are employed.

Different components (see **Table 2**) are used as stabilizer agents such as ammonium chloride and Na_2EDTA in palladium–ammine complex compounds. When NH_4Cl is used as stabilizer and hypophosphite is the reducer, the bath stability is reached because the concentration of $[Pd(NH_3)_4]^{2+}$ remains constant.[4] Instead, the Na_2EDTA stabilizer ability is achieved by a ligand substitution. However, the resulting solution requires higher temperature for metal reduction than ammonia based baths, due to its higher stability.[4]

Table 1 Components of an electroless plating bath

Component	*Purpose*
Metal salt	Source of metal to be deposit
Reducing agent	To provide the electrons to the metal reduction
pH adjuster	pH adjustment
Complexing agent	To form metal complex avoiding the excess of free metal ion
Additives	To improve bath stability or deposit properties

Table 2 Composition of electroless plating baths of different metals

Metal	*Metal salt*	*Complexing agent*	*Stabilizer*	*Proposed complex ion*	*Reducing agent*	*pH Adjuster*	*pH*	*T (K)*	*References*
Pd	$PdCl_2$	NH_4OH	NH_4Cl	$[Pd(NH_3)_4]^{2+}$	$NaPO_2H_2$		11	308–333	[4]
	$[Pd(NH_3)_4]Cl_2$		Na_2EDTA		H_2NNH_2		11	313–333	
Ag	$AgNO_3$	NH_4OH	Na_2EDTA	$[Ag(NH_3)_2]^+$	H_2NNH_2		11	308–323	[10,11]
				$[Ag(NH_3)_2]^+$	CH_2O		8–9	293	[12]
Cu	$CuSO_4 \cdot 5H_2O$ or $Cu(NO_3)_2 \cdot 2H_2O$, or $CuCl_2 \cdot 2H_2O$	Na_2EDTA	$(C_2H_5)_2NCS_2Na.3H_2O$	$[Cu(EDTA)]^{2-}$	CH_2O	NaOH	12–13.5	298–328	[13–15]
Au	$NaAu(Cl)_4 \cdot 2H_2O$ $AuCl_3$ $HCl \cdot 4H_2O$	Na_2SO_3 and $Na_2S_2O_3 \cdot 5H_2O$		$[Au(SO_3)(S_2O_3)]^{3-}$	*L*-$C_6H_8O_6$	NaOH	10	323–333	[16]
Ru	$RuCl_3 \cdot 3H_2O$	NH_4OH		$[Ru(NH_3)_4(OH)Cl]^+$	H_2NNH_2		11	308–333	[17]
		$NaNO_2$		$[RuNO(NH_3)_4(OH)]^{2+}$	H_2NNH_2		9.5–13	308–353	[18]
		NH_4OH and NaOH			H_2NNH_2			RT[a]	[19]
					$NaPO_2H_2$		11	303	
		NaOH	NH_4Cl				11	303	
	$K_2[Ru(NO)Cl_5]$	NH_4OH	H_3NO				9.5–13	308–353	
Ni	$NiCl_2 \cdot 6H_2O$	NH_4OH		$[Ni(NH_3)_6]^{2+}$	$NaBH_4$		11		[20]
		$Na_3C_6H_5O_7$		$[Ni(C_6H_5O_7)(H_2O)_2]^{2+}$	$NaBH_4$	NaOH	12	313	[21]
	$NiSO_4 \cdot 4H_2O$				H_2NNH_2	NaOH	10–12	353–363	[22]
	$NiCl_2 \cdot 6H_2O$, etc.				$NaPO_2H_2$		8.5–9.5	311–315	[23]
	$Ni(OCOCH_3)_2 \cdot 4H_2O$	Na_2EDTA			H_2NNH_2	NaOH	8–11.5	343–368	[24]
	$NiCl_2 \cdot 6H_2O$		Pb^{2+}		$(CH_3)_2NHBH_3$		4–6	333	[25]
Co	$CoCl_2 \cdot 2H_2O$	NH_4OH	NH_4Cl		$NaBH_4$	NaOH	11		[26]
		$Na_3C_6H_5O_7$ and $CH_3COONa \cdot 3H_2O$			$NaPO_2H_2$	NaOH		368	[27]
		$Na_3C_6H_5O_7$			H_2NNH_2	NH_4OH and NaOH	11–13	333–363	[28]

[a]RT, Room temperature.

3.1.2 Electroless Deposition of Pure Metals

3.1.2.1 Palladium

The electroless deposition of palladium coatings has been widely reported in the literature.[4,29,30] The deposition from a hydrazine plating bath was first reported by Rhoda[31] in 1959 using palladium in the form of tetra-amine di-chloride $[Pd(NH_3)_4]Cl_2$.

It was found[29] that the deposition rate increases with temperature, hydrazine, and Pd concentration. A spontaneous precipitation in the bulk of the bath occurs in the absence of EDTA, which is commonly utilized as stabilizer. On the other hand, a decrease in the plating rate with time was observed, which was attributed to the catalytic decomposition of hydrazine by palladium. One of the major challenges of the development of the homogeneous palladium coating was the improvement in the stability of the plating bath by a proper selection of additives and stabilizers.

Ma *et al.*[30,32] reported a detailed experimental study conducted to model the electroless palladium plating kinetics. They analyzed the effect of temperature, initial Pd and hydrazine concentration, and agitation speed on the plating deposition rate. It was shown that hydrazine was the limiting reactant for the studied range of initial Pd metal ion concentrations (between 8.2 and 24.5 mM). Furthermore, it was demonstrated that the ELP of Pd was strongly affected by the external mass transfer in the absence of agitation (**Figure 4(a)**). An increase in both the Pd deposition rate and solution conversion was observed with the agitation rate up to about 400 rpm. A higher agitation rate did not produce further improvements (**Figure 4(a)**).

The morphology of the Pd coatings is significantly affected by the rate of agitation. In the film without agitation, the surface morphology is composed of small tightly knitted Pd clusters (**Figure 4(b)**). On the other hand, the morphology formed by the bath agitation at a rate of 50 rpm was under the shape of loosely packed small clusters. In the case of Pd plating, at an agitation rate of 200 rpm and later at 400 rpm, the SEM images suggested that the Pd deposition was noticeably more uniform and smooth in appearance with relatively larger clusters and cauliflower-like morphology (**Figure 4(b)**).[32]

3.1.2.2 Nickel

The plating baths for electroless deposition of Ni are composed mainly of nickel sulfate (source of Ni), sodium hypophosphite (reducing agent), and chemicals to prevent precipitation of insoluble nickel hydroxide. They are operated at temperatures between 333–358 K and the pH is maintained in an acid range for bath stability. However, the evolution of hydrogen could lower the pH; to prevent this, alkaline salts of Na and K or ammonium ions are usually added to the bath. For plating baths with hypophosphite as reducing agent, a wide range of plating baths with pH ranging from 4 to 11 has been reported. During electroless Ni deposition, P is co-deposited. At low pH values, coatings with higher phosphorous content (up to 25 at% at pH 4) are obtained. In the alkaline range, films with less than 1 at% of phosphorous are synthesized. One important pH-dependent property of nickel coatings is the fact that films grown using acidic baths exhibit good adhesion characteristics to steel. Very likely, this is why those film types are more common in industry. Alkaline baths tend to have a higher deposition rate with the concomitant result of decreased stability.[33]

In addition to hypophosphite, three reducing agents are frequently used to nickel electroless deposition: sodium borohydride ($NaBH_4$) (pH 12–14), hydrazine (pH 8–11), and DMAB $(CH_3)_2NHBH_3$, (pH 6–10). Hydrazine based plating baths are used to obtain pure nickel coating. However, the instability of the baths at high temperature and the cost of hydrazine have limited its use at industrial level.[34]

The Ni coatings grown in acidic bath using hypophosphite (high P content) have an amorphous or liquid-like structure.[35] Heat treatment to about 603 K produces semi-crystalline face-centered-cubic (fcc) nickel interspersed with intermetallic

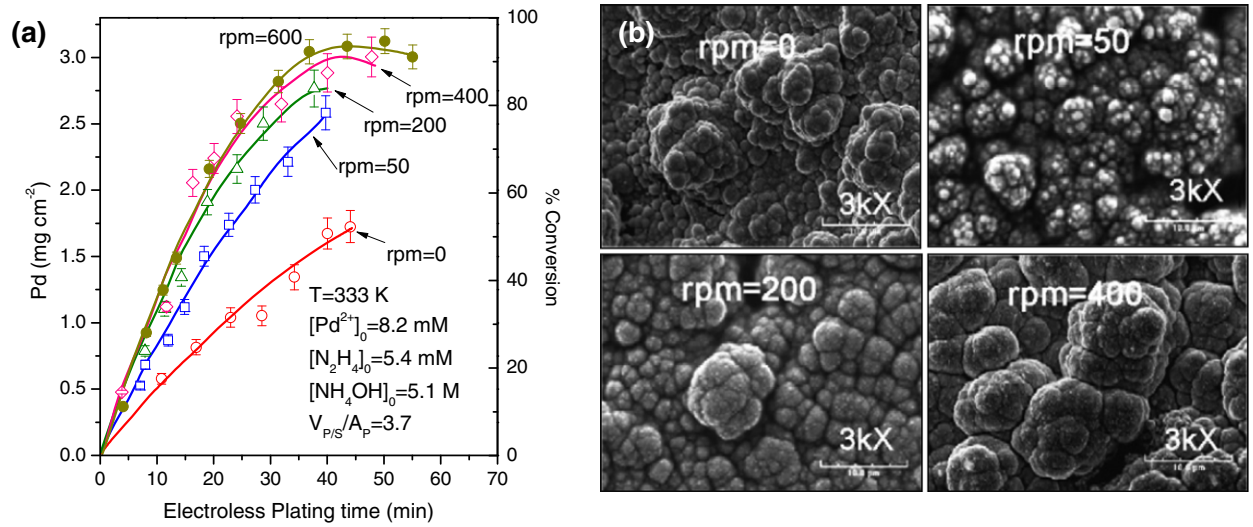


Figure 4 Effect of plating bath agitation on: Pd plating rate (a) and coating morphology (b). Reprinted from Ayturk, M. E.; Ma, Y. H. Electroless Pd and Ag Deposition Kinetics of the Composite Pd and Pd/Ag Membranes Synthesized from Agitated Plating Baths. *J. Memb. Sci.* **2009**, *330*, 233–245. © Elsevier 2009.

compounds such as Ni_3P; the grain size of the Ni fcc structure increases when temperature increases.[35]

3.1.2.3 Silver

The plating baths used in the Ag deposition are very unstable and short-lived, with the formation of silver power throughout the solution. It has been found that the addition of small amounts of 3-iodotyrosine or 3, 5-diiodotyrosine improves the bath stability. Considering that the bath stability are markedly affected by the pH, Kubota and Koura[36] studied the effect of different synthesis parameters. They found that as the plating time increases, the pH of the bath changes with the concentration of silver nitrate, mainly at an initial pH below 10.5.

The deposition rates for the electroless Ag plating are strongly influenced by the temperature and hydrazine concentration. Baths containing $AgNO_3$, NH_4OH, and hydrazine are unstable at temperatures higher than 333 K, due to the evaporation of excess NH_4OH.[30] Even though a higher concentration of the reducing agent resulted in an increase in the deposition rate, the stability of the silver bath was altered as evidenced by a decrease in the pH of the bath (<10). At a hydrazine concentration of 5.4 mM (range studied 1.8–5.4 mM), the bulk precipitation of the Ag metal was evidenced when the processes were conducted without agitation.[30] On the other hand, the ELP of silver is strongly affected by the external mass transfer. In the same way as for Pd depositions, the agitation rate produces an increase in the silver deposition rate and the conversion of the plating reaction (**Figure 5(a)**).

Ma *et al.*[30,32] reported that the Ag electroless process produces deposits with nonuniform growth with a tendency to grow more in the perpendicular direction to the surface of porous stainless steel substrates. As it can be seen in **Figure 5**, the silver deposition morphology was considerably affected by the bath agitation. The silver morphology of films synthesized in static baths (0 rpm) consisted of randomly distributed clusters with different shapes and sizes (**Figure 5(b)**). On the other hand, the morphology of films obtained in a bath with stirring produced relatively more uniform clusters. Due to the agitation of the plating bath, the heat dissipation via convection is further enhanced, minimizing both heat and mass transfer limitations and resulting in faster plating rates, with higher conversions. Together with the bath agitation, increased plating temperature and reducing agent concentration assist in forming uniform and improved nucleation sites, thus allowing higher conversions and faster plating rates.[30]

3.1.2.4 Copper

The plating solutions used for copper electroless deposition are often composed of copper sulfate, a complexing agent such as EDTA, a reducing agent, a stabilizer, and NaOH to adjust the pH. Traditional ELP uses formaldehyde as reducing agent; however, other reducing agents have also been used, namely glyoxylic acid, hypophosphite, sodium bisulfate ($NaHSO_3$) and sodium thiosulfate pentahydrate ($Na_2S_2O_3 \cdot 5H_2O$). The selection of the bath compositions depends on some empirical rules.[37] It has been pointed out that in order to allow the complexing of all cupric ions, the ratio of EDTA/Cu should be set about 2.5, whereas pH values are best adjusted between 12.5 and 13.5. So far, various attempts have been made to improve plating quality as well as rate and bath stability[38,39] Kaliaguine and coworkers[37] found that the concentration of EDTA and NaOH in the plating bath is the most important factor affecting the deposition rate of Cu. The Cu deposition was enhanced by increasing the concentration of NaOH, $CuSO_4$, and HCHO and decreasing the EDTA content.

The surface morphology evolution of copper deposits obtained under several conditions using formaldehyde or glyoxylic acid as reducing agent has been reported[40] in the literature. Due to the acidic nature of glyoxylic acid and its

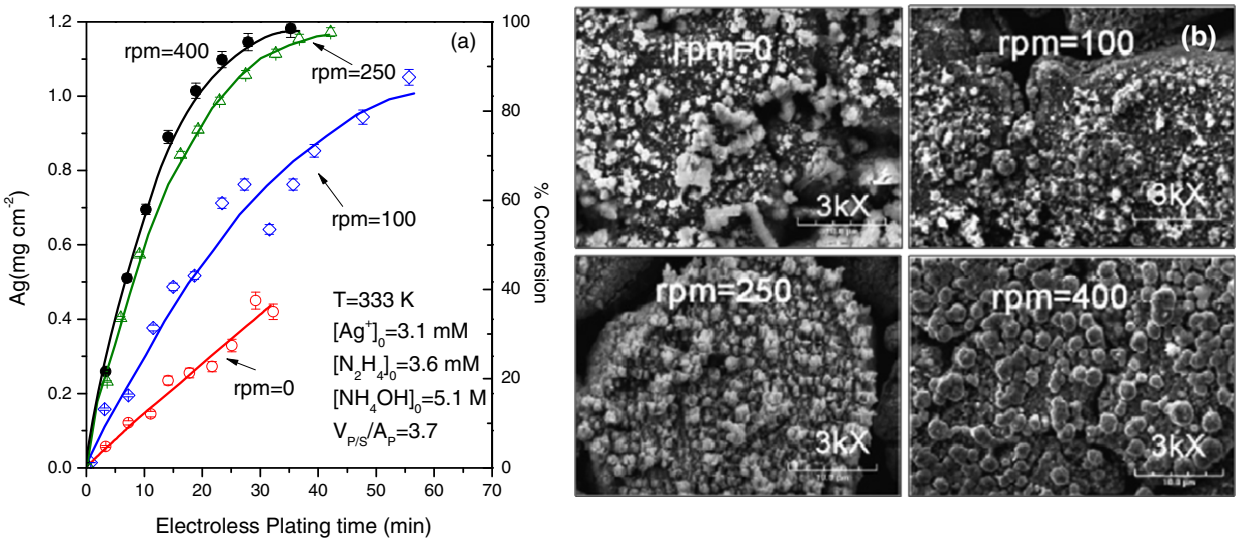


Figure 5 Effect of plating bath agitation on: Ag plating rate (a) and coating morphology (b). Reprinted from Ayturk, M. E.; Ma, Y. H. Electroless Pd and Ag Deposition Kinetics of the Composite Pd and Pd/Ag Membranes Synthesized from Agitated Plating Baths. *J. Memb. Sci.* **2009**, *330*, 233–245. © Elsevier 2009.

high sensitivity to temperature and concentration, it is not so easy to control the plating bath containing glyoxylic acid as it is to control those with formaldehyde. In addition, the used concentration of the copper sulfate is relatively low when a lower concentration of glyoxylic acid is employed at high temperature. With the increase of the glyoxylic acid concentration, the plating bath becomes unstable at 343 K, which makes the solution unable to sustain prolonged plating. When the temperature is lowered to 318 K, although the concentration of glyoxylic acid is even higher, the plating remains relatively stable. By replacing formaldehyde with glyoxylic acid, it is possible to obtain a smoother surface in the electroless copper deposit, which could be due to the fine grains on the surface of the deposits from glyoxylic acid solutions in the early stage of the plating process. In a plating bath with a high concentration of glyoxylic acid and at high temperature (343 K), although the 120 min deposit has large grains on the surface, the surface morphology of the earlier stage deposit consists of small grains. At low temperature (318 K), plating baths with a high concentration of glyoxylic acid and formaldehyde give the smoothest surface finish.[40]

3.1.3 Palladium Binary Alloys

Electroless deposition has been widely used to synthesize several binary and ternary palladium based alloys in order to be used as membranes for hydrogen separation within other applications. Investigations of film compositions and structures, and the effect that synthesis variables produce on them are of great importance in order to develop new materials and improve their properties. Even though it is a widely used technique for the synthesis of Pd and Pd-alloy films, one of the major problems related to the ELP method is the difficulty in obtaining a uniform alloy composition on thickness. Alloying is most commonly achieved by the coating-diffusion method. This technique consists in the sequential or co-deposition of the metals followed by high-temperature diffusion treatment under reductive (H_2) or inert (Ar, N_2) atmosphere to promote the alloy formation. In order to obtain layers without composition gradients on thickness, treatments at high temperatures and longer times are required for sequential electroless deposited layers. On the other hand, the simultaneous deposition of two metals facilitates the contact between the pure metals and improves alloy formation. With the aim of achieving uniform alloy coatings through electroless deposition, a substantial amount of study has been carried out on a wide variety of support materials (metals and ceramics) and using several characterization techniques. X-ray diffraction (XRD) is widely used to study the phase evolution and/or phase transition under annealing conditions. The morphology and atomic composition of both the top and cross section view of the films are determined by Scanning Electron Spectroscopy (SEM) coupled with Energy Dispersive Spectroscopy (EDS). In order to study the surface segregation under annealing and permeation conditions, X-ray photoelectron (XPS) and Low energy ion scattering (LEIS) spectroscopies have been employed to determine the composition of the near-surface region and top-most surface layer, respectively.

3.1.3.1 Sequential and Co-Deposition of PdAg Alloys

As it is well known, palladium and silver are completely soluble in the solid state and form the fcc (face-centered-cubic) phase in all the composition range. The synthesis and characterization of both sequential deposition[41,42] and co-deposition[43] of PdAg have been widely reported in the literature using hydrazine-based palladium plating baths. Films obtained by sequential deposition need stronger heat treatments, longer times or higher temperatures for alloy formation compared with films obtained by co-deposition. Nevertheless, simultaneous deposition presents certain difficulties in obtaining films with homogeneous morphology and desired bulk composition. Ma *et al.*[42] presented a comprehensive work regarding the isothermal nucleation and growth kinetics of PdAg alloy phase by using *in situ* time-resolved high-temperature X-ray diffraction (HTXRD). The HTXRD data indicated that the formation of the fcc PdAg alloy was observed once the target annealing temperature was reached. However, the extent of the phase transformation for the film annealed at 823 K was smaller than the one observed for the films annealed at 773 and 873 K (**Figure 6**). From the SEM top-surface view, it could be seen that the typical surface morphology of the films annealed at 773 and 823 K was in the form of dendrite silver, in contact with the underlying Pd layer. For the film annealed at 823 K, large clusters of Ag dendrites were observed, which presented varying sizes and shapes with respect to the annealed morphologies at 773 and 873 K. As a result, the predominant presence of Ag-dendrites significantly affected the contact area and the planar shape of the original interface between the Pd and Ag layers. The presence of defects and imperfections in the morphology can also have a substantial effect on the nucleation and growth processes, and thus in the formation of the PdAg alloy phase. The higher defect density observed in the film annealed at 823 K could be the reason for the lower extent of alloy formation at this temperature (**Figure 6(a)**). From the EDS data, it was possible to observe a more heterogeneous distribution of Pd and Ag in the thickness of the film annealed at 823 K, compared with those annealed at 773 and 873 K (**Figure 6(b)**). The agreement between the HTXRD kinetics data, the cross section SEM images and the EDS line scans indicated that the deposition morphology had a significant effect on the PdAg alloy phase growth kinetics. From the HTXRD experiments, the authors reported a quantitative analysis of the PdAg alloy phase nucleation and growth kinetics of annealing at 773, 823, and 873 K. The difference in estimated activation energies of deposition might be related to the presence of heterogeneous nucleation sites, defects and imperfections at the original interface between Pd and Ag layers.

The effect of deposition time on morphology and homogeneity on PdAg alloy formation was studied by Bosko *et al.*[11] They prepared PdAg membranes by sequential deposition on top of alumina or NaA modified porous stainless steel substrates. By reducing the thickness of each deposition step to *ca.* 1 ± 0.1 μm, the PdAg alloy formation was obtained with thermal treatment at 773 K in H_2 atmosphere during 110 h.[11] The EDS analyses of the film with shorter deposition cycles showed homogeneous atomic composition up to 15–20 μm deep. As shown in **Figure 7**, the PdAg (90 min) film showed a

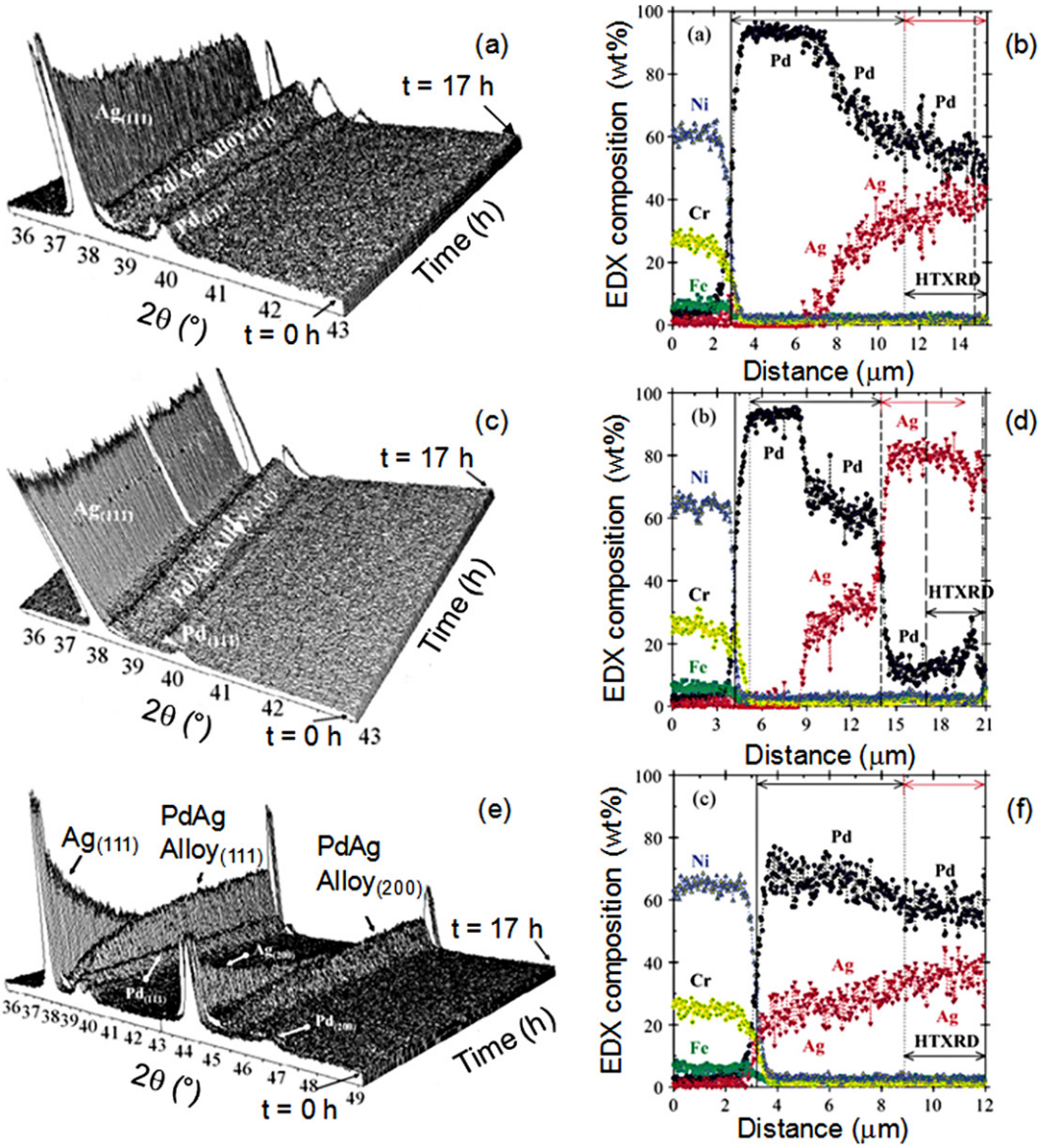


Figure 6 *In situ* time-resolved HTXRD data and EDS cross sectional line scans for isothermal annealing in hydrogen at: 773 K (a, b), 823 K (c, d), and 873 K (e, f). Reprinted from Ayturk, M. E.; Payzant, E. A.; Speakman, S. A.; Ma, Y. H. Isothermal Nucleation and Growth Kinetics of Pd/Ag Alloy Phase via *in situ* Time-Resolved High-Temperature X-Ray Diffraction (HTXRD) Analysis. *J. Memb. Sci.* **2008**, *316*, 97–111. © Elsevier 2008.

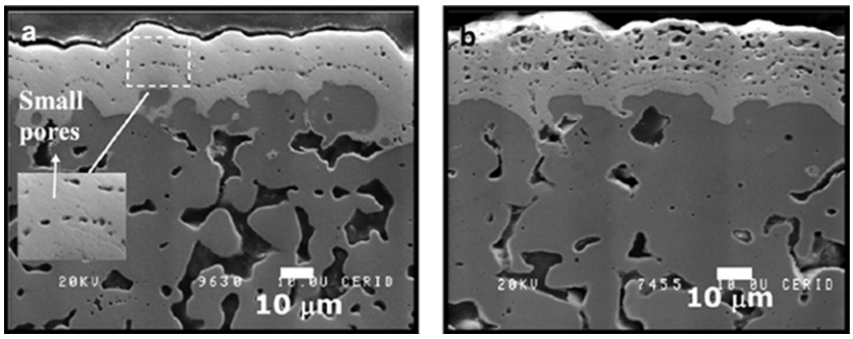


Figure 7 Effect of electroless deposition time on morphology of PdAg sequentially deposited films. Reprinted from Bosko, M. L.; Lombardo, E. A.; Cornaglia, L. M. The Effect of Electroless Plating Time on the Morphology, Alloy Formation and H_2 Transport Properties of Pd–Ag Composite Membranes. *Int. J. Hydrog. Energy* **2011**, *36*, 4068–4078. © Elsevier 2011.

compact film with few defects formed between two well-defined layers. On the other hand, the film synthesized with shorter deposition cycles showed a higher defect density in thickness (Figure 7). This difference was related to the dendritic growth of silver layers. Therefore, these results suggest that the use of a higher number of Ag depositions increased the detrimental effect of the silver dendritic growth.

The co-deposition of PdAg alloys has also been reported in the literature[43,44] Yeung *et al.*[43] studied the effect of plating parameters on the microstructure and performance of co-deposited PdAg membranes synthesized from hydrazine-based plating baths containing Pd and Ag precursors. The presence of Ag in the plating bath inhibited the deposition of Pd resulting in a decrease of the overall deposition rate. Co-deposition of Pd and Ag was favored for plating solutions with low ammonium content, elevated temperatures, and a moderate hydrazine/metal ratio.

3.1.3.2 Sequential and Co-Deposition of PdRu Alloys

The PdRu alloys could be deposited by sequential deposition or co-deposition followed by annealing at high temperature. Sequential plating may not produce fully homogeneous films considering the elevated Tammann temperature of metals ($T_{\text{TammannRu}} = 1310$ K, $T_{\text{TammannPd}} = 914$ K), while the composition of some co-plated films has been shown to vary with plating time, concentration of reducing agent, metal ion concentration and synthesis temperature.[17]

The synthesis of PdRu alloy films in the range of 5–10 wt% of Ru from a EDTA-free bath was reported by Way *et al.*[45] The coating composition is enhanced in Pd content with respect to the bath. In this study, these authors claimed that the incorporation of Ru to the plating bath improves the substrate coverage allowing to obtain thinner films. On the other hand, Braun *et al.*[17] studied the effect of synthesis variables on the morphology, substrate adherence and composition of PdRu co-deposited films. Films prepared using EDTA-free plating baths present more heterogeneous morphology if compared with films prepared with EDTA under the same conditions (Figure 8). For the PdRu coatings obtained without EDTA and higher hydrazine concentrations (Figures 8(b) and 8(f)), a higher dendritic morphology with growth in height were observed. On the other hand, the film with the lowest concentration of hydrazine (Figures 8(b) and 8(d)) presents a less heterogeneous morphology, probably due to a lower reaction rate.

Homogeneous and defect-free films were obtained employing baths at low pH, moderate to high agitation speeds and high concentration of hydrazine, using EDTA as a stabilizer and temperatures near 323 K (Figures 8(a), 8(c), and 8(e)).

3.1.3.3 Sequential Deposition of PdCu Alloys

We have found only one article in the literature reporting co-deposition of PdCu alloys by electroless methods. In this study, the authors used palladium–cyanide complexes and formaldehyde as reducing agent.[46] The preparation of PdCu alloys by ELP is commonly achieved by the sequential deposition of Pd and Cu layers followed by annealing at high temperature. For sequential deposition, the plating of Pd using a palladium–ammonia complex on top of a Cu layer could not be performed since ammonia partially dissolves copper. Hence, palladium should be plated first followed by copper and then, the deposits should be annealed.

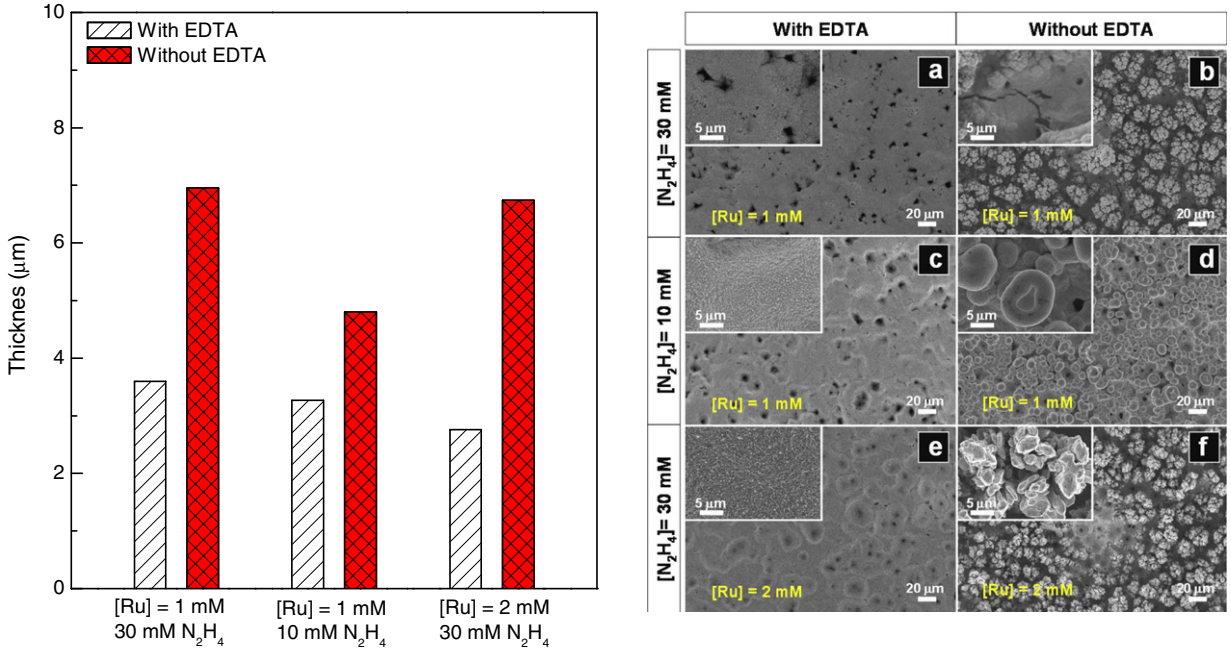


Figure 8 Hydrazine concentration effect on PdRu film morphology synthesized with EDTA (a, c, e, and g) and without EDTA (b, d, f, and h). Electroless deposition conditions: [Ru + Pd] = 10 mM, [Ru] = 10 mM, T = 323 K, pH 11.5. Three 1 h co-depositions. Reprinted from Braun, F.; Tarditi, A. M.; Cornaglia, L. M. Optimization and Characterization of Electroless Co-Deposited PdRu Membranes: Effect of the Plating Variables on Morphology. *J. Memb. Sci.* **2011**, *382*, 252–261. © Elsevier 2011.

The PdCu system is structurally different from the PdAg where only the fcc phase is formed throughout the composition range and temperature. Palladium and copper are not fully miscible below 873 K. The system forms a continuous series of disordered fcc solid solution above 873 K and at all temperatures when the palladium composition is higher than 65 at%. At a composition of palladium about 40 at% and ordered bcc (body-centered-cubic) phase with a CsCl like structure is found below 873 K. Additionally, there exist two more structure types with a Cu_3Au related lattices at Cu compositions higher than 70 at%.[47]

HTXRD has been used by Ma *et al.*[48] to study the Pd–Cu phase transformation of electroless films deposited on top of porous stainless steel substrates. During the annealing at temperatures between 773 and 873 K, there can be a maximum of five phases present, namely pure Pd and pure Cu phases, the Pd-rich and Cu-rich fcc phases and one bcc phase. The application of the Avrami model indicated that the nucleation and growth of the fcc phase were one dimensional in nature. The rate-limiting process of the solid-state transformation was the bulk diffusion of Cu into Pd. To completely form the fcc phase (with *ca.* 15 at% Cu) at 773 K, annealing during 225 h would be needed.[48]

After annealing, the morphology of the layer looks like a porous Pd/Cu layer on top of a nonporous Pd/Cu alloy. Ma *et al.*[48] claimed that the porous Pd/Cu alloy was caused by the Kirkendall effect which occurred when two metals with unequal diffusion coefficients underwent interdiffusion. In this case, the voids were formed when Cu atoms diffused faster than the Pd atoms. The Kirkendall porosity has been previously observed on the Cu side of Pd/Cu diffusion couples. Another reason for the voids could be the fcc–bcc transition. Indeed, the change in the lattice structure and the lattice parameter could cause irreversible structural transformation.

3.1.3.4 Sequential Deposition of PdAu Alloys

The PdAu alloy formation from ELP of sequential palladium and gold layers on top of ceramic tubes was studied by Goldbach *et al.*[49] The authors deposited a thin film of gold on top of a Pd layer. For the deposition of the Au layer, they used a cyanide-free plating bath. The analysis of the alloy formation as a function of time at different temperatures showed that the alloying of the separate metal layer required about 168 h at 873 K and more than 500 h at 773 K under hydrogen stream. In contrast, Tarditi *et al.*[16] reported fcc PdAu alloy formation at 773 K during 120 h in hydrogen stream for multilayered Pd/Au films synthesized on top of porous stainless steel disks. The difference observed could be attributed to the fact that Goldbach *et al.*[50] prepared a bilayered Pd/Au film consisting in a thin gold layer on top of a Pd film, whereas Tarditi *et al.* deposited a multilayer film alternating layers of Pd and Au.

In order to optimize the synthesis and homogeneous alloy formation in thickness, Goldbach *et al.*[50] reported the synthesis of PdAu nanostructured layers. The as-synthesized samples are formed by *ca.* 30 nm wide Au layers and 250 nm wide Pd layers sequentially deposited on top of ceramic support tubes (Figure 9). The veined multilayer pattern observed by SEM-EDS in the as-prepared film disappeared and the Pd and Au EDS traces became flat after one day of annealing at 773 K

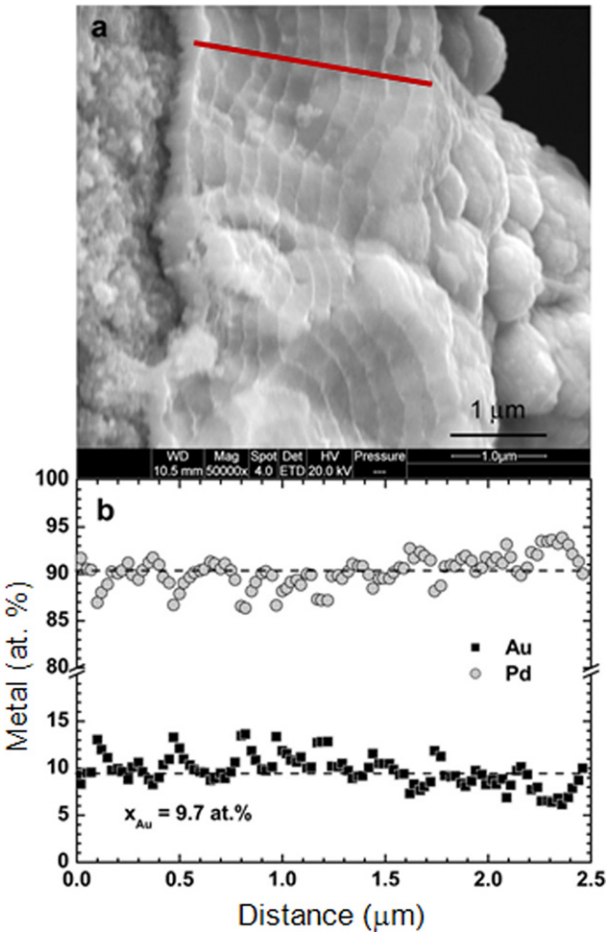


Figure 9 Cross sectional SEM image of freshly prepared Pd/Au multilayer film (a); EDS scan along the line marked in the SEM image (b). Reprinted from Braun, F.; Tarditi, A. M.; Cornaglia, L. M. Optimization and Characterization of Electroless Co-Deposited PdRu Membranes: Effect of the Plating Variables on Morphology. *J. Memb. Sci.* **2011**, *382*, 252–261. © Elsevier 2011.

under atmospheric H_2 pressure, which indicated that the homogenization of the multilayer proceeded rapidly under those circumstances. The improved alloying of nanostructured PdAu electroless deposited films could be attributed to the much extended interface between the two metals in comparison with a bilayer film with the same total thickness.

3.1.4 Palladium Ternary Alloys

Recently, there has been increasing interest in studying the synthesis and characterization of some Pd-based ternary alloys because of their superior properties concerning hydrogen permeability and/or chemical resistance. Ternary alloys containing copper or gold have a higher H_2S resistance corrosion than pure palladium membranes which experiment surface and bulk formation of PdS_4. Cornaglia and coworkers[13,51–54] reported the synthesis and characterization of PdCuAu, PdCuAg, PdAgAu ternary alloys. The alloys films were synthesized on top of porous stainless steel substrates by

sequential electroless deposition of the pure metals. A summary of the compositions of the plating bath and the experimental conditions used for the electroless deposition of Pd, Cu, Au, Ru, and Ag are shown in Table 3. Prior to the metal deposition, the sensitizing-activation of the substrate using a $SnCl_2$ and $PdCl_2$ acidic solution was performed at room temperature for all the alloys.

3.1.4.1 PdAgAu Alloys

PdAgAu ternary alloys with different atomic composition ($Pd_{83}Ag_2Au_{15}$, $Pd_{74}Ag_{14}Au_{12}$, $Pd_{78}Ag_9Au_{13}$, and $Pd_{75}Ag_{16}Au_9$) have been obtained by the sequential electroless deposition method on top of porous stainless steel disks previously modified with alumina or ZrO_2.[51,52] Palladium, silver, and gold were deposited in this order.[52] The three-metal deposition cycle was repeated for the films to achieve a target thickness of ~14 μm. The ternary films were annealed at 773 or 873 K in H_2 to promote metallic interdiffusion and alloy formation. The XRD patterns after annealing at 773 K during 120 h in hydrogen stream display an incomplete fcc alloy formation as illustrated by the appearance of small shoulders in the main peaks assigned to the fcc structure (Figure 10). These shoulders are more pronounced in the film with higher silver content (Figure 10(b)). With a second annealing at 873 K for 48 h, a complete alloy formation was evidenced (Figure 10),[52] displaying a homogeneous alloy composition on thickness.[51] The PdAgAu film with higher

Table 3 Composition and experimental conditions for the Pd, Ag, Cu, Au, and Ru baths used for the synthesis of the binary and ternary alloys synthesized by electroless plating

	Pd	*Ag*	*Cu*	*Au*	*Ru*
$PdCl_2$ (g L^{-1})	3.6	–	–	–	–
$AgNO_3$ (g L^{-1})	–	0.5	–	–	–
$CuSO_4 \cdot 5H_2O$ (g L^{-1})	–	–	20	–	–
NH_4OH (mL L^{-1})	650	650	–	–	–
$Na_2EDTA \cdot 2H_2O$ (g L^{-1})	67	67	30	–	–
N_2H_4 1 M (mL L^{-1})	10	10	–	–	–
HCHO (37%) (mL L^{-1})	–	–	14	–	–
NaOH (g L^{-1})	–	–	20	0.2	102
EDA (ppm)	–	–	100	–	–
$K_4Fe(CN)_6 \cdot 3H_2O$ (ppm)	–	–	35	–	–
$(C_2H_5)_2NCS_2Na \cdot 3H_2O$ (ppm)	–	–	5	–	–
$AuCl_3$ $HCl \cdot 4H_2O$ (mmol L^{-1})	–	–	–	7.5	–
Na_2SO_3 (mol L^{-1})	–	–	–	0.1	–
$Na_2S_2O_3 \cdot 5H_2O$ (mol L^{-1})	–	–	–	0.1	–
L-$C_6H_8O_6$ (mol L^{-1})	–	–	–	0.3	–
HCl (mmol L^{-1})	–	–	–	–	0.12
$RuCl_3 \cdot 3H_2O$ (mmol L^{-1})	–	–	–	–	3.08
pH	11	11	12	10	11.5–14
Temperature (K)	323	323	298	333	30–80

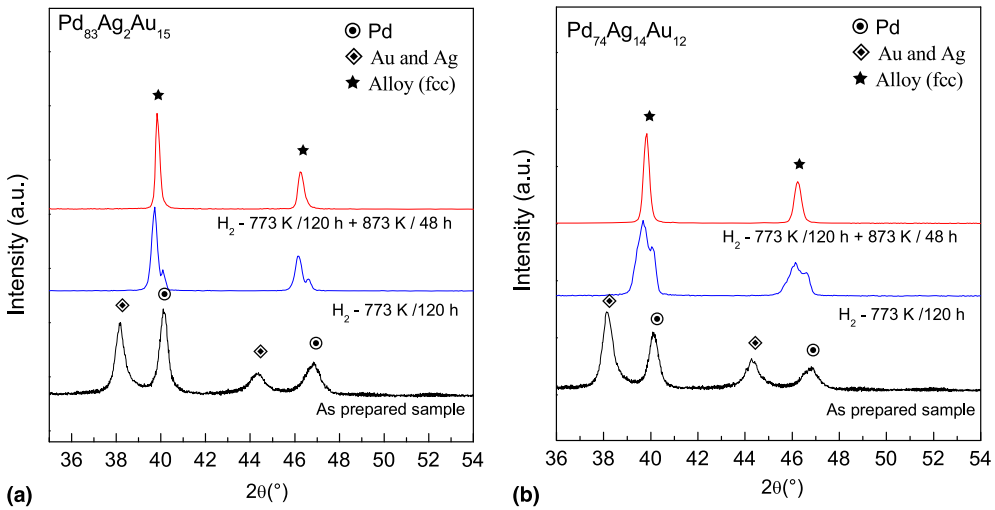


Figure 10 Effect of the annealing temperature on the PdAgAu fcc alloy formation for: $Pd_{83}Ag_2Au_{15}$ (a) and $Pd_{74}Ag_{14}Au_{12}$ (b) films. Reprinted from Braun, F.; Miller, J. B.; Gellman, A. J.; *et al.* PdAgAu Alloy with High Resistance To Corrosion by H_2S. *Int. J. Hydrog. Energy* **2012**, *37*, 18547–18555. © Elsevier 2012.

silver atomic composition ($Pd_{74}Ag_{14}Au_{12}$) presents a more heterogeneous morphology with a higher density of defects (Figure 10), which could be related to the heterogeneous nucleation and dendritic growth of silver deposits obtained by the electroless method.

Way and coworkers[55] also investigated the PdAuAg alloys deposited on top of porous zirconia-coated stainless steel tubes (YSZT). The YSZT was activated for Pd ELP by spraying a solution of Pd acetate in chloroform onto the substrate using an airbrush, followed by a heat treatment in air to 623 K to decompose the organic ligand. Prior to the plating, the activation layer was reduced by submerging the substrate in a mixture of ammonium hydroxide, hydrazine, and water. In this case, the metal deposition was in the order Pd, Au, and Ag. The sample was annealed at 773 K during 120 h in H_2(3.5%)/Ar. From the XRD spectra, it could be observed that the PdAuAg peaks are not symmetric, which indicates that complete alloy formation did not occur.

3.1.4.2 PdAgCu Alloys

In order to obtain homogeneous PdAgCu alloys, palladium, silver and copper were deposited in this sequence by electroless deposition on top of ZrO_2 modified porous stainless steel disks.[53] Plating times for Pd (323 K), Ag (333 K), and Cu (303 K) were adjusted to achieve the desired metal composition. After electroless deposition of Cu, the films were immediately immersed in 0.01 M HCl to neutralize any residual plating solution, followed by rinsing with DI water and ethanol to facilitate drying and prevent oxidation of the copper layer. In addition, Cu on the surface partially or completely dissolved in the plating bath. Therefore, the first metal layer applied to the support was always Pd, then Ag and finally a Cu layer was applied on top of the Pd–Ag layers. The film was then heated up to 773 K in hydrogen atmosphere in order to form a homogeneous palladium–silver–copper alloy by thermal diffusion. After annealing at 773 K for 48 h, it was possible to observe the formation of two phases, the fcc and bcc of the PdAgCu alloy (Figure 11). When the annealing time increased, the fcc/bcc ratio increased,[54] which is consistent with the data reported in the literature for the PdCu binary alloy.[56] Although Ag was deposited between Pd and Cu, no peaks corresponding to the PdAg binary alloy were observed in the patterns even after 162 h up to 773 K (Figure 11).

The fraction of the fcc and bcc phases (X_{bcc} and X_{fcc}) for the PdCuAg synthesized films was estimated from the integrated intensities of their main peaks, (110) and (111) for the bcc and the fcc phase, respectively. In order to apply this procedure to obtain the total concentration of palladium, it was assumed that as the Ag concentration in the bulk is low it does not introduce any considerable modification in the lattice parameter and therefore does not modify the data obtained from these expressions.[13,53] Then, the concentration of Pd in each phase was calculated from the lattice parameter using the equations previously reported.[56] The evolution of X_{bcc} and X_{fcc} as a function of annealing time at 773 K is shown in Figure 11(c). After 162 h at 773 K in H_2, only the feature corresponding to the fcc phase was observed by XRD (Figure 11) for a PdAgCu film with a palladium atomic composition of about 72%.[53]

SEM surface micrographs of the PdAgCu samples show a uniform and smooth morphology, with no evidence of dendritic growth.[53] It is well known that the Cu surface morphology of samples prepared by electroless method exhibits much smaller agglomerated particles than those observed in the Pd plating films where the typical cauliflower structure is present.

3.1.4.3 PdCuAu Alloys

PdCuAu ternary alloys with different composition were synthesized by the sequential electroless deposition technique on

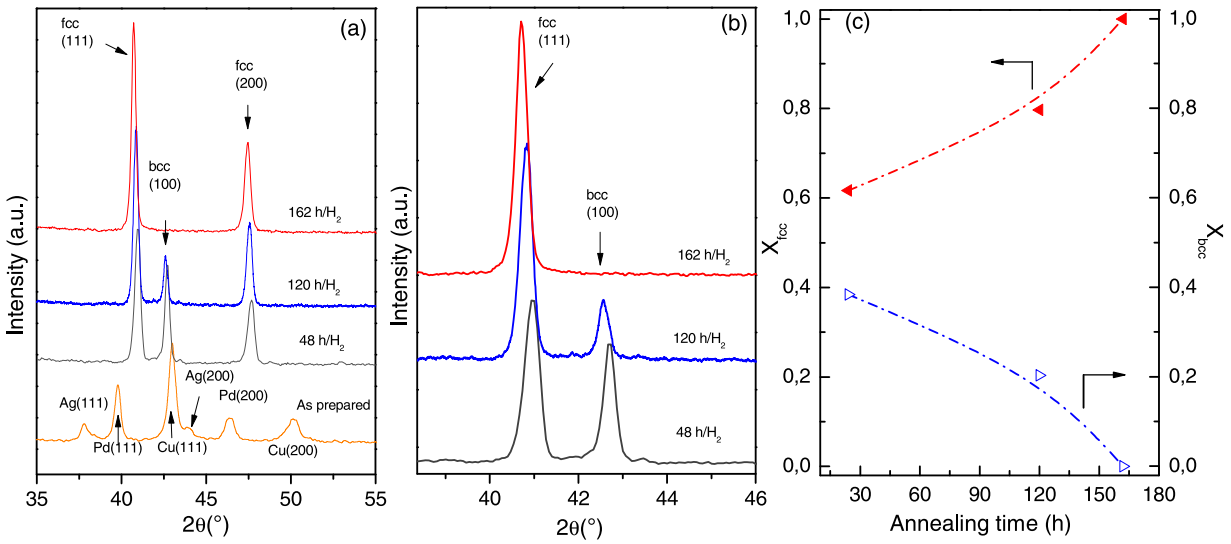


Figure 11 X-ray diffraction patterns of the PdAgCu ternary alloy films corresponding to the as synthesized samples and after annealing up to 773 K in H_2 at different times (a). Short scan of the (111) fcc peak and the (100) bcc peak for the PdAgCu film (b). X_{fcc} and X_{bcc} as a function of annealing time. Reprinted from Tarditi, A. M.; Cornaglia, L. M. Novel PdAgCu Ternary Alloy as Promising Materials for Hydrogen Separation Membranes: Synthesis and Characterization. *Surf. Sci.* **2011**, *479*, 246–255. © Elsevier 2011.

top of ZrO_2 modified porous stainless steel disks. For the synthesis of PdCuAu alloy samples, palladium (323 K) was deposited first, followed by Au deposition (333 K). The Cu plating (303 K) was performed on top of the Pd–Au layers, previously activated with $SnCl_2$ and $PdCl_2$. Plating times for Pd, Au, and Cu were adjusted to achieve the desired metal composition in all cases. The sample was then heated up to 773 K in H_2 at atmospheric pressure (101.32 kPa) in order to form a homogeneous palladium–gold–copper alloy by thermal diffusion. To obtain a higher film thickness, a second set of Pd, Au, and Cu layers was applied, followed by a second heat treatment at the same temperature.[54] The samples studied can be divided into two main groups based on their Cu concentration: the $Pd_{60}Cu_{37}Au_3$ and $Pd_{62}Cu_{36}Au_2$ samples, with a higher Cu composition and the $Pd_{70}Cu_{26}Au_4$, $Pd_{67}Cu_{24}Au_9$ and $Pd_{71}Cu_{26}Au_3$ samples with a lower Cu content. XRD patterns of the samples with lower Cu atomic concentration $Pd_{70}Cu_{26}Au_4$, $Pd_{71}Cu_{26}Au_3$ and $Pd_{67}Cu_{24}Au_9$ display complete fcc alloy formation after annealing in hydrogen at 773 K for 120 h. No evidence of the bcc crystalline phase or impurities was detected. In contrast, after annealing at the same temperature for 120 h, the XRD patterns of the $Pd_{60}Cu_{37}Au_3$ and $Pd_{62}Cu_{36}Au_2$ samples indicated the formation of a pure bcc crystal structure. The morphologies of the PdCuAu electroless deposited were homogeneous formed by cauliflower-shaped clusters with well-defined borders. The sample $Pd_{62}Cu_{36}Au_2$ shows a smoother surface, with less defined cluster borders, which could be attributed to the higher Cu content of this sample.[54] The morphology of this sample is similar to that of PdCu samples synthesized by the electroless method.[48]

3.1.5 Applications in Hydrogen Purification

Hydrogen has been considered as an ideal energy carrier for the near future. It can be obtained from renewable raw materials using a variety of energy sources, and it can be transformed into valuable energy forms with high efficiency and without detrimental environmental effects. Moreover, hydrogen is an important raw material in numerous industries, such as computer, metallurgical, chemical, pharmaceutical, fertilizer, and food industries.

Hydrogen can be used for electricity generation in fuel cells with a variety of applications in transportation and stationary power generation. To avoid deactivation of catalytic surfaces in low-temperature PEM fuel cells, H_2 must be nearly free of carbon monoxide, including other impurities such as hydrogen sulfide.

As a result of the increasing demand for high purity hydrogen, palladium-based membranes have received much attention in the last decade.[57–60]

Pd and Pd-alloys are able to separate hydrogen selectively because of the high solubility and diffusivity of this gas in their lattice. Molecular H_2 dissociates on a Pd catalytic surface to form H-atoms, which diffuse through the Pd bulk. The association of the atoms on the opposite surface of the membrane to produce H_2 molecules completes a process that could produce infinite separation selectivity.

The Pd membrane effect on the separation of a H_2 containing mixture is mainly determined by two parameters: permeability and the separation factor. The ideal separation factor (called perm-selectivity or selectivity) is defined as the ratio between a hydrogen pure gas flux to the flux of another pure gas at the same operating conditions.

The hydrogen permeability (Pe) can be expressed by the following equations:

$$\mathrm{Pe} = \frac{J_{\mathrm{H_2}}}{(P_{\mathrm{perm}}^{0.5} - P_{\mathrm{ret}}^{0.5})/L} \quad [15]$$

$$\mathrm{Pe} = D.\mathrm{S} \quad [16]$$

where J_{H2} [mol m^{-2} s^{-1}] is the hydrogen flux, P_{ret} and P_{perm} are the hydrogen partial pressure on the retentate and permeate sides, respectively, and L is the membrane thickness. D and S are the H atom diffusivity and solubility.

The dense metallic membranes can be classified into two groups: self-supported and composite membranes. Self-supported membranes are generally thick (higher than 25 μm) to have physical strength and exhibit inferior hydrogen permeability. Supported or composite membranes are formed by thin Pd-based films supported on porous substrates and constitute an economic option to overcome these limitations.

Generally, there are three main techniques to deposit metallic thin films onto porous supports: ELP, chemical vapor deposition, and physical sputtering. Among the methods developed for coating Pd or Pd-alloy films, ELP gives uniform deposition on complex shapes and any type of supports, produces hardness on the deposited film, and requires very simple equipment.[32,43,61]

Porous ceramic materials, glass, and metal were successfully used as supports for palladium membranes. Ceramic supports have robustness, chemical stability, and superior upper temperature limit. It has been reported that porous ceramic supports with rougher surfaces and larger pores favor the adhesion of the palladium films.[62] Porous metal supports as conductive substrates can be formed into various shapes and have engineered, interconnected porosity with different pore sizes. Furthermore, porous stainless steel (PSS) supports are promising substrates due to their good mechanical strength, more resistance to cracking, operation at high pressures, thermal expansion coefficient similar to that of Pd, and also because of the simplicity of module construction. Composite Pd/PSS membranes, welded on both ends to nonporous stainless steel tubes, can be easily assembled and integrated into an associated process. Nevertheless, the big pores and roughness of the PSS surface impair the preparation of a thin defect-free Pd membrane on porous stainless steel substrates.[63] Then, the pore size of the substrate and its surface roughness could be modified with an intermediate component.[64] The penetration of this material into the pore structure of the substrate would lead to a more compact structure. Thus, when the material is submitted to large temperature changes, the thermal expansion between both components will have lesser effects. This intermediate is also expected to be a diffusion barrier to inhibit the migration of the substrate components to the Pd layer, which will deteriorate the performance of the composite membrane.[65,66]

Yun and Oyama[62] made use of the Pd or Pd alloy layer thickness for a rough estimation of the materials cost, and of

H_2 permeance to evaluate the production yield, for industrial H_2 separations. For this comparison, they selected the ELP method for the deposition of Pd because of its ease of application for any shape or substrate compared with other methods. Substrate material effects were assessed using two factors (top layer thickness and H_2 permeance) for composite Pd membranes prepared by ELP (Figure 12).

Membranes using Vycor glass as a substrate require thicker separation layers to overcome the low mechanical stability of the glass and the difference in the thermal expansion coefficients of the materials. Membranes employing porous stainless steel also need a thick Pd or Pd alloy layer to obtain a continuous separation layer due to the broad distribution of pore sizes and their large size in the metal substrate. Thick Pd or Pd alloy metal layers result in high membrane preparation costs with low H_2 production yield. They concluded that the most desirable Pd membranes for practical applications should be prepared by the ELP technique on porous alumina substrates.

However, they did not consider the cost of porous supports and charges of fabrication. Moreover, in their analysis they did not discuss the effect of diffusion barriers applied to PSS substrates. PdAu layers with very low thickness and high selectivity (<90 000) have been obtained employing Y-ZrO_2/stainless steel porous filters (2.3 μm thick, $Pd_{95}Au_5$ composite membrane).[56]

3.1.5.1 Hydrogen Permeation Properties

Pure palladium films suffer hydrogen embrittlement particularly due to phase transition of the palladium hydride when exposed to hydrogen at temperatures below the critical temperature of 566 K. This hydrogen embrittlement can be overcome by alloying palladium with Ag or Au.[67] In this way, the α–β Pd–H transition temperature significantly decreases thus improving the membrane thermal stability and the tolerance to thermal cycling.

Binary Pd alloys of Au and Ag were also shown to have higher hydrogen permeability than pure Pd by McKinley in 1967[68,69] (Figure 13). This early research was done using cold-worked foils; this fabrication technique produces homogeneous films with precisely controlled compositions. However, the foils produced are generally limited to thicknesses greater than 25 μm.

The reasons for the permeability increase are complex. However, it could be related to the increase of H atom solubility and diffusivity that accompanies the expansion of the Pd lattice by insertion of the relatively large metal atoms.[68] In the case of binary palladium-alloys, Yun and Oyama[62] proposed that H_2 permeance is generally proportional to the average atomic distances of the alloys. This result is in line with the hydrogen permeation mechanism which is controlled by the diffusion of atomic hydrogen through the metal lattice. A longer atomic distance would facilitate this process.

In the last few years, measurements of hydrogen transport through ternary alloy membranes have also been reported.[51,54,70–72] Wang *et al.*[70] synthesized a $Pd_{69}Ag_{30}Ru_1$ alloy membrane by electroless co-deposition and reported that its permeability was three times higher than that of pure Pd. However, the hydrogen selectivity was not reported; hence, the high permeability could be due to the presence of defects.

Employing self-supported membranes, Bredesen and coworkers[71] studied the addition of a number of minor ternary components on PdAg alloys, ~$Pd_{75}Ag_{20}X_5$(X=Au, Mo, Cu, Y) through the magnetron sputtering technique; in all cases, they observed lower H_2 permeability than either pure Pd or the PdAg binary. Coulter *et al.*[72] reported self-supported 25 μm thick $Pd_{86}Au_6Pt_6$ alloy membranes with high H_2 permeabilities that depend on the sputtering conditions.

Authors studied several ternary alloys, PdAgCu, PdCuAu, and PdAgAu, deposited by sequential ELP on porous stainless steel substrates modified with Al_2O_3 or ZrO_2.

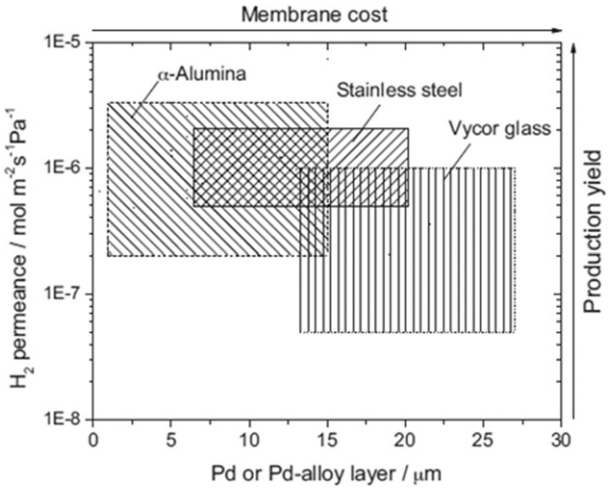


Figure 12 H_2 permeance and top layer thickness of Pd or Pd alloy composite membranes prepared by electroless plating. Reprinted from Yun, S.; Ted Oyama, S. Correlations in Palladium Membranes for Hydrogen Separation: A Review. *J. Memb. Sci.* **2011**, *375*, 28–45. © Elsevier 2011.

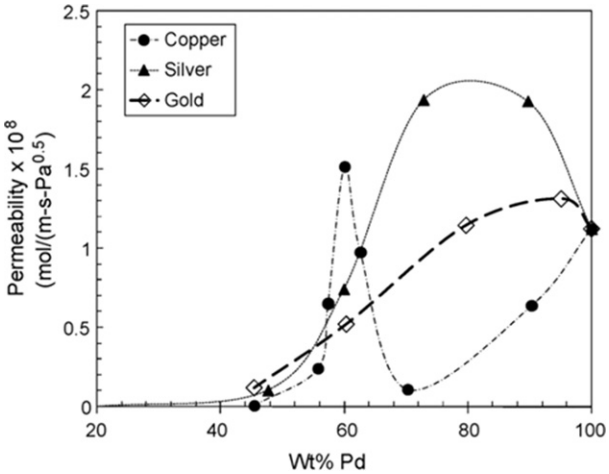


Figure 13 Hydrogen permeability as a function of alloy composition for alloys of palladium with copper, silver, and gold at 623 K. Reprinted from Gade, S. K.; Payzant, E. A.; Park, H. J.; Thoen, P. M.; Way, J. D. The Effects of Fabrication and Annealing on the Structure and Hydrogen Permeation of Pd–Au Binary Alloy Membranes. *J. Memb. Sci.* **2009**, *340*, 227–233. © Elsevier 2009.

Figure 14 shows the hydrogen flux measured for $Pd_{90}Ag_{10}$, $Pd_{98}Ru_2$, $Pd_{91}Au_9$ and both $Pd_{78}Ag_9Au_{13}$ and $Pd_{69}Cu_{14}Au_{17}$ ternary alloys and a Pd reference membrane at different temperatures as a function of $\Delta P^{0.5} = (P_{perm}{}^{0.5} - P_{ret}{}^{0.5})$. Linear relationships between flux and $\Delta P^{0.5}$ confirm that H-atom diffusion is the limiting step of hydrogen transport rates for all films. $Pd_{90}Ag_{10}$, displays the highest hydrogen flow among these films at 723 K. Note that all membranes have thickness equal to 14 μm, except the PdRu layer.

Permeability varied within this membrane set as $Pd_{90}Ag_{10} > Pd_{78}Ag_9Au_{13} > Pd > Pd_{91}Au_9 > Pd_{70}Cu_{13}Au_{17}$. In brief, the PdAgAu ternary membrane displayed lower permeability than the $Pd_{90}Ag_{10}$ alloy membrane, but higher permeability than the other membranes over this temperature range. Note that for all these membranes, the ideal H_2/N_2 selectivity was higher than 10 000.

Hydrogen permeability of related binary and ternary Pd alloys reported by several researchers are summarized in **Table 4**. Relevant examples selected from the literature are included as well as permeability of the membranes presented in **Figure 14** measured at temperatures from 623 to 723 K. The H_2 permeation measurements performed in our group showed that the ternary alloy membrane with less Ag and higher Au content ($Pd_{78}Ag_9Au_{13}$) exhibited higher permeability than the $Pd_{75}Ag_{16}Au_9$ alloy membrane. However, to study the influence of metal composition on permeability, the evaluation of H_2 transport through PdAgAu alloy membranes in a wide range of metal compositions would be necessary.

In the case of PdCuAg alloys, Ling *et al.*[77] using Density Functional Theory (DFT) calculations predicted solubility, diffusivity, and permeability of hydrogen at elevated temperature for a wide range of alloy compositions. From these predictions, they found that the permeability of H increases with Ag concentration for alloys with the same amount of Cu. For a $Pd_{67.1}Cu_{25.9}Ag_7$ ternary alloy, they reported a predicted permeability normalized to pure Pd of about 0.25. This value is close to the data obtained by Tarditi *et al.*[13] for membranes with a similar composition synthesized by the sequential ELP of Pd, Ag, and Cu on top of tube PSS supports.

Zhao *et al.*[76] also investigated a series of PdCuAg membranes with at least 70 at% Pd to elucidate the interdependence between alloy structure and H_2 permeability. They reported compensation between activation energy and the corresponding pre-exponential factor of the H_2 permeation laws obtained for membranes with differing alloy stoichiometry (**Figure 15**). The compensation effect indicates that atomic H diffusion in the bulk PdCuAg alloys remains the permeation rate-determining step down to 2 μm membrane thickness. In addition, the activation energy for H_2 permeation declines with increasing PdCuAg lattice constant, in general. This is in agreement with trends for H binding energies in interstitial lattice sites and transition states of PdCuAg alloys observed in DFT calculations.[77]

The effect of the fabrication method of Pd composite membranes prepared by different methods was evaluated by Yun and Oyama[62] considering H_2/N_2 selectivity and the top layer thickness. However, the H_2 selectivity showed no direct dependence on the Pd thickness but was affected by defects or pinholes on the surface, which are determined not by the thickness but by the quality of the top metal layer. Compared with other membrane preparation techniques, the ELP method allows the easy preparation of Pd membranes using simple equipment and any type of support with high selectivity and low Pd layer thickness.

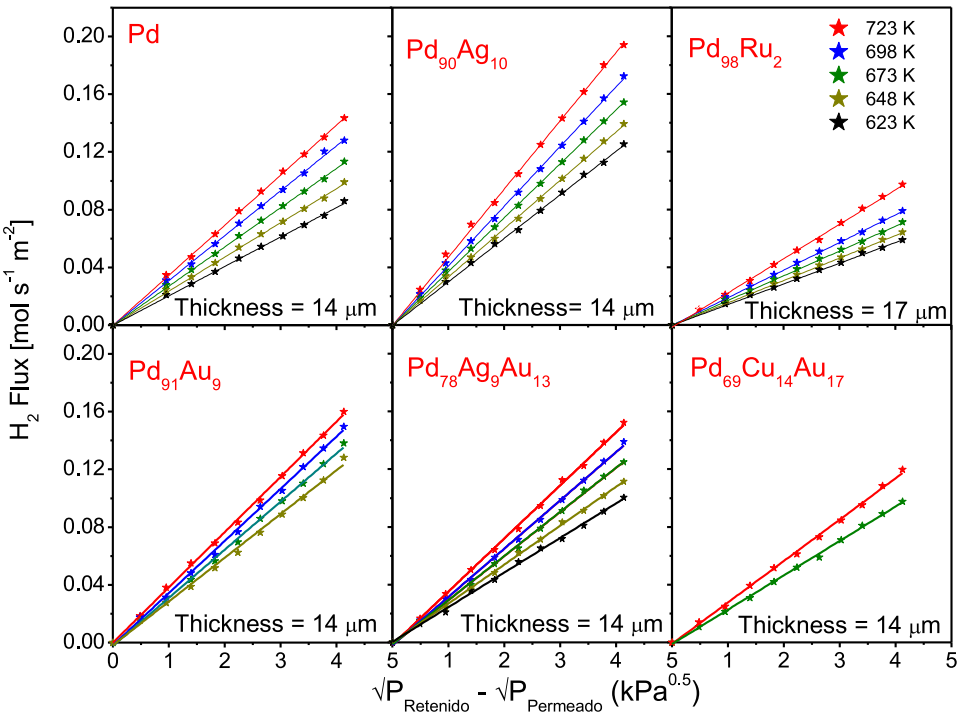


Figure 14 Hydrogen permeation flux as a function of pressure gradient at several temperatures for binary and ternary alloy membranes synthesized by electroless plating.

Table 4 Summary of literature permeability results before and after H_2S exposure for Pd and Pd alloy membranes at several temperatures

Membrane (at%)	*Synthesis*	*Thickness (μm)*	*Temperature (K)/Exposure time (h)*	*Permeability[a] (mol m^{-1} s^{-1} $Pa^{-0.5}$)*	*H_2S treatment*	*Results upon H_2S exposure*	*Reference*
Pd	Foil	25	623/6	1.3×10^{-8}	1000 ppm H_2S/10% He–H_2	Bulk Pd_4S formation	[73]
Pd[b]	ELP	14	673/24	1.2×10^{-8}	100 ppm H_2S in H_2	Bulk Pd_4S formation	[51]
$Pd_{73}Ag_{27}$	CW	>25	623/48	1.9×10^{-8}	3.5 ppm H_2S in H_2	Dull and etched surface	[68]
$Pd_{90}Ag_{10}$[b]	ELP	14	673/24	1.65×10^{-8}	100 ppm H_2S in H_2	Bulk Pd_4S formation	[51]
$Pd_{80}Ag_{20}$[b]	ELP	9.3	673	1.65×10^{-8}	–	–	[30]
$Pd_{67}Cu_{33}$(fcc)[b]	ELP	26	723	1.3×10^{-9}	–	–	[13]
$Pd_{47}Cu_{53}$(bcc)	Foil	25	623/6	1.3×10^{-8}	1000 ppm H_2S/10% He-H_2	Bulk Pd_4S formation	[73]
$Pd_{74}Au_{26}$	CW	>25	623/6	5.1×10^{-9}	66 000 ppm H_2S in H_2	Maintains H_2 flux	[68]
$Pd_{88}Au_{12}$	CW	24	673/100	1.0×10^{-8}	20 ppm H_2S/50% H_2/29% H_2O/19%CO_2/1% CO	High S tolerance and selectivity	[74]
$Pd_{94}Au_6$	MS	11	673/80	1.1×10^{-8}		Pd_4S and $Pd_{2.8}S$ formation	[74]
$Pd_{91}Au_9$[b]	ELP	14	673–723	$1.1–1.5 \times 10^{-8}$	–	–	[16]
$Pd_{95}Au_5$[b]	ELP	2.3	673	1.3×10^{-8}	–	–	[56]
$Pd_{77}Au_{23}$	ELP	4.8	673/24	1.26×10^{-8}	20 ppm H_2S WGS stream	H_2 permeance decreases 50%	[75]
$Pd_{94.5}Au_{5.5}$	ELP	12–16	773/4	4.7×10^{-9}	54.8 ppm H_2S in H_2	65% H_2 flux recovery	[74]
$Pd_{91}Au_9$[b]	ELP	14	673/24	1.1×10^{-8}	100 ppm H_2S in H_2	80% H_2 flux recovery and maintains select.	[51]
$Pd_{87}Au_7Pt_6$	MS	25	673/100	1.0×10^{-8}	20 ppm H_2S/50% H_2/29% H_2O/19%CO_2/1% CO	Pd_4S formation and loss of selectivity	[72]
$Pd_{67}Ag_8Cu_{25}$[b]	ELP	24	723	5.4×10^{-9}	–	–	[13]
$Pd_{84}Ag_5Cu_{11}$	ELP	3.5	673	6.2×10^{-9}	–	–	[76]
$Pd_{85}Ag_{11}Cu_4$[b]	MS	2.2	673/1	7.8×10^{-9}	20 ppm H_2S/90% H_2–N_2	Bulk Pd_4S formation	[71]
$Pd_{69}Ag_{27}Y_4$[b]	MS	2.4	673/1	1.1×10^{-8}	20 ppm H_2S/90% H_2–N_2	Sulfur surface contamination	[71]
$Pd_{76}Ag_{21}Mo_3$[b]	MS	2.3	673/1	5.0×10^{-9}	20 ppm H_2S/90% H_2–N_2	Sulfur surface contamination	[71]
$Pd_{75}Ag_{22}Au_3$[b]	MS	1.9	673/1	8.5×10^{-9}	20 ppm H_2S/90% H_2–N_2	Maintains H_2 flux	[71]
$Pd_{74}Ag_{14}Au_{12}$[b]	ELP	14	623/30	–	1000 ppm H_2S in H_2	No detected bulk sulfides	[52]
$Pd_{78}Ag_9Au_{13}$[b]	ELP	14	673/24	1.3×10^{-8}	100 ppm H_2S in H_2	80% H_2 flux recovery and high selectivity	[51]
$Pd_{75}Ag_{16}Au_9$[b]	ELP	14	673/24	1.2×10^{-8}	100 ppm H_2S in H_2	65% H_2 flux recovery and high selectivity	[51]
$Pd_{67}Ag_{13}Au_{20}$	ELP	9.3	673/24	1.35×10^{-8}	20 ppm H_2S in H_2	70% H_2 flux recovery	[75]
$Pd_{70}Cu_{25}Au_5$[b]	ELP	14	673/24	1.9×10^{-9}	100 ppm H_2S in H_2	75% H_2 flux recovery and high selectivity	[54]
$Pd_{69}Cu_{14}Au_{17}$[b]	ELP	14	673/24	8.7×10^{-9}	100 ppm H_2S in H_2	75% H_2 flux recovery and high selectivity	[54]

[a]Permeability measured in pure H_2 before the H_2S treatment.
[b]H_2/N_2 selectivity >10 000.
Abbreviations: CW, Cold Working; MS, Magnetron Sputtering.

3.1.5.2 H_2S Treatment: Hydrogen Inhibition Transport and Flux Recovery

The effect of H_2S, a common component of fossil-derived syngas, on Pd-based membranes has been studied. H_2S can block hydrogen dissociation sites and can also cause Pd-sulfide formation, which has lower hydrogen permeability than Pd. Alloying Pd with one or more components such as Au or Cu has been employed to improve its response to H_2S.[73,78,79] Most of the literature reports have been focused on H_2S/H_2

mixtures and only few of them studied the effect of CO, CO_2, H_2O, and H_2 mixtures containing H_2S.[74]

PdCu alloys have been extensively studied for sulfur tolerance; their responses to H_2S exposure are complex functions of alloy composition, crystalline phases, and exposure conditions. Alloys with Cu content lower than 30 at% form low-permeability bulk corrosion layers[78] at moderate temperatures, whereas high Cu content alloys exhibit complete inhibition of hydrogen transport, likely due to a combination of surface sulfide formation and site blocking by adsorbed H_2S.[80] In addition, Au has been used to improve the H_2S response of Pd.[79] At low concentrations (Au wt%$\leq$10), Au prevents bulk sulfide formation and partially preserves permeability when exposed to H_2S/H_2 mixtures.[79]

Recently, ternary Pd alloys have been considered for their potential to improve both permeability and H_2S response.[51,54,70–72] The few published reports of the H_2S response of ternary membranes were carried out mainly on self-supported membranes deposited by magnetron sputtering.[71,72] $Pd_{87-89}Au_{7-5}Pt_6$[72] and a series of $\sim Pd_{75}Ag_{20}X_5$ (X=Au, Mo, Cu, Y) alloys[81] synthesized by sputter deposition methods were applied to study H_2S responses in water gas shift and H_2/H_2S mixtures. All Au-containing ternary alloys exhibited the smallest fractional flux loss upon exposure to H_2S.

In our group, we investigated PdAgAu and PdCuAu alloy membranes synthesized by ELP, finding that they do not experience bulk sulfide corrosion even when exposed to 100 ppm H_2S/H_2.[51,52,54]

Seeking to combine the H_2S tolerance of the PdAu and PdCu binary alloys and the high permeability of the PdAg, ternary PdAgAu, and PdCuAu alloys prepared by sequential ELP were investigated. After annealing and pure hydrogen permeation measurements, 100 ppm H_2S/H_2 were added to the feed gas to evaluate the inhibition of H_2 transport by H_2S. Then, after 24 h of H_2S exposure at 663 K, the feed gas was changed back to pure hydrogen to study H_2 flux recovery. Figure 16 shows measured permeabilities as a function of time on stream during H_2S exposure and during subsequent recovery in H_2. All membranes present a large decrease in H_2 permeability after the introduction of H_2S. The primary cause of the rapid decrease is site blocking by adsorbed H_2S.[51] The permeability of pure Pd, and to a lesser extent $Pd_{90}Ag_{10}$, continued to decrease all over the H_2S exposure period, evidence of growth of a low permeability bulk sulfide scale. At the end of

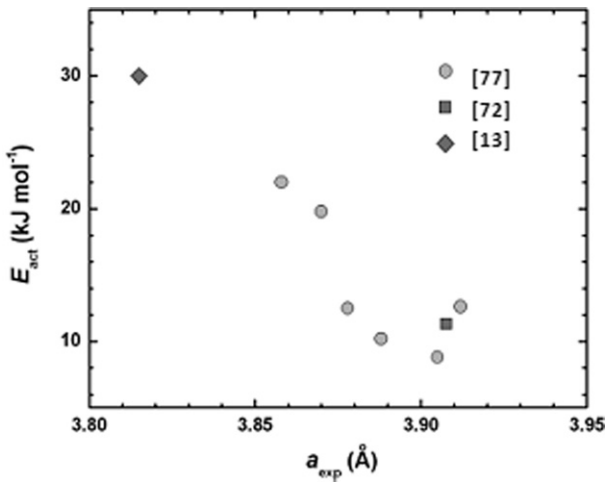


Figure 15 Correlation between the activation energy for hydrogen permeation and the experimental lattice constant of PdCuAg membranes. Reprinted from Zhao, L.; Goldbach, A.; Bao, C.; Xu, H. Structural and Permeation Kinetic Correlations in PdCuAg Membranes. *Appl. Mater. Interfaces* **2014**, *6*, 22408–22416, © Elsevier 2014.

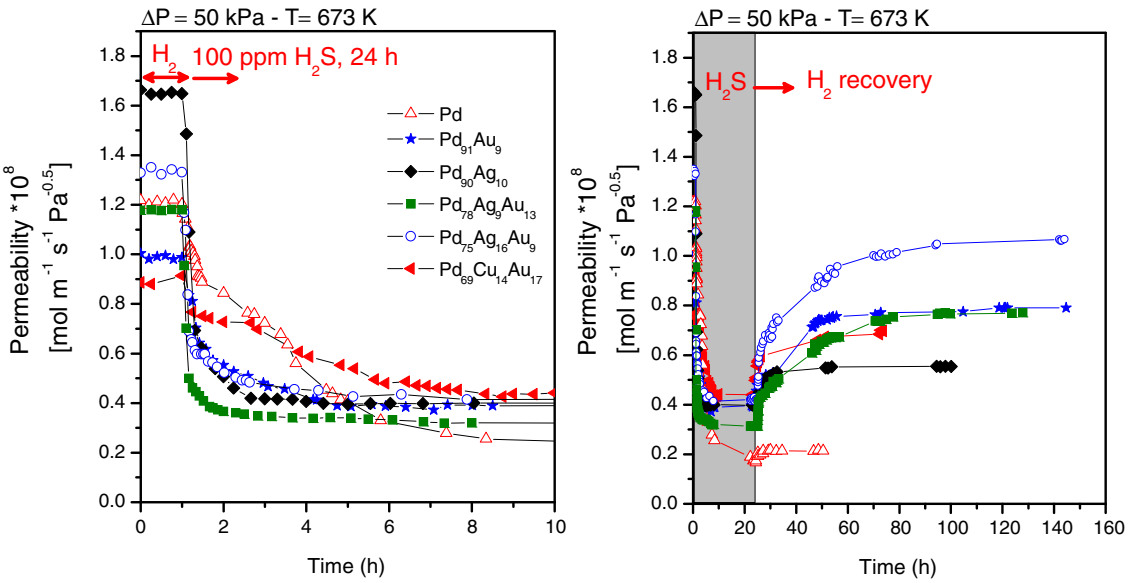


Figure 16 Permeability during the H_2S fed through the membranes as a function of time. H_2S treatment conditions: T=673 K, [H_2S]=100 ppm, time=24 h, ΔP=50 kPa. Reprinted from Braun, F.; Tarditi, A. M.; Miller, J. B.; Cornaglia, L. M. Pd-Based Binary and Ternary Alloy Membranes: Morphological and Perm-Selective Characterization in the Presence of H_2S. *J. Memb. Sci.* **2014**, *450*, 299–307. © Elsevier 2014.

the 24 h H_2S exposure, the membranes displayed the following order of permeability decrease: $Pd_{69}Cu_{14}Au_{17}$ (45% decrease) $< Pd_{91}Au_9 < Pd_{78}Ag_9Au_{13} < Pd_{75}Ag_{16}Au_9 < Pd_{90}Ag_{10} <$ Pd (85% decrease).

Pd and the $Pd_{90}Ag_{10}$ binary membrane showed only very small recoveries upon removal of H_2S, with no significant improvement over time. This behavior is also characteristic of formation of stable, low permeability bulk sulfide layers at the membrane surfaces. The Au-containing ternary alloy membranes displayed high values of H_2 flux recovery. However, none of these alloys recovered all of their original H_2 permeability at 673 K. Strongly adsorbed S and/or formation of thin two-dimensional sulfide layers could prevent the complete recovery at 673 K. XRD analysis of the H_2S-exposed PdAgAu, PdCuAu, and PdAu membranes revealed fcc alloy structure with no evidence of bulk sulfide formation.

To study the effect of temperature on the H_2 recovery, two full cycles of H_2S exposure at 673 K, recovery in H_2 at 673 K, followed by recovery at 773 K were carried out for $Pd_{69}Cu_{14}Au_{17}$ alloy film (Figure 17).[54] The complete hydrogen recovery observed after H_2 treatment at 773 K can be explained by considering two types of S adsorbed on the surface of the films: a weakly adsorbed S, which can be removed at 673 K and a strongly adsorbed sulfur/surface sulfide, which needs a higher temperature to be removed (773 K). The PdCuAu membranes were stable after a total of 550 h, including the annealing at 773K, the pure hydrogen permeation measurements and the H_2S-hydrogen recovery cycles.

The ideal H_2/N_2 selectivity ($< 10\,000$) of the ternary alloy films deposited by sequential electroless deposition on top of porous stainless steel substrates remained unchanged after H_2S treatment followed by hydrogen recovery, suggesting that the exposure/recovery process did not impair the structural integrity of the films.

3.1.6 Surface Properties of Pd Binary and Ternary Alloys

Surface composition is an important parameter in understanding the behavior of alloys in a wide range of applications such as catalysis, corrosion, and membrane separation processes and it is often different from bulk composition. The exposure of an alloy film to different atmospheres (H_2, CO, H_2S) and temperatures can produce preferential surface segregation in either beneficial or detrimental ways. The preparation of Pd-based alloy membranes with controlled metal surface composition and structure is very challenging. For this reason, a quantitative description of the phenomenon is necessary in order to make the appropriate changes in the bulk alloy composition to enhance or inhibit specific segregation behavior.

3.1.6.1 Surface Segregation of Clean Surfaces

XPS and LEIS spectroscopy are the most common techniques employed to determine the composition of the near-surface region and the top-most surface layer, respectively, of the Pd alloy films. Pd surface segregation under hydrogen atmosphere has been reported for the PdAg system. Shu *et al.*,[82] through XPS surface characterization of PdAg self-supported membranes, concluded that the chemisorption of hydrogen induces palladium surface segregation. In the same way, we have previously reported a higher Pd surface concentration in a PdAg sample after treatment in H_2(5%)/Ar at 673 K, when it was compared with the sample without treatment.[83,84]

To estimate the relative atomic distribution of the elements as a function of depth into the surface, both angle-resolved and Ar^+-sputter depth profiling, XPS measurements were performed. In addition, to characterize the top-most atomic layer of the surface region, LEIS spectroscopy analysis was carried out. Angle resolved XPS (ARXPS) experiments provide

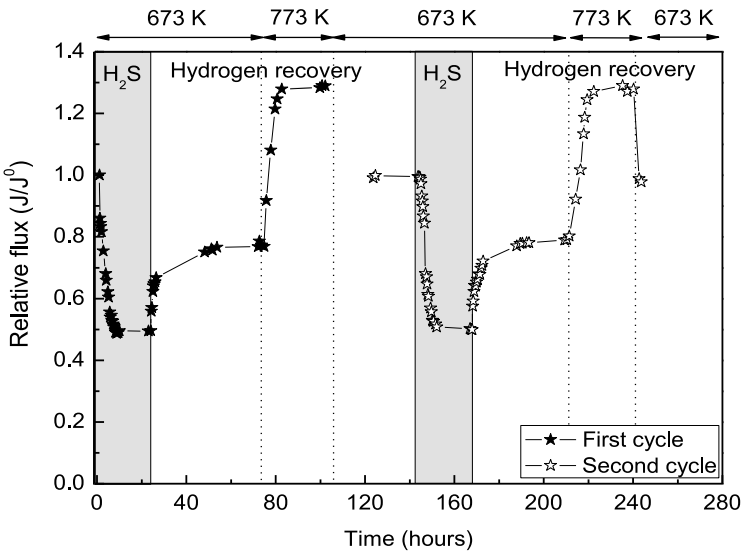


Figure 17 Relative hydrogen flux (J/J^0) during the 100 ppm H_2S/H_2 treatment and subsequent flux recovery for the $Pd_{69}Cu_{14}Au_{17}$ membrane. Reprinted from Tarditi, A. M.; Imhoff, C.; Braun, F.; Miller, J. B.; Gellman, A. J.; Cornaglia, L. PdCuAu Ternary Alloy Membranes: Hydrogen Permeation Properties in the Presence of H_2S. *J. Memb. Sci.* **2015**, *479*, 246–355. © Elsevier 2015.

detailed information about composition within the XPS-accessible near surface of *ca.* 6 atom layers.

Figure 18 summarizes surface characterization data obtained from the $Pd_{67}Cu_{24}Au_9$ (fcc phase) sample after annealing at 773 K for 120 h.[85] ARXPS results show that Cu concentration increased with increasing emission angle (more surface sensitive), while the Pd relative concentration decreased in the same way. These data suggest Cu segregation to the top-most surface region for the fcc $Pd_{67}Cu_{24}Au_9$ alloy.

Additionally, in order to have an indication of the elements distribution in a deeper region, Ar^+-sputtering XPS depth profiles were performed. The atomic compositions of Pd, Cu, and Au as a function of the etching time are plotted in **Figure 18**. The Pd atomic composition decreased with etching time while the Cu concentration increased. At larger depths, the Pd, Cu, and Au concentrations reached steady state, and are close to the bulk compositions measured by EDS. Note that the Ar^+-sputtering depth profile for $Pd_{67}Cu_{24}Au_9$ differed from the element distribution observed in the near-surface region (ARXPS) where Cu segregation to the top-most surface region was observed.

To characterize the top-most atomic layer of the surface region, LEIS analysis using 1 keV He^+ ions was performed. The time-dependence of the LEIS data provides evidence of a changing composition depth profile in the underlying layers due to sputtering effects (**Figure 18**). Note that the Pd concentration increases within the LEIS accessible near-surface region while the Cu concentration decreases, which is in agreement with the results of the ARXPS experiments of $Pd_{67}Cu_{24}Au_9$. For all PdCuAu films, the Pd composition of the near-surface region is above the bulk composition, and the Pd content in the top-most surface region is below that of both the bulk and the near-surface. This pattern could be related to the migration of Cu from the atomic layers immediately below the top-layer to the top-layer, as reported for other alloy systems. In contrast with the Pd and Cu behavior, the Au composition of the PdCuAu ternary alloys determined by XPS and LEIS did not show a significant difference with respect to the bulk composition.

The behavior of several Pd binary and ternary alloy membranes is compared in **Figure 19**. PdCuAu films displayed a similar surface segregation behavior as the PdAu alloy synthesized by the electroless method. In both cases, the near-surface region (XPS) became enriched in Pd with respect to the atomic bulk composition determined by EDS. On the other hand, for the PdCuAg, PdAuAg, PdAg, and PdCu alloys the near-surface region seems to be depleted of palladium with respect to the bulk composition (**Figure 19**). As shown in **Figure 19**, the segregation behavior observed in the PdCuAu electroless deposited films is different from that reported for the PdCuAg alloys, where a co-segregation of Cu and Ag in the near-surface region and Ag-enrichment to the top-most surface layer takes place. This is likely related to a different interaction of the minority component, Au for the PdCuAu system and Ag for the PdCuAg alloy, with the parent PdCu binary.[53,85]

3.1.6.2 Surface Segregation After of H_2S Exposure

The effect of local sulfur contamination at the surfaces of the materials, which may be undetectable by EDS and XRD, were studied on the Pd foil and the ternary alloys after 3 h of H_2S exposure through XPS composition depth profiles. The atomic compositions of Pd, Ag, Au, and S as a function of etching time/depth are shown in Video 1. The Pd foil has a significant sulfur content (S > 10 at%) throughout the ~40 nm profiling experiment. In contrast, the depth profiles of the PdAgAu alloy displays only very weak S signals at the top-surface (etch time = 0), which disappear before the etch depth reaches ~10 nm.

These results suggest that Au also imparts corrosion resistance to the PdAg binary. Au preferentially segregates to the surfaces of both the PdAu binary and the PdAgAu ternary alloys; high surface concentrations of Au are likely linked to the lack of reactivity of the alloy surfaces toward H_2S.

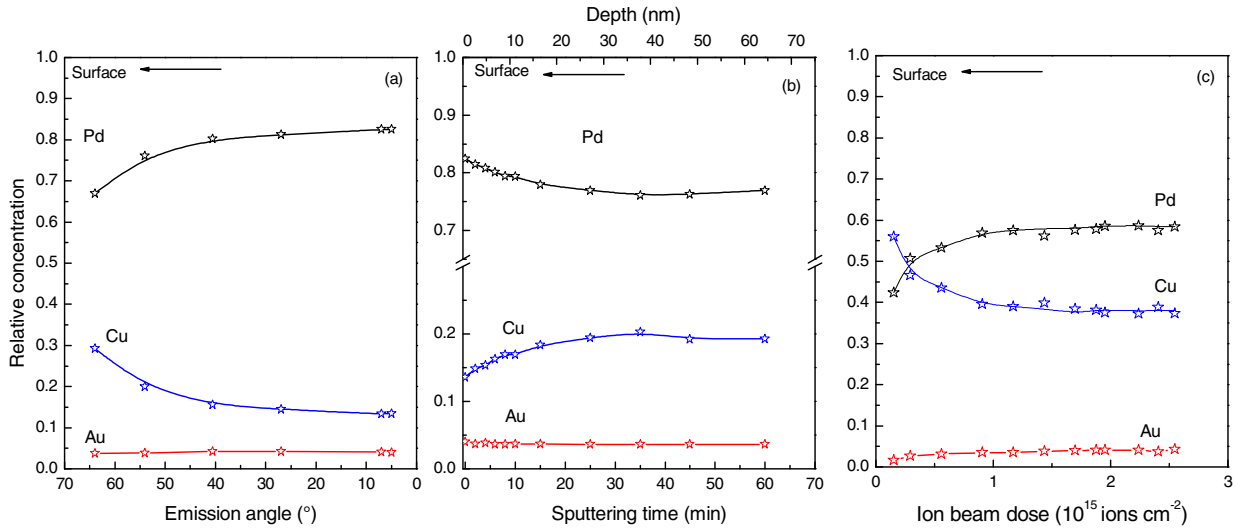


Figure 18 ARXPS and Ar^+-sputtering XPS depth profile (a, b); Pd, Cu, and Au LEIS concentration as a function of the ion dose (c) for the fcc $Pd_{67}Cu_{24}Au_9$ ternary alloy film after annealing up to 773 K. Reprinted from Tarditi, A. M.; Imhoff, C.; Miller, J. B.; Cornaglia, L. Surface Composition of PdCuAu Ternary Alloys: A Combined LEIS and XPS Study. *Surf. Interface Anal.* **2015**, *47*, 745–754. © Elsevier 2015.

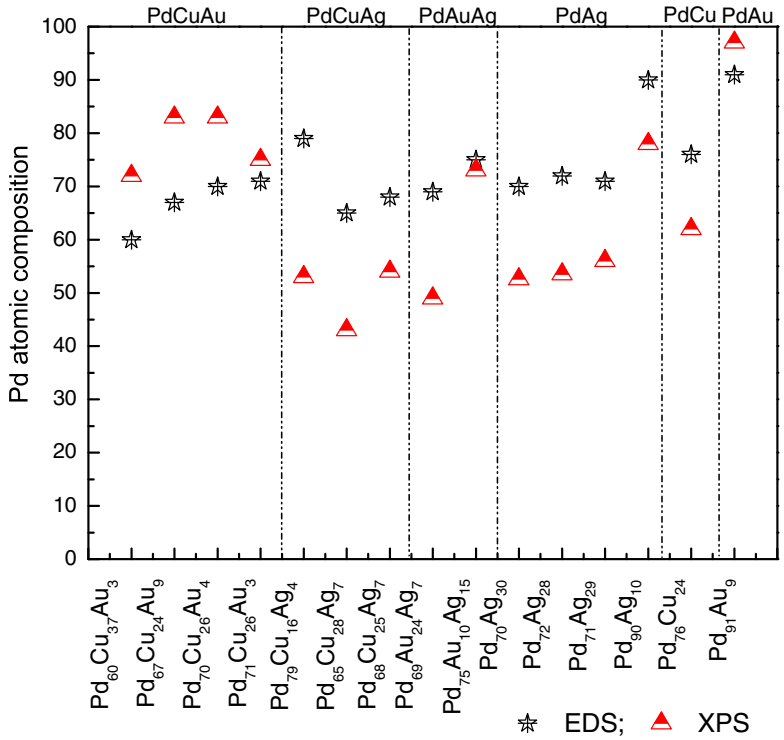


Figure 19 Atomic surface (XPS) and bulk (EDS) composition of Pd-based binary and ternary alloys synthesized by sequential electroless deposition and subsequent annealing at 773 K in hydrogen.

The high H_2S tolerance of the PdAgAu alloys is consistent with the Au enrichment at the surface and the pure-component standard free energies of sulfides formation at 623 K: Au_2S (-8901 J mol^{-1}), Ag_2S ($-63\,427$ J mol^{-1}), and Pd_4S ($-132\,005$ J mol^{-1}).

Our work illustrated the resistance of PdAgAu alloys to bulk corrosion by H_2S. It suggests that fabrication of a ternary alloy membrane based on the high-permeability PdAg binary, but with an Au component specifically for H_2S tolerance, could be an effective strategy for improving the membrane performance in extreme environments.

PdCuAu films also showed low sulfur content on the top-surface after H_2S exposure, which disappears about 10 nm into the bulk. The depth profiles of these films after the hydrogen recovery treatment at 663 K 48 h, followed by treatment at 773 K 24 h, show very low sulfur content ($\sim$3%), in agreement with the hydrogen flux recovery observed through the films.

3.1.7 Conclusions

ELP has been defined as a controlled autocatalytic deposition of a continuous layer on a catalytic surface by the reaction of a metal complex and a chemical reducing agent. Compared with electrodeposition, ELP can cover all surface types, regardless of size, shape, and electrical conductivity of the substrate.

Electroless deposition has been widely used to synthesize several binary palladium-based alloys in order to be used as membranes for hydrogen separation within other applications. For the development of homogeneous Pd coatings when the reducing agent was hydrazine, it was required to improve the stability of the plating bath by means of the proper selection of additives and stabilizers.

One of the major problems related to the ELP method is the difficulty of obtaining a uniform alloy composition on thickness. Alloying is most commonly achieved by the coating-diffusion method that requires temperatures in the 773–873 K range. Much effort is still needed for the development of new plating approaches and plating baths allowing the co-deposition of coatings with a homogeneous composition in thickness, thus avoiding the treatments at high temperatures.

Pd and Pd-alloys are able to separate hydrogen selectively because of the high solubility and diffusivity of hydrogen atoms in their lattice. The H_2 selectivity of Pd membranes is determined not only by the thickness but by the quality of the top metal layer. Compared with other membrane preparation techniques, the ELP method allows the easy preparation of Pd membranes using simple equipment and any type of support with high selectivity and low Pd layer thickness. The employment of an appropriate modifier/diffusion barrier for the porous stainless steel substrate allows obtaining Pd-based layers with very low thickness and high selectivity.

The synthesis and characterization of some Pd-based ternary alloys have been reported because of their superior properties concerning hydrogen permeability and/or chemical resistance. Ternary alloys containing copper or gold present higher H_2S resistance corrosion than the pure palladium membranes which experiment surface and bulk formation of PdS_4.

PdCuAu, PdCuAg, and PdAgAu ternary alloys films were synthesized on top of modified porous stainless steel substrates

by sequential electroless deposition of the pure metals. The ideal H_2/N_2 selectivity ($<10\,000$) remained unchanged after the H_2S treatment followed by hydrogen recovery, suggesting that the exposure/recovery process did not impair the structural integrity of the films.

For all PdCuAu films, Pd composition of the near-surface region is above the bulk composition, the Pd content in the top-most surface region is below that of both the bulk and the near-surface. This pattern could be related to migration of Cu from the atomic layers immediately below the top-layer to the top-layer, as reported for other alloy systems. In contrast, the Au composition did not show a significant difference with respect to the bulk composition. However, in the case of the PdCuAg alloys, a co-segregation of Cu and Ag takes place in the near-surface region as well as a Ag-enrichment to the top-most surface layer.

In the case of PdAgAu alloys, their high resistance to bulk corrosion of H_2S could be related to Au surface segregation. Au preferentially segregates to the surfaces of both the PdAu binary and the PdAgAu ternary alloys; high surface concentrations of Au are likely linked to the lack of reactivity of the alloy surfaces toward H_2S. It suggests that fabrication of a ternary alloy membrane based on the high-permeability PdAg binary alloy could be an effective strategy for improving the membrane performance in extreme environments. However, the evaluation of H_2 transport through PdAgAu alloy membranes in a wide range of metal compositions would be necessary to learn how the metal content influences the H_2 permeability.

Using suitable bath compositions and synthesis strategies, it is possible to synthesize binary and ternary Pd-based alloys to be applied as membranes for hydrogen separation. These synthesis strategies could be useful for the development and improvement of materials for application in other areas as jewelry and dental devices, among others.

See also: 3.15 Electroless Plating as Surface Finishing in Electronic Packaging

References

1. Paunovic, M. Electrochemical Engineering, Electrochemical Deposition. In *Encyclopetdia of Electrochemistry*; Bard, A. J., Stratmann, M., Eds.; Wiley-VCH Verlag GmbH & Co. KGaA: Germany, 2007; pp. 87–158.
2. Xie, L.; Abliz, D.; Li, D. Thin Film Coating for Polymeric Micro Parts. In *Comprehensive Materials Processing*; Hashmi, S., Ed.; Elsevier: Amsterdam, 2014; Vol. 7; pp. 157–170.
3. Paunovic, M.; Schlesinger, M.; Snyder, D. D. Fundamental Considerations. In *Modern Electroplating*, 5th ed.; Schlesinger, M., Paunovic, M., Eds.; John Wiley & Sons: Hoboken, NJ, 2010; pp. 1–32.
4. Rao, C. R. K.; Trivedi, D. C. Chemical and Electrochemical Depositions of Platinum Group Metals and Their Applications. *Coord. Chem. Rev.* **2005**, *249*, 613–631.
5. O'Sullivan, E. J. Fundamental and Practical Aspects of the Electroless Deposition Reaction. In *Advances in Electrochemical Science and Engineering*; Alkire, R. C., Kolb, D. M., Eds.; Wiley-VCH Verlag GmbH: Germany, 2001; pp. 225–273.
6. Ohno, I.; Wakabayashi, O.; Haruyama, S. Anodic Oxidation of Reductants in Electroless Plating. *J. Electrochem. Soc.* **1985**, *132*, 2323–2330.
7. Okinaka, Y.; Osaka, T. Electroless Deposition Processes: Fundamentals and Applications. In *Advances in Electrochemical Science and Engineering*; Gerischer, C. W., Tobias, C. W., Eds.; Wiley-VCH Verlag GmbH: Germany, 1994; pp. 55–116.
8. Djokić, S. S. Electroless Deposition of Metals and Alloys. In *Modern Aspects of Electrochemistry*; Conway, B. E., White, R. E., Eds.; Kluwer Academic/Plenum Publishers: New York, NY, 2002; pp. 51–133.
9. Schlesinger, M. Deposition on Nonconductors. In *Modern Electroplating*, 5th ed.; Schlesinger, M., Paunovic, M., Eds.; John Wiley & Sons: Hoboken, NJ, 2010; pp. 413–420.
10. Koura, N. Electroless Plating of Silver. In *Electroless Plating: Fundamentals and Applications*, 3rd ed.; Mallory, G. O., Hajdu, J. B., Eds.; American Electroplaters and Surface Finishers Society: Orlando, FL, 1990; pp. 441–462.
11. Bosko, M. L.; Lombardo, E. A.; Cornaglia, L. M. The Effect of Electroless Plating Time on the Morphology, Alloy Formation and H_2 Transport Properties of Pd–Ag Composite Membranes. *Int. J. Hydrog. Energy* **2011**, *36*, 4068–4078.
12. Feng, Y.; Yuan, H. Electroless Plating of Carbon Nanotubes with Silver. *J. Mater. Sci.* **2004**, *39*, 3241–3243.
13. Tarditi, A. M.; Braun, F.; Cornaglia, L. M. Novel PdAgCu Ternary Alloy: Hydrogen Permeation and Surface Properties. *Appl. Surf. Sci.* **2011**, *257*, 6626–6635.
14. Bindra, P.; White, J. R. Fundamental Aspects of Electroless Copper Plating. In *Electroless Plating: Fundamentals and Applications*, 3rd ed.; Mallory, G. O., Hajdu, J. B., Eds.; American Electroplaters and Surface Finishers Society: Orlando, FL, 1990; pp. 289–330.
15. Roa, F.; Way, J. D. Influence of Alloy Composition and Membrane Fabrication on the Pressure Dependence of the Hydrogen Flux of Palladium-Copper Membranes. *Ind. Eng. Chem., Res.* **2003**, *42*, 5827–5835.
16. Tarditi, A.; Gerboni, C.; Cornaglia, L. PdAu Membranes Supported on Top of Vacuum-Assisted ZrO_2-Modified Porous Stainless Steel Substrates. *J. Memb. Sci.* **2013**, *428*, 1–10.
17. Braun, F.; Tarditi, A. M.; Cornaglia, L. M. Optimization and Characterization of Electroless Co-Deposited PdRu Membranes: Effect of the Plating Variables on Morphology. *J. Memb. Sci.* **2011**, *382*, 252–261.
18. Okinaka, Y.; Wolowodiuk, C. Electroless Plating of Platinum Group Metals. In *Electroless Plating: Fundamentals and Applications*, 3rd ed.; Mallory, G. O., Hajdu, J. B., Eds.; American Electroplaters and Surface Finishers Society: Orlando, FL, 1990; pp. 421–440.
19. Hyland L. *Electroless Deposition of Group Eight Metal* (Ph.D. thesis), Yorkshire: University of Hull, 1995; pp. 1–166.
20. Mallory, G. The Fundamental Aspects of Electroless Nickel Plating. In *Electroless Plating: Fundamentals and Applications*, 3rd ed.; Mallory, G. O., Hajdu, J. B., Eds.; American Electroplaters and Surface Finishers Society: Orlando, FL, 1990; pp. 1–57.
21. Xu, X.; Cui, Z. D.; Zhu, S. L.; Liang, Y. Q.; Yang, X. J. Preparation of Nickel-Coated Graphite by Electroless Plating under Mechanical or Ultrasonic Agitation. *Surf. Coat. Technol.* **2014**, *240*, 425–431.
22. Agarwal, A.; Pujari, M.; Uppaluri, R.; Verma, A. Efficacy of Reducing Agent and Surfactant Contacting Pattern on the Performance Characteristics of Nickel Electroless Plating Baths Coupled with and without Ultrasound. *Ultrason. Sonochem.* **2014**, *21*, 1382–1391.
23. Tang, X.; Wang, J.; Wang, C.; Shen, B. A Novel Surface Activation Method for Ni/Au Electroless Plating of Acrylonitrile-Butadiene-Styrene. *Surf. Coat. Technol.* **2011**, *206*, 1382–1388.
24. Wen, G.; Guo, Z. X.; Davies, C. K. L. Microstructural Characterization of Electroless-Nickel Coatings on Zirconia Poder. *Scr. Mater.* **2000**, *43*, 307–311.
25. Hassan, H. B.; Hamid, Z. A. Electroless Ni–B Supported on Carbon for Direct Alcohol Fuel Cell Applications. *Int. J. Hydrog. Energy* **2011**, *36*, 849–856.
26. Dai, H.-B.; Liang, Y.; Wang, P.; Cheng, H.-M. Amorphous Cobalt–Boron/Nickel Foam as an Effective Catalyst for Hydrogen Generation from Alkaline Sodium Borohydride Solution. *J. Power Sources* **2008**, *177*, 17–23.
27. Fukuhara, C.; Ohkura, H.; Kamata, Y.; Murakami, Y.; Igarashi, A. Catalytic Properties of Plate-Type Copper-Based Catalysts, for Steam Reforming of Methanol, on an Aluminum Plate Prepared by Electroless Plating. *Appl. Catal. A Gen.* **2004**, *273*, 125–132.
28. Djokić, S. S. Electroless Deposition of Cobalt Using Hydrazine as a Reducing Agent. *J. Electrochem. Soc.* **1997**, *144*, 2358–2363.
29. Ohno, I. Electroless Deposition of Palladium and Platinum. In *Modern Electroplating*, 5th ed.; Schlesinger, M., Paunovic, M., Eds.; John Wiley & Sons: Hoboken, NJ, 2010; pp. 477–482.
30. Bhandari, R.; Ma, Y. H. Pd–Ag Membrane Synthesis: The Electroless and Electro-Plating Conditions and Their Effect on the Deposits Morphology. *J. Memb. Sci.* **2009**, *334*, 50–63.
31. Rhoda, R. N. Electroless Palladium Plating. *Trans. Inst. Metal Finish.* **1959**, *36*, 82.

32. Ayturk, M. E.; Ma, Y. H. Electroless Pd and Ag Deposition Kinetics of the Composite Pd and Pd/Ag Membranes Synthesized from Agitated Plating Baths. *J. Memb. Sci.* **2009**, *330*, 233–245.
33. Schlesinger, M. Electroless Deposition of Nickel. In *Modern Electroplating*, 5th ed.; Schlesinger, M., Paunovic, M., Eds.; John Wiley & Sons: Hoboken, NJ, 2010; pp. 447–458.
34. Steinmetz, P.; Alperine, S.; Friant-Costantini, A.; Josso, P. Electroless Deposition of Pure Nickel, Palladium and Platinum. *Surf. Coat. Technol.* **1990**, *43–44*, 500–510.
35. Guo, Z.; Keong, K. G.; Sha, W. Crystallisation and Phase Transformation Behaviour of Electroless Nickel Phosphorus Platings During Continuous Heating. *J. Alloys Compd.* **2003**, *358*, 112–119.
36. Kubota, A.; Koura, N. Studies of the Electroless Plating of Silver. *J. Met. Fin. Soc. Jpn* **1986**, *37*, 131–136.
37. Shu, J.; Grandjean, B. P. A.; Kaliaguine, S. Effect of $Cu(OH)_2$ on Electroless Copper Plating. *Ind. Eng. Chem. Res.* **1997**, *36*, 1632–1636.
38. Paunovic, M.; Arndt, R. The Effect of Some Additives on Electroless Copper Deposition. *J. Electrochem. Soc.* **1983**, *130*, 794–799.
39. Duffy, J.; Pearson, L.; Paunovic, M. The Effect of pH on Electroless Copper Deposition. *J. Electrochem. Soc.* **1983**, *130*, 876–880.
40. Sha, W.; Wu, X.; Keong, K. G. Electroless Copper Depositions: Surface Morphology Evolution of Electroless Copper Deposits. In *Electroless Copper and Nickel–Phosphorus Plating: Processing, Characterisation and Modelling*, 1st ed.; Wu, X., Keong, Y. G., Eds.; Woodhead Publishing: Cambridge; Philadelphia, PA, 2011; pp. 15–36.
41. Ayturk, M. E.; Engwall, E. E.; Ma, Y. H. Microstructure Analysis of the Intermetallic Diffusion-Induced Alloy Phases in Composite Pd/Ag/Porous Stainless Steel Membranes. *Ind. Eng. Chem. Res.* **2007**, *46*, 4295–4306.
42. Ayturk, M. E.; Payzant, E. A.; Speakman, S. A.; Ma, Y. H. Isothermal Nucleation and Growth Kinetics of Pd/Ag Alloy Phase via *in Situ* Time-Resolved High-Temperature X-ray Diffraction (HTXRD) Analysis. *J. Memb. Sci.* **2008**, *316*, 97–111.
43. Cheng, Y. S.; Yeung, K. L. Palladium–Silver Composite Membranes by Electroless Plating Technique. *J. Memb. Sci.* **1999**, *158*, 127–141.
44. Pacheco, D. A.; Llosa, M. A.; Niwa, S.; *et al.* Preparation of Palladium and Silver Alloy Membrane on a Porous α-Alumina Tube via Simultaneous Electroless Plating. *J. Memb. Sci.* **2005**, *247*, 21–27.
45. Gade, S. K.; Keeling, M. K.; Davidson, A. P.; Hatlevik, O.; Way, J. D. Palladium–Ruthenium Membranes for Hydrogen Separation Fabricated by Electroless Co-Deposition. *Int. J. Hydrog. Energy* **2009**, *34*, 6484–6491.
46. Van den Meerakker, J. E. A. M. On the Mechanism of Electroless Plating. II. One Mechanism for Different Reductants. *J. Appl. Electrochem.* **1990**, *20*, 85–90.
47. Subramanian, P. R.; Laughlin, D. E. Cu–Pd (Copper–Palladium). *J. Phase Equilib.* **1991**, *12* (2), 231–243.
48. Pomerantz, N.; Ma, Y. H.; Payzant, E. A. Isothermal Solid-State Transformation Kinetics Applied to Pd/Cu Alloy Membrane Fabrication. *AIChE J.* **2010**, *56*, 3062–3073.
49. Shi, L.; Goldbach, A.; Zeng, G.; Xu, H. Preparation and Performance of Thin-Layered PdAu/Ceramic Composite Membranes. *Int. J. Hydrog. Energy* **2010**, *35*, 4201–4208.
50. Shi, L.; Goldbach, A.; Xu, H. High-Flux H_2 Separation Membranes from (Pd/Au) n Nanolayers. *Int. J. Hydrog. Energy* **2011**, *36*, 2281–2284.
51. Braun, F.; Tarditi, A. M.; Miller, J. B.; Cornaglia, L. M. Pd-Based Binary and Ternary Alloy Membranes: Morphological and Perm-Selective Characterization in the Presence of H_2S. *J. Memb. Sci.* **2014**, *450*, 299–307.
52. Braun, F.; Miller, J. B.; Gellman, A. J.; *et al.* PdAgAu Alloy with High Resistance to Corrosion by H_2S. *J. Hydrogen Energy* **2012**, *37*, 18547–18555.
53. Tarditi, A. M.; Cornaglia, L. M. Novel PdAgCu Ternary Alloy as Promising Materials for Hydrogen Separation Membranes: Synthesis and Characterization. *Surf. Sci.* **2011**, *605*, 62–71.
54. Tarditi, A. M.; Imhoff, C.; Braun, F.; *et al.* PdCuAu Ternary Alloy Membranes: Hydrogen Permeation Properties in the Presence of H_2S. *J. Memb. Sci.* **2015**, *479*, 246–255.
55. Lewis, A. E.; Zhao, H.; Syed, H.; Wolden, C. A.; Way, J. D. PdAu and PdAuAg Composite Membranes for Hydrogen Separation from Synthetic Water-Gas Shift Streams Containing Hydrogen Sulfide. *J. Memb. Sci.* **2014**, *465*, 167–176.
56. Hatlevik, Ø.; Gade, S. K.; Keeling, M. K.; *et al.* Palladium and Palladium Alloy Membranes for Hydrogen Separation and Production: History, Fabrication Strategies, and Current Performance. *Sep. Purif. Technol.* **2010**, *73*, 59–64.
57. Uemiya, S.; Kato, W.; Uyama, A.; *et al.* Separation of Hydrogen From Gas Mixtures Using Supported Platinum-Group Metal Membranes. *Sep. Purif. Technol.* **2001**, *22–23*, 309–317.
58. Ockwig, N. W.; Nenoff, T. M. Membranes for Hydrogen Separation. *Chem. Rev.* **2007**, *107*, 4078–4110.
59. Paglieri, S. N.; Way, J. D. Innovations in Palladium Membrane Research. *Sep. Purif. Rev.* **2002**, *31*, 1–169.
60. Basile, A.; Gallucci, F.; Tosti, S. Synthesis, Characterization, and Applications of Palladium Membranes. In *Inorganic Membranes: Synthesis, Characterization and Applications; Technology*; Mallada, R., Menéndez, M., Eds.; Elsevier: Amsterdam, 2008; Vol. 13; pp. 255–323.
61. Uemiya, S.; Sato, N.; Ando, H.; *et al.* Separation of Hydrogen Through Palladium Thin Film Supported on a Porous Glass Tube. *J. Memb. Sci.* **1991**, *56*, 303–313.
62. Yun, S.; Ted Oyama, S. Correlations in Palladium Membranes for Hydrogen Separation: A Review. *J. Memb. Sci.* **2011**, *375*, 28–45.
63. Mardilovich, I. P.; Engwall, E.; Ma, Y. H. Dependence of Hydrogen Flux on the Pore Size and Plating Surface Topology of Asymmetric Pd-Porous Stainless Steel Membranes. *Desalination* **2002**, *144*, 85–89.
64. Ma, Y. H.; Akis, B. C.; Ayturk, M. E.; *et al.* Characterization of Intermetallic Diffusion Barrier and Alloy Formation for Pd/Cu and Pd/Ag Porous Stainless Steel Composite Membrane. *Ind. Eng. Chem. Res.* **2004**, *43*, 2936–2945.
65. Yepes, D.; Cornaglia, L. M.; Irusta, S.; Lombardo, E. A. Different Oxides Used as Diffusion Barriers in Composite Hydrogen Permeable Membranes. *J. Memb. Sci.* **2006**, *274*, 92–101.
66. Bosko, M. L.; Yepes, D.; Irusta, S.; *et al.* Characterization of Pd–Ag Membranes After Exposure to Hydrogen Flux at High Temperatures. *J. Memb. Sci.* **2007**, *306*, 56–65.
67. Okazaki, J.; Tanaka, D. A. P.; Tanco, M. A. L.; *et al.* Hydrogen Permeability Study of the Thin Pd–Ag Alloy Membranes in the Temperature Range Across the α–β Phase Transition. *J. Memb. Sci.* **2006**, *282*, 370–374.
68. McKinley, D. Metal Alloy for Hydrogen Separation and Purification. US Patent 3,350,845, 1967.
69. Gade, S. K.; Payzant, E. A.; Park, H. J.; Thoen, P. M.; Way, J. D. The Effects of Fabrication and Annealing on the Structure and Hydrogen Permeation of Pd–Au Binary Alloy Membranes. *J. Memb. Sci.* **2009**, *340*, 227–233.
70. Wang, L.; Yoshiie, R.; Uemiya, S. Fabrication of Novel Pd–Ag–Ru/Al_2O_3 Ternary Alloy Composite Membrane with Remarkably Enhanced H_2 Permeability. *J. Memb. Sci.* **2007**, *306*, 1–7.
71. Peters, T. A.; Kaleta, T.; Stange, M.; Bredesen, R. Development of Ternary Pd–Ag–TM Alloy Membranes with Improved Sulphur Tolerance. *J. Memb. Sci.* **2013**, *429*, 448–458.
72. Coulter, K. E.; Way, J. D.; Gade, S. K.; *et al.* Sulfur Tolerant PdAu and PdAuPt Alloy Hydrogen Separation Membranes. *J. Memb. Sci.* **2012**, *405–406*, 11–19.
73. O'Brien, C. P.; Howard, B. H.; Miller, J. B.; Morreale, B. D.; Gellman, A. J. Inhibition of Hydrogen Transport Through Pd and $Pd_{47}Cu_{53}$ Membranes by H_2S at 350 °C. *J. Memb. Sci.* **2010**, *349*, 380–384.
74. Gade, S. K.; DeVoss, S. J.; Coulter, K. E.; *et al.* Palladium-Gold Membranes in Mixed Gas Streams with Hydrogen Sulfide: Effect of Alloy Content and Fabrication Technique. *J. Memb. Sci.* **2011**, *378*, 35–41.
75. Lewis, A. E.; Zhao, H.; Syed, H.; Wolden, C. A.; Way, J. D. PdAu and PdAuAg Composite Membranes for Hydrogen Separation from Synthetic Water-Gas Shift Streams Containing Hydrogen Sulfide. *J. Memb. Sci.* **2014**, *465*, 167–176.
76. Zhao, L.; Goldbach, A.; Bao, C.; Xu, H. Structural and Permeation Kinetic Correlations in PdCuAg Membranes. *Appl. Mater. Interfaces* **2014**, *6*, 22408–22416.
77. Ling, C.; Semidey-Flecha, L.; Sholl, D. S. First-Principles Screening of PdCuAg Ternary Alloys as H_2 Purification Membranes. *J. Memb. Sci.* **2011**, *371*, 189–196.
78. Iyoha, O.; Enick, R.; Killmeyer, R.; Morreale, B. The Influence of Hydrogen Sulfide-to-Hydrogen Partial Pressure Ratio on the Sulfidization of Pd and 70 mol% Pd–Cu Membranes. *J. Memb. Sci.* **2007**, *305*, 77–92.
79. Chen, C. H.; Ma, Y. H. The Effect of H_2S on the Performance of Pd and Pd/Au Composite Membrane. *J. Memb. Sci.* **2010**, *362*, 535–544.
80. O'Brien, C. P.; Miller, J. B.; Morreale, B. D.; Gellman, A. J. H_2–D_2 Exchange Kinetics in the Presence of H_2S over Pd_4S, $Pd_{70}Cu_{30}$, and $Pd_{47}Cu_{53}$ Surfaces. *J. Phys. Chem. C* **2012**, *116*, 17657–17667.
81. Peters, T. A.; Kaleta, T.; Stange, M.; Bredesen, R. Development of Thin Binary and Ternary Pd-Based Alloy Membranes for Use in Hydrogen Production. *J. Memb. Sci.* **2011**, *383*, 124–134.

82. Shu, J.; Adnot, A.; Grandjean, B. P. A.; Kaliaguine, S. Structurally Stable Composite PdAg Alloy Membranes: Introduction of a Diffusion Barrier. *Thin Solid Films* **1996**, *286*, 72–79.
83. Bosko, M. L.; Miller, J. B.; Lombardo, E. A.; Gellman, A. J.; Cornaglia, L. M. Surface Characterization of Pd–Ag Composite Membranes After Annealing at Various Temperatures. *J. Memb. Sci.* **2011**, *369*, 267–276.
84. Tarditi, A. M.; Bosko, M. L.; Cornaglia, L. M. Alloying and Surface Composition of Model Pd e Ag Films Synthesized by Electroless Deposition. *Int. J. Hydrogen Energy* **2012**, *37*, 6020–6029.
85. Tarditi, A. M.; Imhoff, C.; Miller, J. B.; Cornaglia, L. Surface Composition of PdCuAu Ternary Alloys: A Combined LEIS and XPS Study. *Surf. Interface Anal.* **2015**, *47*, 745–754.

3.2 Tuning of the Microstructure and Surface Topography of Hot-Dip Galvanized Coatings

SMA Shibli, University of Kerala, Thiruvananthapuram, India
R Manu, Sree Vyasa N.S.S. College, Thrissur, India

© 2017 Elsevier Inc. All rights reserved.

3.2.1	**Recent Developments in Metal Composites Incorporated in Hot-Dip Galvanized Coating**	25
3.2.2	**Influence of Metal Oxides on Hot-Dip Galvanization Process**	26
3.2.3	**Methods for Incorporation of Metal Oxide or Composite in the Galvanization Process**	28
3.2.3.1	Formation of Predeposited Metal Oxide Layer: Wet Coating	28
3.2.3.2	Vacuum Coating Techniques	29
3.2.3.3	Direct Blending of Molten Bath with Metal Oxides	29
3.2.3.4	Preoxidation of Steel Prior to Hot-Dip Zinc Coating	29
3.2.4	**Implication of Metal Composites for Performance of Zinc Alloy Coating**	30
3.2.4.1	Physico-Chemical Properties of Metal Oxide Containing Hot-Dip Zinc Coating	30
3.2.4.2	Enhancement in Surface Topographical Characteristics	31
3.2.4.3	Electrochemical Characteristics of the Zinc Coating	32
3.2.5	**Summary**	35
References		35
Relevant Websites		37

3.2.1 Recent Developments in Metal Composites Incorporated in Hot-Dip Galvanized Coating

Despite the advances made in the discovery of new materials that could replace steel in various applications, the extraction and consumption of steel did not show a decrease considering the various statistics on the overall usage of various metals. Steel is used in various forms and it is an integral part in the construction, automobile, and allied industries.[1] Steel undergoes corrosion when exposed to different environments and during its application. There are various techniques to mitigate corrosion of steel structures, such as cathodic protection, anodic protection, alloying, cladding, addition of inhibitors, protective coatings, and metallic coatings. Various types of protective coatings are widely used to prevent corrosion of steel based on the ease of their application and long-term protection. Zinc coating is widely applied because active zinc metal corrodes more preferentially than steel substrate by a cathodic reaction that prevents steel from undergoing corrosion. Different types of zinc coating such as hot-dip galvanizing (batch or continuous), electroplating, metalizing (zinc spraying), mechanical plating, and zinc-rich paint are concomitantly applied on the basis of their application and exposure conditions.

Among them, the hot-dip galvanization process offers a unique combination of superior properties such as high strength, formability, light weight, corrosion resistance, low cost, and recyclability. The process of hot-dip galvanization has seen phenomenal growth during the past decades since its origin back in the eighteenth century. Hot-dip galvanized coatings are known to provide two types of corrosion protection for steel: barrier and galvanic (cathodic). The formation of intermetallic phases or alloys during galvanization depends on the diffusion rate of zinc into the steel substrate and the subsequent alloying reaction between iron and zinc.[2] Such structural modifications during the galvanization process not only improve the performance of the zinc coating but also could dramatically reduce the cost escalation in the process of galvanization. The numerous literature reports from different sources suggest various improvements in the galvanizing process and in the modification of pretreatment or post-treatment of the galvanized specimens. Analyzing the literature reports and reviews, it is clear that the microstructure as well as the surface modification have implications in improving the service span of the galvanized structure.

The performance of hot-dip galvanic coating formed on steel depends not only on the alloy composition of the outer layer but also significantly on the composition of the inner alloy layers at the coating substrate interface and also on the surface topography.[3,4] Further, the presence of barrier layers and through incorporation of certain metal oxides or mixed oxides or preformation of a dispersed metal oxide prior to galvanization can significantly improve the performance of the galvanized coating, thereby improving the coating span when exposed to a myriad of environmental conditions. The main problem of galvanic coating during its outdoor exposure is the noncolumbic loss in the zinc coating without exposing the under-steel substrate. Hot-dip galvanized coating consists of a heterogeneous assembly of different phases composed of mainly Fe and Zn, which are formed due to metallurgical reactions between iron and zinc when a ferrite substrate is immersed into molten zinc.[5] After solidification, the coating consists of an outer layer of 100% zinc (η layer) and inner layers, called alloy layers, consisting of intermetallic phases of iron and zinc such as zeta (ζ) layer (94% Zn–6% Fe), delta (δ) layer (90% Zn–10% Fe), and gamma (Γ)

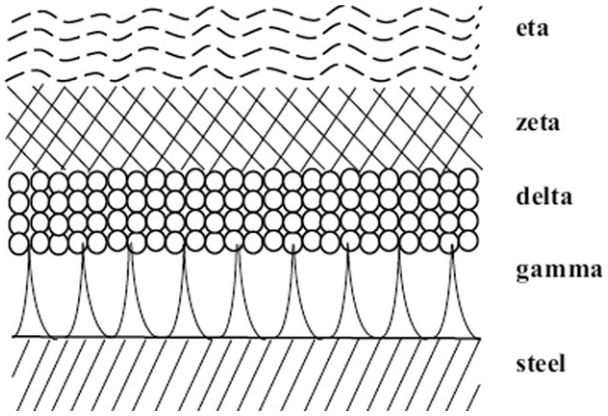


Figure 1 Schematic representation of various alloy layers of Fe and Zn formed by conventional hot-dip zinc coating.

layer (75% Zn–25% Fe), as shown in Figure 1.[6–8] The modification of the Fe–Zn alloy structure during its solidification could definitely improve the metallurgical characteristics of the zinc coating. The modified Fe–Zn alloy layer can be predicted to act as a quasi-stable alloy–oxide layer preventing the penetration of aggressive ions into the coating substrate interface. Thus, by acting as a barrier layer in galvanization, the property of the finished product can be improved. This could have implications in reducing the cost of the process by reducing zinc consumption during galvanization.

As already mentioned, incorporation of certain additives such as metal alloys, metal composites, and mixed metal oxides can modify the alloying character of the Zn–Fe alloy phase, which could improve the inner alloy structure of the galvanized coating. There are various metals such as Al, Mg, Cd, Cu, Ni, Co, Mn, V, and Sb that have been demonstrated to have higher corrosion resistance than pure Zn and that have been used as alloying elements in hot-dip galvanizing.[9–21] However, the thermal processes by which the galvanization reactions progress and different melting temperatures and the solubility of the metals adversely affect the Zn–Fe alloy structure. It remains to be determined whether certain metals have extremely limited solubility due to different melting temperature compared to zinc, and this makes the alloying reaction more complex.

The formation of intermetallic phases or alloys during galvanization depends on the diffusion rate of zinc into the substrate and the subsequent alloying reactions between iron and zinc.[22,23] The bonding strength between the substrate and the coating mainly depends on the surface feature of the metal substrate. The conventional hot-dip process involves laborious steps like degreasing, pickling, fluxing, and heating of the substrate before galvanization. Hence, the formation of the preformed oxide layer or incorporation of metal oxides and metal mixed oxides in the galvanizing bath lead to modifications in the alloy structure of the inner layers. In the present chapter, we discuss various methods including alloying by oxides and formation of a barrier layer as well as a preoxidized layer of metal oxide during hot-dip galvanization process.

There are plenty of literature reports available on modification of molten zinc bath by using metal oxides, rare earth oxides, and mixed oxides that were incorporated in galvanizing bath or formed as a dispersed inner layer or as a superficial layer in conjunction with the Zn–Fe alloy layer. Incorporation of the metal oxides not only could improve the inner alloy structure but also could reduce the consumption of zinc, which makes the process more economical. Metal oxides play a versatile role in the development of heterogeneous catalysis, gas sensors, and corrosion and wear protection materials.[24–29] High-performance hot-dip zinc coatings can be developed by the incorporation of individual and mixed metal oxides such as nano ZnO, nano TiO_2, CeO_2, CeO_2–TiO_2 , Al_2O_3–ZrO_2, FeO, and MnO_2 into the hot-dip zinc coating.[30–37] The incorporation of Al_2O_3–ZrO_2 and Al_2O_3–TiO_2 mixed oxides into galvanizing bath yields aluminium-rich zinc coatings with high sliding and wear resistance. The interior layers of the coatings are also known to possess high stability against corrosion, and many different mechanisms illustrate that corrosion resistance of the coating was improved with these types of additives in the molten zinc bath.[38–42] High corrosion resistance and better physical characteristics of the coating were achieved, as evidenced during analysis by different techniques.

Physical properties such as hardness, thickness, wear resistance, and weldability characteristics of the coating were found to be superior compared to the conventional zinc coating, as evidenced from literature reports.[43–48] The merit of any type of protective coating is the long-term protection it extends to various steel structures exposed to a myriad of exposure conditions. Other than sacrificial action in the case of zinc-rich coating, metal oxide like that in the inner or dispersed layer in the alloy phase could act as a barrier that could mitigate the penetration of certain types of aggressive ions such as Cl^- and ClO_4^- that cause pitting corrosion of steel surfaces and lead to catastrophic failure of giant steel structures. Use of Ni as an alloy metal is a viable alternative to some toxic metals presently used in galvanization.[49–54] It is clear that the extent of barrier protection of the coating was significantly improved, as revealed from various performance analyses including layer-wise electrochemical characterization of the coating under specific conditions.[14] In this case, substantial barrier protection in the coating due to the reinforcement of the metal oxide inner layer or dispersed metal layer was achieved. The interior layers of the coating exhibited relatively higher barrier protection characteristics compared to the outer layer, as evidenced from potential decay analysis of the coated specimens undergoing salt spray test and real-time impedance analysis.

3.2.2 Influence of Metal Oxides on Hot-Dip Galvanization Process

It has been proven that the presence of oxides in the inner layers could modify the Fe–Zn alloy phases, because it is clear that the metal underneath is protected at the same time that sacrificial action of Zn is improved due to the presence of oxides. It is understood that certain rare earth oxides, including Ti and Ta oxides, were also included in the molten zinc

bath.[31,34] These oxides that have their own certain unique alloying reactions when forming alloy phases could improve the property of the galvanized specimens exposed to specific conditions. Incorporation of nano TiO_2 in the hot-dip zinc coating has been known to facilitate phosphating and also to improve paintability of the galvanized structure. The hot-dip galvanized coatings with high corrosion resistance, effective barrier protection, good anti-fouling characteristics, and improved surface quality can be achieved by CeO_2–TiO_2 incorporation.[36,37] These composites not only yield individual characteristics of the additive incorporated in the coating but also provide a new range of reaction modification during the process. But there are certain drawbacks that arise during using these oxides due to their poor wettability in the zinc melt and also due to nonoptimum concentration of the oxide in the melt that lead to reduced homogeneity and distribution of the oxide blended in the zinc melt.

These issues are clearly discussed in this chapter based on the recent research advances made in the field and based on the evidence of various analyses of the improved galvanization process. Wettability of the oxides in the zinc melt can be improved by using relatively small proportions of various oxides that are to be blended with the zinc melt and through agitation and modification of surface morphology of the oxides or composites before blending with molten zinc. The consistency and homogeneity of the melt can be enhanced by blowing inert gases and by uniform mechanical stirring to avoid segregation or settling of metal oxides within the melt. From the literature reports, and based on the results from the authors' preliminary studies, the amount of metal oxides incorporated into the galvanizing bath can be optimized to 1–2 g, depending on which type of oxide is being blended in the melt.

The use of nano zinc oxide, cerium oxide, nickel oxide, titanium oxide, and iron oxide was widely used in various types of zinc coating and protective coating.[55–61] These oxides have certain special properties such as anti-microbial property, photocatalysis, wear resistance, corrosion resistance, and others, which can be well utilized for fabricating hybrid zinc coating for specific applications. One thing to be emphasized is that the amount of nano oxide in the molten zinc bath should be optimized depending on the reaction conditions such as temperature, agitation, and withdrawal speed of the specimen from the molten bath. To obtain homogeneous distribution of the metal oxide within the melt, a lower concentration of metal oxide is usually beneficial in that it could improve the galvanizing reaction between Fe and Zn and it provides reinforcement to the coating with uniform thickness.

Another report sheds light on the effects of micro-sized and nano-sized oxide particles on corrosion resistance and hydrolytic degradation of an epoxy coating during exposure. It was reported that the developed coating has shown better tolerance against corrosive electrolytes when incorporated with nano-sized and micro-sized ZnO particles. The corrosion resistance of the nano composite coating was considerably greater than that of the one reinforced with micro-ZnO particles, as revealed from the literature. The size of the particle has a profound effect on augmenting certain characteristic properties of the deposit. By tuning the size of the nanomaterials and optimizing their amount in the melt, we could modify the inner alloy structure of the deposit. The reinforcement resulted from oxide incorporation, and the modification in the alloy structure of the coating could improve the tolerance of hydrolytic degradation upon exposure to the corrosive electrolyte. Certain physical properties such as hardness, thickness, and wear resistance of the galvanized coating can be improved through incorporation of nanomaterials, which could have some specific applications. The behavior of the epoxy coating reinforced with nanoparticles exposed to corrosive medium reveals that the hardness and cross-linking density of the coating are considerably lower than that of the conventional hot-dipped sample and the sample reinforced with the micro-sized ZnO particles.

Certain other types of metal oxides that were found to be beneficial in enhancing the life of galvanized substrates are ZnO, TiO_2, and CeO_2, which have anti-microbial properties and are also good photocatalysts; therefore, these oxides could be well utilized for zinc coating exposed to water. Titanium dioxide (TiO_2) has been used as a self-cleaning and self-sterilizing material to coat different tools, including sanitary ware, food tableware, and cookware.[62,63] The anti-microbial effects of TiO_2 are activated by its photocatalytic behavior, which is totally dependent on ultraviolet and/or visible light irradiation. The effect of incorporation of titanium dioxide on the physical, electrochemical, and biocidal characteristics of hot-dip galvanic coatings is known to be highly corrosion-resistant with the least biogrowth when used in inclement weather. Although sometimes the metal oxides incorporated in the molten metal can become segregated during the alloy formation, this can be controlled by continuous agitation or by optimizing the concentration and withdrawal speed of the steel coupons from the galvanizing bath. The physical characteristics of the coatings were found to be improved by TiO_2 incorporation. The resistance of the coating against biogrowth can be studied by quantifying the number of microorganisms on the coating surface after immersing in natural sea water containing microorganisms.

Nano ZnO is a promising material due to its easy method of synthesis, nontoxicity, anti-corrosion, and biocidal activities. ZnO that can form a permeation barrier coating[64] is material generally recognized as safe by the US Food and Drug Administration. ZnO nanoparticles are much more effective agents than micropowders for controlling the growth of different microorganisms. Some authors[65–68] have reported that the smaller the particle size, the greater the efficiency in inhibiting bacteria growth. Moreover, several works have proved that the anti-microbial activity is also dependent on the concentration used.[69–72] The higher the concentration of ZnO nanoparticles and microparticles, the higher the antibacterial effect achieved. These results indicate that increasing the active surface area enhances the anti-microbial activity. This observation complements the idea that addition of ZnO nanoparticles in the zinc coating could have beneficial effects in controlling the microbiologically influenced corrosion.

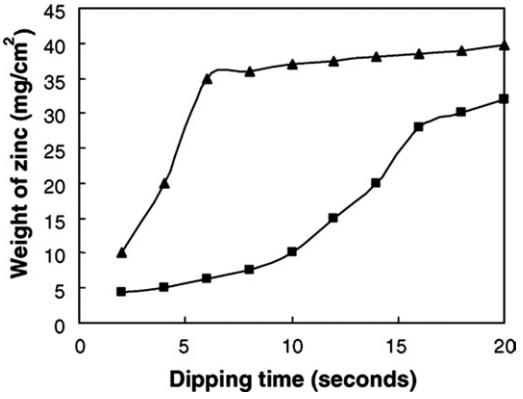


Figure 2 The amount of zinc (mg cm^{-2}) consumed during the galvanization process as a function of dipping time of the substrate: (▲) pure zinc coating and (■) oxide-incorporated coating.

Tuning of thickness is of prime importance and comes into play when using metal oxides in the molten bath. Although obtaining thick intermediate phases is beneficial because it would lengthen the protective life of galvanized coatings, it is not desirable from a mechanical standpoint because the thickness increment of the brittle intermediate phases could facilitate delamination and spalling of the coatings.[73,74] Moreover, excess thickness of the coatings would imply unnecessary use of zinc metal, which is impractical from an economic standpoint. In fact, coating overgrowth is problematic in several types of steels, including silicon-killed steels, where the reaction kinetics between iron and zinc is so rapid that simply reducing the hot-dip duration does not suppress the problem. Under this circumstance, it is advisable to use the process that could provide optimum performance with minimum zinc drainage.

One other work suggests the benefit of the FeO intermediate layer in zinc alloy coating. Presence of iron oxide in the alloy layer creates mixed potential during its exposure, thereby lowering the dezincification process during exposure. The report also contemplates reducing the zinc consumption during galvanization. The amount of iron present in the outermost layer of the iron oxide containing zinc coating can be attributed to the ejection of the oxide layer (FeO) during Fe–Zn outburst reactions. **Figure 2** shows the zinc drainage during galvanization with and without an oxide layer. Moreover, the iron present in the outermost layer could reduce the rate of zinc dissolution, which could not happen in the case of pure zinc coating.

One other important revelation regarding the use of nanomaterials as additives in zinc melt is that it could influence the topography as well as microstructure of the zinc coating. These materials that have high surface area could provide a smooth coating morphology and well-defined grain feature with spangle formation in special cases of zinc coating. This modified surface feature could mitigate the corrosion rate and could reduce the self-corrosion rate of the galvanized coating. The improved surface feature reduces the wetting tendency of the coating during various exposure conditions, and the glossy surface finish could improve the life span of the zinc coating.

3.2.3 Methods for Incorporation of Metal Oxide or Composite in the Galvanization Process

As the issues related to overgrowth and adhesion of the galvanized layer become more pertinent considering the performance and the economics of the galvanized coating for various application, it is necessary to discuss how to optimize the conventional process steps in conjunction with modern improved techniques to develop hybrid coatings that are more advantageous, have better tolerance for corrosion, and are economically viable. Several advanced coating methods were developed that can be suitably mimicked in conventional methods of galvanization through procedural modification and through additive components. The various methods identified involve formation of the monolayer or dispersed layer of metal or an alloy preceding galvanization, thermal decomposition of the substrate under controlled conditions, and blending the molten zinc bath with suitable additives. Each of these methods has its advantage and drawbacks when applied in conjunction with the galvanization process. Blending with suitable additives such as metal oxides, nanomaterials, and alloys is rather simple and beneficial compared to other process modifications.

3.2.3.1 Formation of Predeposited Metal Oxide Layer: Wet Coating

Among the various techniques that can be inculcated in conventional process sequences is the fabrication of a metal, metal oxide, or alloy layer over the steel substrate prior to hot-dip zinc coating. Here, presence of a certain metal layer such as Ni, Mn, ZnO, or Ni–P that serves as a physical barrier could influence the inner layer growth and the consumption of zinc during galvanization. It is clear that formation of a predeposited layer of metal, alloy, or metal oxide could have a profound influence on formation of the inner alloy structure and on the sacrificial action of the pure zinc outer layer during its course of exposure. The dispersed layer or thin layer of metal can be formed through the wet/dry deposition technique. Here, the techniques such as electrodeposition, electroless, dip coating, and vacuum coating are applied based on their suitability. Electrodeposition method can be applied to the substrate using an optimized plating bath for Ni, Zn, Ti, or Fe and by adjusting the rate of deposition through optimizing the current and time. Moreover, by means of electroless coating, an efficient Ni or Ni–P alloy layer can be applied by using a standardized bath where more or less uniform coating than electrodeposition can be obtained over the steel substrate. In dip coating, a thin layer of metal can be formed over the steel substrate by dipping the substrate in a bath of suitable metal salt solution containing a reducing agent. The reducing agent reduces the metal forming as a thin layer over the substrate. The metal oxide dispersed layer can be formed by either electrodeposition or heating the metal surface with the preformed metal layer that forms an oxide layer prior to hot-dip galvanization. During electroless coating, the thickness of the alloy layer can be controlled by adjusting the time of deposition.

One other report delves into formation of iron oxide over steel prior to galvanization. The steel coupons preformed with iron oxides can serve as a barrier layer for galvanized coupons. The iron oxide dispersed layer is formed prior to galvanization by impressing the steel coupons with required current in a suitable medium and the formation of a tenacious oxide layer is affected. Then, galvanization is performed with the oxide inner layer. It has been reported that the iron-rich inner layer can have greater resistance to corrosion than the pure zinc layer in normal galvanized coatings.[75–79]

Electrodeposition of crystalline ZnO thin films from aqueous solutions in the presence of suitable bath reagents has been reported.[80–83] In such cases, a thin film of ZnO is formed by the wet deposition technique, and further widespread studies have been performed by different groups regarding improvement of the coatings.[84–87] Galvanized coatings prepared with a pulse electrodeposited nickel inner layer can be produced with a uniform, void-free structure using a pulse-current waveform upon nickel deposition.[88] The pulse electrodeposition has more advantages than normal electrodeposition, whereby uniform and pore-free deposition with refined grained features can be obtained over the steel substrate. The small pulses of varying time intervals could be generated that ensure refurbishing the substrate or solution interface through replenishing with Ni ions. A typical microstructure of galvanized steels precoated with nickel consists of two apparent Zn–Ni intermediate layers and a nickel layer that survives the galvanization. The uniformity of these layers can be ensured by providing a nickel precoating of adequate thickness in relation to the hot-dip duration.

3.2.3.2 Vacuum Coating Techniques

In vacuum coating, a monolayer or a few layers of metal can be applied by sputtering, which is a chemical vapor deposition technique. The coating can be provided to small and larger area surfaces. One other advantage of vacuum coating is the formation of certain metals that are unable to deposit through the wet coating technique. Ti and Ta or Zr and Ir can be applied as monolayers to the steel substrate through vacuum coating. The monolayer formed by this technique is more adherent, uniform, and compatible to apply further galvanized layers. One other form of thin film formation of metal oxide is by metal organic chemical vapor deposition. The vacuum technique of metal coating is advantageous over other conventional solution phase methods despite its high cost. One thing to be noted here is that the thickness of the coating should not exceed a few monolayers because that could affect the galvanization process.

3.2.3.3 Direct Blending of Molten Bath with Metal Oxides

From the literature review, it is clear that there are many processes by which we can incorporate metal composites as metal oxides and mixed metal oxides through bath modifications that could modify the Fe–Zn alloy layer. Various metal oxides such as ZnO, NiO, FeO, ZrO_2, CeO_2, and TiO_2 have been used as oxides and as composites in galvanized steel substrate. The metal oxides can be directly added to the molten bath or as alloys that could be easily mixed within the molten melt. The amount of additive in the molten bath can be optimized for a homogeneous mix of metal oxide or alloys and the zinc melt. When adding various proportions of metal oxides, care should be taken to avoid agglomeration of oxides over the melt surface. This could ensure a homogeneous distribution of metal oxides within the molten zinc bath. Generally, the molten bath with incorporated oxides is agitated or stirred mechanically to avoid segregation of the oxide particles in the melt.

In this method, the metal composites are first blended in the molten metal bath and the same process as in the case of conventional metal alloy coating follows; therefore, the unique incorporation of various types of metals, alloys, metal oxides, and mixed oxides is possible. The advantage of applying each technique lies in its usage, mode of application, exposure conditions, and cost. Each method has its advantage and drawbacks, but based on the requirements we can shuttle between different conventional techniques in conjunction with modern coating methods.

3.2.3.4 Preoxidation of Steel Prior to Hot-Dip Zinc Coating

The type of steel substrate used in hot-dip zinc coating is noteworthy. For galvanization, steels with different elemental compositions have been used based on their applications for specific purposes. The presence of elements such as Si, Mn, C, Al, and Ti in various steel grades can influence the wetting nature of the steel surface by zinc and on zinc diffusion or penetration, forming various inner alloy layers including zinc consumption. To improve the galvanization process, depending on the steel type, preoxidation and annealing are used under controlled experimental conditions and by using reduced atmosphere. There are some common approaches that are used to improve the wettability of the steel and to develop hot-dip zinc coating with steels with varying alloy contents. One method involves the preoxidation of the steel substrate with high Mn or Si content.[89–96] This forms a porous Mn–Fe mixed oxide layer on the steel surface. The Fe in the mixed oxide should then be chemically reduced during the annealing process by an extremely dry atmosphere and form the Fe_2Al_5 inhibition layer with the dissolved Al from the liquid Zn bath on top of MnO, allowing growth of the Zn layer. The effect of cold rolling the hot-rolled steel with an oxide layer with a thickness of approximately 8 μ improved the wetting property of the steel for galvanization, and this has been investigated in detail.[97]

The preoxidation of the metal surface under controlled conditions in the reducing atmosphere can have a beneficial influence during formation of Fe–Zn alloy phases. There is also a report of an improvement in the wettability by changing the Al concentration in the bath, the bath temperature, and the temperature of the steel.[98] Cho and De Cooman suggest two additional methods: one involving annealing at high dew points to provoke internal Mn oxidation and the other involving flash coating of the surface with pure Fe.[99,100] These methods of pretreatment of steel prior to hot-dip

galvanization improve the wettability, alloying reactions, and other key properties of the coating. Reports are also available regarding corrosion-resistant characteristics of Fe–40Al intermetallic surfaces due to prior oxide formation. The oxidizing behavior of the alloying elements in the surface, if any, can form adherent oxide layers with effective protection characteristics.[57]

3.2.4 Implication of Metal Composites for Performance of Zinc Alloy Coating

Use of various types of metal composites such as metal oxides, mixed metal oxides, and nano metal oxides can have profound effects on the performance of hot-dip galvanized structures. As detailed in the previous section, the metal oxides that are incorporated in the zinc melt could modify the alloy structure and the mechanism of alloy formation between Zn and Fe. It is already proven that nano metal oxides and micro-sized oxides can improve the surface morphology and microstructure of the deposit. This could enhance the corrosion performance of the coating. In the case of metal oxides, one of the shortcomings is its uniform distribution within the zinc melt and its wettability nature. This is surmounted by optimizing the concentration of the additive (composite) and through uniform agitation of the molten melt. The physical and mechanical properties such as hardness, thickness, adhesion, weldability, wear resistance, and porosity of the developed coating with incorporated metal oxides and mixed oxides can be significantly improved in comparison with conventional hot-dip zinc coating. The corrosion tolerance of the galvanized coating may have a marginal improvement in comparison to the normal zinc coating. This has been experimentally proven by results from different electrochemical analyses and also by using certain accelerated corrosion testing. In the case of conventional galvanized steel coupons, the self-corrosion rate of the coating is greater; this behavior of coating deterioration, in addition to its sacrificial action, decreases the life span of the zinc coating. The self-corrosion rate can be drastically reduced in zinc coatings incorporated with metal oxides, as evidenced from a survey of recent research reports.

Different methods and instrumentation techniques are followed to study the efficiency of the developed coating for its overall performance and its applicability to different end uses. Various physico-chemical tests such as hardness, thickness, adhesion weldability, wear resistance, bend test, and smoothness are conducted per the standard test procedure to determine the improvement in the coating and its applicability. Long-term immersion studies are performed to assess the potential decay characteristics of the galvanized coupons under saline conditions. The change in electrode potential with respect to a saturated calomel electrode can be measured at regular intervals for a period of 30 or 60 days, as the condition warrants. Salt spray test can be performed per the ASTM B.117 standard for a period of 30 days at 35 °C to determine the deterioration of the zinc coating under aggressive conditions. The edges of the preweighed coupons should be covered with adhesive tape before placing the coupons in the salt spray chamber. The corroded coupons should be washed with 10% ammonium per sulfate ($[NH_4]_2S_2O_8$) solution at room temperature, dried, and weighed.

The results obtained from various observations predict that there is a remarkable improvement in the performance of the developed hot-dip zinc coating. By examining some of the literatures on the effect of certain oxides on hot-dip zinc-coated products, it is confirmed that these oxides are proven to be beneficial for improving the properties. The incorporation of TiO_2 in the coating has resulted in substantial enhancement of the hardness of the zinc coating. The additional incorporation of Al_2O_3 along with TiO_2 causes little further improvement in the hardness of the coating. The incorporation of TiO_2–ZnO composite in the coating can cause a significantly substantial reduction in thickness of the coating, as also evidenced in other reported studies regarding composite-reinforced hot-dip galvanic coating.[35,101] This could be due to the reinforcement of the metal oxides and the composite nature of the coating.

3.2.4.1 Physico-Chemical Properties of Metal Oxide Containing Hot-Dip Zinc Coating

The hardness value of a coated metal depends on many factors, and the most important one is the composition of the deposit layer. The hardness values for pure zinc-galvanized and galvanized layer over zinc oxide as a barrier layer are 50 and 58 HVN, respectively; however, in the case of Ni–P as a barrier layer, the hardness value is improved up to 70 HVN. The presence of ZnO or Ni–P as a barrier layer not only enhances the adhesion between the steel substrate and the galvanized layer but also inhibits the diffusion of zinc. However, due to the dispersed nature of the barrier layer, a local Fe–Zn outburst reaction occurs, facilitating high zinc diffusion.[46,101] The controlled diffusion of zinc reduces the coating thickness and enhances the adhesion between the coating and the substrate. The interdiffusion also improves the formation of more compact and regular alloy phase formation between Fe and Zn. The presence of mixed oxide composites in the molten zinc bath can reduce the alloying reaction between zinc and iron, resulting in lower thickness of the coating.

Adherence of the coating can be evaluated by first making the steel coupons bent, and then the coating can be tested for appearance of any peeling or cracks. After bending, the surface should not have any surface blemishes or peeling layers. This is in accordance with the already reported evidence on ZnO-incorporated hot-dip zinc coating.[55,101–103] This predicted the good alloying nature and the compact structural characteristics of the coatings. The observation of the thinner coating reveals more compact alloy layers, as observed in the case of zinc coating incorporated with ZnO.

Another type of oxide that shows inferior properties when added to zinc melt is V_2O_5. It is reported that with V_2O_5-incorporated zinc coating there would be several surface cracks, with peeling of outer layers after bend tests.[104] As the thickness of the coating increases, it is likely to develop more surface cracks during bend tests. Generally, incorporation of composites into the coating also results in improvement in

adherence of the coating. This is attributed to the fact that in the presence of inert metallic composites on the surface of the substrate, the diffusion of zinc during galvanization is lowered. The hot-dip zinc coating developed through incorporation of metal oxides and mixed oxides normally reveals a pore-free surface finish that shows the absence of iron on the galvanized surface. This reflects that during alloying mechanisms, zinc uniformly covers itself over steel and the formation of spangles shows good surface features of the zinc coating.

An important set of properties of galvanized steel is its weldability and paintability. It is clear that weldability of the oxide-incorporated coating is superior to conventional galvanized coupons. The surface pore features of the zinc coating prepared with nano oxides improves the paintabillity or phosphatization of the coating, which extends the life of the coating further.

3.2.4.2 Enhancement in Surface Topographical Characteristics

The surface morphology as well as the microstructure of the hot-dip galvanized coating can be significantly improved by the addition of various types of alloys, metal oxides, and inner layer oxides, as reported elsewhere.[37,54,55] It has been reported that incorporation of certain metal oxides could alter the crystal morphology and, depending on the size of the particles incorporated, the crystallite size may also vary.

As discussed, the performance of zinc coating depends not only on the outer surface feature of the coating but also significantly on the microstructure and inner layer morphology of the Fe–Zn alloy layers. Presence of certain oxides such as ZnO, TiO_2, or NiO or the presence of a preformed ZnO, Ni–P, and FeO layer can have a great influence on the improvement of the coating structure and the overall performance of the zinc coating. **Figure 3** shows the Ni-rich inner layer and ZnO inner layer that are formed within the Fe–Zn alloy matrix. Certain metal oxides that act as a barrier or inner oxide layer also improve the surface and grain features of the deposit. The formation of Ni and ZnO inner layers shows that the zinc drains, and thus formation of inner alloys could be controlled such that a uniform and porous surface finish is achieved in the hot-dip zinc coating.

The large crystals created better surface coverage for the coatings incorporated with nano metal oxides. The size of the metal oxides and their distribution in the Fe–Zn alloy phase modifies the microstructure of the coating. Similar to the reported results,[105–107] micropores and cavities are obtained on the surface of these types of coatings. However, the number of the pores is less in the case of the coatings incorporated with nano metal oxides, and this may be due to the surface sealing effect created by nanoparticles compared to micro-sized particles. It should be noted that when using nanoparticles as zinc bath additives, we have to control or tune the size of the particles and their surface features to achieve homogeneous distribution in the melt.

Incorporation of nano metal oxides causes structural refinement of the zinc coating that improves the surface topography of the deposit. Normally, the surface was homogeneous without any surface blemishes or peeled layer, revealing better adhesion of the coating when nano oxides of optimum quantity are incorporated. The surface roughness is normally less compared to conventional hot-dip zinc-coated structures. By optimizing the concentration of additives incorporated in the galvanizing bath, the segregating nature and powdery appearance of the coating can be improved. **Figure 4** shows SEM images of a typical hot-dip zinc coating with ZnO and V_2O_5 incorporated.

Certain metal oxides when added to the molten bath have been found to segregate, and this could lead to an inhomogeneous surface with the appearance of micro-voids caused by

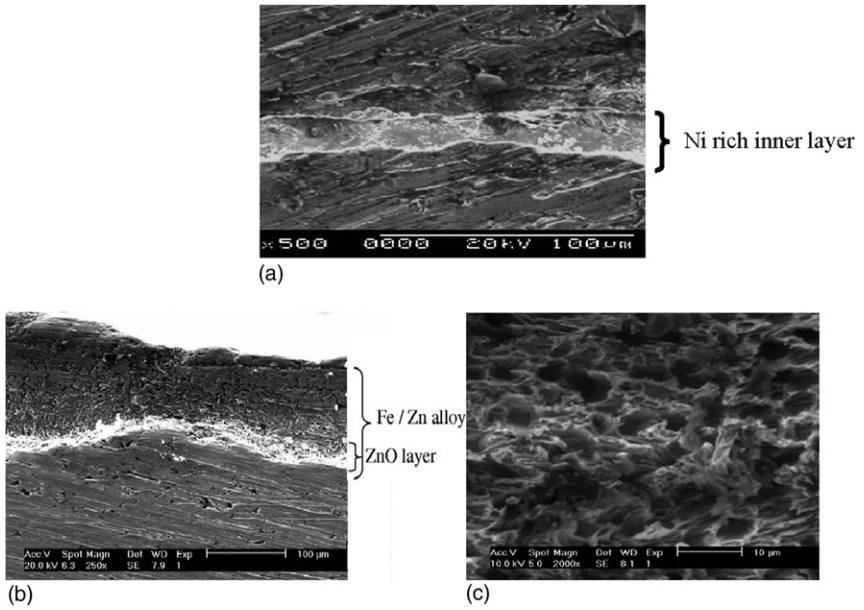


Figure 3 (a) Ni-rich layer, (b) ZnO inner layer, and (c) surface morphology of ZnO-incorporated hot-dip zinc coating.

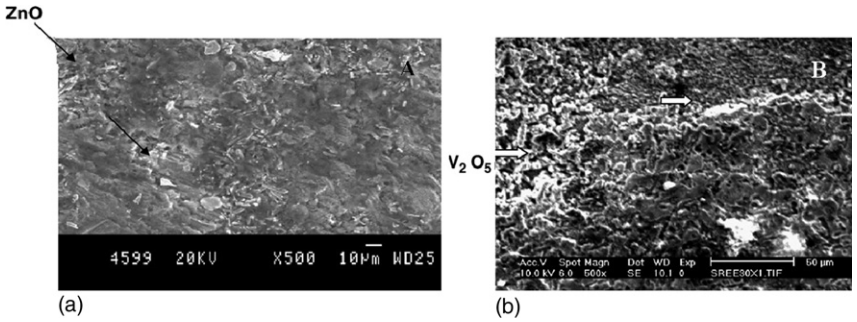


Figure 4 Surface topography of the hot-dip zinc coating with (a) ZnO and (b) V_2O_5.

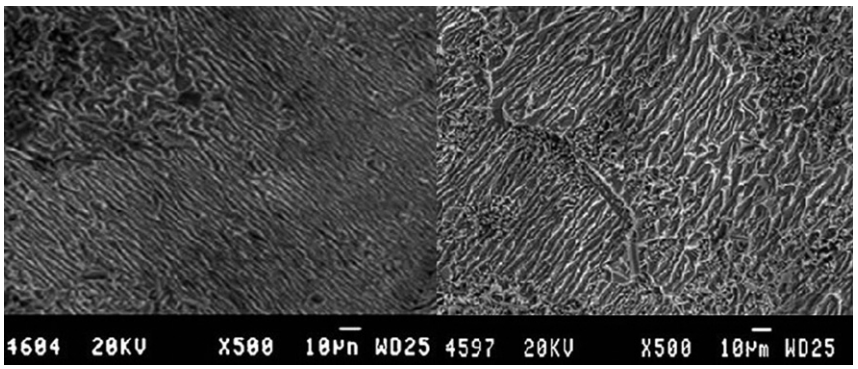


Figure 5 Surface morphology of pure Zn coating and TiO_2-incorporated zinc coating.

segregation. **Figure 4** reveals the segregating nature of surface oxides during the addition of V_2O_5. This can be due to non-wetting behavior of these oxides in the melt that results in formation of surface oxides with ridged morphology. Generally, the ridged spangle surfaces are populated with precipitates present in relatively large size.[108,109] Here, oxides such as ZrO_2 and V_2O_5 undergo segregation above a certain concentration, which leads to poor quality surface features for the galvanized coating. However, these oxides in the form of metal alloys are beneficial for improving characteristic properties of the coating. **Figure 5** shows the surface morphology of a typical zinc coating with pure Zn and one with TiO_2 incorporated.

The pure zinc coating or the coating with 5% Al or Mg alloy results in spangle formation after annealing. The features and size of the spangles depend on the withdrawal speed, temperature, and the alloying reaction with Fe and Zn. A very smooth surface with characteristic spangle formation can be achieved with certain types of oxides and alloy melts in the nano domain, provided that it has an optimum concentration. The nano size and the good wetting property of other oxides such as NiO, MnO_2 , CeO_2, and others can be used for developing hot-dip zinc coating with improved properties and superior surface features.

Color variations in hot-dip zinc coatings occur with changes in molten zinc bath temperature and with different concentrations of Mn. The color change is attributed to the MnO_2 formation. The formation of the Mn oxide film introduces a visible light interference effect with a specific surface color, certain film thickness, and refractive index of oxides. Tomita also reported that the color variations were due to the different thicknesses of the Mn oxide film on the coating surface.[110]

The presence of Mn in the Zn melt can significantly influence the microstructure and Fe–Zn alloy phase distribution. Various literatures indicate that the presence of Mn in Zn melt could promote the δ phase, where we could expect an increase in thickness of the δ-$FeZn_{10}$ phase.[111] This can improve the galvanic character of the hot-dip zinc coating. Mn is a surface-active element in the molten Zn that tends to migrate to the surface from the bulk to form an Mn-rich layer at the surface of the molten Zn. The Mn content at the surface of molten Zn could be more than 10-times higher than that inside the melt and will be oxidized preferentially due to the direct air exposure.[112,113]

3.2.4.3 Electrochemical Characteristics of the Zinc Coating

Important properties that concern the use of zinc coatings are primarily corrosion and formability. The progress of corrosion in different types of galvanized coatings can be investigated by using the electrochemical impedance spectroscopic technique, open circuit potential (OCP) decay, polarization character, weight loss method, and accelerated salt spray test.

Performance of the coating regarding corrosion tolerance under different exposed conditions must be determined. The OCP of the galvanized coupons fabricated with different types of metal oxides shows steady but high negative (cathodic)

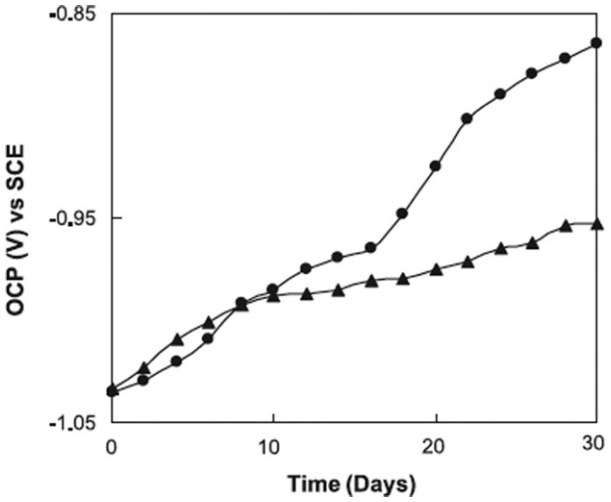


Figure 6 Open circuit potential decay curves of galvanized coupons during long-term immersion test. Medium: 5% NaCl at 30 °C, stagnant condition. (●) Pure zinc coating. (▲) With dispersed Ni under-layer.

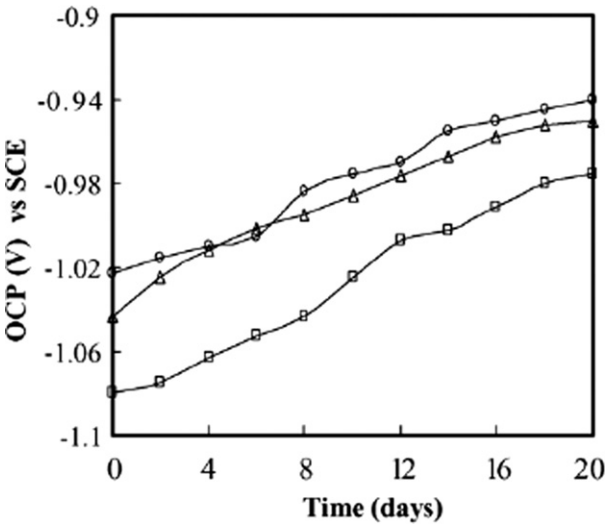


Figure 7 Variation in open circuit potential of the three different galvanized coupons compared to time of exposure during immersion in 5% NaCl solution as a function of nickel concentration in the coating. (○) 0.08% Ni; (Δ) 0.12% Ni; and (□) 0.18% Ni.

potential values during the initial hours of immersion in the electrolyte. The high negative OCP exhibited by the coupons can be attributed to the better alloying reaction between Zn and Fe and to the sacrificial nature of the top pure zinc layer. When Ni is used as barrier layer or a dispersed under-layer, the formation of inner alloys becomes modified. Although corrosion potential of nickel on steel is nobler when compared with steel substrates, nickel can provide some degree of protection by acting as a barrier to aggressive ions.[14,54] The uniformity of the coating, compact layering structure, low surface energy of bright crystals due to their smooth surface, and smaller amount of surface segregation can enhance the polarization tolerance of the coating. The penetration of Cl^- or ClO_4^- ions can also be prevented effectively by the under-layer of nickel coating, as revealed from various reports. Figure 6 shows the potential decay of the pure zinc coating and Ni-dispersed hot-dip zinc coating. Also, regarding the concentration of an additive element, there can be a shift in the potential for exposure. Figure 7 shows the variation in the OCP of the steel coupons with different concentrations of Ni in the alloy layers. Here, the one with the higher concentration of Ni exhibits more cathodic potential initially during the exposure, which can be attributed to the mixed potential of the outermost alloy coating. The shift in cathodic potential is gradual during exposure to 5% NaCl solution, as revealed in Figure 7.

It is clear that we can lower the dissolution rate of zinc in the presence of certain alloying metals such as Ni and Mn, which can act as a barrier layer, thereby significantly reducing the self-corrosion rate of Zn. This is observed with respect to some types of hot-dip zinc coatings containing multiple alloying elements. One other possibility for lower dissolution of Zn is the formation of comparatively stable corrosion products that are formed with certain types of additives that extend protection from corrosion to the underneath substrate.

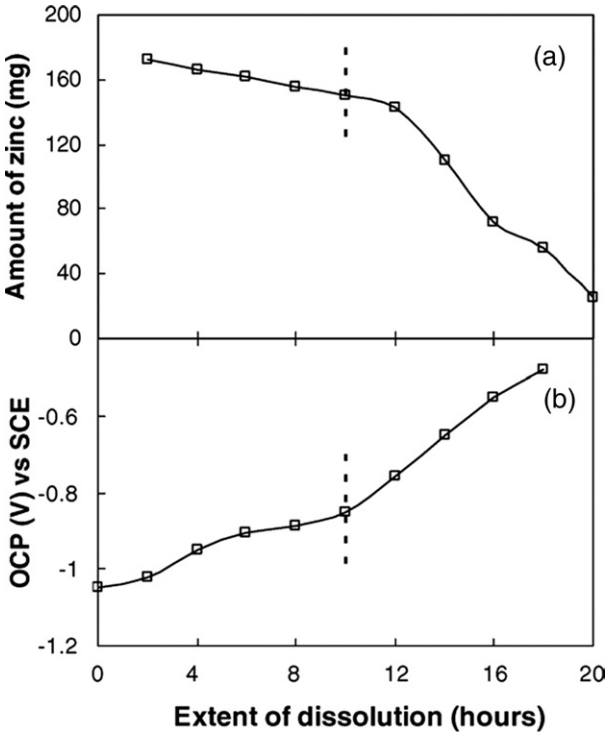


Figure 8 (a) The amount of zinc present in different layers of the galvanic coating formed on iron oxide layer. (b) The variation in open circuit potential (OCP) with respect to exposure of inner/deeper layers of galvanic coating formed on iron oxide layer.

In the case of galvanized coupons containing the highest concentration of nickel, nickel promotes a high rate of diffusion of zinc into the base metal. Nickel concentration increases in the inner layers of the nickel-containing hot-dip zinc coating, as also reported for similar coatings. Hence, any freshly

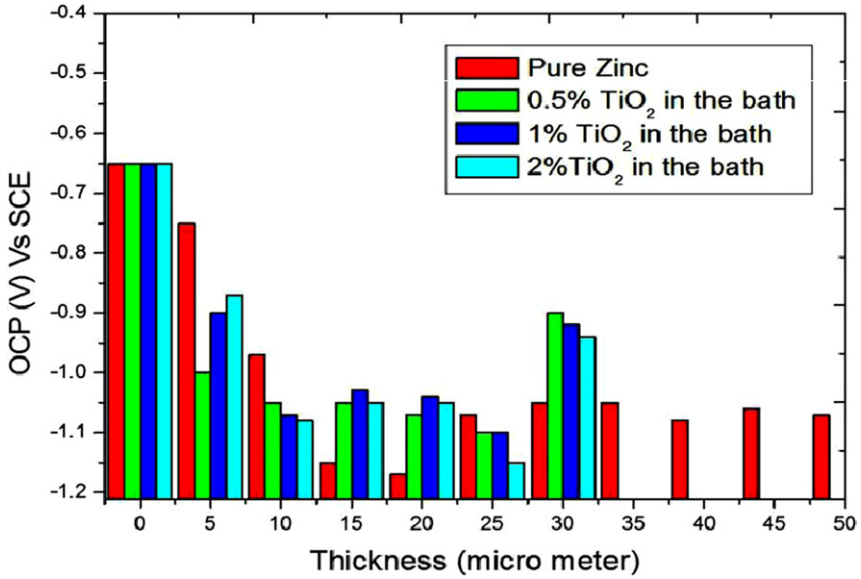


Figure 9 Comparison of layer-wise surface open circuit potential of different galvanic coatings with different concentrations of TiO_2.

opened under-layer should have more influence due to the increase in the concentration of nickel.

In some cases, the presence of oxides within the Fe–Zn alloy layer leads to a decrease in the potential decay of the zinc coating. Thus, it is clear that the zinc coating formed on the iron oxide layer exhibits high corrosion resistance due to the existence of the mixed potential and low dissolution rate of zinc with the optimum pH. The merit of the oxide-containing coating observed during OCP measurements is also notable even though the OCP parameters are not absolute to determine the corrosion rate of the coating. The oxide-containing coating also exhibits very low self-corrosion values among the two types of coatings during prolonged immersion tests. **Figure 8** compares the variation in OCP with the zinc dissolution rate under exposure of 3% NaCl solution.

It has been proven that TiO_2-incorporated hot-dip galvanic coatings can yield high corrosion resistance and less biogrowth on the surface. At the onset of corrosion, the TiO_2-incorporated coupons exhibit lower cathodic potential values do coupons coated with pure zinc. The presence of TiO_2 on the coating surface reduces the active corrosion sites and makes the coating more corrosion-resistant.[113,114] Because TiO_2 and ZnO have comparable band gaps, a synergistic effect of TiO_2 and ZnO could be predicted during the study of biogrowth on the surface of the coupons. Such synergistic action resulting in shift of electronic absorption to high wavelength regions has also been reported in the case of Zn plating with TiO_2.[115] Thus, by identifying suitable metal oxides, we can develop specific coatings to be used in many exposure conditions. **Figure 9** shows the variation in OCP with thickness of the hot-dip zinc coating with various concentrations of TiO_2.

Based on other research, it can be well explained and proven that the incorporation of nano TiO_2 in the phosphating bath can result in coatings with better electrochemical

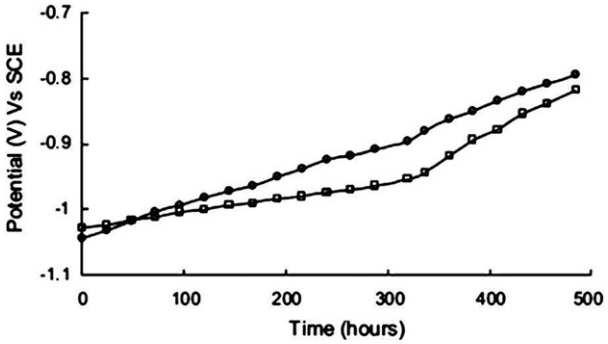


Figure 10 The variation in open circuit potential decay curves of the phosphated zinc coatings immersed in stagnant 0.5 M NaCl solution at 30 ± 2 °C (○, normal phosphate coating; □, TiO_2-incorporated phosphate coating).

stability and enhanced barrier protection characteristics. TiO_2 incorporation effectively reduces the extent of zinc dissolution. The incorporation of TiO_2 reduces the rate of active dissolution of zinc and thereby activates the process of phosphate crystallization, which ultimately yields greater thickness of the phosphate coating. **Figure 10** shows the comparison of the OCP decay curves of the phosphated zinc coating and the TiO_2-incorporated phosphated zinc coating under exposure to 0.5 M NaCl solution. The topography of the nano TiO_2-incorporated Zn coating is shown in **Figure 11**. The incorporation of nano TiO_2 into the phosphating bath can also cause structural refinement of the crystal, leading to the highest surface coverage and resulting in very high surface roughness of the coating. The roles of the nano TiO_2 composites have different mechanisms of action during the process. Their effective distribution depends on which layer is exposed or the composition of the bath (whether molten zinc or phosphating bath). In the phosphating bath, the presence of the oxide acts

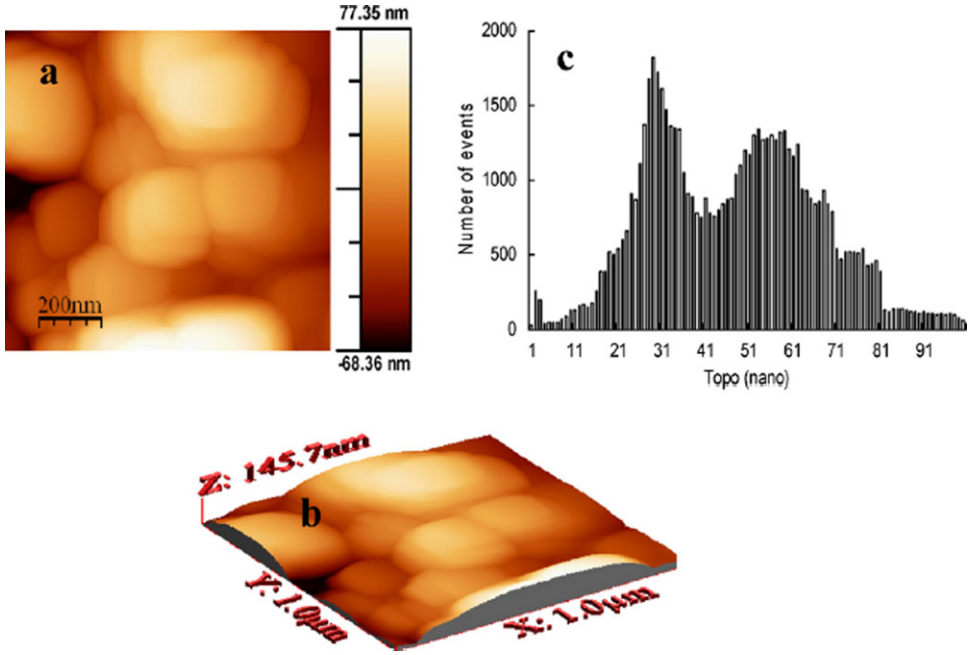


Figure 11 Atomic force micrographs of the TiO_2 coating: (a) two-dimentional image; (b) three-dimentional image; and (c) roughness distribution.

as a regulator and stabilizer to a certain extent and normally leads to a coating with a very high finish.

3.2.5 Summary

In the quest for fabrication of hybrid metal coatings, the co-influence of metal oxides and metal alloys are important for developing new coatings with superior performance for different applications. In the case of hot-dip zinc coating, which is a method that is centuries old, there are plenty of techniques, such as bath modification, pretreatment, and post-treatment, that are able to accommodate the conventional galvanization process. The present chapter highlights the recently developed coating techniques and how they can be concomitantly suited for application in the conventional hot-dip zinc coating process. In the present discussion, we briefly discussed the impact of various metal alloys, metal oxides, and mixed metal oxides on the galvanization process and the performance of the resultant galvanized product. The roles of intermetallic crystals and their *in situ* formation during the course of the galvanizing process are also highlighted.

See also: 3.12 Hot-Dip Galvanizing Process

References

1. Amadeh, A.; Pahlevani, B.; Heshmati-Manesh, S. Effects of Rare Earth Metal Addition on Surface Morphology and Corrosion Resistance of Hot-Dipped Zinc Coatings. *Corros. Sci.* **2002**, *44*, 2321–2331.
2. Reumont, G.; Vogt, J. B.; Iost, A.; Foct, J. The Effects of an Fe–Zn Intermetallic Containing Coating on the Stress Corrosion Cracking Behavior of a Hot-Dip Galvanized Steel. *Surf. Coat. Technol.* **2001**, *139*, 265–271.
3. Dutta, M.; Halder, A. K.; Singh, S. B. Morphology and Properties of Hot Dip Zn–Mg and Zn–Mg–Al Alloy Coatings on Steel Sheet. *Surf. Coat. Technol.* **2010**, *205*, 2578–2584.
4. Marder, A. R. The Metallurgy of Zinc-Coated Steel. *Prog. Mater. Sci.* **2000**, *45* (3), 191–271.
5. Tzimas, E.; Papadimitrou, G. Cracking Mechanisms in High Temperature Hot-Dip Galvanized Coatings. *Surf. Coat. Technol.* **2001**, *145*, 176–185.
6. Sere, P. R.; Culcai, J. D.; Elsner, C. I.; Sarli, A. R. D. Factors Affecting the Hot-Dip Zinc Coatings Structure. *Rev. Metal. Madrid* **1997**, *33*, 376–381.
7. Lin, C. S.; Meshi, M. The Effect of Steel Chemistry on the Formation of Fe–Zn Intermetallic Compounds of Galvanneal-Coated Steel Sheets. *Metall. Mater. Trans. B* **1994**, *25B*, 721–730.
8. Felin, S., Jr.; Barranco, V. XPS Study of the Surface Chemistry of Conventional Hot-Dip Galvanised Pure Zn, Galvanneal and Zn–Al Alloy Coatings on Steel. *Acta Mater.* **2003**, *51*, 5413–5424.
9. Hosny, A. Y.; El-Rafei, M. E.; Ramadan, T. A.; El-Gafari, B. A.; Morsy, S. M. Corrosion Resistance of Zinc Coatings Produced from a Sulfate Bath. *Met. Finish.* **1995**, *93*, 55–59.
10. Allegra, L.; Zoccola, J. C. Aluminum–Zinc-Coated Sheet Steel for Automotive Exhaust, Applications. *Mater. Perform.* **1979**, *18*, 18–21.
11. Fratesi, R.; Roventi, G.; Branca, C.; Simoncini, S. Corrosion Resistance of Zn–Co Alloy Coatings. *Surf. Coat. Technol.* **1994**, *63*, 97–103.
12. Ho-Jong Lee; Jong-Sang Kim. Effect of Ni Addition in Zinc Bath on Formation of Inhibition Layer During Galvannealing of Hot-Dip Galvanized Sheet Steels. *J. Mater. Sci. Lett.* **2001**, *20*, 955–957.
13. Notowidjojo, B.; Wingrove, A. L.; Kennon, N. F. Zinc–0.1% Nickel Coating Silicon Steels. *Mater. Forum* **1989**, *13*, 153–157.
14. Shibli, S. M. A.; Manu, R. Process and Performance Improvement of Hot Dip Zinc Coating by Dispersed Nickel in the Under Layer. *Surf. Coat. Technol.* **2005**, *197*, 103–108.
15. Diaz-Ballote, L.; Ramanauskas, R. Improving the Corrosion Resistance of Hot Dip Galvanized Zinc Coatings by Alloying. *Corro. Rev.* **1999**, *17*, 411–422.
16. Boshkov, N. Galvanic Zn–Mn Alloys – Electrodeposition, Phase Composition, Corrosion Behaviour and Protective Ability. *Surf. Coat. Technol.* **2003**, *172*, 217–226.
17. Munz, R.; Wolf, G. K.; Guzman, L.; Adami, M. Zinc/Manganese Multilayer Coatings for Corrosion Protection. *Thin Solid Films* **2004**, *459*, 297–302.

18. Diaz-Ballote, L.; Ramanauskas, R.; Bartolo-Perez, P. Mn Oxide Film as Corrosion Inhibitor of Zn–Mn Coatings. *Corro. Rev.* **2000**, *18*, 41–51.
19. Ho, M. S. *Atmospheric Corrosion Results of ZM-113 Galvanized Samples After Fifteen Years of Exposure*, Cominco PTC Project No. 84-5-511; 1985.
20. Radeker, W.; Friehe, W. *Proceedings of 7th International Conference on Hot Dip Galvanizing*; Pergamon Press: Paris, 1964; pp. 167–178.
21. Hanna, F.; Nassif, N. Factors Affecting the Quality of Hot-Dip-Galvanized Steel Sheets. *Surf. Technol.* **1984**, *21*, 27–37.
22. Jordan, C. E.; Marder, A. R. Fe–Zn Phase Formation in Interstitial-Free Steels Hot-Dip Galvanized at 450 °C Part II 0.20 wt % Al–Zn Baths. *J. Mater. Sci.* **1997**, *32*, 5603–5610.
23. Price, G. D. S.; Charles, J. A. Effects of Microstructure and of Protective Coatings on the Attack on Steel by Molten Zinc. *J. Iron Steel Inst.* **1973**, 871–874.
24. Jun, F.; Xinzhen, B.; Dejunsi, S.; Zhiquan, J.; Weixin, H. Spectroscopic Studies of Interfacial Structures of CeO_2–TiO_2 Mixed Oxides. *Appl. Surf. Sci.* **2007**, *253*, 8952–8961.
25. Ashraf, P. M.; Shibli, S. M. A. Reinforcing Aluminium with Cerium Oxide: A New and Effective Technique to Prevent Corrosion in Marine Environments. *Electrochem. Commun.* **2007**, *9*, 443–448.
26. Shibli, S. M. A.; Saji, V. S. Co-inhibition Characteristics of Sodium Tungstate with Potassium Iodate on Mild Steel Corrosion. *Corros. Sci.* **2005**, *47*, 2213–2224.
27. Nazeri, A.; Trzaskoma-Paulette, P. P.; Bauer, D. Synthesis and Properties of Cerium and Titanium Oxide Thin Coatings for Corrosion Protection of 304 Stainless Steel. *J. Sol-Gel Sci. Technol.* **1997**, *10*, 317–331.
28. Czerwinski, F.; Smeltzer, W. W. The Early-Stage Oxidation Kinetics of CeO_2 Sol-Coated Nickel. *J. Electrochem. Soc.* **1993**, *140*, 2606–2615.
29. Luo, X. Y.; Zuo, D. W.; Wang, M.; Li, S. L.; Chang, H. Preparation and Hot-Dip Galvanizing Application of CeO_2/Zn Nanocomposite. *Trans. Nonferr. Metal. Soc. China* **2005**, *15*, 203–207.
30. Shibli, S. M. A.; Chacko, F.; Divya, C. Al_2O_3–ZrO_2 Mixed Oxide Composite Incorporated Aluminium Rich Zinc Coatings for High Wear Resistance. *Corros. Sci.* **2010**, *52*, 518–525.
31. Shibli, S. M. A.; Dilimon, V. S.; Antony, S. P.; Manu, R. Incorporation of TiO_2 in Hot Dip Zinc Coating for Efficient Resistance to Biogrowth. *Surf. Coat. Technol.* **2006**, *200*, 4791–4796.
32. Ibanez, R. L.; Barrado, J. R. R.; Martin, F.; Brucker, F.; Leinen, D. Oxide Barrier Coatings on Steel Strip by Spray Pyrolysis. *Surf. Coat.Technol.* **2004**, *188–189*, 675–683.
33. Martin, F.; Lopez, M. C.; Carrera, P.; Barrado, J. R. R.; Leinen, D. XPS Depth Profile Study of Porous Zirconia Films Deposited on Stainless Steel By Spray Pyrolysis: The Problem of Substrate Corrosion. *Surf. Interface Anal.* **2004**, *36*, 8–16.
34. Ayouchi, R.; Martin, F.; Leinen, D.; Barrado, J. R. R. Growth of Pure ZnO Thin Films Prepared by Chemical Spray Pyrolysis on Silicon. *J. Cryst. Growth* **2003**, *247*, 497–504.
35. Shibli, S. M. A.; Chacko, F. Development of Nano TiO_2-Incorporated Phosphate Coatings on Hot Dip Zinc Surface for Good Paintability and Corrosion Resistance. *Appl. Surf. Sci.* **2011**, *257*, 3111–3117.
36. Shibli, S. M. A.; Chacko, F. CeO_2–TiO_2 Mixed Oxide Incorporated High Performance Hot Dip Zinc Coating. *Surf. Coat. Technol.* **2011**, *205*, 2931–2937.
37. Shibli, S. M. A.; Francis, C. Development of Nano CeO_2-Incorporated High Performance Hot-Dip Zinc Coating. *Surf. Coat. Technol.* **2008**, *202*, 4971–4975.
38. Yang, H. L.; Lin, F. C.; Han, E. H. Effects of P/B on the Properties of Anticorrosive Coatings with Different Particle Size. *Prog. Org. Coat.* **2005**, *53*, 91–98.
39. Dhoke, S. K.; Khanna, A. S. Electrochemical Behavior of Nano-Iron Oxide Modified Alkyd Based Waterborne Coatings. *Mater. Chem. Phys.* **2009**, *117*, 550–556.
40. Naderi, R.; Attar, M. M. Electrochemical Study of Protective Behavior of Organic Coating Pigmented with Zinc Aluminum Polyphosphate as a Modified Zinc Phosphate at Different Pigment Volume Concentrations. *Prog. Org. Coat.* **2009**, *66* (3), 314–320.
41. Naderi, R.; Attar, M. M. The Role of Zinc Aluminum Phosphate Anticorrosive Pigment in Protective Performance and Cathodic Disbondment of Epoxy Coating. *Corros. Sci.* **2010**, *52*, 1291–1296.
42. Zhang, X.; Wang, F.; Du, Y. Effect of Nano-Sized Titanium Powder Addition on Corrosion Performance of Epoxy Coatings. *Surf. Coat. Technol.* **2007**, *201*, 7241–7245.
43. Ferkel, H.; Müller, B.; Reihemann, W. Electrodeposition of Particle-Strengthened Nickel Films. *Mater. Sci. Eng. A Struct. Mater.: Prop. Microstruct. Process.* **1997**, *234–236*, 474–476.
44. Narayanan, J.; Wang, H.; Kvit, M. D. *Am. Soc. Mech. Eng. Counc. Rep. Member* **2001**, *95*, 55.
45. Shibli, S. M. A.; Jabeera, B.; Anupama, R. I. Development of ZnO Incorporated Composite Ni–ZnO–P Alloy Coating. *Surf. Coat. Technol.* **2006**, *200*, 3903–3906.
46. Abdel Hamid, Z.; Abdel Aal, A.; Hassan, H. B.; Shaaban, A. Process and Performance of Hot Dip Zinc Coatings Containing ZnO and Ni–P Under Layers as Barrier Protection. *Appl. Surf. Sci.* **2010**, *256*, 4166–4170.
47. Mita, K.; Ikeda, T.; Meada, M. Phase Diagram Study of Fe–Zn Intermetallics. *J. Phase Equilib.* **2001**, *22* (2), 122–125.
48. Pistofidis, N.; Yourlias, G.; Konidaris, S.; Pavilidou, E. I.; Stergiou, A.; Stergioudis, G. The Effect of Bismuth on the Structure of Zinc Hot-Dip Galvanized Coatings. *Mater. Lett.* **2007**, *61*, 994–997.
49. Lee, H. T.; Kim, J. S.; Chang, J. H. *Hangu'k Pyomyon Konghak Hoechi* **1999**, *32*, 157.
50. Lin, C. S.; Lee, H. B.; Hsieh, S. H. Microcracking of Flash Coatings and its Effect on the Zn–Ni Coating Adhesion of Electrodeposited Sheet Steel. *Metall. Met. Trans. A* **1999**, *30*, 437–448.
51. Hall, D. E. Electrodeposited Zinc–Nickel Alloys Coatings – A Review. *Plat. Surf. Finish* **1983**, *70*, 59–65.
52. Sankarapapavinasam, S.; Pushpanaden, F.; Ahmed, M. F. Brighteners for Zinc Nickel Plating. *Met. Fin.* **1989**, *87*, 9–11.
53. Fratesi, R.; Roventi, G. Corrosion Resistance of Zn–Ni Alloy Coatings in Industrial Production. *Surf. Coat. Technol.* **1996**, *82*, 158–164.
54. Shibli, S. M. A.; Manu, R.; Dilimon, V. S. Effect of Nickel-Rich Barrier Layer on Improvement of Hot-Dip Zinc Coating. *Appl. Surf. Sci.* **2005**, *245*, 179–185.
55. Ramezanzadeh, B.; Attar, M. M. Studying the Effects of Micro and Nano Sized ZnO Particles on the Corrosion Resistance and Deterioration Behavior of an Epoxy-Polyamide Coating on Hot-Dip Galvanized Steel. *Prog. Inorg. Coat.* **2011**, *71* (3), 314–328.
56. Lokhande, C. D.; Min, S. K.; Jung, K. W. D.; Joo, O. S. Cathodic Electrodeposition of Amorphous Titanium Oxide Films from an Alkaline Solution Bath. *J. Mater. Sci.* **2004**, *39*, 6607–6610.
57. Shibli, S. M. A.; Manu, R. Improvement of Hot-Dip Zinc Coating by Enriching the Inner Layers with Iron Oxide. *Appl. Surf. Sci.* **2006**, *252*, 3058–3064.
58. Dhoke, S. K.; Khanna, A. S.; Jai Mangal, T. Sinha, Effect of Nano-ZnO Particles on the Corrosion Behavior of Alkyd-Based Waterborne Coatings. *Prog. Org. Coat.* **2009**, *64*, 371–382.
59. Dhoke, S. K.; Khanna, A. S. Effect of Nano-Fe_2O_3 Particles on the Corrosion Behavior of Alkyd Based Waterborne Coating. *Corros. Sci.* **2009**, *51*, 6–20.
60. Shi, H.; Liu, F.; Han, E.; Wei, Y. Effects of Nano Pigments on the Corrosion Resistance of Alkyd Coating. *J. Mater. Sci. Technol.* **2007**, *23* (4), 551–558.
61. Dhoke, S. K.; Khanna, A. S. Study on Electrochemical Behavior of Nano-ZnO Modified Alkyd-Based Waterborne Coatings. *J. Appl. Polym. Sci.* **2009**, *113*, 2232–2237.
62. Fujishima, A.; Rao, T. N.; Tryk, D. A. Titanium Dioxide Photocatalysis. *J. Photochem. Photobiol. C: Photochem. Rev.* **2000**, *1*, 1–21.
63. Chi-Jen Chung; Hsin-I Lin; Hsi-Kai Tsou; Zhi-Yuan Shi; Ju-Liang He. An Antimicrobial TiO_2 Coating for Reducing Hospital-Acquired Infection. *J. Biomed. Mater. Res. Part B: Appl. Biomater.* **2007**, *85B*, 220–224.
64. Fahlteich, J.; Fahland, M.; Schönberger, W.; Schiller, N. Permeation Barrier Properties of Thin Oxide Films on Flexible Polymer Substrates. *Thin Solid Films* **2009**, *517*, 3075–3080.
65. Jones, N.; Ra, B.; Ranjit, K. T.; Manna, A. C. Antibacterial Activity of ZnO Nanoparticle Suspensions on a Broad Spectrum of Microorganisms. *FEMS Microbiol. Lett.* **2008**, *279*, 71–76.
66. Zhang, L.; Jiang, Y.; Ding, Y.; *et al.* Mechanistic Investigation into Antibacterial Behaviour of Suspensions of ZnO Nanoparticles Against *E. Coli. J Nanopart. Res.* **2010**, *12*, 1625–1636.
67. Yamamoto, O. Influence of Particle Size on the Antibacterial Activity of Zinc Oxide. *Int. J. Inorg. Mater.* **2001**, *3*, 643–646.
68. Nair, S.; Sasidharan, A.; Divya Rani, V. V.; *et al.* Role of Size Scale of ZnO Nanoparticles and Microparticles on Toxicity Toward Bacteria and Osteoblast Cancer Cells. *J. Mater. Sci.: Mater. Med.* **2009**, *20*, 235–241.
69. Jin, T.; Sun, D.; Su, J. Y.; Zhang, H.; Sue, H.-J. *J. Food Sci.* **2009**, *74* (1), 47–52.
70. Zhang, L.; Jiang, Y.; Ding, Y.; Povey, M.; York, D. Investigation into the Antibacterial Behaviour of Suspensions of ZnO Nanoparticles (ZnO Nanofluids). *J. Nanopart. Res.* **2007**, *9* (3), 479–489.

71. Sirelkhatim, A.; Mahmud, S.; Seeni, A.; *et al.* Review on Zinc Oxide Nanoparticles: Antibacterial Activity and Toxicity Mechanism. *Nano-Micro Lett.* **2015**, *7* (3), 219–242.
72. Li, J. H.; Honga, R. Y.; Li, M. Y.; Li, H. Z.; Zheng, Y.; Ding, J. Effects of ZnO Nanoparticles on the Mechanical and Antibacterial Properties of Polyurethane Coatings. *Prog. Inorg. Coat.* **2009**, *64*, 504–509.
73. Bennasr, J.; Snoussi, A.; Bradai, C.; Halouani, F. Effect of the Withdrawal Speed on the Thickness of the Zinc Layer in Hot Dip Pure Zinc Coatings. *Mater. Lett.* **2008**, *62*, 2150–2152.
74. Su, X. P.; Wu, C. J.; Liu, D.; Yin, F. C.; Zhu, Z. X.; Yang, S. Effect of Vanadium on Galvanizing Si-Containing Steels. *Surf. Coat. Technol.* **2010**, *205*, 213–218.
75. Vazquez, A. J.; De damborenea, J. J. Corrosion Resistance of Galvanised Coatings in Rural Environments: Retrospective Evaluation. *Br. Corros. J.* **1992**, *27*, 310–314.
76. Frappe, A. L.; Linare, A.; Piessen, P.; Vacher, J. C. *Proceedings of the 14th International Conference on Hot-dip Galvanizing Intergalva '85*, London, EGGA, 1985; pp. 8.1–8.18.
77. Johnsson, T.; Kucera, V. *Proceedings of the 13th International Conference on Hot-dip Galvanizing Intergalva '82*, London, EGGA, 1982; pp. 47.1–47.6.
78. Westerlund, R. *Proceedings of the 12th International Conference on Hot-dip Galvanizing Intergalva '79*, London, EGGA, 1979; pp. 320–327.
79. Jordan, C. E.; Marder, A. R. The Effect of Iron Oxide as an Inhibition Layer on Iron–Zinc Reactions During Hot-Dip Galvanizing. *Metall. Mater. Trans. A* **1998**, *29B*, 479–484.
80. Kathalingam, A.; Kim, M. R.; Chae, Y. S.; Rhee, J. K.; Mahalingam, T. Studies on Electrochemically Deposited ZnO Thin Films. *J. Korean Phys. Soc.* **2009**, *55* (6), 2476–2481.
81. Izaki, M.; Omi, T. Transparent Zinc Oxide Films Prepared by Electrochemical Reaction. *Appl. Phys. Lett.* **1996**, *68*, 2439.
82. Izaki, M.; Omi, T. Electrolyte Optimization for Cathodic Growth of Zinc Oxide Films. *J. Electrochem. Soc.* **1996**, *143*, L53–L55.
83. Peulon, S.; Lincot, D. Cathodic Electrodeposition from Aqueous Solution of Dense or Open-Structured Zinc Oxide Films. *Adv. Mater.* **1996**, *8*, 166–170.
84. Pauporté, Th.; Lincot, D. Heteroepitaxial Electrodeposition of Zinc Oxide Films on Gallium Nitride. *Appl. Phys. Lett.* **1999**, *75*, 3817–3819.
85. Yoshida, T.; Tochimoto, M.; Schlettwein, D.; Wöhrle, D.; Sugiura, T.; Minoura, H. Self-Assembly of Zinc Oxide Thin Films Modified with Tetrasulfonated Metallophthalocyanines by One-Step Electrodeposition. *Chem. Mater.* **1999**, *11*, 2657–2667.
86. Yoshida, T.; Terada, K.; Schlettwein, D.; Oekermann, T.; Sugiura, T.; Minoura, H. Electrochemical Self-Assembly of Nanoporous ZnO/Eosin Y Thin Films and Their Sensitized Photoelectrochemical Performance. *Adv. Mater.* **2000**, *12*, 1214–1217.
87. Yoshida, T.; Oekermann, T.; Okabe, K.; Schlettwein, D.; Funabiki, K.; Minoura, H. Cathodic Electrodeposition of ZnO/Eosin Y Hybrid Thin Films from Dye Added Zinc Nitrate Bath and Their Photoelectrochemical Characterizations. *Electrochemistry* **2002**, *70*, 470.
88. Sa-nguanmoo, R.; Nisaratanaporn, E.; Boonyongmaneerat, Y. Hot-Dip Galvanization with Pulse-Electrodeposited Nickel Pre-Coatings. *Corr. Sci.* **2011**, *53*, 122–126.
89. Blumenau, M.; Barnoush, A.; Thomas, I.; Hofmann, H.; Vehoff, H. Impact of Selective Oxidation During Inline Annealing Prior to Hot-Dip Galvanizing on Zn Wetting and Hydrogen-Induced Delayed Cracking of Austenitic FeMnC steel. *Surf. Coat. Technol.* **2011**, *206*, 542–552.
90. Wang, Y.; Zeng, J. Effects of Mn Addition on the Microstructure and Indentation Creep Behavior of the Hot Dip Zn Coating. *Mat. Des.* **2015**, *69*, 64–69.
91. Arndt, M.; Duchoslav, J.; Steinberger, R.; *et al.* Nanoscale Analysis of the Influence of Pre-Oxidation on Oxide Formation and Wetting Behavior of Hot-Dip Galvanized High Strength Steel. *Corr. Sci.* **2015**, *93*, 148–158.
92. Blumenau, M.; Norden, M.; Friedel, F.; Peters, K. Use of Pre-Oxidation to Improve Reactive Wetting of High Manganese Alloyed Steel During Hot-Dip Galvanizing. *Surf. Coat. Technol.* **2011**, *206*, 559–567.
93. Liu, H.; He, Y.; Li, L. Application of Thermodynamics and Wagner Model on Two Problems in Continuous Hot-Dip Galvanizing. *Appl. Surf. Sci.* **2009**, *256*, 1399–1403.
94. Huin, D.; Flauder, P.; Leblond, J. B. Numerical Simulation of Internal Oxidation of Steels During Annealing Treatments. *Oxid. Met.* **2005**, *64* (1/2), 131–167.
95. Swaminathan, S.; Spiegel, M. Thermodynamic and Kinetic Aspects on the Selective Surface Oxidation of Binary, Ternary and Quarternary Model Alloys. *Appl. Surf. Sci.* **2007**, *253*, 4607–4619.
96. Swaminathan, S.; Rohwerder, M.; Spiegel, M. Temperature and Dew Point Dependent Segregation of Phosphorus And Sulfur in Fe–Mn–P–S Model Alloy. *Surf. Coat. Technol.* **2011**, *205* (16), 4089–4093.
97. He, Y.; Jia, T.; Liu, X.; Cao, G.; Liu, Z.; Li, J. Hot-Dip Galvanizing of Carbon Steel After Cold Rolling with Oxide Scale and Hydrogen Descaling. *J. Iron Steel Res. Intl.* **2014**, *21*, 222–226.
98. Blumenau, M.; Norden, M.; Friedel, F.; Peters, K. Reactive Wetting During Hot-Dip Galvanizing of High Manganese Alloyed Steel. *Surf. Coat. Technol.* **2011**, *205*, 3319–3327.
99. Cho, L.; De Cooman, B. Selective Oxidation of TWIP Steel During Continuous Annealing. *Steel Res. Int.* **2012**, *83* (4), 391–397.
100. Kavitha, R.; McDermid, J. R. Reactive Wetting and In Situ Aluminothermic Reduction of Mn Oxides in Continuous Galvanizing Baths. In *MS&T'10 Conference Proceedings: Advancements in Processing and Properties of Zinc-Coated Advanced High Strength Steels*, Houston, TX, 2010; pp. 1279–1290.
101. Shibli, S. M. A.; Manu, R. Development of Zinc Oxide-Rich Inner Layers in Hot-dip Zinc Coating for Barrier Protection. *Surf. Coat. Technol.* **2006**, *201*, 2358–2363.
102. Nematollahi, M.; Heidarian, M.; Peikari, M.; Kassiriha, S. M.; Arianpouya, N.; Esmaeilpour, M. Comparison Between the Effect of Nanoglass Flake a Montmorillonite Organoclay on Corrosion Performance of Epoxy Coating. *Corros. Sci.* **2010**, *52*, 1809–1817.
103. Behzadnasab, M.; Mirabedini, S. M.; Kabiri, K.; Jamali, S. Corrosion Performance of Epoxy Coatings Containing Silane Treated ZrO_2 Nanoparticles on Mild Steel in 3.5% NaCl Solution. *Corros. Sci.* **2011**, *53*, 89–98.
104. Shibli, S. M. A.; Manu, R.; Beegum, S. Studies on the Influence of Metal Oxides on the Galvanic Characteristics of Hot-Dip Zinc Coating. *Surf. Coat. Technol.* **2008**, *202*, 1733–1737.
105. Bamoulid, L.; Benoit-Marquie, F.; Aries, L.; *et al.* Investigations on Composition and Morphology of Electrochemical Conversion Layer/Titanium Dioxide Deposit On Stainless Steel. *Surf. Coat. Technol.* **2006**, *201*, 2791–2795.
106. El Hajjaji, S.; Maurette, M. T.; Puech-costes, E.; Guenbour, A.; Ben Bachir, A.; Aries, L. Optimisation of Conversion Coatings in Phosphoric Acid Media Using Statistical Experimental Designs. *Br. Corros. J* **1999**, *34*, 273–279.
107. Aries, L.; Roy, J. Secondary Ion Mass Spectrometry and Multireflection Infrared Analyses of Conversion Coatings on Fe–Cr–Al Stainless Steels for Catalysis: Study of Thermal Stability. *Mater. Sci. Technol.* **1994**, *10*, 359–363.
108. Biber, H. E. Scanning Auger Microprobe Study of Hot-Dipped Regular-Spangle Galvanized Steel: Part II. Surface Composition of Chromated Sheet. *Metall. Trans. A, Phys. Metall. Mater. Sci.* **1988**, *19*, 1603–1616.
109. Strutzenberger, J.; Faderl, J. Solidification and Spangle Formation of Hot-Dip-Galvanized Zinc Coatings. *Metall. Mater. Trans. A* **1998**, *29A*, 631–646.
110. Tomita, M.; Yamamoto, S.; Tominaga, C.; Nakayama, K., Colored Zinc Coating. US Patent 5141782A, 1992.
111. Gao, N.; Liu, Y. H.; Tang, N. Y. An Experimental Study of the Liquid Domain of the Zn–Fe–Al–Mn Quaternary System at 460 °C. *J. Phase Equilib. Diffus.* **2010**, *31*, 523–531.
112. Wagner, C. Theoretical Analysis of the Diffusion Processes Determining the Oxidation Rate of Alloys. *J. Electrochem. Soc.* **1952**, *99*, 369–380.
113. Deguchi, T.; Imai, K.; Matsui, H.; Iwasaki, M.; Tada, H.; Ito, S. Rapid Electroplating of Photocatalytically Highly Active TiO_2–Zn Nanocomposite Films on Steel. *J. Mater.Sci.* **2001**, *36*, 4723–4729.
114. Ito, S.; Deguchi, T.; Imai, K.; Iwasaki, M.; Tada, H. Preparation of Highly Photocatalytic Nanocomposite Films Consisting of TiO_2Particles and Zn Electrodeposited on Steel. *Electrochem. Solid-State Lett.* **1999**, *2*, 440–444.
115. Culcasi, J. D.; Sere, P. R.; Elsner, C. I.; Di Sarili, A. R. Control of the Growth of Zinc–Iron Phases in the Hot-Dip Galvanizing Process. *Surf. Coat. Technol.* **1999**, *122*, 21–23.

Relevant Websites

http://www.galvanizeit.org
American Galvanizers Association.
http://www.galvanizingasia.com
Galvanizing Asia.
http://www.hotdipgalvanizing.com
Hot Dip Galvanizing.
http://www.intergalva.com
Intergalva.
http://www.lagalvanizing.com
LA Galvanizing.
http://www.sabregalvanizing.com
Sabre Industries.
http://www.valmont.com
Valmont.

3.3 Surface Finish Coatings

P Sahoo and SK Das, Jadavpur University, Kolkata, India
J Paulo Davim, University of Aveiro, Aveiro, Portugal

© 2017 Elsevier Inc. All rights reserved.

3.3.1	**Introduction**	39
3.3.2	**Classification of Surface Finishing Operations**	39
3.3.3	**Types of Coating Processes**	39
3.3.3.1	Electrochemical Techniques	40
3.3.3.1.1	Electrodeposition	40
3.3.3.1.2	Electroless coatings	40
3.3.3.2	Vapor Depositions	41
3.3.3.2.1	PVD	41
3.3.3.2.2	CVD	41
3.3.3.2.3	Plasma enhanced CVD technique	41
3.3.3.3	Galvanizing	41
3.3.3.4	Powder Coatings	41
3.3.3.5	Diffusion Coatings	42
3.3.3.6	Conversion Coatings	42
3.3.3.6.1	Anodizing	42
3.3.3.6.2	Phosphate coatings	42
3.3.3.6.3	Chromate coatings	42
3.3.3.7	Thermal Spraying	43
3.3.3.7.1	Electric arc spray	43
3.3.3.7.2	Flame spray	43
3.3.3.7.3	Plasma spray	43
3.3.3.7.4	High velocity oxy-fuel	43
3.3.4	**Existing Design of Coating Structures**	43
3.3.4.1	Single-Layer Coatings	45
3.3.4.2	Sandwich Coatings	45
3.3.4.3	Graded Coatings	45
3.3.4.4	Duplex Coatings	45
3.3.4.5	Multilayered Coatings	45
3.3.4.6	Superlattice Coatings	45
3.3.4.7	Multicomponent Coatings	45
3.3.5	**Coating As a Method of Surface Finishing**	45
3.3.5.1	Surface Finishing Facets of Coating	46
3.3.5.1.1	Improving esthetic appeal	46
3.3.5.1.2	Protection against corrosion	46
3.3.5.1.2.1	Barrier protection	47
3.3.5.1.2.2	Cathodic protection	47
3.3.5.1.3	Resistance to wear	48
3.3.5.1.4	Generating smooth and lubricious surface	49
3.3.5.2	Miscellaneous Surface Finish Applications	49
3.3.5.2.1	Hydrophobic coatings	49
3.3.5.2.2	Conformal coatings	49
3.3.5.2.3	Electrical and magnetic properties	50
3.3.5.2.4	Thermal coatings	50
3.3.5.2.5	Rough coatings	50
3.3.5.2.6	Biomedical applications	50
3.3.5.2.7	Optical coatings	50
3.3.6	**Eco-Friendly Coatings (Green Coating)**	50
3.3.7	**Influence of Coating Parameters and Process Optimization**	50
3.3.8	**Surface Finish Measurements of Coatings**	51
3.3.8.1	Coating Thickness	51
3.3.8.2	Adhesion Testing	51
3.3.8.3	Indentation Testing	52
3.3.8.4	Surface Roughness	52

 doi:10.1016/B978-0-12-803581-8.09167-0

3.3.8.5 Measurement of Friction and Wear 52
3.3.8.6 Measurement of Corrosion 52
3.3.9 Effect of Pre-Treatment Processes 54
3.3.10 Selection of Coating for Surface Finish Applications 54
3.3.11 Closure 54
Acknowledgment 55
References 55
Relevant Websites 55

3.3.1 Introduction

Although a particular material can be used to give a physical reality to a design, the former however fails to address every aspects of a foolproof design. A softer material may require a harder surface for protection against wear. A coarser surface may require to be smoothened for lower frictional resistance. An unattractive material may require to be esthetically improved for decorative purposes. Besides, there may be special requirements based on the demand of specific applications. Moreover, corrosion protection is nowadays a universal requirement for maintaining the device service life. All these fall under the purview of surface finishing in which the main idea is to modify the surface of a material in order to impart certain desired characteristics to it. In the absence of surface engineering, finding a material with all-round performance will not only be difficult but also costly.

Around nineteenth century, surface finishing was mainly associated with decorative purposes. However, with the passage of time the focus has shifted toward the 'functional' aspect of the process. Surface finishing is very important today and has been well established through industrial applications, researches, and patents. Various forms of surface finishing exists today, viz., finishing and polishing, conversion coatings (oxidation, anodizing), thermal coatings (carburizing – flame spraying), metal coatings (electrochemical, electroless), physical vapor deposition (PVD), chemical vapor deposition (CVD), organic coatings, etc.

3.3.2 Classification of Surface Finishing Operations

Surface finishing processes are primarily based on the principles of either removal (or reshaping) of the surface of the workpiece or adding and altering the surface with the help of external agents. Machining falls under the purview of the first principle while surface treatment and coatings fall under the purview of the second. Machining, however, smoothens out the material surface only whereas surface coatings employ a second material to be deposited on the first material to endow the specimen with certain properties which the bulk material may not intrinsically possess. The classification of surface finishing operations are given in Figure 1.

3.3.3 Types of Coating Processes

Coatings are a very flexible method of surface finishing. They can be applied on any material irrespective of metal, plastic, ceramic, etc., and over a wide range of thickness varying from a few microns to few millimeters. Coatings can be hard or soft based on the requirements. Hard coatings are in general wear

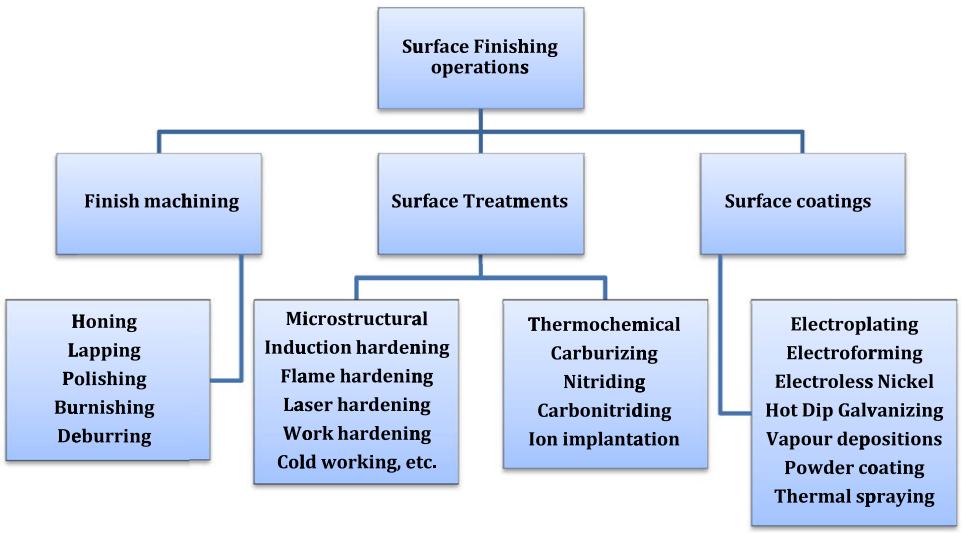


Figure 1 Classification of surface finishing techniques.

resistant while soft coatings exhibit lower friction. Besides, coatings can be deposited with appropriate combination of material to obtain desired properties. For example, certain soft materials can be embedded in the coating to bestow it with self-lubricating property. Moreover, several techniques of coating exist each having its own set of advantages and limitations. Based on the demand of application, a suitable coating process can be chosen.

Surface coating techniques can be further categorized as follows:

- Chemical and electrochemical techniques: electrodeposition, electroless deposition.
- Vapor deposition techniques: PVD, CVD, etc.
- Spraying techniques: thermal spraying, etc.
- Powder coating.

The surface finish coating techniques popularly used nowadays are briefly described in the following sections.

3.3.3.1 Electrochemical Techniques

3.3.3.1.1 Electrodeposition

Electrodeposition employs electricity to reduce cations of a desired material from a solution and coat that material as a thin film onto a conductive substrate surface. The principle works on Faraday's laws of electrolysis. Both the metal to be deposited (anode) and the substrate (cathode) are immersed in an electrochemical bath and direct current (DC) is passed. Sometimes, the bath may contain the salt of the metal to be plated. In that case the anode merely serves the purpose of completing the circuit. The coating rate may depend on the material being coated. Higher thickness can however be achieved by increasing the duration of the coating process. An electroplated layer is usually composed of a single metallic element. Nickel/chromium composites (usually called 'chrome' plating), copper, brass (an alloy), bronze (an alloy), and zinc are used for decorative applications. For functional applications zinc, tin, heavy coatings of nickel, 'hard' chromium, silver, and gold are used. Co-deposition of two or more metals is possible under suitable conditions of potential and polarization (viz., Cu–Zn alloy and Au–Sn alloy).

Electrodeposition is a very popular technique due to its simplicity of operation and bath stability. The process is extensively used in industry in the following areas:

- Protection against corrosion and wear.
- Improving the appearance of a comparatively unattractive material by coating a more expensive material over it as in the case of jewelry.

Electrodeposition suffers from a drawback of non-uniform coating thickness, i.e., the part of the substrate in proximity to the anode (metal source) displays higher thickness compared to the part which is away from the anode. This limitation can be reduced to some extent by using baths where metal ions are in complex form.

Electroplating is used to coat fasteners, jewelry, engineering components, to build up worn components, and sometimes as an undercoat for powder coating and painting.

3.3.3.1.2 Electroless coatings

Electroless nickel coating is a relatively newer technique of coating deposition. Here, coating happens chemically without the use of any electric current. The substrate to be coated is immersed in an electroless bath which typically contains a salt of nickel, a suitable reducing agent, complexing agent, and stabilizer. Apart from these, the bath may also have some other constituents (**Table 1**) depending on the coating to be developed. The cleaned substrate is immersed in the bath and the same is heated. The substrate develops a potential when it is dipped in the bath due to which both positive and negative ions are attracted toward the substrate surface and release their energy through charge transfer process. The basic chemical reactions for electroless coating are given by the following expressions:

$$R^{n+} \rightarrow R^{(n+z)} + ze$$
$$Me^{+z} + ze \rightarrow Me$$

where 'R' indicates the reducing agent and 'Me' indicates the metal to be deposited on a substrate.

Electroless coatings are an ideal choice for surface finishing due to their distinctive advantages, which are as follows:

- Uniform coating occurs even on intricate geometries. This is possible as the constituent elements of the material to be deposited are present in the solution in the form of ions. Since the substrate is fully immersed in the bath and every part of it has equal probability of getting the ions, hence the coating develops uniformly.
- As the coating happens chemically, with suitable activation, coating is possible even on non-conductors, viz., plastics, glass, etc.
- The deposits are often less porous and hence offer barrier protection against corrosive environments. They are found to display superior corrosion resistant capabilities compared to electrodeposited coatings and even hard chrome coatings.
- Electroless nickel coatings exhibit fair hardness (400–600 Hv) in as-deposited conditions which can be further enhanced to more than 1000 Hv with the help of suitable heat treatment. Moreover, with the incorporation of harder particles, viz., SiC, B_4C, etc., the hardness of the coatings can be made comparable to hard chrome coatings.

Table 1 Electroless nickel bath composition and their functions

Component	*Function*
Nickel ion	Source of metal
Reducing agent	Source of electrons
Complexants	Stabilizes the solution by forming nickel complexes
Accelerators	Activates reducing agent and accelerates the deposition
Buffers	Controlling pH (long term)
pH regulators	Regulates pH of solution (short term)
Stabilizer	Prevents solution breakdown by shielding catalytically active nuclei
Wetting agents	Increases wettability of the surfaces to be coated

- Deposits are smooth and have inherent lubricity due to their cauliflower-like microstructure.
- Coatings are solderable and hence can be applied in electrical circuit boards.
- Several materials can be co-deposited with electroless nickel to have customized properties.

3.3.3.2 Vapor Depositions

3.3.3.2.1 PVD

PVD refers to a host of techniques where the material to be deposited is converted to vapor, which is then condensed on to the surface of the substrate in the form of thin coatings. The thickness lies in the range of 0–20 μm. The desired material is ionized and atomized in either of the following ways:

- Physical evaporation
- Plasma sputtering (collisions with other atoms).

In the first method, the material is heated to temperature range of 1000–2000 °C in high vacuum (10^{-8} to 10^{-1} Torr) so that a high vapor pressure is developed, which is sufficient for condensation on the substrate. Alloys and compounds can also be deposited by evaporating separately the constituent elements in proper stoichiometric ratio or by reaction with a gas present in the environment. In case of the latter, an activation of the gases by plasma is often employed to increase its reactivity with the substrate surface. This results in increased adhesion which is normally an issue for plain evaporation-based depositions. The adhesion is poor because of the low kinetic energy of the atoms to be deposited.

In the second method, the material to be coated is ejected from the material surface by bombardment with energetic particles. It is the most widely used vapor deposition technique. In this technique, the coating material is made cathode and an inert gas, mostly Argon is introduced as a medium in which the glow discharge (plasma) is initiated and maintained. The ionized argon atoms are accelerated toward the coating material, whereby they collide resulting in the ejection of coating atoms with high energy. Sputtering can also be combined with a reactive gas giving rise to compound coatings.

Sometimes instead of plasma, an external source of ionization is employed to ionize the coating material. Sputtering process in general results in very good adhesion between the coating and the substrate compared to evaporation technique. This is due to higher kinetic energy of the atoms to be coated. Moreover, in case of sputtering, deposition rates of up to 100 μm h^{-1} can be achieved by the use of magnetrons. Sputtered coatings are commonly used as wear-resistant coatings in applications such as cooking knives and metal-cutting tools.[1] Common coatings applied by PVD include titanium nitride, zirconium nitride, chromium nitride, titanium aluminum nitride, etc.

3.3.3.2.2 CVD

CVD is a coating process in which deposition occurs by the reaction between the hot substrate and its atmosphere containing vapor or gases of the constituents of the coating material. The substrate may be heated by laser or electrical heater to temperatures in excess of 850 °C, which restricts the application of CVD to high melting point substrates only. The pressure in the reaction chamber ranges from 0.5 to 760 Torr. Lower pressure helps in attaining good adhesion and excellent deposit quality. Deposition rate is normally high (upto 40 μmh^{-1}) and is dependent on temperature and pressure. Hard coatings are deposited by this method which include nitrides, carbides, borides, and oxides, as well as structures such as diamond and diamond-like carbon (DLC) which are commonly employed for wear resistance in a variety of industries.

3.3.3.2.3 Plasma enhanced CVD technique

This process employs CVD coupled with glow discharge plasma to deposit coatings. The plasma produces high energy ions which promote deposition and hence the process can be operated at comparatively lower temperatures (up to 600 °C). The plasma also helps in sputtering the workpiece clean before deposition which enhances adhesion between the coating and the substrate.

3.3.3.3 Galvanizing

Galvanizing is the process of applying zinc coating to a more noble metal (popularly steel or iron) to prevent corrosion (rusting). Hot-dip galvanization is the most well-known method in which the steel part is submerged in a bath of molten zinc. In the bath, the iron in the steel metallurgically reacts with the molten zinc to yield a tightly bonded uniform alloy coating, which provides superior corrosion protection to steel. The simplicity of the process provides it with a distinct advantage over other corrosion protection methods. Moreover, galvanizing produces higher thickness coating (about 80 μm) of zinc compared to electroplating (about 25 μm).

Galvanizing is widely used for its ability to resist corrosion. The nature of protection offered by zinc coatings is threefold. First as a barrier, the dense coating covers the total surface and prevents contact with any corrosive environment. Second, if the coating is damaged, due to zinc's sacrificial behavior, corrosion occurs only in zinc. Finally, the natural weathering process helps in developing a natural passive layer on the surface which can then resist corrosion.

Galvanizing is used to protect large steel structural members, roofing material, etc. Tin is also often deposited using the hot-dip technique.

3.3.3.4 Powder Coatings

Powder coating is similar to painting where the substrate to be coated is in the form of a powder. The substrate to be coated is at first made ground and the powder is electrostatically charged. Then the powder is sprayed evenly on the substrate and then baked in an oven so that the powder particles melt and coalesce to form a continuous film. There are two main types of powder available in the market: thermoplastic powders, which will remelt when heated and thermosetting powder, which will not. During the curing process (in the oven), a chemical cross-linking reaction is triggered at the curing

temperature and it is this chemical reaction which gives the powder coating many of its desirable properties.

Powder coating is the youngest of the surface finishing techniques. Its inception was in Australia in around 1965. Powder coating is normally used to produce hard, wear-resistant coatings that are mainly employed for coating of metals, viz., household appliances, aluminum extrusions, drum hardware, and automobile and bicycle parts.

3.3.3.5 Diffusion Coatings

Diffusion coating is a process in which the coating is done on metal components made of iron, nickel, and cobalt under severe operating condition (elevated temperatures and corrosive environment). It provides a dense chemically bonded coating which acts as a diffusion barrier against corrosive environments. Diffusion coating can be done using three processes, viz., solid-state diffusion, liquid-state diffusion, and chemical gas diffusion.

Solid-state diffusion is used with nickel, titanium and iron, among other metals, and the vapor pressure of the coating metal must be lower than the base metal. The coating is performed in a hermetically sealed container with the base metal covered with the powdered coating material. The container is then heated in a vacuum, at a temperature of 1000–1500 °C. The coating metal melts to cover the entire surface of the base metal.

Zinc, chromium, and copper are normally coated through liquid diffusion. Liquid diffusion is usually performed in tank furnaces in which the diffusing metal interacts with the base metal's surface at 800–1300 °C. Complex diffusion coating, viz., chrome calorization and chrome-nickel plating can be achieved through this process.

In chemical gas diffusion, the material to be coated is heated into a gaseous form at a distance from the substrate surface. The gaseous chemical compounds of the coating element react with the base metal, resulting in diffusion of the metal. This gaseous phase consists of halides to ensure sublimation of the diffusing metal on the base metal's surface. The process is usually performed in specially designed furnaces at a temperature of 700–1000 °C.

3.3.3.6 Conversion Coatings

Conversion coating involves the application of a coating by spray or dipping on to a base metal to increase the corrosion protection and also sometimes used as a precursor for developing additional coatings, colors, or primers. Sometimes in conversion coating, a part of the substrate surface is converted into the coating with the help of chemical or electrochemical process. Examples include chromating, phosphating, metal coloring, and oxide coatings. The coatings are usually thin (around 2.5 μm) with a good degree of adhesion.

3.3.3.6.1 Anodizing

Anodizing is a conversion process which is widely used nowadays for surface finishing of aluminum in particular. Anodizing is an electrochemical process in which the natural oxide layer existing on the surface is increased in thickness. As aluminum exists in the anodic side of the galvanic series, it forms oxide readily which is corrosion resistant, hard and abrasion resistant. The naturally occurring layer is very thin (around 0.5 μm) and is susceptible to damage as it is attached to a more ductile material (aluminum). Hence, building up of the layer is necessary to attain the desired corrosion resistant properties.

Anodizing is carried out in the reverse process of electrolytic deposition. During anodizing, the aluminum part is made the anode (positive electrode) in an electrolytic cell consisting of an acid/water solution. The properties attained by the coatings largely depend on the temperature of the bath, for example, at 20 °C, a sulfuric acid anodizing solution will give a soft, transparent clear, easily dyed coating whereas at 5 °C, a hard, dense, and dull gray coating is produced (hard anodizing). A DC electric current is passed between the aluminum that is made the anode (positive terminal), the electrolyte, and a cathode (often lead).

When current is applied, the water in the electrolyte breaks down and oxygen is deposited at the anode. This oxygen combines with the aluminum to form oxide which builds on the oxide film always present on the surface. The acid in the electrolyte tries to dissolve this oxide and produces a porous oxide film on the aluminum surface. Coating thickness up to 25 μm is recommended for external use.

Anodizing produces a high specification metallurgically bonded finish that resists corrosion, abrasion and exposure to industrial, marine and other severe environments. Aluminum, titanium, zinc, cadmium, and magnesium are the metals that are usually anodized. Anodized aluminum is used in the aluminum window frames, commercial building fascia, etc. Aluminum castings are sometimes anodized for engineering purposes to increase surface hardness and abrasion resistance. Aluminum castings contain high levels of alloying metals such as silicon. The inclusion of these materials reduces the transparency of the anodic film and produces a greyish finish not greatly appreciated for decorative purposes. Hence, to avoid this problem, the process is carried out at low temperatures (less than 7 °C).

3.3.3.6.2 Phosphate coatings

This is a chemical conversion coating process through which thin adherent phosphate compound coatings are formed on a metal surface, viz., iron, zinc, or manganese. Among these phosphates, manganese phosphate is more suitable for wear applications. Phosphate coatings are usually applied to carbon steel, low-alloy steel, and cast iron. They can also be applied to zinc, cadmium, aluminum, and tin. Phosphate processes are hard to apply on high alloys for these alloys are likely to be immune to the phosphoric acid. In short, phosphating is one of the most useful non-metallic coatings.

3.3.3.6.3 Chromate coatings

Chromate coatings are similar to phosphate coatings. However, the chromate coatings are formed by the reaction of water solutions of chromic acid or chromium salts. The coatings can be applied to aluminum, zinc, cadmium, and magnesium. The coatings usually have good atmospheric corrosion resistance. Chromate coatings are widely used in protecting common household products, such as screws, hinges, and many hardware items with the yellow–brown appearance.

3.3.3.7 Thermal Spraying

Here the material to be coated (in powder or wire form) is heated to molten form and sprayed with high velocity on the substrate whereby they cool down and solidify to form coating. The heating in general is done electrically, either by arc or plasma. Higher coating thickness ranging up to several millimeters can be obtained through this technique. Thermal sprayed coatings are typically applied to metal substrates, but can also be applied to polymers, ceramics, or any combination thereof. Thermal sprayed coatings can be an effective alternative to several surface treatments including: nickel and chrome plating, nitride coatings, anodizing, etc. However, thermal spray technique has to be applied in line of sight only which poses several restrictions regarding coating of complex geometries and holes.

The thermal spray technique is primarily influenced by the temperature and velocity of the molten particles together with the atmosphere through which the material is sprayed. A schematic diagram of the thermal spray setup is shown in Figure 2. Lower particle velocity results in longer heating duration for the particles which in turn results in the particles attaining higher temperatures. Lower particle velocity results in porous deposits. Besides, if the spraying is conducted in air, oxide formation in coating will be higher.

Thermal spray comprises of four main processes which are as follows.

3.3.3.7.1 Electric arc spray

Electric wire arc thermal spraying utilizes the same principles as employed in wire arc welding systems. The coating material, in wire form, is electrically charged, and then contacted creating an arc. The molten droplets of metal wire are then sprayed onto the substrate using a high velocity air stream to atomize and propel the material. Arc spray coatings are very cost effective and are typically used to apply metals like pure aluminum, zinc, copper, and metal alloys such as stainless steel. Arc spray also allows adjustments to achieve varied coating texture. Electric arc spray is commonly used in automotive, aerospace, defense, infrastructure, etc. Electric arc spraying is also a favorite tool for artists in the creation of sculptures.

3.3.3.7.2 Flame spray

Flame spray, also known as oxy/acetylene combustion spray is recognized as the original thermal spray technique. It makes use of the basic principles of a welding torch with the addition of a high velocity air stream to propel molten particles onto the substrate. The coating material can be in the form of a wire, powder, or rod. Often flame spray coatings are fused after being applied to enhance bond strengths and coating density. The lower temperatures and velocities associated with conventional flame spraying typically result in higher oxides, porosity, and inclusions in coatings. Flame spray can be commonly found in industries such as oil exploration and agriculture. There are many other industries that use flame spray technology including aerospace, infrastructure, machine repair, etc.

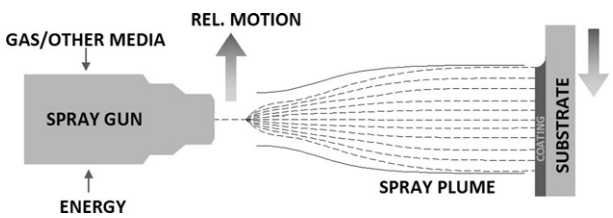


Figure 2 Schematic of thermal spray technique. Adapted from Synthetic Coatings Ltd. Available from: http://www.syntheticcoatings.ie (accessed 29 February 2016).

3.3.3.7.3 Plasma spray

In plasma spray process, plasma state is formed by introducing inert gases between two electrodes. As the plasma gas is heated by the arc, it expands and accelerated through a nozzle. When the gases exit the nozzle of the gun apparatus and return to their normal state, a tremendous amount of heat is released. A powdered coating material is injected into the plasma 'flame,' gets molten and then accelerated onto the substrate.

Because plasma-arc spraying is the most versatile of all the thermal spray processes its application can be found in the widest range of industries. Plasma spray coatings are used commonly in aerospace, automotive, medical devices, agriculture communication, etc. Ceramic coatings are most often applied using plasma spray due to their high melting temperatures.

3.3.3.7.4 High velocity oxy-fuel

The working principle of high velocity oxy-fuel (HVOF) is almost similar to that of flame spray. HVOF involves a closed combustion of fuels, viz., hydrogen, propylene, kerosene, etc. The hot flame is made to exit the chamber through a nozzle where it expands supersonically and propels the coating material toward the substrate. The extreme velocities provide the required kinetic energy which yield coatings that are very dense and very well adhered to the substrate.

Due to its simplicity of operation and quality deposits, HVOF possesses the largest share of the thermal spraying market. It is used to produce wear-resistant coatings, viz., cermets (ceramic and metal mixes), tungsten carbide, etc. As the coatings produced by cermets are very dense they are typically corrosion resistant. Inconel®, Stellite®, stainless steel, and ceramic coatings can also be produced by this method.

The coating processes discussed above are the ones popularly employed in the surface finish industry today. As can be seen each process has its own share of advantages and limitations. The application principle of different coatings processes vary. Moreover, the coatings produced by various processes differ in properties. Hence, an in-depth idea about a coating process is required before selecting it for a particular application. Figure 3 illustrates graphically the coating thickness and process temperature for the relevant coating techniques. The advantages and limitations of each of the processes are given in a nutshell in Table 2.

3.3.4 Existing Design of Coating Structures

Coatings are developed under multiple processes and with various materials, viz., metals, non-metals, composites, etc. Each type of coating may have a distinct set of properties.

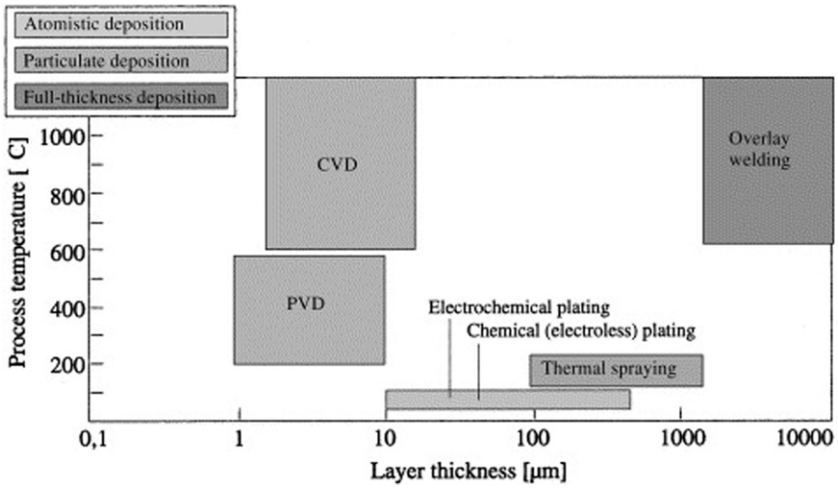


Figure 3 Typical values of process temperature and coating thickness for the surface coating methods. Adapted with permission from Ref. [2]. © Elsevier 2000.

Table 2 Summary of advantages and limitations for the coating methods

Coating process	*Advantages*	*Disadvantages*
Electro/chemical plating	• Corrosion resistance • Low processing temperature • Deposition in bore holes, slots, etc.	• Limited selection of coating materials • Relatively soft coatings • Ecologically problematic treatment baths (include cyanide, heavy metals, fluorides, oils, and greases) • Limited accuracy of surface replication
Diffusion processes	• Corrosion resistance • Good reproducibility	• Relatively soft coatings • Limited selection of base material (must be suitable for nitriding) • Long processing times • Substances from processing are damaging to the environment and to health • Post-treatment required
Chemical vapor deposition (CVD)	• High wear resistance • Economic production of thicker coatings • Suitable for bore holes, slots, etc.	• High processing temperatures • Coatings with several metals (e.g., TiAlN) are not possible • Edges become rounded (coating thickness) • Uses ecologically problematic, toxic metal chlorides
Plasma-assisted chemical vapor deposition (PACVD)	• Significantly lower process temperatures are possible than for CVD • Precise coatings • Low temperatures	• Only limited suitability for bore holes, slots, etc.
Physical vapor deposition (PVD)	• No environmentally damaging materials and emissions, no toxic reaction products • Great variety of coatings can be produced • Coating temperature below the final heat treatment temperature of most steels • Small, precisely reproducible coating thickness (accurate surface replication, true to size) • High wear resistance • Low frictional coefficient	• Bore holes, slots, etc., can only be coated down to a depth equal to the diameter or width of the opening • Corrosion resistant only under certain conditions • In order to achieve a uniform coating thickness, the parts to be coated must be rotated during processing

Besides, within the physical limits of a process, coatings can also be developed with different structures, viz., single layer, multiple layers, reinforced, graded, etc. Each of these structures may also induce some additional advantages in the coating in terms of it properties which may be beneficial to a particular surface finish application. Some of the coating structures

popular in surface finishing industries are discussed in the following texts.

3.3.4.1 Single-Layer Coatings

This is the most widely used coating structure which is easy to produce. Commercial CVD and PVD coatings are made up of one single layer often containing one structure phase. Among the most frequent are TiC, TiN, CrN, alumina (Al_2O_3), and DLC. They are usually applied directly on to the surface of a homogeneous substrate material. Consequently, to provide a high load carrying capacity of the coating composite, the substrate must possess a high hardness and a high Young's modulus. Moreover, many electrolytic and electroless coatings of metals and alloys are produced in single layer. Passivation processes like anodizing by default possesses a single layer structure.

3.3.4.2 Sandwich Coatings

In some cases, several layers of different compositions are applied on the substrate to form a sandwich coating. These types of coatings possess an equivalent property of the individual layers, or, the layers may act in synergy to address a particular issue. Metal-cutting inserts for machining austenitic stainless steel are typically CVD coated with three layers of TiC–Al_2O_3–TiN. TiC accounts for good bonding to the cemented carbide (CC) material, Al_2O_3 provides a good wear resistance at elevated temperatures and, in addition to looking good, TiN gives a clear visual indication of which edges of the insert that have been used. Besides, TiN often reduces the sticking of the work material.

3.3.4.3 Graded Coatings

A graded coating composition or structure improves the load carrying capacity by offering smoother transitions in mechanical properties from those of the hard and stiff coating to those of the softer and more flexible substrate. In this way, the contact load can be distributed over larger areas, which reduces the maximum contact stresses and the stress at the coating/substrate interface.

Successful graded surface layers on steel have been produced by nitriding or carbonizing since many decades, and the examples of forming tools and machine components taking advantage of these treatments are abundant. Today, graded coatings are utilized also in commercial PVD coatings such as Ti(CN). Moreover, graded coatings have also been developed for Ni–P coatings which offer better corrosion resistance compared to the non-graded coatings ones.[3] The grading in Ni–P coatings is developed based on percentage composition of nickel and phosphorous.

3.3.4.4 Duplex Coatings

Since many of the wear-resistant PVD and CVD coatings are relatively brittle, they can only be successfully applied to hard and stiff substrate materials such as hardened steel, CC, or structural ceramics. On softer substrates an intermediate layer acting as a mechanical support for the coating is usually required. For steel and titanium alloys, this support is preferably achieved by nitriding.[4] This combination of nitriding and PVD coating of steel is denoted as duplex coating. Duplex coating of electroless Ni–P/Ni–B are also formed and the compatibility between the layers are found to be good. It is also found that when Ni–P is the outer layer, the corrosion performance of the coating is better while wear resistance is better when Ni–B is the outer layer.

3.3.4.5 Multilayered Coatings

Multilayered coatings are different from sandwich layers by their periodically repeated structure of lamellae of two or more materials. The lamella thickness can vary between a few nanometers to a few tenths of a micrometer. Coatings made of multilayered structures have proved to be harder and significantly tougher than homogeneous coatings of the same materials since the lamellae structure obstructs dislocation and crack propagation.

3.3.4.6 Superlattice Coatings

Multilayered coatings of materials with similar crystal structures tend to form columnar crystals which extend through the whole coating, provided that the thickness of the individual lamellae is sufficiently thin (typically 5–25 nm). Such coatings are referred to as superlattice coatings. One of the first examples of superlattice coatings was obtained by combining TiN/VN and TiN/NbN.[5] Multilayered coating structure can also improve the hardness as well as the toughness, compared to single layers of the same materials.

By selecting a suitable combination of materials for the multilayered structure it is possible to improve the resistance against wear, corrosion, oxidation, high friction, etc. For example, superlattice coatings with thin lamellae of TiN and TaN have shown very good results in cutting of stainless steel. This is believed to be a result of a very good toughness combined with a low affinity of TaN to the work material.[6]

3.3.4.7 Multicomponent Coatings

Additional particles, grains or fibers are present in this type of coating. These additional elements may supplement some of the functionalities of the coatings. They may add to the strength of the coating by reinforcing action or by inherent hardness of the particles. In electroless nickel coatings, composite particles of SiC, B_4C, etc., help in making the coating hard and wear resistant. In contrast, soft particles like polytetrafluoroethylene (PTFE) help in reducing the coefficient of friction of electroless nickel coating. Different coating structures are illustrated in Figure 4.

3.3.5 Coating As a Method of Surface Finishing

Coatings are categorized as adding and altering techniques of surface finishing. They can be developed over the surface of compatible base materials (substrates) using suitable coating

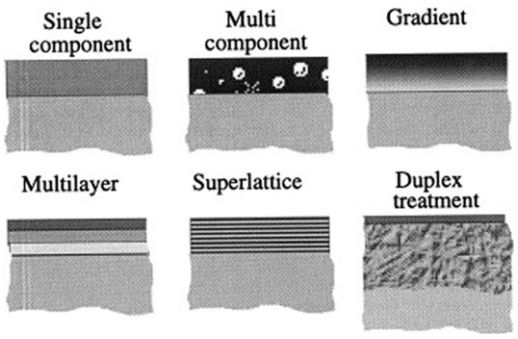


Figure 4 Structures of surface finish coatings. Adapted with permission from Ref. [2]. © Elsevier 2000.

methods. The substrate can be a metal or alloy, plastic, ceramic, i.e., any engineering material based on the application for which it is intended to be used. Depending on the demand of application, surface coatings can improve the esthetic appeal of a material, make the surface smoother and provide resistance against degrading phenomena, viz., corrosion and wear. Improving the esthetic appeal makes the product attractive and increases its marketability while covering the burrs and pits helps in reducing the surface roughness of the product which in turn lowers the frictional resistance. Prevention of corrosion and wear maintains the device performance as well as increases its service life. Moreover, this also eliminates the possibility of accidental hazards and enhances safety. Several types of coating methods exist each having its own set of advantages and limitations. However, with the advancement of technology, several novel coating methods are conceived from time to time which addresses the issues of the previous generation techniques.

Coating is more popular than other surface fishing techniques due to the following reasons:

- The procedure is simple and easy to carry out.
- Many materials and their combinations can be deposited.
- Wide varieties of coating processes exist. The one suitable can be selected.

3.3.5.1 Surface Finishing Facets of Coating

3.3.5.1.1 Improving esthetic appeal

Early applications of coatings within surface finish entity were mainly to improve the appearance of a particular object. Although the focus in the present times has shifted toward obtaining functional coatings, the decorative applications are befitting even today. The decorative applications are motivated by the following factors:

- The ability to compete favorably on an economic basis with decorative electroplating processes, keeping in mind the environmental considerations.
- The ability to provide a broad range of colors.
- Obtain corrosion resistance equivalent to or better than that of the coating process being replaced.
- Use of less expensive substrates.

Electrolytic coatings have for a long while served as a benchmark for decorative applications. Electrolytic coatings have often been used to produce gold plated jewelry and other decorative fittings. However, with passage of time several other coating methods have shown potential to serve in decorative applications. PVD, electroless nickel, chromium, etc., are commonly used for decorative purposes. Chromium plating is commercially used to produce wear-resistant and decorative coatings, but the plating bath contains hexavalent chromium, which has adverse health and environmental effects. Metal or ceramic coatings deposited by PVD are equivalent or superior in performance and are a cost effective alternative to chrome plating in case of decorative applications. Deposited PVD coatings can have a wide range of color. PVD coatings are used to plate watch components including bands, jewelry, eyeglass frames, pen parts (barrels, clips), cigarette lighter cases, knives, and other accessories. In case of jewelry, PVD coating is used to plate TiN which has a typical gold-like appearance. It has the further advantage of abrasion resistance. Now, stainless steel has high hardness and excellent corrosion resistance. TiN coated stainless steel jewelry provides the desired color and durability which has the potential to substitute gold as a cheaper alternative. Another interesting and widespread application of PVD is brass hardware, particularly door and window knobs and faucet parts. While brass hardware is attractive, the corrosion resistance of brass is somewhat limited. Unlike copper, which develops an attractive and uniform green patina on weathering, brass turns a dull dark brown. In order to maintain the attractive finish of highly polished brass hardware, it requires periodical polishing. The recent introduction of zirconium nitride (ZrN) PVD coating onto brass hardware has allowed suppliers of these components to offer 'lifetime' guarantee on surface finish. When deposited to the appropriate stoichiometry, ZrN has a finish that perfectly matches that of brass. It has excellent corrosion resistance, and therefore performs well in applications.

Most PVD is black in color; however, the underlying finish of the metal can affect the reflective properties. Thus, a bead blasted finish will produce a dull deep black appearance, whereas a rough brushed finish may produce a semi glossy finish. This adds a unique professional appearance to the timepiece and virtually eliminates reflective glare.

3.3.5.1.2 Protection against corrosion

Corrosion is a natural phenomenon that involves destructive attack of a metal by its environment so as to cause deterioration in the properties of the metal. Rusting of iron is the most common example of corrosion. Corrosion consumes about 3–5% of the Gross National Product of a nation. Corrosion science is an interdisciplinary area embracing chemistry, materials science, and mechanics. The study of aqueous corrosion processes involves the intersection of chemistry and materials science. But the science of mechanics must be incorporated to understand mechanically assisted corrosion processes, such as stress-corrosion cracking and corrosion fatigue.

Most of the things we encounter in day to day life is either made of metal or has metallic parts, which can get affected by corrosion. Besides, non-metals are also not entirely immune to corrosion. Hence, control of corrosion is vital so that the device service life can be extended. Corrosion protection is one of the primary aspects of surface finishing and coatings are widely used for the same. Electroless nickel, galvanizing, anodizing, etc., are popular for providing good corrosion resistance.

The protection mechanism of coatings against corrosion is normally twofold.

3.3.5.1.2.1 Barrier protection

As the name suggests, barrier protection acts by isolating the base metal from the environment. Barrier protection is perhaps the oldest and most widely used method of corrosion protection. All coatings provide barrier protection to some extent. As long as the barrier remains intact, the base material is protected against corrosion. However, if the barrier is breached, corrosion will begin. To keep the barrier intact, the coating should be strongly adhered to the substrate and also have good abrasion resistance. Hot-dip galvanized coating is widely employed for providing barrier protection to steel. The tightly bonded, impervious nature of zinc makes galvanizing a very good barrier coating. Furthermore, zinc corrodes approximately 1/10–1/40 the rate of steel depending on the environment, making the corrosion rate of a thin zinc coating equivalent to a much thicker steel piece.

3.3.5.1.2.2 Cathodic protection

Barrier protection is the first phase of protection offered by coatings. However, porosity is an issue in almost all the coatings. Presence of pores aids the corrosion products to reach the substrate surface easily. Moreover, coatings may get damaged or delaminated during handling and over a period of time. For these cases galvanic action at the region of contact of the corrosion product with the coating and the substrate determines the protection offered by the coating which is also termed as cathodic protection.

Cathodic protection is a more effective method of resisting corrosion. The cathodic protection depends on whether the coating material is higher than the substrate material in the galvanic series. The galvanic series of metals lists (**Table 3**) metals and alloys in decreasing order of electrical activity in seawater. This arrangement of metals determines what metal will be the anode and cathode when the two are put in an electrolytic cell. Metals higher on the list are anodic to the metals below meaning they provide cathodic or sacrificial protection when the two are connected. Cathodic protection requires changing an element in the corrosion circuit by introducing a new element, thus ensuring that the base metal becomes the cathodic element of the circuit. Hence, the new metal which is anodic corrodes in place of the base metal.

Table 3 Galvanic series of metals

Magnesium	Active (anode)
Zinc	↑
Aluminum	
Cadmium	
Steel/iron	
Lead	
Tin	
Nickel	
Brass	
Bronze	
Copper	
Stainless steel	
Silver	
Graphite	
Titanium	
Gold	
Platinum	Noble (cathode)

Galvanized steel is widely used in applications such as building, automotive body parts, and water distribution systems because of its good resistance to environmental corrosion. It is found that unprotected steel will normally corrode 10–40 times faster than hot-dip galvanized articles; the higher ratios usually being in high-chloride environments. Due to its inertness to high levels UV, hot-dip galvanization is the most popular coating for protecting steel in Australian continent as recommended by 'Galvanizers Association of Australia.'

Hot-dip galvanizing protects steel cathodically which is similar to the sacrificial anode method. From **Table 3**, it is apparent that in the case of hot-dip galvanizing, zinc will preferentially corrode to protect the underlying base steel. In fact, the cathodic protection of hot-dip galvanizing ensures that even if the coating is damaged to the point that bare steel is exposed, no corrosion will begin until all the surrounding zinc is consumed. Cadmium is also used to protect steel by this method.

Corrosion resistance of zinc coating is further improved when the zinc is alloyed with other metal (e.g., Co, Ni, Mn, Al). Some researchers have suggested that the higher protective ability of these systems is due to the corrosion products, zinc hydroxide salts ($Zn(OH)_2$), that formed as a result of interaction with the corrosion medium. Moreover, during the corrosion of zinc in an aerated, neutral solution (0.5 M Na_2SO_4), a passivation layer, which is composed of ZnO in association with $Zn(OH)_2$ is formed on the surface of zinc,[7] which further aids in its anti-corrosion behavior. The effect of pH over the corrosion rate of zinc is depicted in **Figure 5**.

Electroless Ni–P coatings are also widely used for corrosion protection application in a variety of environments. They act as barrier coatings, protecting the substrate by sealing it off from the corrosive environments, rather than by sacrificial action. However, in this respect, only electroless Ni–high P coating is effective in offering an excellent protection, whereas electroless Ni–low P and Ni–medium P coatings are not recommended for severe environments.[8] In general, the corrosion resistance of any alloy depends on the ability to form a surface protective film. Phosphorus can make the corrosion potential increase and the corrosion current decrease, and it promotes the anodic and cathodic reactions during the corrosion process, thereby increasing the anodic dissolution of nickel. Accelerated corrosion of nickel provides prerequisites for concentrating P and thereby for the formation of Ni_3P and Ni_xP_y stable intermediate compounds on the surface, which acts as barrier passive film.

The corrosion behavior of electroless Ni–P coatings is governed by three principal factors, viz., the degree of amorphous state, extent of internal stress, and the percentage of phosphorus content. The combined effect of all of these factors or dominance of any one of these factors is responsible for the observed corrosion behavior. The difference in corrosion resistance between electroless Ni–low P and Ni–high P coatings is in particular due to the difference in structure – a crystalline, inhomogeneous structure for the low P materials, and an amorphous, homogeneous one for the high P materials. Incorporation of specific elements in the electroless Ni–P coatings is found to increase its corrosion protectability. Copper element significantly improved

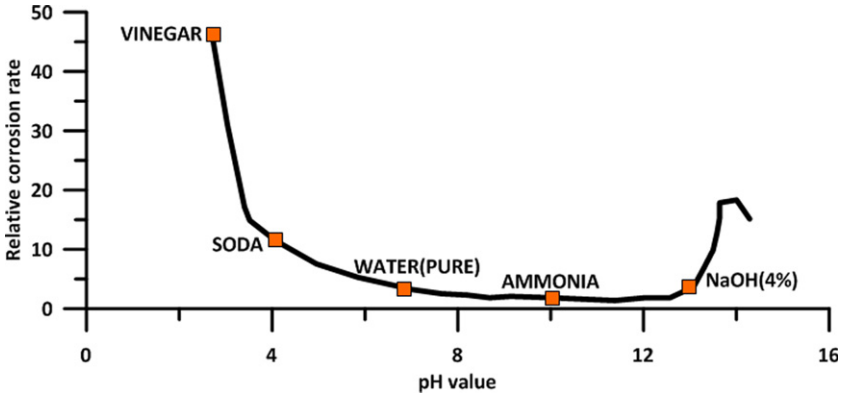


Figure 5 Effect of pH on the corrosion of zinc. Adapted from American Galvanizers Association. Available from: http://www.galvanizeit.org/ (accessed 29 February 2016).

the corrosion resistance of Ni–P coatings. Presence of copper in Ni–W–P deposit also improved its corrosion performance in both brine and acidic environments. Small amount of tin addition can improve the formability of the amorphous phase in Ni–P coating.[9]

Electroless nickel phosphorous coatings have been successfully applied on glass fiber reinforced plastic (GFRP) substrate for making blades of offshore wind turbine installations.[10] An offshore wind turbine should be designed so as to be able to withstand fatigue loads and a hostile environment at all times. Depositing Ni–P coatings on GFRP substrate increase its wear corrosion resistance besides imparting conductivity to resist against damage by lightning strikes. Electroless nickel coating has also been used to improve the wear and wear corrosion properties of carbon fiber reinforced plastic materials, which are frequently utilized in the aerospace, aviation, and automobile industries due to their light weight.[11]

Polyurethane (PU) coatings are employed for different structures today, such as storage tanks, oil and gas pipeline, water and wastewater pipes, bridges and ships to protect them against corrosion and abrasive wear. Chromium, aluminum, and silicon materials can be deposited with the help of diffusion coatings. This in turn makes the base metal develop extreme resistance to corrosion, oxidation, and erosion in its severe working conditions. This proves that the process is highly reliable, enhancing the manufacture of critical components. Diffusion coating is normally used to process gas turbine engine components (vanes, blades, and cases), pump impellers, gate valves, and power generation components.

The electric arc thermal spray technology has been used to coat large objects such as bridges, where aluminum and zinc are deposited to provide corrosion resistance. Flame spray and fuse coatings are produced in these industries to provide wear resistance along with excellent impact resistance.

3.3.5.1.3 Resistance to wear

Wear is a mechanical phenomenon which involves progressive loss of material when two bodies in contact move relative to each other. Mechanical devices suffer wear in operation which also limits their service life. Surface coatings are a way to tackle these deteriorating phenomena. Softer materials, viz., aluminum, magnesium, etc., can be made durable and wear resistant by putting suitable coatings on top. A preferred wear-resistant coating should have a high hardness combined with a relatively low modulus. This is because a high modulus limits the coating's flexibility and overall wear performance. Zeolite materials, with their unique crystalline porous framework, possess this demanding balance. Zeolites' crystallinity offers an exceptional hardness while their porosity provides a relatively low elastic modulus.[12] Zeolite coatings are demonstrated to outperform hard chrome and cadmium coatings in wear and corrosion resistance.

PVD is employed to prevent premature tool failure in cold forging. The wear volume of the coatings TiAlCN, TiC, and Si_3N_4/AlTiN is lower than for the coatings TiAlN and AlCrN.[13] A multilayered structure seems to act beneficially on the mechanical properties and the abrasive wear resistance of thin hard PVD coatings. The overall performance of the multilayered TiN/CrN coating indicates that this coating has a high potential as a tribological coating material. A multilayered coating of TiN/TaN seems to be the best choice for applications where abrasive wear is the predominant wear mechanism.[14]

Polycrystalline diamond coatings can be produced by CVD by using hydrocarbon gas (typically methane) in an excess of hydrogen. The resulting coating shows excellent wear and abrasion resistance. PVD is successfully used on transmission gears and engine parts of racing cars to help those 10 000 + RPM engines increase reliability. Because PVD reduces friction between metal parts less lubrication is necessary and temperatures are generally lower than without coatings. Though PVD coatings are typically only a few microns thick the molecules bond to the surface of the metal in such a way that they are very difficult to remove once applied. This long lasting resilience is what makes PVD so attractive for thousands of mechanical applications.

Tungsten carbide coatings can be put on top of materials like titanium and then subjected to finish grinding to increase its life span multifold. This type of parts can then be employed in landing gears of aero planes and automotive parts. Flame spray and fuse coatings are produced in these industries to provide wear resistance along with excellent impact resistance.

TiNrMoN have proved to be the most interesting multilayer coating, with exceptional tribological properties, when tested against alumina. The low friction properties of MoO_3 indicate

that it would provide good tribological properties also against other counter materials. Again Sn–Ni coatings electrodeposited from a chloride–fluoride-based solution present a somewhat better adhesion and wear resistance, in comparison with the coatings obtained from a pyrophosphate bath.[15]

The results showed that the wear resistance of the nanocomposites was increased by approximately 2–3.5 times compared with unreinforced Ni deposited material.[16] Chromium coatings prepared from a standard electrolyte are widely used in industry to restore parts of machines operating under various conditions and improve their wear resistance. Despite the advantages of these coatings over other materials, their use is limited by the aggressivity of the electrolyte.

Upon a thermal treatment of an electrolytic nickel–boron alloy coating at temperatures of 350–450 °C, the microhardness of the coating increases from 780–830 to 1300–1450 MPa.[17] Similar observations have been made in case of electroless nickel coatings. Electroless Ni–B in particular is found to be suitable for wear-resistant applications. The Taber wear index of Ni–B coating is found to reduce to an astonishing value of 13 after subjected to heat treatment at 400 °C in an atmosphere containing 95% Ar and 5% H_2.[18] Several other soft and hard particulates improve the wear performance of electroless nickel coating which include: alumina, boron carbide, silicon carbide, silicon nitride, silicon oxide, PTFE, and molybdenum sulfide.[9]

Dip coating of silica sol–gel coating reinforced with carbon nano tubes (CNTs) on magnesium alloys substrates displayed good wear resistance behavior.[19] Hard chrome (Cr) coatings are known for their excellent abrasion resistance, low friction coefficient, and their capability to produce thick layers for rebuilding worn parts back to specification. Cadmium (Cd) coatings are critical to aircraft fasteners as a sacrificial wear layer and to provide mild corrosion protection. Ceramic coatings, which are mainly composed of silicon carbide and polymer, showed excellent slurry-resisting performance, and the slurry-resistance is better than that of stainless steel 304, cast iron JM3 and high chrome alloy steel Cr30A. In case of cavitation erosion, a good coating is the one that is able to withstand the load and not flake off, consequently protecting the base material until the next maintenance. PU coatings are found to exhibit low cavitation erosion.[20] Plasma anodizing of aluminum offered a high abrasive wear resistance compared to coatings produced by thermal spray.[21] In case of injection molding of glass reinforced plastic parts for automotive industry, Stellite coatings deposited by cold spray process is found to be sufficiently wear resistant.

Besides possessing corrosion resistant properties, galvanized coatings also offer wear resistance up to some extent. Although the outer layer of galvanized coatings is soft and lacks abrasion resistance, the middle and inners layers are harder and more abrasion resistant than the steel. If the outer layer is removed in operation, the inner harder layers are exposed which give the coating outstanding abrasion resistance so that mechanical damage to galvanized coatings is minimized.

3.3.5.1.4 Generating smooth and lubricious surface

Any part can be made smoother by subjecting it to finer machining processes, viz., grinding, honing, and lapping. The use of these processes implies huge escalation in the production cost of the part. Coating is a method in which these cost can be avoided. Coating when applied on the surface of a part fills the gaps and other discontinuities making the surface smooth. Now, the general objective of applying coating to a surface for any tribology-based application is to impart both smoothness and hardness to the surface so that friction and wear are reduced. Among the two degrading phenomena, friction is a critical factor dictating the efficiency of mechanical assemblies that involve sliding surface contact. It is also partly responsible for wear, which is often the limiting mechanism of device service life. Thus, minimization of the friction of the coating is a vital need. For reduction in friction, sharper peaks, and lower contact condition is desired.

Electrodeposited cobalt coating reinforced by CNTs exhibited lower coefficient of friction than cobalt film at room temperature. However, the coefficient of friction of the composite films increased due to the formation of a significant amount of cobalt oxides on the surface and the dissipation of CNTs at 500 °C.[22] Electroless nickel coatings are inherently smooth and lubricious in nature due to their cauliflower-like microstructure. Addition of certain soft particles, viz., PTFE, graphite and MoS_2 is found to reduce the friction coefficient of electroless nickel coatings further. Introduction of CNTs in nickel matrix showed a very good lubrication property due the self-lubricating property of CNTs.[23]

With the development of low friction coatings such as DLC, smoothness of the substrate surface is now guaranteed. Tungsten disulfide (WS_2) offers low lubricity, with coefficient of friction around 0.03, under extreme load and temperature conditions. SiC–Ni coating produced by pack cementation was found to exhibit self-lubrication properties only at a temperature of 800 °C owing to dense tribo-film which spreads on the wear track.[24] Chrome oxide layer can be corrosion resistant, wear resistant and extremely lubricious. T800 is an alloy of cobalt and is deposited with the help of thermal spraying. It is used to prevent galling between sliding surfaces where lubrication is arduous and to prevent wear and corrosion.

3.3.5.2 Miscellaneous Surface Finish Applications

3.3.5.2.1 Hydrophobic coatings

Making various materials hydrophobic has been a popular topic of research in recent years. A high hydrophobicity is useful for a variety of products and industrial uses, such as self-cleaning fabrics and windows, friction reduction in microfluidic devices, glass wind-shields (that quickly evacuate the water for better visibility in adverse weather conditions) and solar panels.

There have been efforts to develop hydrophobic coatings which can be used in ultra-dry surface applications. Coatings can be sprayed onto objects to make them waterproof. PTFE and fluorinated ethylene propylene are hydrophobic coatings that increase lubricity, desirable in medical applications where devices need to slide easily within the body.

3.3.5.2.2 Conformal coatings

Conformal coatings can change their geometry according to the applied load and pressure. This may be helpful in certain application where undue stresses can be avoided. Moreover,

for fluid sealing applications, a conformal coating will be very helpful as it will maintain the leak-proof joint. Fluoro-polymer rubber coating are developed specifically to seal rougher surface finishes while withstanding high temperatures, long-term coolant and oil exposure, and joint shearing forces.[25]

3.3.5.2.3 Electrical and magnetic properties

CVD is widely used in the semiconductor industry, as part of the semiconductor device fabrication process, to deposit various films including: polycrystalline, amorphous, and epitaxial silicon, SiO_2, silicon germanium, tungsten, silicon nitride, silicon oxynitride, titanium nitride, and various high-k dielectrics. The CVD process is also used to produce synthetic diamonds. Electroless nickel coatings are used to plate printed circuit boards. They also help in metallization of plastic for electrical applications.

3.3.5.2.4 Thermal coatings

Thermal stability is another feature provided by some of the coatings. Thermal endurance may be required in industries, viz., steel industries, power plants, etc. For applications like in turbine blades which are subjected to very high temperatures, thermal barrier coatings like zirconia will enhance its high temperature properties and also extend the life of the blade.

3.3.5.2.5 Rough coatings

For paper industries the drum which needs to grip the paper part can be coated with a tungsten carbide-based coating which is extremely rough. In fact the roughness is so high that the drum can be held by a piece of Velcro.

3.3.5.2.6 Biomedical applications

Titanium and titanium-based coatings show potential for biomedical applications. Coatings of N–TiO_2 showed high corrosion resistance in simulated body fluid in protecting stainless steel.[26]

3.3.5.2.7 Optical coatings

Optical coatings are materials deposited on an optical element, viz., lens or mirror to modify the way in which the element transmits or reflects light. One type of optical coating is an antireflection coating, which reduces unwanted reflections from surfaces, and is commonly used on spectacle and photographic lenses. Another type is the high-reflector coating which can be used to produce mirrors which reflect more than 99.99% of the light which falls on them. Aluminum is used to make mirror surfaces. Silver has higher reflectivity compared to aluminum coatings. UV absorbent coatings are important for protection of human eyes and also increasing the life of the product. Hundreds of alternating layers of a high-mass metal such as molybdenum or tungsten is employed for this purpose. Coatings are also available in some colored lighting, tinted glazing, or sunglasses.

3.3.6 Eco-Friendly Coatings (Green Coating)

With advancement of science and technology, various new coating techniques have emerged. At the same time, the processes which are harmful to humans and pose a threat to the environment have also been identified and continuous effort for searching suitable replacements is on. Hard chrome coating is such a coating which was inevitable in industry even a few years back due to their high resistance against both corrosion and wear. But with time, the high toxicity of the chrome baths and its detrimental effects on environment was realized. With awareness growing this coating is presently in the process of being phased out. Similarly cadmium plating is another such coating for which technologists are in the search for replacement.

Standard chromium plating electrolytes based on chromic acid are among the most dangerous electrolytes in modern industry. Replacement of these electrolytes with those based on trivalent chromium salts is not a solution because the latter are also toxic, and, moreover, coatings formed from these electrolytes developed so far cannot replace coatings deposited from standard chromium plating electrolytes primarily in those cases when the functional properties of chromium coatings are required, for example, their high wear resistance. In recent times due to development of newer coatings, viz., electroless nickel the solution to this problem may be on the horizon. Electroless Ni–B coatings after suitable heat treatment attain hardness values in the vicinity of chrome hardness.

PVD is found to be a suitable alternative to electroplating and other metal finishing processes that use large quantities of toxic and hazardous materials. PVD is a desirable alternative to electroplating and possibly some painting applications because it generates less hazardous waste and uses less hazardous materials (i.e., no plating baths). PVD processes as a substitute for chromium plating in decorative applications represents a development toward an environmentally clean technology.

There are several other environment friendly coating techniques in existence today. It is found that 100% solid PU coatings can comply with the regulations on volatile organic compound emissions. Being virtually non-toxic, zeolites have found potential in medical applications such as in magnetic resonance imaging contrast agents and biocompatible coatings for implants where they produce no hazards to human health. Additionally, zeolites are generally accepted as eco-friendly alternatives in catalysis and in many other applications. Zeolites in thin film or coating form have been shown to have many applications including membranes, sensors, and insulators in computer chips. Electroplated zeolites (ZSM-5) are found to possess more wear resistance than cadmium and chromium coatings. Moreover, the coefficient of friction is also found to be superior.[12] Several research and development labs have also come up with different eco-friendly coatings of their own.

3.3.7 Influence of Coating Parameters and Process Optimization

Present day applications demand greater value and benefit but for a lesser cost. Moreover, due to constant scarcity of resources, it is important that the same product may be used with minimum wastage. This demand for value has kept the focus on getting improved system performance and that too to meet

environmental demand. Coating process optimization seems to be a step toward achieving this goal.

Optimization of the coating process at first involves knowing the different parameters that affect the deposit quality. Then the extent to which a parameter is influential needs to be determined. Finally, the optimization of the process can be carried out with a suitable mathematical- or statistical-based technique. Several studies in this regard have already been undertaken. It is observed that in general for electrolytic Sn–Ni coating, increase in current density during deposition increases the adhesion, wear resistance and absolute hardness of the coating.[15]

Ni matrix reinforced with nano-Al_2O_3 (80 nm in size) MMC coatings with 50–200 μm in thickness were successfully produced by DC electroplating using a modified Watt's type electrolyte. It is found that increasing the surfactant (hexadecylpyridinium bromide) content resulted in increase of Al_2O up to 11.74 vol.% in Ni matrix providing segregation free dispersion of nano-particles. The hardness values of the nano-Al_2O_3 reinforced electrodeposited coatings yielded as high as 641 Hv because of unique dispersion effect.[16] Parametric optimization of the deposition conditions is carried out to improve the hardness of Ni–B coatings and the maximum hardness is found to be about 1400 HV0.1.[27] Optimization of coating parameters is also done for electroless Ni–P coatings which reveal that heat treatment temperature and bath temperature have the most significant influence in controlling wear characteristics of the coating.[28]

It is found that the parameters of the induction-capacitance device have a significant effect on the deposition of chromium coatings from a tetrachromate electrolyte and on the physical and mechanical properties of the coatings. Both the wear resistance and microhardness can be doubles by suitably optimizing the inductance and capacitance values.[29]

3.3.8 Surface Finish Measurements of Coatings

Once a coating is developed, it is necessary to carry out a full-fledged evaluation of the coating so that desired qualities from the coating can be ensured. A coating supposed to provide a certain degree of wear or corrosion resistance should be checked whether it can meet the deliverables. Following are the properties which are normally evaluated for surface finish coatings.

3.3.8.1 Coating Thickness

Thickness is the most basic parameter of a coating. Thickness is very important in terms of corrosion protection. Higher thickness ensures good barrier protection for the coating subjected to corrosive environments. Besides, thickness is also important from wear point of view.

Thickness can be measured by a number of techniques, viz., direct displacement measurement, microscopy, profilometry, gravimetric analysis, electromagnetic methods, etc. Displacement measurement is the most simple thickness measuring technique. In this method the linear distance of blank sample is subtracted from the coated sample to obtain the thickness of the coating. However, this method is highly dependent on the resolution of the measuring instrument. Microscopy method observes the cross cut section of the sample and measures the thickness. The cut section must be evenly ground and polished to get a good view in the microscope. Profilometry measures the step height of a coated and non-coated region to obtain the thickness of the coating. Best results are obtained if the step is abrupt and if surface roughness does not make it too difficult to define the surface planes at the top and bottom of the step. Gravimetric method is a widely used technique to obtain the thickness of the coating. Here, measurements are made of the sample dimensions and the weight of the sample with and without the coating is noted. These measurements are then combined with the knowledge (or assumption) of the coating density to derive an average coating thickness.

Electromagnetic methods exist, which rely on a calibration of magnetic field strength or capacitance with distance. The substrate should be a conductor and should also be ferromagnetic or can be made to generate magnetic fields via induction of eddy currents or, for capacitance methods. Usually a calibration of the electromagnetic sensor response on an uncoated portion of the substrate is required. X-ray fluorescence method relies on calibration of the X-ray absorption of the material to be measured.

3.3.8.2 Adhesion Testing

Adhesion testing of the coating checks the adherence of the coating to the substrate. The simplest test is the straightforward pull-off test. This test uses a stud which is fixed with adhesive on to the coating, which is pulled off using a force-recording mechanical testing system. The force at which the coating gets separated from the substrate is the peel-off force. The maximum strength of the external adhesive poses a limitation to the system. Hence, coatings obtained through PVD and CVD, which in general possess a high degree of adhesion, cannot be measured by this technique.

Higher adhesion strength coatings can be tested by mandrel test or four point bend tests. These test methods apply a stress to the coating-substrate interface by means of a deformation to the entire substrate/coating composite structure. In mandrel testing (Figure 6(a)), a coated test sample is bent over a cylindrical mandrel to a preset angle. If cracking or spalling of the coating occurs before this preset angle, the coating is said to have failed by either cohesive or adhesive failure. In four point bend test, the coating is loaded in four point configuration (Figure 6(b)) so that the coating experiences tensile

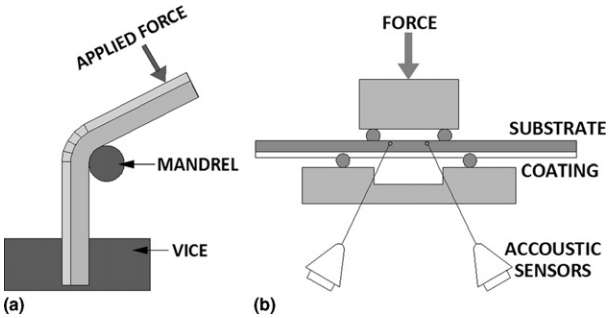


Figure 6 Adhesion tests for coatings (a) Mandrel test and (b) four point bend test.

stress. With increase of applied force, the stress increases and at a certain load (fracture strength of the coating), the coating fails by cracking through its thickness. With further increase in load, more cracks are formed and the strain at which some portion of the coating delaminates and spalls off is known as the adhesion strength of the coating. Rockwell indentation may also be used to evaluate coating adhesion.

3.3.8.3 Indentation Testing

Indentation tests have been popularly employed for measuring the hardness of a material. The basic goal of hardness testing is to quantifiably measure the resistance of a material to plastic deformation. Hardness values offer a comparative measurement of a material's resistance to plastic deformation from a standard source, as different hardness techniques have different scales. For coatings, the thickness plays a decisive part in indentation testing. Higher thickness coatings can be tested with the same instrumentation as for the bulk materials, however, with a lower load. For thin coatings, microhardness testers and nano hardness testers based on Vickers principle is available nowadays. These instruments have very small indenters which are pushed into the coating with very low loads so that effect of substrate hardness does not pollute the results. The indentation thus produced is measured by microscope attached to the system.

3.3.8.4 Surface Roughness

The geometrical parameter of a coating, that is its surface roughness, exerts a fundamental influence on the mechanical integrity of the coating. Accurate measurement of roughness is therefore critical to the evaluation of any coating. The common contact type instrument is the stylus and skid type device. The stylus, often with a diamond probe, is made to traverse the coated surface. The vertical movement of the stylus is recorded and plotted which is then statistically analyzed for obtaining the common roughness parameters. Contact type instrument has the limitation that physical contact with the sample has to be made in order to measure the surface roughness of the coating which is not always feasible. In order to address this issue, non-contact type instruments are available nowadays. These instruments are optically based and normally make use of lasers to capture the surface profile.

3.3.8.5 Measurement of Friction and Wear

As tribological studies are now part and parcel of surface engineering, coatings are subjected to friction and wear tests under near service conditions. Tribo-testing apparatus called tribometers or tribotesters are available which enable one to apply the predetermined load and lubrication if any and obtain the friction and wear behavior from the sample. In most tribometers used in the laboratory, test specimens of simple geometry are utilized in order to start the tests with test conditions as well defined as possible. Usually one of the moving specimens consists of a rotating cylinder or disk against which another solid specimen of different curvature is pressed thus leading to nominal point, line, or flat contact. The operating variables of a tribometer are broadly given by the following quantities: type of motion, load applied, velocity, ambient temperature, and test duration.

- Type of motion: the type of motion is connected with the geometry of the test system and is given by one of the four basic motion types, viz., sliding, rolling, spin, and impact or by a superposition of these basic types.
- Load: the load can be applied by various means to the test system, for example, as a mass (dead load), by a spring, by hydraulic means or by electromagnetic means. For the measurement of the load, force transducers based on strain gauges, inductive elements or pressure-sensitive detectors evaporated on the surface of the specimen in the contact zone are available. The measurement of the load by means of an electro-mechanical force transducer has the great advantage that the normal load signal together with the signal of the friction force can be fed to an electronic divider and the actual value of the friction coefficient (μ = friction force/normal load) can be calculated directly during the test and on real time basis.
- Velocity: for the control of velocity, electronic, or optoelectronic transducers are commercially available. The velocity is an important parameter in tribo testing as much as it determines the lubrication regime within the Stribeck curve. It is also the independent variable in the product of friction force and sliding velocity which gives the friction-induced power loss of a tribo-testing system.
- Temperature: the ambient temperature of the test system is another important operating variable since it determines the thermal state of the system – at least at the initial stage of the test. For the control of the temperature, the following two techniques are utilized most often: thermocouple techniques and infrared-pyrometer techniques.
- Test duration: the set of the operating variables (load, velocity, and temperature) acts on the tribo-testing system as function of time or duration. The test duration also should be selected to be consistent with the nature of the investigation. Attempts are frequently made to shorten the test duration in so-called 'accelerated tests' by increasing the severity of the operating conditions. This procedure, however, is only permissible if the nature of the tribological processes is not changed.

A typical tribotester setup is shown in Figure 7. Here the stationary rectangular specimen is made to slide against a rotating hardened steel roller. Load is applied by a leverage arrangement. The wear is directly measured in terms of depth by a LVDT sensor which is placed just above the specimen. Friction force is captured by a load cell as shown in the Figure. The coefficient of friction is then calculated by the ratio of the friction force and normal load.

3.3.8.6 Measurement of Corrosion

Protection against corrosion is one of the vital objectives of applying any coating. Now, corrosion is a natural process which occurs over a period of time. However, for laboratory-based measurements, the corrosion process is accelerated so that the effects of corrosion could be studied efficiently and in a timely

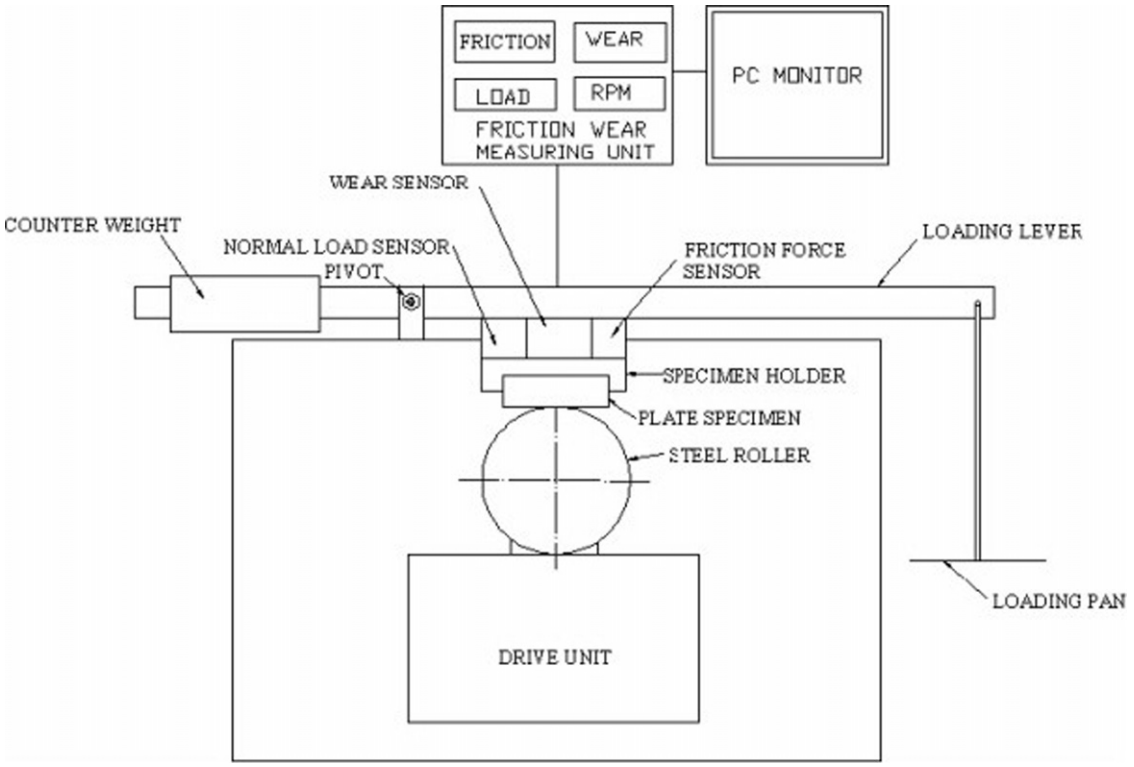


Figure 7 A typical tribotester setup. Adapted with permission from Ref. [30]. © Elsevier 2011.

manner. Corrosion rates for metals undergoing uniform corrosion can be determined by any of the following methods:

- Weight loss
- Weight gain
- Chemical analysis of solution
- Gasometric techniques (when one of the reaction products is a gas)
- Thickness measurements
- Electrical resistance probes
- Inert marker method
- Electrochemical techniques.

Each of the methods mentioned above has an application in either the laboratory or the field. But none of the methods above can provide insights into the underlying mechanism of corrosion-like electrochemical techniques. In addition, electrochemical techniques offer the possibility of mitigating corrosion by controlling the electrode potential. There are many methods of determining the corrosion rate by electrochemical techniques but the DC polarization method and the electrical impedance spectroscopy (EIS) methods using alternating current are the most popular. An instrument known as a potentiostat has control of the voltage across the working electrode-counter electrode pair, and it adjusts this voltage to maintain the potential difference between the working and reference electrodes (which it senses through a high-impedance feedback loop) in accord with the program defined by a function generator. One can view the potentiostat alternatively as an active element whose job is to force through the working electrode whatever current is required to achieve the desired potential at any time.

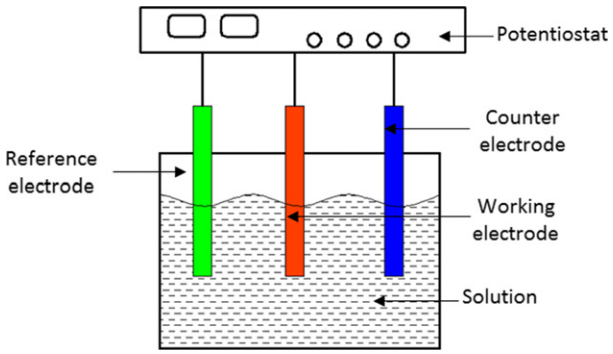


Figure 8 Potentiodynamic polarization setup.

In potentiodynamic polarization tests, the electrochemical cell consists of three electrodes (Figure 8). The coated specimen forms the working electrode which is actually the sample being interrogated. A saturated calomel electrode forms the reference electrode which provides a stable 'reference' against which the applied potential may be accurately measured. A platinum electrode serves as the counter electrode which provides the path for the applied current into the solution. The design of the cell is such that only a known standard area of the specimen is exposed to the electrolyte. The potentiostat is generally controlled via a computer which also captures the polarization data. Through dedicated software it is possible to manually extrapolate the values of E_{corr} (corrosion potential) and I_{corr} (corrosion current density) from the plot.

For EIS tests, the test setup is similar to that of polarization experiments. Electrochemical impedance spectroscopy is

a technique where the cell or electrode impedance is plotted vs. frequency. In case of corrosion studies, EIS is the response of an electrochemical system to AC excitations at frequencies from 100 μm to 100 kHz. In this method, voltage is applied and the current is measured as the response of the system or the vice versa. EIS is a very useful tool to characterize the corrosion properties of various coatings. It estimates with considerable accuracy the corroded area especially during the initial stages of corrosion when this area may not be visible. Hence, EIS allows the early detection and quantification of corrosion that leads to predictions of the useful life of the coating. Moreover, since small amplitude of AC signal is applied to the system, it is virtually a non-destructive method.

3.3.9 Effect of Pre-Treatment Processes

Every successful coating requires a good surface preparation. If the preparation remains incorrect or even inadequate the coating may suffer failure well before the end of its expected service life. In case of galvanizing process, the steel surface has to be thoroughly cleaned as zinc will not metallurgically react with an unclean steel surface. Any failures or inadequacies in surface preparation will immediately be apparent when the steel is withdrawn from the molten zinc, because the unclean areas will remain uncoated and immediate corrective action must be taken. Surface preparation for galvanizing consists of three steps: degreasing, acid pickling, and fluxing. In anodizing, oils and greases are removed in weak alkali solutions and the surface is etched to remove heavy oxides. After rinsing, the aluminum is dipped into a desmut solution to remove the insoluble components of the aluminum which remain on the surface after etching. Finally, the aluminum is rinsed and presented for anodizing. For electroplating, oils and greases are removed in weak to strong alkali solutions (depending on the metal being cleaned and the soils being removed). The surface oxides are removed in acids (strong pickles are used to remove heavy oxides and rust from steel). After rinsing, the parts are presented for electroplating. The vast majority of powder coating failures can be traced to a lack of a suitable surface preparation.

3.3.10 Selection of Coating for Surface Finish Applications

It is very critical to select a coating for a particular surface finish application. Selection of wrong or incompatible coatings could lead to its premature failure due to detachment, delamination, cracking and/or spalling. The selection of a particular surface coating broadly depends on the requirements to be satisfied by the particular component. In any component, the following basic requirements need to be satisfied.[31]

- Mechanical and tribological properties must be sufficient to withstand loads and have a satisfactory working life.
- The process of fabrication should be economic.
- The material should withstand the environmental conditions during its lifetime.

Now typical tribological mechanisms remain same for coatings as for any homogeneous material. The coating shall be selected to match the tribological situation and the life limiting surface damage mechanisms of the intended application. A classification of these mechanisms into three categories is convenient.[32]

- Damage without exchange of material: it involves permanent changes in the component geometry and/or surface topography. Significant parameters include Young's modulus and hardness of coating and substrate. Besides, thickness of the coating is also very important. Coating hardness is the crucial parameter for scratch resistance, while coating toughness or fracture resistance is crucial to resist surface cracking.
- Damage with loss of material (wear): the coating acts as a protective covering on a component. Hence, its wear resistance is of primary concern. If somehow a coating gets damaged and the substrate material is exposed, the service life depends on the wear resistance of the latter. Although a large number of wear mechanisms are described in the literature, the two main categories can be distinguished: wear dominated by coating detachment and wear caused by gradual removal of coating material. The former involves major damage to the coating while the latter often involves mild wear due to abrasion, erosion, chemical dissolution, etc., and does not deviate from the mechanisms causing wear of homogeneous materials.
- Damage with material pick up: work material locally adhered to, for example, the surface of a sheet forming tool used in the automotive industry will inevitably produce indentations or scratches in the surface of the product. Material transfer between the contact surfaces of sliding machine elements is a similar problem often named galling, scuffing, or seizure.

3.3.11 Closure

Coatings are well recognized and widely accepted method of surface finishing. Coatings incorporate different materials together on the substrate surface to have enhanced properties at the surface, which the bulk of the material may not possess. Several methods of coatings are in existence each having its distinct set of advantages and limitations. Among the processes, electrodeposition, electroless deposition, vapor deposition, powder coating, and conversion coatings are a few to be mentioned. Coatings can be applied over any material be it metal or non-metal, conductor or non-conductor, etc., depending on the process. Although previous generation coatings were mainly devoted toward enhancing the esthetic appeal of a component the present coatings primarily address the functional aspect. Depending on the coating material and the process, they can increase the corrosion and wear resistance of a part. Coatings can also make the surface smoother lowering its coefficient of friction. Apart from these there are a host of other applications which coatings can address. The selection of a particular coating for a surface finishing need depends on the requirements to be satisfied for the particular component keeping in mind the ecological concern. Moreover, once

installed, periodic monitoring of the coating health and its maintenance is important to obtain optimum performance from the component.

Acknowledgment

Authors gratefully acknowledge the publishers (Elsevier and others) of a number of technical/research papers used for preparation of this chapter.

See also: 3.16 Hard Coatings on Cutting Tools and Surface Finish

References

1. Mellor, B. G. *Surface Foatings for Protection Against Wear*; Woodhead Publishing Limited: Cambridge, 2006.
2. Hogmark, S.; Jacobson, S.; Larsson, M. Design and Evaluation of Tribological Coatings. *Wear* **2000**, *246*, 20–33.
3. Sankara Narayanan, T. S. N.; Baskaran, I.; Krishnaveni, K.; Parthiban, S. Deposition of Electroless Ni-P Graded Coatings and Evaluation of Their Corrosion Resistance. *Surf. Coat. Technol.* **2006**, *200* (11), 3438–3445.
4. Dingremont, N.; Bergmann, E.; Collignon, P. Application of Duplex Coatings for Metal Injection Moulding. *Surf. Coat. Technol.* **1995**, *72* (3), 157–162.
5. Chu, X.; Barnett, S. A.; Wong, M. S.; Sproul, W. D. Reactive Unbalanced Magnetron Sputter Deposition of Polycrystalline TiN/NbN Superlattice Coatings. *Surf. Coat. Technol.* **1993**, *57*, 13–18.
6. Selinder, T. I.; Nordin, M.; Larsson, M.; *et al.* Performance of PVD TiN/TaN and TiN/NbN Superlattice Coated Cemented Carbide Tools in Stainless Steel Machining. *Surf. Coat. Technol.* **1998**, *105* (1/2), 51–55.
7. Sun, H.; Liu, S.; Sun, L. A Comparative Study on the Corrosion of Galvanized Steel Under Simulated Rust Layer Solution With and Without 3.5 wt% NaCl. *Int. J. Electrochem. Sci.* **2013**, *8*, 3494–3509.
8. Bigdeli, F.; Allahkaram, S. R. An Investigation on Corrosion Resistance of As-Applied and Heat Treated Ni–P/nanoSiC Coatings. *Mater. Des.* **2009**, *30* (10), 4450–4453.
9. Sahoo, P.; Das, S. K. Tribology of Electroless Nickel Coatings – A Review. *Mater. Des.* **2011**, *32* (4), 1760–1775.
10. Lee, C. K. Corrosion and Wear-Corrosion Resistance Properties of Electroless Ni–P Coatings on GFRP Composite in Wind Turbine Blades. *Surf. Coat. Technol.* **2008**, *202* (19), 4868–4874.
11. Lee, C. K. Structure, Electrochemical and Wear-Corrosion Properties of Electroless Nickel–Phosphorus Deposition on CFRP Composites. *Mater. Chem. Phys.* **2009**, *114* (1), 125–133.
12. Chow, G.; Bedi, R. S.; Yan, Y.; Wang, J. Zeolite as a Wear Resistant Coating. *Microporous Mesoporous Mater.* **2012**, *151*, 346–351.
13. Merklein, M.; Schrader, T.; Engel, U. Wear Behavior of PVD-Coatings. *Tribol. Ind.* **2012**, *34* (2), 51–56.
14. Nordin, M.; Larsson, M.; Hogmark, S. Mechanical and Tribological Properties of Multilayered PVD TiN/CrN, TiN/MoN, TiN/NbN and TiN/TaN Coatings on Cemented Carbide. *Surf. Coat. Technol.* **1998**, *106*, 234–241.
15. Jimenez, H.; Gil, L.; Staia, M. H.; Puchi, E. S. Effect of Deposition Parameters on Adhesion, Hardness and Wear Resistance of Sn–Ni Electrolytic Coatings. *Surf. Coat. Technol.* **2008**, *202*, 2072–2079.
16. Gul, H.; Kilic, F.; Aslan, S.; Alp, A.; Akbulut, H. Characteristics of Electro-Co-Deposited Ni–Al_2O_3 Nano-Particle Reinforced Metal Matrix Composite (MMC) Coatings. *Wear* **2009**, *267*, 976–990.
17. Balakai, V. I.; Balakai, I. V. Wear Resistance of Electrolytic Nickel–Boron Alloy Deposited from a Chloride Electrolyte. *Russ. J. Appl. Chem.* **2009**, *82* (9), 1547–1550.
18. Kanta, A. F.; Vitry, V.; Delaunois, F. Wear and Corrosion Resistance of Electroless Nickel–Boron Coated Mild Steel, Vol. 638–642, pp. 846–851. In *6th International Conference on Processing and Manufacturing of Advanced Materials – THERMEC 2009*, Berlin, August 25, 2009; 2010.
19. Lopez, A. J.; Urena, A.; Rams, J. Wear Resistant Coatings: Silica Sol–Gel Reinforced with Carbon Nantubes. *Thin Solid Films* **2011**, *519*, 7904–7910.
20. Qiu, N.; Wang, L.; Wu, S.; Likhachev, D. S. Research on Cavitation Erosion and Wear Resistance Performance of Coatings. *Eng. Fail. Anal.* **2015**, *55*, 208–223.
21. Sieber, M.; Mehner, T.; Dietrich, D. Wear-Resistant Coatings on Aluminium Produced by Plasma Anodising – A Correlation of Wear Properties, Microstructure, Phase Composition and Distribution. *Surf. Coat. Technol.* **2014**, *240*, 96–102.
22. Arai, S.; Miyagawa, K. Frictional and Wear Properties of Cobalt/Multiwalled Carbon Nanotube Composite Films Formed by Electrodeposition. *Surf. Coat. Technol.* **2013**, *235*, 204–211.
23. Chen, X. H.; Chen, C. S.; Xiao, H. N.; *et al.* Dry Friction and Wear Characteristics of Nickel/Carbon Nanotube Electroless Composite Deposits. *Tribiol. Int.* **2006**, *39* (1), 22–28.
24. Zishan, C.; Hejun, L.; Qiangang, F. SiC Wear Resistance Coating with Added Ni, for Carbon/Carbon Composites. *Surf. Coat. Technol.* **2012**, *213*, 207–215.
25. Foster, J. A. Sealing Rougher Surface Finishes Using Conformable Rubber Coating on MLS; SAE Technical Paper 2001-01-0687, 2001, doi:10.4271/2001-01-0687.
26. Wang, H.; Zhang, R.; Yuan, Z.; *et al.* A Comparative Study of the Corrosion Performance of Titanium (ti), Titanium Nitride (TiN), Titanium Dioxide (TiO_2) and Nitrogen-Doped Titanium Oxides (N–TiO_2), as Coatings for Biomedical Applications. *Ceram. Int.* **2015**, doi:10.1016/j.ceramint.2015.05.153.
27. Oraon, B.; Majumdar, G.; Ghosh, B. Improving Hardness of Electroless Ni–B Coatings Using Optimized Deposition Conditions and Annealing. *Mater. Des.* **2008**, *29* (7), 1412–1418.
28. Sahoo, P. Wear Behaviour of Electroless Ni–P Coatings and Optimization of Process Parameters Using Taguchi Method. *Mater. Des.* **2009**, *30* (4), 1341–1349.
29. Gologana, V. F.; Bobanovaa, Zh. I.; Enakib, M. A.; *et al.* Wear Resistant Chromium Coatings Deposited in a Tetrachromate Electrolyte Using an Inductance–Capacitance Device. *Surf. Eng. Appl. Electrochem.* **2014**, *50* (2), 111–116.
30. Das, S. K.; Sahoo, P. Tribological Characteristics of Electroless Ni–B Coating and Optimization of Coating Parameters Using Taguchi Based Grey Relational Analysis. *Mater. Des.* **2011**, *32*, 2228–2238.
31. Sahoo, P. *Engineering Tribology*; Prentice Hall of India: New Delhi, 2005.
32. Hogmark, S.; Jacobson, S.; Vingsbo, O. Surface Damage. In *Friction, Lubrication and Wear Technology: ASM Handbook*; Blau, P. J., Ed.; ASM International: Metals Park, OH, 1992; Vol. 18; pp. 176–183.

Relevant Websites

http://www.galvanizeit.org/
American Galvanizers Association.
http://www.corrosionpedia.com
Corrosion and Abrasion Solutions Ltd.
http://www.engineershandbook.com
Engineer's Handbook.
http://www.syntheticcoatings.ie
Synthetic Coatings Ltd.
http://www.finishing.com
The Finishing Industry.
http://www.tstcoatings.com/thermal_spray_processes.html
Thermal Spray Technologies.

3.4 Residual Stresses in Thermal Spray Coating

AFM Arif and KS Al-Athel, King Fahd University of Petroleum and Minerals, Dhahran, Saudi Arabia
J Mostaghimi, University of Toronto, Toronto, ON, Canada

© 2017 Elsevier Inc. All rights reserved.

3.4.1	**Introduction**	56
3.4.1.1	Sources of Residual Stresses	56
3.4.1.2	Quality Issues	57
3.4.1.3	Importance of Residual Stress Estimation	57
3.4.2	**Experimental Measurement**	58
3.4.2.1	Destructive Methods	58
3.4.2.1.1	Hole-drilling method and layer removal	58
3.4.2.1.2	Material removal by chemical etching	59
3.4.2.2	Nondestructive Methods	59
3.4.2.2.1	Curvature method (*in situ*)	59
3.4.2.2.2	Curvature method (*ex situ*)	59
3.4.2.2.3	Diffraction method	60
3.4.2.2.3.1	X-ray diffraction	60
3.4.2.2.3.2	Synchrotron XRD	60
3.4.2.2.3.3	Neutron diffraction	60
3.4.2.2.4	Micro-RS	60
3.4.2.2.5	Photoluminescence piezo-spectroscopy	61
3.4.2.3	Other Methods	61
3.4.2.4	Residual Stress Measurement Work Done at Centre for Advanced Coatings Technologies	61
3.4.3	**Numerical Estimation**	64
3.4.4	**Summary and Outlook**	68
Acknowledgment		68
References		68

3.4.1 Introduction

Thermal spray coating techniques are very versatile, with different available methods that can be used for a wide range of engineering applications. Thermal spray coating involves a wide range of different techniques such as wire-arc, high velocity oxy-fuel (HVOF), plasma spraying, etc., that are used in many applications (Figure 1). One of the major issues concerning the coating performance is the effect of the residual stresses developed during the coating process on the life and behavior of the coating layer. Measuring these stresses could be very crucial to the evaluation process. Therefore, a lot of research has been done focusing on measuring and calculating the residual stresses quantitatively and qualitatively. Most of the work done was focused on pure experimental techniques to measure the residual stresses during the coating process. Others use a hybrid experimental and analytical procedure to get the stress values. Recently, there has been a lot of work that evolves the use of numerical techniques such as finite element (FE) analysis to calculate the stresses, with the use of experiments for calibrations.

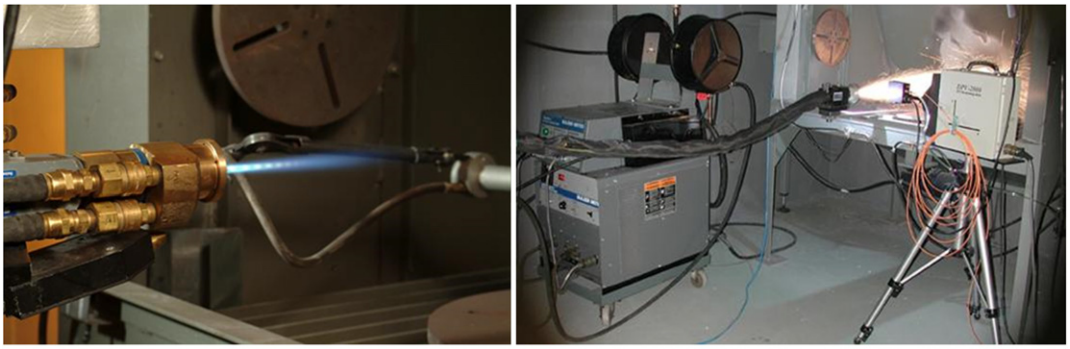


Figure 1 Examples of thermal spray coating techniques, (a) High velocity oxy-fuel spray (left) and (b) wire-arc spray (right). © Centre for Advanced Coating Technologies, University of Toronto.

3.4.1.1 Sources of Residual Stresses

There are two main sources of residual stresses in thermally sprayed coatings. The first is the rapid cooling that happens when the temperature of the sprayed particles drops from the melting temperature to the substrate temperature during the deposition process. This type of stresses is called 'intrinsic,' 'quenching,' or deposition stresses, and has a tensile nature. The second source, and possibly the most contributing, is due to the difference in coefficient of thermal expansion (CTE) between the coating and the substrate. This happens when the coating system temperature starts to drop from the average temperature reached after the deposition process to the room temperature, which is called secondary cooling. The residual stresses are then induced by the mismatch in the thermal shrinkage of the substrate and the coating. In general, if the CTE of the coating is smaller than that of the substrate, compressive residual stresses are likely to form, and vice versa. Aside from the two main reasons, other factors may contribute to the formation of residual stress indirectly. For example, kinetic energy of the coating particles affects the level of the residual stresses formed during deposition. This is related to the coating velocity and particles size.[1,2] Literature shows that the sources of residual stresses in thermal spray coating systems include:

1. Coating deposition process
   - Particles on impact, freeze and contract creating tensile stresses.
   - Largely relieved by the formation of micro-cracks in coatings.
2. Material mismatch stress
   - Generated when coated components cool down to room temperature.
   - Differences in thermal expansion coefficients of coating and underlying substrates.
3. Growth of the Thermally Grown Oxides (TGO)
   - Specially important for thermal barrier coatings (TBCs).
4. Transformation induced stresses
   - Hot corrosion of TBCs.

3.4.1.2 Quality Issues

Many of the process parameters such as the deposition speed, velocity of the spray gun, coating temperature, coating thickness, etc., play an important role in the formation of residual stresses. On the other hand, these parameters cannot be optimized solely based on residual stresses, and the quality of final coating has to be considered as well. The spray parameters must be selected carefully to obtain good quality coatings. A general flow of the coating process steps that affects the quality of the coating can be summarized through the following[3]:

Flow of spray particles → particle impact and deformation → coating formation → splat interactions → formation of pores → coating build up → final coating layer.

Having a clear understanding of the complete process can help in predicting the residual stresses and linking them with the process parameters, microstructure, coating quality, and surface quality.

3.4.1.3 Importance of Residual Stress Estimation

Compressive residual stresses are generally more favorable and their presence may cause no harm to the coating system in many cases, unless they exist in relatively large values. Tensile residual stresses are usually more harmful and raise many coating problems such as:

- initiation and propagation of cracks, which may lead to interface delamination,
- loss in adhesion, and
- fatigue failure.

For example, in TBCs, which are one of the main applications utilizing thermal spray coating, the effect of residual stresses plays a very important role in evaluating the life of the TBC. As shown in **Figure 2**, these cracks could propagate to the stage where complete failure of the coating could occur.[4,5] One of the most common techniques in measuring the residual stresses is by using hole drilling.[2,6,7] Usually in this process, the drilling is carried out gradually at the micro level until the substrate is reached. Since this process involves slow feed rates, high cutting rates, and low drilling depth for every step, it is quite accurate to assume the process generates no stresses. In addition, to ensure no thermally-induced stresses due to the drilling process, a cooling period is applied between every other drilling increment.[7] Then, due to the removal of the material, the residual stresses are released causing deformations to the area surrounding it. Finally, these deformations can be used to measure the strains using strain gages and calculate the stresses knowing the material properties of coating material.

Another experimental technique is the curvature measurements.[8,9] The basic principle in this approach is that after each coating deposition, the thermal mismatch between the coating and the substrate and the rapid cooling of the coating material deposited onto the surface will cause the free contraction of

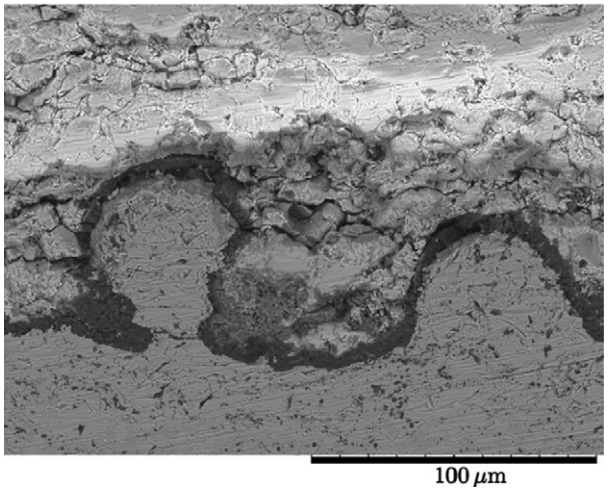


Figure 2 Scanning electron micrograph showing a magnified view of an oxidized thermal barrier coatings showing micro cracking in the vicinity of the thermally grown oxide layer between the top-coat and the bond-coat. The trajectory of the local delamination resides primarily within the top-coat and connects the peaks of the undulations.

the coating to be restricted by the substrate material. This generates internal forces acting between the coating and the substrate that leads to a bending moment causing the material to bend due to the stresses developed within the layers. With more coating layers, more coating thickness will build up and hence an increase in the bending curvature. By correlating the coating thickness and the curvature, the forces and moment balance can be used to calculate the residual stresses developed during the coating process.[10–13]

The curvature measurement method has some variations and can be extended and used along with Raman spectroscopy (RS) to measure the residual stresses.[14] A similar approach can be utilized by chemical substrate removal process[15] where the residual stresses can be calculated from the deflection and curvature of the free standing coating layer alone. The curvature of the coating layer can be evaluated using the same approach using the curvature measurement method, which is based on the classic Stoney equation.[16]

With the advancements in numerical techniques and simulations, new methods have emerged that combines experimental techniques along with numerical analysis. In most of the computational work done in calculating the residual stresses, experiments are used merely to capture the roughness of the coating and substrate interface in addition to the temperature profile. Then, it would be implemented into a FE model where the temperature profile is imposed into the model and the residual stresses are calculated.[2,17,18] The use of finite element methods (FEMs) can be beneficial since only one model needs to be calibrated, and then a variety of analyses can be performed for various coating thicknesses, cooling rates, etc., to calculate the residual stresses.

Other techniques and methods are available that involve a combined experimental and computational approach.[19] Scanning electron microscopy (SEM) can be used to observe the coating profile for any coating process, then object oriented finite element (OOF) is used to calculate the residual stresses.[3,19] This is done by discretizing the coating microstructure into a FE mesh and imposing the temperature profile of the coated sample into the FE model. The model can then be used to calculate the thermal residual stresses developed during the coating process.

3.4.2 Experimental Measurement

Residual stress is an important factor influencing the integrity and performance of thermal spray coatings. Residual stress in thermally sprayed deposits originates from the high-temperature excursions experienced by the material during the process. Residual stress can affect the integrity of the deposit–substrate system as well as its performance and reliability of the entire part. Hence, until now considerable efforts have been made to understand and predict the residual stresses that are generated during the production of thermal spray coatings.[20,21] Different types of techniques were developed for the measurement of residual stresses in thermal spray coatings and all are commonly characterized by two major categories named as destructive method and nondestructive method. The widespread use of each of these methods are fairly restricted because of problems associated with measurement accuracy, spatial resolution, ease of measurement, applicability to a broad range of materials and geometries, feasibility for use as a quality control device in mass production or during service, and flexibility for scaling up from small to large components.[22–24]

3.4.2.1 Destructive Methods

3.4.2.1.1 Hole-drilling method and layer removal

Destructive methods are based on material removal by drilling a hole in the coating/substrate or by grinding off a coating layer. The strain changes are monitored with strain gauges attached to the coating or the substrate, respectively, as shown in **Figure 3**. These methods are capable of determining depth profiling of residual strain. The destructive nature of these conventional techniques limits their use in finished components (e.g., in aerospace applications) and also causes uncertainty in the coating mechanical properties during hole drilling and layer removal (LR).[25] Furthermore, the removal of a layer with uniform thickness is physically very difficult and analyzing the strain gage data is not a simple task. Hence, a numerical method is necessary to validate the experimental results of stress measurement through this method. While the method has been used to evaluate the levels of stress in coatings, it is not really practical for thin or for brittle coatings.

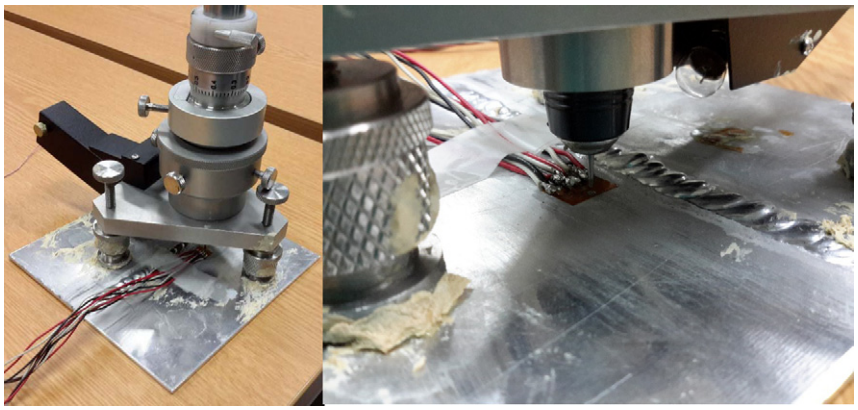


Figure 3 Hole-drilling setup for residual stress measurements.

Numerous researchers have conducted studies based on this approach and have calculated the residual stress of thermal spray coatings.[26–28] For example, Montay *et al.*[29] measured the residual stress gradient in depth of the coating by hole-drilling method (HDM). They calculated the stress by using strain gage rosette.

Greving *et al.*[30] developed a modified LR method for evaluating through-thickness residual stress distributions in thermal spray coatings. The method was experimentally applied to several typical industrial thermal spray coatings. Their results show that the modified LR method is better suited for calculating residual stresses in thermal spray coatings than the conventional LR method. Suresh and Giannakopoulos[31] proposed a general methodology for the determination of surface residual stresses and residual plastic strains using instrumented sharp indentation. This technique can be directly used for residual stress measurements in applications such as thin films, structural coatings, and engineered surfaces whose properties are altered by methods such as mechanical working, etching, ion implantation, case hardening, laser treatments, shot peening, or laser shock peening. Residual stress determination by this continuous load-displacement monitoring during indentation represents a promising alternative and also offers several potential advantages as a possible tool for the mechanical probing of materials. Recently, Sebastiani *et al.*[32] proposed a novel procedure for local residual stress measurement in plasma-sprayed single splats, based on focused ion beam micron-scale ring-core milling and digital image correlation (DIC) for relaxation strain mapping approach. This methodology can give sub-micrometer spatial resolution and it is independent of the splat microstructure. Further, this approach could be applied even to completely amorphous materials.

3.4.2.1.2 Material removal by chemical etching

In 1988, Hobbs and Reiter[33] modified the Hendricks approach[34] and proposed a simple bending theory for determination of residual strain at both the exposed and the interface surfaces in the plasma-sprayed zirconia layer. For this measurement, they prepared individual coating layer by chemical etching. This technique provides a clear insight into the residual stress state of ceramic TBCs. Using the same theory, Yung-Chin Yang[35] measured the residual strain and stress formed in the plasma-sprayed hydroxyapatite coatings. In order to obtain the complete and accurate value and state of the residual stress, the non-stressed free coating layers were produced from the substrate. For this purpose, he used particular types of the substrate and different directions of cooling jets.

3.4.2.2 Nondestructive Methods

3.4.2.2.1 Curvature method (in situ)

Curvature method is a part of nondestructive methods and also the most informative method of residual stress evaluation in thermal spray coatings. In 1909, Stoney derived the formula for this method[36] and it was further developed by Brenner and Senderoff.[37] In 1988, Kuroda *et al.*[38] developed a practical method for *in situ* measurement of both coating thickness and deposition stress during thermal spraying by using this approach. Meantime, Gill and Clyne[39] also measured the residual stress of thermal spray coating by *in situ* curvature approach. Since, numerous curvature measurement methods have been developed and are frequently used to determine the stresses within thermally sprayed coatings and layers.[38–42] This method works based on force and moment balance between the substrate and the coating. During the spray process, the deposition of a layer can induce stresses, which cause the substrate to curve. The resulting changes in curvature during deposition make it possible to calculate the corresponding variations in stress as a function of deposit thickness. Curvature can be measured by contact methods (e.g., profilometry and strain gages) or noncontact methods (e.g., video, laser scanning, grids, and double crystal diffraction topology).[24]

Matejicek and Sampath[43] developed a novel approach based on *in situ* thermoelastic curvature method for determination of stresses and moduli in thermal spray coating with a newly designed instrument and improved the analysis. This approach was based on Kuroda and Clyne's[40] experimental and theoretical treatment with appropriate modifications and improvements. Here the residual stress distribution in the entire sample was determined by superposition of the quenching and thermal stress distributions. For this purpose, the temperature and curvature of the substrate was recorded during the entire deposition process. Quenching stress was determined from the deposition period and thermal stress and coating modulus was determined from the cooling period. Jianguo Zhu *et al.*[44] utilized the three-dimensional digital image correlation (3D DIC) technique to measure the curvature of a thermally sprayed coating sample (**Figure 4**). Then they adopted elastic–plastic FEM to interpret the cross-sectional stress distribution. Their findings predict that the system has several advantages such as a noncontact and full-field optical displacement measurement with high accuracy. The setup is simple and easy to operate with little sample preparation. In addition, the authors believe that 3D DIC has a very high potential and broad application prospects for monitoring of curvature *in situ* by using high-temperature speckles fabrication techniques.

3.4.2.2.2 Curvature method (ex situ)

This is one of the simplest methods to determine the average stress values of thermal sprayed coatings by means of sample preparation, curvature measurement, and the analysis. However, this approach has some limitations and it cannot distinguish a stress gradient and stresses on different phases in coatings. For this measurement, substrate and the coating have to be planar and measurable curvature should be induced without changing the substrate elasticity. The coating and substrate are detached and their respective curvatures are measured. From the difference between the original and final curvatures, the stresses can be calculated.[45–47] This linear approximation stress profile of the coating microstructure was sufficient for certain practical commitments. In 1996, Kesler *et al.*[48] used this *ex situ* curvature measurement method to determine the residual stresses at room temperature. Their result found residual stresses as large as 200 MPa in plasma-sprayed thick Ni–Al_2O_3 composite coatings at room temperature. In principle, this method can be used to determine

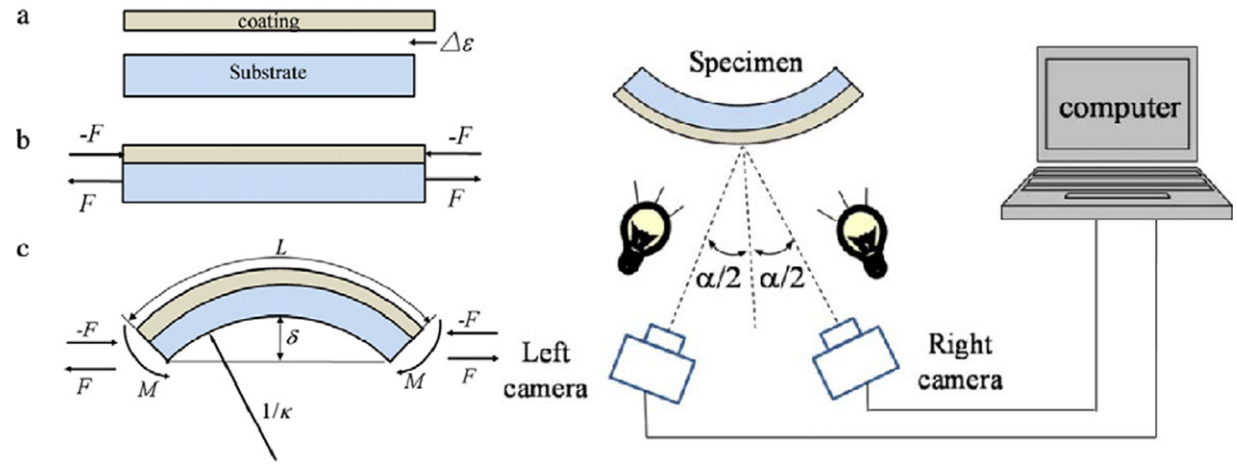


Figure 4 Schematic of the generation of thermal residual stress in a strip coating as a result of the misfit strain, $\Delta\varepsilon$: (a) unconstrained strains due to temperature difference; (b) strain compatibility at interfaces; and (c) bending and balance of bending moment, and the three-dimensional digital image correlation setup.[44]

physical and mechanical properties of layered and graded coatings produced by a number of different processing methods, including physical vapor deposition (PVD).

3.4.2.2.3 Diffraction method

The diffraction method of stress determination is based on the measurement of changes in crystal plane spacing in different directions with respect to the specimen surface, which exhibit themselves as shifts in angular positions of respective diffraction peaks. From this strain determination, stress can be calculated with the use of appropriate elastic constants.[22,49] This nondestructive nature method has plenty of advantages such as phase selectiveness and moderate restrictions on specimen dimensions and repeated measurements on the same specimen. Further, this method has a capability to determine the stresses in each individual phases in composites microstructures by varying the nature of diffraction.[50] Currently different diffraction methods are available and are distinguished by the types of beam source and its power such as X-ray, neutron, electron, and synchrotron X-ray.

3.4.2.2.3.1 X-ray diffraction

This is most the popular method for direct measurement of residual stresses in coating microstructure by observing the shift of selected X-ray diffraction (XRD) peaks. The 'sin2ψ' is the commonly used method to calculate residual stress[51] and numerous investigations have been carried out on row.[20–22,49,50] Low penetration ranges of X-rays (in the order of few ten microns) limit the investigation to a thin surface layer, which may be impractical for coatings with higher thickness and roughness. However, with a modified experimental procedure, the same feature can be used to determine through-thickness stress profiles.

3.4.2.2.3.2 Synchrotron XRD

Synchrotron (or hard) X-rays are alternative for conventional X-rays to measure the residual stress in coating microstructure. Synchrotron sources can be as much as a million times more intense than conventional sources and can provide high energy photons (20–300 keV) that are over a 1000 times more penetrating than conventional X-rays. More penetration depth means this technique is capable of providing high spatial resolution and 3D maps of the strain distribution in coating. Another great advantage that synchrotrons have is that intense narrow beams of 1 mm–10 μm in size are possible. Using this source many attempts have been made to determine the residual stress near the coating surface.[52] Stoica *et al.*[53] applied the X-ray synchrotron radiations to measure the residual stress distribution within the as-sprayed and hot isostatically pressed thermal spray cermet (WC–12Co) coatings. The sin2ψ method was applied with three ψ angles between 7° and 9° at 25 keV and between 12° and 14° at 15 keV.

3.4.2.2.3.3 Neutron diffraction

Neutron diffraction is an alternative to XRD and most of the drawbacks to the use of X-rays have been resolved. The penetrating power of neutrons enables through-thickness stress profiling without any material removal up to several millimeter based on materials. The stress determination in neutron diffraction is based on the same principle as XRD. Lower spatial resolution and challenging experimental procedure limits its usage. However, researchers widely used this method to determine the residual stress of thermal sprayed coatings.[54–57] Ahmed *et al.*[58] successfully applied vertical scanning technique in neutron diffraction experiment and measured the residual strain in 400 μm thick WC–Co thermal spray coatings.

3.4.2.2.4 Micro-RS

Micro-RS is a powerful technique to study the structural changes in the coatings because Raman scattering depends on electron–phonon interactions that are very sensitive to local environments. Due to its sensitivity, it is a suitable technique to identify and study small changes in the stress states of the coatings. This is nondestructive and noninvasive technique and has a high spatial resolution (1 μm or less).[59] This

technique allows measurements in very small areas (micrometer range) for the assessment of the residual stresses in the thermal sprayed coatings cross-section as well in the thin interlayer such as the thermal growth oxides in TBCs.[60,61] Tanaka *et al.*[62,63] measured the residual stress in air plasma-sprayed Y_2O_3 stabilized ZrO_2 TBC by using micro-RS. They used the frequency shift of Raman peak from tetragonal phase ($\approx 640\ cm^{-1}$) for determination of local stress in TBC system. Teixeira *et al.*[64] measured the residual stresses within the PVD bond coating and oxide interlayer by the micro-RS technique in cross-sectioned samples. Further, they introduced micro-displacement laser transducer technique to measure the residual stress within the single as-deposited PVD bond coatings.

3.4.2.2.5 Photoluminescence piezo-spectroscopy

Photoluminescence piezo-spectroscopy (PLPS) is a technique that can be conveniently used to determine the stress in alumina-containing material with high resolution, particularly it is a very useful technique to measure residual stress on TGO layers.[65,66] Zhao and Xiao[67] measured the residual stresses in TBCs by PLPS and compared with indentation technique. Similarly, Dong Liu *et al.*[42] measured the residual stresses of EB-PVD deposited TBC and the TGO layers by RS and PLPS, respectively. However, the direct usage of PLPS has been restricted by the absence of alumina in TBC system.

3.4.2.3 Other Methods

In 1967, Crecraft[68] showed that the acoustoelastic law could be employed for stress measurement of engineering materials. This method provides a macro residual stress over a large volume of engineering material. It also has the advantage of being able to be measured in the bulk area of the material and are therefore well suited to routine inspection operations.[69] However, this method cannot be used in thermal sprayed coating system due to the presence of porosity. Similarly, other existing methods such as magnetic and electrical techniques, thermoelastic and photoelastic methods have certain limitations which restrict their complete utilization for measuring the residual stress in thermal sprayed coatings.[24]

3.4.2.4 Residual Stress Measurement Work Done at Centre for Advanced Coatings Technologies

In 2009, *in situ* curvature measurement device was developed by using a linear variable differential transformer (LVDT) to the measurement of residual stress in single and multilayer coating formations. Further, a new numerical model was developed, employing a commercially available FEM software package, which addressed the shortcomings of the existing models. The numerical model was used to predict the development of internal stresses during deposition of the coatings and their subsequent cooling to room temperature. Resultant predictions were compared with experimental measurements of the curvature of test specimens during deposition to validate the numerical model. Finally, the numerical model was employed to predict the stresses expected under service conditions, incorporating the preexisting internal stresses arising from the deposition process. The multilayer coating developed in this study was predicted to exhibit significantly lower stresses than a conventional coating system.[70]

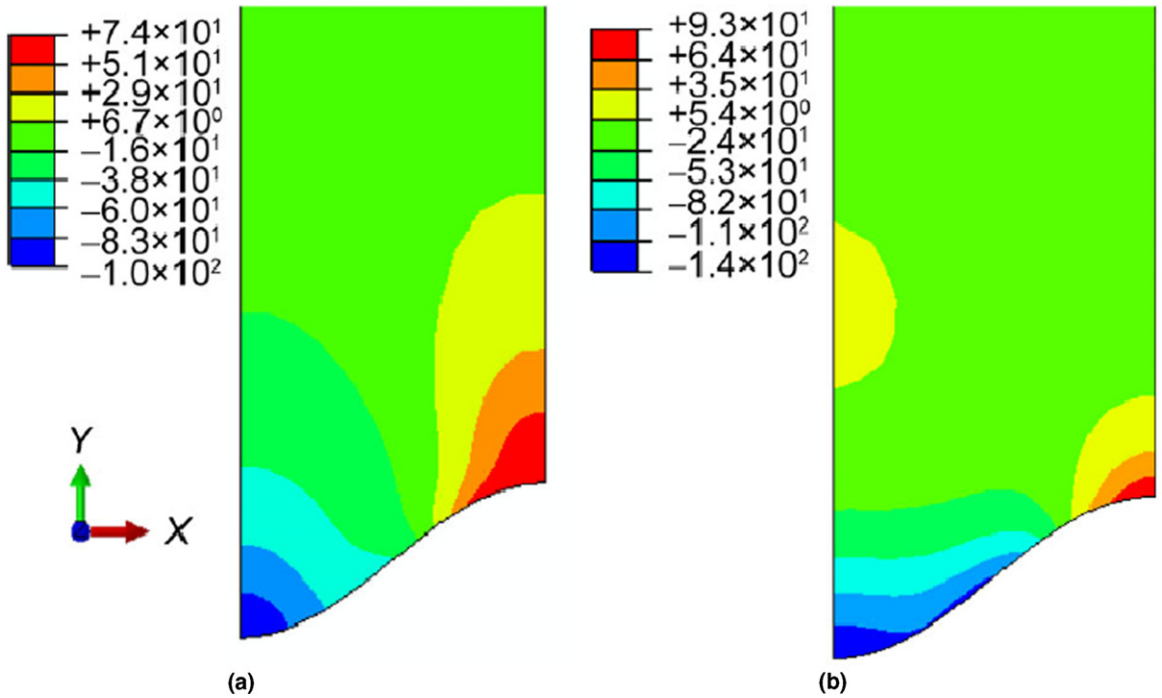


Figure 5 Residual stress σ_{yy} (MPa) in thermal barrier coatings after cooling with thermally grown oxide growth for amplitude A = 20 μm: (a) 3 μm TGO thickness and (b) 5 μm TGO thickness.[72]

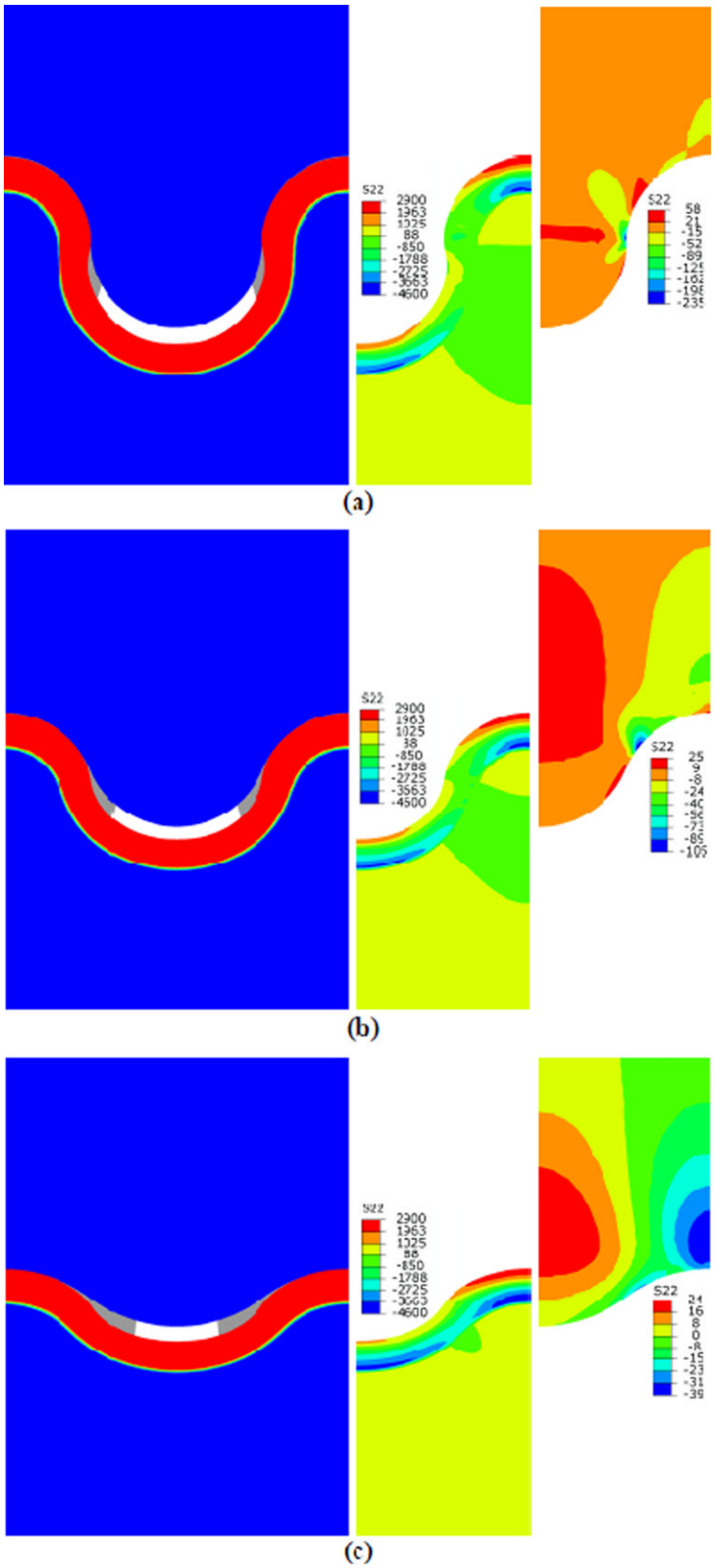


Figure 6 Simulation results and contours of the stress component S_{22} (MPa) in the top-coat and the bond-coat near the thermally grown oxide after 400 h of oxidation at 1050 °C and cool-down to room temperature for undulations with different initial amplitudes of (a) 15 μm, (b) 10 μm, and (c) 5 μm. The cohesive elements that have not yet failed completely are colored gray.[4]

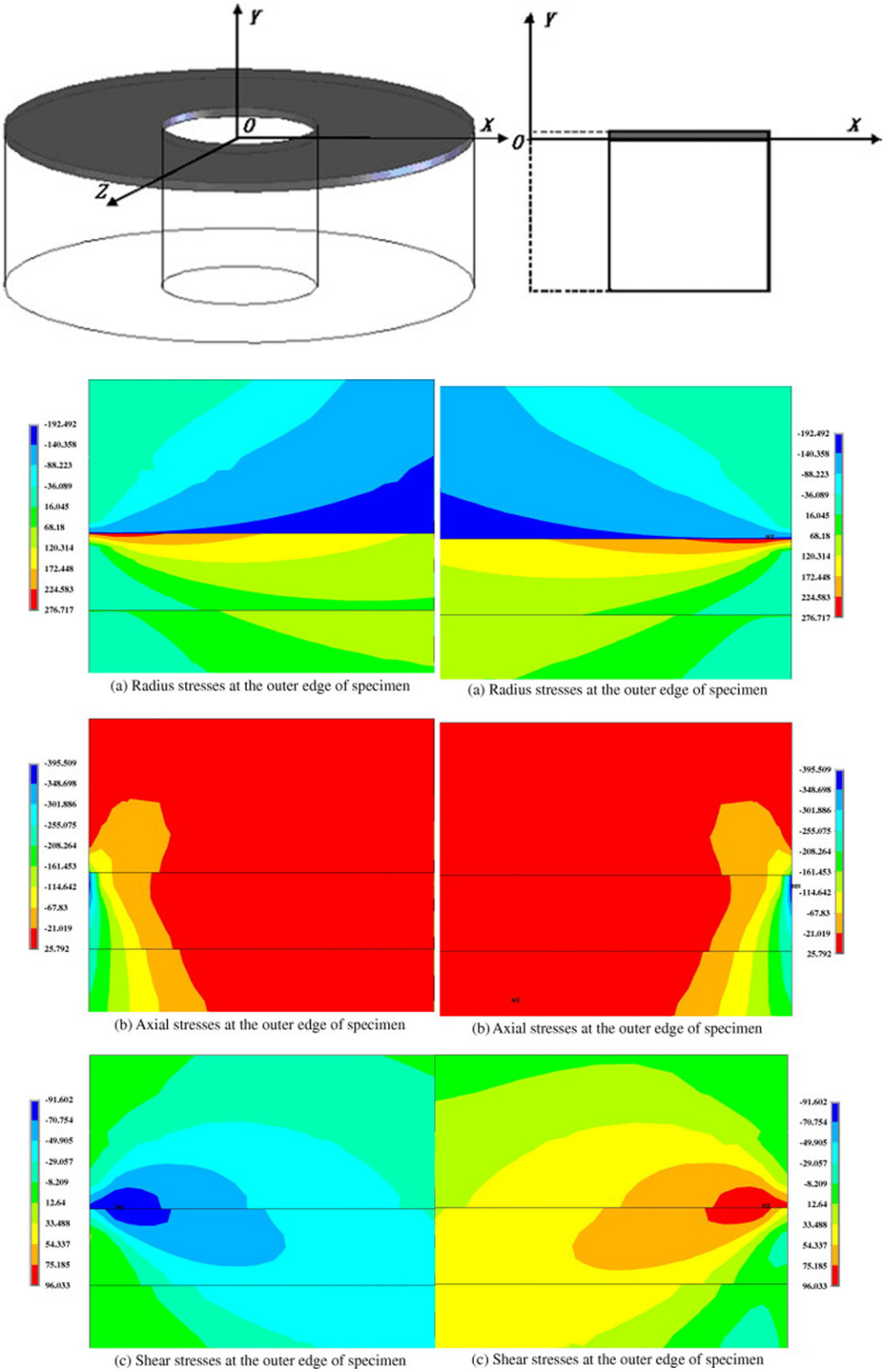


Figure 7 Schematic description of the geometry used in the finite element modeling with distribution of (a) radial, (b) axial, and (c) shear residual stresses (MPa) at the edge of hole (left), and at the outer edge of specimen (right).[79]

3.4.3 Numerical Estimation

Even though few analytical models have been developed,[71] the prediction of residual stresses in thermal spray coatings was mainly carried out using the FEM. This is not surprising as FEM is more popular than other numerical schemes due its flexibility and suitability for modeling complex geometries. For the last few decades,[39] the residual stresses developed in thermal spray coatings has been widely attributed to the mismatch in the CTE between the various layers of the coating system. However, it can be argued that other phenomena such as TGO growth, phase transformations at various interfaces, inhomogeneity of respective layers, surface roughness of the substrate, deposition process parameters, etc., all contribute to the residual stresses even though their contribution is negligible.[72] Therefore, most of the research work carried out considered only the thermal residual stresses which mainly results from the thermal-mismatch stresses developed during cooling of the coating system to room temperature.

Coupled thermal stress analysis with conventional FE formulation is more popular in this field. However, a few modified numerical schemes such as the death and birth scheme, image-based FEM, etc., have recently been used to accurately predict the residual stresses as discussed below.

Starting with computation that was carried out using conventional FE schemes, Limarga *et al.*[73] evaluated the residual stresses induced during the thermal cycling of air plasma-sprayed zirconia TBC using one-dimensional FE model. Coupled thermal–structural elements with creep/plasticity capability and calibrated properties/boundary conditions were used for computation. All the interfaces between the respective layers were assumed to be flat and perfectly bonded. The FE result was validated using RS measurements. The results indicated that large in-plane stresses, which are dependent on cooling rates, are developed at the surface of the coating due to thermal cycling. Consequently, numerous cracks were initiated which result in the failure of the coated samples. The observed discrepancies between the experimental and numerical values were attributed to the use of homogenous, crack-free, and isotropic material model. Similar analysis was carried out by Ng and Gan.[74]

Jianguo Zhu *et al.*[44] investigated the residual stress field and failure mechanism of plasma-sprayed TBC using a two-dimensional plane strain formulation. In addition to the thermal-mismatch stresses, the stresses induced due to sintering/creep, stress relaxation, TGO growth, and surface roughness were included in the calculated residual stresses. A thin section which contains half-amplitude of the sinusoidally-represented surface roughness was used for the computation. The results show that

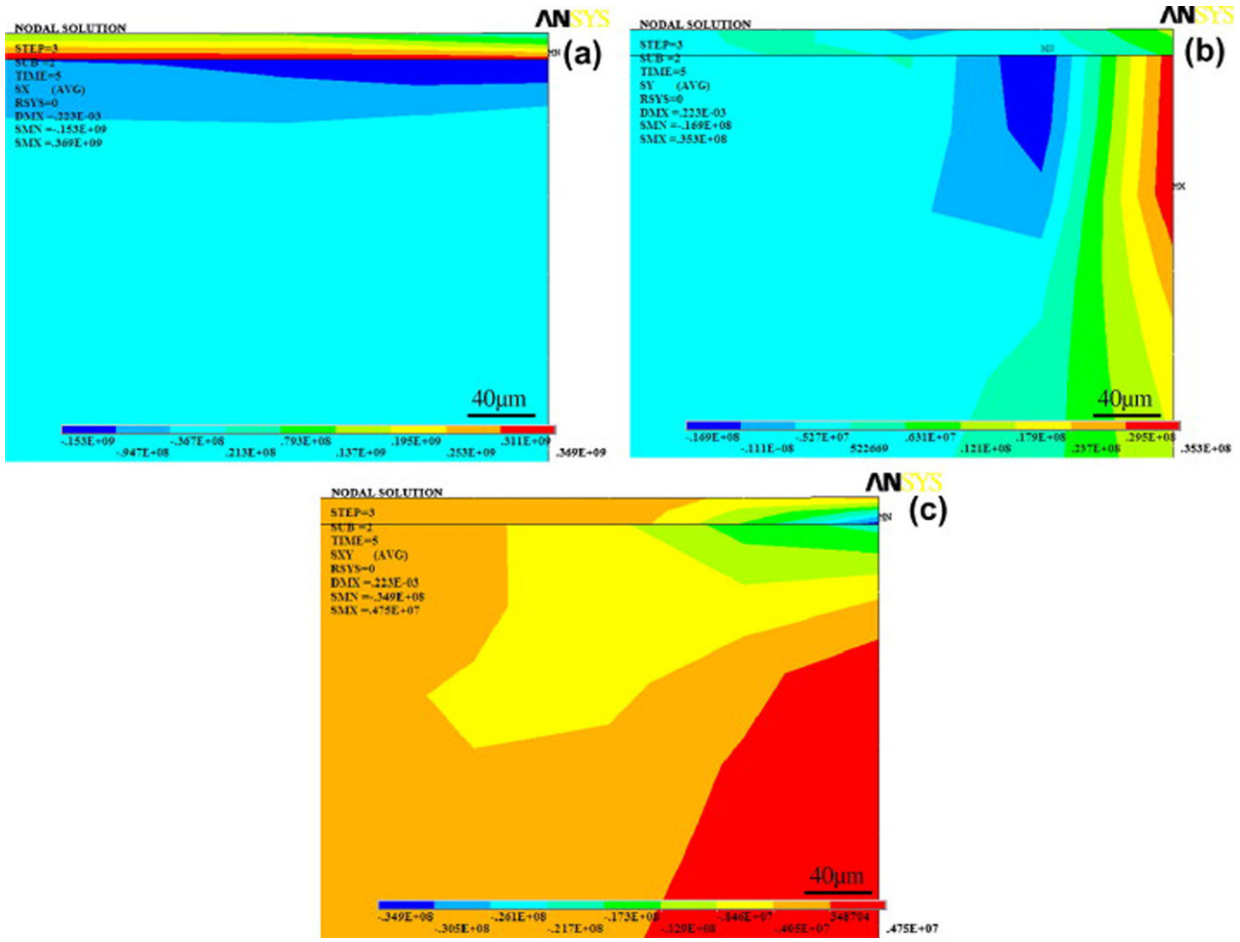


Figure 8 Typical contour plot of stress (MPa) distribution of (a) σ_{xx}, (b) σ_{yy}, and (c) σ_{xy} after the first layer deposition being finished for the LZ/8YSZ thermal barrier coatings (the above layer indicate one layer of the bond-coat).[83]

maximum tensile stress which increases with thermal cycling is developed in a direction perpendicular to the interface (Figure 5). Consequently, the cracks initialize in the high stress regions and propagate along the TBC/bond-coat (BC) interface resulting in the spallation failure of the coating. Therefore, the model has captured the experimentally observed failure mechanism of TBCs qualitatively. However, quantitative comparison of the numerical stress values with experimental values was not made. Similar analysis was carried out by Ranjbar-Far *et al.*[17] and Al-Athel *et al.*[4] (Figure 6).

Zimmerman[75] and Zimmerman *et al.*[76] developed a FE model for the prediction of residual stresses formed from the start of deposition of Ti coating onto Al_2O_3 substrate to when it is cooled to room temperature. The computation was carried out in two stages using a cylindrical sample (geometry). The first stage was a model for the computation of the stress state and temperature distribution induced during the impact of the coating onto the substrate and the layer-by-layer growth of the thickness. The data from the first stage were then transferred to the second stage for the computation of the residual stresses using a thermos-mechanical model. The numerical model was validated by comparing the deflections of the Ti/Al_2O_3 system produced by the detonation method. The results show that the radial residual stresses are higher at the coating/substrate interface and do not depend on the thickness of the sample. Similar analysis was carried out HVOF coatings by Lyphout *et al.*[77] and Bansal *et al.*[78]

Jiang *et al.*[79] carried out a thermo-mechanical analysis of the residual stresses developed in zirconia-based TBC on hollow cylindrical substrate using FEM. Axisymmetric elements with homogenous and isotropic material constitutive model were used for the computation. The FE analysis results the main origin of residual stress in TBC is thermal mismatch between the various layers of the system. Specimen dimension, spray process, coating thickness, and hole radius were also found to have effect on the stress field distribution (Figure 7).

Zhao *et al.*[80] developed a 3D nonlinear thermo-structural model for the multiple layer-by-layer deposition of Al_2O_3–13 wt.%TiO_2/NiCrAl coating on a flat low-carbon steel substrate. A sequentially-coupled approach where thermal analysis results were applied as loads for the computation of residual stresses using the structural model was used. Birth and death element technique was used for simulation of the coating deposition and layer growth. The results show that radial and axial compressive stresses were developed at the interface and BC while tensile stresses were developed at the free edges. They also reported a zig-zag variation of the residual stresses along the depth of the coating. Due to edge effect,

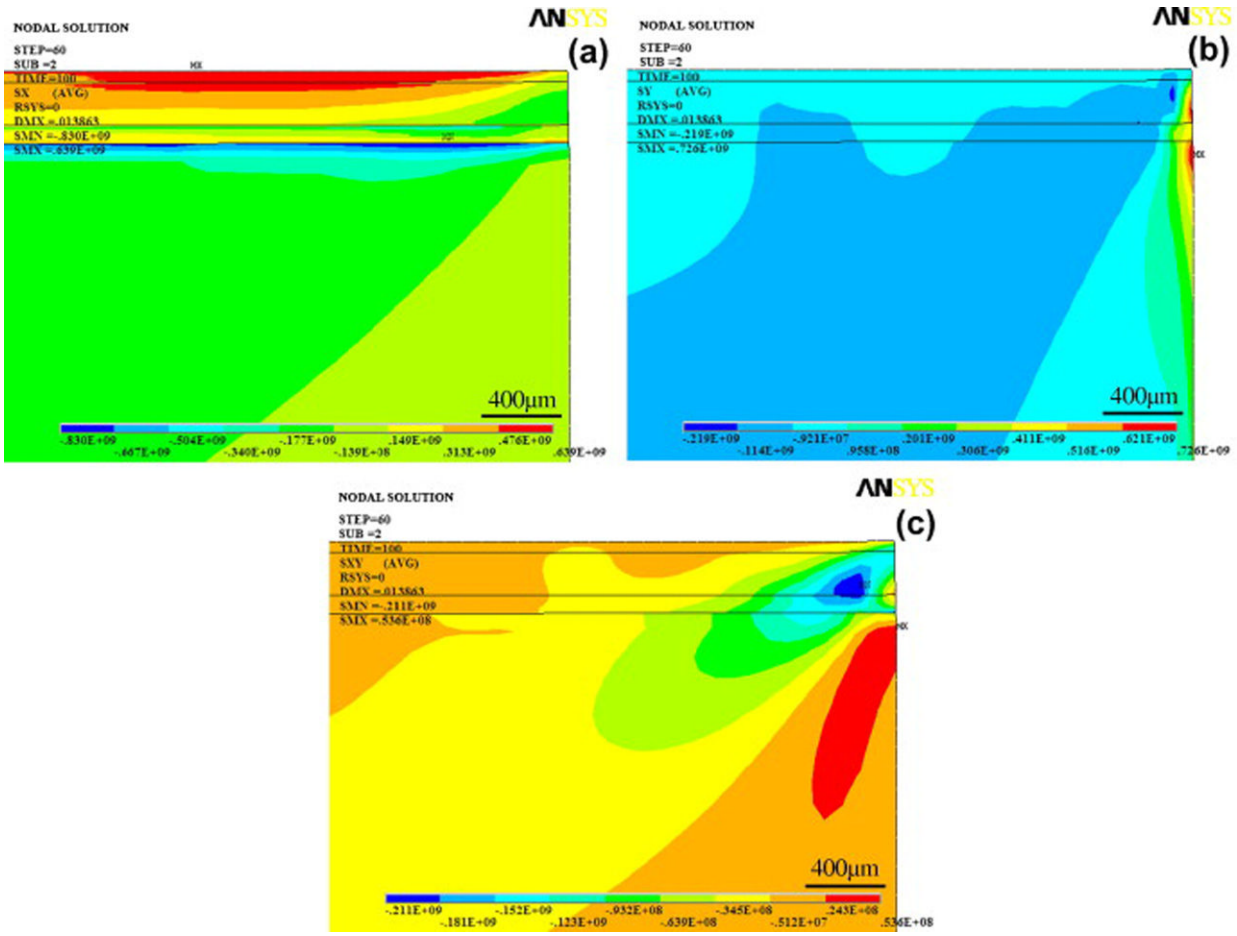


Figure 9 Typical contour plot of stress (MPa) distribution of (a) σ_{xx}, (b) σ_{yy}, and (c) σ_{xy} after the 20 layer deposition being finished for the LZ/8YSZ thermal barrier coatings (100 μm NiCoCrAlY bond-coat, 240 μm 8YSZ ceramic-coat, and 60 μm LZ top-layer).[83]

the model results show the residual stress is compressive with values ranging from 96–296 MPa, which is reasonably comparable with the average experimental (compressive) residual stress of 198 MPa given by XRD.

Liu *et al.*[81] developed a 3D multilayer thermo-mechanical model for the evolution of temperature and residual stress field during the thermal spray of alumina on stainless steel substrate. The influence of the sprayed particles on the substrate and pre-coated ceramic layer temperature was incorporated with the use of the birth and death element technique. The effects of porosities and micro-cracks on the effective properties of the coating were taken account. A tensile stress with small magnitude was obtained within the alumina coating at the end of the process. However, the residual stress became compressive after cooling of the coating to room temperature. Contrary to what was reported by Limarga *et al.*,[73] they observed that a higher cooling rate results in a lower temperature magnitude and lower residual stress within the coating. They validated the model by comparing the simulated deflection of the specimen with experimental measurements. Consequently, the model predicted a residual stress value of -422 MPa which is reasonable comparable to the experimental value of -365 MPa. Furthermore, a similar good comparison was previously obtained by Gan *et al.*[82] for the deposition of nickel–cobalt (NiCoCrAlY) alloy on an aluminum disk (AA1100) substrate. They found that the displacements obtained by the thermo-mechanical FE model compares with the measured one from experiments.

Furthermore, Wang *et al.*[83] predicted the residual stresses developed after deposition of double-ceramic-layer (DCL) $La_2Zr_2O_7$/8YSZ TBCs using birth and death element technique. They found that residual stress was due to quenching and thermal mismatch. The FE results show that the surface and the edge of interface are often the positions of high stress concentration. Their investigations reveal that DCL coating has lower residual stress as compared with the conventional single-layer 8YSZ coating. They further investigated the effect of defects on the residual stresses using a novel method, which uses actual image, i.e., the computational micro-mechanics (CMM) approach. They suggested that DCL coating be used as an ideal coating material in future due to its better thermal insulation effect, sintering resistance ability, and lower residual stress as compared with that of the conventional 8YSZ coating. **Figures 8–10** show the residual stresses after one layer of deposition, 20 layers of deposition, and after cooling.

Wu *et al.*[84] conducted a 2D axisymmetric thermo-structural analysis of the residual stresses developed after the deposition of air plasma spray TBC using the 'modified element birth–death

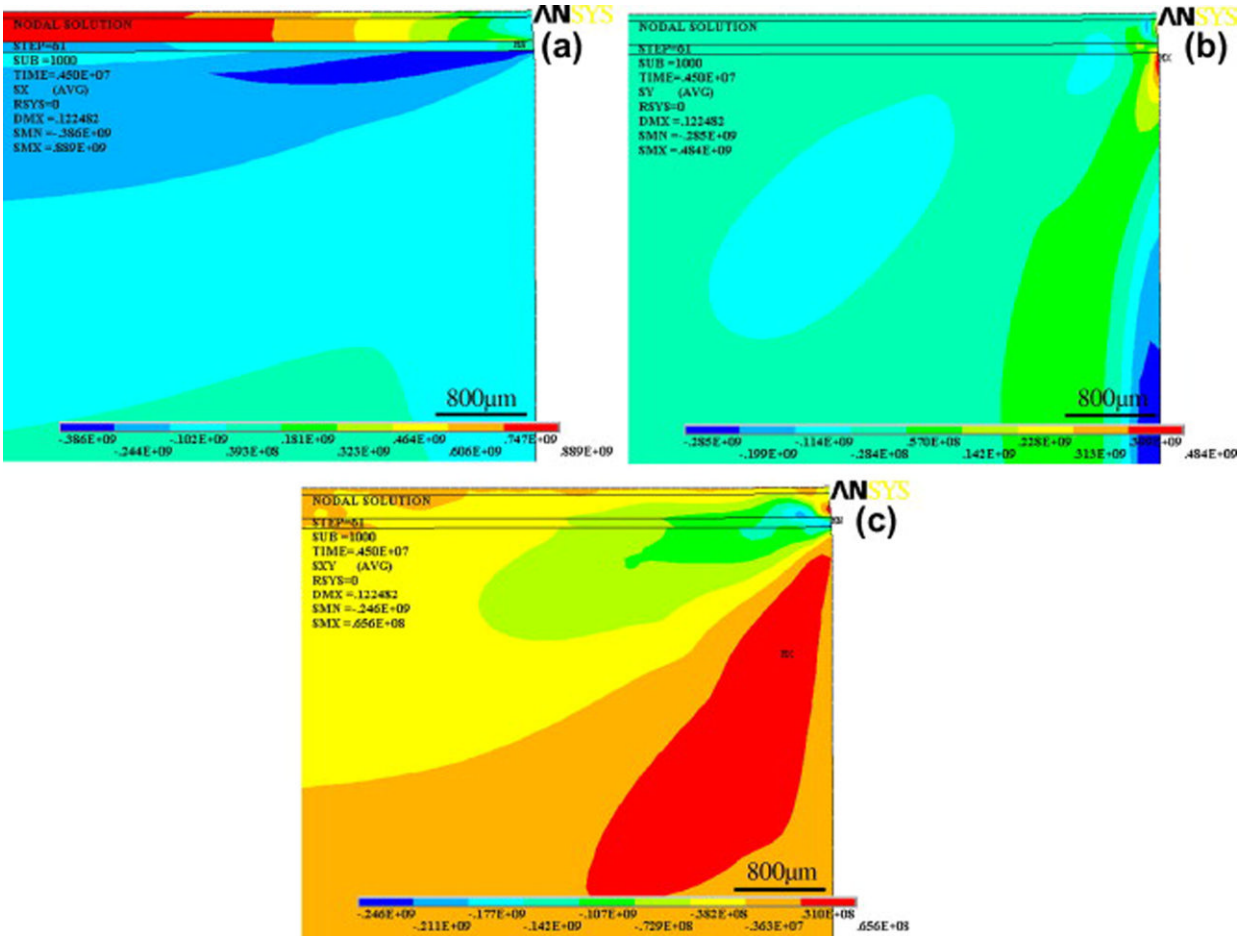


Figure 10 Typical contour plot of stress (MPa) distribution of residual stress of (a) σ_{xx}, (b) σ_{yy}, and (c) σ_{xy} after the LZ/8YSZ thermal barrier coatings being cooled to the ambient temperature (100 μm NiCoCrAlY bond-coat, 240 μm 8YSZ ceramic-coat, and 60 μm LZ top-layer).[83]

technique.' In conventional birth–death element technique, the nodes of the dead elements will not take part in calculation as long as they are inactive. However, nodes of death elements, which are located at the boundaries that are common to both activated and inactivated elements, will move thereby resulting in severe distortion of the inactive elements. To avoid this severe distortion, a 'modified element birth–death technique' was used. Before the computation was done, a group of 'soft/hypothetical elements' with suitable properties were added to appropriate locations within the model. Therefore, these elements could undergo large deformation at low stress levels with little influence on other active elements. The FE results show that the radial residual stress was almost uniform in top-coat layer due to the weakening of the material strength and opening of microcracks under tensile load. Axial residual stresses were found to be higher at the edge of the specimen and the maximum value was found at the BC/substrate interface which might lead to the delamination of the coating. Figure 11 shows the residual stress distribution after the first and the fifth spraying step. The residual displacements obtained using the FEM were found to accurately agree with experimental results obtained by HDM.

Finally, we discuss the papers that used an image-based FE model for the computation. Ghafouri-Azar *et al.*[19] developed 3D stochastic model the deposition of WC–Co coating onto stainless steel substrate using HVOF torch. The model was found to accurately capture the thermal spray process. The simulated microstructure, coating thickness, and percentage porosity were very comparable to experimentally observed ones. The experimental micrograph as well as the simulated microstructure were used with an OOF code developed at the National Institute of Standards and Technology to calculate the residual stresses in the coating. The FE model uses an adaptive meshing technique to discretize the coating microstructure into a mesh suitable for FE analysis. The residual stress values obtained with both the real and computationally generated microstructure were found to be very close. High stresses were found at the substrate/coating interface. The residual stresses were found to increase with coating thickness and coating temperature, and decrease with substrate temperature.

Similarly, Klusemann *et al.*[85] numerically predicted the residual stresses developed in thermal sprayed WC–Co coating that has been subjected to roller burnishing process. They first

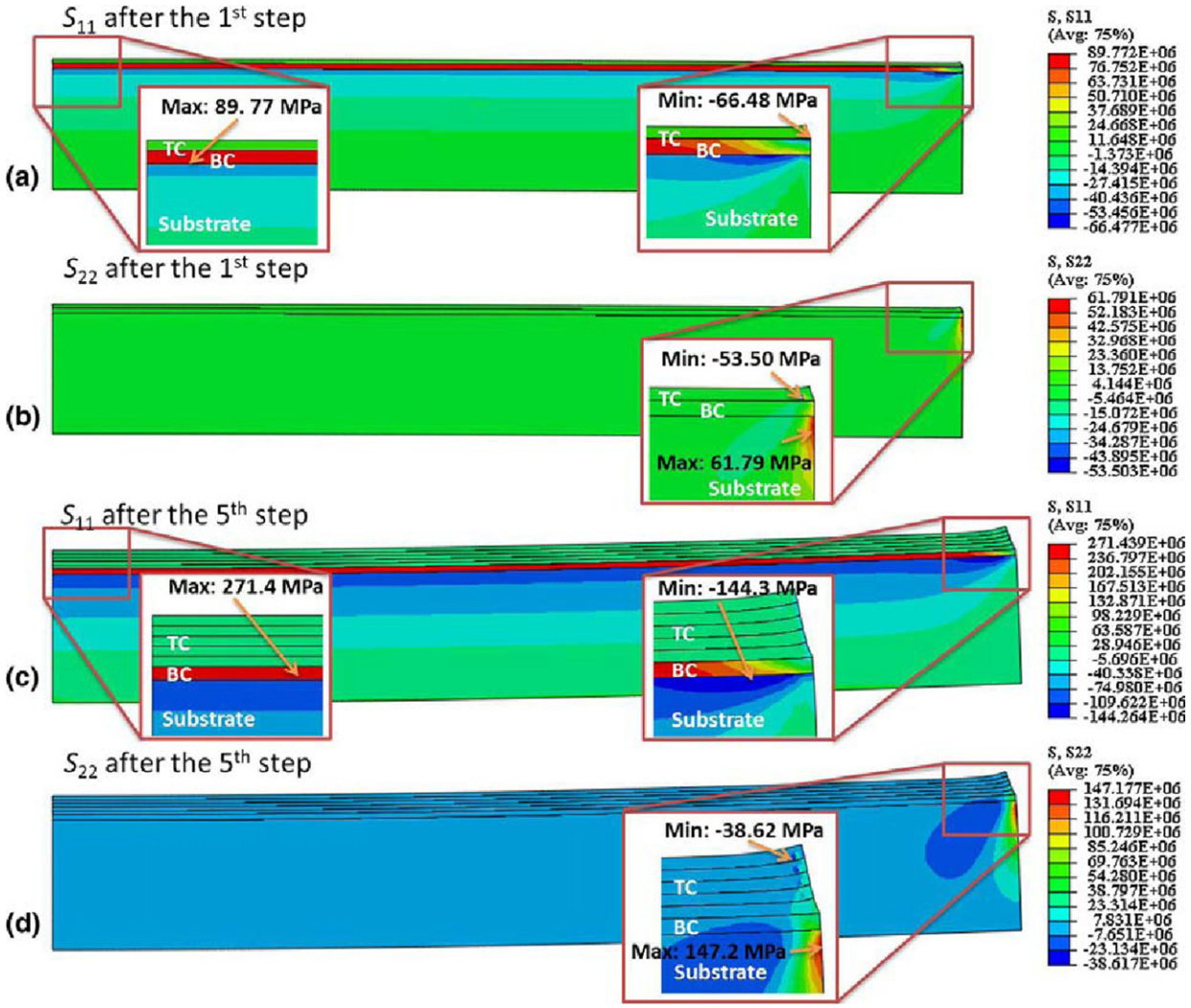


Figure 11 Distributions of residual stress components S_{11} and S_{22} in MPa after the 1st (a and b), and the 5th (c and d) spray steps.[84]

used SEM images to first estimate the effective material properties of the coating before performing a thermo-structural analysis using an optical micrograph for the computation of thermally-induced and rolling-induced residual stresses. The FE results show that compressive residual stresses were developed in the thickness direction after the rolling process, which agrees very well with experiment qualitatively. However, the model shows the development of a layer of tensile stresses the surface of the coating which could not be captured experimentally by HDM. They suggested that computations should be repeated with a 3D image-based model that is coupled with some damage models in order to improve the quality of the results.

3.4.4 Summary and Outlook

It can be seen that the FEM has been successfully used in estimating the residual stresses developed in thermal spray coatings. The FEM has been widely used as compared to other numerical techniques. This is due to its flexibility and suitability for complex or multilayer materials. The residual stresses have been found to be mainly due to thermal mismatch between the various layers of the coating system. However, other phenomenon such as TGO growth, phase transformations at various interfaces, inhomogeneity of respective layers, surface roughness of the substrate, and deposition process parameters; all contribute to the residual stresses even though their contribution is negligible. The results have been shown to be reasonably close to the experimentally measured residual stresses both quantitatively and qualitatively. Therefore, the FEM is a very powerful tool that can be used to predict residual stresses in coatings. But still the following issues need to be addressed in order to improve the effectiveness of FEM in predicting residual stresses:

1. In order to improve the accuracy of the results, a model that incorporates the effect of other processes (such as creep, TGO growth, process parameters, surface roughness, phase transformations, etc.) should be further exploited.
2. As aim of the residual stress prediction is to estimate the lifetime of the coating, future research should relate the developed residual stresses with the coating lifetime when used for specific applications.
3. Even though some image-based FE technique has been used, further investigation should be carried out in order to investigate more about the effect of materials inhomogeneity on the coating life.
4. No reliable coupling of the residual stress model with damage models has been found (to the best of our knowledge). Most of the researchers simply conclude that the high interfacial or residual stresses lead to the spallation or delamination failure of the coatings. Therefore, coupling a multi-scale damage model with the residual stress model may help in understanding more about the failure mechanism of thermal-spray coatings.

Acknowledgment

The authors would like to acknowledge the support of King Fahd University of Petroleum and Minerals through DSR project #SB141002. The contribution of Dr. Yugeswaran to Section 3.4.2 is gratefully acknowledged.

See also: 3.7 HVOF Coating of Nickel Based Alloys: Surface and Mechanical Characteristics

References

1. Santana, Y. Y.; Renault, P. O.; Sebastiani, M.; *et al.* Characterization and Residual Stresses of WC–Co Thermally Sprayed Coatings. *Surf. Coat. Technol.* **2008**, *202* (18), 4560–4565.
2. Santana, Y. Y.; La Barbera-Sosa, J. G.; Staia, M. H.; *et al.* Measurement of Residual Stress in Thermal Spray Coatings by the Incremental Hole Drilling Method. *Surf. Coat. Technol.* **2006**, *201* (5), 2092–2098.
3. Mostaghimi, J.; Chandra, S.; Ghafouri-Azar, R.; Dolatabadi, A. Modeling Thermal Spray Coating Processes: A Powerful Tool in Design and Optimization. *Surf. Coat. Technol.* **2003**, *163*, 1–11.
4. Al-Athel, K.; Loeffel, K.; Liu, H.; Anand, L. Modeling Decohesion of a Top-Coat from a Thermally-Growing Oxide in a Thermal Barrier Coating. *Surf. Coat. Technol.* **2013**, *222*, 68–78.
5. Di Leo, C. V.; Luk-Cyr, J.; Liu, L.; Loeffel, K.; Al-Athel, K.; Anand, L. A New Methodology for Characterizing Traction-Separation Relations for Interfacial Delamination of Thermal Barrier Coatings. *Acta Mater.* **2014**, *71*, 306–318.
6. Ahmed, R.; Fitzpatrick, M. E.; Faisal, N. H. A Comparison of Neutron Diffraction and Hole-Drilling Residual Strain Measurements in Thermally Sprayed Coatings. *Surf. Coat. Technol.* **2012**, *206* (19–20), 4180–4185.
7. Buchmann, M.; Gadow, R.; Tabellion, J. Experimental and Numerical Residual Stress Analysis of Layer Coated Composites. *Mater. Sci. Eng. A: Struct. Mater. Props. Microstruct. Process.* **2000**, *288* (2), 154–159.
8. Kuroda, S.; Fukushima, T.; Kitahara, S. Simultaneous Measurement of Coating Thickness and Deposition Stress during Thermal Spraying. *Thin Solid Films* **1988**, *164*, 157–163.
9. Kuroda, S.; Fukushima, T.; Kitahara, S. Generation Mechanisms of Residual-Stresses in Plasma-Sprayed Coatings. *Vacuum* **1990**, *41* (4–6), 1297–1299.
10. Matejicek, J.; Sampath, S. *In Situ* Measurement of Residual Stresses and Elastic Moduli in Thermal Sprayed Coatings – Part 1: Apparatus and Analysis. *Acta Mater.* **2003**, *51* (3), 863–872.
11. Matejicek, J.; Sampath, S.; Gilmore, D.; Neiser, R. *In Situ* Measurement of Residual Stresses and Elastic Moduli in Thermal Sprayed Coatings – Part 2: Processing Effects on Properties of Mo Coatings. *Acta Mater.* **2003**, *51* (3), 873–885.
12. Zhu, J. G.; Xie, H.; Hu, Z.; Chen, P.; Zhang, Q. Residual Stress in Thermal Spray Coatings Measured by Curvature Based on 3D Digital Image Correlation Technique. *Surf. Coat. Technol.* **2011**, *206* (6), 1396–1402.
13. Zhang, X. C.; Watanabe, M.; Kuroda, S. Effects of Processing Conditions on the Mechanical Properties and Deformation Behaviors of Plasma-Sprayed Thermal Barrier Coatings: Evaluation of Residual Stresses and Mechanical Properties of Thermal Barrier Coatings on the Basis of *In Situ* Curvature Measurement Under a Wide Range of Spray Parameters. *Acta Mater.* **2013**, *61* (4), 1037–1047.
14. Yang, L. X.; Yang, F.; Long, Y.; *et al.* Evolution of Residual Stress in Air Plasma Sprayed Yttria Stabilised Zirconia Thermal Barrier Coatings after Isothermal Treatment. *Surf. Coat. Technol.* **2014**, *251*, 98–105.
15. Gu, L. J.; Fan, X.; Zhao, Y.; *et al.* Influence of Ceramic Thickness on Residual Stress and Bonding Strength for Plasma Sprayed Duplex Thermal Barrier Coating on Aluminum Alloy. *Surf. Coat. Technol.* **2012**, *206* (21), 4403–4410.
16. Stoney, G. G. The Tension of Metallic Films Deposited by Electrolysis. *Proceed. R. Soc. Lond. Ser. A – Contain. Pap. Math. Phys. Charact.* **1909**, *82* (553), 172–175.
17. Ranjbar-Far, M.; Absi, J.; Mariaux, G.; Shahidi, S. Effect of Residual Stresses and Prediction of Possible Failure Mechanisms on Thermal Barrier Coating System by Finite Element Method. *J. Therm. Spray Technol.* **2010**, *19* (5), 1054–1061.
18. Baig, M. N.; Khalid, F. A.; Khan, F. N.; Rahman, K. Properties and Residual Stress Distribution of Plasma Sprayed Magnesia Stabilized Zirconia Thermal Bather Coatings. *Ceram. Int.* **2014**, *40* (3), 4853–4868.
19. Ghafouri-Azar, R.; Mostaghimi, J.; Chandra, S. Modeling Development of Residual Stresses in Thermal Spray Coatings. *Comput. Mater. Sci.* **2006**, *35* (1), 13–26.

20. Clyne, T. W.; Gill, S. C. Residual Stresses in Thermal Spray Coatings and Their Effect on Interfacial Adhesion: A Review of Recent Work. *J. Thermal Spray Technol.* **1996**, *5* (4), 401–418.
21. Xue, M.; Mostaghimi, J.; Chandra, S. Investigation of Splat Curling up in Thermal Spray Coatings. In *Proceedings of the International Thermal Spray Conference,* Seattle, WA; Marple, B. R., Hyland, M. M., Lau, Y. C., Lima, R. S., Voyer, J., Eds.; ASM International: Materials Park, OH, May 15–18, 2006.
22. Brown, S. R.; Turner, I. G.; Reiter, H. Residual Stress Measurement in Thermal Sprayed Hydroxyapatite Coatings. *J. Mater. Sci. Mater. Med.* **1994**, *5*, 756–759.
23. Hill, M. R.; Wei-Yan Lin. Residual Stress Measurement in a Ceramic-Metallic Graded Material. *J. Eng. Mater. Technol.* **2002**, *124*, 185–191.
24. Withers, P. J.; Bhadeshia, H. K. D. H. Overview Residual Stress Part 1 – Measurement Techniques. *Mater. Sci. Technol.* **2001**, *17*, 355–365.
25. ASTM Standard E837–92. Standard Test Method of Determining Residual Stresses by the Hole-Drilling Strain-Gage Method. In *Annual Book of ASTM Standards*; ASTM: Philadelphia, PA, 1992.
26. Dolhof, V.; Musil, J.; Cepera, M.; Zeman, J. Stress Analysis of Thermal Sprayed Coatings Using a Semi-Destructive Hole-Drilling Strain Gauge Method. In *Proceedings of the 8th National Thermal Spray Conference*, Houston, TX, 1995; pp. 445–449.
27. Matejicek, J.; Sampath, S.; Dubsky, J. X-ray Residual Stress Measurement in Metallic and Ceramic Plasma Sprayed Coatings. *J. Therm. Spray Technol.* **1998**, *7* (4), 489–496.
28. Perry, A. J.; Sue, J. A.; Martin, P. J. Practical Measurement of the Residual Stress in Coatings. *Surf. Coat. Technol.* **1996**, *81*, 17–25.
29. Montay, G.; Cherouat, A.; Nussair, A.; Lu, J. Residual Stresses in Coating Technology. *J. Mater. Sci. Technol.* **2004**, *20*, 81–84.
30. Greving, D. J.; Rybicki, E. F.; Shadley, J. R. Through-Thickness Residual Stress Evaluations for Several Industrial Thermal Spray Coatings Using a Modified Layer-Removal Method. *J. Therm. Spray Technol.* **1994**, *3* (4), 379–388.
31. Suresh, S.; Giannakopoulos, A. E. A New Method for Estimating Residual Stresses by Instrumented Sharp Indentation. *Acta Mater.* **1998**, *46* (16), 5755–5767.
32. Sebastiani, M.; Bolelli, G.; Lusvarghi, L.; Bandyopadhyay, P. P.; Bemporad, E. High Resolution Residual Stress Measurement on Amorphous and Crystalline Plasma-Sprayed Single-Splats. *Surf. Coat. Technol.* **2012**, *206*, 4872–4880.
33. Hobbs, M. K.; Reiter, H. Residual Stresses in ZrO_2–8%Y_2O_3 Plasma-Sprayed Thermal Barrier Coatings. *Surf. Coat. Technol.* **1988**, *34*, 33–42.
34. Hendricks, R. C.; McDonald, G. Residual Stress in Plasma-Sprayed Ceramic Turbine Tip and Gas-Path Seal Specimen. *Ceram. Eng. Sci. Proc.* **1983**, *4* (9–10), 802–809.
35. Yung-Chin Yang. Investigation of Residual Stress Generation in Plasma-Sprayed Hydroxyapatite Coatings with Various Spraying Programs. *Surf. Coat. Technol.* **2011**, *205*, 5165–5171.
36. Stoney, G. G. The Tension of Metallic Films Deposited by Electrolysis. *Proc. R. Soc. Lond., A: Contain. Pap. Math. Phys. Charact.* **1909**, *82* (553), 72–175.
37. Brenner, A.; Senderoff, S. Calculation of Stress in Electrodeposits from the Curvature of a Plated Strip. *J. Res. Natl. Bur. Stand.* **1949**, *42*, 105–123.
38. Kuroda, S.; Fukushima, T.; Kitahara, S. Simultaneous Measurement of Coating Thickness and Deposition Stress During Thermal Spraying. *Thin Solid Films* **1988**, *164*, 157–163.
39. Gill, S. C.; Clyne, T. W. Stress Distribution and Material Response in Thermal Spraying Metallic and Ceramic Deposits. *Metall. Trans. B* **1990**, *21*, 377–385.
40. Kuroda, S.; Clyne, T. W. The Quenching Stress in Thermally Sprayed Coatings. *Thin Solid Films* **1991**, *200*, 49–66.
41. Gill, S. C.; Clyne, T. W. Investigation of Residual Stress Generation during Thermal Spraying by Continuous Curvature Measurement. *Thin Solid Films* **1994**, *250*, 72–180.
42. Dong Liu; Rinaldi, C.; Flewitt, P. E. J. Effect of Substrate Curvature on the Evolution of Microstructure and Residual Stresses in EBPVD–TBC. *J. Euro. Ceram. Soc.* **2015**, *35* (9), 2563–2575.
43. Matejicek, J.; Sampath, S. *In Situ* Measurement of Residual Stresses and Elastic Moduli in Thermal Sprayed Coatings Part 1: Apparatus and Analysis. *Acta Mater.* **2003**, *51*, 863–872.
44. Jianguo Zhu; Huimin Xie; Zhenxing Hu; Pengwan Chen; Qingming Zhang Residual Stress in Thermal Spray Coatings Measured by Curvature Based on 3D Digital Image Correlation Technique. *Surf. Coat. Technol.* **2011**, *206*, 1396–1402.
45. Howard, S. J.; Tsui, Y. C.; Clyne, T. W. The Effect of Residual Stresses on the Debonding of Coatings 1: A Model for Delamination at a Bimaterial Interface. *Acta Metall. Mater.* **1994**, *42* (8), 2823–2836.
46. Tsui, Y. C.; Howard, S. J.; Clyne, T. W. The Effect of Residual Stresses on the Debonding of Coatings 2: An Experimental Study of a Thermally Sprayed System. *Acta Metall. Mater.* **1994**, *42* (8), 2837–2844.
47. Scardi, P.; Leoni, M.; Bertini, L.; Bertamini, L. Residual Stress in Partially-Stabilised-Zirconia TBCs: Experimental Measurement and Modelling. *Surf. Coat. Technol.* **1997**, *94–95*, 82–88.
48. Kesler, O.; Finot, M.; Suresh, S.; Sampath, S. Determination of Processing-Induced Stresses and Properties of Layered and Graded Coatings: Experimental Method and Results for Plasma-Sprayed Ni–Al_2O_3. *Acta Mater.* **1997**, *45* (8), 3123–3134.
49. Bolelli, G.; Lusvarghi, L.; Varis, T.; *et al.* Residual Stresses in HVOF-Sprayed Ceramic Coatings. *Surf. Coat. Technol.* **2008**, *202*, 4810–4819.
50. Selvadurai, U.; Hollingsworth, P.; Baumann, I.; *et al.* Influence of the Handling Parameters on Residual Stresses of HVOF-sprayed WC–12Co Coatings. *Surf. Coat. Technol.* **2015**, *268*, 30–35.
51. Cullity, B. D.; *Elements of X-Ray Diffraction*, 2nd ed.; Addison-Wesley: New York, NY, 1978.
52. Korsunsky, A. M.; Wells, K. E.; Withers, P. J. Mapping Two-Dimensional State of Strainusing Synchroton X-Ray Diffraction. *Scripta Mater.* **1998**, *39*, 1705–1712.
53. Stoica, V.; Ahmed, R.; Golshan, M.; Tobe, S. Sliding Wear Evaluation of Hot Isostatically Pressed Thermal Spray Cermet Coatings. *J. Therm. Spray Technol.* **2004**, *13* (1), 93–107.
54. Kesler, O.; Matejicek, J.; Sampath, S.; *et al.* Measurement of Residual Stress in Plasma-Sprayed Metallic, Ceramic and Composite Coatings. *Mater. Sci. Eng.* **1998**, *A257*, 215–224.
55. Scardi, P.; Leoni, M.; Bertini, L.; Bertamini, L.; Crenuschi, F. Strain Gradients in Plasma-Sprayed Zirconia Thermal Barrier Coatings. *Surf. Coat. Technol.* **1998**, *108–109*, 93–98.
56. Matejicek, J.; Sampath, S.; Brand, P. C.; Prask, H. J. Quenching, Thermal and Residual Stress in Plasma Sprayed Deposits: NiCrAlY and YSZ Coatings. *Acta Mater.* **1999**, *47* (2), 607–617.
57. Keller, T.; Margadant, N.; Pirling, T.; Escribano, M. J. R.; Wagner, W. Residual Stress Determination in Thermally Sprayed Metallic Deposits by Neutron Diffraction. *Mater. Sci. Eng.: A* **2004**, *373*, 33–44.
58. Ahmed, R.; Yu, H.; Stewart, S.; Edwards, L.; Santisteban, J. R. Residual Strain Measurements in Thermal Spray Cermet Coatings via Neutron Diffraction. *J. Tribol.* **2007**, *129*, 411–418.
59. Kramer, S.; Faulhaber, S.; Chambers, M.; *et al.* Mechanisms of Cracking and Delamination within Thick Thermal Barrier Systems in Aero-Engines Subject to Calcium–Magnesium–Alumino–Silicate (CMAS) Penetration. *Mater. Sci. Eng.: A* **2008**, *490* (1–2), 26–35.
60. Scrivani, A.; Rizzi, G.; Bardi, U.; *et al.* Thermal Fatigue Behavior of Thick and Porous Thermal Barrier Coatings Systems. *J. Therm. Spray Technol.* **2007**, *16* (5–6), 816–821.
61. Portinha, A.; Teixeira, V.; Carneiro, J.; *et al.* Residual Stresses and Elastic Modulus of Thermal Barrier Coatings Graded in Porosity. *Surf. Coat. Technol.* **2004**, *188–189*, 120–128.
62. Tanaka, M.; Kitazawa, R.; Tomimatsu, T.; Liu, Y. F.; Kagawa, Y. Residual Stress Measurement of an EB–PVD Y_2O_3–ZrO_2 Thermal Barrier Coating by Micro-Raman Spectroscopy. *Surf. Coat. Technol.* **2009**, *204* (5), 657–660.
63. Tanaka, M.; Hasegawa, M.; Dericioglu, A. F.; Kagawa, Y. Measurement of Residual Stress in Air Plasma-Sprayed Y_2O_3–ZrO_2 Thermal Barrier Coating system using Micro-Raman Spectroscopy. *Mater. Sci. Eng.: A* **2006**, *419* (1–2), 262–268.
64. Teixeira, V.; Andritschky, M.; Fischer, W.; Buchkremer, H. P.; Stöver, D. Analysis of Residual Stresses in Thermal Barrier Coatings. *J. Mater. Proc. Technol.* **1999**, *92–93*, 209–216.
65. Qing Ma; Clarke, D. R. Piezospectroscopic Determination of Residual Stresses in Polycrystalline Alumina. *J. Am. Ceram. Soc.* **1994**, *77* (2), 298–302.
66. Qing Ma; Pompe, W.; French, J. D.; Clarke, D. R. Residual Stresses in Al_2O_3–ZrO_2 Composites: A Test of Stochastic Stress Models. *Acta Metall. Mater.* **1994**, *42* (5), 1673–1681.
67. Zhao, X.; Xiao, P. Residual Stresses in Thermal Barrier Coatings Measured by Photoluminescence Piezospectroscopy and Indentation Technique. *Surf. Coat. Technol.* **2006**, *201*, 1124–1131.
68. Crecraft, D. The Measurement of Applied and Residual Stresses in Metals Using Ultrasonic Waves. *J. Sound Vib.* **1967**, *5*, 173–192.
69. Javadi, Y.; Pirzaman, H. S.; Raeisi, M. H.; Najafabadi, M. A. Ultrasonic Inspection of a Welded Stainless Steel Pipe to Evaluate Residual Stresses Through Thickness. *Mater. Des.* **2013**, *49*, 591–601.

70. Samadi, H. *An Alternative Thermal Barrier Coating for Diesel Engines* (Ph.D. thesis); Toronto, ON: Department of Materials Science and Engineering, University of Toronto, 2009.
71. Tsui, Y. C.; Clyne, T. W. An Analytical Model for Predicting Residual Stresses in Progressively Deposited Coatings Part 1: Planar Geometry. *Thin Solid Films* **1997**, *306* (1), 23–33.
72. Zhu, J.; Chen, W.; Xie, H. Simulation of Residual Stresses and their Effects on Thermal Barrier Coating Systems Using Finite Element Method. *Sci. China Physics, Mech. Astron.* **2014**, *58* (3), 1–10.
73. Limarga, A. M.; Vaßen, R.; Clarke, D. R. Stress Distributions in Plasma-Sprayed Thermal Barrier Coatings Under Thermal Cycling in a Temperature Gradient. *J. Appl. Mech.* **2011**, *78* (1), 011003-1–011003-9.
74. Ng, H. W.; Gan, Z. A Finite Element Analysis Technique for Predicting As-Sprayed Residual Stresses Generated by the Plasma Spray Coating Process. *Finite Elem. Anal. Des.* **2005**, *41*, 1235–1254.
75. Zimmerman, J. Finite Element Modelling of the Residual Stresses Induced in Thermally Deposited Coatings. *Arch. Metall. Mater.* **2014**, *59* (2), 593–599.
76. Zimmerman, J.; Lindemann, Z.; Golański, D.; Chmielewski, T.; Włosiński, W. Modeling Residual Stresses Generated in Ti coatings Thermally Sprayed on Al_2O_3 Substrates. *Bull. Pol. Acad. Sci.: Tech. Sci.* **2013**, *61* (2), 515–525.
77. Lyphout, C.; Nylén, P.; Manescu, A.; Pirling, T. Residual Stresses Distribution through Thick HVOF Sprayed Inconel 718 Coatings. *J. Therm. Spray Technol.* **2008**, *17* (5–6), 915–923.
78. Bansal, P.; Shipway, P. H.; Leen, S. B. Residual Stresses in High-Velocity Oxy-Fuel Thermally Sprayed Coatings – Modelling the Effect of Particle Velocity and Temperature during the Spraying Process. *Acta Mater.* **2007**, *55*, 5089–5101.
79. Jiang, Y.; Xu, B. S.; Wang, H. D.; Lu, Y. H. Finite Element Modeling of Residual Stress Around Holes in the Thermal Barrier Coatings. *Comput. Mater. Sci.* **2010**, *49* (3), 603–608.
80. Zhao, H.; Zhang, J.; Wang, Z.; Lin, P.; Wang, Z. Adhesion and Residual Stress of Plasma Sprayed Alumina–Titania Coatings. *J. Adhes. Sci. Technol.* **2015**, *29* (10), 991–1001.
81. Liu, J.; Bolot, R.; Costil, S. Residual Stresses and Final Deformation of an Alumina Coating: Modeling and Measurement. *Surf. Coatings Technol.* **2014**, *268*, 241–246.
82. Gan, Z.; Ng, H. W.; Devasenapathi, A. Deposition-Induced Residual Stresses in Plasma-Sprayed Coatings. *Surf. Coatings Technol.* **2004**, *187* (2–3), 307–319.
83. Wang, L.; Wang, Y.; Sun, X. G.; He, J. Q.; Pan, Z. Y.; Wang, C. H. Finite Element Simulation of Residual Stress of Double-Ceramic-Layer $La_2Zr_2O_7$/8YSZ Thermal Barrier Coatings Using Birth and Death Element Technique. *Comput. Mater. Sci.* **2012**, *53* (1), 117–127.
84. Wu, L.; Zhu, J.; Xie, H. Numerical and Experimental Investigation of Residual Stress in Thermal Barrier Coatings During APS Process. *J. Therm. Spray Technol.* **2014**, *23*, 653–665.
85. Klusemann, B.; Denzer, R.; Svendsen, B. Microstructure-Based Modeling of Residual Stresses in WC–12Co-Sprayed Coatings. *J. Therm. Spray Technol.* **2011**, *21* (1), 96–107.

3.5 Laser Texturing of Materials and Surface Hydrophobicity

BS Yilbas, King Fahd University of Petroleum and Minerals, Dhahran, Saudi Arabia

© 2017 Elsevier Inc. All rights reserved.

3.5.1	**Introduction**	71
3.5.2	**Background**	72
3.5.2.1	PC Sheet	72
3.5.2.2	Alumina Tiles	72
3.5.2.3	Phosphorous Bronze	73
3.5.3	**Experimental Work**	74
3.5.4	**Results and Discussion**	75
3.5.4.1	PC Sheet	75
3.5.4.2	Alumina Tile	78
3.5.4.3	Phosphorous Bronze	81
3.5.5	**Concluding Remarks**	83
Acknowledgments		84
References		84
Relevant Website		85

3.5.1 Introduction

The wetting characteristics of the solid surfaces play an important role in the practical applications. In metal cutting, friction, and bearing applications, the fluid wettability of the surface becomes important because of the requirement of the low friction between two contacted surfaces. The free energy of the solid surface and surface tension of the fluid are two important properties defining the wettability of the fluid on the solid surface; therefore, high surface energy of the solid and low surface tension of the fluid are required for the hydrophilic behavior. In general, the wetting state of the solid surface can be identified through surface hydrophilicity, which takes the form of hydrophilic for high wetting states and hydrophobic for low wetting states. However, hydrophobic surfaces are important when the surface self-cleaning characteristics are required. In this case, dust removal, condensation prevention, and stain-free surfaces can be generated. In nature, the hydrophobic surfaces give rise to a self-cleaning effect. One example of such surfaces is the lotus leaf, for which the surface wetting characteristics are significantly low.[1] A close examination of such surfaces reveals that surface texture and surface energy are two important properties that contribute significantly to the hydrophobicity. Solid surfaces can be textured while mimicking nature; in this case, the surface morphology consisting of micro-/nano-poles can be produced artificially at the solid substrate and modification of surface energy can create hydrophobic behavior of the textured surface. Many methods and processes were introduced to gain the hydrophobic characteristics of the solid surfaces.[2–10] Although the technology and techniques used for the surface texturing are available and, currently, they are part of the research activities in surface engineering, some of the processes are involved complicated steps with high costs. In addition, some of these multistep procedures require harsh conditions or specialized reagents and equipment. Some of these techniques include phase separation,[2] electrochemical deposition,[3] plasma treatment,[7] sol–gel processing,[8] electrospinning,[9] and solution immersion.[10] The surface free energy of solid materials can be modified through chemical and physical processes via altering chemical composition at the surface or coating or by introducing alloying elements. However, micro-/nano-texturing of surfaces have many challenges in terms of cost, processing time, equipment, and skilled manpower requirements. Laser processing of surfaces can be considered as one of the effective ways to texture solid surfaces. In addition, laser processing has several advantages over the other techniques. Some of these advantages include precision of operation, fast processing time, and low cost. High intensity beams are used in laser surface texturing, which triggers evaporation and melting at the surface simultaneously while forming small cavities at the irradiated surface. However, during the texturing process involved with the combination of evaporation and melting, process control is highly critical to achieve the desired texture and hydrophobic characteristics. Because the laser power intensity distribution is Gaussian, the peak power intensity takes place at the irradiated surface. Consequently, the region close to the irradiated spot center evaporates, whereas the region close to the edges of the irradiated spot undergoes melting because of the low incidence of laser power intensity in this region. During the simultaneous occurrence of the evaporation and melting processes, melt flow toward the cavity partially fills the cavity while causing reduction in the cavity size. However, this process can be used as one of the techniques to generate micro-/nano-poles and cavities at the surface. In addition, high-power laser irradiation at the solid surface causes the development of high temperature gradients in the irradiated region. This in turn, gives rise to the formation of high thermal strain in the shallow region of the irradiated surface. In some cases, thermal stress formed in the laser-treated region gives rise to the formation of asperities, such as cracks, voids, and metallurgical defect sites in the irradiated region. Consequently, laser texturing of the solid surfaces process involves with multiphysics and requires

further investigation to explore the physical insight into the processes.

The thermal and mechanical properties of the solid surface plays a vital role in the end product quality of the laser-textured surfaces. This is because of the fact that the absorption coefficient of the incident radiation, evaporation and melting temperatures, latent heat of melting, and thermal diffusivity significantly influence the cavity and melt sizes at the surface. In addition, thermal expansion coefficient, Poisson ratio, elastic modulus, and temperature gradients affect the thermal strain and stress levels in the heated region. Therefore, laser surface ablation characteristics and resulting texture change for different solid substrates; for example, because the thermal and mechanical properties of ceramic, metal, and polymers significantly differ, the resulting laser ablation-induced textures become different and stress levels in the treated layer also differ from each other. Consequently, in the present study, laser-induced texturing of three different materials is presented. These include polycarbonate (PC) sheet, which is widely used as a protective layer at photovoltaic (PV) cells; phosphorus bronze, which has antibacterial characteristics; and alumina, which is a ceramic that has a wide application in industry. The laser texturing process and texture analysis are provided in line with the previous studies.[11–13]

3.5.2 Background

In this section, the relevant literature surveys for the surface processing of the materials selected are provided under the appropriate subheadings.

3.5.2.1 PC Sheet

PC is a durable material. Although it has high impact resistance, it has low scratch resistance and in general, a hard coating is applied for the practical usage. The characteristics of PC are much like those of polymethyl methacrylate (PMMA, acrylic), but PC has superior mechanical properties and is usable over a greater temperature range. PC is highly transparent to visible light, with better light transmission than many kinds of glasses. PC has a high glass transition temperature (147 °C[14]), and it softens gradually above this point. Large plastic deformations can take place in PC sheets without cracking or breaking, thus enabling processing and formation at room temperature using sheet metal techniques, such as bending. This enables the use of PC in prototyping applications without losing its transparency or electrical properties. PC sheet can also be used as a protective cover on PV panels. However, due to dust accumulation over time, optical transmittance of PC sheet decreases and the efficiency of the PV panels is lowered. One method to avoid dust accumulation and to ease dust removal from the surface is to texture the PC surface while creating hydrophobic characteristics. Previously, surface texturing of PC sheet was performed via crystallization of the surface by using acetone.[15] Although the surface texture appears to generate hydrophobic characteristics, the optical transmittance is significantly reduced. However, laser texturing of PC surfaces offers advantages over other chemical methods. In the control gas-assisting environment, a combination of surface evaporation and melting results in micro-/nano-poles while demonstrating hydrophobic characteristics.[15]

Considerable research studies were performed to examine surface hydrophobicity of PC sheets. PC with hydrophilic/hydrophobic coatings for the fabrication of micro-devices was studied by Jang *et al.*[16] They showed that by using hydrophilic treatment of PC, they obtained microchannels that were resistant to organic solvents. Furthermore, by using subsequent hydrophobic treatment, multiple liquids were successfully injected into microchannels sequentially in a valve-free manner. A fabrication and characterization study for superhydrophobic surfaces of PC slab was performed by Zheng *et al.*[17] They indicated that the surface modification introduced the superhydrophobic property to the PC slab, and that abrasive polishing seriously damaged the superhydrophobicity, possibly because the mechanical abrasion removed much of the hydrophobic nano-layers and changed the microstructures in such a way that the surface roughness was considerably reduced and some small areas of bare PC surfaces were exposed. Superhydrophobic and superhydrophilic PC, by tailoring chemistry and nano-texture with plasma processing, was investigated by Palumbo *et al.*[18] They demonstrated that the etching process allowed for formation of nanopillars tens of nanometers wide and up to a micrometer high, which was responsible for the unique behavior. Wetting and other physical characteristics of PC surface textured using laser ablation were presented by Yilbas *et al.*[11] They showed that textured surfaces composed of micro-/nanopores with fine cavities increased the contact angle to hydrophobicity in such a way that contact angles in the range of 120° resulted. Superhydrophobic microtextured PC surfaces were studied by Bhagat and Gupta.[19] They indicated that the microtextured PC could be a perfect master for replication of micro-texture on other types of polymers such as polydimethylsiloxane (PDMS) in bulk and in thin film forms. Hierarchical polymeric textures via solvent-induced phase transformation were examined by Cui *et al.*[20] They demonstrated that the resulting surfaces exhibited high contact angles, low contact angle hysteresis, and complete de-wetting during droplet impact. In addition, theoretical analysis of the wetting and anti-wetting pressures showed that the nanoscale morphology was critical for achieving droplet impact resistance. Nano-texturing of nanocomposites by an innovative and advanced spray system was studied by Banerjee and Balasubramanian.[21] They indicated that the wettability and adhesive property of the nanocomposite resulted in a 131.7° contact angle for the centrifuged spray dryer technique. Stroke asymmetry of tilted superhydrophobic ion track textures was presented by Spohr *et al.*[22] They showed that the tilt orientation of a superhydrophobic surface led to the development of the advancing and receding contact angles, which were against the stroke direction.

3.5.2.2 Alumina Tiles

Alumina tiles are widely used in industry because of high resistance to corrosion, wear, and high temperature. In general, alumina tiles are produced from fine powders through hot

pressing or sintering. Because the powder size, in general, varies between 1 and 3 μm, some micro-/nano-voids are formed among the sintered particles. This limits the practical application of the tiles because of the presence of micro-/nano-pores in the tile structure. The pores can be eliminated through melting and solidification of tiles. However, the bulk melting is expensive because of the high melting temperature and the latent heat of alumina. One of the alternatives is to melt the surface locally using high intensity beams. Laser processing can possibly be used for this purpose; however, the proper settings of laser output power and frequency enable melting and evaporating at the irradiated spot locally at the surface. The combination of melting and ablation can cause texturing of the alumina tile surface. Consequently, laser-controlled processing could provide micro-/nano-textured surfaces and eliminate the localized pores in the vicinity of the tile surface.

Considerable research studies were performed to examine laser treatment of alumina surfaces. Crystallographic and morphological textures in laser surface-modified alumina were examined by Harimkar *et al.*[23] They discussed the interdependence of crystallographic and morphological textures of the surface grains within the framework of faceted growth model. They suggested that the formation of crystal shapes was governed by the relative velocities of certain crystallographic facets. Laser texturing of the alumina surface for improved hydrophobicity was studied by Yilbas *et al.*[12] They indicated that the presence of AlN contributed to hydrophobicity enhancement at the surface. In addition, Wenzel and Cassie–Baxter states were present at the treated surface due to the variation in the surface texture. The effects of laser surface texturing on friction properties of nickel-based composites were investigated by Li *et al.*[24] They demonstrated that the lubricious oxide particles stored in the dimples reduced friction coefficient at elevated temperatures and compensated for the extra lubricant due to the degradation of MoS_2 caused by its oxidation at high temperatures. Laser treatment of polycrystalline alumina and aluminum nitride was studied by Williams *et al.*[25] They indicated that the findings could assist in establishing optimum settings of processing parameters in association with the type, properties, and thickness of the substrates. Morphological modification in laser-dressed alumina grinding wheel material for microscale grinding was investigated by Khangar and Dahotre.[26] The findings revealed that the weight loss in the laser-dressed grinding wheels was lower than that of undressed wheel after grinding. The study of tribological behavior of alumina-doped zinc oxide films grown by pulsed laser deposition was performed by Prasad *et al.*[27] They showed that the presence of dark contrast regions in images of wear scars on $ZnO(Al_2O_3)$ films was due to the presence of a slippery phase. Laser synthesis of composite Al_2O_3–$Y_2Ti_2O_7$ ceramics powder mixtures was performed by Vlasova *et al.*[28] They demonstrated that increasing the alumina content in the initial mixtures increased the saturation of α-Al_2O_3 crystallites on the surface of the layers. Microfabrication of an anodic oxide film by anodizing laser-textured aluminum was studied by Jha *et al.*[29] They demonstrated that microstructures with a depth of a few to several tens of micrometers could be fabricated successfully on the anodic oxide film by using various combinations of laser power density and laser scanning speed. Improvement in the tribological characteristics of Si-DLC coating by laser surface texturing under oil-lubricated point contacts at various temperatures were examined by Amanov *et al.*[30] They indicated that the textured Si-DLC coating led to a lower friction coefficient and wear characteristics as compared to that of the untextured Si-DLC coating throughout the temperature range tested. This behavior could be attributed to the effects of dimples and microstructural alteration due to high-energy action of the pulsating laser beam. Pulsed fiber laser texturing of metals, silicon, and ceramics was performed by Hendow *et al.*[31] They showed that measured values for nanosecond-textured surfaces were in the range of 0.4–2.2 μm and 1.5–5 μm for monocrystalline Si and Al, respectively.

3.5.2.3 Phosphorous Bronze

Extensive research studies reported on laser treatment of bronze surfaces. Laser texturing of sliding surfaces of bearings and pump seals was examined by Antoszewski and Tarelnik.[32] They presented the selection of operating parameters of a picoseconds laser, which was used to produce texturing in elements made of steel, bronze, and silicon carbide. A study of microscopic inspection during laser treatments of artwork was performed by Cacciari *et al.*[33] They developed and tested a dedicated 3D digital microscope by implementing the shape from focus technique, which provided textural and chromatic information for the phenomenological characterization of black crust removal from stones. The tribological properties of the amphiphobic textured metal surface were investigated by Wang *et al.*[34] The findings revealed that a visible transition took place, from a high friction coefficient to low values, when the sliding speed increased. The laser ablation mechanism of bronze-bonded diamond wheels was studied by Chen *et al.*[35] They numerically predicted the average temperature and thickness of the melted layer, ablation velocity, and depth by using different laser power densities. A numerical study on laser ablation of quaternary bronze alloys was performed by Fornarini *et al.*[36] They indicated that the results supported the utilization of ultrafast laser sources for trace detection, despite the residual fractionation occurring in the examined range of fluences that affected the linearity of experimental calibration curves built for tin and lead after internal standardization on copper. The optimization study for the laser dressing of bronze-bonded diamond wheels was introduced by Deng *et al.*[37] The findings revealed that the normal and tangential grinding forces produced by the laser-dressed grinding wheel during grinding were smaller than those of grinding wheels dressed using the conventional mechanical method. Formation of periodic structures by laser ablation of metals in liquids was investigated by Kazakevich *et al.*[38] They showed that for a certain range of laser parameters (fluence and number of laser shots), the surface of the solid target was composed of microcones with a regular structure. The physics of selective evaporation of components during laser ablation of stainless steel was examined by Pershin *et al.*[39] Their findings demonstrated that the mechanism of selective evaporation allowed one to improve precision of the analysis for multicomponent alloys without reference calibration, which increased the practical

importance of the calibration-free laser-induced breakdown spectroscopy. Microstructure and performance of laser cladding on the surface of aluminum bronze was studied by Xu *et al.*[40] They indicated that the microstructure of the lower composite region was cellulated crystal and dendritic crystal. They demonstrated that the high rate of strain developed in the heated region, due to fast cooling rates, resulted in high von Mises stress in the surface region. Laser surface modification treatment of aluminum bronze with B_4C was performed by Yilbas *et al.*[41] They showed that the laser-treated surface produced was relatively free from defects and asperities, with a microhardness that was notably higher than that of the as-received bronze substrate. Laser surface alloying of a marine propeller bronze using aluminum powder was studied by Tang *et al.*[42] They indicated that the galvanic effect between the laser-treated and as-received samples was small, and this was a favorable factor for justifying the use of laser surface alloying with aluminum as a feasible method in the local surface treatment of manganese–nickel–aluminum bronze. Thermal–morphological analysis of laser-treated sintered bronze was performed by Gisario *et al.*[43] They proposed a model to approximate the real operational conditions and predict the most promising settings of the laser system aimed at improving the surface finishing of the metal substrates. Laser embedding of TiC particles into the surface of phosphor bronze-bearing material was presented by Yilbas *et al.*[44] They showed that the microhardness of the laser-treated surface increased almost three times as compared to the base material hardness. Electrochemical testing of the laser-treated bronze surface was studied by Yilbas *et al.*[45] The findings revealed that laser treatment improved the corrosion resistance of the treated surface. In addition, fine grains were formed in the surface region of the laser-treated layer, which were attributed to the long cooling rates at the surface.

3.5.3 Experimental Work

In this section, sets of experiments are provided in line with previous studies.[11–13] The experiments cover the morphological, metallurgical, mechanical, and hydrophobicity testing of the laser-treated surfaces.

The CO_2 laser (LC-ALPHAIII) delivering nominal output power of 2 kW was used to irradiate the workpiece surface. The nominal focal length of the focusing lens was 127 mm. The laser beam diameter focused at the workpiece surface was ~0.25 mm. Nitrogen assisting gas emerging from the conical nozzle and coaxially with the laser beam was used. Laser treatment tests were repeated several times by incorporating different laser parameters and laser parameters resulting in the minimum surface defects, such as small cavities with no cracks or crack networks.

A PC sheet with a thickness of 3 mm was used as the workpiece. The PC sheet was a PBA (*p*-hydroxypheyl) and had excellent optical clarity with high toughness. The PC samples were prepared at $30 \times 30 \times 3\ mm^3$ (width × length × thickness). They were cleaned with distilled water prior to laser treatment. The phosphor bronze with elemental composition (wt%) of 6% Sn, 0.1% P, and balance of Cu was used in the experiments. The samples were prepared from phosphor bronze sheet with a thickness of 3 mm and size of 20 mm × 20 mm (length × width). Alumina (Al_2O_3) tiles (Ceram Tec-ETEC, 2010) with a thickness of 3 mm were used as workpieces.

Material characterization of the laser-treated surfaces was performed using optical microscope, scanning electron microscope (SEM), energy dispersive X-ray spectroscopy (EDS), and X-ray diffraction (XRD). Jeol 6460 electron microscopy is used for SEM examinations and Bruker D8 Advanced with CuKα radiation is used for XRD analysis. Typical XRD settings are 40 kV and 30 mA, and scanning angle (2θ) ranged from 20° to 80°.

Microphotonics digital microhardness tester (MP-100TC) was used to obtain microhardness at the surface of the nitride layer. The standard test method for Vickers indentation hardness of advanced ceramics (ASTM C1327-99) was adopted. Microhardness was measured at the workpiece surface after the laser treatment process. The measurements were repeated five times at each location for consistency of the results.

The XRD technique is used to measure the residual stresses in the laser-treated surface region of phosphorous bronze and alumina tile. The XRD technique provides the data in the surface region of the specimens due to the penetration depth of CuKα radiation into the treated layer (i.e., the penetration depth is approximately 5 μm). The measurement relies on the stresses in the fine-grain polycrystalline structure. The position of the diffraction peak exhibits a shift as the specimen is rotated by an angle (ψ). The magnitude of the shift is related to the magnitude of the residual stress. The relationship between the peak shift and the residual stress (σ) is given by:[46]

$$\sigma = \frac{E}{(1+\upsilon)\sin^2\psi}\frac{(d_n - d_0)}{d_0} \quad [1]$$

where E is Young's modulus, υ is Poisson's ratio, ψ is the tilt angle, d_0 and d_n are the d spacing measured at each tilt angle. If there are no shear strains present in the specimen, then the d spacing changes linearly with $\sin^2\psi$. In the case of alumina, the γ-Al_2O_3 peak (ICDD 29-1486) takes place at 37.5°, which corresponds to the (311) plane with interplaner spacing of 0.239 nm. The linear dependence of d(311) results in a slope of -1.677×10^{-12} m per degree with an intercept of 0.239 nm. The residual stress determined from the XRD technique at the surface vicinity is approximately $-2.1(+0.06/-0.06)$ GPa. In the case of phosphorous bronze, the calculations were performed for $Cu_3N(100)$ planes ($2\theta = 23.44°$) with an interplaner spacing of 0.3844 nm. It should be noted that Cu_3N is identified in accordance with the ICDD 00-055-0308 card. The linear dependence of $d(100)$ results in a slope of $-1.9 \times 10^{-3} \pm 9.12 \times 10^{-5}$ nm and an intercept of $0.3844 \pm 4.75 \times 10^{-3}$ nm. The elastic modulus and Poisson's ratio of phosphor bronze are 96.5 GPa and 0.34,[26] respectively. The residual stress measured is approximately −350 MPa, which is compressive, and the estimated error is ±10 MPa, which is 2.4%. It should be noted that the error is estimated based on three repeats of the XRD measurements and the error related to the measurements is approximately 3%.

In the case of PC sheet, residual stress measurements were performed using the curvature method. The deflection of the workpiece during laser scanning was recorded and the final

deflection was measured using the optical imaging technique. The equation relating deflection Δx to curvature κ is obtained from the geometric relation, which yields:[47]

$$\kappa = \frac{1}{R} = \frac{L_{arc}}{\cos^{-1}\left(1 - \frac{\Delta x}{R}\right)} \quad [2]$$

where L_{arc} is the arc length of the specimen, R is the curvature radius, and Δx is the final deflection due to curvature. The Stony equation[47] is used to obtain the relationship between the residual stress (σ) and the curvature[47]:

$$\sigma = \frac{\kappa E_s t_s^2}{6(1 - \upsilon_s)t_c} \quad [3]$$

where E_s is the elastic modulus, t_s is workpiece thickness, v_s is the Poisson's ratio of the polycarbonate glass, and t_c is the laser-treated layer thickness, which is measured from SEM images.

Scratch resistance of the laser-treated and untreated surfaces was determined from the standard test method in line with the ASTM D7027-05 standard. The linear micro-scratch tester (MCTX-S/N: 01-04300[9]) and scratch hardness measurement data were incorporated in the calculations. According to ASTM D7027-05 standard, scratch hardness (H_s) can be defined as:

$$H_s = \frac{4qP}{\pi w^2} \quad [4]$$

where P is the normal load used in the scratch tests in Newtons, w is the scratch width in millimeters, and q is the dimensionless parameter, which depends on the extent of elastic recovery of the polymer during scratching. In this case, full elastic recovery implies $q=1$, whereas no recovery implies $q=2$.

The wetting experiment was performed using Kyowa (model DM 501) contact angle goniometer. A static sessile drop method was considered for the contact angle measurement. The water contact angle between the water droplet and the heat-treated surface was measured with a fluid medium such as deionized water. Droplet volume was controlled with an automatic dispensing system with a volume step resolution of 0.1 μl. Still images were captured, and contact angle measurements were performed after 1 s of deposition of water droplets on the surface. The contact angle measurements are performed to assess the hydrophobicity of the laser-ablated surface. Because the laser-ablated surface is chemically heterogeneous due to the local nitride formations and nitride dissolutions at the surface, the application of Young's equation[48] is limited in assessing the contact angle. Wenzel[49] and Cassie and Baxter[50] proposed a relationship between the contact angle of a liquid droplet and the surface roughness factor to overcome this limitation. The Wenzel formulation takes the liquid penetration into the rough grooves into account and expresses the contact angle as follows:[51]

$$\cos\theta_w = \frac{r(\gamma_{sv} - \gamma_{sl})}{\gamma_{lv}} \quad [5]$$

where θ_w is the rough surface contact angle, γ_{sv} is the interfacial tension of the solid–vapor interface, γ_{sl} is the interfacial tension of the solid–liquid interface, γ_{lv} is the interfacial tension of the liquid–vapor interface, and r is the surface roughness factor, which is defined as the ratio between the actual and projected surface areas, where $r=1$ for a perfectly smooth surface and $r>1$ for a rough surface. The contact angle equation is expressed as follows:[51]

$$\cos\theta_c = f_1\cos\theta_1 + f_2\cos\theta_2 \quad [6]$$

where θ_c is the apparent contact angle, f_1 is the surface fraction of the liquid–solid interface, f_2 is the surface fraction of the liquid–vapor interface, θ_1 is the contact angle of the liquid–solid interface, and θ_2 is the contact angle for the liquid–vapor interface. In the case of an air–liquid interface, f_1 is the solid–liquid fraction and air fraction (f_2) becomes $(1-f_1)$. For $f_1=0$, the liquid droplet is not in contact with the solid surface; for $f_1=1$, the droplet completely wets the surface.

3.5.4 Results and Discussion

Laser texturing of PC sheet, phosphorous bronze coupons, and alumina tiles are performed. Morphological, metallurgical, mechanical, and surface hydrophobicity are presented according to the materials used in the present study. The findings are in line with the findings of the previous studies.[11–13]

3.5.4.1 PC Sheet

The findings of mechanical, optical, hydrophobicity, and morphological properties are given here and are in line with those of the previous study.[11]

Figure 1 shows optical and SEM micrographs of the laser-treated surface. Laser-treated surface is free from large-scale asperities such as large cracks and voids. Although surface treatment takes place at a constant laser scanning speed, no regular textured patterns are observed at the surface, unlike laser ablation of ceramic surfaces. This is associated with the shallow cavity formation under the controlled ablation at the surface. It should be noted that repetitive pulses with 1500-Hz pulsing frequency are incorporated during the laser ablation process. In this case, overlapping of the irradiated spots due to laser repetitive pulses results in formation of continuous laser scanning tracks, which consist of fine cavities and resolidified sections at the surface. Because laser beam intensity is Gaussian at the workpiece surface, peak intensity occurs at the irradiated spot center. The cavity is formed at the central region of the irradiated spot and melting takes place in the cavity vicinity due to the low laser intensity in this region. However, repetitive laser pulses modify this structure at the surface because of the molten flow from the recently formed cavity near the previously formed cavity. Therefore, surface texture is modified and micro-/nano-pores are formed at the surface. It is evident from the optical image (**Figure 1(a)**) that crystal growth extends radially from the potential nucleation site; however, widespread branching is not visible in the frame of the radial growth. In addition, in some regions (**Figure 1(a)**), intermittent branching takes place, which can be considered as a hallmark of growth to form large spherules. The fine cavity

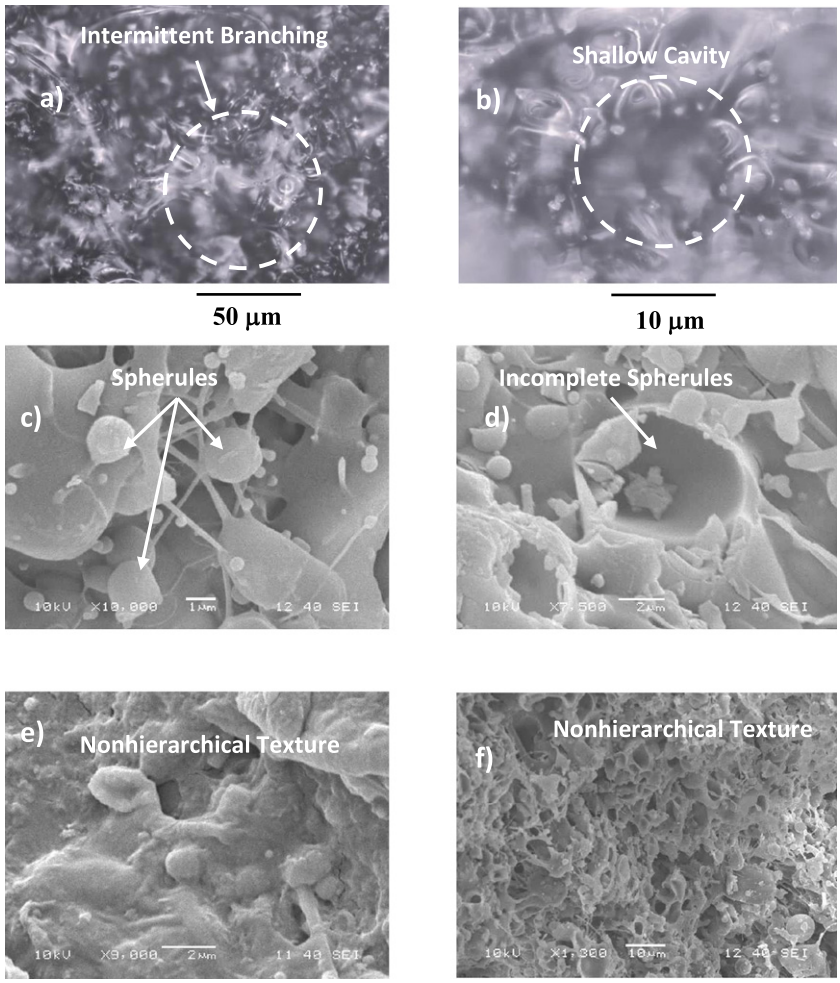


Figure 1 Optical images and scanning electron microscope micrographs of laser-treated surface[11]: (a) optical image demonstrating the crystals formed at the surface and radial growth of crystals and intermittent branching; (b) laser-produced fine shallow cavity and spherules; (c) spherules formed at the surface; (d) incomplete spherules; and (e) and (f) nonhierarchical texture.

formation is also observed in Figure 1(b). Because high-pressure argon is used as assisting gas, no sideways burn-through oxidation reactions are observed at the ablated surface. Surface texture composed of micro-/nano-features is evident from the high-magnification SEM micrograph (Figure 1(a)). Partially formed spherules with varying diameters are also observed from optical and SEM micrographs (Figure 1(b)); however, they do not form hierarchical structure at the surface (Figures 1(c) and 1(d)). This is associated with the varying nucleation density due to nonuniform cooling rates at the surface. Although crystal size varies at the surface, large crystals do not form due to the high cooling rates, unlike those reported for other crystallization processes.[52] Figure 2 shows SEM micrographs of the cross-section of the laser-textured layer. The laser-treated layer consists of fine structures emanating from the surface (Figure 2(b)) and crystal structures formed in the surface region during the solidification process (Figure 2(c)). The laser-treated layer extends almost uniformly along the workpiece surface with a thickness of approximately 2 μm. The fine cavities formed at the surface result in micro-/nano-level waviness contributing to the overall surface texture of the laser-treated layer.

Residual stress formed in the treated layer is determined from the curvature technique. Residual stress obtained from the curvature method is approximately -26 MPa, and the findings reveal that residual stress is compressive. The formation of residual stress is associated with the thermal effect due to high cooling rates and crystallization of the laser-treated surface; in which case, molecular structures are modified in the crystal structure while causing the stress formation after completion of the crystallization process.[53] It should be noted that the volume change due to hydrolysis has an effect on the residual stress formation in the surface region. However, the measurements are performed immediately after the completion of the laser treatment process; therefore, this affect is expected to be insignificant.

Figure 3 shows the friction coefficient of the laser-treated and untreated surfaces. Laser treatment lowers the friction coefficient at the surface, which is associated with enhancement of surface microhardness after the laser treatment process. Laser treatment increases the microhardness of the surface; in which case, microhardness of the untreated surface is 11.2 ± 0.2 HV and that of the laser-treated surface is 25.1 ± 0.9 HV. It should be noted that microhardness

measurements were repeated 10 times at different locations on the laser-treated surface and the error estimated from the hardness data is approximately 0.9 HV. Microhardness variation at the surface is associated with the nonuniform cooling rates and nonuniform distribution of crystal sizes at the surface. However, microhardness enhancement is associated with the crystal structures formed at the surface and high cooling rates that lower the crystal size in the surface region; consequently, a dense crystalline surface results after the laser treatment process. The scar sizes are almost uniform and the scar depth is shallower for the laser-treated and untreated surfaces. The laser-treated surface results in shallow scar depth, which is due to increased hardness at the surface, and no cracks are observed around the scar mark for the laser-treated and untreated surfaces. This demonstrates that the surface fracture toughness reduction due to surface hardness enhancement is not significant. The scratch hardness values of the laser-treated and untreated surfaces are 110 ± 11 MPa and 80 ± 3.2 MPa, respectively. The scratch tests were conducted at different regions of the laser-treated and untreated surfaces. Based on the repeatability of the data, the estimated error is approximately 6% for the laser-treated surface and 4% for the untreated surface.

In general, the laser-treated surface demonstrates the Cassie–Baxter state[50]; in which case, surface texture with low roughness results in air pockets occupying the texture gap while generating hydrophobic behavior at the surface. This situation can be observed from the small value of hysteresis ($\theta_{\text{Advancing}} - \theta_{\text{Receding}}$, where $\theta_{\text{Advancing}}$ is the advancing angle and θ_{Receding} is the receding angle) for the low roughness surface (Table 1). However, in some region at the laser-treated surface, texture changes and surface roughness increases, resulting in nonhydrophobic behavior of the surface, such as

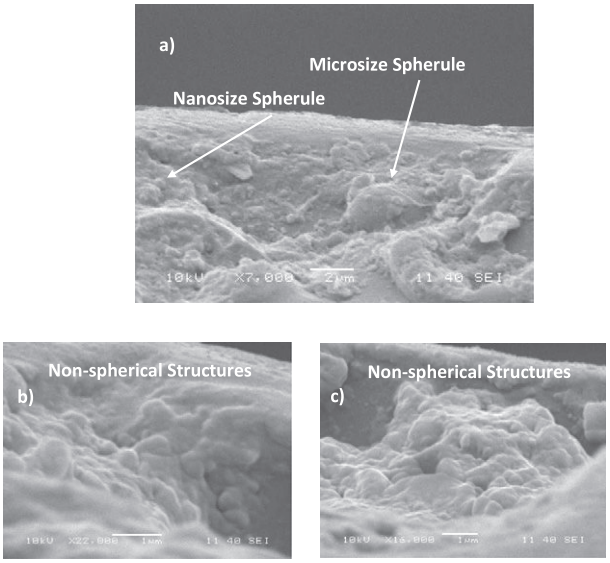


Figure 2 Scanning electron microscope micrographs of the cross-section of the laser-treated layer[11]: (a) spherules at different sizes; (b) nonspherical structures initiating the formation of spherules: and (c) nonspherical dense structure.

Table 1 Contact angles measurement results before and after the laser treatment of polycarbonate sheet[11]

		Contact angle (in degrees)	
		Low roughness	*High roughness*
Laser-treated surface	Advancing	128.2 (+5/−5)	92.3 (+5/−5)
	Receding	121.4 (+5/−5)	78.5 (+5/−5)
Untreated surface	Advancing	84.2 (+5/−5)	–
	Receding	56.6 (+5/−5)	–

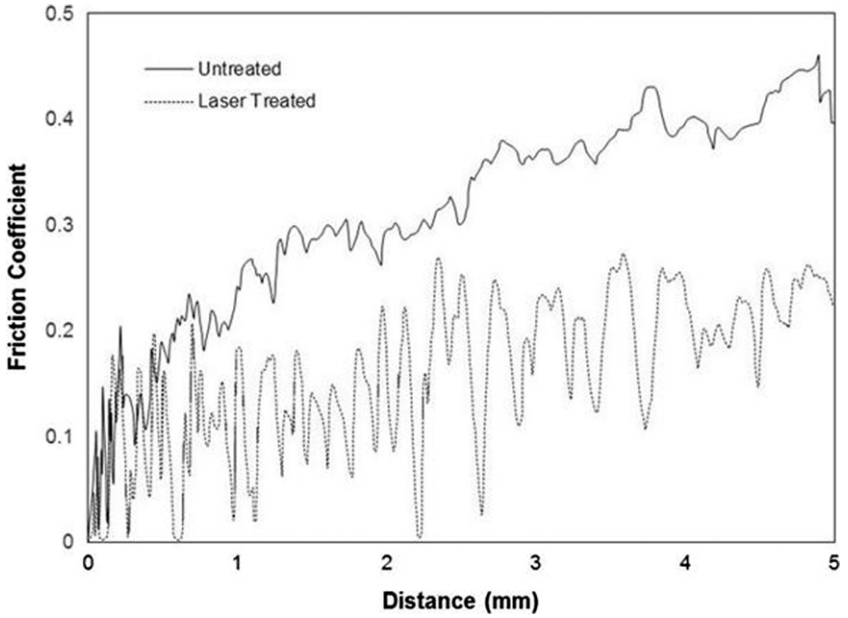


Figure 3 Friction coefficient along the laser-treated and untreated surfaces.[11]

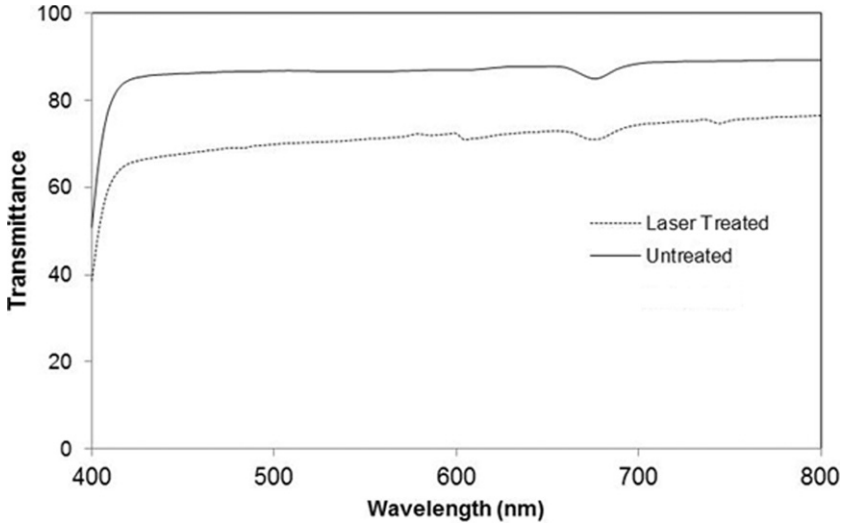


Figure 4 Transmittance data for laser-treated and untreated workpieces.[11]

attainment of a high value of hysteresis (Table 1). This occurs randomly and the total coverage area of this region is small at the laser surface. Consequently, the mixture of hydrophobic states consisting of the Cassie–Baxter and Wenzel states occur at the laser-treated surface. The contact angle measurements reveal that the laser-treated surface demonstrates hydrophobicity across a large area (Table 1, which provides the contact angle data). The roughness factor (f) should be within $0 \leq f \leq 1$ for the hydrophobic surfaces. However, superhydrophobicity is only possible for f values approaching zero. Therefore, f should approach zero for large contact angles in the Cassie and Baxter state. This situation is possible when the surface texture comprises a mixture of micro-/nano-size dimples and pillars, which in turn give rise to the Cassie and Baxter state with large contact angles. This situation is observed in a few locations at the laser-treated surface; in which case, contact angles well in excess of 140° resulted. Figure 4 shows the optical transmittance of the laser-treated and untreated surfaces. The laser-treated surface has less transmittance than that corresponding to the untreated surface. This is associated with the crystal formation at the surface, which alters the absorption characteristics of the incident radiation. Nevertheless, the maximum reduction in the transmittance is approximately 15%, which is significantly low compared to the crystallized surface by the chemical processes, such as immersion in acetone.[54]

3.5.4.2 Alumina Tile

The results obtained for alumina tiles due to mechanical, morphological, and hydrophobic properties are presented and are in line with those of previous study.[12]

Figure 5 shows an optical photograph of the laser-treated workpiece, whereas Figure 6 shows SEM micrographs of the laser-treated surface. The regular ablated tracks can be observed at the laser-treated surface. The tracks are formed during the repetition of the laser pulses at 1500 Hz. To avoid the large-scale cavities at the surface, the laser scanning speed and the laser power intensity are set accordingly after the several

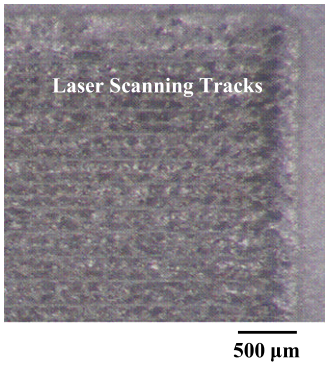


Figure 5 Optical photograph and atomic force microscope micrographs of laser-treated workpiece surfaces.[12]

experimental trials. The maximum depth of the micro-cavities, due to ablation, is approximately 1 µm. The pulse repetitions at the surface modify the micro-cavity shape because of the overlapping of the irradiated spot at the surface. The overlapping ratio of the spots is estimated as 72%, which provides continuous ablation without leaving an unablated gap at the surface. In addition, the overlapping of the irradiated spots modifies the cavity depth such that the initially ablated surface, due to the first pulse, is partially heated by the second consecutive pulse. Because the pulse intensity reduces radially due to Gaussian intensity distribution, the power absorbed by the initially ablated surface due to the second consecutive pulse becomes less because of the workpiece movement during the laser scanning. This, in turn, causes melting rather than ablation in this region; consequently, local flow of molten material fills some part of the previously formed cavity and modifies the geometric features of the cavity surface. Therefore, irregular surface textures with micro/nanoscale dimples are generated at the surface, which can also be seen in the SEM micrographs. The topologic irregularity shows the similarity of the geometric features of the lotus leaf surface.[1] The melting is localized across the small part of the ablated cavity, and no

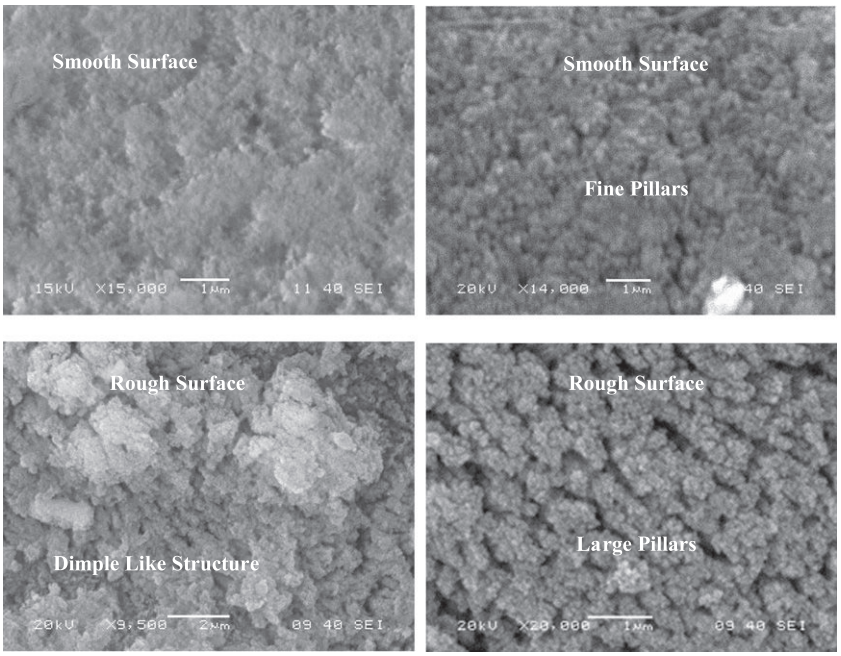


Figure 6 Scanning electron microscope micrographs of laser-treated surfaces.[12] Relatively smooth and rough surfaces.

overflow of molten material is observed across the laser scanning tracks. In addition, the molten flow does not have observable effects on the neighboring cavities. Therefore, the controlled ablation resulted in shallow cavities with dimple-like structures at the surface without large-scale or regular asperities at the surface. Although the cooling rate is high because of the short processing duration and the convection effect of the assisting gas, no crack or crack network is observed at the treated surface. The closed examination of the SEM micrograph reveals that the ablated surface has an irregular texture comprising nano-size grains. The grain refinement at the surface is associated with the high cooling rates and the formation of nitride species at the surface. It should be noted that the use of high-pressure nitrogen as an assisting gas causes the nitride species formation at high temperatures during the ablation process. Moreover, during the laser ablation, evaporated material forms small surface plasma because of the absorption of the incident beam by the vapor front. Because the surface plasma is transiently hot, it contributes to melting at the cavity surface. The surface plasma appears as a bright spot at the irradiated surface during the treatment process. Once the plasma temperature and pressure increase significantly, due to the absorption of the incident beam, the plasma expands rapidly and its thermal effect on the molten flow diminishes. However, the plasma residues appear to be fine dusts at the workpiece surface.

Figure 7 shows SEM micrographs of the cross-section of the laser-treated workpiece. The treated layer extends uniformly 15 μm below the surface because of the constant scanning speed and the steady laser power intensity. Laser ablation at the surface results in fine and dense structures in the surface vicinity, which are attributed to the high cooling rates and the formation of nitride species at the surface. It should be noted that the density of AlN is smaller than the density of Al_2O_3; the volume shrinkage takes place in this region through which the dense structures are formed. Although volume shrinkage results in micro-stress formation in the surface region, no micro-cracks are observed in this region. The overlapping of the laser spots creates a self-annealing effect; in which case, the lately formed cavity site acts like a heating source to the previously formed cavity sites while creating the self-annealing effect. The cooling rates remain high in the region next to the surface vicinity, resulting in small columnar structures. As the depth below the surface increases, the cooling rate becomes slower and relatively larger (as compared to that corresponding to the surface vicinity) columnar structures are formed. As the depth below the surface increases further, large columnar structures replace the grains. The low thermal diffusivity of the substrate material suppresses the extension of the heat-affected zone into the solid bulk. Consequently, the narrow heat-affected zone results between the treated layer and the base material.

Figure 8 shows an X-ray diffractogram for laser-treated and as-received surfaces. The formation of the AlN compound during the laser processing of the surface is evident. The formation of aluminum nitride may take place in two steps. $Al_2O_3 + Al_2O \rightarrow Al_2O + 2CO_2$ (in the first step) and the presence of high-pressure nitrogen as the assisting gas (in the second step) provide $Al_2O + CO + N_2 \rightarrow AlN + CO_2$. A carbonic gas (carbon dioxide) formed during the process escapes from the irradiated surface. AlON compound peak is also observed in the XRD diffractogram. The possible explanation for the formation of AlON is that when the temperature reaches the melting temperature, $Al_2O_3 \rightarrow 2AlO + ½O_2$ is formed. The oxygen atom remains in the alumina structure[55]; however, the presence of N_2 gives rise to $2AlO + N_2 \rightarrow 2AlON$ and formation of the AlON phase. The transformation of the γ-Al_2O_3 phase into thermodynamically stable α- Al_2O_3 is observed when comparing diffractograms of laser-treated and as-received workpiece surfaces. **Table 2** provides the EDS data at three locations on the laser-treated surface. The elemental

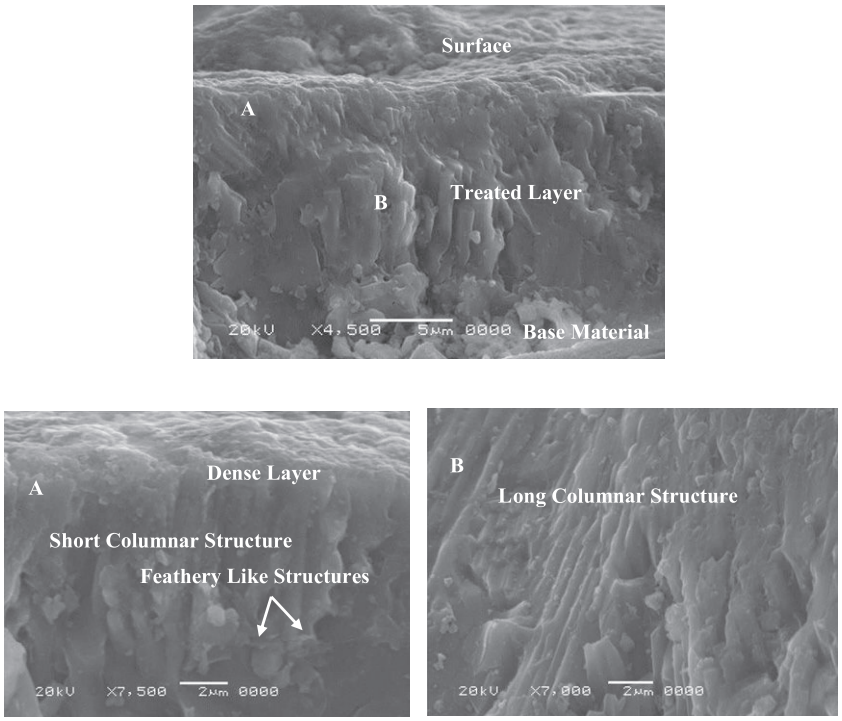


Figure 7 Scanning electron microscope micrographs of cross-section of laser-treated workpiece.[12]

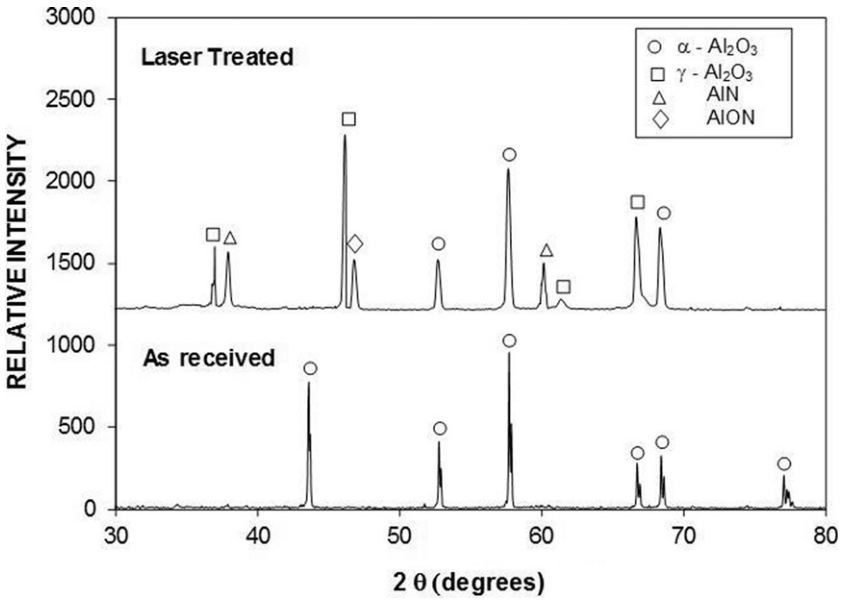


Figure 8 X-ray diffractogram as-received and laser-treated workpiece surfaces.[12]

composition remains uniform at the treated surface. Although the quantification of the light elements involves error in EDS data, the presence of nitrogen is evident, which is attributed to nitride species formation at the surface. **Table 3** gives the microhardness and the residual stress determined from the XRD technique for the laser-treated surfaces. The microhardness increases significantly at the surface, which is approximately 50% more than the base material hardness. The residual stress developed is approximately -2.1 GPa, which is compressive. The formation of a dense layer consisting of fine grains, due to high cooling rates, and nitride phases are responsible for the attainment of high hardness and high residual stress at the surface of the treated surface.

Figure 9 shows photographs obtained from the contact angle measurements, whereas **Table 4** gives the contact angles at different locations at the surface. Because the roughness and

Table 2 Elemental composition of laser-treated surface obtained from EDS data (wt%) for alumina[12]

Spectrum	*N*	*O*	*Al*
Spectrum 1	7.3	37.2	Balance
Spectrum 2	6.2	39.4	Balance
Spectrum 3	7.5	38.2	Balance
Spectrum 4	5.8	40.5	Balance

Table 3 Microhardness and residual stress at the workpiece surface before and after the laser treatment of alumina[12]

	Hardness (HV)	*Residual stress (GPa)*
Laser-treated surface	1650 (+50/−50)	2.1 (+0.06/−0.06)
As-received surface	1150 (+50/−50)	

surface energy alter the wetting properties,[35] the contact angle changes at different locations at the surface. It can be observed from the photographs that in the first case (rough surface), the Wenzel state takes place; therefore, the water droplet penetrates into the grooves and touches the surface without presence of the air gap. In this case, the contact angle attains a slightly low value. However, this behavior is only observed at two out of seven locations where the tests were performed. When comparing the laser-treated and untreated surfaces, it is evident that the contact angle reduces considerably for the untreated surface. The formation of nitride species (AlN) at the treated surface modifies the surface energy such that γ_{sl} reduces. It should be noted that the surface free energy of AlN is 38.3 mJ m^{-2}, whereas it is 68 mJ m^{-2} for Al_2O_3.[56] For the second case, the behavior of the water droplet demonstrates the Cassie and Baxter state; in which case, the fine roughness at the surface results in air pockets, which are captured in the grooves, forming a composite state. According to eqn [6], the f should be within $0 \leq f \leq 1$. Therefore, f should approach zero for large contact angles in the Cassie and Baxter state. This situation can be observed from **Table 4**. Consequently, composite surface texture with the combination of micro-/nano-dimples and pillars results in two states of hydrophobicity at the treated surface, provided that the Cassie and Baxter state dominates over the Wenzel state.

3.5.4.3 Phosphorous Bronze

The results of morphological and metallurgical changes, surface texture, hydrophobicity, and residual stress are discussed and are in line with those of a previous study.[13]

Figure 10 shows SEM micrographs of laser-ablated phosphor bronze surfaces. Laser ablation takes place during the irradiation of repetitive laser pulses along the laser scanning direction; in which case, the ablated surface forms regular laser scanning tracks. Because the laser pulse frequency is 1500 Hz and the laser scanning speed is 0.1 m s^{-1}, overlapping of irradiated spots occurs at the surface. The overlapping ratio is approximately 70% at the surface. Laser intensity distribution is Gaussian and the pulse intensity remains high at the irradiated

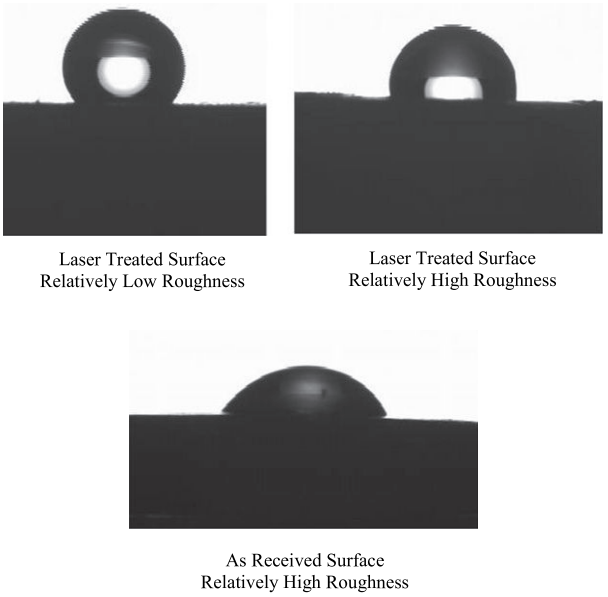


Figure 9 Photographs of water droplet shapes on the sample.[12]

Table 4 Contact angles measurement results before and after the laser treatment of alumina surface[12]

	Contact angle (degrees)	
	Low roughness	*High roughness*
Laser-treated surface	120.8 (+5/−5)	84 (+5/−5)
Untreated surface	63.2 (+5/−5)	

spot center. This, in turn, results in surface evaporation in the region limited to the irradiated spot center, and the melting takes place in the remaining region of the irradiated spot. The melt flow toward the cavity center from its neighborhood modifies the cavity shape and reduces the cavity depth. Therefore, surface texture consisting of micro-/nano-poles and cavities results at the treated surface. The mahogany color in **Figure 11** represents the presence of Cu_3N in the surface region, which is also observed in the X-ray diffractogram, for example, the presence of $Cu_3N(100)$ is associated with the high nitrogen pressure incorporated in the laser treatment process. The presence of a few scattered copper spots is due to the dissolution of Cu_3N at elevated temperatures. In this case, in the near region of the cavity, the surface melts and solidifies rapidly because of the convection cooling of the nitrogen assisting gas; therefore, the dissolution of Cu_3N does not cover the whole surface. Laser-treated surfaces are composed of submicron grains, which are attributed to the rapid solidification and formation of nitrides at the surface region. In addition, the submicron size of the packed particles indicates that each particle contains many single crystals of Cu_3N.[13] Although use of assisting gas increases cooling rates at the surface, no micro-cracks are observed between the packed grains.

Figure 12 shows optical images of the water droplet on the laser-ablated and untreated surfaces, whereas **Table 5** provides the data regarding the contact angle measurements at different

locations at the surfaces. The contact angle varies slightly with the location at the surface, which is attributed to the surface texture variation and the texture composition at the surface. In general, the laser-treated surface demonstrates superhydyrophobic behavior, and the average contact angle of the surface is approximately 142°. Consequently, the texture of the laser-ablated surface, consisting of fine pillars and poles at micro-/nano-scale, results in large contact angles of the water droplet.

Figure 13(a) shows SEM micrographs of the cross-section of the laser-ablated layer. A dense structure consisting of submicron packed particles and extremely fine grains is formed in the surface region (Figure 13(b)). Formation of Cu_3N in the surface region lowers the density and causes volume shrinkage in the dense layer. In addition, the high quench rates in the cooling cycle after laser ablation are responsible for the formation of fine grains in the dense layer. A dendritic structure with elongated grains is observed at some distance below the dense layer (Figure 13(c)). The formation of a dendritic structure indicates the high rate of solidification in this region, and the nonuniform cooling is responsible for the formation of the elongated grains. As the distance below the surface increases further, a cellular structure is formed (Figure 13(d)), which is associated with the relatively lower cooling rates as compared to that of the surface region. EDS data for the elemental composition of the laser-treated surface are given in Table 6. Although quantification of the light elements in EDS data involves error, the presence of nitrogen is evident, which

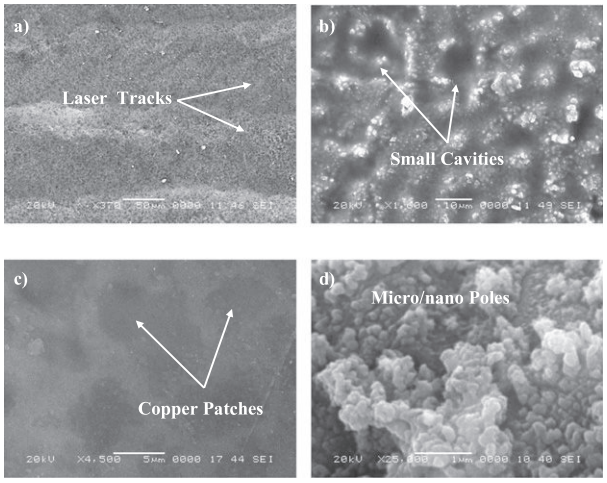


Figure 10 Scanning electron microscope micrographs of laser-ablated surface[13]: (a) regular laser scanning tracks; (b) fine cavities at ablated surface; (c) mahogany color and scattered Cu_3N dissolved spots; and (d) micro-/nano-size surface texture.

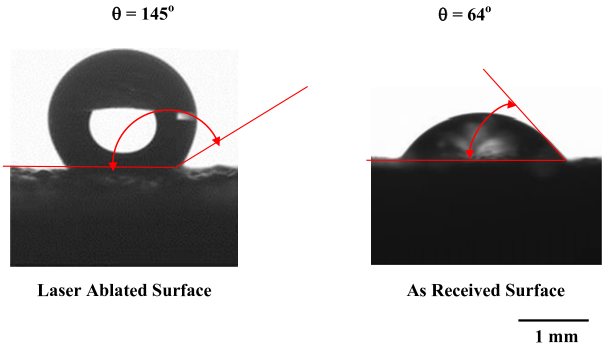


Figure 12 Optical images of water droplets for contact angle measurements.[13]

Table 5 Contact angles measurement results at the surfaces of laser-ablated and as-received phosphorous bronze surfaces[13]

	Contact angle (Degrees)	
	Location 1	*Location 2*
Laser-ablated surface	148 (+5/−5)	141 (+5/−5)
As-received surface	62 (+5/−5)	63 (+5/−5)

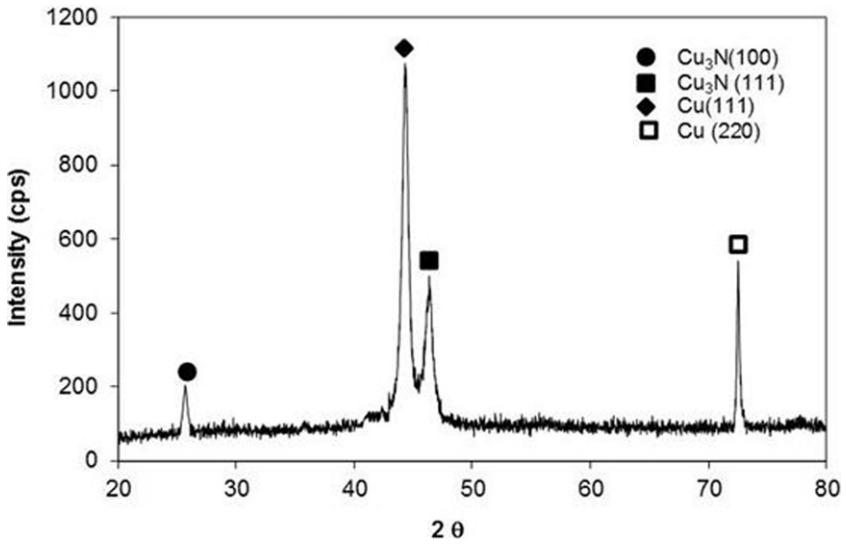


Figure 11 X-ray diffractogram of laser-ablated surface.[13]

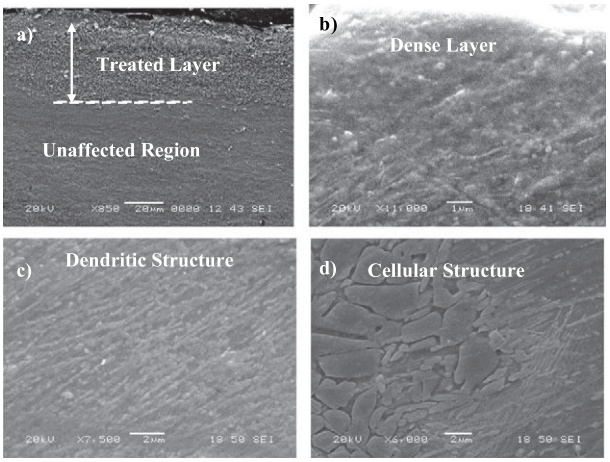


Figure 13 SEM micrographs of cross-section laser-ablated layer[13]: (a) cross-section; (b) small grains; (c) dendritic structure; and (d) cellular structure.

Table 6 EDS data and corresponding locations at the laser-treated surface (wt%) of phosphorous bronze[13]

Spectrum	*N*	*P*	*Sn*	*Cu*
Spectrum 1	7	–	5.7	Balance
Spectrum 2	4	0.1	6	Balance
Spectrum 3	6	0.1	5.8	Balance

Table 7 Microhardness and residual stress for phosphorous bronze[13]

	Hardness (HV)	*Residual stress (MPa)*
Laser-ablated surface	580 (+30/−30)	−350 (+10/−10)
As-received surface	140 (+10/−10)	–

has a high concentration at the surface. The absence of Sn in some EDS spectrums indicates that Sn was evaporated in the surface region during the laser ablation process. The heat-affected zone is shallow without forming a demarcation line between the heat-affected zone and the base material, which is attributed to the high thermal conductivity of the bronze.

The microhardness and residual stress data for the laser-ablated surface are given in Table 7. The microhardness of the laser-ablated surface is high at 580 ± 30 HV, which is almost four-times the hardness of the base material (145 ± 10 HV). This is due to one or all of the following: the dense structure formed in the surface region and the formation of Cu_3N compounds in the surface region after the laser ablation process. The residual stress measured by the XRD technique is approximately −350 ± 10 MPa. Because ablation takes place along the laser scanning tracks, recently ablated regions create a self-annealing effect on the previously ablated regions. This in turn, modifies the cooling rates, particularly below the surface. However, the self-annealing effect created during the cooling period does not significantly alter the stress levels in the surface vicinity because of the convective cooling of the assisting gas at the surface; therefore, the residual stress remains high in the surface region. It should be noted that the residual stress measured is limited to the surface vicinity because the penetration depth of the X-ray radiation is approximately a few micrometers. Although the workpiece surface expands freely during the laser ablation process, the surface vicinity is not free to expand and compressive stresses are formed. This behavior is responsible for the attainment of high residual stress in the surface region. Figure 14 shows the scratch test results used to determine the friction coefficient of the laser-ablated and as-received surfaces.

3.5.5 Concluding Remarks

Laser gas-assisted surface texturing has several advantages over the conventional texturing methods. This is because of the precision of operation, low cost, local treatment, and

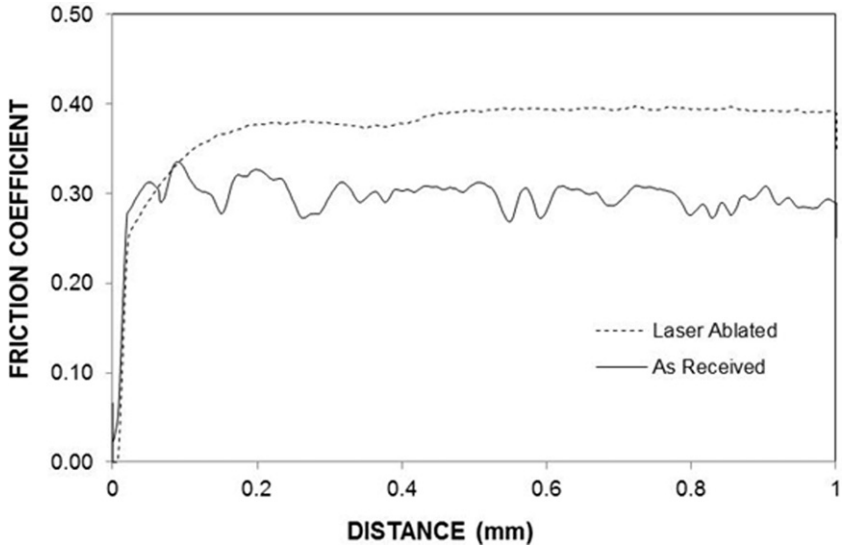


Figure 14 Friction coefficient for laser-ablated and as-received workpiece surfaces.[13]

high-speed processing. A high-intensity laser beam with fine focus spots with a high repetition rate (1500 Hz) is used to irradiate the workpiece surface under the high-pressure nitrogen gas environments. This results in the combination of melting and evaporation at the surface and modifies the cavity size formed at the surface. Therefore, laser surface treatment, which involves the combination and evaporation, gives rise to the surface texture having micro-/nano-poles at the treated surface. In addition, use of nitrogen assisting gas causes the formation of nitride species in the treated surface. In general, the nitride compounds formed at the surface allow the attainment of the low surface energy while improving the surface hydrophobicity. Consequently, the mutual presence of low surface energy and surface texture composed of micro/nano textures results in superhydrophobicity at the surface. However, the use of a high-intensity beam during the texturing of the surface causes formation of high thermal stresses in the surface of the laser-treated region. Therefore, thermally induced stresses become important for using the textured surface in practical applications. The close examination of the residual stress data reveals that the residual stress formed in the laser-treated region is smaller than the yielding limit of the materials, including PC, alumina, and phosphorous bronze. The specific findings are:

- Laser-textured surfaces composed of micro-/nano-texturing, which are due to the combined mode of evaporation and melting at the surface during the texturing. In general, the pole heights vary within the range of 30 nm–1.5 μm, which is true for all the substrate material textured by a laser beam.
- The use of high-pressure nitrogen assisting gas results in nitride compound formation in the surface vicinity of all the substrate materials used for texturing, except PC. The formation of nitride species reduces the surface energy of the textured surfaces.
- The laser-textured surfaces are free from asperities, including large cavities and the micro-cracks. This is associated with the proper selection of the laser texturing parameters.
- Microhardness of the laser-textured surface increases for all the substrate materials used in the study. The microhardness increase can be attributed to the fine grains, which are formed at the surface under the high cooling rates. In addition, formation of nitride species contributes to the microhardness enhancement at the surface.
- The residual stress formed in the laser-treated layer is compressive for all the substrate materials used in the study. This is attributed to the depth of the treated layer, which is shallow (i.e., approximately 20–40 μm).
- The surface hydrophobicity, in general, increases after the laser texturing. However, nonuniform behavior of the laser surface texturing and the mixture of Cassie–Baxter and Wenzel states are observed. Nevertheless, the Cassie–Baxter state covers almost 80% of the total textured surface.

Acknowledgments

The authors acknowledge the support of King Fahd University of Petroleum and Minerals (KFUPM) through the accomplishment of this work.

See also: 3.19 Effect of Surface Roughness on Wetting Properties

References

1. Parker, A. R.; Lawrence, C. R. Water Capture from Desert Fogs by a Namibian Beetle. *Nature* **2001**, *414* (6859), 33–34.
2. Han, J. T.; Xu, X. R.; Cho, K. W. Diverse Access to Artificial Superhydrophobic Surfaces Using Block Co-Polymers. *Langmuir* **2005**, *21* (15), 6662–6665.
3. Shirtcliffe, N. J.; McHale, G.; Newton, M. I.; Chabrol, G.; Perry, C. C. Dual-Scale Roughness Produces Unusually Water-Repellent Surfaces. *Adv. Mater.* **2004**, *16* (21), 1929–1932.
4. Hwang, H. S.; Lee, S. B.; Park, I. Fabrication of Raspberry-Like Superhydrophobic Hollow Silica Particles. *Mater. Lett.* **2010**, *64* (20), 2159–2162.
5. Huang, Y. H.; Wu, J. T.; Yang, S. Y. Direct Fabricating Patterns Using Stamping Transfer Process with PDMS Mold of Hydrophobic Nanostructures on Surface of Micro Cavity. *Microelectron. Eng.* **2011**, *88* (6), 849–854.
6. Yang, T.; Tian, H.; Chen, Y. Preparation of Superhydrophobic Silica Films with Honeycomb-Like Structure by Emulsion Method. *J. Sol-Gel Sci. Technol.* **2009**, *49* (2), 243–246.
7. Kinoshita, H.; Ogasahara, A.; Fukuda, Y.; Ohmae, N. Superhydrophobic/Superhydrophilic Micropatterning on a Carbon Nanotube Film Using a Laser Plasma-Type Hyperthermal Atom Beam Facility. *Carbon* **2010**, *48* (15), 4403–4408.
8. Latthe, S. S.; Imai, H.; Ganesan, V.; Rao, A. V. Superhydrophobic Silica Films by Sol–Gel Co-Precursor Method. *Appl. Surf. Sci.* **2009**, *256* (1), 217–222.
9. Ma, M.; Mao, Y.; Gupta, M.; Gleason, K. K.; Rutledge, G. C. Superhydrophobic Fabrics Produced by Electrospinning And Chemical Vapor Deposition. *Macromolecules* **2005**, *38* (23), 9742–9748.
10. Zhang, X.; Guo, Y.; Zhang, P.; Wu, Z.; Zhang, Z. Superhydrophobic CuO@Cu2S Nanoplate Vertical Arrays on Copper Surfaces. *Mater. Lett.* **2010**, *64* (10), 1200–1203.
11. Yilbas, B. S.; Khaled, M.; Abu-Dheir, N.; *et al.* Wetting and Other Physical Characteristics of Polycarbonate Surface Textured Using Laser Ablation. *Appl. Surf. Sci.* **2014**, *320*, 21–29.
12. Yilbas, B. S.; Khaled, M.; Abu-Dheir, N.; Aqeeli, N.; Furquan, S. Z. Laser Texturing of Alumina Surface for Improved Hydrophobicity. *Appl. Surf. Sci.* **2013**, *286*, 161–170.
13 Yilbas, B. S. Laser Ablation of Phosphor Bronze for Superhydrophobic Surface. *Surf. Eng.* **2015**, doi:10.1179/1743294414Y.0000000325.
14. Frank, F. C.; Tosi, M. On the Theory of Polymer Crystallization. *Proc. R. Soc. Lond. A* **1961**, *263*, 323.
15. Cui, Y. H.; Paxson, A. T.; Smyth, K. M.; Varanasi, K. K. Superhydrophobic Polymer Surface via Solvent-Induced Crystallization. In *Proceedings of the 13th IEEE ITHERM Conference*, Paper No. 978-1-4244-9532-0, 2012; pp. 951–955.
16. Jang, M.; Chan, K.; Lee, N. Y. Modification of Polycarbonate with Hydrophilic/Hydrophobic Coatings for the Fabrication of Microdevices. *Sens. Actuators, B: Chem.* **2014**, *193*, 599–607.
17. Zheng, Z.; Tu, L.; Rao, H.; Qiu, K.; Wang, X.; Fu, S. Fabrication and Characterization of Super-Hydrophobic Surfaces of Polycarbonate Slab. *J. Vac. Sci. Technol.* **2014**, *34* (3), 272–277.
18. Palumbo, F.; Di Mundo, R.; Cappelluti, D.; Dagostino, R. SuperHydrophobic and SuperHydrophilic Polycarbonate by Tailoring Chemistry and Nano-Texture with Plasma Processing. *Plasma Process. Polym.* **2011**, *8* (2), 118–126.
19. Bhagat, S. D.; Gupta, M. C. Superhydrophobic Microtextured Polycarbonate Surfaces. *Surf. Coat. Technol.* **2015**, *270*, 117–122.
20. Cui, Y.; Paxson, A. T.; Smyth, K. M.; Varanasi, K. K. Hierarchical Polymeric Textures via Solvent-Induced Phase Transformation: A Single-Step Production of Large-Area Superhydrophobic Surfaces. *Coll. Surf. A: Physicochem. Eng. Asp.* **2012**, *394*, 8–13.
21. Banerjee, B. S.; Balasubramanian, K. Nanotexturing of PC/n-HA Nanocomposites by Innovative and Advanced Spray System. *RSC Adv.* **2015**, *5* (18), 13653–13659.
22. Spohr, R.; Sharma, G.; Forsberg, P.; Karlsson, M.; Hallén, A.; Westerberg, L. Stroke Asymmetry of Tilted Superhydrophobic Ion Track Textures. *Langmuir* **2010**, *26* (9), 6790–6796.
23. Harimkar, S. P.; Dahotre, N. B. Crystallographic and Morphological Textures in Laser Surface Modified Alumina Ceramic. *J. Appl. Phys.* **2006**, *100* (2), doi:10.1063/1.2214365. (Article number: 024901).

24. Li, J.; Xiong, D.; Dai, J.; Huang, Z.; Tyagi, R. Effect of Surface Laser Texture on Friction Properties of Nickel-Based Composite. *Tribol. Int.* **2010**, *43* (5–6), 1193–1199.
25. Williams, O.; Williams, M.; Liu, C.; Webb, P.; Firth, P. Laser Micromachining of Polycrystalline Alumina and Aluminium Nitride to Enable Compact Optoelectronic Interconnects. In *Proceedings of the Electronic Packaging Technology Conference, EPTC*, 2009; pp. 920–925. doi: 10.1109/EPTC.2009.5416413.
26. Khangar, A.; Dahotre, N. B. Morphological Modification in Laser-Dressed Alumina Grinding Wheel Material for Microscale Grinding. *J. Mate. Process. Technol.* **2005**, *170* (1–2), 1–10.
27. Prasad, S. V.; Nainaparampil, J. J.; Zabinski, J. S. Tribological Behavior of Alumina Doped Zinc Oxide Films Grown by Pulsed Laser Deposition. *J. Vac. Sci.Technol. A: Vac., Surf. Films* **2002**, *20* (5), 1738–1743.
28. Vlasova, M.; Kakazey, M.; Juarez-Arellano, E. A.; *et al.* Laser Synthesis of Composite Al_2O_3–$Y_2Ti_2O_7$ Ceramics from Al_2O_3–TiO_2–Y_2O_3 Powder Mixtures. *J. Adv. Microsc. Res.* **2013**, *8* (3), 186–194.
29. Jha, H.; Kikuchi, T.; Sakairi, M.; Takahashi, H. Microfabrication of an Anodic Oxide Film by Anodizing Laser-Textured Aluminium. *J. Micromech. Microeng.* **2007**, *17* (10), 1949–1955.
30. Amanov, A.; Watabe, T.; Tsuboi, R.; Sasaki, S. Improvement in the Tribological Characteristics of Si-DLC Coating by Laser Surface Texturing Under Oil-Lubricated Point Contacts at Various Temperatures. *Surf. Coat. Technol.* **2013**, *232*, 549–560.
31. Hendow, S. T.; Ozkan, A. M.; Oliveira, M.; Mottay, E. Pulsed Fiber Laser Texturing of Metals, Silicon, and Ceramics: Comparison of Surface Structural Changes Induced by ns and fs Pulses. In *Proceedings of SPIE 8243 – The International Society for Optical Engineering, Conference on Laser Applications in Microelectronic and Optoelectronic Manufacturing (LAMOM) XVII*, 2012. doi: 10.1117/12.908869.
32. Antoszewski, B.; Tarelnik, V. Laser Texturing of Sliding Surfaces of Bearings and Pump Seals. *Appl. Mech. Mater.* **2014**, *630*, 301–307.
33. Cacciari, L.; Ciofini, D.; Mascalchi, M.; Mencaglia, A.; Siano, S. Novel Approach to the Microscopic Inspection During Laser Cleaning Treatments of Artworks. *Anal. Bioanal. Chem.* **2012**, *402* (4), 1585–1591.
34. Wang, L.; Yan, C.; Wang, Q.; Guo, F.; Hao, X. Study on the Tribological Properties of the Amphiphobic Textured Metal Surface. *J. Huazhong Uni. Sci. Technol.* **2012**, *40* (Suppl. 2), 21–25, (Natural Science Edition).
35. Chen, G.-Y.; Zhu, D.-J.; Peng, K.; You, W.-M.; Li, L.-J.; Mei, L.-F. Ablation Mechanism of Bronze-Bonded Diamond Wheels Dressing by Pulsed Laser. *Chin. J. Lasers* **2007**, *34*, 245–249.
36. Fornarini, L.; Fantoni, R.; Colao, F.; *et al.* Theoretical Modeling of Laser Ablation of Quaternary Bronze Alloys: Case Studies Comparing Femtosecond and Nanosecond LIBS Experimental Data. *J. Phys. Chem. A* **2009**, *113* (52), 14364–14374.
37. Deng, H.; Chen, G. Y.; Zhou, C.; Li, S. C.; Zhang, M. J. Processing Parameter Optimization for the Laser Dressing of Bronze-Bonded Diamond Wheels. *Appl. Surf. Sci.* **2014**, *290*, 475–481.
38. Kazakevich, P. V.; Simakin, A. V.; Shafeev, G. A. Formation of Periodic Structures by Laser Ablation of Metals in Liquids. *Appl. Surf. Sci.* **2006**, *252* (13 (special issue)), 4457–4461.
39. Pershin, S. M.; Lednev, V. N.; Bogatkin, D. E.; Labutin, T. A.; Bunkin, A. F. Physics of Selective Evaporation of Components During Laser Ablation of Stainless Steels. *Quantum Electron.* **2012**, *42* (7), 605–611.
40. Xu, J.-L.; Yang, B.; Gao, W.; *et al.* Microstructure and Performance of Laser Cladding on Surface of Aluminum Bronze. *J. Aeronaut. Mater.* **2009**, *29* (1), 63–67.
41. Yilbas, B. S.; Matthews, A.; Leyland, A.; Karatas, C.; Akhtar, S. S.; Abdul Aleem, B. J. Laser Surface Modification Treatment of Aluminum Bronze with B_4C. *Appl. Surf. Sci.* **2012**, *263*, 804–809.
42. Tang, C. H.; Cheng, F. T.; Man, H. C. Laser Surface Alloying of a Marine Propeller Bronze Using Aluminium Powder. Part II: Corrosion and Erosion–Corrosion Synergism. *Surf. Coat. Technol.* **2006**, *200* (8), 2594–2601.
43. Gisario, A.; Bellisario, D.; Veniali, F. Thermal-Morphological Analysis of Diode Laser Polishing on Sintered Bronze. *Int. J. Mater. Form.* **2010**, *3* (Suppl. 1), 1067–1070.
44. Yilbas, B. S.; Akhtar, S. S.; Karatas, C.; Chatwin, C. Laser Embedding of TiC Particles into the Surface of Phosphor Bronze-Bearing Material. *Surf. Interface Anal.* **2012**, *44* (7), 831–836.
45. Yilbas, B. S.; Toor, I.; Malik, J.; Patel, F.; Karatas, C. Electrochemical Testing of Laser Treated Bronze Surface. *J. Alloy Compds.* **2013**, *563*, 180–185.
46. Khan, R. H. U.; Yerokhin, A. L.; Pilkington, T.; Leyland, A.; Matthews, A. Residual Stress in Plasma Electrolytic Oxidation Coatings on Al Alloy Produced by Pulsed Unipolar Current. *Surf. Coat. Technol.* **2005**, *200*, 1580–1586.
47. Totemeier, T. C.; Wright, R. N. Residual Stress Determination in Thermally Sprayed Coatings – A Comparison of Curvature Models and X-ray Techniques. *Surf. Coat. Technol.* **2006**, *200* (12–13), 3955–3962.
48. Ma, M.; Mao, Y.; Gupta, M.; Gleason, K. K.; Rutledge, G. C. Superhydrophobic Fabrics Produced by Electrospinning and Chemical Vapor Deposition. *Macromolecules* **2005**, *38* (23), 9742–9748.
49. Wenzel, R. N. Resistance of Solid Surfaces tWetting by Water. *Indust. Eng. Chem.* **1936**, *28* (8), 988–994.
50. Cassie, A. B. D.; Baxter, S. Wettability of Porous Surfaces. *Trans. Faraday Soc.* **1944**, *40*, 546–551.
51. Jung, Y. C.; Bhushan, B. Wetting Transition of Water Droplets on Superhydrophobic Patterned Surfaces. *Scr. Mater.* **2007**, *57* (12), 1057–1060.
52. Go, S.; Han, M.; Ahn, Y. Formation of Nanoporous Polycarbonate Surfaces and their Chemical Modification for Superhydrophobicity. *Bull. Korean Chem. Soc.* **2012**, *33* (11), 3899–3902.
53. Zhao, W.; Barsun, S.; Ramani, K.; Johnson, T.; King, R.; Lin, S. Development of PMMA-Precoating Metal Prostheses via Injection Molding: Residual Stresses. *J. Biomed. Mater. Res.* **2001**, *58* (4), 456–462.
54. Ahmed, A. O. M. *Design and Fabrication of Different Textured Surfaces with Improved Hydrophobicity for Photovoltaic Cells' Applications* (MS Thesis); Kingdom of Saudi Arabia: Chemistry Department, KFUPM, 2014.
55. Yilbas, B. S.; Karatas, C.; Arif, A. F. M.; Abdul Aleem, B. J. Laser Gas Assisted Nitriding of Alumina Surfaces. *Surf. Eng.* **2009**, *25* (3), 235–240.
56. Zan, H.-W.; Yen, K.-H.; Liu, P.-K.; Ku, K.-H.; Chen, C.-H.; Hwang, J. Low-Voltage Organic Thin Film Transistors with Hydrophobic Aluminum Nitride Film as Gate Insulator. *Org. Electron.* **2007**, *8*, 450–454.

Relevant Website

www.kfupm.edu.sa
King Fahd University of Petroleum & Minerals.

3.6 Surface Texture Properties of Co–Ni Alloys Formed with Unipolar and Bipolar Plating

J Vazquez-Arenas, Universidad Autónoma Metropolitana – Iztapalapa, México, D.F., México
I Romero-Ibarra, Unidad Profesional Interdisciplinaria en Ingeniería y Tecnologías Avanzadas – IPN, Ciudad de México, México
RH Lara, Universidad Juarez del Estado de Durango, Durango, Mexico
FS Sosa-Rodríguez, Universidad Autónoma Metropolitana, México, D.F., Mexico

© 2017 Elsevier Inc. All rights reserved.

3.6.1	**Introduction**	86
3.6.2	**Materials and Methods**	87
3.6.2.1	Plating of Co–Ni Alloys	87
3.6.2.2	Chemical and Textural Analyses	87
3.6.3	**Results**	88
3.6.3.1	Electrochemical Plating	88
3.6.3.2	XRD and XPS	89
3.6.3.3	AFM and SEM	90
3.6.4	**Conclusions**	94
Acknowledgments		95
References		95
Relevant Websites		95

3.6.1 Introduction

The formation of Co–Ni alloy coatings by plating methods has been strong for many years due to their excellent magnetic properties, hardness, light weight, wear, versatility, abrasion and corrosion resistance, and particularly its prominent catalytic activity.[1–9] The use of this technique to produce these alloys is attractive due to its low cost, flexibility (e.g., deposition as single layer or multi-layer coatings on planar and non-planar substrates), efficiency, and ease of high volume production in contrast with other methods such as sputtering and chemical vapor deposition.[4,10] A significant feature of Co–Ni plating is that alloy composition can be modulated since these metals form homogeneous phases over the whole concentration range.[11] Thus, multiple properties can be explored by only varying its composition. However, as occurs with other iron-group alloys (e.g., Fe–Ni, Fe–Co), the co-deposition is classified as anomalous since the mole fraction of the less noble component cobalt produced in the alloy becomes higher than the $[Co^{2+}]/([Co^{2+}]+[Ni^{2+}])$ ratio in the solution.[11,12]

An extensive amount of research has been intended to investigate this anomalous behavior, suggesting different proposals: faster adsorption rate of the less noble component (e.g., cobalt hydroxide $Co(OH)^{+}_{ads}$) in comparison with the more noble species (e.g., $Ni(OH)^{+}_{ads}$),[13–17] enhanced surface coverage of the less noble $Me(I)_{ads}$ intermediate,[18] formation of intermediate adsorbed species (i.e., $NiCo(III)_{ads}$) which increase the cobalt content in the alloy and release Ni(II) species,[19] differences in electronic structures and liabilities of Co(II) and Ni(II) species on the basis of ligand field theory,[20] and faster charge-transfer of single Co(II) reduction in comparison with Ni(II) reduction.[21–23] Accordingly, there is strong evidence to consider that the phenomena describing this anomaly are presumably arising from intrinsic changes in the electronic structure of the oxidized form of these metals, ion-solvent interactions, as well as transitions states emerging from molecular interactions on the electrode surface, since kinetically the single Co(II) deposition is considerably faster than the Ni(II) one. However, the use of typical quantitative analysis available for electrochemical methods (including mesoscopic to macroscopic scale modeling) is limited to capture the properties of the Co(II) and Ni(II) atomic structures, tracking fast intermediates in the reaction pathway, and collecting quantitative information of the molecular and electronic interactions responsible for such kinetics. Therefore, *Ab initio* methods (i.e., quantum mechanics) need to be used to account for the atomic interactions determining the anomalous behavior of the Co–Ni alloys. To our current state of knowledge, this topic has not been undertaken.

From a practical standpoint, it has been reported that the anomalous behavior of Co–Ni electrodeposition could be overcome through the use of cyclic voltammetry and Pulse Reverse (PR) plating in chloride-based solutions at pH 2 under potentiostatic conditions.[17,24] In these studies, alloy plating was conducted only in chloride electrolyte under stagnant conditions. A subsequent analysis[23] corroborated that the anomalous behavior can be removed with high current efficiencies but only under the above conditions. This effect is due to the high ionic conductivity of Cl^{-}, and the more labile kinetics for metal reduction in the presence of this anion, a requirement to alleviate the anomalous by hastening the dissolution of both metals, particularly Co. On the other hand, sulfate media was not effective to eliminate such behavior, and electrolyte agitation exacerbates anomalous deposition and reduces the current efficiency by enhancing mass transport of Co(II) and H^{+} to and from the cathode surface. These results demonstrate that the pulse plating and PR techniques are tractable to alleviate the anomalous behavior of Co–Ni alloys, regardless of the operation mode, namely potentiostatic or galvanostatic.[17,23,24] Note that galvanostatic operations

 doi:10.1016/B978-0-12-803581-8.09169-4

maintain a constant reaction rate and the potential varies with time; whereas in potentiostatic conditions, the driving force for the reaction (i.e., activity ratio of oxidized/reduced species) remains constant and the reaction rate changes as a function of time. Applied voltage enables a better control of current efficiency and alloy composition, although practical regulation of pulsed voltage is very challenging to attain unlike pulsed current.[25]

The main implications of the use of pulsed techniques in terms of mass transfer effects arises from the continuous depletion of electroactive species in the diffusion layer (outer layer) when subjected to dc operations. During pulse plating, a pulsating diffusion layer (inner) exists close to the electrode surface, as a result of the frequency of the current which generates a pulsating concentration.[25] This concentration profile relaxes when the current is turned off (off-time). If the length of the pulse is short, there is not sufficient time for the diffusion layer to grow into the solution. Metallic cations are furnished to the electrode surface through the outer diffusion layer during the off-time, and this supply enables the relaxation of the pulsating diffusion layer. Note that the concentration gradient is larger in the inner layer (transient) than in the outer one (stationary). Therefore, the depletion of cations in these layers limit the pulse and the average current densities, respectively. Limitations due to mass-transport effects in pulse plating are associated with the fact that the maximum average current density cannot exceed the dc limiting current density, and the length of pulse cannot be longer than the transition time.[25]

The incorporation of adatoms and adions into a crystal lattice (crystallization) has also been connected to the properties of alloy coatings, particularly the morphology and grain refinement. This phenomenon occurs either by the build-up of old crystals, which is enhanced by factors such as: low overpotentials, high surface diffusion rates, and low population of adatoms; or by the formation of new nuclei with demand opposite magnitude (i.e., high overpotentials, low surface diffusion).[25] Pulse current densities are typically higher than the corresponding dc densities, whence the number of surface adatoms during pulse plating is higher than under dc conditions, this leads to an enhancement of nucleation rate and refinement of the grained structure. Although surface diffusion is primarily affected by adsorbates on the cathode surface when additives are added to the plating bath, modulation of the current can also alter this factor. The use of high pulse current densities increases the population of adatoms on the surface so high that there is no enough time for assembling them into the crystal lattice, producing materials with similar properties to those obtained by rapid quenching.

In PR, the critical feature is that cathodic reduction is followed by a period of anodic polarization during each cycle. The purpose of this inversion is to preferentially dissolve the metal (i.e., Co) to lower down in the alloy content, when the anodic voltage or current density are applied.[26] Concerning the micro-structure, this second pulse (anodic) removes metal from areas that tend to overplate during cathodic deposition, which is beneficial to sluggish dendrite formation and improving the plating thickness distribution over complicated shapes. Likewise, PR forces nucleation to start off at each new cathodic pulse, which modifies the alloy structure and grain size. Multiple studies have described significant improvements (i.e., roughness) when compared to dc techniques. However, just a few studies have been intended to comprehensively analyze the structural variations undergone by these alloys when fabricated with the aforementioned techniques, and mainly to understand the influence of mass-transfer during plating. Thus, this cooperative effort is devoted to investigate the textural and structural changes when Co–Ni alloys are formed with dc and PR in chloride media. X-ray diffraction (XRD), scanning electron microscopy (SEM), atomic force microscopy (AFM) and X-ray photoelectron spectroscopy (XPS) are utilized to chemically characterize the texture and structure of the deposits. Additionally, electrochemical characterization is used to determine the influence of mass-transfer on such features.

3.6.2 Materials and Methods

3.6.2.1 Plating of Co–Ni Alloys

The alloys were plated at room temperature in solutions containing 1 M Na_2SO_4 (99.3% purity, Fisher) as supporting electrolyte, 0.1 M $NiCl_2$ (98.1% purity, J. T. Baker), and 0.1 M $CoSO_4$ (99.3% purity, Fisher). The pH in each bath was adjusted to 3. No additives were included in these plating baths to avoid misinterpretation of the effects of pulse plating. All solutions were freshly prepared in deionized water ($\sim$pH 6.8) and deoxygenated with N_2 (Praxair, grade 4.8) prior to experiments.

A 3-electrode cell was used to conduct the electrochemical experiments. The working electrode was a copper (99.999%) disk embedded in nylon with 1.26×10^{-5} m^2 of exposed area. This substrate is not catalytic for hydrogen evolution reaction (HER) unlike other surfaces such as Pt and provides a good conductive surface. No rotation was applied to the electrode to have a better control of the mass transfer of the electroactive species, in order to be able to suppress the anomalous behavior. A pure graphite rod (6.15 mm diameter $\times$ 152 mm long, Alfa AESAR, 99.999%) and Hg–Hg_2SO_4 electrode (Radiometer Analytical) were used as the counter and reference electrodes, respectively. All potentials reported herein correspond to the standard hydrogen electrode scale. Prior to each experiment, the working electrode surface was mechanically polished using SiC-type abrasive of different grades and polished to a mirror finish using Buehler alumina powder (final grain size $\leq$0.05 μm). The electrode was then rinsed with ultrapure water and placed in an ultrasonic bath for 5 min before carrying out the experiments. The three electrodes were connected to a Princeton Applied Research potentiostat/galvanostat model VMP3, interfaced with data acquisition EC-Lab software.

After experiments, samples were washed with deionized water, dried under exposure to N_2 flow, and kept under inert conditions in a desiccator until chemical and textural analyses were carried out.

3.6.2.2 Chemical and Textural Analyses

Plating was carried out using the Galvano static mode for a sufficient period to ensure that a total charge of 2 C was transferred during each experiment. After co-deposition, each working electrode was exposed to a concentrated HNO_3

solution in a vial to dissolve the coating. The solution was then analyzed using an atomic absorption spectrophotometer (Varian Model 220 FS) to obtain the cobalt and nickel composition in the coating.

XRD patterns for the plated samples were obtained using an advanced X-ray diffractometer (Bruker D-8 with geometry Bragg–Brentano) with Cu–Kα radiation ($\lambda = 1.5406$ Å), by performing sweeps from 5° to 70° of 2θ. The diffractometer was operated at 40 kV, 30 mA and the step size used was 0.02°. The XPS analyses were performed using a K-Alpha Thermo Scientific spectrometer with a monochromatized Al–Kα X-rays source (1487 eV), running at a power of 150 W. XPS narrow scans, using an X-ray spot size of 400 μm^2, were collected at 60 eV pass energy. XPS core level spectra were analyzed with Avantage v5.41 software from Thermo Scientific and fitted using a Gaussian–Lorentzian mix function and Shirley type background subtraction used to decompose spectral peaks.

SEM images were collected with a high-field emission microscope JMS-7600 F, using an accelerating voltage of 5.0 kV and equipped with energy dispersive X-ray spectroscopy (EDS) capabilities. The AFM analysis was performed with a Nanosurf easy scan 2 AFM digital system using tapping mode in air to visualize plated alloys (scan rate between 0.5 and 1 Hz). The silicon cantilever showed a free resonance frequency of 13 kHz and a constant of 0.2 N m^{-1} during these experiments. AFM analysis was performed to generate a complete description of the textural properties of Ni–Co alloys.

3.6.3 Results

3.6.3.1 Electrochemical Plating

In general it is recognized that during voltammetry conducted on multiple metallic substrates and electrolytes, H^+ reduction is the reaction occurring at more positive potentials, followed by Ni(II) and Co(II) reduction as thermodynamically predicted.[21–23,26,27] Although the onset of nickel deposition is located at more positive potentials, the kinetics of cobalt deposition is a way faster, whence the anomalous behavior is observed.[20] Once the above reactions become mass-transfer controlled, H_2O reduction proceeds without these limitations. Both H^+ and H_2O reduction contribute as parasitic reactions to the well-known HER. As a result of the occurrence of these processes, one of the following choices needs to be followed in order to suppress the anomalous behavior: (1) an additive has to be added to the electrolyte to form a stable complex with Co(II) or blocking its adsorption, (2) cobalt deposition needs to be forced to occur under mass-transfer control, or (3) the deposit of cobalt needs to overcome dissolution as in pulse-reverse. In this work, the two previous features are combined to control the composition of Co–Ni alloys, namely the use of PR. This approach has been selected since it is a tractable and flexible route unlike the addition of chemical agents.

Table 1 presents the experimental conditions used to form the alloys with dc (M1–M2) and bipolar (M3–M10) techniques. As observed in the pulse plating experiments, the nickel content in the alloy increases as the current density becomes more cathodic, which has been consistently reported for other electrolytes.[21] This behavior results from the faster kinetics of Co(II) deposition which generates a mass-transfer control at lower current densities if compared to nickel deposition. In general, it has been described that the composition of the more noble metal is augmented as the current is made more negative in anomalous deposition, unlike what happens in regular plating.[11] This phenomenon can be confirmed if the partial current densities of the Ni(II), Co(II), and H^+ reduction are plotted as a function of current density (Figure 1). These values can be readily calculated using Faraday's law:

$$j_{Ni} = \frac{z_{Ni}\, m_{Ni}\, F}{M_{Ni}\, t} \quad [1]$$

$$j_{Co} = \frac{z_{Co}\, m_{Co}\, F}{M_{Co}\, t} \quad [2]$$

$$j_{H_2} = j - j_{Ni} - j_{Co} \quad [3]$$

where z_i is the number of electrons transferred [2] to metal i (Ni, Co) during plating, m_i is the mass of species i deposited determined from atomic absorption, F is the Faraday constant (96485.5 C mol^{-1}), M_i is the molecular weight of metal i and t is the electrolysis time. Note that j_{H_2} (partial current density associated to HER, H^+, and H_2O reduction) is obtained from the difference between the total current density and the sum of j_{Ni} and j_{Co}. As observed, j_{Co} (5.28 A m^{-2}) is lower than j_{Co} (34.72 A m^{-2}) and j_{H_2} (10 A m^{-2}) at the lowest current density used in this study (-50 A m^{-2}). Not surprisingly, this behavior results from the faster kinetics of cobalt deposition and a more noble H^+ reduction, respectively. Once that Co(II) concentration becomes rapidly depleted around -250 A m^{-2}, the nickel content surpasses cobalt in the alloy, and the slope of j_{H_2} turns out to be steeper as a result of the onset of H_2O reduction. However, this increase of the nickel composition with more cathodic current densities is not accurately the removal of the anomalous behavior since most likely the deposit is made up of nickel oxides due to a significant occurrence of the HER.[21,23,26] Evidence of such behavior is observed in the lowest current efficiencies obtained under dc conditions for samples M1d–M2 in Table 1, although chemical and textural characterizations should be more conclusive (refer to Sections 3.6.3.2 and 3.6.3.3). Thus, pulsed techniques are utilized below to suppress the anomalous behavior of the Co–Ni alloy without compromising the current efficiency and textural properties of the films. PR (bipolar) is preferred over pulse plating (unipolar) since it has been confirmed that it is the only way (and cyclic voltammetry) to achieve high nickel contents in the deposited alloy.[17,23,24]

The experimental conditions used in the PR are shown in Table 1. The cathodic and anodic amplitudes were selected using cyclic voltammetry (not shown) to favor the nickel deposition at high current efficiencies, and preferentially enhance the dissolution of deposited cobalt, respectively. Typical frequency (t^{-1}) values in pulse plating were evaluated for short (500 Hz) and long cycles (5 Hz), and duty cycles

Table 1 Experimental parameters of the dc and pulse plating experiments conducted in electrolytes containing 0.1 M $NiCl_2$, 0.1 M $CoSO_4$ and 1 M Na_2SO_4 at pH 3

Experiment	*Cathodic amplitude (A m^{-2})*	*Anodic amplitude (A m^{-2})*	*Frequency (Hz)*	*Duty cycle*	*Ni content (wt%)*	*Current efficiency (%)*
M1	−50	–	–	–	13.14	80.00
M1b	−100	–	–	–	20.81	89.21
M1c	−250	–	–	–	37.68	85.74
M1d	−500	–	–	–	48.82	71.43
M1e	−750	–	–	–	49.87	65.30
M2	−1000	–	–	–	57.31	70.34
M3	−600	180	5	50	46.63	62.75
M4	−400	120	5	50	28.1	83.71
M5	−600	180	500	50	49.12	69.39
M6	−400	120	500	50	27.09	85.20
M7	−600	180	5	80	48.31	72.75
M8	−400	120	5	80	46.91	75.70
M9	−600	180	500	80	49.53	17.38
M10	−400	120	500	80	47.68	65.45

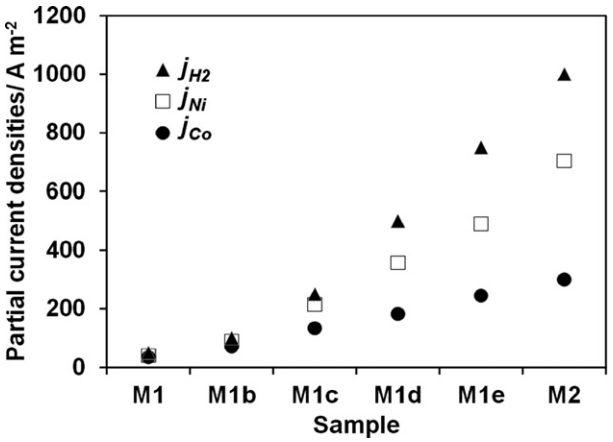


Figure 1 Partial current densities of Ni(II), Co(II), and H^+ reduction calculated for the plating experiments as a function of dc current density.

(i.e., fraction of a cycle elapsed for the cathodic pulse) of 50 and 80%. Note that duty cycles lower than 50% yield very little deposit, regardless of the cathodic current imposed on the electrode, presumably due to a large amount of HER and too much metal dissolved during the anodic pulse. A comparison of the dc and PR conditions reveal that in general, higher nickel contents are obtained for the alloys formed using the anodic pulse, and similar current efficiencies are obtained if considered that the deposits formed with PR undergo oxidation. A trend is observed in current efficiency, the higher the anodic amplitude is, the lower the current efficiency will be. In spite of this trend, the current efficiencies are relatively high for the PR technique. Another important finding described in Table 1 is that the current efficiency decreases as the frequency is raised. This effect benefits the HER since less time is enabled to elapse during each cathodic cycle and less depletion of Co (II) and Ni(II) species will occur close to the electrode surface, whence H^+ and H_2O reduction effectively competes with the alloy formation. A similar effect occurs with the nickel content, which decreases as the frequency is raised. This results from the same point discussed above, Co(II) reduction is considerably faster, thus, if less depletion of this species takes place during the cathodic pulse, the nickel content will not augment in the alloy, unless the duty cycle is increased up to 80% (refer to M7–M10 samples in Table 1), where the nickel composition virtually becomes constant. Using these long duty cycles, the depletion of Co(II) is ensured by using a cathodic pulse lasting 4/5 of the total cycle. However, it should be bear in mind that high frequencies around 500 Hz compromise the current efficiency due to the competitive reduction between Ni(II) and H^+ species.

PR has been used to alleviate the anomalous behavior of Co–Ni alloys at relatively high current efficiencies; however, systematic information of the textural and morphological properties is scarce in the literature. Below, XRD and XPS analysis are conducted to accurately determine the alloy composition and structure, while AFM and SEM are utilized to study the morphological features of the deposits.

3.6.3.2 XRD and XPS

Figure 2 shows XRD patterns (XRD) obtained for the Co–Ni alloys plated using direct current (M1–M2) and PR (M3–M10) at the experimental conditions shown in Table 1. In general, all XRD patterns exhibit two intense peaks at ~43.4° and ~50.6° of 2θ values that correspond to (111) and (200) planes of elemental FCC copper crystalline phase, which has been as used as substrate to conduct the deposits. These peaks were determined using the standard powder diffraction card PDF, copper file 04–009–2090.[28] No oxide copper crystalline species were observed. The XRD patterns contain no evidence of the presence of either pure nickel or cobalt phases, suggesting the formation of a solid solution. Likewise, no oxide metals were indexed, most likely due to their low content to be detected by the technique. Figure 2 displays two more peaks at ~ 44.36° and ~51.6°, corresponding to Co–Ni alloys, and their concentration rely on the experimental conditions as formerly determined with atomic absorption (refer to Table 1). Sample M1 formed at the lowest current density of the dc conditions presents peaks with low intensity in comparison

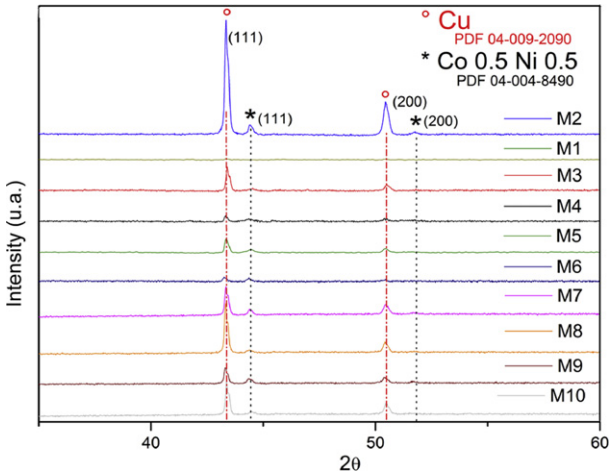


Figure 2 X-ray diffraction spectra obtained for Co–Ni alloys deposited at different experimental conditions shown in **Table 1**.

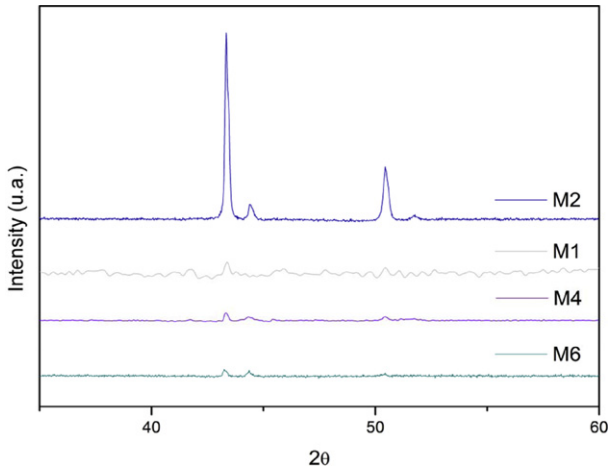


Figure 3 X-ray diffraction spectra obtained for Co–Ni alloys deposited at different experimental conditions shown in **Table 1** (M1, M2, M4, and M6).

with other samples. Presumably, this behavior results from a low amount of deposit as a result of a significant occurrence of a more noble H^+ reduction, and overcoming activation energies for metal reduction (i.e., overpotential). Note that the detection limit of atomic absorption is lower compared to XRD. On the other hand, M2 is a more crystalline material since it was formed at the most cathodic current density ($-1000\,A\,m^{-2}$), whereby a thick deposit was achieved, regardless of the existence of H_2O reduction. All samples show two peaks related to the Co–Ni alloy, that approximately match the nickel composition presented in **Table 1**. Samples M2, M3, and M5 were indexed to PDF 04–004–8490 that is associated to the ~0.5 nickel and ~0.5 cobalt alloy concentration.

Figure 3 shows a comparison of Co–Ni alloys formed by dc current and PR with different Ni wt% and 50% of duty cycles. According to the chemical analysis performed with the atomic absorption, sample M1 contains 13.14 wt% of nickel, M2 contains 57.31 wt% of nickel, while M4 28.08 wt% and M6 27.09 wt%. These analyses are representative of the nickel content obtained with XRD.

Table 2 Weight percentages determined using X-ray photoelectron spectroscopy for the Co–Ni alloys plated with dc and pulse plating experiments conducted according to the conditions shown in **Table 1**. XPS data were fitted to core Ni 2p3, Co 2p, O 1s, and C 1s level spectra

Experiment	*Ni 2p3 (wt%)*	*Co 2p (wt%)*	*O 1s (wt%)*	*C 1s (wt%)*
M1	14.9	81.1	2.2	1.8
M3	51.0	48.5	0.2	0.3
M4	15.5	78.8	4.1	1.6
M6	24.3	73.2	1.3	1.3

Further chemical analysis for the Co–Ni alloys (M1, M4, and M6) with a different Ni wt% was performed using XPS to corroborate the alloy composition. **Table 2** shows the wt% obtained for these samples by fitting the XPS experimental data to core Ni 2p3, Co 2p, O 1s, and C 1s level spectra. As observed, M1, M4, and M6, respectively, contain 14.9, 15.5, and 24.3 wt% Ni (refer to Section 3.6.2.2 for further details of calculations), while the same alloys analyzed with atomic absorption presented 13.14, 28.08, and 27.09 wt% Ni, confirming that the Co–Ni composition can be determined with atomic absorption, XRD and XPS. Likewise, the alloys exhibiting around 50 wt% Ni can be accurately determined with these techniques (i.e., M3). Note that C and O atoms are detected in very low concentrations for all samples. This analysis does not provide details whether the oxygen belongs to oxides/hydroxides formed in the electrolyte or in contact with air, but it provides sufficient experimental evidence to consider that an important contribution (C, O) arises from CO adsorption on the samples surfaces. It is worth mentioning that slight changes in composition are observed among different techniques. This is due to the variation in composition of the samples with depth, which is sensitive to the surface irradiation of the material with the beam of the technique (e.g., XPS, XRD), and only atomic absorption is able to determine the overall composition by dissolving the entire deposit.

3.6.3.3 AFM and SEM

AFM technique was used in an attempt to assess the influence of plating conditions, such as duty cycle, frequency, cathodic and anodic amplitudes, on the textural properties of Co–Ni alloys formed under dc and PR conditions. **Figure 4** shows AFM images collected on M1–M6 alloys formed under the experimental conditions shown in **Table 1**. The morphology of M1, M3, and M5 alloys exhibits sub-micron grains that are homogenously distributed and appear fairly similar to each other. Note that M1 grains are larger compared to M3 and M5, presumably, due to the influence of H^+ reduction in the formation of M1 and also its lower nickel content. On the other hand, the textural features of M2, M4, and M6 (refer to **Table 1**) alloys differ from the characteristics of the

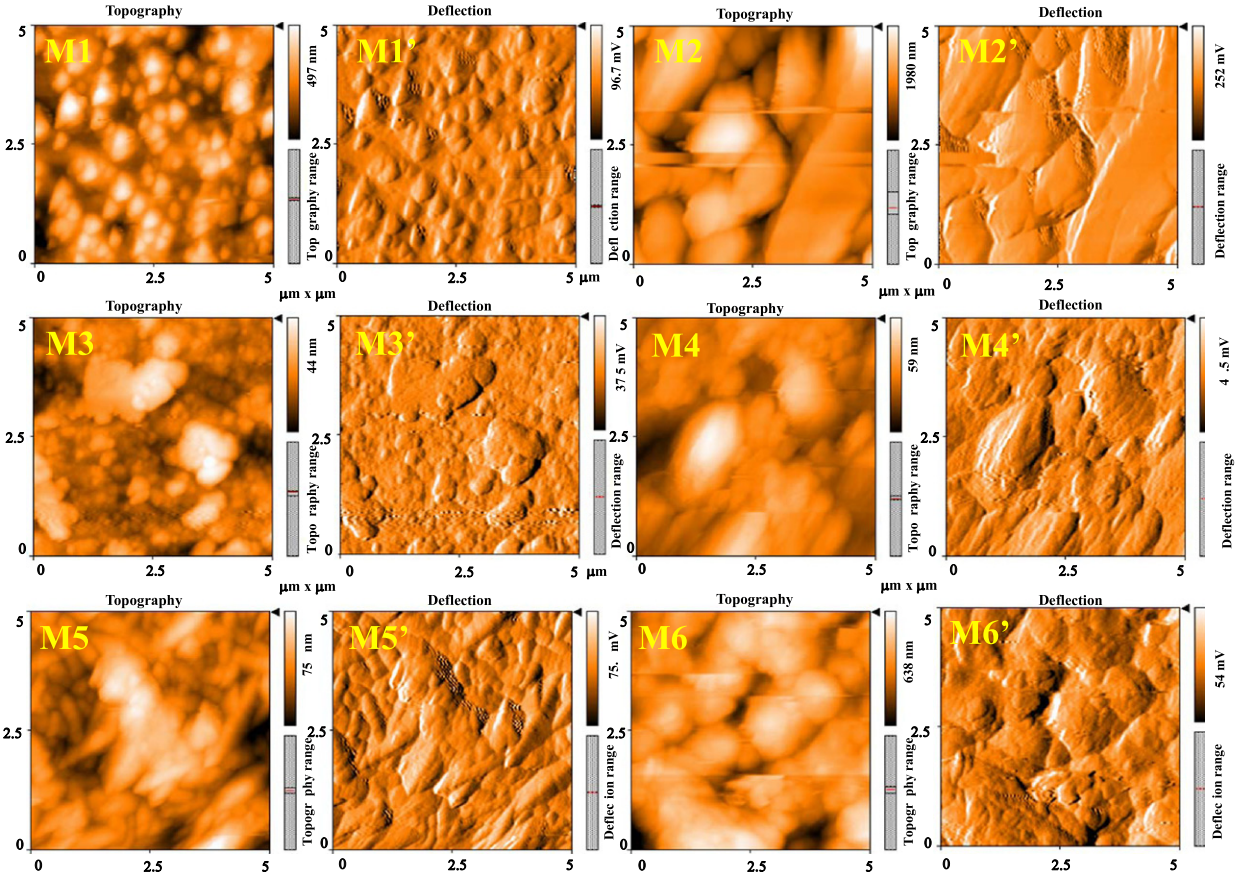


Figure 4 AFM images (topography and deflection modes) collected for plated Co–Ni alloys at different experimental conditions shown in **Table 1** (M1–M6). Scan rate used between 0.5 and 1 Hz.

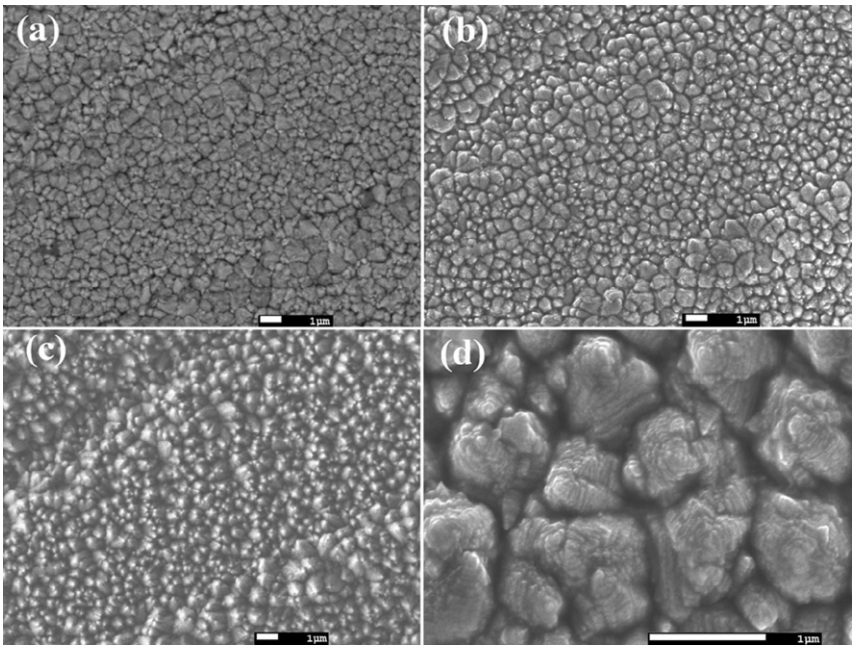


Figure 5 SEM images of Co–Ni alloys deposited under dc conditions using a cathodic amplitude of -50 A m^{-2} (M1), and acquired with different detectors: (a) A low angle backscatter detector (LABe), (b) an upper detector (SEI), (c) a lower detector (LEI), and (d) magnification of (c).

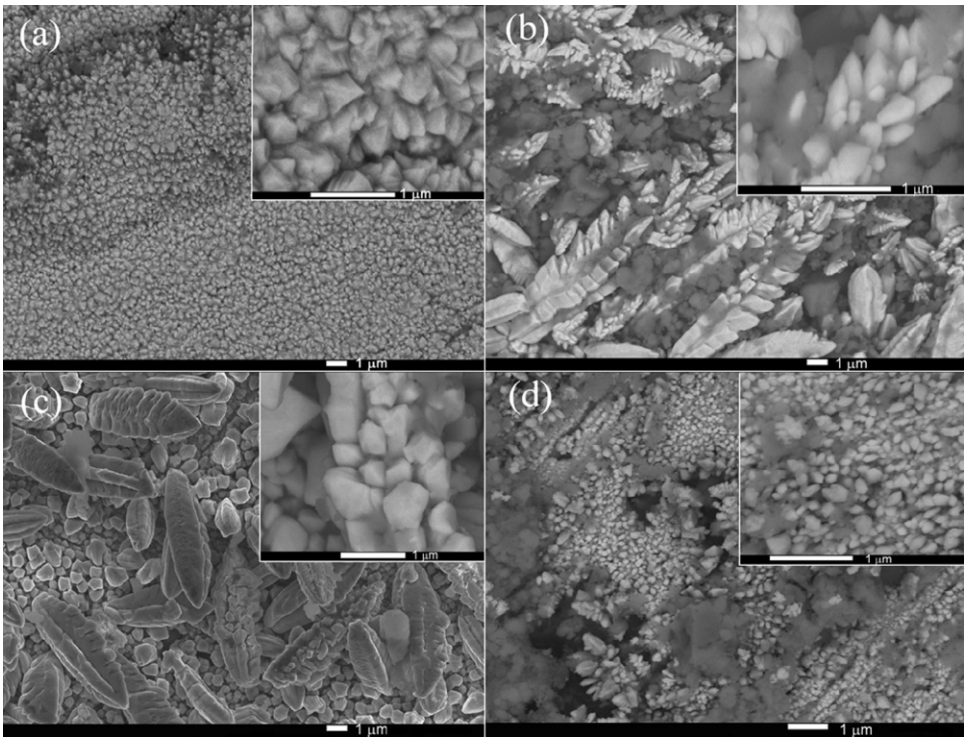


Figure 6 SEM micrographs of Co–Ni alloys deposited at different experimental conditions shown in Table 1. The cathodic amplitudes used to conduct the plating are: (a) -50 (M1), (b) -500 (M1d), (c) -750 (M1e) and (d) -1000 A m^{-2} (M2).

aforementioned systems, but are similar each other (Figure 5). M2 is a particular case since it is formed with an important input of the H_2O reduction, thus, similar to M1 sample is difficult to draw its morphology only on the basis of the nickel content. For M4 and M6 alloys, the sub-micron grains are stretched out, and they appear to be well interconnected each other. Surprisingly, the similarity of the textural properties could result from the same nickel content and current efficiency obtained for both alloys, unlike the more agglomerated flattened shapes collected for M2, resulting from a considerable gas evolution on the electrode surface, and most likely involving metal oxides/hydroxides.

The microstructure of the Co–Ni alloys (M1–M6) was also analyzed with SEM, in order to draw the influence of the plating parameters on this property. Figure 5 shows SEM micrographs of the M1 alloy (Table 1) acquired with different detectors: (a) at low angle backscatter detector (LABe), (b) secondary electron imaging, an upper detector (SEI), (c) secondary electron a lower detector (LEI) and (d) a magnification of the sample obtained. As observed in Figure 5(a), the LABe detector enables observing particles with high spatial resolution and the absence of contrast clearly shows a homogeneous surface sample. The morphology of the sample is uniform and a difference in contrast due to differences in the chemical composition of the sample is not observed. Figure 5(b) shows the SEI mode image. Edges and contours of the particles are defined and the sample reveals roughness and relief. Figure 5(c) shows the LEI mode that provides topological information. The surface of the sample is uniform without defects, holes, and impurities incorporation during plating due to a low input of H^+ reduction (refer to current efficiency in Table 1), although the grains are large. Figure 5(d) reveals the magnification of the pyramidal-like particles deposited over copper. Co and Ni are miscible and form stable alloys at room temperature. The pyramidal-shaped grain size is around 1 μm. The crystal structure, particle shape, and size of the electrochemically obtained Co–Ni alloy deposits considerably depend on current density. According to the nickel content, the alloy showed uniformity and homogeneity of the surface chemical composition at this cathodic amplitude (-50 A m^{-2}). These images are consistent with the AFM analysis conducted for the same sample (Figure 4), which concludes that submicron sized grains have a homogeneous distribution.

Figure 6 shows SEM images of Co–Ni alloys formed under the following dc cathodic amplitudes: (a) -50 (M1), (b) -500 (M1d), (c) -750 (M1e), and (d) -1000 A m^{-2} (M2). The morphologies of the deposited particles are significantly different, depending on the imposed current density. At -50 A m^{-2} (Figure 6(a)), the surface is homogeneous and the crystal size is less than 0.5 μm (sub-micron order). Crystals display sharp edges and pyramidal-like morphology. When the cathodic amplitudes are increased to -500 and -750 A m^{-2} (Figures 6(b) and 6(c), respectively), a bimodal particle morphology is observed. The bimodal particle morphology consists in semi-spherical grains size less than $\sim$0.5 μm and there are elongated particles around $\sim$10 μm. In particular, the elongated particles obtained at -750 A m^{-2} exhibit a smooth surface. Larger grains are obtained in both conditions, and the edges are smoothed in comparison

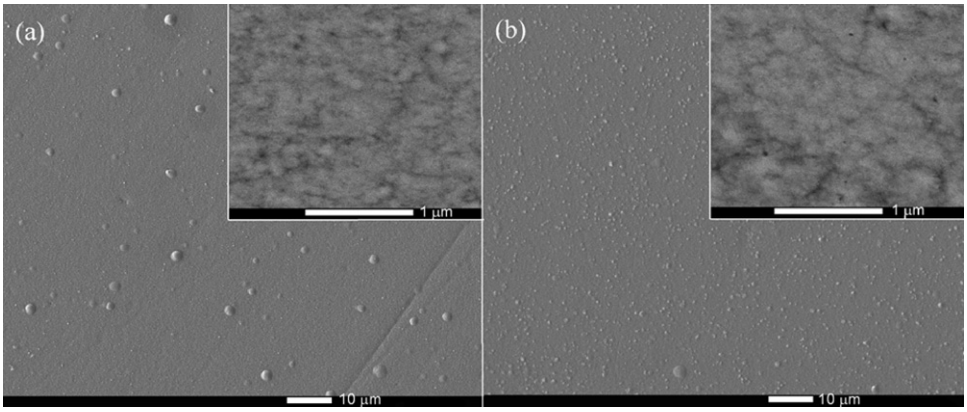


Figure 7 SEM micrographs of Co–Ni alloys deposited using pulse reverse at 5 Hz and 5% of duty cycle (Table 1): (a) sample M3 and (b) sample M4.

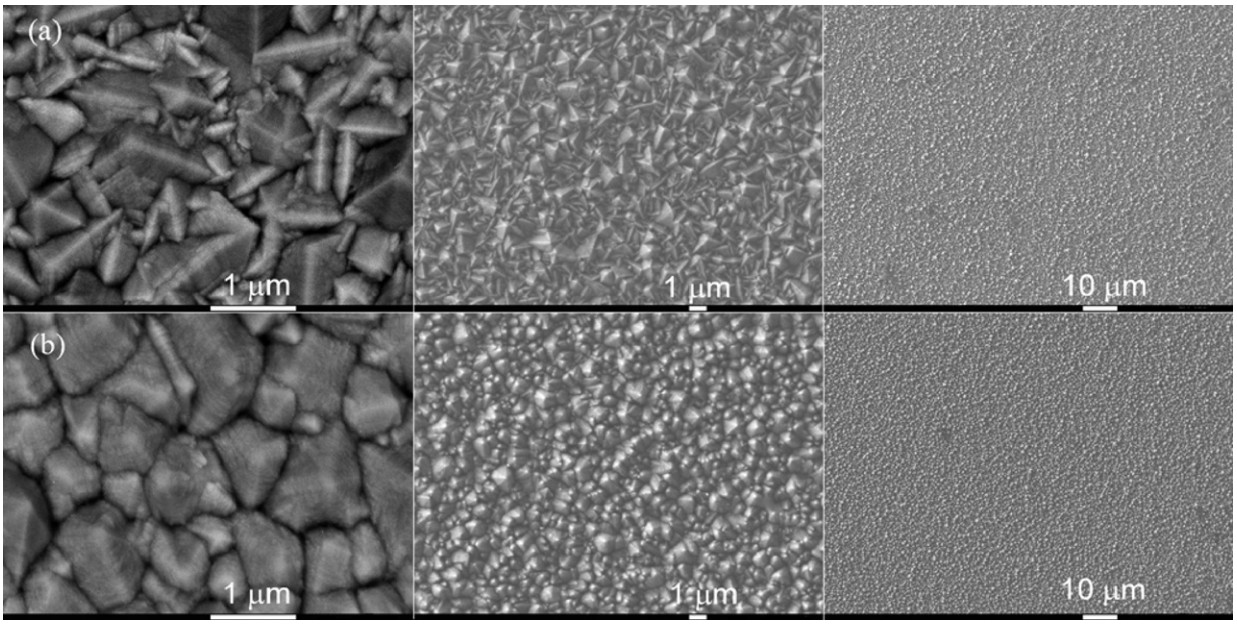


Figure 8 SEM micrographs of Co–Ni alloys deposited using pulse reverse at 500 Hz and 50% of duty cycle: (a) sample M5 and (b) sample M6.

with the dc operation condition obtained at $-50\ A\ m^{-2}$ (M1). The appearances of pyramidal-shaped grains are not observed under these conditions. At $-1000\ A\ m^{-2}$ (M2, Figure 5(d)), the grains formed are coarser, spherical, denser, and more pack together to yield a more compact structure, although some holes appear all over its surface. The bimodal particle morphology loss the elongated shape. High deposit rate promotes high defect densities and impurity incorporation, which can be the cause of decreasing alloy grain size. Although the nickel content in the alloy plays an important role to refine the grain size (e.g., sample M2), the parasitic reaction (HER) also exerts some influence in the morphology of the alloy as noted in Figure 6, where H_2O reduction becomes dominant and H^+ reduction enters the mass-transport control as the current density becomes $-1000\ A\ m^{-2}$.

When PR conditions are imposed on the electrode surface, different microstructures are obtained in comparison with dc plating. Figure 7 shows SEM micrographs collected for M3 (a) and M4 (b) samples and 5% of duty cycle. As observed, smooth surfaces are observed for both alloys, suggesting that the anodic pulse favorably modifies the alloy structure and grain size, and improves the roughness. The morphology exhibits a more compact surface aggregation instead of the rocky-rod or bimodal particle shape. These results agree with the AFM images (Figure 4).

Figure 8 shows SEM images of samples M5 (a) and M6 (b), prepared at 500 Hz and 50% of duty cycles at different magnifications. Once again, smooth and homogeneous surfaces are observed at lower magnifications for both samples. At $-600\ A\ m^{-2}$ (M5, Figure 8(a)) a pyramidal morphology with shape edges is observed, and particles size distribution is broad. Also, the grains are more stretched out and flattened compared to M6. At $-400\ A\ m^{-2}$, the particle size distribution is narrower and the grains are coarser than

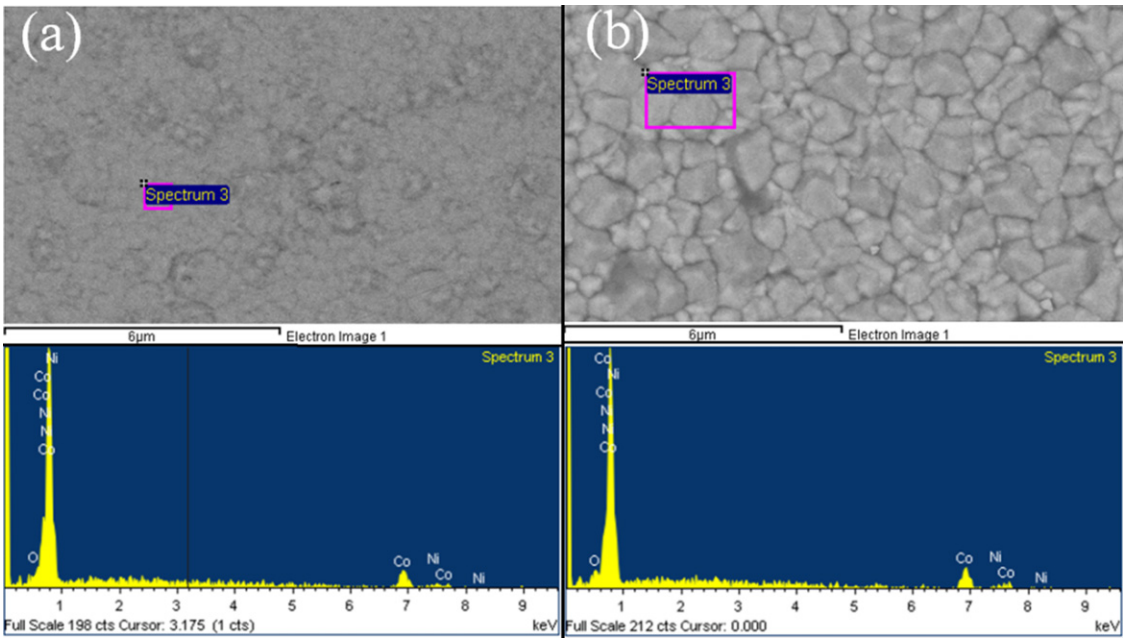


Figure 9 Energy Dispersive Spectroscopy measured for Co–Ni alloys: (a) sample M4 and (b) sample M6.

the sample M5. The morphology reveals sub-micron grains homogeneously distributed. The nickel content could modify the grain size and the particle size distribution. Results are in accordance with **Figure 4**, showing AFM images for these samples.

Figure 9 shows EDS spectra of samples M4 and M6. At lower frequencies (sample M4, **Figure 7(a)**), the Ni concentration is 28 wt%, while with the increase of frequency (sample M6, **Figure 8(b)**) the Ni content decrease to 27.7 wt%. All nickel concentrations in the samples were estimated with the EDS and the results were similar to XPS measurements. Also, these results agree with the atomic adsorption measurements shown in **Table 1**. Overall, the morphology of electrodeposited alloy depends strongly of the deposit parameters. The surface morphology of the deposits is determined by the nature of the electrochemically active ions or complexes and kinetics of the electrocrystallization processes.

3.6.4 Conclusions

Co–Ni alloy formed with plating methods is classified as anomalous behavior, where the less noble component (Co) experiences a kinetically faster kinetics in comparison with the nobler component (Ni), whereby way larger contents of Co in the alloy are typically obtained during deposition. Although such behavior is displayed in most electrolytes, it has been observed that electrolytes containing chloride mitigates this effect. Therefore, mixed sulfate–chloride electrolytes (0.1 M $NiCl_2$, 0.1 M $CoSO_4$ and 1 M Na_2SO_4 at pH 3) have been used to fabricate Co–Ni alloys, along with PR techniques which have assisted the removal of the anomalous behavior. Likewise, analysis conducted with pulse plating have been devoted to determine the influence of mass transfer modulated with plating parameters (cathodic and anodic amplitudes, frequency, duty cycle) on the nickel content, current efficiency and textural properties of the alloys. Using only dc plating, the nickel content in the alloy increased as the dc current density becomes more cathodic, since Co(II) deposition entered the mass-transfer region; and current efficiencies dropped at low and high cathodic current densities due to H^+ and H_2O reduction, respectively.

Higher nickel contents and similar current efficiencies were obtained in the alloys when they were subjected to anodic amplitudes like in PR. Duty cycles lower than 50% yielded very little deposit, regardless of the cathodic current imposed on the electrode, presumably due to a large amount of HER and too much metal dissolved during the anodic pulse. Plating proceeded under lower current efficiencies when the anodic amplitude was increased, and both efficiency and nickel content decayed as the frequency was raised, since less time was enabled to elapse during each cathodic cycle whence less depletion of Co(II) and Ni(II) species occurred close to the electrode surface. In summary, better results in terms of nickel composition and current efficiency were obtained using duty cycles of 80% with a frequency of 5 Hz, and anodic amplitudes of 120 A m^{-2}. This behavior resulted from a prolonged depletion of Co(II) and H^+, which forced these species to become mass-transport controlled without experiencing a significant nickel dissolution.

Chemical analysis revealed that the techniques of atomic absorption, XRD and XPS were able to determine an accurate alloy composition, producing the same results. XRD patterns collected for the alloys provided no evidence of the presence of either pure nickel or cobalt phases. Likewise, no oxide metals related to variation of the surface pH due to HER were found, presumably as a result of their low content. Adsorption of CO on the sample surfaces was determined using XPS.

Textural properties (micro-structure, morphology) were evaluated with AFM and SEM. These techniques showed that

larger grains with a more significant roughness are obtained when dc conditions are used to form the alloys. At low currents ($-50\ A\ m^{-2}$), crystals displayed sharp edges and pyramidal-like morphology and the surface was relatively homogeneous, while at intermediate currents (-500 to $-750\ A\ m^{-2}$) a bimodal particle morphology was observed, consisting of semi-spherical grains size lower than $\sim 0.5\ \mu m$ combined with elongated particles around $\sim 10\ \mu m$. At $-1000\ A\ m^{-2}$, the grains formed were coarser, spherical, denser, and more packed together to yield a more compact structure, although some holes appeared all over its surface. PR generated finer grains and way more smooth surfaces if compared to dc plating. Although, the parasitic reactions (current efficiency) and the nickel content exert some influence in the morphology and micro-structure of the Co–Ni alloys. It was determined that the plating mode is more determining than the aforementioned parameters due to a better control of the mass-transport of the electroactive species and their electrocrystallization phenomena. Although, different morphologies (i.e., pyramidal) can be deposited using PR. It was found that frequency is a crucial plating parameter to control in order to fabricate Co–Ni alloys with enhanced features, since it more frequently removes unstable regions of the deposit (e.g., dendrites) and create more nuclei.

Acknowledgments

I Romero-Ibarra is acknowledged as recipient of the program '*Catedras CONACYT.*' Financial support is greatly appreciated from CONACYT (Grants No. 2010–155698, 2012–183230, 2013–205416, and 2014–237343). The authors acknowledge the technical support of J. Romero and R. Rosas.

See also: 3.1 Electroless Plating of Pd Binary and Ternary Alloys and Surface Characteristics for Application in Hydrogen Separation. 3.2 Tuning of the Microstructure and Surface Topography of Hot-Dip Galvanized Coatings

References

1. Lowenheim, F. A. *Modern Electroplating*, 3rd ed.; John Wiley & Sons: New York, NY, 1974.
2. Fenineche, N.; Coddet, C. Effect of Electrodeposition Parameters on the Microstructure and Mechanical Properties of Co–Ni Alloys. *Surf. Coat. Technol.* **1990**, *41*, 75–81.
3. Brossard, L.; Messier, C. Effect of Cobalt Deposits on Nickel Substrates on the Oxygen Evolution Reaction in KOH. *J. Appl. Electrochem.* **1993**, *23*, 379–386.
4. Landolt, D. Electrochemical and Materials Science Aspects of Alloy Deposition. *Electrochim. Acta* **1994**, *39*, 1075–1090.
5. Andricacos, P. C.; Robertson, N. Future Directions in Electroplated Materials for Thin-Film Recording Heads. *IBM J. Res. Dev.* **1998**, *42*, 671–680.
6. Duch, M.; Esteve, J.; Gomez, E.; Perez-Castillejos, R.; Valles, E. Electrodeposited Co–Ni Alloys for MEMS. *J. Micromech. Microeng.* **2002**, *12*, 400–405.
7. Duch, M.; Esteve, J.; Gómez, E.; Pérez-Castillejos, R.; Vallés, E. Development and Characterization of Co–Ni Alloys for Microsystems Applications. *J. Electrochem. Soc.* **2002**, *149*, C201–C208.
8. Kim, D.; Park, D.-Y.; Yoo, B. Y.; Sumodjo, P. T. A.; Myung, N. V. Magnetic Properties of Nanocrystalline Iron Group Thin Film Alloys Electrodeposited from Sulfate and Chloride Baths. *Electrochim. Acta* **2003**, *48*, 819–830.
9. Chi, B.; Li, J.; Yang, X.; Gong, Y.; Wang, N. Deposition of Ni–Co by Cyclic Voltammetry Method and its Electrocatalytic Properties for Oxygen Evolution Reaction. *Int. J. Hydrogen Energy* **2005**, *30*, 29–34.
10. Datta, M.; Landolt, D. Fundamental Aspects and Applications of Electrochemical Microfabrication. *Electrochim. Acta* **2000**, *45*, 2535–2558.
11. Brenner, A. *Electrodeposition of Alloys, Principles and Practice*; Academic Press: New York, 1963.
12. Dahms, H.; Croll, I. M. The Anomalous Codeposition of Iron–Nickel Alloys. *J. Electrochem. Soc.* **1965**, *112*, 771–775.
13. Hessami, S.; Tobias, C. W. A Mathematical Model for Anomalous Codeposition of Nickel–Iron on a Rotating Disk Electrode. *J. Electrochem. Soc.* **1989**, *136*, 3611–3616.
14. Sasaki, K. Y.; Talbot, J. B. Electrodeposition of Iron-Group Metals and Binary Alloys from Sulfate Baths II. Modeling. *J. Electrochem. Soc.* **2000**, *147*, 189–197.
15. Grande, W. C.; Talbot, J. B. Electrodeposition of Thin Films of Nickel–Iron: II. Modeling. *J. Electrochem. Soc.* **1993**, *140*, 675–681.
16. Lin, Y.-P.; Selman, J. R. Electrodeposition of Corrosion-Resistant Ni–Zn Alloy: I. Cyclic Voltammetric Study. *J. Electrochem. Soc.* **1993**, *140*, 1299–1303.
17. Bai, A.; Hu, C.-C. Effects of Electroplating Variables on the Composition and Morphology of Nickel/Cobalt Deposits Plated Through Means of Cyclic Voltammetry. *Electrochim. Acta* **2002**, *47*, 3447–3456.
18. Matlosz, M. Competitive Adsorption Effects in the Electrodeposition of Iron–Nickel Alloys. *J. Electrochem. Soc.* **1993**, *140*, 2272–2279.
19. Zech, N.; Podlaha, E. J.; Landolt, D. Anomalous Codeposition of Iron Group Metals II. Mathematical Model. *J. Electrochem. Soc.* **1999**, *146*, 2892–2900.
20. Golodnitsky, D.; Gudin, N. V.; Volyanuk, G. A. Study of Nickel–Cobalt Alloy Electrodeposition from a Sulfamate Electrolyte with Different Anion Additives. *J. Electrochem. Soc.* **2000**, *147*, 4156–4163.
21. Vazquez-Arenas, J.; Altamirano-Garcia, L.; Treeratanaphitak, T.; *et al.* Co–Ni Alloy Electrodeposition under Different Conditions of pH, Current and Composition. *Electrochim. Acta* **2012**, *65*, 234–243.
22. Vazquez-Arenas, J.; Pritzker, M. Steady-State Model for Anomalous Co–Ni Electrodeposition in Sulfate Solutions. *Electrochim. Acta* **2012**, *66*, 139–150.
23. Vazquez-Arenas, J.; Pritzker, M. Effect of Electrolyte and Agitation on the Anomalous Behavior and Morphology of Electrodeposited Co–Ni Alloys. *J. Solid State Electrochem.* **2013**, *17*, 419–433.
24. Bai, A.; Hu, C.-C. Composition Controlling of Co–Ni and Fe–Co Alloys Using Pulse-Reverse Electroplating Through Means of Experimental Strategies. *Electrochim. Acta* **2005**, *50*, 1335–1345.
25. Puippe, J. C., Leaman, F., Eds. *Theory and Practice of Pulse Plating*; American Electroplaters and Surface Finishers Society: Orlando, FL, 1986
26. Vazquez-Arenas, J.; Treeratanaphitak, T.; Pritzker, M. Formation of Co–Ni Alloy Coatings under Direct Current, Pulse Current and Pulse-Reverse Plating Conditions. *Electrochim. Acta* **2012**, *62*, 63–72.
27. Altamirano-Garcia, L.; Vazquez-Arenas, J.; Pritzker, M.; Luna-Sánchez, R.; Cabrera-Sierra, R. Effects of Saccharin and Anions (SO_4^{2-}, Cl^-) on the Electrodeposition of Co–Ni Alloys. *J. Solid State Electrochem.* **2015**, *19*, 423–433.
28. JCPDS – International Center for Diffraction Data, Swarthmore, PA.

Relevant Websites

http://www.bbc.co.uk/schools/gcsebitesize/science/add_aqa/electrolysis/electrolysisrev2.shtml
BBC Report.

http://chempedia.info/info/159770/
Big Chemical Encyclopedia.

https://www.classle.net/book/electrodeposition
Classle.

http://www.finishing.com/index.html
Fishing.com.

http://www.happyplating.eu/
Happy Plating.

http://www.sciencedirect.com/science/book/9781483198071
ScienceDirect.

http://knowledge.electrochem.org/encycl/art-e01-electroplat.htm
The Electrochemical Society.

https://en.wikipedia.org/wiki/Electroplating

3.7 HVOF Coating of Nickel Based Alloys: Surface and Mechanical Characteristics

BS Yilbas, King Fahd University of Petroleum and Minerals, Dhahran, Saudi Arabia

© 2017 Elsevier Inc. All rights reserved.

3.7.1	**Introduction**	96
3.7.2	**Literature Review and Background**	96
3.7.3	**Experimental**	98
3.7.3.1	Fracture Toughness by Indentation Tests	98
3.7.3.2	Residual Stress Measurements by Curvature Method	98
3.7.3.3	Analytical Expression for Residual Stress	99
3.7.3.4	Electro Chemical Tests	99
3.7.4	**Mathematical Modeling**	99
3.7.4.1	Numerical Solution	101
3.7.5	**Findings and Discussions**	101
3.7.5.1	Coating Morphology and Metallurgical Changes	101
3.7.5.1.1	Single layer coating	101
3.7.5.1.2	Two layer coatings	102
3.7.5.2	Laser-Treated Coatings	103
3.7.5.3	Electro Chemical Testing	106
3.7.5.4	Modeling of Laser Treatment of Coating	107
3.7.6	**Concluding Remarks**	108
3.7.6.1	Single Layer Coating	109
3.7.6.2	Two Laser Coating	109
3.7.6.3	Laser Treatment of Coating and Numerical Study	109
3.7.6.4	Corrosion Testing of Coating	109
Acknowledgments		109
References		110
Relevant Website		110

3.7.1 Introduction

Surface finishing of thermal spraying is interesting because of the rough surface texture generated during the spraying process. High velocity oxygen-fuel coating (HVOF) is one of the coating techniques, which is widely used in industry because of its ease of operation, low cost, and efficient processing. In addition, HVOF coatings can protect the underlying surface from the harsh environments such as high temperature, corrosion, and abrasion. The coating can be resistive to erosion, corrosion, and wear depending on the powder properties used for spraying such as Diamalloy 4010 (iron/chrome blend) is widely used for corrosion and wear applications. The combination of these powders in layered structure form is preferable, since it offers advantages over the coating produced by one powders type. The multilayer coating can improve the mechanical properties of the resulting layered structure. The coating can be designed for corrosion or wear protections, which depends on the required functions of the coating. However, multilayer coating can serve for both purposes at the same time. In this case, top coating can be wear resistance and the bottom coating serves for corrosion protection. However, in multilayer coating the coating thickness becomes large and it may not suit in some applications such as the requirements of tight fitting of the surfaces. In addition, the high temperature gradients developed in the coating gives rise to thermal stresses, which limits the practical application of the coatings.

Although considerable research studies were carried out previously to explore the HVOF coating, the challenges for achieving the coating quality and the expected surface finish are still are still in progress. In this chapter, HVOF coating of nickel-based alloys is presented in the light of the previous studies.[1–6] The studies related to spraying, modeling, corrosion assessment and further processing will be given under the appropriate sub-headings.

3.7.2 Literature Review and Background

The progresses made toward achieving the quality of coating are significant over the years. However, some of the selective literature and background work will be provided in the light of the previous studies.[1–6]

The thermal process pertinent to the formation of a WC–Ni coating on low alloy steel by HVOF spraying was studied by Sobolev *et al.*[7] They indicated that the second and subsequent layers of the coating did not have practical influence on the thermal state of the substrate-coating interface. Moreover, the substrate coatings thermal interactions were completely determined by interactions between substrate and the first layer of the coatings. The influence WC–Cr was examined by

 doi:10.1016/B978-0-12-803581-8.09170-0

Zhao *et al.*[8] They indicated that the spray distance had less influence on the wear resistance of coating as compared to those corresponding to the total gas flow rate and the powder feed rate. The mechanical and tribological properties of HVOF thermal sprayed WC–Co coating were investigated by Qiao *et al.*[9] They showed that coatings produced by near nanostructured powders (containing an additive) presented high sliding wear resistance. Investigation into bond strength of Ni and Co composite powders blended with carbides and sprayed by HVOF process onto mild steel surfaces was carried out by Wang *et al.*[10] They found that the bond strength of HVOF coating was correlated well with the spraying parameters, except temperature and particle velocity.

The microstructure of multilayer coatings produced by thermal spray process was examined by Fagoaga *et al.*[11] They showed that the multilayer coatings presented a microstructure composed of alternate phases of chromium carbide cermet and oxides, which were resulted from preferential oxidation of chromium compounds. The mechanical properties of mono and multilayered coatings were examined by David *et al.*[12] They observed that WC–CoCr deposited by HVOF spraying onto P91 steel presented on high fatigue resistance. The bond strength and thermal shock behavior of HVOF sprayed multilayered coating was examined by Wilden *et al.*[13] They showed that HVOF coatings had higher contact of oxygen and higher density than that produced by plasma-sprayed coatings. The mechanical properties of single layer coatings of WC–Co produced by HVOF were examined by Wang *et al.*[14] They indicated that multilayered coatings exhibited better wear resistance under the high load conditions as compared to that corresponding to the single layered coatings. The microstructure and wear resistance of WC–Co coatings thermally sprayed onto tool steel were studied by Pepe *et al.*[15] They introduced the neural network to classify the wear performance of the coatings and indicated that the neural network would be used as an effective tool to classify the wear behavior of the resulting coatings.

The influence of process parameters on molten particle speed and surface temperature and properties of HVOF coatings were investigated by Lih *et al.*[16] They indicated that standoff distance, gun barrel length, and gas flow rate were the most influencing parameters on the coating wear properties. The component repair using HVOF thermal spray was studied by Tan *et al.*[17] They showed that a longer spraying time was required to accomplish repair work on the nitrided components compared to other coatings due to hardened nitrided surfaces resulted in defect sites at the surface during the spraying process. The properties of HVOF NiAl nanostructured coatings were investigated by Hu *et al.*[18] They indicated that spraying was possible to form high quality NiAl nanostructured intermetallic compounds in the coating. Microstructural characteristics of cold-sprayed nanostructured WC–Co coatings was examined by Lima *et al.*[19] The results revealed that there was no degradation of the WC–Co powder during the cold-spray process and uniform WC coating could be produced by the cold-spraying process. The parametric studies on HVOF spraying of MCrAlY coatings were carried out by Lungscheider *et al.*[20] They showed that spray distance, fuel/oxygen ratio and powder feed rate exerted a major influence on microstructure and oxygen content, whereas powder feed gas rate was not significant. The evaluation of through-porosity of HVOF sprayed coatings was carried out by Kowaskita *et al.*[21] The method introduced enabled them to calculate corrosion resistance due to the presence of through-porosity.

The decarburization of WC–Co coating deposited by HVOF process was investigated by Chivavibul *et al.*[22] They showed that the warm spray process did not produced detrimental phases such as W2C and W, which was usually developed due to decarburization of WC. The influence of substrate hardness on decarburization of porous WC-12% Co particles in cold-spraying was investigated by Gao *et al.*[23] They indicated that the properly designs porous cermet powder with certain hardness was a necessary condition to produce hard WC–Co cermet coating. The residual stress formation in the HVOF coating of WC–Co powders onto stainless steel substrate was investigated by Kuroda *et al.*[24] They showed that the residual stress on the surface of the HVOF coating was low and often in tension, but the stress inside the coating was high level of compression. The Young's modulus and fracture toughness of HVOF sprayed bioceramic coatings were examined by Li *et al.*[25] They indicated that the four-point bending test was not suitable for the determination of fracture energy at the coating/substrate interface due to the poor cohesion of the bioceramic coatings. The influences of heat treatment on the abrasion wear behavior of HVOF sprayed WC–Co coatings was examined by Stewart *et al.*[26] They correlated the abrasive wear behavior with the residual stress state, coating integrity, and microstructure.

The residual stress measurement using the curvature method was carried out by Liao *et al.*[27] They showed that temperature history of a part was of paramount importance in stress generation and distribution. The residual stress in HVOF thermally sprayed thick deposits was investigated by Stokes and Looney.[28] They analyzed the change in the stress state from tensile to compressive stress with deposit thickness in terms of quenching and cooling rates. The residual stress generation during thermal spraying was examined by Gill *et al.*[29] They showed that the continuous curvature measurement technique was potentially a reliable and accurate method with a minimum measurement error. The measurement of the residual stress in plasma-sprayed coatings was carried out by Kesler *et al.*[30] They indicated that the respective thermal expansion coefficients and the mechanical properties were the most important factors determining the stress level and the magnitude. The measurement of the residual stress in thermal spray coatings by the incremental hole drilling method was carried out by Santana *et al.*[31] They showed that the nature of the residual stress is tensile and their values were in between 150 and 300 MPa; however, the residual stress was depended on the substrate material, and the process parameters. The residual stress measurement using the curvature method and X-ray diffraction (XRD) technique was carried out by Totemeier and Wright.[32] They indicated that the magnitude of the stresses determined using the curvature method agreed with the XRD results for the coatings, which were sprayed at low particle velocities. However, the stress became compressive for the coatings, which were sprayed at high velocities. The residual stress development in thermal spray coatings was investigated by Ghafouri-Azar *et al.*[33] They indicated that the magnitude of residual stress increased significantly with

increasing the coating thickness. The residual stress development in the HVOF carbide coatings was studied by Pejryd *et al.*[34] They evaluated the coating crack resistance due to bending and low cycle fatigue loads. The residual stress distribution in thermally sprayed coatings was carried out by Otsubo *et al.*[35] They indicated that the residual stress remained almost the same in the coating, except at interface, which reduced from the mean value. The residual stress in HVOF tungsten carbide coating and its effect on the fatigue life were studied by McGrann *et al.*[36] They showed that the fatigue life of the tungsten carbide coating could be determined using the modified layer removal method. The fracture behavior of the brittle coatings was investigated by Bansal *et al.*[37] They showed that the development of the finite element code made it possible to study the effect of various coating parameters in isolation, which was difficult to achieve in an experimental study.

Influence of spraying parameters on electrochemical behavior of HVOF coating was investigated by Planche *et al.*[38] They introduced spraying parameters maximizing the electrochemical resistance of the coating surface. The properties of HVOF sprayed Ni-based alloys with presence of carbides were examined by Hamatani *et al.*[39] They indicated that the inclusion of tungsten carbide in the coating powder improved the corrosion resistance notably. The corrosion behavior of HVOF sprayed steel in sea water was investigated Kawakita *et al.*[40] Their findings revealed that the corrosion took place around the small pore located at the boundary between the splats at the surface. The corrosion behavior of HVOF sprayed and Nd-YAG laser-remelted chromium, nickel chromium coatings were examined by Tuominer *et al.*[41] They showed that laser remelting resulted in the formation of dense oxide layer at the top of the coating as well as full homogenization of the sprayed structure occurred, which in turn improved the corrosion resistance of the surface. The corrosion behavior of HVOF sprayed Inconnel 625 coatings were studied by Zhang *et al.*[42] They indicated that passive current density obtained from the potentiodynamic tests were 10–20 times lower in the liquid fuel coatings than in those sprayed with the gas fuel gun. The corrosion resistance of superheated tubes coated by HVOF thermal spray was investigated by Fukuda and Kawahara.[43] They showed that HVOF coating resulted in high corrosion resistance of the super-heater tubes operating at high temperatures. The corrosion resistance of the HVOF coating was studied by Bolelli *et al.*[44] Their findings revealed that Inconel 625 coating failed to protect the substrate material after 20 h of testing due to inadequate coating conditions.

3.7.3 Experimental

A HVOF coating unit was employed to spray the powders. The spraying parameters selected based on the optimum coating conditions are given in **Table 1**.

Iron/molybdenum blend (Diamalloy 4010) and tungsten carbide cobalt/nickel alloy (Diamalloy 2002) blend powders were used during the coating process. The powder had a particle distribution between 25 and 45 μm with spherical morphology with some small and local satellite attachments.

JEOL JDX-3530 scanning electron microscope (SEM) and EDS are accommodated to obtain photomicrographs of the cross-section and surface of the workpieces after the tests. Microphotonics digital microhardness tester (MP-100TC) was used to obtain microhardness across the depth of the nitride layer. The standard test method for Vickers indentation hardness of advanced ceramics (ASTM C1327–99) was adopted. Microhardness at the surface was measured at the free surface of the workpiece after metallurgical preparation. The workpiece cross-section was also prepared for the microhardness measurements. The measurements were repeated three times at each location.

Table 1 Process parameters of HVOF thermal spray

Oxygen pressure (kPa)	*Fuel pressure (kPa)*	*Air pressure (kPa)*	*Powder feed rate ($m^3\ h^{-1}$)*	*Spray rate ($kg\ h^{-1}$)*	*Spray distance (m)*
1023	590	720	0.85	6.5	0.31

3.7.3.1 Fracture Toughness by Indentation Tests

The indenter test data and crack inhibiting can be used to measure the fracture toughness of the surface. The cracks length (l) covered the distance between the crack tip to the intend. The crack lengths were individually summed to obtain $\sum l$ as described in the previous study.[45] The crack length 'c' from the center of the indent is the sum of individual crack lengths '$\sum l$' and half the indent diagonal length '$2a$.' Therefore, $c = a + \sum l$.[45] However, depending upon the ratio of $\frac{c}{a}$, various equations were developed to estimate the fracture toughness (K). The equation proposed by Evans and Charles[45] was incorporated to estimate the fracture toughness (K) of the surface, which was applicable for $\left(0.6 \le \frac{c}{a} \le 4.5\right)$; therefore,

$$K_c = 0.079\left(\frac{P}{a}\right)^{3/2} \times \log\left(4.5P\frac{a}{c}\right) \quad [1]$$

where P is the applied load on indenter, c is the crack length, and a is the half indent diagonal length.

3.7.3.2 Residual Stress Measurements by Curvature Method

The deflection of the specimen during the coating was recorded and the final deflection was measured using the optical imaging technique.[32] The equation relating deflection Δx to curvature κ is obtained from the geometric relation, which yields:

$$\kappa = \frac{1}{R} = \frac{L_{arc}}{Cos^{-1}\left(1 - \frac{\Delta x}{R}\right)} \quad [2]$$

where L_{arc} is the arc length of the specimen and R is the curvature radius. The Stony equation[32] is used to obtain the relationship the residual stress and the curvature:[32]

$$\sigma = \frac{\kappa E_s t_s^2}{6(1 - \upsilon_s)t_c} \quad [3]$$

where E_s and v_s are the elastic modulus and the Poison's coefficient of the base material, t_s and t_c are the thicknesses of

the base material and the coating, respectively. However, the equation is only applicable for $t_s \gg t_c$.

The measured L_{arc} and Δx, and calculated R values as well as other parameters are used to determine the residual stress.

3.7.3.3 Analytical Expression for Residual Stress

The analytical expression for the residual stress was developed previously is used.[28] The previous expression is based on the thermal expansion mismatched between the coating and the base material. Therefore, the residual stress is:

$$\sigma = \frac{[E_c(T_f - T_R)(\alpha_c - \alpha_s)]}{1 + 2\left(\frac{E_c t_c}{E_s t_s}\right)} \quad [4]$$

where E_c and E_s are the elastic modules of the coating and the base material, t_c and t_s are the coating and base material thicknesses, T_f is the maximum temperature during laser heating, and T_R is the room temperature after the cooling period is over, α_c and α_s are the thermal expansion coefficient of the coating and the base material, respectively.

3.7.3.4 Electro Chemical Tests

Corrosion tests (potentiodynamic polarization and Tafel analysis) on the laser-treated and untreated surfaces were carried out in a three electrode cell, which composed of a specimen as a working electrode, a Platinum wire as a counter electrode, and a saturated calomel reference electrode (SCE). The specimens were degreased in benzene, cleaned ultrasonically, and subsequently washed with distilled water prior to electrochemical tests. The investigations were carried out with an exposed working electrode area of 0.3 cm^2 in 0.5 M NaCl solution at room temperature. The experiments were performed using PCI4/750 Gamry potentiostat and repeated several times to ensure the reproducibility of the data. DC105 corrosion software was used to analyze the Tafel region, while Potentiodynamic polarization experiments were performed at the same scan rate of 0.5mV s^{-1}.

3.7.4 Mathematical Modeling

The mathematical analysis is presented in the light of the previous study.[4] The mathematical analysis covers the formulation of the laser heating of HVOF coating located onto the steel substrate. However, the laser heating analysis is involved with the phase change in the irradiated region. In the analysis, the solid body heat conduction and phase change with temperature-dependent conductivity, internal energy (including latent heat effects), and convection and radiation boundary conditions are considered.

In the case of a moving heat source along the x-axis with a constant velocity U (Figure 1), the energy gain of the substrate material in accordance to Fourier heat transfer equation yields:

$$\rho \frac{\partial(CpT)}{\partial t} = (\nabla(k\nabla T)) + \rho U \frac{\partial(CpT)}{\partial x} + S_o \quad [5]$$

where

$$S_o = I_o \delta (1 - r_f) e^{\left(-\frac{x^2+y^2}{a^2}\right)} \quad [6]$$

I_o is laser power peak density, δ is the absorption coefficient, a is the Gaussian parameter, r_f is the surface reflectivity, ρ is the density, and x and y are the axes while the laser beam scans the surface along the x-axis. The laser beam axis is the z-axis (Figure 1). It should be noted that the laser beam intensity distribution is assumed to be Gaussian at the irradiated surface.

The convective and radiation boundary conditions are considered at the free surface of the workpiece. Therefore, the corresponding boundary condition is:

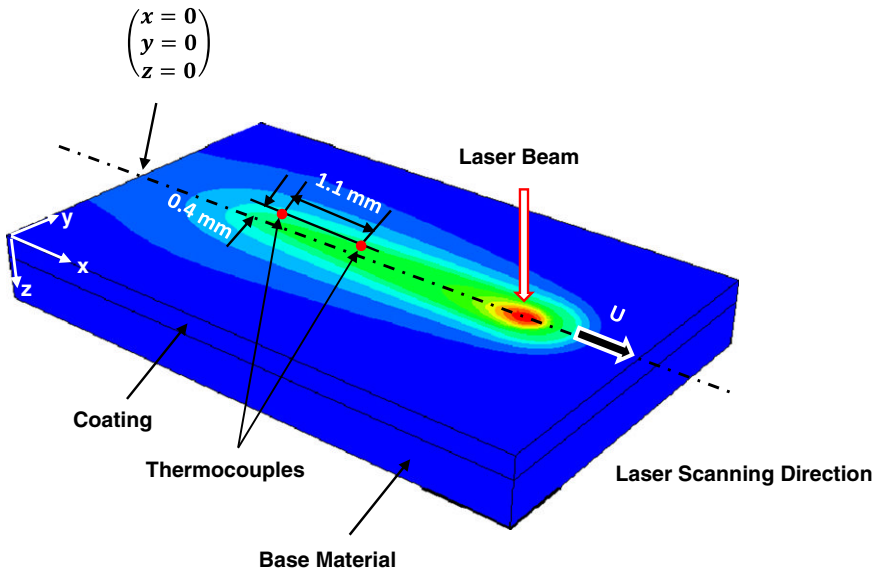


Figure 1 Schematic view of laser scanning of coating and the coordinate system.[4]

At the irradiated surface (top surface):

$$\frac{\partial T}{\partial z} = \frac{h_f}{k}(T_s - T_{amb}) + \frac{\varepsilon\sigma}{k}(T_s^4 - T_{amb}^4) \quad [7]$$

where h_f ($=3000\ \mathrm{W\,(m^2\,K)^{-1}}$) is the forced convection heat transfer coefficient due to the assisting gas.

At the bottom surface:

$$\frac{\partial T}{\partial \gamma} = \frac{h}{k}(T_s - T_{amb}) + \frac{\varepsilon\sigma}{k}(T_s^4 - T_{amb}^4) \quad [8]$$

and

$$\frac{\partial T}{\partial z} = \frac{h}{k}(T_s - T_{amb}) + \frac{\varepsilon\sigma}{k}(T_s^4 - T_{amb}^4) \quad [9]$$

where h ($=20\ \mathrm{W\,(m^2\,K)^{-1}}$) is the heat transfer coefficient due to natural convection, and T_s and T_{amb} are the surface and ambient temperatures, respectively, ε is the emissivity ($\varepsilon=0.9$ is considered), σ is the Stefan–Boltzmann constant ($\sigma=5.67\times10^{-8}\ \mathrm{W\,(m^2\,K^4)^{-1}}$). At far away boundary (at edges of the solution domain) constant temperature boundary is assumed (T=293 K), i.e.,

$$x=\infty\ ;\ \ y=\infty\ ;\ z=t_h \rightarrow T=293\,K \quad [10]$$

where t_h is the thickness of the workpiece. Initially (prior to laser treatment), the substrate material is assumed to be at constant ambient temperature, i.e., $T=T_{\mathrm{amb}}$, which is considered as constant ($T_{\mathrm{amb}}=293$ K).

Equation [1] is solved numerically with the appropriate boundary conditions to predict the temperature field in the substrate material. However, to analyze the phase change problem, the enthalpy method is used.[46] The specific heat capacity is associated with the internal energy gain of the substrate material, i.e., $Cp(T)=\frac{\partial U}{\partial T}$. However, the internal energy gain during the phase change is associated with the latent heat of fusion, which is given separately in terms of solidus and liquidus temperatures (the lower and upper temperature bounds of the phase change range) and the total internal energy associated with the phase change, called the latent heat. Since the primary interest is the stress field developed in the laser irradiated section, the flow field generated in the liquid phase in the surface vicinity during the laser melting process is omitted. It should be noted that the thermal stress field is considered to be almost zero in the melt pool, since only negligibly small hydrodynamic pressures are present in the melt pool.

Solidification involves small strain, so the assumption of small strain is adopted in this work. The thermal strains which dominate thermo-mechanical behavior during solidification are on the order of only a few percent. Several previous solidification models[46] confirm that the solidified metal part indeed undergoes only small deformation during solidification. The displacement spatial gradient is small $\nabla\mathbf{u}=\partial\mathbf{u}/\partial\mathbf{x}$ so $\nabla u{:}\nabla\mathbf{u}\approx1$ and the linearized strain tensor becomes:[47]

$$\varepsilon=\frac{1}{2}\left[\nabla u+(\nabla\mathbf{u})^T\right] \quad [11]$$

The small strain formulation can be used, where Cauchy stress tensor is identified with the nominal stress tensor $\boldsymbol{\sigma}$, and $\mathbf{b}$ is the body force density with respect to initial configuration.

$$\nabla\cdot\boldsymbol{\sigma}(\mathbf{x})+\mathbf{b}=0 \quad [12]$$

The rate representation of total strain in this elastic-viscoplastic model is given by:

$$\dot{\varepsilon}=\dot{\boldsymbol{\varepsilon}}_{e1}+\dot{\varepsilon}_{\mathrm{ie}}+\dot{\varepsilon}_{\mathrm{th}} \quad [13]$$

where $\dot{\boldsymbol{\varepsilon}}_{e1}$, $\dot{\varepsilon}_{\mathrm{ie}}$, $\dot{\varepsilon}_{\mathrm{th}}$ are the elastic, inelastic (plastic + creep), and thermal strain-rate tensors, respectively.

Stress rate $\dot{\sigma}$ depends on elastic strain-rate, and in this case of linear isotropic material and negligible large rotations, it is given by eqn [9] in which ':' represents inner tensor product.

$$\dot{\sigma}=\underline{\underline{\mathbf{D}}}:(\dot{\varepsilon}-\dot{\varepsilon}_{ie}-\dot{\varepsilon}_{th}) \quad [14]$$

$\underline{\underline{\mathbf{D}}}$ is the fourth order isotropic elasticity tensor given by eqn [9]

$$\underline{\underline{\mathbf{D}}}=2\mu\underline{\underline{\mathbf{I}}}+\left(K_B-\frac{2}{3}\mu\right)\mathbf{I}\otimes\mathbf{I} \quad [15]$$

Here μ, K_B are the shear modulus and bulk modulus, respectively, and are in general functions of temperature, while $\underline{\underline{\mathbf{I}}}$, $\mathbf{I}$ are fourth and second order identity tensors and '$\otimes$' is the notation for outer tensor product.

Inelastic strain includes both strain-rate independent plasticity and time-dependent creep. Creep is significant at the high temperatures of the solidification processes and is indistinguishable from plastic strain. The inelastic strain-rate is defined here with a unified formulation using a single internal variable, equivalent inelastic strain $\bar{\varepsilon}_{el}$ characterize the microstructure. The equivalent inelastic strain-rate $\dot{\bar{\varepsilon}}_{el}$ is a function of equivalent stress $\bar{\sigma}$, temperature T, equivalent inelastic strain $\bar{\varepsilon}_{el}$

$$\dot{\bar{\varepsilon}}_{el}=f(\bar{\sigma},T,\bar{\varepsilon}_{el}) \quad [16]$$

$$\bar{\sigma}=\sqrt{\frac{2}{3}\sigma'_{ij}\sigma'_{ij}} \quad [17]$$

where σ' is a deviatoric stress tensor defined in eqn [17].

$$\sigma'_{ij}=\sigma_{ij}-\frac{1}{3}\sigma_{kk}\delta_{ij} \quad [18]$$

The workpiece is assumed to harden isotropically, so the von Mises loading surface, associated plasticity and normality hypothesis in the Prandtl–Reuss flow law is applied:[48]

$$(\dot{\varepsilon}_{ie})_{ij}=\frac{2}{3}\dot{\bar{\varepsilon}}_{el}\frac{\sigma'_{ij}}{\bar{\sigma}} \quad [19]$$

Thermal strains arise due to volume changes caused by both temperature differences and phase transformations, including solidification and solid-state phase changes, i.e.,

$$(\varepsilon_{th})_{ij}=\int_{T_o}^{T}\alpha(T)\,dT\delta_{ij} \quad [20]$$

where α is temperature-dependent coefficient of thermal expansion, and T_o is the reference temperature and δ_{ij} is Kronecker's delta. It is normally accounted for in stress analyses through a temperature-dependent differential thermal expansion coefficient, $\alpha(T)$. ABAQUS/Standard analysis a

spatially varying thermal expansion can be defined for homogeneous solid continuum elements by using a distribution, which includes the tabulated values for the thermal expansion.[46] ABAQUS uses an implicit backward-difference scheme for time integration of both temperature and displacements at every material integration point.[46]

3.7.4.1 Numerical Solution

Finite element discretization was carried out using the ABAQUS software.[46] The fixed boundary conditions are applied on the both ends of the workpiece resembling the experimental laser heating situation. Laser heat flux with Gauss distribution and prescribed velocity of 10 cm s^{-1} along the x-axis through user subroutine DFLUX is applied to the thermal model. The Gauss parameter 'a' is $a = 0.000333$ m, in accordance with the experimental power intensity distribution. The thermal model consisted of two steps. The first step, which lasts 0.05 s, simulates the response of plate under moving laser heat flux. The second step, which lasts for 1000 s, simulated the continued cooling in the model. Cooling was allowed to continue until all of the plate reaches initial temperature (room temperature). The temperature–time history resulted from the thermal analysis is used as input to the thermal stress analysis. The workpiece is considered as an elastic body, which is modeled as von Mises elastic-plastic material with isotropic hardening and with a yield stress that changes with temperature.

3.7.5 Findings and Discussions

The findings of HVOF coating on metallic substrates are presented according to the appropriate sub heading in the light of the previous studies:

3.7.5.1 Coating Morphology and Metallurgical Changes

3.7.5.1.1 Single layer coating

Morphological and metallurgical changes of HVOF coating blended with WC particles and sprayed onto steel 304 surfaces is presented here in. The influence of WC content on the fracture toughness of the resulting coating is discussed in details. Indentation tests and the fracture toughness of the coating surfaces are also included. This section is presented in the light of the previous study.[1]

Figure 2 shows SEM micrographs of the top surface of the coating while Figure 3 shows SEM micrographs of coating cross-section. It is evident from SEM micrograph (Figure 2) that coating is free from cracks and irregularities like voids and large gaps between the splats.

Moreover, addition of WC particles is also partially evident and appeared as dark spots at the surface. In some regions at the surface some loose splats are observed. This situation may occur because of the improper spraying parameters or the powder mixture with non-metallic powders. Nevertheless, this situation is limited with only two samples, which are not considered in the fracture toughness measurements. In the case of cross-sectional view of SEM micrograph (Figure 3), it is evident that splats are bounded through mechanical anchoring. However, some small cavitations and voids are observed at coating-base material interface, which form the irregular patterns in this region. The porosity of the coating changes between 2 and 3%. It is noted that the porosity increases slightly with increasing WC content in the coating, for example, the porosity increase is in the order of 5%. The increase in the porosity is associated with the presence of hard particles in the coating. In this case, during the spraying, splat forms a shape not occupying all the space in the coating once it interacts with the un-deformable hard carbide particle. This situation is also evident from the SEM micrograph that microvoids are formed around the carbide particles. Although the Inconel powder was mixed with carbide particles prior to coating, agglomeration of WC particles occurs in the coating. This forms almost locally scattered small size WC lands in the coating. This situation is more pronounced when WC content is increased in the coating, which may occur because of the spraying process. In this case, small WC particles (2–5 μm) have small mass and during the spraying their momentum becomes less than the Inconel splats. This, in turn, results in early arrival of Inconel splats at the coating and carbide particles arrived at the top of the Inconel splats in a group. This appears as small WC islands in the coating. It should be noted that the melting temperatures of WC particles is much higher

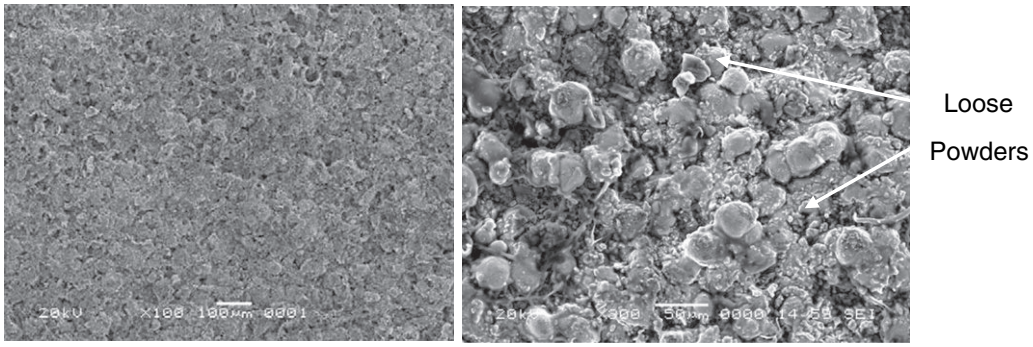


Figure 2 Scanning electron microscope micrographs of top surface of high velocity oxy-fuel coatings.[1]

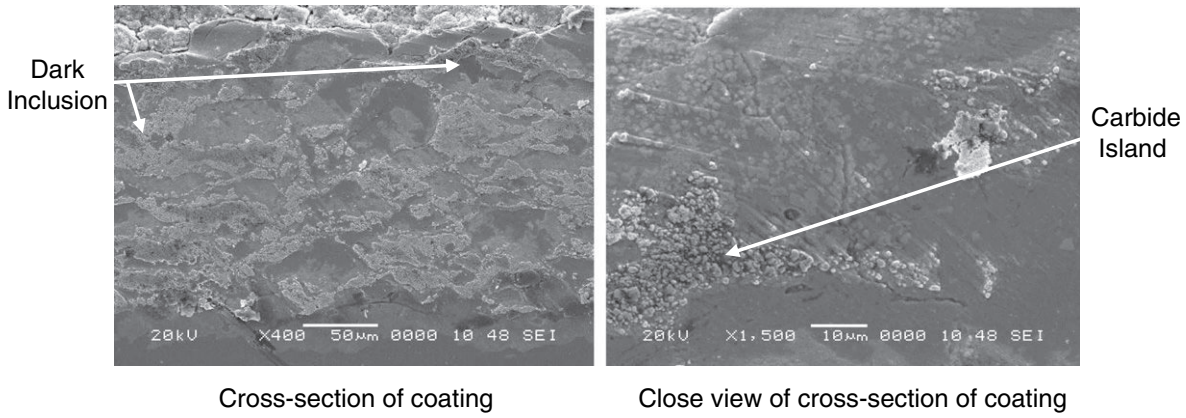


Figure 3 Scanning electron microscope micrographs of cross-section of high velocity oxy-fuel coating.[1]

than that corresponding to Inconel powder; hence, WC particles remain in solid phase during the spraying and remains the same in the coating. The presence of dark inclusion in the coating is the oxides formed during the spraying process. This can also be seen from the EDS line scan, which is shown in Figure 3. It is possible that oxide formation is due to presence of chromium in the Inconel powder. Consequently, high temperature Inconel powders onset of leaving the spraying gun undergo oxidation reactions during the in-flight time. However, depending on the location of the particle in the jet, the splat may undergo severe oxidation reactions. It should be noted that enough oxygen molecules in contact with the powder surface are needed for the oxidation reactions to take place.

Table 2 shows that fracture toughness of the coating surface produced at different WC content. It is evident that increasing WC content in the coating enhances the surface hardness of the resulting coating. This is attributed to the contribution of WC to the overall hardness, since WC hardness is considerably higher than that of Inconel 625. In addition, presence of WC modifies the structure of coating; in which case, rather compact coating is resulted. The fracture toughness of the surface varies with the WC content. Increasing WC in the coating enhances the fracture toughness slightly. This is because of one or all of the following reasons: (1) elastic modules of the coating increases, which is directly proportional to the fracture toughness, (2) increasing hardness, which contributes positively to the fracture toughness, and (3) small voids developed around the carbide particles, which acts as a micro-stress relaxation centers preventing the crack propagation in the surface region. Moreover, improvement in the fracture toughness is considerable despite the fact that the rate of oxide formation is higher due to open atmosphere. In addition, attainment of low fracture toughness for Inconel 625 coating without WC blending is because of the brittle structure formation in the free surface region. The oxide compounds in the surface region are responsible for brittle structure formation in the surface region.

3.7.5.1.2 Two layer coatings

HVOF coating of two-layers consisting of Diamalloy 4010 and 2002 powders onto carbon steel is presented here in. The surface morphology and microstructure of the coating are included in the discussions. This section is presented in the light of the previous study.[2,3]

Table 2 Fracture toughness and elastic modulus obtained from the indentation tests. The error estimated based on the repeats of the indentation test is 5%

	Fracture toughness (MN m$^{-3/2}$)	*E* (GPa)
0% WC	7.4	215
9.3% WC	8.52	240
47% WC	13.3	420

Figure 4 shows SEM micrographs of the top view of the coatings produced by Diamalloy 4010 and 2002 powders it is evident that no loose splats and surface irregularities including voids, cracks, and cavities are observed. However, surface roughness is high because of the presence of the partially molten powders. This is true for the surfaces resulted from both powders. It should be noted that Diamalloy 2002 contains WC, which has a high melting temperature. Consequently, the molten state of the powders requires excessive temperature rise during the spraying process. This can also be observed from the SEM micrographs, i.e., some protruded particles are observed. Moreover, high spraying velocity increases the momentum of the particles and, upon impacting, some particles penetrated into the coating surface. Consequently, the protruded particle distribution is random and they are cover a small area at the coating surface.

Figure 5 shows SEM micrographs for the cross-section of the coatings including single layer coatings produced from Diamalloy 2002 and 4010 powders as well as the two layered coating. It should be noted that the top layer is produced by using Diamalloy 2002 in two layered coating. It is evident that the coating consists of lamellar structure, which is produced during the multi-pass spraying process. Moreover, the porosity in the coating is measured and it is found that the porosity is in the order of 3%. The possible cause of the porosity is due to the presence of the semi-molten and molten splats during the spraying process as well as uneven shapes of the powders. The presence of semi-molten and hard splats is evident and they appear as rounded shapes in the coating; however, this is

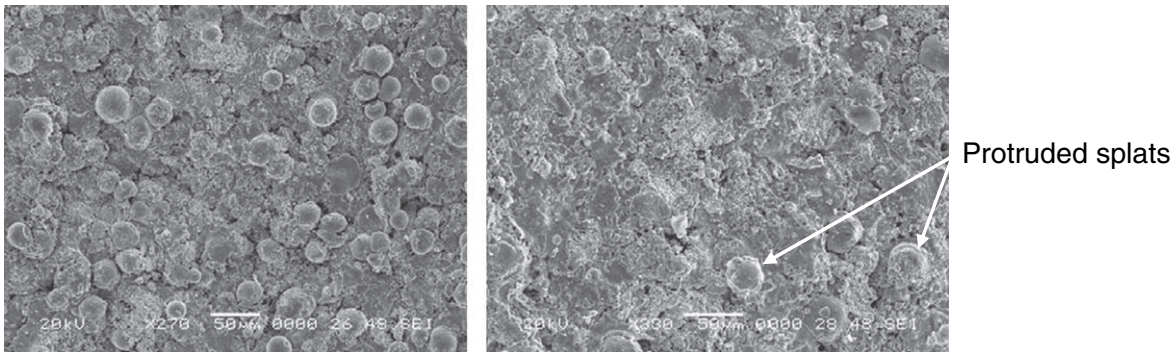


Figure 4 Scanning electron microscope micrographs of top view of coatings produced from Diamalloy 2002 and Diamalloy 4010 powders.[2,3]

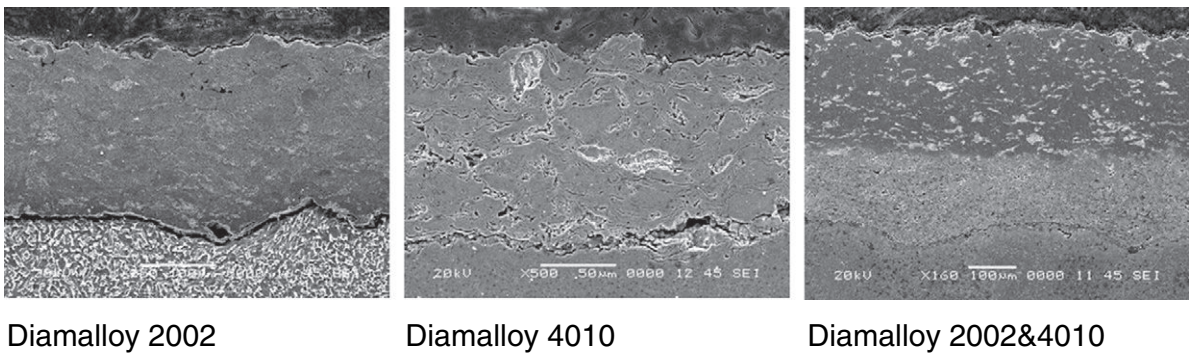


Figure 5 Scanning electron microscope micrographs of cross-sections of single and two layered coatings with two different powders.[2,3]

mainly observed in the surface region of the coatings, particularly for 2002 Diamalloy coating. This is because of the presence of WC in the powders, which requires high temperature for melting. Moreover, some stringers like inclusions are also observed in both coatings. This may be attributed to the oxide formation during the spraying process, i.e., high temperature oxidation occurs around the splats during the spraying process. This situation can also be seen from the EDS line scan. The presence of O_2 shows that oxidation takes place around the splat surface, provided that the oxide layer may not cover the whole surface. This situation is true for both coating produced form Diamalloy 2002 and 4010 powders. The splats are well integrated into the base material at the coating-base material interface. No large cavity or other irregular structure is observed. This indicates that the high velocity of the molten splats were widen over the surface upon high velocity impact. This is particularly true for the coating produced from Diamalloy 4010. In the case of Diamalloy 2002 coating, a small gap of discontinuity is observed at the interface between the coating and the base material, provided the gab is not extended to large area at the interface. This may be because of the presence of WC, which remains at solid phase during the spraying process due to its high melting temperature.

Figure 6 shows indentation marks produced at the surface of Diamalloy 2002 and 4010 coatings as well as in the cross-sections. It is evident the marks produced in Diamalloy 2002 coating is smaller in size than that corresponding to Diamalloy 4010. This is because of the hardness of the Diamalloy 2002 coating due to the presence of WC powders. Moreover, only small cracks are observed around the indentation marks. This is true for all the coatings. The formation of the small size cracks around the indentation marks is unable to determine the surface fracture toughness. However, the fracture toughness may vary over the coating surface despite the fact that the measurement covers the layer area at the surface. Moreover, the cracks produced around the indentation marks are mainly along the direction of lamella structure, which is parallel to the coating surface. This is because of the direction, which is most prone to de-cohesion (easiness of delamination). This is situation is observed from the indentation marks produced at the coating cross-sections. It should be noted that the absence of reasonably large radial cracks does not show the low fracture toughness; however, low tensile strength of the coating. In this case, sharp edge of indenter results in large tensile stresses around the indentation marks.

3.7.5.2 Laser-Treated Coatings

Laser controlled re-melting of HVOF coating diamalloy ((WC-12) Co, Ni, Cr, Fe, Si) particles are presented. Metallurgical changes in the coating prior and after the laser re-melting are included in the discussions. This section is given in the light of the previous study.[4]

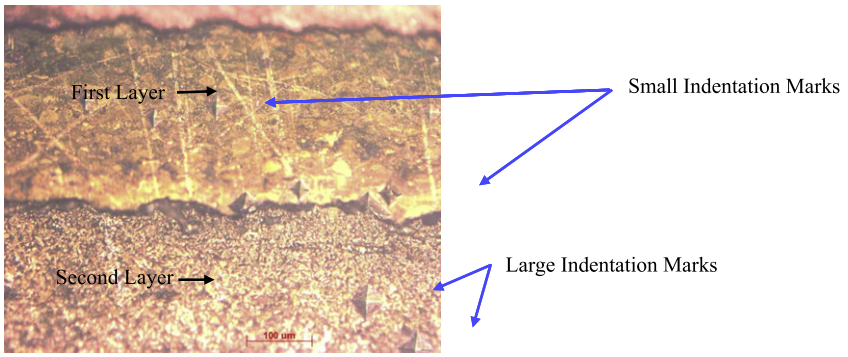


Figure 6 Optical photograph of indentation marks across the two layered coating.[2,3]

Figure 7 shows SEM micrographs of top views of surfaces of as-sprayed coatings and laser-treated coatings. As-sprayed coating surface resembles partially attached splats, which are randomly distributed at the surface. This is associated with the relatively high cooling rates at the surface for the last sprayed powders. In this case, last sprayed powders anchor the free surface of the coating and convection heat transfer from the surface changes the state of the splat from molten to solid at a fast rate. However, the laser treatment re-melts these splats at the surface together with remaining splats in the coating. This, in turn, results in thermal integration of the partially attached splats with the coating. The laser-treated surface is smoother than as-sprayed and it is also free from cracks. Although the cooling rates at the surface are high, initially spayed splats in the coating decrease the cooling rates while generating self-annealing effect at the surface region of the coating. This reduces the stress levels and microcrack formation at the treated surface. Since the laser power intensity is set below the evaporation limit at the coating surface, no cavities are observed at the surface due to avoiding the surface evaporation. The laser scanning tracks are visible at the surface, however, no molten flow between these tracks is observed. The sprayed powder contains WC blend which undergoes oxidation reaction with air at high temperatures releasing the carbonic gas. This, in turn, generates micro-sized gasification holes at the laser-treated surface. The close examination of the treated surface reveals that no micro-sized hole is observable at the surface. Consequently, carbonic gas released from the splats takes place during the in-flight time rather than at the coating surface.

Figure 8 shows SEM micrographs of the cross-section of as-received and laser-treated coatings. As-received coating cross-section consists of molten and partially molten states splats. In addition, locally distributed dark inclusions are also evident indicating oxide particles in the coating. The size of dark inclusions is small, which is associated with the small size powders. In this case, small powder undergoes oxidation reaction during in-flight and form stringers like dark inclusions in the coating. The oxide formation in the coatings is evident from the EDS data, which is given in Table 3. Locally scattered few voids are observed in the coating. However, no major or minor cracks are observed in the coating cross-section. Although thermal expansion coefficients of WC particles and splats are different, thermal strain developed during the cooling period does not cause formation of excessive micro-

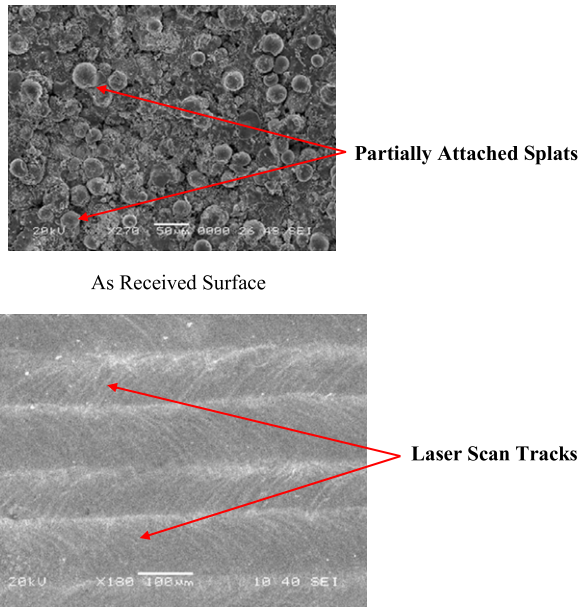


Figure 7 Top view of as-received and laser-treated coating surfaces.[4]

stress around WC blends. Consequently, no micro-cracks network is observed in the coating cross-section. The slow cooling rates in the coating release the thermal strain and lower micro-stress levels around the WC blends. In the case of laser remelted coating, uniform melting along the coating thickness is evident. Laser controlled melting resulted in cellular structure in the coating. Since the cooling rate is non-uniform in the coating, the cell size and their orientation differ in the coating. The differences in thermal conductivity of WC and coating alloy result in non-equilibrium solidification causing the growth of plaques in the liquid layer. This initiates the formation of small cells through a polyphase solidification. The close examination of the coating cross-section also reveals the presence of partially melting of WC blends in the coating. At the interface between the coating and the base material, no boundary defects, such as cracks and separation, or large cavitation are observed. This indicates that no volume shrinkage of the coating occurs in the interface region of the coating.

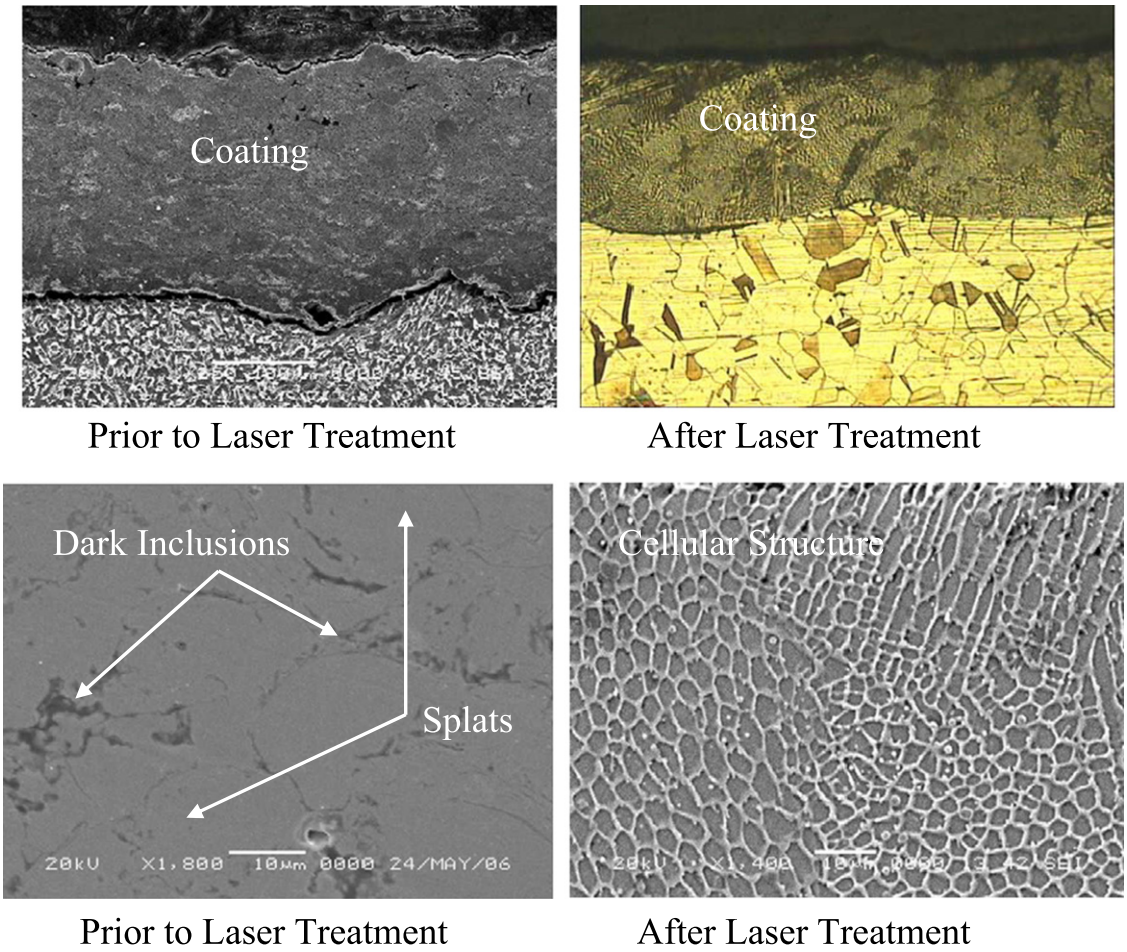


Figure 8 Cross-section of laser coating prior and after the laser treatment process.[4]

Table 3 Elemental composition of diamalloy coating after laser treatment (wt%)

Spectrum	*Si*	*Cr*	*Fe*	*Co*	*O*	*W*	*Ni*
Spectrum 1	1.1	11.5	6.5	1.5	3.5	10.4	Balance
Spectrum 2	1.2	12.2	7.5	1.5	3.4	12.3	Balance
Spectrum 3	2.1	14.0	6.5	2.3	2.8	12.1	Balance

Table 4 gives the residual stress predicted from the simulations and obtained from the measurements using the curvature method. It is evident that the residual stress is lower for as-sprayed coating as compared to that of the laser-treated coating. The self-annealing effect in the coating reduces the residual stress levels in the as-sprayed coatings. In addition, cooling rates after the laser treatment process contributes to attainment of high residual stress in the laser-treated coating. Table 5 gives microhardness test results in the coating prior and after the laser treatment process. Microhardness of the laser-treated coating increases significantly, provided that microhardness in the region of the coating-base material interface is lower than that at the surface region. This is associated with the slow cooling rate in this region, which in turn results in low stress levels in consistent with the stress predictions in this region.

Table 4 The residual stress predicted from the simulations and measured from the curvature technique

	Experiment (MPa)	*Predictions (MPa)*
Laser treated	730	770
As received	520	–

Table 5 Microhardness measurement results prior and after the laser treatment

	Surface (HV)	*Mid-thickness (HV)*	*Interface region (HV)*
Laser treated	680	620	540
As received	570	490	420

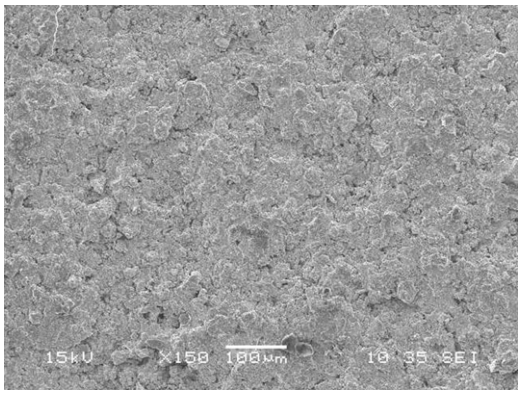


Figure 9 Scanning electron microscope micrograph of the top view of HVOF coated surface.[5]

3.7.5.3 Electro Chemical Testing

HVOF coating of diamalloy on steel substrate and the corrosion resistance of the surface due to 0.5 M NaCl solution is presented in the light of the previous study.[5]

Figure 9 shows SEM micrographs of top view of the coated samples prior to potentiodynamic tests. The coated surface is free from cracks, delimitation, and large size voids. However, partially bonded splats appearing like satellites at the surface are visible from the SEM micrographs. These splats are the last sprayed splats reaching at the surface. Consequently, they are exposed to atmospheric ambient and cools down at a fast rate due to convection heat transfer effects at the free surface. Although high cooling rates results in high temperature gradient at the vicinity of the coated surface, the self-annealing effects of the initially sprayed splats below the coating surface reduces temperature gradient in this region with progressing time. This suppresses the development of thermally induced high stress levels at the surface region. However, presence of the compressive residual stress is evident since the coating and steel substrate slightly bends outwards.

Figure 10 shows SEM micrographs of the cross-section of the coating prior to potentiodynamic tests. It is evident that coating extends uniformly at the steel surface with a thickness of 300 nm are observed in the coating. The coating comprises of lamellar-like structures due to the presence of different sizes of splats in the coating. However, the close examination of SEM micrographs reveals that dark inclusions are present in the coating, which are scattered locally around the splat boundaries. Since the sizes of the dark inclusions are small they appear on boundary separator between the splats. The presence of dark inclusions is attributed to the oxidation of small powders during in-flight. Moreover, small size semi-molten splats at the surface undergo oxidation reactions contributing to stringers like structure at the surface vicinity. The powders sprayed contain 12% WC and melting temperature of WC is high; therefore, these particles remain in solid phase during the spraying process. This increases porosity in the coating. Since the thermal expansion coefficients of WC and the remaining alloying elements are different, stresses are expected to develop around WC particles. This is attributed to the stress development in the coating due to mismatching of thermophysical properties. Nevertheless,

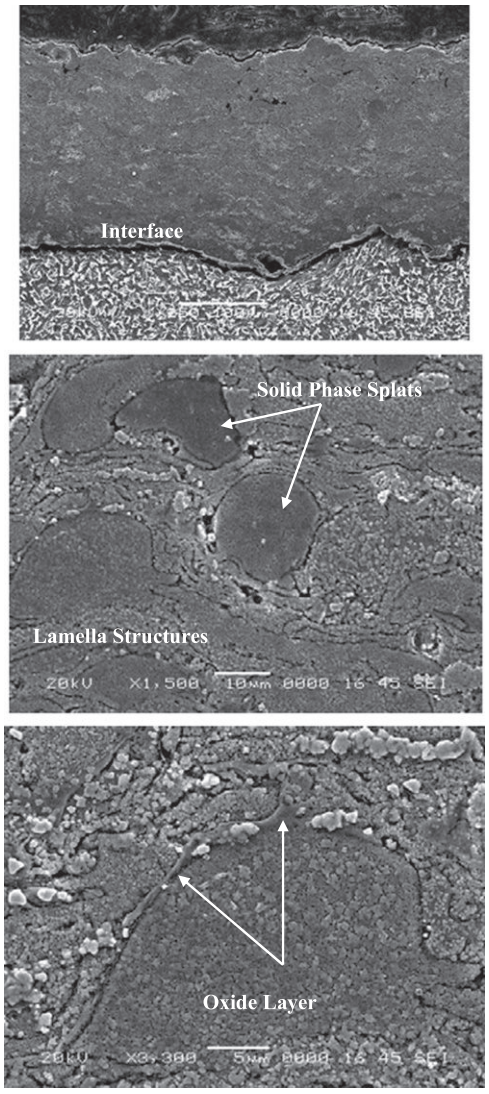


Figure 10 Scanning electron microscope micrograph of cross-section of HVOF coating.[5]

micro-stress developed around WC particles is not large enough to form micro-cracks around the splats, which is also revealed from close examination of SEM micrograph. The dark inclusions and WC particles are hard and brittle and act as the stress centers in the coating. In this case, under the external loads, inclusions break while form large cracks in the coating. Locally scattered few cavities are observed at coating-base material interface, which are attributed to improper anchoring of the splats during the spraying process.

Figure 11 shows the potentiodynamic polarization response of bare carbon steel together with two different kind of HVOF coating using commercial powders, Diamalloy in 0.5 M NaCl solution at room temperature (25 °C). It can be noted by Tafel data as showed in Figure 11 and Table 6 that corrosion rate of 2002 coating was decreased as compared to bare metal. Also the corrosion potentials of 2002 coating was –0.69 V_{SCE} as compare to bare metal, which was –0.53 V_{SCE}. Figure 12 shows SEM micrographs of HVOF coated surfaces after the potentiodynamic tests. The small pit and deep sites

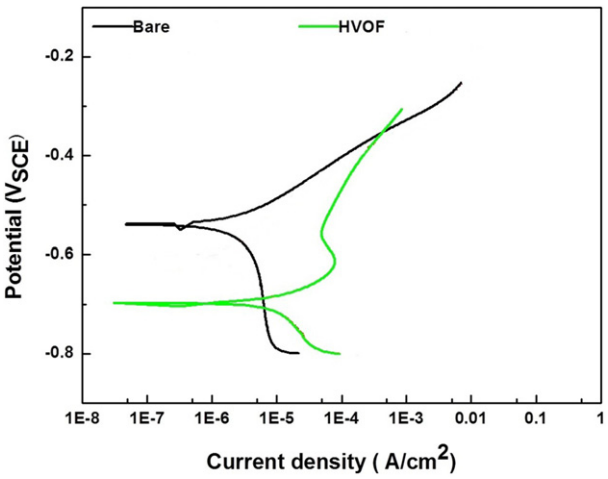


Figure 11 Potentiodynamic polarization response of HVOF coating and base material in 0.5 M NaCl solution at room temperature.[5]

Table 6 Electrochemical test results in 0.5 M NaCl solution at room temperature

	I_{corr} ($10^{-9} \times$ A)	E_{corr} ($10^{-3} \times V_{SCE}$)	*Corrosion rate (mpy)*
Base material	47.9	−538	7.1
HVOF coat surface	30.5	−697	4.5

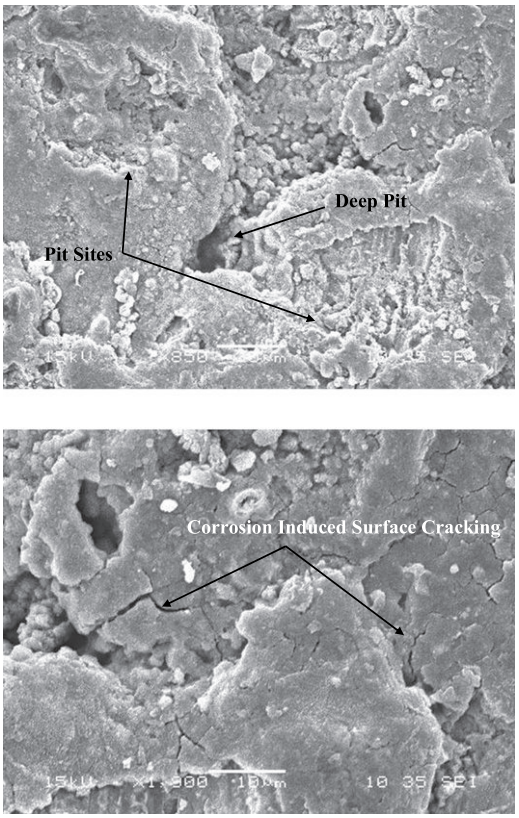


Figure 12 Scanning electron microscope micrographs of pit sites at HVOF coating.[5]

are evident. The presence of deep pit sites is attributed to pores network within the coating, which provides passage to the electrolyte in the coating. This, in turn, causes preferential corrosion around the splat boundaries; consequently corroded splats have higher oxide content. Moreover, a lateral cracking is not observed at the coating surface. This indicates that oxidation induced expansion takes place in the surface region of the coating than at the coating-base material interface. It should be noted that geometrically non-ordered surface texture formed at the coating surface influence the size and depth of the pit sites. The small spacing between the large surface peaks accelerates crevice corrosion while forming the deep pit sites.

3.7.5.4 Modeling of Laser Treatment of Coating

The findings of the model study for laser re-melting of HVOF coating diamalloy (WC-12) Co, Ni, Cr, Fe, Si) is presented in the light of the previous study.[4]

Figure 13 shows temperature distribution along the laser scanning line in the x-axis for different cooling periods. The cooling period starts after $t = 0.05$ s at which the laser power is switched off. Temperature attains high values in the region where the laser power is ceased In this case, temperature exceeds the liquidus temperature of the coating material in the irradiated region while indicating the liquid phase heating in this region. Temperature decays sharply in the neighborhood of the high temperature region, which is more pronounced along $0.005\ \text{m} \le x \le 0.0055$ m. The sharp decay of temperature results in high temperature gradients in this region. Moreover,

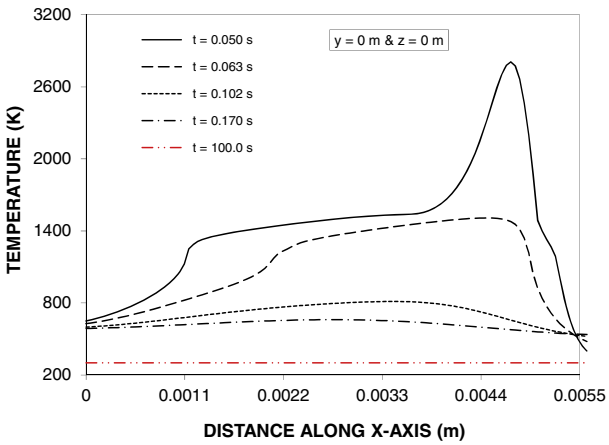


Figure 13 Temperature distribution along the x-axis for different cooling periods.

temperature decay along $0.0011\ \text{m} \le x \le 0.0035$ m is gradual. This is associated with the cooling rate of the initially laser heated region along the x-axis. However, as the cooling period progresses, temperature along the x-axis reduces and almost room temperature is reached at $t = 100$ s of the cooling period. The convection and conduction heat transfer from the laser heated region is responsible for the high cooling rates.

Figure 14 shows von Mises stress variation along the laser scanning line in the x-axis for different cooling periods, which

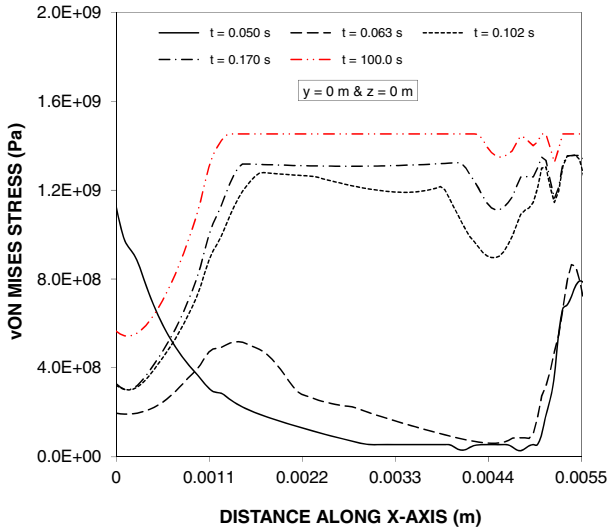


Figure 14 von Mises stress distribution along the *x*-axis for different cooling periods.

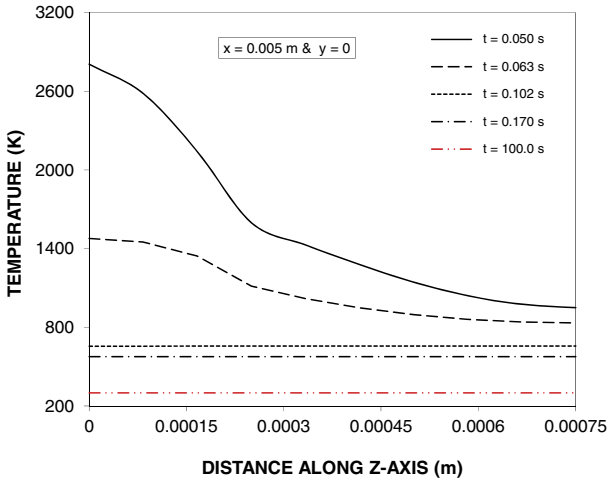


Figure 15 Temperature distribution along the *z*-axis for different cooling periods.

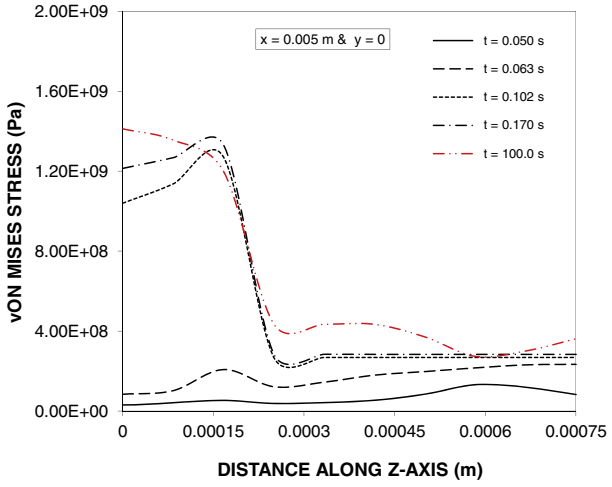


Figure 16 von Mises stress distribution along the *z*-axis for different cooling periods.

are similar to those shown in Figure 13. von Mises stress is low in the region where temperature is high and stress becomes high in the region where temperature decay is sharp. This is attributed to temperature-dependent elastic modulus, which reduces with increasing temperature. In addition, high temperature gradient gives rise to formation of high thermal strain leading to high stress levels in the workpiece. As the cooling period progresses, temperature reduces so that von Mises stress increases. In addition, von Mises stress reduces slightly at the end of cooling period in the region where temperature is initially the highest. This corresponds to the location where the laser beam is switched off. In this case, self-annealing effect of the heated zone in this region is responsible for the stress relaxation. This situation is also observed at different cooling periods toward the end of the cooling cycle.

Figure 15 shows temperature distribution along the *z*-axis in the coating and in the substrate material for different cooling periods. Temperature decay is gradual in the cooling cycle particularly in the surface region of the coating ($z=0$) at the onset of cooling cycle initiation. This is attributed to internal energy gain of the substrate material from the irradiated field just before the laser beam is ceased. Consequently, high rate of energy deposition results in excessive liquid depth and temperature variation in the melt zone becomes small. However, in the interface region between the coating and the base material ($200\ \mu m \leq z = \leq 250\ \mu m$), temperature decays sharply particularly in the cooling period while temperature decay in the base material is gradual. This is attributed to thermal properties of the coating and base material, which are different. Temperature reduces in the coating and the base material as the cooling period progresses; in which case, temperature in the coating and the base material becomes almost the same.

Figure 16 shows von Mises stress distribution along the *z*-axis for different cooling periods. von Mises stress remains low in the coating and base material in the early cooling period due to attainment of low elastic modulus at high temperatures. As the cooling period progresses, von Mises stress attains low values in the surface region. This is associated with high thermal strain developed in the surface region and increasing elastic modulus with reducing temperature. Von Mises stress reduces sharply between the coating and the base material, which is attributed to differences in mechanical properties and thermal expansion coefficients of the coating and the base material. However, high stress field remains almost the same in the coating except the interface region. The attainment of almost uniform stress levels across the coating thickness suggests that no large stress gradients are formed in the coating, except in the interface region. The maximum von Mises stress is on the order of 1.4 GPa.

3.7.6 Concluding Remarks

HVOF coating is established technology for protection of surface from high temperature, corrosion, and wear environments.

However, the research into the improvement of coating quality and the surface finish is still in progress. The important factors affecting the coating quality and the surface finish are large in numbers; however, two of the important factors are the spraying process and the powder quality used during the spraying. Although post-treatment of coating surface improves the coating quality in terms of mechanical properties, the studies on the improvement of surface finish is one of the research areas of the surface finish.

3.7.6.1 Single Layer Coating

The coating surface is free from defects, such as cracks and large size voids. However, irregular pattern of locally scattered contours are observed across the coating and base material interface. WC particles agglomerate in the coating while forming the small carbide islands. This can be attributed to the momentum difference between the carbide particles and the Inconel splats during the spraying process. This situation is more pronounced as the WC content increases in the coating. Oxide compound formation is evident from XRD diffractograms, which also appears as black inclusions around the splats in the coating. The carbonic gas formation during the spraying process alters the carbon content in WC; in which case W_2C is formed in the coating. Elastic modules and microhardness of the coating increases with addition of WC in the coating. The fracture toughness of the surface also increases with increasing WC content in the coating. This is attributed to increase in the elastic modules and microhardness in the surface region. In addition, micro-cavities around the WC particles act like the stress relaxation centers. This, in turn, prevents crack propagation in the surface region.

3.7.6.2 Two Laser Coating

Coatings produced from the Diamalloy 2002 and Diamalloy 4010 give similar surface textures, provided that some scattered protruded splats are observed at the surface for Diamalloy 2002 coating. This can be related to the presence of contains WC, which has a high melting temperature. Coatings produced from both powders formed lamellar structures with the porosity of the order of 3%. No large cavities or irregularities are observed at the coating-base material interface, except Diamalloy 2002 coating. In this case, a locally extended line of discontinuous gab is observed. Oxidation of the some splat surface appears as black inclusions in the coatings; however, the oxide layer does not cover all the surface of the splats. The microhardness measurement reveals that the coating formed by using Diamalloy 2002 has higher hardness than that corresponding to Diamalloy 4010. This is attributed to the presence of WC in the splats. The elastic modulus determined from the indentation tests shows that the elastic modulus of the coating formed form Diamalloy 2002 is higher than that of Diamalloy 4010.

3.7.6.3 Laser Treatment of Coating and Numerical Study

Laser scanning of the coating surface resulted in scanning tracks at the surface and no molten flow across the laser scanning tracks is observed. Uniform melting along the coating thickness is achieved. Although thermal expansion coefficients of WC and neighboring alloying elements in the coating are different, no micro-cracks, or crack network is observed in the laser-treated coating. Due to non-uniform cooling in the coating, cellular structures are observed in different sizes and orientations. The residual stress predicted agrees well with the experimental data. Laser treatment enhances the residual stress levels in the coating as compared to as-sprayed coating. In addition, microhardness of the laser-treated coating increases significantly, particularly in the surface region. Temperature predictions reveal that temperature gradient in the region close to the laser irradiated spot is high. This, in turn, increases von Mises stress in this region. Due to the self-annealing effect of the splats in the coating, von Mises attains slightly lower values in the region where the laser beam is switched off. von Mises stress remains high in the coating, except in the region close to the coating-base material interface; in this case, it reduces notably in this region.

3.7.6.4 Corrosion Testing of Coating

The corrosion resistance of the coating is estimated through potentiodynamic tests in 0.5 M NaCl solution. The findings revealed that the coating consists of a lamella-like structure with the presence of few semi-molten splats. No minor or major cracks observed at the coating surface and the cross-sections. Dark inclusions are observed between the splats due oxidation of small powders during in-flight. In addition, few semi-molten splats are partially attached to the coating surface, which is attributed to the high coating rates at the surface. The residual stress predicted agrees well with its counterpart obtained from the analytical formulation. The residual stress is compressive in nature. The presence of dark inclusions and WC content in the splats contributed to residual stress formation. In this case, mismatch of thermal expansion coefficients between WC and alloying element is responsible for the formation of the micro-stresses around WC. Fracture toughness and microhardness of the coating varies slightly at the surface, which is associated with the WC distribution at the surface; in which case, WC increases microhardness and lowers fracture toughness through enhancing the crack lengths around the indentation mark. HVOF coating improves the corrosion resistance of the base material. However, presence of deep pit sites at the surface suggests the occurrence of preferential corrosion around the splat boundaries. In addition, closely spaced surface texture peaks act as crevice corrosion centers at the surface while initiating the formation of deep pit sites.

Acknowledgments

The author acknowledge the support of King Fahd University of Petroleum, Dhahran, Saudi Arabia for this work.

See also: 2.14 Heat-Treating Copper and Nickel Alloys. 3.13 Finishing and Post-Treatment of Thermal Spray Coatings

References

1. Taha-al, Z. Y.; Hashmi, M. S. J.; Yilbas, B. S. Laser Treatment of HVOF Coating: Model Study and Characterization. *J. Mech. Sci. Technol.* **2007**, *21*, 1439–1444.
2. Al-Shehri, Y. A.; Hashmi, M. S. J.; Yilbas, B. S. HVOF Coating of Diamalloy 2002 and 4010 on Carbon Steel Sheets: Microstructure Examination. *Adv. Mater. Res.* **2011**, *264–265*, 1482–1486.
3. Al-Shehri, Y. A.; Hashmi, M. S. J.; Yilbas, B. S. HVOF Coatings of Diamalloy 2002 and Diamalloy 4010 onto Steel: Tensile and Bending Response of Coatings. *AIP Conf. Proc.* **2010**, *1315*, 1347–1352.
4. Yilbas, B. S.; Akhtar, S. Laser Re-melting of HVOF Coating with WC Blend: Thermal Stress Analysis. *J. Mater. Process. Technol.* **2012**, *212*, 2569–2577.
5. Yilbas, B. S.; Toor, I. H.; Patel, F.; Baig, M. A. Effects of Laser Re-melting on Corrosion Properties of HVOF Coatings. *J. Mater. Eng. Perform.* **2013**, *22* (5), 1505–1511.
6. Al-Fadhli, H. Y.; Stokes, J.; Hashmi, M. S. J.; Yilbas, B. S. HVOF Coating of Welded Surfaces: Fatigue and Corrosion Behaviour of Stainless Steel Coated with Inconel-625 Alloy. *Surf. Coat. Technol.* **2006**, *200*, 4904–4908.
7. Sobolev, V. V.; Guilemany, J. M.; Miguel, J. R.; Calero, J. A. Influence of Thermal Processes on Coating Formation During High Velocity Oxy-Fuel (HVOF) Spraying of WC–Ni Powder Particles. *Surf. Coat. Technol.* **1996**, *82*, 121–129.
8. Zhao, L.; Maurer, M.; Fischer, F.; Dicks, R.; Lugscheider, E. Influence of Spray Parameters on the Particle In-Flight Properties and the Properties of HVOF Coating of WC–CoCr. *Wear* **2004**, *257*, 41–46.
9. Qiao, Y.; Fischer, T. E.; Dent, A. The Effects of Fuel Chemistry and Feedstock Powder Structure on the Mechanical and Tribological Properties of HVOF Thermal-Sprayed WC–Co Coatings with Very Fine Structures. *Surf. Coat. Technol.* **2003**, *172*, 24–41.
10. Wang, Y. Y.; Li, C. J.; Ohmori, A. Examination of Factors Influencing the Bond Strength of High Velocity Oxy-Fuel Sprayed Coatings. *Surf. Coat. Technol.* **2006**, *200*, 2923–2928.
11. Fagoaga, I.; Vivienta, J. L.; Gavin, P.; Bronte, J. M.; Garcia, J.; Tagle, J. A. Multilayer Coatings by Continuous Detonation System Spray Technique. *Thin Solid Films* **1998**, *317*, 259–265.
12. David, C.; Anthymidis, K.; Agrianidis, P.; Tsipas, D. Determination of the Fatigue Resistance of HVOF Thermal Spray WC–CoCr Coatings by Means of Impact Testing. *J. Test. Eval.* **2007**, *35*, 630–633.
13. Wilden, J.; Wank, M.; Steffens, H. D.; Brune, M. New Thermal Barrier Coating System for High Temperature Applications. In *Proceedings of the 15th International Thermal Spray Conference*, Vol. 2, 1998; pp. 1669–1673.
14. Wang, J.; Li, K.; He, X.; *et al.* Effects of Structure and Processing Technique on the Properties of Thermal Spray WC–Co and NiCrAl/WC–Co Coatings. *Mater. Sci. Eng. A* **2004**, *371*, 187–192.
15. Pepe, G.; Looney, L.; Hashmi, M. S. J. Predicting the Wear Resistance of WC–Co Coatings Using Neural Networks. *Int. J. Model. Simul.* **1999**, *19*, 410–417.
16. Lih, W.-C.; Yang, S. H.; Su, C. Y.; Huang, S. C.; Hsu, I. C.; Leu, M. S. Effects of Process Parameters on Molten Particle Speed and Surface Temperature and the Properties of HVOF CrC/NiCr Coatings. *Surf. Coat. Technol.* **2000**, *133–134*, 54–60.
17. Tan, J. C.; Looney, L.; Hashmi, M. S. J. Component Repair Using HVOF Thermal Spraying. *J. Mater. Process. Technol.* **1999**, *92–93*, 203–208.
18. Hu, W.; Li, M.; Fukumoto, M. Preparation and Properties of HVOF NiAl Nanostructured Coatings. *Mater. Sci. Eng.* **2008**, *478*, 1–8.
19. Lima, R. S.; Karthikeyan, J.; Kay, C. M.; Lindemann, J.; Berndt, C. C. Microstructural Characteristics of Cold-Sprayed Nanostructured WC–Co Coatings. *Thin Solid Films* **2002**, *416*, 129–135.
20. Lugscheider, E.; Herbst, C.; Zhao, L. Parameter Studies on High-Velocity Oxy-Fuel Spraying of MCrAlY Coatings. *Surf. Coat. Technol.* **1998**, *108–109*, 16–23.
21. Kawakita, J.; Kuroda, S.; Kodama, T. Evaluation of Through-Porosity of HVOF Sprayed Coating. *Surf. Coat. Technol.* **2003**, *166*, 17–23.
22. Chivavibul, P.; Watanabe, M.; Kuroda, S.; *et al.* Development of WC–Co Coatings Deposited by Warm Spray Process. *J. Therm. Spray Technol.* **2008**, *17*, 750–756.
23. Gao, P. H.; Li, Y. G.; Yang, G. J.; Li, Y. G.; Li, C. X. Influence of Substrate Hardness on Deposition Behavior of Single Porous WC-12 Co Particles in Cold Spraying. *Surf. Coat. Technol.* **2008**, *203*, 384–390.
24. Kuroda, S.; Tashiro, Y.; Yumoto, H.; Taira, S.; Fukanuma, H.; Tobe, S. Peening Action and Residual Stresses in High-Velocity Oxygen Fuel Thermal Spraying of 316 L Stainless Steel. *J. Therm. Spray Technol.* **2001**, *10*, 367–374.
25. Li, H.; Khor, K. A.; Cheang, P. Young's Modulus and Fracture Toughness Determination of High-Velocity Oxy-Fuel-Sprayed Bioceramic Coatings. *Surf. Coat. Technol.* **2002**, *155*, 21–32.
26. Stewart, D. A.; Shipway, P. H.; McCartney, D. G. Influence of Heat Treatment on the Abrasive Wear Behavior of HVOF Sprayed WC–Co Coatings. *Surf. Coat. Technol.* **1998**, *105*, 13–24.
27. Liao, H.; Vaslin, P.; Yang, Y.; Coddet, C. Determination of Residual Stress Distribution from In Situ Curvature Measurements for Thermally Sprayed WC/Co Coatings. *J. Therm. Spray Technol.* **1997**, *6*, 235–241.
28. Stokes, J.; Looney, L. Residual Stress in HVOF Thermally Sprayed Thick Deposits. *Surf. Coat. Technol.* **2004**, *117–118*, 18–23.
29. Gill, S. C.; Clyne, T. W. Investigation of Residual Stress Generation During Thermal Spraying by Continuous Curvature Measurement. *Thin Solid Films* **1994**, *250*, 172–180.
30. Kesler, O.; Matejicek, J.; Sampath, S.; *et al.* Measurement of Residual stress in Plasma-Sprayed Metallic, Ceramic and Composite Coatings. *Mater. Sci. Eng. A* **1998**, *257*, 215–224.
31. Santana, Y. Y.; La Barbera-Sosa, J. G.; Staia, M. H.; *et al.* Measurement of Residual Stress in Thermal Spray Coatings by the Incremental Hole Drilling Method. *Surf. Coat. Technol.* **2006**, *201*, 2092–2098.
32. Totemeier, T. C.; Wright, R. N. Residual Stress Determination in Thermally Sprayed Coatings-a Comparison of Curvature Models and X-Ray Techniques. *Surf. Coat. Technol.* **2006**, *200*, 3955–3962.
33. Ghafouri-Azar, R.; Mostaghimi, J.; Chandra, S. Modeling Development of Residual Stresses in Thermal Spray Coatings. *Comput. Mater. Sci.* **2006**, *35*, 13–26.
34. Pejryd, L.; Wigren, J.; Greving, D. J.; Shadley, J. R.; Rybicki, E. F. Residual Stresses as a Factor in the Selection of Tungsten Carbide Coatings for a Jet Engine Application. *J. Therm. Spray Technol.* **1995**, *4*, 268–274.
35. Otsubo, F.; Kishitake, K.; Terasaki, T. Residual Stress Distribution in Thermally Sprayed Self-Fluxing Alloy Coatings. *Mater. Trans.* **2005**, *46*, 2473–2477.
36. McGrann, R. T. F.; Greving, D. J.; Rybicki, J. R.; Bodger, B. E.; Somerville, D. A. Fatigue Life in Bending and Coating Residual Stress in Tungsten Carbide Thermal Spray Coatings. *J. Therm. Spray Technol.* **1998**, *7*, 546–552.
37. Bansal, P.; Shipway, P. H.; Leen, S. B. Finite Element Modelling of the Fracture Behaviour of Brittle Coatings. *Surf. Coat. Technol.* **2006**, *200*, 5318–5327.
38. Planche, M. P.; Normand, B.; Liao, H.; Rannou, G.; Coddet, C. Influence of HVOF Spraying Parameters on In-flight Characteristics of Inconel 718 Particles and Correlation with the Electrochemical Behaviour of the Coating. *Surf. Coat. Technol.* **2002**, *157*, 247–256.
39. Hamatani, H.; Ichiyama, Y.; Kobayashi, J. Mechanical and Thermal Properties of HVOF Sprayed Ni based Alloys with Carbide. *Sci. Technol. Adv. Mater.* **2002**, *3*, 319–326.
40. Kawakita, J.; Fukushima, T.; Kuroda, S.; Kodama, T. Corrosion Behaviour of HVOF Sprayed SUS316L Stainless Steel in Seawater. *Corros. Sci.* **2002**, *44*, 2561–2581.
41. Tuominen, J.; Vuoristo, P.; Mäntylä, T.; Ahmaniemi, S.; Vihinen, J.; Andersson, P. H. Corrosion Behavior of HVOF-Sprayed and Nd-YAG Laser-Remelted High-Chromium, Nickel-Chromium Coatings. *J. Therm. Spray Technol.* **2002**, *11*, 233–243.
42. Zhang, D.; Harris, S. J.; McCartney, D. G. Microstructure Formation and Corrosion Behaviour in HVOF-Sprayed Inconel 625 Coatings. *Mater. Sci. Eng. A* **2003**, *344*, 45–56.
43. Fukuda, Y.; Kawahara, Y. Evaluation of Corrosion Resistance of Waste Incinerator Superheater Tubes Coated by High Velocity Thermal Spray. *J. Jpn. Inst. Met.* **2002**, *66*, 563–568.
44. Bolelli, G.; Lusvarghi, L.; Giovanardi, R. A Comparison Between the Corrosion Resistances of Some HVOF-Sprayed Metal Alloy Coatings. *Surf. Coat. Technol.* **2008**, *202* (19), 4793–4809.
45. Evans, A. G.; Charles, E. A. Fracture Toughness Determinations by Indentation. *J. Am. Ceram. Soc.* **1976**, *59*, 370–371.
46. ABAQUS. *Theory Manual, Version 6.2*; ABAQUS Inc.: Pawtucket, RI, 2015.
47. Risso, J. M.; Huespe, A. E.; Cardona, A. Thermal Stress Evaluation in the Steel Continuous Casting Process. *Int. J. Numer. Method. Eng.* **2006**, *65*, 1355–1377.
48. Mendelson, A. *Plasticity: Theory and Applications*; Krieger Publishing. Company: Mendelson, Alexzonder, 1983.

Relevant Website

www.kfupm.edu.sa
King Fahd University of Petroleum & Minerals.

3.8 Laser-Based 3D Printing and Surface Texturing

A Selimis and M Farsari, Foundation for Research and Technology – Hellas (FORTH-IESL), Heraklion, Greece

© 2017 Elsevier Inc. All rights reserved.

3.8.1	**Introduction**	111
3.8.2	**SLA**	111
3.8.3	**SLS**	112
3.8.4	**Microscale 3D Printing Techniques**	112
3.8.4.1	Projection Micro-Stereolithography	113
3.8.4.2	Multiphoton Lithography	114
3.8.4.2.1	Multiphoton polymerization	115
3.8.4.2.2	The diffraction limit	116
3.8.4.2.3	Experimental set-up	116
3.8.4.3	Materials for Laser Polymerization	118
3.8.4.3.1	Introduction	118
3.8.4.3.2	Photoinitiators	118
3.8.4.3.3	Organic photopolymers	118
3.8.4.3.3.1	SU-8	119
3.8.4.3.3.2	Hybrid materials	119
3.8.4.4	Applications	119
3.8.4.4.1	Metamaterials	119
3.8.4.4.2	Biomedical applications	121
3.8.5	**Laser-Based Surface Texturing Techniques**	122
3.8.6	**Conclusions**	126
References		126

3.8.1 Introduction

3D printing or additive manufacturing (AM) is described as the process of making a three-dimensional solid object from a digital file using additive processes. A 3D object is created by depositing successive layers of a material according to a computer design.

To print a 3D object, first one needs to have the design. A completely new object can be made in CAD (computer-aided design) file using a 3D-modeling program, such as SolidWorks® or AutoCad®. Alternatively, the copy of an existing object can be made by scanning it using a 3D scanner. Using appropriate software, the 3D model is sliced into horizontal layers, and loaded onto a 3D printer. The 3D printer builds the final object one layer at a time.

A large number of 3D printing techniques is now available, the main differences between them being the way layers are deposited and the materials used. Amongst them, laser-based techniques are very popular, as the laser beam can be focused and directed very accurately.

In this chapter we will detail and compare the most popular laser-based 3D printing techniques. In Sections 3.8.2 and 3.8.3 and we will describe Stereolithography (SLA) and Selective Laser Sintering (SLS), the most industrial of the laser-based 3D printing techniques. In Section 3.8.4 we will concentrate on microscale 3D printing techniques: projection stereolithography (PSL, Section 3.8.4.1) and multiphoton lithography (MPL, Section 3.8.4.2); We will describe extensively the principles and applications of the latter, the most popular and widely used of all microscale 3D printing techniques. Finally, in Section 3.8.5, we will describe how lasers are used to structure the surface of polymers, glasses, semiconductors, and metals.

3.8.2 SLA

SLA is an AM technology for producing 3D objects in a layer-by-layer fashion, by photopolymerizing a photosensitive material with an ultraviolet (UV) laser. The father of SLA is Charles (Chuck) W. Hull; he first coined the term 'stereolithography' and described the apparatus in the 1986 patent "Apparatus for production of three-dimensional objects by stereolithography."[1] There, it is described as "a new and improved system for generating a three-dimensional object by forming successive, adjacent, cross-sectional laminae of that object at the surface of a fluid medium capable of altering its physical state in response to appropriate synergistic stimulation, the successive laminae being automatically integrated as they are formed to define the desired three-dimensional object." It is basically describing a system for making solid objects by successively curing thin layers of a photopolymer using UV light. The patent described a focused UV light beam drawing each layer of the object onto the surface of a vat filled with liquid resin, as shown in **Figure 1**. Also in 1986, C.W. Hull founded 3D Systems Inc.,[2] the first company to develop a commercial SLA system.

In a commercial SLA machine, a focused UV laser beam – nowadays usually the 3rd harmonic of an yttrium aluminum garnet (YAG) laser – is used to photopolymerize an acrylate or epoxy liquid resin.[3] The first (usually sacrificial) layer of the component is built on an elevator platform. At every layer and

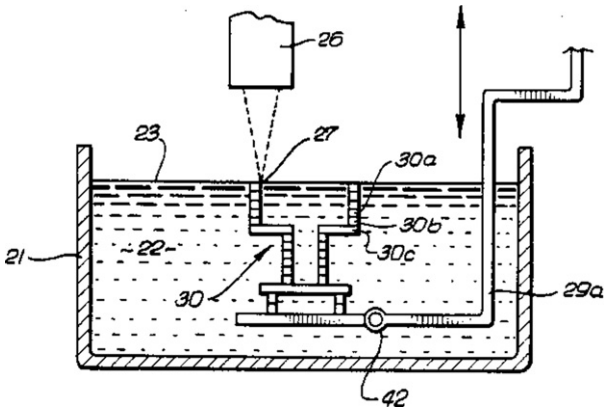


Figure 1 SLA design, as described in the original C.W. Hull patent. Hull, C. W. Apparatus for Production of Three-Dimensional Objects by Stereolithography. U.S. Patent 4,575,330, 1986.

always according to a CAD design, the beam draws a pattern on the surface of the liquid resin, selectively solidifying it and making it adhere to the layer below. After each layer has been 'written,' the elevator platform lowers by a single layer, the built section is re-coated with liquid resin (made flat by employing a re-coating blade), and another layer is 'written.' After the completion of the laser writing, the unexposed photopolymer is removed by immersing the structure in a solvent that dissolves the liquid monomer, and not the polymerized material. To save time, each layer is not fully photopolymerized, but instead the laser traces its exterior, and crosshatches in between. This results in a slice with a honeycomb interior and solid skins on top and bottom, encapsulating liquid resin. After removing the unexposed resin, the 3D object is 'baked' in a UV 'oven,' to solidify the encapsulated liquid resin. Very often the objects made by SLA need to have supporting structures, to avoid deformation due to the piston movement, gravity, and the re-coating blade. These supports need to be removed manually after the completion of the building process.

SLA can produce almost infinitely complex functional prototypes in a time length from a few hours to more than a day. The resolution can be down to 5 μm, while the overall size depends on the type of the machine and the size of the elevator platform. Typically, an SLA machine will be capable of producing components of maximum size $50 \times 50 \times 60\ cm^3$. However, nowadays there are SLA machines, such as the Mammoth,[4] that can produce sizes up to 2 m. On the downside, both photosensitive resins and SLA machines can be very expensive.

The main application of SLA is prototyping; as such, it has been employed by a variety of industries, from medical prototyping to the car industry, where it is routinely used to make polymer prototypes of car engines.

However, the use of SLA models is not limited to prototypes; modern SLA resins provide strong enough models to be machined and make functional synthetic parts, but they are mostly used as master patterns for injection molding and metal casting.

SLA has also been applied in medicine, to fabricate guides for tumor identification and surgery guidance,[5,6] but also for the fabrication of implants and scaffolds for bone and cartilage tissue engineering.[6–10] The materials used in this case can be pure photopolymers, or custom materials such as resins mixed with hydroxyapatite.

3.8.3 SLS

The SLS technique employs a high-power laser to sinter layers of material in powder form, in order to build 3D structures. A typical experimental setup is shown in **Figure 2**. A layer of powder is first deposited on a fabrication piston substrate. The laser beam is scanned over the powder surface following a CAD design. The laser beam heats the powder to melting point and causes the powder particles to melt together to form a solid mass. Subsequent layers are built directly on top of the earlier layers, with new layers of powder deposited on the top of the already sintered layers using a roller.

The materials used for building components in SLS machines can be single component powders (such as metal powders produced by ball milling) or, more commonly two-component powders, coated powders or powder mixtures. Compared to other 3D laser printing techniques, SLS can build components from a wide variety of materials. These can be polymers such as nylon and nylon-coated metal particles,[11–17] polystyrene,[15,18–26] metals such as titanium,[27–35] steel,[36–44] alloys,[32,45–49] and several biomaterials such as hydroxyapatite, polycaprolactone, polylactide, and mixtures of those with other biopolymers.[50–77] Depending on the material, up to 100% density can be achieved with material properties comparable to those from conventional milling methods.

Due to its material versatility and its potential to make very complex geometries directly from computer models, SLS is widely used nowadays. While its original use was in prototyping, it is now used also in custom or limited-run manufacturing to produce end-use parts. One such area is dental implants **Figure 3**[34] and scaffolds for hard and soft tissue engineering. SLS has been extensively used to create hard scaffolds for bone and cartilage tissue engineering,[62,78,79] often employing mixtures of poly-*e*-caprolactone with calcium phosphates as a scaffold material.[80] In soft tissue engineering its use has been more limited; it has been used to melt together poly-*e*-caprolactone layers for cardiac regeneration[81,82]; biodegradable polycaprolactone was also structured in order to grow avidin–biotin human hepatoma Hep G2 cells, for liver tissue engineering. SLS has also been used to make replication masters for biomedical implants.[83]

3.8.4 Microscale 3D Printing Techniques

Progress in technologies such as MEMS and microfluidics has increased the requirement for 3D printing technologies with micro and nano features resolution, using diverse materials, such as ceramics and polymers. In the following paragraphs we describe two laser-based 3D microfabrication techniques: Projection micro-steleolithography and multiphoton lithography.

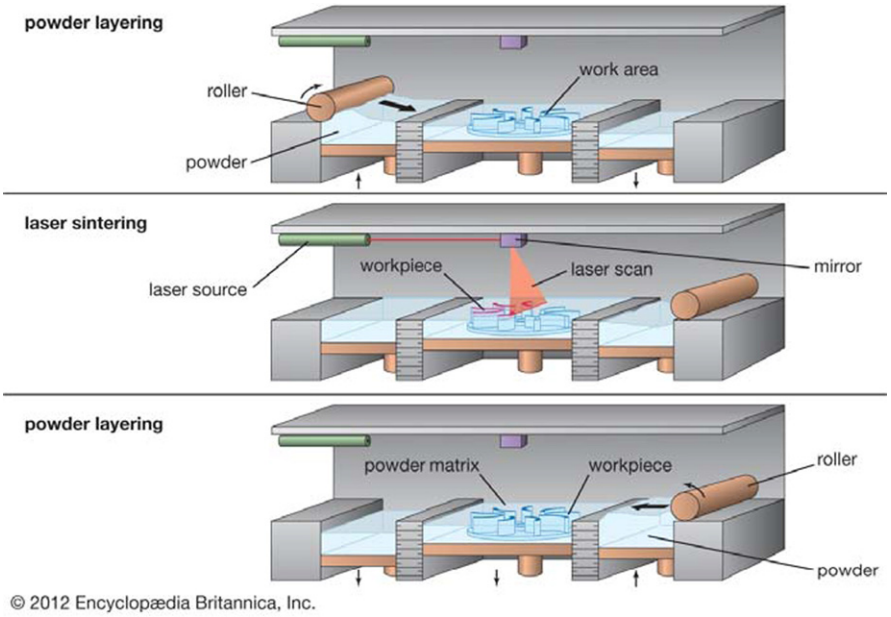


Figure 2 The SLS process, showing (top) the rolling of a thin layer of powder over the work area, (middle) the sintering of powder by a laser beam to build up the workpiece, and (bottom) the rolling of fresh powder over the workpiece to begin a new layer (http://www.britannica.com/technology/3D-printing/images-videos – Encyclopedia Britannica).

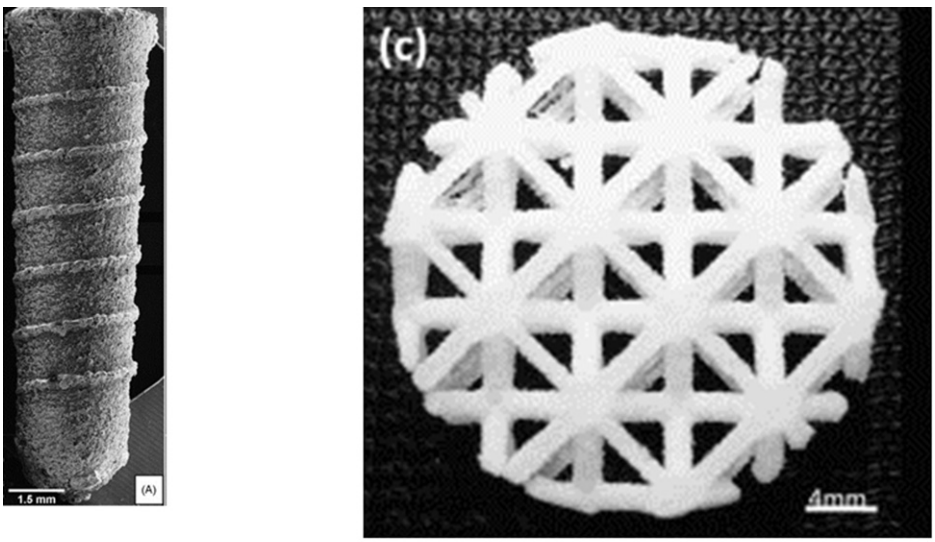


Figure 3 (a) A dental implant made using SLS[34] and (b) poly-*e*-caprolactone scaffolds made using SLS for cardiac regeneration.[82]

3.8.4.1 Projection Micro-Stereolithography

In Section 3.8.2 we described SLA as a technique for fabricating large-scale components and prototypes. The same technique was miniaturized to produce micron scale components,[84] and is now called micro-stereolithography (μSLA). The procedure is exactly the same as in classic SLA, except the beam is focused very tightly, to enable high resolution.

While μSLA worked well, it never became popular for mass production as it was very slow. To overcome this problem, Alain Bertsch and co-workers proposed a new system based on a dynamic mask pattern being projected on the liquid resin surface, therefore photopolymerizing each layer of the pattern in one shot.[85,86] The experimental setup is shown in **Figure 4**. There, the beam of a green laser (515 nm) was modulated by a liquid crystal display (LCD), to project an image on a platform

immersed into the photosensitive resin. As each component layer is made using a single light exposure, the only moving part in the system is the *z*-axis of the component platform.

As the Bertsch system was designed to operate with green light (a wavelength of transparency of the LCD display), it could not use any of the commercially available photosensitive resins designed for classic SLA. This was accomplished by the Chatwin group (Sussex University, UK), who replaced the LCD with a custom-made spatial light modulator (SLM), transparent to the UV.[87–89] Several materials composed for SLA and high-resolution structures were made using this technique (**Figure 5**).[87–90]

Replacing LCDs with SLMs solved the material availability problem but generated others: the low switching speed and low optical density of the refractive elements of the SLM during the *OFF* mode reduce the contrast of the transmitted pattern. In addition, the SLM UV transparency is limited, resulting in energy wastage and overheating (therefore limited lifetime) of the device itself.

At the same time as the Chatwin team developed SLM-based μSLA, digital micromirror devices (DMDs) became available by Texas Instruments.[91] DMD is a reflective array of fast, digital light switches that are monolithically integrated onto a silicon address chip. Used as a projection system, a DMD replaced the SLM in a system implemented by Sun *et al.*,[92] providing high-quality, seamless, all-digital images with exceptional stability and minimal power loss. The quality and resolution of the structures fabricated using this technique was superior to anything presented before (**Figure 6**).

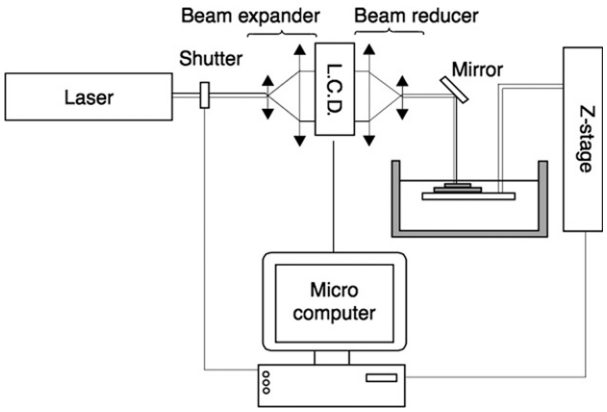


Figure 4 The first projection μSLA set-up using an liquid crystal display as a dynamic mask.[85,86]

The application of DMDs in μSLA is still fairly limited, and most research has focused on improving the process rather than developing applications.[93–96] Again, however, the main area of research applications has been developing microenvironments for cell growth.[97–100]

3.8.4.2 Multiphoton Lithography

Multiphoton Lithography based on the Multiphoton Polymerization of photosensitive materials is a direct laser writing technique that allows the fabrication of three-dimensional structures with submicron resolution.[101–105] The polymerization is based on two-photon absorption (TPA); when the beam of an ultrafast laser is tightly focused into the volume of a transparent, photosensitive material, the polymerization process can be initiated by nonlinear absorption within the focal volume. By moving the laser focus three-dimensionally through the material, 3D structures can be fabricated. The technique has been implemented with a variety of acrylate and epoxy materials and several components and devices have been fabricated such as photonic crystal templates,[106] mechanical devices,[107] and microscopic models.[108] Resolution below 100 nm has been achieved using this technique.[109]

The unique capability of MPL lies in that it allows the fabrication of computer-designed fully 3D structures with resolution beyond the diffraction limit. No other competing technology offers these advantages. Classic 3D prototyping techniques such as UV laser SLA, 3D inkjet printing, and laser sintering can also produce fully three-dimensional structures; however, they cannot provide resolution better than a few microns. On the other hand, lithographic techniques with superior resolution, such as e-beam lithography, cannot produce anything more complicated than high-aspect ratio two-dimensional structures.

In this section we summarize the principles of microfabrication by MPL. We discuss the fundamental principles of multiphoton absorption (MPA) and describe a typical MPL experimental setup. Then we concentrate on materials used for MPL microfabrication, on recent progress in the functionalization of the surface and the bulk of the 3D-fabricated structures, while at the same time discussing applications of the technology.

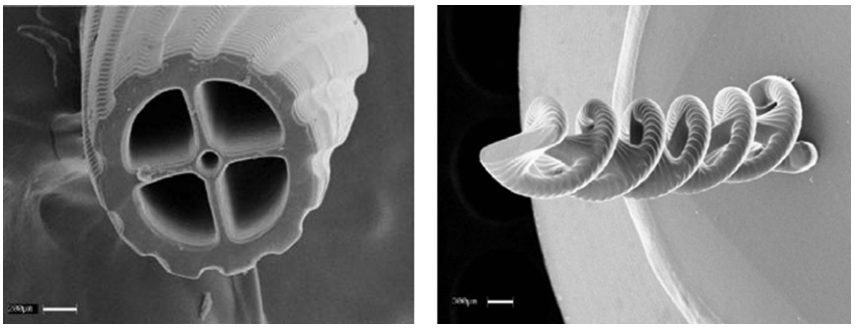


Figure 5 3D structures fabricated using an spatial light modulator as a dynamic mask.[89]

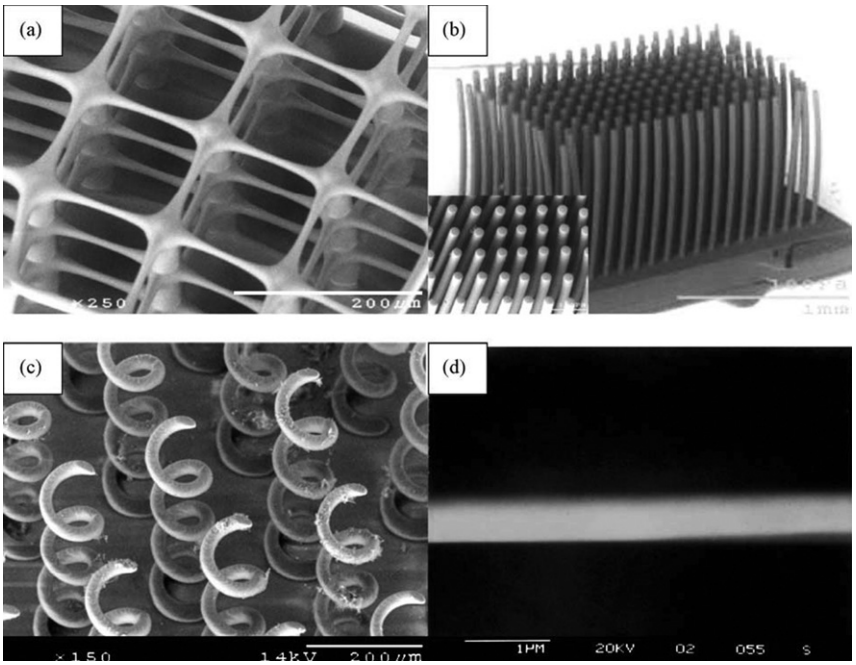


Figure 6 3D complex microstructures fabricated employing a DMD as a dynamic mask. (a) Micro matrix with suspended beam diameter of 5 μm; (b) high aspect-ratio micro rod array consists of 21 × 11 rods with the overall size of 2 mm × 1 mm. The rod diameter and height is of 30 μm and 1 mm, respectively; (c) micro coil array with the coil diameter of 100 m and the wire diameter of 25 μm; and (d) suspended ultra fine line with the diameter of 0.6 μm.[92]

3.8.4.2.1 Multiphoton polymerization

The basis of MPL is the phenomenon of MPA. For simplicity, we will discuss TPA and two-photon polymerization (TPP) – the same rules apply to more than two photons.

There are two types of TPA: sequential and simultaneous. In sequential, the absorbing species is excited to a real intermediate state, then, a second photon is absorbed. The presence of the intermediate energy state implies that the material absorbs at this specific wavelength; it will therefore be a surface effect and will follow the Beer–Lambert law.[3] The simultaneous absorption, on which the MPL technique is based, was originally predicted by Maria Göppert-Mayer in 1931 in her doctoral dissertation.[110] It is defined as "an absorption event caused by the collective action of two or more photons, all of which must be present simultaneously to impart enough energy to drive a transition." This prediction was not experimentally verified until over 30 years later by Werner Kaiser, when the invention of the laser permitted the first experimental verification of the TPA through the two-photon excited fluorescence detection in a europium-doped crystal.[111] In simultaneous absorption, there is no real intermediate energy state, i.e., the material is transparent at that wavelength. Instead, there is a virtual intermediate energy state and TPA happens only if another photon arrives within the virtual state lifetime.[112] For this to occur high intensities are required, which can only be provided by a tightly focused femtosecond (fs) laser beam. This is illustrated in Figure 7; as it can be seen, the electron transition in this case is caused by two photons of energy $h\nu/2$ rather than one of energy $h\nu$.

Ti:Sapphire and near-infrared lasers are widely used for this purpose. They have two main advantages; firstly they have very

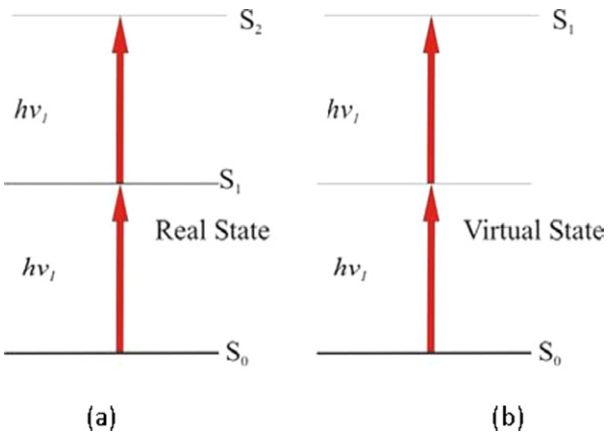


Figure 7 Sequential (a) and simultaneous absorption (b). In the first case the intermediate energy level is an actual energy level, while in the second case it is virtual.

short pulses, in the order of a few tens of femtoseconds, so they do not cause thermal damage. Secondly, their standard wavelength is 780–820 nm, which is twice the wavelength of polymerization of a wide range of photopolymers. In addition, most photopolymers are transparent at around 800 nm, which allows in-volume focusing of the laser beam with minimal scattering.

When the laser is focused tightly into the material, the photoinitiator used to initiate the polymerization will absorb two or more photons and produce radicals. As the material response is proportional to the square of the intensity, this will only happen at the focal point, which, combined with the fact

that the two-photon transition rate is very small, will provide very high-spatial resolution.

Photopolymerization is a light-induced reaction, which converts a liquid or gel monomer into a solid polymer. These reactions require the use of an appropriate photoinitiator, which is a light sensitive molecule that produces an active species upon irradiation with UV, visible, or infrared light. The photoinitiators that have been most extensively used so far are divided into two main categories depending on the nature of generated active species (radicals or cations). An effective initiator has a high-quantum yield in the generation of the active moieties, high-thermal stability and stability in darkness, and is highly soluble in the polymerization medium.

Free-radical polymerizations are chain reactions in which the addition of a monomer molecule to an active chain-end regenerates the active site at the chain-end.

The free-radical photopolymerization mechanism involves at least three different kinds of reactions (Eqn [1a]–[1b]):[113–115]

- The first step is the initiation during which the free-radical initiator is decomposed with light in the presence of monomer to form an active species (Step 1a).
- In the next step, known as the propagation, the initiator fragment reacts with a monomer molecule to form the first active adduct that is capable of being polymerized. Monomers continue to add in the same manner resulting in the formation of macroradicals which are end-active polymers (Step 1b).
- The final step is the termination during which the growth center is deactivated and the final polymer molecules are formed. This step normally involves the reaction between two polymers bearing active centers and can proceed by two different mechanisms, combination or disproportionation, leading to the formation of one or two polymers chains, respectively (Step 1c).

Equations [1a]–[1b] show the TPP process

$$\text{Initiation} \quad I \xrightarrow{h\nu,\, h\nu} I^{*} \longrightarrow R^{\bullet} \qquad [1a]$$

$$\text{Propagation} \quad R^{\bullet} + M \longrightarrow RM^{\bullet} \xrightarrow{M} RMM\cdots \longrightarrow RM_n^{\bullet} \qquad [1b]$$

$$\text{Termination} \quad RM_n^{\bullet} + RM_m^{\bullet} \longrightarrow RM_{n+m}R \qquad [1c]$$

Besides the above, other reactions, such as chain transfer and chain inhibition, often take place and complicate the mechanism of free-radical polymerization.

Photopolymerizations follow the general scheme for any polymerization, however, the use of light, rather than heat, to drive the reaction has certain advantages, such as the elimination of solvent, the high-reaction rates at room temperature, and the spatial control of the polymerization.

3.8.4.2.2 The diffraction limit

Theoretically, the highest resolution that can be achieved by a focused laser beam is given by Abbe's diffraction limit (eqn [2]).[116]

$$\text{Diffraction limit} = \frac{0.5\lambda}{\text{N.A.}} \qquad [2]$$

where λ is the laser wavelength and N.A. is the numerical aperture of the focusing objective; this has fueled the race for ever decreasing wavelengths, such as electron wavelengths and for alternative, non-light patterning techniques such as atomic force microscopy[117–121] and near-field scanning optical microscopy,[122–124] however, these techniques only allow surface and not in-volume patterning. To produce 3D structures with in-volume patterning, and produce photopolymerized voxels smaller than that defined by the diffraction limit, materials with well-defined photopolymerization threshold need to be used.

As the photoinitiator is excited by the laser process, it produces radicals; these radicals are quenched by oxygen and other quenchers in the system. Quenching is a competing effect to photopolymerization and is usually considered detrimental to the process. In MPL, however, it can be used to circumvent the diffraction limit and produce structures of very high resolution. This can be done by modifying the light intensity at the focal volume, in a manner so that the light-produced radicals exceed the quenchers and initiate polymerization only at a region where exposure energy is larger than the threshold. In this case the diffraction limit becomes just a measure of the focal spot size and it does not really determine the voxel size.

3.8.4.2.3 Experimental set-up

A typical experimental setup for the fabrication of three-dimensional microstructures by MPL is shown in **Figure 8**. The laser source typically is a Ti:Sapphire femtosecond oscillator operating at 800 nm; there are also examples in literature where an Optical Parametric Oscillator is used with a Ti:Sapphire laser, to reduce the laser wavelength to visible wavelengths.[109,125] The laser will typically have a pulse length of less than 200 fs and a repetition rate of 50–80 MHz. The energy required for the polymerization process will depend on the material, the photoinitiator and the focusing, but is usually in the order of a few nanojoules per pulse.

The photopolymerized structure is usually generated in a layer-by-layer format. Each layer is formed either using an x–y galvanometric mirror scanner or x–y piezoelectric stages. The main difference between the two cases being that in the former case, the structure remains immobile and the structure is generated by the laser beam moving, while in the latter case the x–y stages move the structure and the laser beam remains immobile. Movement on the z-axis can be achieved using a piezoelectric or a high resolution linear stage.

To achieve the tight focusing conditions required for TPP to occur, a microscope objective needs to be used; when the numerical aperture of the objective is higher than 1, immersion oil is used for index matching. Galvo scanners have to be adapted to accommodate microscope objectives, as usually they are designed to take lenses with long focal lengths.

Beam control can be achieved by either using a fast mechanical shutter or an acousto-optic modulator, while beam intensity control can be achieved using neutral-density filters, a variable attenuator, or a combination of a polarizer and a waveplate.

For the online monitoring of the photopolymerization process a charge-coupled device camera can be mounted behind a dichroic mirror, as shown in **Figure 8**. This is possible

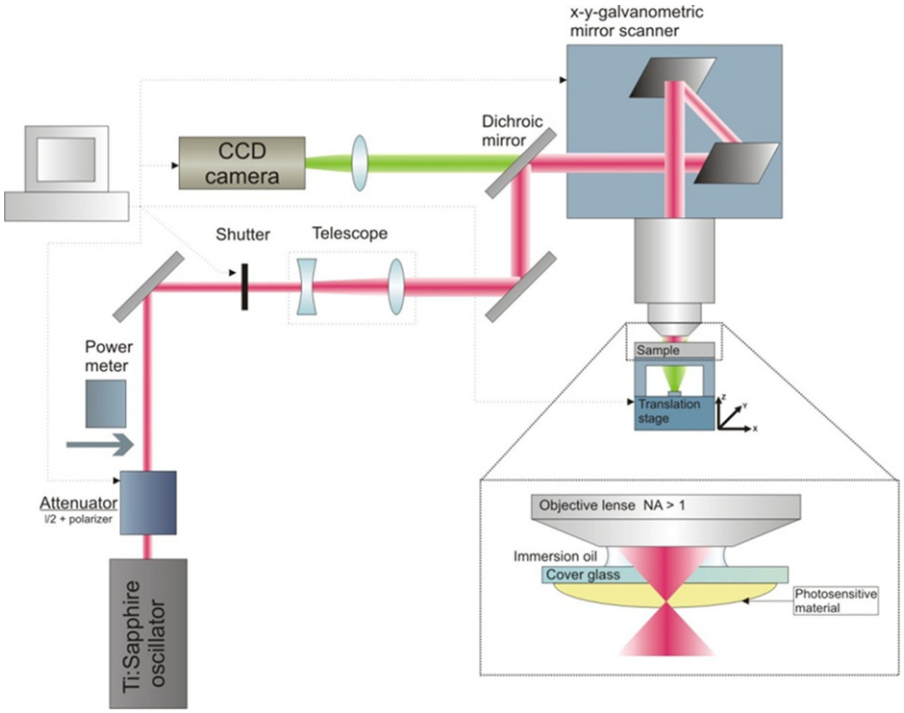


Figure 8 A typical setup for multiphoton polymerization, consisting of a fs laser, a galvanometric mirror scanner, moving stages, directional and focusing optics, and a monitoring camera.

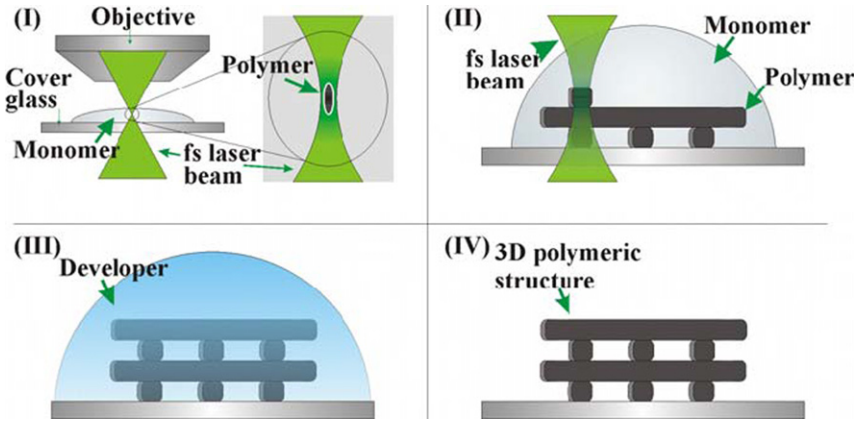


Figure 9 MPL experimental procedure (I) beam focusing, (II) laser writing, (III) development, and (IV) completed structure.

as the refractive index of most photopolymers changes during polymerization, so that the illuminated structures become visible during the building process.

When the photosensitive polymer is in a liquid form, in order to avoid liquid movement as the samples moves, the samples are prepared in a sandwich format between two thin glass coverslips; a spacer needs to be used to maintain sample uniformity. When the sample is a solid or a gel, then there is no need for the sandwich format. To avoid the distortion of the focused laser beam by the built structures, they are fabricated layer-by-layer bottom up with the last layer attached to the glass coverslip.

After the completion of the photopolymerization process and in order to remove the unphotopolymerized resin, the samples need to be developed like in any lithographic process. The developer used and the time for development will depend on the material.

The experimental procedure for fabricating a 3D structure by MPL is shown in Figure 9: (1) The laser beam is tightly focused into the volume of the material. (2) Either the focused beam or the sample move following a computer-generated pattern. (3) After the laser writing of the structure, the sample is immersed into an appropriate developer. (4) The freestanding structure is revealed.

3.8.4.3 Materials for Laser Polymerization

3.8.4.3.1 Introduction

In general, a material suitable for structuring with MPL includes at least two components: (1) a monomer, or a mixture of monomers/oligomers, which will provide the final polymer and (2) a photoinitiator, which will absorb the laser light and provide the active species that will cause this polymerization. Several monomer/oligomer and photoinitiator combinations have been used for this purpose. These are mostly negative photoresists such as hydrogels, acrylate materials,[126,127] the epoxy-based photoresist SU-8,[102] and hybrid materials.[103,128] Recently, redox and Diels–Alder photopolymerization have been also been reported.[129,130] In the following sections, we will discuss briefly these photoinitiators and materials.

3.8.4.3.2 Photoinitiators

During polymerization, a monomer is converted into polymer and this transformation can be induced by light. In classic photolithography, a photoinitiator absorbs the light and produces an active species which causes the photopolymerization. In TPP, however, things are more complicated, and these extra requirements must be fulfilled:[101,126]

- Both the photoinitiator and the monomer/oligomer are transparent at the laser wavelength used, so that the laser beam can be focused inside the volume of the material without being absorbed at the surface.
- The monomer/oligomer needs to be transparent at the TPA wavelength ($\lambda/2$); if it is not, then the photopolymer is likely to be burnt or ablated.
- The photoinitiator needs not only to absorb at the two-photon wavelength, but also to have a high two-photon cross-section, a high radical quantum yield and highly-active radical species generated; typically, if any two of these three are large enough, the initiator will normally be efficient for TPP.

In classic lithography, there are two types of photoinitiators: radical photoinitiators and cationic photoinitators. All the materials developed to date for MPL employ radical photoinitiators; these, upon light irradiation, generate free radicals, which initiate a polymerization process of acrylates or vinyl ethers. Cationic initiators are photo-acid generators that produce cations upon light irradiation and are used for the polymerization of epoxides or vinyl ethers;[113–115] to the best of our knowledge, there are no materials to date, specifically developed for MPL employing cationic polymerization, however, it is employed in the most commonly used photolithography resist, SU-8.

An effective MPL photoinitiator has a high quantum yield in the generation of the active moieties, high thermal stability and stability in darkness, and is highly soluble in the polymerization medium.[131] The most commonly used free-radical photoinitiator is benzophenone and its derivatives.[132,133]

Nowadays, there is a lot of concentrated effort to synthesize fast and efficient photoinitiators specifically for multiphoton applications.[134] In addition, there is a lot of work toward biocompatible photoinitiators, specifically for bio-applications. To this end, classic dyes such as Bengal Rose, Eosin, Nile Red, biomolecules such as flavin mononucleotide, but also novel, synthetic photoinitiators have been used.[127,131,135–141]

3.8.4.3.3 Organic photopolymers

The first materials used for MPL were acrylate photopolymers[142] (Figure 10). These materials have several properties which make them attractive for MPL applications: a wide variety of the full composites or their monomers are commercially available; they are transparent at visible and near-infrared wavelengths, and can therefore be processed by IR and green ultrafast lasers; they can be developed in common, nonaggressive solvents such as isopropanol; they can be polymerized fast and with low shrinkage and, after polymerization, they are mechanically and chemically stable.

Due to their versatile chemistry, acrylate photopolymers have been used in their pure form but also doped with other materials to add them functionality. They have been doped with TiO_2 nanoparticles to increase their refractive index for photonic crystal applications;[143] with CdS nanoparticles for the fabrication of light-emitting 3D structures (Figure 11);[144,145] with metal-binding materials to cover them with metals

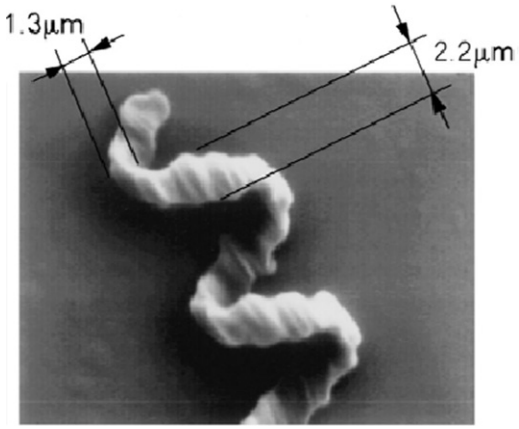


Figure 10 The first 3D structure fabricated by MPL.[142]

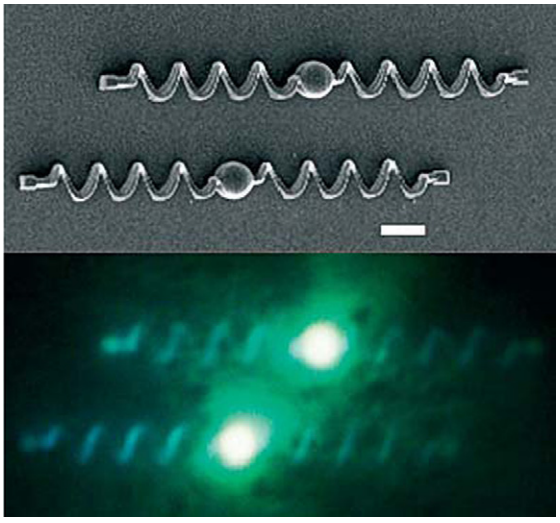


Figure 11 A 3D light-emitting structure.[144]

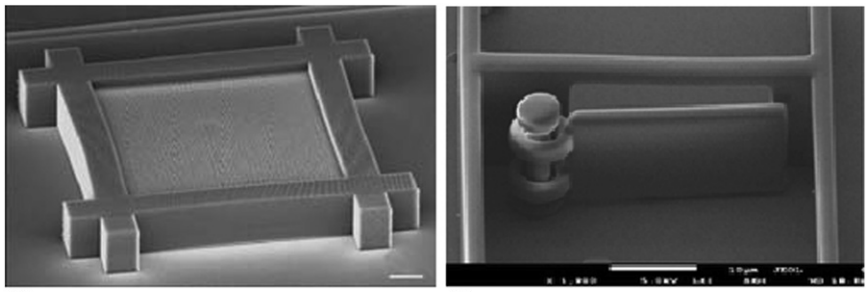


Figure 12 Microstructures fabricated using SU-8. (a) A photonic woodpile structure[108] and (b) A movable microfluidic structure.[158]

using electroless plating;[146,147] with chitosan to make them suitable for bio-applications;[148] with Poly[2-methoxy-5-(2-ethylhexyloxy)-1,4-phenylenevinylene] (MEH-PPV) to make them electroluminescent.[149]

3.8.4.3.3.1 SU-8

SU-8 is a negative, epoxy-based photo-resist commonly used for the fabrication of high-aspect ratio structures, using standard contact lithography. Its absorption maximum is at 365 nm. When exposed to the appropriate light, SU-8's long molecular chains cross-link, causing the material to become insoluble to most common solvents. For this to happen, the SU-8 films require postexposure heat treatment.

The possibility to structure SU-8 by MPL polymerization was first demonstrated by Witzgall *et al.*, who employed single shots from Ti:Sapphire femtosecond amplifier to fabricate small dots.[150] More complex 2D and 3D structures were built by Belfield *et al.* and Kuebler *et al.*, respectively, who worked on the development of novel, efficient photoinitiators for cationic polymerization.[151,152] Since then, SU-8 has been used by a large of the research teams involved in MPL fabrication have used SU-8.[153–157]

SU-8 is thermally stable, transparent in the visible and highly resistant to solvents, acids, and bases. These properties make it suitable for permanent use application; by itself, SU-8 has been employed for the fabrication of photonic (**Figure 12(a)**),[108] microfluidic (**Figure 12(b)**),[158–160] and biomedical structures,[161] while it has also been covered with metal for metamaterial fabrication.

3.8.4.3.3.2 Hybrid materials

Over the last few years, MPL materials research has focused on the development of photosensitive hybrid composites. Especially silicate-only based photopolymers have proved to be a very popular choice, as they can be commercially available and they combine properties of silicate glasses such as hardness, chemical and thermal stability, and optical transparency with the laser processing at low temperatures of organic polymers; properties impossible to achieve with just inorganic or polymeric materials.[125,162–178] The most widely used and studied silicate material is the photopolymer ORMOCER®, commercially available from Microresist Technologies, Germany, and it has been used for a variety of mostly photonic applications, like the optically active polymer microdisk of **Figure 13**.

ORMOCER® and other silicate-only based hybrid materials have provided the possibility to fabricate high-resolution

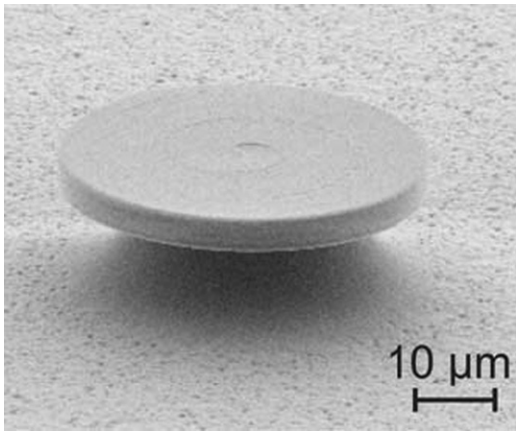


Figure 13 A microdisk fabricated using ORMOCER®.[173]

3D structures. They do not allow, however, the optimization and 'fine-tuning' of the materials properties for specific applications. The versatile chemistry of hybrid composites allows the copolymerization of more than one metal alkoxides; this has been shown to enhance the material's mechanical stability and allows the modification of its optical properties. There are a few examples of composite photosensitive hybrid materials used in MPL applications;[103,133,179,180] Ovsianikov *et al.* showed that under specific fluence conditions, specific material combinations can be structured into complex 3D structures without shrinkage.[181,182] In addition to metal alkoxides, hybrid materials chemistry provides the possibility of the inclusion of functional groups, such as nonlinear optical molecules,[183,184] quantum dots,[185] and metal-binding materials.[186] Zirconium silicates doped with a monomer containing amine moieties were used for the fabrication, for the first time using MPL, of 3D structures selectively metalized with silver (**Figure 14**).[187,188]

3.8.4.4 Applications

3.8.4.4.1 Metamaterials

Metamaterials are artificial materials with properties that do not exist in nature; these properties are due to structure and not material composition. Their name derives from the greek word 'meta,' which means beyond, because these materials have properties that extend beyond materials found naturally. In metamaterials, an assembly of structures can replace the role that atoms and molecules have in conventional materials, resulting in a composite structure with electromagnetic properties beyond

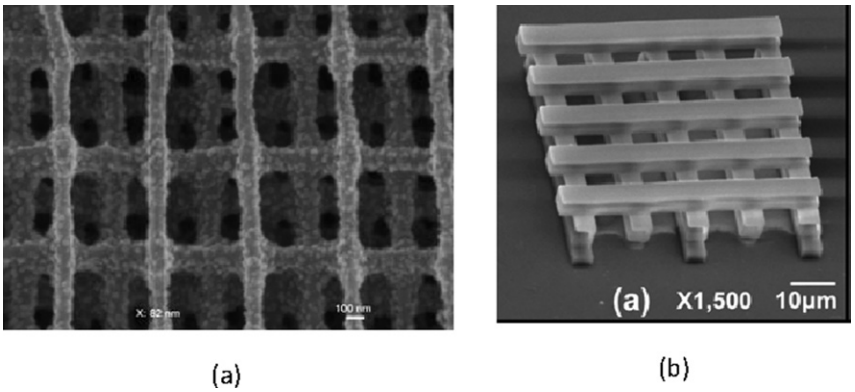


Figure 14 (a) A three-dimensional photonic crystal with sub-100 nm features[187] and (b) an IR polarizer.[188]

anything that can be found naturally, or chemically synthesized. An excellent tutorial on metamaterials can be found in the website of Prof. David R. Smith (Duke University).[189]

Photonic metamaterials consist of nanostructured metalo-dielectric subwavelength building components, and allow the realization of many new and unusual optical properties, such as negative refractive index, magnetism at optical frequencies, perfect absorption, and enhanced optical nonlinearities. Several applications of metamaterials have been proposed, including ultrahigh-resolution imaging systems, compact polarization optics, and cloaking devices.[190] The realization of these applications requires the fabrication of large-scale metallo-dielectric structures, a very challenging task. There has been some limited research into the direct fabrication of metallic 3D structures using multiphoton reduction of metal ions. The quality of the structures, however, has been compromised by the reduced transparency of the metal ion solutions at the laser wavelengths used (500–800 nm).[191,192] Metallic woodpile structures have also been realized experimentally at micron wavelengths using traditional lithographic techniques.[193–195] However, lithographic techniques can accommodate only a very limited number of layers, and aligning each layer with the previous one is difficult.

MPL is the only inherently 3D fabrication technique, with the potential to fabricate 3D structures, but the majority of the materials structurable by MPL are dielectrics. A popular approach is to use MPL to make dielectric structures, and subsequently metallize them. The most successful approaches and their advantages and disadvantages are listed in below:

1. MPL of positive photoresists and filling with gold using electroplating.[196,197] Here, voids are created in a positive tone photoresist using MPL; these are subsequently filled with gold using classic electroplating (**Figure 15**). The main advantage of this technique is that there is no need to remove the photoresist as the refractive index contrast between the gold and the dielectric material is very high. The main disadvantage is that the number of designs that can be structured is limited, as the right apertures of the material removal and gold filling have to be allowed; therefore, this is fundamentally a 2.5D structuring technique.
2. MPL of dielectric structures and nonselective metallization with electroless plating. Here, a standard photolithographic material is used, such as SU-8, for the fabrication of the structures, and subsequently their surface is covered with silver using classic electroless plating.[198–201] Additional processing, to enable the metal adhesion on the surface, is required and the quality, structural integrity, and resolution of the structures depend on the building material and the surface-processing step. The advantage of this technique is that any photopolymer can be used; the disadvantages are that, as the density of the metal-binding sites on the structure cannot be controlled, the metallization quality can vary. In addition, along with the surface of the structures, the substrate is also activated; the metallization is therefore not selective, often requiring an extra step to remove the structures from the metalized substrate.[199]
3. MPL of dielectric structures and selective metallization with electroless plating. Here, a composite doped with the metal-binding sites is employed for the structure fabrication.[147,186,187] The main advantages in this case are that the metallization is selective, and the density and distribution

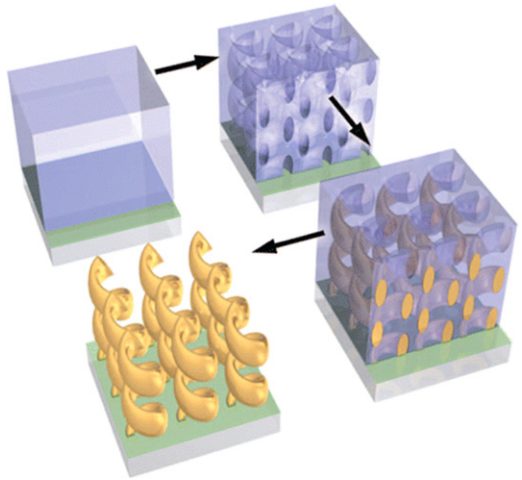


Figure 15 MPL of positive photoresists and filling with gold using electroplating. A positive photoresist is spun onto a glass substrate covered with a 25-nm thin film of conductive indium-tin oxide (ITO) shown in green. After MPL and development, an array of air helices in a block of polymer is fabricated. After electroplating the polymer is removed by plasma etching, leading to an array of freestanding 3D gold helices.[197]

of the metal-binding sites can be controlled. The main disadvantages are that specific metal-binding materials need to be used, and in most cases these were not able to provide the required resolution and structural integrity required for optical metamaterials. Only very recently it was shown that it is possible to use this method for the fabrication of optical nanophotonic devices.[187]

4. MPL of dielectric structures and metallization with chemical vapor deposition (CVD). Here MPL is used to fabricate 3D structures by any material, typically SU-8.[202] The surface of the structures is subsequently activated using plasma etch. Finally, they are covered with silver using CVD. The main advantage of this technique is that any photopolymer can be used, and the resolution and final quality of the structures will depend on that. The main disadvantages are firstly, CVD can only penetrate a small number of structure layers, allowing only a small number of unit cells, and secondly, there is no selectivity; as with the plasma etch, the substrate is activated as well as the structure.

It should also be noted that, recently, there has been reported some work concerning structuring by MPL of transparent conducting materials, such as ionogels.[203,204] However, neither the conductivity nor the resolution of these materials are sufficient for applications in optical metamaterials.

3.8.4.4.2 Biomedical applications

The biomedical applications of MPL can be broadly divided into two categories: biomedical microdevices and scaffolds for cell culture.

The first category, biomedical microdevices, includes devices such as micro-needles for drug delivery, and micromechanic, microfluidic, or optofluidic functional devices.[205,206] Despite the enormous potential of 3D nanostructuring in this field, there are only few examples to date, mostly because there has not been much research into the integration of MPL-made structure into existing micromechanical systems. Only recently, Amato *et al.* employed MPL to build a cell sorter inside a commercial microfluidic chip.[207,208] Most other structures reported are freestanding and have not been integrated into a functional device.[209–216] Special mention should be made to some recent research introducing magnetic materials into the photopolymerizable resin, making possible the contact-free controlled movement to the fabricated devices.[217,218]

The second category, MPL scaffolds for cell culture studies and tissue engineering, has seen an enormous growth over the last few years (Figures 16 and 17). Tissue engineering is the discipline applying the principles of engineering and life sciences toward the development of biological substitutes that restore, maintain, or improve tissue function or a whole organ.[219] An important part of the development of artificial tissue is the choice of scaffold, as it can influence the attachment, migration, and proliferation of cells. 3D cell cultures offer a realistic environment where the functional properties of cells can be observed and manipulated.[220–222] Although producing scaffolds using laser-based, user controlled manufacturing techniques such as MPL or classic SLA is time consuming and therefore costly, recent studies have shown that they can provide tissue engineering solutions for aligned and complex tissue growth. An important advantage is that a controlled topological environment for cell growth can be achieved (Figure 18). In addition, ordered 3D scaffolds are ideally suited for exploring the relationship between 3D topology and cell proliferation. The possibility to manipulate particles in an aqueous solution in order to produce composite material scaffolds with different biological properties selectively localized in space is another advantage of MPL.[223]

Recent reviews by Raimondi *et al.*,[224] Ovsianikov *et al.*,[225] and Selimis *et al.*[104] describe in great detail the use of lasers in tissue engineering applications. In this field, most groups have used permanent scaffolds for hard tissue engineering or investigating cell (including stem cell) growth.[148,161,226–237] More recently, there has been a lot of active research into

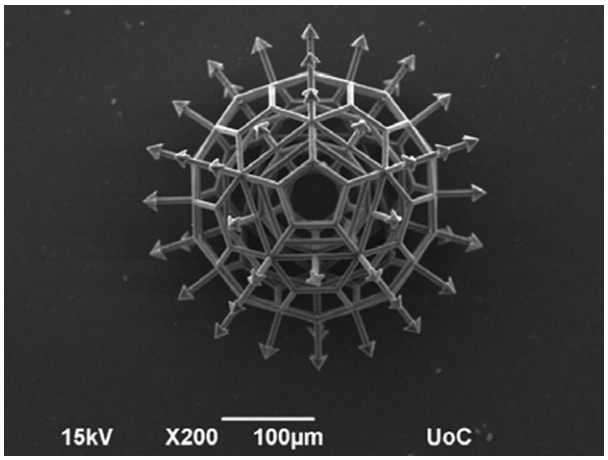


Figure 17 A freestanding micro-scaffold.[227]

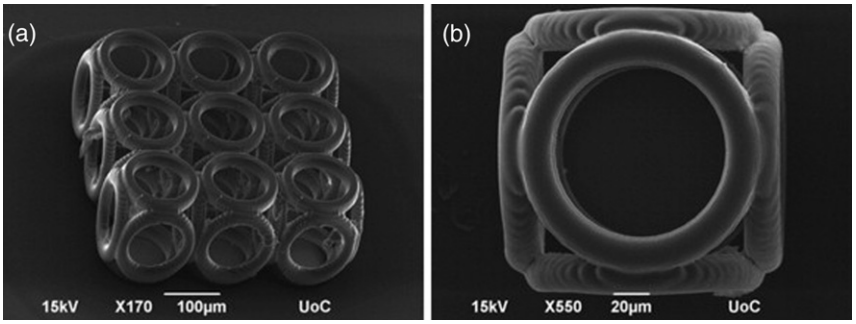


Figure 16 SEM pictures of a 3D artificial scaffolds. (a) A cubic porous scaffold consisting of horizontal and vertical ring structures in 170-fold magnification and (b) a scaffold cell unit in 550-fold magnification.[226]

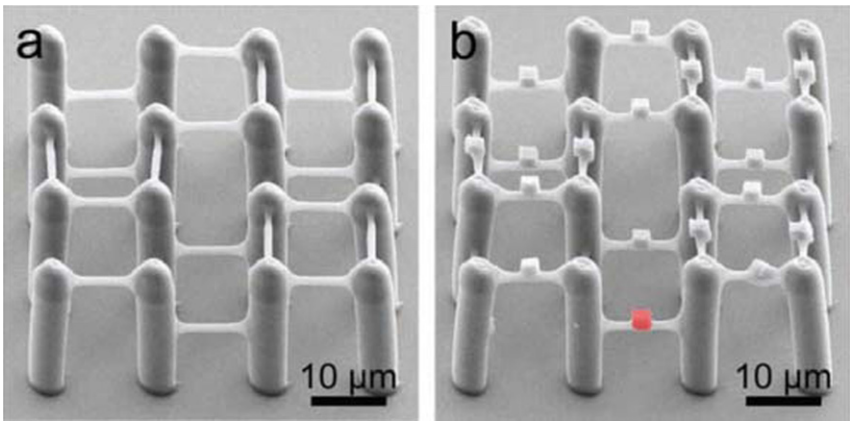


Figure 18 Scanning electron microscopy images illustrating the fabrication of 3D composite polymer scaffolds by sequential MPL. (a) In a first step, 3D frameworks consisting of protein-repellent PEG-DA with 4.8% PETA are polymerized and developed. (b) Frameworks are then cast with Ormocomp and cubes (one cube is highlighted in red) are precisely attached to the PEG-DA beams in a second MPL step.[228]

the synthesis of new, biocompatible and biodegradable materials.[132,238,239]

3.8.5 Laser-Based Surface Texturing Techniques

In general, the assortment of the laser materials processing comprises cutting, drilling, welding, surface hardening, alloying, cladding, rapid prototyping, laser-assisted forming, ablation, and shot peening. In our days, the available laser units can deliver beam with wavelength ranging from the UV to the infrared (IR) spectral region owning continuous or pulsed power density – the laser power may extend from low values (~mW) to extremely high ones as 1–100 W – exhibiting not only both spatial and temporal coherence but low divergence as well.[240,241] Upon the laser materials processing, a portion of an either pulsed or continuous wave laser beam – which incidents on the material surface – is absorbed, while the greater one is reflected. The absorbed photon energy may lead to excitation of valence and/or conduction band electrons, excited electron–phonon interaction within 10^{-11}–10^{-12} s, electron–electron or electron–plasma interaction and electron–hole recombination in a 10^{-9}–10^{-10} s timescale.[242,243] That is to say, extreme heating and cooling rates (typically 10^{3}–10^{10} K s^{-1}) are achieved within the laser-treated region and, most importantly, besides the high total deposited energy density (10^{3}–10^{4} J cm^{-2}), the bulk material temperature is not significantly affected[242,244,245] allowing, thus, the high controlled and precise processing of the material. In any case, toward the achievement of the desired and effective degree of heating and phase transition for the laser surface-processing gamut, the amount of the deposited laser energy density as well as the laser pulse duration should accordingly be picked out. The laser surface processing can be accomplished, *grosso modo*, either without melting (hardening, bending) requiring low power density, with melting (cladding, welding, cutting) necessitating high power density, or, with vaporization (cutting, drilling, ablation) calling for significantly high power density being deposited at ultrashort pulse duration.

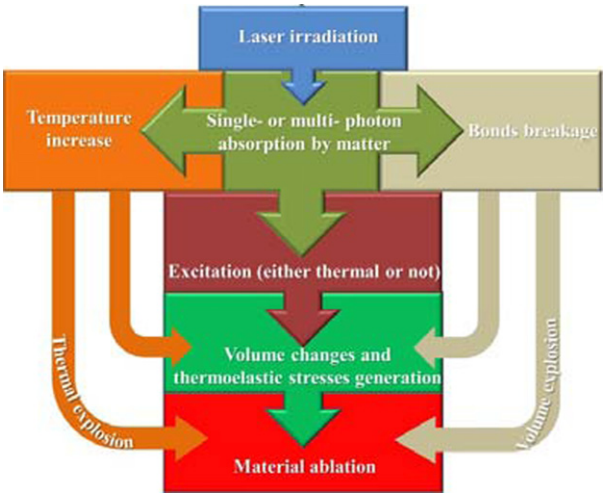


Figure 19 Spectrum of laser-matter interactions leading to material ablation.

In the present section, we shall focus on techniques aiming to the surface roughness modification relying indicatively on laser ablation and laser texturing. The tailoring of surface roughness and topography is very promising for a plethora of applications and the various results found at the literature for metals, ceramics, glasses, and polymers are presented. In general, the formation mechanism(s) underlying the laser-induced topographies remain under study because of the laser machining (LM) process complexity. They are interpreted in terms of material laser ablation (**Figure 19**) based on physical models of molecular dynamic simulations,[246–248] but they do not account for the poorly understood laser-generated effects of plasma plume formation and expansion, oxide formation, optical property changes, nanoparticle shielding, incubation, self-organization as well as for the medium in which the laser processing takes place.[249]

Recently, a detailed theoretical approach concerning the development of various types of self-assembled morphologies, ranging from nano-ripples to periodic microgrooves and quasi-periodic micro-spikes has been reported.[250]

For more than 20 years, laser surface texturing (LST) has proven an efficient and controllable method for producing the texture of micropores on magnetic disk drives[251] and ceramics.[252] LST is, nowadays, an efficient and clean to the environment technique which enables the precise shape and dimension control of induced micro-patterns. It is considered to be the most precocious technique for polymer, metal, ceramic, glass, and semiconductor surface engineering toward the control of wettability,[253–261] the color marking for counterfeit protection,[262,263] the control and improvement of wear resistance and friction coefficient in tribological contact,[264–268] biomimetic,[269–272] and microfluidics[273–275] purposes. LST, relying on material ablation, induces a regular array of a great number of micro-dimples on a surface which meets many challenges in various lubricated applications by friction reduction in conformal lubricated contacts.[273] Indeed, these dimples serve either as traps for wear debris, as reservoir for lubricant under starved lubrication, or, they may enhance the hydrodynamic lubrication mechanism.[274] There have been performed many theoretical and experimental studies concerning the LST contribution to increase the surface adhesion for bonding[275] and to the tribological performance of: (1) lubricating sliding contacts pinpointing at first place the fluid film lubrication – e.g., oil, water, aqueous bovine serum albumin solution[264,265,274,276–286] but, the solid film lubrication[287,288] and, the dry one[289,290] as well, (2) reciprocating automotive components,[291,292] and (3) diamond-like carbon coatings.[293,294] The UV lasers, offering the advantage of reduced surrounding surface overheating over the IR ones, they have been adopted in the surface topography modification of ceramic and hard coatings.[295,296] In advance, LST has also been applied in the fiber laser microgrooves and micro-holes fabrication on the surface of polycrystalline diamond tools,[297] in the tribological properties improvement of Al_2O_3/Mo laminated composites at room and high temperatures,[298] of gray cast iron,[299] of titanium alloy combined with diamond-like carbon films coating technology[300] and of hard TiAlSiN coatings combined with high-energy ion implantation.[301]

Besides the many advantages that LST offers, such as non-contact, good flexibility, and high spatial resolution, its broader application is hindered due to the residual stress and the shrinkage cavity generated by thermal effects during LST process. A surface treatment process for improving several mechanical properties, for example, fatigue, durability, corrosion resistance, and wear performance, of metals is the laser shock peening (LSP) one.[302] It is a cold machining process which relies on the laser-generated shock waves able to induce severe plastic deformation of materials surface: a section of the material to be peened is paint coated and a thin film of water runs over the surface, while, a laser beam passes through the water layer being focused onto a particular target location causing the paint layer to vaporize into plasma.[303] Upon plasma expansion, high pressure (GPa-TPa), short duration (ns), shock waves propagate into the water layer, which confines the energy and increases the pressure pulse intensity within the base material under texturing (**Figure 20**).

It is the amplitude of the laser-induced shock waves that causes the plastic deformation at the surface.[304–306] LSP has been proposed for the fabrication of micro-dimple arrays on copper surface[307] and, it can be applied as a post-processing method for the improvement of surface layers mechanical properties since it induces a compressive residual stress within a depth of more than 1 mm. LSP subsequently to LST has been applied in the case of bionic non-smooth 0Cr18Ni9 stainless steel surfaces fabrication[308] and the effects of LSP and groove spacing on the their wear behavior have been investigated.[302]

The range and variety of the laser-induced microstructures on the surfaces of titanium, stainless steel, aluminum, molybdenum, and copper substrates comprise holes,[253,309–313] bumps or spikes,[254,270,309,314–321] bulges,[322] undulating grooves,[323–325] dimples,[322,326,327] honeycombs,[328] linked nanostructure-textured mound-shaped microstructures,[329] melt-like[312,330] and

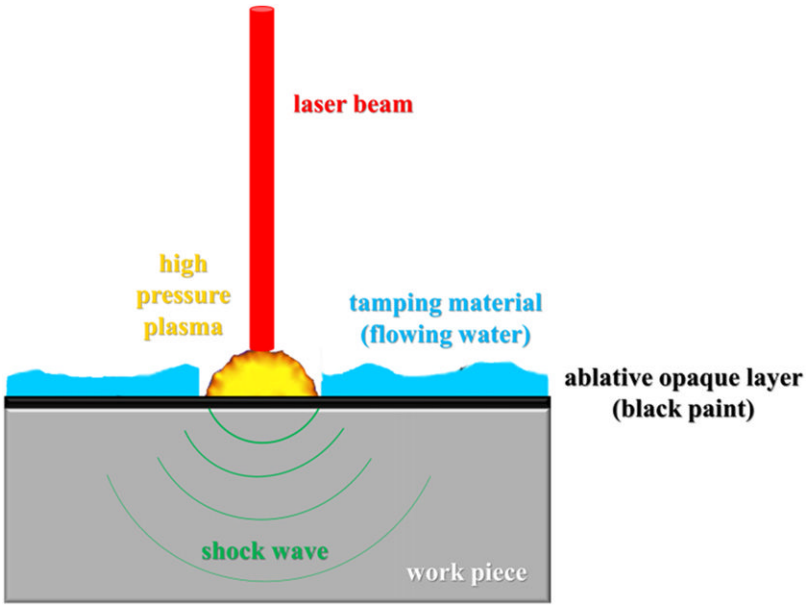


Figure 20 Laser shock peening principle.

cauliflower-like[331] structures. In addition, the formation of laser-induced periodic surface structures, nano-pillars, and micro-columns has also been reported.[332] Other than that, there has been observed the formation of nano-ripples on TiO_2 surface following UV femtosecond laser irradiation,[333] the fs laser nanostructuring of nitrided alloy steels containing Cr,[334] the LST of plasma electrolytically oxidized aluminum 6061 alloy for improved hydrophobicity[335] and the IR fs laser nano- and micro-texturing of a stainless steel surface combined with chemisorption of an hydrophobic agent.[336] In general, the optimization of the laser settings toward a desired surface texture consists a tediously long procedure given the large breadth of the experimental parameters space:[249] laser fluence value, number of applied laser pulses, pulse duration, repetition rate, scanning speed, and number of scans – varying, at the same time, from metal to metal.[337]

In several applications (cutting tools, wearing parts, heat engines, medical implants, construction) for which exceptional physical and mechanical properties are required – such as high hardness, advanced thermal resistance, and chemical stability – the ceramics have established a strong foothold.[338,339] LM has proven a promising tool for their texturing, especially if one takes into account the fact that conventional techniques can hardly face the issue of their machining due to the brittle and hard nature the ceramic materials exhibit.[339–341] There are mainly three ceramic LM techniques: the laser-assisted chemical etching, the LM and the laser-assisted machining (LAM) one.[339,342] In any case, the challenge in the laser micromachining of ceramics lies in the great scattering of common laser wavelengths from their surface restricting, thus, the localized energy absorption.[343]

According to the laser-assisted chemical etching, laser radiation excites the material surface and/or the molecules of an employed appropriate etchant acting, thus, upon the reaction between the material and the etchant. In such a way, the etching rate is mostly affected by the laser fluence value.[344,345]

In LM, the absorbed high-energy density of the incident laser photons causes the breakage of the chemical bonds leading to the material ejection from the irradiated area inducing grooves formation on the ceramic surface.[346,347] The mechanism underlying the material removal deals with material melting, decomposition, and evaporation. The crucial parameter for the process effectiveness employs different properties of the ceramic under treatment each time, such as, reflectivity – especially the multiple reflections in the laser-induced grooves[348] thermal conductivity, specific heat, and latent heats of melting and evaporation.[339,349–351] Alumina owing excellent dielectric strength, thermal stability, and conductivity[352] has been laser textured by CO_2 laser,[353–356] YAG lasers,[357–360] copper vapor laser,[343] KrF laser,[357,361] and near infrared[352] femtosecond laser. In addition, alumina has been laser machined in three dimensions (3D) by 3D laser carving; an industrial technique for ceramic manufacturing of complex shapes based on 3D CAD model slices[362] and by the laser milling technique.[363] In advance, it has been proposed, that, after a focused laser beam scribes two groove-cracks at two intersecting surfaces of a rectangular alumina substrate, a defocused one is applied throughout the length of the groove-cracks, generating, thus, great thermal stress leading to the two groove-cracks link together, requiring much lower energy power compared to the conventional LM technique.[364,365] Several research publications[366,367] report on the use of two laser beams for laser alumina texturing toward the fracture control upon the procedure. Recently, a new methodology has been mentioned for the fabrication of complex-shaped Al_2O_3 ceramic parts by combining LM and gelcasting technique.[368] According to this technique, the unwanted ceramic powders parts are selectively removed by LM specified by a computer program, and the gelcast Al_2O_3 green bodies were machined to a designed shape by a CO_2 laser. Bearings, rocker arms, piston rings, and cams can be made by LM of silicon nitride for automotive, semiconductor, and aerospace industries purposes. CO_2 laser in air[369–371] or under N_2, O_2 gas atmospheres,[372] Nd:YAG laser[373] and excimer laser systems[374] have been employed in the LM of silicon nitride aiming to the micro-cracks minimization. 3D structuring of silicon nitride by employing a relatively new machining process, namely, the laser milling technique relying on CAD data has also been reported,[375] based on an ablation operation leading to the material removal in a layer-by-layer fashion. Another broadly laser-machined ceramic is the silicon carbide. It has been treated by CO_2 laser [70,376,377] in air[373,378,379] or in N_2, O_2 gas atmosphere[372] by Nd:YAG laser[360,378–381] and by KrF laser beam[361] leading to the fabrication of controlled wettability textures.[382,383] The high thermal conductivity and small thermal expansion mismatch with silicon of aluminum nitride justify its widely use in microelectronic substrates and packages[384] and has been laser machined with near-IR and excimer lasers.[359,384,385] The fabrication of pH meters, fuel cells, IR radiators, pressure, and oxygen sensors employs the use of zirconia due to is unique characteristics: low thermal conductivity and friction coefficient, high fracture toughness, and good thermal shock resistance.[386] As the previously mentioned ceramics, it has been textured with Nd:YAG laser,[349,379] CO_2 laser,[370,387] and porous structures are induced upon its XeF laser[377] treatment.[74] LM of blind holes in glass-ceramic sheets have also been applied for inclusion of thermal sensors in the substrate and for fastening the glass-ceramic to other ceramic or metallic components.[388] The LM has also been applied to Al_2O_3–34 wt.% TiC -the induced textured ceramic can be used for high precision parts, such as magnetic head sliders[389,390] and to Si_3N_4/TiC ceramic for wavy grooves fabrication[391] using Nd:YAG laser.[392] As far as it concerns the recent developments in laser texturing of ceramics, there has been reported the formation of alumina precise micro-channels with surface micro-patterns[393] by using LM, imprinting, and a technique of interposing laser-formed sacrificial heat-removable sheets in between ceramic sheets; these features can be used under conditions where chemical and heat resistances are necessary.[394] In addition, it has been mentioned, that, when cutting hard-brittle ceramic biomaterials to prepare scaffold and implant, or, when sectioning them for porosity evaluation, it is better to choose KrF excimer LM.[395]

Unlike LM, in LAM the material removal occurs with no melting of the ceramic, but instead, with a conventional tool following the localized heating of the ceramic by the laser beam. The laser beam deforms the brittle behavior of the ceramic to a ductile one.[339,391] This technique has been applied for the laser texturing of silicon nitride,[391,393,396–403] zirconia,[404,405] magnesia-partially-stabilized zirconia,[406] Al_2O_3,[407–409] and

Inconel 718[410] with carbide and ceramic inserts. A recent publication[411] offers a comparison of LAM technique with conventional machining methods as well as the recent developments in the field.[412]

It seems that laser texturing of ceramics meets the increasing demand for the fabrication of parts owing microscale features for semiconductor, biomedical devices, and optics applications.[413] The rapid, noncontact, and highly flexible nature of the laser process leads to the accurate dimensional design of micro-featured products,[414] for example, of kerfs with depth and width smaller than 100 μm,[339] ensuring the employment of ceramics LM in a great variety of tremendous applications. The Nd:YAG lasers are broadly used compared to the CO_2 ones due to their high-energy density and small focused spot size.[341] However, in most cases, it is a combination of short pulse duration and short wavelength that guarantees best results in many ceramics, with no evidence of melting.[343] New innovations such as short pulsed or femtosecond lasers have drastically decreased the amount of unwanted damage associated with LM.[411] In any case, the conditions of the ceramics laser processing to be selected depend strongly on the material properties and the released constituents upon texturing in order the safety and health requirements to be fulfilled.

Other than that, surface structures can be produced traditionally using lithography with photoresist coating, exposure, and transfer processes[415] or printing, molding, and embossing methods.[416,417] Mask-less laser interference lithography (LIL) enables the large-area periodic structuring with simple equipment.[418,419] This technique relies on the interference of coherent light beams to form a horizontal standing wave for a grating pattern able to be recorded on a photoresist. The period of the structures depends on the laser wavelength and the angle(s)[420] between the -two or more[420–426] incident beams intersection, whereas the laser fluence,[427] the polarization[424,427] as well as the exposure time[428] strongly influence the procedure. By 90° rotation of the sample, and a second exposure, the grid pattern on the photoresist can be defined.[419] LIL has been applied in: the preparation of large-area, long-range ordered ZnO[429,430] and Si[431] nanowires arrays, the micro-lens array fabrication for super-resolution surface nanopatterning,[432] the production of magnetic nano-dot arrays[433,434] and AlGaAs microdisks,[435] the nanostructures fabrication for surface plasmon resonance tuning by gold and silver bimetallic dot arrays,[436] the GaAs solar cells improved efficiency by the induced nanopatterning,[437] and the Cr, Co, Ni, and Ge high-density dot arrays fabrication.[438] One should also mention that there have been textured sixfold symmetry structures on a two-dimensional polymer (SU-8),[439] periodic grating structures on poly(methyl-methacrylate) by soft X-ray laser beam,[440] and nanostructured holes of hexagonal symmetry on tungsten oxide surfaces,[441] via LIL.

LIL on photoresist or as photofluidization lithography has emerged as a technology capable to fabricate templates by irradiating an azo-polymer or a photoresist with interference patterns obtained by using two or more coherent – typically UV – laser beams, mostly operating in continuous wave mode.[442–444] In addition, the LIL-induced nano-patterning structure, following the pattern transfer, can be used in: optical devices,[445] surface plasmon resonance sensors,[446,447] metamaterials,[448] electrodes for cross-bar electronic devices like memories as well as transparent electrodes for light-emitting-diodes and photovoltaic cells,[449] large-area broadband photonic crystal membrane reflectors on glass substrates,[450] biomimetics,[451] micro-sieves for micro-filtration,[452–454] template for self-assembly,[455] field emission panel displays,[456] large-area photonic crystal slabs for visible light,[457] and micro- and nano- fluidics.[458,459] The potential of the LIL technique wider employment in industry has also been mentioned.[460]

Alternatively, the direct laser interference patterning (DLIP) technique enables a scalable process for polymer substrates structuring by direct substrate material ablation, requiring only a single processing step without solvents or heating.[461–463] In DLIP, similarly to LIL, two or more coherent laser beams are brought to interference with each other on a substrate and different one- and two-dimensional periodic patterns are induced by direct ablation of the substrate – with spatial periods ranging from some hundreds nanometers up to several micrometers – in the absence of any masks or templates. The produced patterns are attributed to the periodic light intensity variation and the high light absorption by the material.[464]

Silicon rewards a special dedication since it is an important semiconductor material with numerous applications of broad range, and has erstwhile till recently been laser surface textured for microelectronics, solar cells, or biomedical purposes.[465–472] In general, micro-, submicro-, and nano-periodic patterns[473] (e.g., grooves, pits, spikes) are induced on the Si surface depending on the laser irradiation parameters, the irradiation gas atmosphere or environment[474] affecting the melt material distribution following ablation. In advance, near-field enhanced laser irradiation with micro-nano-sized spheres[475,476] and near-field scanning optical microscope[477,478] have been used. On the contrary, a non-ablative laser surface structuring technique to form a regular array of micro-bumps on Si surface by a 1090 nm continuous wave fiber laser has been proposed,[479] besides the high transparency that Si exhibits at this wavelength. The non-ablative laser-induced micro-bumps formation was attributed to localized Si oxidation.[480] Recently, there has been reported that upon 1064 nm picosecond laser irradiation of Si, micro-nano hierarchical pore structures are formed on its surface, which are subsequently precisely chemically etched and, finally, light-trapping structures are fabricated.[481] LIL has also been applied for the fabrication of two-dimensional photonic crystals in silicon-on-insulator wafers[482] and for Si texturing with thoroughly investigated wetting properties of the induced periodical nano-patterns and hierarchical structures.[483] More recently, there has been reported the case of moth-like[422] as well as of grating, triangle, and square[423] surface structures induced on silicon by multi-beam LIL. Concerning the solar cells applications, sub-micrometer conical and pillar-shaped spikes have been fabricated by irradiating hydrogenated amorphous silicon thin films deposited on glass substrates with hundreds of 800 nm-wavelength, 130 fs-duration laser pulses in air and water environments, respectively.[484] Lately, there has been reported the laser-induced formation of 300 nm period pore arrays on Si combined with electrochemical etching.[485]

Concerning the LST of polymers, a key parameter of the procedure is the polymer molecular weight.[486–489] Low molecular weight polymers with short polymer chains are volatile, whereas, the longer ones of the high molecular weight

polymers melt. In this case, the material removal is due to evaporation from the polymer substrate – upon an explosive boiling procedure – in an ablation plume full of molecular fragments, ions, free electrons, neutral particles, and products from the chemical reactions between the plume components and the irradiation atmosphere. Among the laser textured polymers, poly(methyl-methacrylate) (PMMA) has received the lion's share of the universal applied research interest,[258,486,489–501] for example, for microfluidic devices fabrication, by using mainly UV laser radiation. However, from an application point of view, the thermal damage minimization of the surrounding (the laser irradiated area) material is crucial since it deteriorates both the spatial resolution and the ablation quality.[502] Consequently, the photochemical processes which lead to the so called 'cold' ablation are most preferable. In general, the energy of the UV lasers photons is high enough to induce the direct bond breakage in a strongly absorbing at the irradiation wavelength organic material. It is of great importance the fact that the bulk properties of the laser textured polymers remain intact and, thus, they can be employed in bioengineering applications since the microscale topography may influence several properties, such as wetting properties[260,503] and cell behavior.[504–508]

At the end, it is worth mentioning the recent laser texturing developments at the sake of tissue engineering applications, since they prove the potential spreading of the technique in this rapidly growing interdisciplinary field: the micro-channels on medical needles,[509] the osteoblastic commitment improvement of human mesenchymal stem cells on Ti alloys,[510] the neuronal cells cultivation on Si spikes[470] the fibroblasts cell culture on laser-made chitosan scaffolds[511] and the osteoblast proliferation and morphology on metallic alloys.[512]

3.8.6 Conclusions

This chapter has attempted to cover the laser-based 3D printing and surface texturing techniques which meet the ever increasing challenges and demands of either existing or emerging scientific fields. The superior precision and reproduction, the high working speed, the wide bandwidth of possible materials, and the exceptional degree of flexibility justify the laser fabrication techniques employment in a smorgasbord of human life domains in the industrialized countries: manufacturing, communication, military aspects, health technologies, metrology, reprography, and entertainment. The laser versatility in the ability to create structures of any desired dimension and geometry guarantees the progress of future structuring procedures. Yet, there is a long trail behind the Holy Grail of laser processing capabilities: the controllable fabrication at nanometer scale, which will provide a broad range of technical opportunities with frame and limits left to human imagination.

References

1. Hull, C. W. Apparatus for Production of Three-Dimensional Objects by Stereolithography. U.S. Patent 4,575,330, 1986.
2. 3D SYSTEMS Home Page. Available from: http://www.3dsystems.com (accessed 10 September 2015).
3. Jacobs, P. F. *Rapid Prototyping and Manufacturing: Fundamentals of Stereolithography*; The Society of Manufacturing Engineers (SME): Dearborn, MI, 1992.
4. Mammoth Stereolithography Home Page. Available from: http://manufacturing.materialise.com/mammoth-stereolithography (accessed 10 September 2015).
5. Chang, P. S. H.; Parker, T. H.; Patrick, C. W.; Miller, M. J. The Accuracy of Stereolithography in Planning Craniofacial Bone Replacement. *J. Craniofac. Surg.* **2003**, *14*, 164–170.
6. Kermer, C.; Rasse, M.; Lagogiannis, M.; Undt, G.; Wagner, A.; Millesi, W. Colour Stereolithography for Planning Complex Maxillofacial Tumour Surgery. *J. Craniomaxillofac. Surg.* **1998**, *26*, 360–362.
7. Chu, T. M. G.; Halloran, J. W.; Hollister, S. J.; Feinberg, S. E. Hydroxyapatite Implants with Designed Internal Architecture. *J. Mater. Sci.: Mater. Med.* **2001**, *12*, 471–478.
8. Fisher, J. P.; Vehof, J. W. M.; Dean, D.; *et al.* Soft and Hard Tissue Response to Photocrosslinked Poly(propylene Fumarate) Scaffolds in a Rabbit Model. *J. Biomed. Mater. Res., Part A* **2002**, *59*, 547–556.
9. Hollister, S. J. Porous Scaffold Design for Tissue Engineering. *Nat. Mater.* **2005**, *22*, 354–362.
10. Hutmatcher, D. W.; Sittinger, M.; Risbud, M. V. Scaffold-Based Tissue Engineering: Rationale for Computer-Aided Design and Solid Free-Form Fabrication Systems. *Trends Biotechnol.* **2004**, *22*, 354–362.
11. Berry, E.; Brown, J. M.; Connell, M.; *et al.* Preliminary Experience with Medical Applications of Rapid Prototyping by Selective Laser Sintering. *Med. Eng. Phys.* **1997**, *19*, 90–96.
12. Chung, H.; Das, S. Processing and Properties of Glass Bead Particulate-Filled Functionally Graded Nylon-11 Composites Produced by Selective Laser Sintering. *Mat. Sci. Eng. A-Stuct.* **2006**, *437*, 226–234.
13. Kim, J.; Creasy, T. S. Selective Laser Sintering Characteristics of Nylon 6/Clay-Reinforced Nanocomposite. *Polym. Test.* **2004**, *23*, 629–636.
14. Yan, C.; Shi, Y.; Yang, J.; Liu, J. Preparation and Selective Laser Sintering of Nylon-12 Coated Metal Powders and Post Processing. *J. Mater. Process. Technol.* **2009**, *209*, 5785–5792.
15. Yan, C.; Shi, Y.; Yang, J.; Liu, J. Multiphase Polymeric Materials for Rapid Prototyping and Tooling Technologies and Their Applications. *Compos. Interface.* **2010**, *17*, 257–271.
16. Yan, C. Z.; Shi, Y. S.; Yang, J. S.; Liu, J. H. Preparation and Selective Laser Sintering of Nylon-Coated Metal Powders for the Indirect SLS Process. *Rapid Prototyping J.* **2009**, *15*, 355–360.
17. Zarringhalam, H.; Hopkinson, N.; Kamperman, N. F.; de Vlieger, J. J. Effects of Processing on Microstructure and Properties of SLS Nylon 12. *Mat. Sci. Eng. A-Stuct.* **2006**, *435*, 172–180.
18. Leite, J. L.; Salmoria, G. V.; Paggi, R. A.; Ahrens, C. H.; Pouzada, A. S. A Study on Morphological Properties of Laser Sintered Functionally Graded Blends of Amorphous Thermoplastics. *Int. J. Mater. Prod. Tec.* **2010**, *39*, 205–221.
19. Schmidt, M.; Pohle, D.; Rechtenwald, T. Selective Laser Sintering of PEEK. *Cirp. Ann. Manuf. Techn.* **2007**, *56*, 205–208.
20. Shi, Y.; Wang, Y.; Chen, J.; Huang, S. Experimental Investigation into the Selective Laser Sintering of High-Impact Polystyrene. *J. Appl. Polym. Sci.* **2008**, *108*, 535–540.
21. Shi, Y. S.; Li, Z. C.; Sun, H. X.; Huang, S. H.; Zeng, F. D. Development of a Polymer Alloy of Polystyrene (PS) and Polyamide (PA) for Building Functional Part Based on Selective Laser Sintering (SLS). *Proc. Inst. Mech. Eng. L J. Mater. Des. Appl.* **2004**, *218*, 299–306.
22. Soe, S. P. Improving Dimensional Accuracy in the Production of a CastForm (TM) Polystyrene Pattern for Investment Casting. *Proc. Inst. Mech. Eng., B J. Eng. Manuf.* **2010**, *224*, 1663–1670.
23. Soe, S. P.; Eyers, D. R. FEA Support Structure Generation for the Additive Manufacture of CastForm (TM) Polystyrene Patterns. *Polym. Test.* **2014**, *33*, 187–197.
24. Xu, Z. F.; Zhang, J.; Zheng, H. Z.; Cai, C. C.; Huang, Y. H. Morphology and Mechanical Properties of PS/Al_2O_3 Nanocomposites Based on Selective Laser Sintering. *J. Mater. Sci. Technol. (Shenyang, China)* **2005**, *21*, 866–870.
25. Yan, C.; Shi, Y.; Yang, J.; Liu, J. Investigation into the Selective Laser Sintering of Styrene-Acrylonitrile Copolymer and Postprocessing. *Int. J. Adv. Manuf. Technol.* **2010**, *51*, 973–982.
26. Zheng, H. Z.; Zhang, J.; Lu, S. Q.; Wang, G. C.; Xu, Z. F. Effect of Core-Shell Composite Particles on the Sintering Behavior and Properties of Nano-Al_2O_3/Polystyrene Composite Prepared by SLS. *Mater. Lett.* **2006**, *60*, 1219–1223.

27. Das, S.; Wolhert, M.; Beaman, J. J.; Bourell, D. L. Processing of Titanium Net Shapes by SLS HIP. *Mater. Des.* **1999**, *20*, 115–121.
28. Engel, B.; Bourell, D. L. Titanium Alloy Powder Preparation for Selective Laser Sintering. *Rapid Prototyping J.* **2000**, *6*, 97–106.
29. Fischer, P.; Romano, V.; Blatter, A.; Weber, H. P. Highly Precise Pulsed Selective Laser Sintering of Metallic Powders. *Laser Phys. Lett.* **2005**, *2*, 48–55.
30. Hayashi, T.; Maekawa, K.; Tamura, M.; Hanyu, K. Selective Laser Sintering Method Using Titanium Powder Sheet Toward Fabrication of Porous Bone Substitutes. *JSME Int. J. A Solid M.* **2005**, *48*, 369–375.
31. Tolochko, N. K.; Savich, V. V.; Laoui, T.; *et al.* Dental Root Implants Produced by the Combined Selective Laser Sintering/Melting of Titanium Powders. *Proc. Inst. Mech. Eng. L J. Mater. Des. Appl.* **2002**, *216*, 267–270.
32. Shishkovsky, I. V.; Volova, L. T.; Kuznetsov, M. V.; Morozov, Y. G.; Parkin, I. P. Porous Biocompatible Implants and Tissue Scaffolds Synthesized by Selective Laser Sintering from Ti and NiTi. *J. Mater. Chem.* **2008**, *18*, 1309–1317.
33. Shishkovsky, I. V.; Yadroitsev, I. A.; Smurov, I. Y. Manufacturing Three-Dimensional Nickel Titanium Articles Using Layer-by-Layer Laser-Melting Technology. *Tech. Phys. Lett.* **2013**, *39*, 1081–1084.
34. Traini, T.; Mangano, C.; Sammons, R. L.; Mangano, F.; Macchi, A.; Piatelli, A. Direct Laser Metal Sintering as a New Approach to Fabrication of an Isoelastic Functionally Graded Material for Manufacture of Porous Titanium Dental Implants. *Dent. Mater.* **2008**, *24*, 1525–1533.
35. Williams, J. V.; Revington, P. J. Novel Use of an Aerospace Selective Laser Sintering Machine for Rapid Prototyping of an Orbital Blowout Fracture. *Int. J. Oral Maxillofac. Surg.* **2010**, *39*, 182–184.
36. Chatterjee, A. N.; Kumar, S.; Saha, P.; Mishra, P. K.; Choudhury, A. R. An Experimental Design Approach to Selective Laser Sintering of Low Carbon Steel. *J. Mater. Process. Technol.* **2003**, *136*, 151–157.
37. Childs, T. H. C.; Hauser, C.; Badrossamay, M. Selective Laser Sintering (Melting) of Stainless and Tool Steel Powders: Experiments and Modelling. *Proc. Inst. Mech. Eng., B J. Eng. Manuf.* **2009**, *219*, 339–357.
38. Dewidar, M. M.; Dalgarno, K. W.; Wright, C. S. Processing Conditions and Mechanical Properties of High-Speed Steel Parts Fabricated Using Direct Selective Laser Sintering. *Proc. Inst. Mech. Eng., B J. Eng. Manuf.* **2003**, *217*, 1651–1663.
39. Dewidar, M. M.; Khalil, K. A.; Lim, J. K. Processing and Mechanical Properties of Porous 316L Stainless Steel for Biomedical Applications. *Trans. Nonferrous Met. Soc. China* **2007**, *17*, 468–473.
40. Morgan, R.; Sutcliffe, C. J.; O'Neill, W. Density Analysis of Direct Metal Laser Re-Melted 316L Stainless Steel Cubic Primitives. *J. Mater. Sci.* **2004**, *39*, 1195–1205.
41. Murali, K.; Chatterjee, A. N.; Saha, P.; *et al.* Direct Selective Laser Sintering of Iron-Graphite Powder Mixture. *J. Mater. Process. Technol.* **2003**, *136*, 179–185.
42. Niu, H. J.; Chang, I. T. H. Instability of Scan Tracks of Selective Laser Sintering of High Speed Steel Powders. *Scr. Mater.* **1999**, *41*, 1129–1234.
43. Niu, H. J.; Chang, I. T. H. Selective Laser Sintering of Gas and Water Atomized High Speed Steel Powders. *Scr. Mater.* **1999**, *41*, 25–30.
44. Niu, H. J.; Chang, I. T. H. Selective Laser Sintering of Gas Atomized M2 High Speed Steel Powder. *J. Mater. Sci.* **2000**, *35*, 31–38.
45. Agarwala, M.; Bourell, D.; Beaman, J.; Marcus, H.; Barlow, J. Direct Selective Laser Sintering of Metals. *Rapid Prototyping J.* **1995**, *1*, 26–36.
46. Hunt, J. A.; Callaghan, J. T.; Sutcliffe, C. J.; Morgan, R. H.; Halford, B.; Black, R. A. The Design and Production of Co–Cr Alloy Implants with Controlled Surface Topography by CAD-CAM Method and Their Effects on Osseointegration. *Biomaterials* **2005**, *26*, 5890–5897.
47. Ju, Y.-W.; Eto, H.; Inagaki, T.; Ida, S.; Ishihara, T. Preparation of Ni–Fe Bimetallic Porous Anode Support for Solid Oxide Fuel Cells Using $LaGaO_3$ Based Electrolyte Film with High Power Density. *J. Power Sources* **2010**, *195*, 6294–6300.
48. Tolochko, N.; Mozzharov, S.; Laoui, T.; Froyen, L. Selective Laser Sintering of Single- and Two-Component Metal Powders. *Rapid Prototyping J.* **2003**, *9*, 68–78.
49. Zhang, J.; Shi, Y. S.; Liu, J. H.; Chen, K. H.; Huang, S. H. Investigation into Manufacturing Fe–Cu–C Alloy Parts through Indirect Selective Laser Sintering. *Mater. Sci. Technol.* **2007**, *23*, 333–337.
50. Chua, C. K.; Leong, K. F.; Tan, K. H.; Wiria, F. E.; Cheah, C. M. Development of Tissue Scaffolds Using Selective Laser Sintering of Polyvinyl Alcohol/Hydroxyapatite Biocomposite for Craniofacial and Joint Defects. *J. Mater. Sci.: Mater. Med.* **2004**, *15*, 1113–1121.
51. Duan, B.; Wang, M.; Zhou, W. Y.; Cheung, W. L. Synthesis of Ca–P Nanoparticles and Fabrication of Ca–P/PHBV Nanocomposite Microspheres for Bone Tissue Engineering Applications. *Appl. Surf. Sci.* **2008**, *255*, 529–533.
52. Dyson, J. A.; Genever, P. G.; Dalgarno, K. W.; Wood, D. J. Development of Custom-Built Bone Scaffolds Using Mesenchymal Stem Cells and Apatite–Wollastonite Glass-Ceramics. *Tissue Eng.* **2007**, *13*, 2891–2901.
53. Hao, L.; Salvalani, M. M.; Zhang, Y.; Tanner, K. E.; Harris, R. A. Effects of Material Morphology and Processing Conditions on the Characteristics of Hydroxyapatite and High-Density Polyethylene Biocomposites by Selective Laser Sintering. *Proc. Inst. Mech. Eng. L J. Mater. Des. Appl.* **2006**, *220*, 125–137.
54. Hao, L.; Salvalani, M. M.; Zhang, Y.; Tanner, K. E.; Harris, R. A. Selective Laser Sintering of Hydroxyapatite Reinforced Polyethylene Composites for Bioactive Implants and Tissue Scaffold Development. *Proc. Inst. Mech. Eng. H J. Eng. Med.* **2006**, *220*, 521–531.
55. Kanczler, J. M.; Mirmalek-Sani, S. H.; Hanley, N. A.; *et al.* Biocompatibility and Osteogenic Potential of Human Fetal Femur-Derived Cells on Surface Selective Laser Sintered Scaffolds. *Acta Biomater.* **2009**, *5*, 2063–2071.
56. Lorrison, J. C.; Dalgarno, K. W.; Wood, D. J. Processing of an Apatite–Mullite Glass-Ceramic and an Hydroxyapatite/Phosphate Glass Composite by Selective Laser Sintering. *J. Mater. Sci.: Mater. Med.* **2005**, *16*, 775–781.
57. Peltola, S. M.; Melchels, F. P. W.; Grijpma, D. W.; Kellomaki, M. A Review of Rapid Prototyping Techniques for Tissue Engineering Purposes. *Ann. Med.* **2008**, *40*, 268–280.
58. Shishkovsky, I. V.; Tarasova, E. Y.; Zhuravel, L. V.; Petrov, A. L. The Synthesis of a Biocomposite Based on Nickel Titanium and Hydroxyapatite under Selective Laser Sintering Conditions. *Tech. Phys. Lett.* **2001**, *27*, 211–213.
59. Tan, K. H.; Chua, C. K.; Leong, K. F.; *et al.* Scaffold Development Using Selective Laser Sintering of Polyetheretherketone-Hydroxyapatite Biocomposite Blends. *Biomaterials* **2003**, *24*, 3115–3123.
60. Tan, K. H.; Chua, C. K.; Leong, K. F.; *et al.* Selective Laser Sintering of Biocompatible Polymers for Applications in Tissue Engineering. *Biomed. Mater. Eng.* **2005**, *15*, 113–124.
61. Tan, K. H.; Chua, C. K.; Leong, K. F.; Naing, M. W.; Cheah, C. M. Fabrication and Characterization of Three-Dimensional Poly(ether-Ether-Ketone)/-Hydroxyapatite Biocomposite Scaffolds Using Laser Sintering. *Proc. Inst. Mech. Eng. H J. Eng. Med.* **2005**, *219*, 183–194.
62. Williams, J. M.; Adewunmi, A.; Schek, R. M.; *et al.* Bone Tissue Engineering Using Polycaprolactone Scaffolds Fabricated via Selective Laser Sintering. *Biomaterials* **2005**, *26*, 4817–4827.
63. Wiria, F. E.; Leong, K. F.; Chua, C. K.; Liu, Y. Poly-Epsilon-Caprolactone/Hydroxyapatite for Tissue Engineering Scaffold Fabrication via Selective Laser Sintering. *Acta Biomater.* **2007**, *3*, 1–12.
64. Zhang, Y.; Hao, L.; Salvalani, M. M.; Harris, R. A.; Tanner, K. E. Characterization and Dynamic Mechanical Analysis of Selective Laser Sintered Hydroxyapatite-Filled Polymeric Composites. *J. Biomed. Mater. Res., Part A* **2008**, *86A*, 607–616.
65. Zhou, W. Y.; Duan, B.; Wang, M.; Cheung, W. L. Crystallization Kinetics of Poly(L-Lactide)/Carbonated Hydroxyapatite Nanocomposite Microspheres. *J. Appl. Polym. Sci.* **2009**, *113*, 4100–4115.
66. Zhou, W. Y.; Lee, S. H.; Wang, M.; Cheung, W. L.; Ip, W. Y. Selective Laser Sintering of Porous Tissue Engineering Scaffolds from Poly(L)/Carbonated Hydroxyapatite Nanocomposite Microspheres. *J. Mater. Sci.: Mater. Med.* **2008**, *19*, 2535–2540.
67. Zhou, W. Y.; Wang, M.; Cheung, W. L.; Guo, B. C.; Jia, D. M. Synthesis of Carbonated Hydroxyapatite Nanospheres through Nanoemulsion. *J. Mater. Sci.: Mater. Med.* **2008**, *19*, 103–110.
68. Chua, C. K.; Leong, K. F.; Sudarmadji, N.; Liu, M. J. J.; Chou, S. M. Selective Laser Sintering of Functionally Graded Tissue Scaffolds. *MRS Bull.* **2011**, *36*, 1006–1014.
69. Duan, B.; Cheung, W. L.; Wang, M. Optimized Fabrication of Ca-P/PHBV Nanocomposite Scaffolds via Selective Laser Sintering for Bone Tissue Engineering. *Biofabrication* **2011**, *3*, 015001.
70. Duan, B.; Wang, M.; Zhou, W. Y.; Cheung, W. L.; Li, Z. Y.; Lu, W. W. Three-Dimensional Nanocomposite Scaffolds Fabricated via Selective Laser Sintering for Bone Tissue Engineering. *Acta Biomater.* **2010**, *6*, 4495–4505.
71. Eshraghi, S.; Das, S. Micromechanical Finite-Element Modeling and Experimental Characterization of the Compressive Mechanical Properties of Polycaprolactone-Hydroxyapatite Composite Scaffolds Prepared by Selective Laser Sintering for Bone Tissue Engineering. *Acta Biomater.* **2012**, *8*, 3138–3143.

72. Kolan, K. C. R.; Leu, M. C.; Hilmas, G. E.; Brown, R. F.; Velez, M. Fabrication of 13–93 Bioactive Glass Scaffolds for Bone Tissue Engineering Using Indirect Selective Laser Sintering. *Biofabrication* **2011**, *3*, 025004.
73. Shuai, C.; Gao, C.; Nie, Y.; Hu, H.; Qu, H.; Peng, S. Structural Design and Experimental Analysis of a Selective Laser Sintering System with Nano-Hydroxyapatite Powder. *J. Biomed. Nanotechnol.* **2010**, *6*, 370–374.
74. Shuai, C.; Gao, C.; Nie, Y.; Hu, H.; Zhou, Y.; Peng, S. Structure and Properties of Nano-Hydroxypatite Scaffolds for Bone Tissue Engineering with a Selective Laser Sintering System. *Nanotechnology* **2011**, *22*, 285703.
75. Shuai, C.; Li, P.; Liu, J.; Peng, S. Optimization of TCP/HAP Ratio for Better Properties of Calcium Phosphate Scaffold via Selective Laser Sintering. *Mater. Charact.* **2013**, *77*, 23–31.
76. Xia, Y.; Zhou, P. Y.; Cheng, X. S.; *et al.* Selective Laser Sintering Fabrication of Nano-Hydroxyapatite/Poly-Epsilon-Caprolactone Scaffolds for Bone Tissue Engineering Applications. *Int. J. Nanomedicine* **2013**, *8*, 4197–4213.
77. Zhang, Y.; Hao, L.; Savalani, M. M.; Harris, R. A.; Di Silvio, L.; Tanner, K. E. *In Vitro* Biocompatibility of Hydroxyapatite-Reinforced Polymeric Composites Manufactured by Selective Laser Sintering. *J. Biomed. Mater. Res., Part A* **2009**, *91A*, 1018–1027.
78. Lee, M. Y.; Tsai, W. W.; Chen, H. J.; *et al.* Laser Sintered Porous Polycaprolacone Scaffolds Loaded with Hyaluronic Acid and Gelatin-Grafted Thermoresponsive Hydrogel for Cartilage Tissue Engineering. *Biomed. Mater. Eng.* **2013**, *23*, 533–543.
79. Mazzoli, A. Selective Laser Sintering in Biomedical Engineering. *Med. Biol. Eng. Comput.* **2013**, *51*, 245–256.
80. Lohfeld, S.; Cahill, S.; Barron, V.; *et al.* Fabrication, Mechanical and *In Vivo* Performance of Polycaprolactone/Tricalcium Phosphate Composite Scaffolds. *Acta Biomater.* **2012**, *8*, 3446–3456.
81. Huang, H.; Oizumi, S.; Kojima, N.; Niino, T.; Sakai, Y. Avidin–Biotin Binding-Based Cell Seeding and Perfusion Culture of Liver-Derived Cells in a Porous Scaffold with a Three-Dimensional Interconnected Flow-Channel Network. *Biomaterials* **2007**, *28*, 3815–3823.
82. Yeong, W. Y.; Sudarmadji, N.; Yu, H. Y.; *et al.* Porous Polycaprolactone Scaffold for Cardiac Tissue Engineering Fabricated by Selective Laser Sintering. *Acta Biomater.* **2010**, *6*, 2028–2034.
83. Berry, E.; Marsden, A.; Dalgarno, K. W.; Kessel, D.; Scott, D. J. A. Flexible Tubular Replicas of Abdominal Aortic Aneurysms. *Proc. Inst. Mech. Eng. H J. Eng. Med.* **2002**, *216*, 211–214.
84. Zhang, X.; Jiang, X. N.; Sun, C. Micro-Stereolithography of Polymeric and Ceramic Microstructures. *Sens. Actuators, A* **1999**, *77*, 149–156.
85. Bertsch, A.; Zissi, S.; Jezequel, J. Y.; Corbel, S.; Andre, J. C. Microstereophotolithography Using a Liquid Crystal Display as Dynamic Mask-Generator. *Microsys. Technol.* **1997**, *3*, 42–47.
86. Bertsch, A.; Yezequel, J. Y.; Andre, J. C. Study of the Spatial Resolution of a New 3D Microfabrication Process: The Microstereophotolithography Using a Dynamic Mask-Generator Technique. *J. Photochem. Photobiol. A* **1997**, *107*, 275–281.
87. Chatwin, C.; Farsari, M.; Huang, S. P.; *et al.* UV Microstereolithography System That Uses Spatial Light Modulator Technology. *Appl. Opt.* **1998**, *37*, 7514–7522.
88. Farsari, M.; Huang, S.; Birch, P.; *et al.* Microfabrication by Use of a Spatial Light Modulator in the Ultraviolet: Experimental Results. *Opt. Lett.* **1999**, *24*, 549–550.
89. Farsari, M.; Claret-Tournier, F.; Huang, S.; *et al.* A Novel High-Accuracy Microstereolithography Method Employing an Adaptive Electro-Optic Mask. *J. Mater. Process. Technol.* **2000**, *107*, 167–172.
90. Bertsch, A.; Jiguet, S.; Renaud, P. Microfabrication of Ceramic Components by Microstereolithography. *J. Micromech. Microeng.* **2004**, *14*, 197–203.
91. Hornbeck, L. J. Digital Light Processing for High Brightness, High-Resolution Applications. *SPIE* **1997**, *3013*, 27–40.
92. Sun, C.; Fang, N.; Wu, D. M.; Zhang, X. Projection Micro-Stereolithography Using Digital Micro-Mirror Dynamic Mask. *Sens. Actuators, A* **2005**, *121*, 113–120.
93. Emami, M. M.; Barazandeh, F.; Yaghmaie, F. An Analytical Model for Scanning-Projection Based Stereolithography. *J. Mater. Process. Technol.* **2015**, *219*, 17–27.
94. Lee, M. P.; Cooper, G. J. T.; Hinkley, T.; Gibson, G. M.; Padgett, M. J.; Cronin, L. Development of a 3D Printer Using Scanning Projection Stereolithography. *Sci. Rep.* **2015**, *5*, 9875.
95. Luo, N.; Gao, Y.; Zhang, Z.; Xiao, M.; Wu, H. Three-Dimensional Microstructures of Photoresist Formed by Gradual Gray-Scale Lithography Approach. *Opt. Appl.* **2012**, *42*, 853–864.
96. Xu, K.; Chen, Y. Mask Image Planning for Deformation Control in Projection-Based Stereolithography. *J. Manuf. Sci. E-T ASME* **2015**, *137*, 031014.
97. Choi, J.-W.; Wicker, R.; Lee, S.-H.; Choi, K.-H.; Ha, C.-S.; Chung, I. Fabrication of 3D Biocompatible/Biodegradable Micro-Scaffolds Using Dynamic Mask Projection Microstereolithography. *J. Mater. Process. Technol.* **2009**, *209*, 5494–5503.
98. Han, L.-H.; Mapili, G.; Chen, S.; Roy, K. Projection Microfabrication of Three-Dimensional Scaffolds for Tissue Engineering. *J. Manuf. Sci. E-T ASME* **2008**, *130*, 021005.
99. Wang, S.; Foo, C. W. P.; Warrier, A.; Poo, M. M.; Heilshorn, S. C.; Zhang, X. Gradient Lithography of Engineered Proteins to Fabricate 2D and 3D Cell Culture Micro Environments. *Biomed. Microdevices* **2009**, *11*, 1127–1134.
100. Zhang, A. P.; Qu, X.; Soman, P.; *et al.* Rapid Fabrication of Complex 3D Extracellular Microenvironments by Dynamic Optical Projection Stereolithography. *Adv. Mater. (Weinheim, Ger.)* **2012**, *24*, 4266.
101. Sun, H.-B.; Kawata, S. Two-Photon Photopolymerization and 3D Lithographic Microfabrication; In *NMR 3D Analysis Photopolymerization*; Springer: Berlin, Heidelberg, 2004; pp. 169–273.
102. Juodkazis, S.; Mizeikis, V.; Misawa, H. Three-Dimensional Microfabrication of Materials by Femtosecond Lasers for Photonics Applications. *J. Appl. Phys.* **2009**, *106*, 0511101.
103. Farsari, M.; Chichkov, B. N. Two-Photon Fabrication. *Nature Photon.* **2009**, *3*, 450–452.
104. Selimis, A.; Mironov, V.; Farsari, M. Direct Laser Writing: Principles and Materials for Scaffold 3D Printing. *Microelectron. Eng.* **2015**, *132*, 83–89.
105. Malinauskas, M.; Farsari, M.; Piskarskas, A.; Juodkazis, S. Ultrafast Laser Nanostructuring of Photopolymers: A Decade of Advances. *Phys. Rep.* **2013**, *533*, 1–31.
106. Deubel, M.; Wegener, M.; Linden, S.; von Freymann, G.; John, S. 3D-2D-3D Photonic Crystal Heterostructures Fabricated by Direct Laser Writing. *Opt. Lett.* **2006**, *31*, 805–807.
107. Galajda, P.; Ormos, P. Rotation of Microscopic Propellers in Laser Tweezers. *J. Opt. B Quantum Semiclassical Opt.* **2002**, *4*, S78–S81.
108. Deubel, M.; von Freymann, G.; Wegener, M.; Pereira, S.; Busch, K.; Soukoulis, C. M. Direct Laser Writing of Three-Dimensional Photonic-Crystal Templates for Telecommunications. *Nat. Mater.* **2004**, *3*, 444–447.
109. Haske, W.; Chen, V. W.; Hales, J. M.; *et al.* 65 Nm Feature Sizes Using Visible Wavelength 3-D Multiphoton Lithography. *Opt. Exp.* **2007**, *15*, 3426–3436.
110. Göppert-Mayer, M. Über Elementarakte Mit Zwei Quantensprüngen. *Ann. Phys. (Berlin)* **1931**, *401*, 273–294.
111. Kaiser, W.; Garett, C. G. B. Two-Photon Excitation in CaF_2:Eu^{2+}. *Phys. Rev. Lett.* **1961**, *7*, 229–232.
112. Varadan, V. K.; Jiang, X.; Varadan, V. V. *Microstereolithography and Other Fabrication Techniques for 3D MEMS*; John Wiley & Sons: Chichester, 2001.
113. Stevens, M. P. *Polymer Chemistry: An Introduction*, 3rd ed.; Oxford University Press: New York, NY, 1999.
114. Allcock, H. R.; Lampe, F. W.; Mark, J. E. *Contemporary Polymer Chemistry*; Pearson-Prentice Hall: Upper-Saddle River, NJ, 2003.
115. Hiemenz, P. C.; Lodge, T. P. *Polymer Chemistry*, 2nd ed.; CRC Press: New York, NY, 2007.
116. Born, M.; Wolf, E. *Principles of Optics*, 7th ed.; Cambridge University Press: Cambridge, 1999.
117. Sauer, B. B.; McLean, S. S.; Thomas, R. R.; Tapping Mode, A. F. M. Studies of Nano-Phases on Fluorine-Containing Polyester Coatings and Octadecyltrichlorosilane Monolayers. *Langmuir* **1998**, *14*, 3045–3051.
118. Agarwal, G.; Naik, R. R.; Stone, M. O. Immobilization of Histidine-Tagged Proteins on Nickel by Electrochemical Dip Pen Nanolithography. *J. Am. Chem. Soc.* **2003**, *125*, 7408–7412.
119. Amro, N. A.; Xu, S.; Liu, G. Y. Patterning Surfaces Using Tip-Directed Displacement and Self-Assembly. *Langmuir* **2000**, *16*, 3006–3009.
120. Garno, J. C.; Yang, Y. Y.; Amro, N. A.; Cruchon-Dupeyrat, S.; Chen, S. W.; Liu, G. Y. Precise Positioning of Nanoparticles on Surfaces Using Scanning Probe Lithography. *Nano Lett.* **2003**, *3*, 389–395.
121. Liang, J.; Scoles, G. Nanografting of Alkanethiols by Tapping Mode Atomic Force Microscopy. *Langmuir* **2007**, *23*, 6142–6147.
122. Betzig, E.; Trautman, J. K. Near-Field Optics-Microscopy, Spectroscopy, and Surface Modification Beyond the Diffraction Limit. *Science (Washington, DC, USA)* **1992**, *257*, 189–195.
123. Heinzelmann, H.; Pohl, D. W. Scanning Near-Field Optical Microscopy. *Appl. Phys. A: Mater. Sci. Process.* **1994**, *59*, 89–101.
124. Samori, P. Scanning Probe Microscopies Beyond Imaging. *J. Mater. Chem.* **2004**, *14*, 1353–1366.

125. Straub, M.; Nguyen, L. H.; Fazlic, A.; Gu, M. Complex-Shaped Three-Dimensional Microstructures and Photonic Crystals Generated in a Polysiloxane Polymer by Two-Photon Microstereolithography. *Opt. Mater. (Amsterdam, Neth.)* **2004**, *27*, 359–364.
126. LaFratta, C. N.; Fourkas, J. T.; Baldacchini, T.; Farrer, R. A. Multiphoton Fabrication. *Angew. Chem., Int. Ed.* **2007**, *46*, 6238–6258.
127. Farsari, M.; Filippidis, G.; Sambani, K.; Drakakis, T. S.; Fotakis, C. Two-Photon Polymerization of an Eosin Y-Sensitized Acrylate Composite. *J. Photochem. Photobiol. A* **2006**, *181*, 132–135.
128. Farsari, M.; Vamvakaki, M.; Chichkov, B. N. Multiphoton Polymerization of Hybrid Materials. *J. Opt.* **2010**, *12*, 124001.
129. Kabouraki, E.; Giakoumaki, A. N.; Danilevicius, P.; Gray, D.; Vamvakaki, M.; Farsari, M. Redox Multiphoton Polymerization for 3D Nanofabrication. *Nano Lett.* **2013**, *13*, 3831–3835.
130. Quick, A. S.; Rothfuss, H.; Welle, A.; *et al.* Fabrication and Spatially Resolved Functionalization of 3D Microstructures via Multiphoton-Induced Diels–Alder Chemistry. *Adv. Funct. Mater.* **2014**, *24*, 3571–3580.
131. Li, Z. Q.; Pucher, N.; Cicha, K.; *et al.* A Straightforward Synthesis and Structure–Activity Relationship of Highly Efficient Initiators for Two-Photon Polymerization. *Macromolecules.* **2013**, *46*, 352–361.
132. Claeyssens, F.; Hasan, E. A.; Gaidukeviciute, A.; *et al.* Three-Dimensional Biodegradable Structures Fabricated by Two-Photon Polymerization. *Langmuir* **2009**, *25*, 3219–3223.
133. Bhuian, B.; Winfield, R. J.; O'Brien, S.; Crean, G. M. Investigation of the Two-Photon Polymerisation of a Zr-Based Inorganic-Organic Hybrid Material System. *Appl. Surf. Sci.* **2006**, *252*, 4845–4849.
134. Lu, W.-E.; Dong, X.-Z.; Chen, W.-Q.; Zhao, Z.-S.; Duan, X.-M. Novel Photoinitiator with a Radical Quenching Moiety for Confining Radical Diffusion in Two-Photon Induced Photopolymerization. *J. Mater. Chem.* **2011**, *21*, 5650–5659.
135. Xing, J.; Liu, J.; Zhang, T.; Zhang, L.; Zheng, M.-L.; Duan, X.-M. A Water Soluble Initiator Prepared through Host–Guest Chemical Interaction for Microfabrication of 3D Hydrogels via Two-Photon Polymerization. *J. Mater. Chem. B Mater. Biol. Med.* **2014**, *2*, 4318–4323.
136. Pitts, J. D.; Howell, A. R.; Taboada, R.; *et al.* New Photoactivators for Multiphoton Excited Three-Dimensional Submicron Cross-Linking of Proteins: Bovine Serum Albumin and Type 1 Collagen. *Photochem. Photobiol.* **2002**, *76*, 135–144.
137. Nazir, R.; Danilevicius, P.; Gray, D.; Farsari, M.; Gryko, D. T. Push–Pull Acylo-Phosphine Oxides for Two-Photon-Induced Polymerization. *Macromolecules* **2013**, *46*, 7239–7244.
138. Nazir, R.; Danilevicius, P.; Ciuciu, A. I.; *et al.* Pi-Expanded Ketocoumarins as Efficient, Biocompatible Initiators for Two-Photon-Induced Polymerization. *Chem. Mater.* **2014**, *26*, 3175–3784.
139. Li, Z. Q.; Torgersen, J.; Ajami, A.; *et al.* Initiation Efficiency and Cytotoxicity of Novel Water-Soluble Two-Photon Photoinitiators for Direct 3D Microfabrication of Hydrogels. *RSC Adv.* **2013**, *3*, 15939–15946.
140. Nazir, R.; Bourquard, F.; Balčiūnas, E.; *et al.* Pi-Expanded Alpha, Beta-Unsaturated Ketones: Synthesis, Optical Properties, and Two-Photon-Induced Polymerization. *ChemPhysChem* **2015**, *16*, 682–690.
141. Nazir, R.; Balčiūnas, E.; Buczynska, D.; *et al.* Donor–Acceptor Type Thioxanthones: Synthesis, Optical Properties, and Two-Photon Induced Polymerization. *Macromolecules* **2015**, *48*, 2466–2472.
142. Maruo, S.; Nakamura, O.; Kawata, S. Three-Dimensional Microfabrication with Two-Photon-Absorbed Photopolymerization. *Opt. Lett.* **1997**, *22*, 132–134.
143. Duan, X.-M.; Sun, H.-B.; Kaneko, K.; Kawata, S. Two-Photon Polymerization of Metal Ions Doped Acrylate Monomers and Oligomers for Three-Dimensional Structure Fabrication. *Thin Solid Films* **2004**, *453–54*, 518–521.
144. Sun, Z. B.; Dong, X.-Z.; Chen, W.-Q.; Nakanishi, S.; Duan, X.-M.; Kawata, S. Multicolor Polymer Nanocomposites: In Situ Synthesis and Fabrication of 3D Microstructures. *Adv. Mater. (Weinheim, Ger.)* **2008**, *20*, 914–919.
145. Sun, Z. B.; Dong, X.-Z.; Chen, W.-Q.; Shoji, S.; Duan, X.-M.; Kawata, S. Two- and Three-Dimensional Micro/Nanostructure Patterning of CdS-Polymer Nanocomposites with a Laser Interference Technique and In Situ Synthesis. *Nanotechnology* **2008**, *19*, 035611.
146. Formanek, F.; Takeyasu, N.; Tanaka, T.; Chiyoda, K.; Ishikawa, A.; Kawata, S. Selective Electroless Plating to Fabricate Complex Three-Dimensional Metallic Micro/Nanostructures. *Appl. Phys. Lett.* **2006**, *88*, 083110.
147. Takeyasu, N.; Tanaka, T.; Kawata, S. Fabrication of 3D Metal/Polymer Microstructures by Site-Selective Metal Coating. *Appl. Phys. A: Mater. Sci. Process.* **2008**, *90*, 205–209.
148. Correa, D. S.; Tayalia, P.; Cosendey, G.; *et al.* Two-Photon Polymerization for Fabricating Structures Containing the Biopolymer Chitosan. *J. Nanosci. Nanotechnol.* **2009**, *9*, 5845–5849.
149. Mendoca, C. R.; Correa, D. S.; Marlow, F.; Voss, T.; Tayalia, P.; Mazur, E. Three-Dimensional Fabrication of Optically Active Microstructures Containing an Electroluminescent Polymer. *Appl. Phys. Lett.* **2009**, *95*, 113309.
150. Witzgall, G.; Vrijen, R.; Yablonovitch, E.; Doan, V.; Schwartz, B. J. Single-Shot Two-Photon Exposure of Commercial Photoresist for the Production of Three-Dimensional Structures. *Opt. Lett.* **1998**, *23*, 1745–1747.
151. Belfield, K. D.; Schafer, K. J.; Liu, Y. U.; Ren, X. B.; van Stryland, E. W. Multiphoton-Absorbing Organic Materials for Microfabrication, Emerging Optical Applications and Non-Destructive Three-Dimensional Imaging. *J. Phys. Org. Chem.* **2000**, *13*, 837–849.
152. Kuebler, S. M.; Braun, K. L.; Zhou, W. H.; *et al.* Design and Application of High-Sensitivity Two-Photon Initiators for Three-Dimensional Microfabrication. *J. Photochem. Photobiol. A* **2003**, *158*, 163–170.
153. Teh, W. H.; Durig, U.; Salis, G.; *et al.* SU-8 for Real Three-Dimensional Subdiffraction-Limit Two-Photon Microfabrication. *Appl. Phys. Lett.* **2004**, *84*, 4095–4097.
154. Juodkazis, S.; Mizeikis, V.; Seet, K. K.; Miwa, M.; Misawa, H. Two-Photon Lithography of Nanorods in SU-8 Photoresist. *Nanotechnology* **2005**, *16*, 846–849.
155. Mizeikis, V.; Seet, K. K.; Juodkazis, S.; Misawa, H. Three-Dimensional Woodpile Photonic Crystal Templates for the Infrared Spectral Range. *Opt. Lett.* **2004**, *29*, 2061–2063.
156. Seet, K. K.; Mizeikis, V.; Matsuo, S.; Juodkazis, S.; Misawa, H. Three-Dimensional Spiral-Architecture Photonic Crystals Obtained by Direct Laser Writing. *Adv. Mater. (Weinheim, Ger.)* **2005**, *17*, 541–545.
157. Seet, K. K.; Mizeikis, V.; Juodkazis, S.; Misawa, H. Three-Dimensional Circular Spiral Photonic Crystal Structures Recorded by Femtosecond Pulses. *J. Non-Cryst. Solids* **2006**, *352*, 2390–2394.
158. Wu, D.; Chen, Q.-D.; Niu, L. G.; *et al.* Femtosecond Laser Rapid Prototyping of Nanoshells and Suspending Components towards Microfluidic Devices. *Lab Chip* **2009**, *9*, 2391–2394.
159. Kumi, G.; Yanez, C. O.; Belfield, K. D.; Fourkas, J. T. High-Speed Multiphoton Absorption Polymerization: Fabrication of Microfluidic Channels with Arbitrary Cross-Sections and High Aspect Ratios. *Lab Chip* **2010**, *10*, 1057–1060.
160. Stoneman, M.; Fox, M.; Zeng, C. Y.; Raicu, V. Real-Time Monitoring of Two-Photon Photopolymerization for Use in Fabrication of Microfluidic Devices. *Lab Chip* **2009**, *9*, 819–827.
161. Ovsianikov, A.; Schlie, S.; Ngezahayo, A.; Haverich, A.; Chichkov, B. N. Two-Photon Polymerization Technique for Microfabrication of CAD-Designed 3D Scaffolds from Commercially Available Photosensitive Materials. *J. Tissue Eng. Regen. Med.* **2007**, *1*, 443–449.
162. Houbertz, R.; Domann, G.; Cronauer, C.; *et al.* Inorganic–Organic Hybrid Materials for Application in Optical Devices. *Thin Solid Films* **2003**, *442*, 194–200.
163. Houbertz, R.; Frohich, L.; Popall, M.; *et al.* Inorganic–Organic Hybrid Polymers for Information Technology: From Planar Technology to 3D Nanostructures. *Adv. Eng. Mater.* **2003**, *5*, 551–555.
164. Farsari, M.; Filippidis, G.; Fotakis, C. Fabrication of Three-Dimensional Structures by Three-Photon Polymerization. *Opt. Lett.* **2005**, *30*, 3180–3182.
165. Jun, Y.; Nagpal, P.; Norris, D. J. Thermally Stable Organic–Inorganic Hybrid Photoresists for Fabrication of Photonic Band Gap Structures with Direct Laser Writing. *Adv. Mater. (Weinheim, Ger.)* **2008**, *20*, 606–610.
166. Serbin, J.; Egbert, A.; Ostendorf, A.; *et al.* Femtosecond Laser-Induced Two-Photon Polymerization of Inorganic–Organic Hybrid Materials for Applications in Photonics. *Opt. Lett.* **2003**, *28*, 301–303.
167. Serbin, J.; Gu, M. Superprism Phenomena in Waveguide-Coupled Woodpile Structures Fabricated by Two-Photon Polymerization. *Opt. Exp.* **2006**, *14*, 3563–3568.
168. Serbin, J.; Gu, M. Experimental Evidence for Superprism Effects in Three-Dimensional Polymer Photonic Crystals. *Adv. Mater. (Weinheim, Ger.)* **2006**, *18*, 221–224.
169. Li, J. F.; Jia, B. H.; Zhou, G. Y.; Bullen, C.; Serbin, J.; Gu, M. Spectral Redistribution in Spontaneous Emission from Quantum-Dot-Infiltrated 3D Woodpile Photonic Crystals for Telecommunications. *Adv. Mater. (Weinheim, Ger.)* **2007**, *19*, 3276–3280.
170. Li, J. F.; Jia, B. H.; Gu, M. Engineering Stop Gaps of Inorganic–Organic Polymeric 3D Woodpile Photonic Crystals with Post-Thermal Treatment. *Opt. Exp.* **2008**, *16*, 20073–20080.

171. Woggon, T.; Kleiner, T.; Punke, M.; Lemmer, U. Nanostructuring of Organic–Inorganic Hybrid Materials for Distributed Feedback Laser Resonators by Two-Photon Polymerization. *Opt. Exp.* **2009**, *17*, 2500–2507.
172. Dinca, V.; Kasotakis, E.; Catherine, J.; *et al.* Directed Three-Dimensional Patterning of Self-Assembled Peptide Fibrils. *Nano Lett.* **2008**, *8*, 538–543.
173. Grossmann, T.; Schleede, S.; Hauser, M.; *et al.* Direct Laser Writing for Active and Passive High-Q Polymer Microdisks on Silicon. *Opt. Exp.* **2011**, *19*, 11451–11456.
174. Brasselet, E.; Malinauskas, M.; Zukauskas, A.; Juodkazis, S. Photopolymerized Microscopic Vortex Beam Generators: Precise Delivery of Optical Orbital Angular Momentum. *Appl. Phys. Lett.* **2011**, *97*, 211108.
175. Liu, Z. P.; Li, Y.; Xiao, Y. F.; *et al.* Direct Laser Writing of Whispering Gallery Microcavities by Two-Photon Polymerization. *Appl. Phys. Lett.* **2011**, *97*, 211105.
176. Sun, Q.; Juodkazis, S.; Murazawa, N.; Mizeikis, V.; Misawa, H. Freestanding and Movable Photonic Microstructures Fabricated by Photopolymerization with Femtosecondlaser Pulses. *J. Micromech. Microeng.* **2010**, *20*, 035004.
177. Trull, J.; Maigyte, L.; Mizeikis, V.; *et al.* Formation of Collimated Beams behind the Woodpile Photonic Crystal. *Phys. Rev. A: At., Mol., Opt. Phys.* **2011**, *84*, 033812.
178. Sakellari, I.; Gaidukeviciute, A.; Giakoumaki, A.; *et al.* Two-Photon Polymerization of Titanium-Containing Sol-Gel Composites for Three-Dimensional Structure Fabrication. *Appl. Phys. A: Mater. Sci. Process.* **2010**, *100*, 359–364.
179. Winfield, R. J.; Bhuian, B.; O'Brien, S.; Crean, G. M. Refractive Femtosecond Laser Beam Shaping for Two-Photon Polymerization. *Appl. Phys. Lett.* **2007**, *90*, 111115.
180. Winfield, R. J.; Bhuian, B.; O'Brien, S.; Crean, G. M. Fabrication of Grating Structures by Simultaneous Multi-Spot Fs Laser Writing. *Appl. Surf. Sci.* **2007**, *253*, 8086–8090.
181. Ovsianikov, A.; Viertl, J.; Chichkov, B. N.; *et al.* Ultra-Low Shrinkage Hybrid Photosensitive Material for Two-Photon Polymerization Microfabrication. *ACS Nano* **2008**, *2*, 2257–2262.
182. Ovsianikov, A.; Xiao, S. Z.; Farsari, M.; Vamvakaki, M.; Fotakis, C.; Chichkov, B. N. Shrinkage of Microstructures Produced by Two-Photon Polymerization of Zr-Based Hybrid Photosensitive Materials. *Opt. Exp.* **2009**, *17*, 2143–2148.
183. Farsari, M.; Ovsianikov, A.; Vamvakaki, M.; *et al.* Fabrication of Three-Dimensional Photonic Crystal Structures Containing An Active Nonlinear Optical Chromophore. *Appl. Phys. A: Mater. Sci. Process* **2008**, *93*, 11–15.
184. Zukauskas, A.; Malinauskas, M.; Kontenis, L.; *et al.* Organic Dye Doped Microstructures For Optically Active Functional Devices Fabricated Via Two-Photon Polymerization Technique. *Lith. J. Phys.* **2010**, *50*, 55–61.
185. Jia, B.; Buso, D.; van Embden, J.; Li, J.; Gu, M. Highly Non-Linear Quantum Dot Doped Nanocomposites for Functional Three-Dimensional Structures Generated by Two-Photon Polymerization. *Adv. Mater. (Weinheim, Ger.)* **2010**, *22*, 2463–2467.
186. Terzaki, K.; Vasilantonakis, N.; Gaidukeviciute, A.; *et al.* 3D Conducting Nanostructures Fabricated Using Direct Laser Writing. *Opt. Mater. Exp.* **2011**, *1*, 586–597.
187. Vasilantonakis, N.; Terzaki, K.; Sakellari, I.; *et al.* Three-Dimensional Metallic Photonic Crystals with Optical Bandgaps. *Adv. Mater. (Weinheim, Ger.)* **2012**, *24*, 1101–1105.
188. Kenanakis, G.; Xomalis, A.; Selimis, A.; *et al.* Three-Dimensional Infrared Metamaterial with Asymmetric Transmission. *ACS Photonics* **2015**, *2*, 287–294.
189. Smith, D. R. *META GROUP Home Page*. Available from: http://people.ee.duke.edu/~drsmith/metamaterials.htm (accessed 07 March 2016).
190. Soukoulis, C. M.; Wegener, M. Past Achievements and Future Challenges in the Development of Three-Dimensional Photonic Metamaterials. *Nature Photon.* **2011**, *5*, 523–530.
191. Cao, Y. Y.; Dong, X.-Z.; Takeyasu, N.; *et al.* Morphology and Size Dependence of Silver Microstructures in Fatty Salts-Assisted Multiphoton Photoreduction Microfabrication. *Appl. Phys. A: Mater. Sci. Process.* **2009**, *96*, 453–458.
192. Cao, Y. Y.; Takeyasu, N.; Tanaka, T.; Duan, X.-M.; Kawata, S. 3D Metallic Nanostructure Fabrication by Surfactant-Assisted Multiphoton-Induced Reduction. *Small* **2009**, *5*, 1144–1148.
193. Lin, S. Y.; Moreno, J.; Fleming, J. G. Three-Dimensional Photonic-Crystal Emitter for Thermal Photovoltaic Power Generation. *Appl. Phys. Lett.* **2003**, *83*, 380–382.
194. Lin, S. Y.; Fleming, J. G.; El-Kady, I. Three-Dimensional Photonic-Crystal Emission through Thermal Excitation. *Opt. Lett.* **2003**, *28*, 1909–1911.
195. Fleming, J. G.; Lin, S. Y.; El-Kady, I.; Biswas, R.; Ho, K.-M. All Metallic Three-Dimensional Photonic Crystals with a Large Infrared Band-Gap. *Nature* **2002**, *417*, 52–55.
196. Gansel, J. K.; Latzel, M.; Frolich, A.; Kaschke, J.; Thiel, M.; Wegener, M. Tapered Gold-Helix Metamaterials as Improved Circular Polarizers. *Appl. Phys. Lett.* **2012**, *100*, 101109.
197. Gansel, J. K.; Thiel, M.; Rill, M. S.; *et al.* Gold Helix Photonic Metamaterial as Broadband Circular Polarizer. *Science (Washington, DC, USA)* **2009**, *325*, 1513–1515.
198. Chen, Y.-S.; Tal, A.; Torrance, D. B.; Kuebler, S. M. Fabrication and Characterization of Three-Dimensional Silver-Coated Polymeric Microstructures. *Adv. Funct. Mater.* **2006**, *16*, 1739–1744.
199. Radke, A.; Gissibl, T.; Klotzbücher, T.; Braun, P. V.; Giessen, H. Three-Dimensional Bichiral Plasmonic Crystals Fabricated by Direct Laser Writing and Electroless Silver Plating. *Adv. Mater. (Weinheim, Ger.)* **2011**, *23*, 3018–3021.
200. Hrapovic, S.; Liu, Y. L.; Enright, G.; Bensebaa, F.; Luong, J. H. T. New Strategy for Preparing Thin Gold Films on Modified Glass Surfaces by Electroless Deposition. *Langmuir* **2003**, *19*, 3958–3965.
201. Mallory, G. O.; Hajdu, J. B. *Electroless Plating: Fundamentals and Applications*; American Electroplaters and Surface Finishers Society: Orlando, FL, 1990.
202. Rill, M. S.; Plet, C.; Thiel, M.; *et al.* Photonic Metamaterials by Direct Laser Writing and Silver Chemical Vapour Deposition. *Nat. Mater.* **2008**, *7*, 543–546.
203. Kavanagh, A.; Copperwhite, R.; Oubaha, M.; *et al.* Photo-Patternable Hybrid Ionogels for Electrochromic Applications. *J. Mater. Chem.* **2011**, *21*, 8687–8693.
204. Oubaha, M.; Kavanagh, A.; Gorin, A.; *et al.* Graphene-Doped Photo-Patternable Ionogels: Tuning of Conductivity and Mechanical Stability of 3D Microstructures. *J. Mater. Chem.* **2012**, *22*, 10552–10559.
205. Narayan, R.; Goering, P. Laser Micro-and Nanofabrication of Biomaterials. *MRS Bull.* **2011**, *36*, 973–982.
206. Waldbaur, A.; Rapp, H.; Lange, K.; Rapp, B. E. Let There Be Chip-towards Rapid Prototyping of Microfluidic Devices: One-Step Manufacturing Processes. *Anal. Methods* **2011**, *3*, 2681–2716.
207. Amato, L.; Gu, Y.; Bellini, N.; Eaton, S. M.; Cerullo, G.; Osellame, R. Integrated Three-Dimensional Filter Separates Nanoscale from Microscale Elements in a Microfluidic Chip. *Lab Chip* **2012**, *12*, 1135–1142.
208. Eaton, S. M.; De Marco, C.; Martinez-Vazquez, R.; *et al.* Femtosecond Laser Microstructuring for Polymeric Lab-on-Chips. *J. Biophotonics* **2012**, *5*, 687–702.
209. Schizas, C.; Melissinaki, V.; Gaidukeviciute, A.; *et al.* On the Design and Fabrication by Two-Photon Polymerization of a Readily Assembled Micro-Valve. *Int. J. Adv. Manuf. Technol.* **2010**, *48*, 435–441.
210. Lin, C. L.; Wang, I.; Dollet, B.; Baldeck, P. L. Velocimetry Microsensors Driven by Linearly Polarized Optical Tweezers. *Opt. Lett.* **2006**, *31*, 329–331.
211. Maruo, S.; Hasegawa, T.; Yoshimura, N. Replication of Three-Dimensional Rotary Micromechanism by Membrane-Assisted Transfer Molding. *Jpn. J. Appl. Phys.* **2009**, *48*, 06FH05.
212. Lee, J. T.; George, M. C.; Moore, J. S.; Braun, P. V. Multiphoton Writing of Three-Dimensional Fluidic Channels within a Porous Matrix. *J. Am. Chem. Soc.* **2009**, *131*, 11294–11295.
213. Lin, C. L.; Vitrant, G.; Bouriau, M.; Casalegno, R.; Baldeck, P. L. Optically Driven Archimedes Micro-Screws for Micropump Application. *Opt. Exp.* **2011**, *19*, 8267–8276.
214. Gittard, S. D.; Miller, P. R.; Boehm, R. D.; *et al.* Multiphoton Microscopy of Transdermal Quantum Dot Delivery Using Two Photon Polymerization-Fabricated Polymer Microneedles. *Farad. Discuss.* **2011**, *149*, 171–185.
215. Gittard, S. D.; Narayan, R. J.; Jin, C.; *et al.* Pulsed Laser Deposition of Antimicrobial Silver Coating on Ormocer (R) Microneedles. *Biofabrication* **2009**, *1*, 041001.
216. Gittard, S. D.; Ovsianikov, A.; Akar, H.; *et al.* Two Photon Polymerization-Micromolding of Polyethylene Glycol-Gentamicin Sulfate Microneedles. *Adv. Eng. Mater.* **2010**, *12*, B77–B82.
217. Tian, Y.; Zhang, Y. L.; Ku, J. F.; *et al.* High Performance Magnetically Controllable Microturbines. *Lab Chip* **2010**, *10*, 2902–2905.
218. Tian, Y.; Lu, D. X.; Jiang, H. B.; Lin, X. M. Preparation of a Novel Ferrofluidic Photoresist for Two-Photon Photopolymerization Technique. *J. Magn Magn. Mater.* **2012**, *324*, 3291–3294.
219. Langer, R.; Vacanti, J. P. Tissue Engineering. *Science (Washington, DC, USA)* **1993**, *260*, 920–926.

220. Zhang, S. G.; Gelain, F.; Zhao, X. J. Designer Self-Assembling Peptide Nanofiber Scaffolds for 3D Tissue Cell Cultures. *Semin. Cancer Biol.* **2005**, *15*, 413–420.
221. Abbott, A. Cell Culture: Biology's New Dimension. *Nature* **2003**, *424*, 870–872.
222. Stratakis, E.; Ranella, A.; Farsari, M.; Fotakis, C. Laser-Based Micro/Nanoengineering for Biological Applications. *Prog. Quant. Electron.* **2009**, *33*, 127–163.
223. Dawood, F.; Qin, S. J.; Li, L. J.; Lin, E. Y.; Fourkas, J. T. Simultaneous Microscale Optical Manipulation, Fabrication and Immobilisation in Aqueous Media. *Chem. Sci.* **2012**, *3*, 2449–2456.
224. Raimondi, M. T.; Eaton, S. M.; Nava, M. M.; Laganà, M.; Cerullo, G.; Osellame, R. Two-Photon Laser Polymerization: From Fundamentals to Biomedical Application in Tissue Engineering and Regenerative Medicine. *J. Appl. Biomater. Funct. Mater.* **2012**, *10*, 56–66.
225. Ovsianikov, A.; Mironov, V.; Stampfl, J.; Liska, R. Engineering 3D Cell-Culture Matrices: Multiphoton Processing Technologies for Biological and Tissue Engineering Applications. *Expert Rev. Med. Devices* **2012**, *9*, 613–633.
226. Chatzinikolaidou, M.; Rekstyte, S.; Danilevicius, P.; *et al.* Adhesion and Growth of Human Bone Marrow Mesenchymal Stem Cells on Precise-Geometry 3D Organic–Inorganic Composite Scaffolds for Bone Repair. *Mater. Sci. Eng. C* **2015**, *48*, 301–309.
227. Danilevicius, P.; Rezende, R. A.; Pereira, F. D. A. S.; *et al.* Burr-Like, Laser-Made 3D Microscaffolds for Tissue Spheroid Encagement. *Biointerfaces* **2015**, *10*, 021011.
228. Klein, F.; Richter, B.; Striebel, T.; *et al.* Two-Component Polymer Scaffolds for Controlled Three-Dimensional Cell Culture. *Adv. Mater. (Weinheim, Ger.)* **2011**, *23*, 1341–1345.
229. Psycharakis, S.; Tosca, A.; Melissinaki, V.; Giakoumaki, A.; Ranella, A. Tailor-Made Three-Dimensional Hybrid Scaffolds for Cell Cultures. *Biomed. Mater.* **2011**, *6*, 045008.
230. Malinauskas, M.; Danilevicius, P.; Baltriukiene, D.; *et al.* 3D Artificial Polymeric Scaffolds for Stem Cell Growth Fabricated by Femtosecond Laser. *Lith. J. Phys.* **2010**, *50*, 75–82.
231. Tayalia, P.; Mendonca, C. R.; Baldacchini, T.; Mooney, D. J.; Mazur, E. 3D Cell-Migration Studies Using Two-Photon Engineered Polymer Scaffolds. *Adv. Mater. (Weinheim, Ger.)* **2008**, *20*, 4494–4498.
232. Raimondi, M. T.; Eaton, S. M.; Laganà, M.; *et al.* Three-Dimensional Structural Niches Engineered via Two-Photon Laser Polymerization Promote Stem Cell Homing. *Acta Biomater.* **2013**, *9*, 4579–4584.
233. Terzaki, K.; Kissamitaki, M.; Skarmoutsou, A.; *et al.* Pre-Osteoblastic Cell Response on Three-Dimensional, Organic–Inorganic Hybrid Material Scaffolds for Bone Tissue Engineering. *J. Biomed. Mater. Res., Part A* **2013**, *101*, 2283–2294.
234. Danilevicius, P.; Georgiadi, L.; Pateman, C. J.; Claeyssens, F.; Chatzinikolaidou, M.; Farsari, M. The Effect of Porosity on Cell Ingrowth into Accurately Defined, Laser-Made, Polylactide-Based 3D Scaffolds. *Appl. Surf. Sci.* **2015**, 2–10.
235. Terzaki, K.; Kalloudi, E.; Mossou, E.; *et al.* Mineralized Self-Assembled Peptides on 3D Laser-Made Scaffolds: A New Route toward "Scaffold on Scaffold" Hard Tissue Engineering. *Biofabrication* **2013**, *5*, 045002.
236. Skarmoutsou, A.; Lolas, G.; Charitidis, C. A.; Chatzinikolaidou, M.; Vamvakaki, M.; Farsari, M. Nanomechanical Properties of Hybrid Coatings for Bone Tissue Engineering. *J. Mech. Behav. Biomed. Mater.* **2013**, *25*, 48–62.
237. Maciulaitis, J.; Deveikyte, M.; Rekstyte, S.; *et al.* Preclinical Study of SZ2080 Material 3D Microstructured Scaffolds for Cartilage Tissue Engineering Made by Femtosecond Direct Laser Writing Lithography. *Biofabrication* **2015**, *7*, 015015.
238. Engelhardt, S.; Hoch, E.; Borchers, K.; *et al.* Fabrication of 2D Protein Microstructures and 3D Polymer–Protein Hybrid Microstructures by Two-Photon Polymerization. *Biofabrication* **2011**, *3*, 025003.
239. Turunen, S.; Kapyla, E.; Terzaki, K.; *et al.* Pico- and Femtosecond Laser-Induced Crosslinking of Protein Microstructures: Evaluation of Processability and Bioactivity. *Biofabrication* **2011**, *3*, 045002.
240. Steen, M.; Watkins, K.; *Laser Material Processing*, Vol. 1; Springer-Verlag: New York, NY, 2003.
241. Dutta Majumdar, J.; Manna, I. Laser Material Processing. *Int. Mater. Rev.* **2011**, *56*, 341–388.
242. Dowden, J. *The Theory of Laser Materials Processing: Heat and Mass Transfer in Modern Technology*; Kanopus Publishing Limited: Bristol, 2009.
243. Brown, M. S.; Arnold, C. B. Fundamentals of Laser-Material Interaction and Application to Multiscale Surface Modification. In *Laser Precision Microfabrication*; Sugioka, K., Meunier, M., Piqué, A., Eds.; Springer-Verlag: Berlin, 2010; pp. 91–120.
244. Ready, J. F. Effects due to Absorption of Laser Radiation. *J. Appl. Phys.* **1965**, *36*, 462–468.
245. Rimini, E. *Laser and Electron Beam Interactions with Solids and Materials Processing*; Elsevier: New York, NY, 1982.
246. Miotello, A.; Kelly, R. Laser-Induced Phase Explosion: New Physical Problems When a Condensed Phase Approaches the Thermodynamic Critical Temperature. *Appl. Phys. A: Mater. Sci. Process.* **1999**, *69*, S67–S73.
247. Lewis, L. J.; Perez, D. Laser Ablation with Short and Ultrashort Laser Pulses: Basic Mechanisms from Molecular-Dynamics Simulations. *Appl. Surf. Sci.* **2009**, *255*, 5101–5106.
248. Lorazo, P.; Lewis, L. J.; Meunier, M. Thermodynamic Pathways to Melting Ablation, and Solidification in Absorbing Solids under Pulsed Laser Irradiation. *Phys. Rev. B: Condens. Matter. Phys.* **2006**, *73*, 134108.
249. Tanvir Ahmmed, K. M.; Ling, E. J. Y.; Servio, P.; Kietzig, A.-M. Introducing a New Optimization Tool for Femtosecond Laser-Induced Surface Texturing on Titanium, Stainless Steel, Aluminum and Copper. *Opt. Laser Eng.* **2015**, *66*, 258–268.
250. Tsibidis, G. D.; Fotakis, C.; Stratakis, E. From Ripples to Spikes: A Hydrodynamical Mechanism to Interpret Femtosecond Laser-Induced Self-Assembled Structures. *Phys. Rev. B: Condens. Matter* **2015**, *92*, 041405.
251. Baugmant, P.; Krajnovich, D. J.; Nguyen, T. A.; Tam, A. C. A New Laser Texturing Technique for High Performance Magnetic Disk Drives. *IEEE Trans. Magn.* **1995**, *31*, 2946–2951.
252. Geiger, M.; Roth, S.; Becker, W. Influence of Laser-Produced Microstructures on the Tribological Behaviour of Ceramics. *Surf. Coat. Technol.* **1998**, *101*, 17–22.
253. Wu, B.; Zhou, M.; Li, L.; Ye, X.; Li, G.; Cai, L. Superhydrophobic Surfaces Fabricated by Microstructuring of Stainless Steel Using a Femtosecond Laser. *Appl. Surf. Sci.* **2009**, *256*, 61–66.
254. Noh, J.; Lee, J.-H.; Na, S.; Lim, H.; Jung, D.-H. Fabrication of Hierarchically Micro- and Nano-Structured Mold Surfaces Using Laser Ablation for Mass Production of Superhydrophobic Surfaces. *Jpn. J. Appl. Phys.* **2010**, *49*, 106502.
255. Dahotre, N. B.; Paital, S. R.; Samant, A. N.; Daniel, C. Wetting Behaviour of Laser Synthetic Surface Microtextures on Ti–6Al–4V for Bioapplication. *Phil. Trans. R. Soc. A* **2010**, *368*, 1863–1869.
256. Tseng, S. F.; Hsiao, W. T.; Chen, M. F.; *et al.* Surface Wettability of Silicon Substrates Enhanced by Laser Ablation. *Appl. Phys. A: Mater. Sci. Process.* **2010**, *101*, 303–308.
257. Barberoglou, M.; Zorba, V.; Stratakis, E.; *et al.* Bio-Inspired Water Repellent Surfaces Produced by Ultrafast Laser Structuring of Silicon. *Appl. Surf. Sci.* **2009**, *255*, 5425–5429.
258. De Marco, C.; Eaton, S. M.; Martinez-Vazquez, R.; *et al.* Solvent Vapor Treatment Controls Surface Wettability in PMMA Femtosecond-Laser-Ablated Microchannels. *Microfluid. Nanofluid.* **2013**, *14*, 171–176.
259. Baldacchini, T.; Carey, J. E.; Zhou, M.; Mazur, E. Superhydrophobic Surfaces Prepared by Microstructuring of Silicon Using a Femtoseconf Laser. *Langmuir* **2006**, *22*, 4917–4919.
260. Pazokian, H.; Selimis, A.; Barzin, J.; *et al.* Tailoring the Wetting Properties of Polymers from Hydrophillic to Supehydrophobic Using UV Laser Pulses. *J. Micromech. Microeng.* **2012**, *22*, 035001.
261. Yilbas, B. S.; Khaled, M.; Abu-Dheir, N.; *et al.* Wetting and Other Physical Characteristics of Polycarbonate Surface Textured Using Laser Ablation. *Appl. Surf. Sci.* **2014**, *320*, 21–29.
262. Adams, D. P.; Hodges, V. C.; Hirschfield, D. A.; Rodriguez, M. A.; McDonald, J. P.; Kotula, P. G. Nanosecond Pulsed Laser Irradiation of Stainless Steel 304L: Oxide Growth and Effects on Underlying Metal. *Surf. Coat. Technol.* **2013**, *222*, 1–8.
263. Vorobyev, A. Y.; Cuo, C. Colorizing Metals with Femtosecond Laser Pulses. *Appl. Phys. Lett.* **2008**, *92*, 041914.
264. Etsion, I. State of the Art in Laser Surface Texturing. *J. Tribol.-T. ASME* **2005**, *127*, 248–253.
265. Etsion, I.; Kligerman, Y.; Halperin, S. Analytical and Experimental Investigation of Laser-Textured Mechanical Seal Faces. *Tribol. Trans.* **1999**, *42*, 511–516.
266. Demir, A. G.; Lecis, N.; Previtali, B.; Ugues, D. Scratch Resistance of Fibre Laser Surface Textured TiN Coatings. *Surf. Eng.* **2013**, *29*, 654–659.
267. Xu, D.; Wu, W.; Malhotra, R.; Chen, J.; Lu, B.; Cao, J. Mechanism Investigation for the Influence of Tool Rotation and Laser Surface Texturing (LST) on Formability in Single Point Incremental Forming. *Int. J. Mach. Tools Manuf.* **2013**, *73*, 37–46.
268. Li, J.; Xiong, D.; Wu, H.; Zhang, Y.; Qin, Y. Tribological Properties of Laser Surface Texturing and Molybdenizing Duplex-Treated Stainless Steel at Elevated Temperatures. *Surf. Coat. Technol.* **2013**, *228*, S219–S223.

269. Schmidt, V.; Regina, M. *Laser Technology in Biomimetics. Basics and Applications*; Springer-Verlag: Berlin, Heidelberg, 2013.
270. Kietzig, A.-M.; Hatzikiriakos, S. G.; Englezos, P. Patterned Superhydrophobic Metallic Surfaces. *Langmuir* **2009**, *25*, 4821–4827.
271. White, B.; Sarkar, A.; Kietzig, A.-M. Fog-Harvesting Inspired by the Stenocara Beetle-an Analysis of Drop Collection and Removal from Biomimetic Samples with Wetting Contrast. *Appl. Surf. Sci.* **2013**, *284*, 826–836.
272. Kietzig A.-M.; Lehr J.; Matus L.; Liang F. Laser-Induced Patterns on Metals and Polymers for Biomimetic Surface Engineering. In *Proc. SPIE.*, San Francisco, 2014; pp. 896705–896708.
273. Etsion, I. Improving Tribological Performance of Mechanical Components by Laser Surface Texturing. *Tribol. Int.* **2004**, *17*, 733–737.
274. Olofinjana, B.; Lorenzo-Martin, C.; Ajayi, O. O.; Ajayi, E. O. Effect of Laser Surface Texturing (LST) on Tribochemical Films Dynamics and Friction and Wear Performance. *Wear* **2015**, *332–333*, 1225–1230.
275. Maressa, P.; Anodio, L.; Bernasconi, A.; Demir, A. G.; Previtali, B. Effect of Surface Texture on the Adhesion Performance of Laser Treated Ti6Al4V Alloy. *J. Adhes.* **2015**, *91*, 518–537.
276. Kovalchenko, A.; Ajayi, O.; Erdemir, A.; Fenske, G.; Etsion, I. The Effect of Laser Surface Texturing on Transition in Lubrication Regimes during Unidirectional Sliding Contact. *Tribol. Int.* **2005**, *38*, 219–225.
277. Blau, P. J.; Qu, J.; Riester, L. Effects of LST on Microstructure and Frictional Characteristics of ZrO2 Surfaces under Liquid at Solid Lubrication. In *Proceedings of the World Tribology Congress*, 2005; p. 63197.
278. Krupka, I.; Hartl, M. The Effect of Surface Texturing on Thin EHD Lubrication Films. *Tribol. Int.* **2007**, *40*, 1100–1110.
279. Kovalchenko, A.; Ajayi, O.; Erdemir, A.; Fenske, G. Friction and Wear Behavior of LST under Lubricated Initial Point Contact. *Wear* **2011**, *271*, 1719–1725.
280. Brizmer, V.; Kligerman, Y.; Etsion, I. A Laser Surface Textured Parallel Thrust Bearing. *Tribol. Trans.* **2003**, *46*, 397–403.
281. Braun, D.; Greiner, C.; Scheider, J.; Gumbsch, P. Efficiency of Laser Surface Texturing in the Reduction of Friction under Mixed Lubrication. *Tribol. Int.* **2014**, *77*, 142–147.
282. Wang, T.; Huang, W.; Liu, X.; Li, Y.; Wang, Y. Experimental Study of Two-Phase Mechanical Face Seals with Laser Surface Texturing. *Tribol. Int.* **2014**, *72*, 90–97.
283. Amanov, A.; Watabe, T.; Tsuboi, R.; Sasaki, S. Improvement in the Tribological Characteristics of Si-DLC Coating by Laser Surface Texturing under Oil-Lubricated Point Contacts at Various Temperatures. *Surf. Coat. Technol.* **2013**, *232*, 549–560.
284. Tomanik, E. Modelling the Hydrodynamic Support of Cylinder Bore and Piston Rings with Laser Textured Surfaces. *Tribol. Int.* **2013**, *59*, 90–96.
285. Qin, L.; Lin, P.; Zhang, Y.; Dong, G.; Zeng, Q. Influence of Surface Wettability on the Tribological Properties of Laser Textured Co–Cr–Mo Alloy in Aqueous Bovine Serum Albumin Solution. *Appl. Surf. Sci.* **2013**, *268*, 79–86.
286. Hu, T.; Hu, L.; Ding, Q. The Effect of Laser Surface Texturing on the Tribological Behavior of Ti–6Al–4V. *P. I. Mech. Eng. J-J. Eng.* **2012**, *226*, 854–863.
287. Oksanen, J.; Hakala, T. J.; Tervakangas, S.; *et al.* Tribological Properties of Laser-Textured and Ta–C Coated Surfaces with Burnished WS_2 at Elevated Temperatures. *Tribol. Int.* **2014**, *70*, 94–103.
288. Segu, D. W.; Kim, J.-H.; Choi, S. G.; Jung, Y.-S.; Kim, S.-S. Application of Taguchi Techniques to Study Friction and Wear Properties of MoS_2 Coatings Deposited on Laser Textured Surface. *Surf. Coat. Technol.* **2013**, *232*, 504–514.
289. Xing, Y.; Deng, J.; Feng, X.; Yu, S. Effect of Laser Surface Texturing on Si_3N_4/TiC Ceramic Sliding against Steel under Dry Friction. *Mater. Des.* **2013**, *52*, 234–245.
290. Ripoll, M. R.; Simič, R.; Brenner, J.; Podgornik, B. Friction and Lifetime of Laser Surface–Textured and MoS_2-Coated Ti6Al4V Under Dry Reciprocating Sliding. *Tribol. Lett.* **2013**, *51*, 261–271.
291. Ryk, G.; Kligerman, Y.; Etsion, I. Experimental Investigation of Laser Surface Texturing for Reciprocating Automotive Components. *Tribol. Trans.* **2002**, *45*, 444–449.
292. Zhan, J.; Yang, M. J. The Effects of Dimple Distribution Angle on the Tribology Performance of a Laser Surface Textured Cylinder Piston Ring System. *Laser Eng.* **2014**, *29*, 123–131.
293. Shum, P. W.; Zhou, Z. F.; Li, K. Y. To Increase the Hydrophobicity, Non-Stickiness and Wear Resistance of DLC Surface by Surface Texturing Using a Laser Ablation Process. *Tribol. Int.* **2014**, *78*, 1–6.
294. Shum, P. W.; Zhou, Z. F.; Li, K. Y. To Increase the Hydrophobicity and Wear Resistance of Diamond-Like Carbon Coatings by Surface Texturing Using Laser Ablation Process. *Thin Solid Films* **2013**, *544*, 472–476.
295. Voevodin, A. A.; Zabinski, J. S. Laser Surface Testuring for Adaptive Solid Lubrication. *Wear* **2006**, *261*, 1285–1292.
296. Zeng, D. W.; Li, K.; Yung, K. C.; Chan, H. L. W.; Choy, C. L.; Xie, C. S. UV Laser Micropmachining of Piezoelectric Ceramic Using a Pulsed Nd:YAG Laser. *Appl. Phys. A: Mater. Sci. Process.* **2004**, *78*, 415–421.
297. Su, Y.; Li, L.; He, N.; Zao, W. Experimental Study of Fiber Laser Surface Texturing of Polycrystalline Diamond Tools. *Int. J. Refract. Met. Hard Mater.* **2014**, *45*, 117–124.
298. Fang, Y.; Zhang, Y.; Fan, H.; Hu, T.; Song, J.; Hu, L. Surface Composition-Lubrication Design of Al_2O_3/Mo Laminated Composites-Part I: Influence of Laser Surface Texturing on the Tribological Behavior at 25 and 800 °C. *Wear* **2015**, *334–335*, 23–34.
299. Bathe, R.; Sai Krishna, V.; Nikumb, S. K.; Padmanabham, G. Laser Surface Texturing of Gray Cast Iron for Improving Tribological Behavior. *Appl. Phys. A: Mater. Sci. Process.* **2014**, *117*, 117–123.
300. He, D.; Zheng, S.; Pu, J.; Zhang, G.; Hu, L. Improving Tribological Properties of Titanium Alloys by Combining Laser Surface Texturing and Diamond-Like Carbon Film. *Tribol. Int.* **2015**, *82*, 20–27.
301. Shum, P. W.; Zhou, Z. F.; Li, K. Y. Friction and Wear Reduction of Hard TiAlSiN Coatings by an Integrated Approach of Laser Surface Texturing and High-Energy Ion Implantation. *Surf. Coat. Technol.* **2014**, *259*, 136–140.
302. Luo, K. Y.; Wang, C. Y.; Li, Y. M.; *et al.* Effects of Laser Shock Peening and Groove Spacing on the Wear Behavior of Non-Smooth Surface Fabricated by Laser Surface Texturing. *Appl. Surf. Sci.* **2014**, *313*, 600–606.
303. Braisted, W.; Brockman, R. Finite Element Simulation of Laser Shock Peening. *Int. J. Fatigue* **1999**, *21*, 719–724.
304. Luo, K. Y.; Lu, J. Z.; Wang, Q. W.; Luo, M.; Qi, H.; Zhou, J. Z. Residual Stress Distribution of Ti–6Al–4V Alloy under Different Ns-LSP Processing Parameters. *Appl. Surf. Sci.* **2013**, *285*, 607–615.
305. Ye, C.; Suslov, S.; Fei, X.; Cheng, G. J. Bimodal Nanocrystallization of NiTi Shape Memory Alloy by Laser Shock Peening and Post-Deformation Annealing. *Acta Mater.* **2011**, *59*, 7219–7227.
306. Lu, J. Z.; Luo, K. Y.; Zhang, Y. K.; *et al.* Grain Refinement Mechanism of Multiple Laser Shock Processing Impacts on ANSI 304 Stainless Steel. *Acta Mater.* **2010**, *58*, 5354–5362.
307. Li, K.; Yao, Z.; Hu, Y.; Gu, W. Friction and Wear Performance of Laser Peen Textured Surface under Starved Lubrication. *Tribol. Int.* **2014**, *77*, 97–105.
308. Lu, J.-Z.; Yang, C.-J.; Zhang, L.; Feng, A.-X.; Jiang, Y.-F. Mechanical Properties and Microstructure of Bionic Non-Smooth Stainless Steel Surface by Laser Multiple Processing. *J. Biomech. Eng.* **2009**, *6*, 180–185.
309. Moradi, S.; Kamal, S.; Englezos, P.; Hatzikiriakos, S. G. Femtosecond Laser Irradiation of Metallic Surfaces: Effects of Laser Parameters on Superhydrophicity. *Nanotechnology* **2013**, *24*, 415302.
310. Kurselis, K.; Kiyan, R.; Chichkov, B. N. Formation of Corrugated and Porous Steel Surfaces by Femtosecond Laser Irradiation. *Appl. Surf. Sci.* **2012**, *258*, 8845–8852.
311. Vorobyev, A. Y.; Cuo, C. Femtosecond Laser Structuring of Titanium Implants. *Appl. Surf. Sci.* **2007**, *253*, 7272–7280.
312. Zuhlke, C. A.; Anderson, T. P.; Alexander, D. R. Formation of Multiscale Surface Structures on Nickel via above Surface Growth and below Surface Growth Mechanisms Using Femtosecond Laser Pulses. *Opt. Exp.* **2013**, 8460–8470.
313. Costil, S.; Lamraoui, A.; Langlade, C.; Heintz, O.; Oltra, R. Surface Modifications Induced by Pulsed-Laser Texturing – Influence of Laser Impact on the Surface Properties. *Appl. Surf. Sci.* **2014**, *288*, 542–549.
314. Fadeeva, E.; Truong, V. K.; Stiesch, M.; *et al.* Bacterial Retention on Superhydrophobic Titanium Surfaces Fabricated by Femtosecond Laser Ablation. *Langmuir* **2011**, *27*, 3012–3019.
315. Kam, D. H.; Bhattacharya, S.; Mazumder, J. Control of Wetting Properties of an AISI 316L Stainless Steel Surface by Femtosecond Laser-Induced Surface Modification. *J. Micromech. Microeng.* **2012**, *22*, 105019.
316. Le Harzic, R.; Breitling, D.; Weikert, M.; *et al.* Pulse Width and Energy Influence on Laser Micromachining of Metals in a Range of 100 Fs to 5 Ps. *Appl. Surf. Sci.* **2005**, *249*, 322–331.
317. Lehr, J.; Kietzig, A.-M. Production of Homogeneous Micro-Structures by Femtosecond Laser Micro-Machining. *Opt. Laser Eng.* **2014**, *57*, 121–129.
318. Nayak, B. K.; Gupta, M. C.; Kolasinski, K. W. Formation of Nano-Textured Conical Microstructures in Titanium Metal Surface by Femtosecond Laser Irradiation. *Appl. Phys. A: Mater. Sci. Process.* **2008**, *90*, 399–402.
319. Nayak, B. K.; Gupta, M. C. Self-Organized Micro/nano Structures in Metal Surfaces by Ultrafast Laser Irradiation. *Opt. Laser Eng.* **2010**, *90*, 940–949.

320. Singh, N.; Alexander, D. R.; Schiffern, J.; Doerr, D. Femtosecond Laser Production of Metal Surfaces Having Unique Surface Structures That Are Broad Band Absorbers. *J. Laser Appl.* **2006**, *18*, 242–244.
321. Oliveira, V.; Ausset, S.; Vilar, R. Surface Micro/Nanostructuring of Titanium under Stationary and Non-Stationary Femtosecond Laser Irradiation. *Appl. Surf. Sci.* **2009**, *255*, 7556–7560.
322. Amanov, A.; Tsuboi, R.; Oe, H.; Sasaki, S. The Influence of Bulges Produced by Laser Surface Texturing on the Sliding Friction and Wear Behavior. *Tribol. Int.* **2013**, *60*, 213–223.
323. Bizi-Bandoki, P.; Benayoun, S.; Valette, S.; Beaugirard, B.; Audouard, E. Modifications of Roughness and Wettability Properties of Metals Induced by Femtosecond Laser Treatment. *Appl. Surf. Sci.* **2011**, *257*, 5213–5218.
324. Prodanov, N.; Gachot, C.; Rosenkratz, A.; Mücklich, F.; Müser, M. H. Contact Mechanics of Laser-Textured Surfaces. *Tribol. Lett.* **2013**, *50*, 41–48.
325. Lin, T. F.; Palmer, T. A.; Meinert, K. C.; Murray, N. R.; Majeski, R. Capillary Wicking of Liquid Lithium on Laser Textured Surfaces for Plasma Facing Components. *J. Nucl. Mater.* **2013**, *433*, 55–65.
326. Xiong, D.; Qin, Y.; Li, J.; Wan, Y.; Tyagi, R. Tribological Properties of PTFE/laser Surface Textured Stainless Steel under Starved Oil Lubrication. *Tribol. Int.* **2015**, *82*, 305–310.
327. Segu, D. Z.; Choi, S. G.; Choi hyouk, J.; Kim, S. S. The Effect of Multi-Scale Laser Textured Surface on Lubrication Regime. *Appl. Surf. Sci.* **2013**, *270*, 58–63.
328. Kim, B. S.; Chung, W. Y.; Rhee, M.-H.; Lee, S.-Y. Studies on the Application of Laser Surface Texturing to Improve the Tribological Performance of AlCrSiN-Coated Surfaces. *Met. Mater. Int.* **2012**, *18*, 1023–1027.
329. Li, Y.; Cui, Z.; Wang, W.; Lin, C.; Tsai, H.-L. Formation of Linked Nanostructure-Textured Mound-Shaped Microstructures on Stainless Steel Surface via Femtosecond Laser Ablation. *Appl. Surf. Sci.* **2015**, *324*, 775–783.
330. Oboňa, J. V.; Ocelík, V.; Rao, J. C.; *et al.* Modification of Cu Surface with Picosecond Laser Pulses. *Appl. Surf. Sci.* **2014**, *303*, 118–124.
331. Demir, A. G.; Furlan, C.; Lecis, N.; Previtali, B. Laser Surface Structuring of AZ31 Mg Alloy for Controlled Wettability. *Biointerfaces* **2014**, *9*, 029009.
332. Cunha, A.; Serro, A. P.; Oliveira, V.; Almeida, A.; Vilar, R.; Durrieu, M.-C. Wetting Behaviour of Femtosecond Laser Textured Ti–6Al–4V Surfaces. *Appl. Surf. Sci.* **2013**, *265*, 688–696.
333. Sabonis, V.; Naujokaitis, A.; Arlauskas, K. Wetting Properties Modification of TiO_2 Layer by Femtosecond UV Pulses. *J. Laser Micro Nanoen.* **2015**, *10*, 24–28.
334. Yasumaru, N.; Sentoku, E.; Haga, M.; Kiuchi, J. Femtosecond-Laser-Induced Nanostructure and High Ablation Rate Observed on Nitrided Alloy Steel. *J. Laser Micro Nanoen.* **2015**, *10*, 33–37.
335. Yilbas, B. S.; Matthews, A.; Karatas, C.; *et al.* Laser Texturing of Plasma Electrolytically Oxidized Aluminum 6061 Surfaces for Improved Hydrophobicity. *J. Manuf. Sci. Eng.* **2014**, *136*, 054501–054509.
336. Saltuganov, P. N.; Ionin, A. A.; Kudryashov, S. I.; *et al.* Fabrication of Superhydrophobic Coating on Stainless Steel Surface by Femtosecond Laser Texturing and Chemisorption of an Hydrophobic Agent. *J. Russ. Laser Res.* **2015**, *36*, 81–85.
337. Lopez, J.; Faucon, M.; Devillard, R.; *et al.* Parameters of Influence in Surface Ablation and Texturing of Metals Using High-Power Ultrafast Laser. *J. Laser Micro Nanoen.* **2015**, *10*, 1–10.
338. U.S. Congress, Office of Technology Assessment. *New Structural Materials Technologies: Opportunities for the Use of Advanced Ceramics and Composites-A Technical Memorandum*; US Government Printing Office: Washington, DC, 1986.
339. Samant, A. N.; Dahotre, N. B. Laser Machining of Structural Ceramics – A Review. *J. Eur. Ceram. Soc.* **2009**, *29*, 969–993.
340. Pandley, P. C.; Shan, H. S. *Modern Machining Processes*; McGraw Hill: New Delhi, 1980.
341. Chryssolouris, G. *Laser Machining Theory and Practice*; Springer-Verlag: New York, NY, 1991.
342. Tuersley, I. P.; Jawaid, A.; Pashby, I. R. Review: Various Methods of Machining Advanced Ceramic Materials. *J. Mater. Process. Technol.* **1994**, *42*, 377–390.
343. Knowles, M. R. H.; Rutterford, G.; Karnakis, D.; Ferguson, A. Micro-Machining of Metals, Ceramics and Polymers Using Nanosecond Lasers. *Int. J. Adv. Manuf. Technol.* **2007**, *33*, 95–102.
344. Bäuerle, D. *Laser Processing and Chemistry*; Springer: New York, NY, 2000.
345. Hibi, Y.; Enomoto, Y.; Kikuchi, K.; Shikata, N.; Ogiso, H. Excimer Laser Assisted Chemical Machining of SiC Ceramic. *Appl. Phys. Lett.* **1995**, *66*, 817–818.
346. Roy, S.; Modest, M. F. CW Laser Machining of Hard Ceramics – I. Effects of Three-Dimensional Conduction, Variable Properties and Various Laser Parameters. *Int. J. Heat Mass Transf.* **1993**, *36*, 3515–3528.
347. Samant, A. N.; Dahotre, N. B. Differences in Physical Phenomena Governing Laser Machining of Structural Ceramics. *Ceram. Int.* **2009**, *35*, 2093–2097.
348. Bang, S. Y.; Roy, S.; Modest, M. F. CW Laser Machining of Hard Ceramics – II. Effects of Multiple Reflections. *Int. J. Heat Mass Transf.* **1993**, *36*, 3529–3540.
349. Kuar, A. S.; Doloi, B.; Bhattacharyya, B. Modelling and Analysis of Pulsed Nd: YAG Laser Machining Characteristics during Micro-Drilling of Zirconia (ZrO_2). *Int. J. Mach. Tools Manuf.* **2006**, *46*, 1301–1310.
350. Samant, A. N.; Du, B.; Dahotre, N. B. *In-Situ* Surface Absorptivity Prediction during 1.06 μm Wavelength Laser Low Aspect Ratio Machining of Structural Ceramics. *Phys. Status Solidi A* **2009**, *206*, 1433–1439.
351. Samant, A. N.; Dahotre, N. B. Absorptivity Transition in the 1.06 μm Wavelength Laser Machining of Structural Ceramics. *Int. J. Appl. Ceram. Tec.* **2011**, *8*, 127–139.
352. Perrie, W.; Rushton, A.; Gill, M.; Fox, P.; O'Neill, W. Femtosecond Laser Micro-Structuring of Alumina Ceramic. *Appl. Surf. Sci.* **2005**, *248*, 213–217.
353. Longfellow, J. High Speed Drilling in Alumina Substrates with a CO_2 Laser. *Am. Ceram. Soc. Bull.* **1971**, *50*, 251–253.
354. Saifi, M. A.; Borutta, R. Optimization of Pulsed CO_2 Laser Parameters for Al_2O_3 Scribing. *Ceram. Bull.* **1975**, *54*, 986–989.
355. Inc. Coherent. *Lasers-Operation, Equipment, Application, and Design*; McGraw Hill: New York, NY, 1980.
356. Chryssolouris, G.; Bredt, J. Machining of Ceramics Using a Laser Lathe. *Proceedings of the Intersociety Symposium on Machining Advanced Ceramic Materials and Components*, Pittsburgh, PA, 1987; pp. 70–72.
357. Samant, A. N.; Dahotre, N. B. Computational Predictions in Single Dimensional Laser Machining of Alumina. *Int. J. Mach. Tools Manuf.* **2008**, *48*, 1345–1353.
358. Hamann, C.; Rosen, H. Laser Machining of Ceramic and Silicon. In *Proceeding of SPIE, High Power Lasers and Their Industrial Applications*, Vol. 801, 1987; pp. 130–137.
359. Glaw, V.; Hahn, R.; Wolf, J.; *et al.* Laser Machining of Ceramics for MCM-D Applications. In *Proceedings of the International Conference Micro Materials Micro Mat'97*, 1997; p. 535.
360. Okamoto, Y.; Sakagawa, T.; Nakamura, H.; Uno, Y. Micro-Machining Characteristics of Ceramics by Harmonics of Nd:YAG Laser. *J. Adv. Mech. Des. Syst.* **2008**, *2*, 661–667.
361. Sciti, D.; Melandri, C.; Bellosi, A. Excimer Laser-Induced Microstructural Changes of Alumina and Silicon Carbide. *J. Mater. Sci.* **2000**, *35*, 3799–3810.
362. Wang, C.; Zeng, X. Study of Laser Carving Three-Dimensional Structures on Ceramics: Quality Controlling and Mechanisms. *Opt. Laser Technol.* **2007**, *39*, 1400–1405.
363. Tsai, C. H.; Chen, H. W. Laser Milling of Cavity in Ceramic Substrate by Fracture-Machining Element Technique. *J. Mater. Process. Technol.* **2003**, *136*, 158–165.
364. Tsai, C. H.; Chen, H. W. The Laser Shaping of Ceramic by a Fracture Machining Technique. *Int. J. Adv. Manuf. Technol.* **2004**, *23*, 342–349.
365. Modest, M. F. Minimization of Elastic Thermal Stresses during Laser Machining of Ceramics Using a Dual-Beam Arrangement. *J. Laser Appl.* **2001**, *13*, 111.
366. Segall, A. E.; Cai, G.; Akarapu, R.; Romasco, A.; Li, B. Q. Fracture Control of Unsupported Ceramics during Laser Machining Using a Simultaneous Prescore. *J. Laser Appl.* **2005**, *17*, 57–62.
367. Tsai, C. H.; Ou, C. H. Machining a Smooth Surface of Ceramic Material by Laser Fracture Machining Technique. *J. Mater. Process. Technol.* **2004**, *155–156*, 1797–1804.
368. Yang, J. L.; Yu, J. L.; Cui, Y. Y.; Huang, Y. New Laser Machining Technology of Al_2O_3 Ceramic with Complex Shape. *Ceram. Int.* **2012**, *38*, 3643–3648.
369. Yamamoto, J.; Yamamoto, Y. Laser Machining of Silicon Nitride. In *International Conference on Laser Advanced Materials Processing-Science and Applications*, 1987; pp. 297–302.
370. Firestone, R. F.; Vesely, E. J., Jr. High Power Laser Beam Machining of Structural Ceramics. In *Intersociety Symposium on Machining of Advanced Ceramic Materials and Components*, 1988; pp. 215–227.
371. Lavrinovich, A. V.; Kryl, Y. A.; Androsov, I. M.; Artemyuk, S. A. Effect of Dimensional Laser Machining on the Structure and Properties of Silicon Nitride. *Powder Metall. Met. Ceram.* **1990**, *29*, 328–332.

372. Shigematsu, I.; Kanayama, K.; Tsuge, A.; Nakamura, M. Analysis of Constituents Generated with Laser Machining of Si_3N_4 and SiC. *J. Mater. Sci. Lett.* **1998**, *17*, 737–739.
373. Samant, A. N.; Dahotre, N. B. *Ab Initio* Physical Analysis of Single Dimensional Laser Machining of Silicon Nitride. *Adv. Eng. Mater.* **2008**, *10*, 978–981.
374. Miyamoto, I.; Marou, H. *Processing of Ceramics by Excimer Lasers. SPIE-Laser Assisted Process II*, Vol. 1279, 1990; p. 66.
375. Pham, D. T.; Dimov, S. S.; Petkov, P. V. Laser Milling of Ceramic Components. *Int. J. Mach. Tools Manuf.* **2007**, *47*, 618–626.
376. Sciti, D.; Bellosi, A. Laser-Induced Surface Drilling of Silicon Carbide. *Appl. Surf. Sci.* **2001**, *180*, 92–101.
377. Copley, S.; Bass, M.; Jau, B.; Wallace, R. Shaping Materials with Lasers. *Laser Mater. Proc.* **1983**, 297–336.
378. Polk, D. H.; Banas, C. M.; Frye, R. W.; Gragosz, R. A. Laser Processing of Materials. *Ind. Heat Exchangers* **1986**, 357–364.
379. Affolter, P.; Schmid, H. G. Processing of New Ceramic Materials with Solid State Laser Radiation. *Spie-High Power Lasers Ind. Appl.* **1987**, *801*, 120–129.
380. Samant, A. N.; Daniel, C.; Chand, R. H.; Blue, C. A.; Dahotre, N. B. Computational Approach to Photonic Drilling of Silicon Carbide. *Int. J. Manuf. Technol.* **2009**, *45*, 704–713.
381. Valentini, F.; Zambotto, I.; Sciti, D.; Silvestroni, L.; Melandri, C.; Guicciardi, S. Microstructure and Nanoindentation Properties of Surface Textures Obtained by Laser Machining and Molding in Silicon Carbide. *Adv. Eng. Mater.* **2013**, *15*, 330–335.
382. Bai, S.; Wang, R.; Li, M. Wettability Control of Laser Textured SiC Surfaces Using Additive Elements. *Ceram. Int.* **2015**, *41*, 5644–5647.
383. Ma, C.; Bai, S.; Peng, X.; Meng, Y. Improving Hydrophobicity of Laser Textured SiC Surface with Micro-Square Convexes. *Appl. Surf. Sci.* **2013**, *266*, 51–56.
384. Lumpp, K. Excimer Laser Machining and Metallization of Vias in Aluminium Nitride. *Mater. Sci. Eng. B* **1997**, *45*, 208–212.
385. Gilbert, T.; Krstic, V. D.; Zak, G. Machining of Aluminium Nitride with Ultra-Violet and Near-Infrared Nd:YAG Lasers. *J. Mater. Process. Technol.* **2007**, *189*, 409–417.
386. Liang, X. Y.; Dutta, S. P. Application Trend in Advanced Ceramic Technologies. *Technovation* **2001**, *21*, 61–65.
387. Yilbas, B. S. Laser Texturing of Zirconia Surface with Presence of TiC and B_4C: Surface Hydrophobicity, Metallurgical, and Mechanical Characteristics. *Ceram. Int.* **2015**, *40*, 16159–16167.
388. Sola, D.; Pena, J. I. Laser Machining and Functional Applications of Glass-Ceramic Materials. *Int. J. Appl. Ceram. Technol.* **2013**, *10*, 484–491.
389. Oliveira, V.; Vilar, R.; Conde, O.; Freitas, P. Laser Micromachining of Al_2O_3–TiC Ceramic. *J. Mater. Res.* **1997**, *12*, 3206–3209.
390. Oliveira, V.; Simoes, F.; Vilar, R. Column-Growth Mechanisms during KrF Laser Micromachining of Al_2O_3–TiC Ceramics. *Appl. Phys. A: Mater. Sci. Process.* **2005**, *81*, 1157–1162.
391. Lei, S.; Shin, Y. C.; Incropera, F. P. Deformation Mechanisms and Constitutive Modelling for Silicon Nitride Undergoing Laser-Assisted Machining. *Int. J. Mach. Tools Manuf.* **2000**, *40*, 2213–2233.
392. Xing, Y.; Deng, J.; Wu, Z.; Cheng, H. Effect of Regular Surface Textures Generated by Laser on Tribological Behavior of Si_3N_4/TiC Ceramic. *Appl. Surf. Sci.* **2013**, *265*, 823–832.
393. Lei, S.; Shin, Y. C.; Incropera, F. P. Experimental Investigation of Thermo-Mechanical Characteristics in Laser-Assisted Machining of Silicon Nitride Ceramics. *J. Manuf. Sci. Eng.* **2001**, *123*, 639–646.
394. Tsumori, F.; Hunt, S.; Osada, T.; Miura, H. Formation of Ceramic Micro-Channel by Combination of Laser Beam Machining and Micro Powder Imprinting. *Jpn. J. Appl. Phys.* **2015**, *54*, 06FM03.
395. Huang, Y. X.; Lu, J. Y.; Huang, J. X. KrF Excimer Laser Precision Machining of Hard and Brittle Ceramic Biomaterials. *Biomed. Mater.* **2014**, *9*, 035009.
396. Rozzi, J. C.; Pfefferkorn, F. E.; Incropera, F. P.; Shin, Y. C. Transient, Three-Dimensional Heat Transfer Model for the Laser Assisted Machining of Silicon Nitride. I. Comparison of Predictions with Measured Surface Temperature Histories. *Int. J. Heat Mass Transf.* **2000**, *43*, 1409–1426.
397. Rozzi, J. C.; Pfefferkorn, F. E.; Incropera, F. P.; Shin., Y. C. Transient Thermal Response of a Rotating Cylindrical Silicon Nitride Workpiece Subjected to a Translating Laser Heat Source. Part I. Comparison of Surface Temperature Measurements with Theoretical Results. *J. Heat Transf.* **1998**, *120*, 899–906.
398. Rozzi, J. C.; Incropera, F. P.; Shin, Y. C. Transient Thermal Response of a Rotating Cylindrical Silicon Nitride Workpiece Subjected to a Translating Laser Heat Source. Part II. Parametric Effects and Assessment of a Simplified Model. *J. Heat Transf.* **1998**, *120*, 907–915.
399. Rozzi, J. C.; Incropera, F. P.; Shin, Y. C. Transient, Three-Dimensional Heat Transfer Model for the Laser Assisted Machining of Silicon Nitride. II. Assessment of Parametric Effects. *Int. J. Heat Mass Transf.* **2000**, *43*, 1425–1437.
400. Rozzi, J. C.; Pfefferkorn, F. E.; Shin, Y. C.; Incropera, F. P. Experimental Evaluation of the Laser Assisted Machining of Silicon Nitride Ceramics. *J. Manuf. Sci. Eng.* **2000**, *122*, 666–670.
401. Tian, T. G.; Shin, Y. C. Thermal Modeling for Laser-Assisted Machining of Silicon Nitride Ceramics with Complex Features. *J. Manuf. Sci. Eng.* **2006**, *128*, 425–434.
402. Tian, Y. G.; Shin, Y. C. Multiscale Finite Element Modeling of Silicon Nitride Ceramics Undergoing Laser-Assisted Machining. *J. Manuf. Sci. Eng.* **2007**, *129*, 287–295.
403. Kim, J.-D.; Lee, S.-J.; Suh, J. Characteristics of Laser Assisted Ma Chining for Silicon Nitride Ceramic according to Machining Parameters. *J. Mech. Sci. Technol.* **2011**, *25*, 995–1001.
404. Pfefferkorn, F. E.; Incropera, F. P.; Shin, Y. C. Heat Transfer Model of Semi-Transparent Ceramics Undergoing Laser-Assisted Machining. *Int. J. Heat Mass Transf.* **2005**, *48*, 1999–2012.
405. Bowman, K. J.; Pfefferkorn, F. E.; Shin, Y. C. Recrystallization Textures during Laser-Assisted Machining of Zirconia Ceramics. In *Textures of Materials, Pts 1 and 2*; Materials Science Forum; Trans Tech Publications Ltd.: Switzerland, 2002; pp. 1669–1674.
406. Pfefferkorn, F. E.; Shin, Y. C.; Tian, Y.; Incropera, F. P. Laser-Assisted Machining of Magnesia-Partially-Stabilized Zirconia. *J. Manuf. Sci. Eng.* **2004**, *126*, 42–51.
407. Chang, C. W.; Kuo, C. P. An Investigation of Laser-Assisted Machining of Al_2O_3 Ceramics Planning. *Int. J. Mach. Tools Manuf.* **2007**, *47*, 452–461.
408. Rebro, P. A.; Shin, Y. C.; Incropera, F. P. Laser-Assisted Machining of Reaction Sintered Mullite Ceramics. *J. Manuf. Sci. Eng.* **2002**, *124*, 875–885.
409. Chang, C. W.; Kuo, C. P. Evaluation of Surface Roughness in Laser-Assisted Machining of Aluminum Oxide Ceramics with Taguchi Method. *Int. J. Mach. Tools Manuf.* **2007**, *47*, 141–147.
410. Germain, G.; Lebrun, J. L.; Braham-Bouchnak, T.; Bellet, D.; Auger, S. Laser-Assisted Machining of Inconel 718 with Carbide and Ceramic Inserts. *Int. J. Mater. Form.* **2008**, *1*, 523–526.
411. Meeker, J.; Segall, A. E.; Semak, V. V. Surface Effects of Alumina Ceramics Machined with Femtosecond Lasers. *J. Laser Appl.* **2010**, *22*, 7–12.
412. Ravindra, D.; Patten, J. Micro-Laser-Assisted Machining: The Future of Manufacturing Ceramics and Semiconductors. *Sensor. Mater.* **2014**, *26*, 417–427.
413. Singh, R.; Alberts, M. J.; Melkote, S. N. Characterization and Prediction of the Heat-Affected Zone in a Laser-Assisted Mechanical Micromachining Process. *Int. J. Mach. Tools Manuf.* **2008**, *48*, 994–1004.
414. Dahotre, N. B.; Harimkar, S. P. *Laser Fabrication and Machining of Materials*; Springer: New York, NY, 2008.
415. Chen, H. L.; Huang, K. T.; Lin, C.-H.; Wang, W. Y.; Fan, W. Fabrication of Sub-Wavelength Antireflective Structures in Solar Cells by Utilizing Modified Illumination and Defocus Techniques in Optical Lithography. *Microelectron. Eng.* **2007**, *84*, 750–754.
416. Gilles, S.; Meier, M.; Prompers, M.; van der Hart, A.; Kugeler, C.; Offenhäusser, A. UV Nanoimprint Lithography with Rigid Polymer Molds. *Microelectron. Eng.* **2008**, *86*, 661–664.
417. Elsner, C.; Zajadacz, J.; Zimmer, K. Replication of 3D-Microstructures with Undercuts by UV-Moulding. *Microelectron. Eng.* **2011**, *88*, 60–63.
418. Hinsberg, W.; Foule, F. A.; Hoffnagle, J.; Sanchez, M.; Wallraff, G.; Morrison, M. Deep-Ultraviolet Interferometric Lithography as a Tool for Assessment of Chemically Amplified Photoresist Performance. *J. Vac. Sci. Technol. B* **1998**, *16*, 3689–3694.
419. Xie, Q.; Hong, M. H.; Tan, H. L.; Chen, G. X.; Shi, L. P.; Chong, T. C. Fabrication of Nanostructures with Laser Interference Lithography. *J. Alloys Compd.* **2008**, *449*, 261–264.
420. Zhang, J.; Wang, Z.; Di, X.; Zhao, L.; Wang, D. Effects of Azimuthal Angles on Laser Interference Lithography. *Appl. Opt.* **2014**, *53*, 6294–6301.
421. Sreekanth, K. V.; Chua, J. K.; Murukeshan, V. M. Interferometric Lithography for Nanoscale Feature Patterning: A Comparative Analysis between Laser Interference, Evanescent Wave Interference, and Surface Plasmon Interference. *Appl. Opt.* **2010**, *49*, 6710–6717.
422. Xu, J.; Wang, Z.; Zhang, Z.; Wang, D.; Weng, Z. Fabrication of Moth-Eye Structures on Silicon by Direct Six-Beam Laser Interference Lithography. *J. Appl. Phys.* **2014**, *115*, 203101.

423. Wang, D.; Wang, Z.; Zhang, Z.; Yue, Y.; Li, D.; Maple, C. Direct Modification of Silicon Surface by Nanosecond Laser Interference Lithography. *Appl. Surf. Sci.* **2013**, *282*, 67–72.
424. Wang, D.; Wang, Z.; Zhang, Z.; Yue, Y.; Li, D.; Maple, C. Effects of Polarization on Four-Beam Laser Interference Lithography. *Appl. Phys. Lett.* **2013**, *102*, 081903.
425. Zhang, Z.; Wang, Z.; Wang, D.; Ding, Y. Periodic Antireflection Surface Structure Fabricated on Silicon by Four-Beam Laser Interference Lithography. *J. Laser Appl.* **2014**, *26*, 012010.
426. Martin-Fabiani, I.; Riedel, S.; Rueda, D. R.; *et al.* Micro- and Submicrostructuring Thin Polymer Films with Two and Three-Beam Single Pulse Laser Interference Lithography. *Langmuir* **2014**, *30*, 8973–8979.
427. Ellman, M.; Rodriguez, A.; Perez, N.; *et al.* High-Power Laser Interference Lithography Process on Photoresist: Effect of Laser Fluence and Polarisation. *Appl. Surf. Sci.* **2009**, *255*, 5537–5541.
428. Yang, H. F.; He, H. D.; Zhao, E. L.; *et al.* Simulation and Fabrication of Nanostructures with Laser Interference Lithography. *Laser Phys.* **2014**, *24*, 065901.
429. Kim, D. S.; Ji, R.; Fan, H. J.; *et al.* Laser-Interference Lithography Tailored for Highly Symmetrically Arranged ZnO Nanowire Arrays. *Small* **2007**, *3*, 76–80.
430. Kim, T.-U.; Sim, J.-A.; Pawar, S. M.; Moon, J.-H.; Kim, J. H. Creation of Nanoscale Two-Dimensional Patterns of ZnO Nanorods Using Laser Interference Lithography Followed by Hydrothermal Synthesis at 90 °C. *Cryst. Growth Des.* **2010**, *10*, 4256–4261.
431. De Boor, J.; Geyer, N.; Wittemann, J. V.; Gosele, U.; Schmidt, V. Sub-100 Nm Silicon Nanowires by Laser Interference Lithography and Metal-Assisted Etching. *Nanotechnology* **2010**, *21*, 095302.
432. Lim, C. S.; Hong, M. H.; Lin, Y.; *et al.* Microlens Array Fabrication by Laser Interference Lithography for Super-Resolution Surface Nanopatterning. *Appl. Phys. Lett.* **2006**, *89*, 1911125.
433. Zheng, M.; Yu, M.; Liu, Y.; *et al.* Magnetic Nanodot Arrays Produced by Direct Laser Interference Lithography. *Appl. Phys. Lett.* **2001**, *79*, 2606–2608.
434. Murillo, R.; van Wolferen, H. A.; Abelmann, L.; Lodder, J. C. Fabrication of Patterned Magnetic Nanodots by Laser Interference Lithography. *Microelectron. Eng.* **2005**, *78–79*, 260–265.
435. Petter, K.; Kipp, T.; Heyn Ch.; Heitmann, D.; Schüller, C. Fabrication of Large Periodic Arrays of AlGaAs Microdisks by Laser-Interference Lithography and Selective Etching. *Appl. Phys. Lett.* **2002**, *81*, 592–594.
436. Liu, C. H.; Hong, M. H.; Cheung, H. W.; *et al.* Bimetallic Structure Fabricated by Laser Interference Lithography for Tuning Surface Plasmon Resonance. *Opt. Exp.* **2008**, *16*, 10701–10709.
437. Cho, K. S.; Mandal, P.; Kim, K.; *et al.* Improved Efficiency in GaAs Solar Cells by 1D and 2D Nanopatterns Fabricated by Laser Interference Lithography. *Opt. Commun.* **2011**, *284*, 2608–2612.
438. Spallas, J. P.; Hawryluk, A. M.; Kania, D. R. Field Emitter Array Mask Patterning Using Laser Interference Lithography. *J. Vac. Sci. Technol. B* **1995**, *13*, 1973–1978.
439. Choi, T.; Jang, J.-H.; Ullal, C. K.; LeMieux, M. C.; Tsukruk, V. V.; Thomas, E. L. The Elastic Properties and Plastic Behavior of Two-Dimensional Polymer Structures Fabricated by Laser Interference Lithography. *Adv. Funct. Mater.* **2006**, *16*, 1324–1330.
440. Ritucci, A.; Reale, A.; Zupella, P.; *et al.* Interference Lithography by a Soft X-Ray Laser Beam: Nanopatterning on Photoresists. *J. Appl. Phys.* **2007**, *102*, 034313.
441. Castro-Hurtado, I.; Tavera, T.; Yurrita, P.; *et al.* Structural and Optical Properties of WO_3 Sputtered Thin Films Nanostructured by Laser Interference Lithography. *Appl. Surf. Sci.* **2013**, *276*, 229–235.
442. Lee, S.; Jeong, Y.-C.; Park, J.-K. Facile Fabrication of Close-Packed Microlens Arrays Using Photoinduced Surface Relief Structures as Templates. *Opt. Exp.* **2007**, *15*, 14550–14559.
443. Lee, S.; Jeong, Y.-C.; Park, J.-K. Unusual Surface Reliefs from Photoinduced Creeping and Aggregation Behavior of Azopolymer. *Appl. Phys. Lett.* **2008**, *93*, 031912.
444. Nalwa, K. S.; Park, J.-M.; Ho, K.-M.; Chaudhary, S. On Realizing Higher Efficiency Polymer Solar Cells Using a Textured Substrate Platform. *Adv. Mater.* **2011**, *23*, 112–116.
445. Seo, J.-H.; Park, J. H.; Kim, S. I.; *et al.* Nanopatterning by Laser Interference Lithography: Applications to Optical Devices. *J. Nanosci. Nanotechnol.* **2014**, *14*, 1521–1532.
446. Arriola, A.; Rodriguez, A.; Perez, N.; *et al.* Fabrication of High Quality Sub-Micron Au Gratings over Large Areas with Pulsed Laser Interference Lithography for SPR Sensors. *Opt. Mater. Exp.* **2012**, *2*, 1571–1579.
447. Xu, L.; Tan, L. S.; Hong, M. H. Tuning of Localized Surface Plasmon Resonance of Well-Ordered Ag/Au Bimetallic Nanodot Arrays by Laser Interference Lithography and Thermal Annealing. *Appl. Opt.* **2011**, *50*, G74–G79.
448. Zhou, Y.; Chen, X. Y.; Fu, Y. H.; Vienne, G.; Kuznetsov, A. I.; Luk'yanchuk, B. Fabrication of Large-Area 3D Optical Fishnet Metamaterial by Laser Interference Lithography. *Appl. Phys. Lett.* **2013**, *103*, 123116.
449. Park, J.-M.; Nalwa, K. S.; Leung, W.; Constant, K.; Chaudhary, S.; Ho, K.-M. Fabrication of Metallic Nanowires and Nanoribbons Using Laser Interference Lithography and Shadow Lithography. *Nanotechnology* **2010**, *21*, 215301.
450. Seo, J.-H.; Park, J.; Zhao, D.; *et al.* Large-Area Printed Broadband Membrane Reflectors by Laser Interference Lithography. *IEEE Photonics J.* **2013**, *5*, 2200106.
451. Siddique, R. H.; Hünig, R.; Faisal, A.; Lemmer, U.; Hölscher, H. Fabrication of Hierarchical Photonic Nanostructures Inspired by Morpho Butterflies Utilizing Laser Interference Lithography. *Opt. Mater. Exp.* **2015**, *5*, 996–1005.
452. van Rjin, C. J. M.; Nijdam, W.; Kuiper, S.; Veldhuis, G. J.; van Wolferen, H.; Elwenspoek, M. Microsieves Made with Laser Interference Lithography for Micro-Filtration Applications. *J. Micromech. Microeng.* **1999**, *9*, 170–172.
453. Kuiper, S.; de Boer, M.; van Rijn, C.; Nijdam, W.; Krijnen, G.; Elwenspoek, M. Wet and Dry Etching Techniques for the Release of Sub-Micrometre Perforated Membranes. *J. Micromech. Microeng.* **2000**, *10*, 171–174.
454. Kuiper, S.; van Wolferen, H.; van Rijn, C.; Nijdam, W.; Krijnen, G.; Elwenspoek, M. Fabrication of Microsieves with Sub-Micron Pore Size by Laser Interference Lithography. *J. Micromech. Microeng.* **2001**, *11*, 33–37.
455. Cheng, J. Y.; Cross, C. A.; Thomas, E. L.; Smith, H. I.; Vansco, G. J. Fabrication of Nanostructures with Long-Range Order Using Block Copolymer Lithography. *Appl. Phys. Lett.* **2002**, *81*, 3657–3659.
456. Fernadez, A.; Nguyen, H. T.; Britten, J. A.; *et al.* Use of Interference Lithography to Pattern Arrays of Submicron Resist Structures for Field Emission Flat Panel Displays. *J. Vac. Sci. Technol. B: Microelectron. Nanometer Struct.-Process., Meas., Phenom.* **1997**, *15*, 729–735.
457. Vogelaar, L.; Nijdam, W.; van Wolferen, H. A. G. M.; *et al.* Large Area Photonic Crystal Slabs for Visible Light with Waveguiding Defect Structures: Fabrication with Focused Ion Beam Assisted Laser Interference Lithography. *Adv. Mater.* **2001**, *13*, 1551–1554.
458. Perez, N.; Tavera, T.; Rodriguez, A.; Ellman, M.; Ayerdi, I.; Olaizola, S. M. Fabrication of Sub-Micrometric Metallic Hollow-Core Structures by Laser Interference Lithography. *Appl. Surf. Sci.* **2012**, *258*, 9370–9373.
459. Wei, Q.; Hu, F.; Wang, L. Formation of Nanotunnels Inside a Resist Film in Laser Interference Lithography. *Langmuir* **2015**, *31*, 5464–5468.
460. Rodriguez, A.; Echeverria, M.; Ellman, M.; *et al.* Laser Interference Lithography for Nanoscale Structuring of Materials: From Laboratory to Industry. *Microelectron. Eng.* **2009**, *86*, 937–940.
461. Lasagni, A. F.; Roch, T.; Langheinrich, D.; Bieda, M.; Wetzig, A. Large Area Direct Fabrication of Periodic Arrays Using Interference Patterning. *Phys. Procedia* **2011**, *12*, 214–220.
462. Roch, T.; Lasagni, A.; Beyer, E. Surface Modification of Thin Tetrahedral Amorphous Carbon Films by Means of UV Direct Laser Interference Patterning. *Diamond Relat. Mater.* **2010**, *19*, 1472–1477.
463. Berger, J.; Grosse Holthaus, M.; Pistillo, N.; Rezwan, K.; Lasagni, A. Ultraviolet Laser Interference Patterning of Hydroxyapatite Surfaces. *Appl. Surf. Sci.* **2011**, *257*, 3081–3087.
464. Müller-Meskamp, L.; Kim, Y. H.; Roch, T.; *et al.* Efficiency Enhancement of Organic Solar Cells by Fabricating Periodic Surface Textures Using Direct Laser Interference Patterning. *Adv. Mater.* **2012**, *24*, 906–910.
465. Her, T.-H.; Finlay, R. J.; Wu, C.; Deliwala, S.; Mazur, E. Microstructuring of Silicon with Femtosecond Laser Pulses. *Appl. Phys. Lett.* **1998**, *73*, 1673–1675.
466. Zorba, V.; Alexandratou, I.; Zergioti, I.; *et al.* Laser Microstructuring of Si Surfaces for Low-Threshold Field-Electron Emission. *Thin Solid Films* **2004**, *453–454*, 492–495.
467. Zorba, V.; Spanakis, E.; Stratakis, E.; *et al.* Silicon Electron Emitters by UV Laser Pulses. *Appl. Phys. Lett.* **2006**, *88*, 1.
468. Simon, P.; Ihlemann, J. Ablation of Submicron Structures on Metals and Semiconductors by Femtosecond UV-Laser Pulses. *Appl. Surf. Sci.* **1997**, *109–110*, 25–29.
469. Borchers, B.; Beskesi, J.; Simon, P.; Ihlemann, J. Submicron Surface Patterning by Laser Ablation with Short UV Pulses Using a Proximity Phase Mask Setup. *J. Appl. Phys.* **2010**, *107*, 063106.
470. Simitzi, C.; Efstathopoulos, P.; Kourgiantaki, A.; *et al.* Laser Fabricated Discontinuous Anisotropic Microconical Substrates as a New Model Scaffold to Control the Directionality of Neuronal Network Outgrowth. *Biomaterials* **2015**, *67*, 115–128.

471. Abbott, M.; Cotter, J. Optical and Electrical Proper Ties of Laser Texturing for Hi Gh-Efficiency Solar Cells. *Prog. Photovolt. Res. Appl.* **2006**, *14*, 225–235.
472. Knüttel, T.; Bergfeld, S.; Haas, S. Laser Texturing of Surfaces in Thin-Film Silicon Photovoltaics – A Comparison of Potential Processes. *J. Laser Micro Nanoen.* **2013**, *8*, 222–229.
473. Tsibidis, G. D.; Stratakis, E.; Loukakos, P. A.; Fotakis, C. Controlled Ultrashort-Pulse Laser-Induced Ripple Formation on Semiconductors. *Appl. Phys. Mater. Sci. Process.* **2014**, *114*, 57–68.
474. Yang, H.; Zhou, L.; He, H.; Qian, J.; Hao, J.; Zhu, H. Textures Induced by a Femtosecond Laser on Silicon Surfaces under Various Environments. *J. Russ. Laser Res.* **2012**, *33*, 349–355.
475. Wang, X. C.; Zheng, H. Y.; Tan, C. W.; Wang, F.; Yu, H. Y.; Pey, K. L. Fabrication of Silicon Nanobump Arrays by Near-Field Enhanced Laser Irradiation. *Appl. Phys. Lett.* **2010**, *96*, 084101–084103.
476. Wysocki, G.; Denk, R.; Piglmayer, K.; Arnold, N.; Bäuerle, D. Single-Step Fabrication of Silicon-Cone Arrays. *Appl. Phys. Lett.* **2003**, *82*, 692–693.
477. Soni, A.; Sundaram, V. M.; Wen, S.-B. The Generation of Nano-Patterns on a Pure Silicon Wafer in Air and Argon with Sub-Diffraction Limit Nanosecond Laser Pulses. *J. Phys. D: Appl. Phys.* **2010**, *43*, 145301.
478. Wen, S.-B.; Greif, R.; Russo, R. E. Background Gas Effects on the Generation of Nanopatterns on a Pure Silicon Wafer with Multiple Femtosecond near Field Laser Ablation. *Appl. Phys. Lett.* **2007**, *91*, 251113.
479. Farrokhi, H.; Zhou, W.; Zheng, H. Y.; Li, Z. L. Non-Ablative Texturing of Silicon Surface with a Continuous Wave Fiber Laser. *Opt. Exp.* **2012**, *20*, 23180.
480. Farrokhi, H.; Zhou, W.; Zheng, H. Theoretical Analysis of Non-Ablative Laser Texturing of Silicon Surface with a Continuous Wave Fiber Laser. *J. Laser Micro Nanoen.* **2015**, *20*, 181–185.
481. Ji, L.; Lv, X.; Wu, Y.; Lin, Z.; Jiang, Y. Hydrophobic Light-Trapping Structures Fabricated on Silicon Surfaces by Picosecond Laser Texturing and Chemical Etching. *J. Photon. Energy* **2015**, *5*, 053094.
482. Prodan, L.; Euser, T. G.; van Wolferen, H. A. G. M.; *et al.* Large-Area Two-Dimensional Silicon Photonic Crystals for Infrared Light Fabricated with Laser Interference Lithography. *Nanotechnology* **2004**, *15*, 639–642.
483. Yang, Y.-L.; Hsu, C.-C.; Chang, T.-L.; Kuo, L.-S.; Chen, P.-H. Study on Wetting Properties of Periodical Nanopatterns by a Combinative Technique of Photolithography and Laser Interference Lithography. *Appl. Surf. Sci.* **2010**, *256*, 3683–3687.
484. Wang, H.; Kongsuwan, P.; Satoh, G.; Yao, L. Femtosecond Laser-Induced Simultaneous Surface Texturing and Crystallization of a-Si:H Thin Film: Morphology Study. *Int. J. Adv. Manuf. Technol.* **2013**, *65*, 1691–1703.
485. Liu, J.; Kleimann, P.; Laffite, G.; Jamois, C.; Orobtchouk, R. Formation of 300 Nm Period Pore Arrays by Laser Interference Lithography and Electrochemical Etching. *Appl. Phys. Lett.* **2015**, *106*, 053107.
486. Nayak, N. C.; Lam, Y. C.; Yue, C. Y.; Sinha, A. T. CO(2)-Laser Micromachining of PMMA: The Effect of Polymer Molecular Weight. *J. Micromech. Microeng.* **2008**, *18*, 095020.
487. Paun, I.-A.; Selimis, A.; Bounos, G.; Kesckemeti, G.; Georgiou, S. Nanosecond and Femtosecond UV Laser Ablation of Polymers: Influence of Molecular Weight. *Appl. Surf. Sci.* **2009**, *255*, 9856–9860.
488. Rebollar, E.; Bounos, G.; Selimis, A.; Castillejo, M.; Georgiou, S. Examination of the Influence of Molecular Weight on Polymer Laser Ablation: Polystyrene at 248 Nm. *Appl. Phys. A: Mater. Sci. Process.* **2008**, *92*, 1043–1046.
489. Bounos, G.; Selimis, A.; Georgiou, S.; Rebollar, E.; Castillejo, M.; Bityurin, N. Dependence of Ultraviolet Nanosecond Laser Polymer Ablation on Polymer Molecular Weight: Poly (Methyl Methacrylate) at 248 Nm. *J. Appl. Phys.* **2006**, *100*, 114323.
490. Wang, Z. K.; Zheng, H. Y.; Xia, H. M. Femtosecond Laser-Induced Modification of Surface Wettability Pf PMMA for Fluid Separation in Microchannels. *Microfluid. Nanofluid.* **2011**, *10*, 225–229.
491. Bartnik, A.; Fiedorowicz, H.; Jarocki, R.; Kostecki, J.; Szczurek, A.; Szczurek, M. Ablation and Surface Modifications of PMMA Using a Laser-Plasma EUV Source. *Appl. Phys. B: Lasers Opt.* **2009**, *96*, 727–730.
492. De Marco, C.; Eaton, S. M.; Suriano, R.; *et al.* Surface Properties of Femtosecond Laser Ablated PMMA. *ACS Appl. Mater. Inter.* **2010**, *2*, 2377–2384.
493. Vannahme, C.; Klinkhammer, S.; Kolew, A.; *et al.* Integration of Organic Semiconductor Lasers and Single-Mode Passive Waveguides into a PMMA Substrate. *Microelectron. Eng.* **2010**, *87*, 693–695.
494. Teixidor, D.; Orozco, F.; Thepsonthi, T.; Ciurana, J.; Rodriguez, C. A.; Ozel, T. Effect of Process Parameters in Nanosecond Pulsed Laser Micromachining of PMMA-Based Microchannels at Near-Infrared and Ultraviolet Wavelengths. *Int. J. Adv. Manuf. Technol.* **2013**, *67*, 1651–1664.
495. Sobon, G.; Sotor, J.; Pasternak, I.; Krajewska, A.; Strupinski, W.; Abramski, K. M. Thulium-Doped All-Fiber Laser Mode-Locked by CVD-Graphene/PMMA Saturable Absorber. *Opt. Exp.* **2013**, *21*, 12797–12802.
496. Klank, H.; Kutter, J. P.; Geschke, O. CO_2-Laser Micromachining and Back-End Processing for Rapid Production of PMMA-Based Microfluidic Systems. *Lab Chip* **2002**, *2*, 242–246.
497. Lawrence, J.; Li, L. Modification of the Wettability Characteristics of Polymethyl Methacrylate (PMMA) by Means of CO_2, Nd: YAG, Excimer and High Power Diode Laser Radiation. *Mater. Sci. Eng. A* **2001**, *303*, 142–149.
498. Cheng, J. Y.; Wei, C. W.; Hsu, K. H.; Young, T. H. Direct-Write Laser Micromachining and Universal Surface Modification of PMMA for Device Development. *Sensor. Actuat. B-Chem.* **2004**, *99*, 186–196.
499. Romoli, L.; Tantussi, G.; Din, G. Experimental Approach to the Laser Machining of PMMA Substrates for the Fabrication of Microfluidic Devices. *Opt. Laser Eng.* **2011**, *49*, 419–427.
500. Yao, L. Y.; Liu, B.; Chen, T.; Liu, S. B.; Zuo, T. C. Micro Flow-through PCR in a PMMA Chip Fabricated by KrF Excimer Laser. *Biomed. Microdevices* **2005**, *7*, 253–257.
501. Hong, T. F.; Ju, W. J.; Wu, M. C.; Tai, C. H.; Tsai, C. H.; Fu, L. M. Rapid Prototyping of PMMA Microfluidic Chips Utilizing a CO_2 Laser. *Microfluid. Nanofluid.* **2010**, *9*, 1125–1133.
502. Dyer, P. E. Excimer Laser Polymer Ablation: Twenty Years On. *Appl. Phys. A: Mater. Sci. Process.* **2003**, *77*, 167–173.
503. Gotoh, K.; Kikuchi, S. Improvement of Wettability and Detergency of Polymeric Materials by Excimer UV Treatment. *Colloid Polym. Sci.* **2005**, *283*, 1356–1360.
504. Malek, C. G. K. Laser Processing for Bio-Microfluidics Applications (Part II). *Anal. Bioanal. Chem.* **2006**, *385*, 1362–1369.
505. Welle, A.; Horn, S.; Schimmelpfeng, J.; Kalka, D. Photo-Chemically Patterned Polymer Surfaces for Controlled PC-12 Adhesion and Neurite Guidance. *J. Neurosci. Methods* **2005**, *142*, 243–250.
506. Pfleging, W.; Bruns, M.; Welle, A.; Wilson, S. Laser-Assisted Modification of Polystyrene Surfaces for Cell Culture Applications. *Appl. Surf. Sci.* **2007**, *253*, 9177–9184.
507. Guber, A. E.; Heckele, M.; Herrmann, D.; *et al.* Microfluidic Lab-on-a-Chip Systems Based on Polymers – Fabrication and Application. *Chem. Eng. J. (Amsterdam, Neth.)* **2004**, *101*, 447–453.
508. Pasparakis, G.; Manouras, T.; Selimis, A.; Vamvakaki, M.; Argitis, P. Laser-Induced Cell Detachment and Patterning with Photodegradable Polymer Substrates. *Angew. Chem., Int. Ed.* **2011**, *50*, 4142–4145.
509. Wang, X.; Xing, Y.; Giovannini, M. Effect of Overlap and Overscan Number in Laser Surface Texturing of Medical Needles. *Appl. Phys. A: Mater. Sci. Process.* **2015**, *120*, 229–238.
510. Cunha, A.; Zouani, O. F.; Plawinski, L.; *et al.* Human Mesenchymal Stem Cell Behavior on Femtosecond Laser-Textured Ti–6Al–4 V Surfaces. *Nanomedicine* **2015**, *10*, 725–739.
511. Castillejo, M.; Rebollar, E.; Oujja, M.; *et al.* Fabrication of Porous Biopolymer Substrates for Cell Growth by UV Laser: The Role of Pulse Duration. *Appl. Surf. Sci.* **2012**, *258*, 8919–8927.
512. Qin, L.; Zeng, Q.; Wang, W.; Zhang, Y.; Dong, G. Response of MC3T3-E1 Osteoblast Cells to the Microenvironment Produced on Co–Cr–Mo Alloy Using Laser Surface Texturing. *J. Mater. Sci.* **2014**, *49*, 2662–2671.

3.9 Hydrophobicity and Surface Finish

A Owais, Beni-Suef University, Beni-Suef, Egypt
M Khaled and BS Yilbas, King Fahd University of Petroleum and Minerals, Dhahran, Saudi Arabia

© 2017 Elsevier Inc. All rights reserved.

3.9.1	**Introduction**	137
3.9.1.1	The Effect of Dust Accumulation on the PV Cell Efficiency	137
3.9.1.2	Historical Background	137
3.9.1.3	Polycarbonates: Properties and Synthesis	137
3.9.1.4	Crystallization Process of PCs	138
3.9.2	**Theoretical Models**	138
3.9.2.1	Fundamentals	138
3.9.2.2	Young's Equation (for Flat Surfaces)	138
3.9.2.3	The Effect of the Chemical Treatment and the Roughness on the Surface Hydrophobicity	139
3.9.2.4	Wenzel and Cassie–Baxter States (for Rough Surfaces)	139
3.9.2.5	Classification of Rough Surfaces	140
3.9.2.6	Self-Cleaning Surfaces	140
3.9.3	**Fabrication Methods and Technologies of Superhydrophobic Surfaces**	140
3.9.4	**The Solid–Liquid Interface and PC-Liquid Acetone**	142
3.9.4.1	AFM Micrographs	142
3.9.4.1.1	Surface topography	142
3.9.4.1.2	Texture profile micrographs	143
3.9.4.2	Scanning Electron Micrographs	144
3.9.4.3	Surface Roughness	144
3.9.4.4	Hydrophobicity Assessments	145
3.9.4.5	Fourier Transform Infrared Technique Characterization	147
3.9.4.6	X-Ray Diffraction Study	147
Acknowledgments		147
References		147

3.9.1 Introduction

A chemical approach is proposed to develop economically feasible hydrophobic surfaces with optimal optical properties. The work includes developing hierarchical superhydrophobic surfaces to significantly improve the hydrophobicity while maintaining the transparency of the solar panels cover, thereby conserving cleaning water and reducing the operational costs. Novel characterization methods are developed to comprehend these characteristics at nanoscale.

3.9.1.1 The Effect of Dust Accumulation on the PV Cell Efficiency

About 5% of the solar light is reflected at the interface between the photovoltaic panel's surface and the air owing to the refractive index difference. During the period of 8 months from the date of the PV cells installation in the desert, dust accumulation, furthermore, was found to reduce the efficiency of the cells' efficiency by 36% due to the surface-transmittance drop. This efficiency reduction extends to be about 72% after 15 years of exposure to the dusty and dry environment of the desert.[2] Therefore, for the PV panels installed in dry environments, the dust particles should not stick over the surfaces of the cells. This may be achievable by texturing the surface to have micro-/nano-patterns in order to mimic the lotus leaf phenomenon as observed from Figure 1.[1]

3.9.1.2 Historical Background

During the last decade, several studies have been performed in order to investigate and improve the different techniques which are used to design hydrophobic surfaces by controlling the surface topography and chemistry.[3] In fact, the idea of developing hydrophobic surfaces is inspired from nature.[4] Lotus leaf has gained the main the focus of the scientists who are interested in this field of research because its surface is rough and hydrophobic as well. Several crop plants also have the same characteristics like the lotus leaves, for example, *Brassica*, *Alchemellia*, and *Lupinus*.[5,6]



Figure 1 A hydrophobic plant leaf.[1]

3.9.1.3 Polycarbonates: Properties and Synthesis

Polycarbonates (PCs) are considered as an organic polymeric material with two subclasses; aliphatic and aromatic. The bisphenol A(2,2-bis(p-hydroxyphenyl) propane)-based PCs (Figure 2) has interesting characteristics like high toughness, high transparency, high heat capability, low water absorbability, low synthesis cost, and ease of decoration; therefore, industrially it is considered one of the most important polymers. Synthesis of PCs includes four different methods: (1) interfacial synthesis, (2) transesterification, (3) oxidative carboxylation, and (4) synthesis using CO_2.[7]

3.9.1.4 Crystallization Process of PCs

Surface texturing and modification of polymers toward achieving surface hydrophobicity and characterization have been of central interest to the researchers.[8–11] The interaction between the PC and acetone is spontaneous and induces crystallization and hence it is utilized to texture the PC surface and form hierarchical superhydrophobic structures.[12] During the crystallization reaction physical changes occur at the surface of the PC due to the phase–phase interaction between the PC surface and the acetone solvent. This physical change leads to create the hierarchical surface pattern with a certain roughness (Figure 3). The semicrystalline polymers have higher chemical resistance compared to the amorphous polymers. An additional important characteristic of the amorphous polymers is the high chain mobility which induces its crystallization.[13] The crystallization of PCs is a very slow process.[13,14] Polymer crystallization process can be induced either thermally or by using organic or inorganic solvents.[15,16] Liang *et al.*[17] used diallyl-orthophtalate as a solvent to induce the PC crystallization process, in the presence of plasticizers. Turska *et al.*[18] treated the PC samples thermally, by heating till 190 °C for about 7 days, in order to get a low degree of crystallization, which is 23% on average. Scientists found that the best organic solvent which can induce the PC crystallization process efficiently is acetone.[19,20]

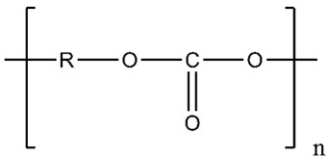


Figure 2 General chemical structure of polycarbonate.[53]

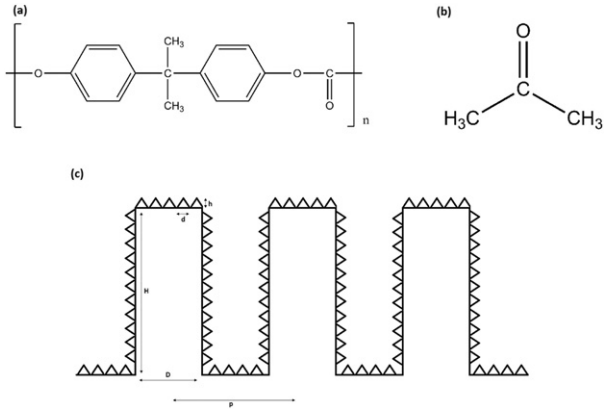


Figure 3 (a) Chemical structures of polycarbonate, (b) chemical structures of acetone, and (c) schematic form of the hierarchical surface; D: diameter, H: height and P: pitch of the circular spherules; h: height and d: diameter of the pyramidal nano-asperities.[12]

3.9.2 Theoretical Models

3.9.2.1 Fundamentals

Surface tension (γ_{LV}) is defined as the force which is responsible for reducing the free liquid's surface area; the unit of this force is N m^{-1} or J m^{-2}.[21] Two forces affect the status of the water droplet over the solid surface, (1) gravitational force and (2) surface tension. The volume of the droplet is the main factor, by which the effecting force is determined. For a water droplet present over a solid surface, interfacial tension forces γ_{SL}, γ_{SV} and γ_{LV} are established, the status of the water droplet, either flattened over the surface or remaining as a sphere, depends upon the balance between these forces.[5]

$$S = \gamma_{SL} + \gamma_{LV} - \gamma_{SV} > 0 \quad [1]$$

Where S: the power of spreading, γ_{SL}: the solid–liquid surface tension, γ_{LV}: the liquid–vapor surface tension, and γ_{SV}: the solid–vapor surface tension.

3.9.2.2 Young's Equation (for Flat Surfaces)

The hydrophobicity of a surface can be identified as the incapability of the surface to interact with water, therefore leading to create a high contact angle (CA), θ (i.e., the angle between the surface and the tangent of the water droplet which is found over it) so as to minimize the contact area between the droplet and the surface. In contrast, if the hydrophilic surface likes water; it makes a small CA, θ, with the water droplet in order to maximize the contact area, thereby leading to droplet-flattening over the surface. The surface is described as hydrophilic if $\gamma_{(SV)} > \gamma_{(SL)}$, the CA is lower than 90°, while, the hydrophobic surface possesses a CA higher than 90° if $\gamma_{(SV)} < \gamma_{(SL)}$ (Figure 4).[5]

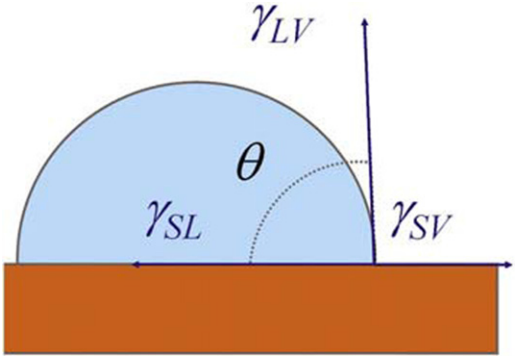


Figure 4 Three-phase contact line diagram of a water droplet on a solid surface.[53,54]

For flat surfaces, there is a mathematical model which illustrates the behavior of a water droplet on such surfaces. Young's equation shows the relation of the three-phase contact line between the droplet and the flat surface[22]:

$$\cos\theta_y = \frac{\gamma_{SV} - \gamma_{SL}}{\gamma_{LV}} \quad [2]$$

3.9.2.3 The Effect of the Chemical Treatment and the Roughness on the Surface Hydrophobicity

The surface roughness does not usually alter the nature of the surface significantly, in other words, it does not transform the hydrophobic surface to be a hydrophilic one or vice versa. The chemical structure and the terminal chemical groups at the materials' surfaces are the only factors that control if the material is hydrophobic or hydrophilic. Coating surfaces with a hydrophobic chemical material can only increase the smooth-surface CA with water up to 120° via lowering the surface energy, while using a hydrophilic chemical as a coating material increases the surface energy, however it can not achieve a CA between the smooth surface and the water droplet lower than 70°. The purpose of texturing the surface is to increase its hydrophobicity or hydrophilicity.[25] Thereby for the hydrophobic and rough surface, the CA can reach more than 160° and, in this case, the surface is called superhydrophobic, whereas for the hydrophilic rough surface, the CA can reach less than 5° and the surface is known as superhydrophilic surface. The contact angles for both the superhydrophobic and the superhydrophilic surfaces are apparent angles, and they are referred back to Cassie–Baxter (θ_{cb}) and Wenzel (θ_w) states, respectively (Figure 5).[26]

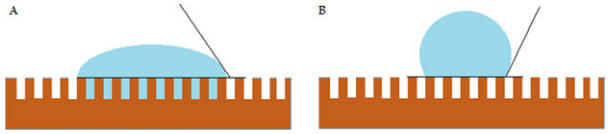


Figure 5 A: Wenzel state, or commonly known as Wenzel impregnated state. The water replaced the air in the gaps and the water droplet flattened, forming an acute angle between its tangent and the surface. B: Cassie–Baxter state. The water droplet is in a semi-sphere shape, forming an obtuse angle between its tangent and the surface.[53,54]

3.9.2.4 Wenzel and Cassie–Baxter States (for Rough Surfaces)

However, not all the surfaces are flat; there are rough surfaces (Figure 6). The water droplet behavior on the rough surface is totally different from the smooth one; in which case, surface texture plays a major role in (1) the degree of the hydrophilicity or the hydrophobicity of the surface and (2) the droplet mobility over the surface. In order to identify the rough surface, basically, it is the surface that has a lower surface energy than the corresponding flat surface of the same material. The energy of the rough surface is lower because if a square with a certain area is taken from a flat surface of a certain material and compared with another square with the same area, which is taken from a rough surface of the same material, more surface area can be found in the rough square because it is a three-dimensional one, while the flat square is only two-dimensional (Figure 6).

Two mathematical models are utilized to study the behavior of the water droplet on the rough surface, Wenzel model and Cassie–Baxter model. In Wenzel model, upon the landing of the water droplet over the rough surface, a water film is produced over the texture because water fills the pockets and therefore replaces the trapped air. According to this case, the water droplet sticks over the surface and does not move, even under the effect of the gravitational force. Wenzel's formula can be formulated as in eqns [3] and [4][23]:

$$\cos\theta_w = r\cos\theta_y \quad [3]$$

$$r = \frac{\text{actual surface}}{\text{geometric surface}} \quad [4]$$

where θ_w: apparent CA (i.e., CA over the rough surface or Wenzel's CA), θ_y: actual CA (i.e., CA over the corresponding smooth surface or Young's CA) and r: roughness factor. This state is non-favorable because it causes stickiness of the water droplet over the surface, so this is against the idea of water droplet rolling which is favorable for self-cleaning surfaces.

In Cassie–Baxter state, there is no water film formation because there is no water-diffusion in the air pockets. However, instead, the water droplet still touches only the

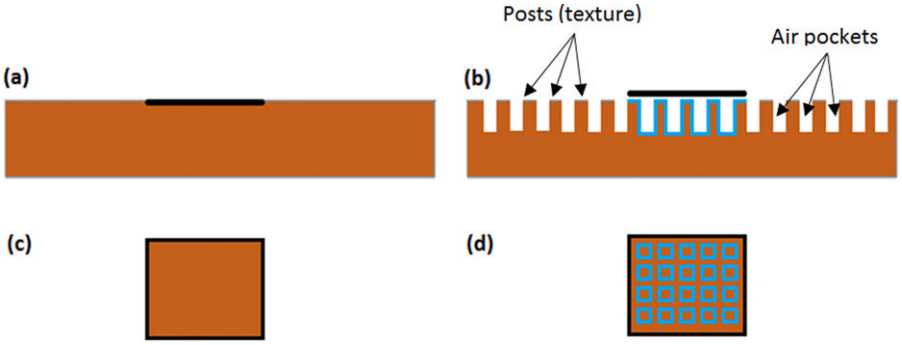


Figure 6 (a) and (b): diagrams illustrate the flat surface and a cross-section of it, and (c) and (d): diagrams illustrate the rough surface and a cross-section of it. From the diagrams, you can see that the rough square has a higher surface area, so a lower surface energy, than the flat square.[53]

tops of the surface-pillars, leaving the areas between them filled with air (eqn [5]). In Cassie–Baxter state, the droplet-curvature is smaller than the gaps due to the weight of the droplet.[5]

$$\cos\theta_{cb} = f_s(\cos\theta_\gamma + 1) - 1 \qquad [5]$$

where θ_{cb}: apparent CA (i.e., CA over the rough surface or Wenzel's CA), θ_γ: actual CA (i.e., CA over the corresponding smooth surface or Young's CA), f_s: the total area of the liquid–air interface.[24]

3.9.2.5 Classification of Rough Surfaces

Designation of rough surfaces can result in three forms of the surface texture: (1) regular, (2) hierarchical, and (3) random textured surface. For the regular rough surfaces, the etching can be done by using photolithography; and this type has a single-scaled roughness; and it is helpful in investigating the droplet behavior over the rough surfaces. The hierarchical rough surfaces, designed by chemical etching, possess complex structures and include roughness of two-scales. However, the random rough surfaces, fabricated by plasma etching, are of multi-scaled roughness.[1]

3.9.2.6 Self-Cleaning Surfaces

Acquiring the self-cleaning property is one of the surface characteristics that are favorable to be present. The self-cleaning feature requires uniform, smooth mobility of the water droplet over the hydrophobic surface. The regular rolling of the water droplet over the hydrophobic surface allows the removal of the accumulated dust particles and contaminants, like in the lotus leaves. The degree of ease and smoothness, with which the water droplet can move over the hydrophobic surface can be measured by measuring (1) the advancing CA (i.e., the CA at the front of the moving water droplet, θ_A; at this point, the volume of the water droplet increases with its motion) and (2) the receding CA (i.e., the CA at the back of the moving water droplet, θ_B; at this point, the volume of the water droplet shrinks with its motion).

The difference between the advancing and receding contact angles results in a new term, called contact angle hysteresis (CAH), θ_h, which is a measurement of the surface homogeneity (eqn [6]) (**Figure 7**). Both, the advancing and receding contact angles are measured at a surface-tilt angle of 1°–30°, for example.

$$\theta_h = \theta_A - \theta_B \qquad [6]$$

Three cases can be found in the values of the CAH: (1) zero or approaching zero value; in this case, the surface is homogeneous and the water droplet rolls smoothly over it, (2) positive value; in this case, the surface is heterogeneous and the water droplet rolls slowly or slides over it, and (3) negative value; in this case the water droplet sticks over the surface. CAH depends on the type of deposited liquid,[27] surface morphology and spaces between the generated textures,[28–31]

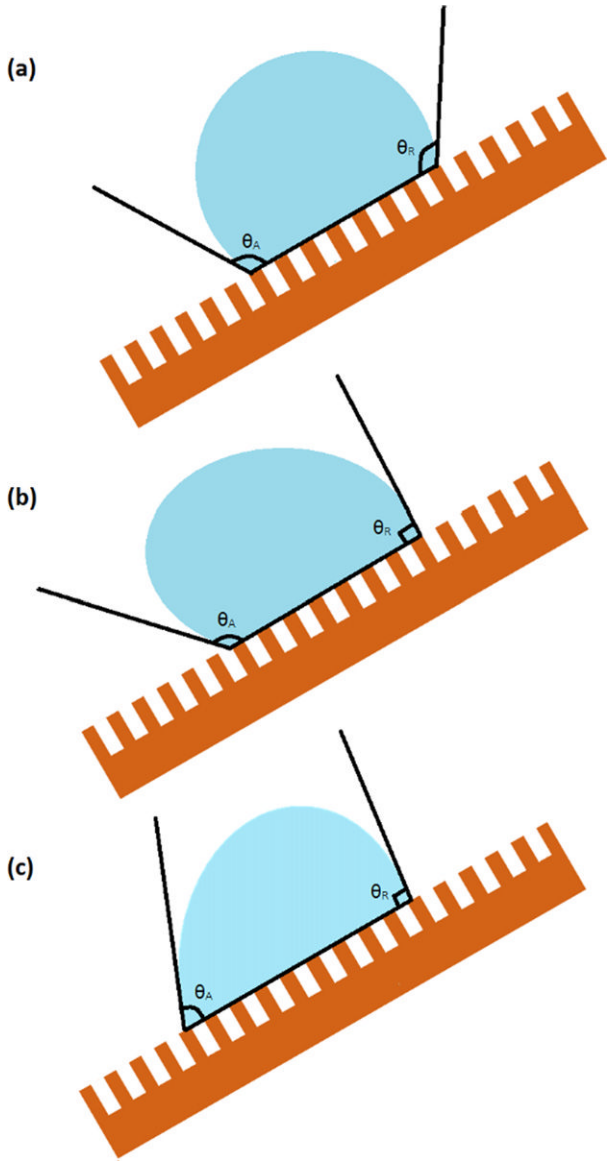


Figure 7 (a) Uniform (contact angle hysteresis (CAH) = zero), (b) nonuniform (CAH = positive value), and (c) nonuniform (CAH = negative value, theoretical case) water droplet movement over the rough hydrophobic surface.[53]

and the type of impregnated liquid in case of lubricant impregnated surfaces.[32,33]

3.9.3 Fabrication Methods and Technologies of Superhydrophobic Surfaces

The designation of a superhydrophobic surface requires the generation of a rough and low-energy surface. The critical problem of increasing roughness is the light reflectance from the rough surface and as a consequence, the decrease of the rough-surface light-transmittance; therefore controlling the surface roughening process should be taken into consideration.[34] Several types of superhydrophobic rough surfaces can

be designed by many techniques; every technique has its own characteristics, advantages, and disadvantages[35]:

1. Photolithography: it is highly controlled and favored in academic studies (to study the effect of varying r and f_s values), however it is very expensive.
2. Colloidal micro- and nano-particles: these types of particles accumulate by self-assembly, can pattern wide surface-areas with multiple scales, and the deposition process is controllable.
3. Template method: a rough surface can be utilized as a negative template and filled up with a material in the liquid state, wait for its hardening, and then get it out. The method is simple and the template can be used for several runs.
4. Etching: several methods of etching, for example, acid, laser, or plasma etching are investigated to create textured surfaces.

One of the crucial applications of the superhydrophobic surfaces is the self-cleaning surfaces. Scientists are spending significant efforts to design an optimized self-cleaning surface, which has the capability of repelling dust particles, by using a variety of methods.[36]

Mimicking the morphologies of natural superhydrophobic surfaces like the lotus leaf structure is the first step to come up with hydrophobicity properties. Template-based techniques, plasma treatment, self-assembly and self-organization, chemical deposition, layer-by-layer (LBL) deposition, colloidal assembly, phase separation, and electrospinning are some of the main methods to develop hydrophobic surfaces.[37–39]

Bruynooghe *et al.*[40] enhanced the light transmittance of the glass surface by coating it with an antireflective material which uses the light-destructive interference phenomenon to reduce the fraction of the scattered light. The coated substrate could be further coated with another coating material, which is hydrophobic (water repelling) and oleophobic (oil repelling) for making it durable and has a self-cleaning property. This top-layer coating included MgF2 (expensive material) in order to make the surface nonreflective. They achieved a CA of 110° after coating with 0.14% reflectance at incident angle of 78° in the spectral region 400–680 nm. Nakajima *et al.*[34] designed boehmite–TiO_2 films, with varied TiO_2 compositions, and a following (heptadecafluorodecyl) trimethoxysilane (FAS-17) coating to be used as superhydrophobic coating materials. Both roughness and CA were studied with different TiO_2 wt.% values. It was noticed that the roughness and CA increase with increasing the TiO_2 wt.%. However, TiO_2-based coatings were affected by UV light, especially at higher TiO_2 compositions, leading to hydrophobicity drop due to the photocatalytic effect (strong oxidation power under UV light) of the TiO_2. Ganbavle *et al.*[41] have used the sol–gel technique of a single step with a view to design a hydrophobic, self-cleaning silica coating material over a glass surface. The coating was tetraethoxysilane (TEOS) based with methyltrimethoxysilane (MTMS) as a co-precursor. The MTMS/TEOS ratio variation, by changing the MTMS concentration versus the hydrophobicity and self-cleaning property was studied; it was found that at the ratio between 0.78–1.57, the water droplet sticked over the surface due to the Cassie-impregnated state, in which a water film was formed on the pillars causing the strong adhesion of the water droplet to the surface; this phenomenon is illustrated in Figure 8. While at the ratio of 7.84, the coating showed a CA of 135°, but with a reduced light transmittance (80%). Lai *et al.*,[42] also designed TiO_2-fluoroalkylsilane thin films, using an electrophoretic deposition method, demonstrating both superhydrophobicity and good transparency (Figures 8 and 9). By Stober method, Chen *et al.*[43] grew hollow silica particles over carbon cores, using chemical vapor deposition (CVD), in order to synthesize a superhydrophobic coating. The achieved CA was 152° with transmittance of 90%, after one coating cycle and 75% after five coating cycles.

Park *et al.*[44] developed superhydrophobic surface with a CA higher than 150° and a hysteresis of lower than 20° by fabricating an ordered microshell array on transparent and flexible polydimethylsiloxane (PDMS) elastomer surface without a need for a low surface energy chemical coating. Verma *et al.*[2] created superhydrophilic nanostructured glass with a CA less than 5° by deposition of thin film of nickel on glass substrates, followed by annealing to create nickel nanoparticles. Their data showed an improvement in the solar cell performance, since net optical transmission increased and the surface was proven to be self-cleaning. Hee *et al.*[45] deposited different thicknesses of TiO_2 film on glass surface by using a simple method. They observed that dust accumulation decreased due to the deposition effect and this effect became more significant when increasing the film thickness.

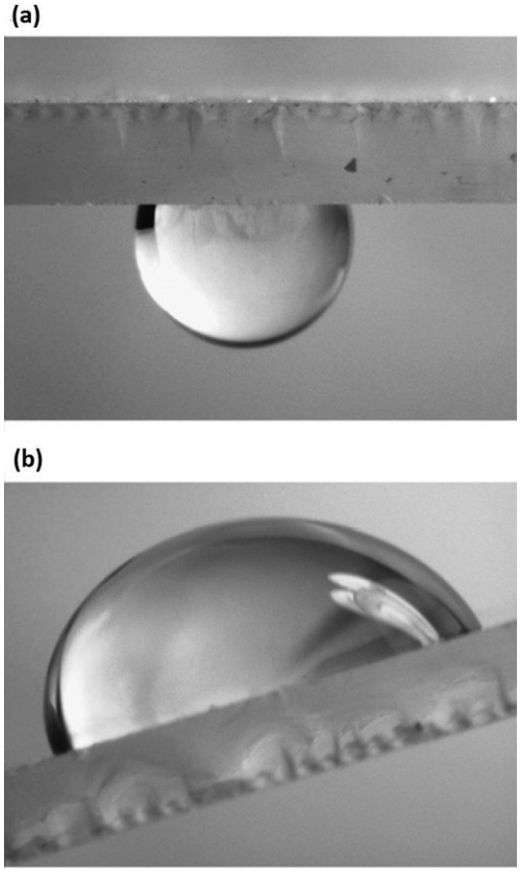


Figure 8 (a) Surface with ratio = 1.57 (Cassie-impregnated state), (b) surface with ratio = 7.84.[41]

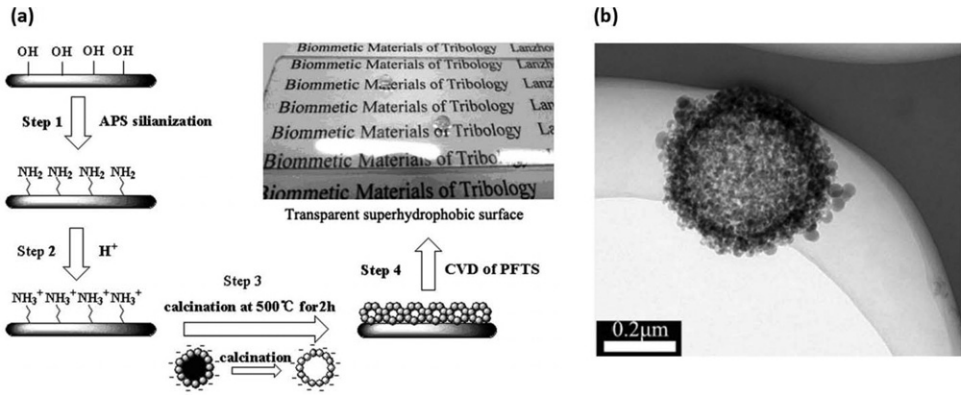


Figure 9 (a) Scheme for the preparation method and (b) hollow silica particles.[43]

However, such dry hydrophobic surfaces do have their limitations; for example, they cannot sustain high impact pressure. During the vapor condensation, surface loses its non-wetting properties. In addition micro-textures can enhance the light reflection. Lubricant impregnated surfaces do overcome limitations. In addition, wet hydrophobic surface exhibit extremely low CAH thus providing better self-cleaning and slippery properties.

Texturing the hydrophobic surfaces enhances the non-wetting properties by increasing the surface geometry while the trapped air between the surface texture posts leads to a superhydrophobic behavior, because the droplets sit partially on air.[31] However, there is a challenge in keeping the air pockets stable between the texture posts. But in case of humid conditions like Kingdom of Saudi Arabia environment, the air pockets can collapse due to dew condensation or evaporation. This occurs at a nanoscale throughout the texture and in turn leads to a highly wetted textured surface.[31] Such effect drew the attention to develop non-wetting surfaces with self-healing properties which are maintained by creating pockets of liquid instead of air by impregnating the texture with lubricant. The lubricant is stabilized by capillary wicking that arises from the micro- or nano-texture.[33] Lui *et al.*[46] fabricated lubricant impregnated surfaces (LIS) by filling organogel-based film on substrate with oil. The surface showed low CAH and self-cleaning efficiency. Wong *et al.*[27] prepared LIS through impregnating ordered epoxy-resin-based nanostructured surfaces and a random network of teflon nano fibrous membranes with lubricant perfluorinated fluids. It has been showed that LIS has the ability to repel different types of low and high surface tension liquids such as water, glycerol, and ethylene glycol. Furthermore, matching the refractive indexes of lubricant fluid and substrate leads to render the micro-texture highly transparent;[27,32] also LIS demonstrated self-healing properties . In case of any surface physical damage, the oil can flow and fill cracks and retain its surface properties.[27] On the other hand, LIS can sustain high drop impact pressure,[27] reduce ice accretion,[27,47,48] and enhances condensation and heat transfer dissipation.[49,50]

The lowest total interface energy state of water droplet represents the thermodynamics stable configuration. It depends on surface texture and impregnated liquid properties such as viscosity, spreading coefficient, and density.[51] Viscosity of oil plays a role in droplet sliding angle and velocity. High viscous oil leads to reduction of the droplet rolling speed and increases the sliding angle.[46,51,52] On the other hand, using high viscous oil can enhance the shearing sustainability of the surface.[49]

3.9.4 The Solid–Liquid Interface and PC-Liquid Acetone

The case study including surface crystallization of PC sheet is presented below toward the surface hydrophobicity assessment in line with the previous study.[53,54]

PC sheets are immersed in pure liquid acetone of different concentrations for different durations. Texture profile micrographs from atomic force microscope (AFM), give detailed images which illustrate the distances between the pillars within the textured surfaces. Roughness mean square and roughness average values, from AFM, are the parameters which give insight into the surface texture and provide information to enhance the hydrophobicity of the surface. All the former characterizations flew in the direction of measuring the contact angles of water droplets over the different textured surfaces as a tool for deducing the surface hydrophobicities.

3.9.4.1 AFM Micrographs

3.9.4.1.1 Surface topography

Several AFM scans are taken for different areas on the smooth PC surface, at different scales (500 nm, 1, 5, 10, 20, and 40 μm). The micrographs ascertain the absence of any kind of texture over the surface of the PC sheet as seen in **Figure 10(a)** with a scanning scale of 40 μm. The elevation that appears at the top-right of the micrograph is due to the sample's general surface morphology due to manufacturing process. **Figures 10(b)–10(f)**, at lower scales, further demonstrate the smoothness of the surface.

Several AFM scans are taken for different areas on the textured PC glass surface, at different scales (500 nm, 1, 5, 10, 20, and 40 μm). The micrographs illustrate clearly the appearance of a new surface texture after the immersion process. In **Figure 11(a)**, with a scanning scale of 40 μm, large spherules appear over the surface after immersing the sample for 10 min. The average size of the spherules, appearing in the figure, is

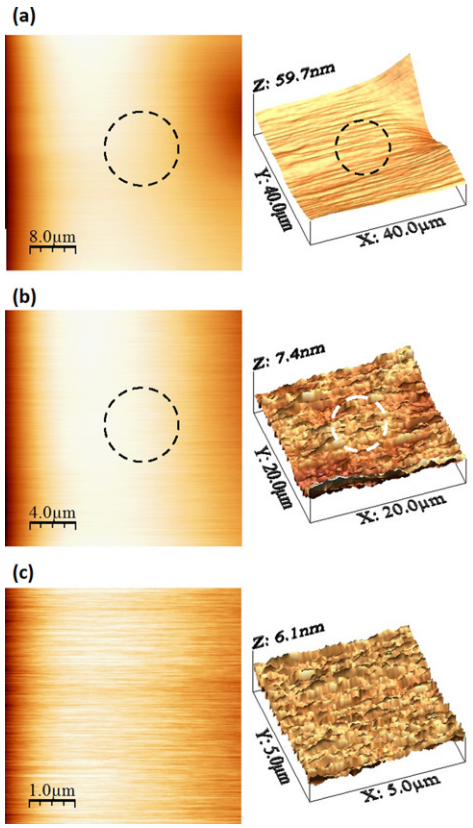


Figure 10 2D and 3D atomic force microscope micrographs at: (a) scale = 40 μm, (b) scale = 20 μm, and (c) scale = 5 μm for a smooth, untreated polycarbonate surface.[53,54]

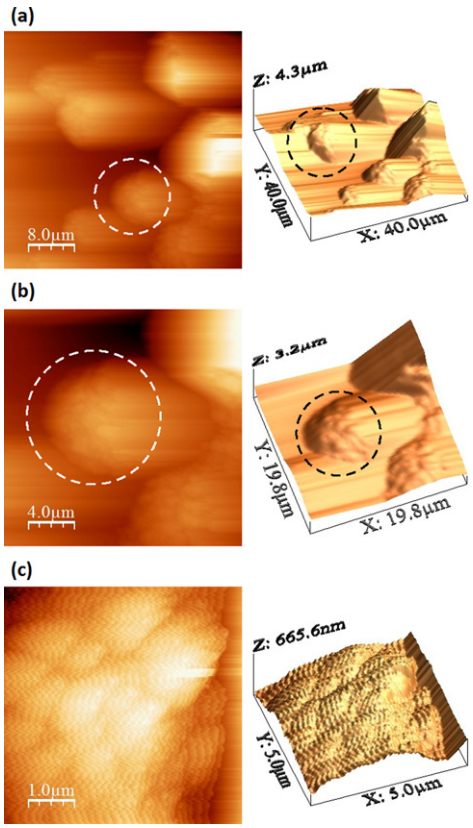


Figure 11 2D and 3D atomic force microscope micrographs at: (a) scale = 40 μm, (b) scale = 20 μm, and (c) scale = 5 μm for a textured polycarbonate surface by immersion in pure liquid acetone for 10 min.[53,54]

nearly 12 μm in width. The lines appearing as tails to the spherules are present due to AFM-tip slipping during the scanning process. In **Figure 11(b)** and at a scale of about 20 μm, the spherule appears more obviously and it can be noticed that the middle spherule is about 10 μm in width. By zooming in and reducing the scanning scale, the surface of the spherule shows more detail. **Figure 11(c)** illustrates that there is texture over the spherule's surface, which is clear also in the 3D micrograph. At lower scales, the surface of the spherule becomes more obvious and the texture over it can be obviously detected. It can be noticed that the surface of the spherule is not homogenous, in other words, the spherule's surface becomes hilly and this hilly surface is full of a grasslike texture, and this can be inferred from the 3D micrograph in **Figure 11(d)**. In both **Figures 11(e)** and **11(f)**, the scales are 1 μm and about 500 nm, respectively.

3.9.4.1.2 Texture profile micrographs

A line profile is drawn on the AFM micrograph and shows the morphology of the smooth PC surface. It can be noticed in **Figure 12**, that the surface texture does not exceed 2 nm in height. This indicates the degree of smoothness of the non-textured PC surface.

The study involves investigating the topology of the textured surface by using surface profile micrographs from AFM in order to follow up the effect of acetone on the PC surface. It is obvious that

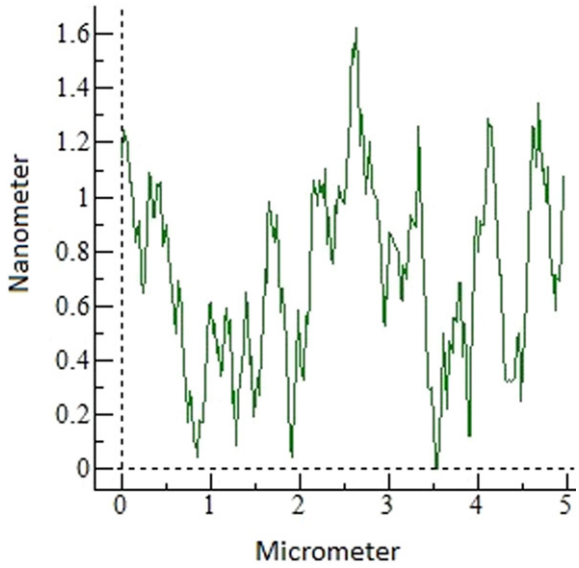


Figure 12 Atomic force microscope texture profile micrographs at 5 μm scale for a smooth untreated polycarbonate surface.[53,54]

through the various scales, from 40 μm to 5 μm, that the surface texture height is in the range of 1.75 μm. In **Figure 13(a)**, the height of the spherules can be measured and it is about 1.8 μm. The width of the middle spherule is about 13 μm. **Figure 13(b)**

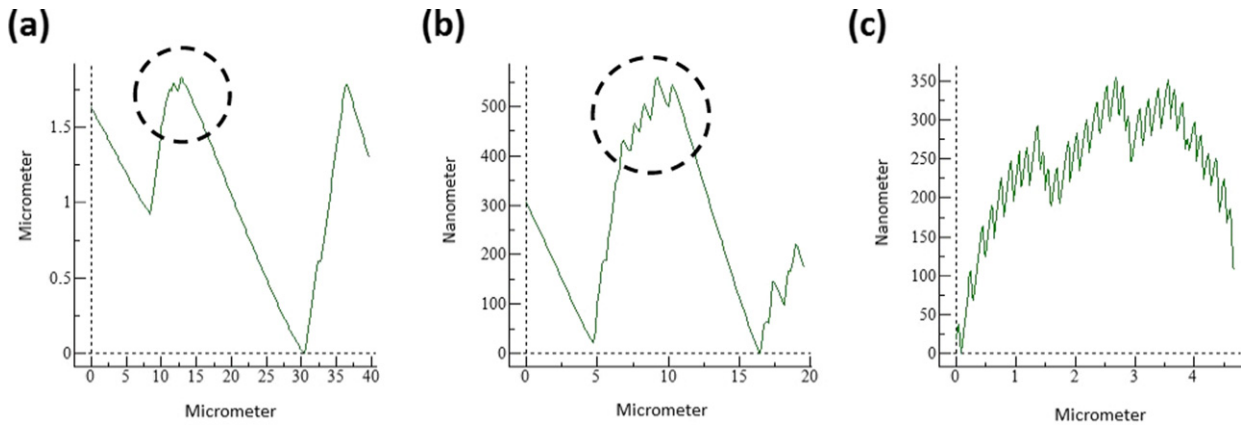


Figure 13 Atomic force microscope texture profile micrographs at: (a) scale = 40 μm, (b) scale = 20 μm, and (c) scale = 5 μm for a textured polycarbonate surface by immersion in pure liquid acetone for 10 min.[53,54]

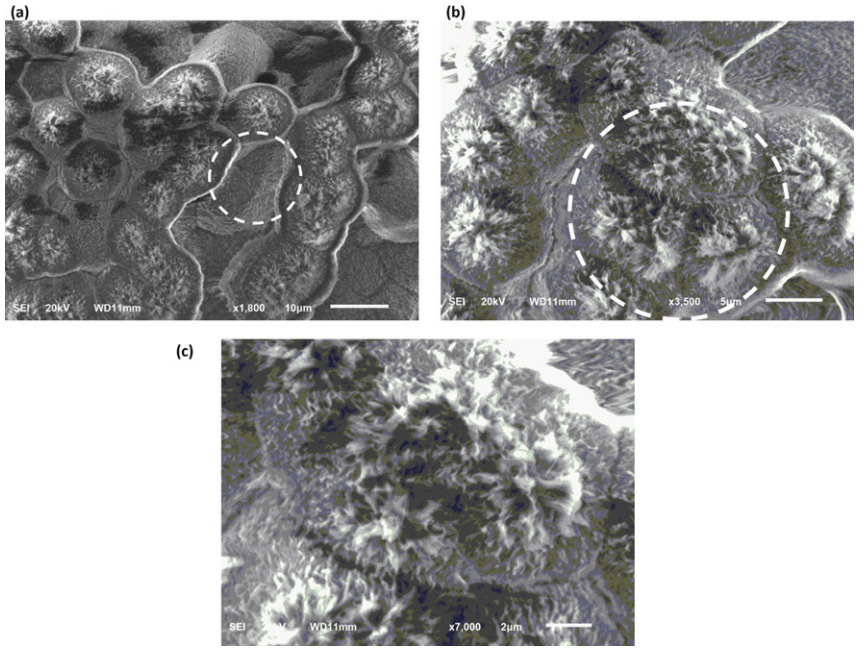


Figure 14 Scanning electron microscope micrographs at: (a) scale = 10 μm, (b) scale = 5 μm, and (c) scale = 2 μm, for a textured polycarbonate surface by immersion in pure liquid acetone for 10 min.[53]

illustrates a single and small spherule of 600 nm in height and nearly 12 μm in width. The texture over the spherule is shown in the figure. In Figure 13(c), a distinctive profile micrograph of the single spherule appears. The spherule contains three small elevations over its surface, each elevation is textured. This promotes the observation of the hilly surface and the grasslike hills, which is pointed out within the description of Figure 11(d).

3.9.4.2 Scanning Electron Micrographs

Scanning electron microscope is used to scan, on different scales, the PC surface after immersion in pure liquid acetone for 10 min. The resulted micrographs support the AFM and texture profile micrographs in proving that the crystallization process resulted in a textured crystallized PC surface with a hierarchical structure (Figure 14).

3.9.4.3 Surface Roughness

Roughness values of PC surfaces can be calculated using the AFM. Surface roughness was given concentration because it is one of the parameters that are responsible for the hydrophobicity of the surface. Roughness values are calculated for two different PC samples for comparison purposes: (1) smooth, untreated PC surface and (2) textured PC surface due to immersion in pure liquid acetone for 10 min. Two values of roughness can be given by the AFM for the single sample's surface, roughness root mean square (RMS) value and roughness average (Ra) value. Table 1 illustrates the Rms and Ra values of different PC samples. It's clear from the values of both the Rms and Ra that the textured PC surface by immersion in pure liquid acetone for 10 min is strongly roughed. This promotes the strong effect of the applied high hydrostatic

pressure on the treated PC surface due to immersion in pure liquid acetone, which allows deep diffusion of the acetone liquid within the polymer layer, leading to complete surface crystallization, pores formation, and as a consequence, high roughness in a very short duration.

3.9.4.4 Hydrophobicity Assessments

CA of the untreated PC surface is measured by dropping a deionized water droplet over the surface and measured using a goniometer. Different areas of the surface are taken into

Table 1 Roughness root mean square (RMS) and roughness average (Ra) values of the smooth (untreated), and solid–liquid interface textured polycarbonate (PC) sheets surfaces[53,54]

Scale (μm)	*Rms values (nm)*		*Ra values (nm)*	
	Smooth PC	*Textured PC*	*Smooth PC*	*Solid–liquid PC*
40	23.99	610	18.85	460
20	11.52	543.1	9.27	407
10	5.26	250	4.19	210
5	2.44	108.44	1.9	87.61
1	0.81	31.1	0.64	25.01
0.5	0.73	27.684 3	0.58	22.743 2

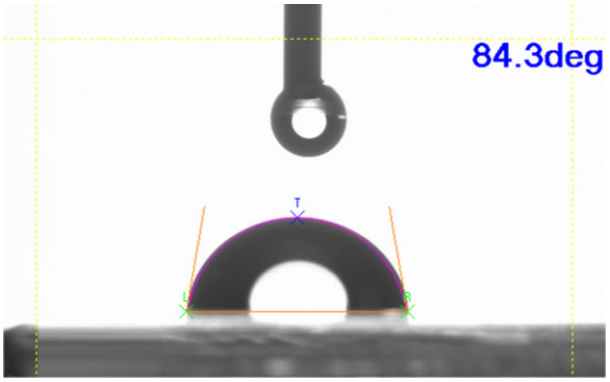


Figure 15 Contact angle of smooth untreated polycarbonate surface.[53,54]

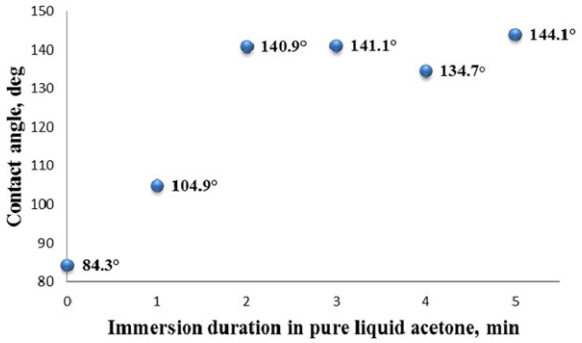


Figure 17 The effect of the immersion duration of polycarbonate sheets in liquid acetone on the contact angle.[53]

Table 2 Calculations of solid fraction values (f_s) of the textured polycarbonate glass samples by immersion in pure liquid acetone[53,54]

Immersion duration (min)	*Apparent CA (θ_{cb})*	*cos $\theta_{cb}+1$*	*Young's CA (θ_y)*	*cos θ_y+1*	*Solid fraction (f_s)*
1	104.9	0.743	84.3	1.099	0.676
2	140.9	0.224	84.3	1.099	0.204
3	141.1	0.222	84.3	1.099	0.202
4	134.7	0.297	84.3	1.099	0.270
5	144.1	0.190	84.3	1.099	0.173

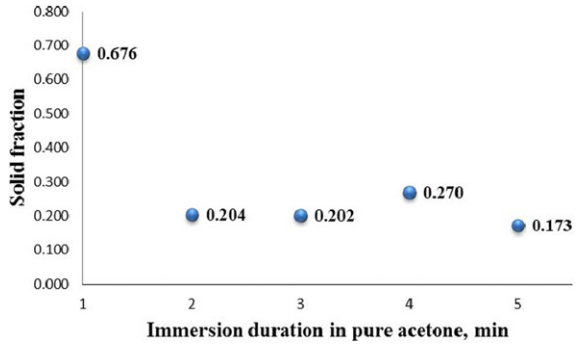


Figure 18 The effect of the immersion duration of polycarbonate in pure acetone liquid on the solid fraction (f_s) value.[53]

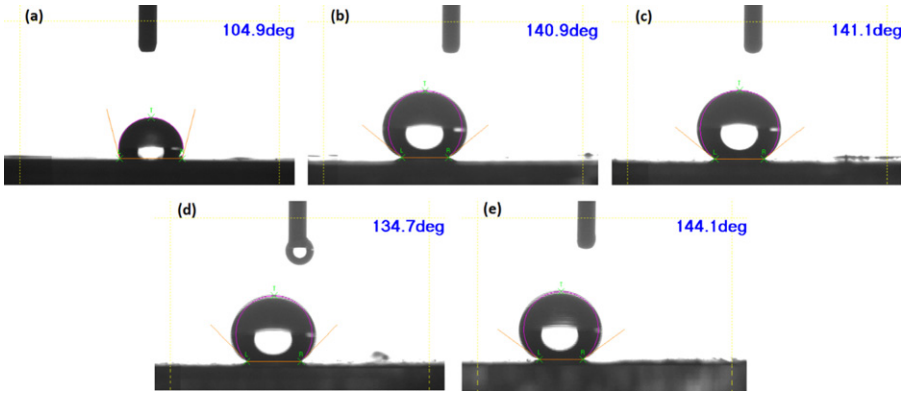


Figure 16 CA of textured polycarbonate sample by immersion in pure liquid acetone for: (a) 1 min, (b) 2 min, (c) 3 min, (d) 4 min, and (e) 5 min.[53,54]

consideration during the measurement. It is found that the average CA is 84.3°; indicating the slight hydrophilicity of the smooth PC surface (Figure 15).

Contact angles for textured PC sheets by pure liquid acetone have been calculated versus the immersion durations in the organic solvent. For an immersion duration of a PC sheet in pure liquid acetone for 1 min, the CA of the surface is 104.9° (Figure 16(a)). By increasing the immersion duration to 2 min, the CA dramatically jumped to 140.9° (Figure 16(b)). Then, by increasing the immersion periods to 3, 4, and 5 min, the contact angles fluctuate between 134.7° and 144.1° (Figures 16(c)–16(e)). Figure 17 illustrates the values of the contact angles of the immersed textured PC samples.

For the hydrophobic surfaces (CA $\theta > 90°$), Cassie–Baxter state can be applied to[24,54] eqn [5]:

$$\cos\theta_{cb} = f_s(\cos\theta_\gamma + 1) - 1$$

where θ_{cb}: the Cassie's (apparent) CA, $\theta_{cb} > 90°$, θ_γ: the Young's CA (CA of the corresponding smooth surface) and f_s: the solid fraction which is in contact with the water droplet. For

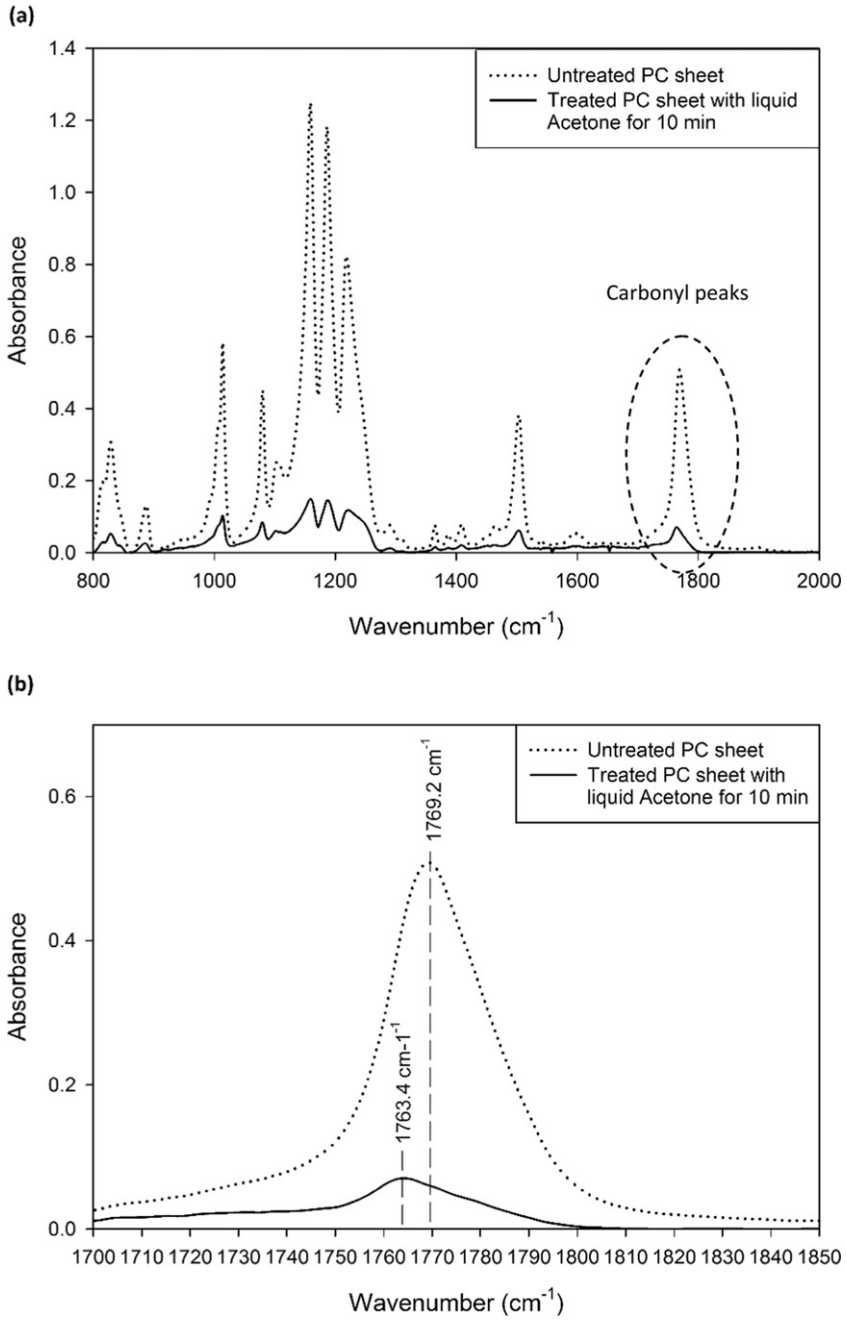


Figure 19 Attenuated total reflectance-Fourier transform infrared spectra of smooth, and liquid acetone-textured polycarbonate (PC) sheets surfaces, (a) whole spectra and (b) carbonyl stretching mode peak.[53,54]

calculating the value of f_s for the single textured hydrophobic surface:

$$f_s = \frac{\cos\theta_{cb} + 1}{\cos\theta_\gamma + 1} \quad [7]$$

Because the apparent contact angles of the textured surfaces, due to immersion in pure liquid acetone for different durations, are larger than 90°, so as a consequence, Cassie–Baxter's state is applicable. Calculations of f_s values for the six different textured surfaces are illustrated in **Table 2** and it is shown in **Figure 18** for different immersion durations.

3.9.4.5 Fourier Transform Infrared Technique Characterization

Fourier transform infrared (FTIR) technique is applied for determining the presence of chemical groups; functional, side, and terminal groups, within a certain chemical compound through the detection of the different stretching and bending modes of the bonds, present in these groups. FTIR technique is used to study the chemical structure of the PC surface before and after the treatment process. In addition, the technique gives an indication on the degree of crystallization of the surface after the treatment process through the peak intensity values. In **Figure 19**, FTIR spectrum of smooth, untreated PCs surface is illustrated. The study focuses on the wavelength at which the peak of carbonyl, C=O, stretching mode appears. Before the exposure to acetone, the peak of carbonyl stretching mode appears at 1764 cm^{-1}, with absorbance value of 0.34. The peak of the phenyl stretching mode appears at 1499 cm^{-1}, with absorbance value of 0.25.

However, in **Figure 19**, FTIR spectrum of textured PC surface, after immersion in pure liquid acetone, is illustrated. The study focuses on the wavelength at which the peak of carbonyl, C=O, stretching mode appears. Before the exposure to acetone, the peak of carbonyl stretching mode appears at 1762 cm^{-1}, with absorbance value of 0.16. The peak of the phenyl stretching mode appears at 1499 cm^{-1}, with absorbance value of 0.08.

Amorphous form of polymer gives a relatively higher degree of freedom to the polymers tail motion.[13] This permits the absorption of larger amounts of energy, and consequently, the performance of stronger vibrations, in case of molecules or groups that have a dipole moment (asymmetric chemical structure).[55]

Dybal *et al.*[56] noticed a shift in the carbonyl peak from 1770 to 1756 cm^{-1} with a tremendous decrease in the peak's intensity. Liu *et al.*[57] related this shift to the material-phase transformation from the amorphous state to the crystalline state. In addition, the decrease in the peak's intensity is related to the phase transformation of the polymer from the amorphous phase, which allows a higher degree of freedom to the chain motions and bond vibrations, to the crystalline phase, in which the molecules are tightly packed and consequently, the vibrations and motions are restricted.[13,58] It is also indicated that the acetone interaction with the PC is a physical process because no new peak emerged after the treatment process.[57]

3.9.4.6 X-Ray Diffraction Study

X-ray diffraction (XRD) technique is used to study the crystalline structure of the textured PC sheet surface. Both the sharpness and strength of the 2θ peak (**Figure 20**) shows clearly that the textured PC sample due to immersion in liquid acetone for 10 min possesses a thick crystalline layer.[54] This comes in agreement the FTIR data (**Figure 19**).

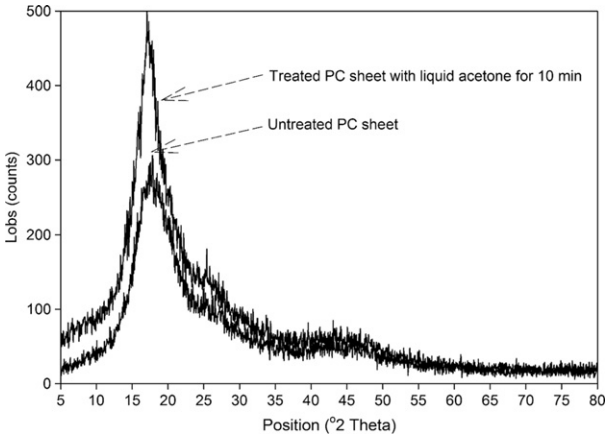


Figure 20 X-ray diffraction data for untreated polycarbonate (PC) sheet, and a textured PC sheet by immersion in pure liquid acetone for 10 min.[53,54]

Acknowledgments

The support of the National Plan for Science, Technology and Innovation (MAARIFAH) – King Abdulaziz City for Science and Technology through the Science and Technology Unit at King Fahd University of Petroleum and Minerals (KFUPM), The Kingdom of Saudi Arabia, through award number (11-ADV2134-04) is acknowledged. The support from the Center of Excellence for Research Collaboration with MIT is also acknowledged for support through projects numbers MIT11111-11112.

See also: 3.19 Effect of Surface Roughness on Wetting Properties

References

1. Blossey, R. Self-Cleaning Surfaces – Virtual Realities. *Nat. Mat.* **2003**, *2*, 301–306.
2. Verma, L. K.; Sakhuja, M.; Son, J.; *et al.* Self-Cleaning and Antireflective Packaging Glass for Solar Modules. *Renew. Energy* **2011**, *36*, 2489–2493.
3. Gao, L.; McCarthy, T. J. A Perfectly Hydrophobic Surface ($\theta A/\theta R = 180/180$). *J. Am. Chem. Soc.* **2006**, *128*, 9052–9053.
4. Yilbas, B.; Khaled, M.; Abu-Dheir, N.; *et al.* Wetting and Other Physical Characteristics of Polycarbonate Surface Textured Using Laser Ablation. *Appl. Surf. Sci.* **2014**, *320*, 21–29.
5. Adamson, A. W.; Gast, A. P. *Physical Chemistry of Surfaces*, 6th ed.; John Wiley and Sons: New York, 1997.
6. Wang, R.; Hashimoto, K.; Fujishima, A.; *et al.* Light-Induced Amphiphilic Surfaces. *Nature* **1997**, *388*, 431–432.
7. Takeuchi, K. Polycarbonates. In *Polymer Science: A Comprehensive Reference*; Möller, K. M., Ed.; Elsevier: Amsterdam, 2012; Vol. 5; pp. 363–376.
8. Tompkins, B. D.; Fisher, E. R. Evaluation of Polymer Hydrophobic Recovery Behavior Following H_2O Plasma Processing. *J. Appl. Polym. Sci.* **2015**, *132*, 41978–41990.
9. Nagel, J.; Bräuer, M.; Hupfer, B.; Grundke, K.; Schwarz, S.; Lehmann, D. Investigations on the Reactive Surface Modification of Polycarbonate by Surface-Reactive Injection Molding. *J. Appl. Polym. Sci.* **2004**, *93*, 1186–1191.

10. Gilliam, M.; Yu, Q. Surface Modification of a Group of Polymers Using a Low Temperature Cascade Arc Torch. *J. Appl. Poly. Sci.* **2007**, *105*, 360–372.
11. Zhang, L.; Yu, H.; Zhao, N.; Dang, Z. M.; Xu, J. Patterned Polymer Surfaces with Wetting Contrast Prepared by Polydopamine Modification. *J. Appl. Poly. Sci.* **2014**, *131*, 41057–41062.
12. Cui, Y.; Paxson, A. T.; Smyth, K. M.; Varanasi, K. K. Hierarchical Polymeric Textures Via Solvent-Induced Phase Transformation: A Single-Step Production of Large-Area Superhydrophobic Surfaces. *Colloids Surf. A: Physicochem. Eng. Asp.* **2012**, *394*, 8–13.
13. de Oliveira, F. L. O.; Leite, M. C. M.; Couto, L. O.; Correia, T. R. Study on Bisphenol-A Polycarbonates Samples Crystallized by Acetone Vapor Induction. *Polym. Bull.* **2011**, *67*, 1045–1057.
14. Fan, Z.; Shu, C.; Yu, Y.; Zaporojtchenko, V.; Faupel, F. Vapor-Induced Crystallization Behavior of Bisphenol-A Polycarbonate. *Polym. Eng. Sci.* **2006**, *46*, 729–734.
15. Aharoni, S. M.; Murthy, N. S. Effects of Solvent-Induced Crystallization on the Amorphous Phase of Polycarbonate of Bisphenol A. *Int. J. Polym. Mater.* **1998**, *42*, 275–283.
16. Sheldon, R.; Blakey, P. Liquid-Induced Crystallization in Polymers. *Nature* **1962**, *195*, 172–173.
17. Liang, G. G.; Cook, W. D.; Sautereau, H. J.; Tcharkhtchi, A. Diallyl Orthophthalate As a Reactive Plasticizer for Polycarbonate. Part 1: Uncured System. *Eur. Polym. J.* **2008**, *44*, 366–375.
18. Turska, E.; Przygocki, W.; Masdowski, M., Crystallization Kinetics of Polycarbonates. I. *J. Polym. Sci. C: Polym. Symp.* **1968**, *16*, 3373.
19. Turska, E.; Janeczek, H. Liquid-Induced Crystallization of a Bisphenol-A Polycarbonate. *Polymer* **1979**, *20*, 855–858.
20. Mercier, J.; Groeninckx, G.; Lesne, M. Some Aspects of Vapor-Induced Crystallization of Polycarbonate of Bisphenol A. *J. Polym. Sci. C: Polym. Symp.* **1967**, *16*, 2059–2067.
21. Bhushan, B.; Jung, Y. C. Natural and Biomimetic Artificial Surfaces for Superhydrophobicity, Self-Cleaning, Low Adhesion, and Drag Reduction. *Prog. Mater. Sci.* **2011**, *56*, 1–108.
22. Young, T. An Essay on the Cohesion of Fluids. *Philos. Trans. R. Soc. Lond.* **1805**, *95*, 65–87.
23. Wenzel, R. N. Resistance of Solid Surfaces to Wetting by Water. *Ind. Eng. Chem.* **1936**, *28*, 988–994.
24. Cassie, A.; Baxter, S. Wettability of Porous Surfaces. *Trans. Faraday Soc.* **1944**, *40*, 546–551.
25. Erbil, H. Y.; Demirel, A. L.; Avcı, Y.; Mert, O. Transformation of a Simple Plastic into a Superhydrophobic Surface. *Science* **2003**, *299*, 1377–1380.
26. Bico, J.; Thiele, U.; Quéré, D. Wetting of Textured Surfaces. *Colloids Surf. A: Physicochem. Eng. Asp.* **2002**, *206*, 41–46.
27. Wong, T.-S.; Kang, S. H.; Tang, S. K.; *et al.* Bioinspired Self-Repairing Slippery Surfaces with Pressure-Stable Omniphobicity. *Nature* **2011**, *477*, 443–447.
28. Dorrer, C.; Rühe, J. Some Thoughts on Superhydrophobic Wetting. *Soft Matter* **2009**, *5*, 51–61.
29. Miwa, M.; Nakajima, A.; Fujishima, A.; Hashimoto, K.; Watanabe, T. Effects of the Surface Roughness on Sliding Angles of Water Droplets on Superhydrophobic Surfaces. *Langmuir* **2000**, *16*, 5754–5760.
30. Quéré, D. Non-Sticking Drops. *Rep. Prog. Phys.* **2005**, *68*, 2495.
31. Smyth, K; Paxon, A.; Kwon, H.-M.; Deng, T.; Varanasi, K.K. Dynamic Wetting on Superhydrophobic Surfaces: Droplet impact and Wetting Hysteresis. In *12th IEEE Intersociety Conference on Thermal and Thermomechanical Phenomena in Electronic Systems (ITherm)*, IEEE, 2010; pp. 1–8.
32. Lafuma, A.; Quéré, D. Slippery Pre-Suffused Surfaces. *Europhys. Lett.* **2011**, *96*, 56001.
33. Smith, J. D.; Dhiman, R.; Anand, S.; *et al.* Droplet Mobility on Lubricant-Impregnated Surfaces. *Soft Matter* **2013**, *9*, 1772–1780.
34. Nakajima, A.; Hashimoto, K.; Watanabe, T.; Takai, K.; Yamauchi, G.; Fujishima, A. Transparent Superhydrophobic Thin Films with Self-Cleaning Properties. *Langmuir* **2000**, *16*, 7044–7047.
35. Shirtcliffe, N. J.; McHale, G.; Atherton, S.; Newton, M. I. An Introduction to Superhydrophobicity. *Adv. Colloid Interface Sci.* **2010**, *161*, 124–138.
36. He, G.; Zhou, C.; Li, Z. Review of Self-Cleaning Method for Solar Cell Array. *Procedia Eng.* **2011**, *16*, 640–645.
37. Boinovich, L. B.; Emelyanenko, A. M. Hydrophobic Materials and Coatings: Principles of Design, Properties and Applications. *Russ. Chem. Rev.* **2008**, *77*, 583.
38. Yan, Y.; Gao, N.; Barthlott, W. Mimicking Natural Superhydrophobic Surfaces and Grasping the Wetting Process: A Review on Recent Progress in Preparing Superhydrophobic Surfaces. *Adv. Colloid Interface Sci.* **2011**, *169*, 80–105.
39. Zhang, X.; Shi, F.; Niu, J.; Jiang, Y.; Wang, Z. Superhydrophobic Surfaces: From Structural Control to Functional Application. *Journal of Materials Chemistry* **2008**, *18*, 621–633.
40. Bruynooghe, S.; Spinzig, S.; Fliedner, M.; Hsu, G. Realization of High Performance AR-Coatings with Dust-and Water-Repellent Properties. *Vakuum in Forschung Und Praxis* **2008**, *20*, 25–29.
41. Ganbavle, V. V.; Bangi, U. K.; Latthe, S. S.; Mahadik, S. A.; Rao, A. V. Self-Cleaning Silica Coatings on Glass by Single Step Sol–Gel Route. *Surf. Coat. Technol.* **2011**, *205*, 5338–5344.
42. Lai, Y.; Tang, Y.; Gong, J.; *et al.* Transparent Superhydrophobic/Superhydrophilic TiO_2-Based Coatings for Self-Cleaning and Anti-Fogging. *J. Mater. Chem.* **2012**, *22*, 7420–7426.
43. Chen, Y.; Zhang, Y.; Shi, L.; *et al.* Transparent Superhydrophobic/Superhydrophilic Coatings for Self-Cleaning and Anti-Fogging. *Appl. Phys. Lett.* **2012**, *101*, 033701-1–033701-4.
44. Park, Y.-B.; Im, H.; Im, M.; Choi, Y.-K. Self-Cleaning Effect of Highly Water-Repellent Microshell Structures for Solar Cell Applications. *J. Mater. Chem.* **2011**, *21*, 633–636.
45. Hee, J. Y.; Kumar, L. V.; Danner, A. J.; Yang, H.; Bhatia, C. S. The Effect of Dust on Transmission and Self-Cleaning Property of Solar Panels. *Energy Procedia* **2012**, *15*, 421–427.
46. Liu, H.; Zhang, P.; Liu, M.; Wang, S.; Jiang, L. Organogel-Based Thin Films for Self-Cleaning on Various Surfaces. *Adv. Mater.* **2013**, *25*, 4477–4481.
47. Kim, P.; Wong, T.-S.; Alvarenga, J.; Kreder, M. J.; Adorno-Martinez, W. E.; Aizenberg, J. Liquid-Infused Nanostructured Surfaces with Extreme Anti-Ice and Anti-Frost Performance. *ACS Nano* **2012**, *6*, 6569–6577.
48. Rykaczewski, K.; Anand, S.; Subramanyam, S. B.; Varanasi, K. K. Mechanism of Frost Formation on Lubricant-Impregnated Surfaces. *Langmuir* **2013**, *29*, 5230–5238.
49. Anand, S.; Paxson, A. T.; Dhiman, R.; Smith, J. D.; Varanasi, K. K. Enhanced Condensation on Lubricant-Impregnated Nanotextured Surfaces. *ACS Nano* **2012**, *6*, 10122–10129.
50. Xiao, R.; Miljkovic, N.; Enright, R.; Wang, E. N. Immersion Condensation on Oil-Infused Heterogeneous Surfaces for Enhanced Heat Transfer. *Sci. Rep.* **2013**, *3*, 1988.
51. De Gennes, P.-G.; Brochard-Wyart, F.; Quéré, D. *Capillarity and Wetting Phenomena: Drops, Bubbles, Pearls, Waves*; Springer: New York, NY, 2004.
52. Butt, H. J.; Kappl, M. *Surface and Interfacial Forces*; John Wiley & Sons: Weinham, 2009.
53. Ahmed, A. O. M. Design and Fabrication of Different Textured Surfaces with Improved Hydrophobicity for Photovoltaic Cells' Applications (M.Sc thesis); Saudi Arabia: King Fahd University of Petroleum and Minerals, 2014; pp. 1–214.
54. Owais, A.; Khaled, M. M.; Yilbas, B. S.; Abu-Dheir, N.; Varanasi, K. K.; Toumi, K. Y. Surface and Wetting Characteristics of Textured Bisphenol-A Based Polycarbonate Surfaces: Acetone-Induced Crystallization Texturing Methods. *J. Appl. Polym. Sci.* **2016**, *133*, 43074–43083.
55. Atkins, P.; de Paula, J. *Atkins' Physical Chemistry*; Oxford University Press: Oxford; New York, NY, 2012.
56. Dybal, J.; Schmidt, P.; Baldrian, J.; Kratochvil, J. Ordered Structures in Polycarbonate Studied by Infrared and Raman Spectroscopy, Wide-Angle X-Ray Scattering, and Differential Scanning Calorimetry. *Macromolecules* **1998**, *31*, 6611–6619.
57. Liu, C. K.; Hu, C. T.; Lee, S. Effect of Compression and Thickness on Acetone Transport in Polycarbonate. *Polym. Eng. Sci.* **2005**, *45*, 687–693.
58. Paragkumar, T.; Edith, N. D.; Six, J.-L. Surface Characteristics of PLA and PLGA Films. *Appl. Surf. Sci.* **2006**, *253*, 2758–2764.

3.10 Atomizers and Finish Properties of Surface Coatings

R Ray and P Henshaw, University of Windsor, Windsor, ON, Canada

© 2017 Elsevier Inc. All rights reserved.

3.10.1	**Introduction**	149
3.10.2	**History**	149
3.10.3	**Types and Methods of Surface Coating**	150
3.10.4	**Droplet Formation and Fate**	150
3.10.4.1	Basic Mechanism	150
3.10.4.2	Formation of Droplets	150
3.10.4.3	Spray Air Contact	151
3.10.4.4	Coating Formation on the Surface	151
3.10.5	**Types and Requirements of Atomizers**	151
3.10.6	**Atomizer and Finishing Properties**	153
3.10.7	**Conclusion**	156
References		156
Relevant Websites		157

3.10.1 Introduction

Atomizers are commonly defined as a mechanical device that can disintegrate a liquid into smaller particles. In surface coating, atomizers create a finer spray and smoother finish than a brush. Atomizers can be optimized, so that up to 85% of the liquid coating ends up on the target and this high transfer efficiency limits air pollution.[1] Although coating is not the only industry associated with atomizers, the development and improvement of the atomizer are closely associated with improvements in the coating industry. The history of their codevelopment is discussed in the next section.

3.10.2 History

The history of surface coating is as old as the history of mankind. Paint is the earliest and most used surface coating in the world. Available evidence was found for the use of paint in Europe by Neanderthal or Cro-Magnon humans around 20 000 years BC. Ancient Aboriginal peoples used paint in North America around 9000 BC.[2] In these prehistoric times, the use of paint was more decorative than functional. The use of paint or other coating materials was seen in Egyptian history, where different organic and synthetic pigments, such as Egyptian blue, were developed.[3] Egyptian blue was made from lime, alumina, silica, soda ash and copper oxides. Their ships were coated with asphalt and balsam oil for preservation and waterproofing.[4] The Japanese and Chinese developed their famous lacquers from Urushi tree sap in order to protect their household instruments from wear and tear. Lacquer is a common term used for wood finish. It can be clear or colored solvent-borne coating.[3] In the fifteenth century, rosin, sandarac, and mastic varnish containing linseed oil were developed in Europe. Thinners were used to decrease the viscosity of paints, which resulted in easier application in cold weather conditions. In the late seventeenth century driers were introduced and the technical preparation of paints was first described by Watkin.[5] Later, the paint and varnish industry slowly started to develop for hand built cars and coaches.[6]

Although surface coating is now widely used for different types of products, other than architectural coatings the early invention and development of coatings was primarily associated with automobiles, masonry, and household products. In modern times, almost every industrial product is coated. In the automotive industry, layers of air drying paints were used in the early twentieth century.[7] Manual sanding and polishing took place after each layer was dried, which meant that several days were required to coat each vehicle. However, during the industrial boom of the Second World War, mass production of vehicles was required and enamel was developed for faster drying and curing. Coincidently, the number of layers was reduced to save time. Enamel is a liquid paint that air dries to a hard finish. These materials can be composed of different types of chemicals. Primers, containing different solvents, synthetic resins, and additive agents were used for corrosion protection, primer surfacers for chip resistance and smoothness, and the top coat for color and weather resistance.[8] In the late 1970s, solvents were recognized as major air pollutants and subsequently, waterborne and electro-deposition paints were introduced. The modern automotive industry applies as many as five coating layers to the exteriors of vehicle bodies.

The spray application of coating has also improved with the changes in coating chemistry. The paint brush was the only instrument used for coatings application up to the nineteenth century. The use of pneumatic guns and pressure pots of paints started being developed in the early twentieth century.[2] Electrodeposition was pioneered by Ford Motor Company in the 1960s for priming their automobiles.[9] This method quickly became popular and other coating industries started using it. However, strict rules for air pollution from the solvents and developing customer attention to color and finishing properties forced the industry to develop improved spraying techniques. Atomizers proved to be efficient and resulted in a better finish and thus became very popular for industrial use.[10]

Nowadays, computer guided robots with different types of atomizers are used in spraying.

3.10.3 Types and Methods of Surface Coating

The various existing paints are classified into three major categories: trade sale paints, industrial coatings, and inorganic coatings.[11] Coatings used on and in structures are the trade sale coatings and can be used for both esthetic and durability issues. For indoor use, appearance and quick drying are major features, while durability is very important for outdoor coating. Protecting the masonry structure remains the major function of this type of coating. Both solvent and water borne paints are used for this purpose.

Industrial coating can be broadly divided into six areas: appliance finishes, automotive finishes, marine coatings, can coatings, coil coatings, and aircraft coatings. Appliance finishes are used on almost all household appliances. Refrigerators, washers, dryers are regularly used, large household appliances where coating is important for their durability and esthetics. The finish of an appliance protects it from corrosion by water, salt, detergent, or even temperature.[12,13] Powder coat, epoxy, and modified acrylics are used as primers, whereas acrylics and alkyds are used as top coats. Flow coats or bell atomizers are used in this process.[13] Zinc phosphate is applied to the bare metal at 1.94–2.26 g m^{-2} when higher corrosion protection is required and iron phosphate is applied at 0.75–1.07 g m^{-2} when lower corrosion resistance can be tolerated.[11]

In the automotive industry, appearance, durability, and corrosion are the major factors affecting the quality of the coating.[11] Primer and topcoats are the major parts of this coating, where primers provide corrosion resistance and topcoat enhances appearance. Both primers and top coats confer different mechanical properties, such as film adhesion to substrates, inter-coat adhesion of different layers, film hardness, and retention of film integrity under deformation, bending, stretching, sharp impact, or stress developed by thermal shock.[11] Durability includes blister resistance or gloss loss due to humidity.[14]

Marine coating is one of the earliest coatings used by mankind and has been in use for the last 2000 years. Different parts of a ship are exposed to different environmental conditions and their coatings differ accordingly. The bottom of a ship is exposed to saltwater corrosion and fouling, while the deck area and the superstructure are exposed to the atmosphere and salt spray. The deck area suffers from regular abrasion and rubbing. The waterline area is exposed to both weather conditions and may be immersed in salt water depending on loading of the ship. These areas need the highest protection with special types of coatings.[15–17]

Can coating is used in both food and non-food type products. Various factors like nature of the product in the can, the type of can, and can manufacturing methods contribute to the type of coating used.[11] In the U.S. food industry, the coating needs to be FDA approved. Some can coatings, like those for cold drinks, should withstand cold temperatures and above-atmospheric pressures for a longer time, whereas cans containing meat products must withstand higher temperatures for a certain period of time.[18]

Coil coatings are mainly used in pre-fabricated products in building components and metal sheating. Coil coated products are pre-coated before assembling the product and allow for optimum use of paint. In this process, metal is cleaned and pre-treated to apply primer. Different types of primers are used depending on the intended exposure. A top coat is applied on top of the primer using rollers. Rollers allow uniform coatings and high production capacity.[11] The most common types of coil coatings are amine alkyds, vinyl alkyds, solution vinyls, thermoset acrylics, organosols, plastisols, etc. However, newer types like silicone polyesters, silicone acrylics, and fluorocarbon coatings are also used by the coil coating industry.[19]

Aircraft coatings are required to be erosion resistant, perform under extreme weather and temperature conditions, and be corrosion resistant. At the same time, the outer coating requires lightning strike resistance and camouflage for military application. Weight is a prime concern in aircraft coating and new developments are underway.[20,21] Hexavalent chromium (CrVI) is used in pre-treatment for corrosion resistance, while epoxy resin primer, and polyurethane enamel top coat are also used.[22]

3.10.4 Droplet Formation and Fate

It is important to know the mechanism of formation of droplets and film of the coating to understand the effects of atomizer properties and parameters on the final finish on the target surface. The basic physics is almost same for most of the atomizers, but their droplet formation technique can vary widely. After the coating is sprayed in the air, significant changes to the droplet occur on contact with the air or other medium. Because most of the atomizers are used in air, the contact between air and spray will be discussed here. It is important to understand evaporation of the coating solvent to understand the surface coating performance on the applied surface.

3.10.4.1 Basic Mechanism

The basic mechanism of atomization has been studied by many researchers, but a final, conclusive understanding of the whole operation is still pending.[37] However, the basic action of atomization is as simple as spraying water from a showerhead or dripping water from a simple capillary tube. Liquid flows along the wall of a capillary tube, forms a sheet of liquid and then is shed in drops.[37,43] These bigger drops may be further disintegrated because of combined internal and external forces and form smaller droplets (spray), which is directed to a surface. Formation of a fluid sheet is different for different types and models of atomizers.

3.10.4.2 Formation of Droplets

The atomization process starts in the atomizer where the fluid is forced through a nozzle. Pressure is applied in the liquid to force it through the nozzle, and as the pressure is released the liquid spreads out. As the length of the liquid front increases, by conservation of mass, the thickness of the liquid front must decrease.[28,79] The breakup of the liquid layer into droplets is a

complex phenomenon which occurs within a very short distance. Pressure, surface tension, and gravitational force are the driving forces to form unstable ligaments of fluid. Upon further propagation of these unstable ligaments, they contract by surface tension and break up into liquid droplets.[28] For different kinds of atomizers the initial ligament formation technique is different. However, after the formation of ligaments the droplets are formed in the same way.

3.10.4.3 Spray Air Contact

When a water droplet travels through the air, it is subject to evaporation and hence a decrease in size. The droplet also cools down due to evaporation and a saturated vapor layer surrounds it. At some point, the droplet reaches its wet bulb temperature. The temperature of the droplet is then lower than the surrounding air temperature, which causes heat flow towards the droplet, and evaporation starts again.[77,78] Thus, the rate of evaporation is not constant and the process is not steady, so the time required for evaporation can be divided into two steps. The first is the time from the formation of droplets to the time when droplets reach their wet bulb temperature. The second is a period of unsteady evaporation. The process continues until the droplet reaches the target surface, or the water completely evaporates. The principle can be applied to other solvents, as well. If the vapor pressure of the coating solvents in the medium is below that of the saturation pressure of the solvents in the medium, evaporation occurs. Evaporation of the droplet in-flight is important for environmental effects and atomizer efficiency as well as the surface finishing quality.

3.10.4.4 Coating Formation on the Surface

When the droplets reach the target surface, they stick to the surface and make a film. If an electrostatic charge is used, the particles lose their charge to the grounded surface.[43] Thus the surface does not repel further droplets from adding to the film. When a liquid drop comes into contact with a target, the drop may follow different scenarios, depending upon the inertia and the target properties. It may deposit into a thin disk, break into secondary and tertiary droplets, or if its inertia and cohesion are high, it may possibly bounce. When inertia is negligible the drop will deposit gently and spread over the surface until equilibrium is reached. If the substrate is roughened, the drop may even splash (lateral spread and rebound) upon impact.[81]

3.10.5 Types and Requirements of Atomizers

Atomizers are available in different types and shapes according to their use. The most common types are the pressure atomizer, rotary atomizer, air assist or air blast atomizer, and effervescent atomizer.[7] Electrostatic charging and ultrasonic atomizers are newer advancements in this area.

Pressure or pressure swirl atomizers are the most common type of atomizer used in the coatings industry. They are also used in aerosol spray cans for deodorants, paint, and air freshener.[7] In a pressure atomizer, the liquid is injected with a tangential velocity component into the swirl chamber. A vortex is produced which develops a low pressure at the axis of the nozzle. When turning on the flow, the external gas is sucked into the center of the vortex, forming an air-core. This forces the liquid to emerge as a cylindrical sheet in the exit orifice, with both axial and tangential velocity components. This causes a conical liquid sheet to form which then breaks down into a spray that has a hollow cone pattern. For finely atomized sprays, the spray angle reduces with distance downstream and the central zone gradually fills with drops, thus forming a solid cone spray.[23] The pressure swirl atomizer is recognized as the most energy efficient method of atomization where pressurized liquid is used, as the method requires a minimum supply pressure to provide a given drop size.[24] The breakup processes of the liquid sheet is generally complex and involves sheet waves, perforations, and ligament breakup. There is usually some repetition in the process which leads to droplet clusters.[24] A typical pressure swirl atomizer is shown in Figure 1. For a pressure swirl atomizer, the pressurized coating forms a ligament of fluid from the sharp edge of the atomizer, which then breaks up into droplets.

A Rotary Bell Atomizer (RBA) is a rotating device used to atomize liquid into spray. In the automotive coating industry, it is a widely used applicator which produces very small droplets and ensures smooth and consistent spray. The RBA allows close-in painting for high transfer efficiency and great penetration into part recesses. It has an excellent pattern control, which limits over-spray considerably for reduced paint waste. A common RBA consists of the following major assemblies: cartridge (optional), valve module, turbine, bell cup, shaping air ring, and the electrostatic system. The cartridge is a detachable vessel which can be refilled. In assembly line spraying, a continuous liquid feeding system is attached to ensure a continuous supply of paint. The valve module controls the flow of liquid by different tubing passages and valves. The turbine is a high speed motor that rotates the bell cup at 10 000–120 000 rpm. The bell is a conical cup attached to the turbine. The liquid is injected into the center of the concave side of the cup and the centrifugal force pulls the paint toward the

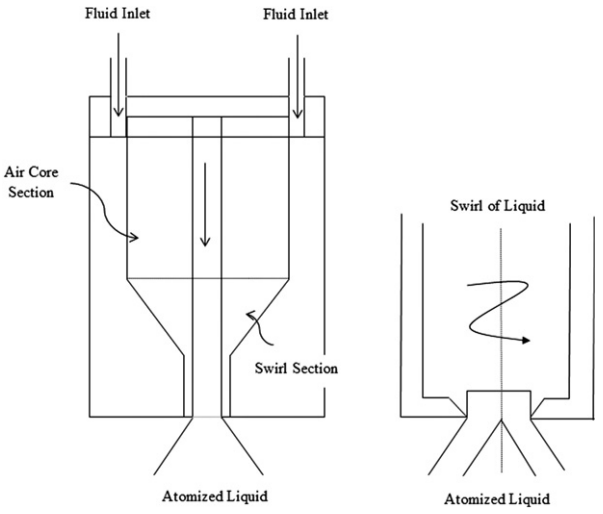


Figure 1 Pressure-swirl atomizer.

edge of the cup.[25,26] The rotating surface may take the form of a flat disk, vaned disk, cup, or slotted wheel.[27] A coaxial air jet termed the shaping air can be used to assist atomization. The shaping air ring has a series of small pinholes along its circumference from which air can be blown onto the outside of the bell circumference to control the spray pattern. The electrostatic system can be used to provide a high voltage (usually between 60 000 and 90 000 V DC) to the spray so that the droplets will be charged and attracted to the grounded target. The RBA can be used without electrostatic charge, but this is rare. Droplets with a high surface charge spontaneously break into smaller droplets. A typical RBA is shown in **Figure 2**.

The process of centrifugal atomization has been studied by several workers, including Hinze and Milborn,[28] Dombrowski *et al.*,[29] and Ray *et al.*[30–32] and has been described in the next section. Hinze and Milborn[28] did the initial investigation of the atomization of liquids using a rotating cup and divided the mechanism of droplet formation into three possible 'stages' depending on the supply rate of the liquid. In stage 1, a very low flow rate is present and a liquid sheet is formed. The sheet deforms by centrifugal forces and drops are formed. With an increased flow, stage 2 occurs where the sheet becomes ligaments of liquid. Higher flow rates increase the thickness and number of ligaments but the ligaments are not sustained long due to disturbances caused by external forces. These ligaments form droplets. If the flow rate is increased more, the ligaments reach their maximum thickness where an extending film is formed from the edge of the cup. This film later converts to a circumferential sinusoidal wave of ligaments and breaks down into droplets. This is termed stage 3.

However, when the rotating speed is high, the atomization process is continuous and occurs at the periphery of the rotating cup or disk. Ligament formation can be made to produce much finer drops if an electrostatic field is applied. Generally, it is found that atomization quality is improved (droplets are smaller) by (1) an increase in rotational speed, (2) a decrease in liquid flow rate, and (3) a decrease in liquid viscosity.

The air assist atomizer and air blast atomizer are almost the same kind of atomizer with a difference in air flowing style. There are beneficial effects of flowing air in assisting the disintegration of a liquid jet or sheet. A well-known disadvantage of the swirl type nozzle is that it has a pressure differential (between the liquid paint and the air) is too low to give good atomization. This problem can be solved using an air assist atomizer and controlling the pressure difference.[7] An extensive variety of air assist atomizers have been designed by various researchers for industrial use in gas turbines and oil-fired furnaces. The details of different types of air assist atomizer can be found in works by Romp,[33] Gretzinger and Marshall,[34] Mullinger and Chigier,[35] and Sargeant.[36] Regardless of the type of design, the primary concept is to impinge a high velocity gas into the liquid. Normally, the liquid has lower velocity and the assisting air can be used both internally and externally. If air is used internally, the spray cone angle is proportional to the decrease of air flow.[37] This type of atomizer is highly appropriate for viscous liquids. Atomization quality is high regardless of the liquid flow rates.[37] If air is used externally, a constant spray angle is produced for any liquid flow. However, external air assist nozzles have a special advantage in that they are less susceptible to air–liquid mixing. Their only drawback is a higher power requirement.[7] A typical internal air assist atomizer is shown in **Figure 3**.

The effervescent atomization technique was developed in the late 1980s by Lefebvre *et al.*[38–40] who called it aerated liquid atomization. In 1990 Buckner *et al.*[41,42] described it as effervescent atomization. This is actually an internal air assist atomizer where high velocity gas and lower velocity liquid go through internal mixing before atomization. But compared to other internal-mixing atomizers, the effervescent atomizer has a lower air flow rate. The air introduced into the liquid forms a bubbly two-phase mixture upstream of the discharge orifice.[38–40] This bubbly mixture has a relatively low density, which occupies most of the total cross-sectional flow area. This phenomenon improves atomization by reducing the characteristic liquid dimensions within the discharge orifice.[41,42] A typical effervescent atomizer is shown in **Figure 4**.



Figure 2 ABB rotary bell atomizer (RB1000 WSC series).

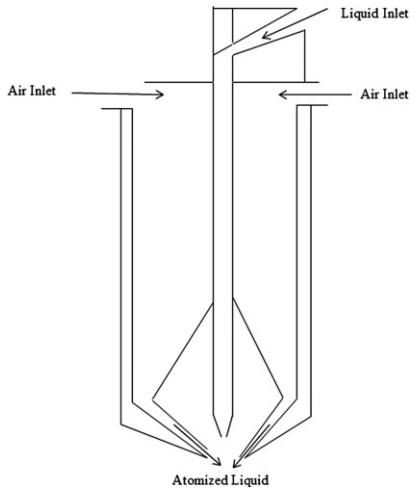


Figure 3 Schematic diagram of an air assist atomizer.

Ultrasonic atomization is a recent advancement where high frequency sound is used to atomize the coating. A simple basic diagram for ultrasonic atomization is given in Figure 5. A disc shaped transducer is used to impart mechanical energy as vibration amplitude in the direction of liquid flow. This vibration causes a transverse wave along the surface of the atomizer, from which droplets form from the peaks in amplitude on the surface.[69] Lord Rayleigh, who is considered as the pioneer of atomization, had started the work on ultrasonic atomization, published in his 'The Theory of Sound' around a century ago. He found that when a liquid is placed in a rotating smooth disk, it creates a vibration perpendicular to the motion of the disk.[43,68] This vibration energy is consumed by the liquid placed on it, which then takes a wave shape. These waves are actually capillary waves which later disintegrate due to the combined action of centrifugal and inertial forces.[43] Normally, atomizers are smaller for higher frequencies, so that less energy is consumed. A higher frequency also creates smaller droplets, which have a smaller maximum flow capacity and create a high transfer efficiency and smooth finish.[69,70]

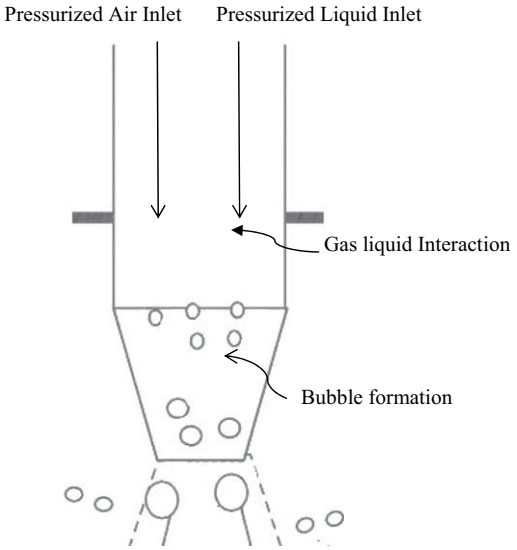


Figure 4 Schematic diagram of an effervescent atomizer.

The ultrasonic atomizers normally create a soft, low-velocity, fine mist which can be controlled to within square micrometers on the target area. This unique feature allows it to be used in different medical equipment, like spray nozzles for the ear, eye or nose.[71,72,80] It has also been used in recent nano-surgery, where protective layers of anti-inflammation medicine coating are used.

Electrostatic application is a technique wherein a high voltage, low current is used in the coating application to entice the spray towards its target. Because of the static charge, the repulsive forces between the particles keep them apart. Normally the charge is applied before or during the droplet formation. Electrostatic application is often used with rotary atomizers which cause a more evenly finished product.[65] The use of electrostatic forces during atomization balances the mechanical forces, like surface tension, and hence a proper combination of coating surface tension, viscosity, and electrostatic charge is required.[66] The precise combination of these three parameters has restricted the use of very high solids content or water borne coatings to get very good results while using electrostatic charge. Electrostatic application is used when coating the application rate is less than 4 $cm^3\ min^{-1}\ cm^{-1}$ of applied length; and the electrostatic charge is between 80–150 kV.[67,68] One of the main benefits of the use of electrostatic application is its higher transfer efficiency, which allows for lower consumption of paint.

3.10.6 Atomizer and Finishing Properties

The finished properties of a surface coating depend upon various other parameters in addition to the spray atomizer itself. Surface cleaning and preparation, coating preparation,

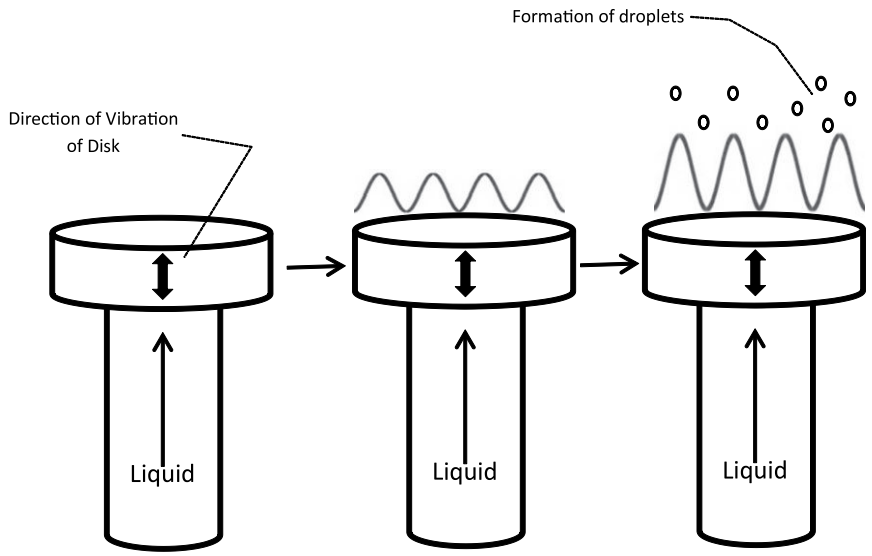


Figure 5 Formation of droplets in an ultrasonic atomizer.

and the spray booth environment influence finishing properties. For any surface and coating type, the surface should be cleaned thoroughly before it can be used for commercial coating. The surface may also require sanding, and primer application. The spray booth should be temperature and humidity controlled to avoid any inconsistencies that would set back production.[58]

The most common finishing problems with surface coatings are blistering, chipping, cracking, cratering, crawling, delamination, dissolution, mottling, and orange peel.[59] Blistering looks like a hollow bubble inside the coating, and generally occurs when sprayed paint is cured. Excessive air flow through the atomizer and improper curing of lower coating layers causes blistering in the final finish. Blistering is only visible after final curing and sometimes can occur after a few months to a few years. The only remedy for blistering is a costly removal and repaint of the surface.[60] Chipping is another problem which can be found anytime from the time of drying to regular use of the surface but mainly occurs after drying. Various portions of the coating can break away. Normally this happens due to incorrect application of the primer and sealer. However, variation of temperature and pressure in the spray booth can also create the problem.[62] Cracking can occur anytime in the cured coating. Normally, it happens in the top coat. High temperature and excessive use of coating are believed to be the major causes behind cracking. This is also a costly problem and repaint is the only remedy.[60,63] Cratering is found immediately after the coating is applied. It looks like a bubble has burst and left a hole in the coated area. Excessive airflow or contamination of the surface are the major causes of this problem. Because the problem is found before drying, it is comparatively cheaper to repaint, but still results in loss of paint and use of labour.[61] Crawling is the excessive waviness of a clear coat. It happens due to uneven or excessive amount of spray. Tapered or faulty atomizers can also create this. The problem can be identified immediately after or during the application of the coating. The clear coat needs to be removed and re-coated to fix this problem.[60] Delamination is a sudden, spur crack and happens on the side. Coating on an unfinished surface, lack of proper airflow, and insufficient drying causes delamination. It is found after drying, and re-painting is the only remedy.[64] Dissolution is not caused by the improper use of an atomizer: rather, it is caused by improper mixing of the coating before application. Mottling is a whitish appearance on the coating surface. Improper or faulty nozzle type and booth temperature are believed to be its major causes. The problem is generally found during spraying and can be fixed immediately.[65] Orange peel is a common problem and is found after drying. It is costly to fix as the problem often arises when the product is with the customer. Lack of surface preparation and improper temperature are the major causes.[60]

In a pressure-swirl atomizer, the liquid flow through a narrow channel results in a higher velocity of the liquid. The liquid pressure was already converted to kinetic energy by the pressure-swirl due to the angular velocity induced in the swirl area. These result in an air vortex which partially blocks the orifice. Both radial and angular velocity exist in the liquid when it emerges from the orifice, taking the shape of a hollow cone. Upon release, these velocities create a high velocity difference between the discharged liquid and the surrounding gas.[28] Pressure-swirl atomizers have better atomization quality than simple nozzles for the same discharge rate. Normally, a high liquid flow rate is maintained and governed by the spill flow rate. A liquid sheet is produced when it passes through the orifice. The liquid sheet thickness and the droplet size decrease with increasing rotating speed. However, the sheet thickness is independent of the flow rate of the discharged liquid.[43] The spray cone angle is independent, but varies with the spill return flow rate.[43]

Different researchers investigated the spray characteristics and performance of pressure swirl atomizers. Taylor[44] and Squire[45] were the pioneers who studied the breakup of liquid sheets generated by swirl atomizers due to liquid film instabilities. Other authors studied the relation between the physical properties of the liquid and droplet diameter. Dexter[46] found that when liquid with suspended solids was used, it did not substantially change the drop size distributions. However, both researchers found that regardless of the type of fluid, surface tension and viscosity play critical roles in the drop size distribution. Stelter *et al.*[47] found that the liquid elasticity was significant for drop formation. An increase of the liquid elasticity increased the average drop diameter and decreased the volume fraction of small droplets in the sprays. Schütz *et al.*[48] used water–glycerol solutions and showed an increase of mean drop size with the increasing flow rate. Rhim *et al.*[24] found that an increase of the liquid flow rate decreased the sheet break-up length, while an increase in the water content increased the break-up length. While using emulsion sprays, Sheng *et al.*[49] found that the mean drop diameter increased with increasing aqueous phase concentration.

Rizk and Lefebvre[50] investigated the impact of geometrical dimensions of a pressure atomizer on the sprays produced. Normally, a very high velocity liquid is used in a pressure swirl atomizer, causing instabilities in the liquid sheet. The liquid sheet breaks up into ligaments and forms a conical shape before the instability converts the ligaments into droplets.[7] The larger droplets populate the outer regions of the spray while moving along their original flight angles. By the same mechanism, the number of smaller droplets is reduced in the core of the spray.[7]

Several investigators worked on RBAs and their effect on liquid atomization. Fraser *et al.*[51] conducted a series of investigations to understand the formation of droplets and liquid sheets during atomization. A rotary atomizer was used with an air spray to confine the fluid spray. They did not find any significant impact of air containment on atomization. However, they found that the initial drop size from the breakup of the liquid sheet was a function of sheet thickness. They concluded that a good finish is dependent on the sheet uniformity and depends on bell speed, flow rate, and viscosity of the fluid.[51]

Di Domenico and Henshaw[52] set up a full factorial two-level DOE matrix to show the relationship between the paint finish appearance and variable RBA parameters: flow rate, bell speed, shaping air, and electrostatic potential. The distinctness of image, surface waviness, and multi-angle color were measured for evaluation. They concluded that a change of particle diameter due to the change in these parameters played an important role in the evaporation of the paint droplets. They hypothesized that greater in-flight evaporation of the spray resulted in a smoother finish.

Corbeels *et al.*[53] investigated the relation between bell speed, flow rate, and mean drop size. A higher bell speed caused higher centrifugal and Coriolis forces and decreased the mean drop size. But, a higher flow rate increased the mean drop size when the bell speed was below 20 000 rpm. The average droplet size increased as a result of increasing the flow rate at constant bell speed. A higher bell speed with a constant flow rate decreased the average drop size and increased the droplet number.

A shadowgraphy technique was used by Basu *et al.*[54] to understand the particle size characteristics of atomization caused by a rotary atomizer. They used metallic, solvent borne, and water borne paints as sprayed liquids. Within the 30 000–50 000 rpm bell speed range, the mean particle size decreased with increasing bell speed; but the rate of decrease fell outside of this range.

In a spray, there is a direct relation between the average droplet size, surface area, and evaporation rate. The higher the drop size, the lower the total surface area and the lower the total evaporation. In an investigation using water spray,[30,31] Ray *et al.* used a Particle Dynamic Analyzer to show the effect on evaporation of different atomization speeds, air flow rates, and water flow rates. They also introduced electrostatic charging while performing the same experiments using clear coat.[32] They held other variables, like atmospheric pressure and temperature constant, and calculated evaporation ($cm^3\,s^{-1}$) between planes 22.5 and 37.5 cm from the atomizer. It was found that the droplet diameter decreased and hence the evaporation increased with higher bell speed or lower flow rate for both water and clearcoat.

Effervescent atomizers are relatively new and various researchers performed detailed experimental studies on them. They tried to compare the performance and spray characteristics of effervescent atomizers over other types of atomizers. The results of this research specify that effervescent atomizers (EAs) exhibit several advantages over conventional pressure or rotary atomizers. Compared to other twin-fluid atomization, air flow-rates are lower in EAs.[55–57] Other conventional atomizers are higher in injection pressure and EAs achieve better atomization.[55,56] EAs have a larger outer orifice diameter, which decreases the chance of fluid clogging. In combustion applications, effervescent atomizer-produced sprays result in lower air pollution due to air existing in the spray core.[55] Research showed that the mean droplet size produced by EAs is relatively unaffected by liquid viscosity, meaning that this single atomizer can be used for a variety of liquids without compromising performance.[7,57] When a liquid with suspended solids is used, EAs have an advantage of less erosion at orifices due to the lower flow rate.[7,57] EAs are more energy efficient compared to pressure or rotary atomizers.

Ultrasonic atomizers are better than traditional atomizers in terms of operating energy requirements. Traditional atomizers use most of their energy to create a velocity difference in order to disintegrate the particles, whereas ultrasonic atomizers use more efficient ultrasonic energy. To achieve full disintegration of the fluid, it is important to operate the atomizer defect-free. The nozzles of the atomizer should be clog-free to get the most uniform coating. Ultrasonic atomizers are free from clogging as the liquid is placed around a sonotrode; a solid vibrating element that does not have any pores to clog.[37]

Bittner *et al.* used an ultrasonic atomizer to study the feasibility of ultrasonic atomization combined with subsequent organic solvent extraction.[73,74] The results of these works showed that ultrasonic technology has the potential for both aseptic processing and upscaling. In the pulmonary drug industry, aerosol spraying is widely used and research is continuing in drug delivery systems by microparticles created using a spray-congealing technique.[75] Passerini *et al.* found that the administration of certain low melting point, poorly soluble drugs can be improved using the ultrasonic atomizer.[76]

The properties of the final finish of the coating depend on the target surface and its application. However, some of the major properties are discussed in the following paragraphs.

Humidity is a vital concern for all types of coating. However, special consideration is given in automotive, marine and aircraft coatings. Condensation resistance is tested for surface coatings used in several food industries and building surface coatings to avoid blistering. For automotive coating, ASTM D714-02 is followed to evaluate the degree of blistering in paints.[82] This standard provides reference photographs to quantify blistering, but the treatment to induce blistering is usually specified by the company purchasing the coated product. The atomization technique, its application method and surrounding pressure and temperature are vital to maintain the proper condensation resistance of the surface.

In the automotive industry salt spray resistance is important, especially in winter countries or marine painting where steel is exposed to salt, the coating should have a standard salt spray resistance capability. In ASTM D610-08 a scale and description of rust ratings are established.[69] The coated steel surface may be exposed to a fog of salt spray, acetic acid, salt/SO_2, or copper and sodium chloride in acetic acid. Though salt spray resistance does not have any direct relation with the atomizer properties, the thickness of the coating sprayed reduces the chance of corrosion due to salt. An even thickness of coating minimizes coating use, and good atomization is a key in this respect.[83]

Weather resistance is important for all the major coating industries except the food industry. The accelerated weathering resistance test is done to find the durability of a coating in different environments. Accelerated weather testing is done with a combination of UV light, cool-down periods, and exposure to moisture or salt spray. Some of the after-paint problems discussed earlier in this section, which are related to paint appearance, are tested here. The final coating should not have any kind of chipping, cracking or flaking. For testing the gloss of the surface, ASTM D523-14 is used.[84] The method uses a Parallel-Beam Glossmeter to measure the reflected light at 60, 20, or 85 degrees from normal. The change in color due to weather (or when comparing two different surfaces) is quantified by ASTM D2244-15a.[85] This method compares coatings by measuring color coordinates based on daylight illumination of color tolerances and color differences between specimens. The differences in color between the standard reference and a test specimen are measured by the use of a colorimeter. Reflectance readings from colorimeter are then converted by computations to color-scale values.

Film adhesion is an important criteria for any surface coating. Since adhesion is the major property which binds coatings on surfaces, a poor adhesion indicates poor quality

of the coating, which may lead to blistering, chipping, and delamination. In the automotive industry, ASTM D3359-09e2 is followed to measure adhesion by the Tape Test[87]. An x-cut is made through the coatings with a razor blade. Pressure sensitive tape is applied to the cut and pulled off. Then the adhesion is assessed qualitatively using a visual scale.

The uniform thickness of coating directly depends on the types of the atomizer and its operating conditions.[86] Studies showed that rotary bell atomizers are the most efficient when automotive coatings are applied.[37]

Abrasion resistance is the property of a coating which resists surface coating wear due to other materials. In the marine industry, abrasion resistance is important as water is always the cause of flat rubbing on the surface. For abrasion resistance ASTM D4060-14 is used, where the abrasion resistance of coatings is measured by the Taber Abraser. The cured coated surface is abraded using rotary rubbing action by a two way rotary abrading wheel. The resulting abrasion marks on the specimen are measured.[87]

3.10.7 Conclusion

The theoretical description in this chapter is a summary of our understanding of the types of surface coating, types of atomizers, and their effects on atomized fluid particles. The durability and esthetic of surface coating are dependent on droplet size distributions, which in turn are dependant on physical properties like surface tension and viscosity of the liquid. The current discussion was limited to the direct effects of the operating conditions of various types of atomizers on the droplet size. However, different defects in surface coating, and their origin in relation with application of coatings are also discussed here.

See also: 3.3 Surface Finish Coatings

References

1. Ghasem, G. N.; Andrew, J. Y.; Lothar, B. *Industrial Sprays and Atomization: Design, Analysis and Applications*; Springer: London, 2013.
2. Boatwritzlit, J. H. Worldwide History of Paint. In *Protective Decorative Coatings, Paints, Varnishes, Licquers Inks*; Matiello, J. J., Ed.; John Wiley & Sons: New York, NY, 1941–1945; Vol. 1; pp. 9–20.
3. Fettis, G. *Automotive Paints and Coatings*; VCH: Basel, 1995.
4. Angelucci, E.; Alberto, B. *The Automobile – From Steam to Gasoline*; McGraw-Hill: New York, NY, 1974; pp. 23–50.
5. Rae, J. B. *The American Automobile: A Brief History*; The University of Chicago Press: Chicago, IL, 1965; pp. 1–18.
6. Armour, A. G.; Wu., D. T.; Antonelli, J. A.; Lowell, J. H. Sixty Years of Automotive Coatings from Lacquers to Oligomers. In *Organic Coatings Their Orgill and Development*; Seymour, R. B., Mark, H., Eds.; Elsevier Science Publishing: New York, NY, 1990.
7. Lefebvre, A. H. *Atomization and Sprays*; Hemisphere Publishing Corporation: New York, NY, 1989.
8. Toda, K.; Salazar, A.; Saito, K. *Automotive Painting Technology: A Monozukuri–Hitozukuri Perspective*; Springer: London; New York, NY, 2012.
9. Weed, F. G. The Finishing of Automotive Equipment and Other Metal Surfaces. In *Protective & Decorative Coatings, Paints, Varnishes, Lacquers & Inks*; Matiello, J. J., Ed.; John Wiley & Sons: New York, NY, 1941–1945; Vol. III, Chapter 14.
10. Hounshell, D. A.; Smith, J. K., Jr *Science & Corporate Strategy*; Cambridge University Press: Cambridge, 1988; pp. 138–146.
11. Paul, S. *Surface Coatings*; John Wiley & Sons: New York, NY, 1986.
12. Shur, E. G. Appliance Finishes. In *Treatise on Coatings*; Myers, R. R., Long, J. S., Eds.; Marcel Dekker: New York, NY, 1975; Vol. 4, Part 1, Chapter 2, p. 86.
13. Miranda, T. J. Recent Advances in Coatings for Household Appliances. In *Proceedings of the 8th International Conference in Organic Coatings Science & Technology*; Athens, Greece, July 12–16, 1982; Vol. III; p. 415.
14. Roberts, D. T., Jr.; Todd, B. H. Evaluation and Modification of the Beckman Variable Angle Accessory for Characterization of Metallic Coatings. *JCT* **1979**, *51* (653), 59.
15. James, D. M. Marine Paints. In *Treatise on Coatings*; Myers, R. R., Long, J. S., Eds.; Marcel Dekker: New York, NY, 1975; Vol. 4, Part I, Chapter 8, p. 415.
16. Ghanem, N. A.; Mcssiha, N. N.; Abd El Malek, M. M.; Ikladious, N. E.; Shaaban, A. F. New Terpolymers with Pendent Organotin Moieties as Antifouling Coatings. *JCT* **1981**, *53* (675), 57.
17. Patton, T. C. Miscellaneous. In *Pigment Handbook*; Patton, T. C., Ed.; John Wiley & Sons: New York, NY, 1973; Vol. 1, p. 931.
18. Gerhardt, G. W.; Seagren, G. W. Coatings for Metal Containers. In *Treatise on Coatings*; Myers, R. R., Long, J. S., Eds.; Marcel Dekker: New York, NY, 1975; Vol. 4, Part I, Chapter 9, p. 483.
19. Lutes, D. K., Sr. Coil Coating – The Continuous Coating of Metal Strip. In *Treatise on Coatings*; Myers, R. R., Long, J. S., Eds.; Marcel Dekker: New York, NY, 1975; Vol. 4, Part I, Chapter 4, p. 237.
20. Prince, D. E. Opportunities in Air Force Coatings Research and Development. *JCT* **1979**, *51* (652), 54.
21. Lewin, J. B. G. Aircraft Finishes. In *Treatise on Coatings*; Myers, R. R., Long, J. S., Eds.; Marcel Dekker: New York, NY, 1975; Vol. 4, Part I, Chapter 1, p. 1.
22. Carlton, G. N. Hexavalent Chromium Exposures During Full-Aircraft Corrosion Control. *AIHA J. (Fairfax, Va)* **2003**, *64*, 668–672.
23. Durdina, L.; Jedelsky, J.; Jicha, M. Experimental Investigation on Spray Characteristics of Pressure-Swirl Atomizers for a Small-Sized Jet Engine. In *12th Triennial International Conference on Liquid Atomization and Spray Systems* (*ICLASS 2012*), Heidelberg, Germany, September 2–6, 2012.
24. Rhim, J.-H. Breakup Length of Conical Emulsion Sheet Discharged by Pressure-Swirl Atomizer. *Int. J. Automot. Technol.* **2001**, *2*, 103.
25. Nordson Corporation. *RA 20 Rotary Atomizer: Close-in Painting Capability with Optimal Coverage, Greater Operating Flexibility and Improved Paint Savings in a Wide Range of Finishing Applications*; Nordson Corporation: Amherst, OH, 2011.
26. Talbert, R. P. *Technology Handbook*; CRC Press: Boca Raton, FL, 2007.
27. Doyle, A.; Moffett, D. R.; Vonnegut, B. Behavior of Evaporating Electrically Charged Droplets. *J. Colloid Sci.* **1964**, *19*, 136–143.
28. Hinze, J. O.; Milborn, H. Atomization of Liquids by Means of a Rotating Cup. *J. Appl. Mech.* **1950**, *17*, 145–153.
29. Dombrowski, N.; Johns, W. The Aerodynamic Instability and Disintegration of Viscous Liquid Sheets. *Chem. Eng. Sci.* **1963**, *18* (3), 203–214.
30. Ray, R.; Henshaw, P.; Biswas, N.; Sak, C. Evaporation of Water Spray from a Rotary Bell Atomizer using a Phase Doppler Anemometer. *Atomization Spray.* **2015**, *25* (7), 539–551.
31. Ray, R.; Henshaw, P.; Biswas, N.; Sak, C. Effects of Bell Speed and Flow Rate on Evaporation of Water Spray from a Rotary Bell Atomizer. *Coatings* **2015**, *5*, 186–194, Special issue: Innovative Coatings for Automotive Industry.
32. Ray, R. *Evaporation of Spray from a Rotary Bell Atomizer* (Ph.D. thesis); Windsor, ON, Canada: University of Windsor, 2015.
33. Romp, H. A. *Oil Burning*; Martinus Nijhoff, Stephen & Company: The Hague, NY, 1937.
34. Gretzinger, J.; Marshall, W. R., Jr. Characteristics of Pneumatic Atomization. *J. Am. Ins. Chem. Eng.* **1961**, *7* (2), 312–318.
35. Mullinger, P. J.; Chigier, N. A. The Design and Performance of Internal Mixing Multi-Jet Twin-Fluid Atomizers. *J. Inst. Fuel* **1974**, *47*, 251–261.
36. Sargeant, M. Blast Atomizer Developments in the Central Electricity Generating Board. In *Proceedings of the 2nd International Conference on Liquid Atomization Spray Systems*, Matiison, WI; 1982; pp. 131–135.
37. Masters, K. *Spray Drying*, 2nd ed.; John Wiley and Sons: New York, NY, 1976.
38. Lefebvre, A. H.; Wang, X. F.; Martin, C. A. Spray Characteristics of Aerated-Liquid Pressure Atomizers. *AIAA J. Prop. Power* **1988**, *4* (4), 293–298.
39. Lefebvre, A. H. A Novel Method of Atomization with Potential Gas Turbine Application. *Indian Def. Sci. J.* **1988**, *38*, 353–362.
40. Roesler, T. C.; Lefebvre, A. H. Studies on Aerated-Liquid Atomization. *Int. J. Turbo Jet Eng.* **1989**, *6*, 221–230.
41. Buckner, H. N.; Sojka, P. E.; Lefebvre, A. H. *Effervescent Atomization of Coal–Water Slurries*; ASME Publ.: Houston, TX, 1990. pp. 105–108, PD-30.

42. Buckner H. N.; Sojka P. E.; Lefebvre A. H. Effervescent Atomization of Non-Newtonian Single Phase Liquids. In *Proceedings of the Fourth Annual Conference on Atomization and Spray Systems*, Hartford, CT; 1990; pp. 93–97.
43. Lefebvre, A. H.; Ballal, D. R. *Gas Turbine Combustion*, 3rd ed.; CRC Press: New York, 2010.
44. Taylor, G. I. The Mechanics of Swirl Atomizers. In *Proceedings of the Seventh International Congress of Applied Mechanics* **1948**, Vol. 2, p. 54.
45. Squire, H. B. Investigation of the Instability of a Moving Liquid Film. *British J. Appl. Phys.* **1953**, *4*.
46. Dexter, R. W., Emulsion Properties and Agricultural Spray Quality. In *Proceedings of the Eighth International Conference on Liquid Atomization and Spray Systems* (*ICLASS*), Pasadena, CA; 2000.
47. Stelter, M. The Influence of Viscoelastic Fluid Properties on Spray Formation from Flat-Fan and Pressure-Swirl Atomizers. *Atomization Spray.* **2002**, *12*, 299.
48. Schütz, S. Atomization of Suspensions with Shear-Thinning Behaviour by Aerodynamic Wave Breakup. *Chem. Eng. Technol.* **2004**, *27*, 619.
49. Sheng, H. Viscosity, Surface Tension, and Atomization of Water–Methanol and Diesel Emulsions. *Atomization Spray.* **2006**, *16*, 1.
50. Rizk, N. K.; Lefebvre, A. H. Internal Flow Characteristics of Simplex Swirl Atomizers. *J. Propul.* **1985**, *1*, 193–199.
51. Fraser, R. P.; Eisenklam, P.; Dombrowski, N.; Hasson, D. Drop Formation from Rapidly Moving Liquid Sheets. *Am. Inst. Chem. Eng. J.* **1962**, *8* (5), 672–680.
52. Di Domenico, J.; Henshaw, P. The Effects of Basecoat Bell Application Parameters on Elements of Appearance for an Automotive Coatings Process. *JCT Res.* **2012**, *9* (6), 675–686.
53. Corbeels, P. L.; Senser, D. W.; Lefebvre, A. H. Atomization Characteristics of a High-Speed Rotary-Bell Paint Applicator. *Atomization Spray.* **1992**, *2*, 87–89.
54. Basu, S. K.; Zhou, J.; Harding, A.; *et al.* Effect of Atomization and Rheology Control Additives on Particle Size and Appearance of Automotive Coatings. In *Proceedings of 15th International Coating Science and Technology Symposium*, St. Paul, MN, September, 2010.
55. Sovani, S. D.; Sojka, P. E.; Lefebvre, A. H. Effervescent Atomization. *Prog. Energy Combust. Sci.* **2001**, *27*, 483.
56. Roesler, T. C.; Lefebvre, A. H. Studies on Aerated-Liquid Atomization. *Int. J. Turbo Jet Eng.* **1989**, *6*, 221–230.
57. Wang, X. F.; Chin, J. S.; Lefebvre, A. H. Influence of Gas Injector Geometry on Atomization Performance of Aerated-Liquid Nozzles. *Int. J. Turbo Jet Eng.* **1989**, *6*, 271–280.
58. Weldon, D. G. *Failure Analysis of Paints and Coatings*; J. Wiley: Chichester; New York, 2001.
59. Lasia, A. *Electrochemical Impedance Spectroscopy and Its Applications*; Springer: New York, NY, 2014. (SpringerLink).
60. Sumon, T.; Lyon, S.; Scantlebury, J. Failure of Aluminium Metal Spray/Organic Duplex Coating Systems on Structural Steel. *Corros. Eng. Sci. Technol.* **2013**, *48* (7), 552–557.
61. Evans, P. L.; Schwartz, L. W.; Roy, R. V. A Mathematical Model for Crater Defect Formation in a Drying Paint Layer. *J. Colloid Interface Sci.* **2000**, *227* (1), 191–205.
62. Doherty, J. Chipping Paint? *Barron's* **2001**, *81* (26), 21–22.
63. Canadian Home Workshop. Paint Problems and Solutions. **2002**, *9* (25), 51.
64. Vatistas, N.; Francioni, V. Anolyte Cells of Electrocoating Paint. I: Anodes, Impurities and Dissolution. *Prog. Org. Coat.* **2009**, *65* (1), 109–115.
65. Saranjam, N.; Chandra, S.; Mostaghimi, J.; Fan, H.; Simmer, J. Orange Peel Formation Due to Surface Tension-Driven Flows Within Drying Paint Films. *J. Coat. Technol. Res.* **2016**, *13* (3), 413–426.
66. Toda, K.; Salazar, A.; Saito, K. *Automotive Painting Technology A Monozukuri-Hitozokuro Perspective*; Springer: Dordrecht, 2011. (Part IV, chapter 6).
67. Kangawa, H.; Lilis, Y.; Takehiko, S.; Masato, M. Effect of Mixture Fraction of Ethanol/Heptane Mixture on Spray Characteristics of Electrostatic Atomization. *Nihon Kikai Gakkai Ronbunshu, B Hen/Trans. Japan Soc. Mech. Eng.* **2011**, *B77* (773), 129–137.
68. Watanabe, H.; Matsuyama, T.; Yamamoto, H. Experimental Study on Electrostatic Atomization of Highly Viscous Liquids. *J. Electrost.* **2003**, *57* (2), 183–197.
69. Wang, Y.; Wakisaka, M. Chitosan Nanofibers Fabricated by Combined Ultrasonic Atomization and Freeze Casting. *Carbohydr. Polym.* **2015**, *122*, 18–25.
70. Avvaru, B.; Patil, M. N.; Gogate, P. R.; Pandit, A. B. Ultrasonic Atomization: Effect of Liquid Phase Properties. *Ultrasonics* **2006**, *44* (2), 146–158.
71. Yasuda, K.; Bando, Y.; Yamaguchi, S.; Nakamura, M.; Oda, A.; Kawase, Y. Analysis of Concentration Characteristics in Ultrasonic Atomization by Droplet Diameter Distribution. *Ultrasonics – Sonochemistry* **2005**, *12* (1), 37–41.
72. Lashmar, U. T.; Provasi, D.; Poole, S. W. Evaluation of the Delivery of Suspensions from an Ultrasonic Nebulizer with and Without the Lung Surfactant 'Exosurf'. *Int. J. Pharm.* **1994**, *103*, 119–123.
73. Bittner, B.; Kissel, T. Ultrasonic Atomization for Spray Drying: A Versatile Technique for the Preparation of Protein Loaded Biodegradable Microspheres. *J. Microencapsul.* **1999**, *16* (3), 325–341.
74. Freitas, S.; Merkle, H. P.; Gander, B. Ultrasonic Atomization into Reduced Pressure Atmosphere – Envisaging Aseptic Spray Drying for Micro-Encapsulation. *J. Controlled Release* **2004**, *95*, 185–195.
75. Rodriguez, L.; Cini, M.; Cavallari, C.; *et al.* Enhanced Release in Ultrasound-Compacted Solid Dosage Form. In *Minutes of European Symposium 'Formulation of Poorly-Available Drugs for Oral Administration';* de Santé, Ed.; Paris, 1999; pp. 409–412.
76. Passerini, N.; Albertini, B.; Gonzáles-Rodríguez, M.; Cavallari, C.; Rodriguez, L. Preparation and Characterization of Ibuprofen-Poloxamer 188 Granules Obtained by Melt Granulation. *Eur. J. Pharm. Sci.* **2002**, *15* (1), 71–78.
77. Ranz, W. E.; Marshall, W. R., Jr. Evaporation from Drops: I. *Chem. Eng. Prog.* **1952**, *48* (3), 141–146.
78. Ranz, W. E.; Marshall, W. R., Jr. Evaporation from Drops: II. *Chem. Eng. Prog.* **1952**, *48* (4), 173–180.
79. Holterman, H. J. *Kinetics and Evaporation of Water Drops in Air.* IMAG Report 2003-12. IMAG: Wageningen, UR, 2003.
80. Niven, R. W.; Ip, A. Y.; Mittelman, S.; Prestrelski, S. J.; Arakawa, T. Some Factors Associated with the Ultrasonic Nebulization of Proteins. *Pharm. Res.* **1995**, *12* (1), 53–59.
81. Bolleddula, D. A.; Berchielli, A.; Aliseda, A. Impact of a Heterogeneous Liquid Droplet on a Dry Surface: Application to the Pharmaceutical Industry. *Adv. Colloid Interface Sci.* **2010**, *159* (2), 144–159.
82. ASTM D714-02, 2009. *Standard Test Method for Evaluating Degree of Blistering of Paints*; ASTM International: West Conshohocken, PA, 2009. DOI:10.1520/D0714-02R09. Available from: www.astm.org.
83. ASTM D610-08, 2012. *Standard Test Method for Evaluating Degree of Rusting on Painted Steel Surfaces*; ASTM International: West Conshohocken, PA, 2012. DOI:10.1520/D0610 08R12. Available from: www.astm.org.
84. ASTM D523-14, 2014. *Standard Test Method for Specular Gloss*; ASTM International: West Conshohocken, PA, 2014. DOI:10.1520/D0523. Available from: www.astm.org.
85. ASTM D2244-15a, 2015. *Standard Practice for Calculation of Color Tolerances and Color Differences from Instrumentally Measured Color Coordinates*; ASTM International: West Conshohocken, PA, 2015. DOI:10.1520/D2244-15A. Available from: www.astm.org.
86. ASTM D3359-09e2, 2009. *Standard Test Methods for Measuring Adhesion by Tape Test*; ASTM International: West Conshohocken, PA, 2009. DOI:10.1520/D3359-09E02. Available from: www.astm.org.
87. ASTM D4060-14, 2014. *Standard Test Method for Abrasion Resistance of Organic Coatings by the Taber Abraser*; ASTM International: West Conshohocken, PA, 2014. DOI:10.1520/D4060-14. Available from: www.astm.org.

Relevant Websites

http://www.paint.org/news/
American Coatings Association News.
http://www.canpaint.com/whats-new/
Canadian Paint and Coatings Association.
http://dsctfocus.org/index.html
Detroit Society of Coatings Technology.
http://corrosion.ksc.nasa.gov/history1.htm
NASA, Corrosion Technology Laboratory.
http://www.journals.elsevier.com/surface-and-coatings-technology
Surface and Coatings Technology.

3.11 Gas Nitriding of H13 Tool Steel Used for Extrusion Dies: Numerical and Experimental Investigation

SS Akhtar, AFM Arif, and BS Yilbas, King Fahd University of Petroleum and Minerals, Dhahran, Saudi Arabia

© 2017 Elsevier Inc. All rights reserved.

3.11.1	**Introduction**	158
3.11.2	**Experimental Procedures**	160
3.11.2.1	Sample Preparation	160
3.11.2.2	Nitriding Cycle Used for Samples	160
3.11.2.3	Nitrided Layer Characterization	160
3.11.3	**Modeling of Gas Nitriding Process**	161
3.11.3.1	Theoretical Background	161
3.11.3.2	Governing Equations and Constitutive Behavior	162
3.11.3.3	Numerical Solution for the Mathematical Model	162
3.11.4	**FE Analysis**	162
3.11.4.1	Geometric Model	162
3.11.4.2	Simulation Model	162
3.11.4.3	Material Model	162
3.11.4.4	Initial and Boundary Conditions	163
3.11.4.5	Solution Procedure	163
3.11.5	**Results and Discussions**	164
3.11.5.1	Influence of Surface Texture on the Nitriding Kinetics	164
3.11.5.1.1	XRD measurement and phase analysis	164
3.11.5.1.2	Morphology of nitrided layers	164
3.11.5.2	Effect of Profile Geometry on the Nitriding Treatment	166
3.11.5.2.1	Geometric features selected for the current study	167
3.11.5.2.2	Metallography and numerical results	167
3.11.5.2.3	Design modifications and recommendations	169
3.11.5.3	Influence of Multiple Nitriding on the Nitriding Kinetics	170
3.11.5.3.1	Morphology of nitride layers	171
3.11.5.3.2	XRD analysis	171
3.11.5.3.3	Comparison of hardness and nitrogen concentration profiles	173
3.11.6	**Conclusions**	175
3.11.6.1	Consideration of Surface Texture on the Nitriding Kinetics	175
3.11.6.2	Consideration of Profile Geometry on the Nitriding Treatment	175
3.11.6.3	Consideration of Multiple Nitriding on the Nitriding Kinetics	176
References		176

3.11.1 Introduction

Aluminum extrusion die is exposed to high temperatures resulting not only from the heated billet but also from heat produced by friction and deformation. Moreover, the die is susceptible to considerable frictional forces at the die bearing land due to high pressure in the extrusion process. In aluminum extrusions, the hard oxide film, which forms instantly on the surface of the extruded metal, causes extensive wear of the die bearing during service. In general, AISI H13 is used for extrusion dies and other tooling components for production of standard aluminum profiles, which are characterized by good resistance to wear, high level of toughness, uniform and high level of machinability, high-temperature strength, and resistance.

Among the different methods available for the enhancement of the surface properties of extrusion dies with complex-shaped cavities, gas nitriding is one of the most efficient; it involves atomic nitrogen from dissociating ammonia gas at temperatures in the range 450–590 °C diffusing into the steel surface. The nitriding of the steel can be visualized bringing N_2 gas into contact with the surface of workpiece under extremely high pressure, which becomes possible by using NH_3 mixed with N_2 or H_2 gas.[1,2,3] Formation of the nitrided case begins through a series of nucleated growth areas on the surface of the steel, a 'compound layer,' with the diffused and reacted nitrides forms beneath the surface called the 'diffusion zone.' The area below the diffusion zone is the core of the steel consisting of tempered martensite. The compound layer occurs as epsilon phase ($\varepsilon - Fe_{2-3}N$), gamma phase ($\gamma' - Fe_4N$), or mixed phase ($\varepsilon + \gamma'$).

In traditional gas nitriding, which has limited control of the growth of the nitrided layer, the process is usually performed in an atmosphere containing partially dissociated ammonia gas at 500–600 °C. In this process, the nitrogen concentration at the surface cannot be properly controlled and oversaturation of the nitrogen can result in excessively porous and brittle superficial

 doi:10.1016/B978-0-12-803581-8.09174-8

'compound layer.' Such an external porous zone has lower hardness, is brittle, and is of spalling nature. It is important to emphasize the fact that the compound layer is very beneficial in the case of hot extrusion dies with regard to wear and corrosion resistance if the porosity is appropriately controlled. Moreover, the conventional nitriding equipment requires frequent monitoring and manual adjustments of atmosphere flow by the operator and, hence, repetitive and consistent results from one process to another cannot be guaranteed. These disadvantages highlight the need for automated controlled gas nitriding. It uses a mixture of ammonia and an additive gas and is controlled by a parameter known as nitriding potential (K_n) instead of the dissociation rate. Due to proper selection of atmosphere composition and adjustment of its flow rate through the retort (i.e., K_n), it is possible to form layers of the required phase composition with the required thickness of individual zones. Mathematically, K_n is the quotient of the partial pressure of the ammonia still present in the retort (the amount of ammonia that has not yet dissociated) and the partial pressure of the hydrogen that has already formed by ammonia dissociation. The nitriding potential can be viewed as the nitriding capability of the atmosphere, and its physical interpretation is that its value strictly corresponds to the equilibrium concentration of nitrogen in the workpiece surface for any given temperature.[4] The ability of the controlled nitriding process for extrusion dies is becoming a requirement in extrusion plants.

Considerable research studies were performed to examine gas nitriding treatment of various alloys with regard to various factors like the surface preparation, die geometry, multiple nitriding, process variables, and others. Sueyoshi *et al.*[5] examined the influence of the mechanical pretreatment on gas nitriding behavior of austenitic stainless steels and found that the nitriding reaction can be enhanced markedly with increasing surface roughness when its value exceeds 6 and 1 μm for SUS310 steel and SUS316 steel, respectively, whereas no reaction is recognized for the surface roughness less than these values. Cselusniak *et al.*[6] showed that a soft and shallow nitrided case is achieved in H13 steel extrusion dies if the bearing surface of the die is not activated before gas nitriding. They suggested that the bearing surface of die should be properly polished for effective nitriding. Bei *et al.*[7] studied the effects of surface ultrasonic peening (SUSSP) on gas nitriding of mild steel. They observed that when gas nitriding at temperatures below 560 °C, SUSSP treatment could not only enhance both diffusion coefficient and mass transfer coefficient dramatically during gaseous nitriding process but also reduce the threshold nitriding potential. With this surface treatment before gas nitriding, the nitriding rate can be accelerated so dramatically that nitriding time can be reduced to the half, or the conventional nitriding temperature could reduce approximately 50%. Wroblewski and Skalski[8] demonstrated that the combination of shot peening with gas nitriding on Armco iron leads to a change in surface layer formation as well as to the improvement in its properties. The plastic deformation generated by the glass shot impacts stimulates diffusion processes and results in increased thickness of nitrided layer in comparison with classical gas nitriding. Baranowska *et al.*[9] investigated that cathode sputtering used as a pretreatment before gas nitriding increases the rate of nitride layer formation in iron. They reported that the ground sample exhibits a thicker nitrided layer after nitriding as compared to the polished sample due to the structural changes observed in the ground samples. They considered surface activation as a positive effect on the gas nitriding kinetics.

Kwon *et al.*[10] studied the growth behavior of the nitrided layer inside a Cr–Mo steel hollow tube with corrugation over the internal surface. They observed differences in the compound and nitrided layer thicknesses on the land and groove surfaces and their dependence on the size of geometric features. Nonuniformity in the nitrided layer thickness and variation with size and shape of the test specimen during plasma nitriding was reported by Ataide *et al.*[11] Alves *et al.*[12] studied the growth behavior of plasma-nitrided layers on AISI 316 stainless workpieces with complex geometry. They found significant differences in thickness and hardness of the resulting nitrided layers as a function of nitriding parameters. The observed thickness of nitrided layers increased with sample height. Tercelj *et al.*[13] studied the ionic and gas nitriding of dies made of H10 tool steel with narrow and deep gaps. A similar type of study was performed by Kugler *et al.*[14] for AISI H13 dies. In both studies, variation in the nitriding depth and compound layer thickness with varying gap sizes were observed. Nayal *et al.*[15] presented a comparison of pulse-plasma-nitrided flat coupons and complexly shaped substrates such as twist drill test bits and showed that the incorporation of nitrogen depends strongly on the substrate geometry. They showed that the amount of nitrogen incorporated at the cutting edge of a drill was systematically higher than in flat coupons nitrided under identical plasma conditions. Reinhold *et al.*[16] performed plasma nitriding in a commercial plasma nitriding facility on various aluminum alloys to study the formation of aluminum nitride layers dependent on the chemical composition and geometry. In addition to simple flat specimens, more complexly shaped samples were investigated to get information about the uniformity of film covering.

Rolinski *et al.*[17] reported that the kinetics of re-nitriding under the plasma nitriding process is a continuation of pre-existing case growth, and long exposure to the nitriding temperatures has a negative effect on the hardness of the 3% Cr–Mo–V steel. Somers *et al.*[18] and Thomas Greßmann[19] have reported that upon long nitriding treatment, the formation of porosity in iron nitrides in the compound layer is very common and can be attributed to the metastable nature of the iron nitrides with respect to the decomposition into iron and molecular nitrogen gas at normal pressure. Czelusniak *et al.*[20] reported that die surfaces require re-nitriding after certain work time. They suggested that die face, unlike die bearing, is exposed to much less wear during the extrusion process, and it may suffer from over-nitriding during the re-nitriding process, resulting in spalling or exfoliating effects.

Hernandez *et al.*[21] proposed a method based on hardness data corresponding to the hardness depth profile of AISI H11 steel in conjunction with Fick's second law. They validated the procedure by computing an estimate of the diffusivity parameters of nitrogen in the α–Fe matrix. Spies *et al.*[22] showed that the main condition for formation of nitrided layers with controlled quality and specified structure is possible by controlling the nitriding potential in the working medium. *In situ* control of a nitriding process with the help of analyzers makes it possible to meet the requirements on the surface layer, prevent disturbance of the equilibrium due to uncontrolled

arrival of oxygen, and ensure the requisite proportion of the gas phases, thus optimizing the structure of the layer and its quality. Mridha and Khan[23] studied the effects of nitriding process variables and prior austenitizing and tempering temperatures for En40B steels gas-nitrided at various temperatures and in different nitriding potentials. They found that surface hardness increases and steeper hardness profiles are obtained with increasing nitriding potential using lower nitriding temperatures. Akhtar *et al.*[24] studied the influence of mechanical pretreatment in terms of surface roughness on nitriding kinetics of AISI H13 tool steel during controlled gas nitriding, and they found that the surface texturing by surface roughening prior to nitriding significantly enhances the nitriding kinetics and is expected to increase wear resistance of H13 steel used for aluminum extrusion die while resulting in its increased service life. Keddam *et al.*[25] presented results of simulation of the diffusion process of nitrogen on pure iron and showed that it is possible to predict both the microstructural nature and the thickness of nitrided layers as well as the nitrogen profile within the formed phases during gas nitriding. Hu *et al.*[26] showed that the change in the concentration field and the factors affecting it can be addressed quickly and accurately using a mathematical model. They also presented a measurement technique for the diffusion coefficient and the activity coefficient of nitrogen.

The purpose of this chapter is to evaluate the applicability of the controlled nitriding process used for the nitriding of AISI H13 dies in the extrusion industry and the benefits that can be achieved in terms of die performance. The study is implemented by undertaking various case studies wherein the H13 specimen is nitrided with the help of automated controlled nitriding equipment with preprogrammed nitriding potential values, and the effects of surface pretreatment, die profile geometry, and multiple nitriding are analyzed both experimentally and numerically. The nitrided layers of samples were compared in terms of microstructure morphology, nitride case depth, hardness depth profile, and quality.

3.11.2 Experimental Procedures

3.11.2.1 Sample Preparation

All the samples used in the current study are H13 tool steel (commercial name: ORVAR 2 Microdized), a typical die steel used for hot extrusion dies with the following composition (%wt): 0.39% C, 1% Si, 0.4% Mn, 5.3% Cr, 1.9% Mo, 0.9% V, and balance Fe. The samples were heat-treated with proper environmental controls using a vacuum furnace to prevent decarburization. The heat treatment cycle included: stress relieving at 650 °C; preheating at 815 °C; austenitizing at 1030 °C; quenching; and double tempering (first at 550 °C and second at 605 °C). After first tempering, the expected embrittling effects of coarse carbide structure, formed by the transformation of retained austenite to tempered martensite, were alleviated by a subsequent second tempering step.

3.11.2.2 Nitriding Cycle Used for Samples

Nitriding technology with state-of-the-art equipment and a user-friendly software program, allowing full automation of all functions, process stages, and safety procedures with closed-loop processing parameters, were used in collaboration with a local industrial setup. The system was capable of maintaining the preset values of nitriding potential ($K_n = p_{NH3}/(p_{H_2})^{3/2}$ where p is the partial pressure of constituting gas). The values of nitriding potentials (K_n) were maintained within certain limits as desired for each processing stage by continuous self-correction. The system set the flows for nitrogen and ammonia according to the preset program. Figure 1(a) shows the variations of temperature and gas flow rate (Q, liters per minute) in the retort during two-stage nitriding. Operating parameters for stage 1 were 490 °C and set-point K_n of 6.4 $(atm)^{-1/2}$; those for stage 2 were 530 °C and set-point K_n of 0.323 $(atm)^{-1/2}$. The furnace was first preheated and equalized to the preset temperature (450 °C) for approximately 3 h. The air in the retort was replaced by the ammonia and nitrogen gas mixture. The filling time (1 h and 40 min) was calculated automatically by the control system based on the furnace volume and incoming gas flow. During each process stage, the temperature and gas flow were controlled to achieve the set-point K_n values, which depend on the ammonia dissociation percentage. The variation of K_n during the nitriding cycle is shown in Figure 1(b) and was recorded at in intervals of 10 min; in which case, K_n variation depicted the decrease of ammonia percentage from stage 1 to stage 2 (i.e., an atmosphere with increased dissociation of ammonia from stage 1 to stage 2). The heat stages were activated automatically, before the next process stage commenced. The times of heating 1 and heating 2 prior to stage 1 and stage 2, respectively, were set to 1 h. The process times for stages 1 and 2 were 1.5 and 3.3 h, respectively. After the second stage, a cooling fan was automatically activated until the preset cooled temperature (110 °C) level was achieved. The total nitriding cycle took approximately 15 h; however, the actual nitriding time was approximately 6.8 h, corresponding to heating 1 through stage 2, as illustrated in Figure 1(a).

3.11.2.3 Nitrided Layer Characterization

The samples were prepared for cross-sections for optical and scanning electron microscopy (SEM). The cross-sections were investigated using an Axioplan 2 imaging optical microscope. The samples were mounted, polished with diamond paste (initially with 3 μm and finally with 0.25 μm), and etched with nital (1 vol% HNO_3 in ethyl alcohol) for approximately 7 s before examination. The SEM micrographs were analyzed with a Jeol JSM-6460LV scanning electron microscope equipped with energy-dispersive spectrometry (EDS). The EDS line-scan technique was used for qualitative analysis of nitrided layer microstructures. X-ray diffraction (XRD) analysis was used to determine phase characterization of nitrided surfaces using LabX XRD-6000 X-ray diffractometer by SHIMADZU. Measurements were performed using Cu–Kα radiation in the scan range of $2\theta = 10^\circ$ to 80° with a step size of 0.02°. International Centre for Diffraction Data (ICDD) database was used for the identification of phases from the positions of diffraction peaks. The microhardness measurements were performed across the cross-sections of the nitrided specimens using a BUEHLER Wirtz Vickers test apparatus under an applied load of 300 g.

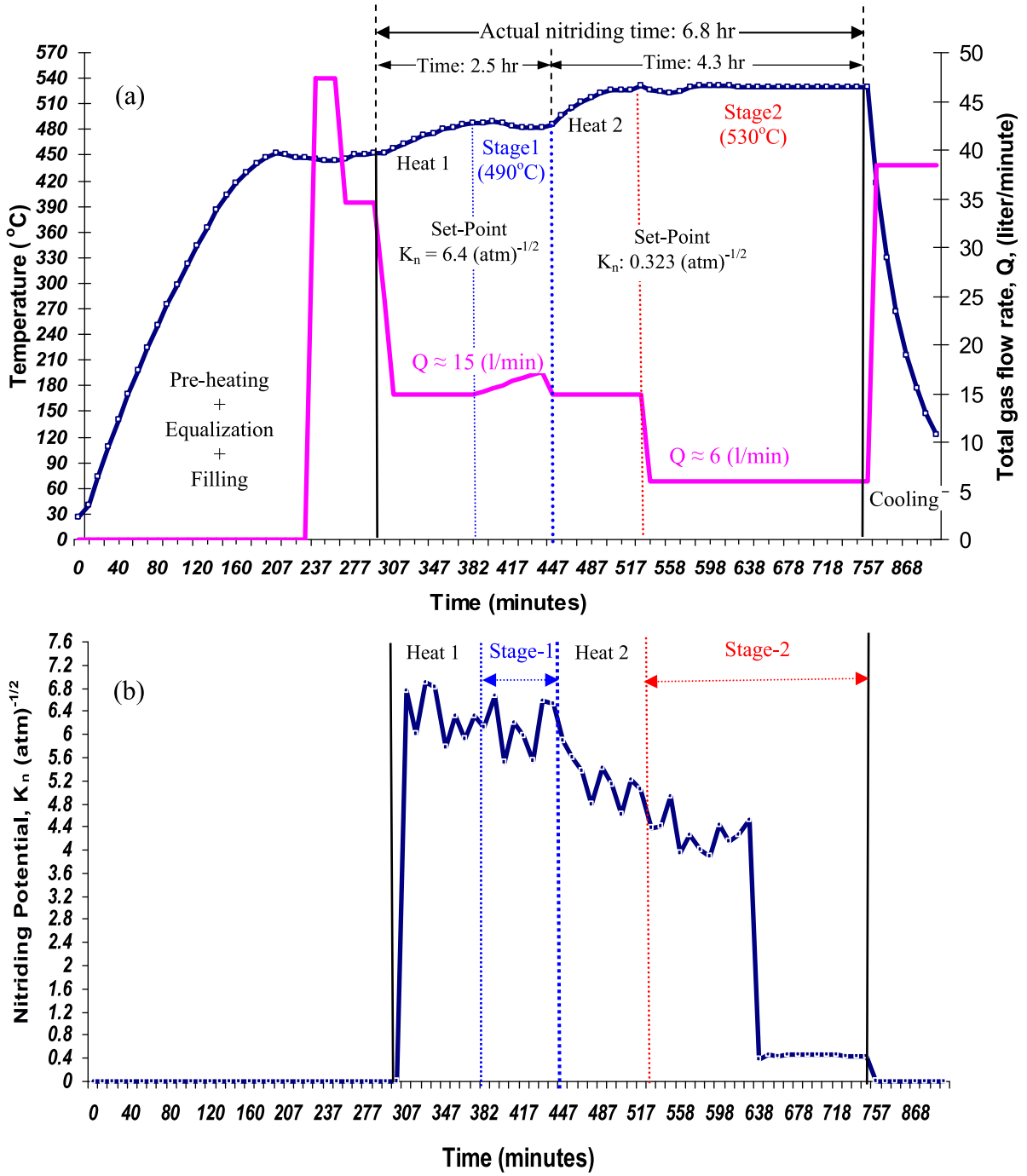


Figure 1 Variations of temperature and flow rate of gas mixture, NH_3 and N_2 (a), and nitriding potential, K_n (b), in the retort during two-stage nitriding of AISI H13 samples.

3.11.3 Modeling of Gas Nitriding Process

3.11.3.1 Theoretical Background

In gas nitriding, atomic nitrogen forms through a catalytic dissociation of ammonia (NH_3) on the surface of steel. This dissociation obeys the following reaction:

$$NH_3 \Leftrightarrow [N] + 3/2(H_2) \quad [1]$$

where [N] represents N dissolved in the steel surface. It is assumed that equilibrium has been established during this reaction. In practice, this means the occurrence of local equilibrium at the workpiece surface. The dimensionless nitriding activity can be expressed as[1]:

$$a_N = K^{(1)} K_n \quad [2]$$

where $K^{(1)}$ is the equilibrium constant for reaction [1] and has the dimensions of pressure, whereas K_n has the dimensions of

(pressure)$^{-1/2}$. The temperature-dependent $K^{(1)}$ is given by:

$$\ln K^{(1)} = 14.05 + (-6594/T) \quad [3]$$

Temperature T in eqn. [3] is between the range of 700–1400 K and should be expressed in Kelvin.

3.11.3.2 Governing Equations and Constitutive Behavior

Gas nitriding is a surface treatment process involving diffusion that is defined by the requirement of mass conservation for the diffusing phase. The governing equation is:

$$\int_V \frac{\partial c}{\partial t} dV + \int_S \mathbf{n}.\mathbf{J}\, dS = 0 \quad [4]$$

where, $c = c(x, t)$ is the mass concentration of the diffusing nitrogen at any point x in the material at any time t, V is any volume whose surface is S, $\mathbf{n}$ is the outward normal to the surface S, $\mathbf{J}$ is the flux of concentration of diffusing phase, and $\mathbf{n}.\mathbf{J}$ is the flux of concentration leaving S. Using the divergence theorem,

$$\int_V \left(\frac{\partial c}{\partial t} + \frac{\partial}{\partial x}\mathbf{J}\right) dV = 0 \quad [5]$$

$$\int_V \left[\delta\varphi\left(\frac{\partial c}{\partial t}\right) + \frac{\partial \delta\varphi}{\partial x}\mathbf{J}\right] dV + \int_S \delta\varphi \mathbf{n}.\,\mathbf{J}\, dS = 0 \quad [6]$$

where $\delta\phi$ is an arbitrary scalar field. Here, ϕ is normalized concentration, $\varphi = c/s$ where s is the solubility of diffusing material in the base material.

The gradient of nitrogen concentration has been formed by increasing the nitrogen concentration at the surface of the steel, which causes the nitrogen atoms to diffuse from the surface to the inside. The diffusion in the solid phase is assumed to be driven by the gradient of concentration, Fick's First Law, which is

$$\mathbf{J} = -D\frac{\partial c}{\partial x} \quad [7]$$

where $\partial c/\partial x$ is the gradient of nitrogen concentration and D is the diffusion coefficient. The units of diffusion coefficient are (length)^2/time and can be expressed as mm^2 per sec. Changing variables, $c = \phi$s, and assuming s as constant, we can write:

$$\mathbf{J} = -sD\left(\frac{\partial \varphi}{\partial x}\right) \quad [8]$$

Introducing the constitutive assumption of eqn [8] into eqn [6] yields:

$$\int_V \left[\delta\varphi\left(s\frac{\partial \varphi}{\partial t}\right) + \frac{\partial \delta\varphi}{\partial x}.sD\left(\frac{\partial \varphi}{\partial x}\right)\right] dV = \int_S \delta\varphi(-\mathbf{n}.\mathbf{J}) dS \quad [9]$$

3.11.3.3 Numerical Solution for the Mathematical Model

Equilibrium in a finite element (FE) model is approximated by a finite set of equations through the introduction of appropriate interpolation/shape functions. Discretized quantities are indicated by uppercase superscripts (e.g., φ^N). The summation convention is adopted for the superscripts. These represent nodal variables, with nodes shared between adjacent elements and appropriate interpolation chosen to provide adequate continuity of the assumed variation. The virtual normalized concentration field is interpolated by:

$$\varphi = \varphi^N N^N \quad [10]$$

where $N^N(x) = N^N(x, y, z)$ are interpolation functions. Then, the discretized equations can be written as:

$$\int_V \left[N^N\left(s\frac{d\varphi}{dt}\right) + \frac{\partial N^N}{dx}.sD\left(\frac{\partial \varphi}{dx}\right)\right] dV = \int_S N^N(-\mathbf{n}.\mathbf{J}) dS \quad [11]$$

Time integration in transient problems utilizes the backward Eularian method; therefore, we can write the integrated equation as:

$$\int_V \left[N^N\left(s\frac{\varphi_{t+\Delta t} - \varphi_t}{\Delta t}\right) + \frac{\partial N^N}{dx}.sD\left(\frac{\partial \varphi_{t+\Delta t}}{dx}\right)\right] dV = \int_S N^N(-\mathbf{n}.\mathbf{J}) dS \quad [12]$$

3.11.4 FE Analysis

3.11.4.1 Geometric Model

The same geometric model is used in the numerical study as it is used in experimental work. As an example, the sample used in experimental and numerical studies related to profile geometry is shown in **Figure 2**. The FE mesh is composed of a linear triangular heat transfer/mass diffusion element with three nodes (type DC2D3). A very fine mesh was needed in the vicinity of the surface to capture the mass diffusion as a result of nitriding. Mesh convergence studies were conducted with respect to the number of elements in the surface region to arrive at the final mesh size.

3.11.4.2 Simulation Model

The actual nitriding cycle (**Figure 1**) is simulated for H13 steel using a sequentially coupled thermal diffusion analysis conducted in ABAQUS. The diffusion simulation is performed by first solving the transient heat analysis for heating 1 and heating 2 prior to constant temperature stage 1 (at 490 °C) and stage 2 (at 530 °C), respectively. The results of the corresponding temperature solution obtained in heat analyses were then coupled with diffusion analysis as a predefined field. A simple interface is provided that uses the output results from the heat transfer analysis to define the temperature field at different times in the mass diffusion analysis.

3.11.4.3 Material Model

For heat analysis, the following material properties for H13 hot work die steel are used: thermal conductivity = 32.65 W m^{-1} K^{-1}; specific heat = 603 J kg^{-1} K^{-1}; and density = 7700 kg m^{-3}.

For diffusion analysis, the following diffusivity D from the experimental work of Hermandez and Cabrera[21] for H11 material is used:

$$D = 0.103 \exp\left(\frac{-83100}{RT}\right) \quad [13]$$

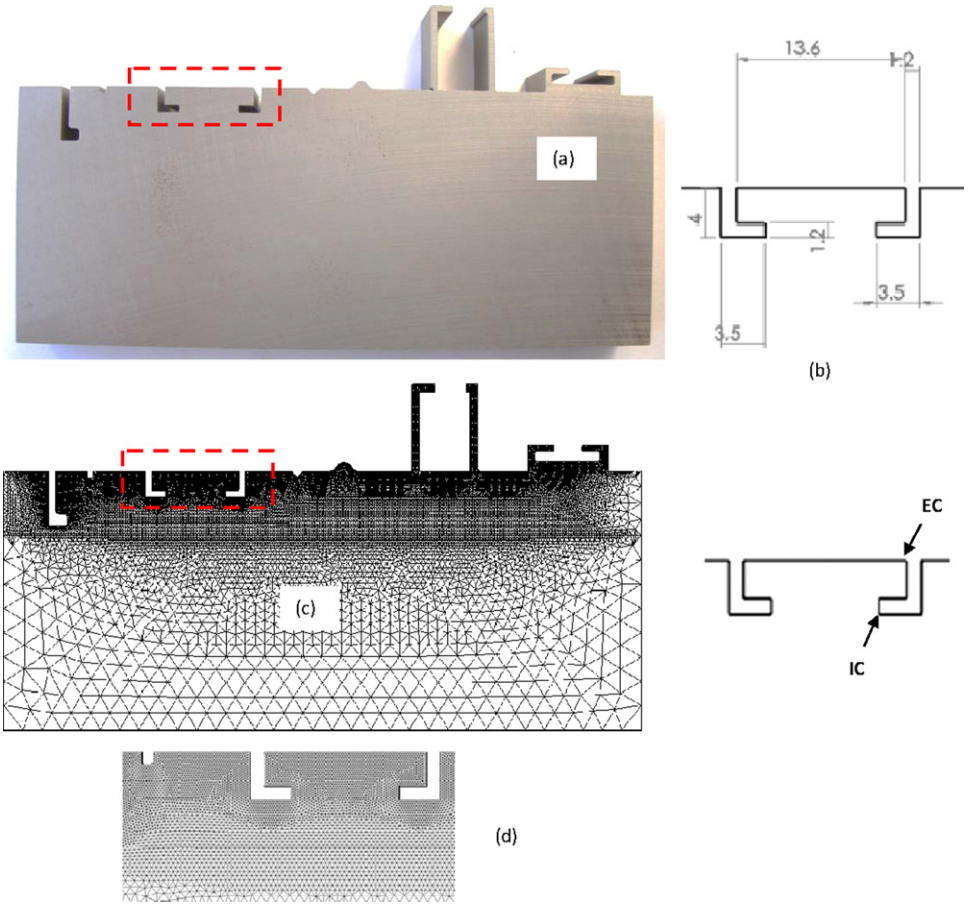


Figure 2 (a) Sample after EDM wire cutting. (b) Dimensional drawings of the studied profile (all dimensions are in mm). (c) Finite element geometric model and mesh layout. (d) The studied profile is shown in close-up.

where the unit of D is in $mm^2\,sec^{-1}$, T is temperature in Kelvin, and $R=8.314\ J\ mol^{-1}\ K^{-1}$ is the universal gas constant.

3.11.4.4 Initial and Boundary Conditions

The driving force for nitrogen transformation from gas to solid is the difference in nitrogen concentration between the gas and solid phases. The flux of nitrogen, J, to the surface of the steel per unit time and per unit surface area is described as[27]

$$J=\beta(C_g-C_s) \qquad [14]$$

where β is the coefficient of mass transfer across the interface and is abbreviated as the mass transfer coefficient, C_g is the nitrogen concentration in the gaseous nitriding medium, and C_s is the nitrogen concentration at the surface of the steel. The units of J are (unit of matter)/(area × time), whereas those of concentration are (unit of matter)/volume. This makes the units of the mass transfer coefficient (length)/time, which can be expressed as mm persec. The unit of matter in both concentration and the flux must be consistent, either as matter or mole or atoms. As atoms, concentration will be in atoms per mm^3, whereas the flux will be in (atoms per mm^2 per sec).

The initial condition is

$t=0,\ C=0$

The external boundary condition is

$$x=0,\quad \beta(C_g-C_s)=-D\frac{\partial c}{\partial x}\Big|_{x=0}$$

where $\frac{\partial c}{\partial x}|_{x=0}$ is the gradient of nitrogen concentration at $x=0$. Surface concentration was taken as zero ($C_s=0$).

3.11.4.5 Solution Procedure

For heat analysis, surface heat flux was applied to increase the temperature during the heating stages of the nitriding cycle. However, no heat analysis was performed for stage 1 and stage 2, and diffusion analysis was conducted at constant temperatures of 490 and 530 °C, respectively. Heat transfer coefficient of 3.5 $W\ m^{-2}\ K^{-1}$ was used.

For diffusion analysis, the following procedure was adopted:

Step 1: The activity in the gas phase (a_N) was first calculated for the nitriding cycle using eqn [2]. $K^{(1)}$ (equilibrium constant for dissociation reaction eqn [1]) was calculated from eqn [3] as a function of temperature in the nitriding cycle. Nitriding potential K_n is known for the nitriding cycle as a function of time (**Figure 1(b)**).

Step 2: To determine nitrogen flux J, eqn [14] to be used as input in ABAQUS, the nitrogen activity (a_N) was converted to

nitrogen wt% using the following relationship[26]:

$$a_N = f_N[\%N] \quad [15]$$

where f_N is the activity coefficient of nitrogen and [%N] is the concentration of nitrogen in steel. Due to the unavailability of f_N for H13 tool steel, the following activity coefficient of nitrogen in 38CrMoAl steel at 500–560 °C has been used[26]:

$$f_N = (2.775 + 2.197[\%N])\exp\left(\frac{-15734}{T} + 13.44\right) \quad [16]$$

Combining eqns [15] and [16], the activity was converted into nitrogen %wt with the help of Engineering Equation Solver (EES) software.

Step 3: The in-process varying nitrogen concentration in %wt. (determined in step 2) was then converted to appropriate concentration of atoms N per mm^3 by considering a unit cell of BCC α-Fe with two atoms with a lattice parameter of 2.87 A°.

Step 4: The mass transfer coefficient, β (to be used in eqn [14]), was determined from the following expression as proposed for 38CrMoAl steel by Hu *et al.*[26]

$$\beta = 0.0621\exp\left(\frac{-6267}{T}\right) \quad [17]$$

where the units of β are mm sec^{-1} and T is in Kelvin.

Step 5: The flux of nitrogen to the surface of the steel in the nitriding cycle (used as input in diffusion simulation in atoms per mm^2 per sec) was determined from eqn [14] by using in-process varying nitrogen concentration C_g (in atoms/mm^3) and mass transfer coefficient β (mm sec^{-1}).

3.11.5 Results and Discussions

The kinetics of gas nitriding of AISI H13 steel with the help of a microscopic investigation of nitride cross-section and FE simulation is considered. FE code ABAQUS is used to simulate the nitriding process using mass diffusion analysis in line with the experimental setup. The nitrided layers were characterized using different techniques, including optical microscopy, SEM, XRD analysis, EDS mapping, and microhardness analysis. Both experimental and numerical results are found in close agreement in terms of nitrogen concentration and corresponding microhardness profiles. The effects of surface texture, multiple nitriding, and profile geometry on the nitriding kinetics have been studied and the findings of the conducted investigations are provided.

3.11.5.1 Influence of Surface Texture on the Nitriding Kinetics

The effect of prenitriding surface texture of AISI H13 steel on the behavior of gas nitriding process under controlled nitriding potential is studied with the aim of finding how efficiently surface activation can be used for better die performance. The nitrided layers of three samples, which were ground, polished, and lapped before nitriding, were studied in terms of morphology of diffusion zone and compound layer, case depth, and hardness depth profile. A sample without surface preparation (designated as unprepared sample) was also included in the investigation for comparison purposes. Samples were polished and lapped using an OMNILAP 2000 lapping machine (South Bay Technology). Surface roughness of the samples was measured by a SJ-400 surface roughness tester (Mitutoyo Corporation, Japan). The samples were cut into two pieces after nitriding and prepared for cross-sections for optical and SEM. The discussions on effect of surface texture are presented in line with the previous study.[24]

3.11.5.1.1 XRD measurement and phase analysis

Figure 3 gives the XRD diffractograms for the surface of unprepared, ground, polished, and lapped samples after gas nitriding treatment. The major phases in the surface of all samples are iron nitrides, which confirm the presence of the superficial compound layer. The major phases identified in the unprepared sample are $\varepsilon - Fe_3N$ corresponding to (110) and (200) planes with small peaks of mixed nitride phases' peak of $\varepsilon - Fe_3N$ (002) + $\gamma' - Fe_4N$ (111) and $\varepsilon - Fe_3N$ (112). Moreover, additional $\varepsilon - Fe_3N$ peaks were also observed corresponding to (101), (103), and (113) planes for surface-treated samples. A small peak of $\varepsilon - Fe_3N$ (110) was also observed in ground and polished samples. The various iron nitride peaks indicate that surface preparation facilitates the incorporation of more nitrogen atoms into the subsurface diffusion zone. High-intensity peaks of α-Fe (110) + CrN (200) in the case of surface-treated samples were observed that can be associated with a thin compound layer. Because the compound layer is thin, it is probable that the Fe and CrN reflections were detected from the subsurface diffusion matrix and not due to the compound layer. No pronounced ferrite (α-Fe) and CrN peaks were detected in untreated samples. This is because the compound layer thickness is longer than the X-ray penetration depth and the Cu–Kα probes to a few microns. The values of lattice spacing (d) corresponding to α-Fe (110) is shown in Table 1. The d-values reduce with increasing prenitriding surface roughness (R_a). These reduced d-values with increasing R_a values are also associated with a corresponding increase in 2θ values. The reduced lattice spacing in ground samples with the highest initial surface roughness of 0.13 ± 0.035 μm after gas nitriding can be associated with the highest compressive stress. The high compressive stress is likely due to comparatively more free atomic nitrogen available to diffuse into the matrix due to more surface activation by the grinding process. This observation is in line with relatively high-nitride XRD peaks in the case of the ground sample. Iron oxide (Fe_2O_3/Fe_3O_4) peaks as revealed in XRD measurements detected from the surface of roughened samples are an indication of oxidation due to partially oxidized rough surfaces prior to the nitriding process.

3.11.5.1.2 Morphology of nitrided layers

The optical microstructures of the nitrided cross-sections of as-received, ground, polished, and lapped samples are shown in Figures 4(a)–4(d). Figure 5 shows the corresponding scanning electron micrographs of the surface vicinity of the nitride layers. All microstructures consist of an internal core of tempered martensite and a nitrided layer at the free surface. The nitrided

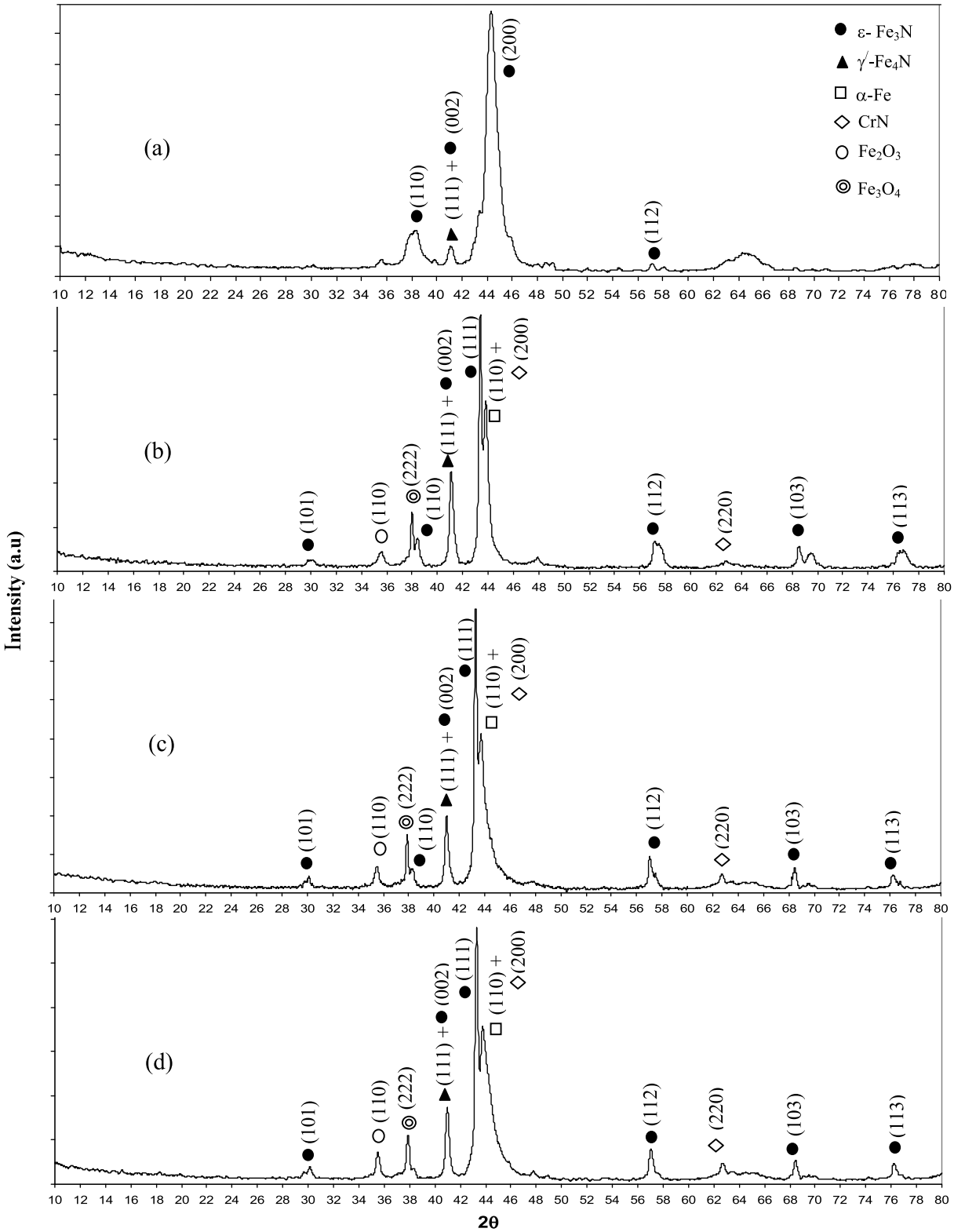


Figure 3 XRD diffractogram recorded from the surface of nitrided AISI H13 samples: (a) as-received sample; (b) ground sample; (c) polished sample; and (d) lapped sample.

layer consists of a diffusion zone with fine nitride precipitates (dark regions in the optical and lamellae structure in the SEM micrographs) and a compound layer at the surface. It is clearly visible from the microstructures that surface texture has significant implications in the thickness and uniformity of the nitrided layer. The shallow and uneven nitride layers in the

Table 1 Prenitriding surface roughness and lattice spacing, 2θ position, and effective case depth of gas-nitrided AISI H13 samples

Sample	R_a *(μm) before nitriding*[a]	*2θ (degree) α-Fe (110)*	*Lattice spacing d (A°) for α-Fe (110)*	*Effective case depth at 700 HV (μm)*
As-received	–	–	–	75
Ground	0.13 ± 0.035	43.80	2.06522	135
Polished	0.08 ± 0.015	43.70	2.06971	120
Lapped	0.04 ± 0.009	43.68	2.07061	85

[a] R_a values are given as average $\pm$ standard deviation.

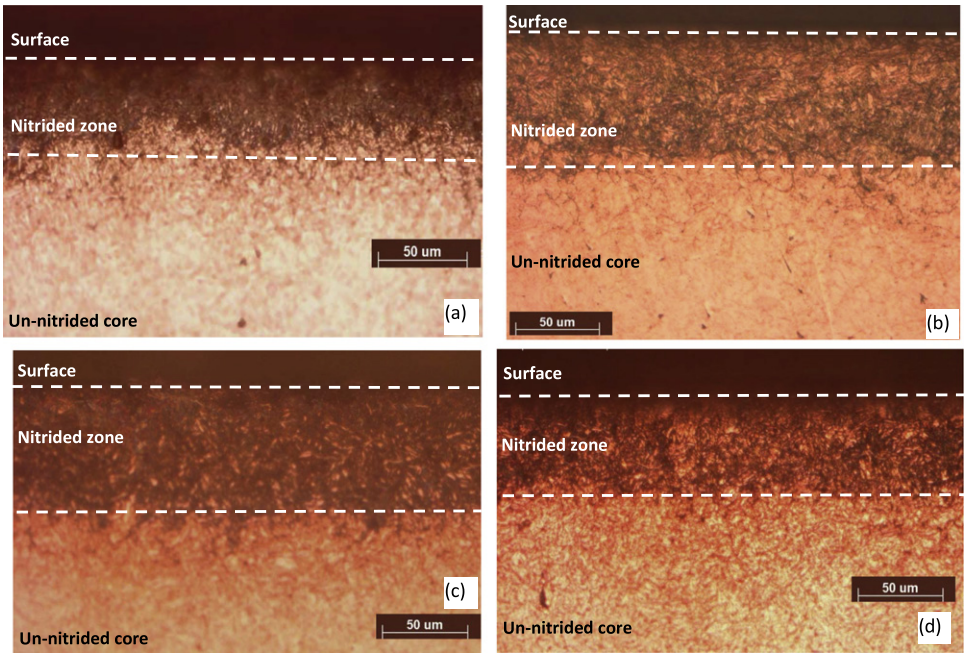


Figure 4 Optical micrographs of nitrided cross-sections: as-received sample (a); ground sample (b); polished sample (c); and lapped sample (d).

case of as-received samples are due to insufficient nitriding treatment, which greatly depends on the ability of free atomic nitrogen to diffuse into the iron matrix. If the surface is not properly textured via mechanical surface treatment, any expected superficial film or deposit, even of infinitesimally small thickness, can partially or completely prevent the access of active nitrogen to the surface, and the availability of nitrogen that manages to get through the film can be insufficient. This, in turn, results in the insufficient quantity of sub-microscopic nitrides that could precipitate during the nitriding cycle, as can be seen from SEM micrographs. Unlike untreated sample surfaces, all the textured surfaces depict deep and uniform diffusion zones with some differences in depths. The diffusion zone increases with increase in initial surface roughness. Moreover, the ground sample resulted in a deep diffusion zone followed by a polished sample. The lapped sample with the lowest surface roughness has the lowest depth of diffusion zone among the textured surface samples. As indicated, the reduced lattice spacing with increased roughness facilitates enhancement of nitrogen diffusion; therefore, the depth of the diffusion zone increases with the increasing surface roughness.

The compound layers formed at the surface of as-received, ground, polished, and lapped samples are shown in Figure 5. Unprepared samples have uneven and thick compound layers as compared to the textured surface samples. The thick compound layer can be strongly associated with slow diffusion rate and nitrogen pressure at the surface. Among the textured surface samples, the ground sample has a more uniform and slightly thicker (2.5–3 μm) compound layer as compared to polished ($\sim$1.5 μm) and lapped ($\sim$1 μm) samples. The thickness of the compound layer of the samples is in line with the thickness of the diffusion zone, which reduces with decreasing surface roughness. This can be associated with high XRD counts of iron nitrides for ground samples, particularly the mixed phase peak of $\varepsilon - Fe_3N\ (002) + \gamma' - Fe_4N\ (111)$, as observed in the XRD diffractogram.

3.11.5.2 Effect of Profile Geometry on the Nitriding Treatment

The influence of most common profile features on the behavior of case hardening quality for AISI H13 tool steel samples were studied both experimentally and numerically. AISI H13 steel samples are manufactured with profiles similar to those used in hot extrusion dies and subsequently gas-nitrided under controlled nitriding potential. Nitrided layers of corner features in the samples are then investigated and uniformity and depth are compared in terms of compound layer and total case depth. Microhardness measurement and both optical and SEM techniques have been used for this purpose. The nitrogen

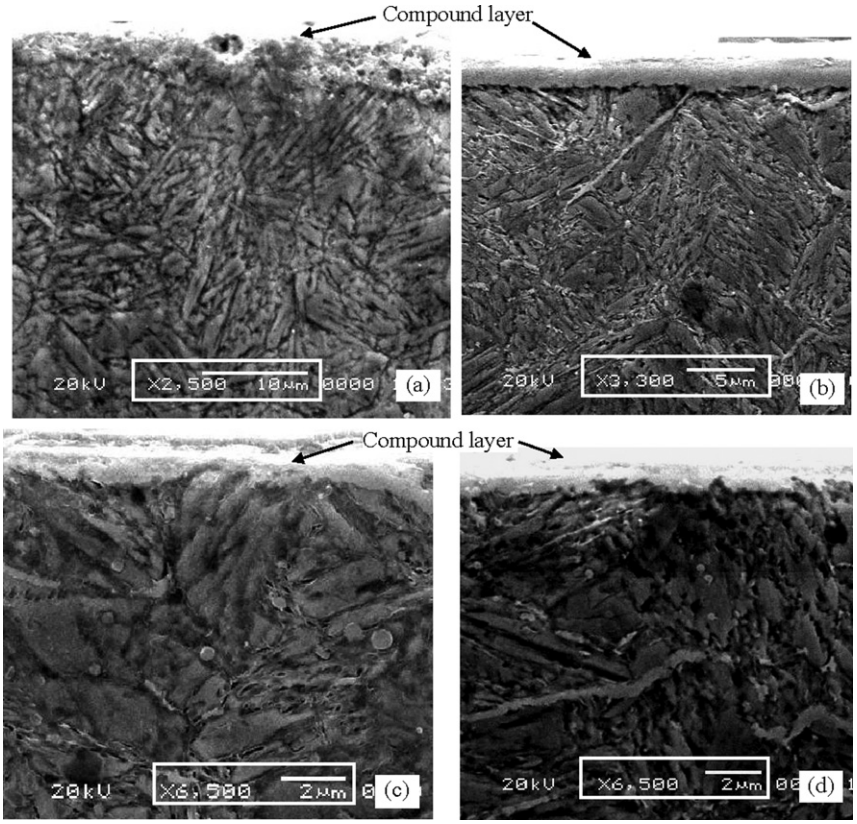


Figure 5 Magnified SEM images of compound layer developed after controlled gas nitriding at the surface of: as-received specimen (a); ground specimen (b); polished specimen (c); and lapped specimen (d).

concentration field is also modeled for corresponding features using the FE method and compared with experimental results. The FE model is then modified for optimum nitride layer formation of these features. Some optimization guidelines are set-up in light of the modified FE models, and recommendations are devised for their implementation to improve the die service life. Discussions of the effects of profile geometry on the nitriding kinetics are presented in line with the previous studies.[27,28]

3.11.5.2.1 Geometric features selected for the current study

The profiles shown in Figure 2 encompass some very common features, such as convex and concave surfaces, flat surfaces, internal corner (IC), external corner (EC), and others. For the present study, only IC and EC were selected based on the fact that these features are the most critical in terms of nitriding layer development.[27] The features reported in the current study are shown in Figure 2, namely EC and IC.

3.11.5.2.2 Metallography and numerical results

Metallographic investigation is performed using optical and scanning electronic microscopes, followed by microhardness measurements to observe the nitride layer formation and its uniformity. The optical and scanning electron micrographs of the nitride cross-sections of the selected features are shown in Figure 6 for corner features, EC, and IC. The corresponding hardness depth profiles are shown in Figure 7. The hardness measurements were taken at a specific location (depth) starting from approximately 25 µm away from the surface. Each indentation point in the hardness depth profiles is the result of average of five measurements at each location.

Numerically predicted nitrided layers developed for the features EC and IC are shown in Figure 8, whereas Figure 9 shows the corresponding variation of nitrogen concentration along the depth for these features.

It can be observed that the compound zone is only visible in SEM micrographs and could not be detected in the optical micrographs due to thinness. The thicknesses of the compound layer at both feature locations is estimated from corresponding SEM micrograph and listed in Table 2. Please refer to previous work[29] for details regarding the formation of the compound layer and morphology of the nitrite layer in relation with the nitriding potential and corresponding nitrogen activity. The critical nitriding potential values and, hence, the nitrogen activities above which the iron nitrides in the compound layer ($\gamma' - Fe_4N$ and $\varepsilon - Fe_3N$) develop were identified from the Lehrer equilibrium diagram. The actual variation of K_n (Figure 1(b)) indicated that the compound layer would form at the surface. It was confirmed from the Lehrer equilibrium diagram that the $\gamma' - Fe_4N$ phase of the compound layer begins to form when K_n of the atmosphere exceeds the upper limit of the nitrogen concentration in the diffusion zone at the nitriding temperature. A further increase in K_n causes the formation of the $\varepsilon - Fe_3N$ phase in the steel surface. The recommended ranges, K_n values, and maximum allowed thickness of

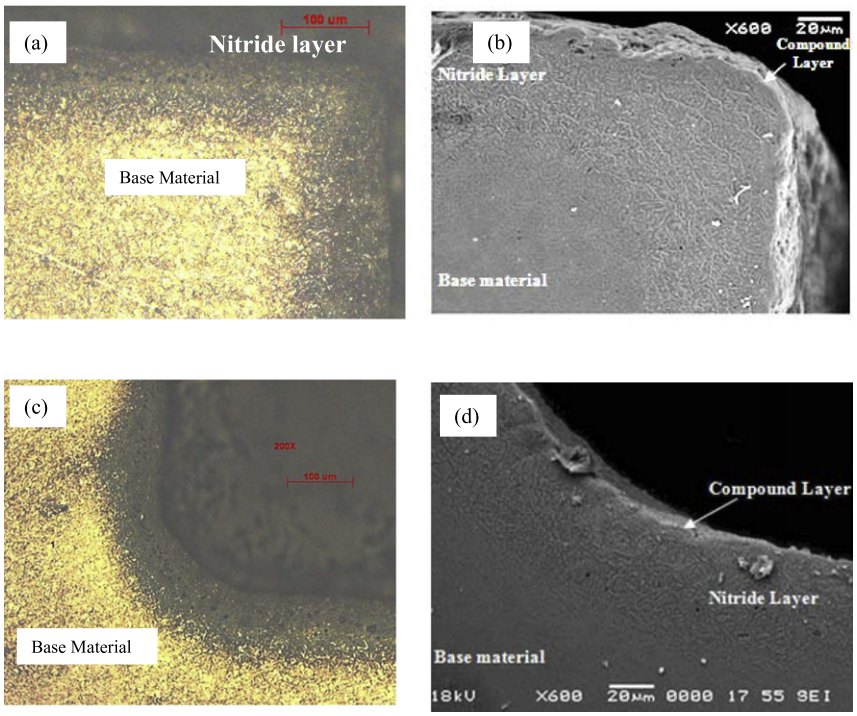


Figure 6 Optical micrographs (a) and scanning electron micrograph (b) observed at the external corner. Optical micrographs (c) and scanning electron micrograph (d) observed at the internal corner.

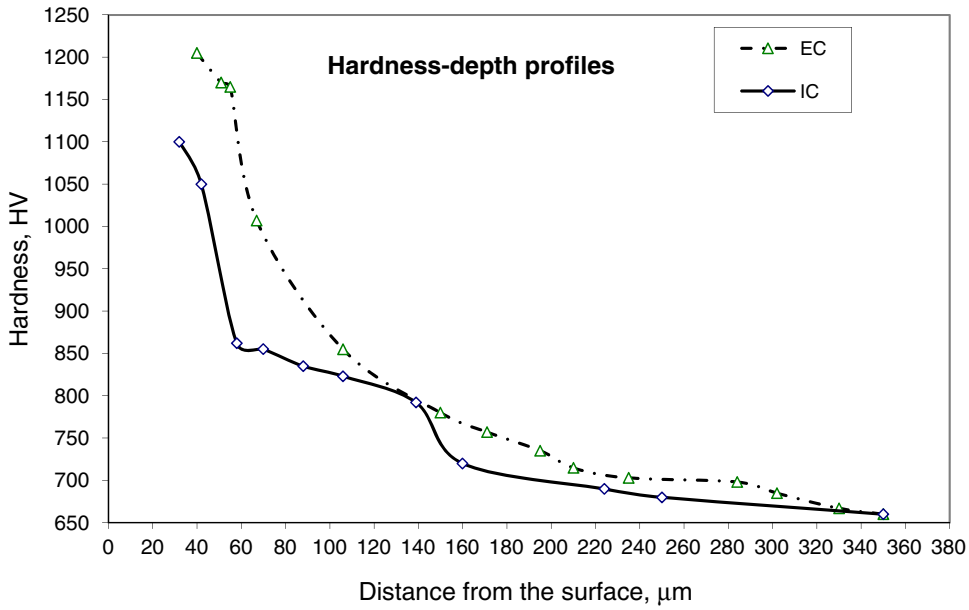


Figure 7 Hardness depth profiles for the external corner and internal corner features.

the compound layer for different classes as classified by AMS per requirement of AMS 2759/10A were used.[30] The thicknesses of the compound layer achieved in both features, EC and IC, are less than the maximum specified by AMS. The compound layer and nitrided depth at each location are given in Table 2.

It can be seen that the pattern of hardness and concentration depth profile are the same for all features, maximum near the surface, and decays toward the core of material. This implies that the nitriding process was successfully performed both experimentally and numerically. Comparing experimental and numerical results, it can be seen that hardness across the nitrided layer cross-section scales fairly well with the decay of nitrogen concentration from surface to core. However, the values of hardness corresponding to any specific depth vary significantly in the samples made of the same material and are

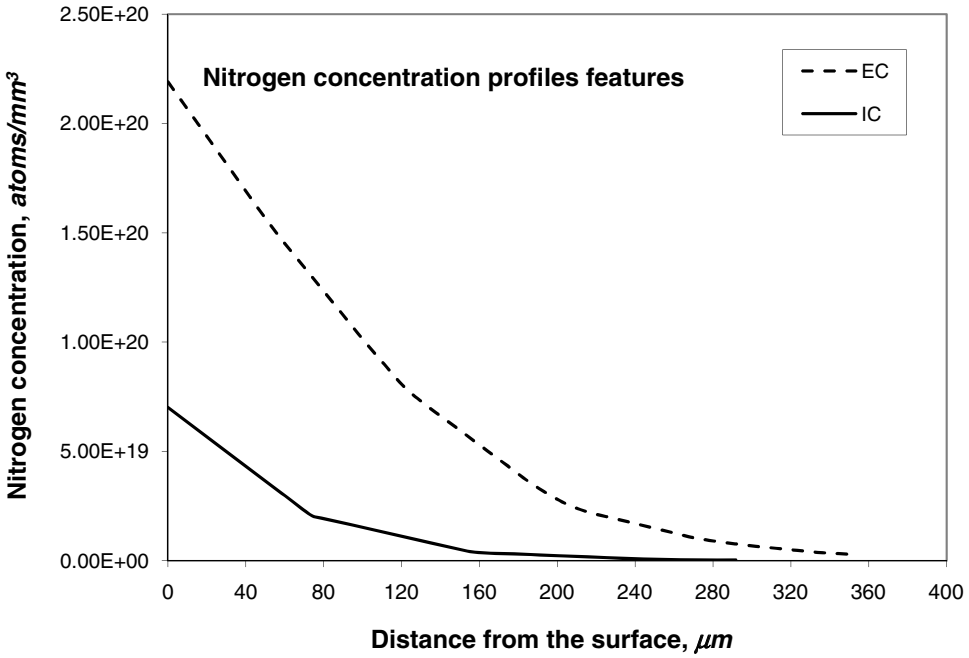


Figure 8 Nitrogen concentration profiles for features of the external corner and the internal corner at the end of nitriding cycle.

nitrided under same conditions. The core hardness was approximately 660 HV in both locations. The nitrided case depth at each feature location is determined from the hardness depth profile (from the experimental study) and the concentration depth profile (from the numerical study). For this purpose, the following criteria are used[27]:

1. Nitriding depth from hardness profile: the depth below the surface at which microhardness is 10% higher than that of the core, as set forth by ASM.[30]
2. Nitriding depth from concentration profile: the depth where the concentration is 10% higher than the average minimum concentration.

Comparing experimental and numerical results, numerically predicted case depths compare well with experimental results for both feature locations. However, slightly higher values can strongly be attributed to nonexact coefficients of diffusion used for diffusion analysis of H13 steel samples. Moreover, in computer simulation, the application of boundary conditions (i.e., surface concentration) is ideal in the sense that it is directly applied to the surface irrespective of the location. However, in the real nitriding process, nitrogen access to different locations is different depending on size, gaps, and orientation of different features (i.e., some locations are exposed and permit easy accessibility but others may be concealed, making it difficult to receive the required nitrogen content).

It can be noted from the micrographs as well as from the numerical predictions that all the flat features of the samples result in uniform and fairly identical nitrided layers. However, the external and ICs significantly influence the uniformity and quality of the nitride formation. The outer corner feature, EC, results in comparatively deeper case depths measured experimentally as well as predicted numerically. This is associated with the simultaneous diffusion from two convergent directions at the corners. Compound layer thickness for these features is less than that found on flat features[27] and are given in **Table 2**; they can be observed from the corresponding SEM micrographs. The hardness curve for the EC feature, EC, is relatively less steep and has a deeper hardening effect, in line with greater case depth. However, oversaturation of nitrogen at the extreme corners resulted in somewhat of a 'corner effect' despite the controlled nitriding process. Such a corner effect results in greatly reduced initial hardness values. As reported by Liliental *et al.*,[4] many problems are experienced with aluminum extrusion dies, with the most common including 'choke' and 'relief' formation when debris from a brittle and spalling nitrided layer at the corner lodges in the die bearing area.

The IC feature has significantly smaller case depths, as can be observed in **Figure 6** (for IC). The pattern of nitrogen diffusion at these locations can be more clearly understood from numerically predicted results (**Figure 9**). Unlike EC features, simultaneous diffusion from two divergent directions results in a reduced nitride case at the corner. As compared to flat surfaces, nonuniformity in the nitrided layer can also be observed. The compound layer developed at the IC is also slightly uneven, and its thickness is approximately 3 μm, which is less than that achieved in flat surfaces.[27]

3.11.5.2.3 Design modifications and recommendations

Based on the present observations, it can be stated without any doubt that die geometric features have a significant effect on the surface hardness, case depth, and compound layer formation, even under the controlled nitriding process. The results of this study highlight the need to include the effect of the die profile on the nitrided layer for optimal die design with improved service life. In the current section, the validated numerical study was extended and some modifications in the path brush features, namely EC and IC, were performed to see

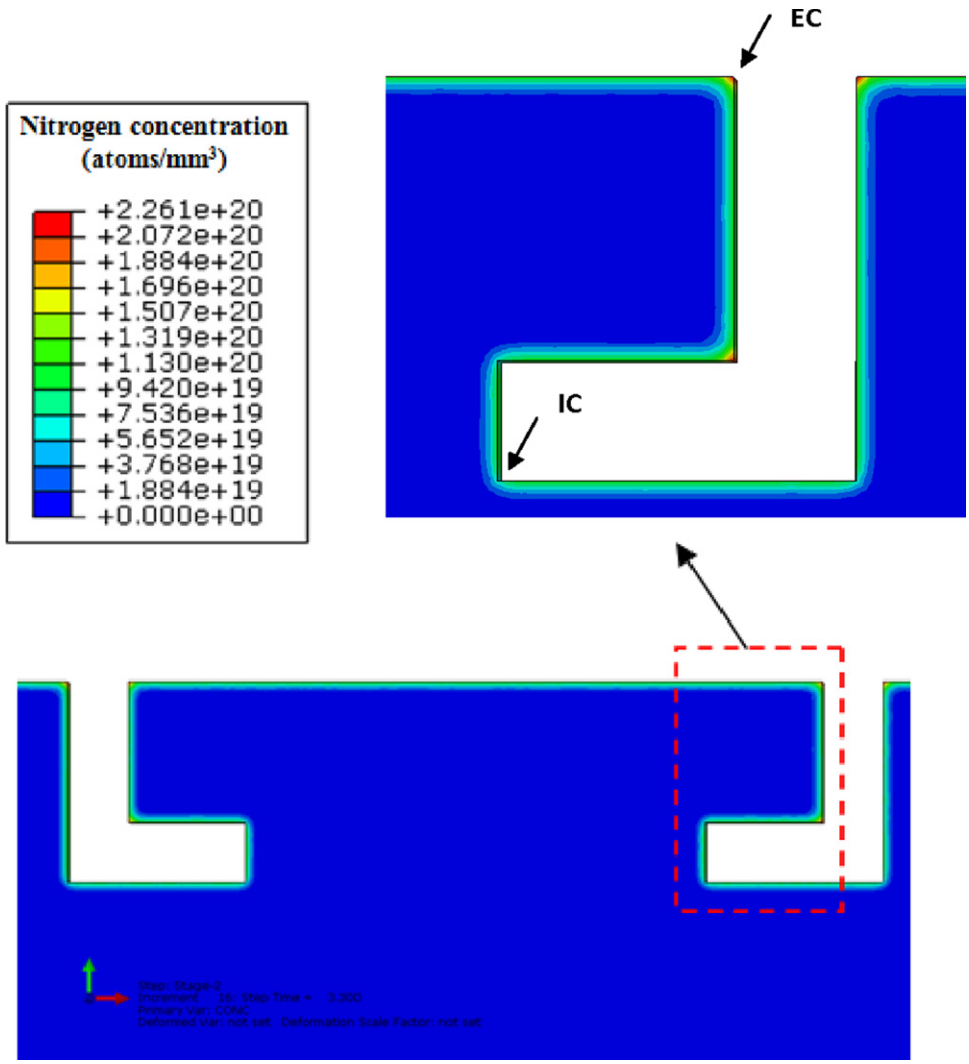


Figure 9 Numerically predicted nitrided layer for features of the external corner (EC) and internal corner (IC) at the end of nitriding cycle. The nitrogen concentration is in atoms per mm^3.

Table 2 Summary of experimental and numerical results

Geometric feature	*Experimental measurements*		*Numerical simulation results*
	Compound layer thickness (μm)	*Minimum case depth (μm)*	*Nitriding depth (μm)*
External corner (EC)	~3–5	208	215
Internal corner (IC)	~3–4	145	160

the effect of geometric shape on the uniformity of nitride layer development on these corner features. As observed, the ECs in the die profiles can present a severe threat to the life of the entire die due to the oversaturation of nitride layer formation. Moreover, the ICs result in the development of a nonuniform nitride layer. Therefore, EC feature and IC feature are modified by incorporating fillets. Two fillet radii, 0.2 and 0.5 mm, are used. Figure 10 shows the effects of external and IC fillets on the nitrogen concentration. It is obvious from the contour plots of the nitrogen concentration that the nitriding layer becomes uniform as we increase the fillet radius from 0 to 0.2 mm to 0.5 mm. It can be observed from Figure 10(c) that incorporation of a fillet at the EC and IC results in uniform growth of nitrogen concentration, which will certainly positively influence the hardness and effectiveness of these corner features. However, it must be remembered that the modified features should not affect the final profile geometry and the desired tolerances of the final extruded section. The suggested modifications in the existing die designs would serve as a baseline for the optimized die designs that will benefit both local and international die manufacturers.

3.11.5.3 Influence of Multiple Nitriding on the Nitriding Kinetics

Repeated nitriding is an indispensable process in the hot extrusion of aluminum profiles and cannot be avoided. The purpose of this section is to examine the effects of the

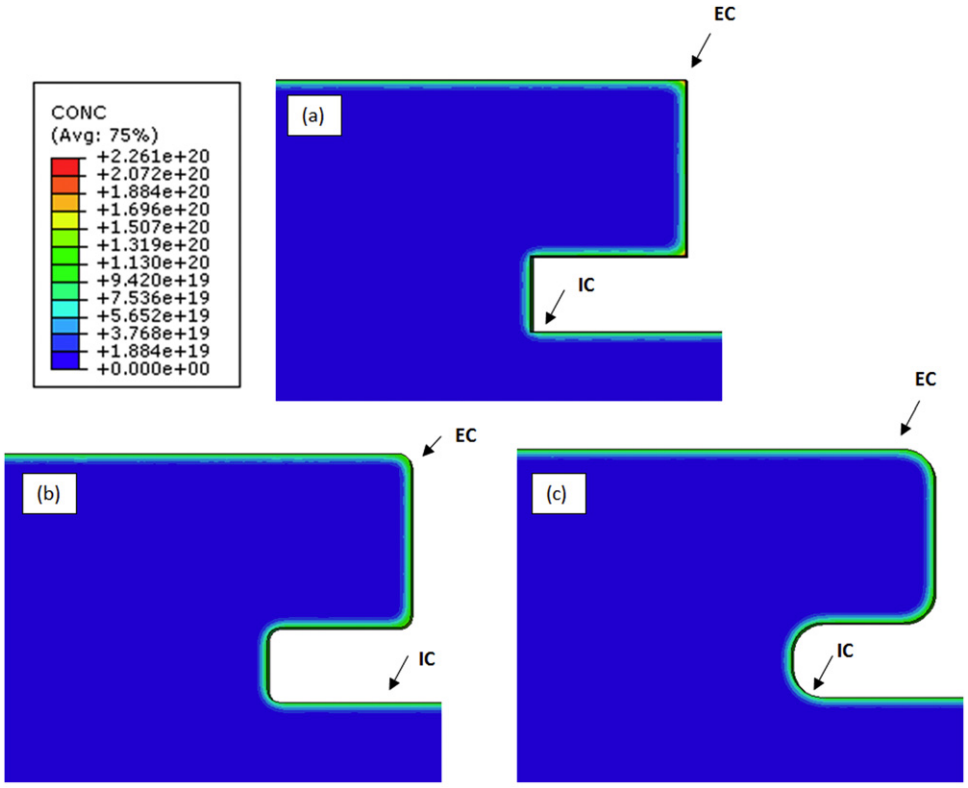


Figure 10 Nitrogen concentration contours for modified external corner (EC) and internal corner (IC) features. (a) Original features, (b) when fillet radius of 0.2 mm is used, and (c) when fillet radius of 0.5 mm is used.

re-nitriding process on the morphology and hardness of the nitride layer when dies are exposed to such practices. The results reported here are in line with the previous study.[31] This study serves as a baseline to identify the re-nitriding conditions through numerical investigation of the process for the extrusion industry. The effect of re-nitriding treatment on the AISI H13 steel surface is studied, both experimentally and numerically, using a two-stage gas nitriding process under controlled nitriding potential, as discussed earlier. The nitride layers of three samples treated with single-, double-, and triple-nitriding processes, respectively, were compared in terms of microstructure morphology, nitride case depth, hardness depth profile, and quality. All the samples were properly heat-treated (quenched and tempered) prior to the nitriding process in line with real extrusion die surface treatment and then subjected to almost the same nitriding cycle during the nitriding and re-nitriding treatments. No prior surface treatment was performed and the samples were re-nitrided with the pre-existing nitride case. Nitrogen concentration profiles predicted from numerical analysis for the cross-sections of single-, double-, and triple-nitrided samples are compared with the hardness profiles of their counterparts obtained from the experiments. The findings reveal that both results are in good agreement.

3.11.5.3.1 Morphology of nitride layers

The variation in total nitride layer thickness in single-, double-, and triple-nitrided sample was found to be significant; it increased from 80 μm in the case of single-nitrided samples to 100 μm for double-nitrided samples and approximately 115 μm for triple-nitrided samples.[31] Multiple-nitrided samples have more dense lamellae colonies, and more precipitates can be observed at the grain boundaries with deeper affect, as shown in Figure 11. This increased amount of precipitates is due to the aggregate long duration at nitriding temperatures during repeated nitriding treatment.

As can be observed from Figure 11, the compound layers in the double- and triple-nitrided samples are much thinner (approximately 1–2 μm) compared to those of single-nitrided samples (4–8 μm). This result is in agreement with previous results[32] indicating that controlled gas nitriding recreates a uniform but thinner nitrided white layer during re-nitriding treatment of H13 dies. It is reported that the critical temperature for the decomposition and compound layer is 500 °C, although in some cases it can start even at 350 °C for hot-working steels.[33] Such decomposition of iron nitride phases in the compound layer at high temperatures results in backward diffusion of nitrogen and destruction of the already existing compound layer. The thinner compound layer during re-nitriding reveals that decomposition of the iron-nitrided phases is dominant compared to re-development of the compound layer during simultaneous re-nitriding treatment.

3.11.5.3.2 XRD analysis

Figure 12 gives the XRD spectrums produced on the surface of nitrided samples and shows the influence of multiple nitriding

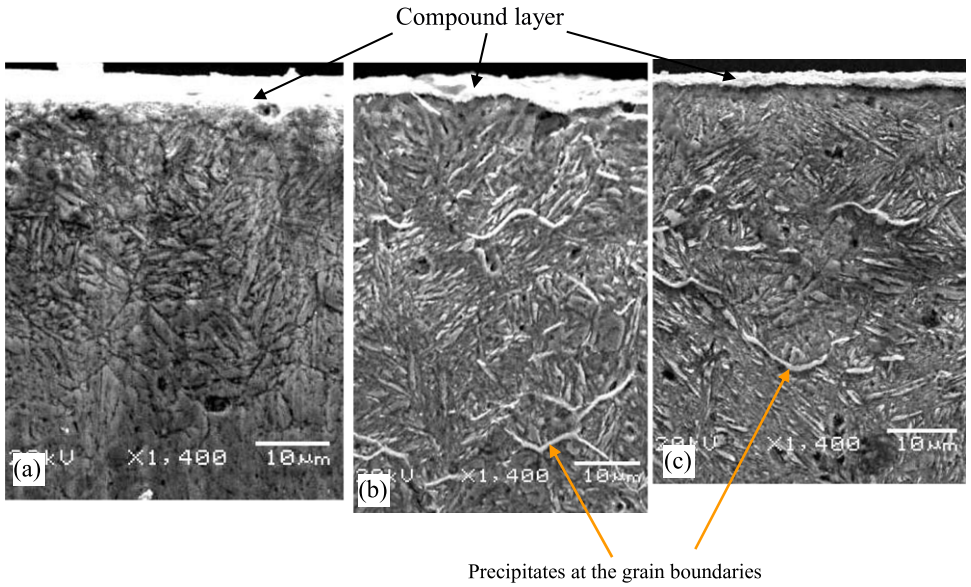


Figure 11 Lamellar structure in the nitrided zone: single-nitrided specimen (a); double-nitrided specimen (b); and triple-nitrided specimen (c).

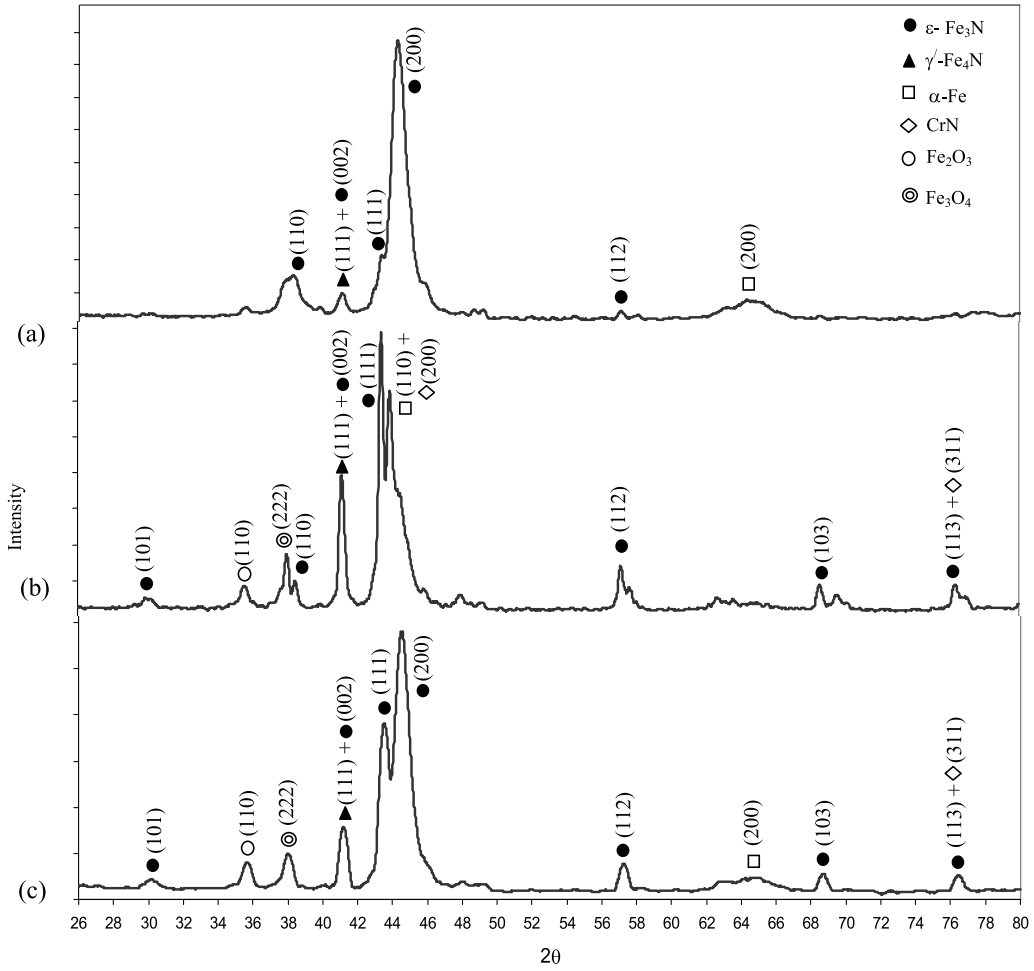


Figure 12 XRD diffractogram recorded from the surface of nitrided AISI H13 samples: (a) single-nitrided sample; (b) double-nitrided sample; and (c) triple-nitrided sample.

treatments on phase formation. As observed, the major phases were identified to be $\varepsilon - Fe_3N$ and $\gamma' - Fe_4N$ in all the three samples, thus confirming the presence of the superficial compound layer. The spectrum related to the single-nitrided sample reveals the presence of a considerably large amount of the $\varepsilon - Fe_3N$ phase compared to the $\gamma' - Fe_4N$ phase, which is relatively close to the monophase ε based on the ratio of ε/γ', as estimated from XED peaks. In contrast, a quite comparable $\gamma' - Fe_4N$ phase in addition to the $\varepsilon - Fe_3N$ phase was detected in double- and triple-nitrided samples, which show that the pre-existing compound layer before re-nitriding significantly affects the fresh compound layer formation in the subsequent re-nitriding process under the same conditions used for un-nitrided sample.

The existence of a comparatively large amount of $\gamma' - Fe_4N$ in multiple nitrided samples can be associated with loss of existing nitrogen (dissolved in $\varepsilon - Fe_3N$) by nitrogen enrichment during the re-nitriding process, which leads to transformation of $\varepsilon - Fe_3N$ to $\gamma' - Fe_4N$. Such a transformation can be attributed to excessive nitriding cycle time during repeated nitriding. It should be mentioned here that the monophase structure ($\gamma' - Fe_4N$ or $\varepsilon - Fe_3N$) of the compound layer is recommended[34] due to homogeneity and increased mechanical properties. In the case of the presence of both phases, relatively higher residual stresses are present in the compound layer due to their different structures (FCC and HCP, respectively), which will result in reduced toughness and generate microcracks under applied stresses. Comparatively narrow full-width at half-maximum (FWHM) observed in the single-nitrided sample XRD peak corresponding to the $\varepsilon - Fe_3N$ phase also indicates less disorder in the compound zone. It is generally recognized[32] that the $\varepsilon - Fe_3N$ phase features better wear resistance than $\gamma' - Fe_4N$. For this reason, $\varepsilon - Fe_3N$ in the compound layer should be viewed as a positive effect for better die performance.

3.11.5.3.3 Comparison of hardness and nitrogen concentration profiles

Figure 13 presents a comparison between the variations in microhardness of the nitride layer as a function of the distance from the surface for single-nitrided and multiple-nitrided samples. In these curves, each point represents the average value of five indentations. The extent of the nitrided regions after repeated nitriding treatment can be compared based on hardness depth profiles. For the initial 15-μm depth of the nitrided zone in the multiple-nitrided samples, reduced hardness was observed: 910 HV for double-nitrided and 860 HV for triple-nitrided samples. This reduced hardness is associated with oxidation and porosity observed in the near-surface diffusion zone. Maximum hardness was found at a depth of approximately 20 μm: 1200 HV for double-nitrided and 1240 HV for triple-nitrided samples. Single-nitrided samples show reduced hardness values in comparison with multiple-nitrided samples, except for the initial depth of 15 μm due to the absence of oxidation and porosity. Hardness depth profile corresponding to the single-nitrided sample behaves in a monotonically decreasing manner with a maximum hardness of approximately 1180 HV at the surface. Comparing double- and triple-nitrided samples, hardness decay toward the core is more gradual and deep in triple-nitrided samples than in double-nitrided samples. The decay of hardness across the nitrided layer cross-section can be strongly related to the decay of nitrogen concentration from surface to core. As explained, near the surface, where the nitrogen supersaturation is maximum, the driving force for nucleation of the lamellae structure is at maximum, causing more abundant and fine structures. The increase of lamellar spacing (coarsening of lamellar structure) with depth induces a pronounced decrease of hardness with depth in the nitrided zone.[35]

Figure 14 shows predicted case depth development after single-, double-, and triple-nitriding treatment simulated

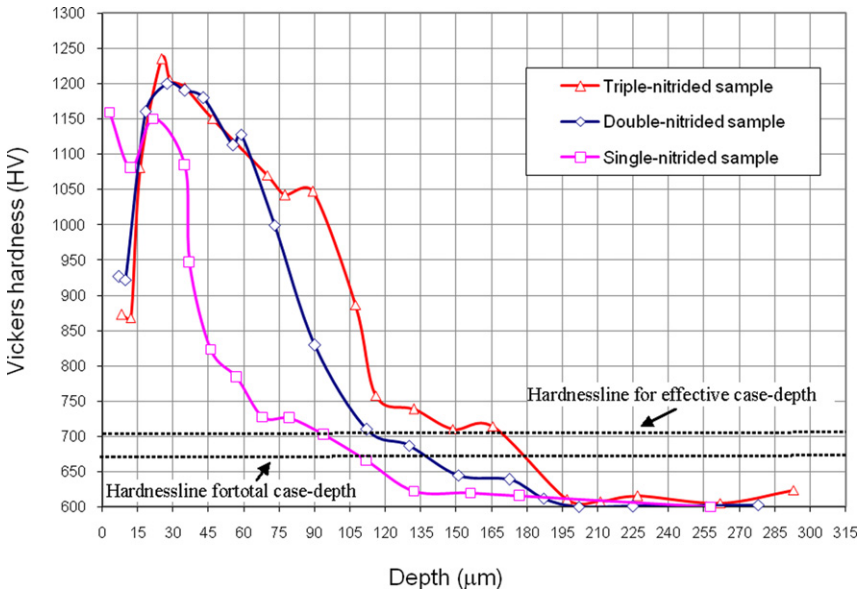


Figure 13 Vickers hardness depth profiles of nitrided cross-section for single-, double-, and triple-nitrided samples: hardness measured under 300 g load.

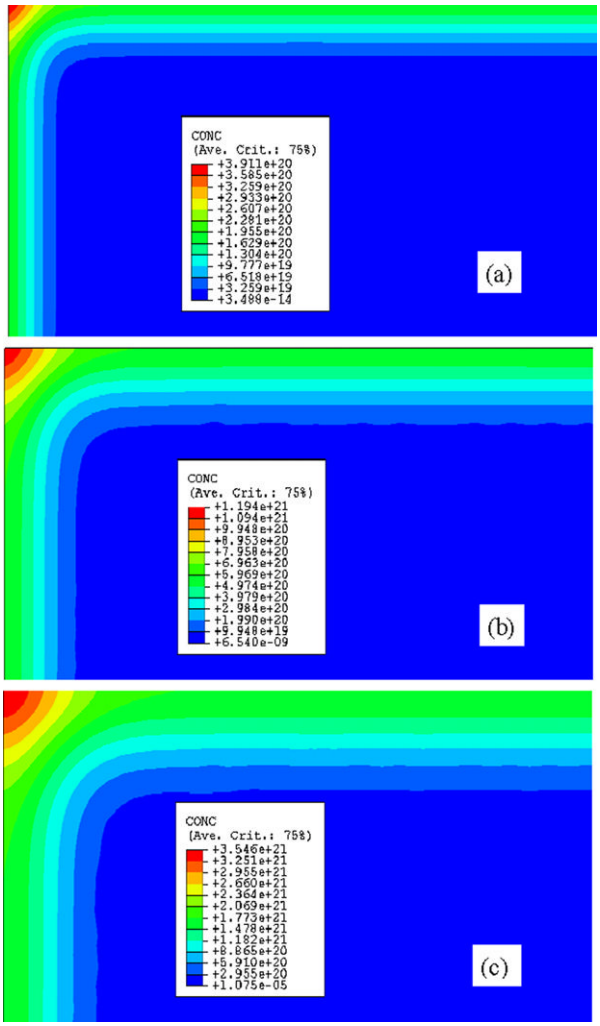


Figure 14 Nitrogen concentration distribution (in atoms per mm^3) and case depth formation at the end of the nitriding cycle: (a) single-nitrided sample; (b) double-nitrided sample; and (c) triple-nitrided sample.

numerically. The corresponding nitrogen mass concentration (in atoms of N per mm^3) profiles are shown in **Figure 15**.

Nitriding depth estimated from numerically obtained concentration profile is based on the depth where the nitrogen concentration is 10% higher than the average minimum concentration, as discussed. **Figures 13** and **15** are used for estimating the case depths from hardness and concentration profiles, respectively. Based on the average core hardness value of 620 HV, the total case depth was obtained corresponding to 680 HV from microhardness profiles of single-, double-, and triple-nitrided samples. The average minimum nitrogen concentration in each case is calculated from the contour legends of **Figure 14**. The comparison of case depth obtained from experimental and numerical results is provided in **Table 3**. Table 3 also provides the effect of multiple nitriding treatments on H13 samples and shows a continuous increase in the case depth with multiple nitriding treatments.

It can be observed that the case depth resulting from FE simulation compares well with experimental measurements. A slight increase in the numerically predicted case depth could be due to two reasons. First, the coefficient of diffusion may not be exact for H13 steel and based on experiments found in the literature. Second, the computer simulation of the diffusion process does not take into account the formation of nitride phases in the form of the superficial compound layer during the nitriding process. These phases significantly reduce the diffusion mechanism due to the reduced coefficient of diffusion. Assuming that the decay of hardness scales fairly well with the decay of nitrogen concentration, concentration depth profiles for single- and multiple-nitrided samples obtained numerically agree well with corresponding hardness depth profiles resulting from experiments. However, a slight difference is found if we compare the depth at which maximum hardness and maximum nitrogen concentration occur. Because numerical simulation did not take into account the compound layer development and porosity effect near the surface, the near-surface hardness values can be ignored when comparing experimental and numerical results.

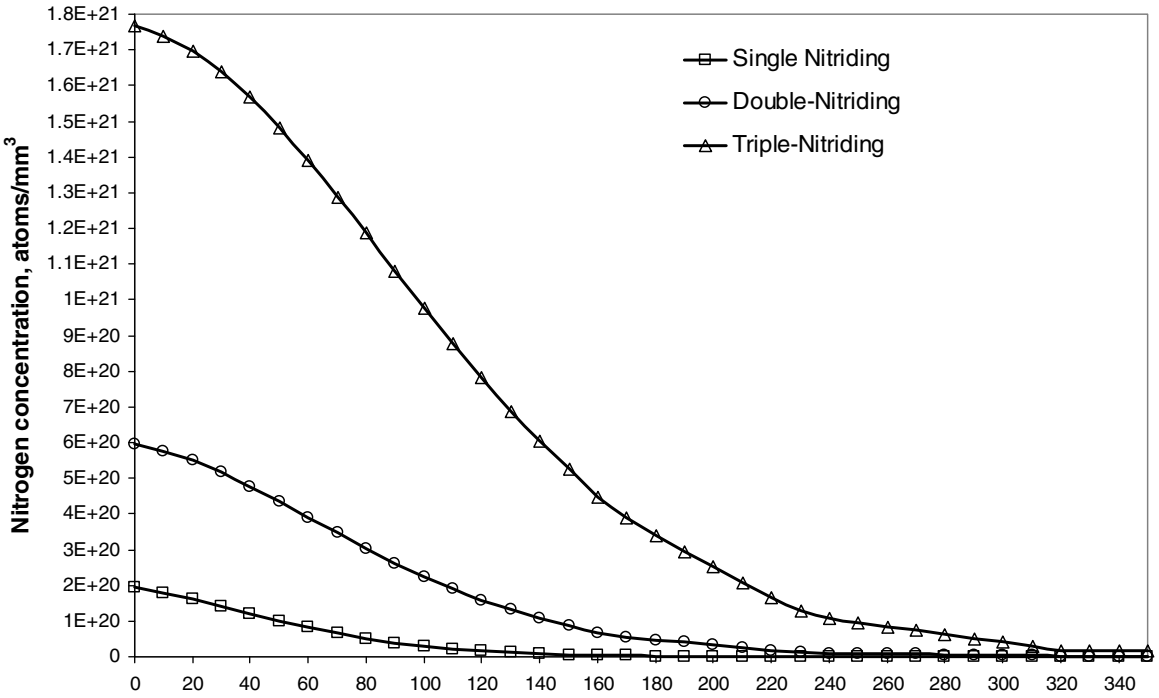


Figure 15 Numerically predicted nitrogen mass concentration as a function of nitriding depth for single-, double-, and triple-nitrided samples.

Table 3 Comparison of nitrided case depth from experimental and numerical studies

Sample	*Nitrided depth (μm)*	
	Experimental results	*Numerical results*
Single-nitrided	105	120
Double-nitrided	135	165
Triple-nitrided	180	200

3.11.6 Conclusions

The conclusions drawn from the current study are grouped into three subsections. In the first subsection, conclusions of the effect of surface texture on the nitriding treatment are presented, whereas in the second section the influence of the profile geometry on the nitriding behavior is discussed. In the laser section, the effect of multiple nitriding is discussed.

3.11.6.1 Consideration of Surface Texture on the Nitriding Kinetics

The influence of mechanical pretreatment (surface texture) in terms of surface roughness on nitriding kinetics of AISI H13 tool steel during controlled gas nitriding was studied. It is found that the surface texturing by surface roughening prior to nitriding enhances significantly the nitriding kinetics and is expected to increase wear resistance of H13 steel used for aluminum extrusion die while resulting in its increased service life. The XRD analysis confirmed that the compound layer consists of iron nitrides mainly $\varepsilon - Fe_3N$ phase and small fraction of $\gamma' - Fe_4N$ phase, which was expected from the values of in-process varying nitriding potential during gas nitriding cycle. Ground sample has more uniform and slightly thicker (2.5–3 μm) compound layer as compared to polished (~1.5 μm) and lapped (~1 μm) samples. Ground sample with high surface roughness exhibits deeper diffusion zone and effective case depth as compared to polished and lapped samples. This can be associated with the reduction in lattice spacing of α-Fe. The reduction in lattice spacing suggests comparatively large number of free atomic nitrogen, which is available for diffusion and induction of high compressive stress at the surface.

3.11.6.2 Consideration of Profile Geometry on the Nitriding Treatment

The geometric features commonly used in the design of aluminum extrusion profiles have been considered to investigate the effect of geometric features on the case hardening of the AISI H13 steel. Numerically predicted case depths compare well with experimental results for EC and IC feature locations, and the current model can be very useful for the die manufacturers during the design stage of die cavities. The EC features resulted in comparatively deep nitride case depth due to simultaneous diffusion from two convergent directions at the corners. The hardness profiles for the EC feature locations are relatively less steep and have a deeper hardening effect, in line with greater case depth. However, oversaturation of nitrogen at the extreme corners resulted in the 'corner effect' despite the controlled nitriding process. It was found that the IC features resulted in reduced nitrided case at the corner due to simultaneous diffusion from two divergent directions. The oversaturation effect in the case of external features and insufficient and nonuniform nitride layer development in the case of

internal features were almost eliminated when the geometry of these features were modified in the FE model by incorporating the fillet. It was found that the incorporation of a 0.5-mm fillet at the external and ICs results in uniform growth of nitrogen concentration. Such a modification is expected to have a certain positive influence on the hardness and effectiveness of these corner features. The results have shown that various die design features can be optimized effectively with the help of the current FE model, keeping in view the target tolerances of various extruded sections.

3.11.6.3 Consideration of Multiple Nitriding on the Nitriding Kinetics

The effect of multiple nitriding on the microstructure of AISI H13 tool steel during controlled gas nitriding treatment was studied. The nitrided layer depth increased with multiple nitriding treatments. Multiple-nitrided samples have more dense lamellae structures of nitrides of alloying elements/α-Fe, and more precipitates were observed at the grain boundaries with deeper effects. The increased amount of precipitates is due to the aggregate long duration of repeated nitriding treatments. Single-nitrided samples reveal the presence of the monophase ε-Fe_3N compound layer in agreement with the nitriding potential values during the nitriding cycle. A mixed phase of γ′-Fe_4N and ε-Fe_3N was detected in multiple-nitrided samples, which can be associated with loss of pre-existing nitrogen dissolved in ε-Fe_3N, which leads to transformation of ε-Fe_3N to γ′-Fe_4N. This mixed-phase microstructure resulted in reduced hardness at the surface. Thinner compound layers were observed in multiple-nitrided samples (approximately 2 μm) compared to single-nitrided samples (approximately 4–8 μm), which is likely due to the fact that the decomposition of iron-nitrided phases in the compound layer is more dominant than re-development of compound layer formation during simultaneous re-nitriding treatment. The case depth and nitrogen concentration depth profiles for single- and multiple-nitrided samples resulting from FE simulation compare well with experimental measurements. Because numerical simulation did not take into account the compound layer development and porosity effect near the surface, a slight difference is found if we compare the depth at which maximum hardness and maximum nitrogen concentration occur. Experimental verification of the nitriding process by FE analysis indicates that the FE model currently developed can serve as a powerful tool to improve the nitriding and re-nitriding cycles of H13 extrusion dies by adjusting the nitriding potential activity, nitriding time, and temperature. Hence, optimization of the nitriding process is viable from the present simulation model of a real-world nitriding cycle.

See also: 3.10 Atomizers and Finish Properties of Surface Coatings

References

1. Mittemeijer, E. J.; Slycke, J. T. Chemical Potentials and Activities of Nitrogen and Carbon Imposed by Gaseous Nitriding and Carburizing Atmospheres. *Surf. Eng.* **1996**, *12* (2), 152–162.
2. Liapina, T. *Phase Transformations in Interstitial Fe–N Alloys* (Ph.D. thesis); Stuttgart: Institut fur Metallkunde der Universitat Stuttgart; Max-Planck-Institut fur Metallforschung, 2005.
3. Díaz, N. V. *Nitriding of Iron-Based Alloys: Residual Stresses and Internal Strain Fields* (Ph.D. thesis); Stuttgart: Max-Planck-Institut fur Metallforschung, 2007.
4. Liliental, W. K.; Czelusniak, A.; Morawski, C. D.; Tymowski, G. J. Getting More Life Out of the Aluminum Extrusion Die by Controlled Gas Nitriding. Nitrex Metal Inc., 1999 (File: T-Tech\TP\PPR\TPAI001.doc).
5. Sueyoshi, H.; Hamaishi, K.; Nakamura, Y.; Kiyofuji, J. Effect of Mechanical Pre-Treatment on Gas Nitriding Behavior in Austenitic Stainless Steels. *Mater. Trans. – JIM* **1996**, *37* (2), 150–156.
6. Czelusniak, A.; Liliental, W. K.; Tymowski, G. *Influence of Die Handling Operations on Performance of Nitrided Aluminum Extrusion Dies*. Nitrex Metal Inc., 1997 (File: T\TP\PPR\ET SE001.doc).
7. Bei, D. H.; Lu, J.; Gu, J. F.; Lu, K.; Pan, J. S. Effects of Surface Nanocrystallization Pre-Treatment on Gas Nitriding Behavior of Mild Steel. *Trans. Mater. Heat Treat.* **2002**, *23* (1), 19–24.
8. Wroblewski, G.; Skalski, K. Properties of Surface Layer Generated by New Combined Process of Burnishing and Nitriding. *Surf. Eng.* **2006**, *22* (2), 138–146.
9. Baranowska, J.; Szczecinski, K.; Wysiecki, M. Increasing of Gas Nitriding Kinetics via Surface Pre-Treatment. *J. Surf. Coat. Technol.* **2002**, *151–152*, 534–539.
10. Kwon, S. C.; Park, M. J.; Baek, W. S.; Lee, G. H. Geometric Effect of Ion Nitriding on the Nitride Growth Behavior in Hollow Tube. *J. Mater. Eng. Perform.* **1992**, *1* (3), 353–358.
11. Ataide, A. R. P.; Alves, C., Jr; Hajeka, V.; Leiteb, J. P. Effects During Plasma Nitriding of Shaped Materials of Different Sizes. *Surf. Coat. Technol.* **2003**, *167*, 52–58.
12. Alves, C., Jr; Silvab da, E. F.; Martinellib, A. E. Effect of Workpiece Geometry on the Uniformity of Nitrided Layers. *Surf. Coat. Technol.* **2001**, *139*, 1–5.
13. Tercelj, M.; Somolej, A.; Vecko-Pirtovesek, T.; Turk, R. The Microstructures and Wear Resistance of Gas-Nitrided and Ionically Nitrided Aisi H10 Dies with Narrow Gaps Designed for Hot Extrusion of Aluminum. *JSME Int. J., Series C: Mech. Syst., Mach. Elem. Manuf.* **2006**, *49*, 121–127.
14. Kugler, G.; Turk, R.; Vecko-Pirtovsek, T.; Tercelj, M. Wear Behavior of Nitrided Microstructures of AISI H13 Dies for Hot Extrusion of Aluminum. *Metalurgija* **2006**, *45* (1), 21–29.
15. Nayal, G.; Lewisa, D. B.; Lembkea, M.; Münza, W. D.; Cockremb, J. E. Influence of Sample Geometry on the Effect of Pulse Plasma Nitriding of M2 Steel. *Surf. Coat. Technol.* **1999**, *111* (2–3), 148–157.
16. Reinhold, B.; Naumann, J.; Spies, H.-J. Influence of Chemical Composition and Geometry on the Nitriding Behavior of Aluminum Alloys. *Harterei-Technische Mitteilungen (Germany)* **1998**, *53* (4), 329–336.
17. Rolinski, E.; LeClaire, F.; Clubine, D.; *et al.* Kinetics of Plasma Nitriding and Renitriding of 3%Cr–Mo–V-Steel. *J. Mater. Eng. Perform.* **2000**, *9* (4), 457–462.
18. Somers, M. A. J.; Mittemeijer, E. J. Layer-Growth Kinetics on Gaseous Nitriding of Pure Iron: Evaluation of Diffusion Coefficients for Nitrogen in Iron Nitrides. *Metallurgical Mater. Trans.* **1995**, *26A*, 57–74.
19. Greßmann, T. *Fe–C and Fe–N Compound Layers: Growth Kinetics and Microstructure* (Ph.D. thesis); Stuttgart: Institut fur Metallkunde der Universitat Stuttgart; Max-Planck-Institut fur Metallforschung, 2007.
20. Czelusniak, A.; Liliental W. K.; Tymowski, G. *Integrated Die Management System-key to Economical Efficiency of an Extrusion Plant*. Nitrex Metal Inc., 2000 (File: T\TP\PPR\;ETSE002.doc).
21. Hermandez, M.; Staia, M. H.; Puchi-Cabrera, E. S. Evaluation of Microstructure and Mechanical Properties of Nitrided Steels. *Surf. Coat. Technol.* **2008**, *202*, 1935–1943.
22. Spies, H.-J.; Le Thien, H.; Biermann, H. B. Controlled Nitriding. *Met. Sci. Heat Treat.* **2004**, *46* (7–8), 272–276.
23. Mridha, S.; Khan, A. A. The Effects of Process Variables on the Hardness of Nitrided 3% Chromium Steel. *J. Mater. Process. Technol.* **2008**, *201*, 325–330.
24. Akhtar, S. S.; Arif, A. F. M.; Yilbas, B. S.; Sheikh, A. K. Influence of Surface Preparation on the Kinetics of Controlled Gas-Nitrided AISI H13 Steels Used in Extrusion Dies. *J. Mater. Eng. Perform.* **2010**, *19* (3), 347–355.
25. Keddam, M.; Djeghlal, M. E.; Barrallier, L.; Salhi, E. Computer Simulation of Nitrided Layers Growth for Pure Iron. *Comput. Mater. Sci.* **2004**, *29*, 43–48.
26. Hu, M.-J.; Pan, J.-S.; Li, Y.-J.; Ruan, D. Mathematical Modeling and Computer Simulation of Nitriding. *Mater. Sci. Technol.* **2000**, *16*, 547–550.
27. Akhtar, S. S.; Arif, A. F. M.; Yilbas, B. S. Nitriding of Aluminum Extrusion Die: Effect of Die Geometry. *J. Mater. Eng. Perform.* **2010**, *19* (3), 401–412.

28. Akhtar, S. S.; Arif, A. F. M. Effect of Profile Corners on the Nitriding Treatment of AISI H13 Hot Extrusion Dies. *J. Manuf. Sci. Eng.* **2014**, *136* (2), 021010.
29. Akhtar, S. S.; Arif, A. F. M.; Yilbas, B. S. Evaluation of Gas Nitriding Process with In-Process Variation of Nitriding Potential for AISI H13 Tool Steel. *Int. J. Adv. Manuf. Technol.* **2010**, *47* (5–8), 687–698.
30. AMS. *Aerospace Material Specification for Automated Gaseous Nitriding Controlled by Nitriding Potential (2579/10A)*. Available from: http://standards.sae.org/ams2759/10/, 2006 (accessed 30 March 2016).
31. Akhtar, S. S.; Arif, A. F. M.; Yilbas, B. S. Influence of Multiple Nitriding on the Case Hardening of H13 Tool Steel: Experimental and Numerical Investigation. *Int. J. Adv. Manuf. Technol.* **2012**, *58* (1–4), 57–70.
32. Howard P.; Dugan, A. Principles of Extrusion Die Management Incorporating New Heat Treatment Technology, In *Presentation at 2nd International Aluminium Extrusion Conference – Gold Coast*, July 2003.
33. Walkowicz, J.; Smolik, J.; Miernik, K. Investigation of the Influence of Ion Etching Parameters on the Structure of Nitrided Case in Hot Working Steel. *Surf. Coat. Technol.* **1999**, *116–119*, 361–366.
34. Hardchrome Engineering. Available from: http://www.hardchrome.com.au/technologies/nitrex-nitriding/ (accessed 30 March 2016).
35. Schacheral, R. E. *Growth Kinetics and Microstructure of Gaseous Nitrided Iron Chromium Alloys* (Ph.D. thesis); Stuttgart: Institut fur Metallkunde der universitat Stuttgart; Max-Planck-Institut fur Metallforschung, 2004.

3.12 Hot-Dip Galvanizing Process

F Ozturk, The Petroleum Institute, Abu Dhabi, UAE
Z Evis, Middle East Technical University, Ankara, Turkey
S Kilic, Ahi Evran University, Kirsehir, Turkey

© 2017 Elsevier Inc. All rights reserved.

3.12.1	Introduction	178
3.12.2	What Is Galvanizing and How Is It Performed?	178
3.12.3	Continuous and Batch Hot-Dip Galvanizing Processes	181
3.12.4	Recent Research and Development Activities in Hot-Dip Galvanizing	183
3.12.5	Presence of Elements in Galvanizing Bath	184
3.12.6	Galvanizing of Advanced High-Strength Steels	185
3.12.7	Failure Mechanisms in Galvanized Steels	187
3.12.8	Conclusion	188
References		188
Relevant Websites		190

3.12.1 Introduction

Galvanizing is a well-known and widely used surface coating process used to protect metals from corrosion.[1,2] In recent years, galvanizing has been updated by applying new procedures. It is very important to obtain optimum coating thickness by putting the sample into a zinc bath for a predetermined immersion time.[3] Increasing the immersion time resulted in a decrease in plasticity of the coating.[3] Corrosion is basically an electrochemical process. It occurs because of differences in electrical potential that exist between dissimilar metals in contact or between small areas on a metal surface in the presence of an electrolyte. Corrosion causes deteriorative loss of a metal as a result of dissolution environmental reactions due to chemical reactions with environment or electrochemical reactions in the inter-zone of the metals in contact. When dissimilar metals are in contact physically, more anodic ones corrode. As one of the controlling techniques of corrosion, a more anodic material is attached to the one to be protected by covering, depositing, or coating methods.[4–9]

Galvanizing has been known since the seventh century. It is a quite simple process that includes immersion in a galvanizing bath and drying processes of the metal pieces. It has been widely used in many industries, such as automotive, construction, electricity distribution towers, heat exchangers, protective barriers, chains, bolts and nuts, traffic signs, lighting poles, and advertising poles.[10,11]

Today, galvanized steels are still the dominant materials used for car bodies. Therefore, many galvanizing plants exist. Electrodeposition and hot-dip galvanizing processes are the main processes for galvanizing automotive body steels.[12] Electrodeposition produces a layer of pure Zn on steel when Zn is applied by using an electricity current. It results in a thinner coating than that attained with hot-dip galvanizing. Generally, it is not suitable for outdoor applications for which a thick coating is required. Its advantages are its brightness, uniform color, and esthetics. There is a strong desire within the automotive industry to move to alternative Zn coating methods offering improved corrosion resistance without increasing coating thickness.[12] It is a known fact that a thick coating increases the cost and decreases the surface quality. For this reason, the hot-dip galvanizing process is an excellent choice for achieving better corrosion properties by adding additional elements or alloys to the Zn bath. The process has several attractive advantages, including low cost, long service life, homogenous surface, flexibility of the process, easy to apply, high resistance to scratches, possible painting, and recycling potential.

In the galvanizing process, the main coating element is zinc (Zn). The position of Zn on the periodic table is the first element of group 12 in the transition metals class. It has a $+2$ ion and hexagonal close-packed crystal structure. Its appearance is blue, and it has very low ductility (brittle nature) at room temperature (RT). Because it has limited slip planes at RT, plastic deformation is limited. Its density is close to that of steel, approximately 7140 kg m^{-3}, and the melting temperature is approximately 400 °C. Electrochemically, Zn has more negative value than iron. Thus, Zn is a metal that is subject to corrosion as an anode. Zn coatings prevent corrosion of the protected metal by forming a barrier and by acting as a sacrificial anode if this barrier is damaged. When exposed to the atmosphere, Zn reacts with oxygen to form ZnO, which further reacts with water molecules in the air to form Zn-hydroxide. Finally, Zn-hydroxide reacts with CO_2 in the atmosphere to yield a thin, impermeable, tenacious, and quite insoluble dull gray layer of Zn-carbonate, which adheres extremely well to the underlying Zn, therefore protecting it from further corrosion. It is well-known that the Zn coating is extensively used for coating steels. In **Figure 1**, galvanizing applications on steel parts and surface appearances are given.

Types of Zn coatings are hot-dip galvanizing, electroplating, spraying, plating, and painting. Among the all galvanizing methods, the hot-dip galvanizing technique is the most common because it results in excellent properties such as high strength and formability, lightweight, corrosion resistance, low manufacturing cost, and recycle potential.[13] Coating thickness varies depending on the working conditions of the material. Therefore, the coating thickness considerably affects the cost of the process.

 doi:10.1016/B978-0-12-803581-8.09175-X

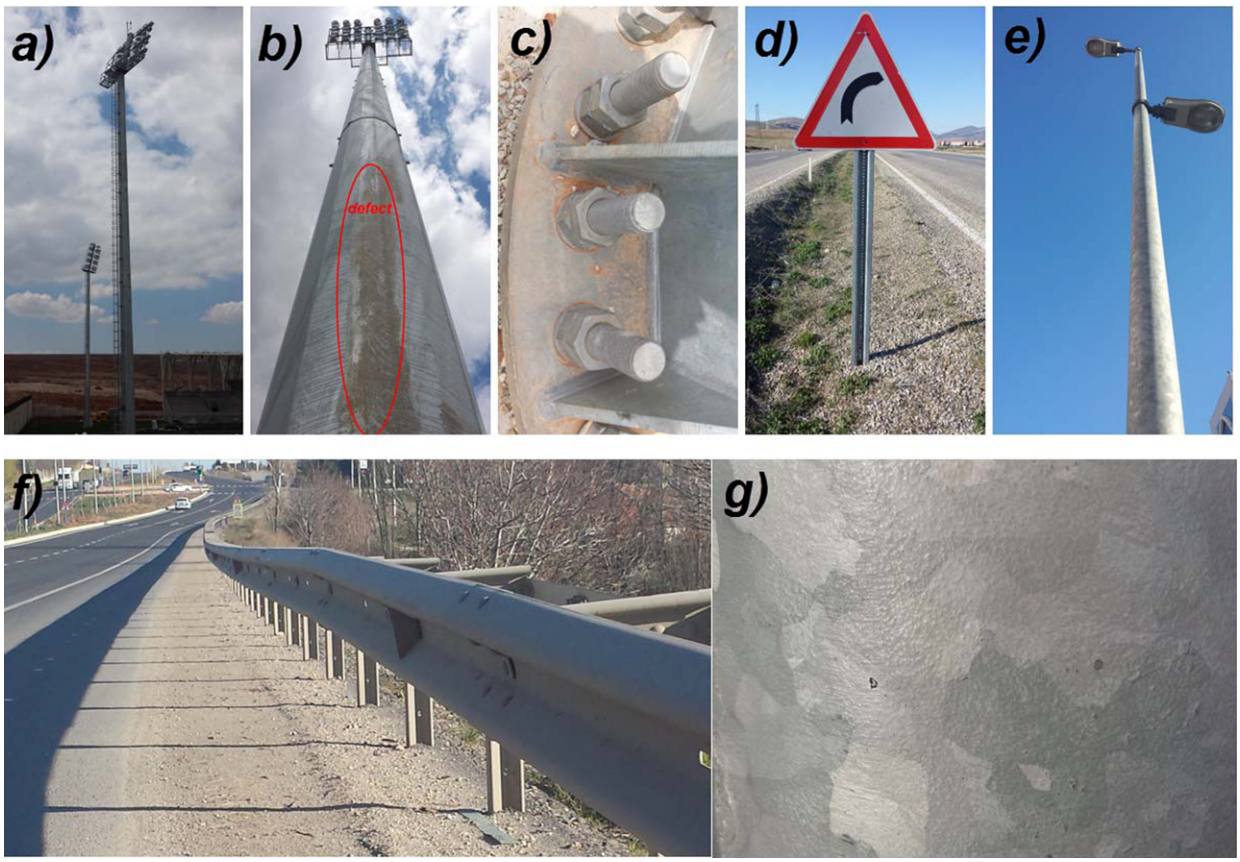


Figure 1 (a) Stadium lighting pole, (b) galvanizing defect, (c) nuts and bolts, (d) traffic sign, (e) lampposts, (f) highway barriers, and (g) galvanized surface appearance.

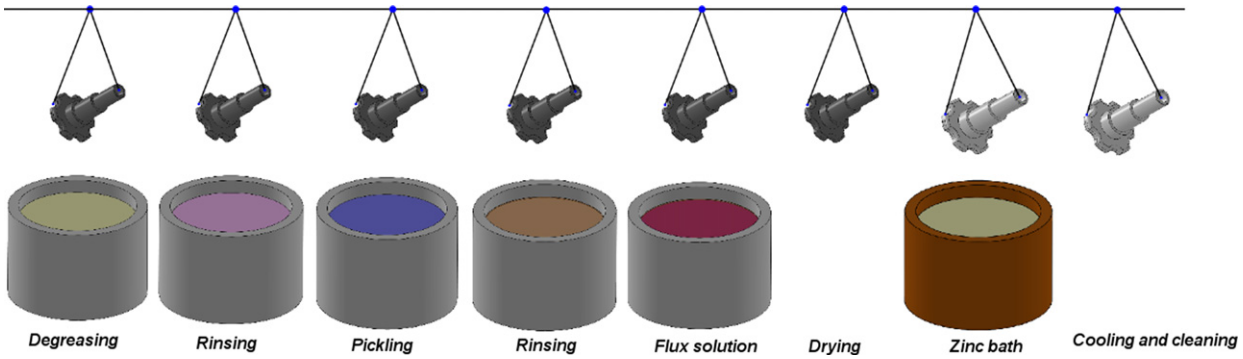


Figure 2 Hot-dip galvanizing process.

3.12.2 What Is Galvanizing and How Is It Performed?

Galvanizing is a simple metallurgically bonded coating process applied in two different ways. These are the hot dip galvanizing process and electrogalvanizing methods. A schematic representation of hot-dip galvanizing is shown in Figure 2. It is well-known that the hot-dip galvanizing process is the most effective and common method to protect steel from corrosion. As seen in this figure, the first step is to degrease the surfaces that will be coated. The good coating is directly related to surface quality. Therefore, part surfaces must be cleaned so that there is no rust and oil, or acceptable coating quality cannot be achieved. First, the rusted surface must be cleaned by performing a surface cleaning operation. If the surface is heavily rusted, then abrasive blast cleaning or mechanical processes including machining might be needed. After blast cleaning, surfaces should be cleaned so they do not contain any oils, paints, greases, or other contaminants. This step involves a process of immersing parts into a degreaser fluid. Degreasers

are usually present in an acid bath. The second step is to rinse the degreased parts with water. The water can be at different temperatures, depending on need. After the surface cleaning process, the following processes are applied, in order: pickling, rinsing, fluxing, drying, galvanizing, and cooling. The fluxing stage is a process required for the binding of Zn to the surface. The temperature of the molten Zn bath is approximately 450 °C. Temperature can be changed slightly depending on the composition of the bath (molten alloy content).

Pickling is a cleaning process in an acid tank filled with either hydrochloric acid or sulfuric acid. These chemicals generally remove rust, mill scale, and other metal oxides. The term 'scale' is typically used to describe the iron oxides that form at high temperatures, such as during hot rolling, annealing in air, or welding. Rust is the product of corrosion of the steel surface when it gets wet. Both types of iron oxides need to be removed prior to the application of the Zn coating. Another rinsing process will take place following the pickling. Fluxing is a protection process involving the cleaned parts. Actually, it coats the parts to prevent part rusting before the galvanizing process (immersion of metal into the bath). There are two different fluxing methods: dry and wet processes. The dry process is performed by prefluxing in a Zn ammonium chloride solution. The wet process uses a molten flux blanket on the Zn bath surface. Flux solution is a slightly acidic solution that contains a combination of Zn chloride and ammonium chloride in the tank. Flux is the same as flux used in soldering. At this stage, the part surfaces are completely free of any oxides or any other contaminants. Any type of contaminants on the surfaces might affect the coating quality and composition. The parts that were fluxed are dried prior to the galvanizing process.

As mentioned previously, the second major step of the galvanizing process is 'galvanizing.' During this step, cleaned parts are submerged into a liquid Zn bath in the tank. During the first minute of immersion in the galvanizing bath, Zn–iron alloy layers grow rapidly on the surfaces of the steels that are most commonly galvanized. Sometimes other elements may be added to the molten Zn bath to obtain desirable properties. Hot dipping not only is a thermal process but also includes chemical reactions and intermixing diffusion reactions. As a result, alloy layers develop. Although only Zn is coated on the outer surface, intermetallic alloys starts to occur between the Zn layer and the base metal's surface, as seen in **Figure 3**. Although pure Zn is coated on the outer layer, compounds consisting of iron are located toward the inner core. New phases developed during coating are shown in **Figure 3**. The interaction of atoms (diffusion) creates a nonuniform coating due to different chemical composition. In the outer zone, the coating is rich in Zn, whereas in inner zone the coating is rich in iron. **Figure 3** indicates several layers that are developed during coating. **Table 1** indicates composition details of each layer developed during galvanizing.

The eta layer is a relatively pure outer coating of Zn. The zeta layers include Zn–iron alloy containing 5.8–6.2% iron. In the delta layer, the amount of Zn is slightly less, with the Zn–iron alloy containing 7–12% iron. The gamma layer just above the base metal is a thin molecular layer containing 21–28% iron. In **Figure 3**, the bottom layer is the base metal. When the galvanizing process is completed, the parts are removed from the tank. The process is usually completed in a short period of time. It may take less than 10 min depending on the desired thickness. The hot-dip galvanized coating usually forms in 3–5 min, depending on the metal thicknesses.

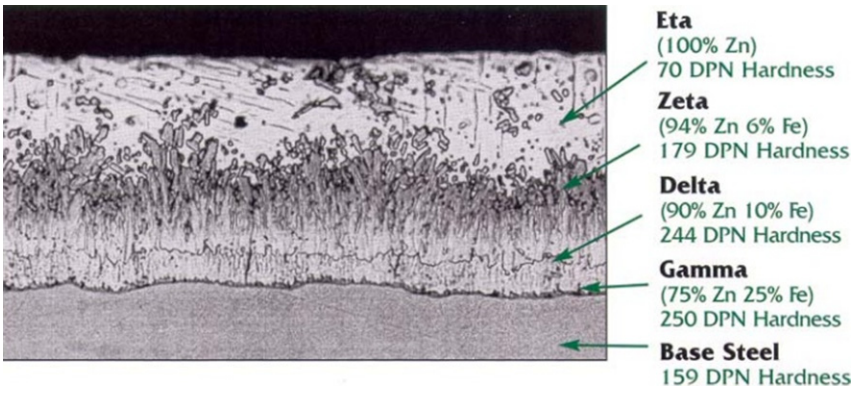


Figure 3 Photomicrograph of batch hot-dip galvanized coating.[2]

Table 1 Composition and properties of alloy layers in batch hot-dip galvanizing[14]

Layer	*Alloy*	*Iron (%)*	*Melting point*		*Crystal structure*	*Alloy characteristics*
			°C	*°F*		
Eta (η)	Zn	0.03	419	787	Hexagonal	Soft, ductile
Zeta (ξ)	$FeZn_{13}$	5.7–6.3	530	986	Monoclinic	Hard, brittle
Delta (δ)	$FeZn_7$	7.0–11.0	530–670	986–1238	Hexagonal	Ductile
Gamma (Γ)	Fe_3Zn_{10}	20.0–27.0	670–780	1238–1436	Cubic	Thin, hard, brittle
Steel base metal	Iron	99+	1510	2750	Cubic	–

In general, coating thicknesses vary from 45 to 85 μ. In the galvanized sheet metals, the amount of Zn is given in terms of gram per square meter (e.g., 80 g m^{-2} Zn).

Finally, parts are removed from the galvanizing tank and transferred to a storage area or quenching tank. Then, post-treatment to enhance the galvanized coating may be applied. This process is generally a quenching process in the water tank. Sometimes the parts are cooled in air.

The second common method of Zn coating is electro-galvanizing, which is applied by setting Zn as an anode and galvanized metal as a cathode in a suitable electrolytic liquid. This process is illustrated in **Figure 4**. Electrogalvanizing is a preferred process if the temperature of molten Zn bath can damage the piece to be galvanized. Also, it is applied to the decorative items for which surface quality is an important issue. Coating thickness should be usually up to 20 μ. Low coating thickness is the main disadvantage of the process.

In the galvanizing process, coating thickness, alloy structure, and finish of galvanized coatings are influenced by surface condition and material compositions. Increasing the period of immersion in the galvanizing bath will not increase the coating thickness, except in the case of silicon (Si)-containing steel. Grit blasting increases the coating area and creates plastic deformation, which makes surfaces highly reactive to molten Zn. Surface thickness is determined depending on the application under which substrate is to be used. It is a fact that a thick coating has a longer life but poor surface appearance.

The amount of elements can have major effects on the structure, appearance, and properties of galvanized coatings.[15–17] The most critical elements are Si and phosphorous (P) in the galvanizing process. In extreme cases, coatings can be excessively thick, brittle, and easily damaged. Si causes excessively thick coatings. Excessive growth in coating thickness takes place on steels with Si contents in the range 0.04–0.14%. Growth rates are less for steels containing between 0.15 and 0.22% Si, but they are more with increasing Si levels above 0.22%. Presence of P (such as approximately 0.05%) in steel produces a marked increase in reactivity of steel with molten Zn and rapid coating growth. When present in combination with Si, P can have a disproportionate effect, producing excessively thick galvanized coatings. As a guide to the suitability of steels containing Si and P for galvanizing, the following criteria should be applied:

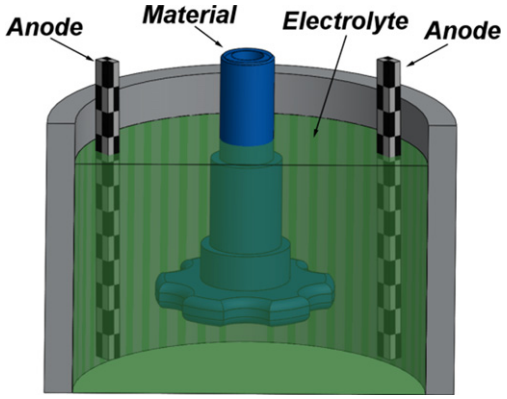


Figure 4 Electrogalvanizing method.

$\%Si < 0.04\%$ and $\%Si + (2.5 \times \%P) < 0.09\%$. Galvanized coatings on Si steels are usually dull gray or patchy gray in color with a rough finish, and they may be brittle. Coating service life is proportional to the increased thickness and is unaffected by appearance, provided that the coating is sound and continuous. In general, the thickness, adherence, and appearance of galvanized coatings on Si and P steels are outside the control of the galvanizer.

Obtaining a proper bonding zone during the hot-dip process is important to achieve the desired galvanizing benefit. The thicker Zn coating does not always mean a longer working life. Alloy layers are hard and brittle, so cracking on the coating layer may occur and propagate easily in any force application case. If any post process will be applied on the part, such as deep drawing after galvanizing, then the alloy layer has to be thin and suitable to prevent formation of cracks. Also, if the part is already fabricated and no additional forming is required, then the thicker Zn coating means a longer working life, but the thicker Zn coating requires additional process time and cost.[18–20]

Double dipping, or galvanizing two times, will not increase the thickness of the galvanized coating and may adversely affect the coating appearance. The terms 'double dipping' and 'double-end dipping' are sometimes confused. Double-end dipping is a method of galvanizing articles too long for the available bath by immersing one end of the work at a time. However, it was previously mentioned that coatings of double layers by galvanizing and organic coatings increase the service life of galvanized steels under various environments.[21,22]

Designing the galvanizing process is very important in terms of the finished product. Consistent section size is important for good galvanizing. Molten Zn should flow freely and easily. Ventilation is necessary to prevent air traps. Folds and tight curves should be avoided as much as possible.

After the galvanizing process, visual inspection takes place to check Zn on the materials. It is often possible to see improper coatings, and even in some areas no Zn is reached. Zn thickness is measured at various locations of coating and checked to see whether desired thickness is achieved. Thickness gages are used for measurement. Variations in colors are checked. Actually, color variations are related to the composition of the steel. For example, silicon steel has a dull surface appearance.[23]

For the packing of the galvanized products, no metal straps are used because they damage the coating. Only plastic straps are used as much as possible. If they are stacked together, then air flow circulation between surfaces should be allowed because, otherwise, moisture will form and rust will occur. It is a key point that moisture should always be eliminated and stacked items should be kept dry. The stacks need to be ventilated during transportation. The finished product is always labeled, indicating how material is coated and the thickness of the coating.

3.12.3 Continuous and Batch Hot-Dip Galvanizing Processes

Hot-dip galvanizing processes can be performed as continuous or batch, depending on the need and application. A continuous

process is only limited for sheet, strip, and wires. The coated sheet is then blanked or sheared and formed into a final part. The aforementioned steps are automated in the process. The process can easily be controlled and very accurate thickness can be achieved. The other method is the batch hot-dip galvanizing process, which is a discrete process used after fabrication of the parts. Parts as small as fasteners to as large as bridge structural girders can be galvanized using the batch method. In continuous process, wherein the steel is immersed for a very brief time, the batch process requires the part to be immersed for much longer times.

The continuous hot-dip galvanizing process is suitable for galvanizing coiled sheet metal. When the coil at the entry end finishes, another coil is welded to the tail of the previous one, as seen in **Figure 5**. Therefore, process may continue for days. Tension at both ends of the line provides additional constraint to sheet metal. This constraint prevents thermal distortion of thinner sheet metal. Also, thinner sheets (up to 0.15 mm) can be galvanized, avoiding distortion as an advantage. As a disadvantage, thickness is limited up to 6 mm.

Generally after galvanizing, sheet metals undergo post-deformation processes such as deep drawing or roll forming. Therefore, it is vital to not damage the coating layer during deformation after the galvanizing process. The thinner coating allows more intricate deformation without any damage on the coating layer. Because the alloy layer is hard and brittle, the fineness of the alloy layer is essential for good formability.

The thickness of the galvanic layer can be controlled by the speed of the production line and the addition of aluminum (Al) to the Zn bath. Production line speed can be 200 m s^{-1}. Sometimes this speed may not be enough due to thinner coat requirements during continuous hot-dip galvanizing processes. Al can be added to decrease the diffusion speed. A slow Zn–iron reaction rate leads to formation of a thinner coating layer.[24–26]

A batch hot-dip galvanizing process is suitable for bigger workpieces. A thicker coating layer can be achieved without any thermal distortion. As seen in **Figures 2** and **6**, fluxing can be applied in two ways: dry or wet. In a study of dip galvanizing, a wire was coated in a molten zinc bath after being treated in a nitrogen (N) and hydrogen (H) atmosphere and fluxing.[3] In the dry method, fluxing is applied before the Zn bath. In the wet method, flux is added into the Zn bath. Due to the fact that density of flux is less than that of Zn, flux floats on the molten Zn bath upper surface. When the part starts to enter the Zn bath process, it is first covered with flux and then is dipped in the Zn bath.

For both methods, the galvanizing process consists of common subprocesses like surface preparations (cleansing, rinsing, pickling, fluxing), galvanizing (dipping into molten Zn bath), and final inspection. The ability of the coating layer to stick to base metal depends on surface preparations.

Lead (Pb) or bismuth (Bi) can be used to easily dispose of excessive Zn after the dipping process. When Si content in the base metal is high, nickel (Ni) can be added to improve the galvanizing process. **Table 2** gives a general summary about both methods and shows a comparison of both methods.

Steels were continuously reheated (annealed) at different temperatures before the galvanizing in another study.[27] Moreover, a reducing atmosphere removed the oxides formed at RT that were present at the surface.[27] Rather than the

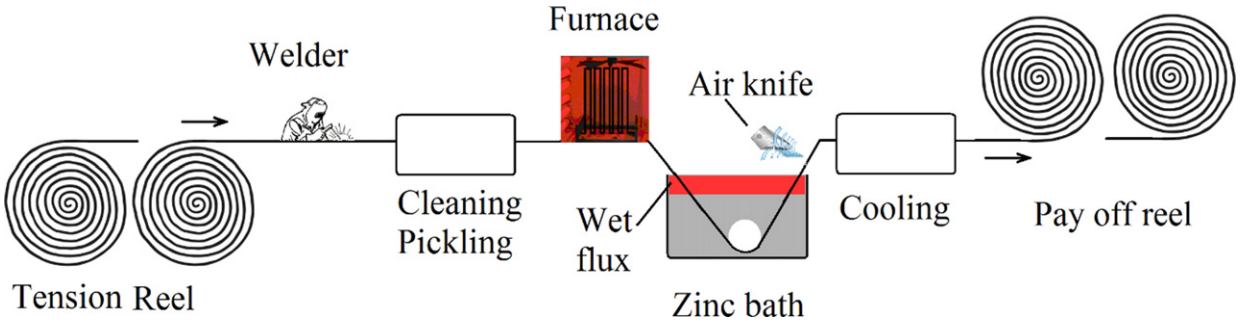


Figure 5 Schematic of continuous hot-dip galvanizing process.

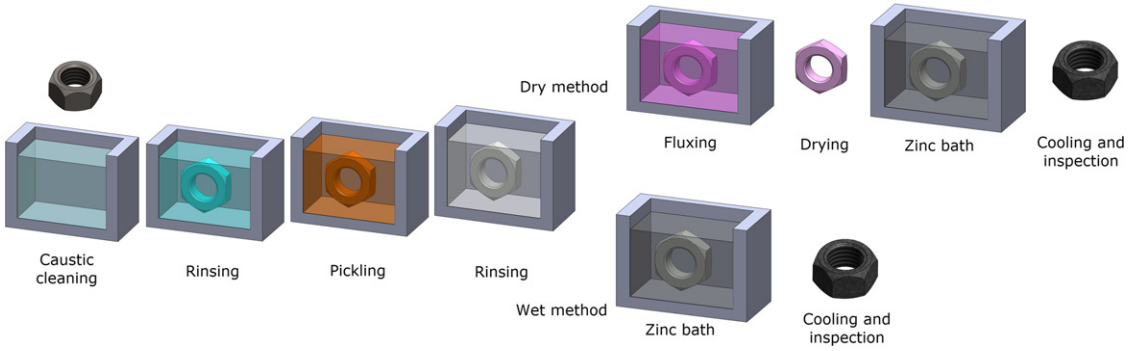


Figure 6 Batch hot-dip galvanizing process.

Table 2 Properties of hot-dip galvanizing processes

	Continuous hot-dip galvanizing	*Batch hot-dip galvanizing*
Part thickness	Sheet metals (very thin, limited to 6 mm)	Only thicker parts due to thermal distortion of thin parts
Zn bath ingredient	Al (slows the reaction)	–
Speed of process	Very high speed	Slower than continuous process

reheating temperatures of 550 and 650 °C, at 750 °C the carbides formed at the steel surface were dissolved.[27] This reheating temperature was observed as the best condition for galvanizing.[27] Furthermore, cooling conditions affect the grain size of the coatings.[28]

Si-killed steels were Zn-coated with a high-temperature hot-dip galvanizing procedure.[29] However, it was found that immersion time did not affect the coating thickness and presence of the phases during coating.[29] High-temperature hot-dip galvanizing resulted in higher hardness values than those of normal galvanizing at moderate temperatures.[29] High-temperature hot-dip galvanizing resulted in coating with minute amounts and phases.[29] Steels were fully coated in high-temperature ranges of 520–555 °C; the conventional galvanizing temperature is 455 °C.[30]

Bicao *et al.*[31] investigated the effect of Zn galvanizing bath temperature on coating morphology and thickness. Samples were galvanized at a bath temperature between 450 and 530 °C.[31] When the galvanizing temperature was between 450 and 470 °C, galvanized coating was coherent and a delta layer and a compact zeta layer were at the top.[31] A very thick Zn coating was observed after a galvanizing bath temperature of 480 °C.[31] When the bath temperature was increased to more than 500 °C, the delta phase was mainly observed during the coating.[31]

3.12.4 Recent Research and Development Activities in Hot-Dip Galvanizing

Research has been conducted to attain better corrosion behavior from the hot-dip coated steels.[12,32–34]

Metallic coatings containing magnesium (Mg) have been widely investigated. Several studies have been published regarding Mg addition to Zn coating. Hosking *et al.*[12] reviewed the effect of the addition of Mg to a Zn bath. They showed that steel coated with Zn–Mg has greater corrosion resistance in a sodium chloride–containing atmosphere than conventional Zn-coated steel with a similar coating thickness. They proposed a proper mechanism with the following guidelines:

- Quenching of oxygen reduction reactions at the cathodes by the formation of protective magnesium hydroxide.
- Decreased oxygen reduction facilitates the formation of stable simonkolleite.
- Hydroxides associated with simonkolleite formation are neutralized by carbonization at the cathodes.
- Magnesium hydroxide at the cathodes is transformed into carbonate-containing hydroxides, which in turn facilitate further formation of protective simonkolleite.

Prosek *et al.*[33] showed that Zn–Mg alloy containing from 1 to 32 wt% Mg, pure Zn, and pure Mg was contaminated with sodium chloride and exposed to humid air for 28 days. They found that Mg was substantially decreased as a result of weight loss of ZnMg alloys in atmospheric conditions in the presence of chloride. The effect of Mg was most profound at 4–8 wt% Mg in the structure. Finally, they recommended that 'the optimal corrosion protection of ZnMg alloys in atmospheric conditions is related to combination of relatively noble free corrosion potentials close to that of Zn and the presence of Mg-based films with good stability and barrier properties.' Hausbrand *et al.*[32] studied the progress of the corrosive degradation of the alloy coating–paint interface. They proposed a degradation mechanism model. Results reveal that adjusting the composition of the Mg–Zn oxide at the coatings can inhibit anodic delamination. Schuerz *et al.*[35] studied the corrosion behavior of steel sheets coated with Zn and Zn–Al–Mg with a thickness of 7 μ tested in a salt environment. They found that the corrosion resistance of steel coated with Zn–Al–Mg was better than steel coated with Zn. They concluded that the transformation of the Zn–Al–Mg coating into the Al-rich oxide layer is the key reaction in the corrosion process and is necessary for improvement. Dutta *et al.*[10] studied hot-dip Zn–Mg and Zn–Mg–Al alloy coatings on steel sheets. They studied both low and high Mg contents in Zn–Mg alloy. The results indicate that the Zn–Mg–Al bath shows better corrosion resistance than pure Zn and Zn–Mg baths. It was also mentioned that Al addition suppressed the oxidation of Mg. This improves the coating quality enormously. It was also pointed out that the Mg oxide layer is more protective than the Zn oxide layer. Li *et al.*[36] investigated the effects of Mg addition (0, 0.5, 1.5, and 2.5 wt%) on the microstructure and corrosion resistance of Galvalume coating (Zn–55Al–1.6Si). Results show that a new intermetallic phase ($MgZn_2$) appears in the Zn-rich interdendritic area of the Mg-containing Galvalume coating. The corrosion product formed on Zn–55Al–1.6Si–1.5Mg coating displays a densely packed microstructure, showing the best barrier protection characteristics. It was obvious that Mg improves the corrosion performance. This issue was reported many times in the past for Zn and Zn–Al coatings.

Formation of the Fe–Al inhibition layer was discussed previously.[37] They characterized the formed inhibition layer on TiNb-stabilized interstitial-free (IF) steel after a short galvanizing process. They determined heterogeneous growth of Fe_2Al_5. Higher growth was seen on Zn side. In a computational study, production sequencing problems related to a continuous galvanizing line of a company were solved in a progressive way by developing a simple model and a proposed tabu search algorithm.[38]

Doehlert design was applied to reduce the Zn consumption in the galvanizing bath, along with considering the effects of bath temperature, immersion time, and the withdrawal speed.[39] The substrate alloy relation to the coating of Zn-free layers can be controlled by the galvanizing bath temperature.[39] It was shown that coating thickness can be adjusted by changing the

immersion time.[40] The amount of unalloyed Zn adhered to the substrate can be controlled with withdrawal speed.[39] Therefore, it was shown that the galvanizing process and steps can be optimized to obtain a coating with a minimum thickness without changing the composition of the galvanizing bath.[39] In this study, optimum operating conditions for bath temperature, immersion time, and withdrawal speed were found to be 444 °C, 90 s, and 4 m min^{-1}, respectively.[39] However, sample dimensions and geometries are also important factors affecting the physical properties.[39]

Texture greatly affects the coating properties. Pure Zn galvanizing bath temperature under hot-dip galvanizing conditions resulted in (0001) plane texturing of Zn after solidification.[28] The presence of Al and copper (Cu) in the galvanizing Zn bath also triggers some texture formation.[28] When Pb is added to this galvanizing bath, this texture formation starts to diminish and dentritic growth starts to form.[28] Moreover, the presence of Ni in the galvanizing bath also starts to decrease the texture formation.[28,41]

When elements of Sb, Bi, tin (Sn), Al, or Pb are present in the galvanizing bath, large grains (spangles) are formed at the coatings.[28,42–45] Presence of these elements changes the surface tension of the Zn and orientation of Zn grains.[15] Therefore, spangles are highly requested by customers purchasing hot-dip galvanized coatings.[15] Moreover, addition of Pb in the galvanizing bath decreases the coating thickness and Zn consumption.[28]

As a result of formation of large bright spangles on the coating, smooth surfaces form and textures with (0001) basal planes form.[43] However, dull spangles result in formation of other planes.[43] Moreover, large and dull spangles diminish the corrosion characteristics of the hot-dip galvanized coatings.[44]

3.12.5 Presence of Elements in Galvanizing Bath

One or more alloying elements may be added to the bath to improve coating performance. Therefore, in the hot-dipping galvanizing process, various alloying elements in galvanizing bath affect the coating properties.[46] Recent research and development activities for this purpose have been summarized as follows. Galvanizing bath can be adjusted by adding small amounts of various elements such as Al, Pb, Ni, Bi, germanium (Ge), titanium (Ti), Cu, Cadmium (Cd), Sn, and others to improve the coating morphology, thickness, quality, appearance, and adherence to the substrate.[42,46–52] Moreover, additives such as Al, Bi, Mg, Ni, and others are commonly used in galvanizing baths to increase the Zn fluidity and its diffusion.[52,53]

The corrosion performance of Zn coatings could be improved with the deposition of a zinc–manganese (Zn–Mn) coating because Mn protects the Zn due to its anodic behavior.[54] This method is faster and easier and produces thinner coatings.[55] Hosking *et al.*[12] noted, 'There is a desire within the automotive industry to move to alternative Zn coatings offering improved corrosion resistance without increasing coating thickness. Thinner (less than 7 μ) metallic coatings are attractive as they may alleviate processing difficulties such as spalling of the coating during forming and brass formation on spot welder electrodes.' Moreover, Pistofidis *et al.*[55] pointed out, 'Mn islands are very beneficial with regard to the corrosion performance of the coating, because they act as sacrificial anodes that protect Zn.'

Wang *et al.*[37] investigated the interaction between the Al in the Zn bath and the surface oxides formed by selective oxidation on 1.2Si–1.5Mn transformation-induced plasticity (TRIP) steel during hot-dip galvanizing. Results show that the SiO_2 films were the most stable of the oxides and were barely reduced by the amorphous $xMnO \cdot SiO_2$ oxide that reacted with Al to form a Si–Mn–Al-containing oxide.[23] Presence of Al in the Zn bath can reduce surface oxides such as MnO, Cr_2O_3, SiO_2, and others on the steel substrate.[56] Al in the galvanizing bath controls the coating morphology and formation of intermetallic compounds of Fe–Zn.[40] Low concentrations of Al (such as less than 0.09 wt% Al) resulted in formation of a coating with eta, zeta, delta, and gamma phases.[50] Moreover, high concentrations of Al (such as more than 0.16 wt%) resulted in thick coatings with high concentrations of Zn and presence of the eta phase.[50] Therefore, growth of the Zn–Fe phases is generally adjusted by including 0.18–0.30% Al in the galvanizing bath.[49] Due to the presence of Al in the galvanizing bath, development of Fe–Zn intermetallic compounds can be inhibited.[49]

The effect of Si on the galvanizing reaction is generally called the Sandelin effect, which prevents the formation of a stable and passivating layer in the bath. Sn, Ni, and Al have moderate Sandelin effects. Chromium (Cr) slows the kinetics of metallurgical reactions.[17]

The influence of Ni is important with respect to the development of the Zn/iron alloy layer, especially when galvanizing steels containing high Si. This development is still quite new and all the metallurgical aspects related to the addition of small amounts of nickel are still being discovered. The reaction between Fe and Zn can be suppressed by adding a small amount of Fe and Al, forming Fe_2Al_5.[57–59]

Hot-dip galvanized coatings comprise essentially pure Zn, provided that controlled amounts of Al or Si are added to the molten Zn bath to suppress the formation of intermetallic Zn–iron. Surfaces coated with the hot-dip process possess generally very large grains that are called spangles when elements of Pb, Sb, and Bi are added to the bath with aluminum.[42,48,52]

Peng *et al.*[60] studied typical spangles on a batch hot-dip of Zn–0.05Al–0.2Sb alloy coating. They observed shiny, feathery, and dull types of spangles. It was determined that antimony (Sb) segregates extensively on the spangle surface. The segregation degree increases from shiny to feathery to dull spangles. The hot-dip coating process has received more attention in recent years due to its beautiful appearance. Many galvanizers have attempted to develop processes for decoration purposes.[60–63]

The effect of vanadium on galvanizing Si-containing steel was studied by Su *et al.*[64] Three different steels with effective Si contents of 0.158, 0.242, and 0.363 wt%, were immersed for 0.5–8 min in Zn baths with four levels of vanadium (V), ranging from 0 to 0.16 wt%. Results reveal that addition of V to the bath suppresses Si reactivity; it was known that Si caused an excessively thick coating. The excessive growth in coating thickness takes place on steels with Si contents in the range of 0.04–0.14%. Thick coating causes poor adhesion, which

affects the quality of the coating. Steels with high Si contents (Si > 0.05%) can be successfully coated in a galvanizing bath containing 0.04% Ni and 0.1% Bi.[51] For steels with high Si content, coatings with the same or better quality can be obtained with using less Ni in the galvanizing bath.[51] Moreover, improved properties were obtained for Zi–Ni–Bi alloys, which can be used in industrial applications as an alternative to the galvanizing baths containing Pb, especially considering the associated health issues.[11]

The presence of Cu and Cd changes the coating phases because of the formation of intermetallics in the coatings, whereas Sn (up to 3% in the galvanizing bath) does not contribute any change in coating phase and thickness.[46] However, presence of Cu in the galvanizing bath results in poor adherence of the coating to the substrate.[46] Di Cocco *et al.*[50] studied the effect of Cu, Sn, and Ti additions in the coating baths for an ipersandelin steel. Results indicate that Cu, Pb, and Sn do not change the morphology of the intermetallic phases. Ti results in the presence of an outer layer characterized by a double phase and a brittle dispersed phase. Moreover, a small amount (0.04%) of Ti in the galvanizing bath makes the coating more stable, delays the combination of Fe–Zn, and inhibits the growth of Fe–Zn intermetallic compounds.[49]

In addition to the above elements, strontium improves both the adhesive strength and corrosion resistance of hot-dip galvanized coating.[65] V_2O_3 is commonly included in the galvanizing bath because it is included at coatings under atmospheric conditions for galvanic corrosion.[53,66] However, ZnO resisted to galvanic corrosion of the coatings better than V_2O_3.[13]

3.12.6 Galvanizing of Advanced High-Strength Steels

In recent years, a tremendous amount of research has been performed to determine how to use advanced high-strength steels (AHSS) in the automotive industry to reduce fuel consumption and lighten the structure by using a thin sheet instead of a thick sheet without sacrificing performance and safety.[67,68] AHSS are developed by steelmakers in accordance with the requirements of the automotive industry (passenger safety, lightness, fuel economy, formability). Examples of steels in this group are martensitic steels, dual phase (DP), TRIP, complex phase steel, twinning-induced plasticity (TWIP), and others. The use of AHSS has increased dramatically in past two decades. As an example, **Figure 7** displays steel usage in some car models.[69] Although these steels have very attractive properties, they have some problems. One of them is a galvanizing issue.

A number of problems in the Zn coating against corrosion of AHSS steel have been addressed by several investigators.[56,70–72] In these steels, alloying elements such as Mn, Si, molybdenum (Mo), Cr, and others during recrystallization annealing lead to the formation of oxide on the steel surface.[73–75] **Figure 8** indicates four methods to prevent Zn coating defects in the hot-dip galvanizing process for AHSS steels. This oxide layer leads to poor results in the galvanizing process.[76] In the hot-dip galvanizing process of AHSS steel, bare spots, flaking of the Zn layer, and cracks with deformation occur.[76] Ti–IF and DP steel annealing time and the composition of the protective atmosphere of H_2–N_2 at a low dew point were examined by Cvijović *et al.*[77] As a result of this study, it was observed that Mn, Al, Si, and Cr make oxide in all conditions, but these high Mn and Si concentrations increase the concentration of nonwettable $MnSiO_3$ particles in DP steel. Also, although the increase of annealing time led to an increase in surface oxide layer, the increase of H_2 in the created gas atmosphere helps to increase the wettability. Khondker *et al.*[78] investigated the effect of oxidation potential of an annealing atmosphere in DP steel. In the experimental study, they emphasized that Mn causes important selective oxidation. However, they have found that before dipping, Mn oxides on the steel surface provide good coating adhesion to annealed samples.

Cold-rolled steels have much better Zn coatings than hot-rolled steels.[79] However, many studies have been performed to increase the Zn coating of the hot-rolled steels.[79]

Liu *et al.*[80] investigated the galvanizing ability of TRIP steel, which has four different chemical compositions. Consequently, they stated that the galvanizing ability of the low Si and Mn contents are good, and Al in the Zn bath makes a good contribution to galvanization. Galvanizing ability can be greatly increased with the optimization of critical factors (steel composition, dew point, and bath chemistry).[81] In another study of galvanizing of TRIP steel,[82] it was emphasized that the TRIP steel is not suitable for traditional hot-dip galvanizing due to the high Si content, defects on the steel surface occur, and the Zn coating does not have good quality. In the

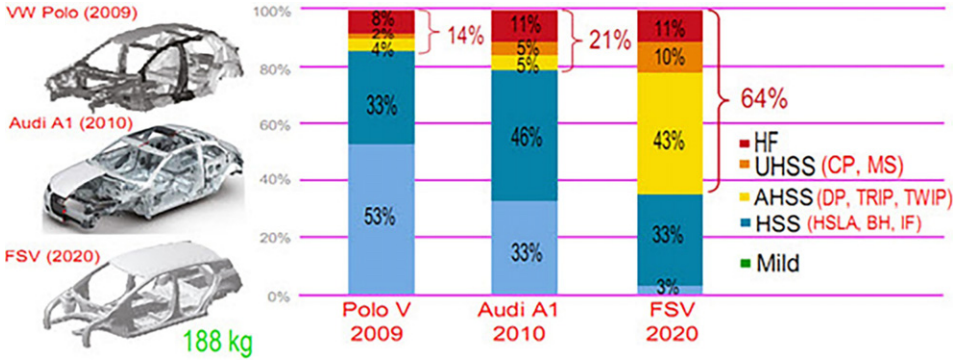


Figure 7 The use of AHSS in some automotive models.[69]

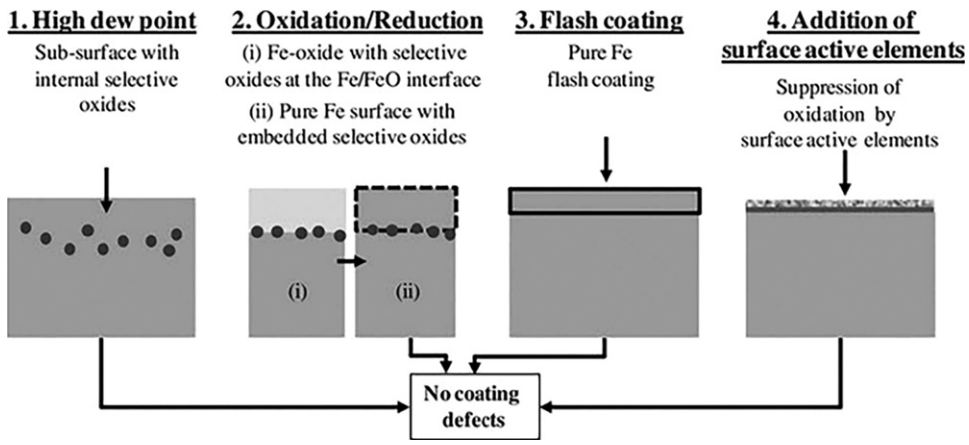


Figure 8 Schematic illustration of the four proposed methods to prevent Zn coating defects in the hot-dip galvanizing process in AHSS steel.[73]

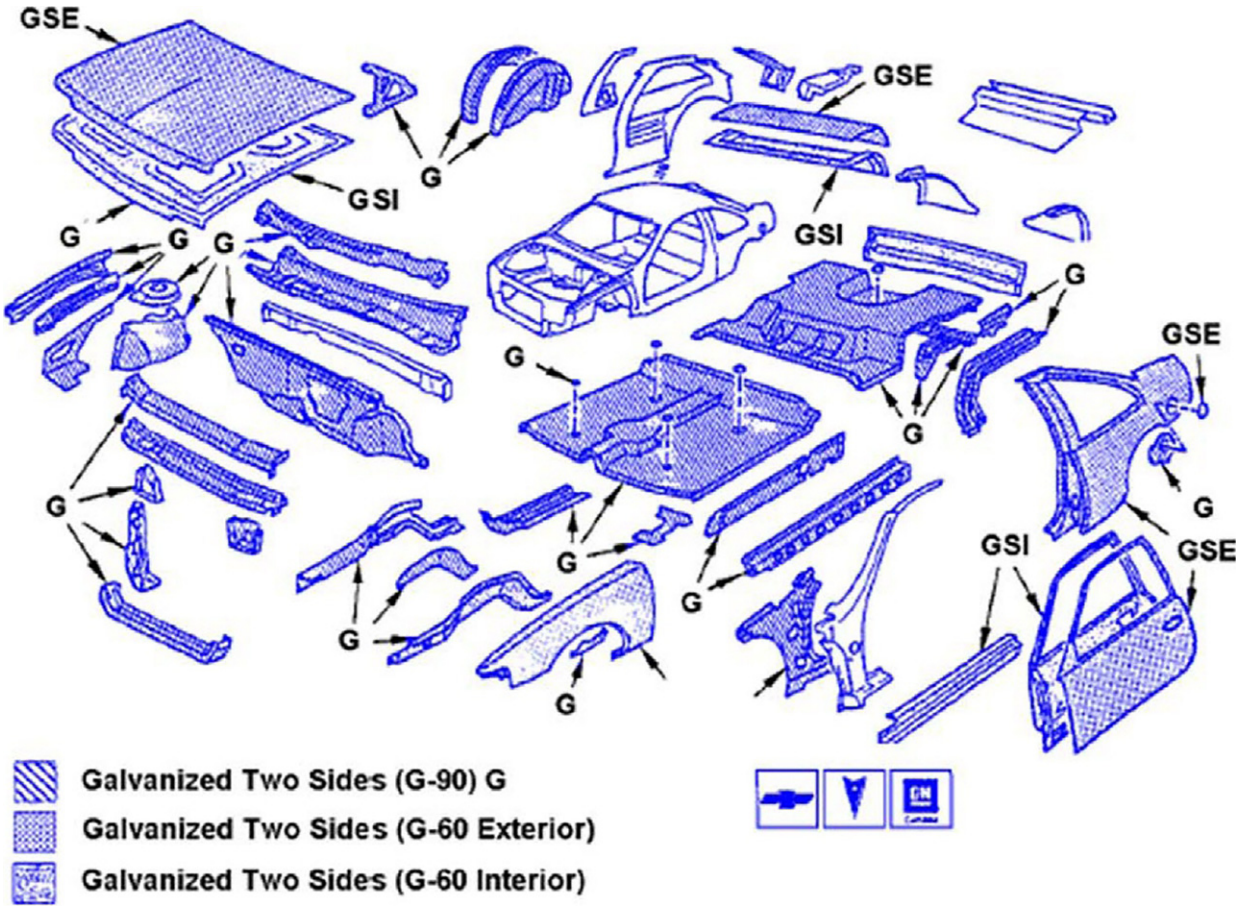


Figure 9 Galvanizing applications in the automotive parts.[84]

galvanizing of AHSS steel, various technological methods (precoating, preoxidation, and dew point control) are recommended.[83]

Galvanized parts are shown in Figure 9.[84] In AHSS steel galvanizing operations, one of the most common problems is galling. Galling is the removal of coating or the adhesion during metal-forming processes. During the forming of galvanized AHSS parts, factors between die material and coating have been investigated.[37,85] Details of the galling process are illustrated in Figure 10.

TWIP steel, which is a new material for the automotive industry, hot-dip galvanizing, and hydrogen-induced delayed cracking problems were examined by Blumenau *et al.*[86] In this work, for the first time, the effect of selective oxidation on

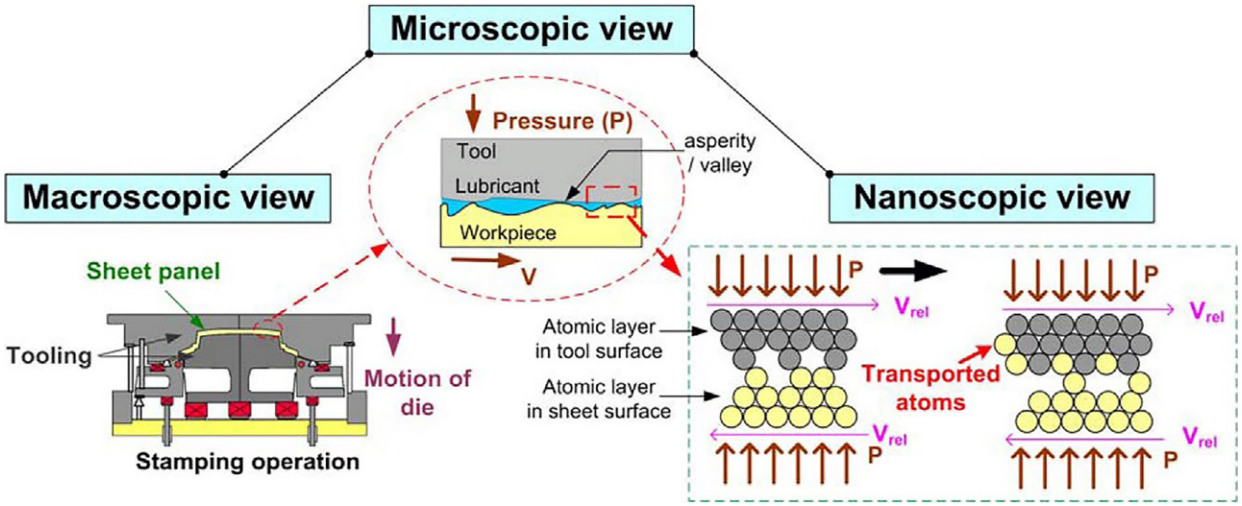


Figure 10 Schematic representation of galling process.[84]

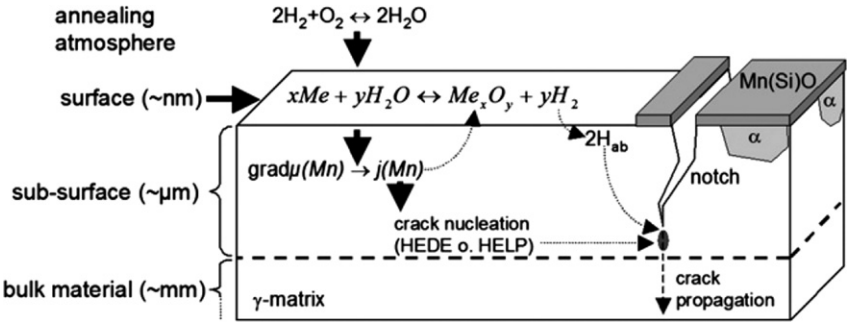


Figure 11 Schematic representation of the proposed model.[86]

hydrogen-induced delayed cracking was verified. Their models are displayed in Figure 11. The models emphasize that removal of solid solute Mn on the subsurface plays a key role.

The hot-dip galvanizing process was applied to dual-phase steel by Belousov *et al.*[87]; high-strength steel sheets (strength, 450–600 MPa) were produced. In another study, the effect of heat treatment was examined in the dual-phase steel, which is made with hot-dip galvanizing and, and was sensitive to the yield strength of the annealing program regardless of the total elongation.[88]

3.12.7 Failure Mechanisms in Galvanized Steels

In the hot-dip process, some unwanted microstructures and failures have commonly been seen. It is known that the presence of cracks in the coatings weakens the coating barrier.[11] Failure mechanisms during galvanizing were investigated by a European project and were prepared to show and share these problems with industries.[89] The most common problem is liquid metal-assisted cracking (LMAC), as shown in Figure 12. This is a condition that occurs only when there is contact with the molten Zn. LMAC is a failure that quickly passes to a brittle structure with a covering of a normally ductile metal or with



Figure 12 Liquid metal-assisted cracking.[92]

contact with a liquid metal.[90] LMAC can occur after galvanizing or may occur when there is a subsequently applied force. Even a small crack in a working environment under successive loads can become a very large crack. Figure 13 shows cracks forming during galvanizing.[89] Repair is performed using a welding method to eliminate this problem. Numerous



Figure 13 Photo of cracking occurring during galvanization.[89]

studies have been performed to attempt to protect against this cracking.[90,91]

Many environmental factors affect the failure of steel parts (or structures) during galvanizing.[89] At a galvanizing temperature of 450 °C, a decrease in impact and strength values of the structural steels was generally observed.[89] Moreover, it was observed that Zn–Bi–Pb–Sn baths resulted in more brittle coatings than the Zn–Pb baths.[89] Surface roughness as a result of fluxing increases the probability of local embrittlement formation similar to notch-like effects.[89]

Liu *et al.*[93] showed that presence of Cl^- can cause the formation of pitting corrosion, which increases corrosion rate as the temperature increases. Moreover, the polarization resistance increases with increasing hydrostatic pressure.

Coatings formed after galvanization at 560 °C in a pure Zn bath were investigated by three-point bending.[94] Crack population and statistical analyses results indicate applied strain on the coating affects the crack density created during three-point bending. However, coating thickness did not contribute any statistical information in terms of crack density.[94] Moreover, the density of cracks acted as a barrier to stop crack propagation at the thickness of the outer Zn-rich layers.[94]

3.12.8 Conclusion

In this chapter, hot-dip galvanizing processes were addressed due to their high application in the coating of automotive body materials. Mg–Zn coatings have been identified as a potential next generation of galvanized steel. Addition of Mg to the Zn bath can improve corrosion performance without increasing the thickness of coating. Effects of various elements present in the galvanizing bath were discussed related to coating properties. Improvements in AHSS galvanizing is a challenging issue and more efforts are still needed in this regard.

See also: 3.1 Electroless Plating of Pd Binary and Ternary Alloys and Surface Characteristics for Application in Hydrogen Separation. 3.2 Tuning of the Microstructure and Surface Topography of Hot-Dip Galvanized Coatings

References

1. Cambel, J. W. *Corrosion, Vol. 13*; *ASM Handbook*; ASM: New York, NY, 1999.
2. American Galvanizers Association (AGA). Available from: http://courtgalvanizinginc.com/wp-content/uploads/2012/04/Zinc_Coatings.pdf, 2006 (accessed 30 March 2016).
3. Szota, J. G. Steel Wire Galvanizing by the VERT-DOWN Method. *J. Mater. Process. Technol.* **1995**, *55*, 134–139. doi:10.1016/0924-0136(95)01933-2.
4. Coburn, S. K. *Cost-Effectiveness of Hot-Dip Galvanizing for Exposed Steel*; Transportation Research Board, National Research Council: Washington, DC, 1984.
5. Hanley, H. R. *Hot Dip Galvanizing; A Review Of The Process*, Rolla (MO), University of Missouri; School of Mines and Metallurgy, Bulletin, Technical Series, 1940.
6. Maass, P.; Peissker, P.; Ahner, C. *Handbook of Hot-Dip Galvanization*; Wiley-VCH: Weinheim, 2011.
7. Spowers, W. H.; Polansky, V. S. *Hot-Dip Galvanizing Practice*, 1st ed.; Penton Publishing Co.: Cleveland, 1938.
8. Texas Transportation Institute. *Hot-Dip Galvanizing*; Highway Department: College Station, TX, 1966.
9. van Eijnsbergen, J. F. H. *Duplex Systems: Hot-Dip Galvanizing Plus Painting*; Elsevier: Amsterdam; New York, NY, 1994.
10. Dutta, M.; Halder, A. K.; Singh, S. B. Morphology and Properties of Hot Dip Zn–Mg and Zn–Mg–Al Alloy Coatings on Steel Sheet. *Surf. Coat. Technol.* **2010**, *205*, 2578–2584. doi:10.1016/j.surfcoat.2010.10.006.
11. Gallego, A.; Gil, J. F.; Castro, E.; Piotrkowski, R. Identification of Coating Damage Processes in Corroded Galvanized Steel by Acoustic Emission Wavelet Analysis. *Surf. Coat. Technol.* **2007**, *201*, 4743–4756. doi:10.1016/j.surfcoat.2006.10.018.
12. Hosking, N. C.; Ström, M. A.; Shipway, P. H.; Rudd, C. D. Corrosion Resistance of Zn–Magnesium Coated Steel. *Corros. Sci.* **2007**, *49*, 3669–3695. doi:10.1016/j.corsci.2007.03.032.
13. Shibli, S. M. A.; Meena, B. N.; Remya, R. A Review on Recent Approaches in the Field of Hot Dip Zn Galvanizing Process. *Surf. Coat. Technol.* **2015**, *262*, 210–215. doi:10.1016/j.surfcoat.2014.12.054.
14. GalvInfoNote 9, Continuous Hot-Dip Galvanizing versus GENERAL (BATCH) GALVanizing, Rev 2.1, 2003.
15. Jordan, C. E.; Marder, A. R. Fe–Zn Phase Formation in Interstitial-Free steels Hot-Dip Galvanized at 450 °C: Part I 0.00 wt% Al–Zn Baths. *J. Mater. Sci.* **1997**, *32*, 5593–5602. doi:10.1023/A:1018680625668.
16. Kozdras, M. S.; Niessen, P. Surface Effects in Batch Galvanizing of Silicon Containing Steels. *Mater. Sci. Technol.* **1990**, *6* (8), 681–686. doi:10.1179/mst.1990.6.8.681.
17. Petit, E. J.; Grosbety, Y.; Aden-Ali, S.; Gilgert, J.; Azari, Z. Microstructure of the Coating and Mechanical Properties of Galvanized Chromium-Rich Martensitic Steel. *Surf. Coat. Technol.* **2010**, *205*, 2404–2411. doi:10.1016/j.surfcoat.2010.09.032.
18. Martinez, M. A.; Sanz, P.; Ruiz, M. L.; Fabrellas, B.; Abad, E.; Rivera, J. Evaluation of the Spanish Hot Dip Galvanising Sector as a Source of Polychlorinated Dibenzo-p-Dioxins and Polychlorinated Dibenzofurans. *Chemosphere* **2008**, *71*, 1127–1134. doi:10.1016/j.chemosphere.2007.10.038.
19. Balzer, H.; Hoehne, M.; Noll, R.; Sturm, V. New Approach to Online Monitoring of the Al Depth Profile of the Hot-Dip Galvanised Sheet Steel Using LIBS. *Anal. Bioanal. Chem.* **2006**, *385*, 225–233. doi:10.1007/s00216-006-0347-z.
20. Verma, D. K.; Shaw, D. S. An Evaluation of Airborne nickel, Zn, and Lead Exposure at Hot Dip Galvanizing Plants. *Am. Ind. Hyg. Assoc. J.* **1991**, *52*, 511–515.doi:10.1080/15298669191365135.

21. van Eijnsbergen, J. F. H. Duplex Systems. Hot-Dip Galvanizing Plus Painting. Book Review. *Progr. Org. Coat.* **1996**, *28*, 149. doi:10.1016/0300-9440(96)80490-5.
22. van Eijnsbergen, J. F. H. Duplex Systems. Hot-Dip Galvanizing Plus Painting. Book Review. *Corros. Sci.* **1996**, *38*, 171. doi:10.1016/S0010-938X(96)90028-1.
23. Galvanizing Asia. *Hot Dip Galvanizing – Process, Applications, Properties*. Available from: http://www.galvanizingasia.com/pdfs/page9-25.pdf, 2016 (accessed 30 March 2016).
24. Ahmadi, P. N.; Rafiezadeh, E. Effect of Aluminum on Microstructure and Thickness of Galvanized Layers on Low Carbon Silicon-Free Steel. *Int. J. Iron Steel Soc. Iran* **2009**, *6* (1), 25–29.
25. GalvInfo Center. *The Role of Aluminum in Continuous Hot-Dip Galvanizing in: GalvInfoNote* 2.4. Available from: http://galvinfo.com/ginotes/GalvInfoNote_2_4.pdf (accessed 3 March 2016).
26. Lazik, S.; Esling, C.; Wegria, J. Cracking in Zn Layers on Continuous Galvanized Sheets A Review. *Texture. Microstruct.* **1995**, *23*, 131–147, 10.1155/TSM.23.131.
27. Chattopadhyay, A.; Subramanya Sarma, V.; Murty, B. S.; Haldar, A.; Bhattacharjee, D. Studies on Hot Rolled Galvanized Steel Sheets: Effect of Reheating on Galvanizing. *Surf. Coat. Technol.* **2009**, *203*, 3465–3471. doi:10.1016/j.surfcoat.2009.05.005.
28. Pavlidou, E.; Pistofidis, N.; Vourlias, G.; Stergioudis, G. Modification of the Growth-Direction of the Zinc Coatings Associated with Element Additions to the Galvanizing Bath. *Mater. Lett.* **2005**, *59*, 1619–1622. doi:10.1016/j.matlet.2004.08.045.
29. Verma, A. R. B.; van Ooij, W. J. High Temperature Batch Hot-Dip Galvanizing. Part 1. General Description of Coatings Formed at 560 °C. *Surf. Coat. Technol.* **1997**, *89*, 132–142. doi:10.1016/S0257-8972(96)02941-6.
30. Verma, A. R. B.; van Ooij, W. J. High Temperature Batch Hot-Dip Galvanizing. Part 2. Comparison of Coatings Formed in the Temperature Range 520–555 °C. *Surf. Coat. Technol.* **1997**, *89*, 143–150. doi:10.1016/S0257-8972(96)02940-4.
31. Bicao, P.; Jianhua, W.; Xuping, S.; Zhi, L.; Fucheng, Y. Effects of Zinc Bath Temperature on the Coatings of Hot-Dip Galvanizing. *Surf. Coat. Technol.* **2008**, *202*, 1785–1788. doi:10.1016/j.surfcoat.2007.07.044.
32. Hausbrand, R.; Stratmann, M.; Rohwerder, M. Corrosion of Zn–Magnesium Coatings: Mechanism of Paint Delamination. *Corros. Sci.* **2009**, *51* (9), 2107–2114. doi:10.1016/j.corsci.2009.05.042.
33. Prosek, T.; Nazarov, A.; Bexell, U.; Thierry, D.; Serak, J. Corrosion Mechanism of Model Zn–Magnesium Alloys in Atmospheric Conditions. *Corros. Sci.* **2008**, *50*, 2216–2231. doi:10.1016/j.corsci.2008.06.008.
34. Yadav, A. P.; Nishikata, A.; Tsuru, T. Degradation Mechanism of Galvanized Steel in Wet–Dry Cyclic Environment Containing Chloride Ions. *Corros. Sci.* **2004**, *46* (2), 361–376. doi:10.1016/S0010-938X(03)00153-7.
35. Schuerz, S.; Fleischanderl, M.; Luckeneder, G. H.; *et al.* Corrosion Behaviour of Zn–Al–Mg Coated Steel Sheet in Sodium Chloride-Containing Environment. *Corros. Sci.* **2009**, *51*, 2355–2363. doi:10.1016/j.corsci.2009.06.019.
36. Li, S.; Gao, B.; Tu, G.; *et al.* Effects of Magnesium on the Microstructure and Corrosion Resistance of Zn–55Al–1.6Si Coating. *Constr. Build. Mater.* **2014**, *71*, 124–131. doi:10.1016/j.conbuildmat.2014.08.023.
37. Wang, W.; Wang, K.; Zhao, Y.; Hua, M.; Wei, X. A Study on Galling Initiation in Friction Coupling Stretch Bending with Advanced High Strength Hot-Dip Galvanized Sheet. *Wear* **2015**, *328–329*, 286–294. doi:10.1016/j.wear.2015.02.058.
38. Valls Verdejo, V.; Angeles Perez Alarco, M.; Pilar Lino Sorli, M. Scheduling in a Galvanizing Line. *Comput. Oper. Res.* **2009**, *36*, 280–296. doi:10.1016/j.cor.2007.09.006.
39. Bennasr, J.; Snoussi, A.; Bradai, C.; Halouani, F. Optimization of Hot-Dip Galvanizing Process of Reactive Steels: Minimizing Zinc Consumption Without Alloy Additions. *Mater, Lett.* **2008**, *62*, 3328–3330. doi:10.1016/j.matlet.2008.02.067.
40. De Abreu, Y.; Da Silva, A.; Ruiz, A.; Requiz, R.; Angulo, N.; Alanis, R. Study of Zinc Coatings on Steel Substrate Attained by Two Different Techniques. *Surf. Coat. Technol.* **1999**, *120–121*, 682–686. doi:10.1016/S0257–8972(99)00358–8.
41. Vourlias, G.; Pistofidis, N.; Stergioudis, G.; Tsipas, D. The Effect of Alloying Elements on the Crystallization Behaviour and on the Properties of Galvanized Coatings. *Cryst. Res. Technol.* **2004**, *39*, 23–29. doi:10.1002/crat.200310144.
42. Asgari, H.; Toroghinejad, M. R.; Golozar, M. A. On Texture, Corrosion Resistance and Morphology of Hot-Dip Galvanized Zn Coatings. *Appl. Surf. Sci.* **2007**, *253*, 6769–6777. doi:10.1016/j.apsusc.2007.01.093.
43. Jin-tang, L.; Xin-hua, W.; Chun-shan, C.; Gang, K.; Jin-hong, C.; Qiao-yu, X. Crystallographic Research of Spangle on Hot Dip Galvanized Steel Sheets. *Trans. Nonferr. Met. Soc. China* **2007**, *17*, 351–356. doi:10.1016/S1003-6326(07)60097-1.
44. Asgari, H.; Toroghinejad, M. R.; Golozar, M. A. Relationship Between (00.2) and (20.1) Texture Components and Corrosion Resistance of Hot-Dip Galvanized Zinc Coatings. *J. Mater. Process. Technol.* **2008**, *198*, 54–59. doi:10.1016/j.jmatprotec.2007.06.068.
45. Asgari, H.; Toroghinejad, M. R.; Golozar, M. A. Effect of Coating Thickness on Modifying the Texture and Corrosion Performance of Hot-Dip Galvanized Coatings. *Curr. Appl. Phys.* **2009**, *9*, 59–66. doi:10.1016/j.cap.2007.10.090.
46. Katiforis, N.; Papadimitriou, G. Influence of Copper, Cadmium and Tin Additions in the Galvanizing bath on the Structure, Thickness and Cracking Behaviour of the Galvanized Coatings. *Surf. Coat. Technol.* **1996**, *78*, 185–195. doi:10.1016/0257-8972(94)02408-1.
47. Borhan-Tavakoli, A. Mécanime d'Action du Germanium Lors de la Galvanisation a 723 K (450 °C) Dans un Bain Aluminisé. *J. Jpn. Inst. Met.* **1985**, *26*, 101, 10.2320/matertrans1960.26.101.
48. Chang, S.; Shin, J. C. The Effect of Antimony Additions on Hot Dip Galvanized Coatings. *Corros. Sci.* **1994**, *36*, 1425–1436. doi:10.1016/0010-938X(94)90190-2.
49. Culcasi, J. D.; Sere, P. R.; Elsner, C. I.; Di Sarli, A. D. Control of the Growth of Zinc–Iron Phases in the Hot-dip Galvanizing Process. *Surf. Coat. Technol.* **1999**, *122*, 21–23. doi:10.1016/S0257-8972(99)00404-1.
50. Di Cocco, V.; Iacoviello, F.; Natali, S. Damaging Micromechanisms in Hot-Dip Galvanizing Zn Based Coatings. *Theor. Appl. Fract. Mech.* **2014**, *70*, 91–98. doi:10.1016/j.tafmec.2014.05.003.
51. Fratesi, R.; Ruffini, N.; Malavolta, M.; Bellezze, T. Contemporary Use of Ni and Bi in Hot-Dip Galvanizing. *Surf. Coat. Technol.* **2002**, *157*, 34–39. doi:10.1016/S0257-8972(02)00137-8.
52. Pistofidis, N.; Vourlias, G.; Konidaris, S.; Pavlidou, E.; Stergioudis, G. The Combined Effect of Nickel and Bismuth on the Structure of Hot-Dip Zn Coatings. *Mater. Lett.* **2007**, *61*, 2007–2010. doi:10.1016/j.matlet.2006.08.002.
53. Shibli, S. M. A.; Manu, R.; Beegum, S. Studies on the Influence of Metal Oxides on the Galvanic Characteristics of Hot-Dip Zinc Coating. *Surf. Coat. Technol.* **2008**, *202*, 1733–1737. doi:10.1016/j.surfcoat.2007.07.033.
54. Rieger, P. H. *Electrochemistry*; Prentice-Hall International: New York, NY, 1987.
55. Pistofidis, N.; Vourlias, G.; Konidaris, S.; Pavlidou, E.; Stergiou, A.; Stergioudis, G. Microstructure of Zn Hot-Dip Galvanized Coatings Used for Corrosion Protection. *Mater. Lett.* **2006**, *60*, 786–789. doi:10.1016/j.matlet.2005.10.013.
56. Liu, H.; He, Y.; Li, L. Application of Thermodynamics and Wagner Model on Two Problems in Continuous Hot-Dip Galvanizing. *Appl. Surf. Sci.* **2009**, *256*, 1399–1403. doi:10.1016/j.apsusc.2009.08.095.
57. Hirose, S.; Itoh, T.; Makita, M.; *et al.* Defect Structure of Deformed Fe_2Al_5 Intermetallic Compound. *Intermetallics* **2003**, *11*, 633–642. doi:10.1016/S0966-9795(03)00050-5.
58. Shawki, S.; Hamid, Z. A. Effect of Aluminium Content on the Coating Structure and Dross Formation in the Hot-Dip Galvanizing Process. *Surf. Interface Anal.* **2003**, *35*, 943–947. doi:10.1002/sia.1608.
59. Munroe, P. R.; Laksmi, C. S.; Gleeson, B. Effects of 0.1 and 0.2 wt.% Aluminium Addition to Zinc on the Interdiffusion between Zinc and Iron at 400 °C. *Mater. Sci. Eng.: A,* **1998**, *251* (1), 87–93. doi:10.1016/S0921-5093(98)00641-8.
60. Peng, S.; Lu, J.; Che, C.; Kong, G.; Xu, Q. Morphology and Antimony Segregation of Spangles on Batch Hot-Dip Galvanized Coatings. *Appl. Surf. Sci.* **2010**, *256* (16), 5015–5020. doi:10.1016/j.apsusc.2010.03.046.
61. Kazumi, N., Yasuhide, M., Kenichiro, M. Hot-Dip Zn–Al–Sn Alloy Coated Steel Sheet Excellent in Spangle Uniformity and Corrosion Resistance. Japan Patent 2001207249, 2001.
62. McDevitt, E.T. Molten Al–Zn Alloy Bath Microalloyed with Borides for Small Spangle Size on Hot-Dip Coated Steel Strip, EP02027947 to ISG Technologies Inc., 2004.
63. McDevitt, E.T., Friedersdorf, F.J., Rommal, H.E.G. Composition for Controlling Spangle Size, a Coated Steel Product, and a Coating Method. US Patent 20050181229, 2005.
64. Su, X.; Wu, C.; Liu, D.; Yin, F.; Zhu, Z.; Yang, S. Effect of Vanadium on Galvanizing Si-Containing Steels. *Surf. Coat. Technol.* **2010**, *205* (1), 213–218. doi:10.1016/j.surfcoat.2010.06.037.
65. Vagge, S. T.; Raja, V. S. Influence of Strontium on Electrochemical Corrosion Behavior of Hot-Dip Galvanized Coating. *Surf. Coat. Technol.* **2009**, *203*, 3092–3098. doi:10.1016/j.surfcoat.2009.03.026.
66. Chassagneux, E.; Thomas, G. Studies on V_2O_5 Induced Hot Corrosion. *Mater. Chem. Phys.* **1987**, *17*, 273–284. doi:10.1016/0254-0584(87)90149-0.
67. Ozturk, F.; Polat, A.; Toros, S.; Picu, R. C. Strain Hardening and Strain Rate Sensitivity Behaviors of Advanced High Strength Steels. *J. Iron Steel Res. Int.* **2013**, *20* (6), 68–74. doi:10.1016/S1006-706X(13)60114-4.
68. Ozturk, F.; Toros, S.; Kilic, S. Tensile and Springback Behavior of DP600 Advanced High Strength Steel at Warm Temperatures. *J. Iron Steel Res. Int.* **2009**, *16* (6), 41–46. doi:10.1016/S1006-706X(10)60025-8.
69. Ruifrok, R. *TATA Steel: Light Weight Steel Solutions in Automotive Design.* Available from: http://www.han.nl/onderzoek/nieuws/more-weight-to-lightweigh/_attachments/presentatie_tata_steel_han_automotive_symposium_22-11-12.pdf, 2016 (accessed 30 March 2016).

70. Liu, H.; Li, F.; Shi, W.; *et al.* Challenges in Hot-Dip Galvanizing of High Strength Dual Phase Steel: Surface Selective Oxidation and Mechanical Property Degradation. *Surf. Coat. Technol.* **2012**, *206*, 3428–3436. doi:10.1016/j.surfcoat.2012.02.001.
71. Sagl, R.; Jarosik, A.; Angeli, G.; Haunschmied, T.; Hesser, G.; Stifter, D. Tailoring of Oxide Morphology and Crystallinity on Advanced High-Strength Steel Surfaces Prior Hot-Dip Galvanizing. *Acta Mater.* **2014**, *72*, 192–199. doi:10.1016/j.actamat.2014.03.037.
72. Sagl, R.; Jarosik, A.; Stifter, D.; Angeli, G. The Role of Surface Oxides on Annealed High-Strength Steels in Hot-Dip Galvanizing. *Corros. Sci.* **2013**, *70*, 268–275. doi:10.1016/j.corsci.2013.01.039.
73. Cho, L.; Kim, M. S.; Kim, Y. H.; De Cooman, B. C. Influence of Minor Alloying Elements on Selective Oxidation and Reactive Wetting of CMnSi TRIP Steel During Hot Dip Galvanizing. *Metall. Mater. Trans. A* **2014**, *45A*, 4486. doi:10.1007/s11661-014-2394-y.
74. Kim, M. S.; Kwak, J. H.; Kim, J. S.; Liu, Y. H.; Gao, N.; Tang, N.-Y. Galvanizability of Advanced High-Strength steels 1180TRIP and 1180CP. *Metall. Mater. Trans. A* **2009**, *40A*, 1904. doi:10.1007/s11661-009-9880-7.
75. Lin, K. C.; Chu, P. W.; Lin, C. S.; Chen, H. B. Galvanizing and Galvannealing Behavior of CMnSiCr Dual-Phase steels. *Metall. Mater. Trans. A* **2013**, *44A*, 2690. doi:10.1007/s11661-013-1612-3.
76. Li, F.; Liu, H.; Shi, W.; Liu, R.; Li, L. Hot Dip Galvanizing Behavior of Advanced High Strength Steel. *Mater. Corros.* **2012**, *63*, 396–400. doi:10.1002/maco.201005905.
77. Cvijović, I.; Parezanović, I.; Spiegel, M. Influence H_2–N_2 Atmosphere Composition and Annealing Duration on the Selective Surface Oxidation of Low-Carbon Steels. *Corros. Sci.* **2006**, *48*, 980–993. doi:10.1016/j.corsci.2005.02.022.
78. Khondker, R.; Mertens, A.; McDermid, J. R. Effect of Annealing Atmosphere on the Galvanizing Behavior of Dual-Phase Steel. *Mater. Sci. Eng.: A* **2007**, *463*, 157–165. doi:10.1016/j.msea.2006.09.116.
79. Chattopadhyay, A.; Subramanya Sarma, V.; Murty, B. S.; Haldar, A.; Bhattacharjee, D. Studies on Hot-Rolled Galvanized Steel Sheets: Segregation of Alloying Elements at the Surface. *Scr. Mater.* **2008**, *59*, 522–525. doi:10.1016/j.scriptamat.2008.04.040.
80. Liu, H.; Shi, W.; He, Y.; Li, L. The Effect of Alloy Elements on Selective Oxidation and Galvanizability of TRIP-Aided Steel. *Surf. Interface Anal.* **2010**, *42*, 1685–1689. doi:10.1002/sia.3368.
81. Teck Resources. *Meeting the Challenges of Galvanizing Advanced High Strength Steels*. Available from: https://tr.scribd.com/doc/305490064/Galvanizing-AHSS, 2016 (accessed 30 March 2016).
82. Mahieu, J.; De Cooman, B.; Claessens, S. Galvanizability of High-Strength Steels for Automotive Applications. *Metall. Mater. Trans. A* **2001**, *32*, 2905–2908. doi:10.1007/s11661-001-1042-5.
83. Jin, Y. Development of Advanced High Strength Steels for Automotive Applications. *La Metallurgia Italiana* **2011**, *6*.
84. Kim, H., *Prediction and Elimination of Galling in Forming Galvanized Advanced High Strength Steels (AHSS)* (PhD Thesis), Columbus, OH: The Ohio State University, 2008.
85. Kim, H.; Han, S.; Yan, Q.; Altan, T. Evaluation of Tool Materials, Coatings and Lubricants in Forming Galvanized Advanced High Strength Steels (AHSS). *CIRP Ann. – Manuf. Technol.* **2008**, *57*, 299–304. doi:10.1016/j.cirp.2008.03.029.
86. Blumenau, M.; Barnoush, A.; Thomas, I.; Hofmann, H.; Vehoff, H. Impact of Selective Oxidation During Inline Annealing Prior to Hot-Dip Galvanizing on Zn Wetting and Hydrogen-Induced Delayed Cracking of Austenitic FeMnC Steel. *Surf. Coat. Technol.* **2011**, *206*, 542–552. doi:10.1016/j.surfcoat.2011.07.081.
87. Belousov, V. A.; Petrenko, P. A.; Tkachenko, V. A. Production of High Strength Hot Galvanized Sheet From Dual Phase Steel. *Steel Transl.* **2010**, *40* (8), 773–776. doi:10.3103/S096709121008019X.
88. Pan, E.; Di, H.; Jiang, G.; Bao, C. Effect of Heat Treatment on Microstructures and Mechanical Properties of Hot-Dip Galvanized DP Steels. *Acta Metall. Sin. (English Letters)* **2014**, *27* (3), 469–475. doi:10.1007/s40195-014-0066-y.
89. Carpio, J.; Casado, J. A.; Alvarez, J. A.; Gutierrez-Solana, F. Environmental Factors in Failure During Structural Steel Hot-Dip Galvanizing. *Eng. Fail. Anal.* **2009**, *16*, 585–595. doi:10.1016/j.engfailanal.2008.02.006.
90. The British Constructional Steelwork Association. BCSA and GA Publication No. 40/05, 2005.
91. Rudd, W.; Wen, S.; Langenberg, P.; *et al.* Final Report. Research Fund for Coal and Steel. Directorate-General for Research. European Commission, 2007.
92. NSC Technical Report. Available from: http://www.newsteelconstruction.com/wp/rare-problem-can-be-easily-avoided/ (accessed 3 March 2005).
93. Liu, S.; Sun, H.; Zhang, N.; Sun, L. The Corrosion Performance of Galvanized Steel in Closed Rusty Seawater. *Int. J. Corros.* **2013**, *2013*. doi:10.1155/2013/267353.
94. Tzimas, E.; Papadimitriou, G. Cracking Mechanisms in High Temperature Hot-Dip Galvanized Coatings. *Surf. Coat. Technol.* **2001**, *145*, 176–185. doi:10.1016/S0257-8972(01)01323-8.

Relevant Websites

www.galvanizeit.org/
American Galvanizers Association.
http://www.galvanizing.org.uk
Galvanizer's Association.
http://www.gaa.com.au/
Galvanizer's Association of Australia.
http://www.galvanizingasia.com
Galvanizing Asia.

3.13 Finishing and Post-Treatment of Thermal Spray Coatings

MM Verdian, Islamic Azad University, Najafabad, Iran

© 2017 Elsevier Inc. All rights reserved.

3.13.1	**Introduction**	191
3.13.2	**Mechanical Finishing**	192
3.13.2.1	Turning; Milling and Machining	193
3.13.2.2	Grinding	193
3.13.2.2.1	Conventional grinding	193
3.13.2.2.2	Abrasive belt grinding	194
3.13.2.3	Polishing Techniques	194
3.13.2.3.1	Superfinishing and honing	194
3.13.2.3.2	Hand stoning and buffing	194
3.13.2.3.3	Tumbling and burnishing	194
3.13.2.3.4	Lapping	194
3.13.2.4	Effect of Finishing on Coatings Characteristics and Properties	194
3.13.2.5	Modeling the Finishing Processes	195
3.13.3	**Thermal Post-Treatments**	195
3.13.3.1	Fusing of Self-Flux Alloys	195
3.13.3.2	Remelting	196
3.13.3.2.1	Laser remelting	196
3.13.3.2.2	Electron beam remelting	196
3.13.3.2.3	TIG remelting	196
3.13.3.3	Solid State Heat Treatment	197
3.13.3.3.1	Pressure-assisted sintering	197
3.13.3.3.2	Pressure-less sintering and annealing	197
3.13.3.3.3	Austempering	198
3.13.3.4	Diffusion Annealing of Aluminum and Chromium	199
3.13.4	**Sealing**	199
3.13.4.1	The Basics	199
3.13.4.2	Organic Sealers	199
3.13.4.3	Inorganic Sealers	199
3.13.4.3.1	Aluminum–phosphate	199
3.13.4.3.2	Enameling	200
3.13.4.3.3	Electroplating	200
3.13.4.3.4	Sealing using glass formers	200
3.13.4.3.5	Sol–gel	200
3.13.4.3.6	Chemical treatment	200
3.13.4.3.7	Chemical vapor deposition	200
3.13.4.3.8	Molten metal or oxide penetration	200
3.13.5	**Other Processes**	200
3.13.5.1	Friction Stir Processing	200
3.13.5.2	Plasma Electrolytic Oxidation	202
3.13.5.3	Sol Infiltration	202
3.13.5.4	Physical Vapor Deposition	202
3.13.5.5	Ion Implantation	202
3.13.5.6	Shot Peening and Rolling	203
3.13.5.7	Laser Engraving	203
3.13.5.8	Thermochemical Processing	203
3.13.6	**Summary and Conclusion**	204
References		204
Relevant Websites		206

3.13.1 Introduction

Thermal spray processes involves spraying fine molten or semi-molten particles onto substrates to form a coating layer (Figure 1).[1] The feedstock materials can be in the form of wire or powder. The electrical sources can be used to heat the feedstock such as arc or plasma spraying systems. The combustion is another source of heat which

is used in flame and high velocity oxy-fuel (HVOF) spraying.[1–4]

The typical microstructure of a thermally sprayed coating is shown in Figure 2.[5] A lamella structure is observed due to flattening of particles when striking into the substrate. The inflight surface oxidation of particles results in presence of oxides in the coatings. The porosity of coatings is also arisen form vacant spaces between splats. The roughness is evident in sprayed coatings due irregularities of splats at the surface.

Many kinds of metallic, ceramic, polymeric, and composite materials can be deposited using thermal spray processes. The composition of feedstock material, pre-treatment of substrate and spraying method affect the performance of the as-sprayed coatings. The finishing and post-treatment of as-sprayed coatings are often inevitable. The control of roughness and dimension is the main reason for finishing of coatings. In the case of thermal treatment, microstructural improvement may be considered. While chemical treatment is used to seal the open pores. Recently, other post-treatments were used to achieve novel microstructures. The service life of coatings depends also on final treatments.

3.13.2 Mechanical Finishing

The as-sprayed coatings are relatively rough. Depend on the spraying method and coating material, the as-sprayed roughness (R_a) can vary between 3 and 40 μm approximately.[1–4] The high roughness can results in:

- Increased friction and wear
- Leakage of fluid and unsuitable sealing in mechanical systems and in parts like valves
- Out of tolerance dimensions

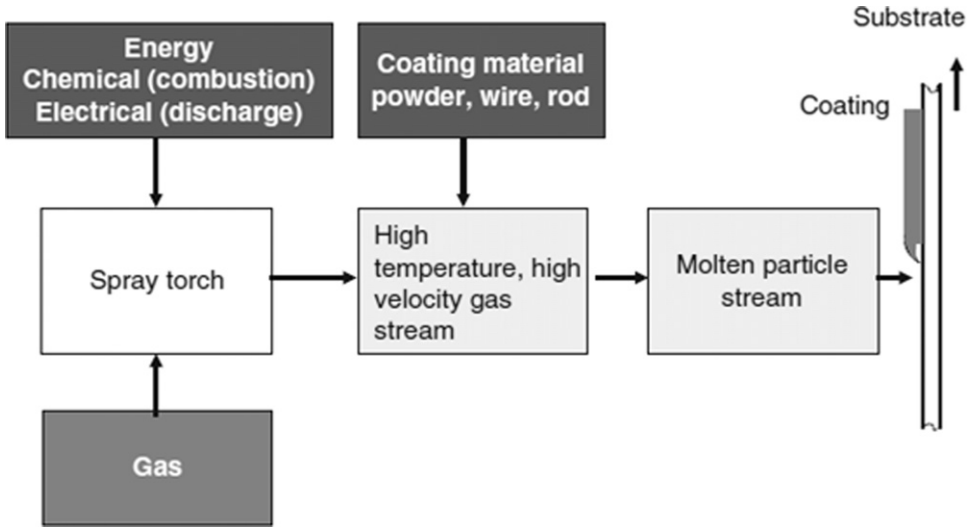


Figure 1 Schematics of thermal spray procedures.[3]

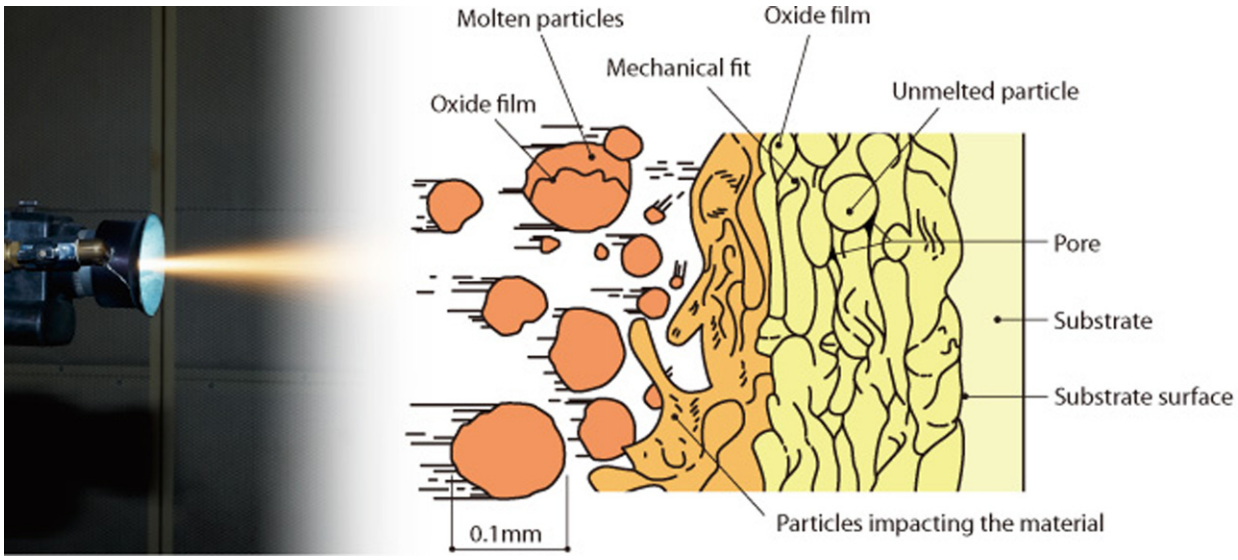


Figure 2 The nature of thermal spray coatings.[5]

To eliminate the deleterious effects of roughness and to ensure the desired dimensions, the coatings are often turned and ground. In some cases, the as-sprayed coatings may be used. Decorative coatings or corrosion resistant coatings are the examples. However, the final roughness and dimension depends on the application criteria.

3.13.2.1 Turning; Milling and Machining

Turning of thermal spray coatings is performed to remove as-sprayed roughness and to control the dimensions. Due to different bonding and microstructural conditions of the coatings in comparison to those of bulk materials (cast or wrought alloys), the use of traditional turning techniques may not be successful. As a result, the coating may be impaired or the tool may be failed. The problems during turning may be arisen form one or more following reasons[3,4]:

- Presence of porosity which may cause pull-out of coating;
- Lamella structure of coatings; the improper machining may results in debonding;
- Mechanical substrate-coating bonding which is relatively weak in comparison to physical and metallurgical bonds;
- Low machinability of some coating materials like cermets or ceramics;
- Penetration of coolants or lubricants through the coating;
- Thickness of coating; the over pressure can be remove all the coating layers to reach the substrate especially in thinner coatings.

The metallic coatings can be turned without any significant concern. However, cermet coatings must be carefully turned using carbide tools. In the case of brittle ceramic coatings, machining is not performed due to catastrophic failure of coatings. The lubricants and coolants (if used) may penetrate through the open pores after turning. So, the turning process must be performed carefully. Due to splat granular structure of coatings, crumble chips are formed during machining. The machined surface seems to be dull with fine pores.[1–4]

For machinable thermal spray coatings, carbide tools are generally used for turning. Use of other kinds of tools, can increase tool wear significantly. Tool angles recommended for turning using carbide tools are seen in **Figure 3**.[3] High-speed steel tools can be used for machining of metallic coatings. Some recommendation for wheel speed can be found elsewhere.[4]

The machining process is started by removal of heavy sprayed material at the end of part. The speed of rough machining is lower than that of finish machining twice. The depth of cutting can be up to 0.75 mm. Sometimes multi-passes are necessary for machining. 0.13–0.25 mm on the radius must be remained for finishing.[4]

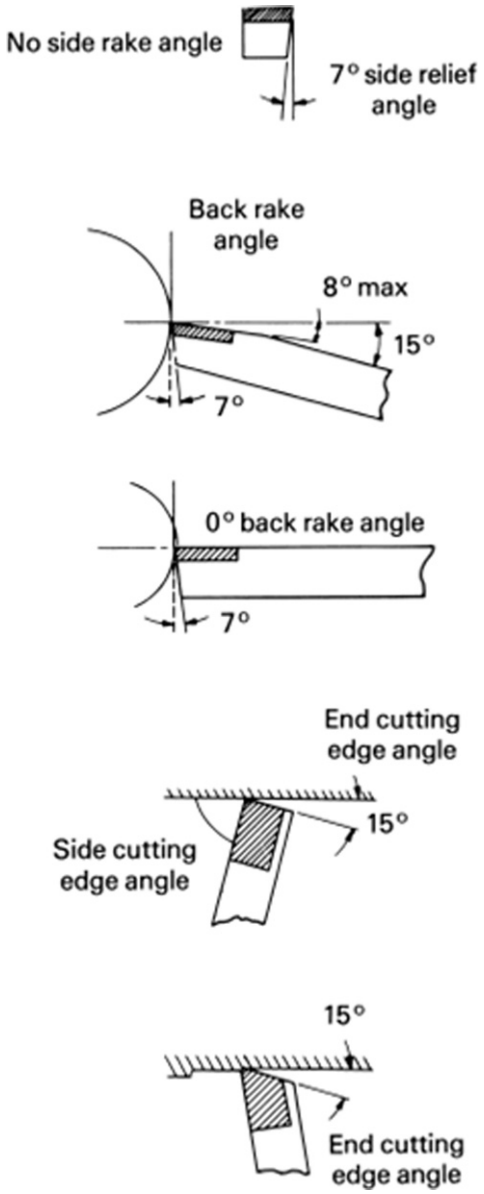


Figure 3 Tool angles recommended for machining of thermal spray coatings using carbide tools.[3]

3.13.2.2 Grinding

3.13.2.2.1 Conventional grinding

In comparison to machining (turning), grinding provides better finish and tolerance but is more expensive. In addition, the machining cannot be applied on ceramic coating so the grinding is inevitable. However, the material removal is much lower than that in machining. The coating thickness after grinding is close to final size ($\pm 5\,\mu m$).[1] Outside diameter grinders, internal grinders and surface grinders can be used for grinding. In the case of complex shapes, the machines with six axes or ultrasonic machining or CNC may be used.[1,4] As mentioned above, the finishing of thermal spray coatings is different from that of conventional materials due to specific microstructural aspects. So, the consideration must be taken to avoid coating failure or tool wear. Due to better freedom in wheel and abrasive selection, wet grinding is preferable. In this case, the hard wheel can be used to improve surface finish and decrease dressing (it should be noted that due to loading of wheel face or wear of abrasive grains, the wheel may be dresses by diamond tool).[4]

The type of grinding wheel (the material, grit size, and bond type) is selected based on microstructure and hardness of coating and the required finishing. To decrease the tool wear, the coarse grain wheel containing low binder can be used. For ceramic coatings, boron nitride and diamond are used. WC-based cermets require diamond wheels. In the case of metallic coatings, SiC, or Al_2O_3 wheels can be used. The details of wheel selection can be found in thermal spray literature.[4]

The sharp wheels must be used to cut without overheating. The wheels must provide free cutting action. The wheel must be compatible with operation and equipment. The grit size is usually between 37 and 180 μm. finer grit size can be used for better finish but the grits may penetrate through the coating via open pores. Vitrified bonds are mostly used for grinding due to good chemical and thermal resistance (for speeds up to 33 m s^{-1}). For higher speeds (up to 48 m s^{-1}), resin bonded materials can be used.[1,4]

The important parameters during grinding are[1–4,6]:

- Wheel speed: the lower wheel speed is, the softer action is expected. The wheel speed must be controlled to achieve best grinding performance and decrease wheel wear. It was reported that super high-speed grinding of HVOF WC–Co coating, results in improved grinding efficiency, the surface finish and the wheel life.
- Work speed: the increase in part speed, finishing is performed better.
- Area of contact: by increase of pressure (at contact area), the grinding depth decreased. In such conditions, the narrow wheels are more effective than wide ones.
- Use of water or lubricant: wet grinding is preferred especially in the case of hard coatings due to decrease cracking, overheating, and blistering. Water soluble oils are used with antiwelding agents.

In the final stage of grinding, the sparking must be avoided. The cracking or delamination of coating may occur during grinding due to exceeding pressure especially in the case of ceramic coatings or coatings with low adhesion strength.[3]

3.13.2.2.2 Abrasive belt grinding

Coated abrasive belts can be used for grinding and finishing. The advantages are low overheating, no need to dressing, low cost and ability to be changed easily. The coated part can be place on a lathe or mounted in a fixture. The part is rotated or transverses under the head of belt. The belt speed varies between 30 and 40 m s^{-1} while the speed of the specimen is between 0.13 and 1 m s^{-1}. The speeds must be controlled depending on size of part and type of coating. The grit size is selected based on required surface finish and rate of material removal. It is difficult to minimize the out of roughness using this technique.[1,4]

3.13.2.3 Polishing Techniques

Polishing is somewhat similar to grinding when the used abrasives are finer. The surface roughness (R_a) down to 1 μm (even near to 0.2 μm) can be obtained using polishing procedures. To achieve lower roughness, lapping techniques may be used.

3.13.2.3.1 Superfinishing and honing

Superfinishing involves rotation of the part against an abrasive stone or a tape. The lubricant and solvents are determining factors in superfinishing. The higher viscosity of fluid is, the finer finishing is attained. Honing rules and results are similar to those in superfinishing.[4]

3.13.2.3.2 Hand stoning and buffing

Buffing and hand stoning can be performed using paper, stone, wheel, or stick. Soft metal coatings like zinc and aluminum are easily stoned. Coarse abrasive are used firstly then finer ones. Cermets and ceramics can be stoned to achieve a light finish.[4]

3.13.2.3.3 Tumbling and burnishing

Tumbling is done using a rotating tub including water and abrasives. In the case of burnishing, hard ball are used. These processes are economically when a large number of small parts are present or the part has uncommon contours.[4]

3.13.2.3.4 Lapping

Lapping is a finishing process in which abrasive agents are suspended in oil or grease. High surface finish can be obtained by lapping (R_a of 0.05–0.1 μm). Low speed and high pressure result in the best finishes. Fused coatings must be lapped drily.[1,4]

3.13.2.4 Effect of Finishing on Coatings Characteristics and Properties

In the practical point of view, it is important to understand the effect of finishing on functional properties of the coatings. The change in coating properties can be rationalized in two terms; (1) the change in surface conditions due to the elimination of roughness and removal of superficial layers and (2) the change in coating body structure such as generation of residual stresses, formation of microcracks, or splat pull-out. As a result, the adhesion and cohesion strength, microhardness, fracture toughness, fatigue, wear, and corrosion resistant can be altered after grinding.

Corrosion resistant coating can be used in both as-sprayed and ground conditions depending on the application. The effect of grinding on corrosion resistance is complicated. As-sprayed coatings usually show higher corrosion rate due to formation of local galvanic cells on the surface (increased surface area). However, the corrosion resistant can be lowered if microcracks are produced during grinding. The microcracks can act as local electrochemical cells or enhance penetration of electrolyte through the coating body. Guilemany *et al.*[7] reported that grinding of HVOF-sprayed NiTi increases the corrosion rate due to formation of microcracks inside the coating. Moskal *et al.* investigated the effect of grinding on morphology and thickness of oxides formed after oxidation of plasma sprayed NiCrAlY at 1000 and 1100 °C. It was found that the oxide thickness is higher in the case of as-sprayed coating.[8]

Erosion resistance of as-sprayed and ground of WC–Co–Cr coatings fabricated by detonation gun and HVOF processes was investigated. The ground samples showed better erosion

resistance due to generation of compressive residual stresses in the coatings.[9] In the case of sliding wear applications, the coatings are often used in polished conditions as friction and wear increases with roughness. As-sprayed coatings are rarely used for wear applications. The role of grinding on plain and fretting fatigue behavior of detonation gun sprayed Cu–Ni–In coating on Al–Mg–Si alloy was investigated. Ground coatings exhibited better resistance due to better surface finish and residual compressive stresses at the surface.[10]

Masoumi *et al.*[11] investigated the effect of grinding on adhesion strength and residual stresses in HVOF WC–10Co–4Cr coating. The porosity content increased in ground coatings due to loading between part and wheel. The microhardness, adhesion and cohesion strength improved after grinding. All these results were discussed based on compressive residual stresses. The ceramic coatings are more susceptible to cracking during grinding process due to lower fracture toughness. Liu *et al.*[12] investigated the modeling of residual stresses in nano-ceramic coatings. It was found that the grinding temperature and parameters affect the type and magnitude of residual stresses. By selecting optimum conditions, beneficial compressive stresses can be expected. The high grinding temperature can also favor phase transformation in some coatings such as WC–Co during grinding.[13]

3.13.2.5 Modeling the Finishing Processes

In recent years, efforts have been made to model finishing processes. An analytical model was investigated by Hiegemann *et al.*[14] to predict roughness thermal spray coatings after ball burnishing where the surface asperities were simulated by pyramids. The deformation of these pyramids was modeled by considering acting forces. There was a good agreement between the theoretical and experimental results. Rausch *et al.* used constructive solid geometry technique to model grinding process using a geometric-kinematic simulation. The model was used for optimizing the grinding procedure and predicting surface topography. Cutting tool durability was modeled using statistical approaches in 40C130 steel coating. Friction has been also analyzed in burnished and ground WC–12Co coatings. Arc sprayed WC–Fe and HVOF WC–Co coating were ground on a machining center by using mounted points. A force model was proposed based on the design and analyzes of computer experiments.[15] The mathematical models composed of linear terms were used to model the role of grinding parameters on the grinding force during grinding of HVOF WC–Co–Cr coating.[16]

Partition coefficient was also modeled to a thermo-mechanical approach during grinding of HVOF WC–Co–Cr coatings. The maximum temperature was measured using finite element solution. The temperature in arc of cut was measured using a novel grindable thermocouple.[17]

3.13.3 Thermal Post-Treatments

Thermal treatment of coatings involves various heating procedures such as remelting, fusing, sintering and annealing. The goals can be listed as[1–4]:

- elimination of pores and splat boundaries to improve cohesion strength and enhancing in bonding strength by creation of metallurgical bonding between coating and substrate;
- improvement in thermal shock resistance or fracture toughness due to microstructural refinement and metallurgical bonding;
- microstructural modifications such as stress relieving;
- to complete the reaction between elements; for example, formation of final compounds like intermetallics;
- crystallization of amorphous coatings;
- to enhance wear and corrosion resistance by eliminating open pores.

3.13.3.1 Fusing of Self-Flux Alloys

Self-fluxing alloys are alloys which can form a low melting point borosilicate phase during heat treatment (fusion). These Ni or Co-based coatings contain B and Si elements reacting with metal oxides to form a borosilicate phase. Cr is added to the alloy to improve corrosion resistance. The formation of B-bearing precipitates such as $Cr_2Ni_3B_6$ precipitate[18] may be responsible for increase of hardness after fusing. Borosilicate acts as a deoxidizer. In addition, the melting point of this phase is 300 or 400 lower than that of the matrix alloy. So, a kind of liquid phase sintering occurs. As a result, the pores are eliminated and the cohesion strength increases. Due to low density of the borosilicate phase, it comes to the surface and can be removed by grinding. The fusing temperature is between 1000 and 1100 °C (it is selected based on chemical composition of the coating). Due to high-temperature of process, the coating diffusion occurs at the interface so metallurgical bonding is formed. About 10–20% shrinkage occurs during fusing because of pore elimination.[1–4] Fused self-flux coatings show good impact resistance as well as desirable wear and corrosion behavior. Fusing process can be performed by flame (torch), furnace, induction, or even laser. The details of fusing procedures can be found below.

Torch heating is widely used for fusing of self-flux alloys because it is cost-effective and rapid. A single or multi jet troch pass can be used. Natural flame is used for Ni-alloys and slightly reducing flame for Co-alloys. Acetylene or propane is used as fuels. The coated part is preheated to 760–870 °C before achieving fusing range. The flame must be low speed or in the case of cylindrical parts, the motion of part must be low to prevent loss of molten metal. The key factor in torch fusing is temperature control which depends on operator skills (based on color and flow). The process can be also performed automatically.[1–4]

In comparison to torch fusing, the use of furnace fusing results in better temperature control and high production rate. It is useful for thin coatings, flat samples, large parts, and irregular shapes. The most advantage of this method is less thermal shock due to controlled heating and cooling rate. Argon, vacuum, and hydrogen can be used as furnace atmosphere. Due to saved time and energy, induction fusing has been developed rapidly especially for large parts.[1–4] Laser can be used for fusing if parameters are controlled well and proper preheating. However, it is more expensive than conventional methods.

Houdková *et al.*[19] investigated the effect of four different fusing treatments (furnace, flame, induction, and laser treatment) on microstructure and properties of flame and HVOF-sprayed NiCrBSi alloy. All fusing procedures resulted in elimination of splat boundaries and improvement in corrosion, hardness, and wear resistance. The main difference was the dilution between coating and substrate, which was noticeable in the case laser fusing. It may be confusing that the laser treated samples showed the thickest diffusion layer. However, laser process parameters were selected to obtain fully melted and crack-free structure. So, the interfacial regions may incorporate in the laser process and the dilution has increased.

Although self-flux alloys can be deposited on various substrates, however, fusing treatment may encounter problems. Fusing treatment cannot be performed on low melting point alloys like Al and Cu alloys. When there is a large difference between thermal expansion of coating and substrate, the fusing may result in cracking or spallation of the coating. In such cases, slow cooling and heating rates or preheating are preferred. In the case of insufficient wetting or melting or overheating, the porosity may remain. For large parts or complex shapes, non-uniform heating may be observed. The distortion is another possible problem which may occur during fusing that can be controlled by proper heating and cooling rates.[1–4]

3.13.3.2 Remelting

In recent years, some efforts have been made to remelt thermal spray coatings. The main goals are to remove splat structure and pores, formation of metallurgical bonding and improvement in fracture toughness and impact resistance as well as corrosion and wear resistance. After remelting, a rapidly solidified structure is attained which shows refined microstructure.

Laser remelting has been used extensively due to precision control and position. Electron beam is another source for remelting but needs high vacuum. Tungsten inert gas (TIG) process was also used as a cost-effective process but may invilve dilution (up to 30%).

3.13.3.2.1 Laser remelting

Laser remelting has been used due to controlled heating and melting. Many types of coatings including wear or corrosion resistant coatings, biomedical coatings, and thermal barrier coatings were subjected to remelting. The types of lasers used for remelting are:

- continuous CO_2 lasers with powers up to 5 kW;
- continuous CO_2 lasers with powers in order of 100 W;
- pulsed Nd/YAG lasers;
- power diode lasers with powers in order of few kW.

The reflection coefficient must be considered to control the laser absorption by the surface. In the case of coating materials with low thermal conductivity (such as ceramics), the micro or macrocracks may be formed during the treatment.[2]

Flame sprayed polyether ether ketone (PEEK) coatings deposited on 304 L stainless steel were remelted using Nd:YAG, CO_2 or diode lasers. The adhesion improved and the porosity decreased after remelting.[20] The remelting of metallic and cermet coatings has been investigated extensively. Ceramic coating remelted by laser includes wear resistant coatings like Al_2O_3–TiO_2 and Cr_2O_3 coatings, thermal barrier coatings such as YSZ and hydroxyapatite (HAp).[1]

3.13.3.2.2 Electron beam remelting

Electron beam was used for post-spray treatment of small areas. In spite of small spot size, it is very costly and needs high vacuum ($<10^{-4}$ Pa). So, electron beam was used less in comparison to laser.[2]

Electron beam treatment of arc sprayed FeCrAl coatings resulted in discrete bulged nodules composed of Fe–Cr column grains and improvement in corrosion behavior.[21] HVOF CoNiCrAlY coating treated by electron beam showed one thin and homogenous oxide layer after cyclic oxidation.[22] Improvement in oxidation resistance has been seen also for YSZ coatings.[23]

3.13.3.2.3 TIG remelting

TIG process has been used both for remelting and surface alloying purposes. The procedure is similar to TIG surfacing process. It is cheaper than laser, but, the control of heat and position is difficult. The high dilution (up to 30%) is the main limitation of this method.

Decreases of porosity and roughness and improvement in adhesion were observed after remelting of Cr_3C_2/Ni–Al and W_2C–WC/Co cermet coatings.[24] Role of lanthanum oxide addition and remelting on flame sprayed Ni–WC coating was investigated.[25] The microhardness and wear resistance of remelted coatings were higher than those of as-sprayed coating. Fe-based amorphous composite coatings deposited using arc spraying were subjected to TIG remelting.[26] The porosity decreased after remelting and a metallurgical bonding was formed at interfacial region. A dendritic microstructure formed after remelting while the hardness increased. Remelting of FeNiCrAlBRE self-flux alloy coatings fabricated by high velocity arc spraying was investigated.[27] The microstructure changed from lamellar to cellular structure after remelting. As a result, the defects decreased and wear resistance improved.

Tungsten-rich dendrites and W_6Co_6C and Fe_6Co_6C carbides were observed after remelting of plasma sprayed WC–Co coating. The hardness increased from 900 to 1250 HV after remelting and wear resistance improved.[28] A diffusion layer (diluted region) was observed between remelted coating and substrate. The cross-section of as-sprayed and TIG-remelted coatings are seen in **Figures 4(a)** and **4(b)**, respectively.

Ceramic coatings such as Al_2O_3–TiB_2 coating were also remelted using modified TIG process (**Figure 5**). This is an arc-independent technique unlike traditional TIG process. The results showed that the porosity and roughness decreases after remelting.[29]

Fe–Al intermetallic coatings were fabricated on steel substrate using arc spraying of Al coating and subsequent TIG remelting (**Figure 6**).[30] The dilution of coating with substrate resulted in formation of Fe–Al intermetallic phases. The Al layer was 200 μm thick while the intermetallic layers were 500 μm (**Figure 7**).

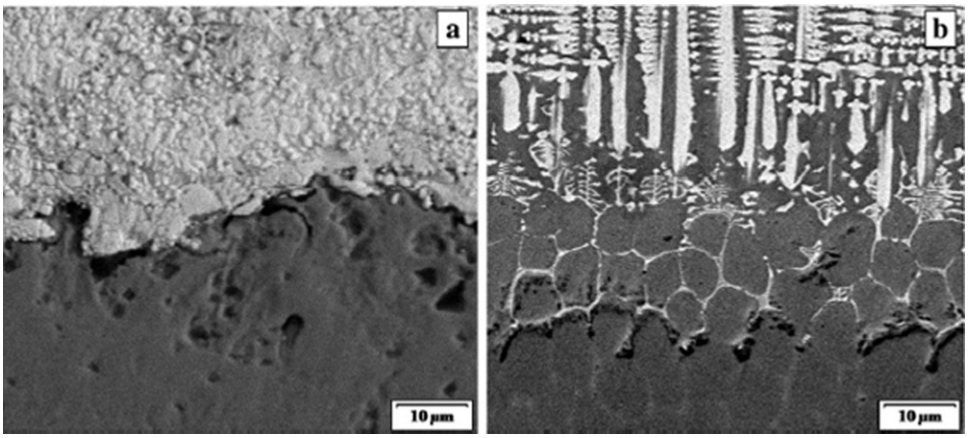


Figure 4 The cross-section of (a) plasma sprayed and (b) TIG-remelted WC–Co coatings.[28]

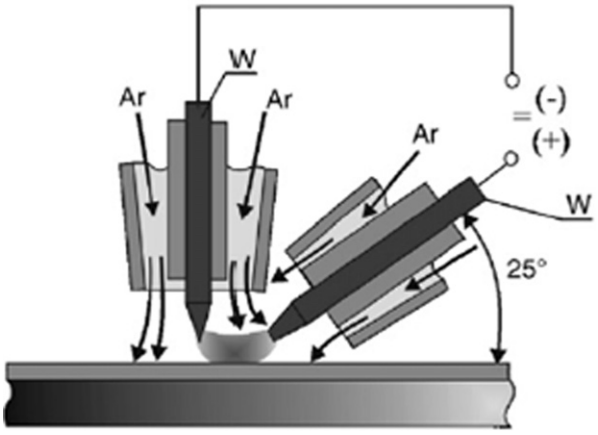


Figure 5 Modified TIG process used for remelting of ceramic coatings.[29]

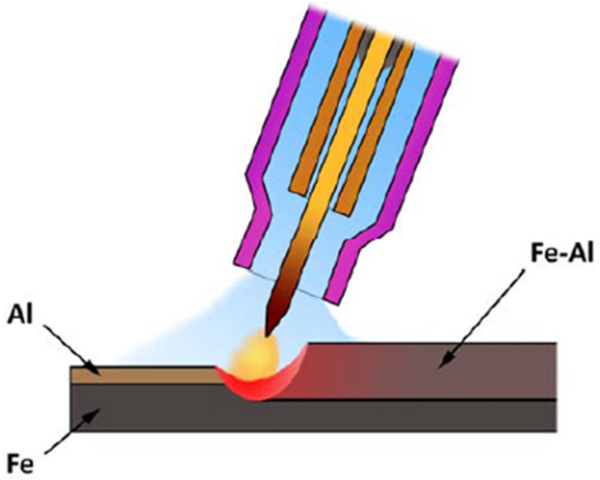


Figure 6 Schematic of TIG remelting of Al coatings to produce Fe–Al intermetallics on steel susbtrate.[30]

3.13.3.3 Solid State Heat Treatment

3.13.3.3.1 Pressure-assisted sintering

Pressure-assisted processes like hot isostatic pressing (HIP) and spark plasma sintering (SPS) and pressure-less procedures like microwave and furnace sintering have been used as post-treatments of thermal spray coatings. Sintering processes are performed at 0.7–0.8 of melting point of final compound. Solid state diffusion occurs at these temperatures so that the porosity decreases. The pressure enhances the densification. In addition, metallurgical bonding is formed at interface while cohesion strength increases.[1,2] The goals are similar to those of remelting. The advantage of sintering versus remelting is absence of cast structure and decreased thermal stresses. The main limitations of pressure-assisted sintering are (1) size limitation for large parts and (2) high running costs.

HIP is a hot consolidation process in which high-pressures (up to 300 MPa) is applied on the powder samples at high temperatures (0.7–0.8 of absolute melting point of final compounds). The sample is sealed using a glass vessel or metallic foil.[1,2] Then, the pressure is applied using an inert gas. This process is ordinary used for P/M parts but has been developed for thermal spray coating. It is costly and can be performed only on small parts. So, it has not found widespread application.

SPS is a rapid sintering process. In this method, a current applied through the electrodes attached to the graphitic die. The Joul effect is responsible for heating of metallic materials. In addition, the formation of plasma (in the presence of inert gas) between the particles generates heat and favors the diffusion. So, SPS process is faster than other sintering processes even than HIP. The time of sintering in SPS about 10–20 min and the temperature is about 0.6 of melting point of final compound. The uniaxial pressure is applied which is in order of tens of MPa. SPS has been used to improve the properties of ceramic coatings such as YSZ.[1,2]

3.13.3.3.2 Pressure-less sintering and annealing

Sintering procedure can be done without application of pressure. It is cheaper than pressure-assisted sintering. The large pores may remain after sintering unlike pressure-assisted approaches while the open pores can be closed. The different atmospheres like argon, vacuum, hydrogen, nitrogen, and other gas mixtures can be used.

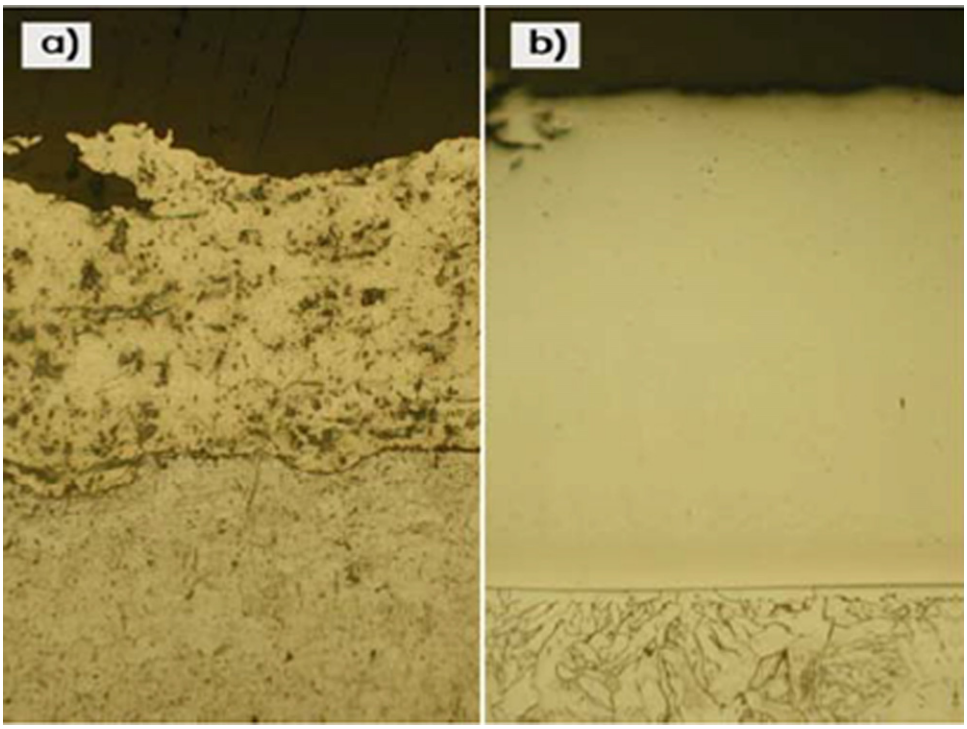


Figure 7 Optical micrograph of the cross-section of as-sprayed Al coating (a) before and (b) after TIG remelting.[30]

Frodelius *et al.*[31] investigated the phase transitions during annealing of HVOF-sprayed Ti_2AlC coating on hastelloy X substrate. As-sprayed coatings were composed of Ti_2AlC, Ti_3AlC_2, TiC, Ti–Al, and oxides. Up to 500 °C no new phase was formed. Between 550 and 700 °C, the amount Ti_3AlC_2 increased. Above 700 °C, Ti_2AlC formed from TiC and Al. The decomposition of Ti_2AlC and Ti_3AlC_2 was observed and TiC and Al_2O_3 were formed at 900–1100 °C.

HVOF WC–Co and NiCr–Cr_3C_2 on steel substrate were annealed at 500 for 24 h and at 550 °C for 5.5 h. It was found that the hardness of WC–Co increased from 1200 to 1500 HV after annealing at 500 °C. The microstructure of this coating was homogenized after post-treatment. The voids formed at coating/substrate interface in the case of NiCr–Cr_3C_2 coating.[32]

Microwaves are waves with the wavelength of in order of millimeter to meter. In microwave sintering, electromagnetic energy is transformed into thermal energy. The papers investigated microwave sintering of thermal spray coatings are scanty. APS YSZ coatings were treated using microwave for solid oxide fuel cell applications. The results showed that the ionic conductivity of sintered coatings was higher than that of as-sprayed coating by on order of magnitude.[33]

Thermally sprayed intermetallic coatings were investigated in recent years for wear, aqueous, and high-temperature corrosion applications. The intermetallic powders are often selected as feedstock. However, the activated powders can be used due to lower costs. In this case, the reaction may be incomplete during spaying due to rapid heating and cooling. Post-spray heat treatment can be performed to complete the reactions. There are a few papers dealing with this matter.

Mechanically activated Ni–Ti powders were sprayed using vacuum plasma spraying process. The as-sprayed coatings were somewhat porous but unreacted Ni and Ti were present in the coatings. After heat treatment at 900 °C, the elements fully reacted and a diffusion layer was formed between coating and substrate.[34]

Two studies were formed by arc spraying using different wires. Al wire as cathode and steel wire as anode were melted using arc spraying.[35] No intermetallic phase was formed during spraying but heat treatment of coatings at 550 and 650 °C resulted in formation of Fe–Al intermetallic phases while Fe was still present. A similar study was performed using Mg wire as cathode and Al as anode on Mg substrate. Intermetallic phases were not formed during spraying while annealing at 430 °C, the elements reacted completely.[36]

Due to rapid cooling involved during praying (10^5 K s^{-1}), amorphous structures can be deposited depending on glass formability of the feedstock. These coatings show good corrosion resistance. Crystallization heat treatment can be performed to form nanocrystalline structure to improve hardness and wear resistance. The crystallization temperature is selected based on thermal analysis.[1] It must be noted that the crystallization temperature is lower than that of sintering processes to avoid grain growth.

3.13.3.3.3 Austempering

Austempering heat treatment (or molten salt heat treatment) has been performed on plasma sprayed WC-based coatings. A two-step heat treatment including immersion of samples at 870 °C for 30 min and subsequent quenching in another salt at 315 °C was performed. The results of that study showed that undesirable W_2C phase can be eliminated and metallurgical bonding can be obtained after austempering. The hardness increased after post-treatment due to compressive residual stresses.[37]

3.13.3.4 Diffusion Annealing of Aluminum and Chromium

Diffusion annealing is used to diffuse the aluminum into a metallic substrate or another coating to improve high-temperature corrosion resistance. Diffusion of Al coating into steel or silicon bronze is performed at about 870 °C. An Al-rich surface layer id formed which exhibit good oxidation resistance due to formation of Al_2O_3 protective layer.[4]

Ti-49 at.% Al alloy has been aluminized by applying 100 μm arc sprayed Al and subsequent induction diffusion annealing at 1100 °C under Ar atmosphere. The annealing time varied between 2 and 30 min. $TiAl_3$ was formed as the outermost layer which grew by increases the annealing time. The intermediate layers between the top layer and substrate consisted of Ti_2Al_5, $TiAl_2$, and Al-rich TiAl. The aluminized coating, exhibited better oxidation resistance at 900 °C in air.[38]

Al coating and be deposited as a top coat on another coating. The diffusion treatment results in formation of a ternary coating such as FeCrAl and NiCrAl. NiCr or FeCr is deposited first and the Al is applied. Finally, the diffusion treatment is performed.

Belluci *et al.*[39] investigated the role of pack aluminizing on high-temperature corrosion resistance of HVOF Fe–Cr coating in a simulated coal-fired energy system. The oxide layer formed on as-sprayed coating was not protective due to vaporization of Cr(VI)oxide hydroxide in the presence of oxygen and water. Al-modified coatings showed better resistance due to thin Al_2O_3 layer. Post-treatment had no deleterious effect on adhesion of coating as no new interface was formed after aluminizing.

Recently, heat treating of NiCrBSiFe/Al system was investigated at temperature range of 500 to 700 °C for 3 h. $NiAl_3$ phase was formed gradually based on the temperature. Ni-islands were firstly formed which then enriched in Al to form Ni_3Al. The treated coatings showed superior oxidation resistant at 700 and 800 °C due to formation of dense Al_2O_3 layer. In the case of as-sprayed coatings, iron oxides were detected at substrate-coating interface, which reveals the high porosity results in decrease in protectiveness of as-sprayed coatings.[40]

Several attempts have been also made to diffuse Al into thermally sprayed MCrAlY coatings using chemical vapor deposition (CVD),[41] pack cementation,[42–46] or cathodic arc deposition.[47] This process is called 'over aluminizing.' Over aluminizing is often used to control the thermally grown oxide when MCrAlY used as a bond coat for TBCs. It can be also used to improve oxidation and hot corrosion resistance of MCrAlY top coats. Pt–Al coatings were also deposited on CoNiCrAlY coating by applying PVD Pt coating and subsequent aluminizing.[46] The results showed that the adhesion of Pt-aluminized coating during cyclic oxidation was better than that of as-sprayed and aluminized coating.

The pack cementation process has been used to densify plasma sprayed $NiCr/Cr_2C_3$. The results showed that the hardness increases after post-treatment.[48]

3.13.4 Sealing

3.13.4.1 The Basics

The porosity is one of characteristics of thermal spray coatings. The pores may be interconnected. The presence of such defects may results in penetration of corrosives medium or other unwanted materials through the coating body. In some applications, sealing enhances dielectric constant of coatings. The application of sealer can be useful were leakage is important in mechanical processes.[1–4] Anodic coatings like Zn and Al may be sealed to increase life time. Cathodic coatings like stainless steel or copper must be sealed if open pore is present. Ceramic coatings are also sealed for corrosion applications.

The conventional sealing involves penetrating a liquid sealer through the coating via capillary effect. Then, the sealer is cured to be solidified. A sealer must have low viscosity to penetrate through the coating. The chemical and thermal resistance of the sealer in service condition as well as safe and health aspects must be considered. Atmospheric sealing is performed by spraying, brushing, and immersion. The efficiency of this method depends on sealer wettability. But it can be performed on large parts. The sealing can be performed under vacuum (low pressure) or high pressures. Both methods are suitable only for small parts. High pressure method enhances the penetration of sealer. Low pressure method can remove air and moisture from the pores.[1–4] The sealer may be organic or inorganic which is discussed below.

3.13.4.2 Organic Sealers

The main organic sealers are used for post-treatment of thermal spray coatings are[1–4]:

- Paints which are water or solvent soluble. They are air dried.
- Waxes, greases, and oils.
- Phenolics (including epoxy phenolics) which must be air dried or heat cured.
- Epoxy resins which have one part as catalyst.
- Polyesters which have one part as catalyst or must be heat cured.
- Polyurethans which have one part as catalyst or must be air dried.
- Linseed oils which must be air dried.
- Polyimides which are heat cured.
- Coal tars which are air dried. They are used for submerged parts in salt or fresh water.
- Silicon resins which are air dried. Aluminum–silicon resins can be used at service temperatures up to 480 °C.
- Vinyls which are air dried for use in temperatures lower than 65 °C.
- Anaerobics which are cured in absence of air.

3.13.4.3 Inorganic Sealers

Inorganic sealing are used usually for high-temperature applications where organic sealer are not applicable. Various techniques such as aluminum phosphate, Cr diffusion, sol–gel, impregnation, electroplating, and other chemical processes can be used to seal the coatings.

3.13.4.3.1 Aluminum–phosphate

An aqueous solution containing aluminum hydroxide and phosphoric acid is applied to the surface. The subsequent heat

treatment is often performed at 100, 200, and 400 °C, respectively, to complete the dehydration process and to form aluminum phosphate. This process has been used to seal Al_2O_3, Cr_2O_3,[49,50] and YSZ coatings.[51]

It has been shown that the application of alumina/aluminum phosphate sealer can improve hot corrosion resistance of HVOF NiCr–Cr_2C_3 coatings. The sealer was applied by nylon brushing and air curing at room temperature.[52]

3.13.4.3.2 Enameling

HVOF CoNiCrAlY coatings were subjected to enamel coating using SiO_2-based feedstock. The results showed that the hot corrosion resistance and oxidation resistance at 900 °C improved after the post-treatment.[53] After vacuum annealing, enamel powders were place on coated samples and then heated to 1000 °C.

3.13.4.3.3 Electroplating

Ni electroplating has been used to seal arc sprayed hastelloy[54] and APS Al_2O_3[55] coatings. The electrodeposition seals the open pores and a forms top Ni coat as a barrier. In the case of hastelloy coating, the corrosion resistance improved after sealing. In the case of Al_2O_3 coating, the wear resistance and hardness improved.

3.13.4.3.4 Sealing using glass formers

Glass forming agents such as SiO_2 were used for sealing. The agent is applied and then the softening heat treatment is performed.[56] This process was used to seal YSZ coatings for solid oxide fuel cell applications.

3.13.4.3.5 Sol–gel

In sol–gel process an organic precursor and a metal ion containing liquid (sol) is used. The precursor penetrates through the open pores and forms a gel then. Finally, calcination process can be used. Sol–gel alumina process has been used to seal ceramic and cermet coatings.[57]

3.13.4.3.6 Chemical treatment

Nitrate solution has been used for sealing of YSZ coating for solid oxide fuel cell application. The densification was performed using aqueous solution of zirconium and yttrium. After sealing procedure, the coated samples were dried at 500 °C for 30 min to decompose nitrate. The post-treatment improved the electrical resistance by 30%.[58]

Hydroxide solutions were used for improvement in bioactivity of vacuum plasma sprayed Ti coating on carbon fiber-reinforced PEEK (CF-PEEK) substrate. The coated samples were immerged in 10 M NaOH solution. It was found that the mentioned procedure was effective to fabricate bioactive coatings for texture engineering applications.[59]

HVOF HAp–TiO_2 coatings were chemically treated using different processes. Using the alkaline treatment, a nanostructured sodium hydroxycarbonate was formed on the surface and biocompability improved. The collagen-treated coatings also showed better biological response.[60]

3.13.4.3.7 Chemical vapor deposition

CVD process has been used to seal the Al_2O_3–TiO_2 and Al_2O_3 coatings. H_2–$AlCl_3$–CO_2 gas mixture was used to react at 1000 °C. CVD coating with the phase structure of α-Al_2O_3 and thickness of 10–20 μm were produced. The corrosion resistance of Al_2O_3–TiO_2 improved after CVD process. However, Al_2O_3 were cracked during CVD cycle treatment due to mismatch between thermal expansion coefficient Cu substrate and Al_2O_3 coating. The CVD was not able to close these cracks.[61]

A duplex HVOF-sprayed WC–Co–Cr/CVD DLC coatings were deposited on aluminum substrate. DLC coating was composed of an interlayer of (Cr), a graded intermediate Cr–W/C and WC/C layers. The application of thin top coated decreased friction and wear but the corrosion resistance was not changed due to low thickness and presence of defects (pores) in CVD layer. Cermet layer had no effect of microstructure and properties of CVD layer but load carrying ability of the cermet layer (due to higher thickness) resulted in better scratch resistance. However, due to limited adhesion of CVD and sprayed layers spallation occurred at interfacial region.[62]

3.13.4.3.8 Molten metal or oxide penetration

Molten metals can be used for sealing. It penetrates through the coating. The melting point the sealer metal must be lower than that of coating. The process was used for cermet and ceramic coatings. In this regard, liquid Mn was used to seal YSZ coatings.[63,64] Cu infiltration has been also used for Ti–Mo coatings.[65]

Molten oxide infiltration is a novel sealing process. A multicomponent oxide with relatively low melting point is used a plate on the coated surface. The components are then heat treated in a furnace to melt the oxide and to perform the penetration process.[66,67] The penetration temperature depends on the melting point of oxide. It has been reported that sealing of APS 316 L coating using MnO–SiO_2 oxides improves the corrosion resistance of the coatings in salt spray procedure.[66,67]

3.13.5 Other Processes

3.13.5.1 Friction Stir Processing

Friction stir processing (FSP) is a solid state thermomechanical surfacing process. In this process, a rotating pin (**Figure 8**) is traversed along the specific path on the surface of component. The friction between the part and the tool results in heat generation. Simultaneously, the superficial layer deforms plastically in the front of pin. It is like a thermomechanical process. As a result, microstructural and grain refinement and homogenization occur at the surface.[68]

In recent years, efforts have been made to improve microstructure and mechanical properties of thermally sprayed coatings using FSP. However, the utilization of this post-spray technique has not been extensive.

HVOF WC–CrC–Ni coatings were modified by FSP using a sintered WC–Co tool.[69] Scanning electron microscope (SEM) micrograph of as-sprayed coating is shown in **Figure 9**. The thickness of coating was 300 μm. In macroscopic scale, no visible damage was detected, but the porosity is present in the coating. After FSP (**Figure 10**), the thickness decreased to about 150 μm due to stirring and compressive stresses. Under the coating layer, stir zone and heat affected zone are observed.

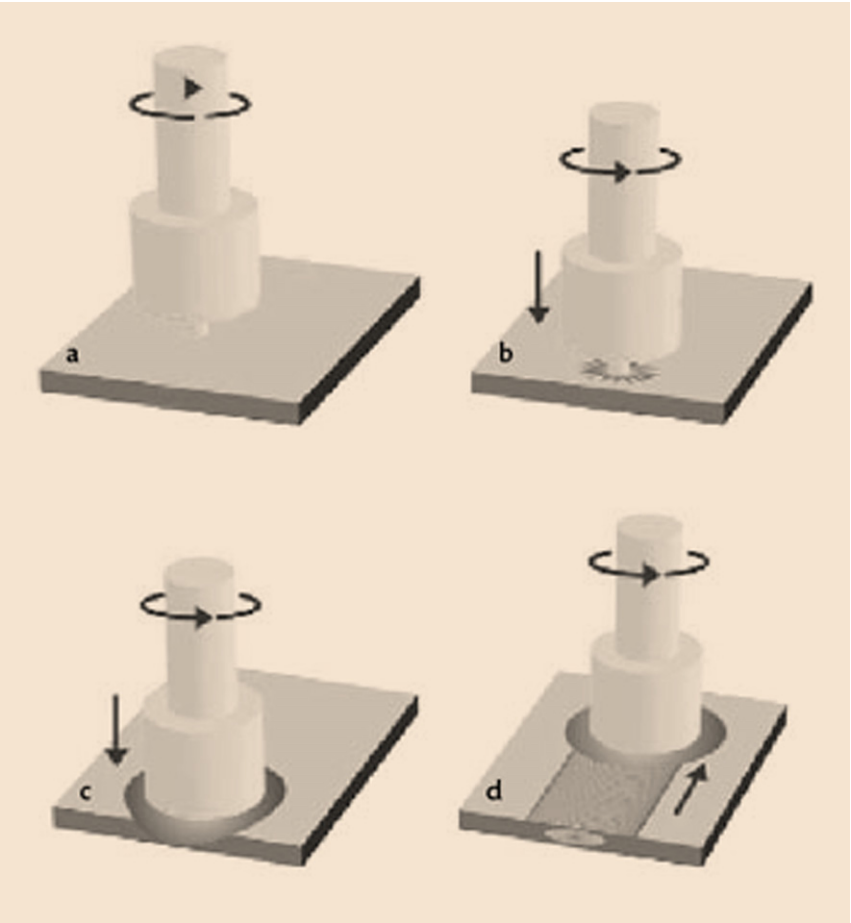


Figure 8 Schematics of friction stir processing.[68]

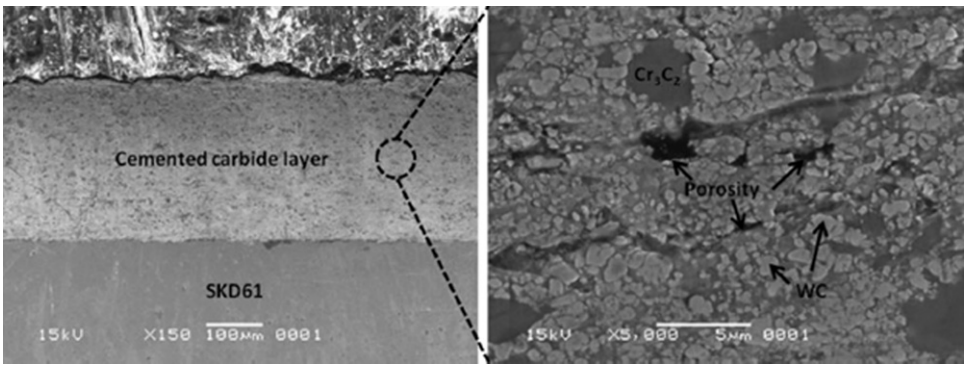


Figure 9 Scanning electron microscope micrograph of the cross-section of as-sprayed WC–CrC–Ni coating.[69]

SEM micrograph of the modified coating layer is shown in Figure 11. The pores disappeared and WC rearranged after FSP due to plastic deformation of Ni binder and an irregular interface was formed after FSP. Although the fracture toughness was not significantly after FSP, but the hardness of coatings increased from 1200 to 2000 HV.

In 2014, Mazaheri *et al.*[70] investigated the effect of FSP on microstructure and tribological properties of HVOF-sprayed A356/Al_2O_3 composite coating. A 200 μm thick coating was subjected to FSP. After FSP, a uniform distribution of Al_2O_3 particles was observed. The hardness and wear resistance increased after FSP. The effect of FSP on microstructure of arc sprayed high-Cr steel coatings was also evaluated. After FSP, the porosity was significantly decreased the microstructure was refined. It was shown that hardness and wear resistance of FSPed layer were two and seven times higher than that of

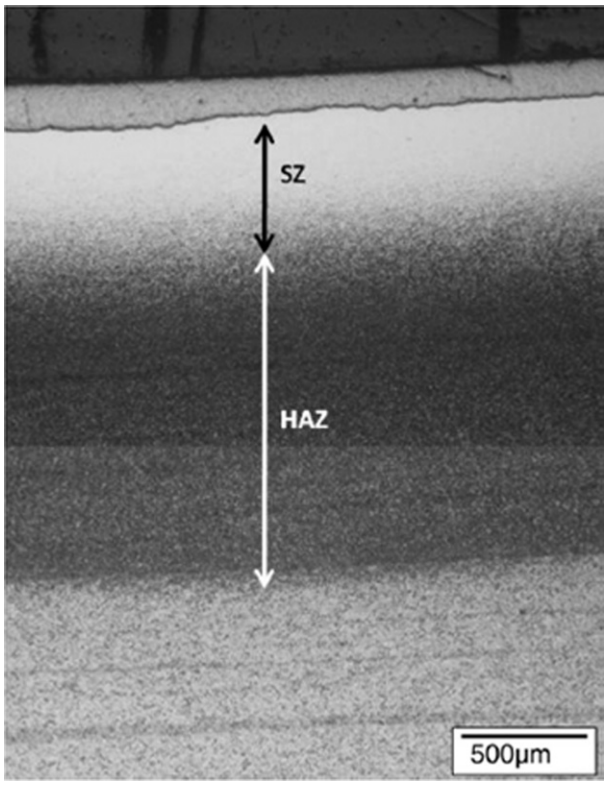


Figure 10 Scanning electron microscope micrograph of the cross-section of WC–CrC–Ni coating after friction stir processing.[69]

as-sprayed coating.[71] Flame sprayed Ni–Cr–Al Coating was also modified by FSP.[72] Grain size refinement occurred after FSP while a composite layer with good density was formed.

3.13.5.2 Plasma Electrolytic Oxidation

Plasma electrolytic oxidation (PEO) is a conversion surface treatment usually applied to light alloys like aluminum, titanium, and magnesium. The substrate is immerged in a liquid electrolyte as an anode. The electrical potential is applied to oxidize the surface of substrate. The voltage is so high (100–1000 V) to modify the structure of the coatings.[73,74] PEO process has been performed on arc sprayed aluminum coatings on carbon steel substrate in a liquid composed of KOH and liquid glass. Dense and uniform layers were formed in optimum conditions (**Figure 11**). The wear resistance was significantly improved wile high hardness (up to 2000 HV) was observed. Micro-arc oxidation (MEO) of arc sprayed Al, Al–6Mg, and Al–12Si coatings on low alloy steel were investigated. Ceramic coatings mainly composed of Al_2O_3 were obtained after MEO. The coatings showed high hardness.[74]

3.13.5.3 Sol Infiltration

Plasma sprayed Al_2O_3–Cr_2O_3 coatings deposited on Al_2O_3 were subjected to sol-infiltration and heat treatment.[75] The goal was to investigate effects of sintering stresses on cracking behavior of coatings for high-temperature applications. Fine microcracks were observed at coating/substrate interface in the

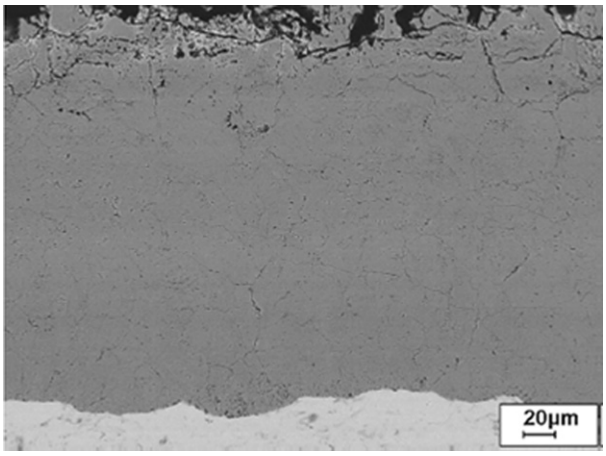


Figure 11 Scanning electron microscope micrograph of the cross-section of plasma electrolytic oxidation coating on arc sprayed aluminum.[74]

case of as-sprayed coating while after heat treated at 1550 °C severe delamination of coating was seen. The SiO_2 sol-infiltration (by immersing the coated specimen in ethyl silicate solution containing 25% SiO_2) was performed before heat treatment.

3.13.5.4 Physical Vapor Deposition

The use of PVD coatings as a post-treatment is not widespread. Ti–TiN_x coating was deposited on Ti6Al4V alloy using reactive plasma spraying process. The coatings were 50 μm thick. Then, a 2 μm TiN coating was applied by PVD. The friction coefficient of thermal spray coating was not significantly changed by application of TiN (at loads of 10, 20, and 30 N applied in wear tests). The weight loss of duplex coatings decreased by one order of magnitude at load of 10 N in comparison to that of as-sprayed coatings. At higher loads, the changes were not significant.[76]

3.13.5.5 Ion Implantation

Ion implantation is a surface modification technology in which accelerated ions (with the 10–200 keV energy) impact into a solid surface. The process can change chemical or tribological properties of the surface although the infected layers are too thin (less than 100 nm).[77,78]

Vacuum plasma sprayed CoNiCrAlY coatings implanted with Nb and N ions.[77] The oxidation resistance of coatings was evaluated at 1150 °C in air for 50 and 100 h was investigated. Ion implantation resulted in broadening of diffraction lines in X-ray diffractogram. The thickness of TGO reduced in the case of implanted coatings. This improves the service life of thermal barrier top coat. Another study was performed to investigate the effect of Al and Nb ion implantation on oxidation behavior of vacuum plasma sprayed CoNiCrAlY coatings at 1100 °C.[78] Nb-implanted coatings showed superior resistance due to formation of a dense Al_2O_3 scale. In the case of Al implantation, a non-protective spinel layer was formed during oxidation.

Ion implantation has been also used to improve tribological properties of coatings. It has been reported that N-ion implantation improve wear resistance of flame sprayed iron-base coatings.[79] Similar results were obtained for plasma sprayed Cr_2O_3 coatings.[80] In this regard, CrN and β-Cr_2N precipitates were formed in the N-ion implanted surface layer.

3.13.5.6 Shot Peening and Rolling

Shot peening is controlled impingement of metallic spheres stream in to a substrate to produce compressive stress. Shot peening can be used to improve fatigue resistance of coatings by introducing compressive stresses onto surface. In addition, the surface pores may be closed upon peening. Peening has been used for aircraft turbine parts. It was also shown the cavitation resistance of zinc coating improved after post-spray rolling.[1–4]

Shot peening has been performed to improve surface condition and oxidation resistance of CoCrAlY bond coat on Ni-based superalloys. YSZ top coat was deposited using EB-PVD, which showed good thermal cycling behavior (1643 cycles at 1020 °C).[81]

The fatigue strength of WC–10Ni coated AISI 4340 steel increased from 750 to 850 MPa after peening.[82] The fretting wear resistance of WC–17% Co coating on 30NiCrMo steel was not changed by shot peening but friction coefficient decreased. Such a coating was deposited on Al7050-T7451 alloy by HVOF process.[83] The fatigue strength of substrate increased after coating application. However, the resistance decreased after peening due to local roughening of coating which accelerated crack nucleation.

3.13.5.7 Laser Engraving

Laser engraving is formerly used for manufacturing Anilox rolls in printing industry.[84] The precise amount of ink is transferred by these rolls (in the flexographic printing machine). In the engraving process, fine patterns are produced on plasma sprayed ceramic coatings (like Figure 12) by local vaporizing the surface. CO_2 laser are mostly used but Nd-doped YAG laser were used too. Cr_2O_3, Al_2O_3, and Al_2O_3–TiO_2 coating were laser engraved.

3.13.5.8 Thermochemical Processing

Plasma nitriding (PN) and nitrocarburizing were performed on HVOF stainless steel coating.[85] In that work, the effects of PN and nitrocarburizing on HVOF-sprayed stainless steel. 17–4 PH (as a precipitation hardening grade), 316 (as an austenitic grade), and 410 (as a martensitic grade) were investigated. All coatings showed low porosity. After nitriding in $N_2 + H_2$ environment, a thick nitrided layer composed of a compound layer and a diffusion layer were formed. The thinnest nitride layer was corresponded to 316 coating with FCC structure while the thickest layers was formed on 410 coating with BCC structure (Figure 13). Plasma nitrocarburizing in C_2H_2 environment resulted in thicker nitride layers in comparison to those formed after nitriding. The thickest layer was formed on 410 coating like that in nitrided specimens.

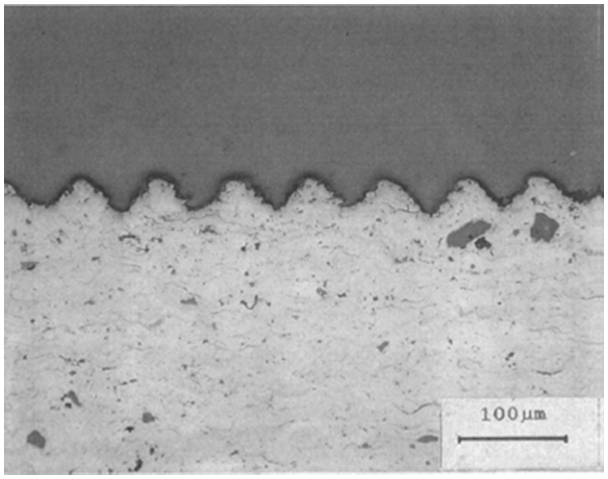


Figure 12 Scanning electron microscope micrograph of the cross-section of laser-engraved coating.[84]

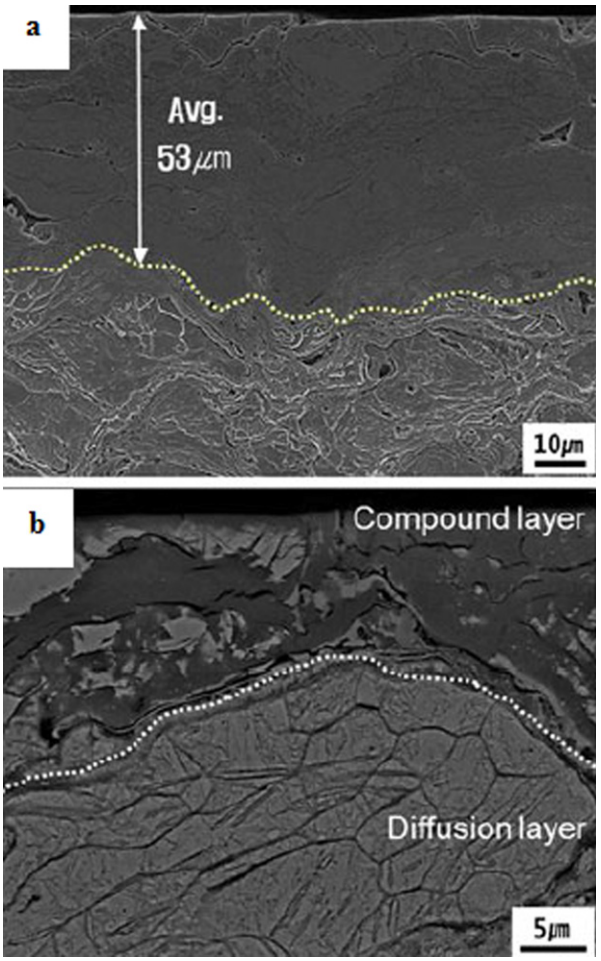


Figure 13 Cross-section of plasma nitride 410 stainless steel coating.[85]

The surface hardness of nitrided and nitrocarburized coatings were greater than 1300 HV 0.01 (three times higher than those of as-sprayed coatings) due to the presence of hard nitride

precipitates such as CrN, Fe_3N, and Fe_4N. The highest microhardness was observed in the case of 410 coating (above 1450 HV) due to formation of Cr23C6. 410 coating after thermochemical treatment, showed the best load bearing capacity due to the high thickness of nitrided or nitorcarburized layer.

3.13.6 Summary and Conclusion

Thermal spray coatings are widely used for various applications such as wear, corrosion, thermal and electrical insulation, and other applications. The nature of thermal spray coatings is different from that of bulk materials and even from other types of coatings. The lamella structure, porosity, oxides, and rough as-sprayed surface are the main characteristics of these coatings. In many applications, as-sprayed coatings cannot be used and additional treatment is necessary. Finishing and grinding is needed where smooth surfaces must be produced. Sealing procedures are applied to seal the open pores to improve corrosion resistance. Remelting and solid state heat treatment can be also performed to improve impact resistance and fracture resistance as well as corrosion behavior. Using remelting procedures, the microstructure of coatings changes completely and a rapidly solidified structure is attained. During solid-state heat treatment, the microstructure is partially changed to form a sintered structure. Some post-treatments were performed in recent years to obtain unique microstructures. In this regard, PEO, FSP, PVD, ion implantation, and thermochemical processing can be mentioned. These processes have not found widespread industrial applications but seem to be promising. It should be noted that the application of post-treatment is not always beneficial. Economic and technical limitations must be considered. In addition, as-sprayed coatings can be satisfactorily used in many industrial applications. The main challenges regarding post-treatments may be summarized as:

- investigating the effect of post-treatment on characteristics and properties using experimental or modeling procedures;
- development of cost-effective and environmentally friendly post-treatments with less technical limitations;
- the combination of thermal spray procures with other coating or surface modification technologies.

See also: 3.7 HVOF Coating of Nickel Based Alloys: Surface and Mechanical Characteristics. 3.14 High Velocity Oxy-Fuel Spraying and Surface Finish

References

1. Fauchais, P. L.; Heberlein, J. V. R.; Boulos, M. I. *Thermal Spray Fundamentals From Powder to Part*; Springer: New York, NY, 2014.
2. Pawlowski, L. *The Science and Engineering of Thermal Spray Coatings*; 2nd ed.; Wiley: Southern Gate, 2008.
3. Davis, J. R., Ed. *Handbook of Thermal Spray Technology*; ASM: Materials Park, OH, 2004.
4. AWS:TS-85. *Thermal Spraying, Practice, Theory and Application*; American Welding Society: Miami, 1985.
5. OSAKA FUJI Corporation. Available at: http://www.ofic.co.jp/en/r_and_d/thermalspraying/images/ph_01.jpg (accessed 26 Febuary 2016).
6. Guo, L.; Yi, J.; Sheng, X.-M. Experimental Research on HVOF Sprayed WC–Co Coating at Super High Speed Grinding. *Hunan Daxue Xuebao/J. Hunan Univ. Nat. Sci.* **2012**, *39* (9), 23–27.
7. Guilemany, J. M.; Cinca, N.; Dosta, S.; Benedetti, A. V. Corrosion Behavior of Thermal Sprayed Nitinol Coatings. *Corros. Sci.* **2009**, *51*, 171–180.
8. Moskal, G.; Niemiec, D. Influence of Surface Condition on Oxides Layer Morphology on NiCrAlY Coating During Oxidation at Temperature 1000 °C and 1100 °C. *Solid State Phenom.* **2015**, *227*, 385–388.
9. Murthy, J. K. N.; Raob, D. S.; Venkataraman, B. Effect of Grinding on the Erosion Behavior of a WC–Co–Cr Coating Deposited by HVOF and Detonation Gun Spray Processes. *Wear* **2001**, *249*, 592–600.
10. Rajasekaran, B.; Ganesh Sundararaman, S.; Joshi, S. V.; Sundararajan, G. Effect of Grinding on Plain Fatigue and Fretting Fatigue Behavior of Detonation Gun Sprayed Cu–Ni–In Coating on Al–Mg–Si Alloy. *Int. J. Fatigue* **2009**, *31*, 791–796.
11. Masoumi, H.; Mohsen Safavi, S.; Salehi, M. Effect of Grinding on the Residual Stress and Adhesion Strength of HVOF Thermally Sprayed WC–10Co–4Cr Coating. *Mater. Manuf. Process.* **2014**, *29* (9), 1139–1151.
12. Liu, W. X. Study Progress on Grinding Surface Residual Stresses for Nano-Ceramic Coatings. *Adv. Mater. Res.* **2013**, *753–755*, 277–280.
13. Li, D.-D.; Kuang, J.; Chen, Q.-Q.; Hu, D.-J.; Xu, L.-M. Temperature and Phase Transformation in Grinding Process of WC–Co Coating. *Shenyang Gongye Daxue Xuebao/J. Shenyang Univ. Technol.* **2014**, *36* (5), 532–536.
14. Hiegemann, L.; Weddeling, C.; Ben Khalifa, N.; Tekkaya, A. E. Prediction of Roughness After Ball Burnishing Of Thermally Coated Surfaces. *J. Mater. Process. Technol.* **2015**, *217*, 193–201.
15. Tekkaya, A. E.; Kleiner, M.; Biermann, D.; *et al.* Friction Analysis of Thermally Sprayed Coatings Finished by Ball Burnishing and Grinding. *Prod. Eng.* **2013**, *7* (6), 601–610.
16. Masoumi, H.; Safavi, S. M.; Salehi, M. Grinding force, Specific Energy and Material Removal Mechanism in Grinding of HVOF-Sprayed WC–Co–Cr Coating. *Mater. Manuf. Process.* **2014**, *29* (3), 321–330.
17. Lefebvre, A.; Sinot, O.; Torrance, A. A.; Lipinski, P. Determination of the Partition Coefficient for the Grinding of a Hard WC–Co–Cr Coating with a Diamond Wheel. *Mach. Sci. Technol. Int. J.* **2014**, *18* (4), 585–602.
18. Arabi, H.; Rastegari, S.; Ramezani, V.; Valefi, Z. Influence of Heat Treatment Parameters, Temperature and Time, on Wear and Microhardness of NiCrBSi Flame Sprayed Coatings Applied on CK45 Substrates. *Iran. J. Mater. Sci. Eng.* **2013**, *10* (2), 1–10.
19. Houdková, S.; Smazalová, E.; Vostřák, M.; Schubert, J. Properties of NiCrBSi Coating, as Sprayed and Remelted by Different Technologies. *Surf. Coat. Technol.* **2014**, *253*, 14–26.
20. Soveja, A.; Costil, S.; Liao, H.; Sallamand, P.; Coddet, C. Remelting of Flame Spraying PEEK Coating Using Lasers. *J. Therm. Spray Technol.* **2010**, *19* (1–2), 439–447.
21. Shengzhi, H.; Dongyun, H.; Limin, Z. Microstructure and Corrosion Resistance of FeCrAl Coating After High Current Pulsed Electron Beam Surface Modification. *Procedia Eng.* **2012**, *27*, 1700–1706.
22. Marginean, G.; Utu, D. Cyclic Oxidation Behaviour of Different Treated CoNiCrAlY Coatings. *Appl. Surf. Sci.* **2012**, *258* (20), 8307–8311.
23. Mei, X. X.; Liu, Y.; Ma, X.; Wang, N. Structure and Performance of YSZ Thermal Barrier Coatings Irradiated by High Intensity Pulsed Ion Beam. *Adv. Mater. Res.* **2012**, *538–541*, 2377–2381.
24. Iwaszko, J.; Nitkiewicz, Z. Solidification Microstructure of Plasma Sprayed and Remelted Carbide Coatings (Cr_3C_2/Ni–Al, W_2C–WC/Co). *Mater. Manuf. Process.* **2002**, *17* (2), 169–176.
25. Dhakar, B. M.; Dwivedi, D. H. K.; Sharma, S. Influence of TIG Remelting and Re(La_2O_3) Addition on Microstructure, Hardness and Wear of Ni–WC Composite coating. In *Supplemental Proceedings, Vol. 1: Materials Processing and Interfaces TMS (The Minerals, Metals & Materials Society)*, 2012; pp. 603–608.
26. Xie, D. J.; Liu, Z. D.; Hu, W. Q.; Wang, Y. T. An Experimental Study on the Properties of fe-Based Amorphous Composite Coatings Prepared by Different Processes. *Adv. Mater. Res.* **2011**, *239–242*, 2137–2141.
27. Tian, H. L.; Weib, S. C.; Chen, Y. X.; Tong, H.; Liu, Y.; Xu, B. S. Surface Remelting Treated High Velocity Arc Sprayed FeNiCrAlBRE Coating by Tungsten Inert Gas. *Phys. Procedia* **2013**, *50*, 322–327.
28. Ghadami, F.; Heydarzadeh Sohi, M.; Ghadami, S. Effect of TIG Surface Melting on Structure and Wear Properties of Air Plasma-Sprayed WC–Co Coatings. *Surf. Coat. Technol.* **2015**, *261*, 108–113.

29. Cheng, H. C.; Li, Z. X.; Shi, Y. W. Effects of TIG Surface Treating on Microstructural Characteristics and Mechanical Properties of Al_2O_3–TiB_2 Coating by APS. *Mater. Sci. Technol.* **2011**, *27* (1), 194–200.
30. Gontarz, G.; Golański, D.; Chmielewski, D. Properties of Fe–Al Type Intermetallic Layers Produced by AC TIG Method. *Adv. Mater. Sci.* **2013**, *13* (3), 5–16.
31. Frodelius, J.; Johansson, E. M.; Córdoba, J. M.; Per Eklund, O. M.; Hultman, L. Annealing of Thermally Sprayed Ti_2AlC Coatings. *Int. J. Appl. Ceram. Technol.* **2011**, *8* (1), 74–84.
32. Richer, M.; Leszczyńska-Madej, B. Effect of the Annealing on the Microstructure of HVOF Deposited Coatings. *J. Achiev. Mater. Manuf. Eng.* **2011**, *46* (1), 95–102.
33. Zhang, C.; Zhang, G.; Leparoux, S.; *et al.* Microwave Sintering of Plasma-Sprayed Yttria Stabilized Zirconia Electrolyte Coating. *J. Eur. Ceram. Soc.* **2008**, *28*, 2529–2538.
34. Bram, M.; Ahmad-Khanlou, A.; Buchkremer, H. P.; Stover, D. Vacuum Plasma Spraying of NiTi Protection Layers. *Mater. Lett.* **2002**, *57*, 647–651.
35. Chen, Y.; Liang, X.; Wei, S.; Liu, Y.; Xu, B. Heat Treatment Induced Intermetallic Phase Transition of Arc-Sprayed Coating Prepared by the Wires Combination of Aluminum-Cathode and Steel-Anode. *Appl. Surf. Sci.* **2009**, *255*, 8299–8304.
36. Xu, R.; Song, G. Post-Heat Treatment of Arc-Sprayed Coating Prepared by the Wires Combination of Mg-Cathode and Al-Anode to form Protective Intermetallic Layers. *Appl. Surf. Sci.* **2011**, *257*, 3097–3102.
37. Lenling, W. J.; Smith, M. F.; Henfling, J. A. *Beneficial Effects of Austempering Post-Treatment on Tungsten Carbide Based Wear Coatings, Thermal Spray Research and Applications*; ASM International: Materials Park, OH, 1991; pp. 227–232.
38. Sasaki, T.; Yagi, T.; Watanabe, T.; Yanagisawa, A. Aluminizing of TiAl-Based Alloy Using Thermal Spray Coating. *Surf. Coat. Technol.* **2011**, *205*, 3900–3904.
39. Bellucci, A.; Bellini, S.; Pileggi, R.; Stocchi, D.; Tuurna, S. Effect of Al Enrichment by Pack Cementation of FeCr Coatings Deposited by HVOF. *J. Therm. Spray Technol.* **2015**, *24* (1–2), 244–251.
40. Chaliampalias, D.; Andronis, S.; Pliatsikas, N.; *et al.* Formation and Oxidation Resistance of Al/Ni Coatings on Low Carbon Steel by Flame Spray. *Surf. Coat. Technol.* **2014**, *255*, 62–68.
41. Rizzi, G.; Scrivani, A. Development of CVD Overaluminising Process on Different CoNiCrAlY Bond Coats Deposited by Vacuum Plasma Spray (VPS), Low Pressure Plasma Spray (LPPS) and High Velocity Oxygen Fuel (HVOF). In *TMS Annual Meeting 2007, 136th TMS Annual Meeting*, Orlando, FL, 25 February 2007 to 1 March 2007; 2007; Code 71555; pp. 61–68.
42. Mohammadi, M.; Jahromi, S. A. J.; Javadpour, S.; Kobayashi, A.; Shirvani, K. Hot Corrosion Behavior and Microstructural Change of Al-Gradient CoNiCrAlYSi Coatings, Produced by LVPS and Diffusional Processes. *Oxid. Met.* **2012**, *78* (1–2), 17–30.
43. Bababdani, S. M.; Nogorani, F. S. Overaluminizing of a CoNiCrAlY Coating by Inward and Outward Diffusion Treatments. *Metall. Mater. Trans. A* **2014**, *45* (4), 2116–2122.
44. Góral, M.; Pytel, M.; Cmela, W.; Drajewicz, M. The Influence of Overaluminizing on TGO Formation on Thermal Barrier Coatings Deposited by Low Pressure Plasma Spraying and Chemical Vapour Deposition Methods on Rene 80 Nickel Superalloy. *Solid State Phenom.* **2015**, *227*, 321–324.
45. Itoh, Y.; Saitoh, M. Mechanical Properties of Overaluminized MCrAlY Coatings at Room Temperature. *J. Eng. Gas Turbine. Power* **2005**, *127* (4), 807–813.
46. Lee, J.-H.; Tsai, P.-C.; Lee, J.-W. Cyclic Oxidation Behavior and Microstructure Evolution of Aluminized, Pt-aluminized High Velocity Oxygen Fuel Sprayed CoNiCrAlY Coatings. *Thin Solid Films* **2009**, *517* (17), 5253–5258.
47. Jiang, J.; Zhao, H.; Zhou, X.; Tao, S.; Ding, C. Oxidation Resistance of Vacuum Plasma Sprayed CoNiCrAlY Coatings Modified by Filtered Cathodic Vacuum Arc Deposition Aluminizing. *J. Therm. Spray Technol.* **2013**, *22* (1), 69–74.
48. Takeuchi, J.; Murata, Y.; Harada, Y.; Tomita, T.; Nakahama, S.; Go, T. An Improvement of Cr_3C_2–NiCr Sprayed Coatings Followed by Chromium Diffusion Treatment. In *Thermal Spray: Meeting the Challenges of the 21st Century*; Coddet, C., Ed.; ASM International: Materials Park, OH, 1998; pp. 1425–1430.
49. Leivo, E. M.; Vippola, M. S.; Sorsa, P. P. A.; Vuoristo, P. M.; Mantyla, T. A. Wear and Corrosion Properties of Plasma Sprayed Al_2O_3 and Cr_2O_3 Coatings Sealed by Aluminum Phosphates. *J. Therm. Spray Technol.* **1997**, *6* (2), 205–210.
50. Ahmaniemi, S.; Vippola, M.; Vuoristo, P.; Mantyla, T.; Buchmann, M.; Gadow, R. Residual Stresses in Aluminium Phosphate Sealed Plasma Sprayed Oxide Coatings and their Effect on Abrasive Wear. *Wear* **2002**, *252*, 614–623.
51. Ahmaniemi, S.; Vuoristo, P.; Mantyla, T.; Gualco, C.; Bonadei, A.; Di, R. Thermal Cycling Resistance of Modified Thick Thermal Barrier Coatings. *Surf. Coat. Technol.* **2005**, *190*, 378–387.
52. Chatha, S. S.; Sidhu, H. S.; Sidhu, B. S. The Effects Of Post-Treatment on the Hot Corrosion Behavior of the HVOF-Sprayed Cr_3C_2–NiCr Coating. *Surf. Coat. Technol.* **2012**, *206*, 4212–4224.
53. Xie, D.; Xiong, Y.; Wang, F. Effect of an Enamel Coating on the Oxidation and Hot Corrosion Behavior of an HVOF-Sprayed Co–Ni–Cr–Al–Y Coating. *Oxid. Met.* **2003**, *59* (5/6), 503–516.
54. Panadda, N.; Koiprasert, H. Improved Corrosion Resistance of Thermally Sprayed Coating via Surface Grinding and Electroplating Techniques. *Surf. Coat. Technol.* **2006**, *201*, 737–743.
55. Westergard, R.; Hogmark, S. Sealing to Improve the Wear Properties of Plasma Sprayed Alumina by Electro-Deposited Ni. *Wear* **2004**, *256*, 1153–1162.
56. Caron, N.; Bianchi, L.; Methout, S. Development of a Functional Sealing Layer for SOFC Applications. *J. Therm. Spray Technol.* **2008**, *17* (5–6), 598–602.
57. Armada, S.; Tilset, B. G.; Pilz, M.; Liltvedt, R.; Bratland, H.; Espallargas, N. Sealing HVOF Thermally Sprayed WC–CoCr Coatings by Sol–Gel. *Methods* **2011**, *20* (4), 917–925.
58. Li, C.-J.; Ning, X.-J.; Li, C. X. Effect of Densification Processes on the Properties of Plasma-Sprayed YSZ Electrolyte Coatings for Solid Oxide Fuel Cells. *Surf. Coat. Technol.* **2005**, *190*, 60–64.
59. Shi, J. M.; Ding, C. X.; Wu, X. Q. Preparation of Bioactive and Porous Titanium Coating by Vacuum Plasma Spraying and Chemical Treatment. In *Thermal Spray 2001: New Surfaces for a New Millenium*; Berndt, C. C., Khor, K. A., Lugscheider, E. F., Eds.; ASM International: Materials Park, OH, 2001; pp. 593–597.
60. Melero, H.; Garcia-Giralt, N.; Fernández, J.; Díez-Pérez, A.; Guilemany, J. M. Comparison of *In Vitro* Behavior of As-Sprayed, Alkaline-Treated and Collagen-Treated Bioceramic Coatings Obtained by High Velocity Oxy-Fuel Spray. *Appl. Surf. Sci.* **2014**, *307*, 246–254.
61. Mantyla, T.; Vuoristo, P.; Kettunen, P. Chemical Vapor Deposition Densification of Plasma Sprayed Oxide Coatings. *Thin Solid Films* **1984**, *118*, 437–444.
62. Bolelli, G.; Bonferroni, B.; Coletta, G.; Lusvarghi, L.; Pitacco, F. Wear and Corrosion Behaviour of HVOF WC–CoCr/CVD DLC Hybrid Coating Systems Deposited Onto Aluminium Substrate. *Surf. Coat. Technol.* **2011**, *205*, 4211–4220.
63. Ohmori, A.; Zhou, Z.; Inoue, K. Improvement of Plasma-Sprayed Ceramic Coating Properties by Heat-Treatment with Liquid Mn. In *Thermal Spray Industrial Applications*; Berndt, C. C., Sampath, S., Eds.; ASM International: Material Park, OH, 1994; pp. 543–548.
64. Knuuttila, J.; Sorsa, P.; Mantyla, T. Sealing of Thermal Spray Coatings by Impregnation. *J Therm. Spray Technol.* **1999**, *8* (2), 251–257.
65. Ito, H.; Nakamura, R.; Shiroyama, M. Infiltration of Copper into Titanium Molybdenum Spray Coatings. *Surf. Eng.* **1988**, *4*, 35–38.
66. Wang, J.; Shinozaki, N.; Zengb, Z.; Sakoda, N.; Fukami, N. Penetration Treatment of Plasma Spray SUS316L Stainless Steelcoatings by Molten MnO–SiO_2 Oxides. *Appl. Surf. Sci.* **2015**, *325*, 132–138.
67. Wang, J.; Shibasaki, S.; Miyoshi, N.; Shinozaki, N.; Zeng, Z.; Sakoda, N. Penetration Treatment of Plasma Spray SUS316L Stainless Steel Coatings by Molten Multi-Component Oxides. *Surf. Coat. Technol.* **2014**, *252*, 173–178.
68. Mishra, R. S.; De, P. S.; Kumar, N. *Friction Stir Welding and Processing Science and Engineering*; ASM International: Materials Park, OH, 2007.
69. Yoshiaki, M.; Fujii, H.; Mizuno, T.; Abe, G.; Nagaoka, T.; Fukusumi, M. Modification of Thermally Sprayed Cemented Carbide Layer by Friction Stir Processing. *Surf. Coat. Technol.* **2010**, *204*, 2459–2464.
70. Mazaheri, Y.; Karimzadeh, F.; Enayati, M. H. Tribological Behavior of A356/Al2O3 Surface Nanocomposite Prepared by Friction Stir Processing. *Metall. Mater. Trans. A* **2014**, *45*, 2250–2259.
71. Rahbar-Kelishami, A.; Abdollah-Zadeh, A.; Hadavi, M. M.; Seraj, R. A.; Gerlich, A. P. Improvement of Wear Resistance of Sprayed Layer on 52100 Steel by Friction Stir Processing. *Appl. Surf. Sci.* **2014**, *316*, 501–507.
72. Zhu, L. K.; Zhou, X. P.; Fang, Y. Z.; Xu, F. Ni–Cr–Al Coating Layer Modified by Friction Stir Processing – Analysis of Microstructure and Element Diffusion. *Adv. Mater. Res.* **2015**, *1095*, 616–619.
73. Pokhmurskii, V.; Nykyforchyn, G.; Student, M.; *et al.* Plasma Electrolytic Oxidation of Arc Sprayed Aluminium Coatings. *J. Therm. Spray Technol.* **2007**, *16* (5–6), 998–1004.
74. Levent, C. K.; Ustel, F.; Ozel, A.; Mimaroglu, A. Micro Arc Oxidation of Wire Arc Sprayed Al-Mg6, Al-Si12, Al Coatings on Low Alloyed Steel. *Engineering* **2011**, *3*, 680–690.

75. Marple, B. R.; Voyer, J.; Béchard, P. Sol Infiltration and Heat Treatment of Alumina-Chromia Plasma Sprayed Coatings. *J. Eur. Ceram. Soc.* **2001**, *21*, 861–868.
76. Casadei, F.; Tului, M. Combining Thermal Spraying and PVD Technologies: A New Approach of Duplex Surface Engineering for Ti Alloys. *Surf. Coat. Technol.* **2013**, *237*, 415–420.
77. Byon, E.; Zhang, S.; Lee, S. H.; Lee, G. H.; Kwon, S. C. Effect of Ion Implantation on Growth of Thermally Grown Oxide in MCrAlY Coating for TBC. *Surf. Coat. Technol.* **2010**, *205*, S435–S438.
78. Jiang, J.; Zhao, H.; Zhou, X.; Taoa, S.; Ding, S. The Effect of Ion Implantation on the Oxidation Resistance of Vacuum Plasma Sprayed CoNiCrAlY Coatings. *Appl. Surf. Sci.* **2012**, *261*, 422–430.
79. Byeli, A. V.; Belotserkovskii, M. A.; Kukareko, V. A. Microstructure and Wear Resistance of Thermal Sprayed Steel Coatings Ion Beam Implanted with Nitrogen. *Wear* **2009**, *267* (9–10), 1757–1761.
80. Zhang, G.-S.; Wei, M.-Q. Friction and Wear Behavior of Cr_2O_3 Coating Implantated with Nitrogen Ions. *Mocaxue Xuebao/Tribology* **2006**, *26* (5), 422–426.
81. Zhou, Z. H.; Sheng, K. G.; Li, H. F.; Xu, H. B.; Zhang, C. G.; Wang, L. Effects of Shot Peening Process on Thermal Cycling Lifetime of TBCs Prepared by EB-PVD. *Chin. J. Aeronaut.* **2005**, *20*, 145–147.
82. Junior, G. S.; Voorwald, H. J. C.; Vieira, L. F. S.; Cioffi, M. O. H.; Bonora, R. G. Evaluation of WC–10Ni Thermal Spray Coating With Shot Peening on the Fatigue Strength of AISI 4340 Steel. *Procedia Eng.* **2010**, *2*, 649–656.
83. Kubiak, K.; Fouvry, S.; Marechal, A. M.; Vernet, J. M. Behaviour of Shot Peening Combined with WC–Co HVOF Coating Under Complex Fretting Wear and Fretting Fatigue Loading Conditions. *Surf. Coat. Technol.* **2006**, *201*, 4323–4328.
84. Pawlowski, L. Technology of Thermally Sprayed Anilox Rolls: State of Art, Problems and Perspectives. *J. Therm. Spray Technol.* **1996**, *5*, 317–335.
85. Gayoung, P.; Bae, G.; Moon, K.; Lee, C. Effect of Plasma Nitriding and Nitrocarburizing on HVOF-Sprayed Stainless Steel Coatings. *J. Therm. Spray Technol.* **2013**, *22* (8), 1365–1372.

Relevant Websites

http://www.fwgts.com/
Gartner Thermal Spray.
http://www.gordonengland.co.uk/
Gordon England.
www.gtv-mbh.com
GTV.
http://www.metallisation.com/
Metallisation.
www.praxairsurfacetechnologies.com
Praxiar.
www.sulzer.com
Sulzer.
http://www.thermalspray.com/
Thermal Spray Company.
http://www.tstcoatings.com/post-spray_capabilities.html
TST Engineered Solutions.

3.14 High Velocity Oxy-Fuel Spraying and Surface Finish

H Singh, Indian Institute of Technology Ropar, Rupnagar, India
M Kaur and N Bala, Baba Banda Singh Bahadur Engineering College, Fatehgarh Sahib, India

© 2017 Elsevier Inc. All rights reserved.

3.14.1	**Introduction**	207
3.14.2	**HVOF Spray Process**	207
3.14.2.1	History	207
3.14.2.2	Principle	207
3.14.2.3	Process Technical Details and Spray Parameters	207
3.14.2.4	Mechanism of Coating	209
3.14.2.5	HVOF Coating Characteristics	209
3.14.3	**Comparison with Other Thermal Spray Techniques**	210
3.14.4	**Surface Finish Guidelines for HVOF Spraying**	210
3.14.5	**HVOF Spray and Surface Finish**	211
3.14.5.1	Pre-Deposition Surface Finish	211
3.14.5.2	As-Sprayed Surface Finish	213
3.14.5.2.1	Automobile industry	213
3.14.5.2.2	Power generation industry	213
3.14.5.2.3	Surface roughness of bondcoats in thermal barrier coatings	213
3.14.5.3	Post-Deposition Surface Finish	215
3.14.6	**Concluding Remarks**	217
References		217
Relevant Websites		219

3.14.1 Introduction

Thermal spraying was mentioned for the first time in the patents of Swiss engineer Max Ulrich Schoop (1870–1956) at the beginning of the twentieth century.[1] It is a group of coating techniques, in which a jet of combustion products along with the injected powder particles are directed toward substrate material to form surface coating. Various thermal spraying techniques include arc spraying (AS), plasma spraying (PS), high velocity oxy-fuel (HVOF) spraying, detonation-gun (D-gun) spraying, and cold spraying (CS). Among these techniques, HVOF spraying offers the possibility to develop high-quality coatings, with several advantages such as increased hardness, lower value of porosity, low-oxide content, and good corrosion and wear resistance. That is why; HVOF spraying has attracted worldwide attention within the field of surface engineering. This chapter describes HVOF spray technology and its applications in relation to surface finishing. Some literature studies have been included to explain the role of HVOF spraying to achieve surface finish for some specific applications.

3.14.2 HVOF Spray Process

3.14.2.1 History

Thorpe *et al.*[2] reported that HVOF spray technology was invented in 1958 by Union Carbide, which is currently known as Praxair Surface Technologies, Inc. The technique was first introduced commercially in 1974 by Browning. Bick and Jürgens[3] and Kreye *et al.*[4] among others agreed that the initial work was conducted at the Thayer School of Engineering, Hanover, USA. According to Pawlowski,[5] HVOF spray torch to be used was developed at the end of the 1970s and at the beginning of the 1980s.[5]

3.14.2.2 Principle

To formulate a desired coating, HVOF spray process utilizes a blend of thermal and kinetic energy transfer. The melting and acceleration of powder particles take place.[6] The gases which can be used for this process are propane, acetylene, oxygen, propylene, methyl acetylene propadiene (MAPP-stabilized gas), hydrogen, methane, ethylene, SPRAL 29 kerosene, and LPG. The chosen gases are injected into the combustion chamber of the spray torch at high pressure, and are ignited. The resulting gas jet achieves supersonic speeds with Mach number greater than one. The selected coating powder to be deposited is fed axially into a spray gun, where it interacts with hot gas stream and gets melted, and propelled toward the workpiece surface to be coated (Tan *et al.*[6]). This process results in dense thermal spray coatings on the substrates. Voyer and Marple[7] stated that owing to high kinetic energy of the powder particles striking the substrate surface, the particles need not to be completely molten to form good quality HVOF coatings. Furthermore, improved gas heating and acceleration permit better heat/momentum transfer to the particles.[8]

3.14.2.3 Process Technical Details and Spray Parameters

Different HVOF spray systems have been manufactured by several companies in various designs and process-capabilities. For instance, a cross-section of a commercial Sulzer Metco

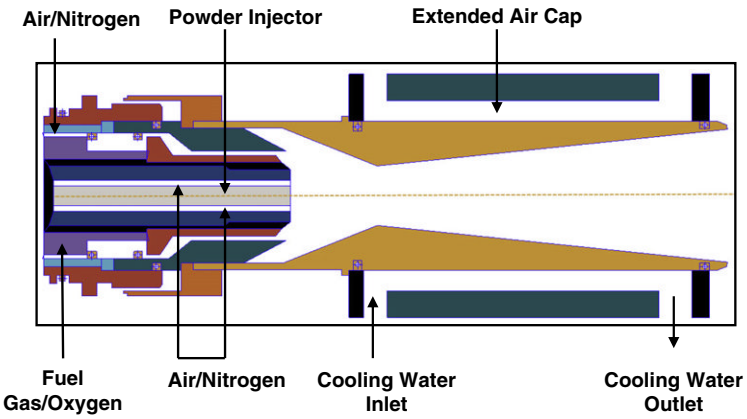


Figure 1 The high velocity oxy-fuel (HVOF) process (Lugscheider *et al.*[9]).

Diamond Jet Hybrid (DJ) HVOF system is shown in Figure 1.[9] The system comprises a spray torch, flow meter unit, powder feed unit, and an air and gas supply unit. To obtain good quality coatings and depending upon the requirement of the user, the mixture of oxygen and fuel gas or hydrogen (H_2) is used.[10] The fuel gases are mixed in the combustion chamber of the gun. Afterwards, these thoroughly mixed gases are expelled out from the nozzle and ignited in the exterior to gun. Ignited gases form a round flame configuration that surrounds the powdered material as it flows through the gun. Ignition temperatures in the range of 2760–3315 °C can be achieved depending on the fuel. The value of flame velocity reaches above 1200 m s^{-1}. In this way, the powder stream is provided with uniform heating, melting, and acceleration by the circular flame.[10] In the HVOF process, the powder particles attain supersonic velocities with a Mach number in the range of 1.5–2.0.[11]

HVOF spray apparatus is available with various gun designs and capacities in the market. Every system is different in design but are based on same fundamental principles. The supersonic gas velocities are achieved by the combination of high pressure (over 3 bar) and gas flow rates of several hundred liters per minute.[12] The HVOF systems are roughly divided into the first, second, and third generation systems. In the first two generations guns, the pressurized burning of gaseous fuel with oxygen is used to generate an exhaust jet traveling at a speed of about 2000 m s^{-1}.[12]

The primary difference between the first and second generation is the design of the nozzle. Oksa *et al.*[12] reported that in the first generation HVOF systems, there is relatively large combustion chamber and a straight nozzle.[12] Maximum of one Mach velocities can be achieved with this design. In the second generation there is de Laval nozzle, which enables over Mach 1 velocities at the diverging part of the nozzle. For instance, about 2–3 kg h^{-1} of WC–Co is sprayed under standard spray conditions in these systems with the power level of about 100 kW.[12] The third generation systems are designed with higher combustion chamber pressures from 8 bar up to as far as 25 bar and for power levels ranging from 100–300 kW. These systems are capable of having spray rates up to about 10 kg h^{-1}. The key differences between all these generations are summarized in Table 1.[12]

Table 1 The key differences between three generations of HVOF systems[12]

	Nozzle type	*Power level (kW)*[a]	*Combustion chamber pressure (bar)*	*Kg h^{-1} (WC–Co)*
1st generation	Straight	80	3–5	2–6
2nd generation	De laval	80–120	5–10	2–10
3rd generation	De laval	100–300	up to 25	10–12

[a]Total heat output.

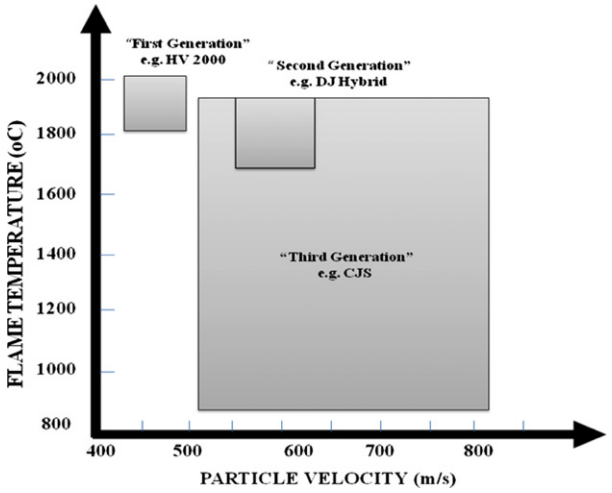


Figure 2 Flame temperature vs. particle velocity for the first, second, and third generation HVOF spray systems.[12]

Scientifically, the main parameters affecting the coating formation are particle velocity (v) and particle temperature (T) together with substrate characteristics.[12] These parameters decide the coating buildup process and the coating deposit formation. Particle velocity and particle temperature both affect the deposit microstructure and the deposit efficiency. Figure 2 schematically shows the trend in HVOF spray process development.[12] The trend has been toward faster particle velocities, higher gas pressures, and lower particle temperatures.

3.14.2.4 Mechanism of Coating

According to Pawlowski,[13] when a particle strikes substrate or grit blasted surface, it may be molten, semi-molten or solid. It all depends upon the melting temperatures of the particle relative to the flame temperature. The final microstructure of the deposit results from the state of the particle when it exits the combustion zone (Pawlowski[13]). At high velocities, rapid solidification of small globules gives rise to lamellar grain structure of the HVOF coatings, which flatten upon striking a colder substrate surface (Stokes[14]). Fantassi *et al.*[15] and Moreau *et al.*[16] reported that at first, the particle is melted and expelled out from the spray gun. It impacts the substrate and the impact creates a shock wave inside the lamella and in the substrate. Post-impact makes the particle into a 'pancake' shape lamella or splat (with reasonable particle velocities and reasonable heat contents) or a flower type lamella (connected with a higher velocity of the particle and a higher heat content) when the solidification process takes place as represented in **Figure 3**. Spreading of the splat is restrained by surface tension when a molten droplet reaches at a surface at high velocity. Else the extremities of the splat will either become weak, and break off or form small spherical drops (Stokes[14]). Kanouff *et al.*[17] in their studies made clear that the substrate surface roughness has a great influence on the splat formation and adherence loss occurs if an insufficient amount of surface roughness is present whilst spraying.

Stokes[14] explained the coating buildup for the HVOF spraying process. According to him, a coating is developed by the buildup of individual particles which strike a substrate. In one pass of the spray gun, a layer of 5–15 lamellae thickness is formed, however, it all depends upon the various processing parameters such as spray distance, powder feed rate, particle size, and the torch's linear speed.[14] Therefore, to build up a coating across the workpiece, several passes of spray gun are needed. In the meantime, the coating layer deposited by the first pass may be subjected to oxidation and cooling. Due to the difference in temperatures between the first and second layer, on the second pass, the temperature of earlier layer, which may be partially solidified, cools the second layer. The final coating may contain 5–200 passes of deposited material. Further, the coating is cooled down to room temperature. During this period the thermal stresses generate, often leading to crack formation in the coating or separation from the substrate.[14] As per the opinion of Stokes,[14] when a molten or semi-molten particle strikes the substrate or previously deposited material, solidification starts and a columnar deposit structure is developed. Moreover, Pawlowski[13] reported that the deposit structure may transform to a brick wall type structure where a low rate of heat removal is experienced between the particle and the adjoining material interface, due to substrate oxidation and/or surface roughness. In either case the solidification within each lamella will repeat itself as the coating builds up to the required thickness.[13]

3.14.2.5 HVOF Coating Characteristics

The key to the success of HVOF is the extremely high kinetic energy that is produced and transferred from the HVOF unit to the substrate using space-age rocket propulsion technology.[18,19] Typical velocities approach 1500 m s^{-1} to over 2200 m s^{-1}, depending on the hardware selected. With both thermal and kinetic energy, the high velocity particles are almost embedded into the substrate to form a superior coating with the following characteristics:[18]

- High density
- High bond strengths (in excess of 8.27×10^7 N m^{-2})
- Negligible porosity (with no interconnecting porosity)
- Metal working capabilities
- Essentially stress free
- Greater hardness
- Greater thickness
- Low thermal input (substrate temperature less than 149 °C which ensures that the original mechanical properties are preserved and no stress relieving is required).

Therefore, the HVOF coatings have high density, increased thickness capability, smoother surface finish, lower oxide levels, low porosities, less effect of the environment during the spray process and better corrosion and wear resistance properties (Kinos[18] and Khor and Leh[19]).

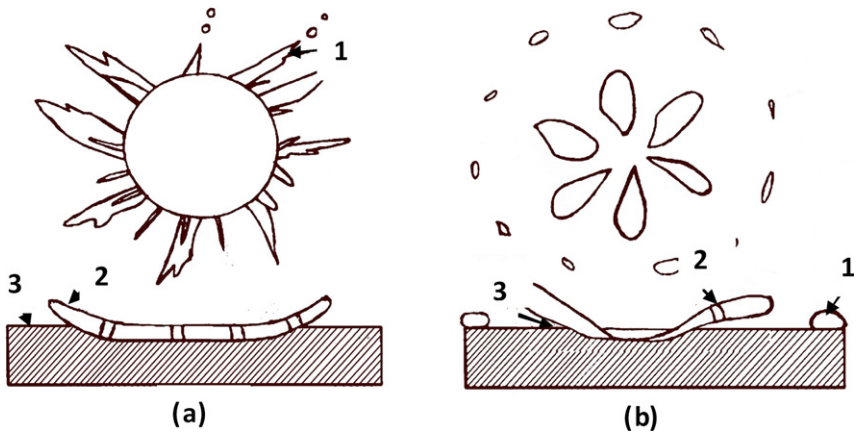


Figure 3 Primary morphologies of lamellae/splat obtained from sprayed particles: (a) pancake; (b) flower; (1) corona; (2) crack; (3) deformed substrate (Fantassi *et al.*[15] and Moreau *et al.*[16]).

3.14.3 Comparison with Other Thermal Spray Techniques

Pawlowski[5] presented a comparison of HVOF spraying with the other thermal spray processes and concluded that the principles of this technique are similar with a variation in the way of burning the fuel medium in oxygen.[5] This is done to attain a relatively lower temperature supersonic gas jet for the deposition of heat sensitive materials in facilities that function at ambient pressures and temperatures. It has been mentioned that the burning is continuous for HVOF, whereas repetitive for D-gun spray process. The HVOF spray process is a low-temperature process compared with other techniques. Moreover, the procedure requires minimal base metal preparation and can be directly applied to the working tools. These benefits enable HVOF to be a promising and popular process.[20–22] Jacobs *et al.*[23] suggested that in terms of particle condition, the HVOF spraying has many advantages over the other thermal spray processes including:

- More uniform and efficient particle heating, due to the high turbulence experienced by the particles within the combustion chamber.
- Much shorter exposure time in flight due to the high particle velocities.
- Lower surface oxidation due to short particle exposure time compared to other thermal spraying techniques.
- Reduced mixing with ambient air once jet and particles leave the gun.
- Lower ultimate particle temperatures compared to other processes such as plasma or arc guns, as these processes operate at temperatures of 16 000 and 6000 °C as opposed to 3000 °C in the HVOF (oxygen/propylene mixture) process.

The literature indicates that HVOF spray technique is a rapidly developing thermal spray technology for depositing surface coatings to combat high-temperature corrosion and wear. Even this technique has challenged vacuum PS technique, which is comparatively expensive to set up (capital costs approximately $2 000 000).[23] In addition, with the availability of handy HVOF spraying equipments, the process provides the possibility of on-site applications in the real boiler and other heavy-duty installations, which are not possible with other techniques such as PS, D-gun, chemical vapor deposition (CVD), physical vapor deposition (PVD), carbonization, and laser cladding. In high-temperature applications, the HVOF coatings possess relatively low porosity and high degradation characteristics.[24] Kirsten *et al.*[25] established experimentally that HVOF spray technique is a flexible dry-coating technology with less environmental impact. It covers many applications with a variety of possible coating materials. Table 2 presents a comparison of the typical parameters of various thermal spray techniques.[25]

3.14.4 Surface Finish Guidelines for HVOF Spraying

Based upon their research work, Greene Tweed,[27] established the optimum surface finish for the HVOF coatings. HVOF coatings are now replacing hard chrome plating in the aerospace industry; therefore the definition of optimum surface finish for the coatings has been modified. For instance, the interesting feature to notice is that how the chrome and HVOF interact with seals and bearings in dynamic applications. It has been reported that with growing time in service, the chrome surface finish will 'polish' and become smoother. On the other hand in spite of the accumulation of dynamic cycles with seals and bearings, the HVOF surfaces have been found to remain relatively uniform. Greene Tweed,[27] recognized separate recommendations for chrome-plated and HVOF-coated surfaces. The definitions of the surface roughness parameters as found in ISO 4287 for finished HVOF-coated surfaces are reproduced here[27]:

Ra: The arithmetic means of a surface finish profile within a sampling length.[27]

Rp: The largest peak height of a surface finish profile within a sampling length measured from the mean line (Figure 4). This parameter can be used to measure the potential aggression of the surface. A lower value of Rp is recommended for HVOF spray tungsten and carbide particles, to assure that no irregularly high peaks are present that could act to slice the seals and bearings.[27]

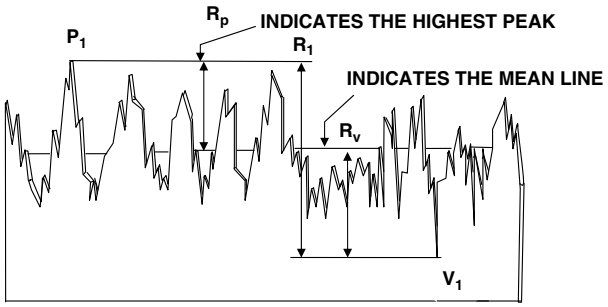


Figure 4 Surface roughness parameter Rp.[27]

Table 2 Characteristic parameters of several thermal spray techniques (Karthikeyan[25])

Parameter	*Wire arc*	*Plasma*	*HVOF*	*Cold spray*
Jet temperature (K)	~6000	~13 000	~5500	300–900
Jet velocity ($m\,s^{-1}$)	50–100	800–1500	1000–2000	1000–2500
Gas	Air, N_2, Ar	Ar, H_2, N_2, He	CH_4, C_3H_6, H_2	Air, N_2, He
Gas flow rates ($N\,m^{-1}$)	500–3000	40–150	400–1100	1000–3300
Power (KW)	2–5	40–200	150–300	5–10
Feedstock ($g\,min^{-1}$)	150–2000	10–80	15–50	20–80
Deposition density (%)	80–95%	90–95%	95%	95%

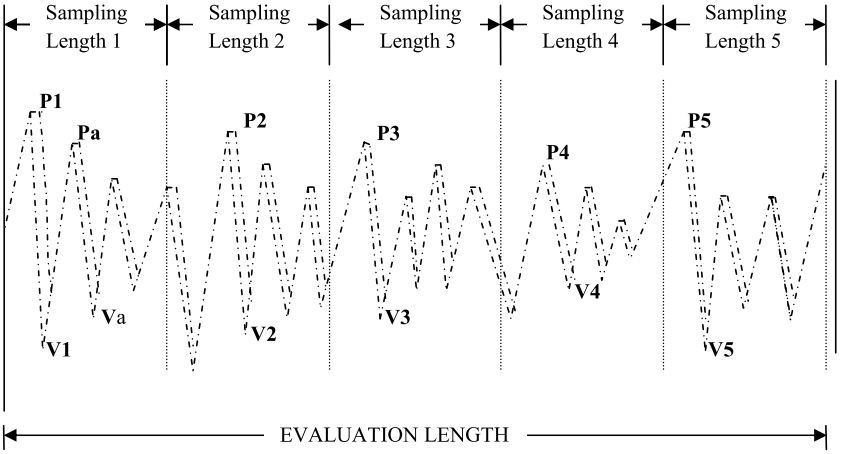


Figure 5 Surface roughness parameter Rz.[27]

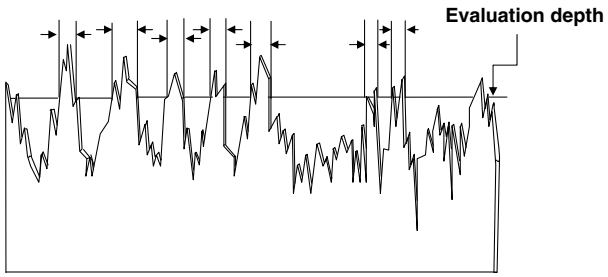


Figure 6 Surface roughness parameter Rmr.[27]

Rz: As reported by Greene Tweed,[26] the Rz surface roughness parameter is the average of the sum of the largest valley depth to the highest peak of a surface finish profile within a sampling length (Figure 5). The Rz value provides an indication of the surface's potential to maintain the desired lubrication to the seal as boundary layer lubrication present on the surface can be beneficial to decrease the friction and wear on the seal.

Rmr (tp): It is defined as the ratios of the material length at a specific depth for a surface finish profile. The parameter provides information on the relative material ratio at a specific evaluation depth (Figure 6).

Values for the surface finish parameters for HVOF as recommended by Greene Tweed[27] are as follows:

Ra = Maximum 4 μin (0.1 μm)
Rp = Maximum 8 μin (0.2 μm)
Rz = Maximum 40 μin (1.0 μm).

Since HVOF spray process utilizes hard, dense particles such as tungsten and carbides, the literature recommends that greater care in the preparation of the runout is required as compared to traditional chrome coatings. The following common criteria have been suggested in the preparation of HVOF runout[27]:

1. Long fade out is preferred – For HVOF coatings it is preferred to have much longer blending of the coating. The amount of the blend is to be determined by the manufacturing methodology and hardware geometry.
2. Hardware geometry – To create a more reliable, benign runout, the HVOF coating can be feathered along the tapered geometry (Figure 7). The termination of HVOF in advance of a chamfer or radius makes it more hard to fade out the coating, therefore increasing the possibility of the runout being aggressive to seals during installation.[27]

3.14.5 HVOF Spray and Surface Finish

In this section, surface finish issues related to the development of high quality HVOF-sprayed coatings have been discussed. Some specific studies have also been added so as to elaborate the issues with the help of experimental data.

3.14.5.1 Pre-Deposition Surface Finish

Thermal spray process requires adequate surface preparation in order to have good coating adhesion/substrate adhesion. For wear and erosion applications the adhesion of the coating to the substrate plays a vital role. If adequate bonding of a coating is required then the substrate has to be prepared properly. First and foremost is the cleanliness of the substrate surface followed by roughening the substrate using grit blasting or any other technique.[28] Surface preparation is most of the time necessary before the coating elaboration to ensure the best contact between the molten particles and the surface. The coating/substrate interfacial adhesion can then be improved. Various mechanisms related to the bonding of coating-substrate constitute an important aspect of the theory of thermal spray technology. Therefore, the investigations related to this aspect have attracted a great deal of attention in the past few decades.[29–32] For a thermal spraying process the different mechanisms of the coating-substrate adhesion can be classified as given[33]:

1. Mechanical interlocking effect,
2. Physical bond, and
3. Chemical–metallurgical bond.[33]

In case of a conventional spray process where particle velocity is comparatively low, the bonding between the coating and

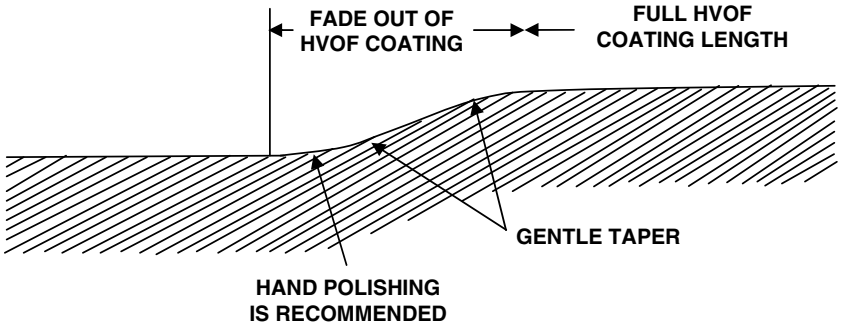


Figure 7 HVOF coating runout.[27]

the substrate is mainly dependent on the mechanical interlocking. The mechanical interlocking is further dependent on the substrate surface roughness and the solidification of the impacting particles, which are in the form of droplets. Investigations show that in case of conventional thermal spraying processes an increase in the roughness of the substrate surface as well as an improvement in the melting state of spray particle leads to an improvement in the adhesive strength of the coating.[34–38]

Wang *et al.*[39] conducted experiments in order to study how the substrate roughness affects the adhesive strength of HVOF-sprayed coatings. NiCrBSi coatings were deposited using HVOF spraying on the mild steel substrate surfaces of different roughness. The spraying gun used for the purpose was CH-2000 HVOF system in which propane gas was used as a fuel gas. The pressures of the propane and oxygen were 0.35 and 0.55 MPa, respectively. The flow of oxygen was set to 439 l min^{-1}, whereas that of propane 45 l min^{-1}. For the powder feed gas nitrogen at a pressure of 0.35 MPa was used. Throughout the spraying process the spray distance from the gun exit to the substrate surface was kept at 210 mm. In order to obtain different roughness, the substrates were prepared before the spraying; which was done by sandblasting or grinding with different sizes of grits. The surface of one set of samples was polished. Profilometer (TR240, Shidai) was used to measure the surface roughness and also to record the surface profile. For each sample, the calculated roughness Ra was the average of surface roughness measured at six different positions. The following conclusions were made:[39]

- For the recorded value of the substrate surface (Ra) less than 1.7 μm, similar adhesive characteristic were obtained for the HVOF NiCrBSi coatings to that of those coatings that were deposited on a polished substrate. Ineffective adhesion was observed at the substrate/coating interface.
- For the substrate surface roughness value more than Ra 5.8 μm, there was an increase in adhesive strength with an increase in the surface roughness. The adhesive strength of the coating was increased with the increase in the roughness of the substrate surface.
- For a practical rough substrate the coating reached a limited adhesive strength of about 40 MPa. The result was in accordance with the general observations about the effects of surface roughness on the adhesion of thermally sprayed coatings.
- For the coating deposited with completely melted alloy particles no improvement in the adhesive strength was observed with the increase in the substrate roughness when the adhesion reached to 40–50 MPa.[39]

The impact of roughness on the fatigue behavior was studied by Gonzalez-Hermosilla *et al.*[40] For this they deposited WC-10 Co–Cr cermet coating on SAE 1045 steel by HVOF spray technique. For conducting the fatigue tests rotating bending conditions ($R = -1$) were employed. Specimens were prepared having different surface roughness, including as-polished, fine grinding (abrasive paper grit 400), grit blasted with alumina particles of two different sizes (<1 and <3 mm, respectively), as-grit blasted specimens employing alumina particles of 3 mm in size. It was concluded that initiation of fatigue crack was delayed at deep notches because of presence of cermet coating and grit blasting lead to embedment of alumina particles at the steel substrate. In comparison with the as-polished specimens this led to an inconsequential fatigue strength debit of the coated one. On the other hand, fine grinding weakened the mechanical bonding of the coating, which lead to the delamination of the coating from the substrate at raised maximum alternating stresses. It was observed that though grit blasting improved the adhesion of coating, it also introduced flaws that initiated the formation of fatigue cracks.[40]

To explore the influence of varying surface roughness and chemistry on the formation of polyether ether ketone (PEEK) coatings on ANSI stainless steel 304 was subjected to various substrate pretreatments.[41] HVOF and assisted combustion high velocity air fuel (AC-HVAF) thermal spray techniques were used to deposit single splats and coatings of PEEK respectively. The three substrate pretreatments used for the work were as received degreased, etched, and steel grit blasted. X-ray photoelectron spectroscopy (XPS) analysis was done and the results showed that the etched substrate had the most chemically clean surface. This was confirmed by contact angle measurement which showed that the etched substrate had the lowest contact angle which indicated good wetting properties. This was followed by the degreased and the steel grit blasted substrates. Along with the Ra value the skewness parameter was also used for the description of the surface profile. As indicated by the roughness and skewness values of the treated substrates the steel grit blasted surface possessed the maximum roughness value in comparison to the etched and degreased substrates. The roughness value of etched and degreased substrates were found to be an order of magnitude lower than the roughness values of the steel grit blasted surface. While the skewness was found to be positive on the etched substrate, it

was found to be slightly negative on the steel grit and negative on the degreased substrate. Splats per mm^2 were highest on the steel grit blasted substrate followed by degreased and etched surface as depicted by PEEK single splat image analysis. From these results it was concluded that for ANSI304 stainless steel surface a positive skewness can be obtained using an etching process. For surfaces possessing appropriate topography the mechanical interlocking factor predominates than surface chemistry for room temperature substrates. Hence it may be established that PEEK coatings deposited by HVOF and AC-HVAF thermal spraying onto stainless steel surfaces and for ANSI304 stainless steel surfaces with comparable roughness and PEEK coatings on surfaces with positive skewness showed a better coating adhesion in comparison to similar surfaces with negative skewness.[41]

3.14.5.2 As-Sprayed Surface Finish

HVOF spray technique is best recommended for carbide matrix coatings.[42] Carbide coatings sprayed by HVOF render good hardness, wear, and abrasion resistance characteristics and have perfect alternative for hard chrome plating.[42] Harvey[43] mentioned in his study that adhesive strength at the coating and substrate interface for a typical HVOF-sprayed coating can be 10 times higher than that obtainable from other thermal spraying processes. HVOF spraying is considered a valid process to deposit cermet coatings (WC–Co and Cr_3C_2–NiCr) of low porosity content (about 1%) due to the high particle velocity and low flame temperature. Specifically HVOF spraying allows creating denser and less oxidized coatings than conventional thermal spray technologies. Perry *et al.*[44] reported that during the development of the HVOF coatings, no significant thermal and mechanical alterations of the substrate are usually observed. Moreover, Kaur *et al.*[10] mentioned that the HVOF coatings are used in applications requiring the highest density and strength that are not available from most other thermal spray processes. New applications that previously were not suitable for thermal spray coatings are now becoming viable. In the aeronautical industry, the HVOF coatings are considered as a standard for spraying of carbides and many applications. These industries were previously using electrolytic chromium and have now been replaced by carbides and alloys sprayed by the HVOF process.[45]

3.14.5.2.1 Automobile industry

Nowadays, automobile industry is a growing market for thermal spraying and number of coating applications is increasing steadily.[5] A few examples of HVOF coatings' applications are mentioned in **Table 3**. Picas *et al.*[42] studied the behavior of HVOF CrC75 (NiCr20) 25 coatings deposited on a steel substrate with a thickness of approximately 150 μm. In order to achieve very fine surface finish, dense, and coherent microstructure of the coating, they sprayed the HVOF carbide coatings from three different agglomerated feedstock powders with various powder size distributions. Taylor–Hobson rugosimeter–profilometer was used to measure the surface roughness values with a cut-off of 0.8 mm. With fine powder size distribution and optimized HVOF spray parameters, they succeeded in developing the as-sprayed HVOF CrC75 (NiCr20) 25 coatings with the lower value of surface roughness Ra as 2.0 μm (**Table 3**). The authors recommended the use of efficient and economic 'clean' HVOF technology to coat different type of critical mechanical components like valves, pistons, piston rings, rods, hydraulic components thereby considered to replace the hazardous hard chromium plating technology.

3.14.5.2.2 Power generation industry

Slurry erosion of turbine components is a very serious problem in the hydraulic power plants all around the globe, for instance in those situated in Himalayan regions of India.[46–47] The hydraulic turbine components such as guide vanes, top and bottom ring liners, labyrinths, runner blades, inlet valve seals, etc. are mainly affected by slurry erosion, which are usually protected by surface coatings. Therefore, Goyal *et al.*[48] deposited WC–10Co–4Cr and Al_2O_3–13(TiO_2) coatings on CF8M turbine steel by HVOF spray process and studied their performance under slurry erosion conditions. The coatings were developed at M/S Metallizing Equipment Company Private Limited, Jodhpur, India, by using commercial HVOF thermal spray system (HIPOJET2700). Surface roughness tester (SurftestSJ301, Mitutoyo) was used to measure the surface roughness values on the uncoated and coated specimens. The spray parameters and the Ra values are reported in **Table 3**. The authors observed higher erosion rates in the early cycles of experimentation. The authors reported that the initial roughness of the specimens could be the possible reason for this behavior. The higher material removal rate during the initial period might have resulted due to the micropeaks and valleys which exist on the surface of the specimens. However, once the surfaces became smooth, the erosion rate became, by and large, steady. The HVOF-sprayed WC–10Co–4Cr coating was found to be protective against the slurry erosion of the base steel.

3.14.5.2.3 Surface roughness of bondcoats in thermal barrier coatings

Thermal barrier coatings (TBCs) have been widely used in order to obtain more efficient and durable hot section components in gas turbine engines.[49,50] TBCs normally consist of a thermally insulating ceramic topcoat and an oxidation-resistant metallic bondcoat on the substrate.[51,52] MCrAlY (M¼Ni, and/or Co) is typically used as a bondcoat as it offers a good thermal expansion match between the substrate and the topcoat. In addition to that it also protect the substrate from oxidation and hot corrosion. A thermally grown oxide (TGO) formation takes place at the bondcoat/topcoat interface when in service at high temperatures. This TGO is responsible for the durability and failure of TBCs.[53–55] The roughness of the bondcoat is a critical factor which is responsible for the effective lifetime of TBCs. Bondcoat roughness depends on the technique used for deposition of coating. In addition to that it has been noticed that the properties of feedstock powders and spraying parameters also influence the microstructure and roughness of the bondcoats.[55,56] Studies done by various researchers proved that the condition of the bondcoat surface had a substantial effect on the lifetime of TBCs.[56–59]

In the work done by Ni and Zhou[60] HVOF spray technique was used to deposit NiCrAlY bondcoat with an aim to investigate the effect of three different types of surface modifications namely grit blasting, shot-peening, and vacuum treatment on

Table 3 Typical applications of HVOF spraying[42,48]

Component	*Coating material*	*Coating function and requirements*	*HVOF gun details*	*Spray parameters*		*Coating characterization results*
Valves, pistons, piston rings, rods, and hydraulic critical mechanical components	CrC75 (NiCr20) 25	Friction and wear properties	C-CJS HVOF gun (nozzle configuration k5.2 (Thermico, Germany)	Hydrogen flow rate taken ($m^3\ h^{-1}$) Fuel (kerosene) flow rate ($l\ h^{-1}$) Oxygen flow rate ($m^3\ h^{-1}$) N_2 powder feeding ($m^3\ h^{-1}$) Powder feed rate ($kg\ h^{-1}$) Deposit efficiency (%) Density taken in ($g\ cm^{-3}$)	0.8 8–12 6 45 4 55 6.6	• Surface roughness value with very fine powder size particles <5 μm (Ra-2.0 μm) • Dense and coherent microstructure obtained[42]
Hydro turbine components	WC–10Co–4Cr; $Al_2O_3 + 13TiO_2$; $Cr_3C_2 + 25$NiCr, Cr_2O_3; CoNiCrAlY	Slurry erosion	HVOF thermal spray system (HIPOJET2700)	Air pressure ($kg\ cm^{-2}$) Oxygen flow rate (slpm) Fuel (LPG) flow rate (slpm) Air-flow rate (slpm) Powder feed rate ($g\ min^{-1}$) Fuel pressure ($kg\ cm^{-2}$) Oxygen pressure ($kg\ cm^{-2}$) Spray distance (cm)	5.5 270 60–65 650 28 6.5 10.0 20	• Surface roughness values for WC–10Co–4Cr coating, Ra-4.27 μm and for $Al_2O_3 + 13TiO_2$ Coating, Ra-4.55 μm • Surface roughness values for $Cr_3C_2 + 25$NiCr coating, Ra-3.34 μm and for Cr_2O_3 coating, Ra-2.83 μm • Surface roughness values for CoNiCrAlY coating, Ra-4.58 μm[48]

the thermal cycling lifetime of TBCs. The main objective of the investigation was to study the morphology and composition of TGO, and also to explore the failure mechanism of the coating. NiCrAlY bondcoat was prepared by HVOF spray on nickel-based superalloy using a commercial Met Jet III (metallization) gun. The fuel used for the deposition was kerosene and carrier gas was nitrogen. After the successful deposition of the coating three different types of surface finishing modifications were employed as given below[60]:

- Grit blasting of the specimens by using alumina grit of 250 mm size,
- Shot-peening of the specimens by using glass grit of 250 mm size, and
- Preoxidation heat treatment under vacuum conditions using working pressure of $3–7 \times 10^{-3}$ Pa for 2 h at 1050 °C to obtain different surface morphologies of the coatings.

After the above mentioned procedure 8 wt% Y_2O_3–ZrO_2 powders were deposited by air plasma spray (APS) onto the surfaces of the HVOF-sprayed NiCrAlY coating. The results exhibited better thermal shock resistance in case of surface-modified TBCs. In case of TBCs with the as-sprayed bondcoat, failure took place within the topcoat as well as at the interface between spinels and the topcoat. For the shot-peening, grit blasting, and vacuum treatment TBC systems the failure was noticed mostly within the topcoat. TGO observed on as-sprayed bondcoat was found to consist of $Ni(Al,Cr)_2O_4$ spinels on the outer layer and a Al_2O_3 phase in the inner layer. A continuous and uniform Al_2O_3 was observed after surface modification. It was noticed that the presence of mixed oxides (spinels) on the as-sprayed bondcoat enhanced the failure of TBCs. It was concluded that the formation of a continuous and uniform Al_2O_3 after surface modifications was instrumental in the enhancement of the thermal cycling life of TBCs.[60]

The influence of processing parameters on the microstructure of overlay coatings has been studied by several authors. Rajasekaran *et al.*[61] observed that MCrAlY overlay coatings sprayed by HVOF process had considerable variations in the microstructure and roughness subject to powder grain size and spraying parameters, such as spray distance and/or

powder flow rate. Pant *et al.*[62] found that the microstructural properties of the MCrAlY overlay coating sprayed by high-energy HVOF were dependent on the type of gun used for the spraying process. An investigation of Perez[63] showed that the intersplat porosity can be greatly reduced by optimization of APS spray parameters, and the MCrAlY overlay coating density becomes similar to that sprayed by HVOF. All the above results showed that even in the frame of one spraying method, it is possible to produce bondcoats with large differences in microstructures and roughness profiles using different powder particles sizes, spraying parameters, or spraying guns.

Nowak *et al.*[64] investigated the influence of change in morphology and roughness profile on the lifetime of APS–TBC systems. For this purpose bondcoats of the same chemical composition were deposited using different thermal-sprayed techniques namely HVOF, VPS, and two kinds of a double-layered bondcoat having a base coating of HVOF and a thin outer layer 'flashcoat'sprayed by APS. The lifetime evaluation was done using cyclic oxidation testing at 1120 °C. The bondcoat roughness profile was correlated with the lifetime of APS–TBC systems using standard bondcoat roughness parameters, which included arithmetic average height (Ra) and maximum height of the profile (Ry), of the as-received TBC systems. Apart from the standard Ra and Ry calculations, fractal analysis of the bondcoat roughness profiles was also executed using the commercially available software Sfrax 1.0.[65] The three TBC systems chosen for the quantitative roughness evaluation were HVOF bondcoat, VPS bondcoat, and APS-flashcoat. Initially a standard roughness evaluation was done by calculating the Ra and Ry values. The results of the evaluated roughness values are reproduced in **Table 4**.

The arithmetic mean roughness (Ra) values of the evaluated bondcoats were found to vary between 11.2 μm for the HVOF bondcoat and 13.2 μm for the system with optimized APS-flashcoat. The TBC system which possessed the smallest bondcoat roughness, i.e., HVOF bondcoat showed the shortest lifetime. Further, the system possessing the highest roughness had the longest lifetime. It was observed that the parameters which were used for the APS-flashcoat spraying strongly effected the lifetime of the TBC system. It was noticed that a slight variation in spraying parameters for the APS-flashcoat led to formation of a porous and discontinuous layer. This led to shortening of lifetime of the respective TBC-system (which was even shorter than that of the system with flat HVOF bondcoat) as a result of rapid breakaway oxidation of the flashcoat.[64]

The performance of TBC specimens having NiCoCrAlYHfSi bond coatings deposited by HVOF spraying technique on superalloy 1483 and X4 substrates was assessed in dry and wet air in 1 h furnace cycles at 1100 °C.[66] Specimens of 1483 and X4 superalloys having size 16 mm diameter and 2 mm thickness were prepared by machining followed by grit blasting. Finally, the prepared specimens were coated using ~125 μm NiCoCrAlYHfSi (Amdry 386) by the HVOF process in two stages. In the first stage a finer (−44/+16 μm) powder was used and the second stage consisted of coarser (−90/+38 μm) powder in order to attain a higher roughness. After the deposition of the coatings, these were annealed in a vacuum of 10^{-4} Pa (10^{-6} Torr) for 4 h at 1080 °C. APS technique was utilized for the top coatings of 8 wt% Y_2O_3-stabilized ZrO_2 (YSZ) on one side of the coupons in thickness range of 190–240 μm. Cyclic oxidation test were conducted in a groups of four specimens at each condition. In order to characterize the thermally grown alumina scale three were coated with an APS YSZ topcoat and the fourth was tested without YSZ. Compared to an earlier study of NiCoCrAlYHfSi bond coatings, the HVOF bond coatings were found to be rougher having a value of Ra = 8 μm, which was nearer to commercial HVOF coatings.[66] It was observed that for the TBC coatings deposited on the X4 substrates cycled in air with 10% water vapor, the increase in the roughness value from Ra = 5 to 8 μm did not have much effect on the average TBC lifetime. The presence of 10% water vapor decreased the average TBC lifetime for 1483 by 13%, however, in both wet and dry conditions, the lifetimes for this substrate were 30–50% below those observed for X4 substrates. The main cause of this behavior was the lower Al content and higher Ti content in 1483. Roughness and residual stress in the alumina scale were measured on specimens without a ceramic top coating and it was concluded that the change in substrate or the addition of water vapor had no effect on the same. **Figure 8** summarizes the average TBC lifetimes measured in this study and compares these results to those obtained earlier on the same X4 substrate, but with a lower roughness HVOF bond coating.[67]

Table 4 Results of bondcoat roughness evaluation using conventional procedures combined with TBC lifetimes during thermal cycling[64]

Bondcoat	*HVOF bondcoat*	*VPS bondcoat*	*APS-flashcoat*
Ra (μm)	11.3	12.9	13.2
Ry (μm)	65	91	90
Lifetime at 1120 °C	108 h	252 h	344 h

3.14.5.3 Post-Deposition Surface Finish

HVOF spraying enables deposition of relatively thick coatings which are suitable for engineering applications including

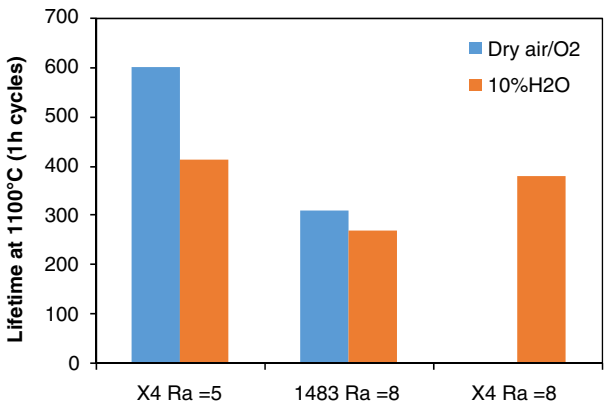


Figure 8 Average lifetimes for air plasma spray Y_2O_3-stabilized ZrO_2 coated X4 and 1483 specimens with high velocity oxy-fuel NiCoCrAlYHfSi type bond coatings exposed in 1-h cycles at 1100 °C in dry and wet environments: The data with the lower roughness is from a previous study.[66]

resistant to wear. The resultant coatings are economical, easy-to-achieve and offer excellent protection. As a result, these coatings have found applications in various industrial fields.[68,69] Though many coatings are deposited near-net shape but still their finishing is mostly required. For coatings that exhibit such a grade of protection, the finishing process can be troublesome. It can be time consuming and expensive, accounting for up to 50% of the manufacturing cost. Moreover, wrong finishing operations may lead to the deterioration of the coating precision and surface integrity.[70] It has been stated that grinding is the most commonly adopted method for finishing of hard materials[71,72] such as that of thermal-sprayed coatings. However, grinding can be comparatively costly and may occasionally reduce the performance of the coating.[72]

Abrasive fluidized bed (AFB) technology was proposed by Barletta *et al.*[73] to finish high speed axial-symmetric components coated by HVOF. The changes in the coating morphology according to the operational parameters and the related material removal mechanisms were investigated. Further, the closest conformity of the processed coatings with the dimensional tolerances were also evaluated. **Figure 9** shows that the trend of roughness parameters versus abrasive size at 12 000 rpm. Ra and Rz improved after the first finishing step with the biggest abrasive (mesh size 46) and improved slightly when smaller abrasives (mesh size 80 and 120) were used. Ra and Rz improved from approximately 7 and 35 µm to approximately 2 and 10 µm. Rdq (i.e., slope), related to the local coarseness of the surface and, therefore, to its capability to reflect the incident light, decreased after the first finishing step from 22 to 10 µm. RSm increased from 0.2 to approximately 0.26 mm as the morphology changed from the initial micro-corrugated topography of the partially melted or unmolten Stellite 6.[74]

It was concluded from the study that Al_2O_3 abrasives are suitable to finish the coatings leading to a satisfying morphology and the process does not have a significant impact on

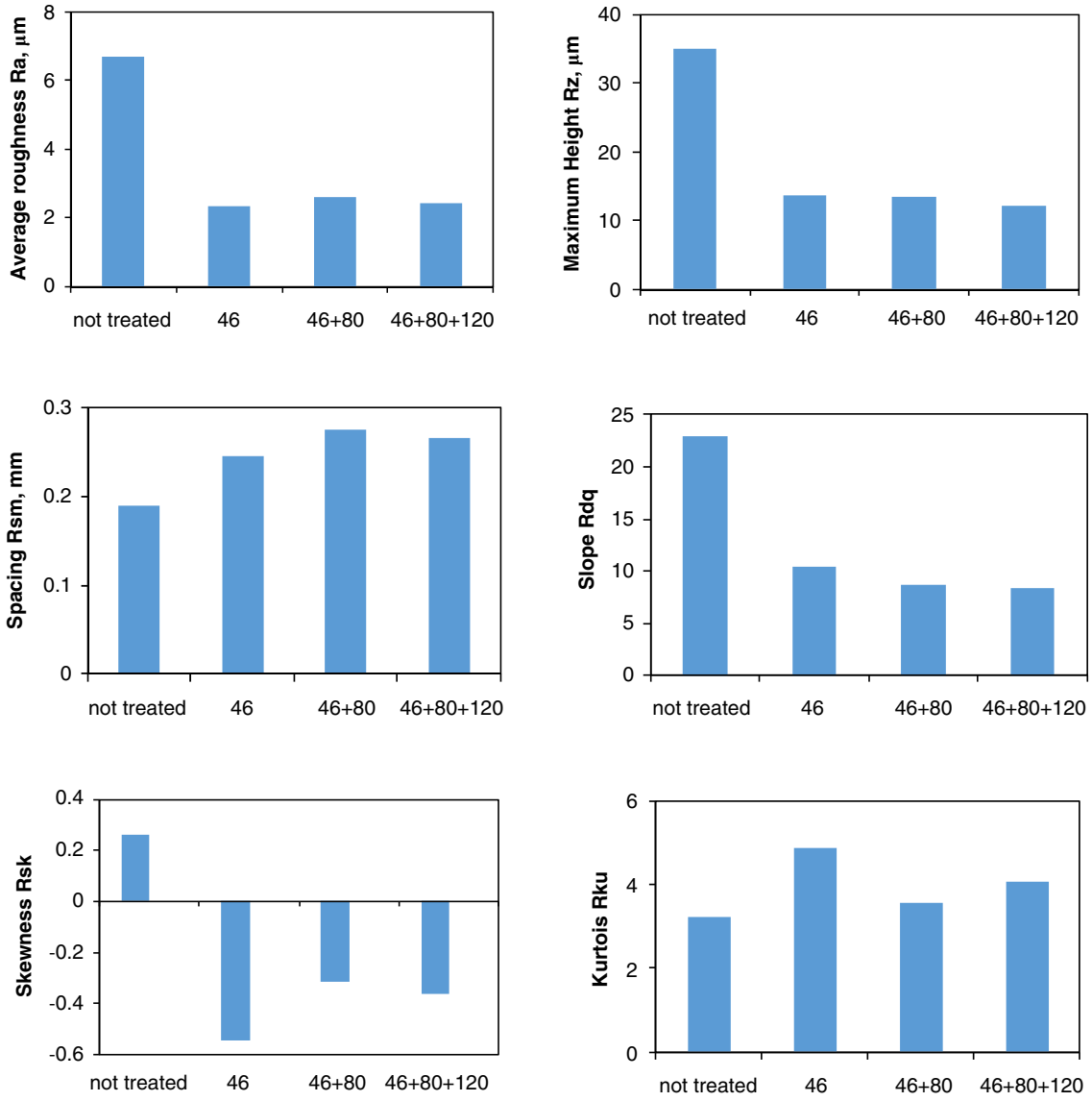


Figure 9 Trend of roughness parameters vs. abrasive size at 12 000 rpm.[73]

the dimensional properties with moderate material removal (−0.3% in the starting radius). Hence, the study demonstrated the feasibility of AFB to machine hard coatings. The technique has been suggested to be flexible and suitable to wider industrial applications. Moreover, this process permits to obtain end-products with a high standard. Furthermore, it is low cost, safe, easy to automate and eco-friendly process.[73]

Surface roughness characterization of thermally sprayed and precision machined WC–Co and Alloy-625 coatings was carried out by Zhong *et al.*[75] It was established that commercial machines and tools could be used for the machining of difficult-to-machine coating surfaces. The surface finish of the machined coatings was also characterized. The thermal spraying processes used for depositing the coating were AS and HVOF spraying. Optimization of the surface finishing of the coatings was done on the basis of surface finish and time required using different machining techniques. Machined samples were then examined using stylus roughness testers. Surface roughness parameters (Ra and Rq) were measured using different cut-off lengths, sampling lengths, and numbers of sampling in order to characterize the scaling behavior of the surfaces. Whereas the diamond turning process of WC–Co lead to high material removal rates, on the other hand diamond grinding of WC–Co resulted in good surface finish with relatively high material removal rates.[75] It was found that the surface roughness heights of the machined surfaces were dependent on the scale of cut-off length as a power law. For WC–Co coatings deposited by the HVOF process mirror like surfaces were achieved by fine grinding operation using a fine diamond wheel. When cubic boron nitride (CBN) grinding was done on the HVOF-sprayed WC–Co coatings some problems with loading of grinding wheels were observed. However no such loading problem was observed when diamond grinding was conducted.[75]

3.14.6 Concluding Remarks

In this chapter, HVOF thermal spray technique, its comparison with other thermal spray processes and its applications in relation to the surface finishing have been reviewed. HVOF techniques have developed extensively over the last two decades from the first generation HVOF systems to the third generation HVOF systems. New modifications and improvements of the technology have been introduced. Nowadays, HVOF thermal spray process is being accepted by many industries due to the advantage of being applied on-site on the surface of the components and superior coating properties. The HVOF spray process retains the composition of the coating material to a greater extent and has been shown to produce coatings with low porosity, low-oxide content, better density, better coating cohesive strength and bond strength in comparison with other thermal spray processes. Furthermore, it is evident from literature studies that with increasing time in service, the HVOF-coated surfaces have been found to remain relatively constant regardless of the accumulation of dynamic cycles with seals and bearings in dynamic applications. Surface preparation is vital before the coating deposition process in order to improve the coating/substrate interfacial adhesion. Certain preprocessing techniques are utilized to remove grease and other contaminants from the surface which also help to change the physicochemical properties and/or surface morphology for better adhesion of the same. Among the commonly used techniques, degreasing and sandblasting are used in most cases. Investigations done by various researchers prove that for TBCs the condition of the bondcoat surface roughness had a significant effect on the overall lifetime of the same. The bondcoat can be subjected to grit blasting, shot-peening or certain preoxidation heat treatment processes in order to obtain different surface finish. For optimizing the surface finish after the coating deposition different machining techniques like grinding, diamond turning and AFB technology have been recommended.

See also: 3.13 Finishing and Post-Treatment of Thermal Spray Coatings

References

1. Simunovic, K. Welding Engineering and Technology. In *Thermal Spraying*; Slobodan, K., Ed.; Encyclopedia of Life Support Systems (EOLSS): Oxford, 2010; pp. 1–25.
2. Thorpe, M. L.; Richter, H. J. A Pragmatic Analysis and Comparison of HVOF Processes. *J. Therm. Spray Technol.* **1992**, *1* (2), 161–170.
3. Bick, H.; Jürgens, W. Advanced High Velocity Thermal Spraying of Metallic and Ceramic Powders. In *Proceedings of the 10th International Thermal Spray Conference*, DVS, Düsseldorf, Germany, 1983; pp. 92–94.
4. Kreye, H.; Fandrich, D.; Müller, H. H.; Reiners, G. *Microstructure and Bond Strength of WC–Co Coatings Deposited by Hypersonic Flame Spraying, in Advances in Thermal Spraying*; Pergamon Press: New York, NY, 1986; pp. 121–128.
5. Pawlowski, L. *The Science and Engineering of Thermal Spray Coatings*; John Wiley & Sons Ltd.: Chichester, 2008.
6. Tan, J. C.; Looney, L.; Hashmi, M. S. J. Component Repair Using HVOF Thermal Spraying. *J. Mater. Process. Technol.* **1999**, *92–93*, 203–208.
7. Voyer, J.; Marple, B. R. Thermal Spray Processing of WC–Co Nanomaterials. In *Thermal Spraying: Surface Engineering via Applied Reasearch*; Berndt, C. C., Ed.; ASM International: Montreal, QC, 2000; pp. 895–904.
8. Berndt, C. C. *Thermal Spray Technology-Course Proceedings, Organized by International Advanced Research Centre for Powder Metallurgy and New Materials (ARCI)*, Hyderabad, India, 2014.
9. Lugscheider, E.; Herbst, C.; Zhao, L. Parameter Studies on High-Velocity Oxy-Fuel Spraying of MCrAlY Coatings,. *Surf. Coat. Technol.* **1998**, *108–109*, 16–23.
10. Kaur, M.; Singh, H.; Prakash, S. A Survey of the Literature on the Use of High Velocity Oxy-Fuel Spray Technology for High Temperature Corrosion and Erosion-Corrosion Resistant Coatings. *Anticorros. Method Mater.* **2008**, *55* (2), 86–96.
11. Kaur, M.; Singh, H.; Prakash, S. High-Temperature Behavior of a High-Velocity Oxy-Fuel Sprayed Cr_3C_2–NiCr Coating. *Metall. Mater. Trans. A* **2012**, *43*, 2979–2993.
12. Oksa, M.; Turunen, E.; Suhonen, T.; Varis, T.; Hannula, S. P. Optimization and Characterization of High Velocity Oxy-Fuel Sprayed Coatings: Techniques. *Mater. Appl. Coat.* **2011**, *1*, 17–52.
13. Pawlowski, L. *The Science and Engineering of Thermal Spray Coatings*; Wiley: New York, NY, 1995.
14. Stokes, J. *The Theory and Application of the HVOF Thermal Spray Process*; Dublin City University: Dublin, 2005.
15. Fantassi, S., Vardelle, M., Fauchais, P., Moreau, C. Investigation of the Splat Formation versus Different Particulate Temperatures and Velocities Prior to Impact. In *Proceedings of International Thermal Spray Conference*, Florida, USA, 1992; pp. 755–760.
16. Moreau, C.; Cielo, P.; Lamontagne, M. Flattening and Solidification of Thermal Sprayed Particles. In *Proceedings International Thermal Spray Conference*, Florida, USA, 1992; pp. 761–766.

17. Kanouff, M. P.; Neiser, R. A., Jr; Roemer, T. J. Surface Roughness of Thermal Spray Coatings Made with Off-Normal Spray Angles. *J. Therm. Spray Technol.* **1998**, *7* (2), 219–228.
18. Kinos, T. *Proceedings of NTPC*, 1994; p. 357.
19. Khor, K. A.; Leh, N. L. *Proceedings of NTSC*, 1993; p. 613.
20. Tucker, R. C.; Ashari, A. A.; Coddet, C., Eds. *Proceedings of 13th ITSC*, Nice, France, 1992; p. 75.
21. Hwang, S. Y., Seong, B. G., Ohmori, A., Eds. *Proceedings of 14th ITSC*, Kobe, Japan, 1995; p. 59.
22. Li, C. J., Sonoya, K., Ji, G. C., Wang, Y. Y., Coddet, C., Eds. *Proceedings of 15th ITSC*, Nice, France, 1998; p. 287.
23. Jacobs, L.; Hyland, M. M.; Bonte, M. De Comparative Study of WC–Cermet Coatings Sprayed via the HVOF and the HVAF Process. *J. Therm. Spray Technol.* **1998**, *7* (2), 213–218.
24. Hussain, N.; Shahid, K. A.; Khan, I. H.; Rahman, S. Oxidation of High-Temperature Alloys (Superalloys) at Elevated Temperatures in Air: I. *Oxid. Metals* **1994**, *41* (3–4), 251–269.
25. Kirsten, A.; Oechsle, M.; Moll, R. HVOF-Sprayed Materials Replace Hard-Chromium Plating. *Sulzer Tech. Rev.* **2006**, *1*, 4164–4166.
26. Karthikeyan, J. *Cold Spray Technology: International Status and USA Efforts*; ASB Industries Inc.: Barberton, OH, 2004; pp. 1–14.
27. Greene Tweed Surface finish/Product Data, 2007. Available from: www.gtweed.com (accessed 3 March 2016).
28. Tucker, R. C., Ed. *Introduction to Coating Design and Processing. ASM Handbook, Volume 5A: Thermal Spray Technology*; ASM International: Materials Park, OH, 2013
29. McPherson, R. The Relationship between the Mechanism of Formation, and Properties of Plasma-Sprayed Coatings Microstructure. *Thin Sol. Films* **1981**, *83*, 297–310.
30. Weiss, H. Adhesion of Advanced Overlay Coatings: Mechanisms and Quantitative Assessment,. *Surf. Coat. Technol.* **1995**, *71*, 201–207.
31. Li, L.; Wang, X. Y.; Wei, G.; Vaidya, A.; Zhang, H.; Sampath, S. Substrate Melting during Thermal Spray Splat Quenching. *Thin Sol. Films* **2004**, *468*, 113–119.
32. Khor, K. A.; Li, H.; Cheang, P. Significance of Melt-Fraction in HVOF Sprayed Hydroxyapatite Particles, Splats and Coatings. *Biomaterials* **2004**, *25*, 1177–1186.
33. Pawlowski, L. *The Science and Engineering of Thermal Spray Coating*; John Wiley & Sons: Chichester, 1995.
34. Mellali, M.; Fauchais, P.; Grimaud, A. Influence of Substrate Roughness and Temperature on the Adhesion/Cohesion of Alumina Coatings. *Surf. Coat. Technol.* **1996**, *81*, 275–286.
35. Fauchais, P.; Vardelle, M.; Vardelle, A.; Bianchi, L. Plasma Spray: Study of the Coating Generation. *Ceram. Int.* **1996**, *22*, 295–303.
36. Hutson, A. L.; Niinomi, M.; Nicholas, T.; Eylon, D. Effect of Various Surface Conditions on Fretting Fatigue Behavior of Ti–6Al–4V. *Int. J. Fatigue* **2002**, *24*, 1223–1234.
37. Berndt, C. C.; Leigh, S. H. Evaluation of Off-Angle Thermal Spray. *Surf. Coat. Technol.* **1997**, *89*, 213–224.
38. Amada, S.; Hirose, T. Influence of Grit Blasting Pre-Treatment on the Adhesion Strength of Plasma Sprayed Coatings: Fractal Analysis of Roughness. *Surf. Coat. Technol.* **1998**, *102*, 132–137.
39. Wang, Y. Y.; Li, C. J.; Ohmori, A. Influence of Substrate Roughness on the Bonding Mechanisms of High Velocity Oxy-Fuel Sprayed Coatings. *Thin Sol. Films* **2005**, *485*, 141–147.
40. Gonzalez-Hermosilla, W. A.; Chicot, D.; Lesage, J.; *et al.* Effect of Substrate Roughness on Fatigue Behaviour of SAE 1045 Steel Coated withWC–10Co–4Cr Cermet Deposited by HVOF Thermal Spray. *Mater. Sci. Eng.: A* **2010**, *527* (2010), 6551–6561.
41. Patel, K.; Doyle, C. S.; Yonekura, D.; James, B. J. Effect of Surface Roughness Parameters on Thermally Sprayed PEEK Coatings,. *Surf. Coat. Technol.* **2010**, *204*, 3567–3572.
42. Picas, J. A.; Forn, A.; Matthaus, G. HVOF Coatings as an Alternative to Hard Chrome for Pistons and Valves. *Wear* **2006**, *261* (5–6), 477–484.
43. Harvey, D. The Tough Truth-Wear-Resistant Coatings Using High Velocity Oxy-Fuel. *Ind. Lubr. Tribol.* **1996**, *48*, 11–16.
44. Perry, J. M.; Neville, A.; Hodgkiess, T. A Comparison of the Corrosion Behaviour of WC–CoCr and WC–Co HVOF Thermally Sprayed Coatings by In Situ Atomic Force Microscopy (AFM). *J. Therm. Spray Technol.* **2002**, *11* (4), 536–541.
45. Grasset, G. Projection Thermique et Codeposition Electrolytique, Deux Alternatives. In *1st International Meeting on Thermal Spraying*; Pawlowski, L., Ed.; ENSCL, Lille, December 3–4, 2003; pp. 197–202 (unpublished conference proceedings).
46. Sharma, D. P.; Singh, S. Operational Problems of Water Turbine in U.P. with Special Reference to Tiloth Power Station. In *Proceedings of all India Seminar on Metallurgical Problems in Power Projects*, 1987; pp. 18–35.
47. Naidu, B. S. K. Developing Silt Consciousness in the Minds of Hydropower Engineers. In *Proceedings of the 1st International Conference on Silting Problems in Hydropower Plants*, 1999; pp. 1–36.
48. Goyal, D. K.; Singh, H.; Kumar, H.; Sahni, V. Slurry Erosion Behaviour of HVOF Sprayed WC-10Co-4Cr and $Al_2O_3 + 13TiO_2$ Coatings on a Turbine Steel. *Wear* **2012**, *289*, 46–57.
49. Khan, A. S.; Nazmy, M. MCrAlY Bond Coating and Method of Depositing Said MCrAlY Bond Coating. U.S. Patent No. 7,264,887 B2, 4 September 2007.
50. Evans, H.; Taylor Oxidation of High-temperature Coatings. *Proc. Inst. Mech. Eng.* **2006**, *220*, 1–10.
51. Goward, G. Progress in Coatings for Gas Turbine Airfoils. *Surf. Coat. Technol.* **1998**, *108–109*, 73–79.
52. DeMasi-Marcin, J. T.; Gupta, D. K. Protective Coatings in the Gas Turbine Engine. *Surf. Coat. Technol.* **1994**, *68–69*, 1–9.
53. Yamazaki, Y.; Fukanuma, H.; Ohno, N. Effect of Interfacial Roughness of Bond Coat on the Residual Adhesion Strength of a Plasma Sprayed TBC System after Thermal Cycle Fatigue. *J. Sol. Mech. Mater. Eng.* **2010**, *4* (2), 196–207.
54. Eriksson, R.; Sjorstrom, S.; Brodin, H.; Johansson, S.; Ostergren, L.; Li, X. H. TBC Bond Coat–Topoat Interface Roughness: Influence on Fatigue Life and Modelling Aspects. *Surf. Coat. Technol.* **2013**, *236*, 230–238.
55. Hsueh, C. H.; Haynes, J. A.; Lance, M. J.; *et al.* Effect of Interface Roughness on Residual Stresses in Thermal Barrier Coatings. *J. Am. Ceram. Soc.* **1999**, *82* (4), 1073–1075.
56. Zhang, D. B.; Gong, S. K.; Xu, H. B.; Wu, Z. Effect of Bond Coat Surface Roughness on the Thermal Cyclic Behavior of Thermal Barrier Coatings. *Surf. Coat. Technol.* **2006**, *201*, 649–653.
57. Che, C.; Wu, G. Q.; Qi, H. Y.; Huang, Z.; Yang, X. G. Effect of Bond Coat Surface Roughness on Oxidation behavior of Air Plasma Sprayed Thermal Barrier Coatings. *Surf. Eng.* **2008**, *24* (4), 276–279.
58. Matsumoto, M.; Hayakawa, K.; Kitaoka, S.; *et al.* The Effect of Preoxidation Atmosphere on Oxidation Behavior and Thermal Cycle Life of ThermalBarrier Coatings. *Mater. Sci. Eng.: A* **2006**, *441*, 119–125.
59. Ni, L. Y.; Wu, Z. L.; Zhou, C. G. Effects of Surface Modification on Isothermal Oxidation Behaviour of HVOF-Sprayed NiCrAlY Coatings. *Prog. Nat. Sci.: Mater. Int.* **2011**, *21* (2), 173–179.
60. Liyong, Ni.; Zhou, C. Effects of Surface Modifications on Thermal Cycling Lifetime of Thermal Barrier Coatings with HVOF NiCrAlY Bond Coat. *Prog. Nat. Sci.: Mater. Int.* **2012**, *22* (3), 237–243.
61. Rajasekaran, B.; Mauer, G.; Vassen, R. Enhanced Characteristics of HVOF-Sprayed MCrAlY Bond Coats for TBC applications. *J. Therm. Spray Technol.* **2011**, *20* (6), 1209–1216.
62. Pant, B. K.; Arya, V.; Mann, B. S. Development of Low-Oxide MCrAlY Coatings for Gas Turbine Applications. *J. Therm. Spray Technol.* **2007**, *16* (2), 275–280.
63. Perez, E. *Development of APS MCrAlY Dense Bond Coats, UTSR Summer Fellowship Program Project Report*. Available from: http://citeseerx.ist.psu.edu/viewdoc/download?rep=rep1&type=pdf&doi=10.1.1.205.7334, 2006 (accessed 13 April 2016).
64. Nowak, W.; Naumenko, D.; Mor, G.; *et al.* Effect of Processing Parameters on MCrAlY Bondcoat Roughness and Lifetime of APS–TBC Systems. *Surf. Coat. Technol.* **2014**, *260*, 82–89.
65. Surfract. Available from: http://www.surfract.com/sfrax.html (accessed 3 March 2016).
66. Haynes, J. A.; Unocic, K. A.; Lance, M. J.; Pint, B. A. Impact of Superalloy Composition, Bond Coat Roughness and Water Vapor on TBC Lifetime with HVOF NiCoCrAlYHfSi Bond Coatings. *Surf. Coat. Technol.* **2013**, *237*, 65–70.
67. Haynes, J. A.; Unocic, K. A.; Pint, B. A. Effect of Water Vapor on the 1100 °C Oxidation Behavior of Plasma-Sprayed TBCs with HVOF NiCoCrAlX Bond Coatings. *Surf. Coat. Technol.* **2013**, *215*, 39–45.
68. Ernst, P.; Barbezat, G. Thermal Spray Applications in Power Train Contribute to the Saving of Energy and Material Resources. *Surf. Coat. Technol.* **2008**, *202*, 4428–4431.
69. Vassen, R.; Kassner, H.; Stuke, A.; Hauler, F.; Hathiramani, D.; Stover, D. Advanced Thermal Spray Technologies for Applications in Energy Systems. *Surf. Coat. Technol.* **2008**, *202*, 4432–4437.
70. Karimi, A.; Verdon, C.; Barbezat, G. Microstructure and Hydroabrasive Wear Behaviour of High Velocity Oxy-Fuel Thermally Sprayed WCCo(Cr) Coatings. *Surf. Coat. Technol.* **1993**, *57*, 81–89.

71. Stephenson, D. J.; Hedge, J.; Corbett, J. Surface Finishing of Ni–Cr–B–Si Composite Coatings by Precision Grinding. *Int. J. Mach. Tool. Manuf.* **2002**, *42*, 357–363.
72. Murthy, J. K. N.; Rao, D. S.; Venkataraman, B. Effect of Grinding on the Erosion Behaviour of a WC–Co–Cr Coating Deposited by HVOF and Detonation Gun Spray Processes. *Wear* **2001**, *249*, 592–600.
73. Barletta, M.; Guarino, S.; Vesco, S.; Gisario, A.; Tagliaferri, V. Abrasive Fluidized Bed (AFB) Finishing of Thermally Sprayed Cobalt–Chromium Coatings. *Manuf. Lett.* **2013**, *1*, 1–4.
74. Sidhu, H. S.; Sidhu, B. S.; Prakash, S. Solid Particle Erosion of HVOF Sprayed NiCr and Stellite-6 Coatings. *Surf. Coat. Technol.* **2007**, *202*, 232–238.
75. Zhong, Z. W.; Peng, Z. F.; Liu, N. Surface Roughness Characterization of Thermally Sprayed and Precision Machined WC–Co and Alloy-625 Coatings. *Mater. Charact.* **2007**, *58*, 997–1005.

Relevant Websites

http://www.bodycote.com/en/services/surface-technology/hvof-coating.aspx
Bodycote.
http://www.gtweed.com/docs/design-tools/SurfaceFinish__AS_US.pdf
Greene Tweed.
http://www.praxairsurfacetechnologies.com/
Praxair Surface Technologies.
http://samples.sainsburysebooks.co.uk/9780470754078_sample_381415.pdf
Sainsbury's eBooks.
http://www.surfacetechnology.co.uk/
Surface Technology.
http://www.tstcoatings.com/index.php?page=HVOF.html
TST Engineered Coating Solutions.

3.15 Electroless Plating as Surface Finishing in Electronic Packaging

MA Azmah Hanim, Universiti Putra Malaysia, Serdang, Malaysia

© 2017 Elsevier Inc. All rights reserved.

3.15.1	**Introduction to Surface Finish Systems**	220
3.15.1.1	Surface Treatment	221
3.15.2	**Electroless Plating Baths in Electronic Packaging**	222
3.15.2.1	EN Plating	223
3.15.2.2	Electroless Palladium Plating	224
3.15.2.3	Electroless Gold Plating	226
3.15.3	**Conclusion**	228
References		228

3.15.1 Introduction to Surface Finish Systems

The flip chip is a type of interconnection used in electronic packaging. The main components of the flip chip consist of thin layers of metal called under bump metallurgy (UBM) on the die bond pads, layers of metal called top-surface metallurgy (TSM) on the substrate bond pads, and solder bumps on the UBM, as shown in Figure 1. The term 'surface finish' refers to the TSM layers.

The decision to use a surface finish is based on the premise that the desired level of solderability could not be realized with the conditions of the substrate surface at the time of soldering.[1] Inadequate substrate solderability can arise during the course of one of two general pretexts:

1. Similar to the case of glasses, ceramics, or refractory metals, the underlying base metal is isolated from the molten solder by a finish that provides the solderable layer to which the solder wets and over which it spreads to form the joint.
2. The applied finish simply coats the base metal to seal it against excessive oxidation. The surface finish is either dissolved into the solder, as is typically the case with metal coatings, or dissipated by the heat process just before the solder starts spreading, like those associated with several organic coatings.

Other than solderability protection, the application of this one-layer or multi-layer thin film on the metallization pads is also needed to provide adhesion and to act as a solder diffusion barrier, a solder wetting layer, and a corrosion-resistant layer.[2,3] Usually, the solder used contains a high percentage of tin (Sn). Because of Sn's high diffusivity and reactivity with copper (Cu; the metallization pad), this will result in rapid Cu–Sn intermetallic growth. Intermetallics, although needed to form a good bond, may reduce the solder's thermal fatigue life, if present in excessive quantities, due to their brittle nature.[4] This is one of the reasons why surface finishes are very important. Figure 2 illustrates the effect of a surface finish on the solderability and the process of solder joint formation.

It is also of great importance that the thicknesses of the solderable and protective layers (surface finish system) are closely controlled. If the solderable layer (which is usually the diffusion barrier layer) is too thin, then it might be fully consumed during soldering, thus exposing the liquid solder to the underlying base metal surface and, in the process, defeating the purpose of acting as a diffusion barrier. If dissolution of the

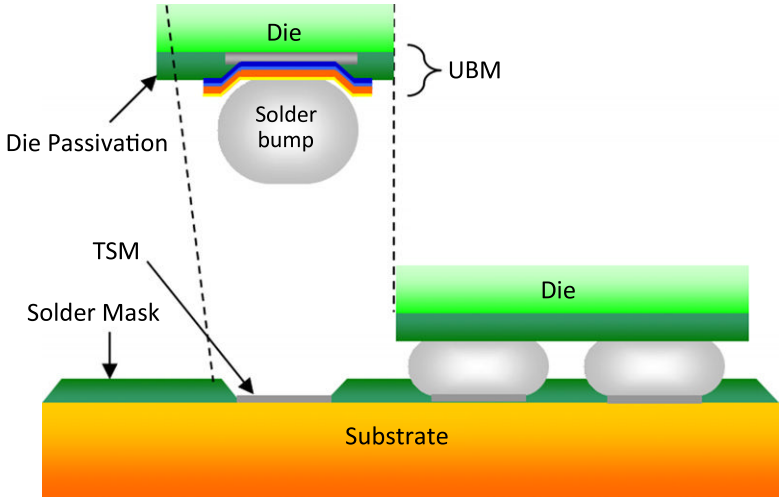


Figure 1 Flip chip solder joint.

 doi:10.1016/B978-0-12-803581-8.09177-3

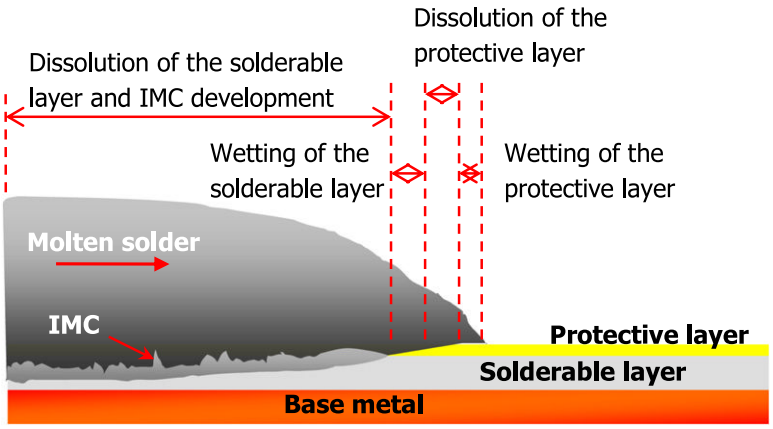


Figure 2 Schematic diagram of the phenomena that occurs in the solderable and protective finishes during the wetting and spreading of liquid solder.[1]

solderable layer occurs, then it may lead to the degradation of the solder joint's properties. If it is too thick, then it is not only undesirable from an economic view point but also detrimental to the solder joint's reliability. Thick coatings are always associated with high residual stress and contaminants from the plating bath. High residual stresses will lead to delamination of the solderable layer from the base metal surface.[1,5]

As the world moves forward toward adapting to stricter environmental standards, the entire electronics industry needs to re-evaluate its manufacturing practices. Implementation of restriction of the use of hazardous substances in countries around the world has moved innovation forward by leaps and bounds to determine new lead-free products that meet these requirements. In addition, the package also has to be able to withstand the higher assembly temperatures of lead-free solder alternatives.[6] In summary, it can be said that a good surface finish must be able to produce the following: acceptable metallurgical properties between the substrate and the solder; an inert property at ambient and/or reflow conditions over time; excellent wetting properties with the solder; and flat with controllable thickness.[7]

For the manufacturers of electronic packaging, hot-air solder leveling (HASL) has been the dominant final finish for the majority of printed circuit boards. However, it is the largest source of lead used in the industry. In addition to the need for lead-free materials, the other drivers that are pushing the electronics industry to consider HASL alternatives are cost and technology. Thus, as technology has evolved, a series of alternate surface finishes has been created, tested, and implemented for use throughout the printed circuit industry. Some finishes are widely used and others are used for very specific applications.

Regardless of the material type used for the surface finishing, electroless, and immersion plating seem to be the available methods for surface finish deposition in electronic packaging. This is due to the fact that electroless and immersion plating allow the fabrication of isolated metal patterns on insulating substrates.[8] Some of the surface finish systems available for electronic packaging using the electroless and immersion processes are:

1. Electroless nickel (EN)/immersion gold
2. EN/electroless gold
3. EN/electroless palladium/immersion gold
4. Immersion silver
5. Immersion tin
6. Direct immersion gold.

In the process in which metal is deposited from an aqueous solution, both electroless and immersion plating meet the requirements of chemical deposition. However, the electroless and immersion techniques differ in terms of their deposition mechanisms and the final results. Electroless plating is basically a chemical reduction process depending on the catalytic reduction of a metallic ion in an aqueous solution containing a reducing agent, with subsequent deposition of the metal without the use of electrical energy. The substrate itself can be catalytic or activated by the use of displacement deposits of palladium compounds or galvanic coupling with a catalytic metal. After the reaction is initiated, the metal deposited serves as the catalyst, ensuring the continuous build-up of the metal. For immersion, however, the more noble material will be deposited on the less noble through displacement. The process will stop as soon as the substrate is completely covered by the metal coating. The immersion process requires no reducing agents in the bath solutions.[9–11] In this research article, attention is focused on electroless plating solutions.

3.15.1.1 Surface Treatment

Electroless plating, like any other process, has its own advantages and weaknesses, as listed in **Table 1**.[8,12]

In electroless plating, the surface preparation of the substrate is a very important procedure. The solderability of the surface finish can deteriorate due to the exposure of the surfaces to deposited air-borne contaminants such as dust, 'acid rain' components, lubricant aerosols, or even tarnishing chemicals. The nature and magnitude of these contaminants will depend on the localized plant environment, as well as on any nearby industrial and agricultural operations. For example, in EN deposition, not all substrates are catalytic and could initiate plating without requiring additional activation steps. Nickel, steel, and aluminum substrates can initiate electroless

Table 1 Advantages and weaknesses of electroless plating

No.	*Advantages*	*Weaknesses*
1.	Capability to deposit thin films of metal on nonconducting surfaces (e.g., glass, ceramics, polymers)	Complex plating bath solution containing metal complex ions, reducing agents, pH adjustments, buffering components, and additives that may age, by-product reaction affecting the deposition, homogenous nucleation of the plating solution, nucleation on defects or nonselected surfaces, or failure to nucleate due to contamination or problems with the catalytic surface
2.	Requires relatively simple tools; plating bath and plating bath solution	Most of the plating solutions are hazardous to the environment (e.g., gold plating solution containing cyanide, nickel plating solution with thiourea as a stabilizing agent); need a proper method to dispose of the solution after plating
3.	Constant thickness of plated layer regardless of shape	Stringent control of the chemicals, temperature, and pH is needed according to each plating solution's specification

deposition with standard preparation cycles. However, copper and brass are not catalytic and require additional activation steps to ensure plate initiation.[1]

Alkaline soak cleaning is the traditional first step in the preparation cycle. The type of soils to be cleaned and the type of substrate determine the step or approach to solving the potential cleaning problem. The variety of soils commonly found in a plating facility includes machine drawing lubricants, buffing compounds, chlorinated oils, and waxes.[13] There are many more types of material that can be categorized as soils, including dirt, smut, oxides, rust, and heat scale. These types of soils are primarily handled during the activation process. Once a specific cleaning strategy has been chosen, factors such as operating temperature, concentration, and agitation become important considerations.[13]

Rinsing is the most critical part of the pretreatment process. According to Durkin,[13] increasing the rinsing time effectively removes these materials at the surface interface, although the films remaining contain minimal wetting agent or surfactant. In most cases, this condition is not harmful to the next process stage. It is also easy to visualize that a simple rinsing scheme, moving the substrate up and down as one wishes, is not likely to be very effective. Increasing the time (up to 2 min) of the rinses following the alkaline cleaning processes is recommended to ensure that the films remaining on the surface interface area are adequately removed.

After rinsing, activation is the most critical step in the preparation process. After cleaning the oils from the surface, all oxides need to be removed to allow proper atomic bonding of the plate to the substrate. The activation process can be broken down into different types or groups. The most common types are acid activation based on acid salts, mineral acids such as sulfuric acid or hydrochloric acid, and activators based on citric acid. The choice of which acids to use and their strength depend on the type and condition of the metal to be plated. Hydrochloric acid should not be used because chlorides may be detrimental to the EN deposit if corrosion resistance of the deposit is an important requirement. Other activators in the cleaning line include electro-cleaners, electrolytic acids, and nickel copper strikes. For nonconductive substrates, activators based on palladium chloride are commonly used.[13]

Immediately after the activation process, the substrate is immersed inside the plating solution, following the respective plating solution requirements such as temperature and pH. The actual deposition and its kinetics are defined in the following way:[8]

1. Transport of the constituents (i.e., metal complexes, reducing agents, other ions, additives) in the electrolyte toward the catalytic surface.
2. Adsorption of the constituents onto the surface.
3. Intermediate reactions involved in metal complex reduction and decomposition and the absorbed reducing agent oxidation. There are many possible intermediate reactions, and the rate depends on the catalytic seed as well as the absorbed species concentration.
4. Desorption of unreacted species, intermediates, and products.
5. Transport of the unreacted species, intermediates, and products away from the substrate.

After the initial step of nucleation, the metals grow following the deposition reaction as long as there is no significant depletion of any electrolyte compound or loss of the substrate catalytic properties.[8] The understanding of the process, stability, precision, and cost reduction in the electroless plating process has improved according to the technology evolution.

3.15.2 Electroless Plating Baths in Electronic Packaging

When selecting an alternative surface finish, the key parameters to consider are solderability, ambient stability, high-temperature stability, suitability for use with lead-free solders, solder joint integrity, and cost.[14] Currently, there are several alternative surface finishes using the electroless and/or immersion deposition techniques, which are used or are being explored for future use in the lead-free industry. The surface finishes are[5,12,15]:

1. EN/immersion gold
2. EN/electroless gold
3. EN/electroless palladium/immersion gold
4. Immersion silver
5. Immersion tin
6. EN/immersion silver

Based on this list, commonly there are only three types of electroless baths involved. These are EN, electroless palladium, and electroless gold solutions.

3.15.2.1 EN Plating

EN plating is undoubtedly the most important catalytic plating process that results in uniform deposits in use today. Several advantages, like its low cost, the easy formation of a continuous and uniform coating on the surface of a substrate with a complex shape, and the capability of depositing on either conductive or nonconductive parts, have attracted great interest from academia and industry. EN plating has unique chemical and mechanical properties and therefore is increasingly being used.[16] Some of these properties are:

1. Uniformity
2. Excellent corrosion resistance
3. Wear and abrasion resistance
4. Solderability
5. High hardness
6. Amorphous and microcrystalline deposits.

The chemical and physical properties of an EN coating depend on its composition, which, in turn, depends on the formulation and operating conditions of the EN plating bath. Typically, the constituents of an EN solution are[17–19]:

1. A source of nickel ions, usually nickel sulfate or nickel chloride; the nickel concentration is normally between 5 and 11 g l^{-1}.
2. A reducing agent to supply electrons for the reduction of the nickel. Several reducing agents are used in EN plating, including sodium hypophosphite, amineboranes, sodium borohydrite, and hydrazine. However, approximately 70% of EN is deposited from solutions reduced by sodium hypophosphite. This reduces the nickel ions and reacts with water at catalytic surfaces to form orthophosphite, which accumulates in solution and eventually precipitates as nickel phosphate. Because hydrogen ions are a by-product of these reactions, the pH of electroless solutions will decrease during normal operations.

The electrochemical mechanism, whereby catalytic oxidation of the hypophosphite yields electrons at the catalytic surface, which, in turn, reduces the nickel and hydrogen ions, is illustrated as follows[20]:

$$H_2PO_2^- + H_2O \rightarrow H_2PO_3^- + 2H^+ + 2e^- \quad [I]$$

$$Ni^{2+} + 2e^- \rightarrow Ni \quad [II]$$

$$2H^+ + 2e^- \rightarrow H_2 \quad [III]$$

$$H_2PO_2^- + 2H^+ + e^- \rightarrow P + 2H_2O \quad [IV]$$

The atomic hydrogen mechanism, whereby atomic hydrogen is released as a result of the catalytic dehydrogenation of the hypophosphite molecules adsorbed at the surface, is illustrated as follows:

$$H_2PO_2^- + H_2O \rightarrow HPO_3^{2-} + H^+ 2H_{ads} \quad [V]$$

$$2H_{ads} + Ni^{2+} \rightarrow Ni + 2H^+ \quad [VI]$$

$$H_2PO_2 + H_{ads} \rightarrow H_2O + OH^- + P \quad [VII]$$

The adsorbed active hydrogen [VI] then reduces the nickel at the surface of the catalyst:

$$(H_2PO_2)^{2-} + H_2O \rightarrow H^+ + (HPO_3)^{2-} + H_2 \quad [VIII]$$

Simultaneously, some of the absorbed hydrogen reduces a small amount of the hypophosphite at the catalytic surface to water, hydroxyl ions, and phosphorus [VII]. Most of the hypophosphite present is catalytic, which is oxidized to orthophosphite and gaseous hydrogen [VIII], causing low efficiency of EN solutions for the alloy coating while the deposition of nickel and phosphorus continues. Usually, 5 kg of sodium hypophosphite is required to reduce 1 kg of nickel, for an average efficiency of 37%.[21,22] The coefficient of utilization of the hypophosphite varies with the nature of the buffer additive; the highest degree of utilization of the hypophosphite was observed in the solution containing sodium acetate, and the lowest was observed with sodium citrate. The main characteristic of the process is the change in the composition of the solution. The concentration of nickel salt and hypophosphite is decreased and the concentration of the acid is increased during the process of deposition. This causes lowering of the deposition rate.[22]

3. Suitable complexing agents: added to control nickel ion activity that will, if too high, result in the complete decomposition of the solution when the sodium hypophosphite is added. The complexing agents also function as buffers and suppress the tendency for nickel to precipitate as hydroxide. Complexing agents control the rate of the deposition reaction, the rate of change of pH, the phosphorus content of the deposit, the bath stability, the tendency to form insoluble nickel phosphate, and the ease of solution control.
4. Stabilizers/inhibitors: used in minute quantities to completely eliminate the tendency for spontaneous decomposition of the plating solution and the deposition of metal on the walls of the plating tank, pipes, and other equipment.
5. Energy: catalytic reactions, such as EN plating, require energy that is supplied in the form of heat to proceed. The quantity of energy required by the system or added to it is one of the most important factors affecting the kinetics and the rate of the deposition reaction.

The major factor affecting EN plating is the bath composition. **Table 2** shows typical EN bath formulations, both acidic and alkaline. However, other factors such as pH, temperature, and the surface area of the substrate also affect the plating process.[16] Nickel deposits obtained from acid solutions have a very bright and smooth surface. As the pH increases to become more alkaline, the nickel content of the deposit increases or phosphorus decreases. Temperature also has a significant effect on the rate of the plating process. The plating rate increases with the increase in temperature and, after a certain point, the quality of the plating deteriorates because it will be difficult to

Table 2 Typical electroless nickel bath formulations[23]

	Acid	*Alkaline*
Temperature	77–93 °C	26–95 °C
pH	4.4–5.2	8.5–14
Deposition in 1 h	12.7–25.4 μm	10–12.7 μm
Metal salt	Nickel sulfate Nickel chloride	Nickel sulfate Nickel chloride
Reducing agent	Sodium borohydride Sodium hypophosphite Dimethylamine borane (DMAB) Hydrazine	Sodium borohydride Sodium hypophosphite Dimethylamine borane (DMAB) Hydrazine Diethylamine borane (DEAB)
Complexing agent	Citric acid Sodium citrate Succinic acid Proprinic acid Glycolic acid Sodium acetate	Citric acid Sodium citrate Succinic acid Lactic acid Glycolic acid Sodium acetate Sodium pyrophosphate
Stabilizer	Fluoride compounds Heavy metal salts Thiourea Thioorganic compounds (i.e., mercaptobenzothiazole, MBT) Oxy anions (i.e., iodates)	Thiourea Heavy metal salts Thioorganic compound Triethanolamine Thallium salts Selenium salts
pH adjustment	Ammonium hydroxide Sulfuric acid	Ammonium hydroxide Sulfuric acid Caustic soda Sodium hydroxide

maintain the pH of the solution. This temperature depends on each solution used.

Generally, there are three main types of EN coatings: nickel–phosphorus, nickel–boron, and poly-alloys. Nickel–boron is very often used in industrial applications for its as-plated hardness, which is higher than that of nickel–phosphorus. The boron content can vary from 0.1 to 10%. The reducing agent used is dimethylamine boron or sodium borohydride, depending on the desired alloy composition. Poly-alloys are a combination of nickel, boron, or phosphorus and other metals such as cobalt, iron, tungsten, rhenium, or molybdenum. Composite deposits such as EN–polytetrafluoroethylene and EN–diamond have been developed for special applications.[23] **Figure 3** shows the general categories of the EN coatings.[19]

EN–phosphorous is by far the most widely used in electronics applications. It is a barrier type of coating and has an autocatalytic chemical reduction process in which the reducing agent is oxidized and Ni^{2+} ions are deposited on the substrate surface. Once the first layer is deposited, it acts as a catalyst for the process. EN–phosphorous coatings are binary alloys of nickel and phosphorous. They are classified as low phosphorous (<6 wt% P), medium phosphorous (6–10 wt% P), and high phosphorous (>10 wt% P) according to Henry[23] and Jothi *et al.*[19]

The phosphorus content of the deposit varies with the bath pH and has a significant influence on the deposit's chemical and physical properties in both the as-plated condition and after heat treatment. Electroless deposits with high phosphorous are obtained in acidic solutions and are either crystalline or amorphous, whereas alkaline solutions have low phosphorous content and are generally crystalline. **Table 3** illustrates the differences in properties between the various nickel–phosphorous coatings.

Because the surface finish will have to go through an elevated temperature for the soldering process, some research has been conducted to study the effect of heating on the EN phosphorus layer. A study by Tomlinson and Wilson[24] found that the nickel–phosphorous layer will start to oxidize at approximately 400 °C; at above 800 °C, the phosphorous will decompose and evaporate from the coating. At above 600 °C, the phosphorous migrates to the surface and the formation of phosphorus oxide has been observed. A kinetic study performed in the same research article at 800–1000 °C showed that the nickel–phosphorus deposit oxidized approximately 100-times faster than pure nickel. The addition of even a small amount of boron to the deposit helps to decrease the amount of oxidation. This finding basically shows that the phosphorus in the nickel–phosphorus layer is the cause of the poor oxidation resistance of the plated layer. Because in electronic packaging the solderability of the surface finishes is one of the most important aspects for consideration, the EN layer will be covered by another plated layer like electroless palladium, electroless gold, or immersion gold to prevent oxidation.

3.15.2.2 Electroless Palladium Plating

Among platinum group metals, palladium is the most inexpensive and is expected to have extensive industrial applications. An example of an electroless palladium plating bath solution is an aqueous solution containing a bivalent palladium salt as a metal source, ammonia as a complexing agent, ethylenediaminetetraacetic acid (EDTA; or a salt thereof) as a stabilizing agent, and hydrazine as a reducing agent.[25] Electroless palladium plating baths can be classified by the reducing agent used. **Table 4** summarizes a few of the bath formulae for two different reducing agents.[26]

Rhoda and Mari[27] developed several electroless palladium plating solutions using hydrazine as a reducing agent. The palladium tetramine complex used in the baths was prepared by the careful addition of ammonium hydroxide to a palladium chloride solution. The solution was then heated to dissolve possible precipitates. EDTA was found to be an effective stabilizer against the spontaneous decomposition of the solution. Bath 1 in **Table 4** was recommended for barrel plating.[27] The hardness of the deposits ranged from 150 to 350 Knoop (25 g load), whereas softer deposits were formed at higher deposition rates. The deposits consisted of a minimum of 99.4% palladium and exhibited a density of 11.96 g cm^{-3}.[27] However, the disadvantage of the hydrazine baths is that the deposition rate decreases drastically after several hours of use, before any significant consumption of the bath constituents

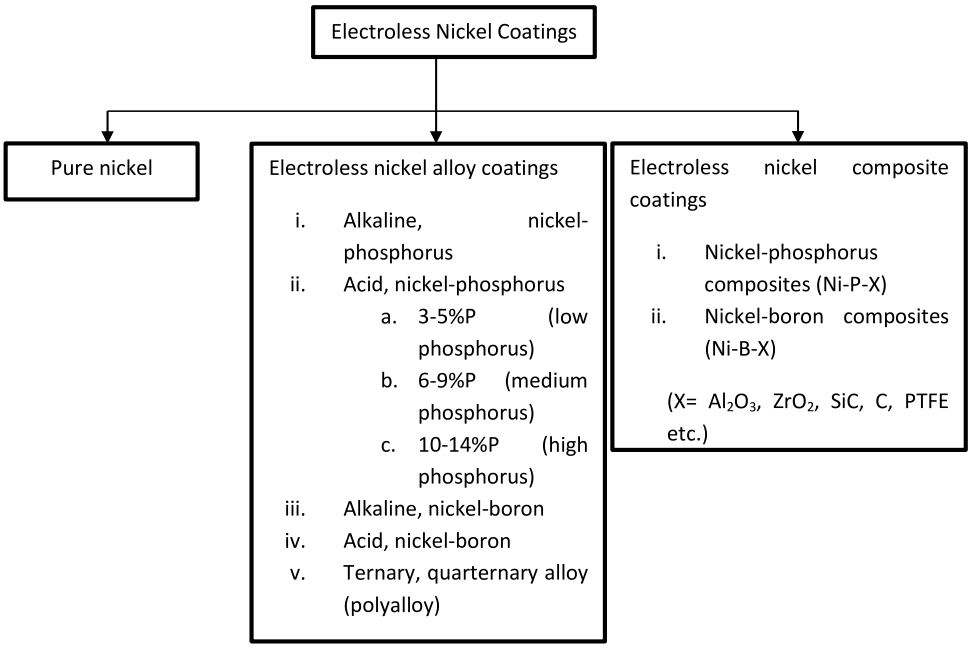


Figure 3 General categories of electroless nickel coatings.[19]

Table 3 The detail of various electroless nickel–phosphorus platings[23]

Phosphorus level	*Phosphorus content*	*Depositions quality*
High	10% or higher	• Excellent corrosion • Easily soldered • Excellent ductility • Nonmagnetic • Excellent diffusion barrier
Medium	6–10%	• Good corrosion resistance in both alkaline and acidic environments • Excellent lubricity • Heat-treatable to 65 RC • Bright, decorative appearance • Mixture of amorphous and microcrystalline phases
Low	Less than 6%	• High as-plated hardness • Excellent wear resistance • Very resistant to corrosion in alkaline environments • High melting point (1200 °C) • Easily soldered • Microcrystalline phase (consisting of many small grains, approximately 2–6 nm in size)

has taken place.[26] Several modified electroless palladium solutions have been designed to solve this problem.[28–30]

The electrochemical aspect of the electroless palladium depositions of baths 3 and 5 in **Table 4** has been studied by Ting *et al.*[29] They reported that the exchange current density for hydrazine (7.8×10^{-5} A cm^{-2}) is higher than that for hypophosphite (2.6×10^{-5} A cm^{-2}). Using electrochemical polarization measurements, Shu *et al.*[28] studied the autocatalytic effect during electroless palladium plating deposition in an alkaline bath containing the palladium–ammine complex, EDTA, and hydrazine. The tetravalent palladium species in the bath may be stabilized through interaction with the co-existing tin oxide in palladium–tin activated substrates.

In most practical electroless palladium plating baths, the palladium–ammine complex is used together with ammonium chloride and hypophosphite as the stabilizer and the reducing agent, respectively.[29,31] A representative make-up for this type of bath, as represented by Pearlstein and Weightman,[31] is shown in **Table 4** as bath 4. The palladium deposits in this bath contained approximately 1.5% phosphorus, and approximately 3 g of sodium hypophosphite monohydrate was consumed to produce 1 g of the electroless palladium

Table 4 Palladium plating bath formula using hydrazine and hypophosphite reducing agents[26]

Bath	*Hydrazine type*			*Hypophosphite type*	
	1	*2*	*3*	*4*	*5*
Palladium (as ammine complex), $[Pd(NH_3)_4]^{2+}$	5.4 g l^{-1}	7.5 g l^{-1}	–	–	–
Palladium chloride, $PdCl_2$	–	–	0.023 M	2 g l^{-1}	0.023 M
Hydrochloric acid, HCl (38%)	–	–	2–8 ml l^{-1}	4 ml l^{-1}	2–8 ml l^{-1}
Ammonium hydroxide, NH_4OH	350 g l^{-1}	280 g l^{-1}	300 ml l^{-1}	160 ml l^{-1}	160 ml l^{-1}
EDTA (disodium salt), Na_2EDTA	33.6 g l^{-1}	8 g l^{-1}	0.1 M	–	–
Ammonium chloride, NH_4Cl	–	–	–	27 g l^{-1}	0.485 M
Hydrazine, $N_2H_4 \cdot H_2O$	0.3 g l^{-1}	–	0.005 M	–	–
Hydrazine (1 M solution)	–	8 ml l^{-1}	–	–	–
Sodium hypophosphate, $NaH_2PO_2 \cdot 2H_2O$	–	–	–	10 g l^{-1}	0.094 M
Temperature (°C)	80	35	60	55	40
Deposition rate (μm h^{-1})	2.5	0.9	2.5	2.5	0.9

Table 5 Electroless palladium plating bath using hydroxylamine[33]

Solution A for 900 ml	
$PdCl_2$	0.3 g dissolved in 9 ml HCl
De-ionized water (DI water)	5 ml
Glacial acetic acid	864 ml
HF (48%)	22 ml
Solution B for 100 ml	
$NH_2OH \cdot HCl$	0.416 g (0.06 M)
KHF_2	0.937 g (0.12 M)
KCl	14.912 g (2.0 M)
Citric acid ($C_6H_8O_7 \cdot H_2O$)	2.101 g (0.1 M)
DI water	100 ml

deposit.[31] Sergienko[32] developed a stable electroless palladium plating bath containing EDTA and hypophosphite.

Other than these two types of reducing agents, Stremsdoerfer *et al.*[33] proposed a new type of electroless deposition of palladium and gold–palladium alloys on a bare n-GaAs surface using hydroxylamine as a reducing agent. The plating bath is composed of two solutions, as shown in Table 5.

Hydrofluoride and potassium chloride, in solutions A and B, respectively, act as stabilizers. The autocatalytic bath for electroless palladium plating on bare n-GaAs as a substrate is prepared by adding a small quantity of solution A to 40 ml of solution B. The bath exhibited a deposition rate of 0.5 μm h^{-1} in the acidic media at 20 °C. The deposits obtained from this bath were well structured and adherent. In addition, Stremsdoerfer *et al.*[34] also reported that the palladium deposited using this bath formed a good metal–semiconductor junction (Pd/n-GaAs junction) by subsequent annealing up to 550 °C. Chepuri and Trivedi[35] reported on the electroless plating of pure palladium from palladium–ethylenediamine complex baths using formic acid as a reducing agent. Electroless pure palladium was deposited using the following basic bath composition: 0.01 M palladium chloride, 0.08 M ethylenediamine, 0.2 M formic acid, and pH 6 at 60 °C. When phosphite or trimethylamine borane was used as a reducing agent, the content of phosphorus in the deposit was reduced.[35]

For application in electronic packaging, palladium and its alloys have also been developed as an economic alternative to gold plating. Even though palladium and gold differ in some of their properties, as listed in Table 6, both materials share the noble character of being highly oxidation-resistant. Electroless palladium shares the desirable attributes of electroless plating in general. However, the soldering process will be easier with a very thin layer of gold on the palladium layer (0.025–0.05 μm).[36] For some applications, even without the gold layer, the solderability of electroless palladium is good enough for electronic packaging.[37]

Other than the applications mentioned, palladium can be used as a soldering preservative and as a barrier inner layer in applications where it is plated directly onto copper circuitry. Palladium, like thin deposits of gold, also can be used as a soldering preservative for electroless nickel-plated copper. Palladium is well known for its catalytic properties in the chemical and automotive industries. Although high cost and application difficulties have limited its use, it is suggested that thin films of electroless plated palladium on a ceramic sponge or other support materials could be used effectively as reaction or auto-emission catalysts.[37]

3.15.2.3 Electroless Gold Plating

The advantages of gold deposition by electroless means are the same as those of EN and electroless palladium. There are a number of formulations available. Many of these have been used in commercial applications, with careful attention being given to bath monitoring and control. Several of the gold salt sources used are potassium gold cyanide, gold chloride, and gold sulfite. By far, potassium gold cyanide is the most common source.[37] Because the gold solution normally contains cyanide compounds, extra precaution is needed in the process and waste treatment of the plating solutions.[12,19] The reducing agents used are also as diverse as the gold source, such as sodium hypophosphite, dimethylamine borane, sodium borohydride, hydrazine, and benzyl alcohol.[37] The formula in Table 7 is reported to plate at a rate of 12–17 μin h^{-1} at 70 °C. The rate is dependent on the benzyl alcohol concentration. A gold film of approximately 35 μin (0.87 μm) requires 2 h immersion in the bath.[38]

Table 6 Comparison of properties, gold versus palladium[37]

Property	*Gold*	*Palladium*
Color	Yellow	Silver/white
Crystal	Face-centered cubic	Face-centered cubic
Resistivity	$2.2 \times 10^8\ \Omega$ m	$10.5 \times 10^8\ \Omega$ m
Magnetic	Diamagnetic	Paramagnetic
Density	19.3 g ml^{-1}	12.0 g ml^{-1}
Molecular weight	197	106
Melting point	1063 °C (1945 °F)	1555 °C (2831 °F)
Boiling point	2660 °C (4820 °F)	3140 °C (5684 °F)
Hardness	20–150 Hv	50–200 Hv
Elongation	44%	24%
Tensile strength	18 ksi	24 ksi
Soluble solder	Complete	Slightly
Maximum thickness	Unlimited	Unlimited
Other	1 oz makes 300 ft^2 foil	Absorbs 900 × vol. H_2
Reacts with	Sulfuric acid, aqua regia, potassium cyanide	Nitric acid, hydrofluoric acid

Table 7 Electroless gold plating formula[38]

Potassium gold cyanide	12–16 g l^{-1}
Diammonium citrate	15–20 g l^{-1}
Citric acid	1–2 g l^{-1}
Benzyl alcohol	2–4% v/v
Temperature	50–70 °C
pH	4–9

Table 8 Formulation for immersion and electroless gold used by Ikuhiro *et al.*[15]

Immersion Au	
$KAu(CN)_2$	0.01 mol dm^{-3}
$K_3(C_6H_5O_7) \cdot H_2O$	0.08 mol dm^{-3}
$[CH_2N(CH_2COOH)_2]_2$	0.3 mol dm^{-3}
$TlSO_4$	1 ppm (as Tl)
pH	4.5
Temperature	90 °C
Electroless Au	
$Na_2[Au(SO_3)_2]$	0.01 mol dm^{-3}
Na_2SO_3	0.1 mol dm^{-3}
$[CH_2N(CH_2COOH)_2]_2$	0.1 mol dm^{-3}
L-Ascorbate	0.25 mol dm^{-3}
$TlSO_4$	3 ppm (as Tl)
pH	7.0
Temperature	60 °C

Table 9 Formulation of electroless gold[9]

	Formula I	*Formula II*	*Formula III*
$KAu(CN)_2$	5 g l^{-1}	1.45 g l^{-1}	1.45 g l^{-1}
KCN	–	6.5 g l^{-1}	11 g l^{-1}
Palladium acetate	0.1–1.0 g l^{-1}	–	–
KOH	–	11.2 g l^{-1}	11.2 g l^{-1}
Ethylenediaminete-traacetic acid (EDTA)	10–15 g l^{-1}	–	–
KBH_4	–	10.8 g l^{-1}	10.8 g l^{-1}
Sodium succinate	5–10 g l^{-1}	–	–
NaEDTA	–	–	5 g l^{-1}
Succinic acid	10–15 g l^{-1}	–	–
Ethanolamine	–	–	50 mL l^{-1}
pH	10.5	–	–
Temperature	75 °C	72 °C	72 °C

Table 10 Effect of palladium acetate on deposition rate and purity[9]

Bath	*Palladium acetate (g l^{-1})*	*Deposition rate (μm h^{-1})*	*Deposited Pd content (wt%)*
1	0.1	0.2	0.04
2	0.5	0.4	0.04
3	1.0	1.0	0.08

When the substrate is immersed in the plating solution, the first reaction is immersion; then, once the substrate is covered with gold, autocatalytic reduction takes place. The electroless gold is deposited as the benzyl alcohol is oxidized. Most electroless gold plating processes require a separate gold immersion deposit, which provides adhesion for the subsequent gold layer and avoids contamination of the gold plating bath, particularly by nickel.[37] In a study conducted by Ikuhiro *et al.*,[15] the plating process of gold consists of two steps. The first step is immersion gold to produce a gold thickness from 0.05 to 0.1 μm, followed by electroless gold plating to produce a gold thickness more than 0.1 μm. Table 8 lists the formula for immersion gold and electroless gold, as used by Ikuhiro *et al.*[15]

Hassan and Ian[9] listed various types of electroless gold plating recipes based on publications at that point in time. From their findings, they developed three formulations for an electroless gold plating bath with minimal agitation requirements because it is not possible to apply vigorous agitation during electroless plating on the complex geometries

needed by some of the available formulations. The first two formulae could deposit up to 2 μm h^{-1} of gold. The substrate used was gold film produced either by electroplating or by vacuum deposition. Table 9 lists the formulations.

The first formula explores the use of the palladium complex as a reductant. Palladium acetate was considered in this study. Table 10 lists the deposition rates of formula I with variable amounts of palladium acetate.

The deposition rate for formula I increases with higher palladium concentration. However, the high cost of palladium acetate mitigates against the use of higher palladium contents. The deposit obtained from this solution was smooth, reflecting the substrate contours, and had a matte, lemon-yellow appearance. However, the bath was not completely stable and decomposition started within approximately 3 h of operating temperatures. Nevertheless, on a small scale, the plating was successful prior to the decomposition process.[9]

Formulas II and III were based on Okinaka's research.[39,40] In formula II, it was found that the decomposition commenced within 1 h of the solution's working life. The initial deposition of 2 μm h^{-1} rapidly decreased with decomposition. It was found that the cyanide increase would help to reduce the rate of decomposition. However, the increase of cyanide also reduces the deposition rate. In formula III, modifications have been made by adding another two stabilizers, EDTA, and ethanolamine. This helps to increase the deposition rate without decreasing the bath stability. The formula was able to produce a consistent deposition rate of 1.5 μm h^{-1} over the course of the 8 h working day. Studies indicated that depletion of the gold content in the bath of up to 50% could be tolerated with no significant reduction in the gold deposition rate.[9]

In the electronics industry, the selection of either electroless or immersion gold plating depends on the final thickness of the gold layer needed for the surface finish application. There are also cases, as mentioned, in which the immersion and electroless solutions were used consecutively. For example, in the EN/immersion gold surface finishes, the three most common failure modes are porous gold, gold embrittlement, and black pad.[41] All of the three mentioned issues are highly related to the mechanisms of gold plating. Therefore, stringent selection of the gold plating solution and the option of immersion or electroless are important and will determine the quality of the surface finish produced.

3.15.3 Conclusion

The literature review indicates that numerous attempts have been made to identify the best formulations and parameters that affect the performance of the three main electroless solution types used in the electronics industry, which are EN, electroless palladium, and electroless gold. The benefits of electroless plating are well understood and discussed; just like any type of processing, it has its own advantages and disadvantages. One type of plating bath may not be suitable for all applications, even in the same field of electronic packaging. Further investigation needs to be conducted to modify, fine-tune, and stabilize the formulations to obtain the necessary final product.

See also: 3.1 Electroless Plating of Pd Binary and Ternary Alloys and Surface Characteristics for Application in Hydrogen Separation

References

1. Vianco, P. T. An Overview of Surface Finishes and Their Role in Printed Circuit Board Solderability and Solder Joint Performance. *Circuit World* **1998**, *25* (1), 6–24.
2. Kumar, A.; He, M.; Chen, Z. Barrier Properties of Thin Au/Ni–P Under Bump Metallization for Sn–3.5Ag Solder. *Surf. Coat. Technol.* **2005**, *198*, 283–286.
3. Se, Y. J.; Kyung, W. P. Eutectic Sn/Pb Solder Bump and Under Bump Metallurgy: Interfacial Reactions and Adhesion. *Solder. Surf. Mount Technol.* **1998**, *10* (3), 29–37.
4. Li, Y. H.; Jenq, G. D. Characterizing Metallurgical Reaction of Sn–Pb Solder with Ni/Cu Under-Bump Metallization by Electron Microscopy. *Thin Solid Films* **2004**, *469–470*, 366–371.
5. Beauvilier, L. The Quest for the Ultimate Surface Finish. *Print. Circuit Des.* **2002**, *19* (6), 27.
6. Menahem, R.; Adam, P.; Michael, O.; Michael, P.; George, M. Review of Capabilities of the ENEPIG Surface Finish. *J. Electron. Mater.* **2014**, *43* (11), 3885–3897.
7. Yee, S.; Ladhar, H. Reliability Comparison of Different Surface Finishes on Copper. *Circuit World* **1998**, *25* (1), 25–29.
8. Diamand, Y. S.; Osaka, T.; Okinaka, Y.; Sugiyama, A.; Dubin, V. 30 Years of Electroless Plating for Semiconductor and Polymer Micro-Systems. *Microelectron. Eng.* **2015**, *132*, 35–45.
9. Hassan, O. A.; Ian, R. A. C. A Review of Electroless Gold Deposition Processes. *Gold Bull.* **1984**, *17* (4), 118–127.
10. Krishnan, K. H.; John, S.; Srinivasan, K. N.; Praveen, J. An Overall Aspect of Electroless Ni–P Depositions – A Review Article. *Metall. Mater. Trans. A* **2006**, *37A*, 1917–1926.
11. David, K. *Chemical Deposition of Metallic Films from Aqueous Solution – Chapter 19*; *Electroless Plating*; William Andrew Publishing/Noyes: New York, NY, 1990. Available from: www.knovel.com.
12. Ernest, L.; Lenora, T. Technically Speaking: Electroless Nickel/Immersion Silver-A New Surface Finish PCB Application. *Met. Finish.* **2013**, *111* (1), 12–19.
13. Durkin, B. Who Really Cares About the Surface Preparation Requirements for the Successful Application of Electroless Nickel? Available from: http://www.pfonline.com/articles/who-really-cares-about-the-surface-preparation-requirements-for-the-successful-application-of-electroless-nickel, 1999 (accessed 17 July 2015).
14. Gilleo, K., Ed. *Area Array Packaging Handbook: Manufacturing and Assembly*; McGraw-Hill Handbooks: New York, NY, 2002.
15. Ikuhiro, K.; Tomohito, K.; Hajime, T.; Hideto, W.; Hideo, H. Influences of Electroless Nickel Film Conditions on Electroless Au/Pd/Ni Wire Bondability. *Trans. Jpn. Inst. Electr. Pack.* **2010**, *3* (1), 78–85.
16. Agarwala, R. C.; Vijaya, A. Electroless Alloy/Composite Coatings: Review. *Sadhana* **2003**, *28* (3–4), 475–493.
17. Mallory, G. O.; Hajdu, J. B. *The Fundamental Aspects of Electroless Nickel Plating*; *Electroless Plating: Fundamentals and Applications*; American Electroplaters and Surface Finishers Society: Orlando, FL, 1990; pp. 1–56.
18. Sudarshan, L. Technically Speaking: Troubleshooting Electroless Nickel Baths. *Met. Finish.* **2013**, *111* (6), 16–19.
19. Jothi, S.; Jianshe, L.; Wei, S. Electroless Nickel, Alloy, Composite and Nano Coatings – A Critical Review. *J. Alloys Compd.* **2013**, *571*, 183–204.
20. Gutzeit, G. Catalytic Nickel Deposition from Aqueous Solution. I–IV. *Plat. Surf. Finish.* **1959**, *46*, 1158–1164.
21. Gaurilow, G. G. *Chemical (Electroless) Nickel Plating*; Porticullis Press: Redhill, 1979.
22. Mallory, G. O. Influence of the Electroless Plating Bath on the Corrosion Resistance of the Deposits. *Plating* **1974**, *61*, 1005.
23. Henry, J. Electroless Coating Part-I. *Met. Finish.* **1984**, *82* (9), 93–94.
24. Tomlinson, W.; Wilson, G. R. The Oxidation of Electroless Ni–B and Ni–P Coatings in Air at 800–1000 °C. *J. Mater. Sci.* **1986**, *21*, 97.
25. Haga, M.; Tsuji, K.; Nawafune, H.; Mizumoto, S.; Uchida, E. Palladium-Base Electroless Plating Solution. U.S. Patent 4, 804, 410, 1989.
26. Ohno, I. Electroless Deposition of Palladium and Platinum: Chapter 20. In *Modern Electroplating (5th ed.)*; Mordechay, S., Milan, P., Eds.; John Wiley and Sons Inc.: New York, NY, 2010; pp. 477–482.

27. Rhoda, R. N.; Mari, M. A. *Palladium Plating by Chemical Reduction*. U.S. Patent US2915406 A, 1958.
28. Shu, J.; Grandjean, B. P. A.; Ghali, E.; Kaliaguine, S. Autocatalytic Effects in Electroless Deposition of Palladium. *J. Electrochem. Soc.* **1993**, *140* (11), 3175–3180.
29. Ting, C. H.; Paunovic, M.; Pai, P. L.; Chiu, G. Selective Electroless Metal Deposition for via Hole Filling in VLSI Multilevel Interconnection Structures. *J. Electrochem. Soc.* **1989**, *136* (2), 462–466.
30. Hsu, C.; Buxbaum, R. E. Electroless and Immersion Plating of Palladium on Zirconium. *J. Electrochem. Soc.* **1985**, *132* (10), 2419–2420.
31. Pearlstein, F.; Weightman, R. *Electroless Deposition of Palladium Alloys*. U.S. Patent US3754939 A, 1972.
32. Sergienko, A. *Bath for the Electroless Deposition of Palladium*. U.S. Patent US3418143 A, 1967.
33. Stremsdoerfer, G.; Perrot, H.; Martin, J. R.; Cléchet, P. Autocatalytic Deposition of Gold and Palladium onto n-GaAs in Acidic Media. *J. Electrochem. Soc.* **1988**, *135* (11), 2881–2886.
34. Stremsdoerfer, G.; Nguyena, D.; Jaffrezic-Renault, N.; Martin, J. R.; Clechet, P. Contact Reactions in Pd / n - GaAs Junctions Formed by Palladium Electroless Deposition. *J. Electrochem. Soc.* **1993**, *140* (2), 519–525.
35. Chepuri, R. K. R.; Trivedi, D. C. Chemical and Electrochemical Depositions of Platinum Group Metals and Their Applications. *Coord. Chem. Rev.* **2005**, *249*, 613–631.
36. Kadija, I.; Abys, J. A.; Kudrak, E. J.; Maisano, J. J. Solderability Characteristics of Palladium, Palladium Nickel, Hard and Soft Gold Electrodeposits. In *Presented in the Proceedings of the 79th AESF Annual Technical Conference SUR/FIN '92*, June 22–25, Atlanta, Georgia, 1992.
37. Don, B.; Jon, B. Electroless Plating Process: Developing Technologies for Electroless Nickel, Palladium and Gold. *Met. Finish.* **1995**, *93*, 55–57.
38. Ganu, G. Electroless Deposition of Gold using Benzyl Alcohol as Reducing Agent. *Plat. Surf. Finish.* **1991**, *78* (8), 70–74.
39. Okinaka, Y. Electroless Gold Deposition Using Borohydride or Dimethylamine Borane as Reducing Agent. *Plating* **1970**, *57*, 914.
40. Okinaka, Y.; Kato, M. Electroless Deposition of Gold: Chapter 21. In *Modern Electroplating*, 5th ed.; Mordechay, S., Milan, P., Eds.; John Wiley and Sons Inc.: New York, NY, 2010; pp. 483–498.
41. Garte, S. M. Porosity. In *Gold Plating Technology*; Reid, F. H., Goldie, W., Eds.; Electrochemical Publications Limited: Glasgow, 1974; pp. 295–315.

3.16 Hard Coatings on Cutting Tools and Surface Finish

H Caliskan, Bartin University, Bartin, Turkey
P Panjan, Jožef Stefan Institute, Ljubljana, Slovenia
C Kurbanoglu, Istanbul Medeniyet University, Istanbul, Turkey

© 2017 Elsevier Inc. All rights reserved.

3.16.1	**Introduction**	230
3.16.2	**Hard Coatings**	231
3.16.2.1	Hard Coating Materials and Design	232
3.16.2.2	Deposition of Hard Coatings	232
3.16.2.3	Multilayer Hard Coatings	233
3.16.2.4	Nanolayer Hard Coatings	234
3.16.2.5	Nanocomposite Hard Coatings	235
3.16.3	**The Effect of Hard Coatings on Workpiece Surface Finish**	235
3.16.3.1	Surface Roughness of Machined Parts	238
3.16.3.2	Residual Stress and Microstructure	239
3.16.4	**Conclusions**	241
References		241
Relevant Websites		242

3.16.1 Introduction

Machining has become main shaping process used in manufacturing of engineering components throughout history. In any machining technology, there is a need for the tools to last long, operate smoothly, and ensure the requested quality of the product (smooth surface, dimensional stability). Thus cutting tools are essential in any machining operation. Due to high competitiveness, tool users are forced to increase tool lifetime, productivity, product quality, and to decrease lubricant consumption. These goals can be partly achieved by modified tool geometry, machining parameters, or tool material improvements. The latter approach has quite strong limitations. Namely, the tool has to be ductile to prevent fracture and hard to decrease tool wear. However, high ductility and high hardness are basically contradictory demands – a material is either hard and with poor ductility, or vice versa. A solution of this problem is to protect the tool made of ductile material (e.g., tool steel) with hard coating. The former ensures resistance to fracture, while hard coating protects the cutting edge against abrasive and mild adhesive wear. Hard coating also reduces the tool temperature by reducing the friction between chip and rake face of a tool. Additionally a relatively low chemical reactivity of coating with workpiece materials ensures protection against welding and thus reduces the adhesive wear. The result of all these effects is that coated tool can operate at higher cutting speed and higher feed rate. Thus hard coating expands the safe zone of cutting tools by minimizing the builtup formation (BUE) and crater wear. Hard protective coatings with high hardness, good resistance to wear, and oxidation, are predominantly transition-metal nitrides with a coating thickness of a few micrometers. Hard protective coatings, deposited by physical vapor deposition (PVD) and chemical vapor deposition (CVD) are the subject of this chapter.

The progress in cutting tool materials, coating techniques, and machine tools has paved the way for machining of materials at higher cutting speeds, higher feed rates or in hardened state. Hard machining operations have potential to be an alternative to grinding and electrical discharge method (EDM) due to their high productivity and flexibility and low environmental waste formation.[1,2] It is important that a workpiece material has good machinability. A workpiece material with high machinability would be described by its low cutting forces, high material removal rate, good surface integrity, precise workpiece dimensions, and low tool wear rate.[3] Hard coatings contribute improvement of these characteristics of machinability.

Carbide tools among other cutting tool materials are frequently preferred in many metal cutting processes owing to their high toughness and satisfactory hardness. However, due to high cutting forces, high contact pressures, high temperatures, and intensive chemical attack at cutting zone in machining process of difficult-to-cut materials[4] (such as hardened steels or nickel and titanium based aviation materials), it is difficult to keep the wear of carbide cutting tools at low level. Notwithstanding that carbide tools have relatively lower cost and higher toughness than Cubic boron nitride (cBN) tools, very often cutting tool change as a result of early tool wear leads to an increase of machine tool run-down time, which affects productivity and manufacturing costs.[5] Therefore, carbide tools need to have high hardness and high oxidation resistance to obtain long lifetime in hard machining, high speed machining, and dry cutting applications. One of the methods used to increase lifetime and thereby machinability of hard materials is deposition of hard coatings on cutting tools. In order to assure performance increase in carbide tools, first TiN, and then TiAlN based thin films, which have high wear resistance and high performance under corrosion or high temperature conditions, was developed.[4,6–8] TiAlN based coatings have frequently been used in dry cutting operations due to the fact that they keep their one phase cubic structure and have high oxidation resistance at cutting processes where temperatures higher than 800 °C comes out.[9,10] In recent years, with

 doi:10.1016/B978-0-12-803581-8.09178-5

development of nanolayer and nanocomposite coatings, superior properties in hard coatings has been obtained.[11–14] Basic characteristics of these advanced hard coatings are high microhardness and toughness together with high adhesion to substrate.

In this chapter, hard coatings deposited on cutting tools will be introduced. After design and production methods are summarized, the effect of hard coatings on surface roughness, cutting forces, and residual stresses will be explained.

3.16.2 Hard Coatings

Hard coatings are thin films which are deposited on tool substrates in order to improve their desired properties such as hardness, friction, wear resistance, and corrosion resistance, while not changing properties of the bulk material.[14] From a functional point of view the most important coating properties are hot hardness, good adhesion to the substrate, and chemical stability. The coating performance can be further improved by optimum coating thickness, fine microstructure, and compressive residual stresses. These properties can essentially be fulfilled only by ceramic materials. In practice, the choice is limited to transition metal nitrides and partly carbides and oxides. Such materials can be reliably deposited in a thin film form by CVD or PVD techniques. In contrast to the CVD methods, the starting material for PVD process is a solid (e.g., titanium), while the volatile elements are usually added as a gas (e.g., nitrogen). The PVD hard coatings have a certain advantages: low deposition temperature preserves cemented carbide toughness, they can be applied to sharp cutting edges, compressive residual stress inhibits microcracks, they have finer grains (smoother surface), higher microhardness, non-equilibrium compositions which are not possible with CVD, their deposition is environmentally clean process.[15,16] The limitations of PVD hard coatings are: thickness limitation due to residual stress, worse adhesion in some cases. Additional drawback is that PVD deposition process is line of sight and hence very complex geometries cannot be coated evenly. In its basic concept a homogeneous (single layer) coating is deposited on the substrate (**Figure 1(a)**). In some cases double layer coating is recommended to be used (**Figure 1(b)**). Thus we can combine for instance the bottom layer having a high hardness (high wear resistance) and the relatively soft top layer with a low friction coefficient. A gradient coating can also be used instead of two discrete layers (**Figure 1(c)**). As an example is TiCN coating, in which the ratio between carbon and nitrogen atoms changes during deposition process. The double layer structure can be repeated several times to achieve a multilayer coating (**Figure 1(d)**). The individual layer thickness can be lowered below 10 nm (while increasing the total number of layers to several hundred). Such a structure is called a nanolayer coating (**Figure 1(e)**). Yet another concept is possible, where during deposition process a two-phase structure (nanocomposite) is formed (**Figure 1(f)**). In these coatings, one phase segregates to the grain boundary of the second phase, where the size of the grains is in the nanometer range. Nanocrystalline TiN embedded in amorphous SiN_x can be given as an example to nanocomposite coatings.[14] Nanostructured coatings generally have higher hardness when compared to conventional coatings.

In the end of 1950s, high speed machine tools started to be used in order to increase machining productivity. However, high cutting speeds or high depths of cut led to the increase of forces at cutting zone and the increase of temperature together with friction and therefore a decrease of cutting tool lifetime. In consequence of researches performed to obtain higher tool life, higher cutting performance, and lower machine tool run-down time, hard coatings such as TiN and TiC started to be deposited on cutting tools by CVD method in the end of 1960s. The CVD coating process is still highly efficient on cemented carbide cutting tools. Due to high deposition temperature (higher than 800 °C) and thermal stresses occurring at coating-substrate interface, CVD technology was unable to transfer to high speed steel (HSS) or other common engineering alloys.[15,17] In the beginning of 1970s, this obstacle was overcome by development of PVD method which provides deposition of hard coatings at temperatures lower than 500 °C.

The first hard coating deposited by PVD method successfully was TiN. Soon after, it was noticed that addition of other elements to the TiN provides enhancement in mechanical and oxidation properties of this coating. As high wear and oxidation resistance, TiAlN coating was used in protection of cutting tools in high temperature cutting applications and today it is still the most commonly used hard coating. PVD process proved to be very flexible due to the fact that it allows deposition of three or more ingradient material at various stoichiometry.[14]

Historical development of hard coatings can be summarized as below:

- In the early 1970s the first CVD hard coatings (TiC) were applied to cemented carbide tools.
- 1975 – first CVD multilayer hard coating combining TiC, TiN, and TiCN layers.
- 1980 – CVD multilayer coating, combining TiC, TiCN, Al_2O_3, and TiN layers.

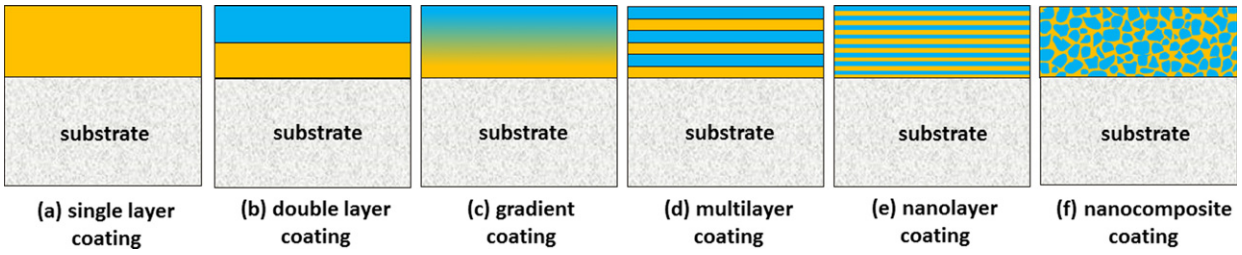


Figure 1 Design of hard coatings.

- 1980 – first low temperature PVD TiN hard coating was first proven on HSS tools.
- 1985 – low temperature PVD TiCN hard coating with gradient composition.
- 1990 – low temperature PVD TiAlN hard coating.
- 1995 – CVD diamond coating multilayer PVD hard coatings (ml–TiN/TiAlN) PVD TiB_2 coating TiAlN/WC–C low frictional PVD hard coating.
- 2000 – first nanolayer coatings (the individual layer thickness can be lowered down to only a few nanometer.
- 2005 – PVD AlCrN first nanocomposite coatings PVD Al_2O_3 coatings.
- 2010 – PVD oxynitride coatings.

Hard coatings are deposited on tools (such as cutting or forming tools[18]) and machine components (such as gears, bearings). Here the goals are to extend their lifetime, to decrease lubricant consumption, to increase productivity and/or to provide machining of new materials. Thus, hard coatings have become an integral part of modern tool technology, and many researches have been dedicated to development of better coating materials and new deposition techniques. The contact between cutting tool-workpiece pair determines the wear resistance of a coating. There is no coating which is universal for each tribological situation. Therefore, various coatings have been improved for certain applications. Nowadays, researches focus on diamond-like carbon (DLC) and oxynitride coatings together with nanocomposite and nanolayer coatings which are applied in industrial manufacturing. Researches continue for coating materials giving better performance in a wide application field.

3.16.2.1 Hard Coating Materials and Design

Production of hard coatings has been carried out using various materials and material combinations until today. As hard coating material, generally, nitrides, carbides, borides, and oxides of transition metals are used. The nitrides used as cutting tool coating material are TiN, TiAlN, CrN, ZrN, TiSiN, TiAlSiN, CrAlN, TiAlCrN, and cBN; carbides are TiC, CrC, and WC.[14,19] TiB_2, is used due to its high hardness and chemical inertness, can be given an example to boride coatings.[20] Al_2O_3 of oxide coatings is among widely used coatings today. DLC, MoS_2, and WC–C are the other coatings used on cutting tools due to their low friction characteristics and they are preferred in other tribological conditions such as gears and bearings.[21,22]

According to the used cutting tool material, workpiece material, and machining method, the ingredients to be used in a coating are determined with the aim of increasing the performance of the cutting tool. Common hard coating properties which should be fulfilled at the cutting edge under operating conditions (high stress and temperature) are[14]

- Good adhesion to the substrate, and between the layers in the case of multilayers (good adhesion to the substrate is a necessary condition for satisfactory performance of the coated tools),
- High hardness at working temperature (hot hardness) of the tool (hard coatings contribute to increased abrasive wear resistance),
- High toughness (coating fracture toughness is as important as hardness),
- Chemical stability and inertness against workpiece material (low solubility of coating material in workpiece material at temperatures encountered during machining),
- Fine-grained microstructure (grain size, grain structure, and grain- and phase boundaries affects the mechanical properties),
- Good oxidation resistance,
- Low coefficient of thermal conductivity for heat to dissipate into the workpiece,
- Coating morphology (relatively smooth PVD hard coatings provide lower cutting forces and ensures better surface finish on the machined part),
- Low friction coefficient,
- Crack retardation by compressive stress,
- Optimal thickness (If it is too thick, then we lose the sharpness of the cutting edge, while thin coating means low wear volume).

There is no hard coating which has all of these properties. Depending on application conditions, some properties of the coating is provided to come to the fore.[23] The early generation of PVD coatings (TiN, TiCN) is still effective at normal machining conditions for carbon and alloys steels. But as speed is increased TiAlN type coatings should be applied due to its better stability at high temperature.[22] TiAlN coating has high oxidation resistance and thermal stability[24] and optimum properties were obtained at 60–70% Al content.[25] As AlTiN coatings are in tendency to transform to cubic hexagonal phase at Al concentrations of higher than 65%, those coatings become metastable.[26] Therefore, with Cr addition, the TiAlN coatings maintain cubic B1 structure at 70% Al concentration and the coating shows high oxidation resistance.[27,28] Cr and Y provide enhancement in oxidation and corrosion resistance. Y also leads decreasing of residual stress, contributing formation of a fine grained structure. CrN has high thermal stability and reduces buildup formation in machining of Ti alloys using Ti based coatings.[22] Zr is useful to increase wear resistance. V addition up to a certain value results in the increase of hardness of TiN. Hardness and chemical inertness of TiAlN increases with Si addition. B addition leads to an increase of wear resistance of Ti–Al based coatings and reduces friction coefficient due to its lubricating property. Hf based nitride and carbide coatings provide improvement in flank and crater wear resistance of cutting tools.[24]

3.16.2.2 Deposition of Hard Coatings

Coatings are deposited by three types of processes which compose of gaseous state, solution state, molten, or semi-molten state processes. Two important characteristic parameters for the coating processes are the thickness of the coatings that can be achieved (from 0.1 μm to 10 mm) and the deposition temperature (from room temperature up to 1000 °C). Two basic deposition processes used in application of hard coatings on cutting tools are CVD and PVD. CVD process is a chemical process which is based on introduction of the material to be deposited in gaseous state into a reaction chamber and then condensation of these gases on to the substrate to form a coating at deposition temperatures in the range of 800–1200 °C.

In PVD process, material is vaporized or sputtered from a solid source (target) and that material is deposited on to the substrate to form a coating.[5] The basic idea of PVD is to transfer the material from the source onto the surface of the substrate. One of the basic requirements is a vacuum environment which ensures that the main free path of evaporated species should be comparable to the source–substrate distance. At the same time the vacuum conditions ensures that the coating contains predominantly the target material, with as few as possible impurities from the ambient atmosphere.

There are many methods, how to release the atoms from the solid target. In evaporation, the atoms are released from the target by heating. In vaporization process, target material is vaporized by one of these methods; resistance evaporation, induction heating, electron beam evaporation, cathodic arc evaporation, or laser beam evaporation. Thereby it is not necessary to reach the target material boiling point. Instead, the target material vapor pressure should be high enough to enable a vapor pressure of about one, which is in standard metals mostly achieved below the melting point. The process is called 'evaporation.' PVD is a line-of-sight process, thus only the surfaces directly exposed toward the source are coated. Due to the geometrical shadowing effect the shaded areas are generally not coated.

In sputtering process, target material is vaporized by bombardment of inert gas ions such as argon. The target atoms can be ejected from the target surface by an elastic collision. General sputtering methods are diode, magnetron, and ion beam sputtering.[5] In the case of diode configuration we ignite plasma between anode (substrate) and cathode (target). This is done by supplying a suitable voltage between the cathode and the anode (about 1 kV) at a suitable pressure (about 1 Pa) of a working gas (typically argon). At these conditions, argon is ionized and these ions bombard the cathode surface with energy of up to 1 keV in our case. Each collision ensures that a few target atoms are ejected from the surface; they reach the substrate surface where they grow as a coating. This process is called 'sputtering.' Diode sputtering is simple but not technologically useful due to low deposition rate ($\sim \mu m\ min^{-1}$) and high temperature of substrates. There are several methods to enhance the ionization of the plasma and thus increase the deposition rate. The most common option is the magnetron sputtering. A magnetron is a device with circularly arranged magnets which form a closed loop of magnetic field, a kind of a magnetic bottle. If a magnetron is placed as a cathode behind the target, this configuration traps the electrons within the closed loop, just above the target. This ensures strongly ionized plasma, which causes heavy bombardment of the target, which in turn provides a high deposition rate. One of the main advantages of magnetron system is the very wide range of materials that can be deposited. PVD processes are also classified according to power sources used in deposition process. In its basic form it is supplied by direct current (DC), at a constant voltage, which is used for deposition of conductive materials. For insulators, an AC power supply is necessary, usually in the radio-frequency (RF) or medium-frequency (MF) regimes. For thermally sensitive materials, a useful compromise is a pulsed-DC mode. It enables a relatively high ionization during the pulse-on phase, and a relatively long pulse-off time allowing the material not to overheat. Recently, short or high power pulsed power sources have been developed. Very high ionization can be obtained with this kind of power sources.[29]

Magnetron sputtering of PVD methods has shown a rapid development. As a result of demand on very quality functional coatings in various sectors and especially in manufacturing processes such as high speed machining and hard metal cutting, recently, magnetron sputtering method is widely preferred in production of many coatings used in industry. The most common coatings deposited by magnetron sputtering method are hard, wear resistant coatings, low friction coefficient coatings, corrosion resistant coatings, decorative coatings, and special optical or electrical property coating.[30] In many cases, the coatings deposited by magnetron sputtering have superior properties than coatings deposited by other PVD processes and have the same function with thicker coatings produced with other surface coating techniques.

3.16.2.3 Multilayer Hard Coatings

Multilayer protective CVD coatings have been deposited on cemented carbide cutting tools for many years. The first multilayer hard coatings were composed from TiC, TiCN, and TiN. Later Al_2O_3 layer was added in such structure. The layers in PVD processes are formed by deposition of coating materials sequentially from different targets. Three different principles are applied for deposition of layered coatings in PVD techniques: (1) sequential switching between two or more sources, (2) rotation of substrates along different spatially separated sources, and (3) changing reactive gas flow.[31] Nowadays, changing output voltage of plasma generator in high power pulsed magnetron sputtering method, the layered structures of the same material can be obtained.[32]

With deposition of multilayer coatings by creating proper material combinations, wear, corrosion, and oxidation resistance of hard coatings have been improved. The first multilayer coating was produced by CVD and then PVD method. Nowadays, multilayer structure is used in most of coatings used industrially.[33,34] The goal of multilayer coatings is to enhance properties and performance of the coating by combining positive characteristics of different coatings. As multilayered sandwich structure provides an increase in coating toughness by means of deflection and branching of the crack energy between layers,[35] the usage of this structure has been useful in cutting processes, for example, milling, where high dynamic loads exist. TEM image of a multilayer CrN/TiAlN coating deposited by magnetron sputtering is given in **Figure 2**. Using a multilayer structure, the columnar structure forming in single layer coatings can be prevented.

Main advantages of multilayer coatings are: (1) Adhesion of a coating to the substrate can be increased[36] and interface layers can be used to provide a gentle transition from coating properties to substrate properties. (2) Sequentially depositing several thin layers with various mechanical properties, stress concentration, and crack propagation conditions can be changed. In the case of a crack formation on coating surface, the crack energy is decreased by deviation and branching of the crack. Conversely, single layer coatings show less resistance to the crack growth. As shown in **Figure 3**, the crack propagates easily onto substrate/cutting tool surface and wide coating

zones are damaged. (3) With deposition of coating layers on the surface, which have individually different properties, for example, corrosion resistance, wear resistance, thermal insulation, electrical conductivity, diffusion barrier, and adhesion to the substrate, the properties of diverse property layer can be improved.[31]

3.16.2.4 Nanolayer Hard Coatings

Nanolayered coatings have excited researchers interest after very high hardness increment obtained in nanolayer TiN/VN coatings.[37] Main reason of the increase in hardness and strength of a nanolayer coating was found to be a large number of interfaces between layers. The change of coating hardness with layer thickness is shown in Figure 4. Maximum hardness was obtained at 5–10 nm bilayer period thickness. In addition, in this bilayer thickness range, the columnar structure seen in single layer coatings was found to change in multilayer superlattice coatings, for example, nanolayer TiAlN coating.[24]

In literature, the difference between multilayer coatings and nanolayer coatings is not described definitely. Generally, high hardness (superhardness) values obtained in nanolayer coating configurations distinguish them from multilayer coatings. The hardness of nanolayer coatings is not equal to average hardness of materials constituting the coating, while the hardness of a multilayer coating is equal to average hardness of materials constituting the coating. Superhardness is commonly seen at layer thickness of 3–10 nm and typically not seen at thickness values higher than 10 nm. An example of the typical nanolayer coating is shown in Figure 5.

The hardness increase in nanolayer coatings is provided by means of interfaces as stated above. Several theories for the

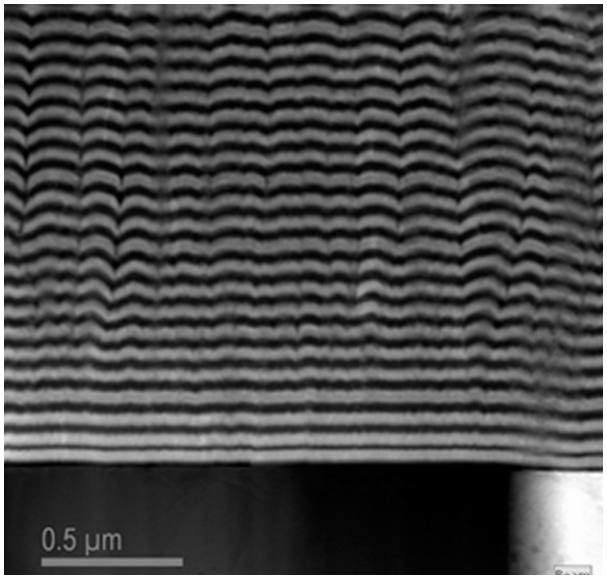


Figure 2 SEM image of CrN/TiAlN layers deposited on a steel substrate.

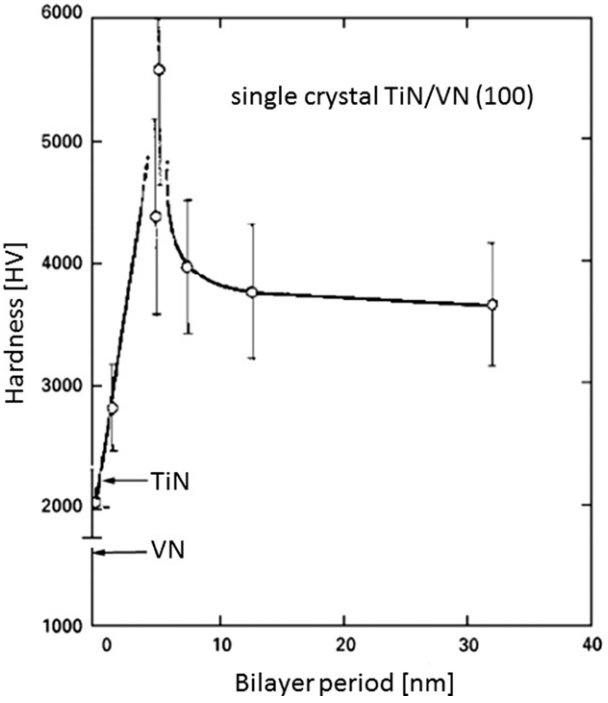


Figure 4 Hardness change of nanolayer TiN/VN coating as a function of bilayer period.[37]

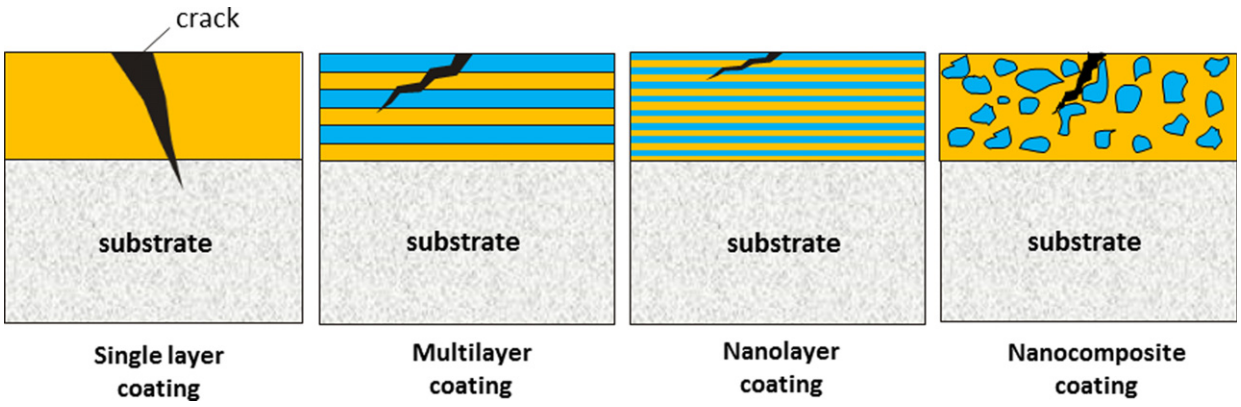


Figure 3 Different crack growths on single layer, multilayer, nanolayer, and nanocomposite coatings.

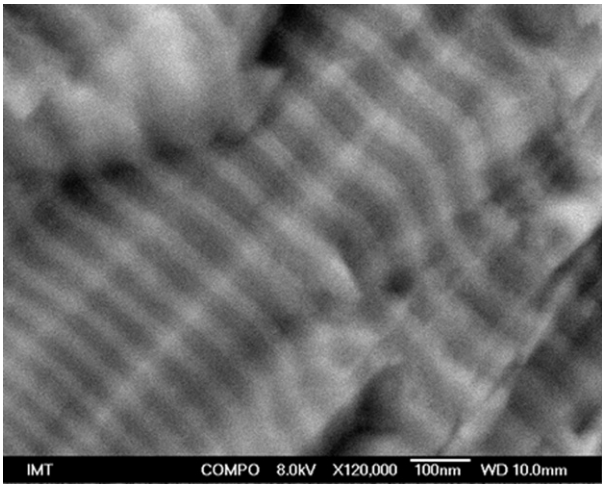


Figure 5 TEM cross sectional image of nanolayer TiN/TiAlN coating.

increase in hardness have been proposed: dislocation blocking by layer interfaces,[38] the Hall–Petch strengthening,[39] the strain effects at layer interfaces[40] and the supermodulus effect.[41] Among these, dislocation blocking has been commonly accepted as a dominant factor in large increase in hardness.[35]

Coating structure plays an important role on fracture toughness of a coating. Nano-multilayer or superlattice coatings are found to show more resistance against microchipping and crack propagation than single layer coatings as shown in **Figure 3**.[24] Moreover, these layers assist to transfer of elements to the surface, which maintains tribo-film formation process in the cutting tool/chip contact region.[42]

3.16.2.5 Nanocomposite Hard Coatings

Nanocomposite coatings are a new generation of materials. A nanocomposite coating composes of at least two phases: a nanocrystalline phase and an amorphous phase, or two nanocrystalline phases.[43] The nanocomposite materials show improved properties due to smaller ($\leq$10 nm) grain sizes compared to those of the conventional materials ($\geq$100 nm). The main property of nanocomposite coatings is an increased hardness. In general more than two times greater hardness can be obtained in a nanocomposite coating compared to that of its harder component. The main reasons of the hardness increase are the dislocation-induced plastic deformation, the nanostructure of materials, and cohesive forces between atoms of neighboring grains.[44]

3.16.3 The Effect of Hard Coatings on Workpiece Surface Finish

In this section, the effect of hard coating application on a cutting tool's performance and the surface finish will be discussed. The relation between hard coatings and cutting process variables and wear mechanisms between tool and workpiece will be explained using experimental results.

The main effects of hard coatings are on surface integrity of the machined material. The term 'surface integrity' is used to describe the attributes of a machined surface (surface topography and properties of subsurface layer) and its relationship to functional performance. Performance characteristics that are most often determined by surface integrity are: fatigue strength, fracture strength, corrosion rate, and tribological behavior (such as friction, wear and lubrication, and dimensional accuracy).[45] A good performance with the machined component can be obtained under service conditions if its surface integrity is high. Thereby, it is highly significant to control the surface integrity in machining processes.[46] Topography, microstructure, texture, surface roughness, metallurgy, hardness, and residual stresses constitute the surface integrity of a machined material.[47] In the following sections, the effect of hard coating on mainly surface roughness and residual stress will be explained.

As stated repeatedly, performance of cutting tools can be enhanced by deposition of a hard coating on tool surfaces. Main reasons for this enhancement are the reduction of adhesion effects between coated tool and workpiece materials, an improvement of abrasive wear resistance, the reduction of the cutting temperature[48,49] and an improvement of the inertness against tribo-oxidation. In addition, an improvement of chip flow can be obtained by a coating with low friction coefficient. The sum of the protective effects provides several times longer tool life than that of uncoated tools and also an increase of machining parameters.[16] The hard coatings enable higher cutting speed and increased tool life, while keeping other cutting conditions the same as with uncoated tools.

Cutting tool dimensions are quite important in terms of workpiece surface finish. The dimensions of component must be maintained during machining to produce accurate parts and to carry out an economically viable process.[48] The tool geometry have been reported to have influence on performance parameters such as surface finish, tool wear, residual stress, white/dark layer, chip form, heat generation, cutting forces, and microhardness variations.[50] Cutting edge profiles of a cemented carbide inserts in turning of Ti6Al4V alloy at cutting speed of 150 m min^{-1} after removal of different volume of material are given in **Figure 6**. It is clearly seen from the figure that the geometry of the cutting edge changes as a result of tool wear on flank and rake faces of the tool due to the mechanisms of abrasion, adhesion, and dissolution–diffusion. Such a geometrical change on the tool results in the increase in cutting temperature and cutting forces, leading to further diffusion wear and buildup edge formation.[51] The most important functions of the hard coating are the separation of the tool material from the counter-face workpiece material (lower diffusion wear) and to reduce wear by hardening the top layer of the surface. Protection of cutting tool with hard coating provides better surface integrity as well as longer tool life when compared to uncoated tools.

To achieve maximum metal cutting productivity, the thickness of the coating has to be optimized. Typical thickness of CVD coatings are 10 μm, while the thickness of PVD coatings are usually less than 5 μm. The thickness of a coating deposited on cutting tools has an influence on the cutting performance. Thickness of a coating, deposited by magnetron sputtering, on the rake and flank face of a cutting tool can be seen on cross-sectional image of the coated tool in **Figure 7**. According to the figure, nose radius of the uncoated tool can be seen to increase

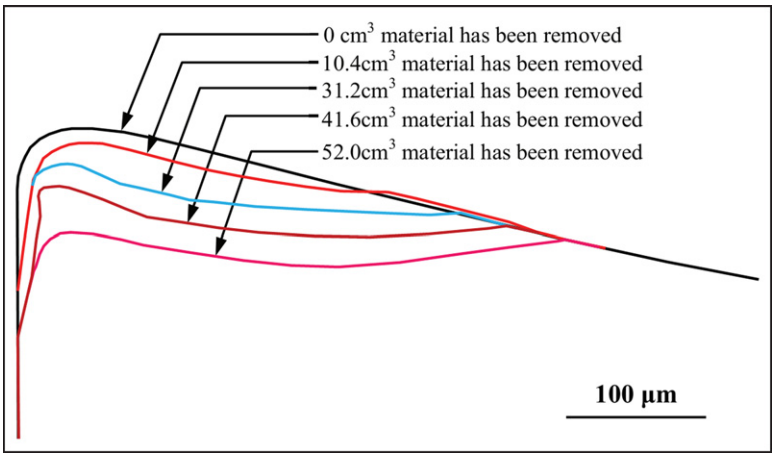


Figure 6 Cutting edge profiles of cemented carbide inserts after different volume of material (Ti6Al4V) have been removed by turning (cutting speed: 150 m min^{-1}).[51]

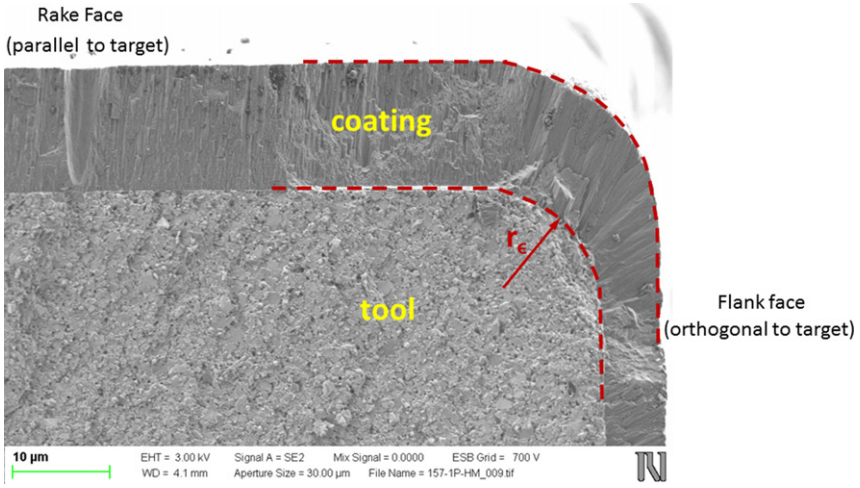


Figure 7 SEM micrograph of cross-sections from a coating grown by magnetron sputtering.

after coating deposition process. This means a geometrical change on the cutting edge. The increase in nose radius of the tool makes cutting tool motion in workpiece difficult, leading to higher cutting forces and temperatures. The higher cutting temperature is the shorter tool life. On the other hand, the extent of the effect of nose radius on cutting forces depends upon the machining condition.[52] If the nose radius is smaller than uncut depth of cut, chip formation occurs easily; otherwise surface roughness may worsen as a result of vibrations.

Besides its effect on nose radius, the thickness of hard coating on cutting tool's rake and flank surfaces are also significant. Due to the configuration of magnetron sputtering process, coating deposition rate is higher on the rake face, which is parallel to target, than the flank face which is orthogonal to target. As well known, thicker coating provide longer lifetime to cutting tools. The thickness value on each tool face should be taken into account to obtain expected tool performance and surface finish. Recently, with developments in magnetron sputtering technique, for example, high power pulse magnetron sputtering, uniform coating thickness can be obtained on tool surfaces.[53]

In addition to the effect of coating thickness on cutting forces and chip formation, the relation between coating's strength and thickness has great significance. Qin *et al.* reported that the residual stresses at the coating–substrate interface will increase with increasing coating thickness. On the other hand, they stated that the increase in coating thickness will commonly raise the resistance of coating cracking and delamination. They obtained longer tool life with diamond coated tools with coating thickness for the thickness range tested due to delay of coating delamination.[52]

Performance of a coated tool is also affected by roughness of the hard coating. The surface topography of hard coatings depends on the topography of bare substrate and the topography induced by the coating deposition process. When tool surface is covered by a hard coating, the surface roughness alters to some extent, depending on the deposition method. During machining scratching of the hard asperities in the

counter-face often occurs and this has the effect of increasing friction and wear. Therefore, the heat generating between the rake face and chip, and between the flank face and finishing face as a result of friction during cutting increases when surface roughness of a coating is high. The highest cutting temperature was obtained with TiAlN/AlCrN among four kinds of coating films, for example, TiN, TiCN, TiAlN, and multilayer TiAlN/AlCrN in milling of hardened steel.[54]

The BUE is one of the principal factors adversely affecting surface finish. It is commonly observed at relatively low cutting speeds. The gradual growth and rapid decay of the size of the BUE causes a saw toothed surface, which is characteristic of the BUE component of surface roughness. In addition, the cutting tip becomes larger and the desirable diameter of the workpiece changes when a builtup-edge is present.[55] The hard coatings with lower friction coefficient prevent sticking of workpiece material on cutting tool edge and provide enhancement in surface quality of machined parts. Due to the fact that DLC coated tools have an excellent smooth surface of $R_a = 0.01$ μm, a low friction coefficient ($\mu = 0.1$) and an excellent anti-adhering property, the formation of builtup edge were prevented in machining of aluminum alloys. Thus, the sharpness of the cutting edge could be maintained, which reduces cutting resistance approximately 50%, and improves the machinability.[56] According to FEM simulations for milling of AlMg2.5 alloy given in **Figure 8**, it seen that chip formation and cutting temperature is affected by DLC coating. In case of DLC coating, a higher chip flow speed was obtained as a result of low friction coefficient of such coating, which produces a large shearing angle, a decreased thickness of chip, and a smaller curl diameter. On the other hand, in case of uncoated cemented carbide tool, the chips were observed to be not susceptible to curl due to higher friction coefficient of the tool.[56]

It was reported many times that hard coatings reduce cutting forces and power consumption due to lower friction coefficients on the rake face of the cutting tools.[57] **Figure 9** clearly designate the influence of hard coating on average cutting force during milling test with CrTiAlN coated and uncoated tools. The cutting forces of uncoated tool increase drastically with the increase of cutting distance, especially at earlier cutting distances. When compared to cutting forces obtained with uncoated tool, that of CrTiAlN coated tool was seen to be much lower and remains stable after a certain cutting distance. It is clearly understood that main reason of reduction in cutting forces and stable milling process is low friction coefficient of CrTiAlN coating.[58]

The influence of DLC coating on cutting forces in machining of AlMg2.5 alloy is shown in **Figure 10**. The principal force, the feed force, and the back force were found to be less for the DLC coated tools than the uncoated ones in all

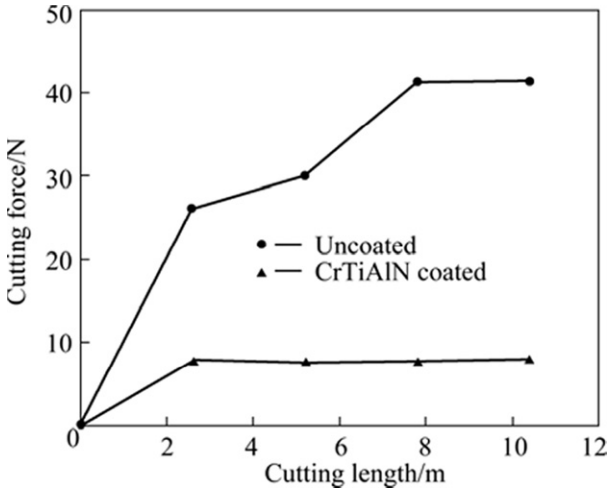


Figure 9 A comparison of cutting force as a function of cutting length during milling test with CrTiAlN coated and uncoated tools.[58]

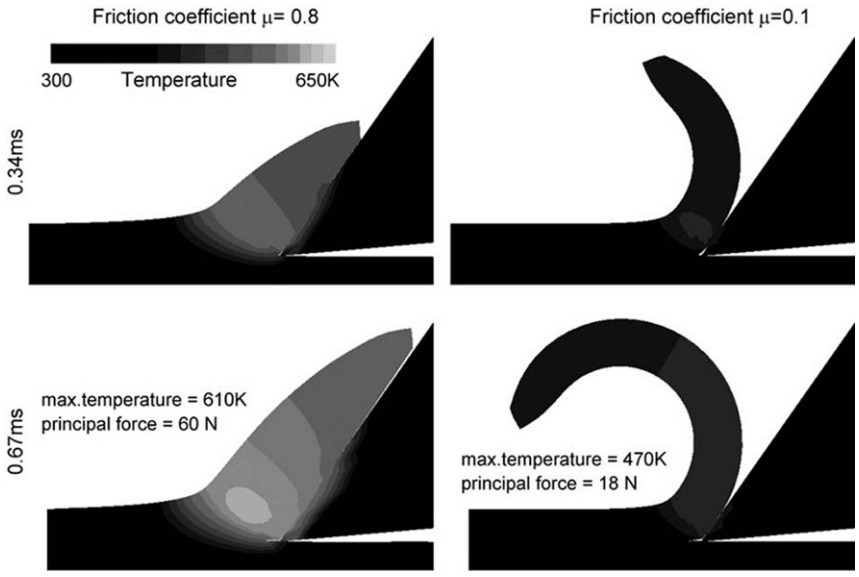


Figure 8 FEM simulation results of types of chip and contours of temperature for AlMg2.5 alloy milling test ($V = 300$ m min^{-1}, $f = 0.15$ mm rev^{-1}, depth of cut 1 mm, lubrication: dry).[56]

cutting tests. In addition, the cutting resistances of DLC coated tools under dry conditions were less than uncoated tools under wet conditions.[56]

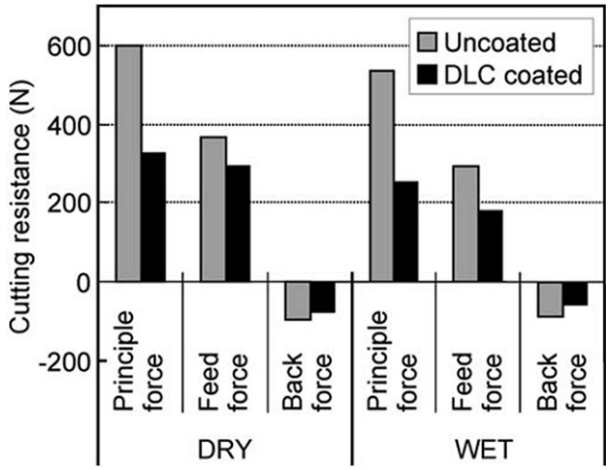


Figure 10 Cutting forces were obtained by averaging the cutting force signals for three teeth during AlMg2.5 alloy machining ($V=300$ m min^{-1}, $f=0.15$ mm rev^{-1}, $a_p=a_e=5$ mm, lubrication: dry).[56]

3.16.3.1 Surface Roughness of Machined Parts

Effect of machining conditions on surface roughness of machined parts is presented in fishbone diagram in **Figure 11**. Surface roughness is affected by many of parameters (nose radius, tool shape, tool material, chip formation, friction in the cutting zone, cutting force variation) and hard coating can be regarded as one of the most important due to its effect on all these parameters. As explained in previous sections, hard coatings as a surface part of a cutting tool material provide improvement in wear resistance and friction characteristics. When considering nose radius, the nose radius increases with the increase of hard coating thickness, resulting in a decrease of surface roughness and an increase of cutting forces. On the other hand, a hard coating protects the shape of cutting tool with higher wear resistance and provides regular chip formation and lower cutting forces as a result of low friction coefficient on the surface.

A better surface roughness with a TiN (PVD) coated cutting tool was obtained in machining of cold-formed carbon steel C15 E4 steel.[60] In face milling of hardened AISI O2 steel using nanolayer AlTiN/TiN and multilayer nanocomposite TiAlSiN/TiSiN/TiAlN coated tools, it was seen that optimum surface roughness changed depending on coating type.[61] A better surface finish was obtained with a-CN/TiAlN coatings after first

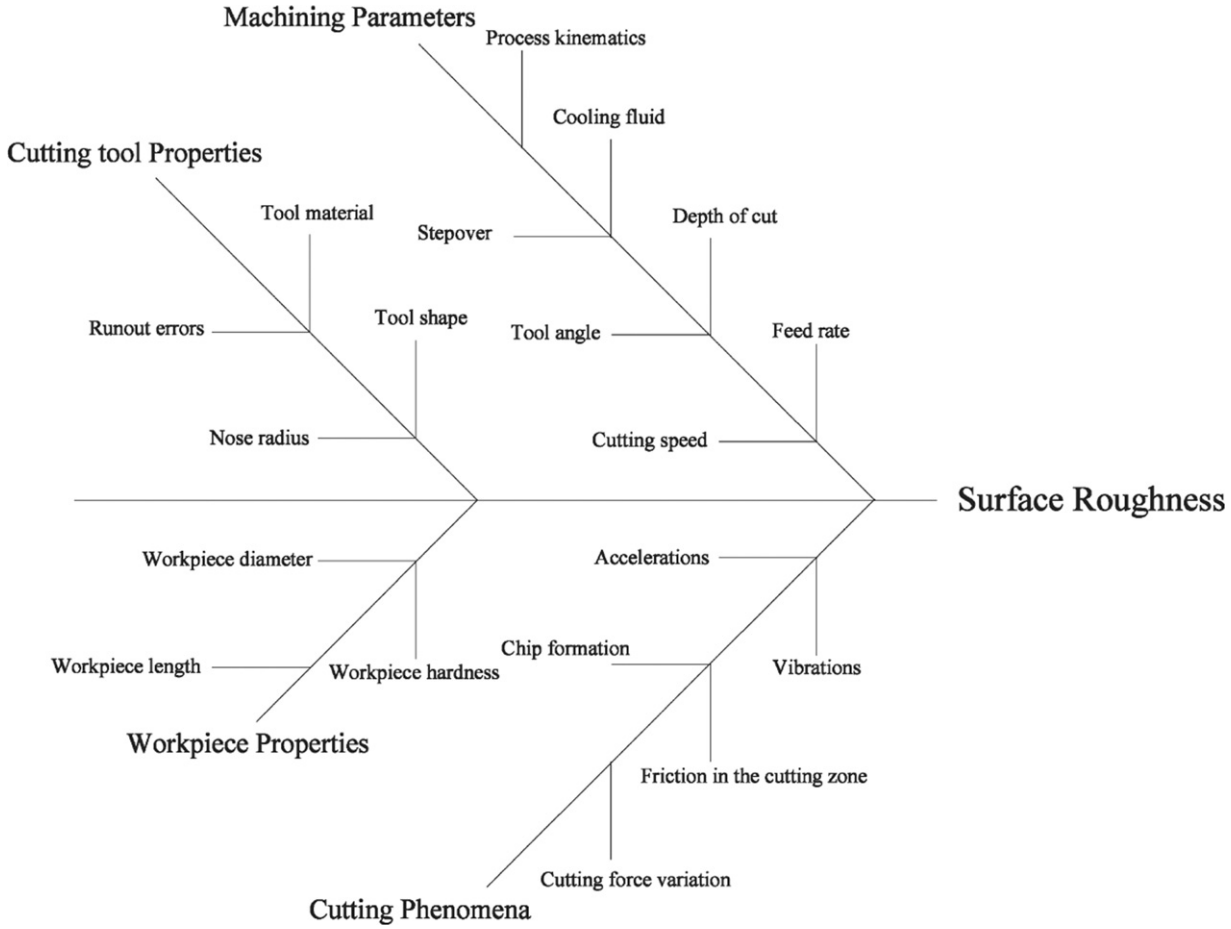


Figure 11 The parameters that affect surface roughness.[59]

pass in face milling of Ti6Al4V alloy. After removal of softer a-CN layer, surface roughness was observed to be similar to that of commercial TiN/TiAlN coated tools.[62]

DLC coatings have excited researchers due to its low friction coefficient and high wear resistance. Under dry conditions, the machined surface roughness of $AlMg_{2.5}$ and $AlCu_{4.5}Si_{12}$ alloys was decreased to about one half using DLC coating as presented in Figure 12.[56]

According to turning test results on the gray cast iron workpiece (260 HB), a lower surface roughness and a higher surface quality were obtained with the coated ceramic tools deposited by PVD or CVD methods, especially in the finish machining process. The uncoated tool gave the highest surface roughness (sample 0). In the case of coating systems (TiN + TiAlSiN + TiN), sample B, and TiCN + TiN (sample F) (Figure 13), a minimum roughness of $R_a = 2.3$ μm was obtained at finish turning. The roughness parameter R_a lower than 2.5 μm was obtained at finish turning for all coating systems, except TiAlN (sample E) and $TiN + Al_2O_3$ (sample G).[63]

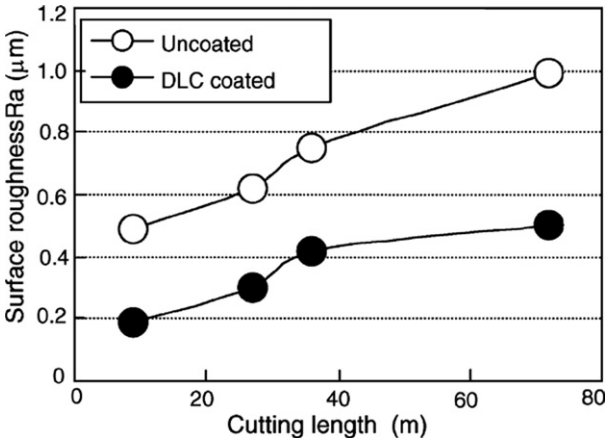


Figure 12 Surface roughness as a function of cutting length during dry machining[56] of workpiece material (AlCu2.5Si18 alloy) using uncoated and DLC coated inserts.

cBN is also a promising coating material due to its higher hardness and wear resistance. Uhlmann *et al.*[64] deposited cBN coating (1.4 μm thickness) on carbide tools. TiAlN was used as interlayer. During machining of Inconel 718 with TiAlN monolayer and TiAlN + cBN coated carbide tools at cutting parameters given in Figure 14, lower roughness and lower resultant cutting force components was obtained with latter ones.[64]

A comparison of cBN tool and coated carbide tools was performed by Okada *et al.*[54] In the case of milling of hardened steel with coated carbide tools, rougher surfaces were generated than those with cBN tools. This was attributed to the difference in roughness of the cutting tool surfaces. Accordingly, smaller workpiece roughness values were obtained with TiN- and TiCN-coated tools than TiAlN- and TiAlN/AlCrN-coated ones. Such behavior was affected with the coated tool's original surface roughness.[54]

3.16.3.2 Residual Stress and Microstructure

The amount of wear on a tool's flank face has critical importance to avoid excessive surface and subsurface damages on the machined components.[65] Especially in hard machining operations on hardened steels, sharpness of a cutting tool considerably effect white layer and residual stress formation on the machined component surface. When sharp tools are used, the surface microstructure remains the same as the bulk material and the surface residual stresses tend to be compressive. Residual stress profiles produced after turning of hardened steel with sharp and worn tools are given in Figure 15. It is seen that in case of the sharp cutting tool, the residual

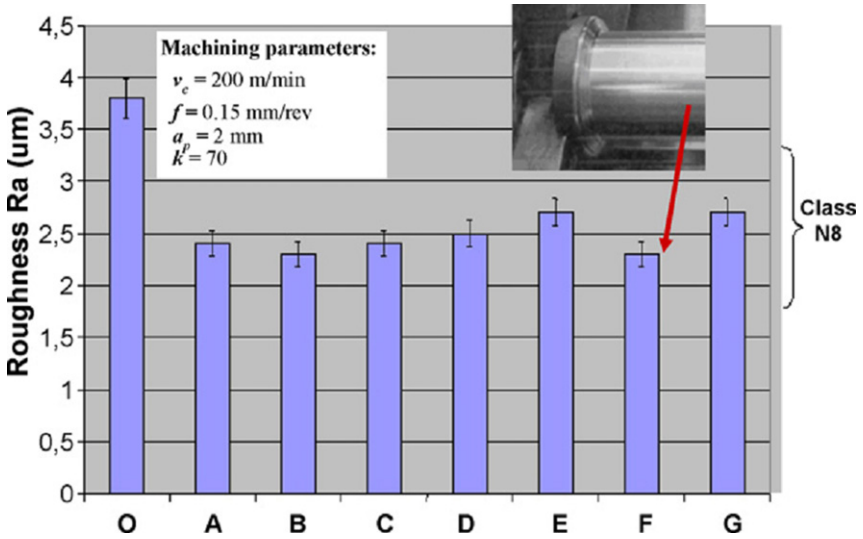


Figure 13 Comparison of the roughness parameter R_a of gray cast iron machined surface with uncoated (sample 0) and different PVD and CVD-coated tools (samples A–G).[63]

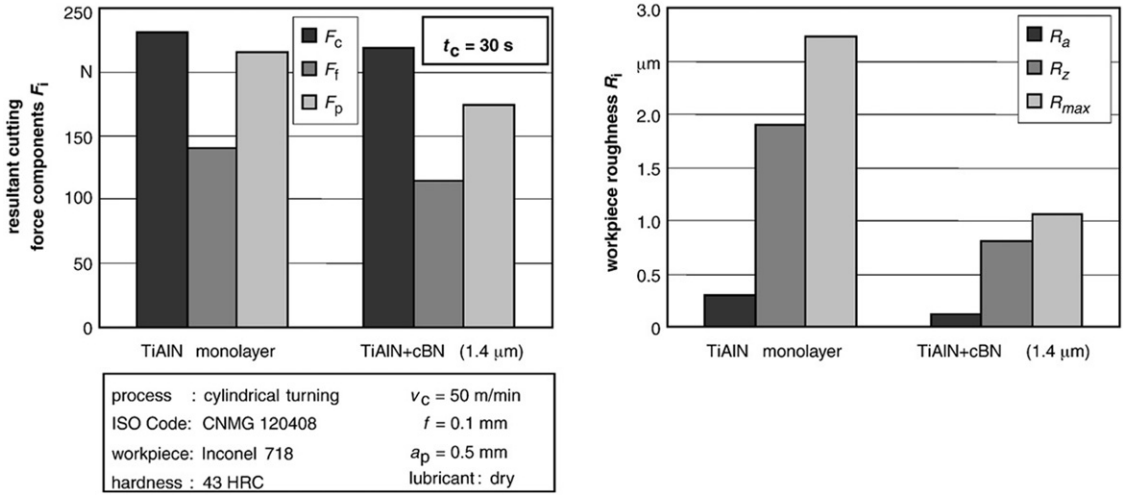


Figure 14 Resultant cutting force components and workpiece roughnesses of cBN coating and TiAlN coating during machining of Inconel 718.[64]

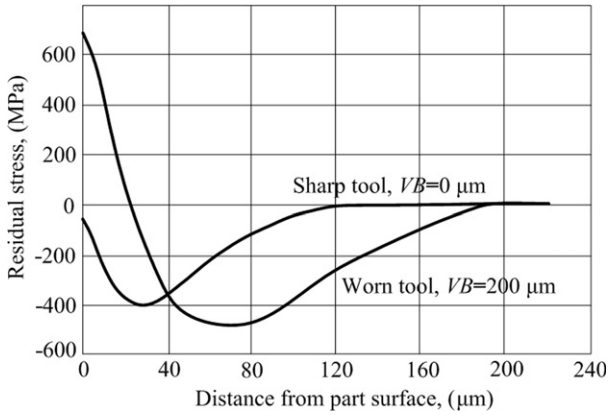


Figure 15 Residual stress depth profiles produced after turning of hardened steel with sharp and worn tools.[55]

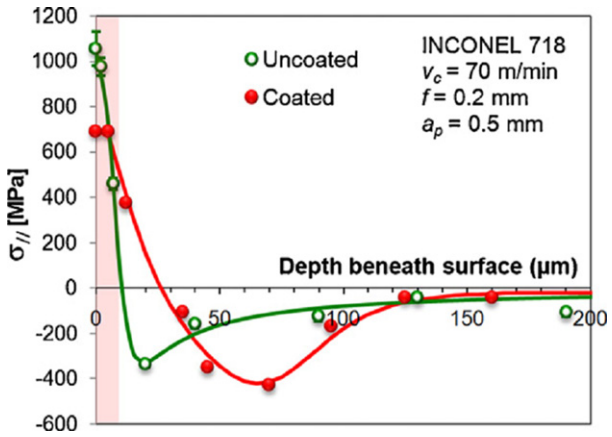


Figure 16 In-depth $\sigma_{//}$ residual stress distribution in machining Inconel 718.[66]

stress at the surface is zero and it becomes compressive below the surface. On the contrary, in case of the worn cutting tool, tensile residual stress occurs at the surface and it becomes compressive at greater distances from the part surface. The residual stress formation with the worn tool was explained in such a way that, with the increase of the tool flank wear, friction between tool flank face/the machine surface increases, leading to higher thermal loads on the surface layer. High cutting temperatures cause to the formation of white layers and a greater tendency to induce tensile residual stresses in the surface layer of the hard machined part.[55]

Figure 16 shows the depth profiles of residual stress induced by machining of Inconel 718 with coated and uncoated cutting tools. Differently from residual stress profiles obtained on hardened steel depicted in Figure 15, residual stresses are tensile at the surface machined with both coated and uncoated tools and the stresses gradually change to compressive values beneath the surface, and then they become equal to the values before machining (around zero MPa). When compared with the coated tools, uncoated tools resulted in higher tensile residual stresses at the surface, lower thickness of tensile layer and lower residual stresses (maximum) in the subsurface.[66]

Figure 17 shows the change of the workpiece surface roughness and of the external tangential residual stress as a function of the cutting speed in hard turning of 27MnCr5 alloy with uncoated cBN tools and TiN coated cBN tools. It is seen that TiN coating provides better surface finish at higher cutting speeds (Figure 17(a)). It can be observed in Figure 17(b) that a TiN coating provides a decrease in the external residual stress between 150 and 350 MPa. A more benefit from TiN coating in terms of residual stress level was obtained at high cutting speeds. The reason of lower residual stress with the TiN coated tools was attributed to the good tribological behavior of TiN coating, which reduces the friction and thereby the mean cutting temperature at the tool/chip interface.[67]

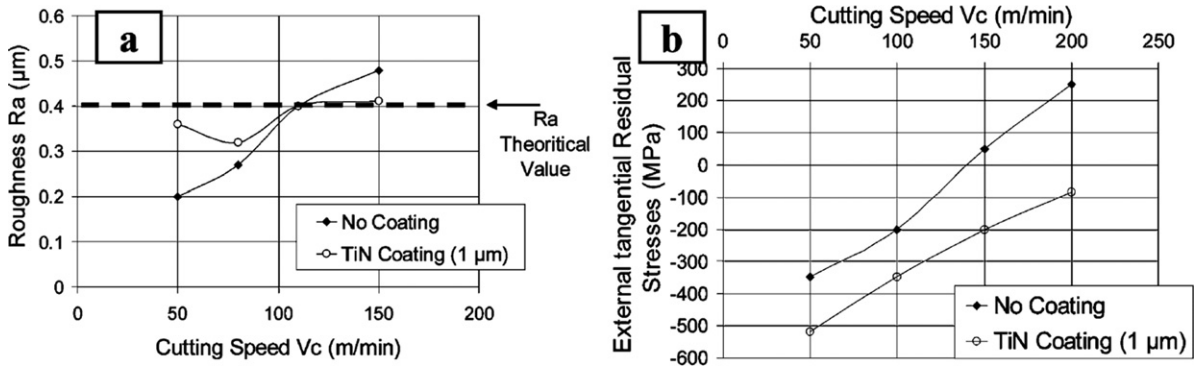


Figure 17 Influence of the TiN coating on external residual stress and roughness after hard turning-27MnCr5, 850 HV0.3, $a_p = 0.15$ mm, TNGA 160408S, f = 0.1 mm rev^{-1}.[67]

3.16.4 Conclusions

In this chapter an outline of the effect of hard coatings on surface finish in machining applications is presented. Main hard coatings designs were introduced and the required properties from a hard coating were summarized. It was shown that cutting performance of cutting tools and surface finish can be significantly improved by deposition of a hard coating on cutting tool materials. The relation of hard coatings with tool wear, cutting temperature, chip formation, surface roughness, and residual stress was discussed in detail.

See also: 3.3 Surface Finish Coatings

References

1. Koshy, P.; Dewes, R. C.; Aspinwall, D. K. High Speed End Milling of Hardened AISI D2 Tool Steel (~58 HRC). *J. Mater. Process. Technol.* **2002**, *127* (2), 266–273.
2. Gopalsamy, B.; Mondal, B.; Ghosh, S.; Arntz, K.; Klocke, F. Investigations on Hard Machining of Impax Hi Hard Tool Steel. *Int. J. Mater. Form.* **2009**, *2* (3), 145–165.
3. Noordin, M. Y.; Venkatesh, V. C.; Sharif, S.; Elting, S.; Abdullah, A. Application of Response Surface Methodology in Describing the Performance of Coated Carbide Tools When Turning AISI 1045 Steel. *J. Mater. Process. Technol.* **2004**, *145* (1), 46–58.
4. Fox-Rabinovich, G. S.; Kovalev, A. I.; Aguirre, M. H.; *et al.* Design and Performance of AlTiN and TiAlCrN PVD Coatings for Machining of Hard to Cut Materials. *Surf. Coat. Technol.* **2009**, *204* (4), 489–496.
5. Holmberg, K.; Matthews, A. *Coatings Tribology: Properties, Mechanisms, Techniques and Applications in Surface Engineering*, 2nd ed.; Elsevier: Oxford, 2009; p. 560.
6. Arndt, M.; Kacsich, T. Performance of New AlTiN Coatings in Dry and High Speed Cutting. *Surf. Coat. Technol.* **2003**, *163–164*, 674–680.
7. Ducros, C.; Sanchette, F. Multilayered and Nanolayered Hard Nitride Thin Films Deposited by Cathodic Arc Evaporation. Part 2: Mechanical Properties and Cutting Performances. *Surf. Coat. Technol.* **2006**, *201* (3–4), 1045–1052.
8. Chen, L.; Wang, S. Q.; Du, Y.; *et al.* Machining Performance of Ti–Al–Si–N Coated Inserts. *Surf. Coat. Technol.* **2010**, *205* (2), 582–586.
9. Knotek, O.; Munz, W. D.; Leyendecker, T. Industrial Deposition of Binary, Ternary, and Quaternary Nitrides of Titanium, Zirconium, and Aluminum. *J. Vac. Sci. Technol. A: Vac. Surf. Films* **1987**, *5* (4), 2173–2179.
10. Witthaut, M.; Cremer, R.; von Richthofen, A.; Neuschütz, D. Improvement of the Oxidation Behavior of Ti1–xAlxN Hard Coatings by Optimization of the Ti/Al Ratio. *Fresenius J. Anal. Chem.* **1998**, *361* (6), 639–641.
11. Chang, Y.-Y.; Wang, D.-Y.; Hung, C.-Y. Structural and Mechanical Properties of Nanolayered TiAlN/CrN Coatings Synthesized by a Cathodic Arc Deposition Process. *Surf. Coat. Technol.* **2005**, *200* (5–6), 1702–1708.
12. Settineri, L.; Faga, M. G.; Gautier, G.; Perucca, M. Evaluation of Wear Resistance of AlSiTiN and AlSiCrN Nanocomposite Coatings for Cutting Tools. *CIRP Ann. – Manuf. Technol.* **2008**, *57* (1), 575–578.
13. Jeong, Y. G.; Kang, M. C.; Kim, J. S.; *et al.* Mechanical Behavior and Cutting Performance of Nano-Multi-Layer TixAl1–xN Coated Tools for High-Speed Machining of AISI D2 Die Steel. *Curr. Appl. Phys.* **2009**, *9* (3, Suppl. 1), S272–S275.
14. Panjan, M. Physical and Chemical Properties of Nanolayered Metal-Nitride Coatings Prepared by Sputtering (Ph.D. Thesis); Ljubljana: University of Ljubljana, 2010.
15. Sproul, W. D. Physical Vapor Deposition Tool Coatings. *Surf. Coat. Technol.* **1996**, *81* (1), 1–7.
16. Knotek, O.; Löffler, F.; Krämer, G. Applications to Cutting Tools. In *Handbook of Hard Coatings*; Bunshah, R. F., Ed.; Noyes Publications: Norwich, NY, 2000; p. 550.
17. Byrne, G.; Dornfeld, D.; Denkena, B. Advancing Cutting Technology. *CIRP Ann. – Manuf. Technol.* **2003**, *52* (2), 483–507.
18. Çalışkan, H.; Erdoğan, A.; Panjan, P.; Gök, M. S.; Karaoğlanlı, A. C. Micro-abrasion Wear Testing of Multilayer Nanocomposite TiAlSiN/TiSiN/TiAlN Hard Coatings Deposited on AISI H11 Steel. *Materiali in Tehnologije/Mater. Technol.* **2013**, *47* (5), 563–568.
19. Quinto, D. T. Twenty-Five Years of PVD Coatings at the Cutting Edge. *SVC Bull.* **2007**, *Fall*, 17–22.
20. Venugopal, K. A.; Tawade, R.; Prashanth, P. G.; Paul, S.; Chattopadhyay, A. B. Turning of Titanium Alloy with TiB_2-coated Carbides under Cryogenic Cooling. *Proc. Inst. Mech. Eng., Part B: J. Eng. Manuf.* **2003**, *217* (12), 1697–1707.
21. Sproul, W. D. Tribological Coatings: From Monolithic to Nanocomposite and Nanolayer Coatings. *SVC Bull.* **2007**, *Fall*, 46–49.
22. Davim, J. P. *Machining: Fundamentals and Recent Advances*; Springer-Verlag: London, 2008.
23. Çalışkan, H. Selection of Boron Based Tribological Hard Coatings Using Multi-Criteria Decision Making Methods. *Mater. Des.* **2013**, *50* (0), 742–749.
24. PalDey, S.; Deevi, S. C. Single Layer and Multilayer Wear Resistant Coatings of (Ti,Al)N: A Review. *Mater. Sci. Eng.: A* **2003**, *342* (1–2), 58–79.
25. Tsutomu, I.; Hiroshi, S. Phase Formation and Characterization of Hard Coatings in the Ti-Al-N System Prepared by the Cathodic Arc Ion Plating Method. *Thin Solid Films* **1991**, *195* (1–2), 99–110.
26. Horling, A.; Hultman, L.; Oden, M.; Sjolen, J.; Karlsson, L. Thermal Stability of Arc Evaporated High Aluminum-Content Ti1–xAlxN Thin Films. *J. Vac. Sci. Technol. A: Vac. Surf. Films* **2002**, *20* (5), 1815–1823.
27. Yamamoto, K.; Sato, T.; Takahara, K.; Hanaguri, K. Properties of (Ti,Cr,Al)N Coatings with High Al Content Deposited by New Plasma Enhanced Arc-Cathode. *Surf. Coat. Technol.* **2003**, *174–175* (0), 620–626.
28. Kovalev, A. I.; Wainstein, D. L.; Rashkovskiy, A. Y.; *et al.* Impact of Al and Cr alloying in TiN-based PVD Coatings on Cutting Performance During Machining of Hard to Cut Materials. *Vacuum* **2009**, *84* (1), 184–187.
29. Sproul, W.D.; Christie, D.J.; Carter, D.C. The Reactive Sputter Deposition of Aluminum Oxide Coatings Using High Power Pulsed Magnetron Sputtering (HPPMS). In *47th Annual Technical Conference Proceedings of Society of Vacuum Coaters*; Dallas, TX, 2004; pp. 96–100.

30. Rossnagel, S. M. Sputter Deposition. In *Opportunities for Innovation: Advanced Surface Engineering*; Sproul, W. D., Legg, K. O., Eds.; Technomic Publishing Company: Switzerland, 1995.
31. Hsieh, J. H.; Liang, C.; Yu, C. H.; Wu, W. Deposition and Characterization of TiAlN and Multi-Layered TiN/TiAlN Coatings Using Unbalanced Magnetron Sputtering. *Surf. Coat Technol.* **1998**, *108–109*, 132–137.
32. Chistyakov, R.; Abraham, B. Advanced Pulsed DC Technology for Material Processing Applications. *Bulletin, Society of Vacuum Coaters*, **2009**, *Fall*, 22–25.
33. Ducros, C.; Benevent, V.; Sanchette, F. Deposition, Characterization and Machining Performance of Multilayer PVD Coatings on Cemented Carbide Cutting Tools. *Surf. Coat. Technol.* **2003**, *163–164*, 681–688.
34. Settineri, L.; Levi, R. Surface Properties and Performance of Multilayer Coated Tools in Turning Inconel. *CIRP Ann. – Manuf. Technol.* **2005**, *54* (1), 515–518.
35. Kumar, C.; Nair, P.; Ramamoorthy, B. Characterization of Multilayer Pvd Nanocoatings Deposited on Tungsten Carbide Cutting Tools. *Int. J. Adv. Manuf. Technol.* **2008**, *38* (5), 622–629.
36. Klocke, F.; Krieg, T. Coated Tools for Metal Cutting – Features and Applications. *CIRP Ann. – Manuf. Technol.* **1999**, *48* (2), 515–525.
37. Helmersson, U.; Todorova, S.; Barnett, S. A.; Sundgren, J. E.; Markert, L. C.; Greene, J. E. Growth of Single-Crystal TiN/VN Strained-Layer Superlattices with Extremely High Mechanical Hardness. *J. Appl. Phys.* **1987**, *62* (2), 481–484.
38. Koehler, J. S. Attempt to Design a Strong Solid. *Phys. Rev. B* **1970**, *2* (2), 547–551.
39. Anderson, P. M.; Li, C. Hall–Petch Relations for Multilayered Materials. *Nanostruct. Mater.* **1995**, *5* (3), 349–362.
40. Kato, M.; Mori, T.; Schwartz, L. H. Hardening by Spinodal Modulated Structure. *Acta Metall.* **1980**, *28* (3), 285–290.
41. Cammarata, R. The Supermodulus Effect in Compositionally Modulated Thin Films. *Scripta Metall.* **1986**, *20* (4), 479–486.
42. Ning, L.; Veldhuis, S. C.; Yamamoto, K. Investigation of Wear Behavior and Chip Formation for Cutting Tools with Nano-Multilayered TiAlCrN/NbN PVD Coating. *Int. J. Mach. Tools Manuf.* **2008**, *48* (6), 656–665.
43. Zhang, S.; Sun, D.; Fu, Y.; Du, H. Recent Advances of Superhard Nanocomposite Coatings: A Review. *Surf. Coat. Technol.* **2003**, *167* (2–3), 113–119.
44. Musil, J. Hard Nanocomposite Coatings: Thermal Stability, Oxidation Resistance and Toughness. *Surf. Coat. Technol.* **2012**, *207*, 50–65.
45. Griffiths, B. *Manufacturing Surface Technology: Surface Integrity and Functional Performance*; Elsevier: Oxford, 2001.
46. Aramcharoen, A.; Mativenga, P. Manufacturing & Laser Processing Group. White Layer Formation and Hardening Effects in Hard Turning of H13 Tool Steel with CrTiAlN and CrTiAlN/MoST-coated Carbide Tools. *Int. J. Adv. Manuf. Technol.* **2008**, *36* (7), 650–657.
47. Grzesik, W. *Advanced Machining Processes of Metallic Materials: Theory, Modelling and Applications*, 1st ed.; Elsevier: Boston, MA, 2008.
48. Robinson, G.; Jackson, M.; Whitfield, M. A Review of Machining Theory and Tool Wear with a View to Developing Micro and Nano Machining Processes. *J. Mater. Sci.* **2007**, *42* (6), 2002–2015.
49. Çalışkan, H.; Kurbanoğlu, C.; Panjan, P.; Čekada, M.; Kramar, D. Wear Behavior and Cutting Performance of Nanostructured Hard Coatings on Cemented Carbide Cutting Tools in Hard Milling. *Tribol. Int.* **2013**, *62*, 215–222.
50. Dogra, M.; Sharma, V. S.; Dureja, J. Effect of Tool Geometry Variation on Finish Turning – A Review. *J. Eng. Sci. Technol. Rev.* **2011**, *4* (1), 1–13.
51. Sun, S.; Brandt, M.; Mo, J. P. Evolution of Tool Wear and its Effect on Cutting Forces During Dry Machining of Ti–6Al–4V Alloy. *Proc. Inst. Mech. Eng. Part B: J. Eng. Manuf.* **2014**, *228* (2), 191–202.
52. Qin, F.; Chou, Y. K.; Nolen, D.; Thompson, R. G. Coating Thickness Effects on Diamond Coated Cutting Tools. *Surf. Coat. Technol.* **2009**, *204* (6–7), 1056–1060.
53. Bobzin, K.; Bagcivan, N.; Immich, P.; Bolz, S.; Cremer, R.; Leyendecker, T. Mechanical Properties and Oxidation Behaviour of (Al,Cr)N and (Al,Cr,Si)N Coatings for Cutting Tools Deposited by HPPMS. *Thin Solid Films* **2008**, *517* (3), 1251–1256.
54. Okada, M.; Hosokawa, A.; Tanaka, R.; Ueda, T. Cutting Performance of PVD-coated Carbide and CBN Tools in Hardmilling. *Int. J. Mach. Tools Manuf.* **2011**, *51* (2), 127–132.
55. Davim, J. P., Ed. *Surface Integrity in Machining*, ISBN: 1848828742; Springer: London, 2010.
56. Fukui, H.; Okida, J.; Omori, N.; Moriguchi, H.; Tsuda, K. Cutting performance of DLC Coated Tools in Dry Machining Aluminum Alloys. *Surf. Coat. Technol.* **2004**, *187* (1), 70–76.
57. Wang, J. The Effect of the Multi-Layer Surface Coating of Carbide Inserts on the Cutting Forces in Turning Operations. *J. Mater. Process. Technol.* **2000**, *97* (1–3), 114–119.
58. Lu, L.; Wang, Q.-M.; Chen, B.-Z.; *et al.* Microstructure and Cutting Performance of CrTiAlN Coating for High-speed Dry Milling. *Trans. Nonferr. Met. Soc.* **2014**, *24* (6), 1800–1806.
59. Benardos, P. G.; Vosniakos, G. C. Prediction of Surface Roughness in CNC Face Milling Using Neural Networks and Taguchi's Design of Experiments. *Robot. Comput.-Int. Manuf.* **2002**, *18* (5–6), 343–354.
60. Kopač, J.; Bahor, M.; Soković, M. Optimal Machining Parameters for Achieving the Desired Surface Roughness in Fine Turning of Cold Pre-formed Steel Workpieces. *Int. J. Mach. Tools Manuf.* **2002**, *42* (6), 707–716.
61. Çalışkan, H.; Kurbanoğlu, C.; Panjan, P.; Kramar, D. Investigation of the Performance of Carbide Cutting Tools with Hard Coatings in Hard Milling Based on the Response Surface Methodology. *Int. J. Adv. Manuf. Technol.* **2013**, *66* (5–8), 883–893.
62. Çalışkan, H.; Küçükköse, M. The Effect of aCN/TiAlN Coating on Tool Wear, Cutting Force, Surface Finish and Chip Morphology in Face Milling of Ti6Al4V Superalloy. *Int. J. Refract. Met. Hard Mater.* **2015**, *50*, 304–312.
63. Soković, M.; Barišić, B.; Sladić, S. Model of Quality Management of Hard Coatings on Ceramic Cutting Tools. *J. Mater. Process. Technol.* **2009**, *209* (8), 4207–4216.
64. Uhlmann, E.; Fuentes, J. A. O.; Keunecke, M. Machining of High Performance Workpiece Materials with CBN Coated Cutting Tools. *Thin Solid Films* **2009**, *518* (5), 1451–1454.
65. Ezugwu, E. O.; Okeke, C. I. Effects of Coating Materials on the Machinability of a Nickel Base, C-263, Alloy. *Tribol. Trans.* **2000**, *43* (3), 549–553.
66. Outeiro, J. C.; Pina, J. C.; M'Saoubi, R.; Pusavec, F.; Jawahir, I. S. Analysis of Residual Stresses Induced by Dry Turning of Difficult-to-Machine Materials. *CIRP Ann. – Manuf. Technol.* **2008**, *57* (1), 77–80.
67. Rech, J.; Moisan, A. Surface Integrity in Finish Hard Turning of Case-Hardened Steels. *Int. J. Mach. Tools Manuf.* **2003**, *43* (5), 543–550.

Relevant Websites

http://www.ist.fraunhofer.de/en/services.html
Fraunhofer Institute for Surface Engineering and Thin Films IST.

https://www.ijs.si/ctp/index_A.html
Jožef Stefan Institute.

3.17 Topological Evaluation of Surfaces in Relation to Surface Finish

P Demircioglu, Adnan Menderes University, Aydın, Turkey

© 2017 Elsevier Inc. All rights reserved.

3.17.1	**Topological Evaluation Methods**	243
3.17.1.1	Contact Surface Measurement Techniques	243
3.17.1.1.1	Portable handheld surface finish instrument	243
3.17.1.1.2	SP	243
3.17.1.1.3	Atomic force microscopy (contact mode)	244
3.17.1.2	Noncontact Surface Measurement Techniques	244
3.17.1.2.1	Confocal microscopy	244
3.17.1.2.2	Focus variation microscopy	245
3.17.1.2.3	CSI	246
3.17.1.2.4	SPM	247
3.17.1.2.4.1	AFM (Noncontact mode)	247
3.17.1.2.4.2	STM	247
3.17.1.2.5	Electron microscopy	247
3.17.1.2.5.1	TEM	248
3.17.1.2.5.2	SEM	248
3.17.1.2.6	Comparison	248
3.17.2	**Characterization of Parameters**	248
3.17.2.1	Primary Profile	250
3.17.2.2	Waviness Profile	250
3.17.2.3	Roughness Profile	250
3.17.3	**Surface Finishing**	254
3.17.4	**Conclusion**	260
References		260

3.17.1 Topological Evaluation Methods

Topological characterization methods are divided into two categories. These are contact and noncontact measurement and evaluation methods. These methods have pros and cons in different aspects. The technological developments are bringing new approaches and solutions. Therefore, evaluation methods for surface characterization should be revised and adapted to new approaching or emerging technologies.

3.17.1.1 Contact Surface Measurement Techniques

In the twentieth century, the attempts for development of the surface instrumentation were initiated by industry and academia. Surface topographical characterization was assessed by the judgment of the inspector either by eye or fingernail. The simplest way to characterize surface structure is visual inspection. The mere eye can tell quite much about larger scale features. The resolution of the human eye is limited to slightly under 100 μm.[1] Because of this reason, it is necessary to have higher spatial resolution measurement systems, which can be used for the surface topographical assessment.

The first contact type stylus profilometer (SP) was developed for the surface topographical characterization by Schmaltz in 1929.[2] After G. Schmaltz, Abbott in 1936[3] and Hobson in 1939[4] advanced the surface inspection and measurement know-how. Early stage evaluation methods were insufficient in order to put a numerical value to the surface texture. Contact type SPs advanced the evaluation methodologies and gave an opportunity to measure the surface parameters for finer and smoother surfaces quantitatively.

3.17.1.1.1 Portable handheld surface finish instrument

Portable handheld surface finish instruments measure multiple roughness parameters using diamond tip drawn across a sample part with motorized traverse mechanism. These instruments produce a set of traceable measurement results including detailed profile graph with one-button operation. Most common types of instruments use standard cutoff values (0.8 mm), accuracy (ranges from 0.1 to 40 μm in R_a), diamond tip with a radius of 5 μm, and traverse length of 5 mm.[5]

There are two common types of surface finish measuring systems as skidded and nonskidded (can be called as skidless). These testers with skidded can measure roughness only (**Figure 1(a)**), whereas skidless testers can evaluate the surface components as form, waviness, and roughness (**Figure 1(b)**). Workpiece belonging to surface being measured is used as a reference surface by skidded instruments, while skidless instruments can use an internal precision surface as a reference. Skid can be used as a mechanical filtering in the measurements. Skid radius is a key factor that determines the obtained results from a tester.

3.17.1.1.2 SP

SPs are supported with the most of the surface finish standards for the prerequisites of the engineering communities and academia (**Figure 2**).[6] A stylus with diamond tip with different

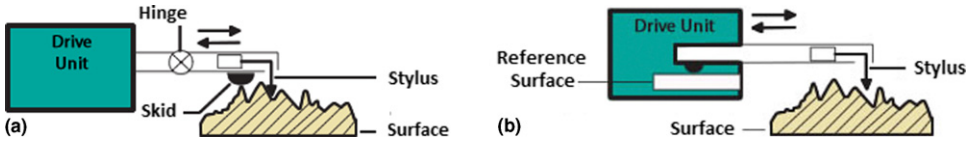


Figure 1 Portable handheld surface finish instrument. (a) with skid and (b) skidless.

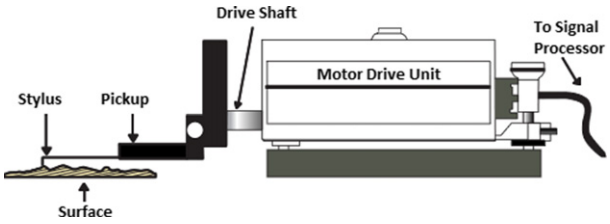


Figure 2 Working principle of stylus profilometer.

sizes (ranges from 20 nm to 50 μm) is moved in vertical stylus displacement on the surface being measured, while the tip is moved laterally across the sample for a predetermined contact force (range from less than 1–50 mg). Measuring range for a typical SP is between 10 nm and 1 mm. An analog signal is produced, as diamond moves mechanically up and down in vertical direction. Generated analog signals by transducer are converted into digital signals, and then this digital information is stored, analyzed, and displayed.

The SPs have pros and cons in different aspects. Software used by these profilometers is compatible with the world's surface finish standards. Stylus instruments are the only instrument types that are fully covered by ISO specification standards and there is good practice guidance available.[7] Obtained measurement results from the SPs are reliable. SPs are more preferable since they have an ability to measure the surface properties of a material with dirty layer, while noncontact measurement systems can measure material surface properties plus surface contaminants. Vertical resolution of these profilometers is usually sub-nanometer level.

The contact type stylus measurement technique has considerable drawbacks that the loaded stylus can damage or scratch the surface being measured, particularly the situation for soft surfaces. The transducer and stylus tips are often fragile, the measurements with these instrument should be applied in a fairly vibration free environment. Consequently, this direct contact measurement method may not be appropriate to be used on a test object undergoing a machining process simultaneously.[8]

3.17.1.1.3 Atomic force microscopy (contact mode)

Atomic Force Microscopy (AFM) is one of the scanning probe microscopy (SPM) techniques. The AFM[9] was developed for imaging the insulating surfaces at atomic resolution levels. For the working principle of AFM, the samples are scanned in 2-axes under the force-sensing probe with tip attached to a cantilever. The interaction between the tip and sample occurs, when the tip is approached to the sample surface with proximity. Therefore, forces between the tip and the sample results in a deflection for the cantilever. The light from a laser is sent to the cantilever, and then reflected light from back of the cantilever is focused on a position sensitive photodetector.[10] Such an optical beam deflection system is sensitive to subnanometer deflections of the cantilever.[11] The AFM performs raster scanning and produces a topographic map of the sample surface (Figure 3(a)). The imaging with contact mode AFM can damage or distort some biological samples (Figure 3(b)).

AFM has abilities to measure the parameters in nanoscale level (Figure 4). These parameters can be:

1. Nanomechanical properties such as elastic modulus, hardness, stiffness, viscoelastic, frictional, etc.
2. Nanochemical properties such as chemical composition of surface features, etc.
3. Nanoelectrical properties such as work function, conductivity, etc.
4. Nanomagnetic properties, for example, magnetostatic field, field gradient above ferromagnets, etc.
5. Texture parameters such as average roughness, maximum peak to valley height, root mean square roughness, 10-point mean height roughness, surface skewness, surface kurtosis, etc.
6. Particle characterization such as parameters, volume, size, shape, and particle surface morphology, etc.

3.17.1.2 Noncontact Surface Measurement Techniques

The invention of noncontact optical techniques is in a sense due to the drawbacks of the contact type stylus measurement techniques. These noncontact measurement methods have ability to measure in-process and the different types of materials. The optical systems and the SPs are two complementary methods.[12] This noncontact environment can also result in much faster measurement times for the optical scanning instruments in the characterization of technical and nontechnical surfaces, while the SPs take more operation time in an aerial scanning mode. 3D noncontact optical surface inspection and measurement methods work with sensor-based approach by being placed at a certain distance from the object. Since optical measurement systems contains many drawbacks such as objective properties, spot size, numerical aperture (NA), field of view (FOV), surface slopes and discontinuities, and multiple scattering, surface finish evaluation results seems to have higher values in other words overestimation of the values of surface texture parameters occurs.

In this section, confocal microscopy, focus variation microscopy, coherence scanning interferometry (CSI), SPM, and electron microscopy as the noncontact methods for measuring surface topography is mentioned.

3.17.1.2.1 Confocal microscopy

The fundamental working principle of confocal microscopy is that only focused-light is sent to detector by means of a spatial

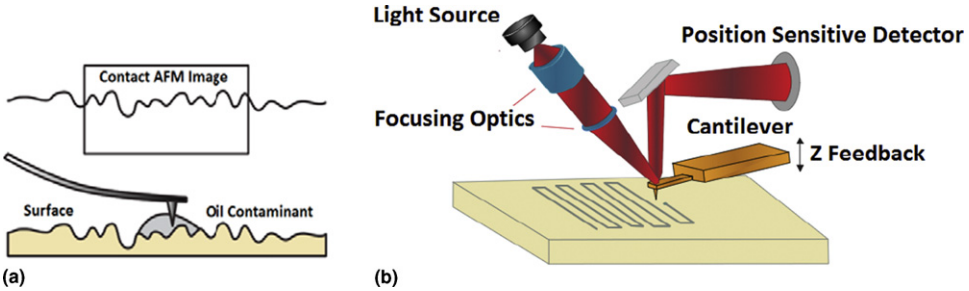


Figure 3 (a) Contact mode AFM imaging and (b) Atomic force microscope (AFM).

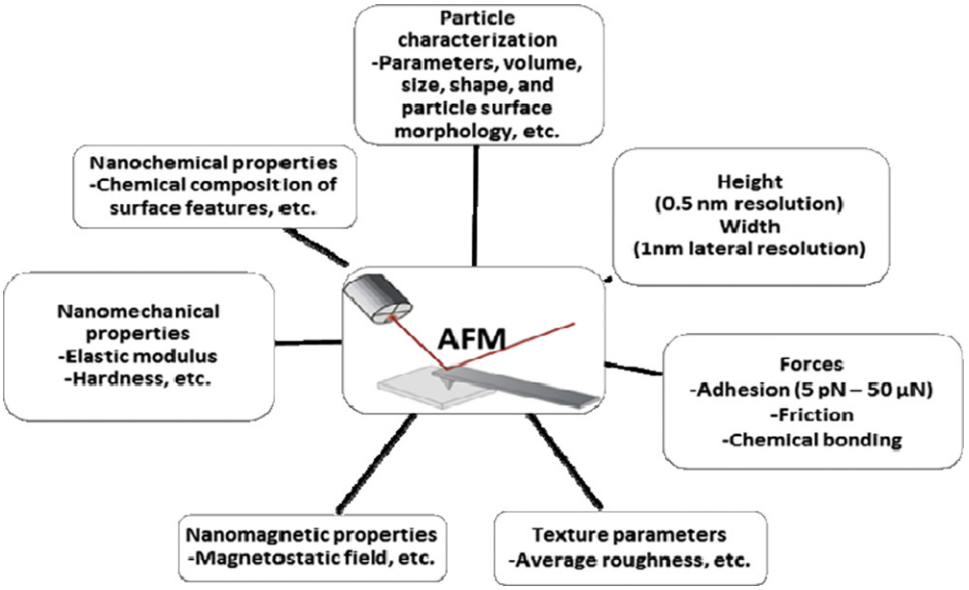


Figure 4 Measurement parameters with AFM.

pinhole placed at the confocal plane of the lens to remove out of focus light. In the late 1800s, Ernst Abbe (The Abbe Criterion) first enlightened that these traditional type fluorescence microscopes have the limits to spatial resolution. The principle of confocal imaging was patented (US patent 3013467) in 1957 by Minsky[13] with the purpose of surpassing the limitations of widefield fluorescence microscopes, since the resolution in confocal microscopy is augmented by eliminating out of focus light. In recent technologies, the confocal microscopy has three main different types of working principles. These principles are named as confocal laser scanning microscopy (CLSM or LSCM) (Figure 5(a)), disk scanning confocal microscopy (DSCM) (Figure 5(b)) and programmable array scanning confocal microscopy (PACM) (Figure 5(c)).

The main differences among confocal microscopes are beam scanning system, motorized scanning disk system, and programmable array scanning system for CLSM, DSCM, and PACM, respectively. In CLSM, beam scanner provides the raster scan of illumination to generate the confocal image. This is obtained by using two mirrors that move in perpendicular directions in order to bend the beam of the light. In DSCM, three different motorized disks are available in the market, these are called as Nipkow disks, parallel slits, and point rotating slit disks. Scanning disk turns and captures light that represents a slice of image from sample surface. In PACM, programmable array takes the roles of beam scanning system in CLSM and motorized disk in DSCM. Programmable array works in a way that only desired lights are taken into account. This each pixel of micro display acts as an illumination and detection element at the same time. Light from out of focus regions falls into neighboring pixels and the signals on the correlated pixels are used to reconstruct confocal image. The array of apertures can be opened or closed.

3.17.1.2.2 Focus variation microscopy

The principle of focus variation was first published by von Helmholtz in 1924.[14] The working principle of these instruments is based on focus variation. The visible light sends through a lens and to a beam splitter, then light goes through objective lens, finally to a sample. The driving unit connected to sample compartment moves vertically to provide in focus, lateral movement of the sample compartment enables the scanning of the sample. Reflected light from the sample goes through objective lens, and passes through semitransparent mirror and tube lenses to the Charge–Coupled Device (CCD) array. In an array, the status of focusing such as out of focus,

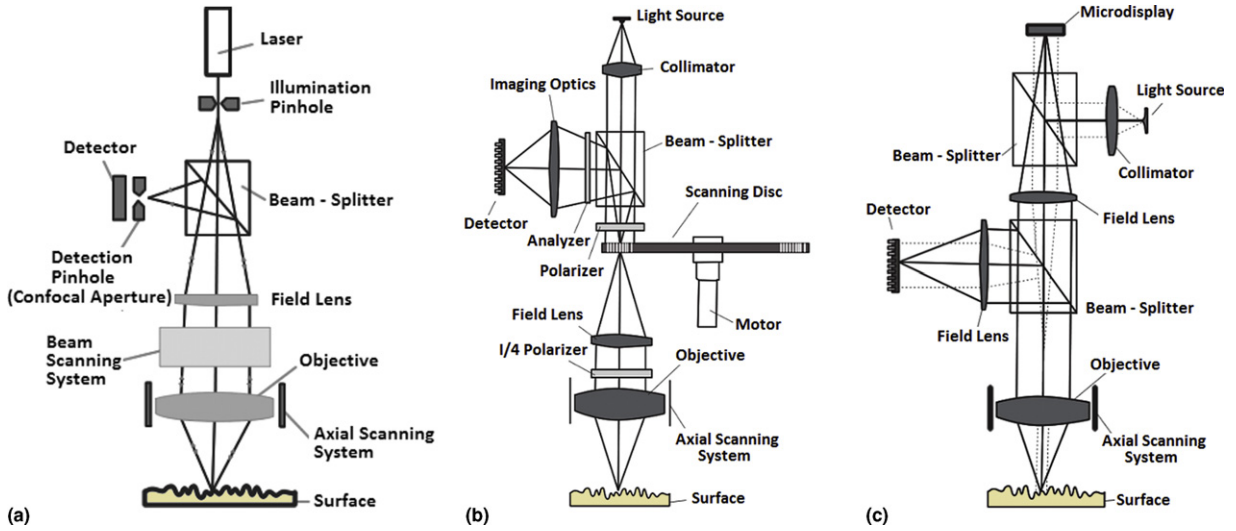
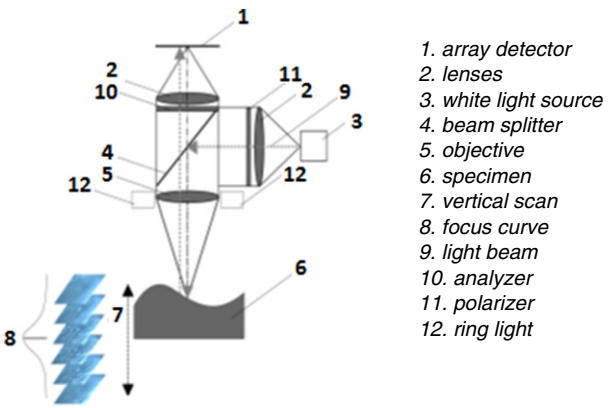


Figure 5 Schematic representation of three working principles of confocal microscopes.[11] (a) Confocal laser scanning microscopy (CLSM or LSCM), (b) disk scanning confocal microscopy (DSCM), and (c) programmable array scanning confocal microscopy (PACM).



1. array detector
2. lenses
3. white light source
4. beam splitter
5. objective
6. specimen
7. vertical scan
8. focus curve
9. light beam
10. analyzer
11. polarizer
12. ring light

Figure 6 Schematic diagram of a typical measurement device based on focus variation.[15]

almost in focus, and in focus is evaluated, calculating the focus information (standard deviation) by 5×5 neighboring pixel values with the pixel values for the point of interest. Working principle of focus variation microscopy is depicted in Figure 6.

3.17.1.2.3 CSI

CSI (Figure 7) is often referred to as vertical scanning white-light interferometry. The light goes through beam splitter to an objective lens and internal reference mirror driven by a piezo-system, finally through the object to be measured. From here, the light is reflected back to the objective, goes through beam splitter, and finally reaches to the digital image sensor. The upper beam splitter directs light from the light source toward the objective lens. The lower beam splitter in the objective lens splits the light into two separate beams. One beam is directed toward the sample and one beam is directed toward an internal reference mirror. The two beams recombine and the recombined light is sent to the detector. Due to the low coherence of the white light source, the optical path length to

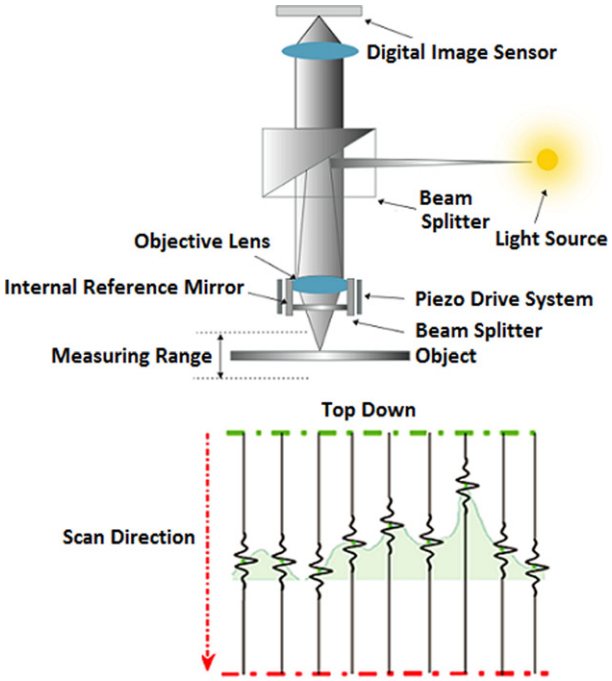


Figure 7 Working principle of coherence scanning interferometry design (upper) with schema of how to build up an interferogram on a surface using CSI. The vertical lines are intensity profiles at the image sensor (lower).[17]

the sample and the reference must be almost identical, for interference to be observed.[16] This characterizes how well a wave can interfere with itself at a different time. The detector measures the intensity of the light as the interferometric objective is actuated in the vertical direction (z-axis) and finds the maximum interference. Each pixel of the sensor measures the intensity of the light and the fringe envelope obtained can be used to calculate the position of the surface.

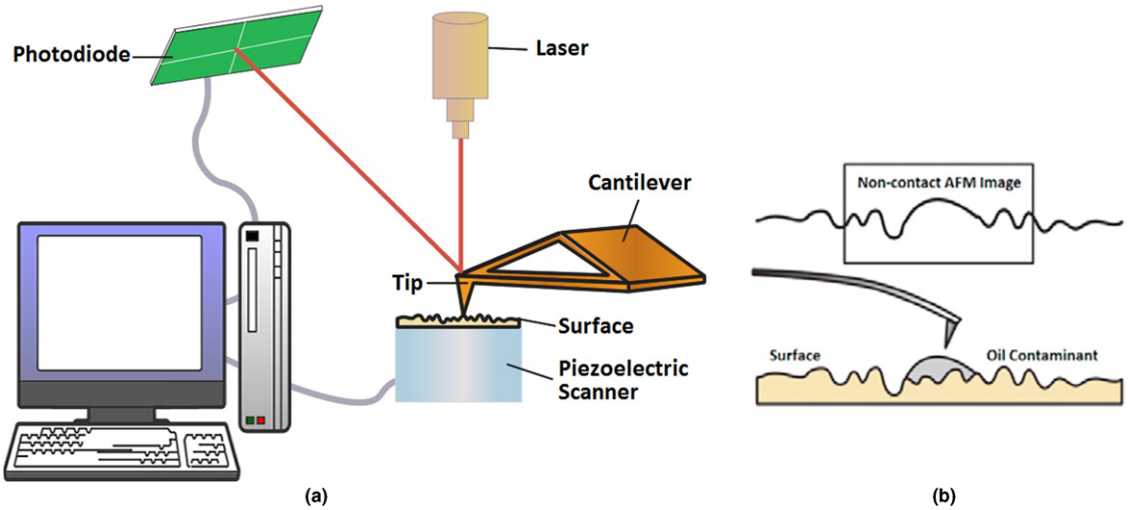


Figure 8 (a) Atomic force microscope and (b) Noncontact mode AFM imaging mode.

3.17.1.2.4 SPM

The Scanning Probe Microscopes (SPMs) represent the fundamental instrumentations for Nanotechnology. Basic principle of SPM has two distinct functions. These are scanning and probing. Scanning is performed by piezo raster 2D (X–Y) scanning, while probing is achieved by a sharp tip mounted to a z-scanner. The most common types of SPMs are noncontact AFM and scanning tunneling microscopy (STM).

3.17.1.2.4.1 AFM (Noncontact mode)

The first Noncontact AFM (NC-AFM) was designed by Martin *et al.* in 1987.[18] Tapping mode or NC-AFM (Figure 8(b)) can be classified in this section, since tip of the instrument does not have contact with sample surface. These types of instruments measure surface topography by utilizing attractive forces (interatomic force) between the tip and the sample surface. NC-AFM uses piezoelectric modulator to obtain the information regarding the surface topography. Piezoelectric modulator enables to keep minimum distance to the sample surface by van der Waals forces between the tip and the sample surface. Therefore, all the time the distance between the tip and the sample surface remains in the same level by z-servo feedback loop control system. The light sends to the cantilever, and then reflected back to photodetector. In photodetector, surface topography information is monitored (Figure 8(a)).

3.17.1.2.4.2 STM

The STM is based on the quantum mechanical tunneling effect (Figure 9). Binnig and Rohrer developed this system in 1981 (at IBM Zürich) and earned the Nobel Prize in Physics in 1986.[19] For an STM, average lateral and depth resolutions are considered to be 0.1 and 0.01 nm, respectively. With this resolution, individual atoms within materials are routinely imaged and manipulated. STM performs well for all conductive materials. However, it is possible to measure even biological materials such as DNA. Working principle of these instruments is that extremely fine conducting material creates tunneling effect with conductive samples. In theory, when a quantum object is sent on a material with a thick barrier, this quantum object bounces off. If the barrier is thinner, it has the ability to pass through the object. Metals are made of atoms and electrons. Electrons come off the metal surface, when electric current passes through the tip. This produces a tunnel effect. Low current is amplified by a current amplifier. Distance control and scanning unit enable to control the voltage goes to the piezoelectric tube. Thus, the tip is moved, and then finally data is recorded and displayed.

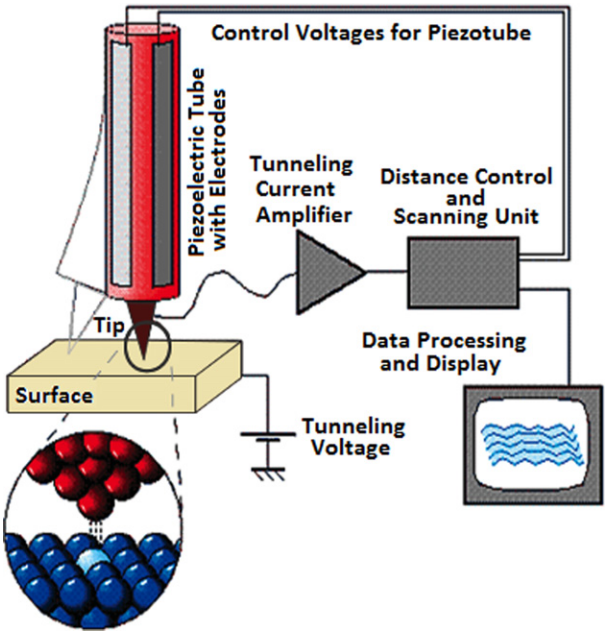


Figure 9 Working principle of scanning tunneling microscopy.[20]

3.17.1.2.5 Electron microscopy

The working principle of electron microscopes is that the system uses a beam of electrons instead of the light to produce an image of the sample specimen. There are two types of

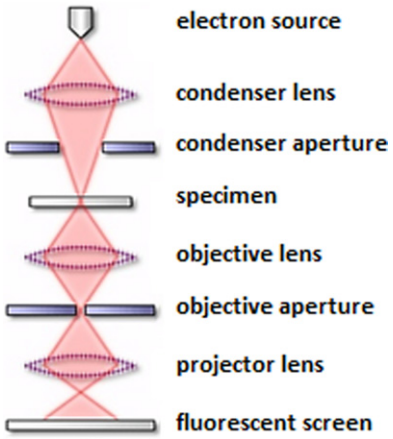


Figure 10 Schematic representation of transmission electron microscopy.

electron microscopes. These are Transmission Electron Microscopy (TEM) and Scanning Electron Microscopy (SEM). Generally, TEM and SEM utilize electromagnetic and/or electrostatic lenses to keep up the path of electrons. The resolution of these systems depends upon the wavelength of the irradiation used to create an image. Reducing the wavelength increases the resolution. Thus, the resolution of the image obtained from the microscope can be increased if the accelerating voltage of the electron beam is increased. Hans Busch was a pioneer of electron optics and laid the theoretical basis for the electron microscopy in 1920s. Knoll and Ruska[21] succeeded in magnifying an electron image. The first prototype of electron microscopy was actually built by Ruska in 1933 and was capable of resolving to 50 nm. In this section, the working principles of TEM and SEM are explicitly depicted.

3.17.1.2.5.1 TEM

In these instruments (Figure 10), instead of using light, electrons are produced and transmitted through an ultrathin specimen (semitransparent for electrons) as an electron beam. Like in spectroscopy, electrons passing through a specimen interact with the atoms in sample. As a result of the specimen characteristics, the properties of transmitted electron beam changes. The transmitted electron beam is projected on a fluorescent screen, and then the information is captured from fluorescent surface to create the TEM image. In other words, TEM contains a high voltage electron beam emitted by a cathode and formed by magnetic lenses. The electron beam partly transmitted through the ultrathin specimen carries information about the structure of the specimen. The spatial information is magnified by a series of magnetic lenses, and finally the image formed on a fluorescent screen. The image detected by a CCD camera played and recorded in real time.

3.17.1.2.5.2 SEM

In contrast to the TEM, SEM (Figure 11) produces the images using secondary electrons which are emitted from a specimen hit by the electrons of the primary beam. In SEM, the electron beam is scanned across the surface being measured in a raster scan with the detectors for building up an image by mapping the detected signals with the beam position. Since primary

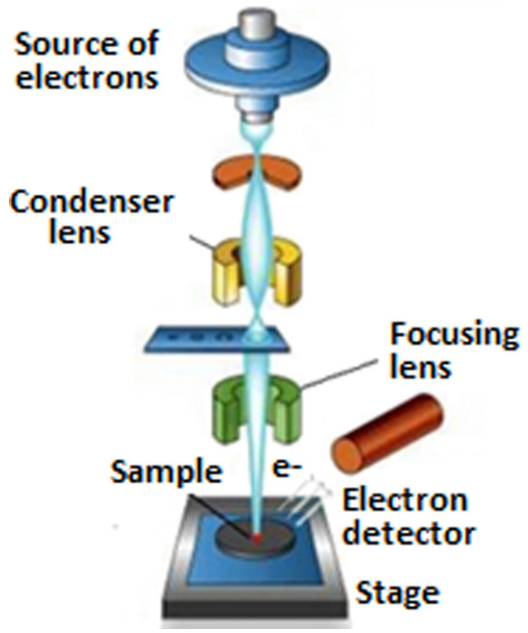


Figure 11 Schematic representation of scanning electron microscopy.

beam electrons have more energy than secondary electrons, secondary electrons from the atoms are kicked away by primary electrons and scattered electrons carry information regarding the surface properties of the specimen. Therefore, SEM is a vital measurement technique for the surface finish studies.

3.17.1.2.6 Comparison

Table 1 gives the comparison of the measurement and inspection techniques.

The sensitivity of instruments using cantilever beam with tip are affected by stiffness, size, and material type of the tip. TEM requires a special environmental conditioning such as vacuum, while SEM and others does not require. When compared in terms of cost and complexity, TEM and SEM require special lenses and optics, and have the highest cost among others in investment. STM tip should be conducting, can be simply cut freshly by normal wire cutter. STM works with the very top atom at the freshly cut tip, providing to atomic resolution. AFM tip should be sharp enough to get good resolution (fat-tip effect), and also AFM tip should be stiff enough to sense the atomic interaction with sample surface. AFM tip is not necessary to be conducting, but STM tip should be conductive.

From coarse to very fine surface finishes, it is important to test a specimen with proper instruments and to make decision with above mentioned measurement and inspection methods. Therefore, surface finishing and quality measurements can be done using above instruments. In surface finish measurement studies or in industry, crucial task is that the selection of proper measurement methods according to surface finish.

3.17.2 Characterization of Parameters

Surface texture refers to the surface irregularities such as peaks and valleys, produced on a surface by any forming processes.

Table 1 Comparison of the measurement and inspection techniques

Criteria	*Contact stylus*	*Noncontact optical*	*AFM*	*STM*	*TEM*	*SEM*
Type of probe	Tip	Light beam	Tip	Tip	Electron beam	Electron beam
Type of contact	Contact	Noncontact	Contact and Noncontact	Noncontact	Noncontact	Noncontact
Source	Mechanical-electrical energy	Photons	Mechanical-electrical energy/Photons	Atomic forces	Electrons	Electrons
Detection	Transducer	Photodetector	Photodetector	Photodetector	Fluorescent scene	CCD
Sample preparation	Little/Not required	Little/Not required	Required	Required	Required	Required
Spatial Resolution	0.1 μm–1 mm	0.5 μm	20 nm	2.5 nm	2 nm–1 μm	10 nm
Z-Resolution	0.3 nm	0.1 μm	Sub-nanometer/ Angstrom	0.2 nm	100 nm	2 nm
Z-Range	50 μm	20 μm	5 μm	100 nm	2 μm	2 μm
Output	2D/3D	2D/3D	3D	3D	2D	3D

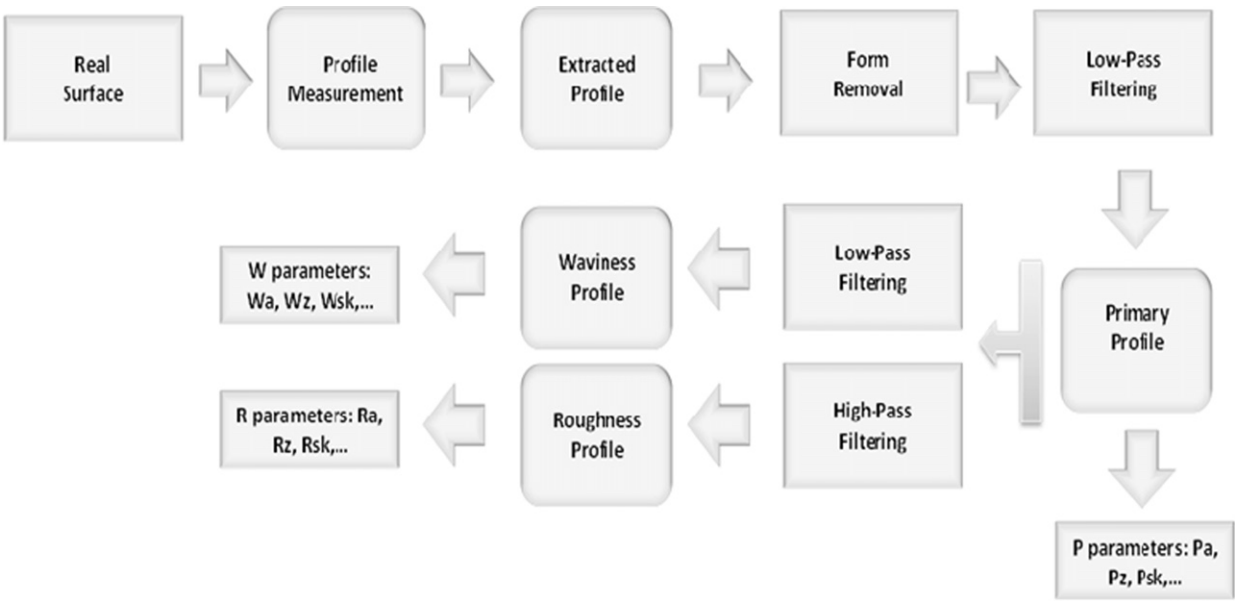


Figure 12 Surface topography evaluation schema.

Form, waviness, and roughness are basic components of a surface texture, which is much more associated with the roughness, since in practice surface roughness is most commonly used and measured. Forms typically appear due to the errors occurring from machining. This is commonly known as straightness errors. Waviness is a result of various vibrations during machining process related to both machine tool and outside sources like work deflection, vibration, heat treatment, and other similar factors. Roughness occurs as a result of feed-rate tool geometry, tool condition, the process used, and hardness and other variations in material characteristics. Since form, waviness, and roughness appears due to different factors mentioned above, it is possible to remove these errors with analyses. The removal of errors can be accomplished using selected filters or cutoff values. In this section, primary profile, waviness, and roughness are detailed explicitly.

Surface parameters are obtained using two types of profiling techniques. These techniques are based upon height measurements. These height measurements are made along a line (profile method) or over an area (raster area methods). Both types of techniques develop quantitative knowledge of the surface peaks and valleys by point measurement using high resolution probe. Surface topography evaluation schema (Figure 12) indicates how primary profile, waviness, and roughness are obtained using digital filters. Firstly, a profile signal is extracted from a surface using any profilometer such as with mechanical/optical probe. The extracted profile refers to the sampled and digitized signal. Then, form removal process is applied to the extracted profile signal. This refers to removal of errors caused by geometry of sample part/measurand. After the removal of form type, low-pass filter is applied to the obtained signal. The result is the primary profile signal. The primary profile parameters such as P_a, P_z, P_{sk}, etc.,

are obtained from primary profile signals. Low-pass filtering is applied to the primary profile signal and therefore, waviness profile signal is obtained. Parameters obtained from these signals are W_a, W_z, W_{sk}, etc. High-pass filter is applied to the primary profile signal. Then the roughness profile signal is obtained. Roughness parameters are R_a, R_z, R_{sk}, etc.

3.17.2.1 Primary Profile

The primary profile is acronym as *P*, which is the profile after low-pass filtering the measuring values using the cutoff wavelength λ_s. The short-wave profile parts in the signal are cutoff and evaluated within the sampling length (cutoff). This equals to the measured length or the length of the measured surface profile.[22] The primary profile signal obtained from a surface texture using low-pass filter is shown in **Figure 13(a)**. The profile is a superimposed image of roughness, waviness, and profile. **Figure 13(a)** shows the surface texture profile signal for a surface while **Figure 13(b)** illustrates the signals for original signal plus primary profile signal.

3.17.2.2 Waviness Profile

The waviness profile is acronym as *W*, which results from low-pass filtering the primary profile with the cutoff wavelength λ_c and high-pass filtering with the cutoff wavelength λ_f. Waviness profile is evaluated over the measured length l_n, which is composed of several sampling lengths l_w. The single measured length l_w corresponds to the cutoff wavelength λ_f of the high-pass filter. The original signal is illustrated in **Figure 14(a)**. The waviness profile signal obtained from a primary profile signal using low-pass filter is shown in **Figure 14(b)**.

3.17.2.3 Roughness Profile

The roughness profile is acronym as *R*, which results from high-pass filtering the primary profile with the cutoff wavelength λ_c. Roughness profile is evaluated over the measured length l_n, which is composed of five single measured lengths l_r. The single measured length l_r corresponds to the cutoff wavelength λ_c of the primary profile filter. The original signal is illustrated in **Figure 15(a)**. The roughness profile signal (**Figure 15(b)**) is obtained from a primary profile signal using high-pass filter.

Table 2 shows the 2D surface profile parameters, their corresponding equations, and graphical representations. Here, for each 2D parameter, definitions are given with their equations in order to use in surface topological calculation and evaluations. Furthermore, graphical representations for each surface parameter are depicted so as to illustrate the phenomena how 2D surface parameters are withdrawn for the best comprehension.

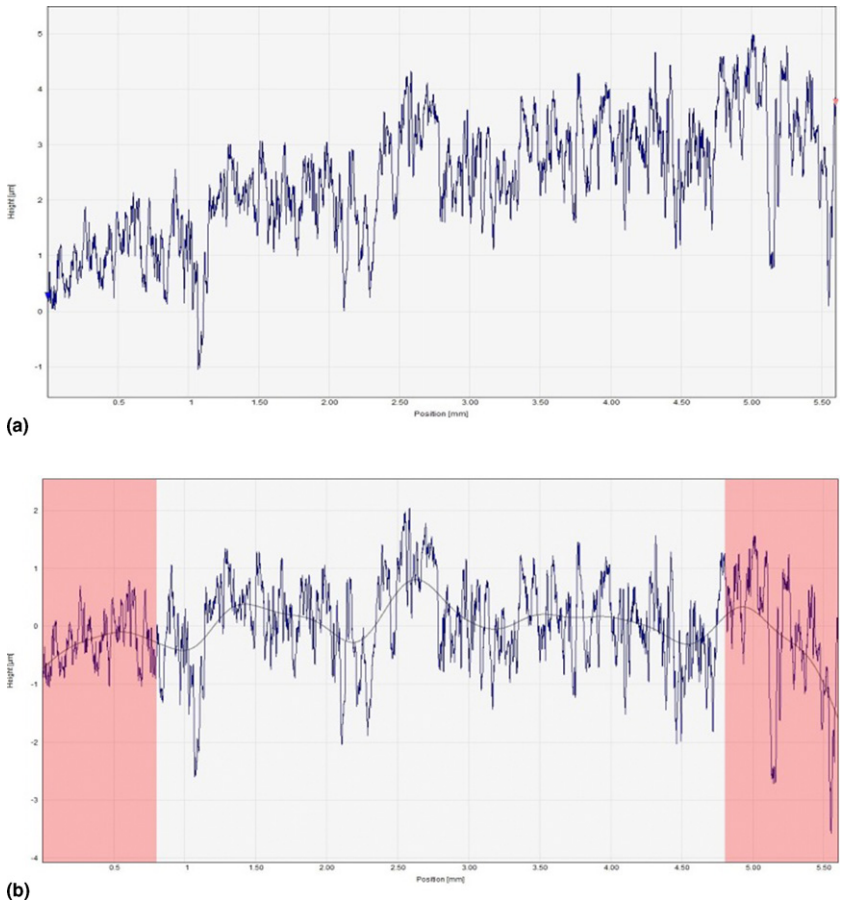


Figure 13 Surface profile signals. (a) Original and (b) Original + Primary profile.

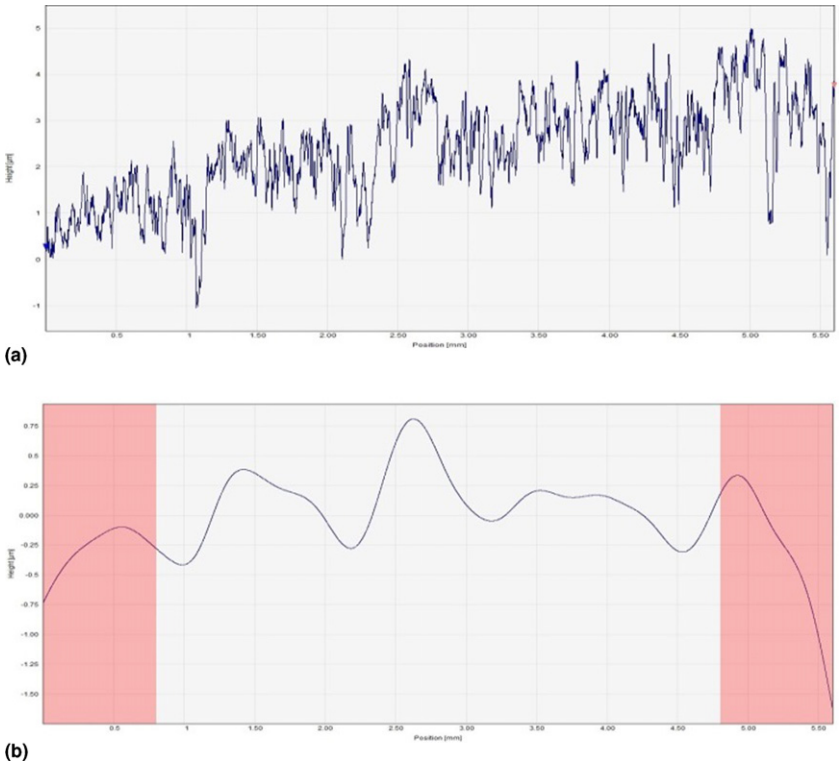


Figure 14 Surface profile signals. (a) Original and (b) Waviness.

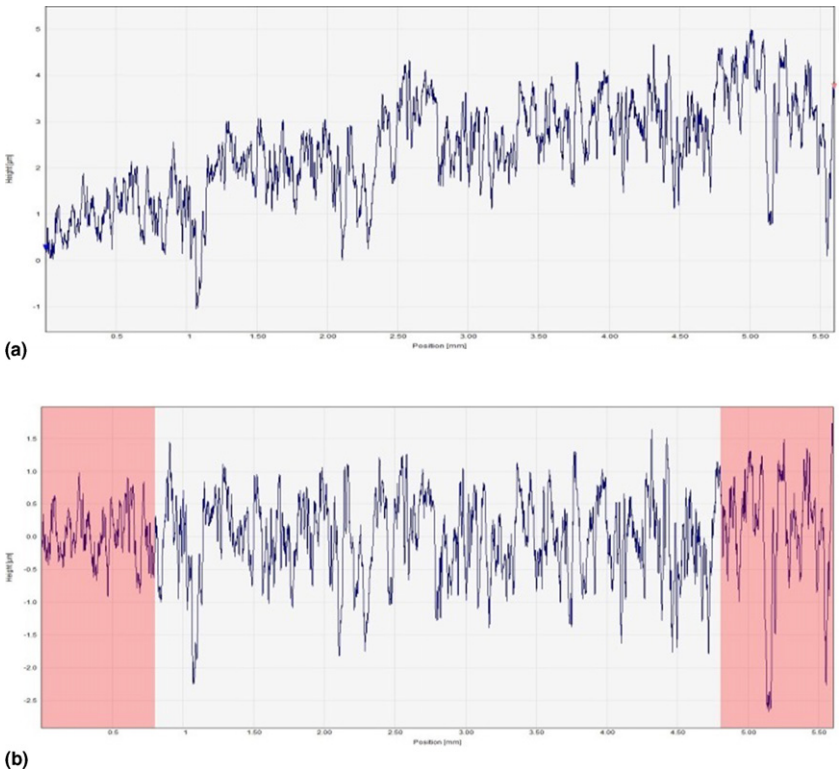
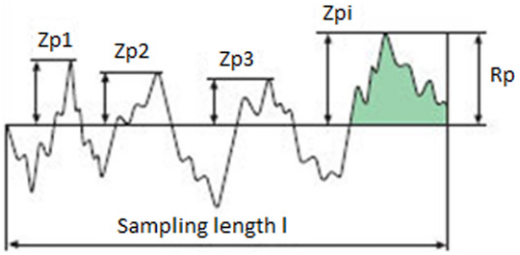
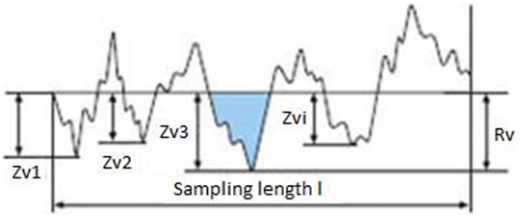
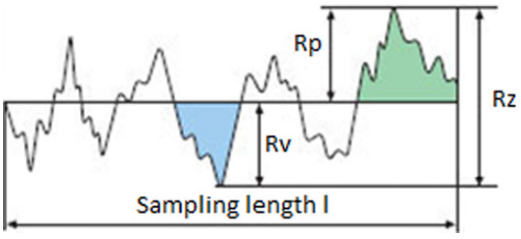
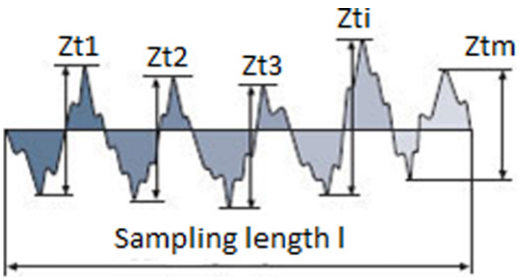
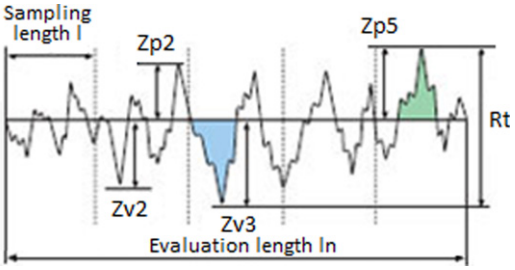


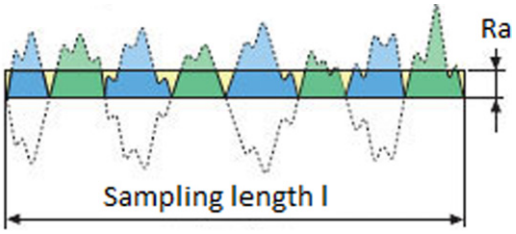
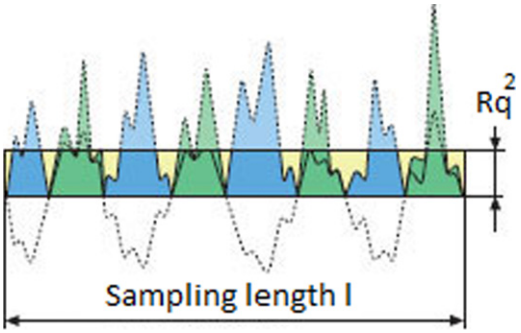
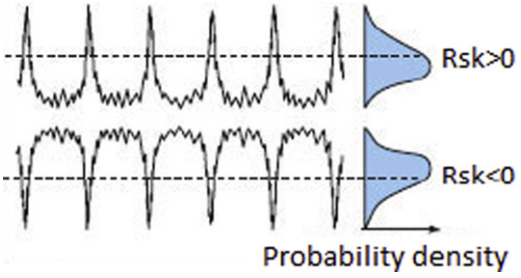
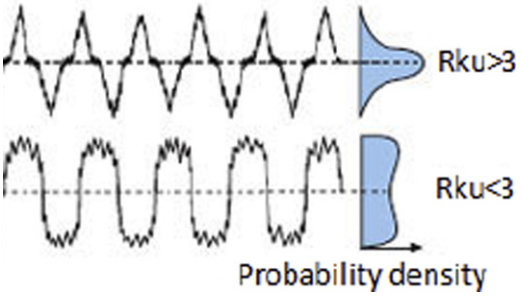
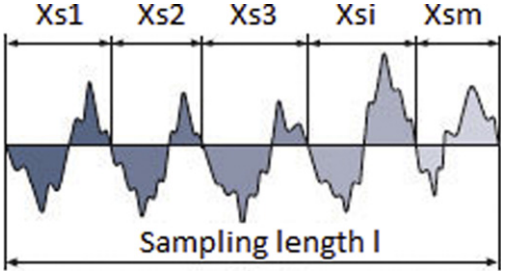
Figure 15 Surface profile signals. (a) Original and (b) Roughness.

Table 2 2D surface profile parameters[23,24]

2D surface profile parameters	*Equation with description*	*Graphical representation*
Amplitude parameters (peak to valley)		
Maximum profile peak height *Rp*, *Wp*, and *Pp*	$Rp = \max(Zp(x))$ Largest profile peak height *Zp* within a sampling length.	
Maximum profile valley depth *Rv*, *Wv*, and *Pv*	$Rv = \min(Zp(x))$ Largest profile valley depth *Zv* within a sampling length.	
Maximum height of profile *Rz*, *Wz*, and *Pz*	$Rz = Rp + Rv$ Sum of height of the largest profile peak height *Rp* and the largest profile valley *Rv* within a sampling length.	
Mean height of profile elements *Rc*, *Wc*, and *Pc*	$Rc = \frac{1}{m}\sum_{i=1}^{m} Zti$ Mean value of the profile element heights *Zt* within a sampling length.	
Total height of profile *Rt*, *Wt*, and *Pt*	$Rt = \max(Zpi) + \max(Zvi)$ Sum of height of the largest profile peak height *Rp* and the largest profile valley *Rv* within an evaluation length.	

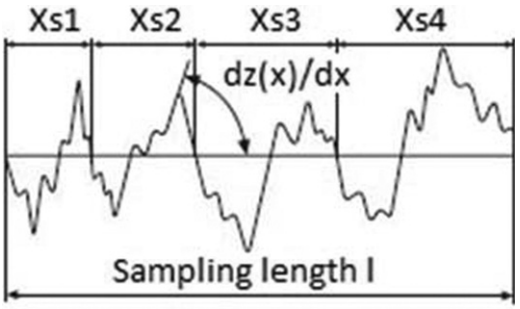
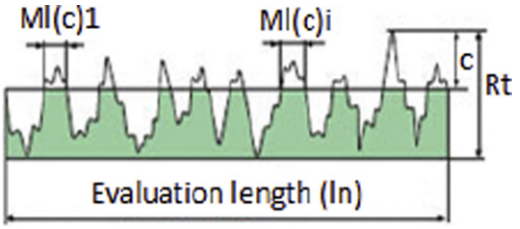
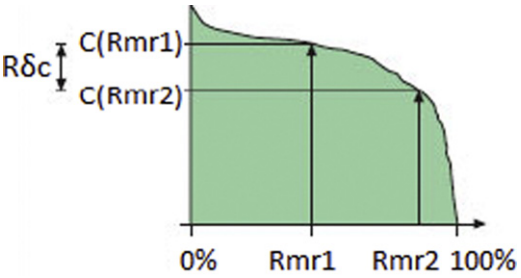
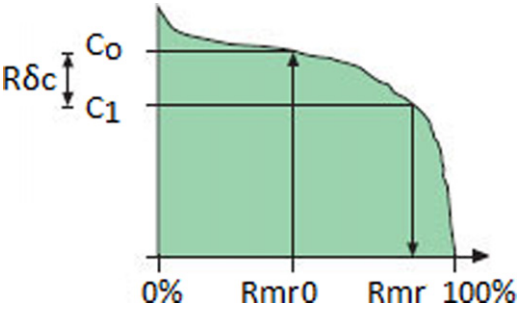
(*Continued*)

Table 2 Continued

2D surface profile parameters	*Equation with description*	*Graphical representation*
Amplitude parameters (average of ordinates)		
Arithmetical mean deviation of the assessed profile *Ra*, *Wa*, and *Pa*	$Pa, Ra, Wa = \frac{1}{l}\int_0^l \lvert Z(x)\rvert \mathrm{d}x$ Arithmetic mean of the absolute ordinate values $Z(x)$ within a sampling length.	
Root mean square deviation from the assessed profile *Rq*, *Wq*, and *Pq*	$Pq, Rq, Wq = \sqrt{\frac{1}{l}\int_0^l Z^2(x)\mathrm{d}x}$ Root mean square value of the ordinate values $Z(x)$ within a sampling length.	
Skewness of the assessed profile *Rsk*, *Wsk*, and *Psk*	$Rsk = \frac{1}{Rq^3}\left[\frac{1}{lr}\int_0^{lr} Z^3(x)\mathrm{d}x\right]$ Quotient of mean cube value of the ordinate values $Z(x)$ and cube *Pq*, *Rq*, *Wq*, respectively, within a sampling length.	
Kurtosis of the assessed profile *Rku*, *Wku*, and *Pku*	$Rku = \frac{1}{Rq^4}\frac{1}{lr}\int_0^{lr} Z^4(x)\mathrm{d}x$ Quotient of mean quartic of the ordinate values $Z(x)$ and 4th power of *Pq*, *Rq*, *Wq*, respectively, within a sampling length.	
Spacing Parameters Mean width of profile elements *Rsm*, *Wsm*, and *Psm*	$Rsm = \frac{1}{m}\sum_{i=1}^{m} Xsi$ Mean value of the profile element width *Xs* within a sampling length.	

(*Continued*)

Table 2 Continued

2D surface profile parameters	*Equation with description*	*Graphical representation*
Hybrid Parameters Root mean square slope of the assessed profile $R\Delta q$, $W\Delta q$, and $P\Delta q$	$R\Delta q = \sqrt{\frac{1}{l}\int_0^l \left[\frac{d}{dx}Z(x)\right]^2 dx}$ Root mean square value of the ordinate slopes dZ/dx within a sampling length.	
Curves Related Parameters Material ratio of the profile $Rmr(c)$, $Wmr(c)$ and $Pmr(c)$	$Rmr(c) = \frac{1}{ln}\sum_{i=1}^{m} Ml(c)i$ Ratio of the material length of the profile elements $Ml(c)$ at a given level c to the evaluation length.	
Profile section height difference $R\delta c$, $W\delta c$, and $P\delta c$	$R\delta c = c(Rmr1) - c(Rmr2)$ $: Rmr1 < Rmr2$ Vertical distance between two section levels of given material ratio.	
Relative material ratio Rmr, Wmr and Pmr	$Rmr = Rmr(c_1)$ $C_1 = C_0 - R\delta c$ $C_0 = C(Rmr0)$ Material ratio determined at a profile section level $R\delta c$, related to a reference C_0.	

3D surface profile parameters are listed with their corresponding equations in Table 3. Here, for each 3D parameter, definitions are given with their equations in order to use in surface topological calculation and evaluations. This areal information is needed to have better results for surface evaluation since 3D parameters contain more information than information obtained from profiling.

3.17.3 Surface Finishing

All machining processes leave characteristic topographic features on the surfaces of components. Surface finishing is a very wide range of industrial processes. These processes change and modify the surface of produced sample to reach the desired properties. From deburring processes to a variety of technological processes,

Table 3 3D surface profile parameters[25]

3D surface profile parameters	*Equation with description*
Amplitude characterization	$Sa = \iint_a \lvert Z(x,y)\rvert \, dxdy$
	Sa: The average deviation of the surface
	$Sq = \sqrt{\iint_a (Z(x,y))^2 dxdy}$
	Sq: The root mean square deviation of the surface
	$Ssk = \frac{1}{Sq^3} \iint_a (Z(x,y))^3 dxdy$
	Ssk: Skewness of surface height distribution
	$Sku = \frac{1}{Sq^4} \iint_a (Z(x,y))^4 dxdy$
	Sku: Kurtosis of surface height distribution
	$Sz = \frac{\sum_1^5 \lvert \text{Peak Heights}\rvert + \sum_1^5 \lvert \text{Valley Depths}\rvert}{5}$
	Sz: Ten point height of the surface
Spatial characterization	$Sds = \frac{\text{Number of Peaks}}{\text{Area}}$
	Sds: Density of summits
	$Str = \frac{\text{Length of fastest decay}(0.2) \text{ of ACF in any direction}}{\text{Length of slowest decay}(0.2) \text{ of ACF in any direction}}$
	Str: Texture aspect ratio; ACF = Auto correlation function
	Sal = Length of fastest decay of ACF to 0.2 in any direction
	Sal: Fastest decay auto correlation length
	Std = Major direction of lay derived from APSDF
	Std: Texture direction of surface; APSDF = Angular power spectral density function
Hybrid characterization	$Sdq = \sqrt{\frac{1}{A}\int_0^{Lx}\int_0^{Ly} \left(\frac{\partial Z(x,y)}{\partial x}\right)^2 + \left(\frac{\partial Z(x,y)}{\partial y}\right)^2 dydx}$
	Sdq: Root-mean square surface slope
	$Ssc = \frac{1}{A}\int_0^{Lx}\int_0^{Ly} \left(\frac{\partial^2 Z(x,y)}{\partial x^2}\right) + \left(\frac{\partial^2 Z(x,y)}{\partial y^2}\right) dydx$
	Ssc: Mean summit curvature
	$Sdr = \frac{(\text{Total surface area}) - (\text{Cross sectional area})}{\text{Cross sectional area}}$
	Sdr: Developed surface area ratio
Functional characterization	$Sbi = \frac{Sq}{\text{True height}(0.05)} = \frac{1}{h(0.05)}$
	Sbi: Surface bearing index
	$Sci = \left(\frac{Vv(h_{0.05}) - Vv(h_{0.80})}{A}\right) \div Sq$
	Sci: Core fluid retention index; smoother = Smaller sci
	$Svi = \left(\frac{Vv(h_{0.80})}{A}\right) \div Sq$
	Svi: Valley fluid retention Index; good fluid retention = larger *Svi*

(*Continued*)

Table 3 Continued

3D surface profile parameters	*Equation with description*
	$Sm = \left(\frac{Vm(h_{0.10})}{A}\right)$
	Sm: Surface material volume – Volume from top to 10% bearing area
	$Sc = \left(\frac{Vv(h_{0.10}) - Vv(h_{0.80})}{A}\right)$
	Sc: Core void volume – Volume enclosed 10–80% bearing area
	$Sv = \left(\frac{Vv(h_{0.80}) - Vv(h_{1.00})}{A}\right)$
	Sv: Surface void volume – Volume from 80 to 100% bearing area

Table 4 Adding and altering methods

Adding and altering methods	*Working principle*	*Topological evaluation of surface finish*	*Applications*
Blanching	Whitening of a surface using acid or coating with tin.	0.4–0.8 μm	Tin based productions, etc.
Case hardening	Hardening of surface such as flame and induction hardening, carburizing, nitriding, cyaniding, carbonitriding, ferritic nitrocarburizing.	0.3–0.5 μm	Screws, firing pins and rifle bolt faces, or engine camshafts, etc.
Ceramic glaze	Coating of vitreous materials to fuse with ceramic using fire.	0.3–0.5 μm	Coloring, water-proofing, and decorating purposes, etc.
Cladding	Bonding of two different metals by pressing/extruding two metals through a die/rolling two metal sheets with high pressure.	0.5–1 μm	Heat exchangers, coins productions, etc.
Corona treatment	Modificating surface using electrically discharge plasma.	0.5–1 μm	Polyethylene, polypropylene, vinyl, PVC, PET, metalized surfaces, etc.
Diffusion processes	Diffusing carbon or nitrogen to a metal surface.	0.5–1 μm	Gears, crankshafts, valve parts, extruder screws, die-casting tools, forging and extrusion dies, injectors, and plastic-mold tools, etc.
→Carburizing	Diffusing carbon to a metal surface.		
→Nitriding	Diffusing nitrogen to a metal surface.		
Electroplating	Coating metal objects with a thin layer of a different metal.	0.5–1 μm	Circuits of cell phones, computers, and other electronic devices, etc.
Galvanizing	Coating steel with zinc to provide long term corrosion protection and abrasion resistance with hot metal bath or Electro-deposition.	150 μm	Building and construction, etc.
Gilding	Coating metals and nonmetals with gold leaf, gold flakes, brass, etc.	NA	Hand application and glueing, electroplating, etc.
Glazing	Glazing by spraying, dipping, pouring, and painting etc.	NA	Ceramic glaze, insulated glazing, etc.
Knurling	Producing indentations on a part of a workpiece.	NA	Tool handles, mechanical pencils, and the control knobs on electronic equipment, etc.
Painting	Applying paint, pigment, color, or other medium to a surface.	NA	Knives, sponges, and airbrushes, etc.
Passivation/Conversion coating	Coating with a chemical or electro-chemical process.	NA	Microelectronics, photovoltaics, etc.
→Anodizing	Increasing thickness of the natural oxide layer on metal surface by forming the anode electrode of an electrical circuit.	Usually, the higher the anodizing voltage, the more roughening occurs.	Baseball bats, signs, furniture, surgical trays, motorcycle, architectural molding, etc.
→Bluing	Heating the steel until a blue oxide film appears without chemicals.	NA	Guns, firearms, razor blades, etc.
→Chromate conversion coating	Applying chromate conversion coating to substrate to passivate steel, aluminum alloys.	NA	Aircraft industry, everyday items such hardware, tools, etc.

(*Continued*)

Table 4 Continued

Adding and altering methods	*Working principle*	*Topological evaluation of surface finish*	*Applications*
Phosphate conversion coating	Spraying to the surface with dilute solution of phosphoric acid and phosphate salts to form phosphates layer.	NA	Application of supplemental coatings: lubricants, sealers, oil, etc.
◆◆ Parkerizing	The process involves submerging the metal part into a phosphoric acid solution.	NA	Automobiles, firearms, etc.
→Plasma electrolytic oxidation	Producing oxide coatings on metals, using higher potentials, so that discharges occur, resulting plasma modifies structure of the oxide layer.	NA	Aerospace and defense (gearboxes, gear bearing carriers, etc.).
Plasma spraying	Producing coatings on structural materials into the plasma jet, emanating from a plasma torch.	NA	Corrosion protection, medical implants, etc.
Powder coating	Producing thicker coatings without sagging, and producing minimal appearance differences between horizontally coated surfaces and vertically coated surfaces.	NA	Automobile parts, bicycle frames and parts, etc.
Thin-film deposition	Depositing a thin film of material onto a substrate or onto previously deposited layers.	Sub-micrometer and nanometer	Electronic semiconductor devices and optical coatings, etc.
→Chemical vapor deposition (CVD)	Depositing thin films of materials on wafers or other substrates.		
→Electroplating/ Electrodeposition	Using electrical current to reduce metal cations in an electrolytic solution in order to coat a conductive object with a thin adherent layer, modifying the surface properties.		Car parts, bath taps, kitchen gas burners, wheel rims, and coins such as pennies, etc.
→Electrophoretic deposition (EPD)	Suspending colloidal particles in a liquid under the electric field, depositing onto an electrode.		Automobile bodies and parts, tractors and heavy equipment, electrical switch gear, industrial products, etc.
→Mechanical plating/ Peen plating/ Mechanical deposition/Cold welding	Descaling and removing soil from the workpiece in tumbler without electrical charge passing through the plating medium.		Nails, screws, nuts, washers, stampings, springs, clips, and sintered iron components, etc.
→Sputter deposition	Removing atoms from a solid target's surface, projecting them into gas phase from condensing on another surface.		Photovoltaics, flat panel display, etc.
→Physical vapor deposition (PVD)	Depositing thin films by the condensation of a vaporized form of the desired film material onto workpiece surfaces.		Aerospace, Dies, and molds, Automotive, Surgical/Medical, Cutting tools, Fire arms, etc.
→Vacuum plating	Depositing layers of material atom-by-atom/ molecule-by-molecule on a solid surface at below atmospheric pressure (i.e., vacuum).		Metallic films, semiconductor films, solar cells, automotive applications, etc.
Vitreous enamel/ Porcelain enamel	Fusing a thin layer of glass at high temperature on to the surface of a metal.	NA	Jewelry and decorative art, housing and interior walls of major kitchen appliances, chemical reactors and pharmaceutical process tanks, etc.

surface finishing covers a wide-ranging of industries and applications. The main functions of the surface finishing are the improvement of the surface appearance, the enhancement of the corrosion resistance and the impartment of the required surface properties. Surface finishing processes can be categorized by how they affect the workpiece as adding or altering finishing (**Table 4**) and removing or reshaping finishing (**Table 5**).

Table 6 represents the general characteristics of machining processes.[26] This table gives detail information regarding the process, their characteristics, tolerances, and roughness values. Here, it is clear that each machining process produce different surface topography. Average roughness values for each machining process prove that each machining process results in different surface texture.

Table 7 explicitly indicates the general characteristics of advanced machining processes.[26] Information regarding the process, their characteristics, tolerances and roughness values are detailed.

Table 5 Removing and reshaping methods

Removing and reshaping methods	*Working principle*	*Topological evaluation range*	*Applications*
Abrasive blasting	Propelling a stream of abrasive material against a surface under high pressure to smooth a rough surface.	NA	The lettering and engraving on most modern cemetery monuments and markers, etc.
→Sandblasting	Producing 3D-signage. These signs often incorporate gold leaf overlay and crushed smalts.		Refurbish buildings, cleaning boat hulls, brick, stone, concrete work, etc.
Burnishing	Burnishing smears the texture of a rough surface and makes it shinier.	0.125–0.5 μm	The inner ring of the ball bearing, burnishing tools, etc.
Chemical-mechanical planarization (CMP)	Using abrasive chemical slurry, to remove material and making any irregular topography the wafer flat.	Sub-micrometer and nanometer	Semiconductor devices, photolithographic applications, etc.
Electropolishing	Removing surface imperfections from a sample to polish, passivate, deburr metal parts using chemicals and electrical current.	Sub-micrometer and nanometer	Drums of washing machines, surgical devices, etc.
Flame polishing	Exposing the material to a flame smooths tension of the surface out.	Sub-micrometer	Glass pipettes, electronic industry, IC encapsulation, etc.
Gas cluster ion beam	Bombarding to a surface by a beam of high energy nano cluster ions using gas cluster ion beam.	Sub-nanometer	Semiconductor devices, optical thin films, fixed disk memory systems.
Grinding	Using a rotating abrasive wheel to smooth the flat surface of materials to reach an ideal surface for a functional purpose.	0.1–1.6 μm	Sealing surfaces between cylinder head and cylinder liner and between cylinder liner and engine frame, etc.
Industrial etching/ Chemical milling	Using baths of temperature-regulated etching chemicals to remove material to attain the desired shape.	Sub-micrometer and nanometer	Printed circuit board, semiconductor, integrated circuits and microelectromechanical systems etc.
Linishing	Using grinding or belt sanding techniques to improve the flatness of a surface and produces a matt finish.	0.1–3.2 μm	Profiles with square and rectangular section, etc.
Mass finishing processes/Vibratory finishing	Deburring, radiusing, smoothing, polishing and degreasing the mass produced parts by mechanical/chemical means.	Sub-micrometer and nanometer	Metal parts, etc.
Pickling	Remove impurities from ferrous metals with a solution called pickle liquor containing strong acids.	Pickled surfacing increases roughness range (2–6 μm)	Jewelry, sheet steel, plate, coil, etc.
Polishing	Rubbing the surface or using a chemical action in order to create a smooth and shiny surface.	0.05–0.5 μm	Household cleaners, car polish, stone polishing, jewelry, plastics, brake linings, ball bearings, aerospace, etc.
→Buffing	Smoothing the surface using an abrasive and a work wheel or a leather strop.		Automotive, aviation, composite, marine, etc.
→Lapping	Rubbing two surfaces together with an abrasive by hand movement or using a machine.		Aircraft and motor manufacturers, electronics companies, clockmakers, toolmakers, etc.
Peening/Shot peening	Bombarding to a metal part by tiny balls of steel, stainless steel, cut-wire, glass, or ceramic shot.	Shot peening treatment increases roughness range (1–6 μm)	Crankshafts, gears, torsion bars, springs, valves, exhaust manifolds, blades, disks, turbines, etc.
Superfinishing	Using bonded abrasive stick moved with a reciprocating motion and pressed against the surface to be finished (similar to honing).	0.025–0.2 μm	Computer memory drums, sewing machine parts, automotive cylinders, bearing components, pistons rods, axles, shafts, clutch plates, etc.
Magnetic field-assisted finishing	Using a magnetic field to force abrasive particles against the target surface.	Sub-micrometer and nanometer	Medical components, fluid systems, optics, dies and molds, microelectromechanical systems, etc.

Table 6 General characteristics of machining processes

Process	*Characteristics*	*Commercial tolerances (± mm)*	*Roughness average,* R_a *(μm)*
Turning	Turning and facing operations are performed on all types of materials; requires skilled labor; low production rate, but medium to high rates can be achieved with turret lathes and automatic machines, requiring less skilled labor.	Fine: 0.05–0.13, Rough: 0.13, Skiving: 0.025–0.05	0.4–6.3
Boring	Internal surfaces or profiles, with characteristics similar to those produced by turning; stiffness of boring bar is important to avoid chatter.	0.025	0.4–6.3
Drilling	Round holes of various sizes and depths; requires boring and reaming for improved accuracy; high production rate; labor skill required depends on hole location and accuracy specified.	0.075	1.6–6.3
Milling	Variety of shapes involving contours, flat surfaces, and slots; wide variety of tooling; versatile; low to medium production rate; requires skilled labor.	0.13–0.25	0.8–6.3
Planing	Flat surfaces and straight contour profiles on large surfaces; suitable for low-quantity production; labor skill required depends on part shape.	0.08–0.13	1.6–12.5
Shaping	Flat surfaces and straight contour profiles on relatively small workpieces; suitable for low-quantity production; labor skill required depends on part shape.	0.05–0.13	1.6–12.5
Broaching	External and internal flat surfaces, slots, and contours with good surface finish; costly tooling; high production rate; labor skill required depends on part shape.	0.025–0.15	0.8–3.2
Sawing	Straight and contour cuts on flats or structural shapes; not suitable for hard materials unless the saw has carbide teeth or is coated with diamond; low production rate; requires only low skilled labor.	0.8	1.6–25

Table 7 General characteristics of advanced machining processes

Process	*Characteristics*	*Commercial tolerances (± mm)*	*Roughness average,* R_a *(μm)*
Chemical machining	Shallow removal (up to 12 mm) on large flat or curved surfaces; blanking of thin sheets; low tooling and equipment cost; suitable for low production runs.	0.025–0.1 mm min^{-1}	1.6–6.3
Electrochemical machining	Complex shapes with deep cavities; highest rate of material removal; expensive tooling and equipment; high power consumption; medium to high production quantity.	V: 5–25 DC; A: 2.5–12 mm min^{-1}, depending on current density	0.2–3.2
Electrochemical grinding	Cutting off and sharpening hard materials, such as tungsten–carbide tools; also used as a honing process; higher material removal rate than grinding.	A: 1–3 A mm^{-2}; typically 1500 mm^3 m^{-1} in per 1000 A	0.1–1.6
Electrical-discharge machining (EDM)	Shaping and cutting complex parts made of hard materials; some surface damage may result; also used for grinding and cutting; versatile; expensive tooling and equipment.	V: 50–380; A: 0.1–500; typically 300 mm^3 min^{-1}	0.05–6.3
Wire EDM	Contour cutting of flat or curved surfaces; expensive equipment.	Varies with workpiece material and its thickness	0.8–1.6
Laser-beam machining	Cutting and hole making on thin materials; heat-affected zone; does not require a vacuum; expensive equipment; consumes much energy; extreme caution required in use.	0.50–7.5 m min^{-1}	0.2–6.3
Electron-beam machining	Cutting and hole making on thin materials; very small holes and slots; heat-affected zone; requires a vacuum; expensive equipment.	1–2 mm^3 min^{-1}	0.2–6.3
Water-jet machining	Cutting all types of nonmetallic materials to 25 mm and greater in thickness; suitable for contour cutting of flexible materials; no thermal damage; environmentally safe process	Varies considerably with workpiece material	0.1–3.2

(*Continued*)

Table 7 Continued

Process	*Characteristics*	*Commercial tolerances (± mm)*	*Roughness average, R_a (μm)*
Abrasive water-jet machining	Single or multilayer cutting of metallic and nonmetallic materials.	Up to 7.5 m min^{-1}	0.1–1.6
Abrasive-jet machining	Cutting, slotting, deburring, flash removal, etching, and cleaning of metallic and nonmetallic materials; tends to round off sharp edges; some hazard because of airborne particulates.	Varies considerably with workpiece material	0.1–1.6

3.17.4 Conclusion

In this chapter, topological evaluations with regard to surface finish were discussed in three subsections. These subsections were so vital in order to comprehend the relationships among topological parameters and evaluation methods, instruments and surface finish, which is the outcome from the machining process. It is so significantly meaningful that knowing the weaknesses of measurement tools and instrumentation can enlighten and enrich the topological evaluation methods for surface finish evaluation. Today's topological evaluation methods are using the product surface finish evaluations after machining process. However, tomorrow's topological evaluation methods will have data from the instruments during machining process. It is hoped that for further future evaluations, multisensory approaches integrated with experimental models will provide advance information for surface finishes.

See also: 3.18 Evaluation of Surface Finish Quality Using Computer Vision Techniques

References

1. Blunt, L.; Stout, K. J. *Three-Dimensional Surface Topography*; Penton Press: London, 2000.
2. Whitehouse, D. J. *Surfaces and Their Measurement*; Butterworth-Heinemann: Waltham, MA, 2004.
3. Abbott, J.; Firestone, A. A New Profilograph Measures Roughness of Finely Finished and Ground Surfaces. *Automot. Ind.* **1933**, *69*, 204–207.
4. Sherwood, K. F.; Crookall, J. R. Surface Finish Measurement. *Proc. Inst. Mech. Eng.* **1967**, *182*, 68.
5. Demircioglu, P. Surface Topographical Evaluation of Coated Cutting Tools with Different Coating Technologies. *Measurement* **2014**, *47*, 893–902.
6. Tay, C. J.; Wang, S. H.; Quan, C.; Shang, H. M. *In Situ* Surface Roughness Measurement Using a Laser Scattering Method. *Opt. Commun.* **2003**, *218*, 1–10.
7. Giusca, C. L.; Leach, R. K. *Calibration of Stylus Instruments for Areal Surface Texture Measurement. NPL Good Practice Guide*; National Physical Laboratory: Middlesex, 2011.
8. Demircioglu, P.; Durakbasa, M. N. Investigations on Machined Metal Surfaces through the Stylus Type and Optical 3D Instruments and Their Mathematical Modeling with the Help of Statistical Techniques. *Measurement* **2011**, *44* (4), 611–619.
9. Binning, G.; Quate, C. F.; Gerber, C. Atomic Force Microscopy. *Phys. Rev. Lett.* **1986**, *56* (9), 930–933.
10. Cuenat, A. Scanning Probe and Particle Beam Microscopy. In *Fundamental Principles of Engineering Nanometrology*; Leach, R. K., Ed.; Elsevier: Oxford, 2010, Chapter 7, pp. 177–210.
11. Leach, R. K., Ed. *Optical Measurement of Surface Topography*; Springer: Berlin, 2011.
12. Demircioglu P. Comparison of Stylus and Optical Methods: Evaluation of High Precision Surface Structures and their Mathematical Modeling with the Help of Statistical Techniques (Published Ph.D thesis); Germany: LAP Lambert Academic Publishing, 2010.
13. Minsky M. Microscopy Apparatus, U.S. Patent 3,013,467, 1957.
14. Helmholtz, H. L. F. *Helmholtz's Treatise on Physiological Optics*; Optical Society of America: Washington, DC, 1924.
15. Danzl, R.; Helmli, F.; Scherer, S. Focus Variation – A Robust Technology for High Resolution Optical 3D Surface Metrology. *J. Mech. Eng.* **2011**, *57* (3), 245–256.
16. Hecht, E. *Optics*; Pearson: San Francisco, CA, 2003.
17. Deraoui, A.; Mallat, K.; Cornet, A.; Defrance, P. Optical Properties of Micro and Nanostructured Bioinspired Materials. *Int. J. Opt. Appl.* **2014**, *4* (2), 31–39.
18. Martin, Y.; Williams, C. C.; Wickramasinghe, H. K. Atomic Force Microscope-Force Mapping and Profiling on a Sub 100-Å Scale. *J. Appl. Phys.* **1987**, *61*, 4723–4729.
19. Binnig, G.; Rohrer, H. Scanning Tunneling Microscopy. *IBM J. Res. Dev.* **1986**, *30* (4), 355–369.
20. Bai, C. *Scanning Tunneling Microscopy and Its Applications*; Springer-Verlag: New York, NY, 2000.
21. Ruska, E. The Development of the Electron Microscope. *Biosci. Rep.* **1987**, *7* (8), 607–630.
22. ISO 3274, Geometrical Product Specifications (GPS) – Surface Texture: Profile Method – Nominal Characteristics of Contact (Stylus) Instruments; 1996 (Last Reviewed in 2012).
23. ISO 4287, Geometrical Product Specifications (GPS) – Surface Texture: Profile Method – Terms, Definitions and Surface Texture Parameters; 1997 (Last Reviewed in 2015).
24. ISO 4288, Geometrical Product Specifications (GPS) – Surface Texture: Profile Method – Rules and Procedures for the Assessment of Surface Texture; 1996 (Last Reviewed in 2013).
25. ISO 25178–2, Geometrical Product Specifications (GPS) – Surface Texture: Areal – Part 2: Terms, Definitions and Surface Texture Parameters; 2012.
26. Kalpakjian, S.; Schmid, S. R.; Kok, C. W. *Manufacturing Processes for Engineering Materials*; Pearson-Prentice Hall: London, Singapore, 2008.

3.18 Evaluation of Surface Finish Quality Using Computer Vision Techniques

I Bogrekci and P Demircioglu, Adnan Menderes University, Aydın, Turkey

© 2017 Elsevier Inc. All rights reserved.

3.18.1	**Surface Finish Quality**	261
3.18.2	**Imaging Systems for Surface Characterization**	261
3.18.2.1	Imaging Systems	261
3.18.2.2	Basics of Image Acquisition for CV	264
3.18.2.3	Basics of Image Processing and Analysis for CV	267
3.18.3	**Surface Evaluation Methods with CV**	267
3.18.3.1	FFT	271
3.18.3.2	WT	273
3.18.3.3	Line Scanning	273
3.18.3.4	Speckle Infusion	273
3.18.3.5	Morphological Evaluations	274
3.18.3.5.1	Blob analyses	274
3.18.3.5.2	Edge enhancement and detection	274
3.18.4	**Concluding Remarks**	274
References		274

3.18.1 Surface Finish Quality

Surface finish occurs during the manufacturing process. For precise manufacturing, surface finish topological characterization methods are divided into two categories. These are contact and noncontact measurement and evaluation methods. These methods have pros and cons in different aspects. The technological developments are bringing new approaches and solutions. Therefore, evaluation methods for surface characterization should be revised and adapted to new approaching or emerging technologies.

Table 1 lists the machining processes corresponding to surface roughness value and their tolerances.[1] Each machining process produces a variety of surface finish, which has a range of roughness values (R_a). Also, each process consists of tolerance limits for manufacturing.

In order to achieve the desired surface finish, the evaluation of the surface parameters should be determined properly. With the development of novel and recent measurement techniques, the introduction and the usage of new materials and coating technologies has enabled us to evaluate and verify different characteristics of surface parameters in two- (2D) and three dimensions (3D). The measurement of surface texture can be used to determine the surface roughness in which some parameters such as R_a, the area between the roughness profile and its central line, and R_z, the average maximum height of roughness profile, etc. describe the roughness in values. These surface roughness parameters are generally measured and evaluated by a diamond stylus profilometer (SP).[2–4] These contact type profilometers are supported with the most of the surface finish standards for the needs of the engineering and research communities.[5–9] The verification of computer vision (CV)-based surface parameters determinations are generally performed using the values obtained from the contact stylus type profilometers.

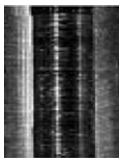
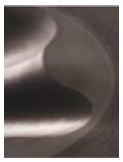
3.18.2 Imaging Systems for Surface Characterization

3.18.2.1 Imaging Systems

There are numbers of imaging methods in order to characterize surfaces (Table 2).[10–14] These methods use the photons, electron beam, atomic forces, and mechanical–electrical energy in order to produce the image of a specimen. The different energy sources are used. The main idea here is to obtain information regarding the surface/specimen. Light/energy source, optics, detectors, and software are the main components of these imaging systems. Images are the output of these systems. Hardware and drivers for capturing images are used to form images. Depending upon the software specifications, there are available image processing and analyses algorithms in the software. Some of the below mentioned imaging systems require sample preparation. The resolutions of these systems vary in micron to nano levels.

The sensitivity of instruments using cantilever beam with tip are affected by stiffness, size, and material type of the tip. Transmission Electron Microscopy (TEM) requires a special environmental conditioning such as vacuum, while Scanning Electron Microscopy (SEM) and others does not require. When compared in terms of cost and complexity, TEM and SEM require special lenses and optics, and have the highest cost among others in investment. Scanning Tunneling Microscopy (STM) tip should be conducting, and it can be simply cut freshly by normal wire cutter. STM works with the very top atom at the freshly cut tip, providing to atomic resolution. Atomic Force Microscopy (AFM) tip should be sharp enough to get good resolution (fat-tip effect), and also AFM tip should be stiff enough to sense the atomic interaction with sample surface. AFM tip is not necessary to be conducting, but STM tip should be conductive. Computed tomography (CT) instruments for conventional medical applications provide

Table 1 Machining processes related to surface finish quality

Process	*Images*	*Commercial tolerances (± mm)*	*Roughness average, R_a (μm)*
Turning		Fine: 0.05–0.13; Rough: 0.13; Skiving: 0.025–0.05;	0.4–6.3
Boring		0.025	0.4–6.3
Drilling		0.075	1.6–6.3
Milling		0.13–0.25	0.8–6.3
Planing		0.08–0.13	1.6–12.5
Shaping		0.05–0.13	1.6–12.5
Broaching		0.025–0.15	0.8–3.2
Sawing		0.8	1.6–25

resolution of 1–2 mm for meter–decimeter-scale objects. Common industrial CT systems have high-resolution instruments. These instruments provide resolution of 100–200 μm for decimeter–centimeter-scale objects. Microfocal ultrahigh-resolution instruments provide resolution of a few tens of microns for centimeter–millimeter-scale objects.

X-ray based CT is a noncontact and nondestructive technique for visualizing interior features within solid objects, and for obtaining digital information from their 3D geometries and properties. CT is dependent upon X-ray absorption of the elemental composition and the density of the sample and the distance the X-rays traverse through the sample. Tomography with X-ray tubes has a spatial resolution of about 10 μm within an object size of a few millimeters for industrial and materials science applications.

X-ray tomographic microscopy (XTM) is a noncontact and nondeformative technique for visualizing the material structures by utilizing intense, highly collimated synchrotron radiation. XTM can be used for the characterization of surface topography.

Table 2 Imaging systems for surface characterization

Criteria	*Noncontact optical*	*AFM*	*STM*	*TEM*	*SEM*	*CT/XTM*	*CV*
Type of probe	Light beam	Tip	Tip	Electron beam	Electron beam	Electron beam	Light beam
Type of contact	Noncontact	Contact and noncontact	Noncontact	Noncontact	Noncontact	Noncontact	Noncontact
Source	Photons	Mechanical–electrical energy/Photons	Atomic forces	Electrons	Electrons	Electrons	Photons
Detection	Photodetector	Photodetector	Photodetector	Fluorescent scene	CCD	CCD	Photodetector/ CCD
Sample preparation	Little/Not required	Required	Required	Required	Required	Not required	Not required
Spatial Resolution	0.5 μm	20 nm	2.5 nm	2 nm–1 μm	10 nm	0.37 μm	<1 μm
Z-Resolution	0.1 μm	Sub-nanometer/ Angstrom	0.2 nm	100 nm	2 nm	–	–
Z Range	20 μm	5 μm	100 nm	2 μm	2 μm	–	–
Output	2D/3D	3D	3D	2D	3D	2D/3D	2D/3D

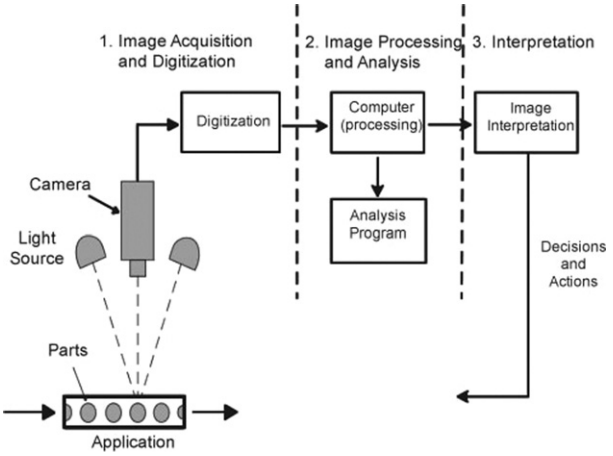


Figure 1 A typical computer vision application.[15]

From coarse to very fine surface finishes, it is important to test a specimen with proper instruments and to make decision with above mentioned measurement and inspection methods. Therefore, surface finishing and quality measurements can be done using above instruments. In surface finish measurement studies or in industry, crucial task is that the selection of proper measurement methods according to surface finish.

A typical CV system consists of image acquisition and digitization, image processing and analysis, and interpretation, decision and action (**Figure 1**). In image acquisition part, light source, frame grabbers, and camera are essential components. The selection of each unit and combining them to have working CV system require specialty. However, it can be learnt. In image processing and analysis part, a computer and commercial image processing packages/user developed codes using Matlab, Visual C++, OpenCV, Matrox Library etc., are necessary components. In image interpretation part, the derivation of useful spatial information from images is the task of image interpretation. The detection (searching for objects), identification (recognition of certain target), delineation (outlining the recognized target for mapping purposes), enumeration (counting certain phenomena from the image),

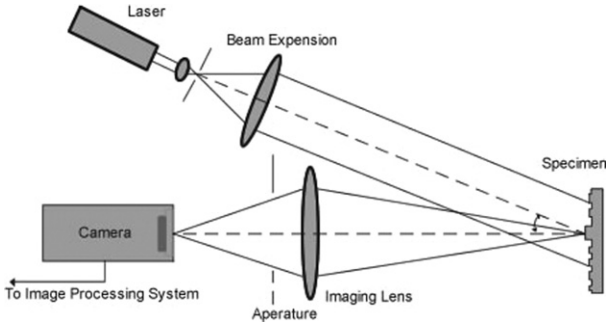


Figure 2 Surface measurement by computer vision.[15]

mensuration (measuring the area, the volume, the amount, and the length of certain target from an image) are pillar of image interpretation. Image interpretations are based upon some elements. These are listed here:

1. Image tone, gray level, or multispectral gray-level vector,
2. Image texture,
3. Pattern,
4. Association,
5. Shadow,
6. Shape,
7. Size,
8. Site.

In decision and action part, the desired action is properly selected using the results or information derived from image processing, analysis, and interpretations. Here, an expert system/decision support system/user developed codes of criteria can be used to start or to give commands to execute the required action.

Figure 2 demonstrates the surface measurement by CV. Here, a camera, a laser light source, apertures, and lenses are used for surface measurement. Light from laser is sent through aperture and beam expansion lens to the surface of the sample. The reflected light from the sample goes through imaging lens and aperture to the camera. The image is then obtained.

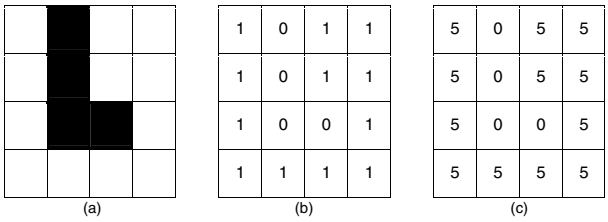


Figure 3 Binary imaging representation of 4 by 4 pixel array: (a) image, (b) DN values, and (c) voltages (volt).[16]

3.18.2.2 Basics of Image Acquisition for CV

Imaging is the creation of images from a physical scene using a camera or similar device. Imaging can be studied by dividing the area into two as analog and digital imaging. Currently, digital imaging is dominating the imaging world. A digital image may be created directly from a physical scene by a camera or similar devices. Alternatively, it may be obtained from another image in an analog medium, such as photographs, photographic film, or printed paper, by an image scanner or similar device.

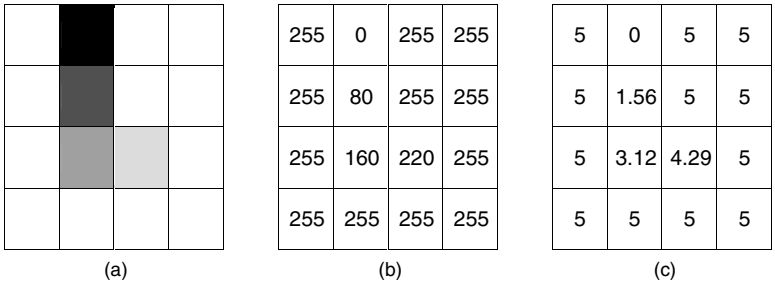


Figure 4 Gray level imaging representation of 4 by 4 pixel array: (a) image, (b) DN values, and (c) voltages (volt).[16]

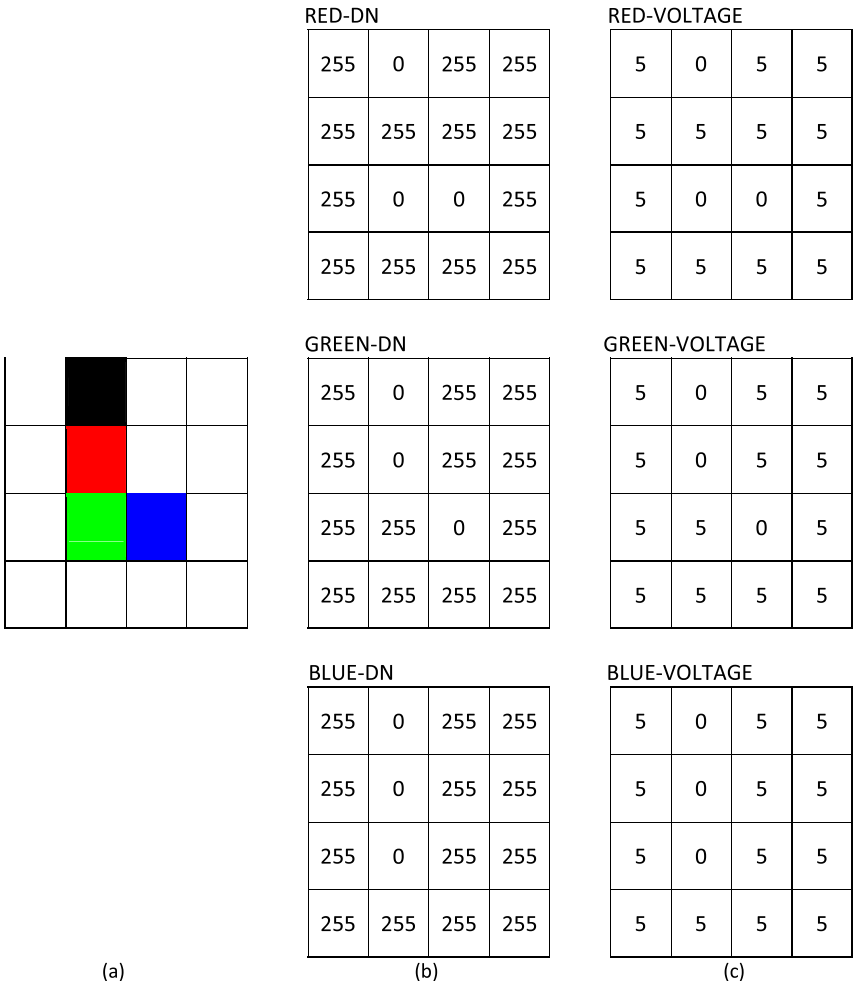


Figure 5 Color imaging representation of 4 by 4 pixel array: (a) image, (b) DN values, and (c) voltages (volt).[16]

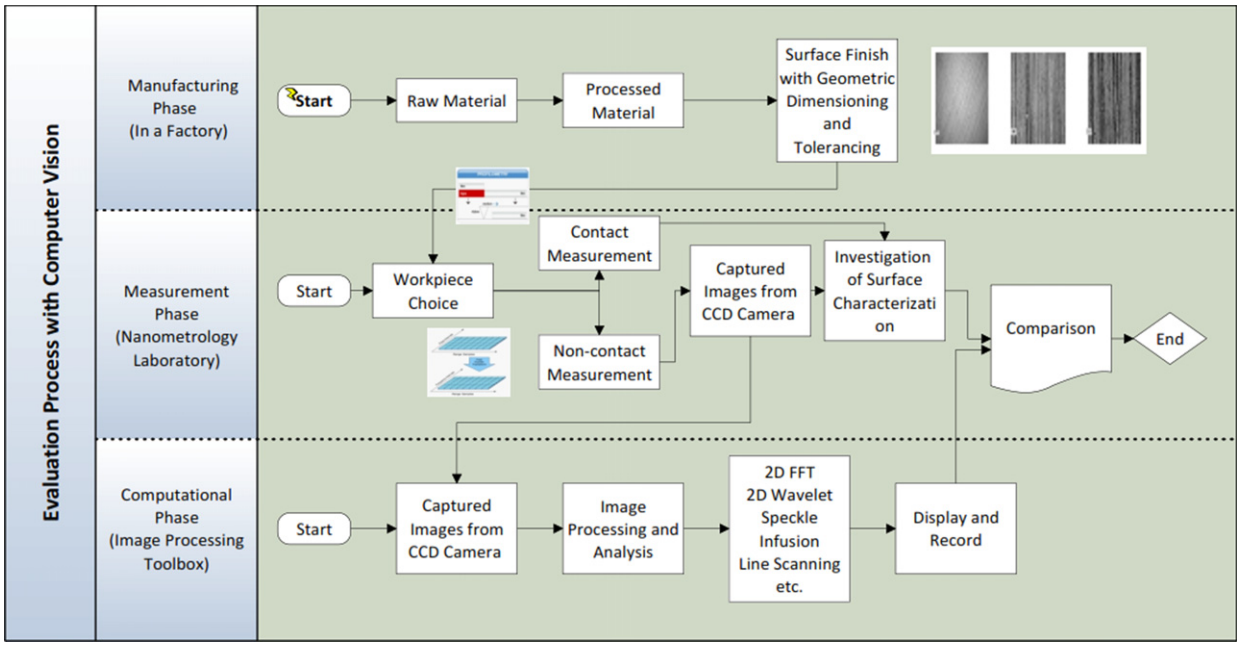


Figure 6 Evaluation process with computer vision.

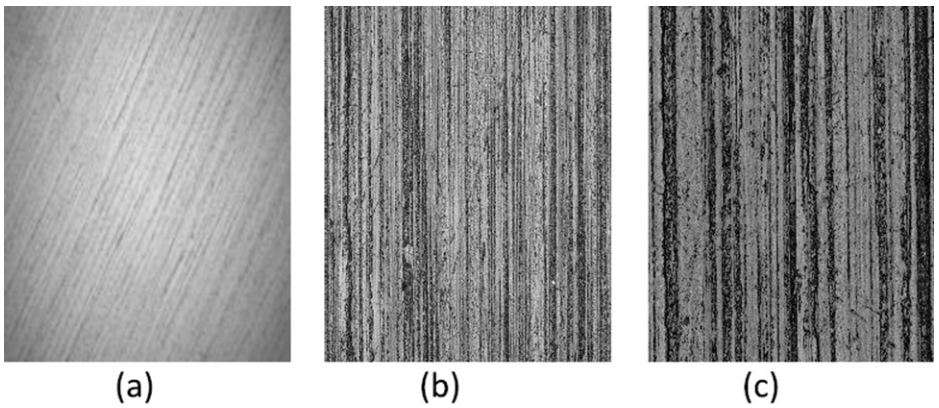


Figure 7 The images taken from the workpieces: (a) Ground surface (R_a=0.498 μm), (b) Front milled surface (R_a=2.382 μm), and (c) Face turned surface (R_a=3.984 μm).[17]

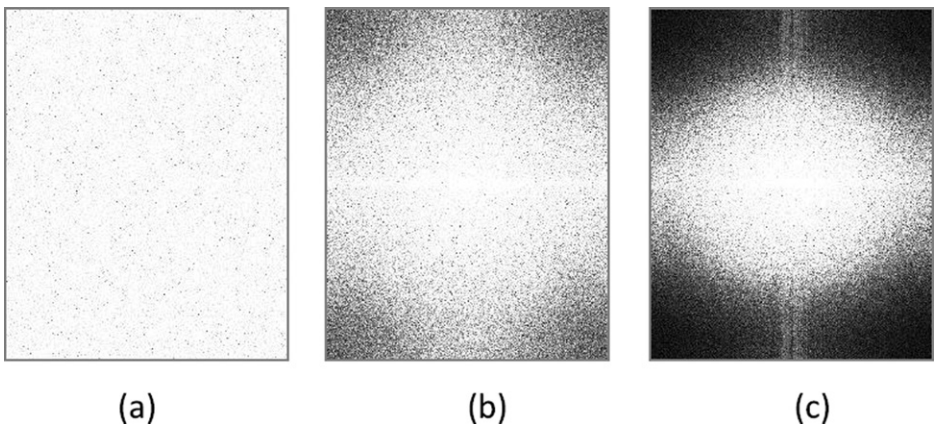


Figure 8 The images after FFT analysis: (a) Ground surface (R_a=0.498 μm), (b) Front milled surface (R_a=2.382 μm), and (c) Face turned surface (R_a=3.984 μm).[17]

There have been so called imaging practices in science without using a camera or similar device. Ultrasound images can be given as an example. Many technical images; such as those acquired with tomographic equipment, side-scan sonar, or radio telescopes are actually obtained by complex processing of nonimage data. This digitalization of analog real-world data is known as digitizing, and involves sampling (discretization) and quantization.

Figure 3 illustrates the binary imaging representation of L shaped-item. Digital numbers (DNs) are given in Figure 3(b) and array voltage representation is shown in Figure 3(c). An example of 4 by 4 pixel array detector is given here. It is assumed that minimum voltage level is 0 V while the maximum voltage level is 5 V. When L shaped black colored item is fixed to the white board, the image appears as seen in Figure 3(a). The voltage levels of each detector are observed as in Figure 3(c). Finally DN values of the image matrix would be as Figure 3(b) for 2 bit representation.

Figure 4 illustrates the monochrome imaging representation of L shaped-item colored with black and different tones of grays for 8 bit imaging system. DNs are given in Figure 4(b) and array voltage representation is shown in Figure 4(c). An example of 4 by 4 pixel array detector is given here. It is assumed that minimum voltage level is 0 V while the maximum voltage level is 5 V. When L shaped black and gray colored item is fixed to the white board, the image appears as seen in Figure 4(a). The voltage levels of each sensor are observed as in Figure 4(c). Finally DN values of the image matrix would be as Figure 4(b) for 8 bit representation.

Up to now non-spectral imaging is explained, in this approach, the light from the physical scene comes to the detector via optics with no spectral fragmentations. The detector sensitivity and digitalization of frame grabber/AD converter are main factors in non-spectral imaging. The light intensity/the amount of the reflection is the essential determinant factor in sensing. When we come to the color imaging, sort of fragmentations of the light into different wavelengths occurs.

Figure 5 illustrates the color imaging representation of L shaped-item colored with black, red, green, and blue for 8 bit imaging system. DNs are given in Figure 5(b) for red, green, and blue (RGB). The array voltage representations are shown in Figure 5(c) for RGB. An example of 4 by 4 pixel array detector is given here. It is assumed that minimum voltage level is 0 V while the maximum voltage level is 5 V. When L shaped black, red, green, and blue colored item is fixed to the white board; the image appears as seen in Figure 5(a). The voltage levels of each sensor are observed as in Figure 5(c) for RGB. Finally DN values of the image matrix would be as Figure 5(b) for 8 bit representation. For imaging, there are few significant factors that affect the quality of the image. These can be explained as stated below:

1. CCD/CMOS detector pixel size,
2. f-value (focal length) for focusing optics,
3. The distance between the object and the camera,
4. Light intensity,
5. Aperture size,
6. Shutter speed,
7. ADC digitization resolution (8, 16, 24 bit).

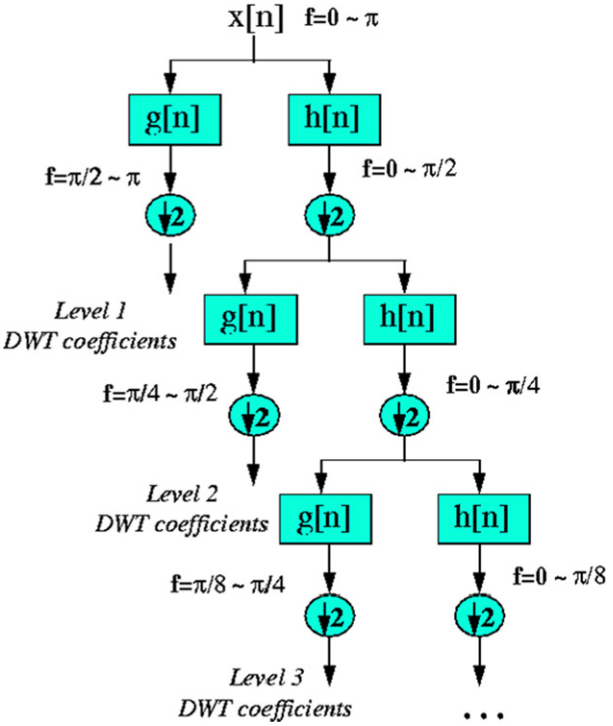


Figure 10 Application of wavelet transform using low-pass and high-pass filters.[20]

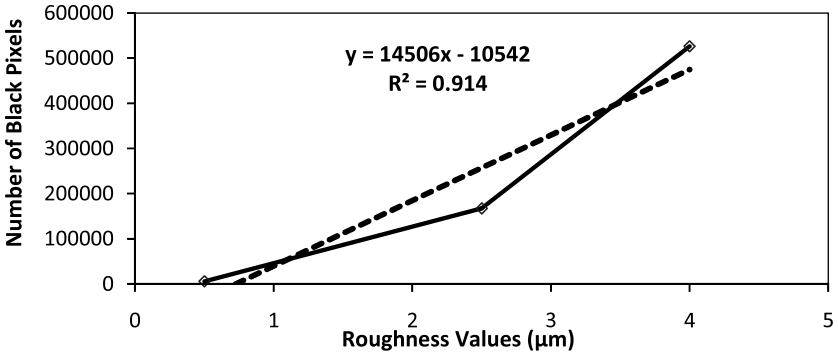


Figure 9 The number of black (dark) pixels from FFT images taken from images of workpieces: (a) Ground surface (R_a=0.498 μm), (b) Front milled surface (R_a=2.382 μm), and (c) Face turned surface (R_a=3.984 μm).[17]

3.18.2.3 Basics of Image Processing and Analysis for CV

The parameters stated above are the main factors which defines the quality of images. Spatial resolution is one of the most important key factors. Imaging mostly involves alteration, subtraction, addition, multiplication, and division etc., of DNs at 2D matrix within or with other 1D/2D matrix or constant. In imaging, some of image processing techniques can be stated below:

1. Resampling,
2. Resizing,
3. Color space processing,
4. Filtering (low pass, high pass, band pass, edge filtering etc.),
5. Pattern recognition,
6. Blob analysis,
7. Contrast enhancement,
8. Geometric corrections/calibrations/enhancements,
9. Transformations (Fourier, wavelet etc.).

Above mentioned techniques are some of the commonly used techniques. However, there are many more image processing techniques used for image processing.[16]

3.18.3 Surface Evaluation Methods with CV

All machining processes leave characteristic topographic features on the surfaces of components. Surface finishing is a very wide range of industrial processes. These processes change and modify the surface of produced sample to reach the desired properties. From deburring processes to a variety of technological processes, surface finishing covers a wide-ranging of industries and applications. The main functions of the surface finishing are the improvement of the surface appearance, the enhancement of the corrosion resistance and the impartment of the required surface properties.

Surface finishing processes can be categorized by how they affect the workpiece as removing or reshaping finishing and adding or altering finishing.

The main objective here for surface evaluation with CV is that rapid, cost-effective, real-time measurements of surfaces can be easily conducted. In order to perform better measurements, a calibration for the camera is necessary. If the sample size is fixed for CV measurement, a calibration without any object/marker can be performed. In CV surface characterization, μm–nm/pixel should be determined before any further evaluation is conducted. Spatial resolution in this case is very important parameter in order to classify the instruments. Higher spatial resolution cameras can give out more information. Spatial resolution in a way can be arranged by the distance between a camera and an object.

Evaluation process with CV can be categorized into two sections apart from manufacturing phase before calibration. A part is manufactured using conventional, additive, precision etc., manufacturing techniques. The obtained workpiece is then scanned using 2D/3D surface measurement instruments. The profile, waviness, and roughness parameters are then computed.

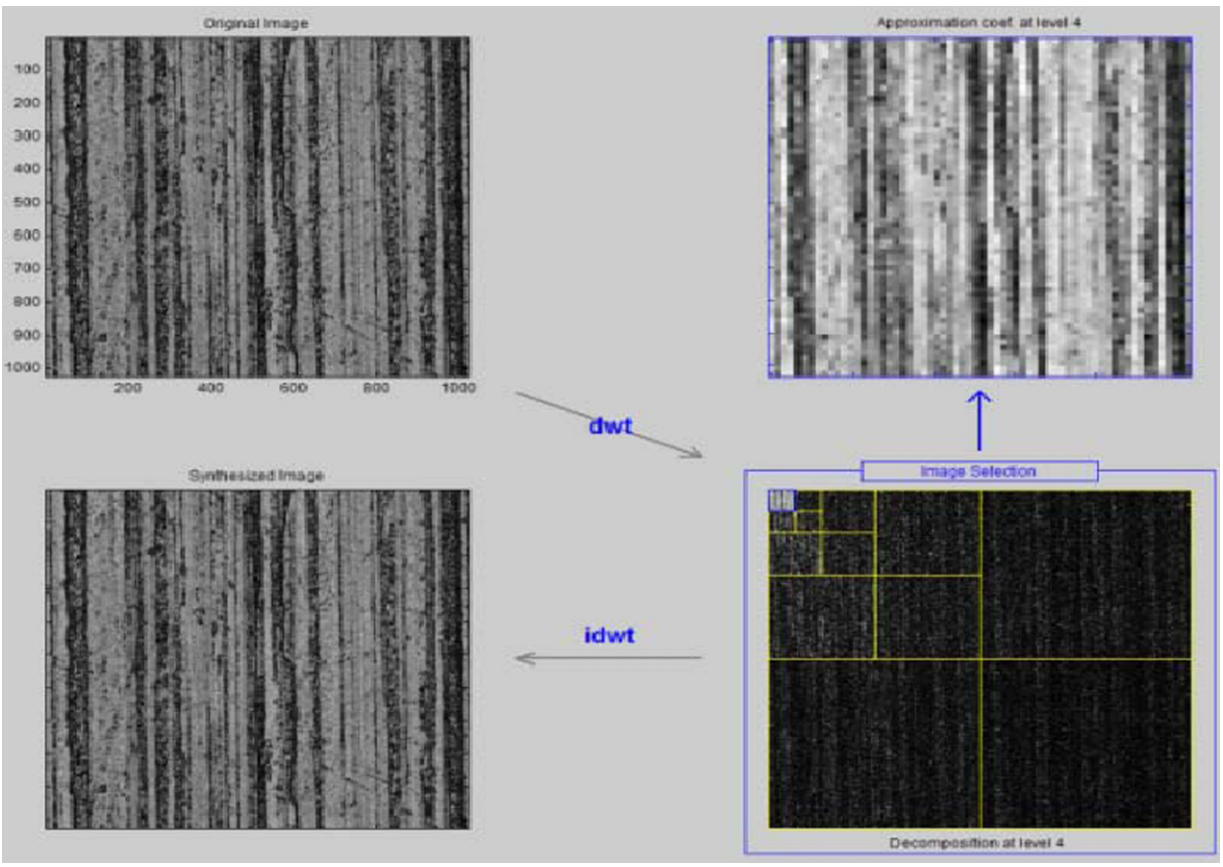


Figure 11 Wavelet transform procedure.[21]

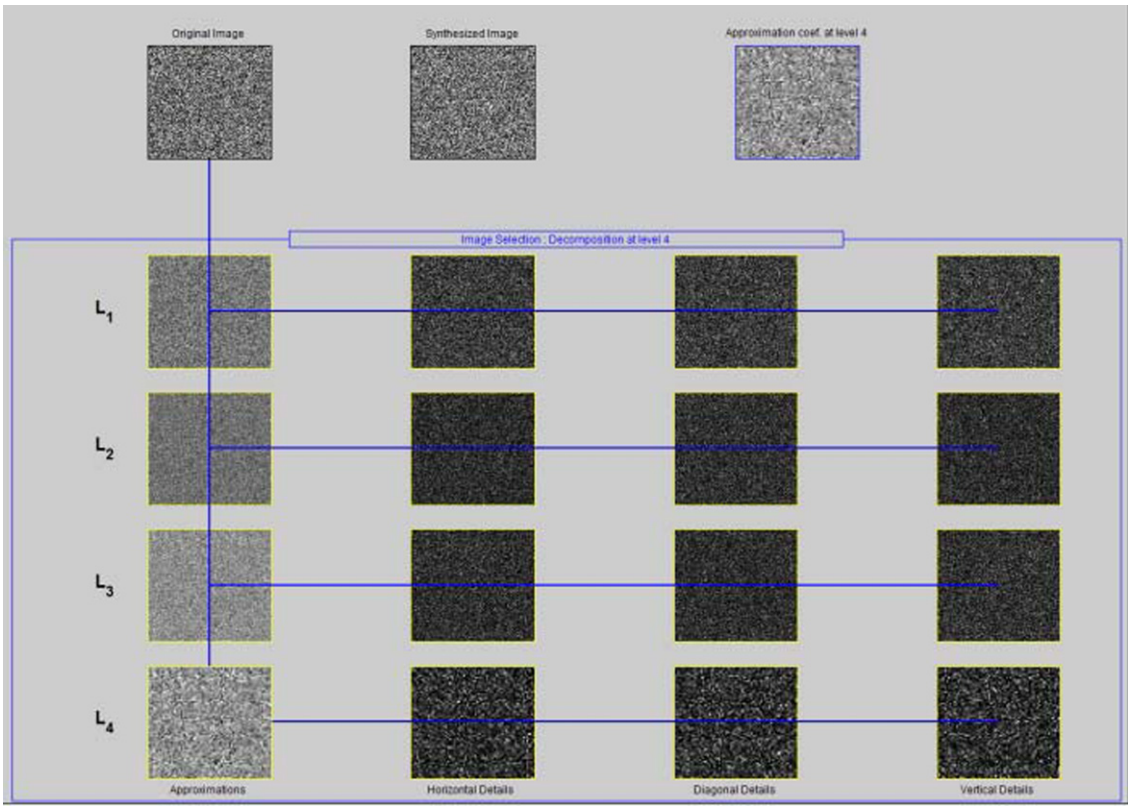


Figure 12 Wavelet transform for the grounded surface.[21]

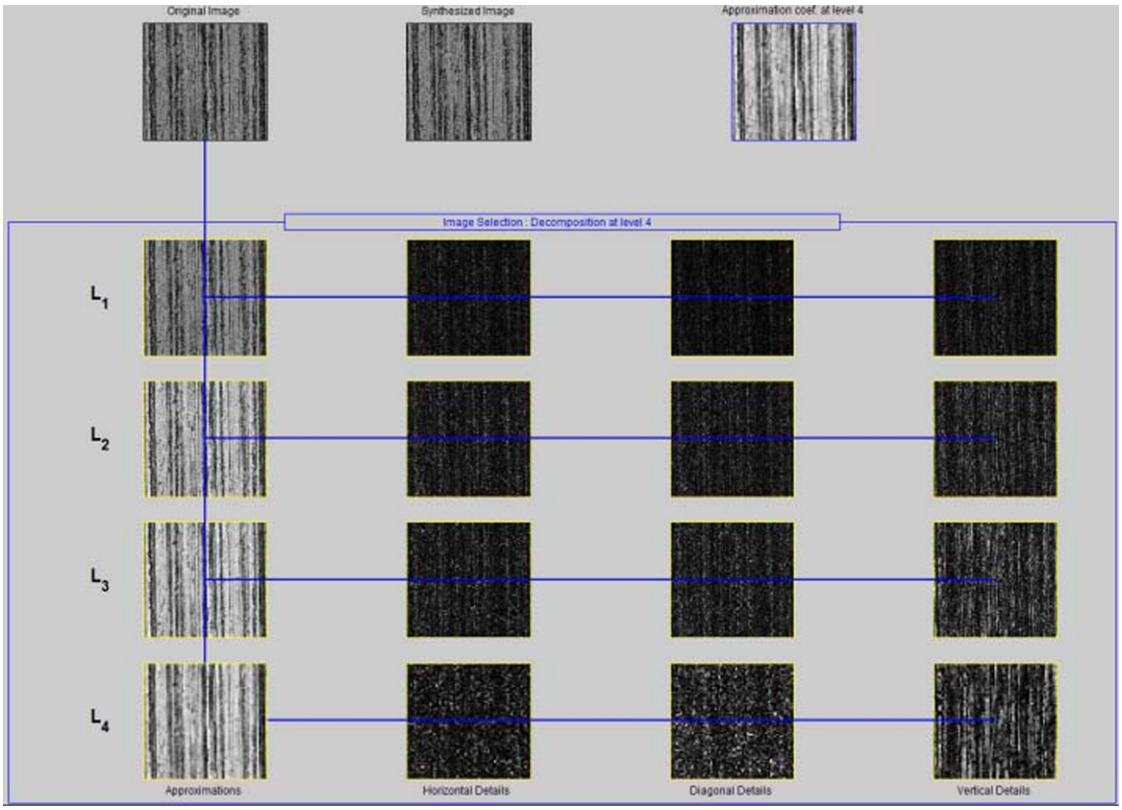


Figure 13 Wavelet transform for the front milled surface.[21]

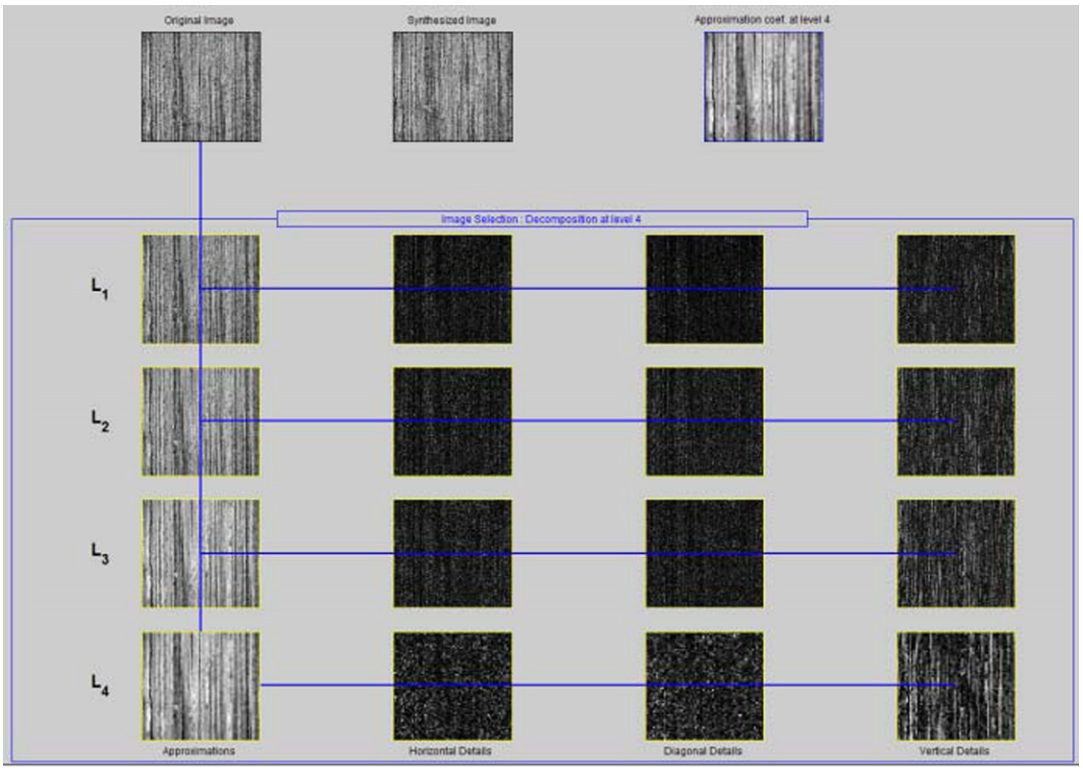


Figure 14 Wavelet transform for the face turned surface.[21]

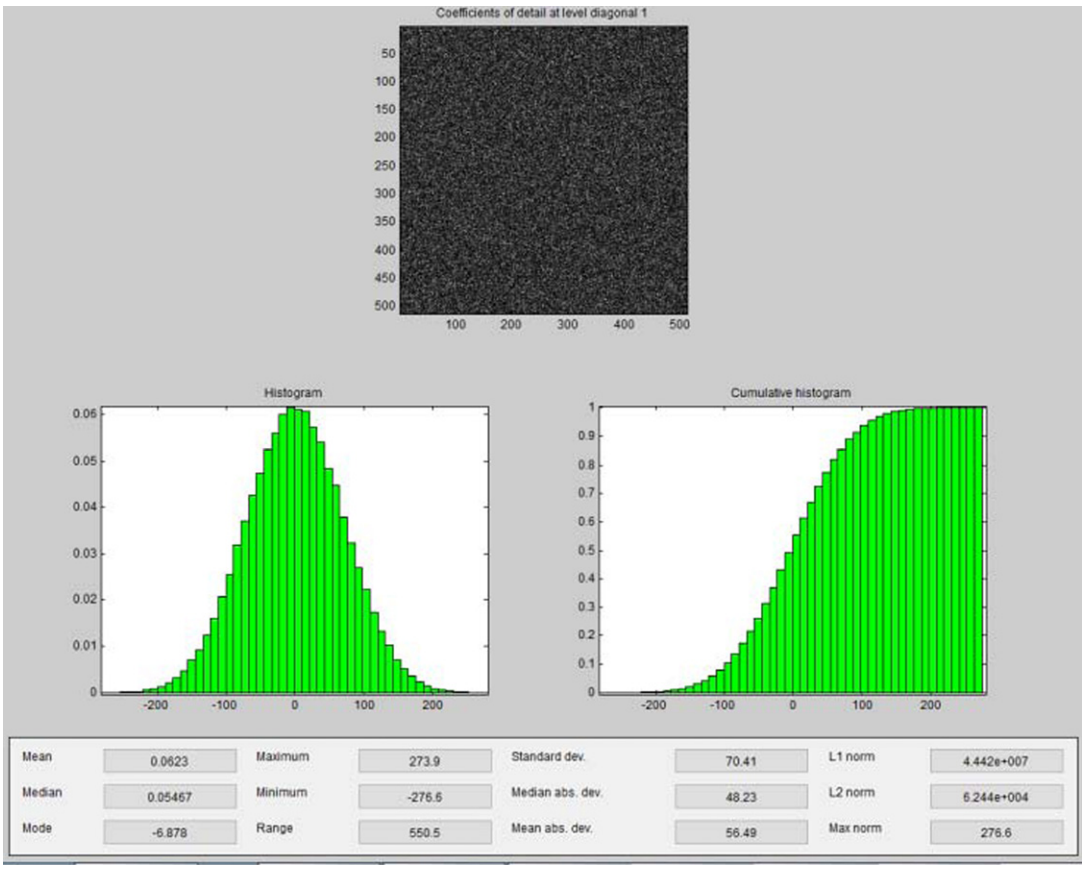


Figure 15 Statistical results from wavelet transform for the grounded surface.[21]

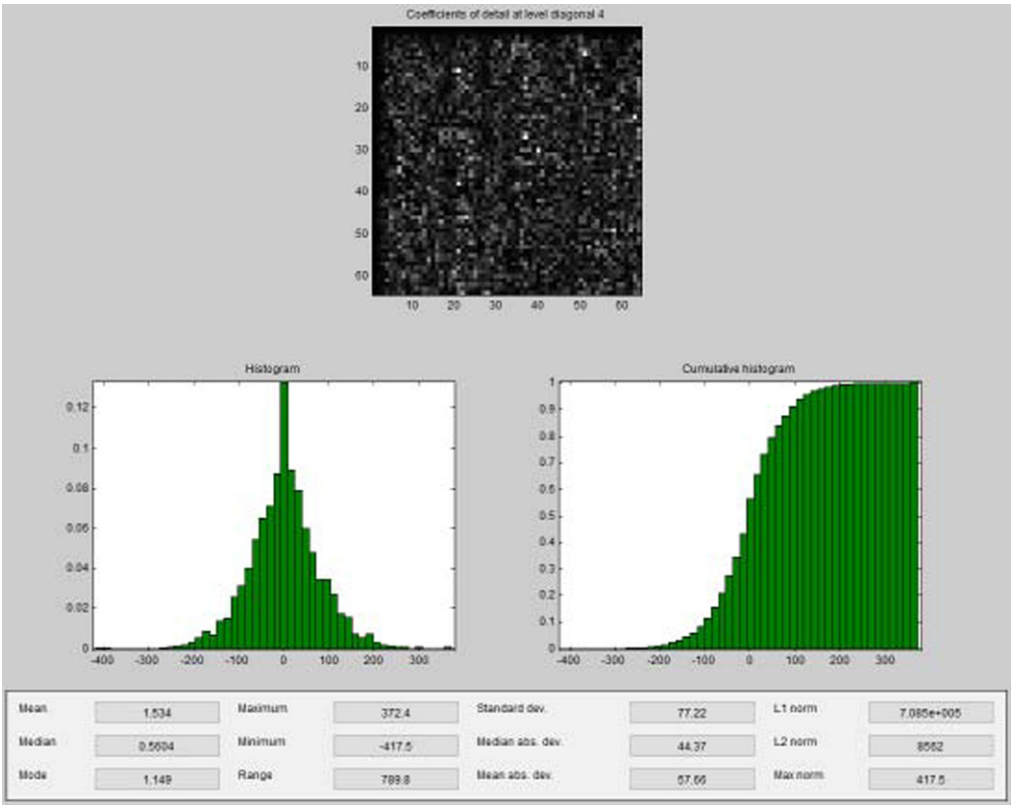


Figure 16 Statistical results from wavelet transform for the front milled surface.[21]

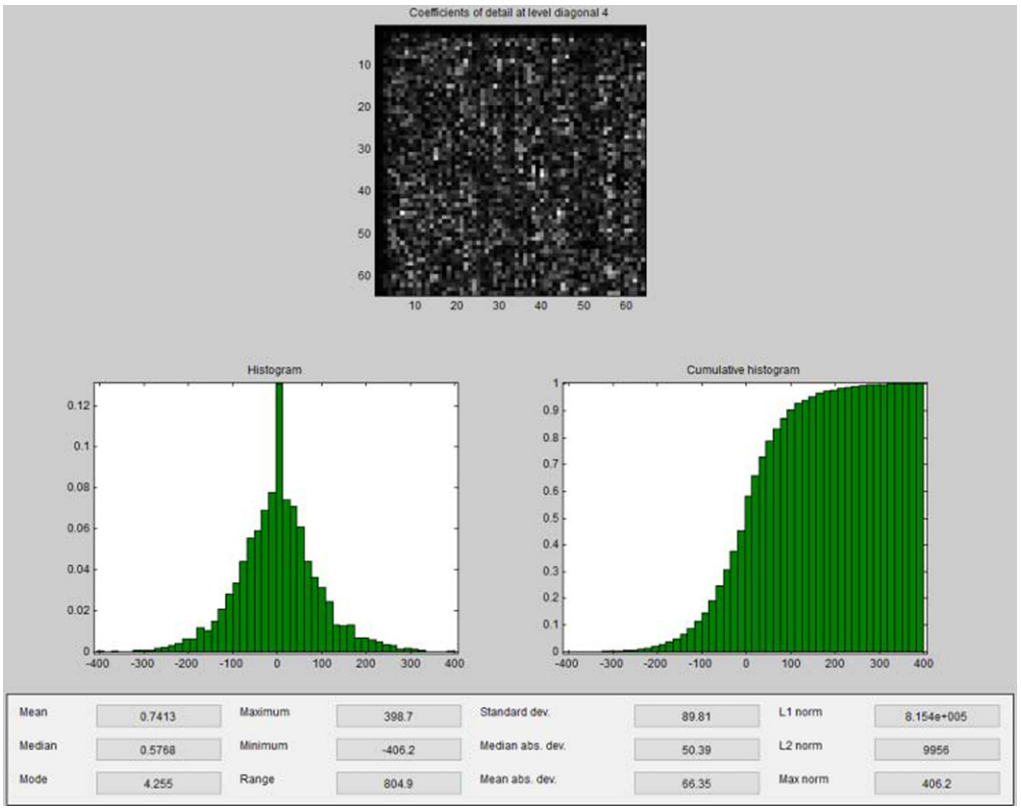


Figure 17 Statistical results from wavelet transform for the face turned surface.[21]

In computational phase, image processing, and analyses algorithms are applied to find out the surface parameters (Figure 6).

In recent years, there have been many researches regarding the surface characterization using CV. CV studies focus on image acquisition, processing, and analysis. Each phase is so vital in order to perform right measurement. In image acquisition phase, camera specifications such as the field of view (FOV), aperture size, focal length, shutter speed, pixel size, zooming, ADC type (x bit), lighting specifications; light type (Led, laser, ambient, fluorescent lamp, incandescent etc.), the position of lighting (rear, front, side, structured etc.), intensity variation by the time, scattering, and environmental conditions; temperature, dust, and moisture can affect the performance of measurements.

Several investigations have been performed to inspect surface roughness of a workpiece by using image processing techniques. The same location of each captured image as shown is processed and analyzed using image processing software. Mostly, the names of the techniques carried out are Line scanning, Speckle, 2D Fast Fourier Transform (FFT), 2D Wavelet Transform (WT) image processing techniques.

In this chapter, for better comprehension, three parts with three different surface roughness parameters are taken as a case study. Then, each image analysis technique is applied to these images. The distinction of surface roughness parameters are observed after the application of these algorithms to these images.

Figure 7 shows the images taken from workpieces manufactured by conventional manufacturing processes such as grinding, milling, and turning. Surface parameters are measured and calculated using standard instruments and their software. The computed surface parameters in this study are a variety of surface parameters such as R_z, R_a, R_q, R_t, taken as R_a values.[18] These values are the average values from ten measurement points. The results from analysis are as follows: R_a values are 0.498, 2.382, and 3.984 μm for ground, front milled, and face turned surfaces, respectively.

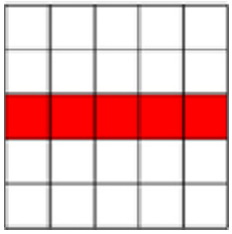


Figure 18 Line scanning representation.[20]

3.18.3.1 FFT

The Fourier Transform is used if the geometric characteristics of a spatial domain image are desired.[19] Because the image in the Fourier domain is decomposed into its sinusoidal components, it is easy to process certain frequencies of the image. The 2D FFT algorithms transform the spatial domain image into the frequency domain image to identify the major influencing factors. The captured color images of samples produced by different manufacturing techniques are transformed into gray level 8 bit images. Eight bit gray images are binarised using different threshold level such as 0.2 threshold level. Binarised images are analysed using FFT. The percentages of black and white pixel numbers of the transformed images are then computed in order to validate with other surface parameter determination methods. Here is the example how the number of white and black pixels are computed.

Calculation of the percentage of black pixels (PBP) is presented below:

$$\mathrm{PBP} = \frac{\mathrm{TNBP}}{\mathrm{TNP}} \times 100 \qquad [1]$$

where,

PBP is the percentage of black pixels (%),

TNBP is the total number of black pixels in the image,

TNP is the total number of pixels in the image.

Calculation of the percentage of white pixels (PWP) is presented as follows:

$$\mathrm{PWP} = \frac{\mathrm{TNWP}}{\mathrm{TNP}} \times 100 \qquad [2]$$

where,

PWP is the percentage of white pixels (%),

TNWP is the total number of white pixels in the image,

TNP is the total number of pixels in the image. Then, the comparison between the images taken from different surface topographical structures is conducted.

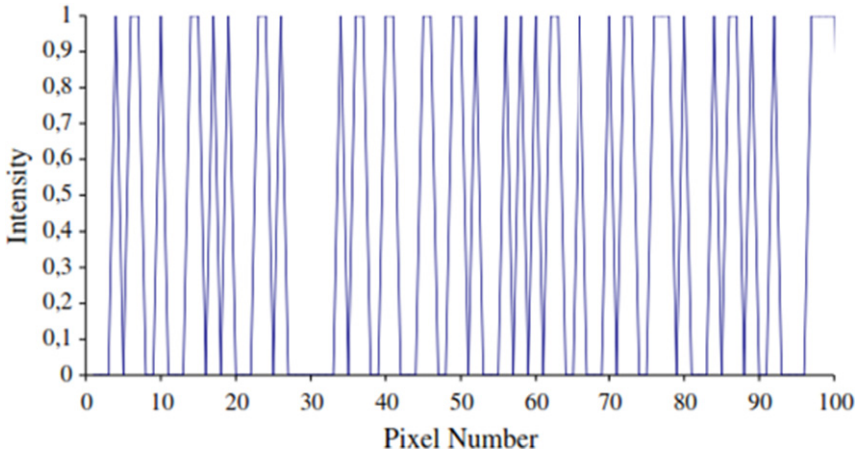


Figure 19 The signal taken from the image workpiece manufactured by grinding (R_a=0.498 μm).[17]

Figure 8 illustrates the results of 2D FFT analyses. Figures 8(a)–8(c) clearly indicates that as the roughness increases the diameter of white pixels blob decreases. Additionally, the number of black pixels increases as the roughness of surface increases.

Figure 9 shows the relationship between the number of black pixels and surface roughness values obtained from standard measurement methods.[6–9] The number of black pixels in the image increases with increase in surface roughness values. Also, as the surface roughness values increases, the

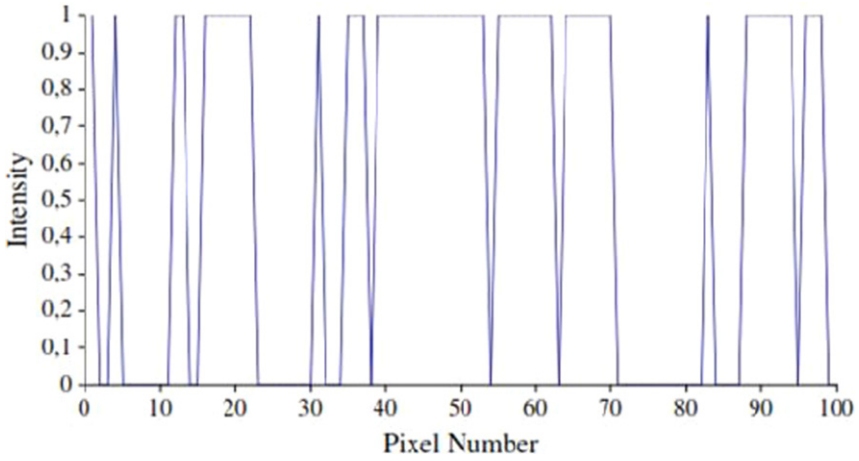


Figure 20 The signal taken from the image workpiece manufactured by milling (R_a=2.382 μm).[17]

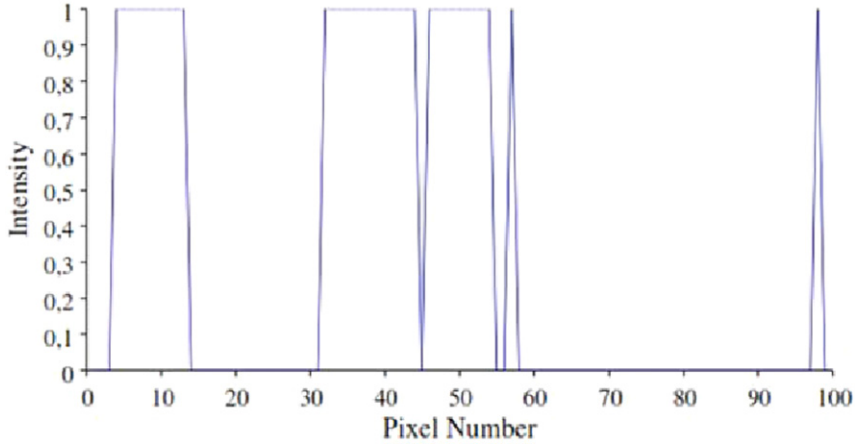


Figure 21 The signal taken from the image workpiece manufactured by turning (R_a=3.984 μm).[17]

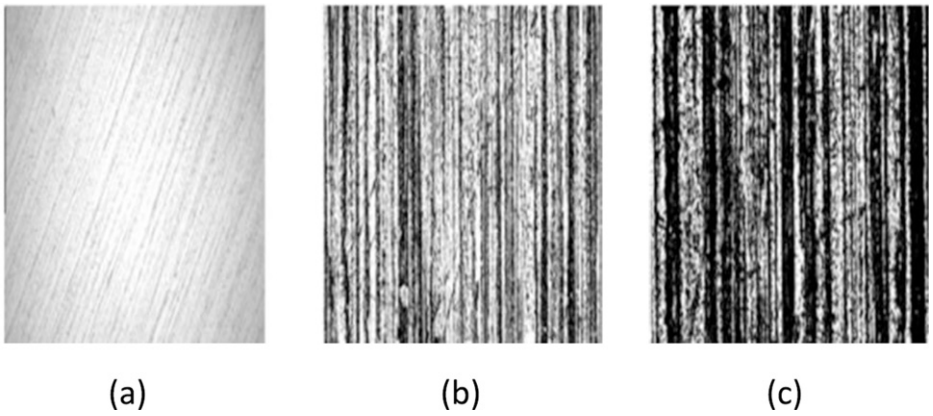


Figure 22 The speckle images added to binarised images of workpieces (a) Ground surface (R_a=0.498 μm), (b) Front milled surface (R_a=2.382 μm) and (c) Face turned surface (R_a=3.984 μm).[17]

number of white pixels in the image decreases. The regression equation and the coefficient of determination for the relationship between black pixels and surface roughness values are given at eqn [3].

$$Y_{bp} = 145\ 061 * R_a - 105\ 427 \quad (R^2 = 0.91) \qquad [3]$$

where,

Y_{bp} is the number of black pixels

R_a is surface roughness.

3.18.3.2 WT

WT works as decomposing the image into its frequencies but preserving the information coming from spatial domain. Decomposition can be explained as the application of filtering. The filtering here is the implementation of low-pass and high-pass filters, accordingly (**Figure 10**).

Figure 11 indicates the WT procedure. **Figures 12–14** demonstrate the WT results for the surface images captured from workpieces manufactured by conventional techniques such as grinding, front milling, and face turning.

The statistical results from WTs for the surface images captured from workpieces manufactured by conventional techniques such as grinding (**Figure 15**), front milling (**Figure 16**), and face turning (**Figure 17**) are illustrated.

Statistical results from discrete wavelet transform analysis indicate that standard deviations derived from the images decomposed at level 4 have significant relationship with R_a values for ground, front milled, and face turned surfaces, respectively (*Stdv*: 70.41, 77.22, 89.81, and R_a: 0.498, 2.382 and 3.984 μm).[21]

3.18.3.3 Line Scanning

True color images are binarised. DN values of binarised images are collected from the selected lines using line scanning technique. **Figure 18** illustrates how information is picked up from the image for further analysis by line scanning.[20]

The results of line scanning as an image processing techniques from **Figures 19–21** clearly indicate that pulse numbers are different for each surface. The number of pulses is 28, 11, and 5 respectively for ground, front milled, and face turned surfaces. Also pulse widths of signals confirm that pulse widths increase with increase in surface roughness.

3.18.3.4 Speckle Infusion

Speckle is the random pattern of bright (white pixels) and dark (black pixels) regions that is observed when a surface is illuminated with a highly coherent light beam. When the illuminating beam is reflected from a surface, the optical path difference between various wavelets with different wavelength would result in interference showing up as a granular pattern of intensity termed as speckle. The properties of this speckle pattern are used for estimation/quantification of roughness parameters. The spatial properties of the speckle pattern can be related to the surface characteristics. For example, surface roughness may be extracted from the information provided by speckle pattern.[17,22] For example, when Matlab is used for image processing, the function in image processing toolbox is presented as 'J=imnoise (I,'speckle',v).'

The function adds multiplicative noise to the image I, using the eqn [4] below,

$$J = I + n * I \qquad [4]$$

where, n is uniformly distributed random noise with mean 0 and variance v. The default value in the toolbox for v is 0.04.

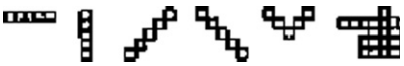


Figure 23 Image particle-finding method.[20]

Table 3 Blob analysis description

Color	*Description*
Green	All the particles found in an image
Blue	The smallest particles
Yellow	Small particles
Red	Big particles
Pink	The biggest particles

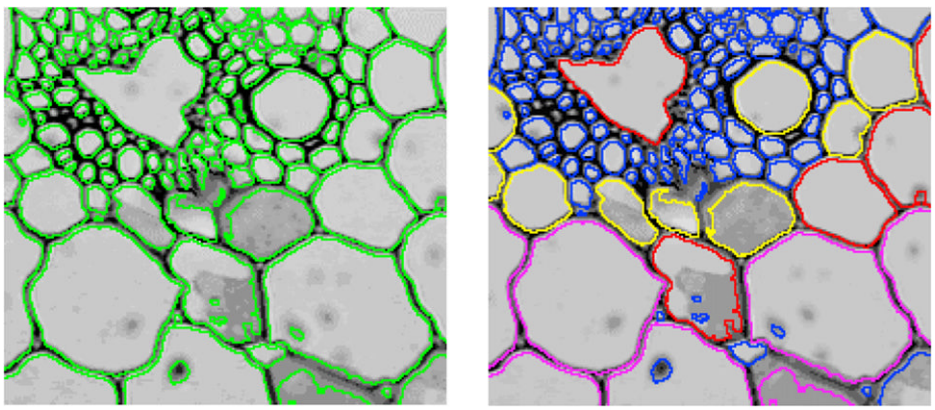


Figure 24 Visual (Blob) sieving: (a) Found particles and (b) Classified particles.[20]

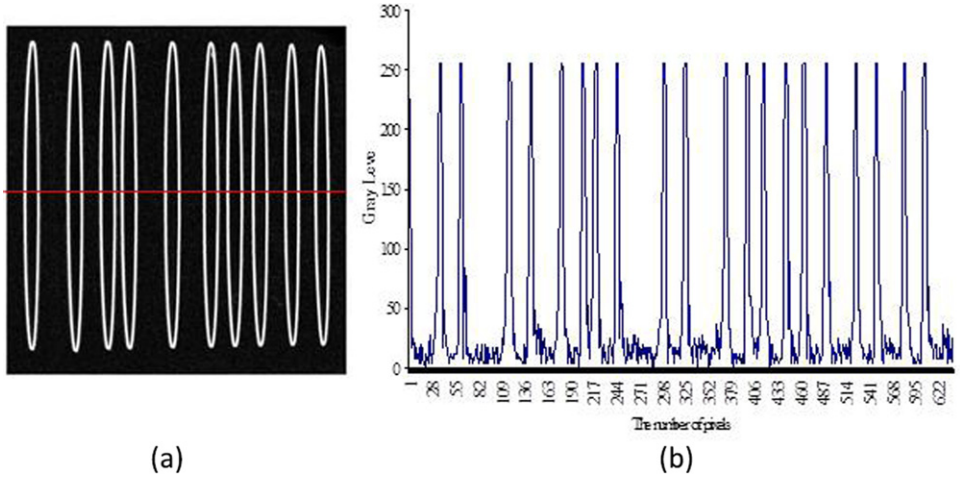


Figure 25 Signal extraction with line scanning method from an (a) edge-detected image and (b) extracted signal.[23]

This technique adds multiplicative noise to the image. The variance of the added random noise in this study is 0.05.

Speckle analyses results are shown in **Figure 22**. **Figures 22(a)–22(c)** clearly indicate that as the roughness increases the both sharpness and color distinctions increase. Also, surface texture becomes more recognized.

3.18.3.5 Morphological Evaluations

3.18.3.5.1 Blob analyses

In the image sieving method, images are resampled to the X by X pixel frames. Then the Color level is decreased to the 16 gray (4 bit) and the image particles are found. This is shown pictorially in **Figure 23**. In particle finding method, decision is made whether neighboring pixel is the part of the same particle with the selected pixel or not. The criteria can be standard deviation of the selected pixel.

In particle finding procedure, a particle is defined as a number of connected pixels within a particular grayscale range, specified by low and high threshold values. After finding the particles in an image the software is trained by picking up the same size particles for each class. In this case, the four classes are determined. The mean, minimum, maximum numbers of area and perimeter and also particle numbers of each class in the images are computed. The results are shown as the found particles (**Figure 24(a)**) and the classified particles (**Figure 24(b)**). **Table 3** also explains the description for blob analysis results. Blue, yellow, red, and pink refer to particle size range from small to large.[20]

3.18.3.5.2 Edge enhancement and detection

Obtaining accurate size information is not easy task. **Figure 25** illustrates how size information from an image was obtained. Red line shows that data is retrieved from the image (see **Figure 25(a)**). Extracted signal which represents gray level values for pixel positions is illustrated in **Figure 25(b)**. DN values over 250 suggest that there is an edge in that pixel location. In theory, the more the frequency of signal extracted from across the images the more the particle number in that axis, because each peak value represents the one edge in the image.

3.18.4 Concluding Remarks

In this chapter, surface finish quality evaluations with CV/Machine Vision are discussed in three subsections. These subsections are surface finish quality, imaging systems for surface characterization, and surface evaluation methods by CV. These subsections are so vital in order to comprehend the relationships among surface quality parameters, imaging instruments, and surface finish. With the advance of new technologies, machine vision techniques would be used widely in the industry for the characterization of surface finish quality. Rapid and real-time measurement capability of machine vision systems could improve and develop the technique for the characterization of surface parameters in the future.

See also: 3.17 Topological Evaluation of Surfaces in Relation to Surface Finish

References

1. Kalpakjian, S.; Schmid, S. R.; Kok, C. W. *Manufacturing Processes for Engineering Materials*; Pearson-Prentice Hall: London; Singapore, 2008.
2. Blunt, L.; Stout, K. J. *Three-Dimensional Surface Topography*; Penton Press: London, 2000.
3. Whitehouse, D. J. *Surfaces and Their Measurement*; Butterworth-Heinemann: Waltham, MA, 2004.
4. Leach, R. K., Ed. *Optical Measurement of Surface Topography*; Springer: Berlin, 2011.
5. Demircioglu, P. Surface Topographical Evaluation of Coated Cutting Tools with Different Coating Technologies. *Measurement* **2014**, *47*, 893–902.
6. ISO 3274, Geometrical Product Specifications (GPS) – Surface Texture: Profile Method – Nominal Characteristics of Contact (Stylus) Instruments; 1996 (Last Reviewed in 2012).
7. ISO 4287, Geometrical Product Specifications (GPS) – Surface Texture: Profile Method – Terms, Definitions and Surface Texture Parameters; 1997 (Last Reviewed in 2015).
8. ISO 4288, Geometrical Product Specifications (GPS) – Surface Texture: Profile Method – Rules and Procedures for the Assessment of Surface Texture; 1996 (Last Reviewed in 2013).
9. ISO 25178–2, Geometrical Product Specifications (GPS) – Surface Texture: Areal – Part 2: Terms, Definitions and Surface Texture Parameters; 2012.
10. Danzl, R.; Helmli, F.; Scherer, S. Focus Variation – A Robust Technology for High Resolution Optical 3D Surface Metrology. *J. Mech. Eng.* **2011**, *57* (3), 245–256.

11. Hecht, E. *Optics*; Pearson: San Francisco, CA, 2003.
12. Martin, Y.; Williams, C. C.; Wickramasinghe, H. K. Atomic Force Microscope-Force Mapping and Profiling on a Sub 100-Å Scale. *J. Appl. Phys.* **1987**, *61*, 4723–4729.
13. Binnig, G.; Rohrer, H. Scanning Tunneling Microscopy. *IBM J. Res. Dev.* **1986**, *30* (4), 355.
14. Ruska, E. The Development of the Electron Microscope. *Biosci. Rep.* **1987**, *7* (8), 607–630.
15. Groover, M. P. *Automation, Production Systems, and Computer-Integrated Manufacturing*; Prentice Hall: Upper Saddle River, NJ, 2015 (ISBN-13: 9781292076119).
16. Bogrekci, I. Spectral Imaging Versus Non-Spectral Imaging. In *Computer Vision*; Yoshida, S. R., Ed.; Nova Science Publisher: New York, 2011; pp. 269–284.
17. Demircioglu, P.; Bogrekci, I.; Durakbasa, M. N. Micro Scale Surface Texture Characterization of Technical Structures by Computer Vision. *Measurement* **2013**, *46*, 2022–2028.
18. Demircioglu P. *Comparison of Stylus and Optical Methods: Evaluation of High Precision Surface Structures and Their Mathematical Modeling with the Help of Statistical Techniques* (Published Ph.D. thesis). Germany: LAP Lambert Academic Publishing; 2010 (ISBN:978–3–838390215).
19. Arunachalam, N.; Ramamoorthy, B. Fourier Transform Based Texture Measures for Grinding Wheel Condition Monitoring Using Machine Vision. *IJMTM* **2010**, *21*, 112–121.
20. Bogrekci I. *Soil Tilth Sensing: Soil Sensing Technologies* (Published Ph.D. thesis); Germany: LAP Lambert Academic Publishing, 2010 (ISBN:978–3–83838085–8).
21. Bogrekci, I.; Demircioglu, P.; Cerci, Y.; Deniz, C. Roughness Measurement Verification of the Surface Structures Produced by Different Manufacturing Techniques Using Wavelet Transform. In *11th International Symposium on Measurement and Quality Control (ISMQC2013)*, 2013; pp. 60–63.
22. Dhanasekar, B.; Mohan, N. K.; Bhaduri, B.; Ramamoorthy, B. Evaluation of Surface Roughness Based on Monochromatic Speckle Correlation Using Image Processing. *Precis. Eng.* **2008**, *32*, 196–206.
23. Bogrekci, I.; Godwin, R. J. Development of Image Processing Technique for Soil Tilth Sensing. *Biosys. Eng.* **2007**, *97*, 323–331.

3.19 Effect of Surface Roughness on Wetting Properties

H Mojiri and M Aliofkhazraei, Tarbiat Modares University, Tehran, Iran

© 2017 Elsevier Inc. All rights reserved.

3.19.1	**Introduction**	276
3.19.2	**Surface Wettability**	277
3.19.2.1	Wettability on a Flat Surface	277
3.19.2.2	Wettability on Rough Surfaces	277
3.19.2.3	Contact Angle Hysteresis	278
3.19.2.3.1	Film pressure contact angle hysteresis	279
3.19.2.4	Methods of Contact Angle Hysteresis Measurement	279
3.19.2.4.1	The Wilhelmy method	279
3.19.2.4.2	The methods of suction and injection (sessile drop)	280
3.19.2.4.3	Tilted surface method	281
3.19.2.5	Wetting Free Energies	281
3.19.2.6	Contact Angle and Corrosion Resistance	282
3.19.2.7	Common Methods of Producing Superhydrophobic Surfaces	282
3.19.2.7.1	SAMs	282
3.19.2.7.2	Fatty acid monolayers	282
3.19.2.7.3	Organosilicon-derivative monolayers	282
3.19.2.7.4	Organic adsorbed sulfur on the metal	283
3.19.2.7.5	Silanes	283
3.19.2.7.6	Stearic acid ($CH_3(CH_2)_{16}CO_2H$)	285
3.19.2.7.7	Tetradecanoic acid	286
3.19.2.7.8	Benzoic acid ($C_7H_6O_2$ or C_6H_5COOH)	286
3.19.3	**Topography of the Rough Surface**	286
3.19.3.1	Characteristics of the Rough Surface	286
3.19.3.2	Random Surface Roughness Static Analysis	289
3.19.3.3	Roughness of Fractal Surfaces	290
3.19.3.4	Creation of a Rough Substrate and Its Modification Using Low Surface Energy Materials	292
3.19.3.4.1	Etching and lithography	292
3.19.3.4.2	Sol-gel process	292
3.19.3.4.3	Colloid accumulation and layer method	293
3.19.3.4.4	Electrochemical reaction and deposition method	293
3.19.3.4.5	Other methods	294
3.19.4	**The Relationship between Roughness and Surface Wettability**	294
3.19.4.1	The Analysis of the Contact Angle	295
3.19.4.1.1	Flat surface	295
3.19.4.1.2	Effect of surface area on the contact angle of a rough surface	295
3.19.4.1.3	Composite solid–liquid–air interface	296
3.19.4.1.4	The effect of edge and variation of surface slope	297
3.19.4.2	Calculation of the Contact Angle for Selected Surfaces and Surface Modification	298
3.19.4.2.1	2D periodic profiles	298
3.19.4.2.1.1	Saw-toothed periodic profile	298
3.19.4.2.1.2	Periodic profile	298
3.19.4.2.2	3D surfaces	298
3.19.4.2.2.1	An array of inequalities with the same shapes and sizes	298
3.19.4.2.2.2	Random rough surface	300
3.19.4.3	Modification of Surfaces to Achieve the Highest Contact Angle	300
3.19.4.3.1	Modification on the basis of monoscale roughness profiles	300
3.19.4.3.2	Modification on the basis of multiscaled roughness profiles	301
3.19.5	**Conclusion**	303
References		303
Relevant Websites		305

 doi:10.1016/B978-0-12-803581-8.09181-5

3.19.1 Introduction

Each substance ends at a point or place. This point or place is the surface and it is not an actual end point, but rather a point to distinguish two states or physical concepts. On the surface of a liquid, the molecules have fewer neighbors in comparison with the bulk volume. As a result, the energy interaction is evident in the surface tension, γ_{LV}, a force that is applied to decrease the area of the free surface of the liquid. Traditionally, the surface tension can be assumed as a force in the unit of the length, which can be counted in Newtons per meter squared or in energy for the units of the surface (Joule per meter squared).[1] The surface tension, γ_{LV}, implies an interface between liquid and vapor, which is an example of surface tensions. Two other interfaces, including solid–liquid and solid–vapor, create the surface tensions of γ_{SV} and γ_{SL}. The equilibrium between these surface tensions decides that a droplet on a solid surface will have a droplet form or will change to a layer form.[2] As shown in recently published work, the lexicology of the word 'wettability' has not been clearly paraphrased. So, we aim to elucidate it here.

The words 'hydro,' 'phobic,' and 'philic' are derived from Greek and mean water, fear, and adoration, respectively. These words are used to define the interaction of water and other materials. As an example, these words are used to classify liquids and solids based on their solubility in water and based on their wettability.[3] Many surfaces in the nature have superhydrophobic and self-cleaning properties. For example, the wings of the butterfly and the leave of some plants (including cabbage and Indian cress) have the aforementioned properties. The best example is the lotus leaf.

The electron microscope pictures of the lotus leaf show some protrusion parts that are 20–40 μm away from each other and are covered with a rough surface with a waxy structure. Numerous studies confirm that this coarsened structure is a combination of micrometer and nanometer scale, with low surface energy; this combination causes a contact angle higher than 150°, low slide angle, and self-cleaning effect. Surfaces with such properties are called 'superhydrophobic.' Some natural examples do not show this two-scaled structure, and there are some questions about the necessity of this two-scaled structure, which is discussed in Section 3.19.2 from the wettability point of view.[4] Before 1996, little attention was given to the superhydrophobic surfaces that were based on the connection of the static contact angle of the water and the geometry of the rough surface. In 1997, two German botanists, Neinhuis and Barthlott, using scanning electron microscope (SEM) discovered the two-scaled structure of the lotus leaf and investigated its chemical composition. That study revealed two important guidelines for researchers who study superhydrophobic surfaces: the roughening of the surface of materials with low surface energy and the modification and creation of the rough surfaces using materials with low surface energy. Therefore, the unusual surface wettability in nature can be created by controlling the microstructure of the geometry of the surface and low surface energy. After that discovery (by German scientists), much research and many review articles related to the superhydrophobic surfaces were published, which explained the applications of the superhydrophobic surface. These applications include self-cleaning windshields of cars, optical equipment, windowpanes, and anti-fog and anti-corrosion coatings. In many reviews and research articles, the 'lotus effect' was investigated and the microscaled/nanoscaled structure was suggested to create and develop superhydrophobic surfaces (Figure 1).[5]

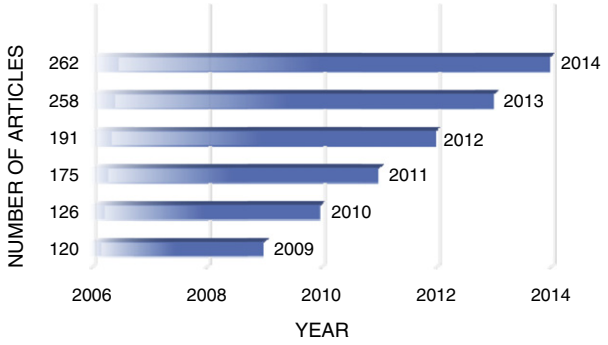


Figure 1 The bar chart of the articles in the past 6 years. Cao, L. *Superhydrophobic Surface: Design, Fabrication, and Applications*; University of Pittsburgh: Pittsburgh, PA, 2011.

3.19.2 Surface Wettability

3.19.2.1 Wettability on a Flat Surface

When a liquid droplet is on a physically and chemically homogeneous surface (Figure 2), wettability of the surface is determined by the chemical composition of the surface. The contact angle of a flat surface (or inherent contact angle θ_{flat}) can be related to three free surface energies in the Young equation: free surface energy of the intersections of solid–vapor (γ_{SV}), solid–liquid (γ_{SL}), and liquid–vapor (γ_{LV}) (Figure 2).[6]

$$\text{Cos}\,\theta_{flat} = \frac{\gamma_{SV} - \gamma_{SL}}{\gamma_{LV}} \quad [1]$$

In which the γ_{SL} is approximated using the following equation:[6]

$$\gamma_{SL} = \gamma_{SV} + \gamma_{LV} - 2\sqrt{\gamma_{SV} * \gamma_{LV}} \quad [2]$$

According to eqns [1] and [2], by increasing the free surface energy of solid–vapor (γ_{SV}), the hydrophobia increases. It has been reported that the intersection with the lowest surface energy belongs to the trifluoromethyl group (6 mN m^{-1}), which with a contact angle of 120° has the highest surface contact angle of water on the flat surface. Increasing the hydrophobicity requires manipulation of surface topography.

Modifying the contact angle of samples, with the aim of hydrophobizing the hydrophilic surface, requires reduction of surface energy, with different methods, of low-energy materials that are placed on the surface. The most common and most popular of them are silanes[8,9] and fluoropolymers.[10,11]

3.19.2.2 Wettability on Rough Surfaces

The effect of surface roughness on wettability was discussed by Wenzel in 1936, and later by Cassie and Baxter in 1944. Wenzel suggested that when a surface becomes rough, the area of the affected surface increases, resulting in more of a tendency for

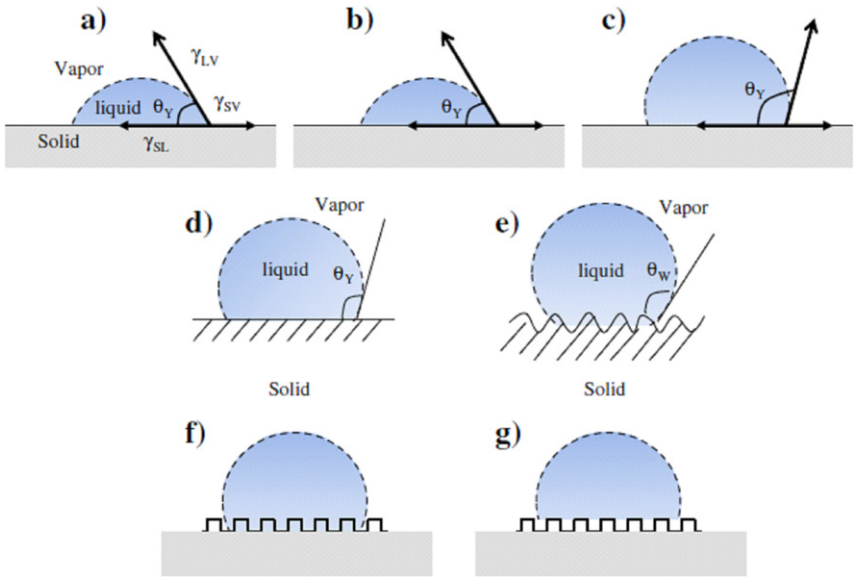


Figure 2 Schematic illustration of contact angle: (a) contact angle of Young's equation; (b) hydrophilic surface; (c) hydrophobic surface; (d) a smooth solid surface; (e) a rough solid surface; (f) homogeneous (Wenzel state) wetting regime; and (g) heterogeneous (Cassie–Baxter state) wetting regime.[7]

water to be more widespread on the hydrophilic surface and in the increased contact of liquid and the surface; spreading on the rough hydrophobic surface decreases to decrease the contact angle. These two states are more favorable from a thermodynamic point of view. A key assumption is that the water is completely in contact with the surface, which is named the Wenzel state (**Figure 2(f)**). The relation between superficial contact angles (θ_{rough}) in the coarse surface and inherent contact angle (θ_{flat}) can be explained by the Wenzel equation.[6]

$$\cos\theta_{rough} = r\cos\theta_{flat} \quad [3]$$

Where r is the roughness factor and is defined as a ratio of the real surface to the horizontal surface. Because r is always higher than 1 for a rough surface, the equation predicts that if $\theta_{flat} > 90$, then $\theta_{rough} > \theta_{flat}$, and if $\theta_{flat} < 90$, then $\theta_{rough} > \theta_{flat}$. So, in the Wenzel state, the surface roughness increases the hydrophobia of the hydrophobic surface and also increases the hydrophilicity of the hydrophilic surface.[6]

It seems impossible for the water to follow surface bumps of the hydrophobic substrate to keep complete contact with the solid surface. That is because in this state, the energy of complete contact is higher than that of partial contact with the surface. It is possible that air gets trapped between the water and the texture of the surface. As a result, the water contacts the surface of the solid–vapor composite and shapes the droplet. This is called the Cassie state (**Figure 2(g)**). The superficial contact angle is explained in the Cassie state with the Cassie–Baxter equation. $\text{Cos}\theta_{LV}$ is the fraction of surfaces that are in contact with the air.

$$\cos\theta_{rough} = \varphi_s * \cos\theta_{flat} + \varphi_v * \cos\theta_{LV} = \varphi_s * \cos\theta_{flat} - (1 - \varphi_s) \quad [4]$$

Where φ_s and φ_v are the fraction of solid in contact with water ($\varphi_s + \varphi_v = 1$). Because the contact angle of water in the air is 180°, the trapped air significantly increases the superficial hydrophobicity of the surface. According to eqn [4], reduction of φ_s, increases the θ_{rough} and results in hydrophobicity. In the Cassie equation, surface roughness has no effect that can be obtained using the roughness number of eqn [5].[12]

$$\cos\theta = r\cos\theta_{flat} - \varphi_v * (r\cos\theta_{flat} + 1) \quad [5]$$

For a system in which the water is in contact with the coarse solid surface, one of the two states can happen. Equations of Wenzel and Cassie cross-over at the critical point of θ_c.[6]

$$\cos\theta_c = -\frac{1 - \varphi_s}{r - \varphi_s} \quad [6]$$

When $\cos\theta_{rough}$ increases, the energy of the system reduces linearly. So, when the water is in contact with the surface of the solid and $\theta_c > \theta_{flat}$, the Wenzel thermodynamic state is more stable. Because $r > 1$ and $\varphi_s < 1$, Q_c is always higher than 90°. With this kind of roughness, when $\theta_c < \theta_{flat}$, the Cassie state occurs on hydrophobic surfaces. All the aforementioned equations are for homogeneous or uniform roughness. So, the general state for the Cassie surface contact angle is provided by eqn [7] (see **Figure 3**).

$$\cos\theta_{composite} = f_1(x,y) * \cos\theta_1 + f_2(x,y) * \cos\theta_2 \quad [7]$$

3.19.2.3 Contact Angle Hysteresis

Another parameter in addition to the contact angle, which is measured in the static state, is needed to specify the wettability.

The hysteresis of the contact angle is the difference between the advancing contact angle (θ_A) and receding contact angle (θ_R), which appears due to the roughness and the heterogeneity of the solid surface. 'Hysteresis' of the contact angle has been derived from the shape of the contact angle in the mobile surface method. In the mobile surface method, the intersection moves slowly and creates advancing and receding contact angles (**Figure 4**). If the roughness is the first agent to be

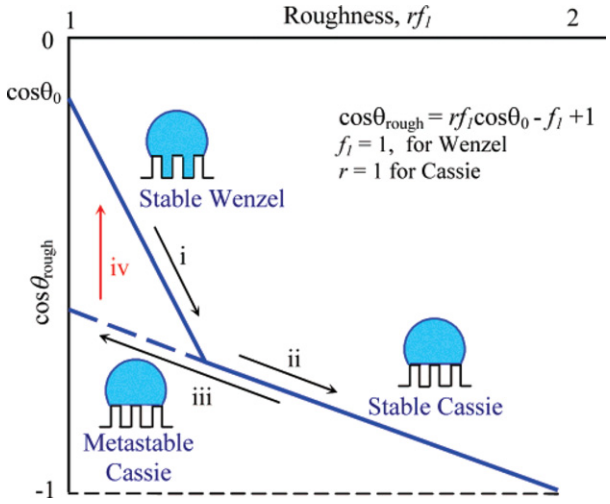


Figure 3 Wetting hysteresis for a superhydrophobic surface. Contact angle as a function of roughness. The stable Wenzel state (i) can transform into the stable Cassie state with increasing roughness (ii). The metastable Cassie state (iii) can abruptly transform (iv) into the stable Wenzel state. The transition from (i) to (ii) corresponds to equal Wenzel and Cassie states of free energies, whereas the transition in (iv) corresponds to significant energy dissipation and thus is irreversible.[13]

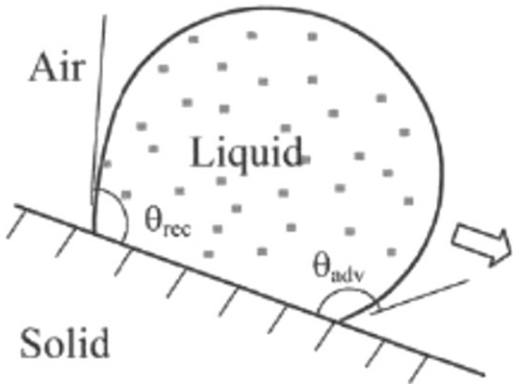


Figure 4 Schematic of a droplet on a tilted substrate showing advancing and receding contact angle.[13]

calculated, then the contact angle measured from the Young equation is meaningless.[14] The advancing and receding angles have the most and least Gibbs free energies, respectively. The barrier of energy for the surface to achieve the least energy is very high. This unstable energy level can be eliminated using vibration, but the least energy still cannot be achieved.

3.19.2.3.1 Film pressure contact angle hysteresis

In most of the intersection systems, it has been observed that the contact angle depends on this concept of how the liquid advances on the dry surface or how it recedes on a wet film surface. Because of the film pressure, free energy of the solid surface, γ_{sf}, changes, which can be determined with eqn [1], in which π is the film pressure. This equation cannot be applied to the Cassie state and is only calculated for the Wenzel state.

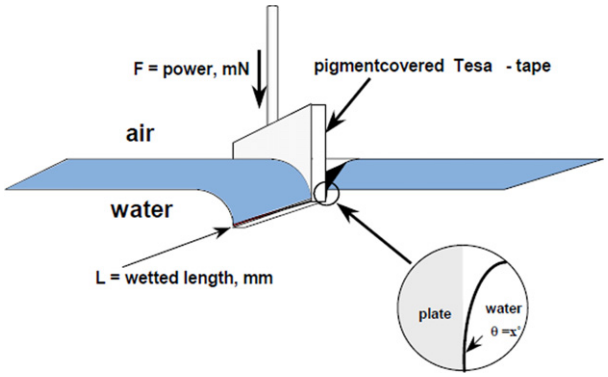


Figure 5 Modified 'Wilhelmy plate' technique.[16]

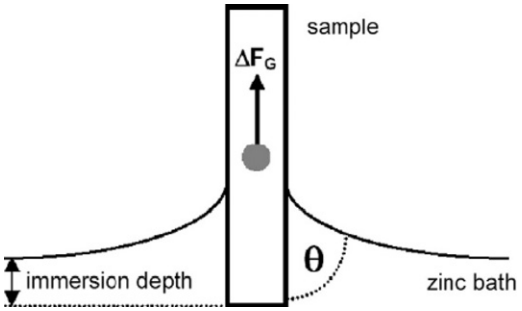


Figure 6 Applied Wilhelmy plate methodology with partially dipped sample.[18]

$$\gamma_{sf} = \gamma_{SV} + \pi = \gamma_{SV} + \gamma_{LV}(\cos\theta_R - \cos\theta_A) \quad [8]$$

Because the spreading of the droplet is not spontaneous, it is accompanied by increasing free energy of the solid surface in the territory of the receding droplet. As a result, π would be positive. If the liquid remains after receding of the droplet, then eqn [2] can be used.[15]

$$\gamma_{SV} = \frac{\pi*(1+\cos\theta_A)^2}{(1+\cos\theta_R)^2 - (1+\cos\theta_A)^2} \quad [9]$$

3.19.2.4 Methods of Contact Angle Hysteresis Measurement

3.19.2.4.1 The Wilhelmy method

In Figures 5 and 6, we can see the schematic of the Wilhelmy plate technique. The F force for partial soaking of a flat surface in a solution is as given in the equation, where P is the wetted perimeter of the surface, γ is the surface tension of the liquid, θ is the contact angle of the vapor–solid–liquid, ρ is density of the liquid, A is the area of the cross-section of the surface, h is the soaking depth, and g is the gravity constant.[14]

$$F(h) = P\gamma\cos B - pAhg \quad [10]$$

In the dynamic position, for capillary number, $Ca = \eta v/\gamma$ less than 10^{-15}, where η is the viscosity of the liquid and v is the speed of contact line movement of the air–solid–liquid; the dynamic contact angle is almost equal to the static contact angle. So, if the applied force on the surface, F, is recorded during the cycle of testing, slow soaking, and exiting of the test

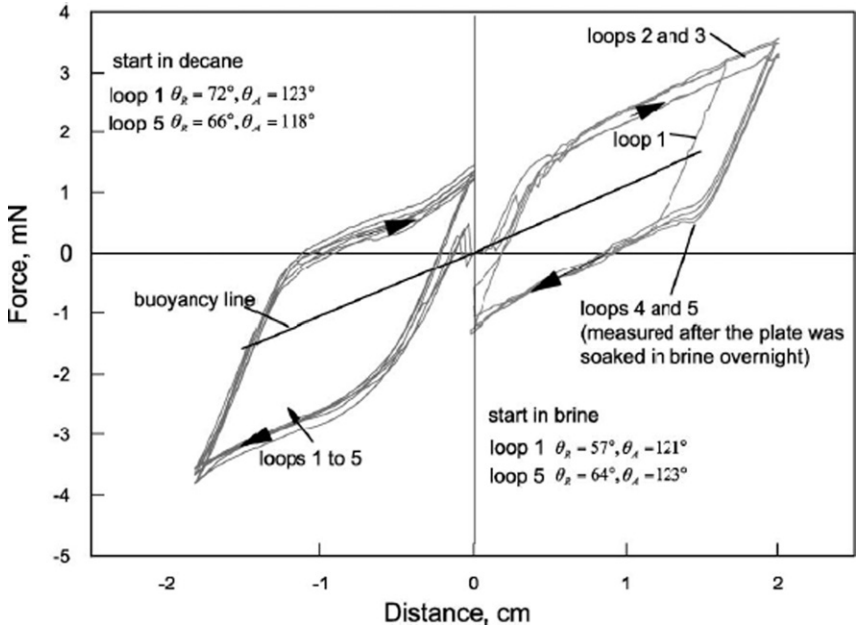


Figure 7 Force–distance diagrams for plates prewetted in 0.1 NaCl brine and aged in A95 crude oil for 10 days at 80 °C.[17]

liquid, then that diagram of F as a function of soaking depths, h, should be linear with the slope of $-\rho Ag$ and γ-intercept of $P\gamma\cos B$. For porous and hygroscopic materials, the weight of the surface might change during the cycle of the testing due to the absorption and desorption of the liquid. So, the measured force is in the form of eqn [11]. $F_w(t)$ is the weight of absorbed water during time.[14]

$$F(h,t) = P\gamma\cos\theta + F_W(t) + \rho Agh \qquad [11]$$

The results of the Wilhelmy test are shown in the diagrams in Figure 7. The hysteresis of the contact angle that results in a difference of force is clear in the results. As the distance of the two parallel lines increased, the more hysteresis of the contact angle that was recorded for the samples with different wettabilities. One of the advantages of this method is that it gives a mean value of different places on the sample, and its disadvantage is that it needs symmetry in the sample and indirect data that should be converted to the contact angle. In Figure 8, a real diagram of the Wilhelmy test results from the zinc samples with oxide coatings is shown. Shifting of the diagram to the more positive values shows a reduction in the contact angle. In fact, it is the distance between advancing and receding hysteresis of the contact angle that is reduced. The slope of the diagram shows the buoyancy force, which has a direct relation with the width of the sample, and these variations occur because of the physical heterogeneity of the sample.

The results of the Wilhelmy diagrams are dependent on the surface of the solid sample, and the condition of the solution also has an effect.

Figure 9(a) shows the profile of force and soaking depths for a wetted sample with no buoyancy effect detected. Figure 9(b) shows the effect of buoyancy as the slope of the sample; this effect could be eliminated with measurement of hysteresis of the contact angle at the crossover point with the surface for these samples. In Figure 9(c), the weight of the sample increases with the process and absorbs the liquid. This method can be used for the porous materials that have a constant soaking rate and the absorbed weight changes. Figure 9(d) shows the required force for the sloping of the nonwetted sample into the liquid as a function of soaking depths. At first, the force does not increase because the contact angle is more than 90° and repels water, but the negative slope of the diagram still exists because of the buoyancy.

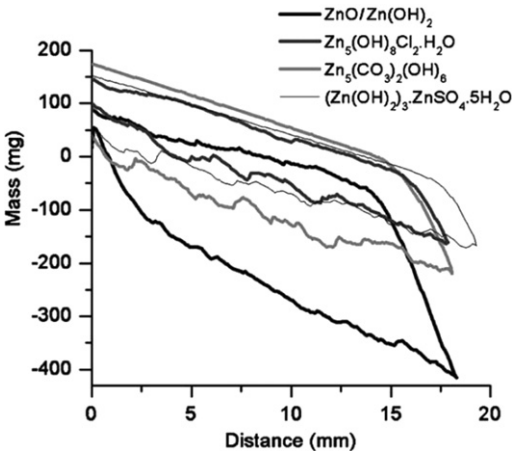


Figure 8 The Wilhelmy diagram showing the variation of the weight as a function of soaking distance in water for the zinc surfaces with oxide coating.[19]

3.19.2.4.2 The methods of suction and injection (sessile drop)

It is usually achieved with expansion and shrinkage of the droplet, using a needle to drag the droplet, and applying water to the droplet. This method is also known as slow dynamic contact angle. A droplet is poured on the surface and the

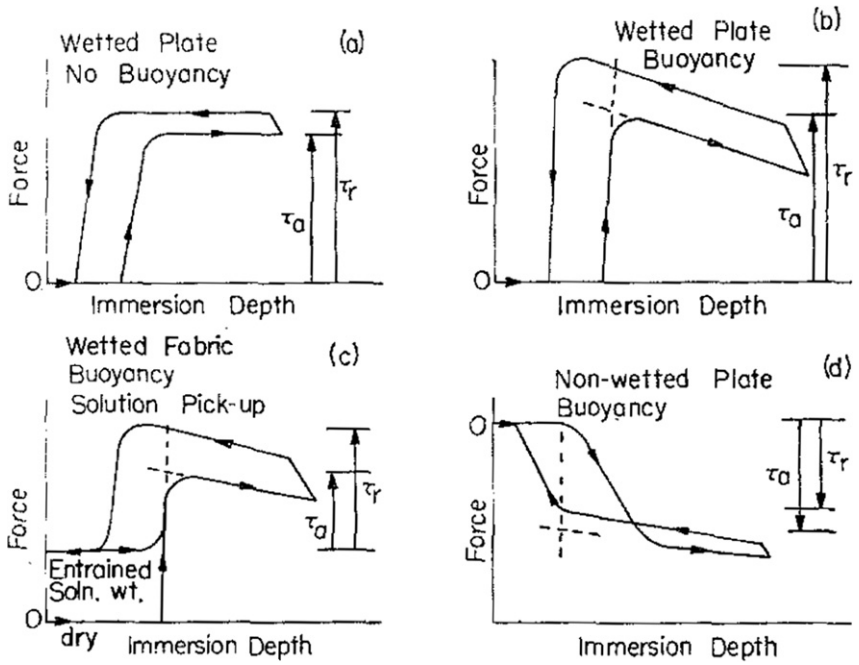


Figure 9 The profile of the ideal force and soaking depths for different solid samples. Each shows how the advancing and receding adhesive forces, T_a and T_r, are calculated.[20]

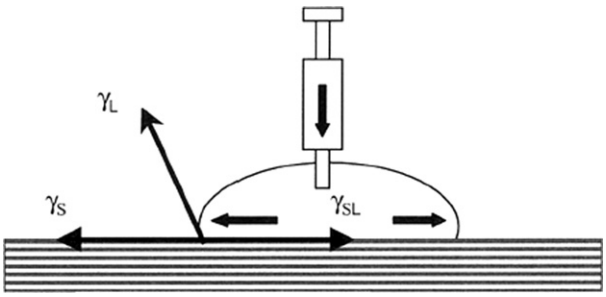


Figure 10 Schematic representation of the measurement of advancing contact angle.[21]

contact angle is measured. For the advancing contact angle, the liquid is injected into the droplet using a needle, and the volume of the droplet would increase continuously but the diameter of the droplet would remain steady (see **Figure 10**). The contact angle would also increase. In a second, the increased diameter and the contact angle would be at maximum value, and that value would be the advancing contact angle. For the receding contact angle, instead of injecting, the liquid would be suctioned; the minimum value during reduction of diameter is the receding contact angle. The limitation of this method is that several measurements of different areas of the sample should be performed and the mean value should be reported.

3.19.2.4.3 Tilted surface method

To investigate the hysteresis of the contact angle, a small droplet of approximately 5 µl should be placed on the flat surface. Then, up to the position that the droplet starts moving on the surface, the surface should be tilted. Then, the advancing and receding contact angles should be calculated using picturing and picture analysis. **Figure 11** shows some states of the droplet during this method. The limitation of this method is investigating the dynamic angle in the low velocities.

This method can be performed in a slightly different way: the droplet could be placed on the tilted surface, followed by blowing on the droplet (**Figure 12**). The droplet would grow in volume and, during moving of the droplet, the hysteresis of the contact angle should be calculated. As the droplet grows bigger, it should start sliding at a minor angle. Low contact angles are mostly in the Wenzel surface state and high contact angles are mostly in the Cassie state. When the hysteresis of the contact angle increases, it is possible that the advancing and receding contact angles are different from each other. Contact angle hysteresis could occur in the Wenzel or Cassie states at a constant value; the equilibrium contact angle requires prediction of the state of the surface (**Figure 13**).

The sliding angle is the least tilted angle of the substrate that causes the droplet to move. The connection between hysteresis of the contact angle with the sliding angle follows from eqn [12].[6]

$$\frac{Mg(\sin\alpha)}{W} = \gamma_{LV} * (\cos\theta_R - \cos\theta_A) \qquad [12]$$

Where α is the sliding angle, g is the gravity acceleration, M is the mass of the droplet, and w is the area of the wetting. From eqn [12], it seems that the sliding angle depends on the size and shape of the droplet. So, the smaller hysteresis of the contact angle results in a smaller sliding angle, and a constant droplet size could be used to compare the wettability.

3.19.2.5 Wetting Free Energies

To measure wetting free energies variations in a sessile droplet on a solid surface, a thermodynamic model with the assumption



Figure 11 The states of the liquid droplet (nonadhesive, adhesive, sliding) for the tilted droplet method.[22]

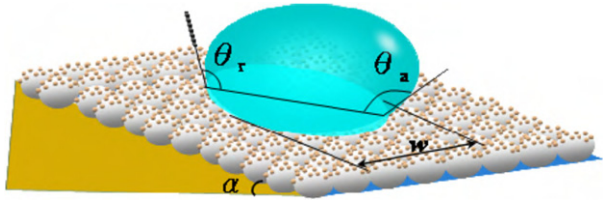


Figure 12 Schematic illustration of the liquid droplet that starts to slide down a tilted plate.[23]

of an adsorption mechanism has been identified. This model resulted in direct specification of the wetting free energies from contact angle data without any knowledge of solid–vapor–liquid interface tension. In this model, it has been assumed that the chemical potential of the surface of the solid is equal to the liquid droplet, the chemical potential of the liquid is dependent on the internal pressure of the droplet, the internal pressure of the droplet is dependent on the variation of the curvature of the droplet on the surface, and the droplet has a spherical shape at first but, after being placed on the surface, it becomes a part of wetting free energies.

Finally, a formula was achieved for wetting free energies as a function of the advancing contact angle (it is approximate to the equilibrium state in static position), which is mentioned in eqn [13]. **Figure 14** shows the wetting free energies as a function of advancing contact angle. With an increasing contact angle, the wetting free energies decrease exponentially and arrive at zero, which seems to be the tendency of the liquid when the wetting has been eliminated; according to eqn [5], liquid has no tendency to adhere to the surface.[24]

$$\Delta G = \left(\frac{1}{3}\right)(RT)*\ln\left[\left(\frac{1}{4}\right)(2+\cos\theta)(1-\cos\theta)^2\right] \qquad [13]$$

3.19.2.6 Contact Angle and Corrosion Resistance

Corrosion of metals in the electrolyte is dependent on the surface reactions, and any agent that repels corrosion agents or reduces the reaction rate can increase corrosion resistance, for example, inhibitors that reduce the contact surface or coatings that reduce the contact surface and increase the resistance. One of these agents is the contact angle of water on the surface. Many studies investigated the effect of the superhydrophobic contact angle on the corrosion rate.

The polarization test has been performed on anodized aluminum with modified surface energy using molten myristic acids (**Figure 15**). The superhydrophobic sample has more corrosion potential and less corrosion current; of course, it shows a passive state. The contact angle of the coating was 154° and the results of the electrochemical impedance show that the polarization resistance values for superhydrophobic and anodized surfaces were 337 and 27.94 kΩ, respectively.

3.19.2.7 Common Methods of Producing Superhydrophobic Surfaces

There are many physical and chemical methods for producing superhydrophobic surfaces that can be performed using two procedures. The first way is the modification of the rough hydrophilic surface with a hydrophobic layer. The second way is roughening of the hydrophobic surface. There are different physical and chemical methods to produce the hydrophobic surfaces, such as solution and laser etching, soaking, chemical vapor deposition (CVD), plasma vapor deposition (PVD), electroplating, electrospinning, anodizing, self-assembled monolayers (SAMs), synthesis, and sol-gel.

3.19.2.7.1 SAMs

SAMs are ordered molecule connections that are created on the surface of the solids with adsorption of a surfactant (**Figure 16**). This simple process has made the SAMs inherently producible, which are technologically attractive for superlattice production and surface engineering. In this 2D system, the ordering is produced by spontaneous chemical synthesis in an intersection as a system that is approaching equilibrium. Even though the surface is not limited to the long-chain molecules, SAMs of long-chain hydrocarbons are the most common complements for the supermolecular structures.

3.19.2.7.2 Fatty acid monolayers

Spontaneous absorption of long-chain *n*-alkanoic acid ($C_nH_{2n+1}COOH$) has been studied in recent years. This is an acid–base reaction and is the driving force for creation of the surface salt between the carboxylate anion and the surface cathode of the metal. These layers are placed on the oxides, but their chemical absorption on the amorphous oxides is not unique. It has been discovered that on the surface of AgO, two atoms of oxygen carboxylate connect to the surface symmetrically, whereas on the surfaces of CuO and Al_2O_3, the carboxylate, which has been connected to the surface asymmetrically, shows an angle approximating to zero (**Figure 17**).

3.19.2.7.3 Organosilicon-derivative monolayers

Monolayers of alkylchlorosilan, alkylalkoxysilanes, and alkylaminosilane need a hydroxylated surface as a substrate to be created. The driving force for this self-assembly is the creation of the connection with the position of polysiloxane that is to

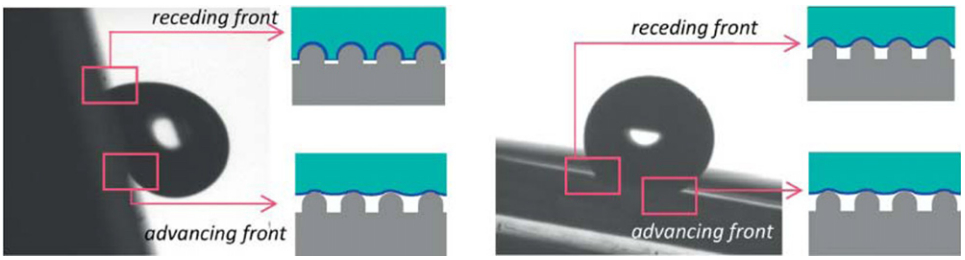


Figure 13 (Left) The droplets slides on the hydrophobic surface. Observed strong hysteresis (contact angle of 72°) can explain the difference in the wetting ability, which is due to the surface fraction of the liquid in contact with the air or the solid in the advancing and receding contact angles. (Right) The droplet moves on another surface with low contact angle hysteresis and with low surface energy. There is little difference between the fraction of solid in contact with the two sides.[22]

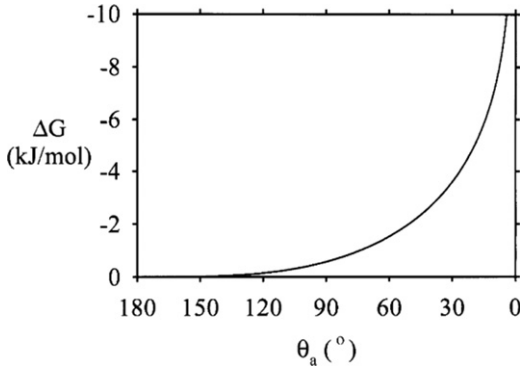


Figure 14 Variation of wetting free energies as a function of the advancing contact angle.[24]

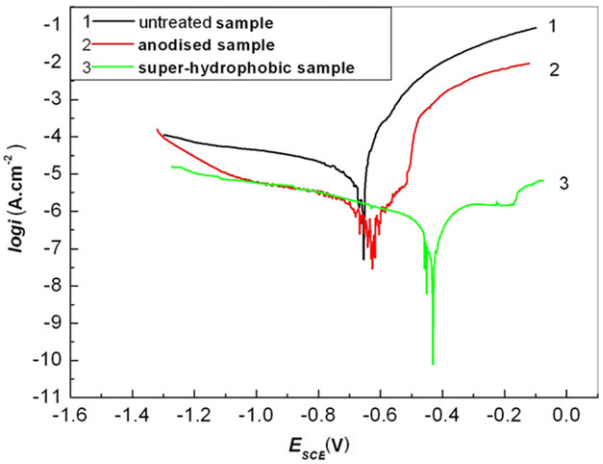


Figure 15 Polarization diagram of the untreated, anodized, and superhydrophobic samples in sterile sea water with 2 mVs^{-1}.[25]

connect with the surface of the silanol group with Si–O–Si bounds. The substrate, which was successfully prepared for these monolayers, includes silicon oxide, aluminum oxide, quartz, glass, mica, zinc selenide, germanium oxide, and gold. Because the substrates in the creation of SAMs are amorphous silanes, arrangement of alkyl chains in silane alkyl SAMs is specified below the structure of the polysiloxane chain. The recreating ability of the alkyltrichlorosilan is still a problem because the quality of the created monolayer is dependent on the reaction conditions. The coating time was different, from 90 min to 24 h. atomic-force microscopy (AFM) has proven the island structure of the partial monolayer. Researchers have discovered that the octadecyltrichlorosilane (OTS) of monolayers on mica is created with the nucleation of island hillsides with fractal dimensions that increase with the increase of the surface covering. In the OTS film, there are pinholes up to 100 nm wide.

3.19.2.7.4 Organic adsorbed sulfur on the metal

Sulfur and selenium complements have a high tendency to surface on transition metals. This is probably due to the creation of multiple bonds with the surface metal clusters. The kinetics of the alkanethiol absorption on the surface of gold (Au, 111) in relatively dilute solutions (millimolar) shows that there are two different absorption kinetics. First, there is a very fast step that results in a contact angle that reaches the value limit, and the thickness is 80–90% of the maximum value. Then, there is a slow step that takes hours, resulting in contact angle and thickness at the maximum values. The first step, which is explained by Longmire absorption under the control of diffusion, is highly dependent on the concentration of thiol. In a concentration of 1 mM, it takes approximately 1 min; in the concentration of 1 μM, it takes more than 100 min. The second step can be explained by crystallizing, which the alkyl chains avoid in their disordered manner and enter the unit cells. So, the first step of kinetics is dependent on the reaction of the head surface, and the activation energy might depend on the adsorbing sulfur electron density. In other words, the second step of kinetics is related to the disorder of the chain, different components of the chain–chain (bipolar–bipolar and others) reaction, and the movability of the chains.

3.19.2.7.5 Silanes

Silanes are a wide branch of materials that are used for these purposes, but they can be considered a subbranch of fluoroalkyksilanes (FAS). The synthesis of the silica fluor nanoparticles is performed by methods like spin coating. An agent in a group of fluorine particles is proven using the Fourier transform infrared spectroscopy (FTIR) method and indicating the presence of Si–O–Si and C–F bonds.

FAS can makes agents for silica particles using the sol-gel process. Fluorine silica can be produced with the Stober standard

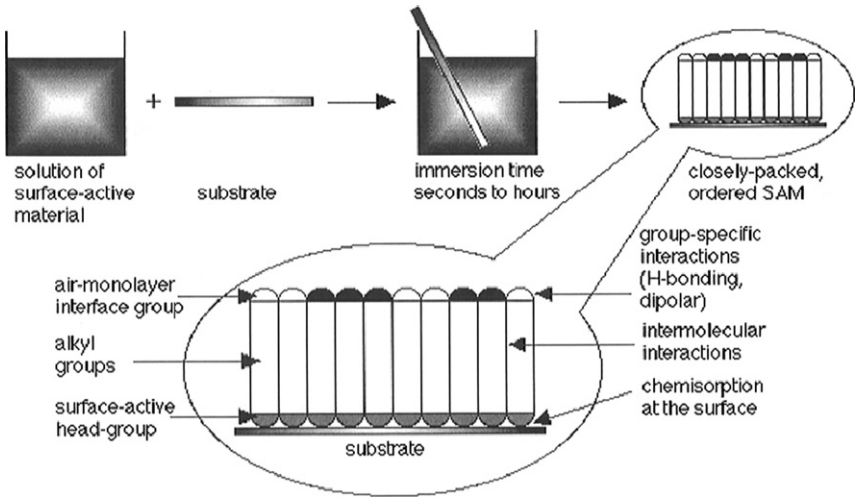


Figure 16 Self-assembled monolayers can be created by single soaking of the substrate in a solution of surface-activated material. The driving force for spontaneous creation of the 2D connection was the formation of a chemical connection of molecules with surface and intermolecular reactions.[26]

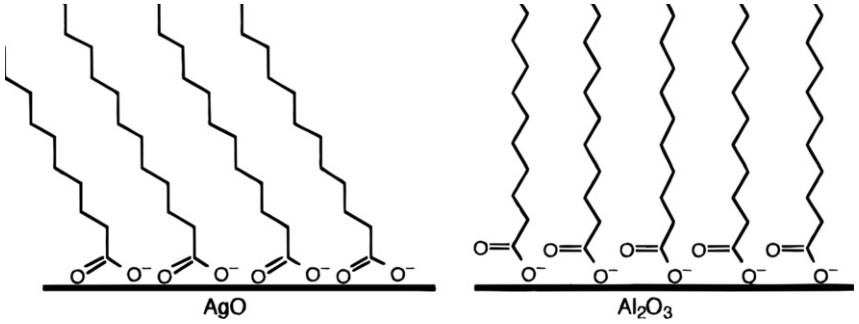


Figure 17 Monolayer of fatty acid on Al_2O_3 and AgO.[26]

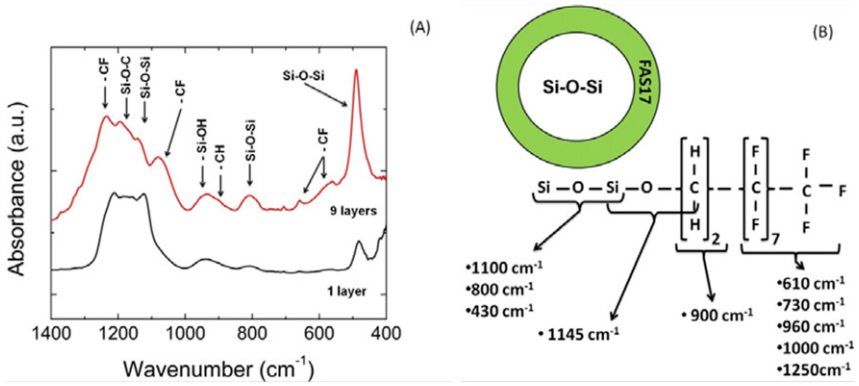


Figure 18 (a) The transform infrared spectroscopy (infrared reflection-absorption spectroscopy (IRRAS)) for fluorine silica nanoparticles of the aluminum coating as a function of quantity of layers. (b) Agented silica nanoparticles with a thin layer of FAS17 on the infrared spectrum.[27]

process. Ethanol and ammonium hydroxide are mixed at 50° in a container. Tetraethoxysilane (Si $(OC_2H_5)_4$; TEOS) is added to the solution, droplet by droplet, while stirring. The transparent mixture is opaque because of the formation of silicon nanoparticles. The sensitized silica nanoparticles in a solution of ethanolic fluor alkyl silane or FAS 17 ($C_{16}H_{19}F_{17}O_3Si$) have more agents. With the spin-coating process, aluminum, glass, and silicon can be coated with fluorine silica nanoparticles. This coated film on a hot surface at 70° is too dry for vaporizing water and ethanol. The agented silica nanoparticles can be identified using infrared spectroscopy (Figure 18). With seven layers of coating, the contact angle is 150°. In one layer, the

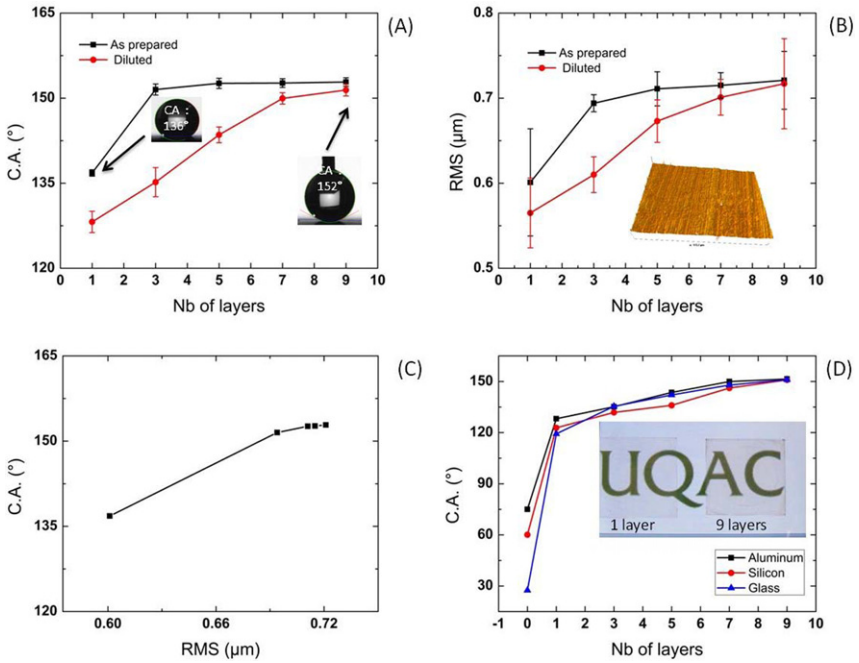


Figure 19 (a) Variation of contact angle of water. (b) Root mean square (RMS) roughness as a function of coating layers using prepared (black) and dilute solution (red). (c) The connection between the water contact angle and RMS roughness for prepared solution on aluminum. (d) Variation of the water contact angle as a function of quantity of the coating layers using dilute solution on different substrates. The transparency of the coating is illustrated.[27]

roughness of the coating has not achieved the appropriate value and the contact angle is low. With the increasing layers, the roughness achieves the appropriate value and the contact angle increases (Figure 19).

3.19.2.7.6 Stearic acid ($CH_3(CH_2)_{16}CO_2H$)

Stearic acid is a saturated fatty acid that can deposit on the surface in special conditions. This acid is insoluble in water and soluble in ethanol. The copper substrate should be cleaned, pickled, and soaked in 10% volume HNO_3 for oxide elimination. The clean sample should be soaked in ethanolic stearic acid solution (0.01 M) and 30 V DC should be applied. The anode and cathode should be made of copper. Studying the X-ray powder diffractometer (XRD) peaks proves the existence of copper stearate components resulting from the reaction of stearic acid with copper. The resulting component was studied using SEM (Figure 20). These components provide the necessary roughness and low energy of hydrophobia so the contact angle arrives at 153° and so the hysteresis of the contact angle decreases. Other researchers created a self-assembled layer on porous alumina using stearic acid.[28] This method was performed on anodized aluminum in 0.01 volume of stearic acid solution in ethanol for 30 min without applying any potential and superhydrophobia was achieved.[29]

Due to the insolubility of stearic acid, it cannot be applied to sedimentation of magnesium stearate in an aqueous solution. With the addition of soda to stearic acid sodium, stearate would form, which is completely soluble in water. Magnesium stearate can be created by a reaction of magnesium sulfate, which is soluble in water, with sodium stearate, and the magnesium stearate would deposit in solution because it is insoluble in water. If magnesium chloride exists in solution other than magnesium stearate, then sodium chloride would also be produced. Of course, there is the possibility of its creation from a magnesium ion solution. The melting point of magnesium stearate is 85.5 °C, but the calcium stearate produced from the reaction of calcium oxide and stearic acid melts at 155 °C. Stearic acid was applied on the zinc oxide nanorods and the contact angle increased. The zinc oxide (Figure 21) produced was soaked in a solution of 0.002 M *n*-Hexane stearic acid and shows a contact angle of 151° and negligible hysteresis. The FTIR analysis shows that the bonding of the carboxyl group was broken and transformed to the carboxylate bidentate on the surface of zinc oxide.

Another method of creation of surfaces with high contact angles is hydrophobizing of particles, such as ceramics, and then depositing them on the surface.[32–34] Zinc oxide dry powder (0.209 g) and stearic acid (0.0595 g) in the ethanol solution (10 ml) should be mixed for 1 h with a constant speed at 75 °C. Then, the mixture should be aged for 2–3 h. The resulting suspension is used to create the thin film on the glass using the dip coating method. Then, it should be dried at 80 °C. To investigate the effect of stearic acid, samples were coated with different amounts. The researchers calculated an angle of 178° for the sample with an 8%M concentration of stearic acid and zinc oxide. This is because zinc oxide nanoparticles provide the required roughness and stearic acid provides low surface energy. In higher percentages, the contact angle decreases due to reduction of roughness. Hydrophobizing of the magnesium can be performed using a simple methods of soaking in a superhydrophobized ethanol solution with 0.05 mol l^{-1} stearic acid[35] (see Figure 22).

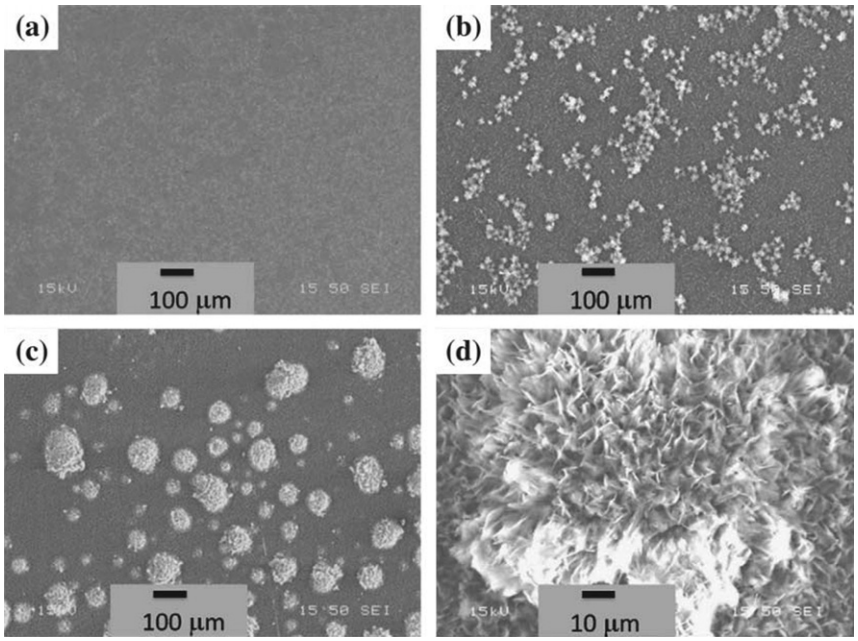


Figure 20 Scanning electron microscope (SEM) images of anodic surface of copper electrode after applying 30 V DC potential in ethanolic stearic acid solution for (a) 0.5 H, (b) 1.5 H, (c) 3 H, and (d) morphology of one single particle for 3 H.[30]

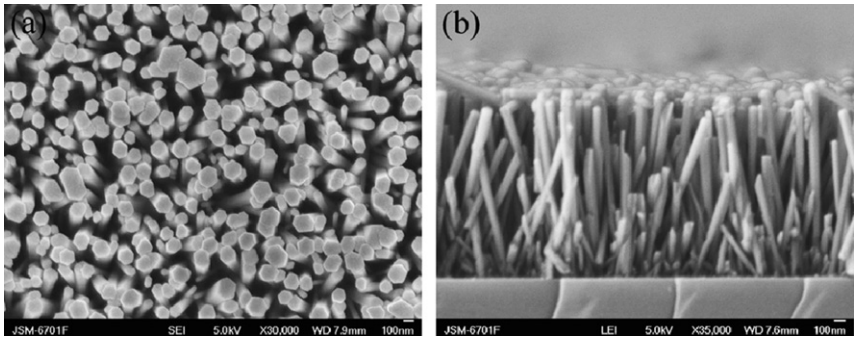


Figure 21 (a) Scanning electron microscope (SEM) tops and (b) cross-section of the zinc oxide nanorods after the first step.[31]

3.19.2.7.7 Tetradecanoic acid

Tetradecanoic is a hydrocarbon fatty acid like stearate that can react with metals and that creates a hydrophobic component on the surface. Copper (Figure 23) should be soaked in 0.01 M tetradeconoic acid solution in ethanol at room temperature for 3–5 days. Because of the oxygen in the environment, the copper will corrode, the copper ions react with the tetradecanoic, and the component is created. Finally, copper tetradecanoic can be created in cluster form and provides the hydrophobic condition of the copper specimen at 162°.

3.19.2.7.8 Benzoic acid ($C_7H_6O_2$ or C_6H_5COOH)

Benzoic acid is a colorless crystal solid that can reduce the energy of the surface in a reaction. This acid can be dissolved in water at less than 3 g per liter. A thin film of silver is created at room temperature on a clean copper substrate with simple soaking in blue silver nitrate solution with or without the presence of adequate concentrations of benzoic acid during a specified period of time. Silver attaches to the surface with a displacement reaction, the hydroxyl benzoic acid group attaches to the surface of copper and silver, and the superhydrophobic surface engenders an angle of 162° (Figure 24).

3.19.3 Topography of the Rough Surface

3.19.3.1 Characteristics of the Rough Surface

A rough surface (see Figure 25) (to be more specific, the intersection of liquid– solid, gas–solid, or solid–vacuum) has a complex structure and characteristics depending on the nature of the material and surface preparation. All the surfaces of solids, whether natural or artificial, regardless of production method, have disorders. No machine can produce a molecular flat surface for common materials. Even the flattest surfaces

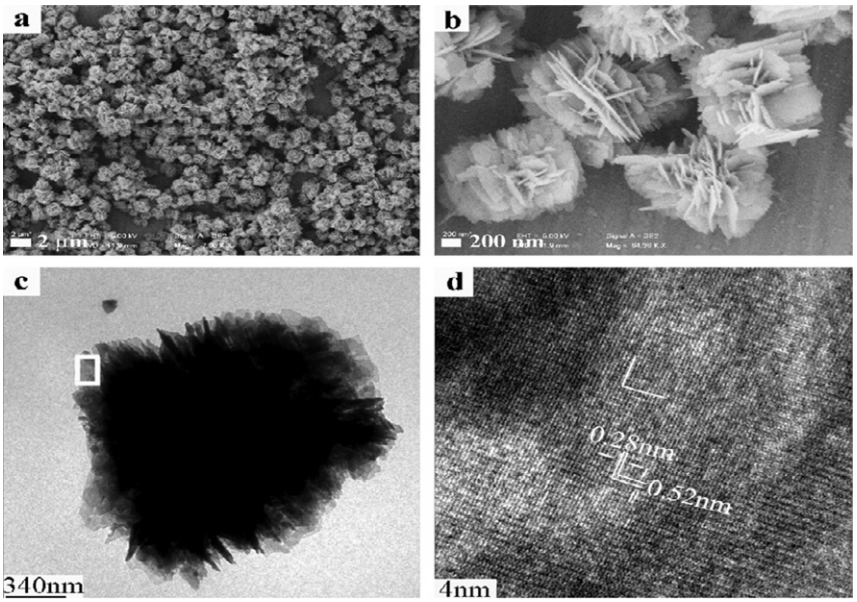


Figure 22 Field emission scanning electron microscope (FESEM) and transmission electron microscopy (TEM) images of the zinc oxide samples. (a) Panoramic FESEM image. (b) FESEM image with higher magnification. (c) TEM image of hierarchical microholes. (d) High-resolution transmission electron microscopy (HRTEM) image of a nanosheet with a distinct square.[32]

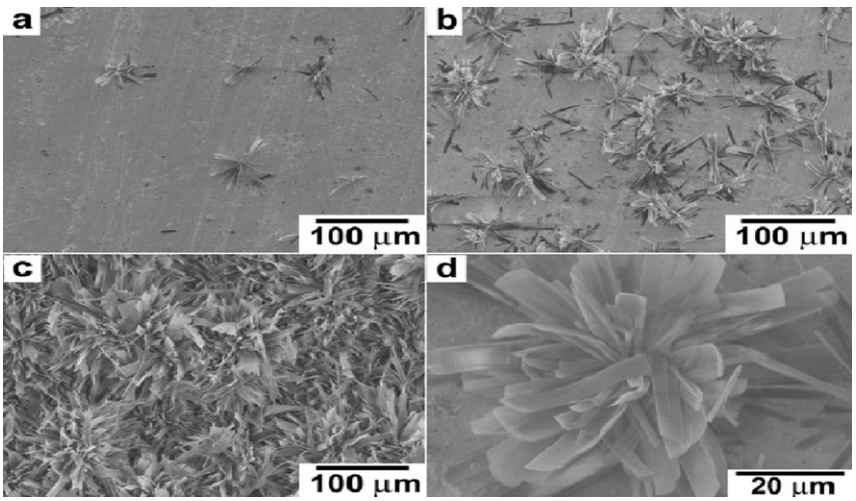


Figure 23 Scanning electron microscope (SEM) image of copper tetradecanoic plus surface of the copper during soaking. Soaking times: (a) 4 h; (b) 16 h; and (c) 72 h. (d) Higher-magnification image of a unique flower-shaped structure of a single cluster.[36]

have disorders because of cleavage of some crystals (such as graphite or silica). Their height is on the atomic scale. Engineering surfaces usually contain the following:

- Wavy conditions
- Roughness
- Lay
- Imperfections

Wavy conditions are a result of vibrations from machine production or collision during production. These conditions involve disorders with relatively long wavelengths (usually some microns). Roughness is produced by surface vibration of the short wavelengths that are defined by the ledges (local maximum) or valley (local minimum). Lay is the main path of the main pattern that usually occurs during production. Undesirable and unexpected imperfections and unintentional discontinuities exist in texture.[38,39]

The difference between the properties of different kind of roughness is an issue that is related to the conditions, application, detachments limits, and measurement tools.

Generally, it is not possible for all properties to be measured simultaneously. The word 'hardness' has many meanings, and this can cause many problems. This is because of the concept that for one resolution, a value that is reported as a maximum on the surface profile might be reported as a minimum for another resolution.

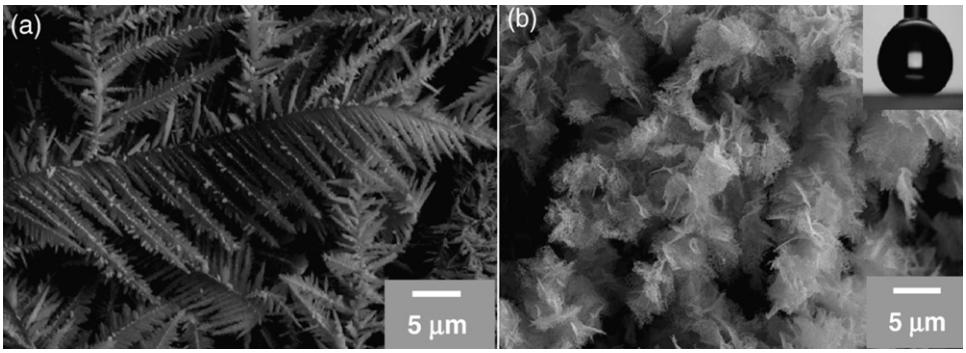


Figure 24 Scanning electron microscope (SEM) image of deposited silver on the copper substrate in the galvanic reaction exchange in silver nitrate solution (a) without benzoic acid and (b) with benzoic acid and an image of a water droplet on the surface.[37]

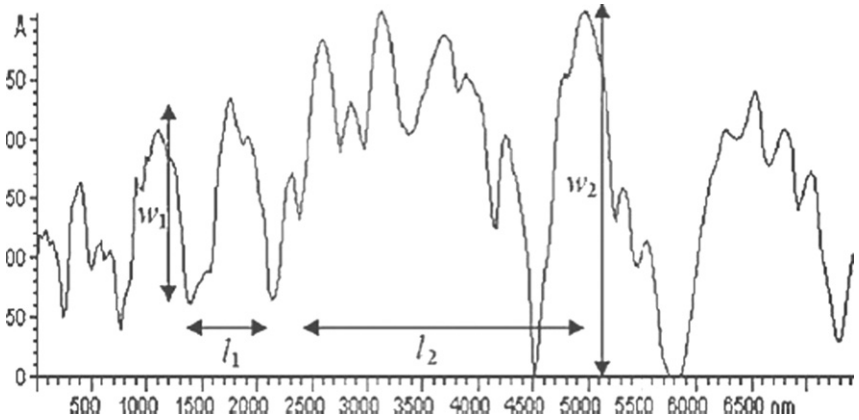


Figure 25 A rough surface.[40]

There are a variety of tools for measurement of surface roughness. Mechanical tools (contacting) and optical tools (not contacting) are applied for measurements of roughness on macroscales and microscales.[38,39]

The mechanical pen method includes amplifying and recording of the vertical movements of the tip of the pen, which moves with a constant speed on the surface. The pen is usually mechanically coupled with a capacitor sensor or linear indignant differential transformer. When the pen starts scanning the surface, the corresponding analog signal amplifies and converts to a digital signal. The detachment limit of the profile depends on the dimensions of the pen's tip. The sharper the tip, the more details of the profile that can be achieved.

Optical methods are based on the reflection of light from the surface. This method includes reflection methods that are dependent on the medical mirror. In the gloss meter method, measurements are performed by applying diffusion reflection and optical intersection methods, which are applied in many commercial methods. Using noncontact methods, there is the possibility of surface damage.

Many methods have been developed for measurements of roughness on microscales and macroscales. The family of instruments used based on scanning tunneling microscope (STM) and AFM are named scanning probe microscopy (SPM). For STM, which was developed in the 1980s, a small, sharp, metallic tip is placed near the surface (0.3–1 nm). As soon as the voltage is applied between the tip and the surface of the sample, the tunneling current is recorded, which is proportional to the distance between the tip and the surface. When the tip scans the sample, the profile of the height of the sample is recorded in nanometers up to the detachment limit.

AFM is a combination of STM principles and the measuring pen. For AFM, the tip of the pen (with diameter of a few nanometers) is placed at the end of a long (a few micrometers), strong cantilever. The deviance of the cantilever is measured by identifying the position of the reflected laser beam. During the contact mode, the tip of the pen scans the sample and the inequality map is achieved up to the detachment limit (in nanometers).

In the noncontact mode, the noncontact force of van der Waals in front of the tip of the pen causes deviation of the prop. When the hardness of the cantilever is identified, this deviation can be converted to the units of the force (with a detachment limit measured in nano-Newtons). AFM can be performed in normal environments as well as in a vacuum.[41,42]

SEM can also be applied to study the properties of the surface. This method has several limitations. First, it is difficult to achieve quantitative information from SEM. Second, the scope field of the SEM is limited. SEM requires a vacuum. In addition, a conductor is required for isolating the sample. For biological samples, there is a technique called environmental scanning electron microscopy (ESEM), which performs the measurements

in controlled conditions of humidity and pressure. Advanced methods of material analyses include X-ray spectroscopy, Raman spectroscopy, electron diffraction, and some other methods.

In addition to the surface disorders, the surfaces of the solids include different regions or different layers such as chemical absorption layers (0.03 nm), physical absorption layers (0.03–3 nm), and some layers that have reacted chemically (1–100 nm). In chemical absorption layers, the surface of the solid creates bonds with the absorbed species that are of the covalent type and share electrons. With increasing cell absorption layers, there is no chemical bond between the substrate and absorbed material, and the forces are van der Waals. The van der Waals forces are relatively weak (<10 kJ mol^{-1}) in long ranges in comparison with the strong forces (40–400 kJ mol^{-1}) in short ranges (in atomic ranges, which are approximately 0.3 nm). The common absorption agents include oxygen, water vapor, and hydrocarbons resulting from an environment that can be dense on the surface. Although the chemical absorption layer is a monolayer, the physical absorption layer can contain different layers of molecules. A layer that has bonded chemically is significantly thicker and includes many molecular layers. A common example of the chemically reacted layer is an oxide layer on metallic substrates.

3.19.3.2 Random Surface Roughness Static Analysis

There are many quantitative parameters for specifying random roughness properties of the surface (see Figure 26). This means that they are all derived from a specified form. These parameters include vibrating parameters and space parameters.[38,39,43] The most common vibrating parameter is root mean square (RMS) or standard deviation from the central mean line.

For a 2D roughness profile, $Z(x)$ is defined as the central mean line calculated from the mean of the absolute value of the vertical deviation from the profile mean line (see Figure 27).

$$R_a = 1/L \int_0^L |z - x| dx \quad [14]$$

where L is the length of the sample.

$$m = \int_0^L Z dx \quad [15]$$

and RMS-squared can be attained from eqn [16].

$$\sigma^2 = 1/L \int_0^L (z - x)^2 dx \quad [16]$$

Because the coarse surfaces profile can have the same RMS, the other parameters for identifying the details of the surface profile are needed. Two other statistic parameters are skewness and kurtosis, which can be represented using the following normalized forms:

$$SK = 1/\sigma^3 L \int_0^L (z - x)^3 dx \quad [17]$$

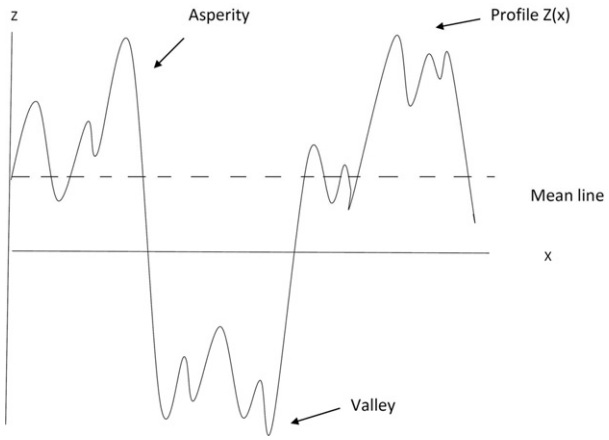


Figure 27 Schematic of the rough surface profile.

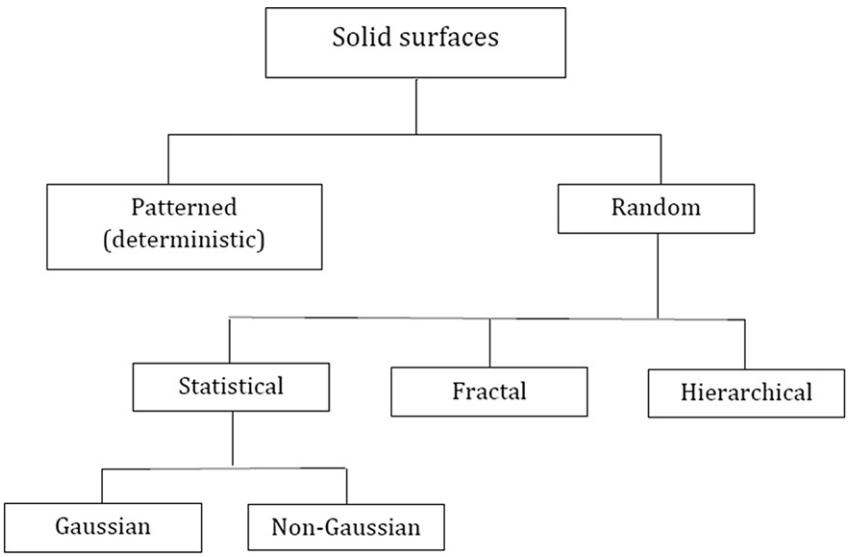


Figure 26 Typology of the rough surfaces.

$$k = 1/\sigma^4 L \int_0^L (z-x)^4 \mathrm{d}x \quad [18]$$

A surface with negative skewness has more local maximums above the mean line (Figure 28(a)), whereas for a positive skewness it is opposite (Figure 28(b)). Similarly, a surface with low kurtosis has more local maximums above the mean line in comparison with a high elongation surface. It is noticeable that although these parameters were defined for 2D surfaces, they can be easily generalized for 3D surfaces.[38,39]

The cumulative probability distribution function p (h) is connected to the random variable Z (h), which is defined as the possibility of the occurrence of $Z(x)<h$ and is written as:

$$p(h) = (z<k) \text{ Probability} \quad [19]$$

It is common for the structure of the random data to be defined as the slope of the distribution function, which is known as the probability density function (PDF) and is represented as:

$$p(z) = \mathrm{d}p(z)/\mathrm{d}z \quad [20]$$

The integral of PDF is equal to P (z), and the area under the curve of the PDF should continue.[38,39]

In many of the practical cases, random information tends to follow normal or Gaussian distribution that, in the case of PDF, is represented as follows:

$$p(z) = \frac{1}{\sigma\sqrt{2\pi}} \exp\left(-\frac{(z-m)^2}{2\sigma^2}\right) \quad [21]$$

where m is mean and σ is the standard deviation. For simplicity, the Gaussian function is usually pictured as a function of a normalized variable of $Z = \frac{z-m}{\sigma}$.

$$p(z^*) = \frac{1}{\sqrt{2\pi}} \exp\left(-\frac{z^{*2}}{2}\right) \quad [22]$$

The Gaussian equation has SK=0 and K=3.[39]

Gaussian distribution is found in nature and practical applications when a random quantity is the sum of so many random agents that affect each other independently. When an engineering surface is formed, many random agents are related to the roughness, and in many of these cases the height of the roughness follows Gaussian distribution. Such surfaces are called Gaussian surfaces.

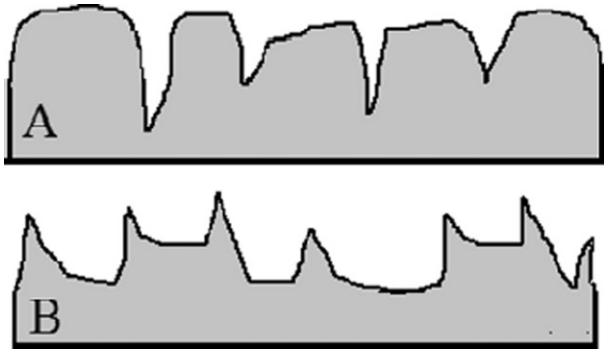


Figure 28 Surfaces with negative (a) and positive (b) skewness.[44]

To introduce spatial distribution of random roughness, the correlation function, defined here, is used.

$$c(\tau) = \lim_{L\to\infty} \frac{1}{L\sigma^2} \int_0^L [z(x)-m][z(x+z)-m]\mathrm{d}x \quad [23]$$

This function identifies the correlation between two measured variables in the distance of τ from each other, for example, $Z(x)$ and $Z(x+\tau)$.

This function can be attained from a comparison between the $Z(x)$ function with the same τ shifted function. The function c (τ) goes to zero if there is no static correlation between z values separated by the value of τ. In contrary, this function has values different than zero. There are several engineering surfaces that have an exponential self-correlated function.

$$c(\tau) = \exp\left(-\frac{\tau}{\beta}\right) \quad [24]$$

where β is the length of correlation and/or a length that the correlation function is reduced to by a small component of its primary value. In this β, the distance function is reduced to the value of $1/e$. In many cases, the value of β^*, which is equal to 2.3 β, is used as the correlation length, and the function is reduced to 10% of its main value.[38,39]

For a Gaussian surface with a self-correlated function, σ and β are two parameters with length dimensions that easily define the roughness. Although σ is a height parameter that determines the height of an inequality (hardness), β is a length parameter that determines the length of an inequality. The absolute mean value of the slope is proportionate to the σ/β^*, whereas the mean curve is proportionate to the β^*/σ. For a Gaussian surface, σ is related to the RMS because $\sigma = \sqrt{\pi/2}$.[38,39] The parameters σ and β^* are suitable parameters for specifying many random surfaces. It should be noted that a Gaussian surface has just one inherent length parameter, β^*, and one vertical parameter, σ. Thus, it cannot specify manifold scaled roughness.

3.19.3.3 Roughness of Fractal Surfaces

Roughness measurement parameters such as σ and β^* are sensitive to the scale; this is because of the measurement apparatus detachment limit (limits of the sample intervals or short wavelength) and the scan height (the limit of the long wavelength). Because the roughness is made of many overlapping wavelengths, all of them affect the cumulative values of σ and β^*. Wavelengths shorter or higher than the sample intervals have no effect on the roughness parameters. So, the measured roughness parameters are dependent on the limitations of the short and long wavelengths. These considerations are not just a result of the measurements or the limitations of the measurement apparatuses. In practical cases that are accompanied by contact, inequalities can be introduced as a component of the roughness that is formed during contact and forms a contact point. So, the height and length of the contact points for rough surfaces are important and might cause wavelength limitations during the contact.

A surface consists of a lot of roughness. The differences in the height of surfaces and other parameters of roughness

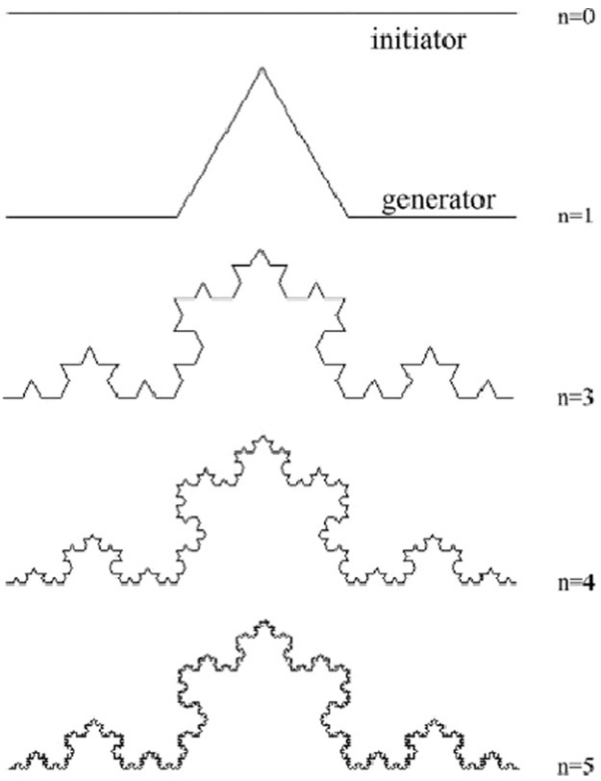


Figure 29 Construction of the triadic Koch curve.[46]

are dependent on the detachment limit of the roughness measurement tools. By increasing the detachment limit of the roughness measurement tools, smaller details can be observed. When a surface grows continuously, the roughness details can be observed in nanoscale. The roughness is structurally the same at all the magnifications. Self-affinity can be identified by fractal geometry.

Archad[45] suggested that a rough surface is covered with inequalities with specified extents, but few inequalities exist.

He proved that an elastic surface with a hierarchical structure, which is similar to fractal geometry, can result with approximately linear dependence on the actual contact surface with the normal force. This is in agreement with the linear dependence on the friction force of the contact surface, which is due to the adhesion and can confirm the coordination between friction force and normal applied force.

Self-similarity surfaces and diagrams were investigated in the early 1920s. An important property of these diagrams and surfaces is that they have small dimensions. When a linear scale is magnified using a specified factor of α, the size of the diagram or the area is altered proportionally to α^D. This is due to the possibility of more detailed observations at higher magnifications. When the Koch diagram (see **Figure 29**) with a length of L is magnified with an agent of $\alpha=3$, the length is $4L$. Therefore, the fractal scales would vary between $D=\frac{\ln(4)}{\ln(3)}=1.26$, 1, and 2. Even though the fractal curves provide the same self-similarity magnification in all directions, contrary to most mathematical functions applied in engineering, fractal curves have no intersection. The word self-affinity (see **Figure 30**) has little meaning.

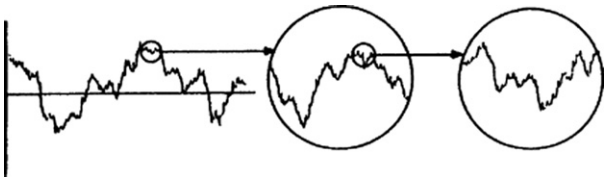


Figure 30 Qualitative description of statistical self-affinity for a surface profile.[53]

In the 1970s, there word fractal was introduced and self-similarity and self-affinity theories were widely popular. Fractal geometry can be applied in a wide scope of physical problems, from the beach line of the oceans to the turbulence of the fluids. Fractal geometry is a general tool that can be applied for noncontinuous behaviors that cannot be studied using traditional continuous functions calculations.

In the 1980s, it was suggested that fractal geometry can be applied to identify the properties of rough surfaces.[47–52] Majumdar and Bhushan (1990) suggested that the self-affinity function has important properties of a self-affinity surface profile.

$$z(x)=G^{(D-1)}\sum_{n=n_j}^{\infty}\frac{\cos 2\pi\gamma^n x}{\gamma^{(2-D)n}} \qquad [25]$$

$\Upsilon>1;\ 1<D<2$

where D is the fractal dimension, G is a dimensionless constant for scaling, and Y^n indicates the surface roughness frequency. D is dimensionless and G has the dimension of the length, and they both indicate a fractal profile. Ganti and Bhushan[48] developed this analysis and considered the side detachment power of the apparatus as an inherent length unit. This analysis considers the extended surface properties of the two parameters of fractal geometry – fractal scale and intensity coefficient – that are theatrically independent for each surface and apparatus. Ganti and Bhushan[48] presented a technique for simulation of fractal surface profiles.

Some engineering surfaces are measured to confirm the extended fractal analysis, especially for magnetic tapes, thin film hard disks, steel disks, plastic disks, and diamond films, which have different hardness. For a surface with different roughness, the fractal dimension stays steady. Although the constant of scaling varies with the variation of the height of the surface (σ^2) for an apparatus, the simulated σ has the same trend as the measured σ (equal up to small scanned lengths). The coefficient of friction for all surfaces has a logical relationship with the constant of scaling.

Almost no type of self-similarity can be found up to any specific length scale (e.g., molecular scale) or limited high-frequency (short wavelength), ω_h, with higher magnification of the profile. In the same conditions, there is limited low frequency (long wavelength), $\omega_{h.}$ in fractal behavior.[50] It should be noted that a fractal profile has no specific parameter on the length scale. Even though the limitations of short and long wavelengths significantly create these parameters of the length scale, $\frac{1}{\omega_l}$ and $\frac{1}{\omega_h}$, during the contact of two coarse surfaces, the parameters such as number of inequalities in contact and the real surface in contact are dependent on the limitations of short and long wavelengths as exponential functions, and the exponential functions are dependent on D and G.

3.19.3.4 Creation of a Rough Substrate and Its Modification Using Low Surface Energy Materials

The methods of creation of the superhydrophobic surfaces using materials with low surface energy are usually a single-step process that benefits from the ease of the process. However, they are always limited to a small group of materials. Here, the superhydrophobic surfaces are created using a completely different strategy with coarse substrates and modification of materials with low surface energy. The wettability divides the surface from the bulk properties and enhances the applicability of the superhydrophobic surfaces.

There several methods for fabrication of coarse surfaces, including laser with the plasma/chemical etching, lithography, sol-gel process, dissolution method, colloid accumulation method, layer method, reaction and electrical/chemical deposition, electrospinning, and CVD. Also, there are many methods for chemical edification of the surface. For example, a covalent bond can be created between gold and alkyltiol. Silanes are usually applied for reduction of surface energy. Absorption and coating can also change the chemistry of the surface.

3.19.3.4.1 Etching and lithography

Etching is a direct and effective method for fabrication of rough surfaces. Etching has many methods, including plasma etching,[54,55] laser etching,[56,57] and chemical etching.[58,59] All of these methods have been applied for the fabrication of superhydrophobic surfaces. For example, Teshima *et al.*[55] achieved a transparent superhydrophobic surface from a polymer substrate (poly(ethylene terephthalate) (PET)) using oxygen etching by means of plasma, which increased the CVD by using (tetramethylsilane (TMS)) an advancing agent. Qian and Shen[58] suggested a simple method for roughening the surface using chemical etching of the selected dislocation on polycrystalline metals including aluminum. After modification by flouroalkylosilanes, the metallic etched surface showed hydrophobicity.

Lithography (e.g., photolithography, lithography of electron beam, lithography of X-ray, soft lithography, nanolithography) is an accepted method for producing a large area with a periodic pattern in nanoscale and microscale.[60,61] Abdolsalam *et al.*[62] performed a systematic study of wettability of gold surfaces using a plating method for molds with submicron scales and investigated the role of the size of the holes and their shape in the wettability control. Matrin *et al.*[63] produced an ordered array of nanoholes and vertical nanorods using electron beam lithography and plasma lithography. They achieved a contact angle of 164° and hysteresis of 1° for the surface with vertical long rods with arc tips after hydrophobizing using octadecyl trichlorosilane. Using photolithography, complex surfaces with hydrophobic patterns and superhydrophilic properties were reported by Notsu *et al.*[64] (see **Figure 31**).

3.19.3.4.2 Sol-gel process

The sol-gel process is used for manufacturing superhydrophobic surfaces from many types of materials.[65–70] In many investigations, due to the presence of materials with low surface energy in the sol-gel process, there is no other hydrophobizing process. For example, Shirtcliff *et al.*[67] produced a porous sol-gel foam of Organo-trithoxysile that shows both superhydrophobic behavior and superhydrophilic behavior when exposed to high temperatures. Shang *et al.*[69] presented a method whereby transparent superhydrophobic surfaces were produced by modifying silicate-based films using fluorinated silanes instead of mixing low-energy materials in sol. In the same case, Wu

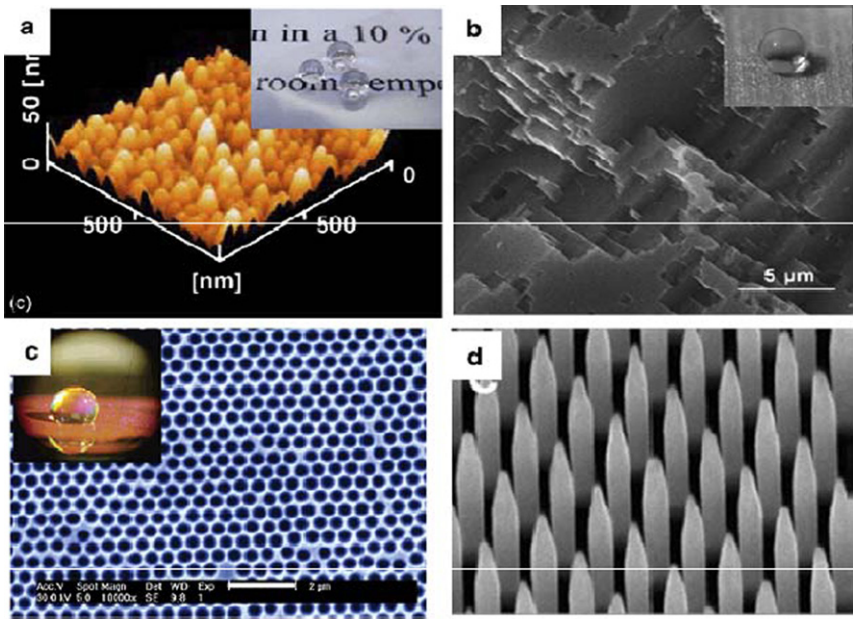


Figure 31 Superhydrophobic surfaces produced by etching and lithography. (a) atomic-force microscopy (AFM) picture of poly(ethylene terephthalate coated by tetramethylsilane (TMS) layer after oxygen plasma modification.[55] (b) Scanning electron microscope (SEM) image of aluminum surface etched by Beck dislocation etchant for 15 seconds at room temperature and a picture of a droplet on the surface after coating by fluoroalkyl silanes (inset).[58] (c) SEM picture of a gold film in a spherical submicron mold, deposited electrically.[62] (d) SEM picture of nanopilars after hydrophobizing. The diameter of the pillars is approximately 120 nm.[63]

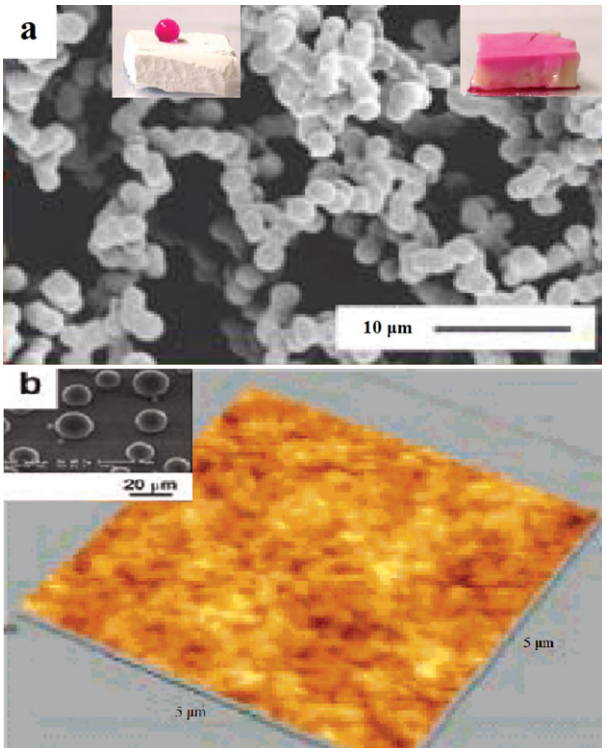


Figure 32 Superhydrophobic surfaces produced by sol-gel process. (a) Scanning electron microscope (SEM) image of MTEOS sol-gel foam. Inset pictures show fenol fetalein in water on the sol-gel foam, tempered at 390 °C (left) and 400 °C (right).[67] (b) Atomic-force microscopy (AFM) picture of sol-gel film containing 30 wt% silicate colloid. Picture area: 55 μm^2. Inset picture shows the chilled water vapor on this film.[68]

et al.[70] produced a ZnO-based surface in a microstructure using chemical processing; after coating, superhydrophobia was achieved using long-chain alkanoic acids (see Figure 32).

3.19.3.4.3 Colloid accumulation and layer method

This is a rich method for manufacturing thin coatings on a molecular scale on the film, and the chemistry used in this method involves static interaction and hydrogen bonding. Recently, the layer-by-layer (LBL) method has been used for manufacturing superhydrophobic rough surfaces.[71–74] For example, Zhai *et al.*[75] used LBL for manufacturing a pH-sensitive multilayer from poly allylamine hydrochloride and poly acrylic acid that forms a beehive structure on the surface after appropriate acid modification. As Zhang *et al.*[71,72,76] revealed, this method can be combined with electrochemical deposition to form superhydrophobic surfaces (Figure 33(a)).

Accumulation via colloid systems shows that the roughness creates an appropriate surface for superhydrophobicity.[77–79] Ming *et al.*[78] prepared a surface with two scales of roughness containing raspberry-shaped particles. These particles were formed from a covalent bond between silica particles in the amine agent group with a size of 70 nm and silica particles of an epoxy agent with a size of 700 nm. The reaction was between the amine groups and epoxy. The surface was superhydrophobic after modification by polydimethylsiloxane (Figure 33(b)).

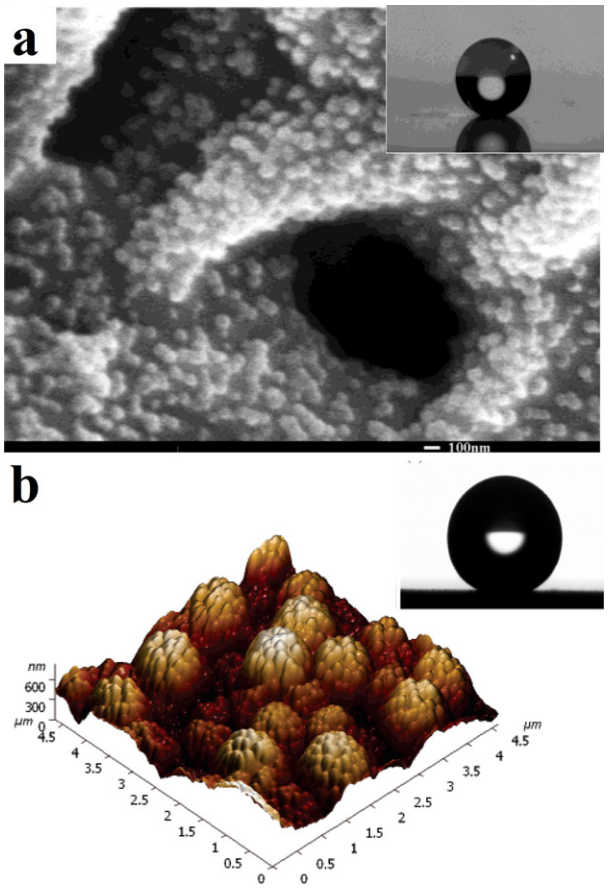


Figure 33 Superhydrophobic surfaces containing two scales of roughness produced by (a) the layer method[75] and (b) the colloid method.[78]

3.19.3.4.4 Electrochemical reaction and deposition method

This method is widely used for the preparation and creation of superhydrophobic surfaces. For example, Zhang *et al.*[76] showed that surfaces that have been coated using the electrochemical deposition method with gold dendritic clusters on an indium–tin oxide electrode and that have been modified using a multilayer poly-electrolyte show superhydrophobic properties after deposition of a single monolayer of *n*-dodecanethiol. Shirtcliff *et al.*[80] produced a copper piece with two scales of roughness using an electroplating and simulation technique. That piece of copper was similar to a 'chocolate with pieces of candy.' More hydrophobizing was performed using fluorocarbons; with superhydrophobizing, a contact angle of 160° was achieved. The Cho group[74] recently created a superhydrophobic surface similar to a lotus leaf using an electrochemical reaction of copper or copper–tin alloy on ferrous plates using sulfur gas and subsequent modification using perfluorosilanes. It should be noted that chemical bed deposition is applied for producing nanostructure surfaces. For example, Hosono *et al.*[81] applied this technique to manufacture a brucite cobalt hydroxide nano-pin, and a contact angle higher than 178° after modification and use of laric acid was achieved (see Figure 34).

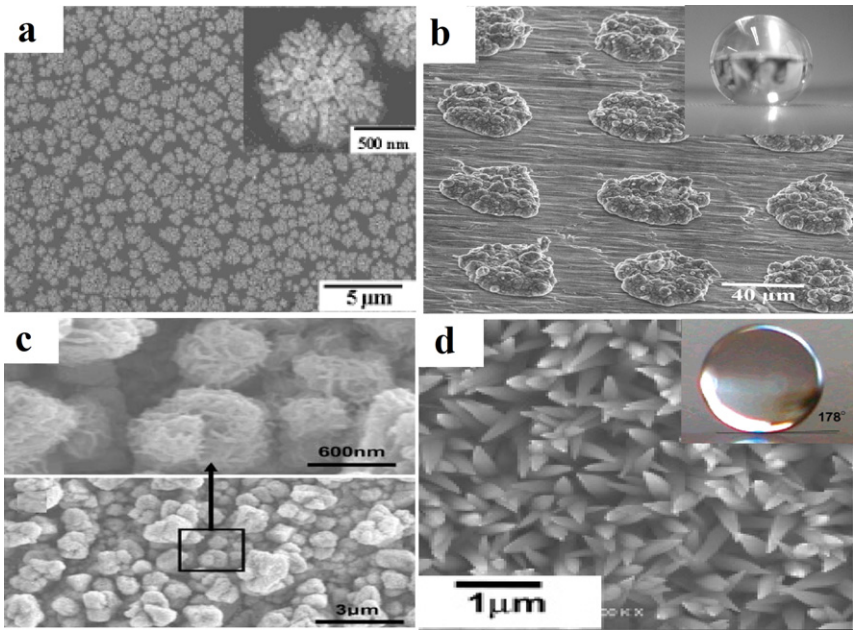


Figure 34 Scanning electron microscope (SEM) image of superhydrophobic surfaces manufactured using electrochemical deposition or chemical bed deposition. (a) Gold cluster produced on indium–tin oxide electrode and modified using a multilayer polyelectrolyte.[76] (b) The surface of copper with two roughness scales and the droplet on it (inset).[80] (c) The surface of the copper after the electrochemical reaction with sulfur gas.[74] (d) Nano-pin of brucite cobalt hydroxide-laric acid and its contact angle (inset).[81]

3.19.3.4.5 Other methods

Electrospinning is a powerful technique for manufacturing very small fibers and has been studied by many groups for its use in manufacturing superhydrophobic surfaces.[82–88] Electrospinning of a hydrophobic material promotes it to a superhydrophobic in one single step. Ma *et al.*[87] showed that superhydrophobia with a high contact angle of 170° can be achieved by applying a thin layer of compact fluorinated polymer coating to the electrospinned samples using incipient chemical vapor deposition. CVD and PVD have been widely used for chemical modification and creation of nanosurfaces. Haung *et al.*[89] created a stable hydrophobic surface that consists of carbon nanotubes that were created using CVD on a catalyst layer of Fe–N. Superhydrophobia was achieved after the creation of the thin layer of ZnO.

3.19.4 The Relationship between Roughness and Surface Wettability

A surface is considered a superhydrophobic surface if the contact angle is approximately 180°. The contact angle depends on many different factors, including surface roughness, preparation method, and cleanliness of the surface.[38,39,90] One of the methods for increasing the hydrophilic and hydrophobic properties is increasing the surface roughness. Wenzel[91] presented a model based on reduction of net energy during droplet extension on the rough surface. A rough surface has a bigger solid–liquid intersection, which results in higher net energy, and this concept will increase the contact angle for a hydrophobic surface and reduce the contact angle for a hydrophilic surface. Another model was represented by Cassie and Baxter[92] that uses a solid–liquid–air interface that can affect the contact angle of very rough surfaces. It has been proven in the laboratory that the roughness that alters the contact angle is in agreement with the Wenzel model. Yost *et al.*[93] found that roughness can increase the wettability of a copper sample with the eutectic weld of tin–lead. This system has a contact angle of 15–20° for flat surfaces. They concluded that the contact angle increases for wetting liquids. Erbil *et al.* measured the contact angle of polypropylene; they found that there is an increase of roughness when the contact angle increases.

In the past decade, scientists focused on natural hydrophobic materials. There are some plants leaves, including lotus, that have a high contact angle with water.[94,95] These leaves are covered with a range of different waxes that are a combination of large hydrocarbon molecules with a thickness of 1 nm and high hydrophobic properties. These surfaces are rough due to the existence of epidermis bump cells, which create inequalities (**Figure 35**). Other examples of biologic surfaces are the wings of a duck and of a butterfly. Their stripy surfaces create some air pockets that prevent complete contact with water. The study and simulation of biological substances are referred to 'biomimetics,' which is derived from the Greek word 'bio mimesis' and means biological imitation. Artificial hydrophobic surfaces can be achieved by chemical modification accompanied by materials with low surface energy, including polytetrafluorothilen, silicones, and waxes, and/or directly from roughening of hydrophobic surfaces.

When two solid materials make contact in the presence of a wetting material, surface tension is usually created. This surface tension results in normal surface tension force that can increase the tangential force of friction. The magnitude of the surface tension force is dependent on the contact inequalities

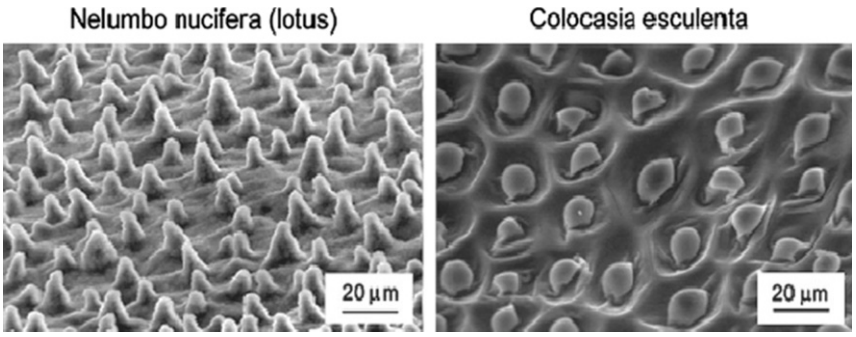


Figure 35 Micrographs of two hydrophobic leaves: *Nelumbo nucifera* (lotus) and *Colocasia esculenta*.[96]

and the diameter inequalities, and these are dependent on roughness, surface tension of the liquid, and the contact angle. The contact angle depends on surface roughness. So, roughness affects the wet friction force. This impact was previously neglected.

3.19.4.1 The Analysis of the Contact Angle

The dependence of the contact angle on the surface tension of the liquid contacting the surface of a rough solid and a flat surface has been considered. Also, the effects of the contact point and sharp edge on the contact angle have been discussed.

3.19.4.1.1 Flat surface

It is well known that the atoms and molecules of the surface of liquids or solids contain higher energy in comparison with bulk atoms or molecules; this results in surface tension or free surface energy and is considered an important surface property. This property can be claimed quantitatively by free surface energy or surface tension that is equal to the equivalent needed work for creation of unit cells at a constant volume and temperature. When a solid contacts a liquid, the molecular interaction decreases the energy to below the energy level for each individual surface. This is claimed by the Dupre equation.

$$W_{SL} = \gamma_{SA} + \gamma_{LA} - \gamma_{SL} \quad [26]$$

where W_{SL} is the work of adhesion in the unit of area between two surfaces, γ_{SL} and γ_{SA} are surface energy (surface tension) of solids against air and liquids, and γ_{LA} is the surface energy of liquid against air.[38,90]

If a droplet of liquid is on the surface of the solid, the surfaces of the liquid and solid maintain equilibrium, and a specific angle called the static contact angle is formed. The contact angle can be identified using the general energy of the system in the minimum state.[90] The total energy, E_{tot}, can be obtained from the following equation:

$$E_{tot} = \gamma_{LA} * (A_{LA} + A_{SL}) - W_{SL} * A_{SL} \quad [27]$$

where A_{LA} and A_{SL} are areas where liquid contacts solid and air. It has been assumed that the droplet is small enough to neglect the potential energy of gravity. In the equilibrium state, dE_{tot} is zero, resulting in the following equation:

$$\gamma_{LA} * (dA_{LA} + dA_{SL}) - W_{SL} * dA_{SL} \quad [28]$$

For a droplet in constant volume, geometrical considerations can be applied:

$$\frac{dA_{LA}}{dA_{SL}} = \cos\theta_0 \quad [29]$$

By combining eqns [26], [28], and [29], the contact angle can be determined with the famous Young equation (eqn [4]).

$$\cos\theta_0 = \frac{\gamma_{SV} - \gamma_{SL}}{\gamma_{LV}} \quad [30]$$

Using eqn [5], the static contact angle can be calculated if the surface tensions are clear.

3.19.4.1.2 Effect of surface area on the contact angle of a rough surface

The Young equation is only applicable for flat solid surfaces. If the surface is rough, then it affects the contact angle in two ways. The first is the increased contact area A_{SL}, and the second is the effect of sharp edges (see **Figure 36**).

If the droplet size is small in comparison with the normal roughness value, then the roughness distribution cannot affect the contact angle. We consider a rough solid surface with the normal value of roughness, which is smaller than the droplet (100 μ or bigger), guarantees the Young equation, and realizes that effective surface tension can be a complicated function of the surface roughness. For a droplet that is placed on the surface, eqn [29] can be modified as:[91]

$$\mathrm{Cos}\,\theta = \frac{dA_{LA}}{dA_F} = \frac{A_{SL}}{A_F} * \frac{dA_{LA}}{dA_{SL}} = R_F \mathrm{Cos}\,\theta_0 \quad [31]$$

where θ is the contact angle of the coarse surface, A_f is the flat contact point of solid–liquid and/or the reflection of the solid–liquid A_{SL} surface on the horizontal surface, and R_f is the roughness factor defined as:

$$R_F = \frac{A_{SL}}{A_F} \quad [32]$$

Equation 31 shows that if the liquid surface wets the solid surface, ($\mathrm{Cos}\theta_0 > 0$), then it can wet the surface with a contact angle of $\theta_0 > \theta$ because $R_f > 1$. In addition, for nonwetting liquids ($\mathrm{Cos}\theta_0 < 0$), the contact angle would be bigger for the rough surfaces in comparison with flat ones ($\theta_0 < \theta$). The

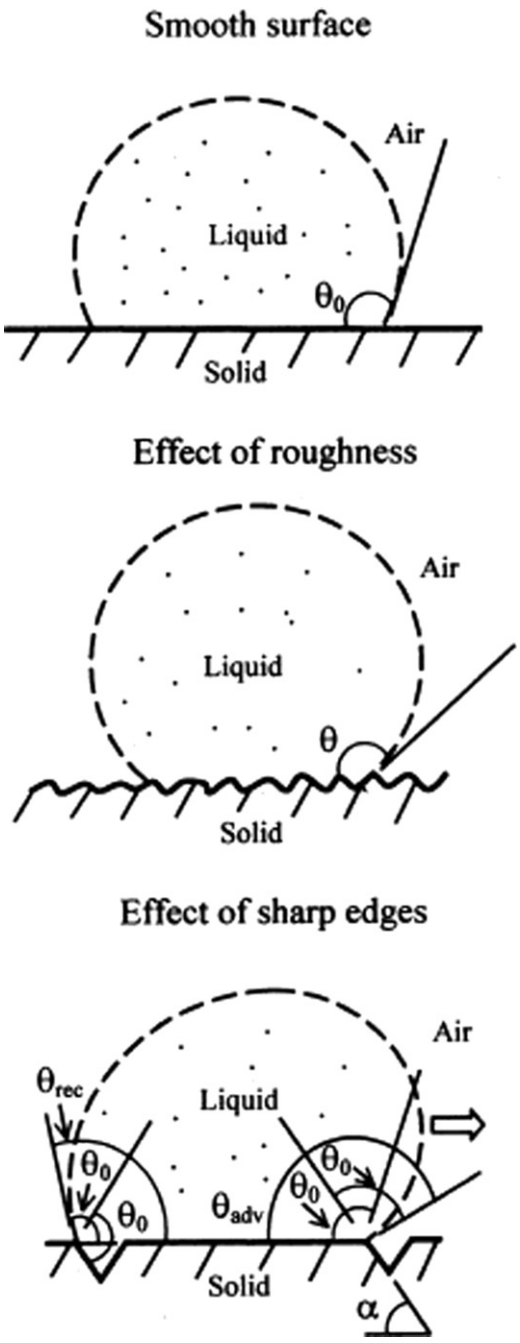


Figure 36 The liquid droplet in contact with a solid flat surface; the contact angle is θ_0. The rough surface, contact angle of θ, and a surface with sharp edges are also show. For a droplet moving on a sharp edge from left to right (declared with the arc), the contact angle on the sharp edge can have any value between the contact angle on the horizontal surface and the sloped surface. This effect can cause the difference in the advancing and receding contact angles.[96]

dependence of the contact angle on the roughness coefficient is represented in **Figure 37** for different values of the θ_0.

3.19.4.1.3 Composite solid–liquid–air interface

It is claimed that the eqn [31] is only qualified for the mean values of R_f when $-1 < R_f \mathrm{Cos}\theta < 1$. With high roughness, a

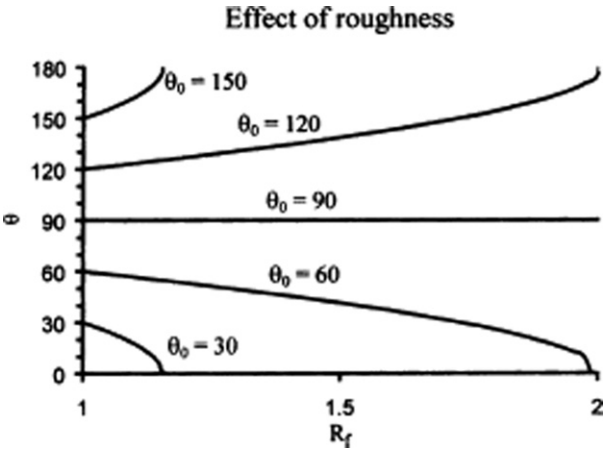


Figure 37 Contact angle for the rough surface (θ) as a function of the roughness factor (R_f) for the contact angles for a flat surface (θ_0).[97]

wetting liquid would be completely absorbed by the holes of the roughness. A nonwetting liquid cannot defuse in the holes with a high slope, which is due to the formation of the air pockets and will result in the creation of a combined intersection of solid–liquid–air, which is shown in **Figure 38(a)** for flat and saw-toothed profiles. The contact point's air–liquid will not increase with an increase of roughness.[98]

The creation of a composite interface of a saw-toothed profile with the slope of α for a flat profile is shown in **Figure 38(a)**. To determine whether the interface is liquid–solid or combined, the pure energy variation dE_{tot} should be considered, which is in agreement with the ds displacement of the liquid–air surface along the sloped wall of the groove. For the liquid–air interface, $dE_{tot} < 0$, from the energy point of view, liquid is most likely to fill the groove. Although for a composite interface, $dE_{tot} > 0$, from the energy point of view, liquid is most likely to leave the groove. The variation of energy is dependent on the α angle, and the critical value of this slope, called α_0, can be calculated using the equation $dE_{tot} = 0$.

$$dE_{tot} = dA_{SL} * \gamma_{SL} + dA_{LA} * \gamma_{LA} = -2\gamma_{LA} \cos\alpha_0 \, ds$$

$$+2(\gamma_{SL} - \gamma_{SA})ds = 0 \qquad [33]$$

By applying eqn [5] in eqn [8], the resulted can be $\mathrm{Cos}\alpha_0 = \mathrm{Cos}\theta_0$.

$$\alpha_0 = 180 - \theta_0 \qquad [34]$$

For small slopes ($\alpha < \alpha_0$), the total energy variation is negative and the intersection is solid. For high slopes ($\alpha > \alpha_0$), this variation is positive and the intersection is combined (as shown in **Figure 38(a)**).

Cassie and Baxter[92] developed the Wenzel equation. The Wenzel equation was developed for the homogenous solid–liquid interface and composite interface. For this purpose there are two interfaces: a liquid–air interface with the surrounding environment and a mixed interface under the droplet, which contains the solid–liquid, liquid–air, and air–solid interfaces. For the area of a geometrical component of a flat interface of solid–liquid and air–liquid under the droplet, φ_{SL} and φ_{LA}, the

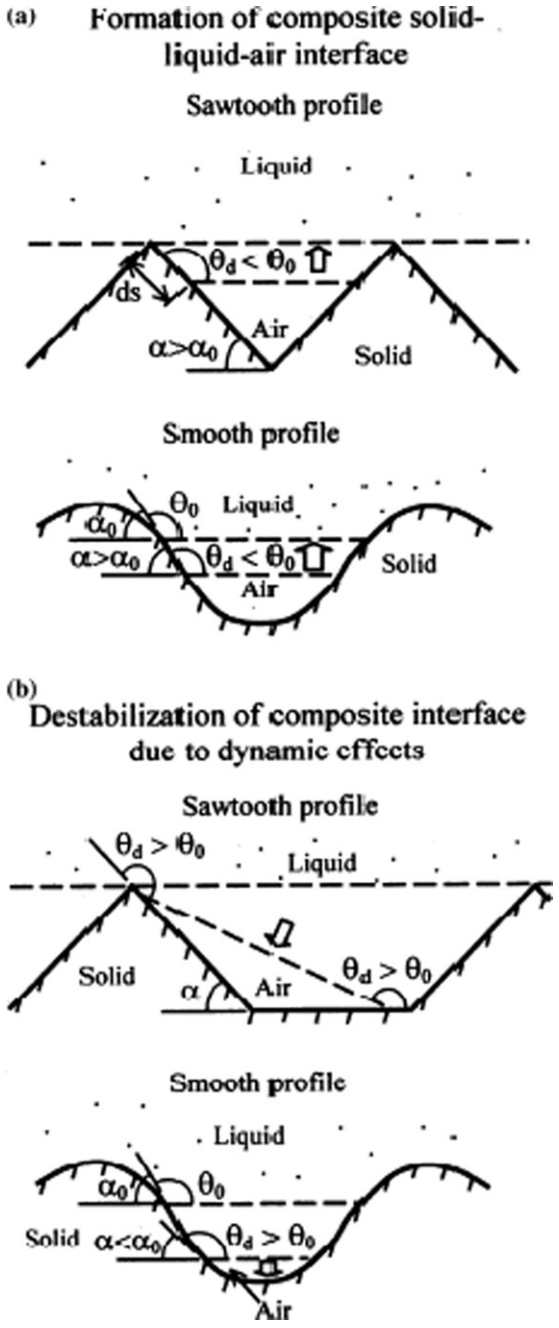


Figure 38 (a) Creation of a combined intersection of solid–liquid–air for saw-toothed and flat profiles. (b) Instability of composite interface for flat and saw-toothed profiles according to dynamic effects. The dynamic contact angle $\theta_d > \theta_0$ is proportional to the advancing liquid–air intersection, whereas $\theta_d < \theta_0$ is proportional to the receding interface.[97]

area of the composite flat interface is equal to:

$$A_C = \varphi_{SL} * A_C + \varphi_{LA} * A_C = R_F A_{SL} + \varphi_{LA} A_C \qquad [35]$$

To calculate the contact angle in a state similar to calculating eqn [31], the differential surfaces of the air–liquid interface under the droplet, $\varphi_{LA}\ dA_c$, should be subtracted from the total differential surface of liquid–air:

$$\cos\theta = R_F * \varphi_{SL} * \cos\theta_0 - \varphi_{LA} \qquad [36]$$

According to eqn [36], for the roughness factor limit, high φ_{SL} approaches zero while φ_{LA} tends toward 1, and as a result θ tends toward 180°. Although the Cassie–Baxter model explains no dependence of φ_{SL} and φ_{LA} on the roughness factor and does not explain under what condition the combined intersection can be created. Johnson and Dieter showed that the combined homogenous interface has a relationship with two semi-stable states of the droplet. Although it might be possible for a system to have a composite interface geometrically, from the energy point of view, it is more likely that liquid penetrates the inequalities and creates a homogenous interface. Marmur[99] formulized the geometrical conditions for a surface in which the energy of the system is comparatively minimum and a composite interface might exist. Patankar[100] suggested that the existence of the interface in a combined or homogenous form is dependent on the history of the system. For example, the droplet is created on the surface or is deposited there. The mentioned analyses are not in agreement with the concept that both homogenous and composite interfaces can exist simultaneously. To investigate the possibility of the creation of the composite interface, stability should be analyzed. It has been assumed that the composite interface is stable, as extracted from the equation. It was assumed that the advancing liquid–air interface stays horizontal. This assumption is difficult to justify when the distances between inequalities are long or when the slope changes are slowed. In these cases, the air–liquid interface can easily be unstable because of imperfections of the profile or dynamic effects such as surface waves. This can result in creation of the homogeneous solid–liquid interface. **Figure 38(b)** shows the instability of the combined interface when there is a long distance between inequalities and when there is a flat profile with liquid filling the groove. In a point of the liquid–air intersection, if the local angle of that point with the surface of solid is higher than θ_0, then eventually the liquid fills the groove. Equation [36] predicts the contact angle; because the possibility of instability has been neglected, development of a random approach with attention given to the probability of an unstable composite interface and other probabilities of semi-stable states has been suggested.

3.19.4.1.4 The effect of edge and variation of surface slope

A sharp edge can pin the interface of the air–liquid–solid (which is known as a triple line). In other words, it can place the interface in a contact angle different than θ_0. This effect has been shown in the discontinuous line of **Figure 36**, in which a droplet displaces among a grooved solid surface. On the edge, the contact angle is not specified and can hold any value between the contact angles of a flat surface or a sloped surface. For a droplet moving from left to right, this triple line is stuck on the edge point until it is able to cross the sloped surface. In **Figure 36**, the variation in the surface slope at the edge is the reason for this sticking. Because of this concept, the advancing contact angle (dynamic advancing contact angle or $\theta_{adv} = \theta_0 + \alpha$) is higher than θ_0, whereas the receding contact angle (dynamic receding contact angle or $\theta_{rec} = \theta_0 + \alpha$) is less than θ_0. This phenomenon is known as the hysteresis of the contact angle.[90,98] The amplitude of the hysteresis is defined as $\theta_{adv} - \theta_{rec}$. The liquid can

easily move along the surface if the hysteresis of the contact angle is a small. In the same conditions, the hysteresis of the contact angle can exist if the slope changes slowly. The transition to the composite interface can decrease the contact area of the liquid–solid. As a result, the liquid would be in contact with solid just during the peak of inequalities and where the slope variation is small and the triple line trapping is less. Therefore, the transition to the composite interface can reduce the hysteresis of the contact angle and the droplet would move easily.

3.19.4.2 Calculation of the Contact Angle for Selected Surfaces and Surface Modification

Figure 39 shows the different roughness profiles of the 2D and 3D surface profiles. According to this analysis, modification of roughness for the contact angle can be performed.

3.19.4.2.1 2D periodic profiles

3.19.4.2.1.1 Saw-toothed periodic profile

We assumed a saw-toothed profile surface with a tooth angle (or the overall slope) of α (see Figure 39). The roughness factor can be calculated by using eqn [7]:

$$R_F = \frac{A_{SL}}{A_F} = (\mathrm{Cos}\ \alpha)^{-1} \qquad [37]$$

By applying eqn [31], the contact angle can be achieved:

$$\mathrm{Cos}\ \theta = \frac{\mathrm{Cos}\ \theta_0}{\mathrm{Cos}\ \alpha} \qquad [38]$$

Increasing the value of α up to the critical value of α_0, represented using eqn [9], transfers the complete contact of liquid–air to the air–liquid–solid interface and eqn [38] can no longer be applied. Appling the value of $\alpha=\alpha_0$ obtained from eqn [34] in eqn [13], the value of θ, which is correlated to α_0, can be attained. The critical value of α_0 can be correlated to the contact angle of 180°. This means that by increasing the angle of the tooth up to the critical value, a surface with an approximate contact angle of 180° for a specific θ_0 can be created. The sharp edge can result in trapping the triple line and a lack of tendency for the creation of a saw-toothed profile. The saw-toothed profile can create the roughness in the direction of the grooves and open head capillary tubes can amplify the wettability, which is undesirable.

3.19.4.2.1.2 Periodic profile

Considering function, the Fourier equation, and the mathematical equations related to it, it can be concluded[101] that a combined intersection can be unstable and eqn [36] cannot be applied. So, the sinus intersection is not proposed for manufacturing superhydrophobic surfaces. In addition, the sinusoidal profile can create roughness in the direction of the grooves and open head capillary tubes can amplify the wettability, which is undesirable (see Figure 39).

3.19.4.2.2 3D surfaces

The profile analysis shows the critical roughness parameters when contact lines are parallel to the grooves. The 3D surfaces of more general practical cases accompanied by different types of roughness are presented here.

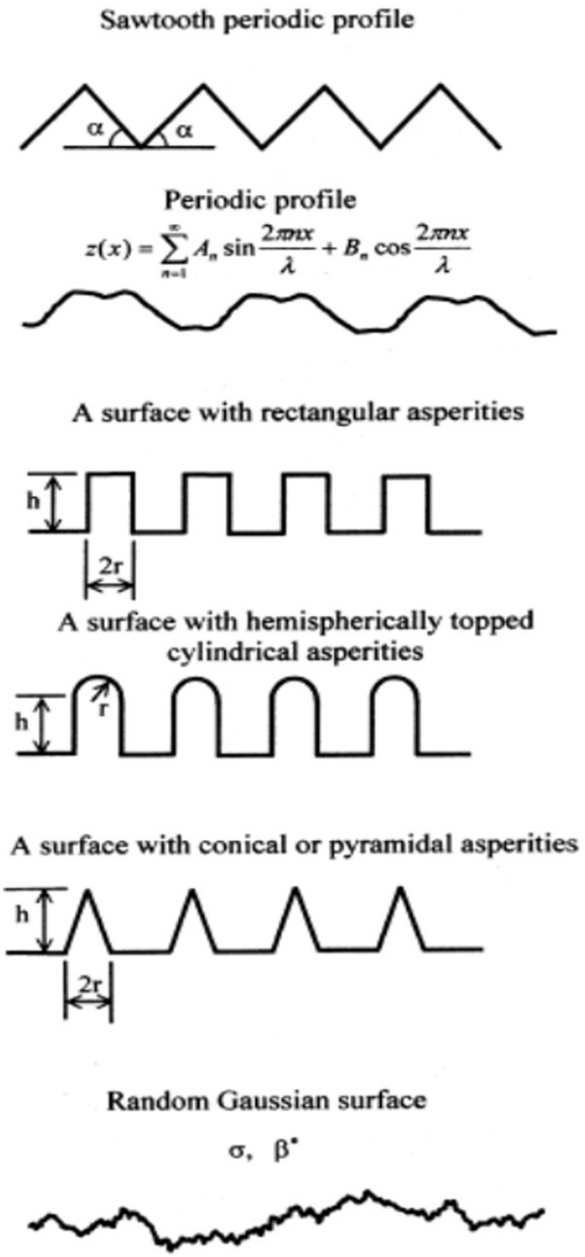


Figure 39 Schematic of the different rough surfaces.[97]

3.19.4.2.2.1 An array of inequalities with the same shapes and sizes

In this section we describe surface profiles that contain inequalities with the same shapes and sizes as rectangular inequalities, formulize the mathematical functions for them, and subsequently calculate the contact angle and roughness factor. It is necessary to introduce parameter η, which is the density of inequalities in the unit of area, and also parameter ρ, which is the parameter of classification and identifies the classification of the inequalities.

To identify the critical values of the roughness parameters of the interface, whether the local slope can achieve a value higher than the critical value of α_0 and whether the interface has a tendency to stabilize should be analyzed. Performing

these analyses is difficult due to the complexity of the problem. It can be approximately determined that by increasing the mean value of the diagram's slope, both parameters of the local slope increase and instability of the intersection decreases because the surface would be less flat. Therefore, we assume that, in a case similar to 2D profile, the absolute value of the line's slope is responsible for the transition to the composite interface of air–liquid–solid; for rectangular, hemispheric head, pyramidal, and conical inequalities, the mean value of the final slope, m, is equal to multiple density inequalities and the flat surface is reflected in the absolute value of the mean slope (which is equal to two values of the slope direction ratio).

$$m = \eta\pi r2(h/r) = \eta\pi hr \qquad [39]$$

The critical value can be obtained using the same trend for eqn [18].

$$m_0 = \eta\pi hr = \tan(180 - \theta_0) = \tan(-\theta_0) \qquad [40]$$

According to the applied equations in this section, for the value of $\theta_0 = 120^\circ$ for rectangular, hemispheric head, pyramidal, and conical profiles, the contact angle tends toward 180° before the critical value of roughness gets to the value of h/r which is shown in **Figure 40**.

The equations in this study are used for calculating the contact angle of the lotus leaf and results are compared to the measured data. The lotus leaf almost has a head of hemispheric inequality and is covered with wax, as shown in **Figure 35**.[94,95] The static contact angle for the droplet of water on the surface of the wax has been a reported to be 104° by Craig[102] and 103° by Kamusewitz.[103] According to the information provided by Wagner,[95] the amount of inequalities in a lotus leaf is approximately 3400 mm^{-2} ($\eta = 0.0034$ μm). The mean diameter of the head of hemispheric inequalities is 10 μm and the ratio of the slope is approximately 1. According to the equations, these

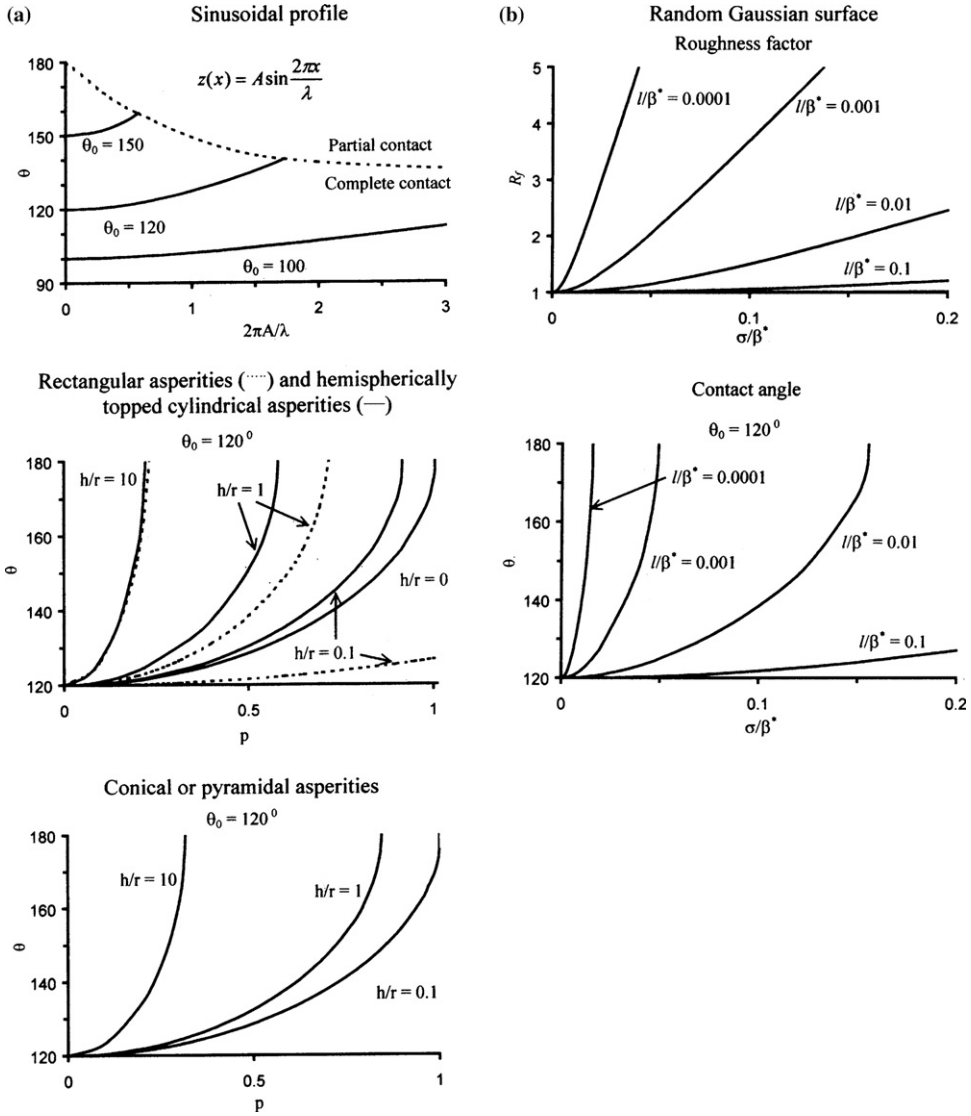


Figure 40 (a) The contact angle of a rough surface (θ) as a function of surface parameters for the surfaces with sinusoidal, rectangular, cylindrical, hemispheric head, pyramidal, and conical profiles. (b) Dependence of roughness factor and the contact angle of a coarse surface on the roughness parameters for a Gaussian surface.[97]

values yield a roughness factor of 4 and a contact angle of 160° (using $\theta_0 = 104°$ for the wax). The contact angle for the droplet of water on the lotus leaf has been reported as 162°.[94]

3.19.4.2.2.2 Random rough surface

A simple, random rough surface can be assumed as the interface of a flat surface, and a 2D random process can be identified using height distribution and correlation function. Many rough natural and engineering surfaces can be identified using a Gaussian height distribution and exponential correlation function.[38,39] In this case, a rough surface can be introduced by standard deviations and two other parameters including: height of inequalities σ and the length of correlation β^*. The length of correlation is a space parameter and can be used as a criterion for the measurement of roughness. This parameter is responsible for horizontal scaling, and σ is used for vertical scaling. The measured roughness is dependent on the limits of measurement of long and short wavelengths.[38,39]

Also, the absolute value of the slope of the Gaussian surface has a Gaussian distribution with a mean value as represented here:

$$m = \frac{\sigma}{I}\sqrt{\frac{1 - \left[\exp\left(-\frac{\beta^*}{L}\right)\right]^2}{\pi}} \qquad [41]$$

where L is the range of samples or the range of short wavelength, which is the distance between the data points during measurement.[104] For a surface, the measurement ranges are given with a limit of wavelength lower than Gaussian roughness and is compared with the atomic scale.

To determine the critical values of the roughness parameters, we assumed that the absolute mean value of the slope is enough for the transition of the air–liquid–solid interface. The critical value of the Gaussian is equal to:

$$m_0 = \left(\frac{\sigma}{L}\sqrt{\frac{1 - \left[\exp\left(-\frac{\beta^*}{L}\right)\right]^2}{\pi}}\right) = \tan(-\theta_0) \qquad [42]$$

Figure 40(b) shows the dependence of the roughness factor on the σ/β^*. It is clear that the roughness factor and the contact angle increase with the increase of σ/β^*. According to eqn [42], it can be shown that for the value of $\theta_0 = 120°$, the contact angle arrives at 180° before the critical parameters of roughness, which has been demonstrated for the values of σ/β^* and L/β^*. It is notable that for most engineered and natural Gaussian surfaces the ratio of $\sigma/\beta^* \ll 0.1$, and the mean value of the slope is very small ($m \ll 1$). So, the more that roughness is lower than the critical value, the more difficult it is achieve the high contact angle with a random Gaussian area with a real value of σ/β^*.

3.19.4.3 Modification of Surfaces to Achieve the Highest Contact Angle

3.19.4.3.1 Modification on the basis of monoscale roughness profiles

Among all the surface types, the highest contact angle can be achieved through the saw-toothed profile, rectangular, spherical head, pyramidal, and conical inequalities. As we predicted, this saw-toothed profile is undesirable due to the sharp edges that might trap the triple line and the grooves that might increase the wettability. Therefore, preventing hysteresis of the contact angle is necessary to prevent the age inequalities with the sharp edges, because they might trap the triple line. The best inequalities are the spherical ones.

Two-tiered roughness that involves two wavelengths has been assumed by some researchers as the agent for reduction of wettability.[105] Nonetheless, this is similar to involving the sharp edges, which is undesirable, and results in instability of the combined intersection of air–liquid–solid.

According to the equations and the results in **Figure 40**, the maximum of the contact angle can be achieved by increasing the ratio of h/r and the scaling parameters of ρ. The maximum value of the slope direction ratio can be achieved by increasing the height of inequality. The maximum of scaling parameters can be achieved by hardening the scaling of inequalities.

The square of scaling parameter, ρ, is equal to the ratio of the ground area of the inequalities to the overall surface area. So, the higher the ρ, the higher the density of the scaling. For circular inequalities, the square of inequalities distribution results in ½ r scaling of the rows in the unit of area with ½ r of inequalities in the unit of length of each row. More density of the scaling of inequalities can be achieved using a hexagonal distribution of inequalities (see **Figure 41**). This distribution pattern can result in the scaling of $1/\sqrt{3}\ r$ of the inequality rows in the unit of length with the ½ r inequality or $\eta = \frac{1}{2\sqrt{3}r}$, resulting in:

$$\rho = r\sqrt{\pi\eta} = \sqrt{\frac{\pi}{2\sqrt{3}}} = 0.952 \qquad [43]$$

Therefore, it can be advised that for the modification of surfaces, spherical head inequalities with a hexagonal scale and a high slope direction ratio should be used. It has been mentioned that some plants have a tendency for inequality distribution similar to hexagonal distribution.

Another shape that creates scaling density is pyramidal inequality with a squared base. To prevent the sharp edges, the

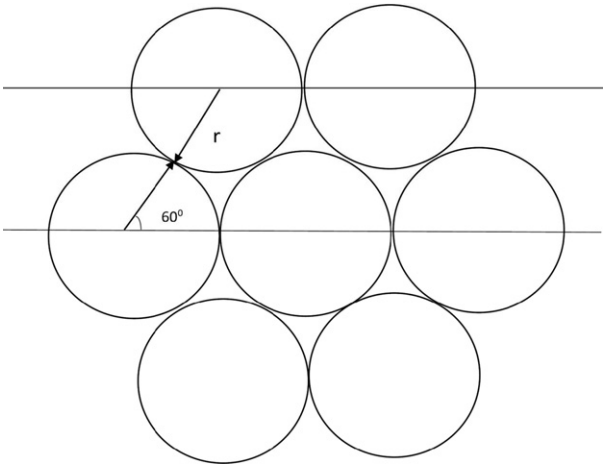


Figure 41 Hexagonal pattern of circular inequality scaling for the highest density of scaling.

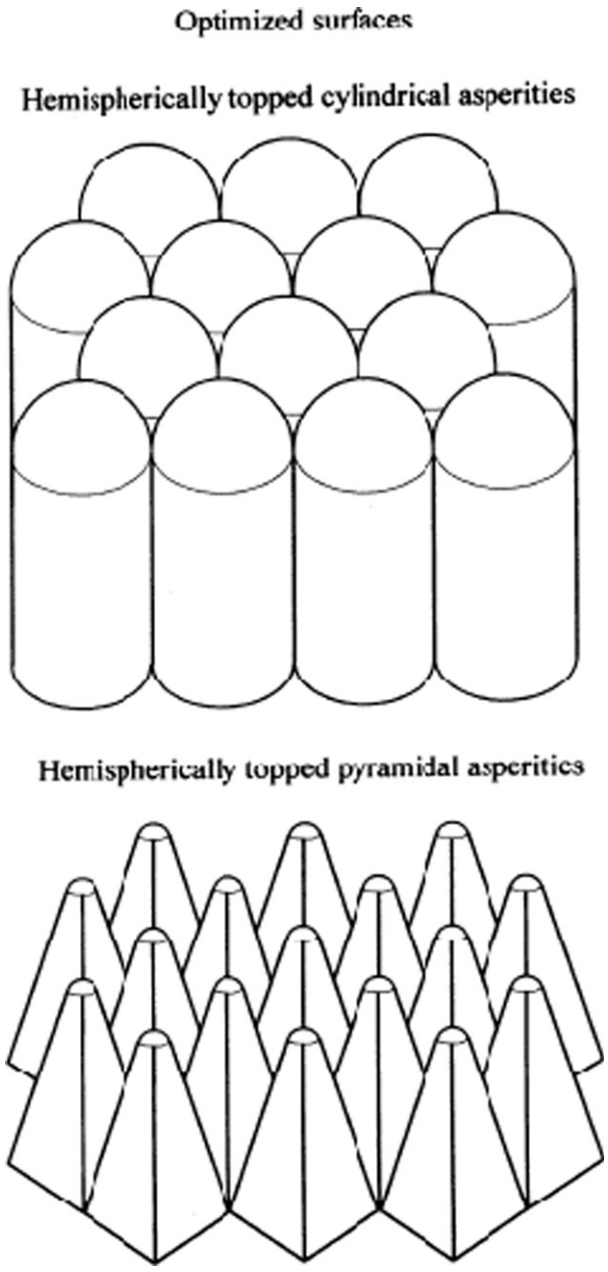


Figure 42 The modified distribution of cylindrical hemispherical head inequalities and pyramidal inequalities with the squared base and rounded heads. The squared bases provide higher scaling density but involve unwanted sharp edges.[96]

head of inequalities should be rounded to the hemispherical shape (see **Figure 42**). The rectangular inequalities do not provide any space for the diffusion of liquids. So, for the inequalities with the square base, the pyramidal shape should be used. It should be mentioned that valleys with round edges have the same effect as inequalities on the contact angle.

The diameter of the specific inequalities, r for a circular base or $2r$ for a square base, should be small in comparison with normal droplets. The high limit of the droplet size can be estimated according to this necessity because the effect of gravity is small in comparison with the surface tension (a bigger droplet tends to be divided into many small droplets). The gravimetric energy of the droplet is given by the density, ρ, which is multiplied by volume, the constant of gravity, and diameter.

$$W_g = \left(\frac{4}{3}\right)\pi r^3 \rho g r \qquad [44]$$

The energy related to the surface tension can be calculated by multiplying the area of the surface in the surface tension:

$$W_S = 4\pi r^2 \gamma_{LA} \qquad [45]$$

Because $W_g \ll W_s$, the maximum diameter of the droplet can be calculated as:

$$r_{max} \ll \sqrt{\frac{3\gamma_{LA}}{\rho g}} \qquad [46]$$

The usual quantities of water, $\rho = 1000\ \mathrm{kg\ m^{-3}}$ and $\gamma_{LA} = 72\ \mathrm{mJ\ m^{-2}}$, result in $r_{max} \ll 4.7$ mm. Although these little droplets tend to unite and create bigger droplets, the minimum diameter of the droplet only limits the molecular scale; therefore, it is desirable for r to be as small as possible.

Briefly, it can be said that the highest contact angle and the lowest hysteresis of the contact angle can be obtained by hemispherical head inequalities with the scaling pattern of hexagonal or pyramidal inequalities with rounded heads. These suggestions can be used for manufacturing superhydrophobic surfaces.

For wetting, the roughness of the liquid can reduce the contact angle according to eqn [31]. So, for manufacturing superhydrophobic surfaces by using the roughness effect, a hydrophobic layer (film) is needed. The hydrophobic coating is a known method of increasing the hydrophobia of materials.[106]

3.19.4.3.2 Modification on the basis of multiscaled roughness profiles

The effects of multiscaled roughness (hierarchical) on the modification of superhydrophobic structures of solid surfaces have been studied theatrically. Three kinds of alternative surface topography have been demonstrated regarding the effects of additional roughness scales on the transition contact angle of wet surfaces. This can be performed by calculation of the Gibbs energy of a droplet, which is dependent on the position of the liquid–air interface inside the grooves and the geometry of the contact angle (the contact angle has been considered a variable for Gibbs energy). In this study the wetting system is considered a 2D system that contains a cylindrical droplet on a 2D rough surface that is chemically homogeneous. The selection of this system is due to the ease of calculations. The qualitative results of 2D calculations have been compared to the 3D reality.[107,108]

Three roughness topography includes sinusoidal bumps with three roughness scales, flat head rods with three roughness scales, and self-similarity and triadic Koch with four roughness scales. The geometrical details have been shown in **Figure 43**. These topographies have been selected because they

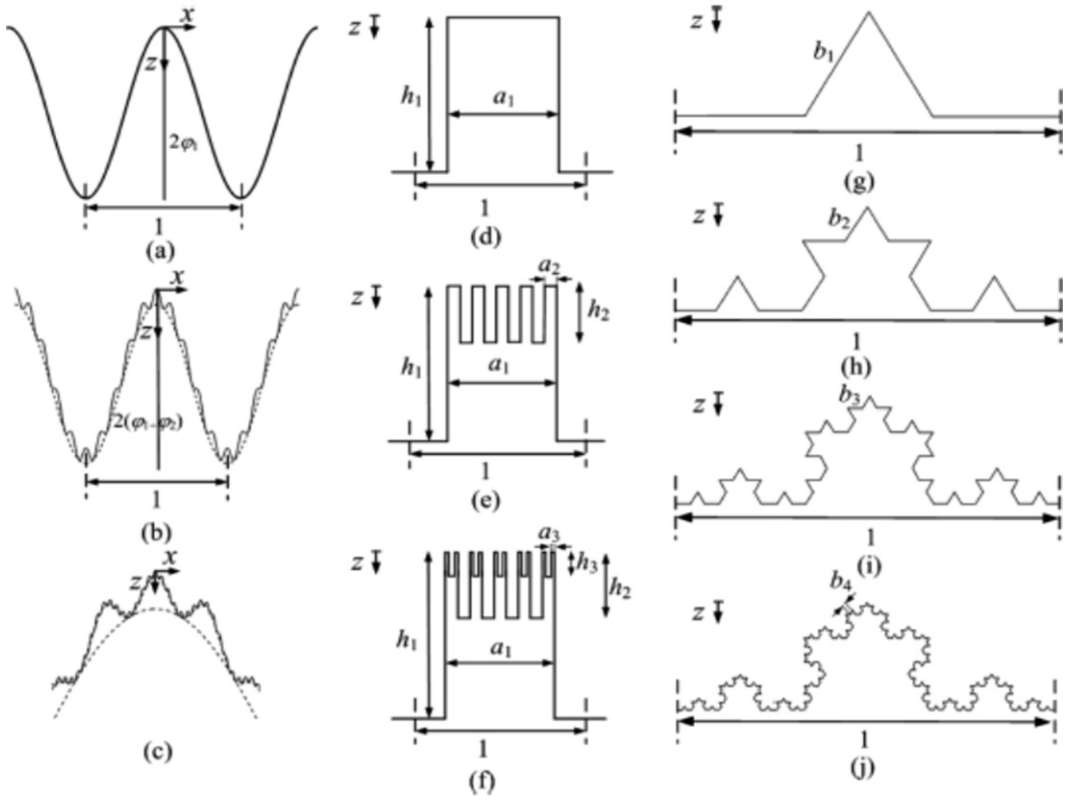


Figure 43 The unique topography cells of 2D solid surfaces. Three scales of sinusoidal surface topography are shown (a–c). (c) Picture has been magnified in comparison with the two other pictures. Three scales of flat head rods are shown (d–f). Four scales of roughness of the artificial surface of triadic Koch are shown (g–j).[117]

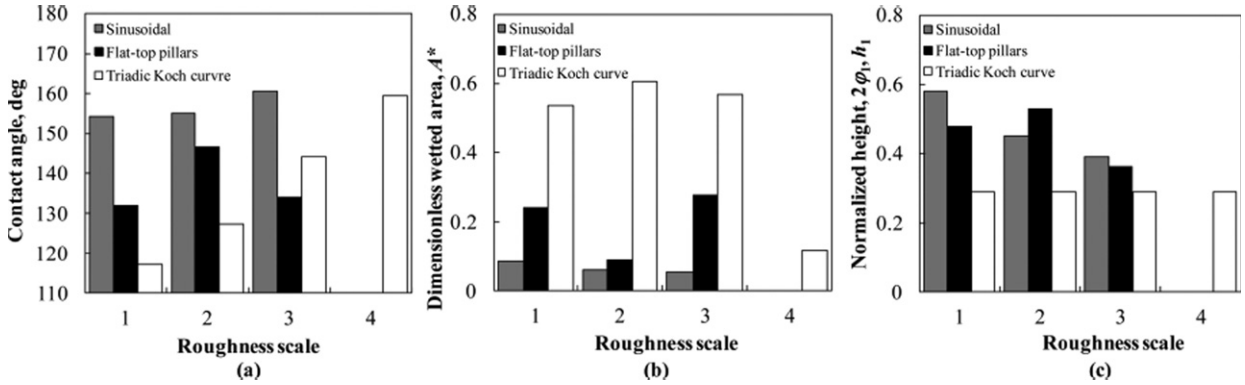


Figure 44 Comparison between three topographies in the transition point and between the Wenzel and Cassie–Baxter states, but not for the triadic Koch diagram because the transition point is not clearly identified. (a) The most stable contact angles. (b) Scale of less wetted areas. (c) Height of roughness composition.[117]

exist in nature as well as in artificial sensitized surfaces. The sinusoidal topography is similar to lotus leaf inequalities and is produced using microscaled techniques with different scales of roughness. The topography of flat head rods is widely used for modification to achieve a high contact angle and low contact angle hysteresis.[109–114] The triadic Koch diagram is a fractal example that has been analyzed to investigate whether the fractal nature can result in unique properties.[115,116]

An important practical criterion for nonwettability is the wetted area (the contact angle of liquid–air), which identifies the ability of sliding on the surface. This wetted surface is usually smaller (or much smaller) in the Cassie–Baxter state wettability equation in comparison to the Wenzel state, even when the contact angles are equal. These wetted surfaces might be difficult to measure in laboratory conditions (usually the sliding angle is reported), but with design calculations they can be explained.

The second important criterion for nonwettability is the thermodynamical stability of the Cassie–Baxter state in comparison with the Wenzel state. The transition point between

these states, according to stability, occurs when the contact angles are equal. This transition angle is the main criterion because the contact angle of the design surface must be equal to or higher than the transition angle. This might be difficult in some cases, including the triadic Koch diagram because of the impossibility of detecting the exact transition point because the variables might not be continuous (see **Figure 44**).

The mechanical stability of rough surfaces is dependent on the height of the roughness among all other parameters. Therefore, height is an important parameter that should be considered.

The modification of the design for a hydrophobic surface is a complicated process that contains many other parameters. Also, the modification process should begin with identifying the lowest wetted surface and the lowest values of properties in the transition contact angle.

By increasing the quantity of roughness scales, the following differences occur in 2D systems: (1) for sinusoidal surfaces, the transition contact angle slowly increases and the wetted surface slowly decreases, but the composition of the roughness significantly increases; (2) for flat head rods, the variations are not uniform; the minimum of the wetted surface is achieved at the maximum of the contact angle, but in the maximum of the height the composition of the roughness can be attained; and (3) for roughness of the triadic Koch diagram, according to the definition, the high property is constant and the Cassie–Baxter state is only stable when four scales of roughness exist.

3.19.5 Conclusion

By comparing three 2D topographies, it can be concluded that multiscaled roughness is better, but this strongly depends on the geometrical basis of the roughness. Therefore, there is no guarantee for the benefit of multiscale roughness. Among all the studied examples, sinusoidal topography is the most applicable because it has the lowest contact surface and the highest contact angle, and has height similar to that of other topographies. This conclusion is similar to the previous conclusion regarding single-scale roughness. This is in agreement with the superhydrophobic surfaces in the nature, including the bumps of the lotus leaf. Generally, it seems that the round headed properties are more beneficial in comparison with sharp edges for superhydrophobicity.

See also: 3.9 Hydrophobicity and Surface Finish

References

1. Tohidi, N. Thermodynamic of Metallurgical Engineering & Materials, Tehran University **2003**, *3*, 175–178.
2. Shirtcliffe, N. J.; *et al.* An Introduction to Superhydrophobicity. *Adv. Colloid Interface* **2010**, *161* (1), 124–138.
3. Marmur, A. Hydro-Hygro-Oleo-Omni-Phobic? Terminology of Wettability Classification. *Soft Matter* **2012**, *8* (26), 6867–6870.
4. Ma, M.; Hill, R. M. Superhydrophobic Surfaces. *Curr. Opin. Colloid Interface Sci.* **2006**, *11* (4), 193–202.
5. Latthe, S. S.; *et al.* Superhydrophobic Surfaces Developed by Mimicking Hierarchical Surface Morphology of Lotus Leaf. *Molecules* **2014**, *19* (4), 4256–4283.
6. Cao, L. *Superhydrophobic Surface: Design, Fabrication, and Applications*; University of Pittsburgh: Pittsburgh, PA, 2011.
7. Kim, B.; *et al.* Stable Superhydrophobic Si Surface Produced by Using Reactive Ion Etching Process Combined with Hydrophobic Coatings. *Surf. Coat. Tech.* **2013**, *232*, 928–935.
8. Hwang, H. S.; Lee, S. B.; Park, I. Fabrication of Raspberry-Like Superhydrophobic Hollow Silica Particles. *Mater. Lett.* **2010**, *64* (20), 2159–2162.
9. Latthe, S. S.; *et al.* Superhydrophobic Silica Films by Sol–Gel Co-Precursor Method. *Appl. Surf. Sci.* **2009**, *256* (1), 217–222.
10. Woodward, I.; *et al.* Micropatterning of Plasma Fluorinated Super-Hydrophobic Surfaces. *Plasma Chem. Plasma Process.* **2006**, *26* (5), 507–516.
11. Ofir, Y.; *et al.* Controlled Fluorination of FePt Nanoparticles: Hydrophobic to Superhydrophobic Surfaces. *Adv. Mater.* **2007**, *19* (22), 4075–4079.
12. Nosonovsky, M.; Bhushan, B. *Multiscale Dissipative Mechanisms and Hierarchical Surfaces: Friction, Superhydrophobicity, and Biomimetics*; Springer Science & Business Media: Heidelberg, 2008.
13. Nosonovsky, M.; Bhushan, B. Patterned Nonadhesive Surfaces: Superhydrophobicity and Wetting Regime Transitions. *Langmuir* **2008**, *24* (4), 1525–1533.
14. Mittal, K. L. *Contact Angle, Wettability and Adhesion*, Vol. 4; CRC Press: Boca Raton, FL, 2006.
15. Pogorzelski, S. J.; *et al.* A Novel Methodology Based on Contact Angle Hysteresis Approach for Surface Changes Monitoring in Model PMMA-Corega Tabs System. *Appl. Surf. Sci.* **2012**, *258* (8), 3652–3658.
16. Stiller, S.; *et al.* Investigation of the Stability in Emulsions Stabilized with Different Surface Modified Titanium Dioxides. *Colloid Surface A* **2004**, *232* (2), 261–267.
17. Blumenau, M.; *et al.* Wetting and Reactive Wetting During Hot-Dip Galvanizing of High Mn alloyed Steel with Zn–Al–Mg Baths. *Surf. Coat. Tech.* **2012**, *206* (19), 4194–4201.
18. Xie, X.; Morrow, N. R.; Buckley, J. S. Contact Angle Hysteresis and the Stability of Wetting Changes Induced by Adsorption from Crude Oil. *J. Petrol. Sci. Eng.* **2002**, *33* (1), 147–159.
19. Muster, T. H.; Neufeld, A. K.; Cole, I. S. The Protective Nature of Passivation Films on Zinc: Wetting and Surface Energy. *Corros. Sci.* **2004**, *46* (9), 2337–2354.
20. Bendure, R. L. Dynamic Adhesion Tension Measurement. *J. Colloid Interface Sci.* **1973**, *42* (1), 137–144.
21. Gindl, M.; *et al.* A Comparison of Different Methods to Calculate the Surface Free Energy of Wood Using Contact Angle Measurements. *Colloid Surface A* **2001**, *181* (1), 279–287.
22. Di Mundo, R.; Palumbo, F. Comments Regarding 'An Essay on Contact Angle Measurements'. *Plasma Process. Polym.* **2011**, *8* (1), 14–18.
23. Hsieh, C.-T.; Wu, F.-L.; Chen, W.-Y. Sliding Behavior of Oil Droplets on Nanosphere Stacking Layers with Different Surface Textures. *Appl. Surf. Sci.* **2010**, *256* (23), 7253–7259.
24. Extrand, C. A Thermodynamic Model for Wetting Free Energies from Contact Angles. *Langmuir* **2003**, *19* (3), 646–649.
25. He, T.; *et al.* Super-Hydrophobic Surface Treatment as Corrosion Protection for Aluminum in Seawater. *Corros. Sci.* **2009**, *51* (8), 1757–1761.
26. Ulman, A. Formation and Structure of Self-Assembled Monolayers. *Chem. Rev.* **1996**, *96* (4), 1533–1554.
27. Brassard, J.-D.; Sarkar, D.; Perron, J. Fluorine Based Superhydrophobic Coatings. *Appl. Sci.* **2012**, *2* (2), 453–464.
28. Feng, L.; *et al.* Superhydrophobic Alumina Surface Based on Stearic Acid Modification. *Appl. Surf. Sci.* **2011**, *257* (9), 3959–3963.
29. Wu, R. M.; *et al. Fabrication of a Super-Hydrophobic Micro-Nanoporous Aluminum Surface by Anodic Oxidation*; *Applied Mechanics and Materials*; Trans Tech Publ, 2012.
30. Huang, Y.; Sarkar, D.; Chen, X.-G. A One-Step Process to Engineer Superhydrophobic Copper Surfaces. *Mater. Lett.* **2010**, *64* (24), 2722–2724.
31. Zhang, J.; Zhang, J. A Facile Method for Preparing a Non-Adhesive Superhydrophobic Zno Nanorod Surface. *Mater. Lett.* **2013**, *93*, 386–389.
32. Wang, Y.; Li, B.; Xu, C. Fabrication of Superhydrophobic Surface of Hierarchical ZnO Thin Films by Using Stearic Acid. *Superlattices Microstruct.* **2012**, *51* (1), 128–134.
33. Li, Y.; *et al.* Fabrication of Hierarchical ZnO Architectures and Their Superhydrophobic Surfaces with Strong Adhesive Force. *Inorg. Chem.* **2008**, *47* (8), 3140–3143.
34. Li, Y.; *et al.* Superhydrophobic Bionic Surfaces with Hierarchical Microsphere/SWCNT Composite Arrays. *Langmuir* **2007**, *23* (4), 2169–2174.

35. Wang, Y.; *et al.* Super-Hydrophobic Surface on Pure Magnesium Substrate by Wet Chemical Method. *Appl. Surf. Sci.* **2010**, *256* (12), 3837–3840.
36. Wang, S.; Feng, L.; Jiang, L. One-Step Solution-Immersion Process for the Fabrication of Stable Bionic Superhydrophobic Surfaces. *Adv. Mater.* **2006**, *18* (6), 767–770.
37. Sarkar, D.; Saleema, N. One-Step Fabrication Process of Superhydrophobic Green Coatings. *Surf. Coat. Tech.* **2010**, *204* (15), 2483–2486.
38. Bharat, B. *Principles and Applications of Tribology*, 2nd ed.; Wiley: New York, NY, 1999.
39. Bhushan, B. *Introduction to Tribology*; John Wiley & Sons: New York, NY, 2002.
40. Nabiyouni, G.; Farahani, B. J. Anomalous Scaling in Surface Roughness Evaluation of Electrodeposited Nanocrystalline Pt Thin Films. *Appl. Surf. Sci.* **2009**, *256* (3), 674–682.
41. Bhushan, B. *Handbook of Micro/Nano Tribology*; CRC Press: Boca Raton, FL, 1998.
42. Bhushan, B. *Introduction to Nanotribology and Nanomechanics*; Springer: Berlin; Heidelberg; New York, NY, 2005.
43. Thomas, T. *Rough Surfaces*; Longman: London; New York, NY, 1982.
44. Sharifi-viand, A.; Mahjani, M. G.; Jafarian, M. Determination of Fractal Rough Surface of Polypyrrole Film: AFM and Electrochemical Analysis. *Synth. Met.* **2014**, *191*, 104–112.
45. Archard, J. Elastic Deformation and the Laws of Friction. In *Proceedings of the Royal Society of London A: Mathematical, Physical and Engineering Sciences*; The Royal Society, 1957.
46. Jiang, Y.; *et al.* Influence of Geometrical Distribution of Rock Joints on Deformational Behavior of Underground Opening. *Tunn. Undergr. Sp. Tech.* **2006**, *21* (5), 485–491.
47. Gagnepain, J.; Roques-Carmes, C. Fractal Approach to Two-Dimensional and Three-Dimensional Surface Roughness. *Wear* **1986**, *109* (1), 119–126.
48. Ganti, S.; Bhushan, B. Generalized Fractal Analysis and Its Applications to Engineering Surfaces. *Wear* **1995**, *180* (1), 17–34.
49. Ling, F. F. Scaling Law for Contoured Length of Engineering Surfaces. *J. Appl. Phys.* **1987**, *62* (6), 2570–2572.
50. Majumdar, A.; Bhushan, B. Role of Fractal Geometry in Roughness Characterization and Contact Mechanics of Surfaces. *J. Tribol.* **1990**, *112* (2), 205–216.
51. Majumdar, A.; Bhushan, B. Fractal Model of Elastic-Plastic Contact between Rough Surfaces. *J. Tribol.* **1991**, *113* (1), 1–11.
52. Mandelbrot, B. B.; Passoja, D. E.; Paullay, A. J. Fractal Character of Fracture Surfaces of Metals. *Nature* **1984**, *308*, 721–722.
53. Zou, M.; *et al.* A Monte Carlo Method for Simulating Fractal Surfaces. *Physica A* **2007**, *386* (1), 176–186.
54. Shiu, J.-Y., Kuo, C.-W., Chen, P. Fabrication of Tunable Superhydrophobic Surfaces. in Smart Materials, Nano-, and Micro-Smart Systems. In *Proceedings of the SPIE 5648, Smart Materials III*; International Society for Optics and Photonics, 2004; p. 325.
55. Teshima, K.; *et al.* Transparent Ultra Water-Repellent Poly (Ethylene Terephthalate) Substrates Fabricated by Oxygen Plasma Treatment and Subsequent Hydrophobic Coating. *Appl. Surf. Sci.* **2005**, *244* (1), 619–622.
56. Jin, M.; *et al.* Super-Hydrophobic PDMS Surface with Ultra-Low Adhesive Force. *Macromol. Rapid Comm.* **2005**, *26* (22), 1805–1809.
57. Song, X.; *et al.* Fabrication of Superhydrophobic Surfaces by Self-Assembly and Their Water-Adhesion Properties. *J. Phys. Chem. B* **2005**, *109* (9), 4048–4052.
58. Qian, B.; Shen, Z. Fabrication of Superhydrophobic Surfaces by Dislocation-Selective Chemical Etching on Aluminum, Copper, and Zinc Substrates. *Langmuir* **2005**, *21* (20), 9007–9009.
59. Guo, Z.; *et al.* Stable Biomimetic Super-Hydrophobic Engineering Materials. *J. Am. Chem. Soc.* **2005**, *127* (45), 15670–15671.
60. Fürstner, R.; *et al.* Wetting and Self-Cleaning Properties of Artificial Superhydrophobic Surfaces. *Langmuir* **2005**, *21* (3), 956–961.
61. Callies, M.; *et al.* Microfabricated Textured Surfaces for Super-Hydrophobicity Investigations. *Microelectron Eng.* **2005**, *78*, 100–105.
62. Abdelsalam, M. E.; *et al.* Wetting of Regularly Structured Gold Surfaces. *Langmuir* **2005**, *21* (5), 1753–1757.
63. Martines, E.; *et al.* Super-Hydrophobicity and Superhydrophilicity of Regular Nanopatterns. *Nano Lett.* **2005**, *5* (10), 2097–2103.
64. Notsu, H.; *et al.* Super-Hydrophobic/Super-Hydrophilic Patterning of Gold Surfaces by Photocatalytic Lithography. *J. Mater. Chem.* **2005**, *15* (15), 1523–1527.
65. Feng, X.; *et al.* Reversible Super-Hydrophobicity to Super-Hydrophilicity Transition of Aligned ZnO Nanorod Films. *J. Am. Chem. Soc.* **2004**, *126* (1), 62–63.
66. Feng, X.; Zhai, J.; Jiang, L. The Fabrication and Switchable Superhydrophobicity of TiO_2 Nanorod Films. *Angew. Chem. Int. Ed.* **2005**, *44* (32), 5115–5118.
67. Shirtcliffe, N. J.; *et al.* Porous Materials Show Superhydrophobic to Superhydrophilic Switching. *Chem. Commun.* **2005**, *25*, 3135–3137.
68. Hikita, M.; *et al.* Super-Liquid-Repellent Surfaces Prepared by Colloidal Silica Nanoparticles Covered with Fluoroalkyl Groups. *Langmuir* **2005**, *21* (16), 7299–7302.
69. Shang, H.; *et al.* Optically Transparent Superhydrophobic Silica-Based Films. *Thin Solid Films* **2005**, *472* (1), 37–43.
70. Wu, X.; Zheng, L.; Wu, D. Fabrication of Superhydrophobic Surfaces from Microstructured ZnO-based Surfaces Via a Wet-Chemical Route. *Langmuir* **2005**, *21* (7), 2665–2667.
71. Shi, F.; Wang, Z.; Zhang, X. Combining a Layer-by-Layer Assembling Technique with Electrochemical Deposition of Gold Aggregates to Mimic the Legs of Water Striders. *Adv. Mater.* **2005**, *17* (8), 1005–1009.
72. Zhao, N.; *et al.* Combining Layer-by-Layer Assembly with Electrodeposition of Silver Aggregates for Fabricating Superhydrophobic Surfaces. *Langmuir* **2005**, *21* (10), 4713–4716.
73. Jisr, R. M.; Rmaile, H. H.; Schlenoff, J. B. Hydrophobic and Ultrahydrophobic Multilayer Thin Films from Perfluorinated Polyelectrolytes. *Angew. Chem. Int. Ed.* **2005**, *44* (5), 782–785.
74. Han, J. T.; *et al.* Fabrication of a Bionic Superhydrophobic Metal Surface by Sulfur-Induced Morphological Development. *J. Mater. Chem.* **2005**, *15* (30), 3089–3092.
75. Zhai, L.; *et al.* Stable Superhydrophobic Coatings from Polyelectrolyte Multilayers. *Nano Lett.* **2004**, *4* (7), 1349–1353.
76. Zhang, X.; *et al.* Polyelectrolyte Multilayer as Matrix for Electrochemical Deposition of Gold Clusters: Toward Super-Hydrophobic Surface. *J. Am. Chem. Soc.* **2004**, *126* (10), 3064–3065.
77. Shiu, J.-Y.; *et al.* Fabrication of Tunable Superhydrophobic Surfaces by Nanosphere Lithography. *Chem. Mat.* **2004**, *16* (4), 561–564.
78. Ming, W.; *et al.* Superhydrophobic Films from Raspberry-Like Particles. *Nano Lett.* **2005**, *5* (11), 2298–2301.
79. Zhang, G.; *et al.* Fabrication of Superhydrophobic Surfaces from Binary Colloidal Assembly. *Langmuir* **2005**, *21* (20), 9143–9148.
80. Shirtcliffe, N. J.; *et al.* Dual-Scale Roughness Produces Unusually Water-Repellent Surfaces. *Adv. Mater.* **2004**, *16* (21), 1929–1932.
81. Hosono, E.; *et al.* Superhydrophobic Perpendicular Nanopin Film by the Bottom-Up Process. *J. Am. Chem. Soc.* **2005**, *127* (39), 13458–13459.
82. Singh, A.; Steely, L.; Allcock, H. R. Poly [Bis (2, 2, 2-trifluoroethoxy) Phosphazene] Superhydrophobic Nanofibers. *Langmuir* **2005**, *21* (25), 11604–11607.
83. Ma, M.; *et al.* Electrospun Poly (Styrene-Block-Dimethylsiloxane) Block Copolymer Fibers Exhibiting Superhydrophobicity. *Langmuir* **2005**, *21* (12), 5549–5554.
84. Jiang, L.; Zhao, Y.; Zhai, J. A Lotus-Leaf-Like Superhydrophobic Surface: A Porous Microsphere/Nanofiber Composite Film Prepared by Electrohydrodynamics. *Angew. Chem.* **2004**, *116* (33), 4438–4441.
85. Acatay, K.; *et al.* Tunable, Superhydrophobically Stable Polymeric Surfaces by Electrospinning. *Angewandte Chemie International Edition* **2004**, *43* (39), 5210–5213.
86. Gu, Z.-Z.; *et al.* Artificial Silver Ragwort Surface. *Appl. Phys. Lett.* **2005**, *86* (20), 201915.
87. Ma, M.; *et al.* Superhydrophobic Fabrics Produced by Electrospinning and Chemical Vapor Deposition. *Macromolecules* **2005**, *38* (23), 9742–9748.
88. Shang, H.; *et al.* Nanostructured Superhydrophobic Surfaces. *J. Mater. Sci.* **2005**, *40* (13), 3587–3591.
89. Huang, L.; *et al.* Stable Superhydrophobic Surface Via Carbon Nanotubes Coated with a ZnO Thin Film. *J. Phys. Chem. B* **2005**, *109* (16), 7746–7748.
90. Israelachvili, J. N. *Intermolecular and Surface Forces: With Applications to Colloidal and Biological Systems (Colloid Science)*; Academic Press: London, 1992.
91. Wenzel, R. N. Resistance of Solid Surfaces to Wetting by Water. *Ind. Eng. Chem.* **1936**, *28* (8), 988–994.
92. Cassie, A.; Baxter, S. Wettability of Porous Surfaces. *J. Chem. Soc.* **1944**, *40*, 546–551.
93. Yost, F.; Michael, F.; Eisenmann, E. Extensive Wetting Due to Roughness. *Acta. Metall. Mater.* **1995**, *43* (1), 299–305.

94. Neinhuis, C.; Barthlott, W. Characterization and Distribution of Water-Repellent, Self-Cleaning Plant Surfaces. *Ann. Bot.* **1997**, *79* (6), 667–677.
95. Wagner, P.; *et al.* Quantitative Assessment to the Structural Basis of Water Repellency in Natural and Technical Surfaces. *J. Exp. Bot.* **2003**, *54* (385), 1295–1303.
96. Bhushan, B. Nanotribology and Nanomechanics of MEMS/NEMS and BioMEMS/BioNEMS Materials and Devices. *Microelectron Eng.* **2007**, *84* (3), 387–412.
97. Nosonovsky, M.; Bhushan, B. Roughness Optimization for Biomimetic Superhydrophobic Surfaces. *Microsys. Technol.* **2005**, *11* (7), 535–549.
98. Eustathopoulos, N.; Nicholas, M. G.; Drevet, B. *Wettability at High Temperatures*, Vol. 3; Elsevier: New York, NY, 1999.
99. Marmur, A. Wetting on Hydrophobic Rough Surfaces: To Be Heterogeneous or Not to Be? *Langmuir* **2003**, *19* (20), 8343–8348.
100. Patankar, N. A. On the Modeling of Hydrophobic Contact Angles on Rough Surfaces. *Langmuir* **2003**, *19* (4), 1249–1253.
101. Zhou, X.; De Hosson, J. T. M. Influence of Surface Roughness on the Wetting Angle. *J. Mater. Res.* **1995**, *10* (08), 1984–1992.
102. Craig, R.; Berry, G.; Peyton, F. Wetting of Poly-(Methyl Methacrylate) and Polystyrene by Water and Saliva. *J. Phys. Chem.* **1960**, *64* (5), 541–543.
103. Kamusewitz, H.; Possart, W.; Paul, D. The Relation between Young's Equilibrium Contact Angle and the Hysteresis on Rough Paraffin Wax Surfaces. *Colloid Surface A* **1999**, *156* (1), 271–279.
104. Whitehouse, D.J.; Archard, J. The Properties of Random Surfaces of Significance in Their Contact. In *Proceedings of the Royal Society of London A: Mathematical, Physical and Engineering Sciences*; The Royal Society, 1970.
105. Herminghaus, S. Roughness-Induced Non-Wetting. *Europhys. Lett.* **2000**, *52* (2), 165.
106. Mahadik, S. A.; Pedraza, F. D.; Relekar, B. P.; Parale, V. G.; Lohar, G. M.; Thorat, S. S. Synthesis and Characterization of Superhydrophobic–Superoleophilic Surface. *J. Sol-Gel Sci. Technol.* **2016**, *78* (3), 1–7.
107. Bittoun, E.; Marmur, A. Chemical Nano-Heterogeneities Detection by Contact Angle Hysteresis: Theoretical Feasibility. *Langmuir* **2010**, *26* (20), 15933–15937.
108. Marmur, A.; Bittoun, E. When Wenzel and Cassie Are Right: Reconciling Local and Global Considerations. *Langmuir* **2009**, *25* (3), 1277–1281.
109. Li, W.; Amirfazli, A. Hierarchical Structures for Natural Superhydrophobic Surfaces. *Soft Matter* **2008**, *4* (3), 462–466.
110. Sajadinia, S. H.; Sharif, F. Thermodynamic Analysis of the Wetting Behavior of Dual Scale Patterned Hydrophobic Surfaces. *J. Colloid Interface Sci.* **2010**, *344* (2), 575–583.
111. Liu, T.; *et al.* Thermodynamic Analysis of the Effect of the Hierarchical Architecture of a Superhydrophobic Surface on a Condensed Drop State. *Langmuir* **2010**, *26* (18), 14835–14841.
112. Liu, H.; Zhang, H.; Li, W. Thermodynamic Analysis on Wetting Behavior of Hierarchical Structured Superhydrophobic Surfaces. *Langmuir* **2011**, *27* (10), 6260–6267.
113. Cha, T.-G.; *et al.* Nanoscale Patterning of Microtextured Surfaces to Control Superhydrophobic Robustness. *Langmuir* **2010**, *26* (11), 8319–8326.
114. Kwon, Y.; *et al.* Design of Surface Hierarchy for Extreme Hydrophobicity. *Langmuir* **2009**, *25* (11), 6129–6136.
115. Synytska, A.; *et al.* Wetting on Fractal Superhydrophobic Surfaces from "Core – Shell" Particles: A Comparison of Theory and Experiment. *Langmuir* **2009**, *25* (5), 3132–3136.
116. Yan, H.; *et al.* Super Water-Repellent Surfaces with Fractal Structures and Their Potential Application to Biological Studies. *Colloid Surf. A* **2006**, *284*, 490–494.
117. Bittoun, E.; Marmur, A. The Role of Multiscale Roughness in the Lotus Effect: Is It Essential for Super-Hydrophobicity? *Langmuir* **2012**, *28* (39), 13933–13942.

Relevant Websites

www.IOSS.org
: International Ocular Surface Society.

www.Nace.org
: National Association of Corrosion Engineers.

3.20 Surface Preparation and Adhesion Tests of Coatings

M Jokar and M Aliofkhazraei, Tarbiat Modares University, Tehran, Iran

© 2017 Elsevier Inc. All rights reserved.

3.20.1	**Introduction**	306
3.20.2	**Preparation of the Sample's Surface**	307
3.20.2.1	Grinding	307
3.20.2.2	Sanding	307
3.20.2.3	Polishing and Burnishing of the Samples	307
3.20.2.3.1	Mechanical polishing	307
3.20.2.3.2	Electro polishing and burnishing	308
3.20.2.4	Etching	308
3.20.2.4.1	Chemical etching	308
3.20.2.4.2	Electro etching	308
3.20.2.5	Posttreatment, Additional Operations and Different Methods of Surface Analyses	308
3.20.3	**Conversion Coatings**	311
3.20.3.1	Chromate	313
3.20.3.2	The Hexavalent Non-Chromic Coatings	320
3.20.3.3	Replacement Schedule	320
3.20.3.4	The Comparison of the Hexavalent and Trivalent Chromes	322
3.20.3.5	Phosphating	323
3.20.4	**Polyurethane Coating**	325
3.20.5	**Sol–Gel**	327
3.20.6	**Electro Deposition**	330
3.20.7	**Conclusions**	332
References		333
Relevant Websites		335

3.20.1 Introduction

A good adhesion property, which is defined through the processing, test, and service condition, is one of the most fundamental necessities of each substrate coating system. A large number of factors define a good adhesion property and many of them are too difficult without assuring gradual process. The process has been developed in an empirical manner, and has been thereby aided by some of the basic intended factors like giving a good adhesion property or other properties, which are vital for a good adhesion. From this point of view, it seems that one can make an acceptable decision in terms of doing some influential works in obtaining, good a adhesion, or which method is correct to test the adhesion property. ASTM has defined the adhesion in the form of a condition which two surfaces absorb each other either through valence forces, or by interlocking with mechanical forces, by becoming coalescence.[1] In **Figure 1** the diverse reasons of the adhesion coating to the substrate can be observed.

In engineering applications, adhesion is the physical resistance of the interface between regions of a material system. These interfaces have been found in the grain boundaries, abrasion and failure surfaces, and also, in substrate-film systems. Failure adhesion is defined as the separation in/or near the interface in a large space, which usually occurs under tension. The ultimate result of failure or changing the shape of materials is adhesion disruption, and it may depend on the properties of substrate material in the nearness of the interface, materials within phase, or material coating. Adhesion resistance is an irreversible macroscopic property of the system that can be tested. A good adhesion takes place, when the intersection region is not disrupted under circumstances of service, or unacceptable low tensions. To have a good adhesion, mechanical properties of intersectional materials, are very important points. These intersectional materials presumably have different properties, composition, and microstructures other than the rest mass of the materials. An intersection can be sharp or penetrating, rough or smooth. Formation and presence of the intersection region can possibly affect the composition, tension, or microstructures. Tensions that might wipe out the adhesion are involving mechanically (tension, pressure, communal, shock, etc.), chemically (corrosion, solubility), and temperature/time (penetrating reactions). The residual film stresses, may cause disruption. The major methods for acquiring the adhesion comprising are: reducing the surface energy, high failure energy for the intersection region, or using bonding agents in order to obtain new surface. Deposition process and variables of the procedure may have an important effect on the results of adhesion through the changing of nucleation growth and deposition properties. Deposition operations may be used to increase the adhesion. These operations containing: heating, ion mixing, and penetration of the free active particles in the intersection. Heating the couple substrate film causes the tension releasing in many of the systems. We can make changes in adhesion under confined situations anytime, and this procedure may be

 doi:10.1016/B978-0-12-803581-8.09201-8

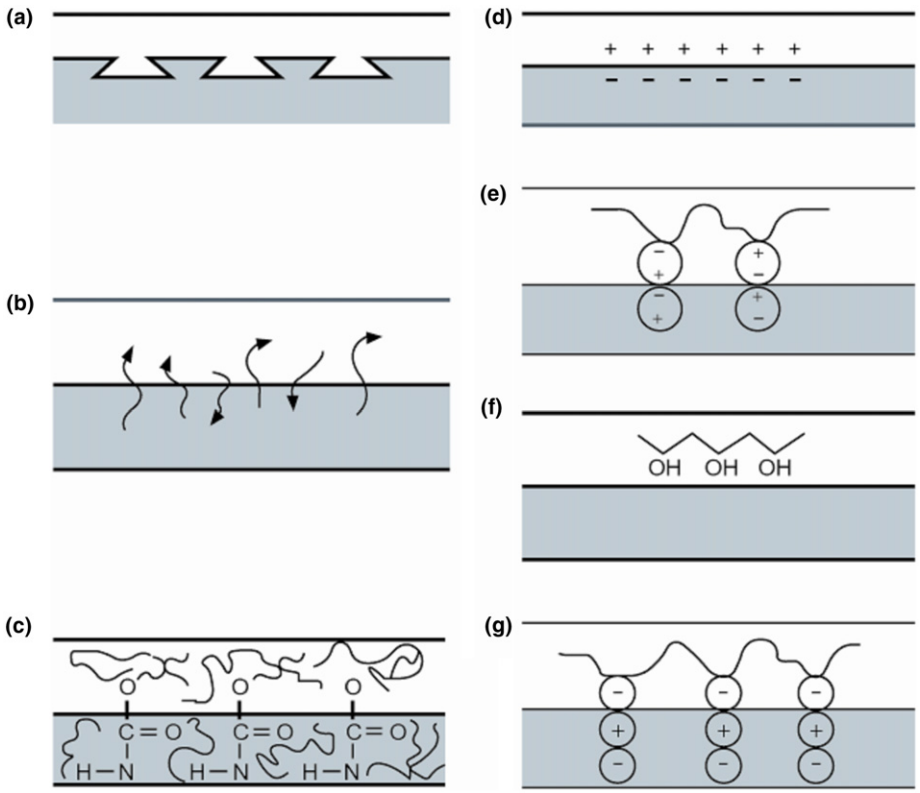


Figure 1 Physical and chemical reasons of adhesion between coating and substrate (a) mechanical connecting, (b) penetration, (c) chemical bonding, (d) contact charging, (e) bipolar interaction, (f) hydrogen bonding, and (g) mirror bonding in metals.[1]

occurred by tension releasing and particle penetrating in intersection.[2]

3.20.2 Preparation of the Sample's Surface

3.20.2.1 Grinding

Grinding is applied to smooth the samples and remove the sharp edges and deep grooves created by cutting tools. During the grinding, the sample should be kept cool with water or other cooling liquids, to prevent from microscopic structure changes of the samples that may occur.

3.20.2.2 Sanding

After disappearing of the lines and unevenness caused by the cutting tool during grinding, sanding operations are respectively applied on the sanders 60, 100, 200, 400, 600, 800, 1000, and 2000. The sander number 60 is the roughest and 2000 is the softest.

The most considerable points during sanding: the direction of sanding has altered from a sander to another one, and each time it is rotated with the amount of 90° in the case of fading the former lines and creates vertical lines over the previous. By the softer sander, we can do the sanding smoother with the lower pressure but spending more time. Sanding should be done on the sanders that water flows over them to not contaminate the former coarser particles next to the sander surface. After finishing sanding operations, the samples should be washed, dried, and then transferred to the next phase.

3.20.2.3 Polishing and Burnishing of the Samples

Polishing is carried out to completely wiping out the remained lines through the samples during the sanding.

3.20.2.3.1 Mechanical polishing

Mechanical polishing is done on a rotating disk covered with a felt, and is sprayed with a very fine abrasive materials (e.g., aluminum oxide or magnesium oxide). Because of, not creating grooves on the samples, brush or the felt that is employed here, should be thick and have no hard particles especially dust. At the entire period of polishing, it is necessary to smear the felt with suspended aluminum dust in water frequently. Grading of the aluminum oxide particles is different and we usually polish hard materials such as steel and cast iron with coarser aluminum powder rather than the soft metals like aluminum and lead. The alumina is in two forms: allotropic alpha (hexagonal) and gamma (cubic). The polishing properties of these two forms are different, so that alpha alumina acts faster in abrasion of metals and is more suitable for rough polishing, while gamma alumina prepares a polished surface with the high quality, so it is apt for the final polishing. Sometimes, it is utilized magnesium oxide for polishing aluminum and its alloys. This substance absorbs the carbonic gas of the air and produces carbonate. Therefore, aluminum oxide is usually used in the metallurgy laboratory. A disk with a velvet coating and diamond powder is being used to obtain a mostly polished surface and devoid of any grooves. Often, it is better to use an appropriate lubricant such as alcohol for diamond paste, to

remaining free or rising up the power of cutting powder of diamond particles, and also to increase the life of velvet coating.

3.20.2.3.2 Electro polishing and burnishing

An electronic or electrolytic polishing is defined as dissolution of a metal surface in an electrolytic solution. This kind of polishing is used in metallographic parts, stainless steels, copper alloys, magnesium, zirconium, aluminum alloys, and other metals that their polishing is typically formed by the mechanical methods. Here, the studied sample case is in the role of anode, a sheet of stainless steel in case of cathode, and electrolyte is in the role of the solvent. By the above mechanism, the unevenness of segment surface is solved, and the surface changing of layers created during the sanding, is entirely removed.[2]

3.20.2.4 Etching

Etching is defined as a metal surface corrosion by the corrosive liquid; that is usually kind of an acid. Some metals show their microscopic structure without etching (after polishing) such as emerging layer and spherical graphite in gray and ductile cast iron. In a microscopic investigation of polished samples, only properties such as porosity, type and distribution of inclusions, and corrosion cracks can be observed. During the etching the areas of surface with high energy-like grain boundaries are corroded, and the grading of segments would be appearing. Also, grains and different phases of the material have different corrosion rate, and this is another point to recognizing them from each other. In the case of metals that are consisting of different phases, different constituent components with varied intensities are corroded, and this happens because of the lack of equality of solution between various phases of a metal in the etch solution. High energy locations such as impurities, displacements, and grain boundaries are intensely corroded in touch with the etch solution, and are seen as darker areas under the microscope. Etching process is doing in both electrolytic and chemical methods.

3.20.2.4.1 Chemical etching

Chemical etching is the most common process that is used for disclosure of the microstructure of a substance. The goal of chemical etching is to clarify the different comprising phases of the sample. To be appeared the structure of iron and non-iron alloys, there are different types of etching solutions. The most famous etching solutions for microetching of carbon and alloy steels are Nital 2% and Picral 4%. Since both solutions have the same etching properties, usually they are used instead of each other. But, under some conditions, selecting an etching solution may cause remarkable differences. For example, in a low carbon steel with the substructure of perlite and ferrite, the 2% nital solution etches grain boundaries of ferrite and therefore causing to ultra-etching of perlite. On the other hand, the 4% picral solution etches the pearlite phase, but has no effects on ferrite grain boundaries. The sample is put under microscopic studies, after suspending into the etch solution and then drying. The most sufficient way to dry the samples is using drying devices. With the advent of any problem and damage surface of samples such as ultra-etching, it is necessary to polish and etch the samples again.

3.20.2.4.2 Electro etching

Electro etching is an imposing corrosion in the presence of an electrolyte and electrical current. This method is hardly used in carbon and alloy steels, but is applied for the alloys that are impenetrable, or their reaction with the chemical materials is slow. Stainless steels, heat resistant alloys, nickel based alloys, cobalt and chrome alloys are materials that the electrolytic etching is used to them. In this mechanism, the polished sample (anode) is suspended into the electrolyte, and a positive voltage is applied to it. The consumption, current and voltage used in electrolyte etching, is usually less than the voltage and current needed to electro polishing. Electro polishing is not only a method to finalizing and suitable surface payment in many laboratorial works but also a very adequate way to prepare the surface for coating deposition. The most important industrial parameters for determining the quality and durability of the coatings, is the quality of the adhesion. The effect of electro polishing in adhesion amount of the hard chrome coating has been investigated, and grooving test in additional to gloss meter searches, and optical and electron microscopes, have been used to determine the adhesion amount. The results of various experiments demonstrate that the electro polishing process causes a distinct increase in adhesion of the hard coating chrome, but amount of adhesion is dependent on the type of consumption solution, time, and the current density. Results showed that increasing of time of electro polishing samples in current densities above 225 A dm^{-1}, may causes in decrease of surface roughness, arising of glossiness, and also increasing of the adhesion. The relation between adhesion and surface roughness which is obtained by the use of electro polishing, indicating this matter that the bonding strength has a little mechanical locking and, in turn, mostly depends on penetrating theories and chemical bonding.[3]

As an instance, researchers have investigated the zirconium oxide as a preparation or pretreatment before applying due to the aluminum alloy, and having used the coating without chrome. In this way, by the sol–gel mechanism, the thin ZrO_2 coating has been deposited over the Al2024 with the use of spraying technology; and for doing the adhesion test, the zirconium oxide surface is covered with organic polymer. Adhesion and the electrochemical behavior of the coating have been investigated. The applied coating has increased resistance to the corrosion and adhesion.[4]

Galvanized steel is used for various technology applications, and this process is traced back to its high corrosion resistance. The protection capabilities of zinc are rising by applying a thicker coating, or painting the substance metal with the suitable polish. The main problem in painting the zinc is reaching to the good adhesion of color to the galvanized steel. If preparation or pretreatment be done with appropriate acid formulation, it could obtain an excellent adhesion, and then the study taken coatings with scanning electron microscope (SEM), X-ray diffraction, and energy dispersive analysis of X-rays analysis.[5] **Table 1** is a classification of these type articles.

3.20.2.5 Posttreatment, Additional Operations and Different Methods of Surface Analyses

In this section some posttreatment, additional operations and different methods of surface analyses were studied. For example,

Table 1 Investigation of pretreatment type, substance, coating contents, and acquired results of them

Treatment type	*Base metal*	*Coating type*	*Results*	*Adhesion*	*References*
ZrO_2 coatings and hybrid organic–inorganic coatings	AA2024 aluminum alloy	ZrO_2	Cerium nitrate introduced in hybrid organic–inorganic films evidences an inhibition effect on corrosion processes, which can be attributed to cerium compounds	Promote adhesion	4
Pretreatment procedures	Galvanized steel	Alkyd resin + 3% HsP (water-borne resin, water-borne acrylic-styrene copolymer + phosphoric acid) + 3% $HsPO_4$ (vinyl resin + 3% $HsPO_4$)	It is possible to develop effective acid pretreatments for galvanized steel by a correct formulation and an adequate application	The adhesion of binders strongly depended on the nature of the conversion layer	5
Pretreatment of magnesium-based components	High-pressure die-cast AM30 magnesium alloy	Siloxane-based lubricant	Good corrosion performance homogeneity over the entire component optimized concerning defects, pores, and impurities	Good topcoat adhesion	6
Epoxy nanocomposite	St-37 type steel	Nano-sized ZnO particles	Excellent corrosion resistance, good paint adhesion, and low cost	Good paint adhesion	7
Pretreatment processes in powder coating	Hot rolled steel (HRS)	After pretreatment and dry-off process, all test panels were painted in an electrostatic powder coating booth. White industrial triglycidyl isocyanurate-free polyester powder coating was used	Zinc phosphate conversion coating gave the best performance, and zirconium-based nanostructured conversion coating was superior to that of iron phosphate conversion coatings on HRS	Best adhesion	8
Pretreatments epoxy resin was applied on the pretreated steel substrates	Cold-rolled carbon steel panels	γ-glycidoxypropyltrimethoxysilane	Reduced the disruption of interfacial bonds at the binder/substrate interface. Addition of 2 wt.% cerium nitrate into the silane formulation led to the maximum efficiency of resultant coating	Improvement of cathodic disbondment and also dry and wet adhesion of epoxy coating	9
Cerium-based conversion coatings as pretreatments	AA606	R_2 and constant phase element CPE2	Improved the quality of coatings	Excellent polyester coating adhesion was found independently on aluminum surface pretreatment	10
Altered migration and adhesion potential	Human bone marrow stromal	–	The basal migration of m-NSC was significantly reduced compared with MSC (6 versus 27 out of 10 000 cells migrated within 6 h).	Adhesion of m-NSC to the filter membrane was delayed and not affected by IGF1 or PDGFbb: 90% of MSC, but only 20% of m-NSC, adhered within 1 h, with 90% of m-NSC adhering within 3 h	11

(*Continued*)

Table 1 Continued

Treatment type	*Base metal*	*Coating type*	*Results*	*Adhesion*	*References*
Fiber metal laminates	Aluminum 2024	ARALL (aramid-reinforced aluminum laminate) based on aramid fibers, GLARE (glass-reinforced aluminum laminate) based on high strength glass fibers and CARALL (carbon-reinforced aluminum laminate) based on carbon fibers	Offer several advantages such as better damage tolerance to fatigue crack growth and impact damage especially for aircraft applications	Adhesively bonded fiber metal laminates have been shown to be far more fatigue resistant than equivalent mechanically bonded structures	12
Epoxy-bonded	AA6060 aluminum	Hydrated aluminum oxide deposited Ti (and Zr) oxide only covered a small fraction of the total surface area, mainly located at the cathodic – Al(Fe,Mn)Si particles	The conversion coating formed in pH 4.0 solution was relatively thick over a considerable area fraction of the AA6060 surface. Under similar coating conditions, the thickness of deposited Ti–Zr oxide layer surrounding the particles was observed to be of the order 50–100 nm	Promoted adhesion	13
Powder coated aluminum alloy	Aluminum (1050) sheet	Aluminum hydroxide	Relatively good performance of the powder coating is due to a high ohmic resistance of the coating prior to and after saturation with water, low water solubility of the coating itself and good adhesion of the coating to the substrate	Improved the dry adhesion performance	14
Cleaner technologies	–	–	Most of the factors identified in the empirical literature could be drivers and barriers to innovation depending on the circumstances, time, and contexts in which they are considered	If a firm perceives that consumers have little willingness to pay for more expensive products, this might deter it from investing in cleaner technologies. The signals from the market must be the right ones	15
Cryoblasting involves bombarding a substrate with carbon dioxide particles	Aluminum and its alloys, 5251 alloy	Degreased-only aluminum 5251 alloy coupon	This method will be elective for other metals. To solvent degreasing or as the first stage, to replace organic solvents, in a multi-stage pretreatment	Would be expected to benefit adhesion	16

(*Continued*)

Table 1 Continued

Treatment type	*Base metal*	*Coating type*	*Results*	*Adhesion*	*References*
PEG-based coatings other protein-resistant surfaces PEG and other coatings release- and contact-based antimicrobial coatings	Most metallic surfaces	Protease-based anti-fouling films photoactivated self-cleaning films release-based approach	Resistance to adhesion of biocontaminants or degradation of the biocontaminants	Preventing the adhesion of proteins or microbes involves the functionalization of surfaces with PEG or oligo (ethylene glycol) groups	17
Auto-catalytic plating based on a wet blast system	Ferrous iron	$Zn_3(PO_4)_2 + 2Fe_3(PO_4)_2$	Improvement in physical properties of the coatings and the reduction of effluent problems	Excellent adhesion of very fine grained crystals, which exhibit good corrosion and lubrication characteristics	18
Laser technology	Commercially available 2024-T3 and 7075-T6 aluminum; 4130 steel; GM3006 fiberglass/epoxy, IM7/977-3 graphite/epoxy, and AMS3902 Kevlar composite materials; and metallic honeycomb core	Replace chemical stripping and dry media blasting in coatings removal applications	Any of the lasers tested due to the potential to exceed recommended IR and UV levels	Paint adhesion tests also yielded that the process is suitable for use on all material	19

the methods of Simmons and Beard have been applied to hydroxylated iron surfaces to determine the values of pK I and pK II using anion and cation exchange. Results showed that a value of IEPS ~10 was obtained, which is good agreement with published data. The values of surface coverage obtained in these experiments are lower than the predicted results from those obtained in model experiments.[20] In other research SHIMIZU studied the route toward the enhanced understanding the corrosion and filming behavior of aluminum and its alloys. Results showed that the combined use of the ultramicrotomy approach and atomic force microscopy is expected to play a great role in enhancing the understanding of the corrosion and filming behavior of aluminum and aluminum alloys, as well as for other metals.[22] **Table 2** shows some examples of this type of articles.

3.20.3 Conversion Coatings

The terms, conversion coating, is referred to the coatings that are created by the reaction of the atomic layers of the metal surface with anions that are produced at the center of the metals. Therefore, the process of creating conversion coating is a controlled process that has been formed artificially, and finally creates a layer on the metal surface. This layer has a strong connection with the base metal, and practically is insoluble in water and intervening environment, and also, is a good electrical insulator.

Many investigators have introduced and applied different conversion coatings such as the coating based on elements: lanthanum, zirconium, potassium, cerium, zinc chromate coatings, phosphate chromate, non-chromate, etc., on various substrate like aluminum, copper, steel or magnesium, and as it is expected, these coatings, after enactment, observing and assessing their specific morphology of the coatings have achieved an excellent adhesion and corrosion resistance. Although, the magnesium alloys have low densities and high mechanical properties, but their applications have been restricted because of their weak corrosion resistance. The investigators have studied different conversion coatings to solve the problem. As an, example we can see below the conversion coatings based on cerium, zirconium, and niobium on the AM50 alloy, that they have obtained desired results with the contribution of electrochemical calculations, leading to polarization curves and electrochemical impedance spectroscopy, and also, the difficult procedure of inspecting the corrosion resistance such humidity and salt spray. Adhesion has been improved in addition to corrosion resistance improvement.[25] For example, to applying a cerium-based conversion coating, the aluminum 7075 samples are suspended into sodium nitrate solution, and adequate coverage is achieved at room temperature and specified time. This coating can be used by spraying or other methods.[10]

Another sample is lanthanum-based conversion coating on the Mg–8Li alloy. For exerting this coating, the substrate metal is prepared first. Then it is put in the bath containing considered elements (in this example lanthanum, and bath comprising lanthanum nitrate), and after each phase, samples are washed with distilled water. Finally, the applied coating has been dried with air and is to analyze.[26] Nevertheless,

Table 2 Posttreatment types, substrate, coating contents, and obtained results

Treatment type	*Base metal*	*Coating type*	*Results*	*Adhesion*	*References*
2.5 wt.% $(NH_4)_3PO_4$ posttreatment after silica treatment	A6092/SiC/17.5p aluminum metal	Si–P composite coatings	Provide a maximum localized corrosion protection to AMMC. The surface morphology of Si–P composite coatings and the ability to protect AMMC substrate from localized corrosion in Cl-media were examined as a function of phosphate treatment time	Excellent adhesion	14
Inorganic surfaces	Pure iron	Hydroxylated iron	The values of surface coverage obtained in these experiments are lower than that predicted from the or those obtained in model experiments	–	20
Hygrothermal ageing and thermal shock	C151 Cu alloy black Cu oxide	Cu oxide	Prevention of corrosion and oxidation of Cu leadframes and substrates	Improving the interfacial adhesion with organic adhesives	21
Corrosion and filming behavior	Pure aluminum specimens	The Al_2Fe particles are oxidized during anodizing in sulfuric acid solution\forming a porous type oxide containing iron and having a texture similar to \but slightly higher than\that grown over the surrounding matrix surface	Improve mechanical strength\corrosion resistance	Improve the adhesion strength	22
Hydrofluoric (HF) treatment	Mg-2.5 wt.%, Zn-0.5 wt.%, Zr alloy	MgF_2 protective coating	HF treatment improves the corrosion resistance of Mg–Zn–Zr alloy and slows down the release rate of Mg^{2+} into the anticoagulated blood	–	23
Plasma treatment	AA 2024-T3	Hexafluoroethane layer deposited on the trimethylsilane plasma polymer substrate	Specific chemical changes take place in the first several days after film formation. These changes can be summarized according to elemental species and specific components	Improve adhesion of primer coatings	24

magnesium alloys has low density despite their good mechanical properties, but their utilizations have been somewhat limited from their weak corrosion resistance point of view. For solving this issue, investigators have reviewed diverse conversion coatings based on cerium, zirconium, and niobium over the AZ91 alloy in the following; that with the help of electrochemical impedance spectroscopy, and as well as, any dissimilar methods have been investigated. In the end, they have acquired favorable outcomes relating to corrosion resistance, including humidity and salt spraying. Corrosion resistance and adhesion have also been meliorated.[25] As it is seen in the **Figure 2**, with the increasing of the immersion time, current density and potential have reduced. Therefore, the corrosion resistance has been raised, also.

Figure 3 is the results of the magnesium alloys X-ray photoelectron spectroscopy experiments with the cited conversion coating at the room temperature. As it is shown, the obtained coating includes zirconium oxides, cerium oxide, niobium

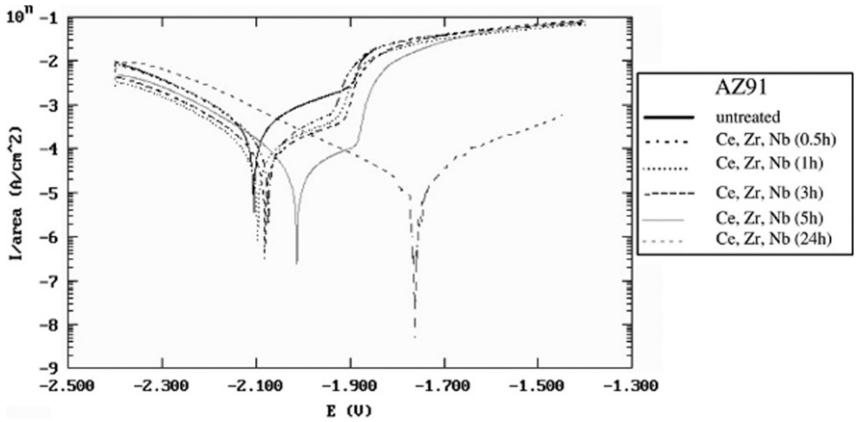


Figure 2 The polarization curve of AZ91 alloy according to the maintenance time in the bath Ce–Zr–Nb into the sodium sulfate solution.[25]

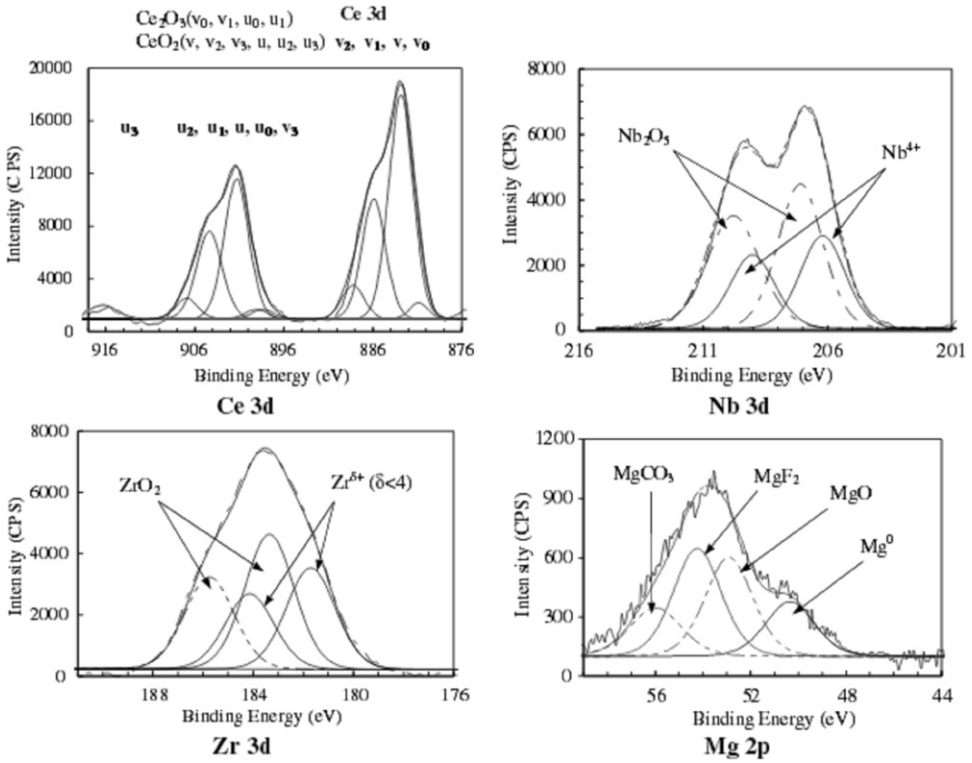


Figure 3 Chemical spectra X-ray photoelectron spectroscopy of the AZ91 alloy containing components Ce–Nr–Nb after 5 h keeping in the bath at the room temperature.[25]

oxide, and magnesium oxide. Table 3 demonstrates the various examples regarding this field.

3.20.3.1 Chromate

Chromate method is one of the processes of the conversion coatings that has progressed and developed widespread during the last two decades. The term of 'chromate' called to chemical and electrochemical operations of metals and the metal coating solutions which there are chromate acid, chrome, or dichromate in them. The consequence of such treatments is to create a protective conversion coating including components trivalent and hexavalent chromium on the metal surface. It has been known well the preventing properties from corroding of materials through the chromate. By adding small amounts of the substance to the water circulating system, the surface of metal is being coated and so, being prevented of corrosion. Chromate coatings are applied widely in products of industries like: machine manufacturing, electric, electronic, telecommunications, and auto engines industries. They also play a major role by replacing some certain metals instead of metals having less half-life. As an example, chromated zinc, which is replaced

Table 3 Classification of conversion coating type, substrate, coating contents, and obtained analysis

Treatment type	*Base metal*	*Coating type*	*Results*	*Adhesion*	*References*
Cerium-based conversion coatings	AA606	R_2 and constant phase element CPE2	Improved the quality of coatings	Excellent polyester coating adhesion was found independently on aluminum surface pretreatment	10
Ce, Zr, and Nb-based conversion coating	AZ91 and AM50 magnesium alloys	Coating includes $CeO_2 \cdot Ce_2O_3$, ZrO_2, Nb_2O_5, MgO, and MgF_2	Increased corrosion potential, decreased corrosion and anodic dissolution current densities, and increased polarization and charge transfer resistances	Excellent paint adhesion	25
Lanthanum-based conversion coating	Mg–8Li alloy	$La(OH)_3$	The electrochemical results revealed that the lanthanum-based conversion coating possessed better corrosion resistance than the Mg–8Li substrate	Good adhesion to substrate	26
The relative proportion of coherent crystalline regions increases with time	The amorphous alumina evolves toward a partially crystalline form during the drying of the coating and with ageing	Crystallized mixed oxide such as Fe $(Cr,A1)_2O_4$. Moreover, $A1_2O_3$ phases which prevented the thermal oxidation of the stainless steel	Fe–17% Cr ferritic stainless steel	Conversion alumina coatings	27
Conversion coating produced by the permanganate-based system	Strip of galvanized steel	The manganese oxide-aluminum oxide	Extra thickness is due to the slow formation of the coating, which provides a more corrosion-resistant surface	Excellent paint adhesion due to the large number of attachment points available to the applied coating	28
The manganese oxide, zinc oxide conversion coating produced by the permanganate-based system	Zinc and zinc alloys	Chromium: 17%; zinc: 12%; carbon 10%; oxygen: 54%; aluminum 6%; and trace: copper and fluorine (less than 2%)	Will more easily accept applied coatings and/or resist corrosion. They are rather thin (not more than 6000 nm on zinc), quickly and easily formed, easily scratched	If used to improve upon paint adhesion – they are coated shortly after being formed to prevent degradation of the conversion coating	29
Lithium-based conversion coating. All coatings were painted with the 10P4-2-primer epoxy resin	AA2024-T3 aluminum alloy	Non-chromate (LBCC-DIP, LBCC-POL-5 and LBCCM. POL-45) and chromate conversion-coated surfaces (ALOD)	Non-chromate conversion-coated surfaces are very porous, while the chromate conversion-coated surfaces are more uniform non-chromate films they protect the AA2024-T3 aluminum alloy against corrosion since the corrosion rate of surfaces covered with these film were lower than the one of surfaces covered with the chromate films	The adhesion between primer epoxy and the conversion coating films is better for the chromate film than for the non-chromate films proposed in this work	30

(*Continued*)

Table 3 Continued

Treatment type	*Base metal*	*Coating type*	*Results*	*Adhesion*	*References*
Conversion Coating	Cold-rolled steel	Nano-structured metal oxide, titanic, and/or zirconic composite	Provide phosphate-free and environmentally friendly pretreatment, which has corrosion protection	Paint adhesion properties at least equal to iron phosphate	31
Conversion coatings	Fe–17% Cr ferritic stainless steel	Conversion coating (sulfuric acid)/ alumina, N: conversion coating (nitric acid)/ alumina, P: conversion coating (phosphoric acid)/ alumina	The conversion coating obtained in phosphoric or nitric acid baths present low concentration of sulfur at the surface and the same morphology of standard conversion coating obtained in sulfuric acid	Conversion coating obtained in nitric acid modified by alumina deposit, have the best effect on the thermal oxidation resistance of the stainless steel, equivalent to standard coatings	32
Conversion alumina coating	Stainless steel Fe–17% Cr stainless steel	Duplex conversion – alumina coating	An efficient thermal barrier character thiosulfate and nitric acid concentrations have an important influence on the formation of conversion coating	Strong interfacial adhesion and must be very porous	33
Conversion coating growth in sulfuric acid medium	Carbon steel	Electrochemical alumina deposit	High roughness and high real surface area	Strong interfacial adhesion	34
Barium phosphate chemical conversion coating	Mg alloys	An under layer of mixed amorphous phosphates and a top layer of crystalline $BaHPO_4$	Improved corrosion resistance of the AZ31 magnesium alloy with the barium phosphate coating, with the two-layer coating being more corrosion resistant than a single under layer coating	The top layer exhibits a lower adhesion than the under layer	35
Zirconium-based conversion coating (ZrCC)	Mild steel	Oxide–hydroxide of zirconium and adsorbed fluoride ion on the mild steel surface	A drastic improvement of adhesion bonding between organic coating and steel substrate. Zirconium-based conversion layer could increase the chemical and/or physical interaction between epoxy organic coating and the steel substrate leading to enhancement of adhesion strength of the base substrate	ZrCC increased adhesion strength of mild steel to the organic coating and the zirconium treated mild steel adhesion performance is better than that of the three cationic phosphate layer	36
Chemical conversion coatings	Plain carbon steel (0.5–0.8% carbon by weight)	Bonderite 245 treated 15 N 20 plain carbon steel surface	The initial glycidoxypropyl-trimethoxysilane treated single lap shear (SLS) joints demonstrated mainly cohesive failure of the adhesive when observed optically. Following exposure for up to 8 weeks the	Good adhesion	37

(*Continued*)

Table 3 Continued

Treatment type	*Base metal*	*Coating type*	*Results*	*Adhesion*	*References*
			failure was always mainly cohesive with limited apparent interfacial failure observed after as little as 2 weeks		
Fluoacid-based conversion coatings	Aluminum alloy (6063-T52)	Stoichiometry suggests that the ZrF_6^{2-} complex is broken upon integration into the substrate oxide	Provide chrome-equivalent corrosion protection and facilitate the adhesion of paint. Polymer choice is critical in assuring good performance	Enhance paint or lacquer adhesion	38
ZrCC	Cold-rolled steel	$ZrO_2 \cdot 2H_2O \cdot H_2ZrF_6$	According to zirconium energy dispersive spectrometer (EDS) map, uniform distribution of Zr along the surface of treated sample was observed. ZrCC can increase corrosion performance of fully painted systems	Adhesion tests exhibited considerable high values	39
Chemical conversion coating	Aluminum	Alumina	To restore corrosion protection and ensure paint adhesion after plastic media blasting	Excellent adhesion	40
Zinc phosphate coatings	AA6061 alloy	$AlPO_4$	Give strong adhesive bonding and improve corrosion resistance	Strong adhesive bonding	41
Conversion coating	Copper	Cupric oxide	Black oxide was originally developed for multilayered printed circuit boards (PCBs). To enhance the adhesion between organic prepreg layers and copper foils. The main benefits of copper oxide coating in the PCB applications are the increased available surface area for bonding through the rough, porous copper oxide crystals and the passivation of the copper surface to prevent its contamination during the manufacturing processes at elevated temperature	Applied onto the copper substrate to improve its interfacial adhesion with polymeric adhesive	42
Hydrotalcite conversion coatings	Aluminum aerospace alloys AA2024 (Al–4Cu–1.5Mg) panels were coated with a nitrate-based hydrotalcite coating (NO_3HT)	NO_3HT	Adsorption of the anionic SLS would decrease the negative surface charge of the hydrotalcite (HT) surface and decrease the electrostatic attraction of the	Increased adhesion is believed to be due to the increased wettability of the HT	43

(*Continued*)

Table 3 Continued

Treatment type	*Base metal*	*Coating type*	*Results*	*Adhesion*	*References*
			chloride anion. The adsorption of the cationic Adogen should increase the adsorption of the chloride ion		
HT-based conversion coatings	Aluminum alloy panels for adhesion testing. The alloy used was AA2024-T3 (Al/4Cu/1.5Mg	CO_3HT, NO_3HT, and S_2O_8 HT conversion coating powders	Increased epoxy adhesion can be achieved by modification of the wettability or electrostatic characteristics of the HT coatings	Increase the adhesion	44
Conversion coating	Clad 2024-T3 aluminum alloy	Oxide layer sol–gel-treated epoxy aluminum joint	Macrorough structures drive the crack to within a thin epoxy layer close to the polymer–metal interface, which enhances the initial strength of the sol–gel-reinforced interface	Enhanced adhesion	45
Phosphating	Steel	$Fe(H_2PO_4)_2$	Improved corrosion resistance, wear resistance	Highly adherent to the underlying metal	46
Chromate/phosphate conversion coating	1050 Al alloy	Aluminum hydroxide and polymer-oxide bonds and different mixture compounds	Good corrosion performance highest surface free energies	Best adhesion strength	47
Zinc phosphate coating	AZ91D magnesium alloy	$Zn_3(PO_4)_2$ H_2O, Zn, $AlPO_4$, and $MgZn_2(PO_4)_2$	Good corrosion resistance	The adhesion of paint on the zinc phosphate coating was better than that of paint on chromate conversion coating due to the microporous structure of the phosphate coating	48
Oxide films	Pure aluminum	Alumina	Improved performance in corrosion resistance of these metals is the improvement of the hydration resistance of the oxide film or the oxidocoating interface	Improved performance in adhesion	49
Conversion coatings	High purity aluminum	Chlorinated rubber primer	Anti-corrosion primer performance	Conversion coatings were mainly employed to improve metal-polymer bonds. The adhesion performances of polymer–metal interfaces were attributed to mechanical interlocking	50
Deleterious effects of water	Metal/epoxy interface by the presence of water	Metal/epoxy interface	Chemical conversion-coated samples were found to be much more stable in wet	Maximum bond strength	51

(*Continued*)

Table 3 Continued

Treatment type	*Base metal*	*Coating type*	*Results*	*Adhesion*	*References*
			conditions compared to samples without conversion coating		
New oxide layers	AA2024-T3 aluminum alloy sheets	Oxide layers and cerium-based conversion coatings cerium oxyhydroxide layers	Improvements in the mechanical performance after adhesive bonding	Increased adhesion	52
Hydrotalcite conversion coating on	Mg alloy	Double hydroxide (Mg–Al LDH) film	The results suggest that the LDH film has the potential to become an environmentally friendly replacement for increasingly regulated chromate conversion coatings	The cross cutting showed that the adhesion between the film and the substrate was very strong, which enhances its potential for practical application	53
Conversion coating is composed of pyrophosphate with a flower-like microstructure	Carbon steel	Conversion coating contains P, Fe, and O elements $FeH_{10}(PO_4)_4$	This conversion coating presents much better anti-wax performance than carbon steel and heat-treated carbon steel in water-contained crude oil	Has a special wettability, which is super-oleophobic with low oil-adhesion in water and hydrophilic in oil	54
Conversion coatings	Aluminum alloy 6061-T6	Hydrated Ce(III)/Ce (IV) oxide	Increase in corrosion resistance	Improved adhesion	55
Coating degradation and delamination process.	Phosphated steel	Additional paint, wax, or sealer coatings	Long-term degradation processes leading to the failure of high performance coatings can differ in mechanism from those important for coatings that fail quickly	–	56
Zinc–aluminum–chromium conversion coating	Metal surface	Zinc and aluminum existed mostly as zero-valent zinc and zero-valent aluminum, but chromium existed mostly as trivalent chromium oxide	At the same time, the chromic acid in the treatment chemical reacted with the metal surface of the substrate forming a chemical bond providing strong adhesion	Good adhesion	57
Conversion coatings	AZ31 magnesium alloy	Cerium hydroxides/oxides	The coating was at two-layer structure. The adhesive weakness between the surface layer and the inside layer was a crucial factor that limited the coating protection ability	Poor adhesion	58
Chemical conversion and organic coatings	AZ91D Mg alloy by precision die-casting	Corrosion product, consisting of MgO, $Mg(OH)_2$, and $Mg_2(OH)_3Cl$ filled up the blisters	Scanning electron microscope/EDS and Fourier transform infrared analysis showed the blistering initiated because of *in situ* loss of adhesion at the organic coating/substrate interface,	If the conversion coating is contaminated in any way adhesion will be poor and mostly result in blister formation on contaminated spots	59

(*Continued*)

Table 3 Continued

Treatment type	*Base metal*	*Coating type*	*Results*	*Adhesion*	*References*
			caused by contamination and/or corrosion		
Ceramic conversion coating and layer-by-layer polymeric coating combinations	AZ31 magnesium alloy	$Mg(OH)_2$ following sodium hydroxide treatment and rinsing in distilled water	Improve the corrosion resistance and cellular integration of these implants with the native tissue, while delivering vital drugs or biological elements to the site of implantation	Improved biocompatibility, cellular adhesion, and proliferation in comparison to the un-coated alloy surface	60
Conversion coating	AZ31B and A2017, A6022	$Mg(OH)_2$ coating on AZ31B and Boehmite on A6022	Higher tensile shear strength (16 MPa) with epoxy resin. In the acrylic resin, $Mg(OH)_2$ coating on AZ31B and Boehmite on A6022 had a tensile shear strength of 14 MPa	It is obvious that these conversion coatings can be alternatives to chromate conversion coatings as surface treatment for adhesion of magnesium alloys and aluminum alloys	61
Conversion coating	EN AW-6082-T6 aluminum alloy	Al(Fe,Mn)Si	The technique may thus provide useful information about the adhesion behavior of heterogeneous conversion-coated aluminum surfaces	Application of a chromate-free Ti–Zr-based treatment also increased adhesion, but the adhesion force varied significantly due to the presence of a Al (Fe,Mn)Si particles causing non-uniform deposition of the conversion coating	62
Four types of conversion coatings amorphous iron phosphate, heavy zinc phosphate, and three types of modified zinc phosphates that utilized one or more metal cations in addition to zinc	Steel	Polycrystalline conversion coatings	Conversion coatings that consist of large crystals tend to produce poor results under tensile forces, due to fracture or breakage of the large crystals when subjected to torque and impact forces	Improved adhesion of organic finishes	63
Conversion coating	AZ31B Mg	$Mg(OH)_2$	Excellent pitting corrosion resistance has been demonstrated mechanism of the ionic liquid (IL) conversion coating formation: IL molecules breakdown before reacting with the metal surface	–	64
Conversion coatings amorphous iron phosphate, heavy zinc phosphate, and three types of modified zinc	Steel	Mixture of hopeite $[(Zn_3(PO_4)_2 _94 H_2O]$ and phosphophyllite $[(Zn_2Fe(PO_4)_2 _94 H_2O]$ mixture of	Enhanced ability for bonding to organic coatings large corrosion barrier	Provide an amorphous base with enhanced surface area for bonding. curing adhesives are used	65

(*Continued*)

Table 3 Continued

Treatment type	*Base metal*	*Coating type*	*Results*	*Adhesion*	*References*
phosphates that utilized one or more metal cations in addition to zinc		hopeite and rhombic scholzite crystals [$Zn_2Ca(PO_4)_2$ _92 H_2O]; the percentage of metals incorporated into the conversion coating mixture of vivianite and magnetite		to create the rubber-to-metal bond	

by the metals coated with cadmium can be mentioned. The objectives of using chromated metals including:

a. Increasing the corrosion resistance of the metal or protective metal coatings, in the recent case, it is likely led to prolonging the first coming out of corrosion on the base metal and coating metal.
b. Decreasing the surface damages generated from finger traces (surface scratches).
c. Raising adhesion of the paint and other organic coatings.
d. Staining or better acceptance of decorative coatings.

The high consumption of these coatings in the industry is because of creating properties such as corrosion resistance, and improving the color traits or coating of the surface. For instance, conversion coating of chrome with the use of the permanganate system over the galvanized steel can be investigated.[28] As a well understood case, researchers in the multi-components coating for magnesium have used a chemical conversion process without acid washing, and the sample has been put in the bath comprising elements of P, Al, Mg, K, Ca, Mn, Zn, and O. Obtained coating includes multi-component oxides of mentioned elements, and caused to improve the corrosion resistance of the cited alloy.[66] In another essay, the AZ91D magnesium alloy has been etched with sodium chloride, then has been suspended in Nanomyte DT-60 for 10 min at the room temperature. During this process, alloy sheets that were initially gray, have been covered with a bright yellow micrometer 2–3 layers. This yellow layer, that is the considered coating, has been increased durability and stability of the alloy in various environments.[67] **Table 4** denotes the samples of chromate conversion coating properties, and obtained results of applying them.

3.20.3.2 The Hexavalent Non-Chromic Coatings

Nowadays, most of converting and surface coatings of steel parts, especially parts that are utilized in vehicles containing hexavalent chrome. The excellent capability of surface protection and corrosion resistance are the reasons of this general exploitation. But environmental and health problems and hazards relating to hexavalent chrome, have made the industrialized countries that are the greatest costumes of these coatings, to regulate some programs to remove and replace these materials. The July first 2007 was the deadline for the elimination the certain form of chrome metal and replacing chrome-free coatings in the coatings of auto parts of the European Union. The table below represents the comparison between adhesion and the type of the failure in the coating. As it is observed, in the case of chromate, failure was taken place in the primer, and in the case of the coating-free sample; it has occurred in the substrate, and chromate coating has led to increasing of the adhesion.[80] **Figure 4** is the weight reduction curve and the coating type of the AZ92A magnesium alloy samples. The weight reduction of the MLTC + MLT coatings, chromate and the coating-free sample has respectively risen. The corrosion rate of the chromated sample is five times less than the coating-free sample.[80]

Table 5 demonstrates samples with conversion chromate coating, properties, and the results of applying them.

3.20.3.3 Replacement Schedule

On September 18, 2000 the parliament of Europe put on the agenda the elimination of harmful substances to the environment in manufacturing auto parts. The plan of the Committee consisted of determining a deadline that the members being ensured that in auto parts, elements such as lead, mercury, cadmium, and hexavalent chrome will not be used. These parts including connectors, press parts, casting parts, machining parts, and accessorial parts which are employed from zinc coatings, dichromate coatings, and chrome coatings for corrosion protection of them. In the case of hexavalent chromes, in the beginning, it was declared the program of limiting authorized total amount to maximum 2 g amount in each automobile until 2003. But, since this procedure does not give a standard method concerning analyzing the use of chrome, and there is not any other solution for replacing all hexavalent chrome coatings, belonging to the Europe Agreement with the EU Auto industry[85] an agreeable gradual program was approved with the name of eliminating hexavalent chrome. The steps of the plan were the followings:

1. Stopping shiny and blue chromatic systems until July 2002.
2. Stopping yellow chromatic systems until 2003.
3. Elimination of hexavalent chrome in zinc systems until the January 1, 2005.
4. Elimination of hexavalent chrome in the surfaces of black and olive chromatic coatings until the July 2007.

Table 4 Different chromate conversion coating, substrate, coating contents, and obtained results of them

Treatment type	*Base metal*	*Coating type*	*Results*	*Adhesion*	*References*
Chromate conversion coatings (CCCs)	Metal such as cold-rolled steel, galvanized steel, and copper and aluminum alloys	Silane films	A superior application method because of more uniform and compactness of prepared films and thereby the best barrier properties compared with other application methods. The properties of the silane, as a corrosion-resistant pre-treatment coating, may significantly improve by the incorporation of rare earth salts and nanoparticles	Excellent adhesion and good barrier properties	9
Conversion coating produced by the permanganate-based system	Strip of galvanized steel	The manganese oxide-aluminum oxide	Extra thickness is due to the slow formation of the coating, which provides a more corrosion-resistant surface	Excellent paint adhesion due to the large number of attachment points available to the applied coating	28
Chromium VI as alternative oxidizing species, sodium molybdate, tungstate and vanadate, and ammonium molybdate, $(NH_4)6Mo_7O_{24} \cdot 4H_2O$	Zinc galvanized steel	$Cr(OH)_3$, $CrO(OH)$ and $ZnCr_2O_4$	Both improve the corrosion resistance and enhance the chemical adhesion of organic coatings	Enhance the chemical adhesion of organic coatings	68
CCCs cerium and rare earth oxide-based coatings cerium oxides	2024-Al varying amounts of Ni^{2+} and Mn^{2+}	Al–Cu–Mg(ZPO coating crystals at the edge of the particle but not over most of its central area). CeO_2, $Ce(OH)_4$, and $Ce(OH)_3$	More easily accept applied primer and/or paint and offers corrosion resistance in the event that the covering layer is damaged	Adhesive coating	69
CCC	Aluminum, Grade 1050	Insulating oxide film on aluminum	Chromating will provide enhanced corrosion resistance	Increase the adhesion of paints or other subsequently applied coatings	70
Alternative treatment to CCC	AA 6082 aluminum alloy	Deposition of films of $CeO_2 \cdot 2H_2O$ (or $Ce(OH)_4$ on aluminum alloys in a few minutes at room temperature with or without a catalyst	Coatings obtained without a catalyst had some interesting properties though EIS revealed that their performances still did not equal those of CCC	The catalyst also improved the adhesion of the $CeO_2 \cdot 2H_2O$ layer but has dramatic effects on the anti-corrosion properties	71
CCCs	Al 2024-T3	Cr^{3+} hydroxide	Inhibition of Al corrosion is derived from both inhibition of oxygen reduction and inhibition of metal dissolution reactions mainly due to a delay in the onset of pitting	Excellent adhesion	72
CCCs sol–gel chemistry-based coating	Aluminum	Cr(VI), alodine film oxide materials	Improve corrosion resistance and paint adhesion	Improve paint adhesion	73

(*Continued*)

Table 4 Continued

Treatment type	*Base metal*	*Coating type*	*Results*	*Adhesion*	*References*
		hybrid organic/ inorganic			
CCCs	Commercial purity rolled aluminum	Chromate film	Good paint and lacquer adhesion	Improve the adhesion strength	74
Conversion coatings	99.99% pure aluminum	Hydrated chromium oxide/hydroxide and chromium phosphate	Improve corrosion resistance and paint adhesion	Enhancing adhesion	75
CCCs	5083 aluminum alloy	Epoxy paints were applied to the chromate and non-chromate treatment surfaces	Corrosion propagation from the scratched area in the painted samples with chromate treatment was lower than for the non-chromate coated surfaces coating system including chromate treatment presented lower corrosion current densities, higher polarization resistance, and less negative corrosion potential than the corresponding values obtained for the non-chromate conversion-coated surfaces	Adhesion of coating systems (including chromate treatment) was better than the adhesion of non-CCCs	76
Failure of chromate-treated aluminum bonded in lap shear configuration using a structural epoxy paste	2219 Al alloy was treated with Alodine 1200	Chromium is present in the conversion coating as both Cr(III) and Cr(VI) species, and that other components are present at the conversion coating surface, some in a reduced form	High strength and good toughness durable in high and low temperatures, thermal cycling, radiation, atomic oxygen exposure	Excellent adhesion	77
0.5 g $Fe(NH_4)(SO_4)_2 \cdot 12H_2O$ to 20 ml of 0.05 M $K_4Fe \cdot (CN)_6 \cdot 3H_2O$ solution [Fe(II):Fe (III)51:1]	Aluminum alloys, such as AA 2024-T3 aircraft alloy	CCCs have	Corrosion-resistant coating strongly coating	Adhesive coating	78
CCCs	A sandwiched type of electro-galvanized (EG) steel sheet	Bonded with poly (vinyl butyral) (PVB)	Enhanced both initial tensile shearing strength (TSS) and the joint durability in the corrosive environment. Improvement on the shearing properties of the EG steel sandwiches	Good adhesion of TSS equal to 17.8 MPa	79

3.20.3.4 The Comparison of the Hexavalent and Trivalent Chromes

The danger of skin cancer increases in utterly subjecting to the hexavalent chrome coatings. The hexavalent chrome is the only form of chrome that penetrates into the cell membrane of human beings, and subsequently destroys cells. This action creates environmental pollutions during the destruction or recovery of the vehicles. Nonetheless, hexavalent chrome gives the best corrosion resistance of the conversion and surface coatings. Trivalent chrome is safe for the environment and health problems, but its corrosion protection properties are not as similar as hexavalent chrome. So, it is necessary to use a topcoat in most cases, and this issue increases the cost of the coating. Practically, controlling the coating bath corresponded to trivalent chrome and sustainable maintenance of it

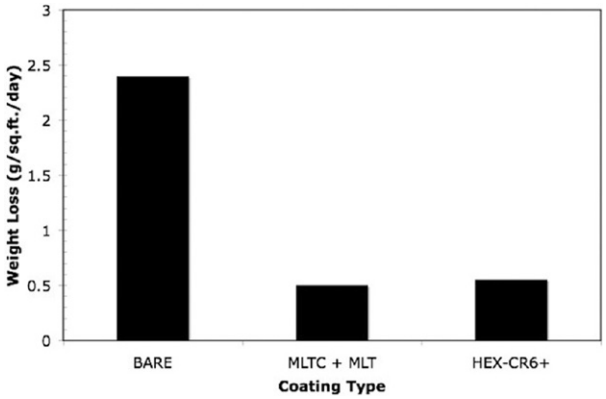


Figure 4 Weight reduction curve and the coating type of the sample, with AZ92A magnesium alloy.[80]

is thoroughly problematic. On the other hand, appearance and quality facet also is not feasible to stay stable. The coating adhesion to the metal is less, as well. The trivalent chrome coatings are cheaper than hexavalent ones. For example, this value for trivalent shiny blue chrome is approximately 10–20%. But, as discussed above, with regard to having less corrosion protection properties of trivalent chrome, and computation in the use of a topcoat, the cost of the coating increases. On the other side, coatings comprising trivalent chrome prominently involve the exploitation of oxidizing agents, which converts them into the hexavalent chrome in the coated surfaces. Nevertheless, the use of hexavalent chrome coatings creates not only a better corrosion resistance but also an easier operation and higher stability.[85]

3.20.3.5 Phosphating

Phosphate–zinc coating (plating) is one of the first conducted plating in the industry.

This plating is done both in the forms of immersion and spray. The purpose of phosphating is improving the color adhesion, increasing the corrosion resistance, aiding to alteration of cold deforms, and raising the surface abrasion resistance. Consisting materials of the zinc–phosophating bath are zinc oxide, phosphoric acid, nitrites, or nitrates (as a catalyst) and distilled water. Phosphate coating as a conversion coating is the result of reaction between iron parts and phosphate solution. This reaction takes place only in the surface of parts. This process along with decreasing and sometimes pickling, have been recognized as preparation of the components. This coating is in the form of dark rainbow in the iron group phosphates, and dark gray to black crystals in either zinc or magnesium group phosphates. By using activators and accelerators, the appearance changes in unevenness and the size of phosphate crystals could be made up. Phosphate coatings are applied to three general purposes following:

1. Increasing color adhesion: phosphate crystals increase the color adhesion by creating roughness on the surface of the parts.
2. Raising corrosion resistance: phosphate crystals are suitable sites for maintaining anti-corrosion oils longer, by creating roughness over the surface of the components. It also prevents rusting of the screws and nuts, while welding of the parts to each that is carried out. This application is called anti-galling.
3. Wire tension of sheets, pipes, or rods: phosphate crystals are an appropriate carriage for preserving tension oils or powders by creating roughness, which makes better lubricating through crushing the crystals in the tension process or pressing, in addition to increasing the quality of the parts and avoid the lines and scratches.

Electrical properties of the phosphate coating are given below:

Zinc oxide: this substance is used as a basic ion of zinc; this material has been exerted between similar components because of many aspects such as being more economical and cheaper, easier transportation and usage, and also, produced in diverse grades.

Phosphoric acid: this substance is used as a base for phosphate ion. It is also a supplier of some required acids in terms of acid washing process and dissolution of iron ion from the part's surface.

Nitric acid: generally, this material is applied for: (1) regulating the free acid and total acid, and as a result regulating the deposition grain size. (2) pH regulating, and (3) supplier of the nitrate ion. If its value heightens, because of increasing free acid, coating with finer grains is obtained.

Nickel ion: nickel salts are used in this process as facilitators, meanwhile Nickel itself gets deposited on the surface and causes the darkness of sediment.

The coating process: the coating process is commenced over the metal surface firstly, with processes of oxidation and releasing the iron ion in suspension. At this stage, initially, the metal surface is oxidized through the various oxidations existing in suspension, and two positively charged iron ions are released into the bath. At this phase, the amount of acid bath and type of oxidizing play decisive role in the speed and type of reaction in the acid washing. For two common oxidizers, nitrate and chlorate, following reactions can be considered:

$$4Fe + NaNO_3 + 10H^+ \rightarrow 4Fe^{2+} + NH_4{}^+ + Na^+ + 3H_2O$$

$$3Fe + NaClO_3 + 6H^+ \rightarrow 3Fe^{2+} + NaCl + 3H_2O$$

In these kinds of reactions in addition to surface acid washing, released hydrogen ion from the surface part also combined with the oxidizing material and as a result, impedes of releasing hydrogen gas from the surface of the material. It is so called that releasing of the hydrogen gas from these surfaces leads to increasing the thickness of the iron-saturated layer and hence, it takes more time to become supersaturated; so, the overall speed of the process is decreased; because the layer that is stationary on the part's surface must initially be saturated by metal ions in the favor of getting ability of depositing crystals on the part's surface by the cited layer. After saturating of the solution, zinc phosphate crystals are formed over the surface and deposited on the piece. The mechanism of deposition includes nucleation and growth steps. The type of oxidizer, solution composition, temperature, and pH are also the agents that affected this mechanism.

Table 5 Classification of the types of non-chromic coatings, substrate, coating contents, and obtained results

Treatment type	*Base metal*	*Coating type*	*Results*	*Adhesion*	*References*
The manganese oxide, zinc oxide conversion coating produced by the permanganate-based system	Zinc and zinc alloys	Chromium: 17%; zinc: 12%; carbon 10%; oxygen: 54%; aluminum: 6%; and trace: copper and fluorine (less than 2%)	Will more easily accept applied coatings and/or resist corrosion. They are rather thin (not more than 6000 nm on zinc), quickly and easily formed, easily scratched	If used to improve upon paint adhesion – they are coated shortly after being formed to prevent degradation of the conversion coating	29
Multi-elements complex coating	AZ91D magnesium alloy	$Ca_{0.965}Mg_2Al_{16}O_{27}$, $Mn_5 \cdot 64P_3$, $ZnAl_2O_4$, and $(Mg_{0.66}A_{l0.34})(Al_{0.83}Mg_{0.17})_2O_4$	Good corrosion resistance	Can provide better protection to the substrates of magnesium alloy	66
Chromate-free conversion coating	Magnesium alloys Mg AZ91D	NANOMYTE PT-60	Anti-corrosion performance exhibits less corrosion than other chromate and non-chromate industry standards	Excellent adhesion	67
Replacement to the conventional hexavalent chromium-based chemfilm technologies for magnesium alloys	Cast AZ92A-T6 magnesium alloy	Conversion coating, hexavalent chromated, and trivalent chromium treated	The new non-chromated conversion coating technology could be a drop-in replacement to the conventional hexavalent chromium-based conversion coatings	Coated samples had relatively higher pull-off adhesion value of 3140 psi compared to the hexavalent chromated samples (2542 psi)	80
Chrome-free conversion coating	Magnesium, aluminum and zinc, and their respective alloys	Oxidation of magnesium, aluminum, and zinc	Electrical conductivity, filiform, and neutral salt-spray corrosion resistance	With the same level of adhesion and secondary corrosion resistance as that found in chrome containing conversion coating systems	81
Conversion coating	AZ91D magnesium alloy	$K_2HPO_4 \cdot KMnO_4$	Corrosion resistance of the conversion coating by phosphate-permanganate solution is matched to that of the conversion coating by traditional chromate solution, but for the corrosion resistance after painting, the former is better than the later	Good adhesion to matrix	82
Chrome-free nanocomposite sol–gel coatings	AA5083	Tetraethylorthosilicate and 3-glycidoxypropyl-trimethoxysilane	Minimum corrosion current density	Strong adhesion	83
Created by Cr(III), Cr (VI), Cr(III)-Co(II), and Cr(III)-Ni(II) conversion coatings. Epoxy nanocomposites	Hot-dip galvanized steel (HDG) samples	Epoxy nanocomposite on the HDG steel samples, treated by different kind of conversion coatings	Improve the corrosion n resistance of the epoxy coating on HDG. Decrease of contact angle (φ) and increase of surface roughness (*Ra*) of the pretreated HDG samples were obtained	Increase of the adhesion strength	84

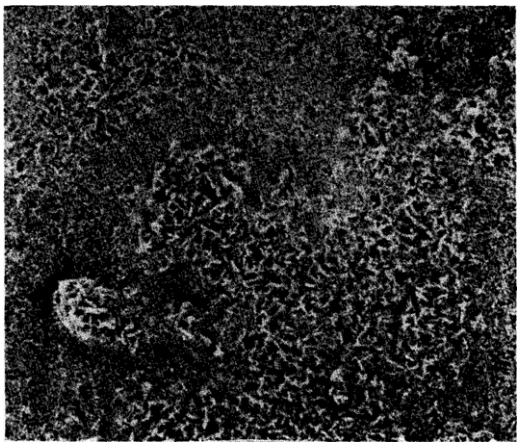


Figure 5 The scanning electron microscope image of the zinc phosphate coating applied over the galvanized steel.[28]

The conventional reaction of forming coating is followed by:

$$3Zn^{2+} + 6H_2PO^{2+} \rightarrow 4Zn_3(PO_4)^{2-} + 4H^{4+} + H_2PO_4^-$$

However, relying on the composition of a solution, other reactions can take place as follows:

$$2Zn^{2+} + 4H_2PO^{2+} + 4Fe \rightarrow Zn_2Fe(PO_4)^{2+} + 2H^+ + H_2 + 2H_2PO_4^-$$

$$2Zn^{2+} + 6H_2PO_4^- + Ca \rightarrow CaZn_2(PO_4)^{2+} + 4H^{4+} + H_2PO_4^-$$

Each phase that is made in these reactions, has different properties.

For instance, in the third reaction of this category $CaZn_2(PO_4)_2$, it is observed that by applying that on the coating, the roughness of the coating is decreased.[86] **Figure 5** shows the SEM image of the zinc phosphate coating over the galvanized steel. The thin crystalline structure of this coating is a the result of high forming speed of coating and because of the presence of active regions, gives the best color adhesion.[28]

Figure 6 is the SEM image of the galvanized steel with the cited chromate coating. Over passing of immersion time and being thickened of the coating, the corrosion resistance properties have been modified. Also, the created roughness on the surface, provides the conditions of good adhesion for subsequent layer.[28] The potentiodynamics of the sample without coating and the sample containing zinc phosphate coating, that has been applied over the 6061 aluminum alloy shows that the phosphated sample has more negative potential and, relative to other sample is more active.[41] The test results of adhesion and corrosion resistance show that both cases improve with applying this coating.[41] The **Table 6** shows several samples of the applied phosphate coatings on different substances in which adhesion and other coating properties have been investigated.

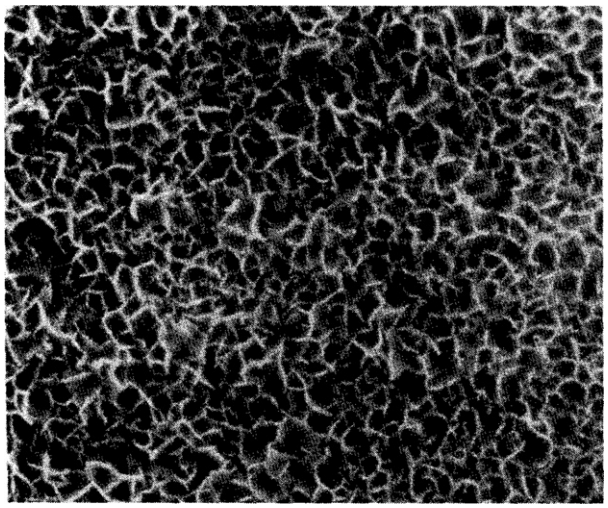


Figure 6 Scanning electron microscope image of the thick zinc phosphate coating over the galvanized steel.[28]

3.20.4 Polyurethane Coating

Outdoor usages and using a polyurethane coating in front of the UV ray increase durability of the coating system, and ultimately the structure itself is affected. Applying this coating is recommended over the available and compatible anti-corrosive liners and intermediates in sites and environments with different atmospheric conditions. Using in the acute acidic situations is not recommended. The coating has good adhesion to most metals. Marine and steel structural coatings, bridges, exterior surfaces of tanks, refiners, petrochemical plants, the final coating for protection of metal structures in acute and corrosive environments that the color and loss stability are required, metallic structures in chemical and petrochemical industries, power stations, waste water treatment plants, decks and the ship's hull are some of its applications either.[95]

This coating, as the last layer, undertakes the protecting of the surface and underlying layers of the coating system against the climatic situations. The high resistance against the ultraviolet radiations is distinguished characteristic of this color. Flexibility and high hardness have caused to the extraordinary efficiency in the difficult mechanical conditions.

- High adhesion and hardness on the metallic surfaces.
- Excellent case against ultra-radiation.
- Supplying supreme endurance in marine and industrial ambient.
- Resistant to water, impact and abrasion.
- Very good stability against climatic changes and extreme weather environments.[95]

Preparing and spraying steps: the needed surface should be clean and devoid of any pollution, fat, oil, and humidity. The cleaning operation is done by proper detergents. If the paint is directly applied on the surface, the surface should thoroughly be prepared. After preparation of the surface, the color components are mixed through the certain mixing ratio (according to the guidelines), and stirred with an appropriate stirrer until obtaining a uniform and homogenous mixture.

Table 6 Scrutinizing variety of phosphate coatings, substrate, coating contents and the handled results of them

Treatment type	*Base metal*	*Coating type*	*Results*	*Adhesion*	*References*
Zinc phosphate coatings	AA6061 alloy	$AlPO_4$	Give strong adhesive bonding and improve corrosion resistance	Strong adhesive bonding	41
Phosphating	Steel	$Fe(H_2PO_4)_2$	Improved corrosion resistance, wear resistance	Highly adherent to the underlying metal	46
Zinc phosphate coating	AZ91D magnesium alloy	$Zn_3(PO_4)_2$ H_2O, Zn, $AlPO_4$, and $MgZn_2(PO_4)_2$	Good corrosion resistance	The adhesion of paint on the zinc phosphate coating was better than that of paint on CCC due to the microporous structure of the phosphate coating	48
Phosphated substrates were coated with epoxy coatings	Galvanized steel specimens	Manganese modified phosphate conversion coating and primer, calcium modified phosphate conversion coating and primer	Enhance paint or lacquer adhesion and promote corrosion resistance	Improves the adhesion of organic coatings due to removal of strong organic contaminations and alteration of oxide layer	50
Conversion coatings	High-strength cold-rolled sheet steel supplied by the Bethelehem Steel Corporation	$Zn_3(PO_4)_2 \cdot 2H_2O$	The suppression and controllability of the crystal growth of Zn–Ph conversion coatings precipitated on high-strength cold-rolled steels depends primarily on the internal diffusion and segmental chemisorption of polyelectrolytes having functional carboxylic acid and sulfonic acid pendant groups on the embryonic crystal faces	Promoting adhesive strength	87
Copper on zinc phosphate conversion coatings	Al 2024-T3 alloy	Cu 2p spectra from the sample coated by solution containing 1 ppm Cu^{2+}	Cu in phosphating solutions that aim to meet the overall challenge of forming coatings that can improve the passivation of different Al alloy surfaces	Increased adhesion	88
Phosphatizing coating	Bare 2024-T3 Al panel	ISPC painted on chromated	Superior paint performance improved durability of paint	Improved adhesion	89
Conversion coatings	Steel	Polyacrylic acid (PAA) modified zinc phosphate crystal	Improve both resistance to corrosion and topcoat adherence. It has been reported that the addition of PAA reduces the size of crystallites, which leads to greater film ductility	Improved adhesion properties	90

(*Continued*)

Table 6 Continued

Treatment type	*Base metal*	*Coating type*	*Results*	*Adhesion*	*References*
Zinc phosphate conversion coatings	Metal surface	Metal oxide	Promote excellent paint adhesion and corrosion resistance	Excellent paint adhesion	91
Organic coatings	Low carbon steel sheets	Phosphatized and painted	Chromium passivation plus iron phosphates had very limited protective action	Metal paint adhesion is poor because of coating delamination enhanced by the parallel use of protection by magnesium anodes	92
Electrogalvanized steels (EGS)	1006 cold-rolled steel coated with electroplated zinc (Ford E 60 Electrozinc 60 G), supplied by Advanced Coating Technologies, Inc.	Zn and Ph-coated EGS substrates	Good protection layers against corrosion EGS surfaces. having poor adherence to polymeric topcoats were transformed into chemically and physically reactive surfaces by depositing hopeite	Improving adhesion to the polyurethane topcoating	93
Coating degradation and delamination process	Phosphated steel	Additional paint, wax, or sealer coatings	Long-term degradation processes leading to the failure of high performance coatings can differ in mechanism from those important for coatings that fail quickly	–	94

Table 7 Polyurethane coating, substrate, coating contents, and conclusions

Treatment type	*Base metal*	*Coating type*	*Results*	*Adhesion*	*References*
Thermoplastic polyurethane elastomer is co-molded with galvanized steel	Galvanized steel	Aminopropyl trimethoxysilane amino silane	The model, compared to experimental results, also revealed that it is important to account for internal stresses, mostly for treatments leading to low intrinsic interfacial shear strength values	The best silane treatments led to mixed cohesive–interfacial failure, while other treatments showed a purely interfacial failure	97

In order to dilute and adjusting the viscosity of color tinnier gradually add to the color, and stirred to the getting desired uniform composition. This coloring is applicable by airless spray, air spray, immersion methods, electrostatic spray, brush, and a roller. And, the unpainted and damaged parts on a small-scale can be repaired by brush.[96]

Researchers have investigated thermoplastic Polyurethane Elastomer adhesion to galvanized steel over the following article. When the thermoplastic polyurethane elastomer is applied to the galvanized steel, adhesion, and durability of that have a great dependence on chemical bonding thermoplastic polyurethane elastomer-metal. Aminopropyl trimethoxysilane gamma amino silane deposits under various parameters such as solvent type and pH. The preparation processes include sanding, pickling, air flow, and a zinc phosphate conversion coating. Polyurethane adhesion to the substrate was assessed by tensile tests and showed the desired results.[97] In **Table 7**, an example of presented papers has been studied.

3.20.5 Sol–Gel

This method is usually used for producing materials, as an example metal oxide starting from a colloidal solution (sol) that is as a precursor substance for an interconnected network (gel) of discrete particles or network polymers. Precursor substances typically include alkoxide and metal salts (such as chlorides, nitrates, and acetates) that are put under different hydrolysis and polymerization reactions. Generally, sol is

introduced as a stable suspension containing solid colloidal or polymeric particles in a liquid. These particles can be amorphous or crystalline. Solid colloidal particles that are nanosized dimensions are formed through two reactions. Simply said, sol is a mixture of solids with various sizes between 1 and 100 nm in water that are not deposited. It is comprised of:

1. Hydrolysis: through the effect of salt dissolved in water, the metal cathode ions establish complex with water. In this state, the pair electron transfer from water molecules to empty orbitals of transited metal cathode ion is possible. Hydrogen's particle charge is increased and water molecule catches acidic properties. According to the acidity of the water, types of hydrolysis reactions can be obtained. In general, raising the density of the metal ions cause to increasing the bridges of metal ions by AKSU and HYDROKSU ligands, and increasing the number of hydrogen existed in ligands and so an easier hydrolyzes.
2. Condensation: this reaction is done through two different friendly nuclear mechanisms and depends on the neighboring numbers of metals. When the needed neighboring number is provided, condition is done by a substituted friendly nuclear reaction, and when the needed neighboring number of metal is not provided, there is friendly coral additive.[98]

The condition reaction is actually a kind of polymerization itself, and is divided in two sections:

1. Alishan: a condition process that makes hydroxide bridges between two metals.
2. Axylishen: a condition reaction in which oxygen bridges between two metals occurred.

Sol formation is generally divided into two categories:

1. Formation of real solution from the considered precursors (alkoxide precursors or metal salt precursors) into the solvent that can contain water, alcohol, or acid.
2. Formation of the colloidal solution (sol) through the converting the metallic atoms to the metallic complexes by hydrolysis and condition reactions, that are actually the creator reactions of colloidal particles; by conducting these reactions, particles are getting larger and reaching the colloidal particle dimensions from 1 nm to approximately 100 nm. At this level of experiment, nanoparticles that are usually amorphous have been formed.
3. Stabilizing the colloidal particles and deterring them from depositing by a stabilizing agent. This agent can be controlled either by curbing the environmental factors such as pH controlling, sol temperature, the amount of sol is stirring, or by adding chemical materials.

Gel is a continuous three dimensional porous network that has inserted a liquid phase into itself. In most of sol–gel systems, the formation of the gel is followed by creation covalent bonds, and gel is not reversible; this means that, it has not the capability of reversing to sol state. If the acquired gel assets, bonds aside from other covalent bonds, it could be reversible. The types of gel based on formation mechanism:

Colloidal gels: in colloidal gel, the network is created by agglomeration (sticking) of the colloidal particles.

Polymeric gels: in polymeric gel, the network has a polymeric microstructure; in other words, it consists of polymeric units which are making up the gel.

The processes of the gel formation: after three steps that were mentioned in the formation of sol, the formation processes of gel that actually are in the sequence of sol formation steps depending on the types of gel (colloidal or polymeric) are followed as:

1. If gel is colloidal, it is obtained through sticking the colloidal particles to each other by weak van der Waal's forces as a result of evaporation of the solvent surrounding the colloidal particles.
2. If gel is polymeric, that means the surround of colloidal particles would compose of molecules which are susceptible to forming a polymeric matrix. In this case colloidal particles are stabilized like raisins in a raisin cake. Therefore, it can be led to stabilizing this polymeric network by changing the surrounding agents such as pH, temperature and time regulation, or adding chemical materials. Then, it can be gotten rid of the polymeric network around the gel by contriving it into an oven, and we will then just have nanoparticles at this level of function. Eventually, by putting the obtained product in the oven being aware of the minimum calcination temperature, the amorphous nanoparticles can be transformed into crystalline nanoparticles. Aluminum and its alloys are used expansively in



Figure 7 The scheme of the coating system (a) conversion, (b) new sol–gel coating, and (c) the technology of non-chromium super primer.

the industries of marine, aerospace, and Auto industries. This metal has good mechanical and physical properties, but it has not acceptable corrosion and abrasion resistance because of its porosity. Typically, chromate coating is used for preparation of the surface; although, it is forbidden the usage of chrome compositions due to causing cancer diseases.[98]

The hybrid sol–gel coating based on silica is an appropriate alternative to chromate compositions because of forming the

Table 8 Sol–gel coating type, substrate, coating contents, and acquired results

Treatment type	*Base metal*	*Coating type*	*Results*	*Adhesion*	*References*
Conversion coating	Clad 2024-T3 aluminum alloy	Oxide layer sol–gel-treated epoxy aluminum joint	Macrorough structures drive the crack to within a thin epoxy layer close to the polymer–metal interface, which enhances the initial strength of the sol–gel-reinforced interface	Enhanced adhesion	45
Nanocomposite sol–gel coatings	AA5083	Tetraethylorthosilicate and 3-glycidoxypropyl-trimethoxysilane	The evaluation of the result obtained from abrasion shows cohesive and interfacial wear with abrasive and adhesive mechanisms, respectively. Liquid impact results show cohesive failure of the coatings without any sign of delamination	Good mechanical properties of optimum nano-composite coatings, such as excellent adhesion to the substrate (4.74 MPa)	98
Sol–gel-based hybrid coatings	316 l stainless steel	Titanium-isopropoxide and 3-glycidoxypropyl-trimethoxysilane	A three dimensional network of –Si–O–Si– linkages environment-friendly technology with number of advantages like room temperature synthesis, chemical inertness, high oxidation and abrasion resistance, excellent thermal stability, very low health hazard	Excellent adhesion to metal as well as to the subsequent coat via strong covalent bond	99
Hybrid nanocomposite sol–gel coatings	Aluminum 5083 alloy	Fourier transform infrared spectra of the hybrid films for different samples	Exhibit excellent mechanical properties as well as adhesive to the substrate	Maximum adhesion of coating to the substrate	100
Hybrid sol–gel	Aluminum alloy AA2024	Two different types of coating were applied: a non-inhibited film consisting of two layers (non-inhibited system) and a similar film doped with cerium nitrate in an intermediate	Improve corrosion behavior of aluminum alloys	Improved adhesion	101
Sol–gel	Mg	MgF_2 coating on Mg and the HA coating on MgF	Improved the corrosion resistance and the bioactivity of Mg. The coating layers were uniform, dense and strongly adhered to the Mg substrate without any posttreatment. The double coating layer effectively reduced the Mg corrosion rate and prevented the formation of any by-products in the SBF solution	Strong adhesion to the Mg substrate, with a bonding strength of 34 MPa the bonding strength of HA coating on the MgF_2 (25 MPa) was slightly higher than the HA coating on the bare Mg (22 MPa)	102

SiloxaneDance network. Hybrids have been noteworthy to researchers because of having both polymeric and ceramic material's properties.[98] In other case, the SEM image of low carbon stainless steel 316 with and without sol–gel coating after polarization test showed that the sample without coating has been locally and uniformly eroded and there were cavities on it; while there were fine cracks on the coated sample.[99] To resolve this problem, multi-layer and sophisticated systems below have been proposed, and the best results have been obtained with the help of super primer as shown in **Figure 7**.[98]

As it is observed, coating of tetraethylorthosilicate and glycidoxypropyltrimethoxysilane over the aluminum alloy resulted in increasing corrosion resistance of this alloy. In addition, uniformity and homogeneity of this coating to improve the adhesion.[100] **Table 8** consists of the hybrid and nanocomposite sol–gel coatings have been applied to diverse substances and led to increasing the adhesion properties and improving mechanical properties, abrasion resistance and corrosion resistance.

3.20.6 Electro Deposition

Electro deposition is a strong method for coating the surface. The main electrodeposits' properties are abrasion resistance, hardness, formability, porosity, inner tensions, coating adhesion, and corrosion resistance. All of these properties and characteristics can be changed by selecting a few numbers of variations such as temperature, component's concentrations, pH of electrolyte, current density, condition of electrolytic current, and using the electrolytic additives. Creating a surface coating by the way of electro deposition may comprise a variety numbers of important processes, including the preparation of the substrate, coating formation, and final checkout. The thickness of applied deposit is controlled through operations in a constant time and a constant current density. As it is derived from the Faraday law for electrolysis, for an intended metal (M) which is deposited from the location of its ions (M^{z+}), the following relationship is established:

$$M^{z+} + Z^{e-} \rightarrow M$$

Under constant circumstances with constant current density (I), thickness rate of the coating (X) develops related to time which is described through the following equation:

$$dx/dt = (MI\varphi/\rho AzF)$$

As M is the molar weight of materials, φ current efficiency, ρ density of the sheeted layer, A deposited space, z the number of transferred electrons, and F is Faraday constant. Hence, with the assumption that current efficiency is 100%, with a given current density and knowing the electrode ambiance, the coating thickness can be stabilized for each metal by time, so that this phenomenon for the selection of materials that use 1 A dm^{-1} current density; deposited thickness can be altered from several single layers up to hundreds micrometers.[103] There are two hypothesis:

1. 100% current efficiency, which cannot be real, although reaching to 100% efficiency may be possible in some systems.
2. Deposit density is in equilibrium to the density of pure metal, which also this case is not essential against high porosity of some deposits. The current efficiency and density of the coatings that are in the formation of electrolytic deposits are decreased by raising the current density. Generally, in order to decoration of electrolytic deposits, they have to be smooth and flawless and also mirror-polished. While engineering does not need special decorative coatings, deposits should be compressed and homogenized. They also have to coat all substrates. Some intermediate depositions lead to electrolytic deposit over the unacceptable surface coatings. This case, also, comes to pass by using high current densities which resulting in irregular settlements. The more applicable method to developing and changing the structure and appearing electrolytic depositions is integrating the additives in the electrical plating bath.[104] In addition to pure metals, alloys (double, triple, and complex), oxide layers, conductive polymers, and composition layers can be produced by using electrolytic methods. A wide range of engineering applications could be manufactured by electrolytic deposition that involving conductive coatings for electronic

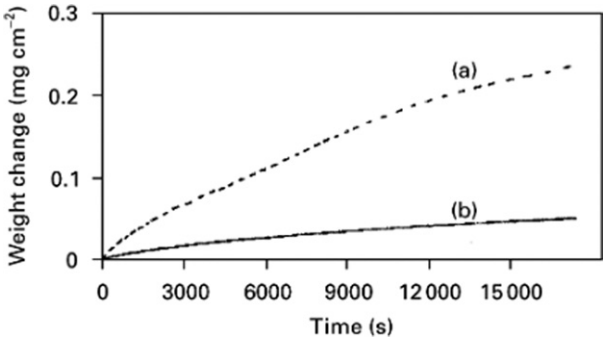


Figure 8 The graph of weight changing (a) steel without coating and (b) steel with electrolytic coating relied on time with temperature 1000 °C.[106]

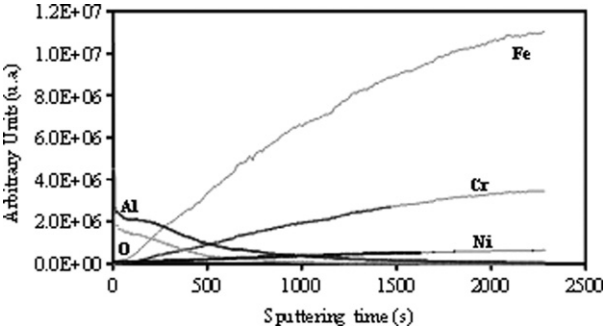


Figure 9 The distribution profile of elements in the alumina deposition according to the bombarding time.[106]

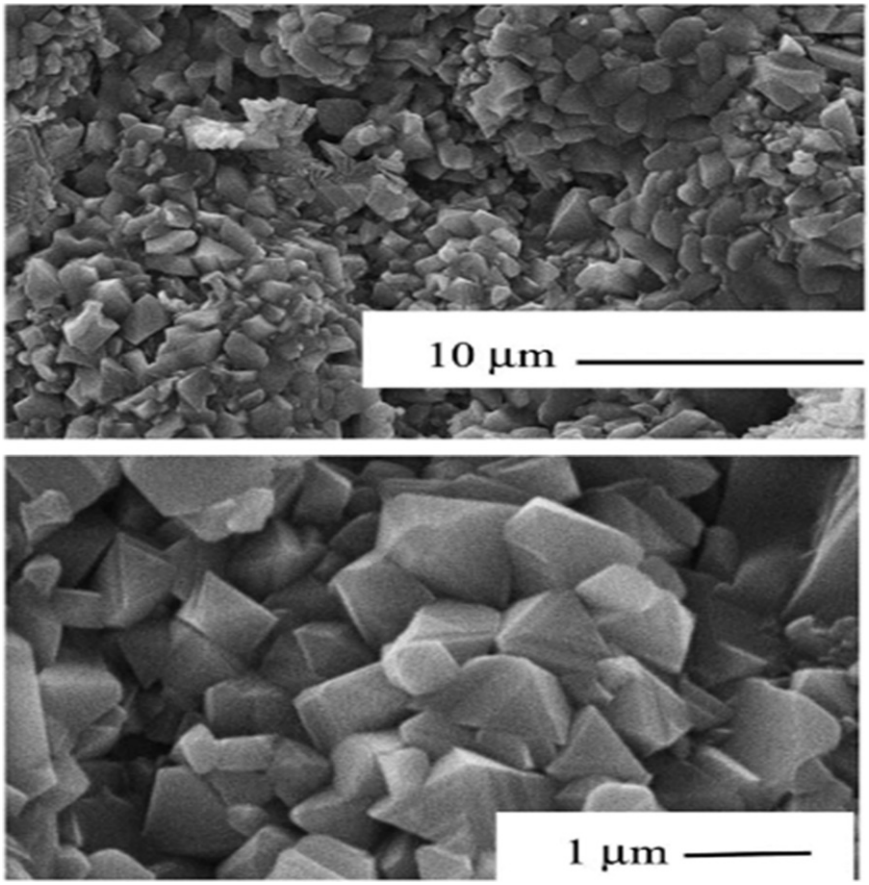


Figure 10 The scanning electron microscope image of formed alumina coating in air 1000° after oxidizing for 8 h.[106]

industry, tribological layers for mechanic engineering and nano structures for specific magnetic semi-conductors and optical applications. Coatings are categorized in metallic, composite and anodized groups. This classification is based on the relation between process conditions and deposit features. Electrolytic deposition can be categorized into two separate methods:

1. Electrolytic deposition: soluble ionic components that are mainly metal ions, decrease at the cathode and obtain from depositing an electrolytic deposition layer of the electrolytic solution. Anode can be either soluble or insoluble.
2. Electrophoretic deposition: deposited material exists in the form of fine powder in the electrolyte. Selective absorption, which has been done on the particles, separating ions of the particles, encountering bipolar molecules or electron transferring in solution, all create charges over the particles. When a surface charge is applied, the electrical potential between anode and cathode initially causes surface separation which had been coated. Electrolytic coatings can be applied in different classifications. Their range is wide from simple homogenous layers to complex multi-depositions. Electrolytic depositions can be getting proper to special applications.[105] Morphology and properties of electrode-deposited metal coatings vary according to many factors containing electrolyte bath composition, coating method, deposition thickness, and electrolyte temperature. As it is said, the electrolyte or immersion method is a way to apply coating that is done generally on stainless steel, aluminum, and magnesium. Such properties that these kinds of coatings create are excellent adhesion and appropriate roughness along with corrosion resistance.[105] **Figure 8** shows the corrosion resistance or weight loss with time for the samples with and without coating. It is obvious that, the alumina coating applied on an authentic stainless steel has improved the corrosion resistance of the alloy.[106]

The **Figure 9** shows the profile distribution of different elements in the applied Alumina coatings over the austenitic stainless steel with the passing of the bombarding time. It is clear that by passing of the bombarding time, the percent of alumina has been reduced, in contrast to increasing of Fe.[106]

The **Figure 10** is the SEM image of applied alumina coating on austenitic stainless steel. As it can be seen, the alumina structure with complicatedly mixed crystals contributes to the creation of a penetrable boundary layer and increase the corrosion resistance and on the other hand, appropriate surface roughness makes it ready for the subsequent coating application.

Table 9 Different electrolytic coatings, substrate, coatings contents, and obtained results

Treatment type	*Base metal*	*Coating type*	*Results*	*Adhesion*	*References*
X-ray photoelectron spectroscopy	Pure aluminum	Alumina	Improved performance in corrosion resistance of these metals is the improvement of the hydration resistance of the oxide film or the oxidocoating interface	Improved performance in adhesion	49
Electrolytic alumina deposit	Austenitic stainless steel	Alumina	Improving the resistance to thermal oxidation	Strong interfacial adhesion with the substrate	106
Alumina coatings	Fe–Cr–Al alloy	Crystallized alumina coating	Conductive and porus enough to permit during the electrolysis for the aluminum salt modifies the oxidation kinetics of the alloy very high temperature resistance	Strong adhesion	107
Aluminum hydroxide deposited from an aqueous solution of an aluminum salt	Fe–17% Cr ferritic stainless steel	Precipitation of aluminum oxyhydroxide	Fabrication of thermal barrier on a metal conversion coating substrate	Excellent adhesion	108
Electrodeposited ZnN	Steel sheet	4-nitrothiophenold and 4-nitrobenzenediazonium	Improve the corrosion properties as well as the durability of the hybrid coating. Functionalities depending on the rest of the molecule structure such as lubrication and adhesion	Excellent adhesion	109
Electrodeposited	AZ91 Mg alloy	$Mg(OH)_2$	Superior corrosion resistance for the coated AZ91 Mg alloy as the corrosion current density decreased, for coated specimen and the corrosion potential increased at the same condition	Maximum bond strength	110
Deposits of alumina added or not with yttrium	Fe–17% Cr stainless steel	Alumina	Yttrium improved the protecting character of alumina coating; reduces the rate of oxidation and increase the adhesion of deposits	Enhances its adhesion	111
Plasma electrolytic oxidation	Aluminum (Al), magnesium (Mg), titanium (Ti), and their alloys	Substrate metal oxides (such as Al_2O_3, TiO_2, and MgO on Al, Ti, Mg and their alloys, respectively) complex oxides and compounds which involve the components presented in the electrolytes	Poor tribological properties, such as low wear resistance, high friction coefficient and difficulty to lubricate, have seriously restricted their extensive applications	Superior wear resistance, large thickness, high microhardness and good adhesion to substrates	112

In the following essays in Table 9, it has been reviewed electrolytic coatings that have been applied on the various substrates and caused to improve the mechanical properties, hardness, and adhesion and corrosion resistance.

3.20.7 Conclusions

Adhesion is the physical resistance of an interface between regions of the material system. Such interfaces have been

found in the grain boundaries, surface abrasion and failures, as well as, in the substrate-film systems. To evaluate the adhesion quality and amount of it in the substrate-film systems, different coatings containing preparations, supplementary operations, conversion coatings, chromate, phosphate, polyurethane and sol–gel coatings, and electrolytic depositions have been scrutinized in the forms of tables. As it was obviously inferred, the type of preparation process and supplementary operation play a vital role in the adhesion quality of surfaces. Then phosphate and chromate conversion coatings were analyzed, which the results demonstrated an increase and improvement of diverse properties especially adhesion. Polyurethane coatings modify the morphology of the surface and sol–gel coatings increase adhesion properties, reformed of mechanical properties, abrasion resistance, and corrosion resistance. In the end, electrolytic deposition coatings lead to improving mechanical properties, hardness, adhesion, and corrosion resistance.

See also: 3.21 Powder Metallurgical Processing of NiTi Using Spark Plasma Sintering

References

1. ASTM B571-97. *Standard Practice for Qualitative Adhesion Testing of Metallic Coatings*; ASTM International: West Conshohocken, PA, 2013.
2. Higgins, G. L.; Hullcoop, R. S.; Turgoose, S.; Bullough, W. 4.01 – Surface Pretreatment. In *Shreir's Corrosion – Volume 4: Management and Control of Corrosion*; Richardson, T. J. A., Ed.; Elsevier, 2010, pp. 2483–2493. Available from: http://www.sciencedirect.com/science/referenceworks/9780444527875 (accessed 4 April 2016).
3. Sato, K.; Shikida, M.; Laermer, F. Wet and Dry Etching. In *Comprehensive Microsystems*; Gianchandani, Y., Tabata, O., Zappe, H., Eds.; Elsevier, 2008, Vol. 1, pp. 183–233, Available from: http://www.sciencedirect.com/science/referenceworks/9780444521903 (accessed 4 April 2016).
4. Andreatta, F.; *et al.* Development and Industrial Scale-Up of ZrO2 Coatings and Hybrid Organic–Inorganic Coatings used as Pre-Treatments Before Painting Aluminium Alloys. *Progr. Org. Coat.* **2011**, *72* (1–2), 3–14.
5. Romagnoli, R.; Vetere, V. F.; del Amo, B. Effective Acid Pre-Treatments for Galvanised Steel. *Surf. Coat. Int. Part B: Coat. Trans.* **2003**, *86* (4), 301–307.
6. Blawert, C.; da Conceicao, T. F.; Kainer, K. U.; Izquierdo, P.; Klose, S. G.; Hche, D. Influence of Die Lubricants on Pickling and Conversion Treatment of High-Pressure Die-Cast AM30 Magnesium Alloy. *Adv. Eng. Mat.* **2012**, *14*, 227–235.
7. Ramezanzadeh, B.; Attar, M. M. Evaluation of the Effects of Surface Treatments on the Cathodic Delamination and Anticorrosion Performance of An Epoxy-Nanocomposite on Steel Substrate. *J. Coat. Technol. Res.* **2013**, *10* (1), 47–55.
8. Tepe, B.; Gunay, B. Evaluation of Pre-Treatment Processes for HRS (Hot Rolled Steel) in Powder Coating. *Prog. Org. Coat.* **2008**, *62* (2), 134–144.
9. Zaferani, S. H.; *et al.* Using Silane Films to Produce an Alternative for Chromate Conversion Coatings. *Corrosion* **2012**, *69* (4), 372–387.
10. Živković, Lj. S.; Jegdić, B. V.; Popić, J. P.; Bajat, J. B.; Mišković-Stanković, V. B. The Influence of Ce-Based Coatings as Pretreatments on Corrosion Stability of Top Powder Polyester Coating on AA6060. *Prog. Org. Coat.* **2013**, *76*, 1387–1395.
11. Habisch, H. J.; Fiedler, J.; Ludolph, A. C.; Storch, A.; Brenner, R. E. Altered Migration and Adhesion Potential of Pro-neurally Converted Human Bone Marrow Stromal Cells. *Cytotherapy* **2008**, *10*, 824–833.
12. Koch, A. Chemical Pretreatment of Metal Surfaces. *Sheet Met. Ind.* **1984**, *61*, 132–133.
13. Lunder, O.; *et al.* Effect of Pre-Treatment on The Durability of Epoxy-Bonded AA6060 Aluminium Joints. *Int. J. Adhes. Adhes.* **2004**, *24* (2), 107–117.
14. Mirabedini, S. M.; *et al.* Adhesive Strength of Powder Coated Aluminium Substrates. *Int. J. Adhes. Adhes.* **2005**, *25* (6), 484–494.
15. Montalvo, C. General Wisdom Concerning the Factors Affecting the Adoption of Cleaner Technologies: A Survey 1990–2007. *J. Clean. Prod.* **2008**, *16* (Suppl. 1), S7–S13.
16. Brewis, D. M.; Critchlow, G. W.; Curtis, C. A. Cryoblasting as a Pretreatment to Enhance Adhesion to Aluminium Alloys: An Initial Study. *Int. J. Adhes. Adhes.* **1999**, *19* (4), 253–256.
17. Harris, S. Powder Coating Solutions. *Polym. Paint Colour J.* **2006**, *196*, 8.
18. Darkins, P. D. A New System for Conversion Coatings. *Tribology* **1974**, *7* (3), 107–112.
19. Klingenberg, M. L.; *et al.* Transitioning Laser Technology to Support Air Force Depot Transformation Needs. *Surf. Coat. Technol.* **2007**, *202* (1), 45–57.
20. Kim, J. K.; Lebbai, M.; Woo, R. S. C. Effects of Hygrothermal Ageing and Thermal Shock on Reliability of Interfacial Adhesion between Black Oxide Coated Copper Substrate and Epoxy Resin. *Composite Interfaces* **2005**, *12*, 739–756.
21. Shimizu, K.; *et al.* Ultramicrotomy – A Route Towards the Enhanced Understanding of the Corrosion and Filming Behaviour of Aluminium and Its Alloys. *Corros. Sci.* **1998**, *40* (7), 1049–1072.
22. Watts, J. F.; Gibson, E. M. The Determination of the Acid-Base Properties of Inorganic Surfaces by X-ray Photoelectron Spectroscopy. *Int. J. Adhes. Adhes.* **1991**, *11* (2), 105–108.
23. Ye, X.-Y.; *et al.* The Influence of HF Treatment on Corrosion Resistance and In Vitro Biocompatibility of Mg–Zn–Zr Alloy. *Front. Mater. Sci. China* **2010**, *4* (2), 132–138.
24. Moffitt, C. E.; *et al.* XPS Analysis of the Aging of Thin, Adhesion Promoting, Fluorocarbon Treatments of DC Plasma Polymers. *Plasma. Polym.* **2001**, *6* (4), 193–209.
25. Ardelean, H.; Frateur, I.; Marcus, P. Corrosion Protection of Magnesium Alloys by Cerium, Zirconium and Niobium-Based Conversion Coatings. *Corros. Sci.* **2008**, *50*, 1907–1918.
26. Yang, L.; *et al.* Lanthanum-Based Conversion Coating on Mg–8Li Alloy. *Appl. Surf. Sci.* **2008**, *255* (5, Part 1), 2338–2341.
27. Aries, L.; *et al.* Electrochemically Induced Alumina Coatings on Stainless Steel: Composition and Behaviour at High Temperature. *J. Appl. Electrochem.* **1996**, *26* (6), 617–622.
28. Bibber, J. An Overview of Nonhexavalent Chromium Conversion Coatings – Part II: Zinc. *Met. Finish.* **2002**, *100* (2), 98–102.
29. Bibber, J. W. Non-Chrome-Containing Conversion Coatings for Zinc and Zinc Alloys. Environmentally Friendly Alternatives Provide Equal or Better Adhesion and Corrosion Resistance as Conventional Methods. *Met. Finish.* **2008**, *106*, 41–46.
30. Castro, M. R. S.; *et al.* Adhesion and Corrosion Studies of a Lithium Based Conversion Coating Film on the 2024 Aluminum Alloy. *Thin Solid Films* **2004**, *457* (2), 307–312.
31. Droniou, P.; Fristad, W. E.; Liang, J.-L. Nanoceramic-based Conversion Coating: Ecological and Economic Benefits Position Process as a Viable Alternative to Phosphating Systems. *Met. Finish.* **2005**, *103* (12), 41–43.
32. El Hajjaji, S.; *et al.* Effect of Treatment Baths Nature on the Characteristics of Conversion Coatings Modified by Electrolytic Alumina Deposits. *Corros. Sci.* **2000**, *42* (6), 941–956.
33. El Hajjaji, S.; *et al.* Duplex Conversion – Alumina Coating on Stainless Steel for High Temperature Applications. *Surf. Coat. Technol.* **1998**, *110* (1–2), 40–47.
34. El Hajjaji, S.; *et al.* Optimization of Conversion Coatings: Study of the Influence of Parameters with Experimental Designs. *Appl. Surf. Sci.* **2000**, *165* (2–3), 184–192.
35. Chen, Y.; Luan, B. L.; Song, G. L.; Yang, Q.; Kingston, D. M.; Bensebaa, F. An Investigation of New Barium Phosphate Chemical Conversion Coating on AZ31 Magnesium Alloy. *Surf. Coat. Technol.* **2012**, *210*, 156–165.
36. Ghanbari, A.; Attar, M. M. Surface Free Energy Characterization and Adhesion Performance of Mild Steel Treated Based on Zirconium Conversion Coating: A Comparative Study. *Surf. Coat. Technol.* **2014**, *246* (0), 26–33.
37. Critchlow, G. W.; *et al.* Chemical Conversion Coatings for Structural Adhesive Bonding of Plain Carbon Steels. *Int. J. Adhes. Adhes.* **2000**, *20* (2), 113–122.
38. Deck, P. D.; Moon, M.; Sujdak, R. J. Investigation of Fluoacid Based Conversion Coatings on Aluminum. *Prog. Org. Coat.* **1998**, *34* (1–4), 39–48.
39. Eivaz Mohammadloo, H.; *et al.* A Comprehensive Study of the Green Hexafluorozirconic Acid-based Conversion Coating. *Prog. Org. Coat.* **2014**, *77* (2), 322–330.
40. Dunn, M. H. *Post Processing Requirements for Plastic Bead Processing on Aluminum*. SAE Technical Papers, 1987.
41. Kok, W. H.; *et al.* Formation of Zinc Phosphate Coatings on AA6061 Aluminum Alloy. *J. Mater. Sci.* **2001**, *36* (16), 3941–3946.

42. Lebbai, M.; Kim, J. K.; Szeto, W. K. Surface Characteristics and Adhesion Performance of Black Oxide Coated Copper Substrates With Epoxy Resins. *J. Adhes. Sci. Technol.* **2003**, *17*, 1543–1560.
43. Leggat, R. B.; Taylor, S. A.; Taylor, S. R. Adhesion of Epoxy to Hydrotalcite Conversion Coatings: II. Surface Modification with Ionic Surfactants. *Colloid. Surf. A: Physicochem. Eng. Asp.* **2002**, *210* (1), 83–94.
44. Leggat, R. B.; Taylor, S. A.; Taylor, S. R. Adhesion of Epoxy to Hydrotalcite Conversion Coatings: I. Correlation with Wettability and Electrokinetic Measurements. *Colloid. Surf. A: Physicochem. Eng. Asp.* **2002**, *210*, 69–81.
45. Liu, J.; Berry, D. H.; Seebergh, J. E.; Osborne, J. H.; Blohowiak, K. Y. Effect of Surface Morphology on Crack Growth at a Sol–Gel Reinforced Epoxy/Aluminum Interface. *J. Adhes. Sci. Technol.* **2006**, *82*, 487–516.
46. Narayanan, T. S. N. S. Surface Pretreatment by Phosphate Conversion Coatings – A Review. *Rev. Adv. Mater. Sci.* **2005**, *9*, 130–177.
47. Niknahad, M.; Moradian, S.; Mirabedini, S. M. The Adhesion Properties and Corrosion Performance of Differently Pretreated Epoxy Coatings on an Aluminium Alloy. *Corros. Sci.* **2010**, *52* (6), 1948–1957.
48. Niu, L. Y.; *et al.* A Study and Application of Zinc Phosphate Coating on AZ91D Magnesium Alloy. *Surf. Coat. Technol.* **2006**, *200* (9), 3021–3026.
49. Metson, J. B.; *et al.* X-Ray Photoelectron Spectroscopy Applications to Corrosion and Adhesion at Metal Oxide Surfaces. *Colloid. Surf. A: Physicochem. Eng. Asp.* **1994**, *93* (0), 173–180.
50. Palraj, S.; Jayakrishnan, P.; Raghavan, M. Effect of Conversion Coatings on the Performance of Chlorinated Rubber Primer on Aluminium. *Surf. Coat. Int. Part B: Coat. Trans.* **2003**, *86* (1), 71–74.
51. Kim, G.; Ajersch, F. Surface Energy and Chemical Characteristics of Interfaces of Adhesively Bonded Aluminium Joints. *J. Mater. Sci.* **1994**, *29*, 676–681.
52. Spadaro, C.; Dispenza, C.; Sunseri, C. The Influence of the Nature of the Surface Oxide on the Adhesive Fracture Energy of Aluminium-Bonded Joints as Measured by T-Peel Tests. *Int. J. Adhes. Adhes.* **2008**, *28* (4–5), 211–221.
53. Wang, J.; *et al.* Hydrotalcite Conversion Coating on Mg Alloy and Its Corrosion Resistance. *J. Alloy. Compd.* **2010**, *494* (1–2), 271–274.
54. Wang, Z.; *et al.* A Conversion Coating on Carbon Steel with Good Anti-Wax Performance in Crude Oil. *J. Pet. Sci. Eng.* **2013**, *112* (0), 266–272.
55. Harvey, T. G. Cerium-based Conversion Coatings on Aluminium Alloys: A Process Review. *Corros. Eng. Sci. Technol.* **2013**, *48* (4), 248–269.
56. Holubka, J. W.; Hammond, J. S.; DeVries, J. E.; Dickie, R. A. Surface Analysis of Interfacial Chemistry in Corrosion-Induced Paint Adhesion Loss – 2. Effects of Resin Chemistry and Substrate Pretreatment on Adhesion Loss Mechanism. *J. Coat. Technol. Res.* **1980**, *52*, 63–68.
57. Han, S.; Y.Z.; Yu, S.; Xu, J. Study on Microstructure and the Mechanism of Zinc–Aluminum–Chromium Conversion Coating. *J. Chin. Soc. Corros. Prot.* **2002**, *22*, 273–276.
58. Lingjie, L.; Lei, J.; Yu, S.; Tian, Y.; Jiang, Q.; Pan, F. Formation and Characterization of Cerium Conversion Coatings on Magnesium Alloy. *J. Rare Earths* **2008**, *26*, 383–387.
59. Liu, B.-S.; *et al.* Blistering Failure Analysis of Organic Coatings on AZ91D Mg-Alloy Components. *Eng. Fail. Anal.* **2014**, *42* (0), 231–239.
60. Ostrowski, N.; *et al.* Corrosion Protection and Improved Cytocompatibility of Biodegradable Polymeric Layer-By-Layer Coatings on AZ31 Magnesium Alloys. *Acta Biomater.* **2013**, *9* (10), 8704–8713.
61. Takai, M.; Takaya, M. Influence of Conversion Coating on Magnesium and Aluminum Alloys by Adhesion Method. *Mater. Trans.* **2008**, *49* (5), 1065–1070.
62. Tanem, B. S.; *et al.* AFM Adhesion force Measurements on Conversion-Coated EN AW-6082-T6 Aluminium. *Int. J. Adhes. Adhes.* **2009**, *29* (5), 471–477.
63. Boulos, M. S.; Petschel, M. Coatings for Rubber Bonding and Paint Adhesion. *J. Mater. Eng. Perform.* **1997**, *6* (4), 421–425.
64. Elsentriecy, H. H.; *et al.* Effects of Pretreatment and Process Temperature of a Conversion Coating produced by an Aprotic Ammonium–Phosphate Ionic Liquid on Magnesium Corrosion Protection. *Electrochim. Acta* **2014**, *123* (0), 58–65.
65. Narayanan, T. S. N. Surface Pretreatment by Phosphate Conversion Coatings: A Review. *Rev. Adv. Mater. Sci.* **2005**, *9*, 130–177.
66. Zhao, M.; *et al.* Microstructure and Corrosion Resistance of a Chromium-free Multi-Elements Complex Coating on AZ91D Magnesium Alloy. *Mater. Chem. Phys.* **2006**, *99* (1), 54–60.
67. Bhargava, G.; Allen, F. Self-Healing, Chromate-Free Conversion Coating for Magnesium Alloys. *Met. Finish.* **2012**, *110* (4), 32–38.
68. Almeida, E.; Diamantino, T. C.; Figueiredo, M. O.; Sa, C. Oxidizing Alternative Species to Chromium VI In Zinc Galvanized Steel Surface Treatment. Part 1 – A Morphological and Chemical Study. *Surf. Coat. Technol.* **1998**, *106*, 8–17.
69. Bibber, J. W. Chromate-Free Conversion Coatings for Aluminum. *Plat. Surf. Finish.* **2003**, *90*, 40–43.
70. Gilroy, D.; *et al.* Techniques for Assessing the Protective Properties of Chromated Conversion Coatings – Part I: Aluminum. *Met. Finish.* **1996**, *94* (10), 26–30.
71. Decroly, A.; Petitjean, J.-P. Study of the Deposition of Cerium Oxide by Conversion on to Aluminium Alloys. *Surf. Coat. Technol.* **2005**, *194* (1), 1–9.
72. Kendig, M. W.; Buchheit, R. G. Corrosion Inhibition of Aluminum and Aluminum Alloys by Soluble Chromates, Chromate Coatings, and Chromate-Free Coatings. *Corrosion* **2003**, *59* (5), 379–400.
73. Osborne, J. H. Observations on Chromate Conversion Coatings from a Sol–Gel Perspective. *Prog. Org. Coat.* **2001**, *41* (4), 280–286.
74. Treverton, J. A.; Amor, M. P. High-Resolution SEM Studies of Chromate Conversion Coatings. *J. Mater. Sci.* **1988**, *23* (10), 3706–3710.
75. Oki, M.; Oki, T. K.; Charles, E. Chromate and Chromate–Phosphate Conversion Coatings on Aluminium. *Arab. J. Sci. Eng.* **2012**, *37* (1), 59–64.
76. Eshaghi, A.; Eshaghi, A. Effect of Chromate Conversion Coatings on the Adhesion and Corrosion Resistance of Painted 5083 Aluminum Alloy. *Mater. Sci.* **2012**, *48* (2), 171–175.
77. Kinloch, A. J.; Little, M. S. G.; Watts, J. F. The Role of the Interphase in the Environmental Failure of Adhesive Joints. *Acta Mater.* **2000**, *48* (18–19), 4543–4553.
78. Xia, L.; McCreery, R. L. Structure and Function of Ferricyanide in the Formation of ChromateConversion Coatings on Aluminum Aircraft Alloy. *J. Electrochem. Soc.* **1999**, *146* (10), 3696–3701.
79. Lin, C.-W. Effect of Chromate Conversion Coatings with and without Poly (Acrylic Acid) on the Press Formability, Shearing Properties and Durability of Galvanized Steel Laminates using Poly(Vinyl Butyral) as Core Material. *J. Mater. Sci.* **1999**, *34* (16), 3951–3956.
80. Manavbasi, A.; Nibhanupudi, S.; Bodily, K.; Clarke, T.; Johnson, K.; Estes, B. New Pretreatments and Non-Chromated Chemfilm for Magnesium Alloys. *Met. Finish.* **2012**, *110* (8), 17–22.
81. Bibber, J. W. *"Rohs" Compliant Chrome – Free Conversion Coating for Aerospace Manufacturing*. SAE Technical Papers, 2006.
82. Zhao, M.; *et al.* A Chromium-Free Conversion Coating of Magnesium Alloy by a Phosphate–Permanganate Solution. *Surf. Coat. Technol.* **2006**, *200* (18–19), 5407–5412.
83. Rahimi, H.; *et al.* Optimization of Process Factors for the Synthesis of Advanced Chrome-Free Nanocomposite Sol–Gel Coatings for Corrosion Protection of Marine Aluminum Alloy AA5083 by Design of Experiment. *Prog. Org. Coat.* **2013**, *76* (2–3), 307–317.
84. Ramezanzadeh, B.; Attar, M. M. An Evaluation of the Corrosion Resistance and Adhesion Properties of an Epoxy-Nanocomposite on a Hot-Dip Galvanized Steel (HDG) Treated by Different Kinds of Conversion Coatings. *Surf. Coat. Technol.* **2011**, *205* (19), 4649–4657.
85. Yoshimi, N.; *et al.*, Chromium-Free Coated Steel Sheet, Vol. 87. NKK Technical Review, 2002.
86. Richardson, M. O. W.; Shaw, R. E. 4.02 – Phosphate Coatings. In *Shreir's Corrosion – Volume 4: Management and Control of Corrosion*; Richardson, T. J. A., Ed.; Elsevier: Oxford, 2010, pp. 2494–2502. Available from: http://www.sciencedirect.com/science/referenceworks/9780444527875 (accessed 4 April 2016).
87. Sugama, T.; *et al.* Aspects of the Adhesion and Corrosion Resistance of Polyelectrolyte-Chemisorbed Zinc Phosphate Conversion Coatings. *J. Mater. Sci.* **1988**, *23* (1), 101–110.
88. Sun, X.; *et al.* Some Observations for Effects of Copper on Zinc Phosphate Conversion Coatings on Aluminum Surfaces. *Surf. Coat. Technol.* **2002**, *155* (1), 46–50.
89. Whitten, M. C.; Lin, C.-T. An in Situ Phosphatizing Coating on 2024 T3 Aluminum Coupons. *Prog. Org. Coat.* **2000**, *38* (3–4), 151–162.
90. Wragg, J. L.; *et al.* Characterization of Polyacrylic Acid Modified Zinc Phosphate Crystal Conversion Coatings. *J. Appl. Polym. Sci.* **1993**, *50* (5), 917–928.
91. Giles, T. R., Goodreau, B. H., Fristad, W. E., Kroemer, J., Frank, M. *An Update of New Conversion Coating for the Automotive Industry*. SAE Technical Papers, 2008.
92. Fedrizzi, L.; *et al.* Study of the Corrosion Behaviour of Phosphatized and Painted Industrial Water Heaters. *Prog. Org. Coat.* **2001**, *42* (1–2), 65–74.
93. Sugama, T.; Takahashi, T. Surface Modification of Electrogalvanized Steels by Zinc Phosphate Conversion Coatings. *J. Mater. Sci.* **1995**, *30* (3), 809–823.
94. Holubka, J. W.; Hammond, J. S.; DeVries, J. E.; Dickie, R. A. Surface Analysis of Interfacial Chemistry in Corrosion-Induced Paint Adhesion Loss – 2. Effects of Resin Chemistry and Substrate Pretreatment on Adhesion Loss Mechanism. *J. Coat. Technol. Res.* **1980**, *52*, 63–68.
95. Drobny, J. G. *Handbook of Thermoplastic Elastomers*; William Andrew Publishing: New York, NY, 2007.

96. Hoppe, H.-G.; Wussow, H. -G. In *Polyurethane Handbook;* Oertel, G. (Bayer), Ed.; Hanser Publications: Munich, 1993, p. 412.
97. Hojjati Najafabadi, A.; *et al.* A New Approach of Improving Rain Erosion Resistance of Nanocomposite Sol–Gel Coatings by Optimization Process Factors. *Metall. Mater. Trans. A* **2014**, *45* (5), 2522–2531.
98. Phalippouthe, J. *Sol-Gel: A Low Temperature Process for the Materials of the New Millennium.* Sol–Gel Gateway, 2000.
99. Balgude, D.; Sabnis, A. Sol–Gel Derived Hybrid Coatings as an Environment Friendly Surface Treatment for Corrosion Protection of Metals and Their Alloys. *J. Sol-Gel Sci. Technol.* **2012**, *64* (1), 124–134.
100. Najafabadi, A. H.; *et al.* Sol–Gel Processing of Hybrid Nanocomposite Protective Coatings Using Experimental Design. *Prog. Org. Coat.* **2013**, *76* (1), 293–301.
101. Paussa, L.; *et al.* Inhibition Effect of Cerium in Hybrid Sol–Gel Films on Aluminium Alloy AA2024. *Surf. Interface Anal.* **2010**, *42* (4), 299–305.
102. Jo, J.-H.; *et al. Hydroxyapatite Coating on Magnesium with MgF_2 Interlayer for Enhanced Corrosion Resistance and Biocompatibility. J. Mater. Sci.: Mater. Med.* **2011**, *22* (11), 2437–2447.
103. Gurrappa, I.; Binder, L. Electrodeposition of Nanostructured Coatings and Their Characterization – A Review. *Sci. Technol. Adv. Mater.* **2008**, *9* (4), 043001.
104. *Electrocoating*; The Electrocoat Association: Cincinnati, OH, 2002. ISBN 0-9712422-0-8. Available from: http://www.worldcat.org/title/electrocoating-a-guidebook-for-finishers/oclc/55797879 (accessed 4 April 2016).
105. Koppers, M.; *et al.* Einfluss Der chemischen Umgebung auf Morphologie und Struktur von Magnesiumhydroxid auf Magnesiumoberflächen. *Materialwissenschaft und Werkstofftechnik* **2001**, *32* (1), 88–96.
106. El Hajjaji, S.; El Alaoui, M.; Simon, P.; *et al.* Preparation and Characterization of Electrolytic Alumina Deposit on Austenitic Stainless Steel. *Sci. Technol. Adv. Mater.* **2005**, *6*, 519–524.
107. Aries, L.; *et al.* Preparation and High-Temperature Behaviour of Electrolytic Alumina Film on Fe–Cr–Al Stainless Steel. *J. Mater. Sci.* **1998**, *33* (2), 429–433.
108. Aries, L. Preparation of Electrolytic Ceramic Films on Stainless Steel Conversion Coatings. *J. Appl. Electrochem.* **1994**, *24* (6), 554–558.
109. Berger, F.; Delhalle, J.; Mekhalif, Z. Hybrid Coating on Steel: ZnNi Electrodeposition and Surface Modification with Organothiols and Diazonium Salts. *Electrochim. Acta* **2008**, *53* (6), 2852–2861.
110. Elsentriecy, H. H.; Azumi, K. Electroless Ni–P Deposition on AZ91 D Magnesium Alloy Prepared by Molybdate Chemical Conversion Coatings. *J. Electrochem. Soc.* **2009**, *156*, D70–D77.
111. Lgamri, A.; *et al.* Characterisation of Electrolytically Deposited Alumina and Yttrium Modified Alumina Coatings on Steel. *Surf. Coat. Technol.* **2003**, *162* (2–3), 154–160.
112. Li, Q.; Liang, J.; Wang, Q. Plasma Electrolytic Oxidation Coating on Lightweight Metals. In *Modern Surface Engineering Treatments*; Aliofkhazraei, M., Ed.; Intech, 2013, pp. 75–99, ISBN 978-953-51-1149-8.

Relevant Websites

www.nace.org
NACE: The Worldwide Corrosion Authority.

http://www.sspc.org/
Society for Protective Coatings (formerly Steel Structures Painting Council (SSPC)).

3.21 Powder Metallurgical Processing of NiTi Using Spark Plasma Sintering

K McNamara, J Butler, AA Gandhi, and SAM Tofail, University of Limerick, Limerick, Ireland

© 2017 Elsevier Inc. All rights reserved.

3.21.1	**Introduction**	336
3.21.2	**NiTi SMA**	336
3.21.3	**Methods of Processing NiTi**	337
3.21.3.1	Vacuum Melting	338
3.21.3.1.1	VAR	338
3.21.3.1.2	VIM	338
3.21.3.2	Powder Metallurgy	338
3.21.3.2.1	CS	338
3.21.3.2.2	HIP	339
3.21.4	**SPS**	339
3.21.4.1	Introduction	339
3.21.4.2	SPS of Binary NiTi	340
3.21.4.2.1	Fabrication of binary NiTi using SPS	340
3.21.4.3	SPS of Ternary NiTi	342
3.21.4.3.1	Fabrication of ternary NiTi using SPS	343
3.21.5	**Conclusions**	345
References		345

3.21.1 Introduction

NiTi is a near equiatomic alloy of nickel and titanium. NiTi exhibits unique properties such as shape memory effect (SME), superelasticity, and biocompatibility. Shape memory alloys (SMA) are materials that have the ability to return to a predetermined shape when heated. The unique shape memory and superelastic properties of Nitinol are due to a phase transformation called SME.[1–2]

The melting and production of NiTi is challenging in that it is sensitive to both changes in chemistry and processing. The NiTi transformation temperatures are extremely sensitive to any small variations in the concentration of nickel or titanium.[3–5] Generally SMA are produced by casting, the two most common methods of producing NiTi are vacuum arc remelting (VAR) or vacuum induction melting (VIM) followed by cold or hot working.[3–12] However cast metals have some issues associated with them such as the inability to control chemical composition, segregation, and excessive grain growth which results in poor fatigue properties.[12–14]

An alternate route to casting that became popular in the last 20 years was powder metallurgy. Powder metallurgy became a popular method due to its ability to avoid the problems associated with casting and it allows for better control over the composition of NiTi alloy and can therefore control the transformation temperature.[12,14] Some powder metallurgy processes that are used for NiTi production include conventional sintering (CS),[15–19] hot isostatic pressing (HIP),[12,20–25] metal injection molding (MIM),[26–29] self-propagating high temperature synthesis (SHS),[30–34] and spark plasma sintering (SPS).[14,35–41]

In recent times the SPS technique has emerged as the most efficient powder metallurgical method of melting NiTi. In the SPS process powder particles are uniformly heated to a high density at relatively low temperatures and have a shorter sintering time than CS.[14,42]

In this chapter we review the methods generally used for NiTi fabrication, casting, and powder metallurgy. We concentrate specifically on SPS of binary and ternary NiTi. We also present some of our own work on SPS of binary and ternary NiTi.

3.21.2 NiTi SMA

NiTi is an alloy that contains equiatomic amounts of Nickel and Titanium. It is commonly referred to as Nitinol. The name Nitinol was derived from its place of discovery. In 1962 two researchers William Buehler and Frederick Wang discovered the properties of equiatomic nickel–titanium alloys while doing research at Naval Ordnance Laboratory. This is how the name NiTiNOL was derived, Nickel Titanium Naval Ordnance Laboratory. Nitinol is a SMA.[1]

NiTi exhibits some unique properties such as shape memory and superelasticity. This special property of Nitinol is called SME. SME allows the material to return to its original shape upon heating or cooling.[2] In SME it undergoes a change of crystal structure at a certain temperature called the transformation temperature. Above this transformation temperature NiTi has a crystal structure called austenite and below this transformation temperature the crystal structure is called martensite. This is a reversible transformation so the alloy can transform from one crystal structure to the other and is prompted by a change in temperature or by adding a load to the material.[2]

Figure 1(a) is a stress–strain curve for a SMA that is undergoing SME. In this diagram it can be seen that at high temperature NiTi is in the austenite phase and as previously discussed when a stress is added the NiTi undergoes a phase change from austenite to martensite. But the difference here is that when the stress is removed the NiTi will stay in the martensite phase unless it is heated at which point it will

 doi:10.1016/B978-0-12-803581-8.09202-X

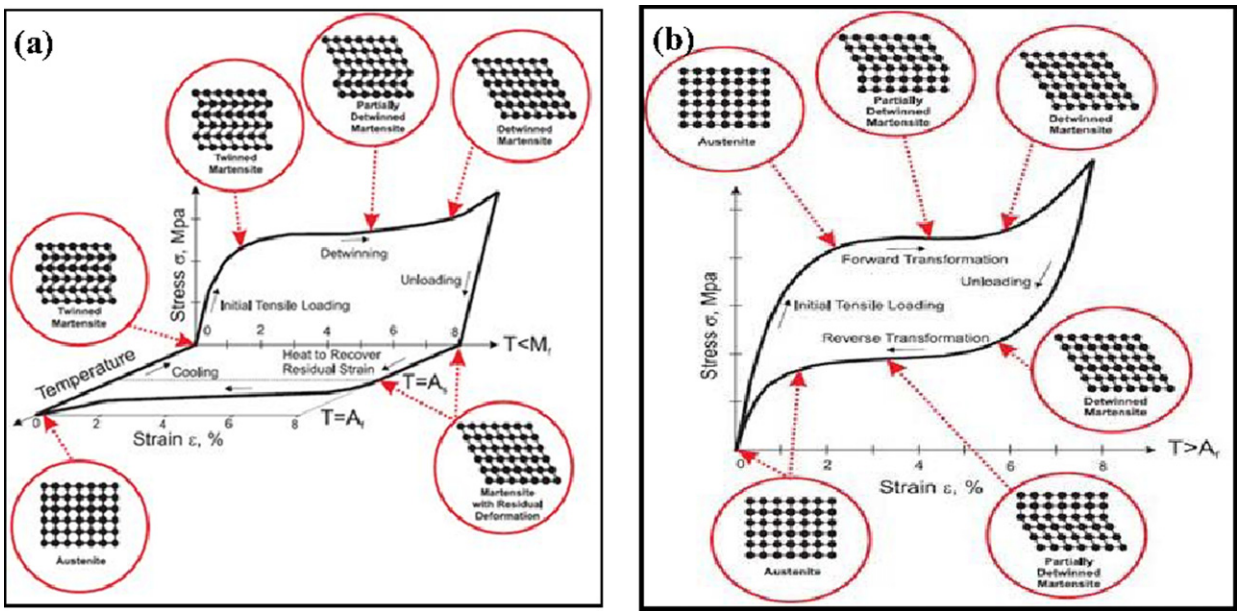


Figure 1 (a) Stress–strain curve for NiTi alloy undergoing shape memory effect and (b) superelastic effect.[43]

return to its original shape.[1,44,45] **Figure 1(b)** is a stress–strain curve for NiTi undergoing superelastic effect. It shows NiTi in the austenite phase but when a stress is added, either cooling or a load is added, it causes the austenite to form detwinned martensite and when the stress is removed the detwinned martensite will return to its austenite state.[1,44,45]

As we know a NiTi alloy is made up of elemental nickel and titanium. What is interesting about this particular alloy apart from its shape memory and superelasticity properties is that it naturally oxidizes to form an oxide layer on the surface. This natural oxide layer is quite thin, 5–10 nm.[46] This layer is mainly composed of titanium dioxide (TiO_2).[47] This TiO_2 layer is what provides the NiTi alloy with its biocompatibility and allows for its use in many biomedical applications. This oxide layer prevents the release of nickel from the alloy into the body. This oxide layer forms from oxygen in the atmosphere that reacts with titanium on the surface of the alloy.[48] It is because of these unique properties that NiTi became widely used in the dental and medical industries in applications such as braces, wire guides, and stents, NiTi is also used in the manufacture of clinical instruments.

3.21.3 Methods of Processing NiTi

The melting and fabrication of NiTi is challenging as it is sensitive to both changes in chemistry and processing. The NiTi transformation temperatures are extremely sensitive to any small variations in the concentration of nickel or titanium. This sensitivity will increase with the nickel content in the alloy. If an alloy has a weight of 55.0% nickel, and if there is even a 1% weight deviation in the concentration of either Ni or Ti, then the transformation temperature will shift by approximately 100 °C. Impurities such as carbon, nitrogen, and oxygen should also be avoided as they can influence the transformation temperature, strength, and ductility of the material. This extreme sensitivity puts a very strict requirement on the alloy melting method that can be used. The alloy melting method needs to be able to control the nickel and titanium ratio so as to not change the transformation temperatures as the alloys SME and superelasticity are dependent on this.[3–5]

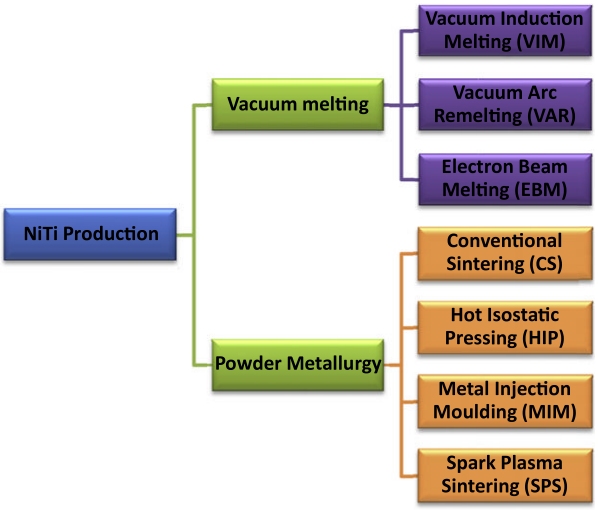


Figure 2 Schematic showing the different ways of producing NiTi.

Figure 2 shows there are two main methods of producing NiTi either by casting or powder metallurgy. Many casting methods include VAR, VIM and electron beam melting (EBM), some of which will be discussed in the next section.[3–5] These methods are the most widely used casting methods for the production of NiTi. Powder metallurgy is another method used to manufacture NiTi. Some of the most commonly used powder metallurgy processes include CS, HIP, MIM, and SPS.[5]

3.21.3.1 Vacuum Melting

3.21.3.1.1 VAR

VAR is a consumable electrode remelting process which is carried out in vacuum and generally used for the production of NiTi. It is not a commonly used method for melting and producing of metals as it is both expensive and time consuming, this method is for specialized materials that oxidize easily. In this method no crucible is used, instead the nickel and titanium are weighted out in the correct ratio and are then packed into a compact. This compact is then used as a consumable electrode. The consumable electrode is melted using an electric arc into a water cooled copper crucible, a frozen skull is formed preventing contamination from the crucible and because of this VAR melting achieves the highest possible purity of the resultant alloy. As the molten metal is formed, the electrode is slowly withdrawn as the metal solidifies at the bottom of the melt pool. Only a small amount of the ingot is molten at any time, so complete mixing throughout the entire ingot does not occur and the ingot must be remelted to achieve a homogeneous mixture.[3–5]

Foroozmehr *et al.*[8] investigated the microstructure during homogenization of NiTi by VAR. As VAR does not rely on electromagnetic forces during melting several remelts of the ingot is necessary to achieve a homogeneous material. A Ti-50%-Ni alloy was prepared via VAR in a water cooled copper crucible. The material was remelted four times to achieve a homogenous mixture at 1000 °C. The microstructure of the material during homogenization was studied using an optical microscope and a scanning electron microscope (SEM). The chemistry and crystal structure of the material was investigated using energy dispersive X-ray spectroscopy (EDS) and X-ray diffraction (XRD). The SEM results showed that the microstructure of the as-cast material was segregated. EDS and XRD results showed that the alloy consisted of monoclinic, Ni_3Ti, and Ti_2Ni phases. It was also found that if the holding time is increased during the homogenization process the amount of the austenite phase increased while other phases decreased. A holding time of 4 h was found to achieve an austenite phase as well as decreasing the hardness of the material.[8]

3.21.3.1.2 VIM

VIM is a process that uses an electrical current to melt metal components in a vacuum environment. For VIM of NiTi, the raw materials are weighed out in the correct ratio and placed in an electrically conductive crucible, usually graphite. An induction coil produces an alternating magnetic field which is the source of the eddy currents that are used to heat the crucible and melt its components. Once molten the induction field and electrodynamic forces stir and mix the melt. This method results in homogenous mixture. There are many advantages to this melting method as the chemistry and transformation temperature of the NiTi can be easily controlled. One disadvantage of this method is that there is some carbon contamination from the graphite crucible, between 200–500 ppm, however this does not affect any of the materials shape memory properties.[3–5] Frenzel *et al.*[9] developed a method to reduce carbon contamination during VIM of NiTi alloy. Graphite crucibles are mainly used in VIM as they have many advantages such as they are cheap, resistant to thermal cracking as well as good electrical properties. Even though the graphite crucibles possess these properties there is still the issue of carbon contamination. Carbon contamination needs to be kept at a minimum in order for NiTi to maintain its unique properties. It was found that if NiTi is melted in a fresh graphite crucible and the nickel is in direct contact with the crucible then the carbon contamination is high. However, it was found that the carbon contamination is lower when the crucible is used a second time. It was shown that the formation of a titanium carbide layer acts as a diffusion barrier. Frenzel *et al.*[9] found that avoiding direct contact between nickel and the graphite crucible reduces the carbon contamination. This is achieved by titanium disk cladding. This is for nickel rich NiTi alloys.[9]

Nayan *et al.*[10] investigated a new novel method of charging for reducing carbon contamination during VIM of NiTi alloys. A certain material arrangement scheme is used for melting the NiTi alloy and reducing the carbon contamination. The main objective of the study is to reduce the contact between the molten titanium and the graphite crucible. This was done by dissolving the titanium in molten nickel. It was found that a titanium carbide layer formed on the crucible after the first melt with a significant titanium loss and high carbon contamination. However it was found that the composition of the desired material was achieved with minimal titanium loss and a significant reduction in carbon contamination. High temperature SMA have a transformation temperature above 100 °C this can be achieved by adding a third element, such as platinum (Pt), palladium (Pd), gold (Au), zirconium (Zr), or hafnium (Hf) to the alloy.[10] Zhang *et al.*[11] investigated melting ternary NiTi alloys by VIM. Various elements such as copper (Cu), iron (Fe), hafnium (Hf), and zirconium (Zr) were added to NiTi as a ternary element to produce a high temperature SMA. A previous technique that was developed was used to keep the carbon contamination to a minimum in this experiment. SEM, EDS and differential scanning calorimetry (DSC) were utilized to investigate the microstructure, chemistry, and transformation temperatures of the ternary alloys. The results showed that ternary NiTiX where X is Cu, Fe, Hf, and Zr can be produced by VIM with low concentration of carbon and oxygen. It was found that microstructural hetrogeneities were present in the samples mainly because of the solidification process. It was found that these could be partly removed by homogenization treatments.[11]

3.21.3.2 Powder Metallurgy

The powder metallurgy route has certain advantages as it can avoid problems such as segregation and excessive grain growth that are often associated with casting. It also offers the ability to control the chemical composition of the alloy. As mentioned earlier in this section some of the most commonly used powder metallurgy processes include CS, HIP, MIM, SHS and SPS. Some examples of the use of NiTi and porous NiTi in CS and HIP will be described later in this section. SPS will be discussed in more detail in the next section.[5,12]

3.21.3.2.1 CS

Sintering is the bonding of particles by diffusion of atoms to reduce surface area. CS is typically performed by pressing

powders into a compact and heating the compact to a point, below the melting temperature, where the atoms can diffuse. Diffusion is a thermally activated process, requiring a minimum energy to begin. As atoms diffuse, some will move into positions that reduce the total surface area and thus reduce the surface energy. The driving force for atoms to move to positions that reduce the surface energy is associated with the stress at the particle surface.[49] The sintering temperature is usually set between two thirds to three quarters of the absolute melting temperature of the metal.[50]

Li *et al.*[15] investigated the properties of porous NiTi prepared by CS of elemental Ni and Ti. Elemental Ni and Ti powders were used in the sintering process, titanium hydride (TiH_2) was added to the mixture as a pore forming agent. The aim of this study was to investigate the effects varying parameters such as sintering temperature, sintering time, and TiH_2 concentration on the porosity, pore size, distribution, and phase composition. The results found that sintering at a lower temperature resulted in the formation of Ni_3Ti phase with pure Ni and Ti also present. Sintering at higher temperature for a longer time resulted in NiTi being the main phase, the pore size and distribution were also found to be homogeneous at higher sintering temperatures.[15] Zhang *et al.*[17] fabricated porous NiTi with gradient porosity and large pore size by CS using ammonium bicarbonate (NH_4HCO_3) as a space holder. Ni and Ti powders were blended with various concentrations of NH_4HCO_3, the porosity, pore size, phase, transformation temperature, and mechanical properties were then investigated. It was found that the porosity and pore size increased linearly with increasing concentration of NH_4HCO_3. The use of NH_4HCO_3 did not have any adverse effect on the phase transformation behavior or microstructure of the alloy. Sample with both high and low porosity were found to have high recoverable strain as well as superelasticity and strength.[17] Li *et al.*[19] produced porous NiTi with controllable pore characteristics by CS and using urea ($CO(NH_2)_2$) particles as space holders. The porosity, pore size, distribution, phase composition, phase transformation, and mechanical properties of the porous NiTi were then analyzed. The results showed that the use of $CO(NH_2)_2$ particles as space holders had no effect on the microstructure of the NiTi Alloy. It was found the when compared with NH_4HCO_3 that the $CO(NH_2)_2$ particles offered higher porosity, strength, and better superelasticity.[18]

3.21.3.2.2 HIP

HIP is a pressure enhanced sintering technique. This technique is used to manufacture dense products.[5,12] For isostatic compaction the powders must be encapsulated in an evacuated gastight welded can. The can transfers the pressure to the powders. This can or mold can be mild steel, stainless, a metal, or a glass capsule. The HIP process subjects powders to simultaneous elevated temperatures of over 1000 °C and pressures of over 98 MPa to eliminate internal micro-shrinkage.[51]

Bram *et al.*[12] investigated the use of HIP to fabricate NiTi shape memory parts. Elemental powders of nickel and titanium were used as the starting material. The powders were homogenized for 24 h in a Turbula mixer. Stainless steel capsules were used for the HIP of NiTi powders. In order to avoid damaging the capsules the powders were pre-compacted. HIP was carried out at a constant pressure of 195 MPa and at various temperatures 850, 950, and 1050 °C for 5 h. After the HIP process the stainless steel capsule was removed by machining. In order to achieve a homogeneous mixture the samples were solution treated at 850 °C for 1 h and water quenched. The water quenched samples were then annealed at 500 °C for 1 h. The microstructure, composition, phase transformation, and mechanical properties of the samples were then analyzed. It was found that HIP carried out at 195 MPa and 1050 °C for 5 h resulted in a dense NiTi sample with good homogeneity. The solution and annealing treatments resulted in the formation of Ni_4Ti_3 precipitates which influences the phase transformation and temperature. Tensile testing showed shape recovery at a low level.[12] Yuan *et al.*[20] manufactured porous NiTi by HIP and investigated the microstructure and transformation behavior of the resulting alloy. Elemental Ni and Ti powders were used for this experiment and were mixed for 4 h. The powders were then pressed to cylindrical green samples at a pressure of 100 MPa using a hydraulic press. HIP was carried out on the samples at pressure of 150 MPa, temperature of 1050 °C for 7 h. The microstructure, transformation temperature, and mechanical properties were then investigated. The results showed that the transformation behavior and superelasticity of porous NiTi is similar to that of dense NiTi.[20]

Yuan *et al.*[21] prepared porous NiTi using capsule free-HIP (CF-HIP). The aim of this experiment was to control the porosity and superelasticity of porous NiTi by monitoring the microstructure, transformation temperature, and mechanical properties. The results showed that porous NiTi with near spherical pores and a homogenous microstructure was fabricated using CF-HIP. After the appropriate thermo-mechanical treatment the porous NiTi alloys exhibit excellent superelastic properties. It was also found that the alloys superelasticity is controlled by the pore size, shape and distribution.[21]

3.21.4 SPS

3.21.4.1 Introduction

SPS was first developed in the 1960s by Inoue *et al.*[52,53] It was a newly developed process for powder sintering and it was expected that sintering assisted by plasma would help develop advanced materials.[54] The SPS or plasma activated sintering (PAS) process is based on the electrical spark discharge phenomenon, where a high energy low voltage pulsed current, momentarily generates spark plasma at high localized temperatures, between powder particles, and causes the surface of the powder particles to vaporize and melt.[14,55] SPS enables compressed powder to be sintered under consistent heating to high density at relatively lower temperatures and in a much shorter time period compared to CS.[14,42] This shorter sintering time is thought to prevent exaggerated grain growth.[56]

The SPS process is a pressure assisted pulsed current sintering method that uses ON-OFF DC pulse energy. This method generates (1) spark plasma, (2) spark impact pressure, (3) Joule heating, and (4) an electrical field diffusion effect. In the SPS process the generation of spark plasma produces a high temperature sputtering event that eliminates adsorbed gas and impurities that exist on the powder particles. The spark impact pressure causes high speed diffusion of the ions and

material transfer. The joule heat generation helps with high speed diffusion of the ions and material transfer and also promotes efficient heating and plastic deformation. The electrical field diffusion effect also promotes high speed diffusion of the ions and material transfer. When the spark discharge appears between the powder particles a high temperature state is generated momentarily, which causes the evaporation and melting of the surface of the powder particles, necks are formed around the area of contact between the particles.[57]

3.21.4.2 SPS of Binary NiTi

Over 20 years ago the interest in using powder metallurgy specifically sintering as a way of processing NiTi began. It was found that this process can avoid problems that are associated with casting methods, VIM and VAR, such as segregation and extensive grain growth.[12] The advantage of using powder metallurgy is the precise control of chemical composition which is important when trying to maintain the unique properties of NiTi. However there are certain difficulties with the powder metallurgy route such as oxidation, porosity, and the tendency to form other NiTi phases.[12,14]

Ye *et al.*[35] studied the properties of amorphous NiTi powders fused via SPS. Mechanically alloyed NiTi powders were used for this experiment. These powders were then consolidated by SPS at a pressure of 50 MPa for 10 min and at different temperatures of 900 and 1100 °C. Various different characterization techniques were used to investigate the crystal structure, transformation temperature, morphology, and chemistry of the consolidated material. The results showed a densified sample was produced with 3 phases (Ni_3Ti, NiTi and $NiTi_2$) present. The formation of 3 phases was due to the inhomogeneous mixture of the powders. It was found that sintering at 900 °C provided a compact sample with a better structure and grain size.[35] Zhao *et al.*[36] investigated the compression behavior of the porous NiTi to use a high energy absorbing material. NiTi was processed with via SPS. Two samples with varying porosities were produced and compared to a dense sample. The dense sample was produced at a pressure of 50 MPa at 850 °C for 5 min. The first porous sample had 13% porosity and was produced at a pressure of 25 MPa at 800 °C for 5 min. The second porous sample had 25% porosity and was produced at a pressure of 5 MPa at 750 °C for 5 min. Compressive tests were carried out at 22 and 15–25 °C to obtain the stress–strain curve of the porous and dense samples. These experimental results were then compared to a model of the stress–strain curve of the porous and dense samples. Experimental results showed that the 13% porosity sample had high ductility and a good microstructure when compared to the 25% porosity sample. The model and experimental results for the 13% porosity NiTi sample were in reasonably good agreement.[36]

Shearwood *et al.*[14] investigated the properties of TiNi nano-powders prepared by SPS. The sintering experiments were carried out at a constant pressure of 30 MPa and at varying temperatures of 700, 800, 900, and 1100 °C. Various different characterization techniques were then carried out on the TiNi nano-powder and sintered samples to analyze their microstructure, chemical composition, crystal structure, and transformation temperatures with the aim to find the ideal sintering temperature. The results showed that the samples sintered at 700 °C had high porosity but had SME. However it was found that the samples sintered above 900 °C suffered from oxidation and loss of SME. The samples sintered at 800 °C produced dense samples with good SME.[14] Fu *et al.*[37] studied the biocompatibility of TiNi nano-powders prepared via SPS. The sintering experiments were carried out at a constant pressure and temperature of 30 MPa and 800 °C for 5 min. The samples were then chemically treated in hydrogen peroxide (H_2O_2) solution at 60 °C for varying times to produce a titania layer on the surface. These samples were then heat treated at 400 °C for 1 h to enhance to bioactivity of the surface. The samples were then characterized to analyze their morphology, chemistry, crystal structure, and transformation temperature. *In vitro* studies were also carried out to determine the biocompatibility of the samples. The results showed that SPS at 800 °C produced a TiNi material with martensitic transformation behavior. A TiO_2 coating was found to have formed on the surface after chemical treatment. This chemical treatment also improved the bioactivity of the TiNi sample. Cell culture results showed the sample to be biocompatible.[37]

Butler *et al.*[39] investigated the production of NiTi wire from elemental nickel and titanium powders fabricated by SPS. Commercially pure powders were used in this experiment. These powders were ball milled for 20 min to obtain a homogeneous equiatomic NiTi powder. These powders were then sintered at a pressure of 50 MPa at 850 °C for 1 and 10 min and at 900 °C for 10 min. Further testing showed that the sample sintered at 900 °C for 10 min was best for extrusion testing. The results showed that SPS reduced the impurities and phases present in as sintered NiTi samples. The resulting wire showed shape memory and superelastic effects as well as low porosity and homogeneity.[39] Zhang *et al.*[41] studied the superelastic effect of porous NiTi prepared by SPS. The Ti and Ni powders were ball milled for 10 h to obtain a homogeneous NiTi powder. After ball milling ammonium hydrogen carbonate (NH_4HCO_3) particles were sieved into the mixture. This was done as a space holder to adjust the porosities of the material. A one step SPS method was carried out at varying temperatures between 800–1050 °C. The samples were then analyzed to determine the pore size, microstructure, crystal structure, compressive strength, and elastic modulus of the material. The results showed NiTi porosity between 10–61%, with an average pore size between 21–415 μm. It was found that the material consisted mainly of NiTi with some Ni_3Ti and Ti_2Ni phases present. It was found that with increasing porosity and pore size the elasticity of NiTi decreased.[41]

3.21.4.2.1 Fabrication of binary NiTi using SPS

A near equiatomic (55.74%Ni, 44.26%Ti) NiTi powder was sintered in a graphite-die (10.4 mm inside diameter). SPS was carried out using Dr. Sinter, SPS-515S model from 700 to 900 °C in vacuum with a holding time of 5 min and a uniaxial pressure ranging from 20 to 50 MPa. The bulk density of the sintered pellets with 10 mm diameter and 1 mm thickness was measured based on the Archimedes' principle. SEM was one of the characterization techniques used to analyze the NiTi samples. The SEM images were able to verify the percentage

porosity/density results. DSC was used to measure the transformation temperatures of each NiTi sample. Equations [1] and [2] were used to calculate the density and porosity of the sintered samples.

$$\text{Density} = \frac{\text{Mass}}{\text{Volume}} = \frac{\text{Weight}}{\pi r^2 h} \quad [1]$$

$$\text{Porosity} = \frac{\text{Theoretical Density} - \text{Actual Density}}{\text{Theoretical Density}} \times \frac{100}{1} \quad [2]$$

Figure 3 below shows a graph of how the calculated percentage density of the NiTi samples varies with pressure and temperature. From the graph it can be seen that density of the NiTi sample increases as both the temperature and pressure increase.

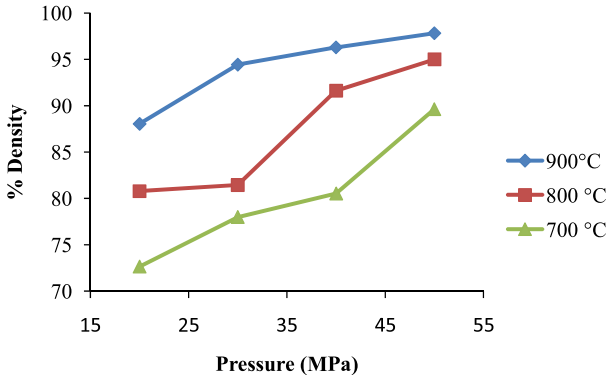


Figure 3 Change of relative density of NiTi as a function of applied pressure during SPS.

SPS at high temperatures and high pressures causes the surface of the NiTi particles to vaporize and melt. The material from both particles then begins to diffuse into neighboring particles. Joule heating is then responsible for the activation of diffusion processes leading to sample compaction and densification. During this process the pores begin to reduce in size and results in the densification of the NiTi sample.

Figures 4(a)–4(c) shows SEM micrographs of the NiTi samples sintered at (a) 900 °C, (b) 800 °C, and (c) 700 °C at a pressure of 50 MPa taken a magnification × 200. From **Figure 4(a)** it can be seen that the particles consolidated well and not many pores are apparent. **Figures 4(b)** and **4(c)** it can be seen that the NiTi powders have not consolidated to form a homogeneous sample.

At a higher temperature diffusion of the melted NiTi powder particles into neighboring particles is faster the pressure being applied to the sample is high so the sample is therefore more compact. In a compacted sample the NiTi powder particles are more tightly packed together, so diffusion into neighboring particles would not take as long and a more compact sample is expected.

DSC was carried out on the samples after sintering. The DSC was used to measure the transformation temperatures of the NiTi samples that were sintered at various temperatures and pressures. From **Figure 5** it can be seen that the results for the NiTi samples sintered at 700 °C/50 MPa, 800 °C/50 MPa, and 900 °C/50 MPa have all been combined into one graph. From the graphs it can be seen that as the temperature decreases the martensite peak moves to the left. As the temperature increases the austenite peak moves from the right to the left. Also from the combined graph it can be seen that the austenite peak decreases in size as the temperature decreases.

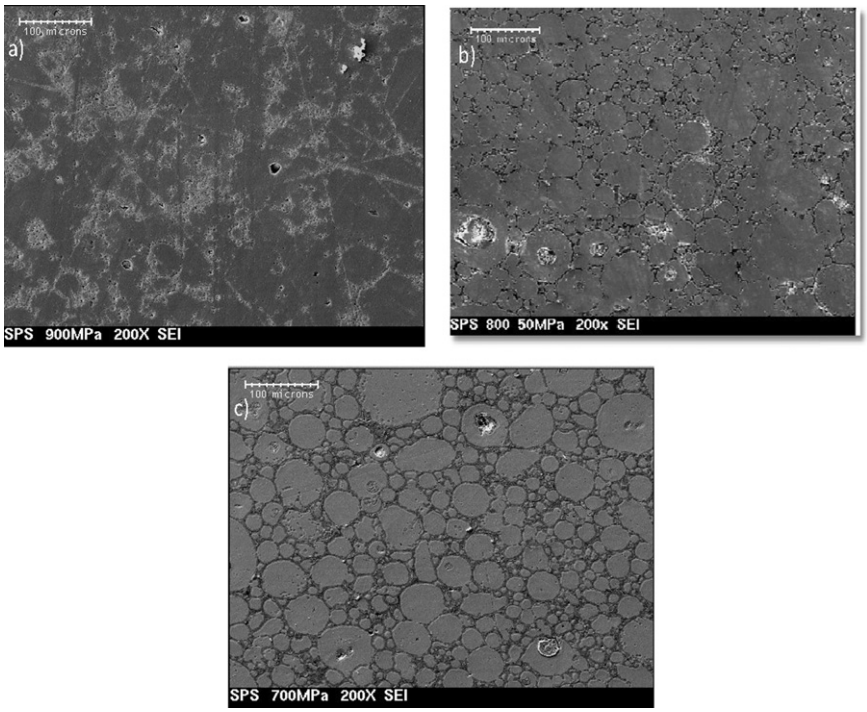


Figure 4 SEM images of SPS sintered NiTi (a) 900 °C (b) 800 °C, and (c) 700 °C 50 MPa.

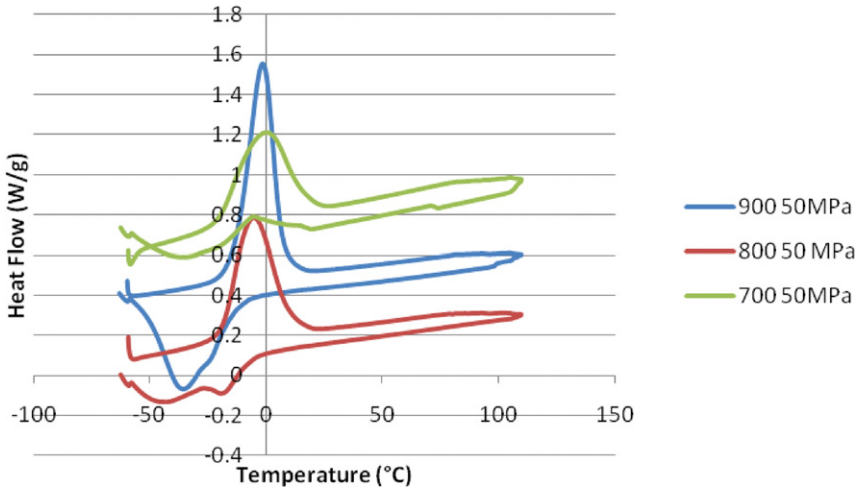


Figure 5 DSC graphs of NiTi sintered at 50 MPa at various temperatures.

This is also seen to be true for the martensite peak. Figure 3(b) shows the DSC curves for the un-sintered NiTi powder. The A_S temperature was found to be -7, A_F temperature was found to be 45, M_S temperature was found to be 12.5, and M_F temperature was found to be -58. If this is compared to the sintered samples it can be seen that the M_F temperature is relatively the same for all the samples only a slight difference is seen. The A_F temperature was found to be 45, these decreases when the NiTi samples are sintered. It was found that as the sintering temperature decreases the A_F temperature increases. The lower the sintering temperature the higher the austenite transformation temperature will be. The M_S temperature of the un-sintered NiTi sample was found to be 12.5 this decreases to negative figures when the NiTi samples are sintered. If this is compared to the sintered NiTi samples it can be seen that as the sintering temperature decreases the M_S temperature of the sintered NiTi samples increases. The A_S temperature for the un-sintered NiTi sample was found to be -7 this decreases as the NiTi samples are sintered. Sintering causes a change in the transformation temperatures of the NiTi samples. It appears that sintering decreases the transformation temperatures of the NiTi alloy.

3.21.4.3 SPS of Ternary NiTi

The primary objectives of adding a ternary element to binary NiTi are to

1. Decrease or increase the hysteresis by adding Cu or Nb, respectively,
2. Lower the Austenite transformation temperatures (Fe, Cr, Co, Al),
3. Increase the Martensite transformation temperatures (Hf, Zr, Pd, Pt, Au),
4. Strengthen the matrix (Mo, W, O, C),
5. Increase radiopacity (Pt, Pd, Ta, W, and rare earths).

Despite the achievements in developing these ternary alloys, over 90% of NiTi used today is still binary NiTi with a nickel content between 49 and 51 at%. The advantages gained by adding these ternary elements are offset by losses in other properties or by huge increases in cost. Of the 10% of NiTi that is alloyed with a ternary element, the approximate order of total estimated volume produced for these alloys can be listed as follows: NiTiFe, NiTiNb, NiTiCr, NiTiCu, NiTiCo, NiTiV, NiTiPt, and NiTiHf.[58] Table 1 below lists the common elements added to NiTi and the effects they will have on the alloys properties.

Although studies have been carried out on VIM of ternary NiTi and SPS of binary NiTi, there are not many reports on SPS of ternary NiTi. Tofail *et al.*[59] investigated the X-ray visibility and metallurgical features of NiTi–Er processed by SPS. Binary NiTi, ErFe, and Er–Ni powders were ball milled for 20 min to obtain a homogeneous mixture. These powders were then sintered using Dr. Sinterlab SPS 515S, with sintering temperature of 760 °C. Hot and Cold working was then carried out on the resulting sample. Various characterization techniques such as SEM, DSC and tensile testing were then carried out on the NiTi–Er sample to investigate the morphology, transformation temperature, and ductility of the sample. The results found that the radiopacity of NiTi improved with the addition of erbium however the austenitic transformation temperature will need to be lowered if the alloy is to be used for superelasticity in biomedical applications.[59] Cristea *et al.*[60] investigated the microstructural and mechanical properties of NiTi and NiTi–Cu fabricated via SPS. Mechanical homogenization and mechanical alloying were used to prepare the homogeneous mixtures. SPS was carried out using HP D25 instrument, sintering was carried out at pressure of 30 MPa and a sintering temperature of 850 °C for 5 min. Various characterization techniques were then used to analyze the samples morphology, chemistry, crystal structure, hardness, and elasticity. The results showed that participates were present in all samples and the mechanically alloyed samples were more homogeneous than the samples that were not mechanically alloyed. The samples that were mechanically alloyed had a higher Vickers hardness when compared to the samples that were not mechanically alloyed. The results from the Young's modulus test showed that the samples were in the austenite phase.[60]

Table 1 List of elements added to NiTi and the effect of ternary additions on workability, radiopacity, transformation temperatures, and hysteresis

Element	*Effects*
Nb	Increases stress hysteresis; improves corrosion resistance and machinability; reasonable ductility; enhances radiopacity [Duerig *et al.*[58]].
Pt	Reduces workability and ductility; usually forms NiTi–PtTi; decreases the TTs up to 10 at% and further additions increase the TTs almost linearly; enhances radiopacity
Ta	Decreases TTs. Results in a radiopacity improvement.
V	Reduces workability and ductility; decreases TTs, can be substituted in small quantities for Ni without seriously impairing the shape memory effect.
Cr	Reduces workability and ductility; decreases TTs, can be substituted in small quantities for Ni without seriously impairing the shape memory effect.
Mn	Reduces workability and ductility; decreases TTs, can be substituted in small quantities for Ni without seriously impairing the shape memory effect.
Al	Reduces workability and ductility; decreases TTs, can be substituted in small quantities for Ni without seriously impairing the shape memory effect.
Co	Workability increases or unaffected; decreases TTs, can be substituted in small quantities for Ni without seriously impairing the shape memory effect.
Fe	Workability increases or unaffected; decreases TTs, can be substituted in small quantities for Ni without seriously impairing the shape memory effect.
Pd	Reduces workability and ductility; Usually forms NiTi–PdTi, decreases the TTs up to 10 at% and further additions increase the TTs almost linearly; enhances radiopacity. Results in a radiopacity improvement. B addition as a quaternary element increases workability.
Au	If substituted for Ni can have a neutral effect or it can increase the TTs. Results in a radiopacity improvement.
Cu	Usually forms as NiTi–CuTi. If substituted for Ni will reduce stress hysteresis; can be substituted for nickel in substantial amounts without affecting the martensitic phase transformation, while fully retaining shape memory and superelasticity; results in a sharp reduction in the hysteresis at approximately 7–8 at%.
Hf	Not as workable or ductile as binary NiTi, NiTiCo, or NiTiFe. If substituted for Ti (Ni $<$ 51%) will increase TTs. More than 30 at% can be added without severely impacting the shape memory effect. Results in a radiopacity improvement.
Ag	Only small amounts added to date. Results in a radiopacity improvement.
Zr	Reduces workability and ductility; If substituted for Ti (Ni $<$ 51%) will increase TTs. More than 30 at% can be added without severely impacting the shape memory effect. Results in a radiopacity improvement.
W	Drastically reduces ductility; results in a radiopacity improvement.

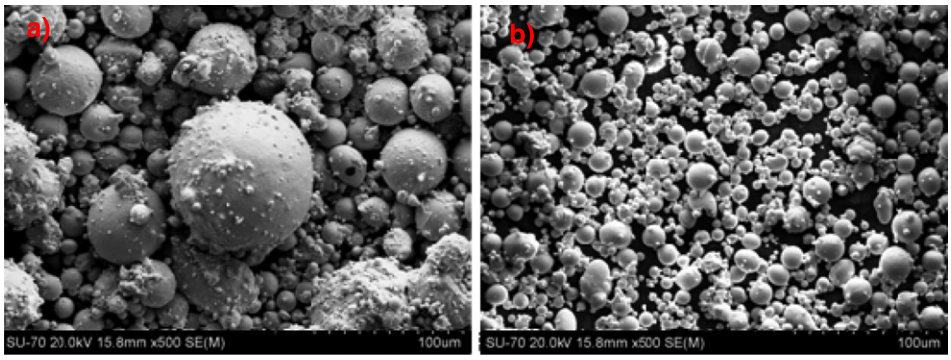


Figure 6 SEM of pre-alloyed gas atomized powders of (a) titanium rich NiTi and (b) nickel rich NiTi starting powders.

3.21.4.3.1 Fabrication of ternary NiTi using SPS

In this experiment ternary NiTiEr was fabricated by SPS. Small nickel rich NiTi powders and Hydrogenated–DeHydrogenated (HDH) erbium powders were ball milled for 20 min. These powders were then sintered at temperature of 800 °C and a pressure 70 MPa using the Dr. Sinterlab SPS 515S.

Figures 6(a) and 6(b) below are SEM images showing pre-alloyed gas atomized NiTi powders. Figure 6(a) shows the morphology and size of these NiTi powders. These powders are titanium rich. Figure 6(b) shows the morphology and size of NiTi powders that are nickel rich.

It can be seen from the SEM images that the gas atomized titanium rich powders have a higher average particle size when compared to gas atomized nickel rich NiTi powders.

Figures 7(a) and 7(b) below show SEM images of NiTi powders ball milled with erbium powders. Figure 7(a) shows SEM images of NiTi powders ball milled with HDH erbium powders. Figure 7(b) shows SEM images of NiTi powders ball milled with nickel erbium powders.

These images highlight the huge variation in powder sizes and indicate that the smaller powders will surround the larger powders during mixing, and ultimately during and after

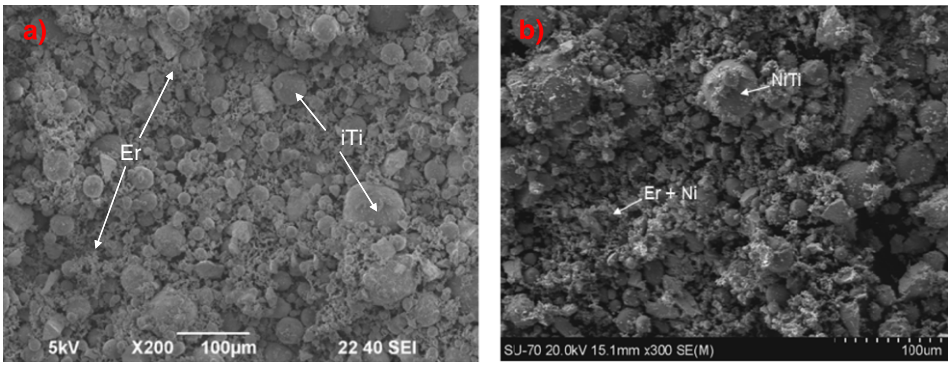
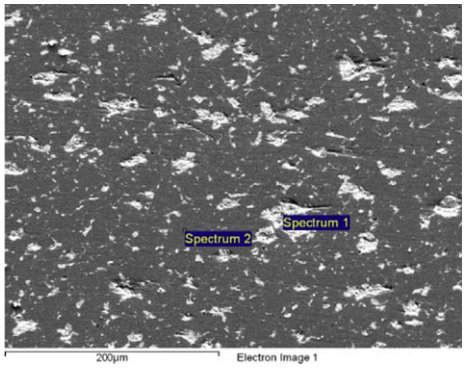


Figure 7 SEM the ball milled (a) NiTi + HDH Er and (b) NiTi + (Er + Ni) starting powders.



Area	Ni	Ti	Er
Spectrum 1	2.61	3.88	93.51
Spectrum 2	50.32	49.57	0.11

Figure 8 SEM/EDS of nickel rich NiTi and HDH Er, sintered at 800 °C and 70 MPa.

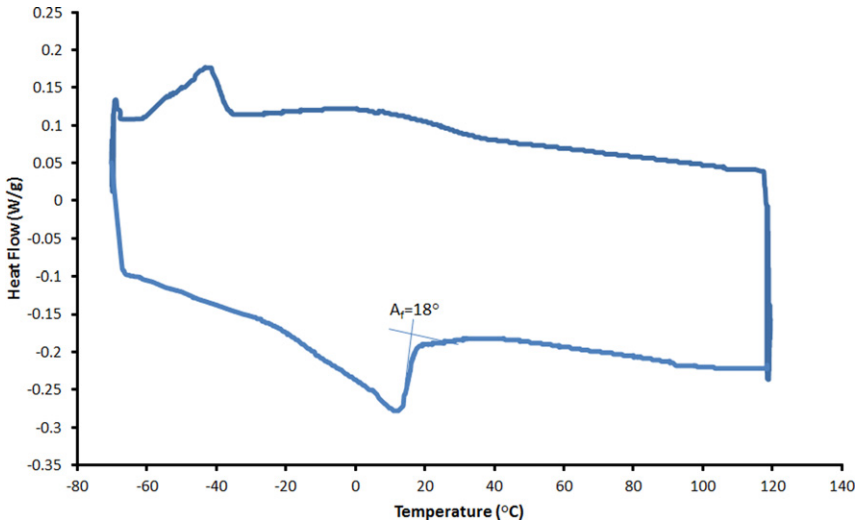


Figure 9 DSC of nickel rich NiTi and HDH Er powder, sintered at 800 °C and 70 MPa.

sintering. While this will not be a problem with the binary alloys, it will cause issues in the ternary NiTiEr alloys if the rare earth powders are finer than the NiTi powders.

SPS was carried out at using both ball milled NiTi and HDH Er powders and NiTi erbium/nickel powders at various temperatures and pressures to find the ideal sintering parameters for the production of ternary NiTiEr. The aim of these experiments was to keep the transformation temperature of the ternary NiTiEr below body temperature and prevent the erbium and nickel from alloying together. It was found that by dropping the sintering to 800 °C and increasing the pressure to 70 MPa, to keep the density >95%, the transformation temperature was more easily controlled.

Figure 8 below shows the microstructure of nickel rich NiTi and HDH erbium powder, using a sintering temperature of 800 °C, temperature ramp rate of 25 °C per minute, and a pressure of 70 MPa.

The hardness was found to be 333 HV in the sintered state. The SEM/EDS analysis showed that the 'HDH Er' was not alloying with the nickel in the nickel rich NiTi powder particles.

Figure 9 shows the DSC graph of nickel rich NiTi and HDH Er powder, sintered at 800 °C and 70 MPa.

This clearly shows that the extra nickel in the nickel rich powder, in combination with the lower sintering temperature, has reduced the A_f transformation temperature to an acceptable level well below body temperature.

3.21.5 Conclusions

This chapter has outlined the main methods of producing NiTi, either by casting or powder metallurgy. Casting, either VIM or VAR, are generally the main methods used to commercially produce NiTi. An alternate route used to casting is powder metallurgy. The main powder metallurgy methods used to produce NiTi such as CS, HIP and specifically SPS were also highlighted in this chapter.

This chapter mainly focused on SPS of NiTi. Some original work on SPS of binary and ternary NiTi was also presented in this chapter. For the binary NiTi work it was concluded that the sample sintered at the higher temperature and pressure has the best qualities that would be required for using this NiTi alloy in products such as stents. From the ternary NiTi work it was found that sintering at lower temperatures and higher pressures resulted in a workable alloy with good transformation temperatures.

See also: 3.20 Surface Preparation and Adhesion Tests of Coatings

References

1. Mantovani, D. Shape Memory Alloys: Properties and Biomedical Applications. *JOM* **2000**, *52* (10), 36–44.
2. Buehler, W. J.; Wang, F. E. A Summary of Recent Research on the NiTinol Alloys and Their Potential Application in Ocean Engineering. *Ocean Eng.* **1968**, *1* (1), 105–120.
3. Hodgson, D.; Russell, S. Nitinol Melting, Manufacture and Fabrication. *Minim. Invasiv. Ther. Allied Technol* **2000**, *9* (2), 61–65.
4. Pelton, A. R.; Russell, S. M.; DiCello, J. The Physical Metallurgy of Nitinol for Medical Applications. *JOM* **2003**, *55* (5), 33–37.
5. Elahinia, M. H.; Hashemi, M.; Tabesh, M.; Bhaduri, S. B. Manufacturing and Processing of NiTi Implants: A Review. *Prog. Mater. Sci.* **2012**, *57* (5), 911–946.
6. Reinoehl, M.; Bradley, D.; Bouthot, R.; Proft, J. The Influence of Melt Practice on Final Fatigue Properties of Superelastic NiTi Wires. In *SMST-2000: Proceedings of the International Conference on Shape Memory and Superelastic Technologies*, Pacific Grove, CA, April, 2000; pp. 397–403.
7. Frenzel, J.; George, E. P.; Dlouhy, A.; Somsen, C.; Wagner, M. X.; Eggeler, G. Influence of Ni on Martensitic Phase Transformations in NiTi Shape Memory Alloys. *Acta Mater.* **2010**, *58* (9), 3444–3458.
8. Foroozmehr, A.; Kermanpur, A.; Ashrafizadeh, F.; Kabiri, Y. Investigating Microstructural Evolution During Homogenization of the Equiatomic NiTi Shape Memory Alloy Produced by Vacuum Arc Remelting. *Mater. Sci. Eng. A* **2011**, *528* (27), 7952–7955.
9. Frenzel, J.; Zhang, Z.; Neuking, K.; Eggeler, G. High Quality Vacuum Induction Melting of Small Quantities of NiTi Shape Memory Alloys in Graphite Crucibles. *J. Alloy. Compd.* **2004**, *385* (1), 214–223.
10. Nayan, N.; Saikrishna, C. N.; Ramaiah, K. V.; Bhaumik, S. K.; Nair, K. S.; Mittal, M. C. Vacuum Induction Melting of NiTi Shape Memory Alloys in Graphite Crucible. *Mater. Sci. Eng. A* **2007**, *465* (1), 44–48.
11. Zhang, Z.; Frenzel, J.; Neuking, K.; Eggeler, G. Vacuum Induction Melting of Ternary NiTiX (X = Cu, Fe, Hf, Zr) Shape Memory Alloys Using Graphite Crucibles. *Mater. Trans.* **2006**, *47* (3), 661–669.
12. Bram, M.; Ahmad-Khanlou, A.; Heckmann, A.; Fuchs, B.; Buchkremer, H. P.; Stöver, D. Powder Metallurgical Fabrication Processes for NiTi Shape Memory Alloy Parts. *Mater. Sci. Eng. A* **2002**, *337* (1), 254–263.
13. Li, B. Y.; Rong, L. J.; Li, Y. Y.; Gjunter, V. E. A Recent Development in Producing Porous Ni–Ti Shape Memory Alloys. *Intermetallics* **2000**, *8* (8), 881–884.
14. Shearwood, C.; Fu, Y. Q.; Yu, L.; Khor, K. A. Spark Plasma Sintering of TiNi Nano-Powder. *Scr. Mater.* **2005**, *52* (6), 455–460.
15. Li, B. Y.; Rong, L. J.; Li, Y. Y. Porous NiTi alloy Prepared from Elemental Powder Sintering. *J. Mater. Res.* **1998**, *13* (10), 2847–2851.
16. Bertheville, B. Porous Single-Phase NiTi Processed under Ca Reducing Vapor for Use as a Bone Graft Substitute. *Biomaterials* **2006**, *27* (8), 1246–1250.
17. Zhang, Y. P.; Li, D. S.; Zhang, X. P. Gradient Porosity and Large Pore Size NiTi Shape Memory Alloys. *Scr. Mater.* **2007**, *57* (11), 1020–1023.
18. Li, D. S.; Zhang, Y. P.; Eggeler, G.; Zhang, X. P. High Porosity and High-Strength Porous NiTi Shape Memory Alloys with Controllable Pore Characteristics. *J. Alloys Compd.* **2009**, *470* (1), L1–L5.
19. Li, H.; Yuan, B.; Gao, Y.; Chung, C. Y.; Zhu, M. High-Porosity NiTi Superelastic Alloys Fabricated by Low-Pressure Sintering Using Titanium Hydride as Pore-Forming Agent. *J. Mater. Sci.* **2009**, *44* (3), 875–881.
20. Yuan, B.; Chung, C. Y.; Zhu, M. Microstructure and Martensitic Transformation Behavior of Porous NiTi Shape Memory Alloy Prepared by Hot Isostatic Pressing Processing. *Mater. Sci. Eng. A* **2004**, *382* (1), 181–187.
21. Yuan, B.; Chung, C. Y.; Zhang, X. P.; Zeng, M. Q.; Zhu, M. Control of Porosity and Superelasticity of Porous NiTi Shape Memory Alloys Prepared by Hot Isostatic Pressing. *Smart Mater. Struct.* **2005**, *14* (5), S201.
22. Yuan, B.; Zhu, M.; Gao, Y.; Li, X.; Chung, C. Y. Forming and Control of Pores by Capsule-Free Hot Isostatic Pressing in NiTi Shape Memory Alloys. *Smart Mater. Struct.* **2008**, *17* (2), 025013.
23. Mentz, J.; Frenzel, J.; Wagner, M. F. X.; *et al.* Powder Metallurgical Processing of NiTi Shape Memory Alloys with Elevated Transformation Temperatures. *Mater. Sci. Eng. A* **2008**, *491* (1), 270–278.
24. Wu, S. L.; Liu, X. M.; Chu, P. K.; Chung, C. Y.; Chu, C. L.; Yeung, K. W. K. Phase Transformation Behavior of Porous NiTi Alloys Fabricated by Capsule-Free Hot Isostatic Pressing. *J. Alloys Compd.* **2008**, *449* (1), 139–143.
25. Bitzer, M.; Bram, M.; Buchkremer, H. P.; Stöver, D. Phase Transformation Behavior of Hot Isostatically Pressed NiTi–X (X = Ag, Nb, W) Alloys for Functional Engineering Applications. *J. Mater. Eng. Perform.* **2012**, *21* (12), 2535–2545.
26. Schöller, E.; Krone, L.; Bram, M.; Buchkremer, H. P.; Ståaver, D. Metal Injection Molding of Shape Memory Alloys Using Prealloyed NiTi Powders. *J. Mater. Sci.* **2005**, *40* (16), 4231–4238.
27. Guoxin, H.; Lixiang, Z.; Yunliang, F.; Yanhong, L. Fabrication of High Porous NiTi Shape Memory Alloy by Metal Injection Molding. *J. Mater. Process. Technol.* **2008**, *206* (1), 395–399.
28. Bram, M.; Bitzer, M.; Buchkremer, H. P.; Stöver, D. Reproducibility Study of NiTi Parts Made by Metal Injection Molding. *J. Mater. Eng. Perform.* **2012**, *21* (12), 2701–2712.
29. Chen, G.; Cao, P.; Wen, G.; Edmonds, N.; Li, Y. Using an Agar-Based Binder to Produce Porous NiTi Alloys by Metal Injection Moulding. *Intermetallics* **2013**, *37*, 92–99.
30. Tay, B. Y.; Goh, C. W.; Gu, Y. W.; *et al.* Porous NiTi Fabricated by Self-Propagating High-Temperature Synthesis of Elemental Powders. *J. Mater. Process. Technol.* **2008**, *202* (1), 359–364.
31. Bassani, P.; Giuliani, P.; Tuissi, A.; Zanotti, C. Thermomechanical Properties of Porous NiTi Alloy Produced by SHS. *J. Mater. Eng. Perform.* **2009**, *18* (5–6), 594–599.
32. Tosun, G.; Ozler, L.; Kaya, M.; Orhan, N. A Study on Microstructure and Porosity of NiTi Alloy Implants Produced by SHS. *J. Alloys Compd.* **2009**, *487* (1), 605–611.
33. Hosseini, S. A.; Alizadeh, M.; Ghasemi, A.; Meshkot, M. A. Highly Porous NiTi with Isotropic Pore Morphology Fabricated by Self-Propagated High-Temperature Synthesis. *J. Mater. Eng. Perform.* **2013**, *22* (2), 405–409.

34. Bassani, P.; Bassani, E.; Tuissi, A.; Giuliani, P.; Zanotti, C. Nonequiatomic NiTi Alloy Produced by Self Propagating High Temperature Synthesis. *J. Mater. Eng. Perform.* **2014**, *23* (7), 2373–2378.
35. Ye, L. L.; Liu, Z. G.; Raviprasad, K.; Quan, M. X.; Umemoto, M.; Hu, Z. Q. Consolidation of MA Amorphous NiTi Powders by Spark Plasma Sintering. *Mater. Sci. Eng. A* **1998**, *241* (1), 290–293.
36. Zhao, Y.; Taya, M.; Kang, Y.; Kawasaki, A. Compression Behavior of Porous NiTi Shape Memory Alloy. *Acta Mater.* **2005**, *53* (2), 337–343.
37. Fu, Y. Q.; Gu, Y. W.; Shearwood, C.; Luo, J. K.; Flewitt, A. J.; Milne, W. I. Spark Plasma Sintering of TiNi Nano-Powders for Biological Application. *Nanotechnology* **2006**, *17* (21), 5293.
38. Majkic, G.; Chennoufi, N.; Chen, Y. C.; Salama, K. Synthesis of NiTi by Low Electrothermal Loss Spark Plasma Sintering. *Metall. Mater. Trans. A* **2007**, *38* (10), 2523–2530.
39. Butler, J.; Tiernan, P.; Gandhi, A. A.; McNamara, K.; Tofail, S. A. M. Production of Nitinol Wire from Elemental Nickel and Titanium Powders Through Spark Plasma Sintering and Extrusion. *J. Mater. Eng. Perform.* **2011**, *20* (4–5), 757–761.
40. Lee, J.; Hwang, J.; Lee, D.; Ryu, H. J.; Hong, S. H. Enhanced Mechanical Properties of Spark Plasma Sintered NiTi Composites Reinforced with Carbon Nanotubes. *J. Alloys Compd.* **2014**, *617*, 505–510.
41. Zhang, L.; Zhang, Y. Q.; Jiang, Y. H.; Zhou, R. Superelastic Behaviors of Biomedical Porous NiTi Alloy With High Porosity and Large Pore Size Prepared by Spark Plasma Sintering. *J. Alloys Compd.* **2015**, *644*, 513–522.
42. Yoo, S.; Groza, J. R.; Sudarshan, T. S.; Yamazaki, K. Diffusion Bonding of Boron Nitride on Metal Substrates by Plasma Activated Sintering (PAS) Process. *Scr. Mater.* **1996**, *34* (9), 1383–1386.
43. McCormick, J. P. *Cyclic Behaviour of Shape Memory Alloys: Material Characterization and Optimization* (Thesis); Atlanta, GA: Georgia Institute of Technology, 2006.
44. Biscarini, A.; Mazzolai, G.; Tuissi, A. Enhanced Nitinol Properties for Biomedical Applications. *Recent Pat. Biomed. Eng.* **2008**, *1*, 180–196.
45. Otsuka, K.; Wayman, C. M. *Shape Memory Materials*; Cambridge University Press: Cambridge, 1999.
46. Feng, B.; Weng, J.; Yang, B.; *et al.* Surface Characterization of Titanium and Adsorption of Bovine Serum Albumin. *Mater. Charact.* **2002**, *49* (2), 129–137.
47. Shabalovskaya, S.; Anderegg, J.; Van Humbeeck, J. Critical Overview of Nitinol Surfaces and Their Modifications for Medical Applications. *Acta Biomater.* **2008**, *4* (3), 447–467.
48. Nolan, M.; Tofail, S. A. M. Density Functional Theory Simulation of Titanium Migration and Reaction with Oxygen in the Early Stages of Oxidation of Equiatomic NiTi Alloy. *Biomaterials* **2010**, *31* (13), 3439–3448.
49. Luke M. T. *Microstructural Evolution of Nickel During Spark Plasma Sintering* (MSc. Thesis); Boise, ID: Boise State University, 2010.
50. Gibson, I.; Rosen, D. W.; Stucker, B. *Additive Manufacturing Technologies: Rapid Prototyping to Direct Digital Manufacturing*; Springer: New York, NY, 2009.
51. Bocanegra-Bernal, M. H. Hot Isostatic Pressing (HIP) Technology and its Applications to Metals and Ceramics. *J. Mater. Sci.* **2004**, *39* (21), 6399–6420.
52. Inoue, K. *Electric-Discharge Sintering*. U.S. Patent 3,241,956, March 22, 1966.
53. Inoue, K. *Apparatus for Electrically Sintering Discrete Bodies*. U.S. Patent 3,250,892, May 10, 1966.
54. Omori, M. Sintering, Consolidation, Reaction and Crystal Growth by the Spark Plasma System (SPS). *Mater. Sci. Eng. A* **2000**, *287* (2), 183–188.
55. Murakami, T.; Kitahara, A.; Koga, Y.; Kawahara, M.; Inui, H.; Yamaguchi, M. Microstructure of Nb–Al Powders Consolidated by Spark Plasma Sintering Process. *Mater. Sci. Eng. A* **1997**, *239*, 672–679.
56. Groza, J. R. Consolidation of Atomized NiAl Powders by Plasma Activated Sintering Process. *Scripta Metallurgica et Materialia* **1994**, *30* (1), 47–52.
57. Tokita, M. Mechanism of Spark Plasma Sintering. In *Proceeding of NEDO International Symposium on Functionally Graded Materials*, Japan, 1999; p. 22.
58. Duerig, T.; Pelton, A.; Trepanier, C. Nitinol. SMST e-Elastic *Newsletter*, 2011.
59. Tofail, S. A. M.; Butler, J.; Gandhi, A. A.; *et al.* X-ray Visibility and Metallurgical Features of NiTi Shape Memory Alloy with Erbium. *Mater. Lett.* **2014**, *137*, 450–454.
60. Cristea, C. D.; Lungu, M.; Balagurov, A. M.; *et al.* Shape Memory NiTi and NiTiCu Alloys Obtained by Spark Plasma Sintering Process. *Adv. Eng. Forum* **2015**, *13*, 83–90.

3.22 Spark Plasma Sintering of Lead-Free Ferroelectric Ceramic Layers

M Karimi-Jafari, K Kowal, E Ul-Haq, and SAM Tofail, University of Limerick, Limerick, Ireland

© 2017 Elsevier Inc. All rights reserved.

3.22.1	**Sintering**	347
3.22.1.1	Sintering Procedure	347
3.22.1.2	Spark Plasma Sintering	348
3.22.1.2.1	History of SPS	348
3.22.1.2.2	Sintering principles and mechanism	349
3.22.1.2.3	Advantages of SPS over conventional sintering	349
3.22.1.2.4	Application of SPS	349
3.22.1.2.4.1	SPS in biomaterials (HAp)	350
3.22.1.2.4.1.1	Microstructural and mechanical properties of spark plasma sintered HAp	350
3.22.1.2.4.1.2	Optical properties of SPS HAp	351
3.22.1.2.4.2	SPS in lead-free ferroelectric ceramics	352
3.22.1.2.4.2.1	BT	353
3.22.1.2.4.2.2	$ANbO_3$	354
3.22.1.2.4.2.3	KNN	355
3.22.1.2.4.2.4	$(Bi_{0.5}Na_{0.5})TiO_3$	355
3.22.2	**Conclusion**	356
References		356
Relevant Websites		357

3.22.1 Sintering

Sintering as a technique has been known for a few millennia and has been used in pottery, tile, and sanitary ware production and fine ceramics. The process itself bases on compression and solidifying powder materials through heat and/or pressure. Sintering is also used extensively in powder metal compactions, a field known as powder metallurgy. Sintering of polycrystalline ceramics has been extensively reported by chemists, physicists, and materials scientists. In recent years, there has been a considerable interest in new sintering methods and their outcome. In materials finish applications, ceramic and metal coatings have been used for longevity, artistic, and decoration purposes. Functional ceramic coatings on metals known as 'cermets' combined hardness and corrosion resistance of ceramics to the toughness and shock resistance of metals and used in cutting tool industry for many decades.

In order to start sintering process, free energy of the system has to be decreased, and pressure becomes the main driving force. Mass transportation kinetics can enhance the process in terms of time efficiency. As a result, diffusion plays an important role in the process, as it is responsible for the transport of the atoms in crystalline solids. Control of the diffusion process is beneficial to the outcome of sintering process, and there are two parameters that have direct effect on diffusion: temperature and concentration of defects in the sample. Defects concentration on its own depends on temperature, gaseous atmosphere, and concentration of dopants and impurities.[1] Furthermore, microstructure is dependent on pre-firing processing variables, however, the effect of controlling variables in firing stage is also critical.

Sintering methods can be divided into two main groups: (1) conventional (free or pressure less) sintering, which is more economical because there is no external pressure and (2) pressure sintering, which employ external pressure during sintering. Pressure sintering can produce material with higher density and finer-grained microstructure.[1]

In conventional methods, there are two important parameters: sintering process steps (duration and temperature) and process environment (vacuum, oxygen, etc.). To heat up the samples two methods can be used: conventional sintering and microwave-assisted sintering. In conventional method, samples are placed in the electrical furnace and heat is being transferred from heating elements, whereas in microwave heating, samples are heated internally due to absorption of microwaves (**Figure 1**).

3.22.1.1 Sintering Procedure

Sintering can include steps such as the burnout of solvents used for binding the powder into a compact form and phase transformation can occur during such processes. Because of this complexity, controlled and multiple-stage processes may be required as presented in **Figure 2**.

The first stage of the process is the burnout of the binder by slow heat up, where duration of the process and the temperature depend on the amount of binder and sample size. The second stage is the low temperature soak during which modification of microstructure is achieved. Chemical homogenization like solid-state reaction or liquid phase formation may occur at this stage. The next step is heating-up to the sintering temperature. Critical parameter during this stage is the heating rate, as the higher the heating rate value, the more the densification occurs. As grains are exposed to high temperature

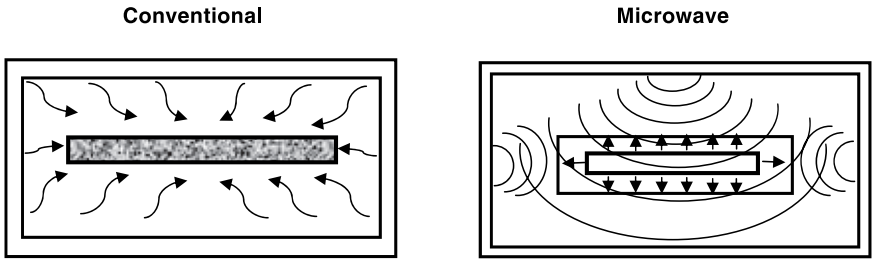


Figure 1 Conventional sintering versus microwave sintering process.[1]

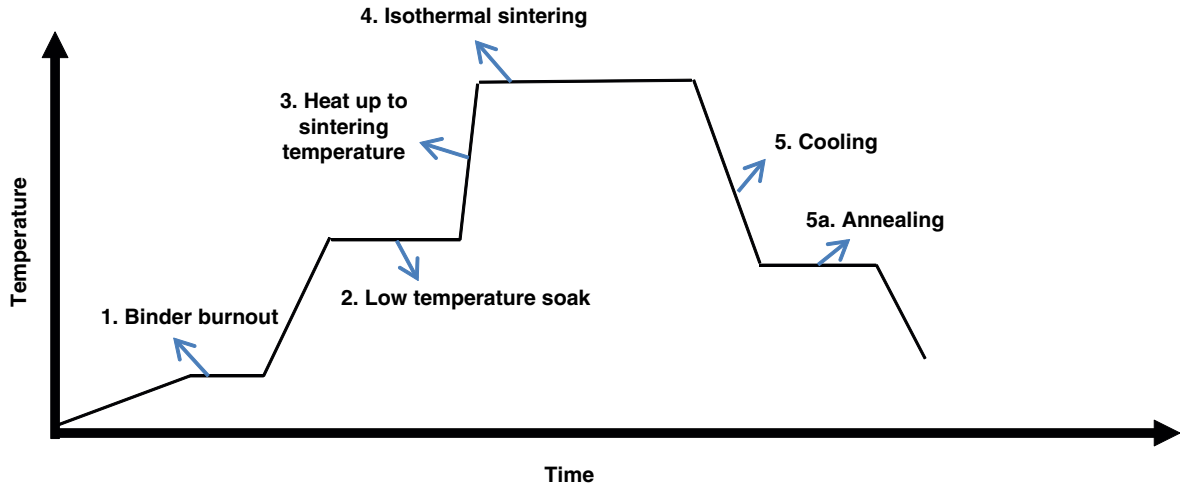


Figure 2 A typical sintering schedule.[1]

for shorter time they do not grow rapidly, and their sizes are finer. The fourth stage is the actual isothermal sintering which leads to final densification. Duration and sintering temperature affect grains coarsening and can cause subsequently abnormal grain growth. For a proper chemical homogenization, sintering time should be extended. The fifth stage is the cool down to the room temperature or in some cases, during cool down an additional annealing step is required to decrease thermal stresses within the sample. Cooling rates can vary depending on the size of the sample, for small samples it can be faster, on the other hand larger samples require slower cooling rate to prevent temperature gradients within the sample that can cause cracking. In order to achieve good structural modification, cooling rate has to be controlled.[1] In practice, some of the above stages may not be needed. For example, green compaction without a binder may not need any binder burnout.

3.22.1.2 Spark Plasma Sintering

Spark plasma sintering (SPS) or pulsed electric current sintering (PECS) are hybrid electrical–mechanical methods used for rapid sintering of metallic and ceramic powders. Pulsed direct electrical current pushed through the sample together with high uniaxial pressure at low atmospheric pressure leads to rapid densification of powders. This process is applicable to sintering of conductive and nonconductive powders. In SPS direct heating of the samples occur by passing electrical current through the sample. High heating rates can be easily achieved, leading to high densification of the powders in a very short time. The high heating rate prevents from undesired grain growth in the sample. Electrical current passes through the sample, and electrical discharge occurs at the contact points of the grains, leading to homogenous heating of the sample. As the result there is a low grain growth and high densification at a very short time, enabling significantly improved or even completely novel materials. The SPS machine consists of following parts: electrodes, two graphite punches (upper and lower), one graphite die, uniaxial pressurizing clamp, vacuum chamber and integrated water cooling system, and controlling system (Figure 3).

Similar to conventional techniques like hot pressing (HP) and hot isostatic pressing (HIP), SPS utilizes simultaneous delivery of heat and pressure. However, there are significant differences between them. In HP and HIP methods, heating rate is much lower than in SPS, as the heating is applied by conventional heating elements in a box furnace. The heat is conveyed to the sample by means of radiation, but it is a very inefficient and slow process. In general high reproducibility, controllability, and speed are the most prominent advantages of SPS over other conventional sintering techniques.

3.22.1.2.1 History of SPS

Sintering assisted by an external electric field was proposed as early as in the 1930s.[3,4] It was based on the combinational use

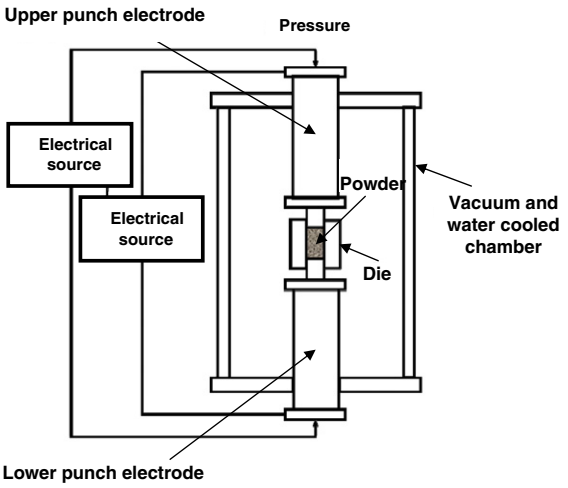


Figure 3 SPS machine schematic.[2]

of electrical heating and pressurized sintering under vacuum or hydrogen gas atmosphere. Electrical discharge sintering was proposed by Inoue in 1960s[5,6] for conductive metallic powders with some of nonconductive materials. In these techniques grains are brought in contact with each other by pressure. By applying electrical current to the sample, ionization and local heating occurs at grain interfaces due to electrical discharge generated at these regions. SPS and plasma activated sintering (PAS) machine was commercially available since 1999.[7] PAS process consists of short pulses of direct current followed by long period of constant direct current. As a result the heating mechanism in the first stage is based on electrical discharge between grains interfaces, while in the second stage resistance heating is the dominant heating mechanism.[7]

3.22.1.2.2 Sintering principles and mechanism

Regarding the differences in the heating mechanisms between SPS and conventional sintering, the densification mechanisms are also different from the diffusion process, which occurs during conventional sintering processes. The process is divided into four steps as shown in **Figure 4**. These steps are: (1) vaporization and solidification, (2) volume diffusion, (3) surface diffusion, and (4) grain boundary diffusion. With the appearance of spark discharge, high temperatures are generated causing vaporization and melting of particles surface, followed by formation of a neck in the contacting area due to volume diffusion. Expansion of necks and plastic deformation of grains occurs leading to densification of the sample.[8] The electrical discharge of SPS process facilitates the removal of oxidized surface of the particles hence, improving the neck formation.[8] Steps 1 and 2 are controlled by voltage breakdown of SPS process. The two last steps depend on Joule effect and applied pressure, which enhances the neck growth and also speed up plastic deformation and finally densification.[8]

Considering the effective parameters in SPS process, compressive pressure is necessary to achieve higher densifications during SPS.[9] As the yield strength of most of the ceramic and metallic materials such as MgO and Al_2O_3 decreases at higher temperatures, once the applied stress reaches the particle yield

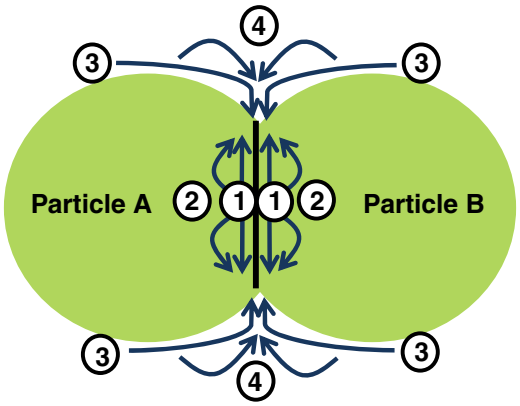


Figure 4 Diffusion process in spark plasma sintering.[7]

stress at a certain temperature, the densification starts the plastic deformation. This mechanism is the main reason of choosing lower sintering temperatures in SPS for materials with low yield strength compared to conventional sintering. However, in high yield strength materials such as YAG (yttrium aluminum garnet, $Y_3Al_5O_{12}$) which keep their high yield strength even at high temperatures, this mechanism is not predominantly active. In these cases, grain rotation and sliding are the main densification mechanisms. Changes of mechanical and electrical properties of the material by temperature determine the main densification mechanism.[9]

3.22.1.2.3 Advantages of SPS over conventional sintering

Direct heating of the sample during the SPS process by electrical discharges facilitates high heating rate. The high heating rate reduces undesired grain growth during the sintering, which is a common drawback in conventional sintering. Furthermore, the simultaneous application of pressure enables setting lower temperatures of sintering compared to conventional sintering. Also, as high temperatures can be reached in short times, sintering takes less time, so SPS can be seen as economically more efficient process.

The research interest in SPS started from two decades ago and has kept its increasing rate until now. It can be obviously seen in the number of papers published on SPS during recent years (**Figure 5**).

3.22.1.2.4 Application of SPS

Because of the advantages of the SPS, there has been a growing interest in using this technology to sinter variety of materials. For instance, it was used to sinter ultra-high temperature materials like WC–Si_3N_4,[10] TiC–ZrC composite,[11] and B_4C.[12] Furthermore, ferroelectric and piezoelectric materials such as $Ba(Zr_{0.2}Ti_{0.8})O_3$,[13] $BaTiO_3$,[14] lead-free materials like $(Na_{0.5}K_{0.5})NbO_3$-$LiTaO_3$[15] have been sintered using SPS. Also, extensive studies were conducted on sintering biomaterials like hydroxyapatite (HAp) by SPS.[16–18]

Considering the broad spectrum of application of SPS in biomaterials and ferroelectric ceramics, following sections of the chapter are focused on sintering these two groups of materials.

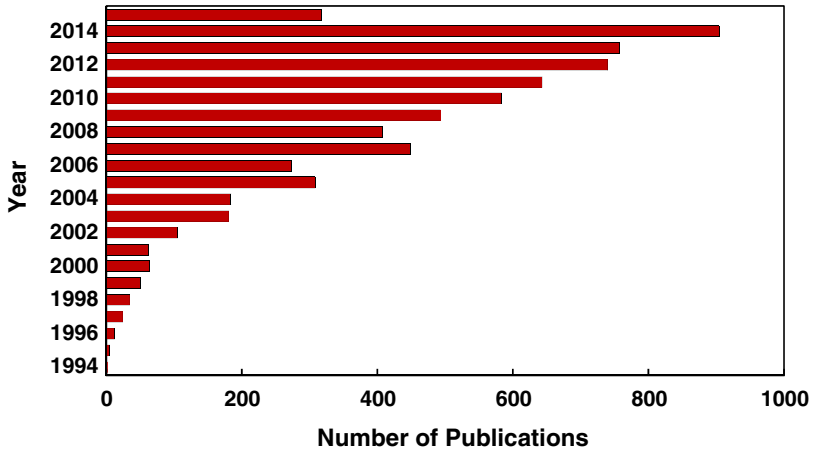


Figure 5 Number of papers published on 'spark plasma sintering' during recent years.

3.22.1.2.4.1 SPS in biomaterials (HAp)

HAp $Ca_{10}(PO_4)_6(OH)_2$ has been used for several years in orthopedic and dental implants, and also in scaffolds enhancing bone growth after hip or knee surgery.[19] The conventional sintering temperature of HAp usually ranges between 1000 and 1500 °C. While porosity of HAp is advantageous for bone growth it is destructive to its mechanical strength and limiting its application. HAps fatigue resistance, tensile and compressive strength depend on total porosity volume after sintering. Furthermore, the dehydroxylation behavior of HAp is another problem, as HAp can be decomposed from its hydrated phase to anhydrous phases such as tricalcium phosphate (TCP) phase at 1200–1450 °C leading to the collapse of HAp structure.[20] The optimum conventional sintering temperature of HAp is reported to be within the range of 1250–1300 °C.[20,21] High sintering temperatures cause grain coarsening, which negatively affects mechanical properties.

High speed, low sintering temperature techniques seem to be beneficial in decreasing the sintering temperature and time, and consequently, prevention of the dehydroxylation and undesired grain growth. Conventional pressure less sintering processes were used to sinter HAp, but methods like HIP, HP, microwave sintering, and SPS have shown promising results in reducing negative effects of conventional sintering. Among all these techniques, SPS has attracted a huge interest due to its high heating rate and application of pressure during sintering.[22] Sintering parameters like: temperature, time, cooling and heating rate, pressure, and atmosphere have been extensively studied by several authors to improve mechanical and biological properties of HAp,[20] produce transparent HAp specimens,[16,18] and also to sinter HAp composite ceramics.[23,24]

3.22.1.2.4.1.1 Microstructural and mechanical properties of spark plasma sintered HAp

Gu *et al.*[2] Sintered HAp at 50 MPa uniaxial pressure with 50 °C min^{-1} heating rate at temperature values varying between 850 and 1100 °C, where holding time was 5 min. The results showed that the optimum densification and best mechanical properties were found in samples sintered at 950 °C, so 300 °C less than in conventional sintering.[2] This drop in sintering temperature is benefits in reducing undesired grain growth and decrease HAp decomposition to TCP. It was reported that the grain growth is negligible until 950 °C.[2] As shown on **Figure 6** the highest relative density (99.6%) was obtained for samples sintered at 950 °C.

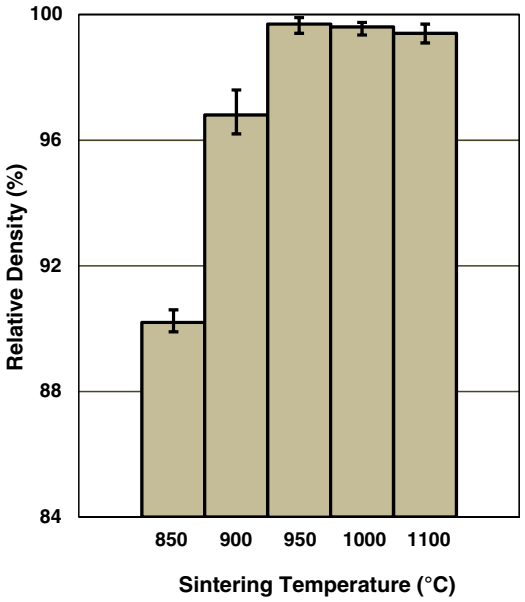


Figure 6 Relative density of HAp sintered by SPS.[2]

Furthermore, samples sintered at 950 °C possessed the highest Young's modulus and Knop hardness. However, above this temperature the grain growth increases rapidly and relative density decreases due to the dehydration of HAp to TCP. The densification process is a two phase process: first one occurs below 900 °C and is linked to the grain boundary diffusion, while a more energetic bulk diffusion process takes place at higher temperatures.

The effect of the initial structural properties such as particle sizes and phase composition on the sintered HAp samples was studied by Cucu *et al.*[25] It was shown that powders with initial smaller particle sizes lead to higher density of sintered samples at lower temperatures. Furthermore, it was reported that the phase decomposition of HAp to TCP during sintering process

hinders the densification of the samples. Consequently, thermal stability of powders can be an important factor in densification process. In addition, particle size and phase composition of the initial powder can affect the final grain size and optical transparency of the samples. Bigger grains and higher TCP phase content in the samples, decreases the transparency.

A comprehensive study on microstructural and mechanical behavior of SPS sintered HAp samples at different sintering temperatures and pressure has been carried out by Li *et al.*[26] They observed that no decomposition of HAp took place up to 1000 °C in vacuum. They also studied the effect of the temperature and pressure on the relative density of the samples. It was shown that sample density increases with higher temperature and pressure a rapid increase of density (from 92 to 98.9%) was observed after increasing the temperature from 800 to 1000 °C at 22.3 MPa.[26] Also, after increasing the pressure from 22.3 to 66.9 MPa at 800° C the density of the samples increased from 92 to 98.9%.

However, it was found that above 900 °C no major variations in density was observed, indicating limitation of temperature impact on the densification of HAp samples. The highest relative density of 99.7% was achieved at 1000 °C and 66.9 MPa. This density is achieved at the sintering temperature, which is about 200–400 °C lower than the conventional sintering temperature. Although higher densities were observed at higher temperatures and pressures, but at the cost of larger grains which resulted in poor mechanical properties of the samples. Hence, the balance between density of the samples and grain size has to be considered with respect to samples mechanical properties. The mechanism that relates the impact of applied pressure and temperature on densification mechanism can be understood into three steps. At temperatures below 850 °C particles are in contact with each other and 'necks' between particles are being formed. In the second stage, within temperature range of 850–900 °C volume and grain boundary diffusion occurs. In this step the density increases and grains grow. During final step, at temperatures higher than 900 °C, continuous pores disappear and closed pores are being formed. These pores are moveable compared to closed pores, and lead to rapid increase in density.[26] Although the densification pressure and temperature depend on the physical and microstructural properties of the powders, the common range of sintering temperature of HAp samples has been reported to be between 900 and 1000 °C depending on various initial powder properties.

The calculated grain growth activation energy based on Arrhenius equation, depicts lower activation energies at higher temperatures and pressures. In this case, the activation energy at 850–900 °C is 55 kcal mol^{-1} and 51 kcal mol^{-1} at 22 and 44.6 MPa, respectively. Lower activation energy was observed at temperatures higher than 950 °C (42 kcal mol^{-1}). This is the main reason of the proliferated grain growth rate at temperature higher than 950 °C. The flexural strength achieved at 44.6 MPa and 950 °C is 131.5 MPa, which is extremely higher than the one achieved by conventional sintering at higher temperatures.[26] Lower flexural strength was observed at higher sintering temperatures than 950 °C, which can be attributed to the higher grain size. It is stated that HAp decomposition, residual stress and grain growth are the main factors in mechanical strength loss of HAp samples.[26] Gradual increase of the optical transparency was observed by increasing sintering temperature and pressure. The highest density and optical transparency was achieved in samples sintered at 1000 °C and 66.9 MPa. The effect of SPS parameters on optical properties of HAp samples will be discussed thoroughly in the next section.

3.22.1.2.4.1.2 Optical properties of SPS HAp

The optical transparency of the HAp in addition to its high chemical stability and biocompatibility,[19] can facilitate its application in new untouched fields. For example, it can be used for applications such as use of confocal microscopy for observation of human cells activities, and transparent window for implantable bio-devices for direct observation of biological activities.[16,18] Spark plasma sintered transparent HAp at temperatures between 800 and 1300 °C under pressure of 30–50 MPa and 5–10 min total sintering time. Local discontinuities such as grain boundaries, microstructural defects, grain size, crystallographic anisotropy, and heterogeneous composition play an important role in the optical properties of HAp ceramics.[16,18] The effect of SPS on crystallographic orientation and finally optical properties of HAp is investigated in our group.[18] The differences in optical transmittance versus sintering temperature are illustrated in **Figure 7**. Samples sintered between 700 and 790 °C with 100 °C min^{-1} heating rate under 50 MPa pressure for 20 min were opaque, while the highest transparency was observed at 900 °C. Samples sintered at higher temperatures were translucent with 40–50% transmittance.[18]

A rapid increase in density was reported in the range between 700 and 900 °C. This trend is almost stopped above 900 °C (**Figure 8**). A comparison between increase of density and transmittance with temperature up to 900 °C showed that the elimination of optical diffraction sources such as pores, grain boundaries, and grain growth are effective in enhancement of both density and transmittance, simultaneously. However, the grain growth above 900 °C resulted in a reduction of the transparency.

The density of the sample sintered at 900 °C is close to the theoretical density and there are not many pores in the structures, which show that the light transmittance is mostly dependent on the samples' microstructure. It was shown that in samples sintered between 700 and 900 °C, *c*-axis is aligned perpendicularly with respect to the uniaxial pressure direction. Eventually, *c*-axis of the most of the grains is perpendicular to the incident light. At temperatures higher than 900 °C there is enough energy available to rotate grains and grow in other directions even under uniaxial pressure. This rotation creates some out of plane grain orientations. This is another reason that can negatively affect the light transmittance after saturation of the density.[18] Consequently, it can be stated that the crystal orientation is one of the most influential factors on optical properties of HAp samples sintered by SPS. HAp crystal orientation plays a considerably important role in protein adsorption. The protein adsorption on *a*-plain of HAp was observed to be extremely higher than that of *c*-plain.[27] These HAps were electrically polarized to show unprecedented piezo, pyro, and ferroelectricity.

In another study, Watanabe *et al.*[27] reported a transparent HAp samples by sintering at 1200 °C with heating rate of

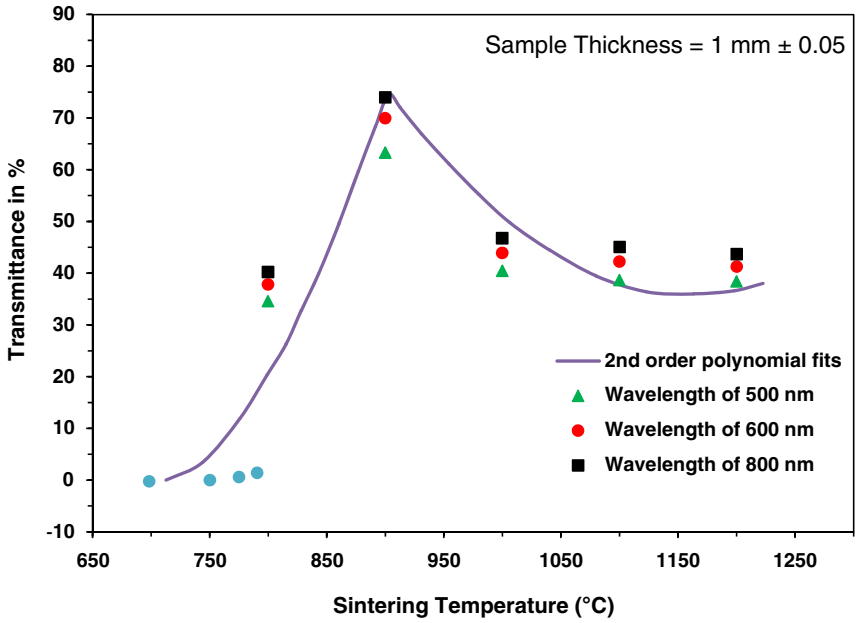


Figure 7 Optical transmittance of the samples sintered at different temperatures.[18]

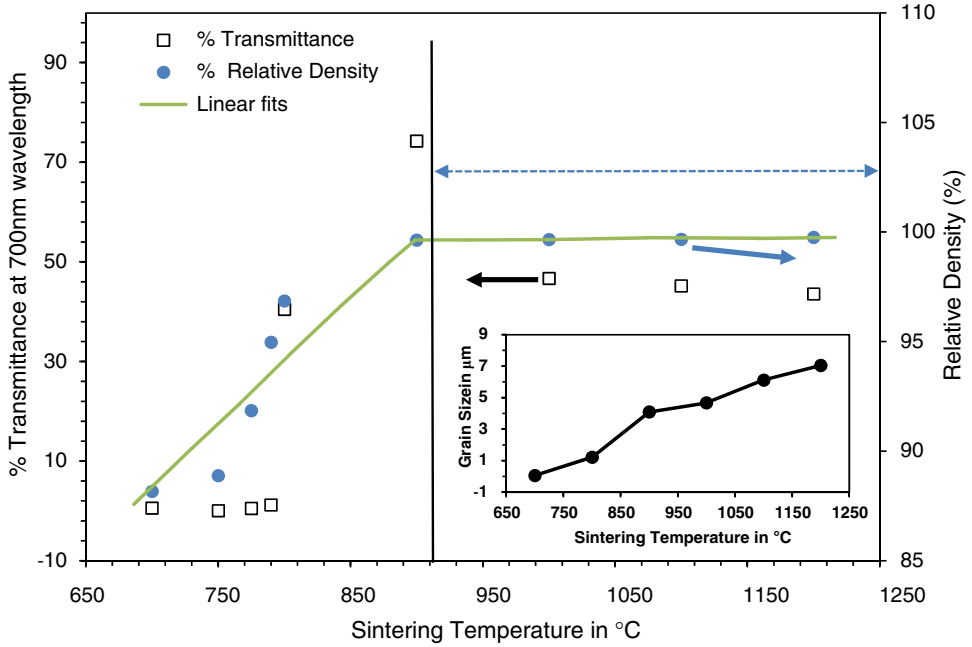


Figure 8 The effect of sintering temperature on relative density, optical transmittance, and grain size of the HAp samples.[18]

50 °C min^{-1} under 50 MPa of applied pressure and 10 min of sintering time.[27] The relative density of 99.7 and 70% transmittance over 700 nm was observed in these samples. This was observed at higher temperature and pressure ranges compared to what Gandhi *et al.*[18] reported. Regardless of the possible different properties of initial powders this can be related to the lower sintering rate that has been exploited in their sintering process. X-ray diffraction pattern of sintered samples in two directions: parallel and perpendicular to the pressure direction shows the effect of sintering pressure on the grains preferential orientation. As it is shown in **Figure 9**, (002) and (004) plains possess the highest intensity in the parallel section. The (100), (200), and (300) plains show the highest intensity in perpendicular direction. It can be deducted that the *c*-plains are formed mainly in perpendicular direction of the sintering pressure.

3.22.1.2.4.2 SPS in lead-free ferroelectric ceramics

Ferroelectricity was discovered in 1921.[28] The ferroelectricity in ceramic materials was found in the 1940s for the first time in barium titanate ($BaTiO_3$).[29] There are other materials within the

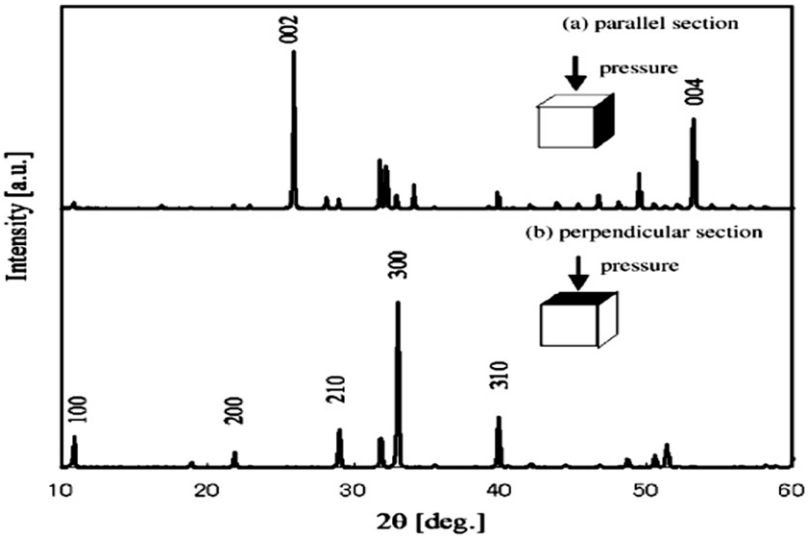


Figure 9 The X-ray diffraction pattern of HAp samples cut in (a) parallel orientation to the pressure and (b) perpendicular orientation to the pressure.[27]

same group of Perovskite structure, which exhibit ferroelectricity such as $PbZr_{1-x}Ti_xO_3$ (PZT), PZT:La (PLZT), $PbTiO_3$ (PT), $Pb(Mg_{1/3}Nb_{2/3})O_3$ (PMN), and $(K_{0.5}Na_{0.5})NbO_3$ (KNN).

One of the most widely exploited ferroelectrics was $PbTiO_3$–$PbZrO_3$ also known as PZT. Because of the new legislations, significantly reducing application of lead in ferroelectric materials,[30] it has drawn attention of academia and industry into new field – lead-free ferroelectric ceramics. Sintering of the lead-free ferroelectric ceramics has been a scope of interest of many researchers during recent years.[31–34] Following lead-free ferroelectrics have been investigated: tungsten bronze type materials, bi-layer structured materials, and Pervoskite type materials.[6] Ferroelectric ceramics such as barium titanate (BT), sodium bismuth titanate (NBT), alkali niobates ($ANbO_3$), for example, potassium niobate, potassium sodium niobate (KNN), and potassium tantalate niobate (KTN) have been investigated as the most promising lead-free ferroelectrics.[35]

Conventional sintering techniques and even high pressure sintering techniques such as cold isostatic press or HIP are not suitable for sintering such materials.[36] The main drawback of conventional sintering of ferroelectrics are the large particle size, high impurity contents as a result of repetitive calcination and grinding processes, and also lower chemical activity.[37] Furthermore, high energy requirements and time consumption are other disadvantages of conventional sintering methods.[35] SPS and microwave sintering are two of the sintering techniques, which most likely suitable for ferroelectric ceramics sintering. However, the simultaneous use of pressure, high heating rate, and direct heating in SPS makes it even more advantageous over microwave sintering.[38]

Accordingly, in this section the SPS sintering of lead-free ferroelectric ceramics and the effect of SPS sintering on their properties is reviewed. In this regard, the SPS process of different lead-free ferroelectrics is discussed.

3.22.1.2.4.2.1 BT

BT as a ferroelectric ceramic is extensively used in various applications such as piezoelectric devices like underwater transducers, sensors, heaters with positive temperature coefficient, and multilayer capacitors.[39,40] These applications require specific properties: high dielectric constants and good resistivity properties in small volumes. BT is an example of material possessing perovskite crystalline structure. It has a cubic structure above its Curie temperature (130 °C) and below that it can have tetragonal, orthorhombic, and rhombohedral structures.[41] BT is mostly synthesized in powder form and because of undesired grain growth during long conventional sintering processes, SPS could prove much better method for sintering such crystalline structure.[42] The whole process leading to sintering of BT usually consists of four steps: BT powder synthesis, powder preparation (grinding/ball milling), sintering, and annealing at lower temperature for a longer time (5–12 h).[43,44]

In one of the first studies on SPS sintering of BT samples, the effect of grain size on ferroelectric properties of BT was investigated.[45] It was shown that the samples with average grain size about 1 μm show the highest values of piezoelectric coefficient d_{33}, planar electromechanical coupling factor k_p, and relative permittivity $\varepsilon'(\varepsilon'=6079$, $d_{33}=519$ pC N^{-1}, and $k_p=39.5\%)$. These values varied with changing grain sizes.[45,46] Consequently, controllable grain growth has a great impact on ferroelectric and piezoelectric properties of BT.[47]

SPS due to its highly controllable process parameters shows a very promising method for BT sintering. As grain size seems to play important role in materials performance, there has been a considerable interest to investigate BT properties with respect to the average grain size. Significant number of papers reported SPS sintering of nano grain size BT samples.[42,43,48] Takeuchi *et al.*[31] used SPS sintering of BT samples in order to achieve submicron grain sizes with acceptable ferroelectric properties. It was shown that SPS sintered samples had smaller grain size (<1 μm) and higher density (>95% relative density) compared to conventionally sintered samples (2–10 μm and 80–90% relative density). Also higher electrical permittivity was observed in samples sintered using SPS method compared to samples prepared by conventional sintering. Samples sintered at lower temperatures showed higher permittivity values. This property was linked to the lower

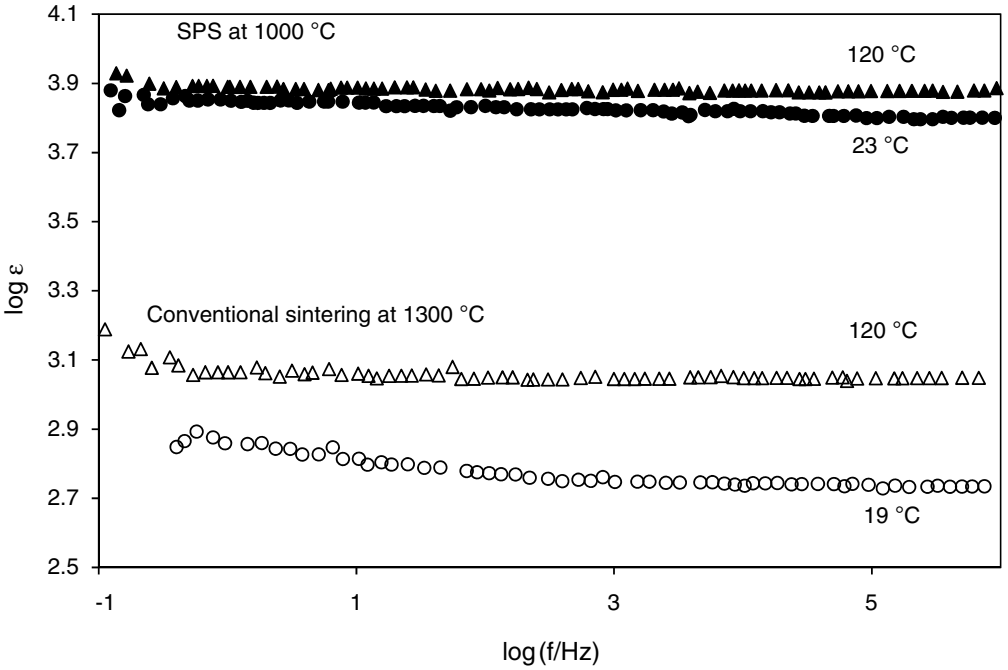


Figure 10 Frequency dependence on permittivity of SPS samples (SPS BT01) and conventionally sintered samples (CH BT01) at two different temperatures.[31]

grain size in samples sintered at lower temperatures. Furthermore, frequency dependence of permittivity in the range of 10^{-1}–10^{6} Hz was lower in SPS sintered samples (**Figure 10**). This was attributed to the removal of air gaps in SPS sintered samples.[31]

Though, it has been stated in many studies that the optimal ferroelectricity can be achieved in samples with average grain size lower than 1 μm.[43,45] The effect of lower grain sizes on the ferroelectricity has not been understood well yet. Felgner *et al.* suggested that the presence of an interconnected low permittivity non ferroelectric grain boundary at low grain size and high grain boundary conditions can decrease the permittivity of the BT samples.[49] In another study, the presence of a dead layer between the grains in samples with grain size of less than 0.5 μm is linked to the reduction of dielectric constant.[43] Other phenomena such as depolarization at small grain sizes,[50] significant decrease in ferroelectric phase transition driving force,[51] the defects of hydroxyl ions residing on the oxygen sites and compensation of the cation vacancies have also been listed as possible reasons of ferroelectricity decrease in grain sizes smaller than 0.5 μm. Deng *et al.* showed piezoelectric properties, phase transition properties, and ferroelectricity[43] in SPS sintered samples with 20 nm grain size. In the studies performed in the temperature from 83 to 437 K shown that all phase transition happens as usual in coarse grain BT samples. Furthermore, post sintering procedures such as thermal annealing have a significant effect on releasing residual stresses, removing excess oxygen vacancies and also, elimination of incorporated hydroxyl groups during SPS process. No significant grain growth has been reported during annealing process.[43] Maiwa *et al.*[44] have observed that as SPS sintered samples of $Ba(Zr_{0.2}Ti_{0.8})O_3$ were dark and deoxidized but after annealing samples would be oxidized and retain a brighter color.

In some other studies barium strontium titanate (BST) has been sintered by SPS in order to achieve transparent ferroelectrics.[32] Transparent ferroelectrics are widely used in electro-optical devices including digital light modulators, optical shutters and switchers, and image memory devices. SPS has shown it applicability in sintering optically transparent samples. This is because its capability in sintering of high density and low grain size samples in short time. To summarize, SPS allows sintering of high density, low grain sized BT samples. The sintered BT samples with grain size lower than 1 μm and higher than 0.5 μm show high dielectric constant, high permittivity, and low frequency dependence of dielectric constant.

3.22.1.2.4.2.2 *$ANbO_3$*

$ANbO_3$ with the common formula of $ANbO_3$ were proposed as a family of lead-free ferroelectric ceramics with perovskite structures in 1950s and 1960s.[52] Ferroelectric materials such as $KNbO_3$ and its solid-state solution with antiferroelectric $NaNbO_3$ given (K, Na)NbO_3 (KNN), (K, Ta)NbO_3 (KTN), (Li, Na)NbO_3 (LNN)[6,53] are among the most prominent alkali niobate structures. The appropriate choice of stable precursors of alkali metals and densification process are the key challenges in the production of lead-free ferroelectric ceramics. For instance, in KNN structure, the volatilization of potassium at high temperatures is the most important problem.

In terms of possible low temperature densification of alkali niobate ferroelectrics several possible solutions have been proposed:

1. electric field or pressure assisted (SPS) sintering,
2. reduction of initial particle size in order to increase the sintering driving force,

3. addition of glass phase,
4. addition of sintering aid agents such as oxide impurities,
5. introduction of lattice defects.[6]

SPS sintering as an electrical field and pressure assisted sintering technique have been used in sintering of low grain size, high density alkali niobate structures. In the following part the SPS sintering of KNN will be discussed further.

3.22.1.2.4.2.3 KNN

The first dense KNN structure was sintered by Jaeger and Egerton in 1962 by HIP techniques,[54] and its high piezoelectricity and Curie temperature were reported. The highest d_{33} reported for KNN was about 416 pC N^{-1}.[55] However, in order to achieve this value in industrial scale there are many points to be considered. SPS with the aforementioned advantages can be a breakthrough in sintering of KNN. Li *et al.* sintered a KNN sample with SPS at 950 °C, for 5 min with heating rate of 100 °C min^{-1}. The sintered sample achieved 99% relative density and grain size range of 200–500 nm.[56] The polarization-electrical field (P-E) hysteresis loop for as-sintered samples, and thermally annealed samples at 900 °C for 1 and 4 h revealed the crucial effects of annealing. The round shape of P-E hysteresis loop of 1 h annealed sample illustrate the insufficiency of annealing time for KNN. On the other hand, the slim polarization hysteresis loop of 4 h annealed samples showed the better elimination of oxygen vacancies. Also, a perfect polarization hysteresis loop was observed when higher bias fields were applied to the samples (**Figure 11**).[56]

Also, according to the initial powder grain size it has been suggested that ultra-fine starting powder can enhance sintering of KNN samples. High energy ball milling processes can be helpful in achieving submicron grain size distribution for initial powders. In this regard it was revealed that the samples with lower grain size distribution can attain higher densities compared to samples with larger grain size distribution. Furthermore, the addition of various oxides for creating low melting point phases and consequently low temperature sintering has been investigated.[6] Although this method can decrease melting point and results in higher density samples, the electrical properties of samples will be also affected by the presence of these new phases.

Some investigations have been done on KNN doped with Li, Sb, and Ta.[57] It was shown that SPS can be very helpful in sintering of dense small grain size samples of $(Na_{0.52}K_{0.44}Li_{0.04})(Nb_{0.86}Ta_{0.06}Sb_{0.08})O_3$ (LTS-KNN). The initial powder with grain size of 11–34 nm was sintered at 750 °C and 120 MPa for 10 min. The final samples had 99.4% relative density and its grain size distribution was in the range of 200–400 nm.[57] In term of ferroelectricity the sample showed a slim polarization curve showing the difficulty in domain walls flip of fine grain ceramic samples. In **Figure 5** $d33$, Kp, ε_{33} T/ε_0 at 1 kHz and tanδ of the annealed ceramic are shown, and they were 296 pC N^{-1}, 49.7%, 920 and 0.025, respectively (**Figure 12**).

3.22.1.2.4.2.4 $(Bi_{0.5}Na_{0.5})TiO_3$

$(Bi_{0.5}Na_{0.5})TiO_3$-$BaTiO_3$ (BNT-BT) has been proposed as a potential replacement for PZT ferroelectrics. Pure BNT with perovskite structure has rhombohedral crystal structure at room temperature. It undergoes a phase transition at 320 °C to tetragonal structure.[58] BNT possesses good ferroelectric properties with high values of remnant polarization $P_r = 38$ μC cm^{-2} with coercive field $E_c = 73$ kV cm^{-1}. BNT has been doped with $BaTiO_3$ in order to improve ferroelectric properties.[59] BNT-BT has been proposed a good candidate to replace PZT ceramics.

SPS has shown a great promise in rapid sintering of BNT-BT ceramics as well. This is because of short sintering time, low sintering temperature and as a result less loss of Bi and Na during sintering process.[59] Since SPS hinders undesired grain growth in BNT-BT samples and thus results in an enhancement of its mechanical strength. It was shown that BNT powder with grain size of around 30 nm, sintered at 900 °C for 5 min under pressure of 65 MPa has the highest relative density (99.62%). The average grain size in the sintered samples was around 50 nm.[5]

According to the ferroelectric properties of sintered samples it was shown that samples sintered at higher temperatures (900 °C) with higher density and grain size have higher

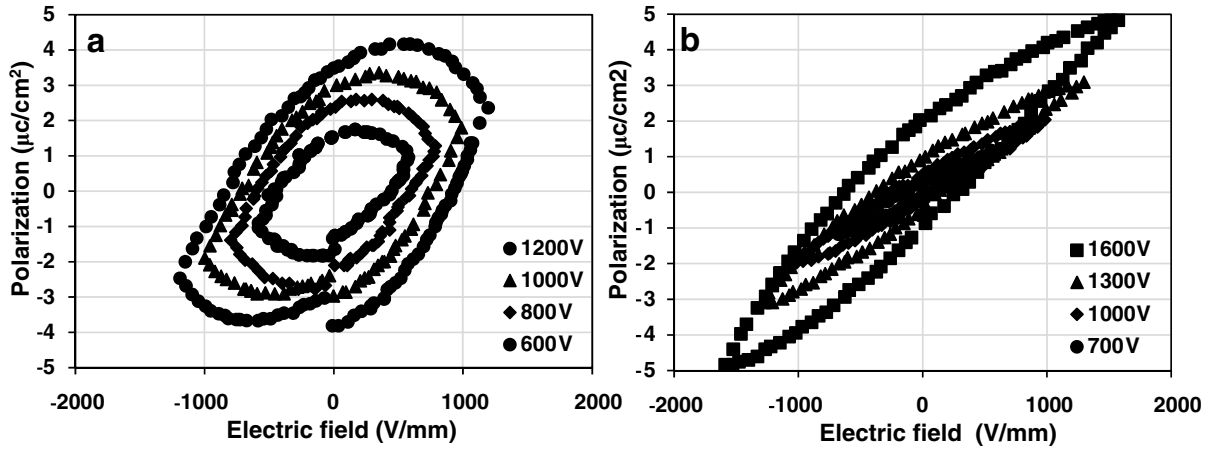


Figure 11 Polarization hystersis curves of $Na_{0.5}K_{0.5}NbO_3$ ceramic spark plasma sintered at 920 °C for 5 min and then annealed for different times in air (a) 1 h and (b) 4 h.[56]

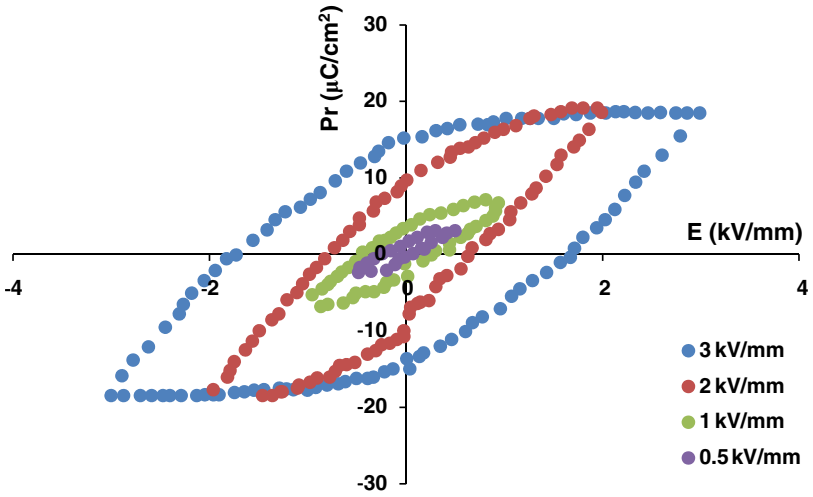


Figure 12 Ferroelectric properties of the annealed LTS-KNN ceramic.[57]

permittivity $\varepsilon_r = 2213$ and loss factor tan $\delta = 5.5$ %. The frequency dependence in all BNT-BT samples shows a decrease in permittivity at higher frequencies.[59]

3.22.2 Conclusion

SPS has shown a huge promise in sintering of biomaterials and lead-free ferroelectric ceramics. In this article, the potential use of SPS in sintering of HAp as a biomaterial with piezoelectric properties and also, in sintering of lead-free ferroelectric ceramics was reviewed. Its main advantages compared to conventional sintering methods are: lower sintering temperature, high heating rate, fast sintering, higher density, and lower grain size distribution in final product. As it was shown, these properties can lead to production of transparent HAp and ferroelectric samples because of high relative density and low grain size of the sample. Furthermore, in case of $ANbO_3$ ferroelectrics the lower sintering time of SPS hinders the technological problem of alkali metals volatilization, which happens during conventional sintering of these materials. To summarize, it can be concluded that SPS is a highly controllable sintering method leading to high density low grain size materials with improved mechanical and electrical properties. Although the current chapter discussed the processing of bulk ceramics but the information gathered here can be used in developing thick films and composite ceramic coatings of such materials.

See also: 3.20 Surface Preparation and Adhesion Tests of Coatings. 3.21 Powder Metallurgical Processing of NiTi Using Spark Plasma Sintering

References

1. Rahaman, M. N. *Ceramic Processing and Sintering*; Taylor & Francis: Boca Raton, FL, 2003.
2. Gu, Y. W.; Loh, N. H.; Khor, K. A.; Tor, S. B.; Cheang, P. Spark Plasma Sintering of Hydroxyapatite Powders. *Biomaterials* **2002**, *23* (1), 37–43.
3. Stojanovic, B. D. Mechanochemical Synthesis of Ceramic Powders with Perovskite Structure. *J. Mater. Process. Technol.* **2003**, *143–144* (0), 78–81.
4. Taylor, G. F. Apparatus for Making Hard Metal Compositions. Gen Electric. US1896854 A, 1933.
5. Kiyoshi, I. Electric-Discharge Sintering. Kiyoshi, Inoue, US3241956 A, 1966.
6. Kiyoshi, I. Apparatus for Electrically Sintering Discrete Bodies. Kiyoshi, Inoue. US24738762A, 1966.
7. Suárez, M.; Fernández, A.; Menéndez, J. L.; *et al.* Challenges and Opportunities for Spark Plasma Sintering: A Key Technology for a New Generation of Materials. In *Sintering Applications*; Ertuğ, B., Ed.; InTech: Rijeka, Croatia, 2013.
8. Diouf, S.; Molinari, A. Densification Mechanisms in Spark Plasma Sintering: Effect of Particle Size and Pressure. *Powder Technol.* **2012**, *221* (0), 220–227.
9. Chaim, R. Densification Mechanisms in Spark Plasma Sintering of Nanocrystalline Ceramics. *Mater. Sci. Eng. A* **2007**, *443* (1–2), 25–32.
10. Zheng, D.; Li, X.; Tang, Y.; Cao, T. WC–Si_3N_4 Composites Prepared by Two-Step Spark Plasma Sintering. *Int. J. Refract. Met. Hard Mater.* **2015**, *50*, 133–139.
11. Li, Y.; Katsui, H.; Goto, T. Spark Plasma Sintering of TiC–ZrC Composites. *Ceram. Int.* **2015**, *41* (5, Part B), 7103–7108.
12. Sairam, K.; Sonber, J. K.; Murthy, T. S. R. Ch.; *et al.* Influence of Spark Plasma Sintering Parameters on Densification and Mechanical Properties of Boron Carbide. *Int. J. Refract. Met. Hard Mater.* **2014**, *42*, 185–192.
13. Maiwa, H. Electromechanical Properties of $Ba(Zr_{0.2}Ti_{0.8})O_3$ Ceramics Prepared by Spark Plasma Sintering. *Ceram. Int.* **2012**, *38* (Supplement 1), S219–S223.
14. Buscaglia, M. T.; Buscaglia, V.; Viviani, M.; *et al.* Ferroelectric Properties of Dense Nanocrystalline $BaTiO_3$ Ceramics. *Nanotechnology* **2004**, *15* (9), 1113–1117.
15. Guo, Y.; Kakimoto, K.-I.; Ohsato, H. $(Na_{0.5}K_{0.5})NbO_3$–$LiTaO_3$ Lead-Free Piezoelectric Ceramics. *Mater. Lett.* **2005**, *59* (2–3), 241–244.
16. Nedelcu, L.; Ioachim, A.; Toacsan, M.; *et al.* Synthesis and Dielectric Characterization of $Ba_{0.6}Sr_{0.4}TiO_3$ Ferroelectric Ceramics. *Thin Solid Films* **2011**, *519* (17), 5811–5815.
17. Gu, Y. W.; Khor, K. A.; Cheang, P. Bone-Like Apatite Layer Formation on Hydroxyapatite Prepared by Spark Plasma Sintering (SPS). *Biomaterials* **2004**, *25* (18), 4127–4134.
18. Gandhi, A. A.; Gunning, R. D.; Ryan, K. M.; Tofail, S. A. The Role of Texturing and Densification on Optical Transmittance of Hydroxyapatite Ceramics. *J. Am. Ceram. Soc.* **2010**, *93* (11), 3773–3777.
19. Hench, L. L. Bioceramics. *J. Am. Ceram. Soc.* **1998**, *81* (7), 1705–1728.
20. Ruys, A. J.; Wei, M.; Sorrell, C. C.; Dickson, M. R.; Brandwood, A.; Milthorpe, B. K. Sintering Effects on the Strength of Hydroxyapatite. *Biomaterials* **1995**, *16* (5), 409–415.
21. Muralithran, G.; Ramesh, S. The Effects of Sintering Temperature on the Properties of Hydroxyapatite. *Ceram. Int.* **2000**, *26* (2), 221–230.
22. Champion, E. Sintering of Calcium Phosphate Bioceramics. *Acta Biomater.* **2013**, *9* (4), 5855–5875.
23. Li, W.; Gao, L. Fabrication of HAp–ZrO_2 (3Y) Nano-Composite by SPS. *Biomaterials* **2003**, *24* (6), 937–940.

24. Klébert, S.; Balázsi, C.; Balázsi, K.; *et al.* Spark Plasma Sintering of Graphene Reinforced Hydroxyapatite Composites. *Ceram. Int.* **2015**, *41* (3, Part A), 3647–3652.
25. Cuccu, A.; Montinaro, S.; Orrù, R.; *et al.* Consolidation of Different Hydroxyapatite Powders by SPS: Optimization of the Sintering Conditions and Characterization of the Obtained Bulk Products. *Ceram. Int.* **2015**, *41* (1, Part A), 725–736.
26. Li, S.; Izui, H.; Okano, M. Densification, Microstructure, and Behavior of Hydroxyapatite Ceramics Sintered by Using Spark Plasma Sintering. *J. Eng. Mater. Technol.* **2008**, *130* (3), 031012.
27. Watanabe, Y.; Ikoma, T.; Monkawa, A.; *et al.* Fabrication of Transparent Hydroxyapatite Sintered Body with High Crystal Orientation by Pulse Electric Current Sintering. *J. Am. Ceram. Soc.* **2005**, *88* (1), 243–245.
28. Richerson, D. W. *Modern Ceramic Engineering: Properties, Processing, and Use in Design*; 2nd ed.; Marcel Dekker, Inc.: New York, NY, 1992.
29. Munir, Z. A.; Quach, D. V.; Ohyanagi, M. Electric Current Activation of Sintering: A Review of the Pulsed Electric Current Sintering Process. *J. Am. Ceram. Soc.* **2011**, *94* (1), 1–19.
30. Mudinepalli, V. R.; Song, S.; Li, J.; Murty, B. A Comparative Study of Structural and Electrical Properties of $Ba_{0.8}Pb_{0.2}TiO_3$ Nanocrystalline Ceramics Prepared by Microwave and Spark Plasma Sintering. *Mater. Chem. Phys.* **2013**, *142* (2), 686–691.
31. Takeuchi, T.; Tabuchi, M.; Kageyama, H.; Suyama, Y. Preparation of Dense $BaTiO_3$ Ceramics with Submicrometer Grains by Spark Plasma Sintering. *J. Am. Ceram. Soc.* **1999**, *82* (4), 939–943.
32. Wu, Y. J.; Wang, N.; Wu, S. Y.; Chen, X. M. Transparent Barium Strontium Titanate Ceramics Prepared by Spark Plasma Sintering. *J. Am. Ceram. Soc.* **2011**, *94* (5), 1343–1345.
33. Chaim, R.; Levin, M.; Shlayer, A.; Estournès, C. Sintering and Densification of Nanocrystalline Ceramic Oxide Powders: A Review. *Adv. Appl. Ceram.* **2008**, *107* (3), 159–169.
34. Chen, F.; Yang, S.; Wu, J.; *et al.* Spark Plasma Sintering and Densification Mechanisms of Conductive Ceramics Under Coupled Thermal/Electric Fields. *J. Am. Ceram. Soc.* **2015**, *98* (3), 732–740.
35. Wu, Y.; Li, J.; Chen, X.; Kakegawa, K. Densification and Microstructures of $PbTiO_3$ Ceramics Prepared by Spark Plasma Sintering. *Mater. Sci. Eng. A* **2010**, *527* (20), 5157–5160.
36. Sindhu, M.; Ahlawat, N.; Sanghi, S.; Kumari, R.; Agarwal, A. Crystal Structure Refinement and Investigation of Electrically Heterogeneous Microstructure of Single Phased Sr Substituted $BaTiO_3$ Ceramics. *J. Alloy. Compd.* **2013**, *575*, 109–114.
37. Groza, J. R.; Zavaliangos, A. Sintering Activation by External Electrical Field. *Mater. Sci. Eng. A* **2000**, *287* (2), 171–177.
38. Guillon, O.; Gonzalez-Julian, J.; Dargatz, B.; *et al.* Field-Assisted Sintering Technology/Spark Plasma Sintering: Mechanisms, Materials, and Technology Developments. *Adv. Eng. Mater.* **2014**, *16* (7), 830–849.
39. Gaffet, E.; Michel, D.; Mazerolles, L.; Berthet, P. Effects of High Energy Ball Milling on Ceramic Oxides. *Mater. Sci. Forum, Trans. Tech. Publ.* **1996**, *235–238*, 103–108.
40. Boldyrev, V. Mechanochemistry and Mechanical Activation. *Mater. Sci. Forum, Trans. Tech. Publ.* **1996**, *225–227*, 511–520.
41. Moulson, A. J.; Herbert, J. M. *Electroceramics: Materials, Properties, Applications*; Chapman and Hall: London; New York, NY, 1990.
42. Kong, L.; Ma, J.; Huang, H.; Zhang, R.; Que, W. Barium Titanate Derived from Mechanochemically Activated Powders. *J. Alloy. Compd.* **2002**, *337* (1), 226–230.
43. Gomez-Yañez, C.; Benitez, C.; Balmori-Ramirez, H. Mechanical Activation of the Synthesis Reaction of $BaTiO_3$ from a Mixture of $BaCO_3$ and TiO_2 Powders. *Ceram. Int.* **2000**, *26* (3), 271–277.
44. Maiwa, H. Structure and Properties of $Ba(Zr_{0.2}Ti_{0.8})O_3$ Ceramics Prepared by Spark Plasma Sintering. *J. Mater. Sci.* **2008**, *43* (19), 6385–6390.
45. Michel, D.; Faudot, F.; Gaffet, E.; Mazerolles, L. Stabilized Zirconias Prepared by Mechanical Alloying. *J. Am. Ceram. Soc.* **1993**, *76* (11), 2884–2888.
46. Komatsubara, S.; Isobe, T.; Senna, M. Effect of Preliminary Mechanical Treatment on the Microhomogenization During Heating of Hydrous Gels as Precursors for Lead Titanate. *J. Am. Ceram. Soc.* **1994**, *77* (1), 278–282.
47. Dorner-Reisel, A.; Schöps, S.; Lenk, A.; Schmutzler, G. Microstructural Comparison of Conventional and Microwave Sintered $BaTiO_3$. *Adv. Eng. Mater.* **2007**, *9* (5), 400–405.
48. Berbenni, V.; Marini, A.; Bruni, G. Effect of Mechanical Milling on Solid State Formation of $BaTiO_3$ from $BaCO_3$–TiO_2 (Rutile) Mixtures. *Thermochim. Acta* **2001**, *374* (2), 151–158.
49. Felgner, K.-H.; Müller, T.; Langhammer, H.; Abicht, H.-P. On the Formation of $BaTiO_3$ from $BaCO_3$ and TiO_2 by Microwave and Conventional Heating. *Mater. Lett.* **2004**, *58* (12), 1943–1947.
50. Clark, I. J.; Takeuchi, T.; Ohtori, N.; Sinclair, D. C. Hydrothermal Synthesis and Characterisation of $BaTiO_3$ Fine Powders: Precursors, Polymorphism and Properties. *J. Mater. Chem.* **1999**, *9* (1), 83–91.
51. Smith, M. B.; Page, K.; Siegrist, T.; *et al.* Crystal Structure and the Paraelectric-to-Ferroelectric Phase Transition of Nanoscale $BaTiO_3$. *J. Am. Chem. Soc.* **2008**, *130* (22), 6955–6963.
52. Hill, D. C.; Tuller, H. L. Ceramic Sensors: Theory and Practice. *Ceram. Mater. Electr.* **1991**, *31*, 265–374.
53. Granzow, T.; Kounga, A.; Aulbach, E.; Rödel, J. Electromechanical Poling of Piezoelectrics. *Appl. Phys. Lett.* **2006**, *88* (25), 252907.
54. Jaeger, R. E.; Egerton, L. Hot Pressing of Potassium-Sodium Niobates. *J. Am. Ceram. Soc.* **1962**, *45* (5), 209–213.
55. Saito, Y.; Takao, H.; Tani, T.; *et al.* Lead-Free Piezoceramics. *Nature* **2004**, *432* (7013), 84–87.
56. Li, J.-F.; Wang, K.; Zhang, B. P.; Zhang, L. M. Ferroelectric and Piezoelectric Properties of Fine-Grained $Na_{0.5}K_{0.5}NbO_3$ Lead-Free Piezoelectric Ceramics Prepared by Spark Plasma Sintering. *J. Am. Ceram. Soc.* **2006**, *89* (2), 706–709.
57. Zhang, H.; Wang, X.; Fang, J.; Zhang, Y.; Li, L. Piezoelectric Properties of Li, Sb, and Ta Co-Doped (K,Na) NbO_3 Ceramics with Fine Grain Size Sintered by SPS Method. *J. Electroceram.* **2013**, *30* (4), 217–220.
58. Jones, G. O.; Thomas, P. A. Investigation of the Structure and Phase Transitions in the Novel A-Site Substituted Distorted Perovskite Compound $Na_{0.5}Bi_{0.5}TiO_3$. *Acta Crystallogr. Sect. B* **2002**, *58* (2), 168–178.
59. Berbecaru, C.; Cernea, M.; Aldica, G. V.; Trusca, R. Structural and Electrical Properties of BNT-$BT_{0.08}$ Ceramics Processed by Spark Plasma Sintering. *World Acad. Sci. Eng. Technol. Int. J. Chem. Mol. Nucl. Mater. Metall. Eng.* **2011**, *5* (7), 533–536.

Relevant Websites

https://en.wikipedia.org/wiki/Spark_plasma_sintering

http://sps.fdc.co.jp/
Fuji Electronics Industrial Co. Ltd.

http://www.totalmateria.com/page.aspx?ID=CheckArticle&site=ktn&NM=292
Total Materia.

3.23 Electrochemical Processing and Surface Finish

NK Jain and S Pathak, Indian Institute of Technology Indore, Indore, India

© 2017 Elsevier Inc. All rights reserved.

3.23.1	**Introduction**	359
3.23.2	**Types of Electrochemical Processes**	360
3.23.3	**EP**	360
3.23.3.1	Principle of EP	360
3.23.3.2	Factors Affecting Quality of Deposition	361
3.23.3.2.1	Effects of current characteristics	361
3.23.3.2.2	Effects of electrolyte parameters	362
3.23.3.2.3	Effects of EP process parameters	363
3.23.3.3	Selection of Deposition Material	364
3.23.3.4	Advantages	364
3.23.3.5	Limitations	364
3.23.3.6	Applications	364
3.23.4	**ECM**	365
3.23.4.1	Working Principle of ECM and Pulsed-ECM	366
3.23.4.2	Material Removal in ECM Process	367
3.23.4.3	Factors Affecting the ECM Process Performance	368
3.23.4.3.1	Electrolyte related parameters	368
3.23.4.3.2	IEG	369
3.23.4.3.3	Current density and voltage	369
3.23.4.3.4	Mass transport phenomenon in ECM	369
3.23.4.4	Capabilities of ECM and Its Effects on Workpiece Material	369
3.23.4.5	Advantages	370
3.23.4.6	Limitations	370
3.23.4.7	Applications	370
3.23.5	**ECG**	371
3.23.5.1	Advantages	371
3.23.5.2	Limitations	371
3.23.5.3	Applications	371
3.23.6	**ECH**	372
3.23.6.1	Process Principle of ECH	372
3.23.6.2	ECH equipment	372
3.23.6.2.1	Finishing of internal cylinders by ECH	372
3.23.6.2.2	Finishing of gears by ECH	373
3.23.6.3	Advantages	374
3.23.6.4	Limitations	375
3.23.6.5	Applications	375
3.23.7	**ECDe**	375
3.23.7.1	Mechanism of ECDe	375
3.23.7.2	Advantages	375
3.23.7.3	Limitations	376
3.23.7.4	Applications	376
3.23.8	**Surface Finish in Various Electrochemical Processes**	376
3.23.8.1	Surface Finish in EP	376
3.23.8.2	Surface Finish in ECM	376
3.23.8.2.1	Selective dissolution	376
3.23.8.2.2	Sporadic breakdown of anodic film	376
3.23.8.2.3	Flow separation and formation of eddies	376
3.23.8.2.4	Evolution of hydrogen gas	376
3.23.8.3	Surface Finish in ECG	377
3.23.8.4	Surface Finish ECH	377
3.23.9	**Summary**	378
References		378

 doi:10.1016/B978-0-12-803581-8.09182-7

3.23.1 Introduction

Electrochemistry deals with the interconversion of chemical energy and electrical energy and finds applications in those daily life products which involve chemical reactions to generate electricity such as batteries, calculators, automobiles, personal gadgets, etc.[1] Electrochemical processes and their derived and hybrid processes are used to meet various processing requirements of the electrically conducting materials. Some worth-mentioning are (1) coating of different materials by electrochemical deposition or electroplating (EP) to improve their surface properties such as corrosion and wear resistance, surface finish, surface integrity, aesthetics, etc.; (2) precision machining of components with a complex shape and difficult to machine materials by electrochemical machining (ECM) process; (3) finishing of intricate components by electrochemical finishing (ECF) process; (4) damage-free grinding of various components by electrochemical grinding (ECG) process; (5) high quality of finishing of gears, cylinders, bushes, sleeves, bearings, etc., by electrochemical honing (ECH) process; (6) removal of different types of burrs with almost no damage to the workpiece by electrochemical deburring (ECDe) process; (7) generating nanoparticles by electrochemical winning (ECW) process; and (8) purification and recycling by electrochemical refining (ECR) process. These processes can easily fabricate difficult-to-fabricate materials namely high strength temperature resistant (HSTR) materials such as superalloys, titanium alloys, stainless steel, copper–beryllium alloys; refractory materials such as tungsten, tantalum, molybdenum, niobium and their alloys; and wear-resistant materials such as nickel, cobalt, chromium and vanadium and their alloys; shape memory alloys, etc. Processing of these materials by conventional processes such as drilling, grinding, boring, turning, lapping, shaping etc. are not able to produce the components with the required quality especially in terms of surface quality and geometric tolerances. The irregularities at the surface and subsurface of components may lead to various undesirable effects such as reduced service life, premature failure, poor load carrying capacity, reduced working efficiency, generation of noise and vibration, etc. These limitations, constantly increasing use of miniature components and ever increasing requirement of high-quality complex shaped components in engineering products have made electrochemical processes as first choice of industries due to its noncontact nature, flexibility, and ease of operation. Therefore, electrochemical processes find many applications in various industries such as aviation, automobile, space, biomedical, consumer products, manufacturing, nuclear, semiconductors, micro- and nano- electromechanical systems (MEMS/NEMS), optics, nano-manufacturing, fashion, etc.

Electrochemical processes involve Faraday's laws governed electrolysis phenomenon in a container called as electrochemical cell which consists of two electrodes (i.e., anode connected to positive terminal of direct current (DC) supply and cathode connected to negative terminal of DC supply) separated by each other by an appropriate interelectrode gap (IEG) and submerged in a suitable electrolyte solution enabling the electrochemical reactions to occur. Some cells have a diaphragm or membrane between the anode and cathode which separates reaction products at anode and cathode. Figure 1 shows a simple electrolysis process for anodic dissolution of iron in brine water. The metallic atoms leave the anode and become ions and the ions move toward the body and become atoms. This process continues and attains

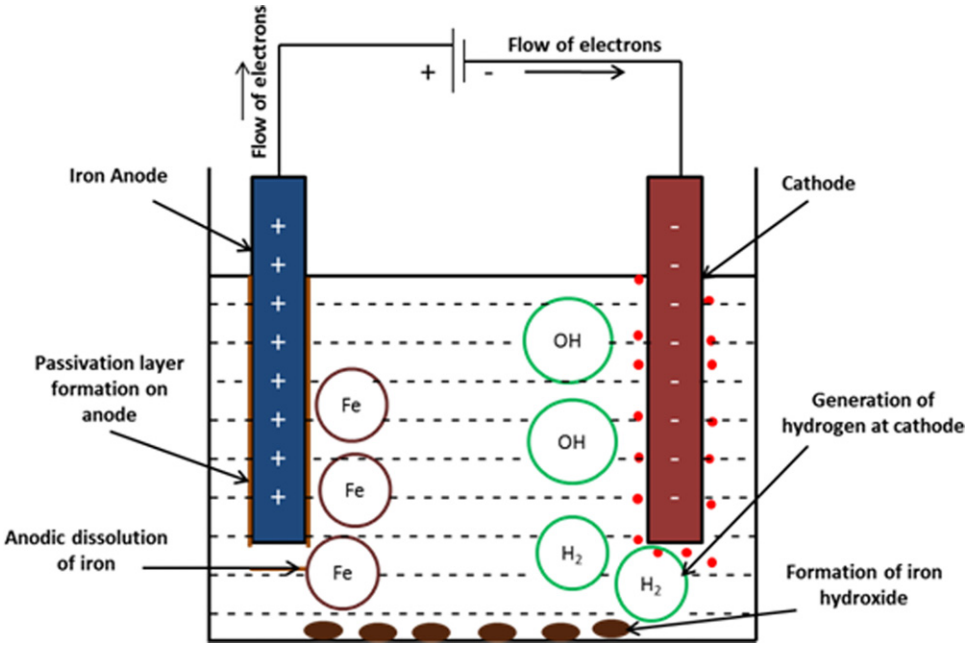


Figure 1 Schematic of a simple electrolysis process.

equilibrium. A potential difference, known as electrode potential exists between a point on the surface of an electrode and an adjacent point in the electrolyte. The electrode potential depends on the combination of electrode and electrolyte. If two different electrodes are submerged in an electrolyte then a potential difference between these electrodes exists which is known as cell 'electromotive force' (cell emf).

The following electrochemical reactions occur when a voltage is applied across the electrodes.

$Fe \rightarrow Fe^{2+} + 2e^{-}$ (at anode; the anodic material dissolves leaving two electrons).

$2H_2O + 2e^{-} \rightarrow H_2\uparrow + 2(OH)^{-}$ (at cathode; water gets the two electrons from the cathode and produces hydrogen gas at cathode and hydroxyl ions).

The positive metal ions move toward the negatively charged cathode. The negatively charged (OH) ions moves toward the positively charged anode and combines with positively charged metal ions to form an insoluble precipitate, i.e., metal hydroxide.

$Fe^{2+} + 2(OH)^{-} \rightarrow Fe(OH)_2$ (Insoluble precipitate)

Faraday's first law of electrolysis states that "the chemical change produced (or amount of any material deposited or dissolved) by flow of electric current through an electrolyte is directly proportional to the quantity of electricity passed through it" and according to Faraday's second law of electrolysis "the amounts of different substances dissolved or deposited by the same quantity of the electricity are proportional to their chemical equivalent weights."

Mathematically, Faraday's laws can be expressed as;

$$m \propto EIt \rightarrow m = \frac{EIt}{F} \rightarrow m = \frac{MIt}{ZF} \quad [1]$$

where,

m = mass of anode material dissolved (grams)

I = amount of current passed (A)

t = time for which current is passed (seconds)

E = chemical equivalent weight of the anode material (grams) $= \frac{M}{Z}$

M = atomic weight of the anode material (grams)

Z = valency of dissolution of the anode material

F = Faraday's constant (F = 96 500 C or A s)

3.23.2 Types of Electrochemical Processes

There are some basic electrochemical processes such as ECM, ECF, ECW, ECR, and various derived and hybrid processes have also been developed to meet the specific requirements for electrochemical processing of the materials and/or product. Table 1 lists these processes.

Table 1 Various types of electrochemical processes and their derived and hybrid versions

Basic electrochemical processes	*Derived and hybrid processes*
• Electrochemical machining (ECM) • Electrochemical finishing (ECF) • Electroplating (EP) • Electrochemical winning (ECW) • Electrochemical refining (ECR) • Electrochemical micro machining (ECMM)	• Electrochemical drilling (ECD) • Electro stream or jet drilling (ESD or EJD) • Shaped tube electro drilling (STED) • Capillary drilling (CD) • Electrochemical turning (ECT) • Electrochemical milling (ECMI) • Electrochemical sawing (ECS) • Electrochemical trepanning (ECTr) • Electrochemical boring (ECB) • Electrochemical broaching (ECBr) • Electrochemical ballizing (ECBz) • Electrochemical deburring (ECDe) • Electrochemical buffing (ECB) • Electrochemical super finishing (ECSF) • Electrochemical grinding (ECG) • Electrochemical honing (ECH) • Electrochemical discharge machining (ECDM) • Electrochemical wire cutting (ECWC)

3.23.3 EP

EP or electrochemical deposition is the application of a metallic coating to an electrically conductive surface by electrolysis phenomenon. It involves passing an electric current through an electrolyte to reduce cations of the coating material and coat that material as a thin film on an electrically conductive workpiece surface. It is an economical technology to protect and enhance the functionality and surface properties of the workpiece. It imparts special or improved properties to the significant surfaces of a part or assembly and/or protecting or enhancing their function in their operating environment. Essentially any electrically conductive surface can be electroplated. The metals and alloy substrates electroplated on a commercial scale are cadmium, chromium, cobalt, copper, gold, indium, iron, lead, nickel, platinum, silver, tin, zinc, brass, bronze, lead–tin, nickel–iron, nickel–cobalt, nickel–phosphorus, tin–nickel, tin–zinc, zinc–nickel, zinc–cobalt, and zinc–iron, etc.[2] Special techniques such as coating with metallic-loaded paints or silver-reduced spray can be used to make nonconductive surfaces such as plastics electrically conductive for EP.[2,3]

3.23.3.1 Principle of EP

Figure 2 depicts schematic of a typical EP cell used for depositing copper using copper sulfate solution. It consists of four major components:

- DC or pulsed DC supply unit: for providing DC power supply between cathode and anode. Usually a rectifier or motor generator is used as DC source to supply the current in the EP cell. The means of regulating the voltage and current maintain their values at the chosen levels.
- Cathode and its positioning means: the substrate material (i.e., workpiece) on which plating is to be done is made as cathode. Its positioning means ensuring its position

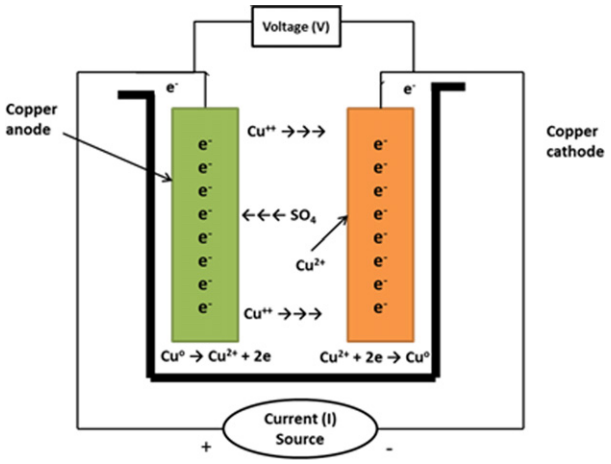


Figure 2 Schematic of a typical electroplating cell.

remains fixed in the in the plating solution and contact with the DC power supply is maintained.

- Anode: the coating material which is to be plated or deposited is made as anode.
- Platers: electrolyte solution is referred as platers. Generally, salt solutions are used as platers.

In an EP process, the deposition reactions at cathode are referred as reduction reactions since electrons are consumed reducing the valence states of the ions involved. The reactions occurring at anode are oxidation reactions in which electrons are liberated and atoms are ionized increasing their valence states. Electrochemical reactions are reversible reactions and independent of each other. They are governed by the condition of material balance, i.e., electrons liberated at the anode must be equal to the number of electrons consumed at the cathode.

For depositing copper using copper sulfate solution, the aqueous solution of electrolyte contains positively charged copper ions and negatively charged sulfate ions. When DC power is supplied, copper from the anode dissolves into the solution leaving two electrons and forming positively charged copper ions (i.e., $Cu \rightleftharpoons Cu^{2+} + 2e^-$) which migrate toward the cathode where they are deionized and are deposited as copper atoms on the anode. The sulfate ions remain unchanged in quantity during the electrolysis.

$$Cu^{2+} + 2e^- \rightleftharpoons Cu(atom)$$

The overall reaction at the anode is the oxidation of water.

$$2H_2O \rightleftharpoons 4H^+ + O_2 + 4e^-$$

If anode material other than copper is used then concentration of Cu^{2+} ions will decrease and that of H^+ ions will increase with time. To avoid and overcome this state, extra copper sulfate must be added to the solution at particular interval of time and the hydrogen ions must be removed by neutralization with an alkali or by using a buffer solution. In practice, the chemical reaction that occurs near the electrode area are more complicated than that shown in Figure 2. Under the influence of an applied potential, rearrangement of ions near the electrode surface results in an electrical double layer called the 'Helmholtz double layer,' followed by the formation of a diffusion layer as shown in Figure 3. These two layers combined are known as 'Gauy–Chapman layer.' Their process sequence is as follows[4]:

- Migration: the hydrated metal ions in the solution migrate toward the cathode under the influence of the applied current as well as by diffusion and convection.
- Electron transfer: at the cathode surface, a hydrated metal ion enters the diffused double layer where the water molecules of the hydrated ion are aligned. Then the metal ion enters the Helmholtz double layer where it is deprived of its hydrate envelope.
- The dehydrated ion is neutralized and adsorbed on the cathode surface.
- The adsorbed atom then migrates or diffuses to the growth point on the cathode surface.

3.23.3.2 Factors Affecting Quality of Deposition

In EP process, the measures of deposition quality namely thickness, composition, density, porosity, surface finish, microstructure, micro-hardness, etc., depend on electrolyte related parameters, current characteristics, EP process, and various types of properties of the workpiece (i.e., cathode) material. Figure 4 lists all these parameters. Out of these parameters those affecting the surface finish and density of the deposition are briefly discussed in following paragraphs.

3.23.3.2.1 Effects of current characteristics

Different types of current and their sources are used for EP. Selection of current source depends on the specific requirements and desired surface quality of the end product. Earlier, alternating current (AC) superimposed on DC (Figure 5(a)) was used as the current source for EP applications; but obtained quality of deposition was not as per requirements and standards because it produces uneven depositions with high values of roughness due to nonuniform current distribution which adversely affects the deposition density and surface finish and may also lead to high porosity in the deposition. Consequently, constant DC is the most commonly used current source in EP applications because it helps in producing a smooth and uniform deposition with high deposition rate and very low or almost negligible porosity. Use of constant DC source makes the process faster. Usually rectifiers or motor generators convert AC to DC. Silicon rectifiers are most commonly used for this purpose. Current characteristics depend on type of its waveform. Most commonly used waveforms are sinusoidal, half-wave and full-wave (Figure 5(b)), periodic reverse (PR) and interrupted (Figure 5(c)), unipolar and bipolar (Figure 5(d)), and pulsed and pulse-reverse (Figure 5(e)). Further developments in DC sources are inclusion of short pulse current (PC) and pulsed reverse current (PRC) in which modulated current waveforms are used to provide a better leveling of the deposition, maximize the surface finish and to minimize the porosity, contamination, etc. Complex current waveforms can be generated by using pulse rectifier: unipolar and bipolar pulses. PR under the proper conditions, produces dense fine-grain, striated, leveled, and bright deposition.[5] A typical PR cycle is 15 s plating and

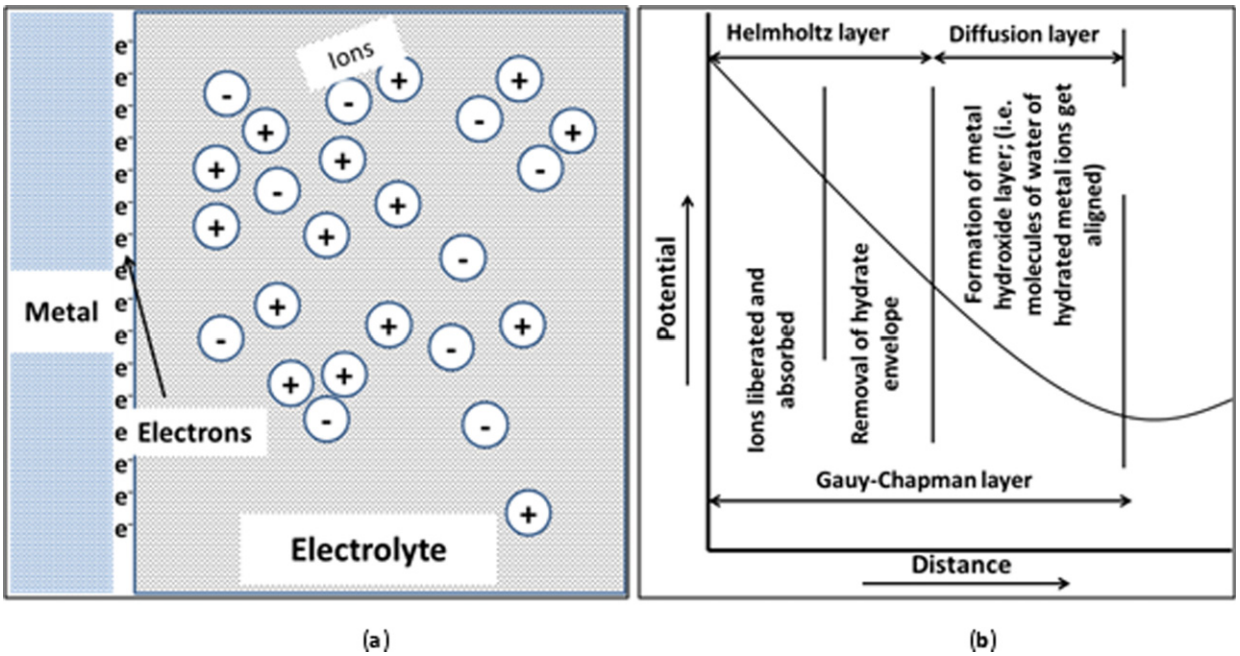


Figure 3 (a) Schematic of ion migrations and (b) graphical representation of Gauy–Chapman layer.

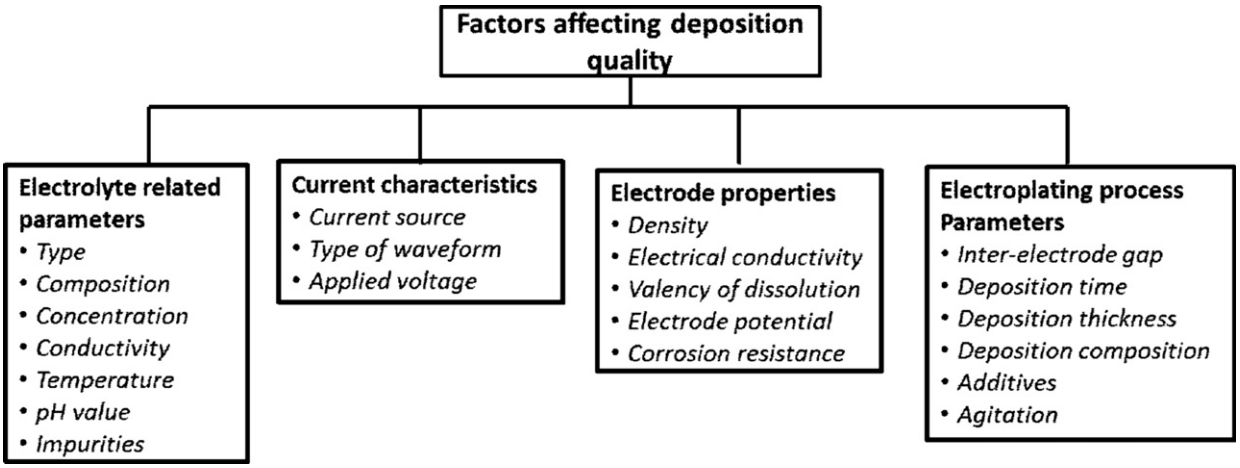


Figure 4 Various parameters affecting deposition quality in the electroplating process.

3 s deplating. Longer the deplating (reversal) cycle, smoother is the deposition.

From the study of effect of pulse power use in EP on current distributions and throwing, it was observed that pulse EP does not affect the primary current distribution, provides less-uniform secondary current distribution, whereas tertiary distribution can be improved by using short-duration high current density pulses as compared to constant DC EP.[5] Deposition quality of some metal and alloy depositions was found to be superior while using pulsed DC than that using constant DC. Some of the advantages of pulse EP are:

- faster deposition rate due to increased permissible current densities,
- denser deposition (i.e., lesser porosity),
- higher purity of deposition and less tendency for impurities to be included in the deposition,
- smoother and finer-grained deposition,
- reduced need or elimination of addition agents,
- less hydrogen evolution thus providing better surface finish and very less hydrogen embrittlement,
- decreased stress in deposition,
- increased Ni or Co contents in alloy-hardened gold deposition with less polymer formation.

3.23.3.2.2 Effects of electrolyte parameters

Electrolyte parameters such as its type, composition, concentration, conductivity, temperature, flow rate, pH value, and impurities greatly affect deposition quality in the EP process.

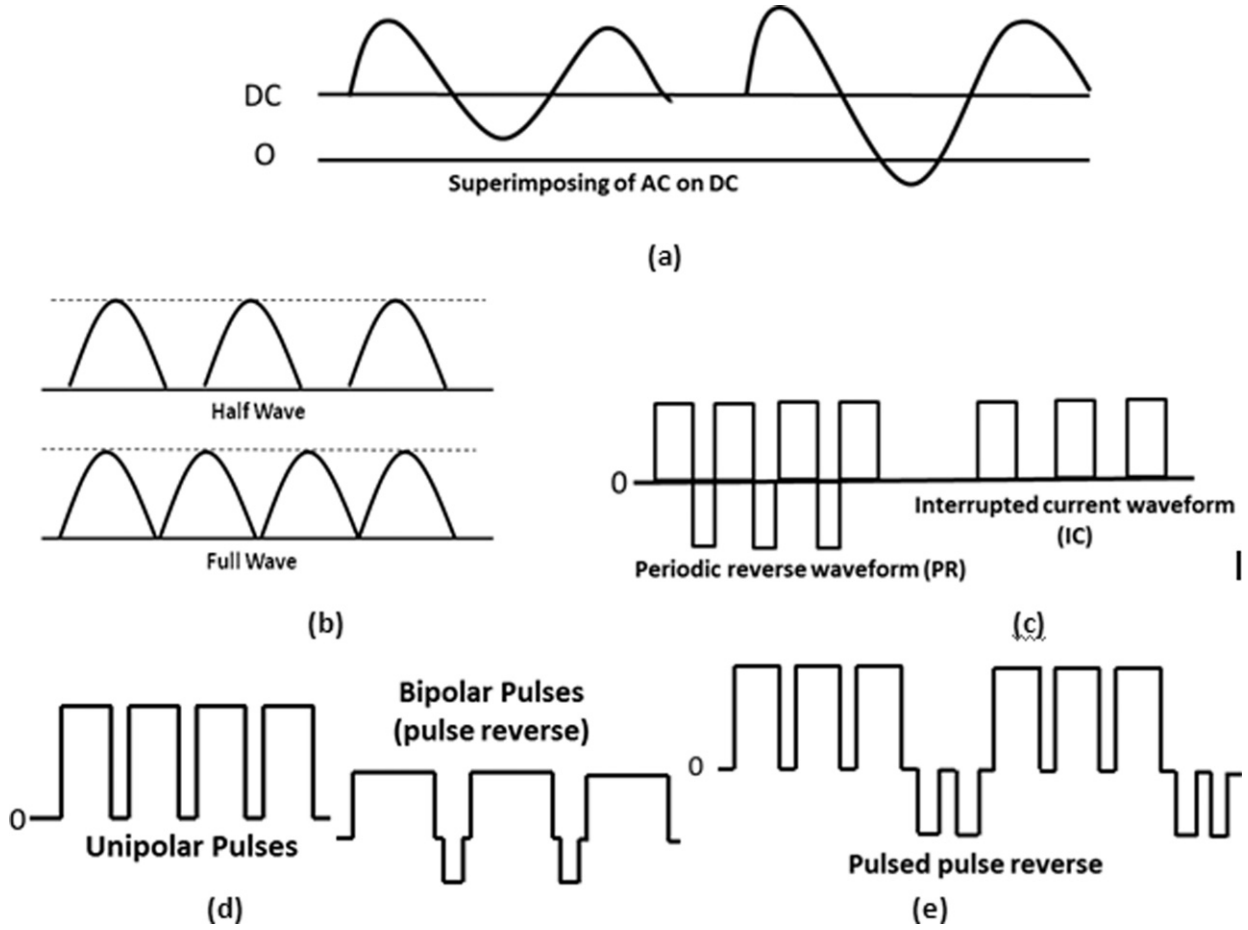


Figure 5 Schematic of different types of electrical waveforms.

Most of these parameters are interdependent and they exert an influence on the structure and functional properties of the deposition. Their accurate prediction is generally very complicated and their optimum ranges can be determined empirically. Type of electrolyte (i.e., salt-based, acidic or alkaline, and passivating or non-passivating) is selected on the basis of physical, mechanical, and electrochemical properties of the electrode material. Role of the electrolyte composition in EP is to facilitate generation and movement of the ions which are to be deposited on the cathodic workpiece and to provide supporting ions. Its other functions are to (1) stabilize the electrolyte, (2) improve electrolyte solution conductivity, (3) to prevent excessive polarization and passivation of the anode, and (4) to provide compatibility with the desired plating conditions. Supporting ions reduces the current shared by the metallic ions or complexes thus making convection (agitation) a more significant factor. EP is mainly dominated by two factors namely, (1) dissolution of the freshly deposited metal atoms on the substrate and (2) formation and absorption of metals hydroxides on the electrode surface.[6] A lower pH value favors the dissolution of freshly deposited material and depresses formation and absorption of the metallic hydroxides. Whereas, higher pH value favors the formation and absorption of metal hydroxides and depresses the dissolution of the freshly deposited metal atoms.

3.23.3.2.3 Effects of EP process parameters

Surface properties of the deposition (i.e., texture, finish, and brightening) by EP are highly affected by the impurities of the electrolytic solution and it is practically impossible to maintain a plating solution free of impurities. This may be due to the fact that the particles deferred in the solution may be attached to the cathodic workpiece surface and resulting in rough and nodular deposition or forming pits if they fall off. Either of these produces adverse effects on surface finish, surface integrity, and corrosion resistance of the deposition.[7] Most common sources of the electrolyte impurities are: impurities in anode, decomposition of additives, dissolution of other deposition chamber parts during EP process, corrosion of auxiliary components of the deposition chamber, improperly cleaned anode and filters, chemicals used for make-up and maintenance, hardness of water, etc. Impurities may lead to poor deposition due to: presence of pitting, poor deposition coverage, poor adhesion, lower cathode efficiency, harder more brittle stressed and darker deposition, cracks in deposition, off-color deposition, etc.[7–11]

Additives are often added to the EP solution to achieve the desired deposition characteristics. They may be organic or colloidal in nature although few of them are soluble inorganic compounds. Their presence might be desired or may be accidental. They are intentionally used to improve the brightening,

leveling, grain-refining, stress-relieving, anti-pitting, etc. of the deposition. Use of additives is found as an important parameter in the EP due to their positive influence on the deposition potential, growth, and structure. Generally, additives promote formation of smooth and shiny coatings and they are added to electrolytic solution in a very small amount. Specific activity of an additive is generally understood in terms of its absorption onto the cathode surface during EP. Additive molecules adsorbed on the cathode surface can affect the activation energy and the rate of charge transfer in the electrochemical reaction and may also influence the mechanism of electrocrystallization.[11,12] They affect the physical and mechanical properties of the deposition. For example, efficiency of the EP process and the characteristics of the Zn–Fe deposition can be improved by employing additives such as glycerin in the plating bath.[13] Recently, various complexing agents such as citrates, tartrates, fluoborates, sulfamates, gluconates, and glycinates have been used. These agents are nontoxic, easily available and their effluent treatment is easier upon degradation.[13,14]

3.23.3.3 Selection of Deposition Material

Selection of suitable coating or deposition material requires understanding and knowledge of the different deposition materials and their properties. Deposition material is chosen primarily on the basis of function and application requirements of the end product. Other factors namely shape, size, product life, cost, wear and corrosion resistance, and operating environment are also to be considered. **Tables 2** and **3** present summary of different metals and alloys along with their applications according to different characteristics of deposition by the EP process. **Table 4** presents comparison of different deposition characteristics for most commonly used depositions by the EP process.

3.23.3.4 Advantages

- Improved corrosion resistance.
- Improved wear resistance.
- Excellent finish and shining.
- Hazardless process.
- Pollution-free process.
- No hydrogen embrittlement.
- No effect on fatigue life.

3.23.3.5 Limitations

- High capital cost.
- Coating on internal diameters cannot be done.
- More time consuming process.
- Plating may not be uniform.

3.23.3.6 Applications

EP is used in many diverse industries including home appliances, jewelry, automotive, aircraft, aerospace, and electronics for both decorative and engineering applications. Purpose of decorative plating is to provide an excellent durability (i.e., surface integrity, and corrosion and wear resistance) and high quality of surface finish and aesthetic properties to the surface of manufactured products by adding a protective layer of different materials. Although, decorative applications have diminished somewhat primarily due to added expenses and problems associated with plant effluent (pollution) control and waste treatment, but its applications in engineering, electroforming, and electronics have increased.[14–17]

- Decoration: coating a more expensive metal onto a base metal surface in order to improve the appearance. Applications are jewelry, furniture fittings, hardware, and tableware.
- Protection: corrosion-resistant coatings such as chromium plating of automobile parts and domestic appliances, zinc and cadmium plating of nuts, screws, and electrical components.
- Wear-resistant coatings such as nickel or chromium plating of bearing surfaces and worn shafts and journals.

Table 2 Summary of different metals and their applications according to characteristics of deposition by the electroplating process

Deposition characteristics	*Metal*	*Applications*
Corrosion resistance	Zn, Cd	Sacrificial coatings, fasteners, and hardware fittings
	Sn	Food containers
	Ni, Cr	Food processing equipment requiring wear resistance
Wear resistance	Ni, Cr, E–Ni,	Aerospace, space, and hydraulics
	Rh, Au	Electronic contacts
High temperature oxidation resistance	Cr, Rh, Pd, Pt	Avionics
Diffusion barrier	Au, Ni	Electronic devices
Decorative	Cu/Ni/Cr	Household appliances and automotive trim
	Ag, Au, Rh	Jewelry
Reflectors	Ag, Rh, Cr	Visible light reflectors
	Au	Infrared reflectors
Soldering and bonding	Pb, Sn, Pb, Cu, Ag, Au	Containers, printed circuits, and other electronic
	Sn, Cd, Ni	Assemblies and chassis
Electroforms	Ni, Cu, Fe, Cr, Co	Radar plumbing, screens, bellows, containers, and molds
Dielectrics	Al,Ti, Ta	Condensers and capacitors coatings

Source: Schwartz, M. Deposition from Aqueous Solutions: An Overview. In Deposition Techniques for Films and Coatings, 2nd ed.; Bunshah, R. F., Ed.; Noyes Publications: Park Ridge, NJ, 1994; pp. 480–590.

Table 3 Summary of different alloys and their applications according to characteristics of deposition by the electroplating process

Deposition characteristics	*Alloy*	*Applications*
Corrosion and wear resistance	Ni–P, Sn–Ni, Sn–Pb	Avionics, computer hard disks, printed circuits boards, electronic assemblies, assemblies and chassis, bearings, corrosion-resistant coatings, and solderable coatings
Decorative and wear resistance	Au–Co, Au–Ni	Jewelry hardened gold alloy deposition for electronic contacts and components with high wear rate
Electroforms and decorative	Co–Ni	Molds for plastics, screens, bellows, and containers
Decorative	Ni–Fe, Cu–Zn, Cu–Sn	Rubber bonding, antique, household appliances, and automobile accessories

Source: Schwartz, M. Deposition from Aqueous Solutions: An Overview. In *Deposition Techniques for Films and Coatings*, 2nd ed.; Bunshah, R. F., Ed.; Noyes Publications: Park Ridge, NJ, 1994; pp. 480–590.

Table 4 Comparison of different deposition characteristics for most commonly used deposition materials by the electroplating process

Deposition characteristics	*Copper deposition*	*Nickel deposition*	*Chromium deposition*	*Nickel and chromium deposition*	*Remarks*
Thickness range (μm)	12.5–500	12.5–500	12.5–500	12.5–500	Grinding required over 200 μm thickness
Hardness (HV)	60–150	200–300	850–950	850–950	Indicates abrasive wear resistance
Corrosion resistance	Very poor	Very good	Poor	Very good	Minimum 50 μm thickness of Ni is required
Low friction anti-stick	Poor	Poor	Excellent	Excellent	Indicates adhesive wear resistance
Resistance to impact	Medium	Very good	Medium	Very good	Thin coats and soft substrates prone to damage
Maximum working temp. (°C)	50	650	650	650	–
Covering complex shapes	Medium	Medium	Very poor	Medium	–
Nontoxicity	Excellent	Very good	Very good	Very good	–
Cost for given thickness	Low	Medium	High	Very high	Depends on shape and size
Typical applications	Lubricant in forming, Heat sink, and selective case hardening	Below or in place of Cr in corrosive condition and printing surfaces	Molds, tools, valves, rams, pistons, shafts, gauges, dies, and saw blades	Marine cranes, hydraulic rams, mine roof supports, and print rolls	–

- Electroforming: manufacture of sieves, screens, dry shaver heads, record stampers, molds, and dies.
- Enhancement: coatings with improved electrical and thermal conductivity, solderability, reflectivity, etc.
- Other applications of EP include salvage of mismachined or worn-out parts and other types of reworking as well as material savings.

3.23.4 ECM

Material removal processes are the most versatile manufacturing process and play a vital role in giving shape to different engineering components. Increased use of high strength and tough materials such as titanium alloy, superalloys, copper, beryllium, etc. in a variety of industries ranging from aerospace to biomedical engineering, found conventional material removal processes to be inefficient in machining these materials and their use may lead to subsurface damage to the workpiece and tool. Conventional machining processes are also found be ineffective in manufacturing the complex and miniature components due to the limited tool size and geometrical limitations. Another limitation with the tools used in the conventional machining processes, is that they may leave rough surfaces or burrs on the machined surface. These roughness and burrs on the machined surfaces are undesirable in most of the engineering applications. For example, in the auto vehicles and other motion machine elements, the roughness in components may cause high noise and vibration and even the parts may lead to premature failures. In biomedical instruments presence of even very small burrs will damage living tissues where these machined parts are used as

implants. In the electronic devices, where a number of components are in close contact, the burrs may lead to short circuits.[18] Limitations of conventional machining processes necessitates the need of an alternative and advanced machining process which is capable of machining the material of any hardness without giving any undesirable effects on the workpiece surface. ECM is emerged as a strong alternative for all the conventional machining process.

3.23.4.1 Working Principle of ECM and Pulsed-ECM

ECM is controlled dissolution of anodic workpiece through electrolysis process governed by Faraday's law of electrolysis. It can be considered as reverse of EP process with certain modifications. In this process, approximately complementary image of cathodic tool is reproduced on the anodic workpiece dissolving it electrolytically but without any deposition in the cathode. It can be used for machining of any electrically conductive material irrespective of its hardness. Figure 6 depicts schematic of a simple ECM setup. It generally uses low value of DC voltage in the range of 8–30 V applied between the anode and a pre-shaped cathode separated by a very small (usually in the range of 0.1–1.0 mm) IEG thus producing a high current density in the range of 10–100 A cm^{-2}. Generally, salt-based electrolytes such as NaCl, $NaClO_3$, $NaNO_3$, or their combination is supplied through the IEG to dissolve the anodic material under the influence of high current density. Products of electrochemical reaction (usually gases and sludge in the form of metal oxides) are flushed away from the IEG by making electrolyte to flow at a rate in the range of 10–50 liter per minute (lpm). The anodic dissolution rate referred as material removal rate (MRR) is governed by Faraday's laws of electrolysis and it depends on the electrochemical properties of the workpiece material, electrolyte properties, and electric current/voltage supplied. Schematic of mechanism of material removal in ECM is presented in Figure 7. There are several process configurations that can be selected based on the requirements and the capabilities of the machine. The various configurations are[18–20]:

- Both the tool and the workpiece are stationary.
- The tool is given linear and rotary motion while the workpiece is stationary.
- Both the tool and the workpiece move.

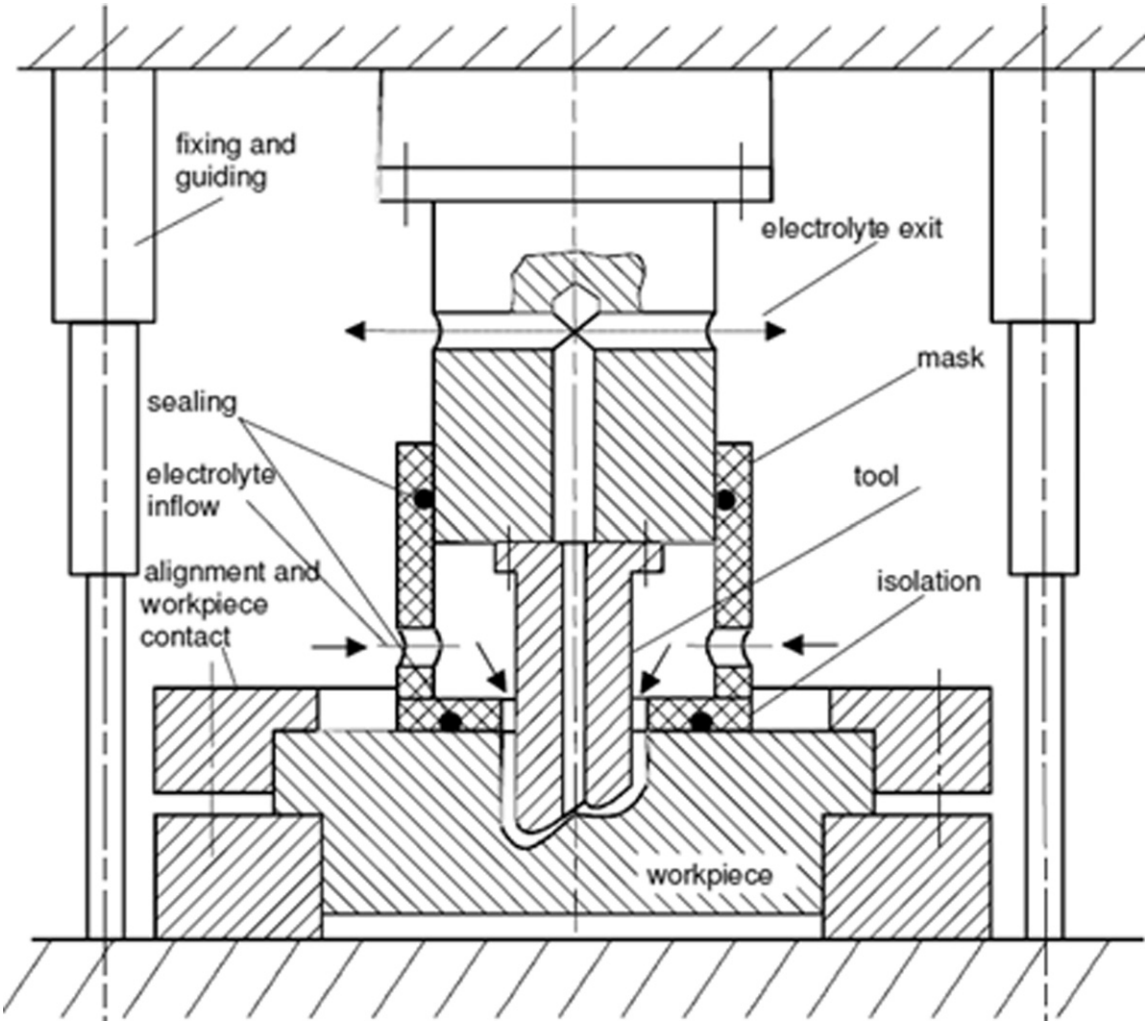


Figure 6 Schematic of a simple electrochemical machining setup.

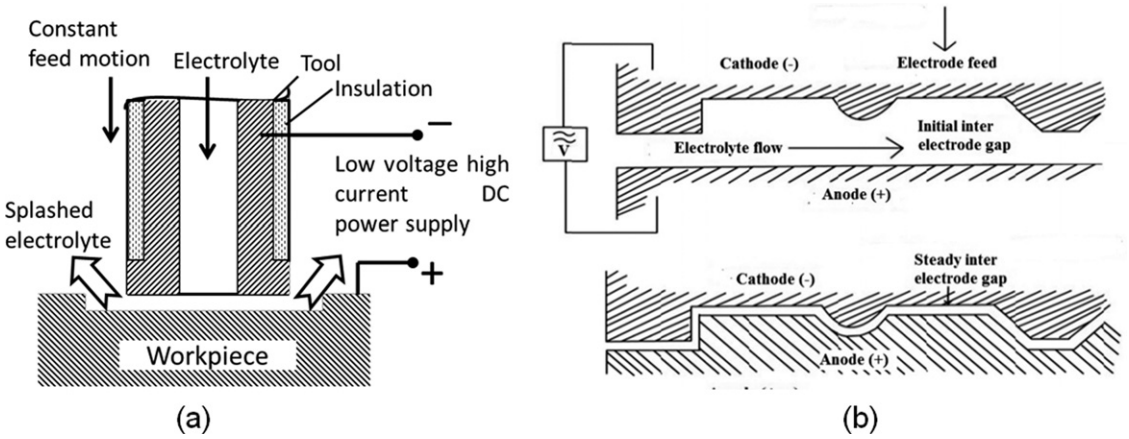


Figure 7 Schematic diagram of (a) working principle and (b) generation of shape on anodic workpiece, in the electrochemical machining process.

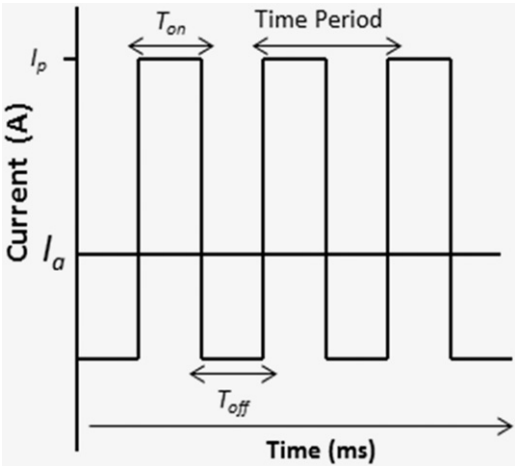


Figure 8 Waveform of the pulsed current.

Further research and development on ECM process and on its derived and hybrid processes are continuing to meet various end product requirements. Pulse electrochemical machining (PECM) is a derived version of ECM in which current is supplied using a pulse generator in the form of short current pulses across the two electrodes. In constant-power ECM, only two parameters related to DC power supply namely current (I) or current density (J) and voltage (V) are the controllable variables. But in PECM, two more additional parameters out of three parameters related to pulsed DC power supply (i.e., pulse-on time '$T_{on,}$' pulse-off time '$T_{off,}$' and duty cycle 'ξ') are also controllable variables. Duty cycle is defined as the ratio of pulse-on time to the total pulse time (eqn. [2]) and is found to have huge impact on the surface quality of the workpiece. A simple waveform of pulsed current is shown in Figure 8. In PECM process, products of electrochemical reaction are flushed away from the IEG during the pulse-off time (T_{off}) which helps in maintaining the clean environment in IEG thus helping electrochemical dissolution to continue resulting in more effective and efficient material removal.

$$\text{Duty cycle}(\xi) = \frac{T_{on}}{T_{on} + T_{off}} 100\% \qquad [2]$$

Introduction of pulse-on and pulse-off times in the ECM leads to higher machining accuracy, better process stability, and suitability for control. These advantages are due to the improved electrolyte flow conditions in the IEG, enhanced localization of anodic dissolution, and small and stable IEG. Although, use of pulsed current slows down the overall process as compared to constant DC supply-based ECM process, but the process becomes more effective as better surface finish and better geometric accuracy can be achieved by PECM.[21]

3.23.4.2 Material Removal in ECM Process

Theoretical expressions for machining time, gravimetric, volumetric, and linear MRR, and current density 'J' in the IEG can be evaluated by using the following equations derived from the Faraday's laws of electrolysis and based on the following assumptions[18–20,22,23]:

- Electrical conductivity of the electrolyte in the IEG remains constant.
- Electrical conductivities of the tool (cathode) and workpiece (anode) are very large ($10^5\ \Omega^{-1}\ \text{cm}^{-1}$) as compared to that of electrolyte ($0.1–1.0\ \Omega^{-1}\text{cm}^{-1}$). Therefore, surfaces of electrodes can be considered as equipotential surface.
- Effective voltage working across the electrodes is $(V - \Delta V)$. Where, ΔV is the total overvoltage at anode and cathode and it is assumed to remain constant.
- Anode dissolves at one fixed valency of dissolution.

$$\text{Machining time} = T_m = \frac{m}{I}\left(\frac{ZF}{M}\right)(\text{seconds}) \qquad [3]$$

$$\text{Gravimetric material removal rate} = Q_g = \eta\left(\frac{M}{ZF}\right)I(\text{g s}^{-1}) \qquad [4]$$

$$\text{Volumetric material removal rate} = Q_v = \eta\left(\frac{M}{ZF\rho_a}\right)I(\text{mm}^3\ \text{s}^{-1}) \qquad [5]$$

Where, η is the current efficiency; ρ_a is the density of the anode material (g mm^{-3}). Ohmic resistance of the electrolyte in the

IEG 'R' is given by

$$R = \frac{\sigma_e Y}{A_p} = \frac{Y}{K_e A_p}\,(\text{Ohm}) \quad [6]$$

Here, σ_e is electrical resistivity (Ω mm) of the electrolyte; K_e is electrical conductivity of the electrolyte ($\Omega^{-1}\,\text{mm}^{-1}$); Y is IEG (mm); A_p is the projected area of the tool face (mm^2), i.e., common area through which current is flowing. Current density in IEG is given by:

$$\text{Current density} = J = \frac{I}{A_p} = \frac{1}{A_p}\,\frac{(V-\Delta V)}{R} = \frac{K_e(V-\Delta V)}{Y} \quad [7]$$

$$\text{Linear material removal rate or penetration rate} = Q_l = \eta\left(\frac{M}{Z\rho_a \text{F}}\right)J \;\; (\text{mm s}^{-1}) \quad [8]$$

Actual rate of change of IEG $\frac{dY}{dt}$ is equal to difference in linear MRR and tool feed rate, i.e.,

$$\frac{dY}{dt} = Q_l - f = \eta\left[\left(\frac{M}{Z\rho_a F}\right)K_e(V-\Delta V)\right]\frac{1}{Y} - f \;\; (\text{mm s}^{-1}) \quad [9]$$

Under the equilibrium condition in the ECM process, the penetration rate 'Q_l' equals to tool feed rate 'f,' i.e., IEG does not change with time. This can be used to obtain expression for equilibrium IEG 'Y_e' from eqn [9] yielding,

$$Y_e = \eta\left[\left(\frac{M}{Z\rho_a \text{F}}\right)K_e(V-\Delta V)\right]\frac{1}{f} \quad [10]$$

3.23.4.3 Factors Affecting the ECM Process Performance

MRR, surface finish, and geometric accuracy of the components machined by ECM depends on parameters related to electrolyte (i.e., type, composition, concentration, temperature, flow rate, pressure, and pH value), properties of the workpiece material (electrochemical equivalent, valency of dissolution, electrode potential, electrical conductivity, and density), ECM process parameters (i.e., IEG, type of power supply, current density, and voltage), and tool design. Following paragraphs discuss them briefly.

3.23.4.3.1 Electrolyte related parameters

Electrolyte is the most important element of ECM system. Generally, an aqueous solution of an appropriate electrolyte is supplied through the IEG at the required flow rate. Main functions of the electrolyte flow are (1) to provide ideal conditions for the electrochemical dissolution of the workpiece material without depositing it on the cathodic tool; (2) flush away the products of ECM formed due to electrochemical reactions (i.e., metal hydroxides and reaction gases); (3) to take away the heat generated due to passage of current and may be due to electrochemical reactions thus maintaining a constant temperature in the IEG; (4) not allowing concentration of ions on the electrodes; and (5) not to allow oxygen evolved at anode to passivate it by forming metal oxides. **Table 5** presents summary of different role/functions of an electrolyte and the required electrolyte property to fulfill each function.

Table 5 Functions and required property of an electrolyte in electrochemical machining process.[18,19,22]

Role or function of electrolyte	*Required electrolyte property*
To complete the electrical circuit and allow large currents to pass	Large electrical conductivity
To sustain required electrochemical reactions	Electrolyte should be such that anode material is continuously dissolved but it is not deposited on the cathode
To carry away the heat generated in the machining zone	Higher specific heat and lower viscosity
To carry away the waste or the materials removed	Good chemical stability
Economics and safety of machining process	Low density, noncorrosive, nontoxic (safe), and inexpensive

Electrolytes used in ECM can be classified as (1) sludging electrolytes, or (2) non-sludging electrolytes. Sludging electrolytes are those which form precipitates as product of electrochemical reactions which remove material from the anodic workpiece, while non-sludging electrolytes dissolve the products of electrochemical reactions. Generally, salt-based electrolytes (i.e., NaCl, $NaNO_3$, $NaClO_3$, KCl, KNO_3, etc.) are sludging electrolytes whereas acidic electrolytes (i.e., HF, HCl, HNO_3, H_2SO_4, etc.), and alkaline electrolytes (i.e., NaOH, KOH, NH_4OH, etc.) are non-sludging electrolytes. Consequently, sludging electrolytes can be reused by filtering them properly and then recirculating them whereas non-sludging electrolytes cannot be reused. Electrolyte can also be classified as passivating and non-passivating electrolytes. Passivating electrolytes contain oxidizing anions such as sodium nitrate ($NaNO_3$) whereas non-passivating electrolytes contain aggressive anions such as sodium chloride. Passivating electrolytes are known to provide better machining quality due to formation of protective oxide layer and oxygen evolution in stray current region.[24,25] Additives such as sodium tartrate, glycerin, and glycol are used to get better results.

In the ECM-based processes, movement of the ions from the cathode toward anode depends on the properties of the electrolyte. Electrolyte conductivity in the IEG is affected by various parameters namely; (1) initial value of IEG, (2) electrolyte concentration, (3) local hydroxide concentration in the electrolyte, (4) bulk and local temperature, and (5) electrolyte pressure and flow rate.[24,26] Selection of an appropriate electrolyte for a particular application depends on the following considerations[27,28]:

- nature of the workpiece material,
- surface finish and dimensional tolerance requirements, and
- required productivity.

Table 6 presents the most commonly used type of electrolytes for different types of alloys. Aqueous solution of $NaNO_3$, NaCl or $NaClO_3$, or their combinations are the most commonly used electrolytes due to the following facts:

- Sodium chloride (NaCl) is more corrosive but its conductivity is very stable over a wide range of pH values.

Table 6 Commonly used type of electrolytes for different alloys[18,19]

Type of alloy	*Preferable electrolytes*
Iron-based alloys	$NaNO_3$, $NaClO_3$, or NaCl
Co–Cr–W-based alloys	NaCl
Ni-based alloys	HCl or mixture of brine and H_2SO_4
Ti-based alloys	10% HF + 10% HCl + 10% HNO_3
WC-based alloys	Strong alkaline solutions

- Sodium nitrate ($NaNO_3$) is less corrosive but it creates a strong passivation layer on the workpiece, due to which less MRR is found in comparison with NaCl. Due to less dissolution of anodic workpiece material better smoothness can be achieved. Also, the electrolytic reactions require higher voltage when using strong passivating electrolyte.

MRR increases with increase in the electrolyte concentration because more ions will be available in the electrolyte solution which increases electrolyte conductivity in IEG enhancing anodic dissolution of the workpiece material. Therefore, concentration of electrolyte should be high but higher concentration may increase passivation effect. Electrolyte conductivity is very sensitive toward electrolyte temperature and increases with it. Electrolyte temperature rises across the IEG due to the use of high current density in IEG. It affects the surface finish and geometric accuracy of the workpiece adversely and may also stop the further machining action in an abrupt manner. Also, higher electrolyte temperature may increase the passivation effect. Electrolyte flow rate is another important parameter to control and optimize the electrolyte conductivity in the IEG. It is a difficult task to maintain the flow of electrolyte in the extremely small IEG without affecting the tool stability.[18–20]

3.23.4.3.2 IEG

Face width of tool electrode and its position with respect to the workpiece determines the IEG between them which is in range of fraction of millimeter. Higher value of IEG necessitates use of higher applied voltage to maintain the required current density in the IEG for the controlled anodic dissolution of workpiece material; but use of higher voltage may give poor surface finish and geometric accuracy. Use of small IEG causes anodic dissolution of workpiece to occur at lower voltage which results in very good surface finish and geometric accuracy; but maintaining small IEG is very difficult and also flow of electrolyte through it because chances of short-circuiting and clogging are very high in a small IEG. Therefore, value of IEG needs to be maintained accurately because any abnormal change in IEG may give poor surface quality of the machined component.[29]

3.23.4.3.3 Current density and voltage

Either constant DC power supply (in ECM) or pulsed DC power supply (in PECM) can be used in ECM-based processes. Constant DC power supply provides continuous current or voltage whereas pulsed power DC supply is used to supply current or voltage in the form of short pulse with specific pulse-on time and pulse-off time. MRR is proportional to the applied voltage. From eqn [5] it can be seen that on increasing the value of voltage the current density will increase which leads to provide a higher MRR. Use of PC has the following advantages [26,30]:

- The sludge products generated from anodic dissolution of workpiece material can be removed during the pulse-off time because formation of the sludge in the narrow IEG might lead to clogging and deposition on the tool which will have an adverse effect on the ECM process.
- It prevents the electrolyte from reaching high temperatures. The use of sufficient pulse-off time allows it to cool down.
- Gap checking and tool repositioning can also be conducted during these pulse pauses to establish the required IEG value before next pulse is on. This leads to significant reduction in the indeterminacy of the IEG and shaping accuracy in the ECM process.

3.23.4.3.4 Mass transport phenomenon in ECM

Mass transport phenomenon plays very important role in controlling the anodic dissolution of workpiece material and in achieving desired level of surface quality because it affects the current density distribution at macroscopic and microscopic levels. Controlled dissolution by mass transport smoothens the surface because IEG at peaks of a surface is smaller than the IEG at the valleys giving more current density and more material removal from the peaks than the valleys (this is referred as 'leveling effect').[24] The anodic leveling can be achieved by three types of nonuniform current distribution, i.e., primary current distribution (Ohmic), secondary current distribution (kinetic), and tertiary current distribution due to nonuniform local mass transport.[25] In ECM, effect of secondary current distribution is negligible if sufficient IEG and electrolyte flow velocity are maintained. Therefore, primary and tertiary current distributions mainly contribute toward smoothening of the workpiece surface. Moreover, influence of the charge transfer kinetics is negligible and differences due to grain orientation, grain boundaries, dislocations, or small inclusions do not play any significant role because of controlled limiting current by mass transport. As a result, material removal at molecular level results in a very smooth surface topography (brightening effect).[24–26]

3.23.4.4 Capabilities of ECM and Its Effects on Workpiece Material

The capabilities of ECM can be judged by knowing its finishing, drilling and cutting capabilities, and its environmental and economic prospects. Table 7 presents the capabilities of ECM process and it can be observed that high geometric accuracy and finishing can be achieved by ECM.

Following are the effects of ECM on the workpiece material:

- Material removal in ECM is smooth and gentle as compared to conventional machining process.
- No effect of ECM on ductility, yield strength, ultimate strength, and micro-hardness of electrochemically machined components.

Table 7 Capabilities of electrochemical machining process

Type	*Capability/characteristics*		*Common value/range (attainable)*
Finishing capabilities	Surface roughness [R_a in μm]		0.4–6.3 (0.05)
	Dimensional tolerance or accuracy [±μm]		50–125 (10)
	Minimum corner radii (mm)		0.2 mm
	Minimum overcut (mm)		0.12 mm
	Minimum surface damage (μm)	Chemical damage	No
		Mechanical damage	No
		Thermal damage	No
Drilling capabilities	Hole diameter (mm)		6.3–75 (3.17)
	Aspect ratio		8
	Hole depth (mm)		127 mm (305)
	Minimum taper (μm/mm)		25
	Maximum number of holes that can be drilled simultaneously		100
	Minimum angle of inclination hole axis with surface		90°
Cutting capabilities	Width of cut (mm)		3.17
	Thickness of cut (mm)		Up to 127 mm
	Range of cutting rate (mm/min)		2.5–12.5
Economic aspects	Initial investment or capital cost		Very high
	Tooling and fixtures cost		Medium
	Power consumption cost		High
	Tool consumption cost		No tool wear
Environmental aspects	Safety		Normal problem
	Toxicity		Normal problem
	Contamination of machining medium		Critical problem

- Depth of work hardened surface in ECM is negligible (approximately 0.001 mm) as compared to turning (0.5 mm) and milling (1.5 mm).
- Hardly any evidence is available about hydrogen embrittlement of electrochemically machined components.
- ECM produces almost stress-free surface.
- Surface finish produced by ECM exhibit better wear resistance, friction resistance, and corrosion resistance than those produced by other processes.
- Compressive residual stresses, that are responsible for higher fatigue strength are very low in ECM process as compared to conventional machining process (approximately 50 kg mm^{-2}). This results in 10–25% lower fatigue strength in the electrochemically machined components.
- Removal of compressive stress layer is primarily responsible for reduction in fatigue strength of electrochemically machined components. Secondary reasons include intergranular attack (IGA) and exposition of micro-cracks and pits at the surface.
- Required fatigue strength can be achieved by some appropriate post-ECM treatment such as mechanical polishing, glass bead blasting, vapor blasting, etc.

3.23.4.5 Advantages

- Performance of ECM is independent of mechanical properties of the workpiece material. Therefore, strength, hardness, toughness, etc., do not affect the measures of ECM; performance such as MRR and surface finish;
- produces burr-free and stress-free surfaces;
- no tool wear due to noncontact nature of the process;
- complex three-dimensional products can be fabricated easily due to its copying nature;
- excellent surface finish can be achieved;
- higher MRR as compared to other unconventional machining processes; and
- no subsurface damage.

3.23.4.6 Limitations

- Very high specific energy consumption (approximately 20 times more as compared to conventional machining processes);
- only electrically conducting material can be machined;
- corrosion of the components of ECM machine, workpiece, and tool due to use of electrolytes;
- design and manufacturing of the ECM tool specially for the complex workpiece is very challenging;
- extreme sharp corners that cannot be machined;
- can cause IGA;
- limited aspect ratio;
- very high initial investment cost;
- high maintenance and tooling cost;
- extremely hazardous while using strong acidic electrolytes; and
- disposal of the used electrolyte is challenging.

3.23.4.7 Applications

- ECM finds various applications in different industries for machining of automobile dies, axial flow turbine blades,

axi-symmetric turbine blades, jet engine parts, chain sprockets, biomedical components, components with micro- and nano- holes, etc.
- Machining and finishing of very complex shaped components.
- Manufacturing of components and machine tools with precise geometry and excellent surface finish (up to 25 μin) can be achieved.
- Machining of heat resistant and hard materials.
- For making deep blind holes of micro-size and pockets.

3.23.5 ECG

ECG is a hybrid finishing process combining advantages of ECM and mechanical grinding processes to produce burr-free, stress-free, and super finished components. Figure 9 depicts the schematic of a simple ECG setup in which the abrasive grinding wheel is made as cathode and while the workpiece is made anode using appropriate DC power supply. ECG grinding wheel is similar to a conventional grinding wheel except that its bonding material is electrically conductive. Commonly used bonding materials are copper, brass, nickel, or copper impregnated resin. Abrasive particles protruding outside from the bonding material of the wheel maintain a constant IEG between the grinding wheel and workpiece. Alumina is the most commonly used abrasive with mesh size in the range of 60–80 μm. Grinding is performed as usual but instead of coolant, a spray of electrolyte is supplied by a nozzle. Both mechanical grinding and ECM take place simultaneously and the grinding wheel is sharpened easily and quickly. The electrolyte takes away the heat and the electrochemical reaction products from the machining zone. Mainly sodium chloride and sodium nitrate is used as electrolyte in ECG.

Majority of the material removal (almost 90–95%) is removed by the electrolytic dissolution of the workpiece material. The role of grinding wheel is only to remove the passivation layer of metal oxide formed on the workpiece surface during the electrochemical dissolution process thus contributing 5–10% of the material removal. Due to very less pressure applied on the grinding wheel in ECG process, life of grinding wheel is more than 10 times than the conventional grinding wheel.[18,19] The ECG process can be used in different forms for different purposes namely electrochemical cylindrical grinding, peripheral or surface grinding, face grinding, form wheel or square grinding, cone wheel grinding, and internal grinding. Main parameters that affect performance, efficiency and effectiveness of ECG process are[31,32]:

- applied voltage and current density,
- type, concentration, and delivery method of electrolyte,
- type, speed, pressure, and running accuracy of the grinding wheel, and
- feed rate of workpiece.

Selection of optimum values of these parameters help to optimize surface finish and MRR.

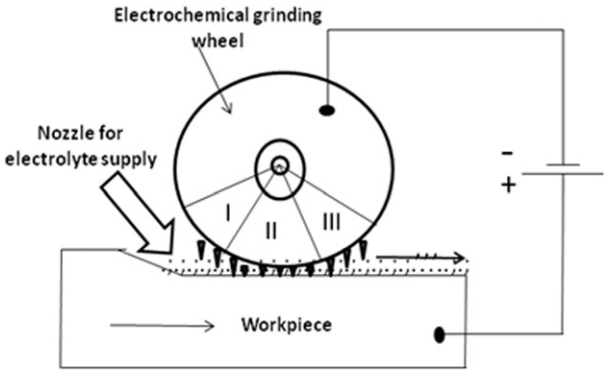


Figure 9 Schematic of electrochemical grinding process.

3.23.5.1 Advantages

- MRR achieved during ECG may be high as 10 times as compared to conventional grinding on hard materials having hardness up to 65 HRC.
- Excellent surface finish under controlled process parameters. Surface finish obtained by ECG ranges from 0.12 to 0.8 μm. Surface finish produced on nonhomogeneous materials during ECG is better than that produced during conventional grinding.
- Minimum inside corner radius of 0.25 mm and outside corner radius of 0.025 mm can be produced by this process.
- No thermal and mechanical damage to workpiece.
- Absence of work hardening.
- No grinding burrs or grind lines over workpiece surface.
- Absence of distortion in thin/fragile/thermo sensitive parts.
- Narrow tolerances can be achieved.
- Longer life of the grinding wheel.
- Relatively small environmental impact because of the reuse of the electrolyte economically viable machining of high grade aerospace components made possible.

3.23.5.2 Limitations

- Process is limited to only electrically conductive materials,
- not suitable for soft materials,
- requires dressing tool preparation for the grinding wheel,
- higher power consumption,
- higher initial investment cost due to specially design and manufacture the grinding wheel, and
- corrosion problem due to use of electrolyte.

3.23.5.3 Applications

- Production of tungsten carbide cutting tools and other tools made of difficult-to-machine materials,
- burr-free sharpening of hypodermic needles,
- grinding of turbine blades made of superalloys,
- form grinding of fragile honeycomb materials used for aerospace applications,
- reprofiling worn locomotive traction motor gear, and
- removal of fatigue cracks from steel structures that have been used for underwater applications.

3.23.6 ECH

ECH is a hybrid superfinishing process which combines capabilities and advantages of ECM with mechanical honing and simultaneously overcoming their individual limitations. Main capabilities of ECM process include: capability to machine/finish material of any hardness, production of stress-free and crack-free surface, higher MRR, and no tool wear. While main capabilities of honing are: ability to correct the geometric errors and controlled generation of functional surfaces. Main limitation of ECM process is passivation of anodic workpiece surface by the metal oxides formed due to evolution of oxygen gas at anode during its electrolytic dissolution. This anode passivation prohibits further electrolytic dissolution of the workpiece. While, major limitations of honing process includes limited life of honing tool, low productivity, incapability of finishing a hardened workpiece, and possibility of mechanical damage (i.e., micro-cracks, hardness alternation, and plastic deformation) to the workpiece material.[33] ECH can be used to correct errors/deviations in geometry/shape such as out-of-roundness or circularity, taper, bell-mouthhole, barrel-shaped hole, axial distortion, boring tool marks, etc., for cylindrical surfaces and ability to correct form errors (i.e., deviations in lead and profile) and location errors (i.e., pitch deviations and runout) for cylindrical and conical gears. Use of pulsed current in the ECH process also helps in enhancing the process performance without requiring higher electrolyte flow rate thus minimizing the size and cost of the equipment for the pulsed-ECH (PECH) processes.[34]

3.23.6.1 Process Principle of ECH

Material removal in ECH is based on a controlled anodic dissolution of workpiece material using a cathodic tool in an electrolytic cell. Generally, a low DC voltage in the range of 8–30 V is applied between anode and cathode separated by a very small value of IEG (usually in the range of 0.1–1.0 mm) which is maintained by the specially designed cathode tool. Current density of the order of 10–100 A cm^{-2} and volumetric MRR in the range of 0.1–1,000 $mm^3\,min^{-1}$ are achieved. Electrolyte should be such that the material removed from the workpiece must not deposit on cathode tool. Products of electrochemical reaction are flushed away from the IEG using an aqueous solution of the salt-based electrolyte such as NaCl, $NaClO_3$, $NaNO_3$, or their combination supplied through the IEG at a flow rate in the range of 10–40 lpm. This helps in maintaining the clean environment in IEG thus helping electrochemical dissolution to continue. The electrolyte flow also takes away the heat generated due to passage of current and possibly due to electrochemical reactions. A passivating layer of metal oxide is generated on the workpiece due to evolution of oxygen at anode which prohibits its further dissolution. Thickness of this protective layer is more at valleys as compared to that on the peaks. The honing tool selectively removes this passivating layer by remaining in continuous contact with the workpiece enabling electrolytic dissolution and mechanical honing to take place simultaneously.[33] Main parameters that affect the performance, efficiency, and effectiveness of ECH process are majorly categorized into three parts, i.e., (1) parameters related to ECM; (2) parameters related to mechanical honing; and (3) parameters related to work material and tooling system. The details these parameters are presented in Table 8.

3.23.6.2 ECH equipment

ECH equipment consists of five subsystems namely (1) DC power supply system; (2) electrolyte supply and cleaning system; (3) specially designed cathode and honing tool; (4) system for providing the required relative motion between the workpiece, cathode, and honing tool; and (5) finishing chamber for housing and holding workpiece, cathode, and honing tool. Out of these subsystems details of DC power supply system and electrolyte supply and cleaning system are similar to those used in the ECM process and described in Section 3.23.4.3. Remaining three subsystems depend on the geometry of the workpiece. These subsystems are described for finishing the internal cylinder and gears in following paragraphs.

3.23.6.2.1 Finishing of internal cylinders by ECH

The tool used for finishing of internal cylinders by ECH is shown in Figure 10. It combines cathode and honing tool in a single unit. It consists of a teflon shaft over which a hollow stainless steel sleeve is fitted. It has even number of equally spaced and radially outward protruding honing sticks on its

Table 8 Parameters that affect the electrochemical honing process performance

Parameters related to electrochemical machining	*Parameters related to mechanical honing*	*Parameters related to workpiece and tooling*
1. Power supply: • Current • Voltage • Pulse-on time • Pulse-off time • Duty cycle 2. Electrolyte • Type • Composition • Concentration • Pressure • Temperature • IEG	1. Speed of rotation 2. Speed of translation 3. Feed mechanism 4. Abrasive • Type • Grit size • Grain size	1. Electrochemical properties of workpiece 2. Mechanical properties of workpiece 3. Tool design

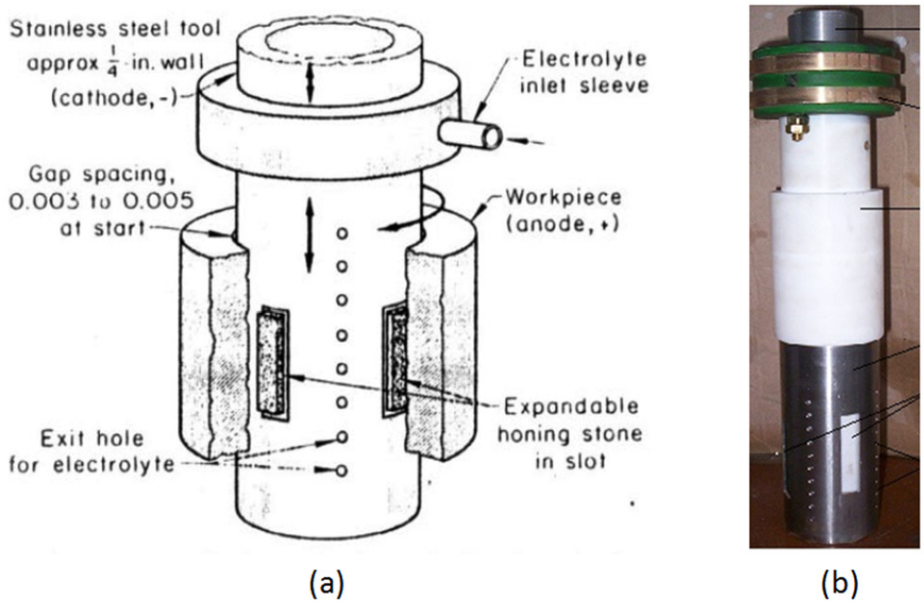


Figure 10 (a) Schematic and (b) photograph of a typical tool for finishing internal cylinders by ECH.[33]

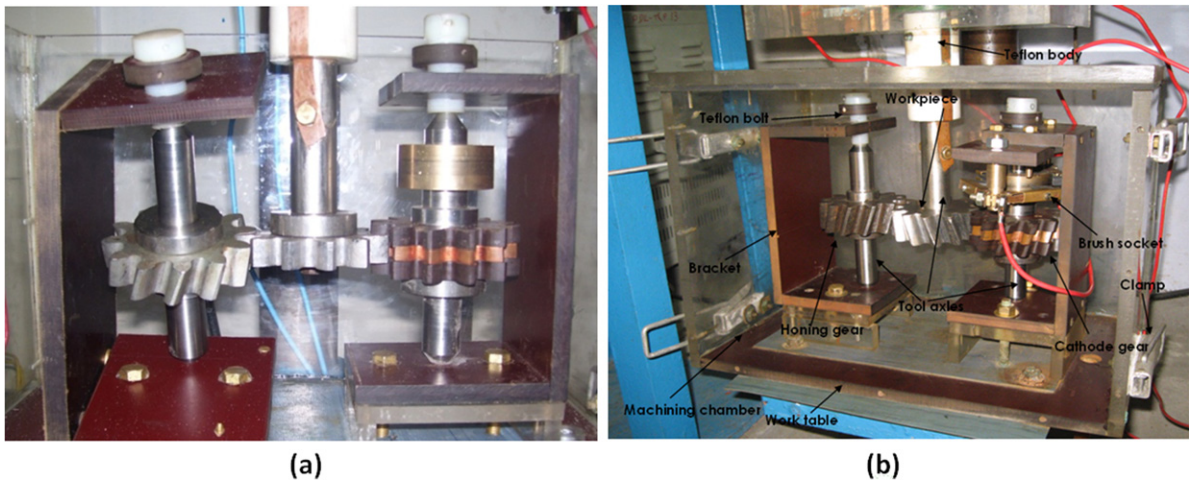


Figure 11 Photographs of machining chamber for high quality finishing of (a) spur gear [35] and (b) helical gear,[36] by the ECH process.

periphery. These sticks are spring controlled which help in adjusting the required honing pressure. These honing sticks act as insulator and amount by which they protrude radially outward determines the IEG between the cylindrical workpiece and the cathode tool. Honing sticks preferentially remove the nonconductive passive layer of metal oxide from the high spots to correct errors or deviations in geometry of the cylindrical workpiece. The electrolyte enters the tool body via a sliding inlet sleeve from which it exits into the IEG through several rows of small holes in the tool body. The electrolyte exits from the top and bottom of the bore. Current is supplied to the tool through a slip-ring copper brush assembly. The tool is provided a precisely controlled combination of rotation and reciprocation simultaneously. Rotary motion is provided by a speed controlled DC servomotor, while reciprocating motion by a microprocessor programmed stepper motor.[33]

3.23.6.2.2 Finishing of gears by ECH

Finishing of gears by ECH requires cathode tool and honing tool to be separate. The workpiece gear meshes with the cathode gear and honing gear simultaneously. Cathode gear is to be specially designed and fabricated in such a way that its electrically conducting portion never touches the anodic workpiece gear thus avoiding short-circuiting and at the same time it maintains the required IEG between the anode and cathode gear. For the cylindrical gears (spur and helical gears) this is ensured by sandwiching a conducting layer between two nonconducting layers and undercutting the conducting layer by an amount equal to the required IEG as compared to the nonconducting layers. The axes of shafts of the workpiece and cathode gears are parallel to each other for finishing the spur and helical gears (Figures 11(a) and 11(b)). The workpiece gear is provided by controllable rotary motion by means of DC

motor while cathode and honing gear rotate by virtue of their tight engagement with the workpiece gear. Since, entire face width of the cathode gear is not electrically conducting therefore a reciprocating motion is also given to workpiece gear by means of a programmable stepper or servomotor to ensure finishing of the entire face width of the cylindrical gear.[35–36] Majority of finishing or material removal is done by the ECM action which occurs between the anodic workpiece gear and the cathode gear while role of the honing action, which takes place between the workpiece and the honing gear, is just to remove selectively the passivation layer of metal oxide formed on the workpiece gear. All the three gears should have same involute profile and same module.

For 'spur gear finishing' by ECH (Figure 11(a)), a helical gear is made as honing gear, it can either be an abrasive impregnated gear or a gear having hardness more than the workpiece gear. It is mounted on a floating stock to ensure dual flank contact between the honing and workpiece gear. The honing gear is mounted in such a way having cross-axis arrangement with the workpiece gear so as to reduce the tooth surface contact and the pressure required for finishing.[35] 'Helical gear finishing' by ECH (Figure 11(b)) does not require the cross-axis arrangement because honing and cathode gears have opposite helix angle to that of the workpiece gear, i.e., if workpiece gear is right-handed helical gear then cathode and honing gears will be left-handed and vice versa.[36]

Finishing of bevel gears by ECH is much more difficult than finishing of cylindrical gears due to their complex geometry which inhibits reciprocation of the workpiece gear required for finishing its entire face width. This problem was solved by Shaikh *et al.*[37] envisaging a novel concept of twin complementary cathode gears as shown in Figure 12(a). In this concept, one of the cathode gears has an electrically conducting layer of copper sandwiched between two nonconducting layers of metalon while, other complimentary cathode gear has a nonconducting layer of metalon sandwiched between two conducting layers of copper. The conducting layers in both the complementary cathode gears are undercut by the required amount of IEG as compared to the insulating layers so as to avoid short-circuiting when these gears mesh with the workpiece gear during the finishing operation. This also ensures that IEG required for electrolytic action is maintained between the workpiece and cathode gears. During the process of anodic dissolution of the workpiece gear material, the electrolyte forms a passivating metal oxide layer on the workpiece gear tooth surface which restricts further finishing by electrolysis action. These passivating layer of metallic oxides generated over the workpiece surface is removed by the honing gear which simultaneously comes in mesh with the workpiece and cathode gears to continue the further finishing by electrolysis action. As the process carries on, the geometric accuracy of the workpiece gear is rapidly improved. Figure 12(b) depicts the photograph of finishing chamber developed by implementing the concept of the twin complementary cathode gears. The tool is provided by a precisely controlled rotation by a speed controlled DC servomotor, while reciprocating motion to the workpiece gear holding shaft for its proper engagement and disengagement with the ECH tools is provided by a microprocessor programmed stepper motor.[38]

3.23.6.3 Advantages

- Material of any hardness (but electrically conducting) can be finished by ECH.
- ECH can achieve surface roughness up to 50 nm and tolerances up to ± 0.002 mm.
- It produces surfaces with distinct cross-hatch lay pattern which is very useful for lubricating oil retention, surfaces with compressive residual stresses required for the components subjected to cyclic loading, and completely stress-free surfaces.
- ECH not only produces high quality surface finish and surface integrity but also has ability to correct errors/deviations in geometry/shape such as out-of-roundness or circularity, taper, bell-mouthhole, barrel-shaped hole, axial distortion, boring tool marks, etc., for cylindrical surfaces and ability to correct form errors (i.e., deviations in lead and profile) and location errors (i.e., pitch deviations and runout) for cylindrical and conical gears.

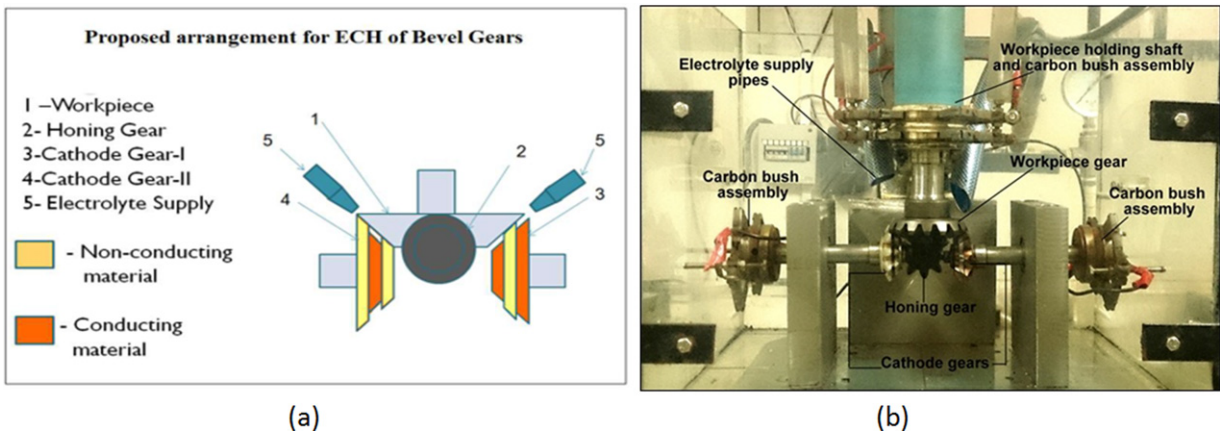


Figure 12 (a) Concept of twin complementary cathode gears for high quality finishing of straight bevel gears by ECH [37] and (b) photograph of the finishing chamber based on this concept.

- It takes less finishing time as compared to ECM and mechanical honing. ECH can finish materials up to 5–10 times faster than mechanical honing and four times faster than internal grinding. Gain is more pronounced for higher material hardness.
- Very less amount of heat is produced thus making it suitable for the processing of parts those are susceptible to heat distortions.
- ECH automatically deburrs the work surface.
- Increased life of abrasive sticks/tool due to very limited role of mechanical honing.
- There is less distortion while finishing thin-walled tubes due to less pressure required between work surface and the honing tool.
- As a by-product, sharp or burred edges of a cross-holes or other intersections which break into the bore are automatically deburred as the main hole is being finished by ECH.

3.23.6.4 Limitations

- It can be used for finishing electrically conductive materials only.
- It is more costly than the mechanical honing due to its electrical, fluid handling elements, need for corrosion protection, costly tooling, and longer setup time. This makes ECH more economical for longer production runs than for tool room and job-shop conditions.
- Difficult to finish the blind holes.
- ECH cannot correct location of hole or perpendicularity.

3.23.6.5 Applications

- ECH can be used to finish the various hard to finish materials such as cast tool steels, high-alloy steels, carbide, titanium alloys, Incoloy, stainless steel, Inconel, and gun steels.
- ECH is an ideal choice for superfinishing, improving the surface integrity, and increasing the service life of the critical components such as internal cylinders, transmission gears, carbide bushings and sleeves, rollers, petrochemical reactors, molds and dies, gun barrels, pressure vessels, etc., which are made of very hard and/or tough, wear-resistant materials, most of which are susceptible to heat distortions.
- ECH is widely used in automobile, avionics, petrochemical, power generation, and fluid power industries.
- It has been used for bore size ranging from 9.5 to 300 mm and length up to 600 mm.

3.23.7 ECDe

Burrs are sharp edged thin crests generally of triangular shape and developed along the edge of a workpiece during various manufacturing operations such as machining, forging, trimming, casting, etc. Burrs may lead to noise generation, hazardous operation of a machine generates friction and wear in the moving parts and it may also affect the fatigue and service life of the component. There are many types of burrs produced by different manufacturing and finishing processes namely: compressive burr, corner burr, edge burr, entrance burr, exit burr, feather burr, flash burr, hanging burr, parting-off burrs, roll over burr, and tear burr.[23] Different type of deburring processes can be classified as mechanical, thermal, abrasive, and electrochemical. The most frequently used method is mechanical. Mechanical deburring is typically carried out manually by a skilled worker resulting in low productivity and higher cost. In thermal deburring, the process difficulties can be eliminated because the workpiece is subjected to a temperature in excess of 1000 °C for few seconds, causing the burrs to ignite and burn-off. The thermal deburring processes require high capital investment and have some technical problems. Typical abrasive deburring processes use abrasive jet, water jet, abrasive water jet, barrel tumbling, spindle finishing, or sand blasting. Due to the higher initial cost and lack of adequate technical data, the use of abrasive jet deburring is also limited.

3.23.7.1 Mechanism of ECDe

ECDe is based on the principle of the anodic dissolution of workpiece material in an electrolytic cell. Figure 13 show the typical arrangement for ECDe for cylinders in which the section of the workpiece which is to be deburred is made anode while the specially designed tool used to deburr the workpiece is made cathode. Those surfaces of the tool where deburring is not required are insulated. In ECDe the IEG between the burrs and the cathode is minimum which results in higher current density helping in faster anodic dissolution of the burrs. When a suitable DC current (50–500 A) is supplied, the burr dissolves forming a controlled radius. During an electrochemical action, current density at the peak of surface irregularities is higher than that elsewhere. Burrs are therefore removed preferentially and the workpiece becomes smooth.[18,39] The deburring tool should also have a similar contour as that of the workpiece thus maintaining an IEG in the range of 0.1–0.3 mm. Use of a rotating and feeding tool electrode enhances the deburring process by creating turbulent flow in the IEG. The spindle rotation is reversed to increase the electrolyte turbulence. Choice of the electrolyte plays an important role in the ECDe process. Aqueous solution of NaCl and $NaNO_3$ are the most commonly used type of electrolytes.

3.23.7.2 Advantages

- ECDe does not induce any mechanical stress or have thermal effects on a workpiece.

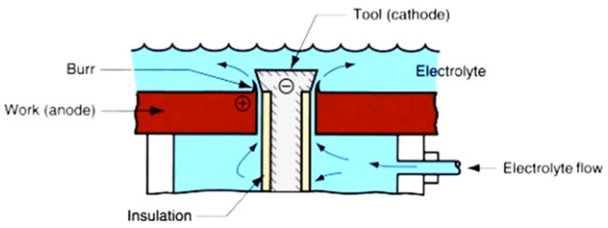


Figure 13 Typical arrangement for electrochemical deburring of a cylinder.

- MRR is independent of the mechanical properties such as hardness and toughness of the machined materials.
- ECDe does not change the physical and chemical properties of a machined surface.
- Elimination of costly hand deburring.
- Very fast deburring process. Normal cycle times for ECDe are between 30 and 45 s.
- Increased product quality and reliability.
- Removal of burrs at the required accuracy, uniformity, proper radius, and clean edge.
- Reduced personnel and labor cost.
- Possibility of automating for higher productivity.

3.23.7.3 Limitations

- It can be used for deburring electrically conductive materials only,
- high power consumption, and
- difficult to remove internal burrs.

3.23.7.4 Applications

- ECDe can be used to deburr gears, spline shafts, milled components, drilled holes, and punched blanks.
- The process is particularly efficient for hydraulic system components such as spools and sleeves of fluid distributors.

3.23.8 Surface Finish in Various Electrochemical Processes

3.23.8.1 Surface Finish in EP

Generally, EP process produces deposition with excellent surface finish in the range of 20–100 nm and shine on the workpiece surface by using controlled EP parameters. Surface finish in EP process depends on the distribution of deposition, leveling, and density of the deposition. Improper and less dense deposition may lead to poor surface finish and high porosity in the deposition. Various additives and levelers in addition to the commonly used EP process parameters (i.e., DC power supply and its related parameters and electrolyte and its related parameters) are used to improve the surface quality of the deposition. Following measures can be used to improve surface finish of the deposition by the EP process:

- stringent control over electrolyte composition and concentration to get good throwing power and use of optimum value of electrolyte temperature and current density,
- minimizing or avoiding the impurities in the electrolyte solution,
- use of pulsed current to achieve clean environment in IEG and uniform deposition,
- use of additive agents such as brighteners, leveling agents, and wetting agents,
- minimizing the convex and concave irregularities in the deposition,
- using optimum value of IEG,
- using conducting or insulating screen and auxiliary anodes, and
- increasing polarization on the cathode.

3.23.8.2 Surface Finish in ECM

Generally ECM process produces very good surface finish but following factors adversely affect surface finish in ECM[40]:

1. selective dissolution,
2. sporadic breakdown of anodic film,
3. flow separation and formation of eddies, and
4. evolution of hydrogen gas.

3.23.8.2.1 Selective dissolution

Each pure material has a particular value of potential at which its electrolytic dissolution occurs. In case of an alloy and metal with impurities, each constituent has its own dissolution potential. In pure metals too, the dissolution potential at grain boundaries is different from those inside the grains. Entire anode surface is equipotential, while electrolyte potential varies across IEG. Consequently, constituents having higher dissolution potential will project away as compared to that of the constituents having lower dissolution potential so as to meet the electrolyte with a lower potential. This results in uneven workpiece surface as depicted in **Figure 14(a)**. Such unevenness can be reduced by increasing the anode potential as shown in **Figure 14(b)**.

3.23.8.2.2 Sporadic breakdown of anodic film

The potential difference between anodic workpiece surface and electrolyte in the region away from the machining area gradually falls and due to this those constituents of the workpiece material that have higher dissolution potentials stops dissolving gradually. This also results in rough workpiece surface. When only few phases remain active and dissolve, a concentration of the electric field results, since active phases occupy a small proportion of the anode surface. Field concentration causes these phases to dissolve very rapidly forming deep pits. Beyond a certain point potential drops to such a low value that no dissolution takes place.

3.23.8.2.3 Flow separation and formation of eddies

Presence of unevenness in the form of peaks and valleys on anode surface causes separation of electrolyte flow and eddy formation. Flow separation may be caused by an improper tool design and improper electrolyte flow path also. Eddy formation leads to higher concentration of metal ions which results in higher concentration over-potential. This causes localized variation in MRRs and consequently unevenness in the machine or finished surface.

3.23.8.2.4 Evolution of hydrogen gas

During the electrochemical dissolution, hydrogen gas is evolved at the cathode. Presence of hydrogen gas reduces electrical conductivity of the electrolyte along its direction of flow. This may result in variable MRR along the flow direction and may deteriorate surface finish of the workpiece.

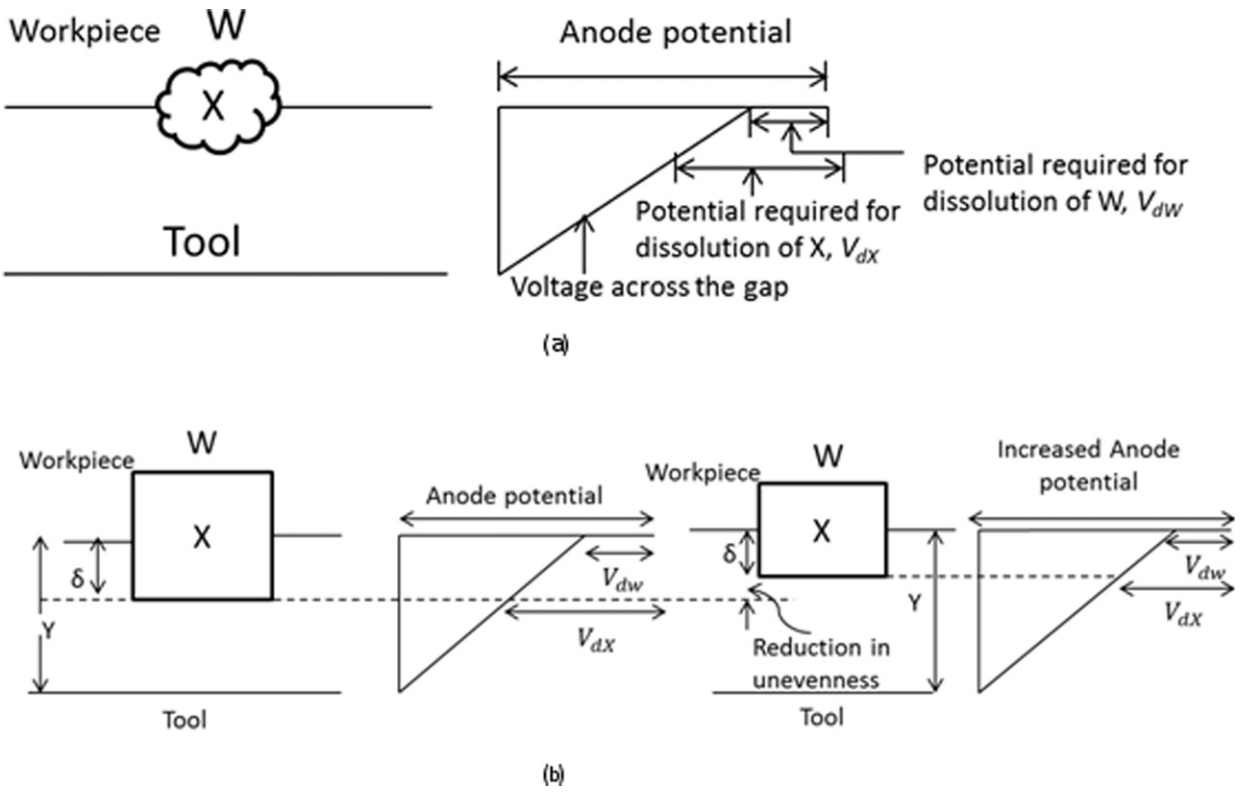


Figure 14 Schematic of (a) unevenness in workpiece surface due to difference in dissolution potential of different phases and (b) reduction in surface unevenness with increase in anode potential.[40]

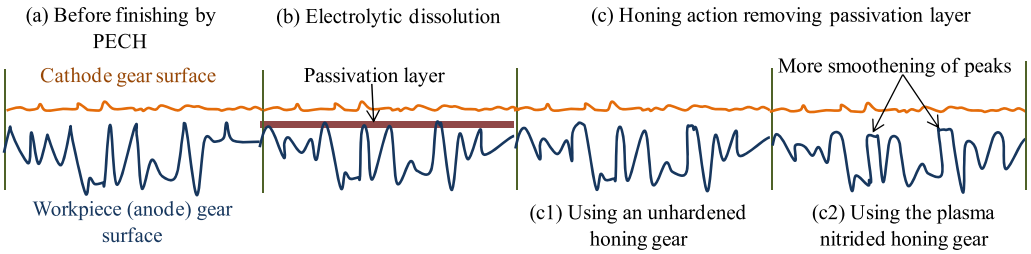


Figure 15 Sequence of finishing the bevel gear by PECH process; (a) before finishing by PECH; (b) after electrolytic dissolution and formation of metallic oxide passivation layer; (c1) after honing action using an unhardened honing gear; and (c2) after honing action using a hardened honing gear.[41]

3.23.8.3 Surface Finish in ECG

ECG process does not produce the typical shiny finish as produced by conventional mechanical grinding process. This is due to the fact that there is no smearing of the material which occurs in the conventional grinding process. Though ECG can achieve surface finish of 0.4 μm or better, it has a matte (dull) rather than a polished look due to the fact that almost 90–95% material removal is due to electrolytic dissolution of the workpiece material and only 5–10% is due to the grinding process. Consequently, above-mentioned causes responsible for poor surface finish in ECM are also applicable to ECG process. Other than ECM related parameters, surface finish in ECG is also affected by speed of grinding wheel and size of abrasive particles used on wheel. Tolerances that can be achieved using ECG depend greatly on the material being cut, the size and depth of cut, and ECG parameters being used. On small cuts, tolerances of 5 μm can be achieved with careful control of the grinding parameters.

3.23.8.4 Surface Finish ECH

ECH can provide the surface finish up to 50 nm using controlled and optimum values of parameters as mentioned in Table 8. In ECH process also, majority of the material removal (90–95%) is due to ECM action only and fraction of material (5–10%) is removed by mechanical honing. Thus factors that adversely affect surface finish in ECM also play major role determining the surface finish obtained ECH process.

Pathak *et al.*[41] have explained the process sequence and mechanism of gear finishing by PECH process as depicted in Figure 15. It can be seen from Figure 15 that during the electrolytic dissolution of the workpiece surface, a metallic oxide passivation layer is formed on its surface prohibiting

Table 9 Comparison of achievable surface finish and tolerance in different conventional and electrochemical processes

Type of process		*Surface finish (μm)*	*Tolerance (mm)*
Conventional machining and finishing processes	Drilling	0.8–12.5	0.03–0.4
	Grinding	0.025–6.3	0.003–0.05
	Boring	0.025–25.0	0.03–0.4
	Broaching	0.4–6.30	0.006–0.3
	Honing	0.025–1.6	0.005–0.04
	Turning	0.025–25.0	0.03–0.5
	Flame cutting	6.3–50.0	0.5–2.0
	Lapping	0.012–0.8	0.005–0.03
	Polishing	0.012–0.8	0.005–0.03
	Shaping	0.4–25.0	0.03–0.5
Electrochemical machining (ECM) and finishing processes	ECM	0.4–6.3	0.05–0.125
	Electroplating	0.05–3.0	–
	Electrochemical grinding	0.013–0.8	0.005–0.05
	Electrochemical polishing	0.1–1.0	0.025–0.025
	Shaped tube electrolytic machining	0.25–6.3	0.005–0.085
	Electrochemical deburring	0.02–1.6	0.005–0.05
	Electrochemical honing	50 nm–2.0	±0.002
	Electrochemical milling frontal	0.01–6.3	0.005–0.5
	Electrochemical milling (side wall)	0.4–15.0	0.025–0.5

its further electrolytic dissolution. Use of an unhardened honing gear (hardness similar to workpiece gear) in the PECH process removes a very small amount of material from some of the highest peaks on the workpiece surface while removing the passivation layer. Whereas, use of a hardened honing gear (30% more harder than workpiece gear) removes material from almost all the peaks on the workpiece surface while scrubbing the passivation layer. This leads to comparatively more reduction in maximum surface roughness which also helps in subsequent electrolytic dissolution to remove some material even from the valley thus giving better and uniform surface finish. They have concluded that honing tool can also participate in material removal process although it must be optimized according to need and system design.

3.23.9 Summary

Surface finish and geometric tolerance of the engineering components plays a vital role in determining their service life, operating performance, and surface integrity. Electrochemical processing of material is found to be superior to the conventional processes due to their ability to machine complex shaped components, machining the harder and tougher materials, excellent surface finish and geometrical accuracy, usefulness in fabrication of miniature components, ease of operation, and higher MRR. **Table 9** presents a comparative analysis of surface finish and tolerance for different conventional processes and electrochemical processes. It can be concluded from this table that electrochemical processes can be used for producing accurate geometry and excellent surface finish.

See also: 3.15 Electroless Plating as Surface Finishing in Electronic Packaging

References

1. Thompson, M. D. *Applied Electrochemistry*; The Macmillan Company: New York, NY, 1914.
2. Jernstedt, G. W. Bright Alloy Plating. U.S. Patent 2530, 697, 1950.
3. Jernstedt, G. W. Plating. Canadian Patent 450, 865, 1948.
4. Schwartz, M. Deposition from Aqueous Solutions: An Overview. In *Deposition Techniques for Films and Coatings*, 2nd ed.; Bunshah, R. F., Ed.; Noyes Publications: Park Ridge, NJ, 1994; pp. 480–590.
5. Dossenbach, O. Current Distribution in Pulse Plating. In *Theory and Practice of Pulse Plating*; Puippe, J.-C., Leaman, F., Eds.; American Electroplaters and Surface Finishing Society: Orlando, FL, 1986; pp. 73–92.
6. Tian, L.; Xu, J.; Xiao, S. The Influence of pH and Bath Composition on the Properties of Ni–Co Coatings Synthesized by Electrodeposition. *Vacuum* **2011**, *86* (1), 27–33.
7. Vetter, K. J. *Electrochemical Kinetics*; Academic Press: NY, New York, 1967; p. 282.
8. Tailor, P. B.; Agrawal, A.; Joshi, S. S. Evolution of Electrochemical Finishing Processes Through Cross Innovations and Modeling. *Int. J. Mach. Tools Manuf.* **2013**, *66*, 15–36.
9. DiBari, G. A. Nickel Plating. In *ASM Handbook-Surface Engineering*, Vol. 5; Reidenbach, F., Eds.; ASM International: Materials Park, OH, 1994, pp. 201–212.
10. Petrocelli, J. V.; Hospadaruk, V.; Di Bari, G. The Electrochemistry of Copper, Nickel and Chromium in the Corrodkote and CASS Test Electrolytes. *Plating* **1962**, *49* (1), 50–59.
11. Fischer, H. Electrodeposition. *Surf. Treat.* **1972**, *73* (1), 239–319.
12. Bockris, J. O'M.; Razumney, G. A. *Fundamental Aspects of Electrocrystallization*; Plenum Press: New York, NY, 1967.
13. Read, H. J. The Effects of Addition Agents on Physical and Mechanical Properties of Electrodeposits. *Plating* **1962**, *49* (6), 602–606.
14. Yoshihara, S.; Ueno, M.; Nagae, Y.; Fujishima, A. Effect of Brightener on Copper Plating: In situ Investigation by the PAS Technique. *J. Electroanal. Chem. Interfacial Electrochem.* **1988**, *243* (2), 475–479.
15. Raub, E.; Müller, K. *Fundamentals of Metal Deposition*; Elsevier: London, 1967; pp. 105–135.
16. Di Bari, G. A. Corrosion of Decorative Electroplated Nickel Chromium Coatings on Steel, Zinc, Aluminum and Plastics. *Met. Finish.* **1977**, *75*, 17–24.
17. Saw, R. L. Toward Protective Decorative Chromium Plating. *Plating* **1961**, *48*, 1310.
18. Jain, V. K. *Advanced Machining Processes*; Allied Publishers Pvt. Ltd: New Delhi, 2002.
19. McGeough, J. *Theory of Electrochemical Machining*; Chapman and Hall Inc.: London, 1974.

20. Wilson, J. F. *Practice and Theory of Electrochemical Machining*; Wiley-Inter Science: New York, NY, 1971.
21. Pathak, S.; Jain, N. K.; Palani, I. A. Improving Surface Quality of Bevel Gears by Pulsed-ECH Process. In *DAAAM International Scientific Book*; Katalinic, B., Tekic, Z., Eds.; DAAAM International: Vienna, 2014; pp. 221–238 (Chapter 19).
22. Bennedict, G. F. *Nontraditional Manufacturing Processes*; Marcel Dekker Inc.: New York, NY, 1987.
23. Groover, M. P. *Fundamentals of Modern Manufacturing*; John-Wiley & Sons: New York, NY, 2000.
24. Datta, M. Anodic Dissolution of Metals at High Rates. *IBM J. Res. Dev.* **1993**, *37* (2), 207–226.
25. Datta, M.; Landolt, D. Fundamentals Aspects and Applications of Electrochemical Micro Fabrication. *Electrochim. Acta* **2000**, *45* (15–16), 2535–2558.
26. Rajurkar, K. P.; Levy, G.; Malshe, A.; *et al.* Micro and Nano Machining by Electro-Physical and Chemical Processes. *Ann. CIRP* **2006**, *55* (2), 643–666.
27. Datta, M. Micro Fabrication by Electrochemical Metal Removal. *IBM J. Res. Dev.* **1998**, *42* (5), 655–670.
28. Rajurkar, K. P.; Zhu, D.; McGeough, J. A.; Kozak, J.; Silva, A. D. New Development in Electrochemical Machining. *Ann. of CIRP* **1999**, *48* (2), 567–579.
29. Kozak, J.; Rajurkar, K. P.; Makkar, Y. Selected Problems of Micro-Electrochemical Machining. *J. Mater. Process. Technol.* **2004**, *149* (1–3), 426–431.
30. Rajurkar, K. P.; Sundaram, M. M.; Malshe, A. Review of Electrochemical and Electrodischarge Machining. *Procedia CIRP* **2013**, *6*, 13–26.
31. Zabroski, S.; Lupak, M.; Poros, D. Wear of Cathode in Electrochemical Grinding of Hardly Machined Materials. *J. Mater. Process. Technol.* **2004**, *149* (1), 414–418.
32. Qu, N. S.; Zhang, Q. L.; Fang, X. L.; Ye, E. K.; Zhu, D. Experimental Investigation on Electrochemical Grinding of Inconel 718. *Procedia CIRP* **2015**, *35*, 16–19.
33. Jain, N. K.; Naik, L. R.; Dubey, A. K.; Shan, H. S. State-of-Art-Review of Electrochemical Honing of Internal Cylinders and Gears. *Proc. IMechE Part B: J. Eng. Manuf.* **2009**, *223*, 665–681.
34. Pathak, S.; Jain, N. K.; Palani, I. A. On Use of Pulsed Electrochemical Honing to Improve Micro-Geometry of Bevel Gears. *Mater. Manuf. Process.* **2014**, *29* (11–12), 1461–1469.
35. Naik, L. R.; Jain, N. K.; Sharma, A. K. Investigation on Precision Finishing of Spur Gears by Electrochemical Honing, In *Proceedings of 2nd International and 23rd AIMTDR Conference*, IIT Madras, India; Shunmugam, M.S., Babu, N.R., Ed., 2008; pp. 509–514.
36. Misra, J. P.; Jain, N. K.; Jain, P. K. Investigations on Precision Finishing of Helical Gears by Electro Chemical Honing (ECH) process. *Proc. IMechE, Part B: J. Eng. Manuf.* **2010**, *224* (12), 1817–1830.
37. Shaikh, J. H.; Jain, N. K.; Venkatesh, V. C. Precision Finishing of Bevel Gears by Electrochemical Honing. *Mater. Manuf. Process.* **2013**, *28*, 1117–1123.
38. Pathak, S.; Jain, N. K.; Palani, I. A. Process Performance Comparison of ECH and PECH for Quality Enhancement of Bevel Gears. *Mater. Manuf. Process.* **2015**, *30* (7), 836–841.
39. Hofy, H. E. *Advanced Machining Processes: Non-Traditional and Hybrid Machining Processes*; McGraw Hill Inc.: New York, NY, 2005.
40. Ghosh, A.; Mallik, A. K. *Manufacturing Science*; Wiley Publication: New York, NY, 2001.
41. Pathak, S.; Jain, N. K.; Palani, I. A. Effect of Honing Gear Hardness on Surface Quality and Micro-geometry Improvement of Straight Bevel Gears in PECH Process. *Int. J. Adv. Manuf. Technol.* **2015**, doi:10.1007/s00170–015–7596-y.

Index

Note
This index is in letter-by-letter order, whereby hyphens and spaces within index headings are ignored in the alphabetization, and it is arranged in set-out style, with a maximum of three levels of heading.

Cross-reference terms in italics are general cross-references, or refer to subentry terms within the main entry (the main entry is not repeated to save space).

Location references refer to the volume number, in bold, followed by the page number.

Major discussion of a subject is indicated by bold page numbers; page numbers suffixed by '*F*' and '*T*' refer to figures and tables, respectively.

A

AA *see* Aluminum Association (AA)
AA sample *see* artificially aged (AA) sample
AA6061 alloy **2**:357
ab initio methods **3**:86
ABAQUS **1**:354, **3**:100–101, **3**:101, **3**:162, **3**:163–164, **3**:164
Abbe Criterion **3**:244–245
abrasion **1**:77
  resistance **3**:156
abrasion resistant high-alloy white irons **2**:276–279
  heat treatment
    of high-chromium white irons **2**:280–281
    of nickel–chromium white irons **2**:277–279
abrasive belt grinding **3**:194
abrasive flow machining (AFM) **1**:98, **1**:116*F*
  advantages **1**:115–116
  applications **1**:116–117
  gear finishing by **1**:115
  limitations **1**:116
  machines **1**:113
    components of **1**:113–115
  parameters of **1**:115
  types **1**:112
    one-way AFM **1**:112, **1**:114*F*
    orbital AFM process **1**:113, **1**:115*F*
    two-way AFM **1**:112–113, **1**:114*F*
  working principle of **1**:112
abrasive fluidized bed (AFB) **3**:216
abrasive jet machine (AJM) **1**:178–180
abrasive material **1**:98–99
abrasive waterjet machining system **1**:157–158
abrasive-assisted wire **1**:249, **1**:249*F*
ABS **1**:443–444
AC *see* alternating current (AC)
acceptance test on fasteners **2**:307
AC-HVAF *see* assisted combustion high velocity air fuel (AC-HVAF)
acoustic emission (AE) **1**:6
acrylate photopolymers **3**:118, **3**:118–119
active compliance toolhead **1**:134, **1**:139, **1**:140*F*, **1**:144
adaptive neuro-fuzzy inference system (ANFIS) models **1**:198, **1**:233–234, **1**:253–258, **1**:254*T*
  ANFIS-based model **1**:233
  development **1**:253–258
  results and discussion **1**:258–259
    electrical parameters effect on WLT **1**:259
    wire electrode parameters effect on WLT **1**:260–262
    workpiece parameters effect on WLT **1**:262
  verification **1**:258
adding and altering methods **3**:256–257*T*
additive agents **3**:376
additive manufacturing (AM) **3**:111
  stereolithography (SLA) **3**:111–112
  selective laser sintering (SLS) **3**:112
additive process for miniature gear manufacturing **1**:511–513
  die casting **1**:514
  injection compression molding (ICM) **1**:518–519
  lithography, electroforming and molding **1**:521–522
  metal injection molding (MIM) **1**:516–518
  micro-powder injection molding (μ-PIM) **1**:519–521
  powder metallurgy (P/M) process **1**:511–513
adhesion **1**:65–66, **1**:77, **3**:306–307, **3**:311
  disruption **3**:306–307
  physical and chemical reasons **3**:307*F*
  resistance **3**:306–307
adhesion strength of coating **3**:51–52
adhesion testing for coatings **3**:51–52
ADI *see* austempered ductile iron (ADI)
advanced high-strength steels (AHSS) **2**:180, **3**:185, **3**:185*F*, **3**:186*F*, **3**:187*F*
AE *see* acoustic emission (AE); algorithm effort (AE); assisting electrode (AE)
aerated liquid atomization **3**:152
aerospace materials **2**:424
AF1410 steel
  heat treatment **2**:185–186, **2**:185*F*
  high-temperature of AerMet 100 steel **2**:187*F*
  microstructures of AerMet 100 steel **2**:186*F*
AFB *see* abrasive fluidized bed (AFB)
AFM *see* abrasive flow machining (AFM); atomic force microscope (AFM); atomic force microscopy (AFM)
Ag electroless process **3**:7
AG40L Sodick electrical discharge machine **1**:302*F*
age hardening **2**:9, **2**:353–354
age-hardening treatment **2**:32–34
aging **2**:181–182, **2**:185–186, **2**:204, **2**:207, **2**:353–356, **2**:373–374, **2**:374–375, **2**:377–378, **2**:377*F*, **2**:378*F*, **2**:388, **2**:389
  artificial **2**:356–357, **2**:357*F*
  determination **2**:388–389
  factors affecting **2**:390
    composition of alloy **2**:390
    plastic deformation **2**:390
    solutionizing treatment system **2**:390
    ultrasonic **2**:390
  natural **2**:354–356, **2**:355*F*, **2**:356*F*
  operation **2**:390
  parameters **2**:389, **2**:389*F*
  pre-conditions and property requirements **2**:388
  quality control **2**:389–390
    key points of operation **2**:390
    properties of aluminum alloys **2**:390
  stress aging **2**:389
  temperature **2**:389, **2**:390
  time **2**:389
  treatment
    effect **2**:328–333
    processes **2**:387–388
AGMA standard *see* American Gear Manufacturers Association (AGMA) standard
AHSS *see* advanced high-strength steels (AHSS)
air assist atomizer **3**:152, **3**:152*F*
air blast atomizer **3**:152
air cylinder pressure control modeling **1**:137
air patenting **2**:22
air plasma spray (APS) **3**:214
  YSZ coatings **3**:198

air spindle speed control modeling **1**:137–138
aircraft coatings **3**:150
air-hardening, medium-alloy cold-work tool steels **2**:217–218*T*, **2**:219–221*T*
AISI *see* American Iron and Steel Institute (AISI)
AISI 304 steel **1**:352
AISI 1050 carbon steel **1**:233–234, **1**:251*T*, **1**:252, **1**:261*F*
AISI 4140 steel **2**:188, **2**:189*F*
AISI D2 tool steel **2**:427
AISI H13 tool steel **3**:159–160, **3**:164, **3**:166–167, **3**:170–171, **3**:175–176, **3**:176
AISI tool steels, chemical composition of **2**:217–218*T*
AJM *see* abrasive jet machine (AJM)
Al–4Cu alloy **2**:378–380, **2**:379*F*
algorithm effort (AE) **1**:87
alkali niobates **3**:353, **3**:354–355
alkaline soak cleaning **3**:222
Al–Li alloy system **2**:358
alloy carbides **2**:228
alloy steels **2**:11
  carburization of *see* carburization of alloy steels
  for gear manufacturing **1**:97
alloy(s) **2**:357, **3**:368, **3**:369*T*
  5456-H39 **2**:338–339
  composition **2**:266, **2**:306, **2**:390, **3**:86–87, **3**:86
  layers **3**:25–26
alloying
  effects on annealing soaking time **2**:251–252, **2**:252*T*
  elements effect on hardenability **2**:65–66, **2**:65*F*, **2**:66*F*, **2**:67*T*
  system of Ti alloys **2**:290
    α stabilizers **2**:290
    β stabilizers **2**:290
    neutral elements **2**:290
alloying elements **2**:11, **2**:11–12
  classification **2**:11–12
  effect of **2**:12–15
    individual alloying elements in summarized form **2**:14–15
    on TTT and CCT curves **2**:15–20
  on eutectoid temperature of steel **2**:13*F*
  on hardness of steel **2**:12*F*
all-purpose aluminum alloys **2**:374, **2**:374*F*
α alloys *see* α-Ti alloys
alpha brass, stress corrosion cracking in **2**:408*F*
α phase **2**:290
  formation of equilibrium **2**:306
  wires **1**:243, **1**:243*F*
α stabilizers **2**:290
alpha–beta aluminum bronzes **2**:409–410
α/β alloys *see* α/β-Ti alloys
α/β-Ti alloys **1**:243–244, **2**:291–292
  heat treatment **2**:301–305
    annealing **2**:305
    change of microstructures during thermochemical process **2**:305*F*
    decomposition of metastable β **2**:306
    normalizing **2**:305
    quenching **2**:305–306
    tempering **2**:306
    thermal treatment effect **2**:306
α-Case **2**:125–126
α-Ti alloys **2**:290–291
  see also β-Ti alloys
  fully α-Ti alloys **2**:290–291
  maximum stress and steady-state stress **2**:297*F*
  near α-Ti alloys **2**:291
alternating current (AC) **3**:361–362
alternative rate cooling **2**:387
alumina **1**:4, **1**:12–13, **3**:72, **3**:74, **3**:307–308, **3**:371
  tiles **3**:72–73, **3**:78–81
    cross-section laser-treated workpiece **3**:80*F*
    laser-treated surfaces **3**:79*F*
    microhardness at work piece **3**:81*T*
    optical photograph **3**:78*F*
    x-ray diffractogram **3**:80*F*
aluminum **1**:281, **2**:14–15, **2**:337
  for gear manufacturing **1**:97
  heat treatment techniques
    digital modeling **2**:391
    new short T6 heat treatment **2**:390–391
    novel multi-stage solutionizing **2**:392–393
    thermo-mechanical treatment **2**:391–392
    thermo-mechanical treatment for non-ferrous alloy **2**:392, **2**:392*F*
    water–air spray cooling **2**:391, **2**:391*F*
aluminum alloys **2**:337, **2**:340–341, **2**:373, **2**:390
  see also Co–Ni alloys
  7050–T7451 aluminum alloy **2**:173
  designation system **2**:337–338, **2**:338*T*
  heat treatment **2**:341–347, **2**:373
    aluminum matrix composites **2**:395–396, **2**:396*F*
    multi-heat treatment on aluminum **2**:393–395
    novel techniques **2**:390–391
    purpose and principles **2**:374
    tempers nomenclature **2**:382
  inspection and quality assurance **2**:368–369
  processes of aging treatment **2**:387–388
  progress in heat treatment **2**:390–391
  properties
    composition of alloy **2**:390
    plastic deformation **2**:390
    solutionizing treatment system **2**:390
    temperature of aging **2**:390
    ultrasonic **2**:390
  technological characteristics of solution treatment **2**:383–384
  temper designations **2**:338–340
Aluminum Association (AA) **2**:337–338
aluminum bronzes, heat treatment of **2**:409–410
aluminum casting die **2**:244
aluminum castings **3**:42
aluminum extrusion die **3**:158
aluminum nitride **2**:93, **2**:108–109, **2**:113
aluminum oxide *see* alumina
aluminum/PMMA mold **1**:448*F*
aluminum–brass wire **1**:240, **1**:240*F*
aluminum–phosphate **3**:199–200
AM *see* additive manufacturing (AM)
American Gear Manufacturers Association (AGMA) standard **1**:507
American Iron and Steel Institute (AISI) **2**:61–62, **2**:215
American National Standards Institute (ANSI) **2**:337–338
  ANSI 35.1 standard **2**:338
ammonia dissociation **2**:114
amorphous polysaccharide **1**:205
analysis of variance (ANOVA) **1**:13–14, **1**:29, **1**:182–183, **1**:306–308
  analysis **1**:19, **1**:21, **1**:22
  for EWR **1**:308*T*
  for MRR **1**:307*T*
ANFIS models *see* adaptive neuro-fuzzy inference system (ANFIS) models
animal fiber **1**:208
ANN *see* artificial neural network (ANN)
annealing **2**:2, **2**:9, **2**:20, **2**:181, **2**:188, **2**:190, **2**:281, **2**:305, **2**:368, **2**:368*T*
  annealing soaking time, alloying effects on **2**:251–252, **2**:252*T*
  diffusion **2**:24
  of ductile irons **2**:262, **2**:266*T*
  full **2**:20
  of gray irons **2**:251
    effects of alloying on annealing soaking time **2**:251–252
    types of annealing **2**:251
  homogenization **2**:24
  incomplete **2**:22
  intercritical **2**:22–23, **2**:23
  isothermal **2**:20–22
    patenting **2**:21–22
  recrystallization **2**:24–27
  spheroidizing **2**:23–24
  subcritical **2**:27
  treatments **2**:300–301
anode **3**:361
anodic coatings **3**:199
anodizing **3**:42
anomalous behavior **3**:86, **3**:86–87, **3**:88, **3**:89
ANOVA *see* analysis of variance (ANOVA)
ANSI *see* American National Standards Institute (ANSI)
ANSYS CFX flow model **1**:450–451, **1**:452, **1**:457, **1**:457–458
Ansys package **2**:167
anti-galling **3**:323
antiphase boundary (APB) strengthening **2**:418–419
APB strengthening *see* antiphase boundary (APB) strengthening
applied Wilhelmy plate methodology **3**:279*F*
APS *see* air plasma spray (APS)
aqueous solutions **2**:54, **3**:199–200
arc spray coatings **3**:43

arc spraying (AS) **3**:207
aromatics-based binder system **1**:476
array micro-holes, continuous machining process of **1**:296–298
Arruda–Boyce constitutive model **1**:147–148, **1**:148
ARs *see* aspect ratios (ARs)
artificial aging **2**:356–357, **2**:357*F*
artificial neural network (ANN) **1**:20, **1**:195, **1**:484
artificially aged (AA) sample **2**:356
AS *see* arc spraying (AS)
'as hot-rolled' sample **1**:18–19
asbestos **1**:209
as-cast matrix **2**:260
aspect ratios (ARs) **1**:173
asperities *see* local maxima
as-quenched castings **2**:264
assisted combustion high velocity air fuel (AC-HVAF) **3**:212–213
assisting electrode (AE) **1**:334
as-sprayed coating **3**:192
as-sprayed surface finish **3**:213
  automobile industry **3**:213
  power generation industry **3**:213
  surface roughness of bondcoats in TBCs **3**:213–215
ASTM A681-94 Standard **2**:215
ASTM C1327-99 standard **3**:74
ASTM D3359-09e2 **3**:155–156
ASTM D7027-05 standard **3**:75
atomic force microscope (AFM) **3**:142, **3**:144–145
  micrographs **3**:142–143
    surface topography **3**:142–143
    texture profile micrographs **3**:143–144
atomic force microscopy (AFM) **1**:421, **3**:87, **3**:90–94, **3**:91*F*
  surface topography **1**:424*F*, **3**:244, **3**:245*F*, **3**:247, **3**:247*F*, **3**:261–262, **3**:282–283, **3**:288
atomic hydrogen mechanism **3**:223
atomization **3**:150–151
  aerated liquid **3**:152
  centrifugal **3**:152
  ultrasonic **3**:153
atomizers
  droplet formation and fate **3**:150
    basic mechanism **3**:150
    coating formation on the surface **3**:151
    formation of droplets **3**:150–151
    spray air contact **3**:151
  and finishing properties **3**:153–156
  types and requirements of **3**:151–153
atoms, diffusion of **2**:400
austempered ductile iron (ADI) **2**:264
austempering **2**:44–45, **2**:253–254, **2**:266–267
  of ductile irons **2**:264–266
    metallurgical variables on properties of ADI **2**:264–266
    two-step austempering heat treatment **2**:268–269
  of gray iron **2**:253–255, **2**:254*F*, **2**:255*F*
    case studies **2**:255, **2**:255*F*
  heat treatment **3**:198
austenite **2**:4–5, **2**:92–93, **3**:336
  characteristic features of **2**:92–93
  effect of austenite composition **2**:93
  excessive retained **2**:93
    effect on properties **2**:93
    major cause **2**:93–94
  reducing retained **2**:94
austenite grain size **2**:93, **2**:94, **2**:95*F*, **2**:96*F*, **2**:97, **2**:97*F*, **2**:234*F*
austenite stabilizer **2**:5
austenitic grain growth **2**:9*F*
austenitic graphitic irons **2**:269–271
  case studies on **2**:272–273
  effects of composition **2**:270–271
  heat treatment **2**:271
austenitic stainless steel **2**:200–204
austenitization **2**:10–11, **2**:10*F*, **2**:154, **2**:154*F*, **2**:156, **2**:162, **2**:185, **2**:192, **2**:193, **2**:195, **2**:196, **2**:200, **2**:205, **2**:224–226, **2**:233, **2**:266
austenitizing temperature **2**:10, **2**:63–64
austenitizing time **2**:50, **2**:63–64, **2**:252
Australian Gear standard **1**:507
autoclave moulding **1**:220
automobile industry **3**:213
auxiliary equipment and application **1**:474*T*
auxiliary mode **1**:41
average method **1**:132, **1**:132*T*, **1**:133
average roughness **1**:15
avian fiber **1**:208
axial stiffness **1**:147
axial/conventional rotary gear shaving **1**:107, **1**:107*F*
Axioplan 2 imaging optical microscope **3**:160
axisymmetric 2D model **1**:195
axisymmetric 3D thermo-physical model **1**:195–196
AZ91 alloy **3**:311–312, **3**:313*F*
AZ91D magnesium **3**:320

B

bainite formation, in steels **2**:42–43
  mechanism of **2**:42–43
bainite reaction curve **2**:15
bainitic heat treatment of malleable irons **2**:258
bainitic transformation **2**:7–8
bake hardening **2**:209, **2**:210–211
ball burnish machining (BEDM) **1**:398, **1**:399*F*
barium strontium titanate (BST) **3**:354
barium titanate (BT) **3**:352–353, **3**:353, **3**:353–354
barreling **1**:355
barrier coating **3**:27
batch hot-dip galvanizing processes **3**:181–183, **3**:182*F*
batch production mode of mass micro-holes **1**:286*F*
Battenfeld Microsystem 50 **1**:443
BCC *see* body centered cubic (BCC)
bcc crystal structure *see* body-centered cubic (bcc) crystal structure
BD *see* bore deviation (BD)
BE/PM *see* blended elemental powder metallurgy (BE/PM)
bearing steel **2**:196–197, **2**:197*F*, **2**:197*T*
  comparison of ELID performance with finishing processes for **1**:379*F*
  cylindrical ELID I grinding, for **1**:378*F*
  effect of finishing operation on **1**:378*T*
BEDG *see* block electrical discharge grinding (BEDG)
BEDM *see* ball burnish machining (BEDM)
benzoic acid **3**:286
Bertsch system **3**:113–114, **3**:114
beryllium bronzes, heat treatment of **2**:410–413
beryllium–copper alloys **2**:415
β alloys *see* β-Ti alloys
β phase **2**:290
  separation **2**:306
beta phase wires **1**:243–244
  cross-section of wire **1**:244*F*
  different processing steps **1**:245*F*
  wires with different coating thickness **1**:245*F*
  X and D types of wire electrodes **1**:244*F*
β stabilizers **2**:290
  ω phase **2**:290
beta–gamma phases **1**:243–244
β-quenching **2**:35
β-Ti alloys **2**:292
  see also α-Ti alloys
  composition, category, transus temperature, source, and year of introduction **2**:314*T*
  heat treatment **2**:311–317
    deformation in $\alpha + \beta$-phase field **2**:317–321
    deformation in β-phase field **2**:313–317
    deformation parameters **2**:316*T*
    grain coarsening in β-phase field **2**:321*F*
    sequence of events during restoration process **2**:320*F*
    SMAs **2**:321–322
    variation in β-transus temperature **2**:313*F*
  pseudo-binary β-isomorphous phase diagram **2**:292*F*
  stabilizers **2**:293*F*
  steady-state stress **2**:296*F*
β-transus temperature **2**:312
$(Bi_{0.5}Na_{0.5})TiO_3$ **3**:355–356
$(Bi_{0.5}Na_{0.5})TiO_3$-$BaTiO_3$ (BNT-BT) **3**:355
bicomponent injection **1**:467
'billet' **1**:524
binary NiTi
  fabrication of **3**:340–342
  spark plasma sintering of **3**:340–342
biodegradability **1**:204
biomedical microdevices **3**:121
biomimetics **3**:294
bipolar pulse **3**:361–362
blackheart malleable iron **2**:257
blended elemental powder metallurgy (BE/PM) **2**:304
blistering, in surface coatings **3**:154
blob analyses **3**:273*F*, **3**:274

block electrical discharge grinding (BEDG) **1**:282
BMC *see* bulk moulding compound (BMC)
BNT-BT *see* $(Bi_{0.5}Na_{0.5})TiO_3$-$BaTiO_3$ (BNT-BT)
body centered cubic (BCC) **2**:5
body-centered cubic (bcc) crystal structure **2**:112, **2**:290
Boltzmann constant **1**:147–148
bonnet polishing **1**:160
bore **1**:26
bore deviation (BD) **1**:39
boring process **1**:26, **1**:41–42
  application in building of tunnel **1**:39–41
  boring bar **1**:26–27, **1**:27
    dynamic properties **1**:34*T*
    with passive damper and accelerometer **1**:30*F*
  cast iron boring machining operation **1**:32*T*
  cutting force measured at Smart Tool **1**:38*F*
  disk cutters **1**:43*F*
  dynamic simulation **1**:34*F*
  experimental and simulated cutting force values **1**:36*F*
  experimental conditions **1**:30*T*, **1**:31*T*
  experimental results **1**:30*T*, **1**:31*T*
  internal turning operation **1**:27
  model parameters **1**:37*T*
  monitoring variables **1**:37*T*
  operations **1**:26, **1**:27–39, **1**:27*F*, **1**:43–44
  surface roughness with passive damper **1**:40*T*
  test trails **1**:29*T*
boron hardenability effect **2**:67–69, **2**:68*F*
bound-abrasive CMP **1**:162
bound-abrasive polishing **1**:162
Bragg's law **1**:415
braiding **1**:218
brass **1**:277
  heat treatment of **2**:406–408
  wire **1**:239–240, **1**:240*F*
    electrode **1**:257*T*, **1**:259, **1**:260*F*, **1**:261*F*
Brinell hardness number (HB) **1**:131–132
Brinell test model **1**:131–132
brines **2**:54
British Standards Institute (BSI) standard **1**:507
bronzes, heat treatment of **2**:408–409
  aluminum bronzes **2**:409–410
  beryllium bronzes **2**:410–413
  silicon bronze **2**:413–414
  tin bronzes **2**:409
BSI standard *see* British Standards Institute (BSI) standard
BST *see* barium strontium titanate (BST)
BT *see* barium titanate (BT)
BUE *see* builtup formation (BUE)
BUEHLER Wirtz Vickers test apparatus **3**:160
buffing process **3**:194
builtup formation (BUE) **1**:1, **1**:11–12, **3**:230, **3**:237
bulk micromachining **1**:329–330
bulk moulding compound (BMC) **1**:219
burnishing **3**:194, **3**:308
burr **1**:139–140
  geometry **1**:141*T*
  reduction **1**:144*F*

C

CA *see* contact angle (CA)
Ca_{10} $(PO_4)_6$ $(OH)_2$ *see* hydroxyapatite (HAp)
CACO technique *see* continuous ant colony optimization (CACO) technique
CAD *see* computer aided design (CAD)
cadmium coatings **3**:49
CAE applications *see* computer aided engineering (CAE) applications
CAH *see* contact angle hysteresis (CAH)
calcium stearate **3**:285
CAM *see* coverage area map (CAM)
capacitor **1**:274, **1**:279
capillary rheometer **1**:477
capsule free-HIP (CF-HIP) **3**:339
carbide tools **3**:230–231
carbon **2**:265, **2**:269, **2**:271
  content hardenability effect **2**:64–65, **2**:64*F*
  content in matrix **2**:248–249
carbon fiber-reinforced PEEK (CF-PEEK) **3**:200
carbon nano tubes (CNTs) **3**:49
carbon steels **2**:222
carburization, methods of **2**:73–74
  gas carburization **2**:78
    advantages **2**:79
    atmospheric conditions for **2**:78–79
    carbon potential **2**:79
    carburizing process **2**:78
    carburizing reactions **2**:78
    carrier gases **2**:79
    disadvantages **2**:79
    safety measures for **2**:79–80
  liquid carburization **2**:76–77
    advantages **2**:77
    carburizing process, high temperature baths **2**:77
    carburizing process, low temperature baths **2**:76–77
    disadvantages **2**:77
    safety precautions **2**:77–78
  plasma carburizing **2**:80–81
    advantages **2**:81
    carburizing process **2**:80–81
    control of carbon supply and case depth **2**:81
  solid/pack carburization **2**:73–74
    advantages **2**:75–76
    carburizing process **2**:73–74
    chemical reactions **2**:74
    decarburization **2**:74–75
    disadvantages **2**:76
  vacuum carburizing **2**:80
    advantages **2**:80
    carburizing process **2**:80
    control of carbon supply and case depth **2**:80
    disadvantages **2**:80
carburization, problems during **2**:102–103
  cracking and exfoliation **2**:104
    prevention **2**:104
  distortion **2**:103–104
    drastic quenching **2**:104
    high temperature hardening **2**:104
    rehardening **2**:104
    release of internal stresses **2**:104
    uneven heating **2**:104
  grinding cracks **2**:105
    prevention **2**:105
  insufficient case depth **2**:103
    prevention **2**:103
  low hardness **2**:103
    decarburization **2**:103
    higher case depth **2**:103
    retained austenite **2**:103
  nonuniform carburizing **2**:103
    prevention **2**:103
  soft spots **2**:104
    prevention **2**:104
  sooting **2**:103
    prevention **2**:103
  uneven case depth **2**:103
    prevention **2**:103
carburization, theory of **2**:81–82
  controlling factors of carburization **2**:82–85
    flow of carbon from the supply source **2**:85–86
    flow of carbon in iron **2**:82–85
  equilibrium state for chemical reaction **2**:82
  Fick's laws of diffusion **2**:81–82
carburization of alloy steels **2**:94
  austenitic stainless steel, low temperature carburization of **2**:98–99
    activation **2**:99–100
    carburizing atmosphere **2**:101
    microstructure of low temperature carburized layer **2**:101
    processing temperature ranges **2**:100–101
  low alloy steels **2**:94
    chromium–nickel steel **2**:94
    molybdenum–nickel steel **2**:94–96
  microalloyed steels **2**:96–98
    niobium-microalloyed steel **2**:98
    vanadium-microalloyed steel **2**:97–98
  tool steels, carburization of **2**:101–102
    cold working tool steel **2**:102
    hot working tool steel **2**:101–102
    mold steel **2**:102
    shock resisting tool steel **2**:102
carburized components, processing sequence for **2**:105
carburized steels, microstructures of **2**:90–91
  austenite **2**:92–93
    characteristic features of **2**:92–93
    effect of austenite composition **2**:93
    excessive retained **2**:93
    reducing retained austenite **2**:94
  martensite **2**:90–91
    formation **2**:90–91
    morphologies **2**:91–92

tempering, effect of **2**:92
transition carbides, role of **2**:92
carburizing **2**:73, **2**:73*F*, **2**:204
diffusion of carbon in iron during **2**:84*F*
heat treatment after carburizing and properties of carburized parts **2**:86–87
direct quench technique **2**:89
double hardening **2**:87–89
heat treatment of gas-carburized steels **2**:90
quenchants for carburized steels **2**:89–90
single hardening with core refinement **2**:87, **2**:88*F*
single hardening without core refinement **2**:87, **2**:87*F*
subzero treatment **2**:90
packing of workpieces in a box for **2**:73*F*
carburizing agent **2**:79
Carreau model **1**:492
Carreau viscosity model **1**:445
Carreau–Yasuda viscosity model **1**:445–446
Case *see* diffusion zone
case depth
insufficient **2**:103
prevention **2**:103
uneven **2**:103
prevention **2**:103
Cassie state **3**:278
Cassie–Baxter states **3**:139–140, **3**:146–147
Cassie-impregnated state **3**:141
cast alloys **2**:340–341, **2**:341*T*, **2**:342*T*, **2**:344–345*T*, **2**:368
heat treatment scheme **2**:358–363, **2**:363*T*, **2**:364*F*, **2**:365–366*T*
cast and forged aluminum alloy parts, tempers for **2**:383, **2**:385*T*
cast irons **2**:436–437, **2**:247
see also gray irons; malleable irons
for gear manufacturing **1**:97
heat treatment **2**:248
matrix structures **2**:248*T*
types **2**:247–248
cast magnesium alloys **2**:36
cast steel, for gear manufacturing **1**:97
castability **2**:270
casting methods **3**:337
casting route **2**:289
Castro Macosko viscosity function **1**:445
cathode
gear **3**:373–374, **3**:373*F*, **3**:374*F*
sputtering **2**:114
cathodic coatings **3**:199
Cauchy–Green deformation tensor **1**:147–148
caul plate **1**:219
CBN *see* cubic boron nitride (CBN)
cBN–TiN-coated carbide tools **1**:63
CCD array *see* Charge–Coupled Device (CCD) array
CCD method *see* central composite design (CCD) method
CCGA *see* cooperative coevolutionary genetic algorithm (CCGA)
CCR *see* critical cooling rate (CCR)
CCT *see* continuous cooling transformation (CCT)
CCT *see* cooling transformation (CCT)
CCT diagram *see* classical time temperature cooling (CCT) diagram
CD's injection mold **2**:223*F*
cellulose **1**:205, **1**:205*F*
cemented carbides **1**:55
centering collar **1**:150*F*
central composite design (CCD) method **1**:225
centrifugal atomization **3**:152
ceramic coatings **3**:43, **3**:49
ceramic injection molding (CIM) **1**:467
ceramic matrix composites (CMC) **1**:173, **1**:212
ceramic(s) **2**:442, **3**:14
coatings **3**:196
composite tools **1**:8
ELID grinding for **1**:370–373
fibers **1**:209
tool materials **1**:55–56
cermets **1**:55, **2**:449, **3**:347
CFD *see* computational fluid dynamics (CFD)
CF-HIP *see* capsule free-HIP (CF-HIP)
CF-PEEK *see* carbon fiber-reinforced PEEK (CF-PEEK)
Charge–Coupled Device (CCD) array **1**:296, **3**:245–246
chatter vibration **1**:5
chemical and textural analyses **3**:87–88
chemical bed deposition **3**:294*F*
chemical etching **3**:308
material removal by **3**:59
chemical mechanical polishing (CMP) **1**:159–160, **1**:365
chemical vapor deposition (CVD) **1**:12–13, **1**:328, **3**:39, **3**:41, **3**:44*T*, **3**:121, **3**:141, **3**:199, **3**:200, **3**:210, **3**:230, **3**:231
CVD-SiC film **1**:378*F*
nitride coatings **2**:132
process **3**:232
chip formation **1**:60–61
chip load **1**:323
chipping, in surface coatings **3**:154
chopped fibers **1**:213
chopper gun **1**:220
chromate **3**:313–320
conversion coating, substrate, coating contents **3**:321–322*T*
non-chromic coatings, substrate, coating contents **3**:324*T*
chromate coatings **3**:42
chromated zinc **3**:313–320
chromium **2**:13–14, **2**:13*F*, **2**:14, **2**:124–125, **2**:271, **2**:277–278, **3**:184
carbides **1**:65
chromium–molybdenum steel **2**:192
chromium coppers **2**:414
chromium hot work tool steels **2**:217–218*T*
chromium nitride **2**:116
chromium plating electrolytes **3**:48
chromium–nickel steel, carburization of **2**:94
CIM *see* ceramic injection molding (CIM)
CIP process *see* cold isostatic pressing (CIP) process
classical time temperature cooling (CCT) diagram **2**:155
c-LBM *see* cover plate laser beam machining (c-LBM)
cleaning system **3**:372
closed die forging **1**:525
CLSM *see* confocal laser scanning microscopy (CLSM)
CMC *see* ceramic matrix composites (CMC)
CMM *see* computational micro-mechanics (CMM)
C-Mold software **1**:472–473
CMP *see* chemical mechanical polishing (CMP)
CNC *see* computer numerical control (CNC)
CNTs *see* carbon nano tubes (CNTs)
CO_2 laser **2**:138, **3**:74
Co-alloys **3**:195
coarse powder (INV1) feedstock **1**:476, **1**:476*F*
coated carbide
inserts **1**:10
tools **1**:48, **1**:50, **1**:56, **1**:59
coated EDM wires **1**:240–241
double-layer-coated wires **1**:241, **1**:242*F*
multilayer-coated wires **1**:241–243, **1**:242*F*, **1**:243*F*
single-layer-coated wires **1**:240–241, **1**:241*F*
coated wire electrode **1**:259–260, **1**:260*F*, **1**:261*F*
coating as a method of surface finishing **3**:45–46
miscellaneous surface finish applications **3**:49
biomedical applications **3**:50
conformal coatings **3**:49–50
electrical and magnetic properties **3**:50
hydrophobic coatings **3**:49
optical coatings **3**:50
rough coatings **3**:50
thermal coatings **3**:50
surface finishing facets of coating **3**:46
barrier protection **3**:47
cathodic protection **3**:47–48
generating smooth and lubricious surface **3**:49
improving esthetic appeal **3**:46
protection against corrosion **3**:46–47
resistance to wear **3**:48–49
coating for surface finish applications, selection of **3**:54
coating methods
advantages and limitations for **3**:44*T*
coating morphology and metallurgical changes **3**:101–102
single layer coating **3**:101–102
two layer coatings **3**:102–103
coating parameters and process optimization, influence of **3**:50–51
coating processes, types of **3**:39–40
conversion coatings **3**:42

coating processes, types of (*continued*)
anodizing **3**:42
chromate coatings **3**:42
phosphate coatings **3**:42
diffusion coatings **3**:42
electrochemical techniques **3**:40
electrodeposition **3**:40
electroless coatings **3**:40–41
galvanizing **3**:41
powder coatings **3**:41–42
thermal spraying **3**:42–43
electric arc spray **3**:43
flame spray **3**:43
high velocity oxy-fuel (HVOF) **3**:43
plasma spray **3**:43
vapor depositions **3**:41
chemical vapor deposition (CVD) **3**:41
physical vapor deposition (PVD) **3**:41
plasma enhanced CVD technique **3**:41
coating structures, existing design of **3**:43–45
duplex coatings **3**:45
graded coatings **3**:45
multicomponent coatings **3**:45
multilayered coatings **3**:45
sandwich coatings **3**:45
single-layer coatings **3**:45
superlattice coatings **3**:45
coating thickness **3**:51
coating(s) **3**:178, **3**:188, **3**:208–209, **3**:235, **3**:323
see also thermal barrier coatings (TBCs); thermal spray coating(s)
coating-diffusion method **3**:8
conversion **3**:311–320, **3**:314–319*T*
deposition process **3**:57
electro deposition **3**:330–332
element **3**:178
hot-dip galvanized **3**:184
metallic **3**:183
polyurethane **3**:325–327, **3**:327*T*
sample's surface preparation **3**:307
sol–gel **3**:327–330, **3**:329*T*
surface **3**:178
system **3**:328*F*
technology **1**:56
thickness **3**:181
cobalt **2**:14, **2**:206
cobalt-bonded tungsten carbides **2**:449–451
cocoa fiber composites **1**:225, **1**:225*T*
cocoa pod husk (CPH) **1**:204
fiber **1**:224–225
coconut oil **1**:2
coefficient of thermal expansion (CTE) **3**:57
coherence scanning interferometry (CSI) **3**:246, **3**:246*F*
coherency strains **2**:381
coil coatings **3**:150
coir fiber-reinforced composite **1**:212
cold chamber die casting process **1**:514
cold compression moldings **1**:219
cold forming **2**:405
cold isostatic pressing (CIP) process **1**:512
cold rolling effect **2**:326–328
cold spraying (CS) **3**:207
cold work tool steels **2**:216, **2**:222*F*
cold working tool steel, carburization of **2**:102
cold-worked (CW) samples **2**:327, **2**:328*F*, **2**:329
colloid accumulation and layer method **3**:293
colloidal gels **3**:328
colloidal micro- and nano-particles **3**:141
Colocasia esculenta **3**:295*F*
combination technology **1**:54–55
combined control system **1**:138–139
combustibility **1**:204
commercial purity titanium (CP Ti) **2**:131, **2**:290, **2**:291, **2**:294*F*
grade 2 flow curves **2**:293–294, **2**:295*F*, **2**:299*F*
heat treatment in **2**:292–293
Co–Mo interaction lends **2**:207
compact manufacturing system **1**:53–54
comparative evaluation **1**:117
compliant microelectrode array fabrication **1**:286–288
composite solid–liquid–air interface **3**:296–297
composite(s) **1**:206–207, **1**:207
advantages and merits **1**:207–208
membranes **3**:14
compound layer **1**:48, **1**:49, **1**:72–74, **2**:120–121
compression ratio (CR) **1**:470
compressive principal stress **1**:134
computational fluid dynamics (CFD) **1**:490
computational micro-mechanics (CMM) **3**:66
computed tomography (CT) **3**:261–262
X-ray based **3**:262
computer aided design (CAD) **3**:111, **3**:111–112
computer aided engineering (CAE) applications **1**:490
computer modeling applications **1**:490*F*
computer numerical control (CNC) **1**:27, **1**:51
controllable component **1**:232
machine **1**:527–529
computer simulation and molded part quality enhancement **1**:490–491
computer vision (CV) **3**:263, **3**:263*F*
basics of image acquisition for **3**:263–266
basics of image processing and analysis for **3**:267
surface evaluation methods with **3**:265*F*, **3**:267–273
2D Fast Fourier Transform (FFT) **3**:271–273
2D Wavelet Transform (WT) **3**:273
blob analyses **3**:274
edge enhancement and detection **3**:274
line scanning **3**:273
morphological evaluations **3**:274
speckle infusion **3**:273–274
confined ablation **1**:409, **1**:409–410, **1**:410*F*, **1**:411, **1**:413*F*
confocal laser scanning microscopy (CLSM) **3**:244–245, **3**:245
confocal microscopes, working principles of **3**:246*F*
confocal microscopy **3**:244–245
conformal coatings **3**:49–50
Co–Ni alloys **3**:86
see also aluminum alloys
atomic force microscopy (AFM) **3**:90–94
chemical and textural analyses **3**:87–88
Co–Ni plating **3**:86
electrochemical plating **3**:88–89, **3**:89*F*, **3**:89*T*
incorporation of adatoms and adions **3**:87
mass transfer effects **3**:87
plating **3**:87
Scanning Electron Microscopy (SEM) **3**:90–94
X-ray diffraction (XRD) **3**:89–90
x-ray photoelectron spectroscopy (XPS) **3**:89–90
conical gears, finishing of **1**:111
by grinding **1**:111
form or non-generative gear grinding **1**:111
generative gear grinding **1**:111
by lapping **1**:111–112
connecting rod hot forging die **2**:243–244, **2**:243*F*
constant-pressure method **1**:104
contact angle (CA) **3**:138, **3**:278*F*, **3**:282
analysis of **3**:295
composite solid–liquid–air interface **3**:296–297
effect of edge and variation of surface slope **3**:297–298
flat surface **3**:295
and corrosion resistance **3**:282
effect of surface area on **3**:295–296
hysteresis **3**:278–279, **3**:297–298
measurement **3**:279–280
contact angle hysteresis (CAH) **3**:140
contact area **1**:121–122, **1**:122–124
Contact Area Map **1**:124, **1**:125
contact area-based path planning **1**:121–122
contact area **1**:122–124
contact mechanics **1**:121–122
continuous polishing path **1**:124–126
coverage area map (CAM) **1**:124
polishing path planning **1**:126–129
step-over size **1**:126
contact force **1**:140–141
contact mechanics **1**:121–122
contact stress modeling **1**:134–135
contact stress-based control **1**:133–134
air cylinder pressure control modeling **1**:137
air spindle speed control modeling **1**:137–138
combined control system **1**:138–139
contact stress modeling **1**:134–135
friction torque modeling **1**:135–136
polishing parameter planning **1**:136–137
pressure tracking control **1**:139
robotic deburring control **1**:139–143
robotic polishing/deburring system **1**:134
contact surface measurement techniques **3**:243

atomic force microscopy **3**:244, **3**:247*F*
portable handheld surface finish instrument **3**:243, **3**:244*F*
stylus profilometer (SP) **3**:243–244, **3**:244*F*
continual induction hardening
computation of **2**:164*F*
numerical model for analysis of **2**:165, **2**:166*F*
software **2**:166*F*
continuous ant colony optimization (CACO) technique **1**:198
continuous cooling transformation (CCT) **2**:255, **2**:304, **2**:304*F*
curve **2**:224
of steels **2**:227*F*
diagram **2**:11
continuous hot-dip galvanizing processes **3**:181–183, **3**:182*F*
continuous phase plate (CPP) **1**:164
continuous polishing path **1**:124–126
continuous surfaces **1**:71
control block diagram **1**:134*F*
closed-loop tool length **1**:142*F*
close loop pressure tracking **1**:140*F*
controlled thermal expansion **2**:270
convective stage *see* liquid cooling stage
conventional grinding **3**:193–194
conventional lap grinding **1**:385*F*
conventional loose-abrasive grinding **1**:154–157
conventional machining processes **3**:365–366
conventional material removal process **1**:268
conventional metallurgy process **2**:216–218
conventional processes **3**:359
conventional sintering (CS) **3**:338–339, **3**:347, **3**:348*F*
SPS advantages **3**:349
conversion coatings **3**:42, **3**:311–320
see also polyurethane (PU) coating
anodizing **3**:313–320
chromate **3**:313–320
chromate coatings **3**:42
hexavalent and trivalent chromes comparison **3**:322–323
hexavalent non-chromic coatings **3**:320
phosphate coatings **3**:42
phosphating **3**:323–325
replacement schedule **3**:320
type, substrate, coating contents **3**:314–319*T*
weight reduction curve **3**:323*F*
cooling
quenching medium **2**:386
rate **2**:386–387, **2**:387*F*
techniques **1**:80–83, **2**:387, **2**:387*F*
temperature range **2**:387
cooling transformation (CCT) **2**:195
cooperative coevolutionary genetic algorithm (CCGA) **1**:43
copolycondensation **1**:217
co-powder injection molding (2C-PIM) **1**:467
copper **1**:4, **1**:173, **1**:186, **1**:276, **2**:265, **2**:271, **3**:3, **3**:7–8
graphite **1**:277
wire **1**:238–239, **1**:240*F*
copper, heat treatment of **2**:405–408
brasses, heat treatment of **2**:406–408
bronzes, heat treatment of **2**:408–409
aluminum bronzes **2**:409–410
beryllium bronzes **2**:410–413
silicon bronze **2**:413–414
tin bronzes **2**:409
chromium coppers **2**:414
copper-base shape memory alloys **2**:415–416
copper–chromium–zirconium alloys **2**:415
copper–nickel–silicon–chromium alloy **2**:415
cupronickels **2**:414
zirconium–copper alloys **2**:414–415
copper and copper alloys **2**:398–400, **2**:399–400
annealing **2**:401–405
homogenization **2**:400–401
stress relieving treatment **2**:405
copper oxide **1**:4
copper tungsten **1**:392–393, **1**:393
copper–beryllium alloys **2**:410–411, **2**:412
copper–tungsten **1**:276
copper–zinc alloy wire electrodes **1**:232
copper–zinc phase diagram **2**:405*F*
core refinement
single hardening with **2**:87, **2**:88*F*
single hardening without **2**:87, **2**:87*F*
corrosion **3**:25, **3**:32
corrosion properties, laser peening **1**:427–429
-like electrochemical techniques **3**:53
measurement of **3**:52–54
protection against **3**:46–47
barrier protection **3**:47
cathodic protection **3**:47–48
resistance **1**:410, **1**:427–429, **2**:270, **3**:27, **3**:282
coating **3**:194
effect of gas nitriding on wear and **2**:131
high silicon irons heat treatment **2**:273–276
testing of coating **3**:109
tests **3**:99
of zinc **3**:48*F*
counter measures **1**:42–43
coupling **1**:209
cover die **1**:514
cover plate laser beam machining (c-LBM) **1**:268–270
coverage area map (CAM) **1**:124, **1**:125*F*, **1**:126*F*
CP Ti *see* commercial purity titanium (CP Ti)
CPH *see* cocoa pod husk (CPH)
CPP *see* continuous phase plate (CPP)
CQ *see* cryo-quenching (CQ)
CR *see* compression ratio (CR)
cracked die, microstructure in **2**:240*F*
cracking, in surface coatings **3**:154
cracking and exfoliation **2**:104
prevention **2**:104
cracking in laser polishing **1**:166
cratering, in surface coatings **3**:154
crawling, in surface coatings **3**:154
critical cooling rate (CCR) **2**:3–4
critical diameter **2**:56–57, **2**:57*F*
evaluation **2**:59, **2**:59*F*
critical resolved shear stress (CRSS) **2**:328
cross '+' micro channel, experiments and simulation for **1**:455–456
cross viscosity model **1**:445, **1**:492
cross-exponential Macosko viscosity model **1**:445–446
cross-linked polymers **1**:217
crowding **1**:126
CRSS *see* critical resolved shear stress (CRSS)
cryogenic machining **1**:80–83
cryogenic treatment (CTs) **2**:279, **2**:285, **2**:422, **2**:422–423, **2**:424–425, **2**:425–426
cryogenic processing
of ferrous alloys **2**:426–427
of nonferrous alloys **2**:445–447
industrial context **2**:423–424
cryogenic processing industry **2**:423–424
current uses of CT process **2**:424
future of CT and applications **2**:424
optimizing CT process **2**:426
technology **2**:425
traditional heat treatment **2**:422
cryonics **2**:422
cryo-quenching (CQ) **2**:425
CryoTech **2**:423
cryotreatments *see* cryogenic treatment (CTs)
crystallite
refinement **1**:429
size **1**:417–418
crystallization **1**:217
crystallization process of polycarbonates **3**:138
CS *see* cold spraying (CS); conventional sintering (CS)
CSI *see* coherence scanning interferometry (CSI)
CT *see* computed tomography (CT)
CTE *see* coefficient of thermal expansion (CTE)
CTs *see* cryogenic treatment (CTs)
cubic boron nitride (CBN) **1**:7, **1**:48, **3**:217, **3**:230–231, **3**:239
cupronickels **2**:414
Curie temperature **3**:353
curing process **1**:220
current density **3**:367, **3**:369
current efficiency **3**:86–87, **3**:88, **3**:92
curvature method **3**:59, **3**:59–60, **3**:97–98
residual stress measurements by **3**:98–99
custom-made vertical injection molding machine **1**:447–448
injection mechanism **1**:448
mold design **1**:448
plasticizing unit and injection mechanism **1**:447–448

cut quality assessment **1**:351
cutting
  edge
    geometry **1**:56–58
    preparation **1**:57*F*
  errors **1**:74–75
  forces **1**:35–36, **1**:58–60, **1**:59*F*, **3**:230, **3**:237, **3**:238*F*
    modeling **1**:75–76
  machine specification **1**:225, **1**:225*F*
  process monitoring method **1**:37
  speed **1**:81
cutting fluids **1**:1–4
  boric acid **1**:4
  coconut oil **1**:2
  extensive research **1**:1–2
  NDM **1**:3
  in turning **1**:4
  twisted nematic liquid crystals **1**:3–4
cutting tool(s) **1**:27, **2**:225*F*, **3**:230, **3**:232
  dimensions **3**:235
  factors due to **1**:6–9
    BUE formation **1**:11–12, **1**:12*F*
    tool coating **1**:12–13
    tool geometry **1**:6–9
    tool wear **1**:9–11
    type of tool edge preparation **1**:7*F*
  materials **1**:55–56
Cu–Zn–Al alloys **2**:415–416
CV *see* computer vision (CV)
CVD *see* chemical vapor deposition (CVD)
CW samples *see* cold-worked (CW) samples
cyanide bath, liquid carburization in **2**:76*F*
cyanide-free plating bath **3**:11
cyclic process **2**:388
cyclic yield strength **1**:431

D

'd vs. $\sin^2\Psi$' technique **1**:415
DC *see* direct current (DC); dislocation cells (DCs)
DC polarization method **3**:53
DCL *see* double-ceramic-layer (DCL)
DCT *see* deep cryogenic treatments (DCT)
DDWs *see* dense dislocation walls (DDWs)
deburring **1**:339–340
decomposition of metastable β **2**:306
deep cryogenic treatments (DCT) **2**:425
deep rolling (DR) **1**:419, **1**:432, **1**:432–433, **1**:432*F*
deep X-ray lithography (DXL) **1**:521
deformation **1**:298, **1**:425–427
  aging **2**:389
  in $\alpha+\beta$-phase field **2**:317–321
  in β-phase field **2**:313–317
  parameters **2**:316*T*
  processes for miniature gear manufacturing **1**:522–523
    extrusion process **1**:524
    forging **1**:525
    hot embossing **1**:526
    stamping **1**:522–523
deionized water **1**:175
delamination, in surface coatings **3**:154
dense dislocation walls (DDWs) **1**:425–426, **1**:427, **2**:176
dense metallic membranes **3**:14
Density Functional Theory (DFT) **3**:16
dental implant **3**:113*F*
deposition **3**:306–307
  of hard coatings **3**:232–233
  stresses **3**:57
depth of cut (DOC) **1**:27, **1**:33
design of experiment (DOE) **1**:251, **1**:483, **1**:484, **1**:486, **1**:487
  for investigation of molded part quality **1**:488*T*
designation system of aluminum alloys **2**:337–338, **2**:338*T*
design-to-manufacturing cycle **1**:75
destabilization treatment **2**:279, **2**:281–282
destructive method
  see also nondestructive methods
  hole-drilling method (HDM) **3**:58–59, **3**:58*F*
  layer removal (LR) **3**:58–59
  material removal by chemical etching **3**:59
deterministic microgrinding (DMG) **1**:158–159
detonation-gun (D-gun) **3**:207
Deutsches Instut fur Normung (DIN) standard **1**:507
dezincification process **3**:28
DF *see* duty factor (DF)
DFT *see* Density Functional Theory (DFT)
D-gun *see* detonation-gun (D-gun)
Diamalloy 4010 and 2002 powders **3**:102, **3**:102–103, **3**:103, **3**:109
diamond grinding **1**:366
Diamond Jet Hybrid (DJ Hybrid) **3**:207–208
diamond-like carbon (DLC) **2**:132, **3**:232
  coatings **3**:239
DIC *see* digital image correlation (DIC)
die casting process **1**:514
  advantages **1**:514–516
  applications **1**:516
  limitations **1**:516
  types **1**:514
die sink (DS) EDM **1**:384–385
dielectric fluid **1**:233, **1**:279–280, **1**:334–335, **1**:390
dielectric liquid **1**:175, **1**:271
dielectric medium **1**:174–177
  fluid **1**:175–177
  gas **1**:177–180
  medium in EDM **1**:277–278
dielectric vibration **1**:174
differential dilatometric technique **2**:18, **2**:19*F*
differential scanning calorimetry (DSC) **1**:477, **2**:329, **3**:340–341, **3**:341–342
diffraction method **3**:60
  neutron diffraction **3**:60
  synchrotron XRD **3**:60
  XRD **3**:60
diffusion
  annealing **2**:24, **3**:198–199, **3**:199
  of atoms **2**:400
  inward diffusion **2**:122–123
diffusion coatings **3**:42
  chemical gas diffusion **3**:42
  liquid diffusion **3**:42
  solid-state diffusion **3**:42
diffusion processes **3**:44*T*
diffusion zone **2**:122–123
diffusional transformation **2**:3–4, **2**:6–7
diffusion-annealed coated wires **1**:243
  alpha phase wires **1**:243
  beta phase wires **1**:243–244
  epsilon phase wires **1**:247, **1**:248
  gamma phase wires **1**:244–247, **1**:245*F*
diffusion-controlled process **2**:117
digital image correlation (DIC) **3**:59
digital micromirror devices (DMDs) **3**:114, **3**:115*F*
digital modeling **2**:391
digital numbers (DNs) **3**:266
digitizing **3**:266
dilute medium **2**:124
dimensional accuracy **1**:74–75
dimensional stability **2**:271–272, **2**:340*T*, **2**:347, **2**:358, **2**:368
dimensional stabilization *see* dimensional stability
dimethylamine borane (DMAB) **3**:3
DIN standard *see* Deutsches Instut fur Normung (DIN) standard
direct ablation mode **1**:409, **1**:410*F*, **1**:411–413
direct blending of molten bath **3**:29
direct current (DC) **3**:233
  supply **3**:359–360, **3**:360, **3**:372
direct laser interference patterning (DLIP) **3**:125
direct quench technique **2**:89
discharge current **1**:235–236
discharge voltage **1**:235–236, **1**:279
disk and ball specimens, wear rate of **1**:377*F*
disk scanning confocal microscopy (DSCM) **3**:244–245, **3**:245
dislocation **1**:408, **1**:417–418, **1**:418, **1**:419–420, **1**:425–426, **1**:426–427, **1**:433
  mechanisms **2**:381–382, **2**:382*F*
  theory **2**:382
dislocation cells (DCs) **2**:176
dislocation lines (DL) **1**:422*F*, **1**:425
dislocation tangles (DTs) **1**:419–420, **1**:422*F*, **2**:176
dispersed metal oxide **3**:25–26
dispersion hardening **2**:381–382, **2**:382*F*
displacement deposition process **3**:1
dissolution, in surface coatings **3**:154
distortion **2**:103–104
DL *see* dislocation lines (DL)
DLC *see* diamond-like carbon (DLC)
DLIP *see* direct laser interference patterning (DLIP)
DMAB *see* dimethylamine borane (DMAB)
DMDs *see* digital micromirror devices (DMDs)
DMG *see* deterministic microgrinding (DMG)
DNs *see* digital numbers (DNs)

DOC *see* depth of cut (DOC)
DOE *see* design of experiment (DOE)
double dipping **3**:181
double shielded TBMs **1**:42
double-ceramic-layer (DCL) **3**:66
double-end dipping **3**:181
double-layer-coated wires **1**:241, **1**:242*F*
double-stage process **2**:109, **2**:120–121
DP steels *see* dual phase (DP) steels
DR *see* deep rolling (DR)
drawdown phenomenon **1**:522–523
droplet formation and fate **3**:150
  basic mechanism **3**:150
  coating formation on the surface **3**:151
  formation of droplets **3**:150–151
  spray air contact **3**:151
DRX *see* dynamic recrystallization (DRX)
dry cutting **1**:2–3, **1**:80
dry EDM **1**:177–180, **1**:278–279
dry etching **1**:330
dry machining **1**:80–83
dry post-processing **1**:167
DSC *see* differential scanning calorimetry (DSC)
DSCM *see* disk scanning confocal microscopy (DSCM)
DTs *see* dislocation tangles (DTs)
dual frequency induction surface hardening **2**:169
dual phase (DP) steels **2**:208–210, **2**:209*T*, **3**:185
  bake hardened **2**:210–211
  dislocations around martensite particle **2**:210*F*
  ferrite–martensite structure **2**:210*F*
  rapid heating producing ultrafine grained **2**:209–210
  transmission electron micrograph **2**:210*F*
dual-phase alpha–beta brasses **2**:408
ductile irons **2**:248, **2**:260
  see also high-alloy irons
  heat treatment **2**:260–262
    annealing **2**:262
    austempering **2**:264–266
    considerations for **2**:261–262
    hardening and tempering **2**:264
    normalizing **2**:262–264
    stress relieving of ductile irons **2**:269
    surface hardening **2**:269
  microstructure **2**:266*F*
ductile mode machining **1**:372
ductile regime machining **1**:325–326
duplex coatings **3**:45
duplex stainless steel **2**:204, **2**:204*F*, **2**:204*T*
duty factor (DF) **1**:235, **1**:236, **1**:279
d-values **3**:164
DXL *see* deep X-ray lithography (DXL)
dynamic recrystallization (DRX) **1**:426, **1**:432

E

EAs *see* effervescent atomizers (EAs); evolutionary algorithms (EAs)
EBM *see* electron beam machining (EBM)
EBSD method *see* electron backscatter diffraction (EBSD) method
EC *see* evolutionary computations (EC)
ECDe process *see* electrochemical deburring (ECDe) process
ECF process *see* electrochemical finishing (ECF) process
ECG process *see* electrochemical grinding (ECG) process
ECH process *see* electrochemical honing (ECH) process
ECM *see* electrochemical machining (ECM)
eco-friendly coatings **3**:50
ECR process *see* electrochemical refining (ECR) process
ECW process *see* electrochemical winning (ECW) process
ED micromilling *see* electrical discharge (ED) micromilling
EDC *see* electrical discharge coating (EDC)
EDDSG process *see* electro-discharge diamond surface grinding (EDDSG) process
EDG *see* electrical discharge grinding (EDG)
edge deburring **1**:143*F*
EDM *see* electrical discharge machining (EDM); electro-discharge machining (EDM)
EDMed SQ **1**:404–405
EDMed surface **1**:392, **1**:396
EDS *see* energy dispersive spectroscopy (EDS)
EDT *see* electrical discharge texturing (EDT)
EDTA *see* ethylenediaminetetraacetic acid (EDTA)
EEM *see* elastic emission machining (EEM)
EES software *see* Engineering Equation Solver (EES) software
effervescent atomizers (EAs) **3**:153*F*, **3**:155
E-glass fiber **1**:208
EIS *see* electrical impedance spectroscopy (EIS)
ejector die **1**:514
elastic emission machining (EEM) **1**:159–160
electric arc spray **3**:43
electric wire arc thermal spraying **3**:43
electrical and magnetic properties **3**:50
electrical discharge (ED) micromilling **1**:333
electrical discharge coating (EDC) **1**:191, **1**:395
electrical discharge grinding (EDG) **1**:270
electrical discharge machining (EDM) **1**:171, **1**:182–186, **1**:270, **1**:270–271, **1**:508, **1**:527–529, **1**:446, **1**:230, **1**:332–333
  see also hard machining; electro-discharge machining (EDM)
  advantages **1**:529
  applications **1**:529–530
  chip **1**:271
  dielectric medium **1**:174–177, **1**:277–278
  electrical discharge (ED) micromilling **1**:333
  electrode material **1**:276
  electrode modification **1**:191–193
  experimental setup **1**:303–304
  hybrid machine for multi-processes of micromachining **1**:271*F*
  limitations **1**:529
  measuring frontal wear of microelectrode **1**:303*F*
  micro-EDM of nonconductive ceramics **1**:333–334
    assisting electrode **1**:334
    dielectric fluid **1**:334–335
    mechanism of material removal **1**:335–337
    recast layer **1**:337–338
  micro wire EDM **1**:333
  μ-EDM **1**:529
  online measurement **1**:301*F*
  PMEDM **1**:180–186
  powder addition **1**:182–186
    performance improvement **1**:182–186, **1**:182*F*, **1**:183*F*, **1**:184*F*, **1**:185*F*, **1**:185*T*
    surface modification **1**:186–188, **1**:187*F*, **1**:188*F*
  process **1**:172, **1**:273*F*
  process parameters **1**:279–280
    electrode wear **1**:280*F*
    fabrication processes of microelectrode **1**:282–283
    performance measure **1**:280
  prospective on process selection **1**:300–303
  pulse generators/power supply **1**:274
  simulation and modeling **1**:193–195
  sparking and gap phenomena **1**:271–272
  ultrasonic vibration assisted EDM **1**:172–173
  wire electrode **1**:236–238, **1**:239*F*, **1**:253*F*
    abrasive-assisted wire **1**:249, **1**:249*F*
    coated EDM wires **1**:240–241
    customized wire shapes **1**:238*F*
    cutting rate improvement **1**:238*F*
    development of **1**:238
    diffusion-annealed coated wires **1**:243
    high tensile strength wires **1**:247–248
    hot dip galvanized wire **1**:249
    plain wires **1**:238–239
    porous electrode wire **1**:249–250, **1**:250*F*
  wires **1**:237
electrical discharge texturing (EDT) **1**:396
electrical impedance spectroscopy (EIS) **3**:53, **3**:53–54
electrical parameters **1**:279
electro chemical testing **3**:99, **3**:105–107
electro deposition **3**:330–332
electro etching **3**:308
electro polishing **3**:308
electro/chemical plating **3**:44*T*
electrochemical deburring (ECDe) process **3**:359, **3**:375, **3**:375*F*
  advantages **3**:375–376
  applications **3**:376
  limitations **3**:376
  mechanism **3**:375

electrochemical deposition **3**:1, **3**:294*F*, **3**:360
  electroplating **3**:1–2
  ELP **3**:2–3
electrochemical finishing (ECF) process **1**:98, **3**:359
electrochemical grinding (ECG) process **1**:98, **3**:359, **3**:371, **3**:371*F*
  advantages **3**:371
  applications **3**:371
  limitations **3**:371
  surface finish in ECG **3**:376–377
electrochemical honing (ECH) process **1**:98, **3**:359, **3**:372, **3**:372*T*
  advantages **3**:374–375
  applications **3**:375
  equipment **3**:372–373
  finishing
    of gears **3**:373–374, **3**:373*F*
    of internal cylinders **3**:372–373
  limitations **3**:375
  photograph of tool for finishing internal cylinders **3**:373*F*
  principle of **3**:372
  surface finish ECH **3**:377–378, **3**:377*F*, **3**:378*T*
electrochemical machining (ECM) **1**:176, **1**:300–301, **1**:338–339, **3**:359, **3**:365–367
  affecting factors **3**:368–369
    advantages **3**:370
    applications **3**:370–371
    capabilities of ECM **3**:369–370, **3**:370*T*
    current density and voltage **3**:369
    electrolyte related parameters **3**:368–369, **3**:368*T*
    IEG **3**:369
    limitation **3**:370
    mass transport phenomenon in **3**:369
  deburring **1**:339–340
  material removal **3**:367–368
  micromachining **1**:338–339
  micro/nano polishing **1**:339
  setup **3**:366*F*, **3**:367*F*
  surface finish **3**:376
    evolution of hydrogen gas **3**:376
    flow separation and formation of eddies **3**:376
    selective dissolution **3**:376, **3**:377*F*
    sporadic breakdown of anodic film **3**:376
  working principle of pulsed-ECM **3**:366–367
electrochemical plating **3**:88–89, **3**:89*F*, **3**:89*T*
electrochemical processing **3**:359–360
  electrochemical deburring (ECDe) **3**:375
  electrochemical grinding (ECG) **3**:371
  electrochemical honing (ECH) **3**:372
  electrochemical machining **3**:365–367
  electrolysis process **3**:359*F*
  electroplating (EP) **3**:360–361
  surface finish in **3**:376
  types **3**:360, **3**:360*T*
electrochemical reaction and deposition method **3**:293
electrochemical refining (ECR) process **3**:359
electrochemical techniques **3**:40
  electrodeposition **3**:40
  electroless coatings **3**:40–41
electrochemical winning (ECW) process **3**:359
electrode
  materials **1**:271
    for EDM **1**:276
    for micro-EDM **1**:277
  modification **1**:191–193, **1**:193*F*
  polarity **1**:279
  potential **3**:359–360
electrode wear ratio (EWR) **1**:275, **1**:280, **1**:280–281, **1**:306–311
  ANOVA for **1**:308*T*
electrode-less ELID
  ELID III **1**:369–370, **1**:370*F*
  ELID IIIA **1**:370, **1**:371*F*
electrodeposition **3**:28, **3**:40, **3**:86–87, **3**:149–150
electro-discharge diamond surface grinding (EDDSG) process **1**:196
electro-discharge machining (EDM) **1**:172*F*, **1**:365, **1**:383–384
  see also hard machining; electrical discharge machining (EDM)
  applications **1**:390
    heat-treated materials **1**:390
    modern semiconductor/composite materials **1**:390
    nonconductive ceramic **1**:390
  categories of **1**:384–388
  die sink (DS) **1**:384–385
  effect on workpiece surface finish **1**:390–394
    ball burnish machining (BEDM) **1**:398–400
    special applications **1**:400–404
    surface alloying using composite (PM) electrode **1**:394–396
    surface modification by conventional electrode materials **1**:392–394
    surface modification by dielectric **1**:396–398
    surface modification using wire EDM **1**:404
  process performance and parameters **1**:388–389
    dielectric fluid **1**:390
    discharge voltage **1**:388–389
    electrode/workpiece material **1**:390
    peak current **1**:389
    polarity **1**:390
    pulse duration and pulse interval **1**:389–390
    pulse waveform **1**:390
    rotational motion of electrode/workpiece **1**:390
  wire-cut (WC) **1**:384–385
electro-finishing method **1**:374–375, **1**:375–376
electroforming **3**:365
electrogalvanizing **3**:181, **3**:181*F*
electroless coating **3**:28, **3**:40–41
electroless deposition **3**:1
  of pure metals **3**:4–6
    Ag **3**:7
    Cu **3**:7–8
    Ni **3**:6–7
    Pd **3**:6
electroless gold, formulation of **3**:227*T*
electroless gold plating **3**:226–228, **3**:227*T*
electroless Ni–B alloy coating **3**:49
electroless nickel (EN) coatings **3**:223–224
  EN–phosphorous coatings **3**:224
  general categories of **3**:225*F*
  nickel–boron **3**:224
  nickel–phosphorus **3**:224, **3**:225*T*
  poly-alloys **3**:224
electroless nickel bath composition and functions **3**:40*T*
electroless nickel coating **3**:40, **3**:49
electroless Ni–P coatings **3**:47, **3**:47–48, **3**:48
electroless palladium plating **3**:224–226
electroless plating (ELP) **3**:1, **3**:2–3, **3**:42, **3**:221
  see also electroplating (EP)
  advantages and weaknesses of **3**:222*T*
  catalytic aspects **3**:3
  conditions and chemical composition **3**:4
  electrolytic cell **3**:2*F*
  mechanistic overview **3**:3–4
  plating baths **3**:2
  surface conditioning **3**:4
electrolysis **1**:371*F*, **3**:359–360, **3**:359*F*
  basic principles of **1**:366*F*
  Faraday's law of **1**:366
electrolyte **3**:368
  flow rate **3**:369
  supply **3**:372
electrolytic coatings **3**:46
electrolytic deposition **3**:331
  electrolytic coatings, substrate, coatings contents **3**:332*T*
electrolytic in-process dressing (ELID) grinding **1**:159, **1**:365–368, **1**:367*F*, **1**:383
  classifications of **1**:368
    electrode-less ELID (ELID III) **1**:369–370
    electrode-less ELID (ELID IIIA) **1**:370
    electrolytic in-process dressing (ELID I) **1**:368, **1**:369*F*
    electrolytic interval dressing (ELID II) **1**:368–369, **1**:370*F*
    ion shot ELID (ELID IV) **1**:370
  components of **1**:366*F*
  vs. electro-discharge machining **1**:405*T*
  experimental setup **1**:368*F*
  honing **1**:375–376
  lap grinding **1**:381, **1**:385*F*
  material deformation **1**:378
  for nano surface finish **1**:370–373
    ceramics **1**:370–373
    coated film **1**:373–374
    metal **1**:374–377
    optical glasses **1**:377–380
    silicon wafer **1**:380–383
  terminology using **1**:366
  for 3-D arc enveloping grinding **1**:384*F*
  wire EDM process **1**:389*F*

electromagnetic and temperature calculations **2**:160
electromagnetic field **2**:159–160, **2**:160, **2**:163
electromagnetic methods **3**:51
electromagnetic stir casting **1**:15
electromotive force (emf) **1**:61–62, **3**:359–360
electron backscatter diffraction (EBSD) method **1**:429
electron beam **3**:196
  remelting **3**:196
electron beam machining (EBM) **1**:332
electron donor parameters **2**:138–139, **2**:139*T*
electron microscopy **3**:247–248
  Scanning Electron Microscopy (SEM) **3**:248, **3**:248*F*
  Transmission Electron Microscopy (TEM) **3**:248, **3**:248*F*
electron transfer **3**:361
electronic packaging
  electroless plating as surface finishing in **3**:**220–229**
electronic speckle pattern interferometer (ESPI) **1**:415
electrophoretic deposition (EPD) **1**:163, **3**:331
  electrodeposition of metals **3**:1
  electroplating features **3**:2
  factors affecting quality of deposition **3**:361–362
  metals and applications **3**:364*T*
  overpotential **3**:2
  types of electrical waveforms **3**:363*F*
electroplated zeolites **3**:50
electroplating (EP) **3**:1, **3**:2*F*, **3**:1–2, **3**:40, **3**:54, **3**:120, **3**:120*F*, **3**:359, **3**:360–361, **3**:361*F*, **3**:365*T*, **3**:200
  see also electroless plating (ELP)
  principle of **3**:360–361
  surface finish in **3**:376
electro-slag remelting (ESR) **2**:241
electrospinning **3**:294
electrostatic application **3**:153
electro-thermal machining process **1**:232
ELI *see* extra low interstitials (ELI)
ELID grinding *see* electrolytic in-process dressing (ELID) grinding
ellipsoid, crowding and unpolished areas for **1**:128*F*
elliptical contact area **1**:124*F*
Ellis model **1**:492
elongation **1**:237
ELP *see* electroless plating (ELP)
embrittlement in maraging steel **2**:207–208
emf *see* electromotive force (emf)
EN coatings *see* electroless nickel (EN) coatings
enameling **3**:200
energy beam micromachining **1**:330–331
  electron beam machining (EBM) **1**:332
  focused ion beam (FIB) **1**:331
    deposition **1**:331
    sputtering **1**:331–332
  laser micromachining **1**:330–331
energy dispersive spectroscopy (EDS) **3**:8, **3**:74, **3**:88, **3**:94*F*
energy dispersive X-ray spectroscopy (EDS/EDX) **1**:250, **1**:251*F*, **1**:373–374, **1**:377*F*, **3**:160, **3**:338
  spectrum analysis **1**:314–317
engineering applications
  bearing steel **2**:196–197, **2**:197*F*, **2**:197*T*
  dual phase steels **2**:208–210, **2**:209*T*
  hadfield steel **2**:197–199, **2**:198*F*, **2**:198*T*
  heat treatment
    of steel casting **2**:211–212, **2**:211*F*
    of TRIP **2**:208
  maraging steel **2**:205–207, **2**:206*F*, **2**:206*T*
  medium-carbon low-alloy steels **2**:181, **2**:188
  silicon steel **2**:195–196
  spring steel **2**:192–195, **2**:192*T*
  stainless steel **2**:199–200
Engineering Equation Solver (EES) software **3**:164
engineering surfaces **3**:286–287
  imperfections **3**:287
  lay **3**:287
  roughness **3**:287
  wavy conditions **3**:287
environmental scanning electron microscopy (ESEM) **3**:288–289
EP *see* electroplating (EP); epoxy resin (EP)
EP additive *see* extreme pressure (EP) additive
EPD *see* electrophoretic deposition (EPD)
epoxy resin (EP) **1**:215–216
ε carbide **2**:40–41
epsilon phase wires **1**:247, **1**:248
equilibrium constant **2**:82
equilibrium polycondensation **1**:217
equilibrium precipitation **2**:374–375, **2**:375–377, **2**:375*F*, **2**:376*F*
equilibrium state for chemical reaction **2**:82
Eringen–Okada equation **1**:446
erosion resistance **2**:270
ESEM *see* environmental scanning electron microscopy (ESEM)
ESPI *see* electronic speckle pattern interferometer (ESPI)
ESR *see* electro-slag remelting (ESR)
eta layer **3**:180–181
etching **3**:141, **3**:292, **3**:292*F*, **3**:308
  and lithography **3**:292
ethylenediaminetetraacetic acid (EDTA) **3**:6, **3**:7, **3**:10, **3**:224
  EDTA-free bath **3**:10
Eularian method **3**:162
Euler–Bernoulli beam equation **1**:33
eutectoid carbon content **2**:5, **2**:6*F*
eutectoid steel **2**:7*F*
  variation of nucleation and growth rate for **2**:7*F*
evaporation **3**:233
evolutionary algorithms (EAs) **1**:87
evolutionary computations (EC) **1**:87
EWR *see* electrode wear ratio (EWR)
excessive retained austenite **2**:93
experimental measurement **3**:58–59
  destructive method **3**:58–59
  experimental methods and measurements **1**:225
  cocoa fiber composites **1**:225
  cutting machine specification **1**:225
  design of experiments **1**:225, **1**:226*T*
  evaluation of cut quality characteristics **1**:225–226, **1**:226*F*
  preparation of cocoa fiber composite **1**:225
  selection of cutting parameters **1**:225, **1**:225*T*
  methods **3**:61
  nondestructive methods **3**:59
  residual stress measurement **3**:61
exponential functions **1**:152
external honing **1**:104
  single helical gear **1**:104*F*
extra low interstitials (ELI) **2**:291
extreme pressure (EP) additive **1**:4
extruding nonferrous alloys **2**:241
extrusion process **1**:221, **1**:524
  advantages **1**:524
  applications **1**:525
  limitations **1**:524–525

F

fabrication
  of microelectrode for batch production **1**:286
  processes of microelectrode **1**:282–283
    hybrid process **1**:294–296
    MBEDG **1**:291–292
    micro-rods by self-drilled holes **1**:293–294
    micro-turning process **1**:292–293
    off-centering **1**:295*F*
    reverse EDM **1**:294
    rotating sacrificial disk **1**:290
    stationary BEDG **1**:290–291
    WEDG **1**:283
  of 3D composite polymer scaffolds **3**:122*F*
face-centered cubic metals (fcc) **1**:427, **2**:199, **3**:6–7, **3**:8
failed bolt, observations on **2**:307–308
  metallurgical analysis **2**:308–309
  visual inspection **2**:307–308
failure adhesion **3**:306–307
failure analysis **2**:311
Faraday's laws **3**:40, **3**:88, **3**:359–360
  first law of electrolysis **3**:360
  second law of electrolysis **3**:360
FAS *see* fluoroalkylsilanes (FAS)
fast Fourier transform (FFT) **1**:6, **1**:29
fatigue **1**:431
  behavior **2**:129
  properties of laser peening **1**:422–425
  thermal fatigue properties of laser-treated surfaces **2**:140
fatty acid monolayers **3**:282
fcc *see* face-centered cubic metals (fcc)
FDM *see* finite difference method (FDM)
Fe–C equilibrium diagram **2**:226*F*
feedstock preparation **1**:516

FEM *see* finite element method (FEM); finite element modeling (FEM)
femtosecond (fs) laser **3**:115, **3**:124, **3**:125
ferrite **2**:4–5, **2**:109
ferrite stabilizers **2**:5
ferritic stainless steel **2**:200, **2**:201*F*, **2**:202*F*, **2**:202*T*
ferritizing annealing **2**:251
ferroelectric materials **3**:349
ferrous alloys **2**:120–123, **2**:127–129, **2**:131
  see also non-ferrous alloy(s); palladium (Pd)
  cryogenic processing **2**:426–427
    case studies **2**:437
    cast irons and pearlitic steels **2**:436–437
    chronological changes in material properties **2**:428–429*T*
    mechanical properties **2**:427
    mechanisms of microstructural change **2**:429–430
    plain carbon steels **2**:434–435
    stainless steels **2**:435–436
    tool steels **2**:430–434
    tribological performance **2**:427–429
  microstructure and phase composition **2**:120–123
    cross-sectional micrographs **2**:121*F*
    hardness vs. depth profiles **2**:124*F*
    nitrided microstructure **2**:122*F*
  nitriding atmosphere **2**:124
  nitriding time and temperature **2**:123–124
  steel composition and heat treatment history **2**:124–125
FESEM *see* field emission scanning electron microscope (FESEM)
FET *see* field-effect transistor (FET)
Fe–Zn alloy phases **3**:26–27, **3**:29–30
FFT *see* fast Fourier transform (FFT)
FI surfaces *see* fully interrupted (FI) surfaces
FIB *see* focused ion beam (FIB)
fiber process **1**:218–219
fiber-reinforced polymer (FRP) **1**:204, **1**:212, **1**:212–215, **1**:213*F*
  advantages and limitations **1**:216*T*
  applications **1**:215
  composites **1**:206–207
  design considerations **1**:216
  disposal and recycling concerns **1**:216
  failure modes **1**:215
  material requirements **1**:215
Fick's equations **2**:117
Fick's first law **3**:162
Fick's laws of diffusion **2**:81–82
Fick's second law **3**:159–160
field emission scanning electron microscope (FESEM) **3**:287*F*
field-effect transistor (FET) **1**:274
filament winding **1**:220–221
filling phase **1**:442
filling-assisted injection molding techniques **1**:444
film adhesion **3**:155–156
film pressure contact angle hysteresis **3**:279
final calibration rigging **1**:150*F*
final thermal-mechanical treatment (FTMT) **2**:391–392
fine alloy carbide particles **2**:228
fine powder (INV2) feedstock **1**:476, **1**:476*F*
finish machining of hardened steel
  cutting edge
    geometry **1**:56–58
    preparation **1**:57*F*
  cutting tool materials **1**:55–56
  hard machining **1**:80–83
    applications **1**:51–53
    industrial applications **1**:52*F*, **1**:53
    workpiece clamping **1**:52–53
  hard machining process modeling **1**:75–76
  machining of hardened steel at different levels **1**:56*F*
  optimization studies in hardened steel machining **1**:86–88
  physical aspects **1**:58–60
    aspect of cutting edges **1**:65*F*
    chip formation **1**:60–61
    cutting forces **1**:58–60, **1**:59*F*
    surface integrity **1**:66–69
    tool–chip interface temperature **1**:61–63
    tool wear patterns and mechanisms **1**:63–66
    tool wear rate progression **1**:66*F*
finish turning **1**:1
  surface finish quality **1**:1
  surface roughness
    development of surface roughness prediction models **1**:19–22
    factors due to cutting tool **1**:6–9
    factors due to machining conditions **1**:1–4
    machining parameters effect **1**:13–17, **1**:18*T*, **1**:19*T*
    optimization studies **1**:19–22
    workpiece material effect **1**:17–19
finite difference method (FDM) **1**:489
finite element analysis **1**:490
finite element method (FEM) **1**:62–63, **1**:75, **1**:195–196, **1**:195*F*, **1**:196*F*, **1**:445, **1**:492, **2**:391, **3**:56, **3**:58, **3**:162
finite element modeling (FEM) **1**:489
finite volume method (FVM) **1**:489
first-order viscosity model **1**:491
'fish-eye' cracks **2**:127–128
fixed-abrasive gear lapping process **1**:101–102
fixed-abrasive grinding **1**:158–159
fixed-abrasive pad polishing **1**:162
fixed-abrasive pellet polishing **1**:162–164
fixed-abrasive polishing **1**:162
  fixed-abrasive pad polishing **1**:162
  fixed-abrasive pellet polishing **1**:162–164
flame hardening **2**:256
flame spray **3**:43
flashless forging **1**:525
flat die forging *see* open die forging
flat surface, wettability on **3**:277
flatness error **1**:74
flip chip solder joint **3**:220, **3**:220*F*
Floe process *see* double-stage process
flow visualization and prediction **1**:489
flow visualization technique **1**:448
fluid application method **1**:1–4
fluid dielectric medium **1**:175–177, **1**:176*F*, **1**:177*F*, **1**:178*F*, **1**:179*F*
fluid jet abrasives **1**:157–158
fluid jet polishing **1**:160
fluoroalkylsilanes (FAS) **3**:283, **3**:283–285
flushability **1**:237
fluxing **3**:180
focus variation microscopy **3**:245–246
focused ion beam (FIB) **1**:268–270, **1**:331
  deposition **1**:331
  machining **1**:164–166
  sputtering **1**:331–332
force-recording mechanical testing system **3**:51
Ford Motor Company **3**:149–150
forging **1**:525
  advantages **1**:525
  applications **1**:526
  limitations **1**:525–526
  quality steel **2**:181, **2**:182–183*F*, **2**:183*T*, **2**:184*F*
    annealing **2**:181
    normalizing **2**:181
  types **1**:525
forging die, premature failure of **2**:240*F*
form cutting tool **1**:508
form grinding
  vs. generative grinding gear **1**:99*F*
  types of **1**:99*F*
fossil-derived syngas **3**:17–18
four point configuration test **3**:51–52, **3**:51*F*
Fourier transform infrared (FTIR) technique **3**:147, **3**:283
fractal geometry **3**:291
fractal surfaces, roughness of **3**:290–291
fracture toughness of the surface **2**:138
free sintering *see* conventional sintering (CS)
free status **2**:373
free-abrasive gear lapping process **1**:101–102
free-contact force machining process **1**:288–289
free-radical polymerizations **3**:116
freestanding micro-scaffold **3**:121*F*
French Gear standard **1**:507
frequency sparks **1**:280
friction **3**:231, **3**:235
  stir welding **1**:430
friction stir processing (FSP) **3**:200–202
friction torque modeling **1**:135–136
FRP *see* fiber-reinforced polymer (FRP)
FSP *see* friction stir processing (FSP)
F-test **1**:352
FTIR technique *see* Fourier transform infrared (FTIR) technique
FTMT *see* final thermal-mechanical treatment (FTMT)
full annealing **2**:20, **2**:251, **2**:251*F*
full width at half maximum (FWHM) **1**:417, **3**:173
fully interrupted (FI) surfaces **1**:71
fully α-Ti alloys **2**:290–291
furnaces **2**:119
  gas circulation **2**:384
fusing **3**:195
  of self-flux alloys **3**:195–196

fuzzy inference system **1**:233
FVM *see* finite volume method (FVM)
FWHM *see* full width at half maximum (FWHM)

G

GA *see* genetic algorithm (GA)
GAE *see* gas assisted etching (GAE)
galling process **3**:187*F*
galvanic series of metals **3**:47*T*
galvanized steel **3**:47, **3**:308
  failure mechanisms in **3**:187–188
galvanizing **3**:41, **3**:178, **3**:178–181, **3**:180*F*, **3**:180*T*
  AHSS **3**:185–187, **3**:185*F*, **3**:186*F*, **3**:187*F*
  galvanizing bath, presence of elements in **3**:184–185
  surface preparation for **3**:54
gamma phase wires **1**:244–247, **1**:245*F*
  cross-section of electrode wire **1**:246*F*
  large-scale diagrammatic view **1**:246*F*
  perspective view and longitudinal section **1**:247*F*
  sheath layer and core **1**:247*F*
gas assisted etching (GAE) **1**:331–332
gas carburization **2**:73, **2**:78
  advantages **2**:79
  atmospheric conditions for **2**:78–79
  carbon potential **2**:79
  carburizing process **2**:78
  carburizing reactions **2**:78
  carrier gases **2**:79
  disadvantages **2**:79
  safety measures for **2**:79–80
gas carburized steel, carburizing cycle of **2**:90*F*
gas carburizing process **2**:78*F*
gas cluster ion beam (GCIB) **1**:164–166
gas dielectric medium **1**:177–180, **1**:179*F*
gas nitrided EN41B steel **2**:131
gas nitriding **2**:108, **2**:109, **2**:112–113, **2**:117–119
  causes and remedies **2**:120
  effects on mechanical properties **2**:127–129
  effects on wear and corrosion resistance **2**:131
  industrial applications **2**:131–132
  nitriding of non-ferrous alloys **2**:108–109
  post-treatment step **2**:119–120
  pre-treatment step **2**:117–119
  recent developments in **2**:132
  set-up **2**:119
  structural alloys **2**:120–123
  thermodynamics of nitriding **2**:109–110
gas nitriding of H13 tool steel **3**:**158–177**
  experimental procedures **3**:160
    nitrided layer characterization **3**:160
    nitriding cycle used for samples **3**:160
    sample preparation **3**:160
  FE analysis **3**:162
    geometric model **3**:162
    initial and boundary conditions **3**:163
    material model **3**:162–163
    simulation model **3**:162
    solution procedure **3**:163–164
  modeling of **3**:160–162
    governing equations and constitutive behavior **3**:162
    numerical solution for the mathematical model **3**:162
    theoretical background **3**:161–162
  nitriding kinetics
    consideration of multiple nitriding on **3**:176
    consideration of surface texture on **3**:175
  nitriding treatment, consideration of profile geometry on **3**:175–176
  results and discussions **3**:164
    effect of profile geometry on nitriding treatment **3**:166–167
    influence of multiple nitriding on nitriding kinetics **3**:170–171
    influence of surface texture on nitriding kinetics **3**:164
  surface preparation **3**:164
gas-carburized steels, heat treatment of **2**:90
gas-carburized tool steels **2**:101–102
gaseous nitrogen **2**:425
gas-phase phenomena **2**:113–114
Gaussian distribution **1**:131, **3**:290
Gaussian power intensity distribution **1**:346
Gaussian surfaces **3**:290
Gauy–Chapman layer **3**:361, **3**:362*F*
GCIB *see* gas cluster ion beam (GCIB)
G-code **1**:139*T*
GEA *see* General Electric Infrastructure Aviation (GEA)
gear **1**:506
  generating process **1**:508
gear burnishing **1**:109–111, **1**:118–119*T*
  advantages **1**:111
  applications **1**:111
  limitations **1**:111
gear burnishing machines **1**:110
  double-die gear burnishing machine **1**:112*F*
  single-die gear burnishing machine **1**:110–111, **1**:112*F*
gear drives **1**:94
gear failures, modes of **1**:94*T*
gear finishing, by AFM **1**:112, **1**:118–119*T*
  advantages **1**:115–116
  AFM machines **1**:113
  AFM parameters **1**:115
  applications **1**:116–117
  components of AFM machine **1**:113–115
  limitations **1**:116
  principle of AFM process **1**:112
  types of AFM process **1**:112
    one-way AFM **1**:112
    orbital AFM process **1**:113
    two-way AFM **1**:112–113
gear finishing process, goals of **1**:95*F*
gear grinding **1**:98, **1**:118–119*T*
  advantages **1**:101
  applications **1**:101
  form or non-generative **1**:98–99
  generative grinding **1**:99–100
    using cup-shaped wheel **1**:100
    using dish-shaped wheel **1**:100
    using rack-tooth worm wheel **1**:100–101
    using threaded wheel **1**:100
  limitations **1**:101
  selection of parameters **1**:101
  types of **1**:98
gear grinding process, different versions of **1**:99*T*
gear hobbing **1**:508–510, **1**:510, **1**:510*F*
  advantages **1**:510
  applications **1**:511
  limitations **1**:510–511
  manufacturing of miniature gear **1**:511*F*
  mini-hob cutters **1**:511*F*
gear honing **1**:103–104, **1**:103*T*, **1**:118–119*T*
  advantages **1**:105
  applications **1**:105
  external honing **1**:104
  internal honing **1**:104
  internal honing over external honing, advantages of **1**:104–105
  limitations **1**:105
  tools used in **1**:104*T*
gear lapping **1**:101–102, **1**:118–119*T*
  advantages **1**:102
  applications **1**:103
  limitations **1**:102
  typical lapping process **1**:102*F*
gear manufacturing processes **1**:96–97
  types of **1**:97*T*
gear materials **1**:97
  abrasives for **1**:103*T*
gear quality
  international standards for **1**:97
  typical applications of **1**:97*T*
gear shape **1**:457–458
gear shaving **1**:105–107, **1**:118–119*T*
  advantages **1**:109
  applications **1**:109
  limitations **1**:109
  mechanism of **1**:106–107
  types of **1**:107
    axial or conventional **1**:107
    diagonal **1**:107–108
    plunge **1**:108–109
    tangential or underpass **1**:108
gear shaving cutters, types of **1**:107*F*
gear shaving process, axes arrangement in **1**:106*F*
gears
  classification of **1**:94
  materials, manufacturing and quality of **1**:96–97
  microgeometry of **1**:95–96
  surface quality of **1**:95
gel **3**:327–328, **3**:328
General Electric Infrastructure Aviation (GEA) **1**:419
generalized Hele-Shaw (GHS) flow model **1**:450
generative grinding **1**:99–100
  using cup-shaped wheel **1**:100, **1**:100*F*
  using dish-shaped wheel **1**:100, **1**:100*F*
  using rack-tooth worm wheel **1**:100–101, **1**:101*F*

generative grinding (*continued*)
using threaded wheel **1**:100, **1**:100*F*
genetic algorithm (GA) **1**:19, **1**:43, **1**:87
geometric simulation model **1**:197
geometrical parameter of coating **3**:52
GFRPs *see* glass-fiber-reinforced plastics (GFRPs)
GHS flow model *see* generalized Hele-Shaw (GHS) flow model
glass fiber composite **1**:204
glass mat thermoplastics (GMT) **1**:219
glass-fiber-reinforced plastics (GFRPs) **1**:204, **1**:206, **3**:48
glass-inserted mold **1**:444
'glow discharge' carburizing **2**:80
glycerin **3**:363–364
GMT *see* glass mat thermoplastics (GMT)
good adhesion property **3**:306
gooseneck casting *see* hot chamber die casting process
GP zones *see* Guinier–Preston (GP) zones
GRA *see* gray relational analysis (GRA)
graded coatings **3**:45
graded cooling **2**:387
grain
boundaries **2**:85*F*
coarsening **2**:8
refinement **1**:418, **1**:420–421, **1**:425, **1**:426, **1**:426*F*, **1**:427
size effect **2**:63, **2**:63*F*
graphite **1**:276–277
graphitization **2**:256
graphitizing annealing **2**:251
gravimetric method **3**:51
gray irons **2**:248
see also cast irons; malleable irons
heat treatment **2**:249–251
annealing **2**:251
austempering **2**:253–255, **2**:254*F*, **2**:255*F*
hardening and tempering **2**:252–253
martempering **2**:255
normalizing **2**:252
stress relieving **2**:249–251
surface hardening **2**:255–256
gray relational analysis (GRA) **1**:223–224, **1**:226
application in optimization of cut characteristics **1**:224–225, **1**:225*F*
determination of optimal joining condition **1**:226
experimental methods and measurements **1**:225
gray relational coefficient calculation **1**:226–227, **1**:227*T*
gray relational grade **1**:227–228, **1**:227*T*, **1**:228*F*
gray system theory **1**:223–224
green coating **3**:50
green cutting **1**:80
grinding **3**:193–194, **3**:307
abrasive belt grinding **3**:194
conventional grinding **3**:193–194
grinding burn **1**:367
grinding cracks **2**:105
prevention **2**:105
grinding fluid **1**:101
grinding wheel speed **1**:101
grinding wheel wear **1**:379
gripper mode **1**:41
Grossmann method **2**:56–57, **2**:60
correlation between **2**:61
multiplying factors **2**:67*T*
ground–equipment–support interactions **1**:41
guided running wire **1**:283
Guinier–Preston (GP) zones **2**:352, **2**:353–354, **2**:412

H

H subdivision state **2**:383
H temper **2**:340*T*
variation **2**:340
H_2S treatment **3**:16–19
H13 steel **2**:235*F*
hadfield steel **2**:197–199, **2**:198*F*, **2**:198*T*
Hall–Petch relation **2**:9
hand lay-up **1**:220, **1**:220*F*
hand stoning process **3**:194
HAp *see* hydroxyapatite (HAp)
hard chrome coatings **3**:49
hard chrome coatings **3**:39–40, **3**:230, **3**:231–232
see also hot-dip galvanized coatings
carbide tools **3**:230–231
deposition **3**:232–233
design **3**:231*F*
effect on workpiece surface finish **3**:235–239
materials and design **3**:232
multilayer **3**:233–234
nanocomposite **3**:235
nanolayer **3**:234–235
hard machining
see also electrical discharge machining (EDM)
applications **1**:51–53
industrial applications **1**:53
industrial applications of hard-part machining **1**:52*F*
workpiece clamping **1**:52–53
cooling techniques applications **1**:80–83
cryogenic machining **1**:80–83
dry machining **1**:80–83
semidry machining **1**:80–83
solid lubricants application **1**:83–86
vegetable oils application **1**:83–86
modeling **1**:75–76
cutting force modeling **1**:75–76
RSs modeling **1**:78–80
tool wear progression modeling **1**:76–78, **1**:78*T*
hard turning **1**:69, **1**:86
hardenability **2**:19–20, **2**:37–38, **2**:50, **2**:249
bands **2**:61–62, **2**:62*F*
boron effect **2**:67–69, **2**:68*F*, **2**:69*F*
carbon content effect **2**:51*F*
criterion for measuring **2**:52–53
mechanism of heat removal during quenching **2**:53
critical cooling rate **2**:51*F*
estimation from chemical composition and austenite grain size **2**:66–67
factors affecting **2**:62–63
alloying elements effect **2**:65–66, **2**:65*F*, **2**:66*F*
austenitizing temperature and time **2**:63–64
carbon content effect **2**:64–65
grain size effect **2**:63, **2**:63*F*
hardness vs. **2**:51–52
Jominy end-quench test **2**:60–61
rockwell hardness **2**:52*F*
hardened steel **1**:47–48
applications
and machining characteristics **1**:49–50
of types **1**:50*T*
machining
characteristics **1**:50*T*, **1**:51*T*
optimization studies in **1**:86–88
soft and hard **1**:48*F*
hardening **1**:47–48, **2**:29–31
double **2**:87–89, **2**:88*F*
of ductile irons **2**:264
factors influencing **2**:31
adequate carbon content to produce hardening **2**:31
austenite decomposition to produce pearlite, bainite, and martensite structures **2**:31–32
heating rate **2**:32
soaking time **2**:32
temperature of heating **2**:32
of gray iron **2**:252–253, **2**:253*F*, **2**:254*F*
case study on **2**:253
heat treatment **2**:19–20
of malleable irons **2**:257–258, **2**:259*F*, **2**:260*F*
single
with core refinement **2**:87, **2**:88*F*
without core refinement **2**:87, **2**:87*F*
hardmetals **2**:449
hardness, low **2**:103
hardness traverse **2**:56–57
hard-part machining (HPM) **1**:47–48
hardened steel **1**:48*F*
industrial applications **1**:52*F*
hard-part turning (HPT) **1**:48–49
qualitative comparison with grinding **1**:48–49, **1**:49*F*
HASL *see* hot-air solder leveling (HASL)
Hastelloy **2**:398, **2**:416
H-atom diffusion **3**:16
HAZ *see* heat-affected zone (HAZ)
hazardless process **3**:364
HB *see* Brinell hardness number (HB)
HCCIs *see* high-chromium cast irons (HCCIs)
HCHCr *see* high carbon high chromium (HCHCr)
HDM *see* hole-drilling method (HDM)
HDPE **1**:443–444
head forging **2**:311
heat preservation **2**:385–386, **2**:386*F*
heat resistance **2**:270
heat treatment **2**:273
high silicon irons **2**:273

heat treatment **2**:2, **2**:273, **2**:292–293, **2**:337, **2**:422
of Al alloys **2**:341–347, **2**:373
Al–4Cu alloy **2**:378–380, **2**:379*F*
all-purpose aluminum alloys **2**:374, **2**:374*F*
annealing **2**:368, **2**:368*T*
for cast alloys **2**:358–363
classification **2**:373, **2**:373*T*
dimensional changes **2**:368
dispersion hardening and dislocation mechanisms **2**:381–382, **2**:382*F*
equilibrium precipitation process **2**:375–377, **2**:375*F*, **2**:376*F*
heat treatment furnaces **2**:341–347
over-aging **2**:380–381, **2**:381*F*
precipitation sequence and aging process **2**:377–378, **2**:377*F*, **2**:378*F*
regression treatment **2**:382, **2**:383*F*, **2**:383*T*
SS and equilibrium precipitation **2**:374–375
strengthening **2**:347–350
stress relief **2**:363–368, **2**:367*F*
sub-classification of solutionizing and aging **2**:373–374
for wrought alloys **2**:357–358
alloying *see* alloying
in α-Ti alloys **2**:292–293
in CP Ti and **2**:292–293
in near α-Ti alloys **2**:291
in α/β-Ti alloys **2**:301–305
annealing **2**:20
austenitic graphitic irons **2**:271
in β-Ti alloys **2**:311–317
of cast irons
carbon content in matrix **2**:248–249
critical temperature ranges **2**:248, **2**:248*F*, **2**:249*T*
hardenability **2**:249
shape and size of castings **2**:249
surface oxidation and decarburization **2**:249
of copper *see* copper, heat treatment of
corrosion resistant high silicon irons **2**:273–276
defects **2**:47–48
overheating **2**:48
quench cracks **2**:47–48
ductile irons **2**:260–262
of gas-carburized steels **2**:90
of gray irons **2**:249–251
hardening **2**:29–31
heat resistant high silicon irons **2**:273
high-chromium white irons **2**:280–281
of malleable irons **2**:256–257
of nickel alloys *see* nickel alloys, heat treatment of
nickel–chromium white irons **2**:277–279
normalizing **2**:27–29
practical aspects of **2**:231–232
austenitization **2**:233
cooling mediums for quenching **2**:233
design, machining, and stress relief **2**:232
heating furnaces **2**:232–233
preheating **2**:233
quality of **2**:234–236
time and temperature of tempering **2**:233–234
processes, types of **2**:5*F*
process variables **2**:9–11
austenitization **2**:10–11
quenching and quenching medium **2**:36–39
stages of **2**:2
heating step **2**:2–3
soaking stage **2**:4
of steel **2**:4–8
common heat treating processes **2**:9
effect of excess heating beyond homogenization **2**:8–9
production of homogeneous austenite **2**:8
steel casting **2**:211–212, **2**:211*F*
tempering **2**:39–42
TRIP **2**:208
troubleshooting **2**:236–237
forging die with premature failure (case study) **2**:239–240
importance of **2**:236–237
ISO VH13 steel **2**:238–239
VF800AT steel **2**:237–238
heat-affected zone (HAZ) **1**:250–251, **1**:251*F*, **1**:391
heating furnaces **2**:232–233
heating rate **2**:3, **2**:384
heating temperature **2**:3–4, **2**:384
heat-treatable alloys **2**:341, **2**:341*T*
heat-treatable aluminum alloys **2**:354
heat-treatment processes **2**:180–181
of AF1410 steel **2**:185–186, **2**:185*F*, **2**:186*F*
of 9Ni4Co steel **2**:184–185
HEL *see* Hugoniot elastic limit (HEL)
Hele-Shaw flow model **1**:444, **1**:444–445, **1**:489
helical gears **3**:373–374, **3**:373*F*
Helmholtz double layer **3**:361
Helmholtz equation **2**:160–161
HER *see* hydrogen evolution reaction (HER)
Hertzian contact **1**:135, **1**:135–136
Hertzian contact theory **1**:122–123
hexavalent chromes **3**:322–323
hexavalent chromium **3**:150
hexavalent non-chromic coatings **3**:320
HIE wire *see* high eagle (HIE) wire
HIF wire *see* high falcon (HIF) wire
high carbon high chromium (HCHCr) **1**:186
high eagle (HIE) wire **1**:238
high falcon (HIF) wire **1**:238
high hawk (HIH) wire **1**:238
high pressure die casting process (HPDCP) *see* die casting process
high real (HIR) wire **1**:238
high sonic (HIS) wire **1**:238
high speed steels (HSS) **1**:50, **1**:106–107, **2**:215, **2**:216–218, **2**:225*F*, **3**:231
microstructure of **2**:216
high strength temperature resistant (HSTR) **3**:359
high temperature stabilization **2**:271
high temperature thermo-mechanical treatment (HT TMT) **2**:392
high tensile strength wires **1**:247–248
molybdenum wire **1**:248
MolyCarb wire **1**:248
steel core wires **1**:248–249, **1**:248*F*, **1**:249*F*
tungsten wire **1**:248
high velocity oxy-fuel (HVOF) **3**:43, **3**:56, **3**:191–192, **3**:207, **3**:208*F*, **3**:208*T*
coatings **3**:209
comparison with thermal spray techniques **3**:209–210
CoNiCrAlY coating **3**:196
HAp–TiO_2 coatings **3**:200
spray **3**:208*F*, **3**:210, **3**:211–213, **3**:213, **3**:214*T*
as-sprayed surface finish **3**:213
history **3**:207
mechanism of coating **3**:208–209
post-deposition surface finish **3**:215–217
pre-deposition surface finish **3**:211–213
principle **3**:207
process technical details **3**:207–208
spray parameters **3**:207–208
surface finish guidelines for **3**:210–211, **3**:212*F*
spray and surface finish **3**:211–213
surface finish guidelines for HVOF spraying **3**:210–211, **3**:212*F*
thermal spray techniques, characteristic parameters of **3**:210*T*
high velocity oxygen-fuel (HVOF) coating of nickel based alloys **3**:**96–110**
corrosion testing of coating **3**:109
experimental **3**:98
analytical expression for residual stress **3**:99
electro chemical tests **3**:99
fracture toughness by indentation tests **3**:98
residual stress measurements by curvature method **3**:98–99
findings and discussions **3**:101–102
coating morphology and metallurgical changes **3**:101–102
electro chemical testing **3**:105–107
laser-treated coatings **3**:103–105
modeling of laser treatment of coating **3**:107–108
laser treatment of coating and numerical study **3**:109
literature review and background **3**:96–98
mathematical modeling **3**:99–101
numerical solution **3**:101
single layer coating **3**:101–102, **3**:109
two laser coating **3**:102–103, **3**:109
high-alloy irons **2**:248, **2**:277*F*
see also ductile irons
heat treatment **2**:269–271
abrasion resistant high-alloy white irons **2**:276–279
austenitic graphitic irons **2**:269–271
heat resistant high silicon irons **2**:273
heat treatment of corrosion resistant high silicon irons **2**:273–276
oxidation resistant high-aluminum irons **2**:276

high-alloy nickel–chromium white irons **2**:277–278
high-carbon, high-chromium cold-work steels **2**:217–218*T*, **2**:219–221*T*
high-carbon high-alloy steels **2**:194
high-chromium cast irons (HCCIs) **2**:284–285
high-chromium white irons heat treatment **2**:280–281
high-molecular-weight polymers **1**:481
high-resolution transmission electron microscopy (HRTEM) **3**:287*F*
high-speed machining (HSM) **1**:51
high-temperature (HT) **2**:340*T*
  batch annealing **2**:195
high-temperature X-ray diffraction (HTXRD) **2**:329, **3**:8, **3**:11
HIH wire *see* high hawk (HIH) wire
HIP *see* hot isostatic pressing (HIP)
HIR wire *see* high real (HIR) wire
HIS wire *see* high sonic (HIS) wire
hob **1**:508–509
hole-drilling method (HDM) **1**:415–416, **3**:57, **3**:58–59, **3**:58*F*
  XRD method vs. **1**:416–417
HOMMELWERKE TURBO RAUHEIT V 6.14 **1**:31
homogeneous austenite
  production of **2**:8
  time–temperature relationship in **2**:11*F*
homogeneous palladium coating **3**:6
homogenization **2**:4, **2**:211
  annealing **2**:24
  treatment **2**:400–401
homogenized and quenched (HQ) sample **2**:327, **2**:328*F*, **2**:329
homopolycondensation **1**:217
honing **3**:194
  gear **3**:373–374
  process **3**:194
Hooke's law **1**:414–415
horizontal micro-EDM working system **1**:289
hot and cold rolling **2**:383
  sheets/plates, tempers for **2**:382–383, **2**:384*T*, **2**:385*T*
hot chamber die casting process **1**:514
hot compression moldings **1**:219
hot dip galvanized wire **1**:249
hot embossing **1**:526
  advantages **1**:526
  applications **1**:527
  limitations **1**:527
hot forged/extruded profiles, tempers for **2**:382, **2**:384*T*
hot forging die, with complex geometry **2**:244
hot forming tools **2**:240
hot isostatic pressing (HIP) **1**:512, **3**:197, **3**:339, **3**:348
hot press processes **1**:218
hot pressing (HP) **3**:348
hot upset forging **1**:525
hot working tool steels **2**:216, **2**:223*F*
  carburization of **2**:101–102
  gas carburizing cycle for **2**:101*F*
hot-air solder leveling (HASL) **3**:221
hot-dip galvanization **3**:41
  composite in **3**:28–29
  influence of metal oxides on **3**:26–28, **3**:28*F*
hot-dip galvanized coatings **3**:184
  see also hard coatings
  alloy layers **3**:26*F*
  composite in galvanization process **3**:28–29
  developments in metal composites incorporated in **3**:25–26
  implication of metal composites **3**:30–31
  metal oxide influence **3**:26–28, **3**:28*F*
hot-dip galvanizing process **3**:47, **3**:178–181, **3**:179*F*, **3**:183*T*, **3**:186*F*, **3**:187
  applications **3**:179*F*
  batch hot-dip galvanizing processes **3**:181–183, **3**:182*F*
  continuous hot-dip galvanizing processes **3**:181–183, **3**:182*F*
  failure mechanisms in galvanized steels **3**:187–188
  galvanizing of AHSS **3**:185–187
  presence of elements in galvanizing bath **3**:184–185
  research and development activities in **3**:183–184
hot-dip zinc coating
  physico-chemical properties of metal oxide containing **3**:30–31
  preoxidation of steel **3**:29–30
hot-work die steel **2**:190
HP *see* hot pressing (HP)
HP9–4–30 steel **2**:184
HPM *see* hard-part machining (HPM)
HPT *see* hard-part turning (HPT)
HQ sample *see* homogenized and quenched (HQ) sample
HRTEM *see* high-resolution transmission electron microscopy (HRTEM)
HSM *see* high-speed machining (HSM)
HSS *see* high speed steels (HSS)
HSS-Co twist drill **1**:211
HSTR *see* high strength temperature resistant (HSTR)
HT *see* high-temperature (HT)
HT TMT *see* high temperature thermo-mechanical treatment (HT TMT)
HTXRD *see* high-temperature X-ray diffraction (HTXRD)
Hugoniot elastic limit (HEL) **1**:409–410
HVOF *see* high velocity oxy-fuel (HVOF)
hybrid design **1**:143–144
hybrid finishing process **1**:98
hybrid materials **3**:119
hybrid process **1**:294–296
  continuous machining process of array micro-holes **1**:296–298
  finishing process **3**:371
  hybridized material removal process **1**:270
  LIGA–micro-EDM hybrid machining process **1**:298–300, **1**:300*F*
  micro-turning–micro-EDM hybrid machining process **1**:294–296
  self-drilled holes–TF-WEDG hybrid machining process **1**:296
  superfinishing process **3**:372
hybrid technology *see* combination technology
hybrid tool, model for **1**:146*F*
hydrazine based plating bath **3**:6
hydrochloric acid **3**:222
hydrofluoride **3**:226
hydrogen **3**:14, **3**:207–208
  applications in hydrogen purification **3**:14–16
  permeability **3**:14
  permeation properties **3**:15–16
    activation energy for **3**:18*F*
    function of pressure gradient **3**:16*F*
    literature permeability results **3**:17*T*
  separation **3**:8
hydrogen evolution reaction (HER) **3**:87, **3**:92–93
hydrolysis **3**:328
hydrophobic coatings **3**:49
hydrophobic surfaces **3**:282
  droplets slides on **3**:283*F*
hydrophobicity and surface finish **3:137–148**
  effect of dust accumulation on PV cell efficiency **3**:137
  historical background **3**:137
  polycarbonates (PCs) **3**:137–138
    crystallization process of **3**:138
  solid–liquid interface and PC-liquid acetone **3**:142–143
    AFM micrographs **3**:142–143
    Fourier transform infrared (FTIR) technique **3**:147
    hydrophobicity assessments **3**:145–147
    scanning electron micrographs **3**:144
    surface roughness **3**:144–145
    X-ray diffraction (XRD) technique **3**:147
  superhydrophobic surfaces
    fabrication methods and technologies of **3**:140–142
  theoretical models **3**:138
    effect of chemical treatment and roughness on surface hydrophobicity **3**:139
    fundamentals **3**:138
    rough surfaces, classification of **3**:140
    self-cleaning surfaces **3**:140
    Wenzel and Cassie–Baxter states **3**:139–140
    Young's equation **3**:138–139
hydroxide solutions **3**:200
hydroxyapatite (HAp) **3**:196, **3**:349, **3**:350
  X-ray diffraction pattern **3**:353*F*
hyperelastic material theory **1**:147–148
hypereutectoid steels **2**:2–3, **2**:16*F*
  annealing of **2**:23, **2**:23–24
hypophosphite **3**:4
hysteresis of contact angle **3**:278–279, **3**:297–298

I

I surfaces *see* interrupted surfaces (I surfaces)
IACS *see* International Annealed Copper Standard (IACS)
IADS *see* International Alloy Development System (IADS)
IBF *see* ion beam figuring (IBF)
ICCO *see* International Cocoa Organization (ICCO)
ICDD database *see* International Centre for Diffraction Data (ICDD) database
ICM *see* injection compression molding (ICM)
ideal critical diameter **2**:59–60, **2**:59*F*, **2**:60*F*
ideal quenching medium **2**:58–59
ideal separation factor **3**:14
IEG *see* interelectrode gap (IEG)
IF steel *see* interstitial-free steel (IF steel)
IGA *see* improved genetic algorithm (IGA); intergranular attack (IGA)
ilmenite **2**:289
IM process *see* injection molding (IM) process
image particle-finding method **3**:273*F*
imaging systems **3**:261–263
  for surface characterization **3**:261–263
IMM *see* injection molding machine (IMM)
immobilization **1**:42
impact wear resistance **2**:437
impression forging *see* closed die forging
improved genetic algorithm (IGA) **1**:20–21
in situ method **3**:59, **3**:60*F*
INCO *see* International Nickel Company (INCO)
incomplete annealing **2**:22–23
Inconel **2**:398, **2**:416
Inconel 625 coating **3**:98, **3**:102
incubation period **2**:7
indentation testing **3**:52
indentation tests, fracture toughness by **3**:98
Indian Standard Specifications (ISS) **1**:507
indirect second stage graphitization **2**:27
induction hardening **2**:154, **2**:256
induction surface hardening *see* surface induction hardening
inductor–hardened body system **2**:168–169
inductor–sprayer system **2**:163, **2**:164, **2**:165–166, **2**:166
industrial coating **3**:150
infrared reflection-absorption spectroscopy (IRRAS) **3**:284*F*
ingot **1**:524
initial contact point **1**:121–122
injection compression molding (ICM) **1**:511, **1**:518–519
  advantages **1**:518–519
  applications **1**:519
  limitations **1**:519
injection electrode ELID grinding system **1**:386*F*
injection molding (IM) process **1**:442, **1**:479
  critical factors influencing part quality in **1**:480
  injection molding cycle **1**:479–480, **1**:479*F*
  modeling of **1**:491–492
    cooling phase of injection molding **1**:496
    feedstock properties and mixing simulation **1**:491–492, **1**:492–493
    filling phase of injection molding **1**:495
    fundamentals of governing equations and boundary conditions **1**:493–494
    melt flow behavior in micro-size channel **1**:494–495
    packing phase of injection molding **1**:495–496
  optimization techniques for **1**:485*F*
    simulation-based **1**:485*F*
  principles of **1**:479
  processing variables of **1**:486*T*
injection molding equipment **1**:467–468
  auxiliary equipment for **1**:473
  feedstock mixing mechanism **1**:468
injection molding machine (IMM) **1**:467–468, **1**:468–470
  based on injection unit **1**:469*F*
  clamping unit **1**:473
  experimental setup of control system for **1**:487*F*
  horizontal **1**:468, **1**:469*F*
  hybrid **1**:468, **1**:469*F*
  mold design **1**:470–472, **1**:471*F*
  part design for micro-PIM **1**:473
  runner and gating system design **1**:472–473, **1**:472*F*
  screw design for **1**:470
  vertical **1**:468, **1**:469*F*
inorganic sealers **3**:199–200
  aluminum–phosphate **3**:199–200
  chemical treatment **3**:200
  chemical vapor deposition **3**:200
  electroplating **3**:200
  enameling **3**:200
  molten metal or oxide penetration **3**:200
  sealing using glass formers **3**:200
  sol–gel process **3**:200
instrumental effects **1**:417
integrated automation system **1**:53–54
intelligent algorithms **1**:487
intended metal **3**:330
intercritical annealing **2**:22–23
interelectrode gap (IEG) **3**:359–360, **3**:369
intergranular attack (IGA) **3**:370
intergranular corrosion **2**:200–201
interlamellar spacing **2**:252
intermediate thermal-mechanical treatment (ITMT) **2**:391–392
intermetallic compounds **2**:374, **2**:378, **2**:390–391, **3**:220
internal honing **1**:104
  external spur gear **1**:105*F*
internal turning **1**:26, **1**:27, **1**:28*F*
International Alloy Development System (IADS) **2**:337–338
International Annealed Copper Standard (IACS) **1**:237, **1**:244, **2**:399
International Centre for Diffraction Data (ICDD) database **3**:160
International Cocoa Organization (ICCO) **1**:204
International Nickel Company (INCO) **2**:416
International Organization for Standardization (ISO) gear standard **1**:507
international tool steel classification standards **2**:219–221*T*
interrupted surfaces (I surfaces) **1**:71
interstitial solid solution **2**:84*F*
interstitial-free steel (IF steel) **3**:183
  recrystallized structure of **2**:26*F*
intrinsic stresses **3**:57
INVAR 36 alloy powders **1**:476*T*
ion beam figuring (IBF) **1**:164–166
ion implantation **2**:125, **3**:202–203
ion shot ELID (ELID IV) grinding **1**:370
  principle of **1**:371*F*
iron **1**:281
  allotropy **2**:218–222
  flow of carbon in **2**:82–85
  and iron–carbide equilibrium **2**:83*F*
iron–carbon alloy **2**:2, **2**:3–4
iron–carbon equilibrium **2**:222
iron–carbon martensites **2**:19–20
iron–iron carbide equilibrium **2**:74, **2**:75*F*
iron–nitrogen system **2**:109–110
  binary phase diagram **2**:110*F*
IRRAS *see* infrared reflection-absorption spectroscopy (IRRAS)
ISO gear standard *see* International Organization for Standardization (ISO) gear standard
ISOMAX **2**:241
isostrain **1**:213
isostress **1**:213
isothermal annealing **2**:20–22, **2**:21*F*
isothermal transformation behavior **2**:6–7, **2**:7–8
ISS *see* Indian Standard Specifications (ISS)
Italian Gear standard **1**:507
ITMT *see* intermediate thermal-mechanical treatment (ITMT)

J

Japanese Gear Manufacturing Association (JGMA) standard **1**:507
Japanese Industrial Standards (JIS) gear standard **1**:507
Jeol 6460 electron microscopy **3**:74
JEOL JDX-3530 SEM and EDS **3**:98
Jeol JSM-6460LV scanning electron microscope **3**:160
JGMA standard *see* Japanese Gear Manufacturing Association (JGMA) standard
JIS gear standard *see* Japanese Industrial Standards (JIS) gear standard
Johnson–Cook equation **1**:76

Jominy end-quench test **2**:60–61, **2**:60*F*, **2**:61*F*
correlation between **2**:61, **2**:61*F*
hardenability bands **2**:61–62

K

kerf variations **1**:223
kerf width **1**:222–223, **1**:349, **1**:351, **1**:358, **1**:358–359, **1**:362–363
different in process **1**:223, **1**:223*F*
variations **1**:223
kerosene **1**:278
kinetics **2**:387
Kirchhoff-Fourier equation **2**:161
Kirkendall effect **3**:11
knitting fiber **1**:218
KNN *see* potassium sodium niobate (KNN)
KOEPFER gantry loader **1**:53–54
Kriging **1**:484
KTN *see* potassium tantalate niobate (KTN)
kurtosis **1**:12

L

lacquer **3**:149
LAM *see* laser-assisted machining (LAM)
Lame equations **2**:161
lamella **3**:209
primary morphologies **3**:209*F*
lamina **1**:213, **1**:214*F*
Langevin function **1**:148
lapping process **3**:194
large step-over size **1**:127*F*
LASER *see* Light Amplification by Stimulated Emission of Radiation (LASER)
laser ablation **3**:122
laser beam processing for surface modifications *see* laser surface: treatment
laser bending **1**:352
experimental **1**:352
mathematical analysis **1**:352–354
results and discussions of **1**:359–361
self-annealing effect **1**:359, **1**:361
laser cutting process **1**:348–350
cut quality assessment **1**:351
evaluation of cut quality **1**:351
factorial analysis **1**:351–352
experimental method **1**:349–350
thermal analysis **1**:349–350
lump parameter analysis for Kerf size **1**:350–351
results and discussions of **1**:357–359
laser drilling **1**:345–347
experimental method **1**:347
hole quality assessment **1**:347–348
evaluation of hole geometric features **1**:347–348
factorial analysis **1**:348
results and discussions of **1**:354–357
qualitative analysis **1**:355–357
quantitative analysis **1**:357
laser interference lithography (LIL) **3**:125, **3**:125–126
laser machining (LM) **1**:344, **3**:122, **3**:124
laser conduction limited heating **1**:345
laser nonconduction limited heating **1**:345
laser micromachining **1**:330–331
laser optics **1**:166
laser peening **1**:408, **1**:409, **1**:409–410, **1**:425–427, **2**:174
advantages and disadvantages and applications **1**:418–419
AFM surface topography **1**:424*F*
confined ablation process **1**:413*F*
conventional shot peening **1**:409
future trends **1**:435
laser beam irradiating material surface **1**:410*F*
laser-peened materials relaxation behavior **1**:431
grain and dislocation evolution during isothermal annealing **1**:434*F*
mechanical relaxation of residual stress **1**:431
thermal relaxation of residual stress **1**:431–435
laser systems **1**:411, **1**:412–413*T*
magnifications of 6061-T6 alloy **1**:430*F*
mechanical and metallurgical effects
corrosion properties **1**:427–429
deformation mechanism **1**:425–427
fatigue properties **1**:422–425
LY12CZ specimens **1**:425*F*
metallurgical modifications during **1**:419–422
tensile properties **1**:425–427
welded joints **1**:429–431
residual stresses
crystallite size and micro-strain **1**:417–418
distribution **1**:416*F*, **1**:424*F*
generation **1**:413–414, **1**:414*F*
measurement of residual stresses **1**:414–415
SEM photographs of laser-peened surfaces **1**:423*F*
shock wave formation **1**:411–413
shot peening vs. **1**:410
stress corrosion cracking test results of SUS304 **1**:429*F*
laser peening without coating (LPWC) **1**:416
laser polishing **1**:166
laser polymerization, materials for **3**:117–118
hybrid materials **3**:119
organic photopolymers **3**:118–119
photoinitiators **3**:118
SU-8 **3**:119
laser shock peening (LSP) principle **3**:123, **3**:123*F*
laser surface
ablation **3**:72
of ceramics **3**:125
modification **1**:408
treatment **2**:137, **2**:140
experimental studies **2**:137–139
phosphorous bronze **2**:139, **2**:141–143, **2**:151
Rene 41 **2**:140–141, **2**:146–151, **2**:151
yttria-stabilized zirconia **2**:139–140, **2**:143–146, **2**:151
laser surface texturing (LST) **3**:123
laser treatment, modeling of
of coating **3**:107–108
laser treatment of coating and numerical study **3**:109
laser(s) **2**:137
beam intensity distribution **2**:137
energy **1**:411
engraving **3**:203
gas-assisted nitriding **2**:132
machining **1**:221–222
melting/ablation parameters **2**:138, **2**:138*T*
remelting **3**:196, **3**:196
shock processing **1**:409–410
surface modification **1**:408
systems for laser peening **1**:411
texturing **3**:71–72, **3**:72
alumina tiles **3**:72–73
experimental work **3**:74–75
PC sheet **3**:72
phosphorous bronze **3**:73–74
results and discussion **3**:75–78
laser-assisted machining (LAM) **1**:331, **3**:124, **3**:124–125
laser-based surface texturing techniques **3**:122–126
laser-matter interactions, spectrum of **3**:122*F*
laser-treated coatings **3**:103–105
laser-treated layer **3**:73–74
laser-workpiece interaction mechanism **1**:345
lath martensite microstructure **2**:92*F*
layer removal (LR) **3**:58–59
LC-ALPHAIII *see* CO_2 laser
LCD *see* liquid crystal display (LCD)
L/D ratio *see* length–diameter (L/D) ratio
lead-free ferroelectric ceramics, SPS in **3**:352–354
lead-free materials **3**:349
lead-free solders **3**:222
least-squares (LS) **1**:88
Lehrer diagrams **2**:110–112
hypothetical surface reactions **2**:111*F*
representation of **2**:111*F*
LEI *see* lower detector (LEI)
LEIS *see* low energy ion scattering (LEIS)
length–diameter (L/D) ratio **1**:31
leveling effect **3**:369
LGVs *see* light goods vehicles (LGVs)
Lifshitz–van der Walls components **2**:139*T*
light alloys **2**:430–431
Light Amplification by Stimulated Emission of Radiation (LASER) **1**:330–331
light goods vehicles (LGVs) **2**:442
LIL *see* laser interference lithography (LIL)
lime-alumina-borosilicate glass *see* E-glass fiber
line scanning **3**:273
linear micro-scratch tester **2**:138

linear polycondensation **1**:217
linear polymers **1**:217
linear variable differential transformer (LVDT) **3**:61
line-of-sight process **3**:233
liquid carburization **2**:73, **2**:76–77
  advantages **2**:77
  carburizing process
    high temperature baths **2**:77
    low temperature baths **2**:76–77
  disadvantages **2**:77
  safety precautions **2**:77–78
liquid carburizing baths
  composition of **2**:77*T*
  sodium cyanide content in **2**:77*T*
liquid cooling stage **2**:53
liquid crystal display (LCD) **3**:113–114, **3**:114, **3**:114*F*
liquid diffusion **3**:42
liquid helium (LHe_2) **2**:423–424
liquid metal-assisted cracking (LMAC) **3**:187–188, **3**:187*F*, **3**:188*F*
liquid nitrogen (LN_2) **2**:422
liquid petroleum **1**:278
LIS *see* lubricant impregnated surfaces (LIS)
liter per minute (lpm) **3**:366
Lithographie Galvanoformung Abformung (LIGA) **1**:322
  LIGA–micro-EDM hybrid machining process **1**:298–300, **1**:300*F*
lithography **3**:292, **3**:292*F*
lithography, electroforming and molding **1**:511, **1**:521–522
  advantages **1**:522
  applications **1**:522
  limitations **1**:522
LM *see* laser machining (LM)
LMAC *see* liquid metal-assisted cracking (LMAC)
local maxima **1**:223
local minima **1**:223
long wavelength **1**:223
loose-abrasive grinding **1**:154–157
  conventional loose-abrasive grinding **1**:154–157
  unconventional loose-abrasive grinding **1**:157–158
loose-abrasive polishing **1**:159–162, **1**:159
lotus effect **3**:277
low alloy steels, carburization of **2**:94
  chromium–nickel steel **2**:94
  molybdenum–nickel steel **2**:94–96
low energy ion scattering (LEIS) **3**:8
low temperature tempered (LTT) martensite **2**:91
low temperature tempering **2**:387
low temperature thermo-mechanical treatment (LT TMT) **2**:392
low-alloy special-purpose tool steels **2**:217–218*T*, **2**:219–221*T*
lower detector (LEI) **3**:91*F*, **3**:92
low-molecular-weight polymers **1**:481
low-pressure injection molding (LPIM) **1**:467
low-pressure PIM (L-PIM) **1**:521
LPIM *see* low-pressure injection molding (LPIM)
L-PIM *see* low-pressure PIM (L-PIM)
lpm *see* liter per minute (lpm)
LPWC *see* laser peening without coating (LPWC)
LR *see* layer removal (LR)
LS *see* least-squares (LS)
LSP principle *see* laser shock peening (LSP) principle
LST *see* laser surface texturing (LST)
LT TMT *see* low temperature thermo-mechanical treatment (LT TMT)
LTS-KNN *see* $(Na_{0.52}K_{0.44}Li_{0.04})(Nb_{0.86}Ta_{0.06}Sb_{0.08})O_3$ (LTS-KNN)
LTT martensite *see* low temperature tempered (LTT) martensite
lubricant impregnated surfaces (LIS) **3**:142
LVDT *see* linear variable differential transformer (LVDT)

M

M05 ⊥ S05 reverse 'T' micro channel **1**:454
M08 + S05 cross '+' micro channel **1**:455–456
machinability **1**:17, **2**:270
machine–fixture–tool–work system (M–F–T–W system) **1**:74
machining **1**:26, **1**:27, **1**:55, **1**:70, **3**:193
  conditions **1**:1–4
    cutting fluids **1**:1–4
    method of fluid application **1**:1–4
    tool vibration **1**:4–6
  factors affecting cut quality **1**:222–223
    kerf width **1**:222–223
    surface roughness **1**:223–224, **1**:224*F*
  of natural fiber-reinforced composite **1**:221–222
  parameters **1**:29, **1**:30
  parameters effect **1**:13–17, **1**:19*T*
    on surface roughness **1**:18*T*
  safety considerations **1**:222
machining processes, general characteristics of **3**:259*T*, **3**:259–260*T*
macro–micro flow model **1**:445
macro flow model **1**:444
macro-gears **1**:506
  shape **1**:458–461
macro-geometry of insert **1**:56–58
macroroughness **1**:223
macro-stress **2**:38–39
magnesium alloys **2**:448
magnesium stearate **3**:285
magnetic resonance imaging (MRI) **1**:206
magnetic spoiling **2**:196
magnetorheological (MR) fluid **1**:161
magnetorheological finishing (MRF) **1**:161
magnetron **3**:233
  sputtering **3**:233
malleable irons **2**:248
  see also cast irons; gray irons
  heat treatment **2**:256–257, **2**:256*T*
    bainitic heat treatment of malleable irons **2**:258
    blackheart malleable iron **2**:257
    hardening and tempering of malleable irons **2**:257–258
    martempering of malleable irons **2**:258
    surface hardening of pearlitic malleable irons **2**:258–260
    whiteheart malleable iron **2**:256–257
malleablizing annealing **2**:256
mandrel **1**:219
  testing **3**:51–52, **3**:51*F*
  wrapping **1**:220
manganese **2**:14, **2**:265, **2**:271
MAPP *see* methyl acetylene propadiene (MAPP)
maraging steel **2**:205–207, **2**:206*F*, **2**:206*T*
  embrittlement in **2**:207–208
  heat-treatment sequence **2**:206*T*, **2**:207, **2**:207*F*, **2**:208*F*
marine coating **3**:150
martempering **2**:43–44, **2**:44*F*
  of gray iron **2**:255
  of malleable irons **2**:258
martensite **2**:7–8, **2**:90–91, **2**:409–410, **3**:336
  finish **2**:424
  formation **2**:90–91
  heating of **2**:226
  microstructure **2**:31*F*, **2**:156
  morphologies **2**:91–92
  tempering, effect of **2**:92
  transition carbides, role of **2**:92
martensite reorientation (MR) **2**:325–326
martensite start (Ms) temperature **2**:255, **2**:264, **2**:266, **2**:282
martensite transformation curve **2**:45*F*
martensitic stainless steel **2**:199–200, **2**:199*T*, **2**:200*F*, **2**:201*F*
martensitic transformation (MT) **2**:3–4, **2**:19–20, **2**:222–224, **2**:322
  in Ti–Ni alloys **2**:322–324
mass flow rate **1**:449
mass transport phenomenon in ECM **3**:369
master decomposition curve (MDC) **1**:480–481
  evaluation of apparent activation energy **1**:481–482
  multistep burnout process **1**:482–483
  single-step burnout process **1**:481
master sintering curve (MSC) **1**:481
material laser ablation **3**:122, **3**:122*F*
material migration **1**:314–317
material removal processes
  conventional process **1**:268
  hybridized process **1**:270
  nonconventional process **1**:268–270
material removal rate (MRR) **1**:101, **1**:154, **1**:154–155, **1**:156, **1**:171, **1**:268–270, **1**:280, **1**:306–311, **3**:366
  ANOVA for **1**:307*T*
mathematical flow model **1**:449–450
  ANSYS CFX flow model **1**:450–451
  MoldFlow flow model **1**:450
  suggestion non-Newtonian viscosity model **1**:451
mathematical modeling **1**:194–195, **1**:194*F*, **1**:448–449

Matlab **3**:273
matrix material, composite types based on **1**:212
  CMC **1**:212
  MMC **1**:212
  PMC **1**:212–215
MBD *see* multibody dynamics (MBD)
MBEDG *see* moving block electrical discharge grinding (MBEDG)
MCS *see* Monte Carlo step (MCS)
MD *see* molecular dynamics (MD)
MDC *see* master decomposition curve (MDC)
MDM *see* modified distance method (MDM)
MDN250 steel **1**:16
mean contact stress **1**:137
mean residual (MR)
  defined **1**:482
mechanical attrition **2**:175*F*, **2**:178
mechanical finishing **3**:192–193
  effect of finishing on coatings **3**:194–195
  grinding **3**:193–194
  modeling finishing process **3**:195
  polishing techniques **3**:194
  turning **3**:193
mechanical pen method **3**:288
mechanical polishing **3**:307–308
mechanical property **2**:374, **2**:382
mechanical stress **2**:241
mechanical surface treatment, recent advances in **2:171–179**
  peening **2**:171–172
    laser peening **2**:174
    shot peening **2**:171–172
    warm peening **2**:173–174
  SMAT **2**:174–176
    mechanism of surface nanocrystallization by SMAT **2**:176
    microstructure characterization of the SMAT **2**:176
    properties of SMAT surface layer **2**:176–178
    SMAT process **2**:175–176
mechanical twins (MTs) **1**:426–427
mechanistic modeling **1**:76
medium-carbon low-alloy steels **2**:181, **2**:188, **2**:188*F*
  chromium–molybdenum steel **2**:192
  forging quality steel **2**:181, **2**:182–183*F*
  heat treatment **2**:184–185, **2**:185–186, **2**:185*F*, **2**:186*F*
  medium-carbon chromium–vanadium steel **2**:192
  nanoscale precipitations hardenable steel **2**:187–188
  Ni–Cr structural steel **2**:189–192, **2**:190*F*, **2**:191*F*
  precipitation hardened martensitic steels **2**:181–184, **2**:184*F*
  press hardenable ultrahigh-strength steel **2**:186–187
  Si-modified 4340 steel **2**:188–189
medium-frequency (MF) **3**:233
MEKP *see* methyl ethyl ketone peroxide (MEKP)
MEMS *see* micro-electromechanical systems (MEMS)
MEMS/NEMS *see* micro/nano electromechanical systems (MEMS/NEMS)
MEO *see* micro-arc oxidation (MEO)
meso-gears **1**:506
metal
  composition **2**:264–266
  deposition **3**:3
  ELID grinding for **1**:374–377
  fibers **1**:209
metal composite
  in hot-dip galvanized coating **3**:25–26
  implication for performance of zinc alloy coating **3**:30–31
    electrochemical characteristics of zinc coating **3**:32–35
    enhancement in surface topographical characteristics **3**:31–32, **3**:31*F*
    physico-chemical properties of metal oxide **3**:30–31
metal injection molding (MIM) **1**:467, **1**:511, **1**:516–518, **1**:517*F*
  advantages **1**:518
  applications **1**:518
  inspection and quality control of MIM products **1**:498–499
  limitations **1**:518
  potential causes and remedies of common defects in **1**:498*T*
  process capabilities **1**:517–518
metal injection molding feedstock, composite and formulation of **1**:478*T*
metal injection molding powders **1**:475*T*
metal matrix composites (MMCs) **1**:10, **1**:212, **1**:232, **2**:446, **3**:51
metal oxide
  direct blending of molten bath with **3**:29
  incorporation methods **3**:28–29
    direct blending of molten bath **3**:29
    formation of predeposited metal oxide layer **3**:28–29
    preoxidation of steel prior to hot-dip zinc coating **3**:29–30
    vacuum coating techniques **3**:29
  influence on hot-dip galvanization process **3**:26–28, **3**:28*F*
metal powder **1**:475–476
  characteristics and test standard **1**:476*T*
metal-cutting process **1**:27
metallic coatings **3**:183
metallic gear materials **1**:506–507
metallography and numerical results **3**:167–169
metallurgical analysis **2**:307, **2**:308–309
metallurgical modifications during laser peening **1**:419–422
metamaterials **3**:119–121
metamodel-based method **1**:484
methyl acetylene propadiene (MAPP) **3**:207
methyl ethyl ketone peroxide (MEKP) **1**:220
methyltrimethoxysilane (MTMS) **3**:141
MF *see* medium-frequency (MF)
Mg-alloys, heat treatment of **2**:36, **2**:36*T*
micro channel fabrication and experimental design **1**:451–452
micro depth of cut of a polishing tool **1**:132–133
micro depth of cut of a single grain **1**:131–132
micro drilling **1**:268
micro flow model **1**:444–445, **1**:446–447
micro gear shape **1**:461
  with 0.3 mm teeth **1**:462
  with 0.5 mm teeth **1**:461–462
  with 1.0 mm teeth **1**:461
micro part fabrication **1**:442–443
micro plastic injection molding **1**:442–444
  custom-made vertical injection molding machine **1**:447–448
    injection mechanism **1**:448
    mold design **1**:448
    plasticizing unit and injection mechanism **1**:447–448
  factors affecting **1**:446
    micro flow model factors **1**:446–447
    pressure **1**:446
    size **1**:447
    temperature **1**:446
    viscosity in micro molding **1**:447
  flow model **1**:444
    macro flow model **1**:444
    macro – micro flow model **1**:445
    micro flow model **1**:444–445
    viscosity for micro injection molding **1**:446
    viscosity model **1**:445–446
  flow observation **1**:444
  literature reviews **1**:447
  machine for **1**:443–444
  macro and micro gear shape molding **1**:457–461
  straight, reverse 'T' and cross '+' micro channel flow **1**:448–450
    experiments and simulation for cross '+' micro channel **1**:455–456
    experiments and simulation for straight channel **1**:452
    mathematical flow model **1**:449–450
    micro channel fabrication and experimental design **1**:451–452
micro wire EDM **1**:333
micro/nano electromechanical systems (MEMS/NEMS) **1**:505–506
micro/nano polishing **1**:339
micro/nano textures **3**:83–84
microalloyed steels, carburization of **2**:96–98
  niobium-microalloyed steel **2**:98
  vanadium-microalloyed steel **2**:97–98
microalloying elements **2**:97
micro-arc oxidation (MEO) **3**:202
micro-crack **1**:312–314
microdrilling **1**:324, **1**:328
micro-EDM (μ-EDM) process **1**:182–186, **1**:273*F*, **1**:385–388, **1**:527, **1**:529
  electrode material for **1**:277
  function and types **1**:272–274
  of nonconductive ceramics **1**:333–334
    assisting electrode **1**:334

dielectric fluid **1**:334–335
mechanism of material removal **1**:335–337
recast layer **1**:337–338
online measurement **1**:301*F*
process parameters **1**:279–280
fabrication processes of microelectrode **1**:282–283
performance measure **1**:280
prospective on process selection **1**:300–303
pulse generators/power supply **1**:274
system configuration **1**:289*F*
WC–Co **1**:304–305
analysis of results **1**:305–306
Microelectro Mechanical System **1**:268
microelectrode
fabrication processes **1**:282–283
measuring frontal wear **1**:303*F*
morphology with thermal properties of materials **1**:282*F*
wear **1**:281*F*
micro-electromechanical systems (MEMS) **3**:112, **3**:359
microfabrication of parts and components **1**:498
microfluidics **3**:112
micro-gears **1**:506
microgeometry of gear **1**:95, **1**:95–96
micro-geometry of insert **1**:56–58
micro-grinding system setup **1**:269*F*
microhardness **2**:330
measurements **2**:94
micro-holes **1**:281*F*, **1**:306*F*
surface characteristics **1**:394*F*
microinjection molding machine (μIMM) **1**:467–468
microinjection molding process **1**:483–486
analytical and numerical methods for **1**:496
application of computer modeling in **1**:489–490
Carreau model **1**:492
computer simulation and molded part quality enhancement **1**:490–491
cooling phase of injection molding **1**:496
cross model **1**:492
developments in simulation of **1**:490
Ellis model **1**:492
feedstock properties and mixing simulation **1**:491–492, **1**:492–493
filling phase of injection molding **1**:495
fundamentals of governing equations and boundary conditions **1**:493–494
melt flow behavior in micro-size channel **1**:494–495
packing phase of injection molding **1**:495–496
power law model **1**:491–492
design of experiment (DOE) approach **1**:483, **1**:484, **1**:486
optimization methods **1**:486–489
parameter control **1**:484–486
process simulation and quality characteristics **1**:496–497
micro-lubrication *see* minimum quantity lubrication (MQL)
micromachining **1**:268, **1:322–343**
electrical discharge machining (EDM) **1**:332–333
electrical discharge (ED) micromilling **1**:333
micro-EDM of nonconductive ceramics **1**:333–334
micro wire EDM **1**:333
electrochemical machining (ECM) **1**:338–339
deburring **1**:339–340
micromachining **1**:338–339
micro/nano polishing **1**:339
energy beam micromachining **1**:330–331
electron beam machining (EBM) **1**:332
focused ion beam (FIB) **1**:331
laser micromachining **1**:330–331
silicon micromachining **1**:328–330
bulk micromachining **1**:329–330
surface micromachining **1**:330
size effect **1**:322–323, **1**:323
tool based **1**:323
ductile regime machining **1**:325–326
microdrilling **1**:324
micromilling **1**:323
minimum quantity lubrication (MQL) **1**:324–325
tooling **1**:326–328
micrometal injection molding (μMIM) **1**:467
fabrication capabilities of **1**:498
micrometal PIM technology **1**:500
micromilling **1**:323
electrical discharge (ED) micromilling **1**:333
experimental setup **1**:269*F*
surface roughness **1**:323
vibration **1**:323–324
micro-mold cavity **1**:272, **1**:300
micro-opto-electro-mechanical systems (MOEMS) **1**:522
microphotonics
digital hardness tester **2**:138
digital microhardness tester **3**:74
micro-powder injection molding (μ-PIM) **1**:467, **1**:511, **1**:519–521
advantages **1**:520–521
applications **1**:521
evolution and product flow in **1**:474*F*
limitations **1**:521
micro-rotating disk electrode (MRDE) **1**:289–290
micro-RS technique **3**:60–61
microsacrificial plastic mold insert MIM (μSPiMIM) **1**:467
microscale 3D printing techniques **3**:112–114
applications **3**:119–121
biomedical **3**:121–122
metamaterials **3**:119–121
laser polymerization, materials for **3**:117–118
hybrid materials **3**:119
organic photopolymers **3**:118–119
photoinitiators **3**:118
SU-8 **3**:119
multiphoton lithography **3**:114–116
diffraction limit **3**:116
experimental set-up **3**:116–117
multiphoton polymerization **3**:114–116
projection micro-stereolithography **3**:112–114
micro-stereolithography (μSLA) **3**:113, **3**:113–114, **3**:114*F*
micro-strain **1**:417–418
micro-stress **2**:38–39
microstructural change mechanisms **2**:429–430
microstructure **3**:25, **3**:28, **3**:29, **3**:87, **3**:94–95
evolution **2**:380*F*
hot-dip galvanized coating **3**:31
micro-total analysis system (μ-TAS) **1**:527
micro-turning
micro-turning–micro-EDM hybrid machining process **1**:294–296
process **1**:292–293
setup **1**:269*F*
microwaves **3**:198
sintering process **3**:348*F*
micro-wire electrical discharge machining (micro-WEDM) **1**:270, **1**:288, **1**:527, **1**:530–531
migration **3**:361, **3**:362*F*
milling process **3**:193
MIM *see* metal injection molding (MIM)
mineral fiber **1**:208–209
mineral oil **1**:278
mineral seal oil **1**:278
MINERALIT® polymer concrete **1**:53–54
miniature gear(s) **1**:505–506, **1**:506, **1**:506*T*
applications **1**:505*F*
comparative evaluation **1**:534–536*T*
gear materials **1**:506–507, **1**:508*F*
manufacturing **1**:507–508
additive process for **1**:511–513
deformative processes for **1**:522–523
spark–erosion-based processes for **1**:527–529
quality of gears and standards **1**:507
subtractive type manufacturing process **1**:508–510
minimum quantity lubrication (MQL) **1**:1–2, **1**:2, **1**:80, **1**:180, **1**:324, **1**:324–325
components **1**:82*F*
minimum surface roughness **1**:22
minor plastic deformation (MPD) layer **1**:425
mixed ceramic inserts **1**:19
mixed oxides **3**:25–26, **3**:26, **3**:30
MLE *see* multilayer electrode (MLE)
MMCs *see* metal matrix composites (MMCs)
MMSE approach *see* multivariate mean square error (MMSE) approach
MODE algorithm *see* multi-objective differential evolution (MODE) algorithm
modeling finishing process **3**:195
modified 'Wilhelmy plate' technique **3**:279*F*

modified distance method (MDM) **1**:87
modified two-domain Tait PVT model **1**:450
MOEMS *see* micro-opto-electro-mechanical systems (MOEMS)
mold cavity **1**:183*F*
mold steel **2**:217–218*T*
  carburization of **2**:102
molded parts, quality of **1**:486
MoldFlow flow model **1**:450
Moldflow Part Advisor filling simulations **1**:450
Moldflow second order model **1**:445
Moldflow software **1**:457–458, **1**:458, **1**:472–473, **1**:491
molding process **1**:219, **1**:219*F*
  bladder molding **1**:219
  chopper gun **1**:220
  compression molding **1**:219–220
  filament winding **1**:220–221
  hand lay-up **1**:220
  mandrel wrapping **1**:220
  pultrusion **1**:221, **1**:221*F*
  resin infusion **1**:221
  vacuum bagging **1**:220
molecular dynamics (MD)
  model **1**:196–197
  simulation **1**:164–166
molten bath, direct blending with metal oxides **3**:29
molten metal penetration **3**:200
molybdenum **2**:14, **2**:115–116, **2**:266, **2**:271, **2**:292, **3**:185
molybdenum disulfide **1**:85–86, **1**:185–186
molybdenum high-speed tool steels **2**:217–218*T*
molybdenum hot work tool steels **2**:217–218*T*
molybdenum nitride **2**:115–116
molybdenum sulfide **1**:4, **1**:212
molybdenum wire **1**:248
molybdenum–nickel steel, carburization of **2**:94–96
MolyCarb wire **1**:248
Monel **2**:398, **2**:416
monoscale roughness profiles **3**:300–301
Monte Carlo method **1**:445
Monte Carlo step (MCS) **2**:353–354
Mössbauer spectroscopy **2**:432
mottling, in surface coatings **3**:154
moving block electrical discharge grinding (MBEDG) **1**:283, **1**:291–292
MP-100TC *see* microphotonics: digital hardness tester
MPA *see* multiphoton absorption (MPA)
MPD layer *see* minor plastic deformation (MPD) layer
MPL *see* multiphoton lithography (MPL)
MPL experimental procedure **3**:117, **3**:117*F*
MQL *see* minimum quantity lubrication (MQL)
MR *see* martensite reorientation (MR); mean residual (MR)
MR fluid *see* magnetorheological (MR) fluid
MRDE *see* micro-rotating disk electrode (MRDE)
MRF *see* magnetorheological finishing (MRF)
MRI *see* magnetic resonance imaging (MRI)
MRR *see* material removal rate (MRR)
Ms temperature *see* martensite start (Ms) temperature
MSC *see* master sintering curve (MSC)
MT *see* martensitic transformation (MT)
MTMS *see* methyltrimethoxysilane (MTMS)
MTs *see* mechanical twins (MTs)
μIM flow channel, physical model for **1**:494*F*
μIM machines and specifications **1**:470*T*
μ-PIM *see* micro-powder injection molding (μ-PIM)
μSLA *see* micro-stereolithography (μSLA)
μSPiMIM *see* microsacrificial plastic mold insert MIM (μSPiMIM)
μ-TAS *see* micro-total analysis system (μ-TAS)
multibody dynamics (MBD) **1**:490
multicomponent coatings **3**:45
multi-heat treatment on aluminum **2**:392*F*, **2**:393–395, **2**:393*F*, **2**:394*F*, **2**:394*T*, **2**:395*F*
multilayer electrode (MLE) **1**:191–192
multilayer hard coatings **3**:233–234, **3**:234*F*
multilayer-coated wires **1**:241–243, **1**:242*F*, **1**:243*F*
multilayered coatings **3**:45
multimedia **1**:500
multi-objective differential evolution (MODE) algorithm **1**:87
multiphoton absorption (MPA) **3**:114
multiphoton lithography (MPL) **3**:111, **3**:114–116
  diffraction limit **3**:116
  experimental procedure **3**:117, **3**:117*F*
  experimental set-up **3**:116–117
  multiphoton polymerization **3**:114–116
multiphoton polymerization **3**:114–116, **3**:117*F*
multiple nitriding, influence of
  on nitriding kinetics **3**:170–171
    comparison of hardness and nitrogen concentration profiles **3**:173–174
    morphology of nitride layers **3**:171
    XRD analysis **3**:171–173
multiple radii inserts **1**:8
multiscaled roughness profiles **3**:301–303
multishot injection molding **1**:467
multi-span Euler–Bernoulli models **1**:27–28
multi-stage solutionizing **2**:392–393
multivariate mean square error (MMSE) approach **1**:87–88

N

NA samples *see* naturally aged (NA) samples
$(Na_{0.52}K_{0.44}Li_{0.04})(Nb_{0.86}Ta_{0.06}Sb_{0.08})O_3$ (LTS-KNN) **3**:355, **3**:356*F*
nano surface generation **1**:365–366
nano ZnO **3**:27
nanocomposite hard coatings **3**:235
nanocrystalline structure **1**:420–421
nanocrystallization **2**:176
  typical features of metals/alloys in **2**:176*T*
nano-electromechanical systems (NEMS) **3**:359
nanofluids **1**:4
nanolayer
  coating **3**:231
  hard coatings **3**:234–235, **3**:234*F*, **3**:235*F*
nanoscale precipitations hardenable steel **2**:187–188
nanostructures **2**:176
natural aging **2**:354–356, **2**:355*F*, **2**:356*F*
natural fiber-reinforced composites **1**:206–207, **1**:218–219
  application of GRA technique **1**:224–225, **1**:225*F*
  fiber-reinforced polymer (FRP) **1**:206–207
  machining **1**:221–222
  manufacturing process **1**:217
  types of composite **1**:212
natural FRP composites **1**:208, **1**:210–212, **1**:218–219
  applications **1**:210
  classification of natural fibers **1**:208
natural-fiber composites **1**:208, **1**:209, **1**:218, **1**:219
naturally aged (NA) samples **2**:356
NBT *see* sodium bismuth titanate (NBT)
NBT problem *see* nominal-the-best (NBT) problem
NC-AFM *see* noncontact AFM (NC-AFM)
Nd:YAG *see* neodymium-doped yttrium aluminum garnet (Nd:YAG)
NDM *see* near-dry machining (NDM)
near α-Ti alloys **2**:291
  flow stress **2**:296*F*
  heat treatment in **2**:291
near dry EDM **1**:180, **1**:180*F*
near-dry lubrication *see* minimum quantity lubrication (MQL)
near-dry machining (NDM) **1**:3
near-infrared (near-IR) **1**:411
near-net shape (NNS) products **2**:301
neat oil **1**:1–2
necklace recrystallization **2**:313
Nelumbo nucifera **3**:295*F*
NEMS *see* nano-electromechanical systems (NEMS)
neodymium-doped yttrium aluminum garnet (Nd:YAG) **1**:411
net-shape microfabrication **1**:467
  future research outlook **1**:499–500
  injection molding equipment **1**:467–468
    auxiliary and other equipment for **1**:473
    clamping unit **1**:473
    feedstock mixing mechanism **1**:468
    injection molding machine (IMM) **1**:468–470
    mold design **1**:470–472
    part design for micro-PIM **1**:473
    runner and gating system design **1**:472–473
    screw design for **1**:470
  microinjection molding process, optimization and simulation of **1**:483–486

analytical and numerical methods for **1**:496
application of computer modeling in **1**:489–490
optimization methods **1**:486–489
parameter control in **1**:484–486
process simulation and quality characteristics for defect-free parts, in PIM **1**:496–497
micrometal powder injection molding **1:466–503**
PIM part fabrication and applications **1**:498
fabrication capabilities of μMIM **1**:498
inspection and quality control of MIM products **1**:498–499
market trend of PIM products **1**:499
powder injection molding (PIM) process **1**:473–476
debinding process **1**:480
feedstock preparation **1**:475–476
injection molding process **1**:479
sintering process **1**:483
neural network model **1**:87
neuro-fuzzy system **1**:255, **1**:255*F*, **1**:256*F*, **1**:257*F*, **1**:258*F*
neutral elements **2**:290
new hot work steels, application and performance of **2**:240–241
case analysis **2**:241–243
aluminum casting die **2**:244
connecting rod hot forging die **2**:243–244
hot forging die with complex geometry **2**:244
warm forging punch **2**:242–243
TENAX 300 and VHSUPER steel, properties of **2**:241
9Ni4Co steel, heat treatment of **2**:184–185
nickel **1**:281, **2**:13–14, **2**:13*F*, **2**:14, **2**:265, **2**:270, **2**:271*F*, **3**:6–7
ion **3**:323
Ni-alloys **1**:432, **3**:195
nickel–cobalt–chromium–molybdenum alloy **1**:427
Ni–Cr structural steel **2**:189–192, **2**:190*F*
Ni–Ti powders **3**:198
nickel alloys, heat treatment of **2**:416
annealing **2**:416
nickel-base superalloys **2**:418–419
precipitation hardening **2**:417–418
solution annealing **2**:416–417
stress equalizing **2**:417
stress relieving **2**:417
Nickel Titanium Naval Ordnance Laboratory **3**:336
nickel–boron **3**:224
nickel–phosphorus layer **3**:224, **3**:225*T*
Ni-hard irons *see* high-alloy nickel–chromium white irons
Nimonics **2**:416
niobium **2**:271
niobium powder injection molding **1**:484*F*
niobium-microalloyed steel, carburization of **2**:98
NiTi **3**:336
binary NiTi, spark plasma sintering of **3**:340–342
methods of processing **3**:337–338
conventional sintering (CS) **3**:338–339
hot isostatic pressing (HIP) **3**:339
powder metallurgy **3**:338–339
vacuum arc remelting (VAR) **3**:338
vacuum induction melting (VIM) **3**:338
stress–strain curve for **3**:337*F*
superelasticity **3**:337, **3**:339
ternary NiTi, spark plasma sintering of **3**:342–345
transformation temperature **3**:336, **3**:337, **3**:338, **3**:341–342, **3**:342
NiTi shape memory alloys (NiTi SMA) **3**:336–337
Nitinol **3**:336
'nitralloy' steels **2**:109
nitric acid **3**:323
nitrided layer characterization **3**:160
'nitrided zone' *see* diffusion zone
nitriding **2**:191–192
kinetics **2**:113–117
steels **2**:108
thermodynamics of **2**:109–110
AlN system **2**:113
Fe–N system **2**:109–110
Lehrer diagrams **2**:110–112
nitriding kinetics **2**:113–117
Ti–N system **2**:112–113
nitriding cycle used for samples **3**:160
nitriding kinetics
consideration of multiple nitriding on **3**:176
consideration of surface texture on **3**:175
nitriding kinetics, influence of multiple nitriding on **3**:170–171
comparison of hardness and nitrogen concentration profiles **3**:173–174
morphology of nitride layers **3**:171
XRD analysis **3**:171–173
nitriding kinetics, influence of surface texture on **3**:164
morphology of nitrided layers **3**:164–166
X-ray diffraction (XRD) measurement and phase analysis **3**:164
nitriding potential **3**:158–159
nitriding treatment, consideration of profile geometry on **3**:175–176
nitriding treatment, effect of profile geometry on **3**:166–167
design modifications and recommendations **3**:169–170
geometric features selected for current study **3**:167
metallography and numerical results **3**:167–169
nitrogen diffusion zone **2**:108
NNS products *see* near-net shape (NNS) products
nodular graphite iron **2**:248
nodular iron *see* ductile irons
nominal-the-best (NBT) problem **1**:87–88
nonabrasive polishing **1**:164–166
nonconforming bodies **1**:121–122
noncontact AFM (NC-AFM) **3**:247
noncontact monitoring system **1**:29
noncontact radiation techniques **1**:62
noncontact surface measurement techniques **3**:244–245
coherence scanning interferometry (CSI) **3**:246, **3**:246*F*
confocal microscopy **3**:244–245
electron microscopy **3**:247–248
Scanning Electron Microscopy (SEM) **3**:248, **3**:248*F*
Transmission Electron Microscopy (TEM) **3**:248, **3**:248*F*
focus variation microscopy **3**:245–246
scanning probe microscopy (SPM) **3**:246–247
atomic force microscopy (AFM) **3**:245*F*, **3**:247
scanning tunneling microscopy (STM) **3**:247, **3**:247*F*
nonconventional material removal process **1**:268–270
nondestructive methods
see also destructive method
diffraction method **3**:60
ex situ **3**:59–60
in situ **3**:59, **3**:60*F*
micro-RS **3**:60–61
PLPS **3**:61
non-dominated sorting genetic algorithm-II (NSGA-II) **1**:87
non-electrical parameters **1**:279
non-ferrous alloy(s) **2**:125–127, **2**:445–447, **2**:32–34
see also ferrous alloys
age-hardening treatment **2**:32–34
aluminum alloys **2**:447–448
annealing of **2**:34
application of heat treatment principles in Mg-alloys **2**:36
cobalt-bonded tungsten carbides **2**:449–451
heat-treat principles of **2**:35–36
magnesium alloys **2**:448
martesite formation in **2**:34–36
microstructure and phase composition **2**:125–127
nitriding
atmosphere **2**:127
time and temperature **2**:127
substrate composition **2**:127
thermo-mechanical treatment for **2**:392
titanium alloys **2**:448–449
nonheat-treatable alloys **2**:341, **2**:341*T*, **2**:343*T*
non-Hertzian contact **1**:135
nonmetallic gear materials **1**:506–507
nonmetallic materials, for gear manufacturing **1**:97
non-sludging electrolytes **3**:368
normalizing **2**:3–4, **2**:9, **2**:27–29, **2**:181, **2**:190, **2**:305
distinctions between annealing and **2**:28–29
ductile irons treatment **2**:262–264
gray iron **2**:252, **2**:252*F*, **2**:253*F*

NSGA-II *see* non-dominated sorting genetic algorithm-II (NSGA-II)
nucleate boiling stage *see* vapor-transport cooling stage
nucleation **2**:63
  aging **2**:389

O

O temper variation **2**:340
OA *see* orthogonal array (OA)
object oriented finite (OOF) element **3**:58
OCP *see* open circuit potential (OCP)
octadecyltrichlorosilane (OTS) **3**:282–283
ODE *see* ordinary differential equation (ODE)
ODS analysis *see* operating deflection shape (ODS) analysis
OFHC *see* oxygen free high conductivity copper (OFHC)
oil-hardening cold-work tool steels **2**:217–218*T*
oils quenching media **2**:54–55, **2**:57*F*, **2**:66*F*
OLED *see* organic light emitting diodes (OLED)
OM *see* optical microscope (OM)
ω phase **2**:290, **2**:306
OMNILAP 2000 lapping machine **3**:164
ON-OFF DC pulse energy **3**:339–340
OO *see* optimizer overhead (OO)
OOF element *see* object oriented finite (OOF) element
open circuit potential (OCP) **3**:32, **3**:33*F*, **3**:34*F*
open die forging **1**:525
open voltage **1**:275
operating deflection shape (ODS) analysis **1**:29
OPS *see* oxide polishing suspension (OPS)
optical coatings **3**:50
optical glass
  ELID grinding for **1**:377–380
  grinding/lapping of **1**:154–157
    fixed-abrasive grinding **1**:158–159
    loose-abrasive grinding **1**:154–157
  polishing of **1**:159–162
    fixed-abrasive polishing **1**:162
    loose-abrasive polishing **1**:159–162
    nonabrasive polishing **1**:164–166
  post-processing of **1**:166–167
    dry post-processing **1**:167
    wet chemical post-processing **1**:166–167
optical methods **3**:288
optical micrographs **3**:168*F*
optical microscope (OM) **1**:252
optical nonlinearity **3**:120
optimal joining condition **1**:226
  calculating gray relational grade **1**:227–228
  gray relational analysis **1**:226
  gray relational coefficient calculation **1**:226–227
  normalization of original data **1**:226, **1**:227*T*
optimization methods
  application of, in injection molding process **1**:486–489
optimization studies in hardened steel machining **1**:86–88
optimizer overhead (OO) **1**:87
orange peel, in surface coatings **3**:154
ordered phase **2**:290
ordinary differential equation (ODE) **1**:493
organic adsorbed sulfur on metal **3**:283
organic light emitting diodes (OLED) **1**:157–158
organic photopolymers **3**:118–119
organic sealers **3**:199
  see also inorganic sealers
organosilicon-derivative monolayers **3**:282–283
ORMOCER® **3**:119, **3**:119*F*
orthogonal array (OA)
  design of **1**:487
Ostwald–de Waele relationship **1**:491
OTS *see* octadecyltrichlorosilane (OTS)
over aluminizing **3**:199
over burning **2**:384
over-aging **2**:380–381, **2**:381*F*
overcut **1**:281–282, **1**:305–306
overhead flood filling **1**:2
overheating or burning **2**:226
oxidation
  post-treatments **2**:119–120
  resistant high-aluminum irons **2**:276
oxide penetration **3**:200
oxide polishing suspension (OPS) **1**:252
oxy/acetylene combustion spray **3**:43
oxygen free high conductivity copper (OFHC) **2**:399

P

PA *see* polysodium acrylate (PA)
PACE *see* plasma-assisted chemical etching (PACE)
pack cementation process **3**:199
PACM *see* programmable array scanning confocal microscopy (PACM)
PACVD *see* plasma-assisted chemical vapor deposition (PACVD)
PAG *see* polyalkylene glycol (PAG)
palladium **3**:6, **3**:42
  see also ferrous alloys; non-ferrous alloy(s)
  Pd binary alloys **3**:8–10
    PdAg alloys sequential and co-deposition **3**:8–10
    PdAu alloys sequential deposition **3**:11
    PdCu alloys sequential deposition **3**:10–11
    PdRu alloys sequential and co-deposition **3**:10
    surface properties of ternary alloys and **3**:19–20
  Pd ternary alloys **3**:11–13
    PdAgAu alloys **3**:12–13
    PdAgCu alloys **3**:13
    PdCuAu alloys **3**:13–14
    surface properties of pd binary alloys and **3**:19–20
  $Pd_{60}Cu_{37}Au_3$ **3**:13–14
  $Pd_{62}Cu_{36}Au_2$ **3**:13–14
Parallel-Beam Glossmeter **3**:155
parameter planning process **1**:136
parking effect **2**:378
partial annealing **2**:368
partially sintered WC/Co tool electrode **1**:396*F*
Particle Dynamic Analyzer **3**:155
particle size distribution (PSD) **1**:476
particle swarm optimization (PSO) **1**:87
particle-reinforced polymer (PRP) **1**:212, **1**:212–215
particulate reinforced aluminum matrix composites (PRAMC) **2**:395–396
PAS *see* plasma activated sintering (PAS)
passive damping **1**:29–30
patenting **2**:21, **2**:21–22
PC *see* pulse current (PC); polycarbonates (PCs)
PC sheet **3**:72, **3**:75–78
  contact angles measurement **3**:77*T*
  optical image **3**:76*F*
  SEM micrographs **3**:77*F*
  transmittance data for laser-treat workpiece **3**:78*F*
PCA *see* principal component analysis (PCA)
PCBN *see* polycrystalline cubic boron nitride (PCBN)
PCD *see* polycrystalline diamond (PCD)
PCVM *see* plasma chemical vaporization machining (PCVM)
PDF *see* probability density function (PDF)
PDMS *see* polydimethylsiloxane (PDMS)
PE *see* polyethylene (PE); pseudoelasticity (PE)
peak current **1**:279
pearlite reaction curve **2**:15
pearlitic steels **2**:436–437
PECH processes *see* pulsed-ECH (PECH) processes
peck-drilling **1**:324
PECM *see* pulse electrochemical machining (PECM)
pectin **1**:205
PEEK *see* polyether ether ketone (PEEK)
peening **2**:171–172
  laser peening **2**:174
  shot peening **2**:171–172
    residual stress and microhardness analysis **2**:172–173
    surface of morphology **2**:172
  warm peening **2**:173–174
    relation between temperature and fatigue life **2**:174
    residual stress in warm peening **2**:174
    warm peening procedure **2**:174
pellet grinding **1**:158
PEO *see* plasma electrolytic oxidation (PEO)
perm-selectivity **3**:14
perovskite structure **3**:352–353
PET *see* poly(ethylene terephthalate) (PET)

Petrov–Galerkin finite element method **1**:445
PFZs *see* precipitate-free zones (PFZs)
phase transformation **2**:3
phosphate
  coating **3**:42, **3**:323
  phosphate–zinc coating **3**:323
  phosphating **3**:323–325
phosphor bronzes **2**:409
phosphoric acid **3**:323
phosphorous **2**:14
phosphorous bronze **2**:139, **2**:141–143, **2**:151, **3**:73–74, **3**:81–83
  see also Rene 41; Yttria-stabilized zirconia
  contact angle measurements **2**:144*F*
  cross-section laser-ablated layer **3**:83*F*
  friction coefficient for laser ablated **2**:144*F*, **3**:83*F*
  laser ablated layer **2**:143*F*
  laser ablated surface **2**:142*F*, **3**:82*F*
phosphorous deoxidized copper **2**:399
photofluidization lithography **3**:125
photoinitiators **3**:116, **3**:118
  cationic **3**:118
  radical **3**:118
photolithography **3**:141
photoluminescence piezo-spectroscopy (PLPS) **3**:61
photonic metamaterials **3**:120
photopolymerization **3**:116
  free-radical **3**:116
  online monitoring of **3**:116–117
photopolymerized structure **3**:116
photosensitive polymer **3**:117
photovoltaic (PV) cells **3**:72
physical evaporation **3**:41
physical metallurgy principles **2**:218–222
  austenitization and quenching **2**:224–226
  carbon steels **2**:222
  iron allotropy **2**:218–222
  martensitic transformation **2**:222–224
  multiple temperings **2**:228–231
  secondary hardness **2**:227–228
  tempering **2**:226–227
physical vapor deposition (PVD) **1**:12–13, **1**:328, **1**:396, **2**:130, **3**:39, **3**:41, **3**:46, **3**:48, **3**:50, **3**:59–60, **3**:202, **3**:210, **3**:230, **3**:231, **3**:233
  advantages and limitations for **3**:44*T*
  nitride coatings **2**:132
  physical evaporation **3**:41
  plasma sputtering **3**:41
π theorem **1**:31
pickling **3**:180
picoseconds laser **3**:73–74
PID controller **1**:139
piezoelectric materials **3**:349
Pilot experiments **1**:31
PIM process *see* powder injection molding (PIM) process
plain carbon steels **2**:11, **2**:434–435
  for gear manufacturing **1**:97
plain EDM wires **1**:238–239
  aluminum–brass wire **1**:240, **1**:240*F*
  brass wire **1**:239–240, **1**:240*F*
  copper wire **1**:238–239, **1**:240*F*
plain-carbon steel **2**:181
planarization rate **1**:162–163
planned cylinder pressure **1**:140*F*
plant fiber **1**:209–210, **1**:209*F*
plasma **1**:234–235
  plasma–assisted nitriding technology **2**:125
plasma activated sintering (PAS) **3**:339, **3**:339–340, **3**:348–349
plasma carburizing **2**:73, **2**:80–81, **2**:81*F*
  advantages **2**:81
  carburizing process **2**:80–81
  control of carbon supply and case depth **2**:81
plasma chemical vaporization machining (PCVM) **1**:164
plasma electrolytic oxidation (PEO) **3**:202
plasma enhanced CVD technique **3**:41
plasma etching **1**:164
plasma nitriding (PN) **3**:203–204
plasma spray **3**:43
plasma spraying (PS) **3**:207
plasma sputtering **3**:41
plasma-arc spraying **3**:43
plasma-assisted chemical etching (PACE) **1**:164
plasma-assisted chemical vapor deposition (PACVD) **3**:44*T*
plastic deformation **1**:409–410, **1**:413, **1**:414, **1**:414*F*, **1**:416–417, **1**:417, **1**:422, **1**:425–427, **1**:432, **2**:173, **2**:174, **2**:175, **2**:176
  high strain rate **1**:420–421
  laser peening causes **1**:419
plastic injection molding **1**:467
  frameworks for optimization of **1**:485*F*
plastic mold **2**:223*F*
plastic mold steels **2**:216
plasticizing unit **1**:447–448
plate martensite microstructure **2**:92*F*
platers **3**:361
Platinum wire **3**:99
plowing force **1**:60
ploy vinylidene fluoride (PVDF) **1**:521
PLPS *see* photoluminescence piezo-spectroscopy (PLPS)
plunge gear shaving **1**:108–109
PM electrode *see* powder metallurgy (PM) electrode
P/M gear **1**:511
PM tool electrodes **1**:396*F*
PMC *see* polymer matrix composites (PMC)
PMDEDM *see* powder-mixed dielectric EDM (PMDEDM)
PMEDM *see* powder mixed electrical discharge machining (PMEDM)
PMMA *see* polymethyl methacrylate (PMMA)
PMND-EDM *see* powder mixed near-dry electrical discharge machining (PMND-EDM)
PN *see* plasma nitriding (PN)
pneumatic ring actuator **1**:147*F*
polarization test **3**:282
polarization-electrical (P-E) field hysteresis loop **3**:355, **3**:355*F*
Polish–Czech project **2**:165–166
polishing parameter planning **1**:136–137
polishing path planning **1**:126–129
polishing stone topography, generation of **1**:130–131, **1**:131*F*
polishing techniques **3**:194
  buffing **3**:194
  burnishing **3**:194
  hand stoning **3**:194
  honing **3**:194
  lapping **3**:194
  superfinishing **3**:194
  tumbling **3**:194
polishing tool **1**:123
  and part **1**:122*F*
polishing/deburring robot **1**:134*F*
polishing/deburring toolhead design **1**:143–144
  experiment on ring actuator stiffness **1**:150–152
  hybrid design **1**:143–144
  ring actuator modeling **1**:147–149
  simulation of ring actuator stiffness **1**:149–150
  toolhead dynamic modeling **1**:144–147
pollution-free process **3**:364
poly vinyl chloride (PVC) **1**:204
poly(ethylene terephthalate) (PET) **3**:292, **3**:292*F*
polyaddition **1**:217–218
polyalkylene glycol (PAG) **2**:55, **2**:56*F*
poly-alloys **3**:224
polycarbonates (PCs) **3**:137–138
  chemical structures of **3**:138*F*
  crystallization process of **3**:138
  PC sheet **3**:72
polycondensation **1**:217
polycrystalline cubic boron nitride (PCBN) **1**:50–51
polycrystalline diamond (PCD) **1**:16, **1**:55, **1**:55–56, **1**:292–293
polycrystalline diamond coatings **3**:48
polydimethylsiloxane (PDMS) **3**:72
  elastomer surface **3**:141
poly-*e*-caprolactone scaffolds **3**:113*F*
polyester **1**:220
polyether ether ketone (PEEK) **1**:216–217, **3**:196, **3**:212–213
polyethylene (PE) **1**:204
polygonization **2**:24–25
polymer crystallization process **3**:138
polymer matrix composites (PMC) **1**:212, **1**:212–215
  fiber-reinforced polymer (FRP) **1**:212–215
  particle-reinforced polymer (PRP) **1**:216–217
polymer(s) **1**:217
  polyaddition **1**:217–218
  polycondensation **1**:217
  polymerization **1**:217
  quenchants **2**:55–56
  quenching **2**:188
polymeric binders, depolymerization of **1**:481
polymeric gels **3**:328
polymerization **1**:217

polymethyl methacrylate (PMMA) **1**:448, **1**:521, **3**:72, **3**:125–126
polyoxymethylene-based binder **1**:476
polypropylene (PP) **1**:204
polysodium acrylate (PA) **2**:55
polytetrafluoroethylene (PTFE) **2**:424, **3**:45
polyurethane (PU) **1**:217, **1**:224–225
polyurethane (PU) coating **3**:48, **3**:49, **3**:325–327
  see also conversion coatings
  substrate, coating contents **3**:327*T*
polyvinyl alcohol (PVA/PVOH) **2**:55
porosity **3**:199
porous electrode wire **1**:249–250, **1**:250*F*
porous stainless steel (PSS) **3**:14
  substrates **3**:7
porous zirconia-coated stainless steel tubes (YSZT) **3**:13
portable handheld surface finish instrument **3**:243, **3**:244*F*
post-deposition surface finish **3**:215–217, **3**:216*F*
potassium chloride **3**:226
potassium sodium niobate (KNN) **3**:353, **3**:355
potassium tantalate niobate (KTN) **3**:353
potentiodynamic polarization tests **3**:53, **3**:53*F*
potentiostat **3**:53
powder coatings **3**:41–42
powder injection molding (PIM) process **1**:467, **1**:473–476
  debinding process **1**:480, **1**:480*T*
    master decomposition curve (MDC), development of **1**:480–481
    solvent **1**:480, **1**:480*T*
    thermal **1**:480, **1**:480*T*
  feedstock preparation **1**:475–476
    binder **1**:476–477
    formulation and characterization **1**:477–479, **1**:479*T*
    metal powder **1**:475–476
  industrial sectors and areas of PIM applications **1**:499*T*
  injection molding process **1**:479
    critical factors influencing part quality in **1**:480
    injection molding cycle **1**:479–480
    principles of **1**:479
  market trend of PIM products **1**:499
  part fabrication and applications **1**:498
    fabrication capabilities of μMIM **1**:498
    inspection and quality control of MIM products **1**:498–499
  sintering process **1**:483
powder metallurgy (P/M) process **1**:511, **1**:511–513, **1**:512*F*, **1**:513, **3**:336, **3**:337, **3**:338–339, **3**:347
  applications **1**:513–514
  route **2**:289
  sintering process on microscopic scale **1**:513*F*
powder metallurgy (PM) electrode **1**:395
powder mixed dielectric (PMD) **1**:180
powder mixed electrical discharge machining (PMEDM) **1**:171–172, **1**:180–186, **1**:181*F*, **1**:278, **1**:279*F*, **1**:398
  see also electrical discharge machining (EDM)
  PMND-EDM **1**:190–191
  powder addition to EDM and micro-EDM **1**:182–186
  powder mixed ultrasonic-assisted EDM **1**:188–190
powder mixed near-dry electrical discharge machining (PMND-EDM) **1**:190–191, **1**:192*F*, **1**:193*F*
powder-mixed dielectric EDM (PMDEDM) **1**:398
powder-mixed micro-EDM process **1**:196
power generation industry **3**:213
power law model **1**:445, **1**:491–492
power supply **1**:274
  pulse waveform and discharge energy **1**:275–276
  RC-type pulse generator **1**:274–275, **1**:274*F*
  transistor-type pulse generator **1**:274, **1**:274*F*
PP *see* polypropylene (PP); pulse reverse (PR)
PRAMC *see* particulate reinforced aluminum matrix composites (PRAMC)
Praxair Surface Technologies **3**:207
PRC *see* pulsed reverse current (PRC)
pre-aged AA6181A alloy **2**:356
precipitate-free zones (PFZs) **2**:351–352
precipitation **2**:3–4
precipitation hardening **2**:353–354, **2**:374–375, **2**:417–418
  martensitic steels **2**:181–184, **2**:184*F*
  stainless steel **2**:204–205, **2**:204*T*, **2**:205*F*
precipitation sequence **2**:377–378, **2**:377*F*, **2**:378*F*
precision
  cutting **1**:224–225, **1**:225, **1**:225*T*
  forging **1**:525
  linear saw **1**:225
precision optics, manufacturing technologies for **1:154–170**
precursor substances **3**:327–328
pre-deposition surface finish **3**:211–213
preheating **2**:4, **2**:233
preoxidation of steel prior to hot-dip zinc coating **3**:29–30
prepreg **1**:219
press casting process **2**:241
pressure **1**:411
  pressure-assisted sintering **3**:197
  pressure-less sintering and annealing **3**:197–198
  sintering **3**:347
pressure tracking control **1**:139
pressure trajectory tracking **1**:141*F*
pressure volume temperature (PVT) **1**:450, **1**:495
pressure-assisted sintering techniques **1**:483
pressureless sintering techniques **1**:483
pressure-swirl atomizer **3**:151*F*, **3**:154
Preston's formula **1**:155
pre-treatment processes, effect of **3**:54
primary chatter **1**:26–27
principal component analysis (PCA) **1**:87–88
probability density function (PDF) **3**:290
process optimization **1**:21
process simulation **1**:193–194, **1**:195
profile geometry, on nitriding treatment **3**:166–167, **3**:175–176
profilometer **2**:439
programmable array scanning confocal microscopy (PACM) **3**:244–245, **3**:245
projection stereo-lithography (PSL) **3**:111, **3**:112–114
protection **2**:385–386, **2**:386*F*
PRP *see* particle-reinforced polymer (PRP)
PS **1**:443–444
PSD *see* particle size distribution (PSD)
pseudoelasticity (PE) **2**:325–326
PSL *see* projection stereo-lithography (PSL)
PSO *see* particle swarm optimization (PSO)
PSS *see* porous stainless steel (PSS)
PTFE *see* polytetrafluoroethylene (PTFE)
PU coating *see* polyurethane (PU) coating
pulse current (PC) **3**:361–362, **3**:367*F*
pulse electrochemical machining (PECM) **3**:367, **3**:367*F*
pulse generators **1**:274
  analysis of RC type **1**:235*F*
  analysis of WEDM **1**:234–236, **1**:235*F*
  chip size and load at different spark energy **1**:236*F*
pulse plating **3**:86–87, **3**:87
pulse reverse (PR) **3**:86–87, **3**:87, **3**:89
pulse waveform
  of controlled pulse generator **1**:389*F*
  and discharge energy **1**:275–276
pulsed electric current sintering (PECS) *see* spark plasma sintering (SPS)
pulsed reverse current (PRC) **3**:361–362
pulsed-ECH (PECH) processes **3**:372
pulse-OFF time **1**:279
pulse-ON time **1**:279
pultrusion **1**:221, **1**:221*F*
pure iron
  and crystalline structures **2**:225*F*
  equilibrium phases of **2**:225*F*
PV cell efficiency, effect of dust accumulation on **3**:137
PV cells *see* photovoltaic (PV) cells
PVA/PVOH *see* polyvinyl alcohol (PVA/PVOH)
PVC *see* poly vinyl chloride (PVC)
PVD *see* physical vapor deposition (PVD)
PVDF *see* ploy vinylidene fluoride (PVDF)
PW-based binder system **1**:476*T*
pyrolysis **1**:480

Q

Q-switched laser system **1**:411
quality
  assurance **2**:368–369
  issues **3**:57
  quality of deposition, factors affecting **3**:361–362, **3**:362*F*
    deposition material selection **3**:364

quantitative methods of measuring hardenability **2**:56–57
critical diameter **2**:56–57, **2**:57*F*
ideal critical diameter **2**:59–60, **2**:59*F*, **2**:60*F*
severity of quench **2**:57–59, **2**:58*F*, **2**:59*T*
quench
cracks **2**:47–48
delay **2**:351
quenched-in vacancies **2**:352–353
sensitivity **2**:351–352
quenchants **2**:169–170
for carburized steels **2**:89–90
quenching **2**:9, **2**:51, **2**:53*F*, **2**:154, **2**:224–226, **2**:305–306, **2**:350–353, **2**:352*F*, **2**:363, **2**:383, **3**:116
cooling mediums for **2**:233
drastic **2**:104
faults **2**:387, **2**:388*T*
mechanism of heat removal during **2**:53
media **2**:53–54, **2**:54*F*, **2**:54*T*
medium **2**:386
and quenching medium **2**:36–39
stresses **3**:57
time **2**:358
transfer time **2**:385–386

R

rack shaving process **1**:107
radial actuation **1**:144–145
radial basis function **1**:484
radial force **1**:59
radial-feed WEDG **1**:283, **1**:283*F*
see also tangential-feed WEDG (TF-WEDG)
radio-frequency (RF) **3**:233
radius of curvature of the part **1**:123
Raman spectroscopy (RS) **3**:58
random rough surface **3**:300
random surface roughness static analysis **3**:289–290
rate-limiting process **3**:11
Rayleigh, Lord **3**:153
RBA *see* Rotary Bell Atomizer (RBA)
RC *see* resistance capacitance (RC)
RCF *see* rolling contact fatigue (RCF)
RC-type pulse generator **1**:274–275, **1**:274*F*
reactive ion etching (RIE) **1**:164, **1**:330
reaustenitization **2**:272
recrystallization **2**:25–26, **2**:27*F*
annealing **2**:24–27
kinetics **2**:26*F*
temperature **2**:403
recursive method **1**:128, **1**:129
redraw wire **1**:238
refrigeration **2**:272
regression
equation models **1**:31
treatment **2**:382, **2**:383*F*, **2**:383*T*
regression and re-aging (RRA) **2**:374
reinforcement **1**:207
remelting **3**:196
electron beam remelting **3**:196
laser remelting **3**:196
TIG remelting **3**:196
removing and reshaping methods **3**:258*T*
Rene 41 **2**:140–141, **2**:146–151, **2**:151
see also phosphorous bronze; Yttria-stabilized zirconia
EDS data **2**:150*T*
laser-treated **2**:148*F*, **2**:149*F*
X-ray diffractogram **2**:150*F*
renewable source **1**:210
replacement schedule **3**:320
residual stress (RS) **1**:48, **1**:69–72, **1**:78–80, **1**:195, **1**:197, **2**:138, **2**:142–143, **2**:145–146, **2**:150–151, **2**:151, **2**:364, **2**:366–368, **2**:405, **3**:57–58, **3**:57*F*, **3**:58, **3**:74
analytical expression for **3**:99
in castings **2**:249
crystallite size and micro-strain **1**:417–418
distribution **1**:416–417, **1**:416*F*, **1**:424*F*
experimental measurement **3**:58–59
generation **1**:413–414, **1**:414*F*
measurement **1**:414–415, **3**:61
by curvature method **3**:98–99
mechanical relaxation **1**:431
and microstructure **3**:239–240, **3**:240*F*, **3**:241*F*
numerical estimation **3**:61–68
quality issues **3**:57
sources **3**:56–57
thermal relaxation **1**:431–435
thermal spray coating techniques **3**:56*F*
resin infusion **1**:221
resin transfer moulding (RTM) **1**:218
resistance capacitance (RC) **1**:274
resistance to tempering **2**:228
resistor **1**:274
response surface methodology (RSM) **1**:16, **1**:69, **1**:233, **1**:484
retained austenite **2**:45–47, **2**:224
stabilization of **2**:234
subzero treatment **2**:46–47
retrogression and re-aging (RRA) **2**:358, **2**:389
reverse EDM (REDM) **1**:294
reverse 'T' shape micro channel, experiments and simulation for **1**:454, **1**:454–455
M05 ⊥ S05 reverse 'T' micro channel **1**:454
modified cross viscosity model for **1**:455
reverted austenite **2**:207
RF *see* radio-frequency (RF)
RIE *see* reactive ion etching (RIE)
ring actuator deformation simulation **1**:149*F*
ring actuator displacement model **1**:148*F*
ring actuator modeling **1**:147–149
ring actuator stiffness **1**:149*F*
experiment on **1**:150–152
simulation of **1**:149–150
ring diaphragm model **1**:148*F*
rinsing **3**:222
robotic deburring control **1**:139–143
robotic polishing and deburring **1:121–153**
contact area-based path planning **1**:121–122
contact area **1**:122–124
contact mechanics **1**:121–122
continuous polishing path **1**:124–126
coverage area map (CAM) **1**:124
polishing path planning **1**:126–129
step-over size **1**:126
contact stress-based control **1**:133–134
air cylinder pressure control modeling **1**:137
air spindle speed control modeling **1**:137–138
combined control system **1**:138–139
contact stress modeling **1**:134–135
friction torque modeling **1**:135–136
polishing parameter planning **1**:136–137
pressure tracking control **1**:139
robotic deburring control **1**:139–143
robotic polishing/deburring system **1**:134
polishing/deburring toolhead design **1**:143–144
experiment on ring actuator stiffness **1**:150–152
hybrid design **1**:143–144
ring actuator modeling **1**:147–149
simulation of ring actuator stiffness **1**:149–150
toolhead dynamic modeling **1**:144–147
surface roughness modeling **1**:129–131
micro depth of cut of a polishing tool **1**:132–133
micro depth of cut of a single grain **1**:131–132
polishing stone topography, generation of **1**:130–131
surface roughness, prediction of **1**:133
rolling contact bearing **2**:197
rolling contact fatigue (RCF) **1**:73–74
room temperature (RT) **2**:339*T*, **3**:178
Rotary Bell Atomizer (RBA) **3**:151–152, **3**:152*F*
rotary gear shaving, diagonal type of **1**:107–108, **1**:108*F*
rotary shaving process **1**:107
axial or conventional type of **1**:107*F*
diagonal type of **1**:108*F*
rotating sacrificial disk **1**:290
rough coatings **3**:50
rough surface **3**:286–287, **3**:288*F*
classification of **3**:140
profile **3**:289*F*
typology of **3**:289*F*
rough surface, topography of **3**:286–289
characteristics of **3**:286–289
random surface roughness static analysis **3**:289–290
roughness of fractal surfaces **3**:290–291
rough substrate and modification, creation of **3**:291–292, **3**:293–294
colloid accumulation and layer method **3**:293
electrochemical reaction and deposition method **3**:293
etching and lithography **3**:292
sol-gel process **3**:292–293
rough turning **1**:1

roughing *see* rough turning
roughness, surface **3**:248–249
roughness and surface wettability, relationship between **3**:294–295
  analysis of contact angle **3**:295
    composite solid–liquid–air interface **3**:296–297
    effect of edge and variation of surface slope **3**:297–298
    effect of surface area on **3**:295–296
    flat surface **3**:295
  calculation of contact angle for selected surfaces and surface modification **3**:298
    2D periodic profiles **3**:298
    3D surfaces **3**:298–300
    periodic profile **3**:298
    saw-toothed periodic profile **3**:298
  surfaces modification to achieve highest contact angle **3**:300–301
    monoscale roughness profiles **3**:300–301
    multiscaled roughness profiles **3**:301–303
roughness measurement parameters **3**:290
roughness of bondcoat **3**:213, **3**:215*T*
RRA *see* regression and re-aging (RRA); retrogression and re-aging (RRA)
RS *see* Raman spectroscopy (RS); residual stress (RS)
RSM *see* response surface methodology (RSM)
RT *see* room temperature (RT)
RTM *see* resin transfer moulding (RTM)
runner and gating system design **1**:472–473, **1**:472*F*
rutile **2**:289

S

SAE *see* Society of Automotive Engineers (SAE)
SAMs *see* self-assembled monolayers (SAMs)
sandblasting **1**:157–158, **1**:158*F*
sanding **3**:307
sandwich coatings **3**:45
sapphire **1**:213
saturated calomel reference electrode (SCE) **3**:99
saturated liquid solution **2**:375
saustenite **2**:109
  grain size **2**:63
    estimation of hardenability **2**:66–67
saw-toothed periodic profile **3**:298
SB *see* shear bands (SB)
SB criterion *see* smaller-the-better (SB) criterion
scanning electron micrographs **3**:144
scanning electron microscope (SEM) **3**:286*F*, **3**:287*F*, **3**:288–289
scanning electron microscopy (SEM) **1**:250, **1**:252*F*, **1**:258*F*, **1**:260*F*, **1**:262*F*, **1**:421, **2**:308–309, **2**:330–331, **3**:8, **3**:58, **3**:74, **3**:87, **3**:90–94, **3**:91*F*, **3**:122*F*, **3**:160, **3**:248, **3**:248*F*, **3**:261–262
scanning probe microscopy (SPM) **3**:244, **3**:246–247
  atomic force microscopy (AFM) **3**:245*F*, **3**:247
  scanning tunneling microscopy (STM) **3**:247, **3**:247*F*, **3**:261–262
SCC *see* stress corrosion cracking (SCC)
SCE *see* saturated calomel reference electrode (SCE)
SCEA *see* side cutting edge angle (SCEA)
Scherrer equation **1**:417
scroll-free turning **1**:55
SCT *see* shallow cryogenic treatments, (SCT)
SDF *see* simultaneous method (SDF)
SE *see* superelasticity (SE)
sealing **3**:199
  anodic coatings **3**:199
  inorganic sealers **3**:199–200
  organic sealers **3**:199
  porosity **3**:199
  using glass formers **3**:200
secondary carbides **2**:228, **2**:231*F*
secondary chatter **1**:5
secondary cooling **3**:57
secondary electron imaging (SEI) **3**:92
secondary hardening **2**:40, **2**:41–42, **2**:228
secondary hardness **2**:227, **2**:227–228
SEDCM *see* simultaneous micro-EDM and micro-ECM (SEDCM)
SEI *see* secondary electron imaging (SEI)
selective laser sintering (SLS) **3**:112, **3**:113*F*
selectivity **3**:14
self-affinity **3**:291
self-annealing effect **2**:137
self-assembled monolayers (SAMs) **3**:282, **3**:284*F*
self-cleaning surfaces **3**:140
self-drilled holes
  EDM micro-rods by **1**:293–294
  self-drilled holes–TF-WEDG hybrid machining process **1**:296
self-excited chatter **1**:26–27
self-monitoring capability **1**:37
self-similarity surfaces and diagrams, investigating **3**:291
self-supported membranes **3**:14
SEM *see* scanning electron microscope (SEM); scanning electron microscopy (SEM)
semicrystalline polysaccharide **1**:205
semidry machining **1**:80–83
semi-ellipsoid part surface **1**:128*F*
semi-solid forming, new short T6 heat treatment for **2**:390–391
sensitization process **3**:4
sequential two-photon absorption **3**:115, **3**:115*F*
series-pattern micro-disk electrode fabrication **1**:288–290
severe plastic deformation (SPD) **1**:418
severity of quench **2**:57–59, **2**:58*F*, **2**:59*T*
SFE *see* stacking fault energy (SFE)
SFs *see* stacking faults (SFs)
shadowgraphy technique **3**:155
shallow cryogenic treatments, (SCT) **2**:425, **2**:427
shape memory alloys (SMA) **2**:321–322, **3**:336, **3**:338
  NiTi **3**:336–337
  phase diagram **2**:322, **2**:326*F*
  Ti–Ni alloys
    MT in **2**:322–324
    precipitation in **2**:324–326
shape memory effect (SME) **2**:321–322, **2**:415–416, **3**:336, **3**:340
shape recovery **2**:328, **2**:332, **2**:333*F*
shaving allowance **1**:106–107
shaving cutter, in gear shaving **1**:105–106
  serration of **1**:106*F*
shaving stock **1**:106–107
shear bands (SB) **1**:426
shear stress **1**:449–450
sheet molding compound (SMC) **1**:518
shock resisting tool steel, carburization of **2**:102
shock waves **1**:425
shock-resisting tool steels **2**:217–218*T*
short-pulse laser **1**:331
shot peening **1**:409, **1**:409*F*, **2**:171–172
  conventional **1**:409
  laser peening vs. **1**:410
  residual stress and microhardness analysis **2**:172–173
  and rolling **3**:203
  surface of morphology **2**:172
shot velocity, surface roughness vs. **2**:172*F*
shrinkage **1**:471, **1**:472, **1**:490, **1**:495, **1**:498–499, **1**:500
SHT *see* solution heat treatment (SHT)
side cutting edge angle (SCEA) **1**:67
signal-to-noise (S/N) ratio **1**:14, **1**:32, **1**:487, **1**:487–488
  experimental results for surface roughness **1**:33*T*
  plots for mean **1**:34*F*
silanes **3**:283–285
Silent Tool **1**:75
silicon **2**:14, **2**:195–196, **2**:196*F*, **2**:265, **2**:271, **2**:293
  Si-modified 4340 steel **2**:188–189
silicon bronze, heat treatment of **2**:413–414
silicon micromachining **1**:328–330
  bulk micromachining **1**:329–330
  surface micromachining **1**:330
silicon nitride **1**:370, **1**:373*F*
silicon wafer, ELID grinding of **1**:380–383
  effect of grain size for **1**:388*F*
  variation of ground surface roughness of **1**:387*F*
silicon wafer thinning process **1**:386*F*
silk fiber **1**:208
silver **3**:7
silver tungsten **1**:277, **1**:392–393, **1**:393
SIMT *see* stress-induced martensitic transformation (SIMT)
simulation and modeling **1**:193–195
  finite element method **1**:195–196, **1**:195*F*, **1**:196*F*
  geometric simulation model **1**:197
  mathematical modeling **1**:194–195, **1**:194*F*

MD model **1**:196–197
sinking EDM simulation method **1**:197
spectroscopic measurement **1**:197
supporting vector machine **1**:197
thermal model **1**:197–198
simultaneous method (SDF) **2**:169
simultaneous micro-EDM and micro-ECM (SEDCM) **1**:176
simultaneous two-photon absorption **3**:115, **3**:115*F*
single raster path **1**:125*F*
single shielded TBMs **1**:42
single-layer coatings **3**:45, **3**:101–102, **3**:109
single-layer-coated wires **1**:240–241, **1**:241*F*
single-phase alpha-aluminum bronzes **2**:409
single-point diamond turning (SPDT) **1**:5
single-stage aging **2**:389
sinking EDM simulation method **1**:197
sintered reaction-bonded silicon nitride (SRBSN) **1**:370, **1**:373*F*
sintering **1**:512, **1**:516–517, **3**:347–348, **3**:348*F*
see also spark plasma sintering (SPS)
sinusoidal topography **3**:303
Sisko model **1**:491
skin fiber **1**:209
SLA *see* stereolithography (SLA)
sliding wear resistance **2**:442
SLM *see* spatial light modulator (SLM)
slow dynamic contact angle **3**:280–281
SLS *see* selective laser sintering (SLS)
sludging electrolytes **3**:368
SMA *see* shape memory alloys (SMA)
small and medium manufacturing enterprises (SMEs) **1**:468
small step-over size **1**:127*F*
small-and medium-sized enterprises (SMEs) **2**:423–424
smaller-the-better (SB) criterion **1**:20
smart mechanical attrition (SMAT) **2**:174–175, **2**:174–176, **2**:175
mechanism of surface nanocrystallization by **2**:176
microstructure characterization of **2**:176
process **2**:175–176
properties of SMAT surface layer **2**:176–178
Smart Tool boring process **1**:36, **1**:38*F*
SMAT *see* smart mechanical attrition (SMAT); surface mechanical attrition treatment (SMAT)
SMC *see* sheet molding compound (SMC)
SME *see* shape memory effect (SME); small and medium manufacturing enterprises (SMEs); small-and medium-sized enterprises (SMEs)
smoothness, of substrate surface **3**:49
S/N ratio *see* signal-to-noise (S/N) ratio
soaking **2**:4
soaking period **2**:4
soaking time **2**:349–350
Society of Automotive Engineers (SAE) **2**:61–62
sodium bismuth titanate (NBT) **3**:353
sodium borohydride **3**:6
sodium chloride **3**:368
sodium cyanide **2**:77–78, **2**:77*T*
sodium nitrate **3**:368, **3**:369
soft spots **2**:104
prevention **2**:104
soft-part machining (SPM) **1**:47–48, **1**:48*F*
sol infiltration **3**:202
solar gas nitriding **2**:132
solar panels **3**:137
sol-gel process **3**:200, **3**:292–293, **3**:293*F*, **3**:327–330, **3**:329*T*
solid contact bearing **2**:197
solid lubricants application **1**:83–86
solid solution (SS) **2**:373, **2**:374–375
hardening **2**:126–127
solid state heat treatment **3**:196–197
austempering heat treatment **3**:198
pressure-assisted sintering **3**:197
pressure-less sintering and annealing **3**:197–198
solid/pack carburization **2**:73–74, **2**:73
advantages **2**:75–76
carburizing process **2**:73–74
chemical reactions **2**:74
decarburization **2**:74–75
disadvantages **2**:76
solid–liquid interface and PC-liquid acetone **3**:142–143
atomic force microscope (AFM) micrographs **3**:142–143
surface topography **3**:142–143
texture profile micrographs **3**:143–144
Fourier transform infrared (FTIR) technique **3**:147
hydrophobicity assessments **3**:145–147
scanning electron micrographs **3**:144
surface roughness **3**:144–145
X-ray diffraction (XRD) technique **3**:147
solid-phase phenomena **2**:113–114
solid-state diffusion **3**:42
solidus temperature **2**:113
Solidworks Plastics software **1**:472–473
solubility **2**:375
solution annealing **2**:416–417
solution heat treatment (SHT) **2**:340*T*, **2**:347–350, **2**:349*F*, **2**:350*F*
solution treatment **2**:272
circulation of furnace gas **2**:384
cooling
process **2**:386
technology **2**:387, **2**:387*F*
criterion and standard **2**:383–384
heating
rate **2**:384
temperature **2**:384
heat preservation **2**:385–386, **2**:386*F*
quenching faults **2**:387
solution treatment and aging (STA) **2**:301
mechanical properties **2**:307*T*
solutionizing **2**:207, **2**:374
process **2**:383
and aging process **2**:379*F*
and aging sub-classification **2**:373–374
sub-classification **2**:373–374
treatment system **2**:390
solution-treated specimen **2**:302, **2**:303*F*
solvent debinding **1**:480, **1**:480*T*
sooting in gas **2**:103
prevention **2**:103
SP *see* stylus profilometer (SP)
spark plasma sintered HAp (SPS HAp) **3**:350
microstructural and mechanical properties **3**:350–351
optical properties **3**:351–352, **3**:352*F*
relative density **3**:350*F*, **3**:352*F*
spark plasma sintering (SPS) **3**:197, **3**:336, **3**:339–340, **3**:348–349, **3**:349, **3**:349*F*
application **3**:349–351
of binary NiTi **3**:340–342
in biomaterials **3**:349–351
diffusion process **3**:349*F*
frequency dependence on permittivity **3**:354*F*
in lead-free ferroelectric ceramics **3**:352–354
principles and mechanism **3**:349
of ternary NiTi **3**:342–345
spark–erosion-based processes
electrical discharge machining (EDM) **1**:527–529
for miniature gear manufacturing **1**:527–529
wire electrical discharge machining (WEDM) **1**:530–531
spatial light modulator (SLM) **3**:114, **3**:114*F*
SPD *see* severe plastic deformation (SPD)
SPDT *see* single-point diamond turning (SPDT)
specific processing energy **1**:475
speckle infusion **3**:273–274
spectroscopic measurement **1**:197
spheroidal graphite iron *see* ductile irons
spheroidization **2**:24, **2**:188
annealing **2**:23–24, **2**:271
of silicon phases **2**:363
spindle speed **1**:138
vs. varied geometry **1**:139*F*
spindle torque **1**:138
SPM *see* scanning probe microscopy (SPM); soft-part machining (SPM)
spray air contact **3**:151
spray parameters **3**:207–208
spray process **3**:207, **3**:208*F*, **3**:210
HVOF coating characteristics **3**:209
mechanism of coating **3**:208–209
principle **3**:207
process technical details **3**:207–208
spray parameters **3**:207–208
spring steel **2**:192–195, **2**:192*T*, **2**:194*F*
SPS *see* spark plasma sintering (SPS)
SPS HAp *see* spark plasma sintered HAp (SPS HAp)
spur gears **3**:373–374
sputtering for FIB micromachining **1**:331–332
sputtering process **3**:29, **3**:41, **3**:233
SRBSN *see* sintered reaction-bonded silicon nitride (SRBSN)
SS *see* solid solution (SS)
SSS *see* supersaturated solid solution (SSS)

STA *see* solution treatment and aging (STA)
stabilized zirconia **2**:140
stacking fault energy (SFE) **1**:421, **2**:176
stacking faults (SFs) **1**:408, **1**:427*F*
stainless steel(s) **2**:199–200, **2**:435–436
  austenitic **2**:200–204, **2**:203*F*, **2**:203*T*
  duplex **2**:204, **2**:204*F*, **2**:204*T*
  ferritic **2**:201*F*, **2**:202*F*, **2**:202*T*
  low temperature carburization of austenitic stainless steel **2**:98–99
    activation **2**:99–100
    carburizing atmosphere **2**:101
    microstructure of low temperature carburized layer **2**:101
    processing temperature ranges **2**:100–101
  martensitic **2**:199–200, **2**:199*T*
  precipitation hardenable **2**:204–205, **2**:204*T*, **2**:205*F*
stalk fiber **1**:209
stamping **1**:522–523
standard WIDAXS40TPDUNR15 boring bar **1**:27
static contact angle **3**:295
static sessile drop method **2**:138, **3**:75
stationary BEDG **1**:290–291
statistical method **1**:223–224
stearic acid **3**:285
steel(s) **2**:422
  core wires **1**:248–249, **1**:248*F*, **1**:249*F*
  for gear manufacturing **1**:97
  heat treatment of **2**:4–8
    common heat treating processes **2**:9
    effect of excess heating beyond homogenization **2**:8–9
    production of homogeneous austenite **2**:8
  heat treatment of casting **2**:211–212, **2**:211*F*
step aging **2**:389
step-over size **1**:126
stereolithography (SLA) **3**:111–112
  design **3**:112*F*
stiffness testing setup **1**:151*F*
stitching **1**:218–219
Stoney equation **3**:58
Stony equation **3**:98–99
straight, reverse 'T' and cross '+' micro channel flow **1**:448–450
  experiments and simulation for cross '+' micro channel **1**:455–456
  experiments and simulation for straight channel **1**:452
  mathematical flow model **1**:449–450
  micro channel fabrication and experimental design **1**:451–452
straight micro channel **1**:452–454
  0.8 mm straight micro channel **1**:452
  modified cross viscosity model for **1**:454
straight oil **1**:1–2
strain-hardened tempers **2**:340*T*
strengthening **2**:292, **2**:341
  by heat treatment
    aging **2**:353–356
    quenching **2**:350–353, **2**:352*F*
    SHT **2**:347–350, **2**:349*F*, **2**:350*F*
stress aging **2**:389
stress corrosion **2**:192
stress corrosion cracking (SCC) **1**:410, **2**:172, **2**:340*T*
  in alpha brass **2**:408*F*
stress equalizing **2**:417
stress relief **2**:232, **2**:363–368, **2**:367*F*
stress relieving **2**:9, **2**:271, **2**:278–279, **2**:417
  annealing **2**:188
  ductile irons **2**:269
  gray irons **2**:249–251, **2**:250–251, **2**:250*F*, **2**:251*T*
  treatment **2**:405
stress-induced martensitic transformation (SIMT) **2**:325–326
stress-rupture effects **1**:214
structural alloys **2**:109, **2**:120–123
  ferrous alloys **2**:120–123
  non-ferrous alloys **2**:125–127
stuffing plunger IMM **1**:467–468
stylus profilometer (SP) **3**:243, **3**:243–244, **3**:244*F*
SU-8 **3**:119
  microstructures fabrication using **3**:119*F*
subcritical annealing **2**:27
subcritical heat treatment **2**:282–283
substrate **3**:1
subtractive type manufacturing process **1**:508–510
subzero treatment **2**:46–47, **2**:90
suction and injection, methods of **3**:280–281
suggestion non-Newtonian viscosity model **1**:451
sulfur contamination **3**:20
super hardening **2**:155
superelasticity (SE) **2**:321–322
superfinishing process **3**:194
superhydrophilic surface **3**:139
superhydrophobia **3**:294
superhydrophobic surfaces **3**:277
  fabrication methods and technologies of **3**:140–142
  production of **3**:282
    benzoic acid **3**:286
    by etching and lithography **3**:292*F*
    by sol-gel process **3**:293*F*
    fatty acid monolayers **3**:282
    organic adsorbed sulfur on metal **3**:283
    organosilicon-derivative monolayers **3**:282–283
    self-assembled monolayers (SAMs) **3**:282
    silanes **3**:283–285
    stearic acid **3**:285
    tetradecanoic acid **3**:285–286
  wetting hysteresis for **3**:279*F*
superlattice coatings **3**:45
supersaturated solid solution (SSS) **2**:373
super-smooth surface **1**:159–160
supporting vector machine **1**:197
surface **1**:252–253
  activation/depassivation **2**:99–100
  coating **3**:178
  composition **3**:19
  conditioning **3**:4
  deformation treatments **2**:267–268
  energy **2**:138, **2**:146
    of zirconia **2**:140
  etching **3**:308
  grinding **3**:307
  hydrophobicity **2**:137, **2**:139, **3**:71–72
  investigation of pretreatment type, substance, coating contents **3**:309–311*T*
  modification **1**:186–188, **1**:187*F*, **1**:188*F*
  morphology **2**:140, **3**:31, **3**:32*F*, **3**:71–72
  nanocrystallization **2**:117
  oxidation and decarburization **2**:249
  polishing and burnishing of samples **3**:307–308
  posttreatment, additional operations and methods **3**:308–311
  posttreatment types, substrate, coating contents **3**:312*T*
  sanding **3**:307
  treatments **2**:422
  wetting **3**:71–72
surface characterization, imaging systems for **3**:261–263, **3**:263*T*
  image acquisition for computer vision **3**:263–266
  image processing and analysis forcomputer vision **3**:267
surface coating
  history **3**:149–150
  techniques **3**:39, **3**:40, **3**:48
  types and methods of **3**:150
surface debris **1**:356
surface evaluation methods with computer vision **3**:267–273
  2D Fast Fourier Transform (FFT) **3**:271–273
  2D Wavelet Transform (WT) **3**:273
  line scanning **3**:273
  morphological evaluations **3**:274
    blob analyses **3**:274
    edge enhancement and detection **3**:274
  speckle infusion **3**:273–274
surface finish **3**:211–213, **3**:220, **3**:254–257, **3**:376
  as-sprayed surface finish **3**:213
  coating as a method of *see* coating as a method of surface finishing
  electrochemical grinding (ECG) **3**:376–377
  electrochemical honing (ECH) **3**:377–378, **3**:377*F*, **3**:378*T*
  electrochemical machining (ECM) **3**:376
  electroplating (EP) **3**:376
  hard coatings effect on workpiece **3**:235–239
  for HVOF spraying **3**:210–211, **3**:212*F*
  parameters **3**:211
  post-deposition surface finish **3**:215–217
  pre-deposition surface finish **3**:211–213
  of thermal spraying **3**:96
surface finish coatings, structures of **3**:46*F*
surface finish measurements of coatings **3**:51
  adhesion testing **3**:51–52
  coating thickness **3**:51
  indentation testing **3**:52

measurement of corrosion **3**:52–54
measurement of friction and wear **3**:52
surface roughness **3**:52
surface finish quality **3**:261
machining processes related to **3**:262*T*
surface finish systems, introduction to **3**:220–222
surface treatment **3**:221–222
surface finishing operations **3**:39
classification of **3**:39, **3**:39*F*
surface hardening **2**:52–53, **2**:53*F*, **2**:249
ductile irons **2**:269
gray iron **2**:255–256
pearlitic malleable irons **2**:258–260, **2**:259–260
surface hydrophobicity
effect of chemical treatment and roughness on **3**:139
surface induction hardening **2:154–170**
austenitization **2**:154, **2**:154*F*, **2**:156, **2**:162
calculation example **2**:163–168
coupled electromagnetic thermal problem **2**:162
electromagnetic field **2**:159–160, **2**:160, **2**:163
idea of **2**:154–158
installations **2**:168–170
Joule losses **2**:159–160, **2**:161, **2**:163
mathematical modeling of **2**:158–163
quenching **2**:154
upper critical temperature **2**:156, **2**:157*F*
surface integrity **1**:66–69, **1**:232, **1**:233–234, **1**:249, **1**:250–251, **1**:262, **1**:282, **3**:235
cutting errors **1**:74–75
dimensional accuracy **1**:74–75
residual stress (RS) **1**:69–72
surface contour plots **1**:69*F*
surface roughness **1**:66–69, **1**:71*F*
white layer effect **1**:72–74
surface mechanical attrition treatment (SMAT) **2**:117, **2**:171
surface micromachining **1**:330
surface nanocrystallization, mechanism of by SMAT **2**:176
surface profile signals **3**:250*F*, **3**:251*F*
surface roughness **1**:66–69, **1**:85–86, **1**:223–224, **1**:224*F*, **1**:227*F*, **1**:280, **1**:311–312, **1**:323, **3**:52, **3**:122, **3**:144–145
bondcoats in thermal barrier coatings (TBCs) **3**:213–215
in finish turning
development of surface roughness prediction models **1**:19–22
factors due to cutting tool **1**:6–9
factors due to machining conditions **1**:1–4
machining parameters effect **1**:13–17, **1**:18*T*, **1**:19*T*
optimization studies **1**:19–22
workpiece material effect **1**:17–19
machined parts **3**:238–239, **3**:238*F*, **3**:239*F*, **3**:240*F*
observations **1**:395*F*
parameter **3**:210*F*, **3**:211*F*
prediction of **1**:133
vs. shot velocity **2**:172*F*
surface finish quality **1**:1
surface roughness modeling **1**:129–131
micro depth of cut of a polishing tool **1**:132–133
micro depth of cut of a single grain **1**:131–132
polishing stone topography, generation of **1**:130–131
surface roughness, prediction of **1**:133
surface segregation
clean surfaces **3**:19–20
H_2S exposure **3**:20–21
surface tension **3**:138, **3**:277
surface texture **3**:248–249
surface topography **3**:25–26, **3**:142–143
characteristics, enhancement in **3**:31–32, **3**:31*F*, **3**:32*F*
evaluation schema **3**:249*F*
hot-dip zinc coating **3**:32*F*
surface ultrasonic peening (SUSSP) **3**:159
surface wettability **3**:277
contact angle and corrosion resistance **3**:282
contact angle hysteresis **3**:278–279
film pressure contact angle hysteresis **3**:279
contact angle hysteresis measurement **3**:279–280
methods of suction and injection **3**:280–281
tilted surface method **3**:281
Wilhelmy method **3**:279–280
flat surface, wettability on **3**:277
rough surfaces, wettability on **3**:277–278
superhydrophobic surfaces production **3**:282
benzoic acid **3**:286
fatty acid monolayers **3**:282
organic adsorbed sulfur on metal **3**:283
organosilicon-derivative monolayers **3**:282–283
self-assembled monolayers (SAMs) **3**:282
silanes **3**:283–285
stearic acid **3**:285
tetradecanoic acid **3**:285–286
wetting free energies **3**:281–282
SUSSP *see* surface ultrasonic peening (SUSSP)
synchrotron XRD **3**:60
synergism **2**:13–14

T

T temper **2**:340*T*
variation **2**:340
T6 temper **2**:358, **2**:373
Taber Abraser **3**:156
Taguchi method **1**:14, **1**:21–22, **1**:487, **1**:489*F*
tangential/underpass rotary gear shaving **1**:108, **1**:108*F*
tangential-feed WEDG (TF-WEDG) **1**:283, **1**:283–284, **1**:283*F*
analysis **1**:284–285
error analysis **1**:284*F*
principle of **1**:283–284
steps **1**:284*F*
TB *see* twin boundary (TB)
TBCs *see* thermal barrier coatings (TBCs)
TBM *see* tunnel boring machine (TBM)
TCP *see* tricalcium phosphate (TCP)
TEM *see* transmission electron microscopy (TEM)
temper(s) **2**:338–339
Al alloys heat treatment **2**:382, **2**:383*T*
for cast and forged aluminum alloy parts **2**:383, **2**:385*T*
for hot and cold rolled sheets/plates **2**:382–383, **2**:384*T*
for hot forged/extruded profiles **2**:382, **2**:384*T*
designations **2**:338–340, **2**:339–340, **2**:339*F*
embrittlement **2**:200
subdivisions **2**:340
temperature
micro injection molding **1**:446
range **2**:387, **2**:387*F*
temperature, time, transformation diagram (TTT) **2**:387
tempering **2**:9, **2**:39–42, **2**:226–227, **2**:306
alloy steels **2**:228
austempering **2**:44–45
ductile irons **2**:264
effect of **2**:92
formation of bainite in steels **2**:42–43
mechanism of **2**:42–43
of gray iron **2**:252–253, **2**:253*F*, **2**:254*F*
case study on **2**:253
of malleable irons **2**:257–258, **2**:259*F*, **2**:260*F*
martempering **2**:43–44
multiple **2**:228–231
processes **1**:47–48
resistance to **2**:228
stages of **2**:40–42, **2**:226
time and temperature of **2**:228*F*, **2**:233–234
template method **3**:141
TENAX 300 steel **2**:241, **2**:241–242, **2**:242*F*
tensile
forces **1**:215
properties **1**:425–427, **2**:327, **2**:331–332
tensile strength (TS) **1**:237, **1**:238–239, **2**:378
TEOS *see* tetraethoxysilane (TEOS)
ternary alloys **3**:11–12
ternary NiTi
fabrication of **3**:342–345
spark plasma sintering of **3**:342–345
tetra-amine di-chloride **3**:6
tetradecanoic acid **3**:285–286
tetraethoxysilane (TEOS) **3**:141, **3**:283–285
tetramethylsilane (TMS) **3**:292, **3**:292*F*
textural properties **3**:90–92, **3**:94–95
texture profile micrographs **3**:143–144

TF-WEDG *see* tangential-feed WEDG (TF-WEDG); tensile strength (TS)
TGA *see* thermogravimetric analysis (TGA)
TGO *see* thermally grown oxide (TGO)
thermal barrier coatings (TBCs) **3**:57, **3**:196, **3**:213, **3**:213–215
thermal coatings **3**:50
thermal debinding **1**:480, **1**:480*T*
thermal deburring processes **3**:375
thermal diffusivity **2**:57
thermal model **1**:192, **1**:194, **1**:197–198
thermal post-treatments **3**:195–196
  diffusion annealing of aluminum and chromium **3**:198–199
  fusing of self-flux alloys **3**:195–196
  remelting **3**:196
  solid state heat treatment **3**:196–197
thermal spray coating(s) **3**:56, **3**:56*F*, **3**:191–192, **3**:192*F*, **3**:200–202
  see also thermal barrier coatings (TBCs)
  experimental measurement **3**:58–59
  mechanical finishing **3**:192–193
  numerical estimation **3**:61–68
  quality issues **3**:57
  residual stress estimation importance **3**:57–58, **3**:57*F*
  sealing **3**:199
  sources of residual stresses **3**:56–57
  thermal post–treatments **3**:195–196
thermal spray process **3**:207, **3**:211
thermal spraying **3**:42–43, **3**:43*F*
  electric arc spray **3**:43
  flame spray **3**:43
  high velocity oxy-fuel (HVOF) **3**:43
  plasma spray **3**:43
  surface finishing of **3**:96
thermal stress **2**:3, **3**:96, **3**:100
thermal treatment effect **2**:306
  composition of alloy **2**:306
  observations **2**:307
  process of manufacture **2**:306–307
thermally grown oxide (TGO) **3**:57, **3**:213
thermally treated tempers **2**:340*T*
thermochemical processing **3**:203–204
thermodynamics **2**:222
thermo-elastic MT **2**:322
thermogravimetric analysis (TGA) **1**:477
thermo-mechanical treatments (TMTs) **2**:324, **2**:389, **2**:391–392
  effects **2**:325–326
  for non-ferrous alloy **2**:392
thermoplastic molding **1**:443
thermoplastic polyurethane (TPU) **1**:211
3D analysis **1**:76
3D artificial scaffolds **3**:121*F*
3D compliance tool model **1**:146*F*
3D cutting geometry **1**:76
three-dimensional digital image correlation technique **3**:59
3D geometric simulation method **1**:194
3D light-emitting structure **3**:118*F*
3D object **3**:111
three-dimensional polycondensation **1**:217
3D printing **3**:111
3D surface profile parameters **3**:255–256*T*
3D surfaces **3**:298–300
3D Systems Inc. **3**:111
threshold force, defined **1**:98
thrusting **1**:41–42
Ti–6Al–4V alloy **1**:432
Ti6Al4V preparation *see* titanium alloy grade 5 (Ti6Al4V) preparation
TiAlN films **1**:373–374
TIG *see* tungsten inert gas (TIG)
tilted droplet method **3**:282*F*
tilted surface method **3**:281, **3**:282*F*
time–temperature–transformation (TTT) diagram **2**:6–7, **2**:7, **2**:13–14, **2**:100–101, **2**:101*F*
  superimposed cooling curve on **2**:17*F*
tin bronzes, heat treatment of **2**:409
Ti–Ni alloys
  MT in **2**:322–324
  precipitation in **2**:324–326
    aging treatment effect **2**:328–333
    cold rolling effect **2**:326–328
    TMT effects **2**:325–326
  three-transformation paths **2**:326*F*
tissue engineering **3**:121
titanium **1**:281, **2**:14, **2**:289
  alloying system **2**:290
  alloys **2**:129–131, **2**:131, **2**:289, **2**:448–449
  α alloys **2**:290–291
  α/β alloys **2**:291–292
  β alloys **2**:292
  casting route **2**:289
  heat treatment **2**:292–293
  high specific strength **2**:289, **2**:289*F*
  powder metallurgy route **2**:289
  stabilizers **2**:293*F*
  stress–temperature map **2**:301*F*
titanium alloy grade 5 (Ti6Al4V) preparation **1**:252, **1**:259*T*
titanium carbide **1**:12–13, **1**:173
titanium carbide percent **1**:193
titanium carbonitride **1**:12–13, **1**:176–177
titanium dioxide **2**:120, **3**:27, **3**:337
titanium nitride **1**:12–13, **2**:125
titanium–nitrogen system **2**:112–113
TMS *see* tetramethylsilane (TMS)
TMTs *see* thermo-mechanical treatments (TMTs)
tonnage steels **2**:215
tool based micromachining **1**:323
  ductile regime machining **1**:325–326
  microdrilling **1**:324
  micromilling **1**:323
    surface roughness **1**:323
    vibration **1**:323–324
  minimum quantity lubrication (MQL) **1**:324–325
  tooling **1**:326–328
tool dynamic model **1**:140
tool life **1**:26–27, **1**:29, **1**:31, **1**:43
tool steels **2**:214–215, **2**:430–434
  carburization of **2**:101–102
    cold working tool steel **2**:102
    hot working tool steel **2**:101–102
    mold steel **2**:102
    shock resisting tool steel **2**:102
  definition **2**:214–215
  families **2**:215–216
    cold work steels **2**:216
    high speed steels (HSS) **2**:216–218
    hot work steels **2**:216
    plastic mold steels **2**:216
  families and classification **2**:215
  heat treatment of **2**:214–245, **2**:218
    quality **2**:234–236
  historical development of **2**:215, **2**:216*T*
  names and classifications **2**:215
  phase transformation **2**:218–222
tool system modeling **1**:142*F*
tool vibration **1**:26–27, **1**:172–173
tool wear **1**:9–11
  patterns and mechanisms **1**:63–66
  progression modeling **1**:76–78, **1**:78*T*
tool wear rate (TWR) **1**:279
tool–chip interface temperature **1**:61–63
toolhead dynamic modeling **1**:144–147
topography **1**:66, **3**:28, **3**:34–35
topological evaluation methods **3**:243
  contact surface measurement techniques **3**:243
    atomic force microscopy **3**:244, **3**:247*F*
    portable handheld surface finish instrument **3**:243, **3**:244*F*
    stylus profilometer (SP) **3**:243–244, **3**:244*F*
  noncontact surface measurement techniques **3**:244–245
    coherence scanning interferometry (CSI) **3**:246, **3**:246*F*
    confocal microscopy **3**:244–245
    electron microscopy **3**:247–248
    focus variation microscopy **3**:245–246
    scanning probe microscopy (SPM) **3**:246–247
  parameters, characterization of **3**:248–250
    primary profile **3**:250
    roughness profile **3**:250–254
    waviness profile **3**:250
  surface finishing **3**:254–257
top-surface metallurgy (TSM) **3**:220
torch heating **3**:195
torque rheometer **1**:477
tough pitch copper **2**:399
TPA *see* two-photon absorption (TPA)
TPP *see* two-photon polymerization (TPP)
TPU *see* thermoplastic polyurethane (TPU)
trade sale coatings **3**:150
transferring time **2**:378
transformation induced plasticity (TRIP) **2**:208, **2**:209*F*, **3**:184
transformation kinetics **2**:7
transformation temperature, defined **3**:336
transformer oil **1**:278
transistor-type pulse generator **1**:274, **1**:274*F*
transmission electron microscopy (TEM) **1**:418, **2**:302, **2**:303*F*, **2**:327, **2**:327*F*, **2**:331, **2**:332*F*, **3**:248, **3**:248*F*, **3**:261–262, **3**:287*F*
triadic Koch curve, construction of **3**:291*F*
triadic Koch diagram **3**:301–302, **3**:302–303, **3**:302*F*
tribological performance **2**:427–429
tribometers **3**:52
tribotesters **3**:52

tricalcium phosphate (TCP) **3**:350
TRIP *see* transformation induced plasticity (TRIP)
trivalent chromes **3**:322–323
troostita **2**:226–227
TSM *see* top-surface metallurgy (TSM)
TTA diagrams **2**:156
tumbling process **3**:194
tungsten (W) **1**:277, **1**:392–393, **1**:393, **2**:14
  wire **1**:248
tungsten carbide (WC) **1**:277, **1**:300–301, **1**:392–393, **1**:393
tungsten carbide coatings **3**:48
tungsten carbide–cobalt (WC–Co) **1**:277, **1**:300–301
  micro-EDM **1**:304–305, **1**:305–306
tungsten high-speed tool steels **2**:217–218*T*
tungsten hot work tool steels **2**:217–218*T*
tungsten inert gas (TIG) **3**:196, **3**:196
tuning of thickness **3**:28
tunnel
  boring process in building **1**:39–41
  support **1**:42
tunnel boring machine (TBM) **1**:39
turning **1**:1, **3**:193
twin boundary (TB) **1**:427
twin screw extruder **1**:468
twin–matrix (T–M) ranges **1**:426–427
twinning-induced plasticity (TWIP) **3**:185, **3**:186–187
twins **1**:408, **1**:426–427
twin-wire EDM system **1**:285–286
TWIP *see* twinning-induced plasticity (TWIP)
two contact bodies **1**:121*F*
two laser coating **3**:102–103, **3**:109
2D cutting geometry **1**:76
2D Fast Fourier Transform (FFT) **3**:271–273
two-dimensional fiber-reinforced polymer **1**:219
2D periodic profiles **3**:298
  periodic profile **3**:298
  saw-toothed periodic profile **3**:298
2D surface profile parameters **3**:252–254*T*
2D Wavelet Transform (WT) **3**:267*F*, **3**:268*F*, **3**:269*F*, **3**:270*F*, **3**:273
two-photon absorption (TPA) **3**:114
  sequential **3**:115, **3**:115*F*
  simultaneous **3**:115, **3**:115*F*
two-photon polymerization (TPP) **3**:115
two-plated mold, typical feature of **1**:471*F*
two-step austempering heat treatment **2**:268–269
two-way shape memory effect (TWSME) **2**:321–322
TWR *see* tool wear rate (TWR)
TWSME *see* two-way shape memory effect (TWSME)
typical heat treatment cycle **1**:484*F*
typical thermogravimetric analysis **1**:481*F*

U

UACEDM *see* ultrasonic assisted cryogenically cooled copper electrode (UACEDM)
UBM *see* under bump metallurgy (UBM)
UHSS *see* ultrahigh strength steels (UHSS)
ultimate tensile strength (UTS) **1**:425, **1**:426, **2**:350
ultrafine grained dual phase steel **2**:209–210
ultrahard high-speed tool steels **2**:217–218*T*
ultrahigh strength steels (UHSS) **1**:47, **2**:190, **2**:190*T*
ultra-high temperature materials **3**:349
ultrahigh-strength steel, press hardenable **2**:186–187, **2**:187*F*
ultraprecision turning **1**:9
ultrasonic assisted cryogenically cooled copper electrode (UACEDM) **1**:173
ultrasonic atomization **3**:153
ultrasonic atomizers **3**:153*F*, **3**:155
ultrasonic vibration assisted EDM **1**:172–173
  dielectric vibration **1**:174
  tool vibration **1**:172–173
  workpiece vibration **1**:173–174
ultrasonic vibration pulse electro-discharge machining (UVPEDM) **1**:172
ultrasonic-assisted EDM, powder mixed **1**:188–190, **1**:188*F*, **1**:189*F*, **1**:190*F*, **1**:191*F*
ultrasonics **1**:157, **1**:159, **1**:161–162
unconventional loose-abrasive grinding **1**:157–158
under aging (UA) copper–beryllium alloys **2**:412
under bump metallurgy (UBM) **3**:220
unipolar pulse **3**:361–362
unsaturated liquid solution **2**:375
unsaturated polyester (UP) **1**:215–216
uphill quenching method **2**:366–368
US Air Force (USAF) **1**:419
UTS *see* ultimate tensile strength (UTS)
UV laser beam **3**:111–112
UVPEDM *see* ultrasonic vibration pulse electro-discharge machining (UVPEDM)

V

VACNTs *see* vertically aligned carbon nanotubes (VACNTs)
vacuum
  bag moulding **1**:220
  coating techniques **3**:29
  environment **3**:233
vacuum arc remelting (VAR) **3**:338
vacuum carburizing **2**:73, **2**:80
  advantages **2**:80
  carburizing process **2**:80
  control of carbon supply and case depth **2**:80
  disadvantages **2**:80
vacuum induction melting (VIM) **3**:338
vanadium **2**:14, **3**:184–185
vanadium-microalloyed steel, carburization of **2**:97–98
vapor blanket stage **2**:53
vapor depositions **3**:41
  chemical vapor deposition (CVD) **3**:41
  physical vapor deposition (PVD) **3**:41
  plasma enhanced CVD technique **3**:41
vapor-transport cooling stage **2**:53
VAR *see* vacuum arc remelting (VAR)
variation in microhardness (VHN) **2**:330*F*
vegetable oils application **1**:83–86
velocimetry interferometer system for any reflector (VISAR) **1**:413
vermicular graphite iron **2**:248
vertical pick-up turning machines **1**:54
vertically aligned carbon nanotubes (VACNTs) **1**:403
VF800AT tool steel **2**:236, **2**:236–237
  analysis of several conditions of heat treatment in **2**:237–238
  microstructures of **2**:238*F*
  nominal chemical composition of **2**:236*T*
  resistance to bending and rupture energy **2**:237*F*
VH13ISO tool steel **2**:236
  analysis of several conditions of heat treatment in **2**:238–239
  microstructures of **2**:239*F*
  nominal chemical composition of **2**:236*T*
VHN *see* variation in microhardness (VHN)
VHSUPER steel **2**:241, **2**:241–242, **2**:242*F*, **2**:244
vibration **1**:4–6, **1**:323–324
vibration-assisted polishing **1**:163
VIM *see* vacuum induction melting (VIM)
vinyl alcohol **1**:213
VISAR *see* velocimetry interferometer system for any reflector (VISAR)
viscosity for micro injection molding **1**:446
viscosity in micro molding **1**:447
viscosity models **1**:445–446, **1**:495
visual sieving **3**:273*F*
voltage **3**:367, **3**:369
voltage vs. displacement relationship **1**:150*F*
volume flow rate **1**:449
von Mises stress distribution **3**:108
von Mises stress variation **1**:359, **1**:359–361
von Mises yielding criterion **1**:414
Vycor glass **3**:15

W

WAIM *see* water-assisted injection molding (WAIM)
warm forging punch **2**:242–243
warm peening **2**:173–174
  relation between temperature and fatigue life **2**:174
  residual stress in warm peening **2**:174
  warm peening procedure **2**:174
water **1**:278
  quenching media **2**:53–54, **2**:57*F*, **2**:58*F*
  water–air spray cooling **2**:391, **2**:391*F*
  water-based dielectrics **1**:278
water-assisted injection molding (WAIM) **1**:467
water-hardening tool steels **2**:217–218*T*
water-in-oil (W/O) emulsion **1**:175
waterjet machining **1**:221–222
water-soluble binder **1**:476

water-to-oil ratio **1**:2
waviness **3**:248–249, **3**:250
wax-based binder system **1**:476, **1**:477
WC *see* tungsten carbide (WC)
weak hardeners **2**:207
wear **3**:230, **3**:230–231, **3**:231
  resistance **2**:131, **2**:270
weather resistance **3**:155
weaving process **1**:218
WEDG *see* wire electrical discharge grinding (WEDG)
WEDM *see* wire electrical discharge machining (WEDM)
weldable malleable irons **2**:256
welded joints **1**:429–431
Wenzel and Cassie–Baxter states **3**:139–140
Wenzel equation **3**:296–297
Wenzel's formula **3**:139
wet chemical post-processing **1**:166–167
wet coating **3**:28–29
wet etchant **1**:329
wet lay-up *see* hand lay-up
wettability **3**:26–27, **3**:27
  on a flat surface **3**:277
  on rough surfaces **3**:277–278
wetting free energies **3**:281–282
wetting hysteresis, for superhydrophobic surface **3**:279*F*
wheel grinding **1**:158–159
wheel truing **1**:379–380
white iron(s) **2**:248
  abrasion resistant high-alloy **2**:276–279
white layer *see* compound layer
white layer thickness (WLT) **1**:183–184, **1**:232, **1**:250–251, **1**:251*F*, **1**:254*T*, **1**:256*F*, **1**:256*T*, **1**:257*T*
  electrical parameters effect **1**:259
  wire electrode parameters effect **1**:260–262
  workpiece parameters effect **1**:262
whiteheart malleable iron **2**:256–257, **2**:257*F*
Widmanstatten ferrite **2**:48, **2**:48*F*
Wilhelmy method **3**:279–280
Wilhelmy test **3**:280
wiper inserts **1**:8
wire electrical discharge grinding (WEDG) **1**:270, **1**:273–274, **1**:283
  compliant microelectrode arrays fabrication **1**:286–288
  fabrication of microelectrode for batch production **1**:286
  radial-feed WEDG **1**:283
  series-pattern micro-disk electrode fabrication **1**:288–290
  TF-WEDG **1**:283–284
  twin-wire EDM system **1**:285–286
wire electrical discharge machining (WEDM) **1**:232, **1**:232*F*, **1**:234–236, **1**:278, **1**:303–304
  see also electrical discharge machining (EDM)
  advantages **1**:531–532
  ANFIS modeling **1**:253–258
  applications **1**:533
  discharge sparks **1**:235*F*
  EDM wire electrode **1**:236–238, **1**:239*F*
  experimental details **1**:251, **1**:253
  fishbone diagram **1**:233*F*
  limitations **1**:532–533
  miniature spur gears **1**:533*F*
  μ-WEDM **1**:530–531
  pulse generator analysis **1**:234–236
  SEM images of micro spur gear **1**:533*F*
  surface characterization **1**:252–253
  white layer and heat-affected zone **1**:250–251
wire electrode **1**:248, **1**:253*T*
wire frame design **1**:130*F*
wire rupture **1**:236
wire-cut EDM **1**:384–385
wire-cut machine **1**:232
WLT *see* white layer thickness (WLT)
W/O emulsion *see* water-in-oil (W/O) emulsion
workpiece **1**:28*F*, **1**:38*F*, **1**:75
  clamping **1**:52–53
  material **1**:3
    effect **1**:17–19
  surfaces **1**:72
  vibration **1**:173–174, **1**:174*F*
workpiece gear, in gear shaving **1**:105–106
woven fibers **1**:213
wrapping of columns **1**:215
wrought alloys **2**:340–341, **2**:341*T*, **2**:342*T*, **2**:344–345*T*
  heat treatment for **2**:357–358, **2**:359–362*T*, **2**:362*T*
wrought aluminum alloys **2**:368
WT *see* 2D Wavelet Transform (WT)

X

XLPA *see* x-ray line profile analysis (XLPA)
XPS *see* x-ray photoelectron spectroscopy (XPS)
X-ray based CT **3**:262
X-ray diffraction (XRD) **1**:414, **1**:414–415, **2**:326–327, **2**:327*F*, **3**:8, **3**:60, **3**:74, **3**:87, **3**:89–90, **3**:90*F*, **3**:338
  analysis **3**:160
  hole-drilling method vs. **1**:416–417
  measurement and phase analysis **3**:164
  technique **3**:97–98, **3**:147
X-ray fluorescence method **3**:51
x-ray line profile analysis (XLPA) **1**:417
x-ray lithography process **1**:521
x-ray photoelectron spectroscopy (XPS) **3**:8, **3**:87, **3**:89–90, **3**:90*T*, **3**:212–213
X-ray tomographic microscopy (XTM) **3**:262
XRD *see* X-ray diffraction (XRD)
XTM *see* X-ray tomographic microscopy (XTM)

Y

Y_2O_3-stabilized ZrO_2 (YSZ) **3**:215, **3**:215*F*
  coatings **3**:196
$Y_3Al_5O_{12}$ *see* Yttrium aluminum garnet (YAG)
YAG *see* Yttrium aluminum garnet (YAG)
yield stress (YS) **2**:389
Young equation **3**:295
  for flat surfaces **3**:138–139
YS *see* yield stress (YS)
yttria-stabilized zirconia **2**:139–140, **2**:143–146, **2**:151
  see also phosphorous bronze; Rene 41
  contact angles measurement **2**:148*T*
  cross-section of laser-treated zirconia layer **2**:146*F*
  laser-treated zirconia surface **2**:145*F*
  water droplet shapes **2**:147*F*
  X-ray diffractogram of laser-treated and as-received **2**:147*F*
yttrium aluminum garnet (YAG) **3**:111–112, **3**:349

Z

Zener–Wert–Avrami function **1**:434
zeolite coating **3**:48
zero-backlash method **1**:104
zigzag path fitting **1**:145*F*
  planning **1**:145*F*
zinc **3**:178, **3**:179–180
  alloys **1**:277
  bath **3**:181, **3**:188
  coating **3**:32, **3**:178, **3**:181
  electrochemical characteristics **3**:32–35, **3**:33*F*, **3**:35*F*
  metal composites for alloy coating **3**:30–31
zinc oxide **3**:285, **3**:286*F*, **3**:287*F*, **3**:323
zinc oxide nanoparticles **3**:285
zinc phosphate **3**:150
zirconium **1**:206
zirconium nitride **3**:46
zirconium nitride PVD coating **3**:46
zirconium–copper alloys **2**:414–415